AD NUMBER

ADB072483

NEW LIMITATION CHANGE

TO

Approved for public release, distribution unlimited

FROM

Distribution authorized to U.S. Gov't. agencies only; Operational use; Mar 82]. Other requests shall be referred to AFWAL/FIGC, Wright-Patterson AFB, OH 45433.

AUTHORITY

AFWAL-DOOS W-PAFB letter

PHOTOGRAPH THIS SHEET

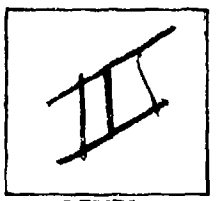

LEVEL

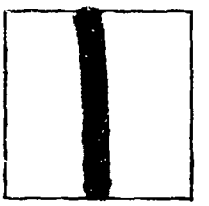

INVENTORY

AD B072483

DTIC ACCESSION NUMBER

AFWAL-TR-83-3048

DOCUMENT IDENTIFICATION Final Rept. Sept. '75 - Sept. '77

Contract F33615-76-C-3061 Apr. '78

"B" Official/Operational Use

DISTRIBUTION STATEMENT

A	R
N	A&I
DTIC TAB	☒
UNANNOUNCED	
JUSTIFICATION	
BY	
DISTRIBUTION /	
AVAILABILITY CODES	
DIST	AVAIL AND/OR SPECIAL
B	

DISTRIBUTION STAMP

DTIC
ELECTE
S APR 18 1983 D
D

DATE ACCESSIONED

88 04 14 166

DATE RECEIVED IN DTIC

PHOTOGRAPH THIS SHEET AND RETURN TO DTIC-DDA-2

DTIC FORM OCT 79 70A

DOCUMENT PROCESSING SHEET

REPORT DOCUMENTATION PAGE		READ INSTRUCTIONS BEFORE COMPLETING FORM
1. REPORT NUMBER AFWAL-TR-83-3048	2. GOVT ACCESSION NO.	3. RECIPIENT'S CATALOG NUMBER
4. TITLE (and Subtitle) USAF STABILITY AND CONTROL DATCOM		5. TYPE OF REPORT & PERIOD COVERED Final Report September 1975-September 1977 6. PERFORMING ORG. REPORT NUMBER
7. AUTHOR(s) R. D. Finck		8. CONTRACT OR GRANT NUMBER(s) F33615-76-C-3061
9. PERFORMING ORGANIZATION NAME AND ADDRESS McDonnell Douglas Corporation Douglas Aircraft Division Long Beach, California 90846		10. PROGRAM ELEMENT, PROJECT, TASK AREA & WORK UNIT NUMBERS 82190110
11. CONTROLLING OFFICE NAME AND ADDRESS Flight Dynamics Laboratory (AFWAL/FIGC) Air Force Wright Aeronautical Laboratories Wright-Patterson Air Force Base, Ohio 45433		12. REPORT DATE April 1978 13. NUMBER OF PAGES 3200
14. MONITORING AGENCY NAME & ADDRESS(if different from Controlling Office)		15. SECURITY CLASS. (of this report) Unclassified 15a. DECLASSIFICATION/DOWNGRADING SCHEDULE

16. DISTRIBUTION STATEMENT (of this Report)

Distribution limited to U.S. Government agencies only; official/operational use, March 1982. Other requests for this document must be referred to AFWAL/FIGC, Wright-Patterson Air Force Base, Ohio 45433.

17. DISTRIBUTION STATEMENT (of the abstract entered in Block 20, if different from Report)

18. SUPPLEMENTARY NOTES

19. KEY WORDS (Continue on reverse side if necessary and identify by block number)

Stability and Control
Aerodynamics
Stability Derivatives
Preliminary Design
Prediction Methods

20. ABSTRACT (Continue on reverse side if necessary and identify by block number)

This report is a collection, correlation, codification, and recording of best knowledge, opinion, and judgment in the area of aerodynamic stability and control prediction methods. It presents substantiated techniques for use (1) early in the design or concept study phase, (2) to evaluate changes resulting from proposed engineering fixes, and (3) as a training on cross-training aid. It bridges the gap between theory and practice by including a combination of pertinent discussion and proven practical methods. For any

20.
Abstract (continued)

given configuration and flight condition, a complete set of stability and control derivatives can be determined without resort to outside information. A spectrum of methods is presented, ranging from very simple and easily applied techniques to quite accurate and thorough procedures. Comparatively simple methods are presented in complete form, while the more complex methods are often handled by reference to separate treatments. Tables which compare calculated results with test data provide indications of method accuracy. Extensive references to related material are also included.

AFWAL-TR-83-3048

USAF STABILITY AND CONTROL DATCOM

R. Fink
McDonnell Douglas Corporation
Douglas Aircraft Division
Long Beach, California 90846

April 1978

Final Report for Period September 1975 - September 1977

FLIGHT DYNAMICS LABORATORY
AIR FORCE WRIGHT AERONAUTICAL LABORATORIES
AIR FORCE SYSTEMS COMMAND
WRIGHT-PATTERSON AFB, OHIO 45433

NOTICE

When Government drawings, specifications, or other data are used for any purpose other than in connection with a definitely related Government procurement operation, the United States Government thereby incurs no responsibility nor any obligation whatsoever; and the fact that the government may have formulated, furnished, or in any way supplied the said drawings, specifications, or other data is not to be regarded by implication or otherwise as in any manner licensing the holder or any other person or corporation, or conveying any rights, or permission to manufacture, use, or sell any patented invention that may in any way be related thereto.

This technical report has been reviewed and is approved for publication.

Donald E Hoak

DONALD E. HOAK
Project Engineer
Control Dynamics Branch

R O Anderson

R. O. ANDERSON, Chief
Control Dynamics Branch
Flight Control Division

FOR THE COMMANDER

Charles R Goss Jr.

CHARLES R. GOSS, Lt Col, USAF
Acting Chief, Flight Control Division
AF Wright Aeronautical Laboratories (AFSC)

If you wish to be placed on our mailing list for revisions to this report, please forward your correct address to AFWAL/FIGC, W-PAFB, OH 45433.

FOREWORD

The current volume entitled "USAF Stability and Control Datcom" has been prepared by the Douglas Aircraft Division of the McDonnell Douglas Corporation under Contracts AF33(616)-6460, AF33(615)-1605, F33615-67-C-1156, F33615-68-C-1260, F33615-70-C-1087, F33615-71-C-1298, F33615-72-C-1348, F33615-73-C-3057, F33615-74-C-3021, F33615-75-C-3067, and F33615-76-C-3061. (The term Datcom is a shorthand notation for data compendium.) This effort is sponsored by the Control Criteria Branch of the Flight Control Division, Air Force Flight Dynamics Laboratory, Wright-Patterson Air Force Base, Dayton, Ohio. The Air Force project engineers for this project were J. W. Carlson and D. E. Hoak. The present volume has been published in order to replace the original work and to provide timely stability and flight control data and methods for the design of manned aircraft, missiles, and space vehicles. It is anticipated that this volume will be continuously revised and expanded to maintain its currency and utility. Comments concerning this effort are invited; these should be addressed to the procuring agency.

CONTRIBUTORS

DOUGLAS AIRCRAFT COMPANY, INC. 1960-1965

MCDONNELL DOUGLAS CORPORATION
DOUGLAS AIRCRAFT DIVISION 1967-1977

PRINCIPAL INVESTIGATORS

R. D. FINCK (1971-)
D. E. ELLISON (1962-1970)
L. V. MALTHAN (1958-1962)

PRINCIPAL COLLABORATORS

D. E. Ellison	Technical Director
R. B. Harris	Technical Advisor
D. E. Drake	Technical Advisor
M. J. Abzug	Technical Advisor
C. S. Thorndike	Technical Editor, 2.1, Sample Problems & Illustrations
R. A. Berg	4.6-, 4.7-, 5.2-, 5.3-, 5.6
G. L. Huggins	6-
R. M. Seplak	4-, 3-
A. C. Blaschke	7-
P. J. Buce	4.3-, 5-, 6-
M. S. Cahn	6-
J. W. Gresham	4-
N. H. Buckingham	4.2-
W. H. Rudderow	6-
C. O. White	4-, 5-
J. L. Lundry	4-
D. P. Marsh	8.1
J. L. Woodworth	8.2
J. Hebert	4-
M. G. Brislawn	9-
W. B. Fisher	6-
H. B. Dietrick	Sample Problems
R. C. Leeds	Graphs & Illustrations
S. L. Fallon	Graphs & Illustrations

TABLE OF CONTENTS

*Subjects for Future Additions

SECTION 1

GUIDE TO DATCOM

Fundamentally, the purpose of the Datcom (Data Compendium) is to provide a systematic summary of methods for estimating basic stability and control derivatives. The Datcom is organized in such a way that it is self-sufficient. For any given flight condition and configuration the complete set of derivatives can be determined without resort to outside information. The book is intended to be used for preliminary design purposes before the acquisition of test data. The use of reliable test data in lieu of the Datcom is always recommended. However, there are many cases where the Datcom can be used to advantage in conjunction with test data. For instance, if the lift-curve slope of a wing-body combination is desired, the Datcom recommends that the lift-curve slopes of the isolated wing and body, respectively, be estimated by methods presented and that appropriate wing-body interference factors (also presented) be applied. If wing-alone test data are available, it is obvious that these test data should be substituted in place of the estimated wing-alone characteristics in determining the lift-curve slope of the combination. Also, if test data are available on a configuration similar to a given configuration, the characteristics of the similar configuration can be corrected to those for the given configuration by judiciously using the Datcom material.

The various sections of the Datcom have been numbered with a decimal system, which provides the maximum degree of flexibility. A "section" as referred to in the Datcom contains information on a single specific item, e.g., wing lift-curve slope. Sections can, in general, be deleted, added, or revised with a minimum disturbance to the remainder of the volume. The numbering system used throughout the Datcom follows the scheme outlined below:

Section: An orderly decimal system is used, consisting of numbers having no more than four digits (see Table of Contents). All sections are listed in the Table of Contents although some consist merely of titles. All sections begin at the top of a right-hand page.

Page: The page number consists of the section number followed by a dash number. Example: Page 4.1.3.2-4 is the 4th page of Section 4.1.3.2.

Figures: Figure numbers are the same as the page number. This is a convenient system for referencing purposes. For pages with more than one figure, a lower case letter follows the figure number. Example: Figure 4.1.3.2-50b is the second figure on Page 4.1.3.2-50. Where a related series of figures appears on more than one page, the figure number is the same as the first page on which the series begins. Example: Figure 4.1.3.2-56d may be found on Page 4.1.3.2-57 and is the 4th in a series of charts. Figures are frequently referred to as "charts" in the text.

Tables: Table numbers consist of the section number followed by an upper case dashed letter. Example: Table 4.1.3.2-A is the first table to appear in Section 4.1.3.2.

Equations: Equation numbers consist of the section number followed by a lower case dashed letter. Example: 4.1.3.2-b is the second equation (of importance) appearing in Section 4.1.3.2. Repeated equations are numbered the same as for the first appearance of the equation but are called out as follows: (Equation 4.1.3.2-b).

The major classification of sections in the Datcom is according to type of stability and control parameter. This classification is summarized below:

Section 1. Guide to Datcom and Methods Summary (present discussion including the Methods Summary)

Section 2. General information

Section 3. Reserved for future use

Section 4. Characteristics at angle of attack

Section 5. Characteristics in sideslip

Section 6. Characteristics of high-lift and control devices

Section 7. Dynamic derivatives

Section 8. Mass and inertia

Section 9. Characteristics of VTOL-STOL aircraft

The information in Section 2 consists of a complete listing of notation and definitions used in the Datcom, including the sections in which each symbol is used. It should be noted that definitions are also frequently given in each section where they appear. Insofar as possible, NASA notation has been used. Thus the notation from original source material has frequently been modified for purposes of consistency. Also included in Section 2 is general information used repeatedly by the engineer, such as geometric parameters, airfoil notation, wetted-area charts, etc.

Sections 4 and 5 are for configurations with flaps and control surfaces neutral. Flap and control characteristics are given in Section 6 for both symmetric and asymmetric deflections. Section 4 includes effects of engine power and ground plane on the angle-of-attack parameters.

The Datcom presents less information on the dynamic derivatives (Section 7) than on the static derivatives, primarily because of the relative scarcity of data, but partly because of the complexities of the theories. Furthermore, the dynamic derivatives are frequently less important than the static derivatives and need not be determined to as great a degree of accuracy. However, the Datcom does present test data, from over a hundred sources, for a great variety of configurations (Table 7-A).

If more than preliminary-design information on mass and inertia (Section 8) is needed, a weights-and-balance engineer should be consulted.

Section 9 is a unified section covering aerodynamic characteristics of VTOL-STOL aircraft, with the exception of ground-effect machines and helicopters. The Datcom presents less information in this area than that presented for conventional configurations because of the scarcity of data, the complexities of the theories, and the large number of variables involved. In most cases the Datcom methods of this section are based on theory and/or experimental data such that their use is

restricted to first approximations of the aerodynamic characteristics of individual components or simple component combinations. However, the Datcom does present a literature summary from over six hundred sources for a great variety of VTOL-STOL configurations (Table 9-A).

It should be noted that the characteristics predicted by this volume are for rigid airframes only. The effects of aeroelasticity and aerothermoelasticity are considered outside the scope of the Datcom.

The basic approach taken to the estimation of the drag parameters in Section 4 has been found to be satisfactory for preliminary-design stability studies. No attempt is made to provide drag estimation methods suitable for performance estimates.

Each of the major divisions discussed above, notably Sections 4, 5, 6, and 7, is subdivided according to vehicle components. That is, the information is presented as wing, body, wing-body, wing-wing, and wing-body-tail sections. The latter three categories generally utilize component information as presented in the first two categories and add the appropriate aerodynamic interference terms. In some cases, however, estimation methods for combined components as a unit are presented. Each section of the Datcom is organized in a specific manner such that the engineer, once familiar with the system, can easily orient himself in a given section. A typical section is diagramed below:

Section Number and Title

General Introductory Material

A. Subsonic Paragraph
   Introductory Material
   Specific Methods
   Sample Problems

B. Transonic Paragraph
   Introductory Material
   Specific Methods
   Sample Problems

C. Supersonic Paragraph
   Introductory Material
   Specific Methods
   Sample Problems

D. Hypersonic Paragraph
   Introductory Material
   Specific Methods
   Sample Problems

References

Tables

Working Charts

In general, each section is organized according to speed regimes. However, Sections 6.3.1 and 6.3.2 are restricted to the hypersonic speed regime and Section 9 to the low-speed transition-flight regime. In a few sections, where applicable, material is included for the rarefied-gas regime as paragraph E. The material for each speed regime is further subdivided into an introductory discussion of the fundamentals of the problem at hand, a detailed outline of specific methods, and sample problems illustrating the use of the methods presented. In the selection of specific methods, an attempt has been made to survey all known existing generalized methods. All methods that give reasonably accurate results and yet do not require undue labor or automatic computing equipment have been included (at least this is the ultimate goal). Where feasible, the configurations chosen for the sample problems are actual test configurations, and thus some substantiation of the methods is afforded by comparison with the test results.

To facilitate the engineer's orientation to those Datcom sections that use a build-up of wing, wing-body, and wing-body-tail components, a Methods Summary has been included at the end of this section. In addition, the methods of Sections 6.1 and 6.2 are also included in the Methods Summary. The contents of the Methods Summary present the following: (1) the wing, wing-body, and wing-body-tail equations available in each speed regime, (2) the sections where the equation components are obtained, (3) the limitations associated with the equations and their respective components (limitations from design charts are not included), and (4) identification of the parameters that are based on exposed planform geometry that are not specified by the subscript e.

Sometimes the same limitations, such as "linear-lift range," may occur for more than one component in an equation. To avoid repetition, the same limitation is not repeated for each component. The list of limitations should not be construed as effectively replacing the discussion preceding each Datcom method. It remains essential to read the discussion accompanying each derivative to ensure an effective application of each method.

Proper use of the Methods Summary will enable the engineer to organize and plan his approach to minimize the interruptions and the time needed to locate and calculate the independent parameters used in the equation under consideration.

The Datcom methods provide derivatives in a stability-axis system unless otherwise noted. Transformations of stability derivatives from one axis system to another are developed in many standard mathematics and engineering texts. In FDL-TDR-64-70, several coordinate systems are defined and illustrated, and coordinate transformation relations are given.

All material presented in the Datcom has been referenced; plagiarizing has been specifically avoided. In general, material that has not been referenced has been contributed by the authors.

In many of the sections, substantiation tables are presented that show a comparison of test results with results calculated by the methods recommended. Geometric and test variables are also tabulated for convenience in comparing these results. Wherever possible, the limits of applicability for a given method have been determined and are stated in the text.

The working charts are presented on open grid, which in general constitute an inconvenience to the user. However, with a few exceptions, the grids used are of two sizes only: centimeter and half-inch grid sizes. This enables the engineer to use transparent grid paper to read the charts accurately.

Another set of documents similar in intent to the Datcom is the "Royal Aeronautical Society Data

Sheets," available from the Royal Aeronautical Society of Great Britain. These documents are particularly useful from the standpoint that foreign source material is strongly represented in them; whereas the Datcom emphasizes American information.

As stated in the introduction, the work on the Datcom will be expanded and revised over the years to maintain an up-to-date and useful document. In order to help achieve this goal, comments concerning this work are invited and should be directed to the USAF Procuring Agency so that the effort may be properly oriented.

METHODS SUMMARY OUTLINE

DERIVATIVE	PAGES
C_D	1-59
C_{l_δ}	1-59 through 1-61
C_n	1-61 through 1-62
C_{n_δ}	1-62

DERIVATIVE	CONFIG.	SPEED REGIME	EQUATION (Datcom
C_{L_α}	W	SUBSONIC	$\frac{C_{L_\alpha}}{A} = \frac{2\pi}{2 + \sqrt{\frac{A^2\beta^2}{\kappa^2}\left(1 + \frac{\tan^2 \Lambda_{c/2}}{\beta^2}\right) + 4}}$
			$C_{L_\alpha} = \underbrace{\left(C_{L_\alpha}\right)_{theory}}_{4.1.3.2}\left[\underbrace{\frac{C_{L_\alpha}}{\left(C_{L_\alpha}\right)_{theory}}}_{4.1.3.2}\right]$
		TRANSONIC	Faired curve between $\left(C_{L_\alpha}\right)_{subsonic}$ and $\left(C_N$
		SUPERSONIC	Figures 4.1.3.2-56a through -60
			$C_{N_\alpha} = \underbrace{K_L}_{4.1.3.2}\left[\underbrace{\left(C_{N_\alpha}\right)_{bw}}_{4.1.3.2}\frac{S_{bw}}{S_W}\underbrace{\left(C_{LE}\right)_{bw}}_{4.1.3.2} + \right.$
			$C_{N_\alpha} = \underbrace{\left[\left(\frac{C_{N_\alpha}}{A}\right)\left(\frac{1+p}{p}\right)\right]}_{4.1.3.2} A\frac{p}{1+p}$
		HYPERSONIC	Figures 4.1.3.2-56a through -60
			$\left(C_{N_\alpha}\right)_{\delta=0} = \frac{4}{\beta}\frac{1}{\sqrt{1 - \frac{\tan^2 \Lambda_{LE}}{\beta^2}}}$
	WB	SUBSONIC	(a) $\left(C_{L_\alpha}\right)_{WB} = \underbrace{\left[K_N + K_{W(B)} + K_{B(W)}\right]}_{4.3.1.2}\underbrace{\left(C_L\right.}_{4.1}$

THODS SUMMARY

)R DERIVATIVE ESTIMATION ion for components indicated)		METHOD LIMITATIONS ASSOCIATED WITH EQUATION COMPONENTS
	Fig. 4.1.3.2-49	Method 1 1. No curved planforms 2. $M \leq 0.8$, $t/c \leq 0.1$, if cranked planforms with round LE
	Eq. 4.1.3.2-b	Method 2 1. Constant-section, delta or clipped-delta configurations ($\Lambda_{TE} = 0$) 2. $0.58 \leq A \leq 2.55$ 3. $0 \leq \lambda \leq 0.3$ 4. $63^{\circ} \leq \Lambda_{LE} \leq 80^{\circ}$ 5. $0.10 \leq t/c \leq 0.30$ 6. $M = 0.2$
sonic		1. Symmetric airfoils of conventional thickness distribution 2. $A \leq 3$ if composite wings 3. $\alpha = 0$
		1. Straight-tapered wings 2. $M > 1.4$ 3. Linear-lift range
$\frac{S_s}{S_W}\underbrace{(C_{LE})_s}_{4.1.3.2} + \underbrace{(C_{N_\alpha})_E}_{4.1.3.2}\frac{S_E}{S_W}\Bigg]$	Eq. 4.1.3.2-h	1. Double-delta and cranked wings 2. Breaks in LE and TE at same spanwise station 3. $1.2 \leq M \leq 3.0$ 4. Linear-lift range
	Eq. 4.1.3.2-ℓ	1. Curved planforms 2. $1.0 \leq M \leq 3.0$ 3. Linear-lift range
		1. Straight-tapered wings 2. Conventional wings of zero thickness 3. Two-dimensional slender-airfoil theory 4. $\alpha = 0$
	Fig. 4.1.3.2-65	1. Straight-tapered planforms 2. Wedge airfoils 3. Two-dimensional slender-airfoil theory 4. $\alpha = 0$
$\frac{S_e}{S_W}$	Fig. 4.3.1.2-a	Method 1 (body diameter)/(wing semispan) ≤ 0.8 (see Sketch (d), 4.3.1.2) (a) Zero wing incidence; wing-body angle of attack varied K_N (based on exposed wing geometry) 1. Bodies of revolution 2. Slender-body theory 3. Linear-lift range $(C_{L_\alpha})_e$ 4. No curved planforms 5. $M \leq 0.8$, $t/c \leq 0.1$, if cranked wings with round LE

DERIVATIVE	CONFIG.	SPEED REGIME	EQUATIONS FOR DERIVATI (Datcom section for compor
C_{L_α} (Contd.)	WB (Contd.)	SUBSONIC (Contd.)	(b) $\left(C_{L_i}\right)_{WB} = \underbrace{\left[k_{W(B)} + k_{B(W)}\right]}_{4.3.1.2} \underbrace{\left(C_{L_\alpha}\right)_e}_{4.1.3.2} \frac{S_e}{S_W}$
			$\left(C_{L_\alpha}\right)_{WB} = \underbrace{K_{(WB)}}_{4.3.1.2} \underbrace{\left(C_{L_\alpha}\right)_W}_{4.1.3.2}$
		TRANSONIC	(Same as subsonic equations)
		SUPERSONIC	(Same as subsonic equations)

ATION ted)	METHOD LIMITATIONS ASSOCIATED WITH EQUATION COMPONENTS
Eq. 4.3.1.2-b	(b) Body angle of attack fixed at zero; wing incidence varied (same limitations as (a) above)
Eq. 4.3.1.2-c	Method 2 (body diameter)/(wing span) is large with delta wing extending entire length of body (see Sketch (c), 4.3.1.2) $(C_{L_\alpha})_W$ 1. No curved planforms 2. $M \leq 0.8$, $t/c \leq 0.1$, if cranked wings with round LE
	Method 1 (body diameter)/(wing span) is small (see Sketch (d), 4.3.1.2) K_N (based on exposed wing geometry) 1. Bodies of revolution 2. Slender-body theory 3. Linear-lift range $K_{B(W)}$ and $k_{W(B)}$ (based on exposed wing geometry) $(C_{L_\alpha})_e$ 4. Symmetric airfoils of conventional thickness distribution 5. $A < 3$ if composite wings 6. $\alpha = 0$
	Method 2 (body diameter)/(wing span) is large with delta wing extending the entire length of the body (see Sketch (c), 4.3.1.2) $(C_{L_\alpha})_W$ 1. Symmetric airfoils of conventional thickness distribution 2. $A < 3$ if composite wings 3. $\alpha = 0$
	Method 1 (body diameter)/(wing span) is small (see Sketch (d), 4.3.1.2) K_N (based on exposed wing geometry) 1. Bodies of revolution 2. Slender-body theory 3. Linear-lift range $K_{B(W)}$ and $k_{W(B)}$ (based on exposed wing geometry) $(C_{N_\alpha})_e$ 4. Breaks in LE and TE at same spanwise station 5. $M > 1.4$ for straight-tapered wings 6. $1.2 < M < 3$ for composite wings 7. $1.0 < M < 3$ for curved planforms

DERIVATIVE	CONFIG.	SPEED REGIME	
C_{L_α} (Contd.)	WB (Contd.)	SUPERSONIC (Contd.)	
	WBT	SUBSONIC	$C_{L_\alpha} = \underbrace{\left(C_{L_\alpha}\right)'_e}_{4.1.3.2} \underbrace{\left[K_N + K_{W(B)} +\right.}_{4.3.1.2}$
			$C_{L_\alpha} = \underbrace{\left(C_{L_\alpha}\right)'_e}_{4.1.3.2} \underbrace{\left[K_N + K_{W(B)} +\right.}_{4.3.1.2}$

METHODS SUMMARY

EQUATIONS FOR DERIVATIVE ESTIMATION (Datcom section for components indicated)	METHOD LIMITATIONS ASSOCIATED WITH EQUATION COMPONENTS
	Method 2 (body diameter)/(wing span) is large with de wing extending entire length of body (see Sketch (c), 4.3.1.2) $\left(C_{N_\alpha}\right)_W$ 1. Breaks in LE and TE at same spanwise sta 2. $M > 1.4$ for straight-tapered wings 3. $1.2 \leq M \leq 3$ for composite wings 4. $1.0 \leq M \leq 3$ for curved planforms 5. Linear-lift range
$\underbrace{\quad\quad}_{K_{B(W)}}' \frac{S_e'}{S'} + \underbrace{\left(C_{L_\alpha}\right)_e''}_{4.1.3.2} \underbrace{\left[K_{W(B)} + K_{B(W)}\right]''}_{4.3.1.2} \underbrace{\left(1 - \frac{\partial \epsilon}{\partial \alpha}\right)}_{4.4.1} \underbrace{\frac{q''}{q_\infty}}_{4.4.1} \frac{S''}{S'} \frac{S_e''}{S''}$ Eq. 4.5.1.1-a	Method 1 $b_W/b_H > 1.5$ 1. (Body diameter)/(wing semispan) ≤ 0.8 (see Sketch (d), 4.3.1.2) 2. $\alpha \leq \alpha_{stall}$ if high aspect ratio and unswept 3. $\alpha << \alpha_{stall}$ if low aspect ratio or swept w $\left(C_{L_\alpha}\right)_e'$ and $\left(C_{L_\alpha}\right)_e''$ 4. No curved planforms 5. $M < 0.8$, $t/c \leq 0.1$, if cranked planforms round LE K_N (based on exposed wing geometry) 6. Bodies of revolution 7. Slender-body theory 8. Linear-lift range $\frac{\partial \epsilon}{\partial \alpha}$ (depends upon method) 9. Straight-tapered wing 10. Other limitations depend upon $\frac{\partial \epsilon}{\partial \alpha}$ predic method $\frac{q''}{q_\infty}$ 11. Valid only on the plane of symmetry
$\underbrace{K_{B(W)}}_{}' \frac{S_e'}{S'} + \underbrace{\left(C_{L_\alpha}\right)_e''}_{4.1.3.2} \underbrace{\left[K_{W(B)} + K_{B(W)}\right]''}_{4.3.1.2} \underbrace{\frac{q''}{q_\infty}}_{4.4.1} \frac{S''}{S'} \frac{S_e''}{S''} + \underbrace{\left(C_{L_\alpha}\right)_{W''(v)}}_{4.5.1.1}$ Eq. 4.5.1.1-b	Method 2 $b_W/b_H < 1.5$ (same limitations as Method 1 above omitting thos of $\partial\epsilon/\partial\alpha$) K_N and $\left(C_{L_\alpha}\right)_{W''(v)}$ (based on exposed wing geomet

DERIVATIVE	CONFIG.	SPEED REGIME	EQUATIONS FOR DERIVATIVE ESTIMAT (Datcom section for components indicate
C_{L_α} (Contd.)	WBT (Contd.)	TRANSONIC	(Same as subsonic equations)
		SUPERSONIC	(Same as subsonic equations)

ARY

ION	METHOD LIMITATIONS ASSOCIATED WITH EQUATION COMPONENTS
	Method 1 $b_W/b_H \geq 1.5$ $\left(C_{L_\alpha}\right)'_e$ and $\left(C_{L_\alpha}\right)''_e$ 1. Symmetric airfoils of conventional thickness distribution 2. $A \leq 3$ if composite planforms 3. $\alpha = 0$ $K_{B(W)}$ (based on exposed wing geometry) K_N (based on exposed wing geometry) 4. Bodies of revolution 5. Slender-body theory 6. Linear-lift range $\frac{\partial \epsilon}{\partial \alpha}$ (depends upon method) 7. Straight-tapered wings 8. Proportional to C_{L_α} $\frac{q''}{q_\infty}$ 9. Conventional trapezoidal planforms 10. Valid only on the plane of symmetry
	Method 2 $b_W/b_H < 1.5$ (same limitations as Method 1 above omitting those of $\partial\epsilon/\partial\alpha$) K_N, $K_{B(W)}$, and $\left(C_{L_\alpha}\right)_{W''(v)}$ (based on exposed wing geometry)
	Method 1 $b_W/b_H \geq 1.5$ $\left(C_{N_\alpha}\right)'_e$ and $\left(C_{N_\alpha}\right)''_e$ 1. Breaks in LE and TE at same spanwise station 2. $M \geq 1.4$ for straight-tapered planforms 3. $1.2 \leq M \leq 3$ for composite planforms 4. $1.0 \leq M \leq 3$ for curved planforms 5. Linear-lift range K_N (based on exposed wing geometry) 6. Bodies of revolution 7. Slender-body theory $K_{B(W)}$ (based on exposed wing geometry) $\frac{\partial \epsilon}{\partial \alpha}$ 8. Straight-tapered wings 9. Other limitations depend upon $\frac{\partial \epsilon}{\partial \alpha}$ prediction method

DERIVATIVE	CONFIG.	SPEED REGIME	EQUATIONS FOR DERIVAT (Datcom section ref comp
C_{L_α} (Contd.)	WBT (Contd.)	SUPERSONIC (Contd.)	
C_{m_α}	W	SUBSONIC	$C_{m_\alpha} = \underbrace{\left(n - \frac{x_{a.c.}}{c_r}\right)}_{4.1.4.2} \frac{c_r}{\bar{c}} \underbrace{C_{L_\alpha}}_{4.1.3.2}$
		TRANSONIC	(Same as subsonic equation)
		SUPERSONIC	(Same as subsonic equation)
		HYPERSONIC	(Same as subsonic equation)

ETHODS SUMMARY

FOR DERIVATIVE ESTIMATION ection for components indicated)	METHOD LIMITATIONS ASSOCIATED WITH EQUATION COMPONENTS
	$\frac{q''}{q_\infty}$ 10. If nonviscous flow field, limited to unswept w 11. If viscous flow field, valid only on the plane o symmetry
	Method 2 $b_W/b_H < 1.5$ (same limitations as Method 1 above omitting those of $\partial\epsilon/\partial\alpha$) K_N, $K_{B(W)}$, and $\left(C_{L_\alpha}\right)_{W''(v)}$ (based on exposed wing geometry)
Eq. 4.1.4.2-d	1. $M \leq 0.6$; however, for swept wings with $t/c \leq 0.04$, application to higher Mach numbe is acceptable 2. Linear-lift range C_{L_α} 3. No curved planforms 4. $M \leq 0.8$, $t/c \leq 0.1$, if cranked planforms wit round LE
	1. Straight-tapered wings 2. Symmetric airfoil sections 3. Linear-lift range C_{L_α} 4. Conventional thickness distribution 5. $\alpha = 0$
	1. Linear-lift range C_{N_α} 2. Breaks in LE and TE at same spanwise statio 3. $M \geq 1.4$ for straight-tapered wings 4. $1.2 \leq M \leq 3$ for composite wings 5. $1.0 \leq M \leq 3$ for curved planforms
	1. $\alpha = 0$ C_{N_α} 2. Straight-tapered wings 3. Conventional wings of zero thickness and wed airfoils 4. Two-dimensional slender-airfoil theory

DERIVATIVE	CONFIG.	SPEED REGIME	EQUATIONS FOR DERIVATIVE (Datcom section for component
C_{m_α} (Contd.)	WB	SUBSONIC	$C_{m_\alpha} = \left(n \quad \frac{x_{a.c.}}{c_r} \right) \frac{c_r}{c}$ C_{L_α} 4.3.2.2 4.3.1.2
		TRANSONIC	(Same as subsonic equation)
		SUPERSONIC	(Same as subsonic equation)

DS SUMMARY

VATIVE ESTIMATION mponents indicated)	METHOD LIMITATIONS ASSOCIATED WITH EQUATION COMPONENTS
Eq. 4.1.4.2-d	$\frac{X_{a.c.}}{C_r}$ (calculations based on exposed wing geometry) 1. Single wing with body (i.e., no cruciform or other multipanel arrangements) 2. $M \leq 0.6$, however, if swept wing with $t/c \leq 0.04$, application to higher Mach numbers is acceptable 3. Linear-lift range C_{L_α} 4. (Body diameter)/(wing span) ≤ 0.8 5. No curved planforms 6. Bod' . of revolution 7. Slender-body theory 8. $M \leq 0.8$, $t/c \leq 0.1$, if swept wing with round LE
	$\frac{X_{a.c.}}{C_r}$ (calculations based on exposed wing geometry) 1. Straight-tapered wings 2. Single wing with body (i.e., no cruciform or other multipanel arrangements) 3. Symmetric airfoils of conventional thickness distribution 4. Linear-lift range C_{L_α} 5. Bodies of revolution 6. Slender-body theory 7. $\alpha = 0$
	$\frac{X_{a.c.}}{C_r}$ (calculations based on exposed wing geometry) 1. Single wing with body (i.e., no cruciform or other multipanel arrangements) 2. Linear-lift range C_{N_α} 3. Breaks in LE and TE at same spanwise station 4. Bodies of revolution 5. Slender-body theory 6. $M \geq 1.4$ for straight-tapered wings 7. $1.2 \leq M \leq 3$ for composite wings 8. $1.0 \leq M \leq 3$ for curved planforms

DERIVATIVE	CONFIG.	SPEED REGIME	EQUATIONS FOR DERIVATIVE ES (Datcom section for components i
C_{m_α} (Contd.)	WBT	SUBSONIC	$C_{m_\alpha}{}^{*} = -\underbrace{\frac{x_{c.g.} - x'}{\bar{c}'}}_{4.5.2.1}\underbrace{\left[K_N + K_{B(W)} + K_{W(B)}\right]'}_{4.3.1.2}\underbrace{\left(C_{L_\alpha}\right)'_e}_{4.1.3.2}\frac{S'_e}{S'}$ $-\underbrace{\frac{x_{c.g.} - x''}{\bar{c}''}}_{4.5.2.1}\underbrace{\left[K_{B(W)} + K_{W(B)}\right]''}_{4.3.1.2}\underbrace{\left(C_{L_\alpha}\right)''_e}_{4.1.3.2}\left(1 - \underbrace{\frac{\partial\epsilon}{\partial\alpha}}_{4.4.1}\right)\underbrace{\frac{q''}{q_\infty}}_{4.4.1}\frac{S''_e}{S''}\frac{S''}{S'}$ *Drag and z terms have been omitted, and small-angle assumptions r to angle of attack; equation as given is valid for most configurations
			$C_{m_\alpha} = -\underbrace{\frac{x_{c.g.} - x'}{\bar{c}'}}_{4.5.2.1}\underbrace{\left[K_N + K_{B(W)} + K_{W(B)}\right]'}_{4.3.1.2}\underbrace{\left(C_{L_\alpha}\right)'_e}_{4.1.3.2}\frac{S'_e}{S'}$ $-\underbrace{\frac{x_{c.g.} - x''}{\bar{c}''}}_{4.5.2.1}\left(\frac{\bar{c}''}{\bar{c}'}\right)\underbrace{\left\{\left[K_{W(B)} + K_{B(W)}\right]''\right.}_{4.3.1.2}\underbrace{\left(C_{L_\alpha}\right)''_e}_{4.1.3.2}\frac{S''_e}{S''}\frac{S''}{S'}\underbrace{\frac{q''}{q_\infty}}_{4.4.1} + \left(C$
		TRANSONIC	(Same as subsonic equations)

METHODS SUMMARY

ATIONS FOR DERIVATIVE ESTIMATION Datcom section for components indicated)	METHOD LIMITATIONS ASSOCIATED WITH EQUATION COMPONENTS
$\underbrace{K_{W(B)}}\Big]' \underbrace{\left(C_{L_\alpha}\right)'_e}_{4.1.3.2} \frac{S'_e}{S'}$ $\underbrace{\quad}\Big]'' \underbrace{\left(C_{L_\alpha}\right)''_e}_{4.1.3.2} \left(1 - \underbrace{\frac{\partial\epsilon}{\partial\alpha}}_{4.4.1}\right) \underbrace{\frac{q''}{q_\infty}}_{4.4.1} \frac{S''_e}{S''} \frac{S''}{S'} \frac{\bar{c}''}{\bar{c}'}$ Eq. 4.5.2.1-d' ed, and small-angle assumptions made with respect is valid for most configurations	Method 1 $b_W/b_H \geq 1.5$ 1. (Body diameter)/(wing semispan) ≤ 0.8 (see Sketch (d), 4.3.1.2) 2. Linear-lift range $\frac{x_{c.g.} - x'}{\bar{c}'}$ (calculations based on exposed planform geometry) 3. Single wing with body (i.e., no cruciform or other multipanel arrangements) 4. $M \leq 0.6$; however, for swept wings with $t/c \leq 0.0$ application to higher Mach numbers is acceptable K_N (based on exposed wing geometry) 5. Bodies of revolution 6. Slender-body theory $\left(C_{L_\alpha}\right)'_e$ and $\left(C_{L_\alpha}\right)''_e$ 7. No curved planforms 8. $M \leq 0.8$, $t/c \leq 0.1$ if cranked planforms with round LE $\frac{\partial\epsilon}{\partial\alpha}$ 9. Straight-tapered wing 10. Other limitations depend upon $\frac{\partial\epsilon}{\partial\alpha}$ prediction method $\frac{q''}{q_\infty}$ 11. Valid only on the plane of symmetry
$\underbrace{K_{W(B)}}\Big]' \underbrace{\left(C_{L_\alpha}\right)'_e}_{4.1.3.2} \frac{S'_e}{S'}$ $\underbrace{K_{B(W)}}\Big]'' \underbrace{\left(C_{L_\alpha}\right)''_e}_{4.1.3.2} \frac{S''_e}{S''} \frac{S''}{S'} \underbrace{\frac{q''}{q_\infty}}_{4.4.1} + \underbrace{\left(C_{L_\alpha}\right)_{W''(v)}}_{4.5.1.1}$ Eq. 4.5.2.1-f' .2	Method 2 $b_W/b_H < 1.5$ (same limitations as Method 1 above, omitting those for $\partial\epsilon/\partial\alpha$) $\frac{x_{c.g.} - x'}{\bar{c}'}$ (calculations based on exposed planform geometry) K_N and $\left(C_{L_\alpha}\right)_{W''(v)}$ (based on exposed wing geometry)
	Method 1 $b_W/b_H \geq 1.5$ $\frac{x_{c.g.} - x'}{\bar{c}'}$ (calculations based on exposed planform geometry) 1. Single wing with body (i.e., no cruciform or other multipanel arrangements) 2. Straight-tapered wings 3. Symmetric airfoils of conventional thickness distribution 4 Linear-lift range

DERIVATIVE	CONFIG.	SPEED REGIME	EQUATIONS FOR DERIVATIVE ESTIMATIO (Datcom section for components indicated)
C_{m_α} (Contd.)	WBT (Contd.)	TRANSONIC (Contd.)	
		SUPERSONIC	(Same as subsonic equations)

ODS SUMMARY

RIVATIVE ESTIMATION components indicated)	METHOD LIMITATIONS ASSOCIATED WITH EQUATION COMPONENTS
	$K_{B(W)}$ (based on exposed wing geometry) K_N (based on exposed wing geometry) 5. Bodies of revolution 6. Slender-body theory $\left(C_{L_\alpha}\right)_e'$ and $\left(C_{L_\alpha}\right)_e''$ 7. $\alpha = 0$ $\frac{\partial \epsilon}{\partial \alpha}$ 8. Proportional to C_{L_α} $\frac{q''}{q_\infty}$ 9. Conventional trapezoidal planforms 10. Valid only on the plane of symmetry
	Method 2 $b_W/b_H < 1.5$ (same limitations as Method 1 above, omitting that for $\partial\epsilon/\partial\alpha$) $\frac{x_{c.g.} - x'}{\bar{c}'}$ (calculations based on exposed planform geometry) K_N, $K_{B(W)}$, and $\left(C_{L_\alpha}\right)_{W''(v)}$ (based on exposed wing geometry)
	Method 1 $b_W/b_H \geq 1.5$ $\frac{x_{c.g.} - x'}{\bar{c}'}$ (calculations based on exposed planform geometry) 1. Single wing with body (i.e., no cruciform or other multipanel arrangements) 2. Linear-lift range K_N (based on exposed wing geometry) 3. Bodies of revolution 4. Slender-body theory $K_{B(W)}$ (based on exposed wing geometry) $\left(C_{N_\alpha}\right)_e'$ and $\left(C_{N_\alpha}\right)_e''$ 5. Breaks in LE and TE at same spanwise station 6. $M \geq 1.4$ for straight-tapered planforms 7. $1.2 \leq M \leq 3$ for composite planforms 8. $1.0 \leq M \leq 3$ for curved planforms $\frac{\partial \epsilon}{\partial \alpha}$ 9. Straight-tapered wings 10. Other limitations depend upon $\frac{\partial \epsilon}{\partial \alpha}$ prediction method

DERIVATIVE	CONFIG.	SPEED REGIME	EQUATIONS FOR DERIVATIVE ESTI (Datcom section for components indi
C_{m_α} (Contd.)	WBT (Contd.)	SUPERSONIC (Contd.)	
C_{L_q}	W	SUBSONIC	$C_{L_q} = \underbrace{\left(\frac{1}{2} + 2\frac{\bar{x}}{\bar{c}}\right)}_{4.1.4.2} \underbrace{C_{L_\alpha}}_{4.1.3.2}$
		TRANSONIC	(Same as subsonic equation)
		SUPERSONIC	$C_{L_q} = \underbrace{C_{L_q}'}_{7.1.1.1} + \underbrace{2\left(\frac{\bar{x}}{\bar{c}}\right)}_{4.1.4.2} \underbrace{C_{N_\alpha}}_{4.1.3.2}$

METHODS SUMMARY

EQUATIONS FOR DERIVATIVE ESTIMATION (Datcom section for components indicated)	METHOD LIMITATIONS ASSOCIATED WITH EQUATION COMPONENTS
	$\frac{q''}{q_\infty}$ 11. If nonviscous flow field, limited to unswept w 12. If viscous flow field, valid only on plane of symmetry
	Method 2 $b_W/b_H \leq 1.5$ (same limitations as Method 1, omitting those of $\partial\epsilon/\partial\alpha$ $\frac{x_{c.g.} - x'}{\bar{c}'}$ (calculation based on exposed planform geom K_N, $K_{B(W)}$, and $\left(C_{L_\alpha}\right)_{W''(v)}$ (based on exposed wing geometry)
Eq. 7.1.1.1-a	$\frac{\bar{x}}{\bar{c}}$ 1. $M \leq 0.6$; however, for swept wings with $t/c \leq 0.04$, application to higher Mach numbe is acceptable 2. Linear-lift range C_{L_α} 3. No curved planforms 4. $M \leq 0.8$, $t/c \leq 0.1$, if cranked wings with round LE
	$\frac{\bar{x}}{\bar{c}}$ 1. Straight-tapered wings 2. No camber C_{L_α} 3. Conventional thickness distribution 4. $\alpha = 0$
Eq. 7.1.1.1-c	1. Straight-tapered wings C'_{L_α} (a) Subsonic LE ($\beta \cot \Lambda_{LE} < 1$) 2 Mach lines from LE vertex may not intersect 3 Wing-tip Mach lines may not intersect on win nor intersect opposite wing tips (b) Supersonic LE ($\beta \cot \Lambda_{LE} > 1$) 4. Valid only if Mach lines from LE vertex intersect TE 5 Foremost Mach line from either wing tip may not intersect remote half of wing $\frac{\bar{x}}{\bar{c}}$ 6. Linear-lift range

DERIVATIVE	CONFIG.	SPEED REGIME	EQUATIONS FOR DERIVATIVE ESTIMATIO (Datcom section for components indicated)
C_{L_q} (Contd.)	W (Contd.)	SUPERSONIC (Contd.)	
	WB	SUBSONIC	$\left(C_{L_q}\right)_{WB} = \underbrace{\left[K_{W(B)} + K_{B(W)}\right]}_{4.3.1.2}\left(\frac{S_e}{S}\right)\left(\frac{\bar{c}_e}{\bar{c}}\right)\underbrace{\left(C_{L_q}\right)_e}_{7.1.1.1} + \underbrace{\left(C_{L_q}\right)_B}_{7.2.1.1}\left(\frac{S_b}{S}\right)\left(\frac{\ell_B}{\bar{c}}\right)$
			$\left(C_{L_q}\right)_{WB} = \underbrace{K_{(WB)}}_{4.3.1.2}\underbrace{\left(C_{L_q}\right)_W}_{7.1.1.1} + \underbrace{\left(C_{L_q}\right)_B}_{7.2.1.1}\left(\frac{S_b}{S}\right)\left(\frac{\ell_B}{\bar{c}}\right)$
		TRANSONIC	(Same as subsonic equations)
		SUPERSONIC	(Same as subsonic equations)

SUMMARY

'VE ESTIMATION ients indicated)	METHOD LIMITATIONS ASSOCIATED WITH EQUATION COMPONENTS
	C_{N_α} 7. $M \geq 1.4$
$\left(\frac{r_B}{c}\right)$ Eq. 7.3.1.1-a	Method 1 (body diameter)/(wing span) is small (see 4.3.1.2 Sketch (d)) $\left(C_{L_q}\right)_e$ 1. No curved planforms 2. Linear-lift range 3. $M \leq 0.6$, however, for swept wings with $t/c \leq 0.04$, application to higher Mach numbers is acceptable 4. $M \leq 0.8$, $t/c \leq 0.1$, if cranked wing with round LE $\left(C_{L_q}\right)_B$ 5. Bodies of revolution
Eq. 7.3.1.1-b	Method 2 (body diameter)/(wing span) is large, with delta wing extending entire length of body (see 4.3.1.2 Sketch (c)) (same limitations as Method 1 above)
	Method 1 (body diameter)/(wing span) is small (see 4.3.1.2 Sketch (d)) $K_{B(W)}$ (based on exposed wing geometry) $\left(C_{L_q}\right)_e$ 1. Straight-tapered wings 2. No camber 3. Conventional thick[illegible] distribution 4. $\alpha = 0$ $\left(C_{L_q}\right)_B$ 5 Bodies of revolution
	Method 2 (body diameter)/(wing span) is large, with delta wing extending entire length of body (see 4.3.1.2 Sketch (c)) (same limitations as Method 1 above)
	Method 1 (body diameter)/(wing span) is small (see 4.3.1.2 Sketch (d)) $K_{B(W)}$ (based on exposed wing geometry) $\left(C_{L_q}\right)_e$ 1. Straight-tapered wings 2. $M \geq 1.4$ 3. Linear-lift range

DERIVATIVE	CONFIG.	SPEED REGIME	EQUATIONS FOR DERIVATIVE ESTIMATIC (Datcom section for components indicated)
C_{L_q} (Contd.)	WB (Contd.)	SUPERSONIC (Contd.)	
	WBT	SUBSONIC	$C_{L_q} = \underbrace{\left(C_{L_q}\right)_{WB}}_{7.3.1.1} + 2\underbrace{\left[K_{W(B)} + K_{B(W)}\right]}_{4.3.1.2}{}''\left(\frac{S_e''}{S'}\right)\underbrace{\left(\frac{x_{c.g.} - x''}{\bar{c}'}\right)}_{4.5.2.1}\underbrace{\left(\frac{q''}{q_\infty}\right)}_{4.4.1}\underbrace{\left(C_{L_\alpha}\right)_e''}_{4.1.3.2}$
			$C_{L_q} = \underbrace{\left(C_{L_q}\right)_{WB}}_{7.3.1.1} + 2\underbrace{\frac{x_{c.g.} - x''}{\bar{c}'}}_{4.5.2.1}\left\{\underbrace{\left[K_{W(B)} + K_{B(W)}\right]}_{4.3.1.2}{}''\left(\frac{S_e''}{S'}\right)\underbrace{\left(\frac{q''}{q_\infty}\right)}_{4.4.1}\underbrace{\left(C_{L_\alpha}\right)_e''}_{4.1.3.2} + \left(C_{L_\alpha}\right.$
		TRANSONIC	(Same as subsonic equations)

ETHODS SUMMARY

OR DERIVATIVE ESTIMATION tion for components indicated)		METHOD LIMITATIONS ASSOCIATED WITH EQUATION COMPONENTS
		(a) Subsonic LE ($\beta \cot \Lambda_{LE} < 1$) 4. Mach lines from TE vertex may not intersect LE 5. Wing tip Mach lines may not intersect on wing nor intersect opposite wing tips (b) Supersonic LE ($\beta \cot \Lambda_{LE} \geq 1$) 6. Valid only if Mach lines from LE vertex intersect TE 7. Foremost Mach line from either wing tip may not intersect remote half of wing $\left(C_{L_q}\right)_B$ 8. Bodies of revolution
		Method 2 (body diameter)/(wing span) is large, with delta wing extending entire length of body (see 4.3.1.2 Sketch (c)) (same limitations as Method 1 above)
$\left(\frac{x_{c.g.} - x''}{\bar{c}'}\right)\left(\frac{q''}{q_\infty}\right)\left(C_{L_\alpha}\right)''_e$ 4.5.2.1 4.4.1 4.1.3.2	Eq. 7.4.1.1-a	Method 1 $b_W/b_H \geq 1.5$ 1. Linear-lift range $\left(C_{L_q}\right)_{WB}$ (based on exposed wing geometry) 2. No curved planforms 3. Bodies of revolution 4. $M \leq 0.6$; however, for swept wings with $t/c \leq 0.04$, application to higher Mach numbers is acceptable 5. $M \leq 0.8$, $t/c \leq 0.1$, if cranked wings with round LE $\frac{q''}{q_\infty}$ 6. Valid only on the plane of symmetry $\left(C_{L_\alpha}\right)''_e$ 7. Additional tail limitations are identical to Items 2 and 5 immediately above
$K_{B(W)}\Big]''\left(\frac{S''_e}{S'}\right)\left(\frac{q''}{q_\infty}\right)\left(C_{L_\alpha}\right)''_e + \left(C_{L_\alpha}\right)_{W''(B)}\Big\}$ .1.2 4.4.1 4.1.3.2 7.4.1.1	Eq. 7.4.1.1-b	Method 2 $b_W/b_H < 1.5$ (same limitations as Method 1 above) $\left(C_{L_q}\right)_{WB}$ and $\left(C_{L_\alpha}\right)_{W''(B)}$ (based on exposed wing geometry)
		Method 1 $b_W/b_H \geq 1.5$ $\left(C_{L_q}\right)_{WB}$ (based on exposed wing geometry) 1. Straight-tapered wings 2. No camber 3. Conventional thickness distribution 4. Bodies of revolution

DERIVATIVE	CONFIG.	SPEED REGIME	EQUATIONS FOR DERIVATIVE ESTIMAT (Datcom section for components indicate
C_{L_q} (Contd.)	WBT (Contd.)	TRANSONIC (Contd.)	
		SUPERSONIC	(Same as subsonic equations)

MMARY

TIMATION ndicated)	METHOD LIMITATIONS ASSOCIATED WITH EQUATION COMPONENTS
	5. $\alpha = 0$ $K_{B(W)}$ (based on exposed wing geometry) $\frac{q'}{q_\infty}$ 6. Conventional trapezoidal planforms 7. Valid only on the plane of symmetry $\left(C_{L_\alpha}\right)_e''$ 8. Additional tail limitations are identical to Items 2, 3, and 5 immediately above
	Method 2 $b_W/b_H < 1.5$ (same limitations as Method 1 above) $\left(C_{L_q}\right)_{WB}$, $K_{B(W)}$, and $\left(C_{L_\alpha}\right)_{W'(v)}$ (based on exposed wing geometry)
	Method 1 $b_W/b_H \geq 1.5$ 1. Linear-lift range $\left(C_{L_q}\right)_{WB}$ (based on exposed wing geometry) 2. Straight-tapered wings 3. Bodies of revolution 4. $M \geq 1.4$ $K_{B(W)}$ (based on exposed wing geometry) (a) Subsonic LE ($\beta \cot \Lambda_{LE} < 1$) 5. Mach line from TE vertex may not intersect LE 6. Wing-tip Mach lines may not intersect on wing nor intersect opposite wing tips (b) Supersonic LE ($\beta \cot \Lambda_{LE} > 1$) 7. Valid only if Mach lines from LE vertex intersect TE 8. Foremost Mach line from either wing tip may not intersect remote half of wing $\frac{q''}{q_\infty}$ 9. If nonviscous flow field, limited to unswept wings 10. If viscous flow field, valid only on plane of symmetry $\left(C_{L_\alpha}\right)_e''$ 11. Additional tail limitations are identical to Items 1 and 4 immediately above
	Method 2 $b_W/b_H < 1.5$ (same limitations as Method 1 above) $\left(C_{L_q}\right)_{WB}$, $K_{B(W)}$, and $\left(C_{L_\alpha}\right)_{W'(v)}$ (based on exposed wing geometry)

DERIVATIVE	CONFIG.	SPEED REGIME	EQUATIONS FOR DERIVATIVE ESTIM (Datcom section for components indic
C_{m_q}	W	SUBSONIC	$\left(C_{m_q}\right)_{M\approx 0.2} = \underbrace{0.7\ c_{l_\alpha}}_{\substack{4.1.1\\4.1.1.2}} \cos \Lambda_{c/4} \left\{ \frac{A\left[\frac{1}{2}\underbrace{\frac{\bar{x}}{\bar{c}}}_{7.1.1.1} + 2\underbrace{\left(\frac{r}{\bar{c}}\right)^2}_{7.1.1.1}\right]}{A + 2\cos\Lambda_{c/4}} + \frac{1}{24}\left(\frac{A^3}{A+\right.\right.$
			$\left(C_{m_q}\right)_{M>0.2} = \left[\frac{\frac{A^3 \tan^2 \Lambda_{c/4}}{AB + 6\cos\Lambda_{c/4}} + \frac{3}{B}}{\frac{A^3 \tan^2 \Lambda_{c/4}}{A + 6\cos\Lambda_{c/4}} + 3}\right] \underbrace{\left(C_{m_q}\right)_{M\approx 0.2}}_{7.1.1.2}$
		TRANSONIC	$C_{m_q} = \frac{\left(C_{L_\alpha}\right)_M - \left(C_{L_\alpha}\right)_{M_{cr}}}{\underbrace{\left(C_{L_\alpha}\right)_{M=1.2}}_{4.1.3.2} - \underbrace{\left(C_{L_\alpha}\right)_{M_{cr}}}_{4.1.3.2}} \left[\underbrace{\left(C_{m_q}\right)_{M=1.2}}_{7.1.1.2} - \underbrace{\left(C_{m_q}\right)_{M_{cr}}}_{7.1.1.2}\right] + \underbrace{\left(C_{m_q}\right)_M}_{7.1.1.2}$
		SUPERSONIC	$C_{m_q} = \underbrace{C'_{m_q}}_{7.1.1.2}\ \underbrace{\left(\frac{\bar{x}}{\bar{c}}\right)}_{7.1.1.1}\ \underbrace{C_{L_q}}_{7.1.1.1}$

METHODS SUMMARY

EQUATIONS FOR DERIVATIVE ESTIMATION (Datcom section for components indicated)		METHOD LIMITATIONS ASSOCIATED WITH EQUATION COMPONENTS
$\underbrace{\quad}_{7.1.1.1}\ \underbrace{\quad}_{7.1.1.1}$ $\left\{\frac{A\left[\frac{1}{2}\frac{\bar{x}}{\bar{c}} + 2\left(\frac{\bar{x}}{\bar{c}}\right)^2\right]}{A + 2\cos\Lambda_{c/4}} + \frac{1}{24}\left(\frac{A^3\tan^2\Lambda_{c/4}}{A + 6\cos\Lambda_{c/4}}\right) + \frac{1}{8}\right\}$	Eq. 7.1.1.2-a	$\frac{\bar{x}}{\bar{c}}$ 1. $M \leq 0.6$; however, for swept wings with $t/c \leq 0.04$, application to higher Mach numbers is acceptable 2. Linear-lift range
$+\frac{3}{B}\Bigg]\underbrace{\left(C_{m_q}\right)_{M=0.2}}_{7.1.1.2}$ $+3$	Eq. 7.1.1.2-b	
$\underbrace{\left(C_{m_q}\right)_{M=1.2}}_{7.1.1.2} - \underbrace{\left(C_{m_q}\right)_{M_{cr}}}_{7.1.1.2}\Bigg] + \underbrace{\left(C_{m_q}\right)_{M_{cr}}}_{7.1.1.2}$	Eq. 7.1.1.2-c	C_{L_α} 1. Symmetric airfoils of conventional thickness distribution 2. $\alpha = 0$ $\left(C_{m_q}\right)_{M=1.2}$ 3. Straight-tapered wings (a) Subsonic LE ($\beta \cot \Lambda_{LE} < 1$) 4. Mach line from TE vertex may not intersect LE 5. Wing-tip Mach lines may not intersect on wings intersect opposite wing tips (b) Supersonic LE ($\beta \cot \Lambda_{LE} > 1$) 6. Valid only if Mach lines from LE vertex intersect TE 7. Foremost Mach line from either wing tip may intersect remote half of wing
	Eq. 7.1.1.2-d	C_{m_q} (a) Subsonic LE ($\beta \cot \Lambda_{LE} < 1$) 1. Mach line from TE vertex may not intersect LE 2. Wing-tip Mach lines may not intersect on wings intersect opposite wing tips (b) Supersonic LE ($\beta \cot \Lambda_{LE} > 1$) 3. Valid only if Mach lines from LE vertex intersect TE 4. Foremost Mach line from either wing tip may intersect remote half of wing C_{L_q} 5. Straight-tapered wings 6. $M \geq 1.4$ 7. Linear-lift range

DERIVATIVE	CONFIG.	SPEED REGIME	EQUATIONS FOR DERIVATIVE ESTIMATION (Datcom section for components indicated)
C_{m_q} (Contd.)	WB	SUBSONIC	$\left(C_{m_q}\right)_{WB} = \underbrace{\left[K_{W(B)} + K_{B(W)}\right]}_{4.3.1.2} \left(\frac{S_e}{S}\right)\left(\frac{\bar{c}_e}{\bar{c}}\right)^2 \underbrace{\left(C_{m_q}\right)_e}_{7.1.1.2} + \underbrace{\left(C_{m_q}\right)_B}_{7.2.1.2} \left(\frac{S_b}{S}\right)\left(\frac{\ell_B}{\bar{c}}\right)^2$
			$\left(C_{m_q}\right)_{WB} = \underbrace{K_{(WB)}}_{4.3.1.2}\underbrace{\left(C_{m_q}\right)_W}_{7.1.1.2} + \underbrace{\left(C_{m_q}\right)_B}_{7.2.1.2}\left(\frac{S_b}{S}\right)\left(\frac{\ell_B}{\bar{c}}\right)^2$
		TRANSONIC	(Same as subsonic equations)

	METHOD LIMITATIONS ASSOCIATED WITH EQUATION COMPONENTS
Eq. 7.3.1.2-a	Method 1 (body diameter)/(wing span) is small (see 4.3.1.2 Sketch (d)) 1. Linear-lift range $\left(C_{m_q}\right)_c$ 2. $M \leq 0.6$; however, for swept wings with $t/c \leq 0.04$, application to higher Mach numbers is acceptable $\left(C_{m_q}\right)_B$ 3. Bodies of revolution
Eq. 7.3.1.2-b	Method 2 (body diameter)/(wing span) is large with delta wing extending entire length of body (see 4.3.1.2 Sketch (c)) (same limitations as Method 1 above)
	Method 1 (body diameter)/(wing span) is small (see 4.3.1.2 Sketch (d)) 1. Linear-lift range $K_{B(W)}$ (based on exposed wing geometry) $\left(C_{m_q}\right)_e$ 2. Straight-tapered wings 3. Symmetric airfoils of conventional thickness distribution 4. $\alpha = 0$ (a) Subsonic LE ($\beta \cot \Lambda_{LE} < 1$) 5. Mach line from TE vertex may not intersect LE 6. Wing-tip Mach lines may not intersect on wings nor intersect opposite wing tips (b) Supersonic LE ($\beta \cot \Lambda_{LE} > 1$) 7. Valid only if Mach lines from LE vertex intersect TE 8. Foremost Mach line from either wing tip may not interesect remote half of wing $\left(C_{m_q}\right)_B$ 9. Bodies of revolution
	Method 2 (body diameter)/(wing span) is large, with delta wing extending entire length of body (see 4.3.1.2 Sketch (c)) (same limitations as Method 1 above)

DERIVATIVE	CONFIG.	SPEED REGIME	EQUATIONS FOR DERIVATIVE ESTIM (Datcom section for components indic
C_{m_q} (Contd.)	WB (Contd.)	SUPERSONIC	(Same as subsonic equations)
	WBT	SUBSONIC	$C_{m_q} = \underbrace{(C_{m_q})_{WB}}_{7.3.1.2} - 2\underbrace{[K_{W(B)} + K_{B(W)}]}_{4.3.1.2}'' \left(\frac{S_e''}{S'}\right)\underbrace{\left(\frac{x_{c.g.} - x''}{\bar{c}'}\right)^2}_{4.5.2.1}\underbrace{\left(\frac{q''}{q_\infty}\right)}_{4.4.1}\underbrace{(C_{L_\alpha})_e}_{4.1.3.2}''$
			$C_{m_q} = \underbrace{(C_{m_q})_{WB}}_{7.3.1.2} - 2\underbrace{\left(\frac{x_{c.g.} - x''}{\bar{c}'}\right)^2}_{4.5.2.1}\left\{\underbrace{[K_{W(B)} + K_{B(W)}]}_{4.3.1.2}''\left(\frac{S_e''}{S'}\right)\underbrace{\left(\frac{q''}{q_\infty}\right)}_{4.4.1}\underbrace{(C_{L}}_{4.1}\right.$

METHODS SUMMARY

S FOR DERIVATIVE ESTIMATION section for components indicated)		METHOD LIMITATIONS ASSOCIATED WITH EQUATION COMPONENTS
		Method 1 (body diameter)/(wing span) is small (see 4.3.1.2 Sketch (d)) 1. Linear-lift range $K_{B(W)}$ (based on exposed wing geometry) $\left(C_{m_q}\right)_e$ 2. Straight-tapered wings 3. $M > 1.4$ (a) Subsonic LE ($\beta \cot \Lambda_{LE} < 1$) 4. Mach line from TE vertex may not intersect LE 5. Wing-tip Mach lines may not intersect on wings nor intersect opposite wing tips (b) Supersonic LE ($\beta \cot \Lambda_{LE} > 1$) 6. Valid only if Mach lines from LE vertex intersect TE 7. Foremost Mach line from either wing tip may not intersect remote half of wing $\left(C_{m_q}\right)_B$ 8. Bodies of revolution
		Method 2 (body diameter)/(wing span) is large with delta wing extending entire length of body (see Sketch (c) 4.3.1.2) (same limitations as Method 1 above)
$\left(\frac{x_{c.g.} - x''}{\bar{c}}\right)^2 \left(\frac{q''}{q_\infty}\right)\left(C_{L_\alpha}\right)''$ 4.5.2.1 4.4.1 4.1.3.2	Eq. 7.4.1.2-a	Method 1 $b_W/b_H \geq 1.5$ $\left(C_{m_q}\right)_{WB}$ (based on exposed wing geometry) 1. Bodies of revolution 2. $M \leq 0.6$; however, if a swept wing with $t/c \leq 0.04$, application to higher Mach numbers is acceptable 3. Linear-lift range $\frac{q''}{q_\infty}$ 4. Valid only on the plane of symmetry $\left(C_{L_\alpha}\right)_e''$ 5. No curved planforms 6. $M \leq 0.8$, $t/c \leq 0.10$, if cranked planforms with round LE
$\left[K_{B(W)} + K_{B(W)}\right]'' \left(\frac{S_e''}{S'}\right)\left(\frac{q''}{q_\infty}\right)\left(C_{L_\alpha}\right)_e'' + \left(C_{L_\alpha}\right)_{W''(v)}$ 4.3.1.2 4.4.1 4.1.3.2 4.5.1.1	Eq. 7.4.1.2-b	Method 2 $b_W/b_H < 1.5$ (same limitations as Method 1 above) $\left(C_{m_q}\right)_{WB}$ and $\left(C_{L_\alpha}\right)_{W''(v)}$ (based on exposed wing geometry)

DERIVATIVE	CONFIG.	SPEED REGIME	EQUATIONS FOR DERIVATIVE ESTIMATION (Datcom section for components indicated)
C_{m_q} (Contd.)	WBT (Contd.)	TRANSONIC	(Same as subsonic equations)
		SUPERSONIC	(Same as subsonic equations)

RY

ON	METHOD LIMITATIONS ASSOCIATED WITH EQUATION COMPONENTS
	Method 1 $b_W/b_H \geq 1.5$ $\left(C_{m_q}\right)_{WB}$ (based on exposed wing geometry) 1. Straight-tapered wings 2. Symmetric airfoils of conventional thickness distribution 3. Bodies of revolution 4. $\alpha = 0$ (a) Subsonic LE ($\beta \cot \Lambda_{LE} < 1$) 5. Mach line from TE vertex may not intersect LE 6. Wing-tip Mach lines may not intersect on wings nor intersect opposite wing tips (b) Supersonic LE ($\beta \cot \Lambda_{LE} > 1$) 7. Valid only if Mach lines from LE vertex intersect TE 8. Foremost Mach line from either wing tip may not intersect remote half of wing $K_{B(W)}$ (based on exposed wing geometry) $\frac{q''}{q_\infty}$ 9. Conventional trapezoidal planforms 10. Valid only on the plane of symmetry $\left(C_{L_\alpha}\right)_e''$ 11. Additional tail limitations are identical to Items 2 and 4 immediately above
	Method 2 $b_W/b_H < 1.5$ (same limitations as Method 1 above) $\left(C_{m_q}\right)_{WB}$, $K_{B(W)}$, and $\left(C_{L_\alpha}\right)_{W''(v)}$ (based on exposed wing geometry)
	Method 1 $b_W/b_H \geq 1.5$ $\left(C_{m_q}\right)_{WB}$ (based on exposed wing geometry) 1. Straight-tapered wings 2. Bodies of revolution 3. $M \geq 1.4$ 4. Linear-lift range $K_{B(W)}$ (based on exposed wing geometry) (a) Subsonic LE ($\beta \cot \Lambda_{LE} < 1$) 5. Mach line from TE vertex may not intersect LE 6. Wing-tip Mach lines may not intersect on wings nor intersect opposite wing tips (b) Supersonic LE ($\beta \cot \Lambda_{LE} > 1$) 7. Valid only if Mach lines from LE vertex intersect TE

DERIVATIVE	CONFIG.	SPEED REGIME	EQUATIONS FOR DERIVATIVE ESTIMATION (Datcom section for components indicated)
C_{m_q} (Contd.)	WBT (Contd.)	SUPERSONIC (Contd.)	
$C_{L_{\dot{\alpha}}}$	$\dot{w}$	SUBSONIC	$C_{L_{\dot{\alpha}}} = 1.5 \underbrace{\left(\frac{x_{a.c.}}{c_r}\right)}_{4.1.4.2} \underbrace{C_{L_\alpha}}_{4.1.3.2} + 3 \underbrace{C_L(g)}_{7.1.4.1}$
		TRANSONIC	(Same as subsonic equation)
		SUPERSONIC	$C_{L_{\dot{\alpha}}} = \frac{\pi A M^2}{2\beta^2} \left[\underbrace{-3G(\beta C)}_{7.1.1.1} \underbrace{F_3(N)}_{7.1.4.1} + \underbrace{2E''(\beta C)}_{7.1.1.1} \underbrace{F_2(N)}_{7.1.4.1} + \frac{1}{M^2} \underbrace{E''(\beta C)}_{7.1.1.1} \underbrace{F_1(}_{7.1.4} \right.$

METHODS SUMMARY

ONS FOR DERIVATIVE ESTIMATION m section for components indicated)		METHOD LIMITATIONS ASSOCIATED WITH EQUATION COMPONENTS
		8. Foremost Mach line from either wing tip may not intersect remote half of wing $\frac{q''}{q_\infty}$ 9. In nonviscous flow field, limited to unswept wings 10. In viscous flow field, valid only on the plane of symmetry $\left(C_{L_\alpha}\right)_e''$ 11. Additional tail limitations are identical to Items 3 and 4 immediately above
		Method 2 $b_W/b_H < 1.5$ (same limitations as Method 1 above) $\left(C_{m_q}\right)_{WB}$, $K_{B(W)}$, and $\left(C_{L_\alpha}\right)_{W''(v)}$ (based on exposed wing geometry)
	Eq. 7.1.4.1-a	1. Triangular planforms 2. Linear-lift range $\frac{x_{a.c.}}{c_r}$ 3. $M \leq 0.6$; however, if swept wing with $t/c \leq 0.04$, application to higher Mach numbers is acceptable $C_L(g)$ 4. $0 < \beta A < 4$
		1. Triangular planforms 2. $M_{cr} \leq M \leq 1.0$ 3. Linear-lift range $\frac{x_{a.c.}}{c_r}$ 4. No camber C_{L_α} 5. Symmetric airfoils of conventional thickness distribution 6. $\alpha = 0$ $C_L(g)$ 7. $0 < \beta A < 4$
$\underbrace{2E''(\beta C)}_{7.1.1.1}\ \underbrace{F_2(N)}_{7.1.4.1} + \frac{1}{M^2}\ \underbrace{E''(\beta C)}_{7.1.1.1}\ \underbrace{F_1(N)}_{7.1.4.1}\Big]$	Eq. 7.1.4.1-b	Method 1 1. Straight-tapered wings 2. $\lambda = 0$ 3. Subsonic LE ($\beta \cot A_{LE} < 1$) 4. Mach line from TE vertex may not intersect LE

DERIVATIVE	CONFIG.	SPEED REGIME	EQUATIONS FOR DERIVATIVE ESTIMATION (Datcom section for components indicated)
C_{L_α} (Contd.)	W (Contd.)	SUPERSONIC (Contd.)	$C_{L_{\dot\alpha}} = \frac{M^2}{\beta^2}\underbrace{(C_{L_{\dot\alpha}})_1}_{7.1.4.1} \quad \frac{1}{\beta^2}\underbrace{(C_{L_{\dot\alpha}})_2}_{7.1.4.1}$
	WB	SUBSONIC	$(C_{L_{\dot\alpha}})_{WB} = \underbrace{\left[K_{W(B)} + K_{B(W)}\right]}_{4.3.1.2}\left(\frac{S_e}{S}\right)\left(\frac{\bar{c}_e}{\bar{c}}\right)\underbrace{(C_{L_{\dot\alpha}})_e}_{7.1.4.1} + \underbrace{(C_{L_{\dot\alpha}})_B}_{7.2.2.1}\left(\frac{S_b}{S}\right)\left(\frac{\ell_B}{\bar{c}}\right)$
			$(C_{L_{\dot\alpha}})_{WB} = \underbrace{K_{(WB)}}_{4.3.1.2}\underbrace{(C_{L_{\dot\alpha}})_W}_{7.1.4.1} + \underbrace{(C_{L_{\dot\alpha}})_B}_{7.2.2.1}\left(\frac{S_b}{S}\right)\left(\frac{\ell_B}{\bar{c}}\right)$
		TRANSONIC	(Same as subsonic equations)

MARY

ATION (ted)	METHOD LIMITATIONS ASSOCIATED WITH EQUATION COMPONENTS
	5. Wing tip Mach lines may not intersect on wings nor intersect opposite wing tips 6. Linear-lift range
Eq. 7.1.4.1-c	Method 2 1. Straight-tapered wings 2. Linear-lift range (a) Subsonic LE ($\beta \cot \Lambda_{LE} < 1$) 3. $0.25 \leq \lambda \leq 1.0$ 4. Mach line from TE vertex may not intersect LE 5. Wing-tip Mach lines may not intersect on wings nor intersect opposite wing tips (b) Supersonic LE ($\beta \cot \Lambda_{LE} > 1$) 6. Valid only if Mach lines from LE vertex intersect TE 7. Foremost Mach line from either wing tip may not intersect the remote half-wing
Eq. 7.3.4.1-a	Method 1 (body diameter)/(wing span) is small (see sketch (d) 4.3.1.2) 1. Linear-lift range $\left(C_{L_\alpha}\right)_e$ 2. Triangular planforms 3. $0 < \beta A < 4$ 4. $M \leq 0.6$; however, if swept wing with $t/c \leq 0.04$, application to higher Mach numbers is acceptable $\left(C_{L_\alpha}\right)_B$ 5. Bodies of revolution
Eq. 7.3.4.1-b	Method 2 (body diameter)/(wing span) is large with delta wing extending entire length of body (see Sketch (c) 4.3.1.2) (same limitations as Method 1 above)
	Method 1 (body diameter)/(wing span) is small (see Sketch (d) 4.3.1.2) 1. Linear-lift range $K_{B(W)}$ (based on exposed wing geometry) $\left(C_{L_\alpha}\right)_e$ 2. Triangular planforms 3. Symmetric airfoils with conventional thickness distribution 4. $0 < \beta A < 4$ 5. $M_{cr} \leq M < 1.0$

DERIVATIVE	CONFIG.	SPEED REGIME	EQUATIONS FOR DERIVATIVE ESTIMATION (Datcom section for components indicated)
$C_{L_{\dot{\alpha}}}$ (Contd.)	WB (Contd.)	TRANSONIC (Contd.)	
		SUPERSONIC	(Same as subsonic equations)
	WBT	SUBSONIC	$C_{L_{\dot{\alpha}}} = \underbrace{\left(C_{L_{\dot{\alpha}}}\right)_{WB}}_{7.3.4.1} + 2\underbrace{\left[K_{W(B)} + K_{B(W)}\right]}_{4.3.1.2}\left(\frac{S''_e}{S'}\right)\underbrace{\left(\frac{x_{c.g.} - x''}{\bar{c}'}\right)}_{4.5.2.1}\underbrace{\left(\frac{q''}{q_\infty}\right)}_{4.4.1}\underbrace{\left(\frac{\partial \epsilon}{\partial \alpha}\right)}_{4.4.1}\underbrace{\left(C_{L_\alpha}\right)''_e}_{4.1.3.2}$

METHODS SUMMARY

ATIONS FOR DERIVATIVE ESTIMATION Datcom section for components indicated)		METHOD LIMITATIONS ASSOCIATED WITH EQUATION COMPONENTS
		$\left(C_{L_{\dot{\alpha}}}\right)_B$ 6. Bodies of revolution
		Method 2 (body diameter)/(wing span) is large with delta wing extending entire length of body (see Sketch (c) 4.3.1.2) (same limitations as Method 1 above)
		Method 1 (body diameter)/(wing span) is small (see Sketch (d) 4.3.1.2) 1. Straight-tapered wing 2. Linear-lift range $K_{B(W)}$ (based on exposed wing geometry) $\left(C_{L_{\dot{\alpha}}}\right)_e$ (a) Subsonic LE ($\beta \cot \Lambda_{LE} < 1$) 3. Mach line from TE vertex may not intersect LE 4. Wing-tip Mach lines may not intersect on wings nor intersect opposite wing tips (b) Supersonic LE ($\beta \cot \Lambda_{LE} > 1$) 5. Valid only if Mach lines from LE vertex intersect TE 6. Foremost Mach line from either wing tip may not intersect remote half-wing $\left(C_{L_{\dot{\alpha}}}\right)_B$ 7. Bodies of revolution
		Method 2 (body diameter)/(wing span) is large with delta wing extending entire length of body (see Sketch (c) 4.3.1.2)(limitations of Method 1)
$\left.\left(\frac{S_e''}{S'}\right)\left(\frac{x_{c.g.} - x''}{\bar{c}'}\right)\left(\frac{q''}{q_\infty}\right)\left(\frac{\partial \epsilon}{\partial \alpha}\right)\left(C_{L_\alpha}\right)_e'\right]_{(W)}''$ 4.5.2.1 4.4.1 4.4.1 4.1.3.2	Eq. 7.4.4.1-a	Method 1 $b_W/b_H \geq 1.5$ 1. Linear-lift range $\left(C_{L_{\dot{\alpha}}}\right)_{WB}$ (based on exposed wing geometry) 2. Triangular planforms 3. $0 < \beta A < 4$ 4. Bodies of revolution 5. $M \leq 0.6$, however, if swept wing with $t/c \leq 0.04$ application to higher Mach numbers is acceptable $\frac{q''}{q_\infty}$ 6. Valid only on the plane of symmetry $\frac{\partial \epsilon}{\partial \alpha}$ 7. Limitations depend upon $\frac{\partial \epsilon}{\partial \alpha}$ prediction metho

DERIVATIVE	CONFIG.	SPEED REGIME	EQUATIONS FOR DERIVATIVE ESTIMATIO (Datcom section for components indicated)
$C_{L_{\dot{\alpha}}}$ (Contd.)	WBT (Contd.)	SUBSONIC (Contd.)	$C_{L_{\dot{\alpha}}} = \underbrace{\left(C_{L_{\dot{\alpha}}}\right)_{WB}}_{7.3.4.1} - 2\underbrace{\left(\frac{X_{c.g.} - X''}{\bar{c}'}\right)}_{4.5.2.1}\underbrace{\left(C_{L_\alpha}\right)_{W''(v)}}_{4.5.1.1}$
		TRANSONIC	(Same as subsonic equations)
		SUPERSONIC	(Same as subsonic equations)

ARY

ION	METHOD LIMITATIONS ASSOCIATED WITH EQUATION COMPONENTS
Eq. 7.4.4.1-b	Method 2 $b_W/b_H < 1.5$ (same limitations as Items 1 through 5 immediately above) $\left(C_{L_{\dot{\alpha}}}\right)_{WB}$ and $\left(C_{L_\alpha}\right)_{W''(v)}$ (based on exposed wing geometry)
	Method 1 $b_W/b_H \geq 1.5$ 1. Linear-lift range $\left(C_{L_{\dot{\alpha}}}\right)_{WB}$ (based on exposed wing geometry) 2. Triangular planforms 3. Symmetric airfoils with conventional thickness distribution 4. $0 < \beta A < 4$ 5. Bodies of revolution 6. $M_{cr} \leq M \leq 1.0$ $K_{B(W)}$ (based on exposed wing geometry) $\frac{q''}{q_\infty}$ 7. Conventional trapezoidal planforms 8. Valid only on the plane of symmetry $\frac{\partial \epsilon}{\partial \alpha}$ 9. Proportional to C_L $\left(C_{L_\alpha}\right)_e''$ 10. $\alpha = 0$ 11. Additional tail limitation is identical to Item 3 immediately above
	Method 2 $b_W/b_H < 1.5$ (same limitations as Items 1 through 6 immediately above) $\left(C_{L_{\dot{\alpha}}}\right)_{WB}$ and $\left(C_{L_\alpha}\right)_{W''(v)}$ (based on exposed wing geometry)
	Method 1 $b_W/b_H \geq 1.5$ 1. Straight-tapered wing 2. Linear-lift range $K_{B(W)}$ (based on exposed wing geometry) $\left(C_{L_{\dot{\alpha}}}\right)_{WB}$ (based on exposed wing geometry) 3. Bodies of revolution (a) Subsonic LE ($\beta \cot \Lambda_{LE} < 1$) 4. Mach line from TE vertex may not intersect LE 5. Wing-tip Mach lines may not intersect on wings nor intersect opposite wing tips

DERIVATIVE	CONFIG.	SPEED REGIME	EQUATIONS FOR DERIVATIVE EST (Datcom section for components in
$C_{L_{\dot{\alpha}}}$ (Contd.)	WBT (Contd.)	SUPERSONIC (Contd.)	
$C_{m_{\dot{\alpha}}}$	W	SUBSONIC	$C_{m_{\dot{\alpha}}} = \underbrace{C_{m_{\dot{\alpha}}}''}_{7.1.4.2} + \left(\frac{X_{c.g.}}{\bar{c}}\right) \underbrace{C_{L_{\dot{\alpha}}}}_{7.1.4.1}$
		TRANSONIC	(Same as subsonic equation)
		SUPERSONIC	(Same as subsonic equation)

METHODS SUMMARY

ATIONS FOR DERIVATIVE ESTIMATION Datcom section for components indicated)	METHOD LIMITATIONS ASSOCIATED WITH EQUATION COMPONENTS
	(b) Supersonic LE ($\beta \cot \Lambda_{LE} > 1$) 6. Valid only if Mach lines from LE vertex intersect TE 7. Foremost Mach line from either wing tip may not intersect remote half-wing $K_{B(W)}$ (based on exposed wing geometry) $\frac{q''}{q_\infty}$ 8. If nonviscous flow field, limited to unswept wings 9. If viscous flow field, valid only on the plane of symmetry $\frac{\partial \epsilon}{\partial \alpha}$ 10. Straight-tapered wings 11. Other limitations depend upon $\frac{\partial \epsilon}{\partial \alpha}$ prediction method $\left(C_{L_\alpha}\right)_c''$ 12. $M \geq 1.4$
	Method 2 $b_W/b_{fl} < 1.5$ (same limitations as Items 1 through 7 immediately above) $\left(C_{L_{\dot\alpha}}\right)_{WB}$ and $\left(C_{L_\alpha}\right)_{W''(v)}$ (based on exposed wing geometry)
Eq 7.1.4.2-a	$C_{L_{\dot\alpha}}$ 1. Triangular planforms 2. $0 < \beta A < 4$ 3. $M \leq 0.6$; however, if swept wing with $t/c \leq 0.04$, application to higher Mach numbers is acceptable 4. Linear-lift range
	$C_{L_{\dot\alpha}}$ 1. Triangular planforms 2. Symmetric airfoils of conventional thickness distribution 3. $0 < \beta A < 4$ 4. $M_{cr} < M \leq 1.0$ 5. Linear-lift range
	$C_{m_{\dot\alpha}}''$ (a) Subsonic LE ($\beta \cot \Lambda_{LE} < 1$) 1. Mach line from TE vertex may not intersect LE 2. Wing-tip Mach lines may not intersect on wings nor intersect opposite wing tips

DERIVATIVE	CONFIG.	SPEED REGIME	EQUATIONS FOR DERIVATIVE ESTIMATIOI (Datcom section for components indicated)
$C_{m_{\dot{\alpha}}}$ (Contd.)	W (Contd.)	SUPERSONIC (Contd.)	
	WB	SUBSONIC	$\left(C_{m_{\dot{\alpha}}}\right)_{WB} = \underbrace{\left[K_{W(B)} + K_{B(W)}\right]}_{4.3.1.2}\left(\frac{S_e}{S}\right)\left(\frac{\bar{c}_e}{\bar{c}}\right)^2 \underbrace{\left(C_{m_{\dot{\alpha}}}\right)_e}_{7.1.4.2} + \underbrace{\left(C_{m_{\dot{\alpha}}}\right)_B}_{7.2.2.2}\left(\frac{S_b}{S}\right)\left(\frac{\ell_B}{\bar{c}}\right)^2$
			$\left(C_{m_{\dot{\alpha}}}\right)_{WB} = \underbrace{K_{(WB)}}_{4.3.1.2}\underbrace{\left(C_{m_{\dot{\alpha}}}\right)_W}_{7.1.4.2} + \underbrace{\left(C_{m_{\dot{\alpha}}}\right)_B}_{7.2.2.2}\left(\frac{S_b}{S}\right)\left(\frac{\ell_B}{\bar{c}}\right)^2$
		TRANSONIC	(Same as subsonic equations)
		SUPERSONIC	(Same as subsonic equations)

MMARY

TIMATION idicated)	METHOD LIMITATIONS ASSOCIATED WITH EQUATION COMPONENTS
	(b) Supersonic LE ($\beta \cot \Lambda_{LE} > 1$) 3. Valid only if Mach lines from LE vertex intersect LE 4. Foremost Mach line from either wing tip may not intersect remote half-wing C_{L_α} 5. Straight-tapered wings 6. Linear-lift range
$\left(\frac{R_B}{\bar{c}}\right)^2$ Eq. 7.3.4.2-a	Method 1 (body diameter)/(wing span) is small (see 4.3.1.2 Sketch (d)) 1. Linear-lift range $(C_{m_\alpha})_e$ 2. Triangular planforms [due to $(C_{L_\alpha})_e$] 3. $0 < \beta A < 4$ 4. $M \leq 0.6$; however, if swept wing with $t/c \leq 0.04$, application to higher Mach numbers is acceptable $(C_{m_\alpha})_B$ 5. Bodies of revolution
Eq. 7.3.4.2-b	Method 2 (body diameter)/(wing span) is large, with delta wing extending over entire length of body (see 4.3.1.2 Sketch (c)) (same limitations as Method 1 above)
	Method 1 (body diameter)/(wing span) is small (see 4.3.1.2 Sketch (d)) 1. Linear-lift range $K_{B(W)}$ (based on exposed wing geometry) $(C_{m_\alpha})_e$ 2. Triangular planforms [due to $(C_{L_\alpha})_e$] 3. Symmetric airfoils of conventional thickness distribution 4. $0 < \beta A \leq 4$ 5. $M_{cr} \leq M \leq 1.0$ $(C_{m_\alpha})_B$ 6. Bodies of revolution
	Method 2 (body diameter)/(wing span) is large, with delta wing extending entire length of body (see 4.3.1.2 Sketch (c)) (same limitations as Method 1 above)
	Method 1 (body diameter)/(wing span) is small (see 4.3.1.2 Sketch (d)) 1. Straight-tapered wings 2. Linear-lift range

DERIVATIVE	CONFIG.	SPEED REGIME	EQUATIONS FOR DERIVATIVE ESTIMATION (Datcom section for components indicated)
$C_{m_{\dot{\alpha}}}$ (Contd.)	WB (Contd.)	SUPERSONIC (Contd.)	
	WBT	SUBSONIC	$C_{m_{\dot{\alpha}}} = \underbrace{\left(C_{m_{\dot{\alpha}}}\right)_{WB}}_{7.3.4.2} - 2\underbrace{\left[K_{W(B)} + K_{B(W)}\right]}_{4.3.1.2}\left(\frac{S_e''}{S'}\right)\underbrace{\left(\frac{X_{c.g.} - X''}{\bar{c}'}\right)^2}_{4.5.2.1}\underbrace{\left(\frac{q''}{q_\infty}\right)}_{4.4.1}\underbrace{\left(\frac{\partial\epsilon}{\partial\alpha}\right)}_{4.4.1}\underbrace{\left(C_{L_\alpha}\right)_e''}_{4.1.3.2}$
			$C_{m_{\dot{\alpha}}} = \underbrace{\left(C_{m_{\dot{\alpha}}}\right)_{WB}}_{7.3.4.2} + 2\underbrace{\left(\frac{X_{c.g.} - X''}{\bar{c}'}\right)^2}_{4.5.2.1}\underbrace{\left(C_{L_\alpha}\right)_{W''(V)}}_{4.5.1.1}$
		TRANSONIC	(Same as subsonic equations)

METHODS SUMMARY

TIONS FOR DERIVATIVE ESTIMATION (com section for components indicated)		METHOD LIMITATIONS ASSOCIATED WITH EQUATION COMPONENTS
		$K_{B(W)}$ (based on exposed wing geometry) $\left(C_{m_{\dot{\alpha}}}\right)_e$ (a) Subsonic LE ($\beta \cot \Lambda_{LE} < 1$) 3. Mach line from TE vertex may not intersect LE 4. Wing-tip Mach lines may not intersect on wings nor intersect opposite wing tips (b) Supersonic LE ($\beta \cot \Lambda_{LE} > 1$) 5. Valid only if Mach lines from LE vertex intersect TE 6. Foremost Mach line from either wing tip may not intersect remote half-wing $\left(C_{m_{\dot{\alpha}}}\right)_B$ 7. Bodies of revolution
		Method 2 (body diameter)/(wing span) is large, with delta wing extending entire length of body (see 4.3.1.2 Sketch (c)) (same limitations as Method 1 above)
$\left(\frac{S_e''}{S'}\right)\left(\frac{x_{c.g.} - x''}{\bar{c}'}\right)^2\left(\frac{q''}{q_\infty}\right)\left(\frac{\partial \epsilon}{\partial \alpha}\right)\left(C_{L_\alpha}\right)_e''$ 4.5.2.1 4.4.1 4.4.1 4.1.3.2	Eq. 7.4.4.2-a	Method 1 $b_W/b_H \geq 1.5$ 1. Linear-lift range $\left(C_{m_{\dot{\alpha}}}\right)_{WB}$ (based on exposed wing geometry) 2. Triangular planforms [due to $\left(C_{L_{\dot{\alpha}}}\right)_e$] 3. $0 < \beta A < 4$ 4. Bodies of revolution 5. $M \leq 0.6$; however, if swept wing with $t/c \leq 0.04$, application to higher Mach numbers is acceptable $\frac{q''}{q_\infty}$ 6. Valid only on the plane of symmetry $\frac{\partial \epsilon}{\partial \alpha}$ 7. Limitations depend upon $\frac{\partial \epsilon}{\partial \alpha}$ prediction method
$\left(C_{L_\alpha}\right)_{W''(c)}$ 4.5.1.1	Eq. 7.4.4.2-b	Method 2 $b_W/b_H < 1.5$ (same limitations as Items 1 through 5 immediately above) $\left(C_{m_{\dot{\alpha}}}\right)_{WB}$ and $\left(C_{L_\alpha}\right)_{W''(c)}$ (based on exposed wing geometry
		Method 1 $b_W/b_H \geq 1.5$ 1. Linear-lift range

DERIVATIVE	CONFIG.	SPEED REGIME	EQUATIONS FOR DERIVATIVE ESTIMATION (Datcom section for components indicated)
$C_{m_{\dot{\alpha}}}$ (Contd.)	WBT (Contd.)	TRANSONIC (Contd.)	
		SUPERSONIC	(Same as subsonic equations)

MARY

MATION icated)	METHOD LIMITATIONS ASSOCIATED WITH EQUATION COMPONENTS
	$\left(C_{m_{\dot{\alpha}}}\right)_{WB}$ (based on exposed wing geometry) 2. Triangular planforms [due to $\left(C_{L_{\dot{\alpha}}}\right)_e$] 3. Symmetric airfoils of conventional thickness distribution 4. $0 \leq \beta A \leq 1.0$ 5. Bodies of revolution 6. $M_{cr} \leq M \leq 1.0$ $K_{B(W)}$ (based on exposed wing geometry) $\frac{q''}{q_\infty}$ 7. Conventional trapezoidal planforms 8. Valid only on the plane of symmetry $\frac{\partial \epsilon}{\partial \alpha}$ 9. Proportional to C_{L_α} $\left(C_{L_\alpha}\right)_e''$ 10. $\alpha = 0$ 11. Additional tail limitation is identical to Item 3 immediately above
	Method 2 $b_W/b_H < 1.5$ (same limitations as Items 1 through 6 immediately above) $\left(C_{m_{\dot{\alpha}}}\right)_{WB}$ and $\left(C_{L_\alpha}\right)_{W''(v)}$ (based on exposed wing geometry)
	Method 1 $b_W/b_H \geq 1.5$ 1. Straight-tapered wings 2. Linear-lift range $\left(C_{m_{\dot{\alpha}}}\right)_{WB}$ (based on exposed wing geometry) 3. Bodies of revolution (a) Subsonic LE: $\beta \cot \Lambda_{LE} < 1$) 4. Mach line from TE vertex may not intersect LE 5. Wing-tip Mach lines may not intersect on wings nor intersect opposite wing tips (b) Supersonic LE: ($\beta \cot \Lambda_{LE} > 1$) 6. Valid only if Mach lines from LE vertex intersect LE 7. Foremost Mach line from either wing tip may not intersect the remote half wing $K_{B(W)}$ (based on exposed wing geometry) $\frac{q''}{q_\infty}$ 8. If nonviscous flow field, limited to unswept wings 9. If viscous flow field, valid only on the plane of symmetry

DERIVATIVE	CONFIG.	SPEED REGIME	EQUATIONS FOR DERIVATIVE ESTIMATIO (Datcom section for components indicated)
$C_{m_{\dot{\alpha}}}$ (Contd.)	WBT (Contd.)	SUPERSONIC (Contd.)	
C_{Y_β}	W	SUBSONIC (Low Speed)	$C_{Y_\beta} = C_L^2 \left[\frac{6 \tan \Lambda_{c/4} \sin \Lambda_{c/4}}{\pi A (A + 4 \cos \Lambda_{c/4})}\right] \frac{1}{57.3} - 0.0001 \lvert\Gamma\rvert$
		(Subcritical)	$\left(\frac{C_{Y_\beta}}{C_L}\right)_M = \frac{A + 4 \cos \Lambda_{c/4}}{AB + 4 \cos \Lambda_{c/4}} \underbrace{\left(\frac{C_{Y_\beta}}{C_L}\right)_{\substack{\text{low} \\ \text{speed}}}}_{5.1.1.1}$
		TRANSONIC	(No method)
		SUPERSONIC	$\frac{C_{Y_\beta}}{\alpha^2} = -\frac{8M^2}{\pi A \beta^2} \frac{1}{57.3} - \frac{0.0001 \lvert\Gamma\rvert}{\alpha^2}$
			$\frac{C_{Y_\beta}}{\alpha^2} = \frac{\pi}{4} AM^2 \underbrace{Q(\beta C)}_{5.1.1.1} \frac{1}{57.3} - \frac{0.0001 \lvert\Gamma\rvert}{\alpha^2}$
	WB	SUBSONIC	$\left(C_{Y_\beta}\right)_{WB} = \underbrace{K_1}_{5.2.1.1} \underbrace{\left(C_{Y_\beta}\right)_B}_{4.2.1.1} \left(\frac{\text{Body Reference Area}}{S_W}\right) + \underbrace{\left(\Delta C_{Y_\beta}\right)_\Gamma}_{5.1.1.1}$
		TRANSONIC	(Same as subsonic equation)
		SUPERSONIC	(Same as subsonic equation)

METHODS SUMMARY

TIONS FOR DERIVATIVE ESTIMATION (com section for components indicated)		METHOD LIMITATIONS ASSOCIATED WITH EQUATION COMPONENTS
		$\frac{\partial \epsilon}{\partial \alpha}$ 10. Limitations depend upon $\frac{\partial \epsilon}{\partial \alpha}$ prediction method $\left(C_{N_\alpha}\right)_e$ 11. $M \geq 1.4$
		Method 2 $b_W / b_H \leq 1.5$ (same limitations as Items 1 through 7 immediately above) $\left(C_{m_{\dot{\alpha}}}\right)_{WB}$ and $\left(C_{L_\alpha}\right)_{W_{(v)}}$ (based on exposed wing geometry)
$\frac{1}{\beta^3} - 0.0001 \lvert\Gamma\rvert$	Eq. 5.1.1.1-a	1. Constant-chord swept wings 2 Linear-lift range
$\frac{\text{Speed}}{1}$	Eq. 5.1.1.1-c	
	Eq. 5.1.1.1-d, -b	1. Rectangular planforms 2 Mach number and aspect ratio greater than that for which the Mach line from LE of tip section intersects TE of opposite tip section $(A\sqrt{M^2 - 1} \geq 1)$
$\frac{0.0001 \lvert\Gamma\rvert}{\alpha^2}$	Eq. 5.1.1.1-e, -b	1 Swept back planforms 2 $\lambda = 0$ 3 Wing is contained within Mach cones springing from apex and TE at center of wing $(\sqrt{M^2 - 1} \cot \Lambda_{LE} \leq 1.0)$
$\left(\frac{\text{Reference Area}}{S_W}\right) + \frac{\left(\Delta C_{Y_\beta}\right)_1}{5.1.1.1}$	Eq. 5.2.1.1-a	$\left(C_{Y_\beta}\right)_B$ 1 Bodies of revolution 2 Linear-lift range
		(same limitations as subsonic above)
		(same limitations as subsonic above)

DERIVATIVE	CONFIG.	SPEED REGIME	EQUATIONS FOR DERIVATIVE ESTIMATION (Datcom section for components indicated)
C_{Y_β} (Contd.)	TB	SUBSONIC	$\left(\Delta C_{Y_\beta}\right)_{V(WBH)} = \underbrace{k}_{5.3.1.1}\underbrace{\left(C_{L_\alpha}\right)_V}_{4.1.3.2}\underbrace{\left(1+\frac{\partial\sigma}{\partial\beta}\right)\frac{q_V}{q_\infty}}_{5.4.1}\frac{S_V}{S_W}$
			$\left(\Delta C_{Y_\beta}\right)_{V\ (WBH)} = \underbrace{\frac{\left(C_{Y_\beta}\right)_{V\ (WBH)}}{\left(C_{Y_\beta}\right)_{V_{eff}}}}_{5.3.1.1}\underbrace{\left(C_{Y_\beta}\right)_{V_{eff}}}_{5.3.1.1}\frac{2S_V}{S_W}$
			(a) $\left(\Delta C_{Y_\beta}\right)_P = -\underbrace{K}_{5.3.1.1}\underbrace{\left(C_{L_\alpha}\right)_P}_{4.1.3.2}\frac{S_{P_e}}{S_W}$
			(b) $\left(\Delta C_{Y_\beta}\right)_{H(B)} = \underbrace{K_{H(B)}}_{5.3.1.1}\underbrace{\left(C_{Y_\beta}\right)_B}_{4.2.1.1}\frac{S_{B_{ref}}}{S_W}$
		TRANSONIC	(No method)
		SUPERSONIC	(a) $\left(\Delta C_{Y_\beta}\right)_P = -\underbrace{K}_{5.3.1.1}\underbrace{\left(C_{N_\alpha}\right)_P}_{4.1.3.2}\frac{S_{P_e}}{S_W}$
			(b) $\left(\Delta C_{Y_\beta}\right)_{H(B)} = \underbrace{K_{H(B)}}_{5.3.1.1}\underbrace{\left(C_{Y_\beta}\right)_B}_{4.2.1.1}\frac{S_{ext}}{S_{ext}}\frac{S_{B_{ref}}}{S_W}$
		HYPERSONIC	

	METHOD LIMITATIONS ASSOCIATED WITH EQUATION COMPONENTS
Eq. 5.3.1.1-b	Method 1 (vertical panels on plane of symmetry) $\left(C_{L_\alpha}\right)_V$ 1. Straight-tapered planforms
Eq. 5.3.1.1-c	Method 2 (twin vertical panels)
Eq. 5.3.1.1-d	Method 3 (horizontal tail mounted on body or no horizontal tail) (a) Contribution of vertical panel $\left(C_{L_{\alpha/p}}\right)$ (based on exposed vertical-tail geometry) 1. No curved planforms 2. $M \leq 0.8$, $t/c \leq 0.1$, if cranked planforms with round LE
Eq. 5.3.1.1-e	(b) Contribution of horizontal tail $\left(C_{Y_{\beta/B}}\right)$ 3. Bodies of revolution 4. Linear-lift range
Eq. 5.3.1.1-f	1. Horizontal tail mounted on body, or no horizontal tail 2. Linear-lift range (a) Vertical-tail contribution K' (based on exposed vertical-tail geometry) $\left(C_{N_\alpha}\right)_p$ (based on exposed vertical-tail geometry) 3 Breaks in LE and TE at same spanwise station 4 $M \geq 1.4$ for straight-tapered planforms 5. $1.2 \leq M \leq 3$ for composite planforms 6 $1.0 \leq M \leq 3$ for curved planforms
Eq. 5.3.1.1-g	(b) Horizontal-tail contribution $\left(C_{Y_\beta}\right)_B$ 7. Bodies of revolution
	Method 1 1 Horizontal tail mounted on a body 2. Not substantiated above $M = 2$ 3 Linear-lift range

DERIVATIVE	CONFIG.	SPEED REGIME	EQUATIONS FOR DERIVATIVE ESTIMATI (Datcom section for components indicated)
C_{Y_β} (Contd.)	TB (Contd.)	HYPERSONIC (Contd.)	(a) $\left(\Delta C_{Y_\beta}\right)_p = \underbrace{K'}_{5.3.1.1}\ \underbrace{\left(C_{N_\alpha}\right)_p}_{4.1.3.2}\ \frac{S_{fe}}{S_W}$
			(b) $\left(\Delta C_{Y_\beta}\right)_{H(B)} = \underbrace{K_{H(B)}}_{5.3.1.1}\ \underbrace{\left(C_{Y_\beta}\right)_B}_{4.2.1.1}\ \frac{S_{act}}{S_{ext}}\ \frac{S_{B_{ref}}}{S_W}$
			$C_p = (\beta \pm \delta)^2 \left(\frac{\gamma+1}{2} \pm \sqrt{\frac{(\gamma+1)^2}{4} + \frac{4}{(M^2-1)(\beta \pm \delta)^2}}\right)$
	WBT	SUBSONIC	$C_{Y_\beta} = \underbrace{\left(C_{Y_\beta}\right)_{WB}}_{5.2.1.1} + \underbrace{\left(\Delta C_{Y_\beta}\right)_{V(WBH)}}_{5.3.1.1}$
			$C_{Y_\beta} = \underbrace{\left(C_{Y_\beta}\right)_{WB}}_{5.2.1.1} + \underbrace{\left(\Delta C_{Y_\beta}\right)_{V(WBH)}}_{5.3.1.1}$
			$C_{Y_\beta} = \underbrace{\left(C_{Y_\beta}\right)_{WB}}_{5.2.1.1} + \sum_p \underbrace{\left(\Delta C_{Y_\beta}\right)_p}_{5.3.1.1}$
		TRANSONIC	(No method)

METHODS SUMMARY

ONS FOR DERIVATIVE ESTIMATION (m section for components indicated)		METHOD LIMITATIONS ASSOCIATED WITH EQUATION COMPONENTS
	Eq. 5.3.1.1-f	(a) Vertical-tail contribution K′ (based on exposed vertical-tail geometry) $\left(C_{N_\alpha}\right)_p$ 4. $M > 3$
$\frac{S_{B_{ref}}}{S_W}$	Eq. 5.3.1.1-g	(b) Horizontal-tail contribution $\left(C_{Y_\beta}\right)_B$ 5. Bodies of revolution
$\frac{4}{(M^2-1)(\beta \pm \delta)^2}$	Eq. 5.3.1.1-h	Method 2 1. Sharp-edged sections 2. $\delta << 1$
	Eq. 5.6.1.1-a	Method 1 (single vertical stabilizer, and horizontal tail at any height or no horizontal tail) 1. Linear-lift range $\left(C_{Y_\beta}\right)_{WB}$ 2. Bodies of revolution $\left(\Delta C_{Y_\beta}\right)_{V(WBH)}$ 3. Straight-tapered planforms
	Eq. 5.6.1.1-a	Method 2 (twin vertical panels) 1. Linear-lift range $\left(C_{Y_\beta}\right)_{WB}$ 2. Bodies of revolution
	Eq. 5.6.1.1-b	Method 3 (horizontal tail mounted on body or no horizontal tail) 1. Linear-lift range $\left(C_{Y_\beta}\right)_{WB}$ 2. Bodies of revolution $\left(\Delta C_{Y_\beta}\right)_p$ (based on exposed vertical-tail geometry) 3. No curved planforms 4. $M \leq 0.8$, $t/c \leq 0.1$, if cranked planforms with round LE

DERIVATIVE	CONFIG.	SPEED REGIME	EQUATIONS FOR DERIVATIVE ESTIMATIO (Datcom section for components indicated)
C_{Y_β} (Contd.)	WBT (Contd.)	SUPERSONIC	$C_{Y_\beta} = \underbrace{\left(C_{Y_\beta}\right)_{WB}}_{5.2.1.1} + \sum_p \underbrace{\left(\Delta C_{Y_\beta}\right)_p}_{5.3.1.1}$
C_{l_β}	W	SUBSONIC	$C_{l_\beta} = C_L\left[\underbrace{\left(\frac{C_{l_\beta}}{C_L}\right)_{\Lambda_{c/2}}}_{5.1.2.1}\ \underbrace{K_{M_\Lambda}}_{5.1.2.1} + \underbrace{\left(\frac{C_{l_\beta}}{C_L}\right)_A}_{5.1.2.1}\right] + \Gamma\left(\underbrace{\frac{C_{l_\beta}}{\Gamma}}_{5.1.2.1}\ \underbrace{K_{M_\Gamma}}_{5.1.2.1}\right) + \theta \tan \Lambda_{c/4}\ \underbrace{\theta \text{ ta}}_{5.}$
			$C_{l_\beta} = C_L\left[-\frac{1}{57.3}\ \frac{2}{3}\ \frac{1}{A}\right] - \Gamma\left(\frac{A}{6}\right)$
			$\frac{C_{l_\beta}}{C_L} = \underbrace{\frac{1}{\left(C_{L_\alpha}\right)_{total}}}_{5.1.2.1}\left\{\underbrace{\left(C_{L_\alpha}\right)_i}_{4.1.3.2}\ \frac{S_i}{S_W}\left[\underbrace{\left(\frac{C_{l_\beta}}{C_L}\right)_{\Lambda_{c/2_i}}}_{5.1.2.1}\ \underbrace{K_{M_{\Lambda_i}}}_{5.1.2.1} + \underbrace{\left(\frac{C_{l_\beta}}{C_L}\right)_{A_i}}_{5.1.2.1}\right]\frac{b_i}{b_W}\right.$ $\left. + \underbrace{\left(C_{L_\alpha}\right)'_o}_{4.1.3.2}\ \frac{S'_o}{S_W}\left[\underbrace{\left(\frac{C_{l_\beta}}{C_L}\right)_{\Lambda'_{c/2_o}}}_{5.1.2.1}\ \underbrace{K_{M_{\Lambda'_o}}}_{5.1.2.1} + \underbrace{\left(\frac{C_{l_\beta}}{C_L}\right)_{A'_o}}_{5.1.2.1}\right]\right\}$
			$\frac{C_{l_\beta}}{C_L} = \underbrace{\left(\frac{1}{C_{L_\alpha}}\right)_{total}}_{5.1.2.1}\left\{\underbrace{\left(C_{L_\alpha}\right)_i}_{4.1.3.2}\ \frac{S_i}{S_W}\left[\frac{1}{57.3}\ \frac{2}{3}\ \frac{1}{A_i}\right]\frac{b_i}{b_W} + \underbrace{\left(C_{L_\alpha}\right)'_o}_{4.1.3.2}\ \frac{S'_o}{S_W}\ \left[\underbrace{\left(\frac{C_{l_2}}{C_L}\right)_A}_{5.1.2.}\right.$

RY

N	METHOD LIMITATIONS ASSOCIATED WITH EQUATION COMPONENTS
Eq. 5.6.1.1-b	1. Horizontal tail mounted on body or no horizontal tail 2. Linear-lift range $\left(C_{Y_\beta}\right)_{WB}$ 3. Bodies of revolution $\left(\Delta C_{Y_\beta}\right)_p$ (based on exposed vertical-tail geometry) 4. Breaks in LE and TE at same spanwise station 5. $M \geq 1.4$ for straight-tapered planforms 6. $1.2 \leq M \leq 3$ for composite planforms 7. $1.0 \leq M \leq 3$ for curved planforms
ΔC_{l_β} n $\Lambda_{c/4}$ 1.2.1 Eq. 5.1.2.1-a	1. Straight-tapered wings 2. $A \geq 1.0$ 3. Uniform dihedral (alternate form is available to account for dihedral) 4. $M \leq 0.6$ 5. $-5^\circ \leq \beta \leq +5^\circ$ 6. Linear-lift range
Eq. 5.1.2.1-a′	1. Straight-tapered wings 2. $A < 1.0$ 3. Uniform dihedral 4. $M \leq 0.6$ 5. $-5^\circ \leq \beta \leq +5^\circ$ 6. Linear-lift range
Eq. 5.1.2.1-b	1. Double-delta and cranked wings 2. A_i and $A_o' \geq 1.0$ 3. No twist 4. No dihedral 5. $M \leq 0.6$ 6. $-5^\circ \leq \beta \leq +5^\circ$ 7. Linear-lift range $\left(C_{L_\alpha}\right)_i$ and $\left(C_{L_\alpha}\right)_o'$ 8. $t/c \leq 0.10$ if cranked wings with round LE
$\Lambda'_{c/2}$ .1 $K_{M_{A_o'}}$ 5.1.2.1 $+\left(\frac{C_{l_\beta}}{C_L}\right)_{A_o'}$ 5.1.2.1 Eq. 5.1.2.1-b	1. Dougle-delta and cranked wings 2. A_i and $A_o' < 1.0$ 3. No twist 4. No dihedral 5. $M \leq 0.6$ 6. $-5^\circ \leq \beta \leq +5^\circ$ 7. Linear-lift range $\left(C_{L_\alpha}\right)_i$ and $\left(C_{L_\alpha}\right)_o'$ 8. $t/c \leq 0.1$ if cranked wings with round LE

DERIVATIVE	CONFIG.	SPEED REGIME	EQUATIONS FOR DERIVATIVE ESTIM. (Datcom section for compo ients indica
C_{l_β} (Contd.)	W (Contd.)	TRANSONIC	$\frac{C_{l_\beta}}{C_L} = \left\{\left[\frac{\overbrace{\left(\frac{C_{l_\beta}}{C_N}\right)_{M=1.4}}^{5.1.2.1}}{\underbrace{\left(C_{N_\alpha}^2\right)_{M=1.4}}_{4.1.3.2}} - \frac{\overbrace{\left(\frac{C_{l_\beta}}{C_L}\right)_{M=0.6}}^{5.1.2.1}}{\underbrace{\left(C_{L_\alpha}^2\right)_{M=0.6}}_{4.1.3.2}}\right]\left(\frac{M-0.6}{0.8}\right) + \frac{\overbrace{\left(\frac{C_{l_\beta}}{C_L}\right)_{M=0.6}}^{5.1.2.1}}{\underbrace{\left(C_{L_\alpha}^2\right)_{M=0.6}}_{4.1.3.2}}\right\}($
		SUPERSONIC	$C_{l_\beta} = -0.061\, C_N \underbrace{\frac{C_{N_\alpha}}{57.3}}_{4.1.3.2}\left[1+\lambda\left(1+\Lambda_{LE}\right)\right]\left(1+\frac{\Lambda_{LE}}{2}\right)\frac{\tan\Lambda_{LE}}{\beta}\left[\frac{M^2\ co}{/}\right.$ $+\Gamma\underbrace{\left(\frac{C_{l_\beta}}{\Gamma}\right)}_{5.1.2.1}$
			$\frac{C_{l_\beta}}{C_N} = -0.061\left[\frac{K_L\overbrace{\left(C_{N_\alpha}\right)_g}^{4.1.3.2}\left(\frac{S_g}{S_W}\right)}{57.3}\right]\left(1+\frac{\Lambda_{LE_g}}{2}\right)\left(\frac{\tan\Lambda_{LE_g}}{\beta}\right)\left[\frac{M^2\cos^2\Lambda_{LE}}{/\ A_g}\right.$ $-0.061\left[\frac{\overbrace{K_L\left(C_{N_\alpha}\right)_{bw}}^{4.1.3.2}\overbrace{\frac{S_{bw}}{S_W}}^{4.1.3.2}}{57.3}\right]\left[1+\lambda_{bw}\left(1+\Lambda_{LE_{bw}}\right)\right]$ $\left(1+\frac{\Lambda_{LE_{bw}}}{2}\right)\left(\frac{\tan\Lambda_{LE_{bw}}}{\beta}\right)\left[\frac{M^2\cos^2\Lambda_{LE_{bw}}}{A_{bw}}+\left(\frac{\tan\Lambda_{LE_{bw}}}{4}\right.\right.$
	WB	SUBSONIC	$C_{l_\beta} = C_L\left[\underbrace{\left(\frac{C_{l_\beta}}{C_L}\right)_{\Lambda_{c/2}}}_{5.1.2.1}\underbrace{K_{M_A}}_{5.1.2.1}\underbrace{K_f}_{5.2.2.1}+\underbrace{\left(\frac{C_{l_\beta}}{C_L}\right)_A}_{5.1.2.1}\right]+\Gamma\left[\underbrace{\frac{C_{l_\beta}}{\Gamma}}_{5.1.2.1},\underbrace{K_{M_\Gamma}}_{5.1.2.1}+\underbrace{\frac{\Delta C_{l_\beta}}{\Gamma}}_{5.2.2.1}\right]+\left($

/

METHODS SUMMARY

EQUATIONS FOR DERIVATIVE ESTIMATION (Datcom section for components indicated)	METHOD LIMITATIONS ASSOCIATED WITH EQUATION COMPONENTS
$\underbrace{\quad}_{4.1.1}$ $\left.\underbrace{\quad}_{M=0.6}\right]\left(\frac{M-0.6}{0.8}\right)+\left[\underbrace{\left(\frac{C_{l_\beta}}{C_L}\right)_{M=0.6}}_{5.1.2.1}\Big/\underbrace{\left(C_{L_\alpha}^2\right)_{M=0.6}}_{4.1.3.2}\right]\underbrace{\left(C_{L_\alpha}^2\right)}_{4.1.3.2}$ Eq. 5.1.2.1-c	1. Straight-tapered wings 2. $-5^\circ \leq \beta \leq +5^\circ$ 3. Linear-lift range $\left(\frac{C_{l_\beta}}{C_N}\right)_{M=1.4}$ 4. Wing tips parallel to free stream 5. No twist 6. Uniform dihedral 7. Foremost Mach line from wing tip may not intersect remote half-wing
$+\Lambda_{LE})\Big]\left(1+\frac{\Lambda_{LE}}{2}\right)\frac{\tan\Lambda_{LE}}{\beta}\left[\frac{M^2\cos^2\Lambda_{LE}}{A}+\left(\frac{\tan\Lambda_{LE}}{4}\right)^{4/3}\right]$ Eq. 5.1.2.1-e	1. Straight-tapered wings 2. No twist 3. Uniform dihedral 4. Linear-lift range C_{N_α} 5. $M \geq 1.4$ $\frac{C_{l_\beta}}{\Gamma}$ 6. Wing tips parallel to free stream 7. Foremost Mach line from wing tip may not intersect remote half-wing
$+\frac{\Lambda_{LE_g}}{2}\left(\frac{\tan\Lambda_{LE_g}}{\beta}\right)\left[\frac{M^2\cos^2\Lambda_{LE_g}}{A_g}+\left(\frac{\tan\Lambda_{LE_g}}{4}\right)^{4/3}\right]\frac{b_g}{b_w}$ $\left.\frac{}{}\right]\left[1+\lambda_{bw}\left(1+\Lambda_{LE_{bw}}\right)\right]$ $\frac{}{}\left(\frac{\tan\Lambda_{LE_{bw}}}{\beta}\right)\left[\frac{M^2\cos^2\Lambda_{LE_{bw}}}{A_{bw}}+\left(\frac{\tan\Lambda_{LE_{bw}}}{4}\right)^{4/3}\right]$ Eq. 5.1.2.1-f	1. Double-delta and cranked wings 2. No twist 3. No dihedral 4. Straight trailing edge 5. Low angles of sideslip 6. Linear-lift range $\left(C_{N_\alpha}\right)_g$ and $\left(C_{N_\alpha}\right)_{bw}$ 7. $1.2 \leq M \leq 3$ 8. $M > 1.4$, if $\Lambda_o > \Lambda_i$ 9. $\Lambda_g < 80^\circ$, if $\Lambda_o > \Lambda_i$
$\underbrace{\left(\frac{C_{l_\beta}}{C_L}\right)_A}_{5.1.2.1}+\Gamma\left[\underbrace{\frac{C_{l_\beta}}{\Gamma}}_{5.1.2.1}\underbrace{K_{M_\Gamma}}_{5.1.2.1}+\underbrace{\frac{\Delta C_{l_\beta}}{\Gamma}}_{5.2.2.1}\right]+\underbrace{\left(\Delta C_{l_\beta}\right)_{\Gamma_W}}_{5.2.2.1}+\theta\tan\Lambda_{c/4}\underbrace{\left(\frac{\Delta C_{l_\beta}}{\theta\tan\Lambda_{c/4}}\right)}_{5.1.2.1}$ Eq. 5.2.2.1-a	1. Straight-tapered wings 2. Uniform dihedral 3. $M \leq M_{fb}$ 4. $5^\circ \leq \beta \leq +5^\circ$ 5. Linear-lift range

DERIVATIVE	CONFIG.	SPEED REGIME	EQUATIONS FOR DERIVATIVE ESTIMATIOI (Datcom section for components indicated)
C_{l_β} (Contd.)	WB (Contd.)	SUBSONIC (Contd.)	
		TRANSONIC	$\frac{C_{l_\beta}}{C_L} = \left\{ \left[\frac{\left(\frac{C_{l_\beta}}{C_N}\right)_{M=1.4} - \left(\frac{C_{l_\beta}}{C_L}\right)_{M_{fb}}}{\left(C_{N_\alpha}^2\right)_{M=1.4} - \left(C_{L_\alpha}^2\right)_{M_{fb}}} \right] \left(\frac{M - M_{fb}}{1.4 - M_{fb}}\right) + \frac{\left(\frac{C_{l_\beta}}{C_L}\right)_{M_{fb}}}{\left(C_{L_\alpha}^2\right)_{M_{fb}}} \right\} \left(C_{L_\alpha}^2\right)_M$ (5.2.2.1; 5.2.2.1; 5.2.2.1; 4.1.3.2; 4.1.3.2; 4.1.3.2; 4.1.3.2; 4.1.3.2)
		SUPERSONIC	$C_{l_\beta} = -0.061\, C_N \frac{C_{N_\alpha}}{57.3} \left[1 + \lambda\left(1 + \Lambda_{LE}\right)\right] \left(1 + \frac{\Lambda_{LE}}{2}\right) \left(\frac{\tan \Lambda_{LE}}{\beta}\right) \left[\frac{M^2 \cos^2 \Lambda_{LE}}{A}\right.$ (4.1.3.2) $+ \Gamma \left[\frac{C_{l_\beta}}{\Gamma} + \frac{\Delta C_{l_\beta}}{\Gamma}\right] + \left(\Delta C_{l_\beta}\right)_{z_W}$ (5.1.2.1; 5.2.2.1; 5.2.2.1)
	TB	SUBSONIC	$\left(\Delta C_{l_\beta}\right)_p = \left(\Delta C_{Y_\beta}\right)_p \frac{z_p \cos \alpha - \ell_p \sin \alpha}{b_W}$ (5.3.1.1)
		TRANSONIC	(No method)
		SUPERSONIC	(Same as subsonic equation)

RY

N	METHOD LIMITATIONS ASSOCIATED WITH EQUATION COMPONENTS
	$\frac{C_{l_\beta}}{C_L}$ 6. $M \leq 0.6$
Eq. 5.2.2.1-d	1. Straight-tapered wings 2. $M_{fb} \leq M \leq 1.4$ 3. $-5° \leq \beta \leq +5°$ $\left(\frac{C_{l_\beta}}{C_N}\right)_{M=1.4}$ 4. Wing tips parallel to free stream 5. Foremost Mach line from wing tip may not intersect remote half-wing $\left(\frac{C_{l_\beta}}{C_L}\right)_{M_{fb}}$ 6. Uniform dihedral 7. Linear-lift range $\left(C_{L_\alpha}\right)_{M_{fb}}$ and $\left(C_{L_\alpha}\right)_M$ 8. Symmetric airfoils of conventional thickness distribution 9. $\alpha \doteq 0$
$E + \left(\frac{\tan \Lambda_{LE}}{4}\right)^{4/3}\Bigg]$ Eq. 5.2.2.1-e	1. Straight-tapered wings 2. $M \geq 1.4$ 3. Linear-lift range $\frac{C_{l_\beta}}{\Gamma}$ 4. Wing tips parallel to free stream 5. Foremost Mach line from wing tip may not intersect remote half-wing 6. Supersonic TE
Eq. 5.3.2.1-a	$\left(\Delta C_{Y_\beta}\right)_P$ (based on exposed vertical-tail geometry for $\left(\Delta C_{Y_\beta}\right)_P$ Method 3) 1. Limitations depend upon $\left(\Delta C_{Y_\beta}\right)_P$ prediction method
	1. Horizontal tail mounted on body or no horizontal tail $\left(\Delta C_{Y_\beta}\right)_P$ (based on exposed vertical-tail geometry) 2. Breaks in LE and TE must be at same spanwise station

DERIVATIVE	CONFIG.	SPEED REGIME	EQUATIONS FOR DERIVATIVE ESTIMATION (Datcom section for components indicated)
C_{l_β} (Contd.)	TB (Contd.)	SUPERSONIC (Contd.)	
		HYPERSONIC	$\left(\Delta C_{l_\beta}\right)_p = \underbrace{\left(\Delta C_{Y_\beta}\right)_p}_{5.3.1.1} \frac{z_p \cos\alpha - \ell_p \sin\alpha}{b_W}$
	WBT	SUBSONIC	$C_{l_\beta} = \underbrace{\left(C_{l_\beta}\right)_{WB}}_{5.2.2.1} + \sum_p \left\{ \underbrace{\left(\Delta C_{Y_\beta}\right)_p}_{5.3.1.1} \left[\frac{z_p \cos\alpha - \ell_p \sin\alpha}{b_W} \right] \right\}$
		TRANSONIC	(No method)

METHODS SUMMARY

ONS FOR DERIVATIVE ESTIMATION om section for components indicated)		METHOD LIMITATIONS ASSOCIATED WITH EQUATION COMPONENTS
		3. Bodies of revolution 4. $M \geq 1.4$ for straight-tapered planforms 5. $1.2 \leq M \leq 3$ for composite planforms 6. $1.0 \leq M \leq 3$ for curved planforms 7. Linear-lift range
	Eq. 5.3.2.1-a	**Method 1** 1. Horizontal tail mounted on body or no horizontal tail 2. $M < 7$ $\left(\Delta C_{Y_\beta}\right)_p$ (based on exposed vertical-panel geometry) 3. $M \geq 1.4$ for straight-tapered planforms 4. $1.2 \leq M \leq 3$ for composite planforms 5. $1.0 \leq M \leq 3$ for curved planforms 6. Linear-lift range z_p and ℓ_p (based on exposed vertical-panel geometry)
		Method 2 1. Horizontal tail mounted on body or no horizontal tail $\left(\Delta C_{Y_\beta}\right)_p$ (based on exposed vertical-panel geometry) 2. Sharp-edge sections 3. $\delta << 1$ z_p and ℓ_p (based on exposed vertical-panel geometry)
		Method 3 1. Horizontal tail mounted on body or no horizontal tail 2. Upper range of hypersonic Mach numbers $\left(\Delta C_{Y_\beta}\right)_p$ (based on exposed vertical-panel geometry) z_p and ℓ_p (based on exposed vertical-panel geometry)
$\left.\dfrac{x - \ell_p \sin\alpha}{b_w}\right]\Bigg\}$	Eq. 5.6.2.1-a	1. Linear-lift range $\left(C_{l_\beta}\right)_{WB}$ 2. Straight-tapered wings 3. Uniform dihedral 4. $M \leq M_{fb}$ 5. $M \leq 0.6$ 6. $5° \leq \beta \leq +5°$ $\left(\Delta C_{Y_\beta}\right)_p$ (based on exposed vertical-tail geometry for $\left(\Delta C_{Y_\beta}\right)_p$ Method 3)

DERIVATIVE	CONFIG.	SPEED REGIME	EQUATIONS FOR DERIVATIVE ESTIMAT (Datcom section for components indicate
C_{l_β} (Contd.)	WBT (Contd.)	SUPERSONIC	(Same as subsonic equation)
C_{n_β}	W	SUBSONIC (Low Speed)	$\frac{C_{n_\beta}}{C_L^2} = \frac{1}{57.3}\left[\frac{1}{4\pi A} - \frac{\tan \Lambda_{c/4}}{\pi A(A + 4\cos \Lambda_{c/4})}\left(\cos \Lambda_{c/4} - \frac{A}{2} - \frac{A^2}{8\cos \Lambda_{c/4}} +\right.\right.$
		(Subcritical)	$\left(\frac{C_{n_\beta}}{C_L^2}\right)_M = \left(\frac{A + 4\cos \Lambda_{c/4}}{AB + 4\cos \Lambda_{c/4}}\right)\left(\frac{A^2B^2 + 4AB\cos \Lambda_{c/4} - 8\cos^2 \Lambda_{c/4}}{A^2 + 4A\cos \Lambda_{c/4} - 8\cos^2 \Lambda_{c/4}}\right)\left(\frac{C_{n_\beta}}{C_L^2}\right.$ 5.1.3
		TRANSONIC	(No method)
		SUPERSONIC	$\frac{C_{n_\beta}}{\alpha^2} = \frac{1}{\pi A^2\beta^2}\left[\frac{4M^2}{3} + 8M^2\frac{x}{\bar{c}} - \pi\left\{\frac{A(1-\beta^2)}{\beta}\ \frac{3+\beta^2}{3\beta^2}\right\}\right]\frac{1}{57.3}$
			$\frac{C_{n_\beta}}{\alpha^2} = \frac{\pi}{3}\left[\underbrace{E''(\beta C)}_{7.1.1.1}\ \underbrace{F_9(N)}_{5.1.3.1} + \left(\frac{A^2}{16}\ \underbrace{F_{11}(N)}_{7.1.1.2} + \frac{x}{\bar{c}}\right)M^2\ \underbrace{Q(\beta C)}_{5.1.1.1}\right]\frac{1}{57.3}$
	WB	ALL SPEEDS	$\left(C_{n_\beta}\right)_{WB} = -\underbrace{K_N}_{5.2.3.1}\ \underbrace{K_{R_\ell}}_{5.2.3.1}\ \frac{S_{B_s}}{S_W}\ \frac{\ell_B}{b}$
	TB	SUBSONIC	$\left(\Delta C_{n_\beta}\right)_p = -\underbrace{\left(\Delta C_{Y_\beta}\right)_p}_{5.3.1.1}\ \frac{\ell_p}{b_W}$

		METHOD LIMITATIONS ASSOCIATED WITH EQUATION COMPONENTS
		1. Linear-lift range $\left(C_{l_\beta}\right)_{WB}$ 2. Straight-tapered wings 3. Wing tips parallel to free stream 4. Foremost Mach line from wing tip may not intersect remote half-wing 5. $M \geq 1.4$ $\left(C_{Y_\beta}\right)_F$ (based on exposed vertical-tail geometry) 6. Additional tail limitation is identical to Item 5 immediately above
$\frac{\sin \Lambda_{c/4}}{A}\Big)\Big]$	Eq. 5.1.3.1-a	1. Linear-lift range
	Eq. 5.1.3.1-b	
	Eq. 5.1.3.1-c	1. Rectangular planform 2. $A\sqrt{M^2 - 1} \geq 1.0$ (Mach number and aspect ratio greater than those for which Mach line from LE of tip section intersects TE of opposite tip section)
	Eq. 5.1.3.1-d	1. $\lambda = 0$ 2. $\sqrt{M^2 - 1} \cot \Lambda_{LE} \leq 1.0$ (Mach number and aspect ratio for which wing lies within Mach cones springing from apex and TE at center of wing)
	Eq. 5.2.3.1-a	1. Linear-lift range
	Eq. 5.3.3.1-a	Method 1 $\left(\Delta C_{Y_\beta}\right)_F$ (based on exposed vertical-tail geometry for $\left(\Delta C_{Y_\beta}\right)_p$ Method 3) 1. Limitations depend upon $\left(\Delta C_{Y_\beta}\right)_p$ prediction method

DERIVATIVE	CONFIG.	SPEED REGIME	EQUATIONS FOR DERIVATIVE E Datcom section for components
C_{n_β} (Contd.)	TB (Contd.)	SUBSONIC (Contd.)	$\left(\Delta C_{n_\beta}\right)_p = -\left(\Delta C_{Y_\beta}\right)_p \dfrac{\ell_p + (x_{a.c.})_p}{b_w}$ (4.1.4.2; 5.3.1.1)
		TRANSONIC	(No method)
		SUPERSONIC	(Same as subsonic equations)
	WBT	SUBSONIC	$C_{n_\beta} = \left(C_{n_\beta}\right)_{WB} + \sum_p \left[-\left(\Delta C_{Y_\beta}\right)_p \dfrac{\ell_p}{b_w}\right]$ (5.2.3.1; 5.3.1.1) $C_{n_\beta} = \left(C_{n_\beta}\right)_{WB} + \sum_p \left[\left(\Delta C_{Y_\beta}\right)_p \left(\dfrac{\ell_p + (x_{a.c.})_p}{b_w}\right)\right]$ (5.2.3.1; 5.3.1.1)

IETHODS SUMMARY

FOR DERIVATIVE ESTIMATION (section for components indicated)	METHOD LIMITATIONS ASSOCIATED WITH EQUATION COMPONENTS
Eq. 5.3.3.1-b	Method 2 $\left(\Delta C_{Y_\beta}\right)_p$ (based on exposed vertical-tail geometry for $\left(\Delta C_{Y_\beta}\right)_p$ Method 3) 1. Limitations depend upon $\left(\Delta C_{Y_\beta}\right)_p$ prediction method $(x_{a.c.})_p$ 2. $M \leq 0.6$; however, if swept planforms with $t/c \leq 0.04$, application to higher Mach numbers is acceptable 3. Linear-lift range
	Method 1 1. Horizontal tail mounted on body, or no horizontal tail $\left(\Delta C_{Y_\beta}\right)_p$ (based on exposed vertical-tail geometry) 2. Breaks in LE and TE at same spanwise station 3. Bodies of revolution 4. $M \geq 1.4$ for straight-tapered planforms 5. $1.2 \leq M \leq 3$ for composite planforms 6. $1.0 \leq M \leq 3$ for curved planforms 7. Linear-lift range
	Method 2 (same limitations as Method 1 above) $\left(\Delta C_{Y_\beta}\right)_p$ (based on exposed vertical-tail geometry)
Eq. 5.6.3.1-a	Method 1 $\left(C_{n_\beta}\right)_{WB}$ 1. Linear-lift range $\left(\Delta C_{Y_\beta}\right)_p$ (based on exposed vertical-tail geometry for $\left(\Delta C_{Y_\beta}\right)_p$ Method 3) 2. Limitations depend upon $\left(\Delta C_{Y_\beta}\right)_p$ prediction method
$\left.\frac{x_{a.c.})_p}{w}\right)\Big]$ Eq. 5.6.3.1-b	Method 2 $\left(C_{n_\beta}\right)_{WB}$ 1. Linear-lift range $\left(\Delta C_{Y_\beta}\right)_p$ (based on exposed vertical-tail geometry for $\left(\Delta C_{Y_\beta}\right)_p$ Method 3) 2. Limitations depend upon $\left(\Delta C_{Y_\beta}\right)_p$ prediction method

2

DERIVATIVE	CONFIG.	SPEED REGIME	EQUATIONS FOR DERIVATIVE ESTIMATION (Datcom section for components indicated)
C_{n_β} (Contd.)	WBT (Contd.)	SUBSONIC (Contd.)	
		TRANSONIC	(No method)
		SUPERSONIC	(Same as subsonic equations)
C_{Y_p}	W	SUBSONIC	$C_{Y_p} = \underbrace{K}_{7.1.2.1}\left[\underbrace{\left(\frac{C_{Y_p}}{C_L}\right)_{C_L=0}}_{\substack{M \\ 7.1.2.1}} C_L\right] + \underbrace{(\Delta C_{Y_p})_\Gamma}_{7.1.2.1}$
		TRANSONIC	(No method)
		SUPERSONIC	Figure 7.1.2.1-10
	WB	SUBSONIC	$C_{Y_p} = \underbrace{K}_{7.1.2.1}\left[\underbrace{\left(\frac{C_{Y_p}}{C_L}\right)_{C_L=0}}_{\substack{M \\ 7.1.2.1}} C_L\right] + \underbrace{(\Delta C_{Y_p})_\Gamma}_{7.1.2.1}$

	METHOD LIMITATIONS ASSOCIATED WITH EQUATION COMPONENTS
	$(x_{a.c.})_p$ 3. $M \leq 0.6$; however, if swept planforms with $t/c \leq 0.04$, application to higher Mach numbers is acceptable 4. Linear-lift range
	Method 1 1. Horizontal tail mounted on body or no horizontal tail $\left(C_{n_\beta}\right)_{WB}$ 2. Linear-lift range $\left(\Delta C_{Y_\beta}\right)_p$ (based on exposed vertical-tail geometry) 3. Breaks in LE and TE at same spanwise station 4. Bodies of revolution 5. $M \geq 1.4$ for straight-tapered planforms 6. $1.2 \leq M \leq 3$ for composite planforms 7. $1.0 \leq M \leq 3$ for curved planforms 8. Linear-lift range
	Method 2 (same limitations as Method 1 above) $\left(\Delta C_{Y_\beta}\right)_p$ (based on vertical-tail geometry)
Eq. 7.1.2.1-a	1. $\alpha \leq \alpha_{stall}$ K 2. Test data for lift and drag $\left(\frac{C_{Y_p}}{C_L}\right)_{\substack{C_L=0 \\ M}}$ 3. $M \leq M_{cr}$
	1. Thin, sweptback, tapered wings with streamwise tips 2. Low lift coefficients
Eq. 7.1.2.1-a	1. (Body diameter)/(wing span) ≤ 0.3 2. $\alpha \leq \alpha_{stall}$ K 3. Test data for lift and drag

DERIVATIVE	CONFIG.	SPEED REGIME	EQUATIONS FOR DERIVATIVE ESTIMA Datcom section for components indicat
C_{Y_p} (Contd.)	WB (Contd.)	SUBSONIC (Contd.)	
		TRANSONIC	(No method)
		SUPERSONIC	Figure 7.1.2.1-10
	WBT	SUBSONIC	$C_{Y_p} = \underbrace{\left(C_{Y_p}\right)_{WB}}_{7.3.2.1} + 2\left[\frac{z - z_p}{b_W}\right] \underbrace{\left(\Delta C_{Y_\beta}\right)_{V(WBH)}}_{5.3.1.1}$
			$C_{Y_p} = \underbrace{\left(C_{Y_p}\right)_{WB}}_{7.3.2.1} + \left[\frac{2z - z_p}{b_W}\right] \underbrace{\left(\Delta C_{Y_\beta}\right)_{V(WBH)}}_{5.3.1.1}$
		TRANSONIC	(No method)
		SUPERSONIC	(No method)
C_{l_p}	W	SUBSONIC	$C_{l_p} = \underbrace{\left(\frac{\beta C_{l_p}}{\kappa}\right)_{C_L=0}}_{7.1.2.2} \underbrace{\left(\frac{\kappa}{\beta}\right)}_{4.1.1.2} \underbrace{\frac{\left(C_{L_\alpha}\right)_{C_L}}{\left(C_{L_\alpha}\right)_{C_L=0}}}_{4.1.3.2} \underbrace{\frac{\left(C_{l_p}\right)_\Gamma}{\left(C_{l_p}\right)_{\Gamma=0}}}_{7.1.2.2} + \underbrace{\left(\Delta C_{l_p}\right)_{drag}}_{7.1.2.2}$ (4.1.3.3)
		TRANSONIC	(No method)

METHODS SUMMARY

EQUATIONS FOR DERIVATIVE ESTIMATION (Datcom section for components indicated)		METHOD LIMITATIONS ASSOCIATED WITH EQUATION COMPONENTS
		$\left(\frac{C_{Y_p}}{C_L}\right)_{C_L=0}$ M 4. $M \leq M_{cr}$
		1. Thin, sweptback, tapered wings with streamw tips 2. (Body diameter)/(wing span) ≤ 0.3 3. Low lift coefficients
$\underbrace{C_{Y_\beta})_{V(WBH)}}_{5.3.1.1}$	Eq. 7.4.2.1-a	Method 1 (conventionally located vertical tails) $\left(C_{Y_p}\right)_{WB}$ 1. (body diameter)/(wing span) ≤ 0.3 2. $\alpha \leq \alpha_{stall}$ 3. Test data for lift and drag 4. $M \leq M_{cr}$ $\left(\Delta C_{Y_\beta}\right)_{V(WBH)}$ 5. Additional or identical tail limitations depend on $\left(\Delta C_{Y_\beta}\right)_{V(WBH)}$ prediction method
$\underbrace{C_{Y_\beta})_{V(WBH)}}_{5.3.1.1}$	Eq. 7.4.2.1-c	Method 2 (vertical tail directly above, or above and slightly behind wing) (same limitations as Method 1 above)
.3.3 $\underbrace{\left.\right)_{C_L}}_{C_L=0}$ $\underbrace{\frac{\left(C_{l_p}\right)_\Gamma}{\left(C_{l_p}\right)_{\Gamma=0}}}_{7.1.2.2}$ $+\underbrace{\left(\Delta C_{l_p}\right)_{drag}}_{7.1.2.2}$	Eq. 7.1.2.2-a	1. $M \leq M_{cr}$ $\left(C_{L_\alpha}\right)_{C_L}$ 2. Symmetric airfoils 3. $1 \times 10^6 \leq R_c \leq 15 \times 10^6$ based on MAC $\left(C_{L_\alpha}\right)_{C_L=0}$ 4. Straight-tapered wings

DERIVATIVE	CONFIG.	SPEED REGIME	EQUATIONS FOR DERIVATIVE ESTIMA (Datcom section for components indicate
C_{l_p} (Contd.)	W (Contd.)	SUPERSONIC	$C_{l_p} = \underbrace{\left[\frac{\left(C_{l_p}\right)_{\text{theory}}}{A}\right]}_{7.1.2.2} A \underbrace{\frac{C_{l_p}}{\left(C_{l_p}\right)_{\text{theory}}}}_{7.1.2.2}$
	WB	SUBSONIC	$C_{l_p} = \underbrace{\left(\frac{\beta C_{l_p}}{\kappa}\right)_{C_L=0}}_{7.1.2.2} \underbrace{\left(\frac{\kappa}{\beta}\right)}_{4.1.1.2} \underbrace{\frac{\overbrace{\left(C_{L_\alpha}\right)_{C_L}}^{4.1.3.3}}{\left(C_{L_\alpha}\right)_{C_L=0}}}_{4.1.3.2} \underbrace{\frac{\left(C_{l_p}\right)_\Gamma}{\left(C_{l_p}\right)_{\Gamma=0}}}_{7.1.2.2} + \underbrace{\left(\Delta C_{l_p}\right)_{\text{drag}}}_{7.1.2.2}$
		TRANSONIC	(No method)
		SUPERSONIC	$\left(C_{l_p}\right)_{WB} = \underbrace{\left(C_{l_p}\right)_W}_{7.1.2.2} \underbrace{\frac{C_{l_p}}{\left(C_{l_p}\right)_{d/b=0}}}_{7.3.2.2}$
	WBT	SUBSONIC	$C_{l_p} = \underbrace{\left(C_{l_p}\right)_{WB}}_{7.1.2.2} + 0.5 \underbrace{\left(C_{l_p}\right)_H}_{7.1.2.2} \left(\frac{S_H}{S_W}\right)\left(\frac{b_H}{b_W}\right)^2 + \left\lvert 2\left(\frac{z}{b_W}\right)\left[\frac{z - z_p}{b_W}\right]\right\rvert (\Delta$

	METHOD LIMITATIONS ASSOCIATED WITH EQUATION COMPONENTS
Eq. 7.1.2.2-d	1. Straight-tapered wings 2. Wing tips parallel to free stream 3. Foremost Mach line from tip may not intersect remote half-wing 4. Supersonic TE
Eq. 7.1.2.2-a	1. (Body diameter)/(wing span) ≤ 0.3 2. $M \leq M_{cr}$ $\left(C_{L_\alpha}\right)_{C_L}$ 3. Symmetric airfoils 4. $1 \times 10^6 \leq R_\ell \leq 15 \times 10^6$ based on MAC $\left(C_{L_\alpha}\right)_{C_L=0}$ 5. Straight-tapered wings
Eq. 7.3.2.2-a	1. Straight-tapered wings. If (body diameter)/(wing span) > 0.3, valid only for triangular wings) 2. Cylindrical or nearly cylindrical bodies $\left(C_{l_p}\right)_W$ 3. Wing tips parallel to free stream 4. Foremost Mach line from tip may not intersect remote half-wing 5. Supersonic TE
Eq. 7.4.2.2-a	Method 1 (conventionally located vertical tails) $\left(C_{l_p}\right)_{WB}$ and $\left(C_{l_p}\right)_H$ 1. Straight-tapered planforms 2. Symmetric airfoils 3. (Body diameter)/(wing span) ≤ 0.3 4. $M \leq M_{cr}$ 5. $1 \times 10^6 \leq R_\ell \leq 15 \times 10^6$ based on MAC $\left(\Delta C_{Y_\beta}\right)_{V(WBH)}$ 6. Additional or identical tail limitations depend on $\left(\Delta C_{Y_\beta}\right)_{V(WBH)}$ prediction method

DERIVATIVE	CONFIG.	SPEED REGIME	EQUATIONS FOR DERIVATIVE ESTIM. (Datcom section for components indica
C_{l_p} (Contd.)	WBT (Contd.)	SUBSONIC (Contd.)	$C_{l_p} = \underbrace{(C_{l_p})_{WB}}_{7.1.2.2} + 0.5 \underbrace{(C_{l_p})_{H}}_{7.1.2.2} \left(\frac{S_H}{S_W}\right)\left(\frac{b_H}{b_W}\right)^2 + \left\| \frac{\ell}{b_W}\left[\frac{2z_{} \quad z_p}{b_W}\right]\right\| ($
		TRANSONIC	(No method)
		SUPERSONIC	(No method)
C_{n_p}	W	SUBSONIC	$C_{n_p} = \underbrace{-C_{l_p}}_{7.1.2.2} \tan\alpha - \underbrace{K}_{7.1.2.3} \left[\underbrace{-C_{l_p}}_{7.1.2.2} \tan\alpha - \underbrace{\left(\frac{C_{n_p}}{C_L}\right)_{\substack{C_L=0 \\ M}}}_{7.1.2.3} C_L \right] + \left(\frac{\Delta C_r}{\theta} \right.$ 7.1.2
		TRANSONIC	(No method)
		SUPERSONIC	$\frac{C_{n_p}}{\alpha} = \underbrace{\left(\frac{C_{n_p}}{\alpha}\right)_{\substack{body \\ axis}}}_{7.1.2.3} + \frac{2x_{c.g.}}{A(1+\lambda)} \underbrace{\left(\frac{C_{Y_p}}{\alpha}\right)}_{7.1.2.1} \left(\underbrace{C_{l_p}}_{7.1.2.2} - \underbrace{C_{n_r}}_{7.1.3.3} \right)$
			$\frac{C_{n_p}}{\alpha} = \underbrace{\left(\frac{C_{n_p}}{\alpha}\right)_{\substack{body \\ axis}}}_{7.1.2.3} + \left[\frac{2x_{c.g.}}{A(1+\lambda)} - \frac{1}{2}\tan\Lambda_{LE} \right] \underbrace{\frac{C_{Y_p}}{\alpha}}_{7.1.2.1} - \underbrace{C_{l_p}}_{7.1.2.2}$
	WB	SUBSONIC	$C_{n_p} = \underbrace{C_{l_p}\tan\alpha}_{7.1.2.2} - \underbrace{K}_{7.1.2.3} \left[\underbrace{C_{l_p}\tan\alpha}_{7.1.2.2} - \underbrace{\left(\frac{C_{n_p}}{C_L}\right)_{\substack{C_L=0 \\ M}}}_{7.1.2.3} C_L \right]$ $+ \underbrace{\left(\frac{\Delta C_{n_p}}{\theta}\right)\theta}_{7.1.2.3} + \underbrace{\left[\frac{\Delta C_{n_p}}{\left(\frac{\partial\alpha}{\partial\delta}\right)_f \delta_f}\right]}_{7.1.2.3} \underbrace{\left(\frac{\partial\alpha}{\partial\delta}\right)_f}_{6.1.1.1} \delta_f$

METHODS SUMMARY

EQUATIONS FOR DERIVATIVE ESTIMATION (Datcom section for components indicated)	METHOD LIMITATIONS ASSOCIATED WITH EQUATION COMPONENTS
$\left(\frac{S_H}{S_W}\right)\left(\frac{b_H}{b_W}\right)^2 + \left\lvert \frac{z}{b_W}\left[\frac{2z - z_p}{b_W}\right]\right\rvert \underbrace{\left(\Delta C_{Y_\beta}\right)_{V(WBH)}}_{5.3.1.1}$ Eq. 7.4.2.2-b	Method 2 (vertical tail located directly above, or above and slightly behind wing) (same limitations as Method 1 above)
$\underbrace{\tan\alpha - \left(\frac{C_{n_p}}{C_L}\right)_{\substack{C_L=0 \\ M}} C_L}_{7.1.2.3}\Big] + \underbrace{\left(\frac{\Delta C_{n_p}}{\theta}\right)\theta}_{7.1.2.3} + \left[\frac{\Delta C_{n_p}}{\underbrace{\left(\frac{\partial\alpha}{\partial\delta}\right)_f \delta_f}_{7.1.2.3}}\right] \underbrace{\left(\frac{\partial\alpha}{\partial\delta}\right)_f \delta_f}_{6.1.1.1}$ Eq. 7.1.2.3-a	1. $M \leq M_{cr}$ 2. Lift coefficients up to stall (if reliable lift and drag data are available) C_{l_p} 3. Straight-tapered wings 4. Symmetric airfoils 5. $1 \times 10^6 \leq R_e \leq 15 \times 10^6$ based on MAC
$\underbrace{\left(\frac{C_{Y_p}}{\alpha}\right)}_{7.1.2.1} - \underbrace{\left(C_{l_p}\right)}_{7.1.2.2} - \underbrace{\left(C_{n_r}\right)}_{7.1.3.3}$ Eq. 7.1.2.3-e	Method 1 Subsonic leading edges ($\beta \cot \Lambda_{LE} < 1$) 1. Straight-tapered wings 2. Streamwise wing tips 3. Low lift coefficients C_{l_p} 4. Foremost Mach line from tip may not intersect remote half-wing 5. Supersonic TE
$\frac{1}{2}\tan\Lambda_{LE}\Big] \underbrace{\frac{C_{Y_p}}{\alpha}}_{7.1.2.1} - \underbrace{C_{l_p}}_{7.1.2.2}$ Eq. 7.1.2.3-g	Method 2 Supersonic leading edges ($\beta \cot \Lambda_{LE} > 1$) (same limitations as Method 1 above)
$C_{l_p}\Big[\underbrace{\tan\alpha - \left(\frac{C_{n_p}}{C_L}\right)_{\substack{C_L=0 \\ M}} C_L}_{7.1.2.3}\Big]$ Eq. 7.1.2.3-a $\underbrace{\left(\frac{\partial\alpha}{\partial\delta}\right)_f \delta_f}_{6.1.1.1}$	1. (Body diameter)/(wing span) ≤ 0.3 2. $M < M_{cr}$ 3. Lift coefficients up to stall (if reliable lift and drag data are available) C_{l_p} 4. Straight-tapered wings 5. Symmetric airfoils 6. $1 \times 10^6 \leq R_e \leq 15 \times 10^6$ based on MAC

DERIVATIVE	CONFIG.	SPEED REGIME	EQUATIONS FOR DERIVATIVE ESTIMATI (Datcom section for components indicated)
C_{n_p} (Contd.)	WB (Contd.)	TRANSONIC	(No method)
		SUPERSONIC	$\frac{C_{n_p}}{\alpha} = \underbrace{\left(\frac{C_{n_p}}{\alpha}\right)_{\substack{\text{body}\\\text{axis}}}}_{7.1.2.3} + \frac{2x_{c.g.}}{A(1+\lambda)} \underbrace{\left(\frac{C_{Y_p}}{\alpha}\right)}_{7.1.2.1} - \underbrace{\left(C_{l_p} - C_{n_r}\right)}_{7.1.2.2\ \ 7.1.3.3}$
			$\frac{C_{n_p}}{\alpha} = \underbrace{\left(\frac{C_{n_p}}{\alpha}\right)_{\substack{\text{body}\\\text{axis}}}}_{7.1.2.3} + \left[\frac{2x_{c.g.}}{A(1+\lambda)} - \frac{1}{2}\tan\Lambda_{LE}\right] \underbrace{\frac{C_{Y_p}}{\alpha}}_{7.1.2.1} - \underbrace{C_{l_p}}_{7.1.2.2}$
	WBT	SUBSONIC	$C_{n_p} = \underbrace{\left(C_{n_p}\right)_{WB}}_{7.3.2.3} - \frac{2}{b_W}\left(\ell_p \cos\alpha + z_p \sin\alpha\right)\left[\frac{z - z_p}{b_W}\right] \underbrace{\left(\Delta C_{Y_\beta}\right)_{V(WBH)}}_{5.3.1.1}$
			$C_{n_p} = \underbrace{\left(C_{n_p}\right)_{WB}}_{7.3.2.3} + 2\left[\frac{z - z_p}{b_W}\right]\left(\Delta C_{n_\beta}\right)_p$
			$C_{n_p} = \underbrace{\left(C_{n_p}\right)_{WB}}_{7.3.2.3} - \left[\frac{\ell_p \cos\alpha + z_p \sin\alpha}{b_W}\right]\left[\frac{2z - z_p}{b_W}\right] \underbrace{\left(\Delta C_{Y_\beta}\right)_{V(WBH)}}_{5.3.1.1}$
			$C_{n_p} = \underbrace{\left(C_{n_p}\right)_{WB}}_{7.3.2.3} + \left[\frac{2z - z_p}{b_W}\right]\left(\Delta C_{n_\beta}\right)_p$

	METHOD LIMITATIONS ASSOCIATED WITH EQUATION COMPONENTS
Eq. 7.1.2.3-e	Method 1 Subsonic leading edges ($\beta \cot \Lambda_{LE} < 1$) 1. Straight-tapered wings 2. Streamwise wing tips 3. (Body diameter)/(wing span) ≤ 0.3 4. Lift coefficients where C_{n_p} varies linearly with C_L C_{l_p} 5. Foremost Mach line from tip may not intersect remote half-wing 6. Supersonic TE
Eq. 7.1.2.3-g	Method 2 Supersonic leading edges ($\beta \cot \Lambda_{LE} > 1$) (same limitations as Method 1 above)
Eq. 7.4.2.3-a	Method 1 (conventionally located vertical tails) $\left(C_{n_p}\right)_{WB}$ 1. Straight-tapered wings 2. Symmetric airfoils 3. (Body diameter)/(wing span) ≤ 0.3 4. $M \leq M_{cr}$ 5. $1 \times 10^6 \leq R_\ell \leq 15 \times 10^6$ based on MAC 6. Lift coefficients up to stall (if reliable lift and drag data are available) $\left(\Delta C_{Y_\beta}\right)_{V(WBH)}$ 7. Additional or identical tail limitations depend on $\left(\Delta C_{Y_\beta}\right)_{V(WBH)}$ prediction method
Eq. 7.4.2.3-b	(same limitations as for Eq. 7.4.2.3-a above) $\left(\Delta C_{n_\beta}\right)_F$ 1. Test data
Eq. 7.4.2.3-c	Method 2 (vertical tails located directly above, or above and slightly behind wing) (same limitations as for Eq. 7.4.2.3-a above)
Eq. 7.4.2.3-d	(same limitations as Method 1 above)

DERIVATIVE	CONFIG.	SPEED REGIME	EQUATIONS FOR DERIVATIVE ESTIMA (Data on section for components indicat
C_{n_p} (Contd.)	WBT (Contd.)	TRANSONIC	(No method)
		SUPERSONIC	(No method)
C_{Y_r}	W	SUBSONIC	(No method)
		TRANSONIC	(No method)
		SUPERSONIC	(No method)
	WB	SUBSONIC	(No method)
		TRANSONIC	(No method)
		SUPERSONIC	(No method)
	WBT	SUBSONIC	$C_{Y_r} = \left(C_{Y_r}\right)_{WB} - \frac{2}{b_w}\left(\ell_p \cos\alpha + z_p \sin\alpha\right)\underbrace{\left(\Delta C_{Y_\beta}\right)_{V(WBH)}}_{5.3.1.1}$
			$C_{Y_r} = \left(C_{Y_r}\right)_{WB} + 2\left(\Delta C_{n_\beta}\right)_p$
		TRANSONIC	(No method)
		SUPERSONIC	(No method)
C_{l_r}	W	SUBSONIC	$C_{l_r} = C_L \underbrace{\left(\frac{C_{l_r}}{C_l}\right)_{C_L=0}^{M}}_{7.1.3.2} + \underbrace{\left(\Delta C_{l_r}\right)_{C_L}}_{7.1.3.2} + \underbrace{\left(\frac{\Delta C_{l_r}}{\Gamma}\right)\Gamma}_{7.1.3.2} + \underbrace{\left(\frac{\Delta C_{l_r}}{\theta}\right)\theta}_{7.1.3.2} +$ [
		TRANSONIC	(No method)
		SUPERSONIC	(No method)

METHODS SUMMARY

TIONS FOR DERIVATIVE ESTIMATION (tcom section for components indicated)		METHOD LIMITATIONS ASSOCIATED WITH EQUATION COMPONENTS
$+ z_p \sin\alpha) \underbrace{\left(\Delta C_{Y_\beta}\right)_{V(WBH)}}_{5.3.1.1}$	Eq. 7.4.3.1-a	1. Aperiodic mode only $\left(C_{Y_r}\right)_{WB}$ 2. Test data $\left(\Delta C_{Y_\beta}\right)_{V(WBH)}$ 3. Additional tail limitations depend on $\left(\Delta C_{Y_\beta}\right)_{V(WBH)}$ prediction method
	Eq. 7.4.3.1-b	$\left(C_{Y_r}\right)_{WB}$ and $\left(\Delta C_{n_\beta}\right)_p$ 1. Test data
$+ \underbrace{\left(\frac{\Delta C_{l_r}}{\Gamma}\right)\Gamma}_{7.1.3.2} + \underbrace{\left(\frac{\Delta C_{l_r}}{\theta}\right)\theta}_{7.1.3.2} + \underbrace{\left[\frac{\Delta C_{l_r}}{\left(\frac{\partial\alpha}{\partial\delta}\right)_f \delta_f}\right]}_{7.1.3.2} \underbrace{\left(\frac{\partial\alpha}{\partial\delta}\right)_f}_{6.1.1.1} \delta_f$	Eq. 7.1.3.2-a	1. $M \leq M_{cr}$ $\left(\Delta C_{l_r}\right)_{C_1}$ 2. No curved planforms 3. No twist or dihedral, if non-straight-tapered wings 4. $t/c \leq 0.1$ if cranked wing with round LE 5. $M \leq 0.6$ 6. Linear-lift range 7. $5^0 \leq \beta \leq 15^0$

DERIVATIVE	CONFIG.	SPEED REGIME	EQUATIONS FOR DERIVATIVE ESTIMATION (Datcom section for components indicated)
C_{l_r} (Contd.)	WB	SUBSONIC	$C_{l_r} = C_L \underbrace{\left(\frac{C_{l_r}}{C_L}\right)_{\substack{C_L=0 \\ M}}}_{7.1.3.2} + \underbrace{\left(\Delta C_{l_r}\right)_{C_L}}_{7.1.3.2} + \underbrace{\left(\frac{\Delta C_{l_r}}{\Gamma}\right)}_{7.1.3.2} \Gamma + \underbrace{\left(\frac{\Delta C_{l_r}}{\theta}\right)}_{7.1.3.2} \theta + \underbrace{\left[\frac{\Delta C_{l_r}}{\left(\frac{\partial \alpha}{\partial \delta}\right)_f}\right.}_{7.1.3.}$
		TRANSONIC	(No method)
		SUPERSONIC	(No method)
	WBT	SUBSONIC	$C_{l_r} = \underbrace{\left(C_{l_r}\right)_{WB}}_{7.3.3.2} - \frac{2}{b_W^2}\left(\ell_p \cos\alpha + z_p \sin\alpha\right)\left(z_p \cos\alpha - \ell_p \sin\alpha\right)\underbrace{\left(\Delta C_{Y_\beta}\right)_{V(W}}_{5.3.1.1}$
			$C_{l_r} = \underbrace{\left(C_{l_r}\right)_{WB}}_{7.3.3.2} - \frac{2}{b_W}\left(\ell_p \cos\alpha + z_p \sin\alpha\right)\left(\Delta C_{l_\beta}\right)_p$
			$C_{l_r} = \underbrace{\left(C_{l_r}\right)_{WB}}_{7.3.3.2} + 2\,\frac{\left(\Delta C_{n_\beta}\right)_p}{\underbrace{\left(\Delta C_{Y_\beta}\right)_{V(WBH)}}_{5.3.1.1}}\left(\Delta C_{l_\beta}\right)_p$
		TRANSONIC	(No method)

UMMARY

ESTIMATION Is indicated)		METHOD LIMITATIONS ASSOCIATED WITH EQUATION COMPONENTS
$\theta + \left[\frac{\Delta C_{l_r}}{\left(\frac{\partial \alpha}{\partial \delta}\right)_f \delta_f}\right]\left(\frac{\partial \alpha}{\partial \delta}\right)_f \delta_f$ 7.1.3.2 6.1.1.1	Eq. 7.1.3.2-a	1. (Body diameter)/(wing span) ≤ 0.3 2. $M \leq M_{cr}$ $\left(\Delta C_{l_r}\right)_{C_L}$ 3. No curved planforms 4. No twist or dihedral, if non-straight-tapered wing 5. t/c ≤ 0.1 if cranked wing with round LE 6. $M \leq 0.6$ 7. Linear-lift range 8. $-5^O \leq \beta \leq +5^O$
$\alpha)\left(\Delta C_{Y_\beta}\right)_{V(WBH)}$ 5.3.1.1	Eq. 7.4.3.2-a	$\left(C_{l_r}\right)_{WB}$ 1. No curved planforms 2. No twist or dihedral, if non-straight-tapered wing 3. t/c ≤ 0.1 if cranked wing with round LE 4. (Body diameter)/(wing span) ≤ 0.3 5. $M \leq 0.6$ 6. $M \leq M_{cr}$ 7. Linear-lift range 8. $-5^O \leq \beta \leq +5^O$ $\left(\Delta C_{Y_\beta}\right)_{V(WBH)}$ 9. Additional or identical tail limitations depend on $\left(\Delta C_{Y_\beta}\right)_{V(WBH)}$ prediction method
	Eq. 7.4.3.2-b	$\left(C_{l_r}\right)_{WB}$ (same limitations as for Eq. 7.4.3.2-a) $\left(\Delta C_{l_\beta}\right)_p$ 1. Test data
	Eq. 7.4.3.2-c	$\left(C_{l_r}\right)_{WB}$ (same limitations as for Eq. 7.4.3.2-a) $\left(\Delta C_{n_\beta}\right)_p$, $\left(\Delta C_{Y_\beta}\right)_{V(WBH)}$, and $\left(\Delta C_{l_\beta}\right)_p$ 1. Test data

DERIVATIVE	CONFIG.	SPEED REGIME	EQUATIONS FOR DERIVATIVE ESTIMATI (Datcom section for components indicated)
C_{l_r} (Contd.)	WBT (Contd.)	SUPERSONIC	(No method)
C_{n_r}	W	SUBSONIC	$C_{n_r} = \underbrace{\left(\frac{C_{n_r}}{C_L^2}\right)}_{7.1.3.3} C_L^2 + \underbrace{\left(\frac{C_{n_r}}{C_{D_0}}\right)}_{7.1.3.3} C_{D_0}$
		TRANSONIC	(No method)
		SUPERSONIC	(No method)
	WB	SUBSONIC	$C_{n_r} = \underbrace{\left(\frac{C_{n_r}}{C_L^2}\right)}_{7.1.3.3} C_L^2 + \underbrace{\left(\frac{C_{n_r}}{C_{D_0}}\right)}_{7.1.3.3}$
		TRANSONIC	(No method)
		SUPERSONIC	(No method)
	WBT	SUBSONIC	$C_{n_r} = \underbrace{\left(C_{n_r}\right)_{WB}}_{7.3.3.3} + \frac{2}{b_W^2}\left(\ell_p \cos\alpha + z_p \sin\alpha\right)^2 \underbrace{\left(\Delta C_{Y_\beta}\right)_{V(WBH)}}_{5.3.1.1}$
			$C_{n_r} = \underbrace{\left(C_{n_r}\right)_{WB}}_{7.3.3.3} + 2 \underbrace{\frac{\left(\Delta C_{n_\beta}\right)_p^2}{\left(\Delta C_{Y_\beta}\right)_{V(WBH)}}}_{5.3.1.1}$
		TRANSONIC	(No method)
		SUPERSONIC	(No method)

ODS SUMMARY

RIVATIVE ESTIMATION components indicated)	METHOD LIMITATIONS ASSOCIATED WITH EQUATION COMPONENTS
Eq. 7.1.3.3-a	1. No twist nor dihedral 2. Lift-coefficient range for which C_{n_r} varies linearly with C_L
Eq. 7.1.3.3-a	1. No twist nor dihedral 2. Lift coefficient range for which C_{n_r} varies linearly with C_L
$\Delta C_{Y_\beta})_{V(WBH)}$ 5.3.1.1	Eq. 7.4.3.3-a 1. Aperiodic mode only $(C_{n_r})_{WB}$ 2. No twist nor dihedral 3. Lift-coefficient range for which C_{n_r} varies linearly with C_L $(\Delta C_{Y_\beta})_{V(WBH)}$ 4. Additional tail limitations depend upon $(\Delta C_{Y_\beta})_{V(WBH)}$ prediction method
Eq. 7.4.3.3-b	(same limitations as for Eq. 7.4.3.3-a above) $(\Delta C_{n_\beta})_p$ 1. Test data

DERIVATIVE	CONFIG.	SPEED REGIME	EQUATIONS FOR DERIVATIVE ESTI (Datcom section for components ind
c_{ℓ_δ} and α_δ	W (two dim)	SUBSONIC	$c_{\ell_\delta} = \left(\frac{\partial c_\ell}{\partial \delta}\right)_\alpha$
			$\alpha_\delta = -\frac{(c_{\ell_\delta})_\alpha}{(c_{\ell_\alpha})_\delta}$
			$\Delta c_\ell = \delta_f \underbrace{\left[\frac{c_{\ell_\delta}}{(c_{\ell_\delta})_{\text{theory}}}\right]}_{6.1.1.1} \underbrace{(c_{\ell_\delta})_{\text{theory}}}_{6.1.1.1} \underbrace{K'}_{6.1.1.1}$
			$\Delta c_\ell = \underbrace{-c_{\ell_\alpha}}_{\text{test data}} \underbrace{\alpha_\delta}_{6.1.1.1} \delta_f$
			$\Delta c_\ell = \underbrace{c_{\ell_\delta}}_{6.1.1.1} \delta_f \underbrace{\eta_1}_{6.1.1.1} \frac{c'}{c}$
			$\Delta c_\ell = \underbrace{\eta_1}_{6.1.1.1} \underbrace{c_{\ell_{\delta_{f_1}}}}_{6.1.1.1} \delta_{f_1}\left(\frac{c + c_1}{c}\right) + \underbrace{\eta_2}_{6.1.1.1} \underbrace{c_{\ell_{\delta_{f_2}}}}_{6.1.1.1} \left(\delta_{f_1} + \delta_{f_2}\right.$
			$\Delta c_\ell = \underbrace{\eta_1}_{6.1.1.1} \underbrace{c_{\ell_{\delta_{f_1}}}}_{6.1.1.1} \delta_{f_1}\left(\frac{c'_2}{c}\right) + \underbrace{\eta_2}_{6.1.1.1} \underbrace{\eta_t}_{6.1.1.1} \underbrace{c_{\ell_{\delta_{f_2}}}}_{6.1.1.1} \delta_{f_2}\left($
			$\Delta c_\ell = \underbrace{-c_{\ell_\alpha}}_{4.1.1.2} \underbrace{\alpha_\delta}_{6.1.1.1} \delta_f$
			$\Delta c_\ell = \left\{\left[\underbrace{1 + k_t\left(\frac{t}{c'}\right)}_{6.1.1.1}\right] \delta_f \left(\underbrace{c_{\ell_{\delta_f}}}_{6.1.1.1} - \underbrace{C'_\mu}_{6.1.1.1}\right) + \underbrace{C'_\mu}_{6.1.1.1} \delta_f + \left[\underbrace{1 + k_t\left(\frac{t}{c'}\right)}_{6.1.1.1}\right] \delta_j \left(c_\ell\right.$ 6.1.

PREVIOUS PAGE IS BLANK

HODS SUMMARY

DERIVATIVE ESTIMATION (for components indicated)		METHOD LIMITATIONS ASSOCIATED WITH EQUATION COMPONENTS
	Eq. 6.1.1.1-a	1. Linear-lift range 2. Other limitations depend upon type of flap (see Equations -c through -j below)
	Eq. 6.1.1.1-b	1. Linear-lift range 2. Other limitations depend upon type of flap (see Equations -c through -j below)
1.1	Eq. 6.1.1.1-c	1. Plain trailing-edge flaps with sealed gaps 2. No beveled trailing edges 3. No compressibility effects
	Eq. 6.1.1.1-d	(a) Single-slotted flaps (b) Fowler flaps 1. Near fully extended position 2. Slot properly developed
	Eq. 6.1.1.1-e	(a) Single-slotted flaps (b) Fowler flaps
$\underbrace{c_{\ell_{\delta_{f_2}}}}_{6.1.1.1} \left(\delta_{f_1} + \delta_{f_2}\right) \frac{c'}{c}$	Eq. 6.1.1.1-h	1. Double-slotted flaps 2. Ratio of forward-flap chord to aft-flap chord ≤ 0.60
$\underbrace{\eta_t}_{1.1.1} \underbrace{c_{\ell_{\delta_{f_2}}}}_{6.1.1.1} \delta_{f_2} \left(1 + \frac{c' - c'_2}{c}\right)$	Eq. 6.1.1.1-i	1. Double-slotted flaps 2. Ratio of forward-flap chord to aft-flap chord $\simeq 1.0$
	Eq. 6.1.1.1-j	1. Split flaps
$\left[1 + \underbrace{k_t\left(\frac{t}{c'}\right)}_{6.1.1.1}\right] \delta_j \left(\underbrace{c_{\ell_{\delta_j}}}_{6.1.1.1} - \underbrace{C'_\mu}_{6.1.1.1}\right) + \underbrace{C'_\mu}_{6.1.1.1} \delta_j \Bigg\} \frac{c'}{c}$	Eq. 6.1.1.1-k	1. Jet flaps (first approximation for multislotted flaps) 2. Linearized thin-airfoil theory 3. No trailing-edge separation 4. No augmentor-wing concept 5. Not valid for low values of C_μ

DERIVATIVE	CONFIG	SPEED REGIME	EQUATIONS FOR DERIVATIVE ESTIM (Datcom section for components indic
c_{ℓ_δ} and α_δ (Contd.)	W (two dim) (Contd.)	SUBSONIC (Contd.)	$\Delta c_\ell = \underbrace{c_{\ell_\delta}}_{6.1.1.1} \delta_f$
			$\Delta c_\ell = \underbrace{c_{\ell_\delta}}_{6.1.1.1} \delta_f \frac{c'}{c}$
			$\Delta c_\ell = \underbrace{-c_{\ell_\alpha}}_{4.1.1.2} \underbrace{\Delta\alpha'_s}_{6.1.1.1}$
$(c_{\ell_\alpha})_\delta$	W (two dim)	SUBSONIC	$(c_{\ell_\alpha})_\delta = \underbrace{(c_{\ell_\alpha})_{\delta=0}}_{4.1.1.2}$ (same as that for flap-retracted section -- see Se
			$(c_{\ell_\alpha})_\delta = \frac{c'}{c} \underbrace{(c_{\ell_\alpha})_{\delta=0}}_{4.1.1.2}$
			$c_{\ell_\alpha} = \left\{ \left[1 + \underbrace{k_t\left(\frac{t}{c'}\right)}_{6.1.1.2} \right] \underbrace{(c'_{\ell_\alpha} - C'_\mu)}_{6.1.1.1} + C'_\mu \right\} \frac{c'}{c}$
			$(c_{\ell_\alpha})_s = (c_{\ell_\alpha})_{\delta=0}$ (same as basic airfoil)
$\Delta c_{\ell_{max}}$	W (two dim)	SUBSONIC	$\Delta c_{\ell_{max}} = \underbrace{k_1}_{6.1.1.3} \underbrace{k_2}_{6.1.1.3} \underbrace{k_3}_{6.1.1.3} \underbrace{(\Delta_{c_{\ell_{max/base}}})}_{6.1.1.3}$
			$\Delta c_\ell = \underbrace{c_{\ell_{\delta_{max}}}}_{6.1.1.3} \underbrace{\eta_{max}}_{6.1.1.3} \underbrace{\eta_\delta}_{6.1.1.3} \delta_f \frac{c'}{c}$

S SUMMARY

ATIVE ESTIMATION nponents indicated)	METHOD LIMITATIONS ASSOCIATED WITH EQUATION COMPONENTS
Eq. 6.1.1.1-f	1. Leading-edge flaps 2. Thin-airfoil theory
Eq. 6.1.1.1-m	1. Thin-airfoil theory (a) Krueger flaps (b) Leading-edge slats
Eq. 6.1.1.1-n	1. Plug or flap spoiler 2. Zero-lift region
ction – see Section 6.1.1.2)	1. Fixed-hinge trailing- and leading-edge flaps 2. $\delta_f \leq 20°$ for plain flaps 3. $\delta_f \leq 30°$ for single-slotted and Fowler flaps 4. $\delta_f \leq 60°$ for double-slotted flaps 5. $\delta_f \leq 45°$ for split flaps 6. No separated flow
Eq. 6.1.1.2-a	1 Translating trailing-edge flaps and leading-edge slats
Eq. 6.1.1.2-b	1. Jet flaps (first approximation for multislotted flaps) 2. Linearized thin-airfoil theory 3. No trailing-edge separation 4. No augmentor-wing concept 5. Not valid for low values of C_μ
	1. Spoilers 2. $\alpha > 0$ 3. $c_\ell < 0$
Eq. 6.1.1.3-a	1. Trailing-edge flaps
Eq. 6.1.1.3-b	1. Thin-airfoil theory (a) Leading-edge flaps 2. No Krueger flaps 3. $\delta_f < 30^o$ (b) Leading-edge slats 4. $\delta_s < 20^o$

DERIVATIVE	CONFIG.	SPEED REGIME	EQUATIONS FOR DERIVATIVE ESTIM (Datcom section for components indic
Δc_m	W (two-dim)	SUBSONIC	$\Delta c_m = \underbrace{\Delta c_\ell}_{6.1.1.1}\left[\frac{x_{ref}}{c} - \underbrace{\left(\frac{x_{c/4}}{c'}\right)}_{6.1.2.1}\left(\frac{c'}{c}\right)\right]$
			Figure 6.1.2.1 -35b
			$\Delta c_{m_{LE}} = \underbrace{c'_{m_{\alpha_{LE}}}}_{6.1.2.1}\left(\frac{c'}{c}\right)^2 \delta_{f_{LE}} + \left(\frac{x_{ref}}{c} + \frac{c'-c}{c}\right)\underbrace{\Delta c_\ell}_{6.1.1.1} + \underbrace{\dot{c}_m}_{4.1.2.1}\left[\left(\frac{c'}{c}\right)^2 - 1\right]$
			$\Delta c_m = \underbrace{(\Delta c_m)_{\delta_{f_{LE}}}}_{6.1.2.1} + \underbrace{\Delta c_{m_\alpha}}_{6.1.2.1} + \underbrace{(\Delta c_m)_{\delta_f}}_{6.1.2.1} + \underbrace{(\Delta c_m)_{\delta_j}}_{6.1.2.1}$
$(c_{m_\alpha})_\delta$	W (two dim)	SUBSONIC	$(c_{m_\alpha})_\delta = (c_{m_\alpha})_{\delta=0}$ (same as that for flap-retracted sections)
			$(\Delta c_m)_\alpha = \underbrace{\Delta c_4 x_2}_{6.1.2.1} + \underbrace{\Delta c_{m_4}}_{6.1.2.1}$
Δc_m	W (two dim)	SUBSONIC	Figure 6.1.2.3-3

ODS SUMMARY

RIVATIVE ESTIMATION r components indicated)	METHOD LIMITATIONS ASSOCIATED WITH EQUATION COMPONENTS
Eq. 6.1.2.1-a	Method 1 1. Plain, split, and multislotted trailing-edge flaps 2. Linear-lift range Δc_{ℓ} (depends upon type of flap)
	Method 2 1. Plain trailing-edge flaps 2. Subcritical Mach numbers 3. Linear-lift range
$\underbrace{c_m}_{1.2.1} \left[\left(\frac{c'}{c}\right)^2 - 1\right] + 0.75 \underbrace{c_{\ell}}_{4.1.1.1,\ 4.1.1.2} \left(\frac{c'}{c}\right)\left(\frac{c'}{c} - 1\right)$ Eq. 6.1.2.1-b	1. Small leading-edge devices 2. Thin-airfoil theory Δc_{ℓ} (depends upon type of flap)
Eq. 6.1.2.1-c	1. Jet flaps (first approximation for multislotted flaps) 2. Linearized thin-airfoil theory 3. No trailing-edge separation 4. No augmentor-wing concept 5. Not valid for low values of C_{μ}
ted sections)	1. Leading- and trailing-edge mechanical flaps 2. No separated flow
Eq. 6.1.2.1-k	1. Jet flaps (first approximation for multislotted flaps) 2. Linearized thin-airfoil theory 3. No trailing-edge separation 4. No augmentor-wing concept 5. Not valid for low values of C_{μ}
	1. Portion of $c_{mc_{\ell}}$ curve below the moment break Δc_{ℓ} (depends upon type of flap)

DERIVATIVE	CONFIG.	SPEED REGIME	EQUATIONS FOR DERIVATIVE (Datcom section for component
c_{h_α}	W (two dim)	SUBSONIC	$c'_{h_\alpha} = \underbrace{\left[\frac{c'_{h_\alpha}}{(c_{h_\alpha})_{theory}}\right]}_{6.1.3.1} \underbrace{(c_{h_\alpha})_{theory}}_{6.1.3.1}$
			$c''_{h_\alpha} = \underbrace{c'_{h_\alpha}}_{6.1.3.1} + 2\underbrace{(c_{\ell_\alpha})_{theory}}_{4.1.1.2}\left[1 - \underbrace{\frac{c_{\ell_\alpha}}{(c_{\ell_\alpha})_{theory}}}_{4.1.1.2}\right]\left(\tan \frac{\phi''_{TE}}{2} - \frac{t}{c}\right.$
			$(c_{h_\alpha})_{balance} = \underbrace{c''_{h_\alpha}}_{6.1.3.1}\left[\underbrace{\frac{(c_{h_\alpha})_{balance}}{c''_{h_\alpha}}}_{6.1.3.1}\right]$
		TRANSONIC	(No method)
		SUPERSONIC	$c_{h_\alpha} = \underbrace{-C_1}_{6.1.3.1} + \underbrace{C_2\,\phi_{TE}}_{6.1.3.1}$
			$c_{h_\alpha} = \underbrace{-C_1}_{6.1.3.1} + \underbrace{\left(\frac{\Delta c_{h_\alpha}}{t/c}\right)}_{6.1.3.1}\frac{t}{c}$

SUMMARY

IVE ESTIMATION nents indicated)		METHOD LIMITATIONS ASSOCIATED WITH EQUATION COMPONENTS
	Eq. 6.1.3.1-a	1. Radius-nose, sealed, trailing-edge flaps 2. Tangent of half the trailing-edge angle = t/c 3. No separated flow 4. Low speeds
$-\frac{t}{c}\Big)$	Eq. 6.1.3.1-b	c'_{h_α} 1. Radius-nose, sealed, trailing-edge flaps 2. Tangent of half the trailing-edge angle ≠ t/c 3. No separated flow 4. Low speeds
	Eq. 6.1.3.1-c	1. Control with nose balance c''_{h_α} 2. Radius-nose, sealed, trailing-edge flaps 3. No separated flow 4. Low speeds
	Eq. 6.1.3.1-e	1. Airfoils with sharp leading and trailing edges 2. Symmetric, straight-sided flaps 3. $c_f/c < 0.5$ 4. Small flap deflections 5. Small angles of attack 6. Flow field supersonic and inviscid 7. No separated flow
	Eq. 6.1.3.1-f	1. Airfoils with sharp leading and trailing edges 2. Symmetric, circular-arc airfoils 3. $c_f/c < 0.5$ 4. Small flap deflections 5. Small angles of attack 6. Flow field supersonic and inviscid 7. No separated flow

DERIVATIVE	CONFIG.	SPEED REGIME	EQUATIONS FOR DERIVATIVE ESTI (Datcom ... for components ind
c_{h_δ}	W (two dim)	SUBSONIC	$c'_{h_\delta} = \underbrace{\left[\frac{c'_{h_\delta}}{(c_{h_\delta})_{theory}}\right]}_{6.1.3.2} \underbrace{(c_{h_\delta})_{theory}}_{6.1.3.2}$
			$c''_{h_\delta} = \underbrace{c'_{h_\delta}}_{6.1.3.2} + 2\underbrace{(c_{l_\delta})_{theory}}_{6.1.1.1}\left[1 - \underbrace{\frac{c_{l_\delta}}{(c_{l_\delta})_{theory}}}_{6.1.1.1}\right]\left(\tan\frac{\phi''_{TE}}{2} - \frac{t}{c}\right)$
			$(c_{h_\delta})_{balance} = \underbrace{c''_{h_\delta}}_{6.1.3.2}\underbrace{\left[\frac{(c_{h_\delta})_{balance}}{c''_{h_\delta}}\right]}_{6.1.3.2}$
		TRANSONIC	(No method)
		SUPERSONIC	$c_{h_\delta} = \underbrace{-C_1}_{6.1.3.2} + \underbrace{C_2\,\phi_{TE}}_{6.1.3.2}$
			$c_{h_\delta} = \underbrace{-C_1}_{6.1.3.2} + \underbrace{\left(\frac{\Delta c_{h_\delta}}{t/c}\right)}_{6.1.3.1}\frac{t}{c}$
$(c_{h_f})_{\delta_t}$	W (two dim)	SUBSONIC	$\left(\frac{\partial c_{h_f}}{\partial \delta_t}\right)_{\alpha,\delta_f} = \left(\frac{\partial c_{h_f}}{\partial \delta_t}\right)_{c_\ell,\delta_f} - \left(\frac{\partial c_{h_f}}{\partial c_\ell}\right)_{\delta_t,\delta_f}\left(\frac{\partial c_\ell}{\partial \alpha}\right)_{\delta_t,\delta_f}\left(\frac{\partial \alpha}{\partial \delta_t}\right)_{c_\ell,\delta_f}$

DERIVATIVE ESTIMATION (for components indicated)		METHOD LIMITATIONS ASSOCIATED WITH EQUATION COMPONENTS
	Eq. 6.1.3.2-a	1. Radius-nose, sealed, trailing-edge flaps 2. Tangent of half the trailing-edge angle = t/c 3. No separated flow 4. Low speeds
$\left(\frac{\phi''_{TE}}{2} - \frac{t}{c}\right)$	Eq. 6.1.3.2-b	1. Radius-nose, sealed, trailing-edge flaps 2. Tangent of half the trailing-edge angle ≠ t/c 3. No separated flow 4. Low speeds
c''_{h_δ}	Eq. 6.1.3.2-c	1. Control with nose balance 2. Radius-nose, sealed, trailing-edge flaps 3. No separated flow 4. Low speeds
	Eq. 6.1.3.2-d	1. Airfoils with sharp leading and trailing edges 2. Symmetric, straight-sided flap 3. $c_f/c < 0.5$ 4. Small flap deflections 5. Small angles of attack 6. Flow field supersonic and inviscid 7. No separated flow
	Eq. 6.1.3.2-e	1. Airfoils with sharp leading and trailing edges 2. Symmetric, circular-arc airfoil 3. $c_f/c \leq 0.5$ 4. Small flap deflections 5. Small angles of attack 6. Flow field supersonic and inviscid 7. No separated flow
δ_f	Eq. 6.1.3.3-a	1. $-18° \leq \delta_t \leq 18°$ 2. Does not account for effects of airfoil thickness, control-surface gaps, control nose balance, and TE angle 3. Low speeds 4. Linear hinge-moment range

DERIVATIVE	CONFIG.	SPEED REGIME	EQUATIONS FOR DERIVATIVE (Datcom section for component
$(c_{h_t})_{\delta_f}$	W (two dim)	SUBSONIC	$\left(\frac{\partial c_{h_t}}{\partial \delta_f}\right)_{\alpha,\delta_t} = \left(\frac{\partial c_{h_t}}{\partial \delta_f}\right)_{c_\ell,\delta_t} - \left(\frac{\partial c_{h_t}}{\partial c_\ell}\right)_{\delta_f,\delta_t}\left(\frac{\partial c_\ell}{\partial \alpha}\right)_{\delta_f,\delta_t}\left(\frac{\partial \alpha}{\partial \delta_f}\right)_{c_\ell,\delta_t}$
C_{L_δ}	W	SUBSONIC	$\Delta C_L = \underbrace{\Delta c_\ell}_{6.1.1.1}\ \overbrace{\left(\frac{C_{L_\alpha}}{c_{\ell_\alpha}}\right)}^{4.1.3.2}\ \underbrace{\left[\frac{(\alpha_\delta)_{C_L}}{(\alpha_\delta)_{c_\ell}}\right]}_{4.1.2\ \ 6.1.4.1}\ \underbrace{K_b}_{6.1.4.1}$
			$\Delta C_L = \underbrace{\Delta c_\ell}_{6.1.1.1}\left[\frac{A_t + \frac{2C'_J}{\pi}}{A_t + 2 + 0.604(C'_J)^{1/2} + 0.876\,C'_J}\right]\frac{S_{W_f}}{S_W}$
			$\Delta C_L = 4\pi d_o\left[\frac{\pi A_t + 2C'_J}{\pi A_t + \underbrace{c'_{\ell_\alpha}}_{6.1.1.1} + 2.01\,C'_J}\right]\frac{\overbrace{\delta_{jeff}}^{6.1.4.1}}{57.3}\frac{S_{W_f}}{S_W}$
		TRANSONIC	$C_{L_\delta} = \underbrace{C_{L_{\delta_{M=0.6}}}}_{6.1.4.1}\ \underbrace{\left(\frac{C_{l_\delta}}{C_{l_{\delta_{M=0.6}}}}\right)}_{6.2.1.1}$

MARY

IMATION licated)	METHOD LIMITATIONS ASSOCIATED WITH EQUATION COMPONENTS
Eq. 6.1.3.4-a	1. $18^{o} \leq \delta_f \leq 18^{o}$ 2. Does not account for effects of airfoil thickness, control-surface gaps, control nose balance, and TE angle 3. Low speeds 4. Linear hinge-moment range
Eq. 6.1.4.1-a	Δc_ℓ (depends upon type of flap) C_{L_α} 1. Mechanical flaps 2. Straight-tapered wings
Eq. 6.1.4.1-b	1. Jet flap IBF configuration 2. Small angles of attack 3. Linearized thin-airfoil theory 4. No trailing-edge separation 5. No augmentor-wing concept 6. Not valid for low values of C_J
Eq. 6.1.4.1-c	1. Jet flap EBF configuration 2. Small angles of attack 3. Linearized thin-airfoil theory 4. No trailing-edge separation 5. No augmentor-wing concept 6. Not valid for low values of C_J
Eq. 6.1.4.1-e	$C_{L_\delta}{}_{M=0.6}$ 1. Straight-tapered wings $C_{l_\delta}{}_{M=0.6}$ 2. Plain trailing-edge flaps 3. $\beta A \geq 2$ 4. $\Lambda_\beta < 60^{o}$ 5. No beveled trailing edges 6. No compressibility effects C_{l_δ} 7. Symmetric airfoils of conventional thickness distribution 8. $\alpha = 0$

DERIVATIVE	CONFIG.	SPEED REGIME	EQUATIONS FOR DERIVATIVE ES (Datcom section for components i
C_{L_δ} (Contd.)	W (Contd.)	SUPERSONIC	$C_{L_\delta} = \left(1 - \underbrace{\frac{C_2}{C_1}}_{6.1.4.1}\phi_{TE}\right)\underbrace{C'_{L_\delta}}_{6.1.4.1}\frac{S_f}{S_W}$
$(C_{L_\alpha})_\delta$	W	SUBSONIC	$(C_{L_\alpha})_\delta = \underbrace{(C_{L_\alpha})_{\delta=0}}_{4.1.3.2}$ (same as for unflapped wings)
			$(C_{L_\alpha})_\delta = \left[\left(\frac{c'}{c} - 1\right)\frac{S_{W_f}}{S_W}\right]\underbrace{(C_{L_\alpha})_{\delta=0}}_{4.1.3.2} + \underbrace{(C_{L_\alpha})_{\delta=0}}_{4.1.3.2}$
			$C_{L_\alpha} = \underbrace{(C_{L_\alpha})_\delta}_{6.1.4.2}\left\{\left[\underbrace{K(A_t, C'_J)}_{6.1.4.2} - 1\right]\underbrace{K_b}_{6.1.4.1} + 1.0\right\} + \frac{C_J(\cos\overbrace{\delta_{leff}}^{6.1.4.1} - 1)}{57.3}$

DERIVATIVE ESTIMATION for components indicated)	METHOD LIMITATIONS ASSOCIATED WITH EQUATION COMPONENTS
Eq. 6.1.4.1-f C'_{L_δ}	1. Leading and trailing edges of the control surface are swept ahead of Mach lines from the deflected controls 2. Control root and tip chords are parallel to the plane of symmetry 3. Controls are located either at the wing tip or far enough inboard so that the outermost Mach lines from the deflected controls do not cross the wing tip 4. Innermost Mach lines from deflected controls do not cross the wing root chord 5. Wing planform has leading edges swept ahead of Mach lines and has streamwise tips 6. Controls are not influenced by tip conical flow from the opposite wing panel or by the interaction of the wing-root Mach cone with the wing tip 7. Symmetric, straight-sided flaps
$(C_{L_\alpha})_{\delta=0}$	1. Nontranslating leading- and trailing-edge flaps 2. No separated flow on wings and flaps 3. No curved planforms 4. $M \leq 0.80$, $t/c \leq 0.1$, if cranked planform with round L
Eq. 6.1.4.2-a $(C_{L_\alpha})_{\delta=0}$	1. Translating leading- and trailing-edge flaps 2. No separated flow on wings and flaps 3. No curved planforms 4. $M \leq 0.80$, $t/c \leq 0.1$, if cranked planform with round L
6.1.4.1 $\frac{\overbrace{\cos \delta_{\text{hinge}}} - 1)}{57.3}$ Eq. 6.1.4.2-b $(C_{l_\alpha})_\delta$	1. Jet flaps 2. $A \geq 5$ 3. No separated flow on wings and flaps 4. No curved planforms 5. $M \leq 0.80$, $t/c \leq 0.1$, if cranked planform with round LE

DERIVATIVE	CONFIG.	SPEED REGIME	EQUATIONS FOR DERIVATIV (Datcom section for compon
$\Delta C_{L_{max}}$	W	SUBSONIC	$\Delta C_{L_{max}} = \underbrace{\Delta c_{\ell_{max}}}_{6.1.1.3} \frac{S_{W_f}}{S_W} \underbrace{K_\Lambda}_{6.1.4.3}$
			$\Delta C_{L_{max}} = 1.28 \left(\frac{c_f/c}{0.18}\right)\left(\frac{b_{slat}}{b_e}\right)^2 \cos^2 \Lambda_{c/4}$
			Figure 6.1.4.3-12
ΔC_m	W	SUBSONIC	$\Delta C_{m_f} = \underbrace{\Delta C_m}_{6.1.5.1} + \underbrace{K_\Lambda}_{6.1.5.1}\left(\frac{A}{1.5}\right)\underbrace{\Delta C_L}_{6.1.4.1} \tan \Lambda_{c/4}$
			$\Delta C_{m_f} = \int_0^{1.0} -\left[\underbrace{c_{\ell_\Lambda}}_{6.1.5.1} \frac{c}{c_{av}} \underbrace{\left(\frac{x}{\bar{c}}\right)}_{6.1.5.1}\right] d\eta$
			$\Delta C_m \left[\underbrace{c_{m_{\delta'_{LE}}}}_{6.1.2.1}\left(\frac{\bar{c}'}{c}\right)+\left(\frac{x_m}{\bar{c}}-\frac{x_{LE}}{\bar{c}}\right)\underbrace{c'_{\ell_\delta}}_{6.1.1.1}\right]\frac{S_{W_f}}{S_W}\delta_f + \left\{\underbrace{C_m}_{\text{test data}}\left[\left(\right.\right.\right.$
			$\Delta C_m = \underbrace{C_{m_m}}_{6.1.5.1} + \underbrace{\eta_t}_{6.1.4.3} \overbrace{C_J}^{6.1.4.1} \underbrace{\frac{\Delta z}{\bar{c}}}_{6.1.5.1} + \sum_{k=1}^{p}\left\{\left[\underbrace{C_\mu}_{6.1.5.1} \overbrace{\frac{\alpha_L}{57.3}}^{6.1.5.1}\right.\right.$
C_{m_δ}	W	TRANSONIC	$C_{m_\delta} = \underbrace{-C_{L_\delta}}_{6.1.4.1} \underbrace{\left(\frac{x}{\bar{c}}\right)}_{6.1.5.1}$

THODS SUMMARY

R DERIVATIVE ESTIMATION)n for components indicated)	METHOD LIMITATIONS ASSOCIATED WITH EQUATION COMPONENTS
Eq. 6.1.4.3-a	1. Mechanical trailing-edge flaps
Eq. 6.1.4.3-b	1. Slats (first-order approximation)
	1. First-order approximation for EBF configuration
Eq. 6.1.5.1-a	1. Linear-lift range 2. $\Lambda_{c/4} < 45^{o}$. ΔC_L (depends upon type of flap) 3. Mechanical flaps 4. Straight-tapered wings
Eq. 6.1.5.1-k	1. Linear aerodynamic control characteristic region C_{ℓ_Λ} (depends upon type of flap) $x/\bar{c}$ 2. Linear-lift range 3. Subcritical Mach numbers
$+\left\{\underbrace{C_m}_{\text{test data}}\left[\left(\frac{\bar{c}'}{c}\right)^2-1\right]+0.75\ \underbrace{C_L}_{\text{test data}}\left(\frac{\bar{c}'}{c}\right)\left(\frac{\bar{c}'-c}{c}\right)\right\}\Delta\eta$ Eq. 6.1.5.1-ℓ	1. Mechanical leading-edge devices 2. Constant flap-chord-to-wing-chord ratio 3. Thin-airfoil theory
$\left[\underbrace{C_\mu}_{6.1.5.1}\ \overbrace{\frac{\alpha_L}{57.3}}^{6.1.5.1}\ \overbrace{\frac{S_K}{S_W}}^{6.1.5.1}-\underbrace{C_{\lambda_k}}_{6.1.5.1}\right]\underbrace{\frac{\Delta x_k}{\bar{c}}}_{6.1.5.1}\Bigg\}$ Eq. 6.1.5.1-u	1. Jet flaps (first approximation for multislotted flap 2. Linearized thin-airfoil theory 3. No trailing-edge separation 4. No augmentor-wing concept 5. Not valid for low values of C_μ
Eq. 6.1.5.1-w	1. Linear aerodynamic control characteristic region C_{L_δ} 2. Straight-tapered wings 3. Plain trailing-edge flaps with sealed gap 4. No beveled trailing edges 5. $\beta A \geq 2$ 6. $\Lambda_\ell < 60^{o}$ 7. Symmetric airfoils with conventional thickness distribution 8. No compressibility effects 9. $\alpha = 0$

DERIVATIVE	CONFIG.	SPEED REGIME	EQUATIONS FOR DERIVATIVE EST (Datcom section for components in
C_{m_δ} (Contd)	W (Contd.)	SUPERSONIC	$C_{m_\delta} = \underbrace{K_1}_{6.1.5.1} \frac{1}{3} \frac{b_1}{\bar{c}} \frac{c_{r_1}}{S_W} \underbrace{C'_{m_\delta}}_{6.1.5.1} \underbrace{K_2}_{6.1.5.1} \frac{1}{2} \frac{b_f}{\bar{c}} \frac{S_f}{S_W} \underbrace{C'_{l_\delta}}_{6.2.1.1} \underbrace{K_3}_{6.1.5.1}$
C_{h_α}	W	SUBSONIC	$C_{h_\alpha} = \frac{A \cos \Lambda_{c/4}}{A + 2 \cos \Lambda_{c/4}} \underbrace{\left(c_{h_\alpha}\right)_{\text{balance}}}_{6.1.3.1} + \underbrace{\Delta C_{h_\alpha}}_{6.1.6.1}$
		TRANSONIC	(No method)
		SUPERSONIC	$\left(C_{h_\alpha}\right)_{t/c} = \left(1 - \underbrace{\frac{C_2}{C_1}}_{6.1.6.1} \phi_{TE}\right) \underbrace{\left(C_{h_\alpha}\right)_{t/c=0}}_{6.1.6.1}$

HODS SUMMARY

DERIVATIVE ESTIMATION (for components indicated)		METHOD LIMITATIONS ASSOCIATED WITH EQUATION COMPONENTS
$\underbrace{C'_{l_\delta}}_{2.1.1} - \underbrace{K_3}_{6.1.5.1} \frac{x_f}{\bar{c}} \frac{S_f}{S_w} \underbrace{C'_{L_\delta}}_{6.1.4.1}$	Eq 6.1.5.1-q	1. Linear aerodynamic control characteristic region 2. Symmetric straight-sided controls 3. Leading and trailing edges of the control surface are swept ahead of Mach lines from the deflected controls. 4. Control root and tip chords are parallel to the plane of symmetry 5. Controls are located either at the wing tip or far enough inboard so that outermost Mach lines from the deflected controls do not cross the wing tip 6. Innermost Mach lines from deflected controls do not cross the wing root chord 7. Wing planform has leading edges swept ahead of Mach lines and has streamwise tips 8. Controls are not influenced by tip conical flow from the opposite wing panel or by the interaction of the wing-root Mach cone with the wing tip. C'_{l_δ} 9. Plain trailing-edge flaps 10. Thin wings
	Eq. 6.1.6.1-a	1. High aspect ratios ($A > 3$) 2. Ends of control surfaces parallel to plane of symmetry 3. Neglects subcritical Mach-number effects 4. Sealed, plain trailing-edge controls c_{h_α} 5. No separated flow 6. Low speeds
	Eq. 6.1.6.1-b	1. Symmetric, straight-sided controls 2. Control root and tip chords are parallel to the plane of symmetry 3. Wing planform has leading edges swept ahead of Mach lines and has streamwise tips 4. Controls are not influenced by tip conical flow from the opposite wing panel or by interaction of the wing-root Mach cone with the wing tip.

DERIVATIVE	CONFIG.	SPEED REGIME	EQUATIONS FOR DERIVAT (Datcom section for compo
C_{h_α} (Contd)	W (Contd.)	SUPERSONIC (Contd.)	$(C_{h_\alpha})_{t/c} = \left\{1 - \frac{\overbrace{2C_2\left(\frac{t}{c}\right)'}^{6.1.6.1}}{\underbrace{3C_1(1+k)}_{6.1.6.1}\cos(\Lambda_{LE} - \Lambda_{HL})}\right\} 2\left[1 + 2\right($
C_{h_δ}	W	SUBSONIC	$C_{h_\delta} = \cos\Lambda_{c/4}\cos\Lambda_{HL}\left[\underbrace{(c_{h_\delta})_{balance}}_{6.1.3.2} + \underbrace{\alpha_\delta}_{6.1.1.1}\underbrace{(c_{h_\alpha})_{balance}}_{6.1.3.1}\right.$
		TRANSONIC	(No method)
		SUPERSONIC	$C_{h_\delta} = \frac{1}{\beta}\left(1 - \underbrace{\frac{C_2}{C_1}}_{6.1.6.2}\phi_{TE}\right)\beta\ \underbrace{C'_{h_\delta}}_{6.1.6.2}$
			$C_{h_\delta} = \frac{1}{\beta}\left\{1 - \frac{4}{3}\underbrace{\frac{C_2}{C_1}}_{6.1.6.2}\left(\frac{t}{c}\right)'\left[1 + 2\left(\frac{x_h}{c}\right)'\right]\right\}\beta\ \underbrace{C'_{h_\delta}}_{6.1.6.2}$

SUMMARY

IVE ESTIMATION nents indicated)	METHOD LIMITATIONS ASSOCIATED WITH EQUATION COMPONENTS
$\left(\frac{x_h}{c}\right)'\Big] \underbrace{-k\left[1 - \left(\frac{x_h}{c}\right)'\right]^2\Big\}}_{6.1.6.1} \underbrace{\left(C_{h_\alpha}\right)_{t/c\,=\,0}}_{6.1.6.1}$ Eq. 6.1.6.1-b with different correction factor	1. Symmetric biconvex airfoil 2. Other limitations identical to Items 2 through 4 immediately above
$\frac{2\cos\Lambda_{c/4}}{A + 2\cos\Lambda_{c/4}}\Big] + \underbrace{\Delta C_{h_\delta}}_{6.1.6.2}$ Eq. 6.1.6.2-a c_{h_δ}	1. High aspect ratios ($A > 3$) 2. Ends of control surfaces parallel to plane of symmetry 3. Neglects subcritical Mach-number effects 4. Sealed, plain trailing-edge flaps 5. No separated flow 6. Low speeds
Eq. 6.1.6.2-b	1. Symmetric, straight-sided controls 2. Leading and trailing edges of the control surface are swept ahead of Mach lines from the deflected controls 3. Control root and tip chords are parallel to the plane of symmetry 4. Controls are located either at the wing tip or far enough inboard so that outermost Mach lines from deflected controls do not cross the wing tip 5. Innermost Mach lines from deflected controls do not cross the wing root chord 6. The wing planform has leading edges swept ahead of Mach lines and has streamwise tips 7. Controls are not influenced by tip conical flow from the opposite wing panel or by interaction of the wing-root Mach cone with the wing tip
Eq. 6.1.6.2-b with different correction factor	1. Symmetric biconvex airfoil 2. Other limitations identical to Items 2 through 7 immediately above

DERIVATIVE	CONFIG.	SPEED REGIME	EQUATIONS FOR DERIVATIVE EST (Datcom section for components inc
C_D	W	SUBSONIC	$C_{D_i} = \frac{\pi A}{m+1}\left[\underset{6.1.7}{G_k} \left\{ \underset{6.1.7}{b_{kk}} \underset{6.1.7}{G_k} - \sum_{n=1}^{k} (1 - \delta_{vn}) \underset{6.1.7}{B_{kn}} \underset{6.1.7}{G_n} \right\} + 2 \sum_{v=1}^{k-1} \underset{6.1.7}{G_v} \left\{ \underset{6.1.7}{b_{vv}} \underset{6.1.7}{G_v} - \sum_{n=1}^{k} (1 - \delta_{vn}) \underset{6.1.7}{B_{vn}} \underset{6.1.7}{G_n} \right\} \sin$
			$\Delta C_{D_{min}} = \underbrace{\Delta c_{d_f}}_{6.1.7} \underbrace{K_b}_{6.1.4.1} + \underbrace{K'}_{6.1.7} \frac{\overbrace{(\Delta C_{L_f})^2}^{6.1.4.1}}{\pi A}$
		TRANSONIC	(No method)
		SUPERSONIC	$\Delta C_{D_{wave}} = \left[\underbrace{\frac{C_{D_{wave}}}{(C_{D_{wave}})_{\delta=0}}}_{6.1.7} - 1 \right] \underbrace{(C_{D_{wave}})_{\delta=0}}_{4.1.5.1}$
C_{l_δ}	W	SUBSONIC	$C_{l_\delta} = \underbrace{\lvert \alpha_\delta \rvert}_{6.1.1.1} \underbrace{C'_{l_\delta}}_{6.2.1.1}$
			$C_l = \underbrace{\frac{C'_{l_\delta}}{2}}_{6.2.1.1} \underbrace{\Delta\alpha'_s}_{6.1.1.1}$
			$(C_l)_{\text{spoiler-slot-deflector}} = \underbrace{K}_{6.2.1.1} \underbrace{(C_l)_{\text{plain spoiler}}}_{6.2.1.1}$

DS SUMMARY

IVATIVE ESTIMATION omponents indicated)		METHOD LIMITATIONS ASSOCIATED WITH EQUATION COMPONENTS
$G_n\}$ 6.1.7		1. No separated flow over control surface 2. Induced drag due to control deflection G_k, G_n, G_v (depends upon type of flap)
B_{vn} $G_n\}$ sin ϕ_v] 6.1.7 6.1.7	Eq. 6.1.7-c	
	Eq. 6.1.7-p	1. No separated flow over control surface 2. Profile drag due to control deflection ΔC_{L_f} (depends upon type of flap)
	Eq. 6.1.7-q	
	Eq. 6.2.1.1-b	1. Plain trailing-edge flaps 2. $\beta A \geq 2$ 3. $\Lambda_\beta < 60°$ 4. $M \leq 0.6$ 5. No separated flow α_δ 6. No beveled trailing edges 7. No compressibility effects
	Eq. 6.2.1.1-c	1. Plug or flap-type spoilers 2. No separated flow C'_{l_δ} 3. Other limitations identical to Items 1 through 4 immediately above
	Eq. 6.2.1.1-f	1. Spoiler-slot-deflector 2. $\beta A \geq 2$ 3. $\Lambda_\beta < 60°$ 4. $M \leq 0.6$ 5. No separated flow $(C_l)_{\text{plain spoiler}}$ 6. Plain flap-type spoiler

DERIVATIVE	CONFIG.	SPEED REGIME	EQUATIONS FOR DERIVATIV (Datcom section for compone
C_{l_δ} (Contd)	W (Contd.)	TRANSONIC	$C_{l_\delta} = \underbrace{(C_{l_\delta})_{M=0.6}}_{6.2.1.1} \underbrace{\frac{C_{L_\alpha}}{(C_{L_\alpha})_{M=0.6}}}_{4.1.3.2}$
		SUPERSONIC	$C_{l_\delta} = \underbrace{\left(1 - \frac{C_2}{C_1}\phi_{TE}\right)}_{6.2.1.1} \underbrace{C'_{L_\delta}}_{6.1.4.1} \frac{S_f}{S_W} \frac{1}{2}\left[\frac{y_i}{b_W} + \left(\frac{b_f}{2b_W}\right)\underbrace{\frac{C_{}}{C'_{}}}_{6.1.}\right.$ 6.2.
			Figure 6.2.1.1-30
		SUBSONIC	$C_{l_\delta} = \frac{1}{2}\left[\left(1 - \frac{\pi A_W}{57.3}\underbrace{\frac{\partial\bar{\epsilon}}{\partial\alpha}}_{4.4.1}\right) + \underbrace{i_{v_{B(H)}}}_{4.3.1.3}\underbrace{\left(\frac{\Gamma}{2\pi\alpha\, Vr}\right)}_{4.3.1.3}\left(\frac{r}{b_{H_e}/2}\right)\right]\underbrace{\eta\left(}_{6.2.1}$

'HODS SUMMARY

ː DERIVATIVE ESTIMATION ɪn for components indicated)		METHOD LIMITATIONS ASSOCIATED WITH EQUATION COMPONENTS
	Eq. 6.2.1.1-g	$(C_l)_{M=0.6}$ (depends upon type of control) C_{L_α} 1. Symmetric airfoils of conventional thickness distribution 2. $A \leq 3$ if composite wing 3. $\alpha = 0$ $\left(C_{L_\alpha}\right)_{M=0.6}$ 4. No curved planform 5. $t/c \leq 0.10$, if cranked planform with round LE
$\left(\frac{b_f}{2b_w}\right)\left[\frac{\overbrace{C'_{l_\delta}}^{6.2.1.1}}{\underbrace{C'_{L_\delta}}_{6.1.4.1}}\right]$	Eq. 6.2.1.1-h	1. Plain trailing-edge flaps 2. Leading (hinge line) and trailing edges of control surfaces are supersonic (swept ahead of Mach lines) 3. Control surfaces are located at wing tip or far enough inboard to prevent outermost Mach lines from control surfaces from crossing wing tip 4. Innermost Mach lines from deflected control surfaces do not cross root chord 5. Root and tip chords of control surfaces are streamwise 6. Controls are not influenced by tip conical flow from opposite wing panel or by interaction of wing-root Mach cone with the wing tip C'_{l_δ} 7. Thin wings C'_{L_δ} 8. Symmetric, straight-sided controls
		1. Plug or flap-type spoilers
$\left.\frac{r}{{}^{y}H_e/2}\right)\Big]\underbrace{\eta\left(\frac{q_H}{q}\right)}_{6.2.1.2}\frac{\bar{y}_H}{b_w}\frac{S_{H_e}}{S_w}\underbrace{\left(C_{L_{\alpha_H}}\right)_e}_{4.1.3.2}$	Eq. 6.2.1.2-a	1. Differentially deflected horizontal stabilizer 2. Horizontal tail mounted on body 3. No separated flow on horizontal tail $\frac{\partial\bar{\epsilon}}{\partial\alpha}$ 4. Straight-tapered wing 5. Other limitations depend upon $\frac{\partial\bar{\epsilon}}{\partial\alpha}$ prediction method $\left(C_{L_{\alpha_H}}\right)_e$ 6. No curved planforms 7. $M \leq 0.8$, $t/c \leq 0.10$, if cranked planform with round LE

DERIVATIVE	CONFIG.	SPEED REGIME	EQUATIONS FOR DERIVATIVE ESTIM (Datcom section for components indic
C_{l_δ} (Contd.)	T (Contd.)	TRANSONIC	(Same as subsonic equation)
			(Same as supersonic equation)
		SUPERSONIC	$C_{l_\delta} = 0.35 \left[\underbrace{i_{v_{B(H)}}}_{4.3.1.3} \underbrace{\left(\frac{\Gamma}{2\pi\alpha\ Vr}\right)}_{4.3.1.3} \left(\frac{r}{b_{H_e}/2}\right) + \underbrace{\left(k_{H(B)} + k_{B(H)}\right)}_{4.3.1.2} \right] \underbrace{\left(C_{N_{\alpha_H}}\right)_e}_{4.1.3.2}$
C_n	W	SUBSONIC	$C_n = \underbrace{K}_{6.2.2.1}\ C_L\ \underbrace{C_{l_\delta}}_{6.2.1.1}\ \frac{(\delta_L - \delta_R)}{2}$
			Figures 6.2.2.1-10, 6.2.2.1-11
			$(C_n)_{\text{spoiler-slot-deflector}} = \underbrace{K}_{6.2.2.1}\ \underbrace{(C_n)_{\text{plain spoiler}}}_{6.2.2.1}$

THODS SUMMARY

R DERIVATIVE ESTIMATION on for components indicated)		METHOD LIMITATIONS ASSOCIATED WITH EQUATION COMPONENTS
		1. Differentially deflected horizontal stabilizer 2. $M < 1.0$ 3. Body-mounted horizontal tail 4. No separated flow on horizontal tail $\frac{\partial \bar{\epsilon}}{\partial \alpha}$ 5. Straight-tapered wing 6. Proportional to C_{L_α} $\left(C_{L_{\alpha_H}}\right)_e$ 7. Symmetric airfoils of conventional thickness distribution 8. $A \leq 3$ if composite wing 9. $\alpha = 0$
		1. $M > 1.0$ (Same limitations as for $M < 1.0$ above except those of $\partial\bar{\epsilon}/\partial\alpha$)
$\underbrace{\left(\quad + k_{B(H)}\right)}_{4.3.1.2}\Big] \underbrace{\left(C_{N_{\alpha_H}}\right)_e}_{4.1.3.2} \frac{\bar{y}_H S_{H_e}}{b_W S_W}$	Eq. 6.2.1.2-c	1. Differentially deflected horizontal stabilizer 2. Body-mounted horizontal tail 3. No separated flow on horizontal tail $\left(C_{N_{\alpha_H}}\right)_e$ 4. Breaks in LE and TE at same spanwise station 5. $M \geq 1.4$ for straight-tapered planforms 6. $1.2 \leq M \leq 3$ for double-delta planforms 7. $1.0 \leq M \leq 3$ for curved planforms
	Eq. 6.2.2.1-a	1. Aileron-type controls 2. No separated flow 3. Neglects contributions due to profile drag C_{l_δ} 4. $\beta A \geq 2$ 5. $\Lambda_\beta < 60°$ 6. No beveled TE 7. No compressibility effect 8. $M \leq 0.6$
		1. Plug and flap-type spoilers 2. $0.02 \leq \delta_s/c \leq 0.10$ 3. $\alpha = 0$
	Eq. 6.2.2.1-b	1. Spoiler-slot-deflector 2. $\alpha = 0$ 3. $\delta_s/\delta_d = 1.0$ $(C_n)_{\text{plain spoiler}}$ 4. Plain, flap-type spoiler

DERIVATIVE	CONFIG.	SPEED REGIME	EQUATIONS FOR DERIVATIV (Datcom section for compone
C_n (Contd.)	W (Contd.)	TRANSONIC	$C_n = \underbrace{(C_n)_{M=0.6}}_{6.2.2.1} \; \underbrace{\frac{C_{L_\alpha}}{(C_{L_\alpha})_{M=0.6}}}_{4.1.3.2}$
		SUPERSONIC	Figure 6.2.2.1-13 Figure 6.2.2.1-14
C_{n_δ}	T	ALL SPEEDS	(No method)

ETHODS SUMMARY

FOR DERIVATIVE ESTIMATION ection for components indicated)	METHOD LIMITATIONS ASSOCIATED WITH EQUATION COMPONENTS
Eq. 6.2.2.1-c	$(C_n)_{M=0.6}$ 1. Aileron-type controls 2. $\beta A \geq 2$ 3. $\Lambda_\beta < 60^\circ$ 4. No beveled TE 5. No separated flow 6. No compressibility effects 7. Neglects contributions due to profile drag $\left(C_{L_\alpha}\right)_{M=0.6}$ 8. Straight-tapered wings C_{L_α} 9. Symmetric airfoils of conventional thickness distribution 10. $\alpha = 0$
	1. Aileron-type controls 2. Neglects contributions due to profile drag
	1. Plug and flap-type spoilers

2.1 GENERAL NOTATION

A complete summary and definition of all notation used in the Datcom is given in this section. The summary is divided into upper and lower case English, upper and lower case Greek, derivatives, and abbreviations. In all cases a general alphabetical listing is used. Throughout the Datcom units are in pounds, feet, seconds, and degrees unless otherwise specified.

A. ENGLISH SYMBOLS

SYMBOL	DEFINITION	SECTIONS
A	aspect ratio of surface, based on total planform, $\frac{b^2}{S}$	Several
A', A''	aspect ratios of forward and aft surfaces, respectively	4.5.1.1 7.4.1.1 7.4.4.1
$\bar{A}$	transonic aspect-ratio similarity parameter, $A\left(\frac{t}{c}\right)^{1/3}$	4.1.4.2
A_D	duct aspect ratio, $\frac{d_e}{c}$	9.3 9.3.1 9.3.2 9.3.3
A_H	aspect ratio of auxiliary horizontal surface, aft tail or canard, $\frac{b_H^2}{S_H}$	Several
A_{H_e}	aspect ratio of exposed horizontal tail	6.2.1.2
$A_H e_H$	effective aspect ratio of horizontal stabilizer	4.5.3.2
A_I	inlet duct area for jet engine	4.6 4.6.1 4.6.3
A_{U_e}	aspect ratio of exposed lower vertical panel	Several
$(A)_V$	geometric aspect ratio of isolated vertical panel, with span and area of panel measured to body center line	Several
A_{V_e}	aspect ratio of exposed upper vertical panel	Several
$(A)_{V(B)}$	aspect ratio of vertical panel in presence of body	Several

SYMBOL	DEFINITION	SECTIONS
$(A)_{V(HB)}$	vertical-panel aspect ratio in presence of horizontal tail and body	Several
A_W	aspect ratio of wing	Several
A_{bw}	aspect ratio of the basic wing	Several
A_e	aspect ratio of exposed (panels joined together) surface, $\frac{b_e^2}{S_e}$	Several
A'_e, A''_e	aspect ratios of forward and aft exposed surfaces, respectively	4.4.1 4.5.1.1 4.5.1.2 7.4.1.1
A_{eff}	1. effective aspect ratio of surface as determined by tip flow separation	4.4.1 5.3.1.1 5.6.1.1
	2. effective aspect ratio of the vertical panel	Several
A'_{eff}	effective aspect ratio of forward surface as determined by tip flow separation	4.5.1.1
$(A_e)_i$	aspect ratio of exposed inboard panels of wing	4.3.2.2
A_f	aspect ratio of flap or control surface, $\frac{b_f^2}{S_f}$	6.1.6.1 6.1.6.2 6.2.1.1
A_g	aspect ratio of glove of a double-delta or a cranked wing	4.1.3.2 5.1.2.1
A_i	1. aspect ratio of that portion of main surface immersed in propeller slipstream, $\frac{b_i}{c_i}$	4.6 4.6.1
	2. aspect ratio of planform formed by the two inboard panels of wing	Several
A_o	aspect ratio of planform formed by the two outboard panels of wing	4.1.5.1 4.1.5.2
A'_o	aspect ratio of planform formed by the two constructed outboard panels of wing	4.1.4.2 4.3.2.2 5.1.2.1
A_s	aspect ratio of a particular spanwise wing section	6.1.5.1
A_t	1. aspect ratio of wing based on total wing area, including flap extension	6.1.4.1 6.1.4.2
	2. aspect ratio of total wing based on extended wing chord, using the particular section value for the chord	6.1.5.1
A_1, A_2	aspect ratio of constructed panels of non-straight-tapered wings	4.1.3.2
a	1. difference in lift-curve slope, or $(C_{L_\alpha}$ at $M_{fb}) - (C_{L_\alpha}$ at $M_a)$	4.1.3.2
	2. $\frac{\tan \Lambda_{HL}}{\beta}$	6.1.6.1

SYMBOL	DEFINITION	SECTIONS
	3. distance from the quarter-chord point of the MAC of the horizontal tail to the plane of tip vortex cores	4.4.1 4.5.1.1 7.4.4.1
	4. major axis of elliptical-body cross section	4.2.1.2 4.2.2.2 4.2.3.1 4.2.3.2
	5. propeller inflow factor	4.6 4.6.4
	6. forward diameter of a cone frustum	4.2.2.1
	7. linear acceleration	8.1
	8. nose diameter of forebody or base diameter of afterbody	4.2.3.1
	9. speed of sound	6.3.2
a_t	speed of sound at nozzle throat	6.3.2
a_0	blade section lift-curve slope	9.1
$a_1, a_2, a_3, \ldots$	diameter at forward end of given body segment	Several
a.c.	aerodynamic center of wing	Several
$(a.c.)_V$	aerodynamic center of the vertical panel	5.3.3.1
B	1. $\sqrt{1 - M^2 \cos^2 \Lambda_{c/4}}$	Several
	2. parameter accounting for changes in circulation	4.7 4.7.1
	3. number of propeller blades	9.1 9.1.1 9.1.3
B_{kn}	parameter in span-loading calculation	6.1.7
B_{vn}	parameter in span-loading calculation	6.1.7
$B_0, B_1, \ldots B_{15}$	drag-due-to-lift regression coefficients	4.3.3.2
B_2	parameter accounting for effect of control-surface and balance-chord ratios on hinge-moment derivative	6.1.6.1 6.1.6.2
b	1. difference in lift-curve slope, or $(C_{L_\alpha} \text{ at } M_{fb}) - (C_{L_\alpha} \text{ at } M_b)$	4.1.3.2
	2. surface span	Several

SYMBOL	DEFINITION	SECTIONS
	3. minor axis of elliptical-body cross section	4.2.1.2 4.2.2.2 4.2.3.1 4.2.3.2
	4. span of slot nozzle (normal to flow direction)	6.3.2
b'	propeller blade chord	9.1 9.1.1 9.1.3
b', b''	total spans of forward and aft surfaces, respectively	Several
$\bar{b}'$	average blade chord	9.1 9.1.1
b_E	span of trailing-edge extension of double-delta and cranked wings	4.1.3.2
b_H	total span of auxiliary horizontal surface, aft tail or canard	Several
b_{H_e}	total span of exposed horizontal tail	6.2.1.2
b_U	span of vertical panel below body center line	Several
b_{U_e}	span of exposed lower vertical panel	Several
b_V	1. span of vertical panel extended to body center line	Several
	2. span of vertical panel for twin vertical panels	5.3.1.1 5.6.1.1
b'_V	partial span of vertical panel for twin vertical panels (see Figure 5.3.1.1-24b)	4.5.1.1 4.5.1.2 5.3.1.1 5.6.1.1
b_{V_e}	span of exposed vertical panel	Several
b_{V_I}	span of vertical stabilizer (tip to fuselage)	Several
b_W	span of wing	Several
b'_W	effective span for unflapped wing	4.7 4.7.1
b_{bw}	span of basic wing	4.1.3.2 4.1.5.1 4.3.3.1 5.1.2.1

SYMBOL	DEFINITION	SECTIONS
b_e	total span of exposed surface	Several
b'_e, b''_e	total spans of exposed forward and aft surfaces, respectively	7.4.1.1
$(b_e)_i$, $(b)_e$	total span of exposed inboard panels of wing	4.3.2.2 4.3.3.1
b_{eff}	effective surface span	4.7 4.7.1 4.4.1
b'_{eff}	effective forward-surface span	4.5.1.1 7.4.1.1
b_f	total span of flaps or control surfaces, measured normal to the plane of symmetry	Several
b'_f	effective span for increment in load due to flaps	4.7 4.7.1
b_g	span of glove of double-delta and cranked wings	4.1.3.2 5.1.2.1
b_i	1. span of planform formed by two inboard panels	2.2.2 4.1.4.2 4.1.5.1 5.1.2.1
	2. total span of a given portion of main surface immersed in propeller slipstream, $2\sqrt{R_p^2 - (z_s + z_w)^2}$	4.6 4.6.1 4.6.3
b_{kk}	parameter in span-loading calculation	6.1.7
b_{max}	minor semiaxis of body cross section	4.2.3.1
b_o	span of planform formed by joining two outboard panels of wing	Several
b'_o	span of planform formed by joining two constructed outboard panels of wing	4.1.4.2 4.3.2.2 5.1.2.1
b_p	propeller blade width at any propeller span station	4.6 4.6.1
b_s	span of spoiler, on one wing panel	6.2.1.1 6.2.2.1
b_{slat}	total span of slats	6.1.4.3
b_v	span of the wing-tip vortices at a given longitudinal station behind a lifting surface	4.4.1 4.5.1.1 7.4.4.1

SYMBOL	DEFINITION	SECTIONS
b'_v, b''_v	vortex spans at the forward and aft surfaces, respectively	Several
b_{vn}	parameter in span-loading calculation	6.1.7
b_{vv}	parameter in span-loading calculation	6.1.7
$b_{v_{ru}}$	span of completely rolled up wing-tip vortices (at distances far downstream from lifting surface)	4.4.1 7.4.4.1
b_1, b_2	span of constructed panels of non-straight-tapered wings	4.1.3.2
b_1, b_2, b_3	vertical span of a given region as defined in Sketch (b) in Section 5.3.1.1	5.3.1.1 5.3.1.2
$b'_{.25,\ .50,\ \ldots}$	propeller blade chord at $\frac{r}{R} = 0.25, 0.50, \ldots$	9.1 9.1.1 9.1.3
$b/(2\ell)$, $\frac{b_W}{2\ell}$	wing slenderness parameter	Several
C	1. thickness correction factor for supersonic wing lift	4.1.3.3 4.1.3.4
	2. roll-moment-of-inertia correction factor for solid component	8.2
$(C_{LE})_{bw}$	leading-edge effect of basic wing on normal-force-curve slope	4.1.3.2
$(C_{LE})_g$	leading-edge effect of glove on normal-force-curve slope	4.1.3.2 4.1.3.4
C_a, C_b, C_c	wing parameters measured to plane of symmetry (see Figure 8.1-22)	8.1
C_0, C_1, ... C_{18}	regression coefficients as a function of Mach number	4.3.2.1
C_1, C_2	1. empirical taper-ratio constants	Several
	2. empirical constants that determine propeller downwash gradients	4.6 4.6.1 4.6.4
	3. Mach-number functions that determine thickness correction factors to supersonic flat-plate aerodynamic derivatives, $C_1 = \frac{2}{\sqrt{M^2 - 1}}$ $C_2 = \frac{(\gamma + 1) M^4 - 4 (M^2 - 1)}{2 (M^2 - 1)^2}$	Several
C_3	1. taper-ratio correction factor for wing aerodynamic center	4.1.4.3
	2. maximum lift-correction factor at transonic speeds	4.1.3.4

SYMBOL.	DEFINITION	SECTIONS
c	1. transonic wing lift-curve slope at M_{fb}	4.1.3.2
	2. chord of airfoil section	Several
	3. duct chord	9.3 9.3.1 9.3.2 9.3.3
	4. nozzle discharge coefficient	6.3.2
c'	1. effective chord of airfoil with deflected extensible-type flap (see Figures 6.1.1.1-44, -45, -46, -48, -51, and 6.1.5.1-60	Several
	2. airfoil chord measured perpendicular to the wing quarter-chord line	6.1.6.1 6.1.6.2
$\bar{c}$, $\bar{c}_W$	wing mean aerodynamic chord	Several
$\bar{c}'$	mean aerodynamic chord of the wing segment affected by the leading-edge device (see Sketch (h), Section 6.1.5.1)	6.1.5.1
$\bar{c}'$, $\bar{c}''$	mean aerodynamic chords of forward and aft surfaces, respectively	Several
c_B	chord at break span station	2.2.2 4.1.3.2 4.1.3.3
$\bar{c}_H$	mean aerodynamic chord of auxiliary horizontal surface, aft tail or canard	4.4.1 4.6 4.6.1 7.4.2.2
$\bar{c}_{H_e}$	mean aerodynamic chord of exposed horizontal-tail panel	4.5.3.1
c'_{LE}	airfoil chord with only leading-edge device extended	6.1.2.1 6.1.5.1
c_V	vertical tail chord at the distance z_H above body center line (see Figure 5.3.1.1-22b)	Several
$\bar{c}_{V_e}$	mean aerodynamic chord of exposed vertical-tail panel	4.5.3.1
$\bar{c}_{W_e}$	mean aerodynamic chord of exposed wing	4.5.3.1
c_a	hypothetical airfoil chord including trailing-edge flap extension and subtracting leading-edge flap extension	6.1.2.1 6.1.5.1
c'_a	extended wing chord due to complete forward-flap extension (see Figures 6.1.1.1-45, -46)	6.1.1.1
$\bar{c}_{\text{area not immersed}}$	mean aerodynamic chord of the wing area not immersed in the slipstream	4.6 4.6.3
c_{av}	average chord of airfoil	6.1.5.1
c_b	balance chord of a control or flap surface	6.1.3.1 6.1.3.2 6.1.6.1 6.1.6.2
c'_b	balance chord of control or flap surface measured perpendicular to the wing quarter-chord line	6.1.6.1

SYMBOL	DEFINITION	SECTIONS
c_{b_t}	chord of tab balance	6.1.3.1 6.1.3.2 6.1.3.3 6.1.3.4
c_{bw}	chord of basic wing	4.1.5.1 4.3.3.1
$\bar{c}_c$	mean aerodynamic chord of a particular control surface	6.3.4
$c_{c.p.}$	wing chord at spanwise center-of-pressure location	6.1.5.1
$\bar{c}_e$	1. mean aerodynamic chord of exposed panel	Several
	2. mean aerodynamic chord of elevator	6.3.4
$\bar{c}'_e$, $\bar{c}''_e$	mean aerodynamic chords of exposed forward and aft surfaces, respectively	7.4.1.1 7.4.1.2 7.4.4.1 7.4.4.2
c_f	flap or control chord measured parallel to plane of symmetry	Several
c'_f	flap or control chord measured perpendicular to the wing quarter-chord line	6.1.6.1
$\bar{c}_f$	mean flap chord	6.1.7
c_{f_i}	chord of a particular segment of a flap of n segments	6.1.2.1 6.1.5.1
$c_{f_{inc}}$	incompressible turbulent flat-plate skin-friction coefficient	4.2.3.1
$c_{f_{LE}}$	chord of the leading-edge flap	6 1.2.1 6.1.5.1
c_{f_r}	root chord of flap or control surface measured parallel to plane of symmetry	6.1.6.1
c_{f_t}	tip chord of flap or control surface measured parallel to plane of symmetry	6.1.6.1
c_{f_1}, c_{f_2}, c_{f_3}	effective chords of combined flap segments as defined by the principle of superposition, shown in Sketch (g), Section 6.1.2.1	6.1.2.1
$c_{f_{\perp LE}}$	chord of leading-edge flap perpendicular to leading edge of airfoil	6.1.5.1
c_i	average chord of that portion of wing immersed in propeller slipstream	4.6 4.6.1 4.6.3
$\bar{c}_i$	mean aerodynamic chord of inboard panel of wing	4.1.5.1 4.1.5.2
$(\bar{c}_i)_e$, $(\bar{c}_o)_e$	mean aerodynamic chords of exposed inboard and outboard panels, respectively, of wing	4.3.3.1
$\bar{c}_{i_H}$	mean aerodynamic chord of that portion of auxiliary surface immersed in propeller slipstream	4.6.3
$\bar{c}_o$	mean aerodynamic chord of outboard panel of wing	4.1.5.1 4.1.5.2 4.3.3.1
$\bar{c}_{p_e}$	mean aerodynamic chord of exposed tail panel	4.5.3.1
c_r	surface root chord	Several

SYMBOL	DEFINITION	SECTIONS
c_r', c_r''	root chords of forward and aft surfaces, respectively	4.5.2.1 7.4.1.1
c_{r_B}	root chord of basic triangular wing (see Sketch (a), Section 7.1.1.1)	5.1.3.1 7.1.1.1 7.1.4.2
$c_{r_{bw}}$	root chord of basic wing of double-delta and cranked wings	4.1.5.1 4.3.3.1 5.1.2.1
c_{r_E}	root chord of trailing edge extension of double-delta and cranked wings	4.1.3.2
c_{r_e}	root chord of exposed surface	Several
c'_{r_e}, c''_{r_e}	root chords of exposed forward and aft surfaces, respectively	4.5.1.2 7.4.1.1
$(c_{r_e})_H$	root chord of exposed horizontal surface	5.3.1.2
$(c_{r_e})_i$	root chord of exposed inboard panels of wing	4.3.2.2
c_{r_f}	root chord of control surface	6.1.5.1
c_{r_g}	root chord of glove of double-delta and cranked wings	4.1.3.2 5.1.2.1
c_{r_H}	root chord of horizontal stabilizer	8.1
c_{r_i}	root chord of inboard panel of wing	4.1.4.2 4.1.5.1 4.3.2.2
$(c_{r_i})_e$	root chord of inboard panel (exposed) of wing	4.3.3.1
c_{r_o}	root chord of outboard panel of wing	4.1.4.2 4.1.5.1 4.3.3.1
c'_{r_o}	root chord of constructed outboard panel of wing	4.1.4.2 4.3.2.2
c_{r_V}	root chord of vertical stabilizer (at fuselage)	8.1
c_{r_W}	root chord of wing	Several
c_{r_1}, c_{r_2}	root chords of constructed panel of non-straight-tapered wings	4.1.3.2
c_s	chord of spoiler	6.2.1.1 6.2.2.1
c_t	1. tip chord of surface	Several
	2. chord of tab, aft of hinge line	6.1.3.1 6.1.3.2 6.1.3.3 6.1.3.4
$\bar{c}_{tc}$	mean aerodynamic chord of control tab	6.3.4
$(c_{t_e})_i$	tip chord of exposed inboard panels of wing	4.3.2.2

SYMBOL	DEFINITION	SECTIONS
c_{t_H}	tip chord of horizontal stabilizer	8.1
c_{t_i}	tip chord of inboard panel of wing	4.1.4.2 4.3.3.1
c_{t_o}	tip chord of outboard panel of wing	4.1.4.2 4.3.2.2
c_{t_V}	tip chord of vertical stabilizer	8.1
c_{t_W}	tip chord of wing	4.1.3.2 5.1.2.1
$c_{\delta\delta}$	extended wing chord due to deflection of leading-edge and trailing-edge flaps (see Sketch (f), Section 6.1.2.1)	6.1.2.1 6.1.5.1
$(c')_{\eta_i}, (c')_{\eta_o}$	effective chords of airfoil with deflected extensible-type flap, at the inboard and outboard edge, respectively, of the flap	6.1.5.1
c_1, c_2	chords of forward and aft flaps, respectively, of a double-slotted flap	6.1.1.1
c_1, c_2, c_3	intersecting flap chord segments that approximate the mean-camber-line distribution of the flap components (see Sketch (e), Section 6.1.2.1)	6.1.2.1 6.1.5.1
$\Delta c_1, \Delta c_2, \Delta c_4, \Delta c_6$	terms analogous to section lift coefficients used in calculating section pitching moments	6.1.2.1 6.1.5.1
$\Delta c_{5_1}, \Delta c_{5_2}, \Delta c_{5_i}$	terms analogous to section lift coefficients for the first, second, and i^{th} trailing-edge flap segments, respectively	6.1.2.1 6.1.5.1
c_1'	flap chord of the forward-flap segment; i.e., for a broken trailing edge the forward-flap segment is extended to form a complete airfoil (see Figure 6.1.1.1-46)	6.1.1.1
$(\bar{c}/4)_V$	the quarter-chord point of the MAC of the vertical panel extending to body center line	Several
$(\bar{c}/2)_{V_e}$	50-percent-chord point of the MAC of exposed vertical panel	5.3.2.1 5.3.3.1
$(\bar{c}/4)_W$	the quarter-chord point of the MAC of the total wing	Several
D	1. total drag	2.1 4.7
	2. empirical factor used in calculating wing lift at high angles of attack	4.1.3.3
	3. diameter of a hemisphere	8.2
	4. propeller diameter	Several
	5. drag force	4.1.3
D′	base diameter of spherical-segment shell	8.2
D_o	body diameter	4.6.4
D_1'	nozzle-exit diameter	4.6.4
d	1. maximum fuselage diameter	Several
	2. $\frac{\tan \Lambda_{TE}}{\beta}$	6.1.6.1

SYMBOL	DEFINITION	SECTIONS
	3. average maximum diameter of fuselage	8.1
	4. outside diameter of a hollow cylindrical element	8.2
	5. equivalent-cylinder diameter for a hemisphere	8.2
	6. base diameter of a spherical nose segment or given frustum	4.2.2.1 4.2.3.1 7.2.1.1 7.2.1.2
	7. average body diameter at the exposed wing root	Several
	8. maximum diameter of forebody or afterbody	4.2.3.1
	9. 2/3 root chord of basic triangular wing	7.1.1.1 7.1.1.2 7.1.4.2
	10. maximum body height at wing-body intersection	5.2.1.1
d', d''	body diameters at the midchord points of the MAC of the forward and aft surfaces, respectively	4.4.1 4.5.1.1 4.5.1.2 7.4.1.1
d_{CB}	duct center-body diameter at exit plane	9.3 9.3.1 9.3.2 9.3.3
d_H	average fuselage width in region of horizontal tail	6.2.1.2
d_{LE}	diameter of leading edge	6.3.1 6.3.2
d_a	diameter at forward end of missile component	8.2
d_b	1. base diameter of body	Several
	2. diameter at aft end of missile component	8.2
	3. base diameter of jet nozzle	4.6.4
$(d_b)_{equiv}$	equivalent base diameter of a non-body-of-revolution configuration	4.2.3.1
d_{cyl}	diameter of cylinder	4.2.1.2 4.2.2.1
d_e	1. average maximum diameter of engine	8.1
	2. exit diameter of duct or nozzle	Several
d_{equiv}	equivalent diameter of a non-body-of-revolution configuration	4.2.1.2 4.2.3.1
$(d_{equiv})_{av}$	average equivalent diameter of non-body-of-revolution configuration	5.2.2.1
d_j	diameter of nozzle exit	4.6.4
d_{max}	maximum diameter of body	4.3.3.1 4.5.3.1

SYMBOL	DEFINITION	SECTIONS
d_n	base diameter of one of n segments of a body	4.2.3.1
d_o	1. base diameter of a spherically blunted body nose	4.2.3.1
	2. theoretical effect of blowing on lift derivative	6.1.4.1
d_p	diameter of ducted propeller	9.3 9.3.1
d_s	diameter of sphere for spherically blunted body noses	Several
d_t	width of nozzle throat	6.3.2
d_0	inside diameter of a hollow cylindrical element	8.2
d_1	upstream pressure interaction length	6.3.1
d_2	downstream interaction length	6.3.1
d_3	distance from reference line to point of intersection of two lines tangent to pressure curve (see Sketch (d), Page 6.3.1-9)	6.3.1
$d_1, d_2, d_3 \ldots$	diameter at aft end of given body segment	Several
$\frac{d}{b}$	ratio of maximum body width to wing span	4.3.2.1
E	empirical constant used in calculating wing lift at high angles of attack	4.1.3.3 4.1.3.4
$E''(\beta C)$	elliptical integral factors of the stability derivative	Several
e	1. Oswald (span) efficiency factor for induced drag	Several
	2. value of error	Several
e^*	induced span efficiency factor (inviscid)	4.1.5.2
e_H	Oswald (span) efficiency factor for induced drag of horizontal stabilizer	4.5.3.2
F	1. general force	4.1.3 8.1
	2. resultant force	4.7 9.2
F_c	1. control force	6.3.2
	2. control-column force (pull force positive)	6.3.4
F_{j_0}	vacuum thrust	6.3.2
F_p	rudder-pedal force (push on left pedal positive)	6.3.4
F_s	elevator stick force (pull force positive)	6.3.4
F_x	1. propeller-wing combination negative-drag force	9.2
	2. duct negative-drag force	9.3

SYMBOL	DEFINITION	SECTIONS
$F_w(\lvert y_{i,o} \rvert)$, $F_w(Y_{i,o})$, $F_{w,o}$	functions used to determine w	4.4.1
$F_1(N)$, $F_2(N)$, $F_3(N)$, $F_4(N)$, $F_5(N)$, $F_6(N)$, $F_7(N)$, $F_8(N)$, $F_9(N)$, $F_{11}(N)$	F(N) factors of the stability derivative	Several
F/T	thrust-recovery factor	9.2 9.2.1 9.2.3
f	1. fineness ratio of body	Several
	2. inflow factor of propeller	4.6 4.6.1
f_A	fineness ratio of body minus the nose	Several
f_C	fineness ratio of cylindrical segment of body	4.2.3.2
f_N	1. fineness ratio of body nose	Several
	2. fineness ratio of body nose and forebody	4.3.2.2
f_{N_o}	fineness ratio of spherically blunted cone extended to cone apex	4.2.3.1
f_b	fineness ratio of boattail	4.2.2.1
$(f)_{equiv}$	equivalent fineness ratio (see Equation 4.3.2.1-d)	4.3.2.2
f_f, $(f)_{forebody}$	fineness ratio of body forebody (see Sketch (a), Section 4.3.2.1)	4.3.2.2
f_{fus}	fineness ratio of fuselage	4.3.3.1
f_n, $(f)_{nose}$	fineness ratio of nose	4.3.2.2
G_c	main-control-surface stick gearing	6.3.4
$G_{c_{max}}$	maximum control-surface stick gearing	6.3.4
$G_{e_{max}}$	maximum elevator stick gearing	6.3.4
G_k, G_n, G_v	span-loading coefficients at spanwise stations k, n, and v, respectively	6.1.7
G_{tc}	control-tab stick gearing	6.3.4
$G(\beta C)$	elliptical integral factors of the stability derivative	7.1.1.1 7.1.1.2 7.1.4.1 7.1.4.2
$\frac{G}{\delta}$	subsonic spanwise loading coefficient	6.1.5.1 6.1.7
$\Delta \frac{G}{\delta}$	increment in spanwise loading coefficient	6.1.5.1

SYMBOL	DEFINITION	SECTIONS
$\left(\frac{G}{\delta}\right)_v$	spanwise-loading coefficient at spanwise station v	6.1.7
$\left(\frac{G}{\delta}\right)_{\eta_i}, \left(\frac{G}{\delta}\right)_{\eta_o}$	spanwise loading coefficient at inboard and outboard ends, respectively, of a flap	6.1.5.1
g	$\frac{\tan \Lambda_{LE}}{\beta}$	6.1.6.1
g', g''	distances parallel to the plane of symmetry from panel apex to the forward end of the MAC of forward and aft panels, respectively	4.5.2.1
H	height of the quarter-chord point of the MAC of the wing above the ground plane	4.7 4.7.1 4.7.4
H_c	hinge moment of main control surface	6.3.4
H_H	height of the quarter-chord point of the MAC of the auxiliary horizontal surface above the ground plane	4.7 4.7.1
H_{tc}	hinge moment of control tab	6.3.4
h	1. average height of fuselage at the wing root chord	5.2.2.1 5.2.3.1 5.6.2.1 5.6.3.1
	2. downward displacement of trailing-vortex sheet from $z = 0$ plane (in this application $z = 0$ is chosen at the quarter-chord point of the MAC of the forward surface)	4.4.1 7.4.4.1
	3. altitude	4.6 4.6.1
	4. maximum height of sonic line above surface (effective jet height)	6.3.2
	5. average height above the ground of the quarter-chord point of wing chord of 75-percent semispan and the three-quarter-chord point of the wing root chord (see sketch on Figure 4.7.1-14)	4.7 4.7.1
h_H	height of aft-surface MAC quarter-chord point above or below the forward-surface root chord, measured in plane of symmetry normal to extended-forward-surface root chord, positive for the aft-surface MAC above the plane of the root chord	Several
$h_{c_r/4}$	height of the quarter-chord point of the wing root chord above the ground	4.7 4.7.1
h_d	distance of deflector lip below surface of wing, perpendicular to wing chord plane	6.2.1.1
h_s	1. distance of spoiler lip above surface of wing, measured from and normal to the airfoil mean line	6.1.1.1 6.2.1.1 6.2.2.1
	2. maximum height of separated boundary layer above the surface	6.3.2
h_v	distance of wing vortex above horizontal tail at tail center of pressure, measured normal to body axis	4.4.1

SYMBOL	DEFINITION	SECTIONS
h_1, h_2	fuselage depths as defined in Figure 5.2.3.1-8	5.2.3.1 5.6.3.1
$\frac{h}{d}$	ratio of maximum canopy height measured from body centerline to body height at the point of maximum canopy height	4.3.2.1
I	moment of inertia (see Figure 8.1-22)	8.1
I_{oy}	moment of inertia about centroidal axis of section	8.1
I_{oy}, I_{ox}, I_{oz}	pitching, rolling, and yawing moments of inertia, respectively, about the centroidal axis of the body	8.1
I_{sp}	jet vacuum specific impulse	6.3.2
$I_{v_{B(H)}}$	vortex interference factor for a lifting surface mounted on the body center line	6.2.1.2
$I_{v_{B(W)}}$	interference factor for effect of body vortex on horizontal panel	4.3.1.3 4.3.1.4
$I_{v_{B(W')}}, I_{v_{B(W'')}}$	interference factors for effects of body vortex on fore and aft panels, respectively	4.5.1.2
$I_{v_{W'(W'')}}$	interference factor for effect of forward panel vortex on aft panel	4.4.1 4.5.1.1 4.5.1.2 7.4.1.1
I_{xx}, I_{yy}, I_{zz}	moments of inertia of the vehicle about x-x axis, y-y axis, and z-z axis, respectively	8.2
$I_{xx}', I_{yy}', I_{zz}'$	moments of inertia of body component about x-x axis, y-y axis, and z-z axis, respectively	8.2
I_y, I_x, I_z	pitching, rolling, and yawing moments of inertia, respectively, about a remote axis	8.1
1	a particular segment of a trailing-edge flap of n segments	6.1.2.1 6.1.5.1
i', i''	angles of incidence of forward and aft surfaces, respectively	4.5.1.2 4.6.1 7.4.1.1
i_H	incidence of auxiliary horizontal surface, aft tail or canard, positive nose up	4.6 4.6.1 4.6.3 4.7.1
i_T	incidence of thrust axis, positive nose up	4.6 4.6.1 4.6.4
i_W	incidence of main surface, positive nose up	Several
Δi_v	total body vortices interference factor	5.3.1.2 5.6.1.2
i_{v_1}, i_{v_2}	body vortex interference factors	5.3.1.2 5.6.1.2

SYMBOL	DEFINITION	SECTIONS
J	1. empirical factor for estimating the lift of wings at high angles of attack	4.1.3.3 4.5.1.2
	2. ducted-propeller advance ratio, $\frac{V_\infty}{nd_p}$	9.3 9.3.1 9.3.2 9.3.3
	3. propeller advance ratio, $\frac{V_\infty}{nD}$	9.1 9.1.1 9.1.3 9.2
	4. jet momentum at the wing trailing edge, $m_j V_j$	6.1.1.1 6.1.4.1
J′	modified advance ratio, J cos α	9.1 9.1.1 9.1.3
J_{0_P}	advance ratio at zero power	9.1 9.1.3
J_{0_T}	advance ratio at zero thrust	9.1 9.1.1 9.1.3
j	one section of a wing of n sections having constant sweep angles within its boundary	4.1.3.2
K	1. factor used to estimate the maximum lift increment of a surface due to propeller power effects	4.6 4.6.2
	2. ratio of rolling-moment coefficient of a spoiler-slot-deflector to that of a plain spoiler	6.2.1.1
	3. parameter accounting for effective wing thickness	4.7 4.7.1
	4. factor accounting for the lift carry-over due to flap deflection on wing sections adjacent to flaps at subsonic speeds	6.1.5.1
	5. factor used to estimate the pitching effectiveness of trailing-edge flaps at transonic speeds	6.1.5.1
	6. surface-element pressure-coefficient constant	4.2.1.2 4.2.2.2
	7. apparent-mass factor	Several
	8. upstream amplification factor (control force normal to the surface normalized with respect to vacuum thrust of sonic nozzle)	6.3.2
	9. pitching-moment-of-inertia correction factor for solid component	8.2
	10. drag-due-to-lift factor	4.1.5.2
	11. ratio of extended wing chord, including extensions of both leading-edge and trailing-edge flaps, to retracted wing chord, $K = c_{\delta\delta}/c$	6.1.2.1
	12. theoretical correction factor for finite aspect-ratio effects on $c_{\ell_{\delta_f}}$, as defined in Equation 6.1.5.1-p	6.1.5.1

SYMBOL	DEFINITION	SECTIONS
	13. constant factor for a given sharp-nosed airfoil section	4.1.5.1 4.3.3.1
	14. empirical correlation factor corresponding to lift-interference factor K_L	4.1.3.2
	15. empirical correlation factor depending upon planform geometry	6.2.2.1
	16. ratio of yawing-moment coefficient of spoiler-slot-deflector to that of a plain spoiler	6.2.2.1
	17. dimensionless correction factor used to extrapolate the potential-flow values to high lift coefficients	7.1.2.1 7.1.2.3
	18. number of propellers	9.2 9.2.1 9.2.3
K'	1. effective apparent-mass factor	Several
	2. flap-span factor	6.1.7
	3. empirical correction factor to section lift increment for nonlinear effects at high flap deflections	Several
K_A	wing-aspect-ratio factor	4.4.1 6.2.1.2
$K_{B(W)}$	ratio of the lift of the body in the presence of the wing to that of the wing alone	Several
K_D	propeller drag factor	4.6 4.6.4
K_H	1. factor accounting for relative size of horizontal and vertical tails	Several
	2. horizontal-tail-location factor	4.4.1 6.2.1.2
$K_{H(B)}$	apparent-mass factor of the horizontal tail in the presence of the body	Several
K_L	1. lift-interference factor for normal-force-curve slope	4.1.3.2 5.1.2.1
	2. pitch-moment-of-inertia correction factor for liquid mass	8.2
K_{M_Γ}	compressibility correction to the dihedral effect used in estimating C_{l_β}	5.1.2.1 5.2.2.1 5.6.2.1
K_{M_Λ}	compressibility correction to the sweep contribution used in estimating C_{l_β}	5.1.2.1 5.2.2.1 5.6.2.1
$K_{M_{\Lambda_i}}$, $K_{M_{\Lambda'_o}}$	compressibility correction to sweep contribution used in estimating C_{l_β} for constructed inboard and outboard panels, respectively, of a composite wing	5.1.2.1

SYMBOL	DEFINITION	SECTIONS
K_N	1. ratio of body-nose lift to that of wing alone	4.3.1.2 4.3.1.3 4.3.1.4 4.5.1.2
	2. propeller normal-force factor	4.6 4.6.1
	3. correlation factor for pressure drag of ogive noses	4.2.3.1 4.3.3.1 4.5.3.1
	4. empirical factor related to sideslip derivative C_{n_β} for body and wing-body interference	5.2.3.1 5.6.3.1
K_{R_ℓ}	empirical Reynolds-number factor	5.2.3.1
$K_{V(B)}$	apparent-mass factor of the upper vertical panel in the presence of the body	Several
$K_{V(BHU)}$	apparent-mass factor of the upper vertical panel in the presence of the body, horizontal tail, and lower vertical panel	Several
$K_{V(BU)}$	apparent-mass factor of the upper vertical panel in the presence of the body and lower vertical panel	Several
$K_{V(BW)}$	apparent-mass factor of the upper vertical panel in the presence of the body and wing	5.3.1.1
$K_{V(BWH)}$	apparent-mass factor of the upper vertical panel in the presence of the body, wing, and horizontal tail	Several
$K_{W(B)}$	1. ratio of the lift of the wing in the presence of the body to that of the wing alone	Several
	2. apparent-mass factor of the wing in the presence of the body	Several
$K_{(WB)}$	ratio of the lift of the wing-body combination to that of the wing alone	4.3.1.2 7.3.1.1 7.3.1.2 7.3.4.2
K_N', $K_{W(B)}'$, $K_{B(W)}'$	appropriate wing-body interference factors for the forward surface	Several
$K_{W(B)}''$, $K_{B(W)}''$	appropriate wing-body interference factors for the aft surface	Several
K_b	factor used in estimating the lift effectiveness of flaps and control surfaces at subsonic speeds	6.1.4.1 6.1.4.2 6.1.5.1 6.1.7
K_{b_k}, $K_{b_{k-1}}$	values of the span factor for outboard and inboard ends, respectively, of the k^{th} wing section	6.1.5.1
$(K_b)_{\eta_i}$, $(K_b)_{\eta_o}$	value of K_b due to a flap extending from the plane of symmetry to the inboard and outboard span stations, respectively, of the actual flap	6.1.4.1 6.1.4.2
K_f	factor used in estimating the body contribution to wing-body C_{l_β}	5.2.2.1 5.6.2.1
K_i	factor used to estimate the body contribution to wing-body C_{Y_β}	5.2.1.1 5.6.1.1
K_m	empirical nonlinear pitching-moment factor	4.1.4.3

SYMBOL	DEFINITION	SECTIONS
K_n	1. factor used to estimate the body contribution to wing-body C_{n_β}	5.2.3.1
	2. Knudsen number	4.2.3.1
K_o	upstream amplification factor of normal sonic nozzle	6.3.2
K_p	1. potential-flow lift parameter	4.2.1.2
	2. conversion factor for a partial-span flap on a sweptback wing	6.1.5.1
$(K_p)_{\eta_i}, (K_p)_{\eta_o}$	value of K_p due to a flap extending from the plane of symmetry to the inboard and outboard span stations, respectively, of the actual flap	6.1.5.1
K_t	hypersonic similarity parameter, $M\frac{t}{c}$, for a wing	4.1.5.1
K_v	viscous-flow lift parameter	4.2.1.2
K_α	factor accounting for the effect of control-surface span in the estimation of the parameter C_{h_α}	6.1.6.1
K_δ	factor accounting for the effect of control-surface span in the estimation of the parameter C_{h_δ}	6.1.6.2
K_θ	pressure-surface slope integral	4.2.1.2 4.2.2.2
K_Λ	1. empirically derived correction factor accounting for the effects of the wing planform	6.1.4.3
	2. flap-span factor	6.1.5.1
$(K_\Lambda)_{\eta_i}, (K_\Lambda)_{\eta_o}$	value of K_Λ due to a flap extending from the plane of symmetry to the inboard and outboard span stations, respectively, of the actual flap	6.1.5.1
K_λ	wing-taper-ratio factor	4.4.1 6.2.1.2
K_{ϕ_U}	cross-coupling interference factor of lower vertical surface	5.3.1.2 5.6.1.2
K_{ϕ_V}	cross-coupling interference factor of upper vertical surface	5.3.1.2 5.6.1.2
K_1	factor accounting for the effect of nacelles and fuselage on wing lift due to power effects	4.6 4.6.1
K_1, K_2, K_3	Mach-number functions used in determining supersonic flap pitching effectiveness	6.1.5.1
$K_1, K_2, K_3, \ldots$	empirical factors used in calculating moments of inertia	8.1
$K_1, K_2, \ldots K_{12}$	geometric and Mach-number parameters used in supersonic hinge-moment-derivation calculations (Page 6.1.6.1-7)	6.1.6.1
$K(A_1, C_J')$	correction factor for blown flaps as a function of jet momentum and aspect ratio	6.1.4.2
k	1. surface-roughness height	Several
	2. factor used in estimating supersonic parameter C_{h_α}	6.1.6.1
	3. the number of the wing section, numbered from fuselage center line outboard	6.1.5.1

SYMBOL	DEFINITION	SECTIONS
	4. empirical factor used in estimating sideslip derivative C_{Y_β}	Several
	5. spanwise station, $\frac{m+1}{2}$	6.1.7
	6. factor used in determining the a.c. location of wing-lift carryover on the body, d/b	4.3.2.2
	7. tab spring effectiveness	6.3.4
$k_{B(H)}$, $k_{H(B)}$	tail-body interference factors	6.2.1.2
$k_{B(W)}$	ratio of lift-curve slope of body in presence of wing to that of wing alone, fuselage at zero angle of attack and wing incidence varying	4.2.1.1 4.3.1.2 4.3.1.3
$k_{W(B)}$	ratio of lift-curve slope of wing in presence of body to that of wing alone, fuselage at zero angle of attack and wing incidence varying	4.3.1.2 4.3.1.3
$k_{W(B)}'$, $k_{B(W)}'$, $k_{W(B)}''$, $k_{B(W)}''$	wing-body interference factors for the forward and aft panels, respectively	4.5.1.2
k_t	airfoil-theory thickness factor	6.1.1.1 6.1.1.2 6.1.4.1
k_1, k_2, k_3	empirical factors used in determining the maximum lift increment due to flap deflection	6.1.1.3 6.1.4.3
$(k_2 - k_1)$	apparent mass factor used in determining the subsonic lift and moment of bodies	Several
$k(\alpha)$	angle-of-attack correction to the horizontal-tail-body interference coefficient	5.2.1.2 5.3.1.2
L	1. general lift force	4.1.2 4.7
	2. equivalent-cylinder length for a hemisphere	8.2
	3. duct lift force, $L = C_L q_\infty S_D$	9.3 9.3.1 9.3.2
	4. airfoil-thickness-location parameter	4.1.5.1 4.3.3.1 4.5.3.1 7.4.2.2
	5. reference length	6.3.1
	6. distance of nozzle from plate leading edge	6.3.2
$L_{.75}$	left-blade position at 3/4-radius point	9.1 9.1.3
$\frac{L}{L_o} - 1$	parameter accounting for effect of image bound vortex on lift	4.7 4.7.1
$(LER)_i$, $(LER)_o$	leading-edge radius of the inboard and outboard panels, respectively, of a wing	4.1.5.2
$\frac{LER}{\bar{c}}$	ratio of leading-edge radius to mean aerodynamic chord taken at the mean aerodynamic chord	4.3.2.1

SYMBOL	DEFINITION	SECTIONS
ℓ	1. reference length	Several
	2. over-all length from wing apex to most aft point on the trailing edge	2.2.2 4.1.3.2 4.1.5.2 4.3.3.2
	3. control-surface linkage arm (see Sketch (f), Section 6.3.4)	6.3.4
ℓ''	distance parallel to longitudinal axis between quarter-chord point of MAC of total forward panel and quarter-chord point of MAC of total aft horizontal panel	Several
ℓ_A	1. length of body minus nose	Several
	2. length of afterbody (see Sketch (a), Section 4.3.3.2)	4.3.2.1 4.3.3.2
	3. length of the boattail segment of a jet nozzle	4.6.4
ℓ_B	1. total length of body	Several
	2. total length of body used as reference length in place of $\bar{c}$	7.2.1.1 7.2.1.2 7.2.2.1 7.2.2.2
	3. length of ogive-cylinder or cone-cylinder segment of body	4.2.2.1
ℓ_C	length of cylindrical segment of a body	4.2.1.1 4.2.1.2 4.2.3.1 4.2.3.2
ℓ_E	length of nozzle past afterbody	4.6.4
ℓ_F	length of flare	4.2.3.2
ℓ_H	1. longitudinal distance from quarter-chord point of the MAC of main surface to quarter-chord point of the MAC of the auxiliary horizontal surface, positive for auxiliary surface behind main surface	Several
	2. distance to the center of pressure of a horizontal stabilizer, measured parallel to the body center line, from the moment reference center	5.6.3.1
	3. distance from the moment reference center to the center of pressure of a horizontal-tail interference side force, measured parallel to the body center line	5.3.3.2 5.6.3.2
ℓ_N	1. length of body nose	Several
	2. length of body nose and forebody	4.3.2.1 4.3.2.2 4.3.3.2
ℓ_{N_o}	length of spherically blunted cone extended to cone apex	4.2.3.1
ℓ_U	distance to the center of pressure of the lower vertical stabilizer (ventral) measured parallel to the body center line, from the moment reference center	Several
ℓ_V	distance to the center of pressure of the upper vertical stabilizer, measured parallel to the body center line, from the moment reference center	Several
$\bar{\ell}_{W(B)}$	distance to center of pressure of the wing-induced body side force measured from the body nose, defined by Equations 5.2.3.2-c, -d	5.2.3.2
ℓ_a, ℓ_b	longitudinal distances from Z-axis to beginning and end stations of body component, respectively	8.2
ℓ_b	length of boattail	4.2.2.1
$\ell_{c.g.}$	longitudinal distance from beginning station of body component to the center of gravity of the component	8.2

SYMBOL	DEFINITION	SECTIONS
ℓ_e	length of engine including propeller	8.1
ℓ_{eff}	distance measured parallel to the forward-surface root chord, between the effective-forward-surface tip quarter chord point and the aft-surface MAC quarter-chord point	4.4.1 4.5.1.1 7.4.4.1
ℓ_{equiv}	length of equivalent body nose, f_{equiv} d	4.3.2.2
ℓ_f	1. longitudinal distance from nose of body to midpoint of wing tip	5.2.2.1 5.6.2.1
	2. length of body forebody	4.3.2.2
	3. length of control	6.3.1
ℓ_{f_i}	free interaction length	6.3.1
ℓ_h	distance from intersection of wing trailing edge with fuselage and the quarter-chord point of the MAC of the horizontal tail	4.2.2.1
ℓ_{r}	1. longitudinal distance from nose of body to exposed root chord of the wing	5.2.2.1 5.2.3.2
	2. length of body nose	4.3.2.2
ℓ_p	1. length of nacelle structure	8.1
	2. distance to the center of pressure of a panel in the empennage, measured parallel to the center line, from the moment reference center	Several
ℓ_s	separation length	6.3.1
ℓ_t	control-tab linkage arm (see Sketch (f), Section 6.3.4)	6.3.4
ℓ_x	distance from moment center to a transverse element, positive where element is forward of moment center	4.2.2.2
ℓ_0	distance from apex of forward-body theoretical cone to face of forward-body segment (see sketch, Page 7.2.1.1-5)	7.2.1.1 7.2.1.2
ℓ_1, ℓ_2	control-surface linkage arms (see Sketch (f), Section 6.3.4)	6.3.4
ℓ_1, ℓ_2, ℓ_3, ...	length of a given segment of a body	Several
ℓ_2	distance measured parallel to the forward-surface root chord, between the forward-surface root-chord aft end and the aft-surface MAC quarter-chord point	4.4.1 4.5.1.1 7.4.4.1
ℓ_3	distance measured parallel to the plane of symmetry, between the forward-surface MAC forward end and the root-chord aft end	4.4.1 4.5.1.1 7.4.4.1
M	1. Mach number	Several
	2. moment	2.1
	3. length of molecular mean tree path for rarefied gas	4.2.3.1
	4. duct pitching moment, $M = C_m q_\infty S_D c$	9.3 9.3.1

SYMBOL	DEFINITION	SECTIONS
ΔM	Mach-number increment	4.1.3.2
$(MAC)_{V_e}$	mean aerodynamic chord of exposed upper vertical panel	5.3.2.1
$M_{C_{D_{w_{peak}}}}{}_{\Lambda_{c/4} = n}$	Mach number for maximum wave-drag increment for swept wing with $\Lambda_{c/4} = n$	4.1.5.1 4.3.3.1 4.5.3.1
$M_{\Delta C_{D_{peak}}}$	Mach number for maximum wave-drag increment	4.1.5.1 4.3.3.1 4.5.3.1
$M_{\left(\frac{\partial C_D}{\partial M}\right)_{C_L = \text{const}} = 0.10}$	Mach number at which the numerical value of the slope of the curve of C_D vs M is 0.10	4.1.5.1
M_D	Mach number for drag divergence	4.1.5.1 4.2.3.1 4.3.3.1 4.5.3.1
$M_{D_{\Lambda_{c/4} = n}}$	Mach number for drag divergence for swept wing with $\Lambda_{c/4} = n$	4.1.5.1 4.3.3.1 4.5.3.1
M_I	initial drag-rise Mach number	4.5.3.1
M_N	Mach number determining if leading edge of wing is supersonic	4.1.5.1
M_a	1. Mach number used in estimating transonic lift-curve slope (see Page 4.1.3.2-13), $M_{fb} + .07$	4.1.3.2
	2. moment-area of a control surface about its hinge axis	6.1.6.1
M_b	Mach number used in estimating transonic lift-curve slope (see Page 4.1 3.2-13), $M_{fb} + .14$	4.1.3.2
M_c	1. Mach number normal to a circular cylinder in steady cross-flow, $M_\infty \sin \alpha$	4.2.1.2 4.2.2.2 4.2.3.2 4.3.3.2
	2. Mach number normal to a circular cylinder in steady cross-flow, $M_\infty \sin \alpha'$	5.2.1.2 5.3.1.2
	3. control-surface moment	6.3.4
M_{cr}	critical Mach number	7.1.1.2
M_e	nozzle-exit Mach number	6.3.2
M_{fb}	force-break Mach number	4.1.3.2 4.1.4.2 5.2.2.1 7.1.1.2
$(M_{fb})_\Lambda$	sweep correction for transonic force-break Mach number	4.1.3.2 4.1.4.2

SYMBOL	DEFINITION	SECTIONS
$(M_{fb})_{\Lambda=0}$	transonic force-break Mach number for zero sweep	4.1.3.2 4.1.4.2
M_o	slope of leading edge	4.4.1
M_p	propeller pitching moment	9.3.1
M_{tc}	tab-surface moment	6.3.4
M_α	local Mach number upstream of interaction	6.3.1
M_1	local Mach number	6.3.2
M_1'	Mach number at nozzle exit	4.6.4
M_∞	free-stream Mach number	Several
$M_\perp$	upstream Mach number normal to the leading edge of the wing	4.1.3.3
$(M_\perp)_{\alpha=0}$	upstream Mach number normal to the leading edge of wing at zero angle of attack	4.1.3.3
m	1. number of spanwise stations on full-span wing	6.1.7
	2. mass	8.1
	3. slope of lifting line	4.4.1
m, n	nondimensional chordwise stations in terms of c	2.2.2
$\dot{m}$	nozzle mass-flow rate	6.3.2
m_i	duct internal mass flow	9.3 9.3.1
m_j	mass flow rate of gas efflux (per section)	6.1.1.1
N	1. normal force	4.1.3
	2. propeller normal force	9.1
	3. ducted-propeller normal force	9.3 9.3.1
N_I	normal force acting at inlet of jet engine due to inclination of inlet to oncoming flow	4.6
N_p	propeller normal force	4.6 9.3.1
n	1. chordwise distance from the wing apex to the pitching-moment reference center measured in root chords, positive for reference center aft of apex	4.1.4 4.1.4.2 4.1.4.3
	2. chordwise distance from wing apex to moment reference center measured in wing mean aerodynamic chords, positive aft	4.7 4.7.3

SYMBOL	DEFINITION	SECTIONS
	3. number of engines	4.6 4.6.1
	4. nondimensional coordinate used in integration of wing-root and wing-tip conical pressures	6.1.6.1
	5. value of sweep angle	4.1.5.1
	6. distance from the face of a given body segment to the desired moment reference axis of the configuration	4.2.2.1 7.2.1.1 7.2.1.2
	7. spanwise station along wing	6.1.7
	8. propeller rotational speed, r.p.s.	9.1 9.3 9.3.1
	9. number of segments of trailing-edge flap	6.1.2.1 6.1.5.1
n'	load factor	4.6 4.6.4 6.3.4
n_i	distance of the desired moment reference center behind the forward face of any given body segment, positive for reference center aft of forward face	4.2.2.1
n_1, n_2	value of i at left- and right-hand wing tips of a swept wing, left and right as viewed from trailing edge to leading edge	4.4.1
P	pressure	6.3.1
P'	ratio of local pressure coefficient to two-dimensional pressure coefficient	6.1.6.1
P_P	plateau pressure	6.3.1
P_e	nozzle-exit pressure	6.3.2
P_o	pressure upstream of separation	6.3.1
P_s	separation pressure	6.3.1
P_α	local pressure upstream of interaction	6.3.1
P_{0_j}	jet plenum pressure	6.3.2
P_1	local pressure	6.3.2
P_2	1. pressure peak value	6.3.1
	2. plateau pressure	6.3.2
P_2'	upstream over-all pressure	6.3.2
P_3	pressure immediately downstream of a transverse jet	6.3.2
P_4	downstream over-all pressure	6.3.2

SYMBOL	DEFINITION	SECTIONS
P_∞	free-stream pressure	6.3.1 6.3.2
p	1. static pressure	Several
	2. cross-section perimeter	4.2.3.1
	3. planform-shape parameter, $S/(b\ell)$	2.2.2 4.1.3.2 4.1.5.2 4.3.3.2
	4. angular velocity in roll	Several
	5. total number of wing sections	6.1.5.1
Δp	static-pressure increment from ambient, $p - p_\infty$	4.6 4.6.1
P_{T_e}	total pressure at jet exit	4.6.1
p_b	base pressure	4.6.4
p_j	jet total pressure	4.6.4
p'_o	internal jet pressure	4.6.4
p_∞	free-stream ambient pressure	4.6.1 4.6.4
q	1. dynamic pressure	Several
	2. angular velocity in pitch	Several
q''	slipstream dynamic pressure	9.2
q_H	average dynamic pressure at an aft horizontal tail	Several
q_V	dynamic pressure at a vertical tail	7.4.2.1 7.4.2.2 7.4.2.3 8.1.2
q_p	average dynamic pressure acting on an aft panel	4.5.3.1
q_s	dynamic pressure in propeller slipstream	4.6
q_l	local dynamic pressure	6.3.2
q_∞	free-stream dynamic pressure	Several
q/p_t, $(q/p_t)_{rel}$	dynamic-pressure ratio for Prandtl-Meyer expansion	4.4.1
q/q_∞	average dynamic-pressure ratio	Several

SYMBOL	DEFINITION	SECTIONS
$\frac{q'}{q_\infty}$	average dynamic-pressure ratio acting on the forward surface	4.5.1.2
$\frac{q''}{q_\infty}$	average dynamic-pressure ratio acting on the aft surface	Several
$\frac{\Delta q}{q}$	dynamic-pressure-loss ratio for points not on the wake center line	4.4.1
$\frac{q_H}{q_\infty}$	effective dynamic-pressure ratio at horizontal tail	4.7 4.7.3
$\frac{\Delta q_H}{q_\infty}$	ratio of the change in dynamic pressure at the horizontal tail	4.6.3
$\frac{\Delta q_s}{q_\infty}$	ratio of the change from free-stream dynamic pressure to slipstream dynamic pressure to the free-stream dynamic pressure	4.6.1 4.6.3
$\left(\frac{\Delta q}{q}\right)_0$	dynamic-pressure-loss ratio at the wake center	4.4.1
R	1. Reynolds number	Several
	2. radial distance from thrust axis to centroid of incremental tail area	4.6.1
	3. reference radius of arbitrary body of revolution	4.2.1.2 4.2.2.2
	4. radius of hemisphere	8.2
	5. propeller radius	Several
	6. leading-edge-suction parameter defined as the ratio of the leading-edge suction actually attained to that theoretically possible	4.1.5.2 4.3.3.2
R'	leading-edge-suction parameter that accounts for the portion of the inboard panel submerged in the body	4.1.5.2
R_L	aerodynamic boost link ratio	6.3.4
$R_{L.S.}$	lifting-surface correlation factor	4.1.5.1 4.3.3.1 7.4.2.2
$(R_{L.S.})_H$	lifting-surface correlation factor of the horizontal-tail panel	4.5.3.1
$(R_{L.S.})_i$, $(R_{L.S.})_o$	lifting-surface correlation factor of the inboard panel and outboard panel, respectively, of the wing	4.3.3.1
$(R_{L.S.})_p$	lifting-surface correlation factor of the tail panel	4.5.3.1

SYMBOL	DEFINITION	SECTIONS
$(R_{L.S.})_V$	lifting-surface correlation factor of the vertical panel	4.5.3.1
$(R_{L.S.})_W$	lifting-surface correlation factor of the wing	4.5.3.1
R_{WB}	wing-body interference factor	4.3.3.1 4.5.3.1
R_b	base radius of body	4.6.4
R_{fus}	maximum fuselage radius forward of propeller plane	9.1 9.1.3
R_i, R_o	leading-edge suction parameter of inboard panel and outboard panel, respectively, of the wing	4.1.5.2
R_j	radius of jet exit	4.6 4.6.1
R'_j	radius of equivalent jet exit	4.6 4.6.1
R_ℓ	Reynolds number	Several
R_{ℓ_L}	Reynolds number based on length	6.3.2
$R_{\ell_{LER}}$	Reynolds number based on the leading-edge radius of the MAC	4.1.5.2 4.3.3.2
$\left(R_{\ell_{LER}}\right)_i$, $\left(R_{\ell_{LER}}\right)_o$	Reynolds numbers based on the leading-edge radius of the MAC of the inboard panel and outboard panel, respectively, of the wing	4.1.5.2
$R_{\ell_{MAC}}$, R_ℓ	Reynolds number based on the length of the mean aerodynamic chord	Several
$R_{\ell_{fus}}$	fuselage Reynolds number	4.3.3.1 4.5.3.1
R_{ℓ_s}	Reynolds number based on distance to the separation point	6.3.2
R_{ℓ_α}	local Reynolds number upstream of interaction	6.3.1 6.3.2
$R^*_{\ell_\alpha}$	reference Reynolds number upstream of interaction	6.3.1
$\left(R_{\ell_\alpha}\right)_{HL}$	Reynolds number at control hinge line, referred to local Reynolds number upstream of interaction	6.3.1

SYMBOL	DEFINITION	SECTIONS
$\left(R_{\ell_\alpha}\right)_{x_o}$	Reynolds number at the point of the beginning of interaction, referred to local Reynolds number upstream of interaction	6.3.1
$\left(R_{\ell_\alpha}\right)_{x_t}$	Reynolds number at transition point, referred to local Reynolds number upstream of interaction	6.3.1
R_{ℓ_∞}	free-stream Reynolds number	6.3.1 6.3.2
R_o	body radius	4.6.4
R_p	propeller radius	Several
R'_1	nozzle-exit radius	4.6.4
$R_{.75}$	right-blade position at 3/4-radius point	9.1 9.1.3
r	1. radius of base of body nose	4.3.1.3
	2. body radius at any station	Several
	3. radius of spherical nose segment	4.2.3.1
	4. body radius	4.3.1.2
	5. $\sqrt{1+\left(\frac{2h}{b}\right)^2}-\frac{2h}{b}$	4.7 4.7.1 4.7.4
	6. radius	8.1
	7. radial distance to propeller blade element	9.1 9.1.1 9.1.2 9.1.3
	8. angular velocity in yaw	Several
	9. average radius of body at vertical-tail exposed root chord	5.3.1.2
	10. average radius of body in the region of the horizontal tail	6.2.1.2
r'	nondimensional coordinate used in integrating wing-root and wing-tip conical pressures	6.1.6.1
r', r''	body radii at the midpoints of the exposed root chords of the forward and aft panels, respectively	4.1.5.2
$\bar{r}$	distance from the axis to the centroid of the total mass	8.1
$r_{LE_{bw}}$	leading-edge radius of basic wing	4.1.5.1 4.3.3.1
r_b	average radius of the body at the wing-body juncture	4.3.3.1
$(r)_{x_o}$	body radius at point where flow ceases to be potential	4.3.3.2

SYMBOL	DEFINITION	SECTIONS
r_1	1. radius of spherical body nose	4.2.1.1 7.2.1.1 7.2.1.2
	2. average body half-depth in the region of the tail panel(s), measured from center line	Several
r_2	average body half-width in the region of the tail panel(s), measured from center line	Several
$\frac{r}{b_W}$	ratio of body radius at exposed-wing-root quarter-chord point or midchord point of forward lifting surface to span of forward surface	4.3.1.3
$\frac{r'}{b'}$	ratio of body radius at root-quarter-chord point or midchord point of exposed forward lifting surface to span of forward surface	4.5.1.2
$\frac{r''}{b''}$	ratio of body radius at exposed-wing-root quarter-chord point at midchord point of aft lifting surface to span of aft surface	4.5.1.2
$(r_1/b)_U$	ratio of average body half-depth in the region of the lower vertical panel to span of lower vertical panel measured to body center line	Several
$(r_1/b)_V$	ratio of average body half-depth in region of the upper vertical panel to span of upper vertical panel measured to body center line	Several
$r_2 \Big/ \frac{b_H}{2}$	ratio of average body half-width in region of horizontal panel(s) to horizontal panel semispan	Several
S	1. cross-sectional reference area of the cylindrical portion of body	4.2.1.2 4.2.2.2
	2. cross-sectional area of body at any point x	4.3.3.1
	3. reference area	4.6 4.6.4 6.3.1
S, S_W	wing area	Several
S'	nose area of forebody or base area of afterbody	4.2.3.1
S', S''	gross planform areas of the forward and aft surfaces, respectively	Several
S_B	frontal area of body	Several
$(S_B)_{ref}$	body reference area	4.3.3.2 5.3.1.1
S_{B_S}	projected side area of body	5.2.1.2 5.2.3.1 5.6.3.1
S_D	duct planform area, $S_D = d_e c$	9.3 9.3.1 9.3.2 9.3.?

SYMBOL	DEFINITION	SECTIONS
S_E	area of trailing-edge extension of double-delta and cranked wings	4.1.3.2
S_H	area of auxiliary horizontal surface, aft tail or canard	Several
ΔS_H	incremental segments of horizontal-tail area	4.6.1
S_{H_e}	area of exposed horizontal-tail panel	4.5.3.1 6.2.1.2
S_{H_i}	area of portion of horizontal tail immersed in propeller slipstream	4.6.3
S_I	total surface area immersed in slipstream	4.6 4.6.4
S_J	streamwise basic wing area ahead of jet flap	6.1.5.1
S_L	area of a loaded region of wing in pressure-moment-area calculations	6.1.6.1
$S_{N_{ref}}$	base area of body nose, πr^2	Several
S_S	wetted or surface area of body excluding base area	Several
$(S_S)_e$	exposed wetted area of body (isolated body minus surface area covered by wing at wing-body juncture)	4.3.3.1 4.5.3.1
S_{U_e}	area of exposed lower vertical panel	Several
S_V	1. area of single vertical panel for configuration with twin vertical panels	5.3.1.1 5.6.1.1
	2. area of upper vertical panel measured to body center line	Several
S_{V_e}	area of exposed upper vertical panel	Several
S_W	wing area	Several
S_{W_e}	area of exposed wing	4.3.3.1 4.5.3.1
S_{W_f}	1. wing planform area including and directly forward of flap area (flap area not included) (see Section 2.2.2)	4.6 4.6.4 6.1.4.2 6.1.4.3
	2. flap-affected wing area, including increase in area due to flap extension	6.1.4.1 6.1.4.2 6.1.5.1
S_{W_i}	wing planform area including and directly forward of flap area immersed in propeller slipstream	4.6.4
S_b	body base area	Several
S_{bw}	area of basic wing	4.1.3.2 4.1.5.1 4.3.3.1 5.1.2.1

SYMBOL	DEFINITION	SECTIONS
$(S_{bw})_e$	area of exposed basic wing	4.3.3.1
S_c	main-control-surface area	6.3.4
S_e	1. area of exposed wing	Several
	2. area of elevator	6.3.4
	3. flow area at duct exit plane, $\frac{\pi d_e^2}{4}\left[1-\left(\frac{d_{CB}}{d_e}\right)^2\right]$	9.3.1
S'_e, S''_e	exposed planform areas of the forward and aft surfaces, respectively	Several
$(S_e)_i$	area of exposed inboard panel of wing	4.3.2.2
S_f	area of flap or control surface	6.1.4.1 6.1.5.1 6.2.1.1
S_g	area of glove of double-delta and cranked wings	4.1.3.2 5.1.2.1
S_i	1. total area of inboard panels of wing	Several
	2. area of portion of wing immersed in propeller slipstream, $b_i c_i$	Several
	3. primary-surface planform area forward of and including the flap area inside the primary-surface tip Mach cone (Figure 6.1.7-28b)	6.1.7
$(S_i)_e$, $(S_o)_e$	areas of exposed inboard and outboard panels, respectively, of wing	4.3.3.1
S_j	area of one section of wing of n sections	4.1.3.2 4.1.3.3
S_k	area of k^{th} wing segment with all flaps retracted	6.1.5.1
S_{ni}	primary-surface planform area forward of and including the flap area outside the primary-surface tip Mach cone (Figure 6.1.7-28b)	6.1.7
S_o	1. total area of outboard panels of wing	Several
	2. cross-sectional area at body station x_o	Several
S'_o	total area of constructed outboard panels of wing	4.1.4.2 4.3.2.2 5.1.2.1
S_p	1. body planform area	4.2.1.2 4.2.2.2 4.2.3.2 4.3.3.2
	2. propeller disk area, πR_p^2	Several
S_{ref}	reference area	Several

SYMBOL	DEFINITION	SECTIONS
S_t	total wing area, including increase in area due to flap extensions	6.1.4.1 6.1.4.2
S_{tc}	control-tab area	6.3.4
S_{wet}	wetted area	4.1.5.1 4.3.3.1 7.4.2.2
$(S_{wet})_e$	wetted area of exposed wing	4.3.3.1 4.5.3.1
$\left[(S_{wet})_H\right]_e$	wetted area of exposed horizontal-tail panel	4.5.3.1
$(S_{wet})_i, (S_{wet})_o$	wetted areas of inboard and outboard panels, respectively, of wing	4.1.5.1 4.3.3.1
$\left(S_{wet_i}\right)_e, \left(S_{wet_o}\right)_e$	wetted areas of exposed inboard and outboard panels, respectively, of wing	4.3.3.1
$\left[(S_{wet})_p\right]_e$	wetted area of exposed tail panel	4.5.3.1
$\left[(S_{wet})_V\right]_e$	wetted area of exposed vertical-tail panel	4.5.3.1
$\left[(S_{wet})_W\right]_e$	wetted area of exposed wing	4.5.3.1
S_x, $S(x)$	body cross-sectional area at any body station, πr^2	Several
S_1, S_2	area of constructed wing panels used to obtain wing lift-curve slope	4.1.3.2 5.1.2.1
S_1, S_2, S_3, . . .	areas on added vertical panel affected by Mach lines emanating from the intersection of exposed leading and trailing edges of all other panels with the body	Several
S_2, S_3	areas of constructed wing panels affected by jet flaps	6.1.5.1
S_{act}/S_{ext}	ratio of actual projected side area of fuselage to that of extended fuselage as determined by Mach lines emanating from leading and trailing edges of exposed root chord of the horizontal panel	Several
T	1. thrust per engine	Several
	2. temperature	6.3.1
	3. factor that accounts for the reduction in longitudinal velocity for wings of infinite span	4.7 4.7.1 4.7.4
	4. product of force and radius	8.1
	5. thrust per propeller or total thrust when used in thrust-recovery factor	9.1 9.1.2 9.2

SYMBOL	DEFINITION	SECTIONS
	6. ducted-propeller thrust	9.3 9.3.1
T_R	transition-strip indicator	4.3.2.1 4.3.3.2
T_{aw}	adiabatic wall temperature	6.3.1
T_c	1. thrust coefficient based on free-stream velocity and propeller disk area, $\frac{T}{q_\infty S_p}$	9.1 9.1.2 9.1.3
	2. propeller thrust coefficient based on free-stream velocity and wing area, $\frac{T}{q_\infty S}$	9.2 9.2.1 9.2.3
T'_c	thrust coefficient per engine, $\frac{2T}{\rho V_\infty^2 S_W}$	Several
T''_c	propeller thrust coefficient based on slipstream velocity and propeller disk area, $\frac{T}{q'' S_p}$	9.2 9.2.1 9.2.3
T_i	total internal axial thrust	9.3 9.3.1
T_{net}	ducted-propeller total net thrust, $(T_i - C_{D_e} q_\infty S_D)$	9.3 9.3.1
T_o	1. free-stream temperature	4.6.4
	2. hovering thrust	9.3.1
T'_o	internal jet temperature	4.6.4
T_p	propeller thrust	9.3.1
T_w	wall temperature	6.3.1
T_α	local temperature upstream of interaction	6.3.1
T_∞	free-stream temperature	6.3.1
t	airfoil maximum thickness	Several
t_c	thickness of control device at hinge line	6.1.3.1 6.1.3.2 6.1.6.1 6.1.6.2
$t_{c.p}$	nondimensional parameter used in calculating moment-arm parameter	6.1.6.1
$t/c, (t/c)_{av}$	average streamwise thickness ratio of lifting surface	Several
$\frac{t}{c'}$	airfoil thickness ratio, based on extended wing chord	6.1.1.1 6.1.1.2 6.1.4.1
$\left(\frac{t}{c}\right)'$	maximum airfoil thickness ratio measured normal to control-surface hinge line	6.1.6.1 6.1.6.2

SYMBOL	DEFINITION	SECTIONS
$\frac{t}{c}$	wing thickness ratio at mean aerodynamic chord	4.3.2.1
$(t/c)_{bw}$	average thickness of the basic wing	4.3.3.1
$(t/c)_{eff}$	effective thickness ratio	4.1.5.1 4.3.3.1 4.5.3.1
$(t/c)_i$, $(t/c)_o$	average streamwise thickness ratios of inboard and outboard panels, respectively, of a lifting surface	4.1.5.1 4.3.3.1
$(t/c)_{max}$	maximum thickness ratio	4.1.3.4 4.5.3.1 4.7
$(t/c)_p$	thickness ratio of tail panel	4.7.1 4.5.3.1
V, V_∞	free-stream velocity	Several
$\overline{V}$	transonic velocity similarity parameter, $\frac{\beta^2}{\left(\frac{t}{c}\right)^{2/3}}$	4.1.4.2
V_B	total body volume	Several
V_N	volume of nose	7.3.1.1
V_T	vertical-tail indicator	4.3.2.1
V_e	1. duct exit velocity	9.3 9.3.1
	2. nozzle exit velocity	6.3.2
	3. equivalent airspeed	6.3.4
V_i	velocity increment of internal mass flow due to power	9.3 9.3.1
V_{i_o}	internal mass-flow velocity with power off	9.3
V_j	1. jet exit velocity	4.6 4.6.1
	2. velocity of gas efflux leaving the trailing edge of the airfoil	6.1.1.1
V'_j	equivalent jet-exit velocity	4.6 4.6.1
$\frac{V_e}{V_\infty}$	exit-velocity ratio	9.3 9.3.1 9.3.2
v	1. any spanwise station on wing	9.3.3 6.1.7
	2. induced-drag factor	4.1.5.2 4.3.3.2

SYMBOL	DEFINITION	SECTIONS
W	weight	4.6 4.6.4 6.3.4 8.2
W_H	weight of horizontal-stabilizer section	8.1
W_L	wing-location index	4.3.2.1
W_P	weight of power-plant section	8.1
W_V	weight of vertical stabilizer	8.1
W_W	weight of wing section including wing carry-through structure	8.1
W_e	weight of engine and propeller	8.1
W_f	weight of fuselage section	8.1
W_{fs}	weight of fuselage structure	8.1
w	1. average body width at the exposed-wing or exposed-tail root chord	5.2.2.1 5.6.2.1
	2. maximum body width	4.3.1.4 5.2.3.1 5.6.3.1
	3. factor used to determine the downwash gradient at a particular point in the flow field not close to the trailing edge of the wing	4.4.1
	4. weight per unit length of element	8.2
	5. induced drag factor	4.1.5.2 4.3.3.2
	6. local vertical disturbance velocity	7.1.1.2
w_a, w_b	weights per unit length at beginning and end stations of body component, respectively	8.2
X	axial force	4.1.3
$\overline{X}$	longitudinal distance of vehicle center of gravity from nose apex	8.2
x	1. distance along airfoil chord, origin at LE	2.2.1 2.2.2 6.1.2.1 6.3.1
	2. distance between the moment center and the a.c. of the lifting surface affected by downwash, positive when a.c. is ahead of moment center	4.5.1.1
	3. parameter accounting for effect of image trailing vortex on lift	4.7 4.7.1

SYMBOL	DEFINITION	SECTIONS
	4. distance of centroid of the area affected by jet power effects from moment reference center, positive for area forward of reference center	4.6.3
	5. distance of the local center of pressure aft of the quarter-chord of the MAC (see Equation 6.1.5.1-j)	6.1.5.1
	6. longitudinal distance from the nose to quarter-chord point of the MAC of the exposed wing panel	4.3.1.3
	7. any station along body	Several
	8. longitudinal distance measured from the wing-root trailing edge aft	4.4.1 7.4.1.1
	9. longitudinal coordinate measured forward from wing leading edge	9.1 9.1.3
	10. longitudinal distance from the body nose to midchord point of the MAC of exposed vertical panel	5.3.1.2 5.6.1.2
	11. distance of origin of moments from the 2/3 c_{r_B} point of the basic triangular wing, measured along the longitudinal axis, positive ahead of the 2/3 c_{r_B} point	5.1.3.1 7.1.1.1
	12. distance of origin of moments from the wing midchord point, measured along the longitudinal axis, positive ahead of midchord point	5.1.3.1
	13. distance of center of loading of a conical-flow region from control hinge axis measured normal to the hinge axis	6.1.6.1
	14. longitudinal distance measured from vertical-tail leading edge to projected quarter-chord of horizontal-tail MAC on to root chord (see sketch, Figure 5.3.1.1-22b)	5.3.1.1 7.4.2.1 7.4.2.2 7.4.2.3
	15. distance from body nose to quarter-chord point of the MAC of exposed horizontal tail in subsonic flow	6.2.1.2
	16. distance from body nose to midchord point of the MAC of exposed horizontal tail in supersonic flow	6.2.1.2
	17. distance from nose to center of pressure of given body segment	4.2.2.1
Δx	1. increment between successive longitudinal stations	4.2.3.2 4.3.3.1 6.1.7
	2. the chordwise distance from the quarter-chord point of the 75-percent-semispan chord to the three-quarter-chord point of the wing root chord, positive when the latter is aft of the former (see Figure 4.7.1-14)	4.7 4.7.1
	3. distance between forward and aft faces of given body segment	4.2.2.1
x'	stations measured from leading to trailing edge of airfoil surface	4.4.1
x', x''	longitudinal distances used in estimating wing pitching moment	4.5.2.1

SYMBOL	DEFINITION	SECTIONS
x', z'	corresponding point on the airfoil for a point x, z in the flow field	4.4.1
x''	location of quarter-chord point of MAC of total aft horizontal panel	7.4.1.1 7.4.1.2 7.4.4.1 7.4.4.2
$\bar{x}$	1. distance between a.c. and c.g., positive when c.g. is ahead of a.c.	Several
	2. longitudinal distance from axes origin to c.g. of component	8.2
	3. chordwise distance between duct moment reference center and installed duct center of pressure, positive for center of pressure ahead of moment reference center	9.3 9.3.2
x_H	distance between vehicle center of gravity and quarter-chord point of horizontal stabilizer MAC (see Figure 4.5.3.2-4)	4.5.3.2
x'_H	distance from jet wake origin to the quarter-chord point of the MAC of the horizontal tail, parallel to the thrust axis	4.6 4.6.1
x_{HL}	distance from nose of configuration to control hinge line	6.3.1
x_I	longitudinal distance between jet inlet and quarter-chord point of wing MAC	4.6 4.6.1 4.6.3
x_{LE}	longitudinal distance from aircraft reference-axis origin to leading edge of mean aerodynamic chord of wing segment affected by leading-edge device	6.1.5.1
$\bar{x}_{LE}$	chordwise distance from apex to leading edge of MAC	2.2.2
x_{MRP}	distance from the leading edge of MAC to the moment reference point, positive for the moment reference point aft of the leading edge of the MAC	6.1.5.1
x_R	point of reattachment pressure rise (see Sketch (a), Page 6.3.1-2)	6.3.1 6.3.2
x_W	longitudinal distance from aerodynamic center of that portion of wing immersed in propeller slipstream to moment-reference-center location, positive for a.c. forward of moment reference center.	4.6 4.6.3
x_a	center-of-lift location of incremental load due to flap deflection, measured positive aft from extended airfoil leading edge parallel to free stream	6.1.2.1
$x_{a.c.}$	1. distance between aerodynamic center and wing apex, parallel to the MAC, positive for a.c. aft of wing apex	Several
	2. airfoil section a.c. position	4.1.2.2
	3. distance between aerodynamic center and airfoil leading edge, parallel to free stream, positive for aerodynamic center aft of leading edge	6.1.2.1
$\Delta x_{a.c.}$	shift in wing aerodynamic center at transonic speeds due to flow separation	4.1.4.2
$x'_{a.c.}$	aerodynamic center of the forward panel, referred to forward-panel apex	4.3.2.2 4.5.2.1
$x''_{a.c.}$	aerodynamic center of the aft panel, referred to aft-panel apex	4.5.2.1
$(x'_{a.c.})'_o$	aerodynamic center of the constructed outboard panel of the wing	4.3.2.2
$(x_{a.c.})_p$	distance between quarter-chord point of MAC of added panel and aerodynamic center of added panel. For supersonic case the distance between the mid-chord point of MAC and aerodynamic center	5.3.3.1 5.6.3.1

SYMBOL	DEFINITION	SECTIONS
$(x_{a.c.})_V$	distance between quarter-chord point of MAC of vertical panel and aerodynamic center of vertical panel	5.3.3.1
x_c	1. axial distance from vertex of body nose to centroid of body planform area	Several
	2. location of hinge line (for corner flow)	6.3.1
	3. fore and aft displacement of control column, positive forward	6.3.4
$x_{c_{max}}$	maximum displacement of control column, positive forward	6.3.4
$x_{centroid}$	distance of the centroid of area of a wing behind the wing apex, parallel to wing MAC and plane of symmetry	2.2.2
$x_{c.g.}$	1. distance between center of gravity and quarter-chord point of wing MAC, parallel to MAC, positive for c.g. aft of MAC	4.5.2.1 4.6 5.3.3.1 7.1.3.3
	2. distance from wing apex to center of gravity, parallel to MAC, positive for c.g. aft of wing apex	Several
$x_{c.p.}$	1. distance from wing apex to center of pressure, parallel to wing chord and plane of symmetry, positive for c.p. aft of wing apex	4.1.4 4.3.2.2
	2. distance from body nose to body center-of-pressure location, positive aft	4.2.2.1 5.2.3.2
	3. distance from airfoil leading edge to center of pressure of incremental load due to flaps, parallel to wing chord, positive for center of pressure aft of leading edge	6.1.2.1
	4. chordwise center-of-pressure location aft of the leading edge for a flapped wing section	6.1.5.1
	5. center-of-pressure location measured relative to the leading edge (two dimensional)	6.3.2
	6. chordwise distance from duct leading edge to center of pressure of unstalled duct, positive aft of duct leading edge	9.3 9.3.2
$x_{c.p._b}$	chordwise center-of-pressure location aft of the leading edge for the basic loading of a plain flap	6.1.5.1
$(x_{c.p.})_b$	center-of-pressure location of boattail, measured aft of the forward face of the boattail	4.2.2.1
$(x_{c.p.})_{\Delta C_N}$	distance of center of pressure of normal-force increment from moment reference point, negative aft	6.3.1
x_{c_V}	parameter accounting for relative positions of the horizontal and vertical tails	5.3.1.1
$(x_{\bar{c}/4})_V$	longitudinal distance between quarter-chord point of MAC of vertical panel and the forward end of its root chord	5.3.3.1
x_e	location of nozzle exit (see Sketch (a), Page 6.3.2-3)	6.3.2
x'_e	distance from jet exit to the quarter-chord point of the MAC of the horizontal tail, parallel to the thrust axis	4.6 4.6.1
x_f	1. distance from airfoil leading edge, parallel to free stream, where total lift increment due to flaps acts	6.1.2.1
	2. distance of the leading edge of the control root chord behind the wing axis of pitch	6.1.5.1
$\bar{x}_f$	longitudinal centroidal distance of fuselage from nose	8.1
$x_{f_1}, x_{f_2}, x_{f_i}$	center-of-lift location of incremental load due to deflection of first, second, and i^{th} flap segment, respectively, measured aft from airfoil leading edge parallel to free stream	6.1.2.1 6.1.5.1

SYMBOL	DEFINITION	SECTIONS
$x_{i(\alpha)}$	distance to center of pressure of wing-induced body side force from juncture of wing leading edge and body at angle of attack	5.2.3.2
$x_{i(\alpha = 0)}$	distance to center of pressure of wing-induced body side force from juncture of wing leading edge and body at zero angle of attack	5.2.3.2
x_j	distance from airfoil leading edge, parallel to free stream, where total lift increment due to jet efflux acts	6.1.2.1 6.1.5.1
x_j'	longitudinal distance from jet wake origin to jet exit, usually considered to be 4.6 times the orifice exhaust radius	4.6 4.6.1
Δx_k	longitudinal distance from moment reference center to chord for zero sweep, defined in x_m definition 4 below, for the k^{th} wing segment	6.1.5.1
x_m	1. longitudinal distance from the body nose to the chosen moment center, positive aft	Several
	2. chordwise distance from duct leading edge to moment reference center, positive aft of duct leading edge	9.3 9.3.2
	3. desired pitching-moment reference point measured positive aft from basic airfoil leading edge paralel to wing chord	6.1.2.1 6.1.5.1
	4. distance from wing leading edge to unique unswept reference line so that the ratio of x_m to local cnord is constant for straight-tapered wings (see Sketch (κ), Section 6.1.5.1)	6.1.5.1
x_o	1. body station where flow ceases to be of a potential nature	Several
	2. function of the slope of the lifting line (m), $\frac{mx}{b/2}$	4.4.1
	3. beginning of pressure interaction	6.3.1
x_p	1. longitudinal distance from intersection of propeller plane with thrust axis and the quarter-chord point of the MAC of the wing	4.6 4.6.1 4.6.3
	2. fore and aft displacement of right rudder pedal, positive forward	6.3.4
x_r	distance from forward end of root chord to intersection of control hinge line with root chord, parallel to wing root chord	6.1.6.1
Δx_r	distance from wing apex to desired moment reference center, measured positive aft	6.1.5.1
x_{ref}	desired pitching-moment reference point, measured positive aft from basic airfoil leading edge parallel to wing chord	6.1.2.1
x_s	1. longitudinal distance from model vertex to point of vortex separation	4.3.1.3 5.3.1.2 5.6.1.2 6.2.1.2
	2. distance from nose of airfoil to spoiler lip, parallel to wing chord (Figure 6.1.1.1-52b)	6.1.1.1 6.2.1.1 5.2.2.1
	3. point of separation pressure rise (see Sketch (a), Page 6.3.1-2)	6.3.1 6.3.2

SYMBOL	DEFINITION	SECTIONS
x_s'	distance from wing leading edge to spoiler hinge line (see Sketch (g), Page 6.2.1.1-6)	6.2.1.1
x_t	1. chordwise position of airfoil maximum thickness	2.2.1 4.1.5.1 4.3.3.1
	2. distance from forward end of tip chord to intersection of control hinge line with tip chord, parallel to root chord	6.1.6.1
	3. transition distance	6.3.1
$x_{(y_c)_{max}}$	chordwise position of maximum camber of airfoil	2.2.1
x_1	1. body station where $\frac{dS_x}{dx}$ first reaches its maximum negative value	Several
	2. distance from intersection of wing leading edge or trailing edge with fuselage and the center of pressure of given body segment (see Sketch (a))	4.2.2.1
$\bar{x}_1$	distance from intersection of wing leading edge with fuselage to forward face of body segment adjacent to the intersection (see Sketch (a))	4.2.2.1
x_1, x_2, x_3	distance parameters used to define section thickness-ratio factor for hexagonal airfoils	4.1.5.1 4.3.3.1
x_1, x_2, x_6	moment arms corresponding to section lift terms Δc_1, Δc_2, Δc_6, respectively	6.1.2.1 6.1.5.1
x_3	point of beginning of downstream pressure rise (see Sketch (a), Page 6.3.2-3)	6.3.2
x_4	point of peak downstream pressure rise (see Sketch (a), Page 6.3.2-3)	6.3.2
$x_{5_1}, x_{5_2}, (x_5)_i$	moment arms corresponding to section lift terms Δc_{5_1}, Δc_{5_2}, Δc_{5_i}, respectively, for the first, second and i^{th} flap segments, respectively	6.1.2.1 6.1.5.1
$\frac{x}{c_v}$	parameter accounting for relative positions of horizontal and vertical tails	5.3.1.1 5.6.1.1
$\frac{x_{a.c.}}{\bar{c}}$	distance of aerodynamic center of wing aft of wing apex, measured in mean aerodynamic chords, positive aft	4.1.4.3
$\frac{x_{a.c.}}{c_r}$	distance of aerodynamic center of wing aft of wing apex measured in root chords, positive aft	4.1.4.2 4.1.4.3 4.3.2.2

SYMBOL	DEFINITION	SECTIONS
$\frac{\Delta x_{a.c.}}{c_r}$	incremental a.c. location accounting for separation effects	4.1.4.2
$\left(\frac{x_{a.c.}}{c_r}\right)_{B(W)}$	value of parameter for body in presence of wing	4.3.2.2
$\left(\frac{x_{a.c.}}{c_r}\right)_{C_L=0}$	aerodynamic-center location at zero lift	4.1.4.3
$\left(\frac{x_{a.c.}}{c_r}\right)_i$	distance of a.c. location of inboard panel of wing aft of apex of inboard panel measured in its root chords	4.1.4.2
$\left(\frac{x_{a.c.}}{c_r}\right)_N$	value of parameter for body nose	4.3.2.2
$\left(\frac{x_{a.c.}}{c_r}\right)_o$	distance of a.c. location of outboard panel of wing aft of the apex of outboard panel, measured in its root chords	4.1.4.2
$\left(\frac{x_{a.c.}}{c_r}\right)_o'$	distance of a.c. location of constructed outboard panel of wing aft of the apex of the constructed outboard panel, measured in its root chords	4.1.4.2 4.3.2.2
$\left(\frac{x_{a.c.}}{c_r}\right)_{W(B)}$	value of parameter for wing in presence of body	4.3.2.2
$\frac{x_{a.c.}'}{c_{r_e}}$	distance of aerodynamic center of wing-body configuration from apex of exposed wing, measured in exposed-wing root chords	4.3.2.2
$\left(\frac{x_{a.c.}'}{c_{r_e}}\right)_{B(W)}$	distance of aerodynamic center of body in presence of the wing from apex of exposed wing, measured in exposed-wing root chords	4.3.2.2
$\left(\frac{x_{a.c.}'}{c_{r_e}}\right)_i$	distance of aerodynamic center of inboard panel of wing from apex of exposed wing, measured in its exposed-wing root chords	4.3.2.2
$\left(\frac{x_{a.c.}'}{c_{r_e}}\right)_N$	distance of aerodynamic center of body nose ahead of wing-body juncture from apex of exposed wing, measured in exposed-wing root chords	4.3.2.2

SYMBOL	DEFINITION	SECTIONS
$\left(\frac{X_{a.c.}}{C_{r_e}}\right)_W$	value of parameter for wing	4.3.2.2
$\left(\frac{X_{a.c.}}{C_{r_e}}\right)_{W(B)}$	distance of aerodynamic center of exposed wing in presence of the body from apex of exposed wing, measured in exposed-wing root chords	4.3.2.2
$\frac{X_{c.p.}}{C_{c.p.}}$	empirically derived chordwise center-of-pressure location of the incremental load due to surface deflection	6.1.5.1
$\left(\frac{X_{c.p.}}{C_{c.p.}}\right)_1$	empirically derived factor of $\frac{X_{c.p.}}{C_{c.p.}}$	6.1.5.1
$\frac{X_{c.p.}}{C_r}$	distance of wing center-of-pressure location, in wing root chords, measured positive aft of wing apex	4.1.4.3
$\left(\frac{X_{c.p.}}{C_r}\right)_{C_L=0}$	wing center-of-pressure location at zero lift	4.1.4.3
$\left(\frac{X_{c.p.}}{C_r}\right)_{C_{L_{max}}}$	wing center-of-pressure location at maximum lift	4.1.4.3
$\left(\frac{X_{c.p.}}{C_r}\right)_{ref}$	wing reference center-of-pressure location	4.1.4.3
$\left(\frac{X_{c.p.}}{C_r}\right)_1$	component of wing center-of-pressure location at maximum lift due to leading-edge sharpness	4.1.4.3
$\Delta\left(\frac{X_{c.p.}}{C_r}\right)_2$, $\Delta\left(\frac{X_{c.p.}}{C_r}\right)_3$, $\Delta\left(\frac{X_{c.p.}}{C_r}\right)_4$	increments of wing center-of-pressure location due to planform geometry	4.1.4.3

SYMBOL	DEFINITION	SECTIONS
$\left(\frac{x_{3D}}{x_{2D}}\right)_i$	ratio of center-of-lift location of a finite-aspect-ratio wing to center-of-lift location of an infinite-aspect-ratio wing for the incremental load due to deflection of the i^{th} trailing-edge flap segment	6.1.5.1
$\left(\frac{x_{3D}}{x_{2D}}\right)_j$	ratio of center-of-lift location of a finite-aspect-ratio wing to center-of-lift location of an infinite-aspect-ratio wing for the incremental load due to jet momentum acting at some angle to trailing-edge camber line	6.1.5.1
$\left(\frac{x_h}{c}\right)'$	distance of the hinge axis behind wing leading edge measured in plane normal to control hinge axis	6.1.6.1 6.1.6.2
Y_{90}, Y_{99}	airfoil ordinates at 90- and 99-percent chord, in percent chords	4.1.1.2 6.1.5.1 7.1.2.2
Y_{90}, Y_{100}	upper-surface ordinates of flap in retracted position at 90- and 100-percent chord, respectively, in fractions of the chord	6.1.1.1
y	1. airfoil ordinate at some value of x	2.2.1
	2. coordinate with origin at midspan of wing leading edge, perpendicular to plane of symmetry	4.4.1
	3. lateral coordinate measured positive to right of plane of symmetry	Several
Δy	1. difference between airfoil ordinate at 6% chord and ordinate at 0.15% chord	Several
	2. lateral distance from thrust axis of one propeller to blade element of another	9.1 9.1.3
	3. spanwise distance on constructed inboard panel = 1/2 b_i	4.1.4.2 4.3.2.2
y (x)	thickness distribution of airfoil	2.2.1
$\bar{y}$	lateral distance from axes origin to c.g. of component	8.2
y_B	spanwise location of break span station	2.2.2
$\bar{y}_H$	1. lateral center-of-pressure coordinate of the horizontal tail, measured from and normal to the longitudinal axis	6.2.1.2
	2. lateral centroidal distance of half horizontal stabilizer from aircraft plane of symmetry	8.1

SYMBOL	DEFINITION	SECTIONS
y_{MAC}	distance of the wing MAC from the plane of symmetry	2.2.2
y_T	spanwise distance from thrust axis to body center line	4.6 4.6.1
$\overline{y}_W$	lateral centroidal distance of half-wing from aircraft plane of symmetry	8.1
$y_{\overline{c}}$	lateral distance to wing mean aerodynamic chord from fuselage center line	6.1.4.2 6.1.5.1
$y'_{\overline{c}}$	lateral distance to mean aerodynamic chord of wing segment affected by the leading-edge device from fuselage center line	6.1.5.1
$y_c(x)$	camber-line distribution of airfoil	2.2.1
$(y_c)_{max}$	maximum ordinate of mean line of airfoil	2.2.1 4.3.2.1 4.3.3.2
y_i	spanwise distance from center line to inboard edge of flap or control surface	6.1.6.1 6.1.6.2 6.2.1.1 6.2.2.1
$y_{i,o}$	distance of inboard corners of horseshoe vortices from plane of symmetry	4.4.1
y_{max}	vertical distance from airfoil chord line to airfoil maximum upper-surface ordinate (see Sketch (a), Section 4.1.4.3)	4.1.4.3
y_o	1. distance of theoretical lateral vortex from plane of symmetry	Several
	2. spanwise distance from center line to outboard edge of flap or control surface	6.1.6.1 6.1.6.2 6.2.1.1 6.2.2.1
y_o, z_o	coordinate axes with origin at c.g. of component	8.2
$\frac{y_{v_1}}{b_V}, \frac{y_{v_2}}{b_V}$	body vortex lateral position at the vertical tail spans (defined by Equation 5.3.1.2-f)	5.3.1.2 5.6.1.2
$\Delta y_\perp$	value of Δy for chord perpendicular to wing leading edge, where Δy is defined above in 1.	Several

SYMBOL	DEFINITION	SECTIONS
Z	parameter used in determining horizontal stabilizer lift coefficient; defined by Equation 4.5.3.2-h	4.5.3.2
z	1. vertical distance between c.g. and quarter-chord point of wing MAC positive for MAC below c.g.	7.1.3.2
	2. vertical distance between c.g. and quarter-chord point of wing root chord, positive for quarter-chord point of root chord below c.g.	7.1.2.1 7.1.2.2 7.3.2.1 7.3.2.2
	3. vertical coordinate with origin at midspan of wing leading edge	4.4.1 4.5.1.1 4.5.1.2
	4. vertical distance from the vortex sheet to the point of interest (usually the quarter-chord point of the MAC of the horizontal tail)	4.4.1 7.4.1.1 7.4.4.1
	5. vertical distance of vertical-tail center-of-pressure location above or below moment-reference-center location	7.4.2.1 7.4.2.2 7.4.2.3
Δz	vertical distance between desired moment-reference-center-chord location and quarter-chord of MAC, positive for wing below desired location	6.1.5.1
z'	vertical distance of the horizontal tail below the body center line	6.2.1.2
z', z''	vertical distance between c.g. and quarter-chord point of forward and aft panel MAC's, respectively	4.5.2.1
$\bar{z}$	vertical distance from axes origin to c.g. of component	8.2
z_H	1. vertical distance between quarter-chord point of horizontal tail and X-axis, positive for tail below X-axis	Several
	2. distance measured normal to the longitudinal axis between the horizontal tail c.p. and the moment reference center, positive for c.p. above longitudinal axis	Several
	3. distance to c.p. of horizontal-tail-interference side force, measured from and normal to the longitudinal axis	5.3.3.2 5.6.3.2
	4. distance from quarter-chord point of wing MAC to quarter-chord point of horizontal-tail MAC, measured normal to longitudinal axis, positive for tail above wing	4.5.1.3
$z_{H_{eff}}$	vertical distance of center line of propeller slipstream from quarter-chord point of horizontal tail MAC (see Figure 4.6-13a), positive for slipstream above horizontal tail	4.6 4.6.3
z_{HL}	distance of hinge line measured from and normal to the X-axis, positive down	6.3.1
z_{H_T}	vertical distance from quarter-chord point of horizontal tail to propeller thrust axis; positive for quarter-chord point above thrust axis (see Figure 4.6-13a)	4.6 4.6.3
z_T	vertical distance from propeller thrust axis to coordinate origin, positive for thrust axis below origin (see Figure 4.6-13)	4.6 4.6.1 4.6.3
z_U	distance normal to the longitudinal axis between the lower-vertical-stabilizer (ventral) center of pressure and the moment reference center (normally negative)	5.3.3.2 5.6.2.1 5.6.3.2

SYMBOL	DEFINITION	SECTIONS
z_V	1. distance normal to the longitudinal axis between the upper-vertical-stabilizer center of pressure and the moment reference center (always positive)	Several
	2. vertical centroidal distance of vertical stabilizer from root chord (at fuselage)	8.1
z_W	1. vertical distance from the quarter-chord point of the wing MAC, to the coordinate origin, positive for wing below the origin (see Figure 4.6-13)	Several
	2. vertical distance from body center line to quarter-chord point of root chord, positive for quarter-chord point below center line	Several
	3. half-width of the wake at any position x	4.4.1 4.5.1.1 4.5.1.2 7.4.1.1
$z_{c.g.}$	vertical distance between c.g. and X-axis, positive for c.g. below X-axis	4.5.2.1 4.6
$\Delta z_{c.g.}$	vertical distance between c.g. and wing MAC quarter-chord, positive above quarter-chord	6.1.5.1
$(z_{c.p.})_{\Delta C_A}$	distance of center of pressure of axial-force increment from moment reference point, positive down	6.3.1
z_j'	distance from jet thrust axis to quarter-chord point of horizontal tail perpendicular to thrust axis, positive for quarter-chord point above thrust axis	4.6 4.6.1
z_o	vertical distance of theoretical vortex above reference plane	Several
z_p	distance normal to the longitudinal axis between the center of pressure of a vertical panel and the moment reference center, positive for the panel above the body	5.6.2.1
z_s	vertical distance from X-axis to propeller-slipstream center line at the quarter-chord of the wing MAC, positive for center line above X-axis (see Figure 4.6-13a)	4.6 4.6.1 4.6.3
$\left(\frac{2z}{b}\right)_{eff}$	effective value of height parameter relative to the displaced vortex	4.4.1
$\left(\frac{2z}{b'}\right)_{eff}$	value of parameter for forward panel	7.4.4.1
$\frac{z_H}{r_l}$	ratio of height of horizontal tail to average half-depth of body in region of horizontal tail (ratio is positive for tail below body center line)	5.3.1.1 5.6.1.1
$\frac{z_{v_1}}{b_V}, \frac{z_{v_2}}{b_V}$	body vortex vertical positions at the vertical tail spans; defined by Equation 5.3.1.2-f	5.3.1.2 5.6.1.2

B. GREEK SYMBOLS

SYMBOL	DEFINITION	SECTIONS
α	1. angle of attack, positive nose up	Several
	2. angular acceleration	8.1
	3. flow deflection angle	6.3.1
$\Delta\alpha$	1. angle-of-attack increment from incipient shock detachment to full detachment, $\alpha' - \alpha^*$	4.1.3.3
	2. change in wing angle of attack due to propeller upwash or downwash, $\frac{-\epsilon_p}{1+\frac{\partial \epsilon_u}{\partial \alpha}}$	4.6.1
	3. increment in angle of attack	4.7 4.7.1
α'	1. angle of attack at end of shock-detachment transition region	4.1.3.3
	2. angle of attack of forward panel	Several
	3. angle of inclination, $\sqrt{\alpha^2+\beta^2}$	Several
	4. an incidence angle defined as $\alpha' = \alpha$ for $0 \leq \alpha \leq 90^o$, and $\alpha' = 180^o - \alpha$ for $90^o \leq \alpha \leq 180^o$	4.2.1.2 4.2.2.2 4.2.3.2
α''	angle of attack of aft panel, $\alpha - \epsilon + i''$	4.1.5.2 4.5.1.2 4.5.2.1
$\overline{\alpha}$	transonic similarity parameter, $\frac{\alpha}{t/c}$	4.1.4.2
α^*	1. angle of attack at which section lift curve begins to deviate from linear variation	Several
	2. angle of attack at incipient shock detachment	4.1.3.3
$\alpha_{C_{L_{max}}}$	wing angle of attack at maximum lift coefficient	Several
$\Delta\alpha_{C_{L_{max}}}$	incremental value of parameter (see Figures 4.1.3.4-21b, -25b)	4.1.3.4
$\alpha'_{C_{L_{max}}}$	wing angle of attack of forward panel at maximum lift coefficient	7.4.4.1
$\left(\alpha_{C_{L_{max}}}\right)_{base}$	base value of parameter	4.1.3.3 4.1.3.4
$\left[\left(\alpha_{C_{L_{max}}}\right)_{base}\right]''_e$	subsonic angle of attack for $C_{L_{max}}$ of exposed aft panel	4.5.1.2

SYMBOL	DEFINITION	SECTIONS
$\left(\alpha_{C_{L_{max}}}\right)_e'$, $\left(\alpha_{C_{L_{max}}}\right)_e''$	angles of attack at maximum lift coefficients of exposed forward and aft panels, respectively	4.1.5.2
$\left(\Delta\alpha_{C_{L_{max}}}\right)_e'$	incremental value of parameter for exposed forward panel	4.5.1.2
$\left(\alpha_{C_{L_{max}}}\right)_W$	value of parameter for wing	4.3.1.4
$\left(\alpha_{C_{L_{max}}}\right)_{WB}$	value of parameter for wing-body combination	4.3.1.4 4.5.1.3
α_D	angle of attack between duct axis and free-stream direction	9.3 9.3.1 9.3.2 9.3.3
α_{FRP}	angle of attack for fuselage reference plane	4.3.1.3
$(\Delta\alpha)_G$	increment in angle of attack at a constant lift coefficient in the presence of the ground	4.7 4.7.1
α_H	angle of attack of horizontal tail or canard surface	4.6.3 4.7.1 6.3.4
$(\Delta\alpha_H)_G$	increment in angle of attack of the horizontal tail in the presence of the ground	4.7 4.7.1
α_L	local angle of attack for a particular spanwise wing section	6.1.5.1
α_T	angle of attack of thrust axis	4.6 4.6.1 4.6.3 4.6.4
α_V	angle of attack of vertical tail	6.3.4
α_W	angle of attack of wing	Several
$\Delta\alpha_W$	change in wing angle of attack ahead or behind the propellers	4.6.1
α_{WB}	wing-body angle of attack	4.5.3.2
α_{break}	angle of attack of wing at which the lift-curve slope becomes nonlinear	4.1.3.3
$\alpha_{c_\ell}{}_{max}$	section angle of attack at maximum lift coefficient	4.1.1 4.1.3.4 4.1.4.3 6.1.1
α_e	equivalent angle of attack for cambered wing	4.1.3.3
$(\alpha_e)_{C_{L_{max}}}$	equivalent angle of attack for cambered wing at maximum lift coefficient	4.1.3.3
α_i	angle of attack for section design lift coefficient	Several
α_{in}	inflow angle at propeller disk	9.1 9.1.3

SYMBOL	DEFINITION	SECTIONS
α_i	angle between jet thrust axis and local velocity at jet intake, $\alpha_T + \epsilon_u$	4.6 4.6.1 4.6.3
α_p	angle between propeller thrust axis and local velocity of propeller plane	4.6 4.6.1 4.6.4
α_s	angle of attack of surface to which main control surface is attached	6.3.4
$\Delta\alpha'_s$	change in section zero-lift angle of attack due to plug-type spoiler	6.1.1.1 6.2.1.1
α_v	angle of attack where onset of vortex lift begins	4.2.1.2
α_δ	control- or flap-effectiveness derivative, $-\frac{\partial \alpha}{\partial \delta}$	Several
$(\alpha_\delta)_{C_L}$	value of α_δ for a wing	6.1.4.1 6.1.5.1 6.1.7
$(\alpha_\delta)_{c_\ell}$	value of α_δ for an airfoil section	6.1.4.1 6.1.5.1 6.1.7
α_0	angle of attack at zero lift	Several
$\Delta\alpha_0$	change in wing zero-lift angle of attack due to linear wing twist	4.1.3.1
$(\alpha_0)_B$	body zero-lift angle of attack	4.3.2.1
$(\alpha_0)_W$	wing zero-lift angle of attack	4.3.2.1
$(\alpha_0)_{WB}$	wing-body zero-lift angle of attack	4.3.2.1
$(\alpha_0)_{\theta=0}$	angle of attack for zero lift of untwisted, constant-section wing	4.1.3.1 4.1.4.3
α_∞	free-stream angle of attack	6.3.2
$\alpha_\perp$	effective angle of attack perpendicular to the wing leading edge, $\tan^{-1}\frac{\tan\alpha}{\cos\Lambda_{LE}}$	4.1.3.1 4.1.3.3
$\frac{d\alpha_{in}}{d\alpha}$	propeller inflow angle of attack gradient	9.1.3
$\dot{\alpha}$	rate of change of angle of attack	7.4.4.1 7.4 4.2
β	1. Mach number parameter, $\sqrt{M^2-1}$ or $\sqrt{1-M^2}$	Several
	2. propeller blade angle at .75 R blade station	Several
	3. angle of sideslip, positive nose left	Several
	4. boattail angle	4.6.4
	5. control-tab gear ratio	6.3.4

SYMBOL	DEFINITION	SECTIONS
$\frac{\beta C_{l_\beta}}{\kappa\Gamma}$	(listed under C_{l_β})	
Γ	dihedral angle, positive wing tips up	Several
Γ', Γ''	dihedral angles of forward and aft surfaces, respectively, positive for wing tips up	4.5.1.1 7.4.1.1
Γ_y	value of circulation at any spanwise station	4.4.1
Γ_o	circulation at zero spanwise station	4.4.1
$\frac{\Gamma}{2\pi\, V r\alpha}$	nondimensional vortex strength	4.3.1.3 4.3.1.4 4.5.1.2 6.2.1.2
$\frac{\Gamma}{2\pi\, \alpha' V r}$	nondimensional vortex strength from Figure 4.3.1.3-15 with α replaced by α'	5.3.1.2 5.6.1.2
$\left[\frac{\Gamma_B}{2\pi\, V r\alpha}\right]'$, $\left[\frac{\Gamma_B}{2\pi\, V r\alpha}\right]''$	nondimensional vortex strengths for the forward and aft panels, respectively	4.5.1.2
$\frac{\Gamma_{yi}}{V\alpha\, b/2}$	circulation strength at $y_{i,o}$	4.4.1
$\frac{\Gamma_{yi+1} - \Gamma_{yi-1}}{V\alpha\, b/2}$	incremental circulation strength	4.4.1
γ	1. ratio of specific heats	Several
	2. angle with origin at wing trailing edge, measured between the zero-angle-of-attack line and the point under consideration	4.4.1 7.4.1.1
	3. dihedral angle of tail	4.5.1.1
	4. jet spreading angle (see Sketch (i), Section 6.1.5.1)	6.1.5.1
Δ_r	ratio of maximum deflections of control tab to main control surface	6.3.4
δ	1. semiwedge nose angle of sharp airfoils or cones	4.1.3.2 4.4.1 6.3.2
	2. flap or control deflection angle (also δ_f), elevators and flaps, positive trailing edge down; ailerons, positive such as to give positive rolling moment; rudder, positive trailing edge left	Several
	3. local slope of the surface of the vertical panel	5.3.1.1
	4. boundary-layer thickness	6.3.1
δ'	1. slope of airfoil surface with respect to free-stream velocity	4.4.1 5.3.1.2 5.6.1.2
	2. flap deflection in plane normal to constant-percent-chord line through $x_{c.p._h}$	6.1.5.1

SYMBOL	DEFINITION	SECTIONS
δ_L	deflection of left-hand control surface	6.2.1.1 6.2.2.1
δ_{LE}	slope of airfoil surface at leading edge	4.4.1
δ_R	deflection of right-hand control surface	6.2.1.1 6.2.2.1
δ_{a_L} or δ_{a_R}	deflection of left or right aileron	6.2.2.1
δ_c	deflection of main control surface	6.3.4
$\delta_{c_{max}}$	maximum deflection of main control surface	6.3.4
δ_d	distance of deflector lip below lower surface of airfoil	6.2.1.1 6.2.2.1
δ_e	1. elevator deflection	6.3.4
	2. equivalent flap deflection due to wing camber and incidence	9.2 9.2.1 9.2.3
$\delta_{e_{max}}$	maximum elevator deflection	6.3.4
δ_{eff}	effective nose wedge angle for sharp-nosed airfoil (see Figure 4.1.3.3-61b)	4.1.3.3
$\delta_{eff_\perp}$	effective nose semiwedge angle for sharp-leading-edge wing, perpendicular to leading edge (see Figure 4.1.3.3-61b)	4.1.3.3
δ_f	1. deflection of flap or control surface (see δ)	Several
	2. force phase angle	9.1 9.1.3
δ_{f_i}	deflection of the i^{th} segment of trailing-edge flap	6.1.2.1 6.1.5.1
$\delta_{f_{LE}}$	deflection of leading-edge device	6.1.2.1
$\delta_{f_1}, \delta_{f_2}$	deflections of forward and aft flaps, respectively, (see Figures 6.1.1.1-45, -46)	Several
$\delta_{f_1}, \delta_{f_2}, \delta_{f_3}$	deflection of first, second, and third segments, respectively, of trailing-edge flaps (see Sketch (f), Section 6.1.2.1)	6.1.2.1
$\delta_{f_{\perp LE}}$	deflection of leading-edge flap, measured perpendicular to airfoil leading edge	6.1.5.1
δ_{i_f}	net turning angle of internal flow including power effects	9.3 9.3.1 9.3.2 9.3.3
δ_{i_o}	turning angle of internal flow with power off	9.3 9.3.1
δ_j	trailing-edge jet momentum angle, with respect to trailing-edge camber line	Several
$\delta_{j_{eff}}$	effective jet deflection angle with respect to airfoil chord	Several
δ_ℓ	deflection of aft flap segment, measured between trailing edge of lower surface of flap segment and line parallel to wing chord	6.1.2.1 6.1.4.1 6.1.4.2 6.1.4.3
δ_{max}	maximum plain-flap deflection for linear aerodynamic characteristics	6.1.3

SYMBOL	DEFINITION	SECTIONS
δ_n	slope of airfoil surface with respect to chord plane	4.4.1
δ_o	boundary-layer thickness at point where interaction begins	6.3.1
δ_s	height of spoiler lip above upper surface of airfoil	6.2.1.1 6.2.2.1
δ_{tc}	deflection of control tab	6.3.4
$\delta_{tc_{max}}$	maximum deflection of control tab	6.3.4
δ_{tt}	deflection of trim tab	6.3.4
δ_u	deflection of primary flap segment, measured between trailing edge of upper surface of flap segment and line parallel to wing chord	6.1.2.1 6.1.4.1 6.1.4.2 6.1.4.3
δ_{vn}	parameter in span-loading calculation	6.1.7
$\delta_\perp$	semiwedge angle measured perpendicular to wing leading edge	Several
$\delta_{\perp HL}$	control deflection measured perpendicular to hinge line	6.1.5.1 6.2.1.1
ϵ	downwash angle in plane of symmetry	Several
$\Delta\epsilon$	1. downwash increment due to flaps 2. downwash increment due to subsonic jet in a subsonic stream	4.4.1 4.6 4.6.1
$\bar{\epsilon}$	1. average downwash over aft surface	4.4.1 6.2.1.2
	2. effective downwash over the wing span	4.6 4.6.4
$\Delta\bar{\epsilon}$	mean-effective-downwash increment	4.6 4.6.1
$(\Delta\epsilon)_G$	increment in downwash due to ground effect in the linear-lift range	4.7 4.7.1
ϵ_H	average downwash angle at the tail	4.4.1 4.5.3.2 4.6.3
$(\Delta\epsilon)_H$	increment in downwash at the tail	4.6.3
ϵ_p	downwash due to propeller power effects	4.6 4.6.1 4.6.3 4.6.4
$\epsilon_{power\ off}$	power-off downwash angle	4.6.3
ϵ_u	upwash angle ahead of the wing	4.6 4.6.1 4.6.3
ϵ_v	downwash at plane of symmetry at height of vortex core	4.4.1
$\epsilon_{z_{slip}}$	upwash induced by propeller slipstream, positive down	9.1 9.1.3

SYMBOL	DEFINITION	SECTIONS
η	1. dimensionless span station, $\frac{y}{b/2}$	Several
	2. ratio of the drag on a finite cylinder to the drag of a cylinder of infinite length	4.2.1.2 4.2.2.2 4.2.3.2 4.3.3.2
	3. angle of sweep of the line intersecting conical-flow regions of wing at angle of attack	6.1.6.1
	4. dimensionless span station, $\cos \frac{v\pi}{m+1}$, $\cos \frac{n\pi}{m+1}$	6.1.7
	5. control-surface efficiency	6.3.4
$\Delta\eta$	increment in dimensionless lateral direction, $\frac{\Delta y}{b/2}$	6.1.4.1 6.1.5.1
$\overline{\eta}$	lateral distance of wing MAC from body center line in semispans	6.1.5.1
η_B	1. dimensionless distance from plane of symmetry to break span station	Several
	2. Mach-number correction to the interference force	5.2.1.2 5.3.1.2
η_W	tail-effectiveness parameter	5.6.1.2
$\eta_{W(U)}$	lower-vertical-stabilizer effectiveness factor	5.6.1.2
$\eta_{W(V)}$	upper-vertical-stabilizer effectiveness factor	5.6.1.2
$\eta'_{\bar{c}}$	dimensionless span station of mean aerodynamic chord of wing segment affected by leading-edge device	6.1.5.1
$\eta_{c.p.}$	spanwise location of the center of pressure of the exposed horizontal tail	6.2.1.2
η_f	dimensionless distance from plane of symmetry to edge of flap or control surface, $\frac{y}{b/2}$	6.1.5.1
η_i	dimensionless distance from plane of symmetry to inboard edge of flap or control surface, $\frac{y_i}{b/2}$	Several
$\Delta\eta_i, \Delta\eta_o$	effective increments in spoiler spanwise inboard and outboard locations, respectively, due to spanwise flow of spoiler wake for partial-span spoilers	6.2.1.1
$\eta_{i_{eff}}, \eta_{o_{eff}}$	effective locations of inboard and outboard ends, respectively, of spoilers	6.2.1.1
η_k, η_{k-1}	dimensionless span stations denoting outboard and inboard ends, respectively, of the kth wing section	6.1.5.1
η_{max}	empirical factor accounting for maximum lifting efficiency	6.1.1.3
η_o	dimensionless distance from plane of symmetry to outboard edge of flap or control surface, $\frac{y_o}{b/2}$	Several
η_t	1. turning-efficiency factor of the aft flap segment	6.1.1.1
	2. static turning efficiency defined as resultant force divided by gross thrust	6.1.4.3 6.1.5.1

SYMBOL	DEFINITION	SECTIONS
η_α	lumped parameter containing the effects of downwash, dynamic-pressure ratio, and Mach number	4.5.1.2
η_δ	empirical factor accounting for changes in flap deflection from the optimum deflection	6.1.1.3
$\eta_0, \eta_1, \eta_2, \eta_3$	dimensionless span stations, from center line outboard on wing	6.1.5.1
η_1	empirical lift-efficiency factor of a single-slotted flap, a vane, or forward-flap segment of double-slotted flap	6.1.1.1
η_2	empirical lift-efficiency factor of the aft-flap segment of a double-slotted flap	6.1.1.1
$\eta\left(\frac{q_H}{q}\right)$	tail-effectiveness factor for configurations with body-mounted horizontal tails	6.2.1.2
θ	1. slope of airfoil mean line at leading edge	2.2.1
	2. linear angle of twist of wing tip with respect to root, negative for washout	Several
	3. ratio of ambient static temperature to jet-exit static temperature	4.6.1
	4. surface slope of cone frustum	Several
	5. shock-wave angle	4.4.1 6.3.1
	6. leading-edge shock angle	5.3.1.2 5.6.1.2
	7. angular pitching velocity	7.1.1.2
	8. slipstream turning angle measured from thrust axis	9.2 9.2.1 9.2.3
	9. spoiler deflection angle	6.2.1.1
	10. body surface slope	4.2.1.2 4.2.2.2
	11. angle of conical divergence	4.6.4
	12. angle of secondary shock	6.3.2
$\Delta\theta$	increment of slipstream turning angle due to wing camber and incidence	9.2 9.2.1
$\tilde{\theta}$	angle between airfoil chord line and line connecting airfoil trailing edge with maximum airfoil upper-surface ordinate (see Sketch (a), Section 4.1.4.3)	4.1.4.3
θ_F	surface slope of flared afterbody	4.2.1.1 4.2.1.2 4.2.2.1
θ_N	1. surface slope of conical body section having a blunted nose	4.2.1.2
	2. surface slope of nose	4.2.3.1 4.3.3.1 5.3.3.1
θ_c	cone angle	4.2.2.1

SYMBOL	DEFINITION	SECTIONS
θ_f	slipstream turning angle adjusted to the condition of zero camber and zero incidence	9.2 9.2.1
θ_1	trailing-edge shock angle	5.3.1.2 5.6.1.2
$\theta_1, \theta_2, \theta_3, \ldots$	local surface slope of body segments	4.2.2.1
κ	ratio of two-dimensional lift-curve slope at appropriate Mach number to $2\pi/\beta$; or, ratio of incompressible two-dimensional lift-curve slope to 2π	Several
Λ_{HL}	sweepback angle of hinge line of flap or control surface	Several
$\Lambda_{H_{c/4}}$	sweep angle of horizontal-tail quarter-chord	4.6 4.6.3
$\Lambda_{LE}, \Lambda_{LE_W}, \Lambda$	sweepback angle of wing leading edge	Several
$\Lambda'_{LE}, \Lambda''_{LE}$	sweepback angles of leading edges of forward and aft surfaces, respectively	4.5.1.1 4.5.1.2 /.4.1.1
$\Lambda_{LE_{bw}}$	sweepback angle of leading edge of basic wing	4.1.3.2 4.1.5.1 4.3.3.1 5.1.2.1
Λ_{LE_e}	sweepback angle of leading edge of exposed wing	4.3.2.2
$(\Lambda_{LE_e})_i$	sweepback angle of leading edge of inboard panel of exposed wing	4.3.2.2
Λ_{LE_g}	sweepback angle of leading edge of glove of double-delta and cranked wings	4.1.3.2 5.1.2.1
Λ_{LE_H}	sweepback angle of horizontal-stabilizer leading edge	4.5.3.1 8.1
$\Lambda_{LE_i}, \Lambda_{LE_o}$	sweepback angles of leading edge of wing inboard and outboard panels, respectively	Several
Λ'_{LE_o}	sweepback angle of leading edge of constructed outboard panels of wing	4.1.4.2 4.3.2.2
Λ_{LE_U}	sweepback angle of lower-vertical-stabilizer leading edge	Several
Λ_{LE_V}	sweepback angle of upper-vertical-stabilizer leading edge	Several
$\Lambda_{LE_1}, \Lambda_{LE_2}$	sweepback angles of leading edge of constructed panels of non-straight-tapered wings	4.1.3.2
Λ_{TE}	sweepback angle of wing trailing edge	Several
$\Lambda_{TE_{bw}}$	sweepback angle of trailing edge of basic wing	4.1.3.2 4.1.5.1 4.3.3.1
Λ_{TE_E}	sweepback angle of trailing edge of extension of double-delta and cranked wings	4.1.3.2

SYMBOL	DEFINITION	SECTIONS
$\Lambda_{TE_i}, \Lambda_{TE_o}$	sweepback angles of trailing edge of wing inboard and outboard panels, respectively	4.1.3.2 4.1.4.2 4.1.5.1
Λ_b	sweepback of constant-percent-chord line through center of pressure of basic loading (see Equation 6.1.5.1-g)	6.1.5.1
Λ_c	complement of leading-edge sweep angle; $\Lambda_c = 90^0 - \Lambda_{LE}$	4.1.3.2 4.1.4.1
$\Lambda_{c/(\ )}$	sweepback angle of a constant-percent-chord line	Several
$\Lambda_{c/2}, \Lambda_{c/2_W}$	sweepback angle of wing 50-percent-chord line	Several
$\Lambda'_{c/2}, \Lambda''_{c/2}$	sweepback angles of 50-percent-chord line of forward and aft surfaces, respectively	4.5.1.1 7.4.1.1
$\Lambda_{3c/4}$	sweepback angle of the three-quarter-chord point of the wing	4.4.1
$\Lambda_{c/2_e}$	sweepback angle of midchord line of exposed wing	4.3.2.2
$\Lambda_{c/2_{eff}}$	effective sweepback angle of midchord line of exposed wing	4.1.3.2 4.1.3.3
$\Lambda_{c/2_i}, \Lambda_{c/2_o}$	sweepback angles of midchord line of wing inboard and outboard panels, respectively	4.1.3.2 4.1.3.3 4.1.4.2 5.1.2.1
$\Lambda_{c/2_j}$	sweepback angle of midchord line of one section of n sections	4.1.3.2 4.1.3.3
$\Lambda'_{c/2_o}$	sweepback angle of midchord line of constructed outboard panel of wing	5.1.2.1
$\Lambda_{c/2_U}$	sweepback angle of the midchord line of the lower vertical stabilizer	5.3.1.1 5.6.1.1
$\Lambda_{c/2_V}$	sweepback angle of the midchord line of the upper vertical stabilizer	5.3.1.1
$\Lambda_{c/4_W}, \Lambda_{c/4}$	sweepback angle of the quarter-chord line of the wing	Several
$\Lambda'_{c/4}, \Lambda''_{c/4}$	sweepback angles of quarter-chord line of forward and aft surfaces, respectively	4.5.1.1 7.4.4.1
Λ_m, Λ_n	sweepback angles of arbitrary chordwise locations	2.2.2
Λ_s	sweepback angle of spoiler hinge line	6.2.1.1
$\Lambda_{(t/c)_{max}}$	sweepback angle of airfoil maximum-thickness line of wing	4.1.5.1 4.3.3.1 4.5.3.1
$\Lambda_{(t/c)_{max_i}}$, $\Lambda_{(t/c)_{max_o}}$	sweepback angles of airfoil maximum-thickness line of wing inboard and outboard panels, respectively	4.1.5.1 4.3.3.1

SYMBOL	DEFINITION	SECTIONS
Λ_β	compressible sweep parameter, $\tan^{-1}\left(\frac{\tan \Lambda_{c/4}}{\beta}\right)$	Several
λ	1. taper ratio, $\frac{\text{tip chord}}{\text{root chord}}$	Several
	2. mean free path (average distance traveled between molecular collisions)	6.3.2
λ', λ''	taper ratios of forward and aft surfaces, respectively	4.5.1.1 7.4.1.1 7.4.4.1
λ_H	taper ratio of horizontal tail or canard surface	Several
λ_{H_e}	taper ratio of exposed horizontal tail	6.2.1.2
λ_U	taper ratio of lower vertical stabilizer, measured from fuselage center line	Several
λ_{U_e}	taper ratio of exposed lower vertical stabilizer	Several
λ_V	taper ratio of upper vertical stabilizer, measured from fuselage center line	Several
λ_{V_e}	taper ratio of exposed upper vertical stabilizer	Several
λ_W	wing taper ratio	Several
λ_{bw}	taper ratio of basic wing	4.1.3.2 4.1.5.1 4.3.3.1 5.1.2.1
λ_e	taper ratio of exposed wing panel	Several
λ'_e, λ''_e	taper ratios of forward and aft exposed surfaces, respectively	4.4.1 4.5.1.1 7.4.1.1
$(\lambda_e)_i$ or $(\lambda_i)_e$	taper ratio of inboard panel of exposed wing	4.3.2.2 4.3.3.1
λ_f	taper ratio of flap or control surface	6.1.4.1 6.1.5.1
λ_g	taper ratio of glove of double-delta and cranked wings	4.1.3.2 5.1.2.1
λ_i, λ_o	taper ratios of wing inboard and outboard panels, respectively	Several
λ'_o	taper ratio of constructed outboard panel of wing	4.1.4.2 4.3.2.2 5.1.2.1
λ_1, λ_2	taper ratios of constructed panels of non-straight-tapered wings	4.1.3.2

SYMBOL	DEFINITION	SECTIONS
μ	Mach angle, $\sin^{-1}\frac{1}{M}$	Several
ν	Prandtl-Meyer angle	4.4.1 5.3.1.2 5.6.1.2
$\Delta\nu$	increment in flow angle between two points on the body surface	4.4.1
ξ	1. any station along body	4.3.3.1
	2. pressure ratio along secondary shock	6.3.2
ξ_{ru}	distance required for complete rollup of wing-tip vortices, measured parallel to the wing root chord from the tip quarter-chord point, in semispans	4.4.1 7.4.4.1
ρ	1. ratio of weight to chord for wing	8.1
	2. air density	4.6 6.3.2
ρ_P	pitch radius of gyration	8.2
ρ_R	roll radius of gyration	8.2
$\rho_{x_o}, \rho_{y_o}, \rho_{z_o}$	radii of gyration at the c.g. of the component	8.2
σ	1. geometric planform parameter, $\frac{A}{4}(1+\lambda)\tan\Lambda_{LE}$	2.2.2 4.1.3.2 4.1.4.3
	2. Prandtl interference coefficient	4.7 4.7.1 4.7.4
	3. sidewash, positive out the left wing	5.4.1
	4. boundary-layer separation angle	6.3.2
	5. air density ratio, ρ/ρ_o	6.3.4
	6. propeller solidity, ratio of blade element area to annular area at 0.75R	9.1 9.1.1 9.1.3
σ_e	effective propeller solidity	9.1 9.1.1 9.1.3
τ	1. one-half the thickness ratio of the forward-facing surface of a wedge airfoil	4.1.5.1
	2. angle denoting an arbitrary position of the ray in the conical-flow field	6.1.6.1
$\tau_{c.p.}$	angle of a ray in the conical-flow field which passes through the center of pressure	6.1.6.1
Φ	effective turning angle	6.1.1.1

SYMBOL	DEFINITION	SECTIONS
ϕ	1. angle of bank of elliptical-cross-section body about its longitudinal axis, measured from the major axis	4.2.1.2 4.2.2.2 4.2.3.2
	2. roll angle	4.3.3.1 6.1.7
	3. angle of inclination normal to body center line, $\tan^{-1}\frac{\beta}{\alpha}$	5.3.1.2 5.6.1.2
	4. angle associated with geometry of separation	6.3.1
	5. inclination of nozzle center line relative to an axis normal to surface	6.3.2
ϕ_{TE}	1. streamwise trailing-edge angle	Several
	2. trailing-edge angle measured normal to control hinge line	6.1.4.1 6.1.5.1 6.1.6.1 6.2.1.1
ϕ'_{TE}	trailing-edge angle based on airfoil ordinates at 90- and 99-percent chord	Several
ϕ''_{TE}	trailing-edge angle based on airfoil ordinates at 95- and 99-percent chord	6.1.3.1 6.1.3.2 6.1.6.1 6.1.6.2
$\phi_{TE_{upper}}$	$\tan^{-1}\frac{Y_{90} - Y_{100}}{0.10}$	6.1.1.1
ϕ_n	span-loading angle calculated at spanwise station n, $\frac{n\pi}{m+1}$	6.1.7
ϕ_v	span loading angle calculated at spanwise station v, $\frac{v\pi}{m+1}$	6.1.7
ϕ_β	lift-efficiency factor for a geared tab system, $1 + \beta C_2/C_1$	6.3.4
Ω	angle used in determination of trim drag (see Figure 4.5.3.2-4)	4.5.3.2

C. CAPITAL-LETTER COEFFICIENTS AND DERIVATIVES

SYMBOL	DEFINITION	SECTIONS
ΔC_A	increment in axial-force coefficient	6.3.1
C_D	drag coefficient, $\frac{\text{drag}}{qS}$	Several
$(C_D)'$	total drag coefficient of the forward panel and body, including wing-body interference	4.5.2.1
$(C_D)''$	total drag coefficient of the aft panel, including wing-body interferences	4.5.2.1
ΔC_D	zero-lift drag coefficient due to flap deflection based on free-stream velocity	9.2 9.2.3
$C_D(\alpha)$	drag due to angle of attack	4.2.3.2 4.3.3.2
$[C_D(\alpha)]_B$	body drag due to angle of attack	4.3.3.2
$[C_D(\alpha)]_{a/b}$	drag due to angle of attack of a body having an elliptical cross section	4.2.3.2
C_{D_A}	wave-drag coefficient based on maximum frontal area of afterbody	Several
ΔC_{D_A}	reduction in afterbody wave-drag coefficient of a body of revolution with elliptic cross section	4.2.3.1
$C_{D_{A(NC)}}$	coefficient of interference drag acting on the afterbody due to the nose and cylindrical section	4.2.3.1 4.2.3.2 4.3.3.1 4.5.3.1
C_{D_b}	base drag coefficient	Several
$(C_{D_b})_B$	base-pressure drag coefficient for the body	4.3.3.1
C_{D_e}	external duct drag coefficient, $\frac{-F_{x_e}}{q_\infty S_D}$	9.3 9.3.1
C_{D_f}	1. skin-friction drag coefficient	Several
	2. power-off zero-lift drag coefficient	9.2 9.2.3
$\Delta(C_{D_f})$	increment of skin-friction drag due to control-surface or flap deflection	6.1.7
$(C_{D_f})_B$	body skin-friction drag coefficient	4.2.3.1 4.3.3.1

SYMBOL	DEFINITION	SECTIONS
$\left(C_{D_f}\right)_b$	zero-lift drag of body exclusive of the base drag, based on body base area	4.2.3.1 4.2.3.2 4.3.3.1 4.5.3.1
$\left(C_{D_f}\right)_H$	compressible skin-friction drag coefficient of horizontal stabilizer, based on total horizontal stabilizer area	4.5.3.1
$\left(C_{D_f}\right)_V$	compressible skin-friction drag coefficient of vertical stabilizer, based on vertical stabilizer area to body center line	4.5.3.1
$\left(C_{D_f}\right)_W$	compressible skin-friction drag coefficient of wing, based on total wing area	4.3.3.1 4.5.3.1
C_{D_H}	drag coefficient of horizontal stabilizer, $\frac{\text{horizontal-tail drag}}{qS_H}$	4.5.3.2 4.6.2
$\left(C_{D_H}\right)_{\alpha_{C_{L_{max}}}}$	horizontal-tail-body drag at stall angle of attack	4.5.1.3
C_{D_i}	induced-drag coefficient	6.1.7
C_{D_L}	drag coefficient due to lift	Several
ΔC_{D_L}	increment in drag due to lift resulting from a breakdown in leading-edge suction at lift coefficients above parabolic-drag-polar region	4.1.5.2
$C_{D_{LE}}$	pressure-drag coefficient of a swept, cylindrical leading edge	4.1.5.1 4.3.3.1
$\left(\Delta C_{D_L}\right)_G$	change in drag due to lift caused by ground effect	4.7 4.7.4
$\left(C_{D_L}\right)_W$	drag due to lift of the wing, based on total wing area	4.3.3.2
$\left(C_{D_L}\right)_{WB}$	drag due to lift of a wing-body configuration	4.3.3.2
$(C_D)_{min}$	minimum drag coefficient	6.1.7
$\Delta C_{D_{min}}$	increment in minimum drag coefficient due to control-surface or flap deflection	6.1.7
$\left(C_{D_{min}}\right)_{flaps\ up}$ or $\left(C_{D_{min}}\right)_{\delta = 0}$	minimum drag coefficient for undeflected control or flap	6.1.7
$C_{D_{N_I}}$	wave-drag coefficient of spherically blunted noses	4.2.3.1 4.3.3.1 4.5.3.1

SYMBOL	DEFINITION	SECTIONS
$\Delta C_{D_{N_1}}$	reduction in forebody wave-drag coefficient of a body of revolution with an elliptic cross section	4.2.3.1
$C_{D_{N_2}}$	wave-drag coefficient of conical or ogive-profile nose, based on maximum frontal area of nose	4.2.3.1 4.3.3.1 4.5.3.1
C_{D_o}	power-off drag coefficient based on free-stream velocity and wing area, $\frac{\text{drag}}{q_\infty S}$	9.2 9.2.3
C_{D_p}	subsonic pressure-drag coefficient	4.2.3.1 4.3.3.1 4.5.3.1
$C_{D_{p_n}}$	pressure-drag coefficient of any of n segments of a body	4.2.3.1
$C_{D_{p_1}}, C_{D_{p_2}}, C_{D_{p_3}}, \ldots$	pressure-drag coefficient of given body segments	4.2.3.1
$\Delta C_{D_{Trim}}$	incremental drag coefficient of horizontal stabilizer including both zero-lift and induced drag	4.5.3.2
C_{D_v}	viscous drag coefficient due to lift	4.1.5.2
C_{D_w}	supersonic wave-drag coefficient of the body	Several
$C_{D_{wave}}$	wave-drag coefficient	6.1.7
$\Delta\left(C_{D_{wave}}\right)$	increment in wave-drag coefficient due to control deflection	6.1.7
$\left(C_{D_{wave}}\right)_{\delta = 0}$ or $\left(\Delta C_{D_0}\right)_{\delta = 0}$	zero-lift wave-drag increment at transonic speeds for undeflected control or flap	6.1.7
$\left(C_{D_w}\right)_B$	wave-drag coefficient of the body	4.3.3.1
$C_{D_{WB}}$	wing-body drag coefficient in absence of ground plane	4.7 4.7.4

SYMBOL	DEFINITION	SECTIONS
$(C_D)_{WB}$	drag coefficient of a wing-body combination at angle of attack	4.3.3.2
$(C_{D_{WB}})_G$	wing-body drag coefficient in the presence of the ground	4.7 4.7.4
$(C_{D_w})_H$	supersonic wave-drag coefficient of the horizontal-tail panel	4.5.3.1
$C_{D_{w_{peak}}}{}_{\Lambda_{c/4}=n}$	maximum wave-drag-coefficient increment for swept wing with $\Lambda_{c/4} = n$	4.1.5.1 4.3.3.1
$C_{D_{w_{peak}}}{}_{\Lambda_{c/4}=0}$	maximum wave-drag-coefficient increment for an unswept wing	4.1.5.1
$(C_{D_w})_V$	supersonic wave-drag coefficient of the vertical-tail panel	4.5.3.1
$(C_{D_w})_W$	supersonic wave-drag coefficient of the wing	4.3.3.1 4.5.3.1
$(C_{D_\alpha})'$	total drag-curve slope of the forward panel and body, including interferences	4.5.2.1
$(C_{D_\alpha})''$	total drag-curve slope of the aft panel and body, including interferences	4.5.2.1
$(C_D)_\delta$	drag coefficient for control surface or flap deflection	6.1.7
$(C_D)_{\delta=0}$	drag coefficient for zero control surface or flap deflection	6.1.7
C_{D_0}	1. zero-lift drag coefficient	Several
	2. profile-drag coefficient of the wing at any given lift coefficient	7.1.3.2 7.1.3.3 7.3.2.2
ΔC_{D_0}	increment of zero-lift wave-drag coefficient at transonic speeds	4.1.5.1 4.3.3.1 4.5.3.1
$(C_{D_0})_B$	total zero-lift drag coefficient of body	4.3.3.1 4.5.3.1
$(\Delta C_{D_0})_{flap}$	increment of zero-lift drag coefficient due to flap deflection	4.6.4
$(\Delta C_{D_0})_{\substack{flaps \\ power\ on}}$	increment of zero-lift drag coefficient for the flap extended and immersed in the propeller slipstream	4.6.4

SYMBOL	DEFINITION	SECTIONS
$(C_{D_0})_H$	zero-lift drag coefficient of horizontal stabilizer, based on total horizontal-stabilizer area	4.5.3.1 4.5.3.2
$(C_{D_0})_i, (C_{D_0})_o$	zero-lift drag coefficients of wing inboard and outboard panels, respectively	4.1.5.1 4.3.3.1
$(C_{D_0})_{\text{lifting surface}}$	zero-lift drag coefficient of lifting surface	4.5.3.1
$(C_{D_0})_{M_D}$	zero-lift drag coefficient at drag-divergence Mach number	4.5.3.1
$(C_{D_0})_{M_I}$	zero-lift drag coefficient at initial drag-rise Mach number	4.5.3.1
$(\Delta C_{D_0})_{\text{power on}}$	increment of zero-lift drag for propeller power	4.6.4
$(\Delta C_{D_0})_s$	increment of skin-friction zero-lift drag coefficient due to propeller slipstream	4.6.4
$(C_{D_0})_V$	zero-lift drag coefficient of vertical stabilizer, based on vertical-stabilizer area to body center line	4.5.3.1 4.5.3.2
$(C_{D_0})_W$	zero-lift drag coefficient of wing, based on total wing area	4.3.3.1 4.5.3.1
$(C_{D_0})_{WB}$	zero-lift drag coefficient of wing-body combination	4.3.3.1 4.3.3.2 4.5.3.1 4.5.3.2
$C_{D_1}, C_{D_2}, C_{D_3}, \cdots$	drag coefficients of various components of body	4.2.3.1
C_{F_c}	control-force coefficient	6.3.2
$(C_{F_c})_{cr}$	corrected control-force coefficient	6.3.2
C_{F_x}	1. negative-drag coefficient based on free-stream velocity and wing area, $\frac{F_x}{q_\infty S}$	9.2
	2. duct negative-drag coefficient based on free-stream velocity and duct planform area, $\frac{F_x}{q_\infty S_D}$	9.3 9.3.2 9.3.3

SYMBOL	DEFINITION	SECTIONS
C_{F_x}''	negative-drag coefficient based on slipstream velocity and wing area, $\frac{F_x}{q''S}$	9.2 9.2.3
$C_{F_{x_e}}$	external duct negative-drag coefficient based on free-stream velocity and duct planform area, $\frac{F_{x_e}}{q_\infty S_D}$	9.3 9.3.1 9.3.3
C_J	three-dimensional trailing-edge jet momentum coefficient for jet-flap configurations	6.1.4.1 6.1.4.2 6.1.4.3 6.1.5.1
C_J'	three-dimensional trailing-edge jet momentum coefficient, based on blown-flap affected area	6.1.4.1 6.1.4.2
C_L	1. lift coefficient, $\frac{\text{lift}}{qS}$	Several
	2. duct lift contribution, $\frac{\text{lift}}{q_\infty S_D}$	9.3 9.3.1 9.3.2
ΔC_L	1. increment in lift due to leading-edge vortex at particular angle of attack (see Sketch (b), Section 4.1.3.2)	4.1.3.2 4.1.4.3
	2. increment in lift beyond the lift coefficient at α_{break}	4.1.3.3
	3. increment of wing lift coefficient due to flap or control-surface deflection	6.1.4.1 6.1.5.1
$(C_L)'$	total lift coefficient of the forward panel and body, including wing-body interference	4.5.2.1 7.4.1.1
C_L''	lift coefficient based on slipstream velocity, $\frac{\text{lift}}{q''S}$	9.2 9.2.1
$(C_L)''$	total lift coefficient of the aft panel, including wing-body interferences	4.5.2.1
$(C_L)_{a/b}$	lift coefficient of a body with elliptical cross section	4.2.1.2
$C_{L_{basic}}$	basic wing lift coefficient excluding leading-edge vortex-induced effects	4.1.4.3
$C_{L_{break}}$	lift coefficient where lift curve becomes nonlinear	4.1.3.3
C_{L_c}	"critical" lift coefficient, where drag-due-to-lift factor is no longer a constant	4.1.5.2
ΔC_{L_c}	lift increment due to control surface	6.3.4
C_{L_d}	conical-camber design lift coefficient for a M = 1.0 design with the designated camber ray line intersecting the wing trailing edge at 0.3 b/2	4.3.2.1
C_{L_e}	lift coefficient resulting from external mass flow	9.3 9.3.1 9.3.2
$(C_L)_e'$	lift coefficient of the exposed forward panel	4.5.1.2

SYMBOL	DEFINITION	SECTIONS
ΔC_{L_f}	increment in wing lift coefficient due to symmetric flap deflection in absence of ground plane	4.7 4.7.1 6.1.7
$\left(C_{L_f}\right)_{WB}$	wing-body lift coefficient including flap effects in absence of ground plane	4.7.1
$\Delta\left(\Delta C_L\right)_{flap}$	empirical factor accounting for flap effects in the presence of the ground	4.7 4.7.1
$C_L(g)$	lift-coefficient correction term	7.1.4.1 7.3.4.1
$\left(\Delta C_L\right)_G$	increment in wing or horizontal tail lift due to the presence of the ground plane	4.7
C_{L_H}	lift coefficient of horizontal tail, $\frac{\text{horizontal-tail lift}}{qS_H}$	4.5.3.2 4.6.3 4.7.1 6.3.4
$\left(\Delta C_L\right)_H$	increment in lift coefficient due to horizontal tail	4.6 4.6.1
$\left(\Delta C_{L_H}\right)_G$	increment in horizontal-tail lift in the presence of the ground	4.7 4.7.3
$C_{L_{H(WBV)}}$	horizontal-tail-body lift in presence of the wing, body, and vertical tail	4.5.1.3
C_{L_i}	lift coefficient resulting from internal mass flow	9.3 9.3.1 9.3.2
$\left(C_{L_i}\right)_{WB}$	rate of change of lift coefficient with wing incidence (fuselage angle of attack held constant)	4.3.1.2
$C_{L_{max}}$	maximum lift coefficient, $\frac{\text{maximum lift}}{qS}$	Several
$\Delta C_{L_{max}}$	1. increment in wing maximum lift coefficient accounting for Mach-number effects	4.1.3.3 4.1.3.4
	2. increment in wing maximum lift coefficient due to propeller power	4.6 4.6.2
	3. increment in wing maximum lift coefficient due to flap deflection	6.1.4.3
$C_{L_{max}}^*$	maximum lift coefficient wing as determined by the low-aspect-ratio method	4.1.3.3
$\left(C_{L_{max}}\right)_{base}$	base value of parameter	4.1.3.3 4.1.3.4
$\left[\left(C_{L_{max}}\right)_{base}\right]_e''$	subsonic maximum lift coefficient of exposed aft panel	4.5.1.2
$\left(C_{L_{max}}\right)_e$	maximum lift coefficient for exposed wing	4.1.3.4

SYMBOL	DEFINITION	SECTIONS
$(C_{L_{max}})_e'$, $(C_{L_{max}})_e''$	maximum lift coefficients of exposed forward and aft panels, respectively	4.1.5.2
$(\Delta C_{L_{max}})_e'$, $(\Delta C_{L_{max}})_e''$	increments in wing maximum lift coefficients accounting for Mach number effects on the forward and aft panels, respectively	4.1.5.2
$(C_{L_{max}})_W$	value of parameter for wing	4.3.1.4
$(C_{L_{max}})_{WB}$	maximum lift coefficient for wing-body	4.3.1.4 4.5.1.3
$(\Delta C_L)_{N_j}$	increment in lift coefficient acting at jet-engine inlet due to inclination of thrust axis to oncoming flow	4.6 4.6.1 4.6.4
$(\Delta C_L)_{N_p}$	increment in lift coefficient due to inclination of propeller plane to oncoming flow	4.6 4.6.1 4.6.3
$C_{L_{nonlinear}}$	lift coefficient above point where the lift curve ceases to be linear	4.1.3.3
C_{L_o}	power-off lift coefficient based on free-stream velocity and wing area, $\frac{L}{q_\infty S}$	9.2 9.2.1 9.2.3
C_{L_p}	lift coefficient due to propeller effects	4.6 4.6.4
$(C_L)_{\substack{power \\ off}}$	lift coefficient of configuration, power off	4.6.1
$(\Delta C_L)_{\substack{power \\ on}}$	increment in lift coefficient due to propeller power	4.6.1 4.6.2
C_{L_q}	pitching derivative, $\frac{\partial C_L}{\partial\left(\frac{q\bar{c}}{2V_\infty}\right)}$	Several
$(\Delta C_L)_q$	increment in lift coefficient due to change in dynamic pressure behind propeller	4.6 4.6.1 4.6.3
C_{L_q}'	value of pitching derivative referred to body axes with origin at wing aerodynamic center	7.1.1.1 7.1.1.2 7.3.1.1
C_{L_q}''	value of pitching derivative referred to body axes with origin at wing leading-edge vertex	7.1.1.1 7.1.1.2
$(C_{L_q})_B$	contribution of the body to pitching derivative C_{L_q}	7.3.1.1 7.4.1.1

SYMBOL	DEFINITION	SECTIONS
$\left(C_{L_q}\right)_e$	contribution of the exposed wing to the pitching derivative C_{L_q}	7.3.1.1 7.3.1.2
$\left(C_{L_q}\right)'_e, \left(C_{L_q}\right)''_e$	contributions of exposed forward and aft panels, respectively, to the pitching derivative C_{L_q}	7.4.1.1
$\left(C_{L_q}\right)_W$	contribution of the wing to the pitching derivative C_{L_q}	7.3.1.1
$\left(C_{L_q}\right)_{WB}$	contribution of the wing-body combination to the pitching derivative C_{L_q}	7.3.1.1 7.4.1.1
C_{L_s}	lift coefficient of surface to which the main control surface is attached	6.3.4
$\left(\Delta C_L\right)_{SE}$	increment in lift coefficient, accounting for the direct influence of the wing shock-expansion field	4.4.1
$\left(\Delta C_L\right)_T$	increment in lift coefficient due to angle of attack of thrust axis	4.6 4.6.1 4.6.4
$\Delta C_{L_{tc}}$	lift loss due to tab	6.3.4
$\Delta C_{L_{trim}}$	incremental lift coefficient required for trim	4.5.3.2
C_{L_V}	vertical-tail lift coefficient	6.3.4
C_{L_W}	1. wing lift coefficient with power effects	4.6 4.6.4
	2. wing lift coefficient, including tab and control deflections	6.3.4
$C_{L_{WB}}$	wing-body lift coefficient in absence of ground plane	4.5.3.2 4.7 4.7.3
$\left(\Delta C_{L_{WB}}\right)_G$	increment in wing-body lift coefficient in the presence of the ground	4.7 4.7.3
$C_{L_{W''(v)}}$	contribution to the lift coefficient due to the effect of the forward-surface vortices on the aft surface	4.5.1.2
C_{L_α}	lift-curve slope, rate of change of lift coefficient with angle of attack, $\frac{dC_L}{d\alpha}$	Several
ΔC_{L_α}	increment in lift-curve slope	4.3.1.2
$\left(\Delta C_L\right)_{\Delta \alpha_W}$	increment in wing lift coefficient due to change in angle of attack induced by propeller flow field	4.6 4.6.1 4.6.3
$C_{L_{\alpha=0}}$	lift coefficient where $\alpha \approx 0$	4.1.3.3
$\left(C_{L_\alpha}\right)'$	1. complete lift-curve slope of forward panel and body, including interferences	4.5.2.1
	2. lift-curve slope of forward panel	4.5.1.2 7.4.4.1
$\left(C_{L_\alpha}\right)''$	1. lift-curve slope of aft panel, including wing-body interference effects	4.5.2.1
	2. lift-curve slope of aft panel	4.5.1.2

SYMBOL	DEFINITION	SECTIONS
$(C_{L_\alpha})_a$	value of the derivative at M_a	4.1.3.2
$(C_{L_\alpha})_B$	lift-curve slope of body	7.3.1.1 7.3.4.1
$(C_{L_\alpha})_b$	value of the derivative at M_b	4.1.3.2
$(C_{L_\alpha})_{basic}$	low-lift-region lift-curve slope, including thickness effects	4.1.3.2 4.1.4.3
$(C_{L_\alpha})_{B(W)}$ or $C_{L_{\alpha_{B(W)}}}$	lift-curve slope of body in presence of wing	4.3.2.2 4.5.2.1 4.5.3.2
$(C_{L_\alpha})_{C_L}$	value of the derivative at a given lift coefficient	5.1.2.2 7.1.2.2 7.3.2.2
$(C_{L_\alpha})_e$	lift-curve slope of the exposed wing	Several
$(C_{L_\alpha})'_e, (C_{L_\alpha})''_e$	lift-curve slopes of the exposed forward and aft panels, respectively	Several
$(C_{L_\alpha})_{fb}$	value of derivative at M_{fb}	4.1.3.2
$C_{L_{\alpha_H}}$	lift-curve slope of the horizontal surface	Several
$(C_{L_{\alpha_H}})_e$	lift-curve slope of the exposed horizontal surface	6.2.1.2
$(C_{L_{\alpha_H}})_{M_H}$	lift-curve slope of the horizontal tail operating at the local Mach number of the flow in the vicinity of the horizontal tail	4.5.1.2
$(C_{L_{\alpha_H}})_{M_\infty}$	lift-curve slope of the isolated horizontal tail at the free-stream Mach number	4.5.1.2
$(C_{L_\alpha})_i$	lift-curve slope of the inboard panel of wing	4.1.4.2 5.1.2.1
$(C_{L_\alpha})_{limit}$	limiting value of lift-curve slope	4.1.3.2
$(C_{L_\alpha})_{\substack{low\\speed}}$ or $\left(\frac{dC_L}{d\alpha}\right)_{\substack{low\\speed}}$	lift-curve slope at low speeds	4.4.1
$(C_{L_\alpha})_M$	value of derivative at a given Mach number	Several

SYMBOL	DEFINITION	SECTIONS
$\left(C_{L_\alpha}\right)_M$ or $\left(\frac{dC_L}{d\alpha}\right)_M$	lift-curve slope at high subsonic Mach numbers	4.4.1
$\left(C_{L_\alpha}\right)_{M_{cr}}$	value of derivative at the critical Mach number	7.1.1.2
$\left(C_{L_\alpha}\right)_N$	value of derivative for nose of body	Several
$C_{L_{\alpha_o}}$	power-off lift-curve slope	9.2.1
$\left(C_{L_\alpha}\right)_o'$	lift-curve slope of the constructed outboard panel of wing	4.1.4.2 5.1.2.1
$\left(C_{L_\alpha}\right)_p$	lift-curve slope of isolated vertical panel mounted on a reflection plane	5.3.1.1
$\left(C_{L_\alpha}\right)_{pred}$	lift-curve slope of cranked wing, predicted by double-delta-wing method	4.1.3.2
$\left(C_{L_\alpha}\right)_{theory}$	value of derivative derived from theory	4.1.3.2
$\left(C_{L_\alpha}\right)_U$	lift-curve slope of isolated lower vertical panel mounted on a reflection plane (the aspect ratio is taken as twice the aspect ratio defined by the average exposed span and exposed area)	Several
$\left(C_{L_\alpha}\right)_V$	1. lift-curve slope of isolated upper vertical panel with effective aspect ratio defined by Equation 5.3.1.1-a	5.3.1.1 5.6.1.1
	2. lift-curve slope of isolated upper vertical panel mounted on a reflection plane (the aspect ratio is taken as twice the aspect ratio defined by the average exposed span and exposed area)	Several
$\left(C_{L_\alpha}\right)_W$	lift-curve slope of the wing	4.3.1.2 4.3.1.3 4.3.3.2
$\left(C_{L_\alpha}\right)_{WB}$	lift-curve slope of the wing-body combination	4.2.2.1 4.3.1.2 4.7 4.7.1
$\left(C_{L_\alpha}\right)_{W\,(B)}$	lift-curve slope of wing in presence of body	4.3.2.2 4.5.2.1
$\left(C_{L_\alpha}\right)_{W_e\,(B)}$	lift-curve slope of the exposed wing in presence of body	4.3.1.2
$\left(C_{L_\alpha}\right)_{W''\,(v)}$	contribution to the lift-curve slope due to the effect of the forward-surface vortices on the aft surface	Several
$\left(C_{L_\alpha}\right)_\delta$	lift-curve slope of flap-deflected wing	6.1.4.2

SYMBOL	DEFINITION	SECTIONS
$\left(C_{L_\alpha}\right)_{\delta=0}$	lift-curve slope of flap-retracted wing	6.1.4.2
$\left(C_{L_\alpha}\right)_{II}, \left(C_{L_\alpha}\right)_{III}$	total lift-curve slopes between $C_{L_{II}}$ and $C_{L_{III}}$, and beyond $C_{L_{III}}$, respectively, (see Sketch (b), Section 4.1.3.2)	4.1.3.2 4.1.4.3
$\delta C_{L_{\alpha_{II}}}, \delta C_{L_{\alpha_{III}}}$	incremental increase in lift-curve slopes starting at $C_{L_{II}}$ and $C_{L_{III}}$, respectively, (see Sketch (b), Section 4.1.3.2)	4.1.3.2
$\frac{\left(C_{L_\alpha}\right)_{test}}{\left(C_{L_\alpha}\right)_{pred}}$	correction factor for subsonic lift-curve slope of cranked wings	4.1.3.2
$C_{L_{\dot\alpha}}$	change in lift coefficient with variation in rate of change of angle of attack, $\frac{\partial C_L}{\partial\left(\frac{\dot\alpha\,\bar c}{2V_\infty}\right)}$	Several
$\left(C_{L_{\dot\alpha}}\right)_B$	value of derivative for body	7.3.4.1 7.4.4.1
$\left(C_{L_{\dot\alpha}}\right)_e$	value of derivative for exposed wing	7.3.4.1 7.3.4.2
$\left(C_{L_{\dot\alpha}}\right)_e''$	contribution of exposed aft panel to acceleration derivative $C_{L_{\dot\alpha}}$	7.4.4.1
$\left(C_{L_{\dot\alpha}}\right)_W$	value of derivative for wing	7.3.4.1
$\left(C_{L_{\dot\alpha}}\right)_{WB}$	value of derivative for wing-body combination	7.3.4.1 7.4.4.1
$\left(C_{L_{\dot\alpha}}\right)_1, \left(C_{L_{\dot\alpha}}\right)_2$	components of the wing contribution to $C_{L_{\dot\alpha}}$	7.1.4.1
C_{L_δ}	rate of change of lift coefficient with wing flap deflection at constant angle of attack, $\frac{d C_L}{d\delta}$	6.1.4.1 6.1.5.1
C_{L_δ}'	lift-effectiveness of one symmetric, straight-sided flap, based on flap area	6.1.4.1 6.1.5.1 6.2.1.1
$\left(\Delta C_L\right)_e$	increment in lift due to inflow velocity of the flow surrounding the jet	4.6 4.6.1 4.6.3
$C_{L_{II}}, C_{L_{III}}$	breaks in lift-curve slope (see Sketch (b), Section 4.1.3.2)	4.1.3.2 4.1.4.3
C_N	1. normal-force coefficient, $\frac{N}{qS}$	Several
	2. normal-force coefficient, $\frac{N}{\rho n^2 D^4}$	9.1

SYMBOL	DEFINITION	SECTIONS
ΔC_N	1. increment in normal-force coefficient	6.3.1
	2. increment in coefficient due to jet-pressure interference on vehicle surfaces	4.6.1
C_N'	1. pseudonormal-force coefficient defined by the equation $C_N' = \frac{C_L}{\cos \alpha}$	4.1.3 4.1.3.3 4.1.3.4 7.4.1.1 9.1
	2. normal-force coefficient based on free-stream velocity and propeller disk area, $\frac{N}{q_\infty S_p}$	
$\left[C_N' @ C_{L_{max}}\right]_e'$, $\left[C_N' @ C_{L_{max}}\right]_e''$	pseudonormal-force coefficients at $C_{L_{max}}$ for exposed forward and aft panels, respectively	4.5.1.2
$\left(\frac{C_N}{C_{N_{cir}}}\right)_{NT}$	ratio of normal-force coefficient for body of noncircular cross section to that for an equivalent body of circular cross section (same cross-sectional area) as determined by Newtonian impact theory	4.2.1.2 4.2.2.2
$\left(\frac{C_N}{C_{N_{cir}}}\right)_{SB}$	ratio of normal-force coefficient for body of noncircular cross section to that for an equivalent body of circular cross section (same cross-sectional area) as determined by slender-body theory	4.2.1.2 4.2.2.2
$(C_N)_{\substack{cone \\ cyl}}$	coefficient for cone-cylinder	4.2.1.2 4.2.3.2
$(C_N)_e$	coefficient for exposed wing	4.3.1.3 4.3.1.4
$(\Delta C_N)_F$	increment in coefficient due to body flare	4.2.1.2 4.2.3.2
$(C_N)_N$	coefficient for nose	4.3.1.3 4.3.1.4
$(\Delta C_N)_N$	increment in coefficient due to body nose	4.2.1.2
C_{N_p}	propeller normal-force coefficient	4.6 4.6.4
C_{N_q}	pitching derivative, $\frac{\partial C_N}{\partial\left(\frac{q\bar{c}}{2V_\infty}\right)}$	7.2.1.1
C_{N_q}'	value of derivative for forward panel	7.2.1.1 7.2.1.2
$(C_N)_W$	coefficient for wing	4.3.1.3
$C_{N_{W''(v)}}$	contribution to the normal-force coefficient due to the effect of the forward-surface vortices on the aft surface	4.5.1.2
C_{N_α}	1. rate of change of normal-force coefficient with angle of attack, $\frac{d C_N}{d \alpha}$	Several
	2. value of derivative for forward panel	Several
	3. value of derivative for propeller	9.1.3

SYMBOL	DEFINITION	SECTIONS
ΔC_{N_α}	increment in normal-force-curve slope of a boattail following a semi-infinite cylinder	4.2.2.1
$\left(C_{N_\alpha}\right)_B$	1. value of derivative for the body	5.2.1.1 7.3.1.1 7.3.1.2 7.3.4.1
	2. value of derivative for the body nose, based on nose frontal area	4.3.2.2
$C_{N_{\alpha_{B\,(W)}}}$	value of derivative for the body in presence of the wing	4.3.2.2
$\left(C_{N_\alpha}\right)_{bw}$	normal-force-curve slope of the basic wing	4.1.3.2 5.1.2.1
$\left(C_{N_\alpha}\right)_E$	value of derivative for trailing-edge extension of double-delta and cranked wings	4.1.3.2
$\left(C_{N_\alpha}\right)_e$	value of derivative for exposed wing	4.3.1.3 4.3.1.4 4.3.2.2 7.3.1.1
$\left(C_{N_\alpha}\right)_e', \left(C_{N_\alpha}\right)_e''$	normal-force-curve slopes of the exposed forward and aft panels, respectively	Several
$\left[\left(C_{N_\alpha}\right)_e\right]_i$	normal-force-curve slope of exposed inboard panel of wing	4.3.2.2
$\left[\left(C_{N_\alpha}\right)_e\right]_{theory}$	theoretical value of derivative for exposed wing	4.3.1.2
$\left[\left(C_{N_\alpha}\right)_{e\ theory}\right]_i$	theoretical value of normal-force-curve slope of exposed inboard panel of wing	4.3.2.2
$\left(\Delta C_{N_\alpha}\right)_F$	increment in normal-force-curve slope of a flared body of revolution following a semi-infinite cylinder	4.2.1.1 4.2.2.1
$\left(C_{N_\alpha}\right)_g$	normal-force-curve slope of glove of double-delta and cranked wings	4.1.3.2 5.1.2.1
$\left(C_{N_{\alpha_H}}\right)_e$	normal-force-curve slope of the exposed horizontal surface	6.2.1.2
$\left(C_{N_\alpha}\right)_i$	normal-force-curve slope of inboard panel of wing	4.1.4.2
$C_{N'_{\alpha\,in}}$	propeller normal-force-curve slope with respect to inflow angle of attack at propeller disk	9.1.3
$\left(C_{N_\alpha}\right)_N$	normal-force-curve slope of nose of body based on total wing area	4.3.1.2 4.3.2.2
$\left(C_{N_\alpha}\right)_o'$	normal-force-curve slope of constructed outboard panel of wing	4.1.4.2
$\left(C_{N_\alpha}\right)_p$	1. propeller normal-force derivative	4.6 4.6.1 4.6.4
	2. normal-force-curve slope of isolated vertical panel mounted on a reflection plane	5.2.1.1

SYMBOL	DEFINITION	SECTIONS
$\left[\left(C_{N_\alpha}\right)_p\right]_{K_N=80.7}$	propeller normal-force derivative for $K_N=80.7$	4.6 4.6.1
$\left(C_{N_\alpha}\right)_{theory}$	theoretical val[illegible]f derivative	Several
$\left[\left(C_{N_\alpha}\right)_{theory}\right]_e$	theoretical value of normal-force-curve slope of exposed wing	4.3.2.2
$\left[\left(C_{N_\alpha}\right)_{theory}\right]_i$	theoretical value of normal-force-curve slope of inboard panel of wing	4.1.4.2
$\left[\left(C_{N_\alpha}\right)_{theory}\right]'_o$	theoretical value of normal-force-curve slope of constructed outboard panel of wing	4.1.4.2 4.3.2.2
$\left(C_{N_\alpha}\right)_U$	normal-force-curve slope of isolated lower vertical panel mounted on a reflection plane (the aspect ratio is taken as twice the aspect ratio determined by the average exposed span and exposed area)	Several
$\left(C_{N_\alpha}\right)_V$	normal-force-curve slope of isolated upper vertical panel mounted on a reflection plane (the aspect ratio is taken as twice the aspect ratio determined by the average exposed span and exposed area)	Several
$C_{N_{\alpha_{W(B)}}}$	normal-force-curve slope of exposed wing in presence of the body	4.3.2.2
$\left(C_{N_\alpha}\right)_1, \left(C_{N_\alpha}\right)_2$	normal-force-curve slopes for constructed panels of non-straight-tapered wings	4.1.3.2 5.1.2.1
$\left(\frac{dC_N}{d\alpha}\right)_{\alpha=0}$	linear normal-force-curve slope for propeller	9.1.3
$C_{N_{\alpha\alpha}}$	nonlinear increment in normal-force coefficient	4.1.3.3 4.1.3.4 4.3.1.3
$\Delta C_{N_{\alpha\alpha}}$	incremental value of coefficient	4.1.3.3
$C_{N'_{\alpha\alpha}}$	value of coefficient at end of shock-detachment transition region	4.1.3.3
$C^*_{N_{\alpha\alpha}}$	value of coefficient at incipient shock separation	4.1.3.3
$\left(C_{N_{\alpha\alpha}}\right)'_e$, $\left(C_{N_{\alpha\alpha}}\right)''_e$	increments in coefficient at $C_{L_{max}}$ for exposed forward and aft surface, respectively	4.5.1.2
$\left(\Delta C_{N_{\alpha\alpha}}\right)'_e$, $\left(\Delta C_{N_{\alpha\alpha}}\right)''_e$	incremental values of coefficient for exposed forward and aft panels, respectively	4.5.1.2

SYMBOL	DEFINITION	SECTIONS
$\left(C_{N_{\alpha\alpha}}\right)_{ref}$	increment in coefficient at $C_{L_{max}}$	4.1.3.3
$\left[\left(C_{N_{\alpha\alpha}}\right)_{ref}\right]'_e$, $\left[\left(C_{N_{\alpha\alpha}}\right)_{ref}\right]''_e$	values of derivatives at $C_{L_{max}}$ for exposed forward and aft panels, respectively	4.5.1.2
$\left[\left(C_{N_{\alpha\alpha}}\right)_{ref}\right]_{WB}$	value of derivative for wing-body combination	4.3.1.3
$\left(C_{N_{\alpha\alpha}}\right)_{theory}$	theoretical value of coefficient	4.1.3.3
$\left(\Delta C_{N_{\alpha\alpha}}\right)_{WB}$	value of increment for wing-body combination	4.3.1.3
$\left(C_{N_{\alpha\alpha}}\right)_{90}$	value of coefficient $\alpha = 90^o$	4.1.3.3
$C_{N_{\dot{\alpha}}}$	rate of change of normal-force coefficient with rate of change in angle of attack	7.2.2.1
$\left(C_{N_{\dot{\alpha}}}\right)_B$	value of derivative for body	7.3.4.1
$\left(C_{N_{\dot{\alpha}}}\right)_e$	value of derivative for exposed wing	7.3.4.1
$\left(C_{N_{\dot{\alpha}}}\right)_{WB}$	value of derivative for wing-body combination	7.3.4.1 7.4.4.1
$\left[\left(C_{N_{\dot{\alpha}}}\right)_1\right]_e$, $\left[\left(C_{N_{\dot{\alpha}}}\right)_2\right]_e$	components to the exposed-wing contribution $C_{N_{\dot{\alpha}}}$	7.3.4.1
$\left(C_{N_1}'\right)'_e$, $\left(C_{N_2}'\right)'_e$	pseudonormal-force coefficients of the exposed forward panel	4.5.1.2
$\left(C_{N_1}'\right)''_e$, $\left(C_{N_2}'\right)''_e$	pseudonormal-force coefficients of the exposed aft panel	4.5.1.2
C_T	thrust coefficient, $\frac{T}{\rho n^2 D^4}$	9.1 9.1.1 9.1.3

SYMBOL	DEFINITION	SECTIONS
C_X	axial-force coefficient	4.2.3.2
$(C_X)_{\alpha = 0}$	axial-force coefficient at zero angle of attack	4.2.3.2
$(C_X)_{\alpha = 180^\circ}$	axial-force coefficient at $\alpha = 180^\circ$	4.2.3.2
C_Y	total side-force coefficient	Several
C_{Y_B}	side-force coefficient of body	5.2.1.2 5.2.3.2
$C_{Y_{H(B)}}$	side-force coefficient of horizontal tail in the presence of the body	5.3.1.2 5.3.3.2 5.6.1.2 5.6.3.2
$C_{Y_{HVU(B)}}$	side-force coefficient of empennage on tail-body configuration	5.3.1.2
$C_{Y_{HVU(WB)}}$	side-force coefficient of empennage on wing-body-tail configuration	5.6.1.2
C_{Y_p}	rotary derivative, $\dfrac{dC_Y}{d\left(\dfrac{pb}{2V_\infty}\right)}$	Several
$(C_{Y_p})_{WB}$	wing-body contribution to the derivative	7.4.2.1
$(\Delta C_{Y_p})_\Gamma$	increment in derivative due to geometric dihedral	7.1.2.1
C_{Y_r}	rotary derivative, $\dfrac{dC_Y}{d\left(\dfrac{rb}{2V_\infty}\right)}$	7.1.3.1 7.1.3.2 7.3.3.1 7.4.3.1
$(C_{Y_r})_{WB}$	wing-body contribution to the derivative	7.4.3.1
C_{Y_U}	side-force coefficient of ventral fin on tail-body configuration	5.3.1.2 5.3.3.2 5.6.1.2
$C_{Y_{U(K,\phi)}}$	side-force coefficient of ventral fin due to interference and cross-coupling of α and β	5.3.1.2 5.6.1.2
$C_{Y_{U(\eta)}}$	side-force coefficient of ventral fin on wing-body-tail configuration	5.6.1.2 5.6.3.2
C_{Y_V}	side-force coefficient of upper vertical tail on tail-body configuration	5.3.1.2 5.3.3.2

SYMBOL	DEFINITION	SECTIONS
$C_{Y_{V(K,\phi)}}$	side-force coefficient of upper vertical tail due to interference and cross-coupling of α and β	5.3.1.2 5.6.1.2
$C_{Y_{V(\Gamma_B)}}$	side-force coefficient of upper vertical tail due to body vortices	5.3.1.2 5.6.1.2
$C_{Y_{V(\eta)}}$	side-force coefficient of upper vertical tail on wing-body-tail configuration	5.6.1.2 5.6.3.2
$C_{Y_{WB}}$	side-force coefficient of wing-body configuration	5.2.1.2 5.6.1.2
$C_{Y_{W(B)}}$	side-force coefficient of the wing in the presence of the body	5.2.1.2 5.2.3.2
$C_{Y_{WBHVU}}$	side-force coefficient of wing-body-tail configuration	5.6.1.2
C_{Y_β}	rate of change of side force with sideslip angle, $\frac{dC_Y}{d\beta}$	Several
$\left(C_{Y_\beta}\right)_B$	value of derivative for body	5.2.1.1 5.3.1.1 5.6.1.1
$\left(\Delta C_{Y_\beta}\right)_{H(BW)}$	increment in C_{Y_β} due to the horizontal tail in the presence of the wing and body	5.3.1.1 5.6.1.1
$\left(\Delta C_{Y_\beta}\right)_{H(BWU)}$	increment in C_{Y_β} due to the horizontal tail in the presence of the wing, body, and lower vertical tail	5.3.1.1
$\left(\Delta C_{Y_\beta}\right)_{HV(BWU)}$	increment in C_{Y_β} due to the horizontal tail and upper vertical tail in the presence of the wing, body, and lower vertical tail	5.3.1.1
$\left(\Delta C_{Y_\beta}\right)_p$	increment in C_{Y_β} due to panel in empennage	Several
$\left(C_{Y_\beta}\right)_U$	value of derivative for lower vertical panel	Several
$\left(\Delta C_{Y_\beta}\right)_{U(WBHV)}$	increment in C_{Y_β} due to lower vertical stabilizer in presence of wing, body, horizontal tail, and upper vertical stabilizer	Several
$\left(C_{Y_\beta}\right)_V$	value of derivative for upper vertical panel	Several
$\left(\Delta C_{Y_\beta}\right)_{V(BWUH)}$	increment in C_{Y_β} due to the upper vertical tail in the presence of the wing, body, lower vertical tail, and horizontal tail	Several
$\left(C_{Y_\beta}\right)_{V_{eff}}$	lift-curve slope of equivalent rectangular vertical panel	5.3.1.1 5.6.1.1

SYMBOL	DEFINITION	SECTIONS
$(\Delta C_{Y_\beta})_{V(WBH)}$	increment in C_{Y_β} due to upper vertical stabilizer in presence of wing, body, and horizontal tail	Several
$(C_{Y_\beta})_W$	value of derivative for wing	5.2.1.1
$(C_{Y_\beta})_{WB}$	value of derivative for wing-body combination	5.2.1.1 5.2.1.2 5.6.1.1
$(\Delta C_{Y_\beta})_\Gamma$	increment in C_{Y_β} due to geometric dihedral	5.2.1.1 5.6.1.1
C_f	skin-friction coefficient for incompressible flow	Several
$(C_f)_B$	turbulent flat-plate skin-friction coefficient of the body including roughness effects	4.3.3.1 4.5.3.1
C_{f_c}	skin-friction coefficient for compressible flow	4.2.3.1 7.4.1.1
$(C_f)_H$	turbulent flat-plate skin-friction coefficient of the horizontal-tail panel	4.5.3.1
$(C_f)_i$, $(C_f)_o$	skin-friction coefficients for incompressible flow of wing inboard and outboard panels, respectively	4.1.5.1
$(C_f)_{inc}$	incompressible, turbulent, flat-plate skin-friction coefficient, including roughness effects, as a function of Reynolds number based on total body length	4.2.3.1
$(C_f)_p$	turbulent flat-plate skin-friction coefficient based on the MAC of the exposed tail panel	4.5.3.1
$(C_f)_V$	turbulent flat-plate skin-friction coefficient of the vertical-tail panel	4.5.3.1
$(C_f)_W$	turbulent flat-plate skin-friction coefficient of the wing including roughness effects	4.3.3.1 4.5.3.1
$(C_{f_W})_i$, $(C_{f_W})_o$	turbulent flat-plate skin-friction coefficients of the wing inboard and outboard panels, respectively, including roughness effects	4.3.3.1
C_{f_0}	vacuum-thrust coefficient	6.3.2
C_h	hinge-moment coefficient, $\frac{\text{hinge moment}}{qS_f c_f}$	6.1.3.2
C_{h_c}	hinge-moment coefficient of control surface	6.3.4
$C_{h_{tc}}$	hinge-moment coefficient of control tab	6.3.4
C_{h_α}	rate of change of hinge moment with angle of attack at constant flap or control deflection, $\frac{d C_h}{d\alpha}$	6.1.6 6.1.6.1

SYMBOL	DEFINITION	SECTIONS
ΔC_{h_α}	increment in derivative accounting for induced-camber effects	6.1.6.1
$\left(C_{h_\alpha}\right)_{t/c}$	hinge-moment derivative for a symmetric, straight-sided control, based on twice the area-moment of the control about its hinge line	6.1.6.1
$\left(C_{h_\alpha}\right)_{t/c=0}$	supersonic flat-plate hinge-moment derivative	6.1.6.1
C_{h_δ}	rate of change of hinge moment with control-surface deflection at constant angle of attack, $\frac{dC_h}{d\delta}$	6.1.6 6.1.6.2
ΔC_{h_δ}	increment in derivative due to induced-camber effects	6.1.6.2
C'_{h_δ}	value of derivative for zero-thickness control surface	6.1.6.2
C_l	rolling-moment coefficient, $\frac{\text{rolling moment}}{qSb}$	Several
C_{l_p}	rotary derivative $\frac{dC_l}{d\left(\frac{pb}{2V_\infty}\right)}$	Several
$\left(C_{l_p}\right)_{C_L}$	value of derivative at a given lift coefficient	7.1.2.2 7.3.2.1 7.3.2.2 7.4.2.2
$\left(\Delta C_{l_p}\right)_{drag}$	increment in derivative due to drag	7.1.2.2 7.4.2.2
$\left(C_{l_p}\right)_H$	horizontal-tail contribution to the derivative	7.4.2.2
$\left(C_{l_p}\right)_{WB}$	wing-body contribution to the derivative	7.4.2.2
$\left(C_{l_p}\right)_\Gamma$	contribution to derivative due to geometric dihedral	7.1.2.2 7.3.2.1 7.3.2.2 7.4.2.2
$\left(C_{l_p}\right)_{\substack{\Gamma=0 \\ C_L=0}}$	derivative at zero lift of wing without dihedral	7.1.2.1 7.1.2.2 7.4.2.2
$\frac{\left(C_{l_p}\right)_{C_{D_L}}}{C_L^2}$	drag-due-to-lift roll-damping parameter	7.1.2.2 7.4.2.2

SYMBOL	DEFINITION	SECTIONS
$\left(\frac{\beta C_{l_p}}{\kappa}\right)_{C_L=0}$	roll-damping parameter at zero lift	7.1.2.2
C_{l_r}	rotary derivative, $\frac{dC_l}{d\left(\frac{rb}{2V_\infty}\right)}$	7.1.3.2 7.3.3.2 7.4.3.2
ΔC_{l_r}	increment in derivative due to geometric dihedral	7.1.3.2
$\left(\Delta C_{l_r}\right)_{C_L}$	semiempirical correction factor used to extrapolate potential-flow values of C_{l_r} to higher lift coefficients	7.1.3.2
$\left(\Delta C_{l_r}\right)_{\substack{\text{side}\\ \text{force}}}$	increment in derivative due to wing side force	7.1.3.2
$\left(C_{l_r}\right)_{WB}$	wing-body contribution to the derivative	7.4.3.2
$\frac{\Delta C_{l_r}}{\Gamma}$	increment in C_{l_r} due to dihedral	7.1.3.2
$\frac{\Delta C_{l_r}}{\theta}$	increment in C_{l_r} due to wing twist	7.1.3.2
C_{l_β}	rate of change of rolling moment with sideslip angle, $\frac{dC_l}{d\beta}$	Several
ΔC_{l_β}	difference between calculated and test values of the derivative	5.1.2.1
$\left(\Delta C_{l_\beta}\right)_p$	increment in C_{l_β} due to panel present in empennage	5.3.2.1 7.4.3.2
$\left(\Delta C_{l_\beta}\right)_U$	increment in C_{l_β} for lower vertical panel	5.3.2.1
$\left(C_{l_\beta}\right)_V$	value of derivative for upper vertical panel	5.3.2.1
$\left(C_{l_\beta}\right)_{WB}$	value of derivative for wing-body combination	5.2.2.1 5.6.2.1
$\left(\Delta C_{l_\beta}\right)_{z_W}$	increment in derivative due to wing height	5.2.2.1 5.6.2.1

SYMBOL	DEFINITION	SECTIONS
$\left(\frac{C_{l_\beta}}{C_L}\right)_A$	contribution of wing aspect ratio to C_{l_β}	5.1.2.1 5.2.2.1 5.6.2.1
$\left(\frac{C_{l_\beta}}{C_L}\right)_{\Lambda_{c/2}}$	contribution of wing sweep to C_{l_β}	5.1.2.1 5.2.2.1
$\left(\frac{C_{l_\beta}}{C_L}\right)_{\Lambda_i}$	contribution of sweep of inboard panel of wing to C_{l_β}	5.1.2.1
$\left(\frac{C_{l_\beta}}{C_L}\right)_{\Lambda'_o}$	contribution of sweep of constructed outboard panel of wing to C_{l_β}	5.1.2.1
$\frac{C_{l_\beta}}{\Gamma}$	dihedral effect on C_{l_β} for uniform geometric dihedral	5.1.2.1
$\left(\frac{C_{l_\beta}}{\Gamma}\right)_{C_L}$	value of parameter at a given lift coefficient	5.1.2.2 5.6.1.2
$\frac{\Delta C_{l_\beta}}{\theta \tan \Lambda_{c/4}}$	wing-twist correction factor	5.1.2.1
$\frac{\beta C_{l_\beta}}{\kappa\Gamma}$	rolling-moment-due-to-sideslip parameter for any symmetric, spanwise distribution of dihedral angle	5.1.2.1
C_{l_δ}	rate of change of rolling moment with control deflection, $\frac{dC_l}{d\delta}$	Several
C_{l_δ}	rolling-moment effectiveness of one symmetric, straight-sided control about its root-chord line	6.1.5.1 6.2.1.1
$C_{l_{\delta_{\perp HL}}}$	value of derivative for control deflection perpendicular to the hinge line	6.2.1.1
C_m	1. pitching-moment coefficient, $\frac{\text{pitching moment}}{qS\bar{c}}$	Several
	2. duct pitching-moment coefficient, $\frac{M}{q_\infty S_D c}$	9.3

SYMBOL	DEFINITION	SECTIONS
ΔC_m	1. increment in pitching-moment coefficient about root-chord midpoint due to leading-edge vortex	4.1.4.3
	2. increment in pitching-moment coefficient	6.1.5.1 6.3.1
$C_{m_{a/b}}$	pitching-moment coefficient of body having elliptical cross sections	4.2.2.2
$C_{m_{C_L}}$	pitching-moment derivative, $\frac{dC_m}{dC_L}$	4.1.4 4.1.4.2 4.3.2.2
$\frac{\Delta C'_m}{C_L}$	ratio of pitching-moment increment to lift increment for a full-span flap on a rectangular wing	6.1.5.1
$\left(\frac{dC_m}{dC_L}\right)_{theory}$	wing pitching-moment-curve slope uncorrected for thickness effects	4.1.4.2
ΔC_{m_f}	increment in coefficient due to flaps at constant angle of attack	6.1.5.1
$(\Delta C_m)_G$	increment in pitching-moment coefficient in the presence of the ground	4.7 4.7.3 4.7.4
$(\Delta C_m)_H$	total change in pitching-moment coefficient of horizontal tail	4.6 4.6.1
$(\Delta C_{m_H})_G$	increment in horizontal-tail pitching moment in the presence of the ground	4.7 4.7.3
$[(\Delta C_m)_{HL}]_{\Delta C_A}$	increment in pitching moment about the hinge line due to axial-force increment	6.3.1
$[(\Delta C_m)_{HL}]_{\Delta C_N}$	increment in pitching moment about the hinge line due to normal-force increment	6.3.1
$(\Delta C_{m_H})_q$	increment in coefficient due to change in dynamic pressure at horizontal tail due to propeller-power effects	4.6 4.6.1 4.6.3
$[C_{m_{H(WBV)}}]_{\alpha C_{L_{max}}}$	horizontal-tail pitching moment at stall angle of attack	4.5.1.3
$(\Delta C_{m_H})_\epsilon$	increment in coefficient due to change in downwash at horizontal tail due to propeller-power effects	4.6 4.6.1 4.6.3
$(\Delta C_m)_L$	increment in coefficient due to change in wing lift caused by propeller power	4.6 4.6.3
C_{m_m}	sum of wing section pitching-moment increments	6.1.5.1

SYMBOL	DEFINITION	SECTIONS
$(\Delta C_{m\ MRP}$	increment in pitching moment about vehicle moment reference point	6.3.1
$(\Delta C_m)_{N_j}$	increment in coefficient due to normal force acting at jet inlet due to inclination of oncoming flow to thrust axis	4.6.3
$(\Delta C_m)_{N_p}$	increment in coefficient due to propeller normal force	4.6 4.6.3
$C_{m_o}(g)$	pitching-moment coefficient correction term	7.1.4.2 7.3.4.2
$(\Delta C_m)_{\substack{power \\ on}}$	total increment in vehicle pitching-moment coefficient at a given angle of attack due to propeller power effects	4.6.3
$(\Delta C_m)_q$	increment in coefficient due to change in propeller-slipstream dynamic pressure	4.6 4.6.3
C_{m_q}	rotary derivative, $\dfrac{\partial C_m}{\partial\left(\dfrac{q\bar{c}}{2V_\infty}\right)}$	Several
C_{m_q}'	1. value of derivative referred to body axis with origin at wing aerodynamic center	7.1.1.2
	2. pitching derivative of body segment based on base area and base diameter and referred to moment center at forward face of segment	7.2.1.2
C_{m_q}''	value of derivative referred to body axis with origin at wing leading-edge vertex	7.1.1.2
$(C_{m_q})_B$	value of derivative for body	7.3.1.2 7.4.1.2
$(C_{m_q})_e$	value of derivative for exposed wing	7.3.1.2
$(C_{m_q})_e'$	value of derivative for exposed forward panel	7.3.1.2 7.4.1.2
$(C_{m_q})_M$	value of derivative at given Mach number	7.1.1.2 7.3.1.2
$(C_{m_q})_{M_{cr}}$	value of derivative at the critical Mach number	7.1.1.2
$(C_{m_q})_W$	value of derivative for wing	7.3.1.2
$(C_{m_q})_{WB}$	value of derivative for wing-body combination	7.3.1.2 7.4.1.2
$(\Delta C_m)_T$	increment in coefficient due to direct thrust force	4.6 4.6.3
$\Delta C_{m\ trim}$	incremental pitching-moment coefficient required for trim	4.5.3.2
$C_{m_{WB}}$	wing-body pitching-moment coefficient, $\dfrac{\text{pitching moment}}{qS\bar{c}}$	4.5.3.2

SYMBOL	DEFINITION	SECTIONS
$\left(\Delta C_{m_{WB}}\right)_G$	increment in wing-body pitching moment in the presence of the ground	4.7 4.7.3
$\left(C_{m_{WB}}\right)_{\alpha_{C_{L_{max}}}}$	wing-body pitching moment at stall angle of attack	4.5.1.3.
C_{m_α}	rate of change of pitching-moment coefficient with angle of attack at constant flap deflection, $\frac{d C_m}{d \alpha}$	Several
C'_{m_α}	pitching-moment-curve slope for body segment	4.2.2.1 7.2.1.2
$\left(C_{m_\alpha}\right)_B$	value of derivative for body	4.3.2.1 7.3.1.2 7.3.4.2
$C_{m_{\dot\alpha}}$	rate of change of pitching-moment coefficient with rate of change of angle of attack, $\frac{\partial C_m}{\partial\left(\frac{\dot\alpha \bar c}{2 V_\infty}\right)}$	Several
$C''_{m_{\dot\alpha}}$	value of pitching derivative referred to body axis with origin at wing leading-edge vertex	7.1.4.2
$\left(C_{m_{\dot\alpha}}\right)_B$	contribution of body to acceleration derivative $C_{m_{\dot\alpha}}$	7.3.4.2 7.4.4.2
$\left(C_{m_{\dot\alpha}}\right)_e$	contribution of exposed wing to acceleration derivative $C_{m_{\dot\alpha}}$	7.3.4.2
$\left(C_{m_{\dot\alpha}}\right)'_e$	contribution of exposed forward panel to the acceleration derivative $C_{m_{\dot\alpha}}$	7.4.4.2
$\left(C_{m_{\dot\alpha}}\right)''_e$	contribution of exposed aft panel to the acceleration derivative $C_{m_{\dot\alpha}}$	7.3.4.2
$\left(C_{m_{\dot\alpha}}\right)_W$	contribution of wing to acceleration derivative $C_{m_{\dot\alpha}}$	7.3.4.2
$\left(C_{m_{\dot\alpha}}\right)_{WB}$	contribution of wing-body combination to acceleration derivative $C_{m_{\dot\alpha}}$	7.3.4.2 7.4.4.2
$\left(C_{m_{\dot\alpha}}\right)_1, \left(C_{m_{\dot\alpha}}\right)_2$	components of the wing contribution to $C_{m_{\dot\alpha}}$	7.1.4.2 7.3.4.2
$\left[\left(C_{m_{\dot\alpha}}\right)_1\right]_e$, $\left[\left(C_{m_{\dot\alpha}}\right)_2\right]_e$	components of the exposed wing contribution to $C_{m_{\dot\alpha}}$	7.3.4.2
C_{m_δ}	rate of change of pitching-moment coefficient with control or flap deflection at constant angle of attack, $\frac{d C_m}{d \delta}$	6.1.5.1
C'_{m_δ}	pitching-moment effectiveness for one symmetric, straight-sided control, based on twice its moment-area about the hinge line	6.1.5.1

SYMBOL	DEFINITION	SECTIONS
$(\Delta C_m)_e$	increment in coefficient due to jet interference effects at the horizontal tail	4.6.3
C_{m_0}	pitching-moment coefficient at zero lift	4.1.4.1 4.1.4.3 4.6.3
ΔC_{m_0}	increment in pitching-moment coefficient at zero lift due to linear twist	4.1.4.1
$C_{m_0}(g)$	pitching-moment-coefficient correction term	7.1.4.2 7.3.4.2
$(C_{m_0})_{\text{area not immersed}}$	pitching-moment coefficient at zero lift for portion of vehicle not immersed in propeller slipstream	4.6 4.6.3
$(C_{m_0})_B$	body zero-lift pitching-moment coefficient without Mach-number effects	4.3.2.1
$(C_{m_0})_i$	pitching-moment coefficient at zero lift of portion of vehicle immersed in propeller slipstream	4.6 4.6.3
$(C_{m_0})_{\text{theory}}$	zero-lift pitching-moment coefficient uncorrected for thickness effects	4.1.4.1
$(C_{m_0})_W$	wing zero-lift pitching-moment coefficient	4.3.2.1
$(C_{m_0})_{WB}$	zero-lift pitching-moment coefficient of the wing-body combination	Several
$(C_{m_0})_{\text{wing-body}}$		
$(C_{m_0})_{\theta=0}$	pitching-moment coefficient at zero lift of untwisted, constant-section wing	4.1.4.1
$\frac{(C_{m_0})_M}{(C_{m_0})_{M=0}}$	Mach-number correction factor	4.3.2.1
C_n	yawing-moment coefficient, $\frac{N}{qSb}$	Several
ΔC_n	yawing moment due to aileron deflection	6.2.2.1
C_{n_B}	yawing-moment coefficient of body	5.2.3.2
$C_{n_{HVU(B)}}$	yawing-moment coefficient of empennage on tail-body configuration	5.3.3.2
$C_{n_{HVU(WB)}}$	yawing-moment coefficient of empennage on wing-body-tail configuration	5.6.3.2
C_{n_p}	rotary derivative, $\frac{dC_n}{d\left(\frac{pb}{2V_\infty}\right)}$	7.1.2.1 7.3.2.1 7.3.2.2 7.4.2.3

SYMBOL	DEFINITION	SECTIONS
$\left(C_{n_p}\right)_M$	value of derivative for a given Mach number	7.3.2.3
$\left(C_{n_p}\right)_{WB}$	wing-body contribution to the derivative	7.4.2.3
$\frac{C_{n_p}}{\alpha}$	supersonic yawing moment due to rolling referred to stability axes with origin at the center of gravity	7.1.2.3
$\left(\frac{C_{n_p}}{\alpha}\right)_{\text{body axis}}$	supersonic yawing moment due to rolling referred to body axes with origin at the wing apex	7.1.2.3
$\left(\frac{C_{n_p}}{\alpha}\right)_{1,2,3}$	supersonic yawing moment due to rolling components -- body axes	7.1.2.3
C_{n_r}	rotary derivative, $\frac{dC_n}{d\left(\frac{rb}{2V_\infty}\right)}$	7.1.3.3. 7.3.3.3 7.4.3.3
$\left(C_{n_r}\right)_{WB}$	wing-body contribution to the derivative	7.4.3.3
$\frac{C_{n_r}}{C_{D_0}}$	low-speed profile-drag yaw-damping parameter	7.1.3.3
$\frac{C_{n_r}}{C_L^2}$	low-speed drag-due-to-lift yaw-damping parameter	7.1.3.3
$C_{n_{VU(B)}}$	yawing-moment coefficient of vertical tail and ventral fin on tail-body configuration	5.3.3.2
$C_{n_{WB}}$	yawing-moment coefficient of wing-body combination	5.2.3.2 5.6.3.2
$C_{n_{WBHVU}}$	yawing-moment coefficient of wing-body-tail configuration	5.6.3.2
C_{n_β}	rate of change of yawing moment with sideslip angle, $\frac{dC_n}{d\beta}$	Several
$\left(\Delta C_{n_\beta}\right)_p$	increment in C_{n_β} due to panel in empennage	Several
$\left(\Delta C_{n_\beta}\right)_V$	increment in C_{n_β} for vertical panel	5.3.3.1
$\left(C_{n_\beta}\right)_W$	value of derivative for wing alone	5.2.3.1
$\left(C_{n_\beta}\right)_{WB}$	value of derivative for wing-body combination	5.2.3.1 5.2.3.2 5.6.3.1

SYMBOL	DEFINITION	SECTIONS
C_{n_δ}	rate of change of yawing moment with control deflection, $\frac{dC_n}{d\delta}$	6.2.2.2
C_p	pressure coefficient $\frac{p - p_\infty}{q_\infty}$	Several
$\Delta C_p, \Delta C_{p_1}$ ...	sums of the pressure coefficients acting on the two sides of a given surface	5.3.1.1
C_{p_b}	base pressure coefficient	4.2.3.1 4.5.3.1 4.6.4
$C_{p_{inc}}$	incipient pressure-rise coefficient	6.3.1
C_{p_o}	two-dimensional pressure coefficient	6.1.6.1
$C_{p_{stag}}$	stagnation-pressure coefficient	4.2.1.2 4.2.2.2
$\left(C_{p_\alpha}\right)_p$	plateau-pressure coefficient referred to local pressure upstream of interaction	6.3.1
$\left(C_{p_\alpha}\right)_{inc}$	incipient pressure-rise coefficient referred to local pressure upstream of interaction	6.3.1
$\left(C_{p_\alpha}\right)_2$	peak value of pressure coefficient referred to local pressure upstream of interaction	6.3.1
C_{p_u}	maximum negative upper-surface section pressure coefficient	4.1.3.2
C_{p_2}	plateau-pressure coefficient	6.3.2
C_{p_∞}	free-stream pressure coefficient	6.3.1
$\left(C_{p_\infty}\right)_p$	plateau-pressure coefficient referred to free-stream pressure	6.3.1
$\left(C_{p_\infty}\right)_\alpha$	local pressure coefficient upstream of interaction referred to free-stream pressure	6.3.1
$\left(C_{p_\infty}\right)_2$	peak value of pressure coefficient referred to free-stream pressure	6.3.1
C_x	drag coefficient	6.3.2
C_{λ_k}	lift contribution to wing section pitching-moment coefficient	6.1.5.1
C_μ	section nondimensional trailing-edge jet momentum coefficient	Several
C'_μ	section nondimensional trailing-edge jet momentum coefficient based on extended airfoil chord	Several

D. LOWER-CASE COEFFICIENTS AND DERIVATIVES

SYMBOL	DEFINITION	SECTIONS
c_d	section drag coefficient, $\frac{\text{drag}}{qc}$	Several
c_{d_c}	cross-flow drag coefficient of circular cylinder of infinite length normal to flow direction	Several
Δc_{d_f}	airfoil-section drag coefficient with flap deflected	6.1.7
c_h	section hinge moment	6.1.3.2
$c_{h_{f_\alpha}}$	flap section hinge moment due to change in angle of attack	6.1.3.1
$\left(c_{h_f}\right)_{\delta_f}$	flap section hinge moment due to flap deflection	6.1.3.2
$\left(c_{h_f}\right)_{\delta_t}$	section hinge-moment derivative of control surface due to tab deflection	6.1.3.3
$c_{h_{t_\alpha}}$	tab section hinge moment due to change in angle of attack	6.1.3.1
$\left(c_{h_t}\right)_{\delta_f}$	section hinge moment derivative of a tab due to control-surface deflection	6.1.3.4
$\left(c_{h_t}\right)_{\delta_t}$	tab section hinge moment due to tab deflection	6.1.3.2
c_{h_α}	rate of change of control section hinge-moment coefficient with angle of attack at control deflection, $\frac{dc_h}{d\alpha}$	6.1.3.1 6.1.3.2 6.1.6.1 6.1.6.2
Δc_{h_α}	increment in derivative accounting for finite control thickness at supersonic speeds	6.1.3.1
c'_{h_α}	hinge-moment derivative (see Page 6.1.3.1-3, Step 1)	6.1.3.1 6.1.6.1 6.1.6.2
c''_{h_α}	hinge-moment derivative (see Page 6.1.3.1-3, Step 2)	6.1.3.1 6.1.6.1
$\left(c_{h_\alpha}\right)_{\text{balance}}$	value of derivative for aerodynamically balanced control surface	6.1.3.1 6.1.6.1
$\left(c_{h_\alpha}\right)_{\text{low speed}}$	value of derivative uncorrected for compressibility	6.1.3.1
$\left(c_{h_\alpha}\right)_M$	value of derivative corrected for compressibility	6.1.3.1
$\left(c_{h_\alpha}\right)_{\text{theory}}$	theoretical value of derivative	6.1.3.1 6.1.6.1

SYMBOL	DEFINITION	SECTIONS
$\frac{\Delta c_{h_\alpha}}{t/c}$	thickness-correction factor for symmetric, circular-arc airfoils	6.1.3.1
c_{h_δ}	rate of change of hinge-moment coefficient with control deflection, $\frac{dc_h}{d\delta}$	6.1.3.2 6.1.6.2
$\Delta c_{h_{\dot\alpha}}$	increment in derivative accounting for thickness effects at supersonic speeds	6.1.3.1 6.1.3.2
c'_{h_δ}	hinge-moment derivative (see Page 6.1.3.2-3, Step 1)	6.1.3.2 6.1.6.2
c''_{h_δ}	hinge-moment derivative (see Page 6.1.3.2-4, Step 2)	6.1.3.2 6.1.6.2
$(c_{h_\delta})_{balance}$	value of derivative for an aerodynamically balanced control	6.1.3.2 6.1.6.2
$(c_{h_\delta})_{low\ speed}$	value of derivative uncorrected for compressibility	6.1.3.2
$(c_{h_\delta})_M$	value of derivative corrected for compressibility	6.1.3.2
$(c_{h_\delta})_{theory}$	theoretical value of derivative	6.1.3.2 6.1.6.2
$\frac{\Delta c_{h_\delta}}{t/c}$	thickness-correction factor for symmetric, circular-arc airfoils	6.1.3.1
c_ℓ	section lift coefficient, $\frac{lift}{qc}$	Several
Δc_ℓ	increment in section lift coefficient due to flap or control deflection	Several
c_{ℓ_i}	design lift coefficient	Several
$c_{\ell_{max}}$	section maximum lift coefficient	Several
$\Delta c_{\ell_{max}}$	increment in section maximum lift coefficient due to flap deflection	6.1.1 6.1.1.3 6.1.4.3
$\Delta_1 c_{\ell_{max}}$	increment in coefficient accounting for effect of camber for airfoils with maximum thickness at 30% chord	4.1.1.4 4.1.3.3
$\Delta_2 c_{\ell_{max}}$	increment in coefficient accounting for effect of camber for airfoils with maximum thickness at positions other than 30% chord	4.1.1.4 4.1.3.3
$\Delta_3 c_{\ell_{max}}$	increment in coefficient accounting for Reynolds-number effects	4.1.1.4 4.1.3.3
$\Delta_4 c_{\ell_{max}}$	increment in coefficient accounting for airfoil-roughness effects	4.1.1.4
$\Delta_5 c_{\ell_{max}}$	increment in coefficient accounting for Mach-number effects	4.1.1.4

SYMBOL	DEFINITION	SECTIONS
$(c_{\ell_{max}})_{base}$	base or reference value of coefficient	4.1.1.4 4.1.3.3
$(\Delta c_{\ell_{max}})_{base}$	base or reference value of coefficient	6.1.1.3 6.1.4.3
$(c_{\ell_{max}})'_e$	section maximum lift coefficient of exposed forward panel	4.1.5.2
c_{ℓ_α}	1. section lift-curve slope, rate of change of section lift coefficient with angle of attack at constant flap deflection, $\frac{dc_\ell}{d\alpha}$	Several
	2. lift-curve slope for wing of infinite span	Several
	3. section lift-curve slope for propeller blade	9.1.3
Δc_{ℓ_α}	increment in section lift-curve slope due to NACA roughness	4.1.1.2
c'_{ℓ_α}	jet-flap section lift-curve slope uncorrected for thickness effects	Several
$(c_{\ell_\alpha})_M$	lift-curve slope corrected for compressibility effects	Several
$(c_{\ell_\alpha})_{theory}$	theoretical value of derivative	Several
$(c_{\ell_\alpha})_\delta$	value of derivative for deflected control or flap conditions	6.1.1.1 6.1.1.2 6.1.5.1
$(c_{\ell_\alpha})_{\delta=0}$	value of derivative for unflapped airfoil, including compressibility effects	6.1.1.2
c_{ℓ_δ}	rate of change of section lift with flap or control deflection at constant angle of attack, $\frac{dc_\ell}{d\delta}$	Several
$c_{\ell_{\delta_a}}$	section lift effectiveness due to deflection of a hypothetical flap	6.1.2.1 6.1.5.1
$c_{\ell_{\delta_f}}$	rate of change of section lift coefficient due to flap deflection	6.1.1.1 6.1.2.1 6.1.4.1
$c_{\ell_{\delta_{f_1}}}, c_{\ell_{\delta_{f_2}}}, c_{\ell_{\delta_{f_i}}}$	theoretical lifting-efficiency factors for first, second, and i^{th} segments, respectively, of trailing-edge flaps	6.1.1.1 6.1.2.1
$c_{\ell_{\delta_j}}$	rate of change of section lift coefficient due to jet deflection	6.1.1.1 6.1.2.1 6.1.4.1 6.1.5.1
$c_{\ell_{\delta_{max}}}$	theoretical maximum lifting effectiveness	6.1.1.3

SYMBOL	DEFINITION	SECTIONS
$(c_{\ell_\delta})_{theory}$	theoretical value of derivative	Several
$(c_{\ell_\delta})_\alpha$	value of derivative at a given angle of attack	6.1.1.1 6.1.5.1
$c_{\ell_{\delta_\perp}}$	value of derivative for control or flap deflection measured perpendicular to hinge line	6.1.6.2
c_{ℓ_Λ}	incremental section lift coefficient due to control deflections	6.1.5.1
$c_{\ell_{\Lambda=0}}$	incremental section lift coefficient as function of span station, referred to basic load line	6.1.5.1
c_m	section pitching-moment coefficient with flaps retracted	6.1.2.1
Δc_m	increment in section pitching-moment coefficient near maximum lift due to flaps and controls	6.1.2.1 6.1.2.2 6.1.2.3 6.1.5.1
dc_m/dc_ℓ	wing section pitching-moment-curve slope	6.1.2.2
$c_{m_{c/4}}$	section pitching-moment coefficient measured about the quarter-chord point	4.1.1 6.1.2.2
Δc_{m_f}	increment in section pitching-moment coefficient at low angles of attack due to flaps and controls	6.1.5.1
c_{m_α}	rate of change of section pitching-moment coefficient with angle of attack, $\frac{dc_m}{d\alpha}$	6.1.2.1 6.1.2.2
Δc_{m_α}	pitching-moment increment due to airfoil angle of attack	6.1.2.1 6.1.5.1
c_{m_δ}	rate of change of section pitching-moment coefficient with flap deflection at constant angle of attack, $\frac{dc_m}{d\delta}$	6.1.2.1
c'_{m_δ}	theoretical flap pitching-moment effectiveness (about the leading edge)	6.1.2.1
$c_{m_{\delta_f}}$	flap pitching-moment effectiveness measured about the leading edge	6.1.2.1
$(\Delta c_m)_{\delta_f}$	pitching-moment increment due to trailing-edge flaps	6.1.2.1 6.1.5.1
$(\Delta c_m)_{\delta_{f_{LE}}}$	pitching-moment increment due to deflection of a leading-edge device	6.1.2.1 6.1.5.1
$c_{m_{\delta_j}}$	rate of change of pitching-moment coefficient measured about the leading edge with respect to the jet deflection	6.1.2.1
$(\Delta c_m)_{\delta_j}$	pitching-moment increment due to jet sheet acting at an angle to trailing-edge camber line	6.1.2.1 6.1.5.1
$c'_{m_{\delta_{LE}}}$	theoretical two-dimensional flap pitching-moment effectiveness about the leading edge	6.1.5.1

SYMBOL	DEFINITION	SECTIONS
c_{m_0}, $\left(c_{m_0}\right)_W$	section pitching-moment coefficient for zero lift	4.1.1 4.1.2.1 4.1.4.1 4.3.2.1
$\left(c_{m_0}\right)_{\text{area not immersed}}$	section pitching-moment coefficient for zero lift of the area not immersed in propeller slipstream	4.6.3
$\left(c_{m_0}\right)_{root}$	section pitching-moment coefficient at zero lift of root section	4.1.4.1
$\left(c_{m_0}\right)_{tip}$	section pitching-moment coefficient at zero lift of tip section	4.1.4.1
Δc_{m_3}, Δc_{m_4}	intermediate terms in determining pitching-moment increments due to leading-edge devices and angle of attack, respectively	6.1.2.1 6.1.5.1

E. PARTIAL DERIVATIVES

SYMBOL	DEFINITION	SECTIONS
$\frac{\partial C_D}{\partial M}$	slope of curve of C_D vs M	4.3.3.1 4.5.3.1
$\frac{\partial \alpha}{\partial \delta}$	rate of change of zero-lift angle of attack with flap deflection	Several
$\frac{\partial \epsilon}{\partial \alpha}$	downwash gradient acting on the aft surface	Several
$\frac{\partial \bar{\epsilon}}{\partial \alpha}$	average downwash gradient acting on the aft surface	4.2.2.1 4.5.1.1
$\left(\frac{\partial \bar{\epsilon}}{\partial \alpha}\right)_{\text{low speed}}$	average downwash gradient acting on the tail at low speeds	4.4.1
$\left(\frac{\partial \epsilon}{\partial \alpha}\right)_M$	downwash gradient acting on the tail at high subsonic Mach numbers	4.4.1
$\left(\frac{\partial \epsilon}{\partial \alpha}\right)_v$	downwash gradient in the plane of symmetry at the height of the vortex core	4.4.1 4.5.1.1 7.4.4.1

SYMBOL	DEFINITION	SECTIONS
$\left(\frac{\partial \epsilon}{\partial \alpha}\right)_{\infty}$	downwash gradient at infinity	4.4.1 4.5.1.1 7.4.4.1
$\frac{\partial \epsilon_p}{\partial \alpha_p}$	downwash parameter due to propeller	4.6 4.6.1 4.6.4
$\frac{\partial \epsilon_u}{\partial \alpha}$	upwash gradient in the plane of symmetry of an unswept wing	Several
$\frac{d\epsilon_{z_{slip}}}{\partial \alpha_{in}}$	induced upwash gradient due to propeller slipstream	9.1.3
$\frac{\partial \sigma}{\partial \beta}$	sidewash parameter	Several
$\left(\frac{\partial c_{h_f}}{\partial c_\ell}\right)_{\delta_t, \delta_f}$	change in section hinge-moment coefficient of a control surface due to lift variation, measured at constant values of tab and flap deflections	6.1.3.3
$\left(\frac{\partial c_{h_f}}{\partial \delta_t}\right)_{c_\ell, \delta_f}$	change in section hinge-moment coefficient of a control surface due to tab deflection, measured at constant values of lift and flap deflection	6.1.3.3
$\left(\frac{\partial c_{h_f}}{\partial \delta_t}\right)_{\alpha, \delta_f}$	change in section hinge-moment coefficient of a control surface due to tab deflection, measured at constant values of angle of attack and flap deflection	6.1.3.3
$\left(\frac{\partial c_{h_t}}{\partial c_\ell}\right)_{\delta_f, \delta_t}$	change in section hinge-moment coefficient of a tab due to lift variation, measured at constant values of flap and tab deflections	6.1.3.4
$\left(\frac{\partial c_{h_t}}{\partial \delta_f}\right)_{c_\ell, \delta_t}$	change in section hinge-moment coefficient of a tab due to control-surface deflection, measured at constant values of lift and tab deflection	6.1.3.4
$\left(\frac{\partial c_{h_t}}{\partial \delta_f}\right)_{\alpha, \delta_t}$	change in section hinge-moment coefficient of a tab due to control-surface deflection, measured at constant values of angle of attack and tab deflection	6.1.3.4

SYMBOL	DEFINITION	SECTIONS
$\left(\frac{\partial c_\ell}{\partial \alpha}\right)_{\delta_f, \delta_t}$	section lift-curve slope of a control surface at constant values of flap and tab deflections	6.1.3.3 6.1.3.4
$\left(\frac{\partial \alpha}{\partial \delta_f}\right)_{c_\ell, \delta_t}$	rate of change of angle of attack due to change in flap deflection at constant values of lift and tab deflection	6.1.3.4
$\left(\frac{\partial \alpha}{\partial \delta_t}\right)_{c_\ell, \delta_f}$	rate of change of angle of attack due to change in tab deflection at constant values of lift and flap deflection	6.1.3.3

F. ABBREVIATIONS

SYMBOL	DEFINITION	SECTIONS
a.c.	aerodynamic center	Several
av	average	Several
c.g.	center of gravity	Several
c.p.	center of pressure	Several
EBF	externally blown flap	Several
FRP	fuselage reference plane	4.5.2.1
fus	fuselage	9.1 9.1.3
HL	hinge line	Several
HM	hinge moment	6.3.1
IBF	internally blown flap	Several
inc	incipient	6.3.1
LE	leading edge	Several
LER	leading-edge radius	Several
MAC	mean aerodynamic chord	Several
max	maximum	Several
MRP	moment reference point	6.1.5.1 6.3.1
ref	reference	Several
SF	safety factor	6.3.2
slip	propeller slipstream	9.1 9.1.3
STOL	short take-off and landing	Several
TE	trailing edge	Several
U	lower vertical stabilizer	Several
V	upper vertical stabilizer	Several
VTOL	vertical take-off and landing	4.6 9 9.1 9.2

2.2 WING PARAMETERS

2.2.1 SECTION PARAMETERS

Airfoil section parameters that are useful in estimating aerodynamic data are presented in this Section. An airfoil-designation summary that has general utility throughout the Handbook is given. Figure 2.2.1-6 gives the trailing-edge angle for standard airfoils. This parameter is used in estimating section lift-curve slopes and control derivatives. Figure 2.2.1-7 gives the leading-edge radius of standard airfoils. This parameter is not used in this Handbook but is used extensively as a correlation parameter in the literature. It is presented for convenience only. The parameter that is used in place of leading-edge radius in the Handbook is the Δ_y parameter (see definition on figure 2.2.1-8). This parameter has been found to be highly successful in correlating data, e.g., see Section 4.1.3.4. It is presented for standard airfoils in figure 2.2.1-8 .

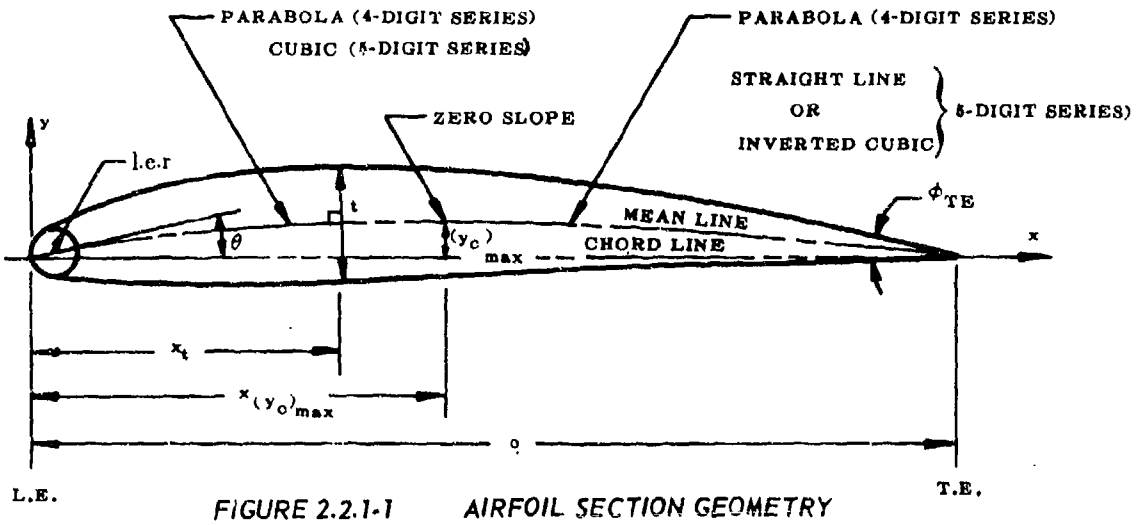

FIGURE 2.2.1-1 AIRFOIL SECTION GEOMETRY

BASIC SYMMETRIC AIRFOIL

- o = chord of airfoil section
- x = distance along chord measured from l.e.
- y = ordinate at some value of x (measured normal to and from the chord line for symmetric airfoils, measured normal to and from the mean line for cambered airfoils)
- y(x) = thickness distribution of airfoil
- $t = 2y_{max}$ = maximum thickness of airfoil
- x_t = position of maximum thickness
- l.e.r. = leading-edge radius
- ϕ_{TE} = trailing-edge angle (included angle between the tangents to the upper and lower surfaces at the trailing edge)

CAMBER MEAN LINE

- $(y_c)_{max}$ = maximum ordinate of mean line
- $y_c(x)$ = shape of mean line
- $x_{(y_c)_{max}}$ = position of maximum camber
- θ = slope of l.e.r. through l.e. equals the slope of the mean line at the l.e.
- c_ℓ = section lift coefficient
- c_{ℓ_i} = design section lift coefficient

AIRFOIL SECTION DESIGNATION

"CLARK Y" AIRFOIL

x_t = 30% CHORD FOR ANY THICKNESS

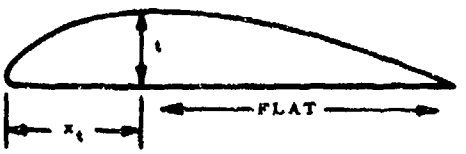

NACA 4-DIGIT SERIES AIRFOILS

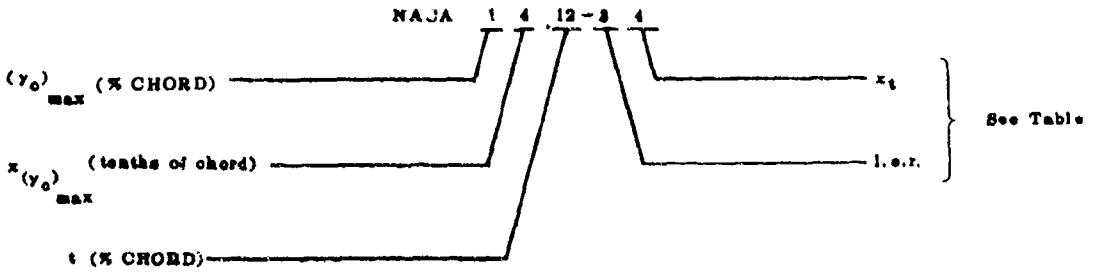

"Dash" numbers (numbers following a dash placed after the standard notation) are expressed only when l.e.r. and/or x_t are different from normal.

FIRST DASH NO.	l.e.r.	SECOND DASH NO.	x_t (% CHORD)
0	Sharp	2	20
3	¼ Normal	3	30 (Normal)
6	Normal	4	40
9	3 × Normal	5	50

GERMAN NOTATION OF NACA 4-DIGIT AND 5-DIGIT SERIES AIRFOILS

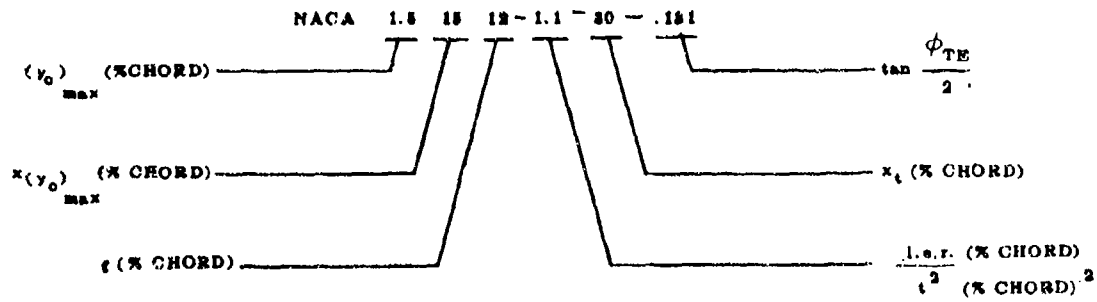

NACA 8-DIGIT SERIES AIRFOIL

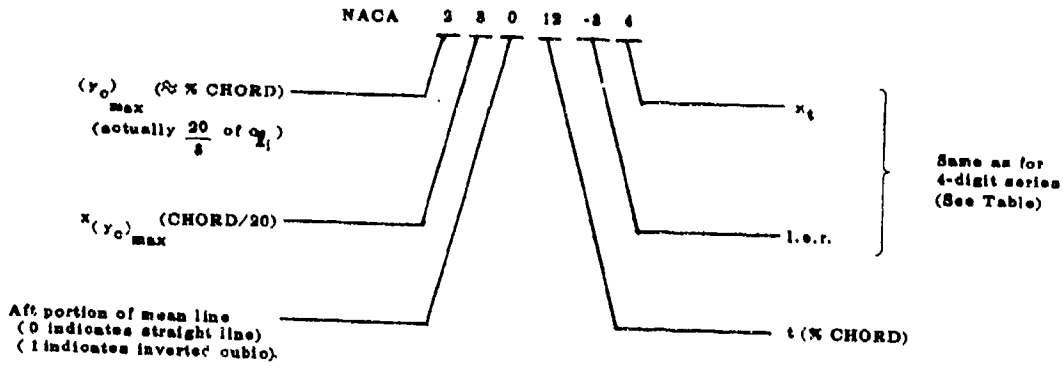

NACA 1- SERIES AIRFOILS

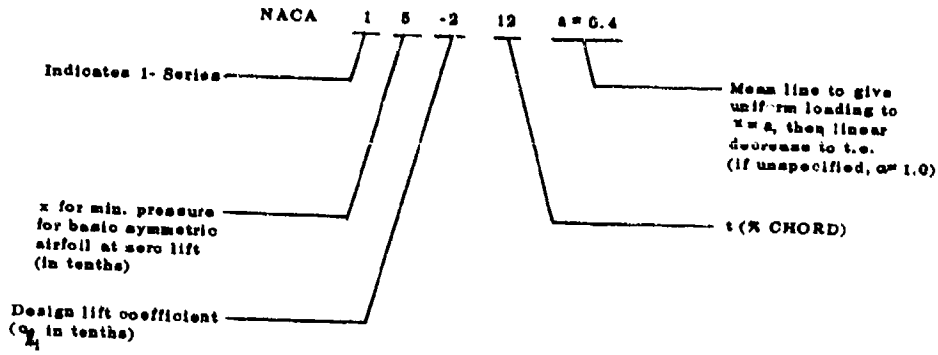

NACA 6- SERIES AIRFOILS

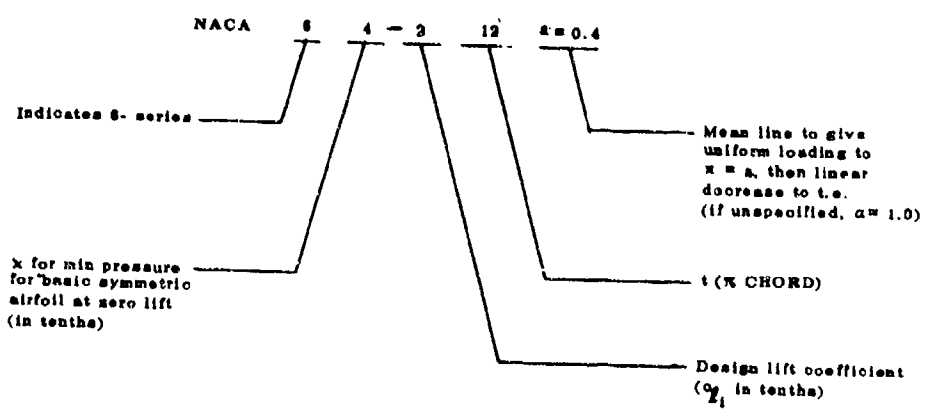

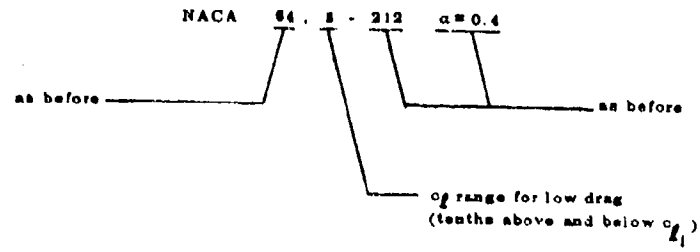

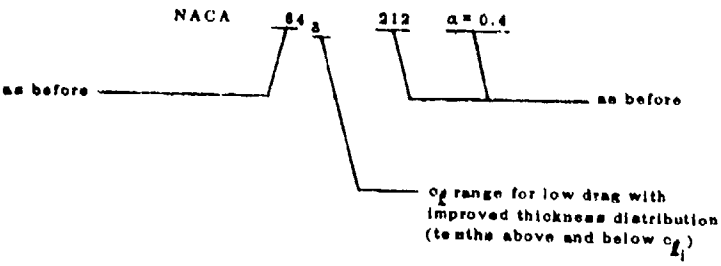

To increase or decrease the airfoil thickness

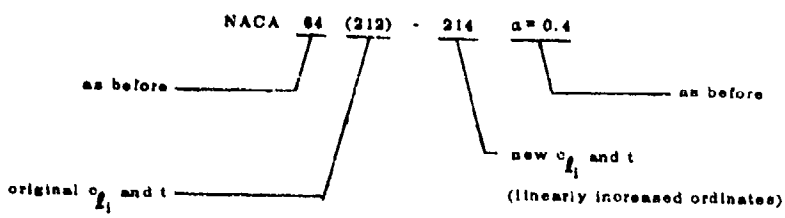

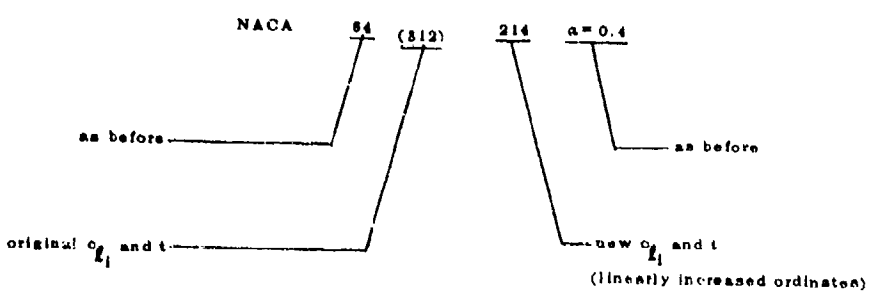

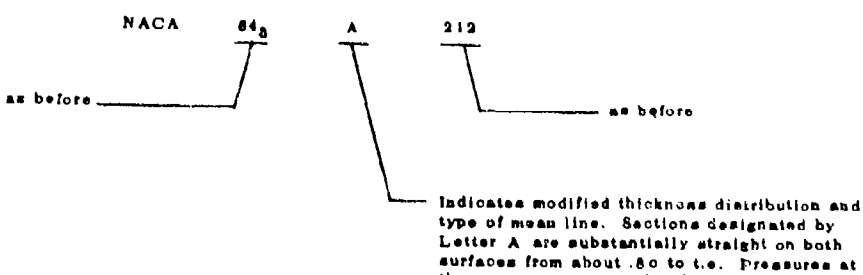

NACA 7- SERIES AIRFOILS

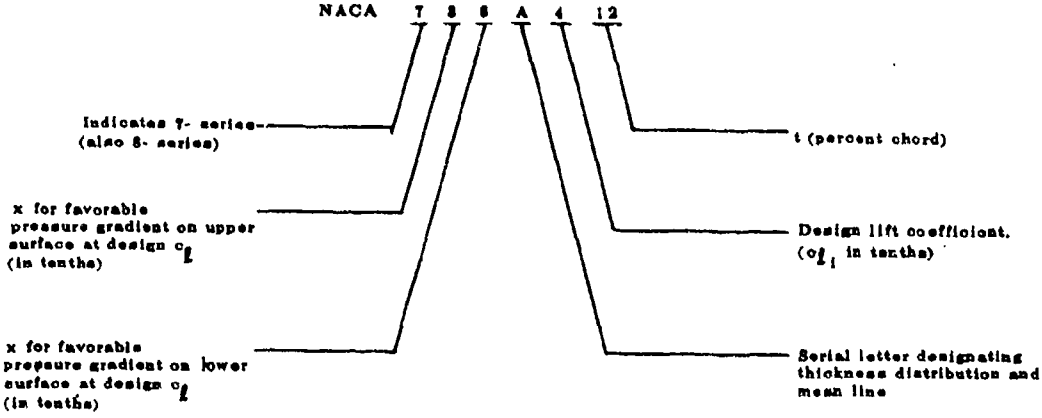

SUPERSONIC AIRFOILS (WEDGE AND CIRCULAR ARC)

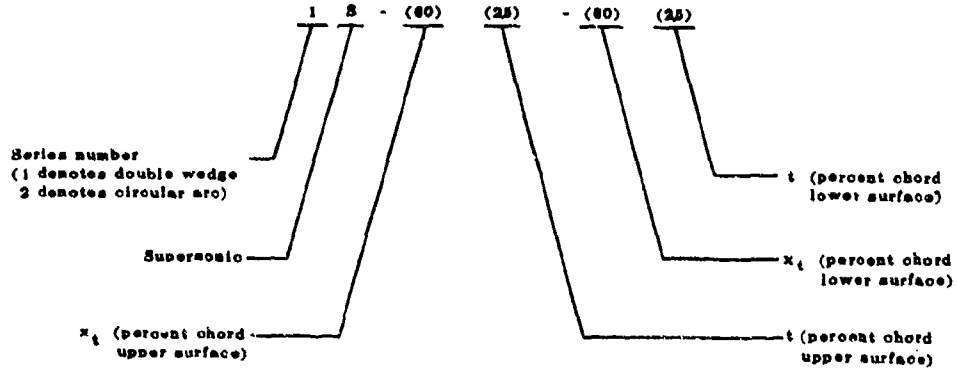

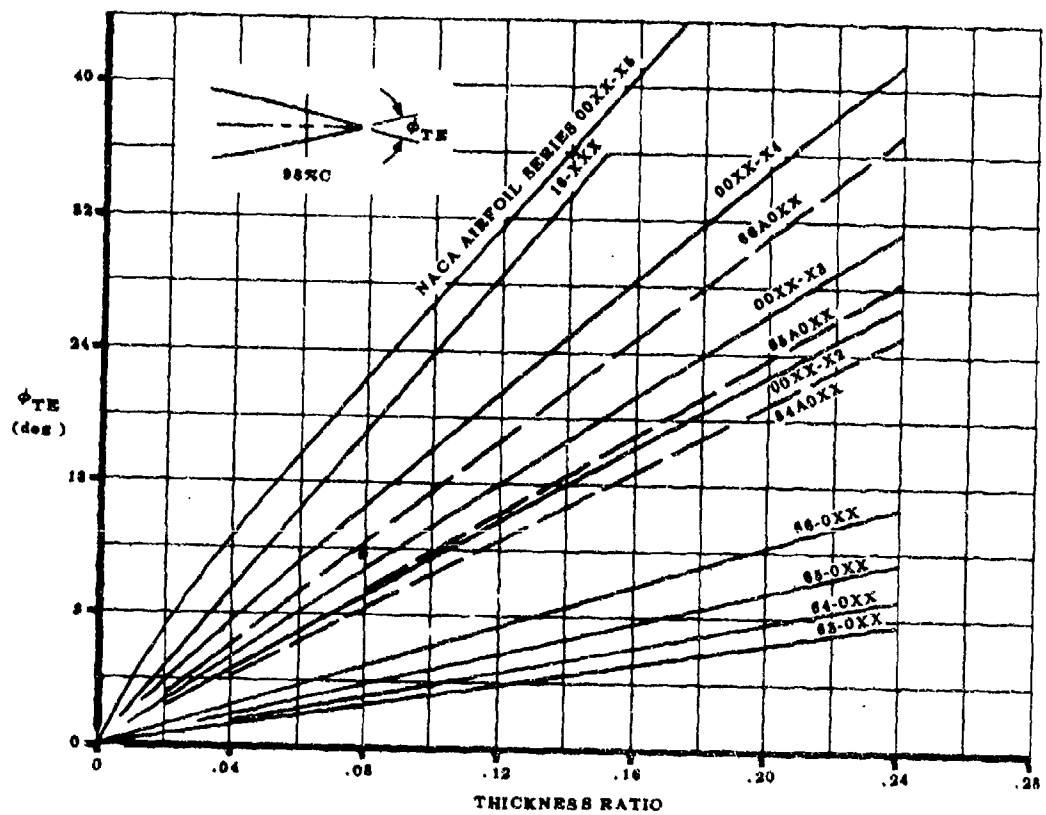

FIGURE 2.2.1-6 VARIATION OF TRAILING-EDGE ANGLE WITH AIRFOIL THICKNESS RATIO

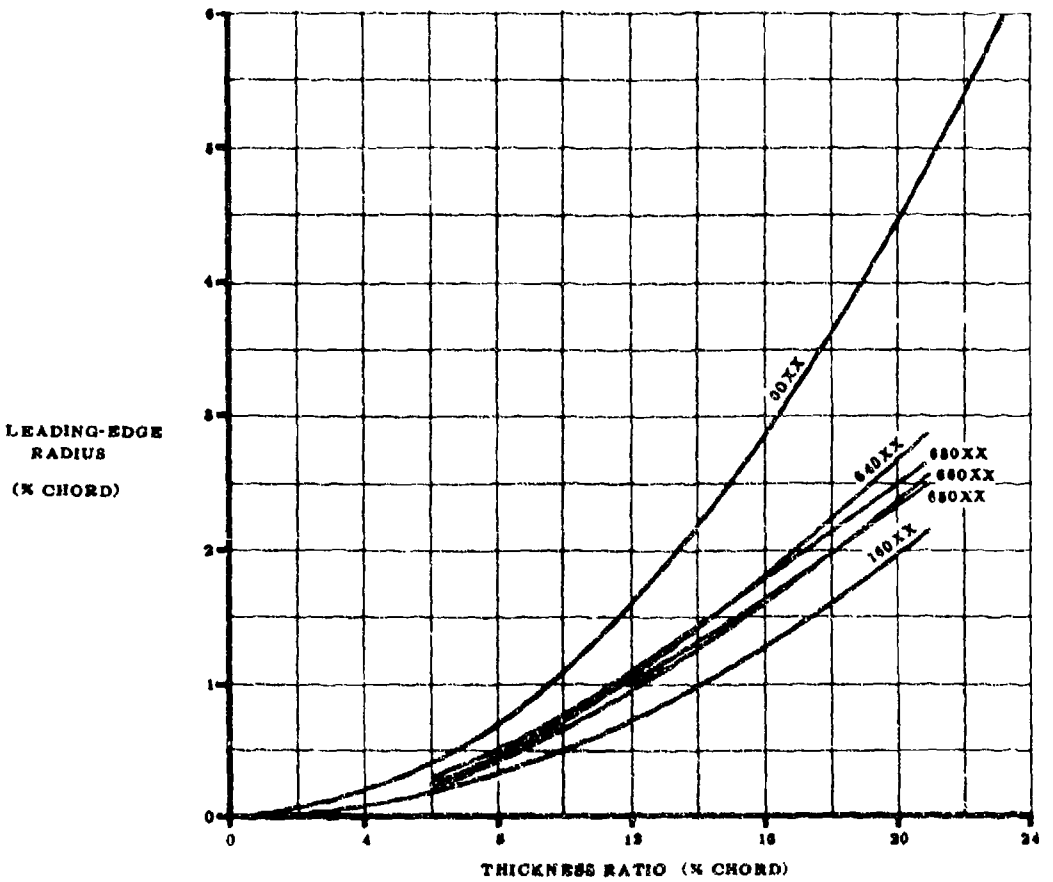

FIGURE 2.2.1-7 VARIATION OF LEADING-EDGE RADIUS WITH THICKNESS RATIO OF AIRFOILS

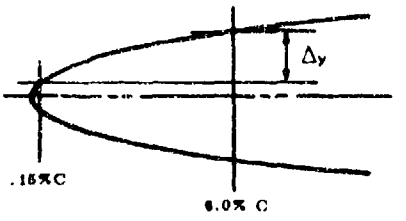

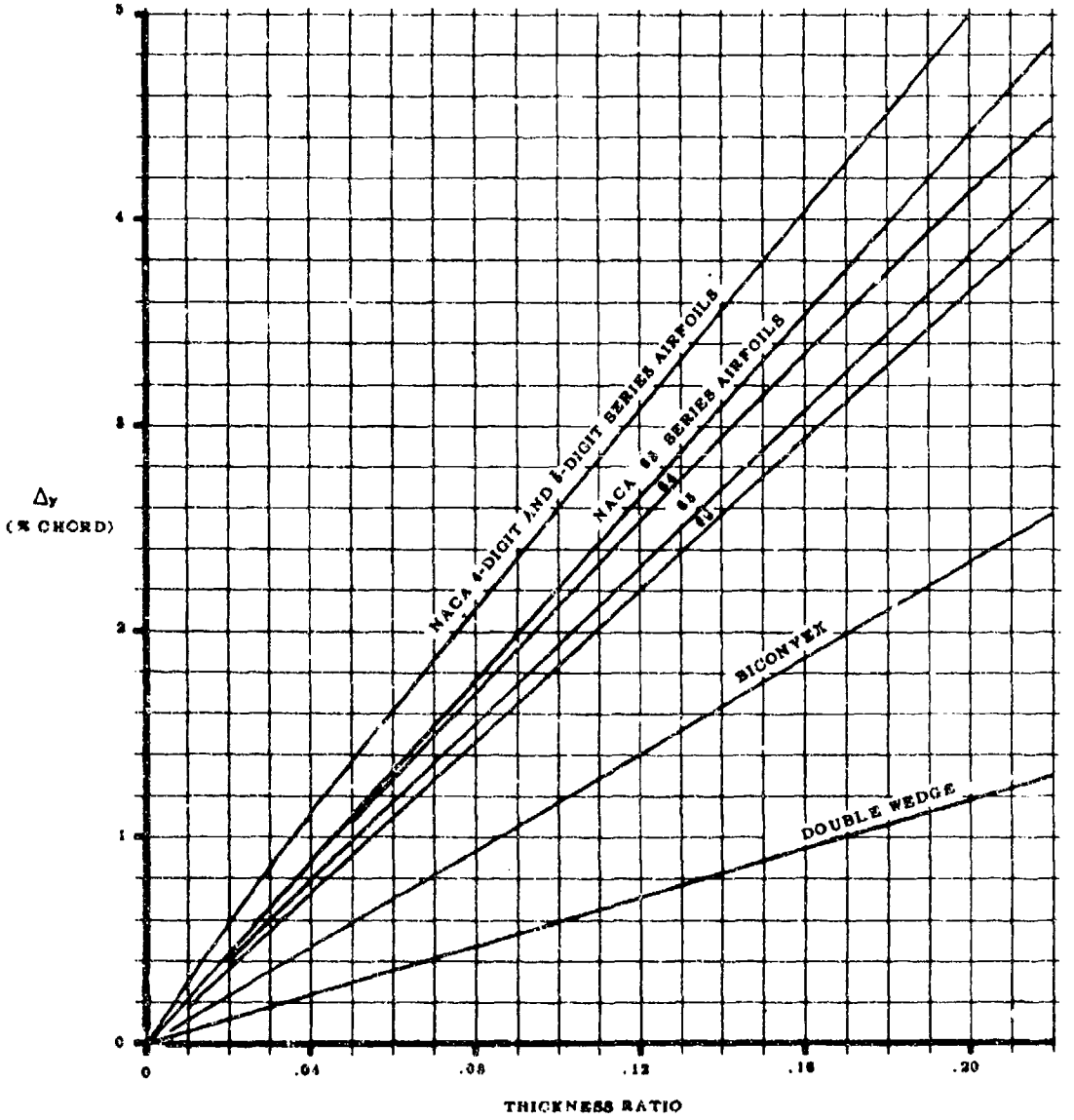

FIGURE 2.2.1-5 VARIATION OF LEADING-EDGE SHARPNESS PARAMETER WITH AIRFOIL THICKNESS RATIO

2.2.2 PLANFORM PARAMETERS

General planform parameters that are useful in estimating aerodynamic data are presented in this section. These parameters are given in equation form for conventional, straight-tapered wings and non-straight-tapered wings.

1. GENERAL PLANFORM PARAMETERS

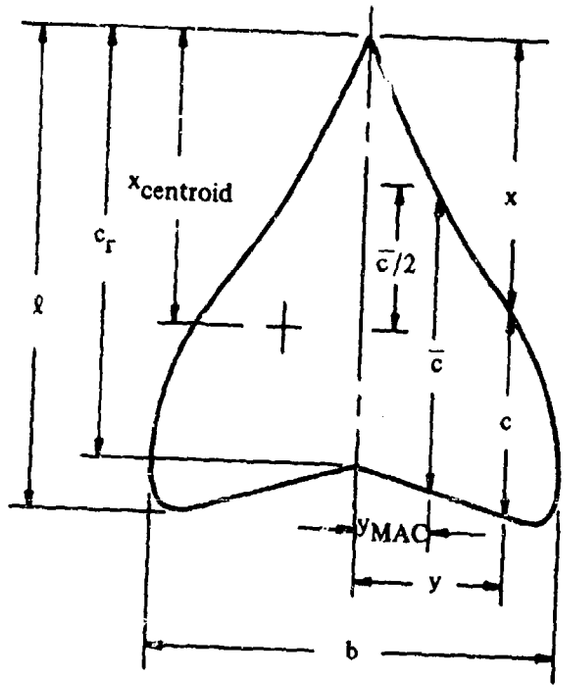

Definitions

A	aspect ratio = b^2/S
b	wing span
$b/(2\ell)$	wing-slenderness parameter
c	chord (parallel to axis of symmetry) at any given span station y
$\bar{c}$	mean aerodynamic chord (MAC)

$$\bar{c} = \frac{2}{S} \int_0^{b/2} c^2 \, dy$$

c_r	root chord
ℓ	over-all length from wing apex to most aft point on trailing edge

p planform-shape parameter = $S/b\ell$

S wing area = $2\int_0^{b/2} c\,dy$

x chordwise location of leading edge at span station y

$x_{centroid}$ chordwise location of centroid of area (chordwise distance from apex to $\bar{c}/2$)

$$x_{centroid} = \frac{2}{S}\int_0^{b/2} c\left(x + \frac{c}{2}\right)dy$$

y general span station measured perpendicular to plane of symmetry

y_{MAC} spanwise location of MAC (equivalent to spanwise location of centroid of area)

$$y_{MAC} = \frac{2}{S}\int_0^{b/2} cy\,dy$$

2. CONVENTIONAL, STRAIGHT-TAPERED PLANFORM PARAMETERS

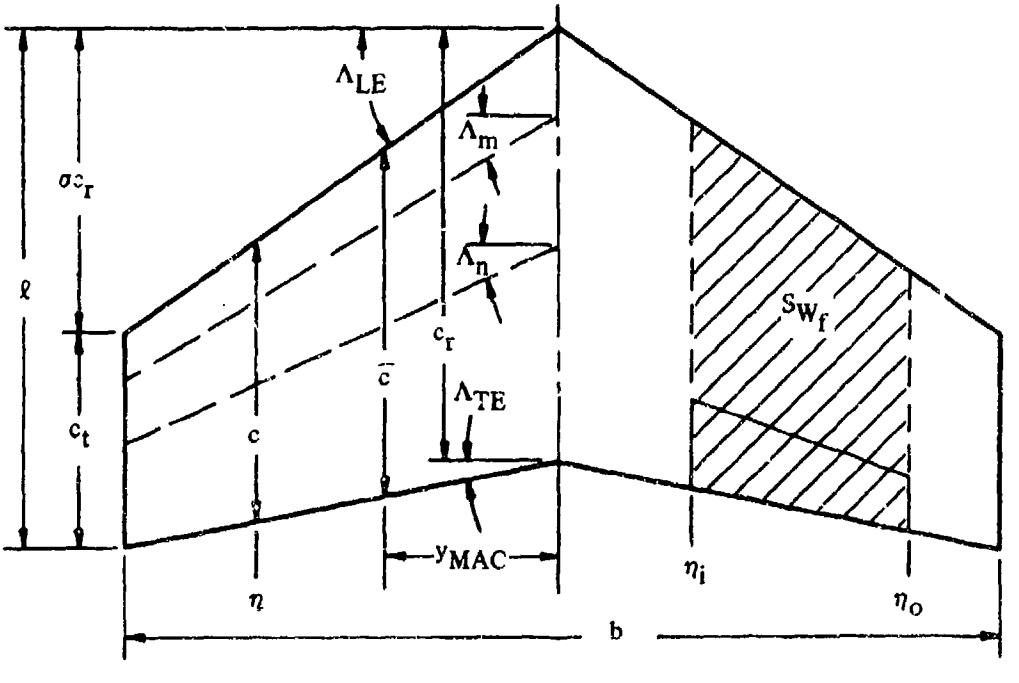

Definitions

b wing span

c chord of wing (parallel to axis of symmetry) at any given span station y

$\bar{c}$	mean aerodynamic chord (MAC)
c_r	root chord
c_t	tip chord
m, n	nondimensional chordwise stations in terms of c
S_{W_f}	wing area affected by trailing-edge deflection
y_{MAC}	spanwise location of MAC
η	nondimensional span station = y/(b/2)
η_i, η_o	nondimensional span stations at inboard and outboard edges of control, respectively.
λ	taper ratio = c_t/c_r
Λ_{LE}	sweep angle of leading edge
Λ_{TE}	sweep angle of trailing edge
Λ_m, Λ_n	sweep angles of arbitrary chordwise locations
σ	ratio of chordwise position of leading edge at tip to root chord length = (b/2) tan Λ_{LE}/c_r

Equations

$$A = \frac{b^2}{S} = \frac{2b}{c_r(1+\lambda)}$$

$$\bar{c} = \frac{2}{3} c_r \frac{1+\lambda+\lambda^2}{1+\lambda}$$

$$S = (b/2)c_r(1+\lambda)$$

$$S_{W_f} = \frac{b}{2}(\eta_o - \eta_i)\, c_r\, [2 - (1-\lambda)(\eta_i + \eta_o)]$$

$$\frac{x_{centroid}}{c_r} = \frac{1}{3}\left(\lambda + \sigma + \frac{1+\lambda\sigma}{1+\lambda}\right)$$

$$\frac{y_{MAC}}{b/2} = \frac{1 - \frac{\bar{c}}{c_r}}{1-\lambda} = \frac{1}{3}\left(\frac{1+2\lambda}{1+\lambda}\right)$$

$$\tan \Lambda_n = \tan \Lambda_m - \frac{4}{A}\left[(n-m)\frac{1-\lambda}{1+\lambda}\right]$$

$$\tan \Lambda_{LE} = \frac{4}{A} \quad (\lambda = 0)$$

$$\sigma = \frac{A}{4}(1 + \lambda) \tan \Lambda_{LE}$$

3. DOUBLE-DELTA AND CRANKED WING PLANFORM PARAMETERS

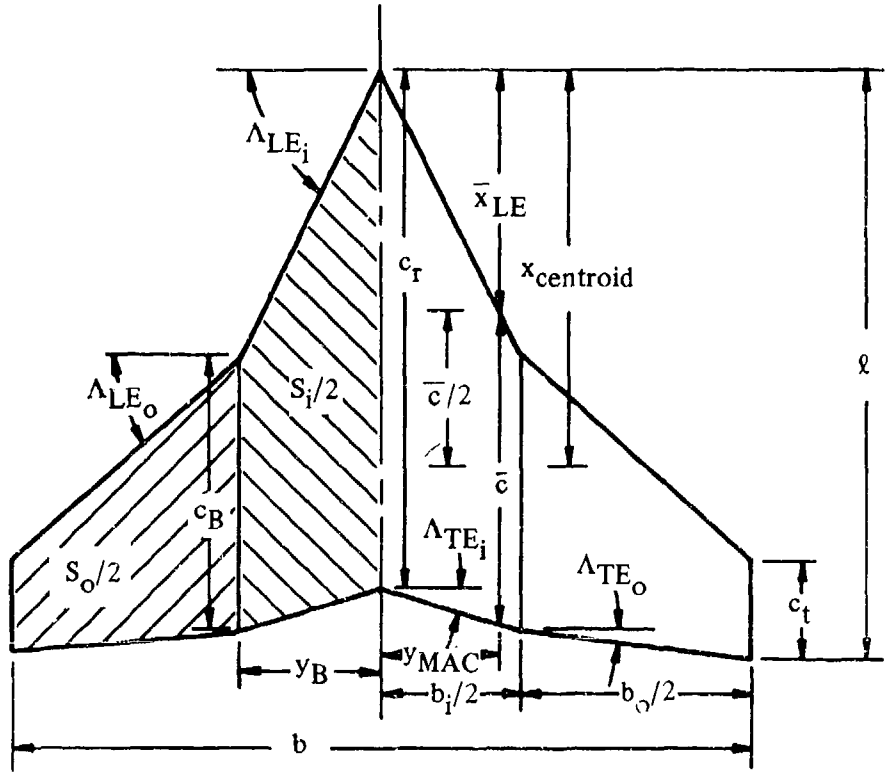

Definitions

b	wing span
b_i	span of planform formed by two inboard panels
b_o	span of planform formed by joining two outboard panels as an isolated wing
$\bar{c}$	mean aerodynamic chord (MAC)
c_B	chord at break span station
c_r	root chord
c_t	tip chord
S_i	total area of inboard panels
S_o	total area of outboard panels

$x_{centroid}$ chordwise location of centroid of area (chordwise distance from apex to $\bar{c}/2$)

$\bar{x}_{LE}$ chordwise distance from apex to leading edge of MAC

y_B spanwise location of break span station

y_{MAC} spanwise location of MAC

$\eta_B = y_B/(b/2)$

$\lambda = c_t/c_r$

$\lambda_i = c_B/c_r$

$\lambda_o = c_t/c_B$

Subscripts

B refers to span station when leading edges and/or trailing edges change sweep angles

i, o refer to inboard and outboard panels, respectively

Equations

$$A = \frac{b^2}{S} = \frac{2b}{c_r\left[(1-\lambda)\eta_B + \lambda_i + \lambda\right]}$$

$$\bar{c} = \frac{2}{S}\int_0^{b/2} c^2\,dy = \frac{\bar{c}_i S_i + \bar{c}_o S_o}{S_i + S_o}$$

$$S = S_i + S_o = \frac{b^2}{A} = (b/2)c_r\left[(1-\lambda)\eta_B + \lambda_i + \lambda\right]$$

$$\frac{x_{centroid}}{c_r} = \frac{\bar{x}_{LE} + \bar{c}/2}{c_r}$$

$$\bar{x}_{LE} = \frac{\left(y_{MAC_i}\tan\Lambda_{LE_i}\right)S_i + \left(y_B\tan\Lambda_{LE_i} + y_{MAC_o}\tan\Lambda_{LE_o}\right)S_o}{S_i + S_o}$$

$$y_{MAC} = \frac{2}{S}\int_0^{b/2} cy\,dy = \frac{y_{MAC_i}S_i + \left(y_B + y_{MAC_o}\right)S_o}{S_i + S_o}$$

$$\eta_B = \frac{b_i}{b} = \frac{1}{1-\lambda}\left(\frac{2b}{Ac_r} - \lambda_i - \lambda\right) = \frac{1}{1-\lambda}\left(\frac{2S}{bc_r} - \lambda_i - \lambda\right)$$

2.3 BODY PARAMETERS

Charts for estimating body volumes and surface areas for various families of profiles are presented in this Section.

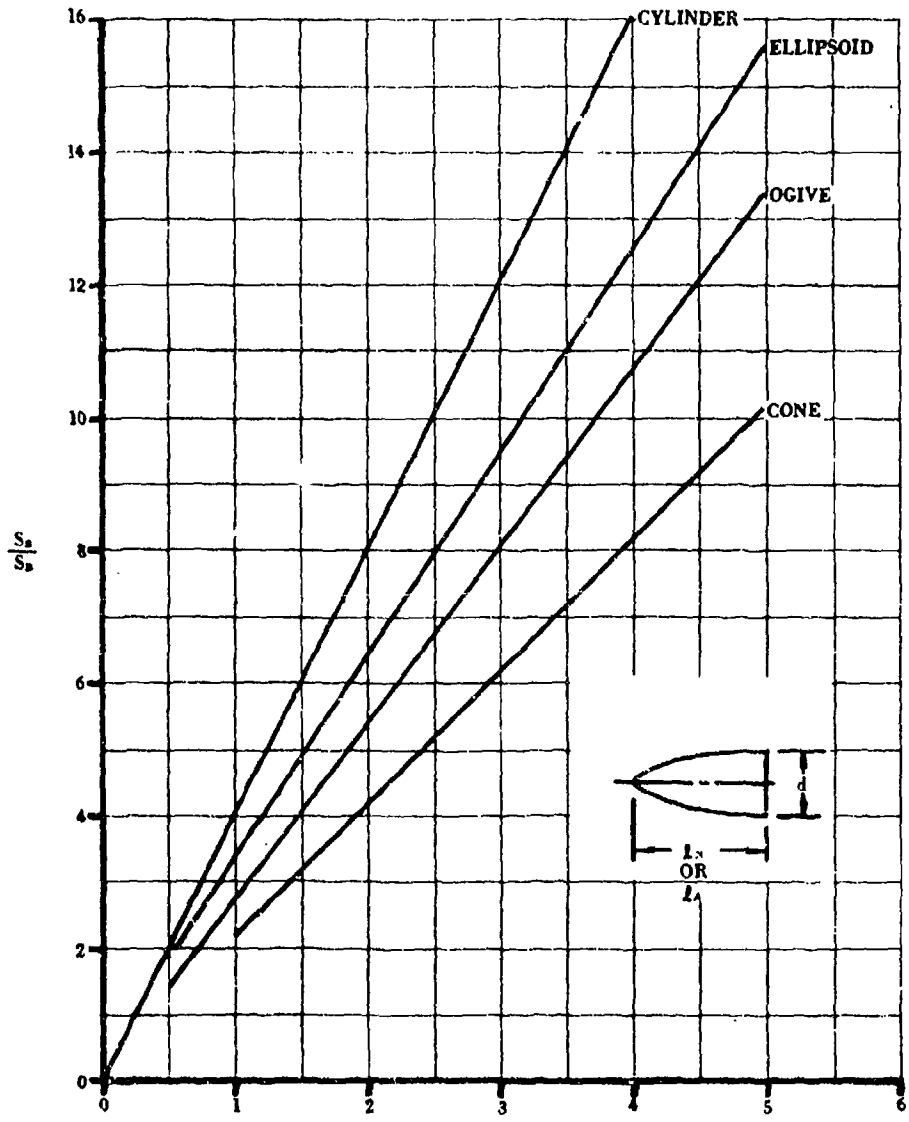

FIGURE 2.3-2 FOREBODY OR AFTERBODY WETTED AREA

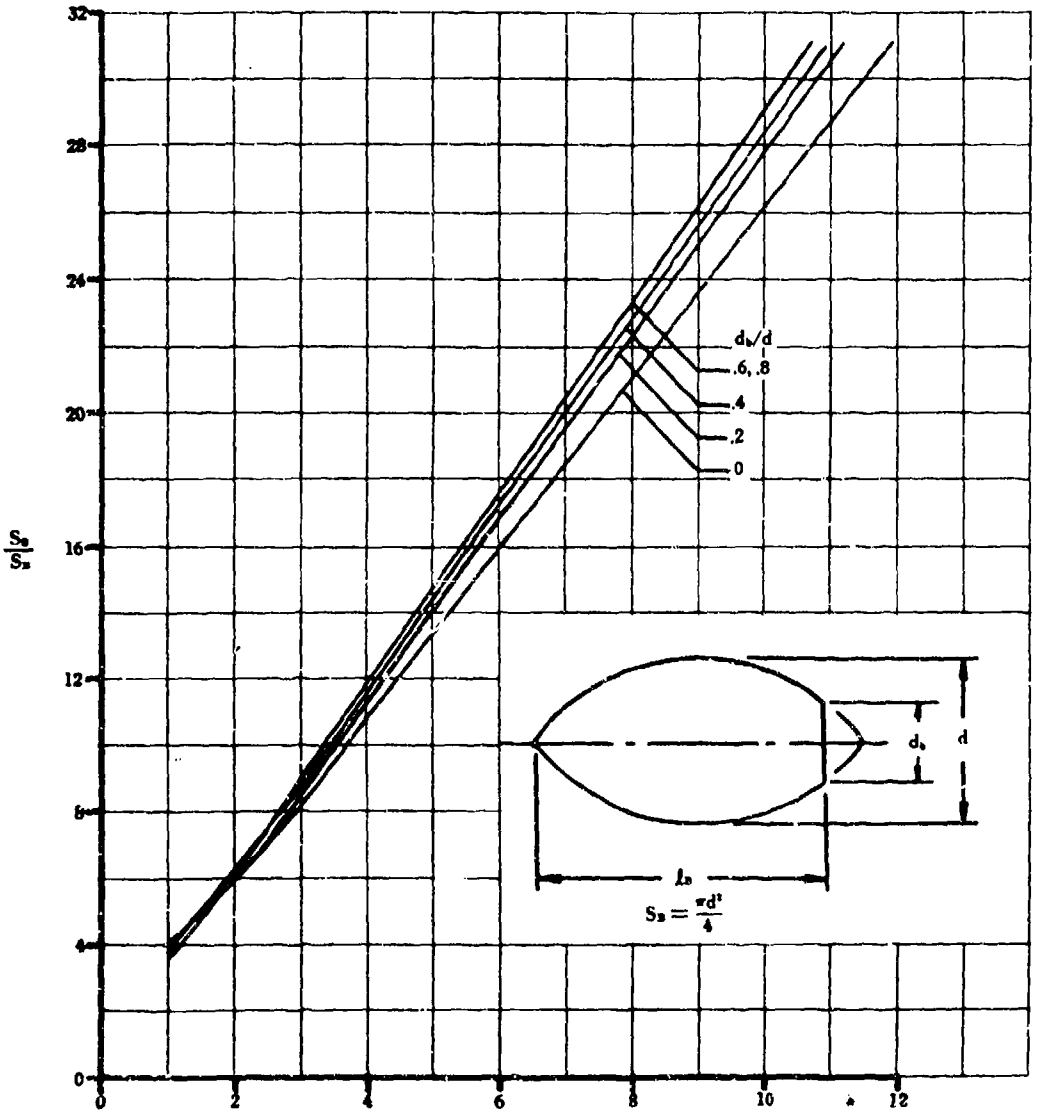

FIGURE 2.3-3 WETTED AREA OF BLUNT-BASE OGIVE BODIES

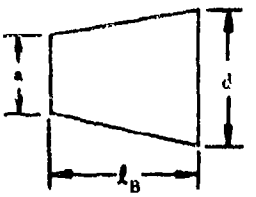

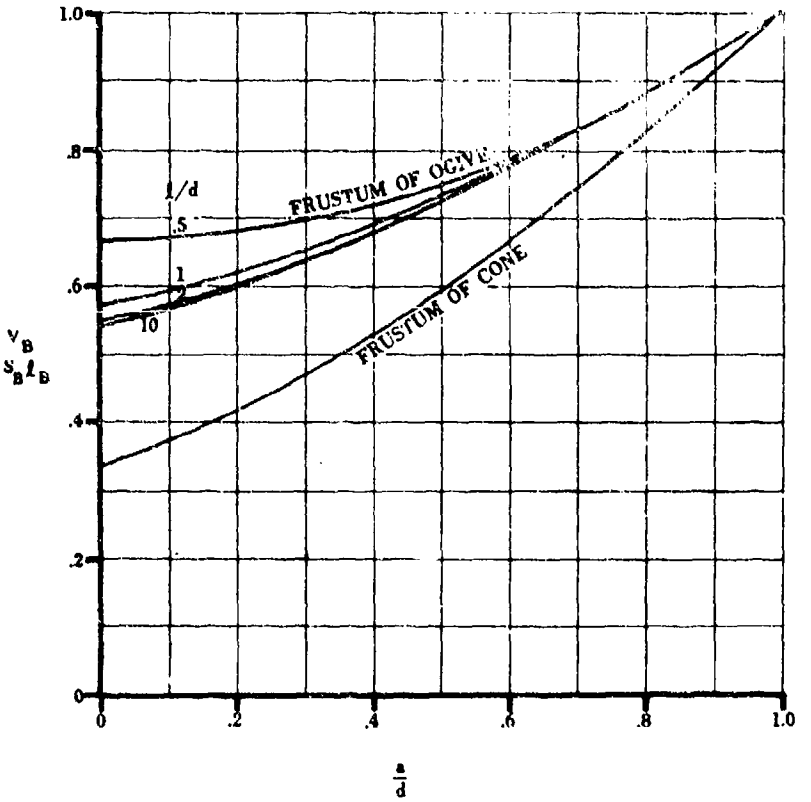

FIGURE 2.3-4 VOLUME OF BODY FRUSTUMS

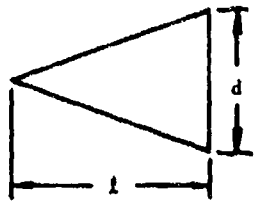

$$S_b = \pi\left(\frac{d}{2}\right)^2$$

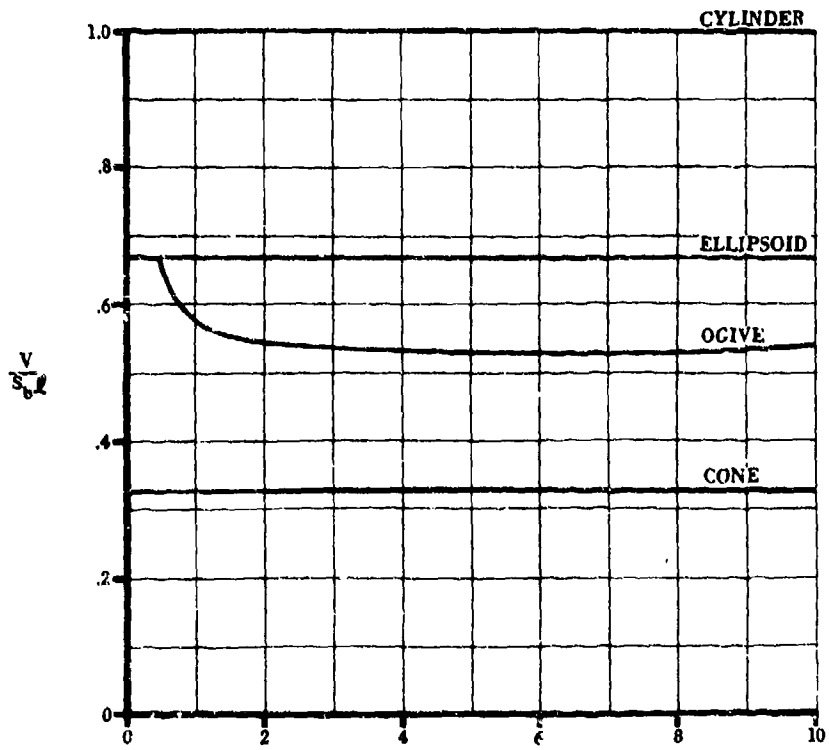

FIGURE 2.3-5 BODY VOLUME

3. EFFECTS OF EXTERNAL STORES

Methods are presented in this section for estimating the effects of externally mounted stores on aircraft stability characteristics. The methods predict the incremental effects due to the installed stores on the aircraft characteristics, not the isolated-store characteristics or the effect of the aircraft on the stores. Section 3 is subdivided as follows:

3.1 Effect of External Stores on Aircraft Lift
3.2 Effect of External Stores on Aircraft Drag
3.3 Effect of External Stores on Aircraft Neutral Point
3.4 Effect of External Stores on Aircraft Side Force
3.5 Effect of External Stores on Aircraft Yawing Moment
3.6 Effect of External Stores on Aircraft Rolling Moment

No suitable general methods have been developed for predicting the effect of stores on aircraft rolling moment, and therefore no Datcom methods have been provided in Section 3.6.

Methods for predicting effects of external stores can be grouped into theoretical, experimental, and empirical, or combinations thereof. Numerous attempts have been made to develop analytical methods for store effects. Reference 1 discusses many of the approaches and provides an extensive bibliography of theoretical methods. The methods tend to be complex and often require elaborate computer programs and extensive computations. Theoretical methods are basically in an early stage of development. They often require simplifications and assumptions which do not lend their application to be generalized over a wide range of loading configurations. Experimental methods include those which utilize increments from flight, wind-tunnel, ballistics or other test data. Access to data and time required for its interpretation are the primary limitations of experimental methods. Reference 1 discusses experimental approaches to computing store effects and provides a bibliography of methods and sources of data. Empirical methods have been developed and documented (References 2 and 3) which seem to provide the best general approach for estimating external-store effects. Empirical methods make use of test-data correlation and theoretical concepts to arrive at prediction equations. The Datcom methods are empirical in nature.

The Datcom methods are taken from Reference 3. Reference 3 is a very comprehensive effort that collected, reviewed, and correlated methods and existing test data to develop generalized prediction equations. Reference 3 also documents wind-tunnel tests which were designed specifically to provide a data base for empirical equation development. A very extensive list of references is also provided.

The Datcom methods in general require that the user provide only aircraft, store, and installation hardware geometric information in order to compute the aerodynamic effects of the store-aircraft combination. In some instances, the user is required to provide clean-aircraft data and isolated-store data. Because the methods are empirical in nature, the physical significance of some terms is not explained. The user should consult References 2 and 3 for additional insight into the method development.

The methods are applicable for wing- and fuselage-mounted conventional stores which are symmetrically or asymmetrically loaded, and are mounted on conventional-type subsonic or supersonic aircraft. This comprises nearly all conventional store configurations encountered. In most instances the methods also account for multiple carriage, mixed and multiple loading cases, and interference effects involving adjacent stores and the fuselage. The methods have not been

substantiated for tip- or tangent-mounted wing stores. Specific limitations and assumptions involving configuration, flight envelope, and data base for method development are discussed in each of the individual sections.

Relatively little substantiation data is provided herein since the method substantiation is well documented in References 2 and 3. Expected accuracies of the methods are discussed in each section.

NOTATION

For the purposes of this section, a store installation refers to all armament-associated hardware including stores at one armament station and external to the clean aircraft. Installation hardware may include pylon, pylon rack, store rack, special adapters and launchers, sway braces, and stores. Typical installation hardware is illustrated in Sketch (a).

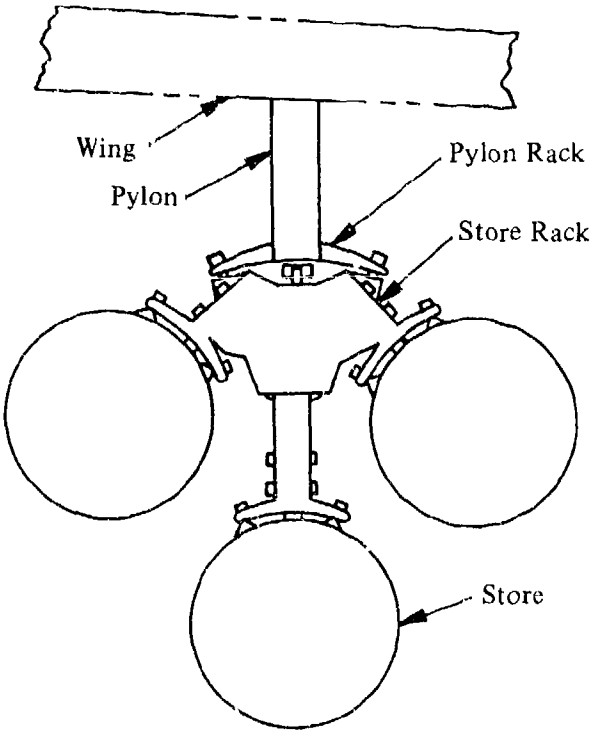

SKETCH (a)

Stores are carried in either a single or multiple carriage mode, and are either pylon- or tangent-mounted. In a single carriage mode, the store is mounted directly on the pylon rack or fuselage. The two multiple carriage modes considered by the Datcom methods are:

TER: Stores are mounted on a triple-ejector rack attached to the pylon rack or fuselage. This rack carries a maximum of three stores.

MER: Stores are mounted on a multiple-ejector rack attached to the pylon rack or fuselage. This rack carries a maximum of six stores.

A general notation list is included in this section for all sections included in Section 3. Since this notation list is quite extensive and the major portion of it includes notation peculiar to the Datcom Methods presented in Section 3, it is not integrated into the notation list presented as Section 2.1.

SYMBOL	DEFINITION
A_W	wing aspect ratio, based on total trapezoidal planform
A_1	longitudinal-location factor (side force)
A_2	store-size correlation factor (side force)
a_1, a_2, a_3	store-diameter correlation factors (drag)
B	basic-store-installation equivalent-parasite-drag area (ft^2) computed at M = 0.9
B_{ASC}	aft-store-cluster contribution (yawing moment)
B_e	protrusion of store fins beyond store body
B_{FSC}	forward-store-cluster contribution (yawing moment)
B_N	basic-store contribution term (side force)
B_P	pylon contribution (side force and yawing moment)
B_R	rack contribution (side force)
B_{SB}	store-body contribution (yawing moment)
B_{SF}	store-fin contribution (yawing moment)
B_X	pylon-longitudinal-location contribution (side force)
B_{xx}	empty-pylon factor (drag)
B_Y	pylon spanwise-location contribution (side force)

SYMBOL	DEFINITION
b_c	maximum vertical store-cluster span (in.), excluding protruding fins
b_e	exposed wing span
b_F	store-fin span (in.)
b_H	span of the aircraft tail
b_W	aircraft wing span
b_1, b_2, b_3	store-row Mach-correlation factors (drag)
C_{D_π}	isolated-store drag coefficient at zero lift
C_{D_0}	clean-aircraft zero-lift drag coefficient
C'_{D_0}	clean-aircraft drag-rise factor
C_L	clean-aircraft lift coefficient
$\left(C_{L_\alpha}\right)_{SB}$	store-body lift-curve slope
$\left(C_{L_\alpha}\right)_{SF}$	store-fin lift-curve slope
$C_{L_{\alpha_{S_{ij}}}}$	free-stream lift-curve slope of store j on installation i
$\left(C_{L_\alpha}\right)_{WB}$	wing-body, clean-aircraft lift-curve slope
C_{n_β}	rate of change of yawing-moment coefficient with sideslip angle
C_{Y_β}	rate of change of side-force coefficient with sideslip angle
ΔC_D	drag-coefficient increment due to external stores
ΔC_L	lift-coefficient increment due to external stores
$\Delta C_{L_{FS}}$	lift-coefficient increment due to fuselage-mounted stores

SYMBOL	DEFINITION
$\Delta C_{L_{WS}}$	lift-coefficient increment due to wing-mounted stores
ΔC_{n_β}	incremental change in C_{n_β}
ΔC_{Y_β}	incremental change in C_{Y_β}
c, c_i, c_{ij}	local wing chord at store or pylon station (in.)
$\bar{c}$	wing mean aerodynamic chord
$c_{p_{low}}$	pylon-bottom chord length (in.)
$c_{p_{top}}$	pylon-top chord length (in.) at wing-pylon juncture
c_r	wing root chord (in.)
D_B	zero-lift equivalent-parasite-drag area (ft^2) due to the basic store installation
D_{EM}	empty-MER equivalent-parasite-drag area (ft^2)
D_{ET}	empty-TER equivalent-parasite-drag area (ft^2)
D_{FLM}	fully loaded MER equivalent-parasite-drag area (ft^2)
D_{FLT}	fully loaded TER equivalent-parasite-drag area (ft^2)
D_{FR}	fuselage-rack equivalent-parasite-drag area (ft^2)
D_I	pylon-store-aircraft-interference equivalent-parasite-drag area (ft^2) at M = 0.9
D_{I_f}	equivalent-parasite-drag area (ft^2) at zero lift due to the mutual interference of store installation and adjacent fuselage
D_{ILP}	installed-loaded-pylon equivalent-parasite-drag area (ft^2)
D_{IM}	store-MER-aircraft-interference equivalent-parasite-drag area (ft^2)
D_{IMR}	installed-MER equivalent-parasite-drag area (ft^2)
D_{IS}	isolated-store equivalent-parasite-drag area (ft^2) at M = 0.90

SYMBOL	DEFINITION
D_{I_S}	zero-lift equivalent-parasite-drag area (ft^2) due to the mutual inteference of adjacent store installations (per pair of adjacent installations)
D_{IT}	store-TER-aircraft-interference equivalent-parasite-drag area (ft^2)
D_{ITR}	installed-TER equivalent-parasite-drag area (ft^2)
D_i	equivalent-parasite-drag area (ft^2) due to lift
D_{LPF}	equivalent-parasite-drag area (ft^2) due to the empty pylon on the fuselage
D_{MRF}	zero-lift equivalent-parasite-drag area (ft^2) due to a MER on the fuselage
D_{MSB}	MER sway-brace equivalent-parasite-drag area (ft^2)
D_{PR}	pylon-rack equivalent-parasite-drag area (ft^2)
D_{TSB}	TER sway-brace equivalent-parasite-drag area (ft^2)
D_X	store-to-aircraft-interference equivalent-parasite-drag area (ft^2)
d_c	minimum clearance between adjacent stores (in.)
d_S	maximum store diameter (in.)
d_{w_A}	maximum width (in.) of the aft-store installation
d_{w_L}	maximum width (in.) of the lead- (most forward) store installation
d_w	defined width (in.) of the store installation not including protruding fins
d_{wing}	distance (in.) from fuselage lower surface at store midpoint to average wing lower surface at wing root
E_u	pylon-height interference factor (drag)
$(FS)_{LE}$	fuselage station (in.) of the nose of the most forward store on the installation or the fuselage station of the leading edge of the pylon for the empty-pylon case
$(FS)_{ref}$	fuselage station (in.) of the moment reference point

SYMBOL	DEFINITION
F_R	ratio of store-fin area (projected onto a horizontal plane) to store-body planform area
$F_1(M)$	MER Mach-effect factor for fuselage-tangent-mounted or fuselage-pylon-mounted installations (pitching moment)
$F_1\left(\bar{x}_{SN_{ij}}\right)$	store longitudinal-placement parameter for TER or MER carriage (pitching moment)
$F_1\left(\bar{x}_{SN_{ij}}, F_R\right)$	store longitudinal-placement and fin-area-ratio parameter for wing pylon-mounted stores (pitching moment)
$F_2(M)$	MER Mach and store-station factor for fuselage tangent-mounted installations (pitching moment)
$F_2(M,j)$	Mach and store-station effect parameter (pitching moment)
$F_{21}\left(\bar{x}_{SN_{ij}}\right)$	store longitudinal-placement factor for wing-pylon-mounted single stores or MER carriage (pitching moment)
$F_{22}\left(\bar{z}_{ij}\right)$	store vertical-placement factor for wing pylon-mounted single stores or MER carriage (pitching moment)
$F_{23}\left(F_R\right)$	store-fin area-ratio factor for wing pylon-mounted single stores (pitching moment)
$F_{23}(M)$	Mach-effect factor for MER carriage (pitching moment)
$F_3(M,j)$	MER Mach and store-station-effect parameter (pitching moment)
h_f	overall fuselage height (in.)
h_p	average pylon height (in.)
I_{S_j}	MER installation neutral-point correlation factor (pitching moment)
K_{AWA}	longitudinal-location factor for multiple rack (lift)
K_{CJK}	pylon Mach-number correlation parameter (drag)
K_{D_1}	store frontal-area factor (drag)
K_{D_2}	wing-sweep-and-location factor (drag)

SYMBOL	DEFINITION
K_{D_3}	tandem-spacing factor (drag)
K_{D_4}	lateral-spacing factor (drag)
K_{D_5}	store-rows factor (drag)
K_{D_6}	stores-per-row factor (drag)
K_{D_7}	store longitudinal-location factor (drag)
K_F	fin constant (side force)
K_f	fuselage proximity-effect parameter (lift)
K_H	pylon-height factor (lift)
K_{HF}	lateral store-to-fuselage clearance parameter (lift)
K_{IF}	installation factor (drag)
K_M	Mach-effect factor (side force)
K_{NB}	nose-shape parameter (pitching moment)
K_{NI}	planform and store-location factor
K_p	pylon-height-effect parameter (lift)
K_{PC}	pylon constant (side force)
K_{PD}	pylon-depth factor (drag)
K_{SD}	store-depth factor (drag)
K_{S_M}	Mach-effect factor for K_{D_1} (drag)
K_{SPAN}	store-installation lateral-placement parameter (lift)
$K_{S_{ij}}$	loading-configuration factor (pitching moment)

SYMBOL	DEFINITION
K_{VF}	fuselage vertical clearance parameter (lift)
K_W	store-installation-width factor (lift)
K_{WING}	wing-location parameter (lift)
K_X	store-placement factor (lift)
K_{xx}	empty-pylon correlation ratio (drag)
K_y	store-installation-depth factor (side force)
K_{y_i}	horizontal-tail span-location factor (pitching moment)
K_{z_i}	horizontal-tail vertical-location factor (pitching moment)
K_Λ	wing-sweep-effect parameter (lift)
K_1	span-location factor (pitching moment)
K_2	longitudinal-correction factor (pitching moment)
K_3	Mach-number-correction factor (pitching moment)
L_{LE}	incremental-lift effect of the longitudinal location of multiple-mounted stores along the local wing chord (lift)
L_R	incremental-lift effect due to carriage-rack installation (lift)
$L_{\alpha_{FS}}$	fuselage-stores incremental-lift effect due to angle of attack (lift)
$L_{\alpha_{WS}}$	wing-stores incremental-lift effect due to aircraft angle of attack (lift)
ℓ_{AFT}	length (in.) of aft-store installation (drag)
ℓ_{ASC}	aft-store-cluster moment arm (in.) (yawing moment)
ℓ_{EM}	length of empty MER (in.)
ℓ_{ET}	length of empty TER (in.)

SYMBOL	DEFINITION
ℓ_m	moment arm (in.) from the moment reference point to the effective point of application of the side-force increment due to external stores (yawing moment)
ℓ_{m_1}	value of ℓ_m for the first of a pair of adjacent store installations (in.) (yawing moment)
ℓ_{m_2}	value of ℓ_m for the second of a pair of adjacent store installations (in.) (yawing moment)
ℓ_n	longitudinal distance (in.) from the store nose of the forward cluster to the store nose of the aft cluster
ℓ_P	pylon moment arm (in.) (yawing moment)
ℓ_S	store-body length (in.)
ℓ_{SB}	store-body moment arm (in.) (yawing moment)
ℓ_{SF}	longitudinal distance (in.) from the store nose to the intersection of the store-fin quarter chord and the store-fin 50% semispan
ℓ_{SP}	maximum store/pylon installation length (in.)
ℓ_x	longitudinal distance (in.) from $(FS)_{LE}$ to the point of side-force application, positive aft
ℓ_1	length of store installation 1.
ℓ_2	length of store installation 2.
M	Mach number
MER	multiple-ejector rack
M_{I_I}	MER adjacent-store separation factor (drag)
M_{I_S}	store-MER-aircraft-interference Mach-correlation factor (drag)
N_{A_i}	total number of asymmetrical external-store installations
N_F	number of store installations adjacent to the fuselage

SYMBOL	DEFINITION
N_I	total number of store installations on the aircraft
N_{I_f}	total number of fuselage-mounted store installations on the aircraft
N_P	total number of pairs of adjacent store installations carried
N_{S_M}	total number of stores attached to the MER
N_{S_T}	total number of stores attached to the TER
N_{S_i}	total number of pairs of symmetrical external-store installations
n_P	number of pylons
n_r	number of stores per row (fuselage mounting)
n_{s_i}	total number of store stations on installation i
P	clean-aircraft drag-rise factor
R_{A_M}	MER aft-longitudinal-placement term (drag)
R_{A_T}	TER aft-longitudinal-placement term (drag)
R_D	basic-stores-correlation factor (side force)
R_{F_M}	MER forward-longitudinal-placement factor (drag)
R_{F_T}	TER forward-longitudinal-placement factor (drag)
R_i	normalized incremental drag due to lift
R_{LC}	aft-store-cluster lateral-clearance factor (yawing moment)
R_{NEG}	adjacent-store interference factor (side force)
R_U	pylon-underside-roughness factor
S_B	maximum fuselage frontal area (ft^2)

SYMBOL	DEFINITION
S_F	store-fin area (in.^{2}) projected onto horizontal plane
S_P	maximum pylon cross-sectional (frontal) area (in.^{2})
S_p	store-body planform area (in.^{2})
S_W	aircraft wing reference area (ft^2)
S_{W_a}	1) affected wing area (in.^{2}) of both wings (for wing-mounted installations); 2) pseudo store installation planform area (in.^{2}) for both installations (for fuselage-mounted installations)
$S_{W_{a_B}}$	pseudo-store-body vertically projected area (in.^{2}) on one wing
$S_{W_{a_F}}$	vertically projected area (in.^{2}) on the wing of the unobstructed, exposed-fin areas of the stores at the given store station for one installation
S_π	store maximum cross-sectional area (ft^2)
T_A	transonic-supersonic correlation factor (drag)
TER	triple-ejector rack
T_F	tandem-stores factor (drag)
T_{I_I}	TER adjacent-store separation factor (drag)
T_{I_S}	store-TER-aircraft-interference Mach-correlation factor (drag)
T_N	distance from the nose of the aft-store installation to the tail of the lead-store installation (in.)
$t_{p_{max}}$	maximum pylon thickness (in.)
$U_{\bar{y}}$	lateral interference factor (drag)
$V_{\bar{x}}$	longitudinal interference factor (drag)
X_A	absolute longitudinal distance (in.) from the trailing edge of one store installation to the trailing edge of the adjacent store installation

SYMBOL	DEFINITION
X_F	absolute longitudinal distance (in.) from the nose of one store installation to the nose of the adjacent installation
X_{OL}	ratio of longitudinal spacing between tandem stores to the store length
x_{AFT}	longitudinal distance from the local wing trailing edge to the trailing edge of the store installation (in.) (or pylon trailing edge for the empty pylon case), positive in the aft direction
$x_{a.c.}$	wing-body aerodynamic-center location of the clean aircraft measured from the leading edge of the mean aerodynamic chord (in.)
x_{FWD}	longitudinal distance from the wing leading edge at the store location to the store/pylon nose (in.), positive for store nose aft of the wing leading edge
x_{ML_i}	distance (in.) from the local wing leading edge to the point midway between the pylon mounting lugs on installation i, positive in the aft direction
$x_{S_{ij}}$	distance (in.) from the leading edge of the mean aerodynamic chord $\bar{c}$, to the point midway between the mounting lugs of the installed store for store j on installation i, positive in the aft direction
$x_{SN_{ij}}$	distance (in.) from the local wing leading edge to nose of store j on installation i, positive in the aft direction
x_r	ratio of the distance between the aircraft nose and the store nose of the most forward store to the aircraft fuselage length
$\Delta x_{n.p.}$	total aircraft neutral-point shift due to external-store installations, positive for aft shift (in.)
$\Delta x_{n.p._1}$	shift in neutral point due to lift transfer from the stores to the clean aircraft, positive for aft shift (in.)
$\Delta x_{n.p._2}$	shift in neutral point due to the interference effects on the wing flow field, positive for aft shift (in.)
$\Delta x_{n.p._3}$	shift in neutral point due to the change in tail effectiveness caused by external stores, positive for aft shift (in.)
$\Delta x'_{n.p._2}$	neutral-point basic-interference-effect term
$\Delta x'_{n.p._3}$	neutral-point horizontal-tail term

SYMBOL	DEFINITION
Y_{A_β}	side-force contribution (ft^2/deg) per degree sideslip due to interference effects from a pair of adjacent external-store installations
Y_{B_β}	basic side-force contribution (ft^2/deg) per degree sideslip due to a symmetrical pair of external-store installations
$\left(Y_{B_\beta}\right)_1$	value of Y_{B_β} for the first of a pair of adjacent installations
$\left(Y_{B_\beta}\right)_2$	value of Y_{B_β} for the second of a pair of adjacent installations
Y_{OD}	ratio of minimum lateral distance between stores (excluding fins) to maximum store diameter
Y_S	minimum lateral clearance (in.) between adjacent store installations
y_i	spanwise distance from the fuselage centerline to the location of installation i
y_i'	spanwise distance from the outboard edge of the fuselage to the location of installation i
y_{ij}	spanwise distance from fuselage centerline to centerline of store j on installation i
$\bar{y}$	fraction of wing semispan location of store station measured from aircraft centerline
ΔY	minimum clearance (in.) between store installation and the fuselage
z	maximum depth of the store installation (in.) measured from the bottom surface of the wing
$\bar{z}$	ratio of vertical distance between average wing lower surface and store centerline to local wing chord
z_e	vertically projected length (in.) of the store installation on the aircraft wing
z_{ij}	distance (in.) from the wing lower surface to the centerline of store j on installation i, positive in the downward direction
z_{T_i}	vertical distance from wing lower surface at installation i to mid-line of the horizontal tail

SYMBOL	DEFINITION
z_w	distance from the top of the fuselage to the midpoint of the wing intersection with the fuselage (in.)
α	aircraft angle of attack
δ	equivalent-parasite-drag area (ft^2)
δ_{S_i}	configuration-related interference parameter (pitching moment)
θ_n	store nose-cone half-angle (deg)

REFERENCES

1. Culley, R. J.: Store Interference Force Prediction Survey. Masters Thesis, California State University, Long Beach, 1975. (U)

2. Gallagher, R. D., and Jimenez, G.: Technique Development for Predicting External Store Aerodynamic Effects on Aircraft Performance. AFFDL-TR 72-24, 1972. (C) Title Unclassified

3. Gallagher, R. D., Jimenez, G., Light, L. E., and Thames, F. C.: Technique for Predicting Aircraft Aerodynamic Effects Due to External Stores Carriage. AFFDL-TR-75-95, Volumes I and II, 1975. (U)

3.1 EFFECT OF EXTERNAL STORES ON AIRCRAFT LIFT

Methods are presented in this section for estimating the change in aircraft lift due to external-store installations. The methods predict an incremental change in lift coefficient, based on wing reference area, which can be added to the clean-aircraft lift coefficient to obtain the aircraft-with-stores lift coefficient. These methods are taken from Reference 1 and are empirical in nature.

Section 3.1 is subdivided as follows:

Section 3.1.1 Lift Increment Due to Wing-Mounted Store Installations

Section 3.1.2 Lift Increment Due to Fuselage-Mounted Store Installations

Section 3.1.3 Total Lift Increment Due to External Stores

Section 3.1.3 presents the method for computing the total incremental lift coefficient due to symmetric and/or asymmetric loading configurations. That section will then refer the user to Section 3.1.1 and/or Section 3.1.2 as appropriate for the loading configuration being analyzed. Due to the nature of the method, the lift increments for wing and fuselage stores are computed separately for pairs of symmetrically-mounted store installations by the methods of Sections 3.1.1 and 3.1.2.

The Datcom methods are applicable to aircraft of conventional design and essentially symmetrical store shapes with no major shape protuberances. The methods are limited to the store-loading configurations and Mach-number ranges presented in Table 3.1-A. The methods are applicable to mixed loading configurations obtained by combining two or more loadings specified in Table 3.1-A. Additional limitations are specifically noted in each of the sections.

TABLE 3.1-A

LOADING AND MACH-NUMBER LIMITATIONS

Mounting Location	Carriage Mode	Mount/Loading Type	Mach-Number Range
Wing	Single	Pylon – Empty	0 → 2.0
		Pylon – Store	
	Multiple	Pylon – Empty MER	0 → 1.6
		Pylon – Full/Partial MER	
		Pylon – Empty TER	
		Pylon – Full/Partial TER	
Fuselage	Single	Tangent	0 → 2.0
		Pylon – Empty	
		Pylon – Store	
	Multiple	Tangent – Empty MER	0 → 1.6
		Tangent – Full/Partial MER	
		Tangent – Empty TER	
		Tangent – Full/Partial TER	
		Pylon – Empty MER	
		Pylon – Full/Partial MER	
		Pylon – Empty TER	
		Pylon – Full/Partial TER	

For most configurations the addition of wing-mounted stores results in a loss of aircraft lift in the subsonic-flight regime. The lift loss generally increases substantially through the transonic speed range, and often reverses to provide positive-lift increments at the higher supersonic speeds ($M > 1.6$).

REFERENCE

1. Gallagher, R. D., Jimenez, G., Light, L. E., and Thames, F. C.: Technique for Predicting Aircraft Aerodynamic Effects Due to External Stores Carriage. AFFDL-TR-75-95, Volumes I and II, 1975. (U)

3.1.1 LIFT INCREMENT DUE TO WING-MOUNTED STORE INSTALLATIONS

A method is presented in this section for estimating the aircraft lift-coefficient increment due to wing-mounted store installations. The method as presented is for estimating the increment due to a pair of symmetric wing-mounted installations. The increment due to a single installation may also be obtained by simply using half the increment due to the pair of symmetric installations.

For most configurations the addition of wing-mounted stores results in a loss of aircraft lift in the subsonic speed range. The lift loss generally increases substantially through the transonic speed range, and often reverses to provide positive lift increments at the higher supersonic speeds.

The Datcom method is taken from Reference 1 and is empirical in nature. The method is applicable to aircraft of conventional design and essentially symmetrical store shapes with no major shape protuberances. The limitations on configuration and Mach-number range are summarized in Table 3.1-A of the preceding section. Additional limitations and assumptions pertaining to the method are listed below:

1. The method is not applicable to wing-tip or wing-tangent-mounted stores.

2. The method has been verified for a Mach-number range between M = 0.6 and M = 2.0 with a few exceptions. Caution should be used in extrapolating the empirical curves beyond the given Mach-number range.

3. The method has not been verified for configurations in which flaps, slats or other flow disrupting devices are deployed.

4. The method gives the best results for an angle-of-attack range from 0 to 8^{O}, although the method can be used for higher angles of attack.

5. The data base used in deriving the method relied heavily on swept-wing tactical-combat-aircraft wind-tunnel data.

6. No method is provided to estimate fuselage and adjacent-store interference effects. These effects may be significant if the separation distances are less than 3 store diameters. Proximity to engine inlets may also be significant.

7. The method is applicable for sideslip angles less than 4^{O}.

The loading configuration capabilities of the method are given in Table 3.1.1-A. Each configuration is assigned a number which is referred to throughout the method. The method is applied separately to each single store installation or symmetrical pair of store installations.

TABLE 3.1.1-A

STORE CONFIGURATION SUMMARY

Configuration			Configuration Number
Mounting	Carriage	Loading	
Pylon	None	Empty	1
	Single	Single	1
Pylon	MER	Empty	2
		Pa. tially Loaded	2
		Full	2
Pylon	TER	Empty	3
		Partially Loaded	3
		Full	3

A. SUBSONIC

DATCOM METHOD

The incremental lift coefficient, based on wing reference area, due to a pair of symmetric wing-mounted external-store installations is given by Equation 3.1.1-a. (For a single installation, this value should be divided by two.)

$$\Delta C_{L_{WS}} = \frac{1}{S_W}\left[(L_R + L_{LE}\, K_{AWA})(K_\Lambda\, K_p + K_f) + L_{\alpha_{WS}}(\alpha - 4.0)\right] \qquad 3.1.1\text{-a}$$

where

S_W is the wing reference area (ft^2).

L_R is an incremental-lift effect due to carriage-rack installation.

For an empty pylon or a pylon-mounted, single-store installation (Configuration 1) L_R is presented over the Mach-number range from 0.6 through 2.0 in Figure 3.1.1-12.

For MER store loading (Configuration 2) or TER store loading (Configuration 3) L_R is presented at M = 0.6, 0.8, and 1.6 in Figures 3.1.1-13 and 3.1.1-14. The value of L_R between M = 0.6 and 0.8 may be obtained by linear interpolation. L_R at M = 1.6 is a single-point value. Over the Mach-number range from $M > 0.8$ to $M < 1.6$, $L_R = 0$ for Configurations 2 and 3.

The term L_R is presented on Figures 3.1.1-12 through 3.1.1-14 as a function of S_{W_a}

where

S_{W_a} is the affected wing area (in.^{2}) of both wings and is given by

$$S_{W_a} = 2\left(S_{W_{a_B}} + S_{W_{a_F}}\right) \qquad 3.1.1\text{-b}$$

where

$S_{W_{a_F}}$ is the vertically projected area (in.^{2}) on one wing of the unobstructed, exposed-fin areas of the stores at the given store station for one installation (See Sketch (a).).

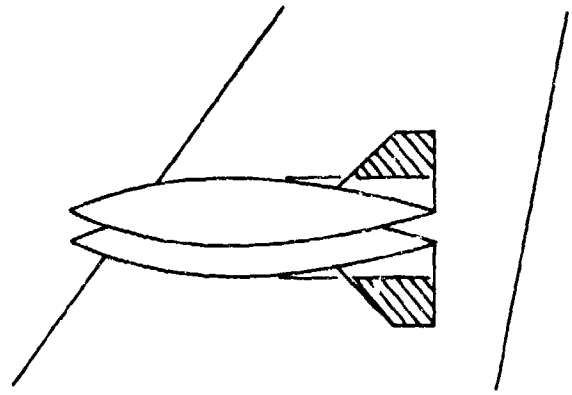

SKETCH (a)

$S_{W_{a_B}}$ is the pseudo-store-body or pylon vertically projected area (in.^{2}) on one wing given by the following geometrical relationships:

1. For $x_{FWD} \geq 0$ and $c \geq (\ell_{SP} + x_{FWD})$:

$$S_{W_{a_B}} = \ell_{SP} d_w \qquad 3.1.1\text{-c}$$

2. For $x_{FWD} \geq 0$ and $c \leq (\ell_{SP} + x_{FWD})$:

$$S_{W_{a_B}} = (c - x_{FWD}) d_w \qquad 3.1.1\text{-d}$$

3. For $x_{FWD} < 0$ and $c < (\ell_{SP} + x_{FWD})$:

$$S_{W_{a_B}} = c d_w \qquad 3.1.1\text{-e}$$

4. For $x_{FWD} < 0$ and $c \geq (\ell_{SP} + x_{FWD})$:

$$S_{W_{a_B}} = (\ell_{SP} + x_{FWD}) d_w \qquad 3.1.1\text{-f}$$

where

x_{FWD} is the longitudinal distance (in.) from the local wing leading edge to the store/pylon nose, positive for store/pylon nose aft of the leading edge. (See Sketch (b).)

c is the local-wing chord (in.) at the store or pylon station. (See Sketch (b).)

ℓ_{SP} is the maximum store/pylon installation length (in.). (See Sketch (b).)

d_w is the defined width (in.) of the store installation, not including protruding fins, given by

1. For an empty pylon:

$$d_w = 1.5 \text{ (maximum pylon width)} \qquad 3.1.1\text{-g}$$

2. For a single store:

$$d_w = d_S \qquad 3.1.1\text{-h}$$

(d_S is the maximum store diameter)

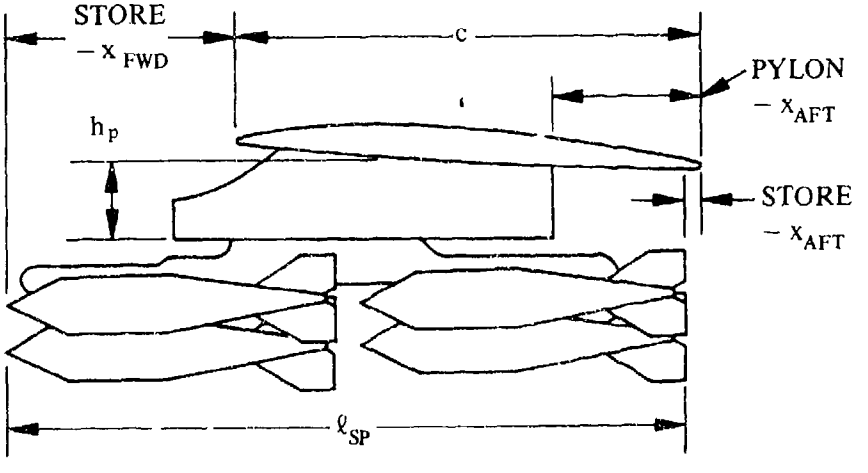

SKETCH (b)

L_{LE} is an incremental-lift effect of the longitudinal location of multiple-mounted stores along the local wing chord. For Configuration 1, $L_{LE} = 0$. For Configurations 2 and 3 $L_{LE} = 0$ at $M \leq 0.8$ and at $M = 1.6$. Over the Mach-number range from $M > 0.8$ to $M < 1.6$ L_{LE} is obtained from Figures 3.1.1-15 and 3.1.1-16 as a function of x_{AFT}/c. The value of x_{AFT} is the longitudinal distance (in.) from the local wing trailing edge to the trailing edge of the store installation (or pylon trailing edge for the empty pylon case), positive in the aft direction. (See Sketch (b).)

K_{AWA} is the longitudinal-location factor for multiple-rack carriage (Configurations 2 and 3) obtained from Figure 3.1.1-17. ($K_{AWA} = 0$ at $M \leq 0.8$ and at $M = 1.6$.)

K_{Λ} is the wing-sweep-effect parameter obtained from Figure 3.1.1-18a.(This parameter is a function of the wing leading-edge sweep angle Λ_{LE}.)

K_p is the pylon-height-effect parameter given by

$$K_p = 1 + K_H K_X K_W \qquad 3.1.1\text{-i}$$

where

K_H is a pylon-height factor obtained from Figure 3.1.1-18b as a function of the average pylon height, h_p (in.). (See Sketch (b).)

K_X is a store-placement factor obtained from Figure 3.1.1-19a as a function of x_{AFT}/c.

K_W is a store-installation-width factor obtained from Figure 3.1.1-19b as a function of h_p/d_w.

K_f is the fuselage proximity-effect parameter where

$$K_f = K_{HF} K_{VF} \qquad 3.1.1\text{-j}$$

and

K_{HF} is a lateral store-to-fuselage clearance parameter obtained from Figure 3.1.1-20b.

K_{VF} is a vertical clearance parameter obtained from Figure 3.1.1-20a.

Note that for a low-wing configuration $K_{HF} = K_{VF} = 0$.

$L_{\alpha_{WS}}$ is an effect due to aircraft angle of attack obtained from Figures 3.1.1-21a through -21h as a function of store-installation type, Mach number, and x_{AFT}/c.

α is the aircraft angle of attack (deg).

Sample Problem

Given: A swept-wing subsonic fighter aircraft from Reference 2, symmetrically loaded as follows:

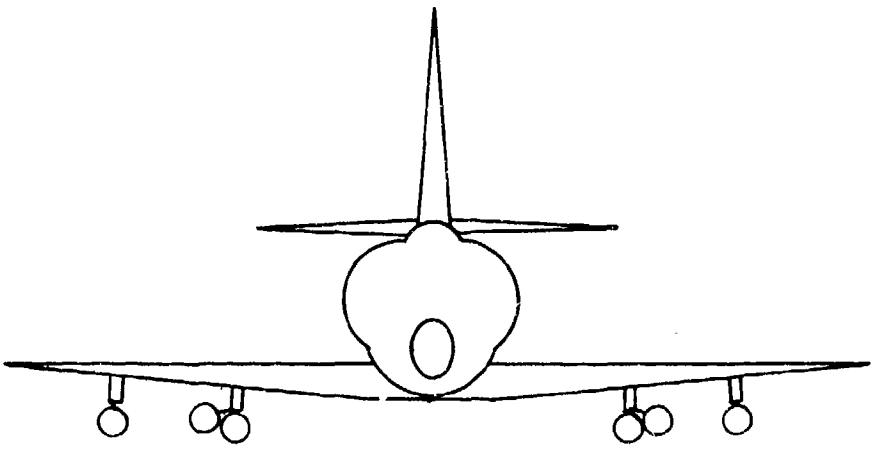

FRONT VIEW

Spanwise Station	Rack Type	Mounting	Store Type	No. of Stores	Configuration Number (Table 3.1.1-A)
Inboard Wing	TER	Pylon	500-lb Bomb	2	3
Outboard Wing	Single	Pylon	500-lb Bomb	1	1

Aircraft Data:

$S_W = 260\ ft^2$ $\quad$ c = 121.5 in. (at inboard sta.)

$\Lambda_{LE} = 42^o$ $\quad$ c = 37.8 in. (at outboard sta.)

Stores Data:

$d_S = 12$ in. $\quad$ $\ell_{SP} = 91.2$ in.

Installation Data:

Location	d_w	$\frac{x_{AFT}}{c}$	$\frac{x_{FWD}}{c}$	h_p	ℓ_{SP}
Inboard Wing	25.6 in.	−0.400	−0.158	11.2 in.	91.2 in.
Outboard Wing	12 in.	−0.210	−0.264	11.2 in.	91.2 in.

Additional Data:

$M = 0.8 \qquad \alpha = 8^{O}$

Geometry of unobstructed, exposed-fin areas required for calculation of $S_{W_{a_F}}$ is shown below.

Compute $\Delta C_{L_{WS}}$ for the inboard wing station (Configuration 3):

$$\ell_{SP} + x_{FWD} = \ell_{SP} + \frac{x_{FWD}}{c} c$$

$$= 91.2 + (-0.158)(121.5)$$

$$= 72.0 \text{ in.}$$

Since $x_{FWD} < 0$ and $c \geq \ell_{SP} + x_{FWD}$

$S_{W_{a_B}} = (\ell_{SP} + x_{FWD})d_w$ (Equation 3.1.1-f)

$= (72.0)(25.6)$

$= 1843 \text{ in.}^2$

To compute $S_{W_{a_F}}$, refer to the planform sketch below of the inboard wing installation:

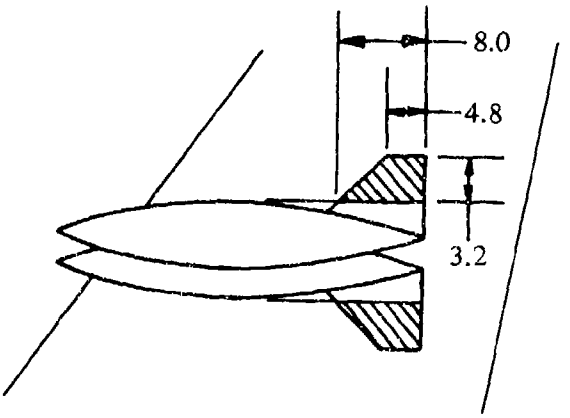

$S_{W_{a_F}}$ is the shaded area of the fins not included in the $S_{W_{a_B}}$ computation.

$$S_{W_{a_F}} = (2)\left(\frac{8.0 + 4.8}{2}\right)(3.2)$$

$$= 41 \text{ in.}^2$$

$$S_{W_a} = 2\left(S_{W_{a_B}} + S_{W_{a_F}}\right) \qquad \text{(Equation 3.1.1-b)}$$

$$= 2\,(1843 + 41)$$

$$= 3768 \text{ in.}^2$$

$L_R = -4.7$ (Figure 3.1.1-14, Configuration 3)

$L_{LE} = 0\ (M \leqslant 0.8)$

$K_{AWA} = 0\ (M \leqslant 0.8)$

$K_A = 1.0$ (Figure 3.1.1-18a)

$K_H = -0.124$ (Figure 3.1.1-18b)

$K_X = 0.30$ (Figure 3.1.1-19a)

$$\frac{h_p}{d_w} = \frac{11.2}{25.6}$$

$$= 0.438$$

$K_W = 1.145$ (Figure 3.1.1-19b)

$K_P = 1 + K_H K_X K_W$ (Equation 3.1.1-i)

$= 1 + (-0.124)(0.30)(1.145)$

$= 0.957$

$K_{HF} = 0, \quad K_{VF} = 0$ (low-wing configuration)

$K_f = K_{HF} K_{VF} = 0$ (Equation 3.1.1-j)

$L_{\alpha_{WS}} = 0.43$ (Figure 3.1.1-21b)

Solution:

$$\Delta C_{L_{WS}} = \frac{1}{S_W}\left[(L_R + L_{LE}K_{AWA})(K_\Lambda K_p + K_f) + L_{\alpha_{WS}}(\alpha - 4.0)\right] \quad \text{(Equation 3.1.1-a)}$$

$$= \frac{1}{260}\left\{[-4.7 + (0)(0)]\,[(1.0)(0.957) + 0] + (0.43)(8.0 - 4.0)\right\}$$

$$= -0.0107 \text{ (inboard wing station)}$$

Compute $\Delta C_{L_{WS}}$ for the outboard wing station (Configuration 1):

$$\ell_{SP} + x_{FWD} = \ell_{SP} + \frac{x_{FWD}}{c}\,c$$

$$= 91.2 + (-0.264)(87.8)$$

$$= 68.0 \text{ in.}$$

Since $x_{FWD} < 0$ and $c \geq \ell_{SP} + x_{FWD}$

$$S_{W_{a_B}} = (\ell_{SP} + x_{FWD})d_w \quad \text{(Equation 3.1.1-f)}$$

$$= (68.0)(12.0)$$

$$= 816 \text{ in.}^2$$

As in the case of the inboard installation, trapezoidal areas of 2 fins extend beyond the projected store body area, $S_{W_{a_B}}$. Since the stores are identical,

$$S_{W_{a_F}} = 41 \text{ in.}^2 \text{ (previously calculated)}$$

$$S_{W_a} = 2\left(S_{W_{a_B}} + S_{W_{a_F}}\right) \quad \text{(Equation 3.1.1-b)}$$

$$= 2\,(816 + 41)$$

$$= 1714 \text{ in.}^2$$

$L_R = -0.8$ (Figure 3.1.1-12, Configuration 1)

$L_{LE} = 0$ (Configuration 1)

$K_{AWA} = 0$ (Applicable for multiple-rack carriage only)

$K_\Lambda = 1.0$ (Figure 3.1.1-18a)

$K_H = -0.124$ (Figure 3.1.1-18b)

$K_X = 0.68$ (Figure 3.1.1-19a)

$\frac{h_p}{d_w} = \frac{11.2}{12.0} = 0.93$

$K_W = 0.175$ (Figure 3.1.1-19b)

$K_p = 1 + K_H K_X K_W$ (Equation 3.1.1-i)

$= 1 + (-0.124)(0.68)(0.175)$

$= 0.985$

$K_{HF} = K_{VF} = 0$ (low-wing configuration)

$K_f = K_{HF} K_{VF} = 0$ (Equation 3.1.1-j)

$L_{\alpha_{WS}} = 0.40$ (Figure 3.1.1-21b)

Solution:

$$\Delta C_{L_{WS}} = \frac{1}{S_W}\left[(L_R + L_{LE} K_{AWA})(K_\Lambda K_p + K_f) + L_{\alpha_{WS}}(\alpha - 4.0)\right] \quad \text{(Equation 3.1.1-a)}$$

$$= \frac{1}{260}\left\{[-0.8 + (0)(0)]\,[(1.0)(0.985) + 0] + 0.40\,(8.0 - 4.0)\right\}$$

$$= 0.00312$$

The calculated values of $\Delta C_{L_{WS}}$ at each wing station are combined with fuselage-store increments in the sample problem of Section 3.1.3 to illustrate a complex loading configuration. Comparison of the calculated results with test data is provided in that section.

B. TRANSONIC

The method presented in Paragraph A of this section is also valid in the transonic speed range. The user is cautioned that the accuracy of the method is less than that expected in the subsonic speed range, and test data should be used whenever possible.

C. SUPERSONIC

The method presented in Paragraph A of this section is also valid in the supersonic speed range. The expected accuracy of the method is comparable to that in the subsonic range. The maximum Mach number provided in the design figures indicates the level to which the method is substantiated. Caution should be used when extrapolating the data beyond the Mach range provided in the figures.

REFERENCES

1. Gallagher, R. D., Jimenez, G., Light, L. E., and Thames, F. C.: Technique for Predicting Aircraft Aerodynamic Effects Due to External Stores Carriage. AFFDL-TR-75-95, Volumes I and II, 1975. (U)

2. Watzke, R. E.: Aerodynamic Data for Model TA-4F Operational Flight Trainer. McDonnell Douglas Corporation Report DAC-67425, 1968. (U)

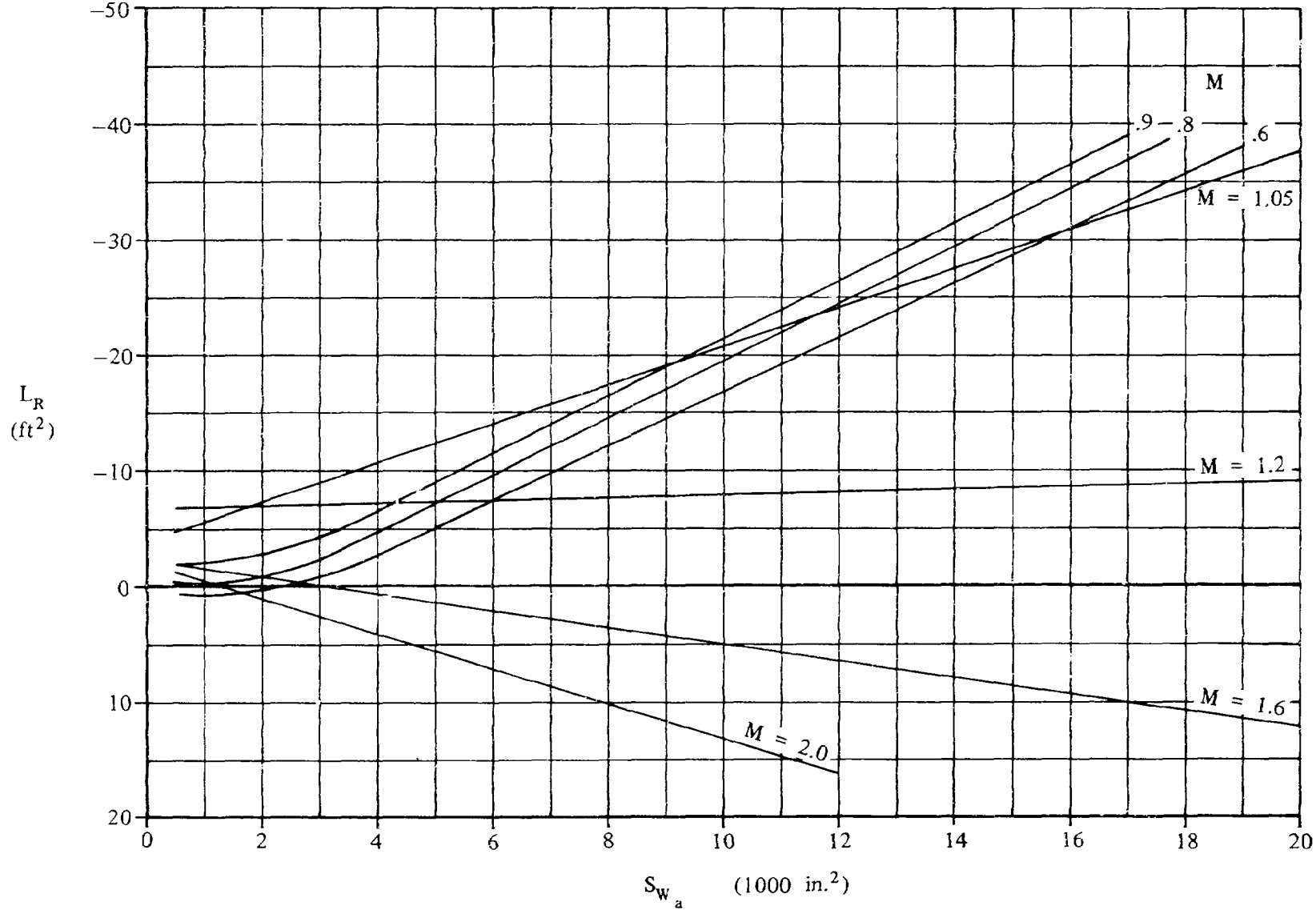

FIGURE 3.1.1-12 INCREMENTAL-LIFT EFFECT DUE TO CARRIAGE-RACK INSTALLATION EMPTY PYLON AND PYLON-MOUNTED SINGLE STORE (CONFIGURATION 1)

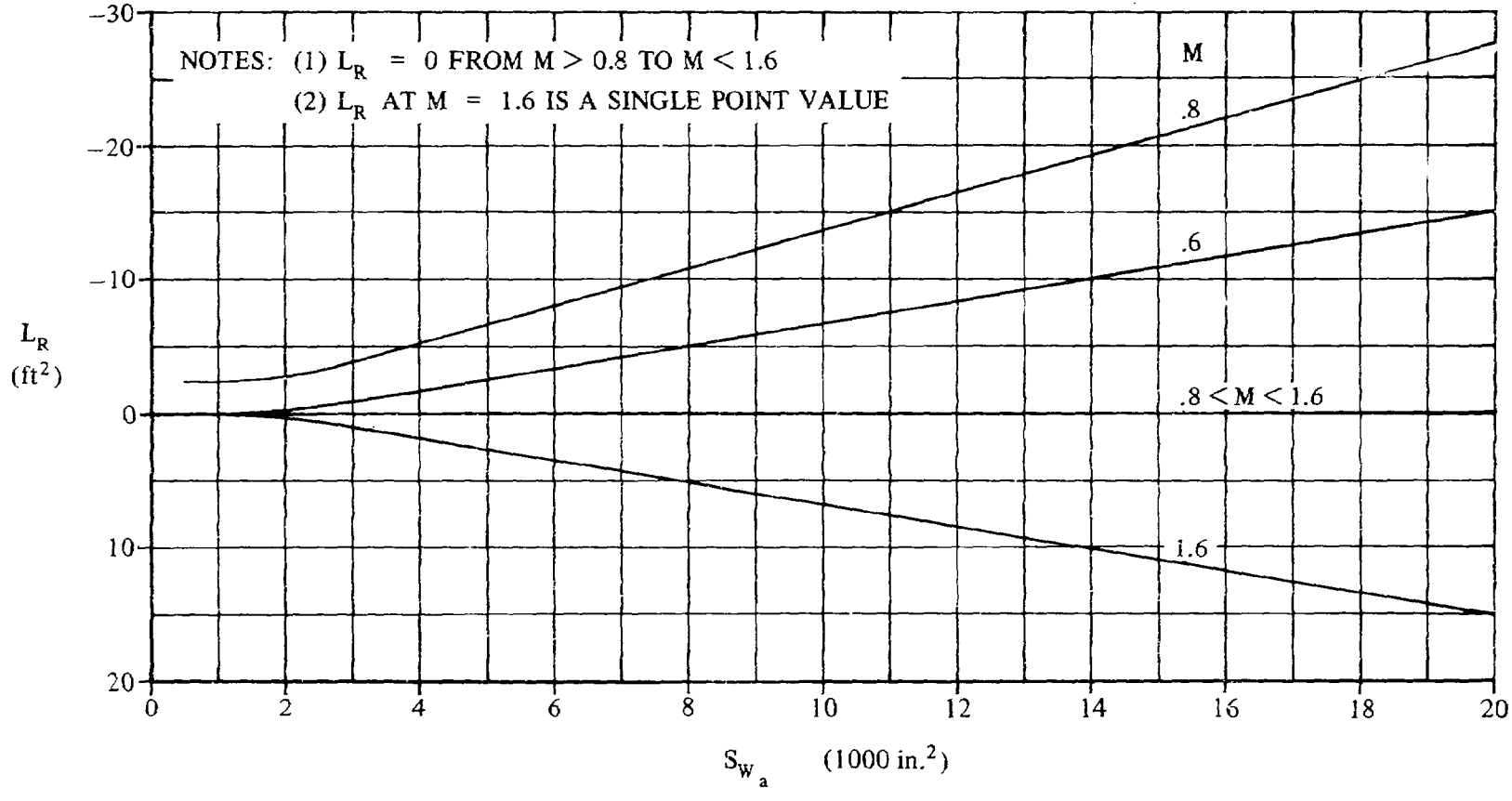

FIGURE 3.1.1-13 INCREMENTAL-LIFT EFFECT DUE TO CARRIAGE-RACK INSTALLATION MER STORE LOADINGS (CONFIGURATION 2)

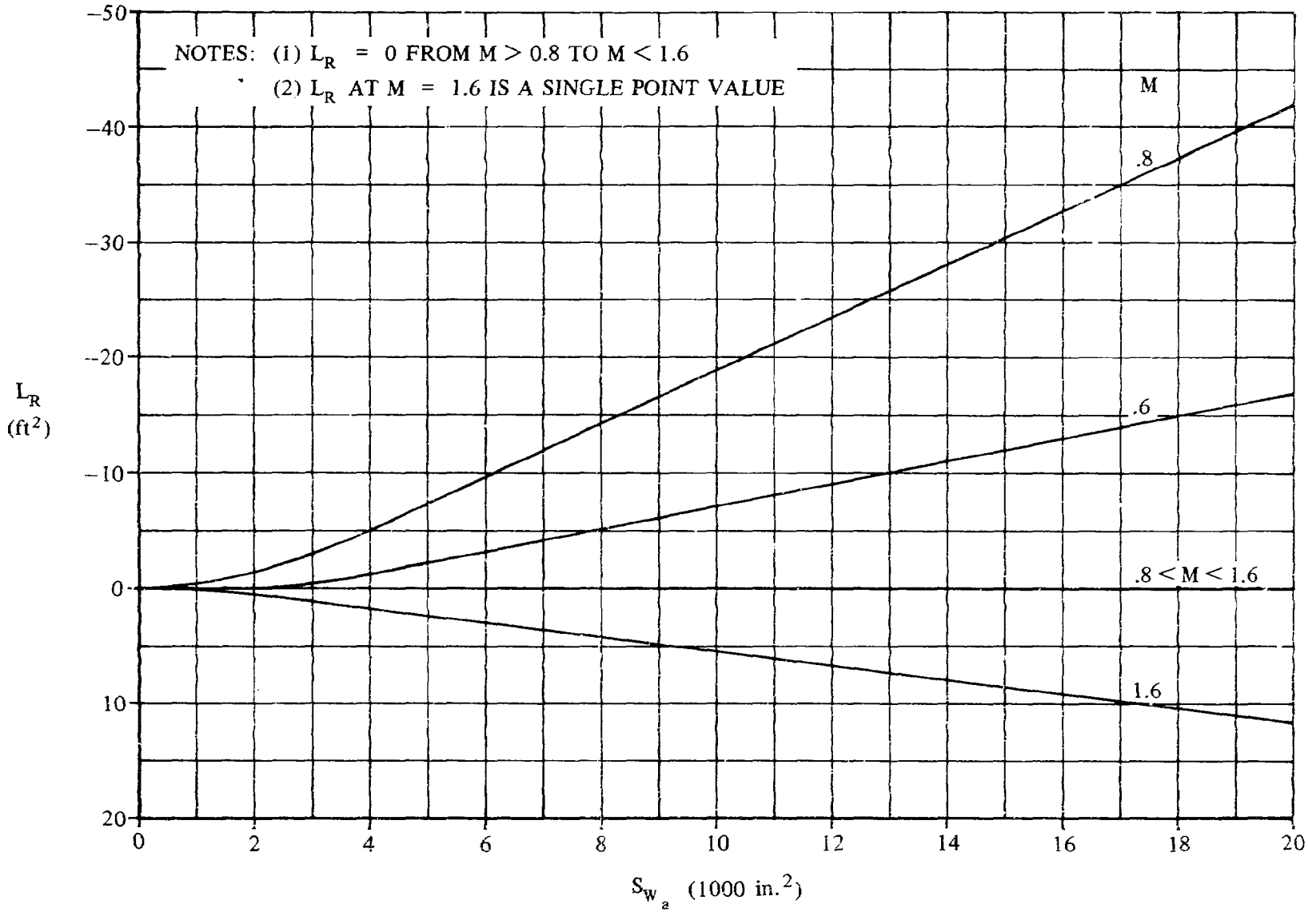

FIGURE 3.1.1-14 INCREMENTAL-LIFT EFFECT DUE TO CARRIAGE-RACK INSTALLATION TER STORE LOADINGS (CONFIGURATION 3)

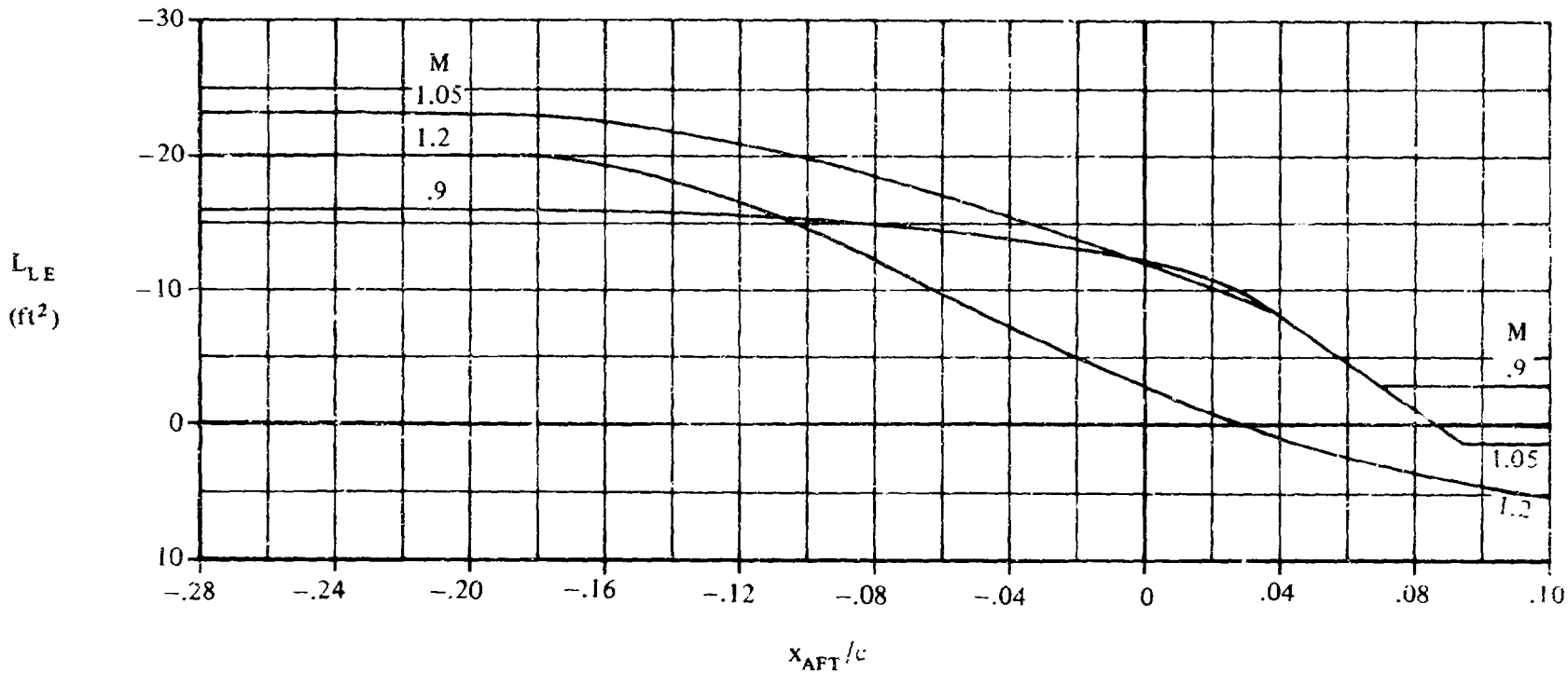

FIGURE 3.1.1-15 INCREMENTAL-LIFT EFFECT DUE TO LONGITUDINAL LOCATION MER STORE LOADINGS (CONFIGURATION 2)

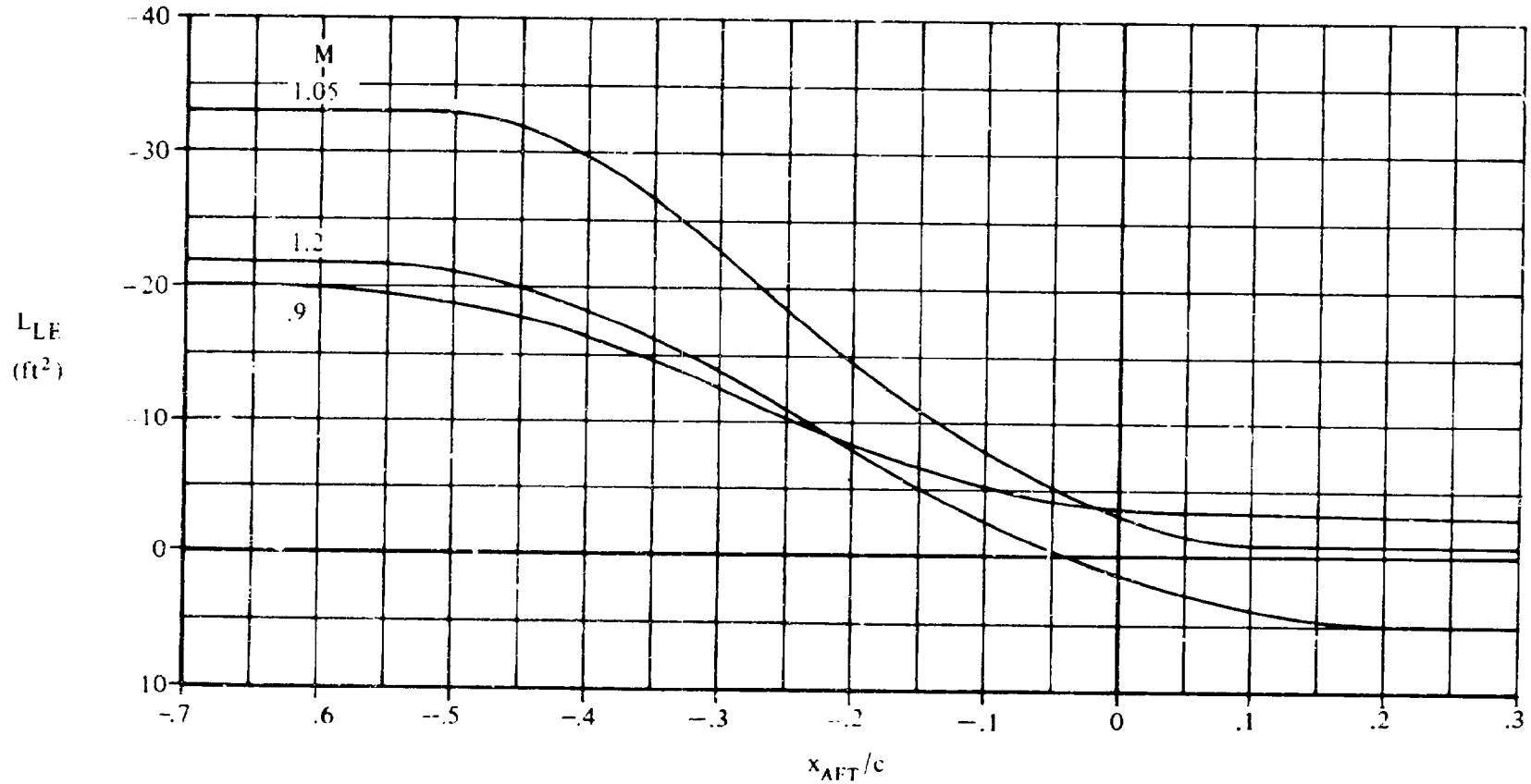

FIGURE 3.1.1-16 INCREMENTAL-LIFT EFFECT DUE TO LONGITUDINAL LOCATION
TER STORE LOADINGS (CONFIGURATION 3)

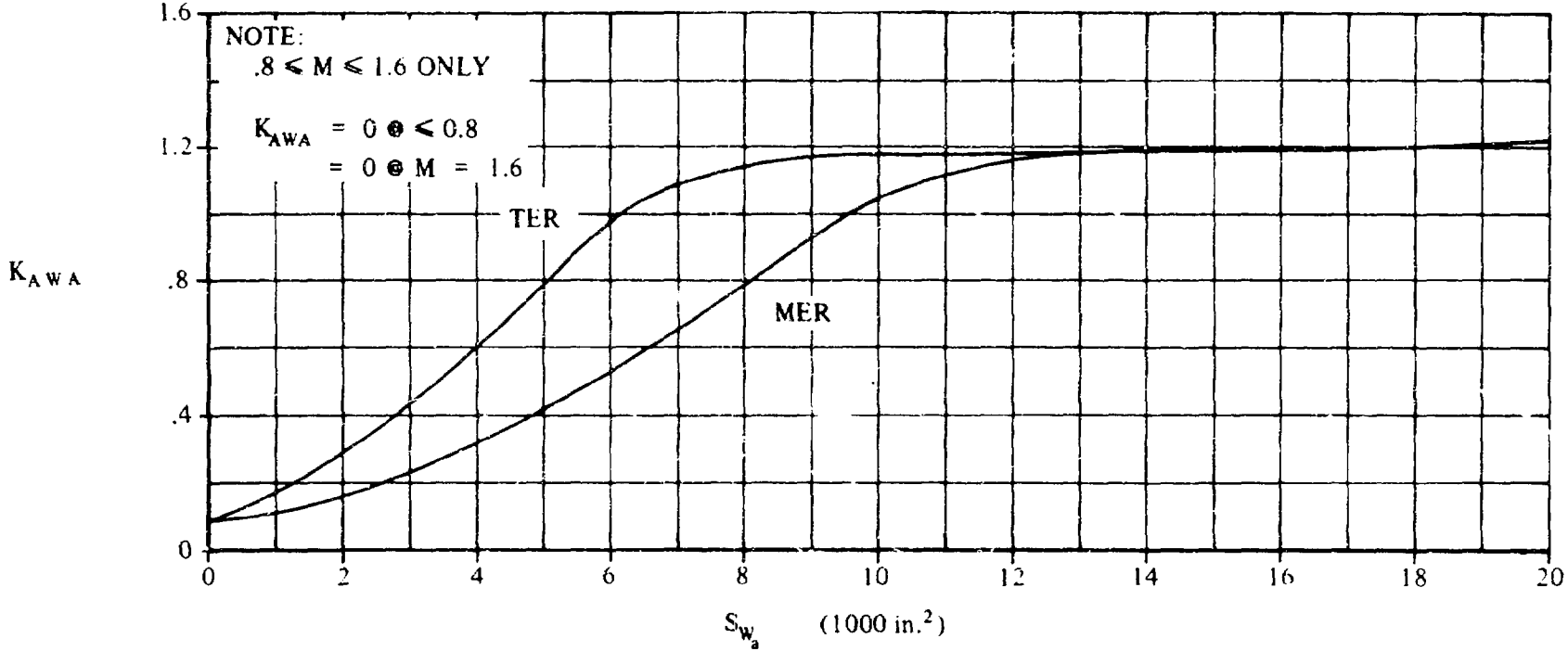

FIGURE 3.1.1-17 EFFECT OF MULTIPLE-RACK TYPE ON LONGITUDINAL-LOCATION FACTOR

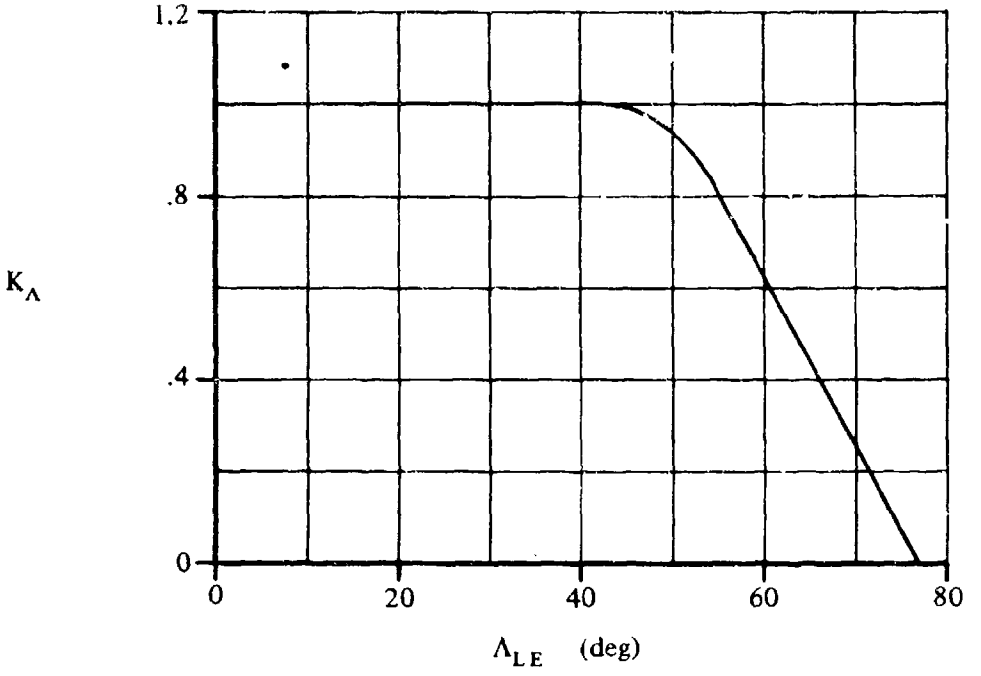

FIGURE 3.1.1-18a WING-SWEEP-EFFECT PARAMETER

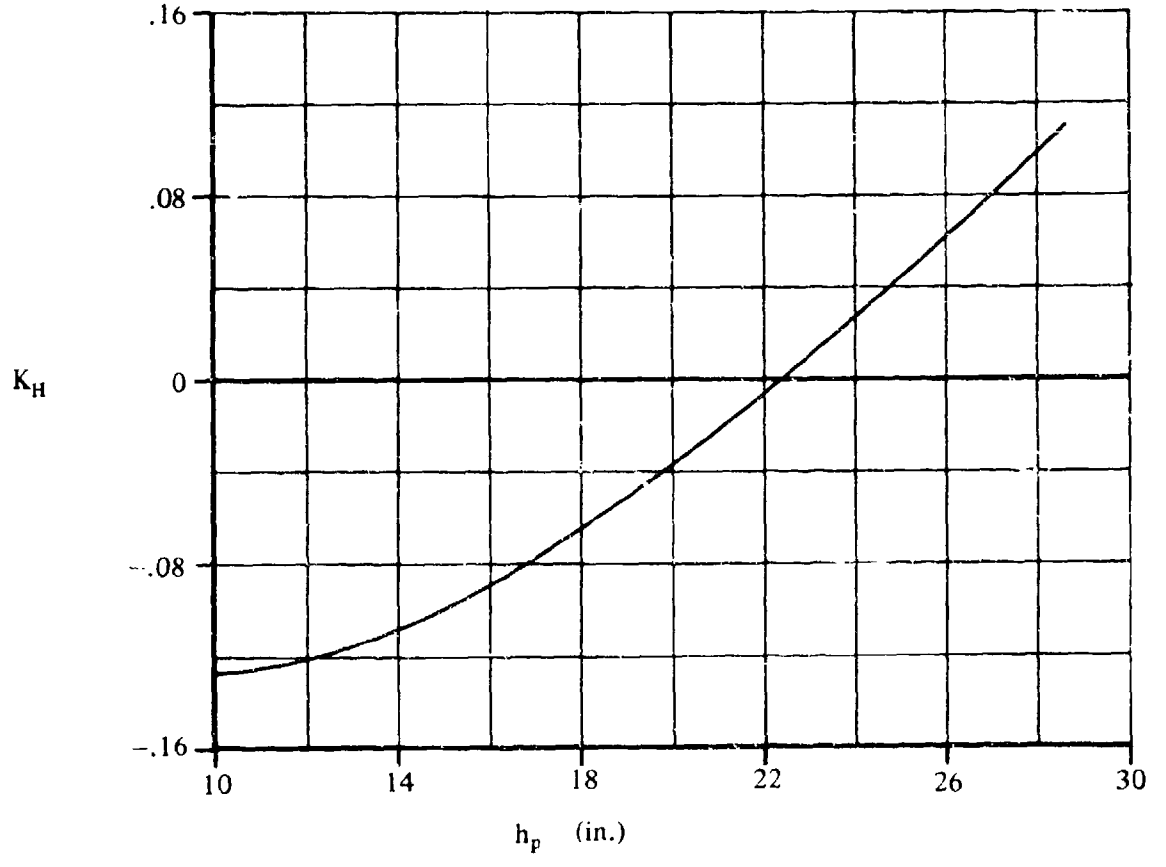

FIGURE 3.1.1-18b PYLON-HEIGHT FACTOR

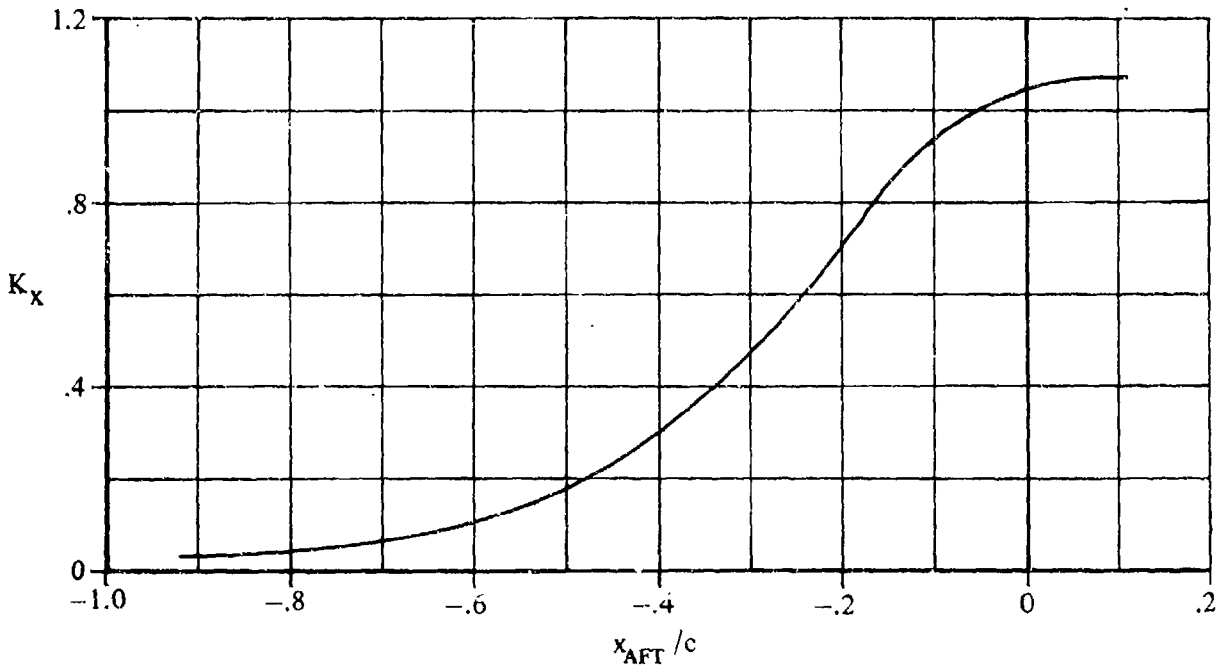

FIGURE 3.1.1-19a STORE-PLACEMENT FACTOR

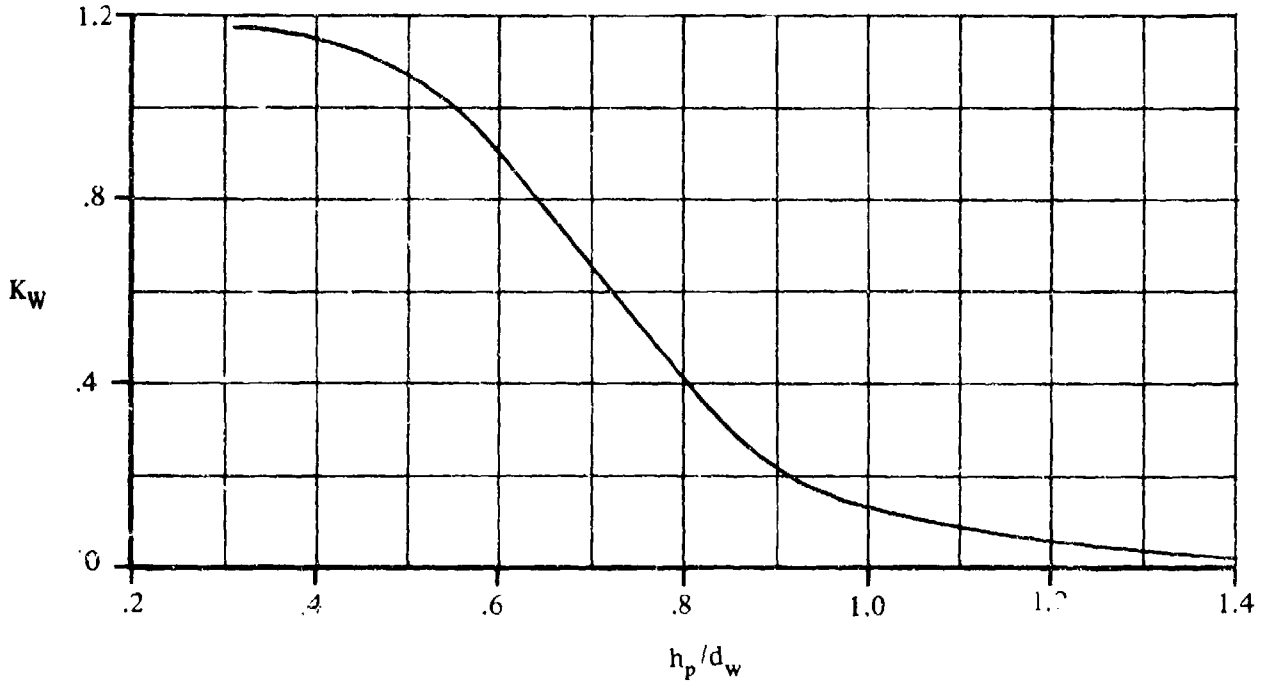

FIGURE 3.1.1-19b STORE-INSTALLATION-WIDTH FACTOR

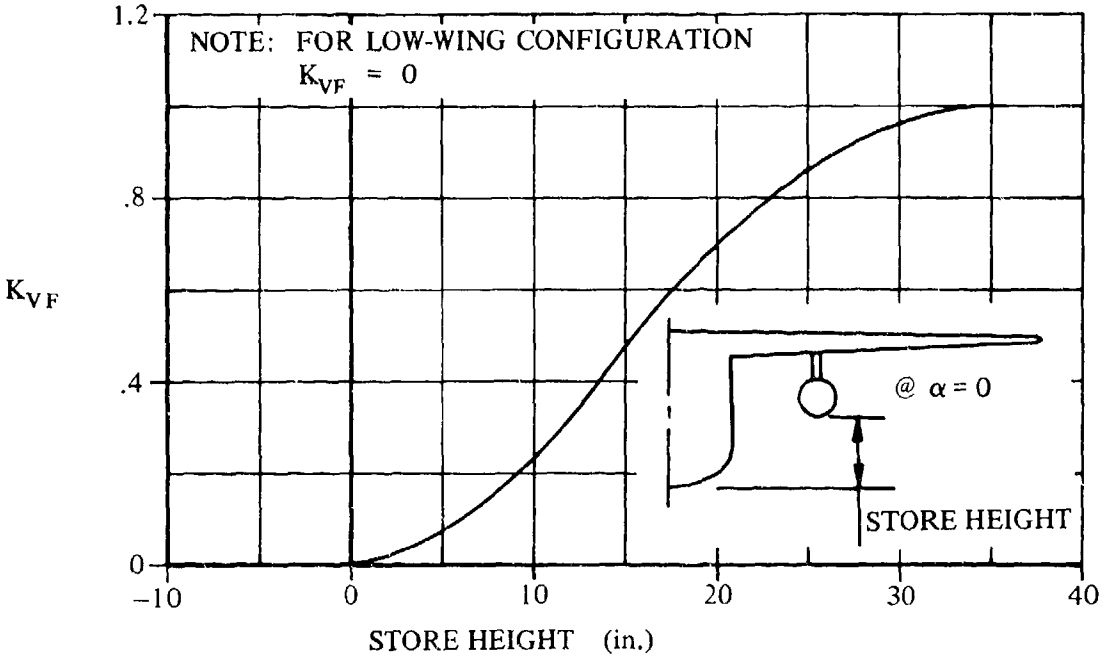

FIGURE 3.1.1-20a VERTICAL CLEARANCE PARAMETER

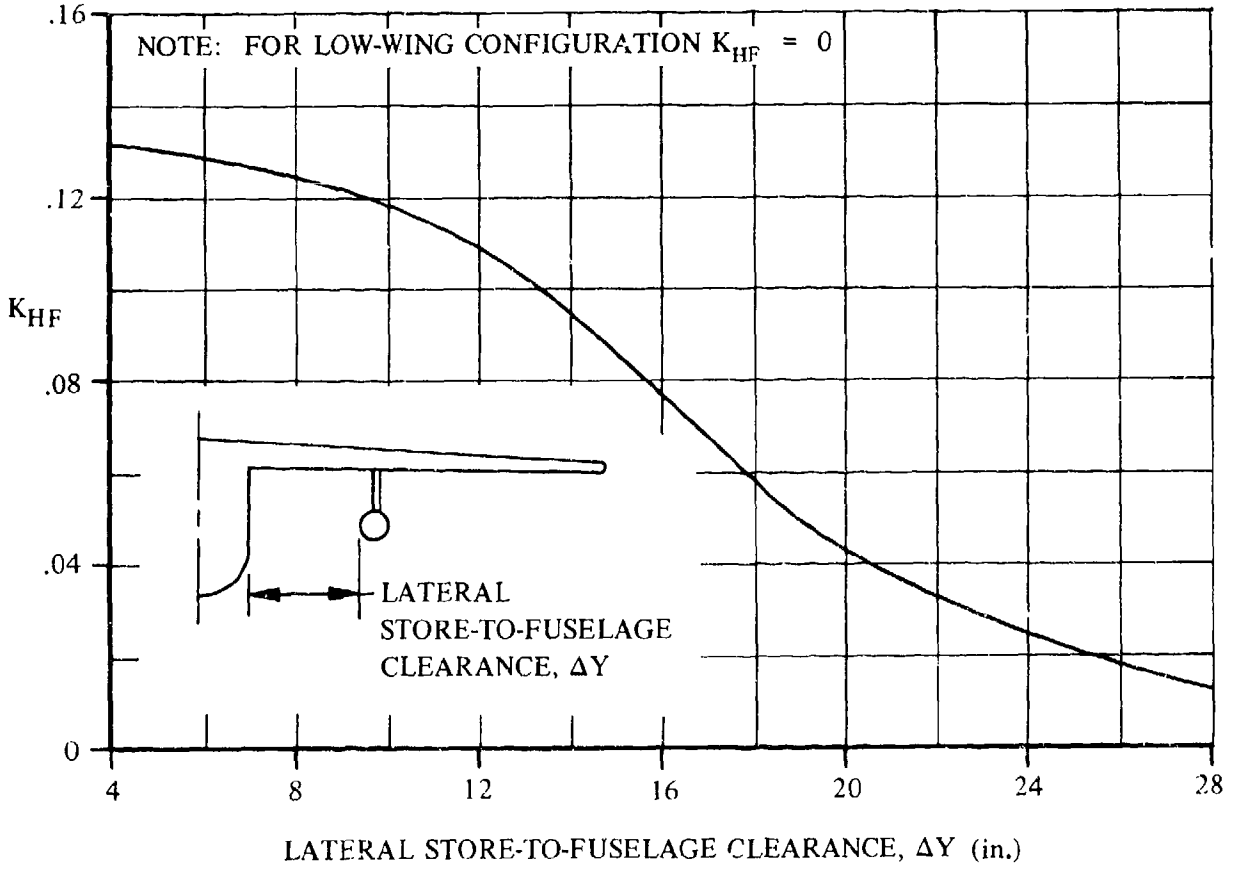

FIGURE 3.1.1-20b LATERAL STORE-TO-FUSELAGE CLEARANCE PARAMETER

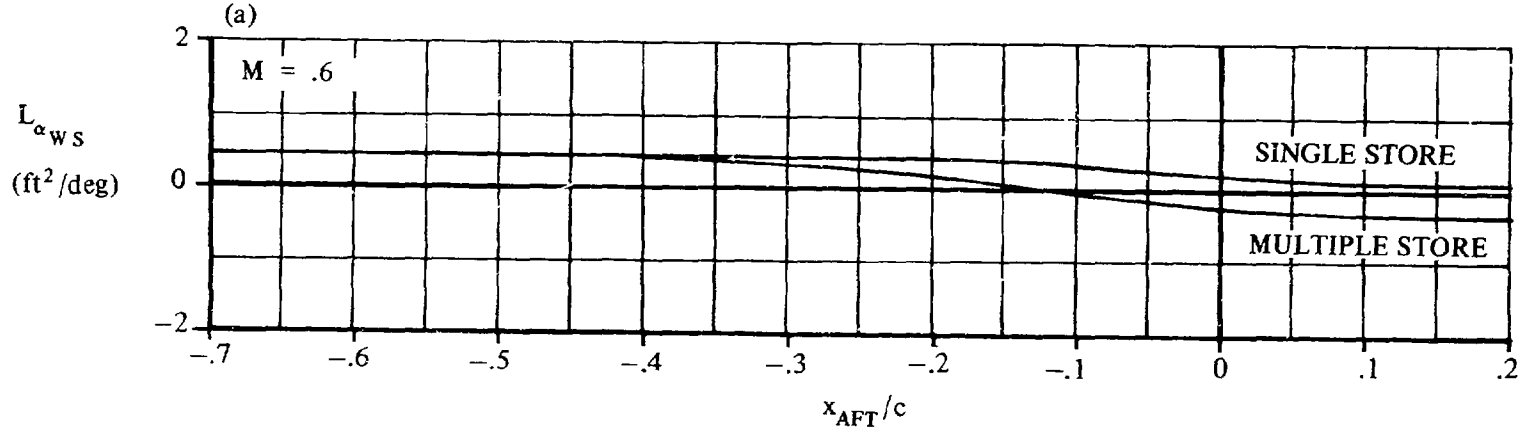

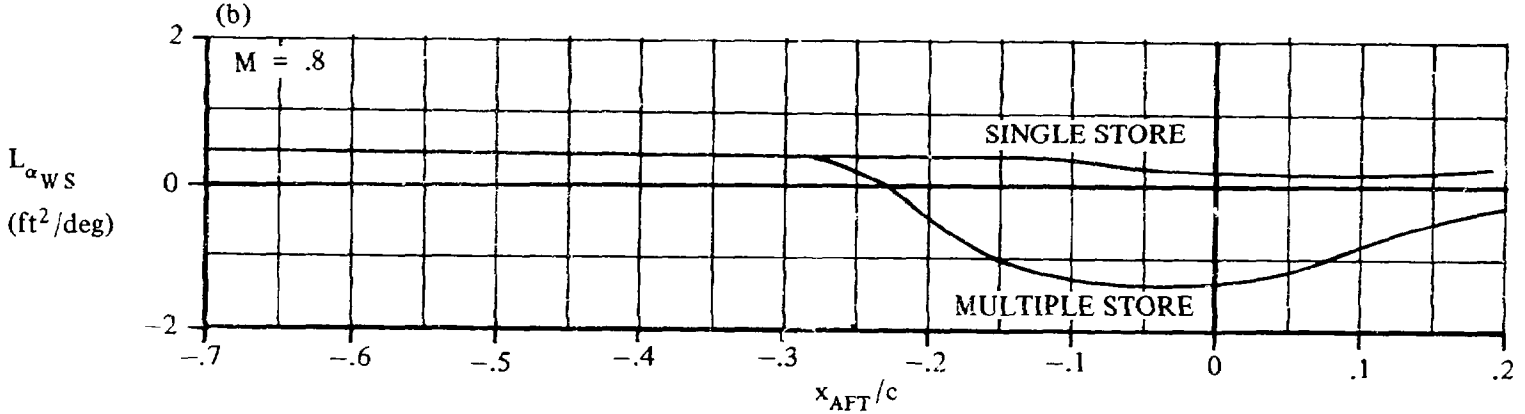

FIGURE 3.1.1-21 INCREMENTAL WING-STORES LIFT EFFECT DUE TO ANGLE OF ATTACK

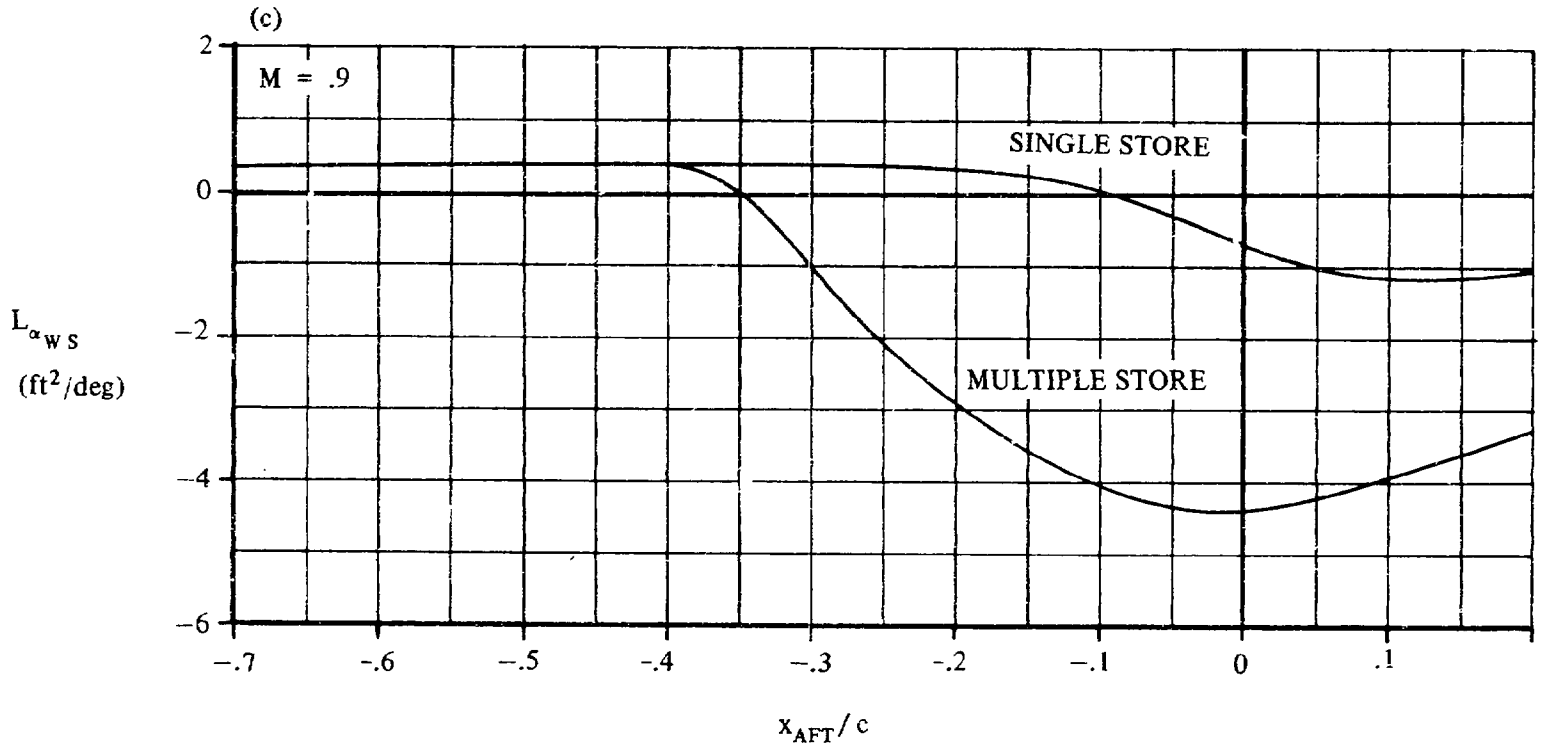

FIGURE 3.1.1-21 (CONTD)

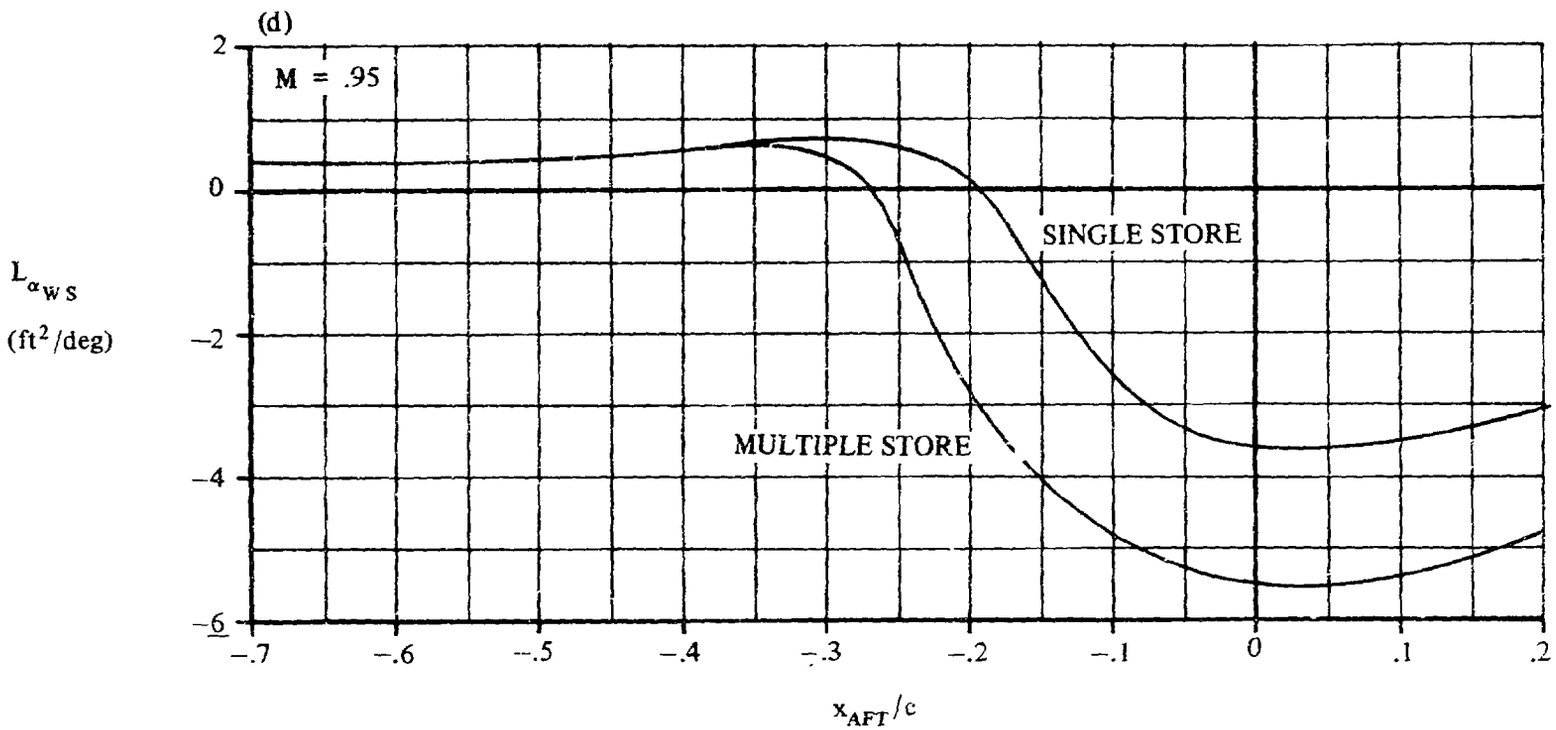

FIGURE 3.1.1-21 (CONTD)

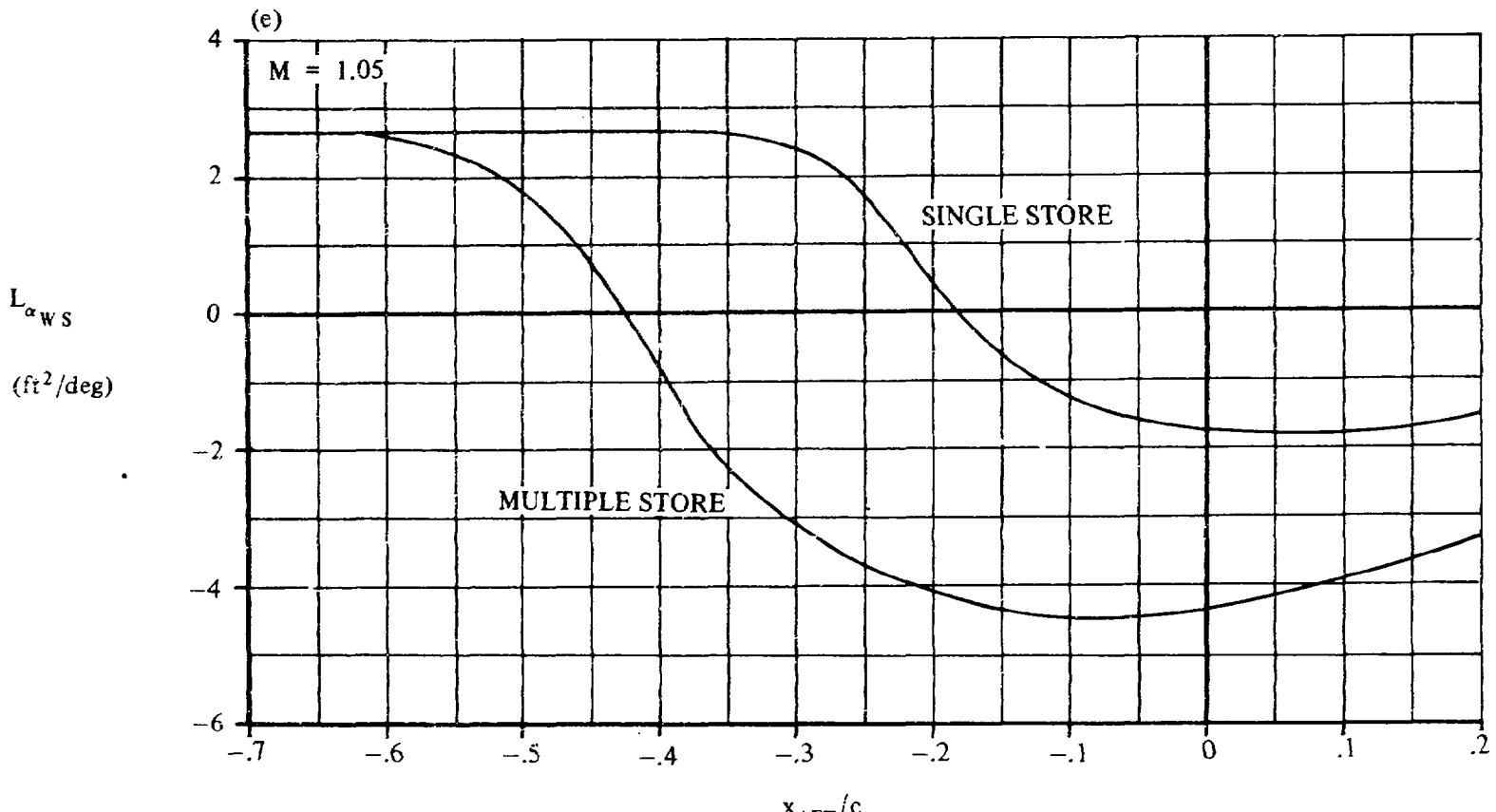

FIGURE 3.1.1-21 (CONTD)

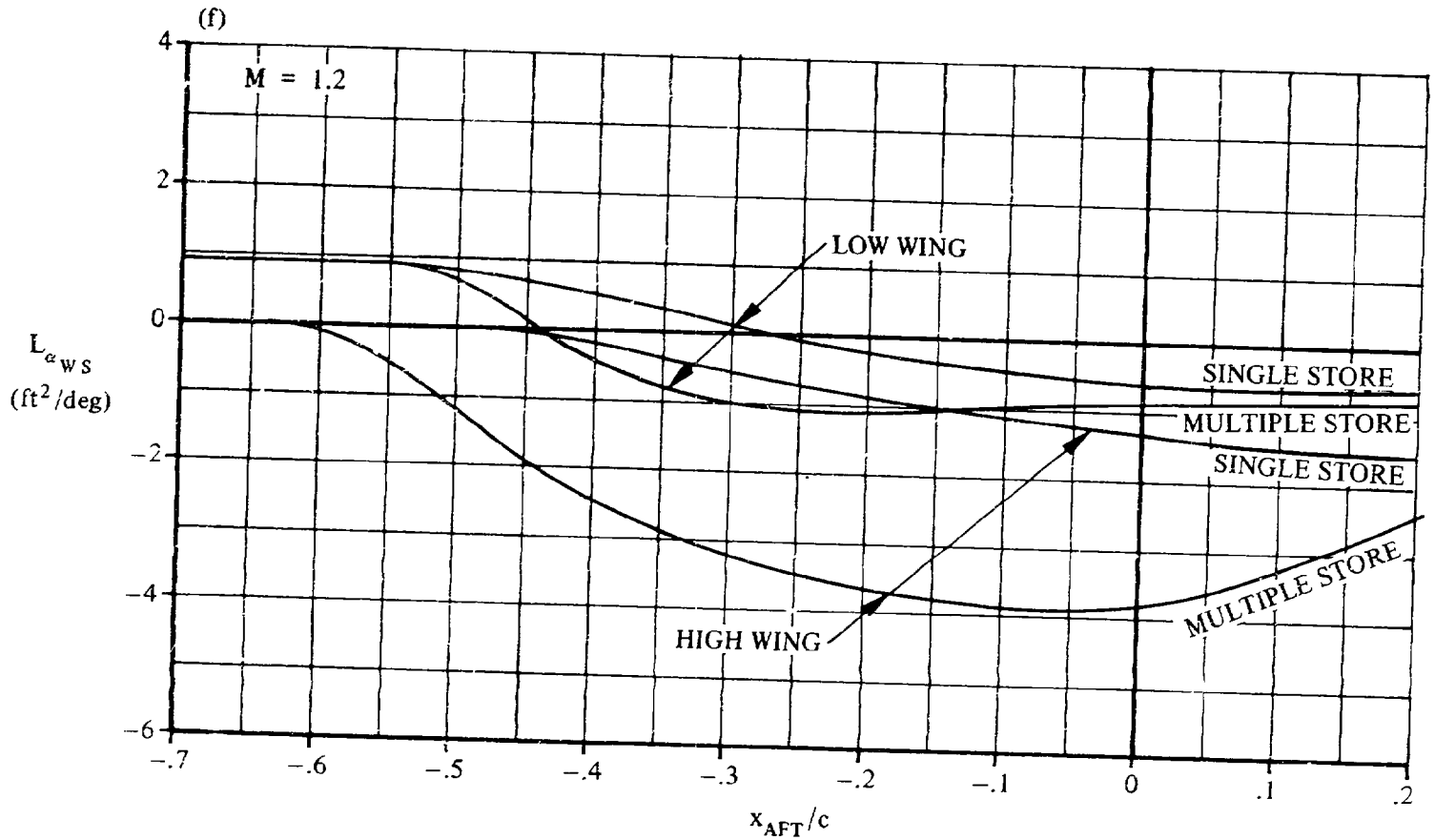

FIGURE 3.1.1-21 (CONTD)

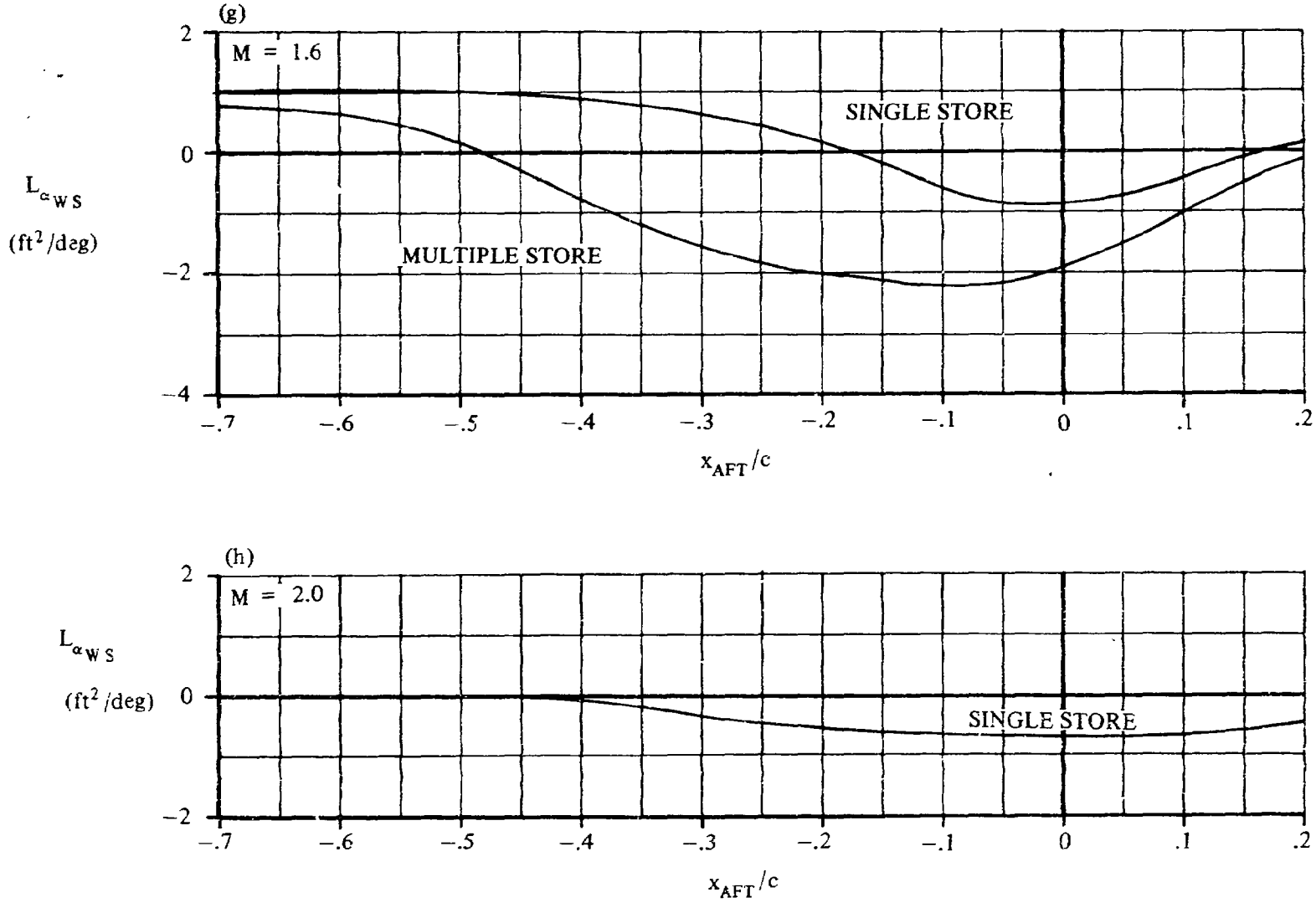

FIGURE 3.1.1-21 (CONTD)

3.1.2 LIFT INCREMENT DUE TO FUSELAGE-MOUNTED STORE INSTALLATIONS

A method is presented in this section for estimating the aircraft lift-coefficient increment due to fuselage-mounted store installations. The method as presented is for estimating the increment due to a pair of symmetric fuselage-mounted installations. The increment due to a single installation may also be obtained by using half the increment due to the pair of symmetric installations.

The Datcom Method is taken from Reference 1 and is empirical in nature. The method is applicable to aircraft of conventional design and essentially symmetrical store shapes with no major shape protuberance. The limitations on configuration and Mach-number range are summarized in Table 3.1-A. Additional limitations and assumptions pertaining to the method are listed below:

1. The method has not been validated for pylon heights greater than 10 inches.

2. The method is limited to store installations which are not mounted beyond 90 percent of the fuselage semispan from the fuselage centerline.

3. The method has been verified for a Mach-number range between M = 0.6 and M = 2.0 with a few exceptions. Caution should be used in extrapolating the empirical curves beyond the given Mach-number range.

4. The method has not been verified for configurations in which flaps, slats or other flow-disrupting devices are deployed.

5. The method gives the best results for an angle-of-attack range from 0 to 8^{o}, although the method can be used for higher angles of attack.

6. The data base used in deriving the method relied heavily on swept-wing tactical-combat-aircraft wind-tunnel data.

7. No method is provided to estimate fuselage and adjacent-store interference effects. These effects may be significant if the separation distances are less than 3 store diameters. Proximity to engine inlets may also be significant.

8. The method is applicable for sideslip angles less than 4^{o}.

The loading configuration capabilities of the method are given in Table 3.1.2-A. Each configuration is assigned a number which is referred to throughout the method. The method is applied separately to each single store installation or symmetrical pair of store installations.

TABLE 3.1.2-A

STORE CONFIGURATION SUMMARY

Store Configuration			Configuration Number
Mounting	Carriage	Loading	
Pylon	None	Empty	1
	Single	Single	1
Tangent	Single	Single	1
Pylon	MER	Empty	2
		Partially Loaded	2
		Full	2
Tangent		Empty	2
		Partially Loaded	2
		Full	2
Pylon	TER	Empty	3
		Partially Loaded	3
		Full	3
Tangent		Empty	3
		Partially Loaded	3
		Full	3

A. SUBSONIC

DATCOM METHOD

The incremental lift coefficient, based on wing reference area, due to a pair of symmetric fuselage-mounted external-store installations is given by Equation 3.1.2-a. (For a single installation, this value should be divided by two.)

$$\Delta C_{L_{FS}} = \frac{1}{S_W}\left[L_R K_{WING} K_{SPAN} + L_{\alpha_{FS}}(\alpha - 4.0)\right] \qquad 3.1.2\text{-a}$$

where

S_W is the wing reference area (ft^2).

L_R is an incremental-lift effect due to carriage-rack installation obtained from Figures 3.1.1-12 through 3.1.1-14 of Section 3.1.1 as a function of Mach number and S_{W_a}. (Refer to the discussion presented in Section 3.1.1 in relation to the Mach-number range and configuration applicability of this parameter.)

where, for fuselage-mounted installations

S_{W_a} is the pseudo store installation planform area ($in.^2$) for both installations, and is given by

$$S_{W_a} = 2\ell_{SP} d_w \qquad 3.1.2\text{-b}$$

where

ℓ_{SP} is the maximum store/pylon installation length (in.). (See Sketch (a).)

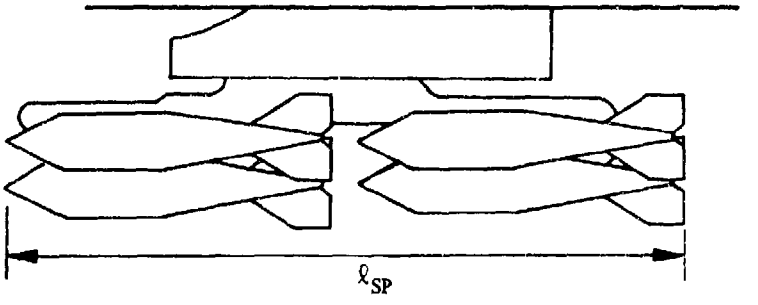

SKETCH (a)

d_w is the maximum width (in.) of the store installation not including protruding fins and is given by

1. For an empty pylon:

$$d_w = 1.5 \times \text{(maximum pylon width)} \qquad 3.1.2\text{-c}$$

2. For a single store:

$$d_w = d_S \qquad 3.1.2\text{-d}$$

(d_S is the maximum store diameter)

K_{WING} is a parameter to account for the effect of wing location on the fuselage. This parameter is obtained from Figure 3.1.2-6 as a function of z_w/h_f where

z_w is the distance from the top of the fuselage to the midpoint of the wing intersection with the fuselage (including canopy protuberances) (See Figure 3.1.2-6).

h_f is the overall height of the fuselage (including canopy protuberances) (See Figure 3.1.2-6).

K_{SPAN} is a parameter to account for the effect of lateral placement of the store installation. The parameter is obtained from Figure 3.1.2-7 and is available for store installations mounted within 90% of the fuselage semispan from the fuselage centerline.

$L_{\alpha_{FS}}$ is an effect due to aircraft angle of attack obtained from Figure 3.1.2-8 as a function of aircraft wing location and Mach number.

α is the aircraft angle of attack (deg).

Sample Problem

Given: A swept-wing subsonic fighter aircraft (Reference 2) loaded with a pylon-mounted MER containing five 500-lb. bombs (two of the bombs are hidden in the front view) located below the fuselage centerline.

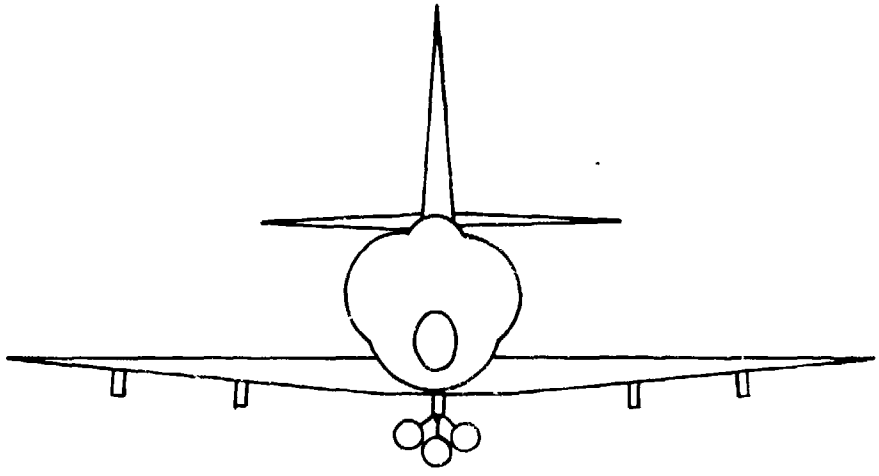

FRONT VIEW

Aircraft Data:

$S_W = 260\ ft^2$ $\qquad z_w/h_f = 0.88$

Stores Data:

$d_S = 12$ in.

Installation Data:

$d_w = 33.6$ in. $\qquad h_p = 11.2$ in. $\qquad \ell_{SP} = 185.6$ in.

Additional Data:

$M = 0.8$ $\qquad \alpha = 0^o$

It is noted from Table 3.1.2-A that this is Configuration Number 2. Since the loading is not a symmetrical pair of installations, the final result will be divided by 2 to obtain the increment for a single installation.

Compute:

$S_{W_a} = 2\ell_{SP} d_w$ (Equation 3.1.2-b)

$= (2)(185.6)(33.6)$

$= 12{,}472 \text{ in.}^2$

$L_R = -17.0$ (Figure 3.1.1-13, Configuration 2)

$z_w/h_f = 0.88$ (Given)

$K_{WING} = 0.93$ (Figure 3.1.2-6)

$K_{SPAN} = 1.0$ (Figure 3.1.2- 7)

$L_{\alpha_{FS}} = 0.15$ (Figure 3.1.2- 8)

Solution:

$$\Delta C_{L_{FS}} = \frac{1}{S_W}\left[L_R K_{WING} K_{SPAN} + L_{\alpha_{FS}}(\alpha - 4.0)\right] \quad \text{(Equation 3.1.2-a)}$$

$$= \frac{1}{260}[(-17.0)(0.93)(1.0) + (0.15)(8.0 - 4.0)]$$

$$= -0.0585 \quad \text{(symmetrical pair)}$$

For a single installation,

$$\Delta C_L = \frac{\Delta C_{L_{FS}}}{2} = \frac{-0.0585}{2} = -0.02925$$

The calculated value of $\Delta C_{L_{FS}}$ is combined with wing-store increments in the Sample Problem of Section 3.1.3 to illustrate a complex loading configuration. Comparison of the calculated results with test data is provided in that section.

B. TRANSONIC

The method presented in Paragraph A of this section is also valid for transonic speeds. The user is cautioned that the accuracy of the method is less than that expected in the subsonic speed range; and test data should be used whenever possible.

C. SUPERSONIC

The method presented in Paragraph A of this section is also valid for supersonic speeds. The expected accuracy of the method is comparable to that in the subsonic range. The maximum Mach number provided in the design figures indicates the level to which the method is substantiated. Caution should be used when extrapolating the data beyond the Mach range provided in the figures.

REFERENCES

1. Gallagher, R. D., Jimenez, G., Light, L. E., and Thames, F. C.: Technique for Predicting Aircraft Aerodynamic Effects Due to External Stores Carriage. AFFDL-TR-75-95, Volumes I and II, 1975. (U)

2. Watzke, R. E.: Aerodynamic Data for Model TA-4F Operational Flight Trainer. McDonnell Douglas Corporation Rept. DAC-67425, 1968. (U)

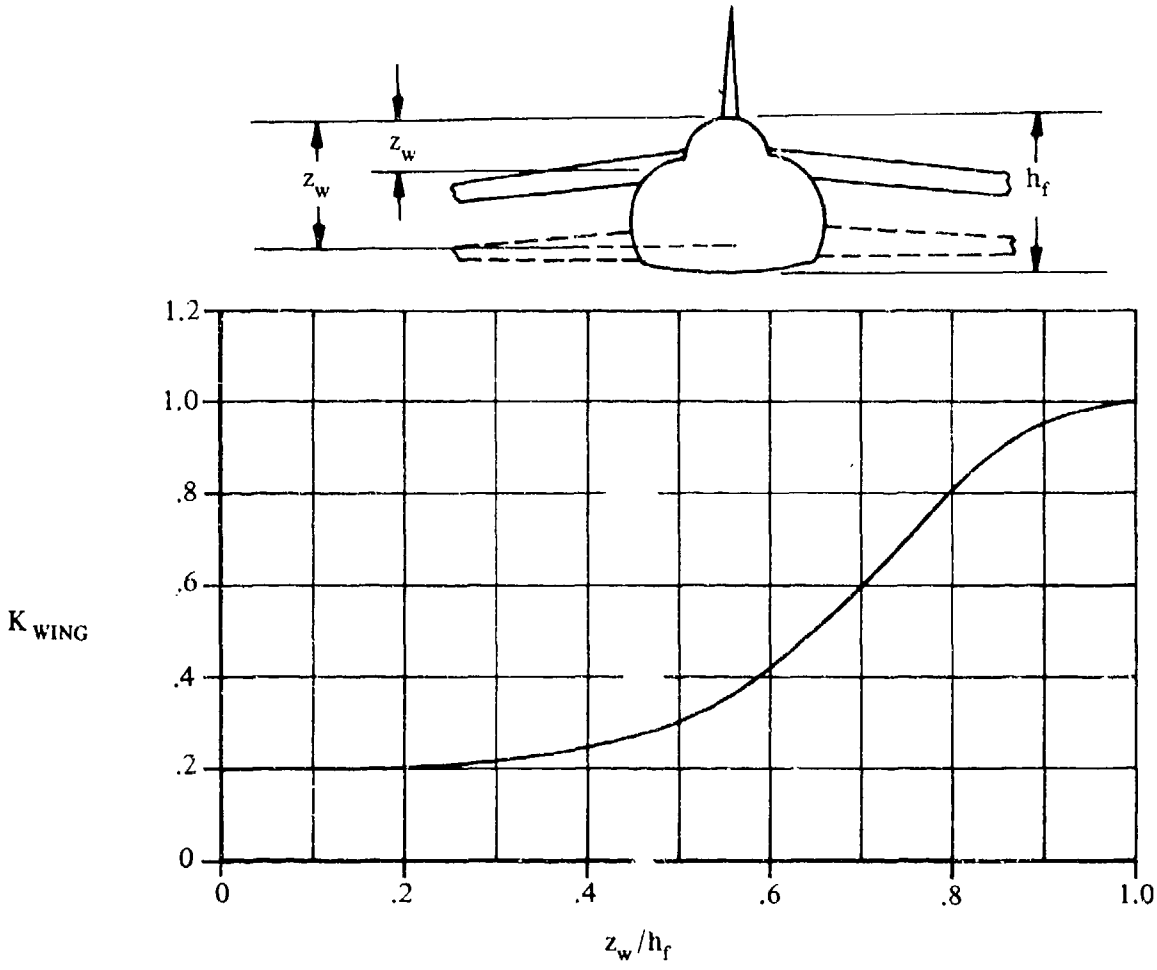

FIGURE 3.1.2-6 WING-LOCATION PARAMETER

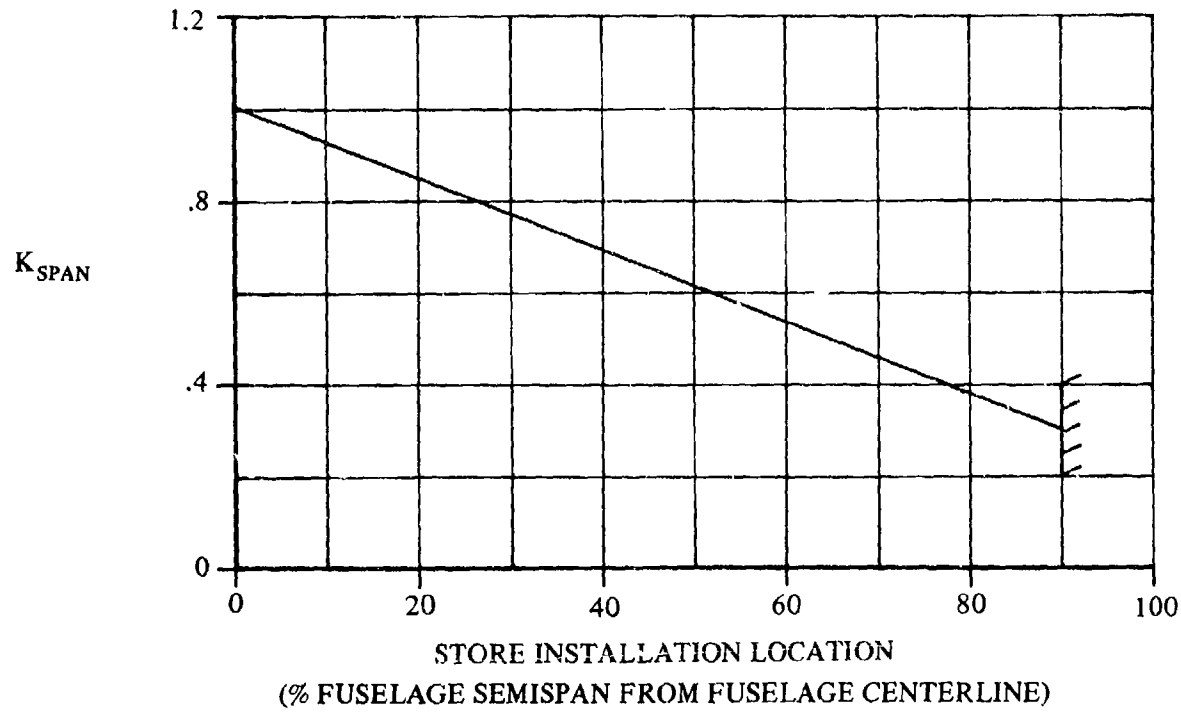

FIGURE 3.1.2- 7 LATERAL-PLACEMENT FACTOR FOR FUSELAGE-MOUNTED STORES

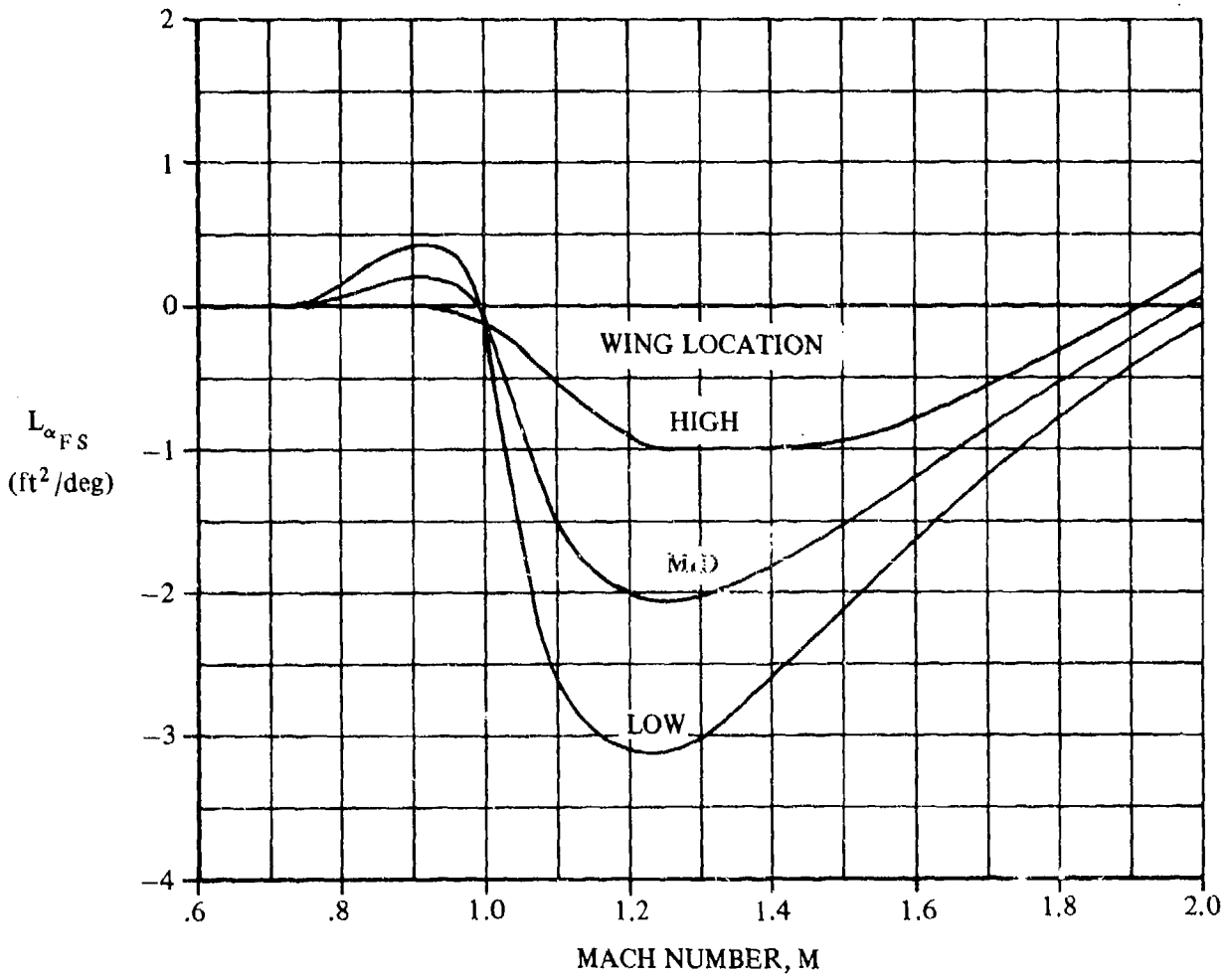

FIGURE 3.1.2- 8 FUSELAGE-STORES INCREMENTAL-LIFT EFFECT DUE TO ANGLE OF ATTACK

3.1.3 TOTAL AIRCRAFT LIFT INCREMENT DUE TO EXTERNAL STORES

A method is presented in this section for estimating the total aircraft lift-coefficient increment due to external-store installations. The method predicts the increments for symmetric, asymmetric, and multiple-installation loading configurations.

The Datcom method is taken from Reference 1 and is empirical in nature. The method is applicable to aircraft of conventional design and essentially symmetrical store shapes with no major shape protuberances. The limitations on configuration and Mach-number range are summarized in Table 3.1-A. Additional limitations and assumptions pertaining to the method are listed below:

1. The method is not applicable to wing-tip or wing-tangent-mounted stores.

2. The method has not been validated for fuselage installations with pylon heights greater than 10 inches.

3. The method for fuselage-mounted stores is limited to installations which are not mounted beyond 90 percent of the fuselage semispan from the fuselage centerline.

4. The method has been verified for a Mach-number range between $M = 0.6$ and $M = 2.0$ with a few exceptions. Caution should be used in extrapolating the empirical curves beyond the given Mach-number range.

5. The method has not been verified for configurations in which flaps, slats or other flow-disrupting devices are deployed.

6. The method gives the best results for an angle-of-attack range from 0 to 8^{o}, although the method can be used for higher angles of attack.

7. The data base used in deriving the method relied heavily on swept-wing tactical-combat-aircraft wind-tunnel data.

8. No method is provided to estimate fuselage and adjacent-store interference effects. These effects may be significant if the separation distances are less than 3 store diameters. Proximity to engine inlets may also be significant.

9. The method is applicable for sideslip angles less than 4^{o}.

The procedure for computing the total lift-coefficient increment requires calculation of the increments for wing and fuselage installations separately by the methods of Sections 3.1.1 and 3.1.2, respectively. The increments for each installation are then summed to obtain the total increment.

A. SUBSONIC

DATCOM METHOD

The total aircraft lift-coefficient increment due to external-store installations and based on wing reference area, S_W, is given by

$$\Delta C_L = \sum_{i=0}^{N_{S_i}} (\Delta C_L)_i + \sum_{j=0}^{N_{A_j}} (\Delta C_L)_j \qquad 3.1.3\text{-a}$$

where

N_{S_i} is the total number of pairs of symmetrical external-store installations.

$(\Delta C_L)_i$ is the incremental lift coefficient due to a pair of symmetrical store installations where:

For wing-mounted installations

$$(\Delta C_L)_i = \Delta C_{L_{WS}} \qquad 3.1.3\text{-b}$$

and $\Delta C_{L_{WS}}$ is calculated in Section 3.1.1.

For fuselage-mounted installations

$$(\Delta C_L)_i = \Delta C_{L_{FS}} \qquad 3.1.3\text{-c}$$

and $\Delta C_{L_{FS}}$ is calculated in Section 3.1.2.

N_{A_i} is the total number of asymmetrical external-store installations.

$(\Delta C_L)_j$ is the incremental lift coefficient due to an asymmetric store installation where:

For wing-mounted installations,

$$(\Delta C_L)_j = \frac{1}{2} \Delta C_{L_{WS}} \qquad 3.1.3\text{-d}$$

and $\Delta C_{L_{WS}}$ is calculated in Section 3.1.1.

For fuselage-mounted installations

$$(\Delta C_L)_j = \frac{1}{2} \Delta C_{L_{FS}} \qquad 3.1.3\text{-e}$$

and $\Delta C_{L_{FS}}$ is calculated in Section 3.1.2.

Reference 1 states that prediction errors for incremental lift are nominally 20 percent. This generally results in an overall accuracy within 2 percent of total aircraft lift. Comparisons of test and calculated results are presented in Reference 1.

Sample Problem

Given: A swept-wing subsonic fighter aircraft from Reference 2, loaded as follows: (This is a combination of the configuration of the Sample Problems from Sections 3.1.1 and 3.1.2.)

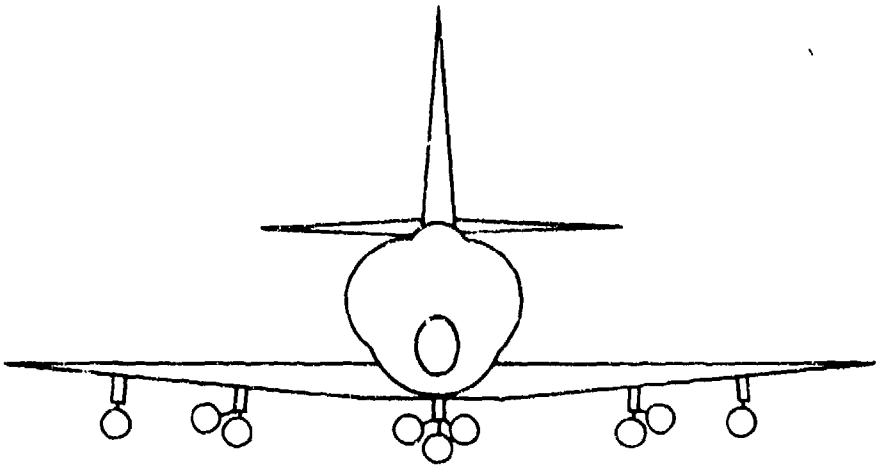

FRONT VIEW

Spanwise Station	Rack Type	Mounting	Store Type	No. of Stores	Configuration Number
Centerline	MER	Pylon	500-lb Bomb	5	2
Inboard Wing	TER	Pylon	500-lb Bomb	2	3
Outboard Wing	Single	Pylon	500-lb Bomb	1	1

Additional Characteristics:

$M = 0.8$ $\alpha = 8^{O}$

(Additional geometric data are provided in the Sample Problems of Sections 3.1.1 and 3.1.2.)

Compute:

$N_{S_i} = 2$ (inboard- and outboard-wing installations)

$N_{A_i} = 1$ (centerline installation)

$(\Delta C_L)_i$ for i = 1,2:

$(\Delta C_L)_1 = \Delta C_{L_{WS}}$ (Equation 3.1.3-b)

where $\Delta C_{L_{WS}}$ is evaluated at the outboard-wing station and computed in the Sample Problem of Section 3.1.1.

$(\Delta C_L) = \Delta C_{L_{WS}} = 0.00312$

$(\Delta C_L)_2 = \Delta C_{L_{WS}}$ (Equation 3.1.3-b)

where $\Delta C_{L_{WS}}$ is evaluated at the inboard-wing station and computed in the Sample Problem of Section 3.1.1.

$(\Delta C_L)_2 = \Delta C_{L_{WS}} = -0.0107$

$(\Delta C_L)_j$ for j = 1:

$(\Delta C_L)_1 = \frac{1}{2}\Delta C_{L_{FS}}$ (Equation 3.1.3-e)

where $\Delta C_{L_{FS}}$ is evaluated at the fuselage-centerline station and computed in the Sample Problem of Section 3.1.2.

$(\Delta C_L)_1 = \Delta C_{L_{FS}} = -0.02925$

Solution:

$$\Delta C_L = \sum_{i=0}^{N_{S_i}} (\Delta C_L)_i + \sum_{j=0}^{N_{A_i}} (\Delta C_L)_j \qquad \text{(Equation 3.1.3-a)}$$

$$\Delta C_L = \sum_{i=0}^{2} (\Delta C_L)_i + \sum_{j=0}^{1} (\Delta C_L)_j$$

$$= 0.00312 - 0.0107 - 0.02925$$

$$= -0.0368$$

Calculated results at additional Mach numbers are shown in comparison to test data from Reference 2 in Sketch (a).

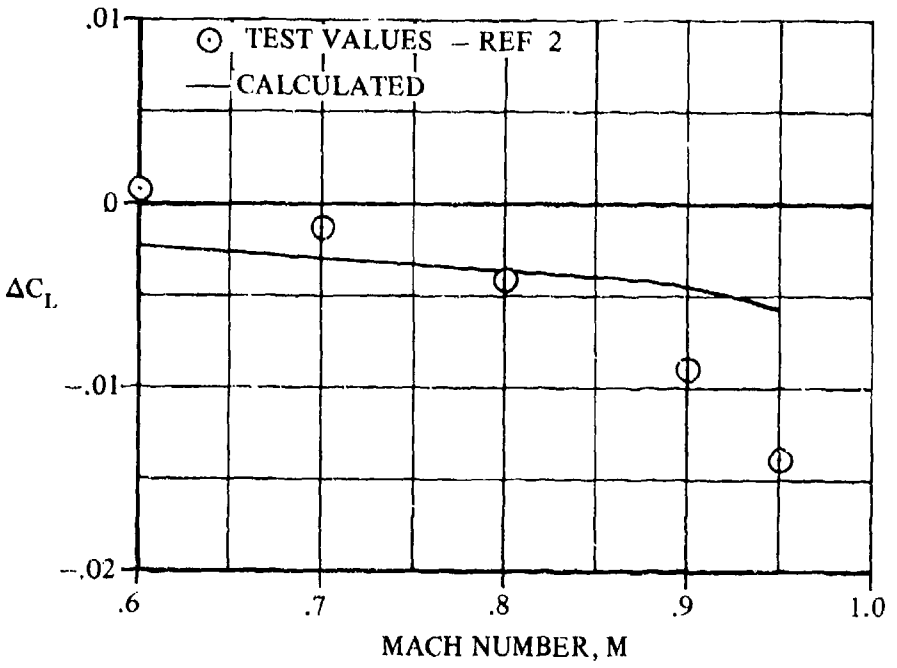

SKETCH (a)

B. TRANSONIC

The method presented in Paragraph A of this section is also valid for transonic speeds. The user is cautioned that the accuracy of the method is less than that expected in the subsonic speed range.

C. SUPERSONIC

The method presented in Paragraph A of this section is also valid for the supersonic speed range. The maximum Mach number provided in the design figures indicates the level to which the method is substantiated.

REFERENCES

1. Gallagher, R. D., Jimenez, G., Light, L. E., and Thames, F. C.: Technique for Predicting Aircraft Aerodynamic Effects Due to External Stores Carriage. AFFDL-TR-75-95, Volumes I and II, 1975. (U)

2. Watzke, R. E.: Aerodynamic Data for Model TA-4F Operational Flight Trainer. McDonnell Douglas Corporation Report DAC-67425, 1968. (U)

3.2 EFFECT OF EXTERNAL STORES ON AIRCRAFT DRAG

Methods are presented in this section for estimating the change in aircraft drag due to external-store installations. The methods predict an incremental change in drag coefficient, based on wing reference area, which can be added to the clean-aircraft drag coefficient to obtain the aircraft-with-stores drag coefficient. These methods are taken from Reference 1 and are empirical in nature.

Section 3.2 is subdivided as follows:

The total drag increment is the sum of the incremental drag at zero lift and the incremental drag due to lift. These components are computed in terms of equivalent-parasite-drag area for each installation by the methods of Sections 3.2.1 and 3.2.2 and are combined to obtain the total-drag-coefficient increment by the method of Section 3.2.3.

The Datcom methods are applicable to aircraft of conventional design and essentially symmetrical store shapes with no major shape protuberances. The methods are limited to the store-loading configurations and Mach-number ranges presented in Table 3.2-A. The methods are applicable to mixed loading configurations obtained by combining two or more loadings specified in Table 3.2-A. Additional limitations are specifically noted in each of the sections that follow.

TABLE 3.2-A

LOADING AND MACH-NUMBER LIMITATIONS

Mounting Location	Carriage Mode	Mount/Loading Type	Mach-Number Range
Wing	Single	Pylon – Empty	0.6 → 2.0
		Pylon – Single Store	
	Multiple	Pylon – Empty MER	0.6 → 1.6
		Pylon – Fully Loaded MER	
		Pylon – Partially Loaded MER	
		Pylon – Empty TER	
		Pylon – Fully Loaded TER	
		Pylon – Partially Loaded TER	
Fuselage	Single	Tangent – One Store	0.6 → 1.6
		Tangent – Two or More Stores	0.6 → 0.9
		Pylon – Empty	0.6 → 2.0
		Pylon – One Store	0.6 → 1.6
		Pylon – Two or More Stores	0.6 → 0.9
	Multiple	Tangent – One Store Installation	0.6 → 1.6
		Pylon – One Store Installation	
Wing or Fuselage		Adjacent Store Installation Interference	0.6 → 1.2
		Additional Drag Due to Lift	0.6 → 1.6

REFERENCE

1. Gallagher, R. D., Jimenez, G., Light, L. E., and Thames, F. C.: Technique for Predicting Aircraft Aerodynamic Effects Due to External Stores Carriage. AFFDL-TR-75-95, Volumes I and II, 1975. (U)

3.2.1 DRAG AT ZERO LIFT

3.2.1.1 BASIC DRAG DUE TO STORE INSTALLATIONS

Methods are presented in this section for estimating the zero-lift equivalent-parasite-drag area due to a store installation. This drag component does not include adjacent-store and fuselage interference effects (see Sections 3.2.1.2 and 3.2.1.3). The Datcom methods are presented for a particular store installation type and loading configuration, and are applied separately to each installation (armament station).

The methods are taken from Reference 1 and are empirical in nature. The methods are applicable to aircraft of conventional design and essentially symmetrical store shapes with no major shape protuberances. The limitations on configuration and Mach-number range are summarized in Table 3.2-A. Additional limitations and assumptions pertaining to the methods are listed below; however, some additional limitations pertaining to a specific method are given in the method descriptions.

1. The empirical design curves used in the methods generally do not provide data below $M = 0.6$, although the methods have been verified for some cases below this speed. Caution should be used when extrapolating the curves beyond the given Mach range.

2. The methods are not applicable to wing-tip and wing-tangent-mounted stores.

3. The methods have not been verified for configurations in which flaps, slats, or other flow-disrupting devices are deployed.

4. The angle-of-attack range is from zero to cruise angle of attack.

5. The data base used in deriving the methods relied heavily on swept-wing tactical-combat-aircraft wind-tunnel data.

6. The methods are applicable for sideslip angles less than 4°.

Methods are presented for the following particular store installation type and loading configurations:

Wing-Mounted Empty Pylon
Wing-Pylon-Mounted Single Store
Wing-Pylon-Mounted Empty MER
Wing-Pylon-Mounted Fully Loaded MER
Wing-Pylon-Mounted Partially Loaded MER
Wing-Pylon-Mounted Empty TER
Wing-Pylon-Mounted Fully Loaded TER
Wing-Pylon-Mounted Partially Loaded TER
Fuselage-Tangent-Mounted Stores (Two or More Single Stores)
Fuselage-Mounted Empty Pylon
Fuselage-Pylon-Mounted Stores (Two or More Single Stores)
Fuselage-Tangent-Mounted Single Store (One Installation)
Fuselage-Tangent-Mounted MER (One Installation)
Fuselage-Pylon-Mounted Single Store (One Installation)
Fuselage-Pylon-Mounted MER (One Installation)

A. SUBSONIC

DATCOM METHODS

The Datcom user should proceed directly to the method appropriate to the particular store installation type and loading configuration of interest.

Wing-Mounted Empty Pylon

The zero-lift equivalent-parasite-drag area (ft^2) due to the basic installation is given by

$$D_B = \left(B_{xx} + K_{xx}\frac{S_P}{144}\right)\left[K_{CJK}\frac{t_{p_{max}}}{0.04}\left(\frac{2}{c_{p_{top}} + c_{p_{low}}}\right)(0.35 + 0.2167R_U)\right] + D_{PR} \qquad 3.2.1.1\text{-a}$$

where

B_{xx} is an empty-pylon drag factor obtained from Figure 3.2.1.1-20 as a function of Mach number and S_p, the pylon frontal area obtained by measuring the maximum cross-sectional area of the isolated pylon.

K_{xx} is an empty-pylon correlation ratio obtained from Figure 3.2.1.1-21a as a function of Mach number and x_{AFT}/c. The value of x_{AFT} is the longitudinal distance (in.) from the local wing trailing edge to the trailing edge of the store installation (or pylon trailing edge for the empty-pylon case), positive in the aft direction. (See Sketch (a).) The value of c is the local wing chord (in.) at the particular store or pylon station. (See Sketch (a).)

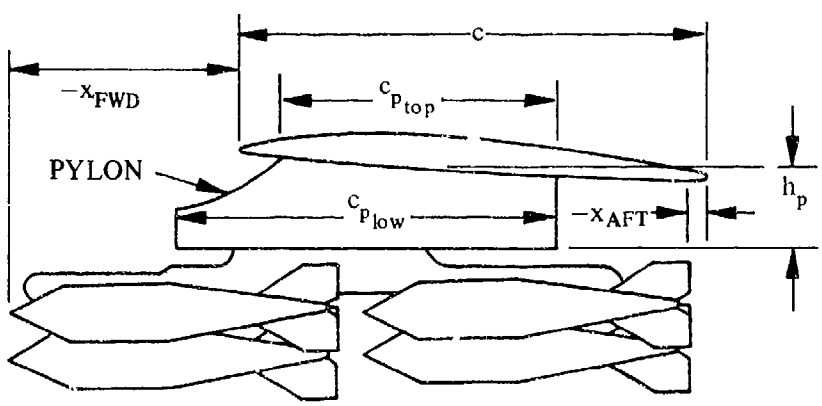

SKETCH (a)

K_{CJK} is a pylon Mach-number correlation parameter obtained from Figure 3.2.1.1-21b as a function of Mach number.

$t_{p_{max}}$ is the maximum pylon thickness (in.).

$c_{p_{top}}$ is the pylon-top-chord length (in.) at the wing-pylon juncture. (See Sketch (a).)

$c_{p_{low}}$ is the pylon-bottom chord length (in.). (See Sketch (a).)

R_U is a pylon-underside-roughness factor given by

R_U = 3, for the pylon-underside case (typical of wind-tunnel model) or for loaded pylons.

R_U = 4, for a rough-pylon-underside case (typical of full-scale hardware). } 3.2.1.1-b

R_U = 5, for an extremely rough-pylon-underside case, i.e., containing large cavities.

D_{PR} is the pylon-rack equivalent-parasite-drag area (ft^2) given by Figure 3.2.1.1.-22a as a function of Mach number.

Wing-Pylon-Mounted Single Store

The zero-lift equivalent-parasite-drag area (ft^2) due to the basic installation is given by separate equations at discrete Mach numbers. To obtain values at intermediate Mach numbers, interpolation must be used.

For M = 0.6:

$$D_B = B + \delta \qquad 3.2.1.1\text{-c}$$

where

B is the equivalent-parasite-drag area (ft^2) computed at M = 0.90 and given by

$$B = D_{ILP} + D_{IS} + D_I \qquad 3.2.1.1\text{-d}$$

where

D_{ILP} is the equivalent-parasite-drag area (ft^2) of the installed loaded pylon given by D_B in Equation 3.2.1.1-a evaluated at M = 0.90 and R_U = 3.

D_{IS} is the isolated-store equivalent-parasite-drag area (ft^2) at M = 0.90, given by

$$D_{IS} = S_\pi C_{D_\pi} \qquad 3.2.1.1\text{-e}$$

where

S_π is the store maximum cross-sectional area (ft^2).

C_{D_π} is the isolated-store drag coefficient at zero lift based on store maximum cross-sectional area. This term can be provided by the user, or can be estimated by using Section 4.2.3.1.

D_I is the equivalent-parasite-drag area (ft^2) due to pylon-store-aircraft interference at M = 0.90, given by

$$D_I = D_X + U_{\bar{y}} V_{\bar{x}} + E_u(22.6 - h_p) \qquad 3.2.1.1\text{-f}$$

where

D_X is the equivalent-parasite-drag area (ft^2) due to store-to-aircraft interference given by Figure 3.2.1.1-22b as a function of x_{AFT}/c, where x_{AFT} and c were previously defined for the wing-mounted empty-pylon case.

$U_{\bar{y}}$ is a lateral drag interference factor (ft) obtained from Figure 3.2.1.1-23a as a function of $\bar{y}$, the fraction of wing semispan location of the store station measured from the aircraft centerline.

$V_{\bar{x}}$ is a longitudinal drag interference factor (ft) obtained from Figure 3.2.1.1-23b as a function of x_{AFT}/c.

E_u is a pylon-height interference factor (ft^2/in.) obtained from Figure 3.2.1.1-23c as a function of x_{AFT}/c.

h_p is the average pylon height (in.). (See Sketch (a).)

δ is the equivalent-parasite-drag area (ft^2) obtained from Figure 3.2.1.1-24 as a function of B.

For M = 0.8:

$$D_B = B + 0.8\delta \qquad 3.2.1.1\text{-g}$$

where B and δ were defined previously.

For M = 0.9:

$$D_B = B \qquad 3.2.1.1\text{-h}$$

where B is given by Equation 3.2.1.1-d.

For M > 0.9, see Paragraphs B and C of this section.

Wing-Pylon-Mounted Empty MER

The zero-lift equivalent-parasite-drag area (ft^2) due to the basic installation is given by

$$D_B = D_{ILP} + D_{MSB} + D_{IMR} \qquad 3.2.1.1\text{-i}$$

where

D_{ILP} is defined in the Wing-Pylon-Mounted Single-Store Case.

D_{MSB} is the MER sway-brace equivalent-parasite-drag area (ft^2) obtained from Figure 3.2.1.1-25 as a function of Mach number.

D_{IMR} is the installed-MER equivalent-parasite-drag area (ft^2) given by

$$D_{IMR} = R_{F_M} + R_{A_M} \qquad 3.2.1.1\text{-j}$$

where

R_{F_M} is a MER forward-longitudinal-placement term (ft^2) obtained from Figure 3.2.1.1-26 as a function of x_{FWD}/c and Mach number, where x_{FWD} is the distance from the local wing leading edge to the store/pylon nose (in.), positive for store nose aft of the local wing leading edge. (See Sketch (a).) The value of c is the local wing chord (in.) at the particular store or pylon station. (See Sketch (a).)

R_{A_M} is a MER aft-longitudinal-placement term (ft^2) obtained from Figure 3.2.1.1-27 as a function of x_{AFT}/c and Mach number, where x_{AFT} was previously defined for a Wing-Mounted Empty-Pylon Case. (See Sketch (a).)

Wing-Pylon-Mounted Fully Loaded MER

The zero-lift equivalent-parasite-drag area (ft^2) due to the basic installation is given by

$$D_B = D_{EM} + 6D_{IS} + D_{IM} \qquad 3.2.1.1\text{-k}$$

where

D_{EM} is the empty-MER equivalent-parasite-drag area (ft^2) given by D_B from Equation 3.2.1.1-i.

D_{IS} is the isolated-store equivalent-parasite-drag area at M = 0.9. (See Equation 3.2.1.1-e.)

D_{IM} is the equivalent-parasite-drag area (ft^2) due to store-MER-aircraft interference, given by

$$D_{IM} = M_{I_S}\left(\frac{z_e^{\,2}\, d_w}{144c} - 30\right) + M_{I_I} \qquad 3.2.1.1\text{-}\ell$$

where

M_{I_S} is a store-MER-aircraft-interference Mach-correlation factor obtained from Figure 3.2.1.1-28 as a function of Mach number.

z_e is the vertically projected length of the store installation on the aircraft wing (in.). (See Sketch (b).)

d_w is the maximum width of the store installation (in.) not including protruding fins. (See Sketch (b).)

c is the local wing chord (in.) at the particular store or pylon station. (See Sketch (a).)

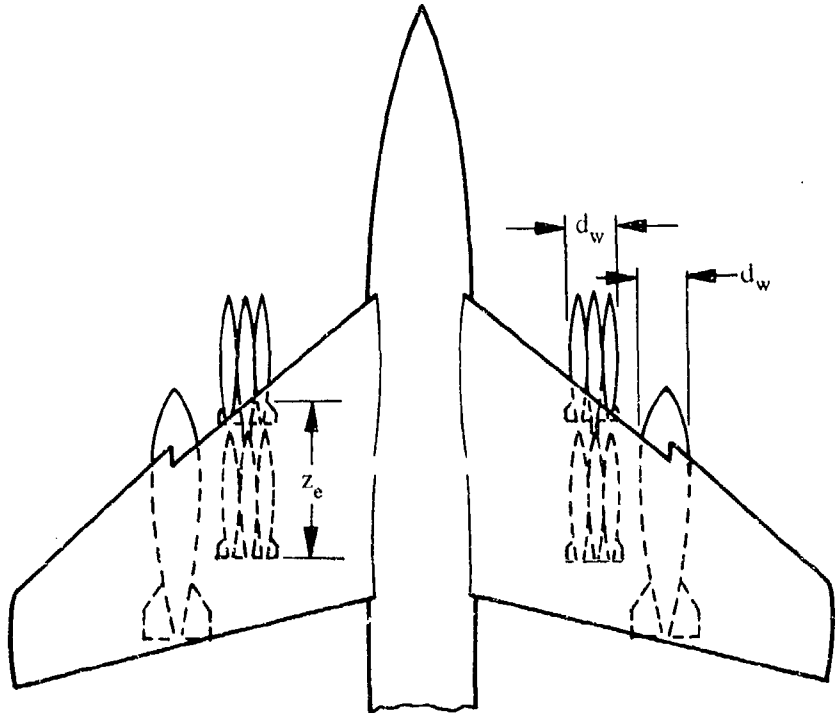

SKETCH (b)

M_{I_I} is a MER adjacent-store separation factor (ft^2) obtained from Figure 3.2.1.1-29 as a function of Mach number and d_c/d_S, where

d_c is the minimum clearance between adjacent stores. (See Figure 3.2.1.1-29.)

d_S is the maximum store diameter.

Wing-Pylon-Mounted Partially Loaded MER

The zero-lift equivalent-parasite-drag area (ft^2) due to the basic installation is given by

$$D_B = D_{EM}\left(1 - \frac{N_{S_M} T_F}{6}\right) + D_{FLM} \qquad 3.2.1.1\text{-m}$$

where

D_{EM} was defined in the Wing-Pylon-Mounted Fully Loaded MER Case.

N_{S_M} is the total number of stores attached to the MER.

T_F is the tandem-stores factor given by

$$\left.\begin{aligned} T_F &= 1.00 \text{ for } N_{S_M} = 1, 5 \text{ or } 6 \text{ stores} \\ &= 1.00 \text{ for } N_{S_M} = 4 \text{ stores total with one store in tandem} \\ &= 0.90 \text{ for } N_{S_M} = 4 \text{ stores total with two stores in tandem} \\ &= 1.0 \text{ for } N_{S_M} = 3 \text{ stores total with one store in tandem} \\ &= 1.10 \text{ for } N_{S_M} = 3 \text{ stores total with none in tandem} \\ &= 0.90 \text{ for } N_{S_M} = 2 \text{ stores total with one store in tandem} \\ &= 1.10 \text{ for } N_{S_M} = 2 \text{ stores total with none in tandem} \end{aligned}\right\} \quad 3.2.1.1\text{-n}$$

D_{FLM} is the zero-lift equivalent-parasite-drag area (ft^2) due to a fully loaded MER given by D_B in Equation 3.2.1.1-k.

Wing-Pylon-Mounted Empty TER

The zero-lift equivalent-parasite-drag area (ft^2) due to the basic installation is given by

$$D_B = D_{ILP} + D_{TSB} + D_{ITR} \qquad 3.2.1.1\text{-o}$$

where

D_{ILP} is defined in the Wing-Pylon-Mounted Single-Store Case.

D_{TSB} is the TER sway-brace equivalent-parasite-drag area (ft^2) obtained from Figure 3.2.1.1-30 as a function of Mach number.

D_{ITR} is the installed-TER equivalent-parasite-drag area (ft^2) given by

$$D_{ITR} = R_{F_T} + R_{A_T} \qquad 3.2.1.1\text{-p}$$

where

R_{F_T} is a TER forward-longitudinal-placement term (ft^2) obtained from Figure 3.2.1.1-31 as a function of x_{FWD}/c and Mach number, where x_{FWD} and c was previously defined for a Wing-Pylon-Mounted Empty-MER Case.

R_{A_T} is a TER aft-longitudinal-placement term (ft^2) obtained from Figure 3.2.1.1-32 (ft^2) as a function of x_{AFT}/c and Mach number, where x_{AFT} was previously defined for a Wing-Mounted Empty-Pylon Case.

Wing-Pylon-Mounted Fully Loaded TER

The zero-lift equivalent-parasite-drag area (ft^2) due to the basic installation is given by

$$D_B = D_{ET} + 3D_{IS} + D_{IT} \qquad 3.2.1.1\text{-q}$$

where

D_{ET} is the empty-TER equivalent-parasite-drag area (ft^2) given by D_B from Equation 3.2.1.1-o.

D_{IS} is the isolated-store equivalent-parasite-drag area (ft^2) at M = 0.9, given by Equation 3.2.1.1-e.

D_{IT} is the equivalent-parasite-drag area (ft^2) due to store-TER-aircraft interference given by

$$D_{IT} = T_{I_S}\left(\frac{z_e^2 d_w}{144c} - 10\right) + T_{I_I} \qquad 3.2.1.1\text{-r}$$

where:

T_{I_S} is a store-TER-aircraft-interference Mach-correlation factor obtained from Figure 3.2.1.1-33 as a function of Mach number.

z_e, d_w and c were previously defined in the Wing-Pylon-Mounted Fully-Loaded-MER Case.

T_{I_I} is a TER adjacent-store separation factor (ft^2) obtained from Figure 3.2.1.1-34 as a function of Mach number and d_c/d_s where d_c and d_s are defined in the Wing-Pylon-Mounted Fully-Loaded-MER Case.

Wing-Pylon-Mounted Partially Loaded TER

The zero-lift equivalent-parasite-drag area (ft^2) due to the basic installation is given by:

$$D_B = D_{ET}\left(1 - \frac{N_{S_T}}{3}\right) + D_{FLT} \qquad 3.2.1.1\text{-s}$$

where

D_{ET} is the empty-TER equivalent-parasite-drag area (ft^2) given by D_B from Equation 3.2.1.1-o.

N_{S_T} is the number of stores attached to the TER.

D_{FLT} is the zero-lift equivalent-parasite-drag area (ft^2) due to a fully loaded TER given by D_B in Equation 3.2.1.1-q.

Fuselage-Tangent-Mounted Stores
(Two or More Single Stores)

The Datcom Method for this configuration is applicable only for 2 or 3 store-row installations mounted on the fuselage bottom surface, and for a Mach-number range of from 0.6 to 0.9. The following additional limitations apply:

1. Same number of stores per row for two- or three-row configurations.
2. Constant fuselage-station location for all stores on a given row.
3. Constant longitudinal space between all stores in tandem, for two- or three-row configurations.
4. Constant lateral space between all stores.
5. Coincident store centerlines for stores in tandem (maximum number of stores in tandem = 3; maximum number of stores/row = 5; staggered store arrangements not included).
6. Effective store-diameter range: 8.0 to 11.5 inches.
7. All stores in one installation must be identical.

Due to the nature of this method, the zero-lift equivalent-parasite-drag area, D_B, is computed for all stores taken together. In order to be consistent with the values of D_B computed by other methods in this section, the entire group of stores is considered to be *one* installation.

The zero-lift equivalent-parasite-drag area (ft^2) due to the basic installation is given by:

$$D_B = n_r D_{FR} + D_{IS} K_{NI} \qquad 3.2.1.1\text{-t}$$

where

n_r is the number of stores per row.

D_{FR} is the fuselage-rack equivalent-parasite-drag area and is a function of the number of rows of stores mounted on the fuselage:

$$D_{FR} = a_1 b_1 \text{ (1 row)} \qquad 3.2.1.1\text{-u}$$

$$D_{FR} = a_1 b_1 + a_2 b_2 \text{ (2 rows)} \qquad 3.2.1.1\text{-v}$$

$$D_{FR} = a_1 b_1 + a_2 b_2 + a_3 b_3 \text{ (3 rows)} \qquad 3.2.1.1\text{-w}$$

where

a_1, a_2, and a_3 are store-diameter correlation factors obtained from Figure 3.2.1.1-35 as a function of the maximum store diameter d_s.

b_1, b_2, and b_3 are store-row Mach-correlation factors obtained from Figure 3.2.1.1-36 as a function of Mach number.

D_{IS} is the isolated-store equivalent-parasite-drag area (ft^2) at M = 0.9, given by Equation 3.2.1.1-e.

K_{NI} is a planform and store-location factor given by

$$K_{NI} = K_{D_1} K_{D_2} K_{D_3} K_{D_4} K_{D_5} K_{D_6} K_{D_7} \qquad 3.2.1.1\text{-x}$$

where

K_{D_1} is a store frontal-area factor given by

$$K_{D_1} = K_{S_M} \left(1 + \frac{3S_\pi}{S_B}\right) \qquad 3.2.1.1\text{-y}$$

where

K_{S_M} is a Mach-effect factor for K_{D_1} obtained from Figure 3.2.1.1-37a as a function of Mach number.

S_π is the store maximum cross-sectional area (ft^2).

S_B is the maximum-fuselage frontal area (ft^2).

K_{D_2} is the wing-sweep-and-location factor obtained from Figure 3.2.1.1-37b as a function of wing leading-edge sweep, wing location, and Mach number.

K_{D_3} is a tandem-spacing factor obtained from Figure 3.2.1.1-38a as a function of Mach number and X_{OL}, the ratio of longitudinal spacing between tandem stores to the store length.

K_{D_4} is a lateral-spacing factor obtained from Figure 3.2.1.1-38b as a function of Y_{OD}, the ratio of the minimum lateral distance (excluding fins) between stores to the maximum store diameter.

K_{D_5} and K_{D_6} are store-rows and stores-per-row correlation factors respectively, obtained by using Table 3.2.1.1-A.

TABLE 3.2.1.1-A

K_{D_5} AND K_{D_6} COMPUTATION

Correlation Factor	No. of Store Rows or Stores Per Row	Figure No. or Value
K_{D_5}	1	Figure 3.2.1.1-39a
	2	Figure 3.2.1.1-39b
	3	1.0
K_{D_6}	1	Figure 3.2.1.1-40
	2	Figure 3.2.1.1-41a
	3	Figure 3.2.1.1-41b

It should be noted that K_{D_5} for the case of 3 store rows is only substantiated for $0.6 \leq M \leq 0.9$.

K_{D_7} is a store longitudinal-location factor obtained from Figure 3.2.1.1-42a as a function of Mach number and x_r, the ratio of the distance between the aircraft nose and the store nose of the most forward store to the aircraft-fuselage length

Fuselage-Mounted Empty Pylon

The Datcom Method for this configuration is applicable for a pylon-frontal-area range of from 20 to 170 square inches, and only for pylons mounted on the bottom surface of the fuselage. The zero-lift equivalent-parasite-drag area (ft^2) due to the basic installation is given by

$$D_B = B_{xx}\left[K_{CJK}\frac{t_{p_{max}}}{0.04}\left(\frac{2}{c_{p_{top}} + c_{p_{low}}}\right)(0.35 + 0.2167R_U)\right] \qquad 3.2.1.1\text{-z}$$

where all of the above terms are defined in the Wing-Mounted-Empty-Pylon Case.

Fuselage-Pylon-Mounted Stores
(Two or More Single Stores)

The Datcom Method for this configuration is subject to the same limitations given for the Fuselage-Tangent-Mounted Stores Case. Due to the nature of the method, the zero-lift equivalent-parasite-drag area, D_B, is computed for all stores taken together. In order to be consistent with the values of D_B computed by other methods in this section, the entire group of stores is considered to be *one* installation. The zero-lift equivalent-parasite-drag area (ft^2) due to the basic installation is given by

$$D_B = n_P D_{LPF} + n_r D_{FR} + K_{SD} K_{PD} K_{NI} D_{IS} \qquad 3.2.1.1\text{-aa}$$

where

n_P is the number of pylons.

D_{LPF} is the zero-lift equivalent-parasite-drag area (ft^2) due to the fuselage-mounted empty pylon given by D_B in Equation 3.2.1.1-z with $R_U = 3.0$.

n_r is the number of stores per row.

D_{FR} is the fuselage-rack equivalent-parasite-drag-area (ft^2) contribution given by Equations 3.2.1.1-u, v, w.

K_{SD} is a store-depth factor obtained from Figure 3.2.1.1-42b as a function of Mach number and X_{OL}, the ratio of longitudinal spacing between tandem stores to the store length.

K_{PD} is a pylon-depth factor obtained from Figures 3.2.1.1-43a through -43o as a function of Mach number, number of rows, number of stores per row, and H_{OD} where

$$H_{OD} = \frac{h_p + 1.5}{d_S} \qquad \text{3.2.1.1-bb}$$

where

h_p is the average pylon height (in.).

d_S is the maximum store diameter (in.).

K_{NI} is a planform and store-location factor defined by Equation 3.2.1.1-x.

D_{IS} is the isolated-store equivalent-parasite-drag area (ft^2) at M = 0.9, given by Equation 3.2.1.1-e.

Fuselage-Tangent-Mounted Single Store
(One Installation)

The zero-lift equivalent-parasite-drag area (ft^2) due to the basic installation is given by

$$D_B = (1 + K_{IF})(D_{PR} + D_{IS}) \qquad \text{3.2.1.1-cc}$$

where

K_{IF} is an installation factor obtained from Figures 3.2.1.1-51a through -51g for single stores, as a function of Mach number, fuselage bottom surface shape (bottom surface either curved or straight), the maximum depth of the store installation measured from the bottom surface of wing z (in.), and the average pylon height (in.) h_p.

D_{PR} is the pylon-rack equivalent-parasite-drag area (ft^2) given by Figure 3.2.1.1-22a as a function of Mach number.

D_{IS} is the isolated-store equivalent-parasite-drag area (ft^2) at M = 0.9, given by Equation 3.2.1.1-e.

Fuselage-Tangent-Mounted MER
(One Installation)

The Datcom Method for this configuration is limited to a single MER installation tangent mounted on the bottom of the fuselage. The zero-lift equivalent-parasite-drag area (ft^2) due to the basic installation is given by

$$D_B = (1 + K_{IF})(D_{PR} + 6D_{IS} + D_{MSB} + D_{MRF}) \qquad 3.2.1.1\text{-dd}$$

where

K_{IF} is an installation factor for tangent-mounted stores obtained from Figures 3.2.1.1-54a through -54g for MER installations.

D_{PR} is the pylon-rack equivalent-parasite-drag area (ft^2) given by Figure 3.2.1.1-22a as a function of Mach number.

D_{IS} is the isolated-store equivalent-parasite-drag area (ft^2) at M = 0.9, given by Equation 3.2.1.1-e.

D_{MSB} is the MER-sway-brace equivalent-parasite-drag area (ft^2) obtained from Figure 3.2.1.1-25 as a function of Mach number.

D_{MRF} is the zero-lift equivalent-parasite-drag area (ft^2) due to MER-rack-to-fuselage interference obtained from Figure 3.2.1.1-57 as a function of Mach number.

Fuselage-Pylon-Mounted Single Store
(One Installation)

The Datcom Method for this configuration is applicable for a pylon-frontal-area range of from 20 to 170 square inches, and only for pylons mounted on the bottom surface of the fuselage. The zero-lift equivalent-parasite-drag area (ft^2) due to the basic installation is given by

$$D_B = (1 + K_{IF})(D_{PR} + D_{IS} + D_{ILP}) \qquad 3.2.1.1\text{-ee}$$

where

K_{IF} is an installation factor as defined for the Fuselage-Tangent-Mounted Single-Store Case, obtained from Figures 3.2.1.1-51a through -51g.

D_{PR} is the pylon-rack equivalent-parasite-drag area (ft^2) given by Figure 3.2.1.1-22a as a function of Mach number.

D_{IS} is the isolated-store equivalent-parasite-drag area (ft^2) at M = 0.9, given by Equation 3.2.1.1-e.

D_{ILP} is the equivalent-parasite-drag area (ft^2) of the installed loaded pylon given by D_B from Equation 3.2.1.1-z with $R_U = 3.0$.

Fuselage-Pylon-Mounted MER
(One Installation)

The Datcom Method for this configuration has the same limitations as the previous case. The zero-lift equivalent-parasite-drag area ( ) due to the basic store installation is given by

$$D_B = (1 + K_{IF})(D_{PR} + 6D_{IS} + D_{ILP} + D_{MRF} + D_{MSB}) \qquad 3.2.1.1\text{-ff}$$

where

K_{IF} is an installation factor as defined for the Fuselage-Tangent-Mounted MER Case, obtained from Figures 3.2.1.1-54a through 3.2.1.1-54g.

D_{PR} is the pylon-rack equivalent-parasite-drag area (ft^2) given by Figure 3.2.1.1-22a as a function of Mach number.

D_{IS} is the isolated-store equivalent-parasite-drag area (ft^2) at M = 0.9, given by Equation 3.2.1.1-e.

D_{ILP} is the installed-loaded-pylon equivalent-parasite-drag area (ft^2) given by D_B from Equation 3.2.1.1-z with $R_U = 3.0$.

D_{MRF} is the zero-lift equivalent-parasite-drag area (ft^2) due to MER-rack-to-fuselage interference obtained from Figure 3.2.1.1-57 as a function of Mach number.

D_{MSB} is the MER-sway-brace equivalent-parasite-drag area (ft^2) obtained from Figure 3.2.1.1-25 as a function of Mach number.

Sample Problem

Given: A swept-wing subsonic fighter aircraft (Reference 2) symmetrically loaded at the inboard wing stations with pylon-mounted TER's, each containing two 500-lb bombs.

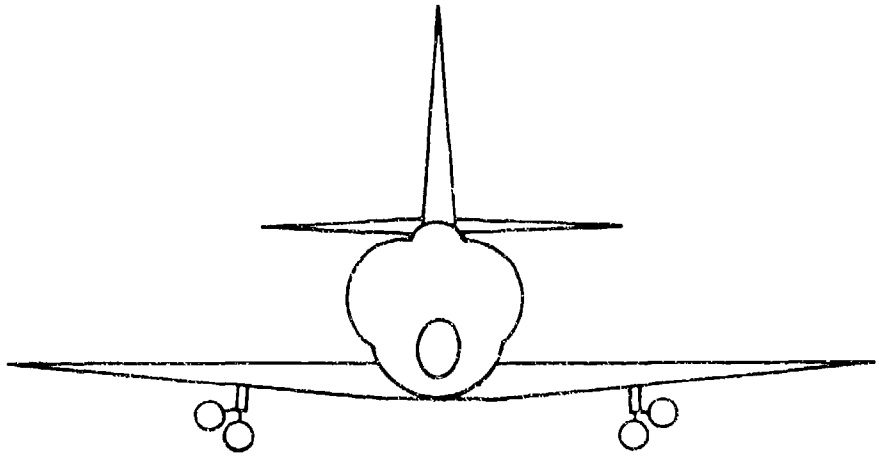

FRONT VIEW

Aircraft Data: c = 121.5 in.

Store Data:

$S_\pi = 0.785\ ft^2$ $C_{D_\pi} = 0.11$ $d_S = 12$ in.

Installation Data:

$S_P = 51.3\ in.^2$ $t_{P_{max}} = 4.7$ in. $c_{P_{top}} = 66.9$ in. $c_{P_{low}} = 66.9$ in.

$x_{AFT} = -49.6$ in. $x_{FWD} = -10.4$ in. $d_c = 3.2$ in. $d_w = 25.6$ in.

$z_e = 70.4$ in.

Additional Data:

M = 0.6

Compute: (Method – Wing-Pylon-Mounted Partially Loaded TER)

Since the installation is symmetrical, only one side need be computed.

$$D_B = D_{ET}\left(1 - \frac{N_{S_T}}{3}\right) + D_{FLT} \qquad \text{(Equation 3.2.1.1-s)}$$

Expand the above equation to identify the terms which need to be computed:

$$D_{ET} = D_{ILP} + D_{TSB} + D_{ITR} \qquad \text{(Equation 3.2.1.1-o)}$$

$$D_{FLT} = D_{ET} + 3D_{IS} + D_{IT} \qquad \text{(Equation 3.2.1.1-q)}$$

Find D_{ILP}:

$$\frac{x_{AFT}}{c} = \frac{-49.6}{121.5} = -0.408$$

$B_{xx} = 0.106$ (Figure 3.2.1.1-20)

$K_{xx} = 0.16$ (Figure 3.2.1.1-21a)

$K_{CJK} = 0.25$ (Figure 3.2.1.1-21b)

$D_{PR} = 0.088\ ft^2$ (Figure 3.2.1.1-22a)

$$D_{ILP} = \left(B_{xx} + K_{xx}\frac{S_P}{144}\right)\left[K_{CJK}\frac{t_{p_{max}}}{0.04}\left(\frac{2}{c_{p_{top}} + c_{p_{low}}}\right)(0.35 + 0.2167R_U)\right] + D_{PR}$$

(Equation 3.2.1.1-a)

$$= \left[0.106 + (0.16)\left(\frac{51.3}{144}\right)\right]\left\{(0.25)\frac{(4.7)}{(0.04)}\frac{(2)[0.35 + (0.2167)3]}{(66.9 + 66.9)}\right\} + 0.088$$

$$= 0.160 \text{ ft}^2$$

Find D_{TSB}:

$D_{TSB} = 0.180 \text{ ft}^2$ (Figure 3.2.1.1-30)

Find D_{ITR}:

$$\frac{x_{FWD}}{c} = \frac{-10.4}{121.5} = -0.0856$$

$R_{F_T} = 0$ (Figure 3.2.1.1-31)

$R_{A_T} = 0.300$ (Figure 3.2.1.1-32)

$D_{ITR} = R_{F_T} + R_{A_T} = 0 + 0.300 = 0.300 \text{ ft}^2$ (Equation 3.2.1.1-p)

Find D_{ET}:

$D_{ET} = D_{ILP} + D_{TSB} + D_{ITR}$ (Equation 3.2.1.1-o)

$= 0.160 + 0.180 + 0.300$

$= 0.640 \text{ ft}^2$

Find D_{IS}:

$D_{IS} = S_\pi C_{D_\pi} = (0.785)(0.11)$ (Equation 3.2.1.1-e)

$= 0.0864 \text{ ft}^2$

Find D_{IT}:

$T_{IS} = 0.005$ (Figure 3.2.1.1-33)

$$\frac{d_c}{d_S} = \frac{3.2}{12} = 0.267$$

$T_{I_I} = 0.40$ (Figure 3.2.1.1-34)

$$D_{I_T} = T_{I_S}\left(\frac{z_e^{\,2}\, d_w}{144c} - 10\right) + T_{I_I} \quad \text{(Equation 3.2.1.1-r)}$$

$$= 0.005\left[\frac{(70.4)^2(25.6)}{(144)(121.5)} - 10\right] + 0.40$$

$$= 0.386 \text{ ft}^2$$

Find D_{FLT}:

$$D_{FLT} = D_{ET} + 3D_{IS} + D_{IT} \quad \text{(Equation 3.2.1.1-q)}$$

$$= 0.640 + (3)(0.0864) + 0.386$$

$$= 1.285 \text{ ft}^2$$

Solution:

$$D_B = D_{ET}\left(1 - \frac{N_{S_T}}{3}\right) + D_{FLT} \quad \text{(Equation 3.2.1.1-s)}$$

$$= 0.640\left(1 - \frac{2}{3}\right) + 1.285 = 1.498 \text{ ft}^2 \text{ (one side)}$$

This result is used in the Sample Problem of Paragraph A of Section 3.2.3 as part of the total-drag-increment computation.

B. TRANSONIC

The method presented in Paragraph A of this section is also valid for transonic speeds with the exception of the following fuselage-mounted configurations which are limited to $M \leqslant 0.9$:

1. Two or more stores tangent-mounted in single-carriage modes.

2. Two or more stores pylon-mounted in single-carriage modes.

The method presented in Paragraph A for the Wing-Pylon-Mounted Single-Store Case requires additional equations in the transonic speed range. Separate equations for D_B are required at discrete Mach numbers as in the subsonic case. To obtain values at intermediate Mach numbers, interpolation must be used.

Wing-Pylon-Mounted Single Store

For M = 0.9:

$$D_B = B \qquad \text{(Equation 3.2.1.1-h)}$$

where

B is given by Equation 3.2.1.1-d.

For M = 0.95:

$$D_B = 0.77\,[(B + T_A S_\pi)P - B] + B \qquad 3.2.1.1\text{-gg}$$

where

B is given by Equation 3.2.1.1-d.

T_A is a transonic-supersonic correlation factor obtained from Figure 3.2.1.1-58a as a function of x_{FWD}, x_{AFT}, and c where

x_{FWD} is the longitudinal distance from the local wing leading edge to the store/pylon nose (in.), positive for store nose aft of the local wing leading edge. (See Sketch (a).)

x_{AFT} is the longitudinal distance (in.) from the local wing trailing edge to the trailing edge of the store installation (or pylon trailing edge for the empty pylon case), positive in the aft direction. (See Sketch (a).)

c is the local wing chord at the local store or pylon station (in.). (See Sketch (a).)

S_π is the maximum store cross-sectional area (ft^2).

P is a clean-aircraft drag-rise factor obtained from Figure 3.2.1.1-58b as a function of the clean-aircraft drag-rise factor, C'_{D_0}, where

$$C'_{D_0} = \frac{C_{D_0} \text{ at } M = 1.05}{C_{D_0} \text{ at } M = 0.6} \qquad 3.2.1.1\text{-hh}$$

where

C_{D_0} is the clean-aircraft zero-lift drag coefficient from test data or estimated from Section 4.5.3.1.

For M = 1.05:

$$D_B = (B + T_A S_\pi)P \qquad 3.2.1.1\text{-ii}$$

where B, T_A, S_π, and P are defined above.

For M = 1.20:

$$D_B = B + T_A S_\pi \qquad 3.2.1.1\text{-jj}$$

where B, T_A, and S_π are defined above.

The user is cautioned that the accuracy of the method is less than that of the subsonic speed range, and test data should be used whenever possible.

C. SUPERSONIC

The method presented in Paragraph A of this section is also valid for supersonic speeds within the Mach-number limits specified in Table 3.2-A. The method presented in Paragraph A for the Wing-Pylon-Mounted Single-Store Case requires the following modification in the supersonic speed range.

Wing-Pylon-Mounted Single Store

For M = 1.60 to M = 2.00:

D_B is obtained from Figures 3.2.1.1-59a and -59b as a function of $B + T_A S_\pi$.

The user should exercise caution in extrapolating the method beyond the specified Mach-number range.

REFERENCES

1. Gallagher, R. D., Jimenez, G., Light, L. E., and Thames, F. C.: Technique for Predicting Aircraft Aerodynamic Effects Due to External Stores Carriage. AFFDL-TR-75-95, Volumes I and II, 1975. (U)

2. Watzke, R. E.: Aerodynamic Data for Model TA-4F Operational Flight Trainer. McDonnell Douglas Corporation Rept. DAC-67425, 1968. (U)

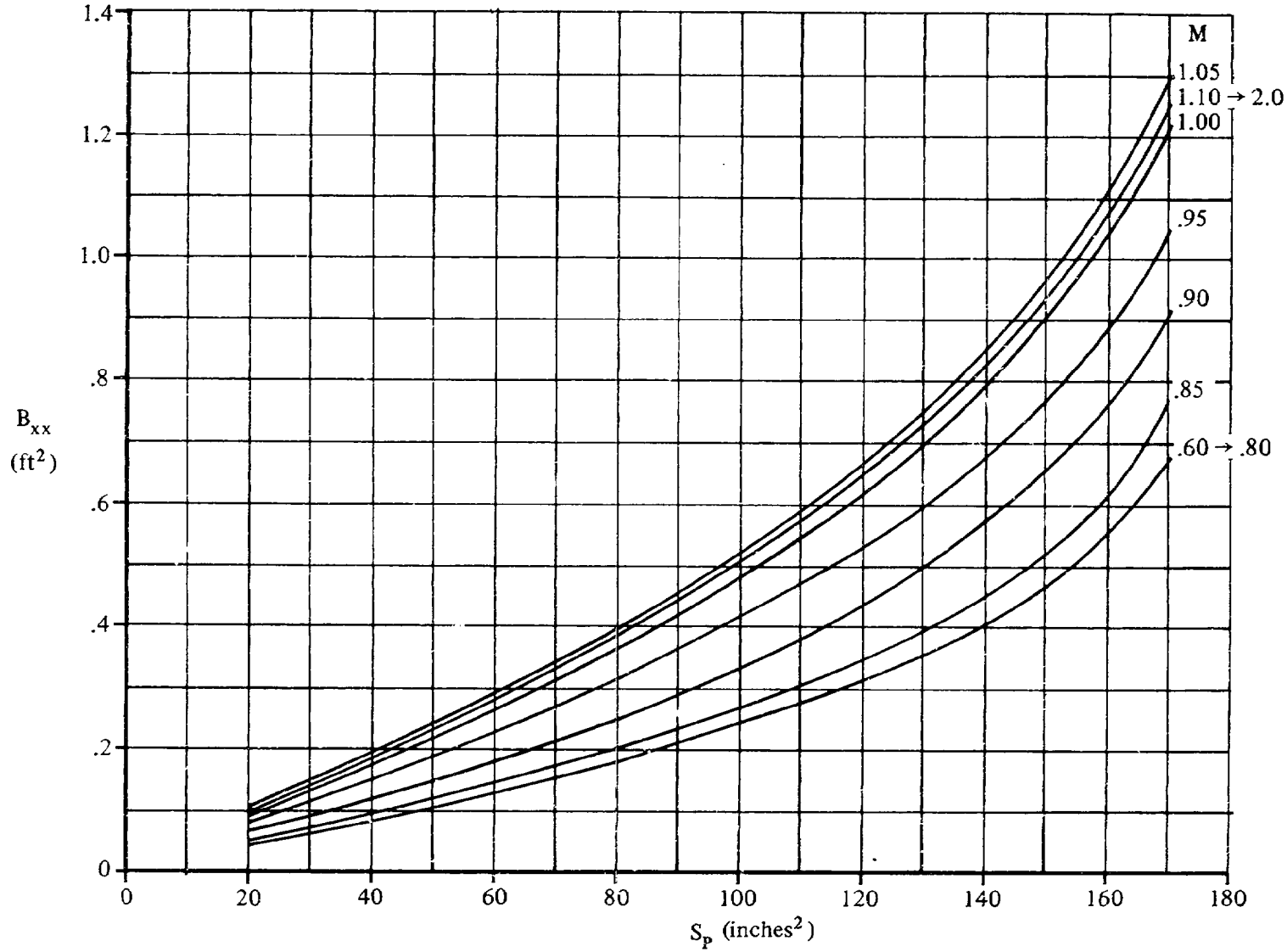

FIGURE 3.2.1.1-20 EMPTY-PYLON DRAG FACTOR

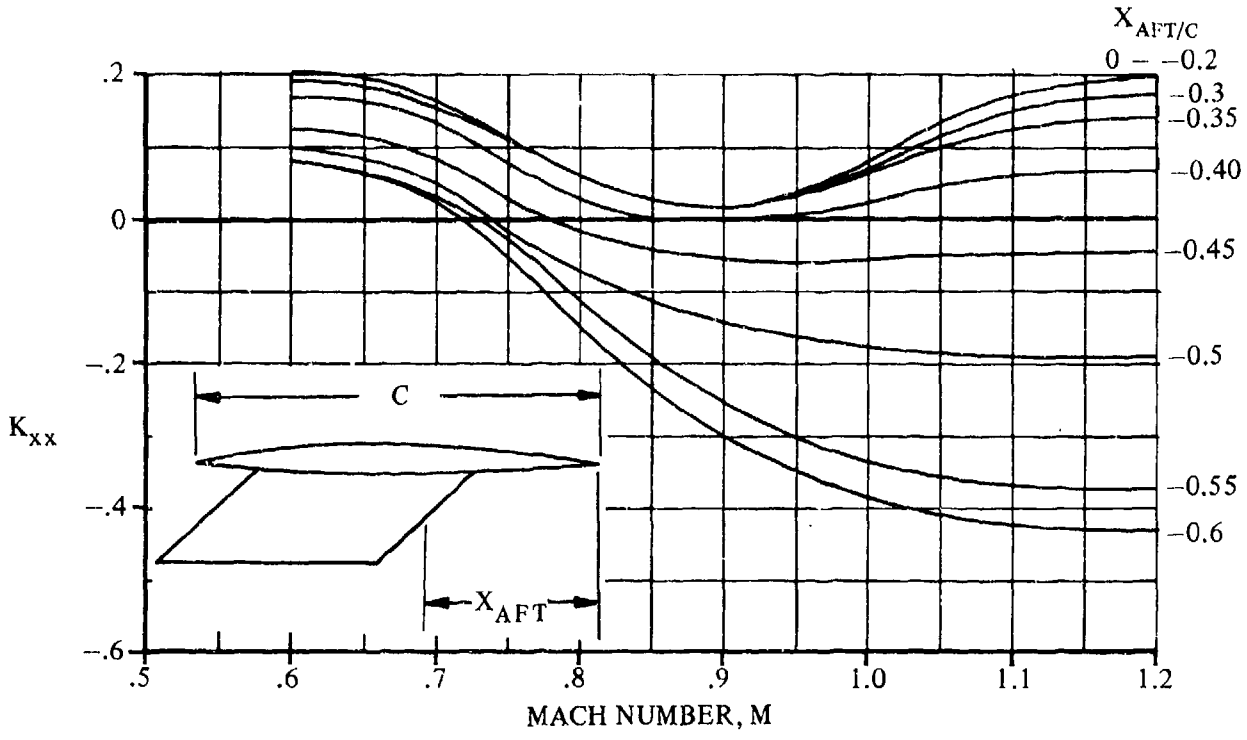

FIGURE 3.2.1.1-21a EMPTY-PYLON CORRELATION RATIO

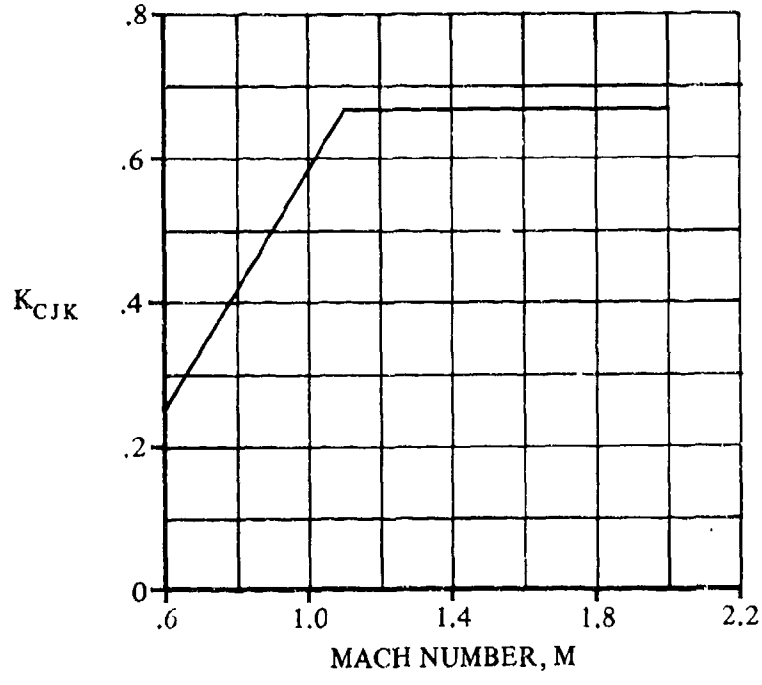

FIGURE 3.2.1.1-21b PYLON MACH-NUMBER CORRELATION PARAMETER

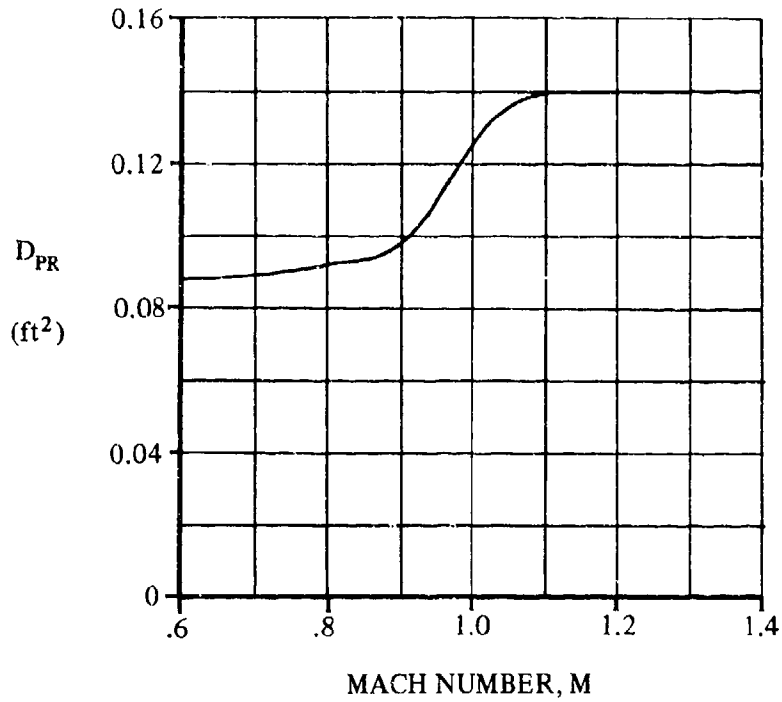

FIGURE 3.2.1.1-22a PYLON-RACK EQUIVALENT-PARASITE-DRAG AREA

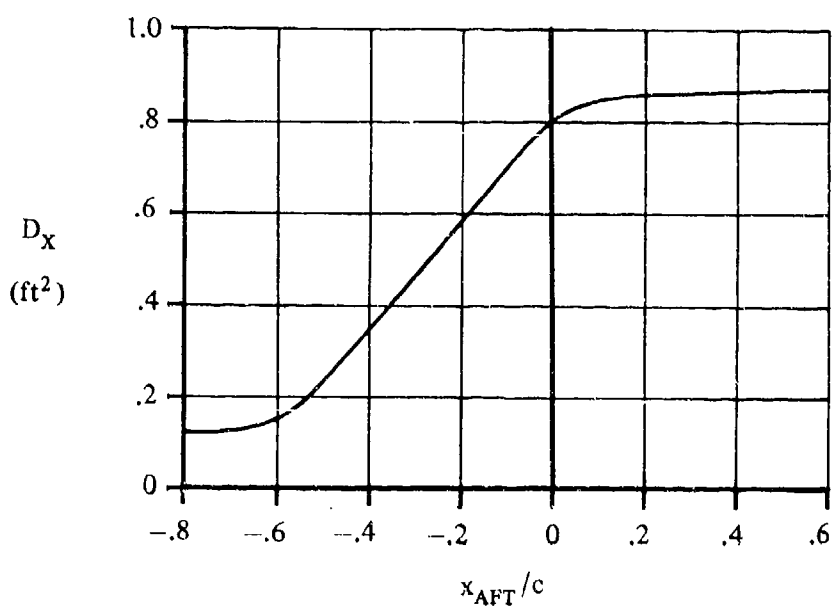

FIGURE 3.2.1.1-22b EQUIVALENT-PARASITE-DRAG AREA DUE TO STORE-TO-AIRCRAFT INTERFERENCE

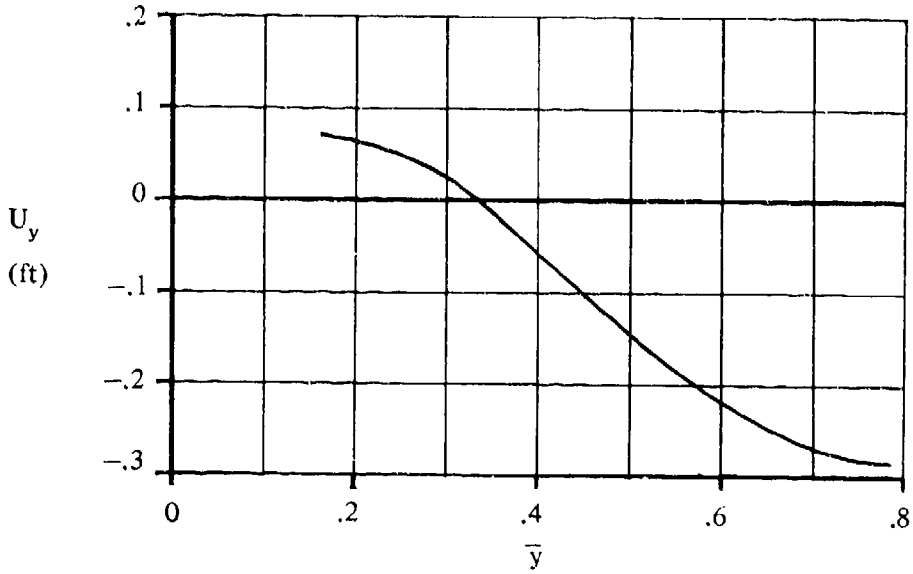

FIGURE 3.2.1.1-23a LATERAL DRAG INTERFERENCE FACTOR

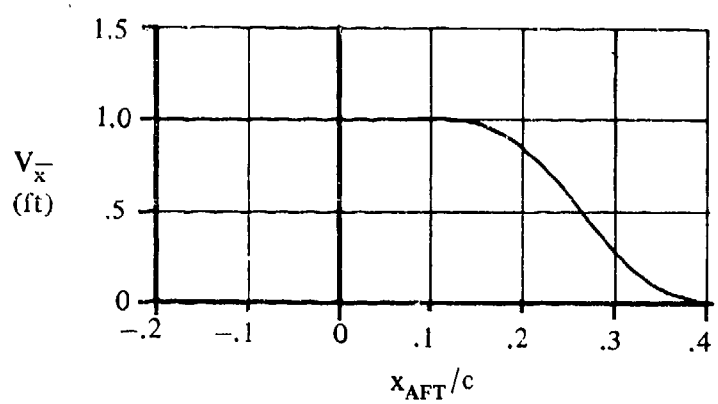

FIGURE 3.2.1.1-23b LONGITUDINAL DRAG INTERFERENCE FACTOR

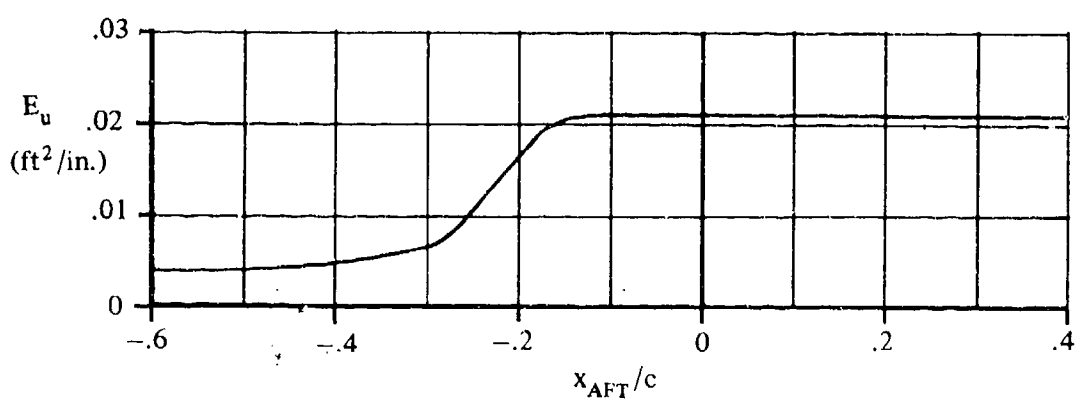

FIGURE 3.2.1.1-23c PYLON-HEIGHT INTERFERENCE FACTOR

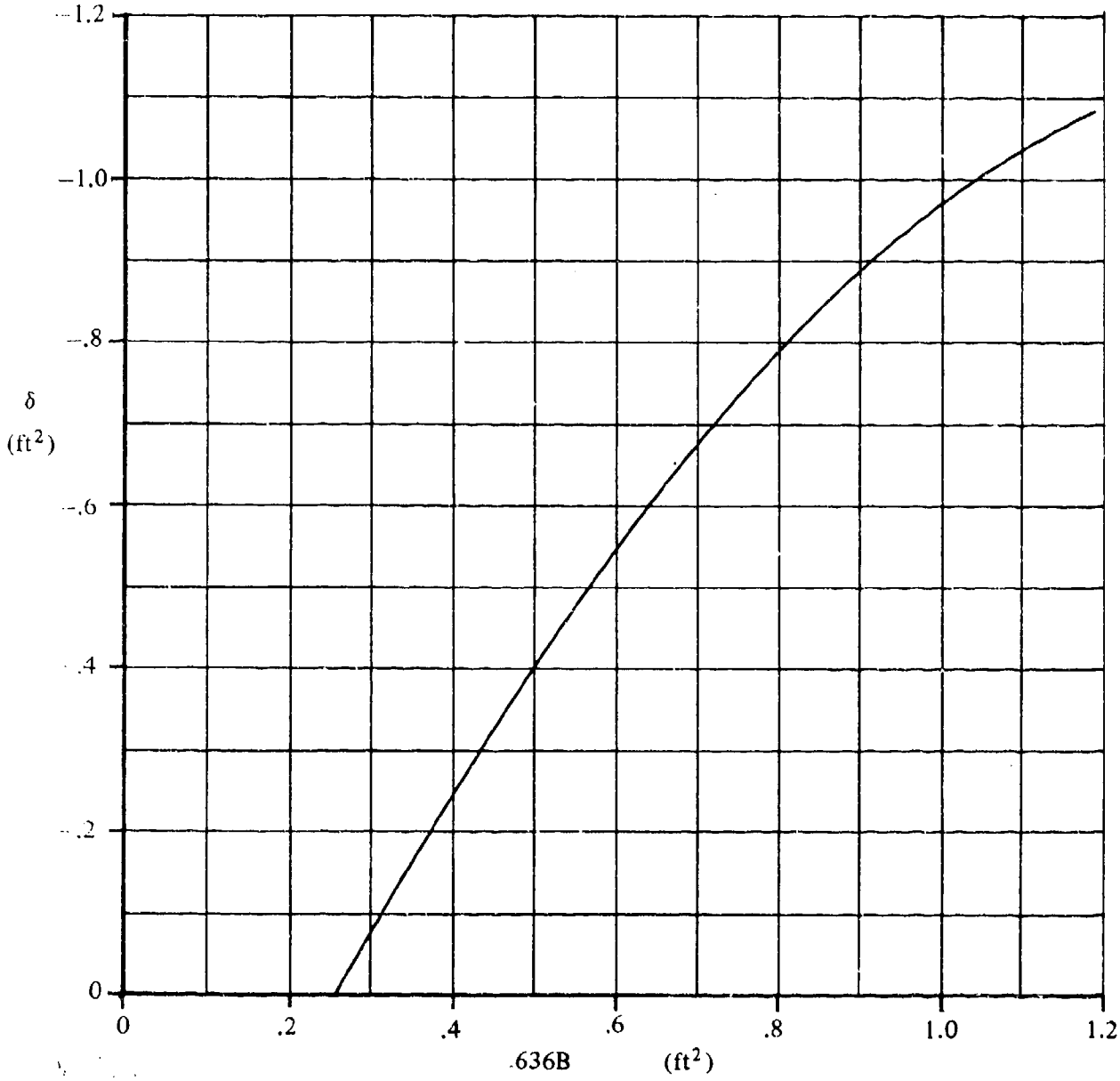

FIGURE 3.2.1.1-24 EQUIVALENT-PARASITE-DRAG AREA

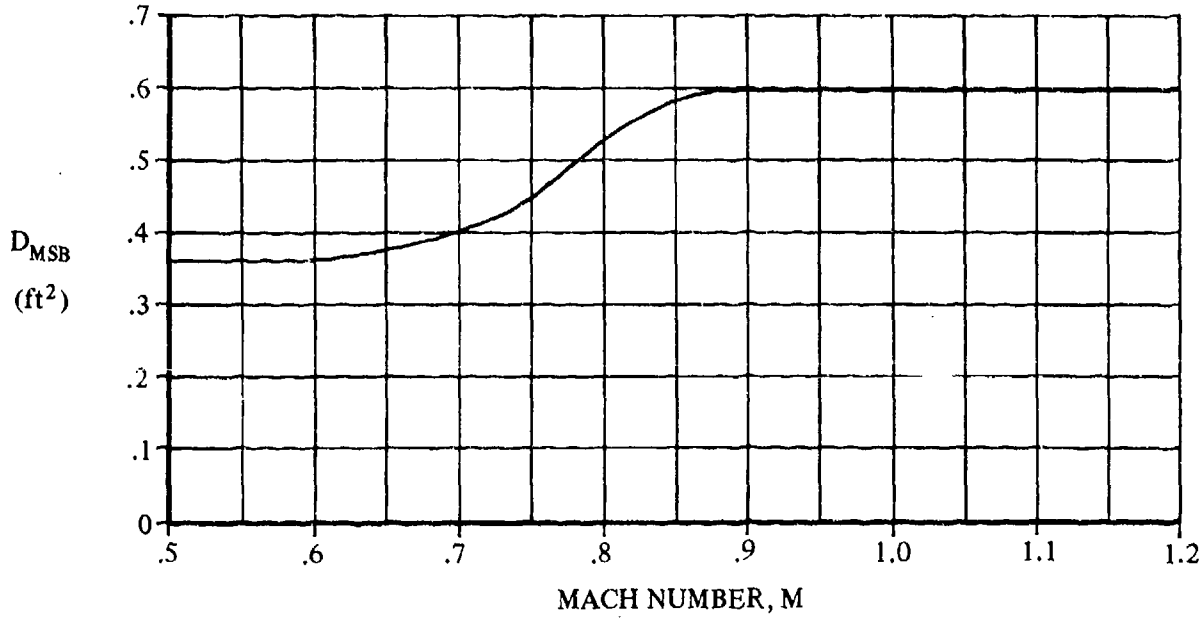

FIGURE 3.2.1.1-25 MER SWAY-BRACE EQUIVALENT-PARASITE-DRAG AREA

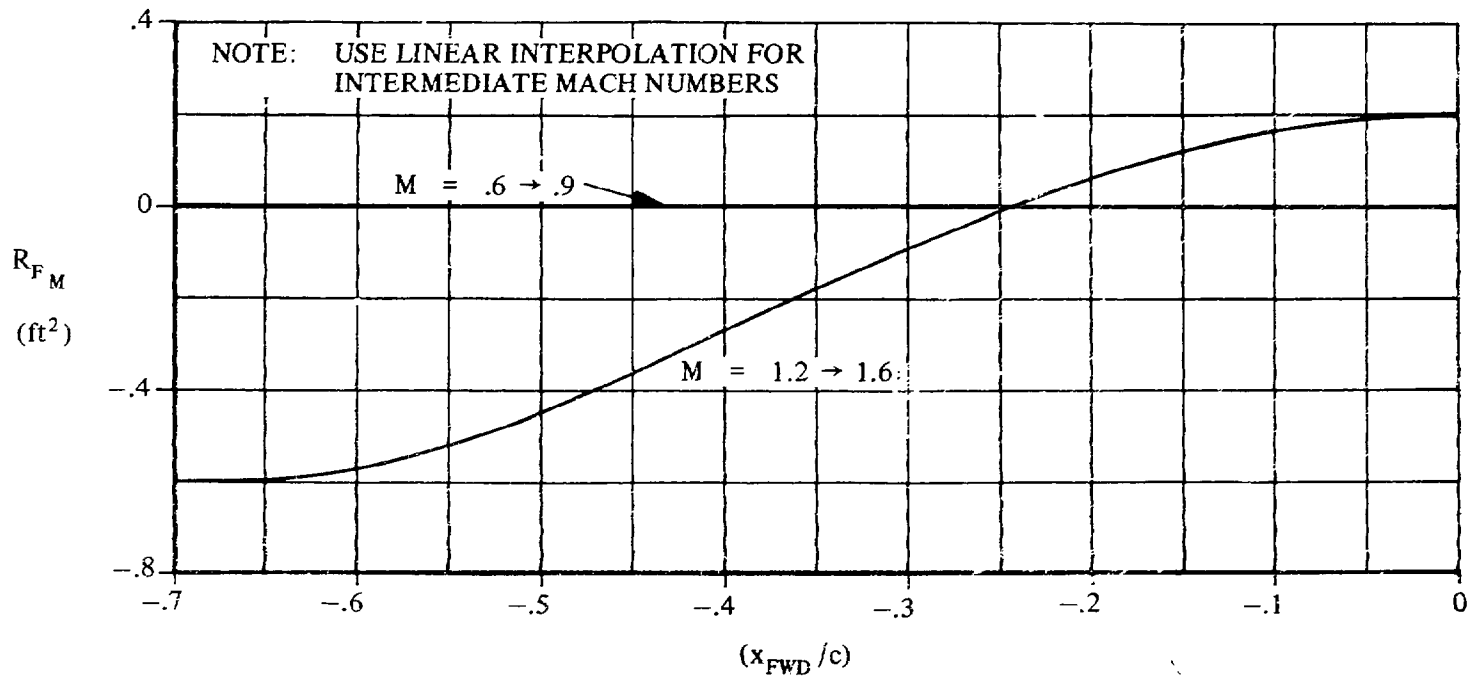

FIGURE 3.2.1.1-26 MER FORWARD-LONGITUDINAL-PLACEMENT TERM

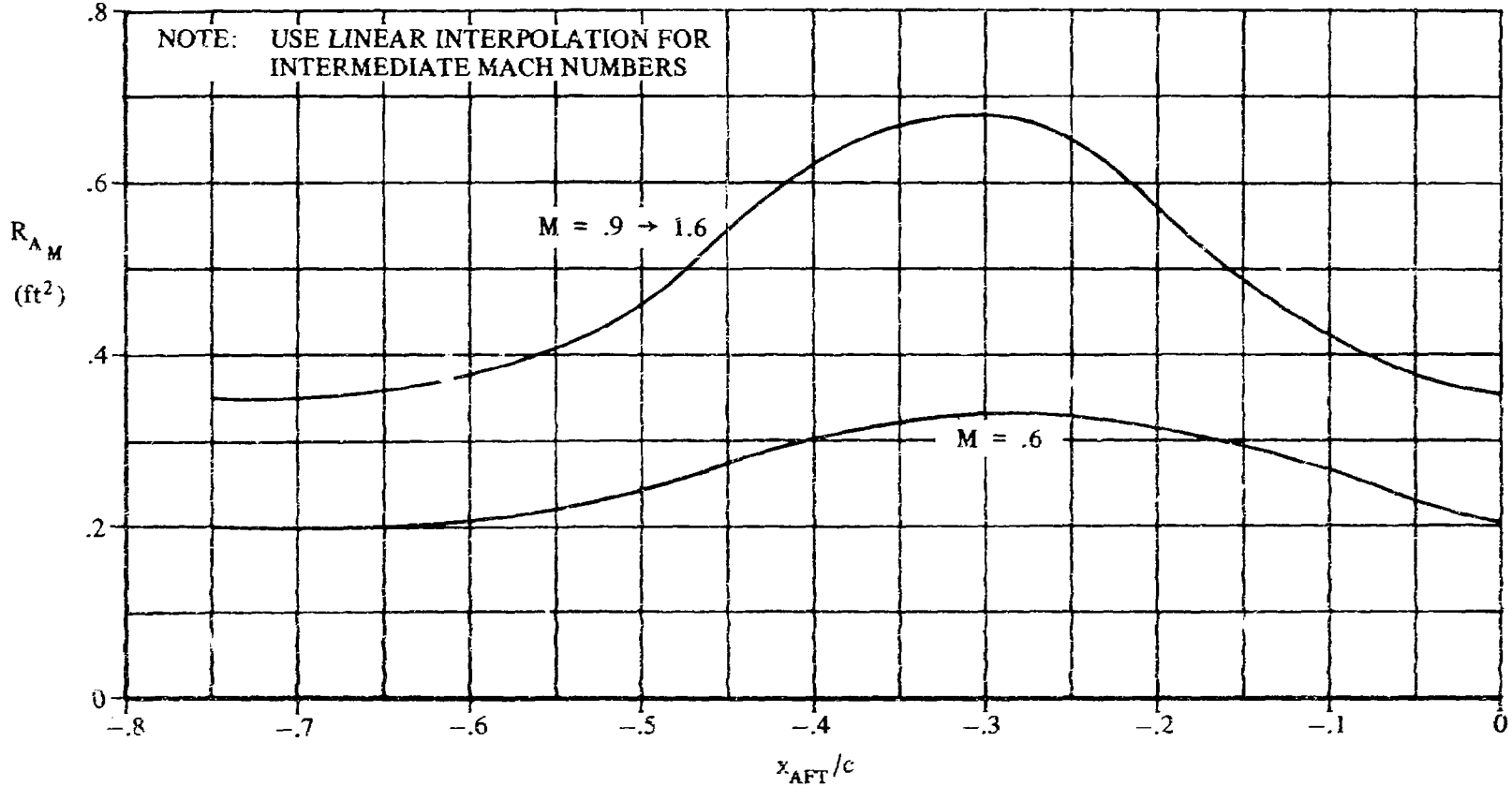

FIGURE 3.2.1.1-27 MER AFT LONGITUDINAL-PLACEMENT TERM

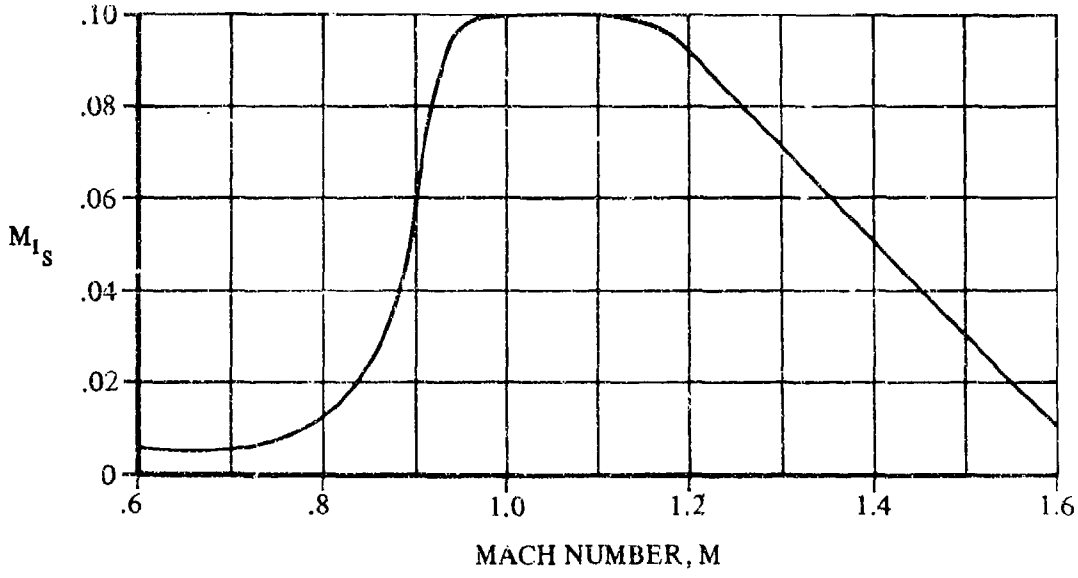

FIGURE 3.2.1.1-28 STORE-MER-AIRCRAFT-INTERFERENCE MACH-CORRELATION FACTOR

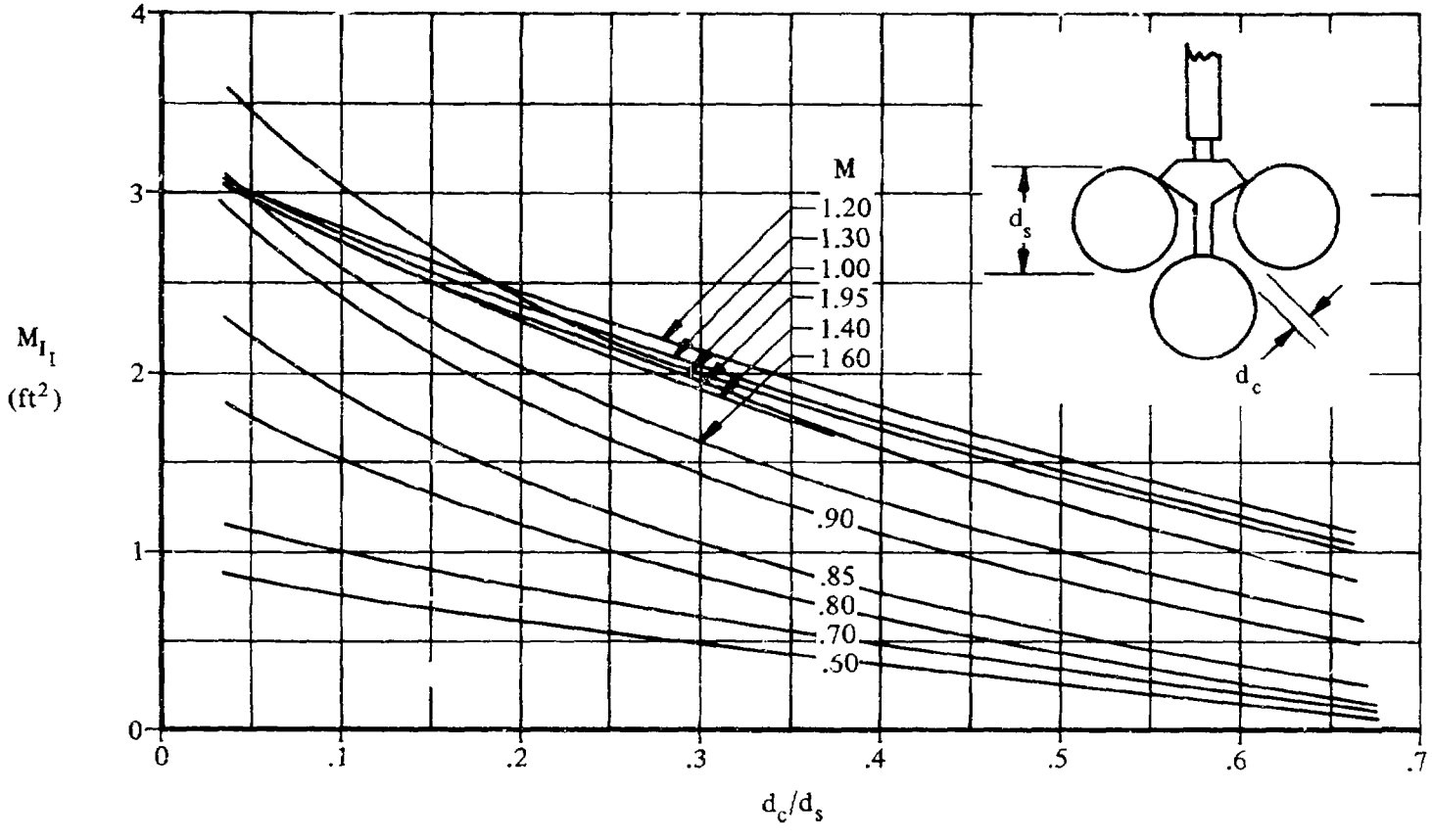

FIGURE 3.2.1.1-29 MER ADJACENT-STORE SEPARATION FACTOR

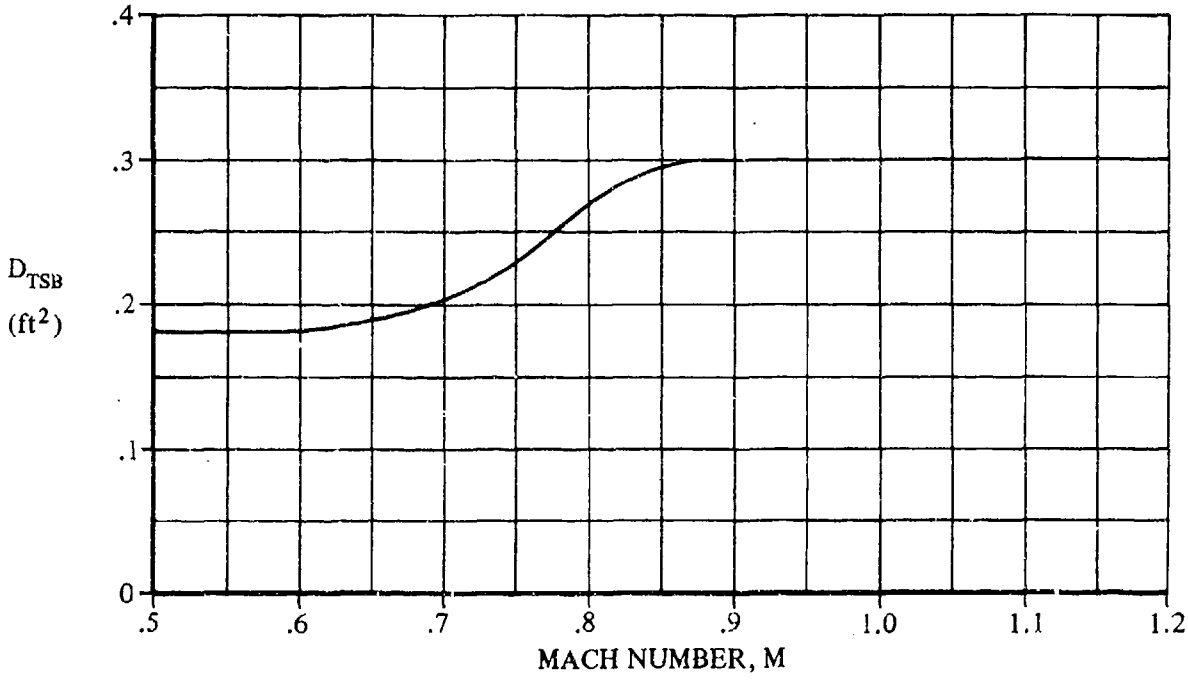

FIGURE 3.2.1.1-30 TER SWAY BRACE EQUIVALENT-PARASITE-DRAG AREA

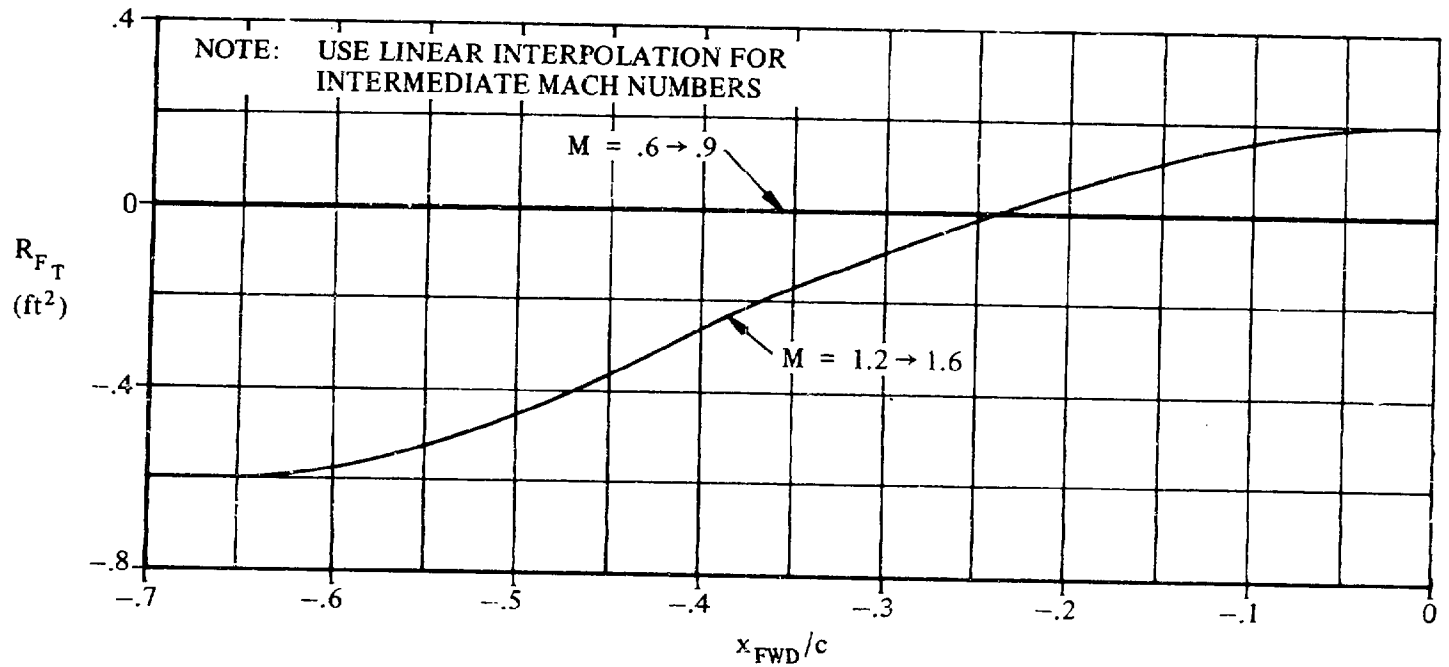

FIGURE 3.2.1.1-31 TER FORWARD-LONGITUDINAL-PLACEMENT TERM

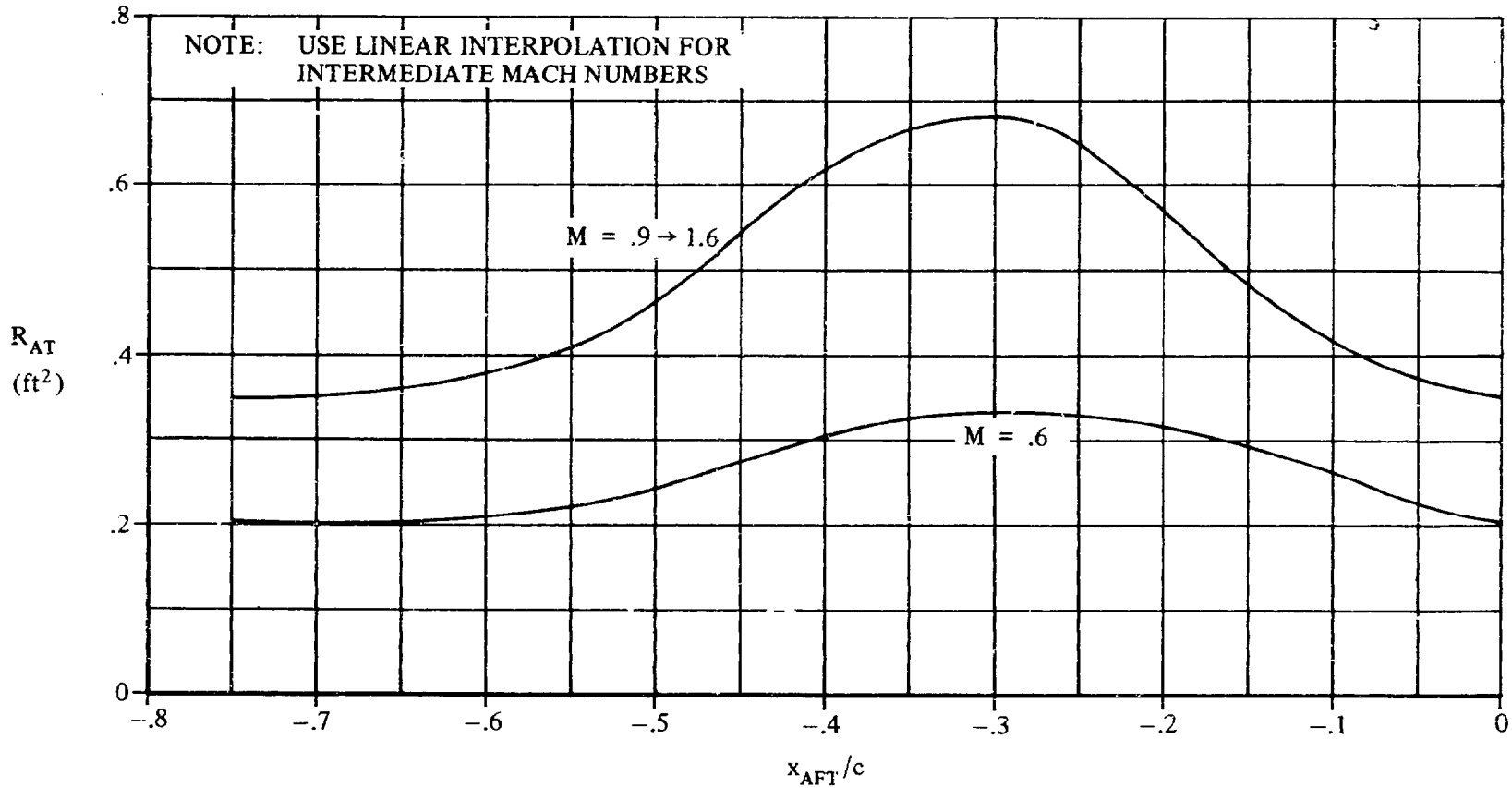

FIGURE 3.2.1.1-32 TER AFT-LONGITUDINAL-PLACEMENT TERM

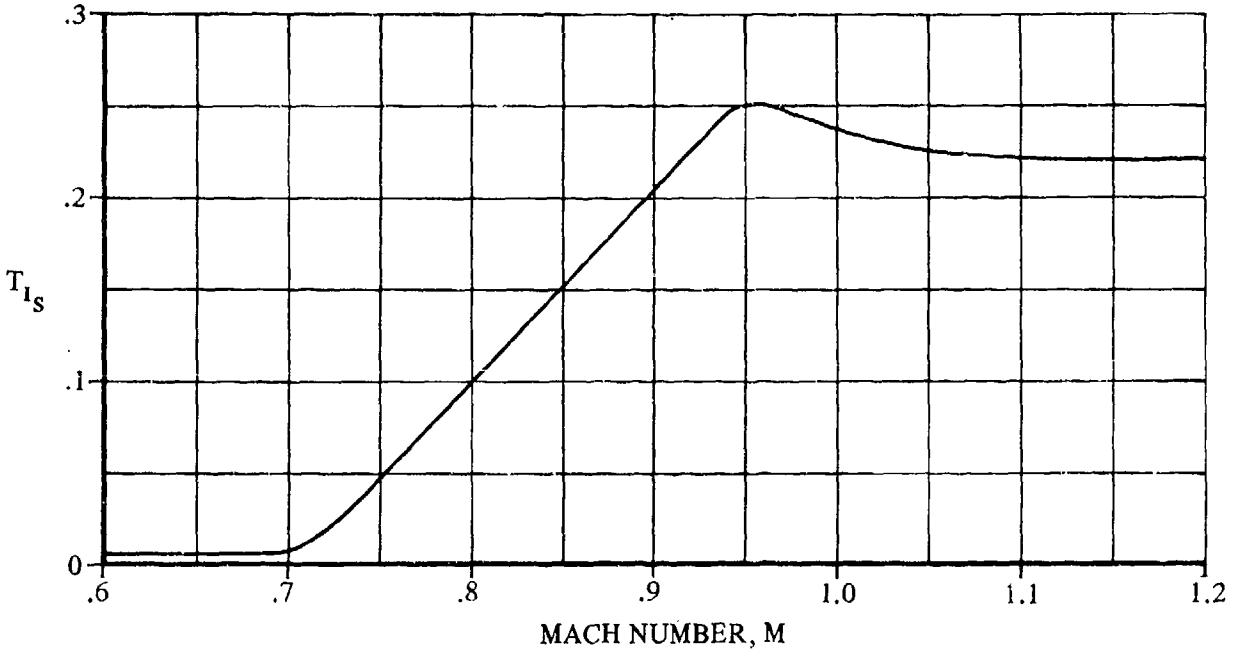

FIGURE 3.2.1.1-33 STORE-TER-AIRCRAFT-INTERFERENCE MACH-CORRELATION FACTOR

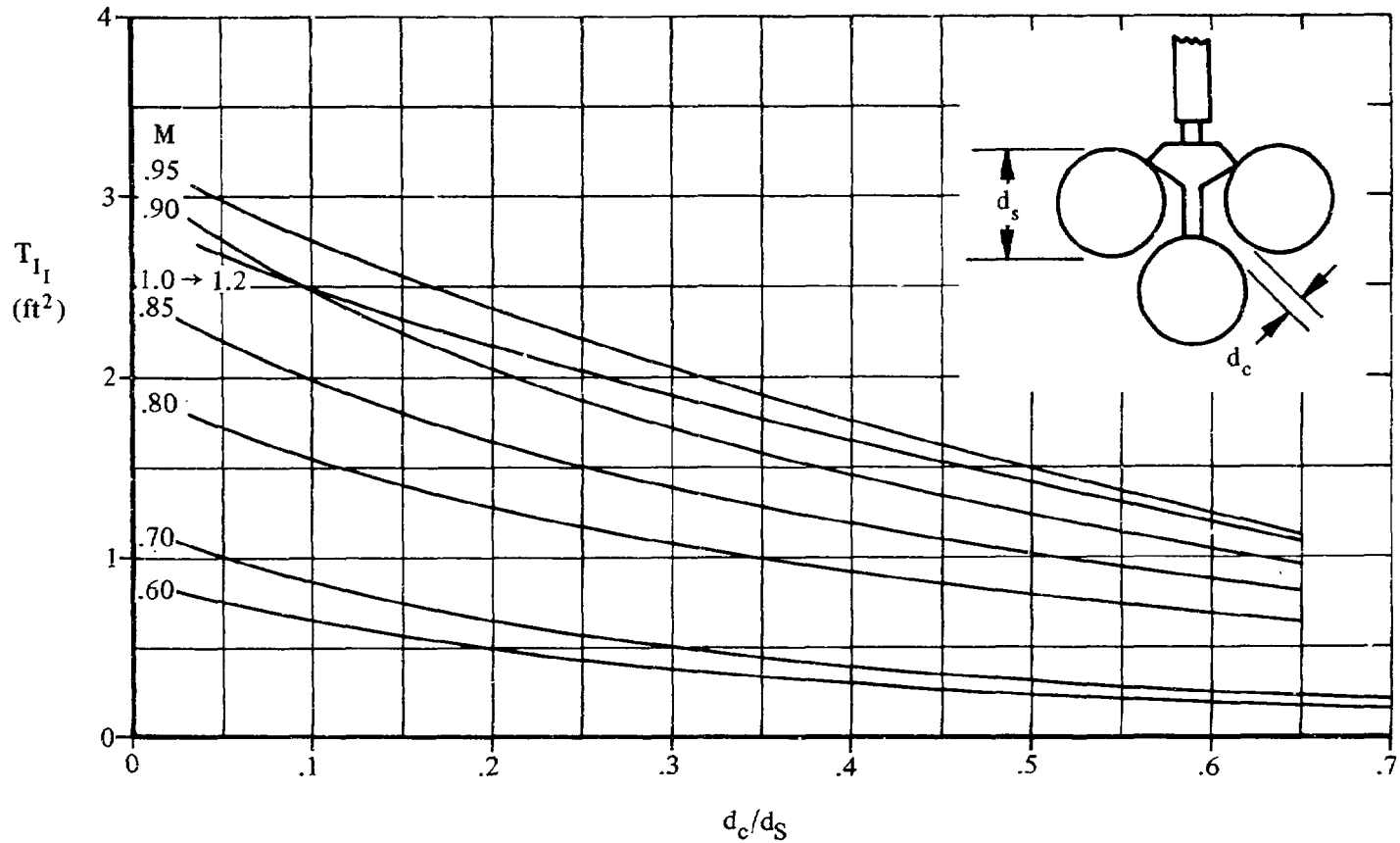

FIGURE 3.2.1.1-34 TER ADJACENT-STORE SEPARATION FACTOR

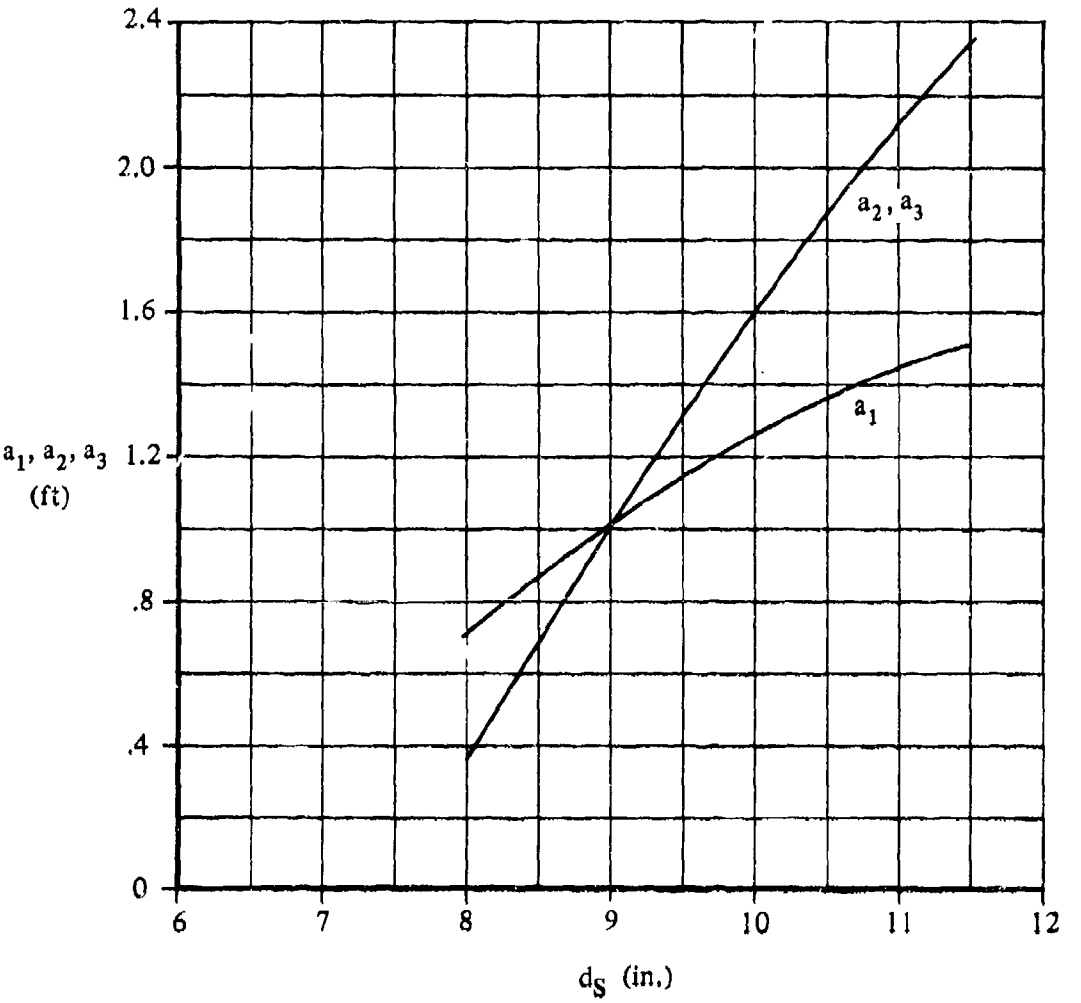

FIGURE 3.2.1.1-35 STORE-DIAMETER CORRELATION FACTORS

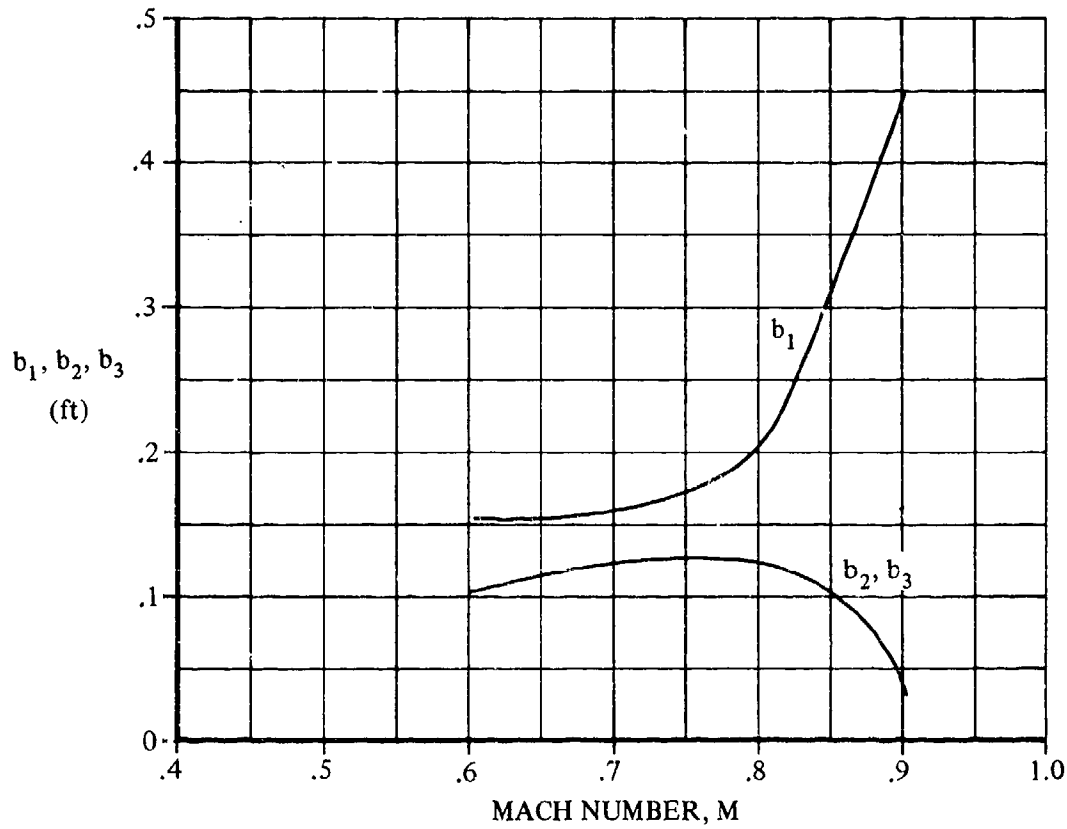

FIGURE 3.2.1.1-36 ROW MACH-CORRELATION FACTORS

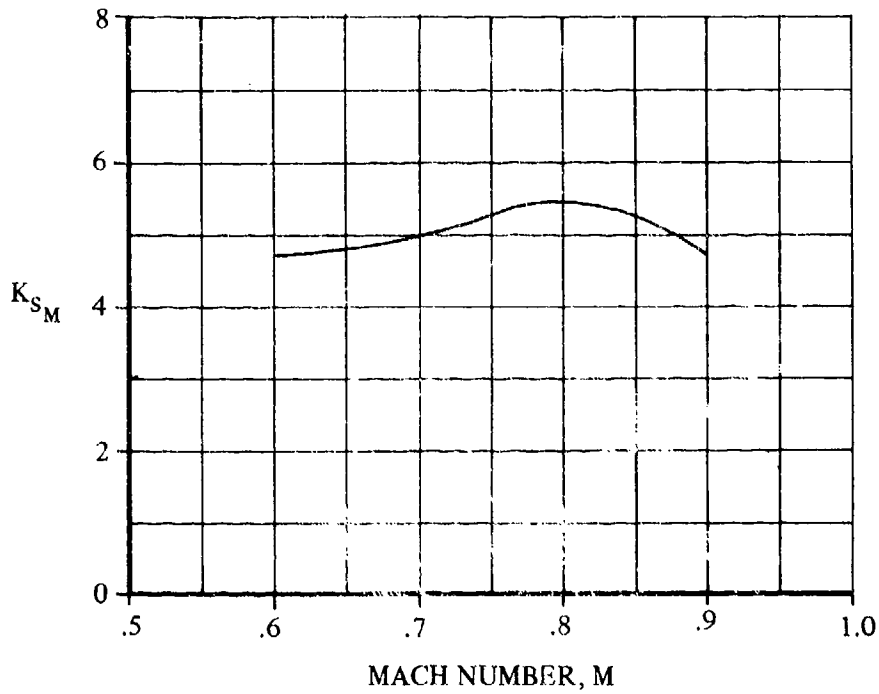

FIGURE 3.2.1.1-37a MACH EFFECT FACTOR FOR K_{D_1}

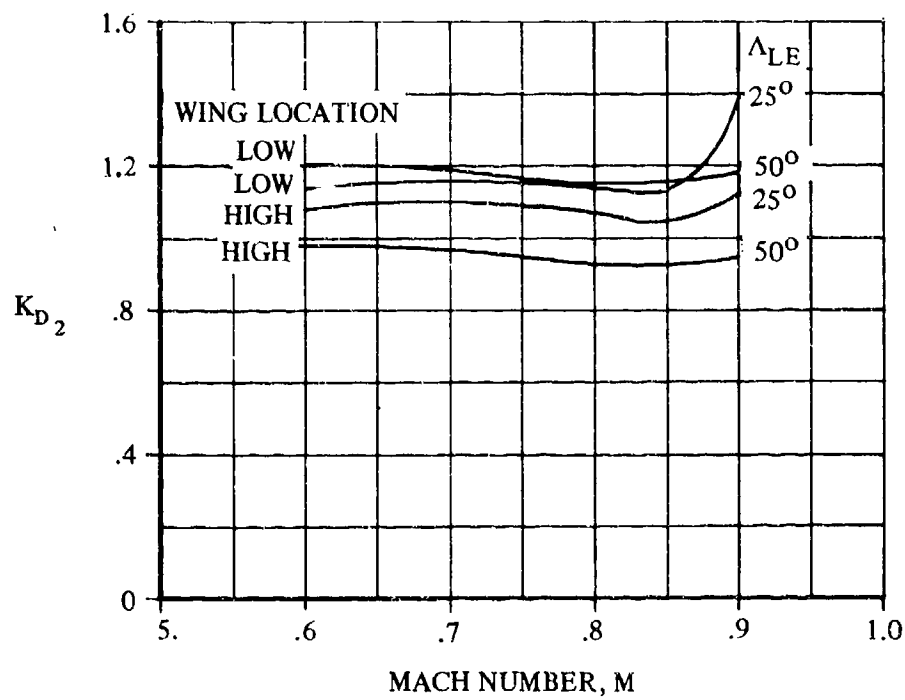

FIGURE 3.2.1.1-37b WING-SWEEP-AND-LOCATION FACTOR

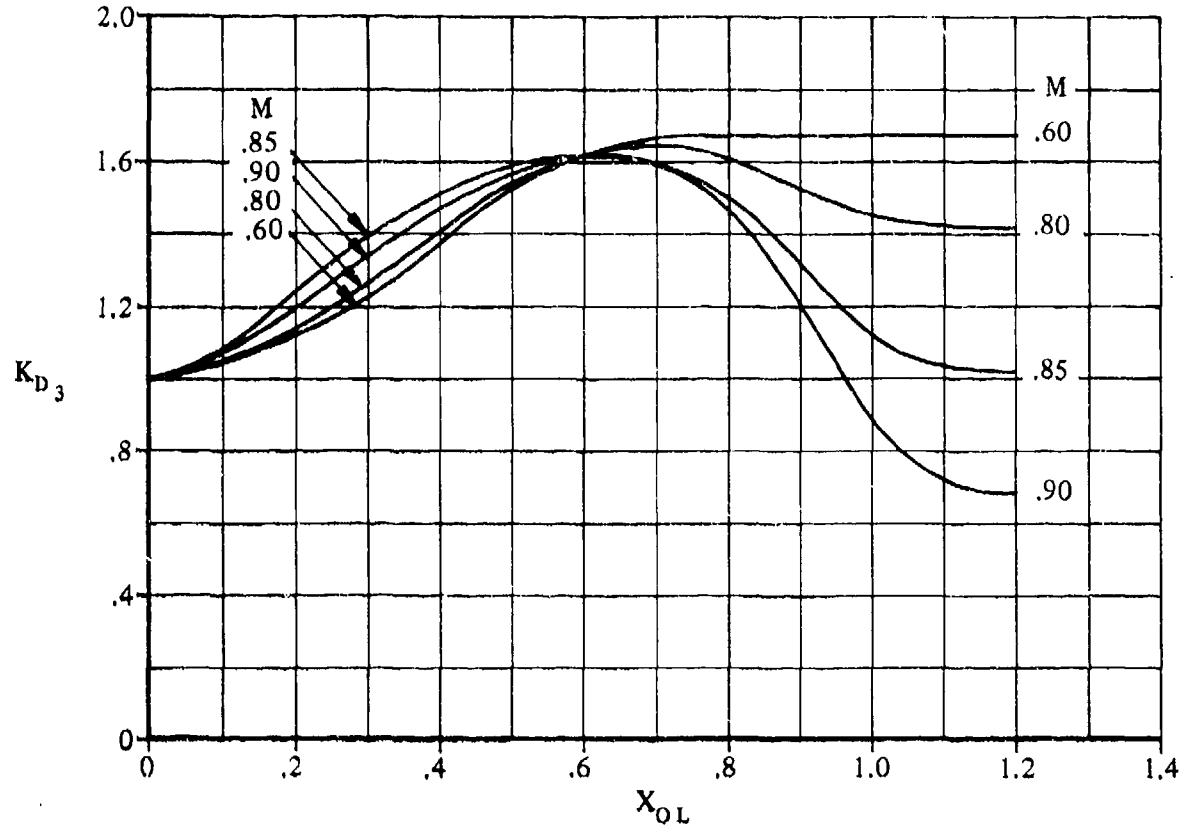

FIGURE 3.2.1.1-38a TANDEM-SPACING FACTOR

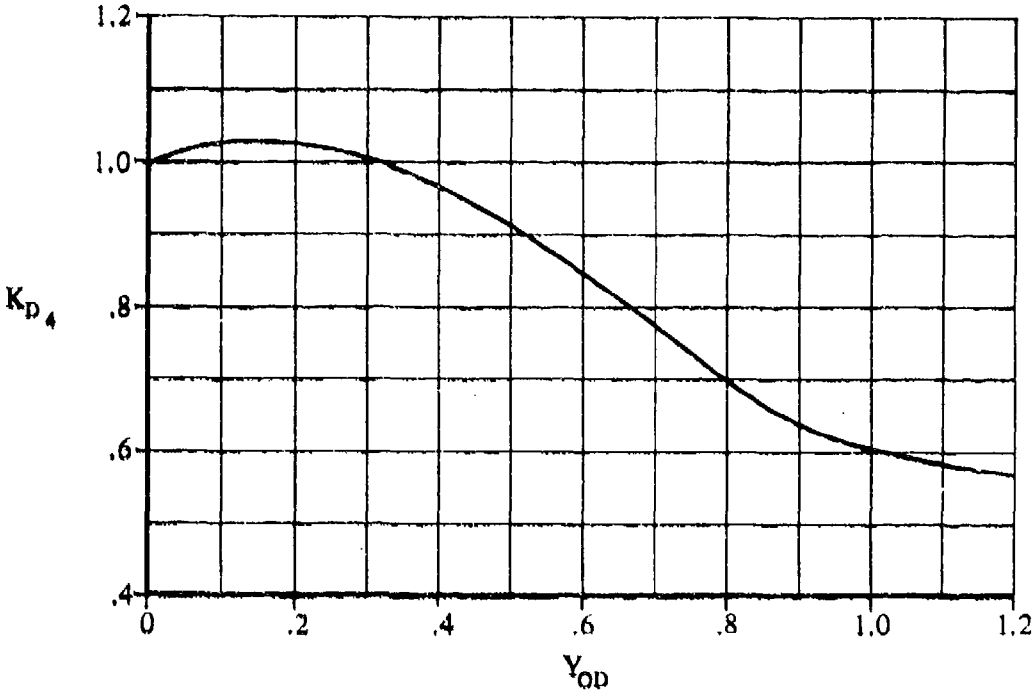

FIGURE 3.2.1.1-38b LATER-SPACING FACTOR

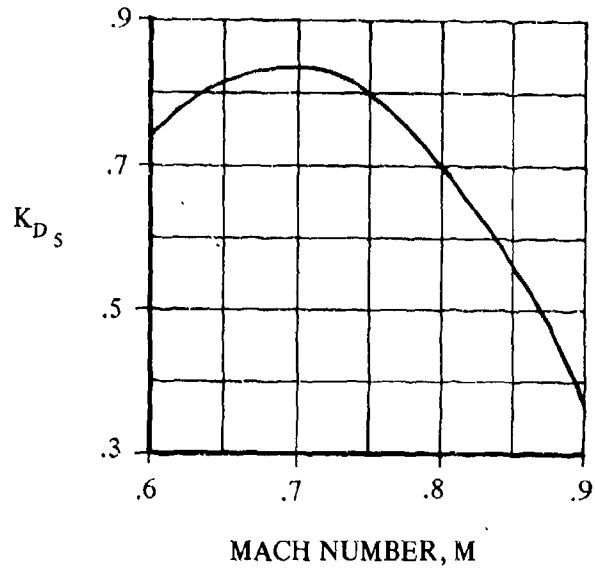

FIGURE 3.2.1.1-39a STORE-ROWS FACTOR FOR ONE ROW

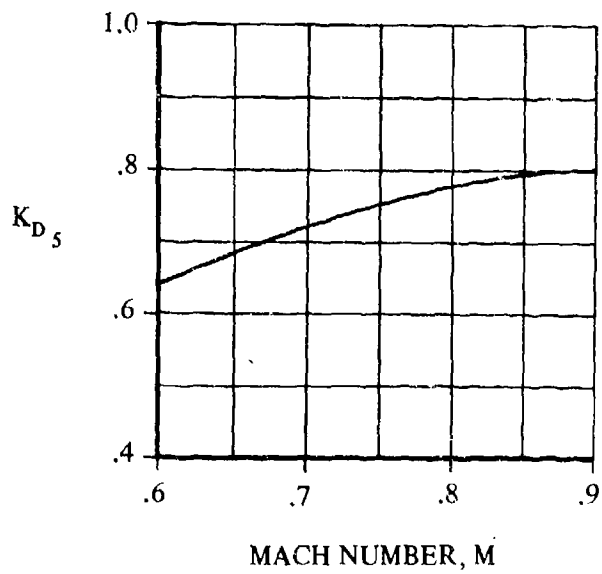

FIGURE 3.2.1.1-39b STORE-ROWS FACTOR FOR TWO ROWS

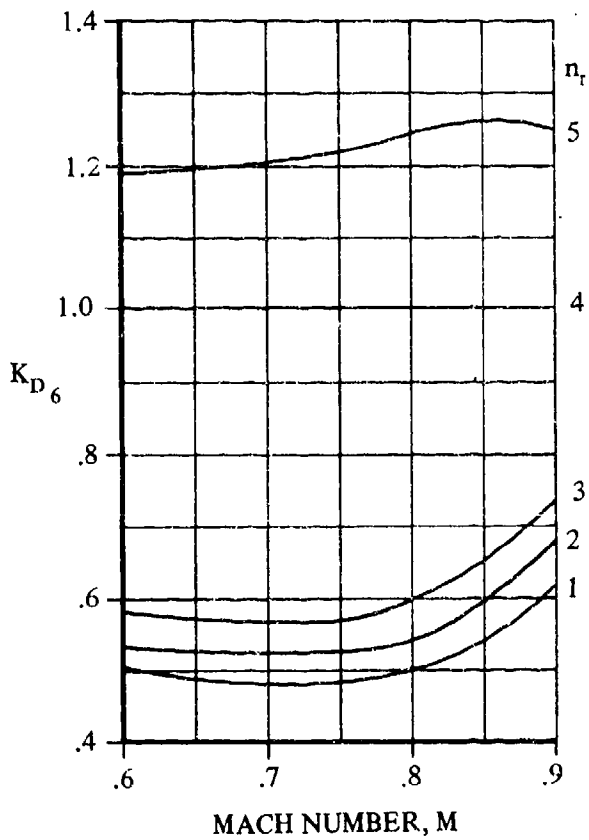

FIGURE 3.2.1.1-40 STORES-PER-ROW FACTOR FOR ONE STORE PER ROW

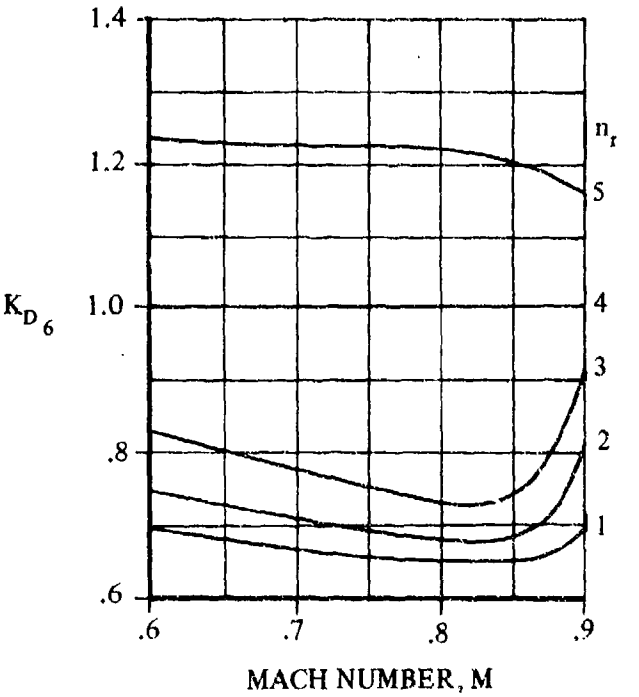

FIGURE 3.2.1.1-41a STORES-PER-ROW FACTOR FOR TWO STORES PER ROW

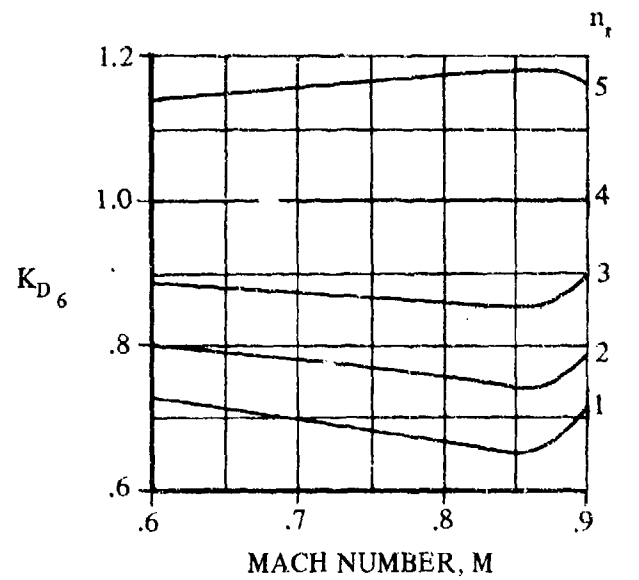

FIGURE 3.2.1.1-41b STORES-PER-ROW FACTOR FOR THREE STORES PER ROW

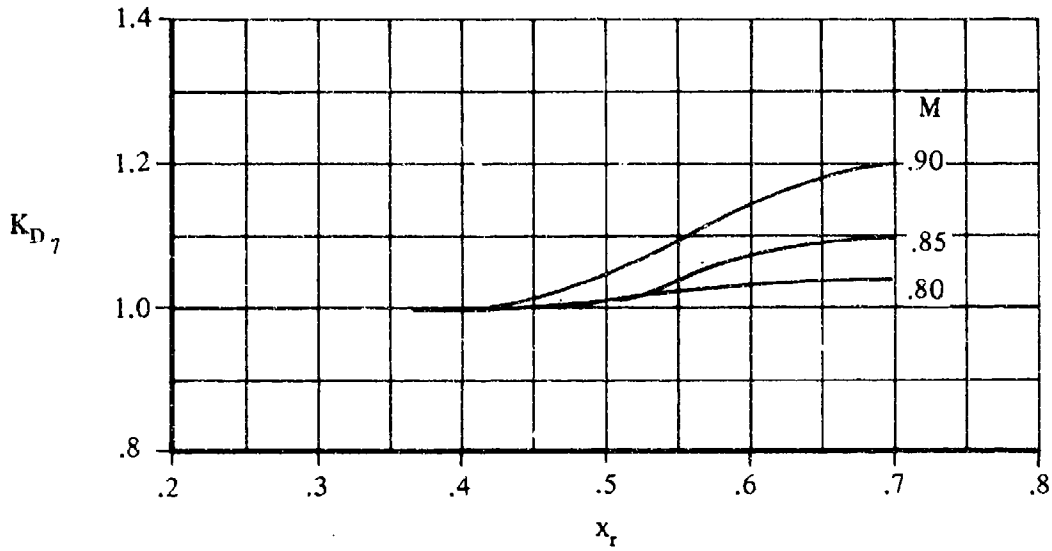

FIGURE 3.2.1.1-42a STORE-LONGITUDINAL-LOCATION FACTOR

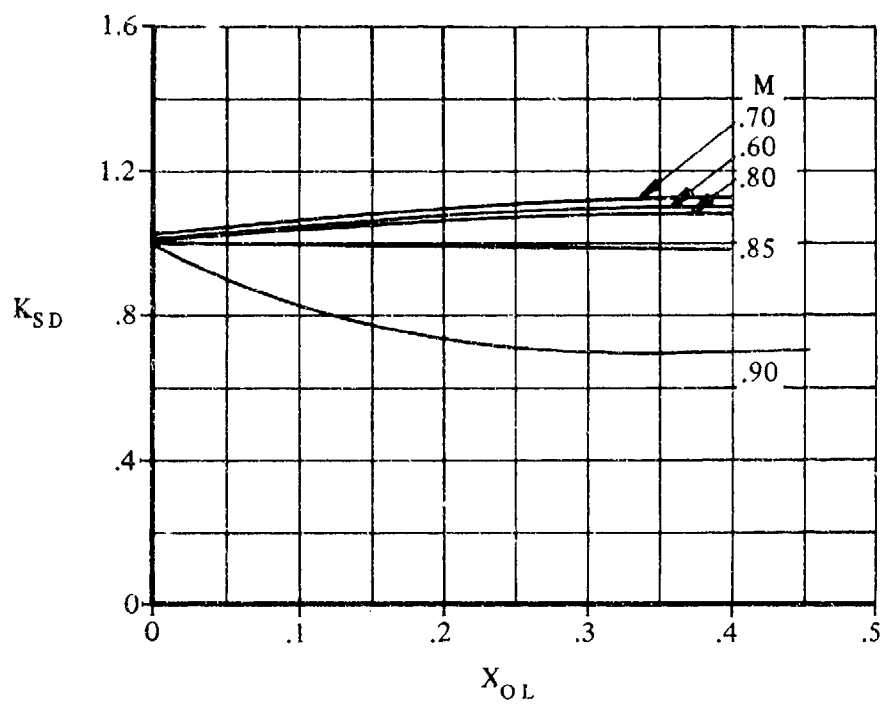

FIGURE 3.2.1.1-42b STORE-DEPTH FACTOR

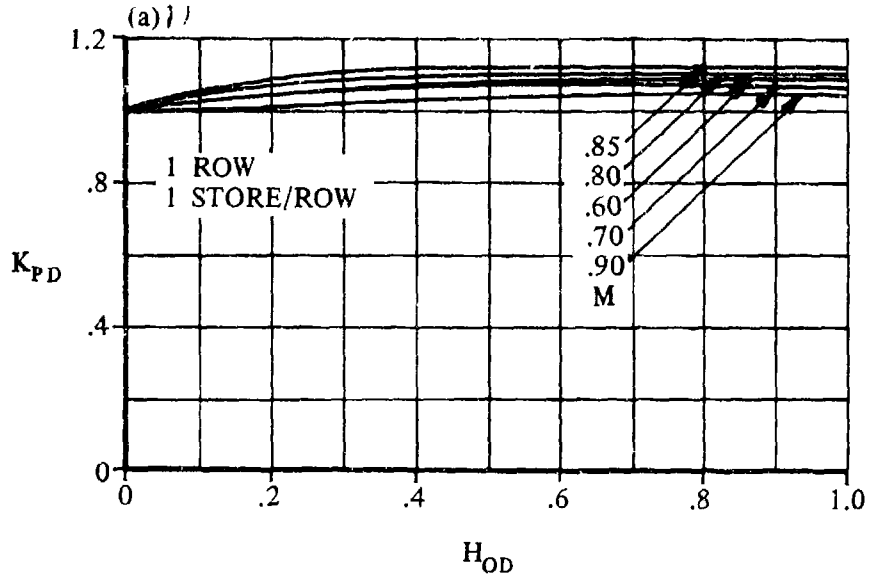

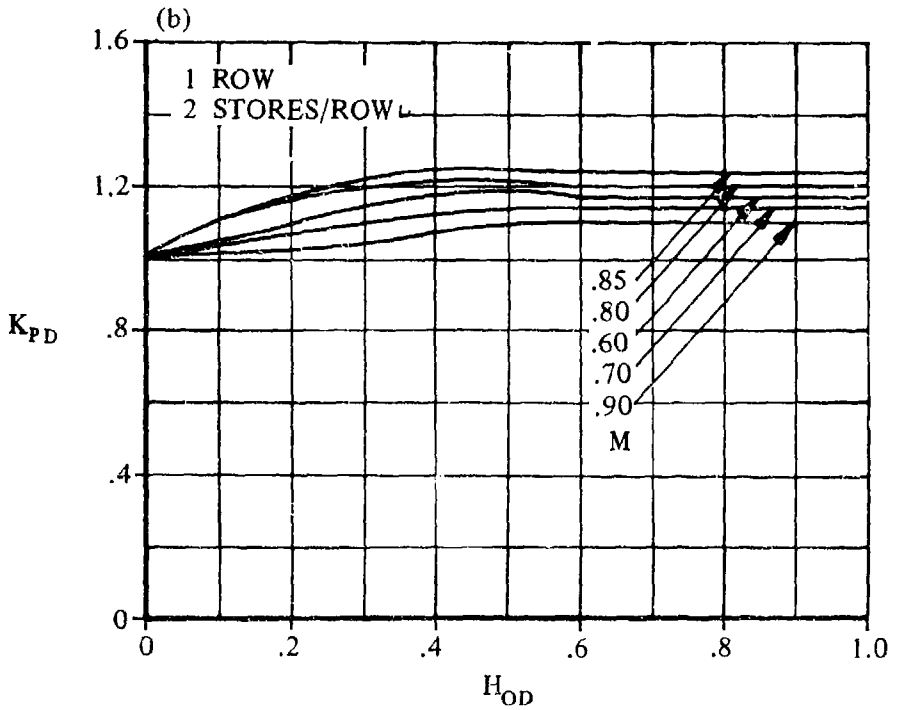

STORE 3.2.1.1-43 PYLON-DEPTH FACTOR

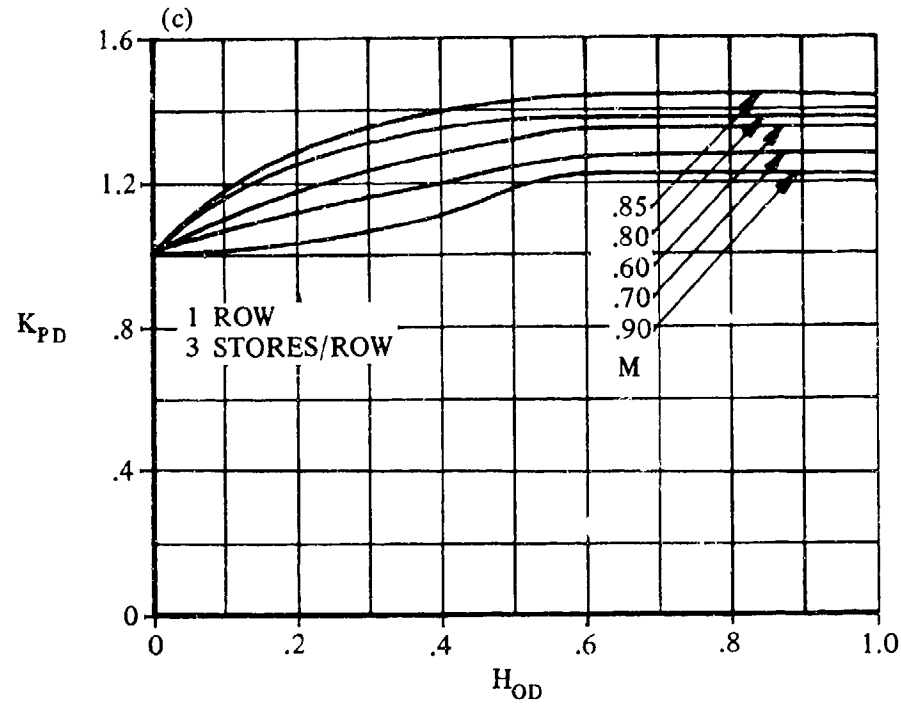

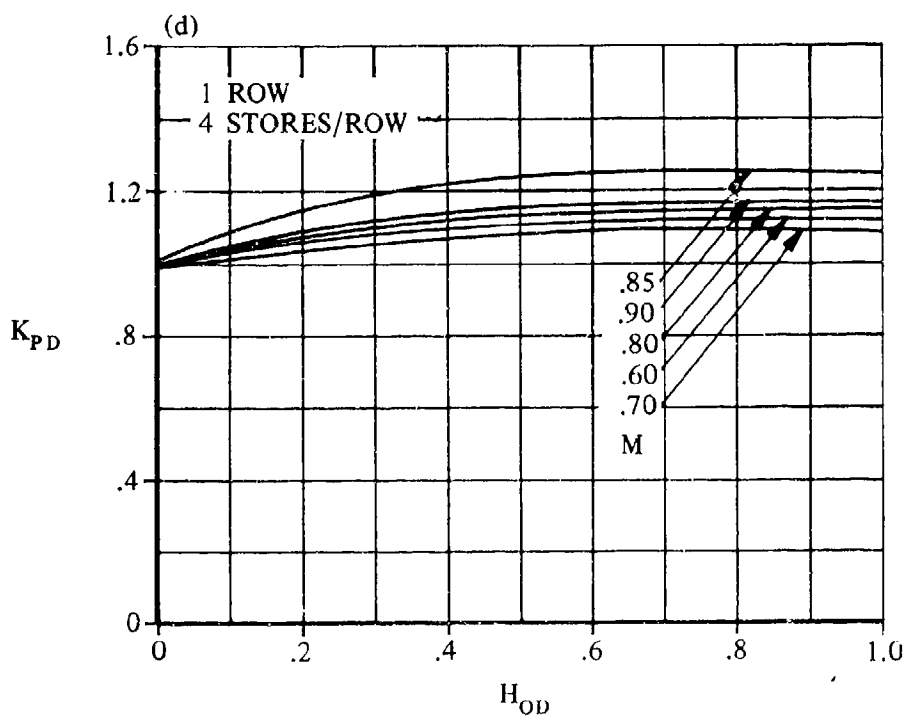

FIGURE 3.2.1.1-43 (CONTD)

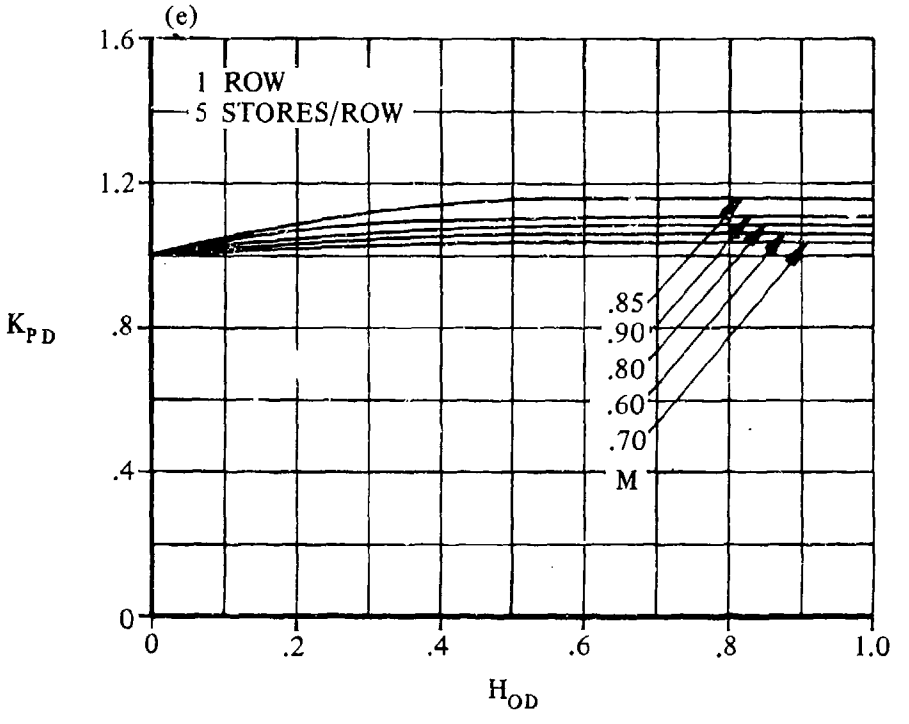

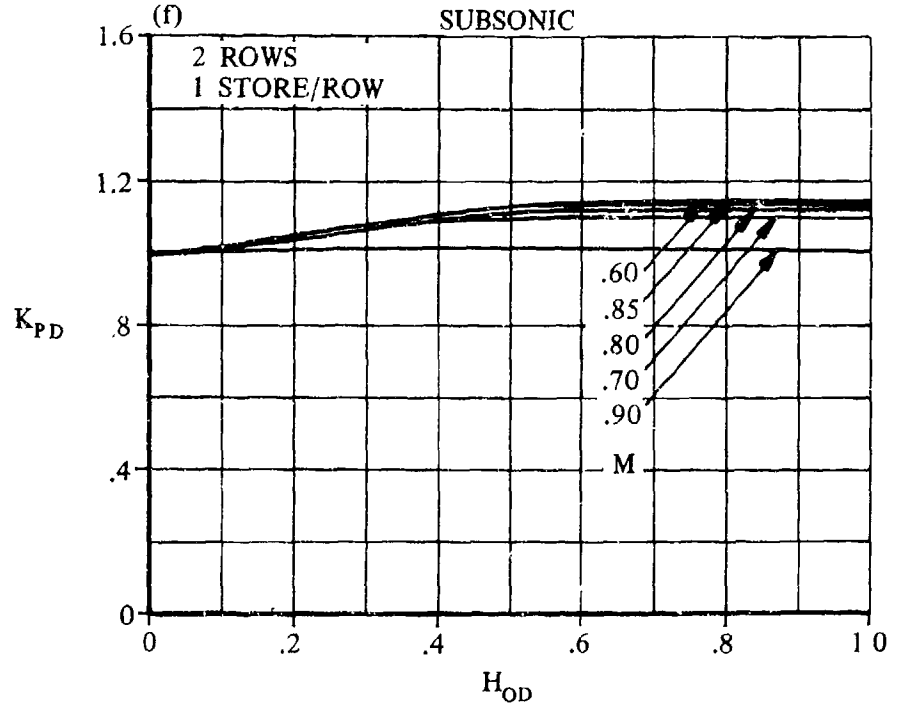

FIGURE 3.2.1.1-43 (CONTD)

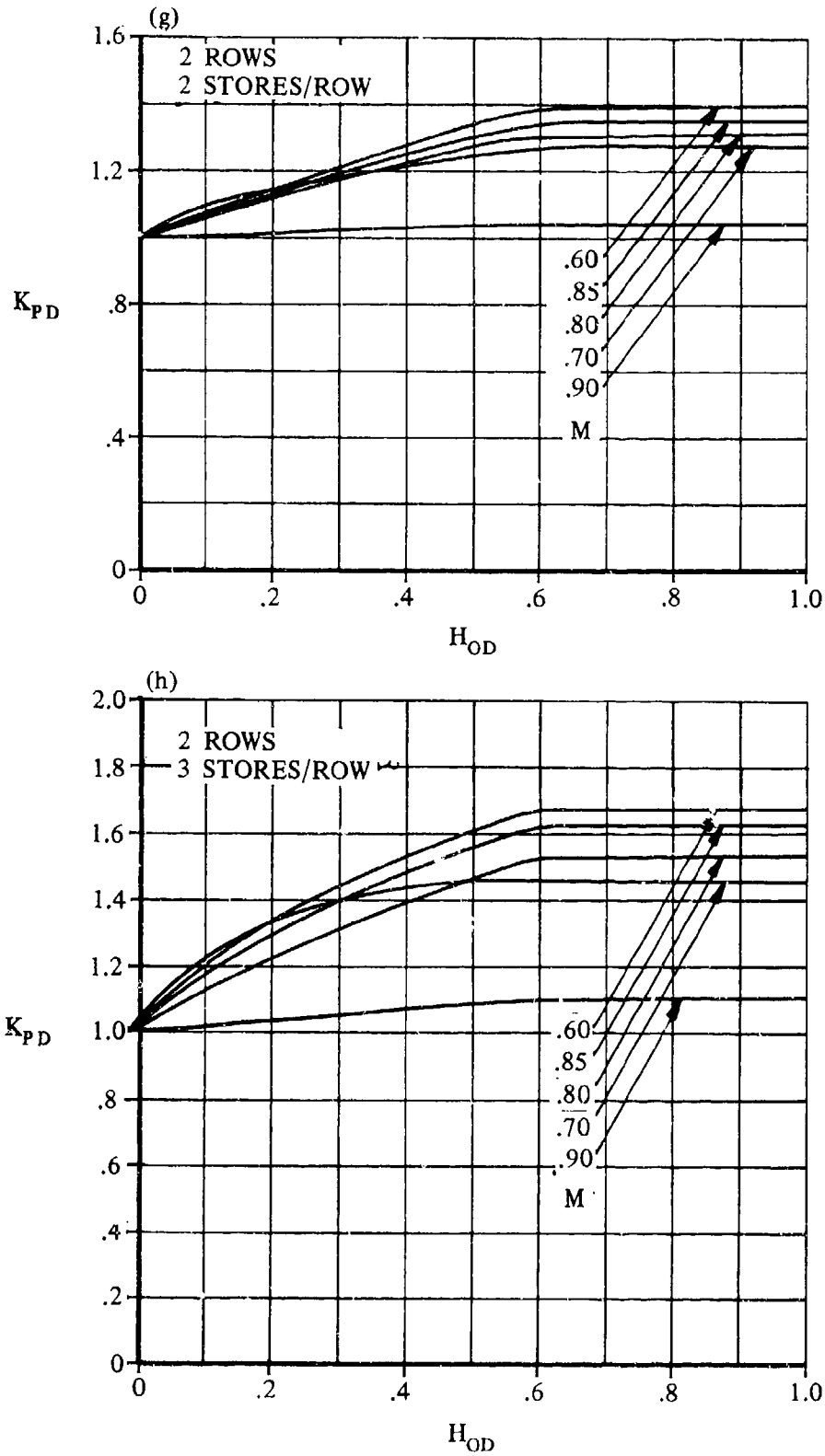

FIGURE 3.2.1.1-43 (CONTD)

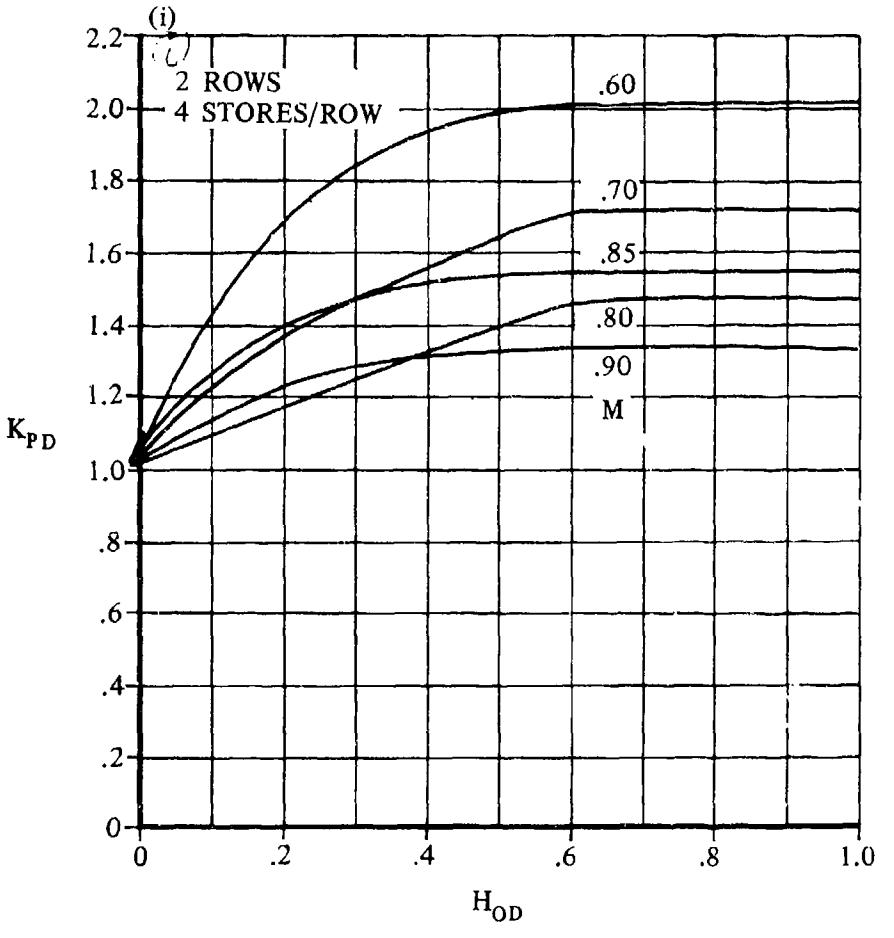

FIGURE 3.2.1.1-43 (CONTD)

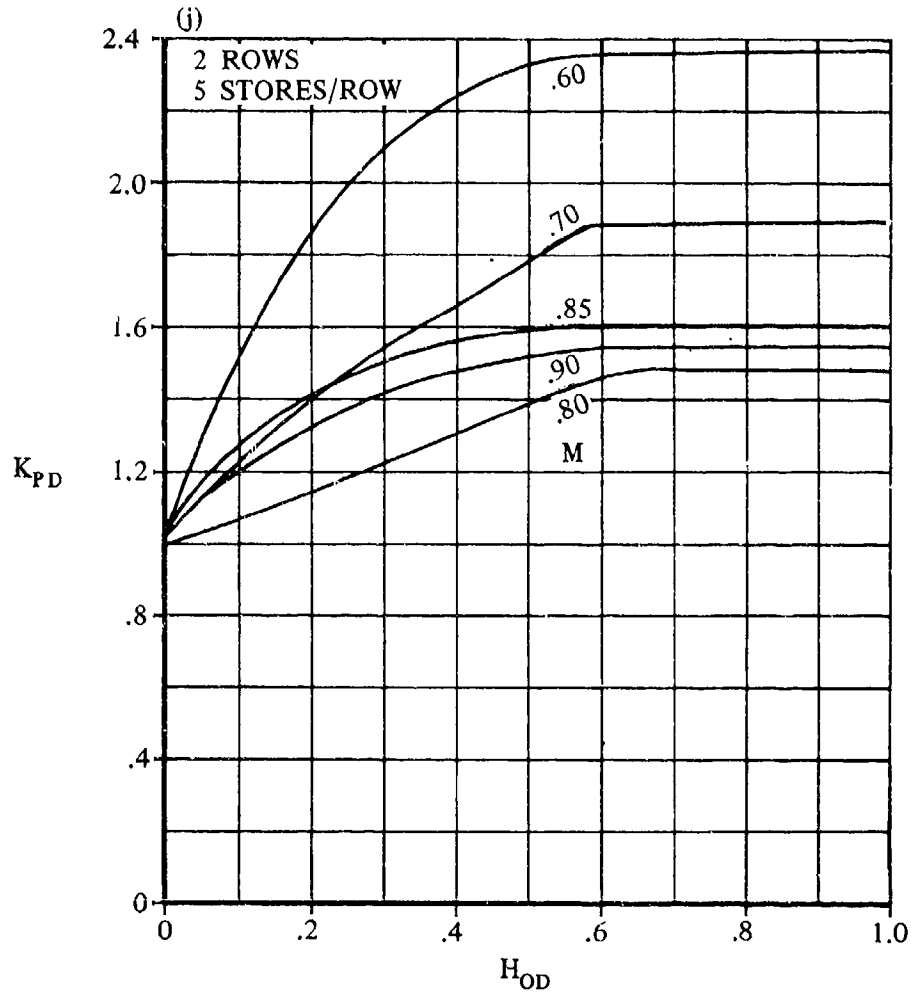

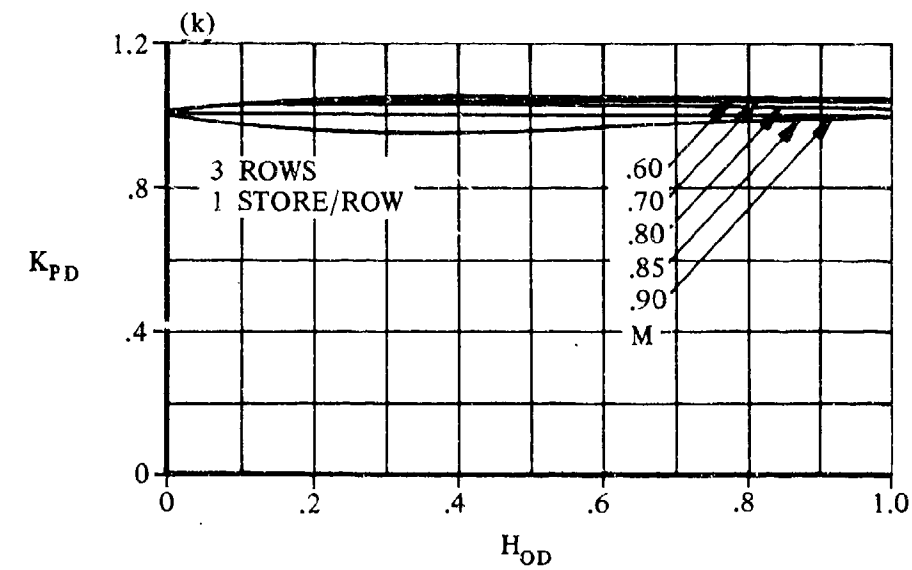

FIGURE 3.2.1.1-43 (CONTD)

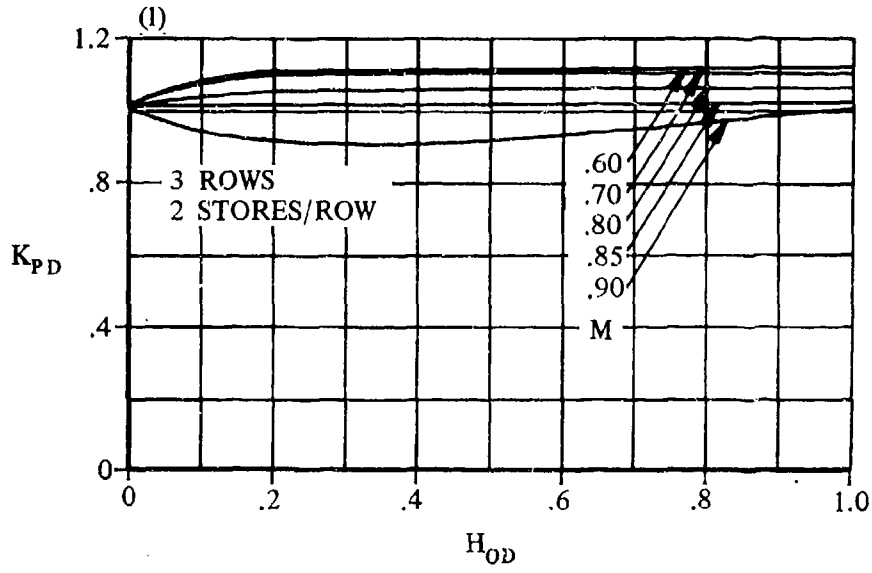

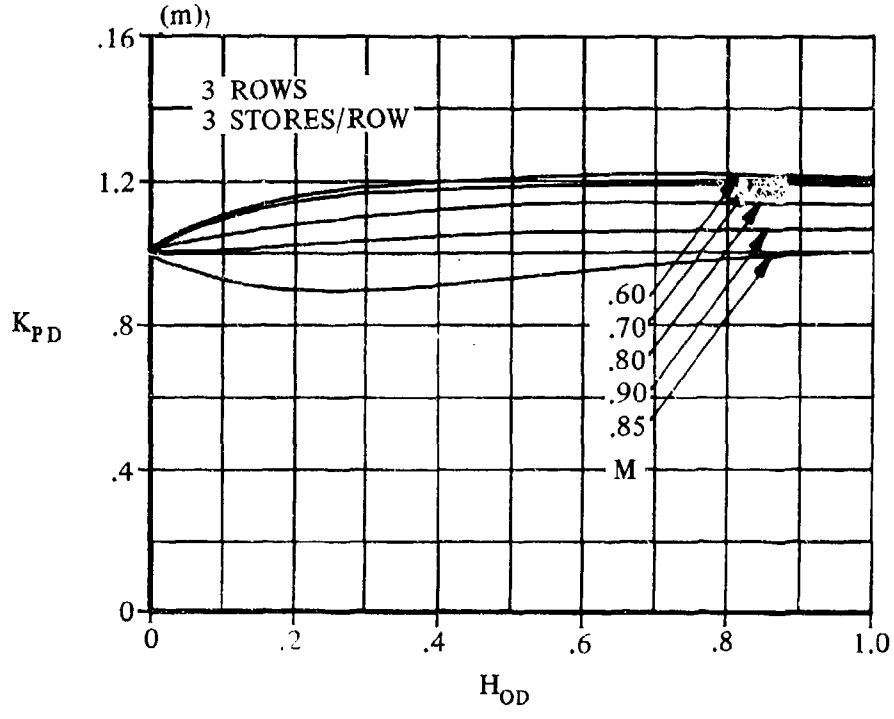

FIGURE 3.2.1.1-43 (CONTD)

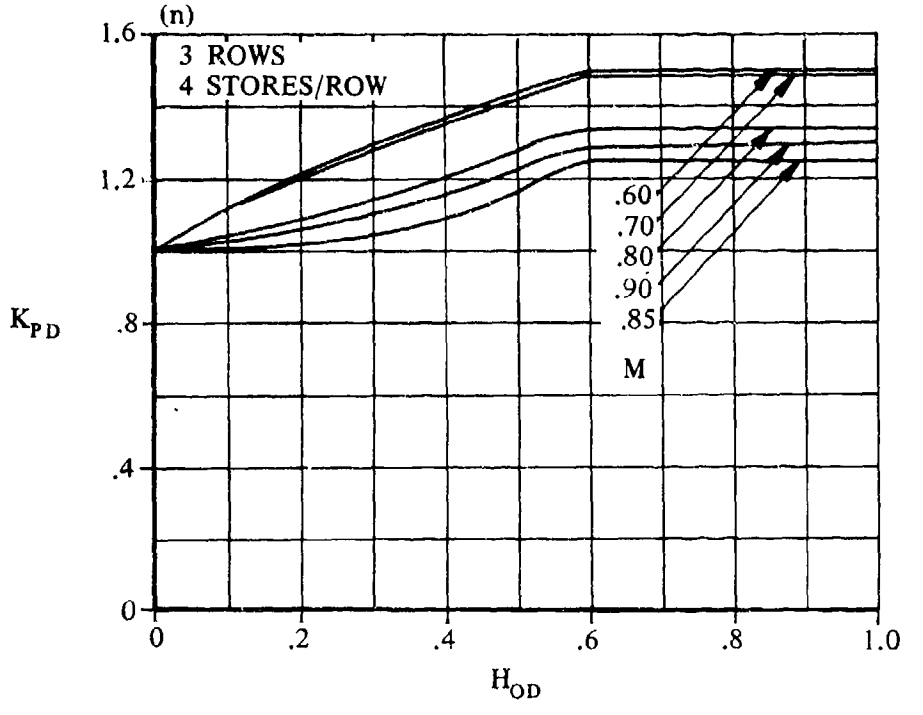

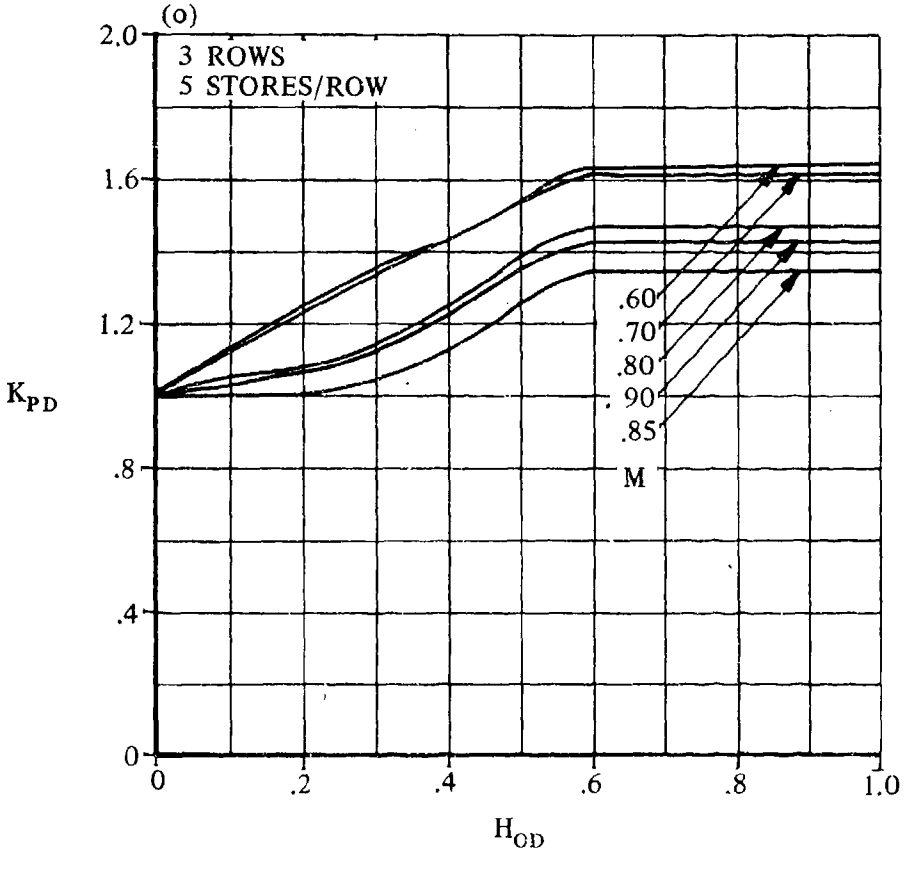

FIGURE 3.2.1.1-43 (CONTD)

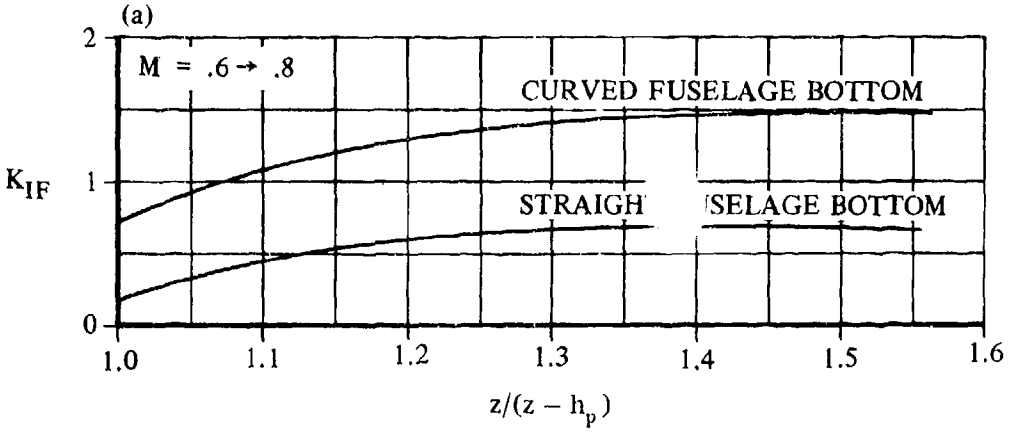

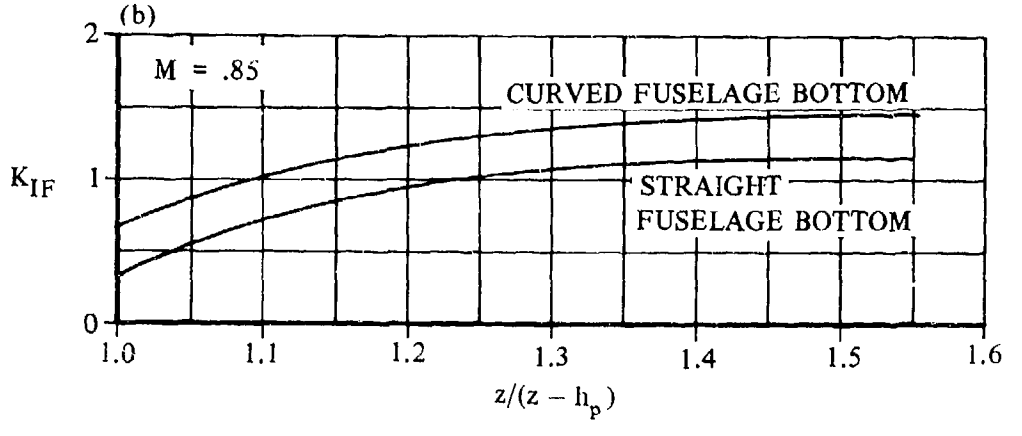

FIGURE 3.2.1.1- 51 SINGLE-STORE INSTALLATION FACTOR

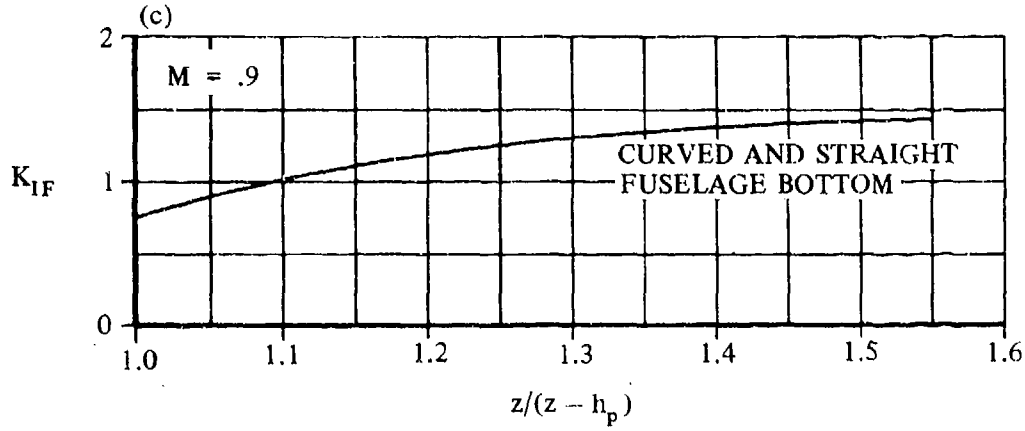

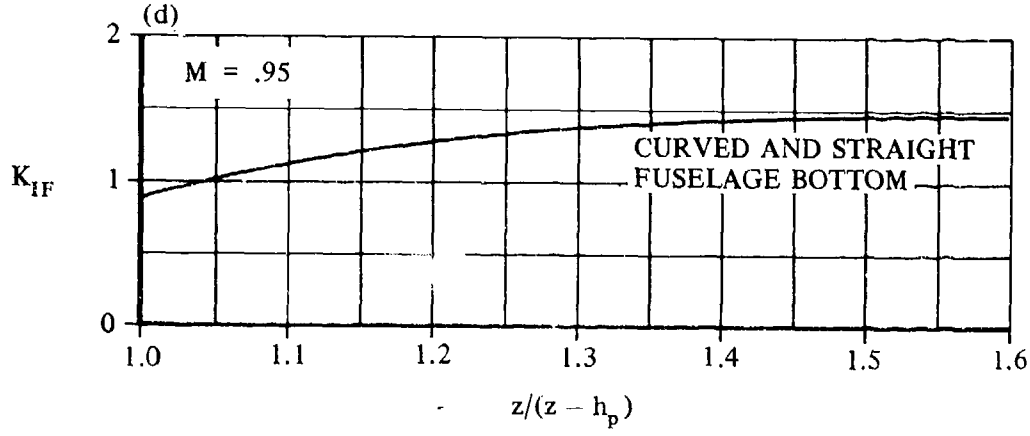

FIGURE 3.2.1.1-51 (CONTD)

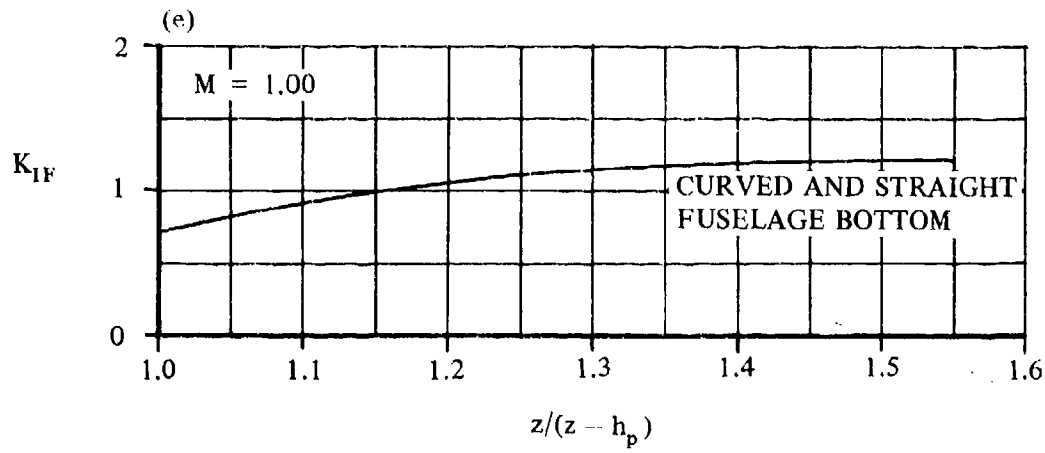

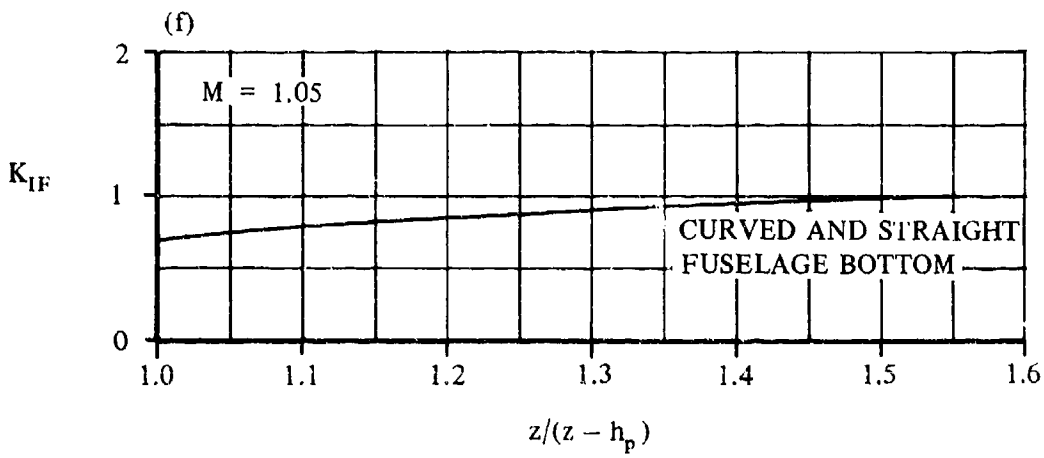

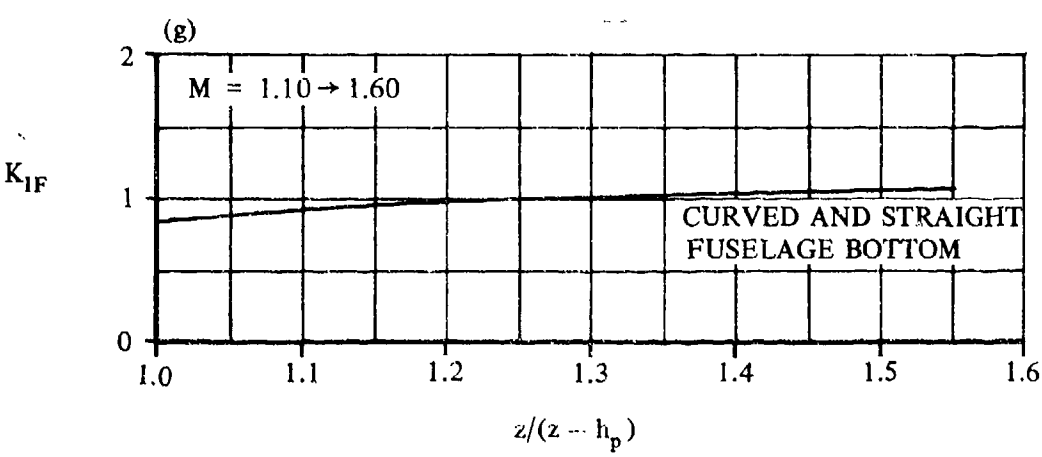

FIGURE 3.2.1.1-51 (CONTD)

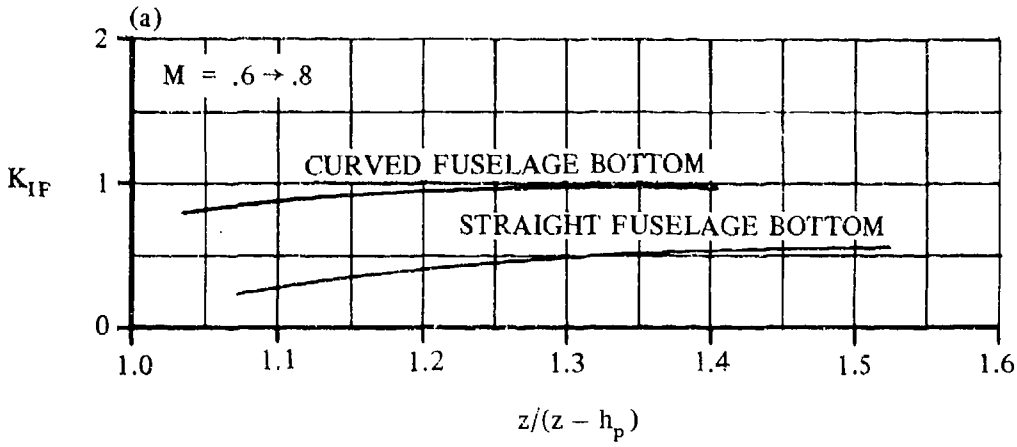

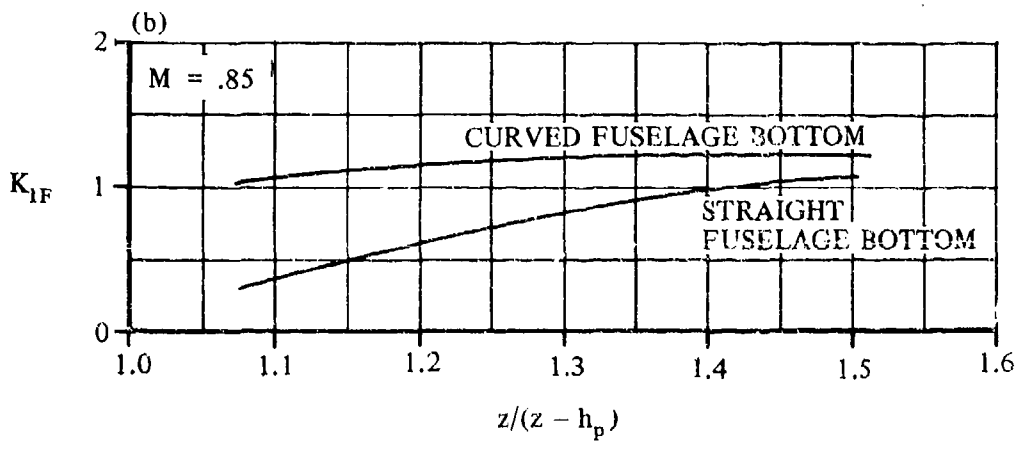

FIGURE 3.2.1.1-54 MULTIPLE-STORES INSTALLATION FACTOR

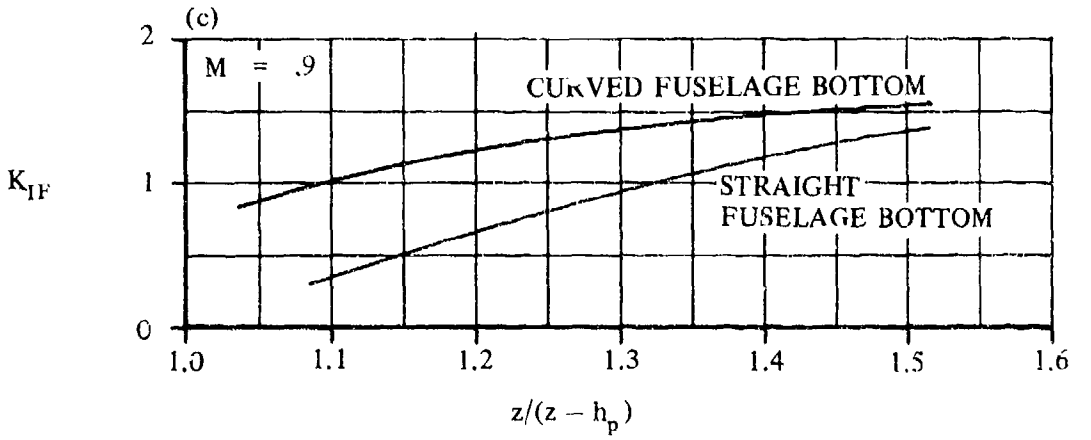

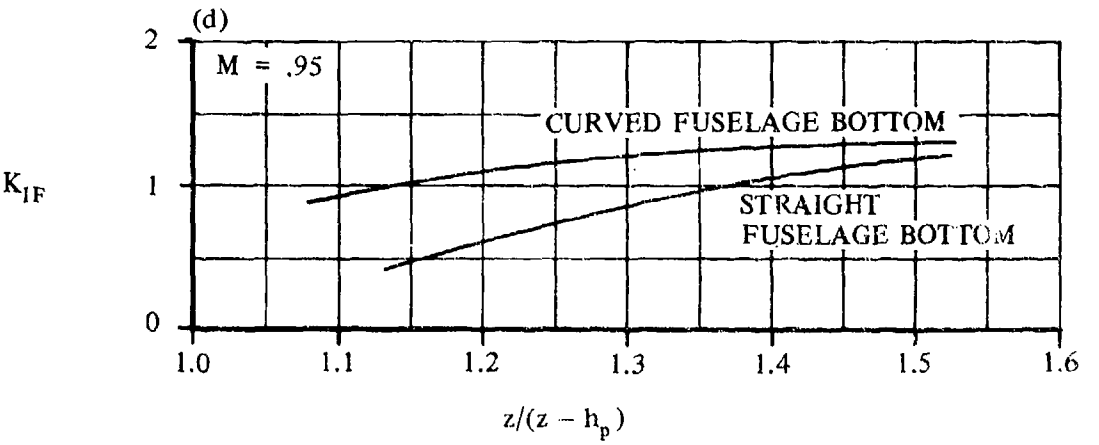

FIGURE 3.2.1.1-54 (CONTD)

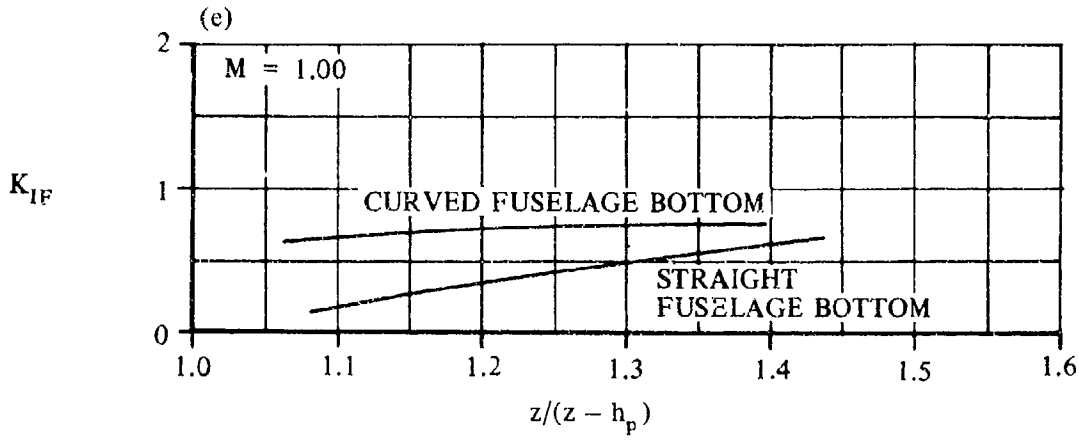

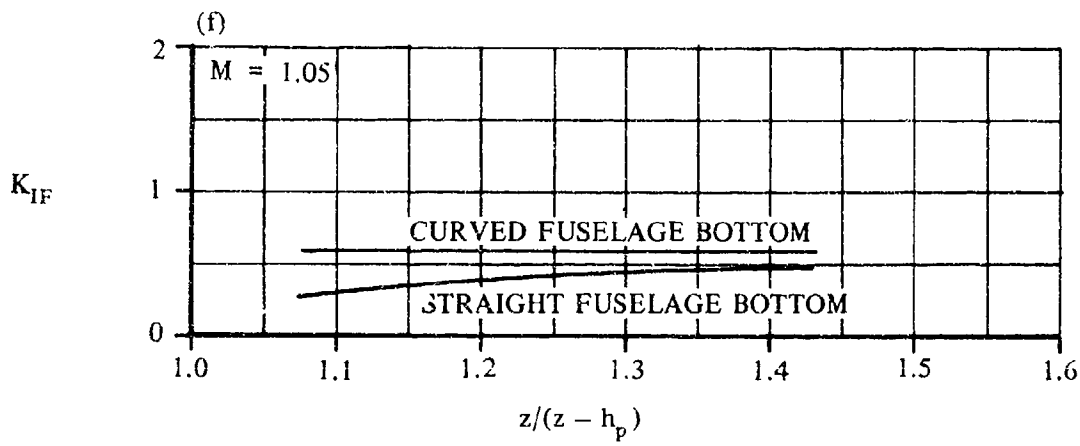

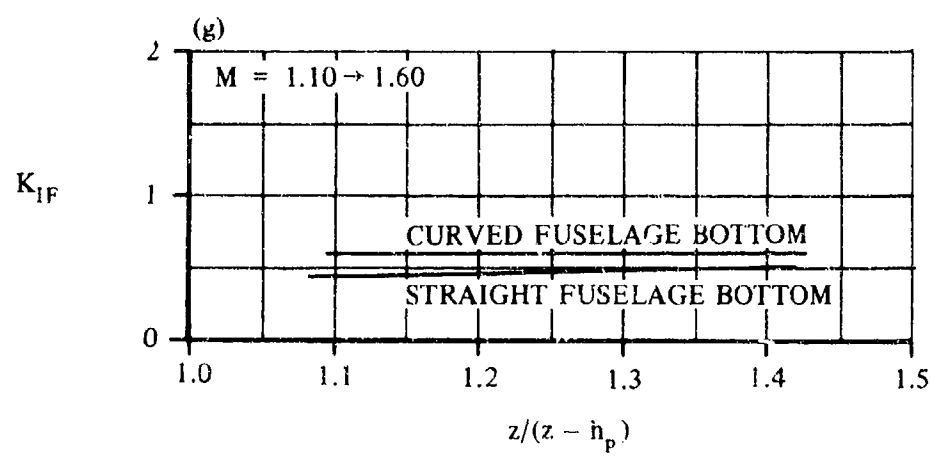

FIGURE 3.2.1.1-54 (CONTD)

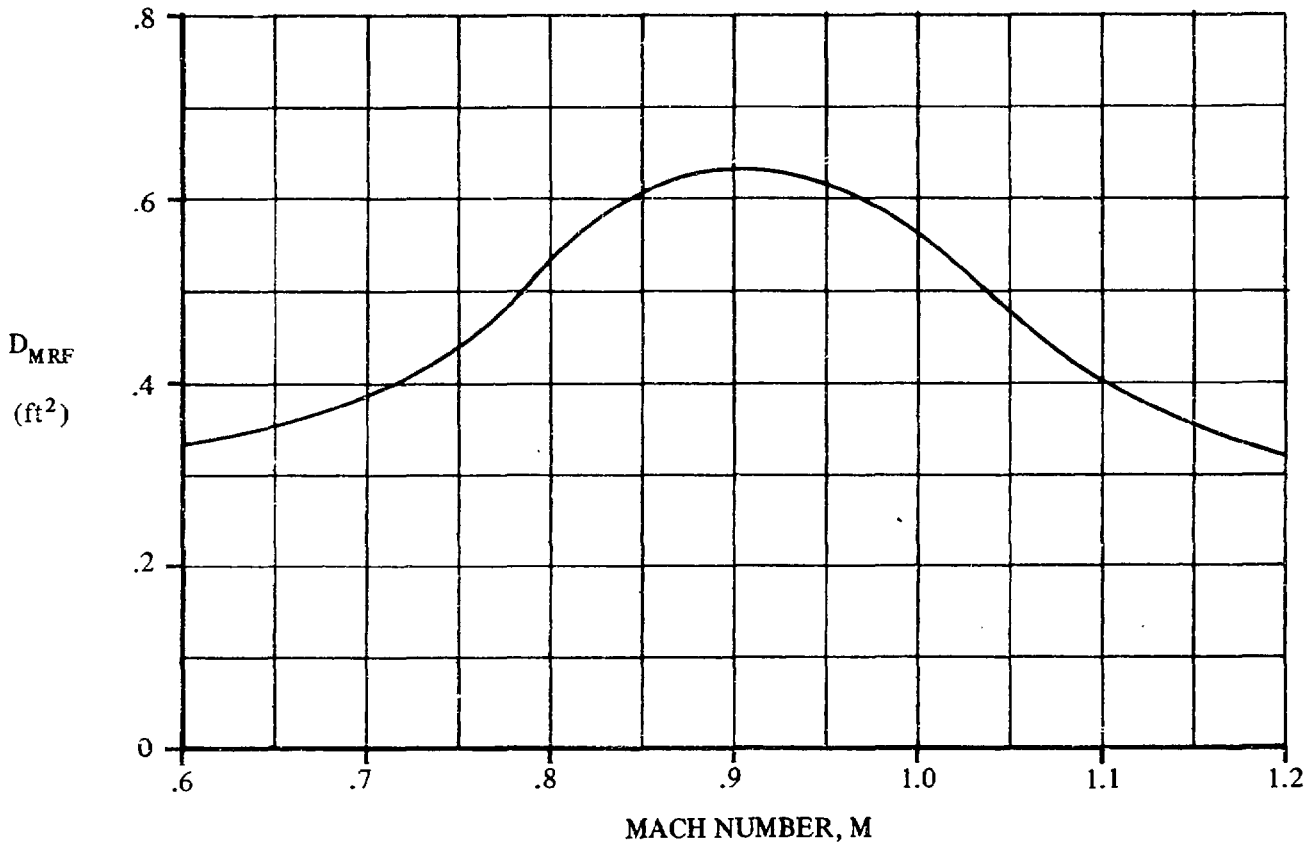

FIGURE 3.2.1.1-57 MER-RACK-TO-FUSELAGE ZERO-LIFT EQUIVALENT-PARASITE-DRAG AREA

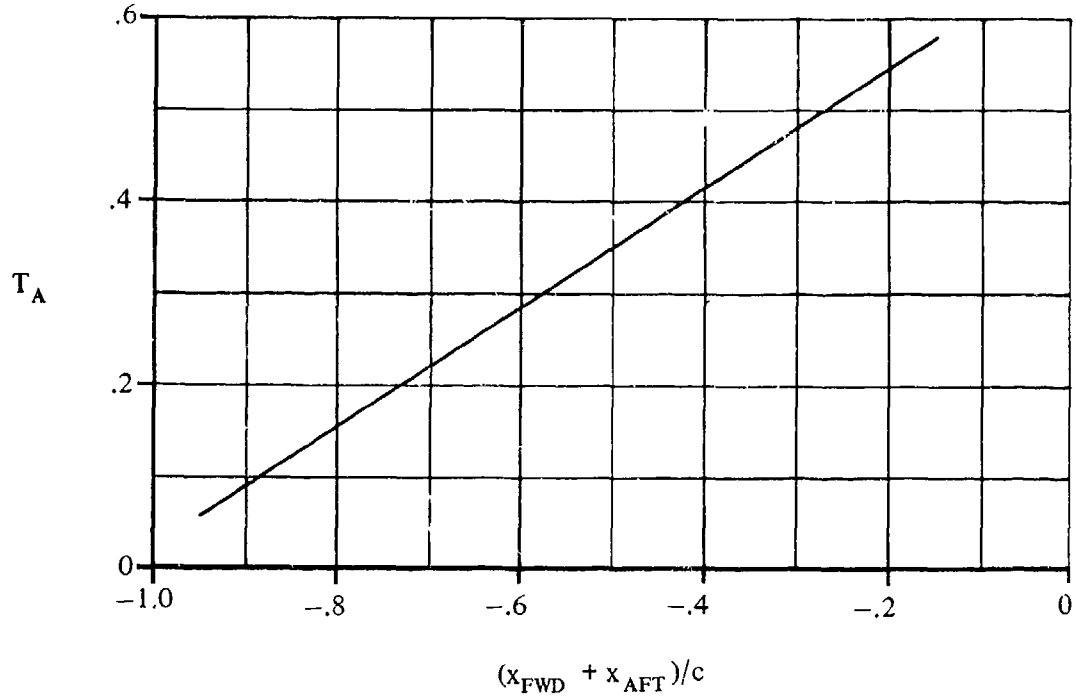

FIGURE 3.2.1.1-58a TRANSONIC-SUPERSONIC CORRELATION FACTOR

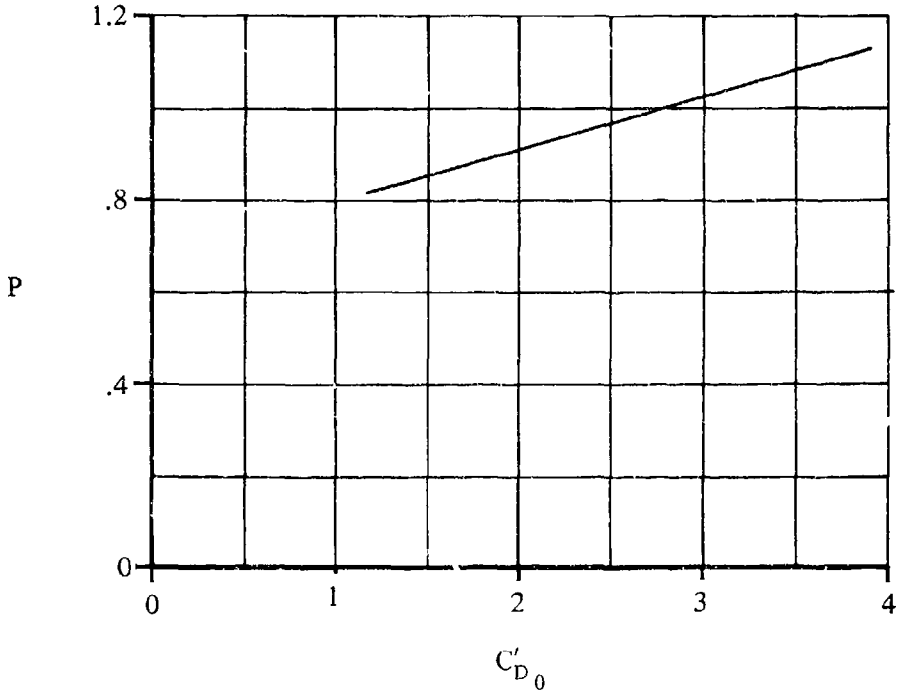

FIGURE 3.2.1.1-58b CLEAN AIRCRAFT DRAG-RISE FACTOR

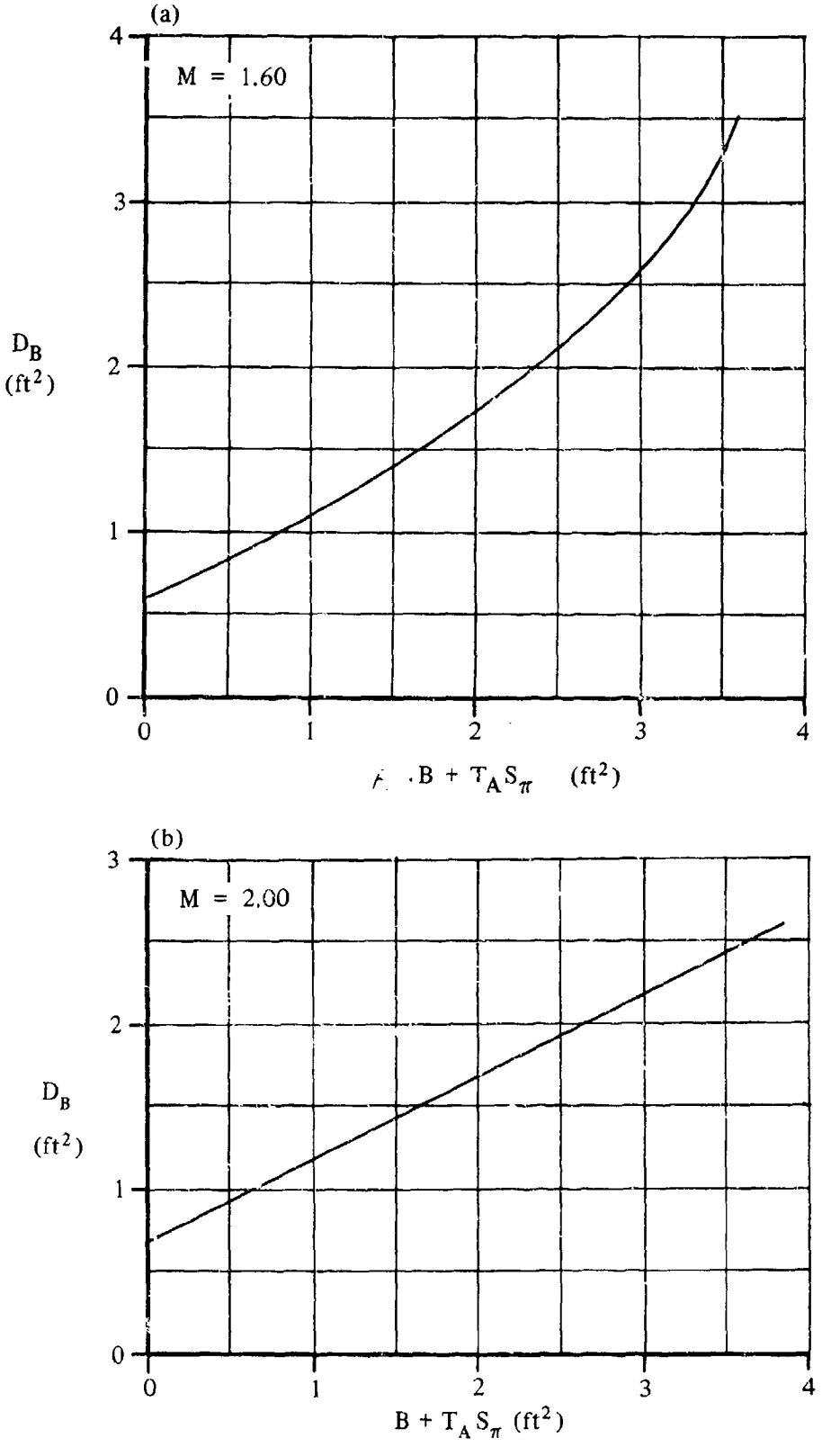

FIGURE 3.2.1.1-59 ZERO-LIFT EQUIVALENT-PARASITE-DRAG AREA FOR A WING-PYLON-MOUNTED SINGLE STORE

3.2.1.2 DRAG DUE TO ADJACENT STORE INTERFERENCE

A method is presented in this section for estimating the zero-lift equivalent-parasite-drag area due to the interference effects of a pair of adjacent store installations. When separate installations are mounted sufficiently close to each other, an interference effect on drag is produced which should be accounted for in the total drag estimate. This effect may be either positive or negative, depending upon the relative positions of the store installations. The effect is computed for each pair of adjacent installations on the aircraft. For example, the aircraft pictured in Sketch (a) would require three computations.

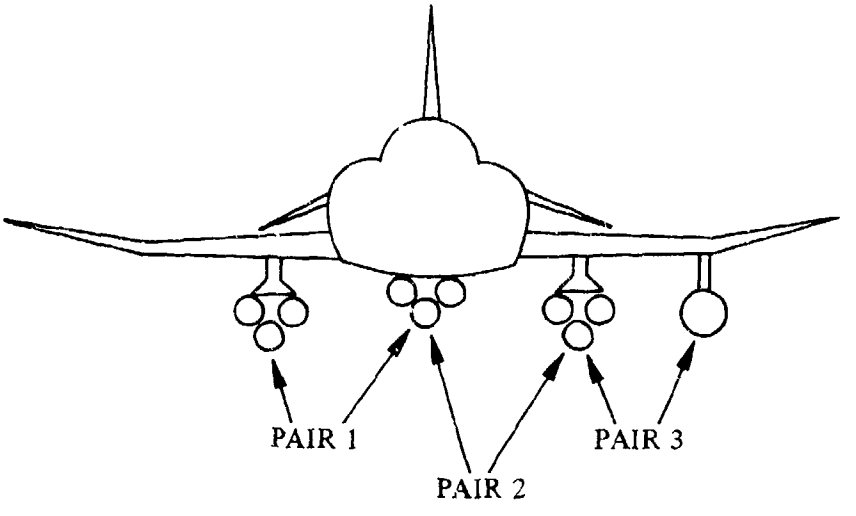

SKETCH (a)

The Datcom Method is taken from Reference 1 and is empirical in nature. The method is applicable to aircraft of conventional design and essentially symmetrical store shapes with no major shape protuberances. The limitations on configuration and Mach-number range are summarized in Table 3.2-A. Caution should be used when extrapolating the curves beyond the given Mach-number range. The method has not been verified for configurations in which flaps, slats, or other flow-disrupting devices are deployed.

A. SUBSONIC

DATCOM METHOD

The zero-lift equivalent-parasite-drag area (ft^2) due to the mutual interference of adjacent store installations per pair of adjacent store installations is given by D_{I_S} where

D_{I_S} is obtained from Figures 3.2.1.2-4a through -4c as a function of Mach number, Y_S, d_{w_L}, d_{w_A}, T_N, and ℓ_{AFT}.

where these terms are illustrated in Sketch (b) and defined as

Y_S is the minimum lateral clearance (in.) between adjacent-store installations (store surface to store surface).

d_{w_L} is the maximum width (in.) of the lead- (most forward) store installation.

d_{w_A} is the maximum width (in.) of the aft-store installation.

T_N is the distance from the nose of the aft-store installation to the tail of the lead-store installation (in.)

ℓ_{AFT} is the length (in.) of the aft-store installation.

It is necessary to use interpolation for Mach numbers not presented in the figures.

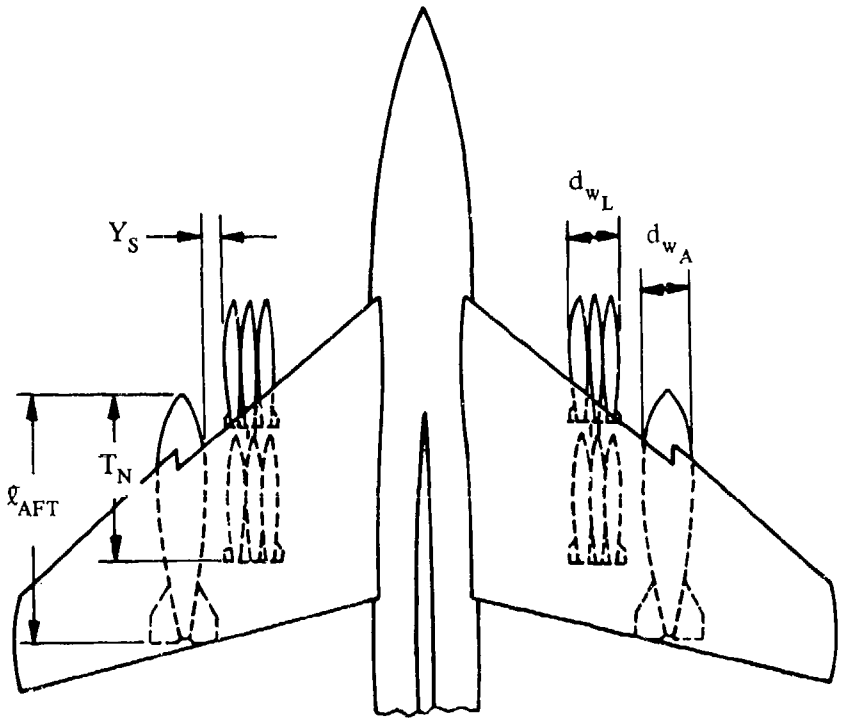

SKETCH (b)

Sample Problem

Given: A swept-wing aircraft symmetrically loaded as shown in Sketch (b).

Stores Data:

Y_S = 10 in. d_{w_L} = 42 in. d_{w_A} = 40 in. T_N = 135 in. ℓ_{AFT} = 205 in.

Additional Data:

M = 0.7

Compute: Referring to Figures 3.2.1.2-4a through -4c, it can be seen that data are presented for M = 0.6, 0.9, and 1.2. It will, therefore, be necessary to obtain D_{I_S} at each of the three Mach numbers and interpolate to obtain the value at M = 0.7.

Compute the independent variables for Figures 3.2.1.2-4a through -4c:

$$\frac{Y_S}{d_{w_L} + d_{w_A}} = \frac{10}{42 + 40} = 0.122$$

$$\frac{T_N}{q_{AFT}} = \frac{135}{205} = 0.659$$

Solution:

At M = 0.6	$D_{I_S} = 0.075$ ft^2	(Figure 3.2.1.2-4a)
At M = 0.9	$D_{I_S} = 0.460$ ft^2	(Figure 3.2.1.2-4b)
At M = 1.2	$D_{I_S} = 0.265$ ft^2	(Figure 3.2.1.2-4c)

Interpolating the above three points at M = 0.7 yields $D_{I_S} = 0.230$ ft^2

B. TRANSONIC

The method presented in Paragraph A of this section is also applicable in the transonic speed range.

C. SUPERSONIC

The method presented in Paragraph A of this section is also applicable in the supersonic speed range. Although no design curves are presented beyond M = 1.2, the existing curves can be cross plotted and extrapolated to M = 1.6 with reasonable success.

REFERENCE

1. Gallagher, R. D., Jimenez, G., Light, L. E., and Thames, F. C.: Technique for Predicting Aircraft Aerodynamic Effects Due to External Stores Carriage. AFFDL-TR-75-95, Volumes I and II, 1975. (U)

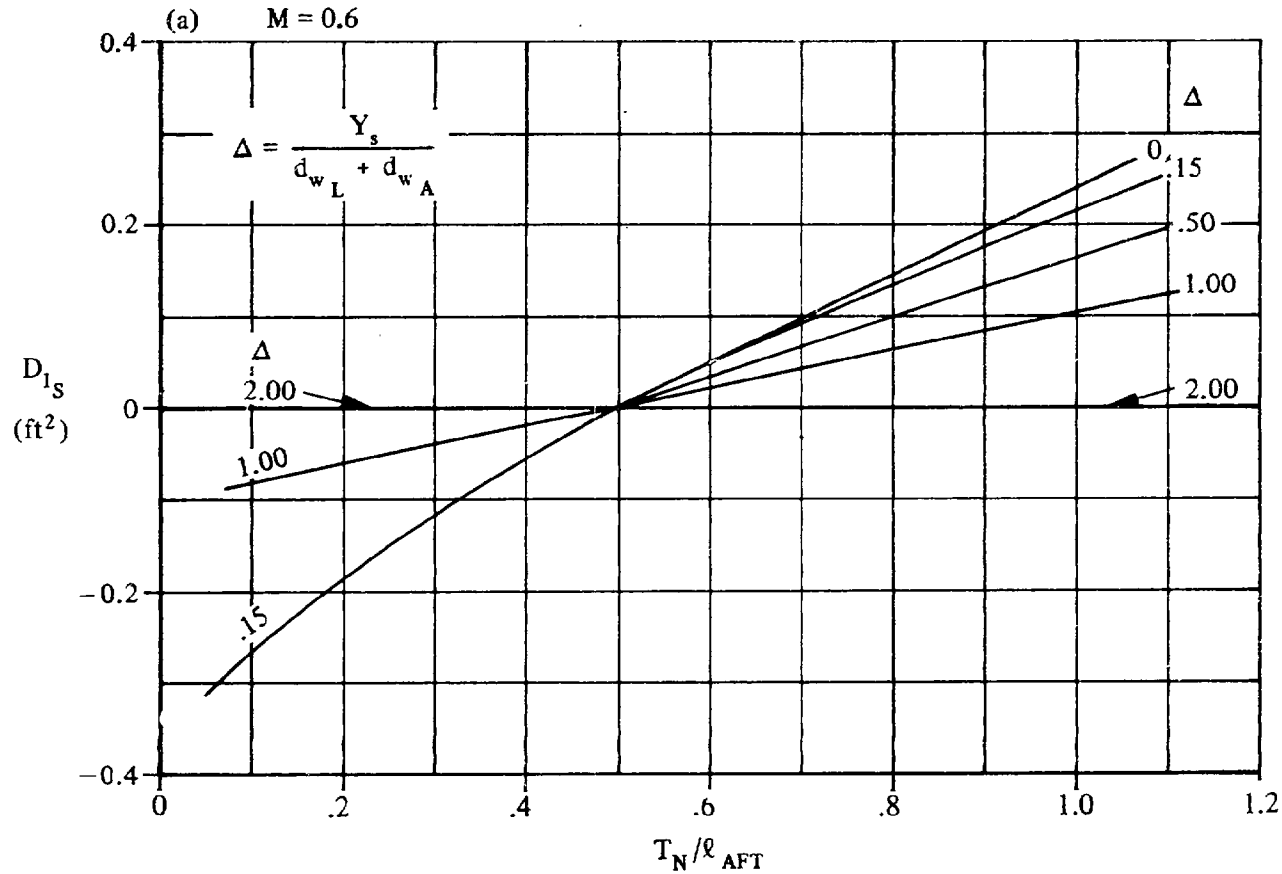

FIGURE 3.2.1.2-4 ZERO-LIFT EQUIVALENT-PARASITE-DRAG AREA DUE TO MUTUAL INTERFERENCE OF ADJACENT STORE INSTALLATIONS

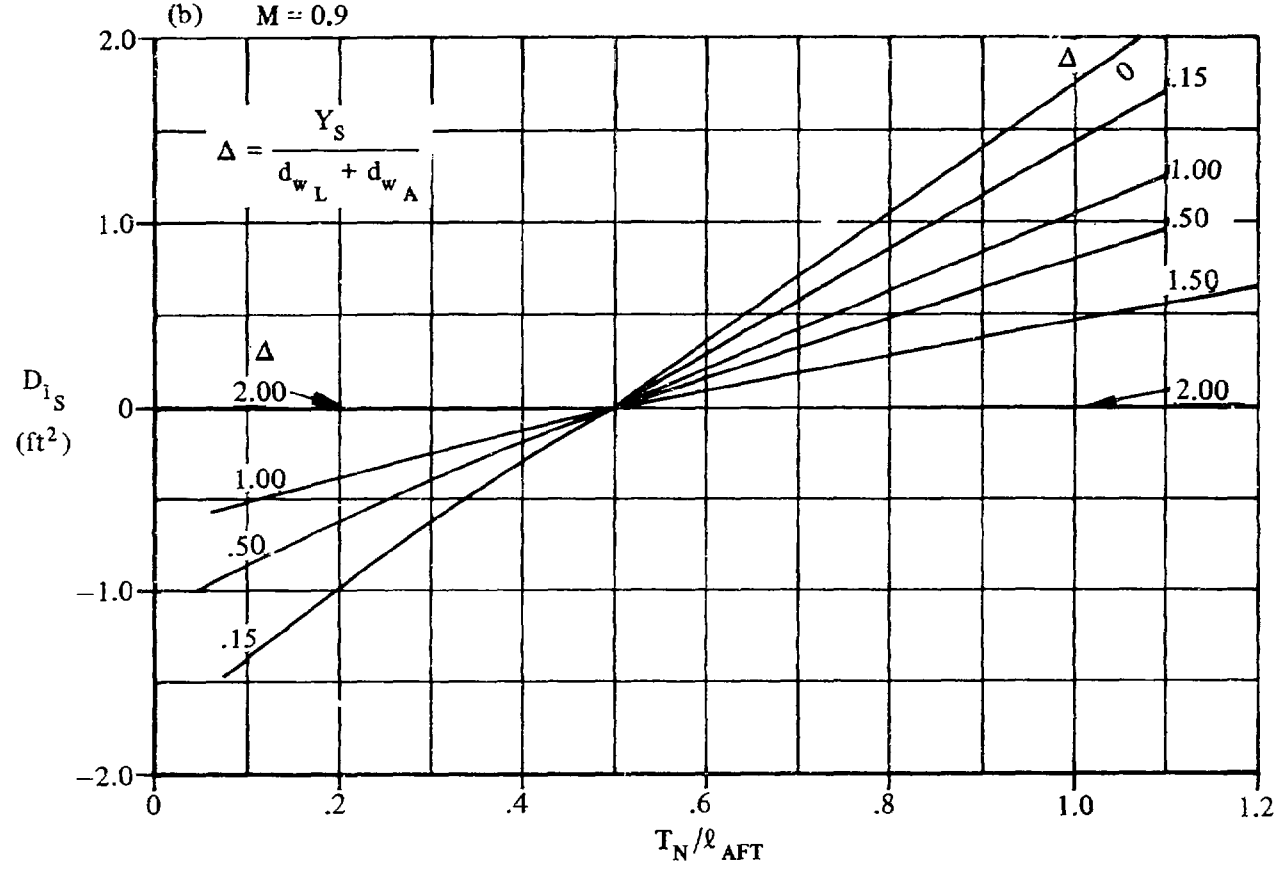

FIGURE 3.2.1.2-4 (CONTD)

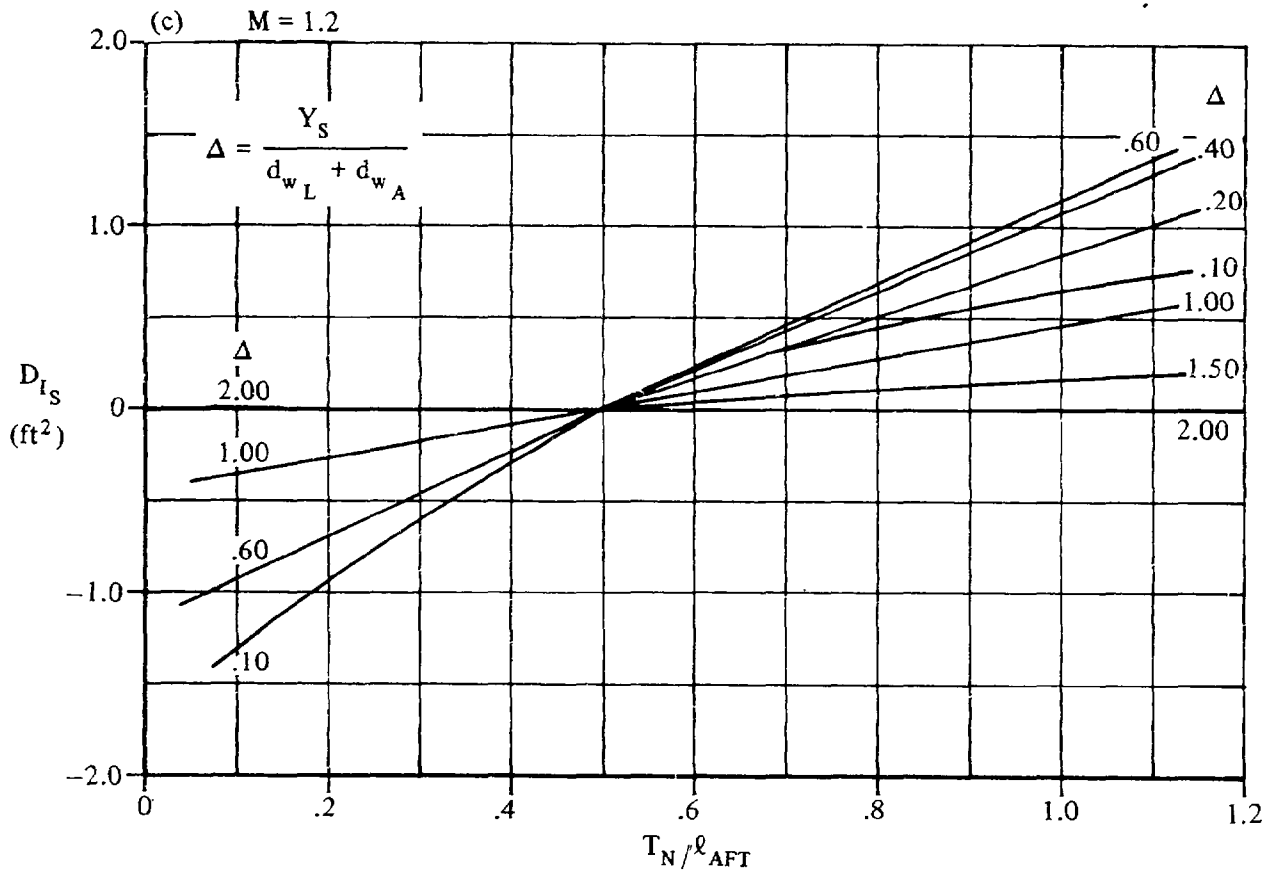

FIGURE 3.1.2-4 (CONTD)

3.2.1.3 DRAG DUE TO FUSELAGE INTERFERENCE

A method is presented in this section for estimating the zero-lift equivalent-parasite-drag area due to the mutual interference effect of a store installation and the adjacent fuselage. This effect is present for wing-mounted stores on high-wing aircraft which are mounted sufficiently close to the fuselage. The interference effect on low-wing aircraft is negligible.

The Datcom Method is taken from Reference 1 and is empirical in nature. The method is applicable to aircraft of conventional design and essentially symmetrical store shapes with no major shape protuberances. The limitations on configuration and Mach-number range are summarized in Table 3.2-A, with the following exception: The method is valid to a maximum Mach number of 0.95. The design curves should not be extrapolated to higher Mach numbers due to the uncertain nature of the interference effects. Caution should be used in extrapolating the curves below M = 0.6. The method has not been verified for configurations in which flaps, slats, or other flow-disrupting devices are deployed.

A. SUBSONIC

DATCOM METHOD

The zero-lift equivalent-parasite-drag area (ft^2) due to the mutual interference of store installation and adjacent fuselage is given by D_{I_f} where D_{I_f} is obtained from Figure 3.2.1.3-3 as a function of Mach number and the minimum clearance between the store installation and the fuselage, ΔY (in.). (See Sketch (a).)

Note that $D_{I_f} = 0$ for low-wing aircraft.

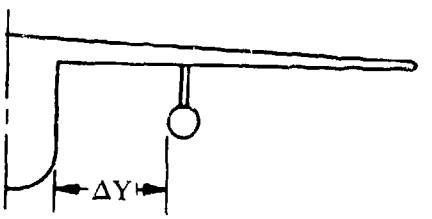

SKETCH (a)

Sample Problem

Given: A high-wing aircraft with a pylon-mounted single store as shown in Sketch (a).

$M = 0.75$ $\Delta Y = 12$ in.

Solution:

$D_{I_f} = 0.290\ ft^2$ (Figure 3.2.1.3-3)

B. TRANSONIC

The method presented in Paragraph A of this section can be applied in the transonic speed range up to a Mach number of 0.95. Extrapolation of the data beyond this Mach number is not recommended due to the uncertain nature of the interference effects.

C. SUPERSONIC

No method is presented to estimate the fuselage-interference effect on drag in the supersonic speed range.

REFERENCE

1. Gallagher, R. D., Jimenez, G., Light, L. E., and Thames, F. C.: Technique for Predicting Aircraft Aerodynamic Effects Due to External Stores Carriage. AFFDL-TR-75-95, Volumes I and II, 1975. (U)

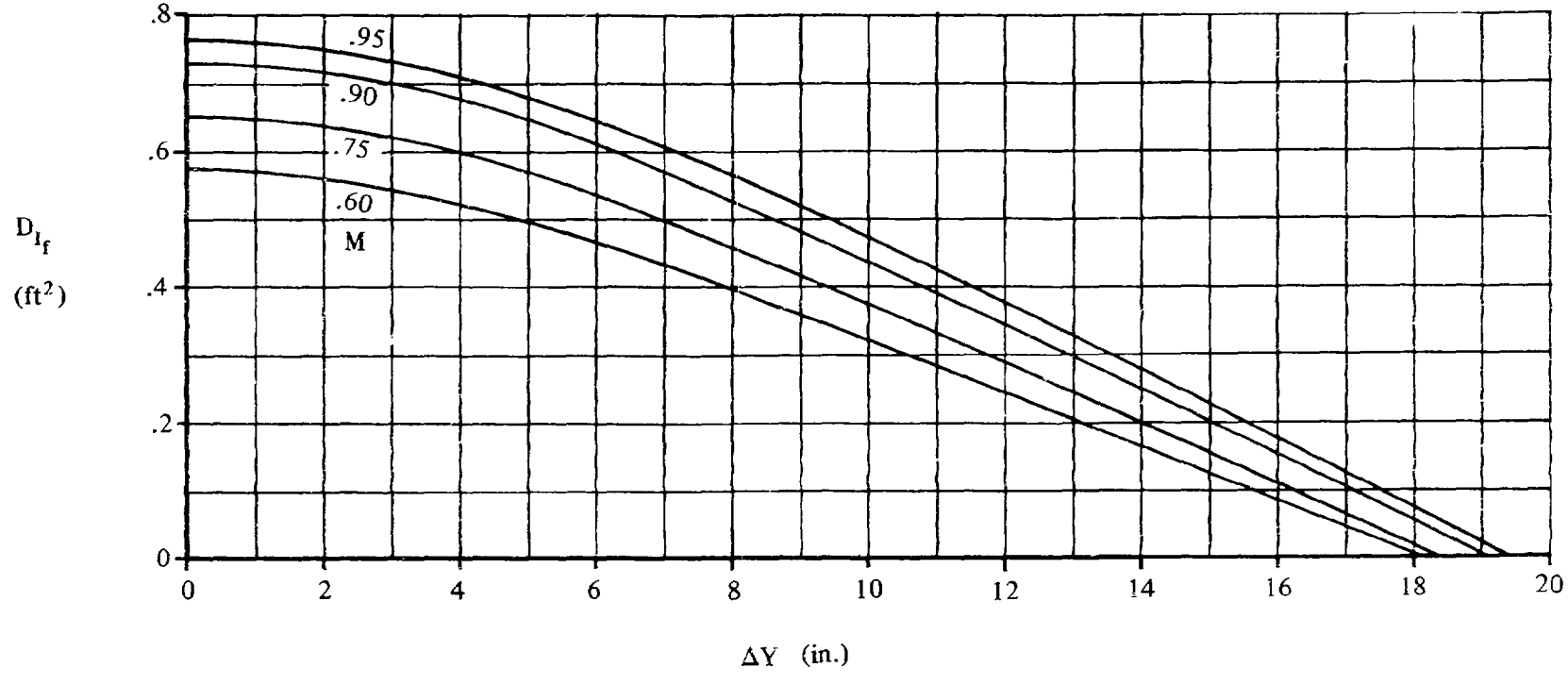

FIGURE 3.2.1.3-3 EQUIVALENT-PARASITE-DRAG AREA DUE TO MUTUAL INTERFERENCE OF STORE INSTALLATION AND ADJACENT FUSELAGE

3.2.2 DRAG DUE TO LIFT

A method is presented in this section for estimating the lift-induced equivalent-parasite-drag area due to an external-store installation. The method is applied separately to each installation (armament station). For all fuselage-mounted store installations, the equivalent-parasite-drag area due to lift is considered to be negligible.

The Datcom Method is taken from Reference 1 and is empirical in nature. The method is applicable to aircraft of conventional design and essentially symmetrical store shapes with no major shape protuberances. The limitations on configuration and Mach-number range are summarized in Table 3.2-A. Additional limitations and assumptions pertaining to the method are listed below:

1. The empirical design curves used in the method do not provide data below M = 0.6, although the method has been verified for some cases below this speed. Caution should be used when extrapolating the curves below the given Mach-number range.

2. The method is not applicable to wing-tip and wing-tangent-mounted stores.

3. The method has not been verified for configurations in which flaps, slats or other flow-disrupting devices are deployed.

4. The angle-of-attack is from zero to cruise angle of attack.

5. The data base used in deriving the method relied heavily on swept-wing tactical-combat-aircraft wind-tunnel data.

6. The method is applicable for sideslip angles less than 4°.

A. SUBSONIC

DATCOM METHOD

The store-installation drag due to lift is a function of aircraft lift coefficient, wing aspect ratio, and an empirical factor. This drag contribution is negative for all configurations for which the method is applicable. For wing-pylon-mounted-store installations, the equivalent-parasite-drag area (ft^2) due to lift is given by

$$D_i = 46.875\, C_L\, A_W\, R_i \qquad 3.2.2\text{-a}$$

where

C_L is the aircraft lift coefficient with store effects based on S_W. This term should be obtained from test data or can be estimated using Sections 3.1.3 and 4.5.1.1.

A_W is the wing aspect ratio, based on the total trapezoidal planform.

R_i is the normalized, incremental drag due to lift obtained from Figure 3.2.2-3 as a function of z, d_w, and Mach number where

z is the maximum depth of the store installation (in.). (See Sketch (a).)

d_w is the maximum width of the store installation (in.). (See Sketch (a).)

It is necessary to use interpolation for Mach numbers not presented in the figures.

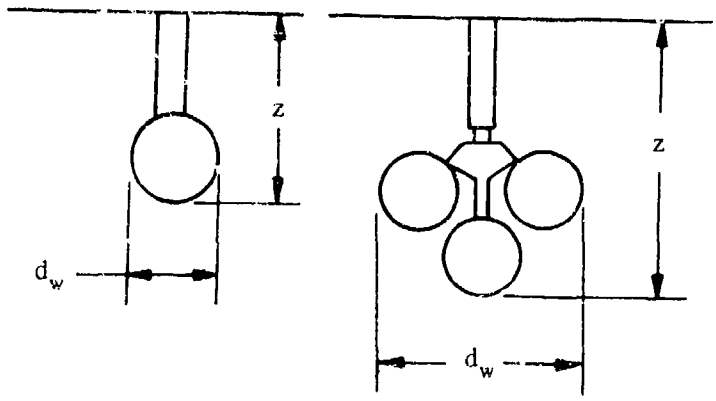

SKETCH (a)

Sample Problem

Given: A swept-wing subsonic fighter aircraft (Reference 2) symmetrically loaded at the inboard-wing stations with pylon-mounted TER's, each containing two 500-lb bombs. This is the same configuration analyzed in the Sample Problem of Paragraph A of Section 3.2.1.1.

Additional Data:

$M = 0.6 \quad \alpha = 8^\circ \quad C_L = 0.185 \quad A_W = 2.91 \quad z = 38.1$ in. $\quad d_w = 25.6$ in.

Compute:

$$\frac{z\, d_w}{144} = \frac{(25.6)(38.1)}{144} = 6.77 \text{ ft}^2$$

$R_i = -0.0025$ (Figure 3.2.2-3)

Solution:

$D_i = 46.875\, C_L\, A_W\, R_i$ (Equation 3.2.2-a)

$= (46.875)(0.185)(2.91)(-0.0025)$

$= -0.063 \text{ ft}^2$

This result is used in the Sample Problem of Paragraph A of Section 3.2.3 as part of the total-drag-increment computation.

B. TRANSONIC

The method presented in Paragraph A of this section is applicable in the transonic speed range.

C. SUPERSONIC

The method presented in Paragraph A of this section is applicable in the supersonic speed range up to a Mach number of 1.6. The user should use caution in extrapolating the method beyond this speed.

REFERENCES

1. Gallagher, R. D., Jimenez, G., Light, L. E., and Thames, F. C.: Technique for Predicting Aircraft Aerodynamic Effects Due to External Stores Carriage. AFFDL-TR-75-95, Volumes I and II, 1975. (U)

2. Watzke, R. E.: Aerodynamic Data for Model TA-4F Operational Flight Trainer. McDonnell Douglas Corporation Report DAC-67425, 1968. (U)

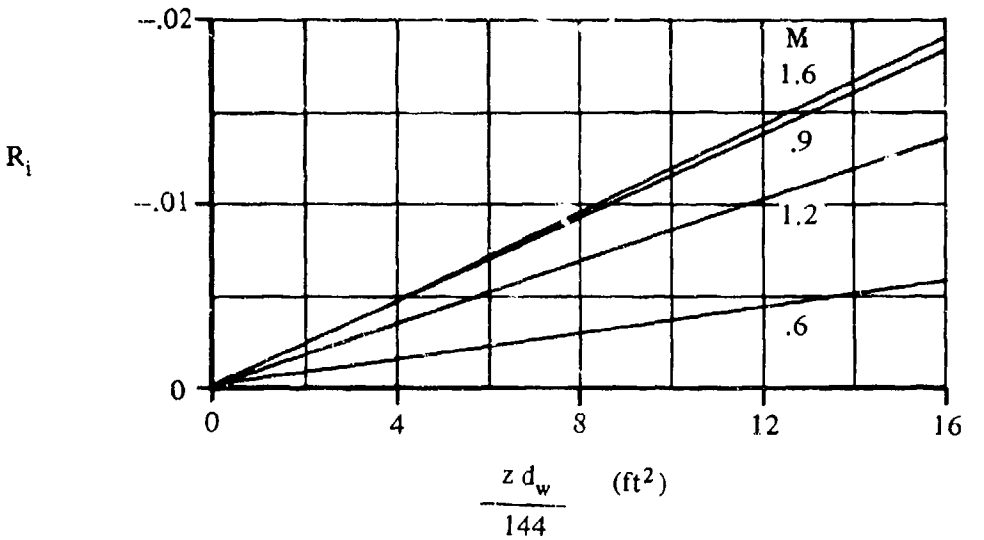

FIGURE 3.2.2-3 NORMALIZED INCREMENTAL DRAG DUE TO LIFT

3.2.3 TOTAL DRAG INCREMENT DUE TO EXTERNAL STORES

A method is presented in this section for estimating the total incremental change in aircraft drag coefficient due to external-store installations. The method predicts the increments for symmetric, asymmetric, and multiple-installation loading configurations. The total drag increment is the sum of the incremental drag at zero lift and the incremental drag due to lift. These components are computed in terms of equivalent-parasite-drag area for each installation by the methods of Sections 3.2.1 and 3.2.2, and combined to obtain the total-drag-coefficient increment by the method of this section.

The Datcom Method is taken from Reference 1 and is empirical in nature. The method is applicable to aircraft of conventional design and essentially symmetrical store shapes with no major shape protuberances. The limitations on configuration and Mach-number range are summarized in Table 3.2-A. Additional limitations and assumptions pertaining to the method are listed below:

1. The method has been verified for the Mach-number range given in Table 3.2-A. The user should use caution in extrapolating the empirical curves beyond the given Mach-number range.

2. The method is not applicable to wing-tip and wing-tangent-mounted stores.

3. The method has not been verified for configurations in which flaps, slats, or other flow-disrupting devices are deployed.

4. The angle-of-attack range is from zero to cruise angle of attack.

5. The data base used in deriving the method relied heavily on swept-wing tactical-combat-aircraft wind-tunnel data.

6. The method is applicable for sideslip angles less than 4^{o}.

The procedure for computing the total-drag-coefficient increment is a summation process in which equivalent-parasite-drag areas for each store installation (armament station) are added together and divided by the wing reference area. Zero-lift-drag contributions are computed by the methods of Section 3.2.1. These include contributions of the basic installation (computed in Section 3.2.1.1), adjacent-store interference (computed in Section 3.2.1.2), and fuselage interference (computed in Section 3.2.1.3). Drag-due-to-lift contributions are computed in Section 3.2.2.

A. SUBSONIC

DATCOM METHOD

The total-aircraft drag-coefficient increment due to external-store installations and based on wing reference area, S_W, is given by

$$\Delta C_D = \frac{1}{S_W}\left\{\sum_{j=1}^{N_I}(D_B)_j + \sum_{k=0}^{N_P}\left(D_{I_S}\right)_k + \sum_{\ell=0}^{N_F}\left(D_{I_f}\right)_\ell + \sum_{m=1}^{N_I}(D_i)_m\right\} \qquad 3.2.3\text{-a}$$

where

S_W is the aircraft wing reference area (ft^2).

N_I is the total number of store installations on the aircraft.

$(D_B)_j$ is the zero-lift equivalent-parasite-drag area (ft^2) at installation j, computed in Section 3.2.1.1.

N_P is the total number of pairs of adjacent-store installations carried. (See Sketch (a).)

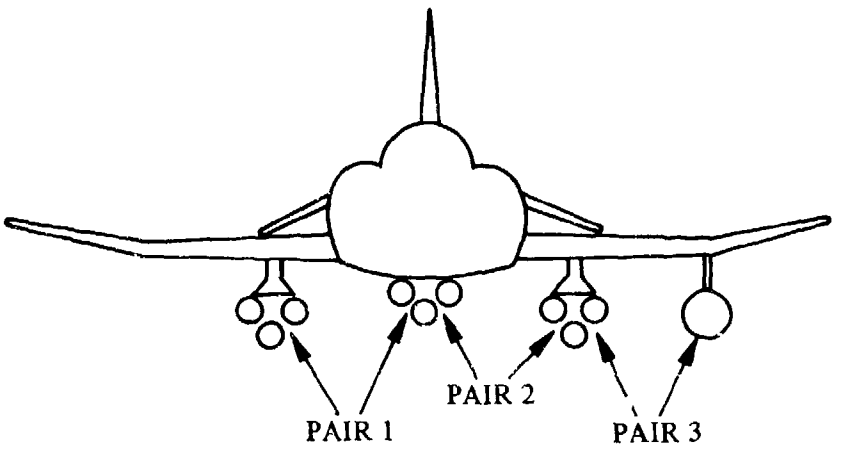

SKETCH (a)

$\left(D_{I_S}\right)_k$ is the zero-lift equivalent-parasite-drag area (ft^2) due to the mutual interference of adjacent-store installations for pair k, computed in Section 3.2.1.2.

N_F is the number of store installations adjacent to the fuselage.

$\left(D_{i_f}\right)_\ell$ is the zero-lift equivalent-parasite-drag area (ft^2) due to the mutual interference of store installation ℓ and adjacent fuselage, computed in Section 3.2.1.3.

$(D_i)_m$ is the drag-due-to-lift equivalent-parasite-drag area (ft^2) at installation m, computed in Section 3.2.2.

Reference 1 states that prediction errors for store incremental-drag are nominally 10 to 15 percent, resulting in an overall accuracy within 5 percent of the total-aircraft-drag coefficient. A comparison of test data with results calculated by this method is provided in Table 3.2.3-A. Additional comparisons of test and calculated results are found in Reference 1.

Sample Problem

Given: A swept-wing subsonic fighter aircraft (Reference 2) symmetrically loaded at the inboard-wing stations with pylon-mounted TER's, each containing two 500-lb bombs. This is the same low-wing configuration presented in the Sample Problems of Paragraph A of Section 3.2.1.1 and Paragraph A of Section 3.2.2.

Additional Characteristics:

$M = 0.6$ $\quad S_W = 260\ ft^2$

(Additional geometric data are provided in the Sample Problems of Sections 3.2.1.1 and 3.2.2.)

$D_B = 1.498\ ft^2$ (1 side) (Sample Problem, Paragraph A, Section 3.2.1.1)

$D_i = -0.063\ ft^2$ (1 side) (Sample Problem, Paragraph A, Section 3.2.2)

$D_{I_f} = 0$ (low-wing configuration)

Compute:

$N_I = 2$ (two store installations)

$N_P = 0$ (No pairs of adjacent store installations)

$N_F = 2$

Solution:

$$\Delta C_D = \frac{1}{S_W}\left\{\sum_{j=1}^{N_I}(D_B)_j + \sum_{k=1}^{N_P}\left(D_{I_S}\right)_k + \sum_{\ell=1}^{N_F}\left(D_{I_f}\right)_\ell + \sum_{m=1}^{N_I}(D_i)_m\right\} \quad \text{(Equation 3.2.3-a)}$$

Expanding and noting that $N_P = 0$ and $\left(D_{I_f}\right)_\ell = 0$,

$$\Delta C_D = \frac{1}{S_W}\left[(D_B)_1 + (D_B)_2 + (D_i)_1 + (D_i)_2\right]$$

$$= \frac{1}{S_W}\left[2D_B + 2D_i\right] \quad \text{(symmetrical installations)}$$

$$= \frac{1}{260}\left[(2)(1.498) + (2)(-0.063)\right]$$

$$= 0.0110$$

Values of ΔC_D at other Mach numbers are shown in comparison to test data from Reference 2 in Sketch (b).

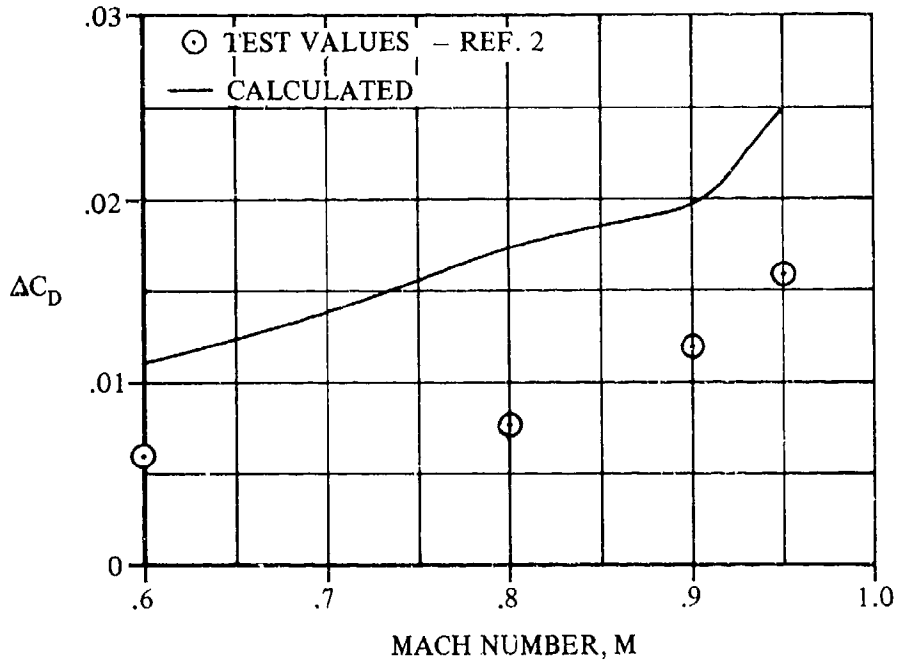

SKETCH (b)

B. TRANSONIC

The method presented in Paragraph A of this section is also valid in the transonic speed range. The user is cautioned that due to the difficulties of predicting drag in the transonic region (especially interference effects), the method is generally less accurate than in the subsonic and supersonic speed ranges.

C. SUPERSONIC

The method presented in Paragraph A of this section is also valid in the supersonic speed range up to the Mach-number limits indicated in Table 3.2-A. Caution should be used when extrapolating data from the figures beyond the given Mach-number range since the method has not been substantiated beyond these limits.

REFERENCES

1. Gallagher, R. D., Jimenez, G., Light, L. E., and Thames, F. C.: Technique for Predicting Aircraft Aerodynamic Effects Due to External Stores Carriage. AFFDL-TR-75-95, Volumes I and II, 1975. (U)

2. Wetzke, R. E.: Aerodynamic Data for Model TA-4F Operational Flight Trainer. McDonnell Douglas Corporation Rept. DAC-67425, 1968. (U)

3. Bonine, W. J., et al.: Model F/RF-4B-C Aerodynamic Derivatives. McDonnell Douglas Corporation Rept. 9842, 1964 (Rev. 1971). (U)

TABLE 3.2.3-A

SUBSONIC EXTERNAL-STORE DRAG
DATA SUMMARY AND SUBSTANTIATION

Ref	Loading Description	α	M	ΔC_D calc	ΔC_D test	ΔC_D calc-test
2	Wing Station Mounting Left Inboard Pylon: Empty	Cruise	0.6	0.00061	0.00060	0.00001
		↓	0.8	0.00066	0.00071	−0.00005
			0.9	0.00087	0.00090	−0.00003
			0.95	0.00113	0.00105	0.00008
	Fuselage Station Mounting Centerline Pylon: Empty	Cruise	0.6	0.00044	0.00061	−0.00017
		↓	0.8	0.00052	0.00076	−0.00024
			0.9	0.00067	0.00098	−0.00031
			0.95	0.00084	0.00117	−0.00033
	Wing Station Mounting Left Inboard Pylon-Mounted Single: 500-lb bomb	Cruise	0.6	0.00141	0.00090	0.00051
		↓	0.8	0.00139	0.00111	0.00028
			0.9	0.00169	0.00195	−0.00026
	Wing Station Mounting Left Inboard Pylon-Mounted TER: 2 500-lb bombs Right Inboard Pylon-Mounted TER: 2 500-lb bombs	Cruise	0.6	0.0110	0.0058	0.0052
		↓	0.8	0.0172	0.0076	0.0096
			0.9	0.0195	0.0117	0.0078
			0.95	0.0250	0.0166	0.0084
	Wing Station Mounting Left Inboard Pylon-Mounted MER: Empty	Cruise	0.6	0.00308	0.00270	0.00038
		↓	0.8	0.00446	0.00344	0.00102
			0.9	0.00540	0.00490	0.00050
			0.95	0.00582	0.00605	−0.00023
3	Fuselage Station Mounting Tangent-Mounted Tandem: 4 missiles	Cruise	0.6	0.00097	0.00100	−0.00003

$$\text{Average Error} \sum \frac{\left|\Delta C_{D_{\text{Calc-Test}}}\right|}{n} = 0.00180$$

3.3 EFFECT OF EXTERNAL STORES ON AIRCRAFT NEUTRAL POINT

Methods are presented in this section for estimating the incremental shift in aircraft neutral point due to external-store installations. By computing a neutral-point shift due to external stores, the methods are actually indicating a stability change in terms of a change in slope of the $C_M - C_L$ curve. For most configurations the effect of store loadings is to destabilize the basic aircraft, although some loadings can result in a stabilizing tendency. The methods are taken from Reference 1 and are empirical in nature.

Section 3.3 is subdivided as follows:

Section 3.3.1 Neutral-Point Shift Due to Lift Transfer from Clean Aircraft.
Section 3.3.2 Neutral-Point Shift Due to Interference Effects on Wing Flow Field.
Section 3.3.3 Neutral-Point Shift Due to Change in Tail Effectiveness.
Section 3.3.4 Total Neutral-Point Shift Due to External Stores.

The total neutral-point shift is the sum of the shifts computed by the methods of Sections 3.3.1, 3.3.2, and 3.3.3.

The Datcom Methods are applicable to aircraft of conventional design and essentially symmetrical store shapes with no major shape protuberances. The methods are limited to the store-loading configurations and Mach-number range presented in Table 3.3-A. The methods are applicable to mixed loading configurations obtained by combining two or more loadings specified in Table 3.3-A. The methods are subject to additional limitations specifically noted in each of the sections that follow.

TABLE 3.3-A

LOADING AND FLIGHT CONDITION LIMITATIONS

Mounting Location	Carriage Mode	Carriage Rack	Mach Number Range	C_L Range
Wing	Single	Pylon	0.6 → 2.0	0 → 0.2
	Multiple	MER – Fully Loaded	0.6 → 1.6	
		MER – Partially Loaded		
		TER – Fully Loaded		
		TER – Partially Loaded		
Fuselage (Centerline)	Single	Pylon		
		Tangent Mounted		
	Multiple	Pylon + MER		
		Tangent MER		

REFERENCE

1. Gallagher, R. D., Jimenez, G., Light, L. E., and Thames, F. C.: Technique for Predicting Aircraft Aerodynamic Effects Due to External Stores Carriage, AFFDL-TR-75-95, Volumes I and II, 1975. (U)

3.3.1 NEUTRAL-POINT SHIFT DUE TO LIFT TRANSFER FROM STORE INSTALLATION TO CLEAN AIRCRAFT

A method is presented in this section for estimating the neutral-point shift due to the transfer of the lifting characteristics from the external-store installations to the clean aircraft. The method predicts a neutral-point shift due to all installations (armament stations) on the aircraft. Wing-flow-field interference and horizontal-tail effects are not included in this section (see Sections 3.3.2 and 3.3.3).

The Datcom Method is taken from Reference 1 and is basically theoretical in concept with empirically-determined factors and coefficients. The method is applicable to aircraft of conventional design and essentially symmetrical store shapes with no major shape protuberances. The limitations on configuration and Mach-number range are summarized in Table 3.3-A. Additional limitations and assumptions pertaining to the method are listed below:

1. The method is not applicable to wing-tip or wing-tangent-mounted stores.

2. The method has been verified for the Mach-number range given in Table 3.3-A. Caution should be used in extrapolating the empirical curves beyond the given Mach-number range.

3. The method has not been verified for configurations in which flaps, slats or other flow-disrupting devices are deployed.

4. The method gives the best results for an angle-of-attack range from 0 to 8^{o}, although the method can be used for higher angles of attack.

5. The data base used in deriving the method relied heavily on swept-wing tactical-combat-aircraft wind-tunnel data.

6. The method is applicable for sideslip angles less than 4^{o}.

7. Fuselage-mounted installations must be located on the fuselage centerline.

8. The method is not applicable to empty multiple racks.

9. The effect of empty pylons on neutral point is considered to be negligible.

The effect due to a pair of symmetrical installations can be computed by doubling the effect of one side.

A. SUBSONIC

DATCOM METHOD

The neutral-point shift in inches, positive for aft shift, due to the transfer of lift from the store installations to the clean aircraft is given by

$$\Delta x_{n.p._1} = \frac{\sum_{i=1}^{N_I} \sum_{j=1}^{n_{s_i}} K_{S_{ij}} C_{L_{\alpha_{S_{ij}}}} \left(x_{S_{ij}} - x_{a.c.}\right)}{C_{L_{\alpha_{WB}}} + \sum_{i=1}^{N_I} \sum_{j=1}^{n_{s_i}} K_{S_{ij}} C_{L_{\alpha_{S_{ij}}}}} \qquad 3.3.1\text{-a}$$

where

N_I is the total number of store installations.

i is the store-installation number.

n_{s_i} is the number of store stations on installation i (including empty stations).

j is the store number on installation i.

$C_{L_{\alpha_{S_{ij}}}}$ is the free-stream lift-curve slope of store j on installation i given by

$$C_{L_{\alpha_{S_{ij}}}} = \frac{375}{S_W}\left[\left(C_{L_\alpha}\right)_{SB}\left(K_{NB}\right) + \left(C_{L_\alpha}\right)_{SF}\right] \text{ (per deg)} \qquad 3.3.1\text{-b}$$

where

S_W is the aircraft wing reference area (ft^2).

$\left(C_{L_\alpha}\right)_{SB}$ is the store-body lift-curve slope (per deg) obtained from Figure 3.3.1-16 as a function of store-body planform area, S_p ($in.^2$).

K_{NB} is a nose-shape parameter given by

$$K_{NB} = 1.0 \text{ for } \theta_n \leqslant 22^o \qquad 3.3.1\text{-c}$$

$$K_{NB} = 1.0 + 0.65\,\frac{(\theta_n - 22)}{68} \text{ for } 22^o < \theta_n \leqslant 90^o \qquad 3.3.1\text{-d}$$

where

θ_n is the store-nose half-cone angle (deg).

$\left(C_{L_\alpha}\right)_{SF}$ is the store-fin lift-curve slope (per deg) given by

$$\left(C_{L_\alpha}\right)_{SF} = (0.191)(10^{-6})(B_e)^2 \qquad 3.3.1\text{-e}$$

where

$$B_e = 0 \text{ for } b_F \leqslant d_S \qquad 3.3.1\text{-f}$$

$$B_e = b_F - d_S \text{ for } b_F > d_S \qquad 3.3.1\text{-g}$$

where b_F and d_S are the store-fin span and maximum store diameter (in.), respectively.

$x_{S_{ij}}$ is the distance (in.) from the leading edge of the mean aerodynamic chord $\bar{c}$, to the point midway between the mounting lugs of the installed store for store j on installation i, positive in the aft direction. (See Sketch (a).)

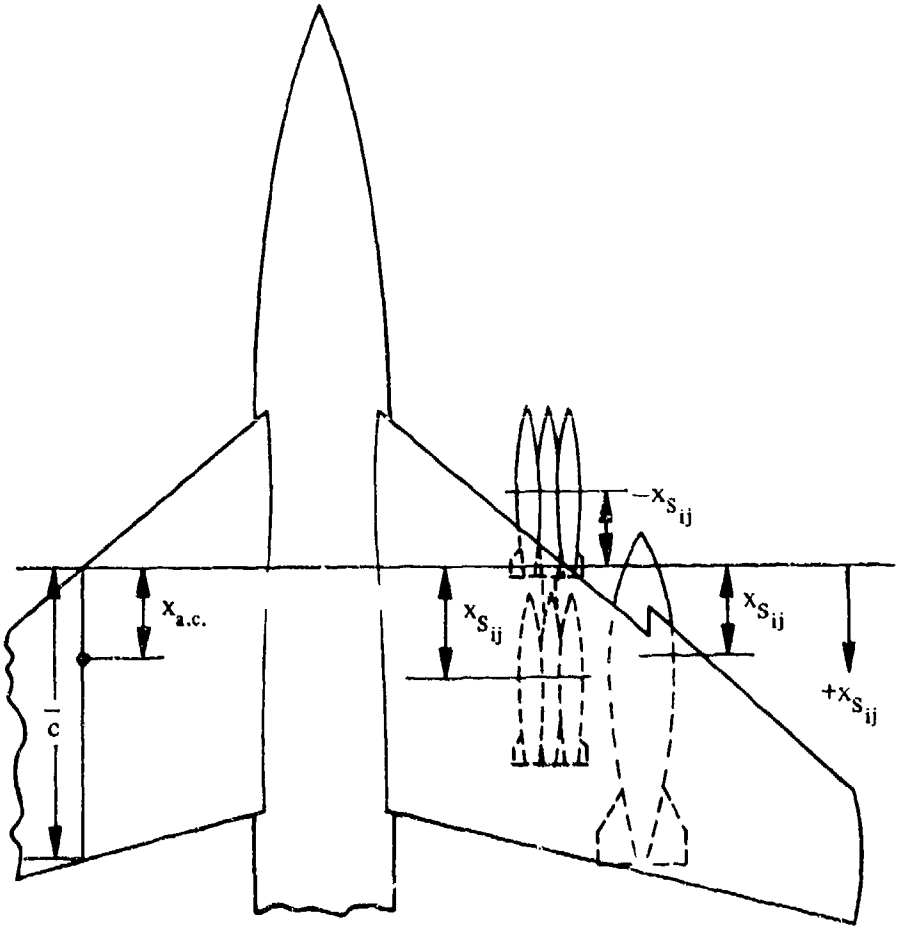

SKETCH (a)

$x_{a.c.}$ is the wing-body aerodynamic-center location of the clean aircraft measured from the leading edge of the wing mean aerodynamic chord (in.). (See Sketch (a).) This value should be obtained from test data or estimated by using Section 4.3.2.2.

$C_{L_{\alpha_{WB}}}$ is the wing-body clean-aircraft lift-curve slope (per deg) obtained from test data or estimated by using Section 4.3.1.2.

$K_{S_{ij}}$ is an empirical factor related to installation type, mounting position, and Mach number and is specified as follows:

1. Wing-Pylon-Mounted Single Store:

In this case $n_{s_i} = 1$ and hence j = 1.

$$K_{S_{ij}} = F_1\left(\bar{x}_{SN_{ij}}, F_R\right) + F_2\left(\bar{x}_{SN_{ij}}, z_{ij}, F_R\right) \quad i = 1, \ldots N_I \qquad 3.3.1\text{-h}$$

where $F_1\left(\bar{x}_{SN_{ij}} F_R\right)$ is a parameter based on store longitudinal placement and fin-area ratio obtained from Figure 3.3.1-17.

where

$$\bar{x}_{SN_{ij}} = \frac{x_{SN_{ij}}}{c_{ij}} \text{ for } j = 1 \qquad 3.3.1\text{-i}$$

where

$x_{SN_{ij}}$ is the distance from the local wing leading edge to nose of store j on installation i, positive in the aft direction (in.). (See Sketch (b).)

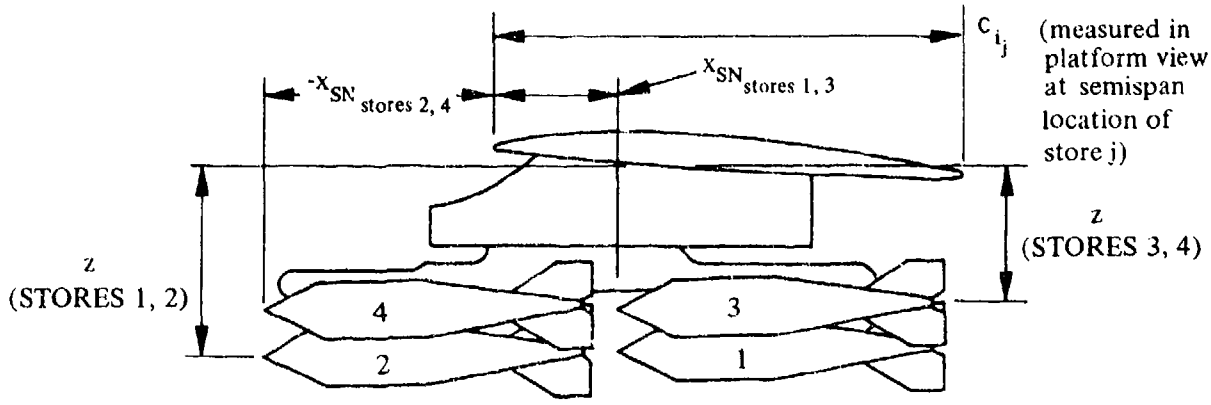

SKETCH (b)

c_{ij} is the local wing chord at the semispan location of store j on store installation i, (in.). (See Sketch (b).)

F_R is given by

$$F_R = \frac{S_F}{S_p} \qquad 3.3.1\text{-j}$$

where

S_F is the store-fin area projected onto a horizontal plane ($in.^2$).

S_p is the store-body planform area ($in.^2$).

$F_2\left(\bar{x}_{SN_{ij}}, \bar{z}_{ij}, F_R\right)$ is given by

$$F_2\left(\bar{x}_{SN_{ij}}, \bar{z}_{ij}, F_R\right) = F_{21}\left(\bar{x}_{SN_{ij}}\right) F_{22}(\bar{z}_{ij})\, F_{23}(F_R) \qquad 3.3.1\text{-k}$$

where

$F_{21}\left(\bar{x}_{SN_{ij}}\right)$ is a store longitudinal-placement factor obtained from Figure 3.3.1-18a where $\bar{x}_{SN_{ij}}$ is given by Equation 3.3.1-i.

$F_{22}(\bar{z}_{ij})$ is a store vertical-placement factor obtained from Figure 3.3.1-18b where $\bar{z}_{ij}$ is obtained from

$$\bar{z}_{ij} = \frac{z_{ij}}{c_{ij}} \text{ for } j = 1 \qquad 3.3.1\text{-}\ell$$

where

z_{ij} is the vertical distance from the average wing lower surface location to the centerline of store j on installation i, positive in downward direction (in.). (See Sketch (b).)

c_{ij} is the local wing chord at the semispan location of store j on store installation i (in.). (See Sketch (b).)

$F_{23}(F_R)$ is a store-fin area-ratio factor obtained from Figure 3.3.1-19a where F_R is given by Equation 3.3.1-j.

2. Wing-Pylon-Mounted TER (For TER installations it is essential that the store stations be identified in the same manner as indicated in Sketch (c).)

$$K_{S_{ij}} = F_1\left(\bar{x}_{SN_{ij}}\right) + F_2(M, j) \quad j = 1, 2, 3 \qquad 3.3.1\text{-m}$$

where

$F_1\left(\bar{x}_{SN_{ij}}\right)$ is a store longitudinal-placement parameter for TER carriage obtained from Figure 3.3.1-19b where $\bar{x}_{SN_{ij}}$ is given by Equation 3.3.1-i.

$F_2(M, j)$ is the TER Mach and store-station effect parameter obtained from Figures 3.3.1-20a through -20c as a function of Mach number and TER store-station number, j, where j refers to the TER station number defined in Sketch (c).

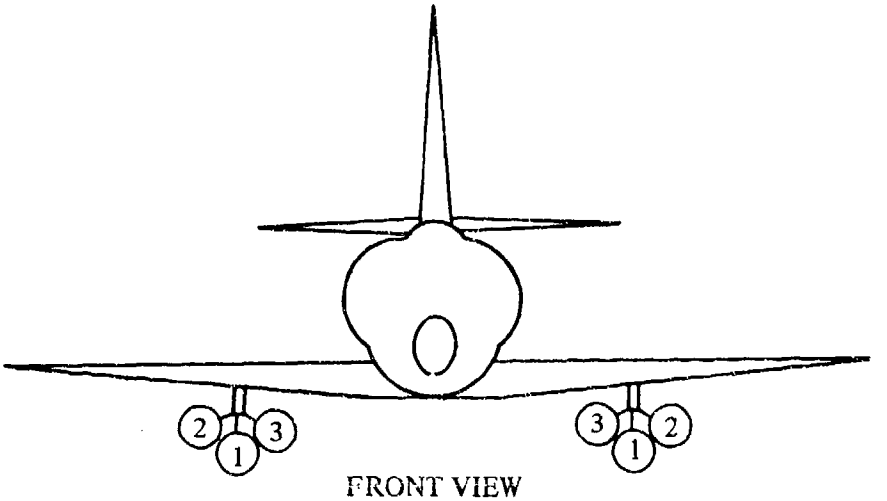

FRONT VIEW

SKETCH (c)

3. Wing-Pylon-Mounted MER (For MER installations it is essential that the store stations be identified in the same manner as indicated in Sketch (d).)

$$K_{S_{ij}} = F_1\left(\bar{x}_{SN_{ij}}\right) + F_2\left(\bar{x}_{SN_{ij}}, \bar{z}_{ij}, M\right) + F_3(M, j) \qquad 3.3.1\text{-n}$$

where

$F_1\left(\bar{x}_{SN_{ij}}\right)$ is a store longitudinal-placement parameter for MER carriage obtained from Figure 3.3.1-21 where $\bar{x}_{SN_{ij}}$ is given by Equation 3.3.1-i.

$F_2\left(\bar{x}_{SN_{ij}}, \bar{z}_{ij}, M\right)$ is given by

$$F_2\left(\bar{x}_{SN_{ij}}, \bar{z}_{ij}, M\right) = F_{21}\left(\bar{x}_{SN_{ij}}\right) F_{22}(\bar{z}_{ij})\, F_{23}(M) \qquad 3.3.1\text{-o}$$

where $\bar{z}_{ij}$ is defined by Equation 3.3.1-ℓ, and

$F_{21}\left(\bar{x}_{SN_{ij}}\right)$ is a MER store longitudinal-placement factor obtained from Figures 3.3.1-22a and -22b.

$F_{22}(\bar{z}_{ij})$ is a MER store vertical-placement factor obtained from Figures 3.3.1-23a and -23b.

$F_{23}(M)$ is a MER Mach-effect factor obtained from Figures 3.3.1-24a and -24b.

$F_3(M, j)$ is the MER Mach and store-station effect parameter obtained from Figures 3.3.1-25a through -25f as a function of Mach number and MER store-station number, j, where j refers to the MER store-station number defined in Sketch (d).

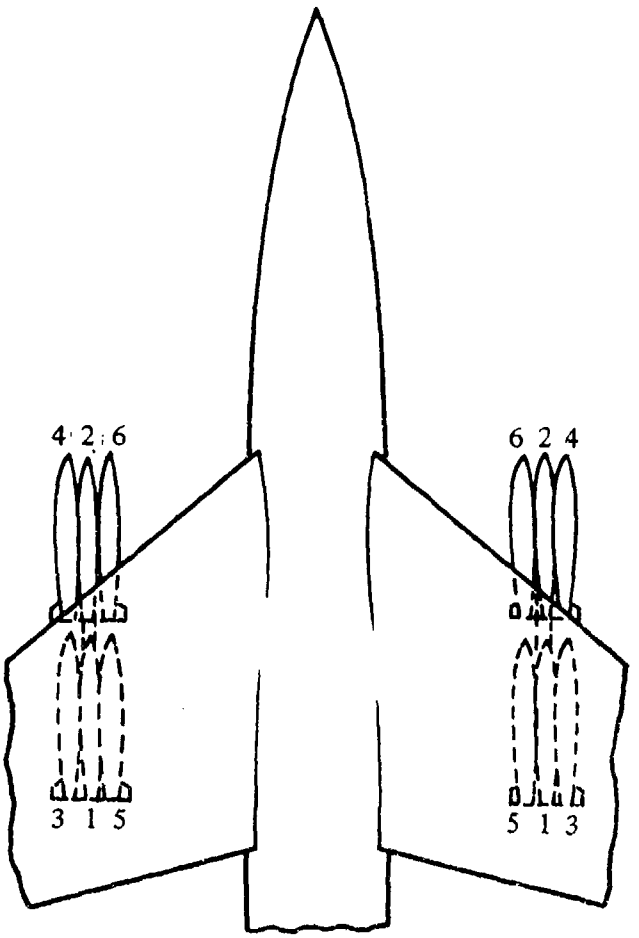

TOP VIEW

SKETCH (d)

4. Fuselage-Centerline-Mounted Single Carriage

In this case $n_{s_j} = 1$ and hence j = 1

$$K_{S_{ij}} = 0.10 \qquad 3.3.1\text{-p}$$

5. Fuselage-Centerline-Tangent-Mounted MER (For fuselage MER installations, use the right wing numbering scheme of Sketch (d) for numbering the store station locations.)

$$K_{S_{ij}} = I_{S_j} [F_1(M) + F_2(M, j)] \quad (j = 1, 2, 3, 4, 5, 6) \qquad 3.3.1\text{-q}$$

where j coincides with the MER station number defined by Sketch (d).

For j = 1, 2

$$I_{S_j} = 1.0 \qquad 3.3.1\text{-r}$$

For j = 3, 4, 5, 6

I_{S_j} is a neutral-point correlation factor for stores on a MER installation obtained from Figure 3.3.1-27a as a function of d_{wing}/c_r where d_{wing} is the distance (in.) from the fuselage lower surface at the store midpoint to the average wing lower surface at the wing root and c_r is the wing root chord (in.).

$F_1(M)$ is a MER Mach-effect factor for fuselage-tangent-mounted installations obtained from Figure 3.3.1-27b as a function of Mach number.

$F_2(M, j)$ is a MER Mach and store-station effect parameter for fuselage-tangent-mounted installations obtained from Figures 3.3.1-28a through -28d as a function of Mach number and MER station, j.

6. Fuselage-Centerline-Pylon-Mounted MER (For fuselage MER installations, use the right wing numbering scheme of Sketch (d) for numbering the store station locations.)

For j = 1, 3, 5 where j are the MER stations defined in Sketch (d),

$$K_{S_{ij}} = I_{S_j} F_1(M) \qquad 3.3.1\text{-s}$$

where

I_{S_j} is defined for Configuration 5.

$F_1(M)$ is a MER Mach-effect factor for fuselage-pylon-mounted installations obtained from Figure 3.3.1-30a as a function of Mach number and MER station, j.

For j = 2,

$$K_{S_{ij}} = F_1(M) \qquad 3.3.1\text{-t}$$

where

$F_1(M)$ is obtained from Figure 3.3.1-45b

For j = 4, 6

$$K_{S_{ij}} = I_{S_j} [F_1(M) + F_2(M, j)] \qquad 3.3.1\text{-u}$$

where

I_{S_j} is defined for Configuration 5.

$F_1(M)$ is a MER Mach-effect factor for fuselage-pylon-mounted installations obtained from Figure 3.3.1-30b as a function of Mach number and MER station, j.

$F_2(M, j)$ is a MER Mach and store-station effect parameter for fuselage-pylon-mounted installations obtained from Figure 3.3.1-31 as a function of configuration and Mach number.

Sample Problem

Given: A swept-wing subsonic fighter aircraft from Reference 2, symmetrically loaded as follows:

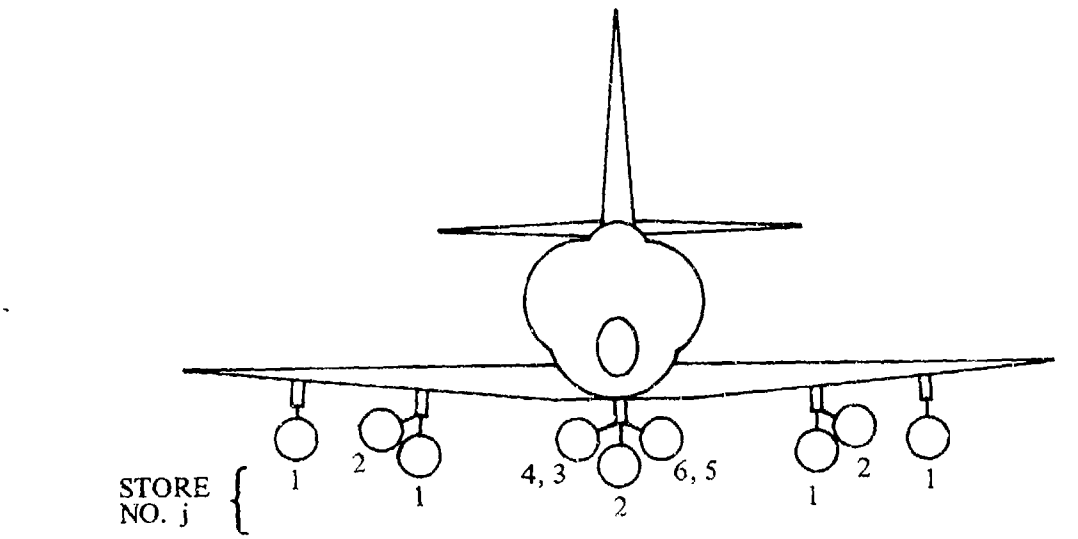

FRONT VIEW

Spanwise Station	Rack Type	Mounting	Store Type	No. of Stores
Centerline	MER	Pylon	500-lb Bomb	5
Inboard Wing	TER	Pylon	500-lb Bomb	2
Outboard Wing	Single	Pylon	500-lb Bomb	1

Aircraft Data:

$S_W = 260\ ft^2$ $\quad \bar{c} = 129.6$ in. $\quad c_r = 186$ in.

$d_{wing} = 0$ $\quad x_{a.c.} = 33.05$ in. $\quad C_{L_{\alpha_{WB}}} = 0.060$ per deg

i	j	Wing Semispan Station, y_{ij} (in.)	c_{ij} (in.)
1,5	1	113.75	87.8
2,4	2	87.00	111.0
2,4	1	78.80	119.0

Isolated-Store Data:

$d_S = 12.0$ in. $\quad S_P = 700\ in.^2$ $\quad S_F = 94\ in.^2$

$b_F = 14.7$ in. $\quad \dot{\theta}_n = 17^o$

Store Installation Data:

Installation Number, i	Store No., j	$x_{SN_{ij}}$ (in.)	$x_{S_{ij}}$ (in.)	z_{ij} (in.)	y_{ij} (in.)
2,4	1	−21.7	31.7	–	78.8.
2,4	2	−30.0	31.7	–	87.0
1,5	1	−23.2	61.2	17.6	113.75
3	3,5	–	71.7	–	0
3	2,4,6	–	−22.4	–	0

Additional Data:

$M = 0.6$ $\quad \alpha = 8^o$

Compute:

To identify the terms that need to be computed, expand Equation 3.3.1-a for the N_I store installations and n_{s_i} stores on each installation. Since the aircraft is symmetrically loaded with respect to the fuselage centerline, installations 1 and 5 are identical, as are 2 and 4. Therefore, it is only necessary to compute the terms (in Equation 3.3.1-a) for installations 1 and 2, and then double their values. The results are then added to the terms for installation 3. The indices for the summation process are summarized in the table below:

i	n_{s_i}	Actual Store Stations Loaded on Installation i
1	1	j = 1
2	3	j = 1, 2
3	6	j = 2, 3, 4, 5, 6

Note that for i = 2, station 3 is not loaded and for i = 3, station 1 is not loaded. Therefore, terms for these locations are set equal to zero.

$\Delta x_{n.p._1}$ numerator (from Equation 3.3.1-a):

$$\sum_{i=1}^{N_I} \sum_{j=1}^{n_{s_i}} K_{S_{ij}} C_{L_{\alpha_{ij}}} \left(x_{S_{ij}} - x_{a.c.}\right) =$$

$$2\left[K_{S_{11}} C_{L_{\alpha_{S_{11}}}} \left(x_{S_{11}} - x_{a.c.}\right) + K_{S_{21}} C_{L_{\alpha_{S_{21}}}} \left(x_{S_{21}} - x_{a.c.}\right)\right.$$

$$\left. + K_{S_{22}} C_{L_{\alpha_{S_{22}}}} \left(x_{S_{22}} - x_{a.c.}\right)\right] + K_{S_{32}} C_{L_{\alpha_{S_{32}}}} \left(x_{S_{32}} - x_{a.c.}\right)$$

$$+ K_{S_{33}} C_{L_{\alpha_{S_{33}}}} \left(x_{S_{33}} - x_{a.c.}\right) + K_{S_{34}} C_{L_{\alpha_{S_{34}}}} \left(x_{S_{34}} - x_{a.c.}\right)$$

$$+ K_{S_{35}} C_{L_{\alpha_{S_{35}}}} \left(x_{S_{35}} - x_{a.c.}\right) + K_{S_{36}} C_{L_{\alpha_{S_{36}}}} \left(x_{S_{36}} - x_{a.c.}\right)$$

$\Delta x_{n.p._1}$ denominator (from Equation 3.3.1-a):

$$C_{L_{\alpha_{WB}}} + \sum_{i=1}^{N_I} \sum_{j=1}^{n_{s_i}} K_{S_{ij}} C_{L_{\alpha_{S_{ij}}}} =$$

$$C_{L_{\alpha_{WB}}} + 2\left[K_{S_{11}} C_{L_{\alpha_{S_{11}}}} + K_{S_{21}} C_{L_{\alpha_{S_{21}}}} + K_{S_{22}} C_{L_{\alpha_{S_{22}}}}\right] + K_{S_{32}} C_{L_{\alpha_{S_{32}}}} + K_{S_{33}} C_{L_{\alpha_{S_{33}}}}$$

$$+ K_{S_{34}} C_{L_{\alpha_{S_{34}}}} + K_{S_{35}} C_{L_{\alpha_{S_{35}}}} + K_{S_{36}} C_{L_{\alpha_{S_{36}}}}$$

For Installation 1 (Wing-Pylon-Mounted Single Store)

$$\bar{x}_{SN_{11}} = \frac{x_{SN_{11}}}{c_{11}} = \frac{-23.2}{87.8} = -0.264 \qquad \text{(Equation 3.3.1-i)}$$

$$F_R = \frac{S_F}{S_P} = \frac{94}{700} = 0.134 \qquad \text{(Equation 3.3.1-j)}$$

$$\bar{z}_{11} = \frac{z_{11}}{c_{11}} = \frac{17.6}{87.8} = 0.200 \qquad \text{(Equation 3.3.1-ℓ)}$$

$$F_1\left(\bar{x}_{SN_{11}}, F_R\right) = -0.035 \qquad \text{(Figure 3.3.1-17)}$$

$$F_{21}\left(\bar{x}_{SN_{11}}\right) = 1.70 \qquad \text{(Figure 3.3.1-18a)}$$

$$F_{22}(\bar{z}_{11}) = 0 \qquad \text{(Figure 3.3.1-18b)}$$

$$F_{23}(F_R) = -0.53 \qquad \text{(Figure 3.3.1-19a)}$$

$$F_2\left(\bar{x}_{SN_{11}}, \bar{z}_{11}, F_R\right) = F_{21}\left(\bar{x}_{SN_{11}}\right) F_{22}(\bar{z}_{11}) F_{23}(F_R) \qquad \text{(Equation 3.3.1-k)}$$

$$= (1.70)(0)(-0.53) = 0$$

$$K_{S_{11}} = F_1\left(\bar{x}_{SN_{11}}, F_R\right) + F_2\left(\bar{x}_{SN_{11}}, \bar{z}_{11}, F_R\right) \qquad \text{(Equation 3.3.1-h)}$$

$$= -0.035 + 0 = -0.035$$

$$\left(C_{L_\alpha}\right)_{SB} = 0.161 \times 10^{-3} \text{ per deg} \qquad \text{(Figure 3.3.1-16)}$$

$$K_{NB} = 1.0 \qquad \text{(Equation 3.3.1-c, } \theta_n < 22^o\text{)}$$

$$B_e = b_F - d_S = 2.70 \qquad \text{(Equation 3.3.1-g, } b_F > d_S\text{)}$$

$$\left(C_{L_\alpha}\right)_{SF} = (0.191)(10^{-6})(B_e^2) \qquad \text{(Equation 3.3.1-e)}$$

$$= (0.191 \times 10^{-6})(2.7)^2$$

$$= 1.392 \times 10^{-6} \text{ per deg}$$

$$C_{L_{\alpha_{S_{11}}}} = \frac{375}{S_W}\left[\left(C_{l_\alpha}\right)_{SB} K_{NB} + \left(C_{L_\alpha}\right)_{SF}\right] \qquad \text{(Equation 3.3.1-b)}$$

$$= \frac{375}{260}\left[(0.161 \times 10^{-3})(1) + 1.392 \times 10^{-6}\right]$$

$$= 0.000233 \text{ per deg}$$

Noting that all stores are identical in this problem,

$C_{L_{\alpha_{S_{ij}}}} = 0.000233$ per deg for all i, j.

For Installation 2 (Wing-Pylon-Mounted TER)

$$\bar{x}_{SN_{21}} = \frac{x_{SN_{21}}}{c_{21}} = \frac{-21.7}{119.0} = -0.182 \qquad \text{(Equation 3.3.1-i)}$$

$$\bar{x}_{SN_{22}} = \frac{x_{SN_{22}}}{c_{22}} = \frac{-30.0}{111.0} = -0.270$$

$$\left.\begin{aligned} F_1\left(\bar{x}_{SN_{21}}\right) &= 0.280 \text{ (centerline sta., j = 1)} \\ F_1\left(\bar{x}_{SN_{22}}\right) &= 0.710 \text{ (shoulder sta., j = 2)} \end{aligned}\right\} \qquad \text{(Figure 3.3.1-19b)}$$

$F_2(M, j) = 0$ for $j = 1$ (Figure 3.3.1-20a)

$F_2(M, j) = 0$ for $j = 2$ (Figure 3.3.1-20b)

$$K_{S_{ij}} = F_1\left(\bar{x}_{SN_{ij}}\right) + F_2(M, j) \qquad \text{(Equation 3.3.1-m)}$$

$$K_{S_{21}} = 0.280 + 0 = 0.280$$

$$K_{S_{22}} = 0.710 + 0 = 0.710$$

For Installation 3 (Fuselage-Centerline-Pylon-Mounted MER)

There are five stores on this installation, therefore determine $K_{S_{ij}} = K_{S_{3j}}$ where $j = 2, 3, 4, 5, 6$

For $j = 2$

$F_1(M) = 0.45$ (Figure 3.3.1-30b)

$K_{S_{ij}} = F_1(M)$ (Equation 3.3.1-t)

$K_{S_{32}} = 0.45$

For $j = 3, 5$

$\frac{d_{wing}}{c_r} = \frac{0}{186} = 0$

$I_{S_j} = 0$ for $j = 3, 5$ (Figure 3.3.1-27a)

$F_1(M) = 0.042$ (Figure 3.3.1-30a)

$K_{S_{ij}} = I_{S_j} F_1(M)$ (Equation 3.3.1-s)

$K_{S_{33}} = K_{S_{35}} = (0)(0.042) = 0$

For $j = 4, 6$

$I_{S_j} = 0$ for $j = 4, 6$ (Figure 3.3.1-27a)

$F_1(M) = 0.45$ for $j = 4, 6$ (Figure 3.3.1-30b)

$F_2(M, j) = 0$ for $j = 4, 6$ (Figure 3.3.1-31)

$K_{S_{ij}} = I_{S_j} [F_1(M) + F_2(M, j)]$ (Equation 3.3.1-u)

$K_{S_{34}} = K_{S_{36}} = (0)[0.45 + 0] = 0$

Substituting into the $\Delta x_{n.p._1}$ numerator:

$$\sum_{i=1}^{N_I} \sum_{j=1}^{n_{s_i}} K_{S_{ij}} C_{L_{\alpha_{S_{ij}}}} \left(x_{S_{ij}} - x_{a.c.}\right) = 2\Big[(-0.035)(0.000233)(61.2 - 33.05) + (0.280)(0.000233)(31.7 - 33.05) + (0.710)(0.000233)(31.7 - 33.05)\Big]$$

$$+ (0.45)(0.000233)(-22.4 - 33.05)$$

$$= -0.006896$$

Substituting into the $\Delta x_{n.p._1}$ denominator:

$$C_{L_{\alpha_{WB}}} + \sum_{i=1}^{N_I} \sum_{j=1}^{n_{s_i}} K_{S_{ij}} C_{L_{\alpha_{S_{ij}}}} = 0.060 + 2\,[(-0.035)(0.000233) + (0.28)(0.000233) + (0.710)(0.000233)] + (0.45)(0.000233)$$

$$= 0.06055$$

Solution:

$$\Delta x_{n.p._1} = \frac{\text{Numerator}}{\text{Denominator}} = \frac{-0.006896}{0.06055} = -0.114 \text{ in.}$$

The calculated values of $\Delta x_{n.p._1}$ are summed with $\Delta x_{n.p._2}$ and $\Delta x_{n.p._3}$ (computed in Sections 3.3.2 and 3.3.3, respectively) in the Sample Problem of Section 3.3.4 to obtain the total shift in neutral point.

B. TRANSONIC

The method presented in Paragraph A of this section is also valid in the transonic speed range. The expected accuracy of the method is less than that in the subsonic speed range.

C. SUPERSONIC

The method presented in Paragraph A of this section is also valid in the supersonic speed range up to a Mach number of 1.6 to 2.0 as indicated in Table 3.3-A. The maximum Mach number provided in the figures should indicate the level to which the method is substantiated. Caution should be used when extrapolating the data beyond the Mach range provided in the figures.

REFERENCES

1. Gallegher, R. D., Jimenez, G., Light, L. E., and Thames, F. C.: Technique for Predicting Aircraft Aerodynamic Effects Due to External Stores Carriage. AFFDL-TR-75-95, Volumes I and II, 1975. (U)

2. Watzke, R. E.: Aerodynamic Data for Model TA-4F Operational Flight Trainer. McDonnell Douglas Corporation Rept. DAC-67425, 1968. (U)

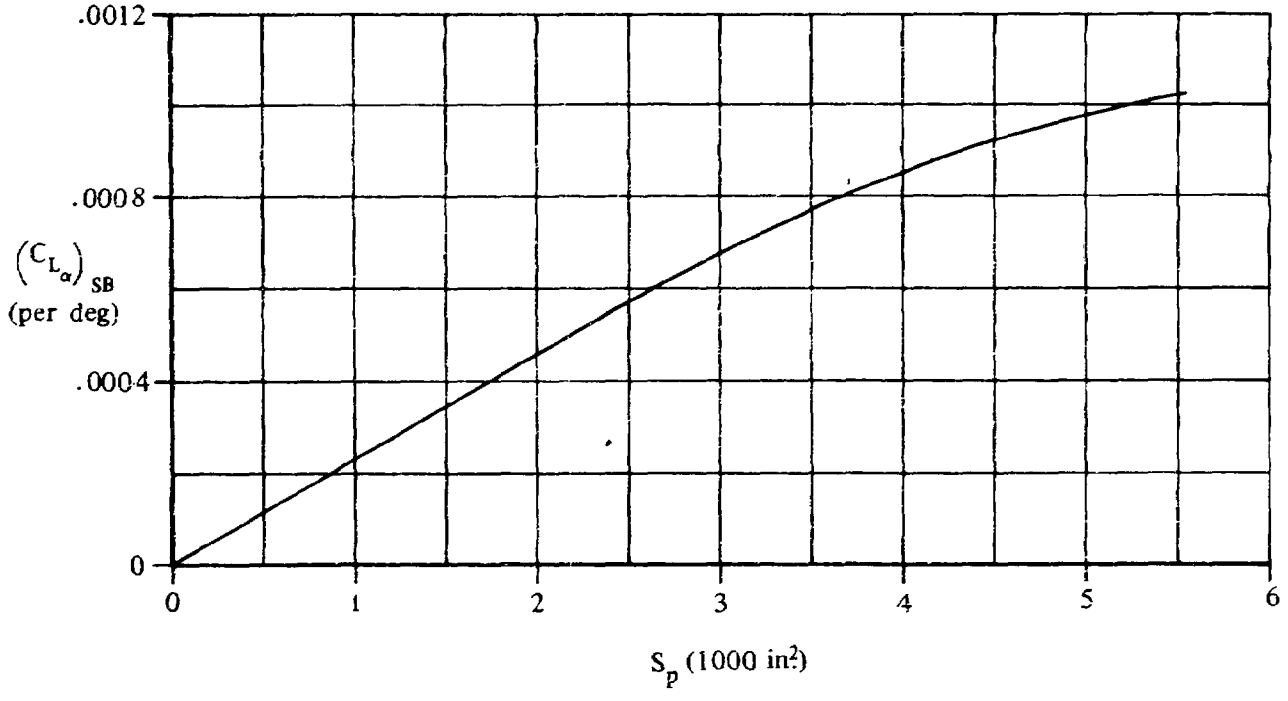

FIGURE 3.3.1-16 STORE-BODY LIFT-CURVE SLOPE

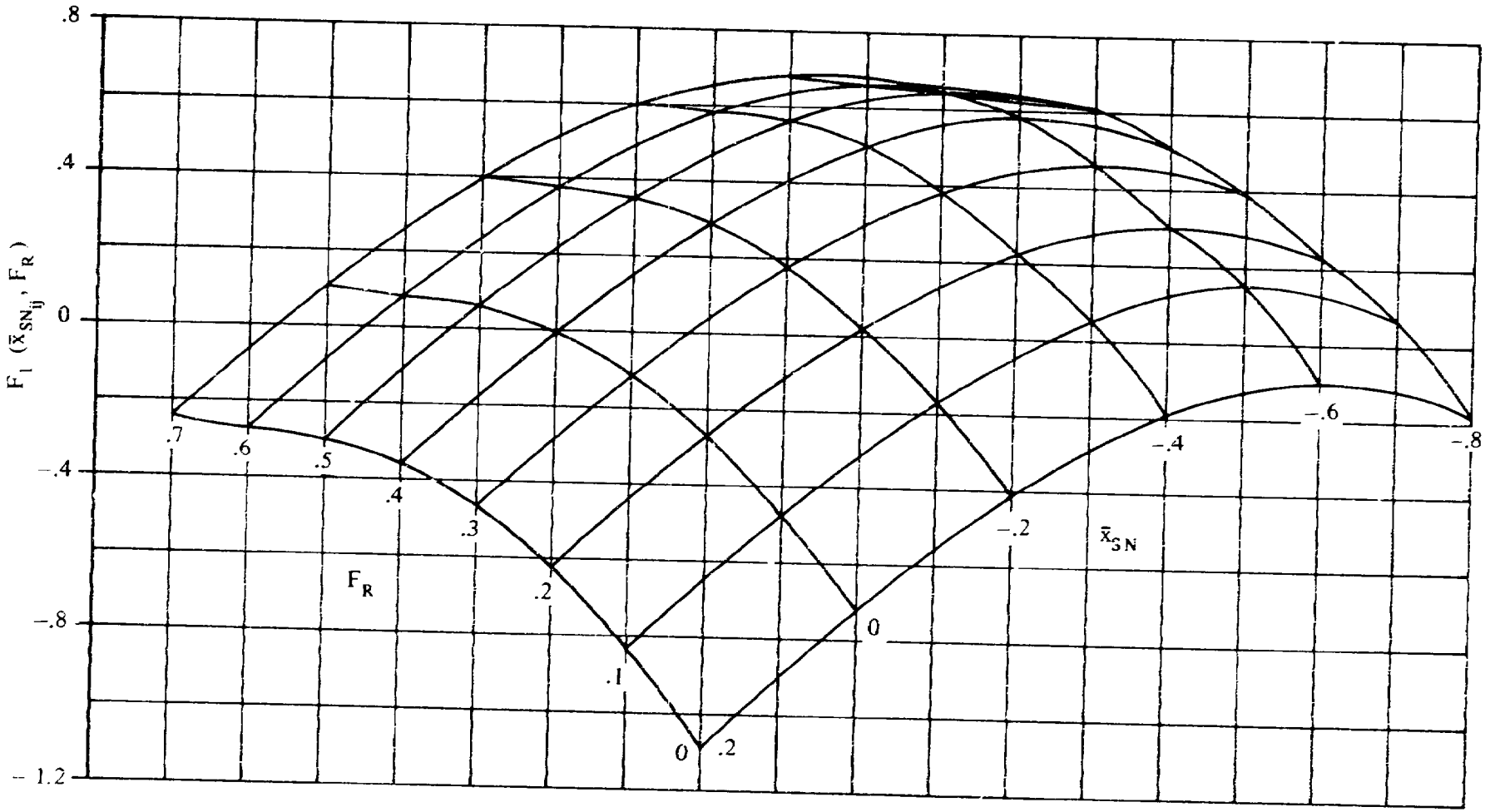

FIGURE 3.3.1-17 STORE LONGITUDINAL-PLACEMENT AND FIN-AREA-RATIO PARAMETER FOR WING-PYLON-MOUNTED SINGLE STORES

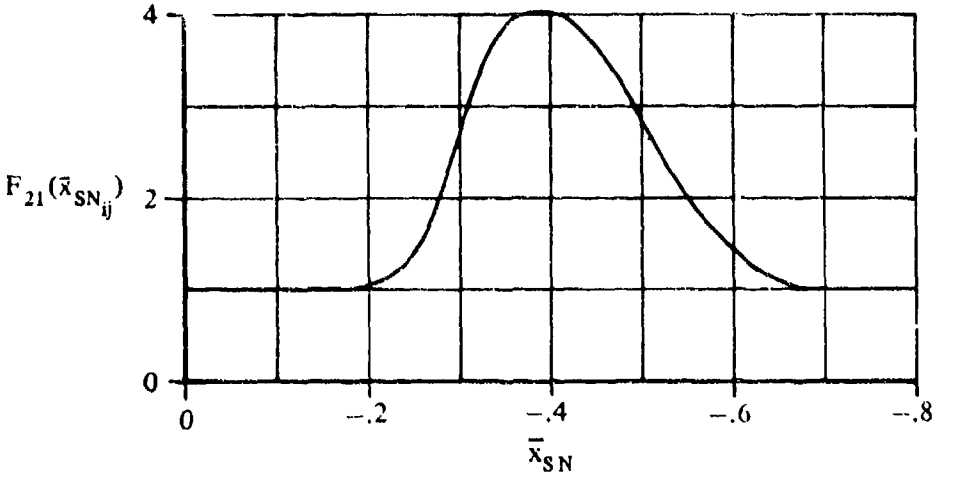

FIGURE 3.3.1-18a STORE LONGITUDINAL-PLACEMENT FACTOR FOR WING-PYLON-MOUNTED SINGLE STORES

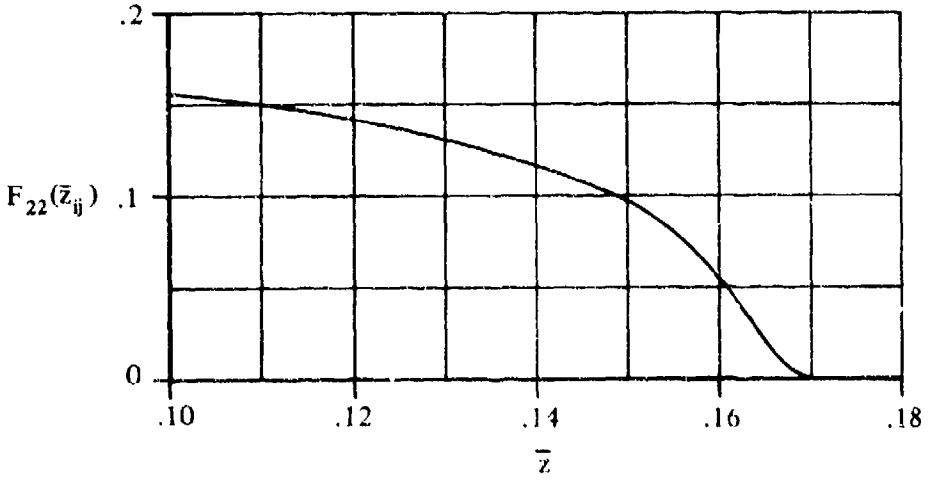

FIGURE 3.1.1-18b STORE VERTICAL-PLACEMENT FACTOR FOR WING-PYLON MOUNTED SINGLE STORES

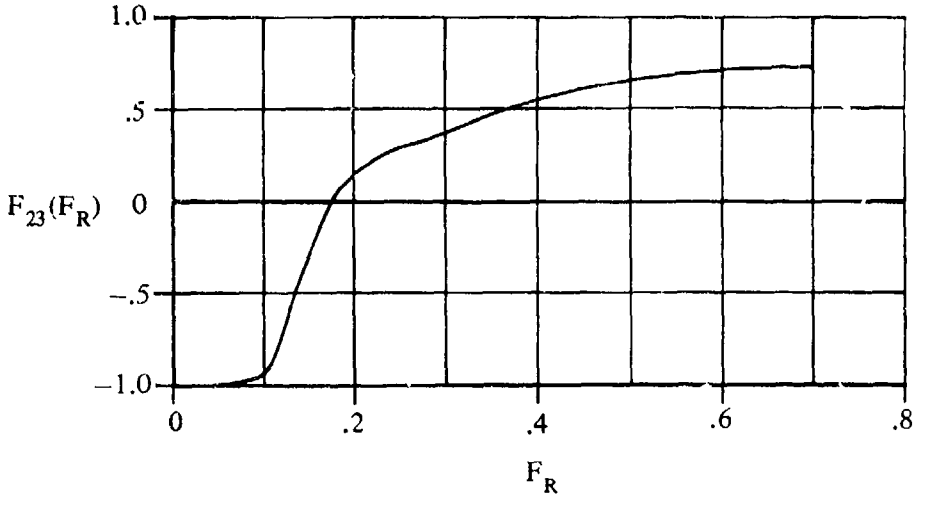

FIGURE 3.3.1-19a STORE-FIN AREA-RATIO FACTOR FOR WING-PLYON-MOUNTED SINGLE STORES

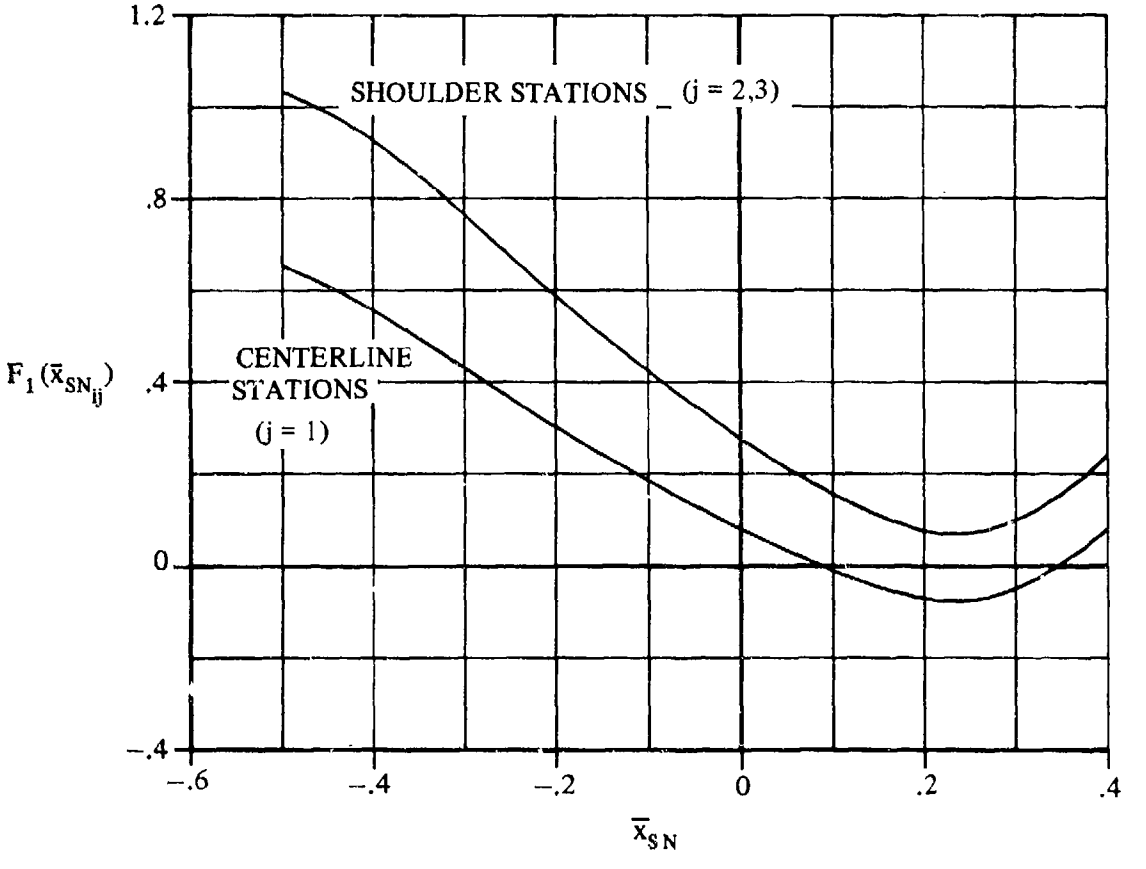

FIGURE 3.3.1-19b STORE LONGITUDINAL-PLACEMENT PARAMETER FOR TER CARRIAGE

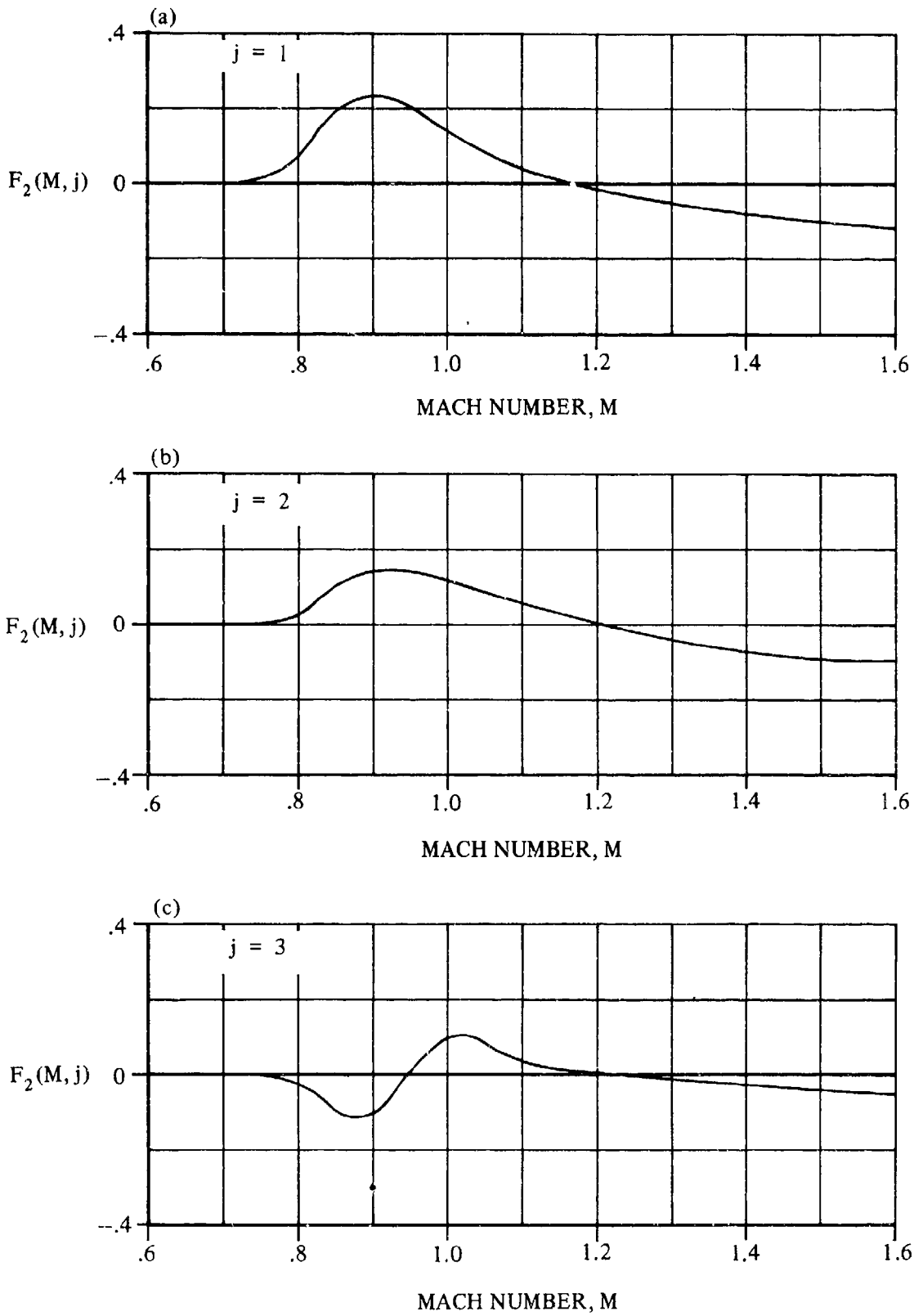

FIGURE 3.3.1-20 TER MACH AND STORE-STATION EFFECT PARAMETER

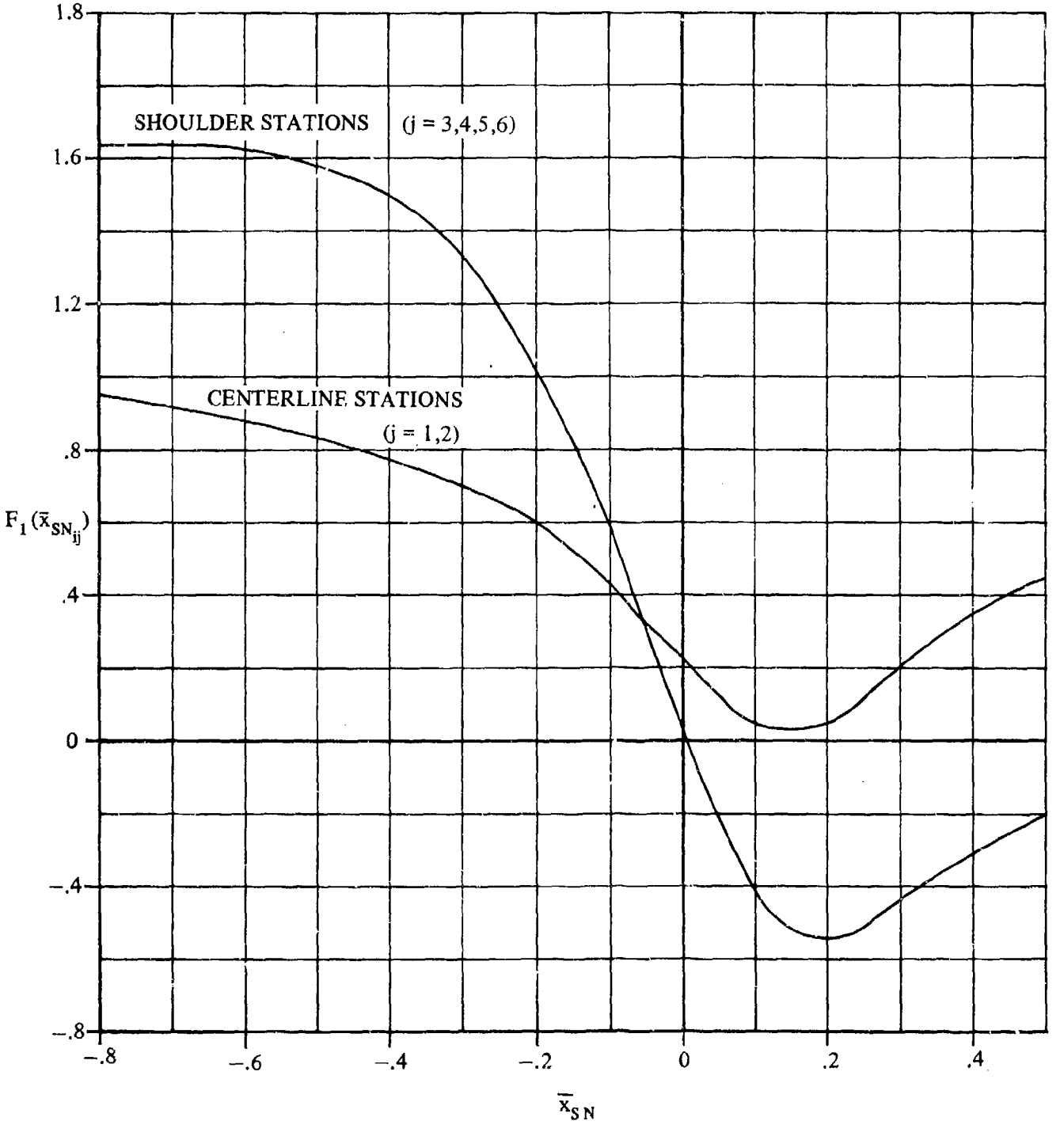

FIGURE 3.3.1-21 STORE LONGITUDINAL-PLACEMENT PARAMETER FOR MER CARRIAGE

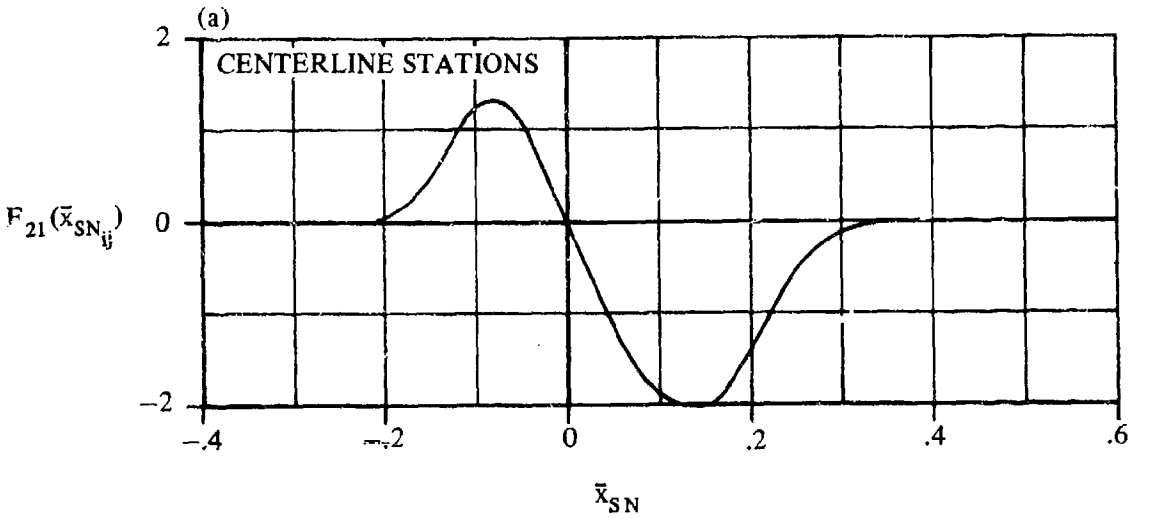

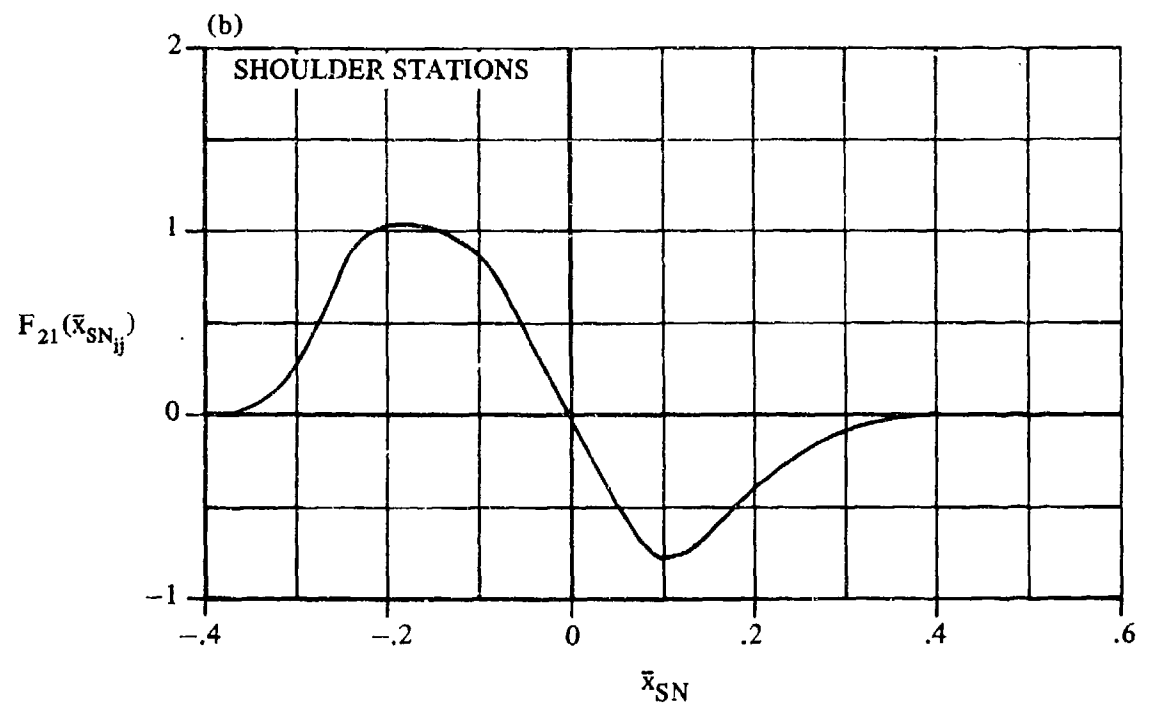

FIGURE 3.3.1-22 STORE LONGITUDINAL-PLACEMENT FACTOR FOR MER CARRIAGE

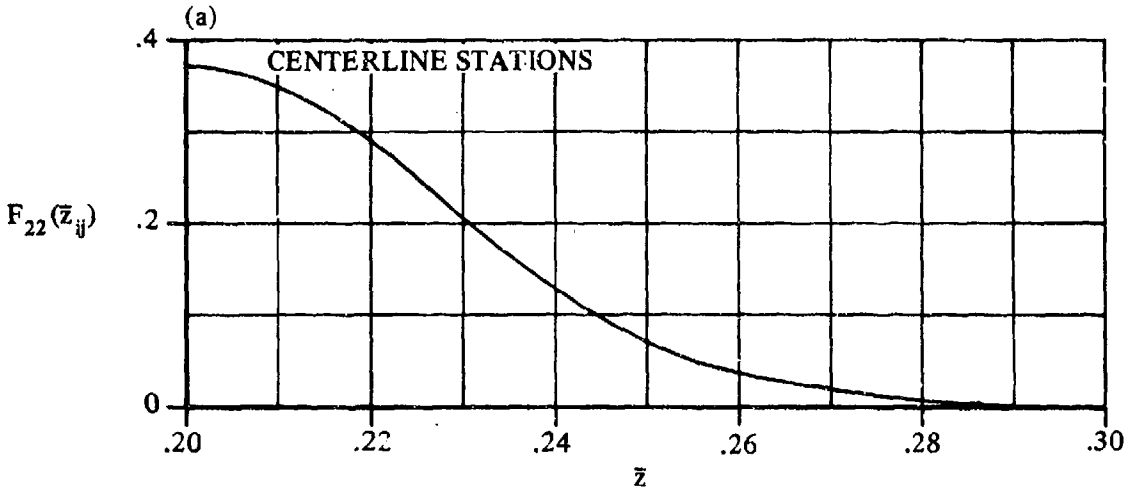

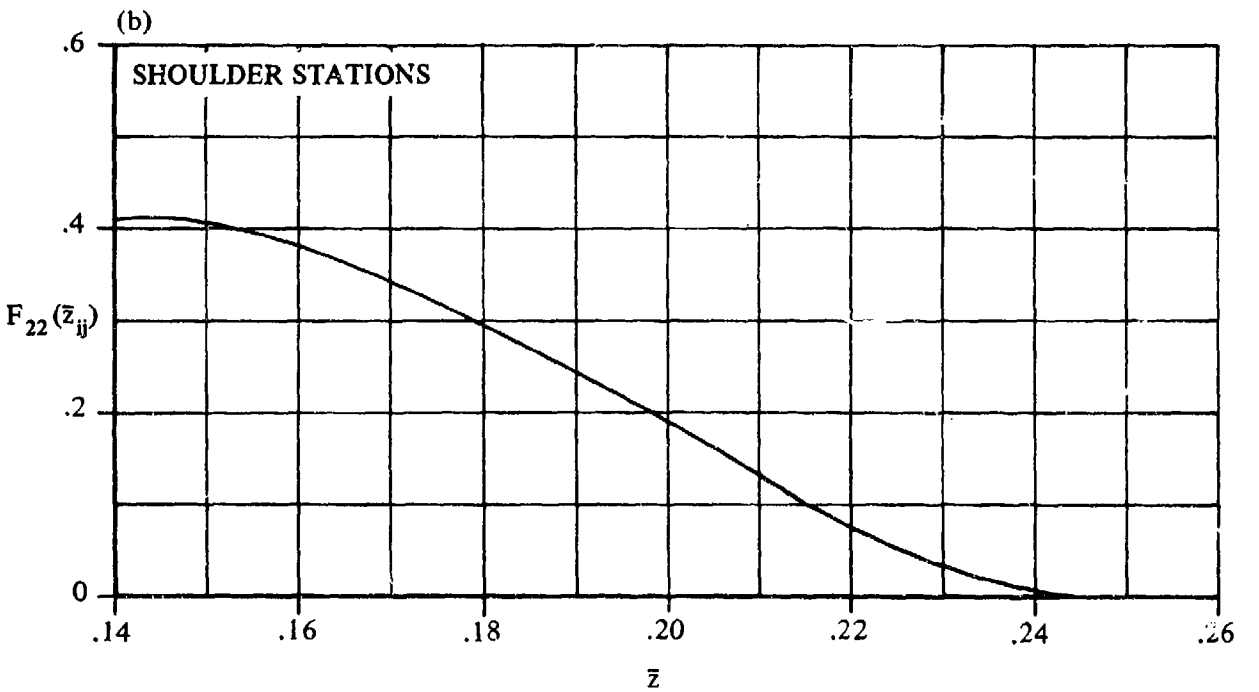

FIGURE 3.3.1-23 STORE VERTICAL-PLACEMENT FACTOR FOR MER CARRIAGE

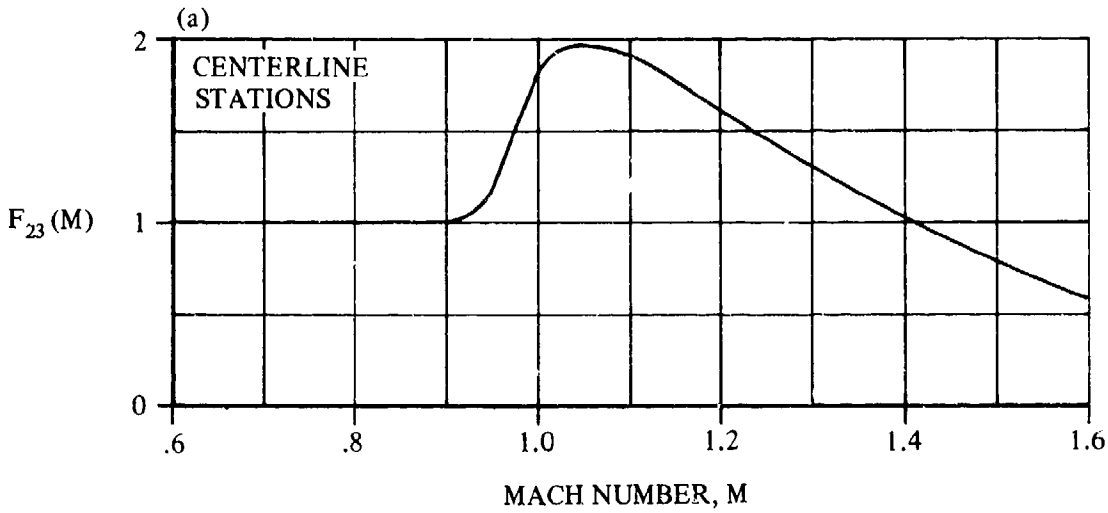

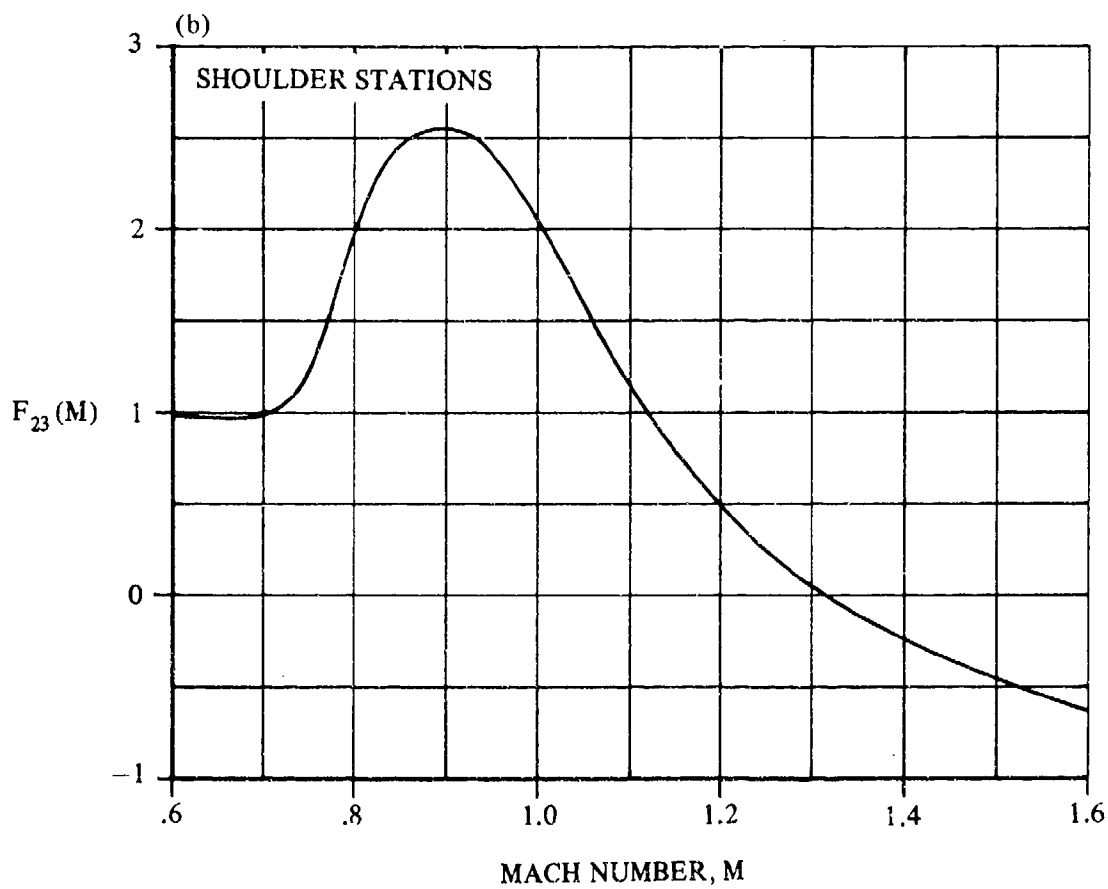

FIGURE 3.3.1-24 MACH-EFFECT FACTOR FOR MER CARRIAGE

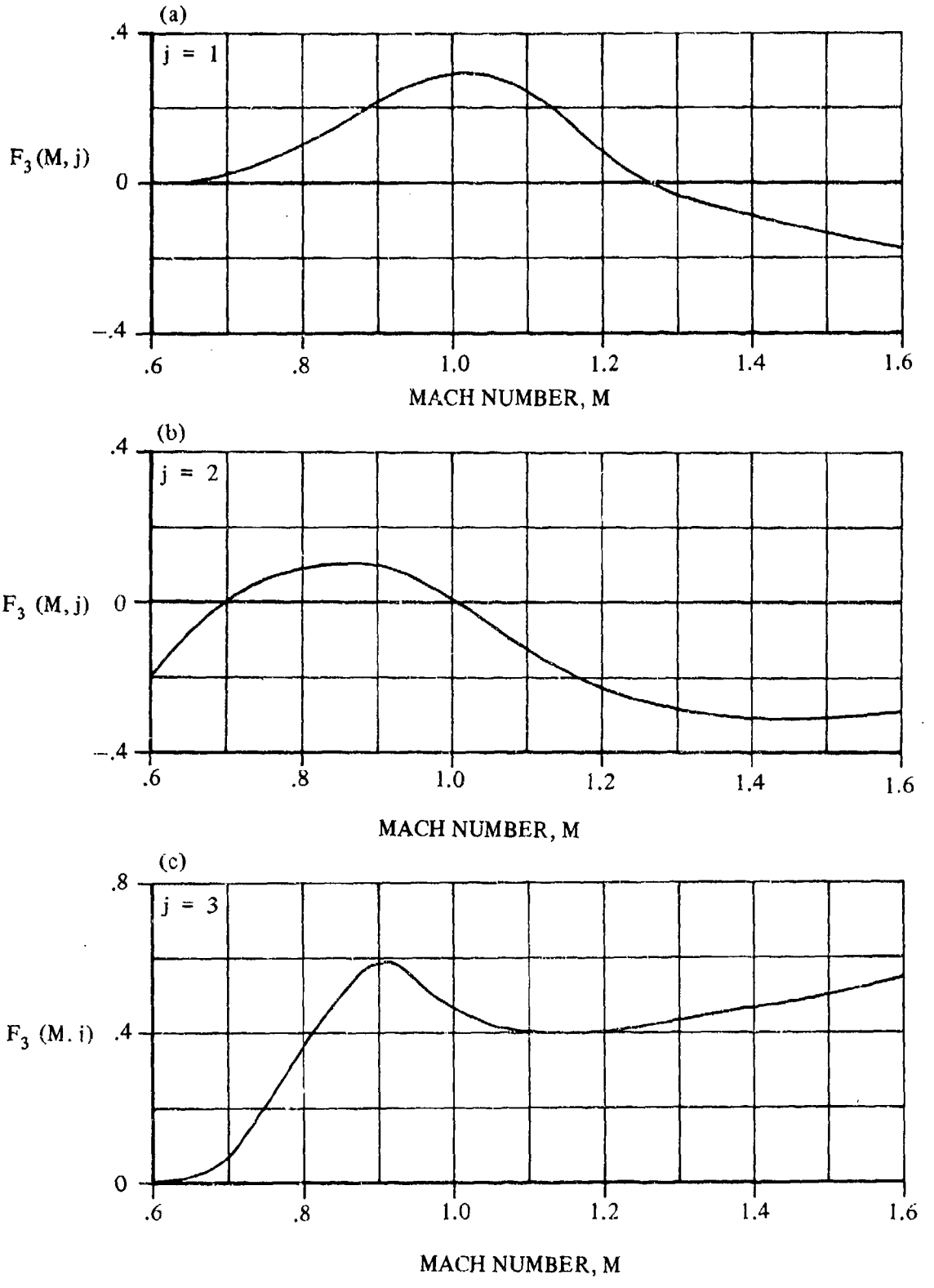

FIGURE 3.3.1-25 MER MACH AND STORE-STATION EFFECT PARAMETER

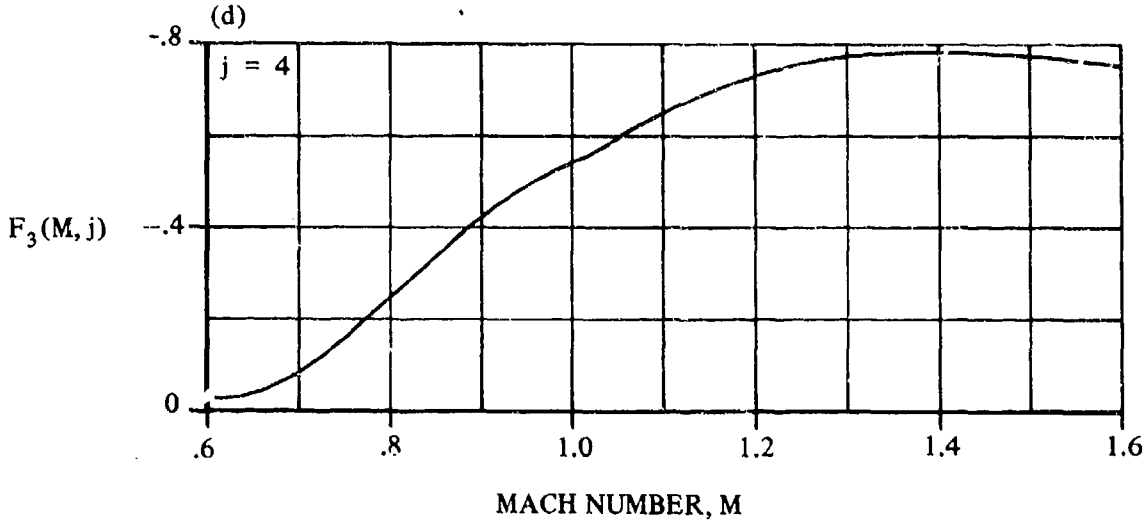

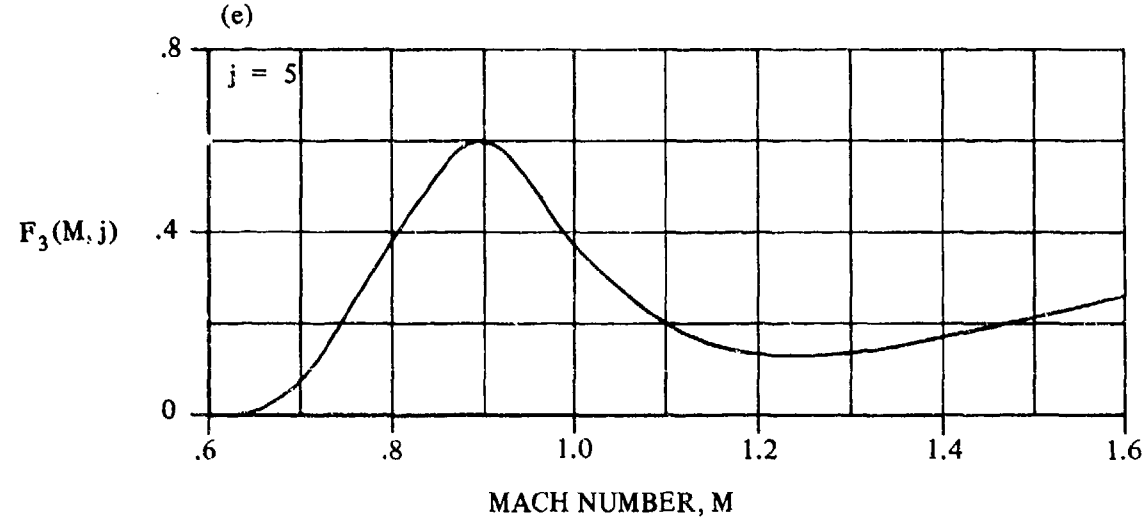

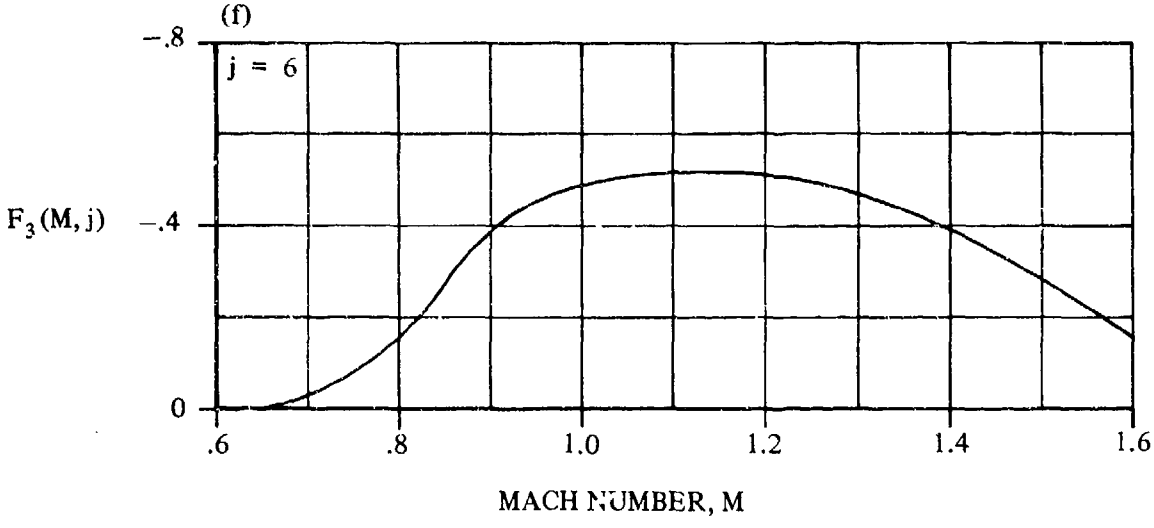

FIGURE 3.3.1-25 (CONTD)

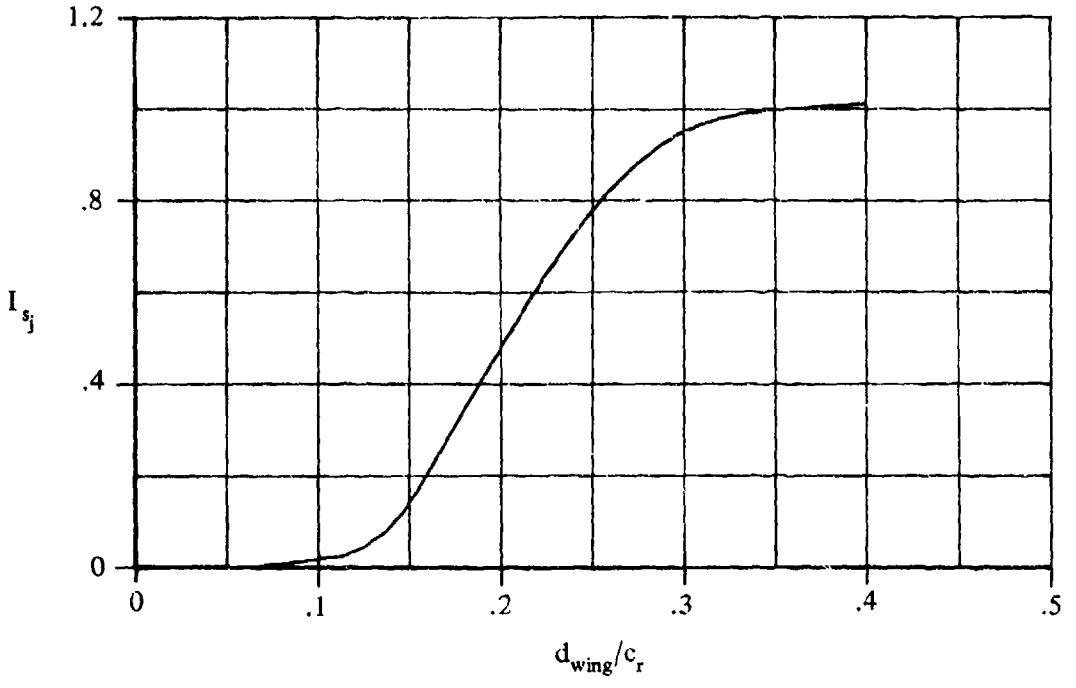

FIGURE 3.3.1-27a MER INSTALLATION NEUTRAL-POINT CORRELATION FACTOR

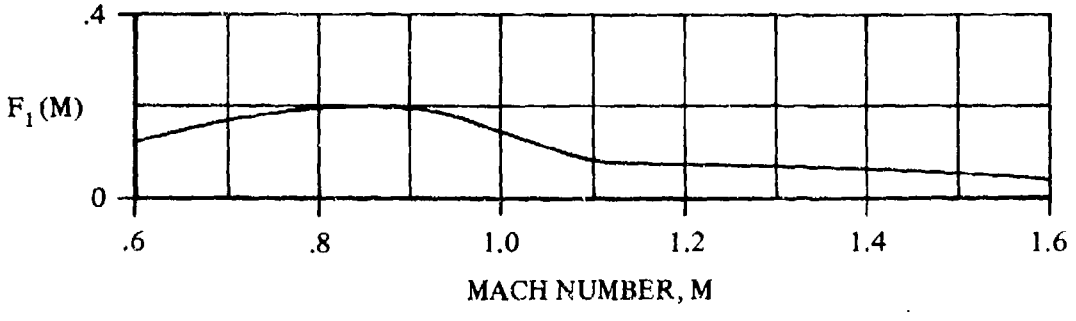

FIGURE 3.3.1-27b MER MACH-EFFECT FACTOR FOR FUSELAGE-TANGENT-MOUNTED INSTALLATIONS

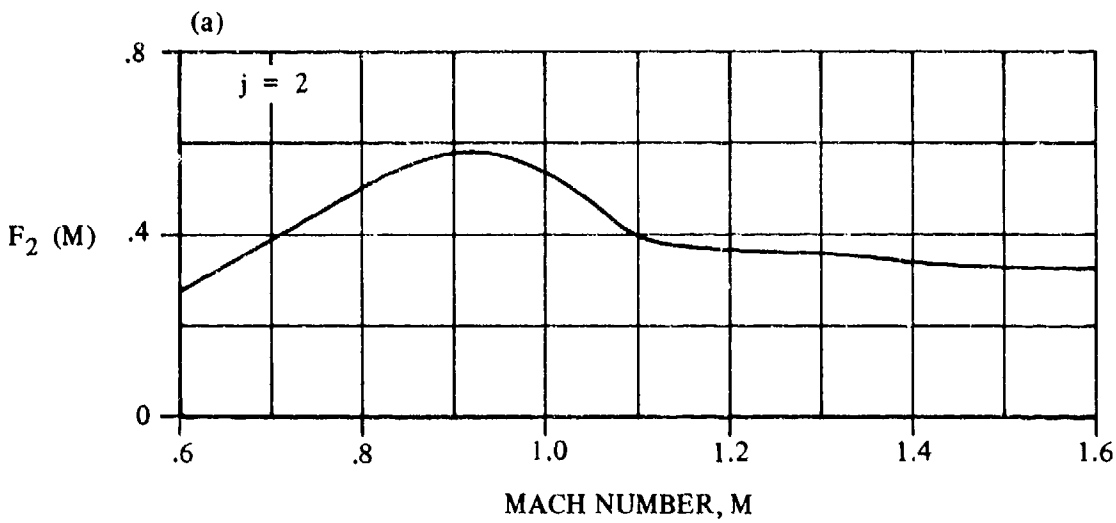

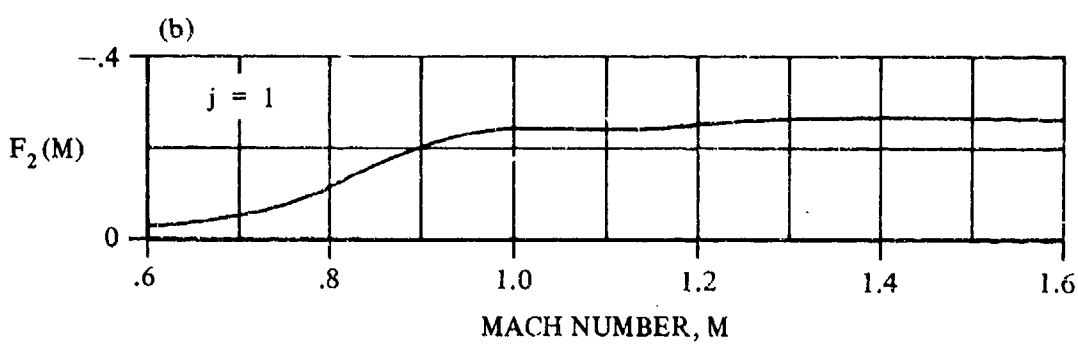

FIGURE 3.3.1-28 MER MACH AND STORE-STATION EFFECT PARAMETER FOR FUSELAGE-TANGENT-MOUNTED INSTALLATIONS

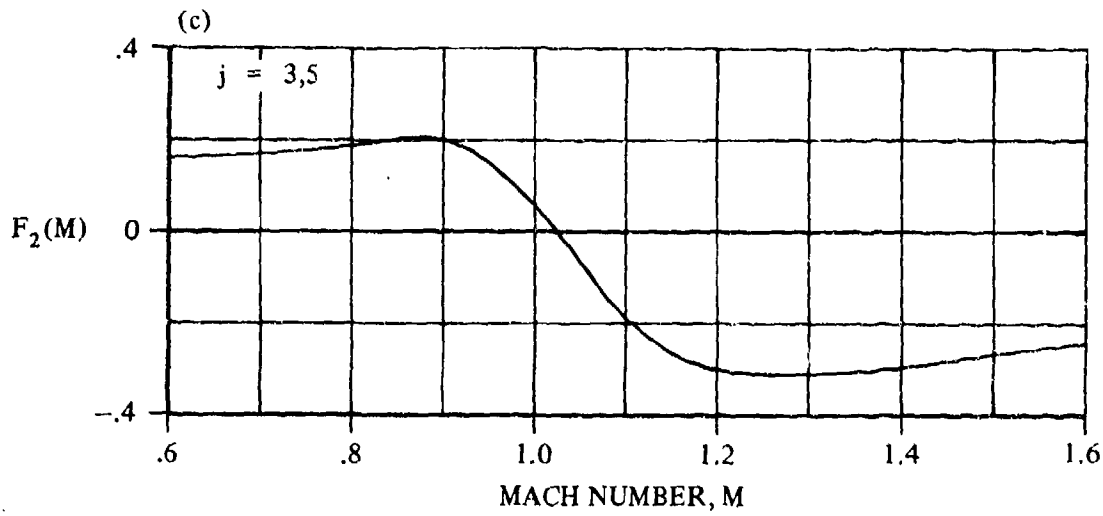

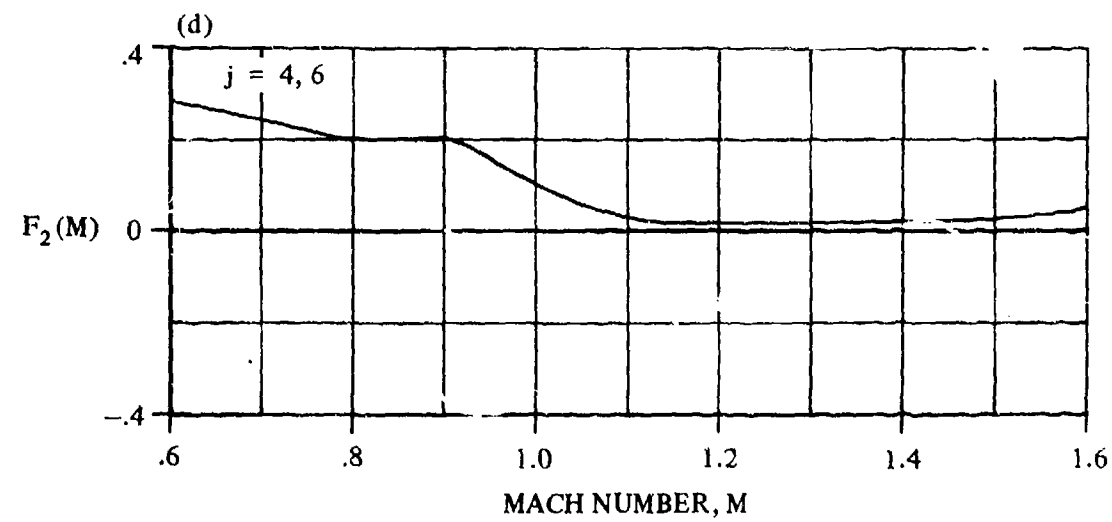

FIGURE 3.3.1-28 (CONTD)

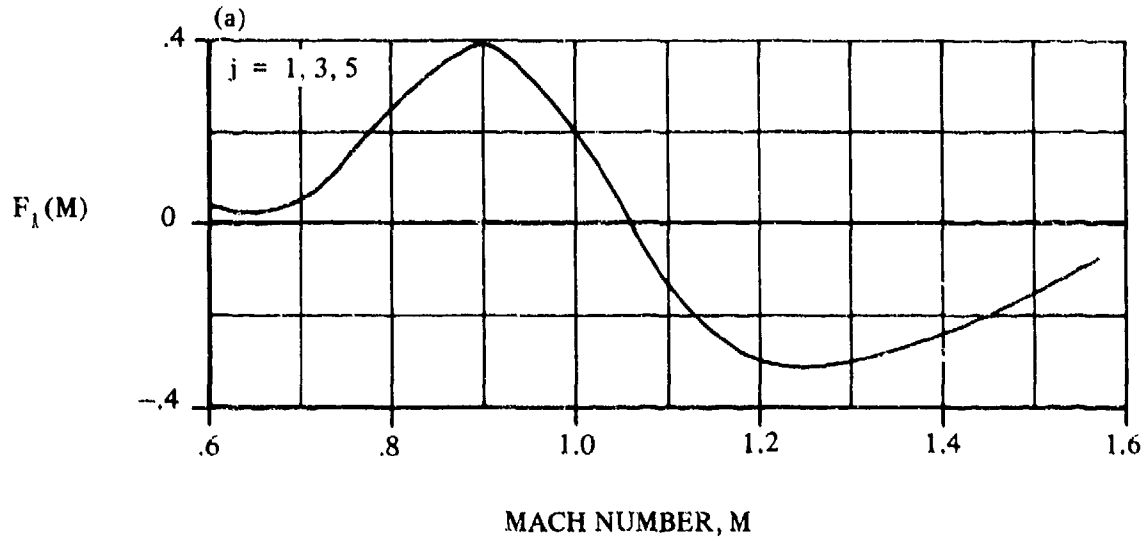

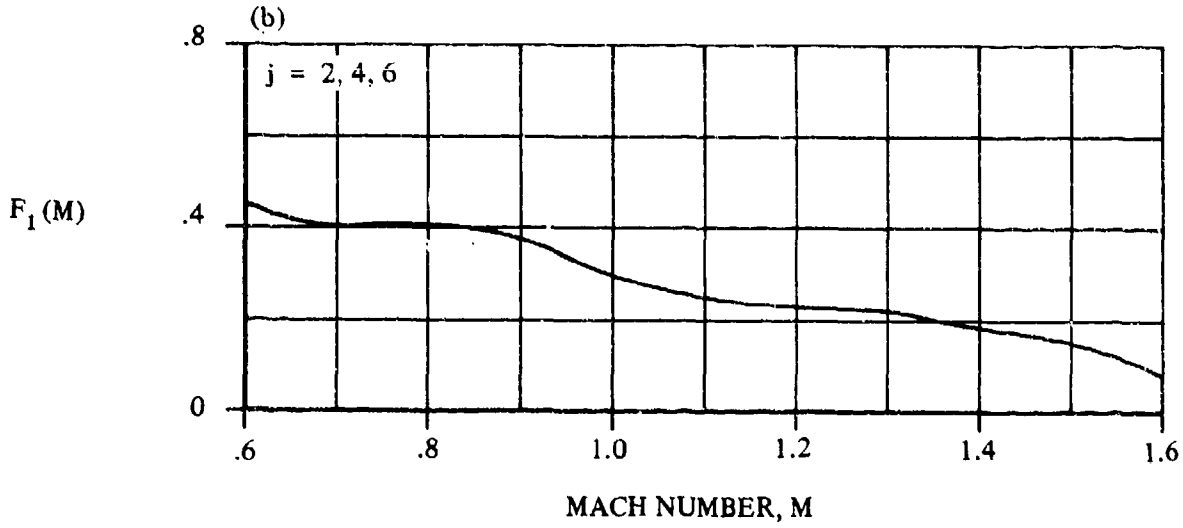

FIGURE 3.3.1-30 MER MACH EFFECT FACTOR FOR FUSELAGE-PYLON-MOUNTED INSTALLATIONS

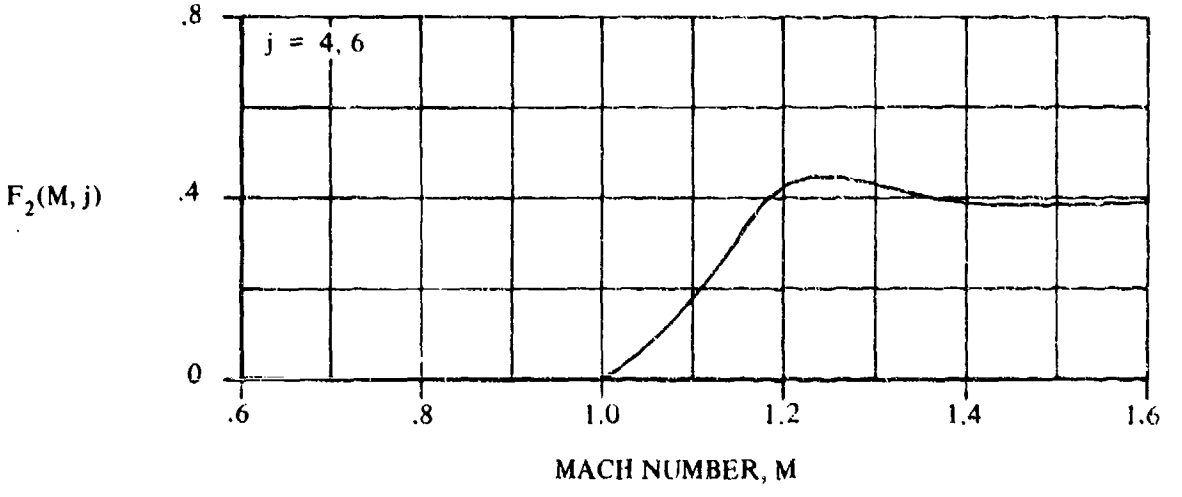

FIGURE 3.3.1-31 MER MACH AND STORE-STATION EFFECT PARAMETER FOR FUSELAGE-PYLON-MOUNTED INSTALLATIONS

3.3.2 NEUTRAL-POINT SHIFT DUE TO INTERFERENCE EFFECTS ON WING FLOW FIELD

A method is presented in this section for estimating the neutral-point shift due to interference effects on the wing flow field from external-store installations. The method predicts a neutral-point shift due to all installations (armament stations) on the aircraft.

The Datcom Method is taken from Reference 1 and is empirical in nature. The method is applicable to aircraft of conventional design and essentially symmetrical store shapes with no major shape protuberances. The limitations on configuration and Mach-number range are summarized in Table 3.3-A. Additional limitations and assumptions pertaining to the method are listed below:

1. The method is not applicable to wing-tip or wing-tangent-mounted stores.
2. The method has been verified for the Mach-number range given in Table 3.3-A. Caution should be used in extrapolating the empirical curves beyond the given Mach-number range.
3. The method has not been verified for configurations in which flaps, slats or other flow-disrupting devices are deployed.
4. The method gives the best results for angle-of-attack range from 0 to 8°, although the method can be used for higher angles of attack.
5. The data base used in deriving the method relied heavily on swept-wing tactical-combat-aircraft wind-tunnel data.
6. The method is applicable for sideslip angles less than 4°.
7. Fuselage-mounted installations must be located on the fuselage centerline.
8. The method is not applicable to empty multiple racks.
9. The effect of empty pylons on neutral point is considered to be negligible.

The effect due to a pair of symmetrical installations can be computed by doubling the effect of one side.

A. SUBSONIC

DATCOM METHOD

The neutral-point shift in inches, positive for aft shift, due to wing flow-field interference effects is given by

$$\Delta x_{n.p._2} = \left(\frac{S_W}{N_I}\right)\left(\sum_{i=1}^{N_I}\sum_{j=1}^{n_{s_i}} C_{L_{\alpha_{S_{ij}}}}\right)\left[\sum_{i=1}^{N_I} \delta S_i \left(\Delta x'_{n.p._2} + K_1 K_2 K_3\right)_i\right] \qquad 3.3.2\text{-a}$$

where

S_W is tl. .. ng reference area (ft^2).

N_I is the total number of store installations on the aircraft.

n_{s_i} is the number of store stations on installation i (including empty stations).

$C_{L_{\alpha_{S_{ij}}}}$ is the free-stream lift-curve slope of store j on installation i (per deg) given by Equation 3.3.1-b.

δ_{S_i} is a parameter related to configuration:

1. For Wing-Pylon Single Carriage:

$$\delta_{S_i} = 20 \qquad \text{3.3.2-b}$$

2. For Wing-Pylon M .R and TER Carriage, and Centerline Single Carriage:

$$\delta_{S_i} = 10 \qquad \text{3.3.2-c}$$

3. For Fuselage-Centerline MER Carriage:

$$\delta_{S_i} = 17.4 \qquad \text{3.3.2-d}$$

$\Delta x'_{n.p._2}$ is a neutral-point basic-interference-effect term obtained from Figures 3.3.2-6a through -6d as a function of configuration and Mach number.

K_1 is a span-location-correction factor obtained from Figures 3.3.2- 8a through - 8c as a function of configuration and $\frac{y_i}{b_W/2}$, where y_i is the wing semispan location of installation i and b_W is the wing span.

Note: For fuselage-mounted installations, $K_1 = 1$.

K_2 is a longitudinal-correction factor obtained from Figure 3.3.2-9a through -9d as a function of x_{ML_i}/c_i, where x_{ML_i} is the distance (in.) from the local wing leading edge to the point midway between the pylon mounting lugs on installation i (positive for the pylon mid-lug point aft of the local wing leading edge), and c_i is the local wing chord (in.) at the semispan location of store installation i. (See Sketch (a).)

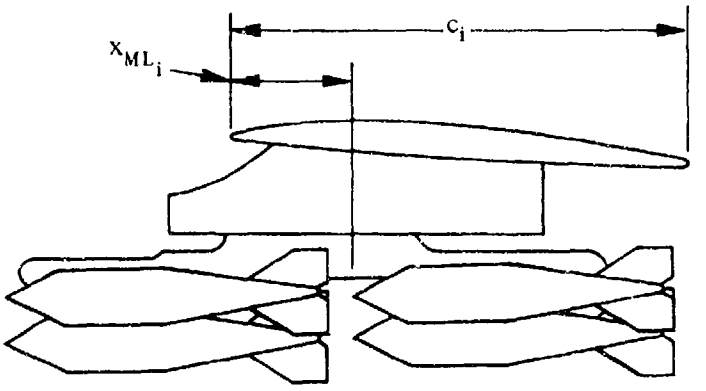

SKETCH (a)

K_3 is a Mach-number-correction factor obtained from Figures 3.3.2-11a through -11d as a function of configuration and Mach number.

Sample Problem

Given: A swept-wing subsonic-fighter aircraft from Reference 2 described in the Sample Problem of Paragraph A of Section 3.3.1.

Additional Data:

$C_{L_{\alpha_{S_{ij}}}}$ = 0.000233 per deg (Sample Problem, Paragraph A, Section 3.3.1)

$M = 0.6$

$b_W/2 = 165$ in.

Installation No., i	1,5	2,4	3
x_{ML_i}/c_i	0.204	0.180	0.445
y_i	113.75	78.8	0

Compute:

$$\frac{S_W}{N_I} = \frac{260}{5} = 52.0 \qquad \text{(first term of Equation 3.3.2-a)}$$

Since all stores are identical and there are a total of 11 stores,

$$\sum_{i=1}^{N_I} \sum_{j=1}^{n_{s_i}} C_{L_{\alpha_{S_{ij}}}} = 11\, C_{L_{\alpha_{S_{ij}}}} \qquad \text{(second term of Equation 3.3.2-a)}$$

$$= (11)(0.000233)$$

$$= 0.00256 \text{ per deg}$$

Since the wing installations 1 and 2 are symmetrical, only one side is calculated and the result multiplied by 2.

δ_{S_1} = 20 (Equation 3.3.2-b)

δ_{S_1} = 10 (Equation 3.3.2-c)

δ_{S_3} = 17.4 (Equation 3.3.2-d)

For Installation 1 (Wing-Pylon-Mounted Single Store)

$\Delta x'_{n.p._2}$ = −0.03 (Figure 3.3.2-6a)

$y_i/(b_W/2)$ = 0.689

K_1 = 0 (Figure 3.3.2-8a)

K_2 = 0 (Figure 3.3.2-9a)

K_3 = −0.39 (Figure 3.3.2-11a)

For Installation 2 (Wing-Pylon-Mounted TER)

$\Delta x'_{n.p._2}$ = −0.02 (Figure 3.3.2-6b)

$y_i/(b_W/2)$ = 0.478

K_1 = 0 (Figure 3.3.2-8b)

K_2 = 0.37 (Figure 3.3.2-9b)

K_3 = −0.25 (Figure 3.3.2-11b)

For Installation 3 (Fuselage-Centerline-Pylon-Mounted MER)

$\Delta x'_{n.p._2}$ = 0.125 (Figure 3.3.2-6d)

K_1 = 1.0 (Fuselage-mounted installation)

K_2 = 1.0 (Figure 3.3.2-9d)

K_3 = 0 (Figure 3.3.2-11d)

$$\sum_{i=1}^{N_I} \delta_{S_i} \left(\Delta x'_{n.p._2} + K_1 K_2 K_3\right)_i = {}_2\delta_{S_1} \left(\Delta x'_{n.p._2} + K_1 K_2 K_3\right)_{i=1} \quad \text{(third term of Equation 3.3.2-a)}$$

$$+ {}_2\delta_{S_2} \left(\Delta x'_{n.p._2} + K_1 K_2 K_3\right)_{i=2}$$

$$+ \delta_{S_3} \left(\Delta x'_{n.p._3} + K_1 K_2 K_3\right)_{i=3}$$

$$= (2)(20)\,[-0.03 + (0)(0)(-0.39)]$$

$$+ (2)(10)[-0.02 + (0)(0.37)(-0.25)]$$

$$+ (17.4)[0.125 + (1.0)(1.0)(0)]$$

$$= 0.575$$

Solution:

$$\Delta x_{n.p._2} = \left(\frac{S_W}{N_I}\right)\left(\sum_{i=1}^{N_I} \sum_{j=1}^{n_{s_i}} C_{L_{\alpha_{S_{ij}}}}\right) \left[\sum_{i=1}^{N_I} \delta_{S_i} \left(\Delta x'_{n.p._2} + K_1 K_2 K_3\right)_i\right] \quad \text{(Equation 3.3.2-a)}$$

$$= (52.0)(0.00256)(0.575) = 0.077 \text{ in.}$$

The calculated value of $\Delta x_{n.p._2}$ is summed with $\Delta x_{n.p._1}$ and $\Delta x_{n.p._3}$ (computed in Sections 3.3.1 and 3.3.3, respectively) in the Sample Problem of Section 3.3.4 to obtain the total shift in neutral point.

B. TRANSONIC

The method presented in Paragraph A of this section is also valid in the transonic speed range. The expected accuracy of the method is less than that in the subsonic speed range.

C. SUPERSONIC

The method presented in Paragraph A of this section is also valid in the supersonic speed range up to a Mach number of 1.6 to 2.0 as indicated in Table 3.3-A. The maximum Mach number provided in the figures should indicate the level to which the method is substantiated. Caution should be used when extrapolating the data beyond the Mach-number range provided in the figures.

REFERENCES

1. Gallagher, R. D., Jimenez, G., Light, L. E., and Thames F. C.: Technique for Predicting Aircraft Aerodynamic Effects Due to External Stores Carriage. AFFDL-TR-75-95, Volumes I and II, 1975. (U)

2. Watzke, R. E.: Aerodynamic Data for Model TA-4F Operational Flight Trainer. McDonnell Douglas Corporation Rept. DAC-67425, 1968. (U)

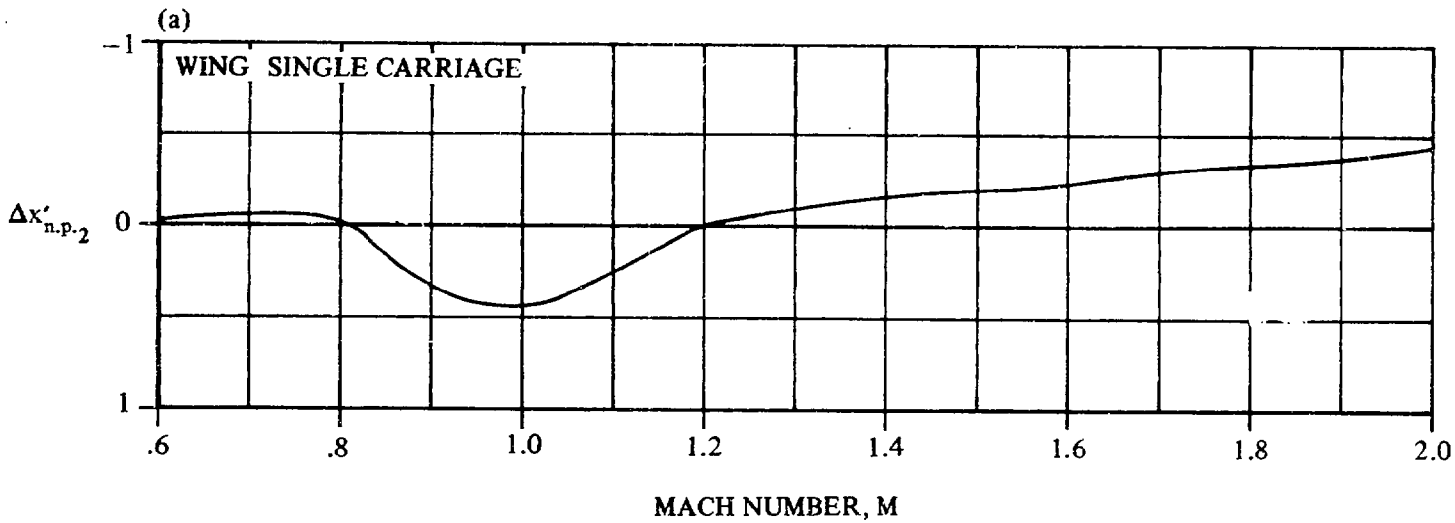

FIGURE 3.3.2-6 NEUTRAL-POINT BASIC-INTERFERENCE-EFFECT TERM

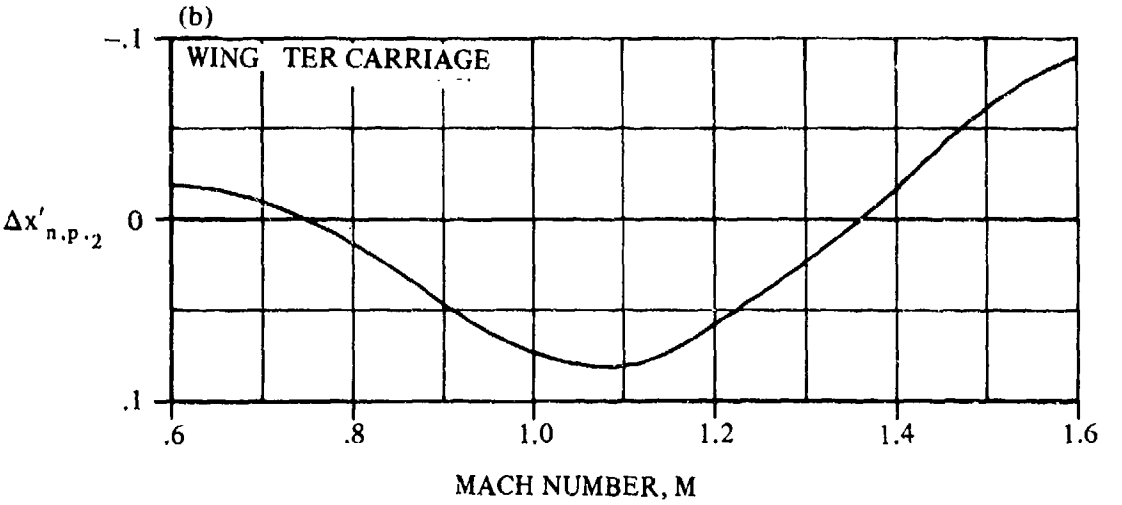

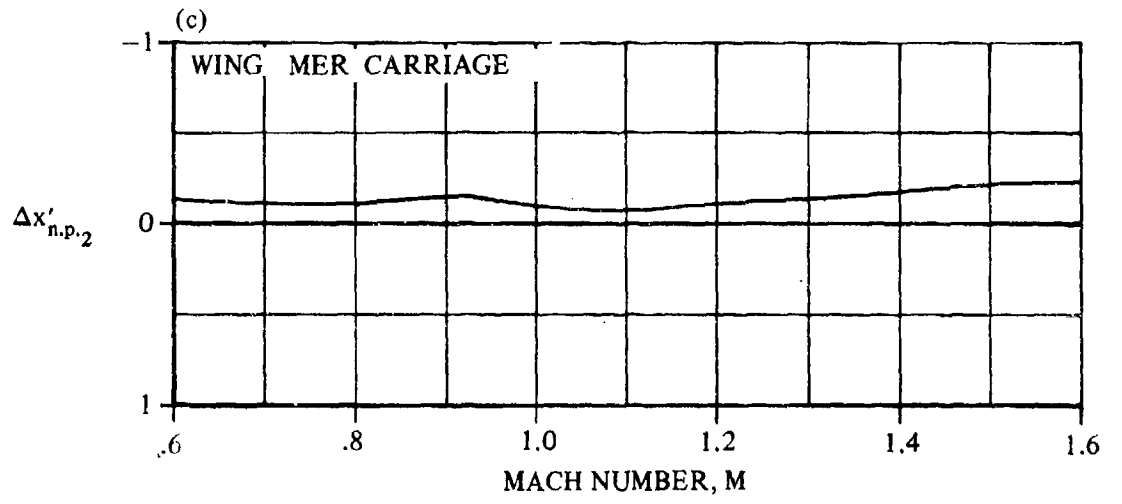

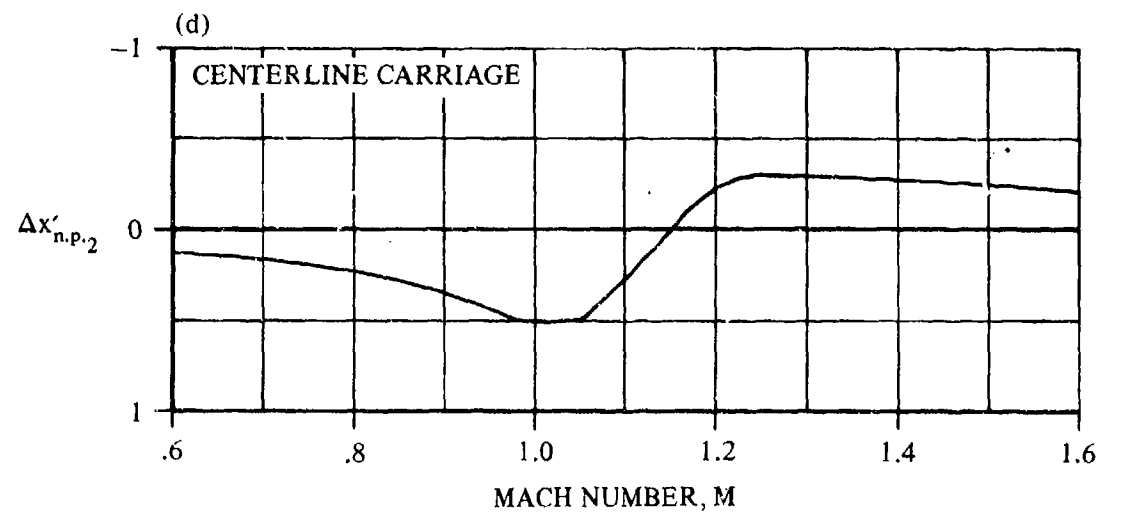

FIGURE 3.3.2-6 (CONTD)

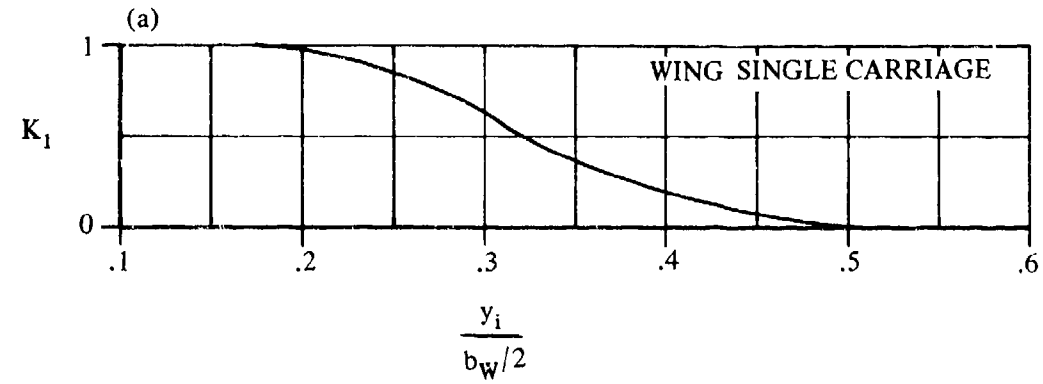

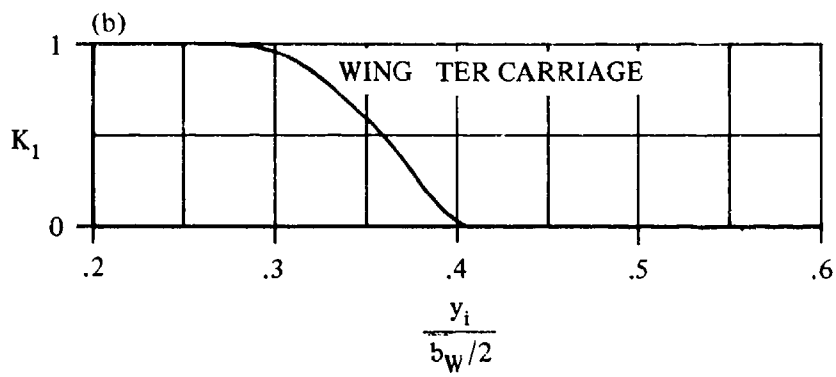

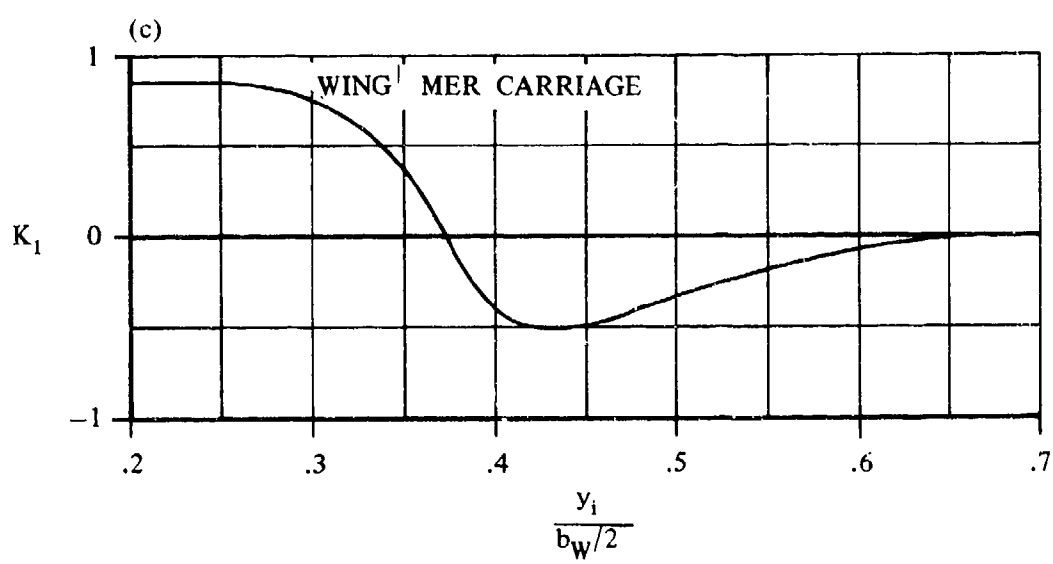

FIGURE 3.3.2-8 NEUTRAL-POINT SPAN-LOCATION-CORRECTION FACTOR

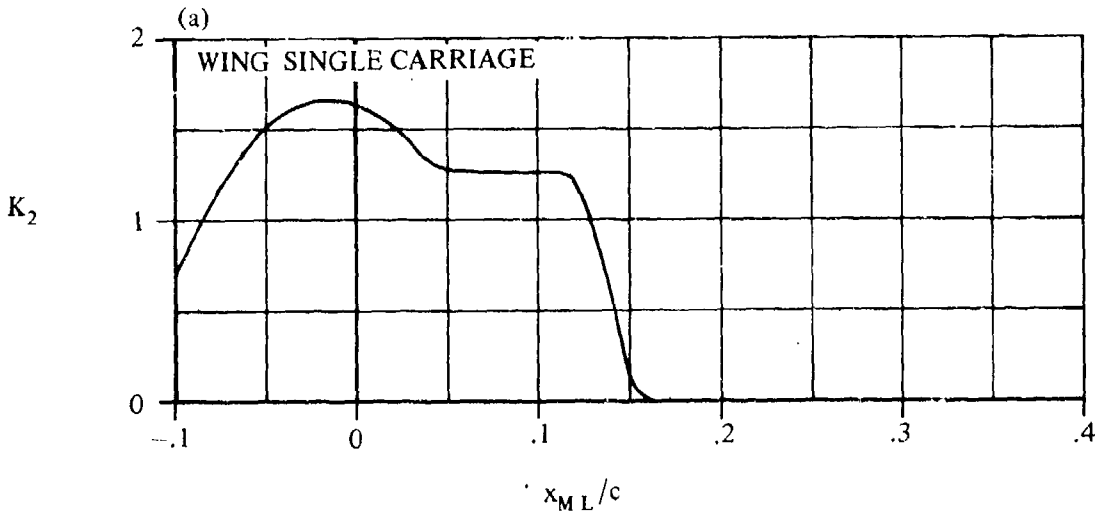

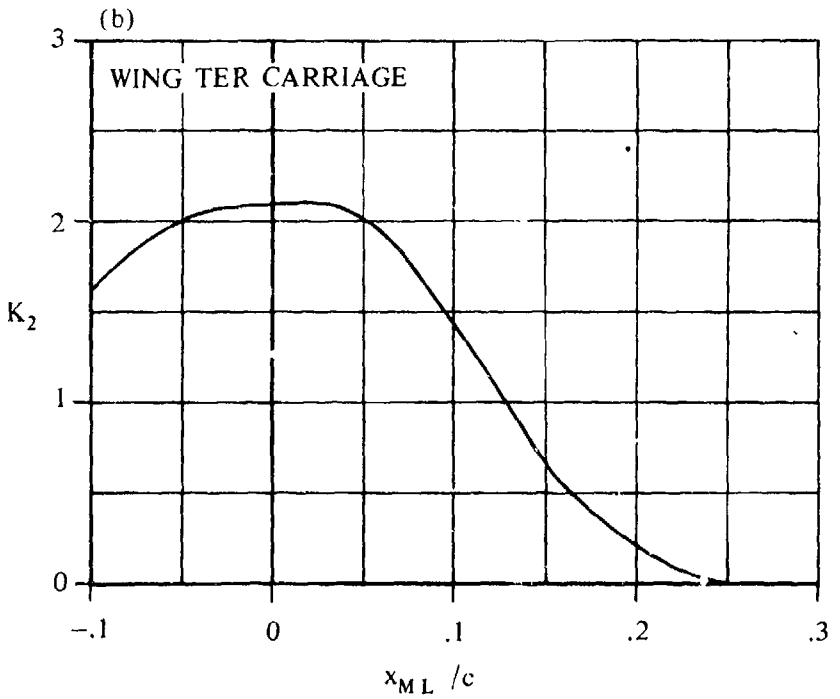

FIGURE 3.3.2-9 NEUTRAL-POINT LONGITUDINAL CORRECTION FACTOR

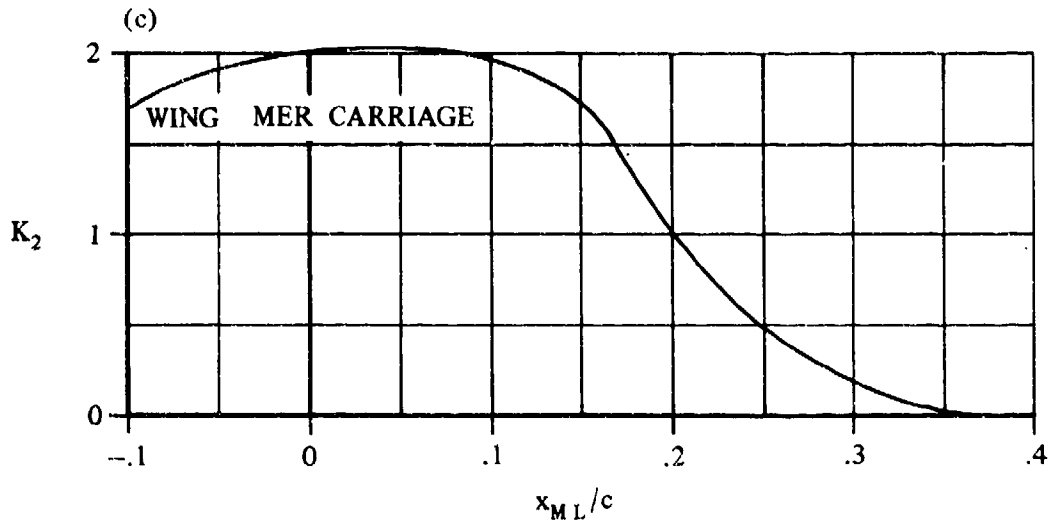

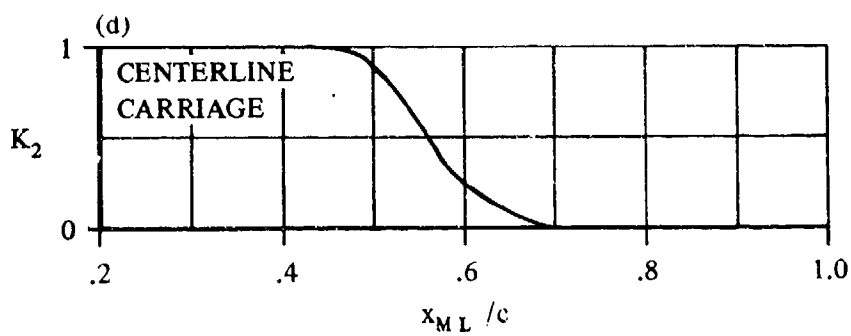

FIGURE 3.3.2-9 (CONTD)

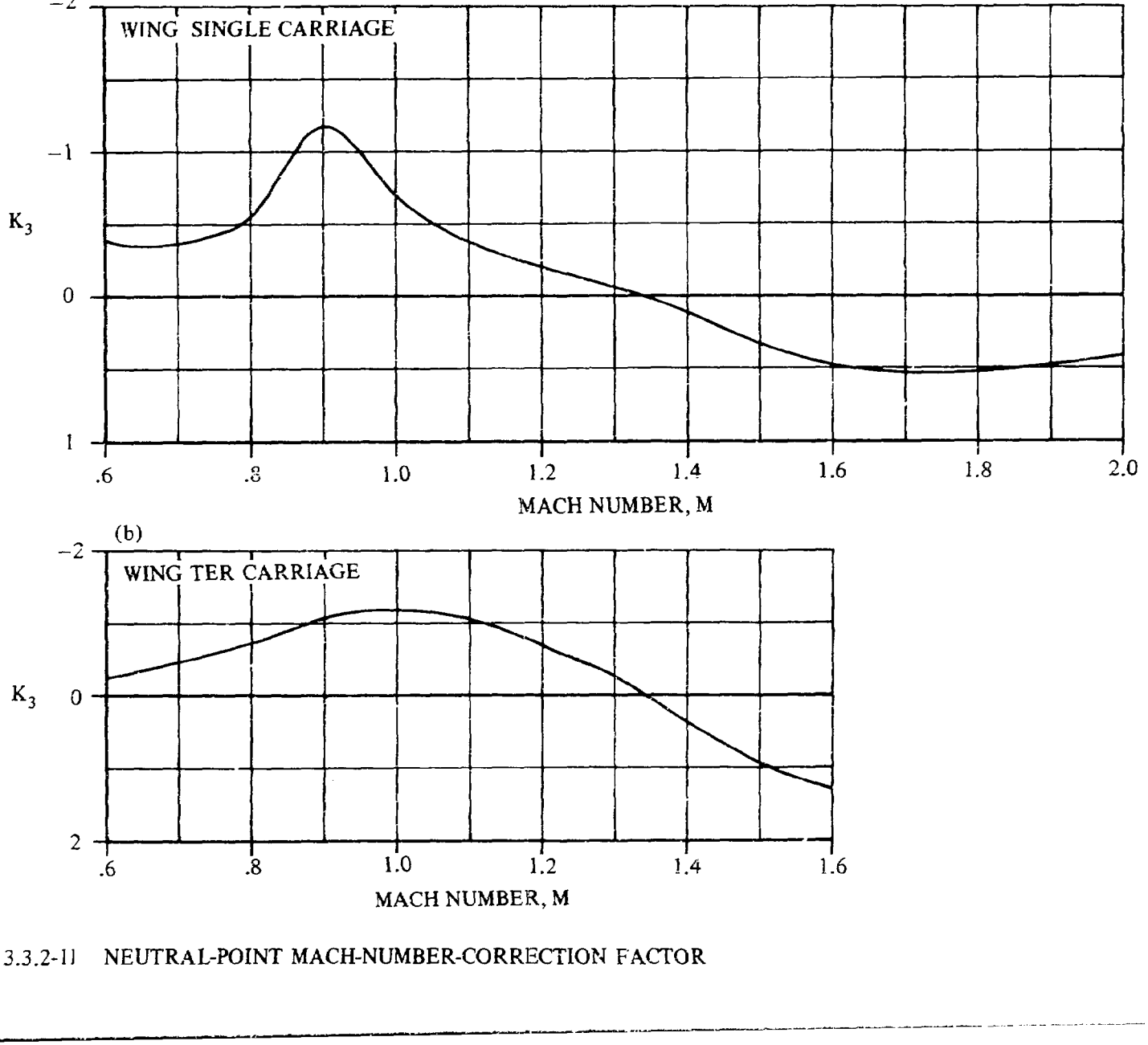

FIGURE 3.3.2-11 NEUTRAL-POINT MACH-NUMBER-CORRECTION FACTOR

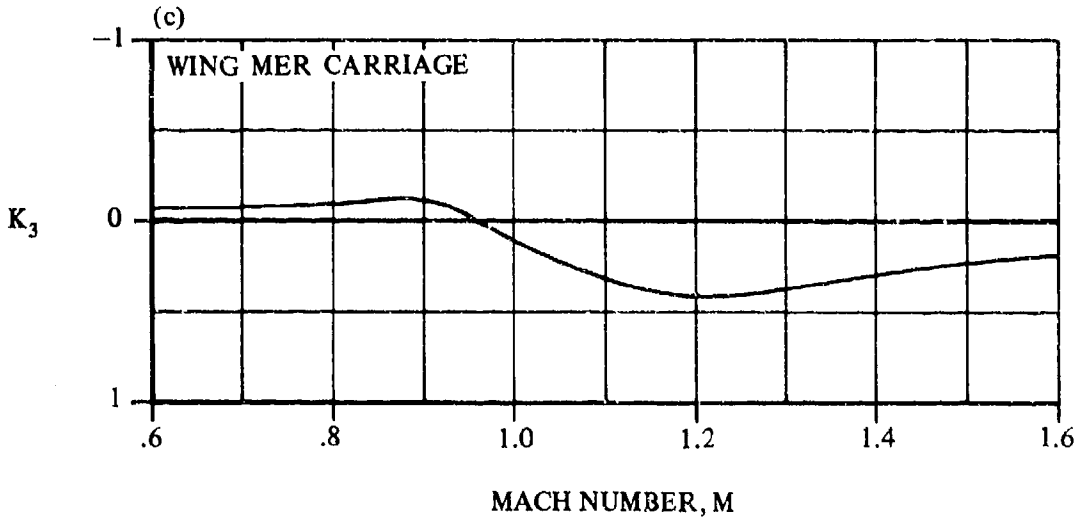

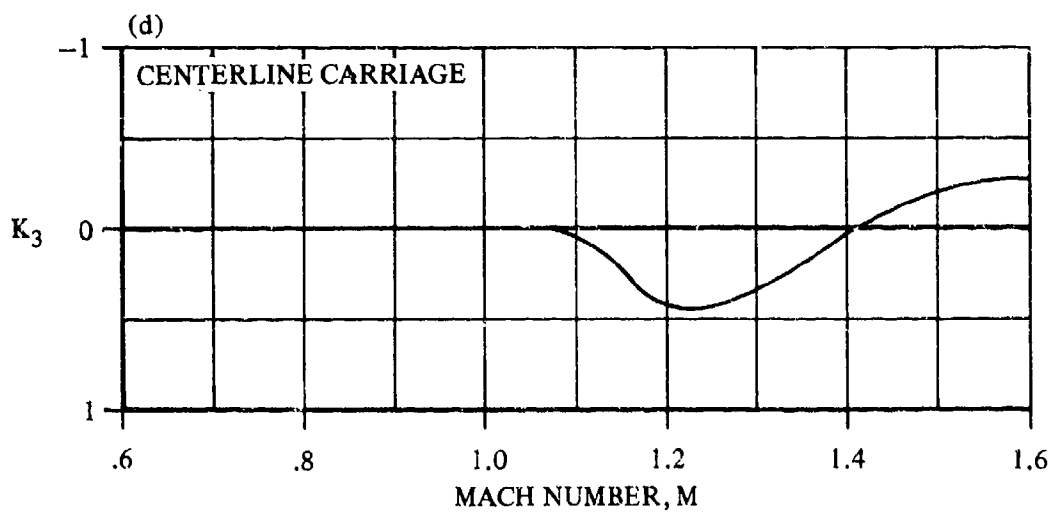

FIGURE 3.3.2-11 (CONTD)

3.3.3 NEUTRAL-POINT SHIFT DUE TO CHANGE IN TAIL EFFECTIVENESS

A method is presented in this section for estimating the neutral-point shift due to the change in horizontal-tail effectiveness caused by wing-mounted external-store installations. The method predicts a neutral-point shift due to all installations (armament stations) on the aircraft.

The Datcom Method is taken from Reference 1 and is empirical in nature. The method is applicable to aircraft of conventional design and essentially symmetrical store shapes with no major shape protuberances. The limitations on configuration and Mach-number range are summarized in Table 3.3-A. The user is cautioned that the neutral-point shift predicted by this method should be considered as only a first approximation because of the limited data base used in deriving the method. Since the method was developed from F-4 and A-7 aircraft wind-tunnel data, special care should be taken when applying the method to aircraft with horizontal-tail spans and vertical locations substantially different from these aircraft. Additional limitations pertaining to the method are listed below:

1. The method has been verified for the Mach-number range indicated in the figures associated with the method. Caution should be used in extrapolating the empirical curves beyond the given Mach-number range.

2. The method has not been verified for configurations in which flaps, slats, or other flow-disrupting devices are deployed.

3. The method is applicable for sideslip angles less than 4^{o}.

The effect due to a pair of symmetrical installations can be computed by doubling the effect of one side.

A. SUBSONIC

DATCOM METHOD

The neutral-point shift in inches, positive for aft shift, due to the change in tail effectiveness from store installations is given by

$$\Delta x_{n.p._3} = \sum_{i=1}^{N_I} \left(\Delta x'_{n.p._3}\right)_i K_{y_i} K_{z_i} \qquad 3.3.3\text{-a}$$

where

N_I is the total number of store installations on the aircraft.

$\Delta x'_{n.p._3}$ is the neutral-point horizontal-tail term obtained from Figures 3.3.3-5a and -5b as a function of configuration and Mach number. For fuselage mounted store installations $\Delta x'_{n.p._3} = 0$.

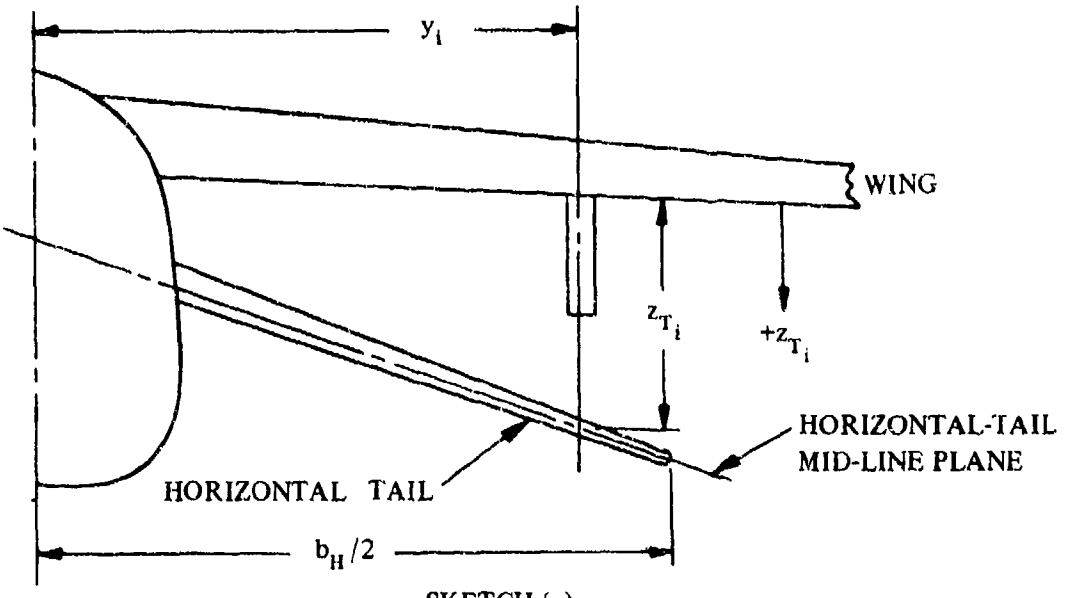

SKETCH (a)

K_{y_i} is the horizontal-tail span-location factor obtained from Figure 3.3.3-6a as a function of $\frac{y_i}{b_H/2}$ where

y_i is the spanwise distance from the fuselage centerline to the location of installation i (illustrated in Sketch (a)).

b_H is the horizontal-tail span (illustrated in Sketch (a)).

K_{z_i} is the horizontal-tail vertical-location factor obtained from Figure 3.3.3-6b as a function of $\frac{z_{T_i}}{b_H/2}$ where

z_{T_i} is the vertical distance from the wing lower surface at installation i to the horizontal-tail mid-line plane (illustrated in Sketch (a)).

Sample Problem

Given: A swept-wing subsonic-fighter aircraft from Reference 2 described in the Sample Problem of Paragraph A of Section 3.3.1. (See Pages 3.3.1-9 and 3.3.1-10 for identification of store installations.)

Additional Data:

$y_1 = y_5 = 113.75$ in.. $y_2 = y_4 = 78.8$ in. $b_H/2 = 68$ in. $M = 0.6$

$z_{T_1} = z_{T_5} = -59.8$ in. $z_{T_2} = z_{T_4} = -59.8$ in.

Compute:

Expand Equation 3.3.3-a to identify the terms that need to be computed, recalling that the wing installations are symmetrically loaded. Installation 3 is a fuselage mounted installation and the contribution of that installation is zero.

$$\Delta x_{n.p._3} = 2\left(\Delta x'_{n.p._3}\right)_1 K_{y_1} K_{z_1} + 2\left(\Delta x'_{n.p._3}\right)_2 K_{y_2} K_{z_2}$$

$\left(\Delta x'_{n.p._3}\right)_1 = 0.48$ (Figure 3.3.3-5a, single carriage)

$\left(\Delta x'_{n.p._3}\right)_2 = 0.80$ (Figure 3.3.3-5b, multiple carriage)

$$\frac{y_1}{b_H/2} = \frac{113.75}{68} = 1.67$$

$$\frac{z_{T_1}}{b_H/2} = \frac{-59.8}{68} = -0.88$$

$$\frac{y_2}{b_H/2} = \frac{78.8}{68} = 1.16$$

$$\frac{z_{T_2}}{b_H/2} = \frac{-59.8}{68} = -0.88$$

$K_{y_2} = 0.57$ (Figure 3.3.3-6a)

Referring to Figure 3.3.3-6a it is seen that $y_i/(b_H/2)$ is beyond the range of the design chart. This suggests that if the store installation is far enough outboard of the tip of the horizontal tail, the increment in neutral-point shift due to that particular installation is negligible. Therefore, for this configuration it is assumed that $K_{y_1} = 0$.

Referring to Figure 3.3.3-6b it is seen that $z_{T_i}/(b_H/2)$ for both Installations 1 and 2 are well beyond the range of the design chart. It seems reasonable to assume that the value of K_{z_i} will asymptotically approach zero as the vertical distance between the store installation and the horizontal tail is increased. Therefore, for this configuration it is assumed that $K_{z_1} = K_{z_2} = 0$.

Solution:

$$\Delta x_{n.p._3} = \sum_{i=1}^{N_I} \left(\Delta x'_{n.p._3}\right)_i K_{y_i} K_{z_i} \qquad \text{(Equation 3.3.3-a)}$$

$$= 2\left(\Delta x'_{n.p._3}\right)_1 \; K_{y_1} K_{z_1} + 2\left(\Delta x'_{n.p._3}\right)_2 \; K_{y_2} K_{z_2}$$

$$= 2(0.48)(0)(0) + 2(0.80)(0.57)(0)$$

$$= 0$$

The calculated value of $\Delta x_{n.p._3}$ is summed with $\Delta x_{n.p._1}$ and $\Delta x_{n.p._2}$ (computed in Sections 3.3.1 and 3.3.2 respectively) in the Sample Problem of Section 3.3.4 to obtain the total shift in neutral point.

B. TRANSONIC

The method presented in Paragraph A of this section is also valid in the transonic speed range.

C. SUPERSONIC

The method presented in Paragraph A of this section is also valid in the supersonic speed range up to a Mach number of 1.6 to 2.0 as indicated in Table 3.3-A. The maximum Mach number provided in the figures should indicate the level to which the method is substantiated. Caution should be used when extrapolating the data beyond the Mach-number range provided in the figures.

REFERENCES

1. Gallagher, R. D., Jimenez, G., Light, L. E., and Thames F. C.: Technique for Predicting Aircraft Aerodynamic Effects Due to External Stores Carriage. AFFDL-TR-75-95, Volumes I and II, 1975. (U)

2. Watzke, R. E.: Aerodynamic Data for Model TA-4F Operational Flight Trainer. McDonnell Douglas Corporation Rept. DAC-67425, 1968. (U)

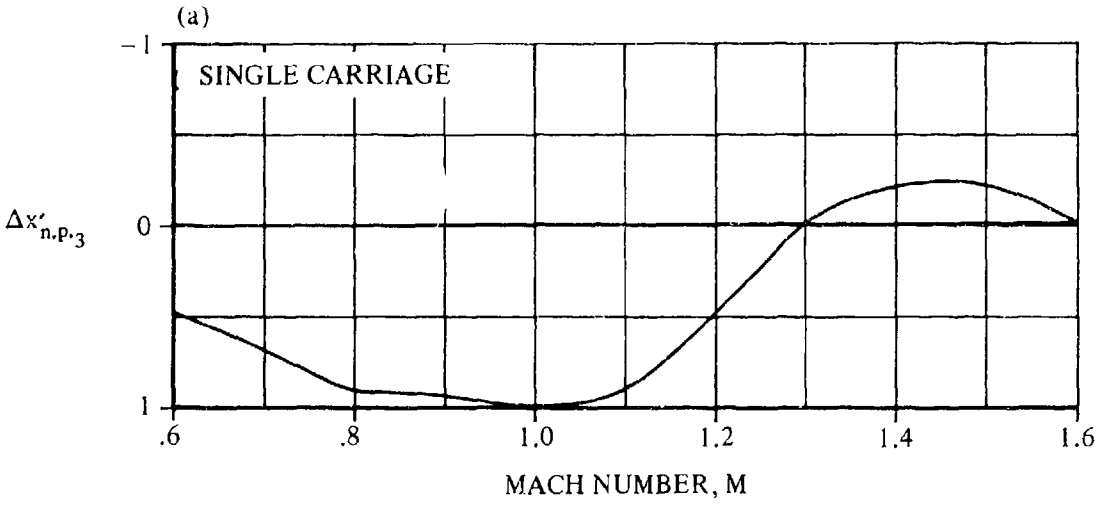

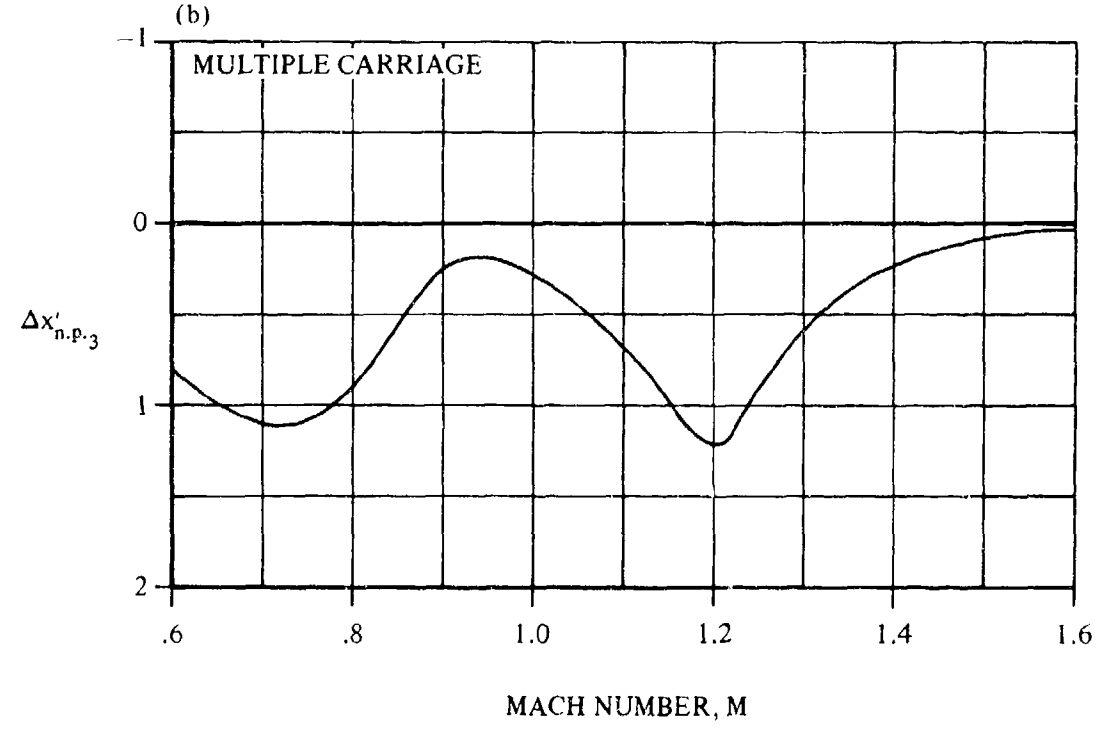

FIGURE 3.3.3-5 NEUTRAL-POINT HORIZONTAL-TAIL TERM

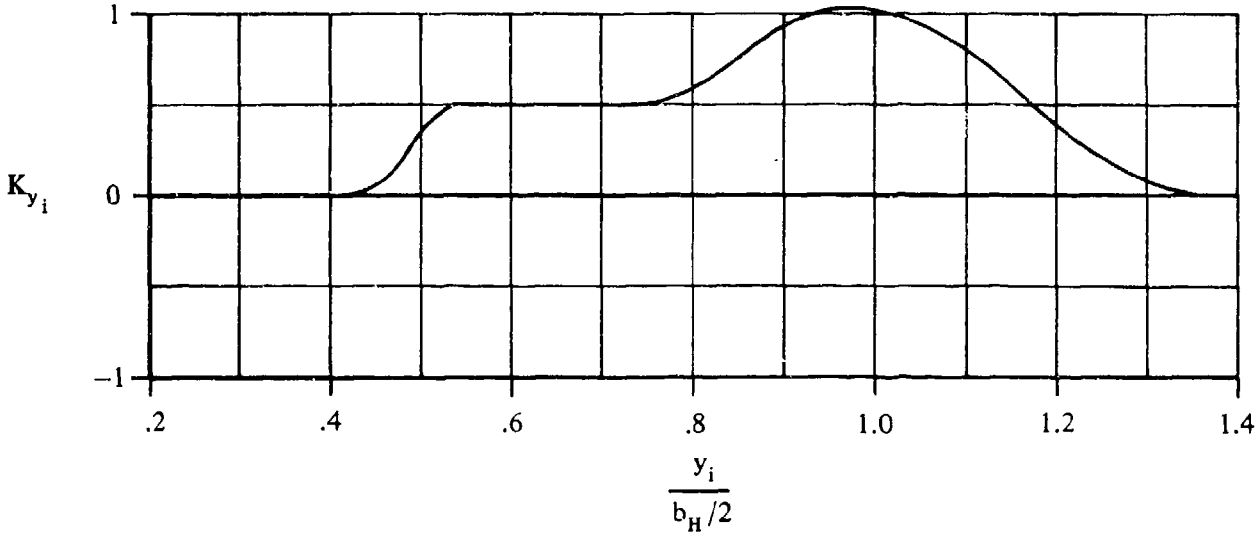

FIGURE 3.3.3-6 a HORIZONTAL-TAIL SPAN-LOCATION FACTOR

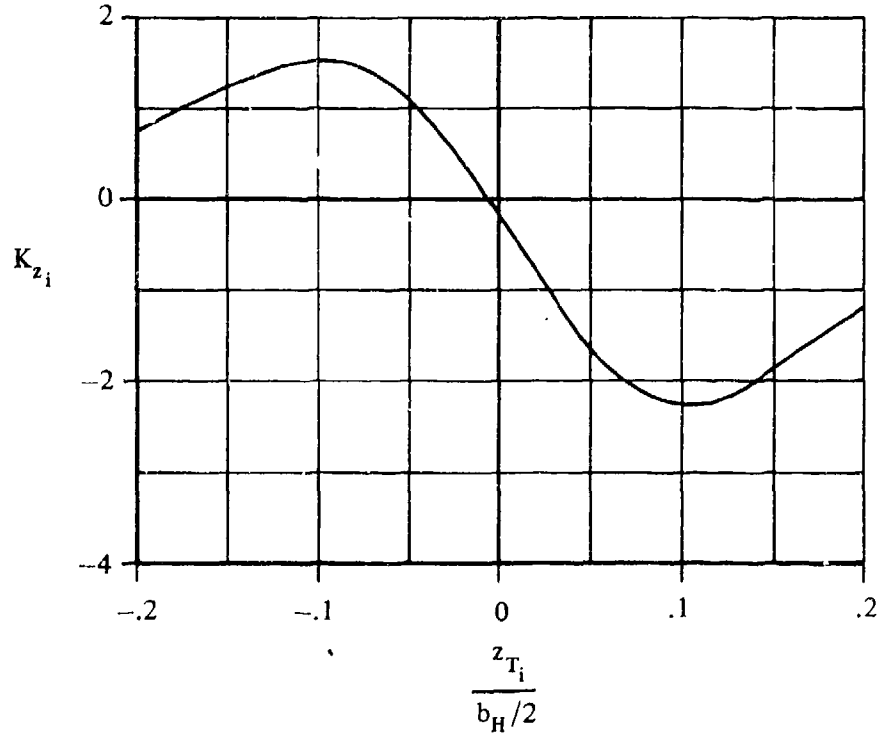

FIGURE 3.3.3-6 b HORIZONTAL-TAIL VERTICAL-LOCATION FACTOR

3.3.4 TOTAL NEUTRAL-POINT SHIFT DUE TO EXTERNAL STORES

A method is presented in this section for estimating the total shift in aircraft neutral point due to external-store installations. The method predicts the neutral-point shift for symmetric, asymmetric, and multiple-installation loading configurations.

The Datcom Method is taken from Reference 1 and is empirical in nature. The method is applicable to aircraft of conventional design and essentially symmetrical store shapes with no major shape protuberances. The limitations on configuration and Mach-number range are summarized in Table 3.3-A. Additional limitations and assumptions pertaining to the method are listed below:

1. The method is not applicable to wing-tip or wing-tangent-mounted stores.
2. Fuselage-mounted installations must be located on the fuselage centerline.
3. The method is not applicable to empty multiple racks.
4. The effect of empty pylons on neutral point is considered to be negligible.
5. The method has been verified for the Mach-number range given in Table 3.3-A. Caution should be used in extrapolating the empirical curves beyond the given Mach-number range.
6. The method has not been verified for configurations in which flaps, slats, or other flow-disrupting devices are deployed.
7. The method gives the best results for an angle-of-attack range from 0 to 8^{o}, although the method can be used for higher angles of attack.
8. The data base used in deriving the method relied heavily on swept-wing tactical-combat-aircraft wind-tunnel data.
9. The method is applicable for sideslip angles less than 4^{o}.

The procedure for computing the total neutral-point shift requires calculation of increments due to lift transfer from stores to aircraft, interference effects on the wing flow field, and change in tail effectiveness. These increments are computed by the methods of Sections 3.3.1, 3.3.2, and 3.3.3, respectively. The increments are computed for the entire loading configuration and then summed by the method of this section to obtain the total increment.

A. SUBSONIC

DATCOM METHOD

The total neutral-point shift in inches, positive for aft shift, due to external-store installations is given by

$$\Delta x_{n.p.} = \Delta x_{n.p._1} + \Delta x_{n.p._2} + \Delta x_{n.p._3} \qquad 3.3.4\text{-a}$$

where

$\Delta x_{n.p._1}$ is the shift in neutral point due to lift transfer from the stores to the clean aircraft (in.), obtained from Section 3.3.1.

$\Delta x_{n.p._2}$ is the shift in neutral point due to the interference effects on the wing flow field (in.), obtained from Section 3.3.2.

$\Delta x_{n.p._3}$ is the shift in neutral point due to the change in tail effectiveness caused by external stores (in.), obtained from Section 3.3.3.

Reference 1 states that the prediction accuracies are such that the predicted values of neutral-point shift are nominally within about 1 inch of the test values 60 percent of the time, and within 4 inches 92 percent of the time.

Sample Problem

Given: A swept-wing subsonic-fighter aircraft from Reference 2 loaded with external-store installations described in the Sample Problem of Paragraph A of Section 3.3.1.

Compute:

$\Delta x_{n.p._1} = -0.114$ in. (Sample Problem, Paragraph A, Section 3.3.1)

$\Delta x_{n.p._2} = 0.077$ in. (Sample Problem, Paragraph A, Section 3.3.2)

$\Delta x_{n.p._3} = 0$ (Sample Problem, Paragraph A, Section 3.3.3)

$\Delta x_{n.p.} = \Delta x_{n.p._1} + \Delta x_{n.p._2} + \Delta x_{n.p._3}$ (Equation 3.3.4-a)

$= -0.114 + 0.077 + 0 = -0.037$ in.

B. TRANSONIC

The method presented in Paragraph A of this section is also valid in the transonic speed range. The expected accuracy of the method is less than that in the subsonic speed range.

C. SUPERSONIC

The method presented in Paragraph A of this section is also valid in the supersonic speed range. The expected accuracy of the method is less than that in the subsonic speed range.

REFERENCES

1. Gallagher, R. D., Jimenez, G., Light, L. E., and Thames, F. C.: Technique for Predicting Aircraft Aerodynamic Effects Due to External Stores Carriage. AFFDL-TR-75-95, Volumes I and II, 1975. (U)

2. Watzke, R. E.: Aerodynamic Data for Model TA-4F Operational Flight Trainer. McDonnell Douglas Corporation Rept. DAC-67425, 1968. (U)

3.4 EFFECTS OF EXTERNAL STORES ON AIRCRAFT SIDE FORCE

A method is presented in this section for estimating the increment in aircraft side force due to external-store installations. The method predicts an incremental change in the side-force-due-to-sideslip derivative, ΔC_{Y_β}, which can be added to the clean aircraft C_{Y_β} to obtain the aircraft-with-stores C_{Y_β}.

The Datcom Method is taken from Reference 1 and is empirical in nature. The method is limited to the store-loading configurations and Mach-number range presented in Table 3.4-A.

TABLE 3.4-A

LOADING AND MACH-NUMBER LIMITATIONS

Mounting Location	Carriage Mode	Mount/Loading Type	Mach-Number Range
Wing	Single	Pylon – Empty	0.6 → 2.0
		Pylon – Store	
	Multiple	Pylon – Empty MER	0.6 → 1.6
		Pylon – Fully Loaded MER	
		Pylon – Empty TER	
		Pylon – Fully Loaded TER	
Fuselage	Single	Tangent	0.6 → 2.0
		Pylon – Empty	
		Pylon – Store	
	Multiple	Tangent – Empty MER	0.6 → 1.6
		Tangent – Fully Loaded MER	
		Tangent – Empty TER	
		Tangent – Fully Loaded TER	
		Pylon – Empty MER	
		Pylon – Fully Loaded MER	
		Pylon – Empty TER	
		Pylon – Fully Loaded TER	

The Datcom Method is applicable to mixed-loading configurations obtained by combining two or more loadings specified in Table 3.4-A. The method was developed from symmetrically-loaded-stores data and is therefore limited primarily to symmetrically-loaded configurations. However, certain asymmetric configurations may be treated by the method. It should be noted that one-half of the incremental side force due to a symmetrical-store loading is not necessarily equivalent to the side force produced by half of that loading carried asymmetrically. Where there are aircraft components near the stores, or if strong lateral flow fields exist due to angle of attack, part of the aerodynamic side force induced by an installation on one side of the aircraft is cancelled by an opposite force on the other side. The Datcom Method is considered applicable to asymmetric configurations for which the sidewash change due to angle of attack is zero and fuselage effects are negligible.

The prediction method was developed from data based on an angle of attack of 5^{o}. No method is provided to account for the effect of angle-of-attack change on side force, but the method is considered to be valid throughout the normal cruise angle-of-attack range.

The method is subject to the following additional limitations and assumptions:

1. The method has been verified for the Mach-number ranges given in Table 3.4-A. Caution should be used in extrapolating the empirical curves beyond the given Mach-number ranges.

2. The method has not been verified for configurations in which flaps, slats, or other flow-disrupting devices are deployed.

3. The store shape is essentially symmetrical with no major shape protuberances.

4. The data base used in deriving the method relied heavily on swept-wing tactical-combat-aircraft wind-tunnel data.

5. No tail effects are included.

6. The method is applicable for sideslip angles less than 8^{o}.

The side-force-derivative increment is composed of a basic contribution due to the store installations and a contribution due to interference between adjacent installations (when separation distance is sufficiently small).

A. SUBSONIC

DATCOM METHOD

The increment in C_{Y_β}, based on wing reference area, due to external-store installations is given by

$$\Delta C_{Y_\beta} = \frac{1}{S_W}\left[\sum_{i=1}^{N_I} \frac{1}{2}\left(Y_{B_\beta}\right)_i + \sum_{j=1}^{N_P}\left(Y_{A_\beta}\right)_j\right] \qquad 3.4\text{-a}$$

where

S_W is the wing reference area (ft^2).

N_I is the total number of store installations.

N_P is the total number of pairs of adjacent-store installations carried. (See Sketch (a).)

Y_{B_β} is the basic side-force contribution (ft^2/deg) per degree sideslip due to a symmetrical pair of external-store installations, calculated in Step 1 below. Since the empirical equations and figures for Y_{B_β} are based on a pair of symmetrical-store installations, Y_{B_β} must be divided by 2 before summing over the total number of installations, thus allowing for the inclusion of asymmetrical loading cases.

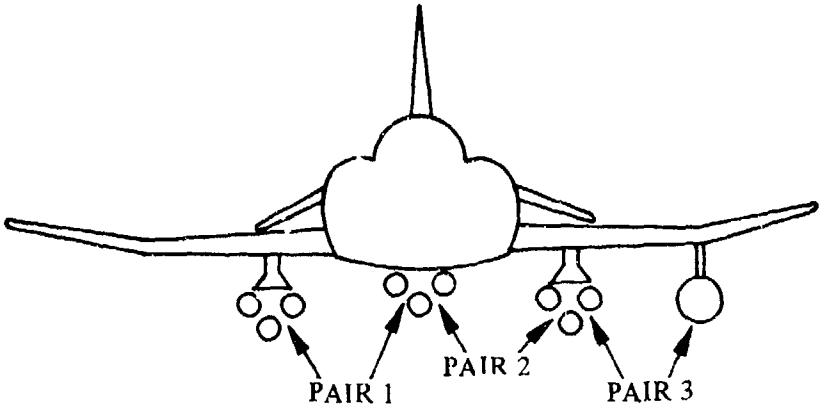

SKETCH (a)

Y_{A_β} is the side-force contribution (ft^2/deg) per degree sideslip due to interference effects from a pair of adjacent external-store installations, calculated in Step 2 below.

ΔC_{Y_β} is computed by using the following steps:

1. Compute Y_{B_β} for each installation.
2. Compute Y_{A_β} for each pair of adjacent installations.
3. Compute ΔC_{Y_β}.

Step 1. Compute Y_{B_β} for each installation:

The various loading configurations are assigned reference numbers in Table 3.4-B.

TABLE 3.4-B

CONFIGURATION SUMMARY

Mounting \ Carriage	Empty	Single	Empty MER	Full MER	Empty TER	Full TER
Wing-Pylon	1	2	3	4	5	6
Fuselage-Tangent	–	7	8	9	10	11
Fuselage-Pylon	12	13	14	15	16	17

$$Y_{B_\beta} = -(B_P + B_R + B_N + B_X + B_Y)\, K_M \qquad 3.4\text{-b}$$

where

B_P is the pylon contribution given by

$$B_P = \frac{K_{PC}\, h_p^{\,2}}{144} \qquad 3.4\text{-c}$$

where

K_{PC} is a pylon constant obtained from Table 3.4-C.

TABLE 3.4-C

PYLON CONSTANT

Configuration	1	2	3	4	5	6	7-11	12	13	14	15	16	17
K_{PC}	.10	.15	.14	.14	.12	.12	0	.10	.15	.14	.14	.12	.12

h_p is the average pylon height (in.). (See Sketch (b).)

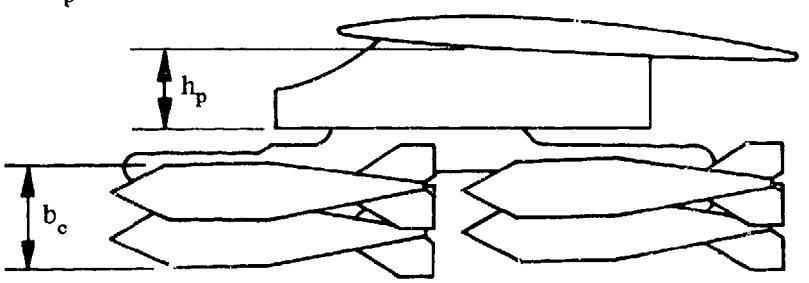

SKETCH (b)

B_R is the rack contribution.

For Configurations 2, 7, and 13 the store contribution is included and

$$B_R = K_F \frac{b_F^2}{144} + \frac{(0.09)\, d_S^2}{144} \qquad 3.4\text{-d}$$

where

K_F is a fin constant given by

K_F = 0.082 for + and X fins

K_F = 0.107 for V fins

b_F is the store-fin span (in.). (Total span measured tip-to-tip. For V fins, the total span of the actual fin and its mirror image.)

d_S is the store maximum diameter (in.).

For other configurations, B_R is given by Table 3.4-D.

TABLE 3.4-D

RACK CONTRIBUTION

Configuration	1	3	4	5	6	8	9	10	11	12	14	15	16	17
B_R	0	.325	.325	.183	.183	.325	.325	.183	.183	0	.325	.325	.183	.183

B_N is the store contribution

For Configurations 1, 3, 5, 8, 10, 12, 14, and 16 $B_N = 0$.

For single-store installations (Configurations 2, 7, and 13), B_N is included in the B_R computation.

For Configurations 4, 6, 9, 11, 15, 17

$$B_N = 0.0666 \left(\frac{b_c}{12}\right)^2 \left(\frac{b_F}{d_S}\right)^3 (R_D + 1) \qquad 3.4\text{-e}$$

where

b_c is the maximum vertical span (in.) of the side projection of the store cluster in a vertical plane, excluding protruding fins. (See Sketch (b).)

R_D is a correlation factor given by Figure 3.4-12 for Configurations 4, 9, and 15. $R_D = 0$ for Configurations 6, 11, and 17. All other terms in Equation 3.4-e have been previously defined.

B_X is the contribution due to pylon longitudinal location.

For fuselage-mounted configurations (Configurations 7-17) $B_X = 0$.

For wing-pylon-mounted configurations (Configurations 1-6), B_X is given by

$$B_X = (B_P + B_R + B_N)(K_{XP} - 1) \qquad 3.4\text{-f}$$

where B_P, B_R, B_N were previously defined and

$$K_{XP} = (1 + A_2)(A_1) \left(\begin{array}{c} K_{XP} \text{ has a maximum} \\ \text{value of 1.0} \end{array}\right) \qquad 3.4\text{-g}$$

where

A_2 is a store-size correlation factor obtained from Figure 3.4-13 as a function of the maximum store diameter, d_S. For Configurations 1, 3, and 5, the value of A_2 is zero.

A_1 is a longitudinal-location correlation factor obtained from Figure 3.4-14 as a function of x_{AFT}/c where

x_{AFT} is the longitudinal distance (in.) from the local wing trailing edge to the trailing edge of pylon, rack, or store as appropriate (i.e., the most aft component), positive in the aft direction. (See Sketch (c).)

c is the local wing chord at the store installation (in.). (See Sketch (c).)

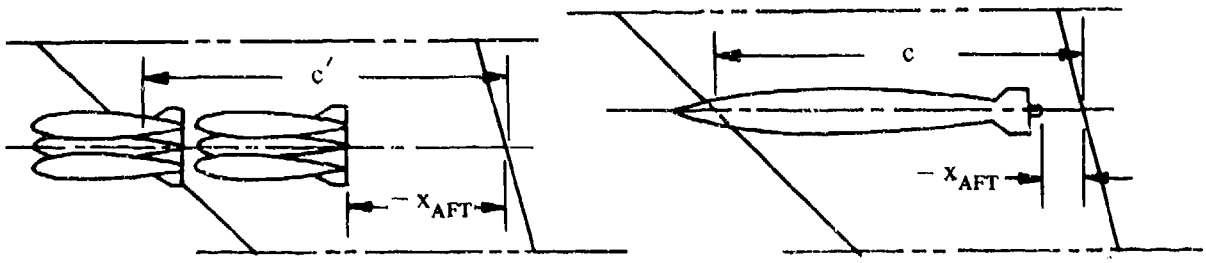

MULTIPLE STORES SINGLE STORE

SKETCH (c)

B_Y is the contribution due to spanwise location of the pylon installation.

For fuselage-mounted configurations (Configurations 7-17),

$$B_Y = 0 \qquad 3.4\text{-h}$$

For wing-pylon-mounted configurations (Configurations 1-6) on low-wing aircraft,

$$B_Y = K_y \left(\frac{y_i}{b_W/2} - 0.350 \right) \qquad 3.4\text{-i}$$

For wing-pylon-mounted configurations on high-wing aircraft,

$$B_Y = K_y \left(\frac{y_i'}{b_e/2} - 0.350 \right) \qquad 3.4\text{-j}$$

where

K_y is a store-installation-depth factor obtained from Figure 3.4-15 as a function of z, the maximum depth (in.) of the store installation.

y_i is the spanwise distance from the fuselage centerline to the location of installation i (illustrated in Sketch (d)).

b_W is the wing span.

y_i' is the spanwise distance from the outboard edge of the fuselage to the location of installation i (illustrated in Sketch (d)).

b_e is the exposed wing span (illustrated in Sketch (d)).

K_M is a side-force Mach-effect factor obtained from Figure 3.4-16 as a function of Mach number and $\frac{y_i'}{b/2}$ where $b = b_W$ for low-wing aircraft, $b = b_e$ for high-wing aircraft, and y_i', b_W, and b_e were previously defined.

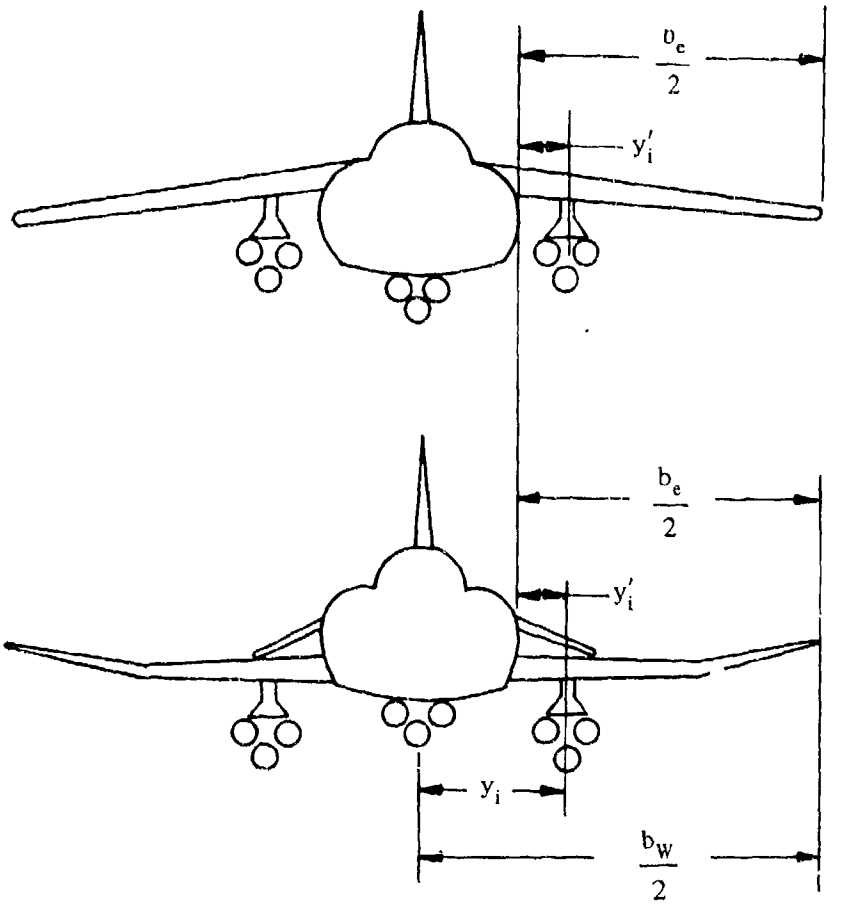

SKETCH (d)

Step 2. Compute Y_{A_β} for each pair of adjacent installations.

Determine the number of pairs of adjacent installations (see Sketch (a)).

Compute Y_{A_β} for each adjacent pair:

$$Y_{A_\beta} = -\left[\left(Y_{B_\beta}\right)_1 + \left(Y_{B_\beta}\right)_2\right] R_{NEG} \qquad 3.4\text{-k}$$

where

$\left(Y_{B_\beta}\right)_1$ is obtained from Equation 3.4-b for the first of the pair of installations.

$\left(Y_{B_\beta}\right)_2$ is obtained from Equation 3.4-b for the second of the pair of installations.

R_{NEG} is an adjacent-store interference factor obtained from Figure 3.4-17 as a function of $(X_F + X_A)/(\ell_1 + \ell_2)$ and Mach number where

X_F is the absolute longitudinal distance from the nose of one store installation to the nose of the adjacent installation. (See Sketch (e).)

X_A is the absolute longitudinal distance from the trailing edge of one store installation to the trailing edge of the adjacent installation. (See Sketch (e).)

ℓ_1 and ℓ_2 are the lengths of the two store installations. (See Sketch e).)

For no adjacent store installations,

$$Y_{A_\beta} = 0 \qquad 3.4\text{-}\ell$$

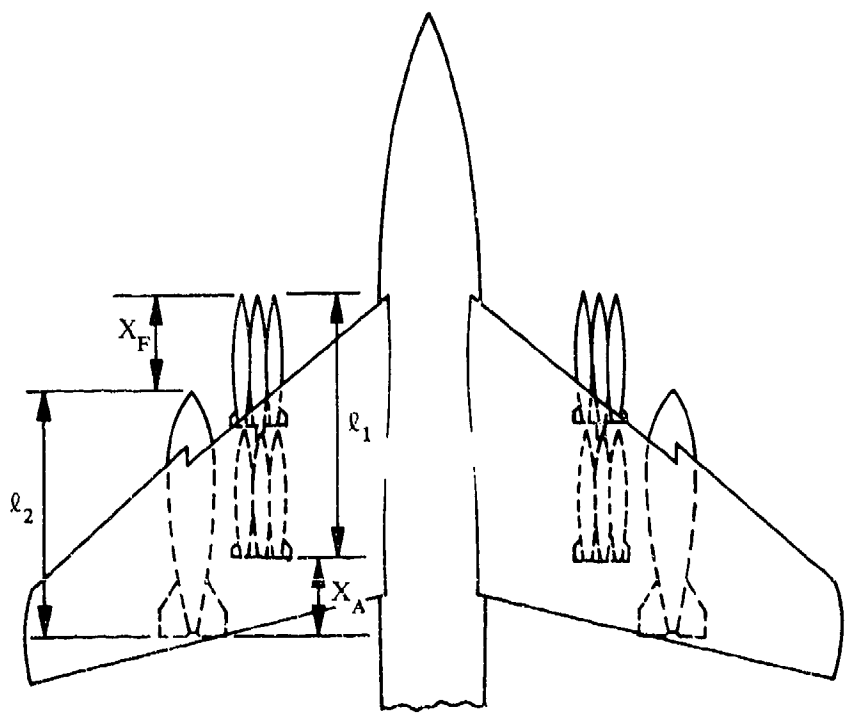

SKETCH (e)

Step 3. Compute ΔC_{Y_β}

ΔC_{Y_β} is computed from Equation 3.4-a by summing the Y_{B_β} values obtained in Step 1 for each installation and the Y_{A_β} values obtained from Step 2 for each pair of adjacent installations.

Reference 1 states that the method nominally results in prediction errors of 10 to 15 percent. A comparison of test data with results calculated by this method is provided in Table 3.4E. Additional comparisons of test and calculated results are found in Reference 1.

Sample Problem

Given: A swept-wing subsonic-fighter aircraft from Reference 2 with one 300-gal tank, pylon mounted on each wing.

Aircraft Data:

$S_W = 260\ ft^2$ Low-wing configuration

Store Data:

$d_S = 26.5$ in. $b_F = 35.06$ in. + type fins

Installation Data:

$h_p = 11.2$ in. $\frac{y_1}{b_W/2} = 0.320$ $\frac{x_{AFT}}{c} = 0.288$ $z = 37.3$ in.

Additional Data:

$M = 0.6$

Compute:

Step 1. Compute Y_{B_β} for each installation. (Since the installations are symmetrical, only one side need be computed). This is Configuration 2 (Table 3.4-B)

$K_{PC} = 0.15$ (Table 3.4-C)

$$B_P = \frac{K_{PC}\, h_P^{\,2}}{144} = \frac{(0.15)(11.2)^2}{144} = 0.1307 \qquad \text{(Equation 3.4-c)}$$

$K_F = 0.082$ (+ type fins)

$$B_R = K_F \frac{b_F^{\,2}}{144} + \frac{(0.09) d_S^{\,2}}{144} \qquad \text{(Equation 3.4-d)}$$

$$= \frac{(0.082)(35.06)^2}{144} + \frac{(0.09)(26.5)^2}{144}$$

$= 1.1389$

B_N is included in the B_R computation (Configuration 2)

$A_2 = 0.365$ (Figure 3.4-13)

$A_1 = 0.77$ (Figure 3.4-14, single store)

$K_{XP} = (1 + A_2)(A_1)$ (maximum value of 1.0) (Equation 3.4-g)

$= (1 + 0.365)(0.77) = 1.05$; use $K_{XP} = 1.0$

$B_X = (B_P + B_R + B_N)(K_{XP} - 1)$ (Equation 3.4-f)

$= (0.1307 + 1.1389 + 0)(1.0 - 1)$

$= 0$

$K_Y = 1.95$ (Figure 3.4-15)

$B_Y = K_Y \left(\frac{y_i}{b_W/2} - 0.350\right)$ (Equation 3.4-i)

$= 1.95\,(0.320 - 0.350) = -0.0585$

$K_M = 1.0$ (Figure 3.4-16)

$Y_{B_\beta} = -(B_P + B_R + B_N + B_X + B_Y)K_M$ (Equation 3.4-b)

$= -(0.137 + 1.1389 + 0 - 0 - 0.0585)(1.0)$

$= -1.211$

Step 2. Compute Y_{A_β} for each pair of adjacent installations. In this case there are no adjacent installations, and $Y_{A_\beta} = 0$.

Step 3. Compute ΔC_{Y_β}:

$$\Delta C_{Y_\beta} = \frac{1}{S_W}\left[\sum_{i=1}^{N_I} \frac{1}{2}\left(Y_{B_\beta}\right)_i + \sum_{j=1}^{N_P}\left(Y_{A_\beta}\right)_j\right] \quad \text{(Equation 3.4-a)}$$

$$= \frac{1}{S_W}\left[\sum_{i=1}^{2} \frac{1}{2}\left(Y_{B_\beta}\right)_i + 0\right]$$

$$= \frac{1}{260}\left[\frac{1}{2}(-1.211) + \frac{1}{2}(-1.211)\right]$$

$= -0.0047$ per deg

Values of ΔC_{Y_β} at other Mach numbers have been calculated and are shown in comparison to test data from Reference 2 in Sketch (c).

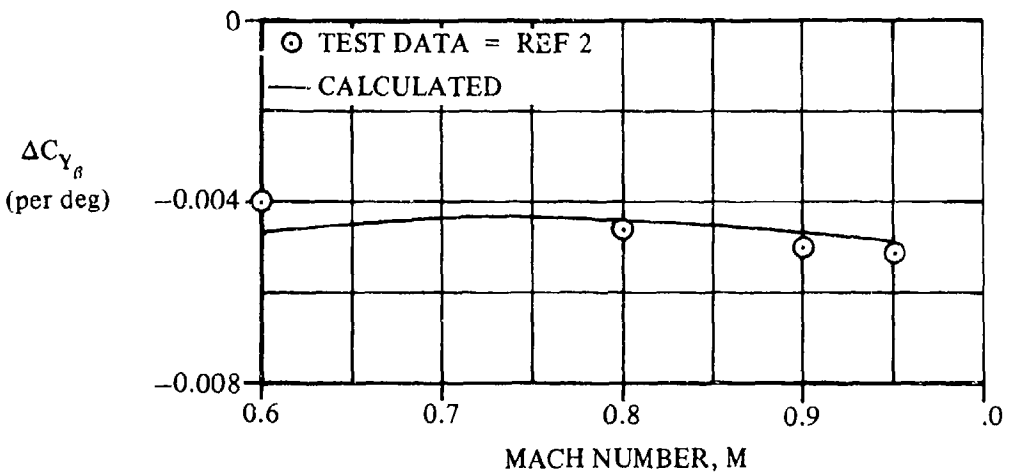

SKETCH (c)

B. TRANSONIC

The method presented in Paragraph A of this section is also valid in the transonic speed range. The user is cautioned that the expected accuracy of the method is less than that expected in the subsonic speed range. A comparison of test data with results calculated by this method at transonic speed is presented in Table 3.4-E.

C. SUPERSONIC

The method presented in Paragraph A of this section is also valid in the supersonic speed range up to a Mach number of 1.6 to 2.0 as indicated in Table 3.4-A. The maximum Mach number provided in the figures should indicate the level to which the method is substantiated by Reference 1. Caution should be used when extrapolating the data beyond the Mach-number range provided in the figures. A comparison of test data with results calculated by this method at supersonic speeds is presented in Table 3.4-E.

REFERENCES

1. Gallagher, R. D., Jimenez, G., Light, L. E., and Thames, F. C.: Technique for Predicting Aircraft Aerodynamic Effects Due to External Stores Carriage. AFFDL-TR-75-95, Volumes I and II, 1975. (U)

2. Watzke, R. E.: Aerodynamic Data for Model TA-4F Operational Flight Trainer. McDonnell Douglas Corporation Rept. DAC-67425, 1968. (U)

3. Bonine, W. J., et al: Model F/RF-4B-C Aerodynamic Derivatives. McDonnell Douglas Corporation Rept. 9842, 1964 (Rev. 1971). (U)

TABLE 3.4-E

SUBSONIC AND SUPERSONIC EXTERNAL-STORE SIDE FORCE DATA SUMMARY AND SUBSTANTIATION

Ref	Loading Description	α (deg)	M	ΔC_{Y_β} calc (per deg)	ΔC_{Y_β} test (per deg)	ΔC_{Y_β} calc-test (per deg)
2	Wing Station Mounting Left Inboard Pylon-Mounted Single: 300-gal tank Right Inboard Pylon-Mounted Single: 300-gal tank	5	0.6	−0.0047	−0.0040	−0.0007
			0.8	−0.0044	−0.0046	0.0002
			0.9	−0.0046	−0.0050	0.0004
			0.95	−0.0048	−0.0051	0.0003
3	Wing Station Mounting Left Inboard Pylon-Mounted Single: Missile Right Inboard Pylon-Mounted Single: Missile	5	0.6	−0.0035	−0.0015	−0.0020
			0.9	−0.0039	−0.0020	−0.0019
			1.2	−0.0042	−0.0028	−0.0014
			1.6	−0.0043	−0.0020	−0.0023
			2.0	−0.0022	−0.0020	−0.0002

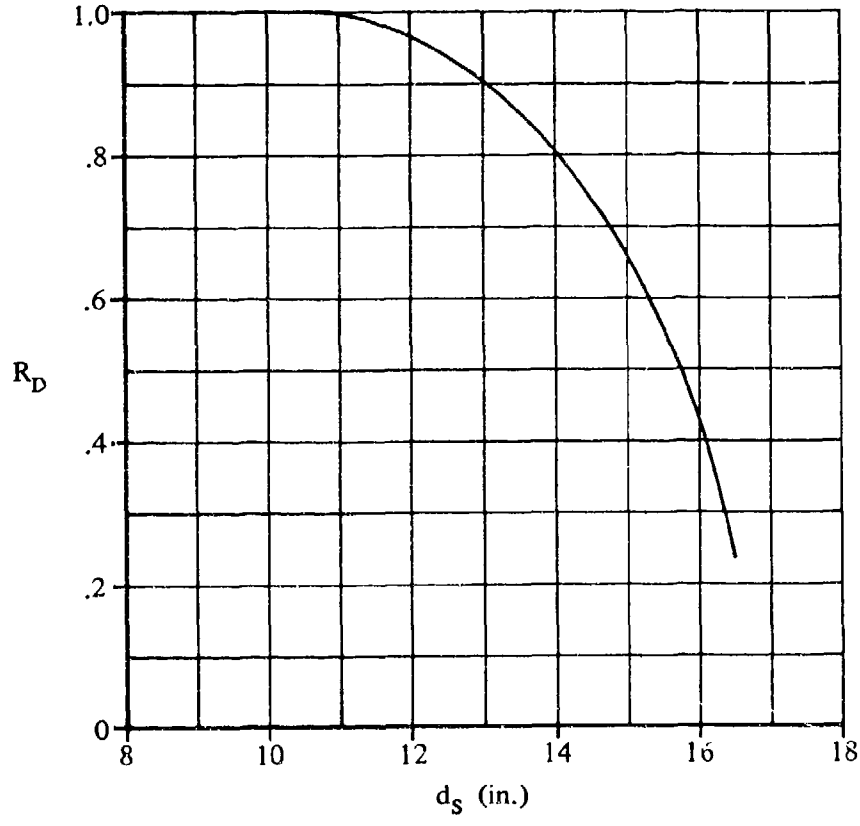

FIGURE 3.4-12 BASIC-STORES-CORRELATION FACTOR

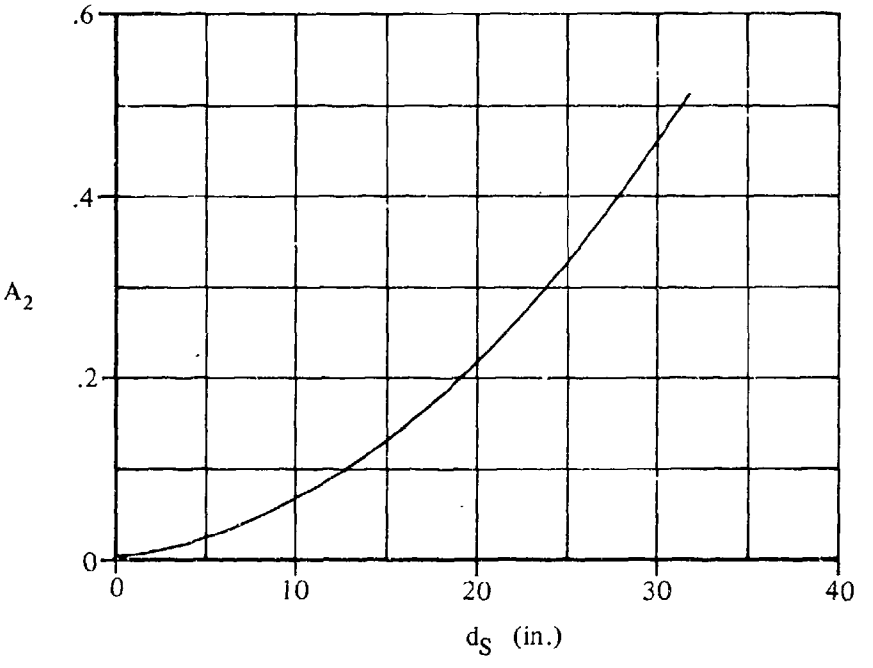

FIGURE 3.4-13 STORE-SIZE CORRELATION FACTOR

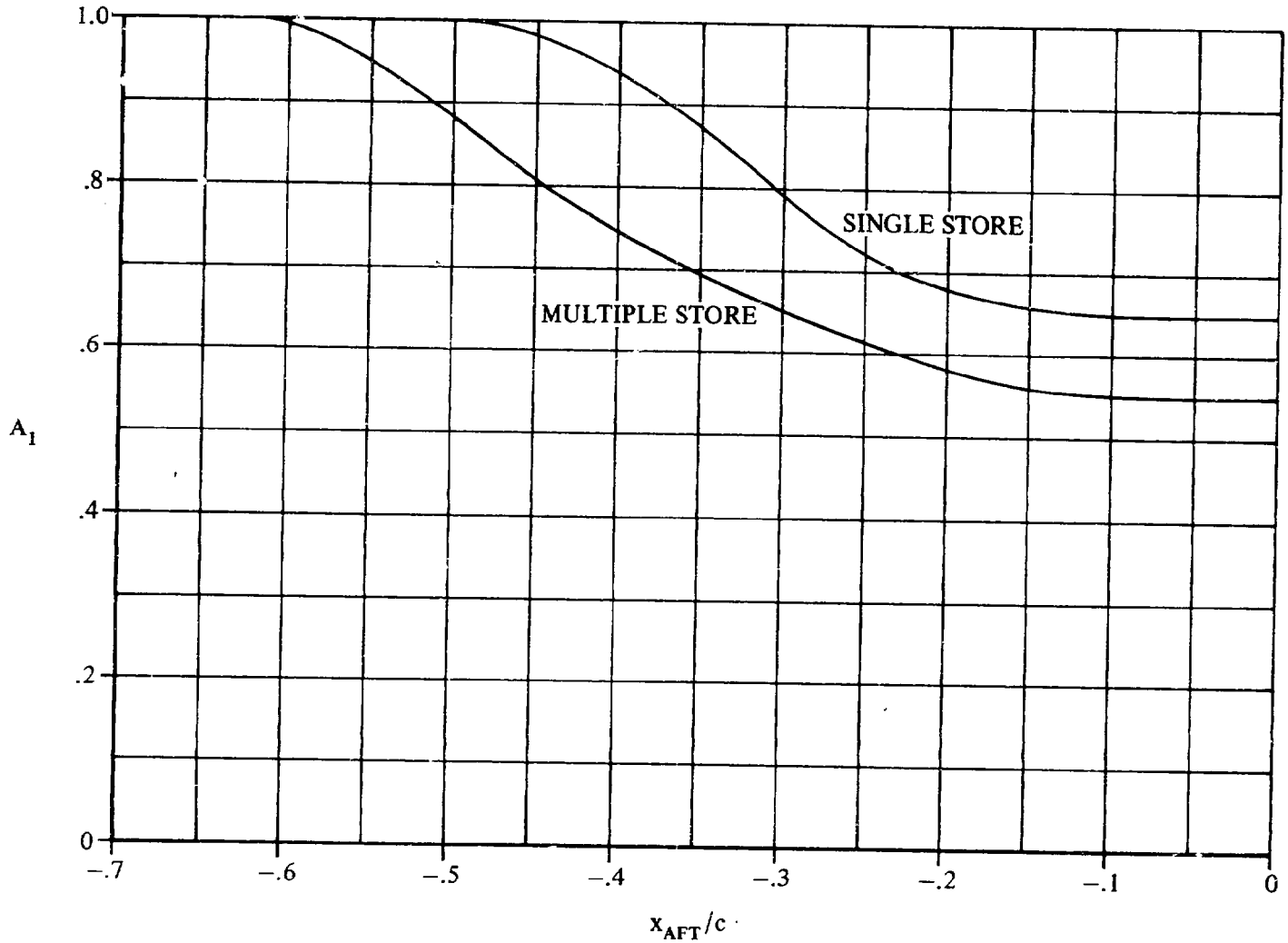

FIGURE 3.4-14 PYLON LONGITUDINAL-LOCATION CORRELATION FACTOR

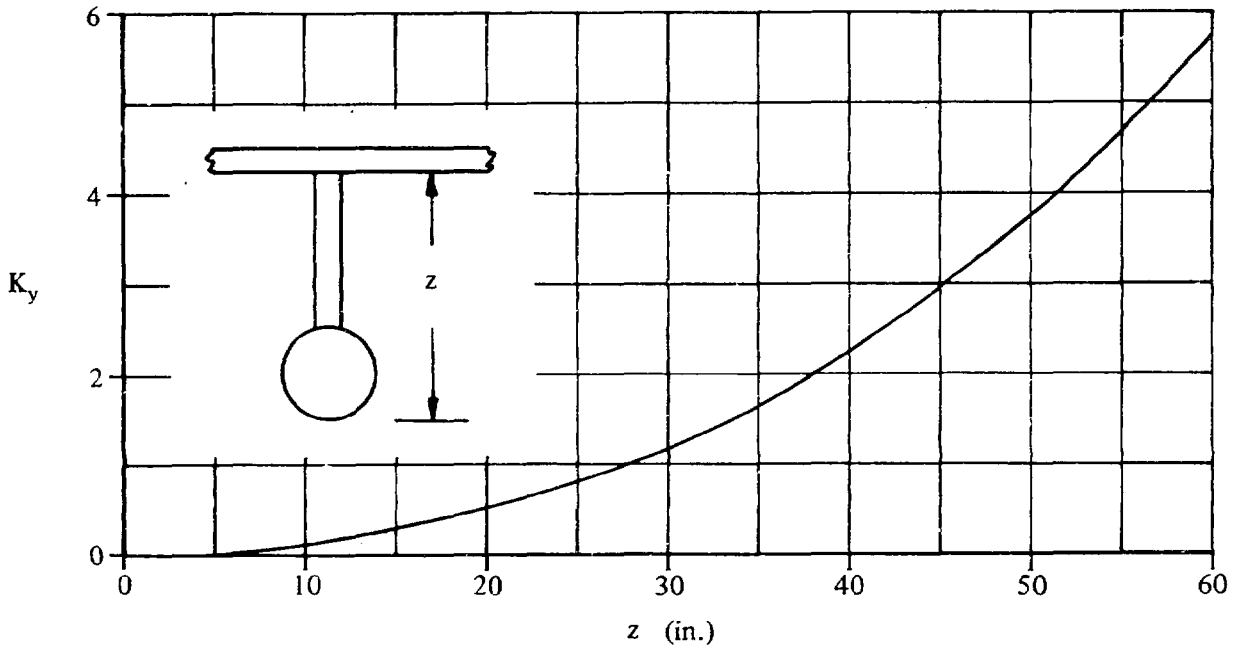

FIGURE 3.4-15 STORE-INSTALLATION-DEPTH FACTOR

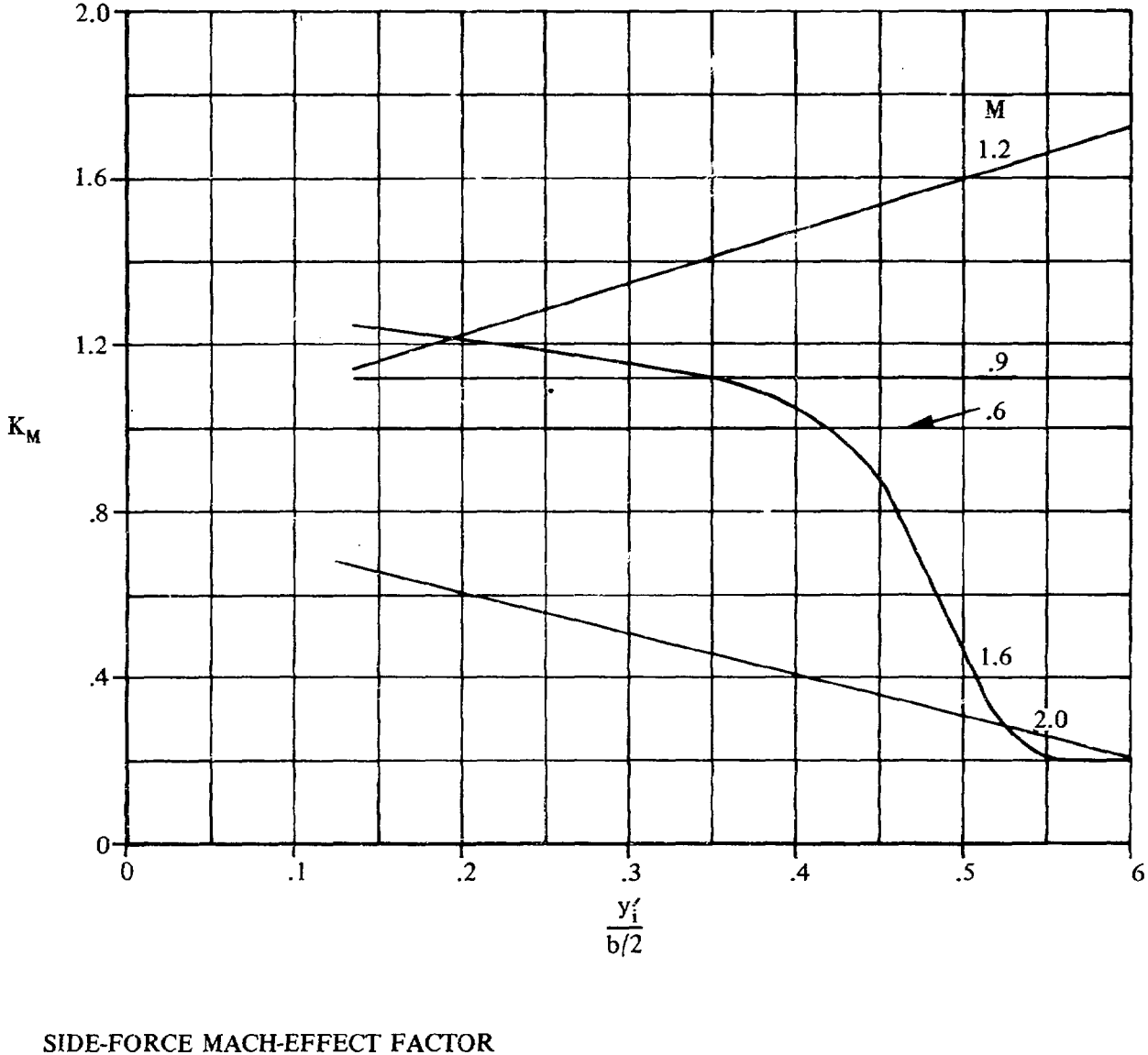

FIGURE 3.4-16 SIDE-FORCE MACH-EFFECT FACTOR

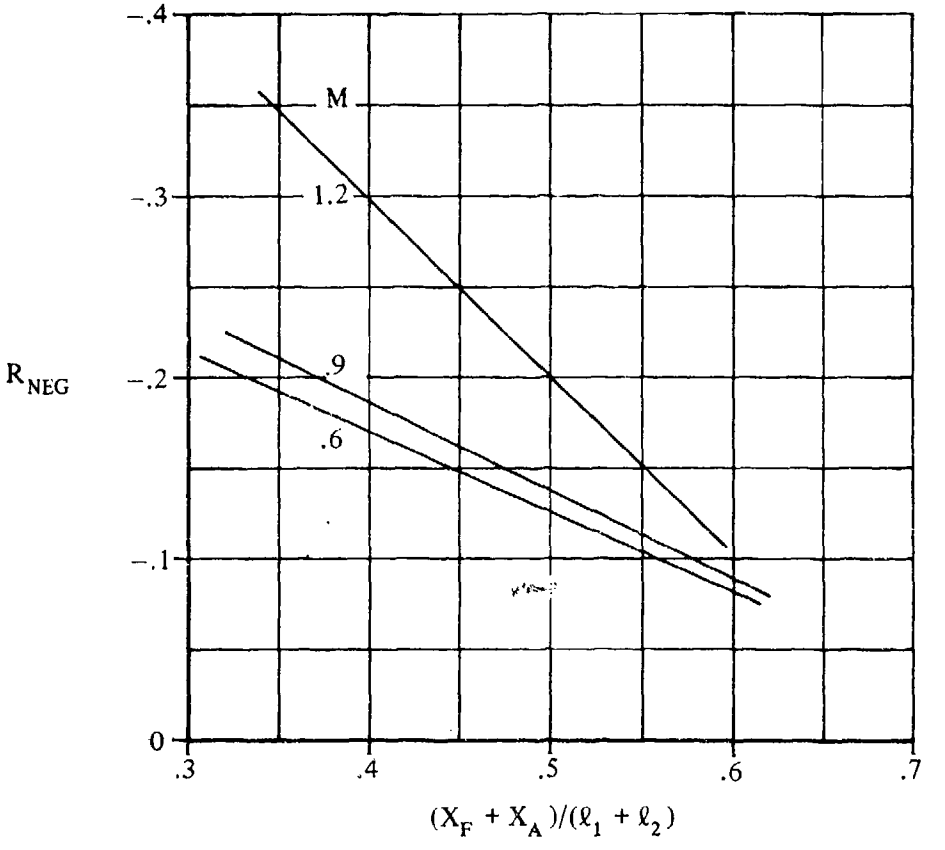

FIGURE 3.4-17 ADJACENT-STORE INTERFERENCE FACTOR

3.5 EFFECT OF EXTERNAL STORES ON AIRCRAFT YAWING MOMENT

A method is presented in this section for estimating the increment in aircraft yawing moment due to external-store installations. For symmetrically-loaded configurations, the increment is primarily due to sideslip. The incremental yawing moment due to asymmetrical loading is composed of a moment due to sideslip and a moment due to drag differential. The moment due to drag differential can be estimated by multiplying the incremental drag coefficient due to the store installation (which may be computed from Section 3.2) by the moment arm from the c.g. to the spanwise location of the installation. The method presented in this section predicts an incremental change in the yawing-moment-due-to-sideslip derivative, ΔC_{n_β}, which can be added to the clean aircraft C_{n_β} to obtain the aircraft-with-stores C_{n_β}.

The Datcom Method is taken from Reference 1 and is empirical in nature. The method requires that the incremental side-force data be provided by the user or computed by the method of Section 3.4. The method is limited to the store-loading configurations and Mach-number ranges presented in Table 3.5-A.

The Datcom Method is applicable to mixed loading configurations obtained by combining two or more loadings specified in Table 3.5-A. The method was developed from symmetrically-loaded-stores data and is therefore limited primarily to symmetrically-loaded configurations. However, certain asymmetric configurations can be treated by the method.

The prediction method was developed from data based on an angle of attack of 5^o. No method is provided to account for the effect of angle-of-attack change on yawing moment, but the method is considered to be valid throughout the normal cruise angle-of-attack range.

TABLE 3.5-A

LOADING AND MACH-NUMBER LIMITATIONS

Mounting Location	Carriage Mode	Mount/Loading	Mach-Number Range
Wing	Single	Pylon – Empty	0.6 → 2.0
		Pylon – Store	
	Multiple	Pylon – Fully-Loaded MER	0.6 → 1.6
		Pylon – Fully-Loaded TER	
Fuselage	Single	Tangent	0.6 → 2.0
		Pylon – Store	
	Multiple	Pylon – Fully-Loaded MER	0.6 → 1.6

The method is subject to the following additional general limitations and assumptions:

1. The method has been verified for the Mach-number ranges given in Table 3.5-A. Caution should be used in extrapolating the empirical curves beyond the given Mach-number ranges.

2. The method has not been verified for configurations in which flaps, slats, or other flow-disrupting devices are deployed.

3. The store shape is essentially symmetrical with no major shape protuberances.

4. The data base used in deriving the method relied heavily on swept-wing tactical-combat-aircraft wind-tunnel data.

5. No tail effects are included.

6. The method is applicable for sideslip angles less than 8^{o}.

The method is based on the premise that yawing moment is the product of the side force and a moment arm from the point of force application to a reference point. Lift and drag effects are neglected. The method is applicable to asymmetric configurations for which the sidewash change due to angle of attack is zero and fuselage effects are negligible.

The yawing-moment-derivative increment is composed of a basic contribution due to the store installations and a contribution due to interference between adjacent installations (when separation distance is small).

A. SUBSONIC

DATCOM METHOD

The increment in C_{n_β} (based on wing reference area and span) due to external stores is given by

$$\Delta C_{n_\beta} = \frac{1}{S_W b_W} \left\{ \sum_{i=1}^{N_I} \left(\frac{1}{2} Y_{B_\beta} \frac{\ell_m}{12} \right)_i + \sum_{j=1}^{N_P} \left[\frac{1}{2} Y_{A_\beta} \left(\frac{\ell_{m_1}}{12} + \frac{\ell_{m_2}}{12} \right) \right]_j \right\} \qquad 3.5\text{-a}$$

where

S_W is the wing reference area (ft^2).

b_W is the wing span (ft).

N_I is the total number of store installations on the aircraft.

Y_{B_β} is the basic side-force contribution (ft^2/deg) per degree sideslip due to a symmetrical pair of external-store installations, obtained from Section 3.4.

N_P is the total number of pairs of adjacent-store installations carried. (See Sketch (a).)

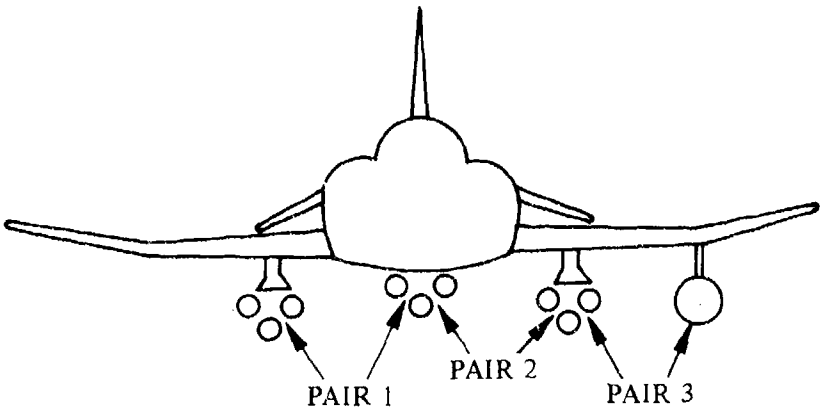

SKETCH (a)

Y_{A_β} is the side-force contribution (ft^2/deg) per degree sideslip due to interference effects from a pair of adjacent-external store installations, obtained from Section 3.4. This term should only be used for single-store installations placed at approximately equal distances below the wing, with minimum lateral separation of 25 to 60 inches between store surfaces of adjacent installations.

ℓ_m, ℓ_{m_1}, ℓ_{m_2} are moment arms (in.) from the moment reference point to the effective point of application of the side-force increment due to external stores, positive in the aft direction. The moment arm for the first of the pair of adjacent installations is ℓ_{m_1}, the second of the pair is ℓ_{m_2}. The value of ℓ_m is given by

$$\ell_m = (FS)_{ref} - [(FS)_{LE} + \ell_x] \qquad 3.5\text{-b}$$

where

$(FS)_{ref}$ is the fuselage station (in.) of the moment reference point.

$(FS)_{LE}$ is the fuselage station (in.) of the nose of the most forward store on the installation or the leading edge of the pylon for the empty pylon case.

ℓ_x is the longitudinal distance (in.) from $(FS)_{LE}$ to the point of side-force application, positive aft. This term is a function of installation type, and is calculated below for various configurations.

Case 1: Wing-Mounted Empty Pylon

$$\ell_x = 0.25\, c_{p_{low}} \qquad 3.5\text{-c}$$

where

$c_{p_{low}}$ is the bottom-pylon-chord length (in.). (See Sketch (b).)

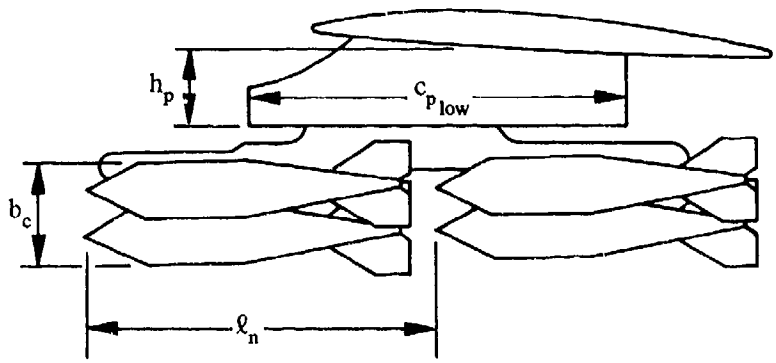

SKETCH (b)

Case 2: Wing- or Fuselage-Pylon-Mounted Single Store

$$\ell_x = \frac{\ell_P B_P + \ell_{SB} B_{SB} + \ell_{SF} B_{SF}}{B_P + B_{SB} + B_{SF}} \qquad 3.5\text{-d}$$

where

ℓ_P is the pylon moment arm (in.) given by

$$\ell_P = 0.25\, c_{p_{low}} \qquad 3.5\text{-e}$$

where $c_{p_{low}}$ is defined above for Case 1.

B_P is the pylon contribution given by

$$B_P = 0.15 \left(\frac{h_p}{12}\right)^2 \qquad 3.5\text{-f}$$

where

h_p is the average pylon height (in.) shown in Sketch (b).

ℓ_{SB} is the store-body moment arm (in.) given by

$$\ell_{SB} = 0.15\, \ell_S \qquad 3.5\text{-g}$$

where

ℓ_S is the store-body length (in.).

B_{SB} is the store-body contribution given by

$$B_{SB} = 0.09\left(\frac{d_S}{12}\right)^2 \qquad 3.5\text{-h}$$

where

d_S is the maximum store diameter (in.).

ℓ_{SF} is the longitudinal distance (in.) from the store nose to the intersection of the store-fin quarter chord and the store-fin 50-percent semispan. (See Sketch (c).)

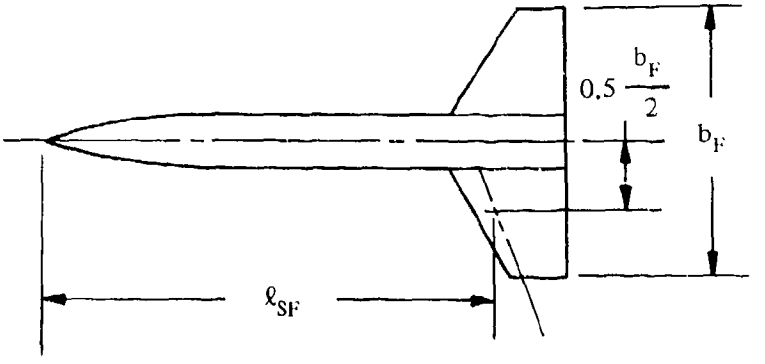

SKETCH (c)

B_{SF} is the store-fin contribution given by

$$B_{SF} = 0.082\left(\frac{b_F}{12}\right)^2 \quad \text{for + or x type fins} \qquad 3.5\text{-i}$$

or

$$B_{SF} = 0.107\left(\frac{b_F}{12}\right)^2 \quad \text{for V type fins} \qquad 3.5\text{-j}$$

where

b_F is the store-fin span (ft) shown in Sketch (c). (For V fins, the total span of the actual fin and its mirror image.)

Case 3: Wing- or Fuselage-Pylon-Mounted Fully-Loaded MER

$$\ell_x = \frac{(0.933)\,\ell_P B_P + 0.5\,\ell_{EM}\,(0.0325) + 0.5\,\ell_S B_{FSC} + \ell_{ASC} B_{ASC}}{B_P + 0.325 + B_{FSC} + B_{ASC}} \qquad 3.5\text{-k}$$

where

ℓ_P is given by Equation 3.5-e.

B_P is given by Equation 3.5-f.

ℓ_{EM} is the length of the empty MER (in.).

ℓ_S is the store-body length (in.).

B_{FSC} is the forward-store-cluster contribution given by

$$B_{FSC} = 0.0666 \left(\frac{b_c}{12}\right)^2 \left(\frac{b_f}{d_S}\right)^2 \qquad 3.5\text{-}\ell$$

where

b_c is the maximum vertical span (in.) of the side projection of the store cluster in a vertical plane, excluding protruding fins. (See Sketch (b).)

b_F and d_S are defined above in Case 2.

ℓ_{ASC} is the aft-store-cluster moment arm given by

$$\ell_{ASC} = 0.5\,\ell_S + \ell_n \qquad 3.5\text{-}m$$

where

ℓ_n is the longitudinal distance (in.) from the store nose of the forward cluster to the store nose of the aft cluster. (See Sketch (b).)

B_{ASC} is the aft-store-cluster contribution given by

$$B_{ASC} = R_{LC} B_{FSC} \qquad 3.5\text{-}n$$

where

B_{FSC} is given by Equation 3.5-ℓ.

R_{LC} is an aft-store-cluster lateral-clearance factor obtained from Figure 3.5-12 as a function of d_S the maximum store diameter.

Case 4: Wing-Pylon-Mounted Fully-Loaded TER

$$\ell_x = \frac{(0.80)\,\ell_P B_P + 0.5\,\ell_{ET}\,(0.182) + 0.5\,\ell_S B_{FSC}}{B_P + 0.182 + B_{FSC}} \qquad 3.5\text{-o}$$

where

ℓ_P is given by Equation 3.5-e.

B_P is given by Equation 3.5-f.

ℓ_{ET} is the length of the empty TER (in.).

B_{FSC} and ℓ_S are defined above in Case 3.

Case 5: Fuselage-Tangent-Mounted Single Store

$$\ell_X = \frac{\ell_{SB} B_{SB} + \ell_{SF} B_{SF}}{B_{SB} + B_{SF}} \qquad 3.5\text{-p}$$

where

ℓ_{SB} is given by Equation 3.5-g.

B_{SB} is given by Equation 3.5-h.

ℓ_{SF} is defined previously in Case 2.

B_{SF} is given by Equations 3.5-i and 3.5-j.

Reference 1 indicates that the method nominally results in average prediction errors of 20 percent from the actual yawing-moment increment. The percent error is highly dependent upon the distance from the aircraft center of gravity to the point of side-force application. When the side force acts through a point near the center of gravity, the percent error may be large even though the moment error is small. A comparison of test data with results calculated by this method is presented in Table 3.5-B. Additional comparisons of test and calculated results are found in Reference 1.

Sample Problem

Given: A swept-wing fighter aircraft from Reference 3 with single pylon-mounted air-to-air missiles mounted on each wing.

Aircraft Data:

$S_W = 530\ ft^2$ $\quad b_W = 38.67\ ft$ $\quad (FS)_{ref} = 317.0\ in.$

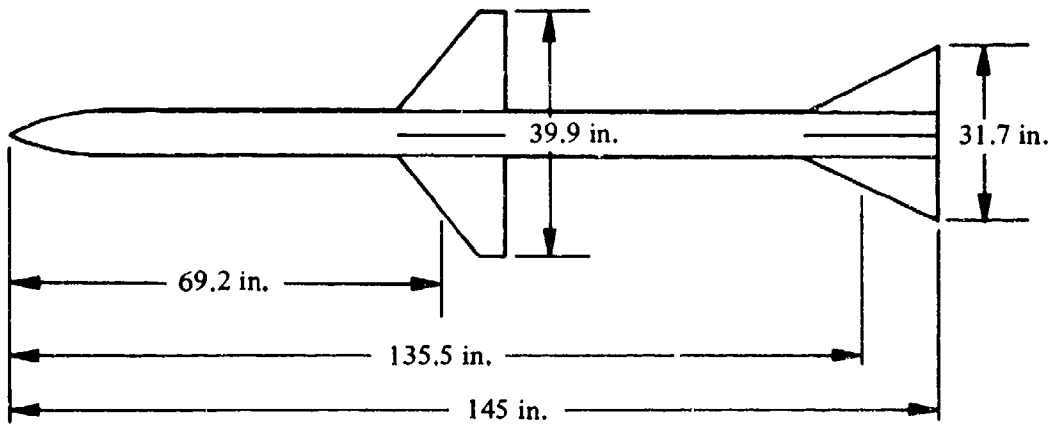

Store Data:

d_S = 8 in. $\quad \ell_S$ = 145 in. $\quad b_F$ (FWD) = 39.9 in.

b_F (AFT) = 31.7 in. $\quad \ell_{SF}$ (FWD) = 69.2 in. $\quad \ell_{SF}$ (AFT) = 135.5 in.

Installation Data:

$c_{p_{low}}$ = 113.8 in. $\quad h_p$ = 18 in. $\quad (FS)_{LE}$ = 182.0 in.

Additional Data:

M = 0.6 $\quad \alpha = 5^o$ $\quad \Delta C_{Y_\beta}$ = –0.0015 per deg

Compute:

Find ℓ_x for each installation. (Only one side need be computed since the installations are symmetrical.) For a wing-pylon-mounted single store:

$$\ell_P = 0.25\, c_{p_{low}} = (0.25)(113.8) = 28.45 \text{ in.} \qquad \text{(Equation 3.5-e)}$$

$$B_P = 0.15\left(\frac{h_p}{12}\right)^2 = (0.15)\left(\frac{18}{12}\right)^2 = 0.3375 \qquad \text{(Equation 3.5-f)}$$

$$\ell_{SB} = 0.15\, \ell_S = (0.15)(145) = 21.75 \text{ in.} \qquad \text{(Equation 3-5-g)}$$

$$B_{SB} = 0.09\left(\frac{d_S}{12}\right)^2 = (0.09)\left(\frac{8}{12}\right)^2 = 0.0400 \qquad \text{(Equation 3.5-h)}$$

Since there are two sets of fins on this store, both sets are accounted for in the computation.

For the forward set of fins,

ℓ_{SF} = 69.2 in.

$$B_{SF} = (0.082)\left(\frac{b_F}{12}\right)^2 = (0.082)\left(\frac{39.9}{12}\right)^2 = 0.907 \text{ ft}^2 \qquad \text{(Equation 3.5-i)}$$

For the aft set of fins,

ℓ_{SF} = 135.5 in.

$$B_{SF} = (0.082)\left(\frac{b_F}{12}\right)^2 = (0.082)\left(\frac{31.7}{12}\right)^2 = 0.572 \qquad \text{(Equation 3.5-i)}$$

$$\ell_x = \frac{\ell_P B_P + \ell_{SB} B_{SB} + \ell_{SF} B_{SF}}{B_P + B_{SB} + B_{SF}} \qquad \text{(Equation 3.5-d).}$$

$$= \frac{(28.45)(0.338) + (21.75)(0.0400) + (69.2)(0.907) + (135.5)(0.572)}{0.338 + 0.0400 + 0.907 + 0.572}$$

= 81.2 in.

Find ℓ_m:

$\ell_m = (FS)_{ref} - [(FS)_{LE} + \ell_x]$ (Equation 3.5-b)

= 317.0 − [182.0 + 81.2]

= 53.8 in.

Since there are no pairs of adjacent store installations, ℓ_{m_1} and ℓ_{m_2} are not computed.

Find Y_{B_β} and Y_{A_β}:

Y_{B_β} and Y_{A_β} are estimated by the method of Section 3.4.

Y_{A_β} = 0 (no adjacent store installations)

Since ΔC_{Y_β} is given, Y_{B_β} can be computed from Equation 3.4-a.

$$\Delta C_{Y_\beta} = \frac{1}{S_W}\left[\sum_{i=1}^{N_I} \frac{1}{2}\left(Y_{B_\beta}\right)_i + \sum_{j=1}^{N_P}\left(Y_{A_\beta}\right)_j\right] \qquad \text{(Equation 3.4-a)}$$

Recalling that $Y_{A_\beta} = 0$ and that there are two installations symmetrically placed,

$$\Delta C_{Y_\beta} = \frac{1}{S_W}(2)\left(\frac{1}{2}\right)Y_{B_\beta}$$

$$Y_{B_\beta} = S_W \Delta C_{Y_\beta}$$

$$= (-0.0015)(530)$$

$$= -0.795 \text{ ft}^2/\text{deg}$$

Find ΔC_{n_β}:

$$\Delta C_{n_\beta} = \frac{1}{S_W b_W}\left\{\sum_{i=1}^{N_I}\left(\frac{1}{2} Y_{B_\beta}\frac{\ell_m}{12}\right)_i + \sum_{j=1}^{N_P}\left[\frac{1}{2} Y_{A_\beta}\left(\frac{\ell_{m_1}}{12} + \frac{\ell_{m_2}}{12}\right)\right]_j\right\} \quad \text{(Equation 3.5-a)}$$

Since $Y_{A_\beta} = 0$, the second term in the above equation drops out. Since the store installations are symmetrical, the above equation reduces to

$$\Delta C_{n_\beta} = (2)\frac{1}{S_W b_W}\left(\frac{1}{2} Y_{B_\beta}\frac{\ell_m}{12}\right)$$

$$= \frac{2}{(530)(38.67)}\frac{1}{2}(-0.795)\left(\frac{53.8}{12}\right)$$

$$= -0.000174 \text{ per deg}$$

Additional values of ΔC_{n_β} at other Mach numbers are shown in comparison to test data from Reference 1 in Sketch (d).

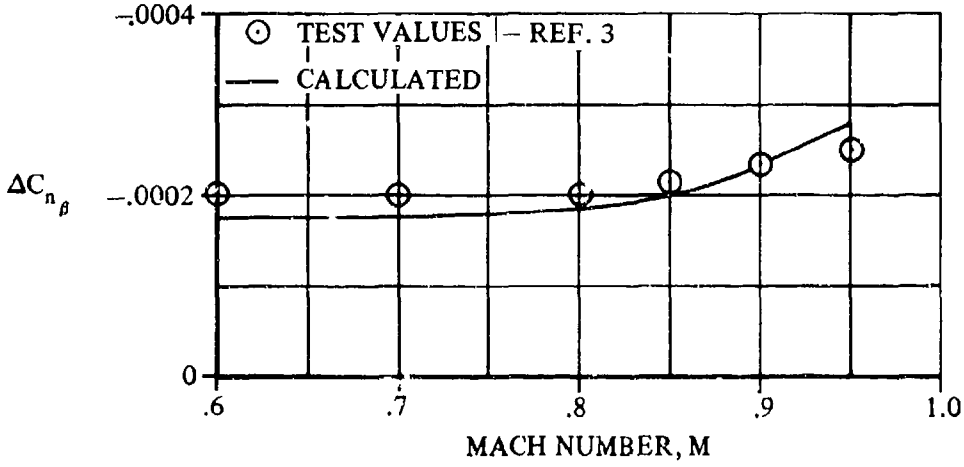

SKETCH (d)

B. TRANSONIC

The method presented in Paragraph A of this section is also valid in the transonic speed range. The user is cautioned that the expected accuracy of the method is less than that expected in the subsonic speed range. A comparison of test data with results calculated by this method at transonic speeds is presented in Table 3.5-B.

C. SUPERSONIC

The method presented in Paragraph A of this section is also valid in the supersonic speed range up to a Mach number of 1.6 to 2.0 as indicated in Table 3.5-A. The maximum Mach numbers provided in the figures of Section 3.4 should indicate the levels to which the method is substantiated by Reference 1. Caution should be used when extrapolating the data beyond the Mach-number range provided in the figures. A comparison of test data with results calculated by this method at supersonic speeds is presented in Table 3.5-B.

REFERENCES

1. Gallagher, R. D., Jimenez, G., Light, L. E., and Thames, F. C.: Technique for Predicting Aircraft Aerodynamic Effects Due to External Stores Carriage, AFFDL-TR-75-95, Volumes I and II, 1975. (U)

2. Watzke, R. E.: Aerodynamic Data for Model TA-4F Operational Flight Trainer, McDonnell Douglas Corporation Rept. DAC-67425, 1968. (U)

3. Bonine, W. J., et al: Model F/RF-4B-C Aerodynamic Derivatives, McDonnell Douglas Corporation Rept. 9842, 1964 (Rev. 1971). (U)

TABLE 3.5-B

SUBSONIC AND SUPERSONIC EXTERNAL-STORE YAWING MOMENT DATA SUMMARY AND SUBSTANTIATION

Ref	Loading Description	α (deg)	M	ΔC_{n_β} calc (per deg)	ΔC_{n_β} test (per deg)	ΔC_{n_β} calc-test (per deg)
2	Wing Station Mounting Left Inboard Pylon-Mounted Single: 300-gal tank Right Inboard Pylon-Mounted Single: 300-gal tank	5	0.6	0.00048	−0.00015	0.00063
			0.8	0.00049	−0.00015	0.00064
			0.9	0.00053	−0.00015	0.00068
			0.95	0.00054	−0.00035	0.00089
3	Wing Station Mounting Left Inboard Pylon-Mounted Single: Missile Right Inboard Pylon-Mounted Single: Missile	5	0.6	−0.00017	−0.00020	0.00003
			0.8	−0.00019	−0.00020	0.00001
			0.9	−0.00023	−0.00023	0
			0.95	−0.00028	−0.00025	−0.00003
			1.2	−0.00032	−0.00045	0.00013
			1.6	−0.00023	−0.00023	0
			2.0	−0.00023	−0.00023	0

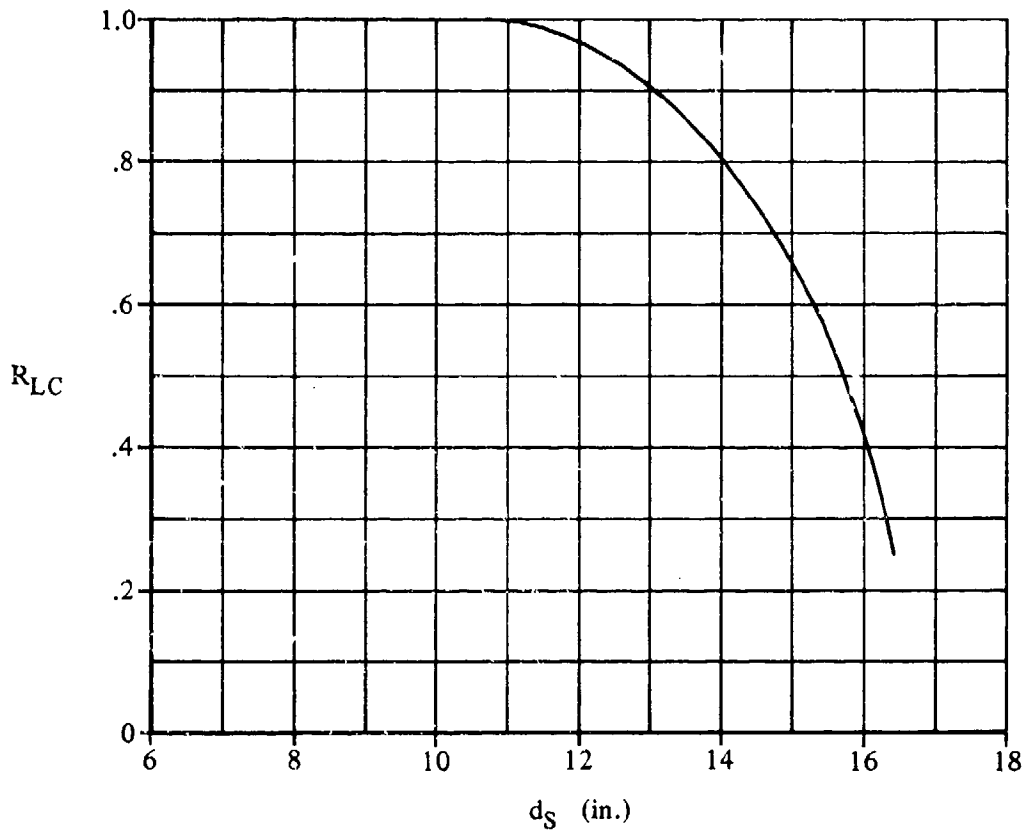

FIGURE 3.5-12 AFT-STORE-CLUSTER LATERAL-CLEARANCE FACTOR

3.6 EFFECT OF EXTERNAL STORES ON AIRCRAFT ROLLING MOMENT

No Datcom Method is provided to estimate the effect of external stores on aircraft rolling moment. No suitable general methods have been developed which provide satisfactory results for a wide range of loading configurations. The user may consult the references cited in Section 3 for available information on prediction of rolling moments.

4.1 WINGS AT ANGLE OF ATTACK

A great deal of theoretical and experimental work has been done toward the development of airfoil sections. Theoretical airfoil design is hampered by the existence of viscous effects in the form of a "boundary layer" of low-energy air between the airfoil surface and the free stream. This boundary layer affects chiefly the section drag and maximum lift characteristics but also has minor effects on lift-curve slope, angle of attack for zero lift, and section pitching-moment coefficient.

Since the boundary layer is influenced by surface roughness, surface curvature, pressure gradient, heat transfer between the surface and the boundary layer, and viscous interaction with the free stream, it is apparent that no simple theoretical considerations can accurately predict all the airfoil characteristics. For these reasons, experimental data are always preferable to theoretical calculations.

Airfoils have been optimized for many specific characteristics, including: high maximum lift, low drag at low lift coefficients, low drag at high lift coefficients, low pitching moments, low drag in the transonic region, and favorable lift characteristics beyond the critical Mach number. Optimization of an airfoil in one direction usually compromises it in another. Thus, low-drag airfoils have poor high-lift characteristics, and high-lift airfoils have low critical Mach numbers.

It is apparent from the above that any generalized charts for airfoil section characteristics, including the ones in this handbook, must be used with caution.

Included in this Section are tabulated NACA experimental and theoretical data that are used and discussed in detail in Sections 4.1.1.1, 4.1.1.2, 4.1.1.3, 4.1.1.4, 4.1.2.1, and 4.1.2.2.

Table 4.1.1-A summarizes experimental data for the NACA four- and five-digit airfoils. Table 4.1.1-B gives corresponding data for the NACA 6-series airfoils. The data, from reference 1, are for smooth-leading-edge conditions and 9×10^6 Reynolds number.

Information is presented on the following airfoil characteristics:

1. angle of attack at zero lift, α_0
2. lift-curve slope, c_{ℓ_α}
3. angle of attack at which the lift curve deviates from linear variation, α^*
4. maximum lift coefficient, $c_{\ell_{max}}$
5. angle of attack for maximum lift coefficient, $\alpha_{c_{\ell_{max}}}$
6. design lift coefficient c_{ℓ_i}
7. angle of attack at design lift coefficient, α_i

From these first five quantities the approximate section lift-curve shape can be synthesized, as illustrated in the following figure:

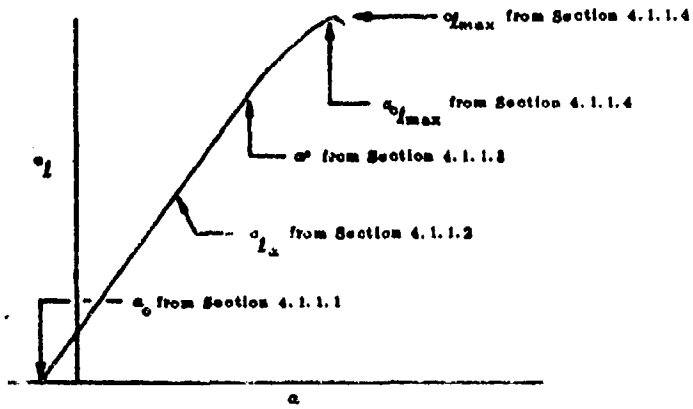

Experimental data for a large number of additional airfoils are available in the literature. These airfoils may be located with the aid of table 4.1.1-C.

Table 4.1.1-D presents theoretical aerodynamic characteristics of various airfoil mean lines. This theoretical information is used to approximate characteristics of NACA-type airfoils for which experimental data are not available.

REFERENCES

1. Abbott, I. H., von Doenhoff, A. E., and Stivers, L. S., Jr.: Summary of Airfoil Data. NACA TR 824, 1945. (U)

2. Pinkerton, R. M., and Greenberg, H.: Aerodynamic Characteristics of a Large Number of Airfoils Tested in the Variable-Density Wind Tunnel. NACA TR 628, 1938. (U)

3. Jacobs, E. N., and Abbott, I. H.: Airfoil Section Data Obtained in the N.A.C.A. Variable-Density Wind Tunnel as Affected by Support Interference and Other Corrections. NACA TR 669, 1939. (U)

4. Jacobs, E. N., Pinkerton, R. M., and Greenberg, H.: Tests of Related Forward-Camber Airfoils in the Variable-Density Wind Tunnel. NACA TR 610, 1937. (U)

5. Jacobs, E. N., Ward, K. E., and Pinkerton, R. M.: The Characteristics of 78 Related Airfoil Sections from Tests in the Variable-Density Wind Tunnel. NACA TR 460, 1933. (U)

6. Loftin, L. K., Jr.: Theoretical and Experimental Data for a Number of NACA 6A-Series Airfoil Sections. NACA TR 903, 1948. (U)

7. Daley, B. N., and Dick, E. S.: Effect of Thickness, Camber, and Thickness Distribution on Airfoil Characteristics at Mach Numbers up to 1.0. NACA TN 3607, 1956. (U)

8. Lindsey, W. F., Stevenson, D. B., and Daley, B. N.: Aerodynamic Characteristics of 24 NACA 16-Series Airfoils at Mach Numbers between 0.3 and 0.8. NACA TN 1546, 1948. (U)

9. Riegels, F. W.: Aerodynamische Profile. Oldenbourg, Munich, 1958. (U)

TABLE 4.1.1-A

EXPERIMENTAL LOW SPEED AIRFOIL SECTION AERODYNAMIC CHARACTERISTICS*

R = 9 x 10^6, Smooth Leading Edge

4- and 5-Digit Airfoils

Airfoil	α_0 (deg)	c_{m_o}	c_{l_α} (per deg)	a.c.	$\alpha_{c_{l_{max}}}$ (deg)	$c_{l_{max}}$	α^* (deg)
0006	0	0	.108	.250	9.0	.92	9.0
0009	0	0	.109	.250	13.4	1.52	11.4
1408	0.8	-.028	.109	.250	14.0	1.35	10.0
1410	-1.0	-.030	.108	.247	14.5	1.50	11.0
1412	-1.1	-.035	.108	.252	15.2	1.68	12.0
2412	-2.0	-.047	.105	.247	16.6	1.65	9.5
2415	-2.0	-.049	.108	.246	16.4	1.68	10.0
2418	-2.3	-.050	.105	.241	14.0	1.47	10.0
2421	-1.5	-.040	.105	.241	16.0	1.47	8.0
2424	-1.5	-.040	.098	.231	16.0	1.29	6.4
4412	-3.5	-.095	.105	.247	14.0	1.67	7.5
4415	-4.3	-.095	.105	.245	15.0	1.64	8.0
4418	-5.5	-.088	.105	.242	14.0	1.52	7.2
4421	-5.5	-.085	.105	.235	16.0	1.47	6.0
4424	-5.5	-.082	.100	.229	16.0	1.36	4.5
23012	-1.4	-.014	.107	.247	15.0	1.79	12.0
23015	-1.0	-.007	.107	.248	15.0	1.72	10.0
23018	-1.2	-.005	.104	.248	16.0	1.60	11.5
23021	-1.2	0	.103	.250	15.0	1.50	10.5
23024	-0.5	0	.097	.231	15.0	1.40	9.7

α^* = angle of attack at which lift curve ceases to be linear.

TABLE 4.1.1-B

EXPERIMENTAL LOW SPEED AIRFOIL SECTION AERODYNAMIC CHARACTERISTICS**

R = 9 x 10^6, Smooth Leading Edge

6-Series Airfoils

Airfoil	α_o (deg)	c_{m_o}	c_{l_α} (per deg)	a.c.	$\alpha_{c_{l_{max}}}$ (deg)	$c_{l_{max}}$	α^* (deg)
63-006	0	.005	.112	.253	10.0	.87	7.7
-009	0	0	.111	.256	11.0	1.15	10.7
63-206	-1.5	-.027	.112	.254	10.5	1.06	6.0
-209	-1.4	-.032	.110	.252	12.0	1.4	10.5
-210	-1.2	-.035	.113	.261	14.5	1.56	9.6
63_1-012	0	0	.116	.265	14.0	1.45	12.5
-212	-2.0	-.035	.114	.262	14.5	1.63	11.4
-412	-2.5	-.075	.117	.271	15.0	1.77	9.6

(Contd.)

**LIFT COEFFICIENTS USED IN THESE CHARTS IS BASED ON CHORD

TABLE 4.1.1-B (Contd)

Airfoil	α_0 (deg)	c_{m_0}	c_{l_α} (per deg)	a.c.	$\alpha_{c_{l_{max}}}$ (deg)	$c_{l_{max}}$	α^* (deg)
63_2-015	0	0	.117	.271	14.5	1.47	11.0
-215	-1.0	-.030	.116	.267	15.0	1.60	8.5
-415	-2.5	-.069	.118	.262	15.0	1.68	10.0
-615	-3.6	-.103	.117	.266	15.0	1.67	8.6
63_3-018	0	0	.116	.271	15.5	1.54	11.2
-218	-1.4	-.033	.116	.271	14.5	1.65	8.0
-418	-2.7	-.064	.116	.272	16.0	1.67	7.0
-618	-3.8	-.097	.116	.267	16.0	1.69	4.2
63_6-021	0	0	.116	.273	17.0	1.58	9.0
-221	-1.5	-.035	.116	.269	15.0	1.44	9.2
-421	-2.8	-.062	.120	.275	16.0	1.48	6.7
63,4-420	-2.3	-.059	.109	.265	14.0	1.42	7.6
63,4-420 a = .5	-2.4	-.037	.111	.265	16.0	1.35	6.0
63(420)-422	-2.2	-.055	.112	.271	14.0	1.36	6.0
63(420)-517	-3.0	-.084	.108	.264	15.0	1.60	8.0
64-006	0	0	.109	.256	9.0	.8	7.2
-009	0	0	.110	.262	11.0	1.17	10.0
64-108	0	-.015	.110	.258	10.0	1.1	10.0
-110	-1.0	-.020	.110	.261	13.0	1.4	10.0
64-206	-1.0	-.040	.110	.253	12.0	1.03	8.0
-208	-1.2	-.039	.113	.257	10.5	1.28	8.5
-209	-1.5	-.040	.107	.261	13.0	1.40	8.9
-210	-1.6	-.040	.110	.258	14.0	1.45	10.5
64_1-012	0	0	.111	.262	14.5	1.45	11.0
-112	-0.8	-.017	.113	.267	14.0	1.50	12.2
-212	-1.8	-.037	.113	.262	15.0	1.55	11.0
-412	-2.6	-.065	.112	.267	15.0	1.67	8.0
64_2-015	0	0	.112	.267	15.0	1.48	13.0
-215	-1.6	-.030	.112	.265	15.0	1.57	10.0
-415	-2.8	-.070	.115	.264	15.0	1.65	8.0
64_3-018	0	.004	.111	.266	17.0	1.50	12.0
-218	-1.3	-.027	.113	.271	16.0	1.53	10.0
-418	-2.9	-.065	.116	.273	14.0	1.57	8.0
-618	-3.8	-.095	.116	.273	16.0	1.58	5.6
64_6-021	0	+.005	.110	.274	14.0	1.30	10.3
-221	-1.2	-.029	.117	.271	15.0	1.32	6.8
-421	-2.8	-.065	.120	.276	15.0	1.42	6.4
65-006	0	0	.105	.255	12.0	.82	7.6
-009	0	0	.107	.264	11.0	1.05	9.8
65-206	-1.6	-.031	.105	.257	12.0	1.03	6.0
-209	-1.2	-.031	.106	.259	12.0	1.30	10.0
-210	-1.6	-.034	.108	.262	13.0	1.40	9.6
65-410	-2.5	-.067	.112	.262	14.0	1.52	8.0

(Contd.)

TABLE 4.1.1-B (Contin.)

Airfoil	α_o (deg)	c_{m_o}	c_{l_α} (per deg)	a.c.	$\alpha_{c_{l_{max}}}$ (deg)	$c_{l_{max}}$	α^* (deg)
65_1-012	0	0	.110	.261	14.0	1.38	10.0
-212	-1.0	-.032	.108	.261	14.0	1.47	9.4
-212 a = .6	-1.4	-.038	.108	.260	14.0	1.50	9.6
-412	-3.0	-.070	.111	.268	15.5	1.66	10.5
65_2-015	0	0	.111	.257	15.0	1.42	11.2
-215	-1.2	-.032	.112	259	15.5	1.58	10.0
-415	-2.6	-.060	.111	.258	16.0	1.61	8.7
-415 a = .5	-2.6	-.061	.111	.264	20.0	1 60	7.0
$65_{(216)}$-114	-0.7	-.019	.112	.268	15.0	1.44	10.5
65(216)-415 a = .5	-3.0	-.057	.106	.267	15.0	1.60	6.0
65_3-018	0	0	.100	.262	17.0	1.44	10.0
-418 a = .5	-3.0	-.081	.112	.266	20.0	1.58	4.4
-618	-4.0	-.100	.110	.272	20.0	1.60	4.9
65_3-018	0	0	.100	.267	16.0	1.37	10.0
-218	-1.2	-.030	.100	.268	16.0	1.48	8.8
-418	-2.4	-.059	.110	.265	16.0	1.64	4.9
-418 a = .5	-2.8	-.058	.118	.267	16.0	1.60	6.0
-618	-4.0	-.102	.113	.276	16.0	1.64	5.2
-618 a = .5	-4.2	-.078	.104	.266	20.0	1.61	5.3
65_4-021	0	0	.112	.267	18.5	1.40	7.4
-221	-1.3	-.039	.115	.274	20.5	1.46	6.0
-421	-2.4	-.066	.116	.272	22.0	1.56	5.0
-421 a = .5	-2.8	-.062	.116	.272	20.0	1.43	5.6
$65_{(421)}$-420	-2.4	-.061	.116	.276	20.0	1.62	4.7
66-006	0	0	.100	.252	9.0	.80	6.5
-009	0	0	.103	.259	10.0	1.05	10.0
66-206	-1.4	- 038	.108	.257	10.5	1.00	7.0
-209	-1.0	-.034	.107	.257	11.0	1.17	9.0
-210	-1.3	-.035	.110	.261	11.0	1.27	10.0
66_1-012	0	0	.106	.255	14.0	1.25	11.2
-212	-1.2	-.032	.102	.259	14.0	1.46	11.6
66_2-015	0	.005	.108	.255	15.5	1.35	12.0
-215	-1.3	-.031	.106	.260	16.0	1.50	11.4
-415	-2.6	-.038	.106	.260	17.0	1.60	10.0
66(215)-016	0	0	.105	.260	14.0	1.35	10.0
-216	-2.0	-.044	.114	.262	16.0	1.55	8.5
-216 a = .6	-1.2	-.030	.100	.257	16.0	1.46	7.0
-416	-2.6	-.066	.100	.255	16.0	1.60	4.0
63A010	0	.005	.108	.254	13.0	1.20	10.0
63A210	-1.5	-.040	.103	.257	14.0	1.48	10.0
64A010	0	0	.110	.258	13.0	1.28	10.0
64A210	-1.5	-.040	.105	.231	2.0	1.44	10.0
64A410	-3.0	-.080	.100	.254	15.0	1.61	10.0
64_1A212	-2.0	-.040	.100	.252	14.0	1.54	11.0
64_2A215	-2.0	-.040	.095	.253	15.0	1.50	12.0

* = angle of attack at which lift curve ceases to be linear.

TABLE 4.1.1-C

BIBLIOGRAPHY OF SUBSONIC AIRFOIL DATA

NOTES: 1. For airfoil designations see Section 2.1.1

2. For a comprehensive coverage of additional airfoil sections see Reference 9.

3. Single asterisk denotes data at positive and negative angles of attack.

Reference 1

N.A.C.A. 67, 1-215
747A315
747A415

Reference 2

BOEING 103*
103A*
106*
106R
111*
111**

SIKORSKY GS-M*
GS-I*

S.T. Ae. 27A

R.A.F. 34

U.S.A. 27*
35-A
35-B*
C-62
C-72*
C-80*
N-22*
N-60
N-60R
N-65
N-69
N-71*
N-75*
N-76*
N-80*
N-81*

GOTTINGEN 387
398*
398-A
398-B
398-R
413
420
429-AG
429-J
436*
532*

CLARK Y*
Y-B
YM-15*
YM-16*
Y-6
Y-8
Y-10
Y-14
Y-15*
Y-22

N.A.C.A. CYH*
-M6*

N.A.C.A. 15
16
17
18
19
20
21*
23
24
25
26
27

N.A.C.A. 22112
23112
24112
25112

Reference 3

N.A.C.A. 0012
0015
0018
0021
0025
0030
2212
2409
4406
4409

N.A.C.A. 23006
23009
43012
43015
43018
63012
63018

Reference 4

N.A.C.A. 0012-63
0012-64
0012-65
23012-33
23012-34
23012-64
21012
22012
24012
25012
32012
33012
34012
42012
43009
43012A
43021
44012
62021
63009
63015
63021
64021

Reference 5

N.A.C.A. 2306
2309
2312
2315
2406
2506
2509

N.A.C.A. 2512
2515
2518
2521
2612
2712

N.A.C.A. 4212
4306
4309
4312
4315
4318
4321
4506
4509
4512
4515
4518
4521
4612
4712

N.A.C.A. 6212
6306
6309
6312
6315
6318
6321
6406
6409
6412
6415
6418
6421
6506
6509
6512
6515
6518
6521
6612
6712

N.A.C.A.** 0006T
0006B
0012T
0012B
0018T
0018B
$2R_1$12
$2R_2$12
0012F_0
0012F_1

Reference 7

N.A.C.A. 63A009
64A004
64A006
64A206
64A506
64A009
64A012
65A009

Reference 8

N.A.C.A. 16-009
16-106
16-109
16-115
16-130
16-209
16-215
16-306
16-309
16-312
16-315
16-321
16-409
16-506
16-509
16-512
16-515
16-521
16-530
16-709
16-712
16-715
16-1009
16-1012

** T = thin nose section B = blunt nose section R = reflexed mean line F = modified T.E.

TABLE 4.1.1-D

THEORETICAL LOW SPEED AERODYNAMIC CHARACTERISTICS OF VARIOUS AIRFOIL MEAN LINES**

Mean Line	c_{ℓ_i}	α_i (deg)	$c_{m_{c/4}}$ at c_{ℓ_i}	
Four-Digit Series				
62	0.8	2.81	-0.118	For other NACA four-digit mean lines, multiply the corresponding* 6-percent camber c_{ℓ_i}, α_i and $c_{m_{c/4}}$ by the ratio of the camber designators, i.e., (2/6), (3/6), (4/6), (5/6)
63	0.6	1.60	-0.134	
64	0.76	0.74	-0.157	
65	0.75	0	-0.187	
66	0.76	-0.74	-0.222	
67	0.80	-1.60	-0.266	
Five-Digit Series				
210	0.30	2.09	-0.008	For other NACA five-digit mean lines, multiply the corresponding* c_{ℓ_i}, α_i and $c_{m_{c/4}}$ by the ratio of camber designators, i.e., (3/2), (4/2), (5/2), (6/2).
220	0.30	1.88	-0.010	
230	0.30	1.65	-0.014	
240	0.30	1.45	-0.019	
250	0.30	1.26	-0.026	
6-Series				
a = 0	1.0	4.56	-0.068	For NACA 6-series airfoils, multiply the corresponding* mean line c_{ℓ_i}, α_i and $c_{m_{c/4}}$ by the ratio of design lift coefficients.
0.1	1.0	4.43	-0.086	
0.2	1.0	4.17	-0.094	
0.3	1.0	3.84	-0.106	
0.4	1.0	3.46	-0.121	
0.5	1.0	3.04	-0.139	
0.6	1.0	2.56	-0.158	
0.7	1.0	2.09	-0.179	
0.8	1.0	1.54	-0.202	
0.9	1.0	0.90	-0.225	
1.0	1.0	0	-0.250	

* "Corresponding" cambers are those for which the chordwise position of maximum camber is the same.

** Lift coefficient is based on airfoil chord.

4.1.1.1 SECTION ZERO-LIFT ANGLE OF ATTACK

Reynolds number and roughness have a small effect on section zero-lift angle of attack. Reference 1 shows that variations due to these causes are usually restricted to less than 1°.

Up to the critical Mach number the effect of compressibility on the zero-lift angle of attack is negligible. Above the critical Mach number, however, compressibility effects can cause large changes in this parameter. Reference 2 presents Mach number effects on some cambered sections.

For supersonic Mach numbers it is advisable to use the method of characteristics or the generalized shock-expansion method (reference 3). The charts and tables of this Section, however, are restricted to low speeds.

HANDBOOK METHOD

Experimental data from reference 4 on the zero-lift angle of attack for NACA four- and five-digit and 6-series airfoils are presented in tables 4.1.1-A and 4.1.1-B, respectively. Data on many additional airfoils may be located in the literature with the help of table 4.1.1-C.

For airfoil series not included in this summary, the theoretical characteristics tabulated in table 4.1.1-D may be used in conjunction with the aforementioned experimental data to derive the zero-lift angle of attack according to the following method. The zero-lift angle of attack is given by the equation (assuming a lift-curve slope of 2π)

$$\alpha_o = k\left(\alpha_i - \frac{57.3}{2\pi} c_{\ell_i}\right) \qquad \text{4.1.1.1-a}$$

$$= k\left(\alpha_i - 9.12\, c_{\ell_i}\right)$$

where c_{ℓ_i} and α_i are the design lift coefficient and angle of attack for the design lift coefficient, respectively. The factor K is empirical (reference 4) and depends upon the airfoil series. For NACA airfoil sections the values are:

K = 0.93 NACA Four-Digit Series
1.08 NACA Five-Digit Series
0.74 NACA 6-Series

Theoretical section design lift coefficients and corresponding angles of attack for NACA four- and five-digit and 6-series airfoils are given in table 4.1.1-D. For airfoils other than those included in table 4.1.1-D, the tabulated values of α_i and c_{ℓ_i} may be linearly scaled, as indicated in the sample problems below and in table 4.1.1-D. The zero-lift angle of attack so obtained may be adjusted by judicious use and comparison with the experimental data of related airfoils. Wherever possible, however, experimental data should be used. The accuracy of this method as compared to experimental data is shown in table 4.1.1.1-A.

SAMPLE PROBLEM

Example 1: Find the theoretical α_o for the NACA 2415 section. The calculation of the theoretical α_o for this section should be based on the NACA 64 mean line, for which

$\alpha_i = 0.74°$ and $c_{l_i} = .76$ (Table 4.1.1-D)

$\alpha_i = (.74)\ 2/6$

$= 0.25°$

$c_{\ell_i} = (.76)\ 2/6$

$= 0.25$

From equation 4.1.1.1-a

$$\alpha_o = .93\left(.25 - \frac{57.3 \times .25}{2\pi}\right)$$

$= -1.91°$

This result compares to $\alpha_o = -2.0°$ experimentally.

Example 2: Find the theoretical α_o for the NACA 65_2 - 415, a = 0.5 airfoil. ($c_{l_i} = .4$)

The NACA a = 0.5 mean line serves as a base in this case, for which the tabulated data of table 4.1.1-D indicate that $\alpha_i = 3.04°$ when $c_{l_i} = 1.0$. The desired value of α_i for the given airfoil is then

$$\alpha_i = 3.04 \times \frac{.4}{1.0}$$

$= 1.22°$

Substitution into equation 4.1.1.1-a yields

$$\alpha_o = .74\left(1.22 - \frac{57.3 \times .4}{2\pi}\right)$$

$= -1.80°$

TABLE 4.1.1.1 A

SUBSONIC ZERO-LIFT ANGLE OF ATTACK

SUBSTANTIATION DATA

Airfoil	α_o, deg Calculated (Equation 4.1.1-a)	α_o, deg Test*	$\Delta\alpha_o$, deg (Calc. - Test)
14xx	-1.0	-1.0 to -0.8	-0.2 to 0
24xx	-1.9	-2.8 to -1.8	-0.1 to +0.4
44xx	-3.8	-4.8 to -3.8	0 to +0.5
230xx	-1.2	-1.4 to -0.8	-0.4 to +0.2
6x - 1xx	-0.7	-1.0 to -0.7	0 to +0.3
6x - 2xx	-1.8	-2.0 to -1.0	-0.8 to +0.7
6x - 4xx	-3.7	-3.9 to -3.2	-0.5 to +0.5
6x - 6xx	-4.0	-4.0 to -3.6	-0.4 to 0
$6x_R$ - 6xx a = .5	-3.7	-4.2	+1.5
$6x_R$ - 2xx a = .5	-1.0	-1.4	+0.4
$6x_R$ - 4xx a = .5	-2.2	-3.0	+0.8
6x - 8xx	-3.4	-3.0	-0.4

*The maximum and minimum values for the experimental values are due primarily to thickness-ratio variations.

$$\text{Average Error} = \frac{\Sigma|\Delta\alpha_o|}{n} = 0.4°$$

REFERENCES

1. Loftin, L. K., Jr., and Smith, H. A.: Aerodynamic Characteristics of 18 NACA Airfoil Sections at Seven Reynolds Numbers From 0.7×10^6 to 9.0×10^6. NACA TN 1945, 1949. (U)

2. Stack, J., and von Doenhoff, A. E.: Tests of 16 Related Airfoils at High Speeds. NACA TR 492, 1934. (U)

3. Eggers, A. J., Jr., Savin, R. C., and Syvertson, C.A.: The Generalized Shock-Expansion Method and Its Application to Bodies Traveling at High Supersonic Airspeeds. Jour. Aero. Sci., April 1955.

4. Abbott, I. H., von Doenhoff, A. E., and Stivers, L. S., Jr.: Summary of Airfoil Data. NACA TR 824, 1945. (U)

5. Pinkerton, R. M., and Greenberg, H.: Aerodynamic Characteristics of a Large Number of Airfoils Tested in the Variable-Density Wind Tunnel. NACA TR 628, 1938. (U)

4.1.1.2 SECTION LIFT-CURVE SLOPE

The theoretical incompressible lift-curve slope (based on the Kutta-Joukowski hypothesis of finite velocity at the trailing edge) may be approximated by the equation (for angles of attack below α^* as given in Section 4.1.1).

$$c_{\ell_\alpha} = 6.28 + 4.7\ t/c \left[1 + .00375\ \phi_{TE}\right] \text{ (per rad)}$$

where ϕ_{TE} is the total trailing-edge angle in degrees. However, boundary-layer effects cause the actual lift-curve slopes to fall considerably below the theoretical values.

On thin wings the loss in lift-curve slope due to Reynolds-number effects is approximately 15 percent at $R_\ell = 10^6$. For thicker wings the losses are further aggravated by the adverse pressure gradient over the rear section due to thickness distribution. To a certain extent this can be correlated with trailing-edge angle. Very thin wings with leading-edge bubble-type separation also suffer additional lift-curve-slope losses. Reference 1 discusses viscous effects on the aerodynamic characteristics of wing sections.

The effects of leading-edge roughness on lift-curve slope can be very severe in some cases. Losses as large as 30 percent, due to the effects of the standard NACA leading-edge roughness, are shown in reference 7.

Up to the critical Mach number of the airfoil section, lift-curve slope follows the Prandtl-Glauert compressibility rule. Beyond the critical Mach number, thick conventional sections suffer large lift-slope changes due to local shock formation on first the upper and then the lower airfoil surfaces. References 2, 3, and 4 show these effects for a series of thick airfoils. An example of Mach-number effects on the lift-curve slope of a thin airfoil is contained in reference 5. Certain airfoils, notably the NACA 8-series (reference 6), are specifically designed to avoid these transonic effects.

Two methods are presented in this section for estimating the airfoil section lift-curve slope at speeds up to the critical Mach number. One uses the large body of available experimental section data, while the other is based on the semiempirical method of reference 8.

No specific methods are presented in the transonic and supersonic speed regimes. Transonic airfoil section characteristics are highly variable with airfoil section, and it is suggested that reference be made to experimental data on the particular airfoil in question. At supersonic speeds theoretical pressure distribution about an arbitrary section can be calculated by generalized shock-expansion theory, second-order theory, or the method of characteristics (see reference 3 of Section 4.1.1.1).

A. SUBSONIC

DATCOM METHODS

1. Method 1

Experimental lift-curve-slope data from reference 7 are presented in table 4.1.1-A for the NACA four- and five-digit airfoils and in table 4.1.1-B for the NACA 6-series airfoils. The effect of the NACA standard roughness on these data is indicated in figure 4.1.1.2-7. The NACA standard roughness is obtained by the use of 0.011-inch carborundum grains applied over the first 8 percent of the 24-inch-chord test models. Experimental lift-curve slopes for many other airfoils may be found in the literature with the aid of table 4.1.1-C.

Low-speed values of c_{ℓ_α} obtained from Section 4.1.1 may be corrected for compressibility effects up to the critical Mach number by application of the Prandtl-Glauert compressibility correction; i.e., $\left(c_{\ell_\alpha}\right)_M = c_{\ell_\alpha}/\beta$.

2. Method 2

This method is basically the semiempirical method of reference 8. The method accounts for the development of the boundary layer for airfoils with transition fixed at the leading edge and with maximum thickness less than approximately 20 percent. The airfoil section lift-curve slope at Mach numbers up to the critical Mach number is given by

$$c\ell_\alpha = \frac{1.05}{\beta}\left[\frac{c\ell_\alpha}{\left(c\ell_\alpha\right)_{\text{theory}}}\right]\left(c\ell_\alpha\right)_{\text{theory}} \qquad 4.1.1.2\text{-a}$$

where

$\left[\frac{\left(c\ell_\alpha\right)}{\left(c\ell_\alpha\right)_{\text{theory}}}\right]$ is an empirical correction factor obtained from figure 4.1.1.2-8a. This factor accounts for the development of the boundary layer towards the airfoil trailing edge. It is related to the Reynolds number with transition fixed at the airfoil leading edge, and the trailing-edge angle defined as the angle between straight lines passing through points at 90 and 99 percent of the chord on the upper and lower airfoil surfaces.

$\left(c\ell_\alpha\right)_{\text{theory}}$ is the theoretical airfoil section lift-curve slope obtained from figure 4.1.1.2-8b. The values of $\left(c\ell_\alpha\right)_{\text{theory}}$ have been determined using the Kutta-Joukowski hypothesis. Since $\left(c\ell_\alpha\right)_{\text{theory}}$ is relatively insensitive to the exact value of the trailing-edge angle, a value of $\phi_{TE} = 20^o$, representing the upper limit of the method, has been chosen as a constant in evaluating this parameter. Consequently, $\left(c\ell_\alpha\right)_{\text{theory}}$ is presented as a function only of airfoil thickness ratio.

β is the Prandtl-Glauert compressibility correction factor $\sqrt{1 - M^2}$.

The constant 1.05 of equation 4.1.1.2-a is an empirical correlation factor based on a large body of test data.

The method is limited to attached flow conditions and must therefore be applied with caution to airfoils with maximum thickness exceeding approximately 0.20c, airfoils with trailing-edge angles greater than approximately 20^o, and airfoils at high angles of attack.

Although the position of transition is important in determining the boundary-layer thickness at the trailing edge, no attempt has been made to estimate the effect of variation of transition position. The available experimental data do not clearly define the behavior of the transition-position movement; consequently, development of general design charts to predict the variation in section lift-curve slope with transition-position movement does not appear feasible. The transition will occur at or near the leading edge on both the upper and lower surfaces of the airfoil for most full-scale practical cases.

A comparison of test data with $c\ell_\alpha$ calculated by this method is presented as table 4.1.1.2-A.

Sample Problem

Method 2

Given: Airfoil tested in reference 9.

NACA 0006 airfoil $\quad M = 0.15; \beta = 0.99 \quad R_\ell = 4.5 \times 10^6 \quad t/c = 0.06$

$$\frac{Y_{90}}{2} = 0.720 \qquad \frac{Y_{99}}{2} = 0.130 \qquad \text{(Y in percent chord)}$$

Compute:

$$\tan\frac{1}{2}\phi'_{TE} = \frac{\frac{Y_{90}}{2} - \frac{Y_{99}}{2}}{9} = 0.066$$

$$\frac{c\ell_\alpha}{(c\ell_\alpha)_{theory}} = 0.880 \text{ (figure 4.1.1.2-8a)}$$

$$(c\ell_\alpha)_{theory} = 6.58 \text{ per rad (figure 4.1.1.2-8b)}$$

Solution:

$$c\ell_\alpha = \frac{1.05}{\beta}\left[\frac{c\ell_\alpha}{(c\ell_\alpha)_{theory}}\right](c\ell_\alpha)_{theory} \quad \text{(equation 4.1.1.2-a)}$$

$$= \frac{1.05}{0.99}\ (0.880)\ (6.58)$$

$$= 6.14 \text{ per rad}$$

$$= 0.107 \text{ per deg}$$

This compares with a test value of 0.103 per degree obtained from reference 9.

REFERENCES

1. Nonweiler, T.R.: The Design of Wing Sections. Aircraft Engineering, Volume XXVIII, Number 329, July 1956. (U)
2. Ladson, C.L.: Two-Dimensional Airfoil Characteristics of Four NACA 6A-Series Airfoils at Transonic Mach Numbers up to 1.25. NACA RM L57F05, 1957. (U)
3. Lindsey, W.F., and Humphreys, M.D.: Effects of Aspect Ratio on Airflow at High Subsonic Mach Numbers. NACA TN 2720, 1952. (U)
4. Gullstrand, T.R.: The Flow Over Two-Dimensional Aerofoils at Incidence in the Transonic Speed Range. KTH Aero TN 27, (Sweden), 1952. (U)
5. Holder, D.W., and Cash, R.F.: Experiments with a Two-Dimensional Aerofoil Designed to be Free from Turbulent Boundary-Layer Separation at Small Angles of Incidence for all Mach Numbers. ARC R&M 3100, 1959. (U)
6. Graham, D.J.: The Development of Cambered Airfoil Sections Having Favorable Lift Characteristics at Supercritical Mach Numbers. NACA TR 947, 1949. (U)
7. Abbott, I.H., von Doenhoff, A.E., and Stivers, L.S., Jr: Summary of Airfoil Data. NACA TR 824, 1945. (U)
8. Anon: Royal Aeronautical Society Data Sheets - Aerodynamics, Vol. II (Wings 01.01.05), 1955. (U)
9. Gambucci, J.B.: Section Characteristics of the 0006 Airfoil with Leading-Edge and Trailing-Edge Flaps. NACA TN 3797, 1956. (U)

10. Sears, R.I.: Wind-Tunnel Data on the Aerodynamic Characteristics of Airplane Control Surfaces. NACA WR L-663, 1943. (U)

11. Loftin, L.K., Jr., and Smith, H.A.: Aerodynamic Characteristics of 15 NACA Airfoil Sections at Seven Reynolds Numbers from 0.7×10^6 to 9.0×10^6. NACA TN 1945, 1949. (U)

12. Berggren, R.E., and Graham, D.J.: Effects of Leading-Edge Radius and Maximum Thickness-Chord Ratio on the Variation with Mach Number of the Aerodynamic Characteristics of Several Thin NACA Airfoil Sections. NACA TN 3172, 1954. (U)

13. Cahill, J.F., and Racisz, S.F.: Wind-Tunnel Investigation of Seven Thin NACA Airfoil Sections to Determine Optimum Double-Slotted-Flap Configurations. NACA TN 1545, 1948. (U)

14. Loftin, L.K., Jr., and Cohen, K.S.: Aerodynamic Characteristics of a Number of Modified NACA Four-Digit-Series Airfoil Sections. NACA TN 1991, 1948. (U)

15. Wenzinger, C.J., and Harris, T.A.: Wind-Tunnel Investigation of N.A.C.A. 23012, 23021, and 23030 Airfoils with Various Sizes of Split Flap. NACA TR 668, 1939. (U)

16. Wenzinger, C.J., and Gauvain, W.E.: Wind-Tunnel Investigation of an N.A.C.A. 23012 Airfoil with a Slotted Flap and Three Types of Auxiliary Flap. NACA TR 679, 1939. (U)

17. Wenzinger, C.J., and Harris, T.A.: Wind-Tunnel Investigation of an N.A.C.A. 23012 Airfoil with Various Arrangements of Slotted Flaps. NACA TR 664, 1939. (U)

18. Ilk, R.J.: High-Speed Aerodynamic Characteristics of Four Thin NACA 63-Series Airfoils. NACA RM A7J23, 1947. (U)

19. Van Dyke, M.D.: High-Speed Subsonic Characteristics of 16 NACA 6-Series Airfoil Sections. NACA TN 2670, 1952. (U)

20. Loftin, L.K., Jr., and Bursnall, W.J.: Theoretical Effects of Variations in Reynolds Number Between 3.0×10^6 and 25.0×10^6 Upon the Aerodynamic Characteristics of a Number of NACA 6-Series Airfoil Sections. NACA TN 1773, 1948. (U)

21. Loftin, L.K. Jr.: Aerodynamic Characteristics of the NACA 64-010 and 0010-1.10 40/1.061 Airfoil Sections at Mach Numbers From 0.30 to 0.86 and Reynolds Numbers From 4.0×10^6 to 8.0×10^6. NACA TN 3244, 1954. (U)

22. Gottlieb, S.M.: Two-Dimensional Wind-Tunnel Investigation of Two NACA 6-Series Airfoils with Leading-Edge Slats. NACA RM L8K22, 1949. (U)

23. Loftin, L.K., Jr., and Bursnall, W.J.: The Effects of Variations in Reynolds Number Between 3.0×10^6 and 25.0×10^6 Upon the Aerodynamic Characteristics of a Number of NACA 6-Series Airfoil Sections. NACA TR 964, 1950. (U)

24. Loftin, L.K., Jr., and Smith, H.A.: Two-Dimensional Aerodynamic Characteristics of 34 Miscellaneous Airfoil Sections. NACA RM L8L08, 1949. (U)

25. Bogdonoff, S.M.: Wind-Tunnel Investigation of a Low-Drag Airfoil Section with a Double Slotted Flap. NACA WR L-679, 1943. (U)

26. Quinn, J.H., Jr.: Wind-Tunnel Investigation of Boundary-Layer Control by Suction on the NACA 65_3-418, $a=1.0$ Airfoil Section with a 0.29-Airfoil-Chord Double Slotted Flap. NACA TN 1071, 1946. (U)

27. Quinn, J.H., Jr.: Wind-Tunnel Investigation of the NACA 65_4-421 Airfoil Section with a Double Slotted Flap and Boundary-Layer Control by Suction. NACA TN 1395, 1947. (U)

28. Braslow, A.L.: Two-Dimensional Wind-Tunnel Investigation of Sealed 0.22 Airfoil-Chord Internally Balanced Ailerons of Different Contour on an NACA $65_{(112)}$-213 Airfoil. NACA TN 1099, 1946. (U)

29. Braslow, A.L., and Loftin, L.K., Jr.: Two-Dimensional Wind-Tunnel Investigation of an Approximately 4-Percent-Thick NACA 66-Series-Type Airfoil Section with a Double Slotted Flap. NACA TN 1110, 1946. (U)

30. Loftin, L.K., Jr.: Theoretical and Experimental Data for a Number of NACA 6A-Series Airfoil Sections. NACA TN 1368, 1947. (U)

31. Kelly, J.A., and Hayter, N.L.F.: Lift and Pitching Moment at Low Speeds of the NACA 64A010 Airfoil Sections Equipped with Various Combinations of a Leading-Edge Slat, Leading-Edge Flap, Split Flap, and Double-Slotted Flap. NACA TN 3007, 1953. (U)

32. Summers, J.L., and Treon, S.L.: The Effects of Amount and Type of Camber on the Variation with Mach Number of the Aerodynamic Characteristics of an 10-Percent-Thick NACA 64A-Series Airfoil Section. NACA TN 2096, 1950. (U)

33. Racisz, S.F.: Investigation of NACA $65_{(112)}$A111 (Approx.) Airfoil with 0.35-Chord Slotted Flap at Reynolds Numbers up to 25 Million. NACA TN 1463, 1947. (U)

TABLE 4.1.1.2-A
SUBSONIC AIRFOIL SECTION LIFT-CURVE SLOPE
DATA SUMMARY AND SUBSTANTIATION
METHOD 2

Ref.	NACA Airfoil Section	M	β	$R_\ell \times 10^{-6}$	$\frac{Y_{90}}{2}$ % c	$\frac{Y_{99}}{2}$ % c	c_{ℓ_α} Calc. (per deg)	c_{ℓ_α} Test (per deg)	e Percent Error
9	0006	0.15	0.99	4.5	0.720	0.130	0.107	0.103	3.9
7	↓	–	1.00	9.0	↓	↓	0.108	0.108	0
↓	0009	–	↓	↓	1.090	0.200	0.108	0.109	-0.9
10	↓	–	↓	2.76	↓	↓	0.101	0.097	4.1
11	0012	<0.15	0.99	3.0	1.448	0.260	0.101	0.103	-1.9
10	0015	–	1.00	2.76	1.810	0.330	0.097	0.097	0
12	0004-1.1	0.30	0.955	1.0	0.622	0.110	0.104	0.106	-1.9
↓	0010-1.1	↓	↓	↓	1.556	0.260	0.097	0.095	2.1
7	1408	–	1.00	9.0	0.965	0.175	0.108	0.109	-0.9
↓	1410	–	↓	↓	1.207	0.220	0.107	0.108	-0.9
↓	1412	–	↓	↓	1.447	0.270	0.106	0.108	-1.9
13	1410	<.18	0.98	6.0	1.207	0.225	0.107	0.106	0.9
14	2408	–	1.00	↓	0.955	0.355	0.107	0.106	0.9
7	2412	–	↓	9.0	1.450	0.260	0.106	0.105	1.0
↓	2415	–	↓	↓	1.810	0.340	0.105	0.106	-0.9
↓	2418	–	↓	↓	2.170	0.400	0.102	0.103	-1.0
11	4412	<0.15	0.99	9.0	1.465	0.270	0.107	0.108	-0.9
↓	4415	↓	↓	6.0	1.825	0.335	0.102	0.105	-2.9
15	23012	0.105	0.99	3.5	1.455	0.265	0.102	0.107	-4.7
16	↓	↓	↓	↓	↓	↓	0.102	0.105	-2.9
17	↓	↓	↓	↓	↓	↓	0.102	0.107	-4.7
11	↓	<0.15	↓	1.0	↓	↓	0.096	0.096	0
↓	↓	↓	↓	3.0	↓	↓	0.101	0.102	-1.0
↓	↓	↓	↓	9.0	↓	↓	0.107	0.107	0
7	↓	–	1.00	↓	↓	↓	0.106	0.107	-0.9
↓	23015	–	↓	↓	1.815	0.335	0.105	0.107	-1.9
11	↓	<0.15	0.99	8.9	↓	↓	0.106	0.104	1.9
↓	↓	↓	↓	6.0	↓	↓	0.103	0.105	-1.9
15	23021	0.105	↓	3.5	2.760	0.500	0.097	0.097	0
7	63-006	–	1.00	9.0	0.383	0.050	0.111	0.112	-0.9
↓	63-009	–	1.00	↓	0.550	0.080	0.112	0.111	0.9
18	63-208	0.30	0.955	1.0	0.496	0.020	0.108	0.106	1.9
↓	63-206	↓	↓	↓	0.383	0.025	0.108	0.110	-1.8
7	↓	–	1.00	9.0	↓	↓	0.111	0.112	-0.9
↓	63-209	–	↓	↓	0.550	0.035	0.112	0.110	1.8
↓	63-210	–	↓	↓	0.604	0.030	0.112	0.113	-1.9
13	↓	<0.18	0.98	↓	↓	↓	0.114	0.110	3.6
19	63-212	0.30	0.955	1.0	0.707	0.030	0.108	0.108	0
18	↓	↓	↓	↓	↓	↓	0.108	0.107	0.9
↓	63-210	↓	↓	↓	0.604	0.030	0.108	0.105	2.9
7	63_1-012	–	1.00	9.0	0.707	0.020	0.112	0.116	-3.4
↓	63_1-212	–	↓	↓	0.707	0.030	0.112	0.114	-1.8
↓	63_1-412	–	↓	↓	0.700	0.015	0.112	0.117	-4.3
11	63_2-415	<0.15	0.99	3.0	0.855	0.037	0.108	0.116	-6.9
↓	↓	↓	↓	6.0	↓	↓	0.112	0.114	1.8
↓	↓	↓	↓	9.0	↓	↓	0.114	0.114	0
20	63_3-018	–	1.00	1.50	0.985	0.025	0.115	0.116	-0.9
7	64-006	–	↓	9.0	0.423	0.030	0.110	0.109	0.9
↓	64-009	–	↓	↓	0.611	0.040	0.111	0.110	0.9
21	64-010	0.3	0.955	3.85	0.671	0.030	0.112	0.120	-6.7
13	64-208	<0.18	0.98	6.0	0.550	0.030	0.111	0.114	-2.6
7	64-206	–	1.00	9.0	0.423	0.020	0.110	0.110	0
↓	64-210	–	↓	↓	0.671	0.035	0.111	0.110	0.9
11	64-409	<0.15	0.99	6.0	0.610	0.025	0.109	0.106	2.8
19	64-212	0.30	0.955	1.0	0.786	0.035	0.107	0.105	1.9

TABLE 4.1.1.2-A (CONTD)

Ref.	NACA Airfoil Section	M	β	R_ℓ x 10^{-6}	$\frac{Y_{90}}{2}$ % c	$\frac{Y_{99}}{2}$ % c	c_{ℓ_α} Calc. (per deg)	c_{ℓ_α} Test (per deg)	e Percent Error
13	64_1-212	<0.15	0.99	6.0	0.786	0.035	0.111	0.115	-3.5
7	64_1-012	–	1.00	9.0	0.786	0.050	0.112	0.111	0.9
↓	64_1-412	–	↓	↓	0.784	0.035	0.112	0.112	0
11	64_1-612	<0.15	0.99	6.0	0.782	0.030	0.111	0.112	-0.9
22	64_1-212	–	1.00	|	0.786	0.035	0.109	0.108	0.9
11	64_2-415	<0.15	0.99	|	0.948	0.035	0.110	0.111	-0.9
↓	64_3-418	↓	↓	↓	1.110	0.045	0.110	0.109	0.9
7	65-009	–	1.00	9.0	0.738	0.040	0.109	0.107	1.9
↓	65-006	–	|	↓	0.510	0.040	0 110	0.105	4.8
23	|	|	|	3.0	|	|	0.105	0.110	-4.5
↓	↓	↓	↓	9.0	↓	↓	0.110	0.111	-0.9
↓	↓	↓	↓	25.0	↓	↓	0.111	0.112	-0.9
7	65-206	–	|	9.0	0.510	0.030	0.110	0.105	4.8
↓	65-209	–	|	|	0.738	0.035	0.110	0.106	3.8
↓	65-210	–	↓	↓	0.810	0.040	0.110	0.108	1.9
13	↓	<0.15	0.99	3.0	↓	↓	0.106	0.106	0
19	65-208	0.30	0.955	1.0	0.664	0.030	0.106	0.105	1.0
↓	65-212	↓	↓	↓	0.946	0.050	0.105	0.102	2.9
7	65_1-012	–	1.00	9.0	0.947	0.050	0.110	0.110	0
|	65_1-212	–	|	|	0.946	0.045	0.110	0.108	1.9
↓	65_1-212 a = .8	–	↓	↓	0.946	0.050	0.110	0.108	1.9
11	65_2-415	<0.15	0.99	1.0	1.141	0.050	0.101	0.106	-4.7
↓	↓	↓	↓	6.0	↓	↓	0.108	0.106	1.9
24	65,3-316 a = .8	–	1.00	8.9	1.240	0.150	0.110	0.109	0.9
26	65,3-118	–	1.00	6.0	1.324	0.060	0.107	0.117	-8.5
25	65_3-418	–	|	1.9	1.316	0.065	0.101	0.104	-2.9
↓	↓	–	|	6.0	↓	↓	0.107	0.111	-3.6
7	65,3-618	–	|	9.0	1.326	0.060	0.110	0.110	0
27	65_4-421	–	|	1.0	1.500	0.060	0.098	0.107	-8.4
↓	↓	–	↓	2.2	↓	↓	0.102	0.104	-1.9
28	65(112)-213	0.15	0.99	8.0	1.026	0.050	0.110	0.102	7.8
7	66-006	–	1.0	9.0	0.666	0.050	0.109	0.100	9.0
↓	66-009	–	↓	↓	0.961	0.060	0.108	0.103	4.9
10	↓	0.10	0.99	2.76	↓	↓	0.103	0.100	3.0
7	66-206	–	1.00	9.0	0.666	0.040	0.108	0.108	0
|	66-209	–	|	|	0.960	0.055	0.107	0.107	0
↓	66-210	–	↓	↓	1.053	0.050	0.107	0.110	-2.7
19	66-206	0.30	0.955	1.0	0.863	0.050	0.103	0.100	3.0
↓	66-212	↓	↓	↓	1.233	0.060	0.101	0.097	4.1
13	66-210	<0.15	0.99	3.0	1.053	0.050	0.103	0.097	6.2
7	66(215)-016	–	1.00	9.0	1.567	0.100	0.105	0.105	0
↓	66(215)-216	–	|	↓	1.565	0.080	0.105	0.114	-7.9
24	66(215)-114	–	↓	6.2	1.400	0.030	0.103	0.108	-4.6
11	66_2-415	<0.15	0.99	3.0	1.490	0.075	0.099	0.099	-1.0
↓	↓	↓	↓	9.0	↓	↓	0.106	0.105	1.0
29	66(215)-214	–	1.00	↓	1.590	0.190	0.105	0.106	-0.9
30	63A010	–	|	6.0	1.037	0.130	0.106	0.106	0
↓	63A210	–	|	9.0	1.030	0.120	0.108	0.103	4.9
7	64A010	–	|	↓	1.062	0.130	0.108	0.110	-1.8
31	|	–	↓	2.0	|	|	0.101	0.098	3.1
↓	|	0.2	0.98	7.0	|	|	0.108	0.107	0.9
30	↓	–	1.00	3.0	↓	↓	0.102	0.108	-5.6
|	64A210	–	|	6.0	1.060	0.120	0.105	0.107	-1.9
↓	64A410	–	↓	9.0	1.062	0.125	0.108	0.105	2.9

TABLE 4.1.1.2-A (CONTD)

Ref.	NACA Airfoil Section	M	β	R_ℓ x 10^{-6}	$\frac{Y_{90}}{2}$ % c	$\frac{Y_{99}}{2}$ % c	c_{ℓ_α} Calc. (per deg)	c_{ℓ_α} Test (per deg)	e Percent Error
32	64A310	0.30	0.955	1.0	1.065	0.110	0.103	0.102	1.0
↓	64A610	↓	↓	↓	1.070	0.125	0.103	0.107	-3.7
↓	64A910	↓	↓	↓	1.035	0.110	0.103	0.103	0
30	64_1A212	–	1.00	6.0	1.260	0.150	0.104	0.104	0
↓	64_2A215	–	↓	9.0	1.550	0.170	0.106	0.101	5.0
33	$65_{(112)}$-A111	–	↓	5.9	1.125	0.165	0.105	0.106	-0.9
7	63A010	–	↓	9.0	1.030	0.130	0.108	0.105	2.9
↓	63A210	–	↓	↓	1.030	0.120	0.108	0.103	4.9
↓	64A210	–	↓	↓	1.060	0.120	0.108	0.105	2.8
↓	64A410	–	↓	↓	1.062	0.125	0.108	0.100	8.0
↓	64_1A212	–	↓	↓	1.260	0.150	0.107	0.100	7.0
↓	64_2A215	–	↓	↓	1.550	0.170	0.106	0.095	11.6

Average Error = $\frac{\Sigma|e|}{n}$ = 2.4%

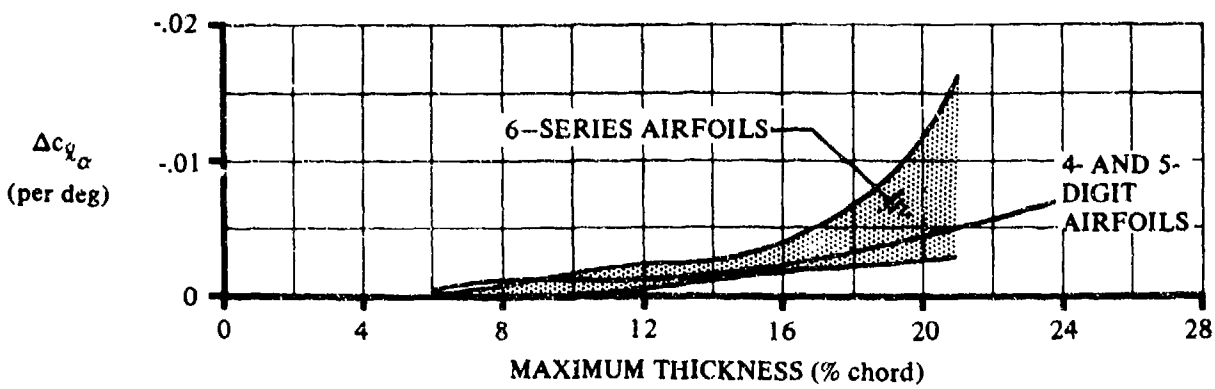

FIGURE 4.1.1.2-7 EFFECT OF NACA ROUGHNESS ON SECTION LIFT-CURVE SLOPE

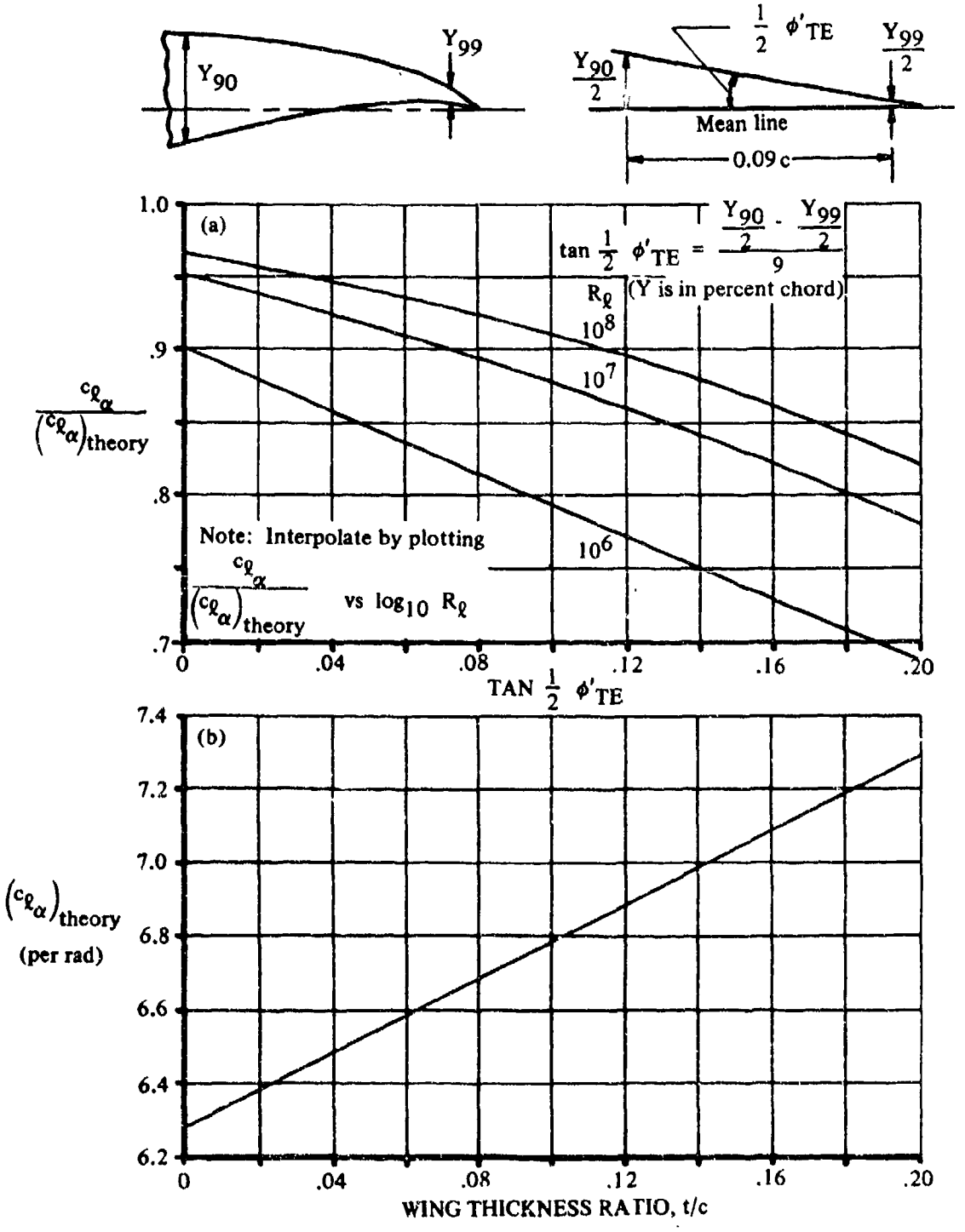

FIGURE 4.1.1.2-8 TWO-DIMENSIONAL LIFT-CURVE SLOPE METHOD 2

4.1.1.3 SECTION LIFT VARIATION WITH ANGLE OF ATTACK NEAR MAXIMUM LIFT

Flow-separation patterns, which determine the stall characteristics of airfoil sections, are due to the effects of viscosity. These flow separation patterns can be classified into three types:

1. Separation near the trailing edge.
2. Separation of the short-bubble type near the leading edge.
3. Separation of the long-bubble type near the leading edge.

A complete discussion of these types of flow separation, as they affect airfoil stall characteristics, is contained in reference 1. They are also discussed in Section 4.1.1.4 with respect to their effect on section maximum lift. Some of the more pertinent factors affecting these stall types are discussed below.

Trailing-Edge Stall

Trailing-edge stall occurs on wings of thickness-to-chord ratios of approximately 12 percent and greater. It is characterized by a gradual separation starting at the section trailing edge and progressing forward with increasing angle of attack. When the separation has moved forward to about the section midchord, maximum lift is reached. The stall for these sections is mild, with a gradual rounding of the lift and moment curves near $c_{l_{max}}$.

Leading-Edge Stall

As the thickness ratio of airfoils decreases, the nose shape becomes progressively sharper. At some point the increasingly severe adverse pressure gradients behind the nose pressure peak cause the lift of the airfoil to be limited by separation starting at the airfoil nose.

Local leading-edge separation on the airfoil upper surface may occur at angles of attack well below those for maximum lift. At these lower angles, the separated laminar boundary layer changes to turbulent and reattaches to the airfoil, leaving a bubble of trapped low-energy air between the separated boundary layer and the airfoil surface. The mechanism of the reattachment is discussed in references 2 and 3. Transition of the boundary layer must precede reattachment, and for this reason the relative stability of the boundary layer at separation is very important. If the boundary-layer Reynolds number based on the displacement thickness is greater than about 450, then transition and reattachment take place in a very short distance, giving rise to a "short bubble". If, on the other hand, the boundary-layer Reynolds number is less than 450, transition and reattachment are considerably delayed, with a resulting "long bubble". The different characteristics of these two bubbles and their effects on stall are discussed below.

. . . . Short-Bubble Leading-Edge Stall

The short bubble is characteristically one percent of the airfoil chord in length and decreases in size with increasing angle of attack. Because of its small size, the bubble has little effect on the section pressure distribution until at some angle of attack the flow abruptly ceases to reattach, thereby separating the flow over the entire upper surface of the airfoil. For this airfoil the lift and pitching-moment curves are quite linear right up to stall. The stall itself is violent, with large changes in lift and pitching moment.

. . . . Long-Bubble Leading-Edge Stall

The long bubble, like the short bubble, consists of a laminar separation followed by a turbulent reattachment. However, as the angle of attack increases, the size of the long bubble also increases until, at maximum lift, the bubble covers the entire upper surface of the airfoil.

For the long-bubble type of separation, the maximum lift achieved is, in general, lower than that for either the short-bubble type or the trailing-edge type. The stall for the long bubble is mild, with gradual rounding of the lift and moment curves.

Reynolds Number Effects

Since the type of bubble formed depends on the Reynolds number of the boundary layer at the point of separation, it is apparent that changes in free-stream Reynolds number can cause the stall of an airfoil to change from one type to another. If the Reynolds number is high enough, boundary-layer transition may take place before the point where laminar separation would occur, and no bubble will be formed at all. The tables and charts pertaining to this section are based primarily on a Reynolds number of 9×10^6. For other Reynolds numbers, reference 4 may be used, which contains a summary of the types of stall to be expected as a function of Reynolds number.

HANDBOOK METHOD

The shape of the section lift curve just below the stall angle of attack can be approximated from a knowledge of the angle of attack at which the lift curve begins to deviate from the linear slope, the maximum lift, angle of attack for maximum lift, and the lift-curve slope. The lift curve just before the stall can then be constructed with acceptable accuracy, as illustrated schematically in Section 4.1.1.

The parameters $c_{\ell_{max}}$, $\alpha_{c_{\ell_{max}}}$, and α_0 are discussed in Sections 4.1.1.4 and 4.1.1.1. The angle of attack α^* at which the lift curve deviates from the linear is tabulated for the NACA four-and five-digit and 6-series airfoils in tables 4.1.1-A and 4.1.1-B, respectively. The data, from reference 5, are for smooth surfaces, 9×10^6 Reynolds number, and low speeds.

REFERENCES

1. McCullough, G. B., and Gault, D. E.: Examples of Three Representative Types of Airfoil-Section Stall at Low Speed. NACA TN 2502, 1951 (U)

2. Crabtree, L. F., and Weber, J.: Some Effects of Flow Separation on Thin Wings With Unswept Leading Edges. R.A.E. Gt. Brit. TN Aero 2405. (U)

3. Crabtree, L. F.: Effects of Leading-Edge Separations on Thin Wings in Two-Dimensional Incompressible Flow. IAS Preprint No. 669, 1957.

4. Gault, D. E.: A Correlation of Low-Speed, Airfoil-Section Stalling Characteristics With Reynolds Number and Airfoil Geometry. NACA TN 3963, 1957 (U)

5. Abbott, I. H., von Doenhoff, A. E., and Stivers, L. S., Jr.: Summary of Airfoil Data. NACA TR 824, 1945. (U)

4.1.1.4 SECTION MAXIMUM LIFT

Subsonic section maximum lift is sensitive to many parameters, including airfoil thickness, location of maximum thickness, camber, position of maximum camber, Mach number, Reynolds number, free-stream turbulence, and airfoil surface condition (roughness). These parameters influence section maximum lift by determining the type of flow separation that limits the lift. Broadly speaking, the separation patterns may be classified into three types:

1. Trailing-edge separation.
2. Leading-edge separation of the short-bubble type.
3. Leading-edge separation of the long-bubble type.

The distinctive features of each of these types of separation are discussed in section 4.1.1.3.

For airfoils that stall as a result of flow separation from the leading edge (thin airfoils), the section maximum lift may be correlated with airfoil-leading-edge geometry. The leading-edge parameter that best correlates the section maximum lift is the Δy-parameter, the difference between the upper-surface ordinates at the 6-percent-chord and 0.15-percent-chord stations, respectively. This parameter is presented as a function of airfoil thickness for several standard airfoils in Section 2.2.1.

For thicker symmetrical airfoils, i.e., those that stall as a result of separation from the trailing edge, a relatively local leading-edge parameter is no longer sufficient. The maximum lift of these sections is correlated by using the position of maximum thickness in addition to the Δy-parameter.

Reference 1 indicates that for thin airfoils there is a maximum lift increment due to camber when the pressure distribution near the nose is identical to that of the corresponding uncambered airfoil. The procedure used in the Handbook is to add an increment of lift, accounting for the effect of camber, to the symmetrical-airfoil maximum lift. Empirically, the increment is a function of maximum-thickness position as well as position and magnitude of maximum camber.

Reynolds number and free-stream turbulence are analogous in their effects on section maximum lift. For thin airfoils an increase in Reynolds number or turbulence causes boundary-layer transition earlier, changing a long-bubble to a short-bubble separation. This increases lift. Roughness, if it causes transition early enough, has the same effect. For thicker airfoils roughness merely decreases the energy of the boundary layer, thus lowering maximum lift.

Mach number effects are very severe on thick airfoils. Maximum lift coefficient begins to drop, starting at $M \approx 0.2$, as illustrated typically in figure 4.1.1.4-8b.

For supersonic speeds, maximum lift can be calculated by the method of reference 2, which makes the assumptions that the upper-surface limit pressure is 70 percent of vacuum and the lower-surface pressure is a function of the total pressure behind a normal shock wave at the free-stream Mach number and the projected area of the lower surface perpendicular to the free-stream direction. Section maximum-lift values obtained by this procedure appear to be slightly low.

HANDBOOK METHOD

In this Section two-dimensional-airfoil maximum-lift information is presented in two forms: tabulated data for specific NACA airfoils and generalized design charts from which the maximum lift of nonstandard airfoils may be approximated. Actual test data should be used whenever possible, however.

Section data for maximum lift and angle of attack for maximum lift for the NACA four- and five-digit airfoils are presented in table 4.1.1-A for smooth-leading-edge conditions, a Reynolds number of 9×10^6, and low speeds. Corresponding information for the NACA 6-series airfoils is presented in table 4.1.1-B. Additional airfoils may be located in the literature with the aid of table 4.1.1-C.

The generalized design charts of this Section are empirically derived from experimental data of references 3, 4, 5, and 6. The section maximum lift coefficient is determined by the equation

$$c_{\ell_{max}} = (c_{\ell_{max}})_{base} + \Delta_1 c_{\ell_{max}} + \Delta_2 c_{\ell_{max}} + \Delta_3 c_{\ell_{max}} + \Delta_4 c_{\ell_{max}} + \Delta_5 c_{\ell_{max}} \qquad 4.1.1.4\text{-a}$$

where the various contributions are obtained as follows:

1. $(c_{\ell_{max}})_{base}$ is obtained from figure 4.1.1.4-5 as a function of Δy and position of maximum thickness. The Δy-parameter for a cambered airfoil is the same as that of the corresponding uncambered airfoil, that is, the uncambered airfoil having the same thickness distribution. This reference value is for uncambered airfoils with smooth leading edges, at 9×10^6 Reynolds number and low speed.

2. $\Delta_1 c_{\ell_{max}}$ accounts for the effect of camber for airfoils having the maximum thickness at 30-percent chord. Figure 4.1.1.4-6 gives $\Delta_1 c_{\ell_{max}}$ as a function of percent camber and maximum-camber location. The percent camber and position of maximum camber for standard NACA airfoils are discussed in Section 2.2.1.

3. $\Delta_2 c_{\ell_{max}}$ amounts to an increment by which $\Delta_1 c_{\ell_{max}}$, the "camber" term for airfoils having their maximum thickness at 30-percent chord, must be modified for airfoils having their maximum thickness at some other position. This increment is obtained from figure 4.1.1.4-7a. (If the maximum thickness is at 30-percent chord, $\Delta_2 c_{\ell_{max}}$ is zero).

4. $\Delta_3 c_{\ell_{max}}$, presented in figure 4.1.1.4-7b, gives the lift increment due to Reynolds number for Reynolds numbers other than 9×10^6.

5. $\Delta_4 c_{\ell_{max}}$, shown in figure 4.1.1.4-8a, gives the lift increment due to roughness. The roughness in this case is the standard NACA roughness and is represented by 0.011-inch grit applied over the first 8-percent chord. This curve is given only as an indication of roughness effects. Actual airplane roughnesses vary considerably and their effects may be quite different from those shown in figure 4.1.1.4-8a.

6. $\Delta_5 c_{\ell_{max}}$ is a correction for Mach numbers greater than approximately 0.2. No generalized charts are presented for Mach number effects. The lift increment due to Mach number should be obtained from test data of similar airfoils when available. Figure 4.1.1.4-8b shows representative effects on particular airfoils.

Table 4.1.1.4-A compares experimental data with results obtained by the use of this method.

SAMPLE PROBLEM

Given:

66_2-415 Airfoil section

$R = 6 \times 10^6$

$M = .10$

Airfoil surface in smooth condition

Compute:

t/c = 15-percent chord*

Position of maximum thickness: 45-percent chord*

Position of maximum camber: 50-percent chord*

Amount of camber: 2.2-percent chord*

$\Delta y = 2.75$ (from Section 2.2.1)

$(c_{\ell_{max}})_{base} = 1.34$ (from figure 4.1.1.4-5)

$\Delta_1 c_{\ell_{max}} = .16$ (from figure 4.1.1.4-6)

$\Delta_2 c_{\ell_{max}} = .08$ (from figure 4.1.1.4-7a)

$\Delta_3 c_{\ell_{max}} = -.02$ (from figure 4.1.1.4-7b)

$\Delta_4 c_{\ell_{max}} = 0$

$\Delta_5 c_{\ell_{max}} = 0$

*See Section 2.2.1 for airfoil description

Solution:

$$c_{\ell_{max}} = (c_{\ell_{max}})_{base} + \Delta_1 c_{\ell_{max}} + \Delta_2 c_{\ell_{max}} + \Delta_3 c_{\ell_{max}} + \Delta_4 c_{\ell_{max}} + \Delta_5 c_{\ell_{max}}$$

$$= 1.56$$

$c_{\ell_{max}} = 1.60$ from test data of reference 4.

TABLE 4.1.1.4-A
AIRFOIL SECTION MAXIMUM LIFT
DATA SUMMARY AND SUBSTANTIATION

Ref.	Airfoil	Position of max. thickness (% chord)	Camber (% chord)	Position of max. camber (% chord)	Δ_y (% chord)	R x 10^{-6}	$(c\ell_{max})_{base}$	$\Delta_1 c\ell_{max}$	$\Delta_2 c\ell_{max}$	$\Delta_3 c\ell_{max}$	$c\ell_{max}$ Calc.	$c\ell_{max}$ Test	Percent Error, %
4	0009	30	0	-----	2.35	9.0	1.36	-----	-----	-----	1.36	1.32	3.0
	1410	30	1.0	40	2.60	9.0	1.46	.11	-----	-----	1.59	1.50	6.0
	2415	30	2.0	40	2.80	9.0	1.57	.06	-----	-.23	1.40	1.40	0
	4412	30	4.0	40	3.08	9.0	1.58	.17	-----	-.18	1.62	1.52	6.6
7	4315	30	4.0	30	2.80	6.0	1.57	.06	-----	-.03	1.60	1.67	-4.2
	4321	30	4.0	30	3.24	6.0	1.41	-.03	-----	-.03	1.35	1.35	-3.6
	6306	30	6.0	30	1.60	6.0	1.02	.04	-----	-.03	1.03	1.05	-1.2
	6309	30	6.0	30	2.35	6.0	1.26	.48	-----	-.01	1.73	1.73	0
4	23012	30	1.5	15	3.06	9.0	1.56	.09	-----	-----	1.67	1.79	-5.6
	23021	30	1.5	15	3.24	9.0	1.41	0	-----	-----	1.41	1.50	-6.0
5	43012	30	3.7	15	3.06	6.0	1.56	.14	-----	0	1.72	1.84	-6.5
	63012	30	3.5	15	3.06	6.0	1.56	.14	-----	0	1.72	1.84	-6.5
8	63-009	35	0	-----	2.00	15.0	1.20	-----	-----	.06	1.26	1.23	2.4
	63-209	35	1.1	50	2.00	25.0	1.20	.03	.16	.06	1.49	1.36	9.6
	63_1-012	35	0	-----	2.68	25.0	1.46	-----	-----	.02	1.48	1.41	5.0
	63_1-212	35	1.1	50	2.68	25.0	1.46	.08	.09	.02	1.65	1.54	7.1
4	63_1-412	35	2.2	50	2.68	9.0	1.46	.17	.09	-----	1.72	1.77	-2.8
	63_2-015	35	0	-----	2.86	9.0	1.46	-----	-----	-----	1.46	1.54	-5.2
	63_2-215	35	2.2	50	2.86	9.0	1.46	.11	-.02	-----	1.57	1.59	-1.3
	64-108	40	.85	50	1.70	9.0	1.06	.03	.20	-----	1.29	1.10	16.4
	64_1-112	40	.85	50	2.52	9.0	1.40	.04	.11	-----	1.55	1.50	3.3
	64_1-012	40	0	-----	2.75	9.0	1.44	-----	-----	-----	1.44	1.50	-4.0
	64_1-212	40	1.1	50	2.75	9.0	1.44	.03	.04	-----	1.51	1.53	-1.3
	64_1-412	40	2.2	50	2.75	9.0	1.44	.07	.04	-----	1.55	1.57	-1.3
	64_2-015	40	0	-----	2.75	9.0	1.44	.11	.04	-----	1.59	1.58	0.6
	64_2-215	40	0	-----	2.90	9.0	1.44	-----	-----	-.10	1.34	1.35	-0.7
	64_2-415	40	2.2	50	2.90	9.0	1.44	.18	.08	-.10	1.59	1.48	7.6
	65-009	45	0	-----	1.98	9.0	1.04	-----	-----	-----	1.04	1.05	-1.0
	65-209	45	1.1	50	1.65	9.0	1.04	.03	.20	---	1.27	1.17	8.5
	65_1-010	45	0	-----	2.30	9.0	1.35	-----	-----	-----	1.35	1.34	0.7
	65_1-410	45	2.2	50	2.30	9.0	1.35	.13	.08	-----	1.56	1.56	0

Average Error in $c\ell_{max}$ = $\frac{\Sigma|\epsilon|}{n}$ = 6.0%

REFERENCES

1. Roshko, A.: Computation of the Increment of Maximum Lift due to Flaps. Douglas Aircraft Company Report SM 23826, 1959. (U)

2. Mayer, J. P.: A Limit Pressure Coefficient and an Estimation of Limit Forces on Airfoils at Supersonic Speeds. NACA RM L8F28, 1948. (U)

3. Pinkerton, R. M., and Greenberg, H.: Aerodynamic Characteristics of a Large Number of Airfoils Tested in the Variable-Density Wind Tunnel. NACA TR 628, 1938 (U)

4. Abbott, I. H., and von Doenhoff, A. E., and Stivers, L. S., Jr.: Summary of Airfoil Data. NACA TR 824, 1945. (U)

5. Jacobs, E. N., and Abbott, I. H.: Airfoil Section Data Obtained in the NACA Variable-Density Tunnel as Affected by Support Interference and Other Corrections. NACA TR 669, 1939. (U)

6. Jacobs, E. N., Pinkerton, R. M., and Greenberg, H.: Tests of Related Forward-Camber Airfoils in the Variable-Density Wind Tunnel. NACA TR 610, 1937. (U)

7. Jacobs, E. N., Ward, K. E., and Pinkerton, R. M.: The Characteristics of 78 Related Airfoil Sections from Tests in the Variable-Density Wind Tunnel. NACA TR 460, 1933. (U)

8. Loftin, L. K., Jr., and Bursnall, W. J.: The Effects of Variations in Reynolds Number between 8.0×10^6 and 25.0×10^6 upon the Aerodynamic Characteristics of a Number of NACA 6-Series Airfoil Sections. NACA TN 1773, 1948. (U)

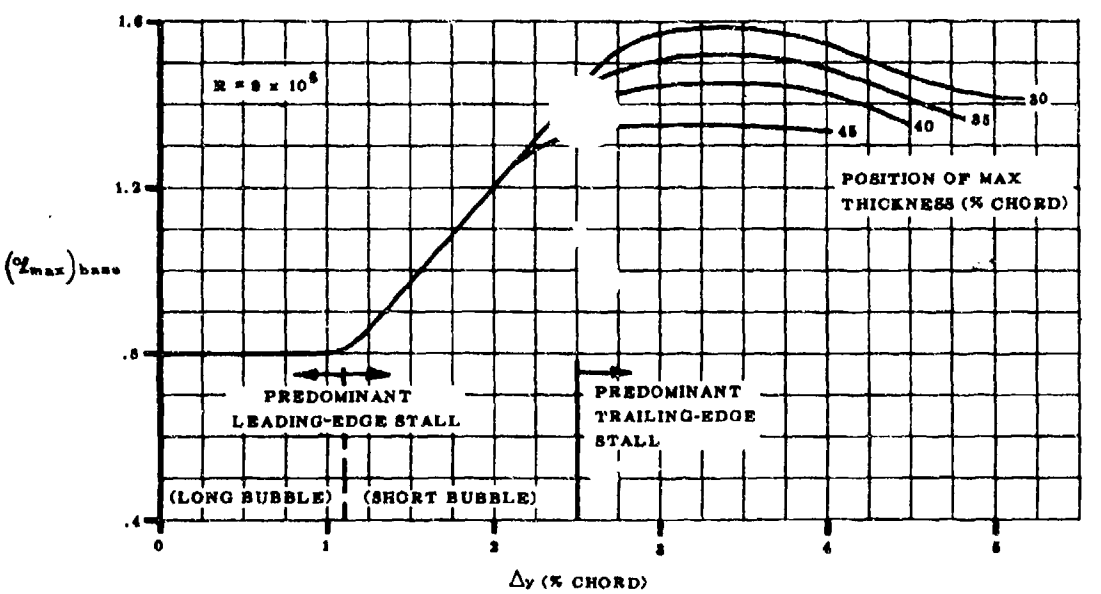

FIGURE 4.1.1.4-5 AIRFOIL SECTION MAXIMUM LIFT COEFFICIENT OF UNCAMBERED AIRFOILS

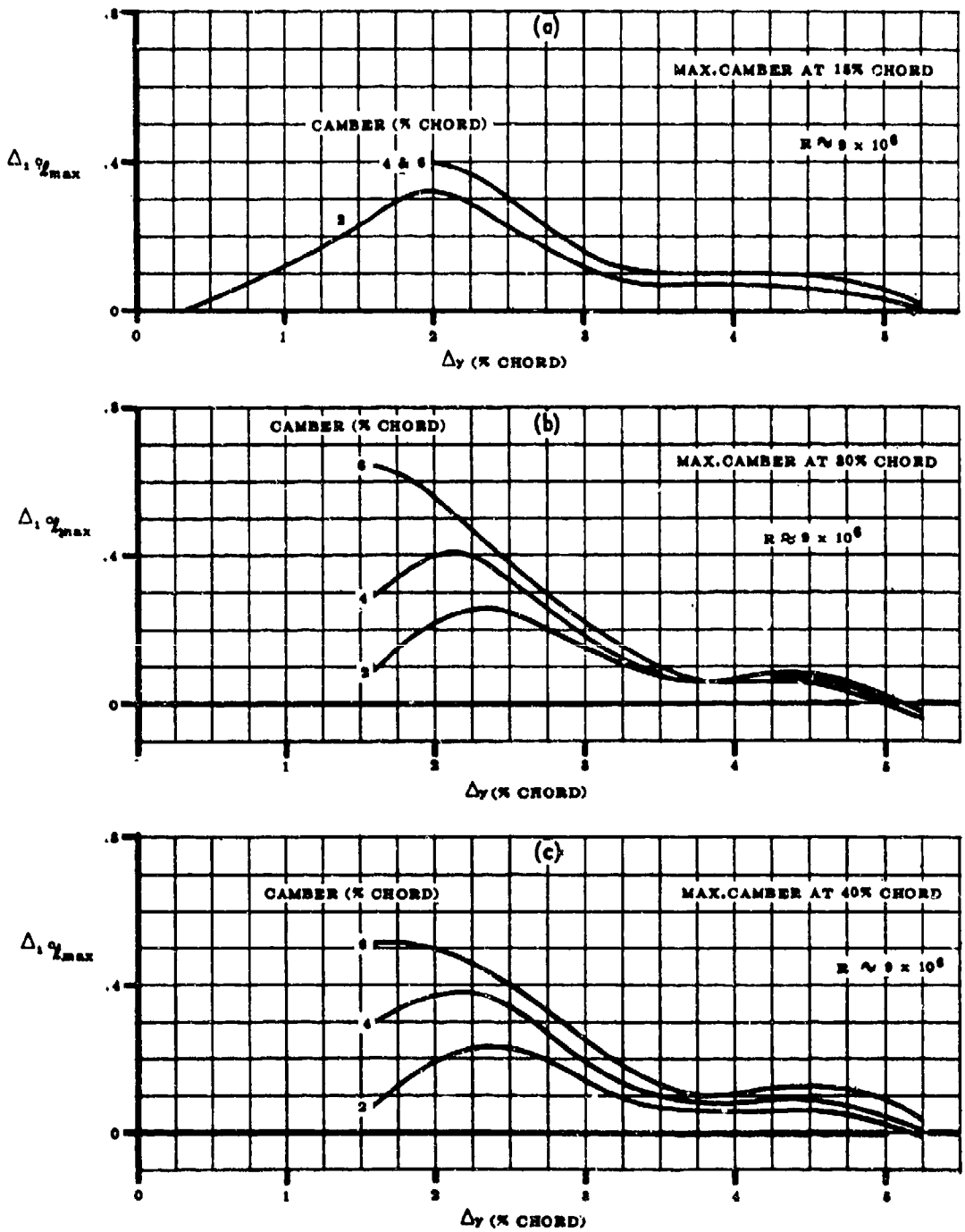

FIGURE 4.1.1.4-6 EFFECT OF AIRFOIL CAMBER LOCATION AND AMOUNT ON SECTION MAXIMUM LIFT

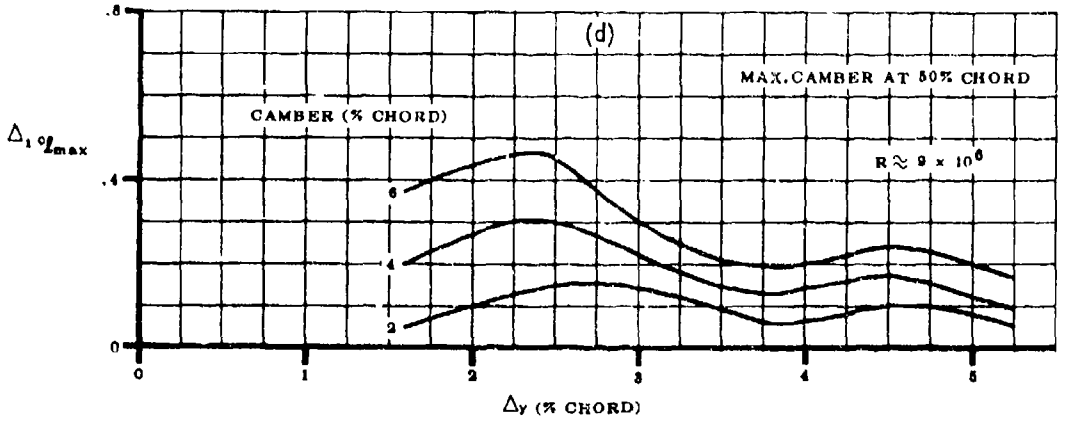

FIGURE 4.1.1.4-6 (Cont'd) EFFECT OF AIRFOIL CAMBER LOCATION AND AMOUNT ON SECTION MAXIMUM LIFT

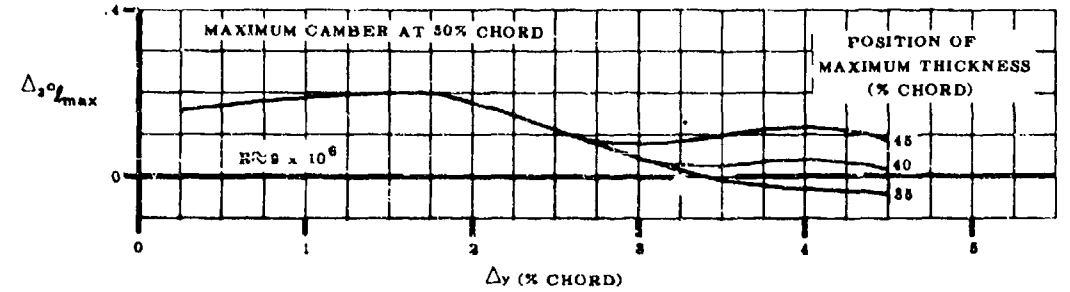

FIGURE 4.1.1.4-7a EFFECT OF POSITION OF MAXIMUM THICKNESS ON SECTION MAXIMUM LIFT

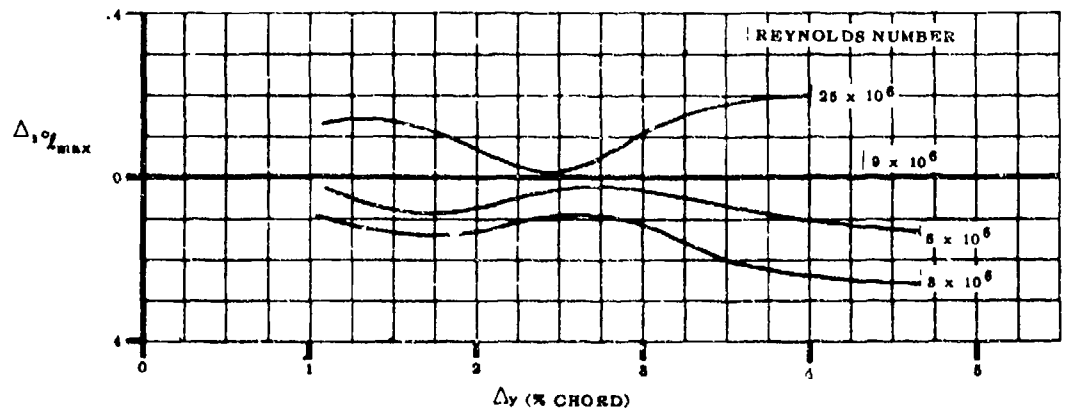

FIGURE 4.1.1.4-7b EFFECT OF REYNOLDS NUMBER ON SECTION MAXIMUM LIFT

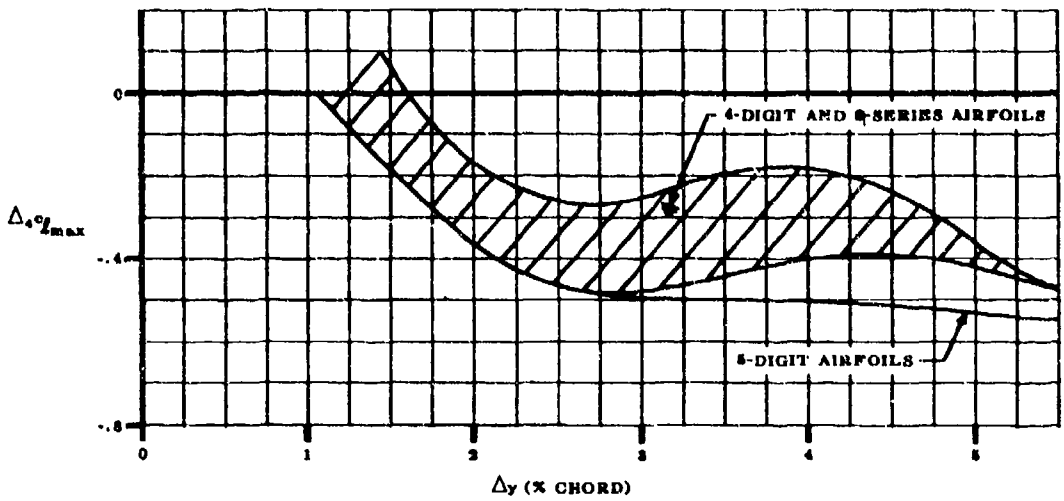

FIGURE 4.1.1.4-8a EFFECT OF NACA STANDARD ROUGHNESS ON SECTION MAXIMUM LIFT

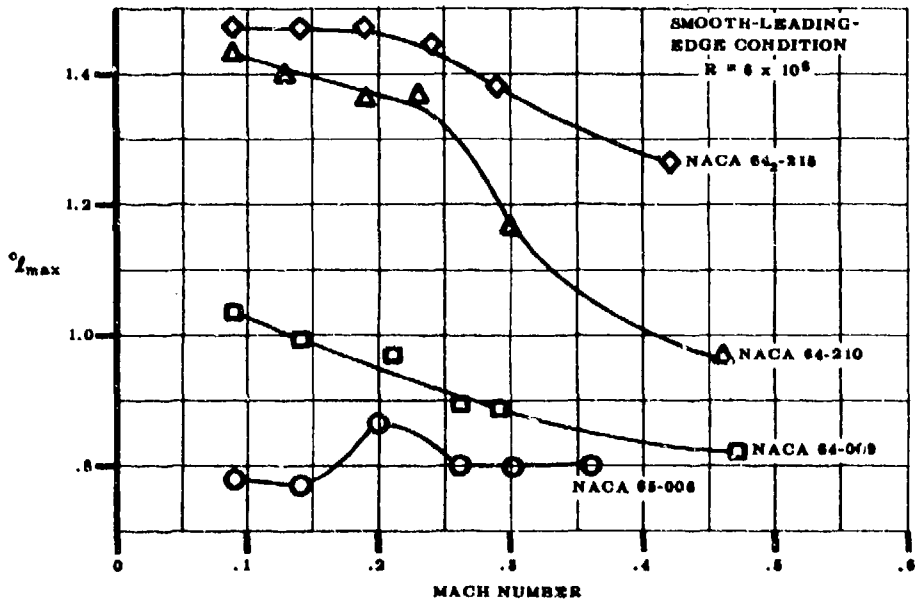

FIGURE 4.1.1.4-8b TYPICAL VARIATION OF SECTION MAXIMUM LIFT WITH FREE-STREAM MACH NUMBER

4.1.2 SECTION PITCHING MOMENT

4.1.2.1 SECTION ZERO-LIFT PITCHING MOMENT

The zero-lift pitching-moment coefficient is included for various NACA four- and five-digit and NACA 6-series airfoil sections in tables 4.1.1-A and 4.1.1-B. These data should be used wherever possible in preference to theoretical data in stability and control calculations.

These tables are applicable to Mach numbers below the critical. Above the critical Mach number, appreciable changes in zero-lift pitching moment may be present because of compressibility effects.

Additional section data may be located in the literature with the aid of table 4.1.1-C.

The theoretical pitching-moment coefficients of the various airfoil mean lines at the design lift coefficients are proportional to the section design lift coefficient or mean-line ordinate (camber) and may be scaled up or down as shown in the sample problems below or in table 4.1.1-D. Since the theoretical thin-airfoil aerodynamic center is at the quarter-chord point, the theoretical zero-lift pitching moment is identical to the theoretical pitching moment about the quarter-chord point at the design lift coefficient, shown in table 4.1.1-D.

Sample Problems

Example 1: Find the theoretical c_{m_0} about the quarter-chord point for the 2415 airfoil. Using the 64 mean line as a base, for which $c_{m_0} = -0.157$(table 4.1.1-D), the required pitching-moment coefficient is

$$c_{m_0} = -.157 \times 2/6$$
$$= -.052$$

The experimental value for this section is -.049 (table 4.1.1-A).

Example 2: Find the c_{m_0} about the quarter-chord point for the NACA 65_3-215, $a = 0.5$ airfoil. The design lift coefficient for this airfoil is 0.2. Using the 6-series mean line for $a = 0.5$, for which $c_{m_0} = -.139$ (table 4.1.1-D), gives the desired pitching-moment coefficient:

$$c_{m_0} = -.139 \times .2$$
$$= -.028$$

4.1.2.2 SECTION PITCHING-MOMENT VARIATION WITH LIFT

A. SUBSONIC

The aerodynamic center of thin airfoil sections is theoretically located at the quarter-chord point. Experimentally, the aerodynamic-center location is a function of section thickness ratio and trailing-edge angle. Experimental data should always be used in preference to the theory.

The summary of experimental aerodynamic characteristics of various NACA four- and five-digit and 6-series airfoil sections given in tables 4.1.1-A and 4.1.1-B includes aerodynamic-center location.

Figure 4.1.2.2-3 presents the generalized aerodynamic center for the useful range of airfoil thickness ratios and trailing-edge angles. Trailing-edge angles, as defined on figure 4.1.2.2-3 are given for standard NACA airfoils in Section 2.2.1. A comparison of experimental data with results based on these charts is shown in table 4.1.2.2-A.

B. SUPERSONIC

Section pitching-moment variation with lift at supersonic speeds is primarily a function of section thickness, thickness distribution, and camber. For conditions where there is no flow separation, shock-expansion theory gives results that are in good agreement with experimental data.

At the higher angles of attack, especially for the thicker sections, flow separation takes place on the upper rear portion of the airfoil. Under these circumstances the experimental center of pressure is farther forward than that predicted by theory.

At very high angles of attack, the shock detaches from the section leading edge. The center of pressure then tends toward the 50-percent-chord point as the angle of attack increases toward 90°

Figure 4.1.2.2-4 gives the position of the center of pressure for three airfoil sections as a function of Mach number, angle of attack, and thickness ratio. These results are calculated from shock-expansion theory (reference 1) and are strictly applicable only when the flow is everywhere attached.

REFERENCE

1. Handbook of Supersonic Aerodynamics, NAVORD Report 1488, Vol 3, Section 6, 1957. (U)

TABLE 4.1.2.2-A

AIRFOIL-SECTION AERODYNAMIC-CENTER POSITION
DATA SUMMARY AND SUBSTANTIATION

Airfoil Section	ϕ_{TE} (deg)	$x_{a.c.}$ Test	$x_{a.c.}$ Calc.	$\Delta x_{a.c.}$ (Calc.-Test)
2421	27.5	.261	.257	—.004
2424	31.4	.231	.232	+.001
4415	19.6	.245	.245	0
4418	23.6	.242	.242	0
4421	27.5	.238	.237	—.001
4424	31.4	.239	.232	—.007
63,-615	4.8	.266	.268	+.002
63,-018	5.7	.271	.271	0
63,-418	5.7	.272	.271	—.001
63,-021	6.6	.273	.274	+.001
63,-221	6.6	.269	.274	+.005
64A010	10.5	.253	.253	0
64,A215	15.8	.252	.252	0
64,A212	13.6	.252	.251	—.001
64-006	2.3	.258	.257	—.001
64-009	3.5	.260	.262	+.002
64,-012	4.6	.259	.265	+.006
64,-015	5.8	.268	.267	—.001
64,-018	6.9	.268	.269	+.001
64,-021	8.1	.273	.272	—.001
65-006	2.9	.256	.256	0
65,-015	7.2	.259	.265	+.006
65,-021	10.1	.270	.269	—.001
66-006	5.6	.258	.253	—.005
66,-015	9.3	.265	.262	—.003
66,-021	13.0	.275	.265	—.010
23024	31.4	.231	.232	+.001
0006	7.9	.250	.249	—.001
1412	15.7	.250	.248	—.002
23012	15.7	.241	.248	+.007
23018	23.6	.241	.242	+.001
23021	27.5	.234	.237	+.003
23024	31.5	.223	.231	+.008

Average Error $= \frac{\Sigma \left| \Delta x_{a.c.} \right|}{n} = 0.003$

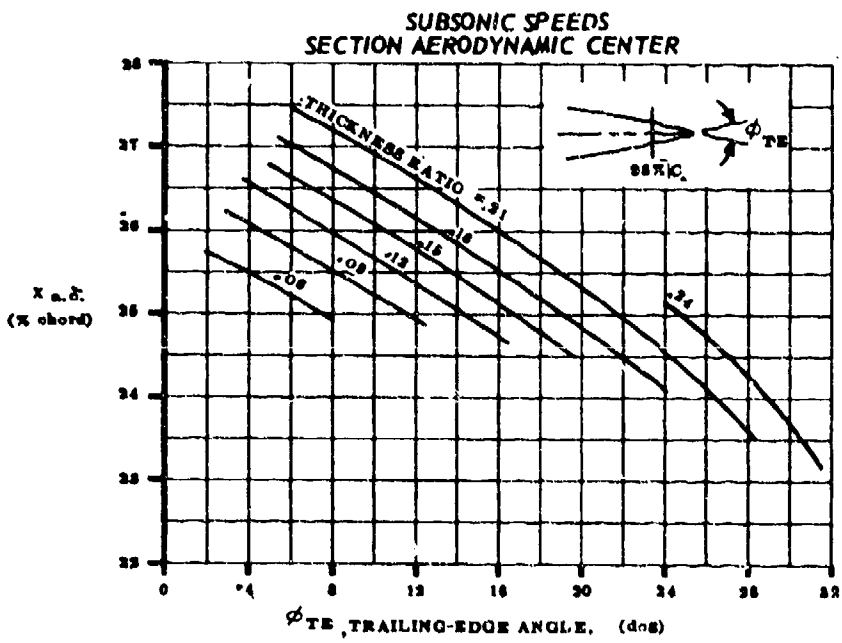

FIGURE 4.1.2.2-3 EFFECT OF TRAILING-EDGE ANGLE ON SECTION AERODYNAMIC-CENTER LOCATION

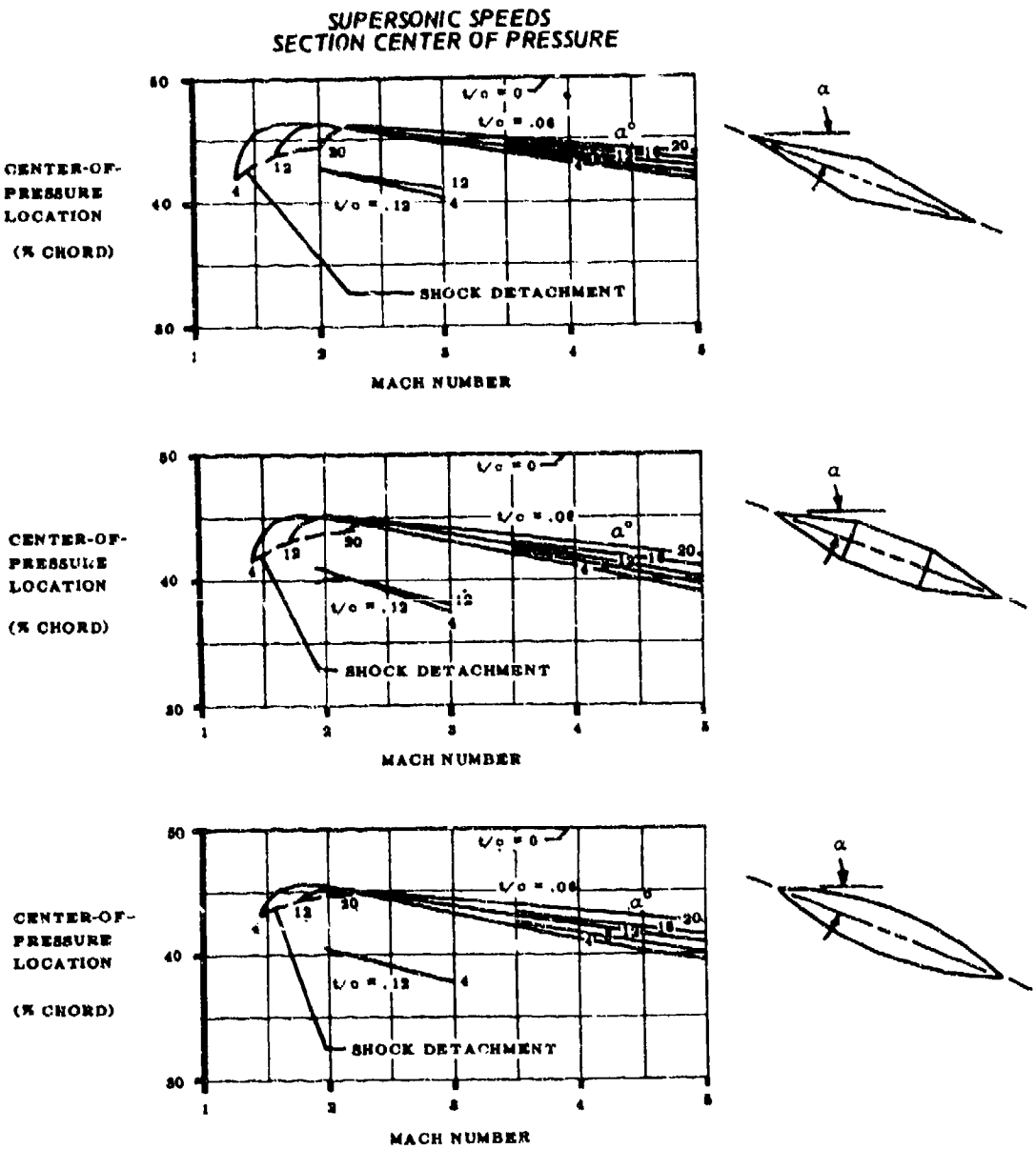

FIGURE 4.1.2.2-4 EFFECT OF THICKNESS AND ANGLE OF ATTACK ON CENTER OF PRESSURE LOCATION

4.1.3 WING LIFT

In the following group of Sections, (4.1.3.1 through 4.1.3.4), methods are presented for calculating the lift and normal force on wings at any angle of attack and any speed. An accurate determination of wing lift characteristics is important, since many other calculations are based on the wing-alone properties, e.g., all wing-body lift estimates and wing and wing-body rolling-moment calculations.

For this reason the approximations that are made in calculating wing lift in certain of the following Sections must be clearly understood in terms of their effect on the accuracy of the resulting numerical values.

The aerodynamic forces acting on a wing may be represented by a single force vector. This vector is conventionally resolved into two orthogonal components. The directions of the components are defined by the axis system selected. The two axis systems used most often are illustrated in the sketch below.

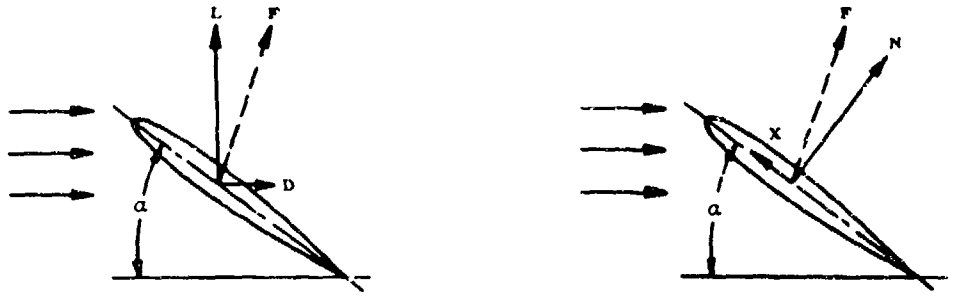

LIFT AXIS SYSTEM NORMAL-FORCE AXIS SYSTEM

In the lift axis system, the force vector F is resolved into components perpendicular and parallel to the free stream. These components are called lift and drag, respectively. In the normal-force axis system, the force vector is resolved into components perpendicular to and parallel to the wing chord, called the normal force and the chord force, respectively.

The equations relating the lift, drag, normal-force, and chord-force coefficients are

$$C_N = C_L \cos \alpha + C_D \sin \alpha \qquad \text{4.1.3-a}$$

$$C_X = - C_D \cos \alpha + C_L \sin \alpha \qquad \text{4.1.3-b}$$

$$C_L = C_N \cos \alpha + C_X \sin \alpha \qquad \text{4.1.3-c}$$

$$C_D = C_N \sin \alpha - C_X \cos \alpha \qquad \text{4.1.3-d}$$

If the resultant force vector is nearly normal to the wing surface, the chordwise force component can be neglected and

$$F \approx N \quad X \approx 0$$

$$C_L \approx C_N \cos \alpha \qquad \text{4.1.3-e}$$

$$C_D \approx C_N \sin \alpha \qquad \text{4.1.3-f}$$

The resultant force vector is nearly normal to the wing surface for all low-aspect-ratio wings and for high-aspect-ratio wings at angles of attack beyond the stall at subsonic speeds. It is also nearly normal to the wing surface for all wings at supersonic speeds. However, for high-aspect-ratio wings at angles of attack below the stall, the resultant force vector is more nearly perpendicular to the free-stream direction than normal to the wing surface.

For purposes of continuity through the complete speed and angle-of-attack envelope it is convenient to introduce a pseudonormal force C_N', defined by the equation

$$C_{N'} = \frac{C_L}{\cos \alpha} \qquad \text{4.1.3-g}$$

As indicated by the discussion above, this $C_{N'}$ is essentially the true normal force for all situations except that of high-aspect-ratio wings at angles of attack below the stall.

In the following Sections $C_{N'}$ is used for C_N throughout. Sample problems in Section 4.1.3.3 show comparisons between experimental C_N values and calculated $C_{N'}$ values, and between experimental and calculated C_L values for several configurations.

4.1.3.1 WING ZERO-LIFT ANGLE OF ATTACK

The method presented in this section is restricted to subsonic speeds. In the transonic and supersonic speed regimes it is suggested that reference be made to experimental data.

A. SUBSONIC

The effect of planform geometry on the zero-lift angle of attack of untwisted, constant-section wings is relatively small. Therefore, the method applied to such planforms is based on airfoil section properties.

For untwisted, constant-section wings the zero-lift angle of attack, taken from reference 1, is

$$(\alpha_0)_{\theta=0} = \alpha_i - \frac{c_{\ell_i}}{c_{\ell_\alpha}} \quad \text{(degrees)} \qquad 4.1.3.1\text{-a}$$

where c_{ℓ_i}, α_i, and c_{ℓ_α} are the section design lift coefficient, angle of attack for design lift coefficient, and section lift-curve slope, respectively. These data may be obtained from Section 4.1.1.

Equation 4.1.3.1-a is applicable to swept wings if the airfoils are defined parallel to the free stream.

If definition of the airfoil section parallel to the free stream is not available for a particular swept wing, then α_0 may be approximated by

$$(\alpha_0)_{\substack{\theta=0 \\ \Lambda}} = \tan^{-1}\left[\tan (\alpha_0)_{\substack{\theta=0 \\ \Lambda=0}} \frac{1}{\cos \Lambda}\right] \quad \text{(degrees)} \qquad 4.1.3.1\text{-b}$$

where

Λ is the sweepback of some constant-percent chord line.

$(\alpha_0)_{\substack{\theta=0 \\ \Lambda=0}}$ is the zero-lift angle of attack of an untwisted, constant-section wing of zero-degree sweepback obtained by using equation 4.1.3.1-a. Values of c_{ℓ_i}, α_i, and c_{ℓ_α} used in equation 4.1.3.1-a are based on the airfoil section in a plane normal to the particular constant-percent chord line.

For wings with constant airfoil sections and linear twist, lifting-line theory may be used as in reference 2 to obtain α_0 as a function of planform geometry. This method uses the equation

$$\alpha_0 = (\alpha_0)_{\theta=0} + \left(\frac{\Delta\alpha_0}{\theta}\right)\theta \quad \text{(degrees)} \qquad 4.1.3.1\text{-c}$$

where

$(\alpha_0)_{\theta=0}$ is the zero-lift angle of attack of the untwisted, constant-section wing, given by equation 4.1.3.1-a.

$\frac{\Delta\alpha_0}{\theta}$ is the change in wing zero-lift angle of attack due to a unit change in linear wing twist. This parameter is obtained from figure 4.1.3.1-4.

θ is the twist of the wing tip with respect to the root section, in degrees (negative for washout). A linear spanwise twist distribution is assumed (all constant-percent points of the local chords lie in straight lines along the span).

Test data have indicated that if the airfoil is cambered the zero-lift angle of attack varies with Mach number, particularly above the critical Mach number. A Mach number correction to be applied to cambered airfoils is presented as figure 4.1.3.1-5. This chart gives the ratio of the zero-lift angle of attack at any subsonic Mach number to the corresponding value at M = 0.3. This chart is based on the data of references 3, 4, and 5 and is to be considered as a first-order approximation only.

Unfortunately, there are not enough data to substantiate the theoretical results as applied to either untwisted or twisted wings. Consequently, experimental data should be used whenever possible.

Sample Problem

Given: An untwisted, constant-section wing.

$A = 6.0 \qquad \Lambda_{c/4} = 6.34^o \qquad \lambda = 0.50 \qquad \theta = 0$

NACA 23012 airfoil (streamwise) $\qquad \frac{Y_{90}}{2} = 1.455 \qquad \frac{Y_{99}}{2} = 0.265$

Low speed; $\beta = 1.0 \qquad R_\ell = 1 \times 10^6$ (based on MAC)

Compute:

$\left.\begin{array}{l} \alpha_i = 1.65^o \\ c_{\ell_i} = 0.30 \end{array}\right\}$ (table 4.1.1-D)

Determine c_{ℓ_α} (Section 4.1.1.2)

$$\tan \frac{1}{2}\phi'_{TE} = \frac{\frac{Y_{90}}{2} - \frac{Y_{99}}{2}}{9} = \frac{1.455 - 0.265}{9} = 0.132$$

$$\frac{c_{\ell_\alpha}}{(c_{\ell_\alpha})_{theory}} = 0.760 \quad \text{(figure 4.1.1.2-8a)}$$

$$(c_{\ell_\alpha})_{theory} = 6.89 \text{ per rad} \quad \text{(figure 4.1.1.2-8b)}$$

$$c_{\ell_\alpha} = \frac{1.05}{\beta}\left[\frac{c_{\ell_\alpha}}{(c_{\ell_\alpha})_{theory}}\right](c_{\ell_\alpha})_{theory} \quad \text{(equation 4.1.1.2-a)}$$

$$= \frac{1.05}{1.0}\ [0.760]\ (6.89) = 5.50 \text{ per rad}$$

$$= 0.096 \text{ per deg}$$

Solution:

$$(\alpha_0)_{\theta=0} = \alpha_i - \frac{c_{\ell_i}}{c_{\ell_\alpha}} \quad \text{(equation 4.1.3.1-a)}$$

$$= 1.65 - \frac{0.30}{0.096}$$

$$= -1.48 \text{ deg}$$

REFERENCES

1. Abbott, I. H., von Doenhoff, A. E., and Stivers, L. S., Jr.: Summary of Airfoil Data. NACA TR 824, 1945. (U)

2. DeYoung, J., and Harper, C. W.: Theoretical Symmetric Span Loading at Subsonic Speeds for Wings Having Arbitrary Plan Form. NACA TR 921, 1948. (U)

3. Granam, D. J.: The Development of Cambered Airfoil Sections Having Favorable Lift Characteristics at Supercritical Mach Numbers. NACA TR 947, 1949. (U)

4. Stack, J., and von Doenhoff, A. E.: Tests of 16 Related Airfoils at High Speeds. NACA TR 492, 1934. (U)

5. Johnson, B. H., Jr., and Shibata, H. H.: Characteristics Throughout the Subsonic Speed Range of a Plane Wing and of a Cambered and Twisted Wing, Both Having 45° of Sweepback. NACA RM A51D27, 1951. (U)

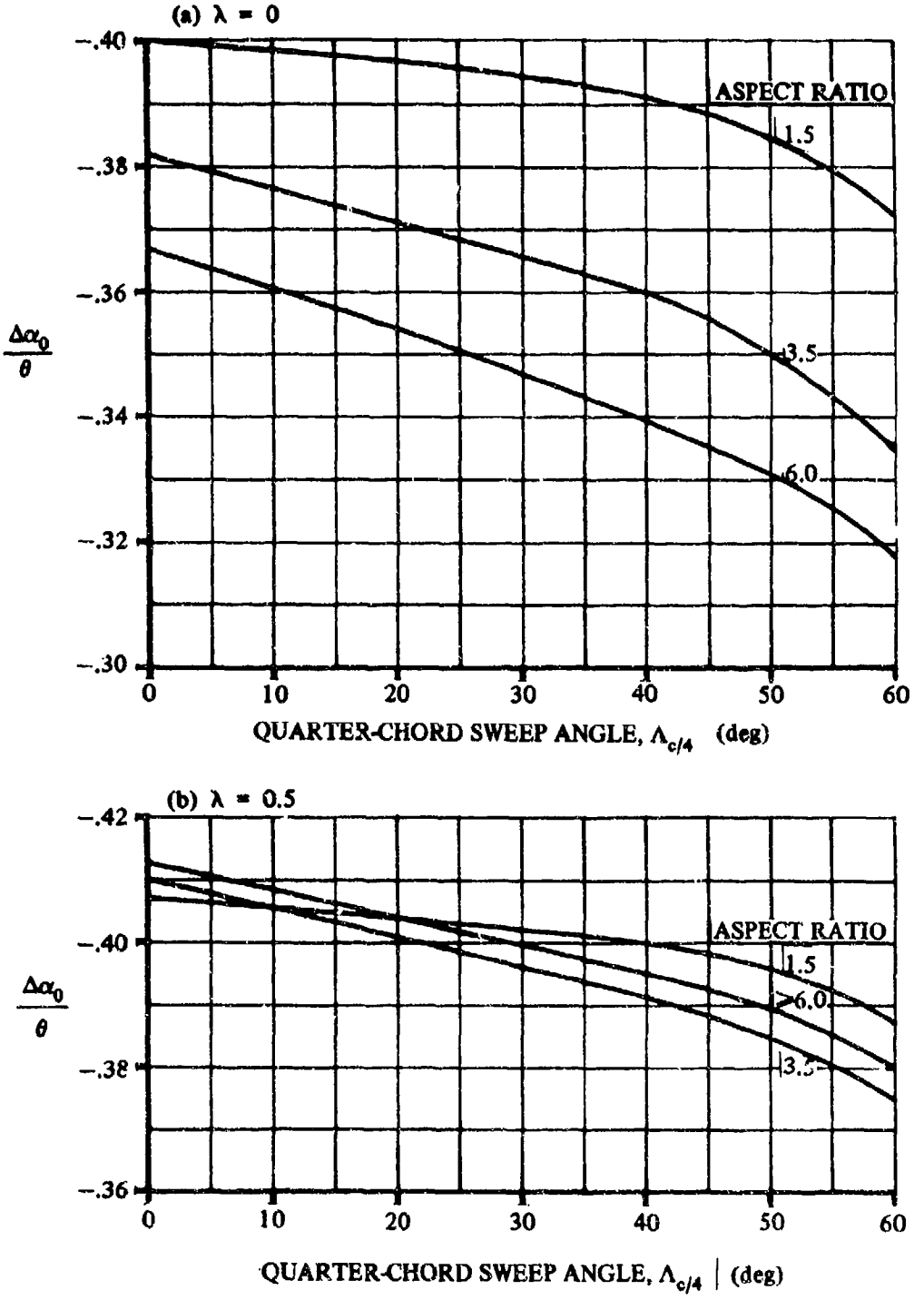

FIGURE 4.1.3.1-4 EFFECT OF LINEAR TWIST ON WING ANGLE OF ATTACK FOR ZERO LIFT

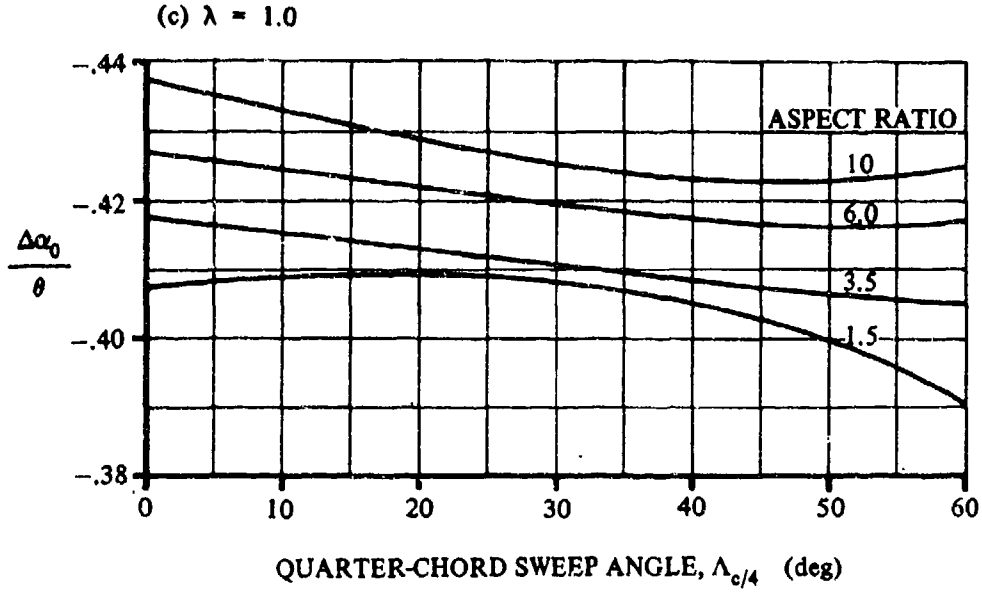

FIGURE 4.1.3.1-4 (CONTD)

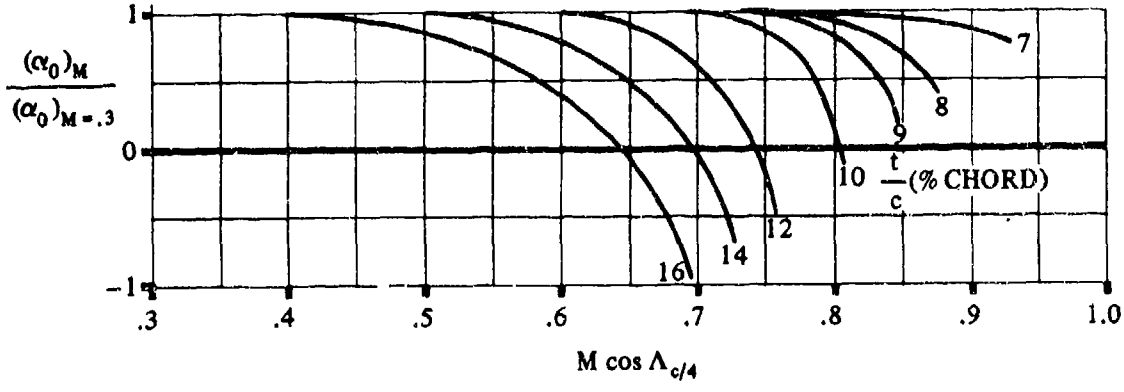

FIGURE 4.1.3.1-5 MACH NUMBER CORRECTION FOR ZERO-LIFT ANGLE OF ATTACK OF CAMBERED AIRFOILS

4.1.3.2 WING LIFT-CURVE SLOPE

The lift on a wing at angle of attack results from the distributed pressures over the surface of the wing. At subsonic speeds, most of the lift on a wing is derived from a region of low pressure on the upper surface near the leading edge. The magnitude and distribution of this pressure field is such that its integrated value over the wing surface results in a force vector that is very nearly perpendicular to the free-stream direction. This is the well-known lift-force vector. The rate of change of this vector with angle of attack is the lift-curve slope $dC_L/d\alpha$, usually written as C_{L_α}.

At supersonic speeds the pressure distribution over the wing is quite different. The pressure integration results in a force vector that is more nearly perpendicular to the wing-chord plane rather than to the free-stream direction. This is called the normal force and its variation with angle of attack in coefficient form is $dC_N/d\alpha$, or C_{N_α}.

For small angles of attack, C_{L_α} is interchangeable with C_{N_α}. At higher angles of attack the distinction is important.

For finite, three-dimensional wings, the free-stream direction with reference to the wing local-airfoil sections is determined by the free-stream angle of attack decreased by the local induced angle of attack. The lift vector is tilted back by an angle equal to the local induced angle. This force vector can be resolved into two components -- one perpendicular to and one parallel to the free-stream direction.

For high-aspect-ratio wings there is a certain justification in using C_{L_α} as C_{N_α} below stall angles, since the induced angle is small. For angles of attack beyond the stall, the total-force vector is essentially normal to the wing chord. For very low-aspect-ratio wings at high angles of attack, the induced effects are large and the local-force vector is tilted back through a large angle.

A. SUBSONIC

Theories for calculating the subsonic lift on three-dimensional wings fall into two general classes, lifting-surface theories and lifting-line theories. Lifting-surface theories, such as those of References 1 and 2, give highly accurate results for both wing lift and pitching moment. Since they are rather difficult to apply, however, they are usually reserved for detailed analyses of specific wings, particularly low-aspect-ratio wings, where the induced-camber and induced-angle-of-attack effects are important.

Lifting-line theories are widely used for calculating the lift-curve slopes of high-aspect-ratio wings, where chord-loading effects are less important. Certain modified lifting-line theories (References 3 and 4) give lift-curve slopes (but not pitching moments) that are quite accurate, even for very low aspect ratios. The explanation for this unexpected accuracy is given in Reference 5.

At subsonic speeds methods are presented for determining the lift-curve slope of the following two classes of wing planforms:

Straight-Tapered Wings (conventional, fixed trapezoidal wings)

Non-Straight-Tapered Wings

Double-delta wings (composite wings with A ≈ 3 or less)
Cranked wings (composite wings with A ≈ 3 or greater)
Curved (Gothic and ogee) wings

These three general categories of non-straight-tapered wings are illustrated in Sketch (a), and their wing-geometry parameters are presented in Section 2.2.2.

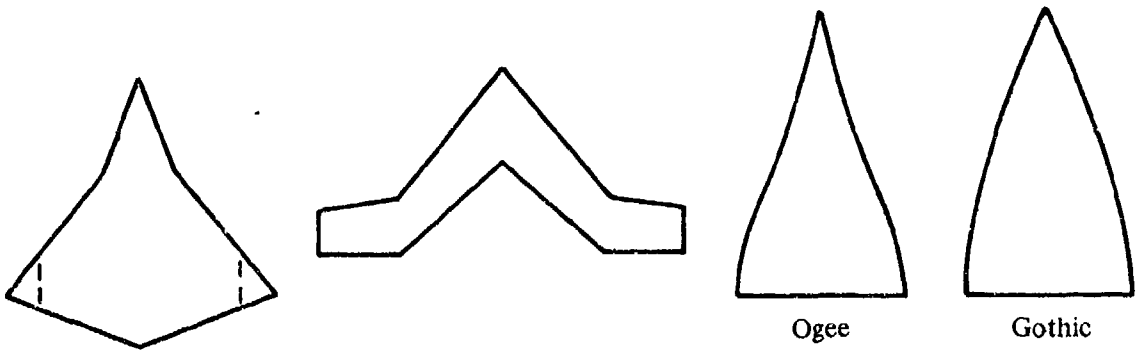

SKETCH (a)

Two separate methods are presented for straight-tapered wings. Method 1, taken from Reference 3, is applicable to the majority of configurations. In this method, the wing taper ratio has been eliminated as a parameter by the use of the midchord sweep angle rather than the conventional quarter-chord or leading-edge sweep angle. This permits a considerable simplification in the presentation of wing-lift-curve-slope information. Because of this simplification, the method of Reference 3 has been chosen for presentation in this section for estimating the lift-curve slope of straight-tapered wings. It gives results that agree with slender-wing theory (Reference 6) at very low aspect ratios and with two-dimensional section data at infinite aspect ratios.

Method 2, taken from Reference 7, is applicable only at M = 0.2 for highly swept, constant-section, low-aspect-ratio, delta or clipped-delta configurations with large thickness ratios; i.e., $0.10 \leqslant t/c \leqslant 0.30$. The unique feature of this method is its consideration of the vortex-induced lift. In contrast to the conventional constant lift-curve slope, this method allows for one or two breaks in the lift-curve slope to account more accurately for the vortex-induced lift contribution.

The lift-curve slopes of non-straight-tapered wings are treated in Reference 8. The planforms investigated include double delta, cranked, and curved (Gothic and ogee). Methods for predicting the lift-curve slope near zero lift for these planforms are based on the work of Spencer in Reference 9. This work consists of an extension of the results presented for conventional wings in Reference 3 to include wings having variation in sweep along the span. Since lift curves of double-delta and curved wings are considered nonlinear throughout the lift range, the lift-curve slope near zero lift is of little significance by itself. On the other hand, experimental results show

that the lift curves for cranked wings (defined as composite wings with aspect ratios approximately three or greater) exhibit a linear range up to approximately eight degrees angle of attack. Consequently, the method of Reference 9, as modified by an empirical correlation factor, is used for the prediction of C_{L_α} for cranked wings with round-nosed airfoils.

DATCOM METHODS

Straight-Tapered Wings

Method 1

The three-dimensional lift-curve slope of conventional wings is presented in Figure 4.1.3.2-49 as a function of wing aspect ratio, midchord sweep angle, Mach number, and section (defined parallel to the free stream) lift-curve slope. The factor κ of Figure 4.1.3.2-49 is the ratio of the two-dimensional lift-curve slope (per radian) at the appropriate Mach number to $2\pi/\beta$; i.e., $(c_{\ell_\alpha})_M / (2\pi/\beta)$. Section lift-curve slope (per degree) is obtained from Section 4.1.1.2.

A sweep-conversion formula is given in Section 2.2.2, from which the midchord sweep for any straight-tapered wing may be determined.

Application of the method is illustrated in the sample problem following the non-straight-tapered-wing methods of this paragraph, and in the sample problems following the straight-tapered-wing methods for transonic speeds in Paragraph B.

Method 2

This semiempirical method is taken from Reference 7, ignoring the small wing-planform nose-radius effects. The semiempirical method was developed by using the test results of Reference 7, correlated with the theoretical predictions based on lifting-surface theory. Because of its semiempirical nature, the method should be restricted to M = 0.2 conditions for highly swept, constant-section, low-aspect-ratio, delta or clipped-delta configurations with the following geometric characteristics:

$$0.58 \leq A \leq 2.55$$

$$0 \leq \lambda \leq 0.3$$

$$63^\circ \leq \Lambda_{LE} \leq 80^\circ$$

$$0.10 \leq t/c \leq 0.30$$

$$\Lambda_{TE} = 0$$

The determination of the breaks in the lift-curve slope ($C_{L_{II}}$ and $C_{L_{III}}$ in Sketch (b)), is contingent upon the availability of section upper-surface pressure data for the particular airfoil section being considered. In the method formulation of Reference 7, the pressure data were derived by means of a computer-program solution for the potential flow equations for two-dimensional incompressible flow, by the method of conformal transformation according to Imai (Reference 10). However, test data from Reference 11 or any other source of valid experimental data will satisfy the requirement.

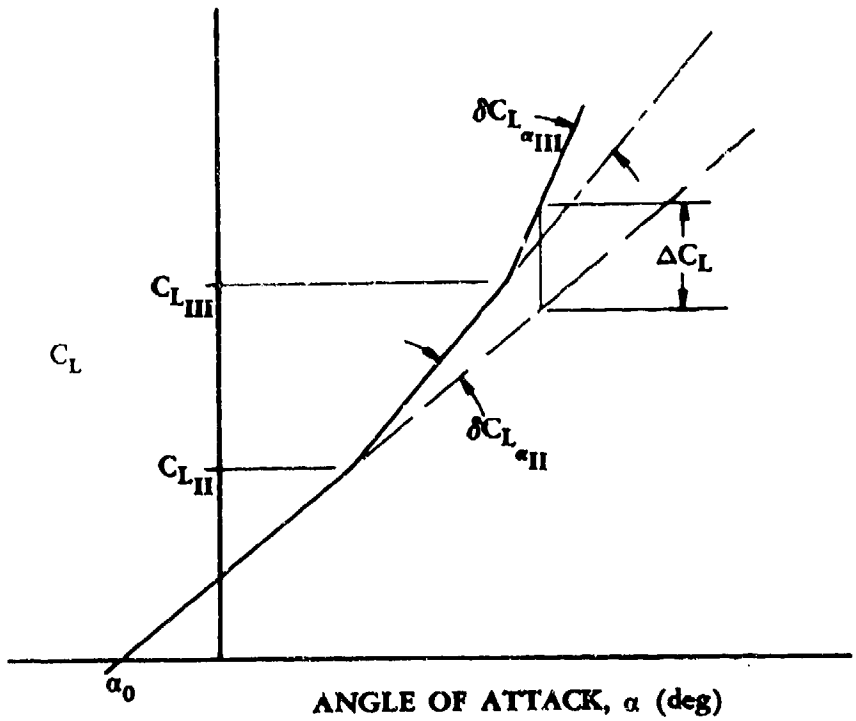

SKETCH (b)

For round-nosed-planform configurations, the reader is referred to Reference 7, where three different planform nose-radius models were tested. Although a procedure was developed to account for the incremental nose-radius effects, it requires a computer-program lifting-surface theory as a basis.

The lift-curve slope for a low-aspect-ratio, delta or clipped-delta wing may be approximated by the following procedure:

Step 1. Determine the low-lift-region lift-curve slope uncorrected for thickness effects by

$$\left(C_{L_\alpha}\right)_{\text{theory}} = 8 \tan^{-1} \frac{\pi A}{16 + \pi A/(1 + 2\lambda \tan \Lambda_{LE})} \qquad 4.1.3.2\text{-a}$$

where

A is the wing aspect ratio.

λ is the wing taper ratio.

Λ_{LE} is the wing leading-edge sweep.

Step 2. Determine the low-lift-region lift-curve slope, based on the wing planform area, by correcting the theoretical value in Step 1 for thickness effects.

$$\left(C_{L_\alpha}\right)_{basic} = \left(C_{L_\alpha}\right)_{theory} \left[\frac{C_{L_\alpha}}{\left(C_{L_\alpha}\right)_{theory}}\right] \qquad 4.1.3.2\text{-b}$$

where

$\left(C_{L_\alpha}\right)_{theory}$ is from Step 1 above.

$\frac{C_{L_\alpha}}{\left(C_{L_\alpha}\right)_{theory}}$ is from Figure 4.1.3.2-50a as a function of aspect ratio, taper ratio, and thickness ratio.

Step 3. Plot the maximum negative upper-surface section pressure coefficient C_{p_u} and its corresponding section lift coefficient c_ℓ on Figure 4.1.3.2-50b for three or four different section lift coefficients. These pressure data are supplied by the user and may be theoretical or taken from a source of experimental data such as Reference 11. When a sufficient number of points have been plotted, fair a smooth line through the points. Now determine where the faired line intersects the value of $\left(C_{L_\alpha}\right)_{theory}$ as determined above in Step 1. The point of intersection determines the value of $C_{L_{II}}$, read on the abscissa scale of the figure. The value for $C_{L_{II}}$ is the lift coefficient where the vortex lift component necessitates the first change in the lift-curve slope (see Sketch (b)). The point of intersection also defines the maximum negative upper-surface section pressure coefficient C_{p_u} used in the next step.

Step 4. Plot the maximum negative upper-surface section pressure coefficient C_{p_u} versus its corresponding nondimensional chordwise location x/c. (These pressure data are supplied by the user as above in Step 3.) Read the chordwise location x/c corresponding to the value of C_{p_u} determined in Step 3.

Step 5. Determine the value of $C_{L_{III}}$ from Figure 4.1.3.2-51 as a function of taper ratio, sweep, thickness ratio, and the chordwise location of C_{p_u}. The value for $C_{L_{III}}$ is the lift coefficient where the vortex lift component necessitates a second change in the lift-curve slope (see Sketch (b)).

Step 6. Determine the value of $\left(C_{L_\alpha}\right)_{limit}$ from the following:

$$\left(C_{L_\alpha}\right)_{limit} = 0.0467 \left(\sin \Lambda_c\right)^{1/4} \text{ (per deg)} \qquad 4.1.3.2\text{-c}$$

where

Λ_c is the complement of the leading-edge sweep angle Λ_{LE}; i.e., $\Lambda_c = 90^\circ - \Lambda_{LE}$.

Step 7. Determine the incremental increase in lift-curve slope $\delta C_{L_{\alpha_{II}}}$ starting at $C_{L_{II}}$ according to the following criteria:

If	Then
$\left(C_{L_\alpha}\right)_{limit} - \left(C_{L_\alpha}\right)_{basic} \geq 0.0067$;	$\delta C_{L_{\alpha_{II}}} = 0.0067$ per deg
$\left(C_{L_\alpha}\right)_{limit} - \left(C_{L_\alpha}\right)_{basic} < 0.0067$;	$\delta C_{L_{\alpha_{II}}} = \left(C_{L_\alpha}\right)_{limit} - \left(C_{L_\alpha}\right)_{basic}$
$\left(C_{L_\alpha}\right)_{limit} \leq \left(C_{L_\alpha}\right)_{basic}$;	$\delta C_{L_{\alpha_{II}}} = 0$

Step 8. Determine the total lift-curve slope in the region between $C_{L_{II}}$ and $C_{L_{III}}$ using

$$\left(C_{L_\alpha}\right)_{II} = \left(C_{L_\alpha}\right)_{basic} + \left(\delta C_{L_\alpha}\right)_{II} \qquad 4.1.3.2\text{-d}$$

where

$\left(C_{L_\alpha}\right)_{basic}$ is from Step 2.

$\left(\delta C_{L_\alpha}\right)_{II}$ is from Step 7.

Step 9. Determine the incremental increase in lift-curve slope $\delta C_{L_{\alpha_{III}}}$ starting at $C_{L_{III}}$ according to the following criteria:

If	Then
$\left(C_{L_\alpha}\right)_{limit} - \left(C_{L_\alpha}\right)_{basic} \geq 0.012$;	$\left(\delta C_{L_\alpha}\right)_{III} = 0.012$ per deg
$\left(C_{L_\alpha}\right)_{limit} - \left(C_{L_\alpha}\right)_{basic} < 0.012$;	$\left(\delta C_{L_\alpha}\right)_{III} = \left(C_{L_\alpha}\right)_{limit} - \left(C_{L_\alpha}\right)_{basic}$
$\left(C_{L_\alpha}\right)_{limit} \leq \left(C_{L_\alpha}\right)_{basic}$;	$\left(\delta C_{L_\alpha}\right)_{III} = 0$

Step 10. Determine the total lift-curve slope in the region beyond $C_{L_{III}}$ using

$$\left(C_{L_\alpha}\right)_{III} = \left(C_{L_\alpha}\right)_{basic} + \left(\delta C_{L_\alpha}\right)_{III} \qquad 4.1.3.2\text{-e}$$

where

$\left(C_{L_\alpha}\right)_{basic}$ is from Step 2.

$\left(\delta C_{L_\alpha}\right)_{III}$ is from Step 9.

The entire lift-curve slope may now be constructed as shown in Sketch (b). (Note that the wing zero-lift angle of attack α_0 is determined by using Section 4.1.3.1.)

No substantiation of this method is possible because of the lack of low-aspect-ratio test data having wing thickness ratios of $0.10 \leqslant t/c \leqslant 0.30$. Application of this method is illustrated in the sample problem on Page 4.1.3.2-8.

Non-Straight-Tapered Wings

Double-Delta Wings

Although the lift-curve slope near zero lift of double-delta wings is of little significance by itself, this C_{L_α} is used in the correlation of nonlinear lift of double-delta wings at subsonic speeds in Section 4.1.3.3.

This method, taken from Reference 9, consists of an extension of the method of Reference 3 by use of an effective value of $\cos \Lambda_{c/2}$, which is defined as the area-weighted average of the local value of $\cos \Lambda_{c/2}$.

The subsonic lift-curve slope of double-delta wings is obtained from the procedure outlined in the following steps:

Step 1. Divide the wing into n sections, each section being assumed to have constant sweep angles within its boundary. (See Section 2.2.2 for wing-geometry parameters.)

Step 2. Using the wing geometry determined in Step 1, obtain $(\cos \Lambda_{c/2})_{eff}$ by

$$\left(\cos \Lambda_{c/2}\right)_{eff} = \frac{1}{S_W} \sum_{j=1}^{j=n} (\cos \Lambda_{c/2})_j \, S_j \qquad 4.1.3.2\text{-f}$$

where

S_W is the total wing area.

j denotes one section of n sections having constant sweep angles within its boundary.

S_j is the total area of one section of n sections.

$(\cos \Lambda_{c/2})_j$ is the cosine of the sweep angle of the half-chord line of one section of n sections

Step 3. Obtain the lift-curve slope by application of the method used to determine C_{L_α} of straight-tapered wings, but with $(\Lambda_{c/2})_{eff}$ used in place of $\Lambda_{c/2}$ in the design chart (Figure 4.1.3.2-49).

Application of this technique is illustrated in the sample problem on Page 4.1.3.2-10.

Cranked Wings

The subsonic lift-curve slope of cranked wings with round-nosed airfoils is obtained by applying an empirical correlation to the method of Reference 9.

The equation for C_{L_α} of cranked wings, taken from Reference 8, is

$$C_{L_\alpha} = \left(C_{L_\alpha}\right)_{pred} \frac{\left(C_{L_\alpha}\right)_{test}}{\left(C_{L_\alpha}\right)_{pred}} \qquad 4.1.3.2\text{-g}$$

where

$\left(C_{L_\alpha}\right)_{pred}$ is the lift-curve slope of the cranked wing, predicted by the method outlined above for the double-delta planform.

$\frac{\left(C_{L_\alpha}\right)_{test}}{\left(C_{L_\alpha}\right)_{pred}}$ is the empirical correlation factor of subsonic lift-curve slope for cranked wings. It is presented as a function of wing aspect ratio and Mach number in Figure 4.1.3.2-52. (All cranked wings analyzed in Reference 8 had round leading edges, and the use of Figure 4.1.3.2-52 is restricted accordingly.)

A comparison of test data for 12 configurations with C_{L_α} of cranked wings having round-nosed airfoils calculated by this method is presented as Table 4.1.3.2-A (taken from Reference 8). The test data are for four wing-alone and eight wing-body configurations. Three of the wing-alone configurations have two breaks in the leading edge. Although no attempt has been made to define the effects of wing thickness ratio, poor accuracy generally results for $t/c > 0.09$. It should also be noted that the calculated accuracy deteriorates as Mach number exceeds 0.80. No configuration had a body-diameter-to-wing-span ratio greater than 0.147 and, consequently, the wing-body interference is considered to be negligible. It is suggested that this method be restricted to values of $M \leq 0.80$ and $t/c \leq 0.10$.

It is suggested that the subsonic lift-curve slope of cranked wings with sharp-nosed airfoils be obtained by direct application of the method outlined for double-delta planforms.

Curved Wings

No method is presented for estimating the subsonic lift-curve slope of curved wings because of their nonlinear lift characteristics.

Sample Problems

1. Method 2

Given: The following straight-tapered, constant-section, low-aspect-ratio, clipped-delta configuration.

$A = 0.823$ $\lambda = 0.18$ $\Lambda_{LE} = 73.5^\circ$ NACA 2412 airfoil

$M = 0.2$

Compute:

$$\left(C_{L_\alpha}\right)_{theory} = 8 \tan^{-1} \frac{\pi A}{16 + \pi A/(1 + 2\lambda \tan \Lambda_{LE})} \quad \text{(Equation 4.1.3.2-a)}$$

$$= 8 \tan^{-1} \frac{0.823\pi}{16 + 0.323\,\pi/[1 + 2(0.18)(3.376)]}$$

$$= 1.195 \text{ per rad} = 0.0209 \text{ per deg}$$

$$\frac{1}{3 + A}\left(\frac{1 - \lambda}{1 + 2\lambda}\right)^2 = \frac{1}{3 + 0.823}\left[\frac{1 - 0.18}{1 + 2(0.18)}\right]^2 = 0.0951$$

$$\frac{C_{L_\alpha}}{\left(C_{L_\alpha}\right)_{theory}} = 0.98 \quad \text{(Figure 4.1.3.2-50a)}$$

$$\left(C_{L_\alpha}\right)_{basic} = \left(C_{L_\alpha}\right)_{theory} \frac{C_{L_\alpha}}{\left(C_{L_\alpha}\right)_{theory}} \quad \text{(Equation 4.1.3.2-b)}$$

$$= (0.0209)(0.98)$$

$$= 0.0205 \text{ per deg} \quad (\text{valid for } C_L < C_{L_{II}})$$

The following pressure data for a NACA 2412 airfoil are (Reference 11):

c_ℓ	C_{P_u}	x/c
0	−0.37	0.30
0.253	−0.56	0.19
0.5	−0.95	0.05

The above data are now plotted on Figure 4.1.3.2-50b. From Figure 4.1.3.2-50b we now obtain a value of 0.222 for $C_{L_{II}}$ at a value of −0.53 for C_{P_u}.

Plot C_{P_u} versus x/c

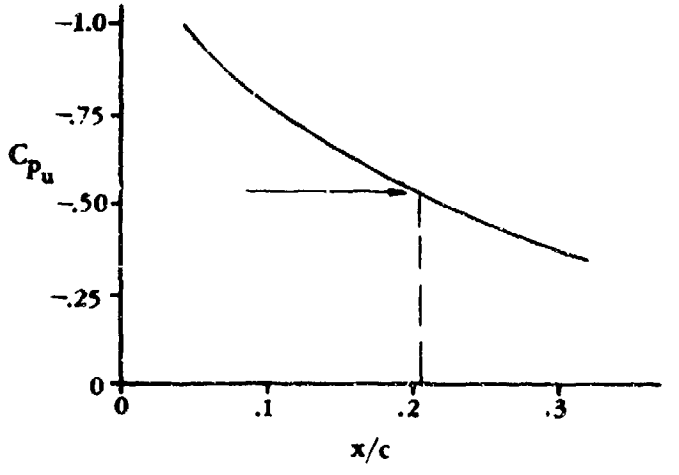

From the above plot x/c = 0.204 for C_{P_u} = −0.53.

$$\frac{x/c}{(1+\lambda)(1-x/c)\tan\Lambda_{LE}} = \frac{0.204}{(1+0.18)(1-0.204)(3.376)} = 0.0643$$

$C_{L_{III}} = 0.467$ (Figure 4.1.3.2-51)

$\Lambda_c = 90^o - \Lambda_{LE} = 90^o - 73.5^o = 16.5^o$

$\left(C_{L_\alpha}\right)_{limit} = 0.0467 (\sin \Lambda_c)^{1/4}$ (Equation 4.1.3.2-c)

$= 0.0467 (\sin 16.5^o)^{1/4}$

$= 0.0342$ per deg

$\left(C_{L_\alpha}\right)_{limit} - \left(C_{L_\alpha}\right)_{basic} = 0.0342 - 0.0205 = 0.0137$

Since $0.0137 > 0.0067$, $\left(\delta C_{L_\alpha}\right)_{II} = 0.0067$ (Step 7)

$\left(C_{L_\alpha}\right)_{II} = \left(C_{L_\alpha}\right)_{basic} + \left(\delta C_{L_\alpha}\right)_{II}$ (Equation 4.1.3.2-d)

$= 0.0205 + 0.0067$

$= 0.0272$ per deg (valid for $0.222 \leq C_L \leq 0.467$)

Since $0.0137 > 0.012$, $\delta C_{L_{\alpha III}} = 0.012$ per deg (Step 9)

$\left(C_{L_\alpha}\right)_{III} = \left(C_{L_\alpha}\right)_{basic} + \left(\delta C_{L_\alpha}\right)_{III}$ (Equation 4.1.3.2-e)

$= 0.0205 + 0.012$

$= 0.0325$ per deg (valid for $C_L > 0.467$)

Solution:

The entire lift curve can now be constructed assuming the wing zero-lift angle of attack α_0 has been determined using Section 4.1.3.1.

2. Non-Straight-Tapered Wings

Given: The cranked-wing planform of Reference 29. (See Section 2.2.2 for wing-planform geometry.)

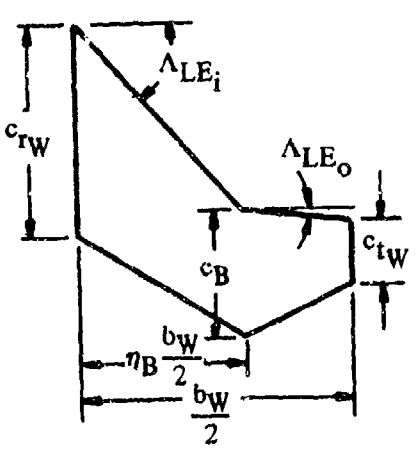

$A_W = 4.0$ $S_W = 2.25$ sq ft $b_W/2 = 18.0$ in.

$\eta_B = 0.6$ $S_i = 1.641$ sq ft $S_o = 0.609$ sq ft

$c_{r_W} = 13.85$ in. $c_B = 8.03$ in. $c_{t_W} = 4.15$ in.

$\lambda_W = 0.30$ $\lambda_i = 0.58$ $\lambda_o = 0.517$

$\Lambda_{LE_i} = 48.6^o$ $\Lambda_{LE_o} = 7.7^o$

$\Lambda_{c/2_i} = 40.9^o$ $\Lambda_{c/2_o} = -7.7^o$

NACA 65A006 airfoil $M = 0.80$; $\beta = 0.60$

Compute:

$$(\cos \Lambda_{c/2})_{eff} = \frac{1}{S_W} \sum_{j=1}^{j=n} (\cos \Lambda_{c/2})_j S_j = \frac{1}{S_W} \left[(\cos \Lambda_{c/2})_i S_i + (\cos \Lambda_{c/2})_o S_o \right]$$

(Equation 4.1.3.2-f)

$$= \frac{1}{2.25} \left[(0.756)(1.641) + (0.991)(0.609) \right] = 0.820$$

$$(\Lambda_{c/2})_{eff} = 34.9^o \; ; \tan (\Lambda_{c/2})_{eff} = 0.6976$$

$$c_{\ell_\alpha} = 6.00 \text{ per rad (Section 4.1.1)}$$

$$c_{\ell_{\alpha_M}} = \frac{c_{\ell_\alpha}}{\beta} = \frac{6.00}{0.6} = 10.0 \text{ per rad}$$

$$\kappa = \frac{c_{\ell_{\alpha_M}}}{(2\pi/\beta)} = \frac{10.0\,(0.6)}{2\pi} = 0.955$$

$$\frac{A}{\kappa} \left[\beta^2 + \tan^2 (\Lambda_{c/2})_{eff} \right]^{1/2} = \frac{4.0}{0.955} \left[0.36 + 0.4866 \right]^{1/2} = 3.85$$

$$\frac{(C_{L_\alpha})_{pred}}{A} = 1.00 \text{ per rad (Figure 4.1.3.2-49)}$$

$$(C_{L_\alpha})_{pred} = 4.00 \text{ per rad}$$

$$\beta A = (0.6)(4.0) = 2.40$$

$$\frac{(C_{L_\alpha})_{test}}{(C_{L_\alpha})_{pred}} = 1.081 \text{ (Figure 4.1.3.2-52)}$$

Solution:

$$C_{L_\alpha} = (C_{L_\alpha})_{pred} \frac{(C_{L_\alpha})_{test}}{(C_{L_\alpha})_{pred}} \text{ (Equation 4.1.3.2-g)}$$

$$= (4.00)(1.081)$$

$$= 4.324 \text{ per rad}$$

$$= 0.0755 \text{ per deg}$$

This compares with a test value of 0.075 per degree from Reference 29.

B. TRANSONIC

The transonic characteristics of wings are very difficult to predict. The current status of the problem is summarized in Reference 12. It is pointed out in this reference that although transonic theory gives results of surprisingly good accuracy in many cases, the mathematical difficulties in solving nonlinear partial differential equations of the mixed elliptic-hyperbolic type have limited its application to a few simple configurations.

On the other hand, wind-tunnel tests cover a wide variety of configurations but are of questionable accuracy because of wall-interference effects. These interference effects are both difficult to determine analytically and difficult to eliminate. Simply testing smaller models is not always sufficient, even in slotted-wall tunnels (Reference 12).

In spite of the uncertainties in test data, the straight-tapered-wing design charts of this section are based largely on experimental data from wind-tunnel tests. This is done because of certain important flow-separation effects not accounted for by theory and because of the limited scope of existing solutions for transonic theory. The limited experimental data for non-straight-tapered wings preclude development of design methods for those planforms at transonic speeds. However, a chart is presented that indicates the trend of transonic data for double-delta wings and for cranked wings with an aspect ratio of approximately three.

Thick, unswept, straight-tapered wings show increases in lift-curve slope with Mach number up to Mach numbers slightly beyond the critical. The slope then drops abruptly to a low value followed by a rise near Mach=1.0 to a value almost as high as the value at the critical Mach number (see Sketch (c), for type "A" wings). This behavior for two-dimensional sections is illustrated in References 13, 14, and 15. Reducing either the aspect ratio or the wing-thickness ratio or both reduces the magnitude of these effects. For very thin wings and for wings of very low aspect ratio these transonic nonlinearities do not exist (see Sketch (c) for type "B" wings). Increasing the sweep angle raises the wing critical Mach number. However, the increase is never as large as that predicted by simple sweep theory. Reference 16 shows that three-dimensional effects in the regions of the wing root and tip prevent the full benefits of sweep from being realized.

The transonic nonlinearities in lift-curve slope are related to the appearance of local shocks located asymmetrically on the upper and lower surfaces of the wing. Prediction of the exact shock-wave location is somewhat involved, since there is an interaction between the shocks on the upper and lower surfaces (Reference 17). Camber, thickness ratio, and thickness distribution all have pronounced effects on section transonic lift characteristics. Proper combination of the above geometric parameters can prevent transonic lift losses even for quite thick sections (Reference 18). Wings that do have large transonic lift losses at zero angle of attack show marked recovery at higher angles of attack (Reference 19).

DATCOM METHODS

Straight-Tapered Wings

The procedure for constructing the transonic lift-curve slope of conventional planforms is outlined in the following steps. In following this procedure, reference should be made to the schematic sketch below. The method is based on data for the untwisted and uncambered wings of References 19 and 47 through 51. These data are compared in Table 4.1.3.2-B with the values calculated from the charts.

The charts are limited to wings having symmetrical airfoils of conventional thickness distribution and are for zero angle of attack only.

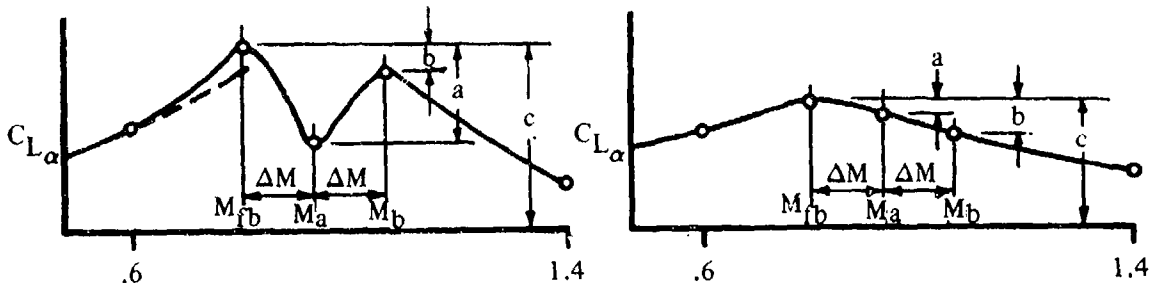

SKETCH (c)

Step 1. Calculate the force-break Mach number M_{fb}. This is obtained from Figure 4.1.3.2-53a for zero wing sweep. A correction for sweep effects is provided by Figure 4.1.3.2-53b.

Step 2. Compute the theoretical lift-curve slope at the force-break Mach number by the method of paragraph A.

Step 3. The actual lift-curve slope at the force-break Mach number is found by means of the ratio $\left(C_{L_\alpha}\right)_{fb}/\left(C_{L_\alpha}\right)_{theory}$ obtained from Figure 4.1.3.2-54a.

Step 4. The abrupt decrease in lift-curve slope above the force-break Mach number is described by the ratio a/c (see Sketch (c)). This ratio is given in Figure 4.1.3.2-54b. The Mach number M_a at which the lift-curve slope reaches its minimum value is

$$M_a = M_{fb} + 0.07$$

The lift-curve slope at M_a is

$$\left(C_{L_\alpha}\right)_a = \left(1 - \frac{a}{c}\right)\left(C_{L_\alpha}\right)_{fb}$$

For wings that do not exhibit large transonic lift losses (Sketch (c)), the lift-curve slope at M_a may still be obtained from the ratio a/c as given in Figure 4.1.3.2-54b. In all cases, c is the lift-curve slope at the force-break Mach number as obtained in Step 3.

Step 5. The subsequent rise in C_{L_α} (Sketch (b)) is given by the ratio b/c as presented in Figure 4.1.3.2-54c. The Mach number at this point is

$$M_b = M_{fb} + 0.14$$

The lift-curve slope is

$$\left(C_{L_\alpha}\right)_b = \left(1 - \frac{b}{c}\right)\left(C_{L_\alpha}\right)_{fb}$$

An identical procedure is used for wings of type "B."

Step 6. The lift-curve slope at M = 0.6 is calculated by the straight-tapered-wing method of Paragraph A of this section.

Step 7. The lift-curve slope at M = 1.4 is calculated by the straight-tapered-wing method of Paragraph C of this section.

Step 8. The complete transonic lift-curve slope between Mach numbers 0.6 and 1.4 can now be constructed by fairing a curve through the points obtained by means of Steps 1 through 7.

Non-Straight-Tapered Wings

During the course of the program reported in Reference 8 an empirical correlation of the lift-curve slope of double-delta and cranked wings at M = 1.0 was achieved. This correlation is presented herein as Figure 4.1.3.2-55. It is suggested that it be used as a guide for fairing between subsonic and supersonic values of C_{L_α} of composite wings with an aspect ratio of three or less.

The configurations used in the correlation vary in aspect ratio from 1.33 to 3.0. The inboard-panel sweepback is 78° for the lower correlation points and 60° for the upper correlation points. Spanwise positions of the leading-edge break η_B vary from approximately 0.30 to 0.70.

Sample Problems

1. Straight-Tapered Wing of Type "A."

Given: Wing tested in Reference 48.

A = 4.0 $\quad \lambda = 1.0 \quad \Lambda_{LE} = 0$ NACA 63A010 airfoil

Compute:

M_{fb} = 0.842 (Figure 4.1.3.2-53a)

$\left(C_{L_\alpha}\right)_{theory}$ at M_{fb}

c_{ℓ_α} = 6.02 per rad (Section 4.1.1)

$$c_{\ell_{\alpha_M}} = \frac{c_{\ell_\alpha}}{\beta}$$

$$\kappa = \frac{c_{\ell_{\alpha_M}}}{(2\pi/\beta)} = \frac{\left(c_{\ell_\alpha}/\beta\right)}{(2\pi/\beta)} = \frac{c_{\ell_\alpha}}{2\pi} = 0.958$$

$$\frac{A}{\kappa}\left[\beta^2_{fb} + \tan^2 \Lambda_{c/2}\right]^{1/2} = \frac{4.0}{0.958}(0.291)^{1/2} = 2.25$$

$$\frac{\left(C_{L_\alpha}\right)_{theory}}{A} = 1.25 \text{ per rad (Figure 4.1.3.2-49)}$$

$$\left(C_{L_\alpha}\right)_{theory} = 5.0 \text{ per rad}$$

$$\frac{\left(C_{L_\alpha}\right)_{fb}}{\left(C_{L_\alpha}\right)_{theory}} = 0.96 \text{ (Figure 4.1.3.2-54a)}$$

$$\left(C_{L_\alpha}\right)_{fb} = 4.80 \text{ per rad}$$

$$\frac{a}{c} = 0.35 \text{ (Figure 4.1.3.2-54b)}$$

$$M_a = M_{fb} + 0.07 = 0.912$$

$$\left(C_{L_\alpha}\right)_a = \left(1 - \frac{a}{c}\right)\left(C_{L_\alpha}\right)_{fb} = 3.12 \text{ per rad}$$

$$\frac{b}{c} = 0.15 \text{ (Figure 4.1.3.2-54c)}$$

$$M_b = M_{fb} + 0.14 = 0.982$$

$$\left(C_{L_\alpha}\right)_b = \left(1 - \frac{b}{c}\right)\left(C_{L_\alpha}\right)_{fb} = 4.08 \text{ per rad}$$

$\left(C_{L_\alpha}\right)_{M=0.6}$ (Paragraph A)

$$\frac{A}{\kappa}\left[\beta^2 + \tan^2 \Lambda_{c/2}\right]^{1/2} = \frac{4.0}{0.958}(0.64)^{1/2} = 3.34$$

$$\frac{\left(C_{L_\alpha}\right)_{M=0.6}}{A} = 1.065 \text{ per rad (Figure 4.1.3.2-49)}$$

$$\left(C_{L_\alpha}\right)_{M=0.6} = 4.26 \text{ per rad}$$

$\left(C_{L_\alpha}\right)_{M=1.40}$ (Paragraph C)

$$1/(\beta A) = 0.255$$

βC_{N_α} = 3.50 per rad (Figure 4.1.3.2-56g)

$\left(C_{N_\alpha}\right)_{M=1.4}$ = 3.57 per rad

Solution:

The complete lift-curve slope as a function of Mach number may now be constructed as shown in the following diagram.

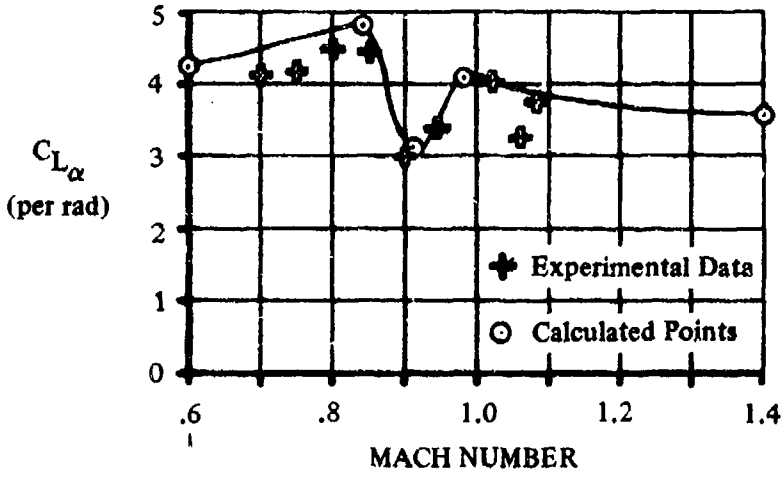

2. Straight-Tapered Wing of Type "B"

Given: Wing tested in Reference 47.

A = 2.67 λ = 0.2 Λ_{LE} = 45° NACA 63A004 airfoil

Compute:

$(M_{fb})_{\Lambda=0}$ = 1.00 (Figure 4.1.3.2-53a)

$\Lambda_{c/2}$ = 26.6°

$(M_{fb})_\Lambda$ = 1.00 (Figure 4.1.3.2-53b)

$\left(C_{L_\alpha}\right)_{theory}$ at $(M_{fb})_\Lambda$

c_{ℓ_α} = 6.47 per rad (Section 4.1.1.2)

$$c_{\ell_{\alpha_M}} = \frac{c_{\ell_\alpha}}{\beta}$$

$$\kappa = \frac{c_{\ell_{\alpha_M}}}{(2\pi/\beta)} = \frac{\left(c_{\ell_\alpha}/\beta\right)}{(2\pi/\beta)} = \frac{c_{\ell_\alpha}}{2\pi} = 1.03$$

$$\frac{A}{\kappa}\left[(\beta_{fb})\Lambda^2 + \tan^2 \Lambda_{c/2}\right]^{1/2} = \frac{2.67}{1.03}(0.251)^{1/2} = 1.30$$

$$\frac{\left(C_{L_\alpha}\right)_{theory}}{A} = 1.435 \text{ per rad (Figure 4.1.3.2-49)}$$

$$\left(C_{L_\alpha}\right)_{theory} = 3.83 \text{ per rad}$$

$$\frac{\left(C_{L_\alpha}\right)_{fb}}{\left(C_{L_\alpha}\right)_{theory}} = 1.085 \text{ (Figure 4.1.3.2-54a)}$$

$$\left(C_{L_\alpha}\right)_{fb} = 4.16 \text{ per rad}$$

$$\frac{a}{c} = 0.005 \text{ (Figure 4.1.3.2-54b)}$$

$$M_a = M_{fb} + 0.07 = 1.07$$

$$\left(C_{L_\alpha}\right)_a = \left(1 - \frac{a}{c}\right)\left(C_{L_\alpha}\right)_{fb} = 4.14 \text{ per rad}$$

$$\frac{b}{c} = 0.075 \text{ (Figure 4.1.3.2-54c)}$$

$$M_b = M_{fb} + 0.14 = 1.14$$

$$\left(C_{L_\alpha}\right)_b = \left(1 - \frac{b}{c}\right)\left(C_{L_\alpha}\right)_{fb} = 3.85$$

$\left(C_{L_\alpha}\right)_{M=0.6}$ (Paragraph A)

$$\frac{A}{\kappa}\left[\beta^2 + \tan^2 \Lambda_{c/2}\right]^{1/2} = \frac{2.67}{1.03}\left[0.64 + 0.251\right]^{1/2} = 2.45$$

$$\frac{\left(C_{L_\alpha}\right)_{M=0.6}}{A} = 1.22 \text{ per rad (Figure 4.1.3.2-49)}$$

$$\left(C_{L_\alpha}\right)_{M=0.6} = 3.26 \text{ per rad}$$

$\left(C_{L_\alpha}\right)_{M=1.4}$ (Paragraph C)

$\beta/\tan \Lambda_{LE}$ = 0.98; A $\tan \Lambda_{LE}$ = 2.67

$\tan \Lambda_{LE} \left(C_{N_\alpha}\right)_{theory}$ = 3.55 per rad (Figure 4.1.3.2-56b)

$\left(C_{N_\alpha}\right)_{theory}$ = 3.55 per rad

Δy = 0.88 (Figure 2.2.1-8)

$\Delta y_\perp = \dfrac{\Delta y}{\cos \Lambda_{LE}}$ = 1.245

$\dfrac{C_{N_\alpha}}{\left(C_{N_\alpha}\right)_{theory}}$ = 0.795 (Figure 4.1.3.2-60)

$\left(C_{N_\alpha}\right)_{M=1.4}$ = 2.82 per rad

Solution:

The complete lift-curve slope as a function of Mach number may now be constructed as shown in the following diagram.

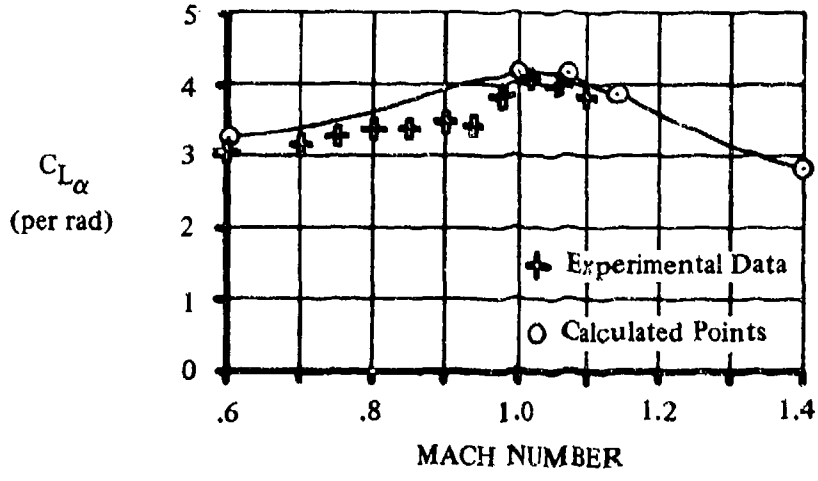

C. SUPERSONIC

Methods are presented for determining the wing normal-force-curve slope of the following two classes of wing planforms:

Straight-Tapered Wings (conventional, fixed trapezoidal wings)

Non-Straight-Tapered Wings

- Double-delta wings
- Cranked wings
- Curved (Gothic and ogee) wings

These three general categories of non-straight-tapered wings are illustrated in Sketch (a) (paragraph A). Their wing-geometry parameters are presented in Section 2.2.2.

At supersonic speeds, the normal-force-curve slope C_{N_α} of conventional, double-delta, and cranked wings is adequately predicted by theoretical calculations except where the effects of thickness become important.

The design charts pertaining to these wing planforms are based on the following references:

Reference 20 – in the region of supersonic leading and trailing edges

Reference 21 – in the region of subsonic leading edges and supersonic trailing edges

Reference 22 – in the regions of tip-root interaction and tip-tip interaction

Reference 23 – in the region of subsonic leading and trailing edges

Reference 6 – for values of $A\beta \leq 1/4$ and $\sigma \leq 1.0$ where $\sigma = 1/4[A(1+\lambda)\tan \Lambda_{LE}]$

References 24 and 25 – for values of $A\beta \leq 1/4$ and $\sigma \geq 1.0$

In addition, an empirically determined "lift-interference factor" from Reference 8 is applied to correlate the results for double-delta and cranked wings. The theoretical results are based on linear theory with the exception of the region where $A\beta \leq 1/4$, which is based on slender-wing theory. Thin airfoils have been assumed in these theories. Thickness effects are not important except for conditions where the Mach lines lie on or near the wing leading edge. Under these conditions the wing-leading-edge shock position is displaced forward from its theoretical position by the finite thickness effects of the leading edge. This displacement results in substantial losses in normal-force-curve slope.

For straight-tapered wings with sharp leading edges, the airfoil nose semiwedge angle (measured perpendicular to the wing leading edge) determines the shock position relative to the wing and hence the normal-force-curve slope. Experimental data indicate that the parameter corresponding to the nose semiwedge angle of the supersonic airfoil is $\Delta y/\cos \Lambda_{LE}$, where Δy is the difference between the upper-surface ordinates expressed in percent chord at the 6-percent- and 0.15-percent-chord stations (Figure 2.2.1-8). This is the same Δy discussed in Section 4.1.3.4 with regard to

airfoil maximum lift. It can be shown that for double-wedge and biconvex airfoils there is a linear relationship between Δy and the leading-edge semiwedge angle, given by

$$\Delta y_{\perp} = 5.85 \tan \delta_{\perp}$$

where

$$\Delta y_{\perp} = \frac{\Delta y}{\cos \Lambda_{LE}}$$

and $\delta_{\perp}$ is the semiwedge angle normal to the leading edge. Either $\delta_{\perp}$ or $\Delta y_{\perp}$, whichever is more convenient, may be used to calculate thickness effects for straight-tapered wings with sharp-nosed airfoils.

Figure 4.1.3.2-60 presents the leading-edge-thickness effect on the normal-force-curve slope of straight-tapered wings in the form of a ratio of actual normal-force-curve slope to theoretical normal-force-curve slope. This chart is empirically derived from the experimental data of Reference 26 of this section and References 11 through 17, 26, and 45, of Section 4.1.3.3.

For double-delta and cranked wings empirical correlation factors for round-nosed and sharp-nosed airfoils (from Reference 8) are applied, which account for leading-edge effects.

The method presented for determining the normal-force-curve slope of curved (Gothic and ogee) wings consists of a semiempirical correlation based on the theoretical results of Squire in Reference 27.

Because of the nonlinear nature of the normal-force curve at high angles of attack, the methods presented for estimating C_{N_α} are limited to low angles of attack.

Wings with inverse taper ($\lambda > 1$) have not been considered. Wings with swept-forward leading edges are included through the use of the reversibility theorem (Reference 28). The reversibility theorem states that the normal-force-curve slope of the wing in forward flight equals the normal-force-curve slope of the same wing in reverse flight at the same Mach number.

DATCOM METHODS

Straight-Tapered Wings

The supersonic normal-force-curve slope of conventional wings is obtained as outlined in the following steps:

Step 1. Obtain the theoretical normal-force-curve slope from Figures 4.1.3.2-56a through 4.1.3.2-56f, except for rectangular wings. The theoretical normal-force-curve slope for rectangular wings must be obtained from Figure 4.1.3.2-56g. These charts should be used for $M \geq 1.4$. For Mach numbers less than 1.4 the transonic method of Paragraph B should be used.

Step 2. For wings approaching the sonic-leading-edge condition, the theoretical C_{N_α} value obtained from Step 1 should be multiplied by the empirical thickness correction factor from Figure 4.1.3.2-60.

Non-Straight-Tapered Wings

Double-Delta Wings

This method, taken from Reference 8, uses the linear-theory design charts of the straight-tapered-wing method with appropriate empirical correction factors. Application of the method requires that the wing planform be broken down as follows (see Sketch (d)):

Basic Wing – the outboard leading and trailing edges extended to the center line.

Glove – a delta wing superimposed over the basic wing. The glove leading edge is that of the inboard panel.

Extension – that portion of the wing behind the trailing edge of the basic wing for wings with broken trailing edges.

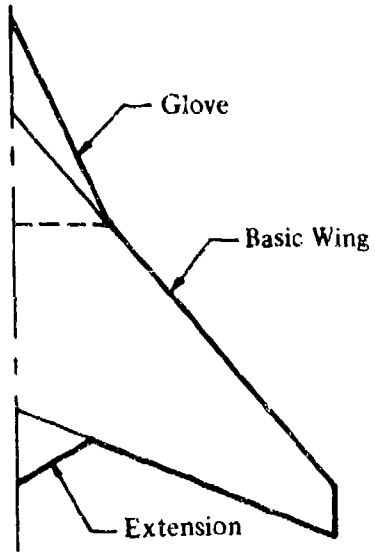

SKETCH (d)

The method is applicable to double-delta wings having breaks in the leading- and/or trailing-edge sweep at only one spanwise station.

The normal-force-curve slope of the total wing is

$$C_{N_\alpha} = K_L \left[\left(C_{N_\alpha}\right)_{bw} \frac{S_{bw}}{S_W} \left(C_{LE}\right)_{bw} + \left(C_{N_\alpha}\right)_g \frac{S_g}{S_W} \left(C_{LE}\right)_g + \left(C_{N_\alpha}\right)_E \frac{S_E}{S_W} \right] \qquad 4.1.3.2\text{-n}$$

where

K_L is an empirically derived "lift-interference factor" obtained from Figure 4.1.3.2-61.

$\frac{S_{bw}}{S_W}, \frac{S_g}{S_W}, \frac{S_E}{S_W}$ are the ratios of the areas of the basic wing, glove, and trailing-edge extension, respectively, to the total wing area. (See Section 2.2.2 for wing-geometry parameters.)

$(C_{N_\alpha})_{bw}, (C_{N_\alpha})_g$ are the normal-force-curve slopes of the basic wing and glove, respectively. $(C_{N_\alpha})_{bw}$ is obtained from Figures 4.1.3.2-56a through 4.1.3.2-56f. $(C_{N_\alpha})_g$ is obtained from either Figure 4.1.3.2-56a or Figure 4.1.3.2-63.

$(C_{LE})_{bw}, (C_{LE})_g$ are empirically derived "leading-edge-effect factors" obtained from Figure 4.1.3.2-62 as functions of Mach number and the respective planform leading-edge sweepback.

$(C_{N_\alpha})_E$ is the normal-force-curve slope of the trailing-edge extension, shown schematically in Sketch (e), and is given by

$$(C_{N_\alpha})_E = \frac{(C_{N_\alpha})_1 \frac{S_1}{S_W} - (C_{N_\alpha})_2 \frac{S_2}{S_W}}{S_E/S_W} \qquad 4.1.3.2\text{-i}$$

where

$(C_{N_\alpha})_1$ is the normal-force-curve slope of a zero-taper-ratio wing with $\Lambda_{LE} = \Lambda_{LE_g}$ and $\Lambda_{TE} = \Lambda_{TE_E}$, obtained from Figure 4.1.3.2-56a or Figure 4.1.3.2-63.

$(C_{N_\alpha})_2$ is the normal-force-curve slope of a zero-taper-ratio wing with $\Lambda_{LE} = \Lambda_{LE_g}$ and $\Lambda_{TE} = \Lambda_{TE_{bw}}$, obtained from Figure 4.1.3.2-56a or Figure 4.1.3.2-63.

$\frac{S_1}{S_W}, \frac{S_2}{S_W}$ are the ratios of the areas of the two zero-taper planforms to the total wing area.

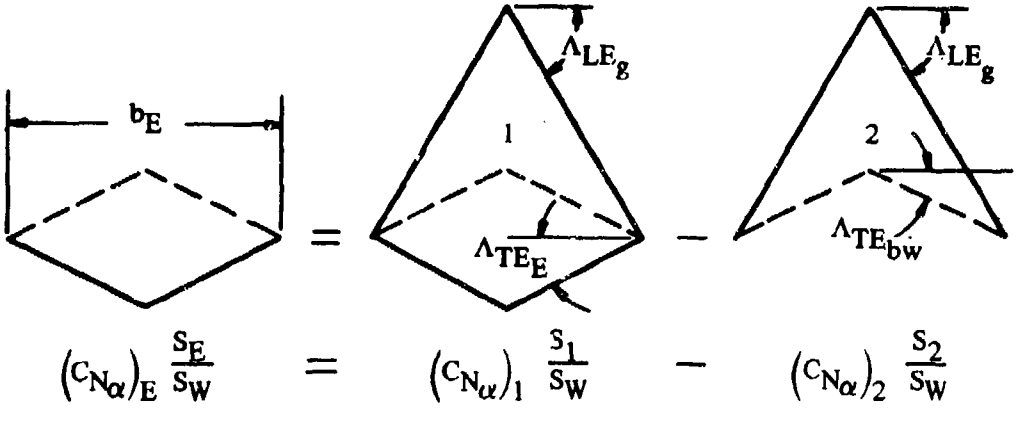

SKETCH (e)

It is recommended that Figure 4.1.3.2-63 be used to obtain the normal-force-curve slopes of the zero-taper-ratio wings rather than Figure 4.1.3.2-56a because of the upper limit of the parameter A tan Λ_{LE} of Figure 4.1.3.2-56a. The use of Figure 4.1.3.2-63 is very convenient since the normal-force-curve slope is presented in the form C_{N_α}/A, which eliminates the necessity of calculating the area of each individual panel.* All that is required to solve Equation 4.1.3.2-i is the total wing planform area S_W and the span b_E of the trailing-edge extension. Using values of C_{N_α}/A from Figure 4.1.3.2-63, Equation 4.1.3.2-i becomes

$$\left(C_{N_\alpha}\right)_E \frac{S_E}{S_W} = \left[\left(\frac{C_{N_\alpha}}{A}\right)_1 - \left(\frac{C_{N_\alpha}}{A}\right)_2\right] \frac{b_E^2}{S_W} \qquad 4.1.3.2\text{-j}$$

Application of this method is illustrated in Sample Problem 1 on Page 4.1.3.2-29.

A comparison of test data for 26 configurations with C_{N_α} of double-delta wings calculated by this method is presented as Table 4.1.3.2-C (taken from Reference 8). All but two of the configurations listed in the table are wing-body combinations, All predictions were made by using the theoretical planform (leading and trailing edges extended to the center line) for the total planform area and neglecting body effects. No configuration had a ratio of body diameter to wing span greater than 0.15; consequently, the wing-body interference is considered to be negligible. The wing-thickness-ratio range covered (0.02 to 0.07) is consistent with current practice and no significant effects of wing thickness ratio are evident.

It should be noted that the maximum error generally occurs on wing-body configurations with large inboard sweep angles ($\Lambda_{LE_i} > 78^\circ$). This can conceivably result from two sources. Configurations with large inboard sweep have a large portion of the theoretical glove planform submerged in the body, making the assumption of negligible wing-body interference effects less valid; and the "leading-edge-effect factors" presented in Figure 4.1.3.2-62 are not well defined for sharp-nosed airfoils at low values of $\beta/\tan \Lambda_{LE}$.

It is recommended that this method be restricted to the Mach-number range, $1.2 \leq M \leq 3.0$ For $M = 1.0$ the empirical correlation presented in Paragraph B should be used.

Another class of double-delta wings of practical interest are those with the outboard wing sweep greater than the inboard wing sweep. No configuration with $\Lambda_{LE_o} > \Lambda_{LE_i}$ was analyzed during the investigation reported in Reference 8; however, a method of approach for treating such configurations is suggested.

Defining the basic-wing breakdown as before results in some additional basic-wing area created forward of the wing sweep break as illustrated in Sketch (f).

*Figure 4.1.3.2-63 may also be applied with equal facility to obtain normal-force-curve slope of the glove. Using $(C_{N_\alpha}/A)_g$ from Figure 4.1.3.2-63

$$\left(C_{N_\alpha}\right)_g \frac{S_g}{S_W} = \left(\frac{C_{N_\alpha}}{A}\right)_g \frac{b_g^2}{S_W}$$

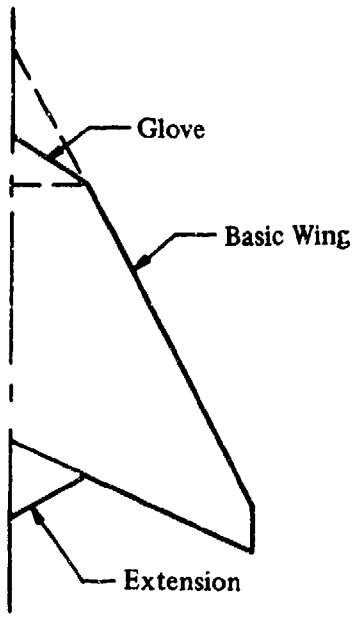

SKETCH (f)

For this class of double-delta wings the normal-force-curve slope of the basic wing is determined by extending the basic-wing leading edge to the configuration center line, calculating the normal-force-curve slope of the extended basic-wing panel, and calculating and subtracting the normal-force-curve slope of the section of the basic-wing panel forward of the wing sweep break. This is shown schematically in Sketch (g).

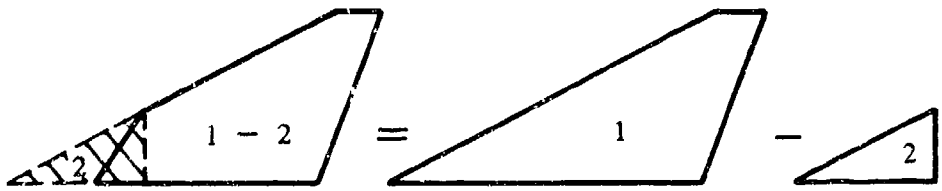

$$\left(C_{N_\alpha}\right)_{bw} \frac{S_{bw}}{S_W} = \left(C_{N_\alpha}\right)_1 \frac{S_1}{S_W} - \left(C_{N_\alpha}\right)_2 \frac{S_2}{S_W}$$

SKETCH (g)

Based on this definition of the normal-force-curve slope of the basic wing, the total wing normal-force-curve slope is given by Equation 4.1.3.2-h with the "lift-interference factor" K_L replaced by K.

$$C_{N_\alpha} = K \left[\left(C_{N_\alpha}\right)_{bw} \frac{S_{bw}}{S_W} (C_{LE})_{bw} + \left(C_{N_\alpha}\right)_g \frac{S_g}{S_W} (C_{LE})_g + \left(C_{N_\alpha}\right)_E \frac{S_E}{S_W} \right] \qquad 4.1.3.2\text{-k}$$

where

K is an empirical correlation factor which corresponds to the "lift-interference factor" K_L. Not enough force data are available to allow correlation of this parameter; however, based on a limited amount of experimental rolling-moment data, K appears to be approximately one.

The remaining parameters are defined as before.

Although not enough data are available to substantiate application of the foregoing analysis to double-delta planforms with $\Lambda_{LE_o} > \Lambda_{LE_i}$, it can be concluded that the method will become less valid for wings employing sharp-nosed airfoils and large outboard sweep angles, since the "leading-edge-effect factors" are not well defined for wings with sharp-nosed airfoils at low values of $\beta/\tan \Lambda_{LE}$.

Application of this method is illustrated in Sample Problem 2 on Page 4.1.3.2-32.

Cranked Wings

The method used to predict the normal-force-curve slope of double-delta wings is also applicable to cranked wings. However, for cranked wings with broken trailing edges the inboard trailing-edge sweep angle may be greater than the outboard trailing-edge sweep angle. Since the basic wing is defined as in the double-delta wing breakdown, this results in some additional area being created behind the inboard trailing edge as illustrated in Sketch (h).

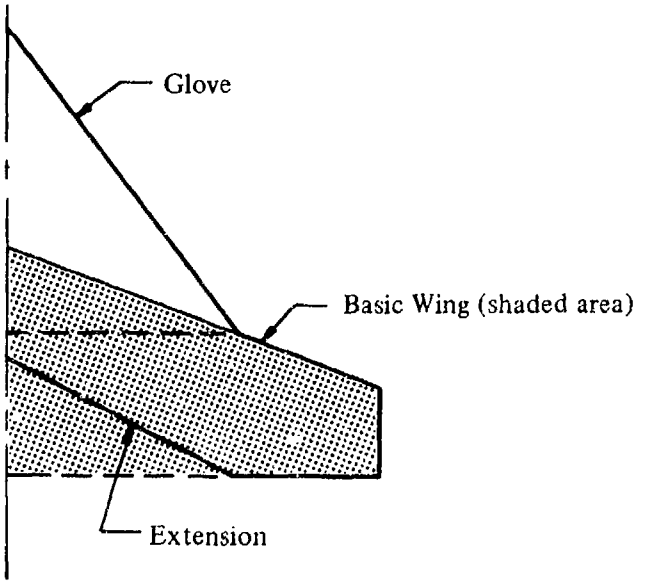

Cranked wing with $\Lambda_{TE_i} > \Lambda_{TE_o}$

SKETCH (h)

This additional area is considered to be the trailing-edge extension. Defining $(C_{N_\alpha})_1$ and $(C_{N_\alpha})_2$ exactly as for the double-delta wing results in a negative normal-force-curve increment for the trailing-edge extension.

This method is applicable to cranked wings having breaks in the leading- and/or trailing-edge sweep at only one spanwise station.

The normal-force-curve slope of the total wing is given by Equation 4.1.3.2-h; i.e.,

$$C_{N_\alpha} = K_L \left[\left(C_{N_\alpha}\right)_{bw} \frac{S_{bw}}{S_W} (C_{LE})_{bw} + \left(C_{N_\alpha}\right)_g \frac{S_g}{S_W} (C_{LE})_g + \left(C_{N_\alpha}\right)_E \frac{S_E}{S_W} \right]$$

where all the parameters are defined under Equation 4.1.3.2-h of the double-delta-wing method.

The normal-force-curve slope of the trailing-edge extension for the case where the inboard trailing-edge sweep angle is greater than the outboard trailing-edge sweep angle is shown schematically in Sketch (i).

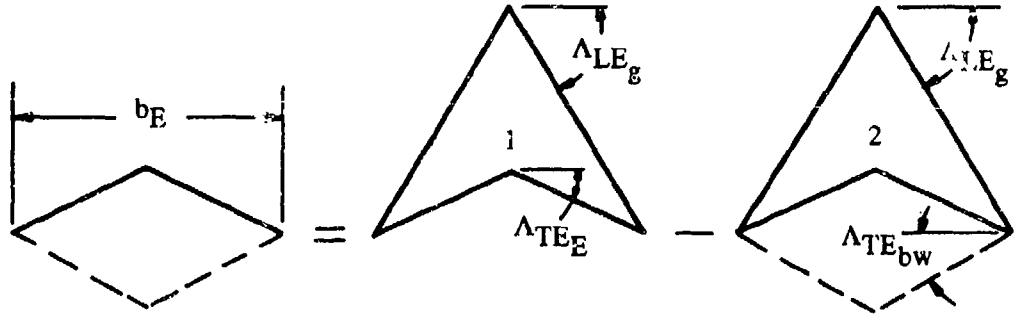

$$\left(C_{N_\alpha}\right)_E \frac{S_E}{S_W} = \left(C_{N_\alpha}\right)_1 \frac{S_1}{S_W} - \left(C_{N_\alpha}\right)_2 \frac{S_2}{S_W}$$

SKETCH (i)

Application of this technique is illustrated in Sample Problem 3 on Page 4.1.3.2-34.

A comparison of test data for seven configurations with C_{N_α} of cranked wings calculated by this method is presented as Table 4.1.3.2-D (taken from Reference 8). The configurations listed in the table are either wing-body combinations or wing-body combinations with nacelles included in the body. The inboard leading-edge sweep angles are generally lower than those on the double-delta wings, which would tend to alleviate the body effects on the glove discussed under the

double-delta-wing method. The wing thickness-ratio range covered (0.02 to 0.08) is consistent with current practice and no significant effects of wing thickness ratio are evident.

Five of the configurations had small ratios of body diameter to wing span and the predictions for those configurations were based on the theoretical planform extended to the body center line. The configurations of References 65 and 66 had nacelles included in the body, and an effective extension was included as part of the planform as shown in Sketch (j). Since the definition of the extension was somewhat arbitrary, this technique should not be considered as a general wing-body prediction technique.

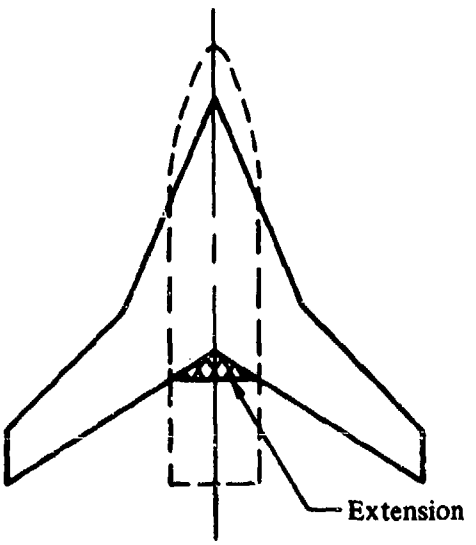

SKETCH (j)

Although all the configurations investigated had round-nosed airfoils, the application of the method to cranked wings with sharp-nosed airfoils should give equally good results except in the low supersonic Mach-number range. The "leading-edge-effect factors" are not well defined for sharp-nosed airfoils at low values of $\beta/\tan \Lambda_{LE}$ and must be considered as a possible source of error at low supersonic Mach numbers.

It is recommended that this method be restricted to the Mach number range, $1.2 \leq M \leq 3.0$. For $M = 1.0$ the empirical correlation presented in Paragraph B can be used for cranked wings with aspect ratios of approximately three.

Curved Wings

This method, taken from Reference 8, is based on the theoretical results of Squire in Reference 27.

The supersonic normal-force-curve slope of curved (Gothic and ogee) planforms is obtained from the procedure outlined in the following steps:

Step 1. Using the given wing geometry calculate the aspect ratio A, the planform shape parameter p, and the wing slenderness parameter $b_W/(2\ell)$. (See Section 2.2.2 for wing-geometry parameters.)

Step 2. At the desired value of $\frac{\beta b_W}{2\ell}$ obtain $\left(\frac{C_{N_\alpha}}{A}\right)\left(\frac{1+p}{p}\right)$ from Figure 4.1.3.2-64.

Step 3. Calculate the supersonic normal-force-curve slope by

$$C_{N_\alpha} = \left[\left(\frac{C_{N_\alpha}}{A}\right)\left(\frac{1+p}{p}\right)\right] A \left(\frac{p}{1+p}\right) \qquad 4.1.3.2\text{-}l$$

Application of this method is illustrated in Sample Problem 4 on Page 4.1.3.2-36.

A comparison of test data for 18 configurations with C_{N_α} of curved wings calculated by this method is presented as Table 4.1.3.2-E (taken from Reference 8). Four of the configurations listed in the table are wing-body combinations with small ratios of body diameter to wing span. The calculations for these configurations were made by using the theoretical planform extended to the body center line and neglecting body effects. All models employed thin wings ($0.008 \leqslant t/c \leqslant 0.06$) with sharp leading edges.

The method provides satisfactory results for low supersonic Mach numbers and may be applied over the Mach number range, $1.0 \leqslant M \leqslant 3.0$.

On some ogee-wing-body configurations the leading-edge sweep becomes very large near the wing-body juncture. For such configurations, unrealistic values of p will be obtained if "good engineering judgment" is not exercised in extending the planform to the center line. The error that could result is illustrated by the somewhat analogous cases of wings W_1, W_4, and W_7 of Reference 79 (see Table 4.1.3.2-E). These configurations are ogee wings with very slender apexes and, consequently, low values of p. It is believed that the slender apex behaves more as a body than as part of the lifting surface. For these wings the method underestimates the normal-force-curve slope from 6.5 to 21.7 percent.

The calculated results for the configuration of Reference 81 are as much as 22 percent in error. However, the model is a sonic-design, blended wing-body configuration with unusual bumps in the wing surface near the wing-body juncture, and it is suspected that the bumps significantly affect the pressure distribution at supersonic speeds. It is significant that at subsonic speeds, test data for this configuration correlate quite well with the predicted lift at angle of attack (see results for Reference 43 in Table 4.1.3.3-D).

The authors of Reference 8 note that moderately low-aspect-ratio wings ($1.5 \leqslant A \leqslant 3.0$) have linear lift-curve slopes up to approximately eight degrees angle of attack at supersonic speeds. However, the low-aspect-ratio-wing ($A \leqslant 1.3$) data of Reference 79 show a break in the lift curve at approximately two degrees angle of attack. Unfortunately, the program reported in Reference 8 did not include an investigation of the supersonic wing-lift variation with angle of attack for irregular-shaped wings.

Sample Problems

1. Double-Delta Wing

Given: Double-delta wing of Reference 58.

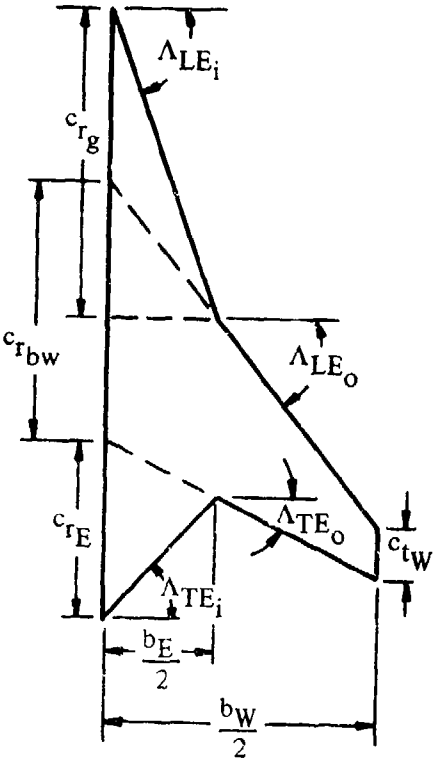

Total Wing

$A_W = 2.42$ $\quad \lambda_W = 0.086$ $\quad b_W = 24.0$ in.

$\Lambda_{LE_i} = 70.67^o$ $\quad \Lambda_{LE_o} = 51.63^o$

$S_W = 238$ sq in. $\quad \eta_B = 0.40$

$\Lambda_{TE_i} = -47.37^o$ $\quad \Lambda_{TE_o} = 26.62^o$

Basic Wing

$A_{bw} = 3.50$ $\quad \lambda_{bw} = 0.20$ $\quad S_{bw} = 164.6$ sq in.

$\Lambda_{LE_{bw}} = \Lambda_{LE_o} = 51.63^o$ $\quad \Lambda_{TE_{bw}} = \Lambda_{TE_o} = 26.62^o$

Glove

$A_g = 1.402$ $\lambda_g = 0$ $\Lambda_{LE_g} = \Lambda_{LE_i} = 70.67^o$ $S_g = 65.7$ sq in.

Extension

$\frac{b_E}{2} = \eta_B \frac{b_W}{2} = 4.8$ in. $\Lambda_{TE_E} = \Lambda_{TE_i} = -47.37^o$

Additional Characteristics:

Sharp-nosed airfoil $M = 2.01; \beta = 1.744$

Compute:

$(C_{N_\alpha})_{bw}$

$\tan \Lambda_{LE_{bw}}/\beta = 0.724$; $(A \tan \Lambda_{LE})_{bw} = 4.421$

$\beta(C_{N_\alpha})_{bw} = 4.24$ per rad (Figure 4.1.3.2-56b)

$(C_{N_\alpha})_{bw} = 2.43$ per rad

$\beta/\tan \Lambda_{LE_{bw}} = 1.38$

$(C_{LE})_{bw} = 0.993$ (Figure 4.1.3.2-62)

$(C_{N_\alpha})_g$ (Since $\lambda = 0$, either Figure 4.1.3.2-56a or 4.1.3.2-63 can be used.) (See footnote on Page 4.1.3.2-23.)

$\beta/\tan \Lambda_{LE_g} = 0.612$; $(A \tan \Lambda_{LE})_g = 3.99$

$\tan \Lambda_{LE_g}(C_{N_\alpha})_g = 4.90$ per rad (Figure 4.1.3.2-56a)

$(C_{N_\alpha})_g = 1.72$ per rad

$(C_{LE})_g = 0.995$ (Figure 4.1.3.2-62)

$(C_{N_\alpha})_E \frac{S_E}{S_W}$ (use Figure 4.1.3.2-63)

$\beta/\tan \Lambda_{LE_l} = \beta/\tan \Lambda_{LE_g} = 0.612$

$$\frac{\tan \Lambda_{TE_1}}{\tan \Lambda_{LE_1}} = \frac{\tan \Lambda_{TE_E}}{\tan \Lambda_{LE_g}} = -0.381$$

$$\left(\frac{C_{N_\alpha}}{A}\right)_1 = 1.58 \text{ (Figure 4.1.3.2-63)}$$

$$\beta/\tan \Lambda_{LE_2} = \beta/\tan \Lambda_{LE_g} = 0.612$$

$$\frac{\tan \Lambda_{TE_2}}{\tan \Lambda_{LE_2}} = \frac{\tan \Lambda_{TE_{bw}}}{\tan \Lambda_{LE_g}} = 0.176$$

$$\left(\frac{C_{N_\alpha}}{A}\right)_2 = 1.07 \text{ per rad (Figure 4.1.3.2-63)}$$

$$\left(C_{N_\alpha}\right)_E \frac{S_E}{S_W} = \left[\left(\frac{C_{N_\alpha}}{A}\right)_1 - \left(\frac{C_{N_\alpha}}{A}\right)_2\right] \frac{b_E^2}{S_W} \text{ (Equation 4.1.3.2-j)}$$

$$= (1.58 - 1.07) \frac{(9.6)^2}{238}$$

$$= 0.197 \text{ per rad}$$

$$\frac{1}{\beta}\left(C_{N_\alpha}\right)_g \frac{S_g}{S_W} = \frac{1}{1.744}(1.72)\left(\frac{65.7}{238}\right) = 0.272$$

$K_L = 0.830$ (Figure 4.1.3.2-61)

Solution:

$$C_{N_\alpha} = K_L\left[\left(C_{N_\alpha}\right)_{bw} \frac{S_{bw}}{S_W} (C_{LE})_{bw} + \left(C_{N_\alpha}\right)_g \frac{S_g}{S_W} (C_{LE})_g + \left(C_{N_\alpha}\right)_E \frac{S_E}{S_W}\right] \text{ (Equation 4.1.3.2-h)}$$

$$= 0.830\left[(2.43)\left(\frac{164.6}{238}\right)(0.993) + (1.72)\left(\frac{65.7}{238}\right)(0.995) + 0.197\right]$$

$$= 0.830\,[1.670 + 0.472 + 0.197]$$

$$= 1.941 \text{ per rad}$$

$$= 0.0339 \text{ per deg}$$

This compares with a test value of 0.0351 per degree from Reference 58.

2. Double-Delta Wing $(\Lambda_{LE_o} > \Lambda_{LE_i})$

Given: The double-delta wing of Reference 75.Configuration has no trailing-edge extension.

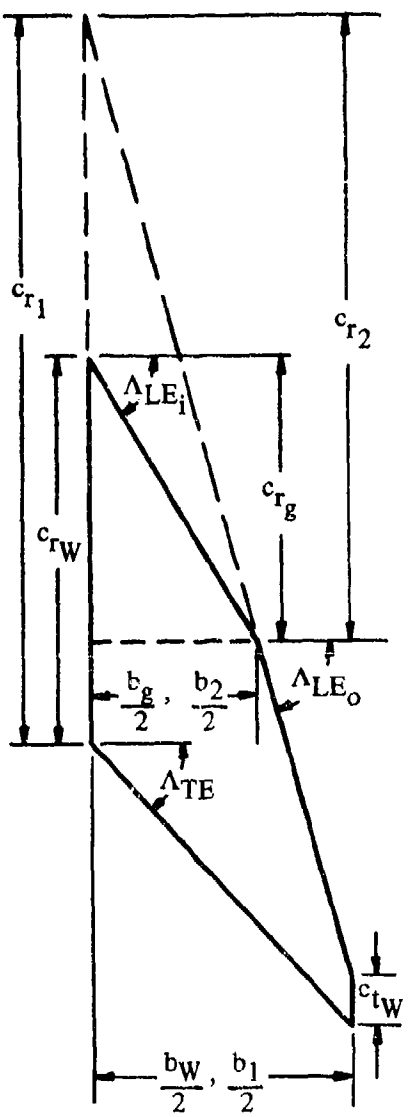

Total Wing

$A_W = 1.86$ $\quad \lambda_W = 0.130$

$\Lambda_{LE_i} = 60^o$ $\quad \Lambda_{LE_o} = 75^o$

$S_W = 275.9$ sq in. $\quad \eta_B = 0.654$

$\Lambda_{TE} = 47.5^o$

Glove

$\frac{S_g}{S_W} = 0.346$ $\quad \lambda_g = 0$ $\quad \Lambda_{LE_g} = \Lambda_{LE_i} = 60^o$

$A_g = 2.31$

Extended Planforms

$\frac{S_1}{S_W} = 1.405$ $\quad \lambda_1 = 0.0698$

$\Lambda_{LE_1} = \Lambda_{LE_o} = 75^o$

$A_1 = 1.327$

$\frac{S_2}{S_W} = 0.745$ $\quad \lambda_2 = 0$

$\Lambda_{LE_2} = \Lambda_{LE_o} = 75^o$

$A_2 = 1.072$

Additional Characteristics

Sharp-nosed airfoil $\quad M = 3.71; \beta = 3.573$

Compute:

$(C_{N_\alpha})_g$

$\tan \Lambda_{LE_g}/\beta = 0.485$; $(A \tan \Lambda_{LE})g = 4.0$

$\beta(C_{N_\alpha})_g$ = 4.0 (Figure 4.1.3.2-56a)

$(C_{N_\alpha})_g$ = 1.12 per rad

$\beta/\tan \Lambda_{LE_g}$ = 2.06

$(C_{LE})_g$ = 1.03 (Figure 4.1.3.2-62)

$(C_{N_\alpha})_{bw} \frac{S_{bw}}{S_W}$

$(C_{N_\alpha})_1$

$\beta/\tan \Lambda_{LE_1}$ = 0.957; $(A \tan \Lambda_{LE})_1$ = 4.94

$\tan \Lambda_{LE_1} (C_{N_\alpha})_1$ = 4.40 per rad (Figures 4.1.3.2-56a through -56c, interpolated)

$(C_{N_\alpha})_1$ = 1.179 per rad

$(C_{N_\alpha})_2$

$\beta/\tan \Lambda_{LE_2}$ = 0.957; $(A \tan \Lambda_{LE})_2$ = 4.0

$\tan \Lambda_{LE_2} (C_{N_\alpha})_2$ = 4.08 (Figure 4.1.3.2-56a)

$(C_{N_\alpha})_2$ = 1.093 per rad

$$(C_{N_\alpha})_{bw} \frac{S_{bw}}{S_W} = (C_{N_\alpha})_1 \frac{S_1}{S_W} - (C_{N_\alpha})_2 \frac{S_2}{S_W}$$

$$= (1.179)(1.405) - (1.093)(0.745)$$

$$= 0.842 \text{ per rad}$$

$\beta/\tan \Lambda_{LE_{bw}}$ = 0.957

$(C_{LE})_{bw}$ = 0.94 (Figure 4.1.3.2-62)

Solution:

$$C_{N_\alpha} = K\left[\left(C_{N_\alpha}\right)_{bw} \frac{S_{bw}}{S_W} (C_{LE})_{bw} + \left(C_{N_\alpha}\right)_g \frac{S_g}{S_W} (C_{LE})_g\right] \quad \text{(Equation 4.1.3.2-k)}$$

$$= 1.0\,[(0.842)(0.94) + (1.12)(0.346)(1.03)]$$

$$= 1.190 \text{ per rad}$$

$$= 0.0208 \text{ per deg}$$

This compares with a test value of 0.024 per degree from Reference 75.

3. Cranked Wing ($\Lambda_{TE_i} > \Lambda_{TE_o}$)

Given: Cranked wing of Reference 32. The inboard trailing-edge sweep angle is greater than the outboard trailing-edge sweep angle. (See Sketches (h) and (i).)

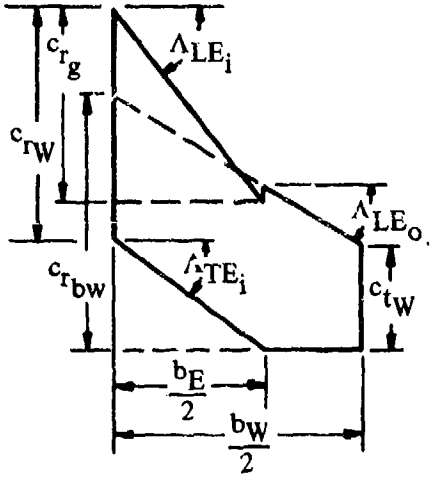

Total Wing

$A_W = 2.91$ $\quad \lambda_W = 0.44$

$\Lambda_{LE_i} = 53.13^o$ $\quad \Lambda_{LE_o} = 32.16^o$

$S_W = 40.04$ sq in. $\quad \eta_B = 0.60$

$\Lambda_{TE_i} = 37.3^o$ $\quad \Lambda_{TE_o} = 0$

Basic Wing

$A_{bw} = 2.73$ $\quad \lambda_{bw} = 0.40$ $\quad \Lambda_{LE_{bw}} = \Lambda_{LE_o} = 32.16^o$

$S_{bw} = 42.77$ sq in. $\quad b_{bw} = 10.8$ in. $\quad \Lambda_{TE_{bw}} = \Lambda_{TE_o} = 0$

Glove

$A_g = 3.0$ $\quad \Lambda_{LE_g} = \Lambda_{LE_i} = 53.13^o$ $\quad S_g = 14.00$ sq in. $\quad \lambda_g = 0$

Extension

$\frac{b_E}{2} = \eta_B \frac{b_W}{2} = 3.24$ in. $\quad \Lambda_{TE_E} = \Lambda_{TE_i} = 37.3^o$

Additional Characteristics

Round-nosed airfoil $\quad M = 1.40;\ \beta = 0.98$

Compute:

$(C_{N_\alpha})_{bw}$

$\tan \Lambda_{LE_{bw}}/\beta = 0.642$; $(A \tan \Lambda_{LE})_{bw} = 1.715$

$\beta (C_{N_\alpha})_{bw} = 3.42$ per rad (Figures 4.1.3.2-56c through -56f, interpolated)

$(C_{N_\alpha})_{bw} = 3.49$ per rad

$\beta/\tan \Lambda_{LE_{bw}} = 1.560$

$(C_{LE})_{bw} = 0.99$ (Figure 4.1.3.2-62)

$(C_{N_\alpha})_g$ (Since $\lambda = 0$, either Figure 4.1.3.2-56a or 4.1.3.2-63 can be used.)

(See footnote on Page 4.1.3.2-23.)

$\beta/\tan \Lambda_{LE_g} = 0.735$; $(A \tan \Lambda_{LE})_g = 4.0$

$\tan \Lambda_{LE_g} (C_{N_\alpha})_g = 4.575$ per rad (Figure 4.1.3.2-56a)

$(C_{N_\alpha})_g = 3.43$ per rad

$(C_{LE})_g = 0.93$ (Figure 4.1.3.2-62)

$(C_{N_\alpha})_E \frac{S_E}{S_W}$ (use Figure 4.1.3.2-63)

$\beta/\tan \Lambda_{LE_1} = \beta/\tan \Lambda_{LE_g} = 0.735$

$\frac{\tan \Lambda_{TE_1}}{\tan \Lambda_{LE_1}} = \frac{\tan \Lambda_{TE_E}}{\tan \Lambda_{LE_g}} = 0.571$

$\left(\frac{C_{N_\alpha}}{A}\right)_1 = 0.650$ per rad (Figure 4.1.3.2-63)

$\beta/\tan \Lambda_{LE_2} = \beta/\tan \Lambda_{LE_g} = 0.735$

$\frac{\tan \Lambda_{TE_2}}{\tan \Lambda_{LE_2}} = \frac{\tan \Lambda_{TE_{bw}}}{\tan \Lambda_{LE_g}} = 0$

$\left(\frac{C_{N_\alpha}}{A}\right)_2 = 1.16$ per rad (Figure 4.1.3.2-63)

$$\left(C_{N_\alpha}\right)_E \frac{S_E}{S_W} = \left[\left(\frac{C_{N_\alpha}}{A}\right)_1 - \left(\frac{C_{N_\alpha}}{A}\right)_2\right] \frac{b_E^2}{S_W} \quad \text{(Equation 4.1.3.2-j)}$$

$$= (0.650 - 1.16) \frac{(6.48)^2}{40.04}$$

$$= -0.535 \text{ per rad}$$

$$\frac{1}{\beta}\left(C_{N_\alpha}\right)_g \frac{S_g}{S_W} = \frac{1}{0.98} (3.43) \frac{(14.00)}{(40.04)} = 1.224$$

K_L = 0.74 (Figure 4.1.3.2-61)

Solution:

$$C_{N_\alpha} = K_L\left[\left(C_{N_\alpha}\right)_{bw} \frac{S_{bw}}{S_W} (C_{LE})_{bw} + \left(C_{N_\alpha}\right)_g \frac{S_g}{S_W} (C_{LE})_g + \left(C_{N_\alpha}\right)_E \frac{S_E}{S_W}\right] \quad \text{(Equation 4.1.3.2-h)}$$

$$= 0.74\left[(3.49) \frac{(42.77)}{(40.04)} (0.99) + (3.43) \frac{(14.00)}{(40.04)} (0.93) - 0.535\right]$$

$$= 0.74\ [3.691 + 1.115 - 0.535]$$

$$= 3.160 \text{ per rad}$$

$$= 0.0552 \text{ per deg}$$

This compares with a test value of 0.0563 per degree from Reference 32.

4. Curved Wing

Given: Ogee wing of Reference 80.

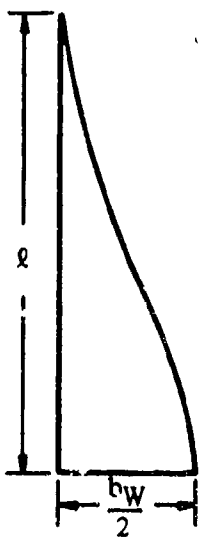

A_W = 1.20 b_W = 12.0 in. ℓ = 20.0 in. S_W = 120 sq in.

M = 1.82; β = 1.52

Compute:

Planform shape parameter

$$p = S_W/(b_W \ell) = (120)/[(12)(20)] = 0.50$$

Wing slenderness parameter

$$b_W/(2\ell) = (12.0)/[(2)(20)] = 0.30$$

$$\frac{\beta b_W}{2\ell} = \frac{(1.52)(12.0)}{(2)(20.0)} = 0.456$$

$$\left(\frac{C_{N_\alpha}}{A}\right)\left(\frac{1+p}{p}\right) = 4.18 \text{ per rad (Figure 4.1.3.2-64)}$$

Solution:

$$C_{N_\alpha} = \left(\frac{C_{N_\alpha}}{A}\right)\left(\frac{1+p}{p}\right) A \left(\frac{p}{1+p}\right) \text{ (Equation 4.1.3.2-}\ell\text{)}$$

$$= (4.18)(1.20)\left(\frac{0.50}{1+0.50}\right)$$

$$= 1.672 \text{ per rad}$$

$$= 0.0292 \text{ per deg}$$

This compares with a test value of 0.0285 per degree from Reference 80.

D. HYPERSONIC

The theoretical normal-force-curve slope of a flat plate at zero angle of attack approaches zero as the Mach number becomes large. The interrelated effects of viscosity, heat transfer, and detached shock waves due to blunt leading edges cause considerable deviations of the normal-force-curve slope from the theoretical values. These effects are discussed more fully in Paragraph D of Section 4.1.3.3. The magnitude of these effects on surface pressures, although large enough to be important under certain conditions, has not been determined. The method presented herein is based on linear theory and is intended only as a first-order approximation of the normal-force-curve slope of straight-tapered planforms at hypersonic speeds.

DATCOM METHOD

The hypersonic portions of Figures 4.1.3.2-56a through 4.1.3.2-56g may be used to obtain a first-order approximation of the normal-force-curve slope at zero angle of attack for conventional wings of zero thickness. For planforms with wedge airfoils an approximation of the normal-force-curve slope at zero angle of attack may be obtained by applying the results of Figure 4.1.3.2-65. This figure, based on two-dimensional supersonic slender-airfoil theory, presents the ratio of C_{N_α} of wedge airfoils to C_{N_α} of flat-plate airfoils.

REFERENCES

1. Multhopp, H.: Methods for Calculating the Lift Distribution of Wings (Subsonic Lifting-Surface Theory). ARC R&M 2884, 1950. (U)

2. Falkner, V.M.: The Calculation of the Aerodynamic Loading on Surfaces of Any Shape. ARC R&M 1910, 1943. (U)

3. Lowry, J.G., and Polhamus, E.: A Method for Predicting Lift Increments Due to Flap Deflection at Low Angles of Attack in Incompressible Flow. NACA TR 3911, 1957. (U)

4. DeYoung, J., and Harper, C.W : Theoretical Symmetric Span Loading at Subsonic Speeds for Wings Having Arbitrary Plan Form. NACA TR 921, 1948. (U)

5. Lawrence H.R.: Lift Distribution on Low Aspect Ratio Wings at Subsonic Speeds. Jour. Aero. Sci., October 1951. (U)

6. Jones, R.T.: Properties of Low-Aspect-Ratio Pointed Wings at Speeds Below and Above the Speed of Sound. NACA TR 835, 1946. (U)

7. Crosthwait, E.L., and Seath, D.D.: Subsonic Characteristics of Low Aspect Ratios. FDL-TDR-64-103, 1965. (U)

8. Benepe, D. B., Kouri, B. G., Webb, J. B., et al: Aerodynamic Characteristics of Non-Straight-Taper Wings. AFFDL-TR-66-73, 1966. (U)

9. Spencer, B.J., Jr.: A Simplified Method for Estimating Subsonic Lift-Curve Slope at Low Angles of Attack for Irregular Planform Wings. NASA TM X-525, 1961. (U)

10. Imai, I., Kaji, I., and Umeda, K.: Mapping Functions of the N.A.C.A. Airfoils into the Unit Circle. Jour. of the Faculty of Science, Hokkaido Univ., Japan, Ser. II, Vol. III, No. 8, 1950. (U)

11. Riegels, F.W.: Aerofoil Sections. Butterworths, London, 1961. (U)

12. Spreiter, J.R.: Aerodynamics of Wings and Bodies at Transonic Speeds. Jour. Aero. Sci., August 1959.

13. Ladson, C.L.: Two-Dimensional Airfoil Characteristics of Four NACA 6A-Series Airfoils at Transonic Mach Numbers up to 1.25. NACA RM L57F05, 1957. (C) Title Unclassified

14. Lindsey, W.F., and Humphreys, M.D.: Effects of Aspect Ratio on Airflow at High Subsonic Mach Numbers. NACA TN 2720, 1952. (U)

15. Gullstrand, T.R.: The Flow Over Two-Dimensional Aerofoils at Incidence in the Transonic Speed Range. KTH (Sweden) Aero TN 27, 1952. (U)

16. Neumark, S.: Critical Mach Numbers for Thin Untapered Swept Wings at Zero Incidence. ARC R&M 2821, 1954. (U)

17. Pearcey, H.H., and Stuart, C.M.: Methods of Boundary-Layer Control for Postponing and Alleviating Buffeting and Other Effects of Shock-Induced Separation. I.A.S. Preprin. Paper FF-22, IAS National Summer Meeting, Los Angeles, California, June 16-19, 1959. (U)

18. Graham, D.J.: The Development of Cambered Airfoil Sections Having Favorable Lift Characteristics at Supercritical Mach Numbers. NACA TR 947, 1949. (U)

19. Polhamus, E.C., and King, T.J., Jr.: Aerodynamic Characteristics of Tapered Wings Having Aspect Ratios of 4, 6, and 8, Quarter-Chord Lines Swept Back 45°, and NACA 63_1A012 Airfoil Sections. NACA RM L51C26, 1951. (U)

20. Harmon, S.M., and Jeffreys, I.: Theoretical Lift and Damping in Roll of Thin Wings With Arbitrary Sweep and Taper at Supersonic Speeds. Supersonic Leading and Trailing Edges. NACA TN 2114, 1950. (U)

21. Malvestuto, F.S., Margolis, K., and Ribner, H.S.: Theoretical Lift and Damping in Roll at Supersonic Speeds of Thin Sweptback Tapered Wings With Streamwise Tips, Subsonic Leading Edges, and Supersonic Trailing Edges. NACA TR 970, 1950. (U)

22. Lapin, E.: Charts for the Computation of Lift and Drag of Finite Wings at Supersonic Speeds. Douglas Aircraft Company Report SM 13480, 1949. (U)

23. Cohen, D.: Formulas for the Supersonic Loading, Lift, and Drag of Flat Sweptback Wings With Leading Edges Behind the Mach Lines. NACA TR 1050, 1951. (U)

24. Mangler, K.W.: Calculation of the Pressure Distribution Over a Wing at Sonic Speeds. ARC R&M 2888, 1955. (U)

25. Mirels, H.: Aerodynamics of Slender Wings and Wing-Body Combinations Having Swept Trailing Edges. NACA TN 3105, 1954. (U)

26. Lampert, S.: Normal-Force Characteristics of Delta Wings at Supersonic Speed. Jour. Aero. Sci., September 1957. (U)

27. Squire, L.C.: Some Applications of 'Not-So-Slender' Wing Theory to Wings With Curved Leading Edges. ARC R&M 3278, 1962. (U)

28. Heaslet, M.A., and Spreiter, J.R.: Reciprocity Relations in Aerodynamics. NACA TR 1119, 1953. (U)

29. Goodson, K.W., and Becht, R.E.: Wind-Tunnel Investigation at High Subsonic Speeds of the Stability Characteristics of a Complete Model Having Sweptback-, M-, W-, and Cranked-Wing Plan Forms and Several Horizontal-Tail Locations. NACA RM L54C29, 1954. (U)

30. Grant, F.C., and Sevier, J.R., Jr.: Transonic and Supersonic Wind-Tunnel Tests of Wing-Body Combinations Designed for High Efficiency at a Mach Number of 1.41. NASA TN D-435, 1960. (U)

31. Mansell, C.J.: Low-Speed Wind-Tunnel Tests on Two Thin Cranked Wings With 60-Degree Sweepback Inboard. ARC R&M 2995, 1957. (U)

32. Wakefield, R.M.: Effects of Wing-Crank, Leading-Edge Chord Extensions and Horizontal-Tail Height on the Longitudinal Stability of Swept-Wing Models at Mach Numbers from 0.6 to 1.4. NASA TM X-92, 1959. (U)

33. Henderson, W.P., and Hammond, A.D.: Low-Speed Investigation of High-Lift and Lateral Control Devices on a Semispan Variable-Sweep Wing Having an Outboard Pivot Location. NASA TM X-542, 1961. (U)

34. Lange, R.H.: Maximum Lift Characteristics of a Wing With the Leading Edge Sweepback Decreasing From 45° at the Root to 20° at the Tip at Reynolds Numbers From 2.4 x 10^6 to 6.0 x 10^6. NACA RM L50A04a, 1950. (U)

35. Kruger, W.: Six Component Measurements on a Cranked Swept-Back Wing. Great Britain Ministry of Supply Translation 816, 1947. (U)

36. Luckert, H.J.: High-Speed Investigations on Various Wing Forms and Wing Sections for the Development of the ARADO 234 Wings. Great Britain Ministry of Supply Translation 279, 1947. (U)

37. Lockwood, V.E., McKinney, L.W., and Lamar, J.E.: Low-Speed Aerodynamic Characteristics of a Supersonic Transport Model With a High Aspect Ratio Variable-Sweep Warped Wing. NASA TM X-979, 1964. (C) Title Unclassified

38. Jernell, L.S.: The Effects of Conical Camber on the Longitudinal Aerodynamic Characteristics of a Variable-Sweep Wing-Fuselage Configuration at Mach Numbers From 0.50 to 3.50. NASA TM X-804, 1964. (C) Title Unclassified

39. Trescot, C.D., Jr., and Spencer, B.J., Jr.: Effect of Reynolds Number on the Low-Speed Longitudinal Aerodynamic Characteristics of Two Variable-Wing-Sweep Airplane Configurations. NASA TM X-434. (C) Title Unclassified

40. Becht, R.E., and Byrnes, A.L., Jr.: Investigation of Low-Speed Aerodynamic Characteristics of a Variable-Sweep Airplane Model With a Wing Having Partial-Span Cambered-Leading-Edge Modifications. NACA RM L52G08a, 1952. (U)

41. Cook, A.M., Greif, R.K., and Aoyagi, K.: Large-Scale Wind-Tunnel Investigation of Low-Speed Aerodynamic Characteristics of Supersonic Transport Model Having Variable-Sweep Wings. NASA TN D-2824, 1965. (U)

42. Spearmen, M.L.: Longitudinal and Lateral Aerodynamic Characteristics at Mach Numbers From 0.60 to 2.20 of a Variable-Sweep Fighter Model With Wing Sweep Angles from 25° to 75°. NASA TM X-710, 1962. (C) Title Unclassified

43. Henderson, W.P.: Low-Speed Aerodynamic Characteristics of a Double-Pivot Variable-Wing-Sweep Airplane Configuration Having Conventional and Outboard Horizontal Tail Surfaces. NASA TM X-773, 1963. (C) Title Unclassified

44. Spencer, B.J., Jr.: Low-Speed Longitudinal Aerodynamic Characteristics Associated With Variations in the Geometry of the Fixed Portion of a Variable-Wing-Sweep Airplane Configuration Having an Outboard Pivot. NASA TM X-625, 1962. (C) Title Unclassified

45. Donlan, C.J., and Sleeman, W.C., Jr: Low-Speed Wind-Tunnel Investigation of the Longitudinal Stability Characteristics of a Model Equipped With a Variable-Sweep Wing. NACA RM L9B18, 1949. (U)

46. Spencer, B.J., Jr.: Stability and Control Characteristics at Low Subsonic Speeds of an Airplane Configuration Having Two Types of Variable-Sweep Wings. NASA TM X-303, 1960. (U)

47. Emerson, H.: Wind-Tunnel Investigation of the Effect of Clipping the Tips of Triangular Wings of Different Thickness, Camber, and Aspect Ratio—Transonic Bump Method. NASA TN 3671, 1956. (U)

48. Nelson, W., and McDevitt, J.: The Transonic Characteristics of 17 Rectangular, Symmetrical Wing Models of Varying Aspect Ratio and Thickness. NACA RM A51A12, 1951. (U)

49. Turner, T.: Effects of Sweep on the Maximum Lift Characteristics of Four Aspect-Ratio 4 Wings at Transonic Speeds. NACA RM L50H11, 1950. (U)

50. Stanbrook, A.: The Lift-Curve Slope and Aerodynamic-Centre Position of Wings at Subsonic and Supersonic Speeds. RAE TN Aero 2328, 1954. (C) Title Unclassified

51. Harris, W.: A Wind-Tunnel Investigation at High Subsonic and Low Supersonic Mach Numbers on a Series of Wings With Various Sweepback, Taper, Aspect Ratio, and Thickness. Part 2. Comparison of Lift and Stability Data. AFTR 6669, 1952. (C) Title Unclassified

52. Luoma, A.V.: Stability and Control Characteristics at Transonic Speeds of a Variable-Wing-Sweep Airplane Configuration With Outboard Panels Swept 113.24° and 75°. NASA TM X-342, 1960. (C) Title Unclassified

53. Bielat, R.P., Robins, A.W., and Alford, W.J., Jr.: The Transonic Aerodynamic Characteristics of Two Variable-Sweep Airplane Configurations Capable of Low-Level Supersonic Attack. NASA TM X-304, 1960. (C) Title Unclassified

54. Ayers, T.G.: Transonic Aerodynamic Characteristics of a Variable-Wing-Sweep Tactical Fighter Model. Phase 1. NASA TM X-1039, 1964. (C) Title Unclassified

55. Ayers, T.G.: Transonic Aerodynamic Characteristics of a Variable-Wing-Sweep Tactical Fighter Model. Phase 2. NASA TM X-1040, 1964. (C) Title Unclassified

56. Re, R.J., and Simonson, A.J.: Transonic Longitudinal Aerodynamic Characteristics of a Variable-Sweep Tactical-Fighter Model With Wing Sweeps of 25°, 65°, 85°, and 106°. NASA TM X-731, 1962. (C) Title Unclassified

57. Alford, W.J., Jr., Luoma, A.V., and Henderson, W.P.: Wind-Tunnel Studies at Subsonic and Transonic Speeds of a Multiple-Mission Variable-Wing-Sweep Airplane Configuration. NASA TM X-206, 1959. (U)

58. Cooper, M., and Sevier, J.R., Jr.: Effect of a Series of Inboard Plan-Form Modifications on the Longitudinal Characteristics of Two 47° Sweptback Wings of Aspect Ratio 3.5, Taper Ratio 0.2, and Different Thickness Distributions at Mach Numbers of 1.61 and 2.01. NACA RM L53E07a, 1953. (U)

59. Anon: Small-Scale Wing-Body Planform Investigation at Mach Numbers from 0.40 to 2.94.Unpublished Data. (U)

60. Durgin, F.A.: A Study of Twist and Camber on Wings in Supersonic Flow. FDL-TDR-64-109, 1964. (U)

61. Kuhns, R.M.: HSWT-083-0 Analysis Report, Supersonic Transport Lifting Fuselage Investigation. Convair San Diego Report AD-SST-012, 1961. (U)

62. Sevier, J.R., Jr.: Aerodynamic Characteristics at Mach Numbers of 1.41 and 2.01 of a Series of Cranked Wings Ranging in Aspect Ratio From 4.00 to 1.74 in Combination With a Body. NASA TM X-172, 1960. (U)

63. Sevier, J.R., Jr.: Effects of Series of Inboard Plan-Form Modifications on the Longitudinal Characteristics of Two Unswept Wings of Aspect Ratio 3.5, Taper Ratio 0.2, and Different Thickness Distributions at Mach Numbers of 1.61 and 2.01. NACA RM L53K11, 1954. (U

64. Anon: Wind-Tunnel Tests of a Series of Wing-Body Configurations for Investigation of Supersonic Lift/Drag Ratios. Unpublished Data. (U)

65. Anon: Unpublished Wind-Tunnel Test Data. (U)

66. Spearman, M.L., and Robinson, R.B.: Effects of Wing Sweep and Horizontal-Tail Position on the Aerodynamic Characteristics at a Mach Number of 2.2 of a Variable-Sweep Airplane Configuration Having an Inboard Wing Pivot. NASA TM X-585, 1961. (U)

67. Landrum, E.J., and Babb, C.D.: Effect of Skewed Wing-Tip Controls on a Variable-Sweep Wing-Fuselage Configuration at Mach Numbers From 2.60 to 4.62. NASA TM X-1031, 1964. (C) Title Unclassified

68. Driver, C., and Spearman, M.L.: Aerodynamic Characteristics at a Mach Number of 2.20 of a Variable-Sweep Fighter Model With Wing Sweeps of 50°, 60°, and 75°. NASA TM X-1041, 1964. (C) Title Unclassified

69. Jernell, L.S.: Aerodynamic Characteristics at Mach Numbers From 2.50 to 4.63 of a Variable-Sweep Model at Sweep Angles from 55° to 75°. NASA TM X-959, 1964. (C) Title Unclassified

70 Landrum, E.J.: Effect of Skewed Wing-Tip Controls on a Variable-Sweep Wing-Fuselage Configuration at Mach Numbers of 1.41 and 2.20. NASA TM X-951, 1964. (C) Title Unclassified

71. Spearman, M.L., and Harris, R.V., Jr.: The Longitudinal and Lateral Aerodynamic Characteristics at Mach Numbers of 1.41 and 2.20 of a Variable-Sweep Fighter Model With Wing Sweeps Varying From 25° to 75°. NASA TM X-759, 1963. (C) Title Unclassified

72. Spearman, M.L., and Robinson, R.B.: Stability and Control Characteristics at a Mach Number of 2.01 of a Variable-Sweep Airplane Configuration Capable of Low-Level Supersonic Attack—Outer Wing Swept 75°. NASA TM X-310, 1960. (C) Title Unclassified

73. Robinson, R.B., and Howard, P.W.: Stability and Control Characteristics at a Mach Number of 2.2 of a Variable-Sweep Airplane Configuration Having a 12-Percent-Thick Wing Swept 75° and an Inboard Pivot Location. NASA TM X-435, 1960. (C) Title Unclassified

74. Foster, G.V., and Morris, O.A.: Stability and Control Characteristics at a Mach Number of 1.97 of an Airplane Configuration Having Two Types of Variable-Sweep Wings. NASA TM X-323, 1960. (U)

75. Foster, G.V.: Stability and Control Characteristics at Mach Numbers of 2.50, 3.00, and 3.71 of a Variable-Wing-Sweep Configuration With Outboard Wing Panels Swept Back 75°. NASA TM X-267, 1960. (U)

76. Spearman, M.L.: Static Longitudinal and Lateral Aerodynamic Characteristics at Mach Numbers of 1.41 and 2.20 of a Model of a Low-Aspect-Ratio 83.5° Delta-Wing Airplane Having Auxiliary Variable-Sweep Wing Panels. NASA TM X-708, 1963. (C) Title Unclassified

77. Shaw, D.S.: Supersonic Investigation of the Static Stability, Performance, and Control of a Variable-Sweep Tactical Fighter Model. Phase 1. NASA TM X-1045, 1965. (C) Title Unclassified

78. Shaw, D.S., and Wassum, D.L.: Supersonic Investigation of the Static Stability, Performance, and Control of a Variable-Sweep Tactical Fighter Model. Phase 2. NASA TM X-1046, 1965. (C) Title Unclassified.

79. Igglesden, M.S.: Tabulated Lift, Drag, and Pitching Moment From Wind-Tunnel Tests on 30 Slender Wings of Ogee and Other Planforms, With Various Thickness Distributions, at M = 1.4 , 1.61, and 1.91. RAE TN Aero 2694, 1960. (U)

80. Squire, L.C., and Capps, D.S.: An Experimental Investigation of the Characteristics of an Ogee Wing From M = 0.4 to M = 1.8. ARC CP 585, 1962. (U)

81. Holdaway, G.H., and Mellenthin, J.A.: Evaluation of Blended Wing-Body Combinations With Curved Plan Forms at Mach Numbers Up to 3.5. NASA TM X-379, 1960. (U)

82. Hicks, R.M., and Hopkins, E.J.: Effects of Spanwise Variation of Leading-Edge Sweep on the Lift, Drag, and Pitching Moment of a Wing-Body Combination at Mach Numbers From 0.7 to 2.94. NASA TN D-2236, 1964. (U)

83. Corlett, W.A., and Foster, G.V.: Aerodynamic Characteristics of a Tailless Fixed-Wing Supersonic Transport Model at Mach Numbers From 1.80 to 2.86. NASA TM X-992, 1964. (C) Title Unclassified

84. Foster, G.V., and Corlett, W.A.: Aerodynamic Characteristics of a Tailless Fixed-Wing Supersonic Transport Configuration at Mach Number 2.20. NASA TM X-960, 1964. (C) Title Unclassified

85. Cook, T.A.: Wind-Tunnel Measurements at Mach Numbers Up to 2.80 of the Effects of Gulling on the Longitudinal and Lateral Stability and Drag of a Cambered, Slender Ogee Wing. ARC CP 803, 1965. (U)

86. Rolls, L.S., Koenig, D.G., and Drinkwater, F.J., III: Flight Investigation of the Aerodynamic Properties of an Ogee Wing. NASA TN D-3071, 1965. (U)

87. Earnshaw, P.B.: Low-Speed Wind-Tunnel Tests on a Series of Cambered Ogee Wings. ARC CP 775, 1963. (U)

88. Keating, R.F.A.: Low-Speed Wind-Tunnel Tests on Sharp-Edged Gothic Wing of Aspect-Ratio 3/4. ARC CP 576 1960. (U)

89. Squire, L.C.: Measurement of Lift and Pitching Moment on 4 Ogee Wings at Supersonic Speeds. ARC CP 673, 1962. (U)

90. Taylor, C.R.: Measurements at Mach Numbers Up to 2.8 of the Longitudinal Characteristics of One Plane and Three Cambered Slender 'Ogee' Wings. ARC R&M 3328, 1961. (U)

91. Isaacs, D.: Measurement at Subsonic and Supersonic Speeds of Longitudinal and Lateral Stability of a Slender Cambered Ogee Wing Including Effects of a Fin, Canopy Nose, and Trailing-Edge Controls. ARC R&M 3390, 1965. (U)

92. Dobson, M.D., and King-Underwood, R.: Wind-Tunnel Tests Between M = .4 and 2.0 on Cambered Wing of Slender Ogee Planform. ARC CP 778, 1965. (U)

93. Eggers, A.J., Jr., Syvertson, C.A., and Kraus, S.: A Study of Inviscid Flow About Airfoils at High Supersonic Speeds. NACA TR 1123, 1953. (U)

94. Creager, M.O.: Surface Pressure Distribution at Hypersonic Speeds For Blunt Delta Wings at Angle of Attack. NASA Memo 5-12-59A, 1959. (U)

95. Messiter, A.F.: Lift of Slender Delta Wings According to Newtonian Theory. AIAA, Vol. I, No. 4, 1963. (U)

96. Olstad, W.B.: Theoretical Evaluation of Hypersonic Forces, Moments and Stability Derivatives For Combinations of Flat Plates, Including Effects of Blunt Leading Edges, by Newtonian Impact Theory. NASA TN D-1015, 1952. (U)

TABLE 4.1.3.2-A
SUBSONIC LIFT-CURVE SLOPE OF CRANKED WINGS
DATA SUMMARY AND SUBSTANTIATION

Ref.	Config.	A	λ_i	λ_o	η_B	Λ_{LE_i}	Λ_{LE_o}	$\frac{d}{b}$	$\frac{t}{c}$	LER	M	$R_{\ell_{max}} \times 10^{-6}$	C_{L_α} Calc.	C_{L_α} Test	• Percent Error
29	WB	4.00	.580	.517	.600	48.6	7.7	.139	.06	Round	.8	2.5 to 3.0	.0755	.0750	0.7
↓	↓	↓	↓	↓	↓	↓	↓	↓	↓	↓	.85	↓	.0773	.0830	−6.9
↓	↓	↓	↓	↓	↓	↓	↓	↓	↓	↓	.9	↓	.0845	.0870	−2.9
30	WB	2.91	.333	.500	.500	57.01	61.7	.139	.04-.03	Round	.6	2.2 to 3.5	.0486	.0490	−0.8
↓	↓	↓	↓	↓	↓	↓	↓	↓	↓	↓	.8	↓	.0536	.0490	9.4
↓	↓	↓	↓	↓	↓	↓	↓	↓	↓	↓	.9	↓	.0587	.0520	12.9
31	WB	3.00	1.0	.075	.549	60	60	.109	.0[illegible]	Round	.18	2.24	.0454	.0455	−0.2
↓	WB	2.98	.455	.654	.583	59	48.5	.097	.06	Round	.18	2.56	.0464	.0460	0.9
32[a]	WB	2.91	.641	.625	.600	53.13	32.18	.147	.06-.03	Round	.6	1.5	.0582	.0590	−1.4
↓	↓	↓	↓	↓	↓	↓	↓	↓	↓	↓	.8	↓	.0657	.0670	−1.9
↓	↓	↓	↓	↓	↓	↓	↓	↓	↓	↓	.9	↓	.0728	.0740	−1.6
↓	WB	2.91	.641	.625	.600	53.13	43.22	.147	.06-.03	Round	.6	1.5	.0565	.0580	−2.6
↓	↓	↓	↓	↓	↓	↓	↓	↓	↓	↓	.8	↓	.0600	.0610	−1.6
↓	↓	↓	↓	↓	↓	↓	↓	↓	↓	↓	.9	↓	.0730	.0660	10.6
33	W	5.20	.339	.268	.379	60.0	25		.045-.06	Round	.13	2.65	.0658	.0632	4.1
34[b]	W	4.18	.531	.686	–	45,30	20		.09	Round	.13	6.0	.0642	.0629	2.1
35[b]	W	5.02	.530	.198	↓	45,30	25		.15	Round	.13	1.9	.0665	.0614	8.3
36[b]	W	6.1	.585	.480	↓	37.03, 28.27	22.63	↓	.105-.09	Round	.550	.6 to 1.0	.0800	.0770	3.9
↓	↓	↓	↓	↓	↓	↓	↓	↓	↓	↓	.602	↓	.0816	.0800	2.0
↓	↓	↓	↓	↓	↓	↓	↓	↓	↓	↓	.649	↓	.0843	.0860	−2.0
↓	↓	↓	↓	↓	↓	↓	↓	↓	↓	↓	.705	↓	.0873	.0910	−4.1
↓	↓	↓	↓	↓	↓	↓	↓	↓	↓	↓	.748	↓	.0907	.0930	−2.5
↓	↓	↓	↓	↓	↓	↓	↓	↓	↓	↓	.777	↓	.0932	.1020	−8.6
↓	↓	↓	↓	↓	↓	↓	↓	↓	↓	↓	.803	↓	.0960	.0945	1.6
↓	↓	↓	↓	↓	↓	↓	↓	↓	↓	↓	.835	↓	.1007	.0960	4.9
37	WBV	8.47	.197	.386	.212	76	16	.062	–	Round	.2	3.6	.0634	(c)	
38	WB	6.18	.294	.463	.308	65	12	.066	.06-.02	Round	.5	.73	.0691		

(a) Notched L.E.
(b) Two breaks in L.E.
(c) This information is classified CONFIDENTIAL.

Average Error = $\frac{\Sigma|\epsilon|}{n}$ = 3.9%

TABLE 4.1.3.2-B
TRANSONIC LIFT-CURVE SLOPES OF STRAIGHT-TAPERED WINGS
DATA SUMMARY AND SUBSTANTIATION

Ref.	Airfoil Section	A	λ	$\Lambda_{c/2}$ (deg)	$R_\ell \times 10^{-6}$	M_{fb}	$(C_{L_\alpha})_{fb}$	M_a	$(C_{L_\alpha})_a$	M_b	$(C_{L_\alpha})_b$	Theoretical (T) Experimental (E)
48	63A010	6	1	0	2.0	.82	6.1	.89	3.2	.96	6.2	T
						.82	6.3	.89	4.1	.95	4.6	E
	63A008	6	1	0	2.0	.84	7.0	.91	5.0	.98	5.9	T
						.84	6.5	.90	5.1	.95	5.5	E
	63A006	6	1	0	2.0	.87	7.9	.94	6.8	1.01	6.9	T
						.87	8.0	.94	6.0	1.01	5.6	E
	63A010	4	1	0	2.0	.84	4.8	.91	3.12	.98	4.08	T
						.84	4.7	.90	3.0	.98	4.2	E
	63A008	4	1	0	2.0	.87	5.4	.94	4.5	1.01	4.5	T
						.86	4.7	.94	4.1	.98	4.7	E
	63A006	4	1	0	2.0	.91	5.9	.98	5.5	1.05	5.1	T
						.94	5.9	.98	5.4	1.05	4.9	E
	63A010	2	1	0	2.0	.98	2.9	1.05	2.9	1.12	2.5	T
						.98	2.7	1.05	2.9			E
	63A008	2	1	0	2.0	1.0	3.1	1.07	3.3	1.17	2.7	T
						1.0	3.4	1.07	3.5			E
	63A006	2	1	0	2.0	1.0	3.3	1.07	3.5	1.14	2.9	T
						1.0	3.2	1.07	3.1			E
	63A010	1	1	0	2.0	1.0	1.4	1.07	1.6*	1.14	1.2	T
						1.0	1.4	1.07	1.5	1.14	1.3*	E
	63A008	1	1	0	2.0	1.0	1.5	1.07	1.7	1.14	1.3	T
						1.0	1.3	1.07	1.5	1.14	1.4	E
	63A006	1	1	0	2.0	1.0	1.6	1.07	1.8	1.14	1.4	T
						1.0	1.3	1.07	1.6	1.14	1.0*	E
49	65A006	4	.6	43.2	.46	.94	4.0	1.01	3.8	1.08	3.5	T
						.94	4.0	1.01	3.9	1.08	3.5	E
	65A006	4	.6	32.5	.46	.93	4.8	1.0	4.4	1.07	4.2	T
						.93	4.8	1.0	4.2	1.07	3.5	E
19	63_1A012	4	.68	43.6	.57	.92	3.6	.99	1.5	1.06	3.0	T
						.92	3.4	.99	2.4	1.1	3.1	E
		6	.56	43.6	.57	.875	4.1	.945	1.4	1.015	3.5	T
						.875	4.7	.995	1.6	1.095	3.3	E
		8	.45	43.6	.57	.875	4.6	.945	1.3	1.015	3.9	T
						.875	4.1	1.0	1.6	1.125	2.9	E
47	63A006	4	0	26.6	2.4	.92	5.2	.99	4.8	1.06	4.5	T
						.92	4.3	.99	4.4	1.06	4.1	E
	63A004	1	.5	33.4	2.9	1.0	1.6	1.07	1.9	1.14	1.5	T
						1.0	1.8	1.07	2.0	1.14	1.9*	E
		1.08	.3	44.0	2.6	1.0	1.7	1.07	1.9	1.14	1.6	T
						1.0	1.9	1.07	1.9	1.14	1.9*	E
		1.67	.2	38.7	2.5	1.0	2.6	1.07	2.9	1.14	2.4	T
						1.0	2.8	1.07	2.9	1.14	2.7*	E
		1.71	.4	26.5	2.7	1.0	2.8	1.07	3.1	1.14	2.6	T
						1.0	2.9	1.07	2.0	1.14	3.0*	E
		2.46	.1	33.5	2.5	1.0	3.7	1.07	3.8	1.14	3.4	T
						1.0	3.7	1.07	3.6	1.14	3.2*	E
		2.67	.2	26.6	2.5	1.0	4.2	1.07	4.1	1.14	3.9	T
						1.0	4.0	1.07	3.9	1.14	3.7*	E

*EXTRAPOLATED VALUES

TABLE 4.1.3.2-C

SUPERSONIC NORMAL-FORCE-CURVE SLOPE OF DOUBLE-DELTA WINGS

DATA SUMMARY AND SUBSTANTIATION

Ref.	Config.	A	λ_i	λ_o	η_B	Λ_{LE_i}	Λ_{LE_o}	$\frac{d}{b}$	$\frac{t}{c}$	LER	M	C_{N_α} Calc.	C_{N_α} Test	% Percent Error
58	WB	3.15	.510	.295	.400	64.07	51.63	.125	.06	Sharp	1.61	.0477	.0462	3.2
		2.86	.407			70.67					1.61	.0442	.0437	1.1
											2.01	.0366	.0355	3.1
		2.86	.407			64.07					1.61	.0458	.0450	1.8
		2.62	.339			70.67					1.61	.0421	.0416	1.2
		2.62	.339			64.07					1.61	.0443	.0431	2.8
		2.42	.292			70.67					1.61	.0411	.0402	2.2
											2.01	.0339	.0351	− 3.4
59	WB	2.01	.416	.302	.313	78	53.3	.127	.03	Sharp[a]	1.10	.0523	.0540	− 3.1
											1.40	.0431	.0440	− 2.0
											2.00	.0332	.0320	3.8
											2.94	.0242	.0230	5.2
		1.96	.295	.344	.405	78	48.5	.127	.03		1.10	.0487	.0500	− 2.6
											1.40	.0405	.0410	− 1.2
											1.98	.0313	.0270	15.9
											2.94	.0227	.0221	2.7
		1.93	.180	.454	.498	78	38.1	.127	.03		1.10	.0476	.0469	1.5
											1.40	.0380	.0363	4.7
											1.98	.0276	.0259	6.6
											2.94	.0205	.0199	3.0
		1.30	.196	0	.414	82	60	.147	.03		1.10	.0322	.0320	0.6
											1.40	.0299	.0280	6.8
											1.98	.0249	.0230	8.3
											2.94	.0194	.0170	14.1
		1.33	.302	.163	.403	82	60	.147	.03	Sharp	1.10	.0350	.0390	−10.3
											1.40	.0323	.0330	− 2.1
											1.98	.0282	.0270	4.4
											2.94	.0207	.0200	3.5
		1.55	.301	0	.400	82	59	.144	.03		1.10	.0382	.0410	− 6.8
											1.40	.0336	.0350	− 4.0
											1.98	.0280	.0280	0
											2.94	.0207	.0210	− 1.4
		1.72	.358	0	.414	77.4	59	.127	.03		1.10	.0421	.0460	− 8.5
											1.39	.0359	.0390	− 7.9
60	W	2.25	.29	0	.415	78	60	− −	.04	Round	3.0	.0221	.0200	10.5
61	W	2.39	.376	0	.126	82.9	50	− −	.07−.03	i-Round	1.2	.0514	.0506	1.6
										o-Sharp	2.0	.0315	.0310	1.6
											3.0	.0216	.0228	− 5.3
											4.0	.0166	.0173	− 4.0

TABLE 4.1.3.2-C (CONTD)

Ref.	Config.	A	λ_i	λ_o	η_B	Λ_{LE_i}	Λ_{LE_o}	$\frac{d}{b}$	$\frac{t}{c}$	LER	M	C_{N_α} Calc.	C_{N_α} Test	e Percent Error
62	WB	2.35	.229	.625	.700	61.7	30	.150	.06	Round[b]		.0520	.0515	1.0
↓	↓	↓	↓	↓	↓	↓	↓	↓	↓	↓	2.01	.0366	.0365	0.3
63	WB	3.15	.508	.295	.400	49.59	20.85	.125	.06	Sharp	2.01	.0363	.0382	− 5.0
		2.86	.407			63.07					2.01	.0346	.0360	− 3.9
		2.62	.339			70.10					2.01	.0328	.0332	− 1.2
		↓	↓			↓					1.61	.0428	.0440	− 2.7
		2.86	.407			49.59					2.01	.0355	.0369	− 3.8
		2.62	.339			63.07					2.01	.0337	.0348	− 3.2
		2.42	.292			70.10					2.01	.0320	.0320	0
		↓	↓			↓					1.61	.0406	.0423	− 4.0
64	WB	2.43	.448	0	.259	78	60	.077	.018–.040	Sharp	2.98	.0232	.0224	3.6
											2.59	.0262	.0254	3.1
											2.20	.0315	.0304	3.6
											1.53	.0402	.0382	5.2
											1.17	.0451	.0459	− 1.7
		1.52	.479	.102	.216	83.35	62	.095	.018–.029		2.98	.0220	.0210	4.8
											2.81	.0231	.0231	0
											2.20	.0280	.0289	− 3.1
											2.59	.0242	.0238	1.7
											1.59	.0344	.0346	− 0.6
		1.26	.627	0	.181	83.0	70	.100	.02		2.98	.0219	.0216	1.4
		↓	↓	↓	↓	↓	↓	↓	↓		2.98	.0219	.0208	5.3
		1.06	.627	.102	.197	83.0	70	.092	.02		2.98	.0201	.0209	− 3.8
											2.98	.0201	.0207	− 2.9
											2.59	.0220	.0228	− 3.5
											2.59	.0220	.0226	− 2.7

(a) These models had theoretically round L.E.'s inboard but were analyzed as sharp due to small size of model and small t/c.

(b) This model had a flat plate wing with a blunt T.E.

$$\text{Average Error} = \frac{\Sigma \mid e \mid}{n} = 3.7\%$$

TABLE 4.1.3.2-D
SUPERSONIC NORMAL-FORCE-CURVE SLOPE OF CRANKED WINGS
DATA SUMMARY AND SUBSTANTIATION

Ref.	Config.	A	λ_i	λ_o	η_B	Λ_{LE_i}	Λ_{LE_o}	$\frac{d}{b}$	$\frac{t}{c}$	LER	M	C_{N_α} Calc.	C_{N_α} Test	e Percent Error
30	WB	2.91	.353	.500	.500	67.01	61.7	.139	.04-.03	Round	1.41	.0456	.0433	5.3
↓	↓	↓	↓	↓	↓	↓	↓	↓	↓	↓	2.01	.0401	0355	13.0
32	WB	2.91	.641	.625	.600	53.13	32.16	.147	.06-.03	Round	1.4	.0552	.0563	− 2.0
↓	↓	↓	↓	↓	↓	↓	43.22	↓	↓	↓		.0568	.0563	0.9
66	WBVN	3.59	.409	.650	.421	70	50	.186	?	Round	2.2	.0375	.0390	−3.8
67	WB	4.43	.389	.464	.404	65	45	.079	.06-.02	Round	2.60	.0299	(a)	
↓	↓	↓	↓	↓	↓	↓	↓	↓	↓	↓	2.96	.0260		
											3.95	.0201		
38	WB	4.43	.389	.464	.404	65	45	.079	.06-.02	Round	1.20	.0660		
↓	↓	↓	↓	↓	↓	↓	↓	↓	↓	↓	2.30	.0343		
											2.60	.0317		
											3.00	.0267		
											3.50	.0212		
65	WBVN	3.80	.374	.289	.297	74.17	50	.211	.08	Round	1.70	.0407	.0390	4.4
↓	↓	↓	↓	↓	↓	↓	↓	↓	↓	↓	2.00	.0345	.0334	3.3
											2.20	.0310	.0324	−4.3
											2.50	.0274	.0289	−5.2

(a) This information is classified CONFIDENTIAL.

Average Error = $\frac{\Sigma \mid e \mid}{n}$ = 4.7%

TABLE 4.1.3.2-E
SUPERSONIC NORMAL-FORCE-CURVE SLOPE OF CURVED (GOTHIC AND OGEE) WINGS
DATA SUMMARY AND SUBSTANTIATION

Ref.	Config.	Planform	A	$\frac{b_W}{2\ell}$	p	$\frac{d}{b}$	$\frac{t}{c}$ (root)	M	C_{N_α} Calc.	C_{N_α} Test	e Percent Error
79	W_1	Ogee	.75	.141	.375	–	.008[a]	1.41	.0180	.0230	−21.7
								1.61	.0178	.0211	−15.6
								1.91	.0175	.0204	−14.2
	W_4		1.00	.188	.375	–	.010[a]	1.41	.0237	.0283	−16.3
								1.61	.0232	.0267	−13.1
								1.91	.0224	.0248	− 9.7
	W_7		1.33	.25	.375	–	.012[a]	1.41	.0305	.0354	−13.8
								1.61	.0297	.0332	−10.5
								1.91	.0275	.0294	− 6.5
	W_{12}		1.00	.25	.500	–	.014[a]	1.41	.0283	.0286	− 1.0
								1.61	.0272	.0262	3.8
								1.91	.0253	.0252	0.4
	W_{32}		1.11	.25	.450	–	.013[a]	1.41	.0293	.0288	1.7
								1.61	.0282	.0270	4.4
								1.91	.0262	.0247	6.1
	W_{10}		.75	.188	.500	–	.012[a]	1.41	.0218	.0219	− 0.5
								1.61	.0213	.0213	0
								1.91	.0205	.0204	0.5
	W_{11}		.75	.25	.667	–	.016[a]	1.41	.0255	.0265	− 3.8
								1.61	.0245	.0253	− 3.2
								1.91	.0227	.0241	− 5.8
	W_{13}		1.00	.25	.500	–	.014[a]	1.41	.0283	.0289	− 2.1
								1.61	.0272	.0265	2.6
								1.91	.0253	.0260	− 2.7
	W_3	Gothic	.75	.25	.667	–	.016[a]	1.41	.0255	.0234	9.0
								1.61	.0245	.0234	4.7
								1.91	.0227	.0229	− 0.9
	W_6		1.00	.333	.667	–	.018[a]	1.41	.0324	.0315	2.9
								1.61	.0300	.0309	− 2.9
								1.91	.0266	.0288	− 7.7
	W_9		1.33	.444	.667	–	.021[a]	1.41	.0392	.0388	1.0
								1.61	.0349	.0373	− 6.4
								1.91	.0307	.0335	− 8.4
	W_{14}		.857	.25	.583	–	.015[a]	1.41	.0268	.0258	3.9
								1.61	.0257	.0243	5.8
								1.91	.0239	.0239	0
	W_{20}		.938	.25	.533	–	.015[a]	1.41	.0277	.0259	6.9
								1.61	.0266	.0254	4.7
								1.91	.0247	.0251	− 1.6
	W_{21}		1.00	.25	.500	–	.015[a]	1.41	.0283	.0289	− 2.1
								1.61	.0272	.0263	3.4
								1.91	.0253	.0261	− 3.1
80	WB	Ogee	1.2	.300	.500	.100	.05	1.00	.0349	.0364	− 4.1
								1.25	.0343	.0351	− 2.3
								1.32	.0338	.0332	1.8
								1.42	.0329	.0327	0.6
								1.61	.0310	.0309	0.3
								1.82	.0292	.0285	1.5

TABLE 4.1.3.2-E (CONTD)

Ref.	Config.	Planform	A	$\frac{b_W}{2l}$	p	$\frac{d}{b}$	$\frac{t}{c}$ (root)	M	C_{N_α} Calc.	C_{N_α} Test	e Percent Error
81	WB	Ogee	2.0	.540	.540	.08	.03	1.00	.0612	.0570	7.4
								1.05	.0614	.0595	3.2
								1.10	.0594	.0610	− 2.6
								1.20	.0553	.0622	−11.1
								1.60	.0418	.0535	−21.9
								1.80	.0378	.0475	−20.4
								2.00	.0347	.0445	−22.0
								2.20	.0318	.0360	−11.7
								2.35	.0304	.0350	−13.1
82	WB	Ogee	1.98	.35	.353	.127	.02	1.40	.0413	.0466	−11.4
								1.98	.0328	.0358	− 8.4
								2.94	.0260	.0238	5.0
85	WB	Ogee	.924	.208	.45	.112	.059	1.4	.0248	.0255	− 2.7
								1.8	.0234	.0227	3.1
								2.2	.0215	.0210	2.4
								2.4	.0207	.0197	5.1
								2.8	.0191	.0182	4.9

(a) Flat Plate Models

Average Error = $\frac{\Sigma|e|}{n}$ = 6.2%

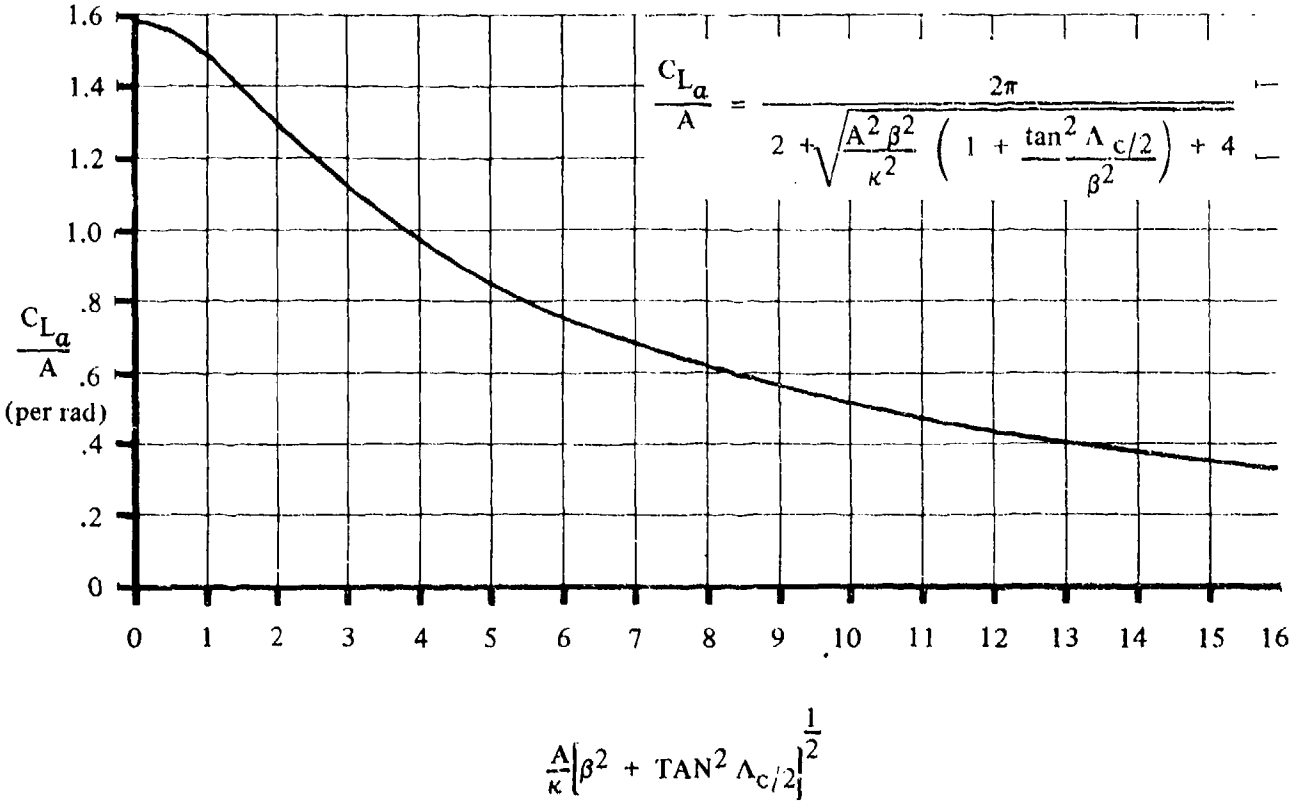

FIGURE 4.1.3.2-49 SUBSONIC WING LIFT-CURVE SLOPE

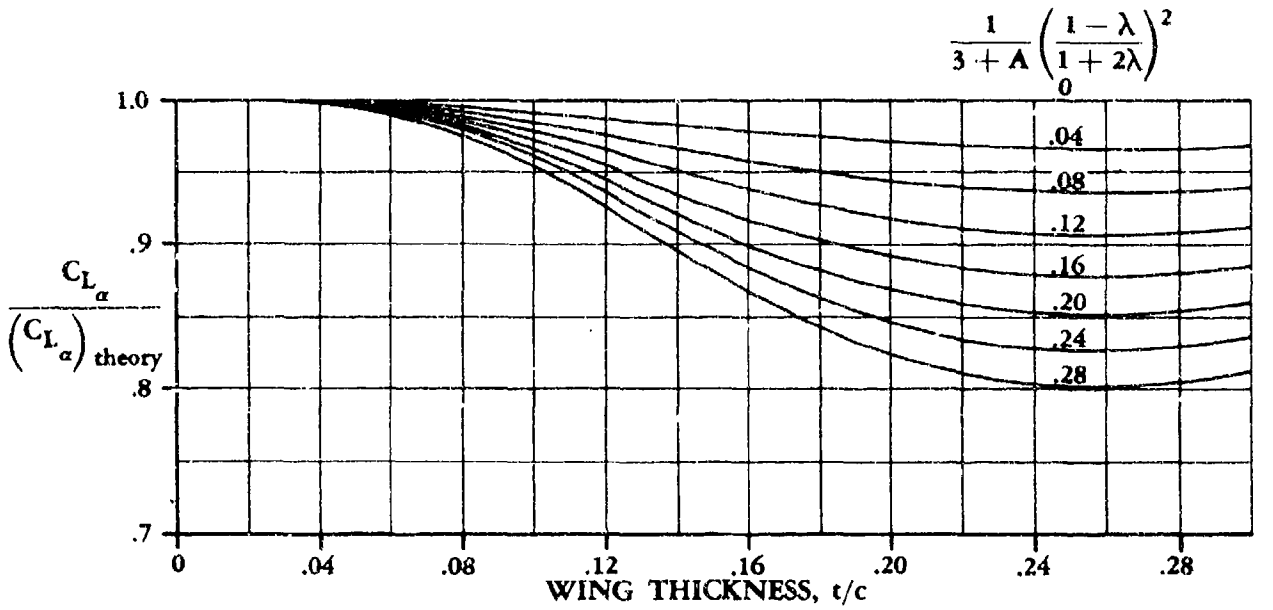

FIGURE 4.1.3.2-50a WING LIFT-CURVE-SLOPE THICKNESS CORRECTION FACTOR

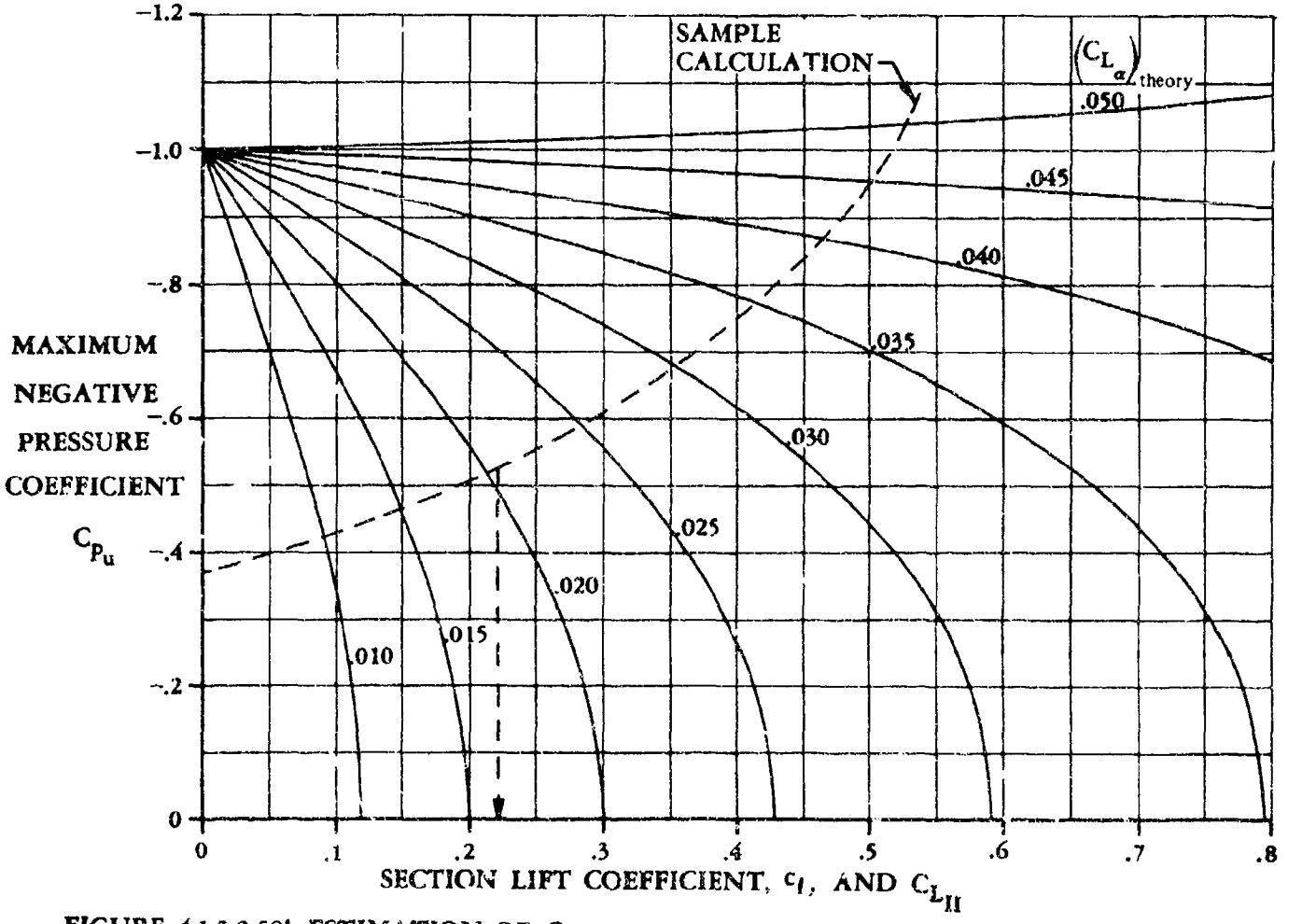

FIGURE 4.1.3.2-50b ESTIMATION OF $C_{L_{II}}$

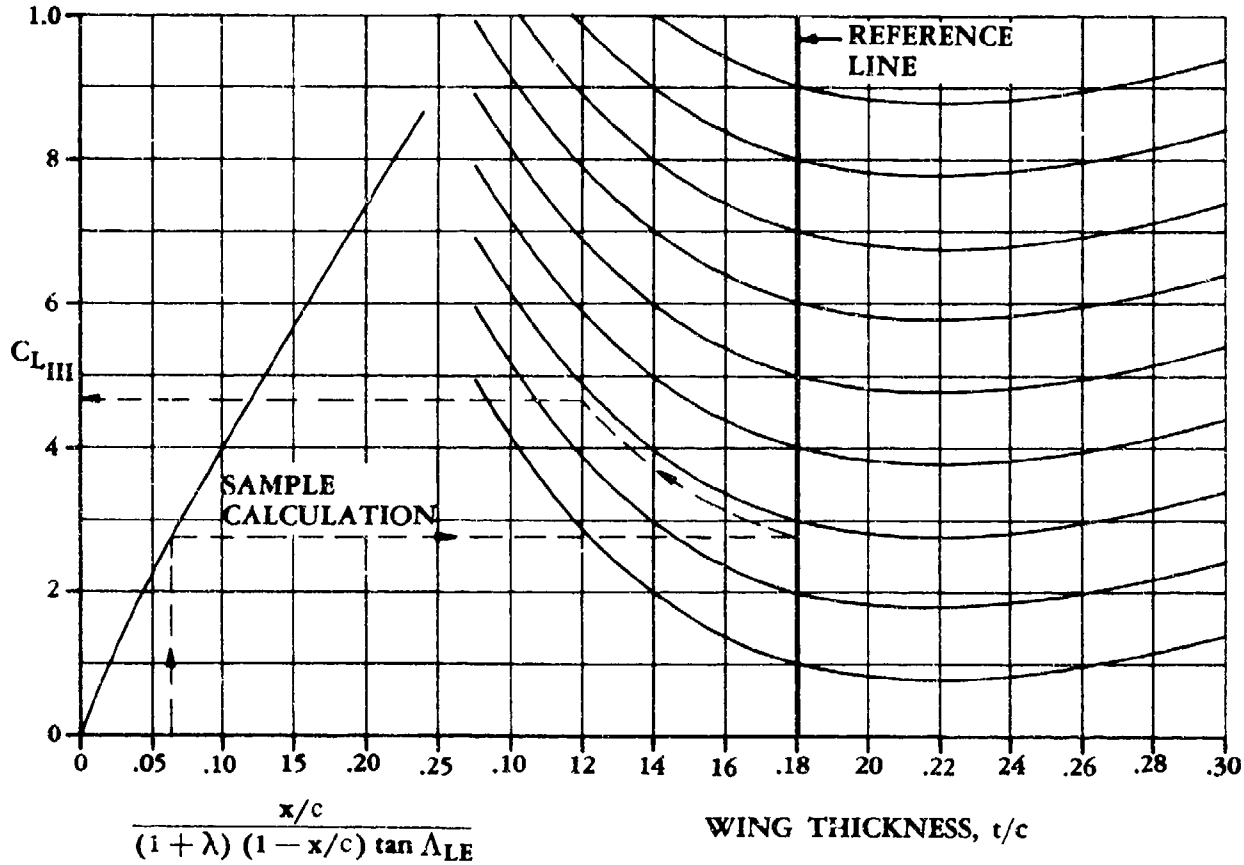

FIGURE 4.1.3.2-51 ESTIMATION OF $C_{L_{III}}$

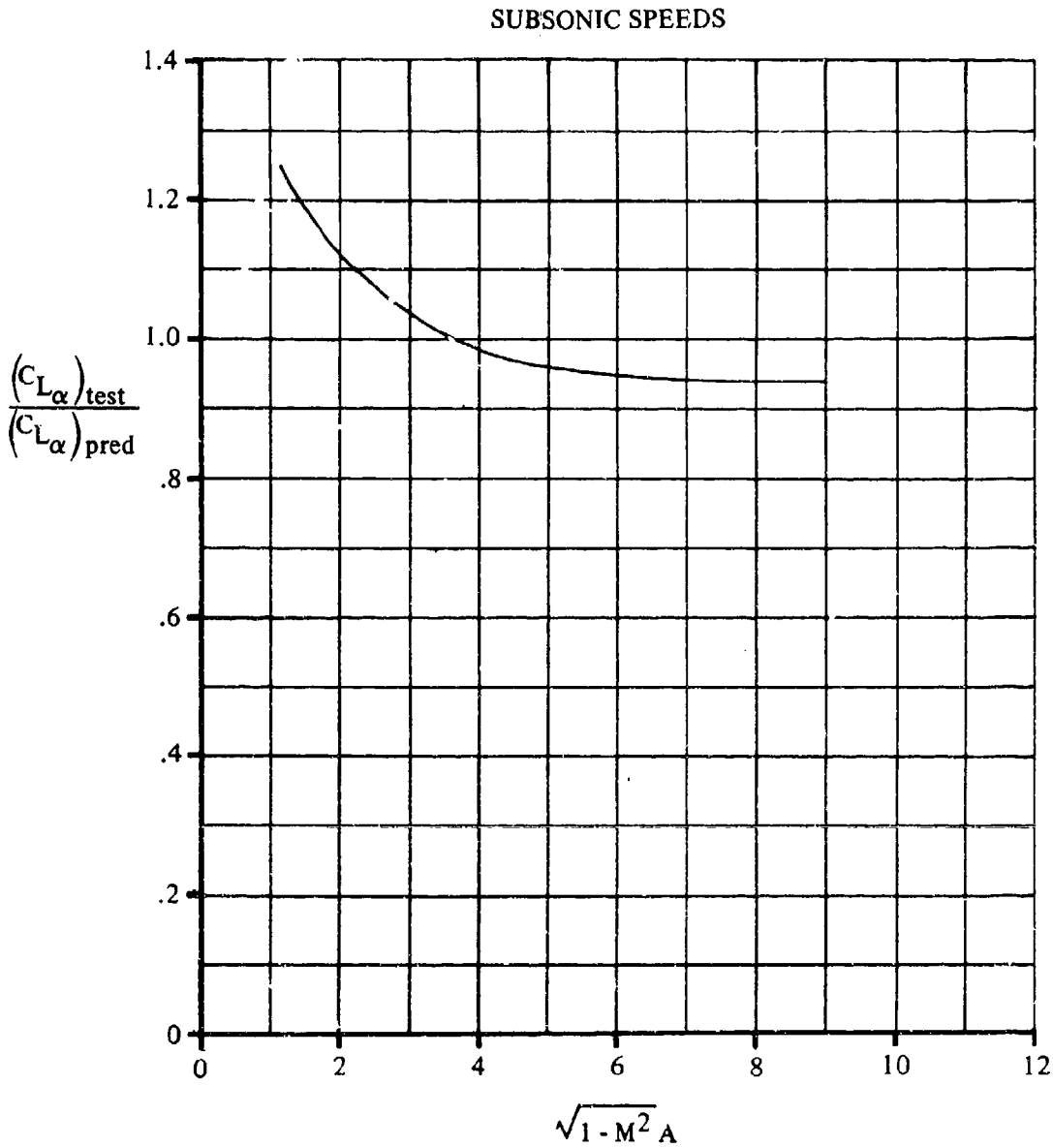

FIGURE 4.1.3.2-52 CORRELATION OF SUBSONIC LIFT-CURVE SLOPE FOR CRANKED PLANFORMS HAVING ROUND-NOSED AIRFOILS

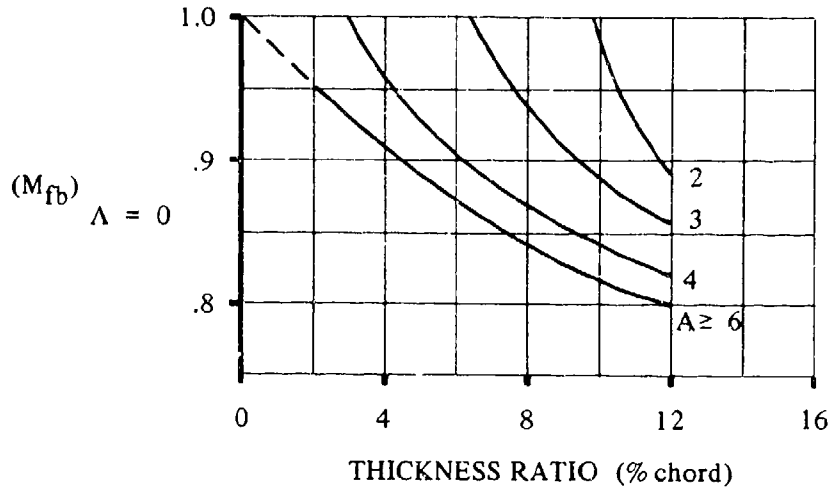

FIGURE 4.1.3.2-53a TRANSONIC FORCE-BREAK MACH NUMBER FOR ZERO SWEEP

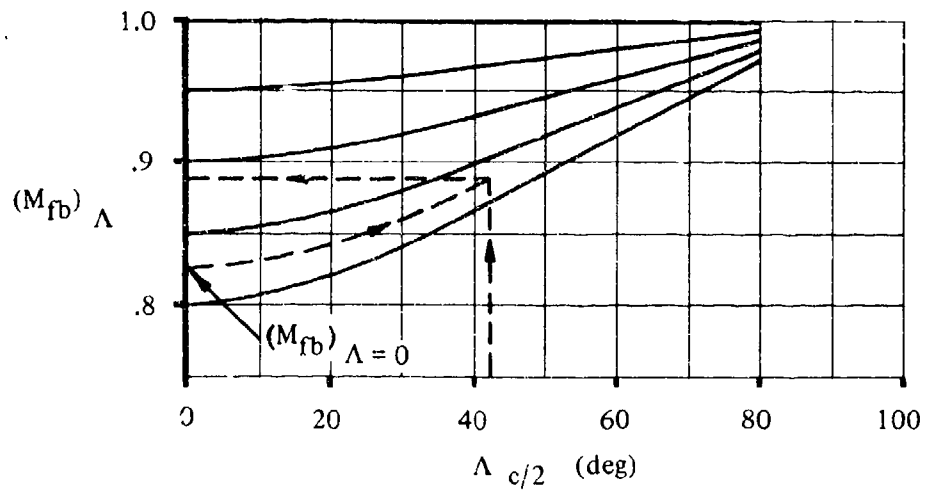

FIGURE 4.1.3.2-53b TRANSONIC SWEEP CORRECTION FOR FORCE-BREAK MACH NUMBER

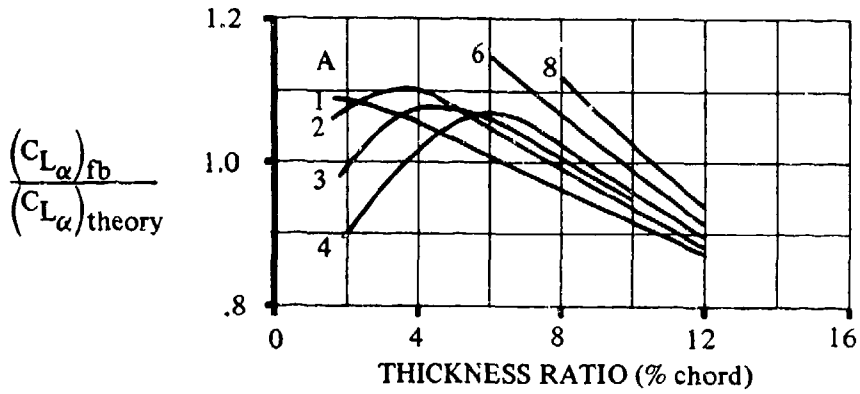

FIGURE 4.1.3.2-54a CORRECTION TO LIFT-CURVE SLOPE AT FORCE-BREAK MACH NUMBER

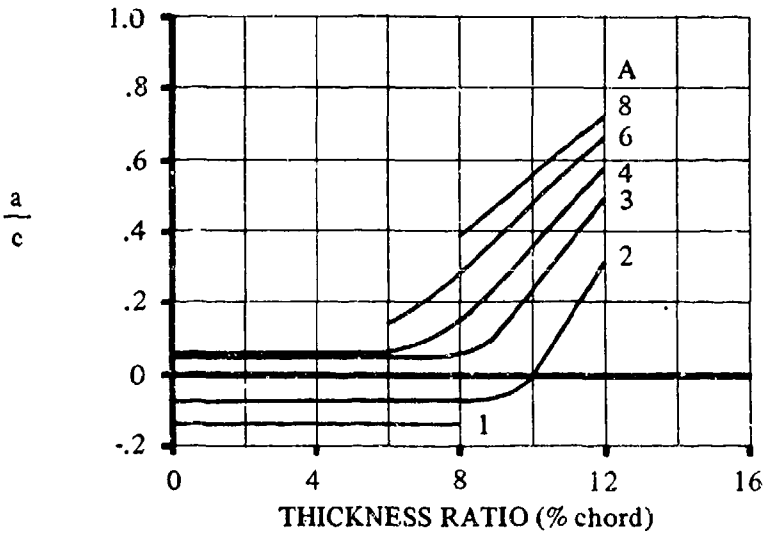

FIGURE 4.1.3.2-54b CHART FOR DETERMINING LIFT-CURVE SLOPE AT M_a

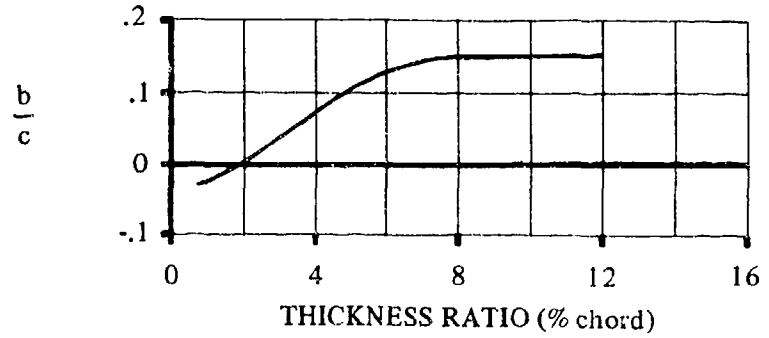

FIGURE 4.1.3.2-54c CHART FOR DETERMINING LIFT-CURVE SLOPE AT M_b

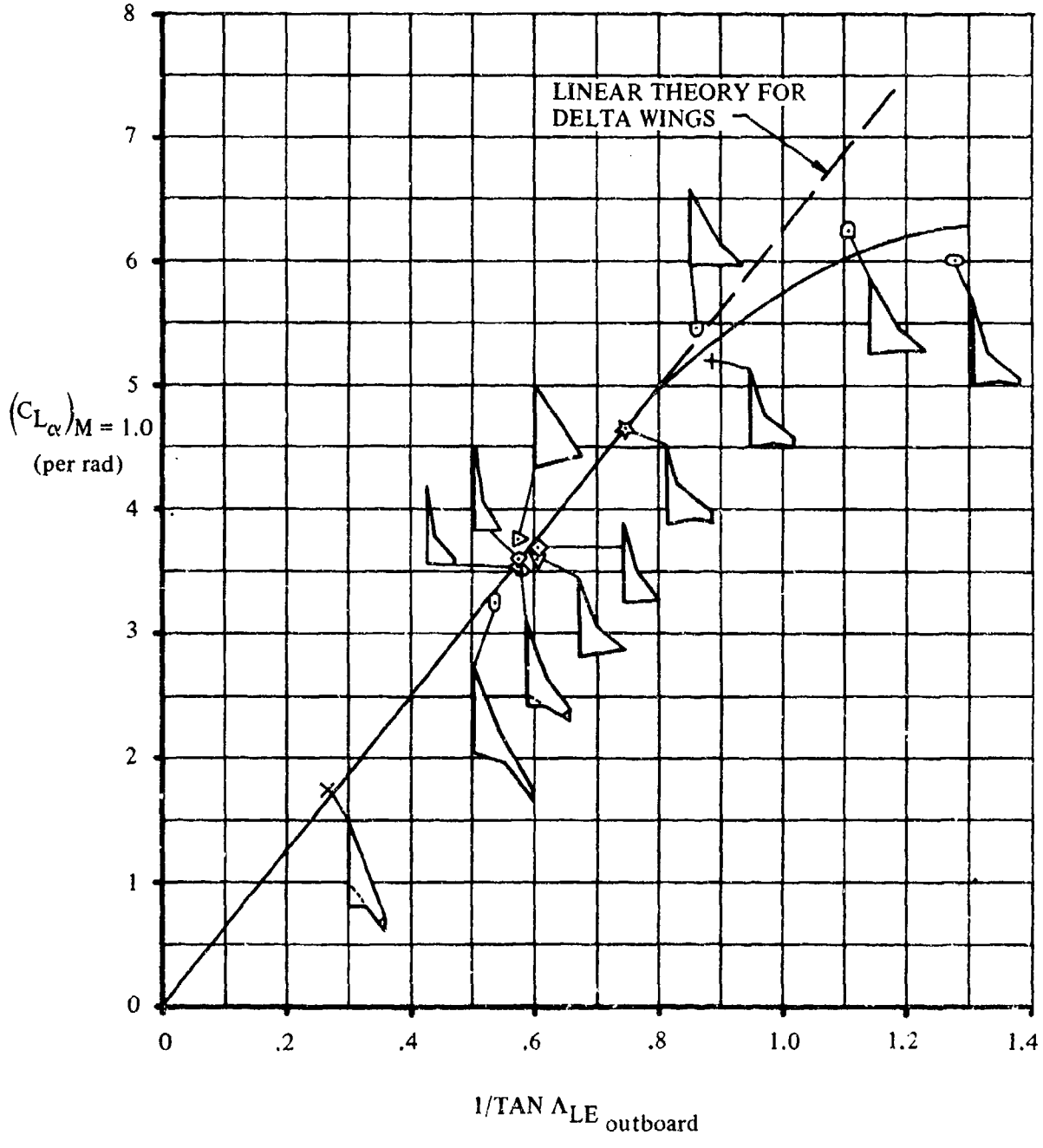

FIGURE 4.1.3.2-55 EMPIRICAL CORRELATION OF LIFT-CURVE SLOPE OF COMPOSITE PLANFORMS AT MACH 1

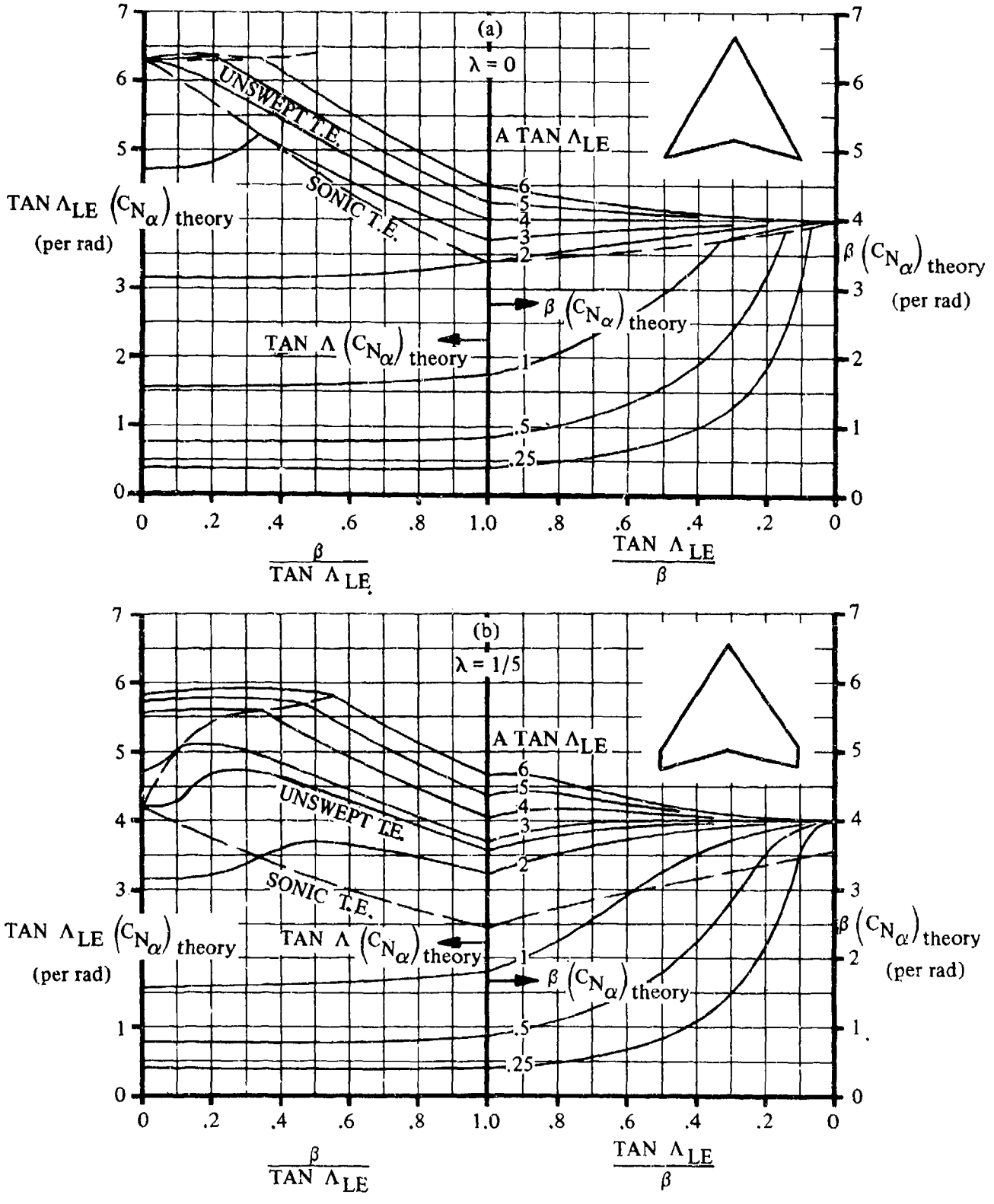

FIGURE 4.1.3.2-56 WING SUPERSONIC NORMAL-FORCE-CURVE SLOPE

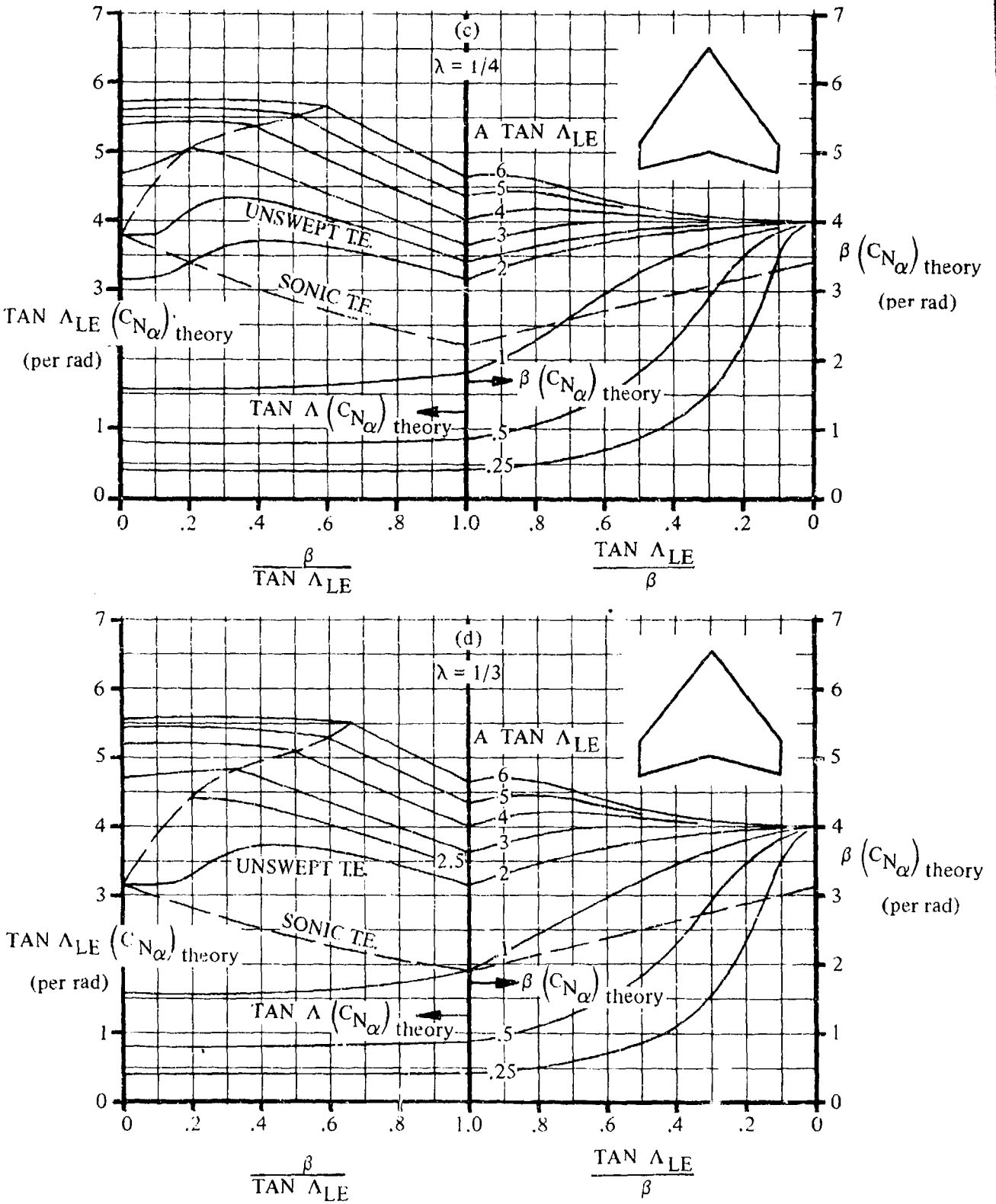

FIGURE 4.1.3.2-56 (CONTD)

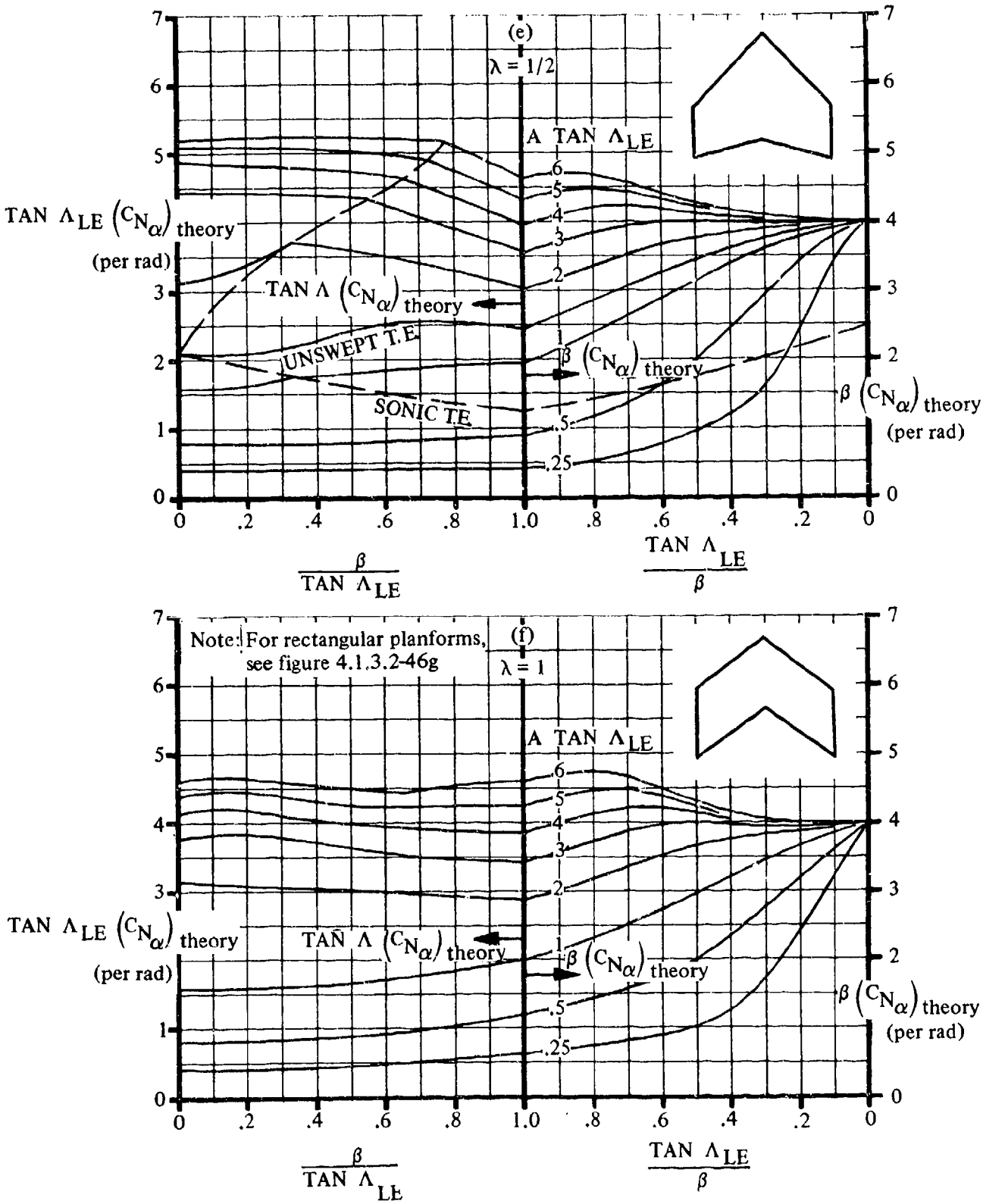

FIGURE 4.1.3.2-56 (CONTD)

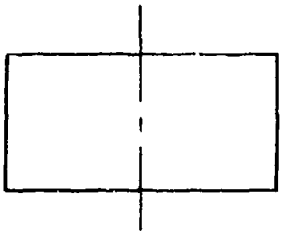

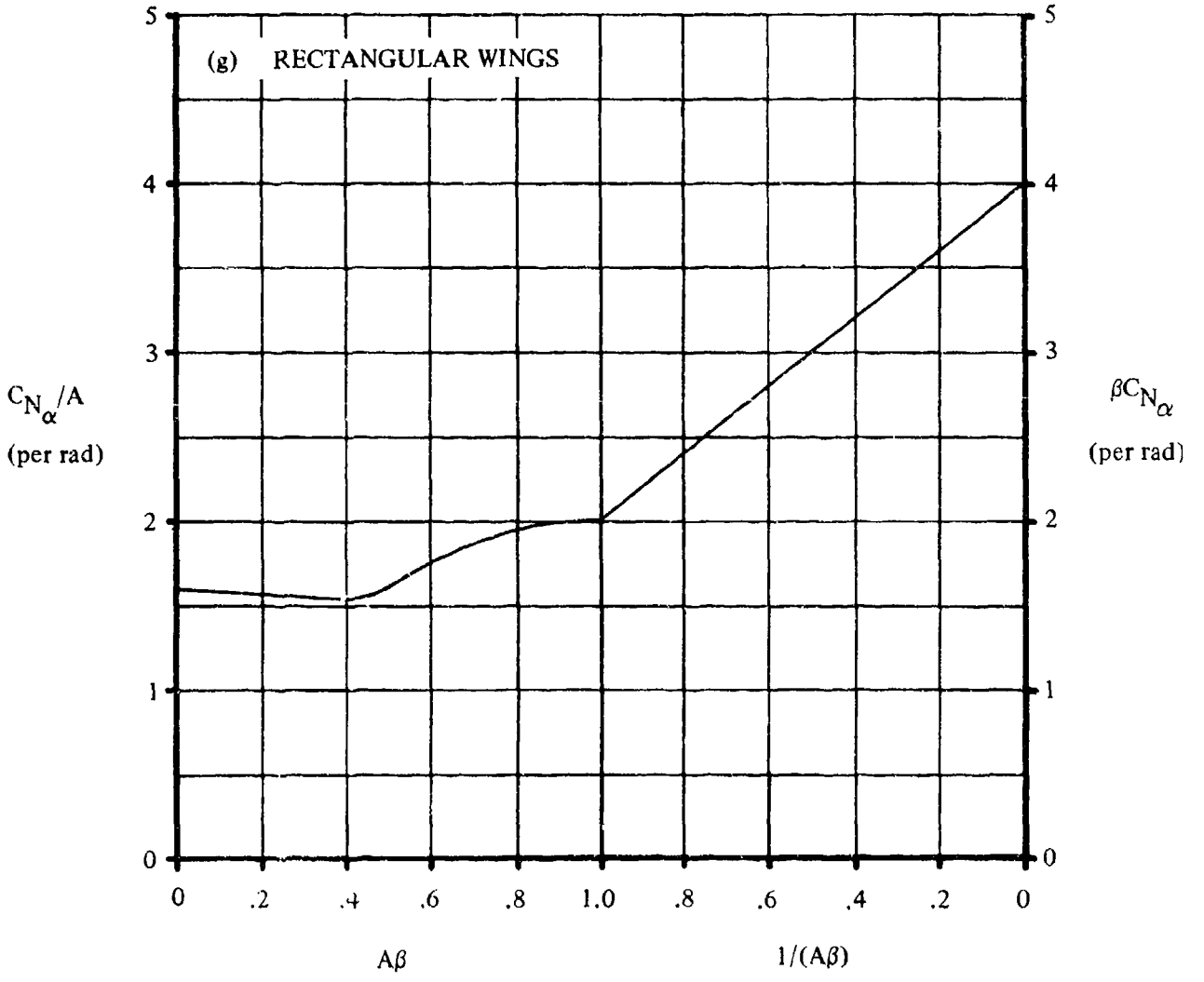

FIGURE 4.1.3.2-56 (CONTD)

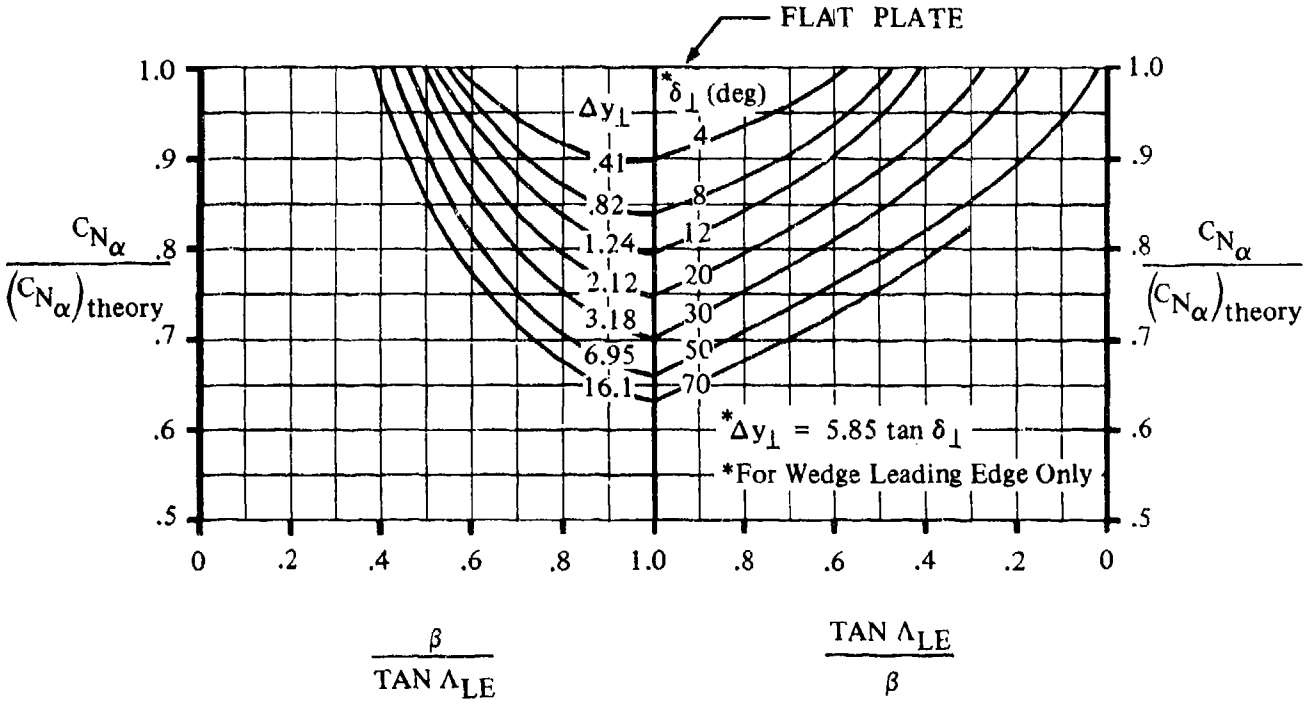

FIGURE 4.1.3.2-60 SUPERSONIC WING LIFT-CURVE-SLOPE CORRECTION FACTOR FOR SONIC-LEADING-EDGE REGION

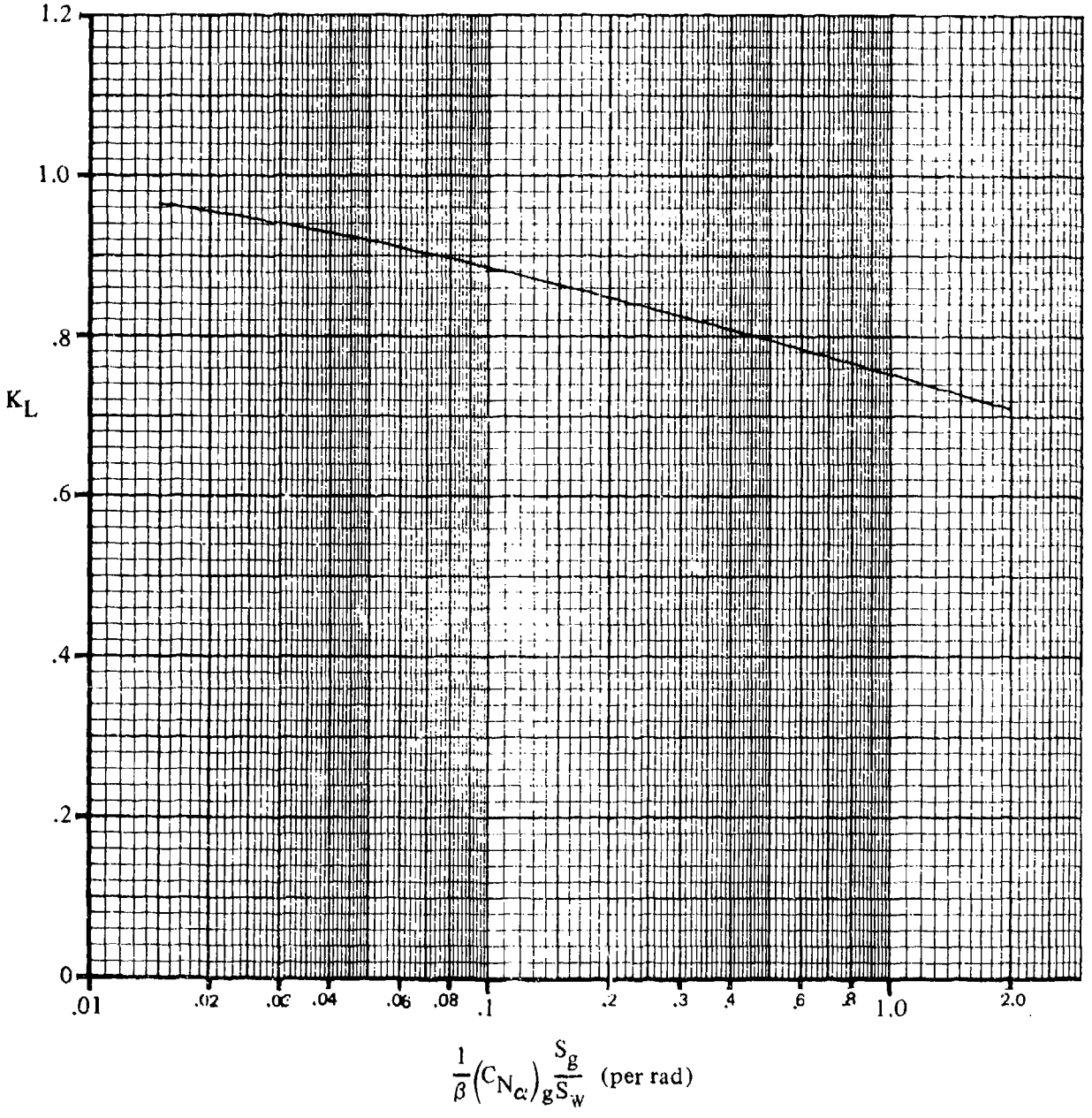

FIGURE 4.1.3.2-61 LIFT-INTERFERENCE FACTOR FOR NORMAL-FORCE-CURVE SLOPE AT SUPERSONIC SPEEDS

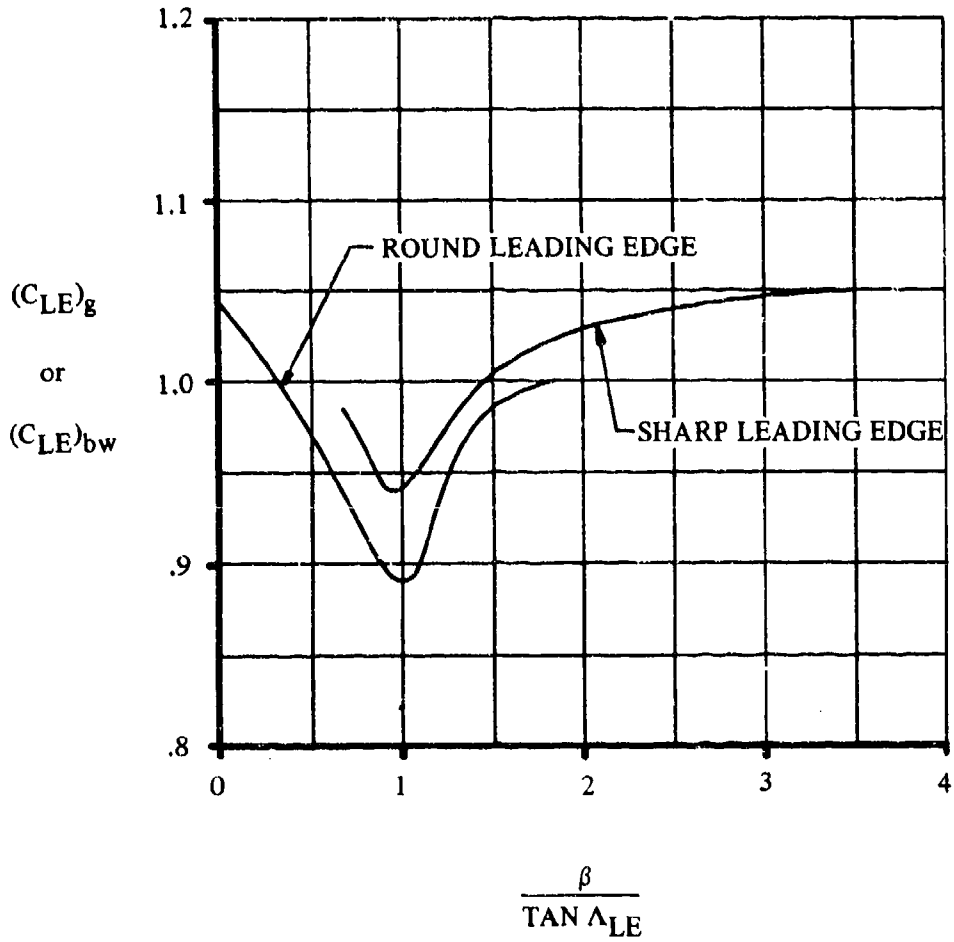

FIGURE 4.1.3.2-62 LEADING-EDGE-EFFECT FACTORS $(C_{LE})_g$ AND $(C_{LE})_{bw}$ FOR NORMAL-FORCE-CURVE SLOPE AT SUPERSONIC SPEEDS

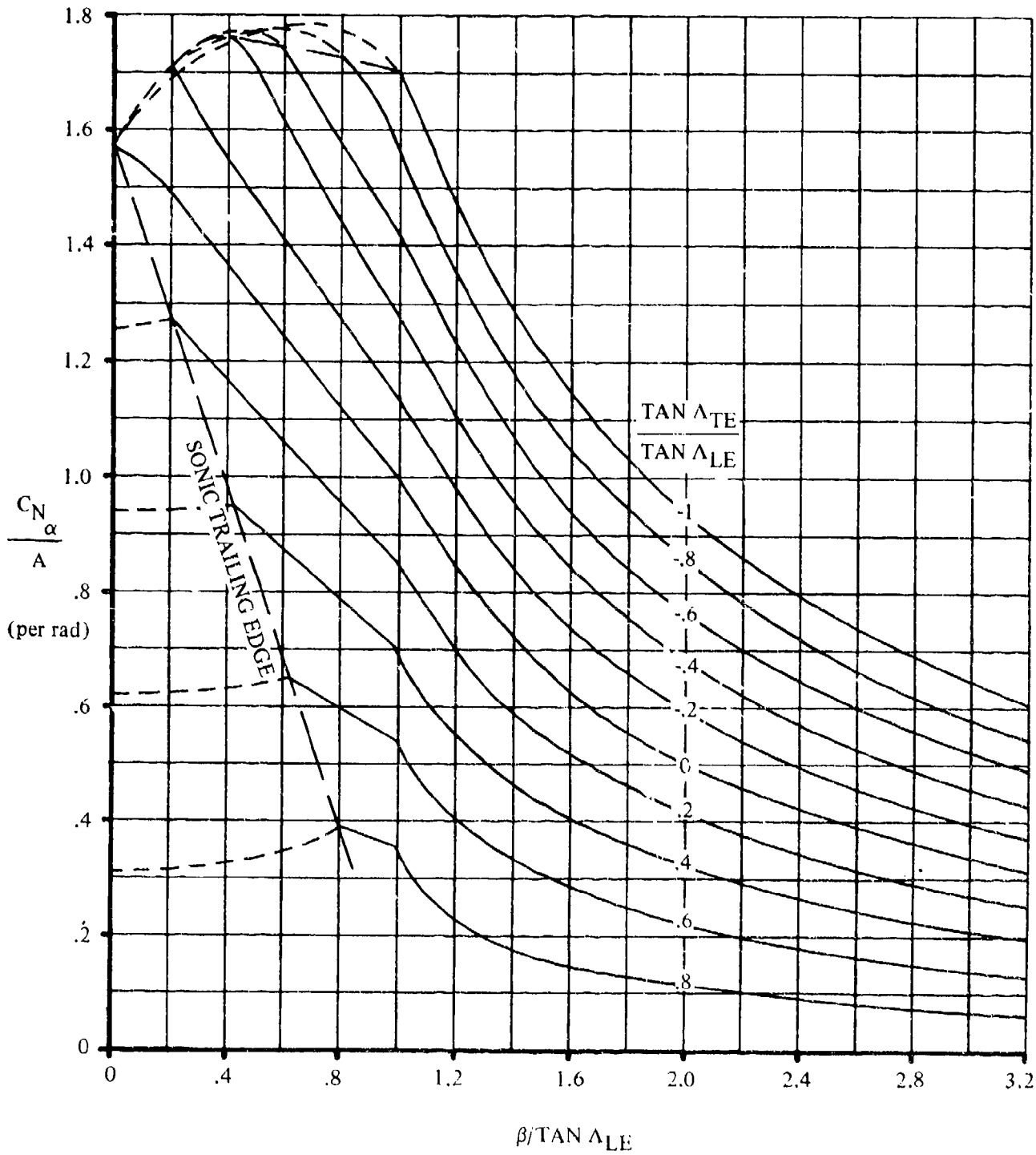

FIGURE 4.1.3.2-63 WING SUPERSONIC NORMAL-FORCE-CURVE SLOPE, $\lambda = 0$

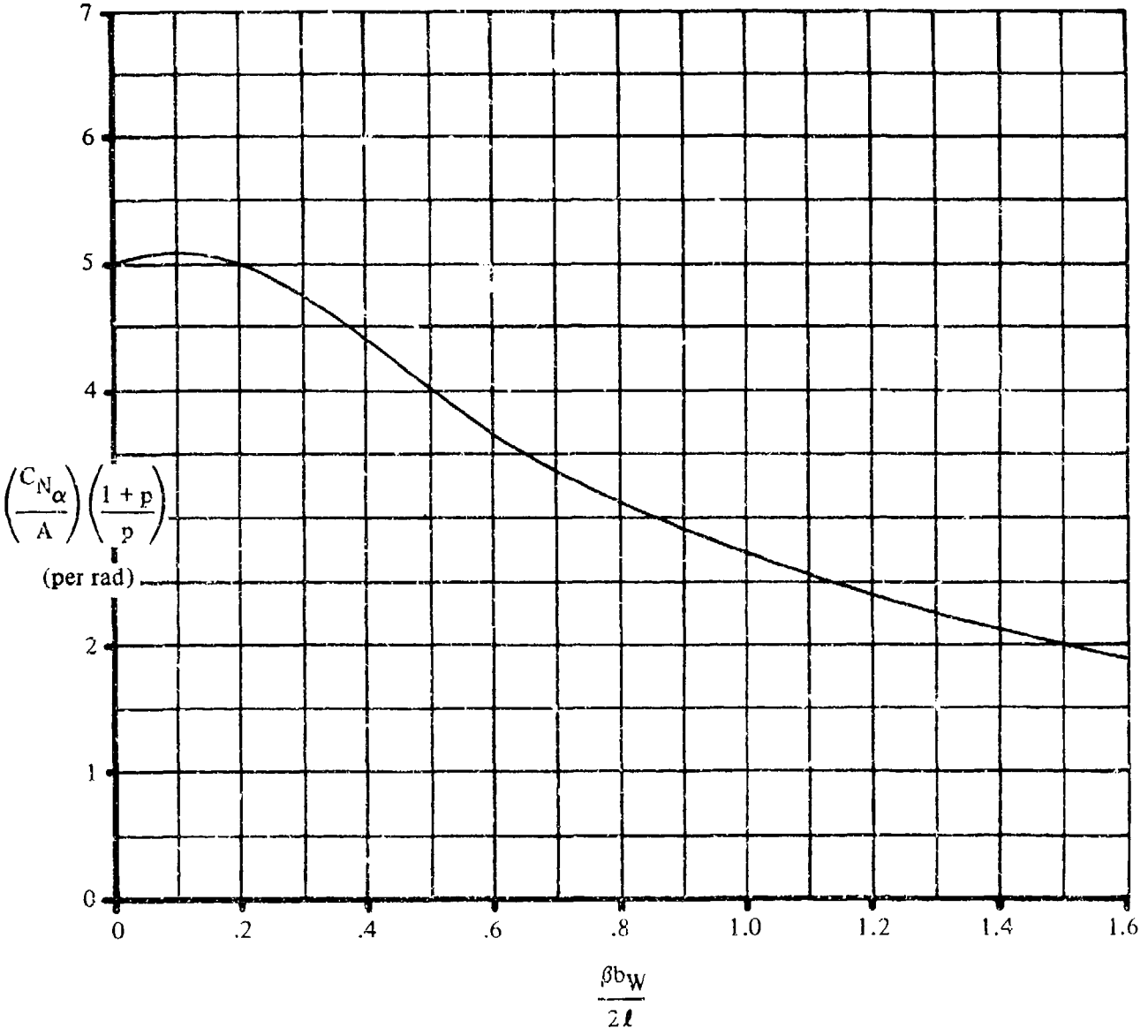

FIGURE 4.1.3.2-64 CORRELATION OF NORMAL-FORCE-CURVE SLOPE AT SUPERSONIC SPEEDS FOR GOTHIC AND OGEE PLANFORMS HAVING SHARP-NOSED AIRFOILS

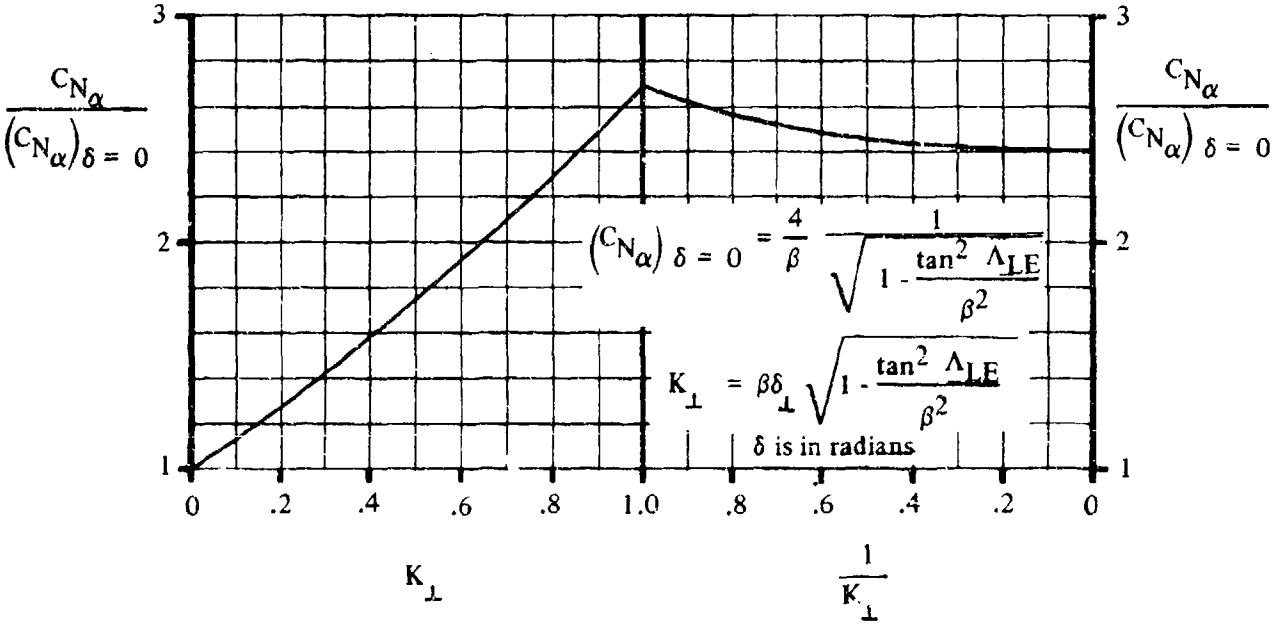

FIGURE 4.1.3.2-65 NORMAL-FORCE-CURVE SLOPE FOR THIN-WEDGE PROFILES FROM TWO-DIMENSIONAL SUPERSONIC-HYPERSONIC SLENDER-AIRFOIL THEORY

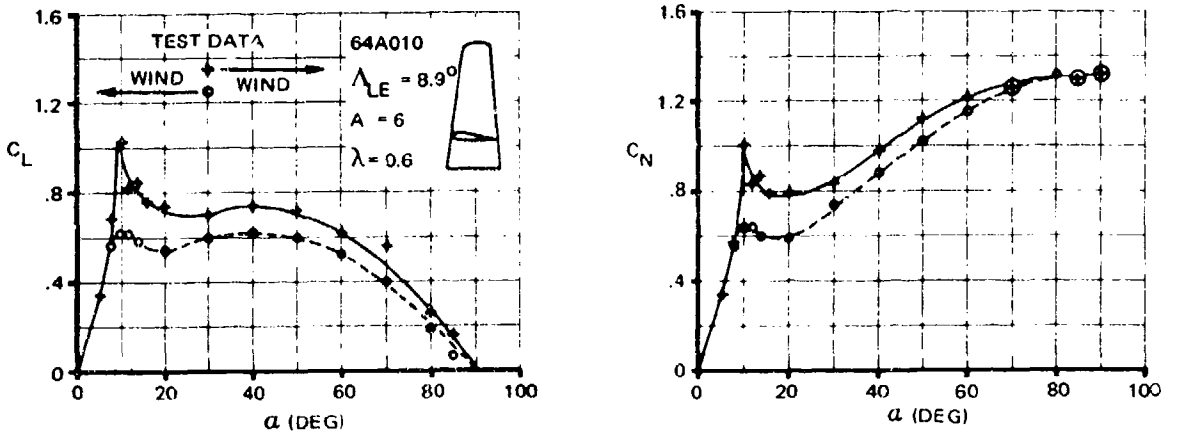

SKETCH (a)

The aspect-ratio-6 wing with the 64A010 airfoil reaches a maximum lift coefficient at a relatively low angle of attack. Following this, the lift drops abruptly and then stabilizes at nearly constant level for approximately the next 30° of angle of attack.

For the same wing with a sharp leading edge (represented by the wing in reverse flow) the maximum lift coefficient is not nearly as large as in the previous case, but the drop subsequent to the maximum lift is also much less. The result is that for angles of attack beyond stall, the lift on the blunt wing is not greatly different from the lift on the sharp wing.

This effect is accounted for in this section by making the drop in lift following maximum lift reflect the difference between the actual maximum lift and the maximum lift determined by the low-aspect-ratio method of Section 4.1.3.4. (This latter method gives results corresponding to those for a thin airfoil.)

For very low-aspect-ratio rectangular wings experimental data (reference 2) occasionally show a hysteresis in the normal-force curve near maximum lift, with different lift-curve shapes, depending on whether the angle of attack is increasing or decreasing. For these wings the results of this section must be applied with caution, since they do not reflect this hysteresis.

Reynolds number was not accounted for in the analysis of this method. There is a Reynolds-number effect on the lift-curve shape for the thicker wings, but within the Reynolds-number limitations listed on the charts the values predicted are of sufficient accuracy for most purposes.

DATCOM METHOD

The general method for estimating the subsonic normal force on conventional, straight-tapered uncambered wings for angles of attack from 0 to 90° is outlined in the following steps:

Step 1. Subsonic Normal Force at Angles of Attack Below the Stall.

The basic equation is

$$\frac{C_L}{\cos \alpha} = C_N' = C_{N_\alpha} \frac{\sin 2\alpha}{2} + C_{N_{\alpha\alpha}} \sin \alpha \, | \sin \alpha | \qquad 4.1.3.3\text{-a}$$

The normal-force-curve slope C_{N_α} is obtained from Section 4.1.3.2.* For high-aspect-ratio

*C_{L_α} is used for C_{N_α}

wings, the lift curve is based on the appropriate section lift-curve slope. For low-aspect ratios and borderline aspect ratios (defined in Section 4.1.3.4), the section lift-curve slope is assumed to be 2π ($\kappa = 1$ in figure 4.1.3.2-49).

The nonlinear coefficient $C_{N_{aa}}$ is calculated as the sum of two terms:

$$C_{N_{aa}} = \left(C_{N_{aa}}\right)_{ref} + \Delta C_{N_{aa}} \qquad 4.1.3.3\text{-b}$$

The reference nonlinear coefficient $\left(C_{N_{aa}}\right)_{ref}$ is based on C'_N at $C_{L_{max}}$ (the normal force at maximum lift), given by

$$C'_N \ @ \ C_{L_{max}} = \frac{C_{L_{max}}}{\cos a_{C_{L_{max}}}} \qquad 4.1.3.3\text{-c}$$

where $C_{L_{max}}$ and $a_{C_{L_{max}}}$ are obtained as outlined in Section 4.1.3.4 for the wing in question. Finally, $\left(C_{N_{aa}}\right)_{ref}$ is given by

$$\left(C_{N_{aa}}\right)_{ref} = \frac{C'_N \ @ \ C_{L_{max}} - C_{N_a}\left(\frac{1}{2}\right)\sin 2a_{C_{L_{max}}}}{\sin a_{C_{L_{max}}}\left|\sin a_{C_{L_{max}}}\right|} \qquad 4.1.3.3\text{-d}$$

The incremental nonlinear lift coefficient $\Delta C_{N_{aa}}$ is now read from figure 4.1.3.3-55a as a function of the parameter J and the ratio of the tangent of the angle of attack in question to the tangent of the angle of attack at $C_{L_{max}}$. The wing-shape parameter J is defined by the equation

$$J = 0.3\ (C_1 + 1)\frac{A}{\beta}\cos \Lambda_{LE}\left\{(C_1 + 1)\ (C_2 + 1) - \left[\frac{(C_2 + 1)\,A \tan \Lambda_{LE}}{7}\right]^3\right\} \qquad 4.1.3.3\text{-e}$$

The constants C_1 and C_2 are the empirical taper-ratio constants of Section 4.1.3.4.

The wing lift coefficient may now be calculated for any angle of attack up to and including the stall by substituting the appropriate values of C_{N_a} and $C_{N_{aa}}$ in equation 4.1.3.3-a.

Step 2. Subsonic Normal Force at Angles of Attack Beyond the Stall.

The equation for the nonlinear coefficient at angles of attack beyond the stall is

$$C_{N_{aa}} = \left(C_{N_{aa}}\right)_{ref} + \left[\left(C_{N_{aa}}\right)_{90^\circ} - \left(C_{N_{aa}}\right)_{ref}\right]\left[1 - \frac{\tan a_{C_{L_{max}}}}{\tan a}\right] + \beta^2 D \frac{C_{N_a}}{2.3}\left(\frac{C_{L_{max}}}{C^*_{L_{max}}}\right)^2 \qquad 4.1.3.3\text{-f}$$

where

$\left(C_{N_{aa}}\right)_{ref}$ is the reference nonlinear coefficient based on C_N' at $C_{L_{max}}$, calculated as outlined in step 1.

$\left(C_{N_{aa}}\right)_{90^o}$ is the normal-force coefficient at $\alpha = 90^o$. At 90^o, $C_{N_{aa}} = C_N'$ since $\sin^2 \alpha = 1$ and $\frac{\sin 2\alpha}{2} = 0$. The quantity C_N' is obtained from figure 4.1.3.3-55b as a function of aspect ratio (references 3 and 4).

β is the Mach number parameter, $\sqrt{1 - M^2}$.

D is an empirical nonlinear term read from the right-hand side of figure 4.1.3.3-55a.

$C_{L_{max}}$ is the maximum lift coefficient obtained as outlined in Section 4.1.3.4 for the wing in question.

$C^*_{L_{max}}$ is the maximum lift coefficient of the wing, calculated by using the low-aspect-ratio method of paragraph B of Section 4.1.3.4. If the wing in question has a low aspect ratio by the definition of Section 4.1.3.4, then $C^*_{L_{max}} = C_{L_{max}}$ and the last term in equation 4.1.3.3-f is $\beta D^2 \frac{C_{N_\alpha}}{2.3}$. If the wing in question has a high aspect ratio by the definition of Section 4.1.3.4, the value of $\left(C_{L_{max}}\right)_{base}$ is obtained from figure 4.1.3.4-23 at $(C_1 + 1)\frac{A}{\beta}\cos \Lambda_{LE} = \frac{4}{\beta}$.

Substituting values of $C_{N_{aa}}$ determined by equation 4.1.3.3-f, together with the value of C_{N_α} from figure 4.1.3.2-49$_b$ into equation 4.1.3.3-a gives the wing normal-force coefficient for angles of attack between the stall angle and 90^o.

For cambered wings the procedure outlined in steps 1 and 2 must be altered slightly. Potential theory states that the lift-curve slope of a wing is unaltered by camber. Thus the lift is defined by

$$C_L = C_{L_\alpha}(\alpha - \alpha_0)$$

where α_0 is the angle of attack for zero lift. For angles of attack below the stall an equivalent angle of attack for the cambered wing is defined as $\alpha_e = \alpha - \alpha_0$. Then, the equations for lift are

$$C_L = C_N' \cos \alpha$$

$$C_N' = C_{N_\alpha}\frac{\sin 2\alpha_e}{2} + C_{N_{aa}} \sin \alpha_e |\sin \alpha_e| \quad \text{(equation 4.1.3.3-a)}$$

where $C_{N_{aa}}$ is given by equation 4.1.3.3-b, but with $\alpha_{C_{L_{max}}}$ replaced by $(\alpha_e)_{C_{L_{max}}}$ in determining

$\left(C_{N_{aa}}\right)_{ref}$ and $\Delta C_{N_{aa}}$; i.e.,

$$\left(C_{N_{aa}}\right)_{ref} = \frac{C'_N \text{ @ } C_{L_{max}} - C_{N_a}\left(\frac{1}{2}\right)\sin 2(a_e)_{C_{L_{max}}}}{\sin (a_e)_{C_{L_{max}}} \left|\sin (a_e)_{C_{L_{max}}}\right|} \quad \text{(equation 4.1.3.3-d)}$$

$\Delta C_{N_{aa}}$ is read from figure 4.1.3.3-55a as a function of J and the ratio $\frac{\tan a_e}{\tan (a_e)_{C_{L_{max}}}}$.

For angles of attack beyond the stall, the linear term vanishes as a approaches 90^o, and the equivalent angle of attack for the cambered wing is defined as

$$a_e = a\left[1 + \frac{a_0}{90^o - a_{C_{L_{max}}}}\right] - \frac{90^o\, a_0}{90^o - a_{C_{L_{max}}}} \qquad 4.1.3.3\text{-g}$$

where a, a_0, and $a_{C_{L_{max}}}$ are measured in degrees. Then, as before,

$$C_L = C'_N \cos a$$

$$C'_N = C_{N_a}\frac{\sin 2a_e}{2} + C_{N_{aa}} \sin a_e \left|\sin a_e\right| \quad \text{(equation 4.1.3.3-a)}$$

where $C_{N_{aa}}$ is given by equation 4.1.3.3-f with $\left(C_{N_{aa}}\right)_{ref}$ calculated as outlined above for the cambered wing at angles of attack below the stall, and $a^* = a_e$.

In applying the above methods to a wing which is on the borderline between a high aspect ratio and a low aspect ratio as defined in Section 4.1.3.4, i.e., $\frac{3}{(C_1 + 1)\cos \Lambda_{LE}} \leqslant A \leqslant \frac{4}{(C_1 + 1)\cos \Lambda_{LE}}$, either the high- or the low-aspect-ratio procedure of Section 4.1.3.4 may be applied to determine the wing maximum-lift characteristics. It is suggested that the low-aspect-ratio procedure be applied as this facilitates application of equation 4.1.3.3-f, since $C^*_{L_{max}} = C_{L_{max}}$.

Three sample problems are included on pages 4.1.3.3-11 through 4.1.3.3-23 to illustrate the calculation procedure for estimating wing lift in the nonlinear angle-of-attack range of conventional, straight-tapered wings. Comparison with experimental data is presented in each case.

Sample problems 1 and 2 emphasize the high-angle-of-attack characteristics of a low-aspect-ratio and a high-aspect-ratio wing, respectively. Comparison is made between the calculated and experimental values for both lift and normal force. Agreement between the calculated and experimental values near stall is not particularly good for the high-aspect-ratio wing. However, the experimental data in this case should be viewed with caution, since it indicates a highly nonlinear lift curve prior to stall for a high-aspect-ratio wing.

Sample problem 3 illustrates the special case of a cambered wing, as well as a more representative comparison of lift at the lower angles of attack.

Non-Straight-Tapered Wings

Semiempirical methods, taken from reference 1, are presented for estimating the nonlinear lift of double-delta and cranked wings at subsonic speeds. The nonlinear lift of double-delta wings is based on the hypothesis that an expression similar to that developed by Küchemann (reference 8) for the nonlinear lift of small-aspect-ratio wings with leading-edge separation may be applied to double-delta planforms. By using such an approach, a correlation proportional to the linear lift-curve slope was developed that is strongly dependent on the inboard-panel geometry. The characteristic behavior exhibited by the experimental data of cranked wings led the authors of reference 1 to conclude that the flow field about these wings is similar to that about a low-aspect-ratio delta wing with leading-edge separation. On the basis of these observations, the nonlinear lift of cranked wings has been related to the correlation for the nonlinear lift of double-delta wings.

The nonlinear lift of curved (Gothic and ogee) wings has been correlated in reference 1 by the empirical method developed by Peckham in reference 9.

The following methods for estimating the nonlinear lift of non-straight-tapered wings are limited to angles of attack of 20° or less.

DATCOM METHODS

Double-Delta Wings

The nonlinear lift of double-delta wings at subsonic speeds is obtained from the procedure outlined in the following steps:

Step 1. Calculate the subsonic wing lift-curve slope C_{L_α} by the method presented for double-delta wings in paragraph A of Section 4.1.3.2.

Step 2. Obtain values of the parameter $\frac{C_L}{C_{L_\alpha}} \frac{A_i}{\eta_B}$ at angles of attack of 4°, 8°, 12°, 16°, and 20° from figure 4.1.3.3-56. This parameter is correlated as a function of wing aspect ratio A, the leading-edge sweepback of the inboard panel Λ_{LE_i}, and the Mach number parameter $\beta = \sqrt{1 - M^2}$. It should be noted that for angles of attack up to 8°, an aspect-ratio dependence exists at Mach numbers above 0.7. Not enough data are available at high subsonic Mach numbers to allow investigation of the aspect-ratio dependence above 8° angle of attack.

Step 3. Calculate C_L by

$$C_L = \left(\frac{C_L}{C_{L_\alpha}} \frac{A_i}{\eta_B}\right) \frac{C_{L_\alpha}}{A_i/\eta_B} \qquad 4.1.3.3\text{-h}$$

where

η_B is the spanwise location of the break in the leading edge expressed in percent of wing semispan.

A_i is the aspect ratio of the planform formed by the two inboard panels

Step 4. Plot calculated values of C_L versus α and fair a curve through the points tangent to C_{L_α} near zero lift.

Application of this technique is illustrated by sample problem 4 at the conclusion of paragraph A (page 4.1.3.3-23).

A comparison of test data for 21 configurations with the nonlinear lift of double-delta wings calculated by this method is presented as table 4.1.3.3-B (taken from reference 1). The largest errors generally occur at $\alpha = 4^{\circ}$ with the accuracy improving as the angle of attack increases. The ratio of body diameter to wing span of the models investigated varied from 0.077 to 0.149, and no apparent effects of relative body size are evident. No significant effects of thickness ratio on lift are evident over the limited thickness-ratio range covered (0.02 to 0.04). The Reynolds numbers of the test data fall into two ranges, 1.04×10^6 to 3.6×10^6 and 17.1×10^6 to 20.3×10^6. Although there are not enough data to allow a quantitative prediction of Reynolds-number effect, it is reasonable to expect that Reynolds number will influence the lift.

Although no attempt was made to define the effect of leading-edge shape on lift, even with round leading edges a highly-swept wing should be expected to have leading-edge separation at the higher angles of attack. With separated flow over the entire leading edge, the resulting vortex pattern should be equivalent to that for a wing with a sharp leading edge. Since the vortex pattern exerts a strong influence on the flow field, at the higher angles of attack the aerodynamic characteristics of wings with round and sharp leading edges should be similar.

It is difficult to assess quantitatively the validity of the aspect-ratio dependence, shown in figure 4.1.3.3-56, at Mach numbers above 0.7. This dependence is based on only nine configurations, and no data are available above 8° angle of attack.

Cranked Wings

The nonlinear lift of cranked wings at subsonic speeds is related to the correlation for the nonlinear lift of double-delta wings presented as figure 4.1.3.3-56. The prediction method consists of a construction procedure for the buildup of lift above the angle of attack at which the lift curve breaks. The break in the lift curve is defined as that point where the lift drops off from the linear value, and the curve itself also becomes nonlinear. The cranked wings examined during the analysis reported in reference 1 showed a break in the lift curve at angles of attack between 6° and 7°. The prediction method is illustrated schematically in sketch (b).

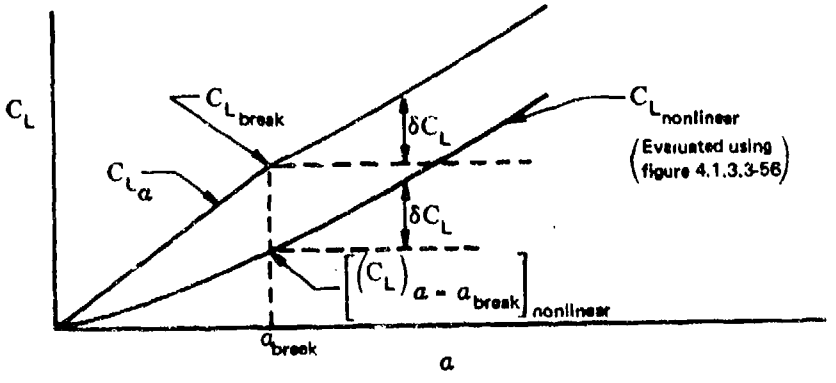

SKETCH (b)

By referring to sketch (b), the nonlinear lift of cranked wings at subsonic speeds is obtained from the procedure outlined in the following steps:

Step 1. Calculate the subsonic wing lift-curve slope C_{L_α} by the method presented for cranked wings in paragraph A of Section 4.1.3.2.

Step 2. Obtain α_{break} as a function of the leading-edge sweepback of the inboard panel from figure 4.1.3.3-57.

Step 3. Calculate $C_{L_{break}}$ by

$$C_{L_{break}} = C_{L_\alpha} \alpha_{break} \qquad 4.1.3.3\text{-i}$$

Step 4. Obtain values of the parameter $\frac{C_L}{C_{L_\alpha}} \frac{A_I}{\eta_B}$ at angles of attack of 4^o, 8^o, 12^o, 16^o, and 20^o from figure 4.1.3.3-56, and calculate $C_{L_{nonlinear}}$ using equation 4.1.3.3-h. (See double-delta-wing method of this paragraph.)

Step 5. Obtain $\left[(C_L)_{\alpha=\alpha_{break}}\right]_{nonlinear}$ by plotting $C_{L_{nonlinear}}$ versus α from step 4, and then calculate δC_L by

$$\delta C_L = \left[C_L - (C_L)_{\alpha=\alpha_{break}}\right]_{nonlinear} \qquad 4.1.3.3\text{-j}$$

Step 6. Add the δC_L values obtained in step 5 to the $C_{L_{break}}$ value obtained in step 3 to obtain the total C_L for each α above α_{break}; i.e.,

$$C_L = C_{L_{break}} + \delta C_L \qquad 4.1.3.3\text{-k}$$

Application of this technique is illustrated by sample problem 5 on page 4.1.3.3-25.

A comparison of test data for seven configurations with the nonlinear lift of cranked wings calculated by this method is presented as table 4.1.3.3-C (taken from reference 1). The ratio of body diameter to wing span of the models investigated varied from 0.062 to 0.147, and no apparent effects of relative body size are evident. No significant effects of thickness ratio on lift are evident over the limited thickness-ratio range covered (0.02 to 0.06).

Before attempting to assess the validity of the method some salient features should be pointed out. The accuracy of the method is strongly dependent on knowing α_{break}. Since the break in the lift curve is essentialy a type of stall phenomenon, Reynolds number may have a significant effect on α_{break}. Unfortunately, a lack of data prevented a detailed study of Reynolds number effects during the correlation reported in reference 1. The method also assumes a sharp discontinuity at α_{break}; however, test data show that as aspect ratio is reduced the break in the lift curve becomes less apparent, and for the lower-aspect-ratio wings the lift curve exhibits a gradual transition from the linear to the nonlinear region. Furthermore, the shape of the nonlinear lift curve is based on the correlation derived for double-delta wings, which is restricted to wings with small or zero trailing-edge sweep angles.

From the foregoing discussion it might be expected that the method would give acceptable results when applied to wings with moderate to high aspect ratios and small or zero trailing-edge sweep angles. Of the seven configurations listed in table 4.1.3.3-C, these conditions are met only by the configurations of references 37, 38, and 39. The average error for the nine calculated points of those references is 4.9 percent.

It is difficult to assess quantitatively the effect of Mach number on the accuracy of the method. However, it should be pointed out that the curves of figure 4.1.3.3-56 have been extrapolated to account for low values

of $\beta \tan \Lambda_{LE_i}$ for the configuration of reference 28 at M = 0.80, 0.85, and 0.90 and for the configurations of reference 36 at M = 0.90.

Since the configurations of references 38 and 39 had twisted and cambered wings, their lift curves were significantly displaced from the origin. In analyzing the test data for these configurations the lift curves were shifted so that $C_{L_{\alpha=0}} = 0$. The calculated results for these configurations compared well with the adjusted test values, indicating that twist and camber have a negligible effect on the shape of the lift curve in the nonlinear region.

Test data show that the lift curve tends to fall off at approximately 16° angle of attack at M = 0.80 and 0.85 for the configuration of reference 28, and at approximately 12° angle of attack throughout the Mach range tested for both configurations of reference 36. This trend indicates that the inboard panel is beginning to stall; consequently, the method should not be expected to give reliable results for these configurations at higher angles of attack.

Curved Wings

The nonlinear lift of curved (Gothic and ogee) wings at subsonic speeds was correlated in reference 1 by Peckham's method (reference 9) where the ratio of lift to the square root of the wing slenderness parameter plotted versus angle of attack converges on a single curve.

The nonlinear lift is obtained from the procedure outlined in the following steps:

Step 1. Using the given wing geometry calculate the wing slenderness parameter $\frac{b_W}{2\ell}$. (See Section 2.2.2 for wing-geometry parameters.)

Step 2. At the desired values of angle of attack obtain $C_L\sqrt{\frac{b_W}{2\ell}}$ from figure 4.1.3.3-58.

Step 3. Calculate C_L at each α by

$$C_L = \frac{C_L}{\sqrt{\frac{b_W}{2\ell}}} \sqrt{\frac{b_W}{2\ell}} \qquad 4.1.3.3\text{-}\ell$$

Application of this technique is illustrated by the sample problem on page 4.1.3.3-28.

A comparison of test data for 11 configurations with the nonlinear lift of curved wings calculated by this method is presented as table 4.1.3.3-D (taken from reference 1). The results indicate that the best accuracy is obtained at the lower Mach numbers and for configurations with aspect ratios near 1.0. Three of the configurations analyzed were wing-bodies, and for these configurations no significant wing-body interference effects were evident. However, it should be noted that no blended wing-body configurations are included in the correlation. Such configurations have a very thick cross section near the apex that should be expected to cause a loss in lift. The two blended wing-body configurations of references 43 and 44 were analyzed during the investigation reported in reference 1, and it was found that the lift predicted using figure 4.1.3.3-58 was about 10 percent higher than test data throughout the angle-of-attack range of both configurations.

Since there is no theoretical basis for this method, it should be used with caution outside the planform parameter ranges covered in the correlation. The correlation of figure 4.1.3.3-58 is based on data from sharp-edged, thin, Gothic and ogee wings with moderate trailing-edge sweep angles (±15°). The planform param-

eter ranges of the data are

$$0.75 \leqslant A \leqslant 2.00$$

$$0.45 \leqslant \frac{S_W}{b_W \ell} \leqslant 0.667$$

$$0.25 \leqslant \frac{b_W}{2\ell} \leqslant 0.54$$

Sample Problems

Conventional, Straight-Tapered Wings

1. High-Angle-of-Attack Characteristics of a Low-Aspect-Ratio Wing.

Given: Delta wing of reference 25.

$A = 2.0$ $\lambda = 0$ $\Lambda_{LE} = 63.5^{o}$ NACA 0005 airfoil (free-stream direction)

$M = 0.2$; $\beta = 0.98$ $R_\ell = 1.2$ to 2.2×10^6 (based on MAC)

$\kappa = 1.0$ (assumed) $\Lambda_{c/2} = 45.2^{o}$

Compute: Angles of attack below the stall

Find $C_{L_{max}}$ and $\alpha_{C_{L_{max}}}$ as outlined in Section 4.1.3.4 and C_{N_α} from Section 4.1.3.2.

$A < \dfrac{3}{(C_1 + 1)\cos \Lambda_{LE}}$; therefore, use low-aspect-ratio method.

$\Delta y = 1.38$ (figure 2.2.1-8)

$C_1 = 0$, $C_2 = 0$ (figure 4.1.3.4-24b)

$(C_1 + 1)\dfrac{A}{\beta}\cos \Lambda_{LE} = \dfrac{2}{0.98}(0.4462) = 0.91$

$\left(C_{L_{max}}\right)_{base} = 1.29$ (figure 4.1.3.4-23a)

$(C_2 + 1)\ A \tan \Lambda_{LE} = 2(2.006) = 4.01$

$\Delta C_{L_{max}} = 0$ (figure 4.1.3.4-24a)

$C_{L_{max}} = \left(C_{L_{max}}\right)_{base} + \Delta C_{L_{max}}$ (equation 4.1.3.4-g)

$= 1.29$

$$\left(a_{C_{L_{max}}}\right)_{base} = 34.6^{o} \text{ (figure 4.1.3.4-25a)}$$

$$A \cos \Lambda_{LE} \left[1 + (2\lambda)^2\right] = 2\,(0.4462)\,[1 + 0] = 0.8924$$

$$\Delta a_{C_{L_{max}}} = -0.1^{o} \text{ (figure 4.1.3.4-25b)}$$

$$a_{C_{L_{max}}} = \left(a_{C_{L_{max}}}\right)_{base} + \Delta a_{C_{L_{max}}} \quad \text{(equation 4.1.3.4-h)}$$

$$= 34.5^{o}$$

Find C_{L_a}

$$\frac{A}{\kappa}\left[\beta^2 + \tan^2 \Lambda_{c/2}\right]^{\frac{1}{2}} = 2.81$$

$$C_{L_a}/A = 1.15 \text{ per rad (figure 4.1.3.2-49)}$$

$$C_{L_a} = C_{N_a} = \left(\frac{C_{L_a}}{A}\right) A = (1.15)\,(2.0) = 2.30 \text{ per rad}$$

Find $\left(C_{N_{aa}}\right)_{ref}$

$$C'_N \;@\; C_{L_{max}} = \frac{C_{L_{max}}}{\cos a_{C_{L_{max}}}} \quad \text{(equation 4.1.3.3-c)}$$

$$= \frac{1.29}{0.8241} = 1.565$$

$$\left(C_{N_{aa}}\right)_{ref} = \frac{C'_N \;@\; C_{L_{max}} - C_{N_a}\left(\frac{1}{2}\right)\sin 2a_{C_{L_{max}}}}{\sin a_{C_{L_{max}}}\left|\sin a_{C_{L_{max}}}\right|} \quad \text{(equation 4.1.3.3-d)}$$

$$\frac{1.565 - 2.30\left(\frac{0.9336}{2}\right)}{(0.5664)^2} = 1.53$$

Find J

$$J = 0.3\,(C_1 + 1)\frac{A}{\beta}\cos \Lambda_{LE}\left\{(C_1 + 1)\,(C_2 + 1) - \left[\frac{(C_2 + 1)\,A \tan \Lambda_{LE}}{7}\right]^3\right\}$$

(equation 4.1.3.3-e)

$$= 0.3\,(1)\left(\frac{2}{0.98}\right)(0.4462)\left\{1 - \left[\frac{2\,(2.006)}{7}\right]^3\right\}$$

$$= 0.222$$

Solution: Angles of Attack Below the Stall

$$\frac{C_L}{\cos\alpha} = C_N' = C_{N_\alpha}\frac{\sin 2\alpha}{2} + C_{N_{\alpha\alpha}}\sin\alpha\,|\sin\alpha| \quad \text{(equation 4.1.3.3-a)}$$

$$C_{N_{\alpha\alpha}} = \left(C_{N_{\alpha\alpha}}\right)_{\text{ref}} + \Delta C_{N_{\alpha\alpha}} \quad \text{(equation 4.1.3.3-b)}$$

$$= 1.53 + \Delta C_{N_{\alpha\alpha}}$$

①	②	③	④	⑤	⑥	⑦	⑧
α (deg)	$\frac{\tan\alpha}{\tan\alpha_{C_{L_{max}}}}$	$\Delta C_{N_{\alpha\alpha}}$ fig. 4.1.3.3-55a	$C_{N_{\alpha\alpha}}$ eq. 4.1.3.3-b 1.53 + ③	$C_{N_{\alpha\alpha}}\sin^2\alpha$	$C_{N_\alpha}\frac{\sin 2\alpha}{2}$	C_N' eq. 4.1.3.3-a ⑤ + ⑥	$C_L = \left(C_N'\cos\alpha\right)$
5	0.126	0.80	2.33	0.018	0.200	0.218	0.22
10	0.266	0.80	2.33	0.070	0.393	0.463	0.46
15	0.390	0.73	2.26	0.161	0.575	0.726	0.70
20	0.530	0.66	2.18	0.285	0.739	0.994	0.93
25	0.680	0.45	1.98	0.354	0.881	1.235	1.12
30	0.840	0.25	1.78	0.445	0.996	1.441	1.26
34.6	1.000	0	1.53	0.491	1.070	1.561	1.29

Compute: Angles of Attack Above the Stall

$$C^*_{L_{max}} = C_{L_{max}} \quad \text{(low-aspect-ratio wing)}$$

$$\left(C_{N_{\alpha\alpha}}\right)_{90^\circ} = 1.20 \text{ (figure 4.1.3.3-55b)}$$

$$\left(C_{N_{\alpha\alpha}}\right)_{\text{ref}} = 1.53 \text{ (calculated on page 4.1.3.3-12)}$$

Solution: Angles of Attack Above the Stall

$$\frac{C_L}{\cos\alpha} = C_N' = C_{N_\alpha}\frac{\sin 2\alpha}{2} + C_{N_{\alpha\alpha}}\sin\alpha\,|\sin\alpha| \quad \text{(equation 4.1.3.3-a)}$$

$$C_{N_{\alpha\alpha}} = \left(C_{N_{\alpha\alpha}}\right)_{ref} + \left[\left(C_{N_{\alpha\alpha}}\right)_{90^\circ} - \left(C_{N_{\alpha\alpha}}\right)_{ref}\right] \left[1 - \frac{\tan \alpha_{C_{L_{max}}}}{\tan \alpha}\right] + \beta^2 D \frac{C_{N_\alpha}}{2.3} \left(\frac{C_{L_{max}}}{C^*_{L_{max}}}\right)^2$$

(equation 4.1.3.3-f)

$$= 1.53 + (1.20 - 1.53) \left[1 - \frac{\tan \alpha_{C_{L_{max}}}}{\tan \alpha}\right] + 0.96\, D \frac{2.30}{2.3} \quad (1)$$

$$= 1.20 + 0.33 \frac{\tan \alpha_{C_{L_{max}}}}{\tan \alpha} + 0.96D$$

① α (deg)	② $\frac{\tan \alpha_{C_{L_{max}}}}{\tan \alpha}$	③ D fig. 4.1.3.3-55a	④ $C_{N_{\alpha\alpha}}$ eq. 4.1.3.3-f 1.2 + .33 ② + .96 ③	⑤ $C_{N_{\alpha\alpha}} \sin^2 \alpha$	⑥ $C_{N_\alpha} \frac{\sin 2\alpha}{2}$	⑦ C'_N eq. 4.1.3.3-e ⑤ + ⑥	⑧ $C_L = \left(C'_N \cos \alpha\right)$
37	0.912	-0.20	1.309	0.474	1.11	1.584	1.26
40	0.819	-0.86	0.654	0.270	1.13	1.400	1.07
45	0.687	-1.43	0.064	0.027	1.15	1.177	0.83
50	0.577	-1.54	-0.088	-0.062	1.13	1.078	0.69
60	0.397	-1.27	0.112	0.084	0.996	1.080	0.54
70	0.250	-0.88	0.438	0.387	0.74	1.127	0.39
90	0	0	1.200	1.200	0	1.200	0

A comparison of the calculated values and the experimental data of reference 25 is presented as sketch (c).

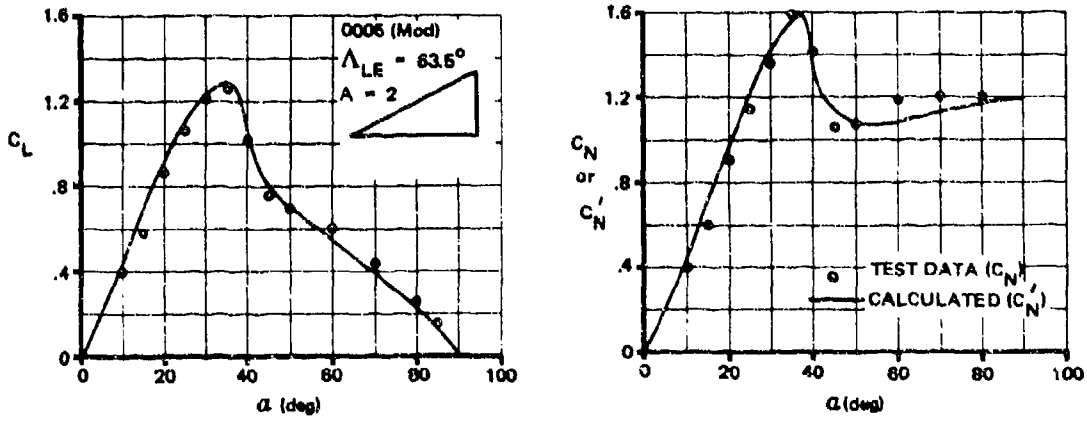

SKETCH (c)

2. High-Angle-of-Attack Characteristics of a High-Aspect-Ratio Wing.

Given: Wing 7 of reference 25.

$A = 6.0 \quad \lambda = 0.5 \quad \Lambda_{LE} = 8.9^{\circ}$ NACA 64A010 airfoil (free-stream direction)

$M = 0.2; \quad \beta = 0.98 \quad R_{\ell} = 1.5$ to 2.2×10^6 (based on MAC)

$\kappa = 1.0$ (assumed) $\quad \Lambda_{c/2} = 2.6^{\circ}$

Compute: Angles of Attack Below the Stall

Find $C_{L_{max}}$ and $\alpha_{C_{L_{max}}}$ as outlined in Section 4.1.3.4 and C_{N_α} from Section 4.1.3.2.

$A > \dfrac{4}{(C_1 + 1) \cos \Lambda_{LE}}$; therefore, use high-aspect-ratio method

$\Delta y = 2.10$ (figure 2.2.1-8)

$c_{\ell_{max}} = 1.23$ at $R_{\ell} = 9 \times 10^6$ (table 4.1.1-B)

$\Delta_3 c_{\ell_{max}} = -0.14$ for $R_{\ell} = 2.0 \times 10^6$ (figure 4.1.1.4-7b, extrapolated)

$c_{\ell_{max}} = 1.23 - 0.14 = 1.09$ (adjusted for test R_{ℓ})

$\dfrac{C_{L_{max}}}{c_{\ell_{max}}} = 0.895$ (figure 4.1.3.4-21a)

$\Delta C_{L_{max}} = 0$ (figure 4.1.3.4-22)

$$C_{L_{max}} = \left(\frac{C_{L_{max}}}{c_{\ell_{max}}} \right) c_{\ell_{max}} + \Delta C_{L_{max}} \quad \text{(equation 4.1.3.4-d)}$$

$$= (0.895)(1.09) = 0.975$$

Find C_{L_α}

$$\frac{A}{\kappa} \left[\beta^2 + \tan^2 \Lambda_{c/2} \right]^{1/2} = 5.89$$

$C_{L_\alpha}/A = 0.76$ per rad (figure 4.1.3.2-49)

$$C_{L_\alpha} = C_{N_\alpha} = \left(\frac{C_{L_\alpha}}{A}\right) A = (0.76)(6) = 4.56 \text{ per rad}$$

$$\Delta\alpha_{C_{L_{max}}} = 1.0^{O} \text{ (figure 4.1.3.4-21b)}$$

$$\alpha_0 = \alpha_i - \frac{c_{\ell_i}}{c_{\ell_\alpha}} = 0 - \frac{0}{0.110} = 0 \text{ (equation 4.1.3.1-a)}$$

$$\alpha_{C_{L_{max}}} = \frac{C_{L_{max}}}{C_{L_\alpha}} + \alpha_0 + \Delta\alpha_{C_{L_{max}}} \text{ (equation 4.1.3.4-e)}$$

$$= \frac{0.975}{4.56/(57.3)} + 0 + 1.0 = 13.3^{O}$$

Find $\left(C_{N_{\alpha\alpha}}\right)_{ref}$

$$C'_N \text{ @ } C_{L_{max}} = \frac{C_{L_{max}}}{\cos \alpha_{C_{L_{max}}}} = \frac{0.975}{0.9732} = 1.002 \text{ (equation 4.1.3.3-c)}$$

$$\left(C_{N_{\alpha\alpha}}\right)_{ref} = \frac{C'_N \text{ @ } C^{*}_{L_{max}} - C_{N_\alpha}\left(\frac{1}{2}\right)\sin 2\alpha_{C_{L_{max}}}}{\sin \alpha_{C_{L_{max}}} \left|\sin \alpha_{C_{L_{max}}}\right|} \text{ (equation 4.1.3.3-d)}$$

$$= \frac{1.002 - 4.56\ \frac{0.4478}{2}}{(0.2300)^2} = -0.359$$

Find J

$C_1 = 0.3$, $C_2 = 1.06$ (figure 4.1.3.4-24b)

$$J = 0.3\,(C_1 + 1)\,\frac{A}{\beta}\cos\Lambda_{LE}\left\{(C_1 + 1)(C_2 + 1) - \left[\frac{(C_2 + 1)\,A\tan\Lambda}{7}\right]^3\right\}$$

(equation 4.1.3.3-e)

$$= 0.3\,(1.31)\,\frac{6}{0.98}\,(0.988)\left\{(1.31)(2.06) - \left[\frac{(2.06)(6)(0.1566)}{7}\right]^3\right\}$$

$$= 6.36$$

Solution: Angles of Attack Below the Stall

$$\frac{C_L}{\cos a} = C'_N = C_{N_a} \frac{\sin 2a}{2} + C_{N_{aa}} \sin a \,|\sin a| \quad \text{(equation 4.1.3.3-a)}$$

$$C_{N_{aa}} = \left(C_{N_{aa}}\right)_{ref} + \Delta C_{N_{aa}} \quad \text{(equation 4.1.3.3-b)}$$

$$C_{N_{aa}} = -0.359 + \Delta C_{N_{aa}}$$

①	②	③	④	⑤	⑥	⑦	⑧
α (deg)	$\frac{\tan \alpha}{\tan \alpha_{C_{L_{max}}}}$	$\Delta C_{N_{\alpha\alpha}}$ fig. 4.1.3.3-55a	$C_{N_{\alpha\alpha}}$ eq. 4.1.3.3-b -.359 + ③	$C_{N_{\alpha\alpha}} \sin^2\alpha$	$C_{N_\alpha} \frac{\sin 2\alpha}{2}$	C'_N eq. 4.1.3.3-a ⑤ + ⑥	$= \left(C'_N \cos \alpha\right)$
5	0.370	2.84	2.48	0.019	0.396	0.415	0.41
10	0.746	1.80	1.44	0.043	0.780	0.823	0.81
13.3	1.000	0	-0.36	-0.019	1.021	1.002	0.98

Compute: Angles of Attack Above the Stall

$C^*_{L_{max}}$ (calculated using the low-aspect-ratio method of Section 4.1.3.4)

$$\left(C_{L_{max}}\right)_{base} = 0.79 \text{ (figure 4.1.3.4-23b at } (C_1 + 1)\frac{A}{\beta} \cos \Lambda_{LE} = \frac{4}{\beta},\ \Delta y = 2.10)$$

$$(C_2 + 1)\, A \tan \Lambda_{LE} = (2.06)(6)(0.1566) = 1.94$$

$$\Delta C_{L_{max}} = -0.08 \text{ (figure 4.1.3.4-24a)}$$

$$C^*_{L_{max}} = \left(C_{L_{max}}\right)_{base} + \Delta C_{L_{max}} \quad \text{(equation 4.1.3.4-g)}$$

$$= 0.79 + (-0.08) = 0.71$$

$$\left(C_{N_{aa}}\right)_{90°} = 1.30 \text{ (figure 4.1.3.3-55b)}$$

$$\left(C_{N_{aa}}\right)_{ref} = -0.359 \text{ (calculated on page 4.1.3.3-16)}$$

Solution: Angles of Attack Above the Stall

$$\frac{C_L}{\cos a} = C'_N = C_{N_a} \frac{\sin 2a}{2} + C_{N_{aa}} \sin a \,|\sin a| \quad \text{(equation 4.1.3.3-a)}$$

$$C_{N_{\alpha\alpha}} = \left(C_{N_{\alpha\alpha}}\right)_{ref} + \left[\left(C_{N_{\alpha\alpha}}\right)_{90^\circ} - \left(C_{N_{\alpha\alpha}}\right)_{ref}\right]\left[1 - \frac{\tan \alpha_{C_{L_{max}}}}{\tan \alpha}\right] + \beta^2 D \frac{C_{N_\alpha}}{2.3}\left(\frac{C_{L_{max}}}{C^*_{L_{max}}}\right)^2$$

(equation 4.1.3.3-f)

$$= -0.359 + (1.3 + 0.359)\left[1 - \frac{\tan \alpha_{C_{L_{max}}}}{\tan \alpha}\right] + 0.96D\left(\frac{4.56}{2.3}\right)\left(\frac{0.975}{0.71}\right)^2$$

$$= 1.3 - 1.659\left(\frac{\tan \alpha_{C_{L_{max}}}}{\tan \alpha}\right) + 3.588D$$

①	②	③	④	⑤	⑥	⑦	⑧
α (deg)	$\frac{\tan \alpha_{C_{L_{max}}}}{\tan \alpha}$	D fig. 4.1.3.3-55a	$C_{N_{\alpha\alpha}}$ eq. 4.1.3.3-f 1.3 -1.66 ② + 3.58 ③	$C_{N_{\alpha\alpha}} \sin^2 \alpha$	$C_{N_\alpha} \frac{\sin 2\alpha}{2}$	C'_N eq. 4.1.3.3-a ⑤ + ⑥	$= \left(C'_N \cos \alpha\right)^{C_L}$
16	0.825	-0.80	-2.94	-0.22	1.21	0.99	0.95
18	0.728	-1.32	-4.64	-0.44	1.34	0.90	0.86
20	0.649	-1.50	-5.16	-0.60	1.47	0.87	0.82
22	0.585	-1.54	-5.20	-0.73	1.58	0.85	0.79
30	0.409	-1.32	-4.11	-1.03	1.97	0.94	0.81
50	0.198	-0.70	-1.54	-0.90	2.25	1.35	0.87
70	0.086	-0.30	0.08	0.07	1.47	1.54	0.53
90	0	0	1.30	1.30	0	1.30	0

A comparison of the calculated values and the experimental data of reference 25 is presented as sketch (d).

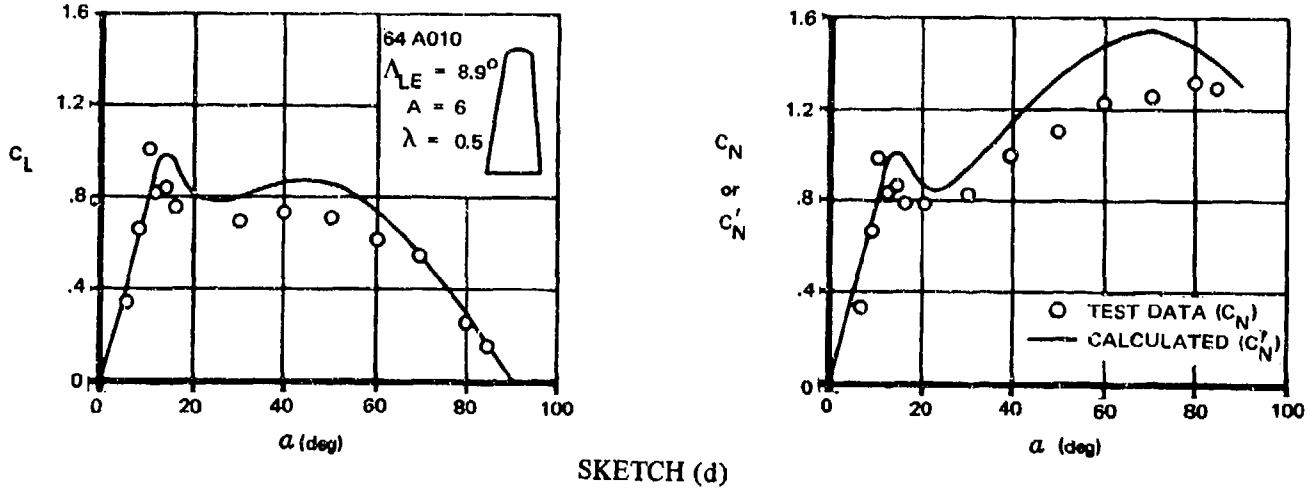

SKETCH (d)

3. Angle-of-Attack Characteristics of a Cambered Wing

Given: The wing of reference 26.

$A = 9.0$ $\lambda = 0.4$ $\Lambda_{LE} = 2.2^{o}$ NACA 63_1 –210 airfoil (free-stream direction)

Position of maximum t/c = 0.45c
Position of maximum camber = 0.50c
Amount of camber = 0.011c

$M = 0.30$; $\beta = 0.954$ $R_\ell = 2.5 \times 10^6$ (based on MAC)

$\kappa = 1.0$ (assumed) $\Lambda_{c/2} = 3.25^{o}$

Compute: Angles of Attack Below the Stall

Find $C_{L_{max}}$ and $\alpha_{C_{L_{max}}}$ as outlined in Section 4.1.3.4 and C_{N_α} from Section 4.1.3.2.

$A > \dfrac{4}{(C_1 + 1)\cos\Lambda_{LE}}$; therefore, use high-aspect-ratio method

$\Delta y = 2.20$ (figure 2.2.1-8)

$\left(c_{\ell_{max}}\right)_{base} = 1.28$ (uncambered wing at $R_\ell = 9 \times 10^6$) (figure 4.1.1.4-5)

$\Delta_1 c_{\ell_{max}} = 0.07$ (figure 4.1.1.4-6d)

$\Delta_2 c_{\ell_{max}} = 0.15$ (figure 4.1.1.4-7a)

$\Delta_3 c_{\ell_{max}} = -0.13$ (figure 4.1.1.4-7b)

$c_{\ell_{max}} = \left(c_{\ell_{max}}\right)_{base} + \Delta_1 c_{\ell_{max}} + \Delta_2 c_{\ell_{max}} + \Delta_3 c_{\ell_{max}}$ (equation 4.1.1.4-a)

$= 1.30 + 0.07 + 0.15 - 0.13 = 1.39$

$\dfrac{C_{L_{max}}}{c_{\ell_{max}}} = 0.90$ (figure 4.1.3.4-21a)

$\Delta C_{L_{max}} = -0.105$ (figure 4.1.3.4-22)

$C_{L_{max}} = \left(\dfrac{C_{L_{max}}}{c_{\ell_{max}}}\right) c_{\ell_{max}} + \Delta C_{L_{max}}$ (equation 4.1.3.4-d)

$= (0.90)(1.39) - 0.105 = 1.15$

$\Delta a_{C_{L_{max}}} = 0.5^{o}$ (figure 4.1.3.4-21b)

Find C_{L_a}

$$\frac{A}{\kappa}\left[\beta^2 + \tan^2 \Lambda_{c/2}\right]^{1/2} = 8.60$$

$C_{L_a}/A = 0.59$ per rad (figure 4.1.3.2-49)

$$C_{L_a} = C_{N_a} = \left(\frac{C_{L_a}}{A}\right)A = (0.59)(9) = 5.31$$

$$a_0 = a_i - \frac{c_{\ell_i}}{c_{\ell_a}} = 0 - \frac{0.2}{0.113} = -1.77^{o} \text{ (equation 4.1.3.1-a)}$$

$$a_{C_{L_{max}}} = \frac{C_{L_{max}}}{C_{L_a}} + a_0 + \Delta a_{C_{L_{max}}} \text{ (equation 4.1.3.4-e)}$$

$$= \frac{1.15}{5.31/(57.3)} + (-1.77) + 0.5 = 11.14^{o}$$

Find $\left(C_{N_{aa}}\right)_{ref}$

$$C'_N \text{ @ } C_{L_{max}} = \frac{C_{L_{max}}}{\cos a_{C_{L_{max}}}} = \frac{1.15}{0.9815} = 1.17 \text{ (equation 4.1.3.3-c)}$$

$$(a_e)_{C_{L_{max}}} = a_{C_{L_{max}}} - a_0 = 12.91^{o}$$

$$\left(C_{N_{aa}}\right)_{ref} = \frac{C'_N \text{ @ } C_{L_{max}} - C_{N_a}\left(\frac{1}{2}\right)\sin 2(a_e)_{C_{L_{max}}}}{\sin (a_e)_{C_{L_{max}}}\left|\sin (a_e)_{C_{L_{max}}}\right|} \text{ (equation 4.1.3.3-d with } a_{C_{L_{max}}} = (a_e)_{C_{L_{max}}}$$

$$= \frac{1.17 - (5.31)\left(\frac{0.4355}{2}\right)}{(0.2235)^2} = \frac{0.0137}{0.0500} = 0.274$$

Find J

$C_1 = 0.43$, $C_2 = 1.09$ (figure 4.1.3.4-24b)

$$J = 0.3\,(C_1 + 1)\frac{A}{\beta}\cos \Lambda_{LE}\left\{(C_1 + 1)(C_2 + 1) - \left[\frac{(C_2 + 1)\,A \tan \Lambda_{LE}}{7}\right]^3\right\} \text{ (equation 4.1.3.3-e)}$$

$$= 0.3\,(1.43)\,\frac{9}{0.954}\,(0.9993)\left\{(1.43)\,(2.09) - \left[\frac{(2.09\,(9)\,(0.0384)}{7}\right]^3\right\}$$

$$= 12.10$$

ution: Angles of Attack Below the Stall

$$\frac{C_L}{\cos\alpha} = C'_N = C_{N_\alpha}\frac{\sin 2\alpha_e}{2} + C_{N_{\alpha\alpha}}\sin\alpha_e\,|\sin\alpha_e| \text{ (equation 4.1.3.3-a with } \alpha = \alpha_e)$$

$$C_{N_{\alpha\alpha}} = \left(C_{N_{\alpha\alpha}}\right)_{ref} + \Delta C_{N_{\alpha\alpha}} \text{ (equation 4.1.3.3-b)}$$

$$C_{N_{\alpha\alpha}} = 0.274 + \Delta C_{N_{\alpha\alpha}}$$

①	②	③	④	⑤	⑥	⑦	⑧	⑨
α (deg)	α_e (deg)	$\frac{\tan\alpha_e}{\tan(\alpha_e)_{C_{L_{max}}}}$	$\Delta C_{N_{\alpha\alpha}}$ fig. 4.1.3.3-55a	$C_{N_{\alpha\alpha}}$ eq. 4.1.3.3-b .274 + ④	$C_{N_{\alpha\alpha}}\sin^2\alpha_e$	$C_{N_\alpha}\frac{\sin 2\alpha_e}{2}$	C'_N eq. 4.1.3.3-a ⑥+⑦	$C_L = (C'_N\cos\alpha)$
0	1.77	0.1349	2.83	3.10	0.0030	0.1639	0.1669	0.167
4	5.77	0.4409	2.83	3.10	0.0313	0.5313	0.5626	0.561
8	9.77	0.7513	1.75	2.02	0.0582	0.8881	0.9463	0.937
10	11.77	0.9092	0.65	0.92	0.0383	1.0601	1.0984	1.082
11.14	12.91	1.00	0	0.27	0.0130	1.1563	1.1693	1.147

Compute: Angles of Attack Above the Stall

$C^*_{L_{max}}$ (Calculated using the low-aspect-ratio method of Section 4.1.3.4)

$$\left(C_{L_{max}}\right)_{base} = 0.79 \text{ (figure 4.1.3.4-23a at } (C_1 + 1)\frac{A}{\beta}\cos\Lambda_{LE} = \frac{4}{\beta},\ \Delta y = 2.20)$$

$$(C_2 + 1)\,A\tan\Lambda_{LE} = (2.09)\,(9)\,(0.0384) = 0.723$$

$$\Delta C_{L_{max}} = -0.105 \text{ (figure 4.1.3.4-24a)}$$

$$C^*_{L_{max}} = \left(C_{L_{max}}\right)_{base} + \Delta C_{L_{max}} \text{ (equation 4.1.3.4-g)}$$

$$= 0.79 + (-0.105) = 0.685$$

$$\left(C_{N_{\alpha\alpha}}\right)_{90^\circ} = 1.37 \text{ (figure 4.1.3.3-55b)}$$

$\left(C_{N_{\alpha\alpha}}\right)_{ref}$ = 0.274 (calculated on page 4.1.3.3-20)

Solution: Angles of Attack Above the Stall

$$\frac{C_L}{\cos \alpha} = C_N' = C_{N_\alpha} \frac{\sin 2\alpha_e}{2} + C_{N_{\alpha\alpha}} \sin \alpha_e |\sin \alpha_e| \quad \text{(equation 4.1.3.3-a with } \alpha = \alpha_e\text{)}$$

$$C_{N_{\alpha\alpha}} = \left(C_{N_{\alpha\alpha}}\right)_{ref} + \left[\left(C_{N_{\alpha\alpha}}\right)_{90^o} - \left(C_{N_{\alpha\alpha}}\right)_{ref}\right] \left[1 - \frac{\tan (\alpha_e)_{C_{L_{max}}}}{\tan \alpha_e}\right] + \beta^2 D \frac{C_{N_\alpha}}{2.3} \left(\frac{C_{L_{max}}}{C^*_{L_{max}}}\right)^2$$

(equation 4.1.3.3-f with $\alpha = \alpha_e$)

$$= 0.274 + (1.37 - 0.274) \left[1 - \frac{\tan (\alpha_e)_{C_{L_{max}}}}{\tan \alpha_e}\right] + 0.91 D \frac{5.31}{2.3} \left(\frac{1.15}{0.685}\right)^2$$

$$= 1.37 - 1.096 \frac{\tan (\alpha_e)_{C_{L_{max}}}}{\tan \alpha_e} + 5.92 D$$

$$\alpha_e = \alpha \left[1 - \frac{\alpha_0}{90^o - \alpha_{C_{L_{max}}}}\right] - \frac{90\ \alpha_0}{90^o - \alpha_{C_{L_{max}}}} \quad \text{(equation 4.1.3.3-g)}$$

$$= \alpha \left[1 - \frac{(-1.77)}{90 - 11.14}\right] - \frac{90\,(-1.77)}{90 - 11.14}$$

$$= 1.022\,\alpha + 2.020$$

① α deg	② α_e deg	③ $\frac{\tan (\alpha_e)_{C_{L_{max}}}}{\tan \alpha_e}$	④ D fig. 4.1.3.3-55a	⑤ $C_{N_{\alpha\alpha}}$ eq. 4.1.3.3-f 1.37 + 1.096 ③ + 5.92 ④	⑥ $C_{N_{\alpha\alpha}} \sin^2 \alpha_e$	⑦ $C_{N_\alpha} \frac{\sin 2\alpha_e}{2}$	⑧ C_N' eq. 4.1.3.3-a ⑥ + ⑦	⑨ $C_L = (C_N' \cos \alpha)$
11.2	13.47	0.9570	-0.05	0.0251	0.0014	1.203	1.204	1.181
12	14.28	0.9006	-0.25	-1.0970	-0.0668	1.269	1.202	1.176
13	15.31	0.8371	-0.70	-3.691	-0.2574	1.328	1.071	1.044

A comparison of the calculated values and the experimental data of reference 26 is presented as sketch (e).

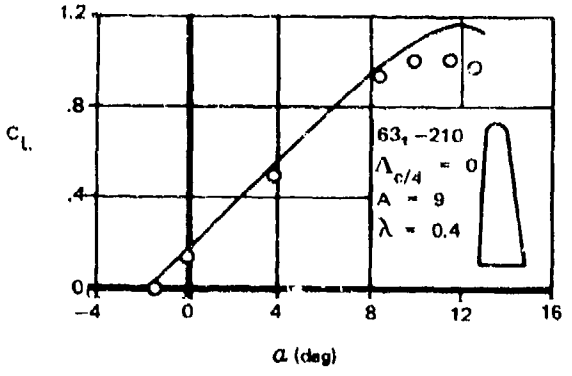

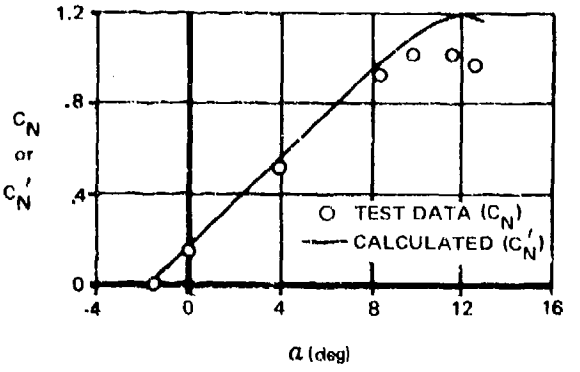

SKETCH (e)

Non-Straight-Tapered Wings

4. Double-Delta Wing

Given: The double-delta wing of reference 27.

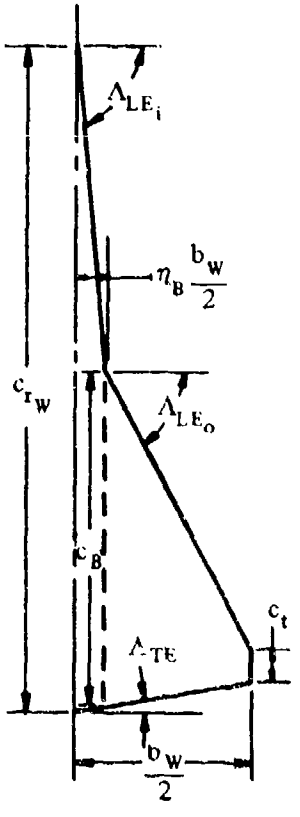

A_W	= 1.49	A_i	= 0.127	S_W	= 9026 sq ft
b_W	= 116 ft	η_B	= 0.180	S_i	= 3437 sq ft
S_o	= 5589 sq ft	λ_W	= 0.0454	λ_i	= 0.483
λ_o	= 0.094	Λ_{TE}	= -10^O	Λ_{LE_i}	= 84.75^O
Λ_{LE_o}	= 62^O	$\Lambda_{c/2_i}$	= 79.5^O	$\Lambda_{c/2_o}$	= 40.7^O

Low Speed; β = 1.0 κ = 1.0 (assumed)

Compute:

C_{L_α} (Section 4.1.3.2)

$$(\cos \Lambda_{c/2})_{eff} = \frac{1}{S_W} \sum_{j=1}^{j=n} (\cos \Lambda_{c/2})_j \, S_j \quad \text{(equation 4.1.3.2-f)}$$

$$= \frac{1}{S_W} (\cos \Lambda_{c/2})_i \, S_i + (\cos \Lambda_{c/2})_o \, S_o$$

$$= \frac{1}{9026} [(0.1822)(3437) + (0.7581)(5589)]$$

$$= 0.5388$$

$$(\Lambda_{c/2})_{eff} = 57.4^\circ; \tan (\Lambda_{c/2})_{eff} = 1.5637$$

$$\frac{A}{\kappa} \left[\beta^2 + \tan^2 (\Lambda_{c/2})_{eff}\right]^{\frac{1}{2}} = 1.49 [1.0 + (1.5637)^2]^{\frac{1}{2}} = 2.77$$

$C_{L_\alpha}/A = 1.16$ per rad (figure 4.1.3.2-49)

$C_{L_\alpha} = 1.728$ per rad

$\beta \tan \Lambda_{LE_i} = (1.0)(10.884) = 10.884$

$$\frac{A_i}{\eta_B} = \frac{0.127}{0.180} = 0.706$$

Solution:

$$C_L = \left(\frac{C_L}{C_{L_\alpha}} \frac{A_i}{\eta_B}\right) \frac{C_{L_\alpha}}{A_i/\eta_B} \quad \text{(equation 4.1.3.3-h)}$$

① α (deg)	② $\beta \tan \Lambda_{LE_i}$	③ $\left(\frac{C_L}{C_{L_\alpha}} \frac{A_i}{\eta_B}\right)$ fig. 4.1.3.3-56	④ C_{L_α} (per rad)	⑤ $\frac{A_i}{\eta_B}$	⑥ C_L eq. 4.1.3.3-h ③④/⑤
4	10.884	0.055	1.728	0.706	0.1346
8	↓	0.127	↓	↓	0.3110
12		0.208			0.5079
16		0.294			0.7196
20		0.380			0.9301

The calculated values of C_L are plotted versus α and a curve faired through the calculated points tangent to C_L near zero lift. (see sketch (f)).

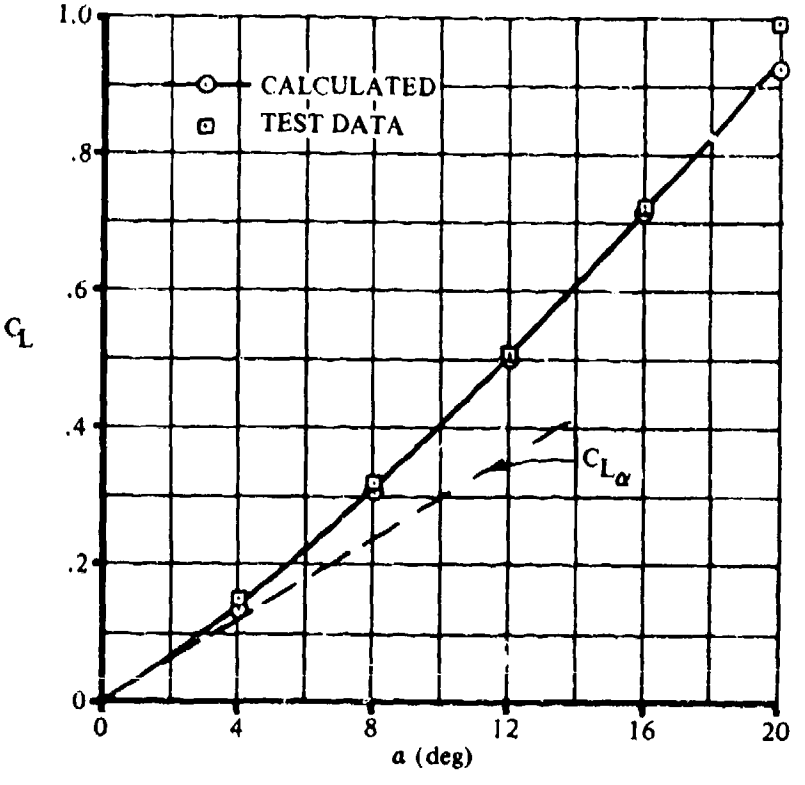

SKETCH (f)

5. Cranked Wing

Given: The cranked wing of reference 28. This is the configuration of the sample problem of paragraph A of Section 4.1.3.2. Some of the characteristics are repeated.

$A_W = 4.0$ $S_W = 2.25$ sq ft $S_i = 1.641$ sq ft $b_W = 3.0$ ft

$\eta_B = 0.60$ $\Lambda_{LE_i} = 48.6^o$ $A_i = 1.97$ $M = 0.80$; $\beta = 0.60$

Compute:

$C_{L_\alpha} = 4.324$ per rad $= 0.0755$ per deg (sample problem, paragraph A, Section 4.1.3.2)

$$\frac{1}{\tan \Lambda_{LE_i}} = \frac{1}{1.1343} = 0.882$$

$\alpha_{break} = 5.9^o$ (figure 4.1.3.3-57)

$C_{L_{break}} = C_{L_\alpha}\, \alpha_{break}$ (equation 4.1.3.3-i)

$= (0.0755)(5.9) = 0.445$

$\beta \tan \Lambda_{LE_i} = (0.6)(1.1343) = 0.681$

$\frac{A_i}{\eta_B} = \frac{1.97}{0.60} = 3.283$

$C_{L_{nonlinear}} = \left(\frac{C_L}{C_{L_\alpha}} \frac{A_i}{\eta_B}\right) \frac{C_{L_\alpha}}{A_i/\eta_B}$ (equation 4.1.3.3-h)

① α (deg)	② $\beta \tan \Lambda_{LE_i}$	③ $\left(\frac{C_L}{C_{L_\alpha}} \frac{A_i}{\eta_B}\right)$ fig. 4.1.3.3-56	④ C_{L_α} (per rad)	⑤ $\frac{A_i}{\eta_B}$	⑥ $C_{L_{nonlinear}}$ eq. 4.1.3.3-h ③④ / ⑤
4	0.681	0.158	4.324	3.283	0.208
8	↓	0.283	↓	↓	0.373
12	↓	0.415	↓	↓	0.547
16	↓	0.555	↓	↓	0.731
20	↓	0.685	↓	↓	0.902

Plot $C_{L_{nonlinear}}$ versus α and read $\left[(C_L)_{\alpha = \alpha_{break}}\right]_{nonlinear}$ at α_{break}.

$\left[(C_L)_{\alpha = \alpha_{break}}\right]_{nonlinear} = 0.285$ (constructed, see sketch (g))

Solution: $\alpha \geq \alpha_{break}$

$C_L = C_{L_{break}} + \delta C_L$ (equation 4.1.3.3-k)

$\delta C_L = \left[C_L - (C_L)_{\alpha = \alpha_{break}}\right]_{nonlinear}$ (equation 4.1.3.3-j)

①	②	③	④	⑤	⑥
α (deg)	C_L (nonlinear)	$(C_L)_{\alpha=\alpha_{break}}$ (nonlinear)	δC_L eq. 4.1.3.3-j ② - ③	$C_{L_{break}}$	C_L eq. 4.1.3.3-k ④ + ⑤
5.9	0.285	0.285	0	0.445	0.445
8	0.373	↓	0.088	↓	0.533
12	0.547		0.262		0.707
16	0.731		0.446		0.891
20	0.902		0.617		1.062

These calculated values of C_L are plotted versus α on sketch (g).

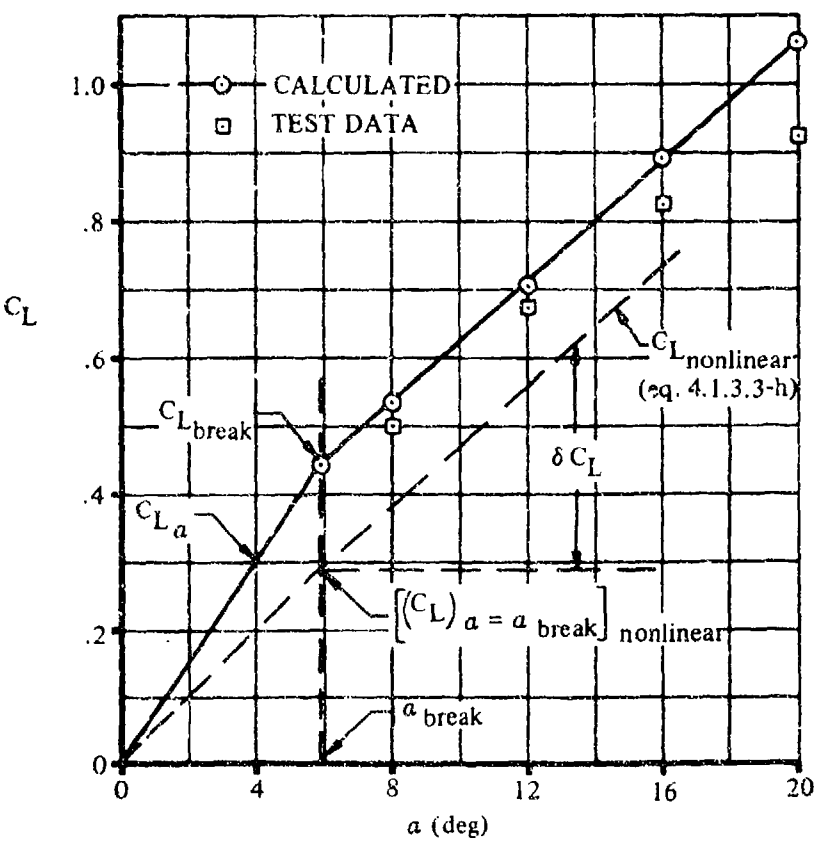

SKETCH (g)

6. Curved Wing

Given: The ogee wing of reference 29.

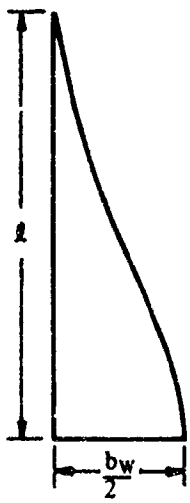

$A = 1.20 \quad b_w = 12.0$ in. $\quad \ell = 20.0$ in.

$M = 0.4$

Compute:

Wing slenderness parameter

$$\frac{b_w}{2\ell} = \frac{12.0}{2(20.0)} = 0.30$$

$$\sqrt{\frac{b_w}{2\ell}} = 0.548$$

Solution:

$$C_L = \frac{C_L}{\sqrt{\frac{b_w}{2\ell}}} \sqrt{\frac{b_w}{2\ell}} \quad \text{(equation 4.1.3.3-}\ell\text{)}$$

①	②	③	④
α (deg)	$C_L \Big/ \sqrt{\frac{b_w}{2\ell}}$ fig. 4.1.3.3-58	$\sqrt{\frac{b_w}{2\ell}}$	C_L eq. 4.1.3.3-ℓ ② ③
4	0.249	0.548	0.136
8	0.525	↓	0.288
12	0.850		0.465
16	1.210		0.664
20	1.580		0.865

These calculated results are compared with test data in table 4.1.3.3-D at angles of attack of 4°, 8°, and 12°.

B. TRANSONIC

No specific charts are presented for determining the transonic lift characteristics of wings at high angles of attack. The best source of information of this type is experimental data on similar configurations, e.g., reference 10. If such information is not immediately available, the method of the following paragraphs may be used as a guide to obtain trends.

For thin, low-aspect-ratio, conventional wings, an indication of the lift characteristics at high angles of attack at transonic speeds may be obtained by the following procedure:

1. Calculate the complete lift curves for $M = 0.6$ and $M = 1.4$ by the methods of paragraphs A and C, respectively, of this section.

2. Obtain the wing lift-curve slope at low angles of attack, as outlined in Section 4.1.3.2, for intermediate Mach numbers.

3. Obtain the wing maximum-lift variation with Mach number and angle of attack for maximum lift as outlined in Section 4.1.3.4.

4. Using as a guide the information determined in the first three steps, construct the approximate lift curves for the range of Mach numbers between 0.6 and 1.4.

For thick, high-aspect-ratio, conventional wings the same procedure may be used except that the transonic lift-curve slopes obtained from Section 4.1.3.2 apply only to the first few degrees of angle of attack and may be misleading if extrapolated to higher angles. Section 4.1.3.2 gives a more detailed discussion of this problem. For any wing, local nonlinearities at high angles of attack are likely to exist at Mach numbers between 0.8 and 0.95. Again, it is best to use experimental data.

C. SUPERSONIC

Conventional, swept wings at supersonic speeds may be conveniently divided into two major categories:

Wings with subsonic leading edges, that is, wings for which $\beta/\tan \Lambda_{LE} < 1$

Wings with supersonic leading edges, that is, wings for which $\beta/\tan \Lambda_{LE} > 1$

The supersonic-leading-edge category may be further subdivided according to whether or not the leading-edge shock is attached or detached.

In order to provide continuity between these various supersonic regimes, as well as with the subsonic regime, the normal-force equation, 4.1.3.3-a, has again been used. As before, the first term is based on linear theory and the second accounts for nonlinear effects. The linear term is taken from Section 4.1.3.2 and the nonlinear coefficient $C_{N_{\alpha\alpha}}$ is given in the charts of this section. The charts of this section are based on references 11 through 19. Table 4.1.3.3-E presents substantiation data and compares the results obtained with this method to experimental data for the subsonic-leading-edge case. Tables 4.1.3.3-F and 4.1.3.3-G present corresponding information for the supersonic-leading-edge cases. Table 4.1.3.3-F is for wings having attached shocks at low angles and detached shocks at high angles. Table 4.1.3.3-G is for wings having detached shocks throughout the angle-of-attack range.

Supersonic Normal-Force Coefficient of Wings with Subsonic Leading Edges

For conventional, swept wings with subsonic leading edges at supersonic free-stream Mach numbers, the nonlinear character of the normal-force curve is primarily a function of $\beta/\tan \Lambda_{LE}$ and to a lesser degree of C_{N_α}. The lift characteristics are similar to the subsonic maximum-lift characteristics of low-aspect-ratio wings, in that the maximum-lift coefficient first increases, then decreases with increasing aspect ratio (see Section 4.1.3.4). As with the subsonic wings, the critical leading-edge sweep angle at which reversal occurs seems to lie between 60° and 65°. Therefore, the influence of C_{N_α} has been separated into two regimes. In the first regime, for sweep angles less than 62.5°, C_{N_α} is used directly as derived from linear theory. In the second regime, for sweep angles greater than 62.5°, the lift-curve slope is modified by an empirical correction factor.

DATCOM METHOD

The procedure for finding the supersonic pseudo normal-force coefficient C'_N of a straight-tapered wing with subsonic leading edges at high angles of attack is as follows:

Step 1. The normal-force-curve slope C_{N_α} for the conventional wing is found from Section 4.1.3.2. This includes the modifying effect of thickness on normal-force-curve slope as given in figure 4.1.3.2-60. In this figure, thickness is represented by $\delta_\perp$, the semiwedge angle normal to the leading edge of wings having sharp leading edges, and by $\Delta y_\perp$, the leading-edge parameter normal to the leading edge of wings having rounded leading edges.

Step 2. An empirical parameter E is found from one of the two following equations:

$$E = C_{N_\alpha} \quad \text{for} \quad \frac{\tan \Lambda_{LE}}{1.92} \leqslant 1$$

$$E = C_{N_\alpha} \left[\frac{\tan \Lambda_{LE}}{1.92} + C \left(\frac{\tan \Lambda_{LE}}{1.92} - 1 \right) \right] \quad \text{for} \quad \frac{\tan \Lambda_{LE}}{1.92} > 1$$

where C is a thickness term from figure 4.1.3.3-59a and $\delta_\perp$ in this figure is the leading-edge parameter normal to the leading edge; for wings having rounded leading edges, $\delta_\perp = \tan^{-1} \dfrac{\Delta y_\perp}{5.85}$

Step 3. The nonlinear coefficient $C_{N_{\alpha\alpha}}$ is found from figure 4.1.3.3-59b as a function of $E \left(\dfrac{\beta}{\tan \Lambda_{LE}} \right)$ and the angle-of-attack parameter $\left[\dfrac{\left(C_{N_\alpha} \right)_{\text{theory}}}{C_{N_\alpha}} \right] \beta \tan \alpha$ or its reciprocal.

Step 4. The total lift and approximate normal-force coefficients are obtained using equation 4.1.3.3-a; i.e.,

$$\frac{C_L}{\cos \alpha} = C'_N = C_{N_\alpha} \frac{\sin 2\alpha}{2} + C_{N_{\alpha\alpha}} \sin \alpha \, |\sin \alpha|$$

Application of this technique is illustrated by the sample problem on pages 4.1.3.3-34 through 4.1.3.3-36.

Supersonic Normal-Force Coefficient of Wings With Supersonic Leading Edges

For conventional wings with supersonic leading edges, the wing leading-edge shock may or may not be attached, depending on the angle of attack and the wing thickness.

When the shock is attached, shock-expansion theory (summarized in reference 20) gives accurate results. Shock-expansion theory states that the pressures acting on a wing are a direct function of the airfoil thickness and profile shape. For the total integrated normal forces, however, little accuracy is lost if the wing is assumed to be a flat plate.

Thickness effects may not be neglected, even approximately, in determining the conditions under which an attached shock will detach. A shock will start to detach whenever the sum of the angle of attack and the semiwedge angle, both measured normal to the leading edge, exceeds the value of an expression given in reference 20; in other words,

$$a_\perp + \delta_\perp > \frac{4}{3\sqrt{3}\,(\gamma+1)} \frac{(M_\perp^2 - 1)^{3/2}}{M_\perp^2}$$

where $M_\perp$ is the Mach number normal to the leading edge and $\gamma = 1.4$. This function is plotted in figure 4.1.3.3-61b. As the angle of attack is increased beyond this value for incipient shock detachment, an angle-of-attack transition region occurs (see sketch (h)), wherein the normal-force characteristics of a given wing gradually come to resemble those of a similar wing of somewhat greater thickness at a lower angle of attack. When the angle of attack reaches the upper limit of the transition region, the shock may be considered to be fully detached.

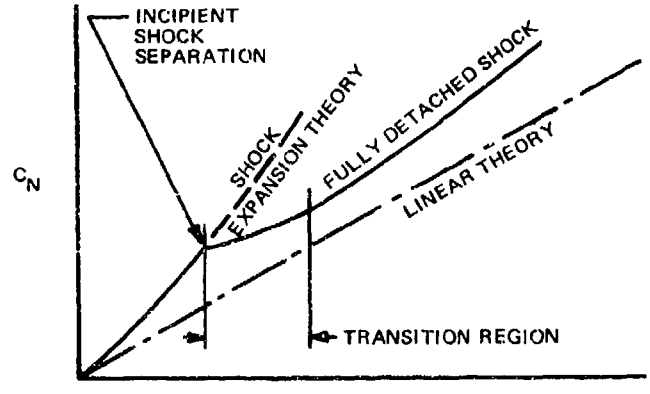

SKETCH (h)

For wings where the leading-edge shock is detached, no theory exists for the prediction of normal forces. However, examination of experimental data shows that a nonlinear force coefficient may be defined and presented in much the same way as was done for supersonic wings with subsonic leading edges. This is to be expected, since a local subsonic region exists near the leading edge when the shock is detached. For these wings, the nonlinear coefficient $C_{N_{aa}}$ is a function of C_{N_a} only.

DATCOM METHOD

The first step is to determine whether the leading-edge shock is attached or detached at zero angle of attack. This is determined by using figure 4.1.3.3-61b. Set $\delta_{eff_\perp}$ (see figure 4.1.3.3-61b) equal to the semiwedge angle of the wing perpendicular to the wing leading edge $\delta_\perp$, and calculate the upstream Mach number perpendicular to the wing leading edge at zero angle of attack by

$$(M_\perp)_{\alpha=0} = M_\infty \sqrt{1 - \sin^2 \Lambda_{LE}}$$

The leading-edge shock condition is then determined by the boundary of figure 4.1.3.3-61b. If the shock is detached, follow procedure (1) below; if the shock is attached, follow procedure (2).

1. Supersonic Wings With Detached Shock at Zero Angle of Attack

The procedure for finding the supersonic pseudo normal-force coefficient C'_N at high angles of attack of a straight-tapered wing with supersonic leading edges and with a detached shock is as follows:

Step 1.a. The derivative C_{N_α} is calculated from Section 4.1.3.2. C_{N_α} is the theoretical normal-force-curve slope of figures 4.1.3.2-56a through 4.1.3.2-56g multiplied by the empirical thickness correction of figure 4.1.3.2-60.

Step 1.b. The equivalent lift-curve slope E is calculated from the appropriate one of the two following equations:

$$E = C_{N_\alpha} \text{ for } \frac{\tan \Lambda_{LE}}{1.92} \leq 1.0$$

$$E = C_{N_\alpha}\left[\frac{\tan \Lambda_{LE}}{1.92} + C\left(\frac{\tan \Lambda_{LE}}{1.92} - 1\right)\right] \text{ for } \frac{\tan \Lambda_{LE}}{1.92} > 1$$

where C is determined from figure 4.1.3.3-59a as a function of the semiwedge angle normal to the leading edge.

The nonlinear coefficient $C_{N_{\alpha\alpha}}$ is determined from figure 4.1.3.3-60a as a function of E and the angle-of-attack parameter used as the abscissa.

Step 1.c. The total lift and approximate normal-force coefficients are obtained using equation 4.1.3.3-a; i.e.,

$$\frac{C_L}{\cos \alpha} = C'_N = C_{N_\alpha} \frac{\sin 2\alpha}{2} + C_{N_{\alpha\alpha}} \sin \alpha \, |\sin \alpha|$$

2. Supersonic Wings With Attached Shock at Zero Angle of Attack

The procedure for finding the supersonic pseudo normal-force coefficient C'_N at high angles of attack of a straight-tapered wing with supersonic leading edges and with an attached shock is as follows:

Step 2.a. The derivative C_{N_α} is calculated from Section 4.1.3.2. C_{N_α} is the theoretical normal-force slope of figures 4.1.3.2-56a through 4.1.3.2-56g multiplied by the empirical thickness correction of figure 4.1.3.2-60.

Step 2.b. Determine the angle of attack α^* at which the shock will start to detach. This is obtained by using figure 4.1.3.3-61b. For unswept wings, the value of $\delta_{eff_\perp}$ at the start of shock detachment is obtained from figure 4.1.3.3-61b at $M_\perp = M_\infty$. Then the angle of attack at which the shock will start to detach is determined by

$$\alpha^* = \delta_{eff_\perp} - \delta_\perp$$

For swept wings $\delta_{eff_\perp}$ must be determined by graphical interpolation, since there is an interdependence between the Mach number and the angle of attack normal to the leading edge. These relations for swept wings are

$$M_\perp = M_\infty \sqrt{1 - \sin^2 \Lambda_{LE} \cos^2 \alpha}$$

$$\alpha_\perp = \tan^{-1}\left(\frac{\tan \alpha}{\cos \Lambda_{LE}}\right)$$

where M_∞ is the free-stream Mach number, $M_\perp$ is the Mach number perpendicular to the leading edge, α is the wing angle of attack, and $\alpha_\perp$ is the angle of attack normal to the leading edge.

For a selected range of α's, calculate $\delta_{eff_\perp}$ and $M_\perp$ using the above equations and the relationship

$$\delta_{eff_\perp} = \alpha_\perp + \delta_\perp$$

Then plot $M_\perp$ versus $\delta_{eff_\perp}$ on figure 4.1.3.3-61b. The intersection of this curve and the boundary curve of figure 4.1.3.3-61b determines the value of $\delta_{eff_\perp}$ at which the shock will start to detach. Then the angle of attack at which the shock will start to detach is determined by

$$\alpha^* = \tan^{-1}\left[\tan(\delta_{eff_\perp} - \delta_\perp) \cos \Lambda_{LE}\right]$$

Step 2.c. The angle-of-attack-transition increment between incipient shock detachment and full detachment is now determined from figure 4.1.3.3-61a. To enter this figure, the nonlinear normal-force coefficient at incipient shock separation $C^*_{N_{\alpha\alpha}}$ must be known. This is read

from figure 4.1.3.3-60b by entering on the abscissa $\left(\beta \tan \alpha \text{ or } \frac{1}{\beta \tan \alpha}\right)$ at the angle of attack corresponding to incipient shock separation as already calculated in step 2.b.

$C^*_{N_{\alpha\alpha}} = C_{N_{\alpha\alpha}}$ is then read from the appropriate β-curve.

Step 2.d. The total lift and approximate normal-force coefficients may now be calculated for the three different angle-of-attack ranges using equation 4.1.3.3-a; i.e.,

$$\frac{C_L}{\cos \alpha} = C'_N = C_{N_\alpha} \frac{\sin 2\alpha}{2} + C_{N_{\alpha\alpha}} \sin \alpha \, |\sin \alpha|$$

where

C_{N_α} is from step 2.a.

$C_{N_{\alpha\alpha}}$ for the attached-shock range is read from figure 4.1.3.3-60b.

$C_{N_{\alpha\alpha}}$ for the fully-detached-shock range is read from figure 4.1.3.3-60a in the manner outlined in step 1.b. of the section on detached shocks.

$C_{N_{\alpha\alpha}}$ in the transition range is interpolated graphically or calculated analytically from the linear-interpolation formula

$$C_{N_{\alpha\alpha}} = C^*_{N_{\alpha\alpha}} - \left(\frac{\alpha - \alpha^*}{\alpha' - \alpha^*}\right)\left(C^*_{N_{\alpha\alpha}} - C'_{N_{\alpha\alpha}}\right)$$

In the above formula the starred quantities are measured at incipient-shock-separation conditions, and primed quantities are measured at the end of the transition region, where the shock is fully detached.

Application of this technique is illustrated by sample problem 2 on pages 4.1.3.3-36 through 4.1.3.3-39.

Sample Problems

1. Supersonic Pseudo-Normal-Force Coefficient of Wing With Subsonic Leading Edge.

Given: Wing 4a of reference 15.

$A = 0.562 \quad \lambda = 0 \quad \Lambda_{LE} = 82^\circ \quad M = 6.9; \quad \beta = 6.83$

Airfoil: 5-percent-thick (free-stream direction) double wedge with maximum thickness at 50-percent chord

Compute:

C_{N_α} (Section 4.1.3.2)

$\delta_\perp$, semiwedge angle normal to wing leading edge

$$\delta_\perp = \frac{\text{semiwedge angle}}{\cos \Lambda_{LE}} = \frac{\frac{1}{2}\left(\frac{0.05}{0.5}\right)}{0.1392}(57.3) = 20.55^\circ$$

$$\frac{\beta}{\tan \Lambda_{LE}} = 0.960 \text{ (subsonic leading edge)}$$

$$A \tan \Lambda_{LE} = 4.00$$

$$\left(C_{N_\alpha}\right)_{\text{theory}} = 0.573 \text{ per rad (figure 4.1.3.2-56a)}$$

$$\frac{C_{N_\alpha}}{\left(C_{N_\alpha}\right)_{\text{theory}}} = 0.750 \text{ (figure 4.1.3.2-60)}$$

$$C_{N_\alpha} = (0.750)(0.573) = 0.430 \text{ per rad}$$

Empirical Parameter E

$$\frac{\tan \Lambda_{LE}}{1.92} = 3.71; \text{ therefore, use second equation listed under step 1.b. of Datcom method.}$$

$$C_{N_\alpha} \frac{\tan \Lambda_{LE}}{1.92} = 1.595$$

$C = 1.30$ (figure 4.1.3.3-59a)

$$E = C_{N_\alpha}\left[\frac{\tan \Lambda_{LE}}{1.92} + C\left(\frac{\tan \Lambda_{LE}}{1.92} - 1\right)\right]$$

$$= 0.43\ [3.71 + (1.30)(3.71 - 1)]$$

$$= 3.11$$

$$E \frac{\beta}{\tan \Lambda_{LE}} = 3.00$$

Solution:

$$C'_N = C_{N_\alpha} \frac{\sin 2\alpha}{2} + C_{N_{\alpha\alpha}} \sin \alpha\ |\sin \alpha| \text{ (equation 4.1.3.3-a)}$$

$C_{N_{aa}}$ is obtained from figure 4.1.3.3-59b.

① α (deg)	② $\frac{C_{N_\alpha}}{(C_{N_\alpha})_{theory}} \frac{1}{\beta \tan\alpha}$	③ $C_{N_{\alpha\alpha}}$ fig. 4.1.3.3-59b	④ $C_{N_{\alpha\alpha}} \sin^2\alpha$	⑤ $C_{N_\alpha} \frac{\sin 2\alpha}{2}$	⑥ C'_N eq. 4.1.3.3-a ④+⑤	⑦ $\left(C'_N \cos\alpha\right)$
8	0.783	0.12	0.002	0.059	0.06	0.06
12	0.517	0.44	0.019	0.087	0.11	0.11
16	0.384	0.64	0.048	0.114	0.16	0.15
20	0.302	0.78	0.091	0.138	0.23	0.22
24	0.247	0.90	0.149	0.160	0.31	0.28
28	0.207	1.00	0.220	0.178	0.40	0.35
32	0.176	1.09	0.306	0.193	0.50	0.42
36	0.151	1.15	0.397	0.204	0.60	0.49
40	0.131	1.22	0.504	0.212	0.72	0.55

2. Supersonic Pseudo-Normal-Force Coefficient of Wing with Supersonic Leading Edge

Given: Wings 1A and 1B of reference 15

$A = 2.31 \quad \lambda = 0 \quad \Lambda_{LE} = 60^\circ \quad M = 6.91; \ \beta = 6.83$

Airfoil: 5-percent-thick double wedge with maximum thickness at 50-percent chord

Compute:

Determine whether the leading-edge shock is attached or detached at zero angle of attack.

$\delta_\perp$ = semiwedge angle normal to wing leading edge

$$\delta_\perp = \frac{\text{semiwedge angle}}{\cos \Lambda_{LE}} = \frac{\frac{1}{2}\left(\frac{0.05}{0.5}\right)}{0.500}(57.3) = 5.7^\circ$$

$$(M_\perp)_{\alpha=0} = M_\infty \sqrt{1 - \sin^2 \Lambda_{LE}} = 3.45$$

For the conditions $(M_\perp)_{\alpha=0} = 3.45$ and $\delta_{eff_\perp} = 5.7^\circ$, the leading-edge shock is attached (see figure 4.1.3.3-61b); therefore, follow procedure (2) of the Datcom method.

C_{N_α} (Section 4.1.3.2)

$$\frac{\tan \Lambda_{LE}}{\beta} = 0.254$$

$$A \tan \Lambda_{LE} = 4.00$$

$$\left(C_{N_\alpha}\right)_{theory} = 0.586 \text{ per rad (figure 4.1.3.2-56a)}$$

$$\frac{C_{N_\alpha}}{\left(C_{N_\alpha}\right)_{theory}} = 1.0 \text{ (figure 4.1.3.2-60)}$$

$$C_{N_\alpha} = 0.586 \text{ per rad}$$

Determine the angle of attack for which the shock will start to detach (α^*).

① α (deg)	② $\tan\alpha$	③ $\frac{\tan\alpha}{\cos\Lambda_{LE}}$	④ $\alpha_\perp$ ($\tan^{-1}$ ③) (deg)	⑤ $\delta_{eff_\perp}$ ($\alpha_\perp + \delta_\perp$) (deg)	⑥ $\cos\alpha$	⑦ $M_\perp = M_\infty\sqrt{1 - \sin^2\Lambda_{LE}\cos^2\alpha}$
4	0.0699	0.1399	7.96	13.7	0.9976	3.48
8	0.1450	0.2901	16.18	21.9	0.9903	3.55
12	0.2121	0.4252	23.04	28.7	0.9781	3.67
16	0.2867	0.5734	29.83	35.5	0.9613	3.82
20	0.3640	0.7280	36.06	41.8	0.9397	4.01
24	0.4452	0.8904	41.68	47.4	0.9135	4.22

Plot $\delta_{eff_\perp}$ versus $M_\perp$ on figure 4.1.3.3-61b. At the intersection of this curve and the boundary curve of figure 4.1.3.3-61b, read $\delta_{eff_\perp}$ at the start of shock detachment.

$$\delta_{eff_\perp} = 38.5^o$$

$$\alpha^* = \tan^{-1}\left[\tan\left(\delta_{eff_\perp} - \delta_\perp\right)\cos\Lambda_{LE}\right]$$

$$= \tan^{-1}\left[\tan\left(38.5 - 5.7\right)\cos 60^o\right]$$

$$= \tan^{-1}\left(0.3223\right) = 17.9^o$$

Solution: Angles of Attack for Fully Attached Shock

$$C'_N = C_{N_\alpha} \frac{\sin 2\alpha}{2} + C_{N_{\alpha\alpha}} \sin\alpha \, |\sin\alpha| \qquad \text{(equation 4.1.3.3-a)}$$

$C_{N_{\alpha\alpha}}$ is obtained from figure 4.1.3.3-60b.

①	②	③	④	⑤	⑥	⑦
α (deg)	$\beta \tan\alpha$	$C_{N_{\alpha\alpha}}$ fig. 4.1.3.3-60b	$C_{N_{\alpha\alpha}} \sin^2\alpha$	$C_{N_\alpha} \frac{\sin 2\alpha}{2}$	C'_N eq. 4.1.3.3-a ④ + ⑤	C_L $(C'_N \cos\alpha)$
4	0.478	0.32	0.002	0.041	0.043	0.043
8	0.960	0.62	0.012	0.081	0.093	0.092
	$\frac{1}{\beta\tan\alpha}$					
12	0.689	0.93	0.040	0.119	0.159	0.156
16	0.510	1.17	0.089	0.155	0.244	0.235
17.9	0.453	1.27	0.120	0.171	0.291	0.277

Solution: Angles of Attack in the Transition Range

$\Delta\alpha = 8.2^\circ$ (figure 4.1.3.3-61a at $C^*_{N_{\alpha\alpha}} = 1.27$)

α' = angle of attack for fully detached shock = $\alpha^* + \Delta\alpha = 26.1^\circ$

$$\left[\frac{C_{N_\alpha}}{(C_{N_\alpha})_{\text{theory}}}\right] \frac{1}{\beta \tan\alpha} = 0.301 \text{ (at } \alpha' = 26.1^\circ)$$

Empirical Parameter E

$\frac{\tan\Lambda_{LE}}{1.92} = 0.902$; therefore, $E = C_{N_\alpha} = 0.586$ (first equation listed under step 1.b. of Datcom method for wings with detached shock)

$C'_{N_{\alpha\alpha}} = 1.23$ (figure 4.1.3.3-60a at $\alpha' = 26.1^\circ$)

$$C_{N_{\alpha\alpha}} = C^*_{N_{\alpha\alpha}} - \left(\frac{\alpha - \alpha^*}{\alpha' - \alpha^*}\right)\left(C^*_{N_{\alpha\alpha}} - C'_{N_{\alpha\alpha}}\right)$$

$$= 1.27 - \left(\frac{a - 17.9}{26.1 - 17.9}\right)(1.27 - 1.23)$$

$$= 1.27 - (a - 17.9)(0.005)$$

$$C'_N = C_{N_\alpha} \frac{\sin 2a}{2} + C_{N_{\alpha\alpha}} \sin a \, |\sin a| \quad \text{(equation 4.1.3.3-a)}$$

① α (deg)	② $C_{N_{0\alpha}}$	③ $C_{N_{\alpha\alpha}} \sin^2\alpha$	④ $C_{N_\alpha} \frac{\sin 2\alpha}{2}$	⑤ C'_N eq. 4.1.3.3-e ③+④	⑥ $\frac{C_L}{\left(C'_N \cos\alpha\right)}$
20	1.26	0.147	0.188	0.335	0.315
24	1.24	0.205	0.218	0.423	0.386

Solution: Angles of Attack for Fully Detached Shock

$$C'_N = C_{N_\alpha} \frac{\sin 2a}{2} + C_{N_{\alpha\alpha}} \sin a \, |\sin a| \quad \text{(equation 4.1.3.3-a)}$$

$C_{N_{\alpha\alpha}}$ is obtained from figure 4.1.3.3-60a.

① α (deg)	② $\frac{C_{N_\alpha}}{(C_{N_\alpha})_{theory}} \frac{1}{\beta \cot\alpha}$	③ $C_{N_{\alpha\alpha}}$ fig. 4.1.3.3-60a	④ $C_{N_{\alpha\alpha}} \sin^2\alpha$	⑤ $C_{N_\alpha} \frac{\sin 2\alpha}{2}$	⑥ C'_N eq. 4.1.3.3-e ④+⑤	⑦ $\left(C'_N \cos\alpha\right)$
28	0.275	1.31	0.289	0.243	0.532	0.470
32	0.234	1.43	0.402	0.283	0.685	0.584
36	0.202	1.46	0.504	0.279	0.783	0.633

D. HYPERSONIC

At hypersonic speeds, the calculation of surface pressures on wings is complicated by several interrelated phenomena. These include the boundary layer, the shock wave, heat transfer between the wing and the gas, dissociation, and ionization. The relative importance of each of these phenomena as they affect the aerodynamic characteristics of wings traveling at hypersonic speeds has not been fully assessed.

Boundary layers affect the surface pressures by the displacement of the inviscid flow. This displacement of the flow also affects the shock-wave pattern and hence the surface pressures. At very low Reynolds numbers the inviscid flow between the boundary layer and the shock wave is entirely absorbed by the boundary layer, and the boundary layer interacts directly with the shock wave. In general, the Reynolds number decreases with increasing Mach number along the flight corridor because of the low densities at the altitudes associated with flight at high hypersonic speeds. Thus boundary-layer effects become important at the higher hypersonic speeds.

Because of aerodynamic heating at hypersonic speeds, lifting surfaces usually use blunt leading edges. Detached shocks are thus present ahead of the wing leading edge. Pressures on the surface near the leading edge behind the detached shock are large compared to oblique-shock, inviscid, flat-plate values at the same angle of attack. This "overpressure" decays with distance from the leading edge in a manner that depends on the free-stream Mach number, leading-edge radius, Reynolds number, and heat-transfer characteristics.

An empirical method presented in references 21 and 22 attempts to account for these Reynolds-number and detached-shock effects. This method combines inviscid-flow theory, blast-wave theory, and a viscous-interaction parameter. The examples presented in references 21 and 22 give some idea of the magnitude of these effects on the surface pressures. Because of the scarcity of test data, however, the range of applicability of this method is undetermined. The accuracy claimed in the references is ±15 percent.

Heat transfer between the gas and the wing surface affects the boundary-layer thickness and hence the surface pressures. The hotter the boundary layer, the thicker it becomes, and vice versa. Gas properties, notably the viscosity and ratio of specific heats, change with temperature. Increasing temperature increases the viscosity and decreases the specific-heat ratio. An indication of the effect of surface temperature on pressure distribution is shown in reference 22.

At high speed and/or low altitudes the extreme temperatures behind the detached shock wave cause dissociation of the atmospheric molecules into their atomic constituents. Under conditions of still higher temperature the atoms ionize and the gas becomes a conducting medium. These phenomena are generally restricted to the leading-edge region. Chapter VIII of reference 23 treats these problems.

Small-disturbance theory has yielded many useful hypersonic similarity forms both for two-dimensional sections and for axisymmetric bodies (chapter II of reference 23). Hypersonic similarity is basically limited to low angles of attack and slender bodies, although successful applications have been made that do not meet these conditions. The hypersonic-similarity concept is discussed and used in Section 4.2.1.2.

The only simple closed-form solution available for the estimation of the normal-force curve of blunt wings at hypersonic speeds is obtained from Newtonian or impact theory (reference 23). Newtonian theory assumes that the component of momentum normal to the surface is canceled (flow remains parallel to the surface after impact), giving rise to a normal force. Several modifications of Newtonian theory that have been developed are discussed in paragraph D of Section 4.2.1.1.

Newtonian theory does not account for many of the real gas interaction effects previously discussed. At high angles of attack or at high Mach numbers the surface pressures attributable to these interactions are small compared to the impact pressures. At low angles of attack or low Mach numbers they are no longer small compared to the impact pressures.

Newtonian theory also assumes that the pressures on the leeward surfaces (those not "seen" from the free-stream direction) are equal to the ambient pressure. Again, this is a good approximation at high angles of attack or high Mach numbers, because the actual pressures on the leeward surfaces compared to those on the forward-facing areas are small. At low Mach numbers or angles of attack the leeward pressures are no longer small compared to the positive pressures, and Newtonian theory gives less accurate results.

The general field of hypersonic flow is treated in references 23 and 24.

DATCOM METHOD

The curves of figures 4.1.3.3-59b through 4.1.3.3-60b are based on test data for the high supersonic Mach numbers and converge to Newtonian-theory flat-plate values for high hypersonic Mach numbers. It is recommended that these charts be used in conjunction with the normal-force-curve-slope information from paragraph C of Section 4.1.3.2 to obtain the total normal-force curve of wings in hypersonic flow.

REFERENCES

1. Benepe, D. B., Kouri, B. G., Webb, J. B., et al: Aerodynamic Characteristics of Non-Straight-Taper Wings. AFFDL-TR-66-73, 1966. (U)

2. Winter, H.: Flow Phenomena on Plates and Airfoils of Short Span. NACA TM 798, 1936. (U)

3. Michael, W. H., Jr.: Flow Studies in the Vicinity of a Modified Flat-Plate Rectangular Wing of Aspect Ratio 0.25. NACA TN 2790, 1952. (U)

4. Bartlett, G. E., and Vidal, R. J.: Experimental Investigation of Influence of Edge Shape on the Aerodynamic Characteristics of Low Aspect Ratio Wings at Low Speeds. Jour. Aero. Sci., Vol. 22, No. 8, August 1955. (U)

5. Anderson, A. E.: An Investigation at Low Speed of a Large-Scale Triangular Wing of Aspect Ratio Two. II — The Effect of Airfoil Section Modifications and the Determination of the Wake Downwash. NACA RM A7H28, 1947. (U)

6. Cahill, J. F., and Gottlieb, S. M.: Low-Speed Aerodynamic Characteristics of a Series of Swept Wings Having NACA 65A006 Airfoil Sections. (Revised) NACA RM L50F16, 1950. (U)

7. Letko, W.: Experimental Determination at Subsonic Speeds of the Oscillatory and Static Lateral Stability Derivatives of a Series of Delta Wings with Leading-Edge Sweep from 30° to 86.5°. NACA RM L57A30, 1957. (U)

8. Küchemann, D.: A Non-Linear Lifting-Surface Theory for Wings of Small Aspect Ratio with Edge Separations. RAE Aero 2540, 1955. (U)

9. Peckham, D. H.: Low-Speed Wind-Tunnel Tests on a Series of Uncambered Slender Pointed Wings with Sharp Edges. RAE Aero 2613, 1958. (U)

10. Emerson, H. F.: Wind-Tunnel Investigation of the Effect of Clipping the Tips of Triangular Wings of Different Thickness, Camber, and Aspect Ratio — Transonic Bump Method. NACA TN 3671, 1956. (U)

11. Gallagher, J. J., and Mueller, J. N.: An Investigation of the Maximum Lift of Wings at Supersonic Speeds. NACA TR 1227, 1955. (U)

12. Kaattari, G. E.: Pressure Distributions on Triangular and Rectangular Wings to High Angles of Attack — Mach Numbers 1.45 and 1.97. NACA RM A54D19, 1954 (U)

13. Bertram, M. H., and McCauley, W. D.: Investigation of the Aerodynamic Characteristics at High Supersonic Mach Numbers of a Family of Delta Wings Having Double-Wedge Sections With the Maximum Thickness at 0.18 Chord. NACA RM L54G28, 1954. (U)

14. Bertram, M. H., and McCauley, W. D.: An Investigation of the Aerodynamic Characteristics of Thin Delta Wings With a Symmetrical Double-Wedge Section at a Mach Number of 6.9. NACA RM L55B14, 1955. (U)

15. Kaattari, G. E.: Pressure Distributions on Triangular and Rectangular Wings to High Angles of Attack — Mach Numbers 2.46 and 3.36. NACA RM A54J12, 1955. (U)

16. Boatright, W. B.: Experimental Study and Analysis of Loading and Pressure Distributions on Delta Wings Due to Thickness and to Angle of Attack at Supersonic Speeds. NACA RM L56I14, 1956. (U)

17. Pitts, W. C.: Force, Moment, and Pressure-Distribution Characteristics of Rectangular Wings at High Angles of Attack and Supersonic Speeds. NACA RM A55K08, 1956. (U)

18. Smith, F. M.: Experimental and Theoretical Aerodynamic Characteristics of Two Low-Aspect-Ratio Delta Wings at Angles of Attack to 50° at a Mach Number of 4.07. NACA RM L57E02, 1957. (U)

19. Hill, W. A.: Experimental Lift of Low-Aspect-Ratio Triangular Wings at Large Angles of Attack and Supersonic Speeds. NACA RM A57I17, 1957. (U)

20. Ames Research Staff: Equations, Tables, and Charts for Compressible Flow. NACA TR 1135, 1953. (U)

21. Creager, M. O.: Surface Pressure Distribution at Hypersonic Speeds for Blunt Delta Wings at Angle of Attack. NASA Memo 5-12-59A, 1959. (U)

22. Creager, M. O.: An Approximate Method for Calculating Surface Pressures on Curved-Profile Blunt Plates in Hypersonic Flow. NASA TN D-71, 1959. (U)

23. Hayes, W. D., and Probstein, R. F.: Hypersonic Flow Theory. Academic Press, New York and London, 1959. (U)

24. Truitt, R. W.: Hypersonic Aerodynamics. The Ronald Press Company, New York, 1959. (U)

25. Koenig, D. G.: Low-Speed Tests of Semispan Wing Models at Angles of Attack from 0^{o} to 180^{o}. NASA Memo 2-27-59A, 1959. (U)

26. Boddy, L. E., and Sutton F. B.: Effects of Wing-Tip Turrets on the Aerodynamic Characteristics of a Typical Bomber-Wing Model. NACA RM A9E09, 1949. (U)

27. Magruder, W. M., et al: Low Speed Characteristics of the Double-Delta SST. Lockheed Horizons, Issue 1, Spring 1965, pp. 28-47. (U)

28. Goodson, K. W., and Becht, R. E.: Wind-Tunnel Investigation at High Subsonic Speeds of the Stability Characteristics of a Complete Model Having Sweepback-, M-, W-, and Cranked-Wing Planforms and Several Horizontal-Tail Locations. NACA RM L54C29, 1954. (U)

29. Squire, L. C., and Capps, D. S.: An Experimental Investigation of the Characteristics of an Ogee Wing from M = 0.4 to M = 1.8. ARC CP 585, 1962. (U)

30. Anon: Small-Scale Wing-Body Planform Investigation at Mach Numbers from 0.40 to 2.94. Unpublished Data. (U)

31. Anon: Large-Scale Double-Delta Wing-Body Planform Investigation at Low Speed. Unpublished Data. (U)

32. Cayot, J. E., and Kuchar, C. E.: System 125A Summary Data Report, Transonic Tests of a 1/30-Scale Model of the WS-125A Airplane (WADC 168). Convair, General Dynamics, F/W Rpt. FZT-25-013, 1957. (C) Title Unclassified

33. Anon: System 125A, Convair Model 25, Summary Data Report, Subsonic Tests of a Preliminary 1/27-Scale Force Model (CVAL 201). Convair, General Dynamics, F/W Rpt. FZT-25-004, 1958. (C) Title Unclassified

34. Grant, F. C., and Sevier, J. R., Jr: Transonic and Supersonic Wind-Tunnel Tests of Wing-Body Combinations Designed for High Efficiency at a Mach Number of 1.41. NASA TN D-435, 1960. (U)

35. Mansell, C. J.: Low-Speed Wind-Tunnel Tests on Two Thin Cranked Wings With 60-Degree Sweepback Inboard. ARC R&M 2995, 1957. (U)

36. Wakefield, R. M.: Effects of Wing-Crank, Leading-Edge Chord Extensions and Horizontal-Tail Height on the Longitudinal Stability of Swept-Wing Models at Mach Numbers from 0.60 to 1.4. NASA TM X-92, 1959. (U)

37. Henderson, W. P., and Hammond, A. D.: Low-Speed Investigation of High-Lift and Lateral Control Devices on a Semispan Variable-Sweep Wing Having an Outboard Pivot Location. NASA TM X-542, 1961. (U)

38. Lockwood, V. E., McKinney, L. W., and Lamar, J. E.: Low-Speed Aerodynamic Characteristics of a Supersonic Transport Model with a High Aspect Ratio Variable Sweep Warped Wing. NASA TM X-979, 1964. (C) Title Unclassified

39. Jernell, L. S.: The Effects of Conical Camber on the Longitudinal Aerodynamic Characteristics of a Variable-Sweep Wing-Fuselage Configuration at Mach Numbers from 0.50 to 3.50. NASA TM X-804, 1963. (C) Title Unclassified

40. Holdaway, G. H., and Mellenthin, J. A.: Evaluation of Blended Wing-Body Combinations with Curved Plan Forms at Mach Numbers up to 3.50. NASA TM X-379, 1960. (U)

41. Hicks, R. M., and Hopkins, E. J.: Effects of Spanwise Variation of Leading-Edge Sweep on the Lift, Drag, and Pitching Moment of a Wing-Body Combination at Mach Numbers from 0.7 to 2.94. NASA TN D-2236, 1964. (U)

42. Earnshaw, P. B.: Low-Speed Wind-Tunnel Tests on a Series of Cambered Ogee Wings. ARC CP 775, 1964. (U)

43. Squire, L. C.: Further Experimental Investigations of the Characteristics of Cambered Gothic Wings at Mach Numbers From 0.4 to 2.0. ARC R&M 3310, 1963. (U)

44. Dobson, M. D., and King-Underwood, R.: Wind-Tunnel Tests Between M = 0.4 and 2.0 on a Cambered Wing of Slender Ogee Planform. ARC CP 778, 1965. (U)

45. Ergebnisse der aerodynamische Versuchsanstalt Goettingen, 1932. (U)

TABLE 4.1.3.3-A
SUBSONIC WING-LIFT VARIATION WITH ANGLE OF ATTACK
DATA SUMMARY AND SUBSTANTIATION

Ref.	A	Λ_{LE}	λ	Δ_y	M	R_ℓ x 10^{-6}	$C_{L_{max}}$	$\alpha_{C_{L_{max}}}$ (deg)	J	α (deg)	C_L Calc.	C_L Test	* Percent Error
3	.25	0	1.0	.745	-0.1	2.1	1.06	45	.139	10	.16	.15	6.6
										20	.45	.417	7.9
										30	.77	.715	7.7
										40	1.02	.986	3.4
										45	1.06	1.06	0
4	1.5	0	1.0	.726	-0.1	2.0	.985	26	.836	5	.21	.190	10.5
										10	.38	.40	- 5.0
										15	.60	.65	- 7.7
										20	.82	.85	- 3.5
										26	.985	*	—
4	1.23	30	.698	.63	-0.1	2.9	1.06	35	.815	5	.17	.175	- 2.8
										10	.375	.38	- 1.3
										15	.6	.66	- 9.1
										20	.815	.85	- 4.1
										25	.98	.98	0
										30	1.05	*	—
										35	1.05	*	—
4	1.5	69.5	0	.26	-0.1	3.0	1.34	35	1.28	5	.185	.175	5.7
										10	.395	.375	5.3
										15	.63	.60	5.0
										20	.875	.86	1.7
										25	1.08	1.11	- 2.7
										30	1.24	1.285	- 3.5
										35	1.34	1.37	- 2.2
5	2	63.4	0	.749	-0.15	14.6	1.37	34.5	.218	5	.22	.22	0
										10	.465	.465	0
										15	.73	.695	5.0
										20	.96	.935	2.7
										25	1.165	1.165	0
										30	1.32	1.345	- 1.8
										34.5	1.37	1.34	2.2

TABLE 4.1.3.3-A (Contd)

Ref	A	Λ_{LE}	λ	Δy	M	R_ℓ x 10^{-6}	$C_{L_{max}}$	$\alpha_{C_{L_{max}}}$ (deg)	J	α (deg)	C_L Calc.	C_L Test	* Percent Error
6	2	48.4	.6	1.2	-0.2	6.0	1.034	27.2	1.08	8	.407	.355	14.6
										12	.575	.575	0
										16	.755	.78	- 3.2
										20	.906	.955	- 5.2
										24	.99	1.033	- 4.2
										27.2	1.02	*	—
6	6	46.2	.6	1.2	-0.2	6.0	1.14	31.7	-4.6	8	.447	.424	5.4
										12	.640	.625	2.4
										16	.80	.78	2.5
										20	.938	.88	6.6
										24	1.045	.972	7.5
										28	1.120	1.026	9.2
										31.7	1.150	*	—
6	4	48.8	.3	1.2	-0.2	6.0	1.06	25.8	1.2	4	.23	.24	- 4.2
										8	.47	.50	- 6.0
										12	.70	.70	0
										16	.88	.90	- 2.2
										20	1.01	1.01	0
										24	1.06	1.07	.9
										25.9	1.06	1.04	1.9
6	4	1.0	1.0	1.2	0.2	6.0	1.026	25.2	.55	8	.442	.40	10.5
										12	.648	.67	- 3.3
										16	.826	.83	- 0.5
										20	.955	.935	2.1
										24	1.032	1.01	2.2
										25.2	1.028	1.015	1.3
										28	.91	.965	- 5.7

Average Error = $\frac{\Sigma \mid e \mid}{n}$ = 3.7%

*Experimental Data Not Available.

TABLE 4.1.3.3-B

SUBSONIC WING-LIFT VARIATION WITH ANGLE OF ATTACK

DOUBLE–DELTA WINGS

DATA SUMMARY AND SUBSTANTIATION

Ref.	Config.	A	λ_i	λ_o	η_B	Λ_{LE_i} (deg)	Λ_{LE_o} (deg)	$\frac{d}{b}$	$\frac{t}{c}$	LER	M	$R\ell_{MAC}$ X 10^{-6}	α (deg)	C_L Calc.	C_L Test	e Percent Error
30	WB	2.01	.416	.302	.313	78	53.3	.127	.03	Sharp[a]	.4	1.04	4	.165	.167	−1.2
													8	.348	.352	−1.1
													12	.559	.555	.7
													16	.77[illegible]	.786	−1.5
													20	[illegible]81	.981	1.0
											.7		4	.186	.194	−4.1
													8	.370	.389	−4.9
											.9		4	.233	.213	9.4
													8	.442	.444	−.5
	WB	1.96	.295	.344	.405	78	48.5	.127	.03	Sharp[a]	.4	1.14	4	.144	.162	−11.1
													8	.305	.324	−5.9
													12	.490	.501	−2.2
													16	.679	.698	−2.7
													20	.869	.892	−2.6
											.7		4	.165	.171	−3.5
													8	.334	.351	−4.8
											.9		4	.208	.189	10.1
													8	.399	.369	8.1
	WB	1.93	.180	.454	.498	78	38.1	.127	.03	Sharp[a]	.4	1.15	4	.130	.137	−5.1
													8	.274	.234	−3.5
													12	.440	.443	−.7
													16	.609	.611	−.3
													20	.781	.780	.1
	WB	1.93	.180	.454	.498	78	38.1	.127	.03	Sharp[a]	.7	1.15	4	.148	.159	−6.9
													8	.308	.319	−3.4
											.9		4	.183	.177	3.4
													8	.357	.345	3.5
	WB	1.30	.196	0	.414	82	60	.147	.03	Sharp[a]	.4	1.70	4	.118	.095	24.2
													8	.239	.222	7.7
													12	.393	.357	10.1
													16	.543	.500	8.6
													20	.701	.642	9.2
											.7		4	.128	.111	15.3
													8	.259	.246	5.3
											.9		4	[illegible]34	.127	5.5
													8	.278	.262	6.1
	WB	1.30	.302	.163	.403	82	60	.147	.03	Sharp[a]	.4	1.47	4	.132	.114	15.8
													8	.269	.273	−1.5
													12	.442	.440	.5

TABLE 4.1.3.3-8 (Contd)

Ref.	Config.	A	λ_i	λ_b	η_B	Λ_{LE_i} (deg)	Λ_{LE_o} (deg)	$\frac{d}{b}$	$\frac{t}{c}$	LER	M	$R_{\ell_{MAC}} \times 10^{-6}$	α (deg)	C_L Calc	C_L Test	e Percent Error
30	WB	1.33	.302	.163	.403	82	60	.147	.03	Sharp[a]	.4	1.47	16	.611	.615	−.7
													20	.787	.790	−.4
											.7		4	.145	.138	5.1
													8	.293	.293	0
											.9		4	.152	.147	3.4
													8	.317	.317	0
	WB	1.55	.301	0	.400	82	59	.144	.03	Sharp[a]	.4	1.38	4	.129	.132	−2.3
													8	.261	.282	−7.4
													12	.428	.446	−4.0
													16	.592	.628	−5.7
													20	.764	.805	−5.1
											.7		4	.141	.145	−2.8
													8	.288	.300	−4.0
											.9		4	.157	.155	1.3
													8	.336	.337	−.3
	WB	1.72	.358	0	.414	77.4	59	.127	.03	Sharp[a]	.4	1.30	4	.151	.142	6.3
													8	.321	.305	5.2
													12	.510	.483	5.6
													16	.706	.682	3.5
													20	.903	.880	2.6
											.7		4	.166	.159	4.4
													8	.312	.333	−6.3
											.9		4	.197	.174	13.2
													8	.332	.365	−9.0
31	WBV	1.87	.488	0	.424	72.6	59	.131	.02-.03	Sharp	.13	17.1	4	.150	.152	−1.3
													8	.340	.336	1.2
													12	.553	.556	−.5
													16	.769	.776	−.9
													20	979	.986	−.7
	WBV	1.46	.482	.189	.484	72.6	59	.149	.02-.03	Sharp	.13	17.3	4	.148	.134	10.4
													8	.335	.327	2.4
													12	.545	.546	−.2
													16	.757	.780	−2.9
													20	.965	1.006	−4.1
	WBV	1.73	.346	0	.551	73.0	59	.131	.02-.03	Sharp	.13	19.3	4	.144	.130	10.8
													8	.323	.308	4.9
													12	.524	.512	2.3
													16	.729	.715	2.0
													20	.930	.912	2.0
	WBV	1.34	.346	.240	.626	73.0	59	.149	.02-.03	Sharp	.13	19.5	4	.137	.136	0.7
													8	.307	.316	−2.8
													12	.498	.520	−4.2
													16	.693	.729	−4.9
													20	.884	.928	−4.7

TABLE 4.1 3.3-8 (Contd)

Ref.	Config.	A	λ_i	λ_o	η_B	Λ_{LE_i} (deg)	Λ_{LE_o} (deg)	$\frac{d}{b}$	$\frac{t}{c}$	L.E.R	M	$R\ell_{MAC} \times 10^{-6}$	α (deg)	C_L Calc.	C_L Test	* Percent Error
31	WBV	1.73	.356	0	.414	77.4	59	.131	.02-.03	Sharp	.13	20.0	4	.143	.150	−4.7
													8	.302	.332	−9.0
													12	.491	.540	−9.1
													16	.685	.746	−8.2
													20	.974	.950	2.5
	WBV	1.34	.356	.210	.475	77.4	59	.149	.02-.03	Sharp	.13	20.3	4	.130	.130	0
													8	.298	.319	−6.6
													12	.484	.520	−6.9
													16	.676	.710	−4.8
													20	.960	.910	5.5
	WBV	1.87	.448	0	.332	77.2	59	.131	.02-.03	Sharp	.13	17.8	4	.146	.150	−2.7
													8	.335	.326	2.8
													12	.524	.541	−3.1
													16	.759	.756	.4
													20	.971	.966	.5
	WBV	1.46	.448	.183	.379	77.2	59	.149	.02-.03	Sharp	.13	18.2	4	.144	.139	3.6
													8	.330	.312	5.8
													12	.538	.525	2.5
													16	.749	.744	.7
													20	.958	.960	−.2
27	WBVN	1.49	.683	.094	.180	84.75	62	.100	?	Sharp	.1	?	4	.135	.150	−10.0
													8	.311	.320	−2.8
													12	.508	.510	−.4
													16	.720	.723	−.4
													20	.930	.995	−6.5
32	WBVN	2.6	.200	0	.710	60	49.20	.090	.033	Round	.7	3.6	4	.214		
											.8		4	.229		
											.9		4	.242		
33	WBVN	2.6	.200	0	.709	60	49.20	.084	.035-.040	Round	.2	3.26	4	.184		
													8	.350		
													12	.531		
													16	.713		
													20	.892		
	WBVN	2.6	.200	0	.709	60	60	.084	.035-.040	Round	.2	3.26	4	.182	(b)	
													8	.345		
													12	.523		
													16	.703		
													20	.879		
	WBVN	3.0	.200	0	.654	60	42.08	.077	.035-.040	Round	.2	3.22	4	.184		
													8	.349		
													12	.529		
													16	.712		
													20	.890		

(a) These models had theoretically round L.E.'s inboard but were analyzed as sharp because of small size of modal and small t/c.

(b) This information is classified CONFIDENTIAL.

$$\text{Average Error} = \frac{\Sigma|\,e\,|}{n} = 4.6\%$$

TABLE 4.1.3.3–C

SUBSONIC WING-LIFT VARIATION WITH ANGLE OF ATTACK
CRANKED WINGS
DATA SUMMARY

Ref.	Config.	A	λ_i	λ_o	η_B	Λ_{LE_i} (deg)	Λ_{LE_o} (deg)	$\frac{d}{b}$	$\frac{t}{c}$	LER	M	$R\ell_{MAC}$ x 10^{-6}	α (deg)	C_L Calc	C_L Test	Percent Error
28	WBV	4.00	.580	.517	.600	49.2	6.6	.139	.06	Round	.80	2.6	8	0.553	0.500	10.6
													12	0.726	0.675	7.6
													16	0.910	0.825	10.3
													20	1.081	0.925	16.9
											.85	2.66	8	0.568	0.530	5.3
													12	0.734	0.690	6.4
													16	0.924	0.865	6.8
													20	1.099	0.995	10.5
											.90	2.81	8	0.603	0.530	13.8
													12	0.794	0.730	8.8
34	WB	2.91	.333	.500	.500	67.01	61.7	.139	.04–.03	Round	.60	2.20	8	0.372	0.370	0.5
													12	0.544	0.575	- 5.4
											.80	2.94	8	0.428	0.390	9.7
													12	0.631	0.585	7.9
											.90	3.30	8	0.477	0.405	17.8
													12	0.701	0.610	14.9
36[a]	WB	2.91	.641	.625	.600	53.13	32.16	.147	.06–.03	Round	.60	1.50	8	0.444	0.480	- 7.5
													12	0.616	0.688	-10.5
													16	0.794	0.835	- 4.9
													20	0.962	0.880	9.3
											.80		8	0.497	0.505	- 1.6
													12	0.693	0.693	0
													16	0.898	0.809	11.0
													20	1.098	0.880	24.8
											.90		8	0.560	0.505	10.9
													12	0.772	0.698	10.6
													16	1.006	0.824	22.0
													20	1.217	0.916	32.9
	WB	2.91	.641	.625	.600	53.13	43.22	.147	.06–.03	Round	.60	1.5	8	0.435	0.500	-13.0
													12	0.602	0.710	-15.2
													16	0.774	0.840	- 7.9
													20	0.937	0.900	4.1
											.80		8	0.452	0.515	-12.2
													12	0.631	0.710	-11.1
													16	0.818	0.825	- 0.8
													20	0.991	0.860	15.2
											.90		8	0.564	0.540	4.4
													12	0.776	0.715	8.5

TABLE 4.1.3.3–C (Contd)

Ref.	Config.	A	λ_i	λ_o	η_B	Λ_{LE_i} (deg)	Λ_{LE_o} (deg)	$\frac{d}{b}$	$\frac{t}{c}$	LER	M	R_ℓ MAC x 10^{-6}	α (deg)	C_L Calc.	C_L Test	* Percent Error
37	W	5.20	.339	.268	.379	60.0	25.0	.147	0.45–0.60	Round	.13	2.65	8	0.490	0.505	- 3.0
↓	↓	↓	↓	↓	↓	↓	↓	↓	↓	↓	↓	↓	12	0.647	0.695	- 6.9
↓	↓	↓	↓	↓	↓	↓	↓	↓	↓	↓	↓	↓	16	0.811	0.875	- 7.3
↓	↓	↓	↓	↓	↓	↓	↓	↓	↓	↓	↓	↓	20	0.969	1.050	- 7.7
38	WBV	8.47	.197	.386	.212	76.0	16.0	.062	–	Round	.20	3.6	8	0.472	(b)	
↓	↓	↓	↓	↓	↓	↓	↓	↓	↓	↓	↓	↓	12	0.594		
39	WB	8.18	.294	.463	.308	65.0	12.0	.066	0.06–0.02	Round	.50	.73	16	0.721		
↓	↓	↓	↓	↓	↓	↓	↓	↓	↓	↓	↓	↓	8	0.512		
													12	0.664		

(a) Notched leading edge

(b) This information is classified CONFIDENTIAL.

Average Error = $\frac{\Sigma |e|}{n}$ = 10.5%

TABLE 4.1.3.3–D
SUBSONIC WING-LIFT VARIATION WITH ANGLE OF ATTACK
CURVED (GOTHIC AND OGEE) WINGS
DATA SUMMARY AND SUBSTANTIATION

Ref.	Config.	Planform	A	$\frac{b_W}{2\ell}$	p	$\frac{d}{b}$	$\frac{t}{c}$ (root)	M	$R_{\ell_{MAC}}$ x 10^{-6}	α (deg)	C_L Calc.	C_L Test	ϵ Percent Error
29	WB	Ogee	1.2	.300	.500	.133	.05	.4	1.7	4	.136	.132	3.0
										8	.288	.285	1.1
										12	.465	.465	0
								.7		4	.136	.132	3.0
										8	.288	.297	-3.0
										12	.466	.489	-4.7
								.8		4	.136	.139	-2.2
										8	.288	.305	-5.6
										12	.466	.499	-6.6
40	WB	Ogee	2.00	.540	.540	.080	.03	.6	8.9	4	.183	.19	-3.7
										8	.386	.385	.3
41	WB	Ogee	1.98	.450	.455	.127	.02	.7	0.58	4	.167	.19	-12.1
										8	.352	.40	-12.0
9	W_1	Gothic	.96	.250	.667	....	.01	.1	2.9	4	.125	.120	4.2
										8	.263	.260	1.2
										12	.425	.425	0
										16	.605	.605	0
	W_2	Gothic	1.00	.333	.667	...	.01	.1	2.9	4	.144	.140	2.9
										8	.303	.310	-2.3
										12	.490	.490	0
										16	.698	.680	2.6
	W_3		1.25	.417	.667					4	.161	.150	7.3
										8	.339	.325	4.3
										12	.549	.532	3.2
	W_4		.94	.306	.651					4	.138	.140	-1.4
										8	.293	.290	1.0
										12	.470	.465	1.1
										16	.668	.659	1.4

TABLE 4.1.3.3–D (Contd)

Ref.	Config.	Planform	A	$\frac{b_W}{2\ell}$	p	$\frac{d}{b}$	$\frac{t}{c}$ (root)	M	$R_{\ell_{MAC}} \times 10^{-6}$	α (deg)	C_L Calc.	C_L Test	e Percent Error
9	W_5	Gothic	1.07	.333	.647	---	.01	.1	2.9	4	.144	.149	-3.4
										8	.303	.312	-2.9
										12	.490	.500	-2.0
										16	.698	.698	0
	W_{11}	Gothic	1.13	.333	.589	---	.01	.1	2.9	4	.144	.150	-4.0
										8	.303	.320	-5.3
										12	.490	.509	-3.7
										16	.698	.706	-1.0
	W_{12}	Gothic	.76	.250	.658	---	.01	.1	2.9	4	.125	.119	5.0
										8	.265	.260	1.9
										12	.425	.423	.5
										16	.605	.608	.5
42	W	Ogee	.927	.209	.450			.18		4	.114	.101	12.9
										8	.240	.230	4.3
										12	.388	.372	4.3
										16	.553	.525	5.3
										20	.722	.683	5.7

Average Error = $\frac{\Sigma \mid e \mid}{n}$ = 3.4%

TABLE 4.1.3.3-E
SUPERSONIC WING-LIFT VARIATION WITH ANGLE OF ATTACK
SUBSONIC LEADING EDGE
DATA SUMMARY AND SUBSTANTIATION

Ref.	A	Λ_{LE} (deg)	λ	Airfoil Section	δ (deg)	M	β	α (deg)	C_L Calc.	C_L Test	e Percent Error
11	1.37	63	1.0	Biconvex (t/c = .06)	15	1.55	1.18	10	0.331	0.358	−7.5
↓	↓	↓	↓	↓	↓	↓	↓	20	0.686	0.722	−5.1
↓	↓	↓	↓	↓	↓	↓	↓	30	0.959	0.944	1.6
↓	↓	↓	↓	↓	↓	↓	↓	40	1.091	1.005	8.5
12	2	63.4	0	Biconvex (t/c = .05)	12.6	1.97	1.70	10	0.344	0.335	2.7
↓	↓	↓	↓	↓	↓	↓	↓	20	0.679	0.630	7.8
↓	↓	↓	↓	↓	↓	↓	↓	30	0.912	0.858	6.3
↓	↓	↓	↓	↓	↓	↓	↓	40	1.030	0.961	5.0
↓	↓	↓	↓	↓	↓	↓	↓	50	1.030	0.958	7.5
16	1.73	66.6	0	65A003	16.8	2.41	2.19	5	0.123	0.132	−6.8
↓	↓	↓	↓	↓	↓	↓	↓	10	0.270	0.268	0.7
↓	↓	↓	↓	↓	↓	↓	↓	15	0.404	0.387	4.4
↓	↓	↓	↓	↓	↓	↓	↓	20	0.520	0.496	4.4
18	0.375	84.6	0	Mod Bicon (t/c = .04)	35	1.96	1.69	10	0.162	0.16	1.2
↓	↓	↓	↓	↓	↓	↓	↓	20	0.387	0.38	1.8
↓	↓	↓	↓	↓	↓	↓	↓	30	0.594	0.58	2.4
↓	↓	↓	↓	↓	↓	↓	↓	40	0.744	0.725	2.6
19	0.375	84.6	0	Mod Bicon (t/c = .04)	35	3.30	3.14	10	0.138	0.131	5.3
↓	↓	↓	↓	↓	↓	↓	↓	20	0.311	0.30	3.6
↓	↓	↓	↓	↓	↓	↓	↓	30	0.488	0.473	3.2
↓	↓	↓	↓	↓	↓	↓	↓	40	0.641	0.62	3.4
19	1	76	0	Mod Bicon (t/c = .04)	15.5	1.96	1.69	10	0.275	0.264	4.2
↓	↓	↓	↓	↓	↓	↓	↓	20	0.562	0.55	2.2
↓	↓	↓	↓	↓	↓	↓	↓	30	0.769	0.779	−1.2
↓	↓	↓	↓	↓	↓	↓	↓	40	0.874	0.892	−2.0

Average Error = $\frac{\Sigma|e|}{n}$ = 4.0%

TABLE 4.1.3.3-F
SUPERSONIC WING-LIFT VARIATION WITH ANGLE OF ATTACK
WITH TRANSITION FROM ATTACHED TO DETACHED SHOCK
DATA SUMMARY AND SUBSTANTIATION

Ref.	A	Λ_{LE} (deg)	λ	Airfoil Section	δ (deg)	M	β	α (deg)	C_L Calc.	C_L Test	e Percent Error
12	2	0	1.0	Biconvex (t/c = .06)	6	1.97	1.7	5	0.176	0.179	−1.6
								10	0.356	0.364	−2.2
								16.8°	0.636	0.622	2.2
								25	0.883	0.861	2.6
								35	1.024	1.023	0.1
								45	1.088	1.075	1.2
13	2.31	60	0	Mod. D.W. (t/c = .06)	24	6.9	6.82	3	0.031	0.0349	−11.2
								6.4°	0.070	0.077	−9.1
								12	0.143	0.147	−2.7
								20	0.287	0.277	3.6
								28	0.465	0.46	1.1
15	4	45	0	Biconvex (t/c = .06)	8	2.46	2.24	3	0.093	0.0927	0.3
								7°	0.218	0.218	0
								12	0.378	0.367	3.0
								18	0.573	0.542	5.7
								25	0.724	0.668	5.2
								35	0.872	0.892	−2.2
								45	0.958	0.988	−3.0
15	2	0	1.0	Biconvex (t/c = .06)	6	2.46	2.24	10	0.281	0.290	−3.1
								20	0.585	0.61	−4.1
								23.8°	0.718	0.731	−1.8
								35	0.90	0.942	−4.4
								45	0.992	1.026	−3.3

Average Error = $\frac{\Sigma|e|}{n}$ = 2.8%

*Angle for incipient shock detachment

TABLE 4.1.3.3-G
SUPERSONIC WING-LIFT VARIATION WITH ANGLE OF ATTACK
DETACHED LEADING-EDGE SHOCK
DATA SUMMARY AND SUBSTANTIATION

Ref.	A	Λ_{LE} (deg)	λ	Airfoil Section	δ (deg)	M	β	α (deg)	C_L Calc.	C_L Test	* Percent Error
25	1.98	64	0	Mod. Flat Pl. (t/c = .02)	21	2.32	2.1	10	0.272	0.287	-5.2
								20	0.574	0.552	3.8
								30	0.838	0.810	3.4
								40	1.0	0.965	3.8
26	4	45	0	Mod. Flat Pl. (t/c = 0.3)	20	2.32	2.1	10	0.298	0.320	-6.8
								20	0.625	0.642	-2.6
								30	0.906	0.936	-3.3
								40	1.076	1.060	1.4
11	1.76	36	1.0	Biconvex (t/c = .11)	16	1.55	1.18	10	0.399	0.404	-1.2
								20	0.765	0.810	-5.6
								30	0.981	1.030	-4.8
								40	1.013	1.076	-5.8
12	4	45	0	Biconvex (t/c = .06)	8	1.97	1.70	5	0.202	0.20	1.0
								15	0.602	0.56	7.5
								25	0.895	0.835	7.2
								35	1.024	1.024	0
								45	1.053	1.088	-3.2
13	1.62	68	0	Mod. D. W. (t/c = .08)	31	6.90	6.82	8	0.084	0.084	0
								12	0.134	0.133	0.8
								16	0.199	0.190	4.7
								20	0.278	0.267	8.2
								24	0.360	0.333	8.1
13	1.29	72.1	0	Mod. D. W. (t/c = .08)	36	6.90	6.82	8	0.077	0.071	8.4
								12	0.124	0.117	6.0
								16	0.180	0.174	3.4
								20	0.244	0.243	0.4
								24	0.309	0.32	-3.4
								28	0.372	0.40	-7.0
13	0.7	80	0	Mod. D. W. (t/c = .08)	62	6.90	6.82	8	0.005	0.058	12.0
								12	0.110	0.102	7.8
								16	0.164	0.158	3.8
								20	0.226	0.220	2.7
								24	0.292	0.288	1.4
								28	0.381	0.359	6.1
15	2	63.4	0	Biconvex (t/c = .06)	12.6	2.46	2.24	10	0.278	0.276	0.7
								20	0.519	0.517	0.4
								30	0.701	0.726	-3.4
								40	0.856	0.904	-5.3
								50	0.919	0.951	-3.4
16	3	53	0	65A003	11	2.41	2.19	5	0.150	0.154	-2.6
								10	0.311	0.296	5.0
								15	0.458	0.443	3.4
								20	0.582	0.559	4.1

Average Error = $\frac{\Sigma |\epsilon|}{n}$ = 4.1%

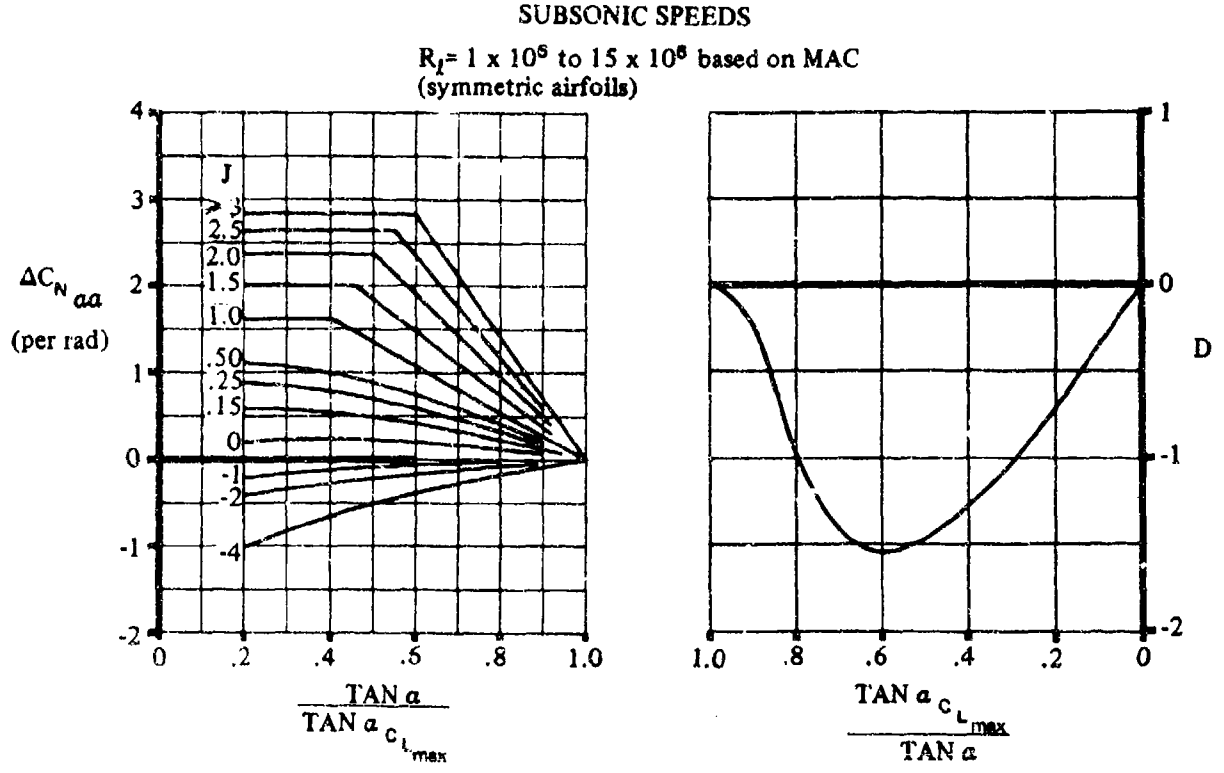

FIGURE 4.1.3.3-55a SUBSONIC LIFT VARIATION WITH ANGLE OF ATTACK

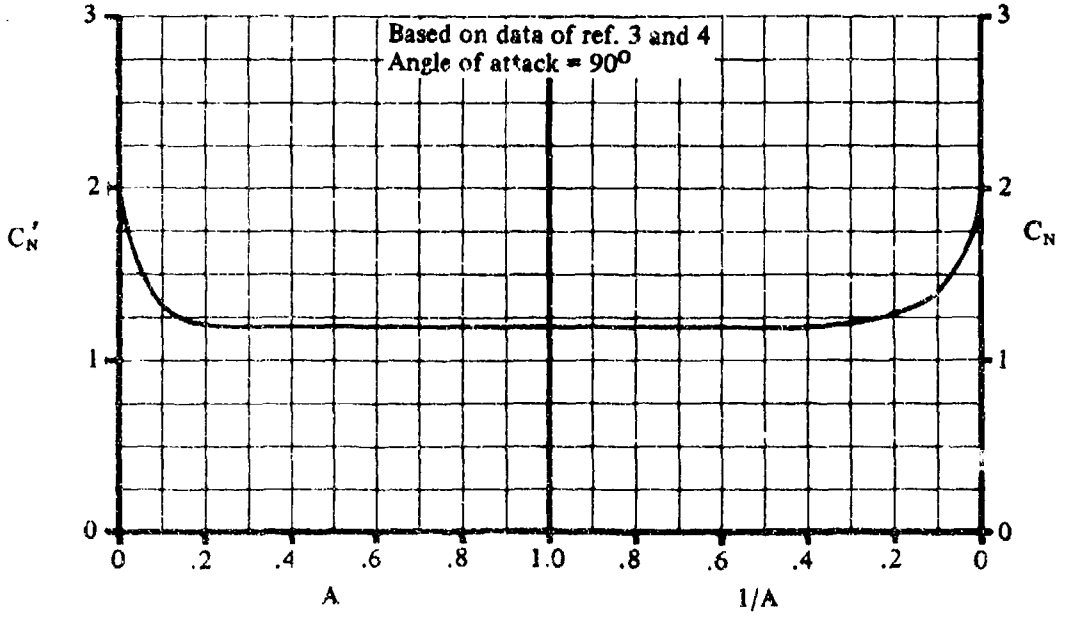

FIGURE 4.1.3.3-55b SUBSONIC LIFT VARIATION WITH WING ASPECT RATIO AT 90° ANGLE OF ATTACK

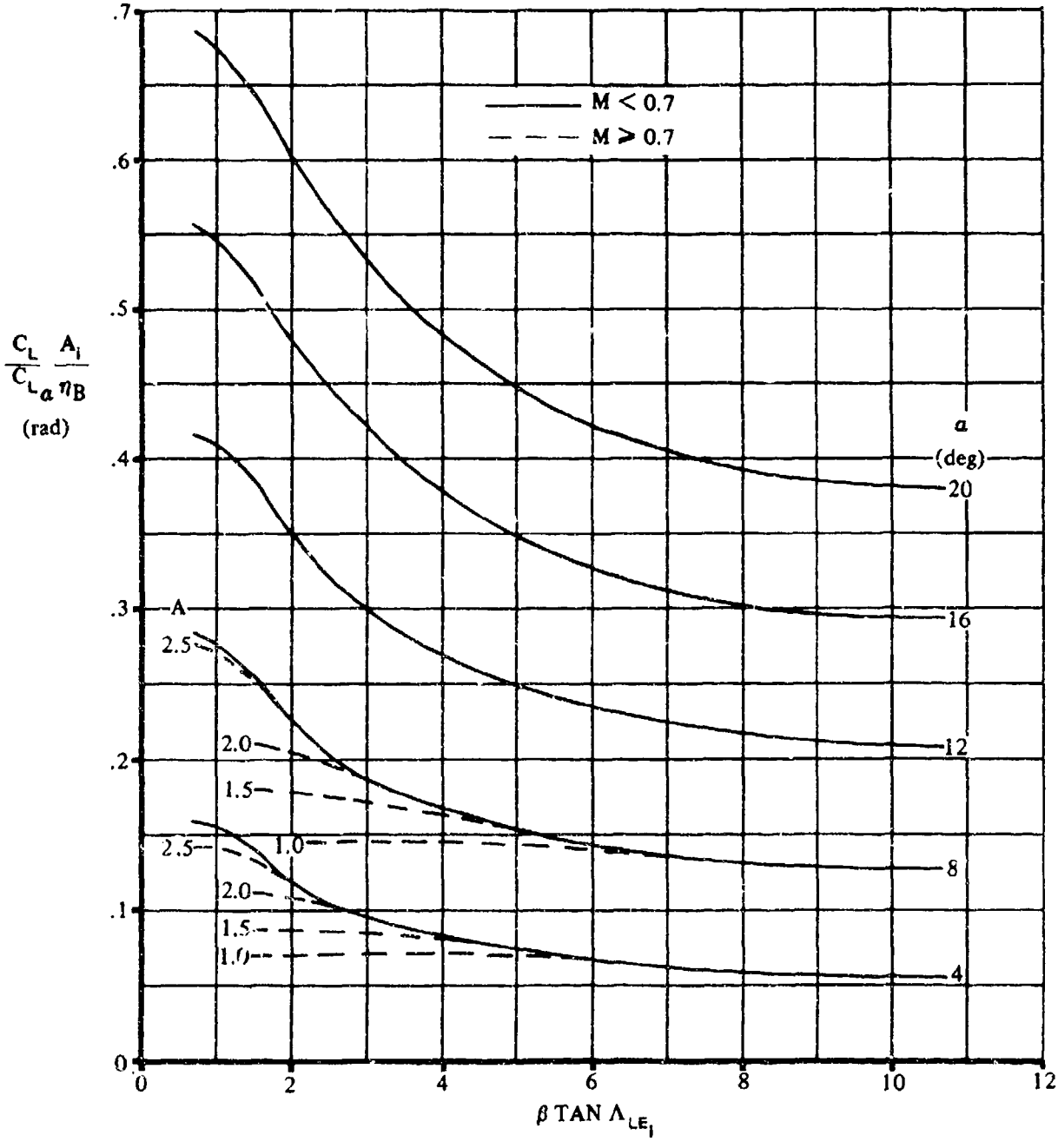

FIGURE 4.1.3.3-56 PREDICTION OF NONLINEAR LIFT OF DOUBLE-DELTA PLANFORMS AT SUBSONIC SPEEDS

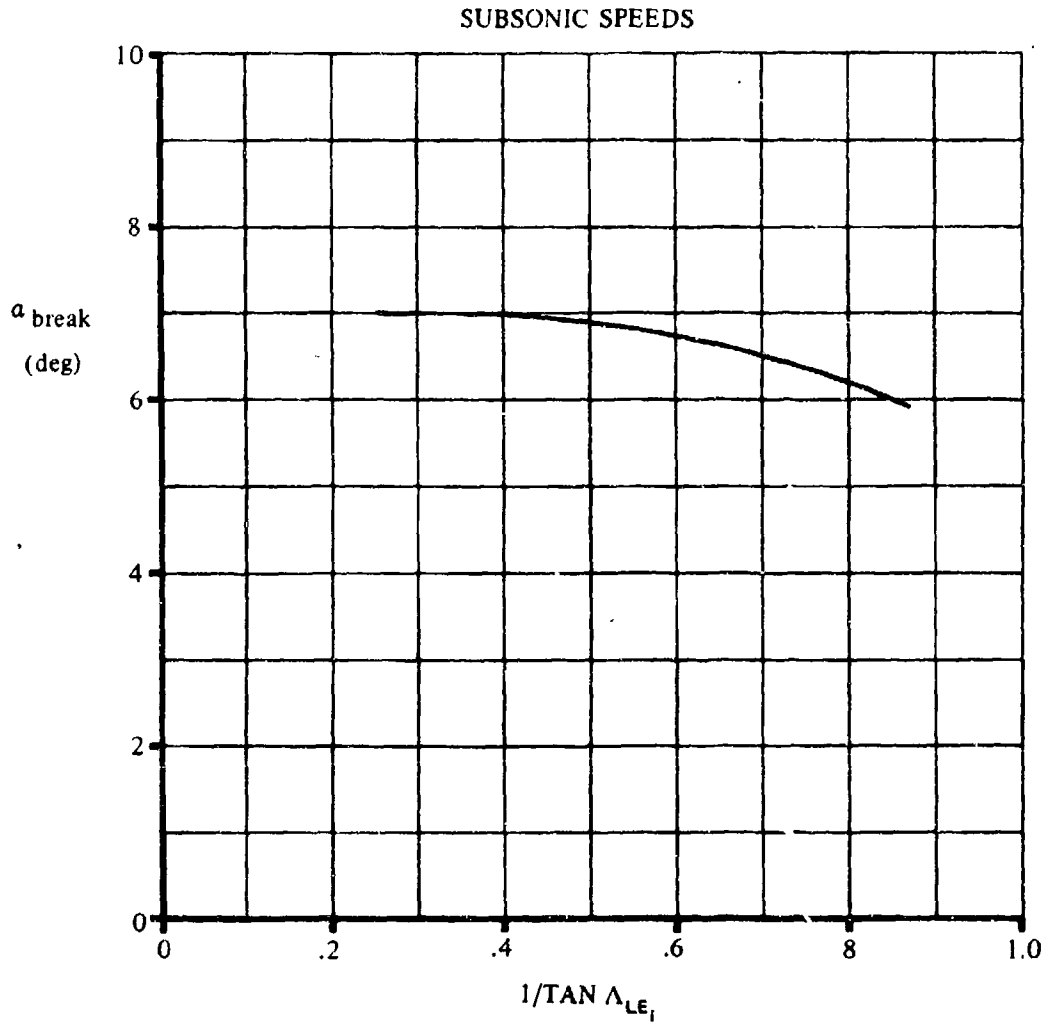

FIGURE 4.1.3.3-57 CORRELATION OF α_{break} FOR CRANKED PLANFORMS OF ASPECT RATIOS GREATER THAN 3 AND HAVING ROUND-NOSED AIRFOILS

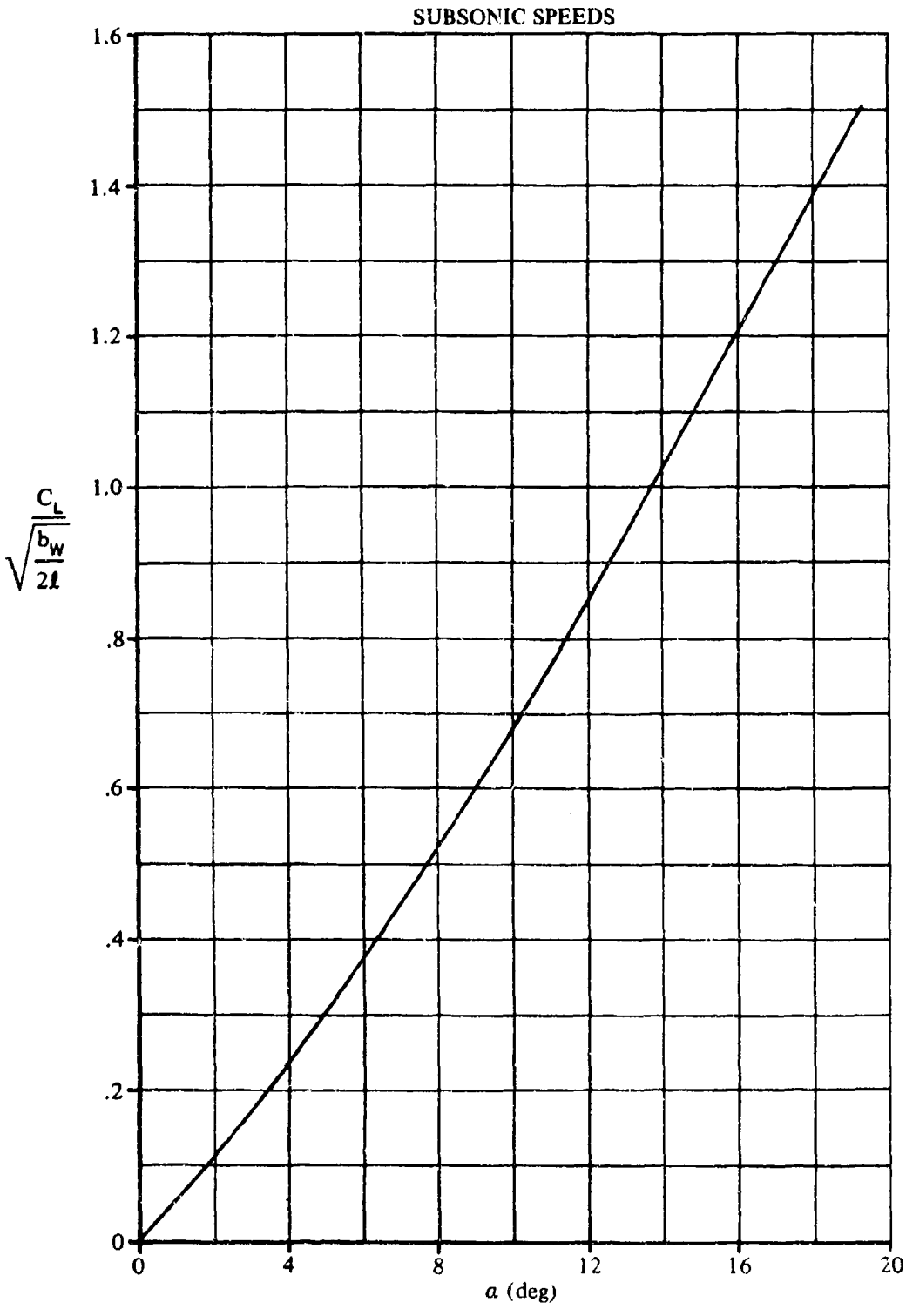

FIGURE 4.1.3.3-58 CORRELATION OF LIFT CURVES OF GOTHIC AND OGEE PLANFORMS

SUPERSONIC SPEEDS

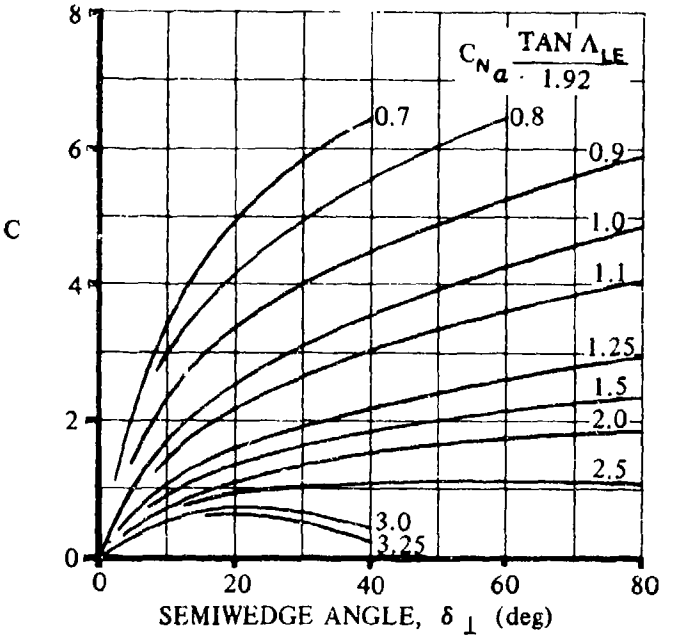

FIGURE 4.1.3.3-59a THICKNESS CORRECTION FACTOR FOR SUPERSONIC WING-LIFT VARIATION WITH ANGLE OF ATTACK

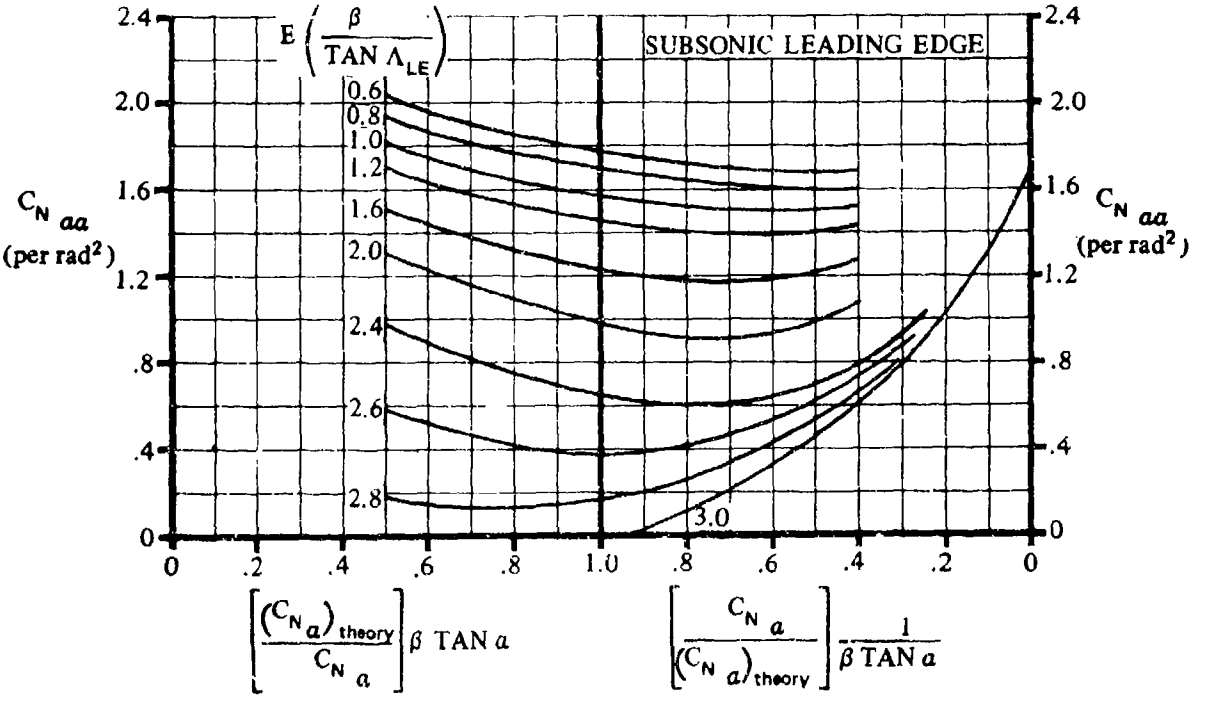

FIGURE 4.1.3.3-59b SUPERSONIC LIFT VARIATION WITH ANGLE OF ATTACK FOR WINGS WITH SUBSONIC LEADING EDGE

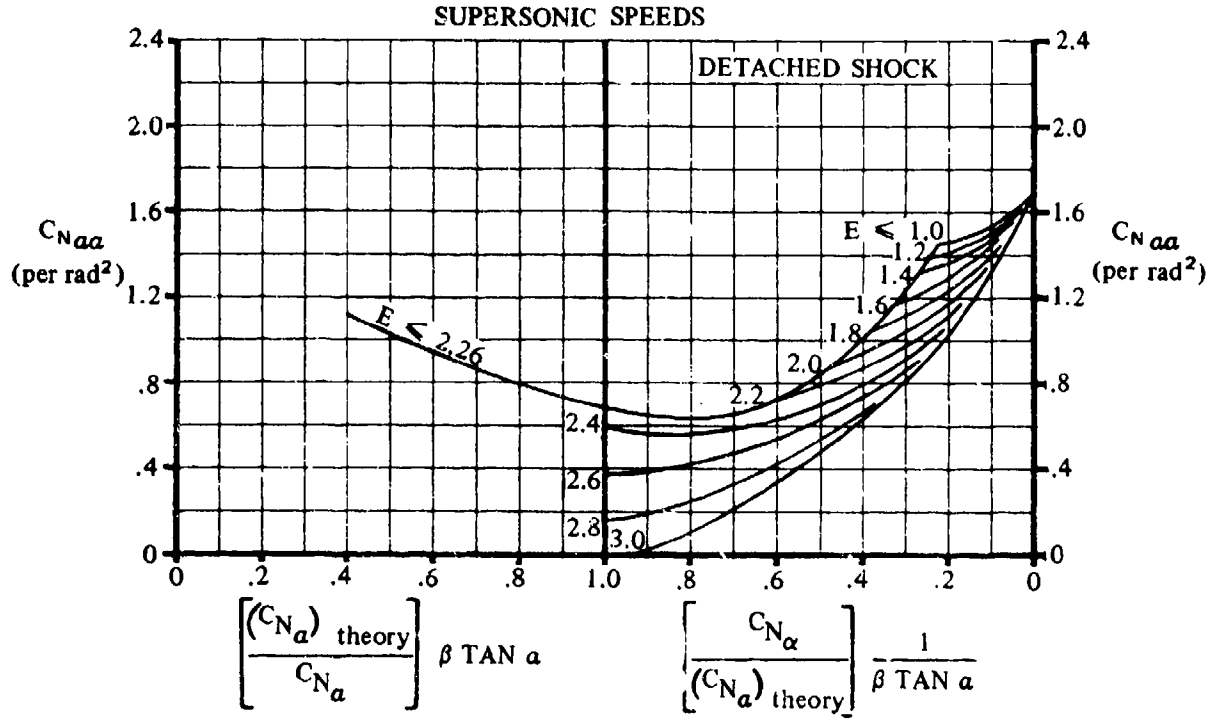

FIGURE 4.1.3.3-60a SUPERSONIC LIFT VARIATION WITH ANGLE OF ATTACK FOR WINGS WITH DETACHED SHOCK

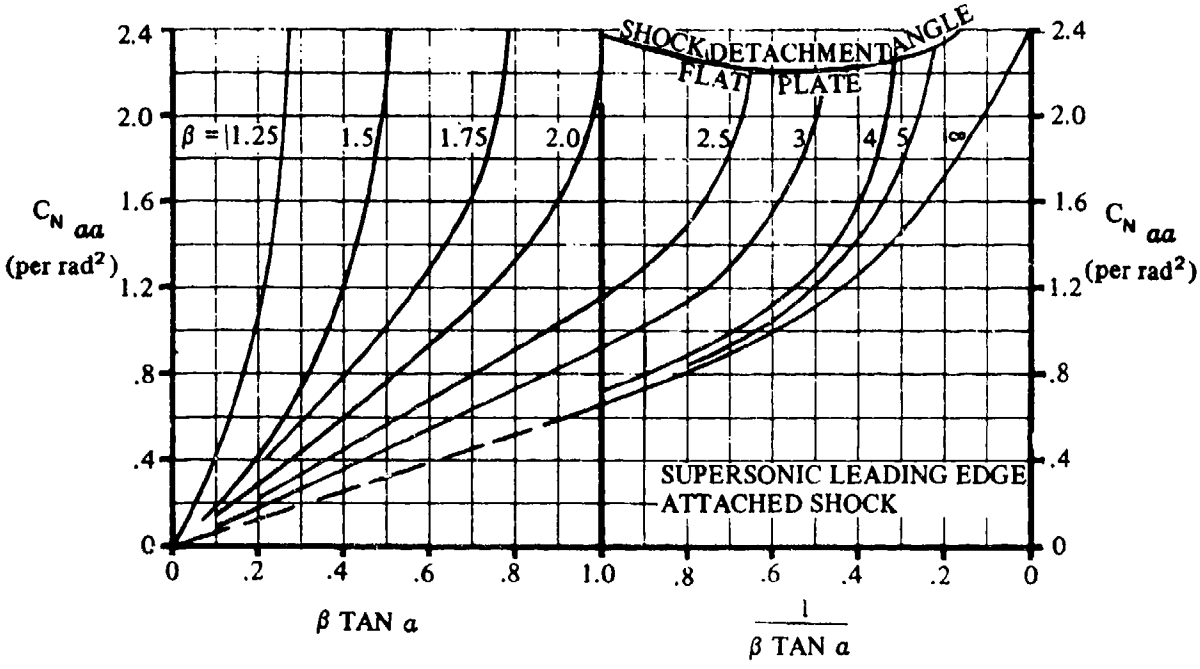

FIGURE 4.1.3.3-60b SUPERSONIC LIFT VARIATION WITH ANGLE OF ATTACK FOR WINGS WITH SUPERSONIC LEADING EDGE-ATTACHED SHOCK

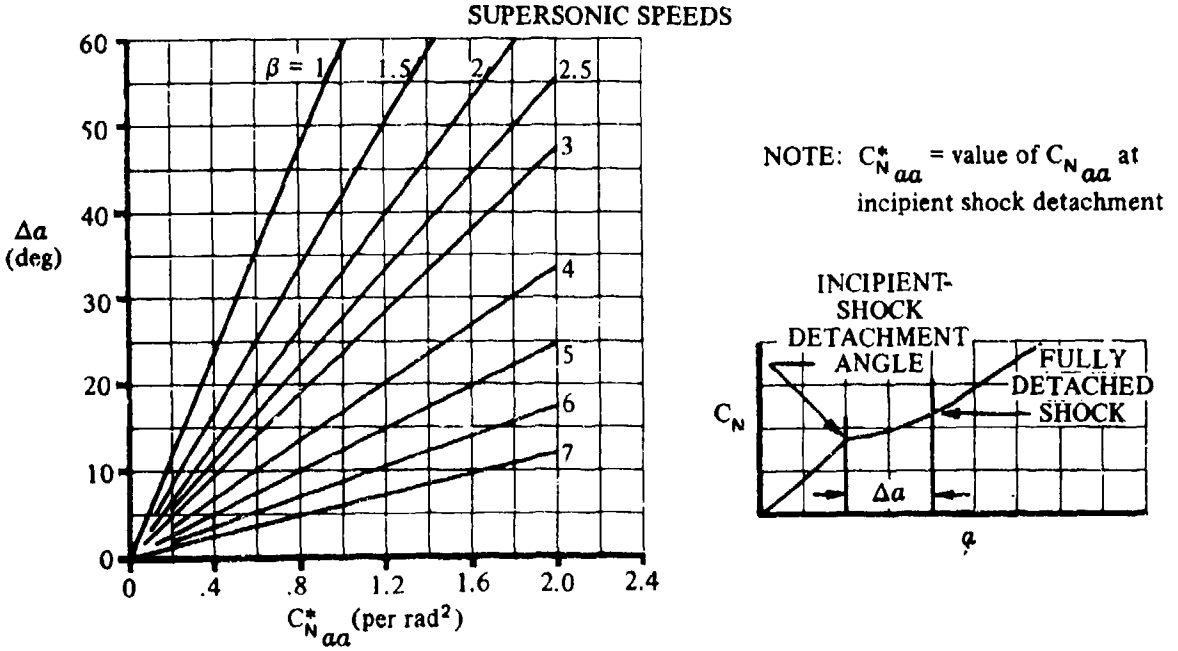

FIGURE 4.1.3.3-61a ANGLE-OF-ATTACK INCREMENT FROM INCIPIENT-SHOCK DETACHMENT TO FULLY DETACHED SHOCK FOR SUPERSONIC WING-LIFT VARIATION WITH ANGLE OF ATTACK

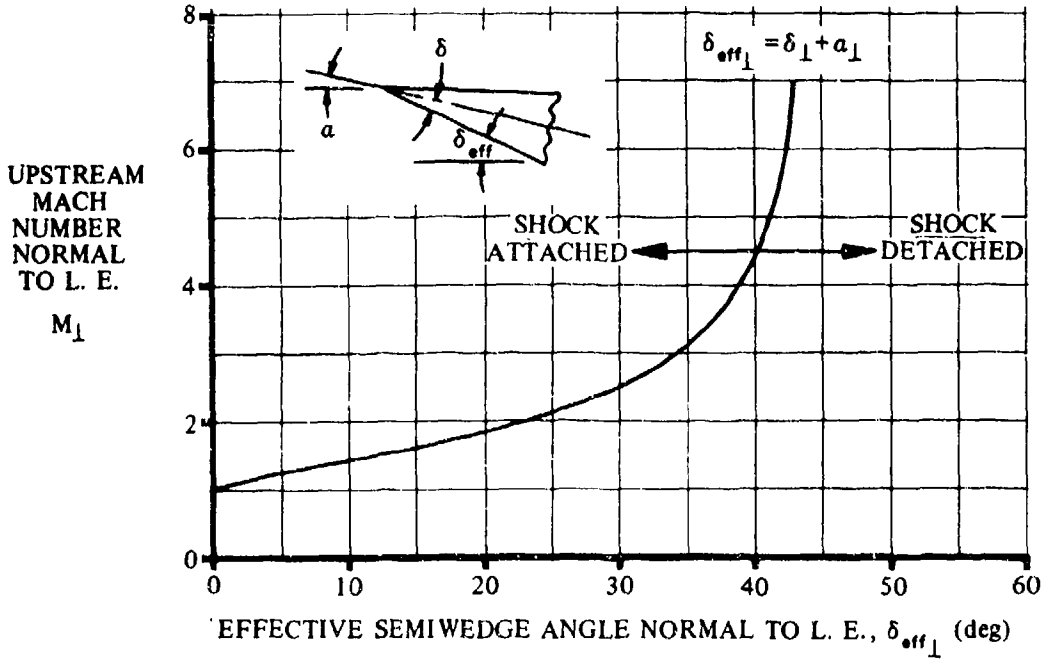

FIGURE 4.1.3.3-61b ANGLE FOR SHOCK DETACHMENT FOR WEDGE AIRFOILS

4.1.3.4 WING MAXIMUM LIFT

Methods are presented in this section for estimating the maximum lift of wings at subsonic, transonic, supersonic, and hypersonic speeds.

A. SUBSONIC

At subsonic speeds the wing maximum lift of high-aspect-ratio wings is directly related to the maximum lift of the wing airfoil section, with planform geometry of secondary importance. However, as the wing aspect ratio decreases, the wing planform shape becomes increasingly more significant. This is especially true for low-aspect-ratio delta-wing or non-straight-tapered planforms where leading-edge vortex effects are prevalent.

The complexity of modern wing designs (twisted wings with varying airfoil sections) precludes the application of empirical methods that yield consistently good results. Thus, the use of more exact theory is necessary for estimating maximum lift. Method 1 presented below requires the user to employ the most accurate wing spanwise-loading computer program available. In case no such program is available to the user, two additional empirical methods are presented. Method 2 is applicable to high-aspect-ratio configurations with constant-section untwisted wings. Method 3 is applicable to low-aspect-ratio configurations with constant-section untwisted wings.

Wing lift characteristics do not change discontinuously from one aspect-ratio regime to another. However, because of the different approaches used in Methods 2 and 3, values calculated by Method 2 will not necessarily match exactly the values of Method 3 for a border-line aspect-ratio configuration.

In general, however, the differences in values obtained by the two methods for the border-line aspect ratios should be small.

Flow Separation and Stalling Characteristics

For high-aspect-ratio wings, the three-dimensional maximum lift and stalling characteristics are, as a first approximation, determined by section properties (see Sections 4.1.1.3 and 4.1.1.4). There are, however, certain three-dimensional effects that may become important. These include the spanwise variations of induced camber and angle of attack, and the effect of spanwise pressure gradient on the boundary layer.

Because of these effects, the stall of three-dimensional wings, even untwisted wings of constant airfoil section, usually starts at some spanwise station and rapidly spreads with increasing angle of attack. Highly tapered wings tend to stall at the tips, while untapered wings tend to stall at the root.

On swept wings the induced effects combine to promote stall at the tip. The induced camber at the tip is negative and the induced angle of attack is high. The spanwise pressure gradient tends to draw the boundary layer from the wing root to the tip. All of these factors promote separation at the wing tip and suppress it at the root. It is therefore very difficult to prevent tip separation at high angles of attack on highly swept wings.

Regardless of where the separation first appears, it is the type of separation that determines the maximum lift. Trailing-edge separation, which is characteristic of thick wings, always results in a loss in maximum lift compared to the airfoil-section maximum lift. Leading-edge separation, where

the flow rolls up into a spanwise vortex, as on thin swept wings, results in an increase in normal force. The magnitude of the increase is related to the strength of the leading-edge vortex. These effects are illustrated by the variations of maximum lift with wing thickness at high sweep angles, as shown in Figure 4.1.3.4-21a. For more details regarding wing flow separation and stalling characteristics, the reader is referred to References 1 and 2.

Reynolds-Number Effects

The salient aspects of the Reynolds-number discussion presented in Reference 2 are presented below. From the available test data results, there appear to be essential differences between the Reynolds-number effects of thin airfoils ($t/c \approx 0.06$), of moderately thick airfoils ($t/c \approx 0.12$), and of thick airfoils ($t/c \approx 0.18$).

The maximum lift of thin airfoils is relatively constant up to a Reynolds number of 10×10^6; but when this Reynolds number is exceeded, the value of maximum lift begins to increase.

With moderately thick airfoils a very large increase of the maximum lift with increasing Reynolds number is found at low Reynolds numbers. However, at Reynolds numbers above 4 to 6×10^6, the maximum lift tends to remain about constant.

The maximum lift of thick airfoils increases gradually up to high Reynolds numbers. At Reynolds numbers above 15×10^6, the maximum lift tends to remain constant.

Mach-Number Effects

Mach-number effects on the maximum lift of unswept, thick wings are quite severe, starting as low as $M = 0.15$. This is to be expected from the analogy with section characteristics (see Section 4.1.1.4). For swept wings the losses due to Mach number are much less than they are for straight wings of a given thickness.

Mach-number effects are due in part to the larger pressure gradients associated with compressible flow. These larger pressure gradients can cause the boundary layer to separate at a lower lift value, thus resulting in a lower maximum lift with increasing Mach number. Large decreases in maximum lift can be related to the problem of shock-induced separation. For a complete discussion of the compressibility effects, the reader is referred to Reference 3.

Interference Effects

It must be recognized that the maximum lift of the wing alone, as given in this section, may be substantially altered by interference effects. The addition of fuselages, nacelles, pylons, and other protuberances can markedly change the aerodynamic characteristics of a given configuration near the stall. Interference effects of this type are discussed in Section 4.3.1.4.

DATCOM METHODS

Method 1

The following method requires that the user have at his disposal an accurate wing spanwise-loading computer program, e.g., a lifting-surface theory computer program. If no such computer program is available, Methods 2 and 3 may be used to approximate the wing maximum lift.

Method 1 is limited to moderately swept configurations where leading-edge vortex effects are not significant. In addition, the spanwise location where stall is first detected should be limited to one local chord-length away from the wing root and tip sections.

Application of the method is as follows:

Step 1. Determine the section $c_{\ell_{max}}$ across the entire span of the wing, based on the appropriate Mach number and local Reynolds number, using Section 4.1.1.4. If section test data are available, they should be used whenever possible, and the appropriate corrections made for Mach number, Reynolds number, and surface roughness as given in Section 4.1.1.4.

Step 2. Plot the section $c_{\ell_{max}}$ from Step 1 as a function of spanwise station η (see Sketch (a)).

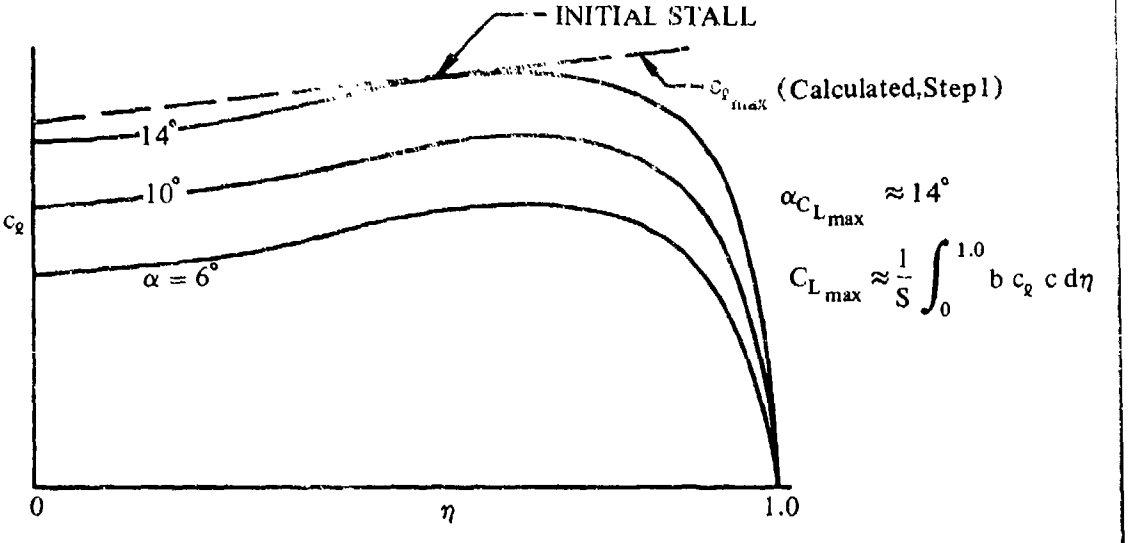

SKETCH (a)

Step 3. Apply the wing spanwise-loading method over a range of angle of attack until a value of the local wing loading coincides or exceeds the local wing $c_{\ell_{max}}$ calculated from Step 1 (see Sketch (a)). The angle of attack at which the spanwise loading coincides with the calculated $c_{\ell_{max}}$ value determines the angle of attack and spanwise position for initial stall. An approximate spanwise location where the stall will first occur can be calculated for an untwisted, tapered wing by

$$\eta_{stall} = 1 - \lambda \qquad 4.1.3.4\text{-a}$$

where λ is the wing taper ratio.

Step 4. Integrate the spanwise loading that coincides with the calculated $c_{\ell_{max}}$ value to obtain the wing $C_{L_{max}}$ value.

Although no substantiation of this method is presented, design experience has shown that the accuracy of this method is superior to that of both Methods 2 and 3.

Method 2

The following method is derived empirically, based on the experimental data of References 4 through 10. This method should therefore be restricted to those untwisted, constant-section, straight-tapered, high-aspect-ratio configurations that satisfy the following relationship:

$$A > \frac{4}{(C_1 + 1)\cos \Lambda_{LE}} \qquad 4.1.3.4\text{-b}$$

where

A is the wing aspect ratio.

C_1 is given as a function of taper ratio in Figure 4.1.3.4-24b.

Λ_{LE} is the sweep of the wing leading edge.

Border-line configurations are those that satisfy the following relationship:

$$\frac{3}{(C_1 + 1)\cos \Lambda_{LE}} \leqslant A \leqslant \frac{4}{(C_1 + 1)\cos \Lambda_{LE}} \qquad 4.1.3.4\text{-c}$$

For these aspect ratios either Method 2 or Method 3 may be used.

If neither Equation 4.1.3.4-b nor -c is satisfied, the low-aspect-ratio procedure presented in Method 3 may be used.

The subsonic maximum lift and angle of attack for maximum lift for those untwisted, constant-section, high-aspect-ratio configurations that satisfy Equation 4.1.3.4-b or -c are given as follows:

$$C_{L_{max}} = \left(\frac{C_{L_{max}}}{c_{\ell_{max}}}\right) c_{\ell_{max}} + \Delta C_{L_{max}} \qquad 4.1.3.4\text{-d}$$

$$\alpha_{C_{L_{max}}} = \frac{C_{L_{max}}}{C_{L_\alpha}} + \alpha_0 + \Delta\alpha_{C_{L_{max}}} \qquad 4.1.3.4\text{-e}$$

The first term on the right side of Equation 4.1.3.4-d is the maximum lift coefficient at M = 0.2, and the second term is the lift increment to be added for Mach numbers between 0.2 and 0.6.

$\frac{C_{L_{max}}}{c_{\ell_{max}}}$ is obtained from Figure 4.1.3.4-21a.

$c_{\ell_{max}}$ is the section maximum lift coefficient at M = 0.2 obtained from Tables 4.1.1-A, -B, or from Section 4.1.1.4.

$\Delta C_{L_{max}}$ is a Mach-number correction obtained from Figure 4.1.3.4-22.

C_{L_α} is the wing lift-curve slope (per degree) for the Mach number under consideration, obtained from test data or Section 4.1.3.2.

α_0 is the wing zero-lift angle for the appropriate Mach number, obtained from test data or Section 4.1.3.1.

$\Delta\alpha_{C_{L_{max}}}$ is obtained from Figure 4.1.3.4-21b. Note that this figure is valid for all subsonic Mach numbers up to 0.6.

The leading-edge parameter Δy, which does not explicitly appear in the equations, must be used in reading values from the charts. The value of Δy is for a streamwise airfoil section and is expressed in percent chord and obtained or approximated from Figure 2.2.1-8.

In calculating $\alpha_{C_{L_{max}}}$ the value of $C_{L_{max}}$ calculated from Equation 4.1.3.4-d is used as the numerator of the first term of Equation 4.1.3.4-e.

A comparison of test values of $C_{L_{max}}$ and $\alpha_{C_{L_{max}}}$ (based on the calculated $C_{L_{max}}$ value) with the corresponding values calculated by this method is shown in Table 4.1.3.4-A.

Method 3.

The following is an empirically derived method (Reference 11) that is applicable to untwisted, symmetrical-section, low-aspect-ratio wings.

Low-aspect-ratio wings at subsonic speeds exhibit extreme nonlinearities in the lift curve at high angles of attack, as shown in the accompanying sketch. Multiple lift peaks exist for many configurations. The charts of this section are for the first peak, as shown by the arrows in Sketch (b).

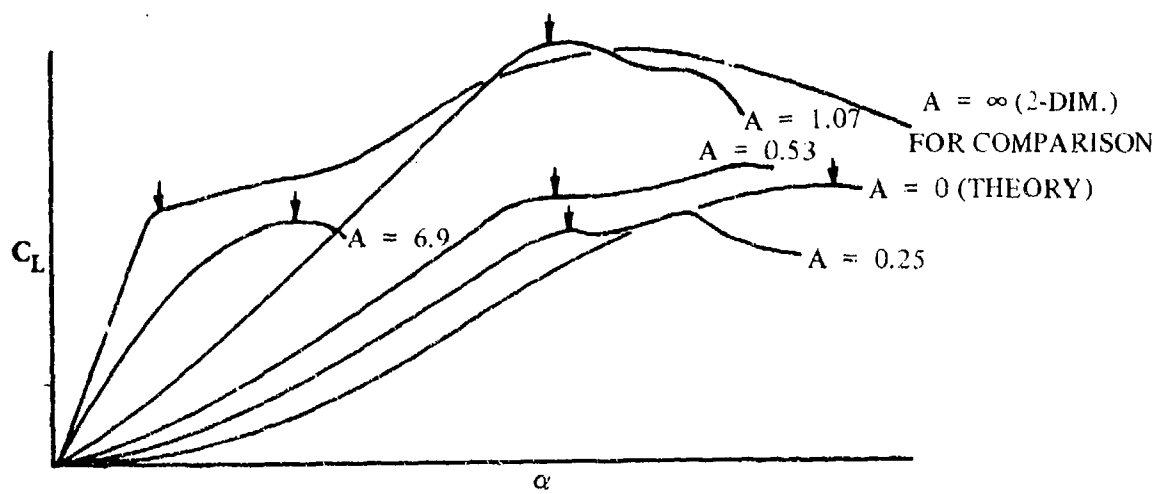

SKETCH (b)

For thin, low-aspect-ratio wings, Reynolds-number effects are small. Within the Reynolds-number and thickness limitations listed on Figures 4.1.3.4-23 through -25, Reynolds number is considered to have no effect.

This method is applicable to those low-aspect-ratio configurations (without considering Mach-number effects) that satisfy the following relationship:

$$A < \frac{3}{(C_1 + 1)\cos \Lambda_{LE}} \qquad 4.1.3.4\text{-f}$$

where

A is the wing aspect ratio.

C_1 is given as a function of taper ratio in Figure 4.1.3.4-24b.

Λ_{LE} is the sweep of the wing leading edge.

Border-line configurations are those that satisfy the following relationship:

$$\frac{3}{(C_1 + 1)\cos \Lambda_{LE}} \leq A \leq \frac{4}{(C_1 + 1)\cos \Lambda_{LE}} \qquad 4.1.3.4\text{-c}$$

For these aspect ratios either Method 2 or Method 3 may be used.

If neither Equation 4.1.3.4-f nor 4.1.3.4-c is satisified, the high-aspect-ratio procedure presented in Method 2 may be used.

The subsonic maximum lift and angle of attack for maximum lift for those untwisted, symmetrical-section, low-aspect-ratio configurations that satisfy Equation 4.1.3.4-f or -c are given as follows:

$$C_{L_{max}} = (C_{L_{max}})_{base} + \Delta C_{L_{max}} \qquad 4.1.3.4\text{-g}$$

$$\alpha_{C_{L_{max}}} = (\alpha_{C_{L_{max}}})_{base} + \Delta\alpha_{C_{L_{max}}} \qquad 4.1.3.4\text{-h}$$

where

$(C_{L_{max}})_{base}$ is the base value of $C_{L_{max}}$ obtained from Figure 4.1.3.4-23a if the position of maximum airfoil-section thickness is forward of the 35-percent-chord point. If the maximum thickness is aft of this point, Figure 4.1.3.4-23b is used. For slab-sided wings the maximum-thickness point is considered to be the first chord-point at which the thickness reaches a maximum. The value of Δy, the leading-edge parameter used in reading these two charts, is obtained or approximated with the aid of Figure 2.2.1-8.

$\Delta C_{L_{max}}$ is the change in the base maximum-lift value. It is obtained from Figure 4.1.3.4-24a as a function of taper ratio, aspect ratio, leading-edge sweep, and Mach number.

$(\alpha_{C_{L_{max}}})_{base}$ is the base value of $\alpha_{C_{L_{max}}}$ obtained from Figure 4.1.3.4-25a. It is a function of aspect ratio, taper ratio, leading-edge sweep, and Mach number.

$\Delta\alpha_{C_{L_{max}}}$ is the change in the base value of angle of attack at maximum lift. It is obtained from Figure 4.1.3.4-25b as a function of taper ratio, aspect ratio, leading-edge sweep, and Mach number.

A comparison of test values of $C_{L_{max}}$ and $\alpha_{C_{L_{max}}}$ with the corresponding values calculated by this method (where $\alpha_{C_{L_{max}}}$ is based on the calculated $C_{L_{max}}$ value) is shown in Table 4.1.3.4-B.

Sample Problems

1. Method 2

Given: The following high-aspect-ratio configuration.

$A = 5.0$ $\quad \Lambda_{LE} = 46.6^{o}$ $\quad \lambda = 0.565$

$R_{\ell} = 2 \times 10^{6}$ $\quad$ Airfoil: NACA 64A010 (free-stream direction)

$C_{L_{\alpha}} = 0.061$ per deg $\quad \alpha_{0} = 0$ $\quad M = 0.4$

Compute:

Determine if the above configuration satisfies the high-aspect-ratio requirement for Method 2, as stipulated in Equation 4.1.3.4-b; i.e.,

$$A > \frac{4}{(C_1 + 1)\cos\Lambda_{LE}}$$

$C_1 = 0.24$ (Figure 4.1.3.4-24b)

$$\frac{4}{(C_1 + 1)\cos\Lambda_{LE}} = \frac{4}{(0.24 + 1.0)\cos 46.6^{o}} = \frac{4}{(1.24)(0.6871)} = 4.69$$

$A = 5.0 > 4.69$

The high-aspect-ratio requirement is satisfied; therefore, Method 2 is applicable to the above configuration.

Determine the maximum lift coefficient at $M = 0.40$

$\Delta y = 2.12\%\, c$ (Figure 2.2.1-8)

$c_{\ell_{max}} = 1.23$ (Table 4.1.1-B)

$\frac{C_{L_{max}}}{c_{\ell_{max}}} = 0.83$ (Figure 4.1.3.4-21a)

$\Delta C_{L_{max}} = -0.053$ (Figure 4.1.3.4-22, interpolated)

$$C_{L_{max}} = \left(\frac{C_{L_{max}}}{c_{\ell_{max}}}\right) c_{\ell_{max}} + \Delta C_{L_{max}} \quad \text{(Equation 4.1.3.4-d)}$$

$$= (0.83)(1.23) + (-0.053)$$

$$= 1.02 - 0.053$$

$$= 0.97$$

Determine the angle of attack at the wing maximum lift

$\Delta\alpha_{C_{L_{max}}} = 6.7^{o}$ (Figure 4.1.3.4-21b)

$$\alpha_{C_{L_{max}}} = \frac{C_{L_{max}}}{C_{L_\alpha}} + \alpha_0 + \Delta\alpha_{C_{L_{max}}} \quad \text{(Equation 4.1.3.4-e)}$$

$$= \frac{0.97}{0.061} + 0 + 6.7$$

$$= 15.9 + 6.7$$

$$= 22.6^{o}$$

2. Method 3

Given: The following low-aspect-ratio configuration.

$A = 1.0$ $\Lambda_{LE} = 45^{o}$ $\lambda = 0.3$

Airfoil: NACA 0005 (free-stream direction)

Maximum thickness @ 30% chord $M = 0.6$

Compute:

Determine if the above configuration satisfies the low-aspect-ratio requirement for Method 3 as stipulated in Equation 4.1.3.4-f; i.e.,

$$A < \frac{3}{(C_1 + 1)\cos\Lambda_{LE}}$$

$C_1 = 0.5$ (Figure 4.1.3.4-24b)

$$\frac{3}{(C_1 + 1)\cos \Lambda_{LE}} = \frac{3}{(0.5 + 1.0)\cos 45^{O}} = \frac{3}{(1.5)(0.7071)} = 2.83$$

$A = 1 < 2.83$

The low-aspect-ratio requirement is satisfied; therefore, Method 3 is applicable to the above configuration.

Determine the maximum-lift coefficient at M = 0.6

$\Delta y = 1.37\%\ c$ (Figure 2.2.1-8)

$\beta = \sqrt{1 - M^2} = \sqrt{1 - (0.6)^2} = 0.80$

$C_2 = 0.91$ (Figure 4.1.3.4-24b)

$$(C_1 + 1)\frac{A}{\beta}\cos \Lambda_{LE} = (0.5 + 1.0)\frac{1}{0.80}\cos 45^{O} = 1.326$$

$(C_{L_{max}})_{base} = 1.12$ (Figure 4.1.3.4-23a)

$(C_2 + 1)\, A \tan \Lambda_{LE} = (0.91 + 1.0)(1) \tan 45^{O} = 1.91$

$\Delta C_{L_{max}} = -0.08$ (Figure 4.1.3.4-24a)

$C_{L_{max}} = (C_{L_{max}})_{base} + \Delta C_{L_{max}}$ (Equation 4.1.3.4-g)

$= 1.12 - 0.08$

$= 1.04$

Determine the angle of attack at the wing maximum lift

$(\alpha_{C_{L_{max}}})_{base} = 30.8^{O}$ (Figure 4.1.3.4-25a)

$A \cos \Lambda_{LE} [1 + (2\lambda)^2] = 1.0 \cos 45^{O} [1 + (0.6)^2] = 0.962$

$\Delta\alpha_{C_{L_{max}}} = 3.5^{O}$ (Figure 4.1.3.4-25b)

$\alpha_{C_{L_{max}}} = (\alpha_{C_{L_{max}}})_{base} + \Delta\alpha_{C_{L_{max}}}$ (Equation 4.1.3.4-h)

$= 30.8 + 3.5$

$= 34.3^{O}$

B. TRANSONIC

No method for high-aspect-ratio wings is presented herein in the transonic speed regime. However, for low-aspect-ratio wings an empirical method is presented.

For low-aspect-ratio wings, the maximum lift at transonic speeds was found to be basically a function of the same variables that were used in the subsonic speed regime (see References 12 through 15). Therefore, the design charts for the transonic speed regime are based on the subsonic design charts.

It should be noted that the transonic maximum-lift coefficient of thick wings may be limited by adverse pitching-moment variations and severe buffeting.

Both of these limitations are associated with extensive flow separation arising from compressibility, shock waves, and adverse pressure gradients.

DATCOM METHOD

The maximum lift and angle of attack at maximum lift for untwisted, symmetrical-section, low-aspect-ratio configurations are determined for Mach numbers between 0.6 and 1.2 by the following procedure:

Step 1. Calculate the maximum lift and angle of attack at maximum lift for the wing under consideration at M = 0.6 by using Method 3 of Paragraph A of this section.

Step 2. Determine the increments in maximum lift and angle of attack at maximum lift at the desired Mach number from Figures 4.1.3.4-26a through -26c. These increments are then added directly to the values obtained at M = 0.6 in Step 1; i.e.,

$$(C_{L_{max}})_M = (C_{L_{max}})_{M=0.6} + \Delta C_{L_{max}} \qquad 4.1.3.4\text{-i}$$

$$(\alpha_{C_{L_{max}}})_M = (\alpha_{C_{L_{max}}})_{M=0.6} + \Delta\alpha_{C_{L_{max}}} \qquad 4.1.3.4\text{-j}$$

A comparison of experimental data with results based on this method is presented in Table 4.1.3.4-C.

Sample Problem

Given: The same low-aspect-ratio configuration used in Sample Problem 2 of Paragraph A.

$A = 1.0$ $\Lambda_{LE} = 45^{\circ}$ $\lambda = 0.3$

Airfoil NACA 0005

$C_{L_{max}} = 1.04$

$\alpha_{C_{L_{max}}} = 34.3^{o}$

$C_2 = 0.91$

$C_1 = 0.50$

} Sample Problem 2, Paragraph A

$M = 1.0$

Compute:

$(C_2 + 1) A \tan \Lambda_{LE} = (0.91 + 1)(1.0)(1.0) = 1.91$

$C_3 = 1.0$ (Figure 4.1.3.4-26b)

$C_3 (C_1 + 1) A \cos \Lambda_{LE} = (1.0)(0.50 + 1)(1.0)(0.7071) = 1.06$

$\Delta C_{L_{max}} = 0$ (Figure 4.1.3.4-26a)

$(C_1 + 1) A \cos \Lambda_{LE} = (0.50 + 1)(1.0)(0.7071) = 1.06$

$\Delta\alpha_{C_{L_{max}}} = 0.5^{o}$ (Figure 4.1.3.4-26c)

Solution:

$C_{L_{max}} = (C_{L_{max}})_{M=0.6} + \Delta C_{L_{max}}$ (Equation 4.1.3.4-i)

$= 1.04 + 0$

$= 1.04$

$\alpha_{C_{L_{max}}} = (\alpha_{C_{L_{max}}})_{M=0.6} + \Delta\alpha_{C_{L_{max}}}$ (Equation 4.1.3.4-j)

$= 34.3 + 0.5$

$= 34.8^{o}$

C. SUPERSONIC

At supersonic speeds the lift is limited by geometric considerations rather than by flow separation. That is, maximum lift is reached when the component of the normal force in the lift direction ceases to increase with angle of attack.

The governing geometric parameters for the determination of maximum lift are those that influence the wing lift-curve slope; i.e., aspect ratio, sweep, taper ratio, and Mach number. It is therefore logical that a good correlating term might include the lift-curve slope. One such parameter that gives good results and is used here is $C_{N_\alpha}/(4/\beta)$.

DATCOM METHOD

For the supersonic case the most accurate way of determining the wing maximum lift is by calculating the normal-force curve (using Sections 4.1.3.2 and 4.1.3.3) and converting it to a lift curve by means of the relationship $C_L = C'_N \cos\alpha$. However, design charts are presented herein for a more rapid procedure of estimating the wing maximum lift.

For Mach numbers greater than 1.4, the supersonic maximum lift and angle of attack at maximum lift may be approximated using Figures 4.1.3.4-27a and -27b. These figures are based on empirical data taken from References 16 through 26, and are presented as a function of C_{N_α} and Mach number ($\beta = \sqrt{M^2 - 1}$). The lift-curve slope C_{N_α} is obtained from test data or from Paragraph C of Section 4.1.3.2.

A comparison of experimental data with results based on this method is presented in Table 4.1.3.4-D.

Sample Problem

Given: The configuration of Reference 18.

$A = 1.96$ $\quad \Lambda_{LE} = 64^\circ$ $\quad C_{N_\alpha} = 1.72$ per rad $\quad M = 2.32$

Compute:

$$\beta = \sqrt{M^2 - 1}$$

$$= \sqrt{(2.32)^2 - 1}$$

$$= 2.093$$

$$\frac{1}{M} = \frac{1}{2.32} = 0.431$$

$$\frac{C_{N_\alpha}}{4/\beta} = \frac{(1.72)(2.093)}{4} = 0.900 \text{ per rad}$$

Solution:

$C_{L_{max}} = 1.02$ (Figure 4.1.3.4-27a)

$\alpha_{C_{L_{max}}} = 41.4^\circ$ (Figure 4.1.3.4-27b)

These compare with test values of $C_{L_{max}}$ of 0.98 and $\alpha_{C_{L_{max}}}$ of 43.8° from Reference 18.

D. HYPERSONIC

The supersonic method of Paragraph C above is used to estimate $C_{L_{max}}$ and $\alpha_{C_{L_{max}}}$ at hypersonic speeds. The parameters that affect $C_{L_{max}}$ at the lower hypersonic Mach numbers are the same as those for the supersonic speeds, i.e., planform parameters. At high hypersonic speeds, $C_{L_{max}}$ is determined primarily by flow impact on the wing lower surface. Newtonian flow theory thus provides a reasonable approximation for $C_{L_{max}}$ values in this speed range. The high hypersonic limit ($1/M \rightarrow 0$) of Figures 4.1.3.4-27a and 4.1.3.4-27b is derived using the Newtonian equation

$$C_L = 2 \sin^2 \alpha \cos \alpha \qquad \text{4.1.3.4-k}$$

REFERENCES

1. Harper, C. W., and Maki, R. L.: A Review of the Stall Characteristics of Swept Wings. NASA TN D-2373, 1964. (U)

2. van den Berg, B.: Reynolds Number and Mach Number Effects on the Maximum Lift and the Stalling Characteristics of Wings at Low Speeds. NLR TR 69025, 1969. (U)

3. Wootton, L. R.: The Effect of Compressibility on the Maximum Lift Coefficient of Airfoils at Subsonic Airspeeds. Jour. of Royal Aero. Soc., Vol. 71, July 1967. (U)

4. Turner, T. R.: Maximum Lift Investigation at Mach Numbers from 0.05 to 1.20 of a Wing with Leading Edge Swept Back 42°. NACA RM L9K03, 1950. (U)

5. Johnson, B. H., Jr., and Shibata, H. H.: Characteristics Througnout the Subsonic Speed Range of a Plane Wing and of a Cambered and Twisted Wing, Both Having 45° of Sweepback. NACA RM A51D27, 1951. (U)

6. Sutton, F. B., and Dickson, J. K.: A Comparison of the Longitudinal Aerodynamic Characteristics at Mach Numbers up to 0.94 of Sweptback Wings Having NACA 4-Digit or NACA 64A Thickness Distributions. NACA RM A54F18, 1954. (U)

7. Schneider, W. C.: A Comparison of the Spanwise Loading Calculated by Various Methods with Experimental Loadings Obtained on a 45° Sweptback Wing of Aspect Ratio 8.02 at a Reynolds Number of 4.0×10^6. NACA TR 1208, 1954. (U)

8. Turner, T. R.: Effects of Sweep on the Maximum-Lift Characteristics of Four Aspect-Ratio-4 Wings at Transonic Speeds. NACA RM L50H11, 1950. (U)

9. Bollech, T. V., and Hadaway, W. M.: The Low-Speed Lift and Pitching-Moment Characteristics of a 45° Sweptback Wing of Aspect Ratio 8 With and Without High-Lift and Stall-Control Devices as Determined from Pressure Distributions at a Reynolds Number of 4.0×10^6. NACA RM L52K26, 1953. (U)

10. Graham, R. R.: Low-Speed Characteristics of a 45° Sweptback Wing of Aspect Ratio 8 from Pressure Distributions and Force Tests at Reynolds Numbers from 1,500,000 to 4,800,000. NACA RM L51H13, 1951. (U)

11. White, C. O.: Maximum Lift Coefficients of Low Aspect Ratio Wings at Subsonic Speeds. Douglas Aircraft Company Report LB 30214, 1959. (U)

12. Nelson, W. H., and McDevitt, J. B.: The Transonic Characteristics of 22 Rectangular, Symmetrical Wing Models of Varying Aspect Ratio and Thickness. NACA TN 3501, 1955. (U)

13. Nelson, W. H., Allen, E. C., and Krumm, W. J.: The Transonic Characteristics of 36 Symmetrical Wings of Varying Taper, Aspect Ratio, and Thickness as Determined by the Transonic-Bump Technique. NACA TN 3529, 1955. (U)

14. Emerson, H. F.: Wind Tunnel Investigation of the Effects of Clipping the Tips of Triangular Wings of Different Thickness, Camber, and Aspect Ratio – Transonic Bump Method. NACA TN 3671, 1956. (U)

15. Few, A. G., Jr., and Fournier, P. G.: Effects of Sweep and Thickness on the Static Longitudinal Aerodynamic Characteristics of a Series of Thin, Low-Aspect-Ratio, Highly Tapered Wings at Transonic Speeds. Transonic Bump Method. NACA RM L54B25, 1954. (U)

16. Anon.: Proposal for a Study of Hypersonic Pressure Over Configurations Having Low Aspect Ratio Delta Wings. Douglas Aircraft Company Report SM 35518, 1958. (U)

17. Ames Research Staff: Equations, Tables, and Charts for Compressible Flow. NACA TR 1135, 1953. (U)

18. Gallagher, J. J., and Mueller, J. N.: An Investigation of the Maximum Lift of Wings at Supersonic Speeds. NACA TR 1227, 1955. (U)

19. Dugan, D. W.: Estimation of Static Longitudinal Stability of Aircraft Configurations at High Mach Numbers and at Angles of Attack Between 0° and $\pm 180^{\circ}$. NASA Memo 1-17-59A, 1959. (U)

20. Kaattari, G. E.: Pressure Distributions on Triangular and Rectangular Wings to High Angles of Attack – Mach Numbers 1.45 and 1.97. NACA RM A54D19, 1954. (U)

21. Kaattari, G. E.: Pressure Distributions on Triangular and Rectangular Wings to High Angles of Attack – Mach Numbers 2.46 and 3.36. NACA RM A54J12, 1955. (U)

22. Bertram, M. H., and McCauley, W. D.: An Investigation of the Aerodynamic Characteristics of Thin Delta Wings with a Symmetrical Double-Wedge Section at a Mach Number of 6.9. NACA RM L55B14, 1955. (U)

23. Pitts, W. C.: Force, Moment, and Pressure-Distribution Characteristics of Rectangular Wings at High Angles of Attack and Supersonic Speeds. NACA RM A55K09, 1956. (U)

24. Boatright, W. B.: Experimental Study and Analysis of Loading and Pressure Distributions on Delta Wings due to Thickness and to Angle of Attack at Supersonic Speeds. NACA RM L56I14, 1956. (U)

25. Smith, F. M.: Experimental and Theoretical Aerodynamic Characteristics of Two Low-Aspect-Ratio Delta Wings at Angles of Attack to 50° at a Mach Number of 4.07. NACA RM L57E02, 1957. (U)

26. Hill, W. A., Jr.: Experimental Lift of Low-Aspect-Ratio Triangular Wings at Large Angles of Attack and Supersonic Speeds. NACA RM A57I17, 1957. (U)

27. Cahill, J. F., and Gottlieb, S. M.: Low-Speed Aerodyanmic Characteristics of a Series of Swept Wings Having NACA 65A006 Airfoil Sections (Revised). NACA RM L50F16, 1950. (U)

28. Rose, L. M.: Low-Speed Investigation of a Small Triangular Wing of Aspect Ratio 2.0. I – The Effect of Combination with a Body of Revolution and Height Above a Ground Plane. NACA RM A7K03, 1948. (U)

29. Graham, D.: Chordwise and Spanwise Loadings Measured at Low Speeds on a Large Triangular Wing Having an Aspect Ratio of 2 and a Thin, Subsonic-Type Airfoil Section. NACA RM A50A04a, 1950. (U)

30. Truckenbrodt, E., and Feindt, E. G.: Investigations on the Stalling Characteristics of Delta Wings in Incompressible Flow. AFOSR TN 57-538, 1957. (U)

31. Winter, H.: Flow Phenomena on Plates and Airfoils of Short Span. NACA TM 798, 1936. (U)

32. Tosti, L.P.: Low-Speed Static Stability and Damping-in-Roll Characteristics of Some Swept and Unswept Low-Aspect-Ratio Wings. NACA TN 1468, 1947. (U)

33. Bartlett, G. E., and Vidal, R. J.: Experimental Investigation of Influence of Edge Shape on the Aerodynamic Characteristics of Low Aspect Ratio Wings at Low Speeds. Jour. Aero. Sci., Vol. 22, No. 8, 1955. (U)

34. Anderson, A. E.: An Investigation at Low Speed of a Large-Scale Triangular Wing of Aspect Ratio Two. II – The Effect of Airfoil Section Modifications and the Determination of the Wake Downwash. NACA RM A7H28, 1947. (U)

35. Jacobs, E. N., and Rhode, R. V.: Airfoil Section Characteristics as Applied to the Prediction of Air Forces and Their Distribution on Wings. NACA TR 631, 1938. (U)

TABLE 4.1.3.4-A
HIGH-ASPECT-RATIO WINGS AT SUBSONIC SPEEDS
DATA SUMMARY AND SUBSTANTIATION

Ref.	t/c	A	Δy (%C)	Λ_{LE} (deg)	M	$Rx10^{-6}$	$C_{L_{max}}$ Calc.	$\alpha_{C_{L_{max}}}$ Calc.	$C_{L_{max}}$ Test	$\alpha_{C_{L_{max}}}$ Test	Percent Error, e	
											$C_{L_{max}}$	$\alpha_{C_{L_{max}}}$
4	0.12	4.0	2.55	42	0.2	2.0	1.02	23.1	0.98	23	4.1	0.4
↓	↓	↓	↓	↓	0.4	3.0	0.93	21.0	0.92	22	1.1	−4.5
					0.6	4.0	0.88	19.6	0.85	20	3.5	−2.0
5	0.075	5.0	1.6	47	0.2	2.0	0.95	23.8	0.98	25	−3.1	−4.8
↓	↓	↓	↓	↓	0.4	2.0	0.91	22.0	0.95	24	−4.2	−5.0
					0.6	2.0	0.91	22.0	0.89	21	2.2	5.2
6	0.11	7.0	2.3	42	0.25	2.0	1.05	19.2	1.07	25.5	−1.9	−24.7
↓	0.10	6.0	2.1	47	0.25	2.0	1.04	21.6	1.06	24	−1.9	−10.0
	0.11	7.0	2.8	42	0.25	2.0	1.02	17.7	1.03	17.5	−1.0	1.1
	0.10	6.0	2.6	47	0.25	2.0	1.00	19.7	1.09	22	−8.3	−10.5
7	0.12	8.0	2.65	46	0.2	4.0	0.98	20.0	1.02	21	−3.9	−4.8
8	0.06	4.0	1.2	37	0.6	0.4	0.83	18.6	0.73	19	13.7	−2.1
↓	↓	↓	↓	47	0.6	0.4	0.92	22.7	0.82	23	12.2	−1.3
				61	0.6	0.4	0.98	29.0	0.89	29	10.1	0
9	0.12	8.02	2.65	46.3	0.19	4.0	0.94	19.0	1.01	21	−6.9	−9.5
10	0.12	8.02	2.65	46.3	0.07	1.5	0.94	19.0	0.90	18	4.4	5.6
↓	↓	↓	↓	↓	0.11	2.2	0.94	↓	0.97	20	−3.1	−5.0
					0.14	3.0	0.94		1.01	22	−6.9	−13.6
					0.19	4.0	0.94		1.01	21	−6.9	−9.5
					0.25	4.8	0.94		1.01	21	−6.9	−9.5

Average Error in $C_{L_{max}} = \frac{\Sigma|e|}{n} = 5.3\%$

Average Error in $\alpha_{C_{L_{max}}} = \frac{\Sigma|e|}{n} = 6.5\%$

TABLE 4.1.3.4-B
LOW-ASPECT-RATIO WINGS AT SUBSONIC SPEEDS
DATA SUMMARY AND SUBSTANTIATION

Ref.	Airfoil Section	%C @ $(t/c)_{max}$	Δy (%c)	A	Λ_{LE} (deg)	M	$C_{L_{max}}$ Calc.	$\alpha_{C_{L_{max}}}$ Calc.	$C_{L_{max}}$ Test	$\alpha_{C_{L_{max}}}$ Test	Percent Error, e	
											$C_{L_{max}}$	$\alpha_{C_{L_{max}}}$
15	65A003	>35	0.60	4.0	45.0	0.6	0.83	20.2	0.87	21.0	−4.6	−3.8
↓	↓	↓	↓	4.0	51.3	↓	0.89	21.7	0.94	22.0	−5.3	−1.4
				4.0	36.8		0.78	19.9	0.83	20.0	−6.0	−0.5
				4.0	26.6		0.72	20.4	0.79	24.0	−8.9	−15.0
				4.0	14.0		0.70	22.1	0.70	20.0	0	10.5
12	63A006	35	1.34	2.0	0	0.4	0.77	19.3	0.75	17.6	2.7	9.7
↓	63A004	35	0.91	1.5	0	0.6	0.85	23.4	0.89	23.5	−4.5	−0.4
	63A004	35	0.91	2.0	0	0.4	0.79	19.3	0.77	17.6	2.6	9.7
13	63A004	35	0.91	2.0	18.5	0.6	0.74	22.5	0.79	19.4	−6.3	16.0
27	65A006	>35	1.17	4.0	45.0	0.2	1.01	25.3	1.01	25.0	0	1.2
↓	65A006	>35	1.17	4.0	48.6	0.2	1.08	25.9	1.09	25.0	−0.9	3.6
28	DW*	<35	0.30	2.0	63.4	–	1.41	34.7.	1.40	36.0	0.7	−3.6
29	0005	<35	1.34	2.0	63.4	0.13	1.30	34.7	1.32	34.5	−1.5	0.6
30	0005	<35	1.34	3.0	53.2	–	0.95	26.2	0.94	24.0	1.0	9.2
31	FP*	<35	0.36	0.03	0	0.08	0.73	44.9	0.69	46.0	5.8	−2.4
↓	↓	↓	0.53	0.134	↓	↓	0.92	44.7	0.83	48.5	10.8	−7.8
			0.86	0.35			1.12	43.9	1.16	41.5	−3.4	5.8
			1.03	0.50			1.16	43.0	1.26	41.5	−7.9	3.6
			1.14	0.66			1.20	41.7	1.31	40.5	−8.4	3.0
			1.46	1.00			1.16	37.2	1.29	39.0	−10.1	−4.6
			1.62	1.25			1.05	31.0	1.16	30.5	−9.5	1.6
			1.79	1.5			0.94	26.2	0.98	24.0	−4.1	9.2
			2.06	2.0			0.80	20.2	0.87	21.0	−8.0	−3.8
32	FP*	<35	0.49	0.5	82.9	–	0.88	35.2	0.86	34.0	2.3	3.5
↓	↓	↓	0.77	1.0	76.0	↓	1.15	35.0	1.12	31.0	2.7	12.9
			1.65	3.0	53.0		0.95	26.2	0.99	25.0	−4.0	4.8
33	DW*	<35	0.26	1.5	69.4	–	1.34	35.0	1.31	31.0	2.3	−12.9
↓	DW*	<35	0.26	1.5	69.4	↓	1.34	35.0	1.37	37.1	−2.2	−5.7

TABLE 4.1.3.4-B (CONTD)
LOW-ASPECT-RATIO WINGS AT SUBSONIC SPEEDS
DATA SUMMARY AND SUBSTANTIATION

Ref.	Airfoil Section	%C @ $(t/c)_{max}$	Δy (%C)	A	Λ_{LE} (deg)	M	$C_{L_{max}}$ Calc.	$\alpha_{C_{L_{max}}}$ Calc.	$C_{L_{max}}$ Test	$\alpha_{C_{L_{max}}}$ Test	Percent Error, e	
											$C_{L_{max}}$	$\alpha_{C_{L_{max}}}$
34	DW*	<35	0.75	2.0	63.4	–	1.37	3[illegible]	1.35	33.0	1.5	5.2
↓	↓	↓	0.75	↓	↓	↓	1.37	34.[illegible]	1.37	33.5	0	3.6
			0.9				1.32	34.7	1.35	34.0	−2.2	2.1
14	63A004	35	0.9	4.0	45.0	0.6	0.82	20.5	0.81	21.0	1.2	−2.4
↓	↓	↓	↓	2.5	58.0	↓	1.02	27.6	1.02	26.0	0	6.2
				3.0	53.2		0.90	23.6	0.90	22.7	0	4.0
				1.33	45.0		1.01	29.6	0.98	24.5	3.1	20.8
				2.67	45.0		0.82	20.7	0.79	21.0	3.8	−1.4
				2.0	53.0		0.91	24.1	0.91	23.2	0	3.9
				1.67	58.0		1.04	27.7	1.06	27.5	−1.9	0.7
				1.62	53.0		0.98	26.4	0.95	23.5	3.2	12.3
				2.15	45.0		0.85	21.8	0.80	21.0	6.2	3.8

*FP = Flat Plate, DW = Double Wedge

Average Error in $C_{L_{max}} = \frac{\Sigma|e|}{n} = 3.7\%$

Average Error in $\alpha_{C_{L_{max}}} = \frac{\Sigma|e|}{n} = 5.8\%$

TABLE 4.1.3.4-C
LOW-ASPECT-RATIO WINGS AT TRANSONIC SPEEDS
DATA SUMMARY AND SUBSTANTIATION

Ref.	A	Λ_{LE} (deg)	Δy	λ	M	Rx10^{-6}	$C_{L_{max}}$ Calc.	$\alpha C_{L_{max}}$ Calc.	$C_{L_{max}}$ Test	$\alpha C_{L_{max}}$ Test	Percent Error, e	
											$C_{L_{max}}$	$\alpha C_{L_{max}}$
12	1.5	0	0.91	1.0	0.6	1.7	0.85	23.4	0.89	23.5	−4.5	−0.4
					0.7	1.8	0.82	22.4	0.87	23	−5.7	−2.6
					0.8	1.9	0.80	22.1	0.87	23	−8.0	−3.9
					0.9	2.0	0.81	22.4	0.92	24	−12.0	−6.7
					1.0	2.1	0.97	24.1	1.02	–	−4.9	–
	2.0	0	1.34	1.0	0.6	1.7	0.73	19.0	0.72	18.5	1.4	2.7
					0.8	1.9	0.72	18	0.70	16.5	2.9	9.1
					0.9	2.0	0.75	18	0.70	16.0	7.1	12.5
					1.0	2.1	0.94	19.5	0.98	20.0	−4.1	−2.5
15	4.0	26.5	0.49	0	0.6	0.75	0.85	18.5	0.83	19.0	2.4	−2.6
					0.8	0.85	0.86	17.5	0.89	21.0	−3.4	−16.7
					0.9	0.87	0.96	18.8	1.01	22.0	−5.0	−14.5
					1.0	0.88	1.25	19.9	1.32	24.0	−5.3	−17.1
					1.1	0.88	1.26	29.5	1.24	26.0	1.6	13.5
13	2.0	18.5	0.49	0.5	0.6	1.4 to 2	0.78	23.3	0.85	21.0	−8.2	11.0
					0.8		0.78	22.3	0.86	19.5	−9.3	14.4
					0.9		0.84	22.5	0.93	18.0	−9.7	25.0
					1.0		1.05	24.6	1.15	22.0	−8.7	11.8
14	3.27	45.0	0.91	0.1	0.6	1.87	0.81	20.5	0.80	20.0	1.2	2.5
					0.8	2.22	0.82	19.5	0.79	17.0	3.8	14.7
					0.9	2.35	0.89	20.5	0.86	23.0	3.5	−10.9
	2.67	45.0	0.91	0.2	0.6	1.92	0.82	20.7	0.79	21.0	3.8	−1.4
					0.8	2.28	0.83	19.7	0.78	21.0	6.4	−6.2
					0.9	2.41	0.89	20.2	0.83	22.0	7.2	−8.2
	2.15	45.0	0.91	0.3	0.6	1.98	0.85	21.8	0.80	21.0	6.3	3.8
					0.8	2.37	0.84	20.8	0.79	21.0	6.3	−1.0
					0.9	2.49	0.88	21.3	0.81	21.0	8.6	1.4
	1.71	45.0	0.91	0.4	0.6	2.07	0.90	24.0	0.86	23.0	4.7	4.3
					0.8	2.46	0.86	23.0	0.84	22.0	2.4	4.5
					0.9	2.59	0.90	23.0	0.84	21.5	7.1	7.0
					1.0	2.69	1.08	24.8	1.00	22.0	8.0	12.7

TABLE 4.1.3.4-C (CONTD)
LOW-ASPECT-RATIO WINGS AT TRANSONIC SPEEDS
DATA SUMMARY AND SUBSTANTIATION

Ref.	A	Λ_{LE} (deg)	Δy	λ	M	$Rx10^{-6}$	$C_{L_{max}}$ Calc.	$\alpha_{C_{L_{max}}}$ Calc.	$C_{L_{max}}$ Test	$\alpha_{C_{L_{max}}}$ Test	Percent Error, e	
											$C_{L_{max}}$	$\alpha_{C_{L_{max}}}$
14	1.33	45.0	0.91	0.5	0.6	2.16	1.01	29.6	0.98	24.5	3.1	20.8
	↓	↓	↓	↓	0.8	2.58	0.93	28.1	0.94	23.5	−1.1	19.6
					0.9	2.72	0.92	28.1	0.93	23.5	−1.1	19.6
					1.0	2.82	1.06	30.0	1.02	26.0	3.9	15.4
	3.00	53.0	0.91	0	0.6	1.86	0.90	23.6	0.90	22.7	0	4.0
	↓	↓	↓	↓	0.8	2.21	0.87	22.3	0.88	22.0	−1.1	1.4
					0.9	2.32	0.90	22.4	0.90	23.0	0	−2.6
					1.0	2.42	1.08	24.2	1.05	24.0	2.9	0.8
	1.29	53.0	0.91	0.4	0.6	2.07	1.09	29.5	1.03	27.0	5.8	9.3
	↓	↓	↓	↓	0.8	2.46	0.99	28.2	0.97	24.0	2.1	17.5
					0.9	2.59	0.97	28.5	0.95	24.0	2.1	18.7
					1.0	2.69	1.10	30.0	1.02	25.0	7.8	20.0
	2.5	58.0	0.49	0	0.6	1.86	1.07	27.2	1.04	27.0	2.9	0.7
	↓	↓	↓	↓	0.8	2.21	1.00	26.0	0.96	23.0	4.2	13.0
					0.9	2.32	1.00	26.2	0.97	24.0	3.1	9.2
					1.0	2.42	1.16	27.9	1.10	25.0	5.5	11.6
	1.67	58.0	0.49	0.2	0.6	1.92	1.06	27.4	1.03	27.0	2.9	1.5
	↓	↓	↓	↓	0.8	2.28	0.99	26.2	0.94	23.5	5.3	11.5
					0.9	2.41	0.99	26.4	0.92	23.5	7.6	12.3

Average Error in $C_{L_{max}} = \frac{\Sigma|e|}{n} = 4.7\%$

Average Error in $\alpha_{C_{L_{max}}} = \frac{\Sigma|e|}{n} = 9.3\%$

TABLE 4.1.3.4-D
WINGS AT SUPERSONIC SPEEDS
DATA SUMMARY AND SUBSTANTIATION

Ref.	M	R x 10^{-6}	A	Λ_{LE} (deg)	$C_{L_{max}}$ Calc.	$\alpha_{C_{L_{max}}}$ Calc.	$C_{L_{max}}$ Test	$\alpha_{C_{L_{max}}}$ Test	Percent Error, e	
									$C_{L_{max}}$	$\alpha_{C_{L_{max}}}$
18	1.9	0.3 to 0.7	1.76	36	1.04	42.3	1.01	42.4	3.0	−0.2
	↓		1.96	64	1.07	40.5	1.06	41.0	0.9	−1.2
	2.32		1.96	64	1.03	41.0	0.98	43.8	5.1	−6.4
	↓		4.0	45	1.07	38.7	1.07	42.6	0	−9.2
			2.0	0	1.02	42.0	0.97	40.8	5.2	2.9
	1.55		1.96	64	1.13	39.5	1.06	41.1	6.6	−3.9
	↓		4.0	45	1.22	34.5	1.13	39.5	8.0	−12.7
			1.76	36	1.09	41.0	1.07	38.1	1.9	7.6
			1.74	0	1.15	38.8	1.14	39.3	0.9	−1.3
23	1.45	1.2 to 6.9	1.0	0	1.07	41.7	1.07	37.7	0	10.6
	1.96		2.0	0	1.07	40.2	1.10	41.5	−2.7	−3.1
	↓		3.0	0	1.09	39.0	1.11	35.0	−1.8	−11.4
	2.43		2.0	0	1.00	42.5	1.05	42.0	−4.8	1.2
	↓		3.0	0	1.01	41.5	1.07	38.0	−5.6	9.2
	3.36		1.0	0	0.89	47.0	0.89	41.7	0	12.7
	↓		2.0	0	0.93	45.0	0.95	41.5	−2.1	8.4
			3.0	0	0.94	44.5	0.95	40.8	−1.1	9.1
26	1.96	2.5 to 6.8	0.375	85	0.772	50.8	0.786	51.0	−1.8	−0.4
	↓		0.667	80	0.86	48.7	0.836	49.0	2.9	−0.6
	2.42		1.0	76	0.92	46.5	0.908	46.0	1.3	1.1
	↓		0.375	85	0.71	53.7	0.746	52.0	−4.8	3.3
			0.667	80	0.814	50.8	0.802	52.0	1.5	−2.3
			1.0	76	0.883	48.3	0.839	46.0	5.2	5.0
	3.30		0.375	85	0.67	54.5	0.687	52.0	−2.5	4.8
	↓		0.667	80	0.774	53.7	0.758	53.0	2.1	1.3
			1.0	76	0.815	51.5	0.815	50.0	0	3.0
21	2.46	1.0 to 3.5	2.0*	0	0.99	42.5	1.00	40.0	−1.0	6.3
	↓		2.0	0	0.99	42.5	1.04	40.0	−4.8	6.3
			2.0*	63	0.97	44.2	0.98	50.0	−1.0	−11.6
			2.0	63	0.97	44.2	0.96	45.0	1.0	−1.8
			4.0*	45	1.04	40.0	1.01	45.0	3.0	−11.1
	3.36	3.4	2.0	63	0.91	45.7	0.84	45.0	8.3	1.6
20	1.45	1.0 to 3.5	4.0*	45	1.21	35.5	1.18	35.0	2.5	1.4
	1.97		4.0*	45	1.11	38.0	1.09	43.0	1.8	−11.6
	↓		2.0*	63	1.02	42.7	1.01	45.0	1.0	−5.1
			2.0*	0	1.07	40.0	1.07	45.0	0	−11.1
			2	0	1.07	40.0	1.08	38.0	−0.9	5.3

*with thickened wing root

Average Error in $C_{L_{max}} = \frac{\Sigma|e|}{n} = 2.6\%$

Average Error in $\alpha_{C_{L_{max}}} = \frac{\Sigma|e|}{n} = 5.6\%$

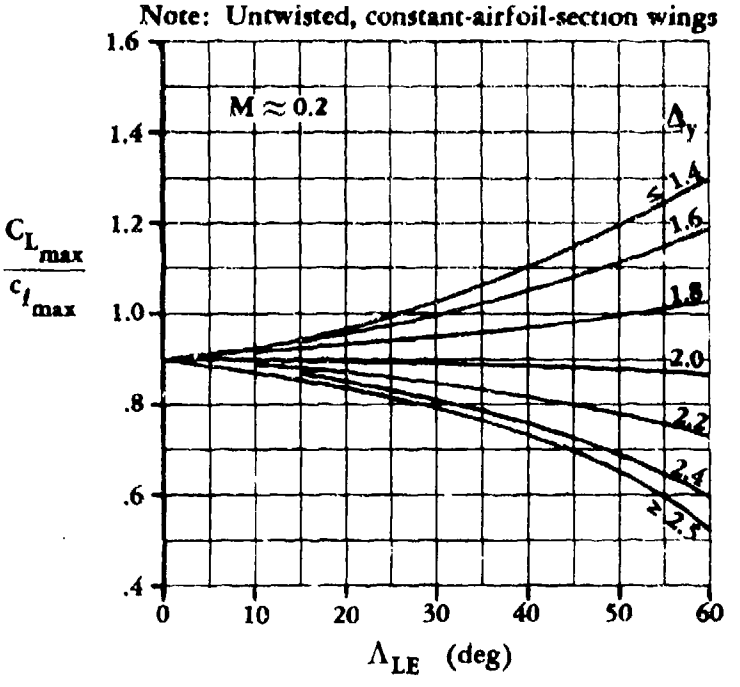

FIGURE 4.1.3.4-21a SUBSONIC MAXIMUM LIFT OF HIGH-ASPECT-RATIO WINGS

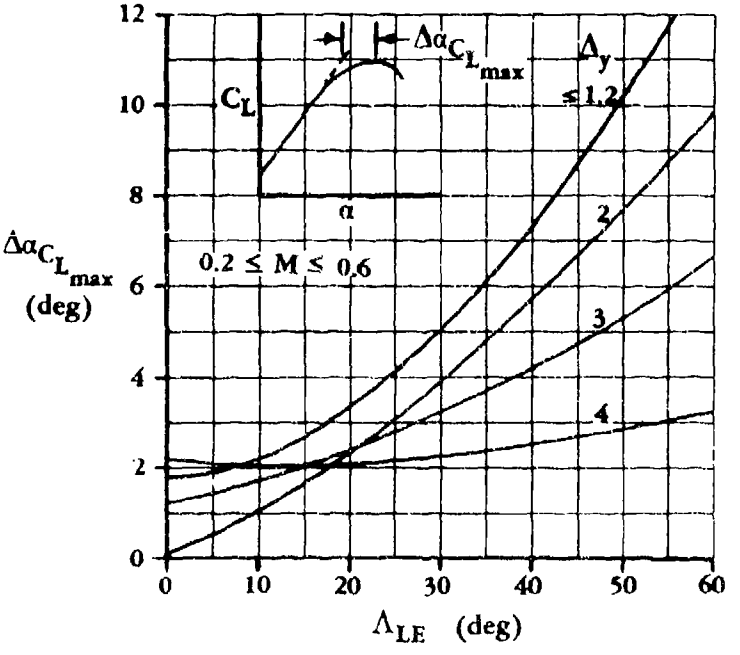

FIGURE 4.1.3.4-21b ANGLE-OF-ATTACK INCREMENT FOR SUBSONIC MAXIMUM LIFT OF HIGH-ASPECT-RATIO WINGS

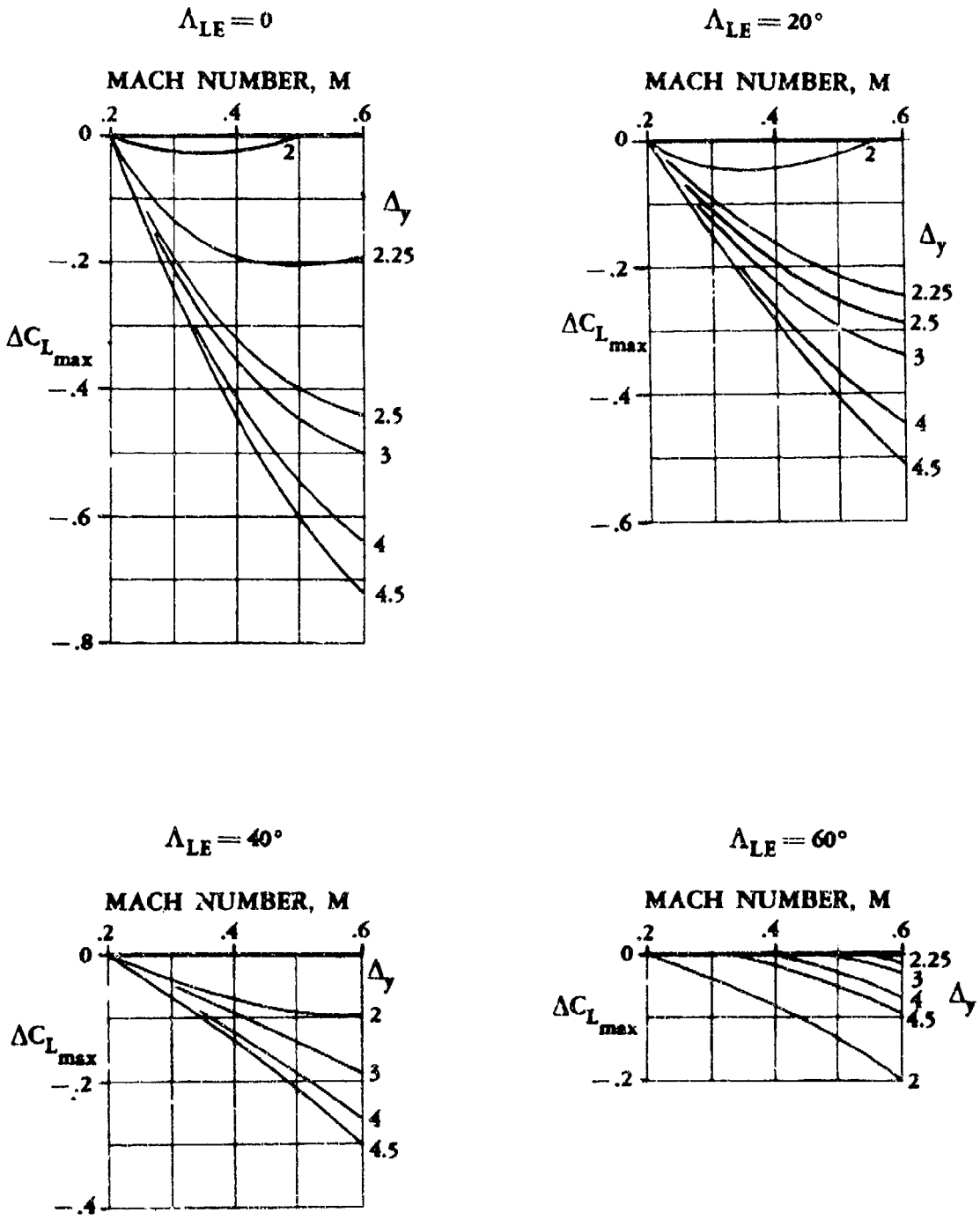

FIGURE 4.1.3.4-22 MACH-NUMBER CORRECTION FOR SUBSONIC MAXIMUM LIFT OF HIGH-ASPECT-RATIO WINGS

Notes: Symmetric airfoils
$R = 1 \times 10^6$ to 10×10^6 based on MAC
Δy for airfoil at MAC

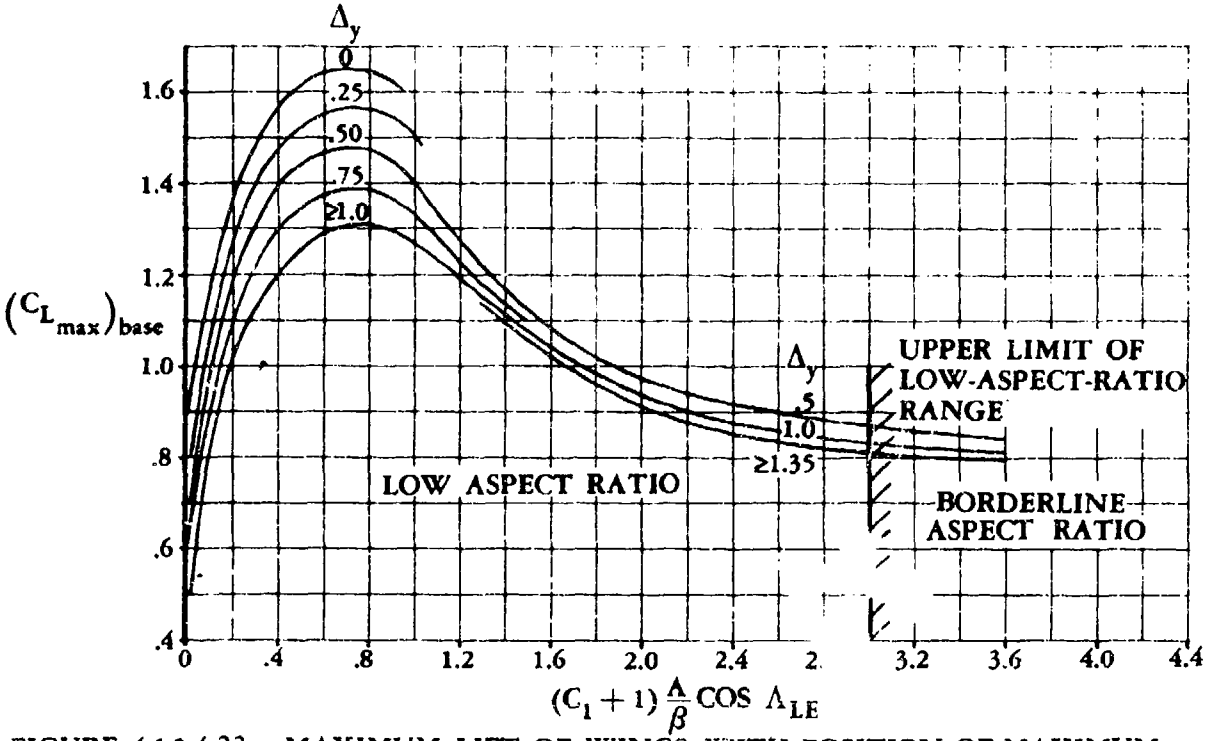

FIGURE 4.1.3.4-23a MAXIMUM LIFT OF WINGS WITH POSITION OF MAXIMUM THICKNESS AT OR FORWARD OF THE 35-PERCENT CHORD

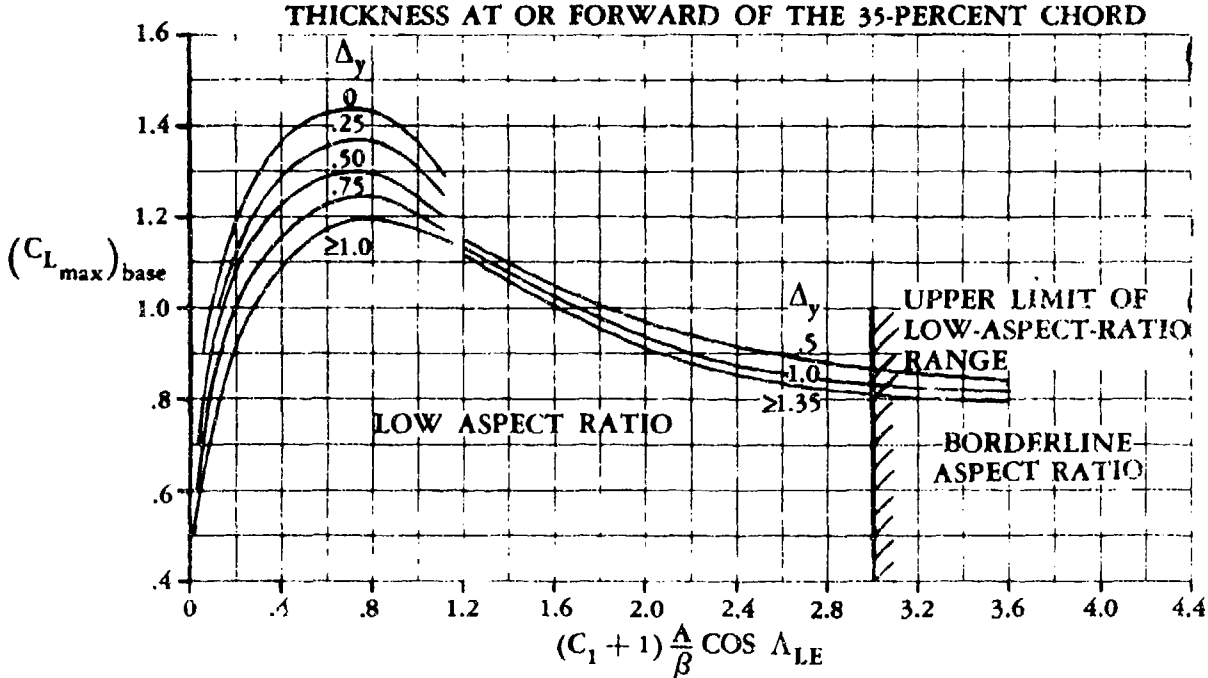

FIGURE 4.1.3.4-23b MAXIMUM LIFT OF WINGS WITH POSITION OF MAXIMUM THICKNESS BETWEEN 35- AND 50-PERCENT CHORD

Notes: Symmetric airfoils
$R = 1 \times 10^6$ to 10×10^6 based on MAC
Δy for airfoil at MAC

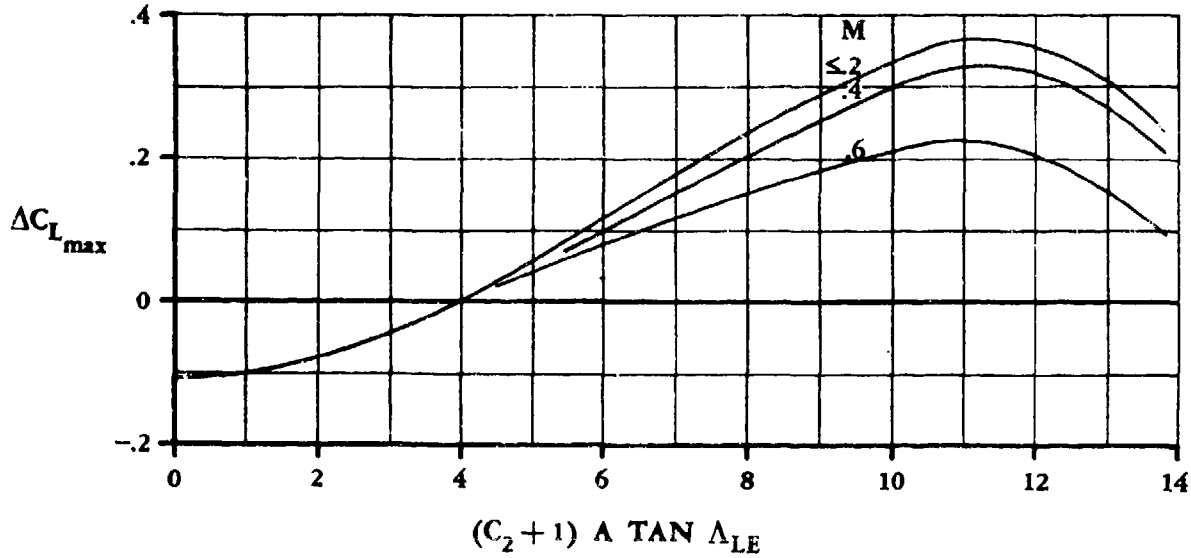

FIGURE 4.1.3.4-24a MAXIMUM-LIFT INCREMENT FOR LOW-ASPECT-RATIO WINGS

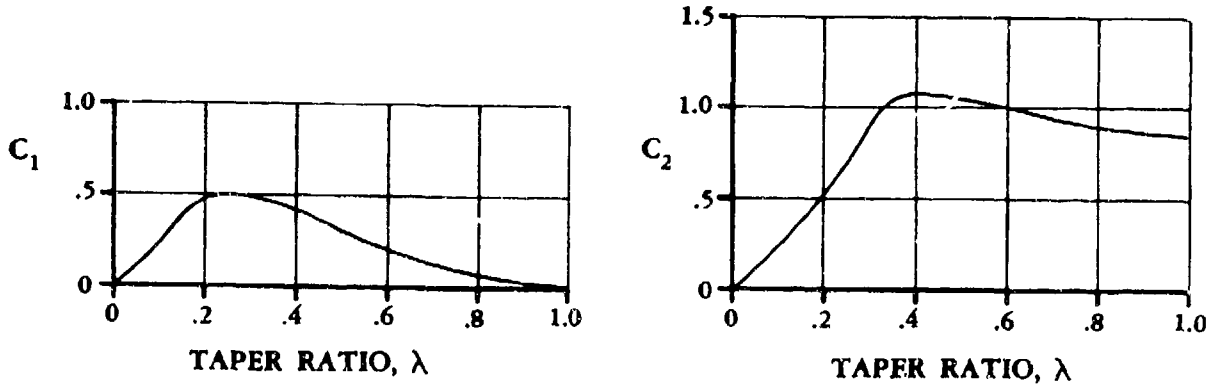

FIGURE 4.1.3.4-24b TAPER-RATIO CORRECTION FACTORS

Notes: Symmetric airfoils
$R = 1 \times 10^6$ to 10×10^6 based on MAC
Δy for airfoil at MAC

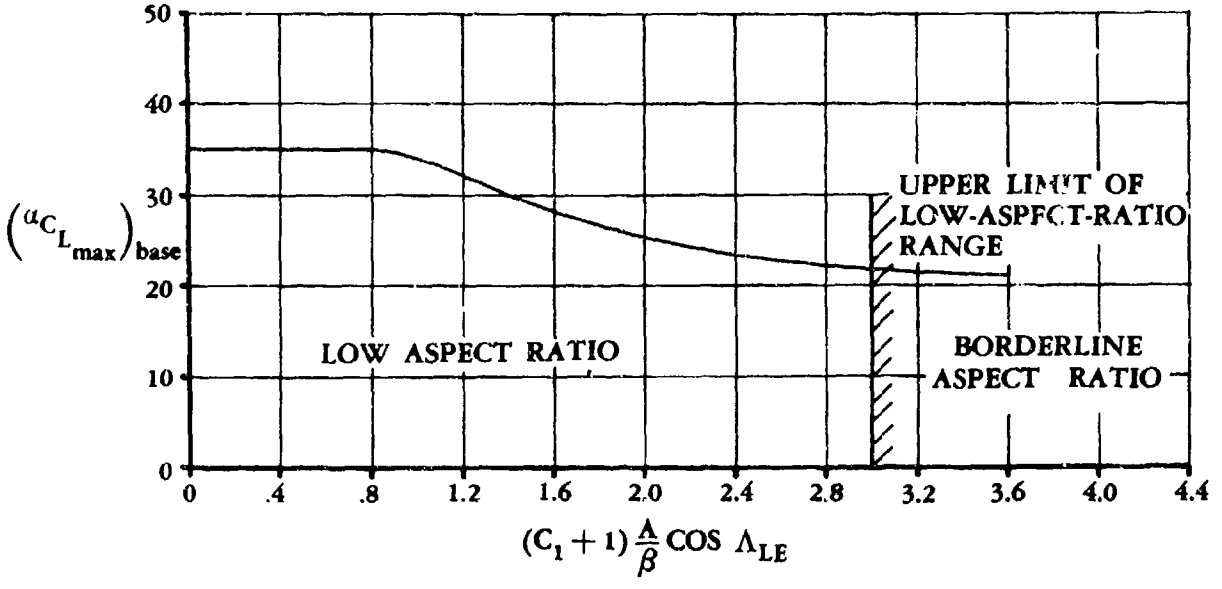

FIGURE 4.1.3.4-25a ANGLE OF ATTACK FOR SUBSONIC MAXIMUM LIFT OF LOW-ASPECT-RATIO WINGS

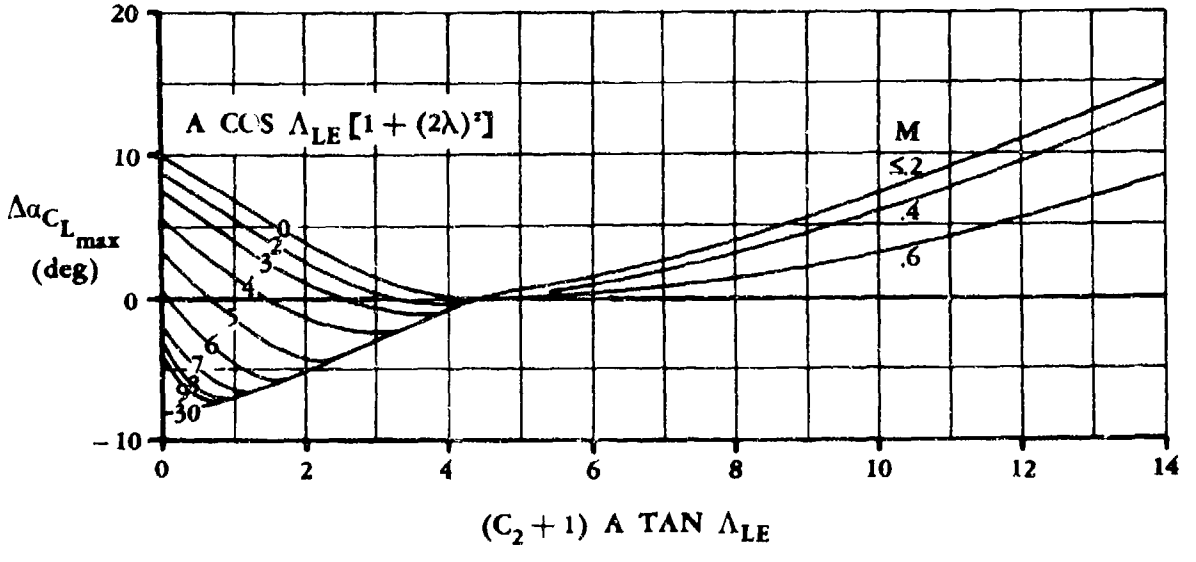

FIGURE 4.1.3.4-25b ANGLE-OF ATTACK INCREMENT FOR SUBSONIC MAXIMUM LIFT OF LOW-ASPECT-RATIO WINGS

TRANSONIC SPEEDS

Notes: Symmetric airfoils

$R = 1 \times 10^6$ to 15×10^6 based on MAC

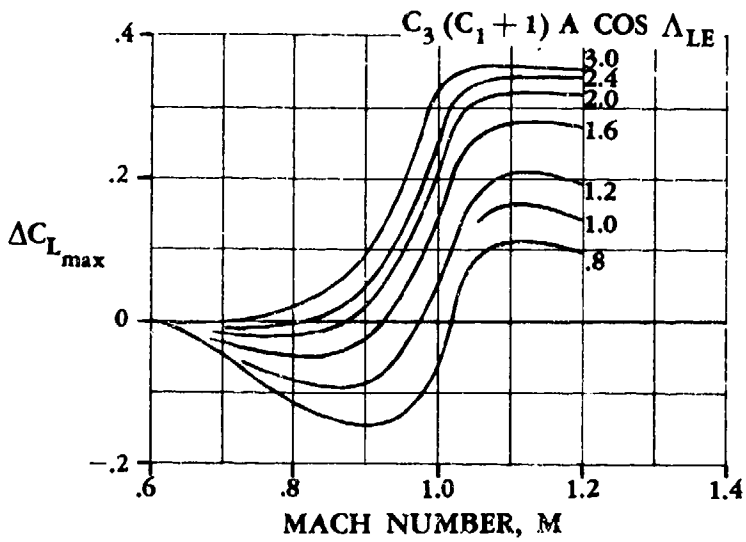

FIGURE 4.1.3.4-26a MAXIMUM LIFT OF LOW-ASPECT-RATIO WINGS

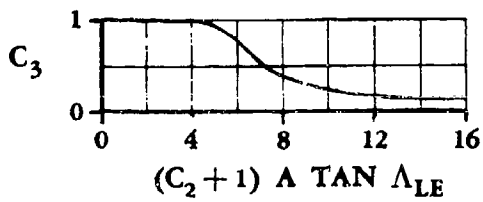

FIGURE 4.1.3.4-26b MAXIMUM-LIFT CORRECTION FACTOR

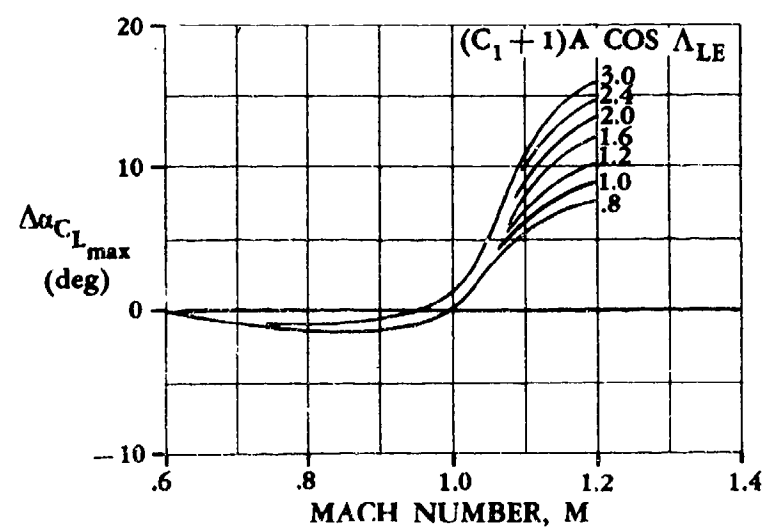

FIGURE 4.1.3.4-26c ANGLE-OF-ATTACK INCREMENT FOR LOW-ASPECT-RATIO WINGS

SUPERSONIC-HYPERSONIC SPEEDS

$1.4 \leq M \leq \infty$

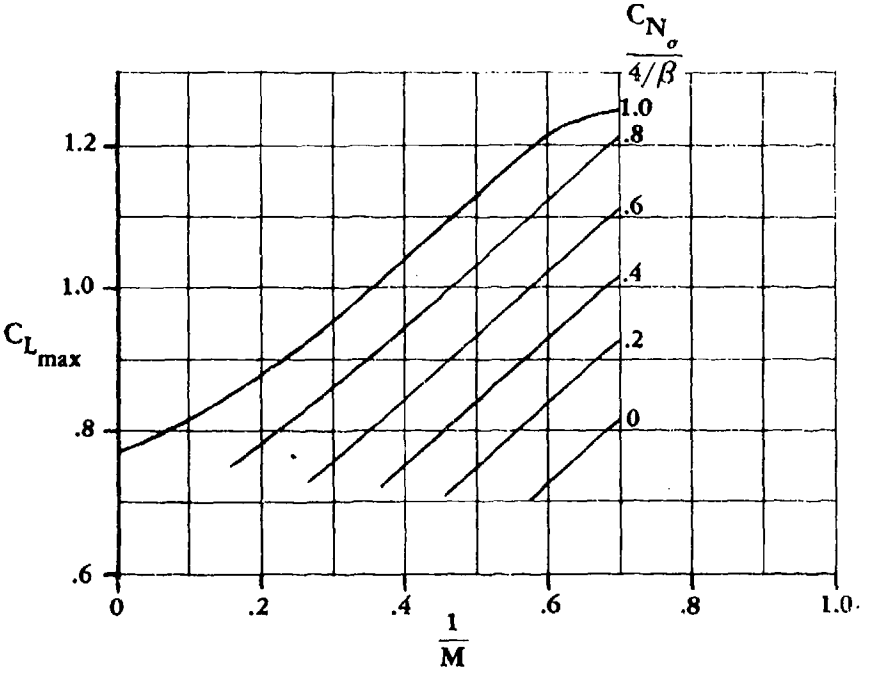

FIGURE 4.1.3.4-27a SUPERSONIC-HYPERSONIC WING MAXIMUM LIFT

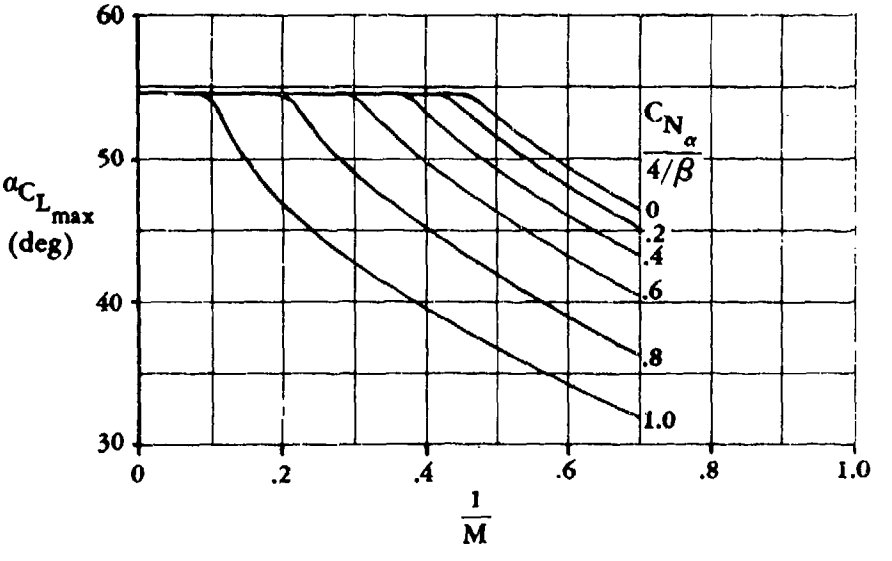

FIGURE 4.1.3.4-27b SUPERSONIC-HYPERSONIC WING ANGLE OF ATTACK FOR MAXIMUM LIFT

4.1.4 WING PITCHING MOMENT

The pitching-moment characteristics of aerodynamic surfaces are conventionally represented by specifying the wing aerodynamic-center location or the wing center of pressure.

The aerodynamic center is defined as that point on the wing plane of symmetry about which the pitching moment is invariant with lift, i.e., $\frac{dC_m}{dC_L} = 0$, for power-off flight of a rigid vehicle at a given Mach number.

The relationship between the wing aerodynamic center and the wing pitching-moment slope about any arbitrary point on the wing root chord is then given by the equation (neglecting wing drag):

$$\frac{dC_m}{dC_L} = -\left(n - \frac{x_{a.c.}}{c_r}\right)\frac{c_r}{c} \qquad 4.1.4\text{-a}$$

where

$\frac{x_{a.c.}}{c_r}$ is the chordwise distance from the wing apex to the aerodynamic center, measured in root chords, positive aft

n is the chordwise distance from the wing apex to the point about which the pitching moment is desired, measured in root chords, positive aft

$\frac{c_r}{c}$ is the ratio of the root chord to the pitching-moment reference chord, generally taken as the wing M.A.C.

$\frac{dC_m}{dC_L}$ is the slope of the wing pitching-moment coefficient about the point n with respect to the lift coefficient

The usefulness of the aerodynamic-center concept lies principally in the convenient way in which it presents pitching-moment information in the linear lift range. Within this range the forces on a wing are simply represented by a lift vector of varying magnitude acting through the aerodynamic center and a constant moment about the a.c. equivalent to the wing zero-lift moment.

The aerodynamic-center concept is often used beyond the linear lift range by specifying the locus of points at which $\frac{dC_m}{dC_L}$ is zero, as a function of lift (or angle of attack). The a.c. curve thus defined represents the successive points at which the surface has "neutral stability."

Center of pressure is defined as that point at which the wing total resultant force intersects the wing chord, i.e., it is the point on the wing chord at which $C_m = 0$.

If the wing center-of-pressure location is known, the wing pitching moment about any other point on the wing chord may be calculated, provided the direction of the resultant-force vector on the wing is also known. This fact, which is apparent from geometrical considerations, is reflected in the equations for determining the moment coefficient from the center of pressure. There are two cases, as follows:

A. Resultant-force vector perpendicular to the wing surface:

$$C_m = -\left(n - \frac{x_{cp}}{c_r}\right)\frac{c_r}{c}\, C_N \qquad 4.1.4\text{-b}$$

B. Resultant-force vector in the lift direction (perpendicular to the free stream):

$$C_m = -\left(n - \frac{x_{cp}}{c_r}\right)\frac{c_r}{c}\, C_L \cos\alpha \qquad 4.1.4\text{-c}$$

In the above equations $\frac{x_{cp}}{c_r}$ is the chordwise distance from the wing apex to the wing center of pressure, measured in

root chords, positive aft.

Since at low angles of attach the resultant-force vector on wings is essentially in the lift direction (see Section 4.1.3), equation 4.1.4-c is applicable. At high angles of attack, the resultant force is more nearly normal to the wing chord and thus equation 4.1.4-b is the more applicable. However, equation 4.1.4-b may also be used at low angles of attack. For the remainder of this Section, it is assumed that equation 4.1.4-b holds at all angles of attack, and that the C_N in this equation is equivalent to the C'_N as defined and discussed in Section 4.1.3.

In the linear lift range, the locations of the center of pressure and the aerodynamic center are the same for wings having symmetrical profiles but not the same for wings having cambered profiles.

Two sets of charts are presented in subsequent Sections. The charts for the linear lift range present the aerodynamic-center location of wings as a function of planform parameters. The charts for the nonlinear lift range give the wing center-of-pressure location also as a function of planform parameters. The two groups of charts taken together permit the calculation of the complete-pitching-moment curve from 0° to 90° angle of attack for symmetrical wings.

For cambered wings, no specific method is presented for calculating the pitching moments beyond the linear lift range. However, for angles of attack beyond the stall, it is not likely that there will be much difference between the pitching moments of symmetrical wings and those of cambered wings.

4.1.4.1 WING ZERO-LIFT PITCHING MOMENT

The methods presented in this section are restricted to subsonic speeds. In the transonic and supersonic speed regimes it is suggested that reference be made to experimental data.

A. SUBSONIC

Two methods are presented for estimating the wing zero-lift pitching moment. Method 1 is general and is applicable to the majority of moderately swept configurations. It is not advisable to use Method 1 for configurations having a quarter-chord-sweep angle greater than 45°. Method 2 is taken from Reference 1 and is applicable only at M = 0.2 for highly swept, constant-section, low-aspect-ratio, delta or clipped-delta configurations with large thickness ratios; i.e., $0.10 \leqslant t/c \leqslant 0.30$.

DATCOM METHODS

Method 1

The low-speed zero-lift pitching moment based on the product of the wing area and mean aerodynamic chord $S_W \bar{c}_W$, for untwisted, constant-section wings with elliptical loading may be approximated by

$$\left(C_{m_0}\right)_{\theta=0} = \frac{A \cos^2 \Lambda_{c/4}}{A + 2 \cos \Lambda_{c/4}} c_{m_0} \qquad 4.1.4.1\text{-a}$$

where c_{m_0} is the section pitching-moment coefficient at zero lift, obtained from Section 4.1.2.1. The airfoil section is defined parallel to the free stream.

For airfoil sections varying along the span

$$\left(C_{m_0}\right)_{\theta=0} = \frac{A \cos^2 \Lambda_{c/4}}{A + 2 \cos \Lambda_{c/4}} \left(\frac{c_{m_{0_{root}}} + c_{m_{0_{tip}}}}{2}\right) \qquad 4.1.4.1\text{-b}$$

where $c_{m_{0_{root}}}$ and $c_{m_{0_{tip}}}$ are the section pitching-moment coefficients at zero lift of the root and tip sections, respectively, both defined parallel to the free stream.

For wings with linear twist, lifting-line theory may be used as in Reference 2 to obtain C_{m_0} by

$$C_{m_0} = \left(C_{m_0}\right)_{\theta=0} + \left(\frac{\Delta C_{m_0}}{\theta}\right)\theta \qquad 4.1.4.1\text{-c}$$

where

$\left(C_{m_0}\right)_{\theta=0}$ is the zero-lift pitching-moment coefficient of an untwisted wing, obtained by using either Equation 4.1.4.1-a or Equation 4.1.4.1-b.

$\frac{\Delta C_{m_0}}{\theta}$ is the change in wing zero-lift pitching-moment coefficient due to a unit change in linear wing twist. This parameter is obtained from Figure 4.1.4.1-5.

θ is the twist of the wing tip with respect to the root section, in degrees (negative for washout). A linear spanwise twist distribution is assumed (all constant-percent points of local chords lie in straight lines along the span).

The effect of Mach number on the wing zero-lift pitching-moment coefficient, up to the critical Mach number, is presented in Figure 4.1.4.1-6. This chart, based on test data, gives the ratio of wing or wing-body zero-lift pitching-moment coefficient in compressible flow to that in incompressible flow. When using this chart, no correction should be made to the section c_{m_0} value. The use of this chart should give reasonable results up to M = 0.8. However, beyond this point the chart should be used with caution, since test data often show abrupt changes in zero-lift pitching moment at high transonic speeds.

The limited availability of test data, coupled with the fact that the wing zero-lift pitching-moment coefficient does not lend itself to accurate experimental measurement, precludes substantiation of this method.

Method 2

This semiempirical method is taken from Reference 1, ignoring the small wing-planform nose-radius effects. The semiempirical method was developed by using the test results of Reference 1, correlated with the theoretical predictions based on lifting-surface theory. Because of its semiempirical nature, the method should be restricted to M = 0.2 conditions for highly swept, constant-section, low-aspect-ratio, delta or clipped-delta configurations with the following geometric characteristics:

$$0.58 \leqslant A \leqslant 2.55$$

$$0 \leqslant \lambda \leqslant 0.3$$

$$63^{\circ} \leqslant \Lambda_{LE} \leqslant 80^{\circ}$$

$$0.10 \leqslant t/c \leqslant 0.30$$

$$\Lambda_{TE} = 0$$

For round-nosed-planform configurations the reader is referred to Reference 1, where three different planform nose-radius models were tested. No incremental nose planform effects are presented here because of their probable configuration dependence.

The wing zero-lift pitching-moment coefficient may be approximated by the following procedure:

Step 1. Determine the section zero-lift pitching-moment coefficient c_{m_0} for the particular airfoil under consideration. Lifting-surface theory was used in the method formulation of Reference 1 to estimate the section zero-lift pitching-moment coefficient. For this reason it is recommended that lifting-surface theory be used, if available, for the prediction of c_{m_0}.

If lifting-surface theory is not available, c_{m_0} may be estimated by using test data; e.g., those listed in Tables 4.1.1-A and -B.

Step 2. Determine a wing zero-lift pitching moment $\left(C_{m_0}\right)_{\text{theory}}$ uncorrected for thickness effects from Figure 4.1.4.1-7 as a function of sweep, taper ratio, and section zero-lift pitching moment. (The value of Λ_c is defined as $\Lambda_c = 90^\circ - \Lambda_{LE}$.)

Step 3. Calculate the wing zero-lift pitching moment C_{m_0}, based on the wing area and wing root chord $S_W c_r$, using the following

$$C_{m_0} = \left[\frac{C_{m_0}}{\left(C_{m_0}\right)_{\text{theory}}}\right] \left(C_{m_0}\right)_{\text{theory}} \qquad 4.1.4.1\text{-d}$$

where

$\dfrac{C_{m_0}}{\left(C_{m_0}\right)_{\text{theory}}}$ is the ratio of zero-lift pitching moment corrected for thickness effects to the uncorrected zero-lift pitching moment. This ratio is obtained from Figure 4.1.4.1-8 as a function of thickness, planform geometry, and the uncorrected wing zero-lift pitching moment.

$\left(C_{m_0}\right)_{\text{theory}}$ is the zero-lifting pitching-moment coefficient uncorrected for thickness effects obtained above in Step 2.

For the particular configurations to which this method is applicable, insufficient data are available to determine the usefulness of Figure 4.1.4.1-6 for estimating Mach number effects.

No substantiation of this method is possible because of the lack of wing-alone low-aspect-ratio test data having thickness ratios of $0.10 \leqslant t/c \leqslant 0.30$.

Sample Problems

1. Method 1

Given: The following straight-tapered wing of Reference 3.

$A = 6.0$ $\quad \lambda = 0.5$ $\quad \Lambda_{c/4} = 9.67^\circ$ $\quad \theta = 0$ $\quad$ Low speed

NACA 2301.2 airfoil (free-stream direction)

Compute:

$c_{m_0} = -0.014$ (Table 4.1.1-A)

Solution:

$$\left(C_{m_0}\right)_{\sigma=0} = \frac{A \cos^2 \Lambda_{c/4}}{A + 2 \cos \Lambda_{c/4}} c_{m_0} \quad \text{(Equation 4.1.4.1-a)}$$

$$= \frac{6(0.9858)^2}{6 + 2(0.9858)} (-0.014)$$

$$= -0.010$$

This compares with a test value of -0.012 from Reference 3.

2. Method 2

Given: The following constant-section, low-aspect-ratio, clipped-delta configuration.

$A = 0.823$ $\lambda = 0.18$ $\Lambda_{LE} = 73.5^{\circ}$

NACA 2412 airfoil $M = 0.2$ $\Lambda_c = 16.5^{\circ}$ (complement of leading-edge sweep)

Compute:

$c_{m_0} = -0.047$ (Table 4.1.1-A)

$4 \tan \Lambda_c (1 + \pi\lambda^2 \tan \Lambda_c) = 4(0.2962)\left[1 + \pi(0.18)^2 (0.2962)\right] = 1.2205$

$\left(C_{m_0}\right)_{\text{theory}} = -0.010$ (Figure 4.1.4.1-7)

$$\frac{C_{m_0}}{\left(C_{m_0}\right)_{\text{theory}}} = 0.91 \quad \text{(Figure 4.1.4.1-8)}$$

$$C_{m_0} = \left[\frac{C_{m_0}}{\left(C_{m_0}\right)_{\text{theory}}}\right] \left(C_{m_0}\right)_{\text{theory}} \quad \text{(Equation 4.1.4.1-d)}$$

$$= (0.91)(-0.010)$$

$$= -0.0091$$

REFERENCES

1. Crosthwait, E. L., and Seath, D. D.: Subsonic Characteristics of Low Aspect Ratios. FDL-TDR-64-103, 1965. (U)

2. DeYoung, J., and Harper, C. W.: Theoretical Symmetric Span Loading at Subsonic Speeds for Wings Having Arbitrary Plan Form. NACA TR 921, 1948. (U)

3. Pearson, H. A., and Anderson, R. F.: Calculation of the Aerodynamic Characteristics of Tapered Wings with Partial-Span Flaps. NACA TR 665, 1939. (U)

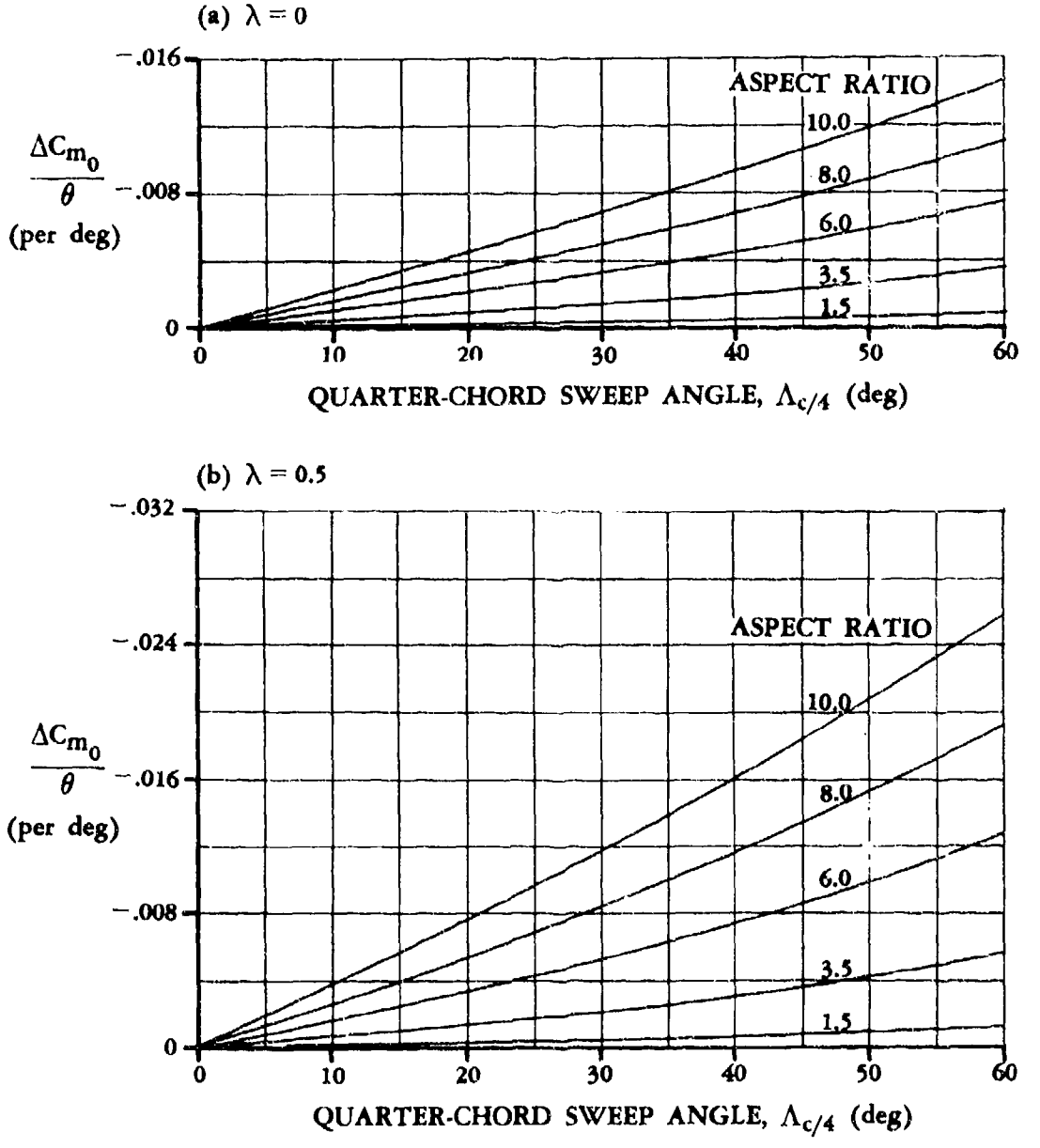

FIGURE 4.1.4.1-5 EFFECT OF LINEAR TWIST ON THE WING ZERO-LIFT PITCHING MOMENT

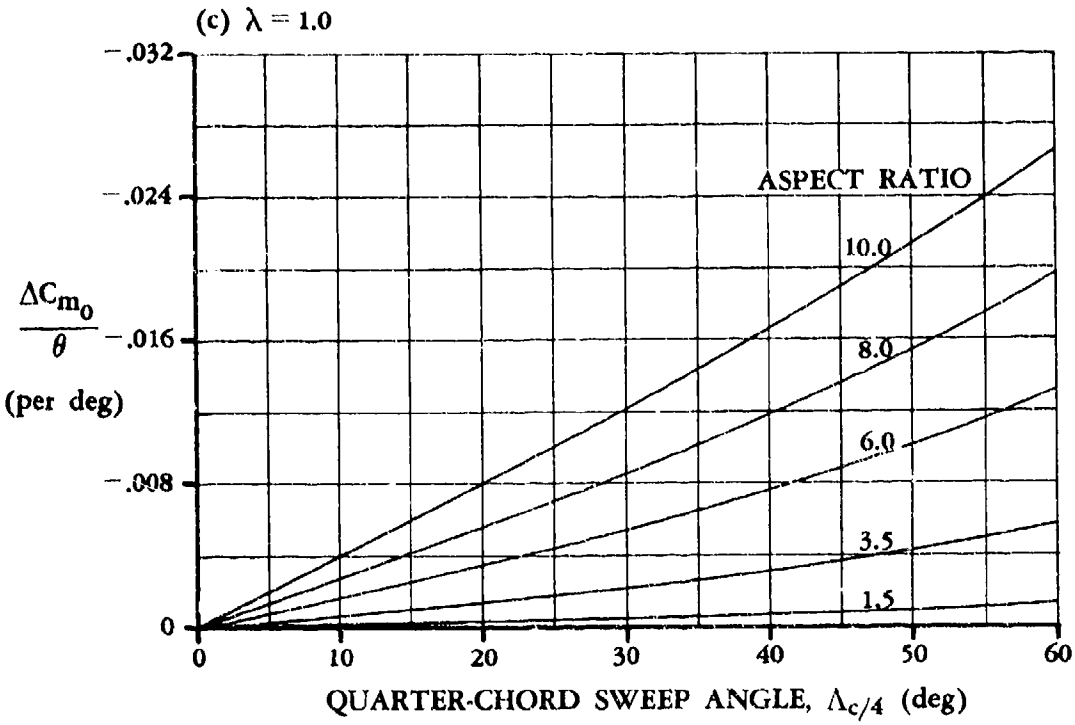

FIGURE 4.1.4.1-5 (CONTD)

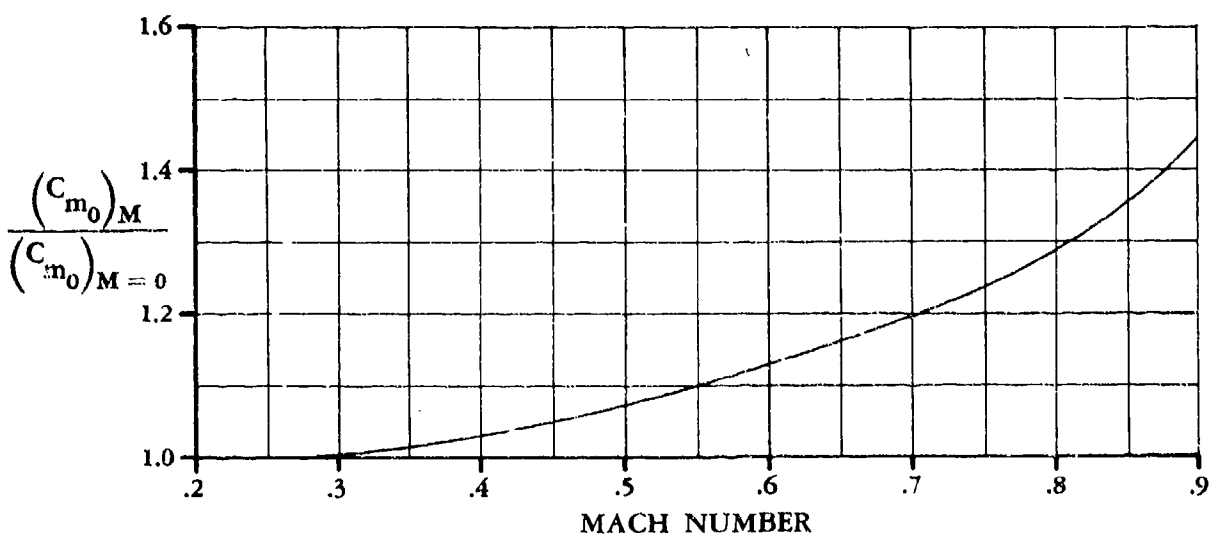

FIGURE 4.1.4.1-6 EFFECT OF COMPRESSIBILITY ON THE WING OR WING-BODY ZERO-LIFT PITCHING-MOMENT COEFFICIENT

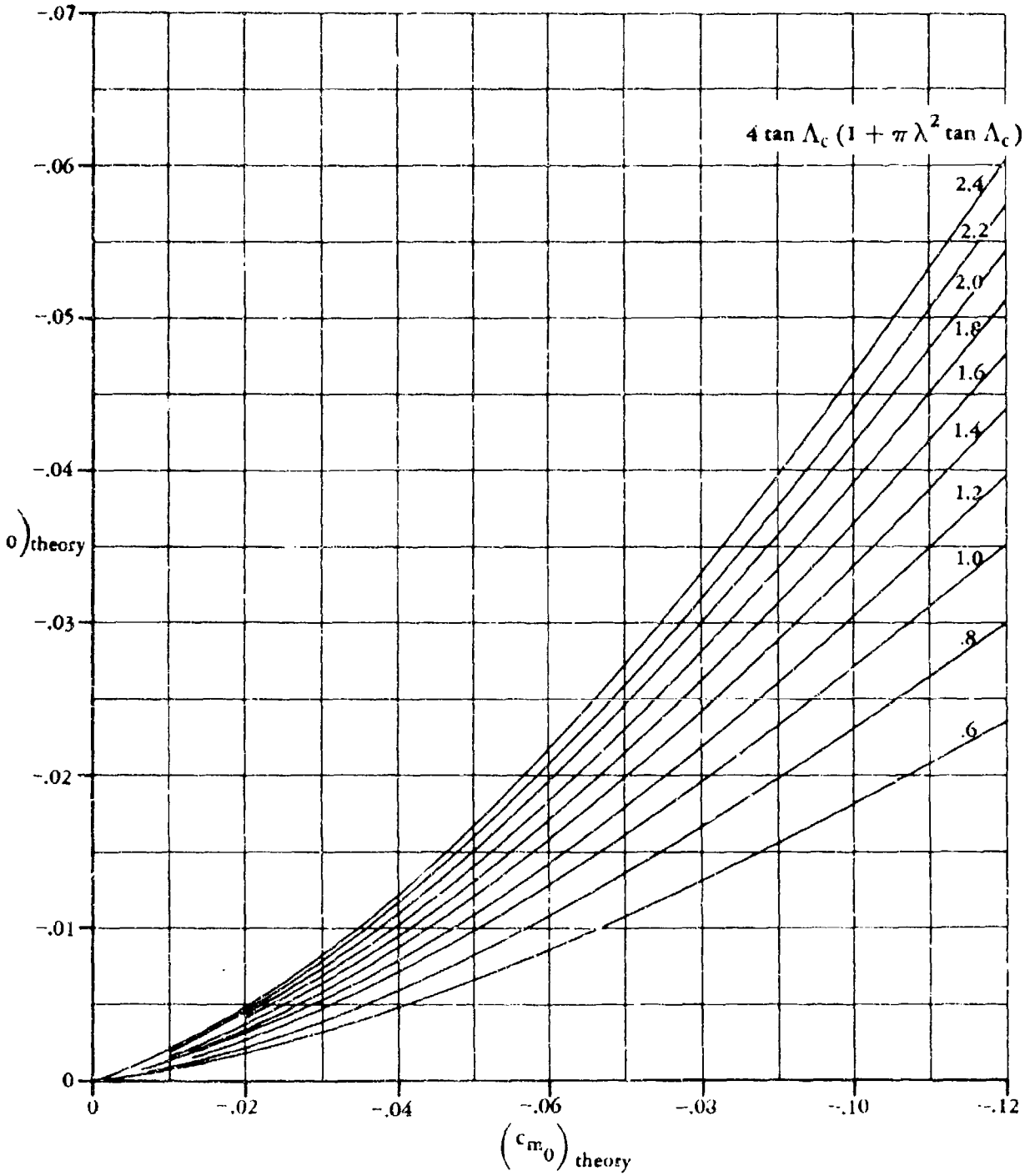

FIGURE 4.1.4.1-7 WING ZERO-LIFT PITCHING MOMENT

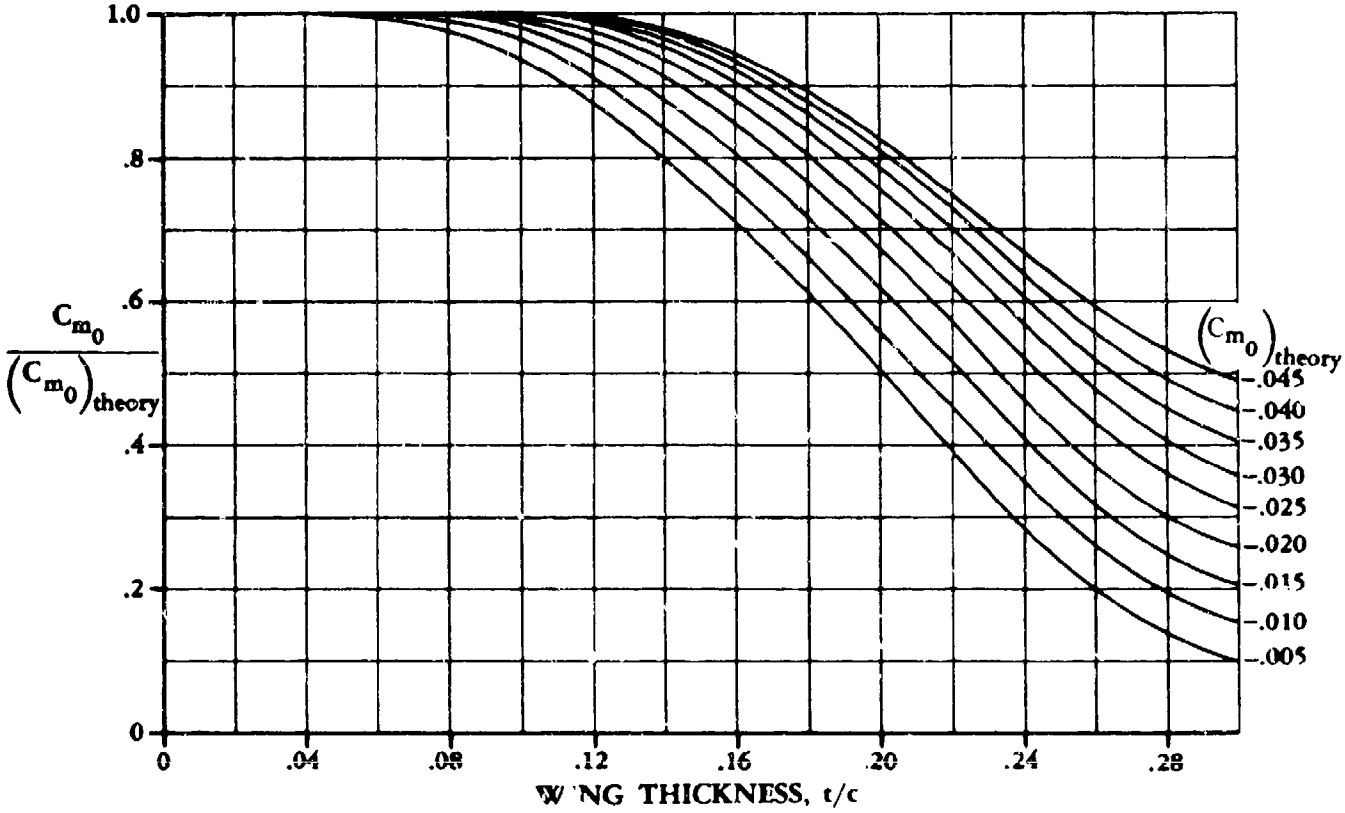

FIGURE 4.1.4.1-8 WING ZERO-LIFT PITCHING-MOMENT THICKNESS CORRECTION FACTOR

4.1.4.2 WING PITCHING-MOMENT-CURVE SLOPE

This section presents methods for calculating the pitching-moment characteristics of wings at low angles of attack at any speed.

The pitching-moment characteristics are generally presented in terms of the wing aerodynamic center. The aerodynamic center (Section 4.1.4) is that point about which the wing pitching moment is invariant with lift. Thus the pitching-moment slope based on the product of the wing area and the mean aerodynamic chord $S_w\bar{c}_w$ about any specified point on the wing chord line may be described by the following equation:

$$\frac{dC_m}{dC_L} = \left(n - \frac{x_{a.c.}}{c_r}\right) \frac{c_r}{\bar{c}} \qquad 4.1.4.2\text{-a}$$

where

$\frac{x_{a.c.}}{c_r}$ is the distance from the wing apex to the aerodynamic center measured in root chords, positive aft.

n is the distance from the wing apex to the desired moment reference center measured in root chords, positive aft.

$\frac{c_r}{\bar{c}}$ is the ratio of the root chord to the mean aerodynamic chord.

A. SUBSONIC

At subsonic speeds methods are presented for predicting the aerodynamic center of the following two classes of wing planforms:

Straight-Tapered Wings (conventional, trapezoidal wings)

Non-Straight-Tapered Wings

Double-delta wings

Cranked wings

Curved (Gothic and ogee) wings

These three general categories of non-straight-tapered wings are illustrated in Sketch (a) of Section 4.1.3.2. Their wing-geometry parameters are presented in Section 2.2.2.

Two methods are presented for estimating the wing pitching-moment-curve slope for straight-tapered wings. Method 1 is general and is applicable to the majority of configurations. Method 2 is applicable only at $M = 0.2$ for highly swept, constant-section, low-aspect-ratio, delta or clipped-delta configurations with large thickness ratios; i.e., $0.10 \leq t/c \leq 0.30$.

All of the basic theories for calculating wing lift apply to wing pitching moments also. However, as is discussed in Section 4.1.3.2, there is no guarantee that a theory that gives accurate results for lift also gives accurate values for moments.

One theory that does give accurate results for both lift and moments of straight-tapered wings over the entire aspect-ratio range is the lifting-surface theory of Reference 1. Although the computation difficulties of this method are not as formidable as those of some other lifting-surface theories, solutions are nevertheless limited to certain specific planforms.

Most of the currently available methods that are applicable to a wide range of configurations are based largely on empirical data. A semiempirical method of this type is presented in Reference 2. The procedure of this reference uses certain simplified theories (see References 3 and 4) to define limiting locations for the aerodynamic-center positions as the wing aspect ratio approaches zero or infinity. For intermediate aspect ratios, some 150 experimental points from 40 different reports are used as a guide in fairing curves between the theoretically determined limits. In this way generalized charts are constructed for straight-tapered wings of arbitrary aspect ratio and taper ratio. Comparison between the aerodynamic-center locations given by the semiempirical method of Reference 2 and the available lifting-surface solutions of Reference 1 shows a high degree of correlation. The charts of Reference 2 also agree well with the other available semiempirical methods of less extensive scope, such as that of Reference 5.

In the Datcom the graphical aerodynamic-center information presented is basically that of Reference 2. However, the charts are presented in a slightly different form, and the effects of Mach number are added by means of the Prandtl-Glauert compressibility correction rule. The design charts for predicting the aerodynamic center are applicable only within the linear-lift range. Thus the charts apply to wings of very low aspect ratio at only very low angles of attack. These charts are directly applicable to straight-tapered wings. In treating non-straight-tapered wings, the wing is divided into two wing panels and the individual lift and aerodynamic center for each panel are used to establish the aerodynamic center for the composite wing.

Within the linear-lift range, profile parameters such as mean camber line, thickness, leading-edge shape, and others appear to have only minor influence on the aerodynamic-center location of either straight-tapered or non-straight-tapered wings.

Reynolds number, on the other hand, can have an appreciable effect. Reference 6 indicates that for a wing of aspect ratio 3 with a 3-percent biconvex section, the aerodynamic center can vary as much as 8 percent of the wing root chord between the Reynolds numbers 2.4×10^6 and 8×10^6. Although this aerodynamic-center shift appears to be larger than usual, it does serve to indicate that wind-tunnel test conditions, such as tunnel turbulence level, model support system, and Reynolds number, can have an important bearing on the experimentally measured aerodynamic chord locations.

DATCOM METHODS

Straight-Tapered Wings

Method 1

Figures 4.1.4.2-26a through 4.1.4.2-26f present the a.c. location for straight-tapered wings at subsonic speeds. These charts give the a.c. location as a fraction of the wing root chord. The charts are based on planform characteristics only and thus are most applicable to low-aspect-ratio wings.

The characteristics of high-aspect-ratio wings are primarily determined by the wing two-dimensional section characteristics. For most airfoil sections the a.c. location is at or near the MAC quarter-chord point. However, if greater accuracy is desired, the a.c. location for the particular airfoil section under consideration may be determined from Section 4.1.2.2.

The applicability of the subsonic portions of Figures 4.1.4.2-26a through 4.1.4.2-26f is limited to $M \leqslant 0.6$. The form of presentation of the charts does not permit an indication of this limit in a manner that is applicable in all situations. Beyond M = 0.6 the a.c. location tends to become dependent on wing profile thickness and shape, as indicated in Paragraph B of this section.

However, for swept wings with $t/c \leqslant 0.04$ the thickness effects are much reduced, and Figures 4.1.4.2-26a through 4.1.4.2-26f may be applied to Mach numbers somewhat higher than M = 0.6.

Method 2

This semiempirical method is taken from Reference 7, ignoring the small wing-planform nose-radius effects. The semiempirical method was developed by using the test results of Reference 7, correlated with the theoretical predictions based on lifting-surface theory. Because of its semiempirical nature, the method should be restricted to M = 0.2 conditions for highly swept, constant-section, low-aspect-ratio, delta or clipped-delta configurations with the following geometric characteristics:

$$0.10 \leqslant t/c \leqslant 0.30$$

$$0.58 \leqslant A \leqslant 2.55 ,$$

$$0 \leqslant \lambda \leqslant 0.3$$

$$63^{\circ} \leqslant \Lambda_{LE} \leqslant 80^{\circ}$$

$$\Lambda_{TE} = 0$$

The nonlinear region of the pitching-moment curve for configurations described above may be approximated by using Method 2 of Section 4.1.4.3.

For round-nosed-planform configurations the reader is referred to Reference 7, where three different planform nose-radius models were tested. No incremental nose planform effects are presented here because of their probable configuration dependence.

The wing pitching-moment-curve slope may be approximated by the following procedure:

Step 1. Calculate the aerodynamic-center location uncorrected for wing thickness effects by the following:

$$\frac{x_{a.c.}}{c_r} = \frac{\frac{2}{3}(1-\lambda) + \frac{1}{2}\left[1 - \frac{\lambda^2}{1+\lambda}\right] \pi \log_e\left(1 + \frac{A}{5}\right)}{1 + \pi \log_e\left(1 + \frac{A}{5}\right)} \qquad 4.1.4.2\text{-b}$$

Step 2. Determine the wing pitching-moment-curve slope uncorrected for wing thickness effects by using a modified form of Equation 4.1.4.2-a, i.e.,

$$\left(\frac{dC_m}{dC_L}\right)_{theory} = n - \frac{x_{a.c.}}{c_r}$$

where

n is the distance from the wing apex to the desired moment reference center, measured in root chords, positive aft. If the semiempirical procedure presented in Method 2 of Section 4.1.4.3 is to be used to determine the nonlinear pitching-moment characteristics, the determination of the moment reference center n is not arbitrary. The moment reference center in this case should be taken at the root-chord midpoint, i.e., $n = 0.5$.

$\frac{x_{a.c.}}{c_r}$ is the distance from the wing apex to the aerodynamic center, measured in root chords, positive aft. This term is obtained from Step 1 above and is uncorrected for thickness effects.

Step 3. Correct the pitching-moment-curve slope for thickness effects, based on the product of wing area and wing root chord $S_W c_r$, by

$$\frac{dC_m}{dC_L} = \left(\frac{dC_m}{dC_L}\right)_{theory} \left[\frac{dC_m/dC_L}{(dC_m/dC_L)_{theory}}\right] \qquad 4.1.4.2\text{-c}$$

where

$\left(\frac{dC_m}{dC_L}\right)_{theory}$ is the wing pitching-moment-curve slope from Step 2, uncorrected for thickness effects.

$\frac{dC_m/dC_L}{(dC_m/dC_L)_{theory}}$ is the wing-thickness-correction factor for the wing pitching-moment-curve slope. This parameter is obtained from Figure 4.1.4.2-29 as a function of $(dC_m/dC_L)_{theory}$ and thickness.

No substantiation of this method is possible because of the lack of low-aspect-ratio test data having wing thickness ratios of $0.10 \leq t/c \leq 0.30$.

Non-Straight-Tapered Wings

The method for predicting the a.c. location near zero lift of non-straight-tapered wings is taken from Reference 8. This method is used for all non-straight-tapered wings. The non-straight-tapered wing is divided into two panels with each panel having conventional, straight-tapered geometry. Then, for each of the constructed panels, the individual lift-curve slope and a.c. are estimated by

treating each constructed panel as a complete wing. The individual lift and a.c. location derived for each constructed panel are then mutually combined in accordance with an "inboard-outboard" weighted-area relationship to establish the predicted a.c. location for the basic non-straight-tapered wing. There is a difference between the construction geometry used to determine the inboard and outboard panels for the double-delta and cranked wings, and that for the curved wings. Application of the method requires that the wings be broken down as defined below.

Double-Delta and Cranked Wings (see Sketch (a))

Inboard Panel – the inboard leading and trailing edges extended to the center line. The tip-chord span station is fixed at the break formed by the discontinuity in the sweep of the leading edge of the composite wing. The constructed inboard panel is designated by subscript i.

Outboard Panel – the leading and trailing edges of the main outboard panel extended inboard to the midpoint between the center line and the break formed by the discontinuity in the sweep of the leading edge of the composite wing. The main outboard panel is designated by subscript o and the constructed outboard panel is designated by a prime and a subscript o.

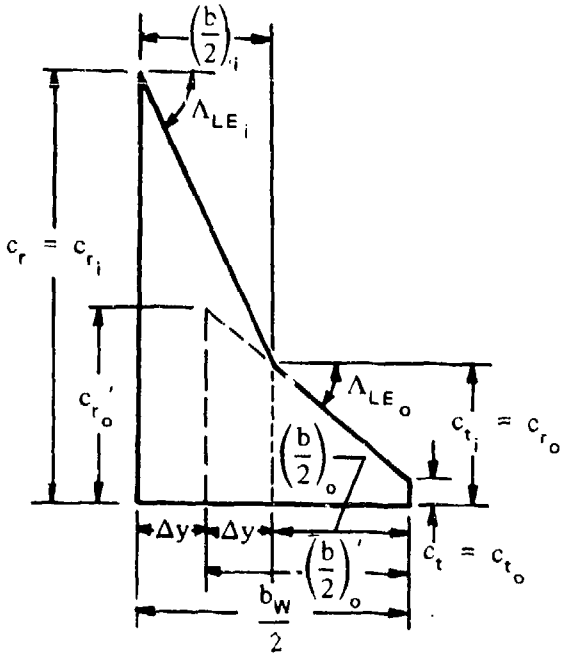

DOUBLE-DELTA WING

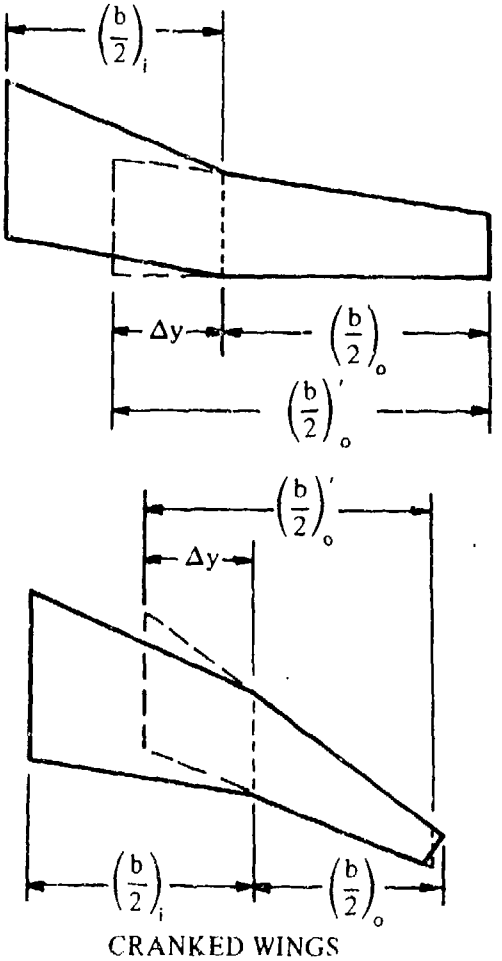

CRANKED WINGS

SKETCH (a)

Many double-delta and cranked wings have non-straight trailing edges with the trailing-edge break occurring at a different span station from the leading-edge break. For such wings the irregular trailing-edge sweep angles of the divided panels are modified by using straight trailing-edge sweep angles for each panel, constructed so that the area moment about the respective wing-panel apex remains approximately the same.

Curved Wings (see Sketch (b))

The basic ogee and Gothic planforms must be modified to divide the wing into two panels having conventional, straight-tapered geometry. The modified inboard and outboard panels are designated in the same manner as noted in the double-delta- and cranked-wing breakdown. Both types of curved wings are divided by the following procedure:

1. The tip chord of the inboard panel is located at one-half of the curved wing semispan; i.e., $\left(\frac{b}{2}\right)_i = \left(\frac{b}{2}\right)_o = 0.50\left(\frac{b_w}{2}\right)$. This locates the span station of the leading-edge break, and tip-chord span station of the constructed inboard panel.

2. The root chord of the constructed outboard panel is located at one-fourth of the curved wing semispan; i.e., c_{r_o}' span station is at $(0.25)\left(\frac{b_w}{2}\right)$.

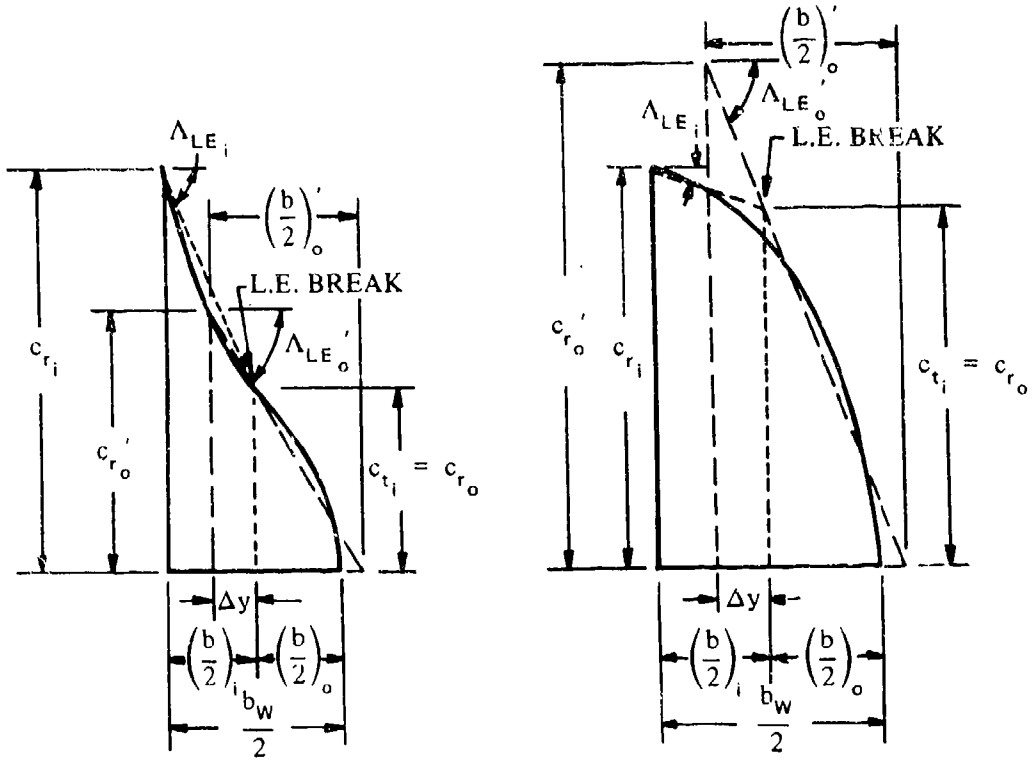

SKETCH (b)

3. The semispan of the constructed outboard panel is 0.85 times the semispan of the basic curved wing; i.e., $\left(\frac{b}{2}\right)'_o = 0.85\left(\frac{b_w}{2}\right)$. This locates the tip of the constructed outboard panel.

4. The tip chord of the constructed outboard panel is zero; i.e., $\lambda'_o = 0$.

5. The leading-edge sweep angles of the two panels are approximated by the use of straight-line segments as shown. Try to maintain an approximately constant area moment for the outboard panel about its apex.

The subsonic aerodynamic-center location of non-straight-tapered wings is obtained from the procedure outlined in the following steps:

Step 1. Divide the non-straight-tapered wing into inboard and outboard panels as discussed above, and determine their pertinent geometric parameters.

Step 2. Determine the lift-curve slope of the constructed inboard panel $\left(C_{L_\alpha}\right)_i$, from Figure 4.1.3.2-49, based on its respective area S_i.

Step 3. Determine the a.c. location of the constructed inboard panel as a fraction of the root chord of the constructed inboard panel $\left(\frac{x_{a.c.}}{c_r}\right)_i$ from Figure 4.1.4.2-26. This a.c. location is aft of the apex of the constructed inboard panel.

Step 4. Determine the lift-curve slope of the constructed outboard panel $\left(C_{L_\alpha}\right)'_o$, from Figure 4.1.3.2-49, based on its respective area S'_o.

Step 5. Determine the a.c. location of the constructed outboard panel as a fraction of the root chord of the constructed outboard panel $\left(\frac{x_{a.c.}}{c_r}\right)'_o$ from Figure 4.1.4.2-26. This a.c. location is aft of the apex of the constructed outboard panel.

Step 6. Convert the a.c. location determined in Step 5 to a fraction of the root chord of the constructed inboard panel and aft of the apex of the constructed inboard panel by

$$\frac{\left(x_{a.c.}\right)'_o}{c_{r_i}} = \left(\frac{x_{a.c.}}{c_r}\right)'_o \left(\frac{c'_{r_o}}{c_{r_i}}\right) - \frac{\Delta y}{c_{r_i}} \tan \Lambda_{LE_o} + \frac{b_i}{2c_{r_i}} \tan \Lambda_{LE_i} \qquad 4.1.4.2\text{-d}$$

Step 7. Calculate the non-straight-tapered-wing aerodynamic center, measured in wing root chords aft of the wing apex, by

$$\frac{x_{a.c.}}{c_r} = \frac{\left(C_{L_\alpha}\right)_i S_i \left(\frac{x_{a.c.}}{c_r}\right)_i + \left(C_{L_\alpha}\right)'_o S'_o \frac{\left(x_{a.c.}\right)'_o}{c_{r_i}}}{\left(C_{L_\alpha}\right)_i S_i + \left(C_{L_\alpha}\right)'_o S'_o} \qquad 4.1. .2\text{-e}$$

The limited availability of experimental data precludes the substantiation of this method for double-delta and cranked wings. No experimental wing-alone double-delta data are readily available for subsonic speeds. Test data for three wing-alone cranked-wing configurations are available. The results of the method applied to those configurations are compared with test results in the data summary presented as Table 4.1.4.2-A (taken from Reference 8).

On the other hand, for curved wings there are enough test data available for a limited substantiation of the method. A comparison of test data for four curved-wing configurations with $x_{a.c.}/c_r$ calculated by this method is presented as Table 4.1.4.2-B (taken from Reference 8). The table also includes two configurations which are wing-body combinations, but the bodies are very small and the wing planform projection effectively blankets nearly all of the body. All the wings investigated have straight trailing edges and one reflex curve in the leading edge. The ranges of Mach number and lift coefficient of the data are:

$$0.09 \leq M \leq 0.9$$

$$0 \leq C_L \leq 0.10$$

Sample Problems

1. Method 2

Given: The following straight-tapered, constant-section, low-aspect-ratio, clipped-delta configuration.

$A = 0.823$ $\quad \lambda = 0.18$ $\quad \Lambda_{LE} = 73.5^\circ$

NACA 2412 airfoil $\quad M = 0.2$

Compute:

$$\frac{x_{a.c.}}{c_r} = \frac{\frac{2}{3}(1-\lambda) + \frac{1}{2}\left[1 - \frac{\lambda^2}{1+\lambda}\right]\pi \log_e\left(1 + \frac{A}{5}\right)}{1 + \pi \log_e\left(1 + \frac{A}{5}\right)} \qquad \text{(Equation 4.1.4.2-b)}$$

$$= \frac{\frac{2}{3}(1-0.18) + \frac{1}{2}\left[1 - \frac{(0.18)^2}{1+0.18}\right]\pi \log_e\left(1 + \frac{0.823}{5}\right)}{1 + \pi \log_e\left(1 + \frac{0.823}{5}\right)}$$

$$= 0.527$$

$$\left(\frac{dC_m}{dC_L}\right)_{theory} = n - \frac{x_{a.c.}}{c_r} \qquad \text{(Modified form of Equation 4.1.4.2-a)}$$

$$= 0.50 - 0.527 \quad = -0.027$$

$$\frac{dC_m/dC_L}{(dC_m/dC_L)_{theory}} = 0.935 \qquad \text{(Figure 4.1.4.2 -29)}$$

$$\frac{dC_m}{dC_L} = \left(\frac{dC_m}{dC_L}\right)_{theory} \left[\frac{dC_m/dC_L}{(dC_m/dC_L)_{theory}}\right] \qquad \text{(Equation 4.1.4.2-c)}$$

$$= (-0.027)(0.935)$$

$$= -0.0252 \qquad \left(\text{based on } S_W c_r, \text{ about } \frac{c_r}{2}\right)$$

2. Non-Straight-Tapered Wings

Given: The cranked wing of Reference 22.

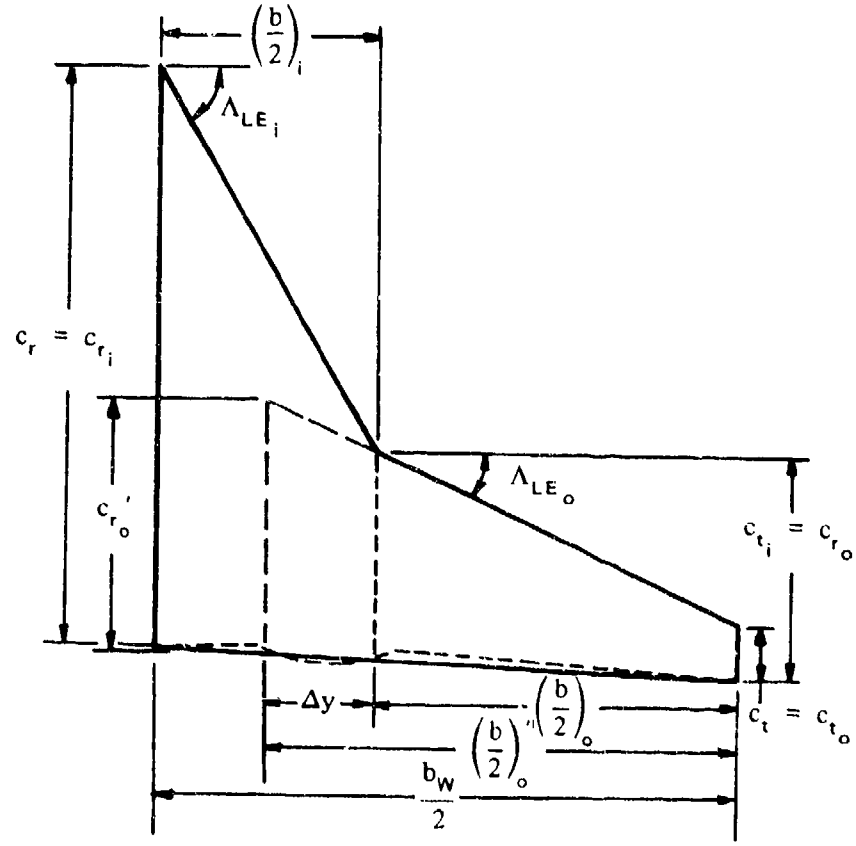

Total-Wing Characteristics:

$A_W = 5.194$ $\quad \lambda_W = 0.090$ $\quad \Lambda_{LE_i} = 60^o$ $\quad \Lambda_{LE_o} = 25^o$

$\eta_B = 0.380$ $\quad c_{r_W} = 50.10$ in. $\quad \frac{b_W}{2} = 50.40$ in.

Constructed Inboard-Panel Characteristics:

$A_i = 1.14$ $\lambda_i = 0.339$ $\Lambda_{LE_i} = 60^o$ $\Lambda_{TE_i} = 1.75^o$

$\left(\frac{b}{2}\right)_i = 19.15$ in. $S_i = 1285$ sq in. $\left(\Lambda_{c/2}\right)_i = 40.9^o$

$c_{r_i} = 50.10$ in. $c_{t_i} = 16.98$ in.

Constructed Outboard-Panel Characteristics:

$A_o' = 6.37$ $\lambda_o' = 0.213$ $\left(\frac{b}{2}\right)_o' = 40.83$ in. $S_o' = 1047$ sq in.

$c_{r_o}' = 21.15$ in. $c_{t_o} = 4.50$ in $\Lambda_{LE_o} = 25^o$ $\Lambda_{TE_o} = 1.75^o$

$\left(\Lambda_{c/2}\right)_o = 14.7^o$ $\Delta y = 9.576$ in.

Additional Characteristics:

$M = 0.13$; $\beta = 0.991$ $\kappa = 1.0$ (assumed)

Compute:

$\left(C_{L_\alpha}\right)_i$ (Section 4.1.3.2)

$$\frac{A_i}{\kappa}\left[\beta^2 + \tan^2\left(\Lambda_{c/2}\right)_i\right]^{1/2} = \frac{1.14}{1.0}\left[(0.991)^2 + (0.8662)^2\right]^{1/2} = 1.50$$

$\left(\frac{C_{L_\alpha}}{A}\right)_i = 1.39$ per rad (Figure 4.1.3.2-49)

$$\left(C_{L_\alpha}\right)_i = \left(\frac{C_{L_\alpha}}{A}\right)_i A_i = 1.39\ (1.14) = 1.58 \text{ per rad}$$

$\left(\frac{x_{a.c.}}{c_r}\right)_i$

$\left(A \tan \Lambda_{LE}\right)_i = (1.14)(1.7321) = 1.975$; $\frac{\beta}{\tan \Lambda_{LE_i}} = \frac{0.991}{1.7321} = 0.572$

$\left(\frac{x_{a.c.}}{c_r}\right)_i = 0.452$ (Figures 4.1.4.2-26a through -26e, interpolated)

$\left(C_{L_a}\right)_o'$ (Section 4.1.3.2)

$$\frac{A_o'}{\kappa}\left[\beta^2 + \tan^2(\Lambda_{c/2})_o\right]^{1/2} = \frac{6.37}{1.0}\left[(0.991)^2 + (0.2623)^2\right]^{1/2} = 6.53$$

$$\left(\frac{C_{L_a}}{A}\right)_o = 0.715 \text{ per rad (Figure 4.1.3.2-49)}$$

$$\left(C_{L_a}\right)_o' = \left(\frac{C_{L_a}}{A}\right)_o A_o' = (0.715)(6.37) = 4.55 \text{ per rad}$$

$$\left(\frac{x_{a.c.}}{c_r}\right)_o$$

$$\left(A \tan \Lambda_{LE}\right)_o' = (6.37)(0.4663) = 2.97; \quad \frac{\tan \Lambda_{LE_o}}{\beta} = \frac{0.4663}{0.991} = 0.471$$

$$\left(\frac{x_{a.c.}}{c_r}\right)_o' = 0.543 \quad \text{(Figures 4.1.4.2-26a through -26e, interpolated)}$$

$$\frac{\left(x_{a.c.}\right)_o'}{c_{r_i}} = \left(\frac{x_{a.c.}}{c_r}\right)_o' \left(\frac{c_{r_o}'}{c_{r_i}}\right) - \frac{\Delta y}{c_{r_i}} \tan \Lambda_{LE_o} + \frac{b_i}{2c_{r_i}} \tan \Lambda_{LE_i} \quad \text{(Equation 4.1.4.2-d)}$$

$$= (0.543)\left(\frac{21.15}{50.10}\right) - \frac{9.576}{50.10}(0.4663) + \frac{19.15}{50.10}(1.7321)$$

$$= 0.802$$

Solution:

$$\frac{x_{a.c.}}{c_r} = \frac{\left(C_{L_a}\right)_i S_i \left(\frac{x_{a.c.}}{c_r}\right)_i + \left(C_{L_a}\right)_o' S_o' \frac{\left(x_{a.c.}\right)_o'}{c_{r_i}}}{\left(C_{L_a}\right)_i S_i + \left(C_{L_a}\right)_o' S_o'} \quad \text{(Equation 4.1.4.2-e)}$$

$$= \frac{1.58\,(1285)\,(0.452) + 4.55\,(1047)\,(0.802)}{1.58\,(1285) + 4.55\,(1047)}$$

$$= 0.697$$

The calculated value compares with a test value of 0.688 from Reference 22.

B. TRANSONIC

Rather than producing linear results as in other speed regimes, application of small-perturbation theory to the transonic regime yields a nonlinear differential equation. This means that at transonic Mach numbers it is not possible to evaluate separately the effects of thickness, camber, and angle of attack, and then to add the individual solutions to obtain the total wing lift and pitching moment. The contributions of each of the above parameters are interrelated, and the wing must be treated as a unit. Theoretical solutions in the transonic speed range are available for only a few specific planforms. Most of the available information on the transonic characteristics of wings is in the form of wind-tunnel test data. As discussed in detail in Section 4.1.3.2, transonic test data are subject to wind-tunnel wall interference effects and must be used with caution.

The use of similarity parameters reduces to a minimum the number of charts required to present test data. Similarity parameters are derived from theoretical considerations and are subject to the limitations of the theory from which they are derived. Although the form of the parameters may be changed by rearranging the variables, the minimum number of parameters for a given theory does not change.

From the nonlinear equations describing transonic flow, it can be shown (Reference 9) that the minimum number of parameters necessary to present complete information in the transonic speed regime is one greater than the number of parameters necessary for the linear theories of both the subsonic and supersonic speed ranges. This means that the number of charts required to present information at transonic speeds is one order of magnitude larger than the number required for either of the other speed ranges.

Only a limited amount of work has been done in organizing transonic test data by means of similarity parameters. The most extensive effort along these lines is given in Reference 10. In this reference, test data from 50 rectangular wings of differing aspect ratio, airfoil thickness, and airfoil section are correlated by means of transonic similarity parameters, with a high degree of success.

For the Datcom, the charts of Reference 10 for rectangular, symmetrical wings at zero angle of attack are adopted directly. Charts for straight-tapered wings of other planform shapes are developed by applying transonic similarity parameters to the experimental data of References 11 through 15. The combined charts for all planforms are presented as Figures 4.1.4.2-30a through 4.1.4.2-30d.

These transonic charts are applicable only to uncambered straight-tapered wings with symmetric airfoil sections at low angles of attack. Wings with cambered airfoils, double-wedge airfoils, and airfoils with blunt trailing edges show different transonic moment and lift characteristics.

Wings with thickness ratios greater than about 7 percent are subject to shock-induced separation effects of significant magnitude. These effects are not accounted for by small-perturbation theory and thus cannot be handled by the similarity parameters of this section. Since there is great similarity between the effects of shock-induced separation on moment and on lift, the treatment of separation-induced moment characteristics in this section is based on the procedure of Section 4.1.3.2 for transonic lift.

DATCOM METHOD

The charts of the Datcom are presented in terms of the transonic similarity parameters of Reference 10. The similarity parameters used for velocity and aspect ratio, respectively, are

$$\bar{V} = \frac{\beta^2}{(t/c)^{2/3}} \text{ and } \bar{A} = A(t/c)^{1/3}$$

The corresponding parameter for angle of attack is

$$\bar{\alpha} = \frac{\alpha}{(t/c)}$$

However, since all of the transonic charts of this section are for low angles of attack such that $\bar{\alpha} \approx 0$, this last parameter does not enter into the calculations.

Figures 4.1.4.2-30a through 4.1.4.2-30d give the a.c. location for symmetrical straight-tapered wings of arbitrary sweep angle, taper ratio, and thickness ratio. For rectangular wings a more thorough presentation of a.c. location as a function of the velocity parameter $\bar{V}$ is given in Figure 4.1.4.2-30d.

The following steps outline the calculation procedure:

Step 1. Determine the aspect-ratio similarity parameter $\bar{A}$.

Step 2. For the appropriate values of λ, A tan Λ_{LE}, and $\bar{A}$, read $\frac{x_{a.c.}}{c_r}$ from Figures 4.1.4.2-30a through 4.1.4.2-30d for values $\bar{V} = \frac{\beta^2}{(t/c)^{2/3}} = -2, -1, 0, +1$. (Cross plots must be made between taper ratios of 0.5 and 1.0.)

Step 3. Determine the Mach numbers corresponding to $\bar{V} = -2, -1, 0, +1$.

Step 4. Calculate $\frac{x_{a.c.}}{c_r}$ for M = 0.6 and M = 1.4 as outlined in the straight-tapered-wing methods of Paragraphs A and C, respectively, of this section.

Step 5. The complete transonic a.c.-location curve can now be constructed by fairing a curve through the points obtained by means of Steps 1 through 4.* (See Sketch (c))

Step 6. The slope of the pitching-moment curve can now be calculated from the equation

$$C_{m_\alpha} = \left(n - \frac{x_{a.c.}}{c_r}\right) \frac{c_r}{\bar{c}} C_{L_\alpha} \qquad 4.1.4.2\text{-f}$$

where C_{L_α} is the lift-curve slope at transonic speeds obtained from Paragraph B of Section 4.1.3.2.

*If the wing under consideration has a thickness ratio greater than 7 percent, the additional Step 7 is required.

Step 7. Determine the incremental a.c. location accounting for separation effects $\frac{\Delta x_{a.c.}}{c_r}$ from Figure 4.1.4.2-33. This increment is applied at the Mach number at which the transonic lift-curve slope reaches its minimum value (M_{fb} + 0.07). The force-break Mach number M_{fb} is obtained during the course of calculating the transonic C_{L_α} values. Application of this a.c. increment and the required fairing technique are illustrated in Sketch (c).

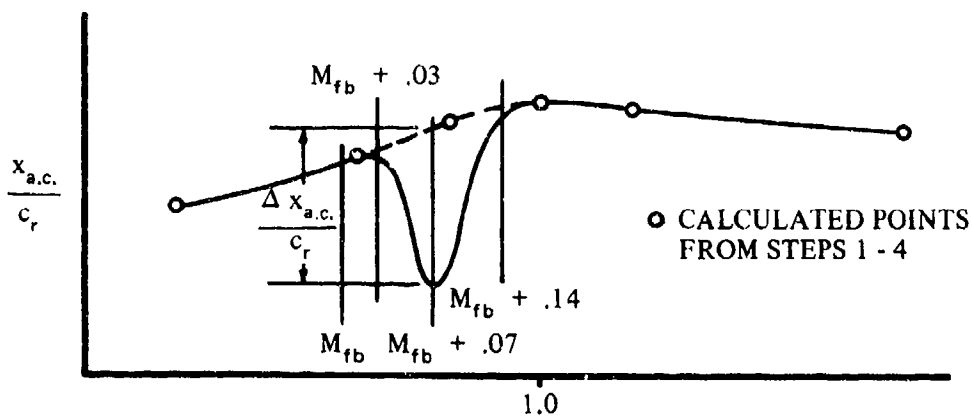

SKETCH (c)

The above sketch represents the a.c. location at zero angle of attack. As the angle of attack is increased, the bucket in the curve near Mach 1 disappears and the shape is more like the dashed portions of Sketch (c).

Sample Problem

Given: The following straight-tapered wing:

$A = 4.0 \qquad \lambda = 0.68 \qquad \Lambda_{LE} = 46.32^o \qquad \Lambda_{c/2} = 43.6^o$

NACA 63A012 airfoil $\quad c_r/\bar{c} = 1.18 \qquad n = 1.09$

Compute:

$$\bar{A} = A\left(\frac{t}{c}\right)^{1/3} = (4.0)(0.493) = 1.972$$

$$A \tan \Lambda_{LE} = (4.0)(\tan 46.32^o) = 4.19$$

Determine $\frac{x_{a.c.}}{c_r}$ for $\bar{V} = -2, -1, 0,$ and $1,$ and the Mach numbers corresponding to $\bar{V}$

$$\bar{V} = \frac{\beta^2}{(t/c)^{2/3}} = \frac{\beta^2}{(0.2433)}; \qquad M = \sqrt{1 + 0.2433\,\bar{V}}$$

$\bar{V}$	M_1 $\sqrt{1 + 0.2433\,\bar{V}}$	$\frac{x_{a.c.}}{c_r}$ Fig. 4.1.4.2-30
-2	.716	1.020
-1	.870	1.055
0	1.000	1.055
1	1.115	1.080

Determine $\frac{x_{a.c.}}{c_r}$ at M = 0.6 and 1.40

$$M = 0.6;\ \beta = 0.80;\ \frac{\beta}{\tan \Lambda_{L.E}} = \frac{0.80}{\tan 46.32^o} = 0.764$$

$$\left(\frac{x_{a.c.}}{c_r}\right)_{M\,=\,0.6} = 1.05 \qquad \text{(Figures 4.1.4.2-26d through -26f, interpolated)}$$

$$M = 1.40;\ \beta = 0.98;\ \frac{\beta}{\tan \Lambda_{LE}} = \frac{0.98}{\tan 46.32^o} = 0.936$$

$$\left(\frac{x_{a.c.}}{c_r}\right)_{M\,=\,1.40} = 1.205 \qquad \text{(Figures 4.1.4.2-26d through -26f, interpolated)}$$

Since (t/c) $>$ 0.07, step 7 of the Datcom method is required.

$\left(M_{fb}\right)\Lambda = 0 = 0.82$ (Figure 4.1.3.2-53a)

$\left(M_{fb}\right)\Lambda = 0.88$ (Figure 4.1.3.2-53b)

M_{fb} is obtained during the course of calculating C_{L_α}. It is shown here, since the calculations for C_{L_α} are not given.

$$A \cos^2 \Lambda_{c/2} = (4.0)(\cos 43.6)^2 = 2.10$$

$\frac{\Delta x_{a.c.}}{c_r} = -0.19$ (Figure 4.1.4.2-33). This correction is applied at $M_{fb} + 0.07 = 0.95$

Construct the transonic a.c. curve using Sketch (c) as a guide.

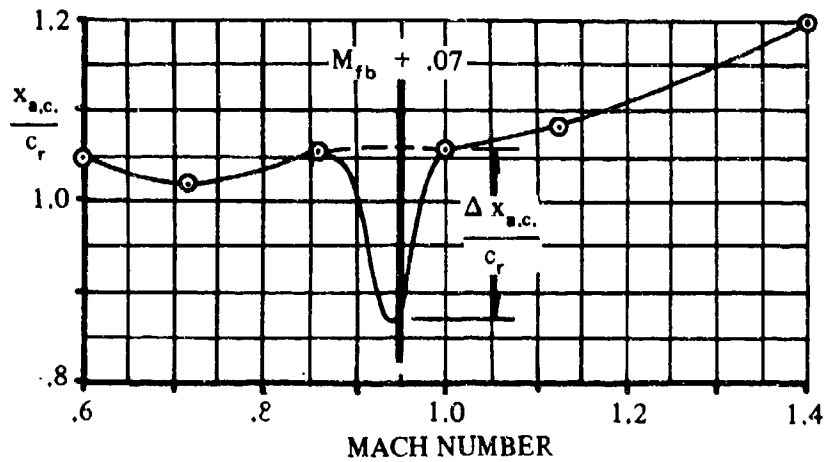

Determine C_{L_a} from Paragraph B, Section 4.1.3.2 (see calculation table below).

Solution:

$$C_{m_a} = \left(n - \frac{x_{a.c.}}{c_r}\right)\frac{c_r}{\bar{c}}\ C_{L_a} \quad \text{(Equation 4.1.4.2-f)}$$

$$= \left(1.09 - \frac{x_{a.c.}}{c_r}\right) 1.18\, C_{L_a}$$

①	②	③	④	⑤
M	$\frac{x_{a.c.}}{c_r}$ (faired curve)	$n - \frac{x_{a.c.}}{c_r}$ 1.09 - ②	C_{L_α} (per deg) Sec. 4.1.3.2, Para. B	C_{m_α} (per deg) Eq. 4.1.4.2-f 1.18 ③ ④
0.70	1.020	.070	.043	.0036
0.87	1.055	.035	.045	.0019
0.95	0.865	.225	.047	.0125
1.00	1.055	.035	.024	.0010
1.10	1.075	.015	.040	.0007

C. SUPERSONIC

Methods are presented for determining the wing aerodynamic-center location of the following two classes of wing planforms:

Straight-Tapered Wings (conventional, trapezoidal wings)

Non-Straight-Tapered Wings

- Double-delta wings
- Cranked wings
- Curved (Gothic and ogee) wings

These three general categories of non-straight-tapered wings are illustrated in Sketch (a) of Section 4.1.3.2. Their wing-geometry parameters are presented in Section 2.2.2.

As is the case at subsonic speeds, the supersonic design charts also present information that is basically that of Reference 2. The effects of Mach number have been accounted for by means of the Prandtl-Glauert compressibility correction, and the resulting design charts are an extension of those used at subsonic speeds. The charts are directly applicable to straight-tapered wings. In treating non-straight-tapered wings, the wing is divided into two panels and the individual lift and aerodynamic-center location for each panel are used to establish the aerodynamic-center location for the composite wing.

The design charts are applicable only in the linear-lift range. Within this range the effects of camber, leading-edge radius, and trailing-edge angle are minor in regard to the aerodynamic-center characteristics.

Although wing profile thickness has little effect on the supersonic wing normal-force-curve slope at low angles of attack, provided the Mach lines do not lie near the wing leading edge (Sections 4.1.3.2 and 4.1.3.3), the situation regarding wing pitching moments is quite different. For unswept wings of high aspect ratio at supersonic speeds, the area influenced by the three-dimensional flow within the tip shock cones is relatively small compared to the large area between the tip shocks, where the flow is two-dimensional. Under these conditions the wing moment characteristics are closely related to the two-dimensional airfoil characteristics. In Section 4.1.2.2 it is shown that for airfoils the aerodynamic center is very much a function of thickness ratio. As a first approximation, the a.c. location for unswept wings at supersonic speeds may be taken as that of the corresponding two-dimensional section.

For swept wings the three-dimensional flow within the shock cones is much larger, and the wing cannot be treated as two-dimensional. Linear theory generally gives satisfactory results for these wings.

As the Mach lines approach the leading edges of wings at supersonic speeds, the lift may deviate considerably from linear-theory lift. These deviations (see Section 4.1.3.2, Paragraph C) are caused by the finite thickness of the wing leading edge, which forces the leading-edge shock to be located at a different position from that predicted by linear theory. For delta wings, at least, these effects on lift are not reflected in the pitching moments. This is perhaps due to the fact that linear theory predicts the same a.c. location for delta wings, whether the leading-edge shock is attached or

detached. For other wings, linear theory does predict minor changes in a.c. location when the leading-edge shock attaches. In general, however, it appears that the role of wing thickness in causing deviations from linear theory at the sonic-leading-edge condition is much less for moments than it is for lift.

DATCOM METHODS

Straight-Tapered Wings

The aerodynamic-center location of swept, straight-tapered wings at Mach numbers greater than 1.4 is obtained from Figures 4.1.4.2-26a through 4.1.4.2-26f. These charts give the a.c. location as a fraction of the wing root chord. For unswept wings, the method of Section 4.1.2.2 for two-dimensional sections in supersonic flow may be used.

Non-Straight-Tapered Wings

The method presented in Paragraph A for predicting the aerodynamic-center location of non-straight-tapered wings is also applicable at supersonic speeds. The normal-force-curve slopes of the constructed inboard and outboard panels are obtained from the straight-tapered-wing design charts of Paragraph C of Section 4.1.3.2 (Figures 4.1.3.2-56a through 4.1.3.2-56f). The a.c. locations of the constructed inboard and outboard panels, measured in root chords of the respective panels, are obtained from the supersonic portion of Figures 4.1.4.2-26a through 4.1.4.2-26f.

Equation 4.1.4.2-e expressed in terms of the normal-force-curve slope is

$$\frac{x_{a.c.}}{c_r} = \frac{\left(C_{N_\alpha}\right)_i S_i \left(\frac{x_{a.c.}}{c_r}\right)_i + \left(C_{N_\alpha}\right)_o' S_o' \frac{\left(x_{a.c.}\right)_o'}{c_{r_i}}}{\left(C_{N_\alpha}\right)_i S_i + \left(C_{N_\alpha}\right)' S_o'}$$

where $x_{a.c.}/c_r$ is the aerodynamic center of the non-straight-tapered wing, measured in wing root chords aft of the wing apex.

The limited availability of experimental data precludes the substantiation of this method for double-delta and cranked wings. No experimental wing-alone cranked-wing data are readily available for supersonic speeds. Test data for one wing-alone double-delta configuration are available (Reference 31). This method predicts the a.c. location for this wing to within about one percent of the test value.

A comparison of test data for three curved-wing configurations with $x_{a.c.}/c_r$ calculated by this method is presented as Table 4.1.4.2-C (taken from Reference 8). One of the configurations is a wing-body combination, but the body is very small and the wing planform projection effectively blankets nearly all the body. All the wings investigated have straight trailing edges and one reflex curve in the leading edge. The Mach-number and lift-coefficient ranges of the data are:

$$1.02 \leqslant M \leqslant 2.60$$

$$0 \leqslant C_L \leqslant 0.10$$

Sample Problem

Given: The ogee wing-body configuration of Reference 29. Since the wing-planform projection blankets nearly all of the body, the combination is treated as a wing-alone configuration.

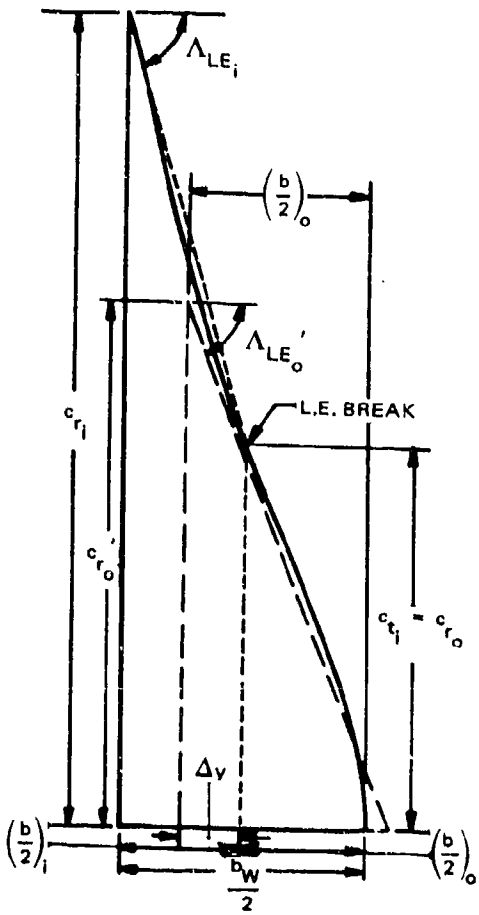

Total-Wing Characteristics:

$A_W = 1.20 \qquad \Lambda_{TE} = 0 \qquad c_{r_W} = 20.0$ in.

$\frac{b_W}{2} = 6.0$ in.

$t/c = 0.05$ (rhombic wing sections – free-stream direction)

Constructed Inboard-Panel Characteristics:

$A_i = 0.407 \qquad \lambda_i = 0.475 \qquad \left(\frac{b}{2}\right)_i = 3.0$ in.

$S_i = 88.5$ sq in. $\qquad c_{r_i} = 20.0$ in. $\qquad c_{t_i} = 9.50$ in.

$\Lambda_{LE_i} = 74.6^o$

Constructed Outboard-Panel Characteristics:

$A_o' = 1.57 \qquad \lambda_o' = 0 \qquad \left(\frac{b}{2}\right)_o' = 5.10$ in.

$S_o' = 66.3$ sq in. $\qquad c_{r_o}' = 13.0$ in. $\qquad \Lambda_{LE_o} = 68.6^o$

$\Delta y = 1.50$ in.

Additional Characteristics:

$M = 1.82; \ \beta = 1.52$

Compute:

$\left(C_{N_\alpha}\right)_i$ (Section 4.1.3.2)

$\left(A \tan \Lambda_{LE}\right)_i = (0.407)(\tan 74.6^o) = 1.477$

$\frac{\beta}{\tan \Lambda_{LE_i}} = \frac{1.52}{\tan 74.6^o} = 0.419$

$\left[\tan \Lambda_{LE} \left(C_{N_\alpha}\right)_{theory}\right]_i = 2.67$ per rad (Figures 4.1.3.2-56c through -56e, interpolated)

$\left[\left(C_{N_\alpha}\right)_{theory}\right]_i = \frac{2.67}{\tan 74.6^o} = 0.736$ per rad

$$\left[\frac{C_{N_\alpha}}{(C_{N\alpha\ \text{theory}})}\right]_i$$

$$\delta_\perp = \frac{\text{semiwedge angle}}{\cos \Lambda_{LE}} = \frac{\frac{1}{2}\left(\frac{0.05}{0.5}\right)}{\cos 74.6^o} (57.3) = 10.8^o$$

$$\Delta y_\perp = 5.85 \tan \delta_\perp = 5.85 \tan 10.8^o = 1.116$$

$$\left[\frac{C_{N_\alpha}}{(C_{N_\alpha})_{\text{theory}}}\right]_i = 1.0 \quad \text{(Figure 4.1.3.2-60)}$$

$$(C_{N_\alpha})_i = \left[\frac{C_{N_\alpha}}{(C_{N_\alpha})_{\text{theory}}}\right]_i \left[(C_{N_\alpha})_{\text{theory}}\right]_i = (1.0)(0.736) = 0.736 \text{ per rad}$$

$$\left(\frac{x_{a.c.}}{c_r}\right)_i$$

$$\left(\frac{x_{a.c.}}{c_r}\right)_i = 0.465 \quad \text{(Figures 4.1.4.2-26a through -26e, interpolated)}$$

$(C_{N_\alpha})_o'$ (Section 4.1.3.2)

$$(A \tan \Lambda_{LE})_o' = 1.57 (\tan 68.6^o) = 4.01$$

$$\frac{\beta}{\tan \Lambda_{LE_o}} = \frac{1.52}{\tan 68.6^o} = 0.596$$

$$\left[\tan \Lambda_{LE} \ (C_{N_\alpha})_{\text{theory}}\right]_o' = 4.92 \text{ per rad} \quad \text{(Figure 4.1.3.2-56a)}$$

$$\left[(C_{N_\alpha})_{\text{theory}}\right]_o' = \frac{4.92}{\tan 68.6^o} = 1.93 \text{ per rad}$$

$$\left[\frac{C_{N_\alpha}}{(C_{N_\alpha})_{\text{theory}}}\right]_o'$$

$$\delta_\perp = \frac{\text{semiwedge angle}}{\cos \Lambda_{LE}} = \frac{\frac{1}{2}\left(\frac{0.05}{0.5}\right)}{\cos 68.6^o} (57.3) = 7.85^o$$

$$\Delta y_{\perp} = 5.85 \tan \delta_{\perp} = 5.85 \tan 7.85^{o} = 0.807$$

$$\left[\frac{C_{N_\alpha}}{(C_{N_\alpha})_{theory}}\right]_o' = 0.965 \quad \text{(Figure 4.1.3.2-60)}$$

$$(C_{N_\alpha})_o' = \left[\frac{C_{N_\alpha}}{(C_{N_\alpha})_{theory}}\right]_o' \left[(C_{N_\alpha})_{theory}\right]_o' = 0.965\,(1.93) = 1.86 \text{ per rad}$$

$$\left(\frac{x_{a.c.}}{c_r}\right)_o$$

$$\left(\frac{x_{a.c.}}{c_r}\right)_o = 0.670 \text{ (Figure 4.1.4.2-26a)}$$

$$\frac{(x_{a.c.})_o'}{c_{r_i}} = \left(\frac{x_{a.c.}}{c_r}\right)_o' \left(\frac{c_{r_o}'}{c_{r_i}}\right) - \frac{\Delta y}{c_{r_i}} \tan \Lambda_{LE_o} + \frac{b_l}{2c_{r_i}} \tan \Lambda_{LE_i} \quad \text{(Equation 4.1.4.2-d)}$$

$$= (0.670)\ \frac{13.0}{20.0} - \frac{1.50}{20.0}\ (2.552) + \frac{3.0}{20.0}\ (3.630)$$

$$= 0.789$$

Solution:

$$\frac{x_{a.c.}}{c_r} = \frac{(C_{N_\alpha})_i\ S_i \left(\frac{x_{a.c.}}{c_r}\right)_i + (C_{N_\alpha})_o'\ S_o'\ \frac{(x_{a.c.})_o'}{c_{r_i}}}{(C_{N_\alpha})_i\ S_i + (C_{N_\alpha})_o'\ S_o'} \quad \text{(Equation 4.1.4.2-e)}$$

$$= \frac{(0.736)\,(88.5)\,(0.465) + (1.86)(66.3)\,(0.789)}{(0.736)\,(88.5) + (1.86)\,(66.3)}$$

$$= 0.677$$

The calculated value compares with a test value of 0.693 from Reference 29.

D. HYPERSONIC

The aerodynamic center of flat-plate straight-tapered wings approaches the area-centroid location as the Mach number becomes large. However, the interrelated effects of viscosity, heat transfer, and detached shock waves due to blunt leading edges cause deviations of the aerodynamic center from the theoretical values. The magnitude of these effects has not been thoroughly evaluated. The hypersonic method of this section is based on linear theory, which gives the location of the aerodynamic center at the area centroid for high Mach numbers.

DATCOM METHOD

The supersonic portions of Figures 4.1.4.2-26a through 4.1.4.2-26f give the a.c. location of straight-tapered wings at zero angle of attack. These charts are derived from linear theory in this region.

REFERENCES

1. Multhopp, H.: Methods for Calculating the Lift Distribution of Wings (Subsonic Lifting-Surface Theory). ARC R&M 2884, 1950. (U)

2. Holmboe, V.: Charts for the Position of t Aerodynamic Center at Low Speeds and Small Angles of Attack for a Large Family of Tapered Wings. SAAB TN 27 (Sweden), 1954. (U)

3. Jones, R.: Properties of Low-Aspect-Ratio Pointed Wings at Speeds Below and Above the Speed of Sound. NACA TR 835, 1946. (U)

4. De Young, J., and Harper, C.: Theoretical Symmetric Span Loading at Subsonic Speeds for Wings Having Arbitrary Plan Form. NACA TR 921, 1948. (U)

5. Anon: Royal Aeronautical Society Data Sheets -- Aerodynamics. Vol. II, (Wings S.08.01.02), 1955. (U)

6. Hunton, L.: Effects of Fixing Transition on the Transonic Aerodynamic Characteristics of a Wing-Body Configuration at Reynolds Numbers from 2.4 to 12 Million. NACA TN 4279, 1958. (U)

7. Crosthwait, E. L., and Seath, D. D.: Subsonic Characteristics of Low Aspect Ratios. FDL-TDR-64-103, 1965. (U)

8. Benepe, D. B., Kouri, B. G., Webb, J. B., et al: Aerodynamic Characteristics of Non-Straight-Taper Wings. AFFDL-TR-66-73, 1968. (U)

9. Warren, C.: Recent Advances in the Knowledge of Transonic Air Flow. Jour. Roy. Aero. Soc., Vol. 60, No. 544, April 1956. (U)

10. McDevitt, J.: A Correlation by Means of Transonic Similarity Rules of Experimentally Determined Characteristics of a Series of Symmetrical and Cambered Wings of Rectangular Plan Form. NACA TR 1253, 1955. (U)

11. Emerson, H.: Wind-Tunnel Investigation of the Effect of Clipping the Tips of Triangular Wings of Different Thickness, Camber and Aspect Ratio -- Transonic Bump Method. NACA TN 3671, 1956. (U)

12. Few, A., Jr., and Fournier, P.: Effects of Sweep and Thickness on the Static Longitudinal Aerodynamic Characteristics of a Series of Thin, Low-Aspect Ratio, Highly Tapered Wings at Transonic Speeds. Transonic-Bump Method. NACA RM L54B25, 1954. (U)

13. Harris, W.: A Wind-Tunnel Investigation at High Subsonic and Low Supersonic Mach Numbers on a Series of Wings with Various Sweepback, Taper, Aspect Ratio, and Thickness. AF TR 6669, 1952. (U)

14. Wiley, H. G.: Aerodynamic Characteristics Extended to High Angles of Attack at Transonic Speeds of a Small-Scale 0° Sweep Wing, 45° Sweptback Wing, and 60° Delta Wing. NACA RM L52I30, 1952. (U)

15. Turner, T. R.: Effects of Sweep on the Maximum-Lift Characteristics of Four Aspect-Ratio-4 Wings at Transonic Speeds. NACA RM L50H11, 1950. (U)

16. Puckett, A. E., and Stewart, H. J.: Aerodynamic Performance of Delta Wings at Supersonic Speeds. Jour. Aero. Sci., Vol. 14, No. 10, October 1947. (U)

17. White, C. O., and Gresham, J. W.: Simplified Design Charts for the Determination of the Approximate Aerodynamic Center Location of Low Aspect Ratio Wings at Small Angles of Attack. Douglas Aircraft Company Report LB 30153, 1959. (U)

18. Kaattari, G. E.: Pressure Distributions on Triangular and Rectangular Wings to High Angles of Attack -- Mach Numbers 2.46 and 3.26. NACA RM A54J12, 1955. (U)

19. Letko, W.: Experimental Determination at Subsonic Speeds of the Oscillatory and Static Lateral Stability Derivatives of a Series of Delta Wings with Leading-Edge Sweep from 30° to 86.5°. NACA RM L57A30, 1957. (U)

20. Smith, F. M.: Experimental and Theoretical Aerodynamic Characteristics of Two Low-Aspect Ratio Delta Wings at Angles of Attack to 50° at a Mach Number of 4.07. NACA RM L57E02, 1957. (U)

21. Bateman, R. E., and Simms, J.: Aerodynamic Investigation of Wing Planforms at Transonic and Supersonic Speeds. Boeing Airplane Company Report D-12131, 1952. (C) Title Unclassified

22. Henderson, W. P. and Hammond, A. D.: Low-Speed Investigation of High-Lift and Lateral-Control Devices on a Semispan Variable-Sweep Wing Having an Outboard-Pivot Location. NASA TM X-542, 1961. (U)

23. Lange, R. H.: Maximum-Lift Characteristics of a Wing with Leading-Edge Sweepback Decreasing from 45^{o} at the Root to 20^{o} at the Tip at Reynolds Numbers from 2.4×10^{6} to 6.0×10^{6}. NACA RM L50A04a, 1950. (U)

24. Kruger, W.: Six-Component Measurements on a Cranked Swept-Back Wing. Great Britain Ministry of Supply Translation 816, 1947. (U)

25. Squire, L. C.: Further Experimental Investigations of the Characteristics of Cambered Gothic Wings at Mach Numbers From 0.60 to 2.0. ARC R&M 3310, 1963. (U)

26. Peckham, D. H., and Atkinson, S. A.: Preliminary Results of Low-Speed Wind-Tunnel Tests on a Gothic Wing of Aspect Ratio 1.0. ARC CP 508, 1960. (U)

27. Keating, R. F. A.: Low-Speed Wind-Tunnel Tests on Sharp-Edged Gothic Wings of Aspect-Ratio 3/4. ARC CP 576, 1961. (U)

28. Spencer, B., Jr., and Hammond, A. D.: Low-Speed Longitudinal Aerodynamic Characteristics Associated With a Series of Low-Aspect-Ratio Wings Having Variations in Leading-Edge Contour. NASA TN D-1374, 1962. (U)

29. Squire, L. C., and Capps, D. S.: An Experimental Investigation of the Characteristics of an Ogee Wing From M = 0.4 to M = 1.8. ARC CP 585, 1962. (U)

30. Taylor, C. R.: Measurements at Mach Numbers up to 2.8 of the Longitudinal Characteristics of One Plane and Three Cambered Slender 'Ogee' Wings. ARC R&M 3328, 1963. (U)

31. Durgin, F. A.: A Study of Twist and Camber on Wings in Supersonic Flow. FDL-TDR-64-109, 1964. (U)

TABLE 4.1.4.2-A
SUBSONIC AERODYNAMIC-CENTER LOCATION OF CRANKED WINGS
DATA SUMMARY

Ref.	Config.	A	λ	η_{β}	$\Lambda_{L.E._i}$ (deg)	Λ_{LE_o} (deg)	M	$\frac{x_{a.c.}}{c_r}$ Calc.	$\frac{x_{a.c.}}{c_r}$ Test	e Percent Error
22	W	5.19	.09	.380	60.0	25.0	0.13	.697	.688	1.3
		4.16	(a)	.430		45.0		.710	.708	0.3
		3.00		.508		60.0		.706	.738	-4.3
		1.89		.654		75.0		.619	.683	-9.4
23	W	4.18	.364	.300[b]	45.0	27.5[b]	0.13	.631	.630	0.2
24	W	5.02	.105	.296[b]	45.0	28.2[b]	0.13	.686	.638	7.5

(a) Raked wing tip

(b) Multi-panel wing approximated by two panels.

Average Error $= \frac{\Sigma |e|}{n} = 3.8\%$

TABLE 4.1.4.2-B
SUBSONIC AERODYNAMIC-CENTER LOCATION OF CURVED WINGS
DATA SUMMARY AND SUBSTANTIATION

Ref.	Config.	Planform	A	$\frac{b_W}{2\ell}$	Λ_{LE_i} (a) (deg)	Λ_{LE_o} (a) (deg)	M	$\frac{x_{a.c.}}{c_r}$ Calc.	$\frac{x_{a.c.}}{c_r}$ Test	e Percent Error
25	W	Gothic	.75	.25	66.0	78.0	.40	.508	.497	2.2
↓	↓	↓	↓	↓	↓	↓	.70	.511	.512	-0.2
							.80	.515	.516	-0.2
							.85	.516	.520	-0.8
							.90	.519	.520	-0.2
26	W	Gothic	1.00	.334	57.2	74.6	.13	.494	.491	0.6
27	W	Gothic	.75	.250	64.0	79.0	.09	.505	.511	-1.2
28	WB	Gothic	1.33	.400	64.6	69.0	.21	.549	.524	4.8
↓	↓	↓	↓	.460	52.0	70.0	↓	.476	.441	8.4
				↓	46.5	↓		.471	.448	5.1
				.500	18.0	72.0		.385	.386	-0.3
				.225	73.0	79.0		.566	.550	2.9
				.500	59.0	65.6	↓	.561	.521	7.7
29	WB	Ogee	1.20	.300	74.6	68.6	.40	.635	.632	0.5
↓	↓	↓	↓	↓	↓	↓	.70	.641	.645	-0.6
							.80	.645	.650	-0.8
							.85	.648	.654	-0.9
							.90	.650	.659	-1.4
30	W	Ogee	.92	.208	80.5	73.3	.30	.696	.691	0.7
↓	↓	↓	↓	↓	↓	↓	.80	.704	.701	0.4

(a) Approximations used in a.c. prediction

Average Error = $\frac{\Sigma|e|}{n}$ = 2.0%

TABLE 4.1.4.2-C
SUPERSONIC AERODYNAMIC-CENTER LOCATION OF CURVED PLANFORMS
DATA SUMMARY AND SUBSTANTIATION

Ref.	Config.	Planform	A	$\frac{b_W}{2\ell}$	Λ_{LE_i} (a) (deg)	Λ_{LE_o} (a) (deg)	M	$\frac{x_{a.c.}}{c_r}$ Calc.	$\frac{x_{a.c.}}{c_r}$ Test	e Percent Error
25	W	Gothic	.75	.250	66.0	78.0	1.02	.542	.528	2.7
							1.25	.549	.557	-1.4
							1.30	.551	.557	-1.1
							1.42	.553	.565	-2.1
							1.61	.556	.580	-4.1
							1.82	.557	.580	-4.0
							2.00	.554	.565	-1.9
29	WB	Ogee	1.20	.300	74.6	68.6	1.25	.676	.693	-2.5
							1.42	.674	.694	-2.9
							1.61	.674	.693	-2.7
							1.82	.677	.693	-2.3
30	W	Ogee	.92	.208	80.5	73.3	1.40	.729	.745	-2.1
							1.80	.723	.740	-2.3
							2.20	.721	.735	-1.9
							2.60	.720	.726	-0.8

(a) Approximations used in a.c. prediction

Average Error = $\frac{\Sigma |e|}{n}$ = 2.3%

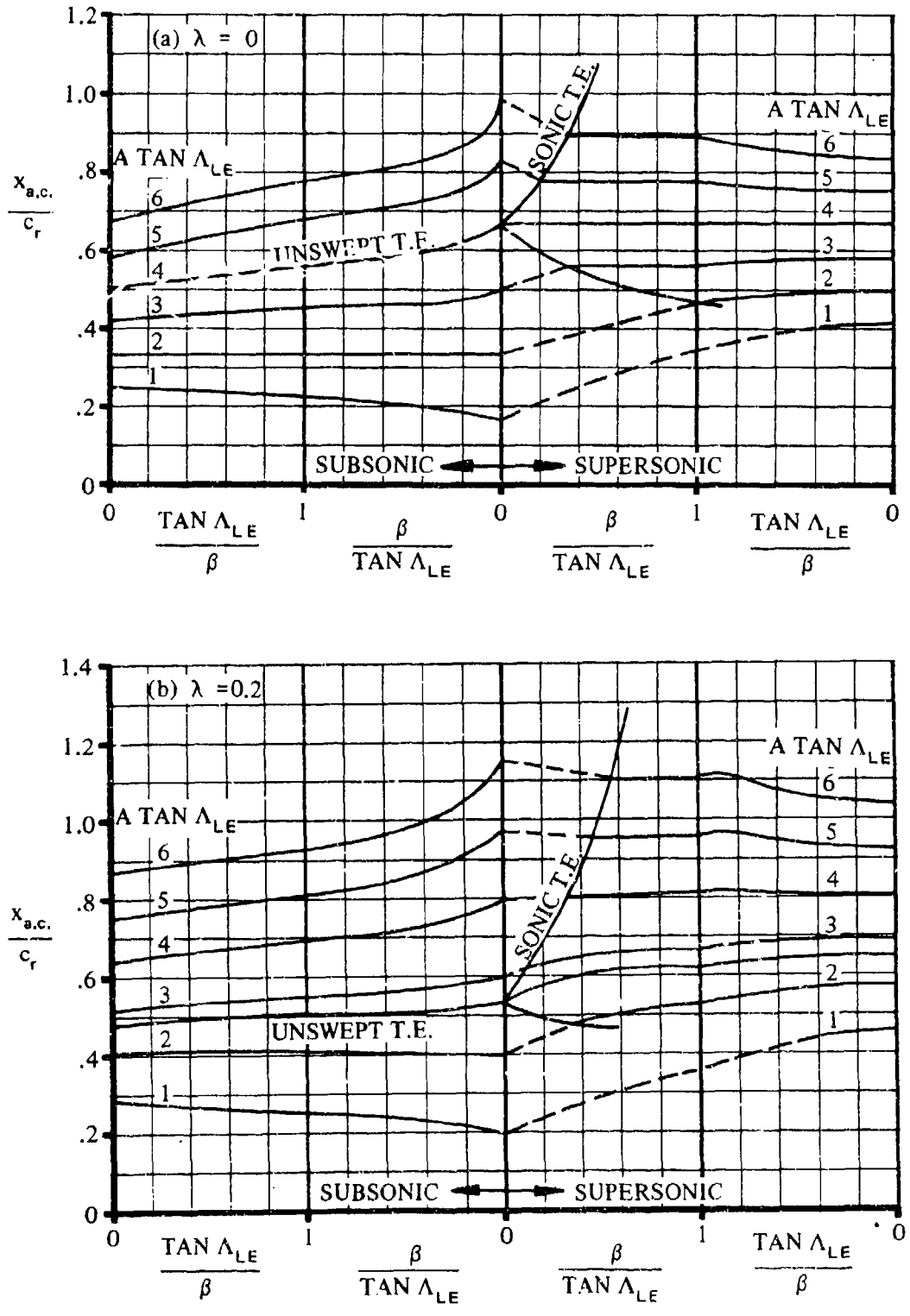

FIGURE 4.1.4.2-26 WING AERODYNAMIC-CENTER POSITION

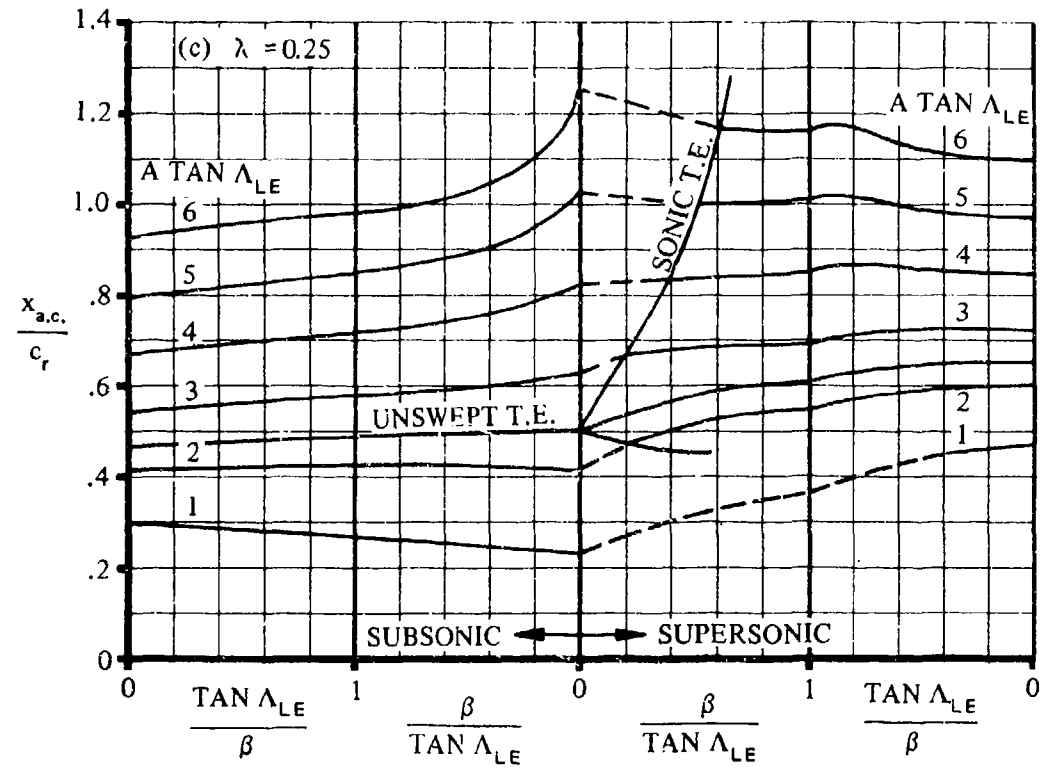

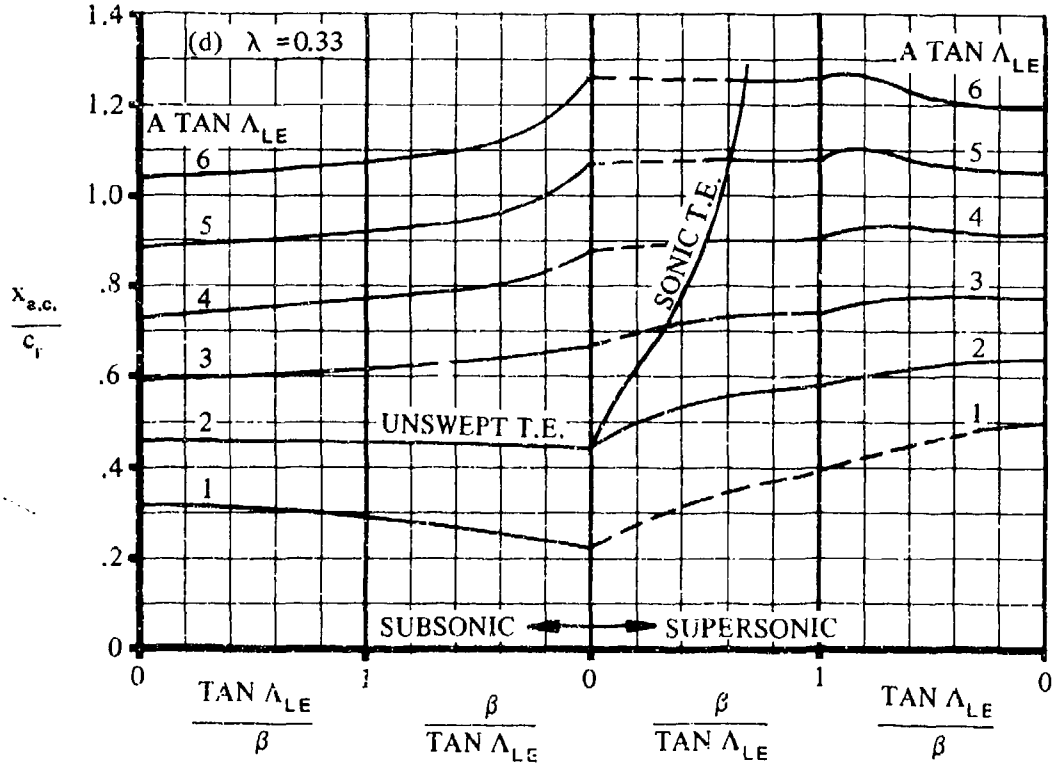

FIGURE 4.1.4.2-26(CONTD)

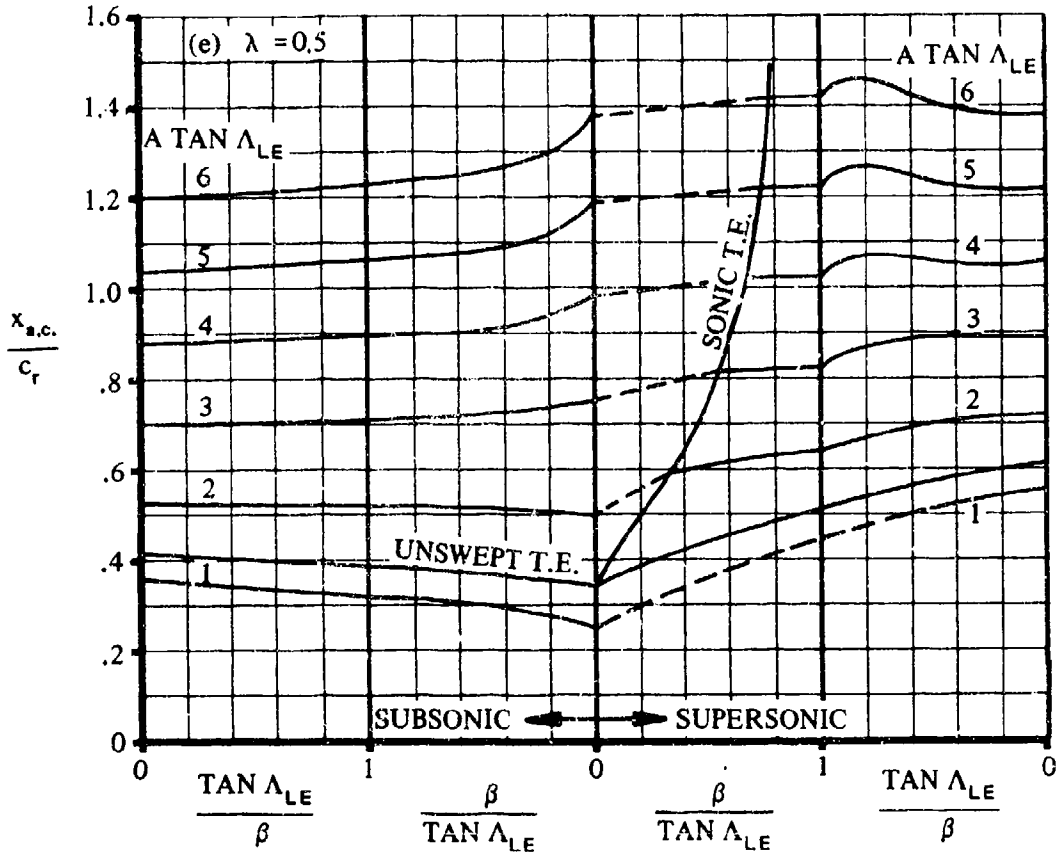

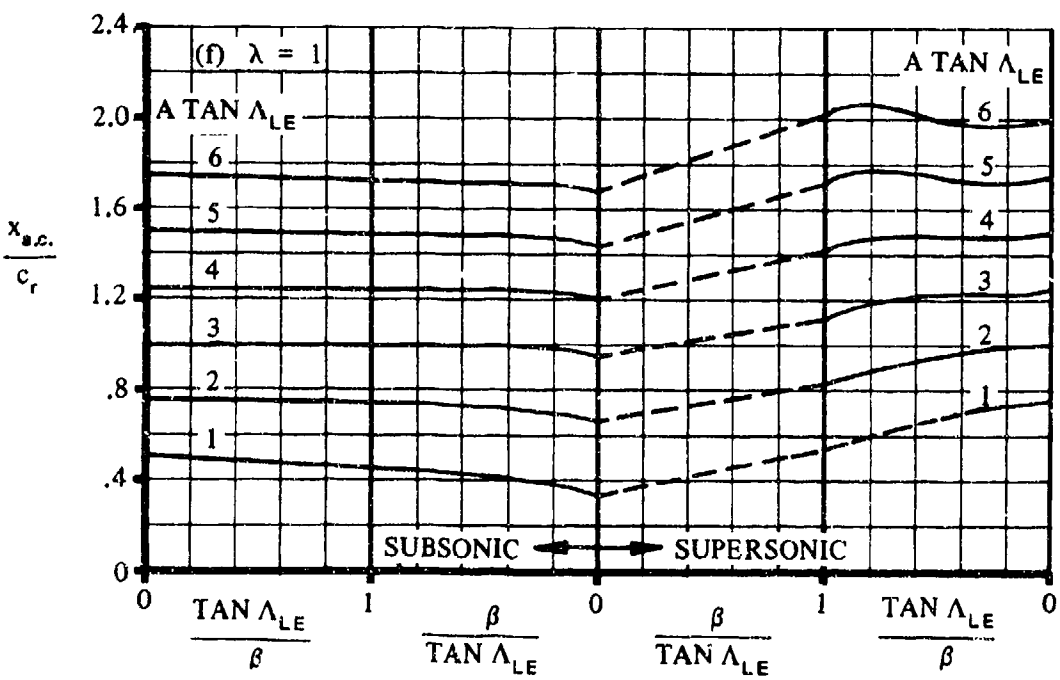

FIGURE 4.1.4.2-26 (CONTD)

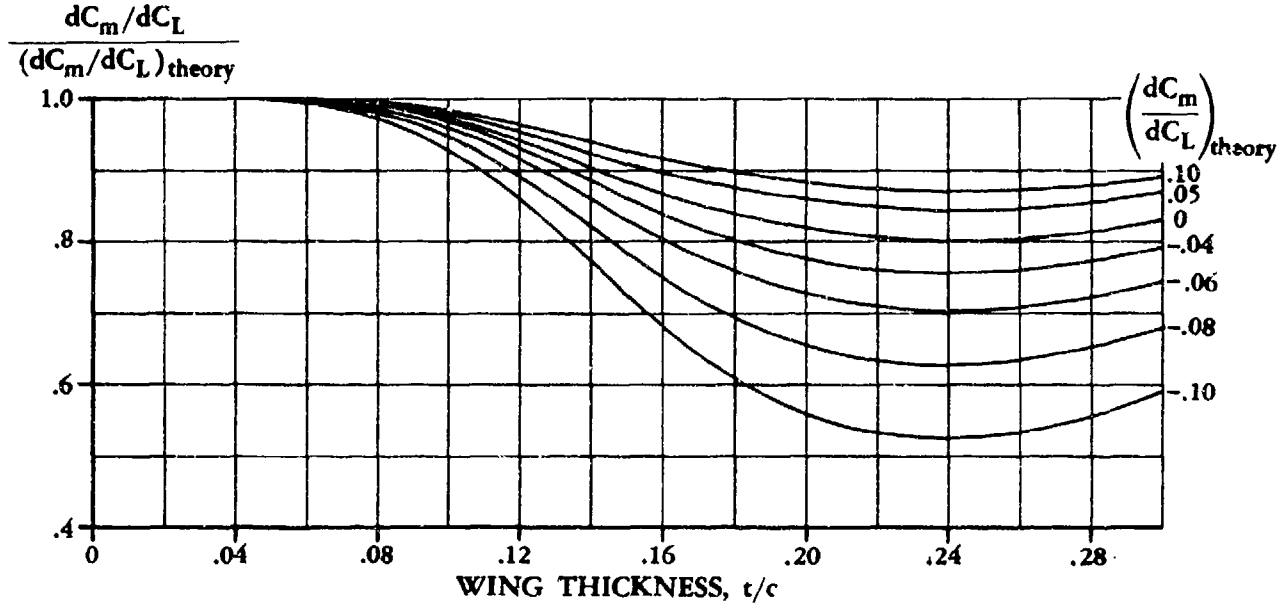

FIGURE 4.1.4.2-29 WING PITCHING-MOMENT-CURVE-SLOPE THICKNESS CORRECTION FACTOR

TRANSONIC SPEEDS

(a) $\lambda = 0$

$\bar{V} = \dfrac{\beta^2}{\left(\dfrac{t}{c}\right)^{2/3}} = 1$ 0 −1 −2

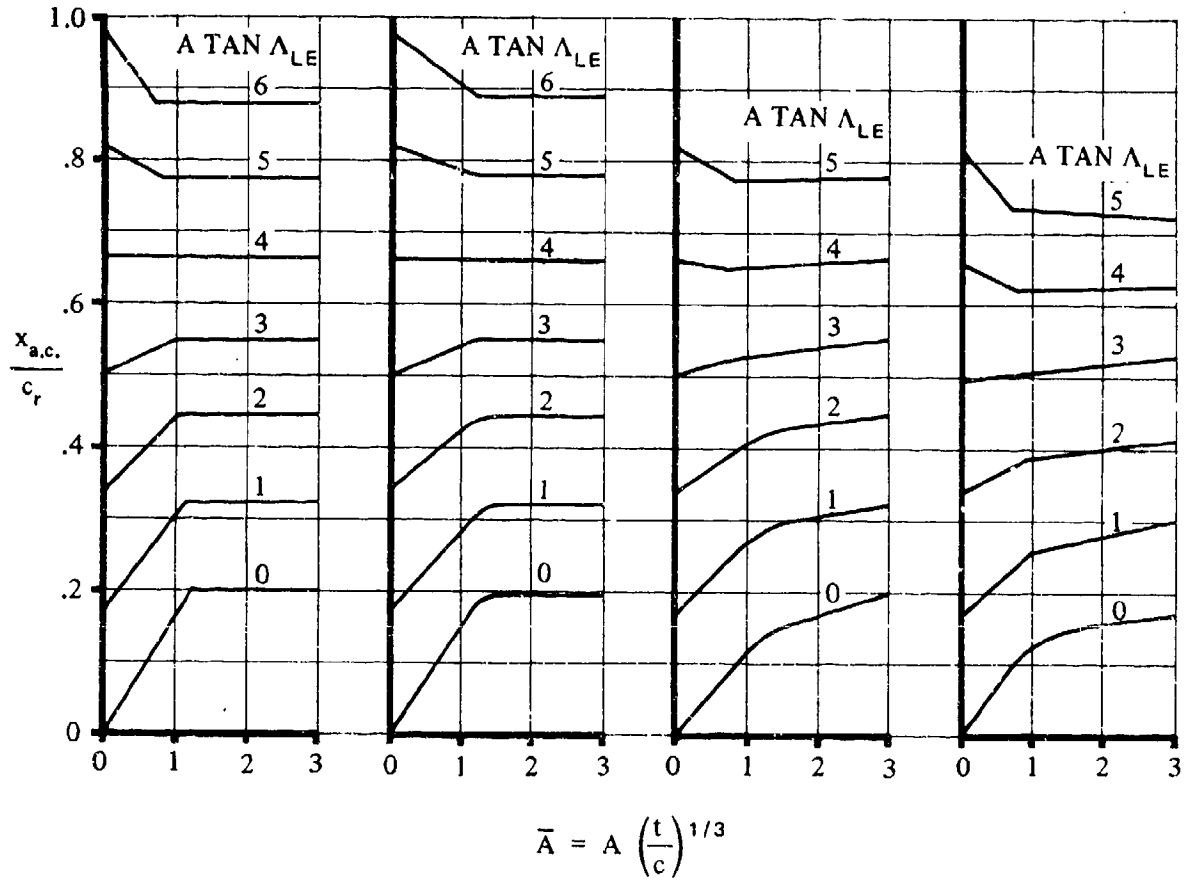

FIGURE 4.1.4.2 -30 TRANSONIC WING AERODYNAMIC-CENTER LOCATION

TRANSONIC SPEEDS

(b) $\lambda = 0.2$

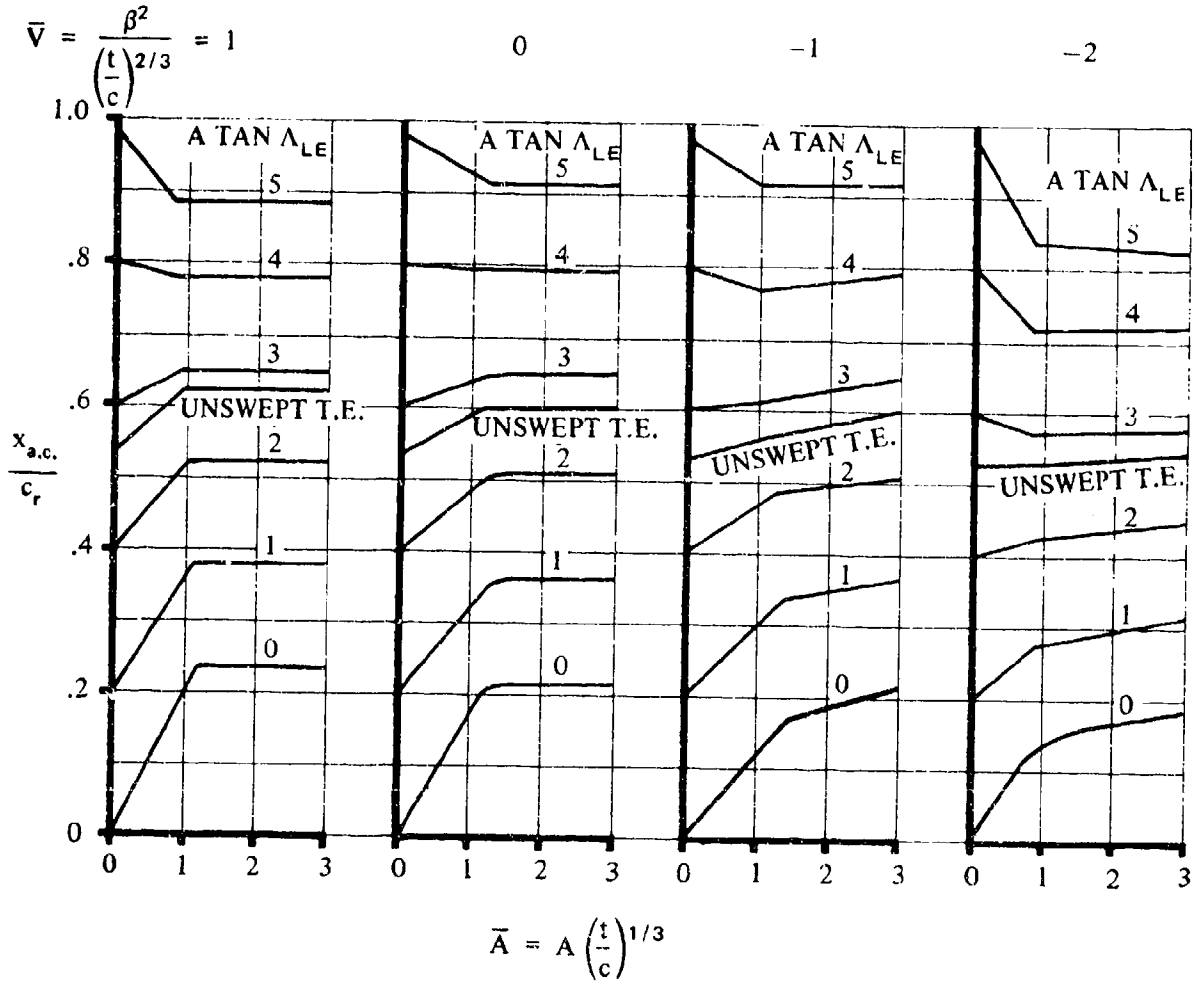

FIGURE 4.1.4.2-30 (CONTD)

TRANSONIC SPEEDS

(c) $\lambda = 0.5$

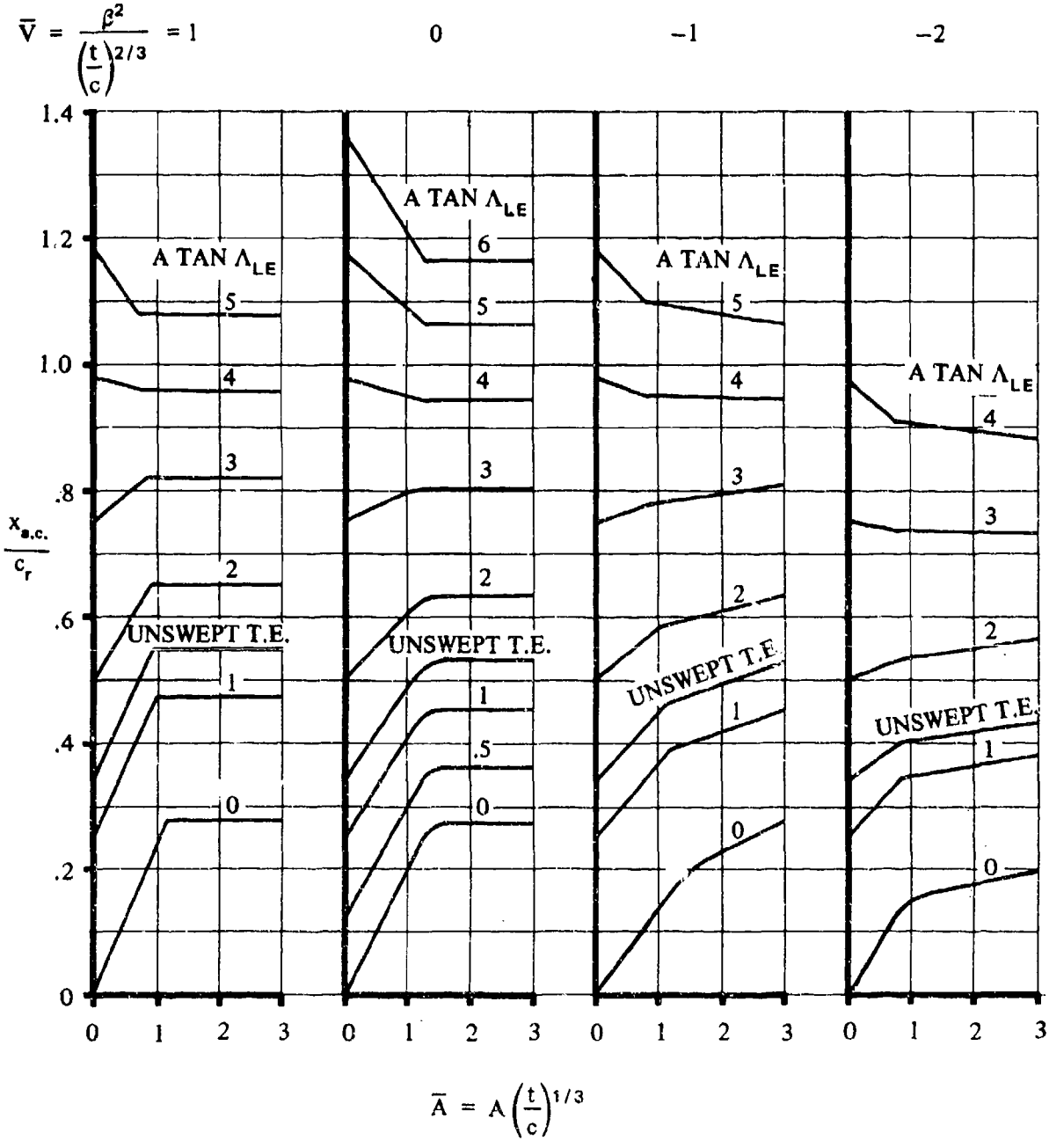

FIGURE 4.1.4.2-30(CONTD)

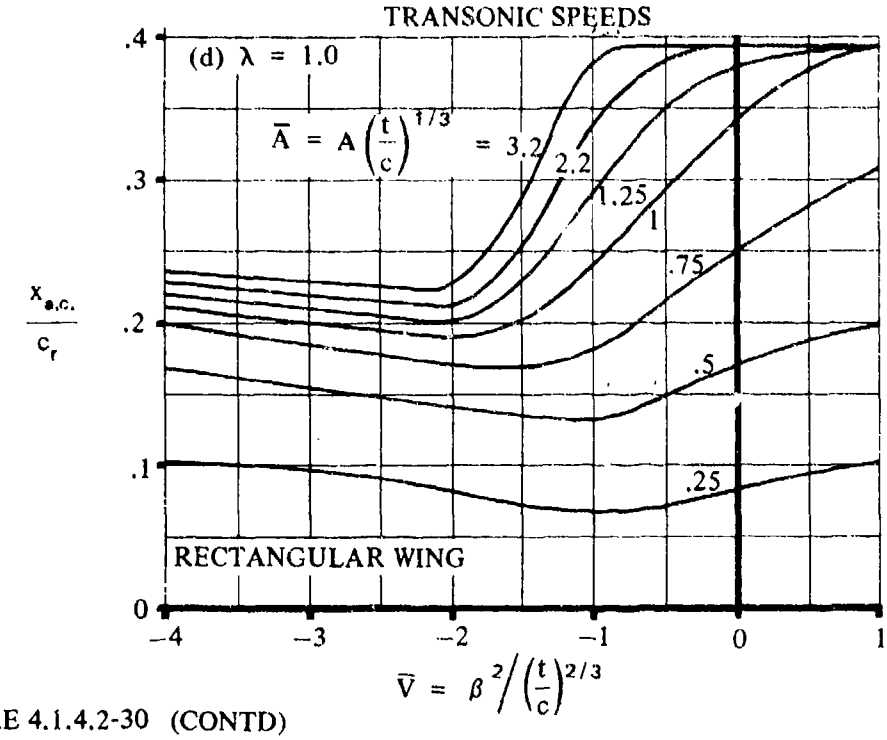

FIGURE 4.1.4.2-30 (CONTD)

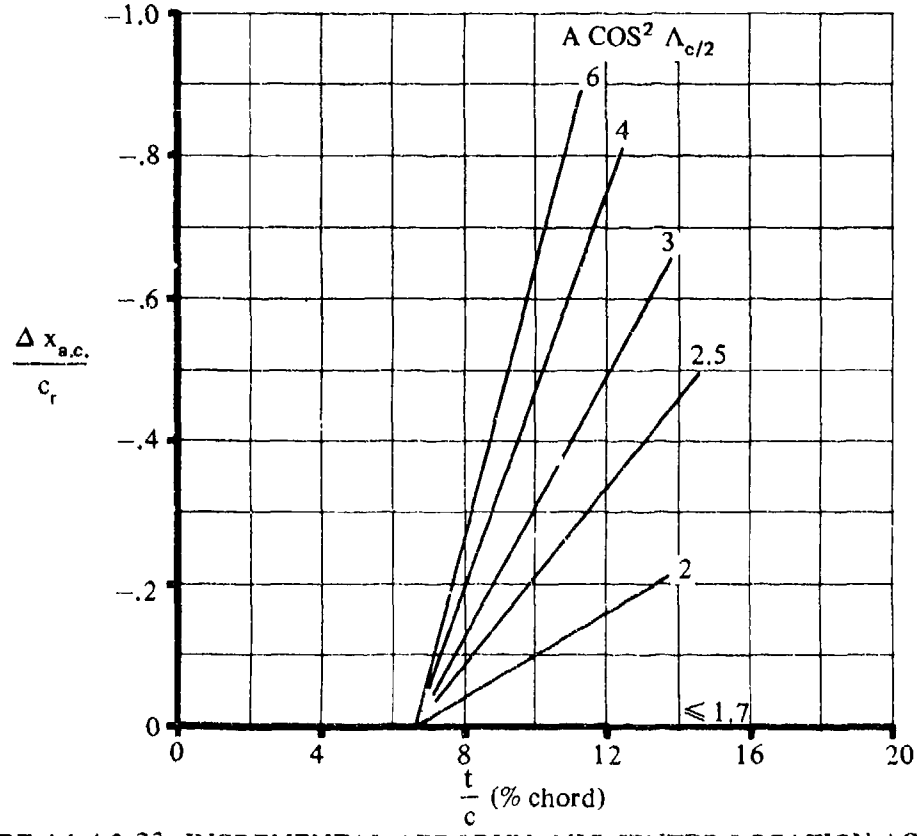

FIGURE 4.1.4.2-33 INCREMENTAL AERODYNAMIC-CENTER LOCATION ACCOUNTING FOR WING SEPARATION EFFECTS

4.1.4.3 WING PITCHING MOMENT IN THE NONLINEAR ANGLE-OF-ATTACK RANGE

Methods are presented herein for estimating the wing pitching-moment coefficient in the nonlinear angle-of-attack region. In the subsonic speed regime methods are presented for both straight-tapered and non-straight-tapered wings. No generalized methods are presented in the transonic or supersonic speed regimes. However, at supersonic speeds a discussion of pitching-moment characteristics is given for rectangular and triangular wings.

A. SUBSONIC

At subsonic speeds empirical methods are presented for predicting the pitching-moment characteristics of the following two classes of wing planforms:

Straight-Tapered Low-Aspect-Ratio Wings

Non-Straight-Tapered Wings (double-delta wings)

No method is presented for evaluating straight-tapered wings of high aspect ratios.* For high-aspect-ratio wings with low sweepback, the center-of-pressure location beyond the linear-lift range moves aft, tending toward the wing midchord at full stall. The magnitude and rate of this trend are variable, depending largely on the particular airfoil section. Insufficient data are available to predict, even from a qualitative standpoint, the pitching-moment characteristics of moderately swept high-aspect-ratio wings beyond the linear-lift range.

For thin, low-aspect-ratio wings there exist areas of flow separation, even at moderate angles of attack. Consequently, for these wings the pitching-moment curve has a tendency to become nonlinear at moderate angles of attack.

Two methods are presented for low-aspect-ratio straight-tapered wings. Method 1 is general and is applicable to most low-aspect-ratio planforms. Method 2 is more restrictive in that it is applicable only at $M = 0.2$ for highly swept, constant-section, low-aspect-ratio, delta or clipped-delta configurations with large thickness ratios; i.e., $0.10 \leq t/c \leq 0.30$. The unique feature of Method 2 is its consideration of the vortex-induced lift and its effect upon the pitching moment.

DATCOM METHODS

Straight-Tapered Wing

Method 1

The following empirical method is applicable to straight-tapered wings that satisfy the following relationship:

$$A \leq \frac{6}{(C_1 + 1)\cos \Lambda_{LE}}$$

*For the purposes of this section, high aspect-ratio wings are those for which $A > \frac{6}{(C_1 + 1)\cos \Lambda_{LE}}$, where C_1 is the empirical taper-ratio factor from Section 4.1.3.4.

where

A is the wing aspect ratio.

C_l is the empirical taper-ratio factor obtained from Figure 4.1.3.4-24b as a function of wing taper ratio.

Λ_{LE} is the sweepback angle of the wing leading edge.

The wing pitching-moment coefficient, based on the product of the wing area and wing MAC $S_W \bar{c}_W$, referred to the desired center-of-gravity location, is given by

$$C_m = \left(n - \frac{x_{c.p.}}{c_r} \right) \frac{c_r}{\bar{c}} C_N \qquad 4.1.4.3\text{-a}$$

where

n is the chordwise distance in root chords from the wing apex to the desired center-of-gravity location, positive aft.

$\frac{c_r}{\bar{c}}$ is the ratio of the wing root chord to the wing mean aerodynamic chord.

C_N is the wing normal-force coefficient, based on the wing area. This parameter should be obtained from test data if available, or by using Equation 4.1.3-a, i.e.,

$$C_N = C_L \cos\alpha + C_D \sin\alpha$$

where

C_L is the wing lift coefficient from test data or from the methods of Sections 4.1.3.1, 4.1.3.2, and 4.1.3.3.

C_D is the wing drag coefficient from test data or from Sections 4.1.5.1 and 4.1.5.2.

α is the wing angle of attack.

It should be noted that in the absence of wing drag data, the normal force may be approximated (see Section 4.1.3.3) by

$$C_N = \frac{C_L}{\cos\alpha}$$

$\frac{x_{c.p.}}{c_r}$ is the wing center-of-pressure location, in wing root chords, measured positive aft from the wing apex. Because of the various relationships used to calculate $\frac{x_{c.p.}}{c_r}$ for angles of attack between 0 and 90°, the following step-by-step procedure is given to facilitate the calculation of $\frac{x_{c.p.}}{c_r}$ versus angle of attack.

Step 1. Calculate the center-of-pressure location at zero lift. The center-of-pressure location at zero lift may be approximated as the aerodynamic center of a wing with a symmetrical airfoil section, at zero angle of attack, which is given in Section 4.1.4.2 as a function of wing planform parameters.

Step 2. Calculate the center-of-pressure location at maximum lift by

$$\left(\frac{x_{c.p.}}{c_r}\right)_{C_{L_{max}}} = \left(\frac{x_{c.p.}}{c_r}\right)_1 + \Delta\left(\frac{x_{c.p.}}{c_r}\right)_2 \qquad 4.1.4.3\text{-b}$$

where

$\left(\frac{x_{c.p.}}{c_r}\right)_1$ is obtained from Figure 4.1.4.3-21a as a function of Δy, the airfoil section leading-edge sharpness parameter. The value of Δy can be obtained from Figure 2.2.1-8.

$\Delta\left(\frac{x_{c.p.}}{c_r}\right)_2$ is obtained from Figures 4.1.4.3-21b and -22a as a function of wing taper ratio, aspect ratio, and leading-edge sweepback.

No specific Mach-number correction is included, because the experimental data show only small and inconsistent shifts up to $M \approx 0.6$.

Caution must be exercised when applying the method of this section to wings having large values of $(C_l + 1) A \cos \Lambda_{LE}$. Configurations of this type show large forward shifts in center-of-pressure location with increasing lift coefficient. This forward shift is related to flow separation and local loss of lift aft of the area centroid. In situations where the forward shift in center of pressure takes place over a small range of lift coefficients, the phenomenon is known as pitch-up. Empirical charts have been developed to define approximate boundaries dividing configurations that show pitch-up from those that do not. One such chart is presented in Figure 4.1.4.3-25.

It is important to recognize that the pitch-up characteristics for any given wing can be strongly modified by wing twist and/or wing-leading-edge devices. An extensive summary of information on pitch-up control devices is given in Reference 1.

Because of their dependence on separation effects, pitch-up characteristics are also sensitive to Reynolds number. Lowering the Reynolds number aggravates pitch-up tendencies, and raising the Reynolds number suppresses them.

The charts for low-aspect-ratio wings apply to untwisted symmetrical-section wings at Reynolds numbers near 6×10^6, based on the mean aerodynamic chord.

Step 3. Calculate the variation of center-of-pressure location between $\alpha = 0$ and $\alpha = \tan^{-1}\left(\frac{\tan \alpha_{C_{L_{max}}}}{0.6}\right)$

a. Determine the stability index from Figure 4.1.4.3-22b as a function of the wing taper ratio, aspect ratio, and leading-edge sweepback.

b. Determine the aspect-ratio index from Figure 4.1.4.3-24a as a function of wing taper ratio, aspect ratio, and leading-edge sweepback.

c. Determine the values of $\Delta\left(\frac{x_{c.p.}}{c_r}\right)_3$ from Figure 4.1.4.3-23a or -23b as a function of the stability index and the ratio of $\frac{\tan\alpha}{\tan\alpha_{C_{L_{max}}}}$ or $\frac{\tan\alpha_{C_{L_{max}}}}{\tan\alpha}$, respectively. (The value of $\Delta\left(\frac{x_{c.p.}}{c_r}\right)_3$ at $\frac{\tan\alpha}{\tan\alpha_{C_{L_{max}}}} = 1$ is zero.)

d. Determine the values of $\Delta\left(\frac{x_{c.p.}}{c_r}\right)_4$ from Figure 4.1.4.3-24b as a function of the aspect-ratio index and the ratio of $\frac{\tan\alpha_{C_{L_{max}}}}{\tan\alpha}$ or $\frac{\tan\alpha}{\tan\alpha_{C_{L_{max}}}}$. (The value of $\Delta\left(\frac{x_{c.p.}}{c_r}\right)_4$ at $\frac{\tan\alpha}{\tan\alpha_{C_{L_{max}}}} = 1$ is zero.)

e. Determine the value of $\left(\frac{x_{c.p.}}{c_r}\right)_{ref}$ by

$$\left(\frac{x_{c.p.}}{c_r}\right)_{ref} = \frac{\left(\frac{x_{c.p.}}{c_r}\right)_{C_{L_{max}}}}{\sin\alpha_{C_{L_{max}}}} - \left(\frac{x_{c.p.}}{c_r}\right)_{C_L=0} \cot\alpha_{C_{L_{max}}} \qquad 4.1.4.3\text{-c}$$

where

$\left(\frac{x_{c.p.}}{c_r}\right)_{C_{L_{max}}}$ is obtained above in Step 2.

$\alpha_{C_{L_{max}}}$ is the angle of attack at maximum lift obtained from Section 4.1.3.4.

$\left(\frac{x_{c.p.}}{c_r}\right)_{C_L=0}$ is the zero-lift center-of-pressure location from Step 1 above.

f. Using the above parameters determine the center-of-pressure location by

$$\frac{x_{c.p.}}{c_r} = \left(\frac{x_{c.p.}}{c_r}\right)_{C_L=0} \cos\alpha + \left[\left(\frac{x_{c.p.}}{c_r}\right)_{ref} + \Delta\left(\frac{x_{c.p.}}{c_r}\right)_3 + \Delta\left(\frac{x_{c.p.}}{c_r}\right)_4\right] \sin\alpha \quad 4.1.4.3\text{-d}$$

Step 4. **Calculate the center-of-pressure location at an angle of attack of 90°. This point is at the area centroid and is found by**

$$\frac{x_{c.p.}}{c_r} = \frac{1}{3}\left(\lambda + \sigma + \frac{1 + \sigma\lambda}{1 + \lambda}\right) \quad 4.1.4.3\text{-e}$$

where

$$\sigma = \frac{1}{4} A (1 + \lambda) \tan \Lambda_{LE} \quad 4.1.4.3\text{-f}$$

where

A is the wing aspect ratio.

λ is the wing taper ratio.

Λ_{LE} is the sweepback angle of the wing leading edge.

Step 5. Calculate the center-of-pressure location between $\alpha = \tan^{-1}\left(\frac{\tan\alpha_{C_{L_{max}}}}{0.6}\right)$ and $\alpha = 90^\circ$ by assuming a linear variation of $\frac{x_{c.p.}}{c_r}$. (The center-of-pressure locations corresponding to $\alpha = \tan^{-1}\left(\frac{\tan\alpha_{C_{L_{max}}}}{0.6}\right)$ and $\alpha = 90^\circ$ are obtained from Steps 3 and 4, respectively.)

A comparison of test data with wing center-of-pressure locations computed by the use of the above procedure is shown in Table 4.1.4.3-A.

Method 2

This semiempirical method is taken from Reference 2, ignoring the small wing-planform nose-radius effects. The semiempirical method was developed by using the test results of Reference 2,

correlated with the theoretical predictions based on lifting-surface theory. Because of its semiempirical nature, the method should be restricted to M = 0.2 conditions for highly swept, constant-section, low-aspect-ratio, delta or clipped-delta configurations with the following geometric characteristics:

$$0.58 \leq A \leq 2.55$$

$$0 \leq \lambda \leq 0.3$$

$$63^{\circ} \leq \Lambda_{LE} \leq 80^{\circ}$$

$$0.10 \leq t/c \leq 0.30$$

$$\Lambda_{TE} = 0$$

For round-nosed-planform configurations the reader is referred to Reference 2, where three different planform-nose-radius models were tested. No incremental nose-planform effects are presented here because of their probable configuration dependence.

This method essentially accounts for the effect of leading-edge vortex-induced lift upon the pitching moment. For details regarding the leading-edge vortex-induced-lift increments, the reader is referred to Method 2 for straight-tapered planforms in Paragraph A of Section 4.1.3.2.

The nonlinear pitching-moment characteristics, taken about the midpoint of the wing root chord and based on the product of the wing area and root chord $S_w c_r$, for a given angle of attack, are estimated by

$$C_m = \left(\frac{dC_m}{dC_L}\right) C_{L_{basic}} + C_{m_0} + \Delta C_m \qquad 4.1.4.3\text{-g}$$

where

$\frac{dC_m}{dC_L}$ is the pitching-moment-curve slope from Method 2 of Paragraph A of Section 4.1.4.2, taken about the root-chord midpoint.

$C_{L_{basic}}$ is the basic wing lift excluding any leading-edge vortex-induced effects, at the particular angle of attack. This value must come from constructing the lift curve using Section 4.1.3.1 for the determination of α_0, and Method 2 of Paragraph A of Section 4.1.3.2 for the determination of $(C_{L_\alpha})_{basic}$.

C_{m_0} is the wing zero-lift pitching moment obtained from Method 2 of Paragraph A of Section 4.1.4.1.

ΔC_m is the pitching-moment increment about the root-chord midpoint due to the leading-edge vortex. This parameter is evaluated at the particular angle of attack using

$$\Delta C_m = \frac{-0.367\,\Delta C_L}{(1 + \cos^2 \Lambda_{LE})(1 + \lambda^2)\cos(\alpha + \bar{\theta})} \qquad 4.1.4.3\text{-h}$$

where

ΔC_L is the lift increment due to the leading-edge vortex at the particular angle of attack (see Sketch (b) in Section 4.1.3.2). This value is obtained using Method 2 of Section 4.1.3.2.

Λ_{LE} is the wing leading-edge sweep.

λ is the wing taper ratio.

α is the wing angle of attack.

$\bar{\theta}$ is the angle between the airfoil chord line and a line connecting the airfoil trailing edge to the airfoil maximum upper-surface ordinate (see Sketch (a)).

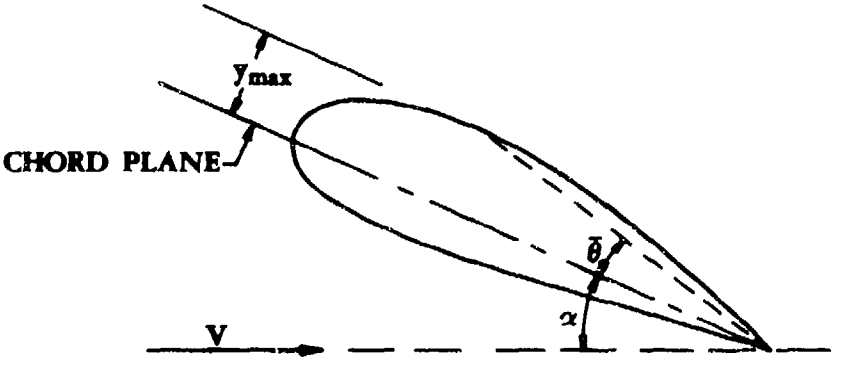

SKETCH (a)

No substantiation of this method is possible because of the lack of low-aspect-ratio test data having wing thickness ratios of $0.10 \leq t/c \leq 0.30$.

Non-Straight-Tapered Wings (Double Delta)

The empirical method (taken from Reference 3) presented herein is applicable only to double-delta wings. This method should be applied with caution because it is based on a limited amount of test data. The test data used in the formulation of the method were obtained for double-delta planforms having the following geometric limitations:

$$60^\circ \leq \Lambda_{LE_i} \leq 83^\circ$$

$$38^\circ \leq \Lambda_{LE_o} \leq 60^\circ$$

$$0.2 \leq \eta_B \leq 0.7$$

The majority of the test data used in the method formulation are wing-body test data, where the body effects have been ignored. The use of wing-body data can be justified because the data exhibit large values for the ratio of wing span to body diameter and because of the scarcity of wing-alone double-delta test data.

For a double-delta wing, the pitching-moment coefficient, based on the product of wing area and wing MAC, referred to the desired reference-center location, is given by

$$C_m = C_{m_0} + C_L \left(n - K_m \frac{x_{a.c.}}{c_r} \right) \frac{c_r}{\bar{c}} \qquad 4.1.4.3\text{-i}$$

where

C_{m_0} is the zero-lift wing pitching-moment coefficient obtained from test data on a similar configuration or from Section 4.1.4.1.

C_L is the wing lift coefficient obtained from test data or from Sections 4.1.3.1, 4.1.3.2 and 4.1.3.3.

n is the chordwise distance in root chords from the wing apex to the desired reference-center location, positive aft.

K_m is the empirical nonlinear pitching-moment factor, obtained from Figures 4.1.4.3-26a through -26f as a function of angle of attack, Mach number, and wing leading-edge sweepback.

$\frac{x_{a.c.}}{c_r}$ is the distance from the wing apex to the aerodynamic center measured in root chords, positive aft. This parameter is obtained from test data or from the double-delta-wing method of Section 4.1.4.2.

$\frac{c_r}{\bar{c}}$ is the ratio of the root chord to the wing mean aerodynamic chord.

No substantiation table of this method is presented, because all available test data were used in the method formulation. However, a sample problem is presented to illustrate the method.

Sample Problems

1. Method 1

Given: Conventional, straight-tapered wing of Reference 4.

$A = 3.0$	$\lambda = 0.143$	NACA 65A003 airfoil	
$\Lambda_{LE} = 51.3^o$	$M = 0.6$	$C_{L_{max}} = 0.94$	$\alpha_{C_{L_{max}}} = 22^o$
$\bar{c} = 0.240$ ft	$c_r = 0.353$ ft	$n = 0.572$	

α (deg)	C_L	C_D
0	0	0.006
8	0.48	0.070
12	0.68	0.145
14	0.76	0.192
16	0.82	0.237
18	0.88	0.300
20	0.92	0.340
22	0.94	0.385
28	0.88	0.475

The variations of C_L and C_D with α, $C_{L_{max}}$, and $\alpha_{C_{L_{max}}}$ have been taken from the test data of Reference 2 to facilitate the calculations.

Compute:

Determine if the straight-taper-wing method is applicable; i.e., if $A \leqslant \frac{6}{(C_1 + 1)\cos \Lambda_{LE}}$.

$C_1 = 0.36$ (Figure 4.1.3.4-24b)

$$A \leqslant \frac{6}{(1.36)(0.6252)}$$

$$\leqslant 7.06$$

The aspect ratio of this configuration is 3.0; therefore, the method is applicable to this particular configuration.

Determine the normal-force coefficient using Equation 4.1.3-a, i.e.,

$$C_N = C_L \cos \alpha + C_D \sin \alpha$$

α	C_L	$\cos \alpha$	C_D	$\sin \alpha$	C_N
0	0	1.0	0.006	0	0
8	0.48	0.9903	0.070	0.1392	0.485
12	0.68	0.9781	0.145	0.2079	0.695
14	0.76	0.9703	0.192	0.2419	0.784
16	0.82	0.9613	0.237	0.2756	0.854
18	0.88	0.9511	0.300	0.3090	0.930
20	0.92	0.9397	0.340	0.3420	0.981
22	0.94	0.9272	0.385	0.3746	1.016
28	0.88	0.8829	0.475	0.4695	1.000

Determine the center-of-pressure location at zero lift

$$A \tan \Lambda_{LE} = (3.0)(1.2482) = 3.7446$$

$$\beta = \sqrt{1 - M^2}$$

$$= \sqrt{1 - 0.36}$$

$$= 0.80$$

$$\frac{\beta}{\tan \Lambda_{LE}} = \frac{0.80}{1.2482} = 0.641$$

$$\left(\frac{x_{a.c.}}{c_r}\right)_{C_L=0} = 0.635 \quad \text{(Figure 4.1.4.2-26, interpolated)}$$

$$\left(\frac{x_{c.p.}}{c_r}\right)_{C_L=0} \cong 0.635$$

Determine the center-of-pressure location at maximum lift

$$\Delta y = 0.6 \quad \text{(Figure 2.2.1-8)}$$

$$\left(\frac{x_{c.p.}}{c_r}\right)_1 = 0.55 \quad \text{(Figure 4.1.4.3-21a)}$$

$$C_3 = 0.28 \quad \text{(Figure 4.1.4.3-21b)}$$

$$(C_3 + 1) A \tan \Lambda_{LE} = (1.28)(3.0)(1.2482) = 4.78$$

$$\Delta\left(\frac{x_{c.p.}}{c_r}\right)_2 = 0.045 \quad \text{(Figure 4.1.4.3-22a)}$$

$$\left(\frac{x_{c.p.}}{c_r}\right)_{C_{L_{max}}} = \left(\frac{x_{c.p.}}{c_r}\right)_1 + \Delta\left(\frac{x_{c.p.}}{c_r}\right)_2 \quad \text{(Equation 4.1.4.3-b)}$$

$$= 0.55 + 0.045$$

$$= 0.595$$

Determine the variation of the center-of-pressure location between $\alpha = 0$ and $\alpha = \tan^{-1}\left(\frac{\tan \alpha_{C_{L_{max}}}}{0.6}\right)$

$$\alpha = \tan^{-1}\left(\frac{\tan \alpha_{C_{L_{max}}}}{0.6}\right)$$

$$= \tan^{-1}\left(\frac{0.4040}{0.6}\right)$$

$$= 33.95^{o}$$

Stability Index = 1.2 (Figure 4.1.4.3-22b)

$A \cos \Lambda_{LE} = (3.0)(0.6252) = 1.8756$

Aspect-Ratio Index = 0.17 (Figure 4.1.4.3-24a)

α	$\frac{\tan \alpha}{\tan \alpha_{C_{L_{max}}}}$	$\Delta\left(\frac{x_{c.p.}}{c_r}\right)_3$ Fig. 4.1.4.3-23a	$\Delta\left(\frac{x_{c.p.}}{c_r}\right)_4$ Fig. 4.1.4.3-24b
8	0.348	−0.20	0.058
12	0.526	−0.12	−0.02
14	0.617	−0.07	−0.04
16	0.710	−0.03	−0.05
18	0.804	0.02	−0.06
20	0.901	0.01	−0.03
22	1.0	0	0
28	0.76*	−0.09**	0.15

$$\left(\frac{x_{c.p.}}{c_r}\right)_{ref} = \frac{\left(\frac{x_{c.p.}}{c_r}\right)_{C_{L_{max}}}}{\sin \alpha_{C_{L_{max}}}} - \left(\frac{x_{c.p.}}{c_r}\right)_{C_{L=0}} \cot \alpha_{C_{L_{max}}} \quad \text{(Equation 4.1.4.3-c)}$$

$$= \frac{0.595}{0.3746} - 0.635\ (2.475)$$

$$= 0.0168$$

*This value is the reciprocal, i.e., $\frac{\tan \alpha_{C_{L_{max}}}}{\tan \alpha} = 0.76$.

**From Figure 4.1.4.3-23b.

$$\frac{x_{c.p.}}{c_r} = \left(\frac{x_{c.p.}}{c_r}\right)_{C_L=0} \cos\alpha + \left[\left(\frac{x_{c.p.}}{c_r}\right)_{ref} + \Delta\left(\frac{x_{c.p.}}{c_r}\right)_3 + \Delta\left(\frac{x_{c.p.}}{c_r}\right)_4\right] \sin\alpha$$

(Equation 4.1.4 3-d)

α	$\cos\alpha$	$\sin\alpha$	$\frac{x_{c.p.}}{c_r}$ (Eq. 4.1.4.3-d)
0	1.0	0	0.635
8	0.9903	0.1392	0.611
12	0.9781	0.2079	0.595
14	0.9703	0.2419	0.594
16	0.9613	0.2756	0.593
18	0.9511	0.3090	0.597
20	0.9397	0.3420	0.596
22	0.9272	0.3746	0.595
28	0.8829	0.4695	0.597

Solution:

$$C_m = \left(n - \frac{x_{c.p.}}{c_r}\right) \frac{c_r}{\bar{c}} C_N \quad \text{(Equation 4.1.4.3-a)}$$

$$= \left(0.572 - \frac{x_{c.p.}}{c_r}\right) \frac{0.353}{0.24} C_N$$

α (deg)	C_N	C_m
0	0	0
8	0.485	−0.0278
12	0.695	- 0.0235
14	0.784	−0.0254
16	0.854	−0.0264
18	0.930	−0.0342
20	0.981	−0.0346
22	1.016	−0.0344
28	1.000	−0.0368

The calculated values are compared with test values from Reference 4 in Sketch (b).

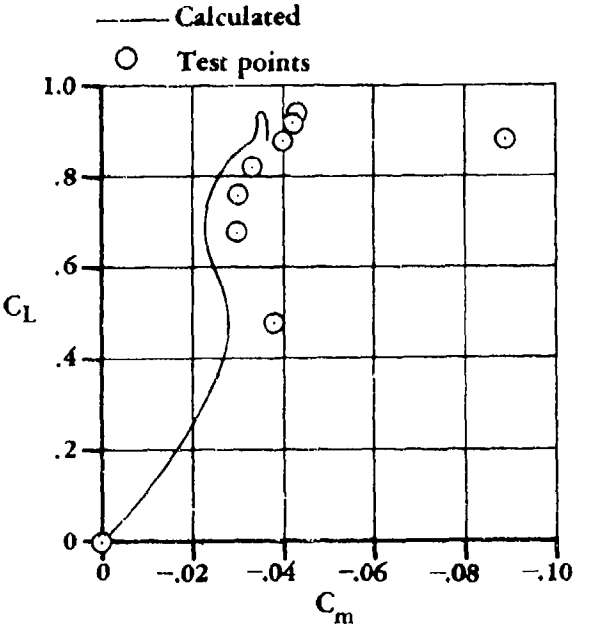

SKETCH (b)

2. Method 2

Given: The following constant-section, low-aspect-ratio, clipped-delta configuration at $\alpha = 20^{\circ}$.

$A = 0.823$ $\quad \lambda = 0.18$ $\quad \Lambda_{LE} = 73.5^{\circ}$ $\quad$ NACA 2412 airfoil

$M = 0.2$ $\quad \theta = 0$ $\quad \bar{\theta} = 6.80^{\circ}$

$\left(C_{L_\alpha}\right)_{basic} = 0.0205$ per deg

$C_{L_{\alpha_{II}}} = 0.0272$ per deg

$C_{L_{\alpha_{III}}} = 0.0325$ per deg

$C_{L_{II}} = 0.222$

$C_{L_{III}} = 0.467$

} (Sample Problem 1 Method 2 Paragraph A Section 4.1.3.2)

$C_{m_0} = 0.0091$ (Sample Problem 2 Section 4.1.4.1)

$\frac{dC_m}{dC_L} = -0.0252$ (Sample Problem 1 Section 4.1.4.2)

Compute:

Determine α_0 using Section 4.1.3.1

$$(\alpha_0)_{\theta=0} = \alpha_i - \frac{c_{\ell_i}}{c_{\ell_\alpha}} \qquad \text{(Equation 4.1.3.1-a)}$$

$\alpha_i = 0.247$

$c_{\ell_i} = 0.253$ } (Table 4.1.1-D)

$c_{\ell_\alpha} = 0.105$ per deg (Table 4.1.1-A)

$$(\alpha_0)_{\theta=0} = 0.247 - \frac{0.253}{0.105}$$

$$= -2.16^{\circ}$$

Now the complete lift curve can be constructed.

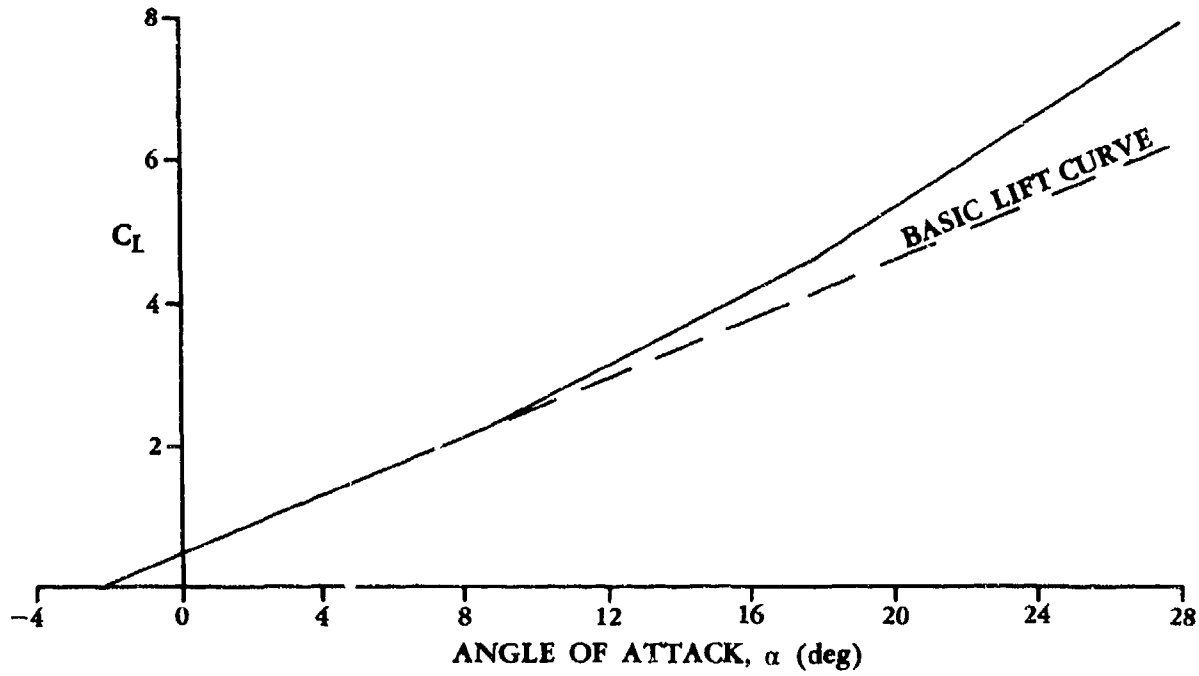

From the constructed lift curve

$\Delta C_L = 0.088$

$C_{L_{basic}} = 0.449$ } at $\alpha = 20^{\circ}$

$$\Delta C_m = \frac{-0.367\,\Delta C_L}{(1+\cos^2\Lambda_{LE})(1+\lambda^2)\cos(\alpha+\bar{\theta})} \qquad \text{(Equation 4.1.4.3-h)}$$

$$= \frac{(-0.367)(0.088)}{(1+0.0806)(1+0.0324)(0.8926)}$$

$$= -0.0324$$

$$C_m = \left(\frac{dC_m}{dC_L}\right) C_{L_{basic}} + C_{m_0} + \Delta C_m \qquad \text{(Equation 4.1.4.3-g)}$$

$$= (-0.0243)(0.449) - 0.0091 - 0.0324$$

$$= -0.0524 \left(\text{based on } S_W c_r, \text{ about } \frac{c_r}{2}\right)$$

3. Double-Delta Wing

Given: The double-delta planform of Reference 5.

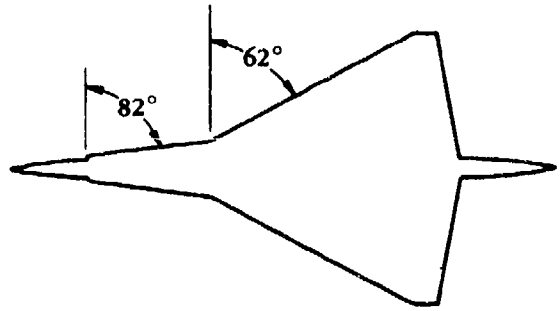

$A = 1.66$ $\quad \bar{c} = 21.68$ ft $\quad S = 505.9$ ft^2 $\quad M = 0.15$

$\left(C_{m_0}\right)_{WB} = 0.016$ $\quad \frac{x_{a.c.}}{\bar{c}} = 1.125$ $\quad n\left(\frac{c_r}{\bar{c}}\right) = 1.04$

α (deg)	C_L
0	−0.06
4	0.10
8	0.29
12	0.51
16	0.74
20	0.96

Compute:

$$\beta = \sqrt{1-M^2} = \sqrt{1-0.0225} = 0.989$$

$$\tan \Lambda_{LE_i} = \tan 82^o = 7.115$$

$$\frac{\beta}{\tan \Lambda_{LE_i}} = \frac{0.989}{7.115} = 0.139$$

Solution:

$$C_m = C_{m_0} + C_L \left(n - K_m \frac{x_{a.c.}}{c_r} \right) \frac{c_r}{\bar{c}} \qquad \text{(Equation 4.1.4.3-i)}$$

$$= C_{m_0} + C_L \left(n \frac{c_r}{\bar{c}} - K_m \frac{x_{a.c.}}{\bar{c}} \right)$$

$$= 0.016 + C_L (1.04 - 1.125 K_m)$$

α (deg)	K_m (Figures 4.1.4.3-26a through -26f)	C_m
0	1.0	0.021
4	0.995	0.008
8	0.985	−0.004
12	0.974	−0.013
16	0.971	−0.023
20	0.967	−0.030

The calculated values are compared with test values from Reference 5 in Sketch (c).

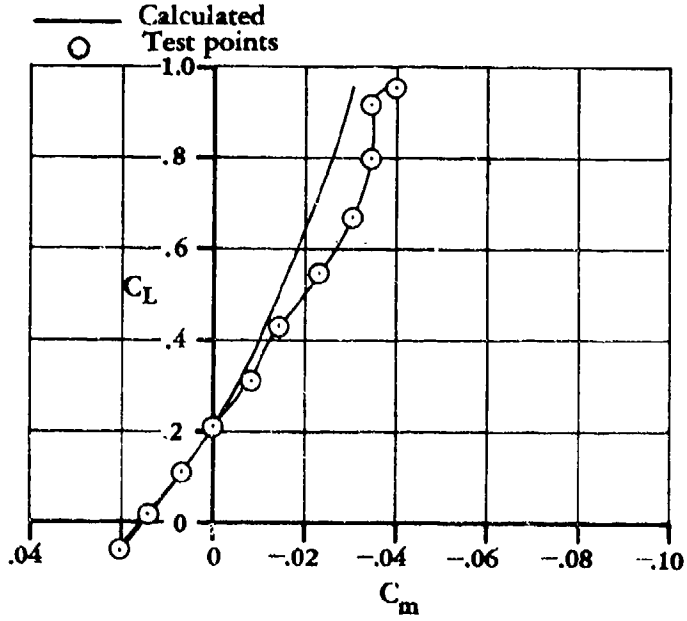

SKETCH (c)

B. TRANSONIC

No generalized handbook method for estimating transonic values of the wing pitching-moment coefficient in the nonlinear angle-of-attack region is available in the literature. For double-delta planforms it is suggested that the method presented in Paragraph A of this section for double-delta planforms be applied with caution.

C. SUPERSONIC

No general method exists for predicting the supersonic pitching moments for wings at high angles of attack. For this reason no charts on this subject are presented in this section. However, a discussion of two particular types of configuration may provide some guides. The two configurations discussed are rectangular and triangular planforms.

Rectangular Wings

For rectangular wings in supersonic flow at low angles of attack there are two principal flow regimes – flow within the influence of the tip shock waves and flow at the center section. Flow within the influence of the tip shock waves is essentially conical in nature, and flow at the wing center section is two dimensional.

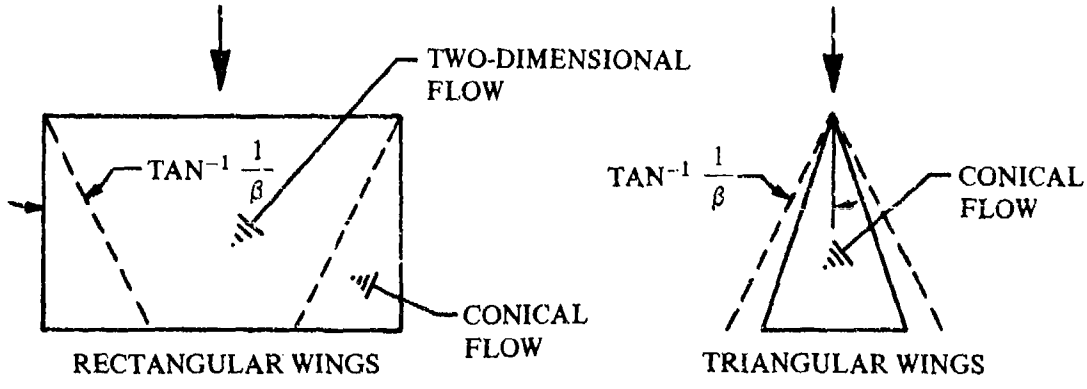

For the wing center section, then, two-dimensional pitching-moment characteristics apply. These are summarized in Section 4.1.2.2.

The effect of the tip influence on the three-dimensional wing is to force the center-of-pressure location forward.

The pitching-moment characteristics of rectangular wings in supersonic flow may be summarized as follows:

1. At low angles of attack the center-of-pressure location moves aft with increasing angle of attack, according to two-dimensional theory.

2. For situations where the tip influence is large compared to that of the two-dimensional region, the center-of-pressure location moves forward with increasing angle of attack. Trailing-edge separation on the wing center section also produces this effect.

3. For angles of attack beyond that at which the wing leading-edge shock detaches, the center-of-pressure location moves aft with increasing angle of attack. At an angle of attack of 90^{o} the wing center-of-pressure location is at the area centroid.

These variations of the center-of-pressure location with angle of attack are illustrated experimentally in the data of Reference 13.

Triangular Wings

For triangular wings the flow is conical over the entire wing. Two conditions apply -- subsonic leading edges and supersonic leading edges.

Triangular Wing with Subsonic Leading Edges

When the triangular wing has leading edges swept well within the Mach cone, slender-body theory applies. Slender-body theory makes no distinction between subsonic and supersonic speeds; therefore, the supersonic triangular-wing characteristics should be very similar to the subsonic triangular-wing characteristics. This is, in fact, the case and supersonic triangular wings with subsonic leading edges show a slight forward shift in center-of-pressure location with angle of attack that is remarkably similar to the subsonic shift. An illustration of this similarity is provided by a comparison of the supersonic data of Reference 14 with calculated subsonic characteristics of the same wing.

Triangular Wings with Supersonic Leading Edges

For triangular wings with supersonic leading edges, the center-of-pressure location changes very little with angle of attack. This is to be expected, since the aerodynamic-center location at zero angle of attack is at the area centroid, which is also the center-of-pressure location at an angle of attack of 90 degrees. Because shock waves separate from the leading edges of triangular wings at relatively low angles of attack (a result of sweep effects; see Section 4.1.3.3), the center of pressure will never be far from the area centroid. Reference 15 gives the center-of-pressure variation of a delta wing with supersonic leading edges.

REFERENCES

1. Furlong, G. C., and McHugh, J. G.: A Summary and Analysis of the Low-Speed Longitudinal Characteristics of Swept Wings at High Reynolds Numbers. NACA TR 1339, 1957. (U)

2. Crosthwait, E. L., and Seath, D. D.: Subsonic Characteristics of Low Aspect Ratios. FDL-TDR-64-103, 1965. (U)

3. Benepe, D. B., Kouri, B. G., Webb, J. B., et al: Aerodynamic Characteristics of Non-Straight-Taper Wings. AFFDL-TR-66-73, 1966. (U)

4. Few, A. G., Jr., and Fournier, P. G.: Effects of Sweep and Thickness on the Static Longitudinal Aerodynamic Characteristics of a Series of Thin, Low-Aspect-Ratio, Highly Tapered Wings at Transonic Speeds, Transonic-Bump Method. NACA PM L54B25, 1954. (U)

5. Corsiglia, V. R., Koenig, D. G., and Morelli, J. P.: Large-Scale Tests of an Airplane Model with a Double-Delta Wing, Including Longitudinal and Lateral Characteristics and Ground Effects. NASA TN D-5102, 1969. (U)

6. McCormack, G. M., and Walling, W. C.: Aerodynamic Study of a Wing-Fuselage Combination Employing a Wing Swept Back 63^{o} -- Investigation of a Large-Scale Model at Low Speed. NACA RM A8D02, 1949. (U)

7. Nelson, W. H., Allen, E. C., and Krumm, W. J.: The Transonic Characteristics of 36 Symmetrical Wings of Varying Taper, Aspect Ratio, and Thickness as Determined by the Transonic-Bump Technique. NACA TN 3529, 1955. (U)

8. Nelson, W. H., and McDevitt, J. B.: The Transonic Characteristics of 22 Rectangular, Symmetrical Wing Models of Varying Aspect Ratio and Thickness. NACA TN 3501, 1955. (U)

9. Johnson, B. H., Jr., and Shibata, H. H.: Characteristics Throughout the Subsonic Speed Range of a Plane Wing and of a Cambered and Twisted Wing, Both Having 45° of Sweepback. NACA RM A51D27, 1951. (U)

10. Cahill, J. F., and Gottlieb, S. M.: Low-Speed Aerodynamic Characteristics of a Series of Swept Wings Having NACA 65A006 Airfoil Sections. (Revised) NACA RM L50F16, 1950. (U)

11 Michael, W. H., Jr.: Flow Studies in the Vicinity of a Modified Flat-Plate Rectangular Wing of Aspect Ratio 0.25. NACA TN 2790, 1952. (U)

12. Foster, G. V., and Griner, R. F.: Low-Speed Longitudinal Characteristics of a Circular-Arc 52° Sweptback Wing of Aspect Ratio 2.84 with and without Leading-Edge and Trailing-Edge Flaps at Reynolds Numbers from 1.6×10^6 to 9.7×10^6. NACA RM L50F16a, 1950. (U)

13. Pitts, W. C.: Force, Moment, and Pressure-Distribution Characteristics of Rectangular Wings at High Angles of Attack and Supersonic Speeds. NACA RM A55K09, 1956. (U)

14. Hatch, J. E., Jr., and Hargrave, L. K.: Effects of Reynolds Number on the Aerodynamic Characteristics of a Delta Wing at Mach number of 2.41. NACA RM L51H06, 1951. (U)

15. Dunning, R. W., and Smith, F. M.: Aerodynamic Characteristics of Two Delta Wings and Two Trapezoidal Wings at Mach Number 4.04. NACA RM L53D30a, 1953. (U)

16. Shortal, J. A., and Maggin, B.: Effect of Sweepback and Aspect Ratio on Longitudinal Stability Characteristics of Wings at Low Speeds. NACA TN 1093, 1946. (U)

TABLE 4.1.4.3-A
SUBSONIC WING-CENTER-OF-PRESSURE POSITION OF STRAIGHT-TAPERED WINGS
DATA SUMMARY AND SUBSTANTIATION

Ref	A	Λ_{LE} (deg)	λ	Airfoil Section	Δy	M	$R \times 10^{-6}$	$\frac{\text{Tan } \alpha}{\text{Tan } \alpha_{C_{L_{max}}}}$	α (deg)	$\left(\frac{x_{c.p.}}{c_r}\right)_{Calc}$	$\left(\frac{x_{c.p.}}{c_r}\right)_{Test}$	e Percent Error
6	3.5	63	0.25	64A006	1.27	0.1	8.0	0	0	1.145	1.123	2.0
								0.2	7.6	1.231	1.181	4.2
								0.4	15.0	1.109	1.070	3.6
								0.6	21.9	1.024	0.994	3.0
								0.8	28.1	0.992	0.973	2.0
								1.0	33.8	0.989	0.983	0.6
7	3	9.5	0.6	63A004	0.87	0.6	1.4	0	0	0.265	0.295	−10.2
								0.2	2.85	0.264	0.253	4.3
								0.4	5.7	0.284	0.273	4.0
								0.6	8.5	0.307	0.293	4.8
								0.8	11.3	0.340	0.340	0
								1.0	14.0	0.365	0.386	−5.4
7	3	18.5	0.33	63A004	0.87	0.6	1.4	0	0	0.275	0.319	−13.8
								0.2	3.4	0.288	0.289	−0.3
								0.4	6.75	0.320	0.301	6.3
								0.6	10.1	0.341	0.344	−0.9
								0.8	13.4	0.363	0.373	−2.7
								1.0	16.5	0.375	0.388	−3.4
7	4	18.5	0.2	63A004	0.87	0.6	1.4	0	0	0.32	0.329	−2.7
								0.2	3.07	0.318	0.310	2.6
								0.4	6.1	0.335	0.328	2.1
								0.6	9.1	0.35	0.352	−0.6
								0.8	12.1	0.364	0.377	−3.4
								1.0	15.0	0.370	0.396	−6.6

TABLE 4.1.4.3-A (CONTD)

Ref	A	Λ_{LE} (deg)	λ	Airfoil Section	Δy	M	R x 10^{-6}	$\frac{\text{Tan } \alpha}{\text{Tan } \alpha C_{L_{max}}}$	α (deg)	$\left(\frac{x_{c.p.}}{c_r}\right)_{Calc}$	$\left(\frac{x_{c.p.}}{c_r}\right)_{Test}$	e Percent Error
8	3	0	1.0	63A004	0.87	0.6	2.0	0	0	0.23	0.25	−8.0
								0.2	3.07	0.225	0.225	0
								0.4	6.1	0.243	0.235	3.4
								0.6	9.1	0.274	0.264	3.8
								0.8	12.1	0.317	0.302	5.0
								1.0	15.0	0.355	0.375	−5.3
8	6	0	1.0	63A006	1.34	0.6	—	0	0	0.25	0.25	0
								0.2	2.44	0.235	0.23	2.2
								0.4	4.9	0.230	0.233	−1.3
								0.6	7.3	0.250	0.242	3.3
								0.8	9.6	0.304	0.294	3.4
								1.0	12.0	0.345	0.344	0.3
9	5	46.5	0.565	64A010	2.1	0.1	2.0	0	0	1.16	1.135	2.2
								0.2	5.3	1.159	1.149	0.9
								0.4	10.6	1.13	1.129	0.1
								0.6	15.6	1.07	1.058	1.1
								0.8	20.5	1.036	1.03	0.6
								1.0	25.0	1.045	1.026	1.9
10	6	46.2	0.6	65A006	1.34	0.1	3.0	0	0	1.355	1.35	0.4
								0.2	7.06	1.338	1.342	−0.3
								0.4	13.9	1.178	1.205	−2.2
								0.6	20.4	1.118	1.165	−4.0
								0.8	25.4	1.162	1.165	−0.3
								1.0	31.8	1.18	1.16	1.7
11	0.25	0	1.0	Flat Plate t/c = 0.02	0.745	0.1	2.0	0	0	0.07	0.10	−30.0
								0.2	11.1	0.318	0.312	1.9
								0.4	21.4	0.357	0.360	−0.8
								0.6	30.4	0.368	0.360	2.2
								0.8	38.1	0.381	0.358	6.4
								1.0	44.4	0.378	0.356	6.2
12	2.84	52.0	0.616	Biconvex t/c = 0.05	0.6	0.12	5.9	0	0	0.856	0.850	0.7
								0.2	5.9	0.858	0.855	0.4
								0.4	11.6	0.877	0.880	−0.3
								0.6	17.1	0.837	0.842	−0.6
								0.8	22.3	0.823	0.823	0
								1.0	27.2	0.824	0.849	−2.9
4	4	51.3	0	65A003	0.6	0.6	0.75	0	0	0.70	0.692	1.2
								0.2	4.5	0.669	0.68	−1.6
								0.4	8.9	0.644	0.65	−0.9
								0.6	13.2	0.628	0.636	−1.3
								0.8	17.3	0.621	0.633	−1.9
								1.0	21.3	0.610	0.630	−3.2
4	3	51.3	0.143	65A003	0.6	0.6	0.78	0	0	0.635	0.620	2.4
								0.2	4.5	0.626	0.618	1.3
								0.4	8.9	0.606	0.619	−2.1
								0.6	13.3	0.595	0.585	1.7
								0.8	17.5	0.596	0.597	−0.2
								1.0	21.5	0.595	0.60	−0.8
Average Error = $\frac{\Sigma \lvert e \rvert}{n}$ = 2.9%												

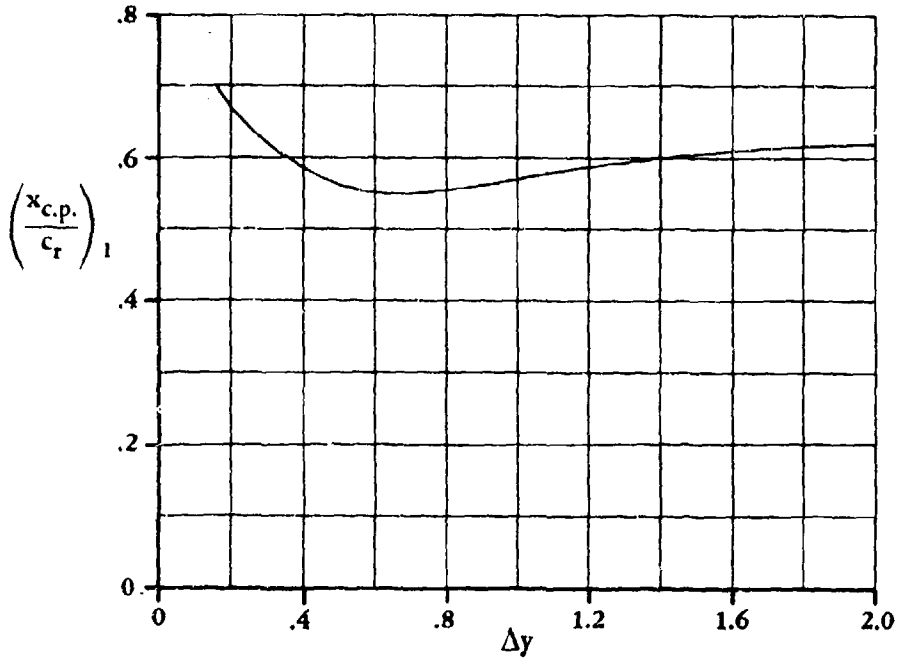

FIGURE 4.1.4.3-21a SUBSONIC CENTER-OF-PRESSURE LOCATION AT MAXIMUM LIFT — EFFECT OF LEADING-EDGE SHAPE

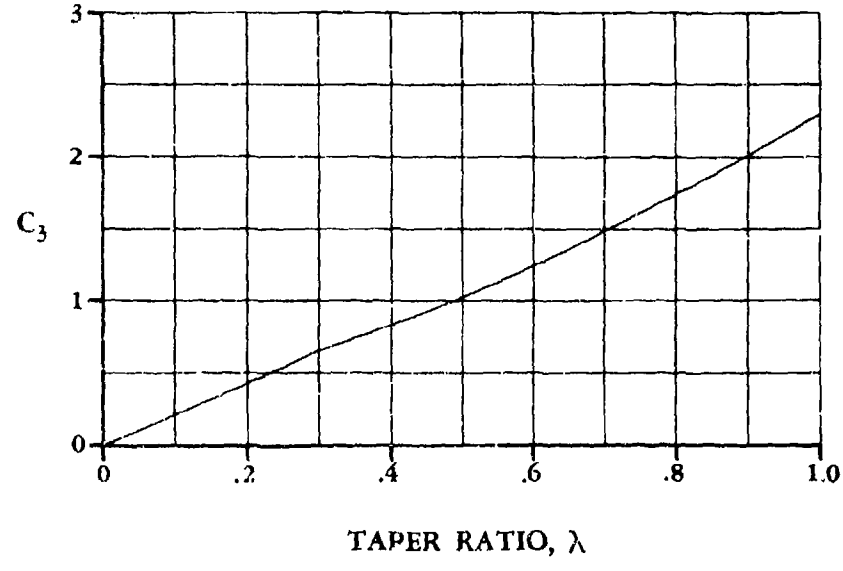

FIGURE 4.1.4.3-21b TAPER-RATIO CORRECTION FACTOR

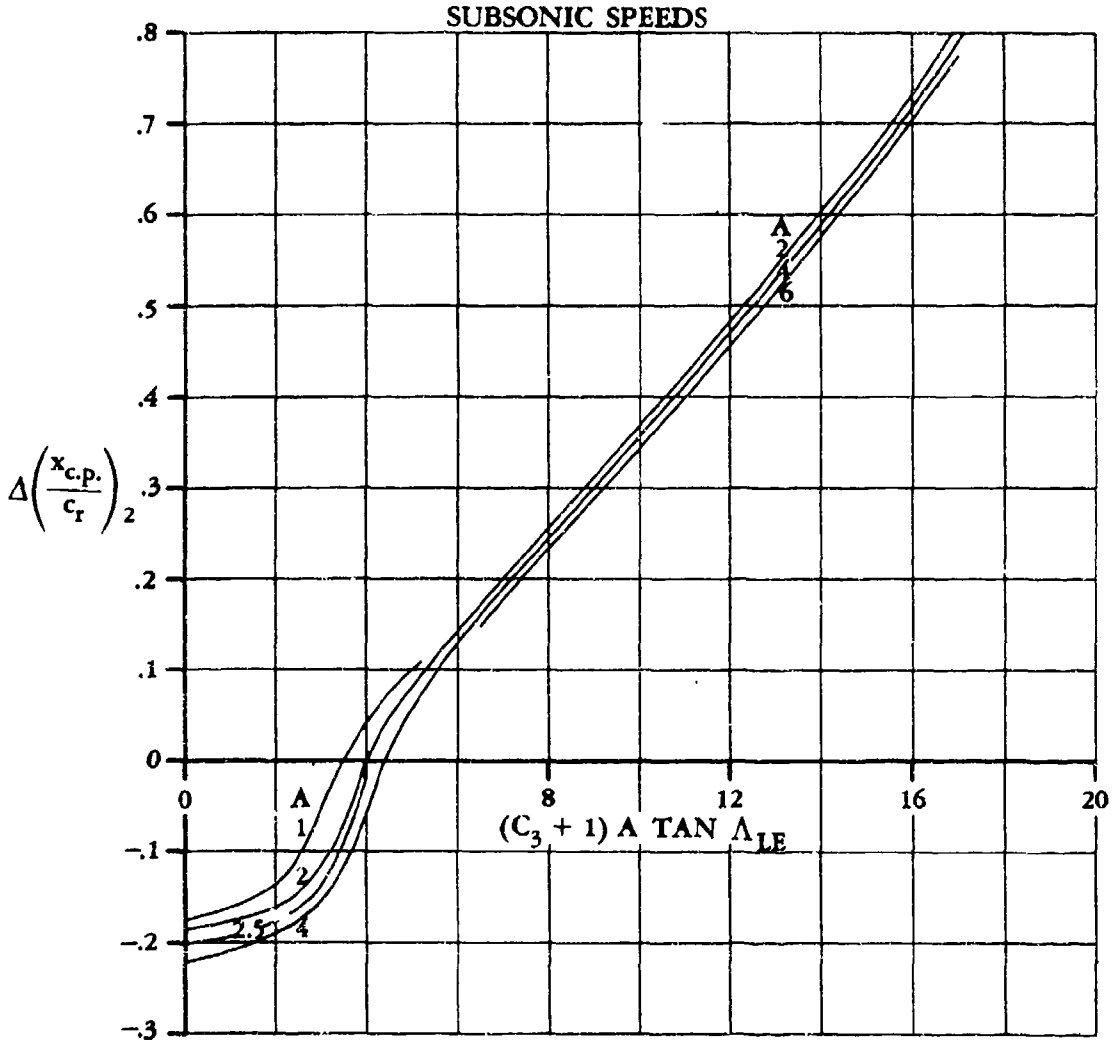

FIGURE 4.1.4.3-22a SUBSONIC CENTER-OF-PRESSURE INCREMENT AT MAXIMUM LIFT — PLANFORM EFFECT

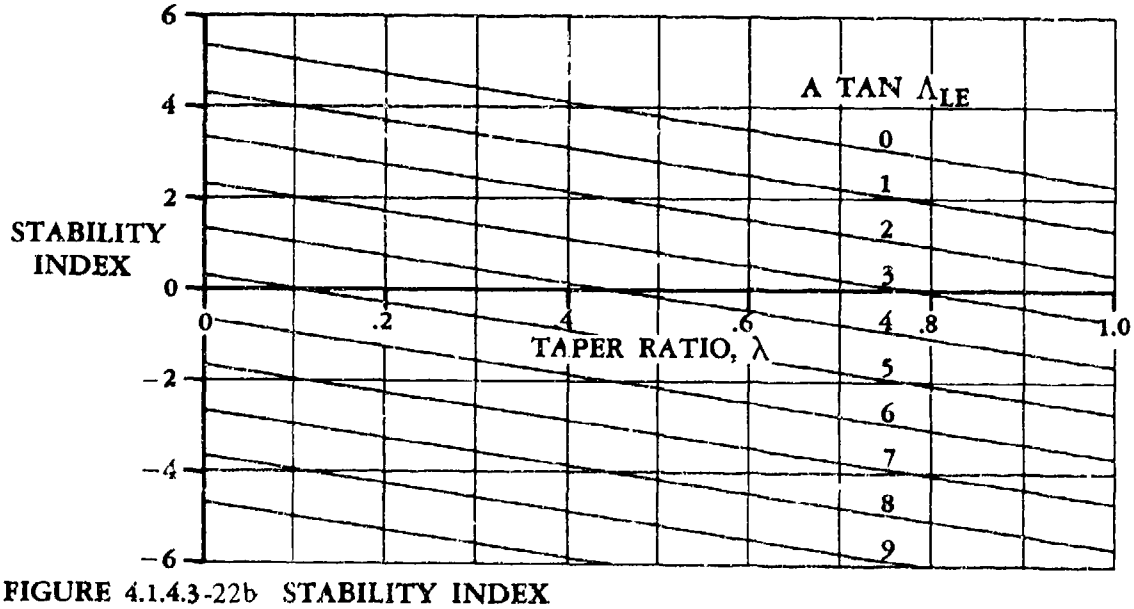

FIGURE 4.1.4.3-22b STABILITY INDEX

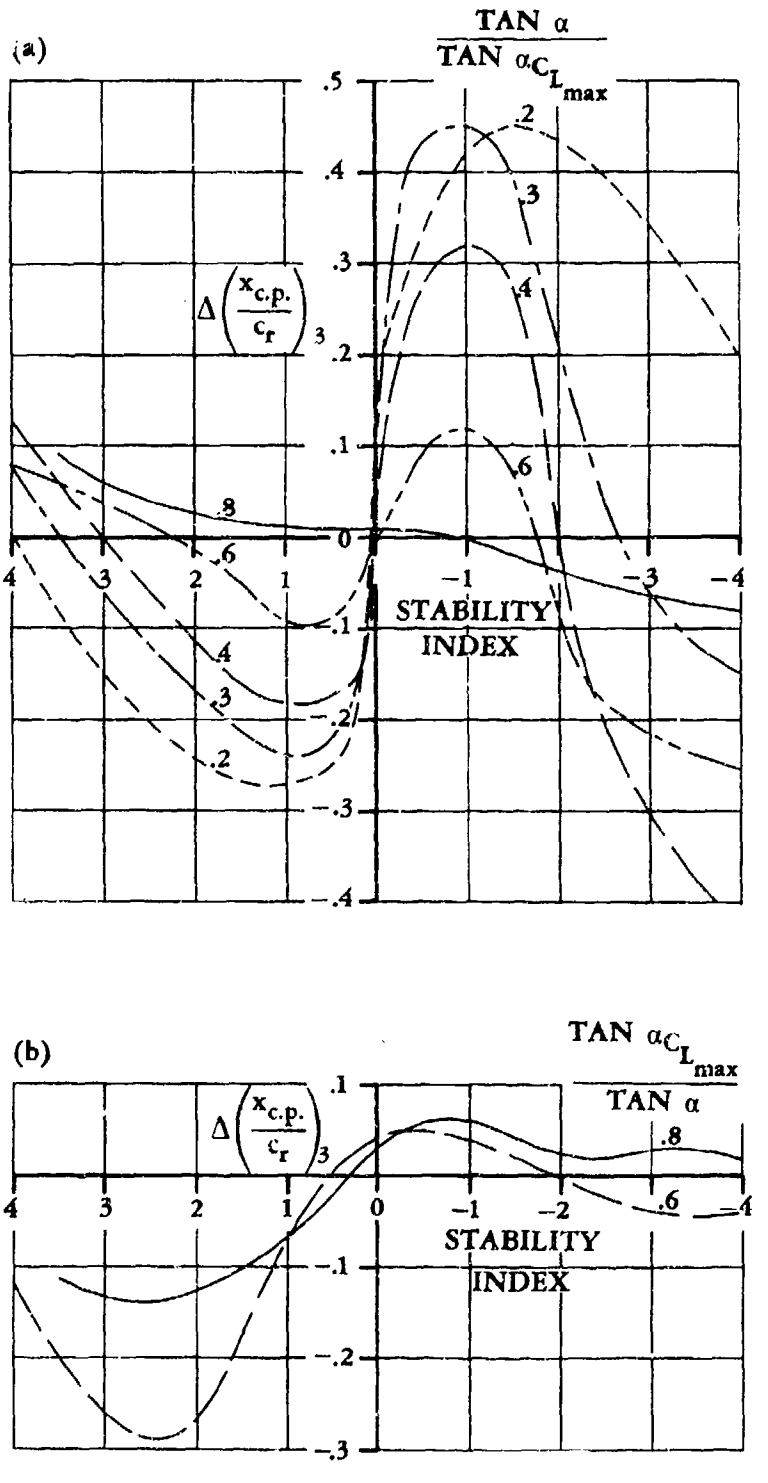

FIGURE 4.1.4.3-23 SUBSONIC WING CENTER-OF-PRESSURE INCREMENT — HIGH ANGLES OF ATTACK

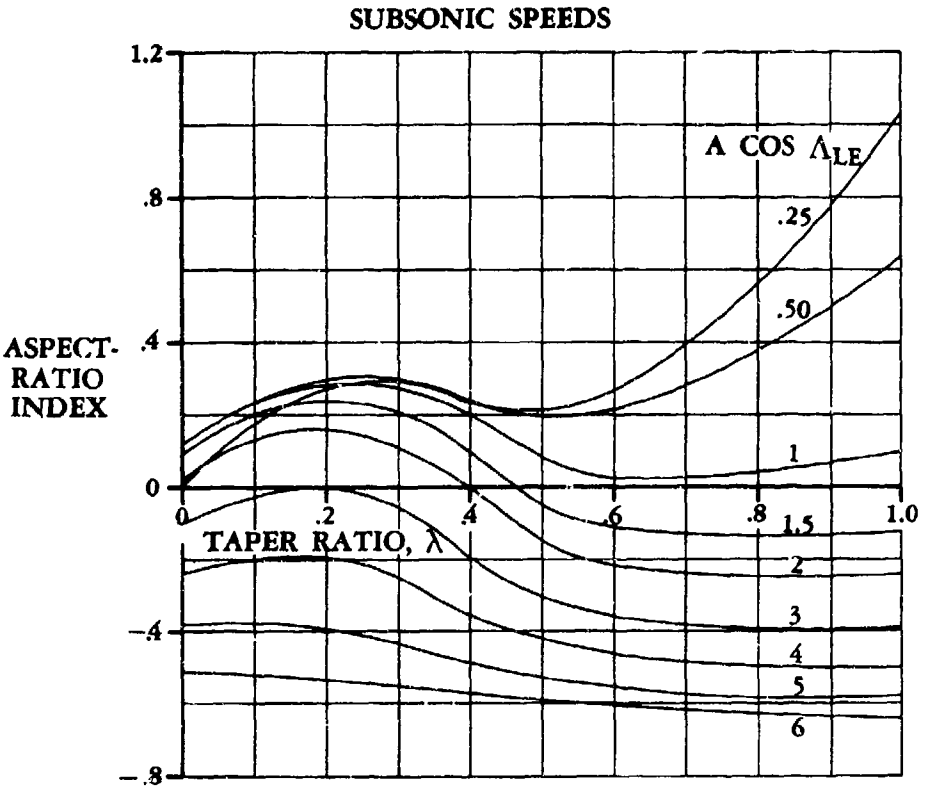

FIGURE 4.1.4.3-24a ASPECT-RATIO INDEX

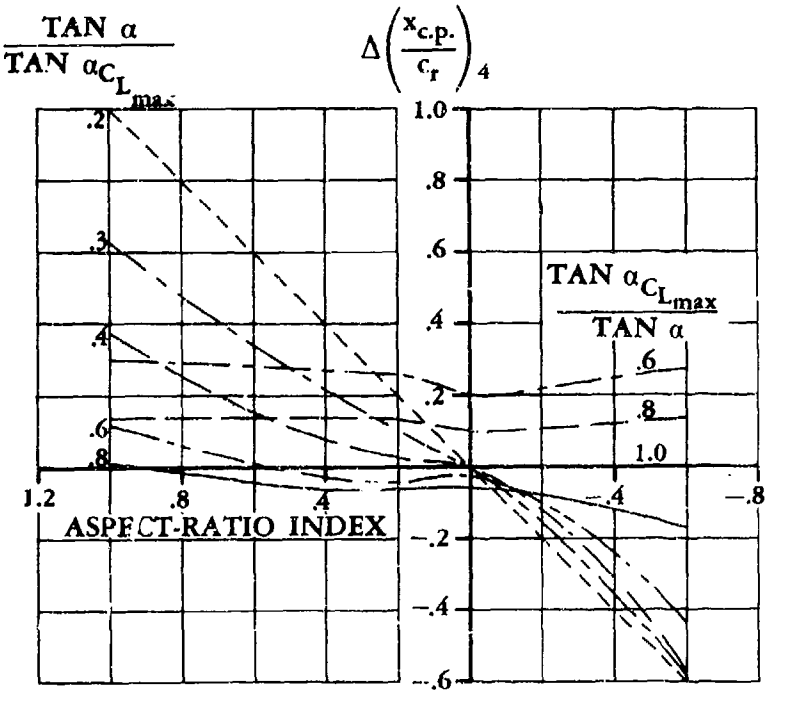

FIGURE 4.1.4.3-24b SUBSONIC WING CENTER-OF-PRESSURE INCREMENT — HIGH ANGLES OF ATTACK

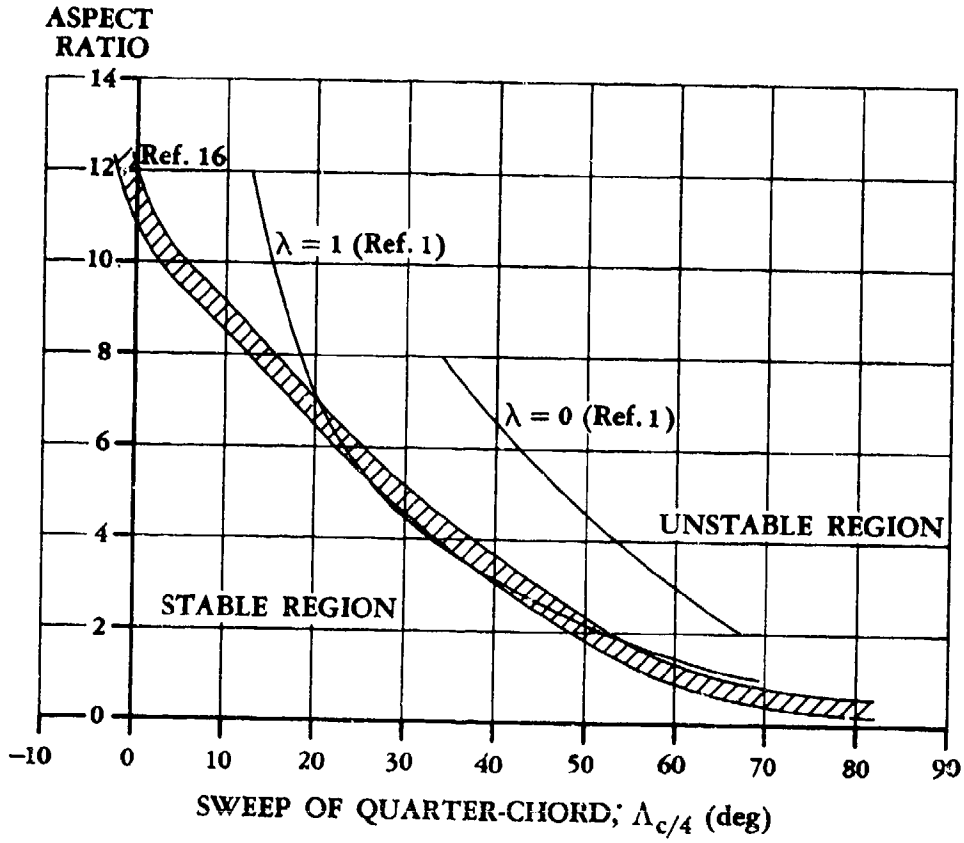

FIGURE 4.1.4.3-25 EMPIRICAL PITCH-UP BOUNDARY

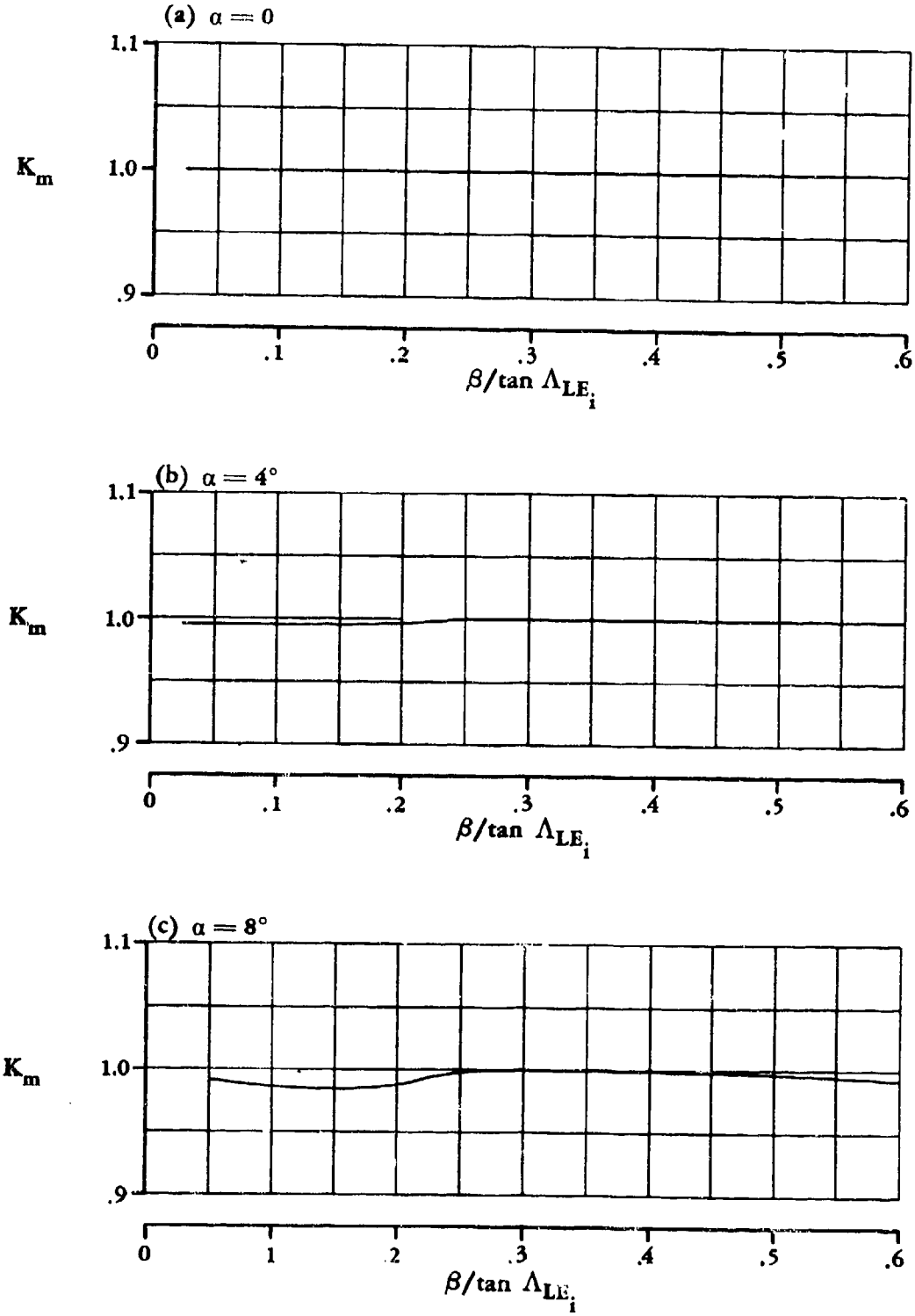

FIGURE 4.1.4.3-26 NONLINEAR PITCHING-MOMENT FACTOR FOR DOUBLE-DELTA WINGS

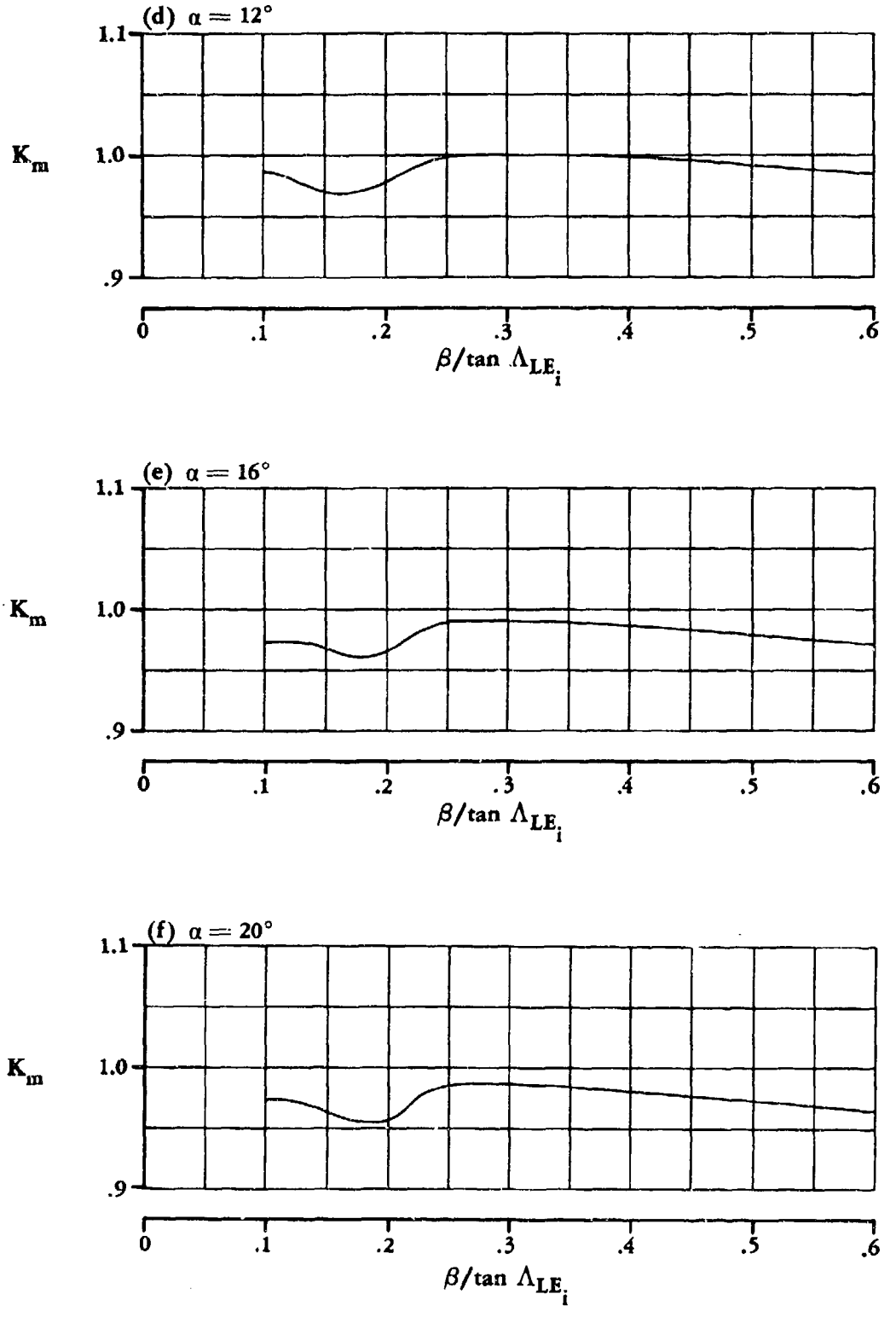

FIGURE 4.1.4.3-26 (CONTD)

4.1.5 WING DRAG

4.1.5.1 WING ZERO-LIFT DRAG

The total zero-lift drag or "profile" drag of a wing is usually considered to be composed of two parts, skin-friction drag and pressure drag. This division of drag is applicable in all speed regimes except the free-molecular-flow regime, where the normal concept of skin friction does not apply.

Skin Friction

Skin-friction drag is caused by shearing stresses within the thin layer of retarded air on the surface of the body known as the boundary layer. The boundary layer arises from the resistance of the viscous fluid to the motion of the body passing through it. Friction drag is extremely important, since it accounts for most of the drag at subsonic speeds and can be a major portion of the drag at high supersonic and hypersonic speeds.

The amount of viscous resistance depends greatly on whether the flow is laminar or turbulent, that is, whether the paths of the fluid particles remain in parallel layers or move in a chaotic or fluctuating fashion from layer to layer. The Reynolds number and the shape of the pressure distribution determine whether the flow over the wing is laminar or turbulent or a mixture of both. For practical considerations, transition from laminar to turbulent flow on a straight wing can be assumed to occur at a Reynolds number of approximately one million, based on distance from the leading edge. This usually corresponds to a position close to the leading edge. Transition will occur at an even lower Reynolds number on a swept wing. Accordingly, the methods presented for the subsonic, transonic, and supersonic regimes are for a fully turbulent boundary layer. In the hypersonic regime, however, the boundary layer is more likely to be laminar, because of the low Reynolds numbers associated with flight in the upper flight corridor.

Pressure Drag

At subsonic speeds pressure drag is usually small compared to skin-friction drag. It is caused by the displacement thickness of the boundary layer, which prevents full pressure recovery at the trailing edge. At transonic and supersonic speeds, pressure drag is identified with wave drag and is quite significant.

A. SUBSONIC

Methods for predicting subsonic zero-lift drag for wings are necessarily empirical and are commonly based on streamwise airfoil thickness ratio. The most frequently used method appears in chapter VI of reference 1 and in such standard references as reference 2. The Datcom method is essentially that of reference 1, but it has been refined by applying a lifting-surface correlation factor from reference 3 which accounts for the increased Reynolds-number length due to spanwise flow.

The Datcom method, taken from reference 3, is applicable to the following two classes of wing planforms:

Straight-Tapered Wings (conventional, trapezoidal planforms)

Non-Straight-Tapered Wings

- Double-delta wings
- Cranked wings
- Curved (Gothic and ogee wings)

DATCOM METHOD

The subsonic wing zero-lift drag coefficient, based on the reference area S_{ref}, is given by

$$C_{D_0} = C_f \left[1 + L\left(\frac{t}{c}\right) + 100\left(\frac{t}{c}\right)^4\right] R_{L.S.} \frac{S_{wet}}{S_{ref}} \qquad 4.1.5.1\text{-a}$$

where

C_f is the turbulent flat-plate skin-friction coefficient from figure 4.1.5.1-26 as a function of Mach number and the Reynolds number based on the reference length ℓ. Figure 4.1.5.1-27 is used in conjunction with figure 4.1.5.1-26 to determine C_f. Figure 4.1.5.1-27 presents the admissible roughness ℓ/k as a function of the Reynolds number based on the reference length.

- ℓ is the reference length in inches—for a wing (or wing panel in the case of composite wings) the length of the mean aerodynamic chord $\bar{c}$.
- k is the surface-roughness height in inches; it depends upon surface finish. Representative values for this parameter can be obtained from table 4.1.5.1-A.

The ratio ℓ/k is computed and figure 4.1.5.1-27 is used to obtain the cutoff Reynolds number. If the cutoff Reynolds number is greater than the computed Reynolds number for the specific configuration, the value of C_f is obtained from figure 4.1.5.1-26 at the computed Reynolds number. If the cutoff Reynolds number is less than the computed Reynolds number, the value of C_f is obtained from figure 4.1.5.1-26 at the cutoff Reynolds number.

$\frac{t}{c}$ is the average streamwise thickness ratio of the wing (or wing panel in the case of composite wings).

L is the airfoil thickness location parameter. $L = 1.2$ for $(t/c)_{max}$ located at $x_t \geq 0.30c$. $L = 2.0$ for $(t/c)_{max}$ located at $x_t < 0.30c$ (x_t is the chordwise position of maximum thickness).

S_{wet} is the wetted area of the wing (or wing panel in the case of composite wings).

S_{ref} is the reference area.

$R_{L.S.}$ is the lifting-surface correction factor obtained from figure 4.1.5.1-28b as a function of the Mach number and the cosine of the sweep angle of the airfoil maximum thickness line of the wing (or wing panel in the case of composite wings). The solid curves of figure 4.1.5.1-28b were developed in reference 4 from wing-alone test data for conventional trapezoidal planforms (including delta wings) having round-nosed airfoil sections. The dashed curves of figure 4.1.5.1-28b are from reference 3 and are arbitrary in the sense that no experimental data are available to justify their use.

Figure 4.1.5.1-28b is used in the following manner:

$R_{L.S.}$	Conventional trapezoidal planforms (including delta wings)	Read value from solid curves.
	Non-straight-tapered wings	Read value from solid curves for outboard panels.
		Read value from dashed curves for inboard panels when $\cos\Lambda_{(t/c)_{max}} < 0.65$.

Non-straight-tapered-wing geometric parameters are presented in Section 2.2.2.

In treating non-straight-tapered planforms equation 4.1.5.1-a is applied to both the inboard and the outboard panels separately (based on a common reference area) and then summed. Curved planforms are approximated by combinations of trapezoidal panels, in which case two such panels are usually sufficient to give a satisfactory result.

For convenience, the bracketed term in equation 4.1.5.1-a is presented in figure 4.1.5.1-28a as a function of t/c and L. It should also be pointed out that the last term in equation 4.1.5.1-a represents the pressure drag of the wing.

Sample Problem

Given: The cranked wing of reference 23.

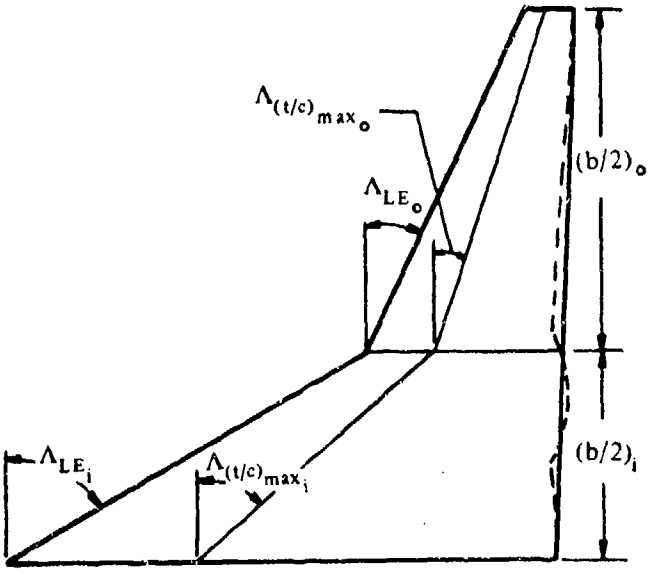

Inboard Panel:

NACA 63A004.5 airfoil (x_t @ 0.35c)

$(t/c)_i = 0.045$ $\quad \left(\frac{b}{2}\right)_i = 1.594$ ft

$\Lambda_{LE_i} = 60^o$ $\quad \Lambda_{(t/c)_{max_i}} = 48.4^o$

$\lambda_i = 0.339$ $\quad c_{r_i} = 4.175$ ft

$A_i = 1.14$ $\quad S_i = 8.91$ sq ft

$\left(S_{wet}\right)_i = 17.82$ sq ft

$\overline{c_i} = 3.02$ ft

Outboard Panel:

NACA 63A006 airfoil (x_t @ 0.35c) $\quad \left(\frac{b}{2}\right)_o = 2.606$ ft $\quad (t/c)_o = 0.06$

$\Lambda_{LE_o} = 25^o$ $\quad \Lambda_{(t/c)_{max_o}} = 18.1^o$ $\quad \lambda_o = 0.265$ $\quad c_{r_o} = 1.415$ ft

$A_o = 5.824$ $\quad S_o = 4.665$ sq ft $\quad \left(S_{wet}\right)_o = 9.33$ sq ft $\quad \overline{c}_o = 0.996$ ft

Additional Characteristics:

$M = 0.13$ $\quad R_\ell = 0.90 \times 10^6$ per ft $\quad$ Smooth surface (assume $k = 0$)

$S_{ref} = S_W = 13.575$ sq ft

Compute:

Inboard Panel

$R_\ell = (0.90 \times 10^6)(\bar{c}_i) = (0.90 \times 10^6)(3.02) = 2.718 \times 10^6$

$\frac{\ell}{k} = \infty$; read $\left(C_f\right)_i$ at calculated R_ℓ

$\left(C_f\right)_i = 0.00372$ (figure 4.1.5.1-26)

$\left[1 + L\left(\frac{t}{c}\right) + 100\left(\frac{t}{c}\right)^4\right]_i = 1.053$ (figure 4.1.5.1-28a, for $L = 1.2$)

$\cos \Lambda_{(t/c)_{max_i}} = \cos 48.4^o = 0.6639$

$\left(R_{L.S.}\right)_i = 0.934$ (figure 4.1.5.1-28b)

$\frac{\left(S_{wet}\right)_i}{S_{ref}} = \frac{17.82}{13.575} = 1.313$

Outboard Panel:

$R_\ell = (0.90 \times 10^6)(\bar{c}_o) = (0.90 \times 10^6)(0.996) = 0.896 \times 10^6$

$\frac{\ell}{k} = \infty$; read $\left(C_f\right)_o$ at calculated R_ℓ

$\left(C_f\right)_o = 0.00451$ (figure 4.1.5.1-26)

$\left[1 + L\left(\frac{t}{c}\right) + 100\left(\frac{t}{c}\right)^4\right]_o = 1.072$ (figure 4.1.5.1-28a, for $L = 1.2$)

$\cos \Lambda_{(t/c)_{max_o}} = \cos 18.1^o = 0.9505$

$\left(R_{L.S.}\right)_o = 1.067$ (figure 4.1.5.1-28b)

$\frac{\left(S_{wet}\right)_o}{S_{ref}} = \frac{9.33}{13.575} = 0.687$

Solution:

$$C_{D_0} = \left(C_{D_0}\right)_i + \left(C_{D_0}\right)_o$$

$$\left(C_{D_0}\right)_i = \left(C_f\right)_i \left[1 + L\left(\frac{t}{c}\right) + 100\left(\frac{t}{c}\right)^4\right]_i \left(R_{L.S.}\right)_i \frac{\left(S_{wet}\right)_i}{S_{ref}} \quad \text{(equation 4.1.5.1-a)}$$

$$= (0.00372)(1.053)(0.934)(1.313) = 0.00480$$

$$\left(C_{D_0}\right)_o = \left(C_f\right)_o \left[1 + L\left(\frac{t}{c}\right) + 100\left(\frac{t}{c}\right)^4\right]_o \left(R_{L.S.}\right)_o \frac{\left(S_{wet}\right)_o}{S_{ref}} \quad \text{(equation 4.1.5.1-a)}$$

$$= (0.00451)(1.072)(1.067)(0.687) = 0.00354$$

$$C_{D_0} = (0.00480) + (0.00354) = 0.00834$$

This compares with a test value of 0.0086 from reference 23.

B. TRANSONIC

The transonic range varies greatly with airfoil shape and thickness, but for the purposes of consistency with the bulk of the Datcom it can be considered to begin at approximately $M = 0.6$ and to end at $M = 1.2$. The drag rise which marks the actual beginning of the transonic range occurs when the local Mach number on some part of the wing exceeds 1.0 and shock waves form on the surface.

Because of the mixed flows, drag in the transonic range does not lend itself either to simple theoretical or to experimental analysis. As in the subsonic regime, the total zero-lift drag can be separated into two parts–skin friction drag due to viscous forces and "wave" or pressure drag due to the viscous dissipation associated with the formation of shock waves on the wing.

In the lower transonic range the shock waves are essentially normal to the surface and serve to decelerate local supersonic flow back to subsonic values. In the upper transonic region there are two shocks, a bow shock ahead of the airfoil and a trailing-edge shock located near the trailing edge. When the bow shock attaches itself to a sharp-nosed airfoil, the entire flow field over the surface becomes supersonic, thus ending the transonic region. For round-nosed airfoils the end of this range is less clearly defined, but it occurs when the bow wave stands very close to the nose and supersonic flow predominates.

Skin Friction

Although it might be reasoned that skin friction should be increased for subsonic compressible flow (lower transonic range) because of the relatively higher local velocities, experimental results show little increase in drag due to viscosity. This is probably due to the compensating effects of Reynolds number and Mach number as well as unpredictable changes in the transition point throughout the Mach number range. Therefore, for the purpose of the Datcom the skin-friction drag will be assumed to be constant and equal to the subsonic value at $M = 0.6$ throughout the transonic range.

Wave Drag

For a given airfoil, it is possible to estimate the critical Mach number and subsequent drag rise accurately. However, the variables involved in a wing design that affect the manner in which the shock waves develop

on the surface, and hence the drag-rise characteristics, are many. They include not only sweep, aspect ratio, taper ratio, and thickness ratio, but also the variations between root and tip in thickness, position of maximum thickness, incidence, and leading-edge geometry. Also, wings designed to fly transonically usually include some treatment, often made by contouring the fuselage, to minimize the "kink" effect at the root and tip. A wing can be designed to become critical from root to tip at the same time and have a flat drag curve with a delayed abrupt steep drag rise. Another wing can be designed which has an identical planform and the same average thickness ratio but has an entirely different shock development, producing a very gradual drag rise starting at a much lower Mach number.

For this reason, it is very difficult to correlate data in this region even on the basis of similarity parameters. The method presented here should be used only for first-order approximations on wings of relatively simple geometry. For cases where the design is aimed at optimizing transonic characteristics, detailed analysis of the isobar development on the wing must be made, in order to arrive at a reasonable drag estimate.

Since the transonic range begins when the first shocks form on the wing and ends when supersonic flow predominates, the amount of wave drag varies from zero at the lower speed to a peak value at the higher speeds within this range. From the standpoint of drag analysis, it is therefore convenient to relate this increase in drag to several parameters. These are discussed below.

The Mach Number for Drag Divergence

The free-stream Mach number at which sonic velocity is first attained on some portion of the wing is called the "theoretical critical Mach number." However, since experimental evidence indicates that there are no abrupt changes in force characteristics until the critical Mach number is exceeded by a substantial amount, it is usual to define the Mach number at which the drag starts to increase rapidly as the drag-divergence Mach number. It is further arbitrarily defined in the literature as the Mach number at which the numerical value of the slope of the curve of C_D vs M is 0.10.

$$M_D = M \left(\frac{\partial C_D}{\partial M} \right)_{C_L = \text{const}} = 0.10 \qquad \text{4.1.5.1-b}$$

The Maximum Wave-Drag Increment and the Mach Number at Which It Occurs

For two-dimensional airfoils, the peak wave drag occurs near M = 1.0. Linear theory predicts a pressure coefficient inversely proportional to $(1 - M^2)$ in high subsonic flow and $(M^2 - 1)$ in supersonic flow; thus indicating a maximum value near 1.0. In practice, however, the magnitude of this peak and the Mach number at which it occurs vary greatly with airfoil thickness, section shape, aspect ratio, and sweep; consequently, no reliable method has been devised to predict these values accurately.

The most useful tools available for correlating data in estimating wave drag in the transonic range are the von Kármán similarity laws (reference 5). These laws state that for two-dimensional flow, the flow pattern over two airfoils must be the same if the value of $(t/c)^{1/3} \mid 1 - M^2 \mid$ has the same value for each airfoil. Hence, if drag is known for one wing section as a function of Mach number, the corresponding quantity for similar sections can be computed by the simple relation $C_D \propto (t/c)^{5/3}$. Extensions of these laws have been made by Busemann and Spreiter to include three-dimensional effects (references 6 and 7).

The Datcom method is applicable only to conventional, trapezoidal planforms.

DATCOM METHOD

The zero-lift drag coefficient of conventional, trapezoidal planforms over the transonic speed regime is approximated by the following steps:

Step 1. Determine the skin-friction drag coefficient at M = 0.60 by

$$C_{D_f} = C_f \left[1 + L\left(\frac{t}{c}\right)\right] \frac{S_{wet}}{S_{ref}} \qquad 4.1.5.1\text{-c}$$

where C_{D_f} is the skin-friction drag coefficient based on the reference area, and the remaining parameters are defined in the Datcom method of paragraph A. This value, calculated at M = 0.6, is assumed to be constant throughout the transonic region.

Step 2. Determine the wave-drag coefficient C_{D_w} at transonic Mach numbers for an unswept wing and construct the curve of C_{D_w} vs Mach number for the appropriate thickness and aspect ratio from figure 4.1.5.1-29. Values of $(t/c)^{1/3}$ and $(t/c)^{5/3}$ are given below to facilitate calculation:

t/c	$(t/c)^{1/3}$	$(t/c)^{5/3}$
0.12	0.493	0.0293
0.11	0.479	0.0254
0.10	0.464	0.0217
0.09	0.448	0.0181
0.08	0.431	0.0148
0.07	0.412	0.0118
0.06	0.392	0.0092
0.05	0.368	0.0068
0.04	0.342	0.00468
0.03	0.311	0.00292
0.02	0.271	0.00147

Step 3. From the curve of C_{D_w} vs M, read $C_{D_{w_{peak}}\Lambda_{c/4}=0}$, $M_{C_{D_{w_{peak}}}\Lambda_{c/4}=0}$, and $M_{D\Lambda_{c/4}=0}$. The Mach number for drag divergence $M_{D\Lambda_{c/4}=0}$ is obtained by a graphical interpretation of equation 4.1.5.1-b; i.e., $M_{D\Lambda_{c/4}=0}$ is read at the point of tangency to the C_{D_w} vs M curve of a line whose slope is $\partial C_D / \partial M = 0.10$.

Step 4. For a wing having sweep, convert values from the straight-wing curve as follows:

$$M_{D\Lambda_{c/4}=n} = \frac{M_{D\Lambda_{c/4}=0}}{(\cos n)^{1/2}} \qquad 4.1.5.1\text{-d}$$

$$C_{D_{w_{peak}}\Lambda_{c/4}=n} = C_{D_{w_{peak}}\Lambda_{c/4}=0} (\cos n)^{2.5} \qquad 4.1.5.1\text{-e}$$

$$M_{C_{D_{w_{peak}}} \Lambda_{c/4} = n} = \frac{M_{C_{D_{w_{peak}}} \Lambda_{c/4} = 0}}{(\cos n)^{1/2}} \qquad 4.1.5.1\text{-f}$$

Step 5. Construct the curve of C_{D_w} vs M for the swept wing by using the values determined in step 4 and the straight-wing curve of C_{D_w} vs M to aid in fairing.

Step 6. The zero-lift drag coefficient is obtained by adding the constant value of skin-friction drag coefficient determined in step 1 to the wave-drag over the transonic speed range determined in step 2 for unswept wings or in step 5 for swept wings.

$$C_{D_0} = C_{D_f} + C_{D_w} \qquad 4.1.5.1\text{-g}$$

Sample Problem

Given: The zero-taper-ratio wing of reference 24.

$A = 4.0$ $\quad \lambda = 0$ $\quad \Lambda_{c/4} = 14.5^o$ $\quad S_{wet} = 1.390$ sq ft

NACA 63A006 airfoil (x_t @ 0.35c)

Additional characteristics:

$R_{\ell_{M=0.6}} = 1.4 \times 10^6$ (based on $\bar{c}$) $\quad S_{ref} = S_W = 0.695$ sq ft

Smooth surface (assume k = 0)

Compute:

Determine the skin-friction drag coefficient.

$\frac{\ell}{k} = \infty$; read C_f at given R_ℓ at M = 0.6.

$C_f = 0.0042$ (figure 4.1.5.1-26)

$$C_{D_f} = C_f \left[1 + L\left(\frac{t}{c}\right)\right] \frac{S_{wet}}{S_{ref}} \qquad \text{(equation 4.1.5.1-c)}$$

$$= 0.0042\,[1 + (1.2)(0.06)]\,\frac{1.390}{0.695}$$

$= 0.0090$ (based on S_W)

Determine and construct the variation of C_{D_w} with Mach number for an unswept wing.

$$A\left(\frac{t}{c}\right)^{1/3} = (4.0)\,(0.392) = 1.568$$

① M	② $\frac{\sqrt{\lvert M^2-1\rvert}}{(t/c)^{1/3}}$	③ $\frac{C_{D_w}}{(t/c)^{5/3}}$ fig. 4.1.5.1-29	④ C_{D_w} ③ (0.0092)
0.85	1.34	0.07	0.00064
0.90	1.11	0.58	0.0053
0.925	0.97	1.10	0.0101
0.95	0.80	1.95	0.0179
0.975	0.57	2.75	0.0253
1.00	0	3.02	0.0278
1.05	0.82	3.10	0.0285
1.10	1.17	3.12	0.0287
1.15	1.45	3.13	0.0288

Plot C_{D_w} vs M for the unswept wing (sketch (a)).

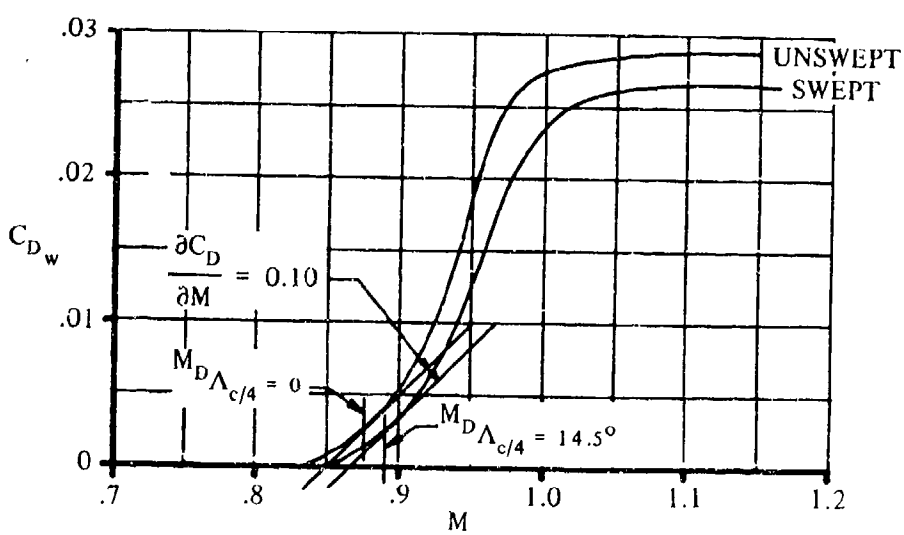

SKETCH (a)

Read the following values from the curve of C_{D_w} vs M for the unswept wing.

$$M_{D_{\Lambda_{c/4}=0}} = 0.875$$

$$C_{D_{w_{peak}\Lambda_{c/4}=0}} = 0.029$$

$$M_{C_{D_{w_{peak}\Lambda_{c/4}=0}}} = 1.10$$

Apply sweep corrections

$$M_{D_{\Lambda_{c/4}=14.5^\circ}} = \frac{M_{D_{\Lambda_{c/4}=0}}}{(\cos 14.5^\circ)^{1/2}} = \frac{0.875}{(0.9681)^{1/2}} = 0.889 \quad \text{(equation 4.1.5.1-d)}$$

$$C_{D_{w_{peak}\Lambda_{c/4}=14.5^\circ}} = C_{D_{w_{peak}\Lambda_{c/4}=0}} (\cos 14.5^\circ)^{2.5} \quad \text{(equation 4.1.5.1-e)}$$

$$= (0.029)\,(0.9681)^{2.5}$$

$$= 0.0267$$

$$M_{C_{D_{w_{peak}\Lambda_{c/4}=14.5^\circ}}} = \frac{M_{C_{D_{w_{peak}\Lambda_{c/4}=0}}}}{(\cos 14.5^\circ)^{1/2}} \quad \text{(equation 4.1.5.1-f)}$$

$$= \frac{1.10}{(0.9681)^{1/2}}$$

$$= 1.12$$

Construct the curve of C_{D_w} vs M for the swept wing using the straight-wing curve to aid in fairing.

Solution:

$$C_{D_0} = C_{D_f} + C_{D_w} \quad \text{(equation 4.1.5.1-g)}$$

① M	② C_{D_f}	③ C_{D_w} sketch (a)	④ C_{D_0} ② + ③
0.85	0.0090	0	0.0090
0.90		0.0035	0.0125
0.925		0.0070	0.0160
0.950		0.0127	0.0217
0.975		0.0197	0.0287
1.000		0.0238	0.0328
1.050		0.0262	0.0352
1.100		0.0265	0.0355
1.150		0.0265	0.0355

The calculated results are compared with test values from reference 24 in sketch (b).

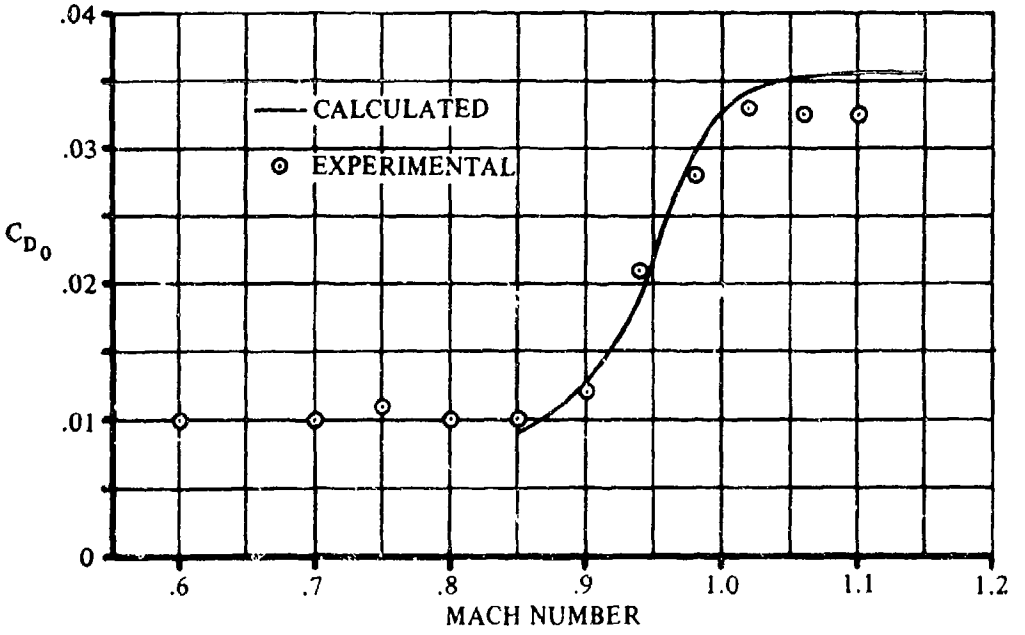

SKETCH (b)

C. SUPERSONIC

Skin Friction

At supersonic speeds it can be shown theoretically that an increase in Mach number results in a decrease in the skin-friction coefficient at constant Reynolds number. This variation, when zero heat transfer is assumed, is due primarily to the variations in temperature and density. In actual cases, where the airplane is transmitting heat to the boundary layer, or where the aircraft is cooled to a point where heat from the boundary layer is transmitted to the skin, the reduction in skin-friction coefficient becomes a function of the heat-transfer condition. The full reduction in skin friction at supersonic Mach numbers is justified only when stabilized conditions and zero heat transfer are attained. Therefore, to obtain accurate supersonic skin-friction coefficients, it is necessary to know the heat-transfer conditions on various portions of a flight vehicle throughout its mission. Since this information can be obtained only by detailed analysis, some assumptions regarding the skin friction are usually made. For flights of long duration, equilibrium (zero heat transfer) is generally assumed. For transient flight, the skin-friction coefficient will vary between the incompressible value and that for zero heat transfer. Another important consideration for estimating the skin-friction drag at supersonic speeds is the Reynolds-number variation throughout the flight regime. The design chart used in the Datcom method presents the turbulent skin-friction coefficient on an insulated flat plate as a function of Mach number and Reynolds number.

Wave Drag

Numerous theories are available for calculating the wave drag of wing planforms at supersonic speeds. No attempt is made to discuss all of these theories and their limitations; however, table 4.1.5.1-B presents a summary of various planforms for which solutions exist. In general, the well-known linear supersonic theory has proved useful in indicating the trends of wing wave drag for the majority of conventional, tapered, trapezoidal planforms with subsonic leading edges (see reference 8).

In discussing the flow regions over a wing, the following general classifications are convenient (see sketch (c)).

Subsonic Wing Leading Edge—If the leading edge of the wing is swept behind the Mach cone, the velocity component normal to the leading edge is subsonic and hence the leading edge is said to be subsonic.

Supersonic Wing Leading Edge--If the leading edge is forward of the Mach cone, the normal velocity component is supersonic and the wing is said to have a supersonic leading edge.

Similar terminology can be applied to the wing trailing edges. For either subsonic or supersonic leading edges the region inside the Mach cone is called the "conical flow" region. In this region the velocity components are constant along rays emanating from the apex and the flow is not influenced by the presence of the tip or trailing edge.

When the leading edge is supersonic, the region outside the Mach cone is called the "two-dimensional flow" region and the velocity distribution in this region is identical to that of an infinite wing having the same leading-edge sweep.

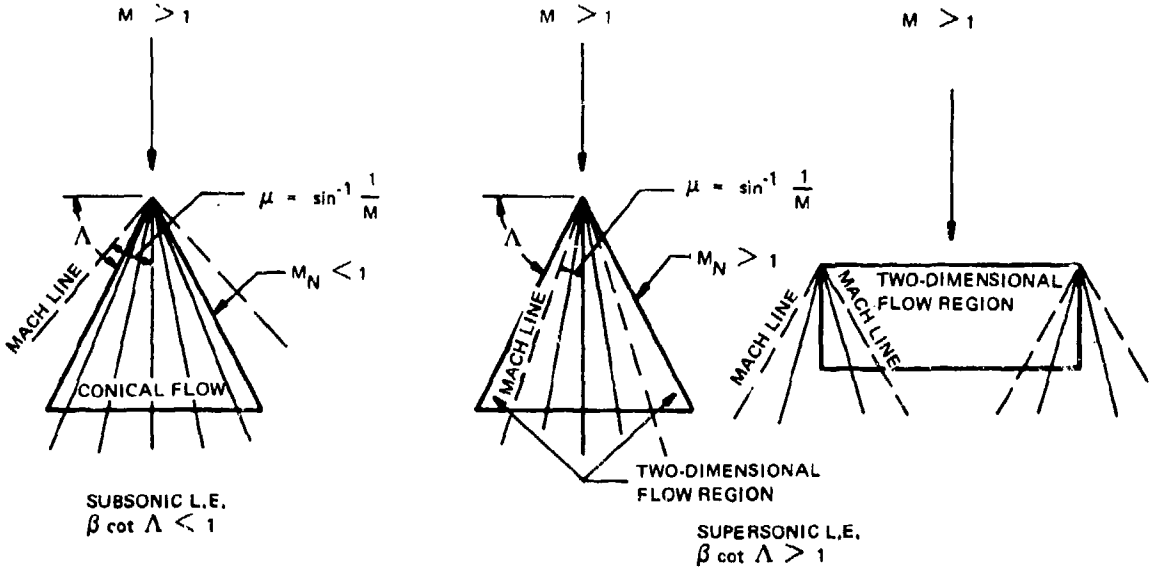

SKETCH (c)

It should be pointed out that due to the approximations of linear theory, kinks occur in the drag curves when lines across which the flow is turned become sonic, namely, leading and trailing edges and ridge lines of polygonal sections. These kinks do not occur in practice, since they correspond to flow conditions for which linear theory is no longer valid.

The Datcom method for estimating supersonic wave drag is taken from reference 3 and is based on the results that have been obtained from linear supersonic theory for the two-dimensional case.

The Datcom method is applicable to the following two classes of wing planforms:

Straight-Tapered Wings (conventional, trapezoidal planforms)

Non-Straight-Tapered Wings

- Double-delta wings
- Cranked wings
- Curved (Gothic and ogee) wings

DATCOM METHOD

The wing zero-lift drag coefficient at supersonic speeds, based on the reference area S_{ref}, is given by

$$C_{D_0} = C_{D_f} + C_{D_w} \qquad 4.1.5.1\text{-h}$$

where C_{D_f} and C_{D_w} are the supersonic skin-friction drag coefficient and the supersonic wave-drag coefficient, respectively, both based on a common reference area, and determined in the following manner:

Skin-Friction Drag Coefficient

The supersonic skin-friction drag coefficient is given by

$$C_{D_f} = C_f \frac{S_{wet}}{S_{ref}} \qquad 4.1.5.1\text{-i}$$

for a conventional, trapezoidal planform, and

$$C_{D_f} = \left(C_f\right)_i \frac{\left(S_{wet}\right)_i}{S_{ref}} + \left(C_f\right)_o \frac{\left(S_{wet}\right)_o}{S_{ref}} \qquad 4.1.5.1\text{-j}$$

for a non-straight-tapered planform.

where

C_f is the turbulent flat-plate skin-friction coefficient from figure 4.1.5.1-26 as a function of Mach number and the Reynolds number based on the reference length ℓ. The reference length ℓ is the mean aerodynamic chord of the wing (or wing panel in the case of composite wings). Figure 4.1.5.1-27 is used in conjunction with figure 4.1.5.1-26 to determine C_f. The procedure for determining C_f is fully explained in the Datcom method of paragraph A.

$\frac{S_{wet}}{S_{ref}}$ is the ratio of the wetted area of the wing (or wing panel in the case of composite wings) to the reference area.

The subscripts i and o refer to the inboard and outboard panels, respectively, of composite planforms.

Curved planforms are approximated by combinations of trapezoidal panels, in which case two such panels are usually sufficient to give a satisfactory result.

Non-straight-tapered wing geometric parameters are presented in Section 2.2.2.

Wave-Drag Coefficient

The form of the equation for the supersonic wave-drag coefficient is in accordance with the results that have been obtained from linear supersonic theory for the two-dimensional case. The effects of changes in wing planform and variable thickness ratio are accounted for by defining an effective thickness ratio and computing the wave-drag coefficient on a basic planform shape. A distinction is made between wings with sharp-nosed airfoil sections and wings with round-nosed airfoil sections.

Wings With Sharp-Nosed Airfoil Sections

For wings with sharp-nosed airfoil sections

$$C_{D_w} = \frac{K}{\beta}\left(\frac{t}{c}\right)^2_{eff} \frac{S_{bw}}{S_{ref}} \qquad 4.1.5.1\text{-k}$$

when the leading edge of the basic wing is supersonic $\left(\beta \cot \Lambda_{LE_{bw}} \geq 1\right)$, and

$$C_{D_w} = K \cot \Lambda_{LE_{bw}} \left(\frac{t}{c}\right)^2_{eff} \frac{S_{bw}}{S_{ref}} \qquad 4.1.5.1\text{-}\ell$$

when the leading edge of the basic wing is subsonic $\left(\beta \cot \Lambda_{LE_{bw}} < 1\right)$.

The subscript bw refers to the basic wing (straight leading and trailing edges), and

S_{bw} is the area of the basic wing – for conventional, trapezoidal planforms, the total wing area. The selection of the basic planform for non-straight-tapered wings is arbitrary, but should deviate as little as possible from the actual wing. Typical non-straight-tapered wings and the basic planforms used in wave-drag estimations are illustrated in sketch (d).

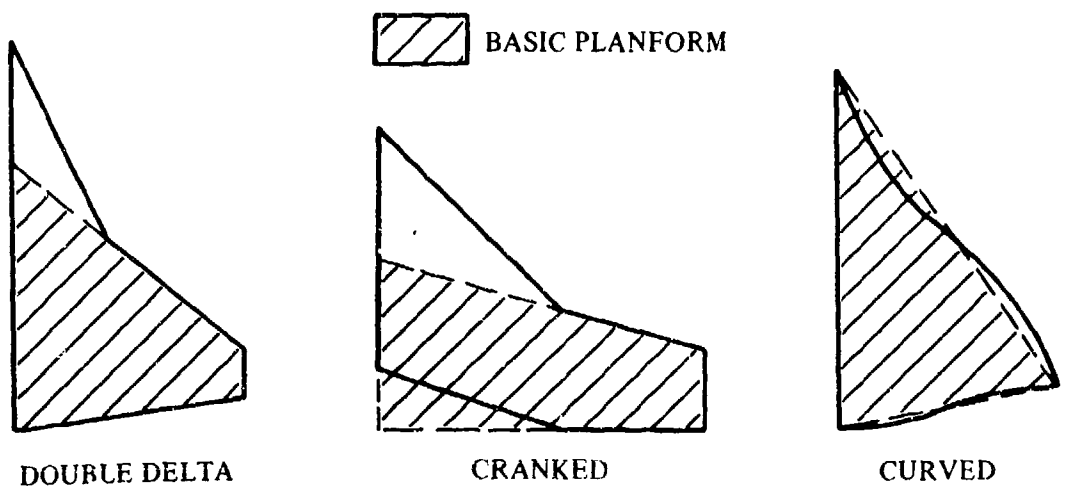

DEFINITION OF BASIC PLANFORMS OF NON-STRAIGHT-TAPERED WINGS FOR SUPERSONIC WAVE-DRAG ESTIMATION

SKETCH (d)

$\left(\frac{t}{c}\right)_{eff}$ is the effective thickness ratio (for a conventional, trapezoidal planform, use the average thickness ratio $(t/c)_{av}$). For a nonstraight-tapered planform the effective thickness ratio is defined in terms of the basic planform and is given by

$$\left(\frac{t}{c}\right)_{eff} = \left[\frac{\int_0^{b/2} \left(\frac{t}{c}\right)^2 c_{bw}\, dy}{\int_0^{b/2} c_{bw}\, dy}\right]^{1/2} \qquad 4.1.5.1\text{-}m$$

where c_{bw} is the chord of the basic wing. Note that in the numerator, the chord of the actual wing and the chord of the basic wing both appear. The denominator is one-half the planform area of the basic wing, so that

$$\left(\frac{t}{c}\right)_{eff} = \frac{\left[\int_0^{b/2} \left(\frac{t}{c}\right)^2 c_{bw}\, dy\right]^{1/2}}{\left(\frac{S_{bw}}{2}\right)^{1/2}} \qquad 4.1.5.1\text{-}m'$$

Numerical integration of the integrand in the numerator is illustrated in the sample problem.

$\Lambda_{LE_{bw}}$ is the leading-edge sweep of the basic wing.

K is a constant factor for a given sharp-nosed airfoil section. For basic wings with variable thickness ratios the K factor is based on the airfoil section at the average chord. K factors for sharp-nosed airfoils are presented in the following table:

SHARP-NOSED AIRFOILS

Basic Wing Airfoil Section	K	Se ı
Biconvex	$\frac{16}{3}$	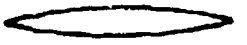
Double Wedge	$\frac{c/x_t}{1 - x_t/c}$	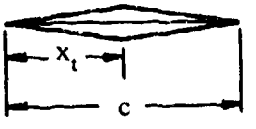
Hexagonal	$\frac{c\,(c - x_2)}{x_1\, x_3}$	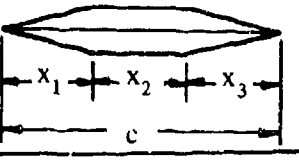

Wings With Round-Nosed Airfoil Sections

Wings with round-nosed airfoil sections exhibit a detached bow wave and a stagnation point, and the pressure-drag coefficient increases as a function of Mach number in a manner similar to the stagnation pressure. Consequently, a constant value of K cannot be used for basic wings with round-nosed airfoils.

The wave-drag coefficient of wings with round-nosed airfoil sections is approximated by adding the pressure drag of a blunt leading edge to the wave drag of the basic wing with an assumed sharp leading edge. By assuming a biconvex shape aft of the leading edge, the wave drag of a round-nosed leading-edge wing is given by

$$C_{D_w} = C_{D_{LE}} + \frac{16}{3\beta}\left(\frac{t}{c}\right)^2_{eff} \frac{S_{bw}}{S_{ref}} \qquad 4.1.5.1\text{-n}$$

when the leading edge of the basic wing is supersonic $\left(\beta \cot \Lambda_{LE_{bw}} \geq 1\right)$, and

$$C_{D_w} = C_{D_{LE}} + \frac{16}{3} \cot \Lambda_{LE_{bw}} \left(\frac{t}{c}\right)^2_{eff} \frac{S_{bw}}{S_{ref}} \qquad 4.1.5.1\text{-o}$$

when the leading edge of the basic wing is subsonic $\left(\beta \cot \Lambda_{LE_{bw}} < 1\right)$.

The second terms on the right-hand side of equations 4.1.5.1-n and 4.1.5.1-o are the wave-drag coefficients of the basic wing with sharp-nosed, biconvex airfoils at the appropriate leading-edge condition, and

$C_{D_{LE}}$ is the pressure-drag coefficient on a swept, cylindrical leading edge obtained as a function of the Mach number and the leading-edge sweep of the basic wing from figure 4.1.5.1-30a or figure 4.1.5.1-30b. The term $\left(2r_{LE_{bw}} \; b_{bw}/\cos \Lambda_{LE_{bw}}\right)$ is the frontal area of the leading edge. For basic wings with variable thickness ratios the leading-edge radius $r_{LE_{bw}}$ is the radius of the section at the average chord.

The correlation of cylindrical leading-edge pressure-drag coefficients is derived in reference 19 and has been substantiated over the Mach number range from 0.5 to 8.0 and for sweep angles from 0 to 75^{o}.

Sample Problem

Given: The double-delta wing designated 6-67-67, of reference 25.

Actual Wing Characteristics:

$A = 2.42$ $\quad \lambda = 0.086$ $\quad \Lambda_{LE_i} = 70.67^{o}$ $\quad \Lambda_{LE_o} = 51.63^{o}$

$\Lambda_{TE_i} = -47.38^{o}$ $\quad \Lambda_{TE_o} = 26.62^{o}$ $\quad \frac{b}{2} = 12.0$ in. $\quad \eta_B = 0.40$

$S_W = S_{ref} = 238$ sq in. $\quad \frac{t}{c}$ varies, (see sketch (e))

Inboard- and Outboard-Panel Characteristics (skin-friction drag calculations):

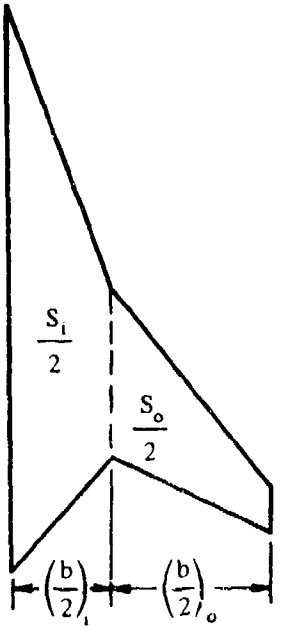

Inboard panel:

$c_{r_i} = 26.58$ in. $\quad \lambda_i = 0.293$ $\quad \overline{c_i} = 18.9$ in.

$S_i = 165$ sq in. $\quad \left(S_{wet}\right)_i = 330$ sq in.

Outboard panel:

$c_{r_o} = 7.77$ in. $\quad \lambda_o = 0.2995$ $\quad \overline{c_o} = 5.54$ in.

$S_o = 73$ sq in. $\quad \left(S_{wet}\right)_o = 146$ sq in.

Basic Wing Characteristics (wave-drag calculations):

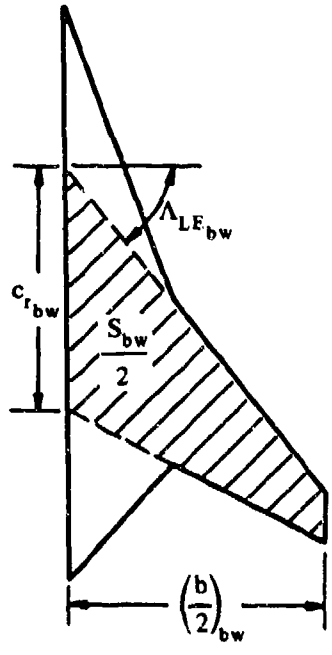

$c_{r_{bw}}$ = 11.43 in. $\quad \lambda_{bw}$ = 0.20

$\Lambda_{LE_{bw}}$ = 51.63° $\quad \Lambda_{TE_{bw}}$ = 26.62°

$\left(\frac{b}{2}\right)_{bw}$ = 12.0 in. $\quad S_{bw}$ = 146.6 sq in.

Airfoil Characteristics:

Hexagonal, sharp leading edge

$\frac{x_1}{c} = \frac{x_2}{c} = \frac{x_3}{c} = \frac{1}{3}$ $\quad (t/c)_{bw}$ = 0.06 (constant)

Additional Characteristics:

M = 2.01; β = 1.744 $\quad$ Smooth surface (assume k = 0)

R_ℓ = 3.35 x 10^6 per ft

Compute:

Skin-friction drag coefficient

Inboard panel

$$R_\ell = (3.35 \times 10^6)(\bar{c}_i) = (3.35 \times 10^6)\left(\frac{18.9}{12}\right) = 5.28 \times 10^6$$

$\frac{\ell}{k} = \infty$; read $\left(C_f\right)_i$ at calculated R_ℓ

$\left(C_f\right)_i$ = 0.00255 (figure 4.1.5.1-26)

Outboard panel

$$R_\ell = (3.35 \times 10^6)(\bar{c}_o) = (3.35 \times 10^6)\left(\frac{5.54}{12}\right) = 1.55 \times 10^6$$

$\frac{\ell}{k} = \infty$; read $\left(C_f\right)_o$ at calculated R_ℓ

$\left(C_f\right)_o$ = 0.00318 (figure 4.1.5.1-26)

$$C_{D_f} = \left(C_f\right)_i \frac{\left(S_{wet}\right)_i}{S_{ref}} + \left(C_f\right)_o \frac{\left(S_{wet}\right)_o}{S_{ref}} \quad \text{(equation 4.1.5.1-j)}$$

$$= (0.00255)\left(\frac{330}{238}\right) + (0.00318)\left(\frac{146}{238}\right)$$

$$= 0.00548 \text{ (based on } S_{ref})$$

Wave-drag coefficient

$$K = \frac{c\,(c - x_2)}{x_1\, x_3} = \frac{1\left(1 - \frac{1}{3}\right)}{\left(\frac{1}{3}\right)^2} = 6.0$$

Determine $(t/c)_{eff}$

The thickness distribution of the actual wing and the chord distribution of the basic wing are shown in sketch (e).

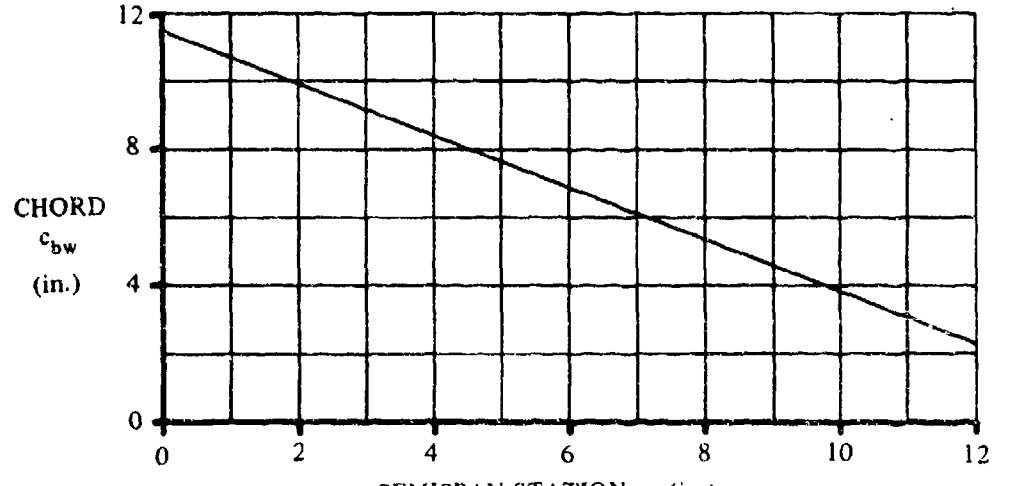

CHORD DISTRIBUTION (BASIC WING)

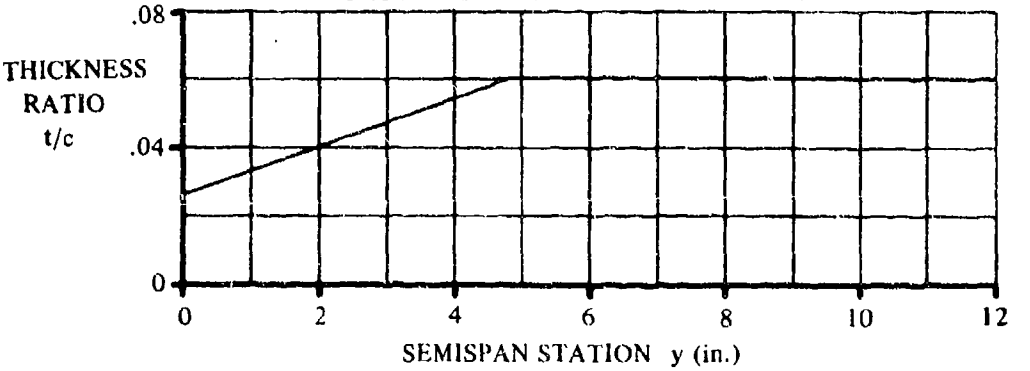

THICKNESS DISTRIBUTION (ACTUAL PLANFORM)

SKETCH (e)

Sketch (f) shows $\left[(t/c)^2\, c_{bw}\right]$ versus spanwise position.

Graphical integration of this curve gives $\int_0^{b/2} \left(\frac{t}{c}\right)^2 c_{bw}\, dy = 0.220$ sq in.

$$\left(\frac{t}{c}\right)^2_{eff} = \frac{\int_0^{b/2} \left(\frac{t}{c}\right)^2 c_{bw}\, dy}{\frac{1}{2} S_{bw}} \qquad \text{(equation 4.1.5.1-m')}$$

$$= \frac{0.220}{\frac{1}{2}(146.6)} = 0.0030$$

$$\left(\frac{t}{c}\right)_{eff} = 0.0548$$

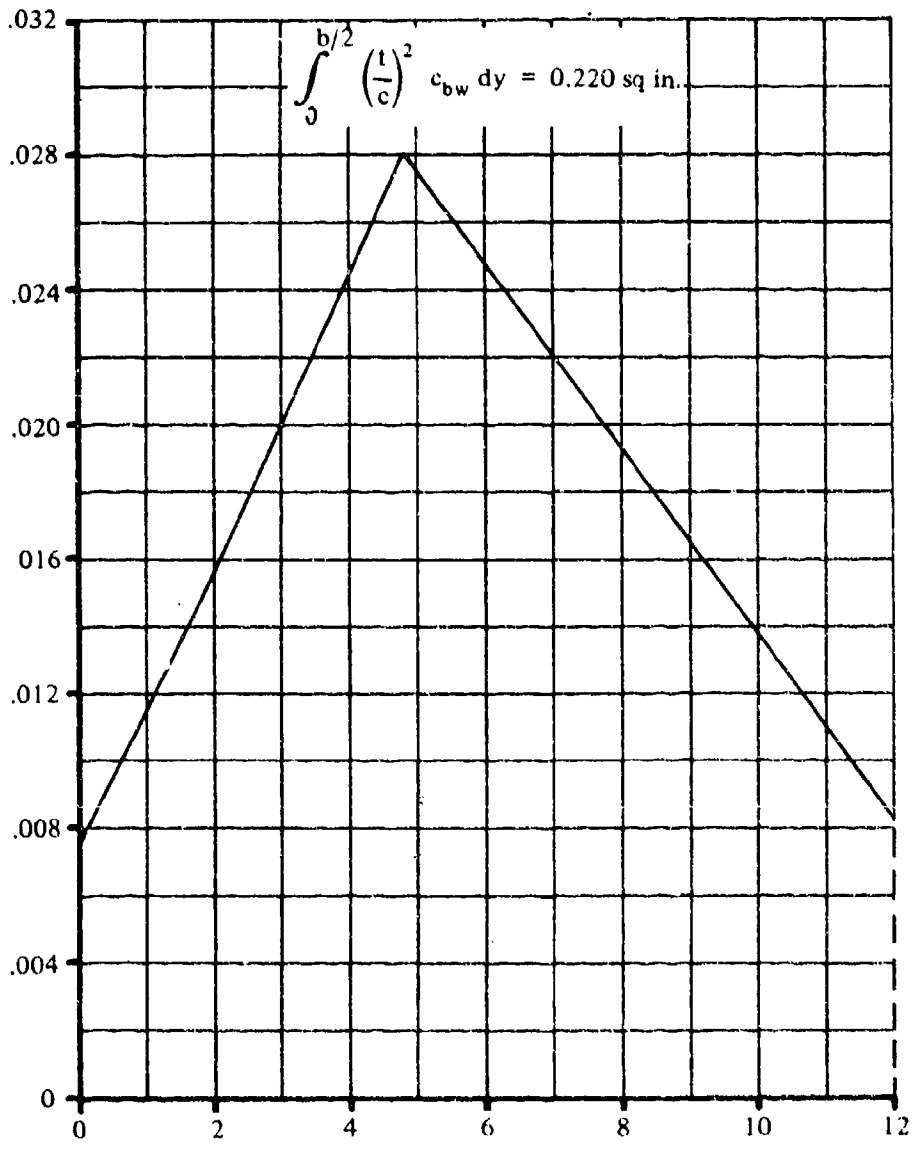

SKETCH (f)

$$\beta \cot \Lambda_{LE_{bw}} = (1.744)(\cot 51.63^{\circ}) = 1.381 \text{ (supersonic leading edge)}$$

$$C_{D_w} = \frac{K}{\beta}\left(\frac{t}{c}\right)^2_{eff}\frac{S_{bw}}{S_{ref}} \quad \text{(equation 4.1.5.1-k)}$$

$$= \left(\frac{6.0}{1.744}\right)(0.0548)^2\left(\frac{146.6}{238}\right)$$

$$= 0.00636 \quad \text{(based on } S_{ref})$$

Solution:

$$C_{D_0} = C_{D_f} + C_{D_w} \quad \text{(equation 4.1.5.1-h)}$$

$$= (0.00548) + (0.00636)$$

$$= 0.01184 \quad \text{(based on } S_{ref})$$

D. HYPERSONIC

The characteristics of hypersonic flow differ from those of supersonic flow in that

1. The shock waves in hypersonic flow lie close to the body causing a strong boundary-layer--shock-wave interaction which exerts an important influence on the flow field. The boundary layer in hypersonic flow may be 10 to 100 times thicker than at low speeds; consequently, a change in the effective body shape results,which in turn brings about a change in the shape of the nose shock wave.

2. High-temperature gas effects become evident at hypersonic speeds.

3. The flow becomes essentially nonlinear in nature.

4. Hypersonic similarity exists. It has been shown that at hypersonic Mach numbers the potential flow of similar airfoils is dynamically similar if the product $\beta(t/c)$ is a constant.

An approximate criterion for defining hypersonic flow is

$$\beta\frac{t}{c} \geq 0.5$$

Since, in hypersonic flow, β is very close to M, the relationship $M(t/c) = K_t$ is used as the hypersonic similarity parameter.

Because of the nonlinearity of hypersonic flow, approximate methods of estimating force characteristics are very desirable. Among the methods used, Newtonian and modified Newtonian theory have proved quite useful. Newtonian theory (reference 20) is based on the assumption that the shock coincides with the wing surfaces and that no friction exists between the wing and the shock layer. The fluid particles ahead of the wing are not disturbed until they encounter the wing surface, at which point the relative momentum normal to the surface is lost and the tangential flow has no further change in velocity. In this case, the air may be visualized as composed of discrete particles, which, after impact, travel parallel to the surface. When the particles reach the free-stream direction, they leave the surface, giving essentially zero pressure on the leeward side.

DATCOM METHOD

The drag at zero-lift is approximated by the drag of the forward-facing surface. Typical values of $C_{D_0}/2\tau^2$ for a wedge, as predicted by Newtonian theory, are presented in the following table from reference 20. (τ is one-half the thickness ratio of the forward-facing surface). It is to be noted that the drag can be reduced as much as one-half by optimization of the shape behind the initial wedge angle.

TYPICAL VALUES OF C_{D_0} FOR A WEDGE

Two-Dimensional
(Reference 20)

Shape	$\frac{1}{2\tau^2} C_{D_0}$	$\frac{C_{D_0}}{(C_{D_0})_{abs.\ opt.}}$
Wedge	1.000	2.000
0.864 Power	0.918	1.836
Proper Optimum	0.770	1.540
Absolute Optimum	0.500	1.000

Note that C_{D_0} is based on frontal area.

Detailed discussions of optimization methods are given in reference 20.

E. RAREFIED GAS

In the previous speed regimes it is assumed that the air behaves as a continuum. At very high altitudes, however, where very low densities are encountered, the actual molecular structure of the air becomes extremely important. Figure 4.1.5.1-32 presents a qualitative division of the various regimes of gas dynamics. It is to be noted that the region of rarefied gases is further divided into regions of varying amounts of rarefaction; i.e., "slip flow" or slightly rarefied, "transition" or moderately rarefied, and "free-molecule flow" or highly rarefied.

Slip Flow

The slip-flow region is of most interest to the aircraft and missile designer. In this region continuum theory becomes questionable, and satisfactory analytical results are uncommon, since the effects of slip flow are usually masked by large compressibility and viscous effects. Figure 4.1.5.1-33 (reference 21) presents test data points for skin friction in slip flow compared with incompressible theory for continuum flow (reference 22). It should be noted that in the subsonic case the test data are generally lower than the theoretical, while at supersonic speeds they are generally higher. This tends to confirm the theory that skin friction in the slip-flow regime is affected by two interrelated phenomena, the interaction of the thick boundary layer with the inviscid flow and the slip at the surface. The former is more important at the higher densities, gradually giving way to the latter for densities extending into the transition regime.

Transition Flow

Present knowledge about the transition regime is extremely limited and will not be covered here.

Free-Molecule Flow

In the free-molecule flow regime, the mean free path of the molecule is large compared to the characteristic dimension of an aerodynamic body in the flow, and the individual gas molecules striking the body do not interact with the surrounding molecules. For this reason the incident flow is assumed to be undisturbed by the presence of the body and no shock waves are expected to form. The boundary layer is very diffuse and has no effect on the flow incident on the body.

The problems associated with free-molecule flow are of particular interest to the satellite designer. In contrast to the other two regimes of rarefied-gas flow, the free-molecule regime can be treated analytically with less difficulty. The drag values of a flat plate with $\alpha = 0$ for diffuse and specular reflection are shown in figures 4.1.5.1-34a and 4.1.5.1-34b, respectively. Diffuse reflection is one in which the velocity of the reflected particles have a Maxwellian velocity distribution (see sketch (g)). Specular reflection is one in which the normal momentum is reversed at the surface and the tangential momemtum remains constant.

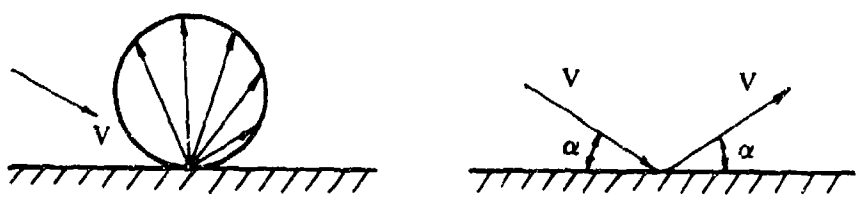

DIFFUSE REFLECTION SPECULAR REFLECTION

SKETCH (g)

REFERENCES

1. Hoerner, S.F.: Fluid-Dynamic Drag. Published by Author,1958. (U)
2. Blakeslee, D.J., Johnson, R.P., and Skevdahl, H.: A General Representation of the Subsonic Lift-Drag Relation for an Arbitrary Airplane Configuration. Rand Report RM 1593, 1955. (U)
3. Benepe, D.B., Kourl, B.G., Webb, J.B., et al: Aerodynamic Characteristics of Non-Straight-Taper Wings. AFF DL-TR-66-73, 1966. (U)
4. Marquardt, R.F.: A General Method for Predicting Subsonic Minimum Drag of an Arbitrary Aircraft Configuration. General Dynamics, F/W MR-A-1261, 1961. (C) Title Unclassified
5. von Karman, T.: The Similarity Laws of Transonic Flow. J. Math. and Physics, Vol. XXVI, No. 3, Oct 1947. (U)
6. Busemann, A.: Application of Transonic Similarity. NACA TN 2687, 1952. (U)
7. Spreiter, J.R., and Alksne, A.: Theoretical Prediction of Pressure Distributions on Nonlifting Airfoils at High Subsonic Speeds. NACA TR 1217, 1955. (U)
8. Flecks, D.: Vergleich der theoretischen und experimentellen Widerstandsbeiwerte im Schall-und Uberschallgebiet. Z. Flugwiss. 6, Heft 2, 1958. (U)
9. Bonney, E.A.: Aerodynamic Characteristics of Rectangular Wings at Supersonic Speeds. Jour. Aero. Sci., Vol. 14, No. 2, Feb. 1947. (U)
10. Puckett, A.E., and Stewart, H.J.: Aerodynamic Performance of Delta Wings at Supersonic Speeds. Jour. Aero. Sci., Vol. 14, No. 10, Oct. 1947. (U)

11. Beane, B.: The Characteristics of Supersonic Wings Having Biconvex Sections. Jour. Aero. Sci., Vol. 18, No. 1, Jan. 1951. (U)

12. Puckett, A.E.: Supersonic Wave Drag of Thin Airfoils. Jour. Aero. Sci., Vol. 13, No. 9, Sept. 1946. (U)

13. Margolis, K.: Supersonic Wave Drag of Sweptback Tapered Wings at Zero Lift. NACA TN 1448, 1947. (U)

14. Margolis, K.: Supersonic Wave Drag of Nonlifting Sweptback Tapered Wings With Mach Lines Behind the Line of Maximum Thickness. NACA TN 1672, 1948. (U)

15. Jones, R.T.: Thin Oblique Airfoils at Supersonic Speed. NACA TN 1107, 1946. (U)

16. Jones, R.T.: Properties of Low-Aspect-Ratio Pointed Wings at Speeds Below and Above the Speed of Sound. NACA TN 1032, 1946. (U)

17. Jones, R.T.: Wing Planforms for High Speed Flight. NACA TR 863, 1946. (U)

18. Bishop, R.A., and Cane, E.G.: Charts of the Theoretical Wave Drag of Wings at Zero-Lift. RAE TN 2421, 1956. (U)

19. Crosthwait, E.L.: Drag of Two-Dimensional Cylindrical Leading Edges. General Dynamics, F/W Rpt. AIM No. 50, 1966. (U)

20. Hayes, W.D., and Probstein, R.F.: Hypersonic Flow Theory. Academic Press, New York, 1959. (U)

21. Emmons, H.W., ed.: Fundamentals of Gas Dynamics. Princeton University Press, Princeton, New Jersey, 1958. (U)

22. Jenour, Z.: Resistance of a Plate in Parallel Flow at Low Reynolds Number. NACA TM 1316, 1951. (U)

23. Henderson, W.P., and Hammond, A.D.: Low-Speed Investigation of High-Lift and Lateral Control Devices on a Semispan Variable-Sweep Wing Having an Outboard Pivot Location. NASA TM X-542, 1961. (U)

24. Nelson, W.H., Allen, E.C., and Krumm, W.J.: The Transonic Characteristics of 36 Symmetrical Wings of Varying Taper, Aspect Ratio, and Thickness as Determined by the Transonic-Bump Technique. NACA RM A53I29, 1953. (U)

25. Cooper, M., and Sevier, J.R., Jr.: Effects of a Series of Inboard Plan-Form Modifications on the Longitudinal Characteristics of Two 47° Sweptback Wings of Aspect Ratio 3.5, Taper Ratio 0.2, and Different Thickness Distributions at Mach Numbers of 1.61 and 2.01. NACA RM L53E07a, 1953. (U)

26. Lin, C.C. (ed.): Turbulent Flows and Heat Transfer. Princeton University Press, Princeton, New Jersey, 1959. (U)

27. Skavdahl, H.: Pressure Drag at Zero Lift for Rounded Leading Edge Wings in the Presence of Bodies. Rand Report RM 1562, 1955 (C) Title Unclassified

28. Blakesley, D.J.: Pressure Drag at Zero Lift in Presence of Body for Wings With Sharp Leading Edges. Rand Report RM 1535, 1955. (C) Title Unclassified

TABLE 4.1.5.1-A
REPRESENTATIVE VALUES OF SURFACE-ROUGHNESS HEIGHT

Type of Surface	Equivalent Sand Roughness k (inches)
Aerodynamically smooth	0
Polished metal or wood	$0.02 - 0.08 \times 10^{-3}$
Natural sheet metal	0.16×10^{-3}
Smooth matte paint, carefully applied	0.25×10^{-3}
Standard camouflage paint, average application	0.40×10^{-3}
Camouflage paint, mass-production spray	$1.20 \cdot 10^{-3}$
Dip-galvanized metal surface	6×10^{-3}
Natural surface of cast iron	10×10^{-3}

TABLE 4.1.5.1-B
SUMMARY OF FINITE WING SOLUTIONS

PLANFORM	SECTION	WAVE-DRAG SOLUTION (ZERO LIFT)	
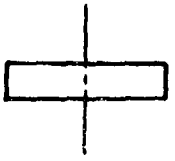		Bonney	Ref. 9
		Bonney	Ref. 9
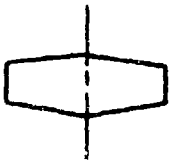		Puckett & Stewart Beane	Ref. 10 Ref. 11
		Beane	Ref. 11
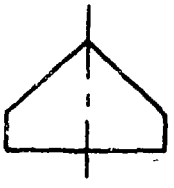		Puckett Margolis	Ref. 12 Ref. 13, 14
		Beane	Ref. 11
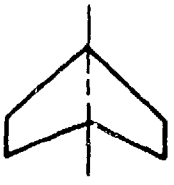		Puckett & Stewart Margolis Bishop & Cane	Ref. 10 Ref. 13, 14 Ref. 18
		Jones Beane Bishop & Cane	Ref. 15, 16, 17 Ref. 11 Ref. 18
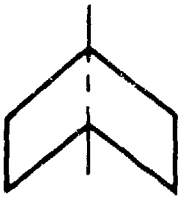	 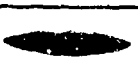 	Bishop & Cane	Ref. 18
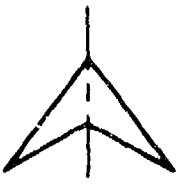	  	Bishop & Cane	Ref. 18

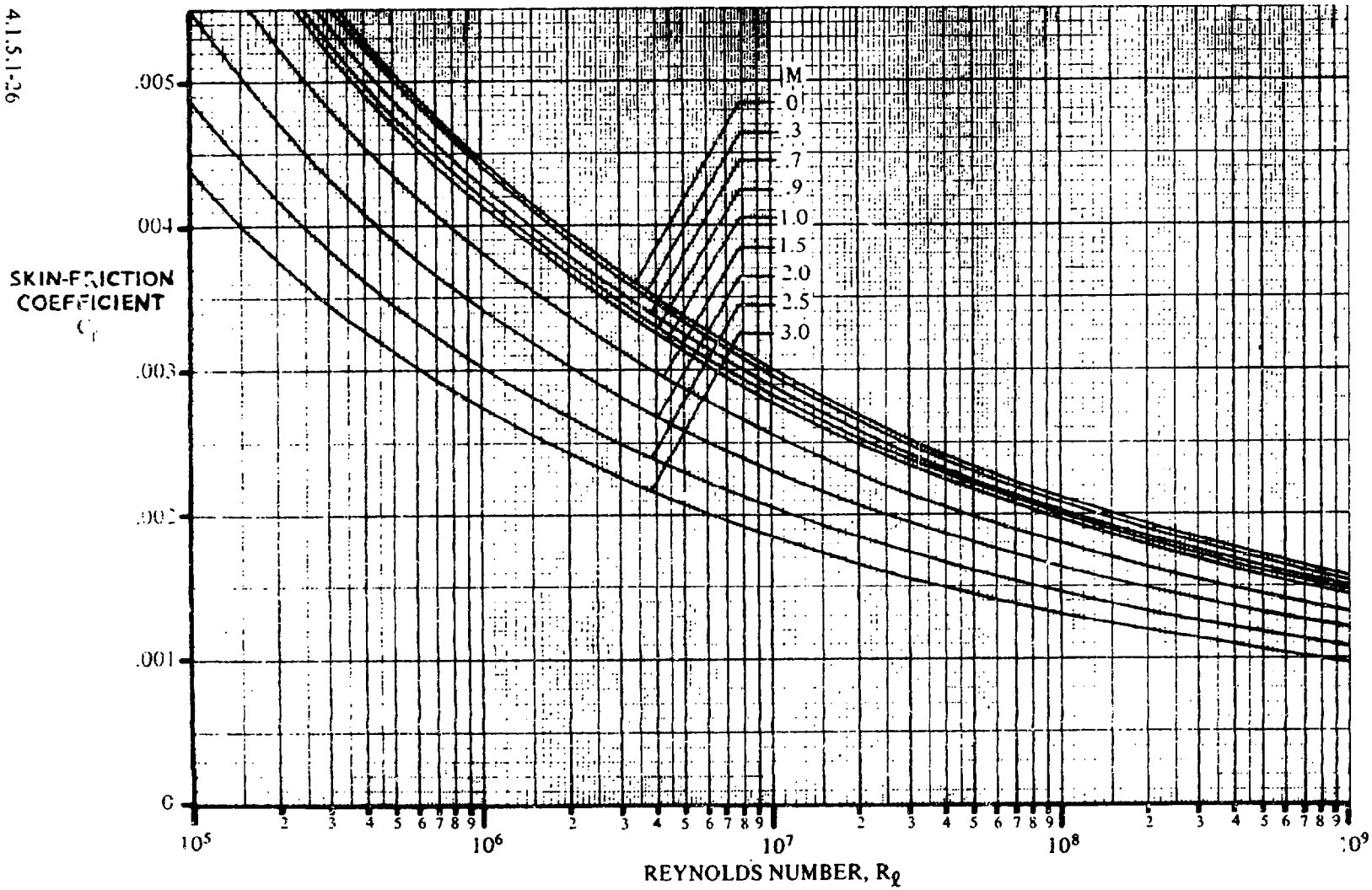

FIGURE 4.1.5.1-26 TURBULENT MEAN SKIN-FRICTION COEFFICIENT ON AN INSULATED FLAT PLATE

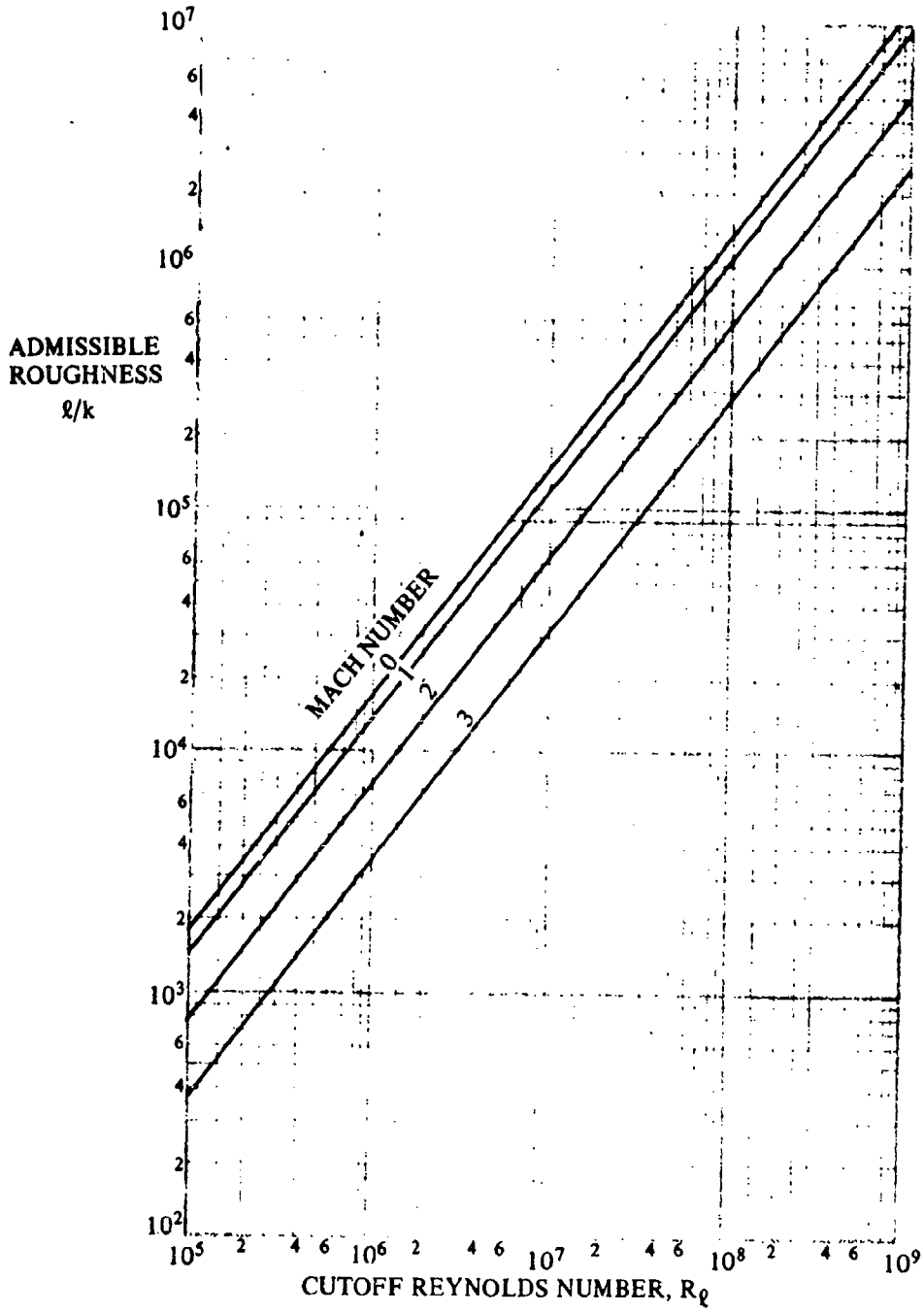

FIGURE 4.1.5.1-27 CUTOFF REYNOLDS NUMBER

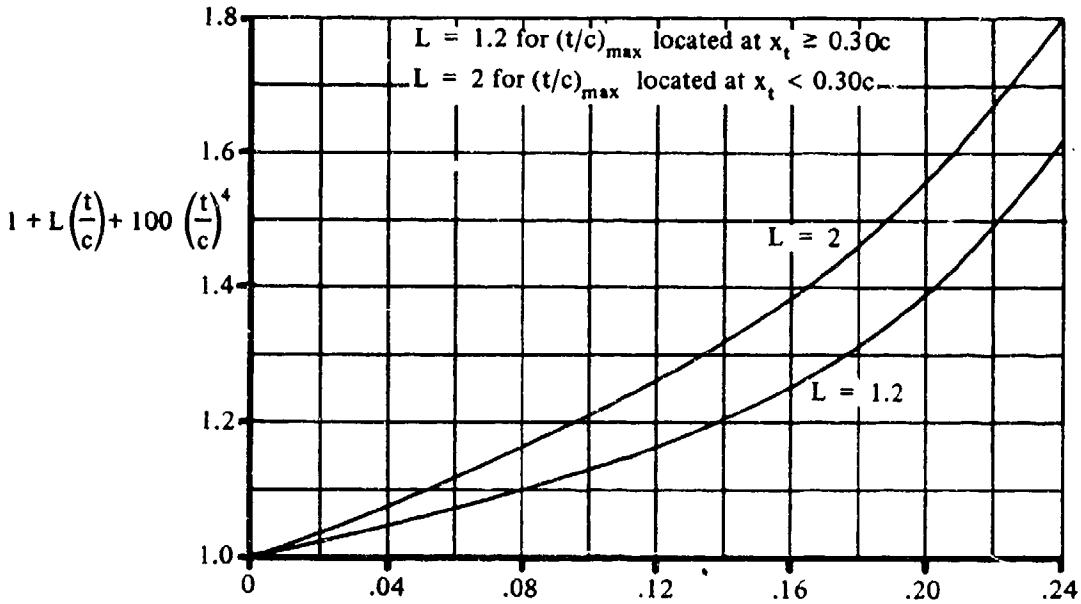

FIGURE 4.1.5.1-28a SUBSONIC WING MINIMUM-DRAG FACTOR

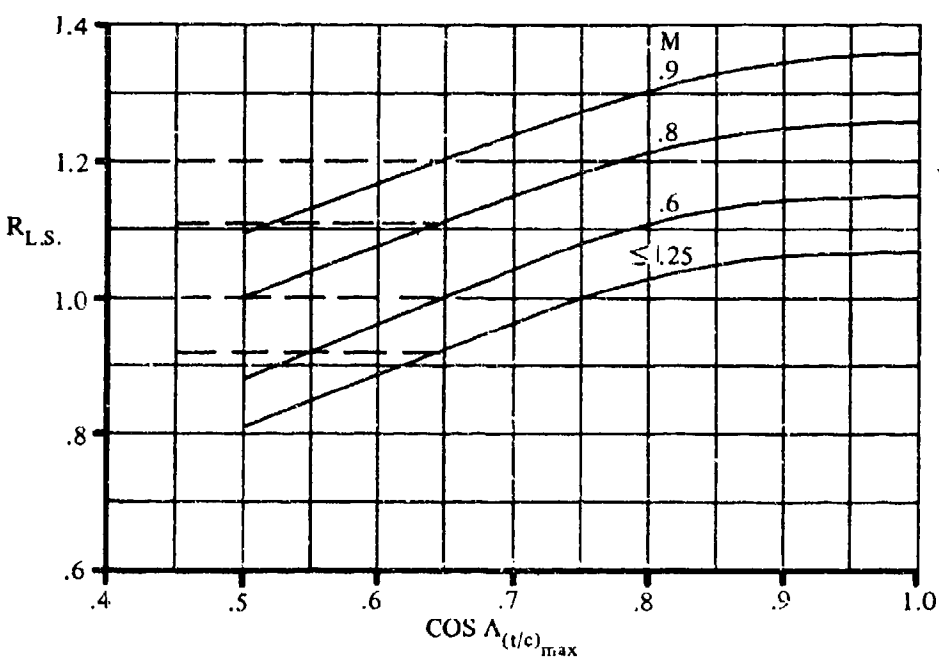

FIGURE 4.1.5.1-28b LIFTING-SURFACE CORRELATION FACTOR FOR SUBSONIC MINIMUM DRAG

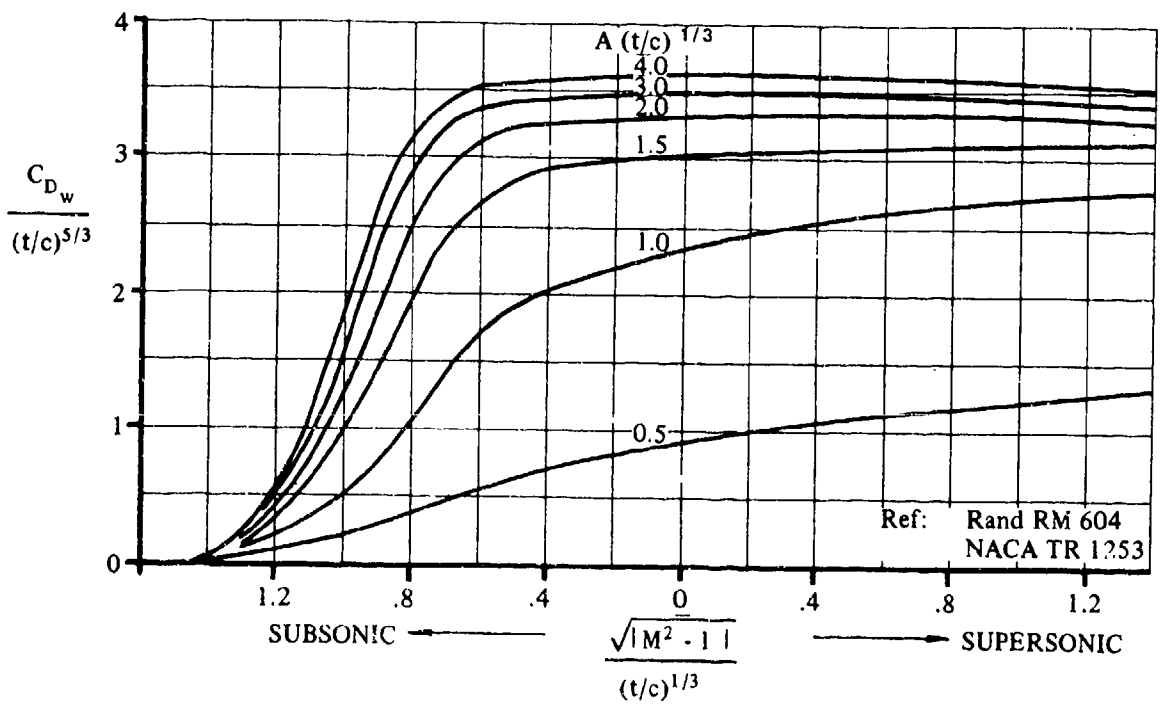

FIGURE 4.1.5.1-29 TRANSONIC ZERO-LIFT WING WAVE DRAG FOR UNSWEPT WINGS AND ROUND-NOSE AIRFOILS

$$C_{D_{LE}}\left[\frac{S_{ref}}{2r_{LE_{bw}}\left(\frac{b_{bw}}{\cos\Lambda_{LE_{bw}}}\right)}\right] = 1.28\,\frac{M^3\cos^6\Lambda_{LE_{bw}}}{1+M^3\cos^3\Lambda_{LE_{bw}}} \quad \text{(Ref. 19)}$$

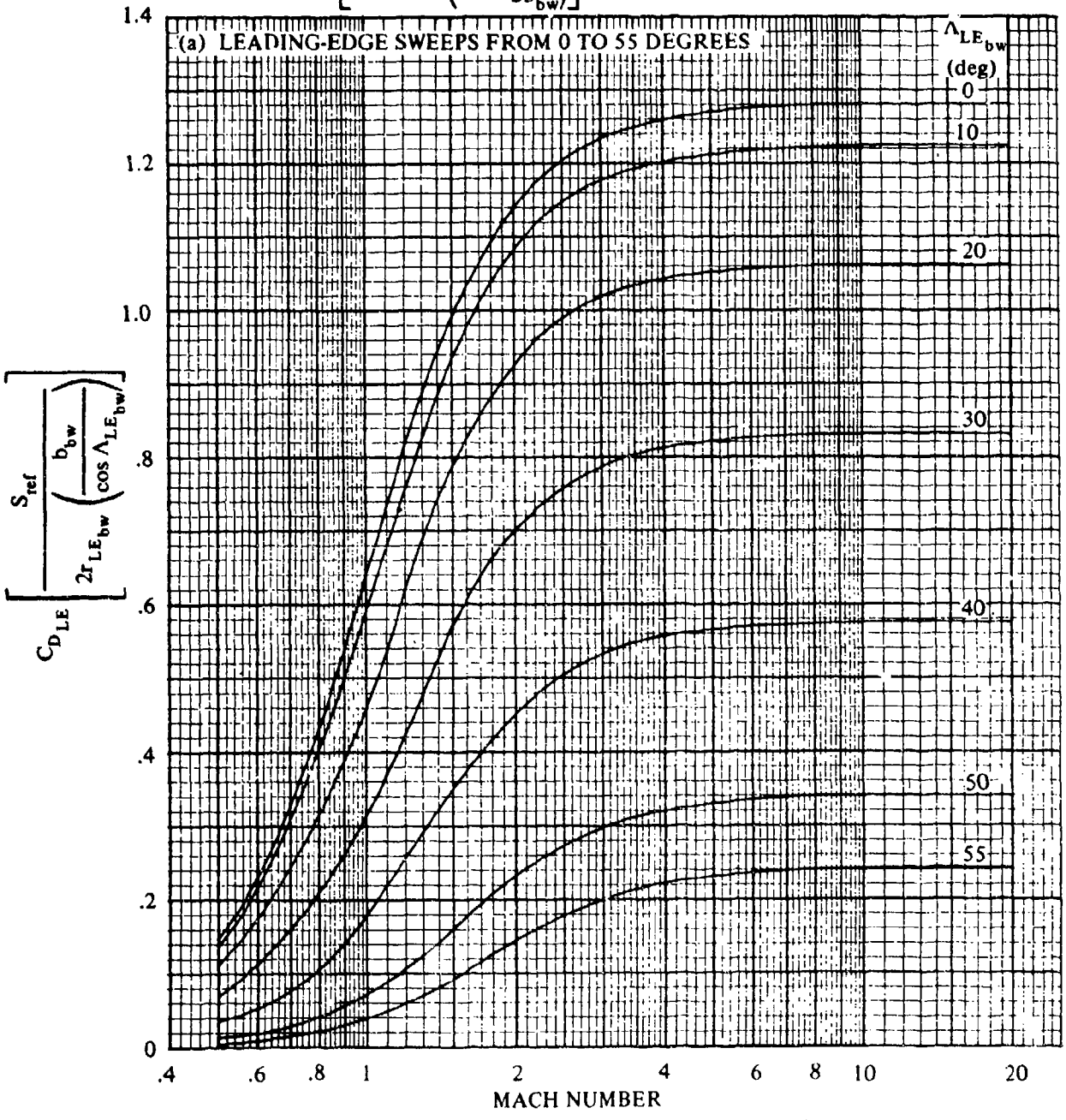

FIGURE 4.1.5.1-30 CORRELATION OF CYLINDRICAL LEADING-EDGE PRESSURE DRAG COEFFICIENTS

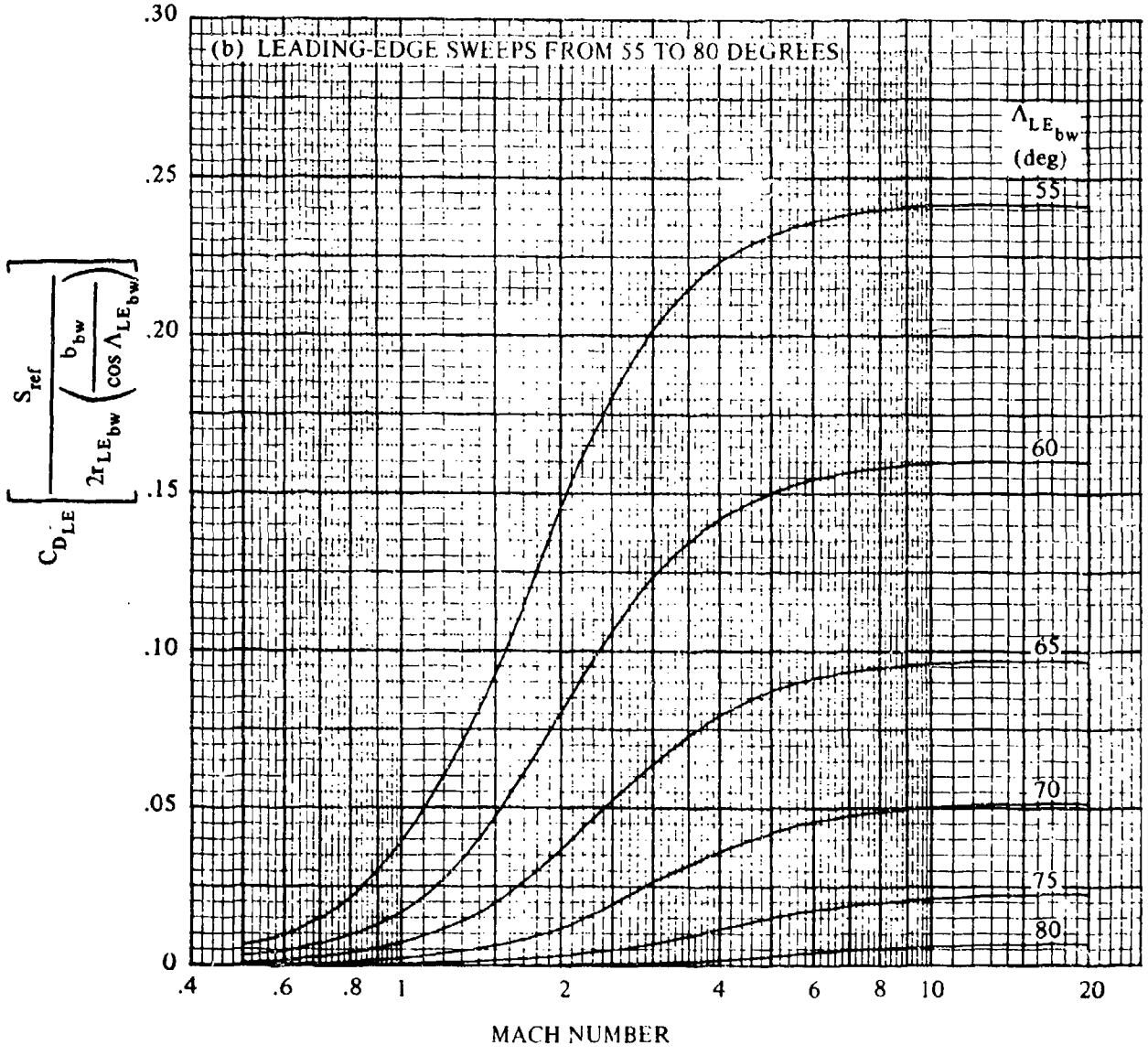

FIGURE 4.1.5.1-30 (CONTD)

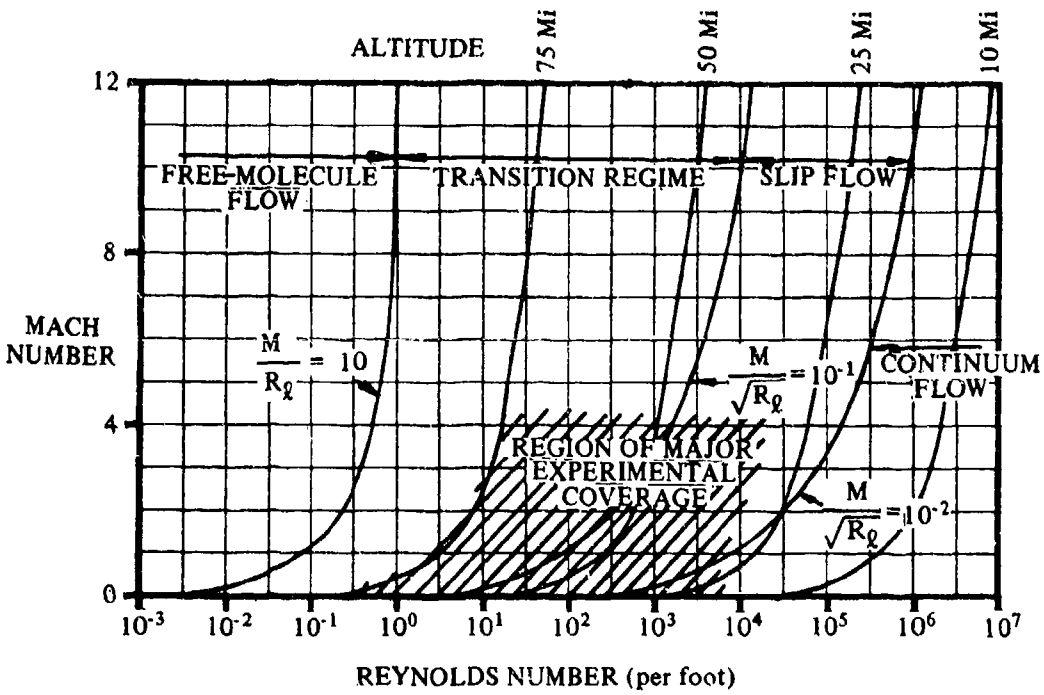

FIGURE 4.1.5.1-32 GENERALIZED RAREFIED GAS FLOW REGIMES

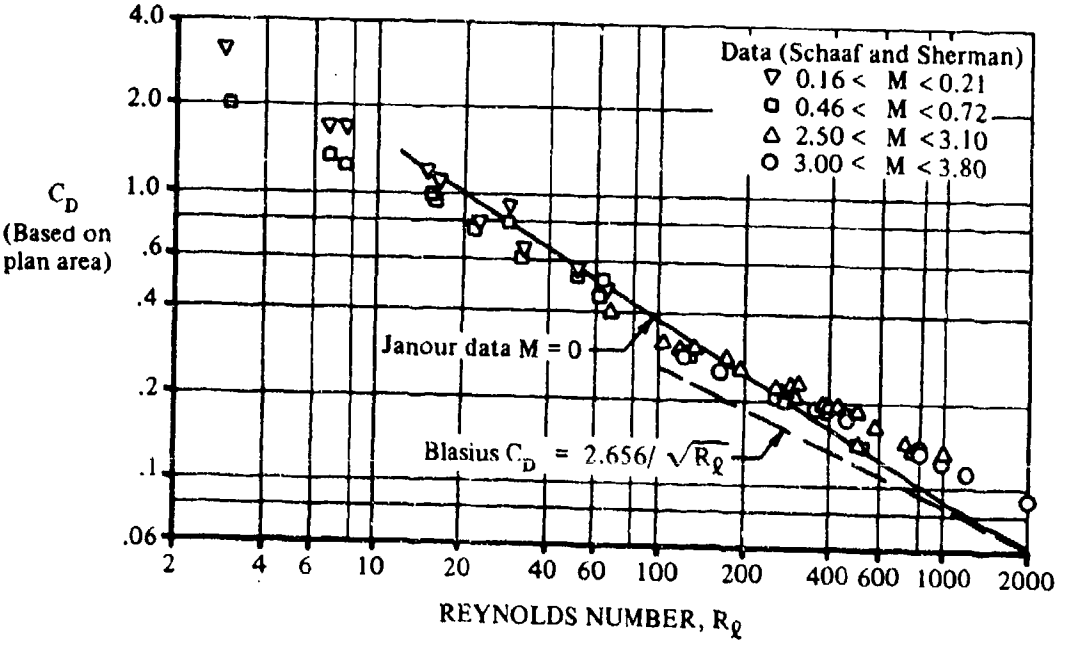

FIGURE 4.1.5.1-33 SKIN FRICTION IN SLIP FLOW

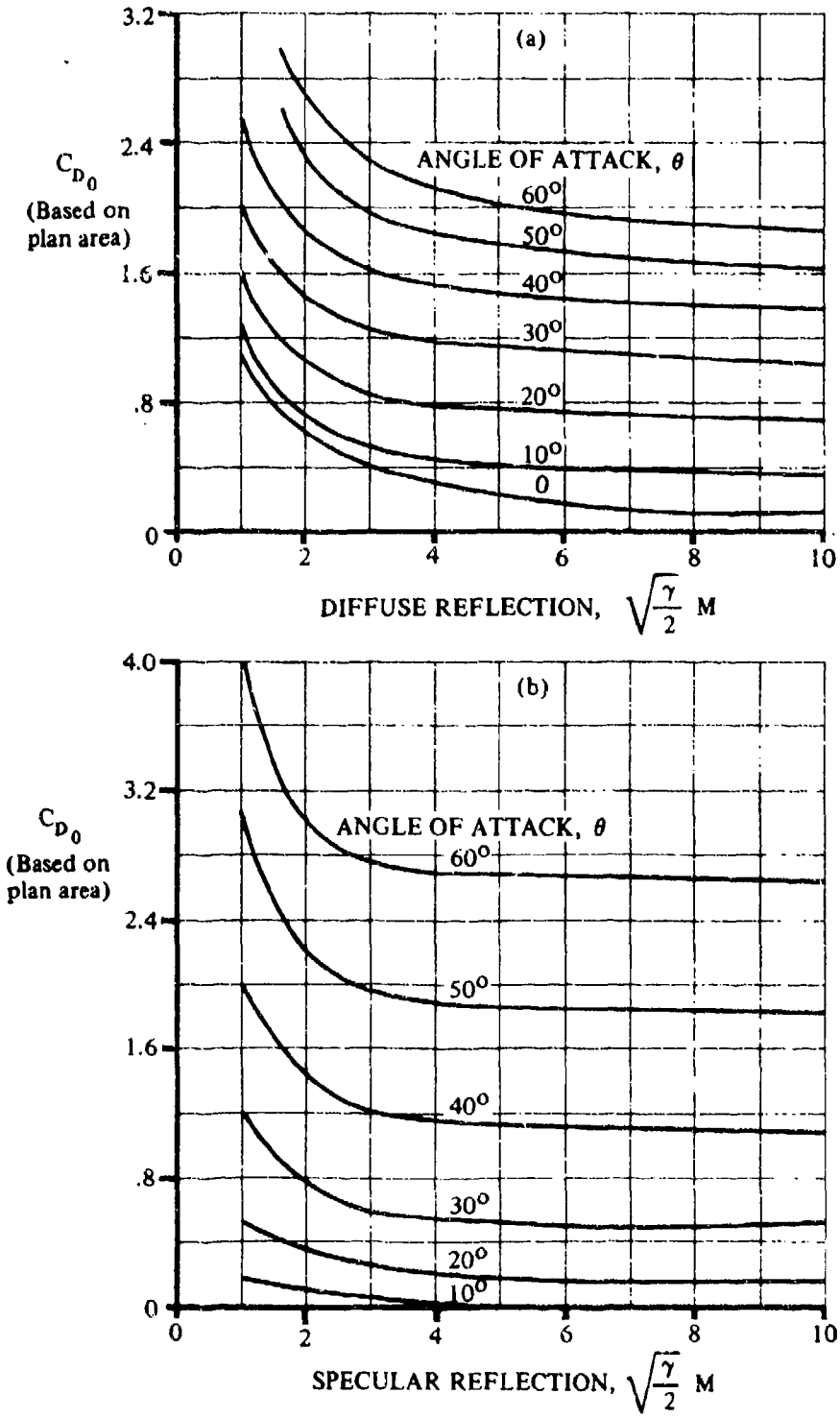

FIGURE 4.1.5.1-34 ZERO-LIFT FLAT-PLATE DRAG FOR FREE-MOLECULE FLOW

4.1.5.2 WING DRAG AT ANGLE OF ATTACK

The drag of a wing at angle of attack can be expressed in the form

$$C_D = C_{D_0} + C_{D_L}$$

where C_{D_0} is the zero-lift drag and the term C_{D_L} represents the drag due to lift. The zero-lift drag of a wing may be obtained by using the methods of Section 4.1.5.1. Methods are presented in this section for estimating the drag-due-to-lift term.

The drag due to lift of a wing increases approximately as the square of the lift coefficient or angle of attack and may be expressed in the form

$$C_{D_L} = \frac{K C_L^2}{\pi A} \qquad 4.1.5.2\text{-a}$$

where K is the drag-due-to-lift factor.

Equation 4.1.5.2-a can further be written as the sum of two terms, the well-known induced drag (or trailing-vortex drag) C_{D_i} and the viscous drag due to lift C_{D_v}, so that

$$C_{D_L} = C_{D_i} + C_{D_v} \qquad 4.1.5.2\text{-b}$$

These drag terms are discussed below.

Induced Drag

The induced drag depends on the wing spanwise loading distribution, since it results from the lift produced by the wing trailing-vortex system. The trailing-vortex system rotates the total wing-force vector rearward, giving the induced-drag component, which increases approximately as the square of the lift coefficient or angle of attack. Induced drag may be expressed as

$$C_{D_i} = \frac{C_L^2}{\pi A e^*} \qquad 4.1.5.2\text{-c}$$

where e^* is the induced span-efficiency factor (or wing span-efficiency factor with $C_{D_v} = 0$).

The theoretical minimum induced drag attainable is obtained from a wing with elliptic span loading, in which case an induced span-efficiency factor of 1.0 represents the theoretically ideal wing.

Viscous Drag Due to Lift

The viscous drag due to lift results from the change in boundary-layer development with lift over the wing. The upper-surface boundary layer increases in thickness as the angle of attack increases, which results in an increase in wing profile drag (skin-friction + pressure drag).

With the induced drag expressed by equation 4.1.5.2-c, the total drag due to lift is given by

$$C_{D_L} = \frac{C_L^2}{\pi A e^*} + C_{D_v} \qquad 4.1.5.2\text{-d}$$

Since the viscous drag due to lift also varies directly with C_L^2, the total drag due to lift is often expressed as

$$C_{D_L} = \frac{C_L^2}{\pi A e} \qquad 4.1.5.2\text{-e}$$

which is of the form of equation 4.1.5.2-a with the drag-due-to-lift factor K expressed as 1/e, where e is the span-efficiency factor, including the effect of viscosity. Therefore, the span-efficiency factor may be expressed in the familiar form

$$e = \frac{1}{\pi A \dfrac{\partial C_{D_L}}{\partial C_L^2}} \qquad 4.1.5.2\text{-f}$$

or, in the more basic form

$$e = \frac{1}{\pi A\left[\dfrac{1}{\pi A e^*} + \dfrac{\partial C_{D_v}}{\partial C_L^2}\right]} \qquad 4.1.5.2\text{-g}$$

The drag-due-to-lift factor is constant over a lift-coefficient range from zero to a certain value of C_L termed the "critical" lift coefficient C_{L_c}. Over this range, referred to as the parabolic-drag region, the variation of drag with C_L^2 is linear (see sketch (a)).

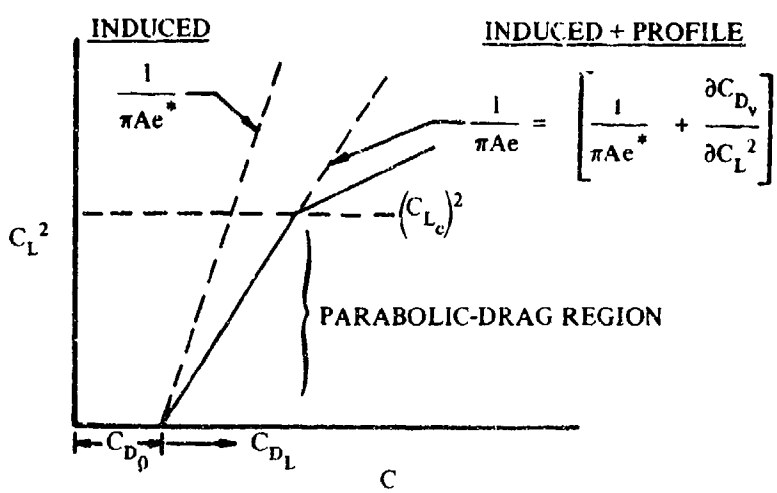

SKETCH (a)

Above C_{L_c} the polar breaks away from a simple parabolic representation because of separation effects, which cause the drag to increase significantly and the drag polar to deviate considerably from the parabolic-drag variation. High sweepback and sharp leading edges promote leading-edge separation at relatively low lift coefficients, resulting in low values of the "critical" lift coefficient.

Cambered and/or twisted wings have a somewhat more complicated drag characteristic. Neither the minimum profile drag nor the minimum induced drag necessarily occurs at zero lift. Sketch (b) illustrates these drag components for a typical cambered and twisted wing. Furthermore, the span-efficiency factor, at any given lift coefficient, varies within wide limits for these wings.

SKETCH (b)

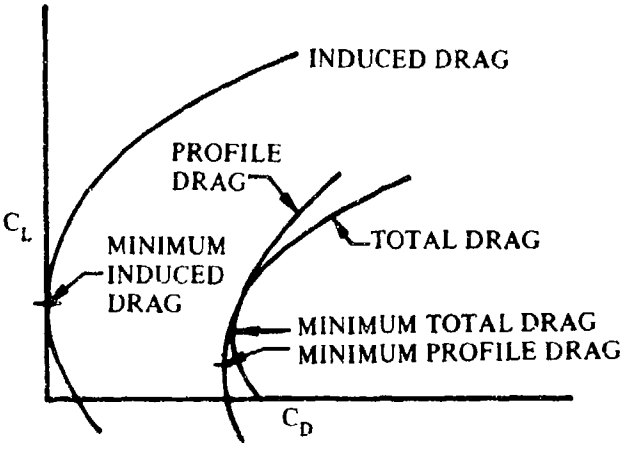

In supersonic flow the wing drag-due-to-lift breakdown is similar to that described above. In addition to the induced drag resulting from the trailing-vortex system (sweptback at the Mach angle), there exists shock-wave drag due to lift resulting from the viscous dissipation associated with the shock waves.

A. SUBSONIC

Many attempts have been made to develop empirical methods for predicting the subsonic span-efficiency factor over the parabolic-drag region. Three recent attempts are reported in references 1, 2, and 3. Frost and Rutherford (reference 1) have used a measure of leading-edge suction as a function of the leading-edge-radius Reynolds number to correlate e based on equation 4.1.5.2-e. This correlation has been further refined in reference 2 to account for planform geometry. In reference 3, Gardner and Weir take a more basic approach to the problem by correlating the viscous drag due to lift as a function of streamwise-thickness ratio and the loss in lift-curve slope due to viscosity. The empirical results of reference 3 are used as the basis of the method presented in reference 4 for estimating the viscous drag due to lift.

At subsonic speeds methods are presented for determining the drag due to lift of the following two classes of wing planforms:

Straight-Tapered Wings (conventional, trapezoidal wings)

Non-Straight-Tapered Wings

- Double-delta wings
- Cranked wings
- Curved (Gothic and ogee) wings

These general categories of non-straight-tapered wings are illustrated in sketch (a) of Section 4.1.3.2. Their wing-geometry parameters are presented in Section 2.2.2.

Straight-Tapered Wings

This method is based on the empirical correlation of the span-efficiency factor as a function of leading-edge suction as presented in reference 1. This correlation is further refined in reference 2 to account for planform geometry. The effect of linear wing twist on the subsonic inviscid induced drag of swept wings is accounted for by the methods of reference 5.

The subsonic drag due to lift of twisted, sweptback wings of straight-tapered planform for lift coefficients up to the "critical" lift coefficient is given by

$$C_{D_L} = \frac{C_L^2}{\pi A e} + C_L \theta \; c_{\ell_\alpha} v + \left(\theta \; c_{\ell_\alpha}\right)^2 \; w \qquad \text{4.1.5.2-h}$$

where

C_L is the wing lift coefficient.

c_{ℓ_α} is the airfoil section lift-curve slope (2π per radian is sufficiently accurate for this method.)

θ is the wing twist, positive for washin (a linear twist distribution is assumed).

v is the induced-drag factor due to linear twist obtained from figures 4.1.5.2-42a through 4.1.5.2-42i.

w is the zero-lift drag factor due to linear twist obtained from figures 4.1.5.2-48a through 4.1.5.2-48i.

e is the span-efficiency factor determined by

$$e = \frac{1.1\left(C_{L_\alpha}/A\right)}{R\left(C_{L_\alpha}/A\right) + (1 - R)\pi} \qquad \text{4.1.5.2-i}$$

where

C_{L_α} is the wing lift-curve slope obtained by the method presented for straight-tapered wings in paragraph A of Section 4.1.3.2.

R is the leading-edge-suction parameter defined as the ratio of leading-edge suction actually attained to that theoretically possible. This parameter is presented in figure 4.1.5.2-53 as a function of leading-edge-radius Reynolds number, Mach number, aspect ratio, and sweepback. The leading-edge-radius Reynolds number $R_{\ell_{LER}}$ is based on the leading-edge radius of the airfoil at the wing mean aerodynamic chord.

For values of the parameter $R_{\ell_{LER}} \cot \Lambda_{LE} \sqrt{1 - M^2 \cos^2 \Lambda_{LE}} > 1.3 \times 10^5$, R is read from figure 4.1.5.2-53b.

For wings with sharp leading edges $R_{\ell_{LER}} = 0$ and $R = 0$. For such configurations the method results in the approximation $C_{D_L}/C_L^2 = 1/(1.1\, C_{L_\alpha})$.

A comparison of test data with results calculated by this method is presented as table 4.1.5.2-A. Most of the configurations listed in the table are wing-body combinations with small values of the ratio of body diameter to wing span. For these configurations, the predictions were made using the total wing planform geometry and neglecting body effects. The ranges of planform and flow parameters of the test data are:

$$2 \leqslant A \leqslant 10.7$$
$$0 \leqslant \lambda \leqslant 0.713$$
$$19.1^\circ \leqslant \Lambda_{LE} \leqslant 63.4^\circ$$
$$0.72 \times 10^6 \leqslant R_{\ell_{MAC}} \leqslant 16.6 \times 10^6$$
$$0.13 \leqslant M \leqslant 0.81$$

Since the effect of camber is not accounted for in the method, no cambered wing data are included in table 4.1.5.2-A.

The limited amount of data available precludes substantiation of the effect of linear wing twist as given in reference 5. The design charts for the induced-drag factor due to linear twist and the zero-lift drag factor due to linear twist have resulted from the use of 59 Weissinger span stations to compute these quantities by means of an automatic digital computer program. In addition, the effect of compressibility on these parameters has been accounted for by applying the Prandtl-Glauert transformation.

Application of the method to an untwisted, sweptback wing is illustrated by sample problem 1 on page 4.1.5.2-9.

Non-Straight-Tapered Wings

Semiempirical methods, taken from reference 2, are presented for estimating the subsonic induced drag of non-straight-tapered wings. The methods presented for double-delta and curved planforms are applicable only to wings with sharp leading edges. In the development of these methods the effect of leading-edge suction was neglected, and the expression used as a basis for the correlation of induced drag was written solely in terms of the normal-force coefficient.

The method presented for cranked planforms is applicable only to wings with round leading edges. All the cranked wings analyzed in reference 2 had round leading edges; therefore, the development of the prediction technique was based on properly accounting for the leading-edge suction force. The resulting method is an extension of the straight-tapered-wing method presented above. It was assumed that given an accurate estimate of the leading-edge-suction parameter on both the inboard and outboard panels of a cranked wing, an effective leading-edge-suction parameter can be estimated by a span-weighted average.

The method presented for cranked wings is applicable in the higher lift-coefficient range where the drag polar deviates from a parabolic variation, as well as in the lower lift-coefficient range. The method presented for sharp-edged double-delta and curved planforms is valid only for the higher lift coefficients. In each case an empirical correlation has been derived that accounts for the effects of flow separation at the higher values of lift coefficient.

Double-Delta Wings

The subsonic induced drag of double-delta wings with sharp leading edges is given by

$$C_{D_L} = 0.95\, C_L \tan\alpha \qquad 4.1.5.2\text{-j}$$

where

C_L is the wing lift coefficient at angle of attack obtained by the method presented for double-delta wings in paragraph A of Section 4.1.3.3.

The constant in equation 4.1.5.2-j is the drag-due-to-lift factor. This factor has been determined during the course of the work reported in reference 2 by plotting test values of $C_{D_L}/(C_L \tan\alpha)$ versus α. This correlation showed that at $\alpha > 8^o$, the ratio of $C_{D_L}/(C_L \tan\alpha)$ approaches 0.95. However, below $\alpha = 8^o$ there was considerable scatter in the data. This is attributed to the inability to determine C_{D_L} accurately from the test data at the lower angles of attack. The method should not be expected to give satisfactory results below $\alpha = 8^o$.

A sample problem illustrating the use of this method is presented on page 4.1.5.2-10.

A comparison of test data with results calculated by this method is presented as table 4.1.5.2-B (taken from reference 2). The test results have been compiled entirely from reference 15 and were the only available low-speed data for sharp-edged double-delta wings. Although all the configurations listed in the table are wing-body combinations, all predictions were made by using the total wing planform geometry and neglecting body effects. Note that at $\alpha = 4^o$ the method does not adequately predict C_{D_L} for sharp-edged double-delta wings.

Since all the test data of table 4.1.5.2-B were included in the drag-due-to-lift-factor correlation, application of the method to configurations with geometric parameters falling outside those of table 4.1.5.2-B should be approached with caution. The ranges of planform parameters used in the correlation are:

$$1.34 \leq A \leq 1.87$$
$$72.6^o \leq \Lambda_{LE_i} \leq 77.4^o$$
$$\Lambda_{LE_o} = 59^o$$
$$0.332 \leq \eta_B \leq 0.628$$

Although the data in table 4.1.5.2-B are for $M = 0.13$, the method should be applicable at higher subsonic Mach numbers, provided an accurate estimation of the C_L versus α variation can be made.

The effects of wing twist and/or camber are not accounted for in the method.

For double-delta wings with round leading edges, it is suggested that the subsonic drag due to lift be approximated by using the method for cranked wings.

Cranked Wings

The subsonic drag due to lift of cranked wings with round leading edges is given by

$$C_{D_L} = \frac{C_L^2}{\pi Ae} + \Delta C_{D_L} \qquad 4.1.5.2\text{-k}$$

where

C_L is the wing lift coefficient.

ΔC_{D_L} is that portion of the drag due to lift resulting from a breakdown in the leading-edge suction at lift coefficients above the parabolic-drag-polar region. An empirical correlation of ΔC_{D_L} as a function of lift coefficient and aspect ratio is presented as figure 4.1.5.2-54.

e is the span-efficiency factor over the parabolic-drag region, given by

$$e = \frac{C_{L_\alpha}/A}{R'\left(C_{L_\alpha}/A\right) + (1 - R')\,\pi} \qquad 4.1.5.2\text{-}\ell$$

where

C_{L_α} is the wing lift-curve slope obtained by the method presented for cranked wings in paragraph A of Section 4.1.3.2.

R' is the effective leading-edge-suction parameter given by

$$R' = R_i(\eta_B) + R_o(1 - \eta_B) \qquad 4.1.5.2\text{-m}$$

where

R_i is the leading-edge suction parameter of the inboard panel, obtained from figure 4.1.5.2-53, but with the parameter $A\lambda/\cos\Lambda_{LE} = 0$.

R_o is the leading-edge-suction parameter of the outboard panel, obtained from figure 4.1.5.2-53 by assuming the outboard panels to be an isolated wing.

The leading-edge-radius Reynolds numbers required to read R_i and R_o from figure 4.1.5.2-53 are based on the leading-edge radius of the mean aerodynamic chord of the inboard and outboard panels, respectively. For values of the parameter $R_{\ell_{LER}} \cot\Lambda_{LE}\sqrt{1 - M^2\cos^2\Lambda_{LE}} > 1.3 \times 10^5$, R_i and/or R_o are read from figure 4.1.5.2-53b.

A sample problem illustrating the use of this method is presented on page 4.1.5.2-11.

A comparison of test data with results calculated by this method is presented as tables 4.1.5.2-C and 4.1.5.2-D (both taken from reference 2). Table 4.1.5.2-C compares the parabolic drag-due-to-lift factor $C_{D_L}/C_L^2 = 1/(\pi Ae)$ with test data. Table 4.1.5.2-D compares the drag due to lift over the nonparabolic region of the drag polar with test data. In table 4.1.5.2-D only the calculated results for references 16 and 18 are based on the predicted value of the parabolic drag-due-to-lift factor. The remainder of the data used the test value of C_{D_L}/C_L^2 combined with ΔC_{D_L} from figure 4.1.5.2-54.

Where test data were available for wing-body configurations, the portion of the inboard panel submerged in the body was accounted for in calculating the parabolic drag due to lift. This was accomplished by defining the effective leading-edge-suction parameter by

$$R' = R_i\left(\eta_B - \frac{d}{b}\right) + R_o(1 - \eta_B) \qquad 4.1.5.2\text{-m}'$$

and basing the leading-edge-radius Reynolds number used to obtain R_i on the leading-edge radius of the mean aerodynamic chord of the exposed inboard panel.

The effect of Reynolds number on the accuracy of predicting ΔC_{D_L} cannot be assessed quantitatively, since all the data used in the empirical correlation were for low Reynolds numbers except those from reference 22. Although a comparison of the data of reference 22 with the low Reynolds-number data shows no effect of Reynolds number, it must be expected that Reynolds number will affect ΔC_{D_L}.

The effect of wing twist is not accounted for in the method. The test data include cambered-wing data, and camber seems to have no effect on ΔC_{D_L}; however, there are not enough data to allow a quantitative evaluation of camber effects.

Finally, it should be pointed out that all the test data of table 4.1.5.2-D were used to derive the ΔC_{D_L} correlation. Therefore, no independent evaluation of the accuracy of the method in the nonparabolic region has been accomplished. In view of this, figure 4.1.5.2-54 should be used with caution outside the range of planform parameters used in the correlation (see figure 4.1.5.2-54).

Curved Wings

The correlation of $C_{D_L}/(C_L \tan \alpha)$, of reference 2, for determining the drag-due-to-lift factor of double-delta wings with sharp leading edges also included data on both Gothic and ogee wings at Mach numbers from 0.1 to 0.7. Therefore, the prediction method is essentially the same as that for double-delta wings.

As previously noted, the correlation for the drag-due-to-lift factor showed considerable scatter in the data below $\alpha = 8^\circ$. Although the data scatter for the curved planforms was not as widely dispersed as that for the double-delta planforms, the method should not be expected to give satisfactory results below $\alpha = 8^\circ$.

The subsonic drag due to lift of curved wings with sharp leading edges is given by equation 4.1.5.2-j; i.e.,

$$C_{D_L} = 0.95\, C_L \tan \alpha$$

where C_L is the wing lift coefficient at angle of attack obtained by the method presented for curved wings in paragraph A of Section 4.1.3.3.

A sample problem illustrating the use of this method is presented on page 4.1.5.2-13.

A comparison of test data with results calculated by this method is presented as table 4.1.5.2-E (taken from reference 2). The test data are for two thin Gothic and two thin ogee wings. It is noted that the calculated results below $\alpha = 8^\circ$ compare more favorably with the test data than those for double-delta wings at low angles of attack. However, since no consistent trend is indicated by the comparison at the lower angles of attack, there is no basis for lowering the angle-of-attack limit below 8°

Since all the data are for low Reynolds numbers, the effect of Reynolds number cannot be assessed. However, it is expected that Reynolds number will affect the results even at low lift coefficients, since leading-edge separation is almost immediate for the sharp-nosed airfoils.

Since all the test data of table 4.1.5.2-E were included in the drag-due-to-lift-factor correlation, application of the method to configurations with geometric parameters falling outside those of table 4.1.5.2-E should be approached with caution. The ranges of planform parameters used in the correlation are:

$$0.75 \leq A \leq 1.98$$

$$0.455 \leq p \leq 0.667$$

$$0.250 \leq \frac{b_W}{2\ell} \leq 0.450$$

The method is limited to thin wings ($t/c < 0.06$). Tests on one 12-percent thick Gothic wing showed less drag due to lift than did the tests on the thin wings. This is attributed to the development of significant suction forces on the forward-facing slopes of the thick wing. The correlation of $C_{D_L}/(C_L \tan\alpha)$ for the 12-percent-thick wing resulted in a constant drag-due-to-lift factor of 0.87.

The effects of wing twist and/or camber are not accounted for in the method.

Sample Problems

1. Conventional, Straight-Tapered Wing

Given: The sweptback wing of reference 14.

Wing Characteristics:

$A = 5.14$ $\lambda = 0.713$ $\Lambda_{LE} = 36.2^o$ $\Lambda_{c/2} = 33.7^o$ $\bar{c} = 1.166$ ft

NACA 65_1A012 airfoil LER = 0.00922c No twist

Additional Characteristics:

$M = 0.75; \beta = 0.661$ $R_{\ell_{MAC}} = 2 \times 10^6$ $R_{\ell_{LER}} = 18.4 \times 10^3$

$\kappa = 1.0$ (assumed)

Compute:

Leading-edge-suction parameter

$$R_{\ell_{LER}} \cot \Lambda_{LE} \sqrt{1 - M^2 \cos^2 \Lambda_{LE}} = (18.4 \times 10^3)(1.3663)\sqrt{1 - (0.75)^2(0.8070)^2} = 20.0 \times 10^3$$

$$\frac{A\lambda}{\cos \Lambda_{LE}} = \frac{(5.14)(0.713)}{(0.8070)} = 4.54$$

$R = 0.803$ (figure 4.1.5.2-53)

$$\frac{A}{\kappa}\sqrt{\beta^2 + \tan^2 \Lambda_{c/2}} = \frac{5.14}{1}\sqrt{(0.661)^2 + (0.6675)^2} = 4.83$$

$$\frac{C_{L_\alpha}}{A} = 0.870 \quad \text{(figure 4.1.3.2-49)}$$

Span-efficiency factor

$$e = \frac{1.1\left(C_{L_\alpha}/A\right)}{R\left(C_{L_\alpha}/A\right) + (1 - R)\,\pi} \qquad \text{(equation 4.1.5.2-i)}$$

$$= \frac{(1.1)\,(0.870)}{(0.803)\,(0.870) + (1 - 0.803)\,\pi} = 0.726$$

Solution:

$$C_{D_L} = \frac{C_L{}^2}{\pi Ae} \qquad \text{(equation 4.1.5.2-h)}$$

$$\frac{C_{D_L}}{C_L{}^2} = \frac{1}{\pi Ae} = \frac{1}{\pi\,(5.14)\,(0.726)} = 0.085$$

This compares with a test value of 0.090 from reference 14.

2. Double-Delta Wing

Given: A double-delta planform of reference 15.

Wing Characteristics:

$A_W = 1.73$ $A_i = 0.409$ $S_W = 560.0$ sq ft $S_i = 407.0$ sq ft

$S_o = 153.0$ sq ft $\Lambda_{LE_i} = 77.4^o$ $\Lambda_{LE_o} = 59^o$ $\Lambda_{TE} = -10^o$

$\eta_B = 0.414$

Additional Characteristics:

$M = 0.13$

Compute:

Variation of C_L with α (Section 4.1.3.3)

The predicted values of C_L versus α for this configuration are listed in table 4.1.3.3-B (This configuration is shown under "reference 31" of the table)

Solution:

$C_{D_L} = 0.95\ C_L \tan \alpha$ (equation 4.1.5.2-j)

α (deg)	C_L table 4.1.3.3-B	tan α	C_{D_L} eq. 4.1.5.2-j
4	0.143	0.0699	0.00950
8	0.302	0.1405	0.04031
12	0.491	0.2126	0.09917
16	0.685	0.2867	0.1866
20	0.974	0.3640	0.3368

The calculated results are compared with test values in table 4.1.5.2-B.

3. Cranked Wing

Given: The cranked wing-body configuration of reference 16. This is the configuration of the cranked-wing sample problem of paragraph A of Section 4.1.3.2.

Wing Characteristics:

$A_W = 4.0$ $A_o = 2.37$ $\Lambda_{LE_i} = 48.6^o$ $\Lambda_{LE_o} = 7.7^o$

$\lambda_o = 0.517$ $\eta_B = 0.60$ NACA 65A006 airfoil LER = 0.00229c

$\bar{c}_i = 0.933$ ft $\bar{c}_o = 0.525$ ft

Additional Characteristics:

$M = 0.80$ $R_\ell = 3.645 \times 10^6$ per ft $\frac{d}{b} = 0.139$

Compute:

Leading-edge-suction parameters, R_i and R_o

Inboard panel:

$$\left(R_{\ell_{LER}}\right)_i = (3.645 \times 10^6)(0.00229\,\bar{c}_i) = (3.645 \times 10^6)(0.00229)(0.933) = 7.79 \times 10^3$$

$$\left(R_{\ell_{LER}} \cot \Lambda_{LE} \sqrt{1 - M^2 \cos^2 \Lambda_{LE}}\right)_i = (7.79 \times 10^3)(0.8816)\sqrt{1 - (0.8)^2 (0.6613)^2}$$

$$= 5.83 \times 10^3$$

$R_i = 0.470$ (figure 4.1.5.2-53, with $\left(A\lambda/\cos \Lambda_{LE}\right)_i = 0$. See definition of R_i, page 4.1.5.2-7)

Outboard panel:

$$\left(R_{\ell_{LER}}\right)_o = (3.645 \times 10^6)(0.00229\,\bar{c}_o) = (3.645 \times 10^6)(0.00229)(0.525) = 4.38 \times 10^3$$

$$\left(R_{\ell_{LER}} \cot \Lambda_{LE} \sqrt{1 - M^2 \cos^2 \Lambda_{LE}}\right)_o = (4.38 \times 10^3)(7.396)\sqrt{1 - (0.8)^2 (0.9910)^2}$$

$$= 1.973 \times 10^4$$

$$\left(\frac{A\lambda}{\cos \Lambda_{LE}}\right)_o = \frac{(2.37)(0.517)}{0.9910} = 1.236$$

$R_o = 0.766$ (figure 4.1.5.2-53)

Effective leading-edge-suction factor

$$R' = R_i\left(\eta_B - \frac{d}{b}\right) + R_o\,(1 - \eta_B) \qquad \text{(equation 4.1.5.2-m')}$$

$$= (0.470)(0.60 - 0.139) + (0.766)(1 - 0.60)$$

$$= 0.523$$

C_{L_α}/A = 1.081 per rad (sample problem, paragraph A, Section 4.1.3.2)

Span-efficiency factor over parabolic-drag region

$$e = \frac{C_{L_\alpha}/A}{R'(C_{L_\alpha}/A) + (1 - R')\pi} \qquad \text{(equation 4.1.5.2-l)}$$

$$= \frac{1.081}{(0.523)(1.081) + (1 - 0.523)\pi}$$

$$= 0.524$$

$$\frac{C_{D_L}}{C_L^2} = \frac{1}{\pi Ae} = \frac{1}{\pi (4.0)(0.524)} = 0.152$$

Solution:

$$C_{D_L} = \frac{C_L^2}{\pi Ae} + \Delta C_{D_L} \qquad \text{(equation 4.1.5.2-k)}$$

$$= \frac{C_{D_L}}{C_L^2} C_L^2 + \Delta C_{D_L}$$

①	②	③	④	⑤	⑥
C_L	C_L/A ①/ 4	ΔC_{D_L} fig 4.1.5.2-54	$\frac{C_{D_L}}{C_L^2}$	$\frac{C_{D_L}}{C_L^2} C_L^2$ ④①^2	C_{D_L} eq 4.1.5.2-k ⑤ + ③
0	0	...	0.152	0	0
0.1	0.025	...		0.0015	0.0015
0.2	0.050	...		0.0061	0.0061
0.3	0.075	...		0.0137	0.0137
0.4	0.100	0.0080		0.0243	0.0323
0.5	0.125	0.0240		0.0380	0.0620
0.6	0.150	0.0510		0.0547	0.1057
0.7	0.175	0.0840		0.0745	0.1585
0.8	0.200	0.1245		0.0973	0.2218

The test values for this configuration are presented in tables 4.1.5.2-C and 4.1.5.2-D for the cranked wing mounted on a circular-ogive body. The calculated results presented in tables 4.1.5.2-C and 4.1.5.2-D take into account the portion of the inboard panel submerged in the body by applying the corrections noted on page 4.1.5.2-7. The leading-edge-radius Reynolds number used to obtain R_i is based on the leading-edge radius of the mean aerodynamic chord of the exposed inboard panel, and the effective leading-edge-suction parameter is determined by using equation 4.1.5.2-m'.

4. Curved Wing

Given: The ogee wing of reference 23. This is the same configuration as the curved-wing sample problem of paragraph A of Section 4.1.3.3.

Wing Characteristics:

$A = 1.20$ $b = 12.0$ in. $\ell = 20.0$ in.

Additional Characteristics:

$M = 0.4$

Compute:

Variation of C_L with α (Section 4.1.3.3)

The predicted values of C_L versus α are obtained from the curved-wing sample problem of paragraph A of Section 4.1.3.3.

Solution:

$C_{D_L} = 0.95\ C_L\ \tan\alpha$ (equation 4.1.5.2-j)

α (deg)	C_L Sec. 4.1.3.3	tan α	C_{D_L} eq. 4.1.5.2-j
4	0.136	0.0699	0.0090
8	0.288	0.1405	0.0384
12	0.465	0.2126	0.0939

The calculated results are compared with test values in table 4.1.5.2-E.

B. TRANSONIC

Test data on straight-tapered wings show that the variation of the drag-due-to-lift parameter C_{D_L}/C_L^2 with Mach number at transonic speeds is somewhat analogous to that of the lift-curve slope. That is, for thick and/or high-aspect-ratio wings this parameter experiences significant deviations with Mach number, while for thin and/or low-aspect-ratio wings this parameter varies uniformly with Mach number (see sketch (c)).

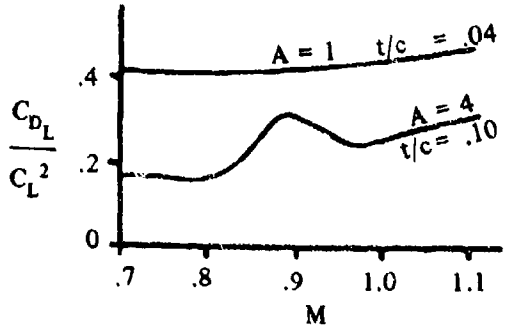

SKETCH (c)

Transonic data on non-straight-tapered wings are too few to allow quantitative analysis of the variation of drag due to lift with Mach number.

The only available approach to the estimation of transonic drag due to lift of conventional, trapezoidal wings appears to be through the use of transonic similarity parameters. This is a particularly useful approach where the quantity of data available for correlation is limited. The method presented, therefore, uses transonic similarity parameters. It should be pointed out, however, that the bulk of existing data at transonic speeds is derived from "bump tests," which are frequently questioned because of the spanwise Mach number gradients.

DATCOM METHOD

The transonic drag due to lift of conventional, trapezoidal planforms of symmetrical section may be approximated by using figures 4.1.5.2-55a through 4.1.5.2-55c for given values of the transonic similarity parameters, $A \tan \Lambda_{LE}$ and $\frac{M^2 - 1}{(t/c)^{2/3}}$

Sample Problem

Given: The following straight-tapered wing from reference 26.

$A = 4.0$ $\quad \lambda = 0$ $\quad \Lambda_{LE} = 45^o$ $\quad$ NACA 63A004 airfoil

Compute:

$(t/c)^{1/3} = 0.342$; $\quad (t/c)^{2/3} = 0.116$; $\quad A(t/c)^{1/3} = 1.368$

$A \tan \Lambda_{LE} = 4.0$

$\frac{M^2 - 1}{(t/c)^{2/3}}$ (see calculation table below)

$\left(\frac{t}{c}\right)^{-1/3}\left(\frac{C_{D_L}}{C_L^2}\right)$ (figures 4.1.5.2-55a and -55b extrapolated, see calculation table below)

Solution:

①	②	③	④
M	$\frac{M^2 - 1}{(t/c)^{2/3}}$	$\left(\frac{t}{c}\right)^{-1/3}\frac{C_{D_L}}{C_L^2}$ fig. 4.1.5.2-55	C_{D_L}/C_L^2 ③ $(t/c)^{1/3}$
0.8	-3.10	0.59	0.202
0.9	-1.64	0.57	0.195
0.94	-1.00	0.57	0.195
0.98	-0.34	0.58	0.198
1.00	0	0.60	0.205
1.05	0.88	0.60	0.205
1.10	1.81	0.59	0.202

The calculated values of C_{D_L}/C_L^2 are compared with test values from reference 26 in sketch (d).

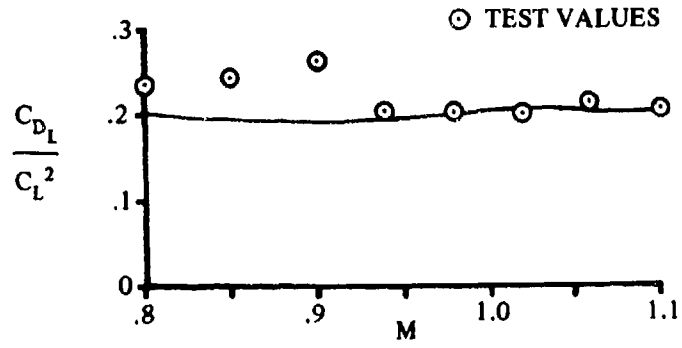

SKETCH (d)

C. SUPERSONIC

At supersonic speeds, wings are generally classified according to whether the Mach number component perpendicular to the leading edge is subsonic or supersonic. A typical presentation of supersonic drag due to lift is shown in sketch (e). For supersonic-leading-edge wings, certain regions of the wing will be in two-dimensional flow where the spanwise pressure loading on the surface is constant.

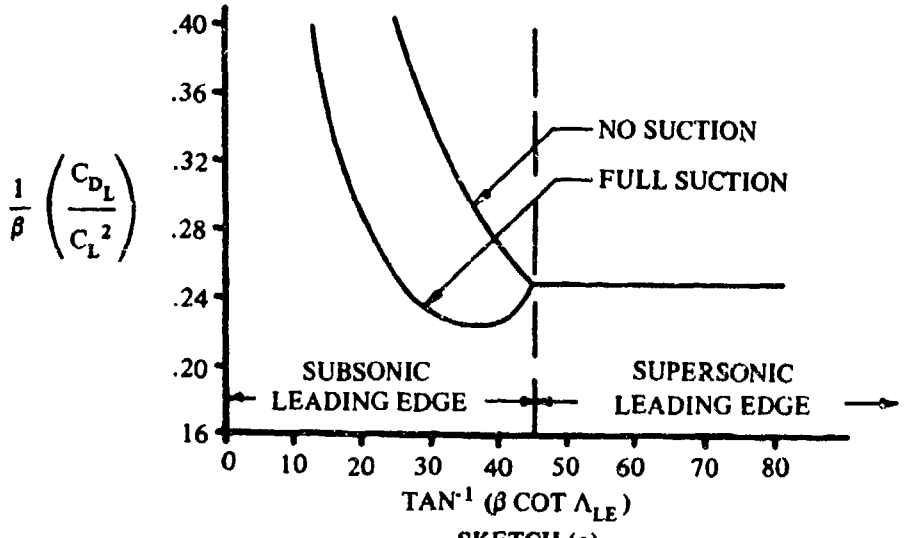

SKETCH (e)

Other portions of the wing are influenced by tip effects and by the wing apex. Three cases are shown in sketch (f). The two-dimensional region has wave drag due to lift, which can be calculated by simple linear theory or by shock-expansion theory. But because the span loading is constant, this region does not produce any vortex drag. The three-dimensional region has shock-wave drag due to lift, but not as much as that of the two-dimensional region. The three-dimensional region also has a drag-due-to-lift contribution associated with the vortex that is shed because of the varying span loading. This phenomenon is exactly like its subsonic counterpart except that the flow field is swept back at the Mach angle.

SKETCH (f)

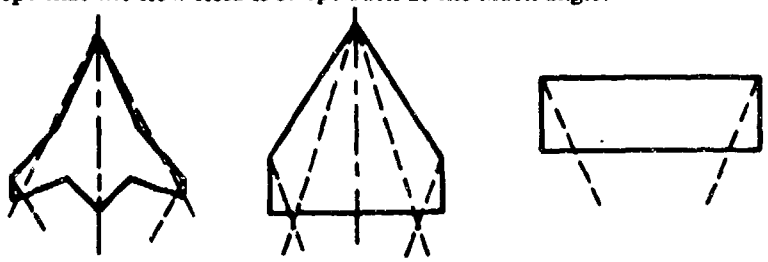

In general, the drag due to lift of a wing quickly approaches the two-dimensional value as the leading edge progresses from the sonic into the supersonic region. The two-dimensional value from linear theory is

$$C_{D_L} = \frac{\beta C_L^2}{4}$$

For subsonic leading edges, no part of the wing is in two-dimensional flow and the span pressure loading, in general, varies continuously across the span. Wave drag due to lift and vortex drag exist as for the supersonic leading-edge case. However, an additional phenomenon occurs. The subsonic Mach number component perpendicular to the leading edge allows leading-edge-suction pressures to develop similar to those that occur on wings in subsonic flow. These suction pressures can cause significant reductions in drag, which, to date, cannot be predicted for a given wing. The amount of suction depends upon the leading-edge shape and the wing-camber shape and distribution. Several authors have, however, calculated the maximum amount of suction attainable for several types of wings (e.g., references 6 and 7). Camber can also produce a significant drag-due-to-lift reduction that is not affected by leading-edge suction. Sketch (e) above shows typical drag reduction due to suction for a cambered delta wing.

Test results for subsonic leading-edge wings generally fall between the limits of wings with no leading-edge suction and wings with full leading-edge suction. For a given test on a cambered wing, however, it is impossible to determine what fraction of the drag reduction is attributable to camber, since camber and leading-edge-suction effects are very similar in nature.

For conditions where the leading edge is slightly supersonic, the theoretical results for cambered wings are less than the two-dimensional value because the forward inclination of the integrated force vector due to the pressures on the cambered portion of the wing persists into the supersonic leading-edge region. In practice, uncambered wings of finite thickness exhibit the same trend, because the leading-edge shock is detached and causes the leading edge to operate at a lower effective Mach number; that is, the airfoil operates at a subsonic leading-edge condition where leading-edge suction can reduce the drag even though the theoretical leading-edge condition is supersonic.

The Reynolds number based on leading-edge radius can also significantly affect the drag due to lift. At low Reynolds number, local leading-edge flow separation can occur with a loss in leading-edge suction. Low Reynolds number also affects the boundary-layer transition point on the wing. In general, increasing Reynolds number causes an increase in friction drag at low angles of attack (forward-moving transition point) and no change in friction drag at high angles of attack (transition point is already forward). Sketch (g) shows the effect of leading-edge-radius Reynolds number based on test data (reference 8). The ordinate of this sketch is the ratio of the induced-drag parameter C_{D_L}/C_L^2 at a Reynolds number of 14×10^3 based on leading-edge radius to the value of the parameter at a given value of leading-edge Reynolds number.

$$\frac{\left(\frac{C_{D_L}}{C_L^2}\right)_{R_{\ell_{LER}} = 14 \times 10^3}}{\left(\frac{C_{D_L}}{C_L^2}\right)_{R_{\ell_{LER}} = \text{Test Value}}}$$

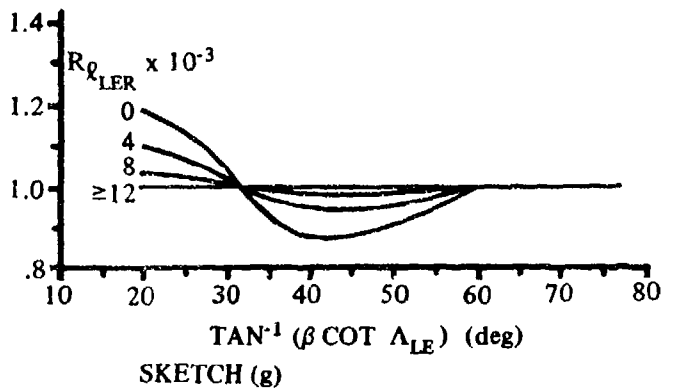

SKETCH (g)

Methods are presented for determining the wing drag due to lift over the parabolic-drag region for the following two classes of wing planforms:

Straight-Tapered Wings (conventional, trapezoidal wings)

Non-Straight-Tapered Wings
- Double-delta wings
- Cranked wings
- Curved (Gothic and ogee) wings

These three general categories of non-straight-tapered wings are illustrated in sketch (a) of Section 4.1.3.2. Their wing-geometry parameters are presented in Section 2.2.2.

The methods presented are based on the conclusions of an analysis of the experimental results of the drag due to lift of slender uncambered wings at supersonic speeds reported in reference 9. It was shown therein that the drag-due-to-lift factor at supersonic speeds collapses into a fairly well-defined single curve when plotted as a function of the wing planform shape and slenderness parameters.

The supersonic design chart presented for non-straight-tapered wings is taken from reference 2, and the parameters used to collapse the data are modifications of those presented in reference 9. The correlation makes no distinction between round and sharp leading edges nor between cambered and uncambered wings.

The parameters used to collapse the data for non-straight-tapered wings in reference 2 have also been applied to uncambered straight-tapered wings. The resulting correlation showed a distinction between straight-tapered wings with round leading edges and those with sharp leading edges.

DATCOM METHODS

Straight-Tapered Wings

The supersonic drag due to lift over the parabolic-drag region for straight-tapered wings is obtained using the procedure outlined in the following steps:

Step 1. Using the given wing geometry, calculate the aspect ratio, the planform shape parameter p, and the wing slenderness parameter $\frac{b_W}{\ell}$. (See Section 2.2.2 for wing-geometry parameters).

Step 2. At the desired value of $\frac{\beta b_W}{2\ell}$ obtain $\pi A \frac{C_{D_L}}{C_L^2} \frac{p}{1+p}$ from the proper design curve of figure 4.1.5.2-58.

Step 3. Calculate the drag due to lift by

$$\frac{C_{D_L}}{C_L^2} = \left[\pi A \frac{C_{D_L}}{C_L^2} \frac{p}{1+p}\right]\left(\frac{1}{\pi A}\right)\left(\frac{1+p}{p}\right) \qquad 4.1.5.2\text{-n}$$

A comparison of test data with results calculated by this method is presented as table 4.1.5.2-F. With one exception, all the configurations listed in the table are wing-body combinations with small ratios of body diameter to wing span. The calculations for these configurations were made by using the theoretical planform extended to the body center line and neglecting body effects. The test configurations are about equally divided between wings with sharp leading edges and those with round leading edges. None of the wings are cambered. The ranges of the planform parameters covered for each leading-edge shape are:

Round Leading Edge	Sharp Leading Edge
$1.313 \leq A \leq 4.0$	$1.5 \leq A \leq 3.5$
$35^{o} \leq \Lambda_{LE} \leq 73^{o}$	$0 \leq \Lambda_{LE} \leq 71^{o}$
$0 \leq \lambda \leq 0.5$	$0 \leq \lambda \leq 1.0$
$0.237 \leq p \leq 0.502$	$0.333 \leq p \leq 0.995$
$0.271 \leq \frac{b_W}{2\ell} \leq 1.00$	$0.333 \leq \frac{b_W}{2\ell} \leq 1.070$

The sample problem presented on page 4.1.5.2-20 for a double-delta wing illustrates the application of the straight-tapered-wing method.

Non-Straight-Tapered Wings

The supersonic drag due to lift over the parabolic-drag region for non-straight-tapered wings is obtained by following the procedure outlined above for straight-tapered wings. The value of the parameter $\pi A \frac{C_{D_L}}{C_L^2} \frac{p}{1+p}$ at the desired value of $\frac{\beta b_W}{2\ell}$ is obtained from figure 4.1.5.2-59. This correlation makes no distinction between wing planforms, between round and sharp leading edges, nor between cambered and uncambered wings.

A comparison of test data with results calculated by this method is presented in table 4.1.5.2-G for double-delta and cranked wings, and in table 4.1.5.2-H (taken from reference 2) for curved wings.

All the configurations listed in table 4.1.5.2-G are wing-body combinations with small ratios of body diameter to wing span. The calculations for these configurations were made by using the theoretical planform extended to the body center line and neglecting body effects. The table includes double-delta wings with both round and sharp leading edges and cranked wings with round leading edges. Some of the wings with round leading edges are cambered. The ranges of the planform parameters of the test data are:

Double-Delta Wings	Cranked Wings
$1.74 \leq A \leq 3.15$	$2.91 \leq A \leq 4.0$
$0.292 \leq p \leq 0.500$	$0.491 \leq p \leq 0.666$
$0.353 \leq \frac{b_W}{2\ell} \leq 0.787$	$0.710 \leq \frac{b_W}{2\ell} \leq 1.333$

The results presented in table 4.1.5.2-H for curved wings with sharp leading edges agree quite well with test data. This is probably due to the fact that the curved planforms have a more limited range of geometric parameters than the double-delta and cranked wings. The ranges of planform parameters of the test data are:

$$0.75 \leq A \leq 1.39$$
$$0.384 \leq p \leq 0.667$$
$$0.208 \leq \frac{b_W}{2\ell} \leq 0.389$$

Sample Problem

Given: The double-delta wing of reference 30 designated X-67-67.

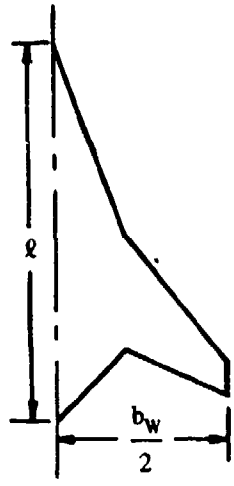

Wing Characteristics:

$A = 2.42$ $\quad S_W = 1.651$ sq ft

$b_W = 2.0$ ft $\quad \ell = 2.22$ ft

Additional Characteristics:

$M = 2.01$; $\quad \beta = 1.742$

Compute:

$$\frac{b_W}{2\ell} = \frac{2.0}{(2)(2.22)} = 0.450$$

$$\frac{\beta b_W}{2\ell} = (1.742)(0.450) = 0.784$$

$$p = \frac{S_W}{b_W \ell} = \frac{1.651}{(2.0)(2.22)} = 0.372$$

$$\frac{1+p}{p} = \frac{1+0.372}{0.372} = 3.688$$

$$\pi A \frac{C_{D_L}}{C_L^2} \frac{p}{1+p} = 0.961 \qquad \text{(figure 4.1.5.2-59)}$$

Solution:

$$\frac{C_{D_L}}{C_L^2} = \left[\pi A \frac{C_{D_L}}{C_L^2} \frac{p}{1+p}\right] \left(\frac{1}{\pi A}\right)\left(\frac{1+p}{p}\right) \qquad \text{(equation 4.1.5.2-n)}$$

$$= (0.961)\left(\frac{1}{2.42\pi}\right)(3.688) = 0.466$$

This compares with a test value of 0.479 from reference 30.

REFERENCES

1. Frost, R.C., and Rutherford, R.: Subsonic Wing Span Efficiency. AIAA Journal, Vol. 1, No. 4, April 1963. (U)

2. Benepe, D.B., Kouri, B.G., Webb, J.B., et al: Aerodynamic Characteristics of Non-Straight-Taper Wings. AFFDL-TR-66-73, 1966. (U)

3. Gardner, D., and Weir, J.: The Drag Due to Lift of Plane Wings at Subsonic Speeds. RAS Journal, Vol. 70, May 1968. (U)

4. Anon: Royal Aeronautical Society, Engineering Sciences Data (Aeronautical Series). Vol. 2, Item 66032, 1966. (U)

5. Lundry, J.: Charts for Obtaining Subsonic Inviscid Induced Drag of Twisted Swept Wings. Douglas Aircraft Company, Report LB-31689, 1964. (U)

6. Puckett, A.E., and Stewart, H.J.: Aerodynamic Performance of Delta Wings at Supersonic Speeds. Jour. Aero. Sci., Vol. 14, No. 10, Oct. 1947. (U)

7. von Kármán, T.: Supersonic Aerodynamics–Principles and Applications. Jour. Aero. Sci., Vol. 14, No. 7, July 1947. (U)

8. Blakeslee, D.J.: Correlation of Wing-Body Drag-Due-to-Lift at Supersonic Speeds for Use in Airplane Design Studies. Rand Report RM 2014, 1957. (C) Title Unclassified

9. Courtney, A.L.: A Collection of Data on the Lift-Dependent Drag of Uncambered Slender Wings at Supersonic Speeds. ARC CP 757, 1964. (U)

10. Hall, C.F.: Lift, Drag, and Pitching Moment of Low-Aspect-Ratio Wings at Subsonic and Supersonic Speeds. NACA RM A53A30, 1953. (U)

11. Graham, R.R.: Low-Speed Characteristics of a 45° Sweptback Wing of Aspect Ratio 8 From Pressure Distributions and Force Tests at Reynolds Numbers from 1,500,000 to 4,800,000. NACA RM L51H13, 1951. (U)

12. Wolhart, W.D., and Thomas, D.F., Jr.: Static Longitudinal and Lateral Stability Characteristics at Low Speed of 60° Sweptback-Midwing Models Having Wings with an Aspect Ratio of 2, 4, or 6. NACA TN 4397, 1958. (U)

13. Kuhn, R.E., and Wiggins, J.W.: Wind-Tunnel Investigation of the Aerodynamic Characteristics in Pitch of Wing-Fuselage Combinations at High Subsonic Speeds–Aspect Ratio Series. NACA RM L52A29, 1952. (U)

14. Tinling, B.E., and Kolk, W.R.: The Effects of Mach Number and Reynolds Number on the Aerodynamic Characteristics of Several 12-Percent-Thick Wings Having 35° of Sweepback and Various Amounts of Camber. NACA RM A50K27, 1951. (U)

15. Anon: Large-Scale Double-Delta Wing-Body Planform Investigation at Low Speed. Unpublished Data. (U)

16. Goodson, K.W., and Beckett, R.E.: Wind-Tunnel Investigation at High Subsonic Speeds of the Stability Characteristics of a Complete Model Having Sweptback-, M-, W-, and Cranked-Wing Planforms and Several Horizontal-Tail Locations. NACA RM L54C29, 1954. (U)

17. Grant, F.C., and Sevier, J.R., Jr.: Transonic and Supersonic Wind-Tunnel Tests of Wing-Body Combinations Designed for High Efficiency at a Mach Number of 1.41. NASA TN D-435, 1960. (U)

18. Henderson, W.P., and Hammond, A.D.: Low-Speed Investigation of High-Lift and Lateral Control Devices on a Semispan Variable-Sweep Wing Having an Outboard Pivot Location. NASA TM X-542, 1961. (U)

19. Lockwood, V.E., McKinney, L.W., and Lamar, J.E.: Low-Speed Aerodynamic Characteristics of a Supersonic Transport Model With a High Aspect Ratio Variable Sweep Warped Wing. NASA TM X-979, 1964. (C) Title Unclassified

20. Jernell, L.S.: The Effects of Conical Camber on the Longitudinal Aerodynamic Characteristics of a Variable-Sweep Wing-Fuselage Configuration at Mach Numbers from 0.60 to 3.50. NASA TM X-804, 1963. (C) Title Unclassified

21. Anon: System 125A, Convair Model 25, Summary Data Report, Subsonic Tests of a Preliminary 1/27-Scale Force Model (CVAL 201). Convair, General Dynamics, F/W, Report FZT-25-004, 1956. (C) Title Unclassified

22. Trescot, C.D., and Spencer, B., Jr.: Effect of Reynolds Number on the Low-Speed Longitudinal Aerodynamic Characteristics of Two Variable-Wing-Sweep Airplane Configurations. NASA TM X-434, 1961. (C) Title Unclassified

23. Squire, L.C., and Capps, D.S.: An Experimental Investigation of the Characteristics of an Ogee Wing from M = 0.4 to M = 1.8. ARC CP 585, 1962. (U)

24. Hicks, R.M., and Hopkins, E.J.: Effects of Spanwise Variation of Leading-Edge Sweep on the Lift, Drag, and Pitching Moment of a Wing-Body Combination at Mach Numbers from 0.7 to 2.94. NASA TN D-2236, 1964. (U)

25. Peckham, D.H.: Low-Speed Wind-Tunnel Tests on a Series of Uncambered Slender Pointed Wings with Sharp Edges. RAE Aero 2613, 1958. (U)

26. Emerson, H.F.: Wind-Tunnel Investigation of the Effect of Clipping the Tips of Triangular Wings of Different Thickness, Camber, and Aspect Ratio--Transonic Bump Method. NACA TN 3671, 1956. (U)

27. Feryn, M.O., and Campbell, J.F.: Effects of Wing Dihedral and Planform on Stability Characteristics of a Research Model at Mach Numbers from 1.80 to 4.63. NASA TN D-2914, 1965. (U)

28. Boyd, J.W., Migotsky, E., and Wetzel, B.E.: A Study of Conical Camber for Triangular and Sweptback Wings. NACA RM A55G19, 1955. (U)

29. Palazzo, E.B., and Spearman, M.L.: Static Longitudinal and Lateral Stability and Control Characteristics of a Model of a 35° Swept-Wing Airplane at a Mach Number of 1.41. NACA RM L54G08, 1955. (U)

30. Cooper, M., and Sevier, J.R., Jr.: Effects of a Series of Inboard Plan-Form Modifications on the Longitudinal Characteristics of Two 47° Sweptback Wings of Aspect Ratio 3.5, Taper Ratio 0.2, and Different Thickness Distributions at Mach Numbers of 1.61 and 2.01. NACA RM L53E07a, 1953. (U)

31. Sevier, J.R., Jr.: Effect of a Series of Inboard Plan Form Modifications on the Longitudinal Characteristics of Two Unswept Wings of Aspect Ratio 3.5, Taper Ratio 0.2, and Different Thickness Distributions at Mach Numbers of 1.61 and 2.01. NACA RM L53K11, 1954. (U)

32. Robins, A.W., Harris, R.V., Jr., and Jackson, C.M., Jr.: Characteristics at Mach Number of 2.03 of a Series of Wings Having Various Spanwise Distributions of Thickness Ratio and Chord. NASA TN D-631, 1960. (U)

33. Wetzel, B.E.: Effect of Taper Ratio on Lift, Drag, and Pitching-Moment Characteristics of Thin Wings of Aspect Ratio 3 with 53.1° Sweepback of Leading Edge at Subsonic and Supersonic Speeds. NACA RM A54J20, 1955. (U)

34. Sevier, J.R., Jr.: Investigation of the Effects of Body Indentation and of Wing-Plan-Form Modification on the Longitudinal Characteristics of a 60° Swept-Wing-Body Combination at Mach Numbers of 1.41, 1.61, and 2.01. NACA RM L55E17, 1955. (U)

35. Holdaway, G.H., and Mellenthin, J.A.: Evaluation of Blended Wing-Body Combinations with Curved Plan Forms at Mach Numbers up to 3.50. NASA TM X-379, 1960. (U)

36. Wakefield, R.M.: Effects of Wing-Crank, Leading-Edge Chord Extensions, and Horizontal-Tail Height on the Longitudinal Stability of Swept-Wing Models at Mach Numbers from 0.6 to 1.4. NASA TM X-92, 1959. (U)

37. Bielat, R.P., Harrison, D.E., and Coppolino, D.A.: An Investigation at Transonic Speeds of the Effects of Thickness Ratio and of Thickened Root Sections on the Aerodynamic Characteristics of Wings With 47° Sweepback, Aspect Ratio 3.5, and Taper Ratio 0.2 in the Slotted Test Section of the Langley 8-Foot High-Speed Tunnel. NACA RM L51I04a, 1951. (U)

38. Spearman, M.L., and Foster, G.V.: Stability and Control Characteristics at a Mach Number of 2.01 of a Variable-Wing-Sweep Configuration With Outboard Wing Panels Swept Back 75°. NASA TM X-32, 1959. (U)

39. Foster, G.V.: Stability and Control Characteristics at Mach Numbers of 2.50, 3.00, and 3.71 of Variable-Wing-Sweep Configuration With Outboard Wing Panels Swept Back 75°. NASA TM X-267, 1960. (U)

40. Sevier, J.R., Jr.: Aerodynamic Characteristics at Mach Numbers of 1.41 and 2.01 of a Series of Cranked Wings Ranging in Aspect Ratio from 4.00 to 1.74 in Combination With a Body. NASA TM X-172, 1960. (U)

41. Kuhns, R.M.: HSWT-083-0 Analysis Report, Supersonic Transport Lifting Fuselage Investigation. Convair, General Dynamics, San Diego, Report AD-SST-012, 1961. (U)

42. Pierce, S.R.: System 125A, Convair Model 25 Summary Data Report, Wind-Tunnel Tests of a 1/125 Scale Model. (JPL Test 20-202), Convair, General Dynamics, F/W, Report FZT-25-006, 1956. (U)

43. Taylor, C.R.: Measurements, at Mach Numbers up to 2.8, of the Longitudinal Characteristics of One Plane and Three Cambered Slender 'Ogee' Wings. ARC R&M 3328, 1963. (U)

TABLE 4.1.5.2-A
SUBSONIC DRAG DUE TO LIFT OF STRAIGHT-TAPERED WINGS
DATA SUMMARY AND SUBSTANTIATION
NO TWIST

Ref.	Config.	A	λ	Λ_{LE} (deg)	NACA Airfoil	$R\ell_{MAC} \times 10^{-6}$	$R\ell_{LER} \times 10^{-3}$	M	$\frac{C_{D_L}}{C_L^2}$ Calc.	$\frac{C_{D_L}}{C_L^2}$ Test	e Percent Error
10	WB	3.0	0	53.1	0003-63	3.1	3.1	0.25	0.251	0.296	-15.2
								0.60	0.242	0.250	- 3.2
						5.9	5.9	0.25	0.215	0.251	-14.3
						10.6	10.6	0.25	0.185	0.217	-14.7
						1.9	1.9	0.61	0.269	0.270	- 0.4
						4.8	4.8	0.61	0.218	0.250	-12.8
		2.0	0	63.4	0003-63	4.9	4.9	0.25	0.336	0.367	- 8.4
								0.60	0.331	0.373	-11.5
						9.3	9.3	0.25	0.291	0.290	0.3
						16.6	16.6	0.25	0.255	0.270	- 5.6
						3.0	3.0	0.61	0.366	0.345	6.1
								0.81	0.353	0.325	8.6
						5.0	5.0	0.61	0.330	0.325	1.5
						7.5	7.5	0.61	0.301	0.325	- 7.4
		4.0	0	45.0	bicanvex t/c = 0.03	2.7	1.215	0.25	0.245	0.245	0
								0.60	0.227	0.240	- 5.4
						5.01	2.25	0.25	0.214	0.226	- 5.3
						9.1	4.095	0.25	0.183	0.180	- 1.7
						1.7	0.765	0.61	0.226	0.216	4.6
						1.7		0.81	0.205	0.195	5.1
						2.9	1.305	0.61	0.225	0.210	7.1
								0.81	0.205	0.190	7.9
						4.2	1.89	0.61	0.208	0.210	- 1.0
								0.81	0.194	0.190	2.1
		2.0	0	63.4	0006-63	1.5	4.12	0.40	0.360	0.350	2.9
								0.60	0.341	0.330	2.7
								0.80	0.334	0.315	6.0

TABLE 4.1.5.2-A (CONTD)

Ref.	Config.	A	λ	Λ_{LE} (deg)	NACA Airfoil	$R\ell_{MAC} \times 10^{-6}$	$R\ell_{LER} \times 10^{-3}$	M	$\frac{C_{D_L}}{C_L^2}$ Calc.	$\frac{C_{D_L}}{C_L^2}$ Test	e Percent Error
10	WB	2.0	0	63.4	0006-63	3.0	8.25	0.24	0.300	0.320	- 6.3
								0.40	0.310	0.290	6.9
								0.60	0.294	0.310	- 5.2
								0.80	0.288	0.310	- 7.1
						5.0	13.75	0.25	0.267	0.262	1.9
						8.0	22.0	0.25	0.240	0.220	9.1
						3.0	8.25	0.61	0.294	0.300	- 2.0
								0.81	0.287	0.290	- 1.0
						7.5	20.6	0.61	0.240	0.240	0
								0.79	0.236	0.254	- 7.1
					0008-63	3.0	21.15	0.24	0.242	0.240	0.8
								0.40	0.240	0.240	0
								0.60	0.238	0.250	- 4.8
								0.80	0.235	0.260	- 9.6
						5.0	35.25	0.25	0.218	0.205	6.3
						8.0	56.4	0.25	0.202	0.195	3.6
						15.0	105.75	0.25	0.188	0.195	- 3.6
		2.0	0.333	45.0	biconvex t/c = 0.03	1.9	0.855	0.61	0.345	0.325	6.2
								0.71	0.338	0.300	12.6
								0.81	0.328	0.302	8.6
						4.8	2.16	0.61	0.306	0.290	5.5
								0.71	0.304	0.290	4.8
								0.81	0.300	0.291	3.1
		3.08	0.388	19.1	biconvex t/c = 0.03	2.4	0	0.25	0.264	0.255	3.5
								0.60	0.244	0.230	6.1
						4.6		0.25	0.264	0.240	10.0
						8.3		0.25	0.264	0.240	10.0

TABLE 4.1.5.2-A (CONTD)

Ref.	Config.	A	λ	Λ_{LE} (deg)	NACA Airfoil	$R\ell_{MAC} \times 10^{-6}$	$R\ell_{LER} \times 10^{-3}$	M	$\frac{C_{D_L}}{C_L^2}$ Calc.	$\frac{C_{D_L}}{C_L^2}$ Test	% Percent Error
10	WB	3.08	0.388	19.1	biconvex t/c = 0.03	1.4	0	0.61	0.243	0.240	1.3
								0.71	0.235	0.235	0
								0.81	0.226	0.220	2.7
						2.4		0.61	0.243	0.245	- 0.8
								0.71	0.235	0.230	2.2
								0.76	0.227	0.230	- 1.3
								0.81	0.226	0.205	10.2
						3.8		0.61	0.243	0.230	5.7
								0.71	0.235	0.220	6.8
								0.81	0.226	0.210	7.6
11	W	8.02	0.450	46.3	63_1A012	3.0	32.1	0.14	0.065	0.068	- 4.4
						4.0	42.8	0.19	0.059	0.062	- 4.8
12	WB	2	0.600	61.7	65A009	1.02	4.16	0.13	0.373	0.340	9.7
		4		60.8		0.72	2.94	0.13	0.308	0.300	2.7
13	WB	2	0.600	48.4	65A006	3.33	7.63	0.40	0.251	0.240	4.6
						3.94	9.02	0.50	0.240	0.240	0
						4.53	10.4	0.60	0.232	0.240	- 3.3
						5.05	11.6	0.70	0.226	0.240	- 5.8
						5.46	12.5	0.80	0.222	0.240	- 7.5
		4	0.600	46.7		2.05	4.69	0.40	0.188	0.173	8.7
						2.42	5.54	0.50	0.172	0.164	4.9
						2.78	6.37	0.60	0.164	0.150	9.3
						3.10	7.10	0.70	0.158	0.155	1.9
						3.35	7.67	0.80	0.153	0.145	5.5
		6	0.600	46.2		1.57	3.60	0.40	0.167	0.160	4.4
						1.86	4.26	0.50	0.156	0.140	11.4
						2.14	4.90	0.60	0.149	0.140	6.4
						2.39	5.47	0.70	0.141	0.135	4.4
						2.59	5.93	0.80	0.135	0.130	3.8

TABLE 4.1.5.2-A (CONTD)

Ref.	Config.	A	λ	Λ_{LE} (deg)	NACA Airfoil	$R\ell_{MAC} \times 10^{-6}$	$R\ell_{LER} \times 10^{-3}$	M	$\frac{C_{D_L}}{C_L^2}$ Calc.	$\frac{C_{D_L}}{C_L^2}$ Test	e Percent Error
14	W	5.14	0.713	36.2	65_1A012	2.0	18.4	0.25	0.086	0.087	- 1.1
								0.40	0.087	0.090	- 3.3
								0.60	0.086	0.093	- 7.5
								0.70	0.085	0.094	- 9.6
								0.75	0.085	0.090	- 5.6
								0.80	0.085	0.094	- 9.6
		10.7	0.500	36.3				0.25	0.057	0.054	5.6
								0.40	0.057	0.056	1.8
								0.60	0.056	0.061	- 8.2
								0.80	0.055	0.061	- 9.8

Average Error = $\frac{\Sigma|e|}{n}$ = 5.8%

TABLE 4.1.5.2-B
SUBSONIC DRAG DUE TO LIFT OF SHARP-LEADING-EDGED
DOUBLE-DELTA WINGS

DATA SUMMARY AND SUBSTANTIATION

Ref.	Config.	A	λ_i	λ_o	η_B	Λ_{LE_i} (deg)	Λ_{LE_o} (deg)	$\frac{c}{b}$	$\frac{t}{c}$	M	$R\ell \times 10^{-6}$ (based on $\bar{c}$)	α (deg)	C_L Calc.	C_{D_L} Calc.	C_{D_L} Test	e Percent Error
15	W8V	1.87	0.488	0	0.424	72.6	59.0	0.131	0.02-0.03	0.13	17.1	4	0.150	0.0100	0.0040	150.0
												8	0.340	0.0450	0.0410	10.7
												12	0.553	0.1117	0.1170	- 4.5
												16	0.769	0.2095	0.2240	- 6.5
												20	0.979	0.3385	0.3520	- 3.8
	W8V	1.46	0.482	0.189	0.484	72.6	59.0	0.149	0.02-0.03	0.13	17.3	4	0.148	0.0098	0.0080	22.6
												8	0.335	0.0441	0.0430	4.0
												12	0.545	0.1101	0.1120	- 1.7
												16	0.757	0.2062	0.2180	- 5.4
												20	0.965	0.3337	0.3520	- 5.2
	W8V	1.73	0.346	0	0.551	73.0	59.0	0.131	0.02-0.03	0.13	19.3	4	0.144	0.0096	0.0070	37.2
												8	0.323	0.0431	0.0430	0.2
												12	0.524	0.1058	0.1080	- 2.0
												16	0.729	0.1986	0.2050	- 3.1
												20	0.930	0.3216	0.3280	- 2.0
	W8V	1.34	0.346	0.240	0.628	73.0	59.0	0.149	0.02-0.03	0.13	19.5	4	0.137	0.0091	0.0100	- 9.0
												8	0.307	0.0410	0.0410	0
												12	0.498	0.1006	0.1060	- 5.1
												16	0.693	0.1888	0.2080	- 9.2
												20	0.884	0.3057	0.3360	- 9.0

TABLE 4.1.5.2-B (CONTD)

Ref.	Config.	A	λ_i	λ_o	η_B	Λ_{LE_i} (deg)	Λ_{LE_o} (deg)	$\frac{d}{b}$	$\frac{t}{c}$	M	$R_{\bar{c}} \times 10^{-6}$ (based on $\bar{c}$)	α (deg)	C_L Calc.	C_{D_L} Calc.	C_{D_L} Test	e Percent Error
15	WBV	1.73	0.356	0	0.414	77.4	59.0	0.131	0.02-0.03	0.13	20.0	4	0.143	0.0095	0.0085	11.8
												8	0.302	0.0403	0.0420	- 4.0
												12	0.491	0.0992	0.1090	- 9.0
												16	0.685	0.1866	0.2110	- 11.6
												20	0.974	0.3368	0.3410	- 1.2
	WBV	1.34	0.356	0.210	0.473	77.4	59.0	0.149	0.02-0.03	0.13	20.3	4	0.130	0.0086	0.0060	43.4
												8	0.298	0.0398	0.0390	2.1
												12	0.484	0.0978	0.1080	- 9.4
												16	0.676	0.1841	0.2050	- 10.2
												20	0.960	0.3320	0.3350	- 0.9
	WBV	1.87	0.448	0	0.332	77.2	59.0	0.131	0.02-0.03	0.13	17.8	4	0.146	0.0097	0.0075	29.4
												8	0.335	0.0447	0.0430	4.0
												12	0.524	0.1058	0.1120	- 5.5
												16	0.759	0.2068	0.2130	- 2.9
												20	0.971	0.3358	0.3360	- 0.1
	WBV	1.46	0.448	0.183	0.379	77.2	59.0	0.149	0.02-0.03	0.13	18.2	4	0.144	0.0096	0.0060	60.0
												8	0.330	0.0441	0.0400	10.3
												12	0.538	0.1087	0.1070	1.6
												16	0.749	0.2040	0.2110	- 3.3
												20	0.958	0.3313	0.3370	- 1.7

Average Error = $\frac{\Sigma|e|}{n}$ = 4.7%

(Excluding values at α = 4°)

TABLE 4.1.5.2-C
SUBSONIC PARABOLIC DRAG DUE TO LIFT OF
ROUND-LEADING-EDGED CRANKED WINGS

DATA SUMMARY

Ref.	Config.	A	λ_i	λ_o	η_B	Λ_{LE_i} (deg)	Λ_{LE_o} (deg)	$\frac{d}{b}$	$\frac{t}{c}$	$(LER)_i$ ($\% \bar{c}_i$)	$(LER)_o$ ($\% \bar{c}_o$)	M	$R\ell \times 10^{-6}$ (based on $\bar{c}$)	C_{D_L}/C_L^2 Calc.	C_{D_L}/C_L^2 Test	e Percent Error
16	WB	4.0	0.580	0.517	0.600	48.6	7.7	0.139	0.06	0.229	0.229	0.80	3.65	0.152	0.154	-1.3
17	WB	2.91	0.333	0.500	0.500	67.0	61.7	0.139	0.04-0.03	0.089	0.067	0.60	3.5	0.320	0.336	-4.8
18	W	5.2	0.339	0.268	0.379	60.0	25.0	---	0.045-0.06	0.149	0.265	0.13	2.65	0.186	0.203	-8.4

Average Error = $\frac{\Sigma|e|}{n}$ = 4.8%

TABLE 4.1.5.2-D
SUBSONIC DRAG DUE TO LIFT BEYOND DRAG POLAR
BREAK FOR ROUND-LEADING-EDGED CRANKED WINGS
DATA SUMMARY AND SUBSTANTIATION

Ref.	Config.	A	λ_i	λ_o	η_B	Λ_{LE_i} (deg)	Λ_{LE_o} (deg)	$\frac{d}{b}$	$\frac{t}{c}$	M	$R\ell \times 10^{-6}$ (based on $\bar{c}$)	C_L	C_{D_L} Calc.	C_{D_L} Test	e Percent Error
16	WB	4.0	0.580	0.517	0.600	48.6	7.7	0.139	0.06	0.80	3.645	0.4	0.0323	0.0300	7.7
												0.5	0.0620	0.0620	0
												0.6	0.1067	0.1060	−0.3
												0.7	0.1585	0.1610	−1.6
												0.8	0.2218	0.2250	−1.4
18	W	6.2	0.339	0.268	0.379	60.0	25.0	---	0.045-0.06	0.13	2.65	0.4	0.0328	0.0321	2.2
												0.5	0.0645	0.0614	5.0
												0.6	0.1010	0.1015	-0.5
												0.7	0.1480	0.1427	3.7
												0.8	0.2040	0.1968	3.7
												0.9	0.2727	0.2619	4.1
												1.0	0.3590	0.3378	6.3
19	WBV	8.47	0.197	0.386	0.212	76.0	16.0	0.062	---	0.20	3.6	0.678	0.0365	(a)	
												0.762	0.0830		
												0.847	0.1720		
20	WB	6.18	0.294	0.463	0.308	65.0	12.0	0.066	0.06-0.02	0.50	0.73	0.618	0.0420		
												0.680	0.0700		
												0.742	0.1120		

TABLE 4.1.5.2-D (CONTD)

Ref.	Config.	A	λ_i	λ_o	η_B	Λ_{LE_i} (deg)	Λ_{LE_o} (deg)	$\frac{d}{b}$	$\frac{t}{c}$	M	$R\ell \times 10^{-6}$ (based on $\bar{c}$)	C_L	C_{D_L} Calc.	C_{D_L} Test	e Percent Error
20	WB	4.43	0.389	0.464	0.405	65.0	45.0	0.080	0.06-0.02	0.50	0.65	0.354	0.0175		
												0.443	0.0365		
												0.532	0.0640		
												0.620	0.1010		
												0.709	0.1470		
												0.797	0.1965		
21	WBVN	3.0	0.200	0	0.654	60.0	42.1	0.077	0.035-0.040	0.20	3.22	0.420	0.0275		
												0.480	0.0420		
												0.540	0.0620		
												0.600	0.0886	(a)	
												0.660	0.1160		
												0.720	0.1470		
	WBVN	4.0	0.200	0.138	0.550	60.0	18.1	0.065	0.035-0.040	0.20	3.07	0.320	0.0135		
												0.400	0.0280		
												0.480	0.0500		
												0.560	0.0811		
												0.640	0.1195		
												0.720	0.1640		
22	WBV	5.95	0.440	0	0.345	60.0	25.0	0.121	0.045	0.36	10.24	0.595	0.0320		
												0.655	0.0500		
												0.714	0.0790		

(a) This information is classified CONFIDENTIAL

Average Error = $\frac{\Sigma|e|}{n}$ = 4.1%

TABLE 4.1.5.2-E
SUBSONIC DRAG DUE TO LIFT OF SHARP-LEADING-EDGED CURVED WINGS
DATA SUMMARY AND SUBSTANTIATION

Ref.	Config.	Planform	A	p	$\frac{b_W}{2\ell}$	$\frac{d}{b}$	$\frac{t}{c}$ (root)	M	$R\ell \times 10^{-6}$ (based on $\bar{c}$)	α (deg)	C_L Calc.	C_{D_L} Calc.	C_{D_L} Test	[a] Percent Error
23	WB	Ogee	1.20	0.500	0.300	0.133	0.05	0.40	1.7	4	0.136	0.0090	0.0080	12.5
										8	0.238	0.0384	0.0360	6.7
										12	0.466	0.0939	0.0980	- 4.2
24	WB	Ogee	1.98	0.455	0.450	0.127	0.02	0.70	0.58	4	0.167	0.0111	0.0110	0.9
										8	0.352	0.0470	0.0485	- 3.1
25	W	Gothic	0.75	0.667	0.250	---	0.01 [a]	0.10	2.9	6.1	0.165	0.0168	0.0136	23.5
										10.1	0.303	0.0613	0.0476	7.8
										14.1	0.465	0.1110	0.1091	1.7
										18.1	0.646	0.2003	0.2016	- 0.6
	W	Gothic	1.25	0.667	0.417	---	0.01 [a]	0.10	2.9	6.15	0.201	0.0208	0.0190	8.4
										10.15	0.389	0.0661	0.0610	8.4
										14.15	0.599	0.1435	0.1420	1.1

(a) Flat-plate models with beveled leading edges; α and C_L are adjusted to account for camber.

Average Error = $\frac{\Sigma|e_i|}{n}$ = 6.6%

TABLE 4.1.5.2-F
SUPERSONIC DRAG DUE TO LIFT OF STRAIGHT-TAPERED WINGS
DATA SUMMARY AND SUBSTANTIATION

Ref.	Config.	A	λ	ρ	$\frac{b_W}{2\ell}$	LER	M	$\pi A \frac{C_{D_L}}{C_L^2}$ Calc.	$\pi A \frac{C_{D_L}}{C_L^2}$ Test	e Percent Error
27	WB	1.313	0.150	0.412	0.271	Round	1.80	2.04	2.00	2.0
							2.16	2.38	2.36	0.8
							2.50	2.71	2.54	6.7
							2.86	3.05	3.34	- 8.7
							3.95	4.09	4.02	1.7
							4.63	4.69	4.70	- 0.2
28	WB	2.0	0	0.500	0.500	Round	1.30	1.81	2.01	-10.0
							1.70	2.57	2.67	- 3.7
							1.90	2.92	2.95	- 1.0
		3.0	0.400	0.484	0.725		1.20	2.02	1.65	22.4
							1.30	2.37	2.05	15.6
							1.50	2.98	2.55	16.9
							1.70	3.54	3.16	12.0
							1.90	4.06	3.79	7.1
29	WB	4.0	0.500	0.320	0.643	Round	1.41	3.34	2.94	13.6
30		3.5	0.200	0.393	0.688	Sharp	1.61	3.39	3.39	0
							2.01	4.54	4.73	4.0
		3.15	0.150	0.437	0.688		1.61	3.14	2.99	5.0
		2.86	0.120	0.441	0.630		1.61	2.89	2.84	1.8
							2.01	3.86	4.09	- 5.6
31	WB	3.50	0.200	0.600	1.050	Sharp	1.61	3.75	3.67	2.2
							2.01	5.09	5.12	- 0.6
		3.15	0.150	0.500	0.787		1.61	3.23	3.34	- 3.3
							2.01	4.36	4.64	- 6.0
32	W	2.5	0.200	0.353	0.441	Sharp	2.03	3.33	2.75	21.1
		1.5		0.646	0.409			2.31	2.29	0.9

TABLE 4.1.5.2-F (CONTD)

Ref.	Config.	A	λ	ρ	$\frac{b_W}{2\ell}$	LER	M	$\pi A \frac{C_{D_L}}{C_L^2}$ Calc.	$\pi A \frac{C_{D_L}}{C_L^2}$ Test	ε Percent Error
33	WB	3.0	0	0.502	0.750	Round	1.20	2.01	2.45	-18.0
							1.30	2.37	2.86	-17.1
							1.50	3.00	3.39	-11.5
							1.70	3.55	3.96	-10.4
							1.90	4.07	4.05	0.5
		3.0	0.200	0.430	0.643		1.20	2.03	2.56	-20.7
							1.30	2.35	2.75	-14.5
							1.50	2.94	3.39	-13.3
							1.70	3.47	3.68	- 5.7
							1.90	3.96	3.94	0.5
		3.0	0.400	0.389	0.585		1.20	2.08	2.32	-10.3
							1.30	2.36	2.54	- 7.1
							1.50	2.94	3.11	- 5.5
							1.70	3.46	3.53	- 2.0
							1.90	3.95	3.64	8.5
24	WB	2.174	0	0.500	0.544	Sharp	1.40	1.87	2.39	-21.8
							.98	3.05	3.21	- 5.0
							2.94	4.76	4.61	3.3
		2.174	0.678	0.960	1.045		1.40	2.26	2.39	- 5.4
							1.98	3.01	3.28	16.2
10	WB	4.0	0	0.500	1.00	Round	1.20	2.50	2.50	0
							1.30	2.98	2.80	6.8
							1.40	3.41	3.30	3.3
							1.53	3.93	3.72	5.6
							1.60	4.19	4.01	4.5
							1.70	4.57	4.30	6.3
		3.08	0.388	0.694	1.07	Sharp	1.20	1.95	1.97	- 1.0
							1.50	3.13	3.25	- 3.7

TABLE 4.1.5.2-F (CONTD)

Ref.	Config.	A	λ	p	$\frac{b_W}{2\ell}$	LER	M	$\pi A \frac{C_{D_L}}{C_L^2}$ Calc.	$\pi A \frac{C_{D_L}}{C_L^2}$ Test	e Percent Error
10	WB	2.0	1.00	0.995	1.00		1.20	1.51	1.57	- 3.8
							1.30	1.87	1.93	- 4.7
							1.40	2.13	2.10	1.4
							1.50	2.41	2.15	12.1
							1.60	2.67	2.32	15.1
							1.70	2.88	2.44	18.0
10	WB	2.0	0.333	0.665	0.672	Sharp	1.20	1.43	1.60	-10.6
							1.30	1.63	1.68	- 3.0
							1.40	1.88	1.78	5.6
							1.50	2.11	2.05	2.9
							1.60	2.33	2.17	7.4
							1.70	2.53	2.46	2.8
34	WB	4.0	0.333	0.237	0.475	Round	1.41	3.38	3.14	7.6
							1.61	4.02	3.90	3.1
							2.01	5.17	4.90	5.5
35	WB	2.0	0	0.500	0.500	Sharp	1.55	2.05	1.95	5.1
							1.80	2.52	2.44	3.3
							1.95	2.78	2.66	4.5
							2.10	3.03	3.05	- 0.7
							2.35	3.45	3.52	- 2.0
							2.50	3.70	3.93	- 5.9
							3.00	4.49	4.66	- 3.6
							3.50	5.29	5.45	- 2.9
		2.0	0	0.333	0.333		2.50	3.41	3.30	3.3
							3.00	4.12	4.37	- 5.7
							3.50	4.81	5.03	- 4.4

TABLE 4.1.5.2-F (CONTD)

Ref.	Config.	A	λ	ρ	$\frac{b_W}{2\ell}$	LER	M	$\pi A \frac{C_{D_L}}{C_L^2}$ Calc.	$\pi A \frac{C_{D_L}}{C_L^2}$ Test	e Percent Error
36	WB	3.0	0.400	0.389	0.584	Round	1.00	1.93	1.93	0
							1.10	1.93	1.98	- 2.5
							1.20	2.08	2.12	- 1.9
							1.30	2.36	2.40	- 1.7
							1.40	2.65	2.60	1.9
		3.0	0.400	0.482	0.723		1.00	1.67	1.72	- 2.9
							1.10	1.71	1.85	- 7.6
							1.20	2.01	2.11	- 4.7
							1.30	2.37	2.36	0.4
							1.40	2.70	2.64	2.3
37	WB	3.50	0.200	0.393	0.588	Round	1.00	1.91	1.86	2.7
							.05	1.91	1.92	- 0.6
							1.10	1.96	1.94	1.0

Average Error = $\frac{\Sigma|e|}{n}$ = 6.4%

Round Leading Edge 6.8%

Sharp Leading Edge 5.8%

TABLE 4.1.5.2-G
SUPERSONIC DRAG DUE TO LIFT OF DOUBLE-DELTA
AND CRANKED WINGS

DATA SUMMARY AND SUBSTANTIATION

Ref.	Config.	Planform	A	p	$\frac{b_W}{2\ell}$	LER	M	$\pi A \frac{C_{D_L}}{C_L^2}$ Calc.	$\pi A \frac{C_{D_L}}{C_L^2}$ Test	e Percent Error
30	WB	Double Delta	3.15	0.359	0.565	Sharp	1.61	3.37	3.32	1.5
			2.86	0.395	0.565			3.14	3.05	3.0
			2.62	0.400	0.525			2.94	2.87	2.4
			2.86	0.335	0.479			3.12	3.27	- 4.6
			2.62	0.365	0.479			2.93	2.99	- 2.0
			2.42	0.372	0.450			2.77	2.88	- 3.8
			2.86	0.335	0.479		2.01	4.04	4.31	- 6.3
			2.42	0.372	0.450			3.54	3.64	- 2.7
31	WB	Double Delta	2.62	0.400	0.525	Sharp	1.61	2.94	3.58	-17.9
			2.42	0.372	0.450			2.77	3.38	-18.0
			3.15	0.500	0.787		2.01	4.83	4.96	- 1.4
			2.86	0.440	0.630			4.30	4.81	-10.6
			2.62	0.400	0.525			3.86	4.68	-17.5
			2.86	0.440	0.630			4.30	4.57	- 5.9
			2.62	0.400	0.525			3.86	4.52	-14.6
			2.42	0.372	0.450			3.54	4.46	-20.6
38	WB	Double Delta	1.86	0.412	0.384	Round	2.01	2.90	2.66	9.0
39	WB	Double Delta	1.86	0.412	0.384	Round	2.50	3.67	2.90	26.6
							3.00	4.47	3.28	36.3
							3.71	5.57	3.97	40.3
34	WB	Double Delta	2.91	0.292	0.425	Round	1.41	2.77	2.65	4.5
							1.61	3.19	3.08	3.6
							2.01	4.07	3.89	4.6

TABLE 4.1.5.2-G (CONTD)

Ref.	Confis.	Planform	A	p	$\frac{b_W}{2\ell}$	LER	M	$\frac{C_{D_L}}{\pi A \frac{C_L}{C_L}^2}$ Calc.	$\frac{C_{D_L}}{\pi A \frac{C_L}{C_L}^2}$ Test	e Percent Error
40	WB	Double Delta	2.67	0.429	0.571	Round	1.41	2.50	2.89	-13.5
							2.01	3.98	4.19	- 5.0
			2.29	0.389	0.444		1.41	2.29	2.70	-15.2
							2.01	3.39	3.83	-11.5
			2.35	0.486	0.571		1.41	2.29	2.54	- 9.8
							2.01	3.65	3.69	- 1.1
			1.95	0.456	0.444		1.41	2.04	2.20	- 7.3
							2.01	3.04	3.26	- 6.7
			2.29	0.389	0.444		1.41	2.29	2.84	-19.4
							2.01	3.39	3.86	-12.2
			2.00	0.364	0.364		1.41	2.17	2.67	-18.7
							2.01	3.05	3.59	-15.0
			2.50	0.467	0.571		1.41	2.39	2.87	-16.7
							2.01	3.81	3.93	- 3.1
			2.06	0.433	0.444		1.41	2.12	2.50	-15.2
							2.01	3.15	3.48	- 9.5
			1.74	0.418	0.364		1.41	1.97	2.19	-10.0
							2.01	2.76	3.12	-11.5
41	WB	Double Delta	2.39	0.295	0.353	I-Round e-Sharp	1.20	2.26	2.44	- 7.3
							2.00	3.46	4.08	-15.2
							3.00	5.26	5.85	- 9.9
42	WBVN	Double Delta	2.60	0.464	0.600	Round	1.76	3.41	3.52	- 3.3
							2.16	4.31	4.22	2.0
							2.56	5.29	5.05	4.5
							3.07	6.15	5.91	4.0

TABLE 4.1.5.2-G (CONTD)

Ref.	Config.	Planform	A	p	$\frac{b_W}{2\ell}$	LER	M	$\frac{C_{D_L}}{\pi A \frac{C_L}{2}}$ Calc.	$\frac{C_{D_L}}{\pi A \frac{C_L}{2}}$ Test	e Percent Error
40	WB	Cranked	4.0	0.666	1.333	Round	1.41	3.96	3.33	18.9
			3.2	0.500	0.800		1.41	2.92	3.10	- 5.8
							2.01	4.94	4.54	8.8
			2.97	0.540	0.800		1.41	2.77	2.99	- 7.4
							2.01	4.69	4.26	10.1
			3.20	0.500	0.800		1.41	2.92	3.52	-17.0
							2.01	4.94	4.67	5.8
36	WB	Cranked	2.91	0.491	0.710	Round	1.00	1.52	2.01	-24.3
							1.10	1.69	2.01	-15.9
							1.20	2.01	2.29	-12.2
							1.30	2.34	2.56	- 8.5
							1.40	2.65	2.74	- 3.3

Average Error = $\frac{\Sigma|e|}{n}$ = 10.7%

Double Delta 10.5%

Cranked 11.6%

TABLE 4.1.5.2-H

SUPERSONIC DRAG DUE TO LIFT OF CURVED PLANFORMS

DATA SUMMARY AND SUBSTANTIATION

SHARP LEADING EDGES

Ref.	Config.	Planform	A	p	$\frac{b_W}{2\ell}$	M	$\frac{C_{D_L}}{\pi A \frac{C_L}{2}}$ Calc.	$\frac{C_{D_L}}{\pi A \frac{C_L}{2}}$ Test	e Percent Error
9	W	Ogee	1.27	0.394	0.244	1.81	2.12	1.90	11.6
						1.91	2.18	2.01	8.5
						2.27	2.47	2.38	3.8
						2.65	2.83	2.77	2.2
						2.95	3.07	3.07	0
	W	Ogee	1.27	0.406	0.269	1.65	1.95	1.90	2.6
						1.84	2.10	2.05	2.4
						2.18	2.38	2.37	0.4
						2.53	2.71	2.71	0
						2.83	2.97	3.05	- 2.6
	W	Ogee	1.20	0.500	0.300	1.00	1.50	1.45	3.4
						1.30	1.56	1.64	- 4.9
						1.60	1.77	1.70	4.1
						1.79	1.94	2.00	- 3.0
	W	Ogee	1.00	0.500	0.250	2.00	1.91	1.82	4.9
	W	Gothic	1.39	0.560	0.389	1.54	1.74	1.82	- 4.4
						1.63	1.92	1.90	1.1
						1.84	2.19	2.07	5.8
						2.06	2.44	2.31	5.6
						2.29	2.70	2.61	3.4
						2.63	3.02	2.93	3.1
						2.61	3.14	3.07	2.3

TABLE 4.1.5.2-H (CONTD)

Ref.	Config.	Planform	A	ρ	$\frac{b_W}{2\ell}$	M	$\frac{C_{D_L}}{\pi A \frac{C_{D_L}}{C_L^2}}$ Calc.	$\frac{C_{D_L}}{\pi A \frac{C_{D_L}}{C_L^2}}$ Test	ε Percent Error
9	W	Gothic	1.09	0.611	0.333	1.55	1.60	1.56	2.6
						1.80	1.82	1.75	4.0
						2.06	2.07	1.94	6.7
						2.31	2.30	2.14	7.5
						2.60	2.57	2.34	9.8
						2.84	2.81	2.55	10.2
9	W	Gothic	1.00	0.667	0.333	1.56	1.53	1.44	6.3
						1.71	1.65	1.56	5.8
						1.87	1.86	1.81	2.8
	W	Gothic	0.75	0.667	0.250	1.00	1.25	1.23	1.6
						1.42	1.30	1.27	2.4
						1.60	1.38	1.32	4.5
						1.82	1.46	1.36	7.4
						1.94	1.55	1.52	2.0
43	W	Ogee	0.924	0.450	0.208	1.40	1.63	1.53	6.5
						1.60	1.69	1.68	0.6
						1.80	1.77	1.80	- 1.7
						2.00	1.87	1.91	- 2.1
						2.20	1.98	2.05	- 3.4
						2.40	2.11	2.18	- 3.2
						2.60	2.23	2.35	- 5.1

Average Error = $\frac{\Sigma|\varepsilon|}{n}$ = 4.1%

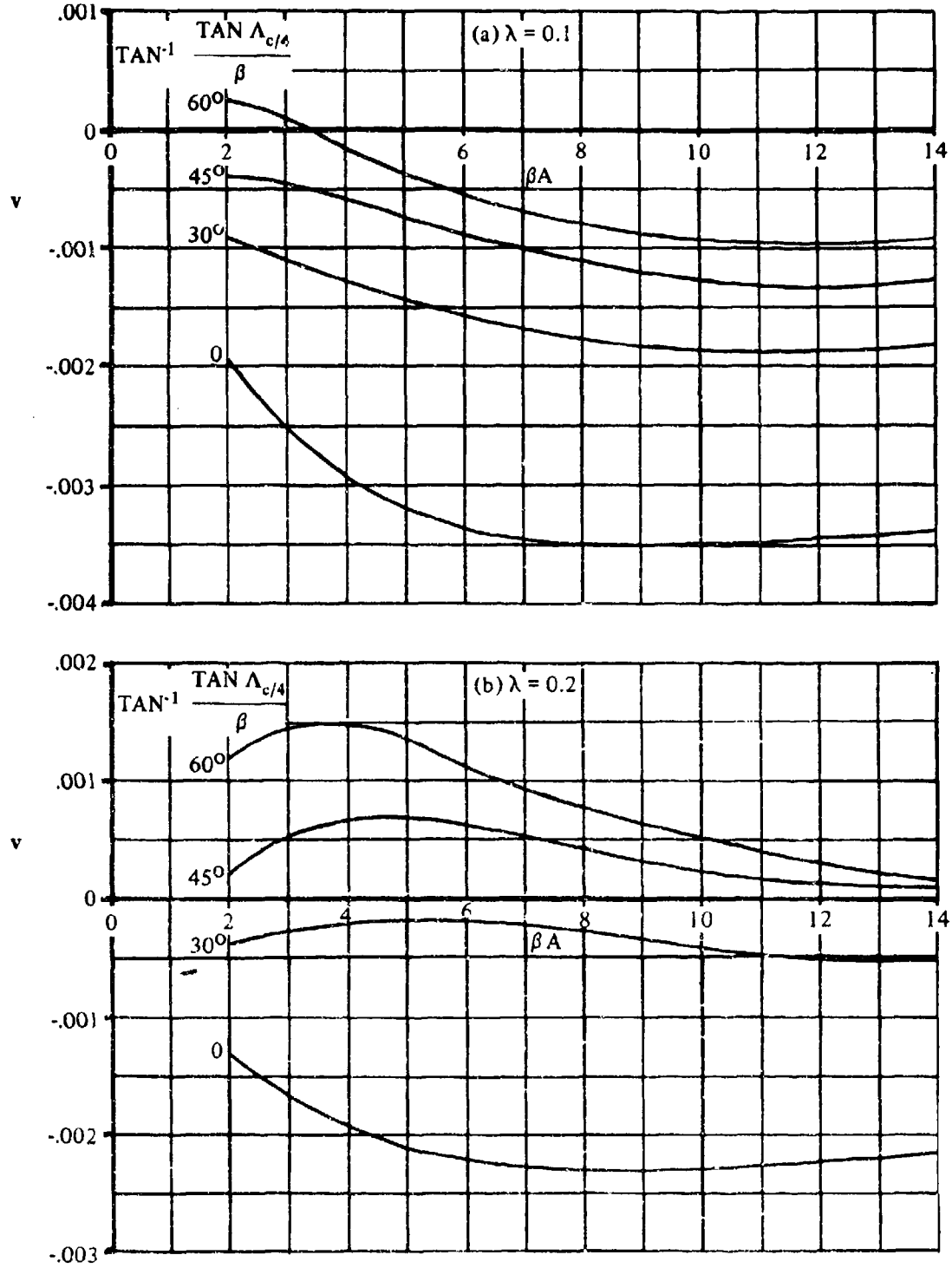

FIGURE 4.1.5.2-42 LIFT-DEPENDENT DRAG FACTOR DUE TO LINEAR TWIST WEISSINGER METHOD

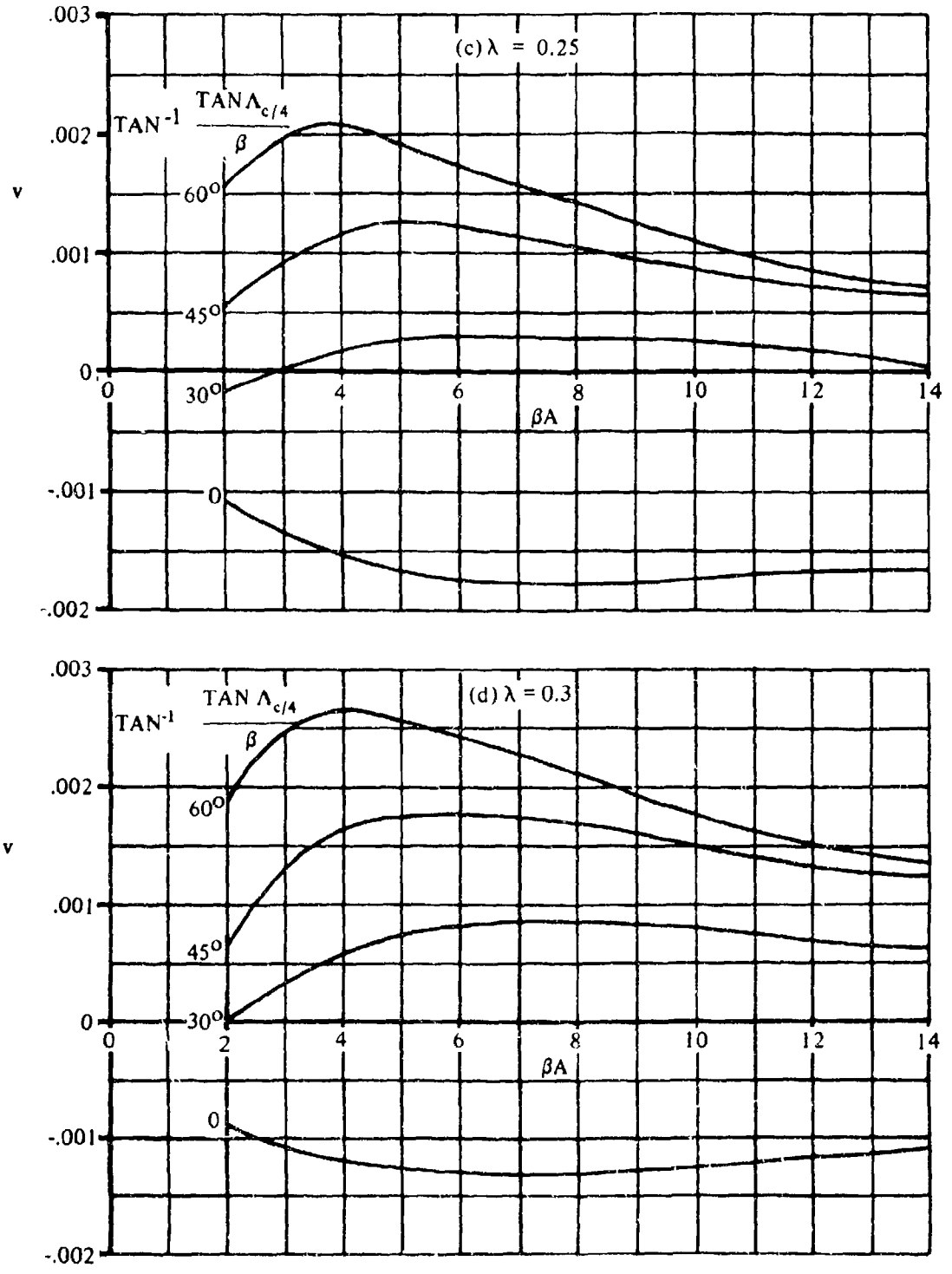

FIGURE 4.1.5.2 -42 (CONTD)

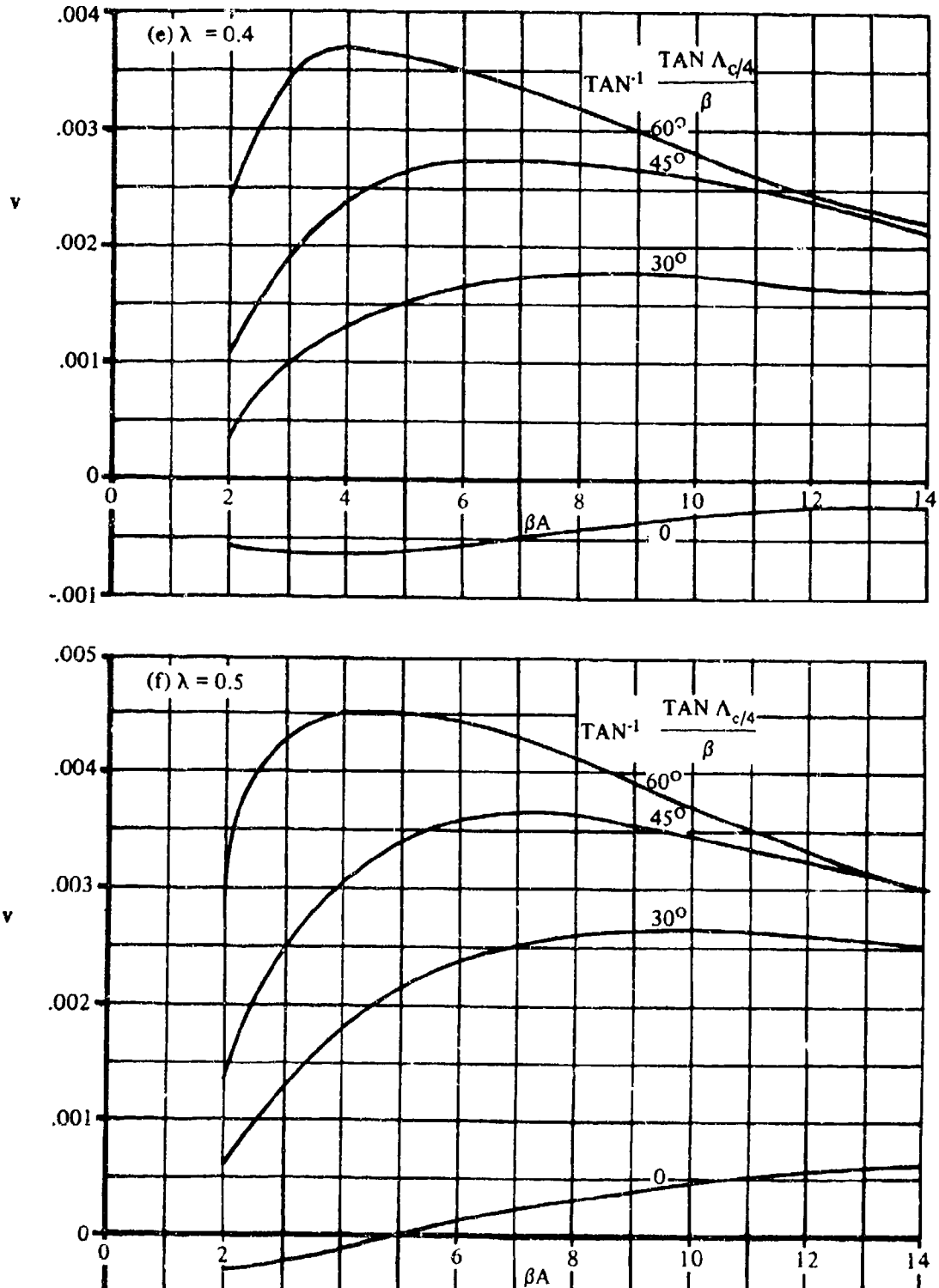

FIGURE 4.1.5.2 -42 (CONTD)

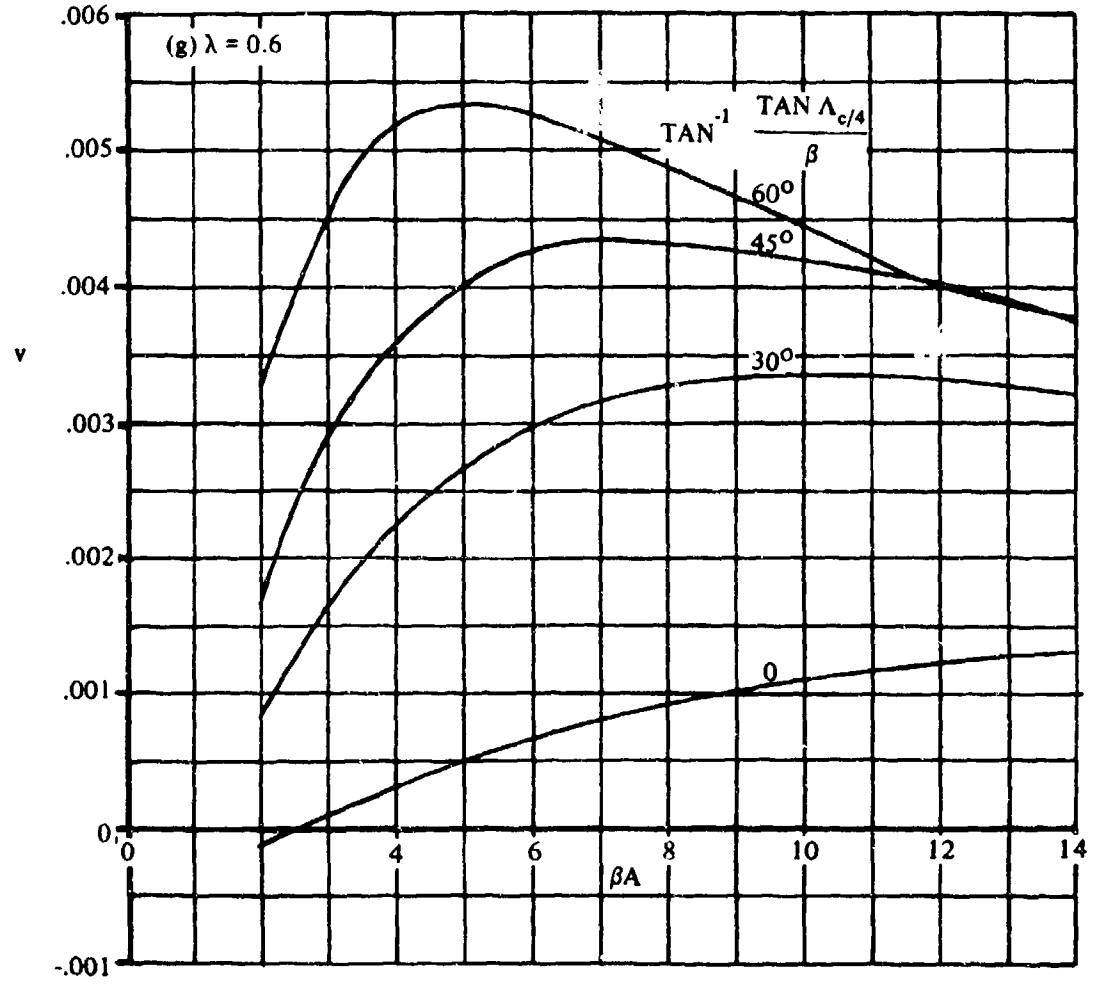

FIGURE 4.1.5.2-42 (CONTD)

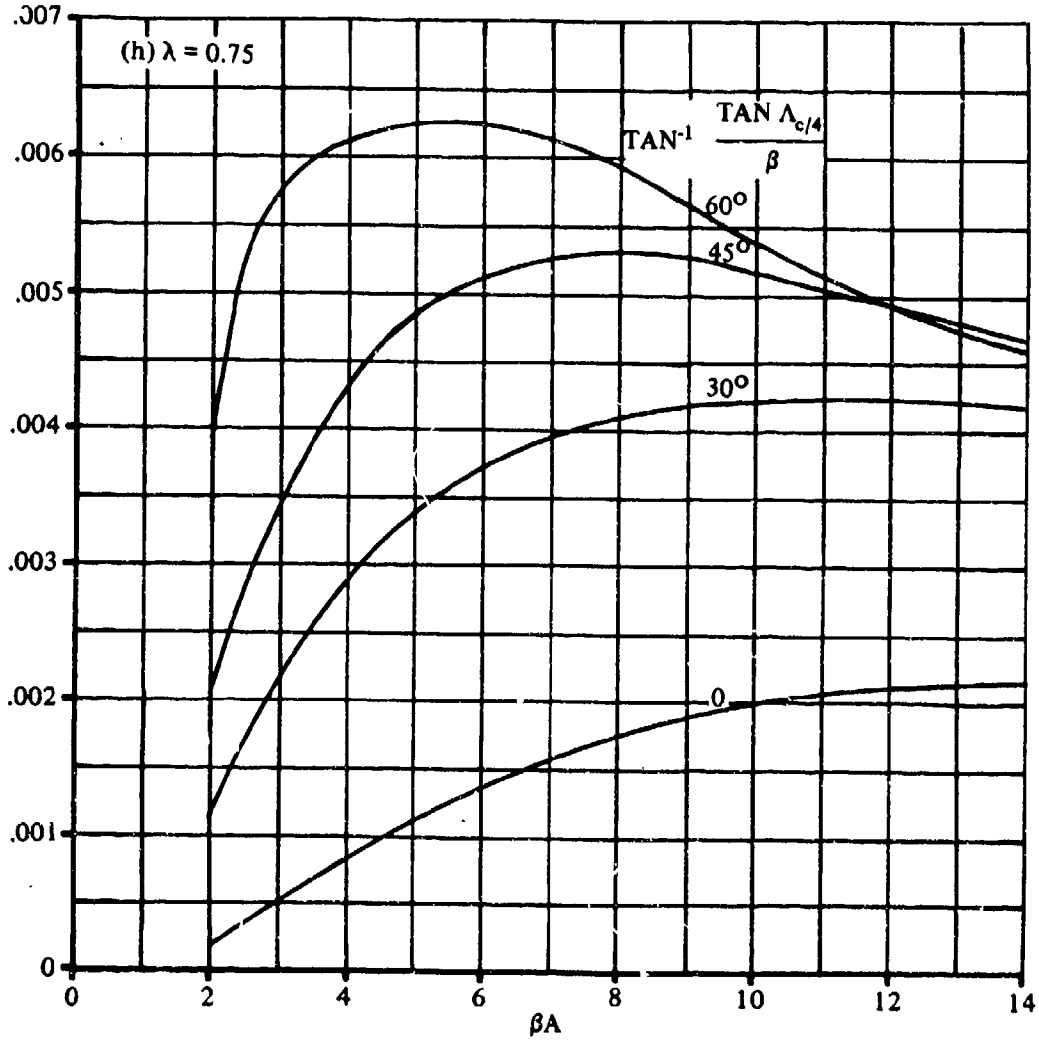

FIGURE 4.1.5.2-42 (CONTD)

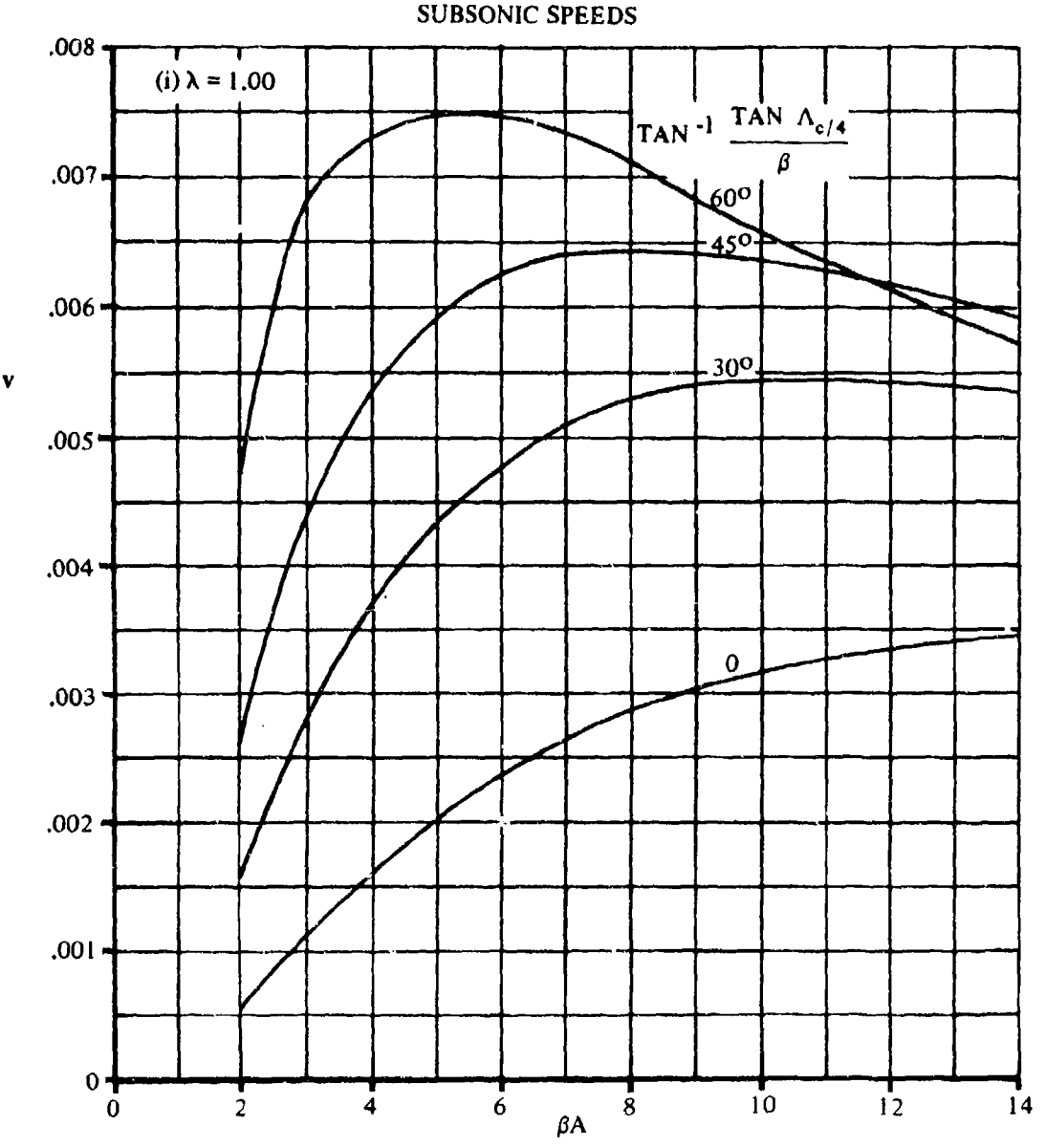

FIGURE 4.1.5.2-42 (CONTD)

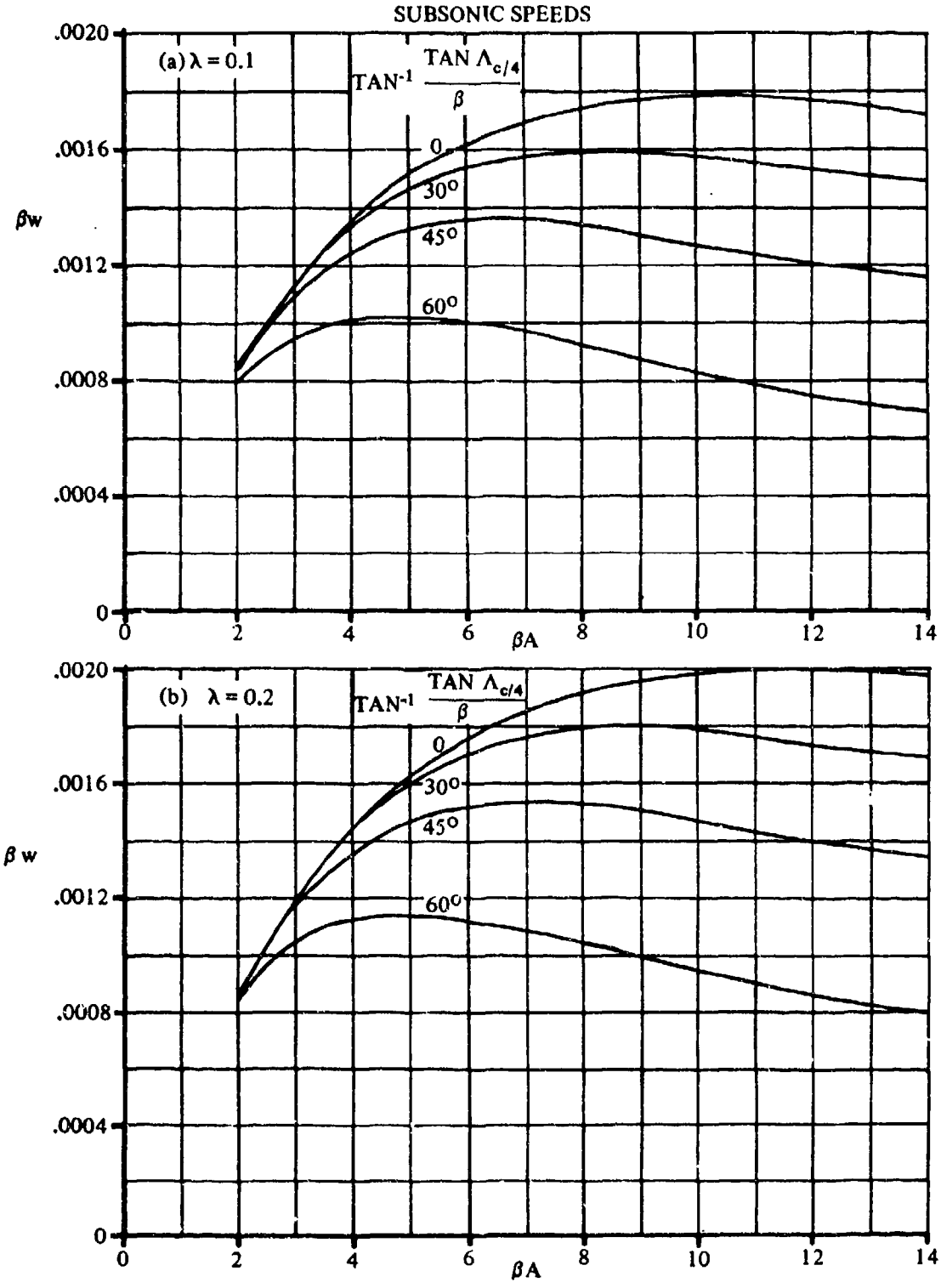

FIGURE 4.1.5.2-48 ZERO-LIFT DRAG FACTOR DUE TO LINEAR TWIST WEISSINGER METHOD

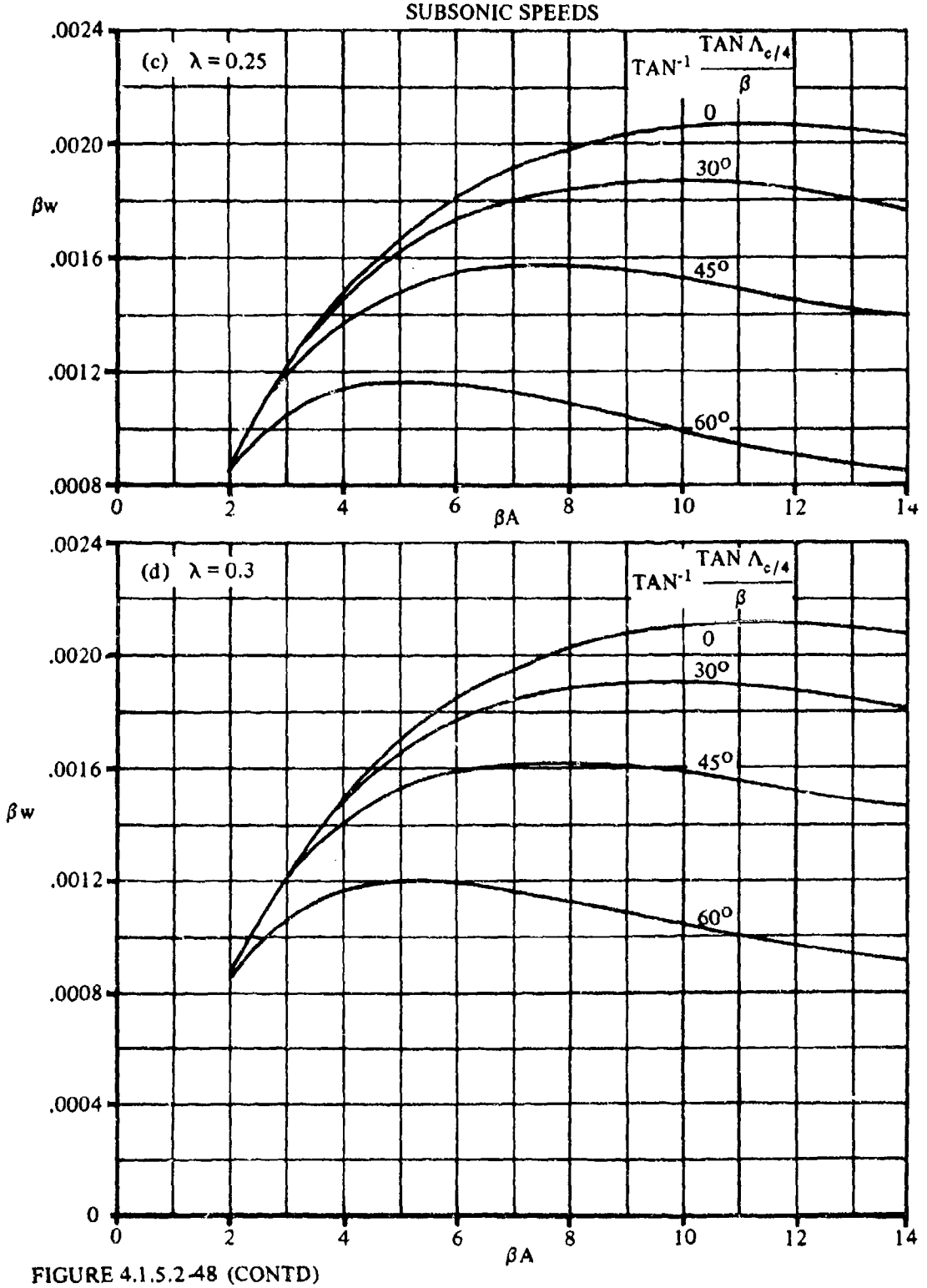

FIGURE 4.1.5.2-48 (CONTD)

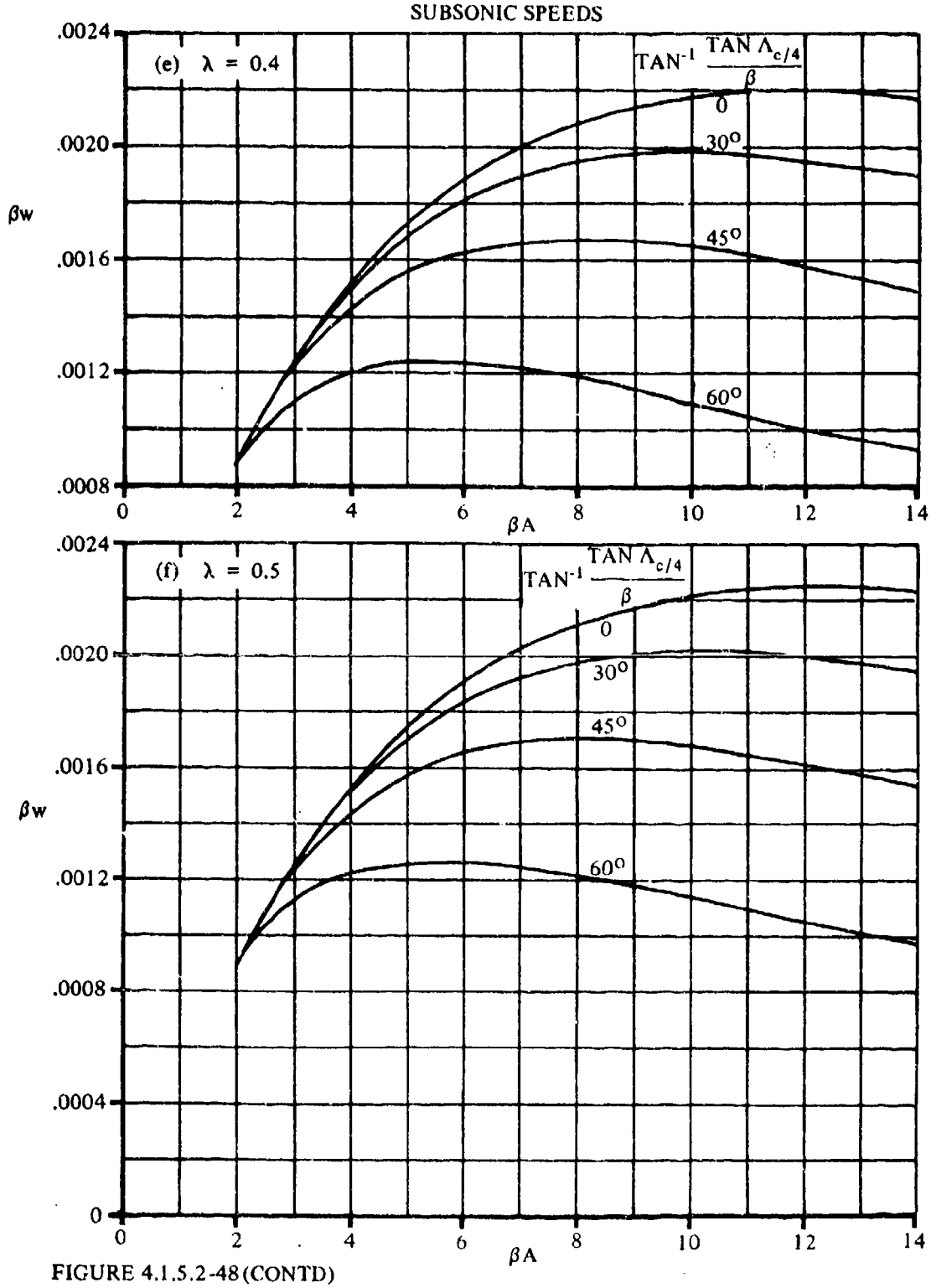

FIGURE 4.1.5.2-48 (CONTD)

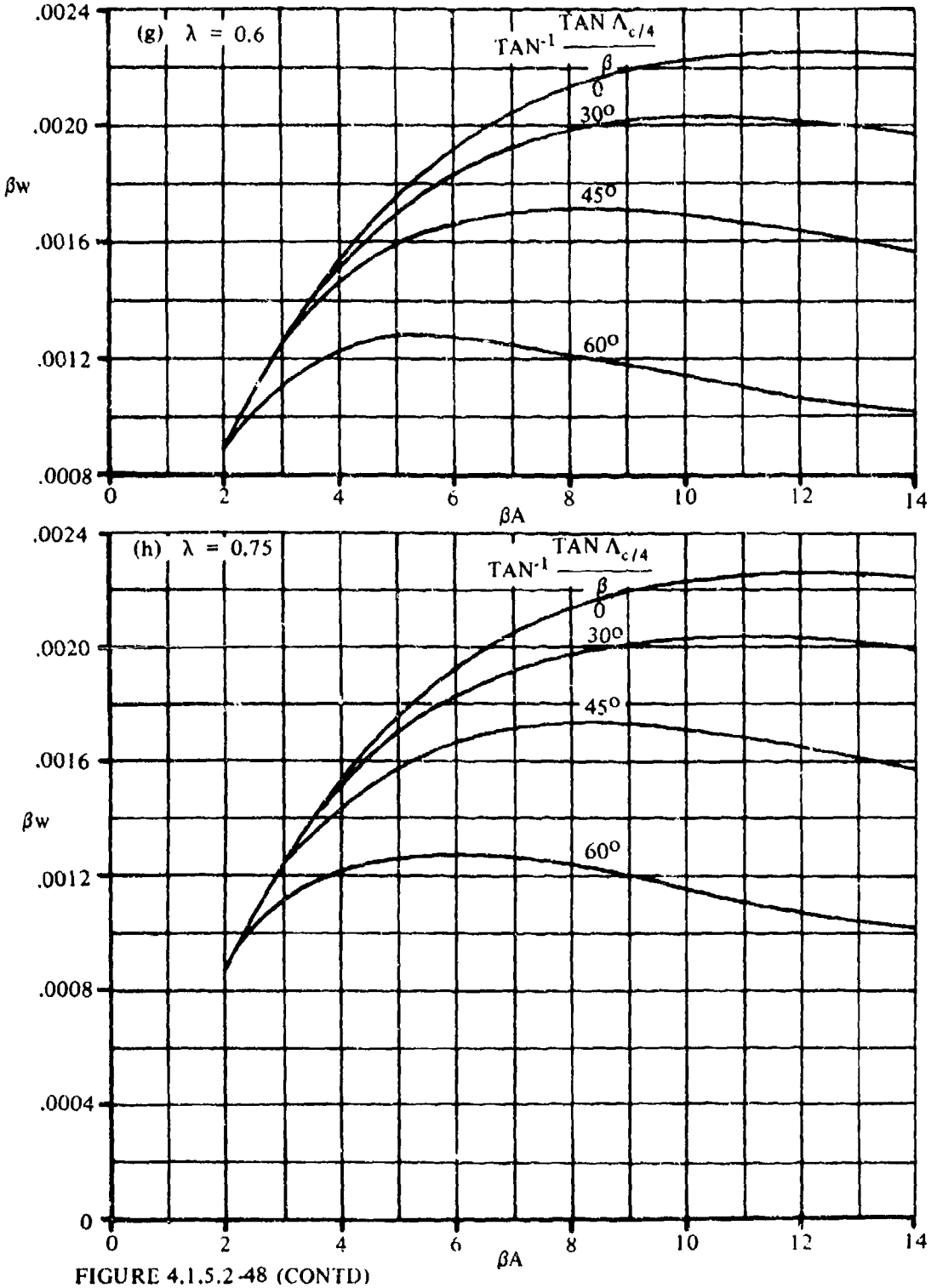

FIGURE 4.1.5.2-48 (CONTD)

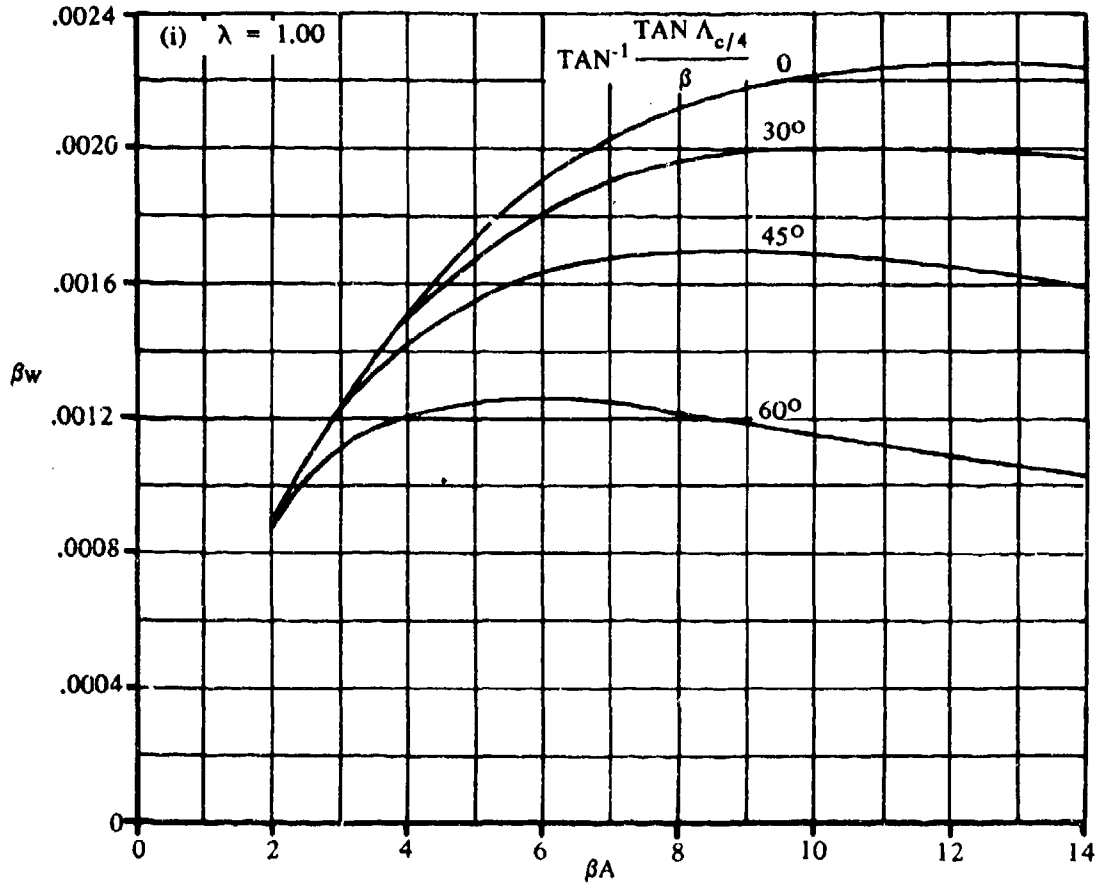

FIGURE 4.1.5.2-48 (CONTD)

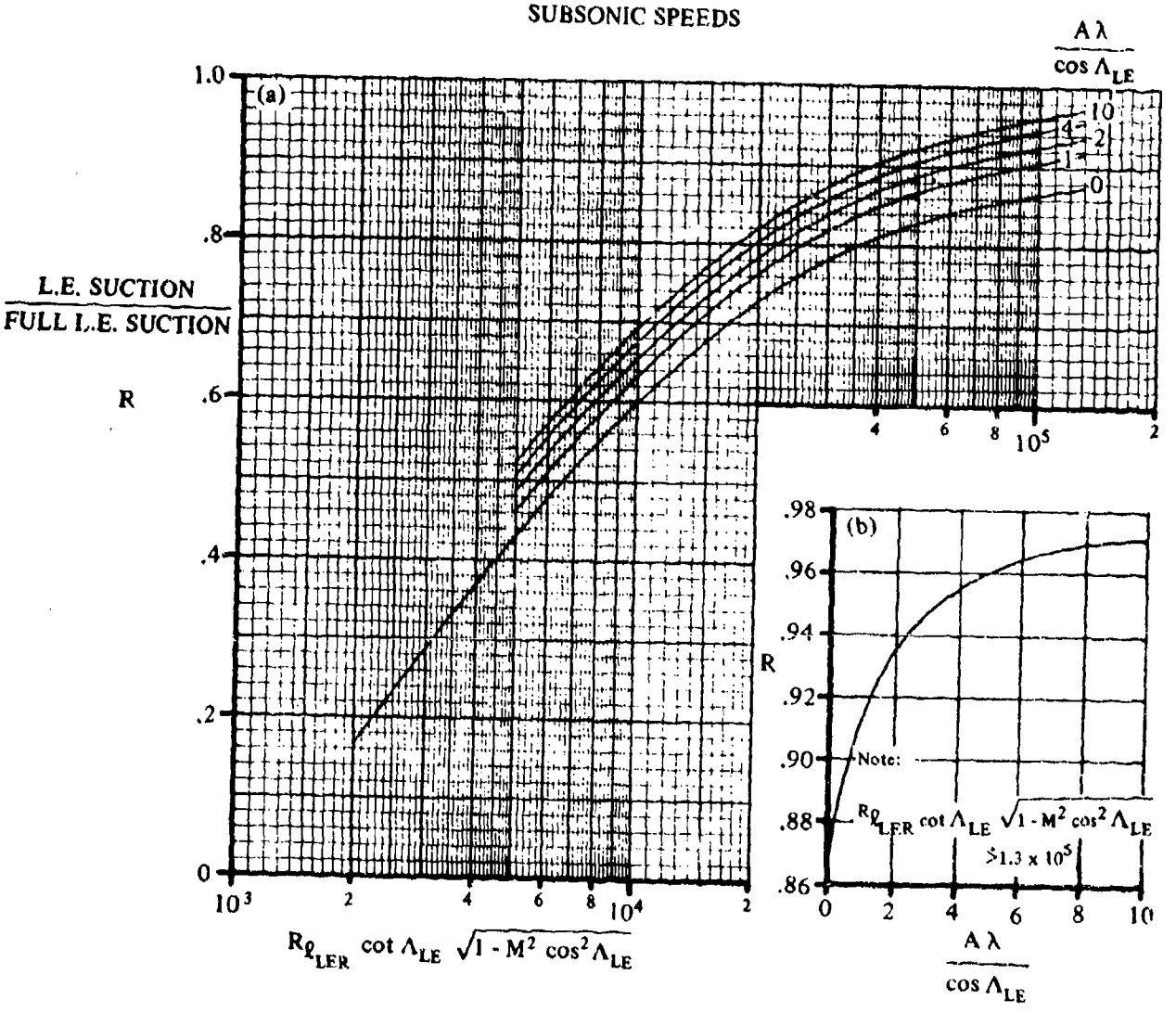

FIGURE 4.1.5.2-53 LEADING-EDGE SUCTION PARAMETER AT SUBSONIC SPEEDS. $M \leq 0.8$

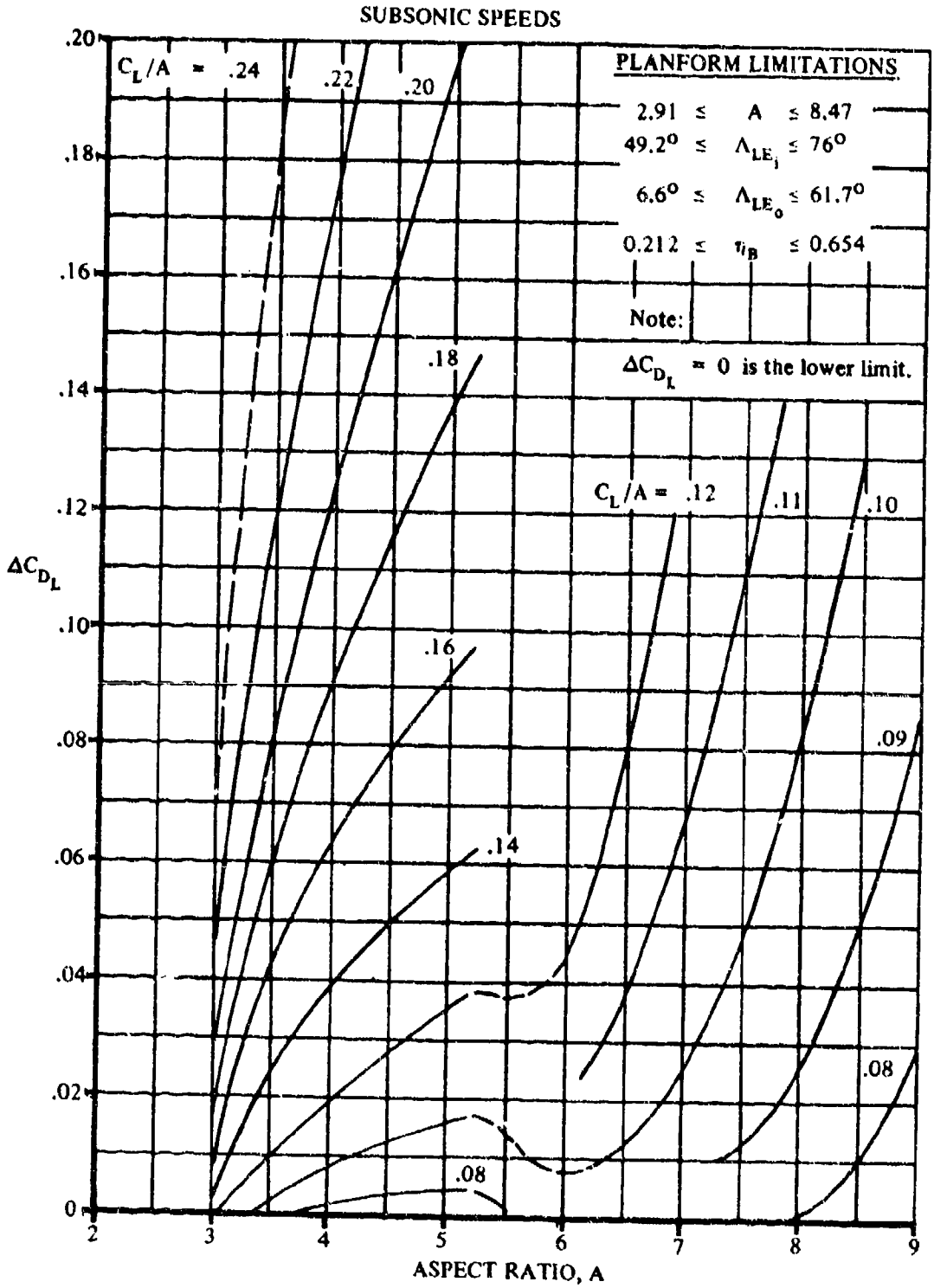

FIGURE 4.1.5.2-54 INDUCED DRAG INCREMENT ABOVE POLAR BREAK FOR CRANKED WINGS HAVING ROUND-NOSED AIRFOILS

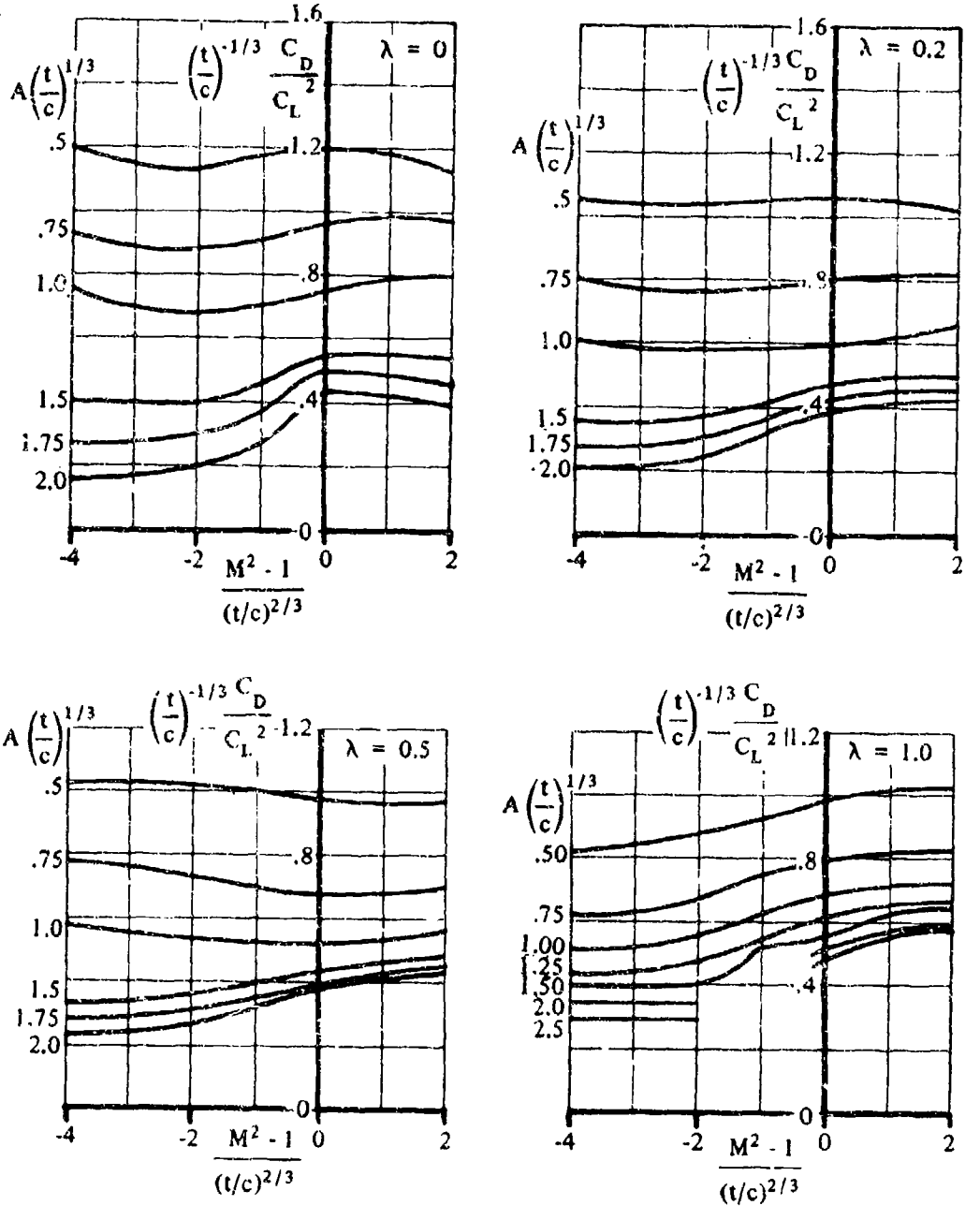

FIGURE 4.1.5.2-55 TRANSONIC DRAG DUE TO LIFT
(a) A TAN $\Lambda_{LE} = 0$

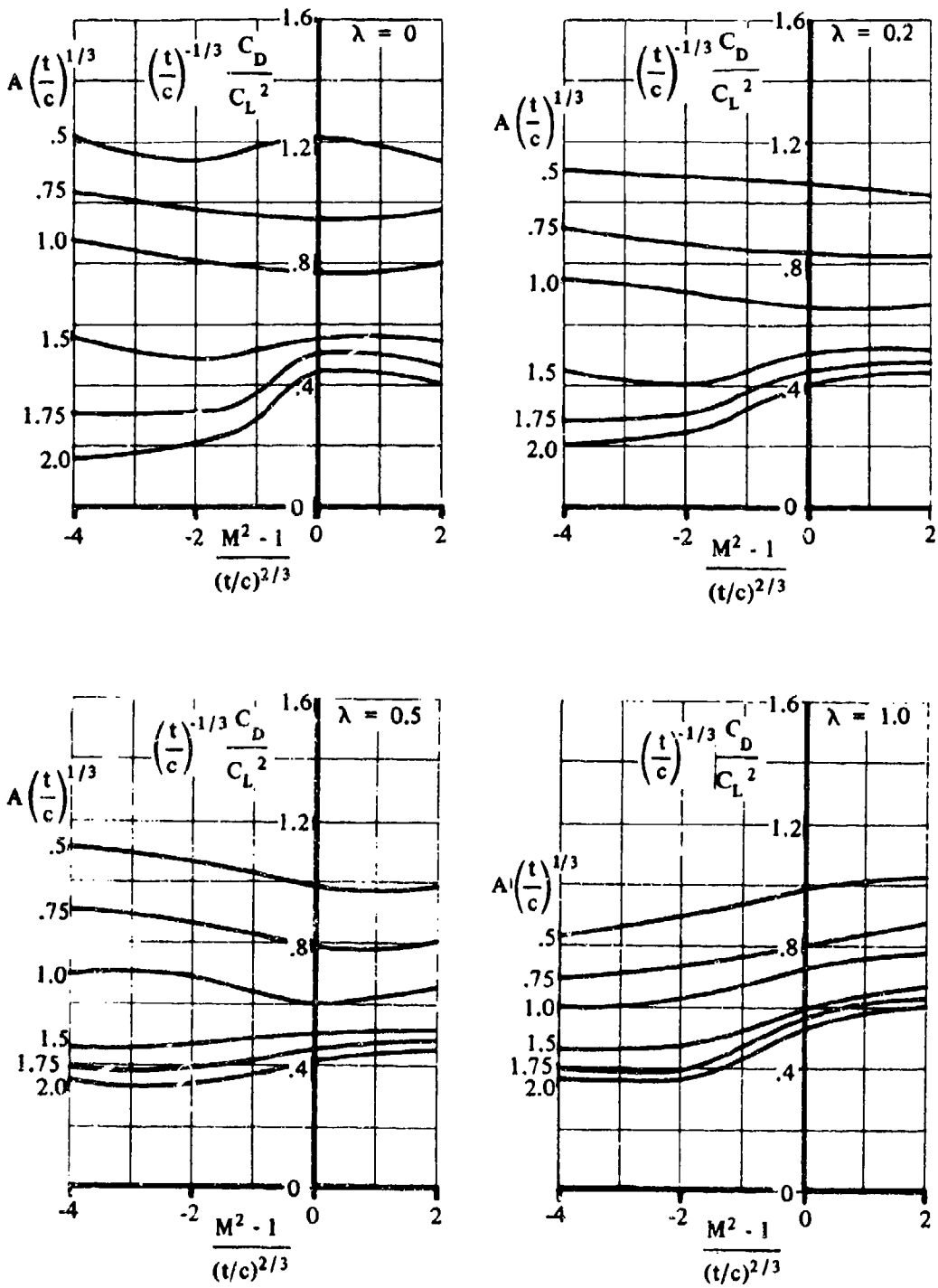

FIGURE 4.1.5.2-55 (CONTD)

(b) A TAN Λ_{LE} = 3

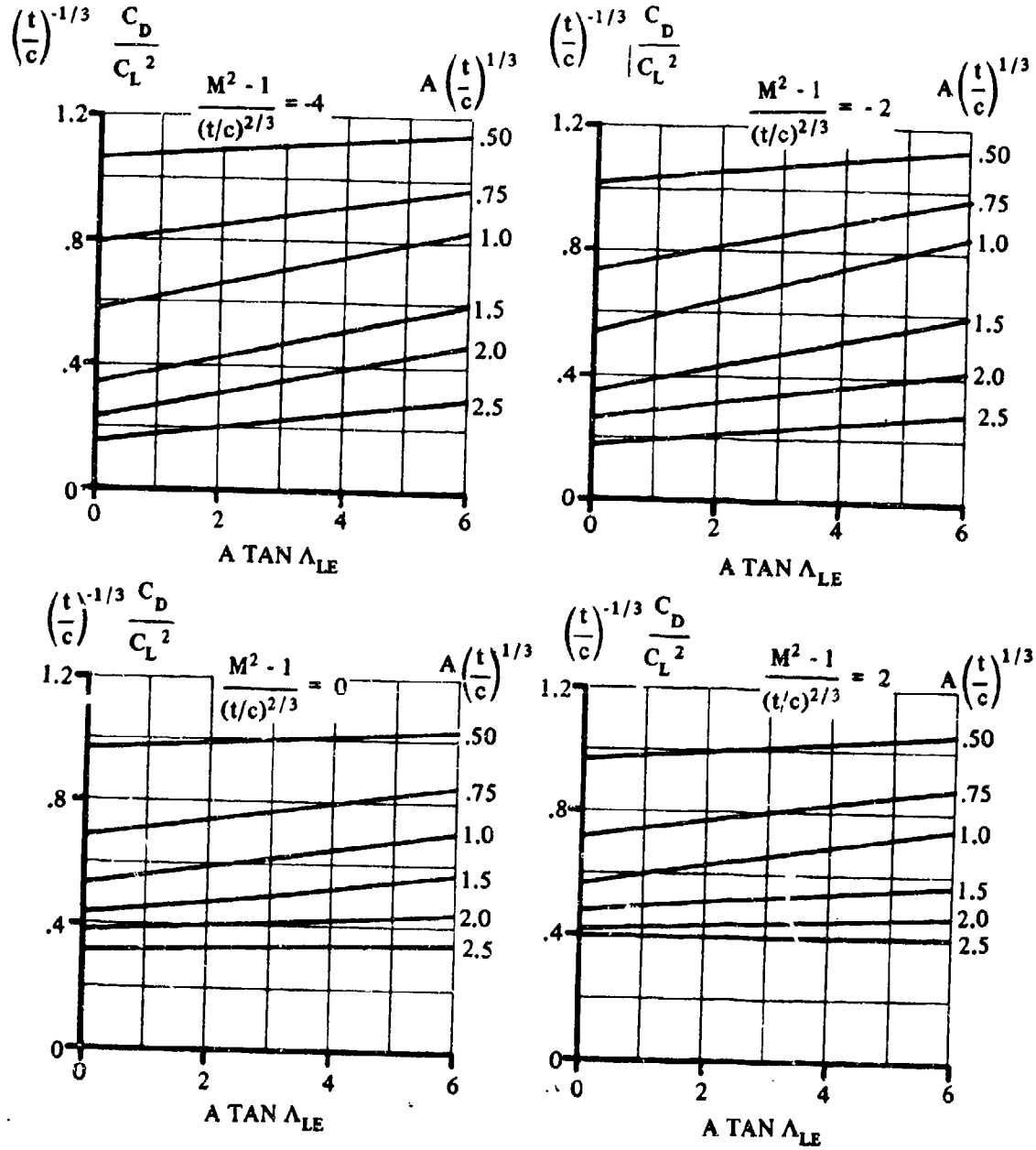

FIGURE 4.1.5.2-55 (CONTD)

(c) TAPER RATIO, $\lambda = 0.50$

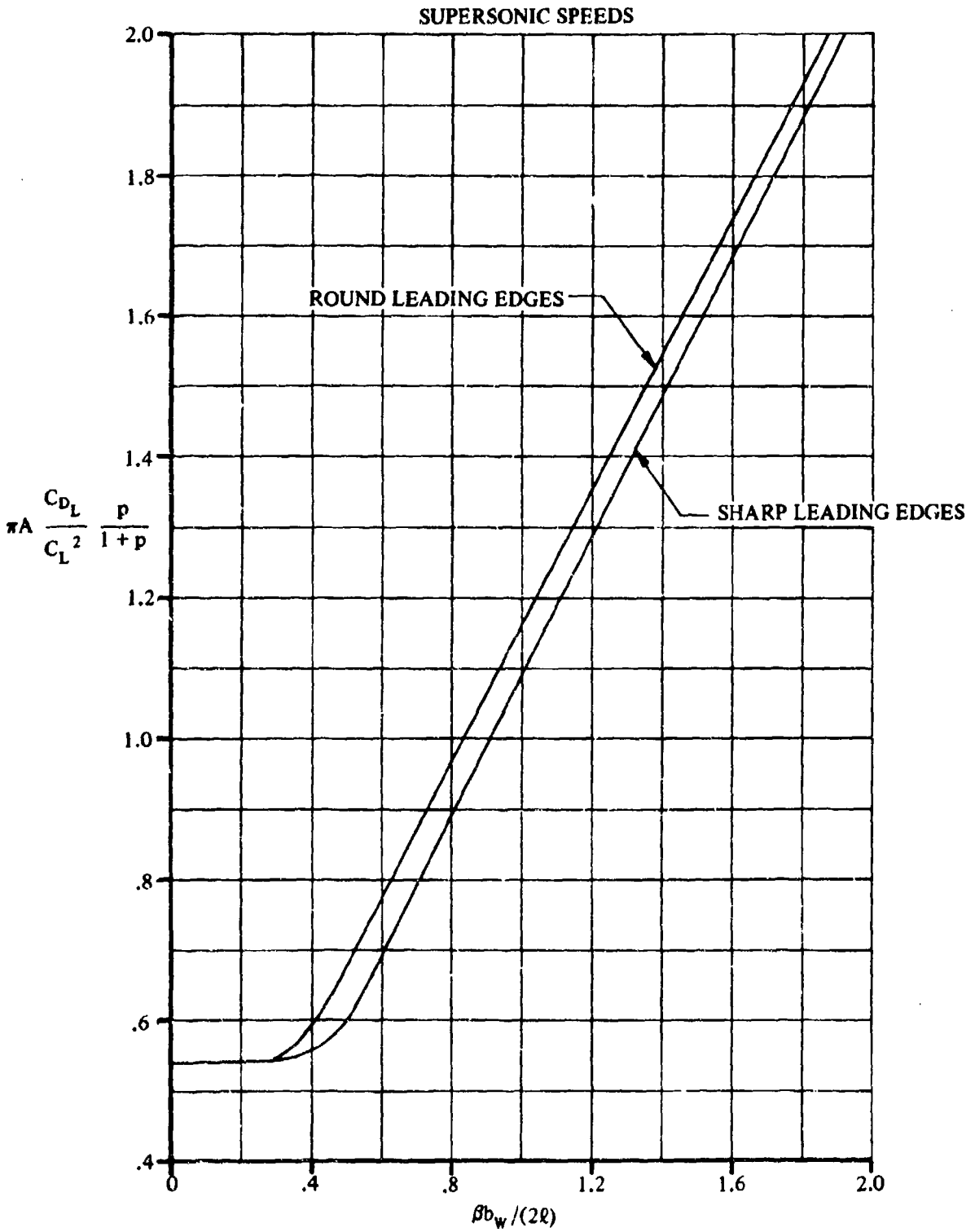

FIGURE 4.1.5.2-58 CORRELATION OF DRAG DUE TO LIFT OF STRAIGHT-TAPERED WINGS

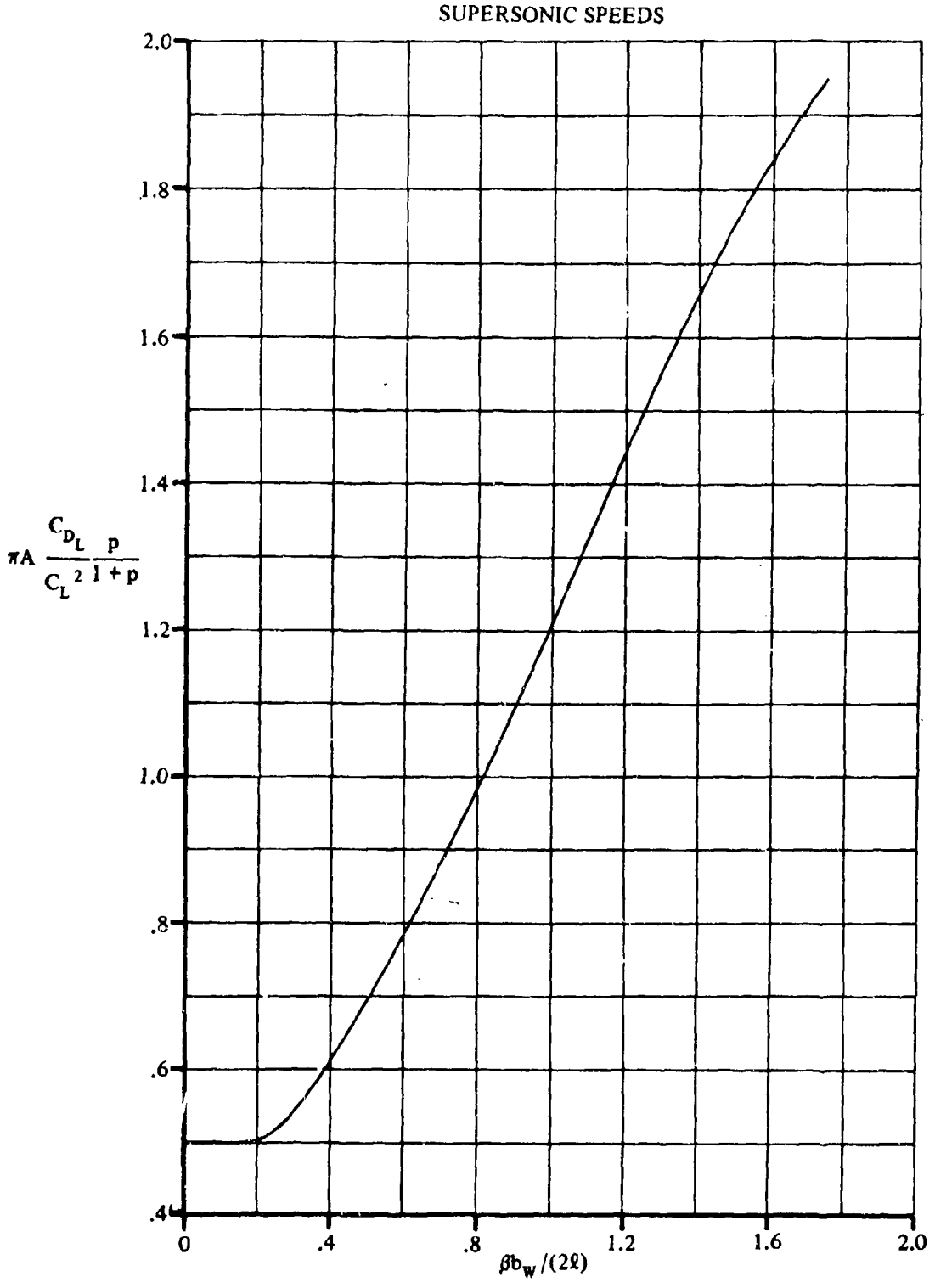

FIGURE 4.1.5.2-59 CORRELATION OF DRAG DUE TO LIFT OF COMPOSITE PLANFORMS

4.2 BODIES AT ANGLE OF ATTACK

4.2.1 BODY LIFT

4.2.1.1 BODY LIFT-CURVE SLOPE

A. SUBSONIC

One of the first attempts to use potential theory for the estimation of lift for bodies of revolution was made by Munk (reference 1). Several similar methods have since been developed that give essentially the same results (references 2 and 3). Potential theory is limited to angles of attack near zero, where viscous cross-flow forces are small. At higher angles of attack the viscous forces become increasingly important (see Section 4.2.1.2).

DATCOM METHOD

The method presented for estimating the lift-curve slope of bodies of revolution at subsonic speeds uses the potential flow term of the expression for body lift from reference 4. The lift-curve slope, based on $V_B^{2/3}$, is

$$C_{L_\alpha} = \frac{2(k_2 - k_1)\, S_o}{V_B^{2/3}} \quad \text{(per radian)} \qquad 4.2.1.1\text{-a}$$

where

V_B is the total body volume.

$(k_2 - k_1)$ is the apparent mass factor developed by Munk and presented in figure 4.2.1.1-20a as a function of body fineness ratio.

S_o is the body cross-sectional area at x_o.

x_o is the body station where the flow ceases to be potential. This is a function of x_1, the body station where the parameter, dS_x/dx first reaches its maximum negative value. x_o and x_1 are correlated in figure 4.2.1.1-20b.

S_x is the body cross-sectional area at any body station.

In many cases it will be possible to determine the location of x_1 by inspection. For cases that are doubtful, the area distribution should be plotted and examined to determine the location where dS_x/dx first reaches its maximum negative value.

The lift-curve slopes of several bodies of revolution, calculated by this method, have been compared with test data in reference 4. In general, the accuracy of the method at angles of attack near zero is good.

For a rapid but approximate estimation, slender-body theory can be used. This gives $C_{L_\alpha} = 2$ per radian, where C_{L_α} is based on the body cross-sectional area at x_o.

No method is available for estimating the lift-curve slope of a body of noncircular cross section. Consequently, test data must be relied upon as the basis for predicting the lift-curve slope of such configurations. A summary of available test data on bodies of noncircular cross section at subsonic speeds is presented as table 4.2.1.1-A.

Sample Problem

Given: An ogive-cylinder-boattailed body of revolution of reference 18.

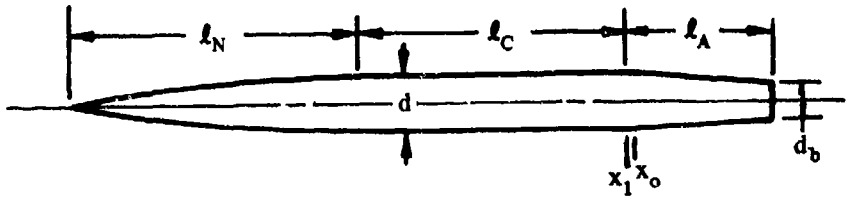

$d = 0.417$ ft $\quad \ell_N = 2.19$ ft $\quad \ell_C = 1.98$ ft $\quad \ell_A = 1.12$ ft

$\ell_B = 5.29$ ft $\quad f = \frac{\ell_B}{d} = 12.7 \quad V_B = 0.537$ cu ft

$x_1 = 4.17$ ft (determined by inspection) $\quad d_b = 0.275$ ft

Compute:

$x_1/\ell_B = 4.17/5.29 = 0.788$

$x_o/\ell_B = 0.793$ (figure 4.2.1.1-20b)

$x_o = (0.793)(5.29) = 4.195$ ft

$(k_2 - k_1) = 0.96$ (figure 4.2.1.1-20a)

$S_o = 0.134$ sq ft

$V_B^{2/3} = 0.537^{2/3} = 0.660$

Solution:

$$C_{L_\alpha} = \frac{2(k_2 - k_1) S_o}{V_B^{2/3}} \quad \text{(equation 4.2.1.1-a)}$$

$$= \frac{2(0.96)(0.134)}{0.660}$$

$= 0.390$ per rad (based on $V_B^{2/3}$)

This compares with a test value of 0.378 per radian, based on $V_B^{2/3}$, from reference 18. The slender-body-theory approximation gives C_{L_α} = 0.406 per radian, based on $V_B^{2/3}$.

B. TRANSONIC

Slender-body theory states that body force characteristics are not functions of Mach number. Experimental data substantially verify this result (references 5, 6, and 7). Any differences in the subsonic value of C_{L_α} obtained from paragraph A and the supersonic value of C_{L_α} obtained from paragraph C should be faired out smoothly in the transonic range.

Transonic test data on bodies of noncircular cross section are available in references 25, 26, and 5 (see table 4.2.1.1-A).

C. SUPERSONIC

Several theoretical methods that have been developed for estimating the lift-curve slope of bodies of revolution are best applied by machine methods. Three of the methods that can be used to estimate characteristics of simple nose-cylinder bodies of revolution at small angles of attack throughout the supersonic range are briefly discussed. They are the slender-body, hybrid, and second-order shock-expansion theories.

Slender-body theory is based on the assumption that the body surface slope (relative to the free stream) is everywhere so small that the boundary conditions may be applied on the axis. This condition is met if β/f_N is small, i.e., if the nose has a large fineness ratio or if the flow is close to sonic speed. Slender-body theory is applicable in the range of values of the parameter β/f_N from 0 to approximately 0.05. Hybrid theory (reference 8), a combination of a second-order axial solution with a first-order cross-flow solution, is applicable for values of β/f_N from approximately 0.05 to 0.40. The second-order shock-expansion method (reference 9), an extension of the general shock-expansion method at small angles of attack, is applicable for values of β/f_N from approximately 0.40 to ∞.

The flow around bodies with boattails can be calculated by Van Dyke's hybrid theory (reference 8). Reference 10 presents a generalized curve for estimating the normal-force-curve slope of boattails, based on the method of reference 8. Lavender and Deep (reference 11) give methods, based on the work of reference 9, for determining the normal-force-curve slope of cone-cylinder-frustums, cone-cylinder-frustum-boosters, and cone-frustum-boosters.

DATCOM METHOD

Empirical design charts are presented for estimating the normal-force-curve slope of bodies of revolution composed of ogival or conical noses and cylindrical afterbodies. In addition, theoretical results are presented for determining the increment in normal-force-curve slope due to the addition of either a boattailed or a flared body of revolution at the end of semi-infinite cylindrical bodies.

Figures 4.2.1.1-21a and 4.2.1.1-21b present C_{N_α}, based on maximum frontal area, for bodies with ogival and conical noses, respectively, and cylindrical afterbodies of varying fineness ratio. The normal-force-curve slopes of two other common nose shapes, the 3/4-power nose and the parabolic nose (1/2-power nose), are not presented directly. However, experimental data indicate that the force characteristics of cones and 3/4-power noses are similar, as are those of ogives and parabolic noses (reference 12). Tests also indicate that the addition of a cylindrical afterbody results in approximately the same increase in lift, irrespective of nose profile shape (reference 13). Therefore figure 4.2.1.1-21a can be used for parabolic-nose-cylinders and

figure 4.2.1.1-21b for 3/4-power-nose-cylinders with sufficient accuracy for most purposes.

The increments in normal-force-curve slope due to the addition of a boattailed or a flared body of revolution at the end of a semi-infinite cylindrical body are presented in figures 4.2.1.1-22a and 4.2.1.1-22b, respectively. Both of these increments are based on the cross-sectional area of the cylindrical body preceding the boattail or the flare. Figure 4.2.1.1-22a is taken from reference 10 and is based on the results of reference 8. Figure 4.2.1.1-22b is based on impact theory.

A comparison of test data with C_{N_α} of ogive-cylinder and cone-cylinder bodies calculated by this method is presented as table 4.2.i.1-B. The ranges of body geometry and Mach number of the test data are:

Cone-Cylinder					Ogive-Cylinder				
0	$\leq$	f_A	$\leq$	10.00	0	$\leq$	f_A	$\leq$	11.00
2.50	$\leq$	f_N	$\leq$	7.00	1.50	$\leq$	f_N	$\leq$	7.00
0	$\leq$	f_A/f_N	$\leq$	3.17	0	$\leq$	f_A/f_N	$\leq$	3.87
1.36	$\leq$	M	$\leq$	5.04	1.28	$\leq$	M	$\leq$	5.04

No method is available for estimating the lift-curve slope of a body of noncircular cross section. Consequently, test data must be relied upon as the basis for predicting the lift-curve slope of such configurations. A summary of available test data on bodies of noncircular cross section at supersonic speeds is presented as table 4.2.1.1-C.

Sample Problem

Given: The cone-cylinder-flare body of reference 27.

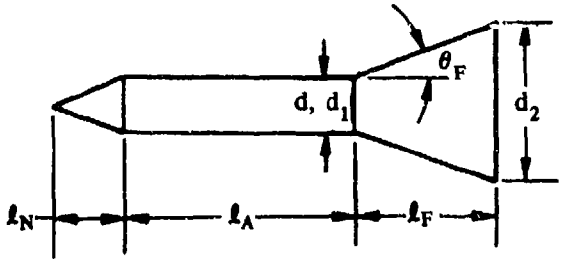

ℓ_N = 1.21 in. ℓ_A = 4.00 in. ℓ_F = 2.40 in.

d = d_1 = 1.0 in. d_2 = 2.75 in.

θ_F = 20°

M = 5.05; β = 4.95

Compute:

Cone-cylinder:

$f_N = \ell_N/d = 1.21$

$f_A = \ell_A/d = 4.00$

$f_A/f_N = 4.0/1.21 = 3.31$

$f_N/\beta = 1.21/4.95 = 0.244$

C_{N_α} = 3.52 per rad (linear extrapolation, figure 4.2.1.1-21b)
(based on cone-cylinder maximum frontal area)

Flare:

$d_2/d_1 = 2.75$

$\dfrac{(\Delta C_{N_\alpha})_F}{\cos^2 \theta_F} = 13.30$ (figure 4.2.1.1-22b)

$(\Delta C_{N_\alpha})_F = 13.30 \quad (\cos 20^o)^2$

$= 11.73$ per rad (based on $\dfrac{\pi d_1^2}{4}$ = cone-cylinder maximum frontal area)

Solution:

$C_{N_\alpha} = C_{N_\alpha}{}_{\text{cone-cylinder}} + (\Delta C_{N_\alpha})_F$

$= 3.52 + 11.73$

$= 15.25$ per rad (based on cone-cylinder maximum frontal area)

This compares with a test value of 17.70 per radian from reference 27.

D. HYPERSONIC

Newtonian impact theory is used for estimating the normal-force-curve slope of bodies of revolution at hypersonic Mach numbers. Newtonian theory assumes that the component of momentum normal to the surface is canceled on impact, thus giving rise to a normal force. The stagnation pressure predicted by Newtonian theory is about ten percent higher than the theoretical adiabatic pressure rise for an infinite Mach number. To correct this overestimation, a modified Newtonian method has been developed in which the assumptions of Newtonian flow are used, but the theoretical stagnation-pressure coefficient for the Mach number being considered is substituted for the Newtonian stagnation-pressure coefficient. Another modification of Newtonian theory considers the centrifugal forces in the flow around bodies of revolution (reference 14). This effect is small for conventional slender noses such as cones and ogives at moderate angles of attack, and the pressure forces on such slender noses are satisfactorily approximated by simple impact theory. For cylindrical afterbodies, inclusion of the effect of the centrifugal forces reduces the estimated normal-force-curve slope approximately ten percent.

Newtonian theory and its modifications are discussed in detail in reference 14. In this work Newtonian analysis is presented for an arbitrary body of revolution and the resulting forces on a cone and cylinder are given. In reference 15 a method of application of Newtonian concepts similar to that of reference 14 is presented. Reference 15 presents design charts which allow the aerodynamic characteristics of arbitrary

bodies of revolution to be obtained without the computation or radial integration of pressure distributions. In reference 16 the modified Newtonian approximation for the pressure distribution on bodies of revolution has been used to derive expressions for the aerodynamic characteristics at zero angle of attack for blunted cones, truncated cones, spherical segments, and rounded-shoulder cylinders. Approximate equations are also presented which may be used in conjunction with the design charts to obtain the zero angle-of-attack characteristics of composite missile components. The Datcom method uses the results of Newtonian impact theory presented in reference 17. This work presents design charts and equations for determining the aerodynamic characteristics of missile shapes composed of one or more cone frustums with or without a spherical nose. In addition, design charts are presented for the special cases of spherically blunted cones and ogives which can be used in conjunction with the results of reference 17.

DATCOM METHOD

The normal-force-curve slope of a body composed of one or more cone frustums with or without a spherical nose, a blunted conical nose, or a blunted ogival nose, based on the body base area, is given by

$$C_{N_\alpha} = \sum_{n=1}^{m} \left(C_{N_\alpha}\right)_n \left(\frac{d_n}{d_b}\right)^2 \qquad 4.2.1.1\text{-b}$$

To apply equation 4.2.1.1-b the body is divided into m segments, the first segment being either a spherical nose, a blunted conical nose, a blunted ogival nose, or a cone frustum, and each succeeding segment a cone frustum. The normal-force-curve slope of a spherical nose, based on its base area, is obtained from figure 4.2.1.1-23. The normal-force-curve slope of a blunted conical or blunted ogival nose, based on their respective base areas, is obtained from figures 4.2.1.1-24 and 4.2.1.1-25, respectively. The normal-force-curve slope of a cone frustum, based on the base area of the specific segment, is obtained from figure 4.2.1.1-26. (Note that a cylinder is considered a cone frustum with $\theta = 0$ and $a/d = 1.0$, and that $C_{N_\alpha} = 0$ by Newtonian impact theory.) The ratio $(d_n/d_b)^2$ refers the normal-force-curve slope to the base area of the configuration.

It should be noted that the design charts used in this method are based on Newtonian theory with no modifications of the stagnation-pressure coefficient or the centrifugal forces.

Sample Problem

Given: Configuration 5115 of reference 45, consisting of a cone-cylinder-frustum body with a spherical nose.

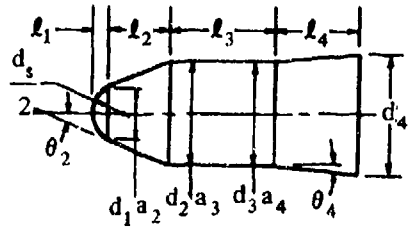

All dimensions in feet

Spherical Segment

$$\ell_1 = 0.18 \qquad \frac{d_s}{2} = 0.36 \qquad d_1 = 0.62$$

Forward Cone Frustum

$$a_2 = 0.62 \qquad d_2 = 1.20$$

$$\ell_2 = 0.72 \qquad \theta_2 = 22.5^\circ$$

Cylinder

$a_3 = 1.20$

$\ell_3 = 1.20$

$d_3 = 1.20$

$\theta = 0$

Rear Cone Frustum

$a_4 = 1.20$

$\ell_4 = 0.96$

$d_4 = d_b = 1.368$

$\theta_4 = 5^\circ$

Compute:

Spherical Segment

$2\ell_1/d_s = 0.18/0.36 = 0.50$

$\left(C_{N_\alpha}\right)_1 = 0.75$ per rad (figure 4.2.1.1-23) $\left(\text{based on } \frac{\pi d_1^2}{4}\right)$

Foreward Cone Frustum

$a_2/d_2 = 0.62/1.20 = 0.517$

$\left(C_{N_\alpha}\right)_2 = 1.250$ per rad (figure 4.2.1.1-26) $\left(\text{based on } \frac{\pi d_2^2}{4}\right)$

Cylinder

$a_3/d_3 = 1.20/1.20 = 1.00$

$\left(C_{N_\alpha}\right)_3 = 0$ (figure 4.2.1.1-26)

Rear Cone Frustum

$a_4/d_4 = 1.20/1.368 = 0.877$

$\left(C_{N_\alpha}\right)_4 = 0.450$ per rad (figure 4.2.1.1-26) $\left(\text{based on } \frac{\pi d_b^2}{4}\right)$

Solution:

$$C_{N_\alpha} = \sum_{n=1}^{m} \left(C_{N_\alpha}\right)_n \left(\frac{d_n}{d_b}\right)^2 \quad \text{(equation 4.2.1.1-b)}$$

$$= (C_{N_\alpha})_1 \left(\frac{d_1}{d_b}\right)^2 + (C_{N_\alpha})_2 \left(\frac{d_2}{d_b}\right)^2 + (C_{N_\alpha})_3 \left(\frac{d_3}{d_b}\right)^2 + (C_{N_\alpha})_4 \left(\frac{d_4}{d_b}\right)^2$$

$$= (0.75) \left(\frac{0.62}{1.368}\right)^2 + (1.250) \left(\frac{1.20}{1.368}\right)^2 + (0) \left(\frac{d_3}{d_b}\right)^2 + (0.450) \left(\frac{1.368}{1.368}\right)^2$$

$$= 0.1540 + 0.9618 + 0 + 0.450$$

$$= 1.566 \text{ per rad} \left(\text{based on configuration base area } \frac{\pi d_b^2}{4}\right)$$

This compares with a test value of 1.719 per radian from reference 45 at a Mach number of 4.04.

REFERENCES

1. Munk, M. M.: The Aerodynamic Forces on Airship Hulls. NACA TR 184, 1924. (U)
2. Upson, R. H., and Klikoff, W. A.: Application of Practical Hydrodynamics to Airship Design. NACA TR 405, 1931. (U)
3. Laitone, E. V.: The Linearized Subsonic and Supersonic Flow About Inclined Bodies of Revolution. Jour. Aero. Sci., Vol. 14, No. 11, 1947. (U)
4. Hopkins, E. J.: A Semiempirical Method for Calculating the Pitching Moment of Bodies of Revolution at Low Mach Numbers. NACA RM A51C14, 1951. (U)
5. McDevitt, J. B., and Taylor, R. A.: Force and Pressure Measurements at Transonic Speeds for Several Bodies Having Elliptical Cross Sections. NACA TN 4362, 1958. (U)
6. McDevitt, J. B., and Taylor, R. A.: Pressure Distributions at Transonic Speeds for Slender Bodies Having Various Axial Locations of Maximum Diameter. NACA TN 4280, 1958. (U)
7. Taylor, R. A., and McDevitt, J. B.: Pressure Distributions at Transonic Speeds for Parabolic-Arc Bodies of Revolution Having Fineness Ratios of 10, 12, and 14. NACA TN 4234, 1958. (U)
8. Van Dyke, M.: First- and Second-order Theory of Supersonic Flow Past Bodies of Revolution. Jour. Aero. Sci., Vol. 18, No. 3, 1951. (U)
9. Syvertson, C. A., and Dennis, D. H.: A Second-Order Shock-Expansion Method Applicable to Bodies of Revolution Near Zero Lift. NACA TR 1328, 1957. (U)
10. Anon: Royal Aeronautical Society Data Sheets – Aerodynamics, Vol. IV (Bodies S.01.03.03), 1958. (U)
11. Lavender, R., and Deep, R.: Application of Second-Order Shock Expansion Theory to Several Types of Bodies of Revolution. Jour. Aero. Sci., Vol. 23, No. 11, 1956. (U)
12. Dennis, D. H., and Cunningham, B. E.: Forces and Moments on Pointed and Blunt-Nosed Bodies of Revolution at Mach Numbers From 2.75 to 5.00. NACA RM A52E22, 1952. (U)
13. Dennis, D. H., and Cunningham, B. E.: Forces and Moments on Inclined Bodies at Mach Numbers From 3.0 to 6.3. NACA RM A54E03, 1954. (U)

14. Grimminger, G., Williams, E. P., and Young, G. B. W.: Lift on Inclined Bodies of Revolution in Hypersonic Flow. Jour. Aero. Sci., Vol. 17, No. 11, 1950. (U)

15. Rainey, R. W.: Working Charts for Rapid Prediction of Force and Pressure Coefficients on Arbitrary Bodies of Revolution by Use of Newtonian Concepts. NASA TN D-176, 1959. (U)

16. Gray, J. D.: Drag and Stability Derivatives of Missile Components According to the Modified Newtonian Theory. AEDC-TN-60-191, 1960. (U)

17. Fisher, L. R.: Equations and Charts for Determining the Hypersonic Stability Derivatives of Combinations of Cone Frustums Computed by Newtonian Impact Theory. NASA TN D-149, 1959. (U)

18. Goodson, K. W.: Effect of Nose Length, Fuselage Length, and Nose Fineness Ratio on the Longitudinal Aerodynamic Characteristics of Two Complete Models at High Subsonic Speeds. NASA Memo 10-10-58L, 1958. (U)

19. Spencer, B., Jr., and Phillips, W. P.: Effects of Cross-Section Shape on the Low-Speed Aerodynamic Characteristics of a Low-Wave-Drag Hypersonic Body. NASA TN D-1963, 1963. (U)

20. Letko, W., and Williams, J. L.: Experimental Investigation at Low Speed of Effects of Fuselage Cross Section on Static Longitudinal and Lateral Stability Characteristics of Models Having 0° and 45° Swept-back Surfaces. NACA TN 3561, 1955. (U)

21. Jacobs, E. N., and Ward, K. E.: Interference of Wing and Fuselage From Tests of 209 Combinations in the NACA Variable-Density Tunnel. NACA TR 540, 1935. (U)

22. House, R. O., and Wallace, A. R.: Wind-Tunnel Investigation of Effect of Interference on Lateral-stability Characteristics of Four NACA 23012 Wings, an Elliptical and a Circular Fuselage and Vertical Fins. NACA TR 705, 1941. (U)

23. King, T. J., Jr.: Wind-Tunnel Investigation at High Subsonic Speeds of Some Effects of Fuselage Cross-Section Shape and Wing Height on the Static Longitudinal and Lateral Stability Characteristics of a Model Having a 45° Swept Wing. NACA RM L55J25, 1956. (U)

24. Sherman, A.: Interference of Wing and Fuselage From Tests of 30 Combinations With Triangular and Elliptical Fuselages in the NACA Variable-Density Tunnel. NACA TN 1272, 1947. (U)

25. Taylor, R. A.: Transonic Aerodynamic Characteristics of Several Bodies Having Elliptical Cross Sections and Various Plan Forms. NASA TN D-14, 1959. (U)

26. Spencer, B., Jr., and Phillips, W. P.: Transonic Aerodynamic Characteristics of a Series of Bodies Having Variations in Fineness Ratio and Cross-Sectional Ellipticity. NASA TN D-2622, 1965. (U)

27. Dennis, D. H., and Syvertson, C. A.: Effects of Boundary-Layer Separation on Normal Force and Center of Pressure of a Cone-Cylinder Model With a Large Base Flare at Mach Numbers From 3.0 to 6.28. NACA RM A55H09, 1955. (U)

28. Buford, W. E., and Shatunoff, S.: The Effects of Fineness Ratio and Mach Number on the Normal Force and Center of Pressure of Conical and Ogival Head Bodies. BRL MR 760, 1954. (U)

29. Delancey, L. M., Jaeger, B. F., and Schroedter, G. M.: The Aerodynamic Characteristics at Mach Number 4.24 of Bodies of Revolution With Varying Lengths and Head Shapes. NOTS TM 358, 1951. (U)

30. Ferri, A.: Supersonic-Tunnel Tests of Projectiles in Germany and Italy. NACA WR L-152, 1945. (U)

31. Walchner, O.: Systematic Wind-Tunnel Measurement on Missiles. NACA TM 1122, 1947. (U)

32. Delameter: Preliminary Analysis of Wind-Tunnel Test Data – First Daingerfield Wind-Tunnel Test Period Preliminary Report. Douglas SM 13256, 1948. (U)

33. Spencer, B., Jr., Phillips, W. P., and Fournier, R. H.: Supersonic Aerodynamic Characteristics of a Series of Bodies Having Variations in Fineness Ratio and Cross-Section Ellipticity. NASA TN D-2389, 1964. (U)

34. Jack, J. R., and Moskowitz, B.: Aerodynamic Characteristics of Two Flat-Bottomed Bodies at a Mach Number of 3.12. NACA RM E53L11b, 1954. (U)

35. Fuller, D. E., Shaw, D. S., and Wassum, D. L.: Effect of Cross-Section Shape on the Aerodynamic Characteristics of Bodies at Mach Numbers From 2.50 to 4.63. NASA TN D-1620, 1963. (U)

36. Lange, R. H., and Wittliff, C. E.: Force and Pressure-Distribution Measurements at a Mach Number of 3.12 of Slender Bodies Having Circular, Elliptical, and Triangular Cross Sections and the Same Longitudinal Distribution of Cross-Sectional Area. NACA RM L56D17, 1956. (U)

37. Jorgensen, L. H.: Inclined Bodies of Various Cross Sections at Supersonic Speeds. NASA Memo 10-3-58A, 1958. (U)

38. Rainey, R. W.: Investigation at Supersonic Speeds of the Effects of Bomb-Bay Configuration Upon the Aerodynamic Characteristics of Fuselages With Noncircular Cross Sections. NACA RM L56H20, 1956. (U)

39. Fuller, D. E., and Campbell, J. F.: Supersonic Lateral-Directional Stability Characteristics of 45° Swept Wing-Body-Tail Model With Various Cross-Sectional Shapes. NASA TN D-2376, 1964. (U)

40. Carlson, H. W., and Gapcynski, J. P.: An Experimental Investigation at a Mach Number of 2.01 of the Effects of Body Cross-Section Shape on the Aerodynamic Characteristics of Bodies and Wing-Body Combinations. NACA RM L55E23, 1955 (U)

41. Jorgensen, L. H.: Elliptic Cones Alone and With Wings at Supersonic Speeds. NACA TR 1376, 1958. (U)

42. Morris, O. A.: Aerodynamic Characteristics in Pitch at a Mach Number of 2.01 of Several Wing-Body Combinations With Wedge Shaped Bodies Located Above and Below at 54.5° Swept Delta Wing. NASA TN D-1823, 1963. (U)

43. Dryer, M., and Luidens, R. W.: Aerodynamic Characteristics of Several Flat-Bottom Configurations at Mach 3.0 and 3.5.NASA Memo 1-2-59E, 1959. (U)

44. Ridyard, H. W.: The Aerodynamic Characteristics of Two Series of Lifting Bodies at Mach Number 6.86. NACA RM L54C15, 1954. (U)

45. Henderson, J. H.: Effect of Nose Bluntness on Normal Force, Pitching Moment, and Center of Pressure on Cone-Cylinder and Cone-Cylinder-Frustum Bodies of Revolution at Mach Numbers of 1.50, 2.18, 2.81, and 4.04. Ordnance Missile Laboratories Redstone Arsenal Rpt. No. GR11F, 1958. (C) Title Unclassified

TABLE 4.2.1.1-A

SUMMARY OF EXPERIMENTAL DATA ON BODIES OF NONCIRCULAR CROSS SECTION

SUBSONIC SPEEDS

Ref.	Nose Shape	Body Cross Section	Afterbody Cross Section	S_b (sq in.)	ℓ_B (in.)	$x_{c.g.}$	w (in.)	h (in.)	p (in.)	c (in.)	ℓ_N (in.)	$f_{N_{equiv}}$	M
19	Ogival Ellipsoid	Horizontal Ellipse	None	18.06	48.0	0.667	5.37	4.29	15.27	2.15	48.0	10.0	0.40
				18.10			5.88	3.92	15.71	1.96			
				18.08			6.79	3.39	16.84	1.70			
				18.12			7.59	3.04	18.16	1.52			
		Vertical Ellipse		18.12			3.04	7.59	18.16	3.79			
				18.08			3.39	6.79	16.84	3.39			
				18.10			3.92	5.88	15.71	2.94			
				18.06			4.29	5.37	15.27	2.68			
20	Ogival Ellipsoid	Square	Square	28.27	45.0	0.533	5.40	5.40	19.88	2.70	18.0	8.33	0.13
						0.565							
		Deep Rectangle	Deep Rectangle			0.533	4.00	7.28	20.84	3.64		8.34	
						0.565							
	Ogival	Shallow Rectangle	Shallow Rectangle			0.533	7.28	4.00		2.00			
						0.565							
21	Rounded	Deep Rectangle	Deep Rectangle	9.29	20.16	see ref.	2.70	3.44	12.28	1.72	8.0	5.86	Low Speed
22	Round	Ellipse	Ellipse	37.17	40.31	0.322	5.20	9.10	23.29	4.55	16.3	5.86	0.107
23	Ogival	Semicircle +Rectangle	Semicircle +Rectangle	22.20	54.72	0.571	5.00	5.00	17.65	2.27	17.8	10.1	0.80–0.92
		Square	Square	24.90					19.60	2.50		9.8	
24	Rounded	Triangle	Triangle	9.29	20.16	see ref.	3.85	3.60	13.23	1.28	8.0	5.24	Low Speed
		Inverted Triangle	Inverted Triangle							2.56			
		Vertical Ellipse	Vertical Ellipse				2.60	4.55	11.62	2.275		5.86	
		Horizontal Ellipse	Horizontal Ellipse				4.55	2.60		1.30			

TABLE 4.2.1.1-A (CONTD)

Ref.	Nose Shape	Body Cross Section		Afterbody Cross Section	S_b (sq in.)	ℓ_B (in.)	$x_{c.g.}$	w (in.)	h (in.)	p (in.)	c (in.)	N (in.)	$f_{N_{equiv}}$	M
25	Ogival Ellipsoid		Ellipse	Ellipse	28.2	61.45	0.50	10.39	3.46	24.30	1.73	36.0	10.24	0.40–1.2
						41.60	0.65						6.93	
					28.3	61.45	0.50	12.00	3.00	27.46	1.50		10.24	
						51.60	0.60						8.60	
						41.60	0.65						6.93	
	Ogival		Circular Segment	Circular Segment	25.1	61.45	0.50	12.00	3.00	25.90	1.50	36.0	10.0	
						51.60	0.60						8.6	
						41.60	0.65						6.9	
26	Ogival Ellipsoid		Horizontal Ellipse	None	12.56	12.00	0.667	4.99	3.27	18.49	1.63	12.0	3.0	0.4–1.4
								5.66	2.83	18.87	1.41			
			Vertical Ellipse					2.83	5.66	18.87	2.83			
			Horizontal Ellipse			20.00		4.99	3.27	18.49	1.63	20.0	5.0	
								5.66	2.83	18.87	1.41			
			Vertical Ellipse					2.83	5.66	18.87	2.83			
			Horizontal Ellipse			28.00		4.99	3.27	18.49	1.63	36.0	10.24	
								5.66	2.83	18.87	1.41			
			Vertical Ellipse					2.83	5.66	18.87	2.83			
5	Ogival Ellipsoid		Vertical Ellipse	Vertical Ellipse	28.3	61.45	–	4.90	7.35	19.62	3.68	36.0	10.24	0.8–1.2
							–	4.24	8.48	21.06	4.24			
							–	3.46	10.38	24.30	5.19			

S_b maximum cross-section area

ℓ_B body length

$x_{c.g.}$ location of moment reference center from body nose (body lengths)

w body cross-section breadth

h body cross-section height

p body cross-section perimeter

c distance from body cross-section (max) centroid to bottom of section

ℓ_N nose length

$f_{N_{equiv}}$ equivalent fineness ratio $= \dfrac{\ell_B}{d_{equiv}}$

where $d_{equiv} = \sqrt{\dfrac{\text{cross-section area}}{0.7854}}$

TABLE 4.2.1.1-B

SUPERSONIC NORMAL-FORCE-CURVE SLOPE OF CONE-CYLINDER
AND OGIVE-CYLINDER BODIES
DATA SUMMARY AND SUBSTANTIATION

Ref.	Nose Shape	M	f_N	f_N	C_{N_α} Calc. (per rad)	C_{N_α} Test (per Rad)	e Percent Error
28	Conical	1.36	2.84	0	1.98	1.79	10.6
				0.24	2.10	1.95	7.7
				0.50	2.22	2.17	2.3
				0.75	2.38	2.34	1.7
				1.66	2.66	2.58	3.1
				2.00	2.70	2.60	3.8
				3.00	2.75	2.58	6.6
				4.00	2.78	2.45	13.5
		1.72		0	1.92	1.78	7.9
				0.50	2.18	2.22	− 1.8
				0.75	2.34	2.38	− 1.7
				1.66	2.68	2.61	2.7
				3.00	2.83	2.60	8.8
				5.00	2.94	2.58	14.0
		3.02		0	1.85	1.83	1.1
				1.66	2.68	2.75	− 6.9
				5.00	3.20	3.27	− 2.1
				7.00	3.28	3.27	0.3
				9.00	3.33	3.20	4.1
		3.55		0	1.86	1.91	− 3.1
				0.24	1.95	1.99	− 2.0
				1.66	2.54	2.76	− 8.0
				4.00	3.10	3.19	− 2.8
				5.00	3.20	3.28	− 2.4
				7.00	3.32	3.43	− 3.2
				9.00	3.37	3.50	− 3.7
		4.00		0	1.85	1.83	1.1
				0.75	2.16	2.23	− 3.1
				2.00	2.64	2.69	− 1.9
				3.00	2.94	2.98	− 1.3
				7.00	3.34	3.32	0.6
13	Conical	3.01	3.00	2.00	2.67	2.82	− 5.3
				4.00	3.10	2.89	7.3
				7.00	3.28	3.10	5.8
			5.00	0	1.89	1.89	0
				2.00	2.56	2.42	5.4
				5.00	2.86	2.48	15.3
			7.00	0	1.95	1.89	3.2
				3.00	2.61	2.65	− 1.5
	3/4 Power	3.01	5.00	2.00	2.56	2.42	5.4
				5.00	2.86	2.56	11.7
	Conical	3.49	3.00	7.00	3.28	3.32	− 1.2
			5.00	5.00	2.89	2.93	− 1.4
			7.00	3.00	2.60	2.73	− 4.8
		4.24	3.00	4.00	3.08	2.80	10.0
				7.00	3.32	3.27	1.5
			5.00	2.00	2.46	2.40	2.5
				5.00	2.93	2.58	9.8
			7.00	0	1.88	1.95	− 3.6
				3.00	2.57	2.29	12.2
		5.04	3.00	2.00	2.61	2.70	− 3.3
				4.00	3.06	2.66	15.1
				7.00	3.35	3.28	2.1

TABLE 4.2.1.1-8 (CONTD)

Ref.	Nose Shape	M	f_N	f_A	C_{N_α} Calc. (per rad)	C_{N_α} Test (per Rad)	e Percent Error
13	Conical	5.04	5.00	0	1.35	2.09	−11.5
				2.00	2.38	2.70	−11.9
				5.00	2.93	2.93	0
			7.00	0	1.85	1.94	− 4.6
				3.00	2.53	2.26	11.9
	3/4 Power	5.04	5.00	2.00	2.38	2.38	0
				5.00	2.93	2.76	6.2
12	Conical	3.49	3.00	0	1.85	1.72	7.6
			5.00	0	1.85	1.79	3.4
		4.01	3.00	0	1.85	1.78	3.9
			4.00	0	1.85	2.07	−10.6
			5.00	0	1.85	1.67	10.8
			7.00	0	1.89	1.99	− 5.0
		5.00	3.00	0	1.85	2.15	−14.0
			4.00	0	1.85	1.84	0.5
			5.00	0	1.85	1.63	13.5
			7.00	0	1.85	2.22	−16.7
29	Conical	4.00	4.00	10.00	3.28	3.37	− 2.7
30	Conical	1.72	2.50	2.50	2.67	3.25	−17.8
		1.99			2.66	3.32	−19.9
		2.64			3.58	3.48	2.9
		3.06			3.53	3.49	1.1
28	Ogival	1.36	2.84	0	2.51	2.41	4.1
				0.24	2.56	2.41	6.2
				0.50	2.60	2.58	0.8
				0.75	2.65	2.61	1.5
				1.00	2.70	2.58	4.7
				1.66	2.72	2.61	4.2
				4.00	2.73	2.58	5.8
		1.72		0	2.47	2.46	0.4
				0.24	2.53	2.52	0.4
				0.50	2.58	2.69	− 4.1
				1.00	2.72	2.75	− 1.1
				1.66	2.79	2.81	− 0.7
				2.00	2.80	2.81	− 0.4
				3.00	2.82	2.81	0.4
				5.00	2.88	2.81	2.5
		3.02		0	2.23	2.46	− 9.3
				0.50	2.42	2.51	− 3.6
				1.66	2.81	3.01	− 6.6
				3.00	3.03	3.38	−10.4
				5.00	3.20	3.38	− 5.3
				7.00	3.30	3.39	− 2.7
				9.00	3.36 extrap	3.21	4.7
				11.00	–	3.38	–
		3.55		0	2.12	2.21	− 4.1
				0.24	2.22	2.26	− 1.8
				0.50	2.32	2.28	1.8
				1.66	2.75	2.70	1.9
				3.00	2.99	3.20	− 6.6
				5.00	3.20	3.27	− 2.1
				7.00	3.31	3.29	0.6
				9.00	3.37	3.32	1.5
		4.00		0	2.04	2.17	− 6.0
				0.75	2.36	2.52	− 6.3
				1.66	2.67	2.81	− 5.0
				2.00	2.76	2.87	− 3.8

TABLE 4.2.1.1-B (CONTD)

Ref.	Nose Shape	M	f_N	f_A	C_{N_α} Calc. (per rad)	C_{N_α} Test (per Rad)	e Percent Error
28	Ogival	4.00	2.84	3.00	2.93	3.04	– 3.6
↓	↓	↓	↓	4.00	3.07	3.15	– 2.5
				5.00	3.20	3.21	– 0.3
				7.00	3.26	3.44	– 5.2
				9.00	3.30	3.59	– 8.1
13	Ogive	3.01	5.00	2.00	2.76	2.72	1.5
↓	↓	↓	↓	5.00	2.87	2.89	– 0.7
	Parabola			2.00	2.76	2.62	5.3
	↓			5.00	2.87	2.60	10.4
	Ogive	5.04		2.00	2.70	2.63	2.7
	↓	↓		5.00	3.02	3.00	0.7
	Parabola			2.00	2.70	2.28	18.4
	Ogive	4.01	3.00	0	2.08	2.04	2.0
	↓	↓	5.00	0	2.35	2.25	4.4
			7.00	0	2.44	2.61	– 6.5
		5.00	3.00	0	1.94	1.93	0.5
		↓	5.00	0	2.24	2.11	6.2
			7.00	0	2.39	2.13	12.2
29	Ogival	4.24	2.50	7.50	3.11	3.15	– 1.3
↓	↓	↓	3.50	6.50	3.22	3.12	3.2
			↓	10.50	3.38	3.56	– 5.1
			4.00	10.00	3.30	3.40	– 2.9
30	Ogival	1.72	2.50	2.50	2.86	3.02	– 5.3
↓	↓	↓	1.50	↓	3.16	3.11	1.6
			3.00		2.80	2.89	– 3.1
		1.28	1.50		2.92	2.93	– 0.3
		1.99	2.50		2.93	3.32	–11.7
		↓	1.50		3.20	3.19	0.3
			3.00		2.85	3.07	– 7.2
			3.50		2.79	2.41	15.8
		2.64	2.50		3.02	3.44	–12.2
		↓	3.00		2.93	3.27	–20.2
			3.50		2.86	3.41	–16.1
		3.06	2.50		3.00	3.52	–14.8
		↓	3.00		2.96	3.24	– 8.6
			3.50	↓	2.88	3.52	–18.2
31	Ogival	1.28	3.50	1.50	2.72	2.76	– 1.4
↓	↓	↓	2.50	2.50	2.70	2.90	– 6.9
		1.72	3.50	1.50	2.76	2.93	– 5.8
		↓	2.50	2.50	2.87	3.15	– 8.9
		1.99	1.50	3.50	3.30	3.45	– 4.3
		↓	3.50	1.50	2.76	3.00	– 8.0
			2.50	1.50	2.76	3.04	– 9.2
			2.50	2.50	2.94	3.24	– 9.3
			3.50	1.50	2.77	3.00	– 7.7
		3.06	3.50	1.50	2.75	2.95	– 6.8
		↓	2.50	2.50	3.00	3.15	– 4.8
32	Ogival	1.73	6.25	9.45	2.62	2.49	5.2
↓	↓	2.00	↓	↓	2.68	2.57	4.3

Average Error = $\frac{\Sigma |e|}{n}$ = 5.55%

Cone-Cylinder 5.9%

Ogive-Cylinder 5.3%

TABLE 4.2.1.1-C

SUMMARY OF EXPERIMENTAL DATA ON BODIES OF NONCIRCULAR CROSS SECTION

SUPERSONIC SPEEDS

Ref.	Nose Shape	Body Cross Section	Afterbody Cross Section	S_b (sq in.)	ℓ_B (in.)	$x_{c.g.}$	w (in.)	h (in.)	p (in.)	c (in.)	ℓ_N (in.)	$f_{N_{equiv}}$	M
33	Ogival Ellipsoid	Horizontal Ellipse	None	12.56	12.00	0.667	4.90	3.27	18.49	1.63	12.00	3.0	1.5–2.86
							5.66	2.83	18.87	1.41			
		Vertical Ellipse					2.83	5.66	18.87	2.83			
		Horizontal Ellipse			20.00		4.90	3.27	18.49	1.63	20.00	5.0	
							5.66	2.83	18.87	1.41			
		Vertical Ellipse					2.83	5.66	18.87	2.83			
		Horizontal Ellipse			28.00		4.90	3.27	18.49	1.63	28.00	7.0	
							5.66	2.83	18.87	1.41			
		Vertical Ellipse					2.83	5.66	18.87	2.83			
34	Semicirc. Cone	Semicircle	Semicircle	1.20	21.00	see rpt.	1.75	0.875	4.50	0.371	11.50	17.0	3.12
	Semiellip. Cone	Semiellipse	Semiellipse	2.40			3.50		7.50			12.0	
35	Cone	Triangle	Triangle	12.44	40.00	0.500	4.48	4.08	13.62	1.36	13.33	10.0	2.5–4.63
		Inverted Triangle	Inverted Triangle							2.72			
		Horizontal Ellipse	Horizontal Ellipse	12.57			4.90	3.27	13.08	1.63			
							5.66	3.83	14.05	1.41			
		Vertical Ellipse	Vertical Ellipse				2.83	5.66		2.83			
	Semicone	Semiellipse	Semiellipse				6.93	2.31	16.18	0.98			
		Inverted Semiellipse	Inverted Semiellipse							1.33			
36	Ogival	Horizontal Ellipse	Horizontal Ellipse	1.13	14.65	see rpt.	1.70	0.87	4.22	4.25	9.00	12.2	3.12
		Vertical Ellipse	Vertical Ellipse				0.87	1.70		0.85			
		Triangle	Triangle				1.23	1.28	4.00	0.50			
37	Ogival	Horizontal Ellipse	Horizontal Ellipse	1.54	14.00	see rpt.	1.71	1.14	4.57	0.571	4.20	10.0	1.98, 3.88
		Vertical Ellipse	Vertical Ellipse				1.14	1.71		0.857			
		Horizontal Ellipse	Horizontal Ellipse				1.98	0.99	4.92	0.495			

TABLE 4.2.1.1-C (CONTD)

Ref.	Nose Shape	Body Cross Section	Afterbody Cross Section	S_b (sq in.)	ℓ_B (in.)	$x_{c.g.}$	w (in.)	h (in.)	p (in.)	c (in.)	ℓ_N (in.)	$f_{N_{equiv}}$	M
37	Ogival	Vertical Ellipse	Vertical Ellipse	1.54	14.00	see rpt.	0.99	1.98	4.92	0.990	4.20	10.0	1.98, 3.88
		Square	Square				1.24	1.24	4.93	0.620			
		Diamond	Diamond				1.75	1.75		0.875			
		Triangle	Triangle				1.89	1.63	5.60	0.544			
		Inverted Triangle	Inverted Triangle							1.090			
		Horizontal Ellipse	Horizontal Ellipse		8.40		1.98	0.99	4.92	0.495		6.0	
		Vertical Ellipse	Vertical Ellipse				0.99	1.98		0.990			
38	Cone	Horizontal Ellipse	Horizontal Ellipse	0.503	8.00	0.500	1.13	0.57	2.81	0.283	1.701	10.0	1.62–2.40
		Vertical Ellipse	Vertical Ellipse				0.57	1.13		0.566			
		Triangle	Triangle										
		Teardrop	Teardrop				0.71	0.95	2.45	0.446			
39	Ogival Cone	Circle	Circle	9.62	39.10	0.454	3.50	3.50	11.00	1.75	12.25	11.17	1.41, 2.20
	Ogival Ellipsoid	Ellipse	Ellipse	14.43				5.26	13.98	2.63		9.09	
	Ogival	Flat-Bottom Teardrop	Flat-Bottom Teardrop	13.02				4.38	13.5[illegible]	1.98		9.61	
		Triangle	Triangle	14.50			4.90	4.42	12.40	1.47		9.09	
		Inverted Triangle	Inverted Triangle							2.95			
40	Ogival	Horizontal Ellipse	Horizontal Ellipse	12.60	42.00	0.697	4.90	3.27	12.94	1.64	14.00	10.50	2.01
		Diamond	Diamond				4.46	4.46	13.12	2.23			
		Triangle	Triangle				4.50	4.10	13.74	1.64			
		Inverted Triangle	Inverted Triangle							2.47			
		Tent	Tent				3.60	4.17	13.14	1.85			
		Inverted Tent	Inverted Tent							2.32			
		Square	Square				3.62	3.62	13.12	1.81			

TABLE 4.2.1.1-C (CONTD)

Ref.	Nose Shape	Body Cross Section		Afterbody Cross Section	S_b (sq in.)	ℓ_B (in.)	$x_{c.g.}$	w (in.)	h (in.)	p (in.)	c (in.)	ℓ_N (in.)	$f_{N_{equiv}}$	M
40	Ogival		90° Teardrop	90° Teardrop	12.60	42.00	0.697	3.89	4.37	12.73	2.02	14.00	10.50	2.01
			Inverted 90° Teardrop	Inverted 90° Teardrop				↓	↓	↓	2.36			
			45° Teardrop	45° Teardrop				3.49	5.02	13.60	2.16			
			Inverted 45° Teardrop	Inverted 45° Teardrop				↓	↓	↓	2.86			
			Vertical Ellipse	Vertical Ellipse				3.27	4.90	12.94	2.45			
			Horizontal Ellipse	Horizontal Ellipse				4.90	3.27	↓	1.64			
			Diamond	Diamond				4.46	4.46	13.12	2.23			
			Triangle	Triangle				4.50	4.10	13.74	1.64			
			Inverted Triangle	Inverted Triangle				↓	↓	↓	2.47			
			Tent	Tent				3.60	4.17	13.14	1.85			
			Inverted Tent	Inverted Tent				3.16	↓	↓	2.32			
			Square	Square				3.62	3.62	13.12	1.81			
			90° Teardrop	90° Teardrop				3.90	4.37	12.73	2.02			
			Inverted 90° Teardrop	Inverted 90° Teardrop				↓	↓	↓	2.36			
			45° Teardrop	45° Teardrop				3.50	5.02	13.60	2.16			
			Inverted 45° Teardrop	Inverted 45° Teardrop				↓	↓	↓	2.86			
			Vertical Ellipse	Vertical Ellipse				3.27	4.90	12.94	2.45			
41	Pointed Ellipsoid		Vertical Ellipse	None	5.73	9.90	see rpt.	2.20	3.29	8.80	1.65	9.90	3.67	1.97, 2.94
								1.57	4.70	11.00	2.35			
								1.10	6.59	14.83	3.29			
						13.50		2.20	3.29	8.80	1.65	13.50	5.00	
			Horizontal Ellipse			9.90		3.29	2.20	↓	1.10	9.90	3.67	
								4.70	1.57	11.00	0.78			
								6.59	1.10	14.83	0.55			

TABLE 4.2.1.1-C (CONTD)

Ref.	Nose Shape	Body Cross Section	Afterbody Cross Section	S_b (sq in.)	ℓ_B (in.)	$x_{c.g.}$	w (in.)	h (in.)	p (in.)	c (in.)	ℓ_N (in.)	$f_{N_{equiv}}$	M
42	Wedge	Rectangle	None	2.80	18.32	see rpt.	2.24	1.25	6.98	0.63	18.32	10.95	2.01
				4.82				2.15	8.78	1.08		8.35	
				3.39			3.85	0.88	9.46	0.44		9.95	
				4.81				1.25	10.20	0.63		8.35	
				6.35				1.65	11.00	0.83		7.27	
				4.82			5.84	0.88	12.72	0.44		8.34	
				6.85				1.25	13.46	0.63		7.00	
			Rectangle	2.69			2.15		6.80		10.22	11.18	
					22.38							13.65	
					26.34							16.13	
				3.59			2.87		8.25			13.95	
43	Conical Duck Bill	Modified Semiellipse	Modified Semiellipse	1.73	17.25	0.584	2.94	1.00	see rpt.	see rpt.	7.12	23.3	3.0
					16.95	0.576					6.93	22.9	
				2.33								19.7	
				1.73		0.569						22.9	
	Conical			102.0	198.1	0.526	21.48	5.52			64.6	34.75	3.0, 3.5
44	Conical Upper Surf	Semicircle on Rectangle	Semicircle on Rectangle	0.50	8.80	see rpt.	0.75	0.75	2.68	0.361	4.3	11.7	6.86
	Cylindrical Upper Surf			1.06			1.50		4.18			8.3	

S_b	maximum cross-section area	p	body cross-section perimeter
ℓ_B	body length	c	distance from body cross-section (max) centroid to bottom of section
$x_{c.g.}$	location of moment reference center from body nose (body lengths)	ℓ_N	nose length
w	body cross-section breadth		
h	body cross-section height	$f_{N_{equiv}}$	equivalent fineness ratio $= \dfrac{\ell_B}{d_{equiv}}$

where $d_{equiv} = \sqrt{\dfrac{\text{cross-section area}}{0.7854}}$

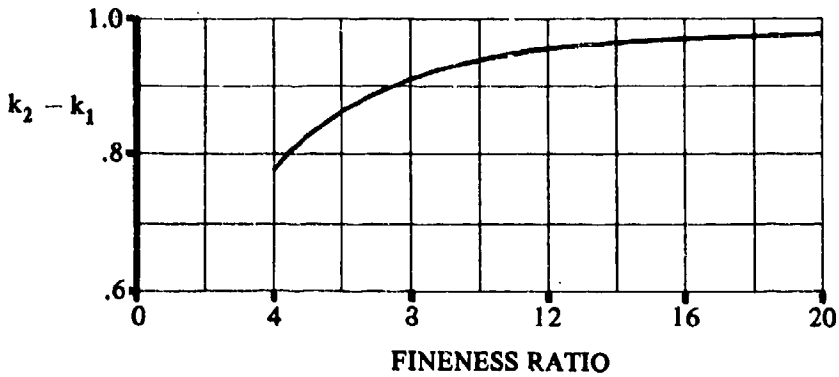

FIGURE 4.2.1.1-20a APPARENT MASS FACTOR

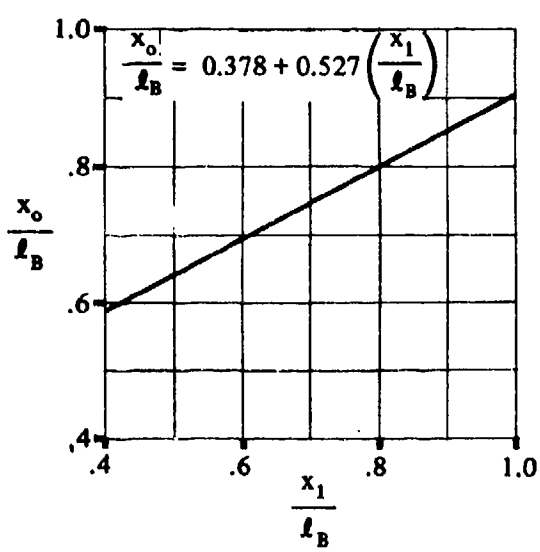

FIGURE 4.2.1.1-20b BODY STATION WHERE FLOW BECOMES VISCOUS

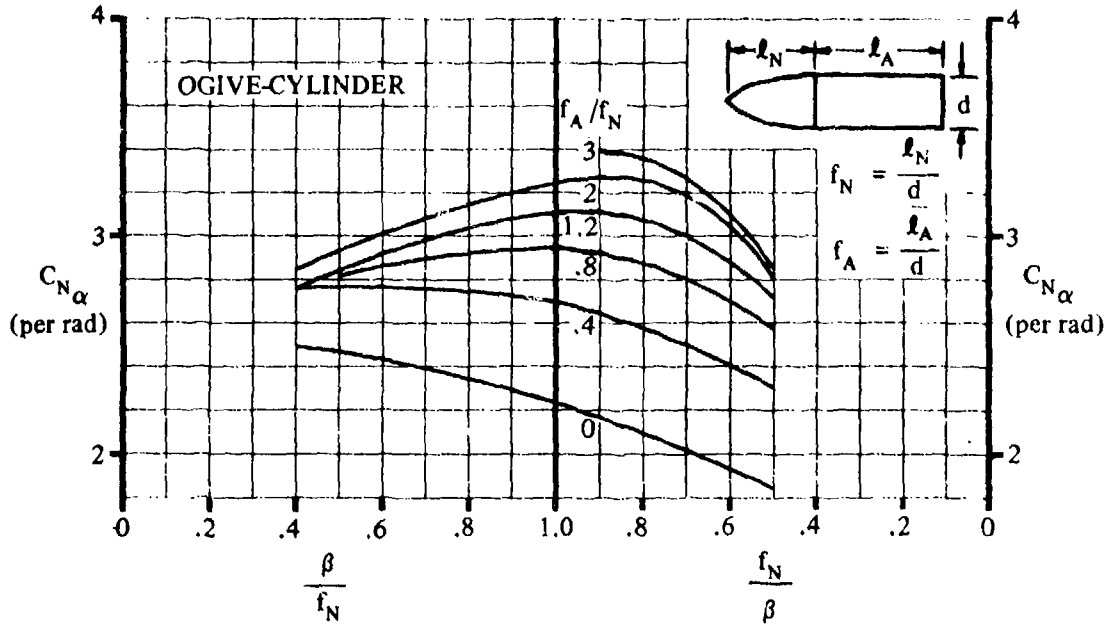

FIGURE 4.2.1.1-21a SUPERSONIC NORMAL-FORCE-CURVE SLOPE FOR OGIVE-CYLINDERS

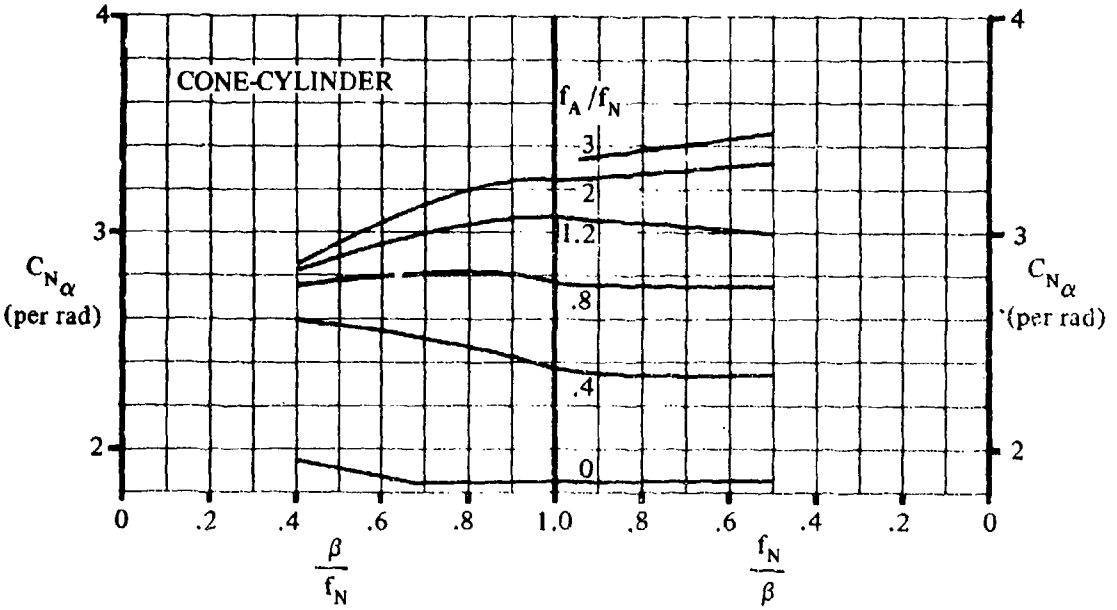

FIGURE 4.2.1.1-21b SUPERSONIC NORMAL-FORCE-CURVE SLOPE FOR CONE-CYLINDERS

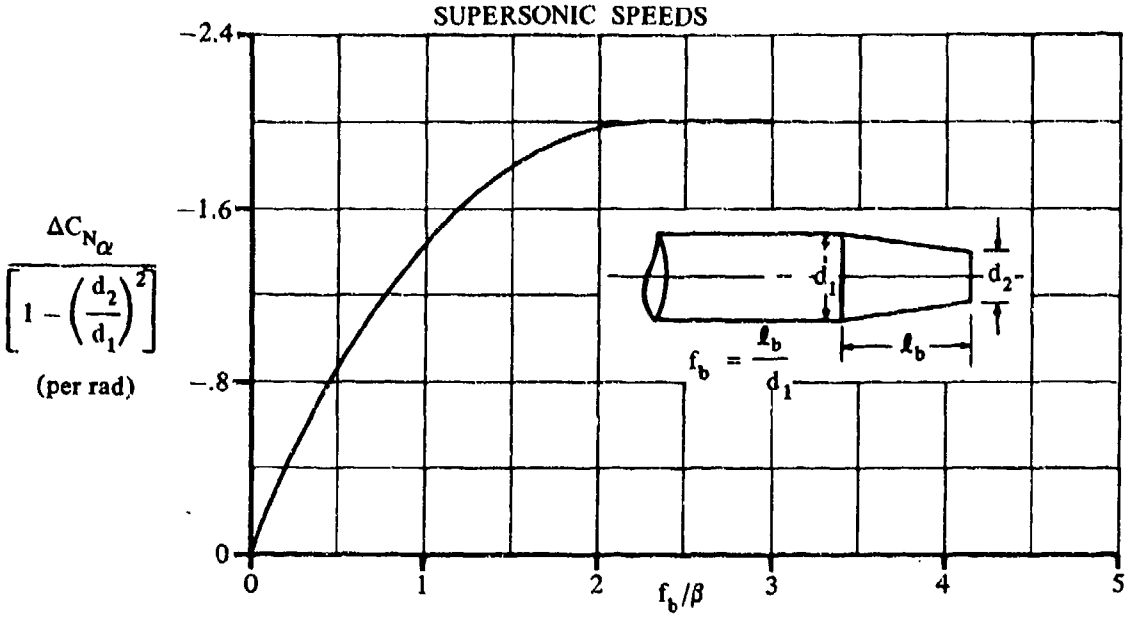

FIGURE 4.2.1.1-22a NORMAL-FORCE-CURVE-SLOPE INCREMENT OF A BOATTAILED BODY OF REVOLUTION FOLLOWING A SEMI-INFINITE CYLINDER

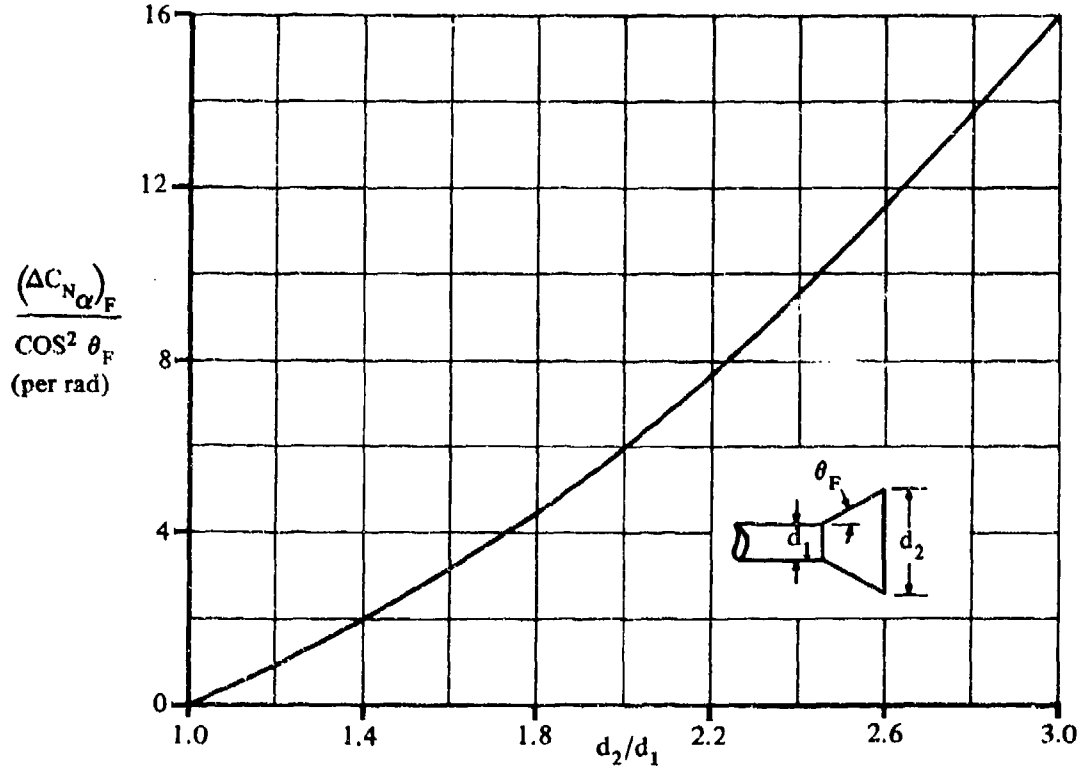

FIGURE 4.2.1.1-22b NORMAL-FORCE-CURVE-SLOPE INCREMENT OF A FLARED BODY OF REVOLUTION FOLLOWING A SEMI-INFINITE CYLINDER – IMPACT THEORY

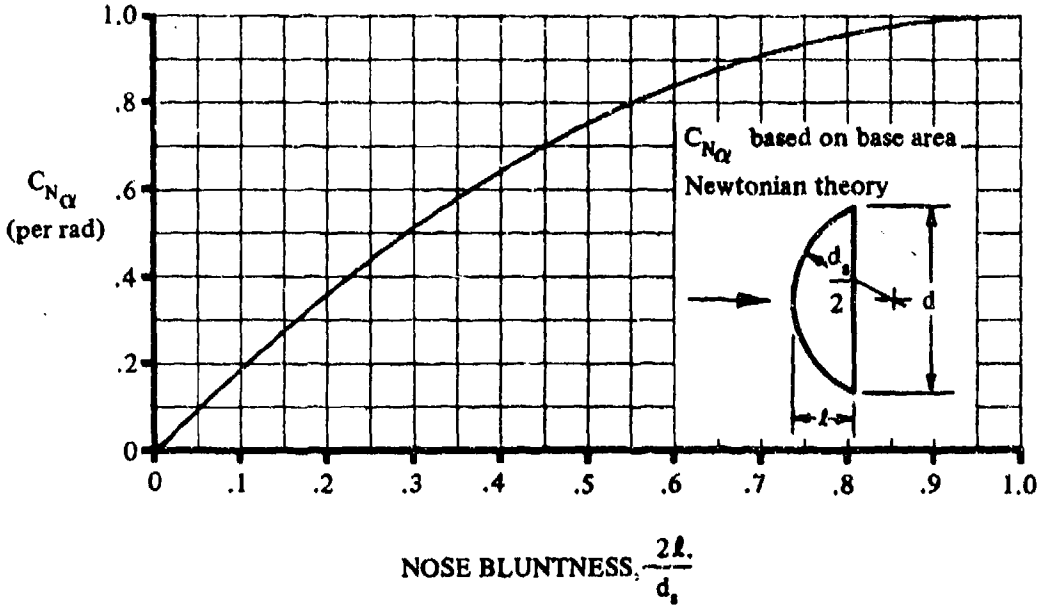

FIGURE 4.2.1.1-23 NORMAL-FORCE-CURVE SLOPE FOR SPHERICAL SEGMENTS

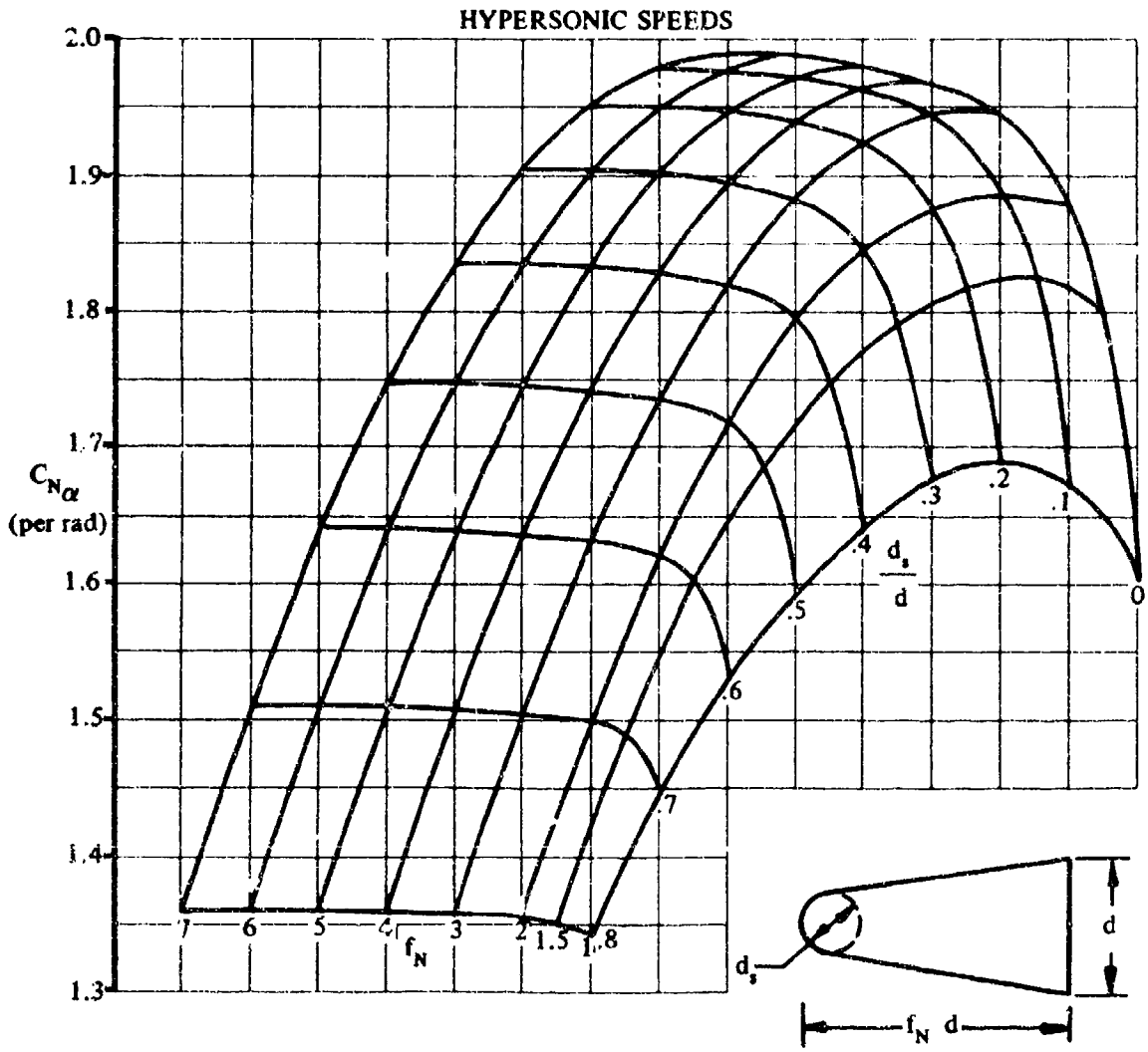

FIGURE 4.2.1.1-24 NORMAL-FORCE-CURVE SLOPE FOR SPHERICALLY BLUNTED CONES

(IMPACT THEORY)

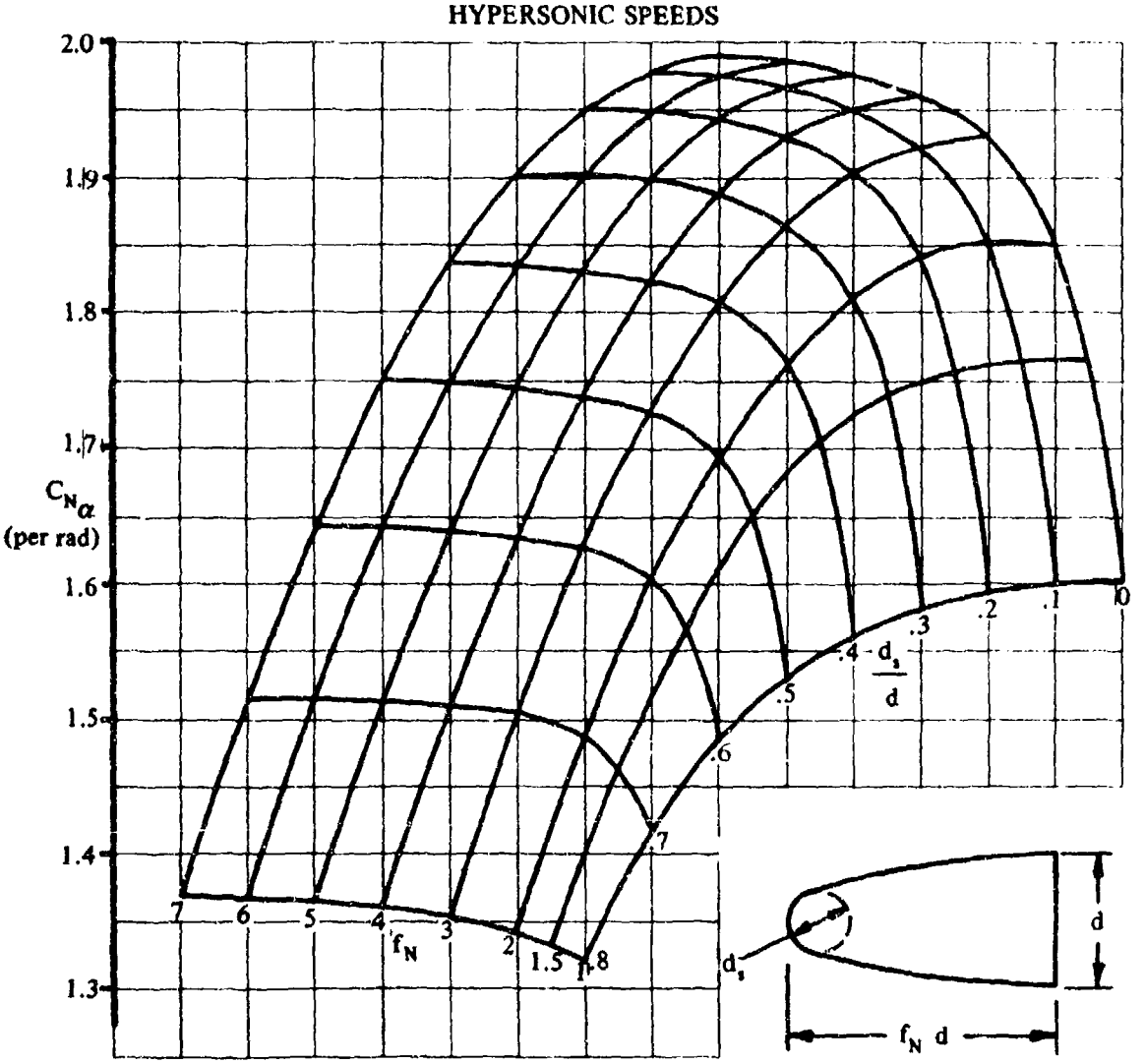

FIGURE 4.2.1.1-25 NORMAL-FORCE-CURVE SLOPE FOR SPHERICALLY BLUNTED OGIVES

(IMPACT THEORY)

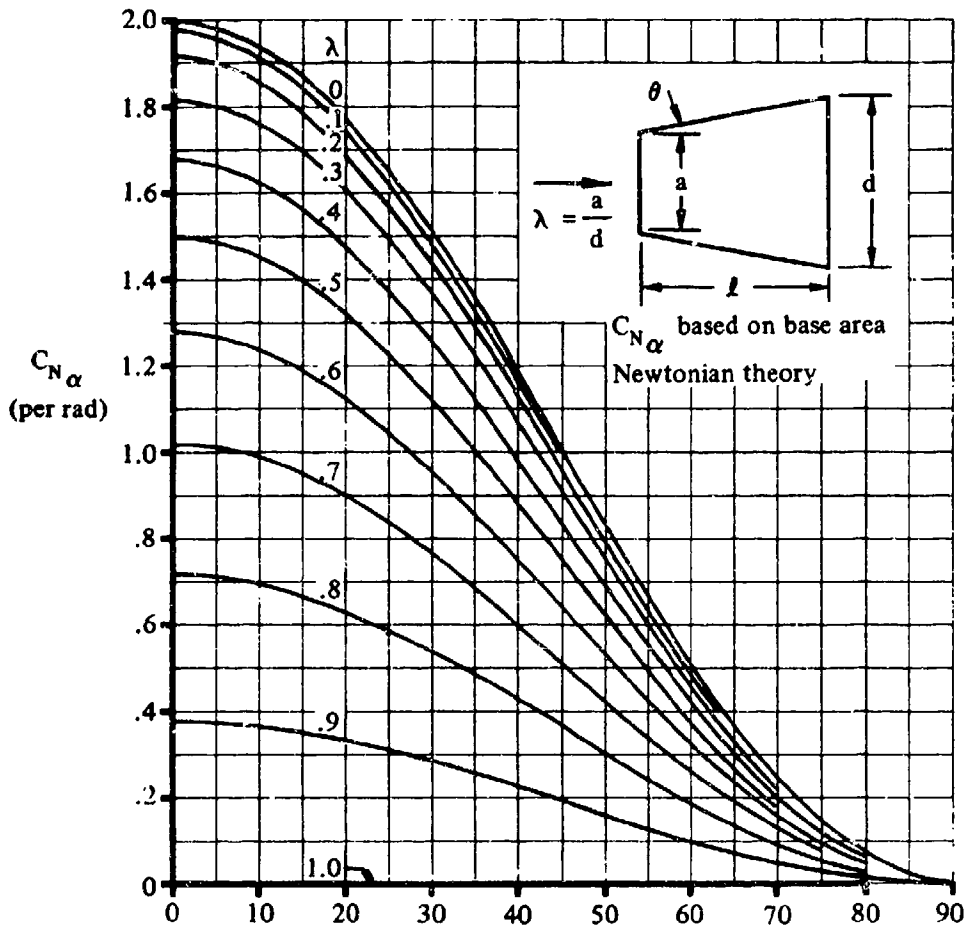

FIGURE 4.2.1.1-26 NORMAL-FORCE-CURVE SLOPE FOR CONE FRUSTUMS

4.2.1.2 BODY LIFT IN THE NONLINEAR ANGLE-OF-ATTACK RANGE

Potential-flow theory shows that the lift on a body is a linear function of angle of attack and is proportional to the body base area. In particular, the lift on a closed body is zero. Slender-body theory also shows that the lift of an inclined body is independent of Mach number from low subsonic to supersonic Mach numbers.

The prediction of body-lift characteristics using potential-flow theory is necessarily limited to those cases where negligible viscous flow separation occurs, i.e., low angles of attack. Divergence between test data and potential-flow predictions can occur at very low angles of attack. Thus, to eliminate the potential-flow-theory angle-of-attack limitation requires consideration of the viscous flow separation effects.

Experimentally, the flow separates over the leeward side of the body, and the normal force increases nonlinearly with angle of attack. A pair of standing body vortices originate near the nose and increase in strength along the length of the body. A cross section of the flow is very similar to the two-dimensional flow about an infinite cylinder with laminar separation. That is, the flow separates in the region of the lateral meridians of the body rather than at points closer to the top meridian, as in turbulent separation. This effect is further accentuated by shocklets that appear (at subsonic speeds) near the maximum half-breadth at about $M \approx 0.4$ and fix the boundary-layer separation. For these reasons a cross-flow drag coefficient for laminar-boundary-layer conditions is used to evaluate viscous cross-flow forces for body lift even though the actual boundary layer is usually turbulent.

Several methods have been developed that assume that the normal forces acting on bodies of revolution at angles of attack can be represented by the linear combination of potential-flow and viscous cross-flow contributions. The lift-curve slope at zero angle of attack is used for the potential-flow term. Some form of cylinder cross-flow drag is used to evaluate viscous cross-flow lift. The methods differ mainly in their treatment of the nonlinear cross-flow term. Some of the better known methods for subsonic and supersonic analyses are discussed below.

In Reference 1 Allen and Perkins assume that the viscous contribution at each station along the body is equal to the steady-state drag of a section of an infinite cylinder placed normal to the flow with velocity $V \sin \alpha$. This method is accurate to within ±10 percent for high fineness-ratio bodies (fineness ratios of approximately 20 or greater). However, the accuracy of the method deteriorates as fineness ratio is decreased.

Kelly, in Reference 2, presents a method that is a refinement of that presented in Reference 1. Kelly uses the hybrid theory of Van Dyke (Reference 3), with a correction for boundary-layer displacement thickness for the potential-flow contribution. For the viscous term, the unsteady cross-flow drag of a cylinder started impulsively from rest is used instead of the steady-state value. This method is limited to cross-flow Mach numbers less than 0.4 and to values of the parameter $2f \tan \alpha \leqslant 9$.

The method of Reference 4 assumes that viscous cross-flow effects occur only on the cylindrical afterbody.

These methods are approximate, however, and each gives accurate answers over a limited range of test conditions. None of them is valid for all conditions.

A. SUBSONIC

Three methods are presented for predicting body lift. The first method, taken from Reference 5, applies only to bodies of revolution and is rather general in its application. It is based on the assumption that the flow is potential over the forward part of the body and has no viscous contribution in this region. On the aft part of the body, the flow is assumed to be entirely viscous, with lift arising solely from cross-flow drag.

The second method applies to bodies of elliptical cross section and bodies of revolution. This method is based on the concept of vortex lift for sharp delta wings as presented in Reference 6. The method as presented herein has been extended to include a set of empirical curves designed to estimate the angle of attack where the onset of vortex lift begins. This modification to the theory is necessary, since the onset of vortex lift for thick bodies does not correspond to that for flat-plate wings, i.e., zero angle of attack. The experimental data used in the correlation are presented in References 7 through 11.

The third method is, in principle, the most general in application, but can be substantiated the least by test data. This method, presented in Reference 12 by Jorgensen, applies to bodies of arbitrary cross section and angles of attack from 0 to 180^{o} in the Mach-number range from 0 to 7. The method is based on the original proposal of Allen (Reference 1), that the cross flow or lift distribution over a body can be expressed as the sum of a slender-body potential term and an empirical viscous cross-flow term. Although the method has been extended in the literature to include bodies with nonconstant cross sections of various types with and without lifting surfaces and afterbodies (References 12 and 13), the lack of substantiating test data has restricted the Datcom method to bodies with constant circular and elliptical cross sections. References are cited to assist in analyzing other configurations. Normal-force coefficient is calculated by this method. See Section 4.2.3.2 for calculation of axial-force coefficient using the method of Jorgensen. The experimental data used in the correlation are presented in References 12, 14, 15, and 16.

As noted above, all methods are applicable to bodies of revolution. It is suggested that Method 1 be used for bodies of revolution at low angles of attack because of its general application and sensitivity to the many possible body profile shapes. It should be noted that for those cases where the predictions from Method 1 diverge from test data (approximately 12^{o} angle of attack or higher), they generally tend to underpredict the lift coefficient. Conversely, the results from Method 2 generally tend to yield estimates that exceed the test data in the high-angle-of-attack range. Therefore, it is recommended that Method 3 be used in the high-angle-of-attack range.

DATCOM METHODS

Method 1

The expression for the lift coefficient of a body of revolution, based on $V_B^{2/3}$, taken from Reference 5, is

$$C_L = \frac{(k_2 - k_1)\, 2\alpha S_o}{V_B^{2/3}} + \frac{2\alpha^2}{V_B^{2/3}} \int_{x_o}^{x_B} \eta\, r\, c_{d_c}\, dx \qquad 4.2.1.2\text{-a}$$

where

$\frac{(k_2 - k_1)\, 2\alpha\, S_o}{V_B^{2/3}}$ is the potential-flow contribution from Paragraph A of Section 4.2.1.1.

α is the angle of attack in radians.

η is the ratio of the drag on a finite cylinder to the drag on an infinite cylinder, obtained from Figure 4.2.1.2-35a.

r is the body radius at any longitudinal station.

c_{d_c} is the steady-state cross-flow drag coefficient of a circular cylinder of infinite length, obtained from Figure 4.2.1.2-35b.

ℓ_B is the body length.

The remaining terms are defined in Paragraph A of Section 4.2.1.1.

The lift coefficients of several bodies of revolution, calculated by the Datcom method, have been compared with test data in Reference 5. In general, the accuracy of the method is satisfactory up to angles of attack of approximately 12^o.

Method 2

The expression for the lift coefficient of bodies of revolution and elliptical cross-section bodies, based on the projected body planform area, is given by

$$C_L = K_p \sin\alpha \cos^2\alpha + K_v \sin^2(\alpha - \alpha_v)\cos(\alpha - \alpha_v) \qquad 4.2.1.2\text{-b}$$

where

K_p is the potential-flow lift parameter, obtained from Figure 4.2.1.2-36a as a function of body aspect ratio.

K_v is the viscous-flow lift parameter, obtained from Figure 4.2.1.2-36b as a function of body aspect ratio.

α is the body angle of attack.

α_v is the angle of attack where the onset of vortex lift begins, obtained from Figure 4.2.1.2-37 as a function of body fineness ratio and thickness ratio.

When $\alpha_v > \alpha$ the viscous-lift contribution (second term) of Equation 4.2.1.2-b is not considered; i.e., it is zero. Thus the second term is considered only for those cases where $\alpha - \alpha_v$ yields a positive value.

The test data used to generate Figure 4.2.1.2-37 were limited to Mach numbers less than 0.6. Therefore it is advisable that Equation 4.2.1.2-b be applied to Mach numbers less than 0.6. For higher Mach numbers the user is referred to the parametric test data contained in References 8 through 11.

A comparison of test data with results calculated by this method is presented in Table 4.2.1.2-A. It should be noted that these test data and all other available test data were used in the development of the empirical curves, which estimate the angle of attack where the onset of vortex lift begins.

In general, the accuracy of the method was found to be satisfactory up to angles of attack of approximately 20°.

For those noncircular cross-section bodies that cannot be analyzed by this method, the user is referred to the summary of available test data on bodies of noncircular cross section at subsonic speeds presented in Table 4.2.1.1-A.

Method 3

The normal-force coefficient* for bodies with circular and elliptical cross sections, based on cross-sectional reference area S, is given by

$$C_N = \left(\frac{C_N}{C_{N_{cir}}}\right)_{SB} \left(\frac{S_b}{S} \sin 2\alpha' \cos\frac{\alpha'}{2}\right) + \left(\frac{C_N}{C_{N_{cir}}}\right)_{NT} \left(\eta c_{d_c} \frac{S_p}{S} \sin^2 \alpha'\right) \qquad 4.2.1.2\text{-c}$$

where

$\left(\frac{C_N}{C_{N_{cir}}}\right)_{SB}$ is the ratio of the normal-force coefficient for the body of noncircular cross section to that for the equivalent body of circular cross section (same cross-sectional area) as determined by slender-body theory. For circular cross sections this ratio is one. For elliptical cross sections this ratio is given by

$$\left(\frac{C_N}{C_{N_{cir}}}\right)_{SB} = \frac{a}{b}\cos^2\phi + \frac{b}{a}\sin^2\phi \qquad 4.2.1.2\text{-d}$$

where

a is the major axis of the elliptical cross section.

b is the minor axis of the elliptical cross section.

ϕ is the angle of bank of the body about its longitudinal axis; $\phi = 0$ with the major axis horizontal, and $\phi = 90^{\circ}$ with the minor axis horizontal.

*The body lift can be determined by $C_L = C_N \cos\alpha + C_X \sin\alpha$ where C_X is obtained from Section 4.2.3.2.

S_b is the body base area.

S is the cross-sectional reference area of the cylindrical portion of the body (can be arbitrarily selected).

α' is an incidence angle defined as $\alpha' = \alpha$ for $0 \leqslant \alpha \leqslant 90^o$ and $\alpha' = 180^o - \alpha$ for $90^o \leqslant \alpha \leqslant 180^o$.

$\left(\frac{C_N}{C_{N_{cir}}}\right)_{NT}$ is the ratio of the normal-force coefficient for the body of noncircular cross section to that for the equivalent body of circular cross section (same cross-sectional area) as determined by Newtonian impact theory. For circular cross sections this ratio is one. For elliptical cross sections this ratio is described below.

When the major axis (a) is perpendicular to the cross-flow velocity,

$$\left(\frac{C_N}{C_{N_{cir}}}\right)_{NT} = \frac{3}{2}\sqrt{\frac{a}{b}}\left\{\frac{-b^2/a^2}{\left(1-\frac{b^2}{a^2}\right)^{3/2}}\log_e\left[\frac{a}{b}\left(1+\sqrt{1-\frac{b^2}{a^2}}\right)\right]+\frac{1}{1-\frac{b^2}{a^2}}\right\}$$

4.2.1.2-e

When the minor axis (b) is perpendicular to the cross-flow velocity,

$$\left(\frac{C_N}{C_{N_{cir}}}\right)_{NT} = \frac{3}{2}\sqrt{\frac{b}{a}}\left[\frac{a^2/b^2}{\left(\frac{a^2}{b^2}-1\right)^{3/2}}\tan^{-1}\left(\sqrt{\frac{a^2}{b^2}-1}\right)-\frac{1}{\frac{a^2}{b^2}-1}\right]$$

4.2.1.2-f

where a and b are as defined above.

η is the cross-flow drag proportionality factor, obtained from Figure 4.2.1.2-35a as a function of body fineness ratio.

c_{d_c} is the cross-flow drag coefficient of the cylindrical section, obtained from Figure 4.2.1.2-35b as a function of cross-flow Mach number M_c, where $M_c = M \sin \alpha$.

S_p is the body planform area. In applying the method to bodies with elliptical cross section, the term S_p in Equation 4.2.1.2-c is based on an equivalent body of revolution with the same cross-sectional area.

Reference 12 discusses methods of computing C_N for bodies with noncircular and nonelliptical cross sections. Reference 13 treats the general case of axially varying cross-sectional shape and bodies with lifting surfaces. However, since substantiating data for these methods are lacking, they have been omitted from the Datcom.

It is noted in Reference 12 that the cross-flow drag coefficient c_{d_c} may be reduced dramatically under the simultaneous conditions of $M_c \leq 0.4$ and $R_\ell \sin\alpha > 10^5$ (R_ℓ is Reynolds number based on diameter). These conditions have only recently been analyzed in detail and have not been included in the Datcom method because of considerable uncertainty in the magnitude and trend of the effects. For more detailed information regarding these effects, the user should refer to Reference 12.

Although the method is applicable up to $\alpha = 180^\circ$, no test verification has been obtained for $\alpha > 60^\circ$ at subsonic speeds. Table 4.2.1.2-B presents substantiation data taken at two Mach numbers. The calculated values for C_N tend to underestimate the test values at high α's. The method is probably less accurate as transonic speeds are approached ($M > 0.9$). It is further recommended that Methods 1 and 2 be used at the low angles of attack whenever possible, since the accuracies of these methods are better substantiated at low α's.

Sample Problems

Method 1

Given: An ogive-cylinder-boattail body of revolution of Reference 20. This is the body of the sample problem of Paragraph A of Section 4.2.1.1.

Body Characteristics:

$d = 5.0$ in. $\quad \ell_N = 26.25$ in. $\quad \ell_C = 23.77$ in. $\quad \ell_A = 13.45$ in.

$d_b = 3.30$ in. $\quad \ell_B = 63.47$ in. $\quad f = \ell_B/d = 12.7$

$(k_2 - k_1) = 0.960$

$V_B^{2/3} = 0.660$ sq ft

$x_o = 50.34$ in.

$S_o = 0.134$ sq ft

(Sample Problem, Paragraph A, Section 4.2.1.1)

Additional Characteristics:

$M = 0.80 \qquad \alpha = 4^\circ, 8^\circ, 12^\circ, 16^\circ, 20^\circ$

Compute:

$$\frac{(k_2 - k_1)\, 2\alpha\, S_o}{V_B^{2/3}} = \frac{(0.960)\,(2)\,\alpha\,(0.134)}{0.660} = 0.390\,\alpha$$

$c_{d_c} = f(M_c);\ M_c = M \sin \alpha$

M_c varies from $0.80 \sin 4^o$ to $0.80 \sin 20^o$; $0.056 \leqslant M_c \leqslant 0.274$

$c_{d_c} = 1.20$ (constant) (Figure 4.2.1.2-35b)

$\eta = 0.710$ (Figure 4.2.1.2-35a)

$$\int_{x_o}^{\ell_B} \eta\, r\, c_{d_c}\, dx = \int_{50.34}^{63.47} (0.710)\,(r)\,(1.20)\, dx$$

$$= (0.710) \left(\frac{2.48 + 1.65}{2}\right) (1.20)\,(63.47 - 50.34)$$

$$= 23.10 \text{ sq in.} = 0.160 \text{ sq ft}$$

Solution:

$$C_L = \frac{(k_2 - k_1)\, 2\alpha S_o}{V_B^{2/3}} + \frac{2\alpha^2}{V_B^{2/3}} \int_{x_o}^{\ell_B} \eta\, r c_{d_c}\, dx \qquad \text{(Equation 4.2.1.2-a)}$$

$$= 0.390\,\alpha + \frac{2\alpha^2}{0.660}\,(0.160)$$

$$= 0.390\,\alpha + 0.485\,\alpha^2$$

α (deg)	α (rad)	C_L (based on $V_B^{2/3}$) Eq. 4.2.1.2-a
4	0.0698	0.0296
8	0.1396	0.0639
12	0.2094	0.1030
16	0.2792	0.1467
20	0.3490	0.1954

The calculated results are compared with test values in Sketch (a).

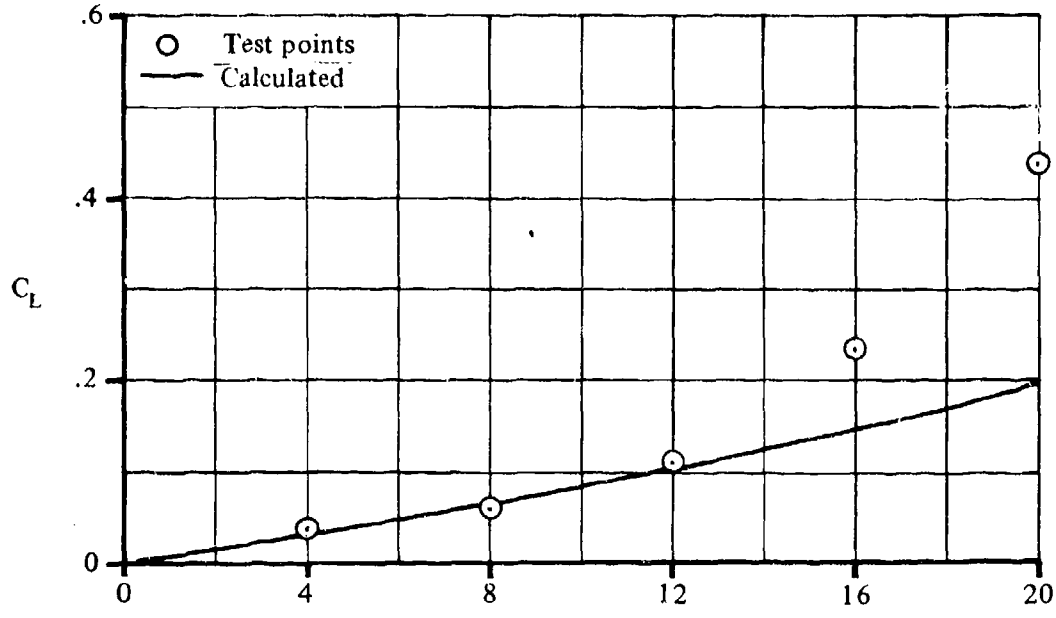

SKETCH (a)

Method 2

Given. The Model A elliptical cross-section body of Reference 11.

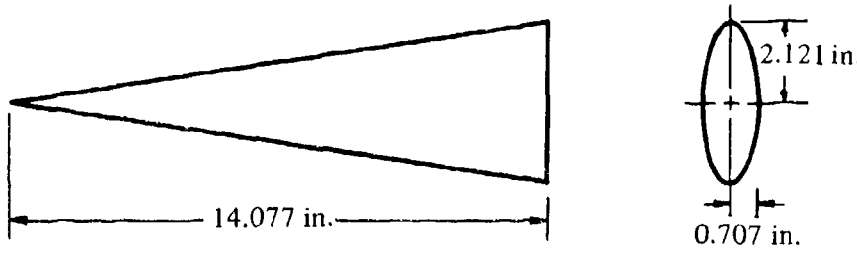

PLANFORM

$S = 29.857$ in.^{2} $A = 0.602$ $S_b = 4.712$ in.^{2}

$M = 0.60$ $R_\ell = 1.4 \times 10^6$

Compute:

$$d_{equiv} = 2\sqrt{\frac{ab}{4}}$$

$$= 2\sqrt{(0.707)(2.121)}$$

$$= 2.45$$

$$f = \frac{\ell_B}{d_{equiv}} = \frac{14.077}{2.45} = 5.74$$

$$\frac{a}{b} = \frac{2.121}{0.707} = 3.0$$

$K_p = 0.85$ (Figure 4.2.1.2-36a)

$K_v = 3.14$ (Figure 4.2.1.2-36b)

$\alpha_v = 4.3^o$ (Figure 4.2.1.2-37)

Solution:

$$C_L = K_p \sin\alpha \cos^2\alpha + K_v \sin^2(\alpha - \alpha_v)\cos(\alpha - \alpha_v)$$ (Equation 4.2.1.2-b)

①	②	③	④
α (deg)	$K_p \sin\alpha \cos^2\alpha$ (Potential component)	$K_v \sin^2(\alpha - \alpha_v)\cos(\alpha - \alpha_v)$ (Vortex component)	C_L ② + ③
0	0	0	0
2	0.0296	0	0.0296
4	0.0590	0	0.0590
6	0.0879	0.0028	0.0907
8	0.1160	0.0131	0.1291
10	0.1432	0.0308	0.1740
12	0.1691	0.0559	0.2250
14	0.1936	0.0879	0.2815
16	0.2165	0.1265	0.3430
18	0.2376	0.1712	0.4088
20	0.2567	0.2215	0.4782

The calculated values are compared with test values from Reference 11 in Sketch (b).

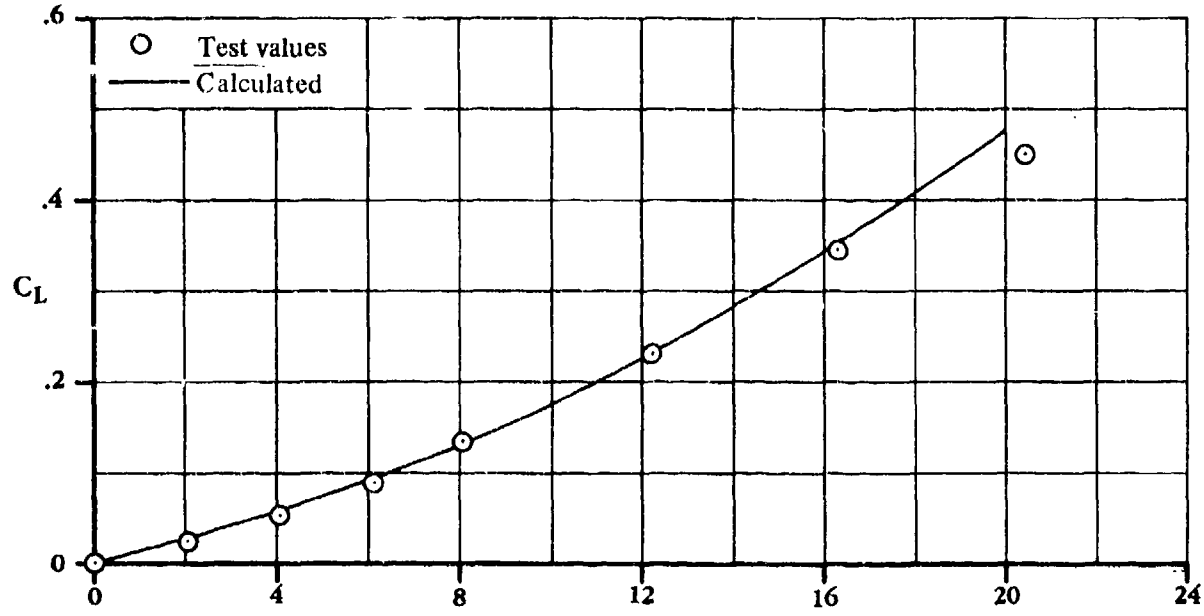

SKETCH (b)

Method 3

Given: Elliptical cross-sectional body with tangent ogive nose of Reference 15.

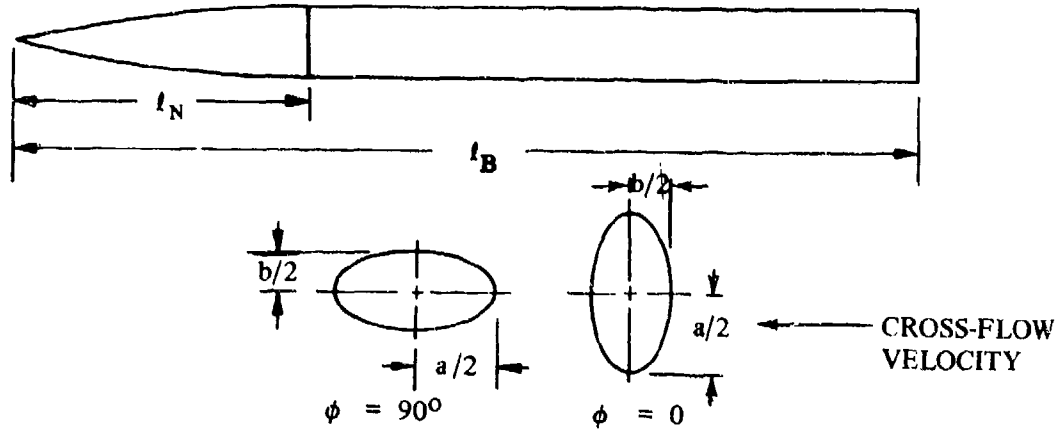

Body Characteristics:

$\frac{a}{2}$ = 4.667 cm $\quad \ell_B$ = 66.0 cm $\quad S_p$ = 392.466 cm^2

$\frac{b}{2}$ = 2.333 cm $\quad \ell_N$ = 19.8 cm

Additional Characteristics:

$\alpha = 50^{o}$ $\phi = 0$ $M = 0.6$ $R_{\ell} = 6.5 \times 10^{5}$ (based on diameter)

and the major axis (a) is perpendicular to cross-flow velocity.

Compute:

$$\alpha' = \alpha = 50^{o}$$

$$S = \frac{\pi ab}{4} = \pi(4.667)(2.333) = 34.206 \text{ cm}^2$$

$$S_b = S = 34.206 \text{ cm}^2$$

$$d = d_{equiv} = 2\sqrt{\frac{ab}{4}} = 6.6 \text{ cm}$$

Slender-body potential-theory term

$$\frac{S_b}{S} \sin 2\alpha' \cos\frac{\alpha'}{2} = \frac{34.206}{34.206}(0.9848)(0.9063) = 0.8925$$

Viscous cross-flow term

$$f = \frac{\ell_B}{d} = \frac{66.0}{6.6} = 10$$

$\eta = 0.685$ (Figure 4.2.1.2-35a)

$$M_c = M \sin\alpha = 0.6\,(0.7660) = 0.46$$

$c_{d_c} = 1.32$ (Figure 4.2.1.2-35b)

$$\eta c_{d_c} \frac{S_p}{S} \sin^2\alpha = (0.685)(1.32)\ \frac{392.466}{34.206}(0.766)^2 = 6.09$$

Ratios for noncircular cross section

$$\left(\frac{C_N}{C_{N_{cir}}}\right)_{SB} = \frac{a}{b}\cos^2\phi + \frac{b}{a}\sin^2\phi \qquad \text{(Equation 4.2.1.2-d)}$$

$$= \frac{4.667}{2.333}(1) + \frac{2.333}{4.667}(0)$$

$$= 2.0$$

$$\left(\frac{C_N}{C_{N_{cir}}}\right)_{NT} = \frac{3}{2}\sqrt{\frac{a}{b}}\left\{\frac{b^2/a^2}{\left(1 - \frac{b^2}{a^2}\right)^{3/2}}\log_e\left[\frac{a}{b}\left(1 + \sqrt{1 - \frac{b^2}{a^2}}\right)\right] + \frac{1}{1 - \frac{b^2}{a^2}}\right\}$$

(Equation 4.2.1.2-e)

$$= \frac{3}{2}\sqrt{\frac{4.667}{2.333}}\left\{\frac{(2.333)^2/(4.667)^2}{\left(1 - \frac{2.333^2}{4.667^2}\right)^{3/2}}\log_e\left[\frac{4.667}{2.333}\left(1 + \sqrt{1 - \frac{2.333^2}{4.667^2}}\right)\right] + \frac{1}{1 - \frac{2.333^2}{4.667^2}}\right\}$$

$$= 2.121\left\{-0.3849 \log_e 3.732 + 1.333\right\}$$

$$= 2.121\left\{-0.3849 (1.3169) + 1.333\right\}$$

$$= 1.752$$

Solution:

$$C_N = \left(\frac{C_N}{C_{N_{cir}}}\right)_{SB}\left(\frac{S_b}{S}\sin 2\alpha' \cos\frac{\alpha'}{2}\right) + \left(\frac{C_N}{C_{N_{cir}}}\right)_{NT}\left(\eta c_{d_c}\frac{S_p}{S}\sin^2\alpha'\right) \quad \text{(Equation 4.2.1.2-c)}$$

$$= 2.0\,(0.8925) + 1.752\,(6.09)$$

$$= 12.45 \text{ (based on body cross-sectional reference area, S)}$$

Additional values have been tabulated below:

M	α (deg)	C_N
0.6	10	1.2
0.6	20	3.2
0.6	30	5.9
0.6	40	9.0
0.6	50	12.5
0.6	60	16.8

The calculated results of the sample problem are compared to test values from Reference 15 in Sketch (c).

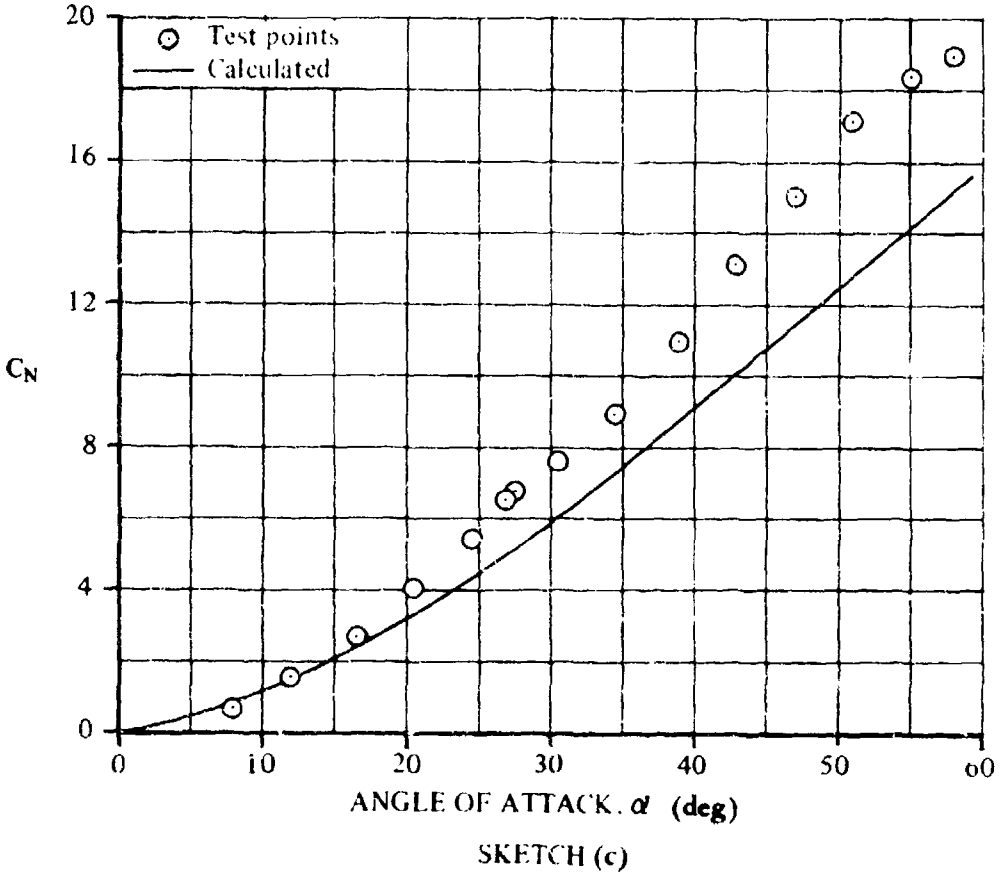

SKETCH (c)

B. TRANSONIC

At transonic Mach numbers, the flow about a body of moderate to large angles of attack is very complex. Analytically, the handling of inviscid mixed subsonic and supersonic flows, which interact at their mutual boundaries, is quite difficult. The presence of the body boundary layer, which may provide an additional mode of interaction between the locally subsonic and supersonic flows, presents an additional complication.

DATCOM METHOD

Because of the analytical difficulties of the problem, no method is given for estimating the transonic lift of a body at angle of attack. It is suggested that subsonic estimates be faired into supersonic results, with experimental data for similar configurations used as a guide in fairing. For bodies of revolution, the reader is referred to the test data of References 17 through 21.

For elliptical cross-section bodies in the transonic speed regime, the reader is referred to the parametric test data presented in References 8 through 11.

C. SUPERSONIC

Three methods are given for predicting body lift.The first method uses the results of the cross-flow analysis presented in Reference 1 to predict the lift on a body of revolution at angle of attack. This result has been modified by Jorgensen in Reference 22 to include bodies of elliptical cross section, and that modification is also presented under Method 1. The cross-flow method of Reference 1 is discussed at the beginning of this section.

The second approach uses hypersonic-similarity concepts that have been adapted to supersonic speeds. The hypersonic-similarity parameters are extended to supersonic Mach numbers by replacing M by β in the hypersonic parameters (Reference 23). Test data for a wide range of cone cylinders for Mach numbers between 1.57 and 4.24 are used in Reference 24 to derive supersonic design charts based on these modified hypersonic-similarity parameters. These charts are presented in this section. They have been slightly modified at the upper limit of their range to make them consistent with the hypersonic charts presented in Paragraph D. These charts can be used for pointed noses other than cones with only small losses in accuracy.

The third method is an improvement on Method 1 developed by Jorgensen in Reference 12. This method calculates the normal-force coefficient up to angles of attack of 180^{o} on bodies with circular and elliptic cross sections. The method is identical to that presented as Method 3 in Paragraph A of this section. It is recommended that this method b used at high angles of attack whenever the first two methods are not applicable

DATCOM METHODS

Method 1

The method presented for predicting the lift of a body of revolution at angle of attack is that of Allen and Perkins, in Reference 1. The lift of bodies of elliptical cross section is that of Reference 1 as modified by Jorgensen in Reference 22.

The lift coefficient of a body of revolution, based on body base area, is

$$C_L = 2\alpha + c_{d_c} \frac{S_p}{S_b} \alpha^2 \qquad 4.2.1.2\text{-g}$$

where

α is the angle of attack in radians.

c_{d_c} is the cross-flow drag coefficient, obtained from Figure 4.2.1.2-35b.

S_p is the body planform area.

S_b is the body base area.

The supersonic lift coefficient at angle of attack of a body having an elliptical cross section, based on body base area, is

$$\left(C_L\right)_{a/b} = \left[\frac{a}{b}\cos^2\phi + \frac{b}{a}\sin^2\phi\right] C_L \qquad 4.2.1.2\text{-h}$$

where

- a is the major axis of the elliptical cross section.
- b is the minor axis of the elliptical cross section.
- ϕ is the angle of bank of the body about its longitudinal axis; $\phi = 0$ with the major axis horizontal and $\phi = 90^o$ with the minor axis horizontal.
- C_L is the lift coefficient of a body of revolution having the same cross-sectional area distribution along its axis as the elliptical-cross-section body of interest. It is given by Equation 4.2.1.2-g.

The Datcom method has been used to calculate the variation of lift coefficient with angle of attack for the bodies of elliptic cross section of Reference 22 and the bodies of revolution of References 1, 22, and 25 through 28. Although the nose shapes of most of the configurations analyzed were tangent ogives, a few bodies of revolution had conical or hemispherical noses. All the afterbodies were straight (no boattail or flare). In general, the calculated results agree well with test data, particularly for angles of attack up to approximately 10^o. The comparison of calculated and test values for the sample problems at the conclusion of Paragraph C of this section is indicative of the degree of accuracy of this method.

Method 2

The alternate method uses hypersonic-similarity parameters that have been adapted to supersonic speeds by the method of Reference 23. The variation of normal-force coefficient with angle of attack for pointed or nearly pointed bodies of revolution is estimated by using Figures 4.2.1.2-38a through -38d, where $\beta = \sqrt{M^2 - 1}$. The normal-force coefficient presented in these design charts is referred to the base area of the configurations.

With the exception of bodies with elliptical cross sections there are no methods for predicting the lift on bodies of noncircular cross section at supersonic speeds. A summary of available test data on bodies of noncircular cross section at supersonic speeds is presented as Table 4.2.1.1-C. It is of interest to note that in Reference 22 (Reference 37 of Table 4.2.1.1-C) the effect of cross-sectional shape on body aerodynamics has been assessed for bodies with circular, elliptic, square, and triangular cross sections. The results for bodies with noncircular cross sections have been compared with results for bodies of revolution having the same axial distribution of cross-sectional area. Data taken from Reference 22 are presented in Sketch (d), which shows the experimental ratio of the lift of bodies with square and triangular cross sections to the lift of the body of revolution having the same axial distribution of cross-sectional area as a function of angle of attack and Mach number.

These data show that at certain angles of bank, noncircular bodies develop considerably more lift than their equivalent bodies of revolution at a given angle of attack. The data of Reference 22 also show that the ratio of lift coefficient for a body of elliptic cross section to that for an equivalent body of revolution is practically constant with change in both angle of attack and Mach number, and that the ratio is given closely by slender-body theory. The slender-body-theory result for the ratio of potential-flow lift for an elliptic body to that for an equivalent body of revolution is the bracketed term in Equation 4.2.1.2-h, i.e., $\left[\frac{a}{b}\cos^2\phi + \frac{b}{a}\sin^2\phi\right]$. No such simple correlation is available for other bodies of noncircular cross section.

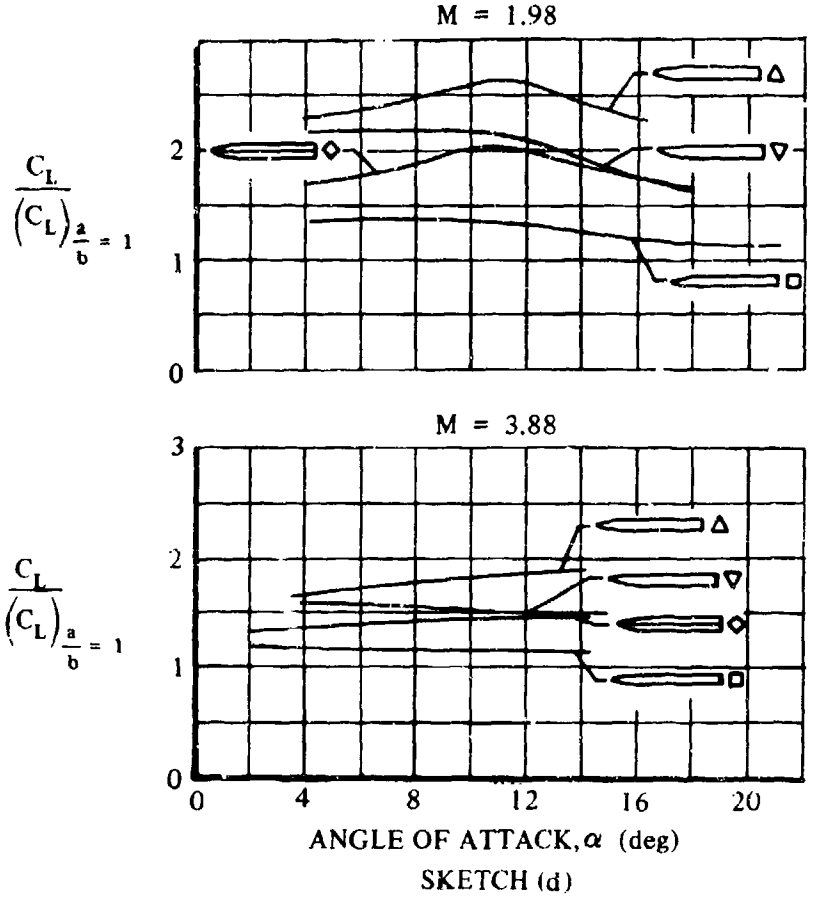

SKETCH (d)

Method 3

The method of Jorgensen for bodies of revolution and bodies with elliptical cross sections, described in Method 3 of Paragraph A of this section, is also applicable throughout the supersonic speed regime up to M = 7. The method is applicable for angles of attack from 0 to 180°.

The cross-flow drag proportionality factor η in Equation 4.2.1.2-c is equal to 1.0 for $M \geq 1.0$.

Comparisons of calculated and test values of C_N are presented in Table 4.2.1.2-C for bodies with circular and elliptical cross sections and various nose shapes. The method is intended primarily for the high-angle-of-attack analysis, and it is recommended that either Datcom Method 1 or 2 be used at low angles of attack.

Sample Problems

1. Method 1

Given: An ogive-cylinder body of Reference 22

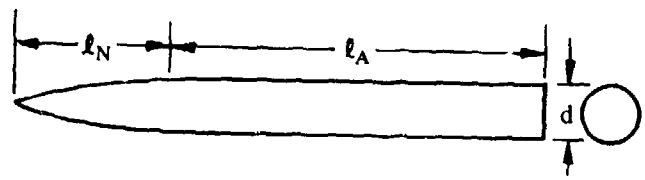

Body Characteristics:

$$f_N = \frac{\ell_N}{d} = 3.0 \qquad f_A = \frac{\ell_A}{d} = 7.0 \qquad f = \frac{\ell_B}{d} = 10.0$$

$d = 1.40$ in. $\qquad S_p = 17.66$ sq in. $\qquad S_b = 1.539$ sq in.

$$S_p/S_b = 11.47$$

Additional Characteristics:

$M = 1.98 \qquad \alpha = 4^o, 8^o, 12^o, 16^o, 20^o$

Compute:

$c_{d_c} = f(\alpha, M)$ (Figure 4.2.1.2-35b) (See calculation table below.)

Solution:

$$C_L = 2\alpha + c_{d_c} \frac{S_p}{S_b} \alpha^2 \qquad \text{(Equation 4.2.1.2-g) (based on } S_b\text{)}$$

① α (deg)	② α (rad)	③ α^2 (rad^2)	④ M_c $M \sin \alpha$	⑤ c_{d_c} Fig. 4.2.1.2-35b	⑥ 2α 2 (2)	⑦ $c_{d_c} \frac{S_p}{S_b} \alpha^2$ (5) (11.47) (3)	⑧ C_L Eq. 4.2.1.2-g (6) + (7)
4	0.0698	0.00487	0.138	1.20	0.1396	0.0670	0.2066
8	0.1396	0.01949	0.276	1.208	0.2792	0.2700	0.5492
12	0.2094	0.04385	0.412	1.275	0.4188	0.6410	1.0598
16	0.2792	0.07795	0.546	1.41	0.5584	1.2600	1.8184
20	0.3490	0.12180	0.677	1.62	0.6980	2.2620	2.9600

2. Method 1

Given: A body of Reference 22 having an elliptical cross section and the same axial distribution of cross-sectional area as the body of revolution of Sample Problem 1.

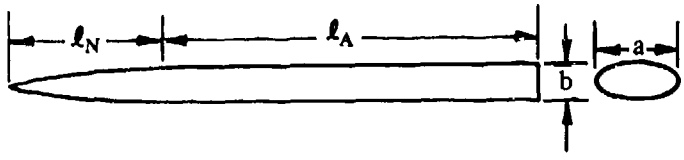

Body Characteristics:

$a = 1.98$ in. $\quad b = 0.99$ in. $\quad a/b = 2.0 \quad \phi = 0$

Additional Characteristics:

$M = 1.98 \quad \alpha = 4^o, 8^o, 12^o, 16^o, 20^o$

Compute:

C_L vs α for a body of revolution having the same cross-sectional area distribution. (from Sample Problem 1)

Solution:

$$(C_L)_{a/b} = \left[\frac{a}{b}\cos^2\phi + \frac{b}{a}\sin^2\phi\right] C_L \qquad \text{(Equation 4.2.1.2-h) (based on } S_b\text{)}$$

$$= [(2.0)(1.0) + 0]\, C_L = 2.0\, C_L$$

α (deg)	C_L Sample Problem 1	$(C_L)_{a/b}$ Eq. 4.2.1.2-h
4	0.207	0.414
8	0.549	1.098
12	1.060	2.120
16	1.818	3.636
20	2.960	5.920

The calculated results of Sample Problems 1 and 2 are compared with test values from Reference 22 in Sketch (e).

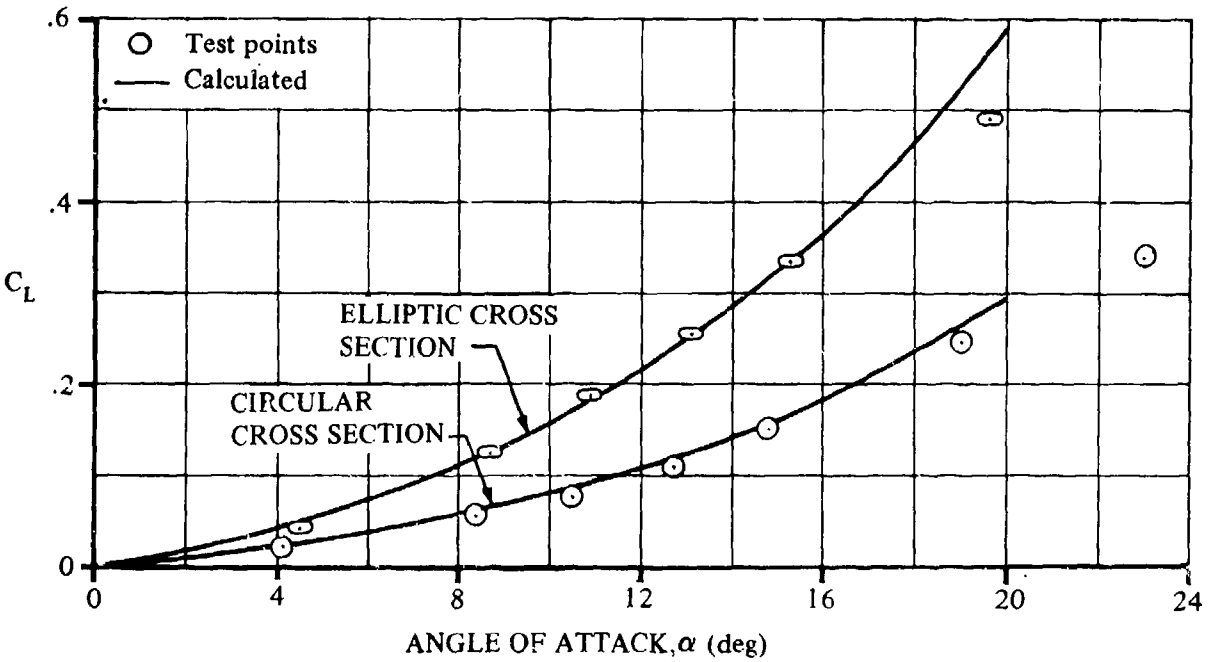

SKETCH (e)

3. Method 3

Refer to Sample Problem 3 in Paragraph A of this section for an example of the application of the method.

D. HYPERSONIC

Three methods are presented for estimating forces on bodies of revolution at hypersonic speeds. One is the hypersonic-similarity method. Another is the Newtonian impact theory and its modifications, discussed in Paragraph D of Section 4.2.1.1. A third method is the method of Jorgensen presented in Paragraphs A and C of this section.

The first method presented in this section is based on hypersonic similarity with Newtonian-theory modifications. Data from References 23 and 29 through 32 have been correlated by means of the hypersonic-similarity parameters and the results extended to high Mach numbers by means of Newtonian theory. These data are limited to pointed, unflared bodies.

The incremental normal-force coefficient due to spherical nose blunting of cones has been calculated by using Newtonian theory. The calculations assume that pressures aft of the intersection of the sphere and the cone are not affected by the blunt nose.

Increments in normal forces due to the addition of flares on cylindrical bodies have also been calculated on the basis of Newtonian flow. Caution should be used in using body flares, however, because they can cause flow separation due to the pressure rise across the shock wave at the beginning of the flare. These separated flows can be unsteady and can cause large losses in lift and moment effectiveness. The conditions that aggravate boundary-layer separation tendencies are large flare angles, lower Mach numbers, high Reynolds number (for a given laminar or turbulent condition), and high wall temperatures. Corner radii or filleting can greatly alleviate this problem. Reference 33 gives some idea of the magnitude of these effects.

The second method is based on Newtonian impact theory. Design charts, taken from Reference 34, are presented for estimating the normal-force characteristics of arbitrary bodies of revolution. These charts are applicable to angles of attack up to 90^{O}.

The third method is the method given by Jorgensen in Reference 12, and presented as Method 3 of Paragraphs A and C of this section. This method calculates the normal-force coefficient up to angles of attack of 180^{O} on bodies with circular and elliptical cross sections. It is recommended that this method be used at high angles of attack whenever the first two methods are not applicable.

DATCOM METHODS

Method 1

The normal-force coefficient for a body composed of a circular cone-cylinder with or without a blunted nose and/or a flared skirt, based on the body base area, is

$$C_N = \left(C_N\right)_{\substack{\text{cone-}\\\text{cylinder}}} \left(\frac{d_{cyl}}{d_b}\right)^2 + \left(\Delta C_N\right)_N \left(\frac{d}{d_b}\right)^2 + \left(\Delta C_N\right)_F \qquad 4.2.1.2\text{-i}$$

where

$\left(C_N\right)_{\substack{\text{cone}\\\text{cylinder}}}$ is the normal-force coefficient of a circular cone-cylinder, based on the cylinder base area. This parameter is obtained from Figure 4.2.1.2-40.

$\left(\Delta C_N\right)_N$ is the increment in normal-force coefficient due to blunting the nose of the cone, based on the base area of the spherical nose segment. This parameter is obtained from Figure 4.2.1.2-42a.

$\left(\Delta C_N\right)_F$ is the increment in normal-force coefficient due to the addition of a flared body of revolution at the end of a semi-infinite cylindrical body, based on the base area of the flared body. This parameter is obtained from Figure 4.2.1.2-42b.

d_{cyl} is the diameter of the cylinder.

d is the diameter of the spherical nose segment. (See Figure 4.2.1.2-42a.)

d_b is the body base diameter.

Method 2

The expression for the normal-force coefficient of an arbitrary body of revolution, based on the body base area, taken from Reference 34, is

$$C_N = \frac{K}{\pi} \frac{\ell_B}{R} \int_0^1 K_\theta \frac{r}{R} d\left(\frac{x}{\ell_B}\right) \qquad 4.2.1.2\text{-j}$$

where

K = 2, according to Newtonian theory, which corresponds to $M_\infty = \infty$ and $\gamma = 1.0$. This value does not account for either Mach number or γ variations, but for pointed bodies with attached shocks it gives results of acceptable accuracy. For blunt bodies the actual value of the stagnation-point pressure coefficient may be used for K:

$$K = C_{P_{stag}} = \frac{\gamma + 3}{\gamma + 1}\left[1 - \frac{2}{\gamma + 3}\,\frac{1}{M_\infty^2}\right] \qquad 4.2.1.2\text{-k}$$

ℓ_B is the body length.

R is the reference radius (radius of the base).

r is the local radius at any body station.

K_θ is a pressure-surface-slope integral factor obtained from Figure 4.2.1.2-43 as a function of angle of attack and the surface slope θ of the body of revolution.

The following steps outline the calculation procedure:

Step 1. From the equation of the body of revolution obtain the expression for the surface slope using the relation

$$\theta = \tan^{-1}\left(\frac{dr}{dx}\right)$$

where θ, dr, and dx are illustrated in Sketch (f).

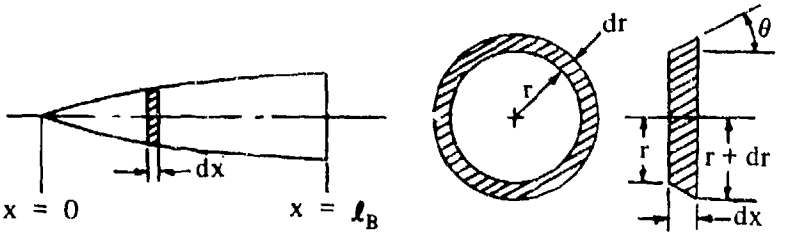

ELEMENT OF SURFACE DETAIL

SKETCH (f)

Step 2. Compute the values of r/R and θ at various longitudinal stations x/ℓ_B.

Step 3. For various x/ℓ_B enter Figure 4.2.1.2-43 with the corresponding θ from Step 2 and obtain K_θ at the desired angle of attack.

Step 4. Plot the product $K_\theta \frac{r}{R}$ versus x/ℓ_B.

Step 5. Obtain C_N by integrating the area under the curve described in Step 4 and multiplying that value by $\frac{K}{\pi} \frac{\ell_B}{R}$.

Method 3

This method is identical to Method 3 presented in Paragraphs A and C of this section. The method is applicable to angles of attack from 0 to 180^o and Mach numbers up to 7. The method has been partially substantiated by test data from Reference 16 in Table 4.2.1.2-C.

The method shows reasonable agreement with test data at hypersonic speeds in the low-angle-of-attack range. Because of the scarcity of substantiating test data, caution should be used when applying the method at higher angles of attack ($\alpha > 25^o$).

Sample Problems

1. Method 1

Given: Configuration 5115 of Reference 35, consisting of a cone-cylinder-frustum body with a spherical nose. This is the configuration of the sample problem in Paragraph D of Section 4.2.1.1.

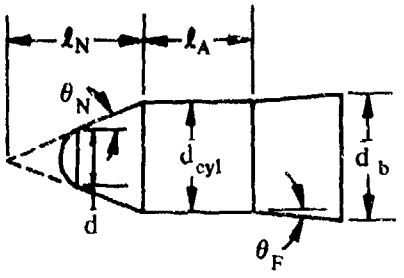

ℓ_N = 1.45 ft ℓ_A = 1.20 ft d = 0.62 ft d_{cyl} = 1.20 ft d_b = 1.268 ft

θ_N = 22.5^o θ_F = 5^o M = 4.04; β = 3.91

Compute:

$$f_A = \frac{\ell_A}{d_{cyl}} = \frac{1.20}{1.20} = 1.00$$

$$f_N = \frac{\ell_N}{d_{cyl}} = \frac{1.45}{1.20} = 1.21$$

$$f_A/f_N = 1.00/1.21 = 0.83$$

$$\beta/f_N = 3.91/1.21 = 3.23$$

$$(d/d_b)^2 = (0.62/1.368)^2 = 0.205$$

$$(d_{cyl}/d_b)^2 = (1.20/1.368)^2 = 0.769$$

$$1 - (d_{cyl}/d_b)^2 = 0.231$$

Solution:

$$C_N = \left(C_N\right)_{\substack{\text{cone-}\\\text{cylinder}}} \left(\frac{d_{cyl}}{d_b}\right)^2 + \left(\Delta C_N\right)_N \left(\frac{d}{d_b}\right)^2 + \left(\Delta C_N\right)_F \qquad \text{(Equation 4.2.1.2-i)}$$

①	②	③	④	⑤	⑥	⑦	⑧	⑨
α (deg)	$\beta\alpha$ (deg)	$(\beta C_N)_{\text{cone-cylinder}}$ Fig. 4.2.1.2-40 interpolated	$(C_N)_{\text{cone-cylinder}}\left(\frac{d_{cyl}}{d_b}\right)^2$ [③/(3.911)] (0.769)	$(\Delta C_N)_N$ Fig. 4.2.1.2-42a	$(\Delta C_N)_N\left(\frac{d}{d_b}\right)^2$ ⑤(0.205)	$\frac{(\Delta C_N)_F}{1-\left(\frac{d_{cyl}}{d_b}\right)^2}$ Fig. 4.2.1.2-42b	$(\Delta C_N)_F$ ⑦(0.231)	C_N (based on S_b) ④+⑥+⑧
0	–	–	–	–	–	–	–	0
10	39.1	1.5	0.295	–0.435	–0.0892	0.40	0.092	0.298
20	78.2	3.5	0.688	–0.820	–0.168	0.92	0.212	0.732
30	117.3	5.4	1.062	–1.125	–0.231	1.66	0.383	1.214
40	156.4	7.8	1.534	–1.350	–0.277	2.55	0.589	1.846

2. Method 2

Given: A second-power body of revolution of fineness ratio 1.0.

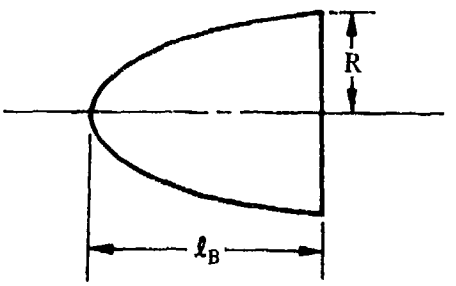

$x = \left(\frac{4}{\ell_B}\right) r^2$ (equation of body) $\quad \ell_B = 2.0$ ft $\quad R = 1.0$ ft

$M_\infty = 3.55 \quad \alpha = 6^o \quad \gamma = 1.40$

Compute:

Determine K for a blunt-nosed body

$$K = \frac{\gamma + 3}{\gamma + 1}\left[1 - \frac{2}{\gamma + 3}\,\frac{1}{M_\infty^2}\right] = 1.77 \qquad \text{(Equation 4.2.1.2-k)}$$

$$\theta = \tan^{-1}\left(\frac{dr}{dx}\right) = \tan^{-1}\left(\frac{1}{4\sqrt{x/\ell_B}}\right)$$

Calculate r/R and θ at various longitudinal stations x/ℓ_B and plot (see Sketch (g)).

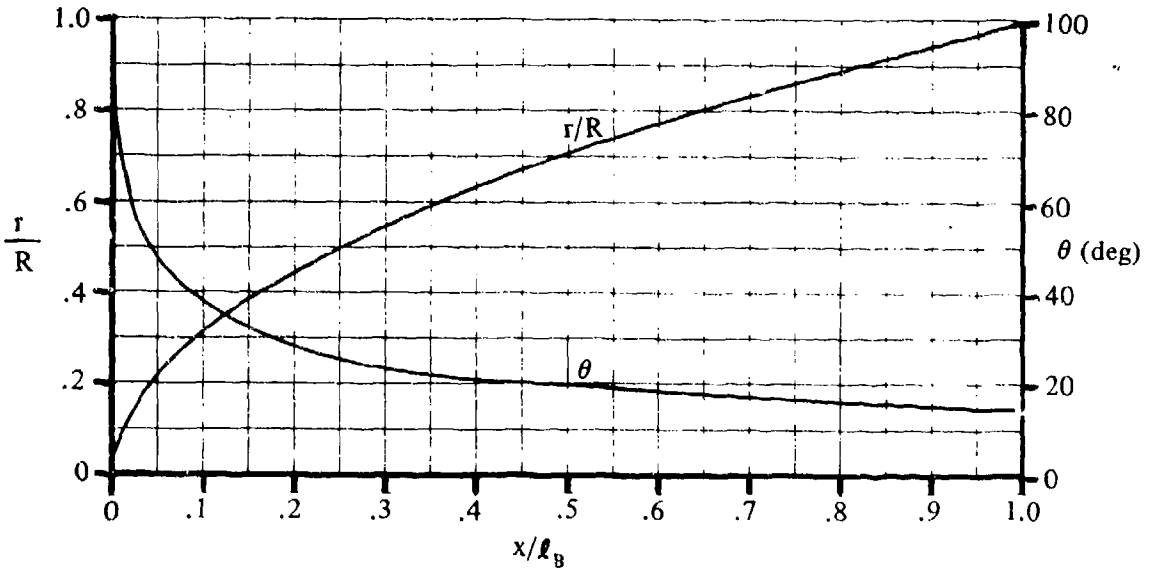

SKETCH (g)

Obtain values for K_θ from Figure 4.2.1.2-43 for various values of θ at $\alpha = 6^o$.

Plot the product of $K_\theta \frac{r}{R}$ versus x/ℓ_B (see Sketch (h)).

Integrate the area under the curve of Sketch (h). $\int_0^1 K_\theta \frac{r}{R} d\left(\frac{x}{\ell_B}\right) = 0.135$

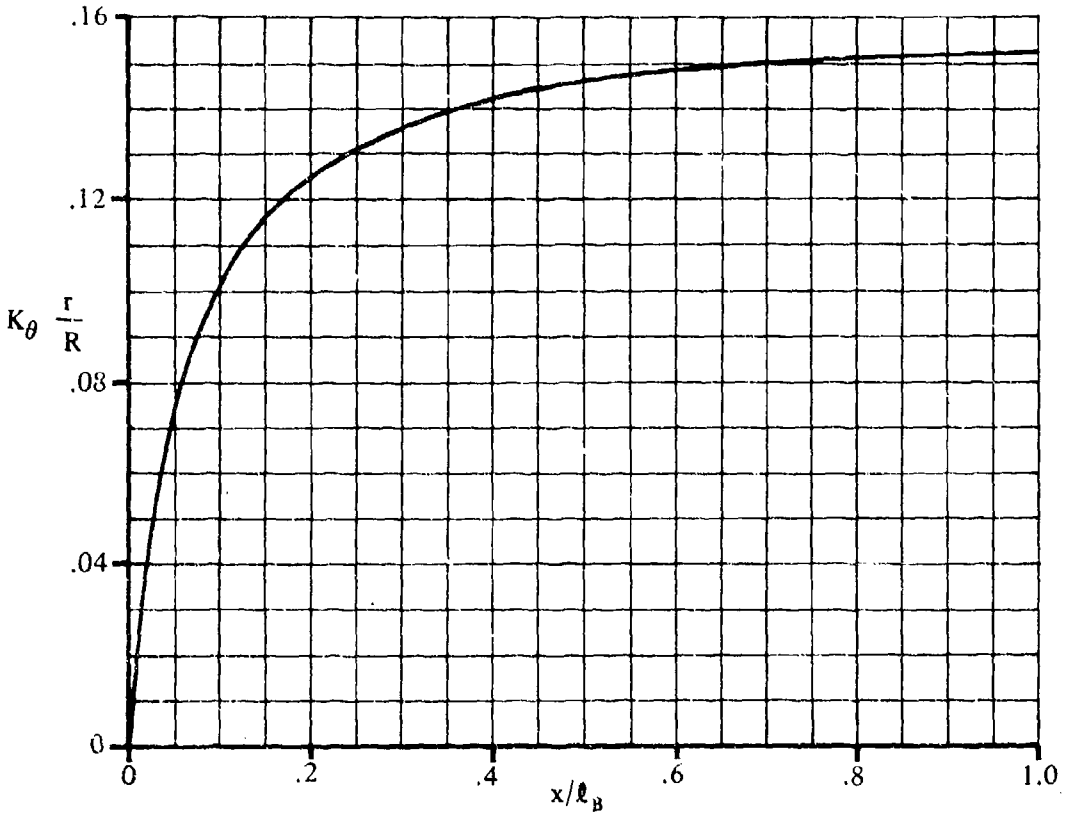

SKETCH (h)

Solution:

$$C_N = \frac{K}{\pi} \frac{\ell_B}{R} \int_0^1 K_\theta \frac{r}{R} d\left(\frac{x}{\ell_B}\right) \quad \text{(Equation 4.2.1.2-j)}$$

$$= \frac{(1.77)(2.0)}{\pi \quad (1.0)}(0.135)$$

$$= 0.152 \text{ (based on } S_b)$$

3. Method 3

Refer to Sample Problem 3 in Paragraph A of this section for an example of the application of the method.

REFERENCES

1. Allen, H. J., and Perkins, E. W.: A Study of Effects of Viscosity on Flow Over Slender Inclined Bodies of Revolution. NACA TR 1048, 1951. (U)

2. Kelly, H. R.: The Estimation of Normal-Force, Drag, and Pitching-Moment Coefficients for Blunt-Based Bodies of Revolution at Large Angles of Attack. Jour. Aero. Sci., Vol. 21, No. 8, 1954. (U)

3. Van Dyke, M. D.: First- and Second-Order Theory of Supersonic Flow Past Bodies of Revolution. Jour. Aero. Sci., Vol. 18, No. 3, 1951. (U)

4. Phythian, J. E., and Dommett, R. L.: Semi-Empirical Methods of Estimating Forces on Bodies at Supersonic Speeds. Jour. Roy. Aero. Soc., Vol. 62, No. 571, 1958. (U)

5. Hopkins, E. J.: A Semiempirical Method for Calculating the Pitching Moment of Bodies of Revolution at Low Mach Numbers. NACA RM A51C14, 1951. (U)

6. Polhamus, E. C.: A Concept of the Vortex Lift of Sharp-Edge Delta Wings Based on a Leading-Edge-Suction Analogy. NACA TN D-3767, 1966, (U)

7. Spencer, B., Jr., and Phillips, W. P.: Effects of Cross-Section Shape on the Low-Speed Aerodynamic Characteristics of a Low-Wave-Drag Hypersonic Body. NASA TN D-1963, 1963. (U)

8. Spencer, B., Jr., and Phillips, W. P.: Transonic Aerodynamic Characteristics of a Series of Bodies Having Variations in Fineness Ratio and Cross-Sectional Ellipticity. NASA TN D-2622, 1965. (U)

9. Spencer, B., Jr.: Transonic Aerodynamic Characteristics of a Series of Related Bodies with Cross-Sectional Ellipticity. NASA TN D-3203, 1966. (U)

10. Taylor, R. A.: Transonic Aerodynamic Characteristics of Several Bodies Having Elliptical Cross Sections and Various Plan Forms. NASA TN D-14, 1959. (U)

11. Stivers, L. S, Jr., and Levy, L. L., Jr.: Longitudinal Force and Moment Data at Mach Numbers from 0.60 to 1.40 for a Family of Elliptic Cones with Various Semiapex Angles. NASA TN D-1149, 1961. (U)

12. Jorgensen, L. H.: Prediction of Static Aerodynamic Characteristics for Space-Shuttle-Like and Other Bodies at Angles of Attack from 0° to 180°. NASA TN D-6996, 1973. (U)

13. Jorgensen, L. H.: A Method for Estimating Static Aerodynamic Characteristics for Slender Bodies of Circular and Noncircular Cross Section Alone and with Lifting Surfaces at Angles of Attack from 0° to 90°. NASA TN D-7228, 1973. (U)

14. Jernell, L. S.: Aerodynamic Characteristics of Bodies of Revolution of Mach Numbers from 1.50 to 2.86 and Angles of Attack to 180°. NASA TM X-1658, 1968. (U)

15. Jorgensen, L. H., and Nelson, E. R.: Experimental Aerodynamic Charateristics for Bodies of Elliptic Cross Section at Angles of Attack from 0° to 58° and Mach Numbers from 0.6 to 2.0. NASA TM X-3129, 1975. (U)

16. Dennis, D. H., and Cunningham, B. E.: Forces and Moments on Inclined Bodies at Mach Numbers from 3.0 to 6.3. NACA RM A54E03, 1954. (U)

17. Hayes, W. C., Jr., and Henderson, W. P.: Some Effects of Nose Bluntness and Fineness Ratio on the Static Longitudinal Aerodynamic Characteristics of Bodies of Revolution at Subsonic Speeds. NASA TN D-650, 1961. (U)

18 Reese, D. E., Jr., and Wehrend, W. R., Jr.: An Investigation of the Static and Dynamic Aerodynamic Characteristics of a Series of Blunt-Nosed Cylinder-Flare Models at Mach Numbers from 0.65 to 2.20. NASA TM X-110, 1960. (U)

19. Polhamus, E. C.: Effect of Nose Shape on Subsonic Aerodynamic Characteristics of a Body of Revolution Having a Fineness Ratio of 10.94. NACA RM L57F25, 1957. (U)

20. Goodson, K. W.: Effect of Nose Length, Fuselage Length, and Nose Fineness Ratio on the Longitudinal Aerodynamic Characteristics of Two Complete Models at High Subsonic Speeds. NASA Memo 10-10-58L, 1958. (U)

21. Coe, P. L., Jr., Chambers, J. R., and Letko, W.: Asymmetric Lateral-Directional Characteristics of Pointed Bodies of Revolution at High Angles of Attack. NASA TN D-7095, 1972. (U)

22. Jorgensen, L. H.: Inclined Bodies of Various Cross Sections at Supersonic Speeds. NASA Memo 10-3-58A, 1958. (U)

23. Van Dyke, M. D.: The Combined Supersonic-Hypersonic Similarity Rule. Jour. Aero. Sci., Vol. 18, No. 7, 1951. (U)

24. Dorrance, W. H., and Norrell, R. G.: Correlation of Cone-Cylinder Normal Force and Pitching Moment Data by the Hypersonic Similarity Rule. Jour. Aero. Sci., Vol. 24, No. 5, 1957. (U)

25. Perkins, E. W., and Jorgensen, L. H.: Comparison of Experimental and Theoretical Normal-Force Distributions (Including Reynolds Number Effects) on an Ogive-Cylinder Body at Mach Number 1.98. NACA TN 3716, 1956. (U)

26. Jack, J. R.: Aerodynamic Characteristics of a Slender Cone-Cylinder Body of Revolution at Mach Number of 3.85. NACA RM E51H17, 1951. (U)

27. Ferri, A.: Supersonic-Tunnel Tests of Projectiles in Germany and Italy. NACA WR L-152, 1945. (U)

28. Delancey, L. M., Jaeger, B. F., and Schroedter, G. M.: The Aerodynamic Characteristics at Mach Number 4.24, of Bodies of Revolution with Varying Lengths and Head Shapes. NOTS TM 358, 1951. (U)

29. Dennis, D. H., and Cunningham, B. E.: Forces and Moments on Pointed and Blunt-Nosed Bodies of Revolution at Mach Numbers from 2.75 to 5.00. NACA RM A52F22, 1952. (U)

30. Resnikoff, M. M.: Optimum Lifting Bodies at High Supersonic Airspeeds. NACA RM A54B15, 1954. (U)

31. Jaeger, B. F., and Morgan, A. J. A.: Review of Experiment and Theory Applicable to Cone-Cylinder and Ogive-Cylinder Bodies of Revolution in Supersonic Flow. NAVORD 5239, 1956. (U)

32. Buford, W. E., and Shatunoff, S.: The Effects of Fineness Ratio and Mach Number on the Normal Force and Center of Pressure of Conical- and Ogival-Head Bodies. BRL MR 760, 1954. (U)

33. Dennis, D. H.: The Effects of Boundary-Layer Separation Over Bodies of Revolution With Conical Tail Flares. NACA RM A57I30, 1957. (U)

34. Rainey, R. W.: Working Charts for Rapid Prediction of Force and Pressure Coefficients on Arbitrary Bodies of Revolution by Newtonian Concepts. NASA TN D-176, 1959. (U)

35. Henderson, J. H.: Effect of Nose Bluntness on Normal Force, Pitching Moment, and Center of Pressure on Cone-Cylinder and Cone-Cylinder-Frustum Bodies of Revolution at Mach Numbers of 1.50, 2.18, 2.81, and 4.04. Ordnance Missile Laboratories Redstone Arsenal Report No. GR11F, 1958. (U)

TABLE 4.2.1.2-A
SUBSONIC BODY LIFT
METHOD 2
DATA SUMMARY AND SUBSTANTIATION

Ref	M	A	a/b	d_{equiv}	ℓ_B/d_{equiv}	α_v Fig. 4.2.1.2-37	α (deg)	$C_{L_{calc}}$	$C_{L_{test}}$	Percent Error e
7	0.4	0.245	1.5	4.80	10.0	7.3	4	0.031	0.024	29.2
							8	0.061	0.063	−3.2
							12	0.113	0.115	−1.7
							16	0.199	0.173	15.0
		0.283	2.0	4.80	10.0	5.5	4	0.041	0.033	24.2
							8	0.089	[illegible]37	2.3
							12	0.174	0.170	2.4
							16	0.295	0.256	15.2
							18	0.368	0.303	21.5
		0.316	2.5	4.80	10.0	4.0	4	0.052	0.051	2.0
							8	0.125	0.134	−6.7
							12	0.243	0.245	−0.8
							16	0.399	0.367	8.7
8	0.4	0.408	1.5	4.0	5.0	12.4	4	0.192	0.20	−4.0
							8	0.377	0.355	6.2
							12	0.549	0.58	−5.3
							16	0.761	0.82	−7.2
							20	1.09	1.12	−2.7
		0.286	1.5	4.0	7.0	8.8	4	0.197	0.21	−6.2
							8	0.387	0.43	−10.0
							12	0.629	0.675	−6.8
							16	1.05	0.97	8.2
							20	1.63	1.46	11.6
		0.786	2.0	4.0	3.0	16.3	4	0.240	0.24	0
							8	0.472	0.45	4.9
							12	0.688	0.665	3.5
							16	0.881	0.89	−1.0
							20	1.087	1.133	−4.1
		0.337	2.0	4.0	7.0	6.7	4	0.257	0.285	−9.8
							8	0.513	0.555	−6.7
							12	0.939	0.95	−1.2
							16	1.556	1.475	5.5
							20	2.343	2.145	9.2

TABLE 4.2.1.2-A (CONTD)

Ref	M	A	a/b	d_{equiv}	ℓ_B/d_{equiv}	α_v Fig. 4.2.1.2-37	α (deg)	$C_{L_{calc}}$	$C_{L_{test}}$	Percent Error e
9	0.5	0.5656	2.0	5.0	5.0	9.1	4	0.055	0.052	5.8
							8	0.108	0.103	4.9
							12	0.165	0.170	−2.9
							16	0.246	0.246	0
							20	0.349	0.343	1.7
		0.3075.	3.0	3.535	7.07	3.45	4	0.0315	0.035	−10.0
							8	0.081	0.084	−3.6
							12	0.158	0.159	−0.6
							16	0.259	0.256	1.2
							18	0.318	0.310	2.6
10	0.4	0.350	3.0	6.0	6.93	3.53	4	0.036	0.044	−18.2
							8	0.090	0.090	0
							12	0.171	0.172	−0.6
		0.311	4.0	6.0	8.60	1.93	4	0.036	0.030	20.0
							8	0.098	0.078	25.6
							12	0.186	0.170	9.4
11	0.6	1.674	3.0	2.45	2.07	12.95	4	0.137	0.125	9.6
							8	0.269	0.250	7.6
							12	0.392	0.380	3.2
							16	0.511	0.510	0.2
							20	0.643	0.675	−4.7
		2.41	3.0	2.45	1.436	16.85	4	0.175	0.160	9.4
							8	0.344	0.320	7.5
							12	0.501	0.465	7.7
							16	0.642	0.625	2.7
							20	0.771	0.780	−1.2

$$\text{Percent Error} = \Sigma \frac{|e|}{n} = 6.9\%$$

TABLE 4.2.1.2-B

SUBSONIC BODY NORMAL FORCE

METHOD 3

DATA SUMMARY AND SUBSTANTIATION

Ref	M	R_ℓ (based on d_{equiv})	a/b	$\frac{\ell_B}{d_{equiv}}$	Nose Shape	α (deg)	$C_{N_{calc}}$	$C_{N_{test}}$	ΔC_N
15	0.6	6.5×10^5	1.0	10	Ogive	10	0.6	0.5	0.1
						20	1.7	1.4	0.3
						30	3.2	2.7	0.5
						40	5.0	4.6	0.4
						50	6.9	6.4	0.5
						60	8.9	8.9	0
	0.9					10	0.6	0.4	0.2
						20	1.7	1.5	0.2
						30	3.3	3.5	−0.2
						40	5.7	6.4	−0.7
						50	8.4	9.8	−1.4
						60	11.1	13.4	−2.3
	0.6		2.0			10	1.2	1.2	0
						20	3.2	3.9	−0.7
						30	5.9	7.3	−1.4
						40	9.0	11.5	−2.5
						50	12.5	16.7	−4.2
						60	15.9	19.2	−3.3
	0.9					10	1.2	1.2	0
						20	3.3	4.3	−1.0
						30	6.2	8.4	−2.2
						40	10.1	14.8	−4.7
						50	15.1	19.1	−4.0
						60	19.7	22.3	−2.6
	0.6		0.5			10	0.3	0.1	0.2
						20	0.8	0.4	0.4
						30	1.6	0.8	0.8
						40	2.6	1.3	1.3
						50	3.5	1.5	2.0
						60	4.5	1.2	3.3
	0.9					10	0.3	0.1	0.2
						20	0.9	0.5	0.4
						30	1.7	1.1	0.6
						40	2.8	2.3	0.5
						50	4.2	5.2	−1.0
						60	5.5	7.0	−1.5

Average Error = $\sum \frac{|\Delta C_N|}{n} = 1.27$

TABLE 4.2.1.2-C

SUPERSONIC AND HYPERSONIC BODY NORMAL FORCE

METHOD 3

DATA SUMMARY AND SUBSTANTIATION

Ref	M	R_ℓ (based on d_{equiv})	a/b	$\frac{\ell_B}{d_{equiv}}$	Nose Shape	α (deg)	$C_{N_{calc}}$	$C_{N_{test}}$	ΔC_N
14	1.50	1.25×10^5	1.0	6	Blunt	35	4.5	5.0	−0.5
						65	10.5	9.0	1.5
						95	11.7	10.0	1.7
				8	Cone	35	4.2	4.5	−0.3
						65	9.7	8.5	1.2
						95	10.7	8.7	2.0
						125	8.6	6.2	2.4
						155	2.6	2.7	−0.1
				9		35	5.4	6.0	−0.6
						65	13.0	10.7	2.3
						95	14.6	11.5	3.1
						125	11.5	8.5	3.0
						155	3.3	7.0	−3.7
				11		35	6.6	7.5	−0.9
						65	16.3	14.0	2.3
						95	18.4	14.6	3.8
						125	14.3	11.5	2.8
						165	1.5	2.0	−0.5
				9	Ogive	35	5.7	6.2	−0.5
						65	13.8	11.5	2.3
						95	15.5	12.0	3.5
						125	12.2	9.5	2.7
						155	3.5	3.8	−0.3
				7		35	4.1	4.7	−0.6
						65	9.4	8.4	1.0
						95	10.4	8.3	2.1
						125	8.4	6.0	2.4
						155	2.6	3.0	−0.4
				11		35	6.5	7.3	−0.8
						65	16.0	13.0	3.0
						95	18.1	14.5	3.6
						125	14.1	10.9	3.2
						155	4.0	4.5	−0.5
	2.86			6	Blunt	35	4.6	4.0	0.6
						65	9.1	8.4	0.7
						95	10.3	10.0	0.3
				8		35	5.8	5.4	0.4
						65	12.0	11.0	1.0
						85	13.6	12.9	0.7

TABLE 4.2.1.2-C (CONTD)

Ref	M	R_ℓ (based on d_{equiv})	a/b	$\frac{\ell_B}{d_{equiv}}$	Nose Shape	α (deg)	$C_{N_{calc}}$	$C_{N_{test}}$	ΔC_N
14	2.86	1.25×10^5	1.0	7	Cone	35	4.3	3.8	0.5
						65	8.4	8.0	0.4
						95	9.4	9.0	0.4
						125	7.3	6.0	1.3
						155	2.8	1.7	1.1
				9		35	5.5	5.2	0.3
						65	11.2	10.5	0.7
						95	12.8	12.0	0.8
						125	9.6	8.1	1.5
						155	3.6	2.4	1.2
				11		35	6.8	6.5	0.3
						65	14.1	13.5	0.6
						95	16.2	15.0	1.2
						125	11.9	10.5	1.4
						155	4.4	3.3	1.1
				9	Ogive	35	5.8	5.5	0.3
						65	12.0	11.0	1.0
						95	13.7	12.6	1.1
						125	10.2	9.0	1.2
						155	3.8	2.6	1.2
				7		35	4.2	4.0	0.2
						65	8.2	7.8	0.4
						95	9.2	8.4	0.8
						125	7.1	5.9	1.2
						155	2.8	1.7	1.1
				9		35	5.4	5.4	0
						65	11.0	10.5	0.5
						95	12.5	11.6	0.9
						125	9.4	8.5	0.9
						155	3.5	2.6	0.9
				11		35	6.7	6.6	0.1
						65	13.8	13.0	0.8
						95	15.9	14.5	1.4
						125	11.8	10.4	1.4
						155	4.3	3.4	0.9
16	4.24	5.4×10^5	1.0	7	Cone	4	0.16	0.22	−0.06
						8	0.49	0.50	−0.01
						12	0.94	0.85	0.09
						16	1.42	1.22	0.20

TABLE 4.2.1.2-C (CONTD)

Ref	M	R_{ℓ} (based on d_{equiv})	a/b	$\frac{\ell_B}{d_{equiv}}$	Nose Shape	α (deg)	$C_{N_{calc}}$	$C_{N_{test}}$	ΔC_N
16	4.24	5.4×10^5	1.0	7	Cone	20	1.90	1.62	0.28
						24	2.39	2.05	0.34
				10		4	0.20	0.26	−0.06
						8	0.59	0.64	−0.05
						12	1.24	1.11	0.13
						16	1.92	1.66	0.26
						20	2.57	2.30	0.27
						24	3.34	3.03	0.31
	5.04	2.6×10^5				4	0.21	0.28	−0.07
						8	0.63	0.65	−0.02
						12	1.23	1.06	0.17
						16	1.81	1.53	0.28
						20	2.45	2.08	0.37
						24	3.23	2.67	0.56
				7	Ogive	4	0.18	0 21	−0.03
						8	0.49	0.46	0.03
						12	0.93	0.78	0.15
						16	1.32	1.14	0.18
	6.28	1.1×10^5			Cone	4	0.19	0.20	−0.01
						8	0.51	0.47	0.04
						12	0.89	0.78	0.11
						16	1.31	1.18	0.13
						20	1.76	1.64	0.12
						24	2.28	2.14	0.14
15	1.2	3.8×10^5	1.0	10	Ogive	10	0.8	0.5	0.3
						20	2.3	2.0	0.3
						30	5.1	4.8	0.3
						40	9.2	8.4	0.8
						50	13.0	11.1	1.9
						60	16.0	14.8	1.2
	1.5					10	0.7	0.5	0.2
						20	2.5	2.6	−0.1
						30	5.8	5.6	0.2
						40	9.4	8.7	0.7
						50	12.4	11.8	0.6
						60	14.7	14.2	0.5
	2.0					10	0.8	0.8	0
						20	2.8	2.8	0
						30	6.0	5.4	0.6

TABLE 4.2.1.2-C (CONTD)

Ref	M	R_ℓ (based on d_{equiv})	a/b	$\frac{\ell_B}{d_{equiv}}$	Nose Shape	α (deg)	$C_{N_{calc}}$	$C_{N_{test}}$	ΔC_N
15	2.0	3.8×10^5	1.0	10	Ogive	40	8.6	8.2	0.4
						50	11.0	11.0	0
						60	13.3	13.0	0.3
	1.2		2.0			10	1.4	1.3	0.1
						20	4.3	5.2	−0.9
						30	9.2	9.8	−0.6
						40	16.3	15.0	1.3
						50	23.0	18.8	4.2
						60	28.3	21.9	6.4
	1.5					10	1.4	1.7	−0.3
						20	4.5	5.4	−0.9
						30	10.2	10.0	0.2
						40	16.8	14.7	2.1
						50	22.2	19.0	3.2
						60	25.9	21.2	4.7
	2.0					10	1.4	1.6	−0.2
						20	5.1	5.1	0
						30	10.7	9.3	1.4
						40	15.4	13.4	2.0
						50	19.5	17.3	2.2
						60	23.4	20.4	3.0
	1.2		0.5			10	0.3	0.2	0.1
						20	1.2	0.7	0.5
						30	2.6	2.2	0.4
						40	4.6	4.6	0
						50	6.5	6.4	0.1
						60	8.0	7.5	0.5
	1.5					10	0.4	0.3	0.1
						20	1.2	0.9	0.3
						30	2.9	2.8	0.1
						40	4.7	5.1	−0.4
						50	6.2	6.9	−0.7
						60	7.4	8.5	−1.1
	2.0					10	0.4	0.4	0
						20	1.4	1.3	0.1
						30	3.0	3.0	0
						40	4.4	4.7	−0.3
						50	5.6	7.4	−1.8
						60	6.6	7.5	−0.9

Average Error = $\sum \frac{|\Delta C_N|}{n} = 0.94$

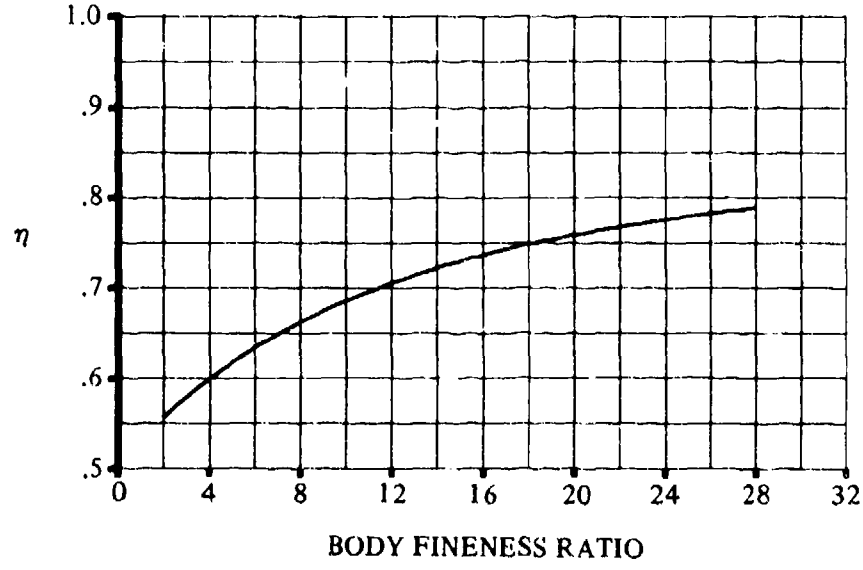

FIGURE 4.2.1.2-35a RATIO OF THE DRAG COEFFICIENT OF A CIRCULAR CYLINDER OF FINITE LENGTH TO THAT OF A CYLINDER OF INFINITE LENGTH

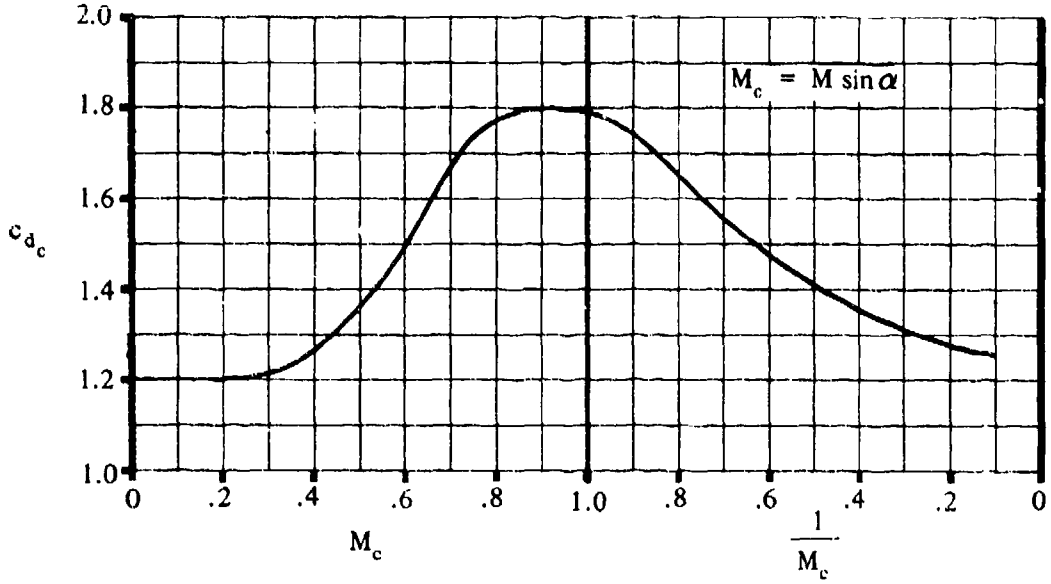

FIGURE 4.2.1.2-35b STEADY-STATE CROSS-FLOW DRAG COEFFICIENT FOR CIRCULAR CYLINDERS (TWO DIMENSIONAL)

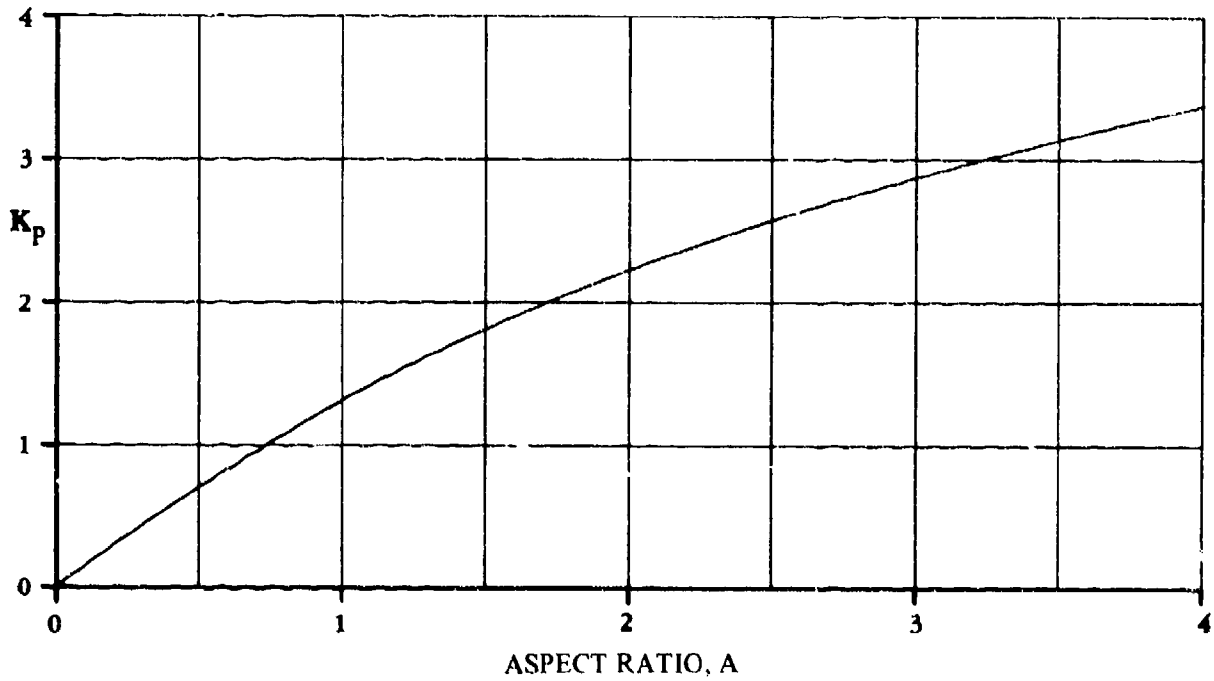

FIGURE 4.2.1.2-36a VARIATION OF POTENTIAL-FLOW LIFT PARAMETER WITH ASPECT RATIO FOR ELLIPTICAL CROSS-SECTION BODIES

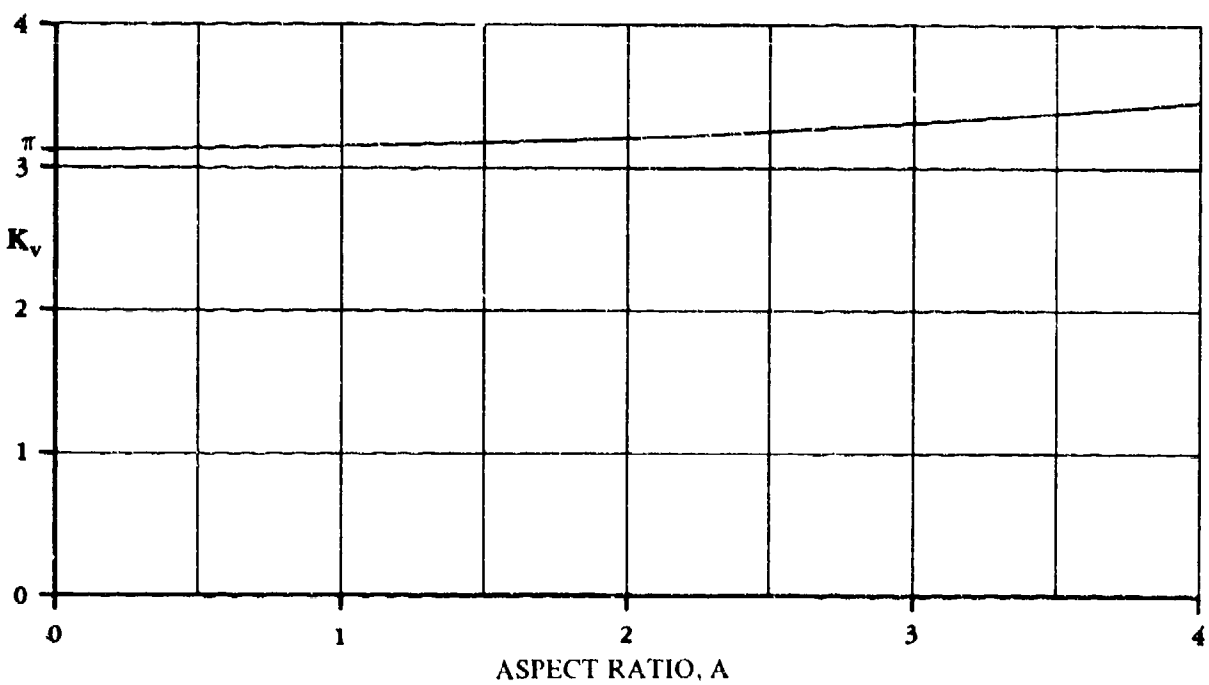

FIGURE 4.2.1.2-36b VARIATION OF VORTEX LIFT PARAMETER WITH ASPECT RATIO FOR ELLIPTICAL CROSS-SECTION BODIES

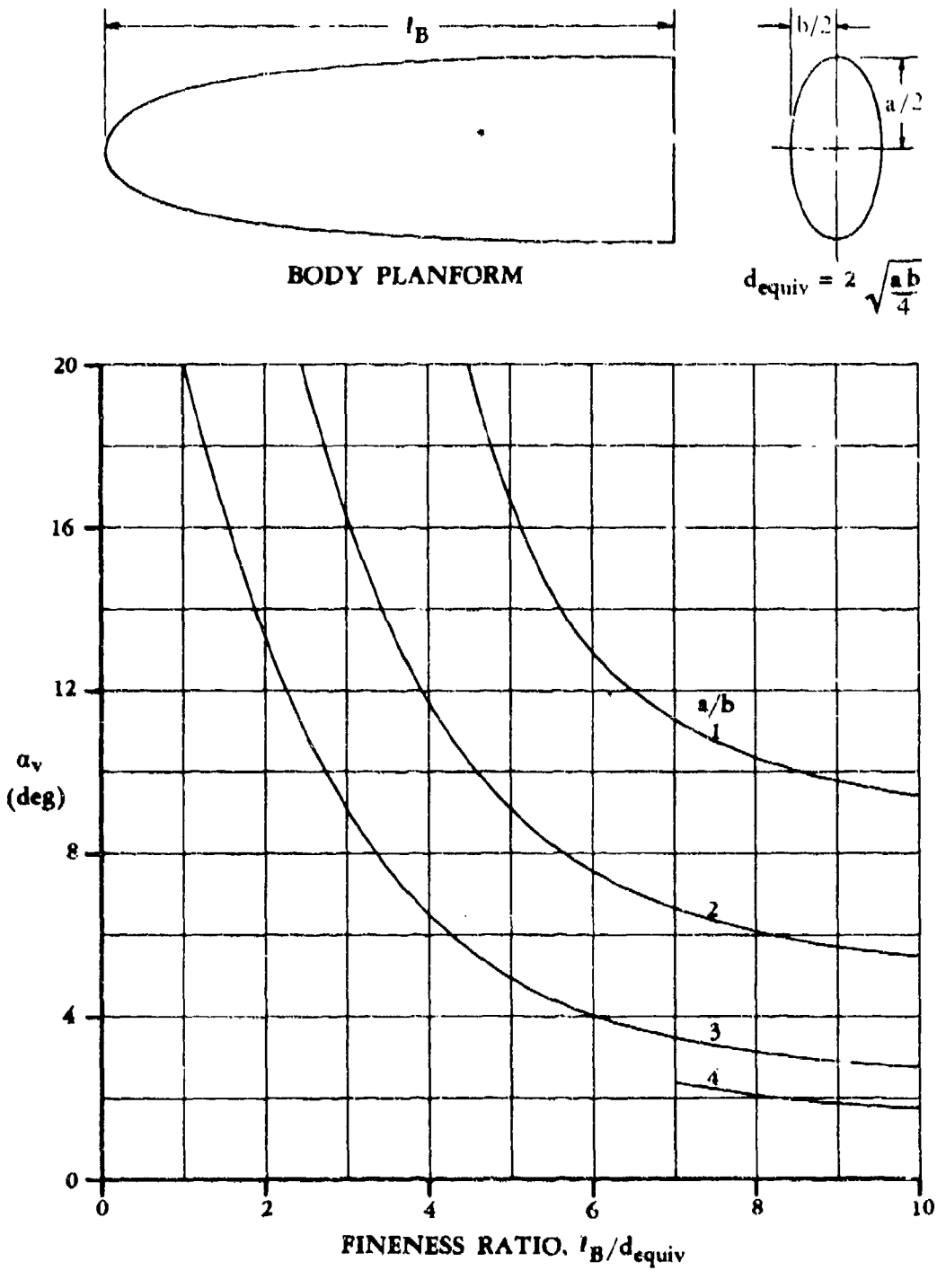

FIGURE 4.2.1.2-37 VARIATION OF ANGLE OF ATTACK FOR ONSET OF VORTEX LIFT WITH FINENESS RATIO AND THICKNESS RATIO FOR ELLIPTICAL BODIES

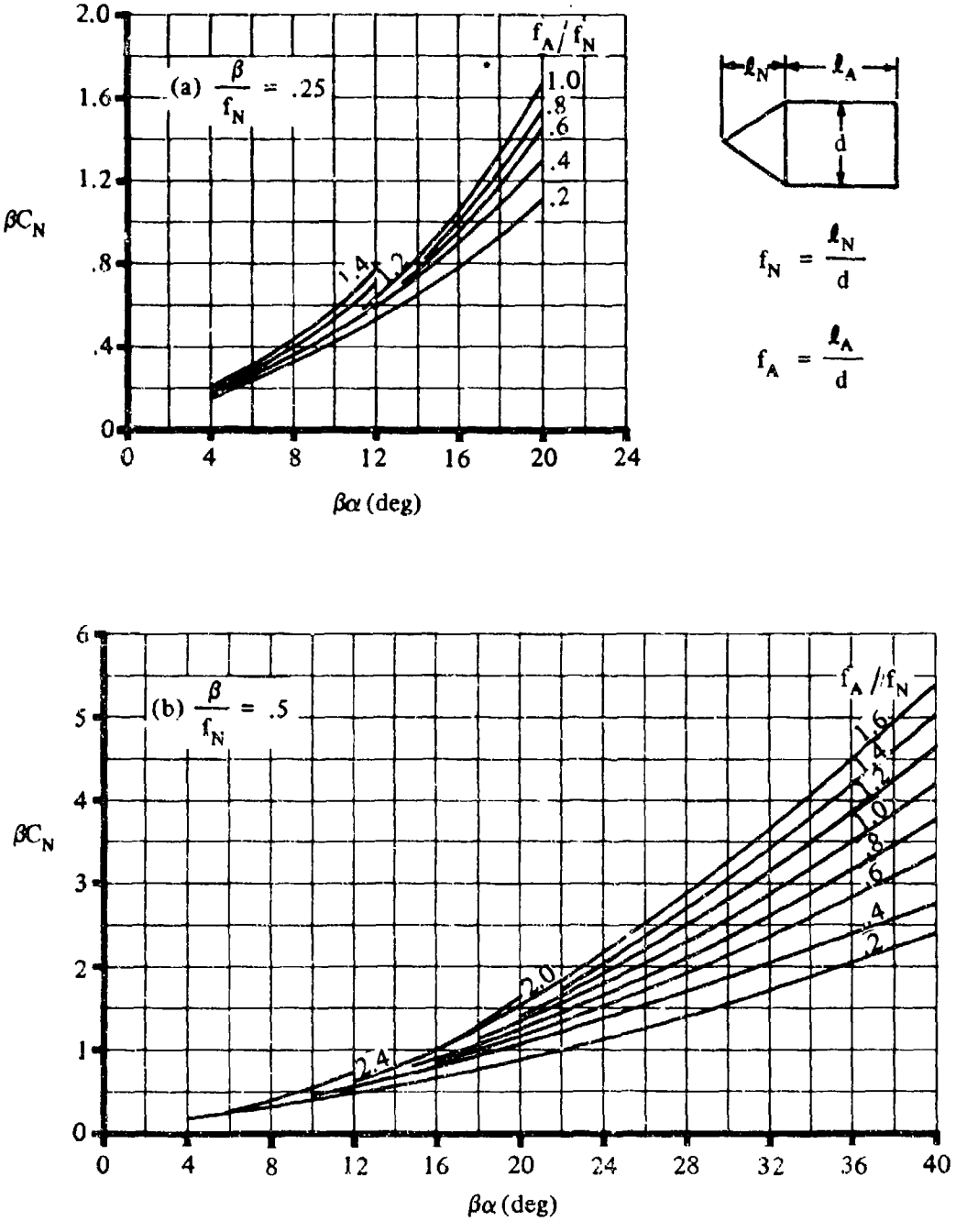

FIGURE 4.2.1.2-38 NORMAL-FORCE COEFFICIENT FOR CONE-CYLINDERS AT SUPERSONIC SPEEDS

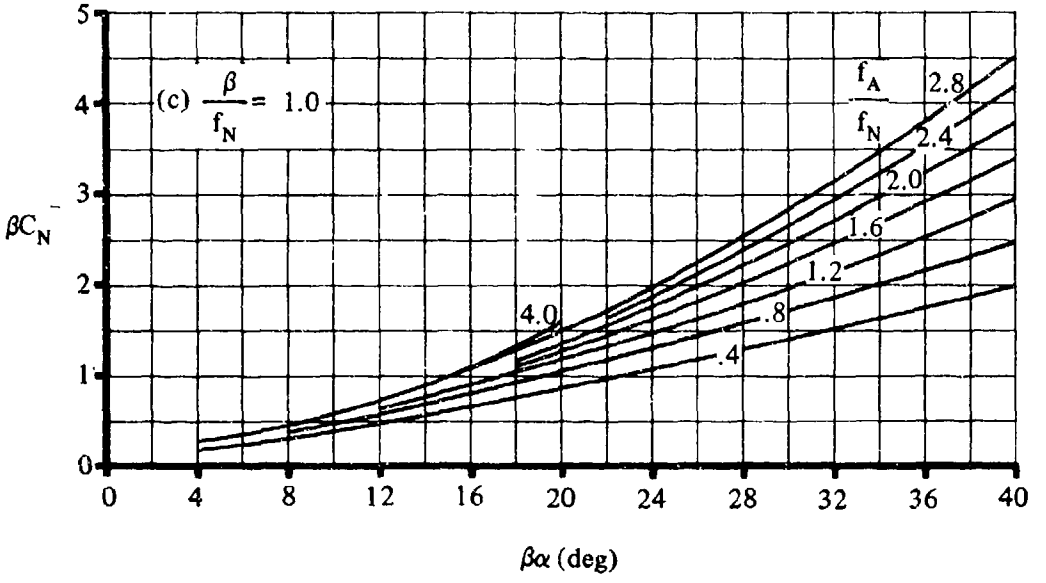

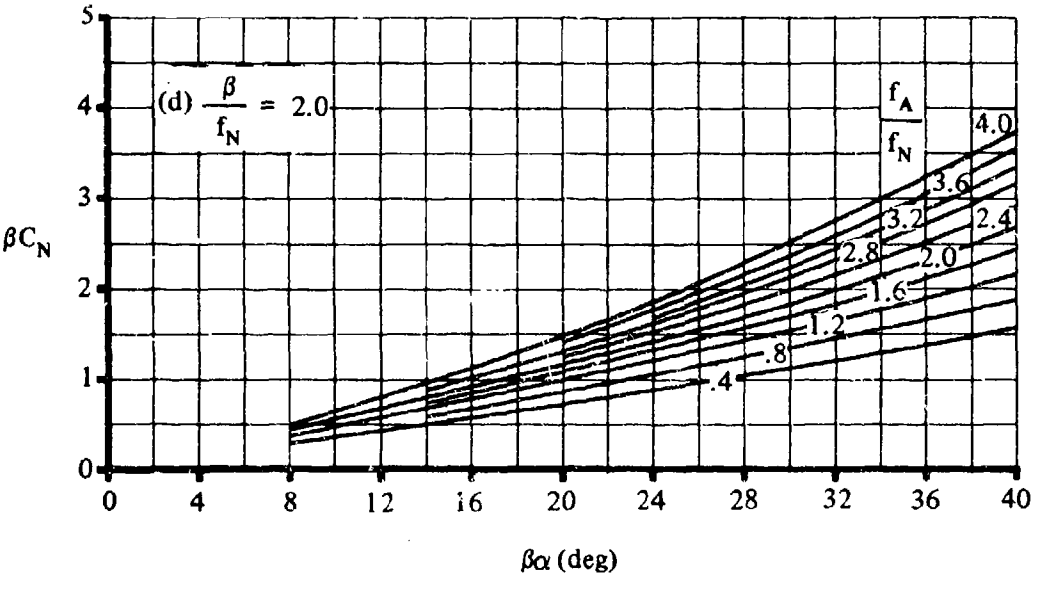

FIGURE 4.2.1.2-38 (CONTD)

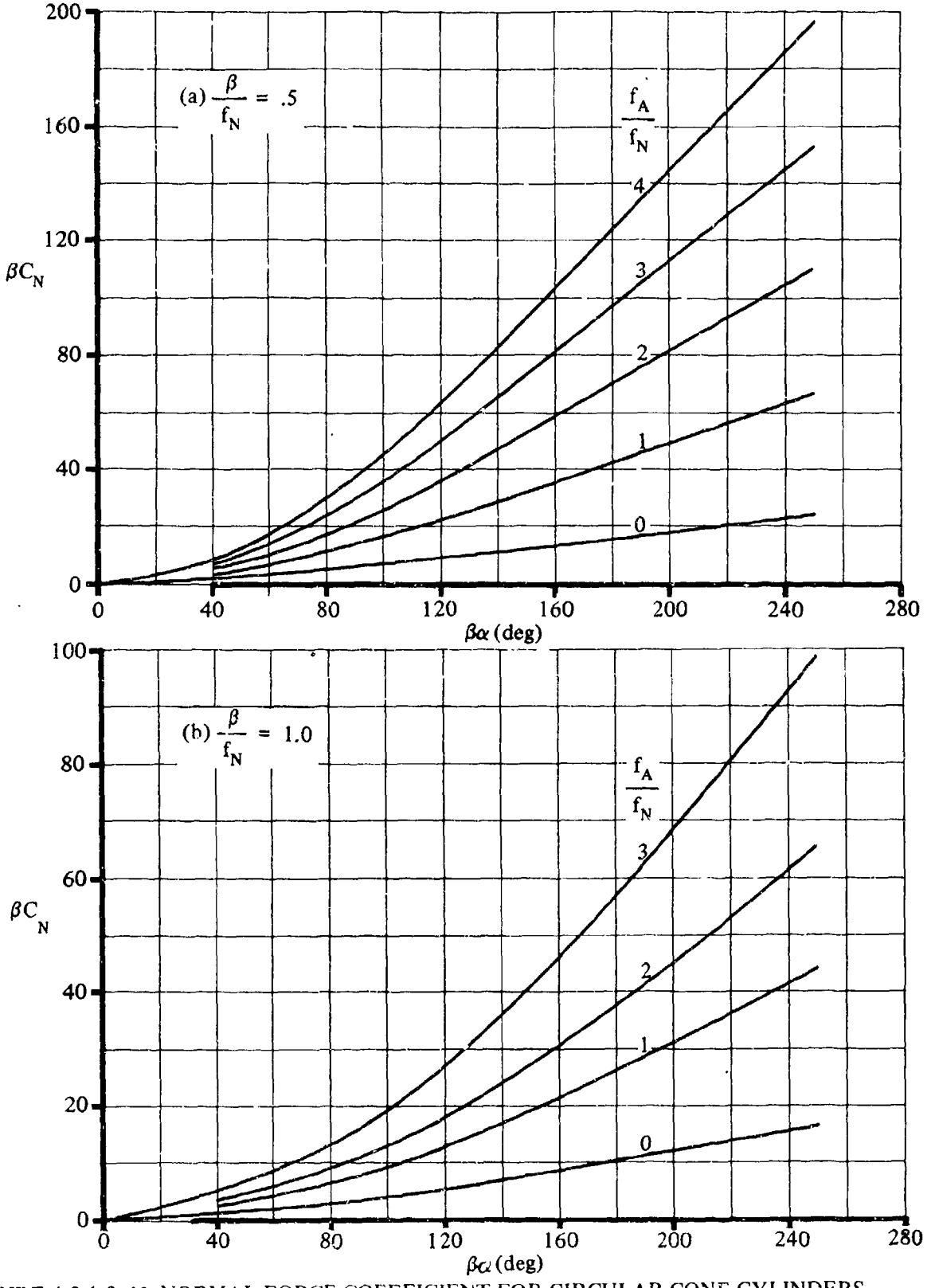

FIGURE 4.2.1.2-40 NORMAL-FORCE COEFFICIENT FOR CIRCULAR CONE-CYLINDERS AT HYPERSONIC SPEEDS

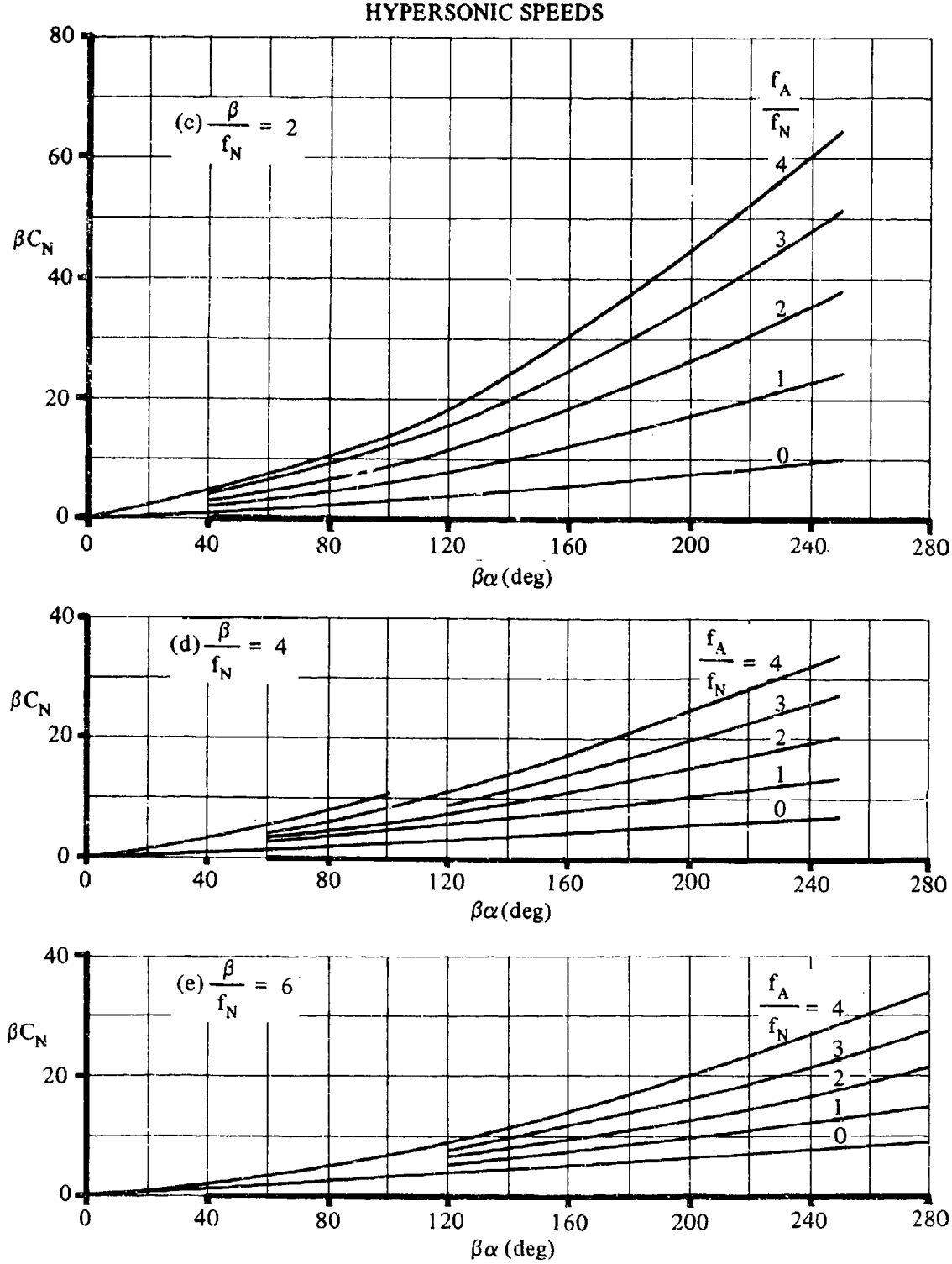

FIGURE 4.2.1.2-40 (CONTD)

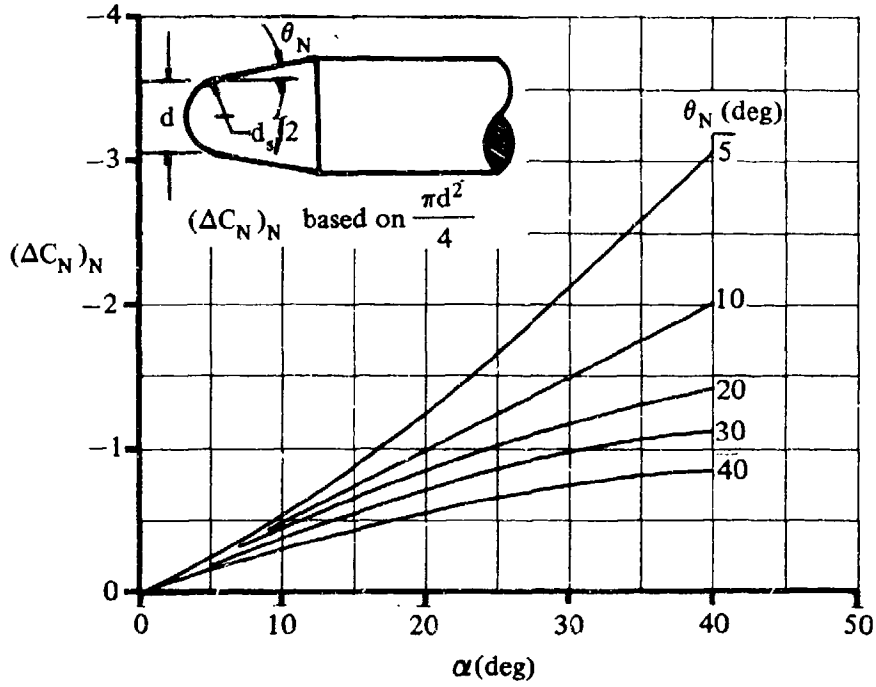

FIGURE 4.2.1.2-42a INCREMENT IN NORMAL FORCE DUE TO NOSE BLUNTING OF A CONE

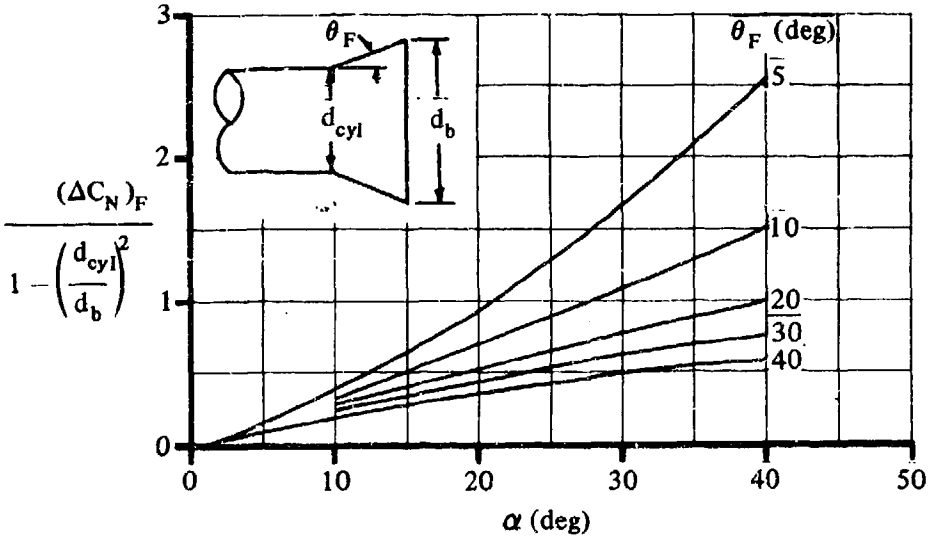

FIGURE 4.2.1.2-42b INCREMENT IN NORMAL FORCE DUE TO BODY FLARE

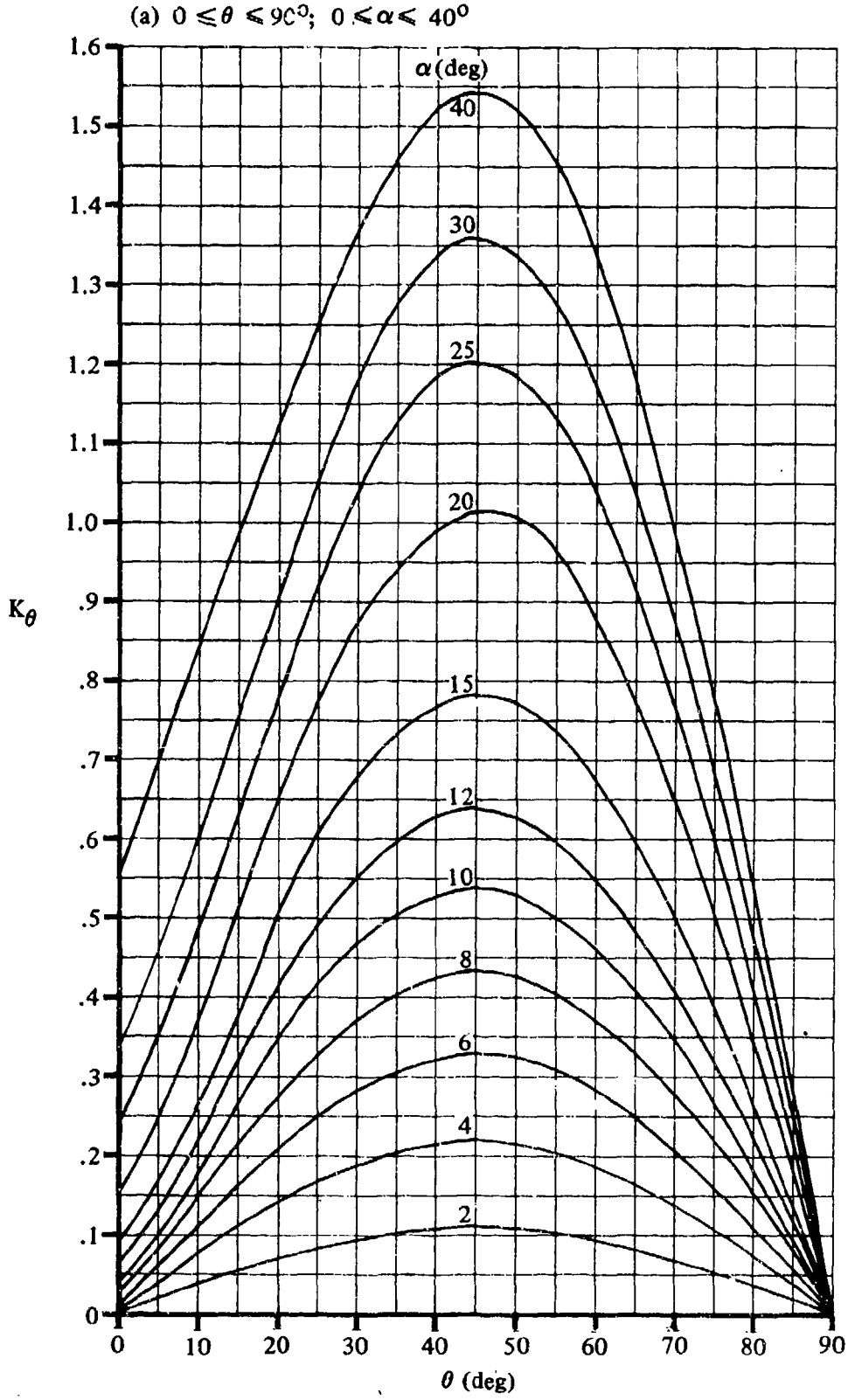

FIGURE 4.2.1.2-43 PRESSURE-SURFACE-SLOPE INTEGRAL FACTOR

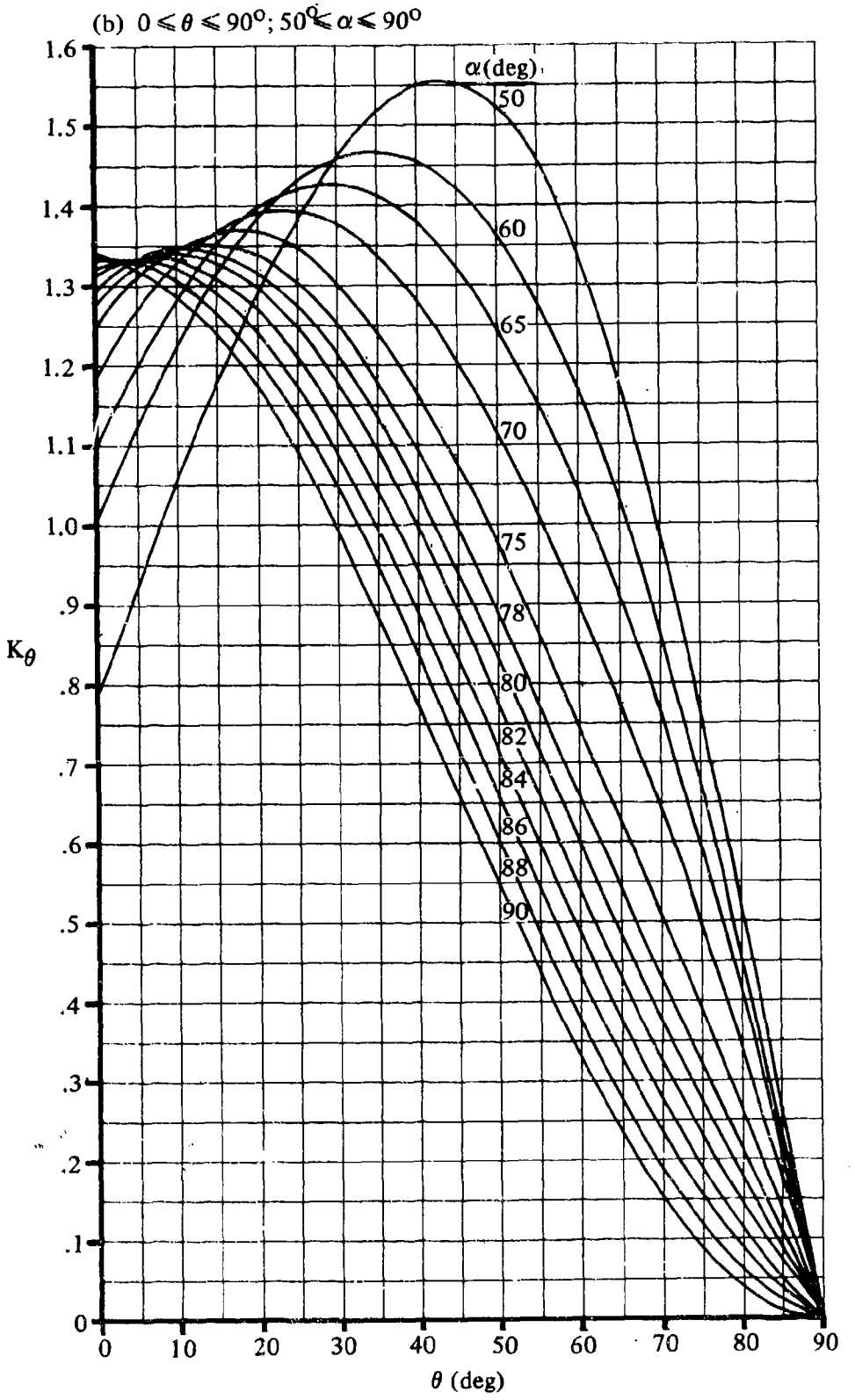

FIGURE 4.2.1.2-43 (CONTD)

4.2.2 BODY PITCHING MOMENT

4.2.2.1 BODY PITCHING-MOMENT-CURVE SLOPE

A. SUBSONIC

Two methods are presented in this section for estimating the body pitching-moment-curve slope at angles of attack near zero. Several additional methods are presented in References 1 through 4 of Section 4.2.1.1. As in the case with lift, moments acting on bodies are frequently considered in the literature to be divisible into two contributions – one due to potential flow over the forward part of the body and the other due to viscous cross flow over the aft part of the body. The general discussion of Section 4.2.1.2 on these flow conditions is directly applicable to this section.

DATCOM METHODS

The two methods presented for calculating the body pitching-moment-curve slope are distinguished from one another in that Method 1 is applicable only to bodies in the presence of a wing flow field; whereas Method 2 is valid only when applied to a body in undisturbed flow.

It is not feasible to present generalized design charts; however, both Equations 4.2.2.1-a and -b can be integrated for any arbitrary body of revolution.

Method 1

Multhopp's method, taken from Reference 1, estimates the body pitching-moment-curve slope in the presence of a wing flow field. This method is valid for bodies of revolution in the low subsonic speed regime. Application of this method is practical only when test data are available for the wing pitching-moment-curve slope of the wing-body combination. This method then allows a separate analysis of the body effects to be made, enabling a build-up of the wing-body pitching-moment-curve slope based on test data for the wing contribution and on this method for the body contribution. If no wing pitching-moment-curve-slope test data are available, the method of Section 4.3.2.2 is recommended for estimating the wing-body pitching-moment-curve slope. The body pitching-moment-curve slope in the presence of a wing flow field, based on the product of wing area and wing MAC $S_W \bar{c}_W$, is given by

$$C_{m_\alpha} = \frac{1}{36.5\, S_W \bar{c}_W} \int_0^{\ell_B} w_f^2 \left(\frac{\partial \epsilon_u}{\partial \alpha} + 1 \right) dx \quad \text{(per degree)} \qquad 4.2.2.1\text{-a}$$

where

S_W is the wing reference area.

$\bar{c}_W$ is the wing mean aerodynamic chord.

ℓ_B is the length of the body.

w_f is the average width of a given body segment (see Sketch (a)).

$\frac{\partial \epsilon_u}{\partial \alpha}$ is the rate of change of upwash with respect to angle of attack. The estimation of $\frac{\partial \epsilon_u}{\partial \alpha}$ varies for various fuselage segments. These definitions of $\frac{\partial \epsilon_u}{\partial \alpha}$ with their respective body segments are presented in Sketch (a). The values of $\frac{\partial \epsilon_u}{\partial \alpha}$ for the body increments forward of the wing are estimated by the curves presented in Figures 4.2.2.1-22a and -22b. The separate curve for the body increment immediately forward of the wing is necessary because of the rapid increase of upwash in this vicinity. Both curves of $\frac{\partial \epsilon_u}{\partial \alpha}$ presented in Figures 4.2.2.1-22a and -22b are based on a wing-body lift-curve slope of 0.0785 per degree. To correct for other values of $\left(C_{L_\alpha}\right)_{WB}$, multiply the values of $\frac{\partial \epsilon_u}{\partial \alpha}$ obtained from these figures by the ratio $\left(C_{L_\alpha}\right)_{WB}/0.0785$. (The values of $\left(C_{L_\alpha}\right)_{WB}$ should be obtained from test data or Section 4.3.1.2 and expressed in units of per degree.) The estimation of $\frac{\partial \epsilon_u}{\partial \alpha}$ for that portion of the body aft of the wing is based on the assumption of a linear variation of downwash from the trailing edge of the exposed wing root chord to the horizontal tail. If the methods of Section 4.4.1 are to be used for estimating $\frac{\partial \bar{\epsilon}}{\partial \alpha}$, the downwash should be calculated for the trailing-edge point of the body; i.e., assume the horizontal-tail MAC quarter-chord point coincides with the trailing edge of the fuselage.

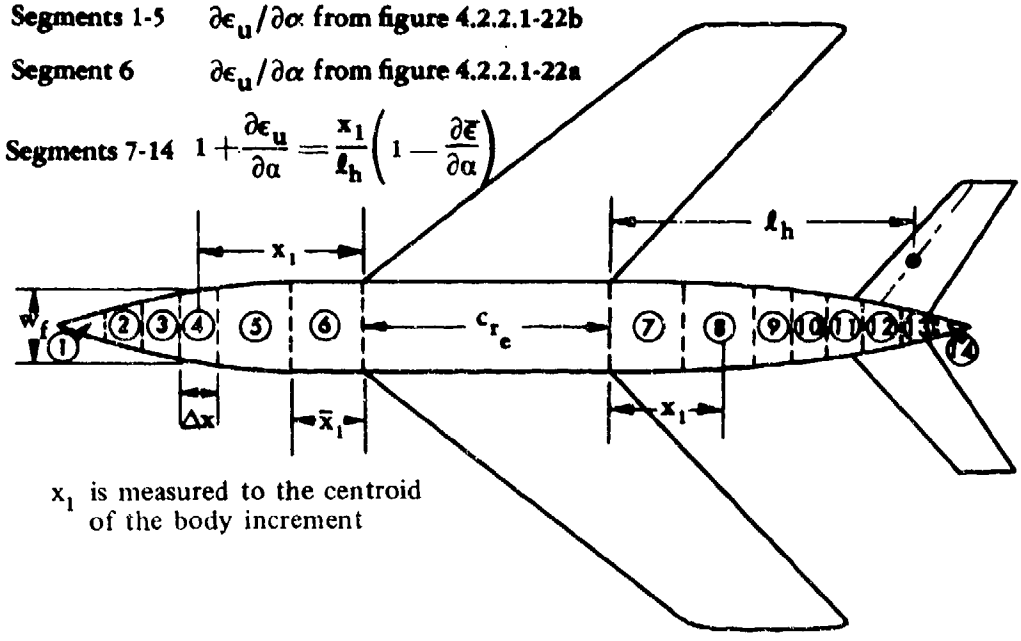

x_1 is measured to the centroid of the body increment

SKETCH (a)

Method 2

The method of Reference 2 is presented for estimating the body pitching-moment-curve slope. Only the potential-flow portion of the method of Reference 2 is applied, limiting the application of the method to angles of attack near zero. The body pitching-moment-curve slope, based on the total body volume V_B, is given by

$$C_{m_\alpha} = \frac{2(k_2 - k_1)}{V_B} \int_0^{x_o} \frac{dS_x}{dx}(x_m - x)\, dx \quad \text{(per radian)} \qquad 4.2.2.1\text{-b}$$

where

$(k_2 - k_1)$ is the apparent mass factor developed by Munk and given in Figure 4.2.1.1-20a.

V_B is the volume of the body.

x_o is the body station where the flow ceases to be potential. It is a function of x_1, the body station where the parameter dS_x/dx first reaches its maximum negative value. The parameters x_o and x_1 are correlated in Figure 4.2.1.1-20b.

S_x is the body cross-sectional area at any body station.

x_m is the longitudinal distance from the nose to the chosen moment center.

x is the location of the center of pressure of a given body segment, measured from the nose.

In many cases it will be possible to determine the location of x_1 by inspection. For cases that are doubtful, the area distribution should be plotted and examined to determine the location where dS_x/dx first reaches its maximum negative value.

The pitching-moment-curve slopes of several bodies of revolution have been calculated by this method and compared with test data in Reference 2. In general, the method has a fair degree of accuracy at angles of attack near zero.

For a rapid but approximate estimation, slender-body theory can be used, which gives

$$C_{m_\alpha} = 2\left(\frac{x_m}{\ell_B} + \frac{V_B}{S_b \ell_B} - 1\right) \quad \text{(per radian)} \qquad 4.2.2.1\text{-c}$$

where C_{m_α} is based on $S_b \ell_B$, S_b being the base area of the body of revolution and ℓ_B the total length of the body of revolution.

No method is available for estimating the pitching-moment-curve slope of a body of noncircular

cross section. Consequently, test data must be relied upon as the basis for predicting the pitching-moment-curve slope of such configurations. A summary of available test data on bodies of noncircular cross section at subsonic speeds is presented as Table 4.2.1.1-A.

Sample Problems

1. Body in the wing flow field

Given: The wing-body configuration of Reference 3

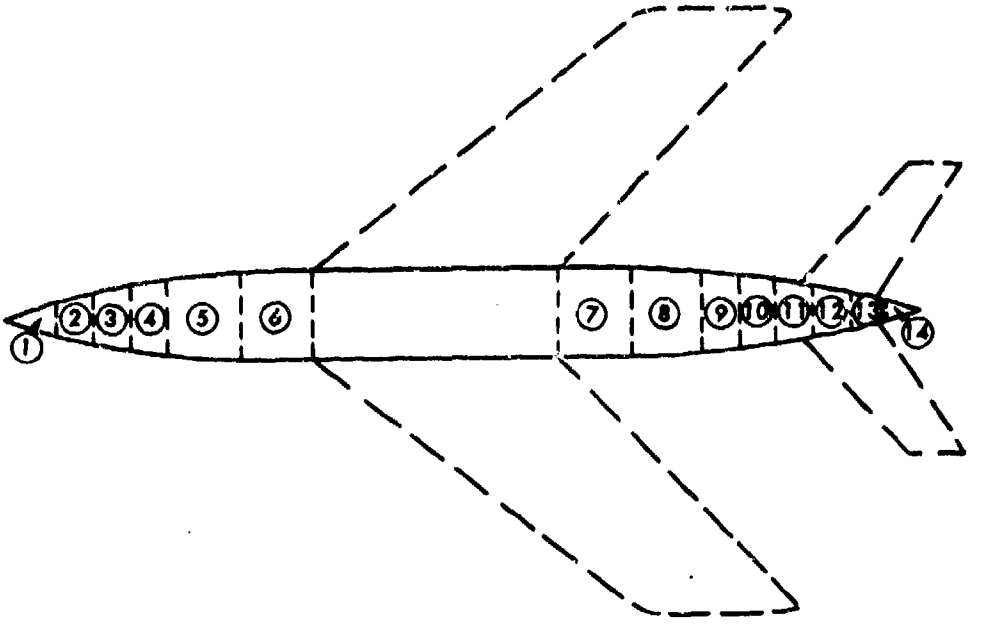

Body Increment	Δx (in.)	w_f (in.)	x_1 (in.)
1	.07	2.7	53.0
2	7	6.9	45.5
3	7	10.3	38.5
4	7	13.4	31.5
5	14	16.1	21.0
6	14	16.8	14.0
7	14	16.8	7.0
8	14	16.1	21.0
9	7	14.1	31.5
10	7	12.7	38.5
11	7	11.1	45.5
12	7	8.2	52.5
13	7	5.1	59.5
14	5.21	1.7	65.6

S_W = 4429 sq in. $\quad \bar{c}_W$ = 39.97 in. $\quad \frac{\partial \bar{\epsilon}}{\partial \alpha}$ = 0.50 (test data)

ℓ_B = 170.95 in. $\quad \ell_h$ = 56.26 in. $\quad \left(C_{L_\alpha}\right)_{WB}$ = 0.047 per degree (test data)

c_{r_e} = 45.67 in.

Compute:

Determine $\frac{\partial \epsilon_u}{\partial \alpha}$ at each body increment

① Body Increment	② $\frac{x_1}{c_{r_e}}$ and $\frac{\bar{x}_1}{c_{r_e}}$	③ $\partial \epsilon_u / \partial \alpha$ Figures 4.2.2.1-22a, -22b	④ $(\partial \epsilon_u / \partial \alpha)_{corrected}$ ③ (0.047)/0.0785
1	1.16	0.14	0.084
2	1.00	0.18	0.108
3	0.84	0.22	0.132
4	0.69	0.27	0.162
5	0.46	0.37	0.222
6	0.31	1.95	1.168

① Body Increment	② $\frac{x_1}{\ell_h}$	③ $\frac{x_1}{\ell_h}\left(1 - \frac{\partial \bar{\epsilon}}{\partial \alpha}\right)$	④ $\partial \epsilon_u / \partial \alpha$ ③ − 1.0
7	0.124	0.062	−0.928
8	0.373	0.187	−0.813
9	0.560	0.280	−0.720
10	0.684	0.342	−0.658
11	0.809	0.404	−0.596
12	0.933	0.467	−0.533
13	1.058	0.529	−0.471
14	1.166	0.583	−0.417

Evaluate $\int_0^{\ell_B} w_f^2 \left(\frac{\partial \epsilon_u}{\partial \alpha} + 1\right) dx$

① Body Increment	② w_f^2 (in.^{2})	③ $\frac{\partial \epsilon_u}{\partial \alpha} + 1$	④ Δx (in.)	$w_f^2\left(\frac{\partial \epsilon_u}{\partial \alpha} + 1\right)\Delta x$ ②③④
1	7.29	1.064	8.07	63.77
2	47.6	1.108	7.0	369.19
3	106.1	1.132	7.0	840.74
4	179.6	1.162	7.0	1460.87
5	259.2	1.222	14.0	4434.39
6	282.2	2.168	14.0	8565.33
7	282.2	0.062	14.0	244.95
8	259.2	0.187	14.0	678.59
9	196.8	0.280	7.0	385.65
10	161.3	0.342	7.0	386.15
11	123.2	0.404	7.0	348.41
12	67.2	0.467	7.0	219.68
13	26.0	0.529	7.0	96.28
14	2.89	0.583	5.21	8.78

$$\sum_{x=0}^{\ell_B} w_f^2 \left(\frac{\partial \epsilon_u}{\partial \alpha} + 1\right) \Delta x = 18{,}106.78 \text{ cu. in.}$$

Solution:

$$C_{m_\alpha} = \frac{1}{36.5\, S_w \bar{c}_w} \int_0^{\ell_B} w_f^2 \left(\frac{\partial \epsilon_u}{\partial \alpha} + 1\right) dx \quad \text{(Equation 4.2.2.1-a)}$$

$$= \frac{18{,}106.78}{(36.5)(4429)(39.97)} = 0.00280 \text{ per degree}$$

No test data are available for the body in the presence of the wing flow field.

2. Potential Flow

Given: The 3/4-power body of revolution of Reference 12.

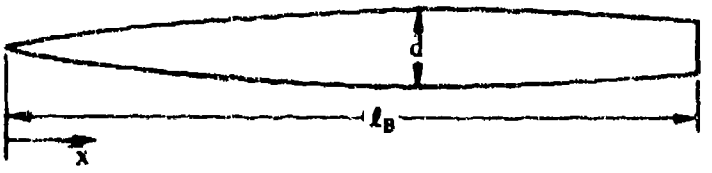

$$r = 0.255\left[1 - \left(1 - \frac{2x}{6.375}\right)^2\right]^{3/4} \qquad \ell_B = 5.036 \text{ ft} \qquad d = 0.510 \text{ ft}$$

$V_B = 0.687$ cu ft $\qquad f = \ell_B/d = 9.87 \qquad x_m = 3.54$ ft $\qquad M = 0.40$

Compute:

Determine x_1

The body station where dS_x/dx first reaches a maximum negative value can be determined by inspection; however, the area distribution is plotted to illustrate the determination of x_1.

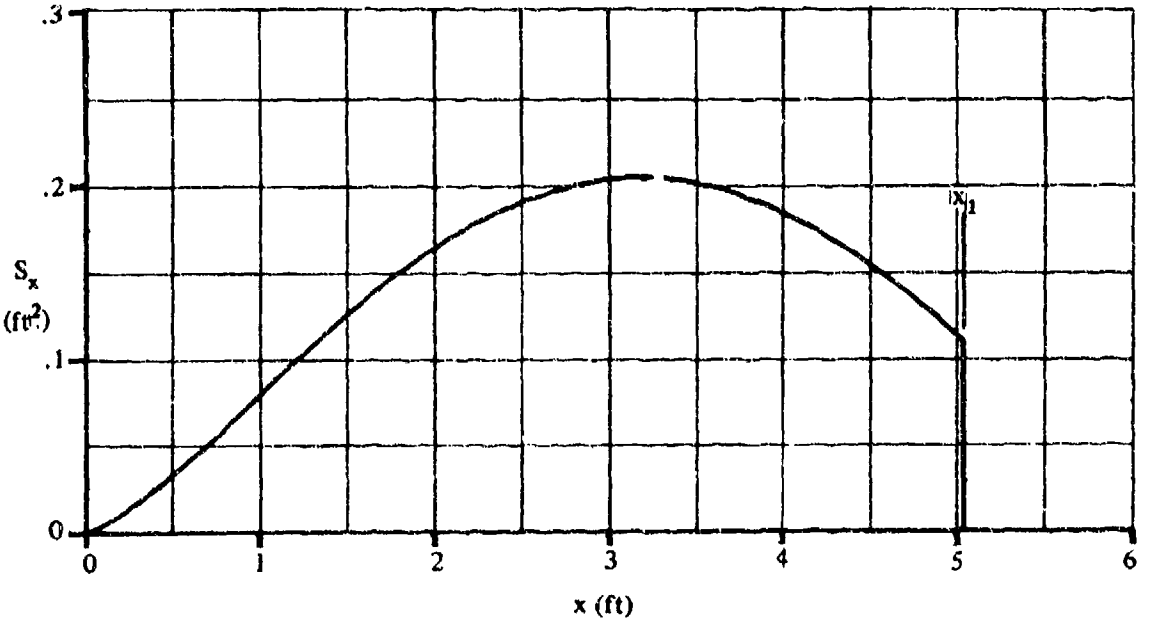

Cross-Sectional Area Distribution

$x_1 = 5.036$ ft

$x_1/\ell_B = 5.036/5.036 = 1.0$

$x_o/\ell_B = 0.905$ (figure 4.2.1.1-20)

$x_o = (0.905)(5.036) = 4.558$ ft

$(k_2 - k_1) = 0.937$ (figure 4.2.1.1-20a)

$$\frac{2(k_2 - k_1)}{V_B} = \frac{2(0.937)}{0.687} = 2.728$$

Evaluate $\int_0^{x_o} \frac{dS_x}{dx} (x_m - x)\, dx$

Station (ft)	r (ft)	S_x (ft^2)	$\frac{dS_x}{dx}\Delta x = \Delta S_x$ (ft^2)	x* (ft)	$(x_m - x)$ (ft)	$\frac{dS_x}{dx}(x_m - x)\Delta x$ (ft^3)
0	0	0				
			0.0317	0.333	3.21	0.102
0.5	0.1005	0.0317				
			0.0468	0.769	2.77	0.130
1.0	0.1581	0.0785				
			0.0376	1.260	2.28	0.086
1.5	0.1922	0.1161				
			0.0472	1.756	1.78	0.084
2.0	0.2280	0.1633				
			0.0270	2.253	1.29	0.0348
2.5	0.2461	0.1903				
			0.0127	2.751	0.79	0.0100
3.0	0.2642	0.2030				
			−0.0016	3.250	0.29	−0.00046
3.5	0.2532	0.2014				
			−0.0166	3.748	−0.21	0.0035
4.0	0.2425	0.1848				
			−0.0327	4.275	−0.74	0.0242
x_o = 4.56	0.2200	0.1521				

$$\sum_{x=0}^{x_o} \frac{dS_x}{dx} (x_m - x)\Delta x = 0.474 \text{ cu ft}$$

Solution:

$$C_{m_\alpha} = \frac{2(k_2 - k_1)}{V_B} \int_0^{x_o} \frac{dS_x}{dx} (x_m - x)\, dx \quad \text{(equation 4.2.2.1-b)}$$

$$= (2.728)(0.474)$$

$$= 1.293 \text{ per rad (based on } V_B)$$

This compares with a test value of 1.369 per radian from reference 12.

*x is taken at the center of volume of each body segment.

3. Slender-Body Theory

Given: The same configuration as sample problem 2.

$x_m = 3.54$ ft $\quad \ell_B = 5.036$ ft $\quad V_B = 0.687$ cu ft $\quad S_b = 0.1103$ sq ft

Compute:

$$x_m/\ell_B = 3.54/5.036 = 0.7029$$

$$\frac{V_B}{S_b \ell_B} = \frac{0.687}{(0.1103)(5.036)} = 1.237$$

Solution:

$$C_{m_\alpha} = 2\left(\frac{x_m}{\ell_B} + \frac{V_B}{S_b \ell_B} - 1\right) \qquad \text{(equation 4.2.2.1-c)}$$

$$= 2(0.7029 + 1.237 - 1)$$

$$= 1.880 \text{ per rad (based on } S_b \ell_B)$$

$$= 1.52 \text{ per rad (based on } V_B)$$

B. TRANSONIC

Slender-body theory states that body force and moment characteristics are not functions of Mach number. Experimental data verify this result (references 4, 5, and 6). Any differences in the subsonic value of C_{m_α} obtained from paragraph A and the supersonic value of C_{m_α} obtained from paragraph C should be faired out smoothly in the transonic range. Experimental data should be used, when available, as a guide in fairing in the transonic range.

Transonic test data on bodies of noncircular cross section are available in references 25, 26, and 5 of table 4.2.1.1-A.

C. SUPERSONIC

Several theoretical methods have been developed that can be used for estimating the moment characteristics of bodies of revolution at supersonic speeds. However, these are best applied by machine methods. Some of these methods are discussed in paragraph C of Section 4.2.1.1.

DATCOM METHOD

An empirical method is presented, based on the data from reference 7, for ogive-cylinder and cone-cylinder bodies at supersonic speeds. Figure 4.2.2.1-23a gives the center-of-pressure location for ogive-cylinders, and figure 4.2.2.1-23b gives the center-of-pressure location for cone-cylinders. The moment slope, based on the product of the maximum frontal area and body length $S_B \ell_B$, is

$$C_{m_\alpha} = \left(\frac{x_m}{\ell_B} - \frac{x_{c.p.}}{\ell_B}\right) C_{N_\alpha} \quad \text{(per radian)} \qquad 4.2.2.1\text{-d}$$

where

$\frac{x_m}{\ell_B}$ is the desired moment-center location in fraction of body length.

$\frac{x_{c.p}}{\ell_B}$ is the center-of-pressure location in fraction of body length, obtained from figure 4.2.2.1-23a or figure 4.2.2.1-23b, depending upon the given configuration.

C_{N_α} is the normal-force-curve slope, based on maximum frontal area of the ogive-cylinder or cone-cylinder body, obtained from paragraph C of Section 4.2.1.1 (figures 4.2.1.1-21a and 4.2.1.1-21b, respectively).

Experimental data from reference 6 indicate that the center-of-pressure location of 1/2-power bodies is closely approximated by corresponding (same fineness ratio) ogive values. This reference also indicates that the center-of-pressure location for 3/4-power bodies is approximately 5 percent of the body length ahead of the corresponding cone location. Figure 4.2.2.1-23a is recommended for 1/2-power bodies. For 3/4-power bodies it is recommended that figure 4.2.2.1-23b be used with the center-of-pressure location moved forward approximately 5 percent from the chart value.

The center-of-pressure location of a boattail at the end of a semi-infinite cylindrical body is presented in figure 4.2.2.1-24. This chart is taken from reference 9 and is based on the results of reference 10.

The moment slope of an ogive-cylinder or cone-cylinder body with a boattail afterbody, based on the product of the maximum frontal area and the length of the ogive-cylinder or cone-cylinder body $S_B\ell_B$, is (see sketch (b))

$$C_{m_\alpha} = (C_{m_\alpha})_{\substack{\text{ogive/cone-}\\\text{cylinder}}} + \left\{\frac{x_m}{\ell_B} - \left[\frac{(x_{c.p.})_b}{\ell_b}\frac{\ell_b}{\ell_B} + \left(1 - \frac{x_m}{\ell_B}\right)\right]\right\} \Delta C_{N_\alpha} \text{ (per radian)} \quad 4.2.2.1\text{-e}$$

where $(C_{m_\alpha})_{\substack{\text{ogive/cone-}\\\text{cylinder}}}$ is obtained from equation 4.2.2.1-d, x_m/ℓ_B is defined above, and

$\frac{(x_{c.p.})_b}{\ell_b}$ is the center-of-pressure location of the boattail in fraction of boattail length, measured aft of the forward face of the boattail. This parameter is obtained from figure 4.2.2.1-24.

$\frac{\ell_b}{\ell_B}$ is the ratio of the boattail length to the length of the ogive-cylinder or cone-cylinder body.

ΔC_{N_α} is the increment in normal-force-curve slope, based on S_B, due to the addition of a boattail to a semi-infinite cylindrical body. This parameter is obtained from paragraph C of Section 4.2.1.1 (figure 4.2.1.1-22a).

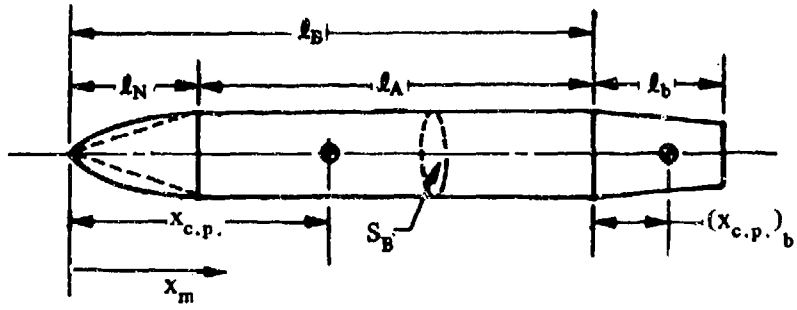

SKETCH (b)

The moment coefficient of a flared body of revolution is taken to be that predicted by impact theory.

The moment slope of an ogive-cylinder or cone-cylinder body with a flared afterbody, based on the product of the maximum frontal area and length of the ogive-cylinder or cone-cylinder body $S_B \ell_B$, is (see sketch (c))

$$C_{m_\alpha} = \left(C_{m_\alpha}\right)_{\substack{\text{ogive/cone-}\\\text{cylinder}}} + C'_{m_\alpha} \frac{d^3}{a^2 \ell_B} + \frac{n}{\ell_B}\left(\Delta C_{N_\alpha}\right)_F \text{ (per radian)} \qquad 4.2.2.1\text{-f}$$

where

$\left(C_{m_\alpha}\right)_{\substack{\text{ogive/cone-}\\\text{cylinder}}}$ is obtained from equation 4.2.2.1-d, and

C_{m_α} is the pitching-moment-curve slope of the flared afterbody about its own front face, based on the product of its base area and base diameter. This parameter is obtained from figure 4.2.2.1-25a.

d is the diameter of the base of the flared body.

a is the diameter of the front face of the flared body.

ℓ_B is the length of the ogive-cylinder or cone-cylinder body.

n is the distance from the face of the flared afterbody to the desired moment reference axis of the configuration, positive aft.

$\left(\Delta C_{N_\alpha}\right)_F$ is the normal-force-curve-slope increment, based on S_B, due to the addition of a flared afterbody behind a semi-infinite cylinder. This parameter is obtained from paragraph C of Section 4.2.1.1 (figure 4.2.1.1-22b).

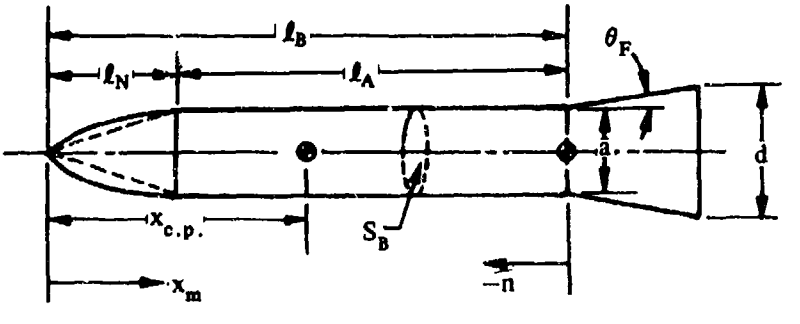

SKETCH (c)

A comparison of test data with C_{m_α} of ogive-cylinder and cone-cylinder bodies calculated by this method is presented as table 4.2.2.1-A. The ranges of body geometry and Mach number of the test data are:

Cone-Cylinder	Ogive-Cylinder
$0 < f_A < 12$	$0 < f_A < 10$
$2.112 < f_N < 12$	$1.5 < f_N < 7$
$0 < f_A/f_N < 2.5$	$0 < f_A/f_N < 2.5$
$1.5 < M < 5.0$	$1.20 < M < 4.24$

No method is available for estimating the pitching-moment-curve slope of a body of noncircular cross section at supersonic speeds. Consequently, test data must be relied upon as the basis for predicting the pitching-moment-curve slope of such configurations. A summary of available test data on bodies of noncircular cross section at supersonic speeds is presented as table 4.2.1.1-C.

Sample Problem

Given: The cone-cylinder-flare body of reference 13. This is the same configuration as the sample problem of paragraph C of Section 4.2.1.1.

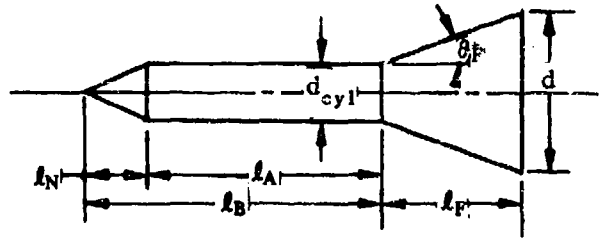

ℓ_N = 1.21 in. ℓ_A = 4.00 in. ℓ_B = 5.21 in.

ℓ_F = 2.40 in. $d_{cyl} = a_{flare}$ = 1.0 in.

$d_{flare} = d$ = 2.75 in. θ_F = 20°

n = −5.21 in. x_m = 0 M = 5.05; β = 4.95

Compute:

Cone-cylinder

$f_N = \ell_N/d_{cyl}$ = 1.21

$f_A = \ell_A/d_{cyl}$ = 4.00

$f_A/f_N = 4.00/1.21 = 3.31$

$f_N/\beta = 1.21/4.95 = 0.244$

$x_{c.p.}/\ell_B = 0.36$ (linear extrapolation) (figure 4.2.2.1-23b)

$C_{N_\alpha} = 3.52$ per rad (based on S_B) (sample problem, paragraph C, Section 4.2.1.1)

$$\left(C_{m_\alpha}\right)_{\substack{\text{cone-}\\\text{cylinder}}} = \left(\frac{x_m}{\ell_B} - \frac{x_{c.p.}}{\ell_B}\right) C_{N_\alpha} \quad \text{(equation 4.2.2.1-d)}$$

$$= (0 - 0.36)(3.52)$$

$$= -1.267 \text{ per rad (based on } S_B\ell_B)$$

Flare:

$\left(\Delta C_{N_\alpha}\right)_F = 11.73$ per rad (based on S_B) (sample problem, paragraph C, Section 4.2.1.1)

$n/\ell_B = -5.21/5.21 = -1.0$

$a/d = 1.0/2.75 = 0.364$

$C'_{m_\alpha} = -1.0$ per rad $\left(\text{based on } \frac{\pi d^3}{4}\right)$ (figure 4.2.2.1-25a)

Solution:

$$C_{m_\alpha} = \left(C_{m_\alpha}\right)_{\substack{\text{cone-}\\\text{cylinder}}} + C'_{m_\alpha} \frac{d^3}{a^2\ell_B} + \frac{n}{\ell_B}\left(\Delta C_{N_\alpha}\right)_F \quad \text{(equation 4.2.2.1-f)}$$

$$= -1.267 + (-1.0)\frac{(2.75)^3}{(1.0)^2(5.21)} + (-1.0)(11.73)$$

$$= -1.267 - 3.992 - 11.73$$

$$= -16.99 \text{ per rad (based on } S_B\ell_B)$$

This compares with a test value of -14.51 per radian from reference 13.

D. HYPERSONIC

Newtonian theory is used in this section to estimate the pitching-moment-curve slope of cone frustums with or without a spherical nose, a blunted conical nose, or a blunted ogival nose. Newtonian impact theory and its modifications are discussed in paragraph D of Section 4.2.1.1.

DATCOM METHOD

Charts that give the pitching-moment-curve slope of cone-frustum bodies and spherical noses are presented in figures 4.2.2.1-25a and 4.2.2.1-25b, respectively. These charts are taken from reference 11 and are based on Newtonian impact theory. By properly combining values from these charts, the total C_{m_α} may be determined for bodies composed of multiple cone frustums with or without spherically blunted noses.

The center-of-pressure locations of spherically blunted cones and ogives are presented in figures 4.2.2.1-26 and 4.2.2.1-27, respectively. These charts are also based on impact theory, and represent a specific application of the method described below for configurations consisting of cone frustums with spherical noses.

The procedure for computing the total pitching-moment-curve slope for a complex body is given in the following steps. The moment values for each individual segment of a multiple cone-frustum body with or without a spherical nose are referred to a moment axis at the front face of that particular segment, and are based on the product of the base area and base diameter of that particular segment.

Step 1. Compute C'_{m_α} for each body segment about its own front face, using figures 4.2.2.1-25a and 4.2.2.1-25b.

Step 2. Transfer the individual moment slopes to a common reference axis by applying the following moment transfer equation to each body segment.

$$C_{m_\alpha} = C'_{m_\alpha} + \frac{n}{d} C_{N_\alpha} \quad \text{(per radian)} \qquad 4.2.2.1\text{-g}$$

where

C_{N_α} is the normal-force-curve slope of the individual cone-frustum or spherical nose segment, based on its own base area, from figures 4.2.1.1-26 and 4.2.1.1-23, respectively.

d is the base diameter of the individual cone-frustum or spherical nose segment.

n is the distance from the front face of a given segment to the desired moment reference axis of the configuration, positive aft.

C'_{m_α} is the pitching-moment-curve slope of an individual segment from figure 4.2.2.1-25a for cone frustums and from figure 4.2.2.1-25b for spherical nose segments. C'_{m_α} is based on the product of the base area and the base diameter of the individual segment.

C_{m_α} is the pitching-moment-curve slope of an individual segment based on the product of the base area and base diameter of the individual segment and referred to a common reference axis.

Step 3. The transferred pitching-moment-curve slopes of the individual body segments are then converted to a common basis by

$$C_{m_\alpha} = \sum_{n=1}^{m} \left(C_{m_\alpha}\right)_n \left(\frac{d_n}{d_b}\right)^3 \quad \text{(per radian)} \qquad 4.2.2.1\text{-h}$$

where the subscript n refers to an individual segment of m segments, and C_{m_α} is referred to a common reference axis and is based on the product of the area and diameter of the base of the configuration $S_b d_b$.

In using figures 4.2.2.1-26 and 4.2.2.1-27 to obtain the pitching-moment-curve slope of spherically blunted cones and ogives, respectively, use is made of equation 4.2.2.1-d, i.e.,

$$C_{m_\alpha} = \left(\frac{x_m}{\ell_B} - \frac{x_{c.p.}}{\ell_B}\right) C_{N_\alpha} \quad \text{(per radian)}$$

where

$\frac{x_{c.p.}}{\ell_B}$ is obtained from figure 4.2.2.1-26 for spherically blunted cones and from figure 4.2.2.1-27 for spherically blunted ogives.

$\frac{x_m}{\ell_B}$ is the desired moment-center location in fraction of body length.

C_{N_α} is the normal-force-curve slope of spherically blunted cones and spherically blunted ogives from figures 4.2.1.1-24 and 4.2.1.1-25, respectively.

C_{m_α} is the pitching-moment-curve slope, referred to a desired moment axis and based on the product of the maximum frontal area and body length $S_B \ell_B$.

Values of C_{m_α} computed by the above method for spherically blunted cones and ogives may be used in conjunction with the results presented for conical-frustum bodies in figure 4.2.2.1-25a, provided the individual results are transferred to a common reference axis and converted to a common basis.

Sample Problem

Given: Configuration 5115 of reference 14, consisting of a cone-cylinder-frustum body with a spherical nose. This is the same configuration as the sample problem in paragraph D of Section 4.2.1.1.

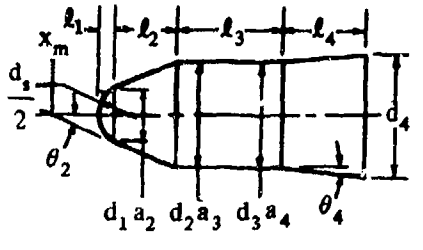

(All dimensions are in feet. x_m located 0.55 ft forward of nose.)

Spherical Segment

$\ell_1 = 0.18 \qquad \frac{d_s}{2} = 0.36 \qquad d_1 = 0.62$

Forward Cone Frustum

$a_2 = 0.62 \qquad d_2 = 1.20 \qquad \ell_2 = 0.72$

$\theta_2 = 22.5^o$

Cylinder

$a_3 = 1.20 \quad d_3 = 1.20 \quad \ell_3 = 1.20 \quad \theta = 0$

Rear Cone Frustum

$a_4 = 1.20 \quad d_4 = d_b = 1.368 \quad \ell_4 = 0.96 \quad \theta_4 = 5^o$

Compute:

Spherical segment

$2\ell_1/d_s = 0.18/0.36 = 0.50$

$C'_{m_{\alpha_1}}$ = −0.430 per rad (figure 4.2.2.1-25b) (based on $\left(\frac{\pi d_1^2}{4}\right) d_1$, and taken about its front face)

$n_1 = -0.55$

$C_{N_{\alpha_1}}$ = 0.75 per rad $\left(\text{based on } \frac{\pi d_1^2}{4}\right)$ (sample problem, paragraph D, Section 4.2.1.1)

$C_{m_{\alpha_1}} = C'_{m_{\alpha_1}} + \frac{n_1}{d_1} C_{N_{\alpha_1}}$ (equation 4.2.2.1-g)

$= -0.430 + \left(\frac{-0.55}{0.62}\right) 0.75$

$= -1.095$ per rad (based on $\left(\frac{\pi d_1^2}{4}\right) d_1$, and taken about x_m)

Forward Cone Frustum

$a_2/d_2 = 0.62/1.20 = 0.517$

$C'_{m_{\alpha_2}}$ = −0.590 per rad (figure 4.2.2.1-25a) (based on $\left(\frac{\pi d_2^2}{4}\right) d_2$, and taken about its front face)

$n_2 = -(0.55 + \ell_1) = -0.73$

$C_{N_{\alpha_2}}$ = 1.250 per rad $\left(\text{based on } \frac{\pi d_2^2}{4}\right)$ (sample problem, paragraph D, Section 4.2.1.1)

$$C_{m_{\alpha_2}} = C'_{m_{\alpha_2}} + \frac{n_2}{d_2} C_{N_{\alpha_2}} \quad \text{(equation 4.2.2.1-g)}$$

$$= -0.590 + \left(\frac{-0.73}{1.20}\right) 1.250$$

$$= -1.350 \text{ per rad (based on } \left(\frac{\pi d_2^{\,2}}{2}\right) d_2, \text{ and taken about } x_m)$$

Cylinder

$a_3/d_3 = 1.20/1.20 = 1.00$

$C'_{m_{\alpha_3}} = 0$ (figure 4.2.2.1-25a)

$n_3 = -(0.55 + \ell_1 + \ell_2) = -1.45$

$C_{N_{\alpha_2}} = 0$ (sample problem, paragraph D, Section 4.2.1.1)

$$C_{m_{\alpha_3}} = C'_{m_{\alpha_3}} + \frac{n_3}{d_3} C_{N_{\alpha_3}} = 0 \quad \text{(equation 4.2.2.1-g)}$$

Rear Cone Frustum

$a_4/d_4 = 1.20/1.368 = 0.877$

$C'_{m_{\alpha_4}} = -0.325$ per rad (figure 4.2.2.1-23a) (based on $\left(\frac{\pi d_b^{\,2}}{4}\right) d_b$, and taken about its front face)

$n_4 = -(0.55 + \ell_1 + \ell_2 + \ell_3) = -2.65$

$C_{N_{\alpha_4}} = 0.450$ per rad $\left(\text{based on } \frac{\pi d_b^{\,2}}{4}\right)$ (sample problem, paragraph D, Section 4.2.1.1)

$$C_{m_{\alpha_4}} = C'_{m_{\alpha_4}} + \frac{n_4}{d_4} C_{N_{\alpha_4}} \quad \text{(equation 4.2.2.1-g)}$$

$$= -0.325 + \left(\frac{-2.65}{1.368}\right) 0.450$$

$$= -1.196 \text{ per rad (based on } \left(\frac{\pi d_b^{\,2}}{4}\right) d_b, \text{ and taken about } x_m)$$

Solution: $= \sum_{n=1}^{m} (C_{m_\alpha})_n \left(\frac{d_n}{d_b}\right)^3$ (equation 4.2.2.1-h)

$$C_{m_\alpha} = (C_{m_\alpha})_1 \left(\frac{d_1}{d_b}\right)^3 + (C_{m_\alpha})_2 \left(\frac{d_2}{d_b}\right)^3 + (C_{m_\alpha})_3 \left(\frac{d_3}{d_b}\right)^3 + (C_{m_\alpha})_4 \left(\frac{d_4}{d_b}\right)^3$$

$$= (-1.095) \left(\frac{0.62}{1.368}\right)^3 + (-1.350) \left(\frac{1.20}{1.368}\right)^3 + 0 \left(\frac{d_3}{d_b}\right)^3 + (-1.196) \left(\frac{1.368}{1.368}\right)^3$$

$$= -0.1019 - 0.9112 + 0 - 1.196$$

$= -2.209$ per rad (based on $\left(\frac{\pi d_b^2}{4}\right) d_b$, and referred to a moment axis at x_m)

REFERENCES

1. Multhopp, H.: Aerodynamics of the Fuselage. NACA TM 1036, 1942. (U)

2. Hopkins, E. J.: A Semiempirical Method for Calculating the Pitching Moment of Bodies of Revolution at Low Mach Numbers. NACA RM A51C14, 1951. (U)

3. Foster, G., and Fitzpatrick, J.: Longitudinal-Stability Investigation of High-Lift and Stall-Control Devices on a 52° Sweptback Wing with and Without Fuselage and Horizontal Tail at a Reynolds Number of 6.8×10^6. NACA RM L8I08, 1948. (U)

4. McDevitt, J. B., and Taylor, R. A.: Force and Pressure Measurements at Transonic Speeds for Several Bodies Having Elliptical Cross Sections. NACA TN 4362, 1958. (U)

5. McDevitt, J. B., and Taylor, R. A.: Pressure Distributions at Transonic Speeds for Slender Bodies Having Various Axial Locations of Maximum Diameter. NACA TN 4280, 1958. (U)

6. Taylor, R. A., and McDevitt, J. B.: Pressure Distributions at Transonic Speeds for Parabolic-Arc Bodies of Revolution Having Fineness Ratios of 10, 12, and 14. NACA TN 4234, 1958. (U)

7. Syvertson, C. A., and Dennis, D. H.: A Second-Order Shock-Expansion Method Applicable to Bodies of Revolution Near Zero Lift. NACA TR 1328, 1957. (U)

8. Dennis, D. H., and Cunningham, B. E.: Forces and Moments on Pointed and Blunt-Nosed Bodies of Revolution at Mach Numbers From 2.75 to 5.00. NACA RM A52E22, 1952. (U)

9. Anon: Royal Aeronautical Society Data Sheets – Aerodynamics, Vol. IV (Bodies S.08.03.03), 1958. (U)

10. Van Dyke, M.: First- and Second-Order Theory of Supersonic Flow Past Bodies of Revolution. Jour. Aero. Sci., Vol. 18, No. 3, 1951. (U)

11. Fisher, L. R.: Equations and Charts for Determining the Hypersonic Stability Derivatives of Combinations of Cone Frustums Computed by Newtonian Impact Theory. NASA TN D-149, 1959. (U)

12. Jones, J. L., and Demele, F. A.: Aerodynamic Study of a Wing-Fuselage Combination Employing a Wing Swept Back 63°. – Characteristics Throughout the Subsonic Speed Range with the Wing Cambered and Twisted for a Uniform Load at a Lift Coefficient of 0.25. NACA RM A9D25, 1949. (U)

13. Dennis, D. H., and Syvertson, C. A.: Effects of Boundary-Layer Separation on Normal Force and Center of Pressure of a Cone-Cylinder Model With a Large Base Flare at Mach Numbers From 3.00 to 6.28. NACA RM A55H09, 1955. (U)

14. Henderson, J. H.: Effect of Nose Bluntness on Normal Force, Pitching Moment, and Center of Pressure on Cone-Cylinder and Cone-Cylinder-Frustum Bodies of Revolution at Mach Numbers of 1.50, 2.18, 2.81 and 4.04. Ordnance Missile Laboratories Redstone Arsenal Rpt. No. GR11F, 1958. (C) Title Unclassified

15. Owens, R. V.: Aerodynamic Characteristics of Spherically Blunted Cones at Mach Numbers From 0.5 to 5.0. NASA TN D-3088, 1965. (U)

16. Ferri, A.: Supersonic-Tunnel Tests of Projectiles in Germany and Italy. NACA WR L-152, 1945. (U)

17. Walchner, O.: Systematic Wind-Tunnel Measurements on Missiles. NACA TM 1122, 1947. (U)

18. Delancey, L. M., Jaeger, B. F., and Schroedter, G. M.: The Aerodynamic Characteristics at Mach No. 4.24 of Bodies of Revolution With Varying Lengths and Head Shapes. NOTS TM 358, 1951. (U)

19 Perkins, E. W., and Jorgensen, L. H.: Comparison of Experimental and Theoretical Normal-Force Distributions (Including Reynolds Number Effects) on an Ogive-Cylinder Body at Mach Number 1.98. NACA TN 3716, 1956. (U)

20 Jack, J. R.: Aerodynamic Characteristics of a Slender Cone-Cylinder Body of Revolution at a Mach Number of 3.85. NACA RM E51H17, 1951. (U)

TABLE 4.2.2.1-A

SUPERSONIC PITCHING-MOMENT-CURVE SLOPE OF CONE-CYLINDER AND OGIVE-CYLINDER BODIES DATA SUMMARY AND SUBSTANTIATION

Ref.	Nose Shape	M	f_N	f_A	$\frac{x_m}{\ell_B}$	C_{m_α} Calc. (per rad)	C_{m_α} Test (per rad)	e Percent Error
13	Cone	1.5	2.836	0	1.0	0.653	0.592	10.3
		1.6				0.650	0.601	8.2
		1.92				0.630	0.592	6.4
		2.0				0.626	0.613	2.1
		2.44				0.620	0.600	3.3
		2.73					0.592	4.7
		3.0					0.597	3.9
		3.0					0.584	6.2
		3.25					0.583	6.3
		3.49					0.579	7.1
		3.8					0.586	5.8
		3.89					0.560	10.7
		4.4					0.571	8.6
		4.46					0.566	9.5
		4.93					0.592	4.7
		1.5	2.112	0	1.0	0.633	0.536	18.1
		1.6				0.626	0.524	19.5
		1.92				0.620	0.549	12.9
		2.0					0.559	10.9
		2.44					0.553	12.1
		2.74					0.553	12.1
		3.0					0.559	10.9
		3.25					0.546	13.6
		3.5					0.560	10.7
		3.8					0.544	14.0
		3.89					0.566	9.5
		4.0					0.552	12.3
		4.4					0.563	10.1
		4.46					0.549	12.9
		4.93					0.572	8.4

TABLE 4.2.2.1-A (CONTD)

Ref.	Nose Shape	M	f_N	f_A	$\frac{x_m}{\ell_B}$	C_{m_α} Calc. (per rad)	C_{m_α} Test (per rad)	e Percent Error
14	Ogive	2.10	3.5	2.5	1.0	1.76	1.80	– 2.2
↓	↓	2.29	↓	↓	↓	1.75	1.85	– 5.4
		2.57				1.74	2.07	–15.9
		2.60				1.75	1.95	–10.3
		2.84				1.74	2.04	–14.7
		3.06				1.73	2.04	–15.2
		1.63	2.5	2.5	1.0	1.89	2.03	– 6.9
		2.03				1.91	2.12	– 9.9
		2.23				1.90	2.29	–17.0
		2.54				1.90	2.18	–12.8
		2.77				1.88	2.26	–16.8
		3.15				1.83	2.07	–11.6
		1.61	2.5	2.5	1.0	1.88	1.64	15.2
		2.02				1.91	1.83	4.4
		2.23				1.90	2.09	– 9.1
		2.59				1.89	2.03	– 6.9
		2.78				1.88	2.11	–10.9
		3.15				1.83	1.96	– 6.6
		1.63	2.5	2.5	1.0	1.89	1.80	5.0
		1.97				1.97	1.89	4.2
		2.25				1.90	1.76	8.0
		2.54				1.90	1.81	5.0
		2.75				1.88	2.05	– 8.3
		3.17				1.82	1.89	– 3.7
	Cone	1.60	2.5	2.5	1.0	1.54	1.57	4.5
	↓	2.03	↓	↓	↓	1.60	1.68	– 4.8
		2.24				1.58	1.66	– 4.8
		2.56				1.56	1.81	–13.8
		2.80				1.54	1.71	– 9.9
		3.15				1.53	1.91	–19.9
	Ogive	1.35	1.5	2.5	1.0	2.16	2.11	2.4
	↓	1.67	↓	↓	↓	2.19	1.86	17.7
		2.08				2.11	1.96	7.7
		2.27				2.05	2.03	1.0
		2.57				1.93	2.21	–12.7
		2.74				1.86	2.12	–12.3
		3.10				1.73	2.09	–17.2
		1.67	3.0	2.5	1.0	1.81	1.91	– 5.2
		2.07				1.81	1.93	– 6.2
		2.28				1.81	1.95	– 7.2
		2.58				1.81	1.93	– 6.2
		2.83				1.79	2.07	–13.5
		3.15				1.77	2.07	–14.5
15	Ogive	1.20	2.5	2.5	1.0	1.83	1.85	– 1.1
↓	↓	1.45	↓	↓	↓	1.87	1.97	– 5.1
		1.99				1.91	2.05	– 6.8
		2.64				1.89	2.01	– 6.0
		3.20				1.81	1.82	– 0.5
		1.20	1.5	3.5	1.0	2.26	2.02	11.9
		1.45				2.31	2.14	7.9
		1.99				2.29	2.42	– 5.4
		2.64				2.03	2.26	–10.2
		3.20				1.80	2.12	–15.1

TABLE 4.2.2.1-A (CONTD)

Ref.	Nose Shape	M	t_N	t_A	$\frac{x_{cp}}{\ell_B}$	C_{m_α} Calc. (per rad)	C_{m_α} Test (per rad)	* Percent Error
15	Ogive	1.20	3.5	1.5	1.0	1.62	1.54	5.2
↓	↓	1.45	↓	↓	↓	1.62	1.65	− 1.8
		1.99				1.61	1.68	− 4.2
		2.64				1.57	1.68	− 6.5
		3.20				1.53	1.57	− 2.5
		2.64	2.5	1.5	1.0	1.63	1.75	− 6.9
		1.99	↓	↓	↓	1.68	1.67	0.6
		2.64	2.5	3.5	1.0	2.08	2.07	0.5
		2.64	2.5	4.5	1.0	2.24	2.26	− 0.9
6	Cone	2.75	3	0	0	−1.23	−1.19	3.4
		3.49					−1.19	3.4
		4.01					−1.22	0.8
		4.45					−1.11	10.8
		2.75	4	0	0	−1.24	−1.26	− 1.6
		4.01				−1.23	−1.39	−11.5
		4.48					−1.48	−16.9
		5.00					−1.23	0
		2.75	5	0	0	−1.27	−1.31	− 3.1
		3.49				−1.23	−1.22	0.8
		4.01					−1.32	− 6.8
		4.48					−1.32	− 6.8
		5.00					−1.17	5.1
		2.75	7	0	0	−1.30	−1.18	10.2
		4.01				−1.26	−1.32	− 4.5
		5.00				−1.23	−1.20	2.5
	Ogive	2.75	3	0	0	−1.23	−1.21	1.7
		4.01	↓			−1.07	−1.15	− 7.0
		2.75	5			−1.33	−1.15	15.7
		4.01	↓			−1.26	−1.25	0.8
		2.75	7			−1.35	−1.35	0
		4.01	↓			−1.32	−1.35	− 2.2
16	Ogive	4.24	3.5	6.5	1.0	2.22	2.12	4.7
↓	↓		4.0	10.0	↓	2.44	2.43	0.4
	Cone	↓	4.0	10.0	↓	2.31	2.14	7.9
17	Ogive	1.98	3.0	7.0	0	−0.69	−0.63	9.5
18	Cone	3.85	12.0	12.0	1.0	1.68	2.18	−22.9

Average Error = $\frac{\Sigma \mid * \mid}{n}$ = 8.0%

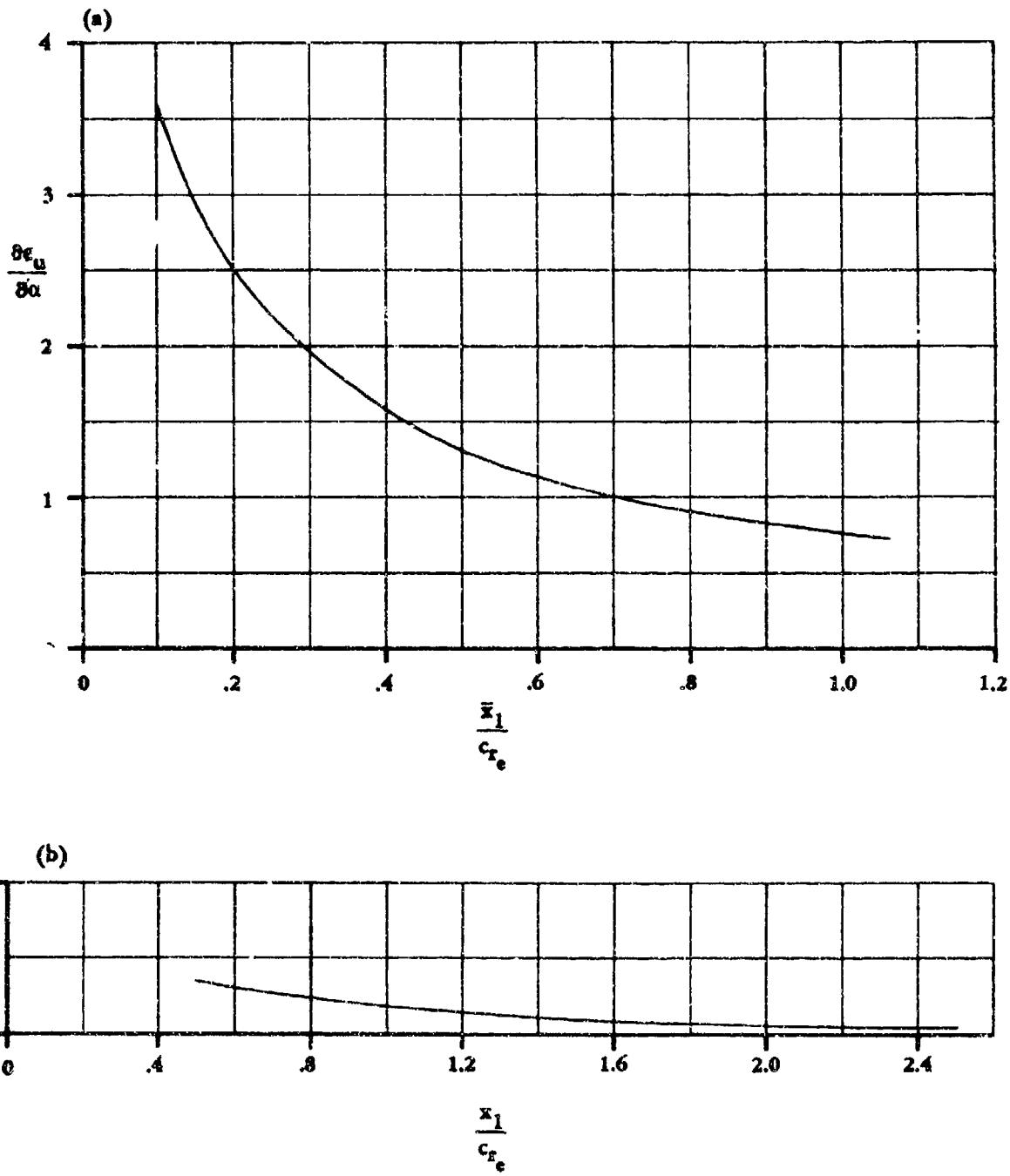

FIGURE 4.2.2.1-22 VARIATION OF UPWASH WITH DISTANCE FROM WING LEADING EDGE

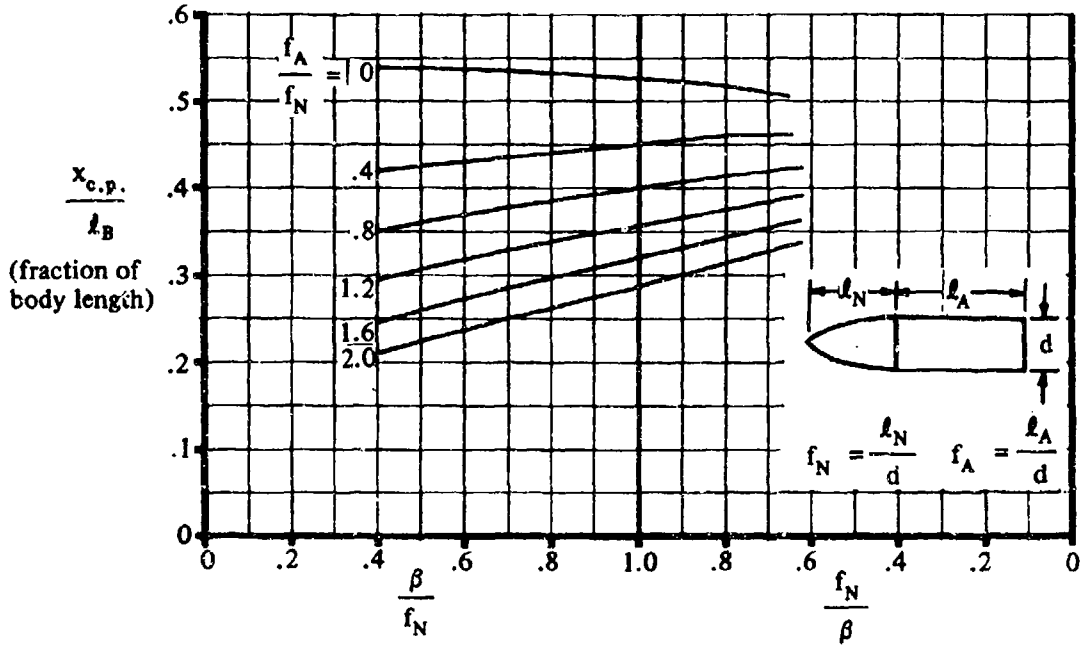

FIGURE 4.2.2.1-23a SUPERSONIC CENTER OF PRESSURE OF OGIVE WITH CYLINDRICAL AFTERBODY

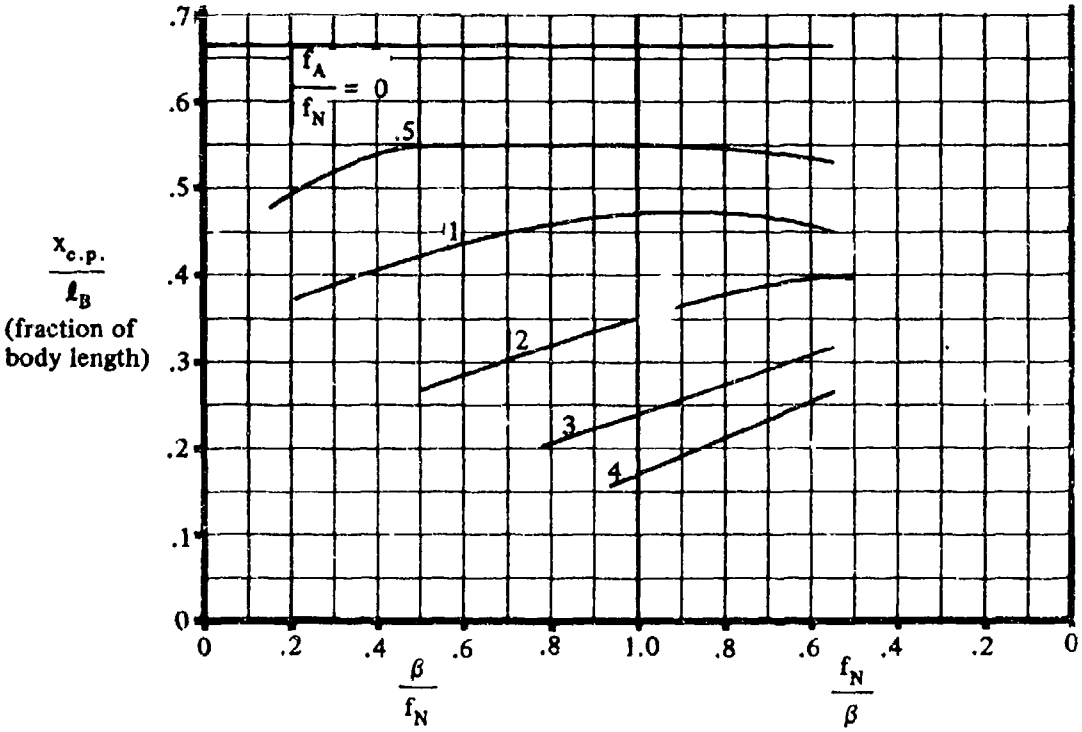

FIGURE 4.2.2.1-23b SUPERSONIC CENTER OF PRESSURE OF CONE WITH CYLINDRICAL AFTERBODY

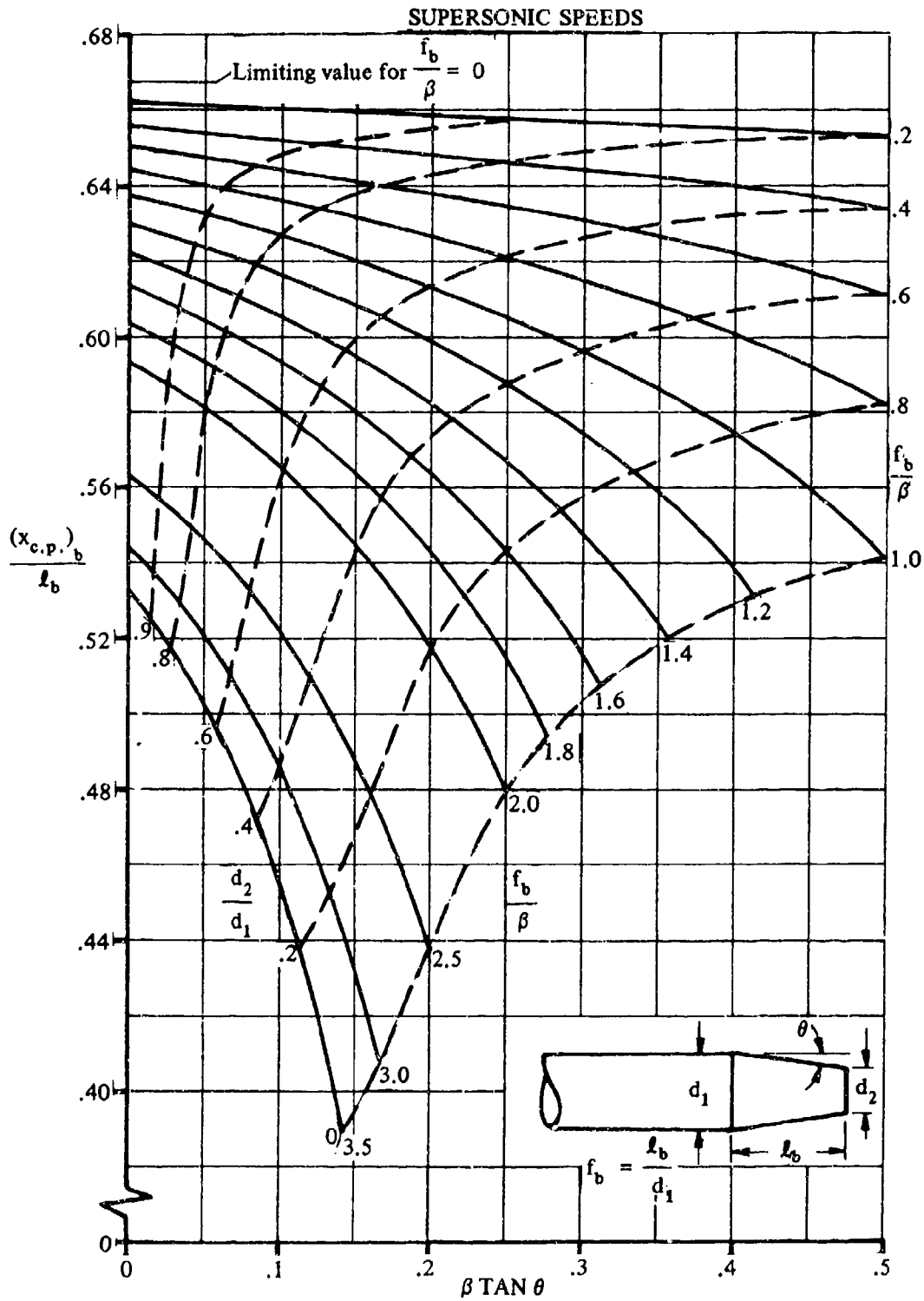

FIGURE 4.2.2.1-24 SUPERSONIC CENTER OF PRESSURE OF BOATTAILED BODY OF REVOLUTION MOUNTED BEHIND A SEMI-INFINITE CYLINDER

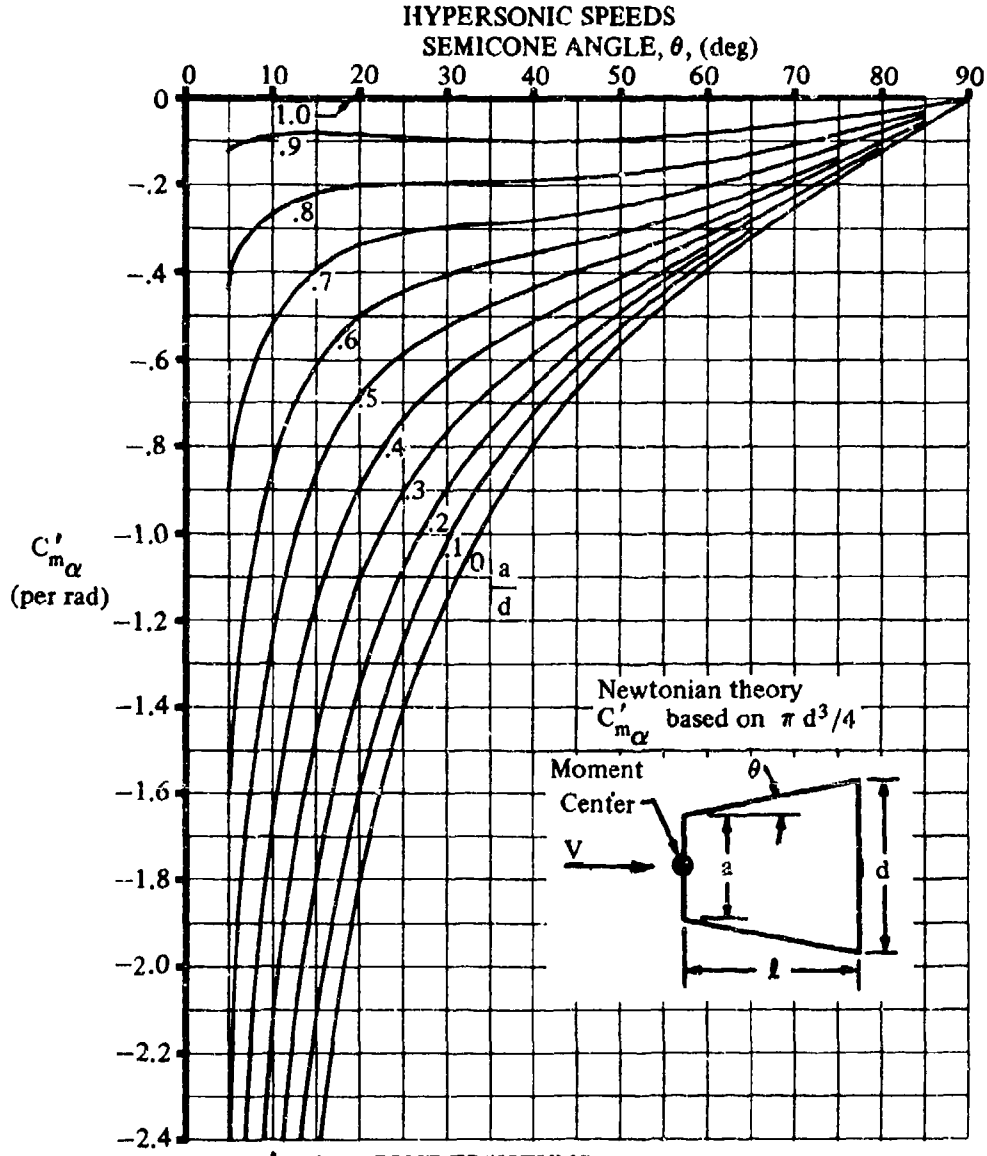

FIGURE 4.2.2.1-25a C'_{m_α} FOR CONE FRUSTUMS

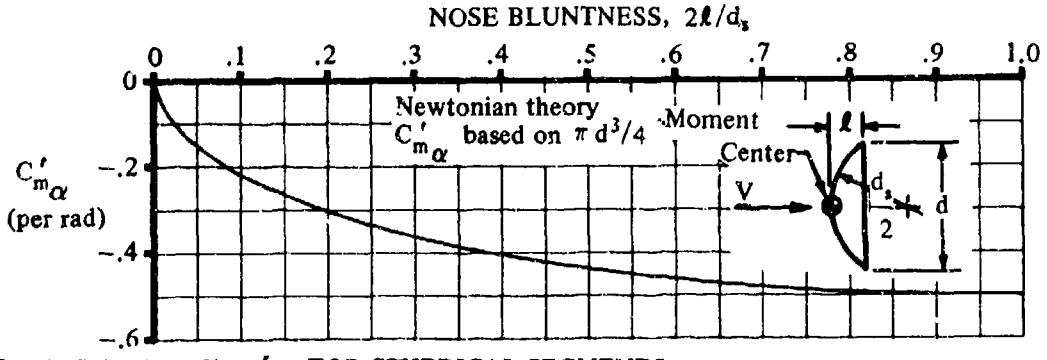

FIGURE 4.2.2.1-25b C'_{m_α} FOR SPHERICAL SEGMENTS

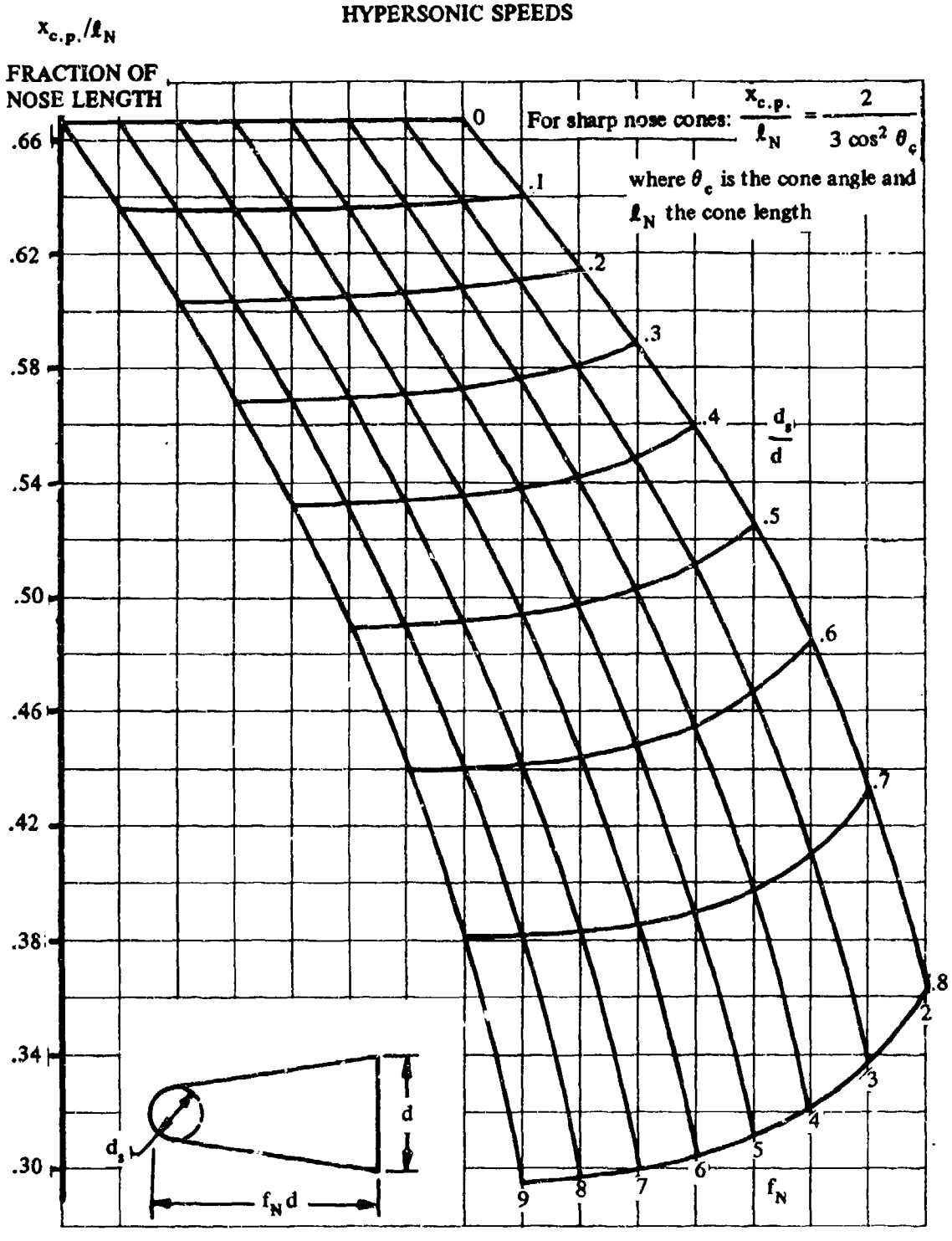

FIGURE 4.2.2.1-26 CENTER OF PRESSURE OF SPHERICALLY BLUNTED CONES (IMPACT THEORY)

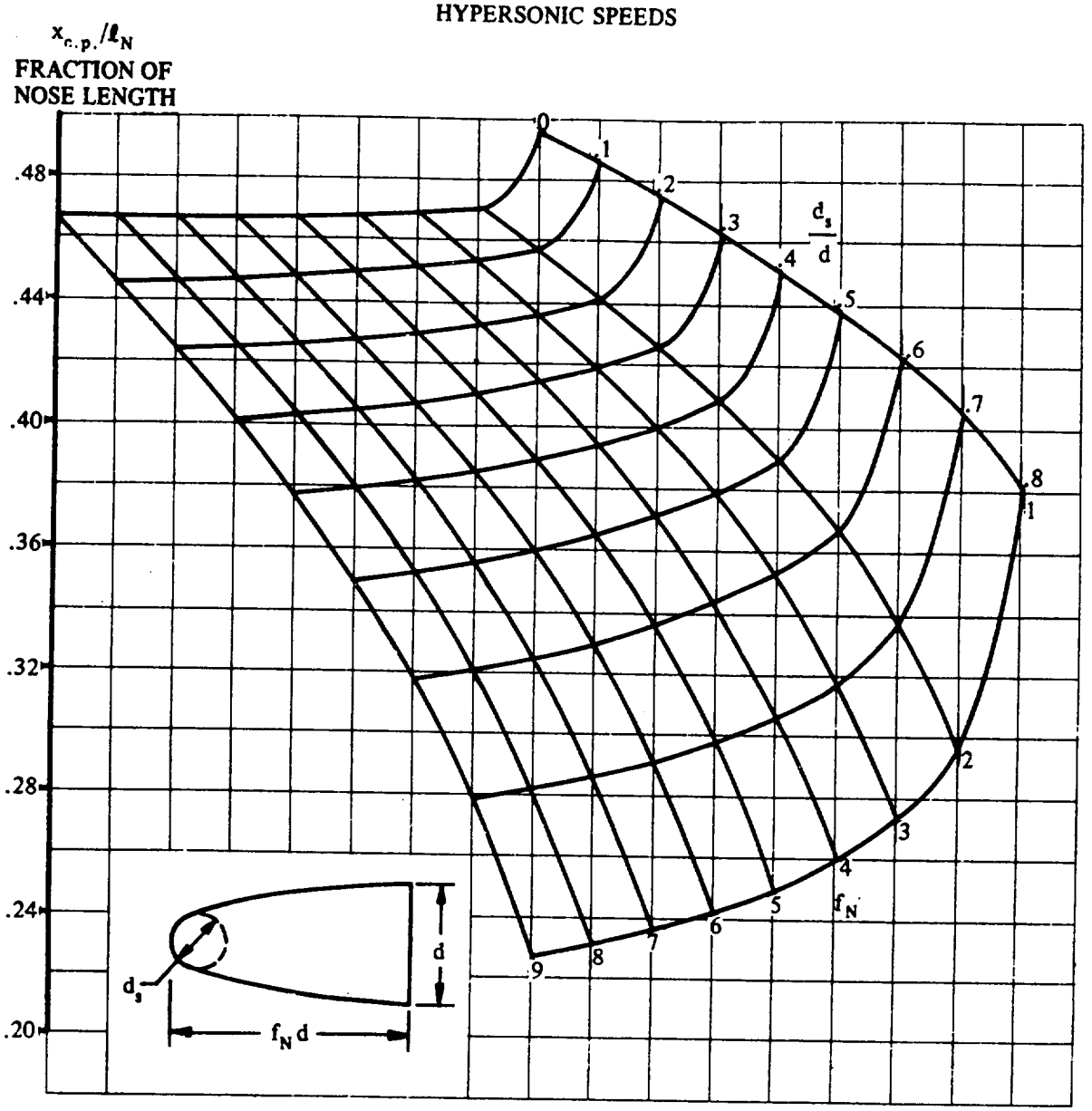

FIGURE 4.2.2.1-27 CENTER OF PRESSURE OF SPHERICALLY BLUNTED OGIVES (IMPACT THEORY)

4.2.2.2 BODY PITCHING MOMENT IN THE NONLINEAR ANGLE-OF-ATTACK RANGE

A. SUBSONIC

Two methods are presented for calculating subsonic pitching-moment coefficient. The first method is applicable to bodies with circular cross sections and angles of attack up to about 12°. This method allows for a variation of the cross-sectional diameter along the length of the body. The second method is applicable to bodies with circular or elliptical cross sections for angles of attack from 0 to 180°. This method has been substantiated only for bodies with a constant cross-sectional size and shape.

DATCOM METHODS

Method 1

As discussed in Section 4.2.1.2, the viscous cross flow over a body at moderate to large angles of attack makes a substantial contribution to both lift and pitching moment. This method for predicting body pitching moment therefore differs chiefly from the method of Section 4.2.2.1 in that the viscous cross forces are considered.

The method of Reference 1 is presented for estimating the pitching moment of a body of revolution at angle of attack, based on the total body volume and referred to an arbitrary moment axis.

$$C_m = \frac{(k_2 - k_1)}{V_B} 2\alpha \int_0^{x_o} \frac{dS_x}{dx}(x_m - x)dx + \frac{2\alpha^2}{V_B} \int_{x_o}^{\ell_B} \eta r c_{d_c}(x_m - x)dx \qquad 4.2.2.2\text{-a}$$

where the terms in the above expression are defined in Paragraph A of either Section 4.2.1.2 or Section 4.2.2.1.

The pitching-moment coefficients of several bodies of revolution, calculated by the Datcom method, have been compared with test data in Reference 1. The method appears to give the best results at the lower angles of attack, but in general the method is satisfactory up to angles of attack of approximately 12°.

Method 2

This method is based on the method of Jorgensen (Reference 2) and consists of the sum of a slender-body potential term and an empirical viscous cross-flow term. The method is applicable to bodies of circular and elliptical cross sections for angles of attack from 0 to 180°. However, it is recommended that Method 1 be used for $\alpha \leqslant 12^{\circ}$. Bodies with other types of cross sections and those with variable cross sections have been investigated by this method (References 2 and 3), but very little substantiating test data are available. A summary of available test data on bodies of noncircular cross section at subsonic speeds is presented as Table 4.2.1.1-A.

The pitching-moment coefficient for bodies of revolution and bodies with elliptical cross sections, based on body cross-sectional reference area and diameter, is determined from the following equations:

For $0 \leqslant \alpha \leqslant 90^{o}$

$$C_m = \left(\frac{C_N}{C_{N_{cir}}}\right)_{SB} \left[\frac{V_B - S_b(\ell_B - x_m)}{Sd}\right] \sin 2\alpha' \cos\frac{\alpha'}{2} + \left(\frac{C_N}{C_{N_{cir}}}\right)_{NT} \eta c_{d_c} \frac{S_p}{S}\left(\frac{x_m - x_c}{d}\right) \sin^2\alpha' \qquad 4.2.2.2\text{-b}$$

For $90^{o} \leqslant \alpha \leqslant 180^{o}$

$$C_m = -\left(\frac{C_N}{C_{N_{cir}}}\right)_{SB} \left(\frac{V_B - S_b x_m}{Sd}\right) \sin 2\alpha' \cos\frac{\alpha'}{2} + \left(\frac{C_N}{C_{N_{cir}}}\right)_{NT} \eta c_{d_c} \frac{S_p}{S}\left(\frac{x_m - x_c}{d}\right) \sin^2\alpha' \qquad 4.2.2.2\text{-c}$$

where

$\left(\frac{C_N}{C_{N_{cir}}}\right)_{SB}$ is the ratio of the normal-force coefficient for the body of noncircular cross section to that for the equivalent body of circular cross section (same cross-sectional area) as determined by slender-body theory. For circular cross sections this ratio is one. For elliptical cross sections this ratio is given by Equation 4.2.1.2-d.

V_B is the total body volume.

S_b is the body base area.

ℓ_B is the body length.

x_m is the distance from the nose to the moment reference center of the body.

S is the cross-sectional reference area of the body (can be arbitrarily selected).

d is the body diameter (or the diameter of an equivalent body of revolution for an elliptic cross section).

α' is an incidence angle defined as $\alpha' = \alpha$ for $0 \leqslant \alpha \leqslant 90^{o}$ and $\alpha' = 180^{o} - \alpha$ for $90^{o} \leqslant \alpha \leqslant 180^{o}$.

$\left(\frac{C_N}{C_{N_{cir}}}\right)_{NT}$ is the ratio of the normal-force coefficient for the body of noncircular cross section to that for the equivalent body of circular cross section (same cross-sectional area) as determined by Newtonian impact theory. For circular cross sections this ratio is one. For elliptical cross sections this ratio is given by Equations 4.2.1.2-e and 4.2.1.2-f.

η is the cross-flow drag proportionality factor, obtained from Figure 4.2.1.2-35a, as a function of body fineness ratio.

c_{d_c} is the cross-flow drag coefficient of the cylindrical section, obtained from Figure 4.2.1.2-35b, as a function of cross-flow Mach number M_c, where $M_c = M \sin \alpha$.

S_p is the body planform area. In applying the method to bodies with elliptical cross section, the term S_p in Equations 4.2.2.2-b and 4.2.2.2-c is based on an equivalent body of revolution with the same cross-sectional area.

x_c is the distance from the nose to the centroid of the body planform area.

This method is applied to bodies of noncircular cross sections in the same manner as Method 3 of Section 4.2.1.2, Paragraph A. Refer to this paragraph for a more detailed explanation of bodies with elliptical cross sections. Bodies with other cross sections are discussed in Reference 3.

It is noted in Reference 2 that the cross-flow drag coefficient may be reduced dramatically under the simultaneous conditions of $M_c \leq 0.4$ and $R_\ell \sin \alpha > 10^5$ (R_ℓ is Reynolds number based on diameter). These conditions have only recently been analyzed in detail and have not been included in the Datcom method because of considerable uncertainty in the magnitude and trend of the effects. For more detailed information regarding these effects, the user should refer to Reference 2.

Calculated results using this method have been compared with test data from Reference 6 in Table 4.2.2.2-A. The method shows fairly good agreement at angles of attack up to 20°, but significantly underestimates the data at higher angles of attack. Caution should be exercised when using this method at subsonic Mach numbers because of the shortage of substantiating test data. It is recommended that Method 1 be used for $0 \leq \alpha \leq 12^\circ$.

Sample Problems

1. Method 1

Given: The 3/4-power body of revolution of Reference 10. This is the same configuration as that in Paragraph A of Section 4.2.2.1.

$$r = 0.255 \left[1 - \left(1 - \frac{2x}{6.375}\right)^2\right]^{3/4} \qquad \ell_B = 5.036 \text{ ft} \qquad d = 0.510 \text{ ft}$$

$$f = \ell_B/d = 9.87 \qquad V_B = 0.687 \text{ cu ft} \qquad x_m = 3.54 \text{ ft}$$

$$M = 0.40 \qquad \alpha = 0 \text{ to } 18^\circ$$

Compute:

$x_o = 4.558$ ft

$$\frac{2(k_2 - k_1)}{V_B} \int_0^{x_o} \frac{dS_x}{dx} (x_m - x)\, dx = 1.293 \text{ per rad}$$ (Sample Problem 2, Paragraph A, Section 4.2.2.1)

$\eta = 0.685$ (Figure 4.2.1.2-35a)

$c_{d_c} = f(M_c)$; $M_c = M \sin \alpha$

M_c varies from 0 to 0.40 sin 18°; $0 \leq M_c \leq 0.1236$

$c_{d_c} = 1.20$ (constant) (Figure 4.2.1.2-35b)

Evaluate $\int_{x_o}^{\ell_B} r\,(x_m - x)\, dx$

Station (ft)	r* (ft)	Δx (ft)	x* (ft)	$(x_m - x)$ ft	$r(x_m - x)\,\Delta x$ (ft^3)
$x_o = 4.56$	0.2037	0.476	4.79	−1.25	−0.121
$\ell_B = 5.036$					

$$\sum_{x_o}^{\ell_B} r(x_m - x)\,\Delta x = -0.121 \text{ cu ft}$$

Solution:

$$C_m = \frac{(k_2 - k_1)}{V_B}\, 2\alpha \int_0^{x_o} \frac{dS_x}{dx} (x_m - x)\, dx + \frac{2\alpha^2}{V_B} \int_{x_o}^{\ell_B} \eta r c_{d_c} (x_m - x)\, dx$$

(Equation 4.2.2.2-a)

$$= 1.293\alpha + \frac{2\alpha^2}{0.687} (0.685)(1.20) \int_{x_o}^{\ell_B} r(x_m - x)\, dx$$

$$= 1.293\alpha - 0.290\alpha^2$$

*x and r are taken at the center of volume of the body segment.

α (deg)	α (rad)	α^2 (rad^2)	C_m (Eq. 4.2.2.2-a)
0	0	0	0
2	0.0349	0.00122	0.0448
4	0.0698	0.00487	0.0888
6	0.1047	0.01096	0.1322
8	0.1396	0.01947	0.1749
10	0.1745	0.03045	0.2168
12	0.2094	0.04385	0.2580
14	0.2443	0.05968	0.2986
16	0.2792	0.07795	0.3384
18	0.3141	0.09866	0.3775

The calculated results are compared with test values from Reference 15 in Sketch (a).

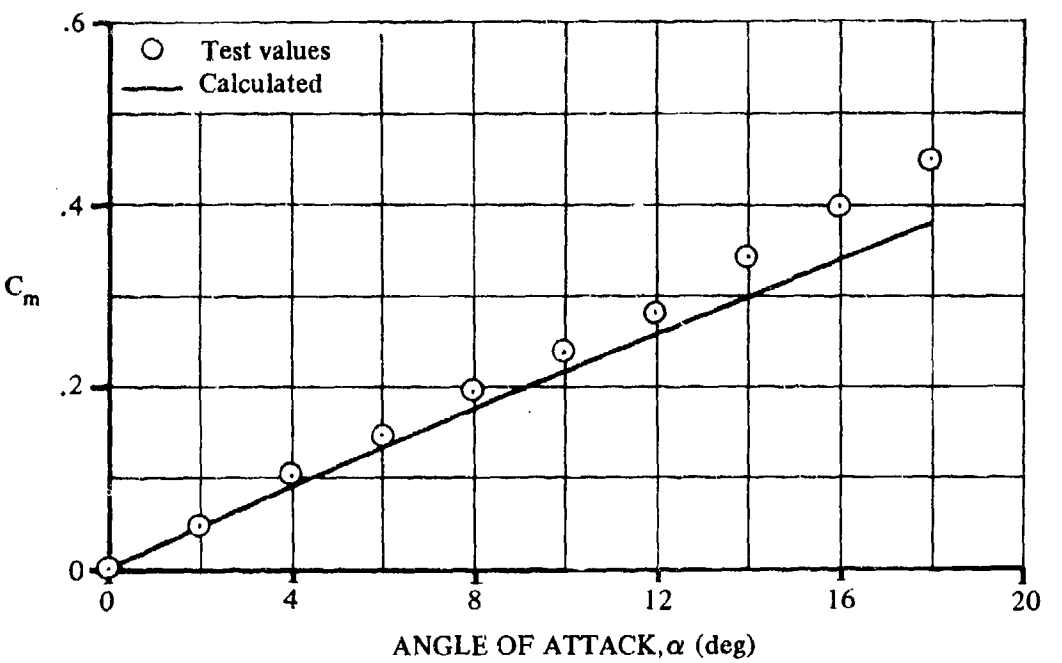

SKETCH (a)

2. Method 2

Given: The elliptical cross-section body with tangent ogive nose of Reference 6. This is the same configuration as given in the sample problem for Method 3 of Paragraph A of Section 4.2.1.2.

Body Characteristics:

$V_B = 1944.64\ cm^3$ $\quad x_c = 36.08\ cm$

$\ell_B = 66.0\ cm$ $\quad x_m = 39.58\ cm$ $\quad S_p = 392.466\ cm^2$

$d = 6.6\ cm$

$S = 34.206\ cm^2$

$S_b = 34.206\ cm^2$

$\left(\frac{C_N}{C_{N_{cir}}}\right)_{SB} = 2.0$

$\left(\frac{C_N}{C_{N_{cir}}}\right)_{NT} = 1.752$

} Sample Problem 3, Paragraph A, Section 4.2.1.2

Additional Characteristics:

$\alpha' = \alpha = 50^o$ $\quad M = 0.6$ $\quad R_\ell = 6.5 \times 10^5$ (based on diameter)

$\phi = 0$

Compute:

Slender-body Potential Term

$\eta = 0.685$

$c_{d_c} = 1.32$

} Sample Problem 3, Paragraph A, Section 4.2.1.2

$$\left(\frac{C_N}{C_{N_{cir}}}\right)_{Sb} \left[\frac{V_B - S_b(\ell_B - x_m)}{Sd}\right] \sin 2\alpha' \cos\frac{\alpha'}{2}$$

$$= (2.0)\left[\frac{1944.64 - 34.206(66.0 - 39.58)}{(34.206)(6.6)}\right](0.9848)(0.9063) = 8.23$$

Viscous Cross-Flow Term

$$\left(\frac{C_N}{C_{N_{cir}}}\right)_{NT} \eta c_{d_c} \frac{S_p}{S}\left(\frac{x_m - x_c}{d}\right) \sin^2\alpha'$$

$$= (1.752)(0.685)(1.32)\left(\frac{392.466}{34.206}\right)\left(\frac{39.58 - 36.08}{6.6}\right)(0.5868) = 5.66$$

Solution:

C_m = slender-body potential term + viscous cross-flow term

= 8.23 + 5.66

= 13.89 (based on Sd)

Additional values have been tabulated below:

M	α (deg)	C_m
0.6	10	3.41
0.6	20	6.87
0.6	30	9.94
0.6	40	12.34
0.6	50	13.89
0.6	60	14.51

The calculated results of the sample problem are compared to test values from Reference 6 in Sketch (b).

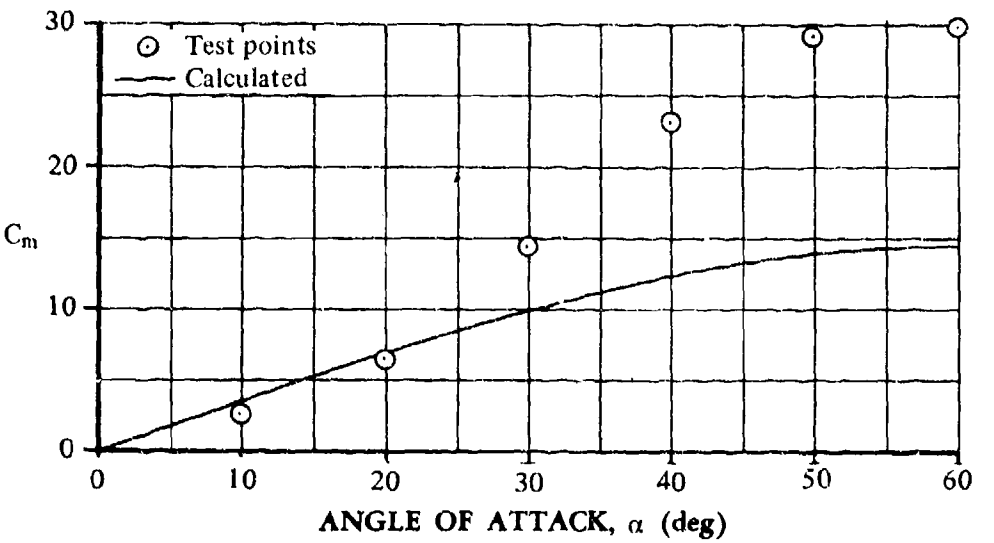

SKETCH (b)

B. TRANSONIC

Transonic flow, which consists by definition of a combination of locally subsonic and supersonic flow regions, is particularly difficult for either theoretical or empirical analysis. The two types of flow interact directly on their mutual boundaries and indirectly through the boundary layer. The resulting flow pattern is highly sensitive to seemingly small changes in geometry. Prediction of transonic body lift is at best an approximation; prediction of transonic body lift distribution is considerably more difficult.

DATCOM METHOD

Because of the difficulty of predicting transonic-flow phenomena to the accuracy required for lift distribution, no Datcom method is given for predicting body pitching moment at transonic speeds. It is suggested that the transonic region be faired smoothly from the subsonic region to the supersonic region.

C. SUPERSONIC

Several theoretical methods have been developed that can be used to estimate the moment characteristics of bodies of revolution at supersonic speeds. Some of these methods are discussed in Paragraph C of Section 4.2.1.2.

Three methods are presented for estimating body pitching moment at supersonic speeds. The first method is based on the method of Allen and Perkins (Reference 7) and includes a modification by Jorgensen (Reference 8) to accommodate bodies with elliptical cross sections. The second approach uses hypersonic-similarity concepts that have been adapted to supersonic speeds (Reference 9). These two methods are discussed in Paragraph C of Section 4.2.1.2. The third method is an improvement on Method 1 developed by Jorgensen in Reference 2. This method extends the capability for calculating pitching moments to 180°. The method is identical to that presented as Method 2 in Paragraph A of this section.

DATCOM METHODS

Method 1

The method presented for predicting the pitching moment of a body of revolution at angle of attack is that of Allen and Perkins, in Reference 7. The method for estimating the pitching moment of bodies of elliptical cross section is that of Reference 7 as modified by Jorgensen in Reference 8.

The pitching-moment coefficient of a body of revolution, based on body base area and body length $S_b \ell_B$ and referred to an arbitrary moment center, is

$$C_m = 2\alpha \left[\frac{V_B}{S_b \ell_B} - \left(1 - \frac{x_m}{\ell_B} \right) \right] + c_{d_c} \frac{S_p}{S_b} \left(\frac{x_m - x_c}{\ell_B} \right) \alpha^2 \qquad 4.2.2.2\text{-d}$$

where x_c is the axial distance from the vertex of the nose to the centroid of the planform area, and the remaining terms are defined in Paragraph C of either Section 4.2.1.2 or Section 4.2.2.1.

The supersonic pitching-moment coefficient at angle of attack of a body having an elliptical cross section, based on body base area and body length $S_b \ell_B$ and referred to an arbitrary moment center, is

$$(C_m)_{a/b} = \left[\frac{a}{b}\cos^2\phi + \frac{b}{a}\sin^2\phi\right] C_m \qquad 4.2.2.2\text{-e}$$

where C_m is the pitching-moment coefficient of a body of revolution having the same cross-sectional area distribution along its axis as the elliptical-cross-section body of interest. It is given by Equation 4.2.2.2-d. The parameters a, b, and ϕ are defined in Paragraph C of Section 4.2.1.2.

The Datcom method has been used to calculate the variation of pitching-moment coefficient with angle of attack for the bodies of elliptic cross section of Reference 8 and for the bodies of revolution of References 7, 8, and 10 through 13. Although the nose shapes of most of the configurations analyzed were tangent ogives, a few bodies of revolution had conical or hemispherical noses. All the afterbodies were straight (no boattail or flare). In general, the calculated results agree well with the test data. The comparison of calculated and test values for the sample problems at the conclusion of this paragraph is indicative of the degree of accuracy of this method.

Method 2

This method uses hypersonic-similarity parameters that have been adapted to supersonic speeds by the method of Reference 9. This method is based on experimental data for a wide range of models for Mach numbers between 1.57 and 2.87. The variation of pitching-moment coefficient with angle of attack for pointed or nearly pointed bodies of revolution is estimated by using Figure 4.2.2.2-26 where $\beta = \sqrt{M^2 - 1}$. The body pitching moment obtained from this chart is referred to the nose apex and is based on the product of body frontal area and the body length $S_B \ell_B$.

A comparison of test data with the pitching-moment coefficient calculated by this method is presented as Table 4.2.2.2-B.

Method 3

This method is the same as Method 2 presented in Paragraph A of this section. The only exception is that the term η in Equations 4.2.2.2-b and 4.2.2.2-c is set equal to 1.0 for $M \geq 1.0$.

The method is applicable to angles of attack from 0 to 180° and Mach numbers up to 7. The method is substantiated by test data from References 4, 5, and 6 in Table 4.2.2.2-C.

The method shows reasonable agreement with most test data, but Methods 1 and 2 are recommended in the low-angle-of-attack range.

With the exception of bodies with elliptical cross sections, there are no Datcom methods for predicting the pitching moment on bodies of noncircular cross section at supersonic speeds. A summary of available test data on bodies of noncircular cross section at supersonic speeds is presented as Table 4.2.1.1-C. In

Reference 8 (Reference 37 of Table 4.2.1.1-C) the effect of cross-sectional shape on body aerodynamics has been assessed for bodies with circular, elliptic, square, and triangular cross sections. These data show that at certain angles of bank, noncircular bodies develop considerably more pitching moment than their equivalent bodies of revolution at a given angle of attack. The data of Reference 8 also show that the ratio of pitching-moment coefficient for a body with elliptic cross section to that for an equivalent body of revolution is practically constant with change in both angle of attack and Mach number. However, no such simple correlation is available for other bodies of noncircular cross section. Method 3 has been applied to other bodies with noncircular and axially varying cross sections by Jorgensen in References 2 and 3. The lack of sufficient substantiating data has precluded inclusion of this application in the Datcom.

Sample Problems

1. Method 1

Given: An ogive-cylinder body of Reference 8. This is the same configuration as that of Sample Problem 1 of Paragraph C of Section 4.2.1.2.

Body Characteristics:

$d = 1.40$ in. $\quad \ell_B = 14.0$ in. $\quad \ell_N = 4.20$ in. $\quad \ell_A = 9.80$ in.

$V_B = 18.56$ cu in. $\quad S_b = 1.539$ sq in. $\quad S_p = 17.66$ sq in.

$S_p/S_b = 11.47 \quad x_c = 7.69$ in. $\quad x_m/\ell_B = 1.0$ (moments referred to body base)

Additional Characteristics:

$M = 1.98 \quad \alpha = 4^o, 8^o, 12^o, 16^o, 20^o$

Compute:

$c_{d_c} = f(M_c) = f(M \sin\alpha)$

α	4^o	8^o	12^o	16^o	20^o	(Sample Problem 1, Paragraph C, Section 4.2.1.2)
c_{d_c}	1.20	1.208	1.275	1.41	1.62	

$$\left[\frac{V_B}{S_b \ell_B} - \left(1 - \frac{x_m}{\ell_B}\right)\right] = \left[\frac{18.56}{(1.539)(14.0)} - (1 - 1.0)\right] = 0.8614$$

$$c_{d_c} \frac{S_p}{S_b} \left(\frac{x_m - x_c}{\ell_B}\right) = c_{d_c} (11.47) \left(\frac{14.0 - 7.69}{14.0}\right) = 5.170\, c_{d_c}$$

Solution:

$$C_m = 2\alpha\left[\frac{V_B}{S_b \ell_B} - \left(1 - \frac{x_m}{\ell_B}\right)\right] + c_{d_c}\frac{S_p}{S_b}\left(\frac{x_m - x_c}{\ell_B}\right)\alpha^2 \quad \text{(Equation 4.2.2.2-d)}$$

$$= 2\alpha(0.8614) + 5.170\, c_{d_c}\alpha^2$$

$$= 1.723\alpha + 5.170\, c_{d_c}\alpha^2$$

α (deg)	α (rad)	α^2 (rad^2)	c_{d_c}	1.723α	$5.170\, c_{d_c}\alpha^2$	C_m Eq. 4.2.2.2-d (based on $S_b\ell_B$)
4	0.0698	0.00487	1.20	0.1203	0.0302	0.151
8	0.1396	0.01950	1.208	0.2405	0.1218	0.362
12	0.2094	0.04386	1.275	0.3608	0.2891	0.650
16	0.2793	0.07798	1.41	0.4812	0.5685	1.050
20	0.3491	0.12185	1.62	0.6015	1.0205	1.622

2. Method 1

Given: A body of Reference 8 having an elliptical cross section and the same axial distribution of cross-sectional area as the body of revolution of Sample Problem 1.

Body Characteristics:

a = 1.98 in. b = 0.99 in. a/b = 2.0 φ = 0

x_m/ℓ_B = 1.0 (moments referred to body base)

Additional Characteristics:

M = 1.98 α = 4°, 8°, 12°, 16°, 20°

Compute:

C_m vs α for a body of revolution having the same cross sectional area distribution and with the moment axis located at the base of the body. (from Sample Problem 1)

Solution:

$$C_m = \left[\frac{a}{b}\cos^2\phi + \frac{b}{a}\sin^2\phi\right] C_m \qquad \text{(Equation 4.2.2.2-e)}$$

$$= [(2.0)(1.0) + 0]\, C_m = 2.0\, C_m$$

α (deg)	C_m Sample Problem 1	$(C_m)_{a/b}$ Eq. 4.2.2.2-e (based on $S_b \ell_B$)
4	0.151	0.302
8	0.362	0.724
12	0.650	1.300
16	1.050	2.100
20	1.622	3.244

The calculated results of Sample Problems 1 and 2 are compared with test values from Reference 8 in Sketch (c)

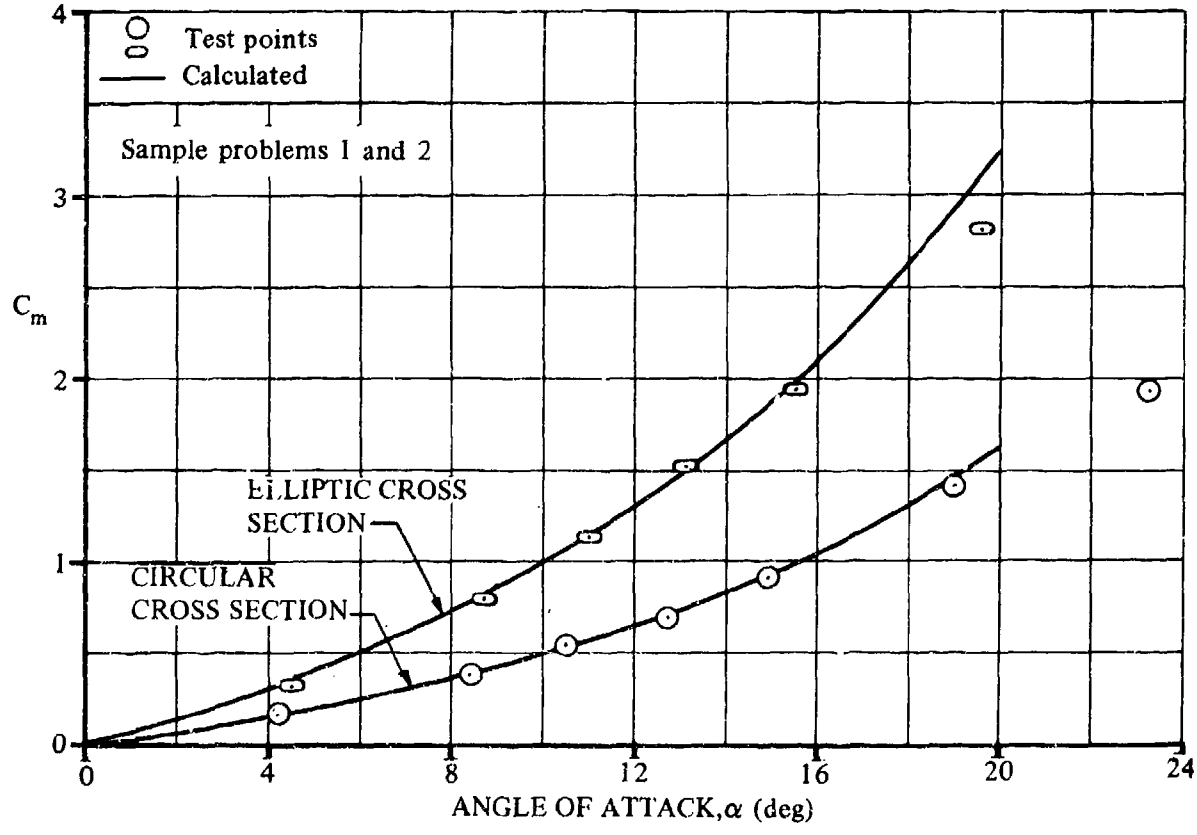

SKETCH (c)

3. Method 2

Given: The ogive-cylinder body of Sample Problem 1.

Body Characteristics:

$d = 1.40$ in. $\quad \ell_N = 4.20$ in. $\quad \ell_A = 9.80$ in.

Additional Characteristics:

$M = 1.98; \quad \beta = 1.71 \quad \alpha = 4^o, 8^o, 12^o$

Compute:

$f_N = \ell_N/d = 4.2/1.4 = 3.0 \quad f_A = \ell_A/d = 9.8/1.4 = 7.0$

$f_A/f_N = 7.0/3.0 = 2.33$

$\beta/f_N = 1.71/3.0 = 0.570$

Solution:

α (deg)	$\beta\alpha$ (deg)	βC_m Fig. 4.2.2.2-26	C_m (based on $S_B\ell_B$) (referred to nose apex)
4	6.84	−0.073	−0.043
8	13.68	−0.275	−0.161
12	20.52	−0.930	−0.544

The calculated results are compared with test values from Reference 8 in Sketch (d). (The test results have been transferred to a moment axis at the nose apex).

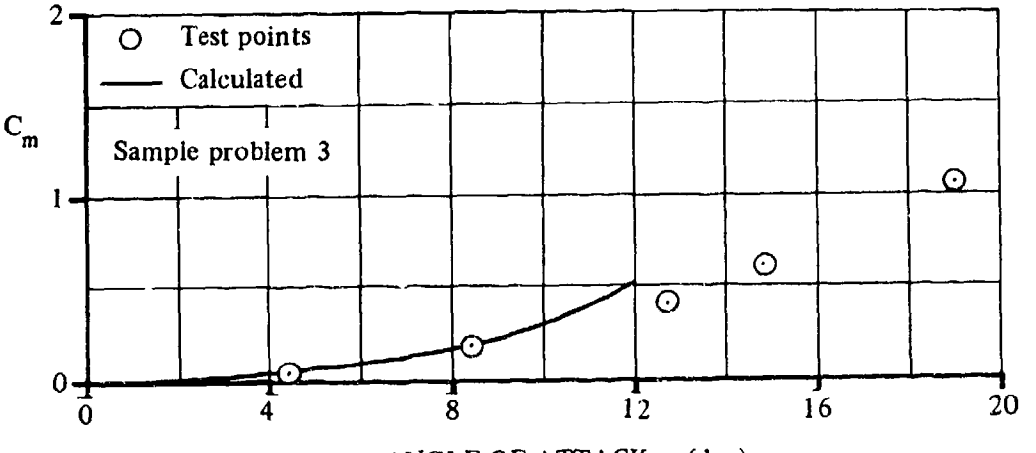

SKETCH (d)

4. Method 3

Refer to Sample Problem 2 in Paragraph A of this section for an example of the application of the method.

D. HYPERSONIC

Three methods are available for estimating the pitching moment of bodies of revolution at hypersonic speeds. The first method, based on Newtonian impact theory and its modifications, is discussed in Paragraph D of Section 4.2.1.1. The second method is the hypersonic-similarity method. The third method is the method of Jorgensen previously presented as Method 3 of Paragraph C of this section.

DATCOM METHODS

Method 1

The expression for the pitching moment of an arbitrary body of revolution, from the modified Newtonian theory of Reference 14, referred to an arbitrary moment center and based on the product of the body base area and body length $S_B \ell_B$, is

$$C_m = \frac{K}{\pi} \frac{\ell_B}{R} \int_0^1 K_\theta \frac{r}{R} \frac{\ell_x}{\ell_B} \, d\left(\frac{x}{\ell_B}\right) \qquad 4.2.2.2\text{-f}$$

where ℓ_x is the distance from the moment center to a transverse element, positive where the element is forward of the moment center. The remaining parameters are defined under Method 2 in Paragraph D of Section 4.2.1.2.

The following steps outline the calculation procedure (Steps 1 through 3 are identical to Steps 1 through 3 of Method 2 of Paragraph D of Section 4.2.1.2):

Step 1. From the equation of the body of revolution obtain the expression for the surface slope using the relation

$$\theta = \tan^{-1}\left(\frac{dr}{dx}\right)$$

where θ, dr, and dx are defined in Sketch (f) of Section 4.2.1.2.

Step 2. Compute the values of r/R and θ at various longitudinanal stations x/ℓ_B.

Step 3. For various x/ℓ_B enter Figure 4.2.1.2-43 with the corresponding θ from Step 2 and obtain K_θ at the desired angle of attack.

Step 4. Plot the product $K_\theta \frac{r}{R} \frac{\ell_x}{\ell_B}$ against x/ℓ_B.

Step 5. Obtain the required value of C_m by integrating the area under the curve described in Step 4 and multiplying by $\frac{K}{\pi} \frac{\ell_B}{R}$.

Method 2

The second method of estimating body pitching moments applies only to ogive-cylinder bodies. This method is based on experimental data for a wide range of models at a Mach number of 4.24. These data have been used to derive a hypersonic design chart (Figure 4.2.2.2-27) based on hypersonic-similarity parameters. The body pitching moment obtained from Figure 4.2.2.2-27, where $\beta = \sqrt{M^2 - 1}$, is referred to the nose apex and is based on the product of the body frontal area and body length $S_B \ell_B$.

Pitching moments calculated by this method are compared with test data in Table 4.2.2.2-D.

Method 3

This method is identical to Method 3 presented in Paragraph C of this section. The method is applicable to angles of attack from 0 to 180° and Mach numbers up to 7. The method has been partially substantiated by the test data from Reference 5 in Table 4.2.2.2-C.

The method shows reasonable agreement with test data at hypersonic speeds in the low-angle-of-attack range. Because of the scarcity of substantiating test data, caution should be used when applying the method at higher angles of attack ($\alpha > 25^\circ$).

Sample Problems

1. Method 1

Given: A second-power body of revolution of fineness ratio 1.0. This is the same configuration as Sample Problem 2 of Paragraph D of Section 4.2.1.2.

$x = \left(\frac{4}{\ell_B}\right) r^2$ (equation of body) $\quad \ell_B = 2.0$ ft $\quad R = 1.0$ ft

$\ell_x/\ell_B = 0.50 - (x/\ell_B)$ (moment center at $0.50\ell_B$)

$M_\infty = 3.55 \quad \alpha = 6^\circ \quad \gamma = 1.40$

$K = 1.77$ (Sample Problem 2, Paragraph D, Section 4.2.1.2)

Compute:

Calculate r/R and θ at various longitudinal stations x/ℓ_B and plot. (See Sketch (g), Sample Problem 2, Paragraph D, Section 4.2.1.2.)

Obtain values of K_θ from Figure 4.2.1.2-43 for various values of θ at $\alpha = 6^\circ$.

Plot the product $K_\theta \frac{r}{R} \frac{\ell_x}{\ell_B}$ versus x/ℓ_B (Sketch (e)).

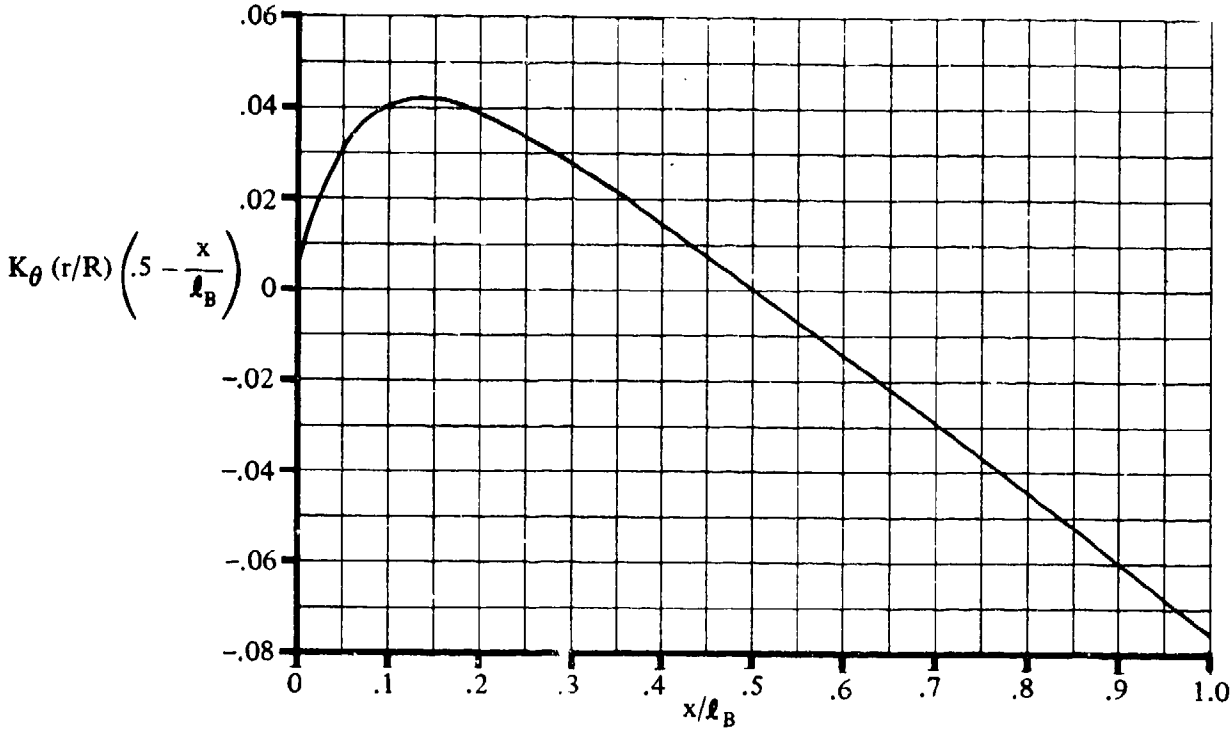

SKETCH (e)

Integrate the area under the curve of Sketch (e).

$$\int_0^1 K_\theta \frac{r}{R}\left(0.50 - \frac{x}{\ell_B}\right) d\left(\frac{x}{\ell_B}\right) = -0.00615$$

Solution:

$$C_m = \frac{K}{\pi}\frac{\ell_B}{R}\int_0^1 K_\theta \frac{r}{R}\frac{\ell_x}{\ell_B}\, d\left(\frac{x}{\ell_B}\right) \quad \text{(Equation 4.2.2.2-f)}$$

$$= \frac{1.77}{\pi}\frac{2}{1}\,(-0.00615)$$

$$= -0.0069 \quad \text{(referred to a moment center at } 0.50\,\ell_B \text{ and based on } S_b\ell_B\text{)}$$

2. Method 2

Given: An ogive-cylinder body of Reference 16.

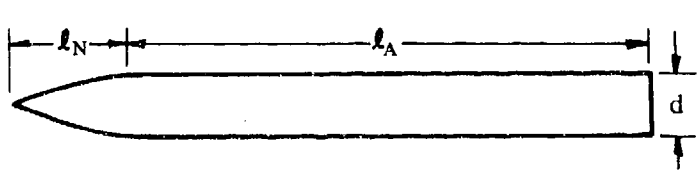

Body Characteristics:

ℓ_N = 2.50 ft ℓ_A = 11.50 ft d = 1.0 ft

Additional Characteristics:

M = 4.24; β = 4.12 α = 2°, 4°, 6°

Compute:

$f_N = \ell_N/d = 2.50$ $f_A = \ell_A/d = 11.50$

$f_A/f_N = 11.50/2.50 = 4.60$ $\beta/f_N = 4.12/2.50 = 1.648$

Solution:

α (deg)	$\beta\alpha$ (deg)	βC_m Fig. 4.2.2.2-27	C_m (based on $S_B\ell_B$) (referred to nose apex)
2	8.24	−0.15	−0.0364
4	16.48	−0.38	−0.0922
6	24.72	−0.79 (extrapolated)	−0.1917
8	32.96	−1.29 (extrapolated)	−0.3131

The calculated results are compared with test values from Reference 15 in Sketch (f).

SKETCH (f)

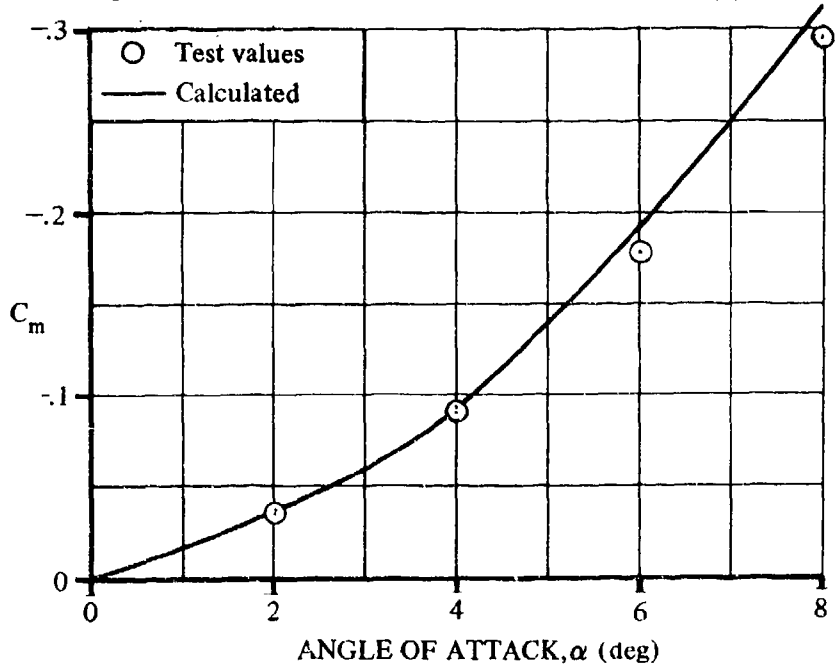

3. Method 3

Refer to Sample Problem 2 in Paragraph A of this section for an example of the application of the method.

REFERENCES

1. Hopkins, E. J.: A Semiempirical Method for Calculating the Pitching Moment of Bo at Low Mach Numbers. NACA RM A51C14, 1951. (U)

2. Jorgensen, L. H.: Prediction of Static Aerodynamic Characteristics for Space-Shuttle-Like and Other Bodies at Angles of Attack from 0^{o} to 180^{o}. NASA TN D-6996, 1973. (U)

3. Jorgensen, L. H.: A Method for Estimating Static Aerodynamic Characteristics for Slender Bodies of Circular and Noncircular Cross Section Alone and with Lifting Surfaces at Angles of Attack from 0^{o} to 90^{o}. NASA TN D-7228, 1973. (U)

4. Jernell, L. S.: Aerodynamic Characteristics of Bodies of Revolution at Mach Numbers from 1.50 to 2.86 and Angles of Attack to 180^{o}. NASA TM X-1658, 1968. (U)

5. Dennis, D. H., and Cunningham, B. E.: Forces and Moments on Inclined Bodies at Mach Numbers from 3.0 to 6.3. NACA RM A54E03, 1954. (U)

6. Jorgensen, L. H., and Nelson, E. R.: Experimental Aerodynamic Characteristics for Bodies of Elliptic Cross Section at Angles of Attack from 0^{o} to 58^{o} and Mach Numbers from 0.6 to 2.0. NASA TM X-3129, 1975. (U)

7. Allen, H. J., and Perkins, E. W.: A Study of Effects of Viscosity on Flow Over Slender Inclined Bodies of Revolution. NACA TR 1048, 1951. (U)

8. Jorgensen, L. H.: Inclined Bodies of Various Cross Section at Supersonic Speeds. NASA Memo 10-3-58A, 1958. (U)

9. Van Dyke, M. D.: The Combined Supersonic-Hypersonic Similarity Rule. Jour. Aero. Sci., Vol. 18, No. 7, 1951. (U)

10. Perkins, E. W., and Jorgensen, L. H.: Comparison of Experimental and Theoretical Normal-Force Distributions (Including Reynolds Number Effects) on an Ogive-Cylinder Body at Mach Number 1.98. NACA TN 3716, 1956. (U)

11. Jack, J. R.: Aerodynamic Characteristics of a Slender Cone-Cylinder Body of Revolution at Mach Number of 3.85. NACA RM E51H17, 1951. (U)

12. Ferri, A.: Supersonic-Tunnel Tests of Projectiles in Germany and Italy. NACA WR L-152, 1945. (U)

13. Delancey, L. M., Jaeger, B. F., and Schroedter, G. M.: The Aerodynamic Characteristics at Mach No. 4.24 of Bodies of Revolution With Varying Lengths and Head Shapes. NOTS TM 358, 1951. (U)

14. Rainey, R. W.: Working Charts for Rapid Prediction of Force and Pressure Coefficients on Arbitrary Bodies of Revolution by Use of Newtonian Concepts. NASA TN D-176, 1959. (U)

15. Jones, J. R., and Demele, F. A.: Aerodynamic Study of a Wing-Fuselage Combination Employing a Wing Swept Back 63^{o} – Characteristics Throughout the Subsonic Speed Range with the Wing Cambered and Twisted for a Uniform Load at a Lift Coefficient of 0.25. NACA RM A9D25, 1949. (U)

16. Jaeger, B. F., and Morgan, A. J. A.: Review of Experiment and Theory Applicable to Cone-Cylinder and Ogive-Cylinder Bodies of Revolution in Supersonic Flow. NAVORD 5239, 1956. (U)

TABLE 4.2.2.2-A
SUBSONIC PITCHING-MOMENT COEFFICIENT
METHOD 2
DATA SUMMARY AND SUBSTANTIATION

Ref	M	R_ℓ (based on d_{equiv})	a/b	$\frac{\ell_B}{d_{equiv}}$	Nose Shape	α (deg)	$C_{m_{calc}}$	$C_{m_{test}}$	ΔC_m
6	0.6	6.5×10^5	1.0	10	Ogive	10	1.7	1.2	0.5
						20	3.4	2.8	0.6
						30	5.2	4.9	0.3
						40	6.4	8.2	−1.8
						50	7.3	10.9	−3.6
						60	7.6	9.7	−1.9
	0.9					10	1.7	1.3	0.4
						20	3.5	3.2	0.3
						30	5.3	7.0	−1.7
						40	6.8	12.5	−5.7
						50	8.1	15.7	−7.6
						60	8.8	14.4	−5.6
	0.6		2.0			10	3.4	2.6	0.8
						20	6.9	6.3	0.6
						30	9.9	14.5	−4.6
						40	12.3	23.1	−11.0
						50	13.9	29.1	−15.3
						60	14.5	29.8	−15.3
	0.9		1.0			10	3.5	2.7	0.8
						20	6.7	8.3	−1.6
						30	10.0	16.7	−6.7
						40	12.9	24.8	−11.9
						50	15.2	29.5	−14.3
						60	16.5	29.0	−12.5
	0.6		0.5			10	0.9	0.4	0.5
						20	1.8	1.3	0.5
						30	2.5	1.7	0.8
						40	3.2	2.5	0.7
						50	3.6	3.5	0.1
						60	3.9	3.3	0.6
	0.9					10	1.0	0.5	0.5
						20	1.7	1.5	0.2
						30	2.6	2.6	0
						40	3.5	5.0	−1.5
						50	4.1	7.5	−3.4

Average Error = $\sum \frac{|\Delta C_m|}{n} = 3.8$

TABLE 4.2.2.2-B

SUPERSONIC PITCHING-MOMENT COEFFICIENT OF OGIVE-CYLINDER BODIES

METHOD 2

DATA SUMMARY AND SUBSTANTIATION

Ref.	M	f_N	f_A	α (deg)	C_m Calc.	C_m Test	e Percent Error
10	1.57	1.12	12.90	4	−.037	−.046	−19.6
	↓	↓	↓	8	−.149	−.116	28.4
	1.86			4	−.035	−.045	−22.2
	↓			8	−.204	−.134	52.2
	2.49			4	−.035	−.032	9.4
	↓			8	−.263	−.246	6.9
	2.87			4	−.043	−.0375	14.7
	↓			8	−.264	−.229	15.3
	1.57	1.50	8.50	4	−.037	−.0311	19.0
	↓	↓	↓	8	−.110	−.0782	40.7
	1.86			4	−.030	−.0385	−22.1
	↓			8	−.140	−.105	33.3
	2.49			4	−.030	−.0225	33.3
	↓			8	−.230	−.193	19.2
	2.87			4	−.040	−.055	−27.3
	↓			8	−.250	−.248	0.8
	1.57	2.50	11.50	4	−.040	−.047	−14.9
	↓	↓	↓	8	−.130	−.126	3.2
	1.86			4	−.045	−.047	− 4.3
	↓			8	−.170	−.143	18.9
	2.49			4	−.050	−.032	56.3
	↓			8	−.270	−.230	17.4
	2.87			4	−.050	−.039	28.2
	↓			8	−.310	−.290	6.9
	1.57	3.00	15.00	4	−.048	−.063	−23.7
	↓	↓	↓	8	−.145	−.147	− 1.4
	2.49			4	−.054	−.0513	5.3
	↓			8	−.325	−.276	17.8
	2.87			4	−.059	−.0647	− 8.8
	↓			8	−.435	−.375	16.0
	1.57	4.00	10.00	4	−.045	−.054	−16.6
	↓	↓	↓	8	−.136	−.140	− 2.9
	1.86			4	−.045	−.0555	−18.9
	↓			8	−.166	−.150	10.7
	2.49			4	−.050	−.0496	0.8
	↓			8	−.259	−.250	3.6
	2.87			4	−.056	−.051	9.8
	↓			8	−.379	−.277	36.8
	1.57	1.12	16.90	4	−.037	−.0517	−28.4
	↓	↓	↓	8	−.190	−.183	3.8
	2.49			4	−.050	−.0592	−15.5
	↓			8	−.340	−.277	22.7
	2.87			4	−.045	−.0554	−18.8
	↓	↓	↓	8	−.349	−.362	− 3.6

$$\text{Average Error} = \frac{\Sigma|e|}{n} = 17.7\%$$

TABLE 4.2.2.2-C

SUPERSONIC PITCHING-MOMENT COEFFICIENT

METHOD 3

DATA SUMMARY AND SUBSTANTIATION

Ref	M	R_ℓ (based on d_{equiv})	a/b	$\frac{\ell_B}{d_{equiv}}$	Nose Shape	α (deg)	$C_{m_{calc}}$	$C_{m_{test}}$	ΔC_m
4	1.5	1.25×10^5	1.0	6	Blunt	35	2.7	1.8	0.9
						65	1.9	1.8	0.1
						95	−0.4	−0.6	0.2
				8	Cone	35	−0.9	−2.0	1.1
						65	−5.2	−4.0	−1.2
						95	−7.4	−7.0	−0.4
						125	−6.6	−8.3	1.7
						155	−2.4	−4.0	1.6
				9		35	−0.9	−2.0	1.1
						65	−7.0	−4.0	−3.0
						95	−10.4	−9.6	−0.8
						125	−9.5	−12.0	2.5
						155	−3.7	−6.2	2.5
				11		35	−0.9	−1.5	0.6
						65	−8.8	−5.0	−3.8
						95	−13.4	−14.0	0.6
						125	−12.5	−16.0	3.5
						165	−2.5	−5.0	2.5
				9	Ogive	35	0.6	0.5	0.1
						65	−4.1	−1.8	−2.3
						95	−7.5	−7.8	0.3
						125	−7.9	−10.5	2.6
						155	−3.6	−5.5	1.9
				7		35	−1.2	−2.0	0.8
						65	−5.4	−4.0	−1.4
						95	−7.3	−7.0	−0.3
						125	−6.3	−7.8	1.5
						155	−2.2	−4.1	1.9
				11		35	−1.4	−1.0	−0.4
						65	−9.5	−5.0	−4.5
						95	−14.0	−15.0	1.0
						125	−12.7	−16.7	4.0
						155	−4.8	−8.7	3.9
	2.86			6	Blunt	35	2.7	0.2	2.5
						65	1.9	0.1	1.8
						95	−0.4	−0.3	−0.1
				8		35	3.6	0.7	2.9
						65	2.6	0.6	2.0
						85	0.5	0.4	0.1

TABLE 4.2.2.2-C (CONTD)

Ref	M	R_ℓ (based on d_{equiv})	a/b	$\frac{\ell_B}{d_{equiv}}$	Nose Shape	α (deg)	$C_{m_{calc}}$	$C_{m_{test}}$	ΔC_m
4	2.86	1.25×10^5	1.0	7	Cone	35	−1.0	−1.8	0.8
						65	−4.3	−4.5	0.2
						95	−6.5	−6.2	−0.3
						125	−5.7	−6.3	0.6
						155	−2.6	−2.2	−0.4
				9		35	−1.0	−1.8	0.8
						65	−5.8	−6.0	0.2
						95	−9.2	−9.0	−0.2
						125	−8.2	−9.3	1.1
						155	−3.9	−3.6	−0.3
				11		35	−1.0	−1.8	0.8
						65	−7.3	−7.5	0.2
						95	−11.9	−11.7	−0.2
						125	−10.8	−12.3	1.5
						155	−5.2	−5.0	−0.2
				9	Ogive	35	0.5	−0.9	1.4
						65	−3.2	−3.9	0.7
						95	−6.7	−6.6	−0.1
						125	−6.9	−7.4	0.5
						155	−3.7	−2.8	−0.9
				7		35	−1.3	−1.4	0.1
						65	−4.5	−4.7	0.2
						95	−6.5	−6.5	0
						125	−5.4	−6.3	0.9
						155	−2.3	−2.5	0.2
				9		35	−1.4	−1.9	0.5
						65	−6.2	−6.4	0.2
						95	−9.4	−9.9	0.5
						125	−8.1	−9.0	0.9
						155	−3.7	−3.5	−0.2
				11		35	−1.5	−2.4	0.9
						65	−7.9	−8.0	0.1
						95	−12.3	−13.6	1.3
						125	−10.9	−12.6	1.7
						155	−5.1	−4.7	−0.4
5	4.24	5.4×10^5	1.0	7	Cone	4	[illegible]4	−0.8	0.4
						8	−1.4	−1.8	0.4
						12	−3.0	−3.2	0.2
						16	−4.8	−4.8	0
						20	−6.5	−6.1	−0.4

TABLE 4.2.2.2-C (CONTD)

Ref	M	R_ℓ (based on d_{equiv})	a/b	$\frac{\ell_B}{d_{equiv}}$	Nose Shape	α (deg)	$C_{m_{calc}}$	$C_{m_{test}}$	ΔC_m
5	4.24	5.4×10^5	1.0	7	Cone	24	−8.5	−7.9	−0.6
	5.04	2.6×10^5		10		4	−0.8	−1.0	0.2
						8	−2.8	−3.1	0.3
						12	−6.0	−4.5	−1.5
						16	−9.0	−7.3	−1.7
						20	−12.4	−9.6	−2.8
						24	−16.5	−12.9	−3.6
					Ogive	4	−0.5	−0.7	0.2
						8	−1.6	−1.7	0.1
						12	−3.1	−2.8	−0.3
						16	−4.6	−4.1	−0.5
	6.28	1.1×10^5			Cone	4	−0.4	−0.6	0.2
						8	−1.5	−1.6	0.1
						12	−2.8	−2.7	−0.1
						16	−4.3	−4.3	0
						20	−6.0	−6.2	0.2
						24	−8.0	−8.5	0.5
6	1.2	3.8×10^5			Ogive	10	1.7	1.6	0.1
						20	3.7	4.2	−0.5
						30	6.1	8.2	−2.1
						40	8.6	10.1	−1.5
						50	10.5	12.0	−1.5
						60	11.5	14.1	−2.6
	1.5					10	1.6	1.8	−0.2
						20	3.9	5.8	−1.9
						30	6.3	7.0	−0.7
						40	8.8	8.3	0.5
						50	10.2	8.9	1.3
						60	10.8	10.8	0
	2.0					10	1.8	2.0	−0.2
						20	4.0	4.1	−0.1
						30	6.5	5.9	0.6
						40	8.3	7.1	1.2
						50	9.5	8.2	1.3
						60	10.1	9.5	0.6
	1.2		2.0			10	3.5	3.4	0.1
						20	7.4	8.3	−0.9
						30	11.6	14.1	−2.5
						40	16.1	17.5	−1.4
						50	19.5	21.6	−2.1

TABLE 4.2.2.2-C (CONTD)

Ref	M	R_ℓ (based on d_{equiv})	a/b	$\frac{\ell_B}{d_{equiv}}$	Nose Shape	α (deg)	$C_{m_{calc}}$	$C_{m_{test}}$	ΔC_m
6	1.2	3.8×10^5	2.0	10	Ogive	60	21.2	23.5	−2.3
	1.5					10	3.5	3.5	0
						20	7.6	8.3	−0.7
						30	12.2	11.4	0.8
						40	16.4	14.5	1.9
						50	18.9	16.1	2.8
						60	19.8	17.5	2.3
	2.0					10	3.5	3.2	0.3
						20	7.6	7.1	0.5
						30	12.5	10.3	2.2
						40	15.6	11.8	3.8
						50	17.6	13.1	4.5
						60	18.6	15.4	3.2
	1.2		0.5			10	0.9	0.9	0
						20	2.0	2.1	−0.1
						30	3.0	4.0	−1.0
						40	4.4	4.5	−0.1
						50	5.2	6.5	−1.3
						60	5.8	8.4	−2.6
	1.5					10	1.0	1.1	−0.1
						20	1.9	2.3	−0.4
						30	3.1	3.7	−0.6
						40	4.4	4.4	0
						50	5.1	5.1	0
						60	5.4	5.4	0
						10	0.8	1.1	−0.3
						20	2.0	2.2	−0.2
						30	3.2	3.2	0
						40	4.1	4.0	0.1
						50	4.8	4.8	0
						60	5.1	4.9	0.2

Average Error = $\sum \frac{|\Delta C_m|}{n} = 1.0$

TABLE 4.2.2.2-D

HYPERSONIC PITCHING-MOMENT COEFFICIENT OF OGIVE-CYLINDER BODIES
METHOD 2
DATA SUMMARY AND SUBSTANTIATION

Ref.	M	f_N	f_A	α (deg)	C_m Calc.	C_m Test	e Percent Error
10	4.24	1.12	8.88	2	−.024	−.021	14.3
				4	−.063	−.060	5.0
				6	−.129	−.130	− 0.8
				8	−.216	−.222	− 2.7
		1.12	12.90	2	−.027	−.026	3.8
				4	−.073	−.071	2.8
				6	−.155	−.146	6.2
				8	−.250	−.255	− 2.0
		1.50	8.50	2	−.029	−.027	7.4
				4	−.070	−.066	6.1
				6	−.146	−.154	− 5.2
				8	−.245	−.239	2.5
		2.50	11.50	2	−.036	−.034	5.9
				4	−.092	−.092	0
				6	−.194	−.175	10.9
				8	−.313	−.296	5.7
		3.00	15.00	2	−.041	−.035	17.1
				4	−.106	−.102	3.9
				6	−.215	−.222	− 3.2
				8	−.332	−.369	−10.0
		3.50	6.50	2	−.034	−.037	−10.8
				4	−.091	−.087	4.6
				6	−.181	−.165	9.7
				8	−.291	−.267	9.0
		4.00	10.00	2	−.039	−.037	5.4
				4	−.102	−.100	2.0
				6	−.201	−.195	3.1
				8	−.335	−.316	6.0
		5.00	5.00	2	− 039	−.041	− 4.9
				4	−.096	−.098	− 2.0
				6	−.187	−.164	14.0
				8	−.311	−.271	14.8
		1.12	16.90	2	−.032	−.036	−11.1
				4	−.092	−.093	− 1.1
				6	−.189	−.170	11.2
				8	−.299	−.262	14.1
		1.50	16.50	2	−.035	−.039	−10.3
				4	−.097	−.101	− 4.0
				6	−.201	−.170	18.2
				8	−.316	−.311	1.6

Average Error = $\frac{\Sigma |e|}{n}$ = 6.8%

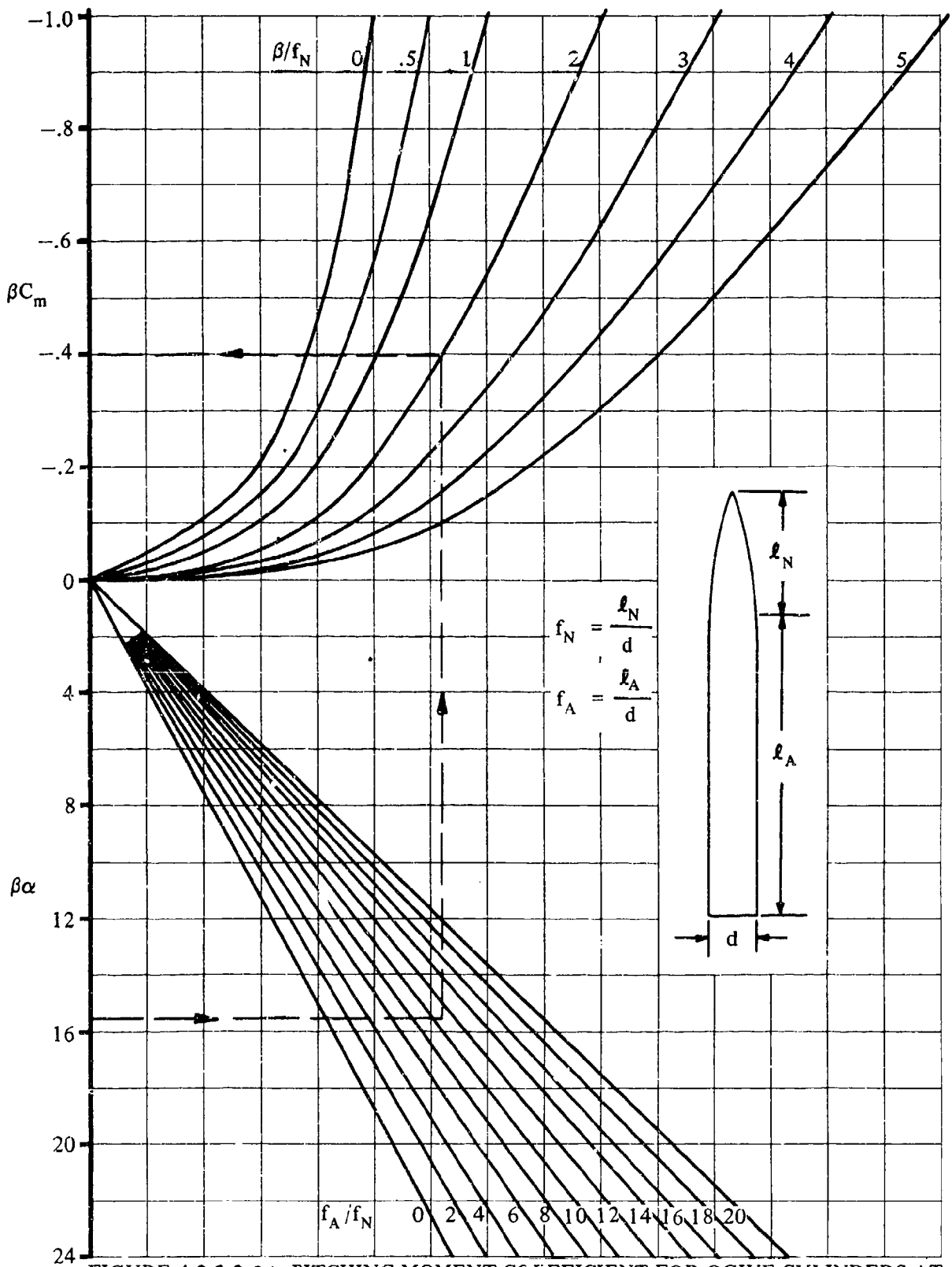

FIGURE 4.2.2.2-26 PITCHING-MOMENT COEFFICIENT FOR OGIVE-CYLINDERS AT SUPERSONIC SPEEDS $1.6 < M < 3.0$

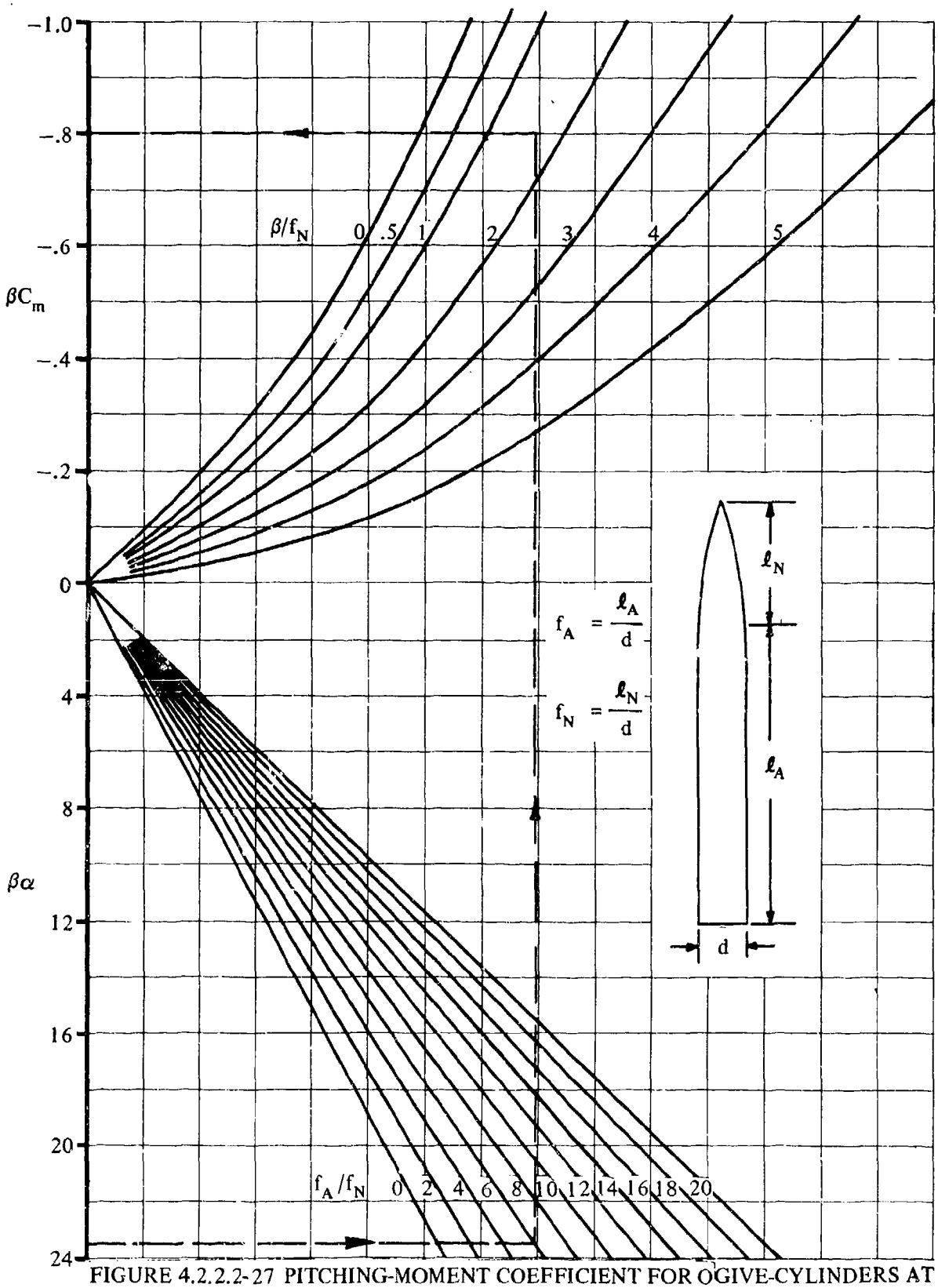

FIGURE 4.2.2.2-27 PITCHING-MOMENT COEFFICIENT FOR OGIVE-CYLINDERS AT HYPERSONIC SPEEDS $3.0 < M < 5.0$

4.2.3 BODY DRAG

4.2.3.1 BODY ZERO-LIFT DRAG

The composition of body zero-lift drag in the various speed regimes is very similar to that for wings (see Section 4.1.5.1). At subsonic speeds the pressure drag of the forebody is generally small and the total drag is composed mostly of skin friction and base drag. For the higher speed regimes the total drag is split significantly between friction and pressure drag.

The methods presented in this section are valid for bodies of revolution. However, excellent approximations can be made for non-body-of-revolution configurations by treating the equivalent body of revolution; that is, the body of revolution that has the same axial area distribution as the actual body.

A. SUBSONIC

At subsonic speeds the total zero-lift drag of smooth slender bodies is primarily skin friction. The Reynolds number based on body length, boundary-layer condition (laminar or turbulent), and surface roughness are important in the determination of the friction drag (see chapter VI of reference 1). For the Datcom these effects are handled the same as for wings (Section 4.1.5.1). A turbulent boundary-layer condition is assumed over the entire body surface.

The pressure drag of a closed body is zero for an inviscid fluid. Actually the displacement of the boundary layer causes an incomplete pressure recovery at the end of the body and a finite pressure drag results. This drag is small for fineness ratios above approximately four but becomes significant for blunt bodies.

The base drag is also generally small, usually less than 10 percent of the total body drag. The most popular approach to the estimation of base drag is to correlate it with the skin-friction drag of the remainder of the body. This approach is discussed in detail in reference 2 and in chapter VI of reference 1. Reference 3 shows that the presence of a wing increases the base pressure (less drag). Tail fins and wind-tunnel stings have the same effect (reference 4). Base pressures are also increased at low Reynolds numbers (reference 5).

DATCOM METHOD

The subsonic zero-lift drag of an isolated body based on the maximum body frontal area is given in reference 6 as

$$C_{D_0} = C_f \left[1 + \frac{60}{(\ell_B/d)^3} + 0.0025 \left(\frac{\ell_B}{d}\right) \right] \frac{S_S}{S_B} + C_{D_b} \qquad 4.2.3.1\text{-a}$$

where the first term on the right-hand side of the equation is the zero-lift drag of the body exclusive of the base drag, and

C_f is the turbulent flat-plate skin-friction coefficient, including roughness effects, as a function of Mach number and the Reynolds number based on the reference length ℓ. This value is obtained from figure 4.1.5.1-26 and is determined as discussed in paragraph A of Section 4.1.5.1. The reference length ℓ is the actual length of the body ℓ_B.

$\frac{\ell_B}{d}$ is the body fineness ratio defined for different types of bodies of revolution as follows:

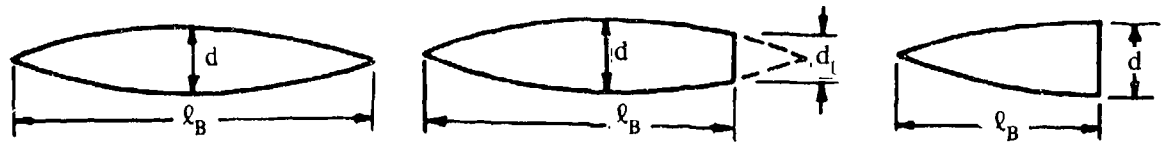

CLOSED BODY BODY HAVING A BLUNT BASE FOREBODY

For non-body-of-revolution configurations the equivalent diameter should be used,

$$d_{equiv} = \sqrt{\frac{\text{cross-sectional area}}{0.7854}}$$

C_{D_b} is the base-drag coefficient, based on the maximum body frontal area, given in reference 1 as

$$C_{D_b} = 0.029 \left(\frac{d_b}{d}\right)^3 \Big/ \sqrt{\left(C_{D_f}\right)_b} \qquad 4.2.3.1\text{-b}$$

where

$\frac{d_b}{d}$ is the ratio of base diameter to maximum diameter (equivalent diameters for non-body-of-revolution configurations).

$\left(C_{D_f}\right)_b$ is the zero-lift drag of the body exclusive of the base as determined by the first term in equation 4.2.3.1-a.

It should be noted that wings or fins (or wind-tunnel stings) can have a sizable effect on base drag.

S_B is the body maximum frontal area.

S_S is the wetted area or surface area of the body excluding the base area. This is normally determined by graphical integration of $\int_0^{\ell_B} p\,dx$, where p is the cross-section perimeter.

The ratio S_S/S_B for a given body can be approximated by using figures 2.3-2 and 2.3-3, which give this ratio for a number of specific body shapes.

The term $0.0025 \frac{\ell_B}{d}$ in equation 4.2.3.1-a represents the pressure-drag contribution.

Sample Problem

Given: The body of reference 54 having an elliptical cross section with a cutoff afterbody.

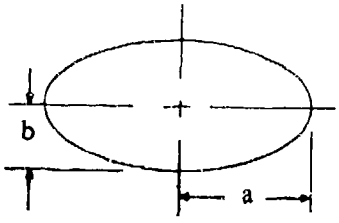

BODY CROSS SECTION
a/b = 3

ℓ_B = 61.45 in. a_{max} = 5.19 in. b_{max} = 1.73 in.

$S_b = 0.25\ S_B$

M = 0.8 $R_\ell = 0.325 \times 10^6$ per in.

Polished metal surface; assume $k = 0.08 \times 10^{-3}$ in.

Compute:

$S_B = \pi ab = \pi(5.19)(1.73) = 28.2$ sq in.

$d_{equiv} = \sqrt{\frac{S_B}{0.7854}} = \sqrt{\frac{28.2}{0.7854}} = 6.0$ in.

$\frac{\ell_B}{d} = \frac{61.45}{6.0} = 10.24$

$\frac{S_S}{S_B} = 31.6$ (extrapolated from figure 2.3-2, ellipsoid with cutoff afterbody)

$R_\ell = (0.325 \times 10^6)(\ell_B) = (0.325 \times 10^6)(61.45) = 1.997 \times 10^7$

$\ell/k = 61.45/(0.08 \times 10^{-3}) = 7.68 \times 10^5$; cutoff $R_\ell = 6.8 \times 10^7$ (figure 4.1.5.1-27)

Since cutoff R_ℓ > calculated R_ℓ, read C_f at calculated R_ℓ.

$C_f = 0.00256$ (figure 4.1.5.1-26)

Determine the zero-lift drag of the body exclusive of base drag.

$$\left(C_{D_f}\right)_b = C_f \left[1 + \frac{60}{(\ell_B/d)^3} + 0.0025\left(\frac{\ell_B}{d}\right)\right]\frac{S_S}{S_B} = 0.00256\left[1 + \frac{60}{(10.24)^3} + 0.0025\,(10.24)\right] 31.6$$

$= 0.0875$ (based on S_B)

$S_b = 0.25\, S_B = (0.25)(28.2) = 7.05$ sq in.

$(d_b)_{equiv} = \sqrt{\frac{S_b}{0.7854}} = \sqrt{\frac{7.05}{0.7854}} = 3.0$ in.

$\frac{d_b}{d} = \frac{3.0}{6.0} = 0.5$

Determine the base drag

$$C_{D_b} = 0.029\left(\frac{d_b}{d}\right)^3 \Big/ \sqrt{\left(C_{D_f}\right)_b} \quad \text{(equation 4.2.3.1-b)}$$

$= 0.029\,(0.5)^3 \,/\, \sqrt{0.0875}$

$= 0.0122$ (based on S_B)

Solution:

$$C_{D_0} = C_f \left[1 + \frac{60}{(\ell_B/d)^3} + 0.0025\left(\frac{\ell_B}{d}\right)\right]\frac{S_S}{S_B} + C_{D_b} \quad \text{(equation 4.2.3.1-a)}$$

$$= 0.0875 + 0.0122$$

$$= 0.0997 \text{ (based on } S_B\text{)}$$

This compares with a test value of 0.0920 from reference 54.

B. TRANSONIC

A fundamental discussion of the transonic aerodynamic characteristics of bodies is given in reference 7 and chapter XVI of reference 1. An extensive bibliography on finned bodies is given in reference 8.

For the Datcom, the general approach consists of predicting the skin friction, the drag-divergence Mach number, and the variation of base drag with Mach number, and the variation of pressure drag for Mach numbers above 1.0. The total drag characteristic as a function of Mach number is then constructed from these estimated characteristics. For the purpose of the Datcom the skin-friction drag is assumed to be constant and equal to the subsonic value at M = 0.6 throughout the transonic range.

DATCOM METHOD

The transonic zero-lift drag coefficient of a body is determined by the following procedure.

Step 1. Calculate the skin-friction drag coefficient at M = 0.6, based on maximum frontal area, by

$$C_{D_f} = C_f \frac{S_S}{S_B} \qquad 4.2.3.1\text{-c}$$

where

C_f is the turbulent flat-plate skin-friction coefficient at M = 0.6, including roughness effects, as a function of the Reynolds number based on the reference length ℓ. This value is obtained from figure 4.1.5.1-26 as discussed in paragraph A of Section 4.1.5.1. The reference length ℓ is the actual length of the body ℓ_B. This value is assumed to be constant throughout the transonic region.

$\frac{S_S}{S_B}$ is the ratio of body wetted area to maximum body frontal area, determined as explained in paragraph A of this section.

Step 2. Calculate the subsonic pressure drag at M = 0.6 by

$$C_{D_P} = (C_f)_{M=0.6}\left[\frac{60}{(\ell_B/d)^3} + 0.0025\left(\frac{\ell_B}{d}\right)\right]\frac{S_S}{S_B} \qquad 4.2.3.1\text{-d}$$

where the individual terms are the same as in equation 4.2.3.1-a. This component of drag is assumed to be constant for $0 < M < 1.0$ and to decrease linearly to zero at $M = 1.2$. (See sketch (a).)

Step 3. Calculate the base-drag coefficient C_{D_b} as a function of Mach number. First calculate the subsonic base drag (at a Mach number of 0.6) as outlined in paragraph A. Figure 4.2.3.1-24 is then used as a guide to determine the base-drag variation with Mach number through the transonic speed range. The chart is based upon the data of references 4 and 9 through 12.

Step 4. The drag-divergence Mach number M_D is obtained from figure 4.2.3.1-25 as a function of body fineness ratio (reference 13). The drag-divergence Mach number is that Mach number at which $\partial C_D / \partial M = 0.10$, and it defines the break in the drag coefficient versus Mach number curve.

Step 5. The wave-drag coefficient C_{D_w} (for parabolic bodies of revolution) is obtained from figure 4.2.3.1-26 as a function of body fineness ratio for Mach numbers between 1.0 and 1.2 (reference 13). Unfortunately, data on other body shapes are extremely limited, and the construction of general charts is not possible at this time. However, for body profiles not too different from parabolic, figure 4.2.3.1-26 can be used as an approximation.

Step 6. The total zero-lift drag is constructed by combining the information of the above steps as illustrated in sketch (a).

$$C_{D_0} = C_{D_f} + C_{D_p} + C_{D_b} + C_{D_w} \qquad \text{4.2.3.1-e}$$

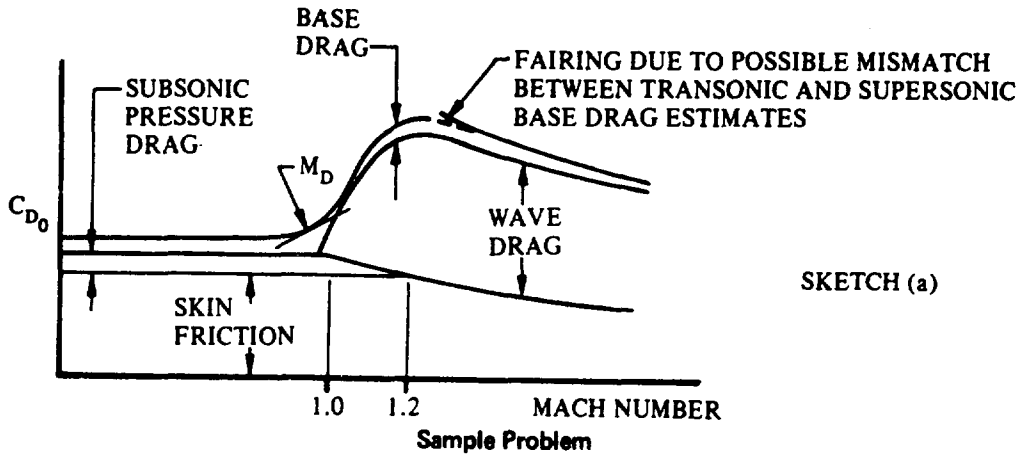

SKETCH (a)

Sample Problem

Given: The parabolic-arc body of revolution with a cutoff afterbody (reference 54).

$\ell_B = 61.45$ in. $\quad d = 6.0$ in. $\quad \ell_B/d = 10.24$ $\quad S_B = 28.2$ sq in.

$S_S/S_B = 30.5$ $\quad d_b/d = 0.50$

$R_{\ell_{M=0.6}} = 1.997 \times 10^7$ (based on ℓ_B)

Polished metal surface; assume $k = 0.08 \times 10^{-3}$ in.

Compute:

The final calculations are presented in table form on page 4.2.3.1-7. Many of the quantities listed below appear as columns in the table.

Skin-friction drag coefficient C_{D_f}

$\ell/k = 61.45/(0.08 \times 10^{-3}) = 7.68 \times 10^5$; cutoff $R_{\ell_{M=0.6}} \approx 6.2 \times 10^7$ (figure 4.1.5.1-27)

Since cutoff R_ℓ > given R_ℓ, read C_f at given R_ℓ.

$C_f = 0.0026$ (figure 4.1.5.1-26 @ M = 0.6)

$$C_{D_f} = C_f \frac{S_S}{S_B} \quad \text{(equation 4.2.3.1-c)}$$

$$= 0.0026\,(30.5) = 0.0793$$

Pressure-drag coefficient C_{D_P}

$$C_{D_P} = (C_f)_{M=0.6} \left[\frac{60}{(\ell_B/d)^3} + 0.0025 \left(\frac{\ell_B}{d} \right) \right] \frac{S_S}{S_B} \quad \text{(equation 4.2.3.1-d)}$$

$$= 0.0026 \left[\frac{60}{(10.24)^3} + 0.0025\,(10.24) \right] 30.5$$

$$= 0.00642$$

This value of C_{D_P} is taken to be constant for $0 < M < 1.0$, then reduced linearly to zero at M = 1.2 (see column (4) of calculation table, page 4.2.3.1-7).

Base-drag coefficient C_{D_b}

$$\left(C_{D_b}\right)_{M=0.8} = 0.029 \left(\frac{d_b}{d} \right)^3 \Big/ \sqrt{\left(C_{D_f}\right)_b} \quad \text{(equation 4.2.3.1-b)}$$

$$\left(C_{D_f}\right)_b = (C_f)_{M=0.6} \left[1 + \frac{60}{(\ell_B/d)^3} + 0.0025 \left(\frac{\ell_B}{d} \right) \right] \frac{S_S}{S_B} \quad \text{(first term, eq. 4.2.3.1-a)}$$

$$= (C_f)_{M=0.6} \frac{S_S}{S_B} + C_{D_P}$$

$$= (0.0026)(30.5) + 0.00642 = 0.0857$$

$$C_{D_b} = (0.029)(0.5)^3 / \sqrt{0.0857} = 0.0124$$

$$\left[\frac{C_{D_b}}{\left(\frac{d_b}{d}\right)^2}\right] = \frac{0.0124}{(0.5)^2} = 0.0496$$

With this value and by using the curves of figure 4.2.3.1-24 as guide lines, obtain values of $\frac{C_{D_b}}{(d_b/d)^2}$ for $0.8 < M < 1.2$. Then $C_{D_b} = \left[\frac{C_{D_b}}{(d_b/d)^2}\right] (d_b/d)^2$ (See columns ⑤ and ⑥ of calculation table, page 4.2.3.1-7.)

Drag-Divergence Mach number M_D

$M_D = 0.982$ (figure 4.2.3.1-25)

Wave-drag coefficient C_{D_w}

The wave-drag coefficient as a f(M) is obtained from figure 4.2.3.1-26) (See column ⑦ of calculation table, page 4.2.3.1-7.)

Solution:

$C_{D_0} = C_{D_f} + C_{D_P} + C_{D_b} + C_{D_w}$ (equation 4.2.3.1-e)

① ② ③ ④ ⑤ ⑥ ⑦ ⑧

M	C_f	C_{D_f} eq. 4.2.3.1-c ② S_S/S_B	C_{D_P}	$\frac{C_{D_b}}{(d_b/d)^2}$ fig. 4.2.3.1-24	C_{D_b} ⑤ $(d_b/d)^2$	C_{D_w} fig. 4.2.3.1-26	C_{D_0} eq. 4.2.3.1-e ③+④+⑥+⑦
0.8	0.0026	0.0793	0.00642	0.0496	0.0124	–	0.0981
0.9			0.00642	0.06	0.0150	–	0.1007
0.95			0.00642	0.075	0.0188	–	0.1045
1.00			0.00642	0.115	0.0288	0.0395	0.1540
1.025			0.00662	0.088	0.0220	0.0580	0.1649
1.05			0.00480	0.065	0.0162	0.0650	0.1653
1.10			0.00320	0.038	0.0095	0.0730	0.1650
1.20			0	0.035	0.0088	0.0770	0.1651

The sample problem results are plotted in sketch (b) along with test values from reference 54.

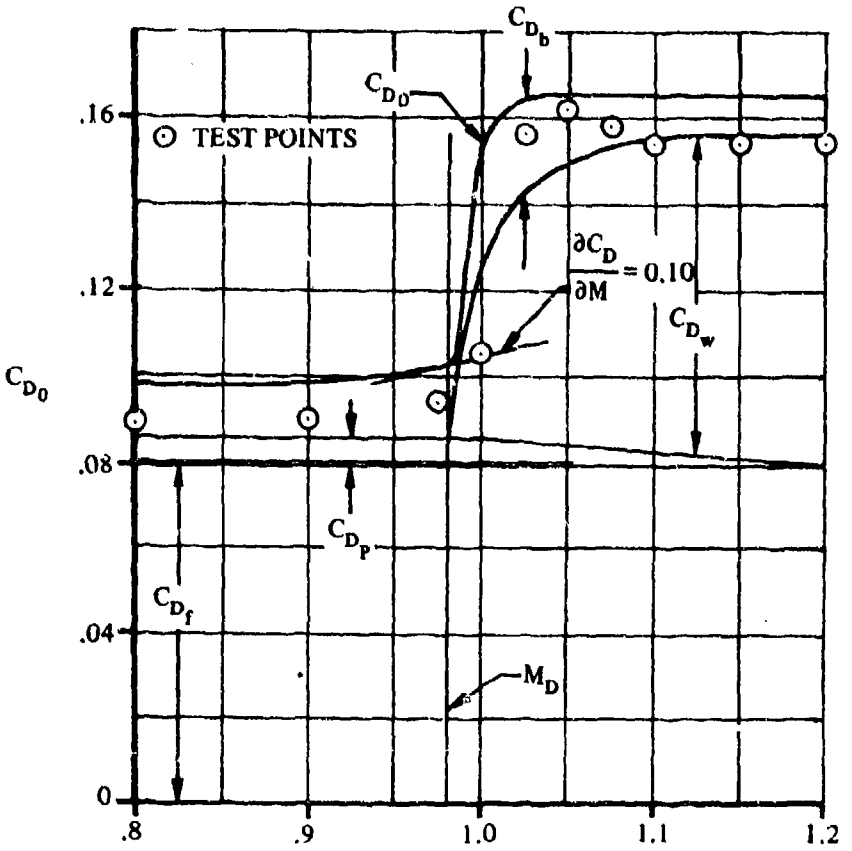

SKETCH (b)

C. SUPERSONIC

The characteristics of compressible skin-friction drag for bodies are similar to those for wings (see paragraph C of Section 4.1.5.1). The skin-friction coefficient decreases with Mach number at constant Reynolds number, and is a function of the ratio of the wall temperature to the free-stream temperature. For the Datcom, zero heat-transfer conditions are assumed; i.e., stabilized flight conditions are assumed. The friction drag for transient flight lies between the incompressible value and the zero heat-transfer value. Another important consideration for estimating the skin-friction drag at supersonic speeds is the Reynolds-number variation throughout the flight regime. The design chart used in the Datcom method is that of Section 4.1.5.1, which presents the turbulent skin-friction coefficient on an insulated flat plate as a function of Mach number and Reynolds number.

Many theoretical solutions are available for estimating the wave drag of the forebody and afterbody. Reference 14 contains an excellent summary of various theories compared to test data. Ten theories are discussed in this reference. It is seen that second-order shock-expansion theory gives the best over-all agreement with data. Many of the theories are seen to give gross errors over certain ranges of the similarity parameters.

Two methods of estimating the forebody and afterbody wave drag are presented in detail in this section. The first is developed in reference 15 and is based on slender-body theory. The second method is based on similarity parameters and is taken from reference 14. For both methods the wave drag is separated into the

forebody drag, the isolated afterbody drag (afterbody preceded by an infinite cylinder), and the interference drag of the forebody and center (cylindrical) section on the afterbody. Charts are presented for forebody and afterbody drag coefficients of straight-element profiles (cones) and parabolic profiles, and for predicting interference-drag coefficients for conical profiles, pointed parabolic profiles, ducted conical profiles, and truncated afterbodies behind pointed parabolic forebodies. Comprehensive charts based on test data giving the effects of nose bluntness are also presented for the first method.

The first method is applicable to both open-nosed and closed-nosed bodies of revolution. The design charts of the second method for predicting the wave-drag coefficient of the nose are restricted to closed-nosed bodies of revolution. Therefore, the second method is restricted accordingly.

A sizable quantity of data on supersonic base drag exists. Charts derived from test data and theory are presented for a wide range of geometric parameters. For the higher supersonic Mach numbers, theory has been used, and at the lower Mach numbers, empirical results have been used. It should be pointed out that the estimation of the afterbody drag of a body cannot necessarily be accomplished independent of the base. The lambda shock which exists near the end of the body separates the boundary layer over the rear portion of the boattail and thus changes both the base pressure and the pressure loading of the boattail. These effects are included in the base-drag charts presented but are not included in the afterbody charts.

DATCOM METHODS

Method 1. Slender-Body Theory

The zero-lift drag coefficient of open-nosed or closed-nosed bodies of revolution, based on the maximum frontal area, is given by

$$C_{D_0} = C_f \frac{S_S}{S_B} + C_{D_{N_2}} + C_{D_A} + C_{D_{A\,(NC)}} + C_{D_{N_1}} + C_{D_b} \qquad 4.2.3.1\text{-f}$$

where

C_f is the turbulent flat-plate skin-friction coefficient, including roughness effects, as a function of Mach number and the Reynolds number based on the reference length ℓ. This value is obtained from figure 4.1.5.1-26 as discussed in paragraph A of Section 4.1.5.1. The reference length ℓ is the total length of the body ℓ_B.

$\frac{S_S}{S_B}$ is the ratio of body wetted area to maximum body frontal area, determined as outlined in paragraph A of this section.

$C_{D_{N_2}}$ and C_{D_A} are the wave-drag coefficients (reference 15) based on maximum frontal area of the nose and afterbody, respectively. Figure 4.2.3.1-27 is for parabolic profile shapes of circular cross section. Figure 4.2.3.1-28 is for conical profile shapes of circular cross section. A drag value obtained from these charts is the drag acting on the oblique surface and does not include the forces acting on the front or rear faces. The external drag of open-nosed bodies can thus be determined.

The wave-drag coefficients of the nose and afterbody of parabolic and conical profile shapes with noncircular cross sections may be approximated by using a forebody or afterbody of circular cross section and of the same area distribution (equivalent body of revolution). In this case values of a and d to be used in figures 4.2.3.1-27 and 4.2.3.1-28 are the equivalent diameters defined as $\sqrt{\frac{\text{cross-sectional area}}{0.7854}}$.

A more exact estimation of $C_{D_{N_2}}$ and C_{D_A} may be made for parabolic and conical profile shapes with elliptic cross sections by using figure 4.2.3.1-29. This figure presents the decrease in wave-drag coefficient, based on maximum frontal area, from the value for the equivalent body of circular cross section to that for a body of elliptic cross section. The wave-drag coefficient of the equivalent body of circular cross section is first obtained from either figure 4.2.3.1-27 or figure 4.2.3.1-28 by using the equivalent diameters. This value is then reduced by the appropriate value of $\Delta C_{D_{N_2}}$ or ΔC_{D_A} obtained from figure 4.2.3.1-29.

$C_{D_{N_1}}$ is the wave-drag coefficient of spherically blunted noses. The extended fineness ratio of the nose is first determined from figures 4.2.3.1-30 and 4.2.3.1-31 for parabolic and conical noses, respectively. This value is then used to determine the wave drag of the spherical nose segment. Figures 4.2.3.1-32a through 4.2.3.1-32f are for combinations of spherical and parabolic noses. Figures 4.2.3.1-38a through 4.2.3.1-38f are for combinations of spherical and conical noses. These latter charts are based on experimental data of references 17 through 27. When interpolation is necessary, several values should be plotted to provide the correct nonlinear variation. Figures 4.2.3.1-30, -31, -32, and -38 are for noses of circular cross section. For noses with noncircular cross sections $C_{D_{N_1}}$ may be approximated by using a nose of circular cross section and of the same area distribution. In this case the values of the equivalent diameters and the fineness ratios based on the equivalent diameters are used in the design charts.

$C_{D_{A\,(NC)}}$ is the interference-drag coefficient acting on the afterbody due to the centerbody (cylindrical section) and the nose. This coefficient is obtained from figure 4.2.3.1-44 for parabolic profiles, from figure 4.2.3.1-46 for conical profiles, and from figure 4.2.3.1-48 for ducted conical profiles (reference 15). For bodies of noncircular cross section the interference drag coefficient may be approximated by using a body of circular cross section and of the same area distribution. In this case the equivalent diameters are used in the design charts.

C_{D_b} is the base-drag coefficient given by

$$C_{D_b} = -C_{P_b}\left(\frac{d_b}{d}\right)^2 \qquad 4.2.3.1\text{-g}$$

where

C_{P_b} is the base-pressure coefficient from figures 4.2.3.1-50 and 4.2.3.1-55 for ogival and conical boattails of circular cross section, respectively. (Although figure 4.2.3.1-50 is derived for ogive boattails, references 28 through 31, it can be applied to parabolic afterbodies if the ratio d_b/d is not small. Actually, if the ratio is small, the magnitude of the base drag would be such as to minimize the importance of large percentage errors.)

$\frac{d_b}{d}$ is the ratio of the base diameter to the maximum body diameter.

For bodies of noncircular cross section the equivalent diameters should be used in the design charts and in equation 4.2.3.1-g.

For bodies of revolution with no boattail the base-drag coefficient is read directly from figure 4.2.3.1-60.

Method 2. Similarity Parameters

An alternate method based on the correlation of test data by using similarity parameters is presented below. The zero-lift drag coefficient of closed-nosed bodies of revolution, based on the maximum frontal area, is given by

$$C_{D_0} = C_f \frac{S_S}{S_B} + C_{D_{N_2}} + C_{D_A} + C_{D_{A\,(NC)}} + C_{D_{N_1}} + C_{D_b} \qquad 4.2.3.1\text{-h}$$

where C_f, S_S/S_B, $C_{D_{A\,(NC)}}$, $C_{D_{N_1}}$, and C_{D_b} are determined as in method 1, and

$C_{D_{N_2}}$ is the zero-lift wave-drag coefficient of the nose obtained from figure 4.2.3.1-61 or 4.2.3.1-62, which are for ogival- and conical-profile noses of circular cross section, respectively. The K_N factor used in figure 4.2.3.1-61 is given in figure 4.2.3.1-63. The chart for cones is based on references 32 through 37 and the chart for ogive noses is based on references 18, 35, and 38 through 40. Slender-body theory and Newtonian theory have also been used. These charts are discussed and substantiated in reference 14.

C_{D_A} is the zero-lift wave-drag coefficient of the afterbody from figure 4.2.3.1-64 or 4.2.3.1-65, which are for ogival and conical afterbodies with circular cross sections, respectively. These charts are based on Van Dyke's second-order theory and the data of reference 41 and are discussed and substantiated in reference 14.

For bodies with noncircular cross sections the component contributions should be based on the equivalent body of circular cross section.

It should be noted that the design charts presented for $C_{D_{N_2}}$ in method 2 are restricted to closed-nosed bodies of revolution.

Sample Problems

1. Method 1. Slender-Body Theory

Given: A cone-cylinder body with the following characteristics (reference 41):

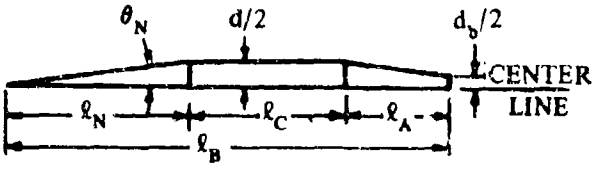

ℓ_B = 129.1 in. $\quad \ell_1 = \ell_N$ = 53.8 in.

$\ell_2 = \ell_C$ = 45.0 in. $\quad \ell_3 = \ell_A$ = 30.3 in.

d = 7.50 in. $\quad d_b$ = 3.28 in.

S_S/S_B = 50.0 $\quad \theta_N = 4^\circ$

Additional characteristics:

M = 1.4; β = 0.980 $\quad R_\ell = 7.6 \times 10^7$ (based on ℓ_B)

Polished metal surface; assume $k = 0.08 \times 10^{-3}$ in.

Compute:

$$\ell/k = \frac{129.1}{0.08 \times 10^{-3}} = 1.61 \times 10^{6}; \text{ cutoff } R_\ell = 2 \times 10^{8} \qquad \text{(figure 4.1.5.1-27)}$$

Since cutoff $R_\ell > 7.6 \times 10^{7}$, read C_f at $R_\ell = 7.6 \times 10^{7}$

$C_f = 0.00192$ (figure 4.1.5.1-26)

Forebody

$$\left(\frac{a_1}{d_1}\right)^2 = 0; \quad \frac{2\ell_1}{\beta d_1} = \frac{2(53.8)}{(0.98)(7.50)} = 14.6$$

$$\left(\frac{2\ell_1}{d_1}\right)^2 = \left[\frac{2(53.8)}{7.50}\right]^2 = 205.8$$

$$C_{D_{N_2}}\left(\frac{2\ell_1}{d_1}\right)^2 = 5.5 \qquad \text{(figure 4.2.3.1-28, extrapolated)}$$

$$C_{D_{N_2}} = (5.5)/(205.8) = 0.0267$$

$C_{D_{N_1}} = 0$ (no bluntness)

Afterbody

$$\left(\frac{a_3}{d_3}\right)^2 = \left(\frac{3.28}{7.50}\right)^2 = 0.191; \quad \frac{2\ell_3}{\beta d_3} = \frac{2(30.3)}{(0.98)(7.50)} = 8.24$$

$$\left(\frac{2\ell_3}{d_3}\right)^2 = \left[\frac{2\,(30.3)}{7.50}\right]^2 = 65.29$$

$$C_{D_A}\left(\frac{2\ell_3}{d_3}\right)^2 = 2.10 \qquad \text{(figure 4.2.3.1-28)}$$

$$C_{D_A} = (2.10)/(65.29) = 0.0322$$

$$\ell_C/\ell_A = \ell_2/\ell_3 = (45)/(30.3) = 1.48$$

$$\ell_N/\ell_A = \ell_1/\ell_3 = (53.8)/(30.3) = 1.78$$

$$C_{D_{A(NC)}}\left(\frac{2\ell_3}{d_3}\right)^2 = 0.27 \quad \text{(figures 4.2.3.1-46b and -46c, interpolated)}$$

$$C_{D_{A(NC)}} = (0.27)/(65.29) = 0.0041$$

$d_b/d = (3.28)/(7.50) = 0.437$; $f_A = \ell_A/d = 30.3/7.50 = 4.04$

$C_{P_b} = -0.055$ (figure 4.2.3.1-55c)

$$C_{D_b} = -C_{P_b}\left(\frac{d_b}{d}\right)^2 \quad \text{(equation 4.2.3.1-g)}$$

$$= -(-0.055)(0.437)^2 = 0.0105$$

Solution:

$$C_{D_0} = C_f\frac{S_S}{S_B} + C_{D_{N_2}} + C_{D_A} + C_{D_{A(NC)}} + C_{D_{N_1}} + C_{D_b} \quad \text{(equation 4.2.3.1-f)}$$

$$= (0.00192)(50.0) + (0.0267) + (0.0322) + (0.0041) + 0 + 0.0105$$

$$= 0.1695 \quad \text{(based on } S_B\text{)}$$

This corresponds to an experimental value of 0.153 from reference 41.

2. Method 1. Slender-Body Theory

Given: The same cone-cylinder body as sample problem 1, except that the nose is spherically blunted.

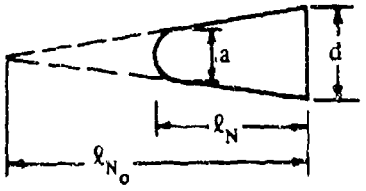

$\frac{a}{d} = \frac{d_s}{d_o} = 0.60$ $\quad \ell_{N_o} = 53.8$ in.

$d = d_o = 7.50$ in. $\quad \ell_N = 24.0$ in.

$\frac{S_S}{S_B} = 45.8$ $\quad \ell_B = 99.3$ in.

$M = 1.40$; $\beta = 0.98$ $\quad R_{\ell} = 5.85 \times 10^7$ (based on ℓ_B)

Polished metal surface; assume $k = 0.08 \times 10^{-3}$ in.

$C_{D_A} = 0.0322$

$C_{D_{A(NC)}} = 0.0041$

$C_{D_b} = 0.0105$

} Afterbody drag components from sample problem 1

Compute:

$$\ell/k = \frac{99.3}{0.08 \times 10^{-3}} = 1.24 \times 10^{6};\ \text{cutoff } R_\ell \simeq 1.60 \times 10^{8} \qquad \text{(figure 4.1.5.1-27)}$$

Since cutoff $R_\ell > 5.85 \times 10^{7}$, read C_f at $R_\ell = 5.85 \times 10^{7}$

$C_f = 0.0020$ (figure 4.1.5.1-26)

Forebody.

$$\left(\frac{a}{d}\right)^2 = 0.36;\ \frac{2\ell_N}{\beta d} = \frac{2\,(24)}{(0.98)\,(7.50)} = 6.53$$

$$\left(\frac{2\ell_N}{d}\right)^2 = \left[\frac{2(24)}{7.50}\right]^2 = 40.96$$

$$C_{D_{N_2}}\left(\frac{2\ell_N}{d}\right)^2 = 1.16 \qquad \text{(figure 4.2.3.1-28)}$$

$$C_{D_{N_2}} = (1.16)/(40.96) = 0.0283$$

$$f_{N_o} = \ell_{N_o}/d_o = (53.8)/(7.50) = 7.17$$

$C_{D_{N_1}} = 0.200$ (figures 4.2.3.1-38a, -38b, -38c; interpolated)

Solution:

$$C_{D_0} = C_f \frac{S_S}{S_B} + C_{D_{N_2}} + C_{D_A} + C_{D_{A(NC)}} + C_{D_{N_1}} + C_{D_b} \qquad \text{(equation 4.2.3.1-f)}$$

$$= (0.0020)\,(45.8) + 0.0283 + 0.0322 + 0.0041 + 0.200 + 0.0105$$

$$= 0.3667 \quad \text{(based on } S_B\text{)}$$

3. Method 2. Similarity Parameters

Given: The same cone-cylinder body as sample problem 1.

$f_N = 7.17$ $f_A = 4.04$ $d_b/d = 0.437$ $\theta_N = 4^{\circ}$ $M = 1.4;\ \beta = 0.98$

$R_\ell = 7.6 \times 10^{7}$ (based on ℓ_B)

Drag components from sample problem 1:

$$C_f \frac{S_S}{S_B} = 0.0960 \qquad C_{D_{A(NC)}} = 0.0041 \qquad C_{D_{N_1}} = 0 \qquad C_{D_b} = 0.0105$$

Compute:

Forebody

$$\beta/f_N = (0.98)/(7.17) = 0.137$$

$$f_N^2 + \frac{1}{4} = (7.17)^2 + \frac{1}{4} = 51.66$$

$$C_{D_{N_2}} \left[(f_N)^2 + \frac{1}{4}\right] = 1.45 \quad \text{(figure 4.2.3.1-62)}$$

$$C_{D_{N_2}} = (1.45)/(51.66) = 0.0280$$

Afterbody

$$f_A^2 = (4.04)^2 = 16.32; \quad \beta/f_A = (0.98)/(4.04) = 0.243$$

$$C_{D_A} (f_A)^2 = 0.53 \quad \text{(figure 4.2.3.1-65)}$$

$$C_{D_A} = (0.53)/(16.32) = 0.0325$$

Solution:

$$C_{D_0} = C_f \frac{S_S}{S_B} + C_{D_{N_2}} + C_{D_A} + C_{D_{A(NC)}} + C_{D_{N_1}} + C_{D_b} \quad \text{(equation 4.2.3.1-h)}$$

$$= 0.0960 + 0.0280 + 0.0325 + 0.0041 + 0 + 0.0105$$

$$= 0.1711 \quad \text{(based on } S_B\text{)}$$

This corresponds to a calculated value of 0.1695 obtained using method 1, and to an experimental value of 0.153 from reference 41.

D. HYPERSONIC

At hypersonic speeds the zero-lift drag of a body is caused primarily by the pressure and friction drag of the nose. The base drag decreases and becomes insignificant at the higher Mach numbers (see figures 4.2.3.1-50, 4.2.3.1-55, and 4.2.3.1-60).

High-speed turbulent skin-friction values are not well defined at the present time. A theory that has had wide acceptance is that of reference 42. The limited experimental data (e.g., reference 43) substantiate this theory reasonably well.

Figures 4.2.3.1-66 and 4.2.3.1-67 are based upon Newtonian impact values at $M \to \infty$ and should give reasonable results for bodies at these speeds. The charts of reference 44 give the drag of bodies of revolution composed of cone frustums and spherical noses based on Newtonian flow. A similar set of charts is contained in reference 45. A more comprehensive set of charts based on Newtonian flow is available in reference 46 for arbitrary bodies of revolution.

DATCOM METHODS

Method 1. Hypersonic Similarity

The method described as method 2 of paragraph C can be used at hypersonic Mach numbers, but with the body skin-friction drag coefficient calculated as outlined in method 2 that follows (see equation 4.2.3.1-j).

Method 2. Newtonian Flow Plus Skin Friction

The zero-lift drag (based on the maximum frontal area) of bodies composed of cone-cylinder frustums and pointed or spherical noses is estimated by adding the pressure-drag coefficient of each segment to the body skin-friction drag coefficient.

$$C_{D_0} = C_{D_f} + \sum_{n=1}^{m} C_{D_{P_n}} \left(\frac{d_n}{d_{max}}\right)^2 \qquad 4.2.3.1\text{-i}$$

The procedure to be followed in evaluating equation 4.2.3.1-i is:

Step 1 Divide the body into m segments, the first segment being the pointed conical or spherical nose and each succeeding segment a cylinder or circular cone frustum. The pressure-drag coefficient for a spherical nose is obtained from figure 4.2.3.1-66. The pressure-drag coefficient of a pointed conical nose, cylinder, or circular cone frustum is obtained from figure 4.2.3.1-67. (Note that the cylinder is considered as a cone frustum with $\theta = 0$ and $a/d = 1.0$, and that the pressure-drag coefficient is zero by Newtonian impact theory.) Figures 4.2.3.1-66 and 4.2.3.1-67 are from reference 44, and are based on Newtonian impact theory. The pressure-drag coefficients from figures 4.2.3.1-66 and 4.2.3.1-67 are based on the base area of the specific segment. The ratio $(d_n/d_{max})^2$ refers the pressure-drag coefficients to the maximum body frontal area.

Step 2 Obtain the body skin-friction drag coefficient by

$$C_{D_f} = 1.02\, C_{f_{inc}} \frac{C_{f_c}}{C_f} \frac{S_S}{S_B} \qquad 4.2.3.1\text{-j}$$

where

$C_{f_{inc}}$ is the incompressible (M = 0), turbulent, flat-plate skin-friction coefficient, including roughness effects, as a function of Reynolds number based on the total length of the body ℓ_B. This value is obtained from figure 4.1.5.1-26 as discussed in paragraph A of Section 4.1.5.1.

$\frac{C_{f_c}}{C_f}$ is the ratio of compressible to incompressible skin-friction coefficient obtained from figure 4.2.3.1-68.

$\frac{S_S}{S_B}$ is the ratio of the body wetted area to maximum body frontal area, determined as outlined in paragraph A of this section.

If method 2 is applied at Mach numbers low enough so that the base drag is significant, the base drag should be added to the results obtained using equation 4.2.3.1-j. Unfortunately, the only base-drag coefficient results available which are compatible with the Newtonian-theory results (restricted to bodies with forward facing slopes or cylinders, in which case the Newtonian results are equal to zero) are those for cylindrical afterbodies. The pressure-drag coefficient for cylindrical afterbodies is presented in figure 4.2.3.1-60 for $M \leq 6$.

Sample Problem

Method 2. Newtonian Flow Plus Skin Friction

Given: A body with the following configuration (reference 54):

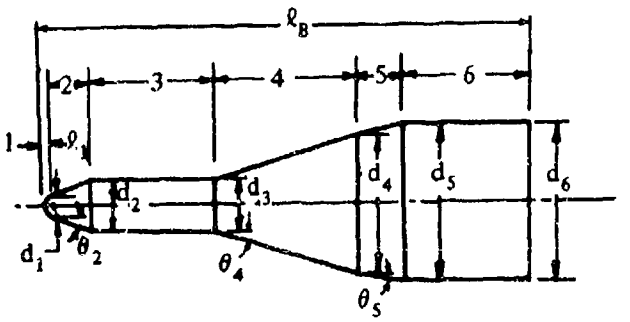

Segment 1: Spherical nose

ℓ_1 = 0.29 in. $d_1 = d_s$ = 0.58 in.

Segment 2: Cone frustum

θ_2 = 20° $a_2 = d_1$ = 0.58 in.

d_2 = 1.50 in.

Segment 3: Cylinder

θ_3 = 0 $a_3 = d_2$=1.50 in.

d_3 = 1.50 in.

Segment 4: Cone frustum

θ_4 = 16.5° $a_4 = d_3$ = 1.50 in.

d_4 = 4.10 in.

Segment 5: Cone frustum

θ_5 = 10.4° $a_5 = d_4$ = 4.10 in.

d_5 = 4.50 in.

Segment 6: Cylinder

θ_6 = 0 $a_6 = d_5$ = 4.50 in.

d_6 = 4.50 in.

Additional characteristics:

S_S/S_B = 8.14 ℓ_B = 14.4 in. M = 4.65 R_ℓ = 7.63×10^6 (based on ℓ_B)

Polished metal surface; assume $k = 0.08 \times 10^{-3}$ in.

Compute:

Determine C_{D_p} of the body segments

Segment 1

$\ell_1/(d_1/2) = (0.29)/(0.58/2) = 1.0$

$C_{D_{p_1}} = 1.0$ (figure 4.2.3.1-66)

Segment 2

$a_2/d_2 = (0.58)/(1.50) = 0.387$

$C_{D_{p_2}} = 0.200$ (figure 4.2.3.1-67)

Segment 3

$a_3/d_3 = (1.50)/(1.50) = 1.0$

$C_{D_{p_3}} = 0$ (figure 4.2.3.1-67)

Segment 4

$a_4/d_4 = (1.50)/(4.10) = 0.366$

$C_{D_{p_4}} = 0.138$ (figure 4.2.3.1-67)

Segment 5

$a_5/d_5 = (4.10)/(4.50) = 0.911$

$C_{D_{p_5}} = 0.010$ (figure 4.2.3.1-67)

Segment 6

$a_6/d_6 = (4.50)/(4.50) = 1.0$

$C_{D_{p_6}} = 0$ (figure 4.2.3.1-67)

Determine the skin-friction drag coefficient C_{D_f}

$\ell/k = 14.4/(0.08 \times 10^{-3}) = 0.18 \times 10^6$; cutoff $R_\ell \simeq 7.5 \times 10^7$ (figure 4.1.5.1-27 at M = 0)

Since cutoff $R_\ell > 7.63 \times 10^6$, read C_f at $R_\ell = 7.63 \times 10^6$

$C_f = 0.00314$ (figure 4.1.5.1-26 at M = 0)

$C_{f_c}/C_f = 0.44$ (figure 4.2.3.1-68)

$$C_{D_f} = 1.02\, C_{f_{inc}} \frac{C_{f_c}}{C_f} \frac{S_S}{S_B} \quad \text{(equation 4.2.3.1-j)}$$

$$= (1.02)(0.00314)(0.44)(8.14) = 0.0115$$

Solution:

$$C_{D_0} = C_{D_f} + \sum_{s=n}^{m} C_{D_{p_n}} \left(\frac{d_n}{d_{max}}\right)^2 \quad \text{(equation 4.2.3.1-i)}$$

$$= C_{D_f} + C_{D_{p_1}} \left(\frac{d_1}{d_6}\right)^2 + C_{D_{p_2}} \left(\frac{d_2}{d_6}\right)^2 + C_{D_{p_3}} \left(\frac{d_3}{d_6}\right)^2 + C_{D_{p_4}} \left(\frac{d_4}{d_6}\right)^2 + C_{D_{p_5}} \left(\frac{d_5}{d_6}\right)^2 + C_{D_{p_6}} \left(\frac{d_6}{d_6}\right)^2$$

$$= 0.0115 + (1.0)\left(\frac{0.58}{4.50}\right)^2 + (0.200)\left(\frac{1.50}{4.50}\right)^2 + 0 + (0.138)\left(\frac{4.10}{4.50}\right)^2 + (0.010)\left(\frac{4.50}{4.50}\right)^2 + 0$$

$$= 0.175 \quad \text{(based on } S_B\text{)}$$

The Mach number of this example is low enough so that the base drag is significant. The base drag coefficient is obtained from figure 4.2.3.1-60 as

$C_{D_b} = 0.055$ (based on S_B)

So, the final result is

$C_{D_0} = C_{D_f} + C_{D_p} + C_{D_b} = 2.30$ (based on S_B)

This result compares favorably with the test value shown in reference 54.

E. RAREFIED GAS

In the discussions of aerodynamic properties presented previously, it has been assumed that the air behaves as a continuous fluid; whereas, at the very low densities encountered at extreme altitudes the actual molecular structure of the air will become important.

By accepted definition (reference 47) a rarefied gas flow is a flow in which the length of the molecular mean free path is comparable to some significant dimension of the flow field. The ratio of these two lengths is called the Knudsen number. If the characteristic length is chosen to be the body dimension used in the definition of Reynolds number, then the Knudsen number can be shown to be given approximately by

$$Kn \approx M/R_{\ell}$$

By the definition given above, the flow can be considered as rarefied if $Kn > 1$. If the flow is very rarefied, say $Kn > 3$ (reference 47) then individual gas molecules strike the surface of the body without interacting with surrounding gas molecules; this flow regime is called free-molecule flow. Between the regime of free-molecule flow and that of continuous gas dynamics (where $Kn \approx 10^{-4}$ or 10^{-5}) lies a large transition region that is not yet clearly defined as to its characteristics.

It is apparent that, if $Kn = 3$ defines the limit for the free-molecule flow regime, the aerodynamics of bodies in this type of flow is of interest only in its application to satellite studies. A Knudsen number of three corresponds to an altitude of roughly 100 miles, if the reference length used is only one foot, with increasing altitude for larger reference dimensions. It seems unlikely that anything resembling a full-size aircraft will attempt to utilize the tenuous atmosphere at these extreme altitudes for a useful purpose without flying at essentially orbital speeds. It is not possible to make any clearcut statements regarding the transition regime. The region likely to be of most interest in aircraft and missile work is that where the flow is just slightly rarefied, that is, where the continuous flow equations are just beginning to become questionable. This is called the slip-flow regime. In the slip-flow regime either the Mach number is large or the Reynolds number is small, by continuum standards. Analysis of the slip-flow regime is difficult, because its characteristics are likely to be masked by compressibility and viscosity effects.

An excellent discussion is presented by Hayes and Probstein (reference 48) concerning the validity of continuum theory as applied to rarefied gas flow. It is concluded that, when properly applied, continuum gas dynamics and viscous flow theory can be useful far into the regime of what is normally considered the domain of kinetic theory.

At the other end of the spectrum, free-molecule flow theory is important for several problems dealing with satellites. Since satellites generally operate in the free-molecule flow regime, it is necessary to estimate the drag coefficient under these conditions in order to predict the perturbations and decay of the orbit, and to use satellite measurements to estimate atmospheric density.

There are many analyses in the literature on the lift and drag of bodies in free-molecule flow (references 47, 49, 50, and 51), since the problem is amenable to analytical solution. In the discussion of reference 47, expressions for the local pressure and shear forces are given in general form, so that these forces can be computed for any type of interaction of the atmospheric molecules with the body surface. At the present, very little is known of the nature of this interaction, and more research is required to establish the type of interaction that may be expected in a specific problem.

Jastrow and Pearse (reference 52) have discussed an additional drag that arises in the flight of a body through a medium containing ions and electrons, as in the ionosphere. The satellite tends to acquire a negative equilibrium electrostatic potential. As a result, atmospheric ions that would otherwise have missed the satellite are drawn into collisions with it, thus increasing the drag.

Integrated drag forces for the simple shapes of the cylinder and sphere are given in reference 47. These data are shown in figure 4.2.3.1-69 for the simplified case in which the surface temperature is equal to the ambient temperature, and for the extremes of specular and fully diffuse reflection.

REFERENCES

1. Hoerner, S.F.: Fluid-Dynamic Drag. Published by Author, 1958. (U)

2. Kurzweg, H.H.: Interrelationship Between Boundary Layer and Base Pressure. Jour. Aero. Sci., Vol. 18, No. 11, Nov. 1951. (U)

3. Morrow, J.D., and Nelson, R.L.: Large-Scale Flight Measurements of Zero-Lift Drag of 10 Wing-Body Configurations at Mach Numbers from 0.8 to 1.6. NACA RM L52D18a, 1953. (U)

4. Hart, R.G.: Effects of Stabilizing Fins and a Rear-Support Sting on the Base Pressures of a Body of Revolution in Free Flight at Mach Numbers from 0.7 to 1.3. NACA RM L52E06, 1952. (U)

5. Chapman, D.R.: An Analysis of Base Pressure at Supersonic Velocities and Comparison with Experiment. NACA TN 2137, 1950. (U)

6. Blakesles, D.J., Johnson, R.P., and Skavdahl, H.: A General Representation of the Subsonic Lift-Drag Relation for an Arbitrary Airplane Configuration. Rand RM 1593, 1955. (U)

7. Spreiter, J.R.: Aerodynamics of Wings and Bodies at Transonic Speeds. Jour. Aero. Sci., Vol. 26, No. 8, August 1959. (U)

8. Stoney, W.E., Jr.: Collection of Zero-Lift Drag Data on Bodies of Revolution from Free-Flight Investigations. NACA TN 4201, 1958. (U)

9. Kelly, T.C.: Transonic Wind-Tunnel Investigation of the Effects of Body Indentation for Boattail and Cylindrical Afterbody Shapes on the Aerodynamic Characteristics of an Unswept-Wing-Body Combination. NACA RM L54A08, 1954. (U)

10. Morgan, F.G., Jr., and Carmel, M.M.: Transonic Wind-Tunnel Investigation of the Effects of Taper Ratio, Body Indentation, Fixed Transition, and Afterbody Shape on the Aerodynamic Characteristics of a 45° Sweptback Wing-Body Combination. NACA RM L54A15, 1954. (U)

11. Katz, E., and Stoney, W.E., Jr.: Base Pressures Measured on Several Parabolic-Arc Bodies of Revolution in Free Flight at Mach Numbers from 0.8 to 1.4 and at Large Reynolds Numbers. NACA RM L51F29, 1951. (U)

12. Peck, R.F.: Flight Measurements of Base Pressure on Bodies of Revolution With and Without Simulated Rocket Chambers. NACA RM L50I28a, 1950. (U)

13. Gollos, W.W.: Transonic and Supersonic Pressure Drag for a Family of Parabolic Type Fuselages at Zero Angle of Attack. Rand Report RM 982, 1952. (C) Title Unclassified

14. Morris, D.N.: A Summary of the Supersonic Pressure Drag of Bodies of Revolution. Jour. Aero. Sci., Vol. 28, No. 7, July 1961. (U)

15. Fraenkel, L.E.: The Theoretical Wave Drag of Some Bodies of Revolution. RAE Aero 2420, 1951. (U)

16. Fraenkel, L.E.: Supersonic Flow Past Slender Bodies of Elliptic Cross-Section. ARC R&M 2954, 1955. (U)

17. Moeckel, W.E.: Experimental Investigation of Supersonic Flow with Detached Shock Waves for Mach Numbers Between 1.8 and 2.9. NACA RM E50D06, 1950. (U)

18. Sommer, S.C., and Stark, J.A.: The Effect of Bluntness on the Drag of Spherical-Tipped Truncated Cones of Fineness Ratio 3 at Mach Numbers 1.2 to 7.4. NACA RM A52B13, 1952. (U)

19. Hart, R.E.: Flight Investigation of the Drag of Round-Nosed Bodies of Revolution at Mach Numbers from 0.6 to 1.5 Using Rocket-Propelled Test Vehicles. NACA RM L51E25, 1951. (U)

20. Anon.: The Drag Coefficient of Very High Velocity Spheres. New Mexico School of Mines, Research and Development Division, Oct. 1949. (U)

21. Chauvin, L.T.: Pressure Distribution and Pressure Drag for a Hemispherical Nose at Mach Numbers 2.05, 2.54, and 3.04. NACA RM L52K06, 1952. (U)

22. Wood, G.P., and Gooderum, P.B.: Method of Determining Initial Tangents of Contours of Flow Variables Behind a Curved, Axially Symmetric Shock Wave. NACA TN 2411, 1951. (U)

23 Winkler, E.M., and Danberg, J.E.: Heat Transfer Characteristics of a Hemispheric Cylinder at Hypersonic Mach Numbers. IAS Preprint 622, Jan. 1956. (U)

24. Stine, H.A., and Wanlass, K.: Theoretical and Experimental Investigation of Aerodynamic-Heating and Isothermal Heat-Transfer Parameters on a Hemispherical Nose with Laminar Boundary Layer at Supersonic Mach Numbers. NACA TN 3344, 1954. (U)

25. Crawford, D.H., and McCauley, W.D.: Investigation of the Laminar Aerodynamic Heat-Transfer Characteristics of a Hemisphere-Cylinder in the Langley 11-Inch Hypersonic Tunnel at a Mach Number of 6.8. NACA TN 3706, 1956. (U)

26. Korobkin, I.: Local Flow Conditions, Recovery Factors and Heat Transfer Coefficients on the Nose of a Hemispheric Cylinder at a Mach Number of 2.8. Navord 2865, May 1953. (U)

27. Ferri, A.: The Influence of Reynolds Numbers at High Mach Numbers. (Abstract) p. 623. Jour. Roy. Aero. Soc., Nov. 1943. (U)

28. Seiff, A., et al: Aerodynamic Characteristics of Bodies at Supersonic Speeds. NACA RM A51J25, 1951. (U)

29. Love, E.S.: The Base Pressure at Supersonic Speeds on Two-Dimensional Airfoils and Bodies of Revolution (With and Without Fins) Having Turbulent Boundary Layers. NACA RM L53C02, 1953. (U)

30. Cubbage, J.M., Jr.: Jet Effects on Base and Afterbody Pressures of a Cylindrical Afterbody at Transonic Speeds. NACA RM L56C21, 1956. (U)

31. Piland, R.O.: Drag Measurements on a 1/6-Scale, Finless, Sting-Mounted NACA RM-10 Missile in Flight at Mach Numbers from 1.1 to 4.04 Showing Some Reynolds Number and Heating Effects. NACA RM L54H09, 1954. (U)

32. Solomon, G.E.: Transonic Flow Past Cone Cylinders. NACA TN 3213, 1954. (U)

33. Seiff, A., and Sommer, S.C.: Experimental Investigation of the Drag of 30°, 60°, and 90° Cone Cylinders at Mach Numbers Between 1.5 and 8.2. NACA RM A52A14b, 1952. (U)

34. Drougge, G.: The Flow Around Conical Tips in the Upper Transonic Range. The Aeronautical Research Institute of Sweden Report No. 25, 1948. (U)

35. Stoney, W.E., Jr.: Transonic Drag Measurements of Eight Body-Nose Shapes. NACA RM L53K17, 1954. (U)

36. Mauersberg, J.D., Thomas, R.E., Ward, V.G., and Von Eschen, G.L.: Blockage and Interference Effects of a Cone-Cylinder Model at Mach Numbers from 0.80 to 1.30. OSU Research Foundation Report SR-4, Jan. 1955. (U)

37. Yoshihara, H.: On the Flow Over a Cone-Cylinder Body at Mach Number One. WADC TR-52-295, 1952. (U)

38. Hieser, G., Henderson, J.H., and Swihart, J.M.: Transonic Aerodynamic and Loads Characteristics of a 4-Percent-Thick Unswept-Wing-Fuselage Combination. NACA RM L54B24, 1954. (U)

39. Johnston, J.F., and Lopatoff, M.: Study by NACA Wing-Flow Method of Transonic Drag Characteristics of a Blunt-Nose Body of Revolution and Comparison with Results for a Sharp-Nose Body. NACA RM L9C11, 1949. (U)

40. Gray, J.D.: Transonic Interference Effects Upon Lift and Drag Measurements in a Slotted Test Section. AEDC-TR-54-47, 1955. (U)

41. Jack, J.R.: Theoretical Pressure Distributions and Wave Drags for Conical Boattails. NACA TN 2972, 1953. (U)

42. VanDriest, E.R.: Turbulent Boundary Layer with Variable Prandtl Numbers. NAA AL 1914, 1951. (U)

43. Sommer, S.C., and Short, B.J.: Free-Flight Measurements of Turbulent-Boundary-Layer Skin Friction in the Presence of Severe Aerodynamic Heating at Mach Numbers from 2.8 to 7.0. NACA TN 3391, 1955. (U)

44. Fisher, L.R.: Equations and Charts for Determining the Hypersonic Stability Derivatives of Combinations of Cone Frustums Computed by Newtonian Impact Theory. NACA TN D-149, 1959. (U)

45. Gray, J.D.: Drag and Stability Derivatives of Missile Components According to the Modified Newtonian Theory. AEDC-TN-60-191, 1960. (U)

46. Rainey, R.W.: Working Charts for Rapid Prediction of Force and Pressure Coefficients on Arbitrary Bodies of Revolution by Use of Newtonian Concepts. NACA TN D-176, 1959. (U)

47. Schaaf, S.A., and Chambre, P.L.: Flow of Rarefied Gases; Section H of Fundamentals of Gas Dynamics; Vol. III of High Speed Aerodynamics and Jet Propulsion: Princeton University Press, 1958. (U)

48. Hayes, W.D., and Probstein, R.F.: Hypersonic Flow Theory. Academic Press, 1959. (U)

49. Stalder, J.R., and Zurick, V.J.: Theoretical Aerodynamic Characteristics of Bodies in a Free Molecule Flow Field. NACA TN 2423, 1951. (U)

50. Ashley, H.: Applications of the Theory of Free Molecule Flow to Aeronautics. Jour. Aero. Sci., Vol. 16, No. 2, Feb. 1949. (U)

51. Schamberg, R.: A New Analytic Representation of Surface Interaction for Hyperthermal Free-Molecule Flow with Application to Neutral-Particle Drag Estimates of Satellites. The Rand Corporation RM 2313, 1959. (U)

52. Jastrow, R., and Pearse, C.A.: Atmospheric Drag on the Satellite. Jour. of Geophysical Research, Vol. 62, No. 3, Sept. 1957. (U)

53. McDevitt, J.B., and Taylor, R.A.: Force and Pressure Measurements at Transonic Speeds for Several Bodies Having Elliptical Cross Sections. NACA TN 4362, 1958. (U)

54. Lust, R.M.: Investigation of the Static Longitudinal Stability Characteristics of a Model of an Intermediate-Range Ballistic Missile at Mach Numbers Between 1.57 and 4.65. NASA TM X-289, 1960. (C) Title Unclassified.

55. Welsh, C.J., and deMorses, C.A.: Results of Flight Tests to Determine Drag of Parabolic and Cone-Cylinder Bodies of Very Large Fineness Ratios at Supersonic Speeds. NACA RM L51E18, 1951. (U)

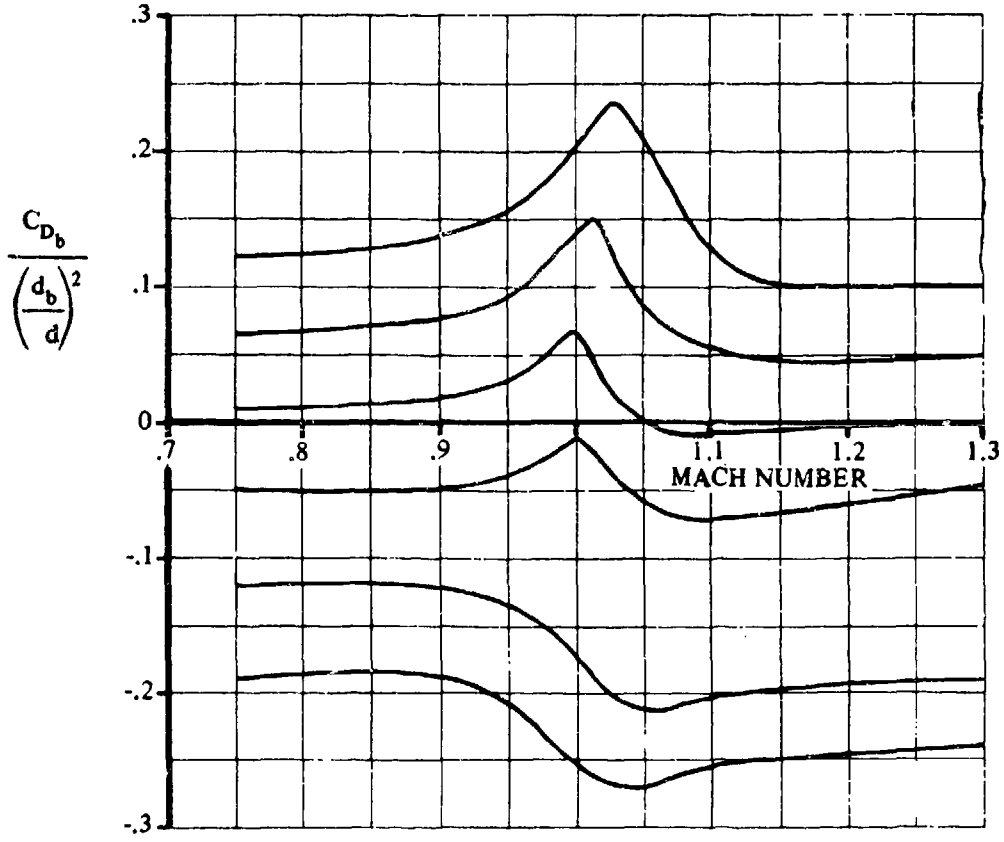

FIGURE 4.2.3.1-24 TRANSONIC FAIRING FOR BASE-PRESSURE COEFFICIENT

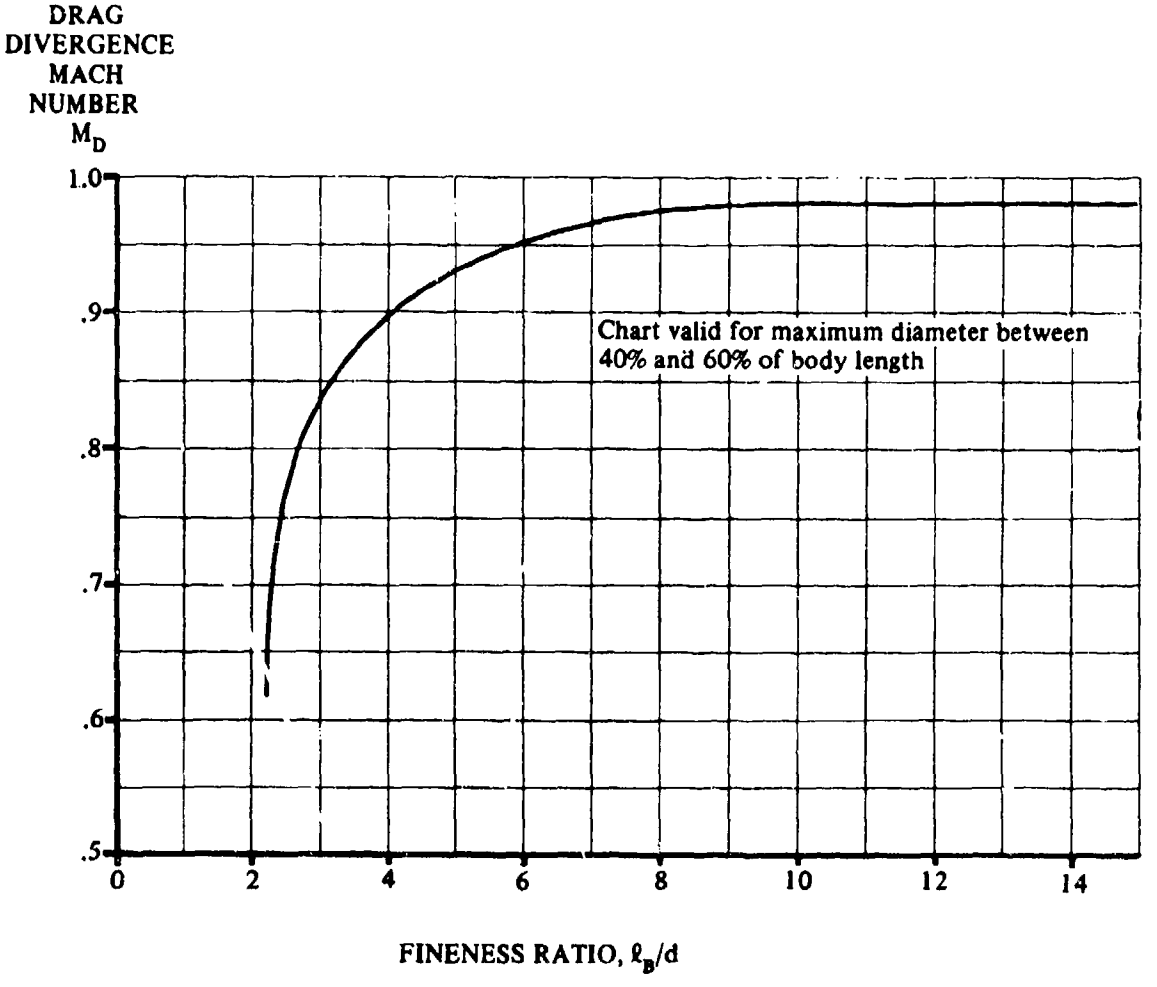

FIGURE 4.2.3.1-25 DRAG-DIVERGENCE MACH NUMBER FOR CLOSED-NOSED BODIES

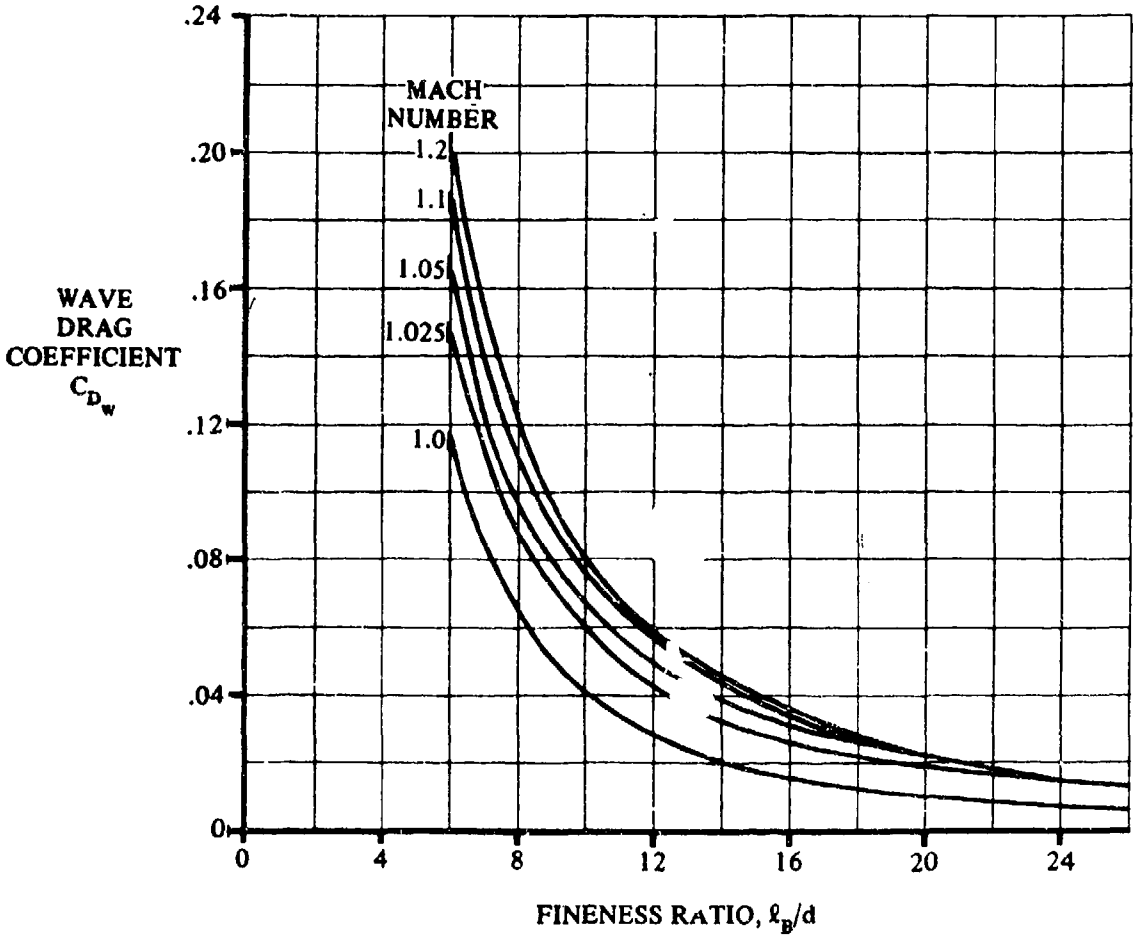

FIGURE 4.2.3.1-26 WAVE DRAG FOR PARABOLIC-TYPE FUSELAGE

Note:

a is the nose diameter of forebody or base diameter of afterbody

d is the maximum diameter of forebody or afterbody

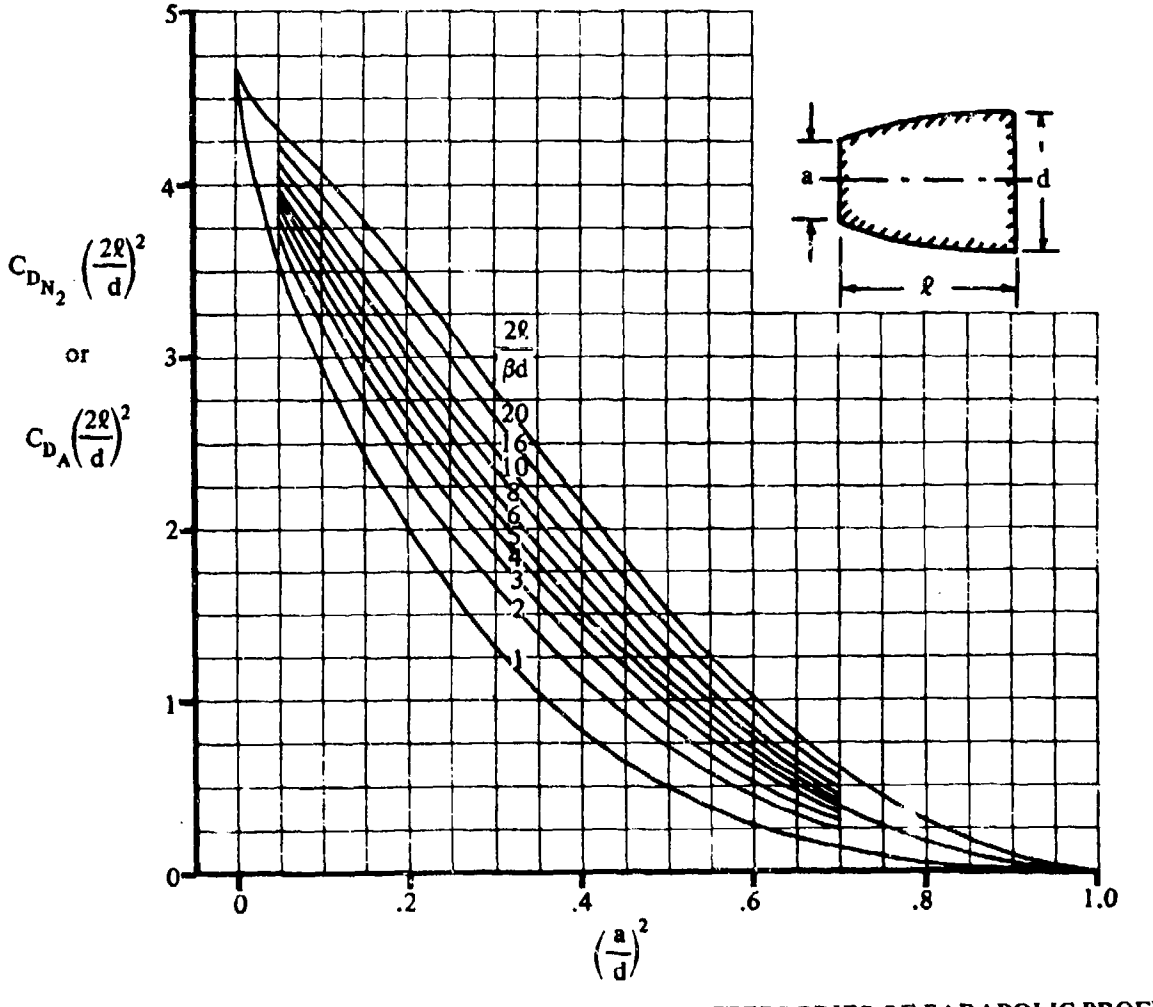

FIGURE 4.2.3.1-27 DRAG OF (SLENDER) FOREBODIES OR AFTERBODIES OF PARABOLIC PROFILE

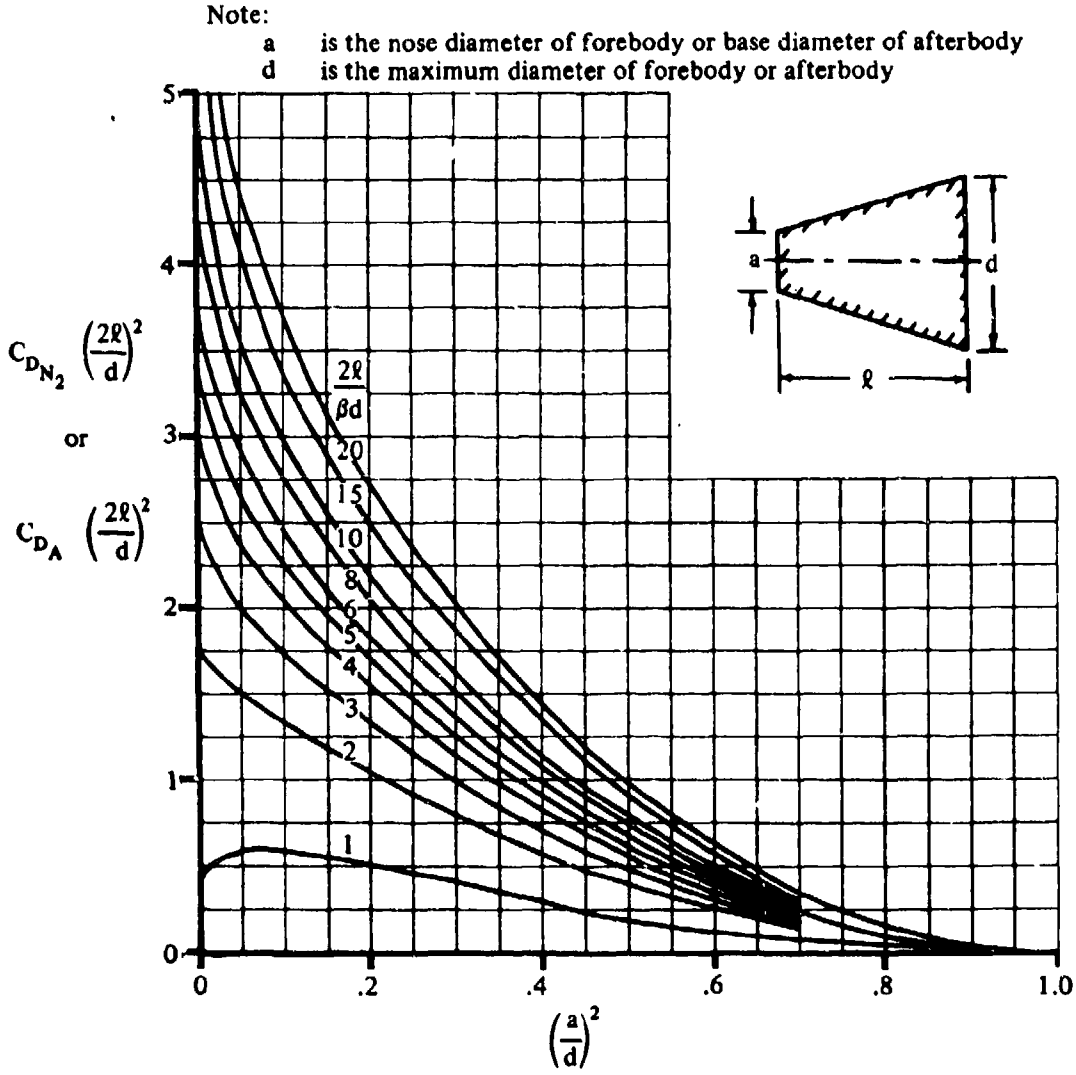

FIGURE 4.2.3.1-28 DRAG OF (SLENDER) CONICAL FOREBODIES OR AFTERBODIES

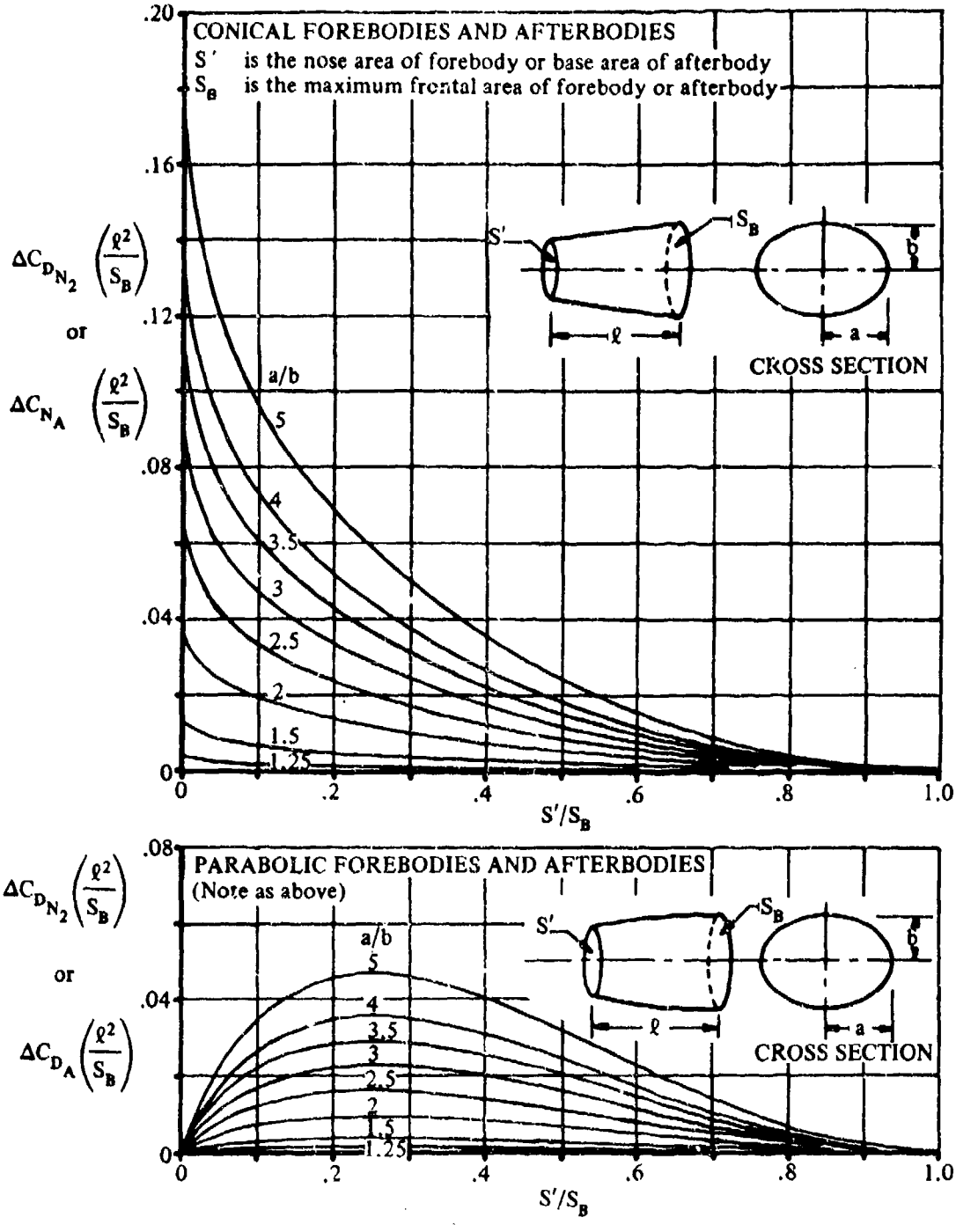

FIGURE 4.2.3.1-29 REDUCTION IN WAVE-DRAG COEFFICIENT DUE TO NONCIRCULAR CROSS SECTION

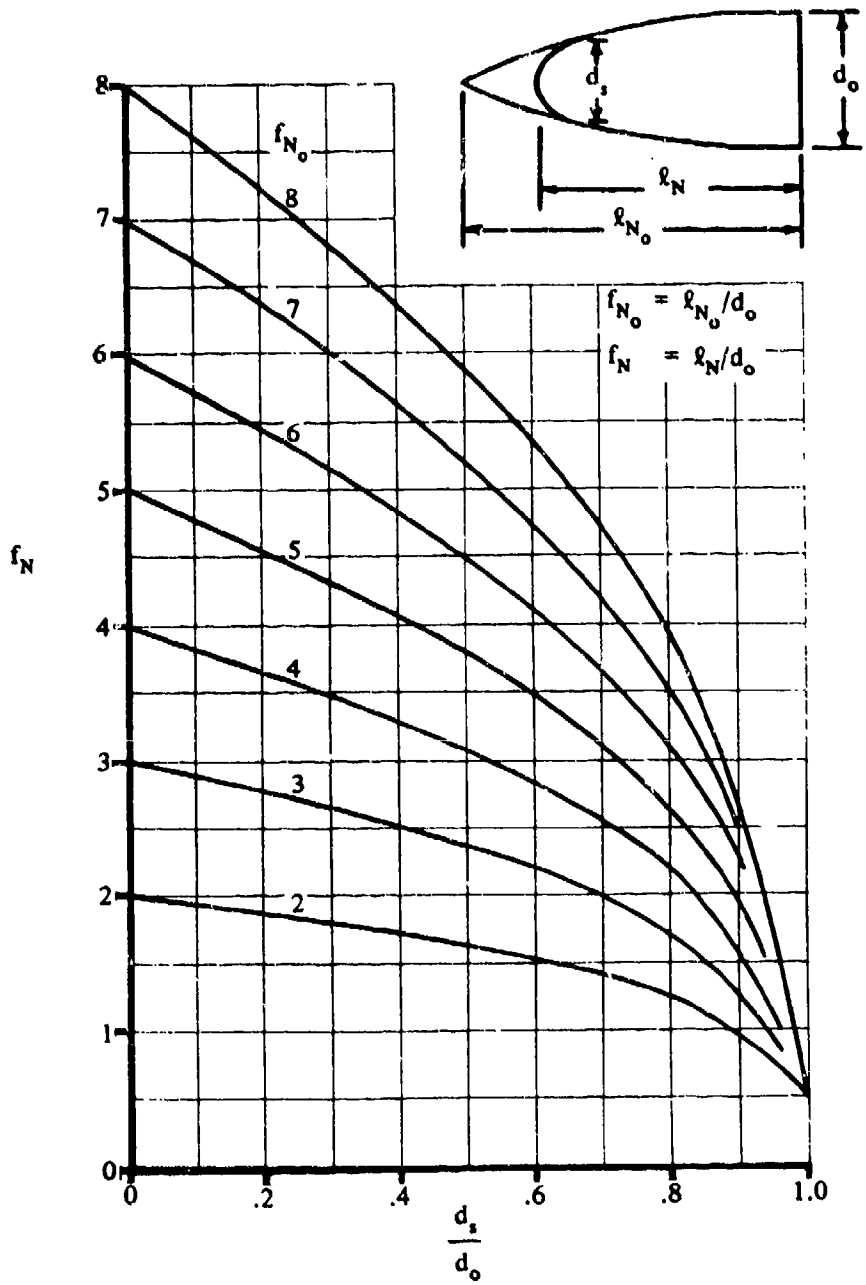

FIGURE 4.2.3.1-30 FINENESS RATIO OF SPHERICALLY BLUNTED OGIVE NOSES

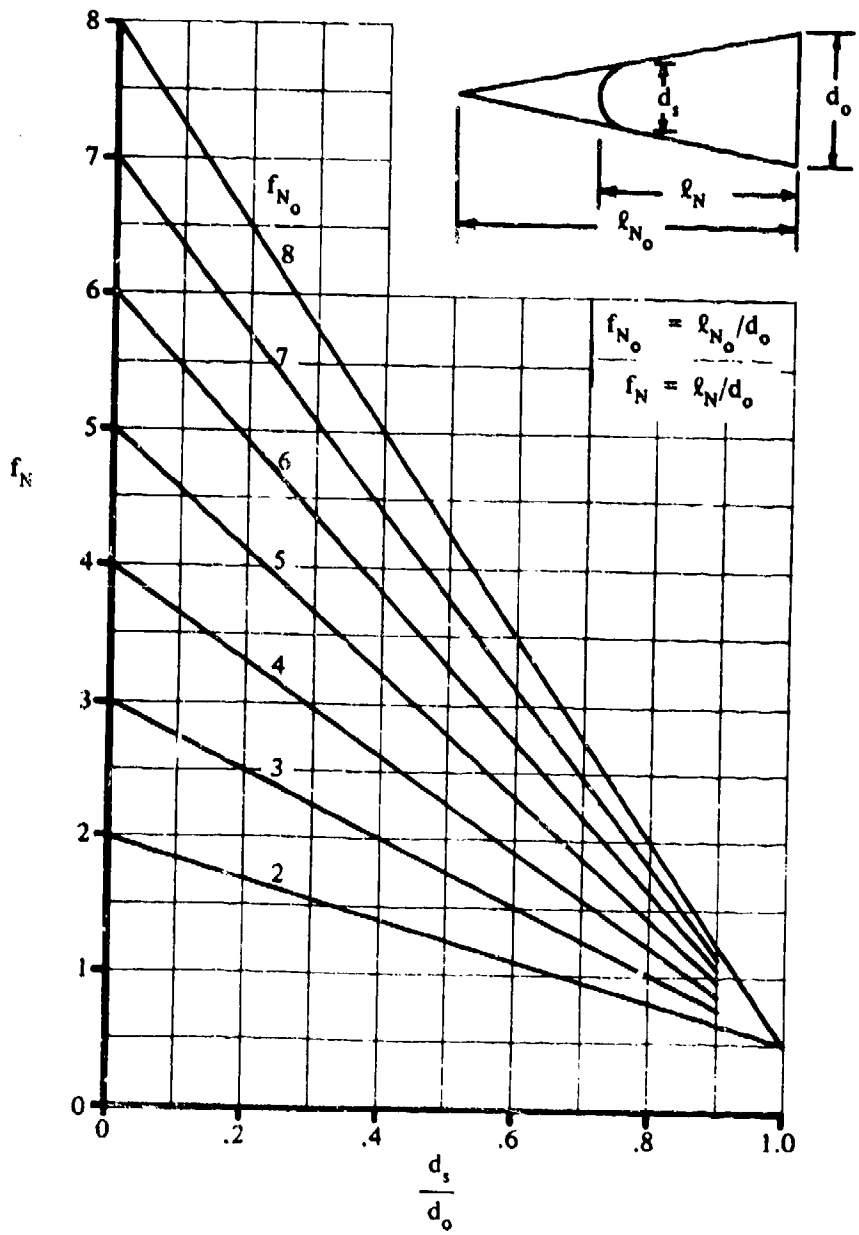

FIGURE 4.2.3.1-31 FINENESS RATIO OF SPHERICALLY BLUNTED CONICAL NOSES

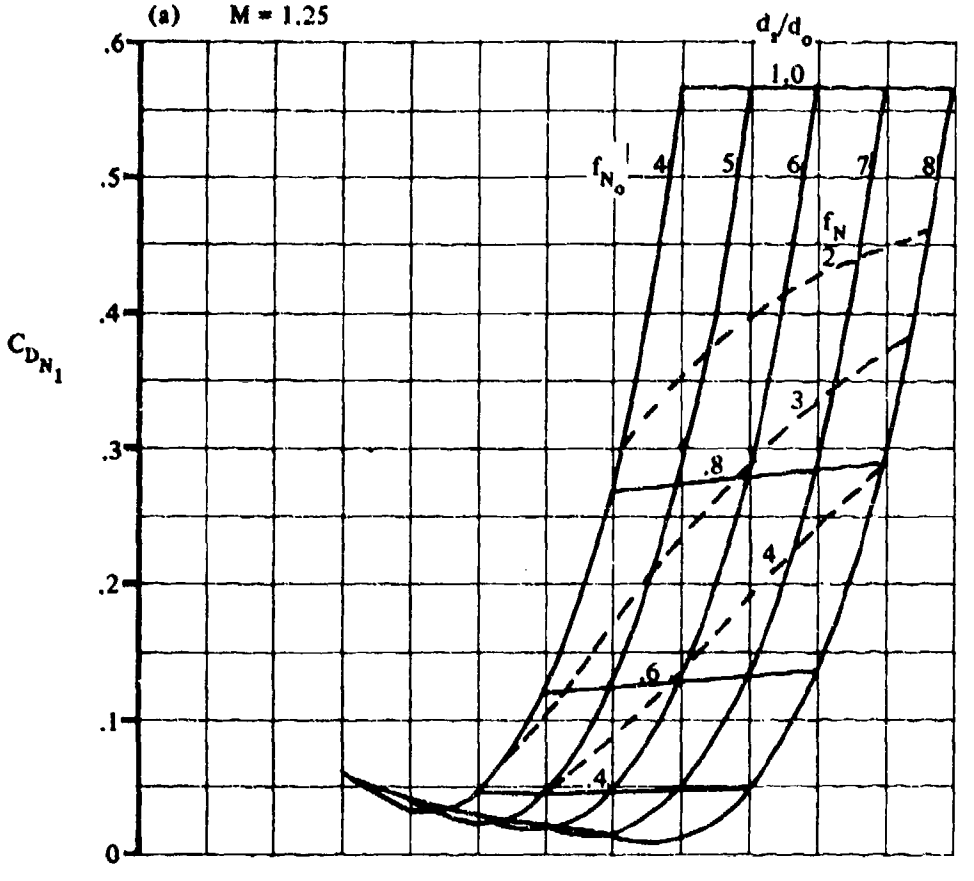

FIGURE 4.2.3.1-32 EFFECT OF BLUNTNESS ON SUPERSONIC PRESSURE DRAG OF SPHERICALLY BLUNTED OGIVES

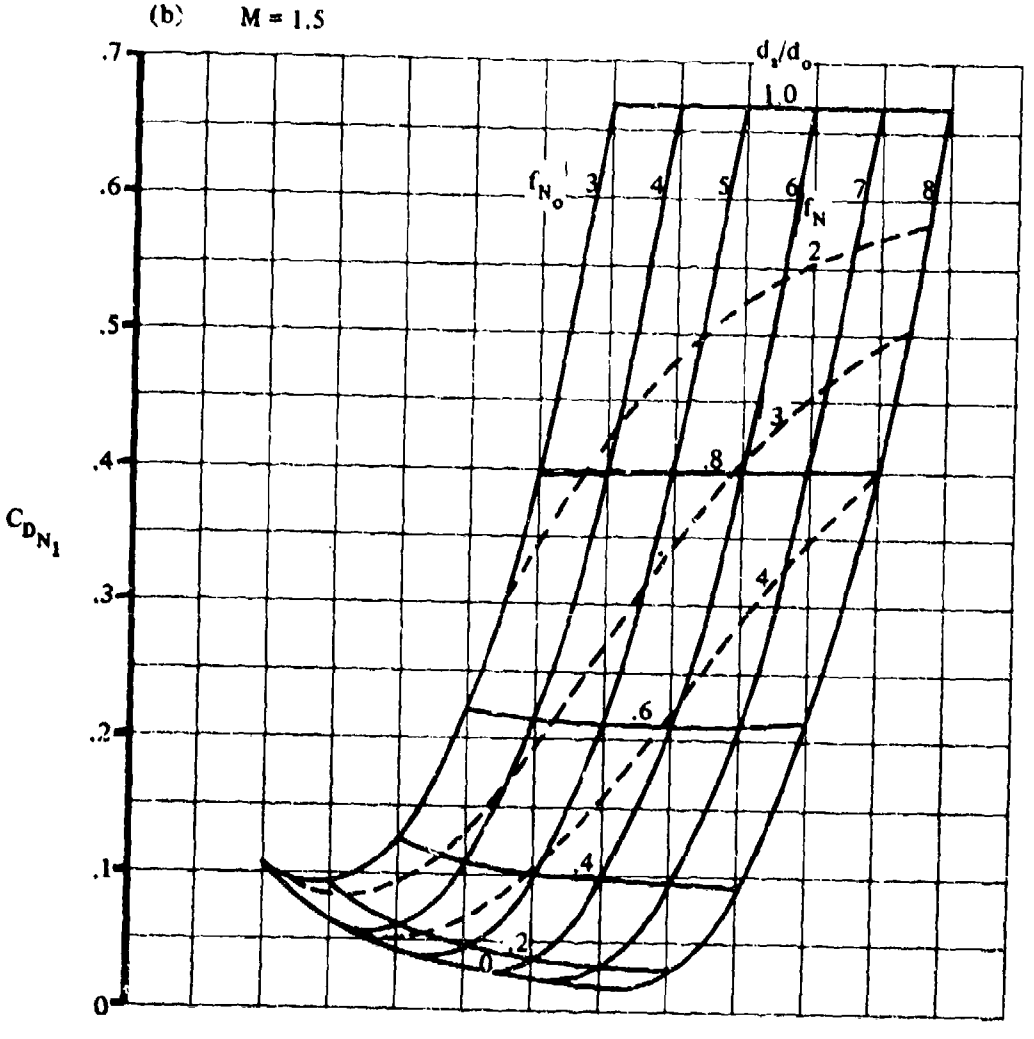

FIGURE 4.2.3.1-32 (CONTD)

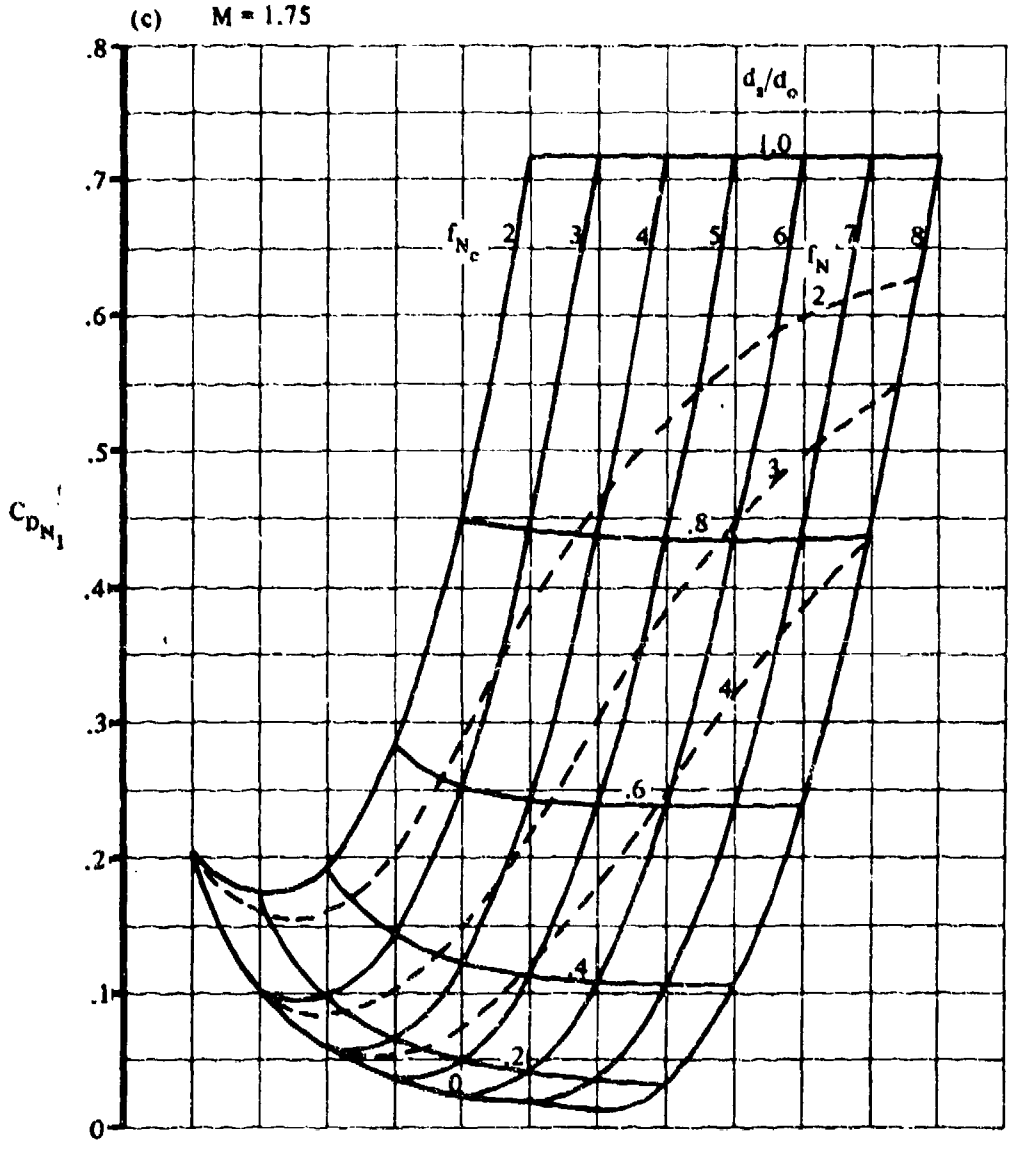

FIGURE 4.2.3.1-32 (CONTD)

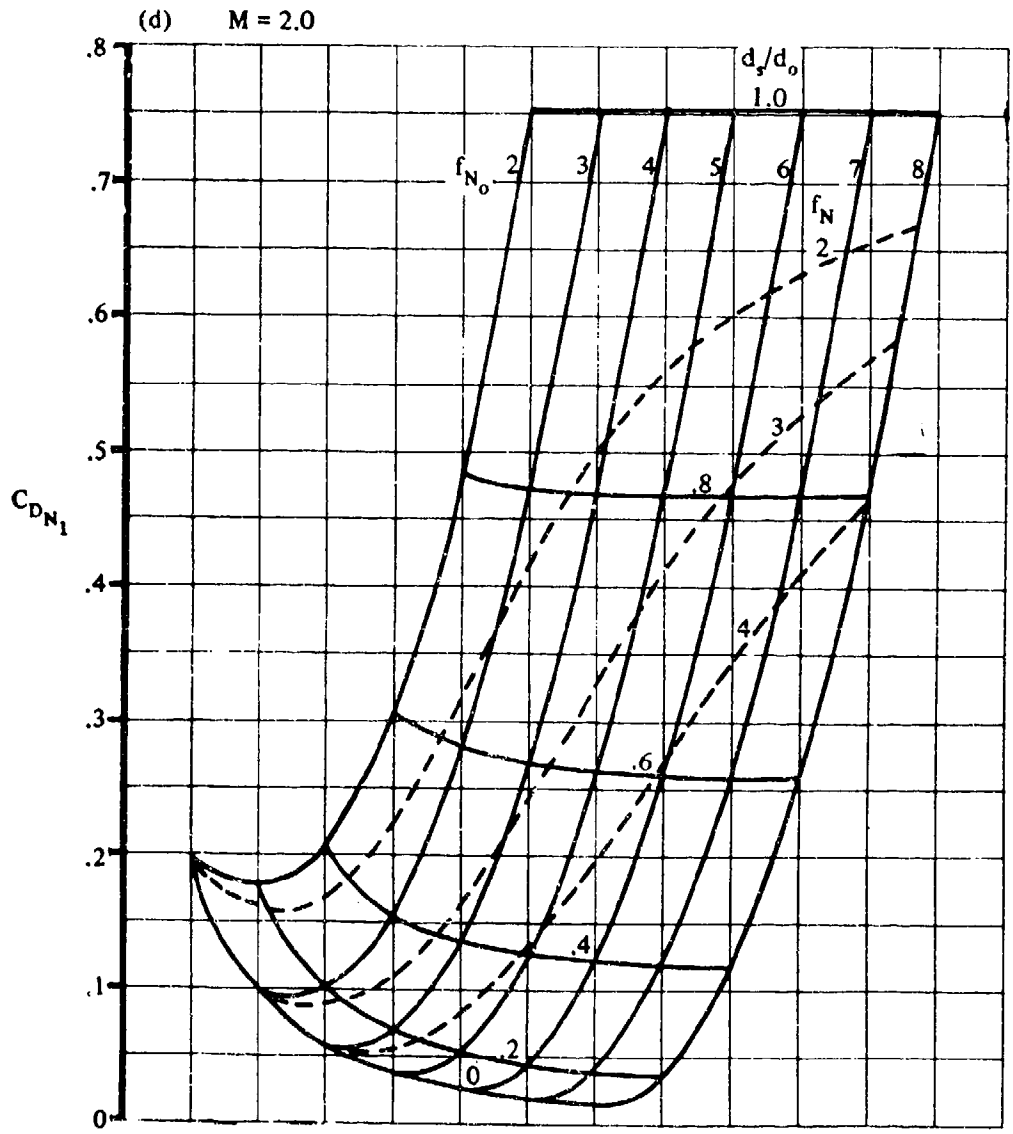

FIGURE 4.2.3.1-32 (CONTD)

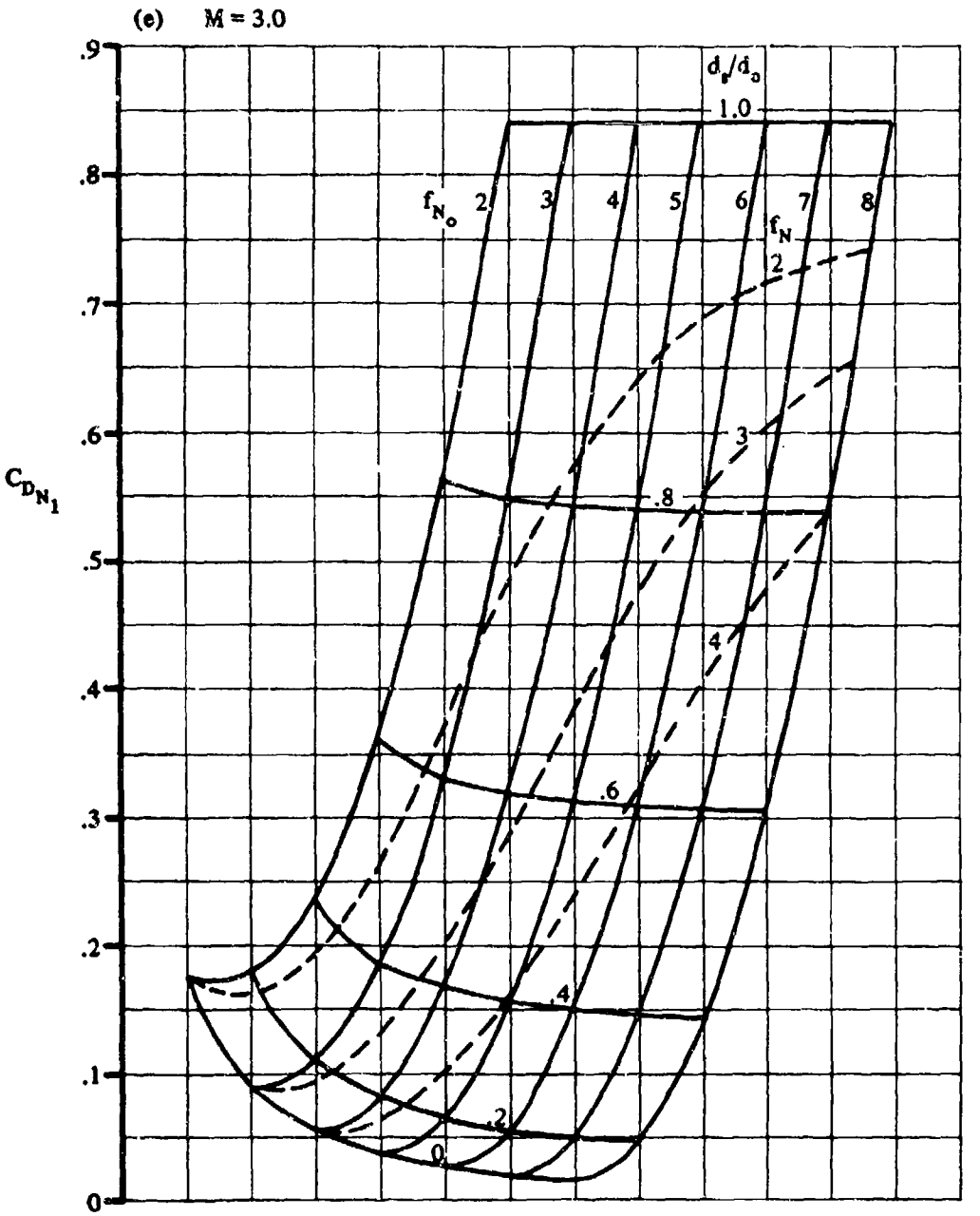

FIGURE 4.2.3.1-32 (CONTD)

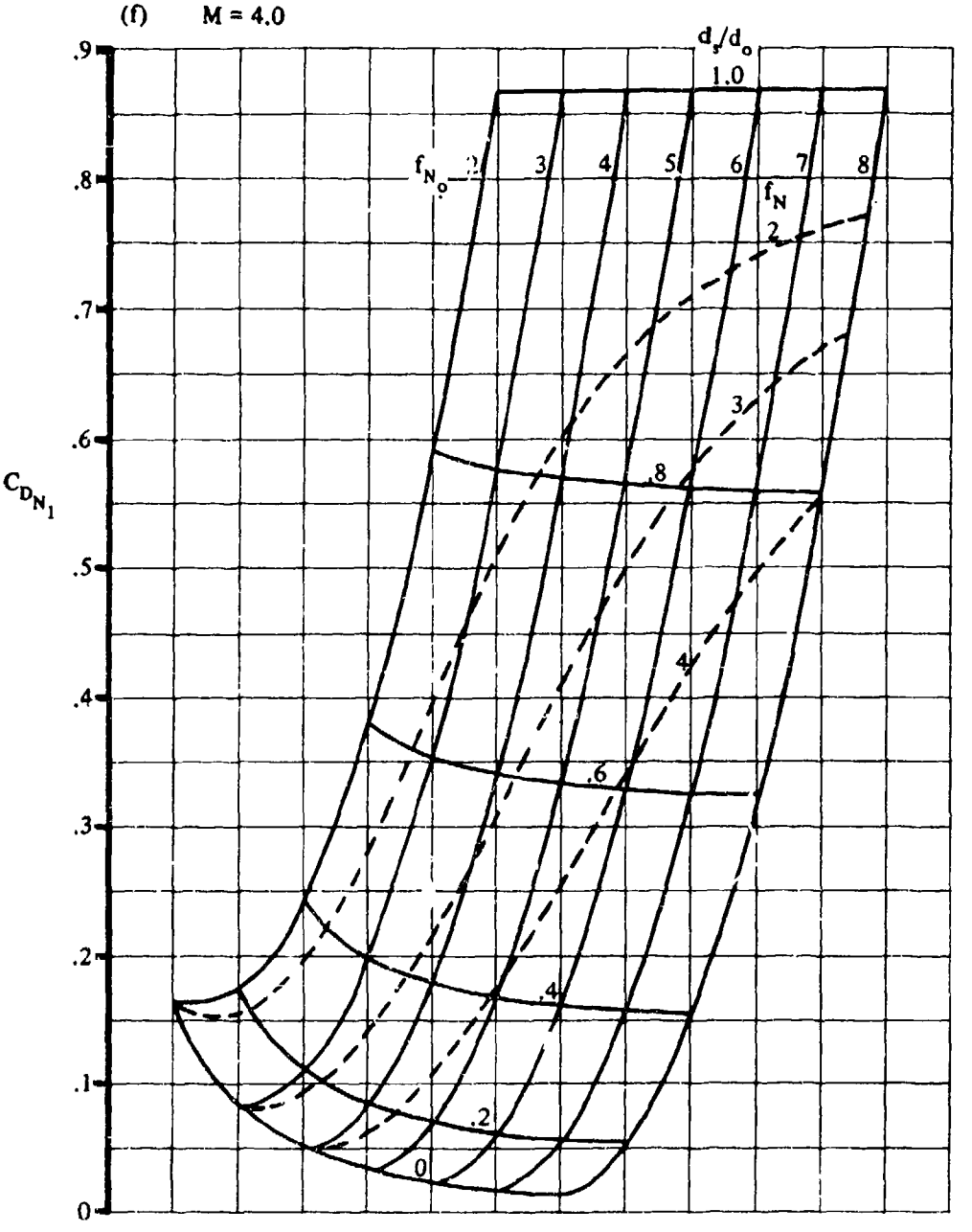

FIGURE 4.2.3.1-32 (CONTD)

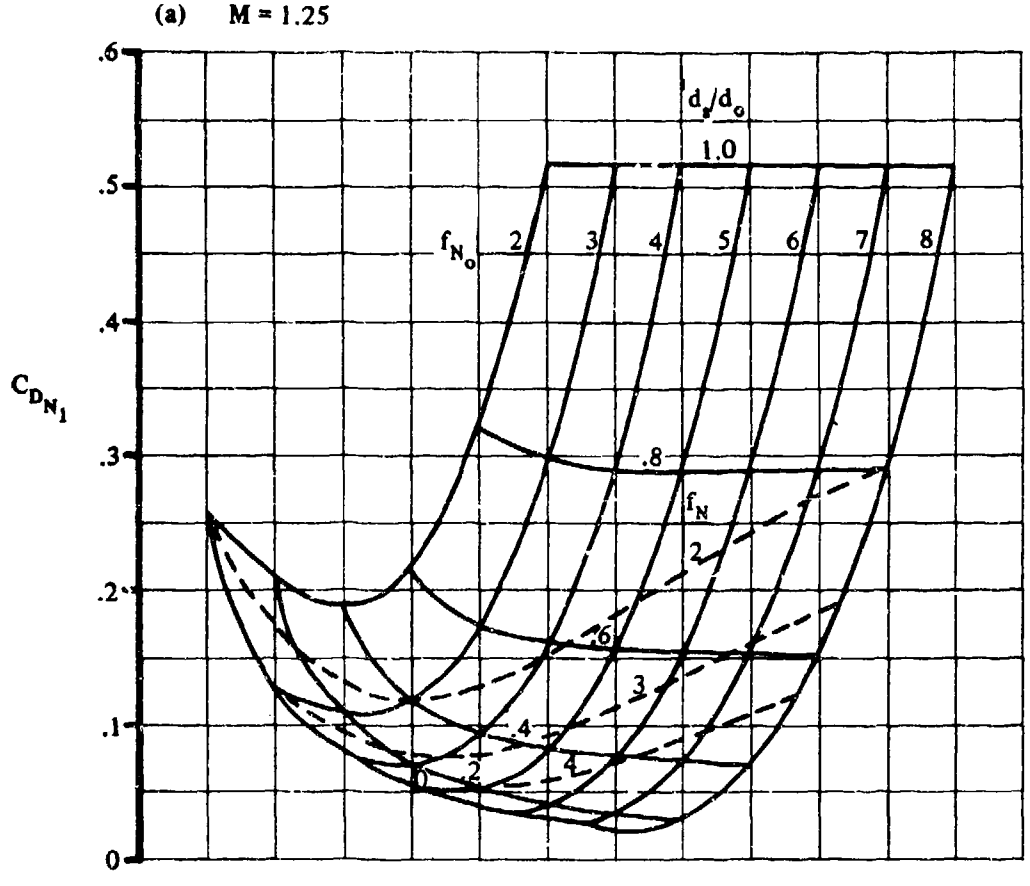

FIGURE 4.2.3.1-38 EFFECT OF BLUNTNESS ON SUPERSONIC PRESSURE DRAG OF SPHERICALLY BLUNTED CONES

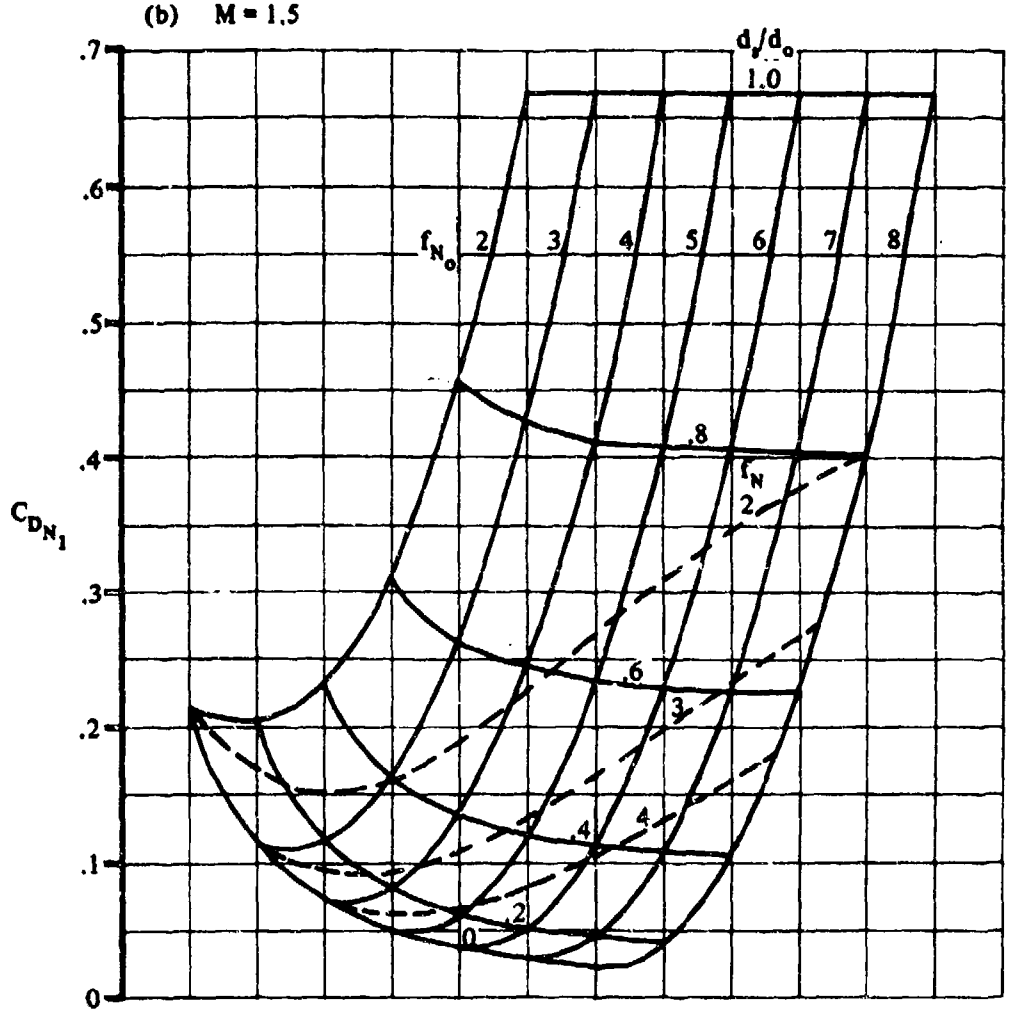

FIGURE 4.2.3.1-38 (CONTD)

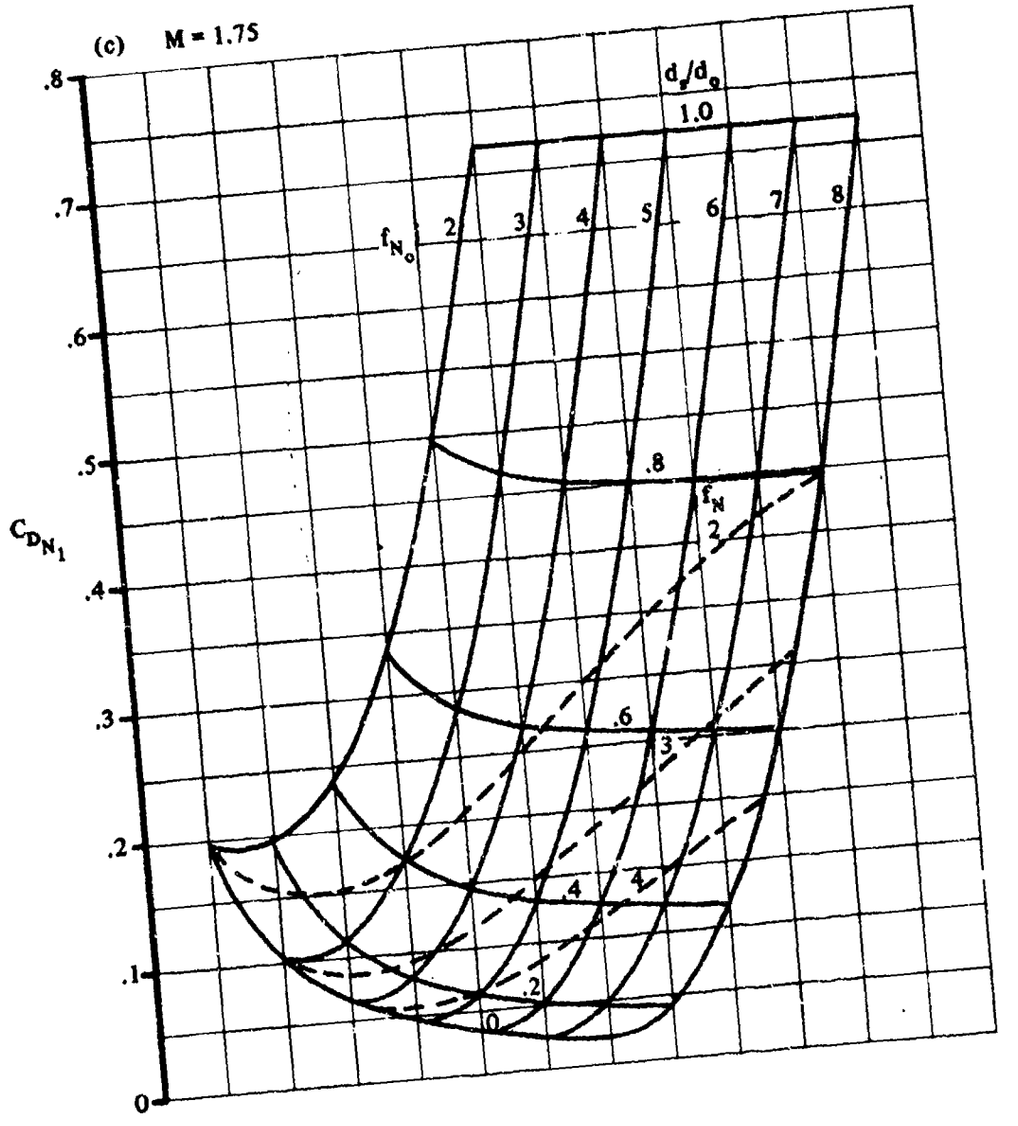

FIGURE 4.2.3.1-38 (CONTD)

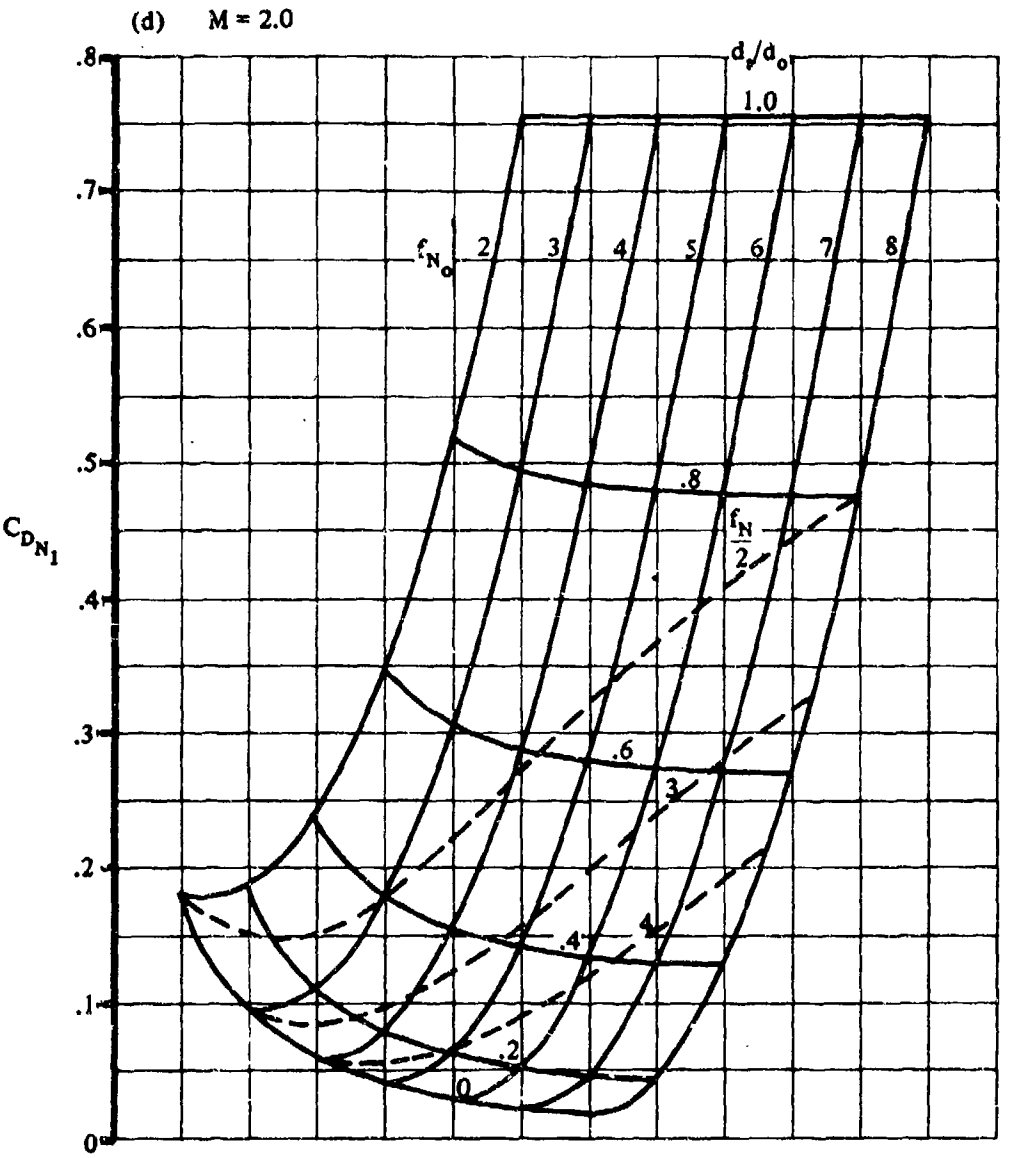

FIGURE 4.2.3.1-38 (CONTD)

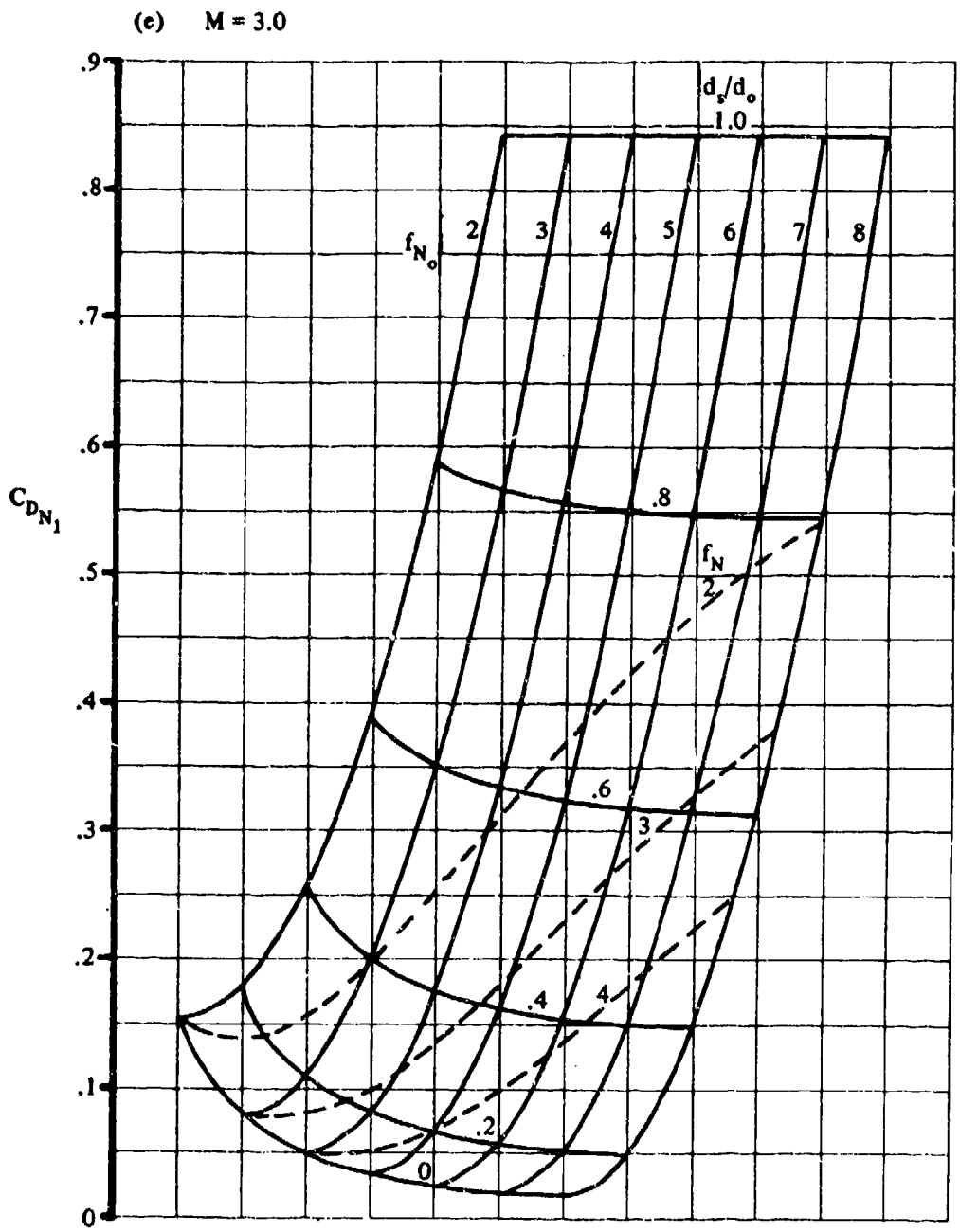

FIGURE 4.2.3.1-38 (CONTD)

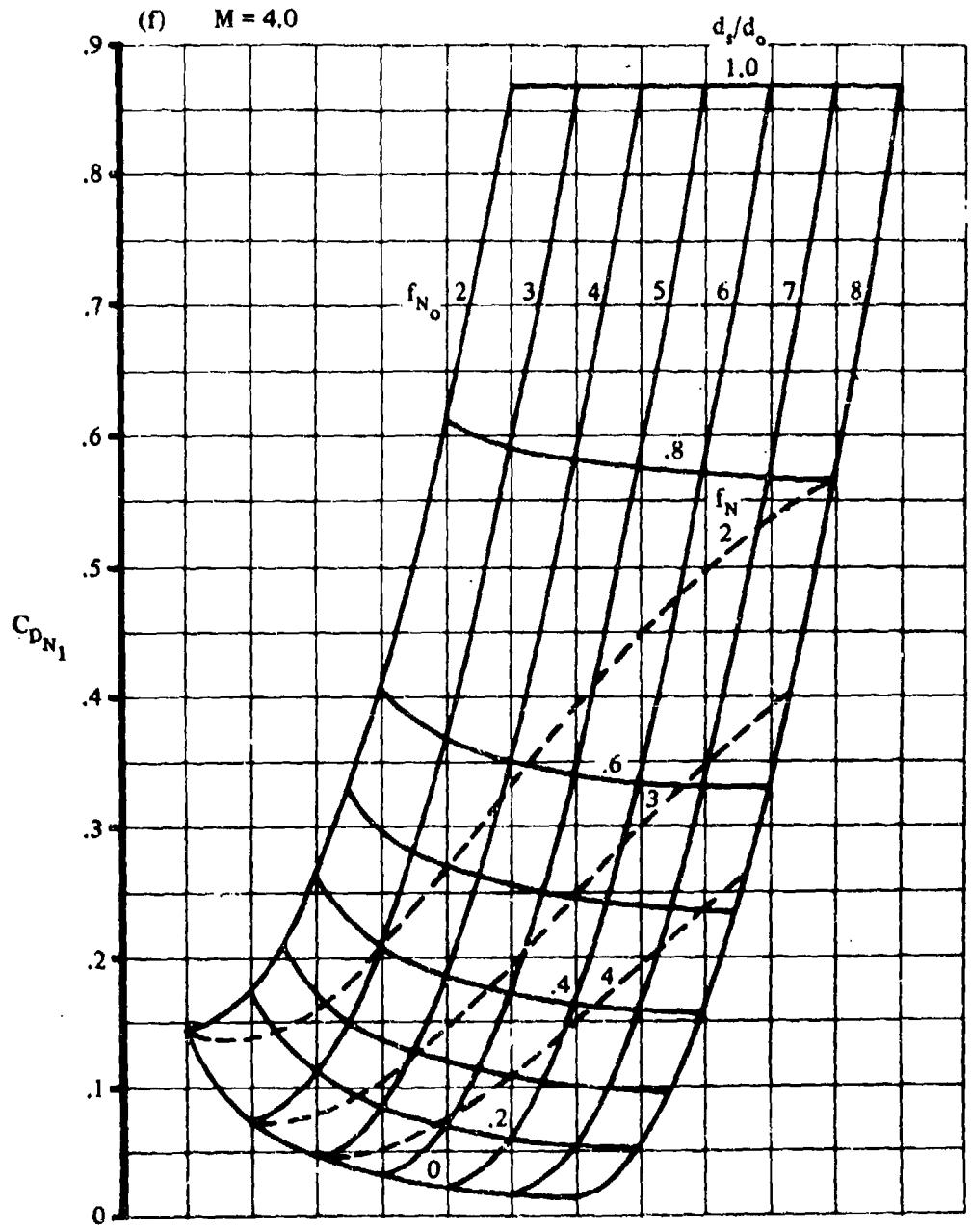

FIGURE 4.2.3.1-38 (CONTD)

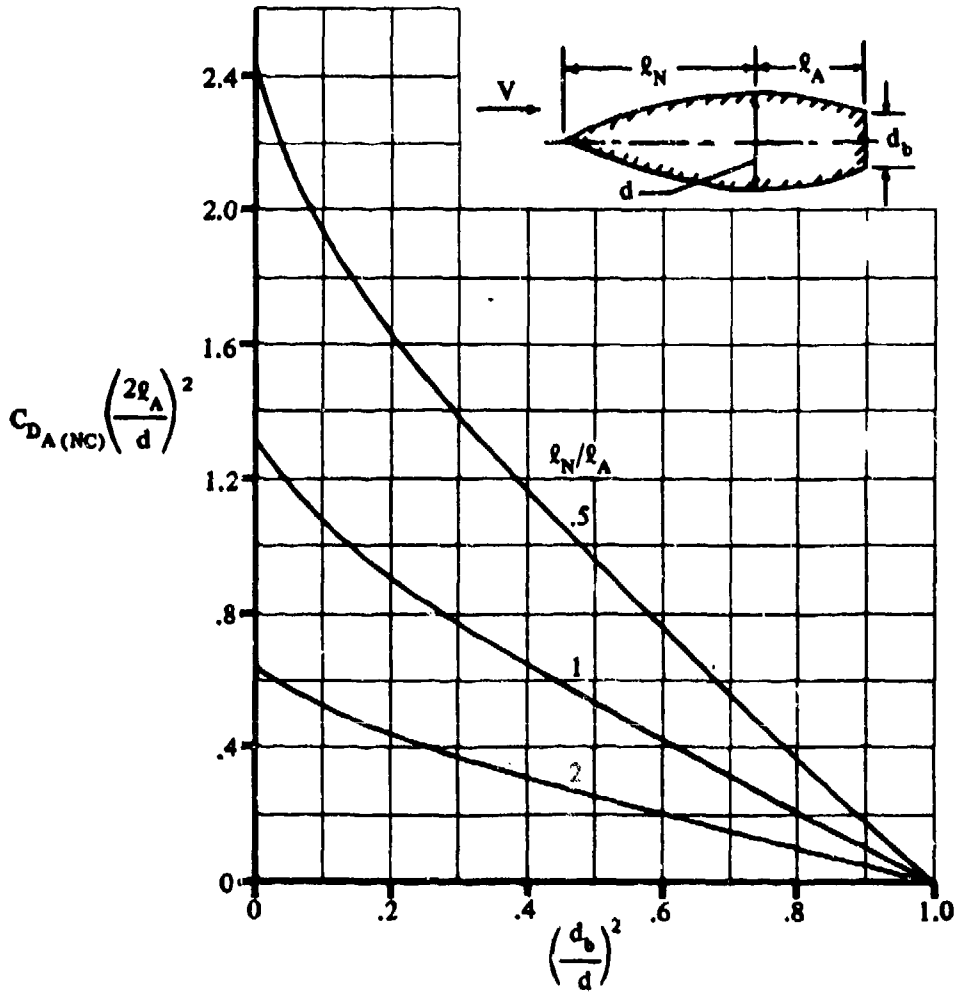

FIGURE 4.2.3.1-44a INTERFERENCE DRAG OF TRUNCATED AFTERBODIES BEHIND POINTED FOREBODIES (PARABOLIC PROFILES: NO PARALLEL PORTION)

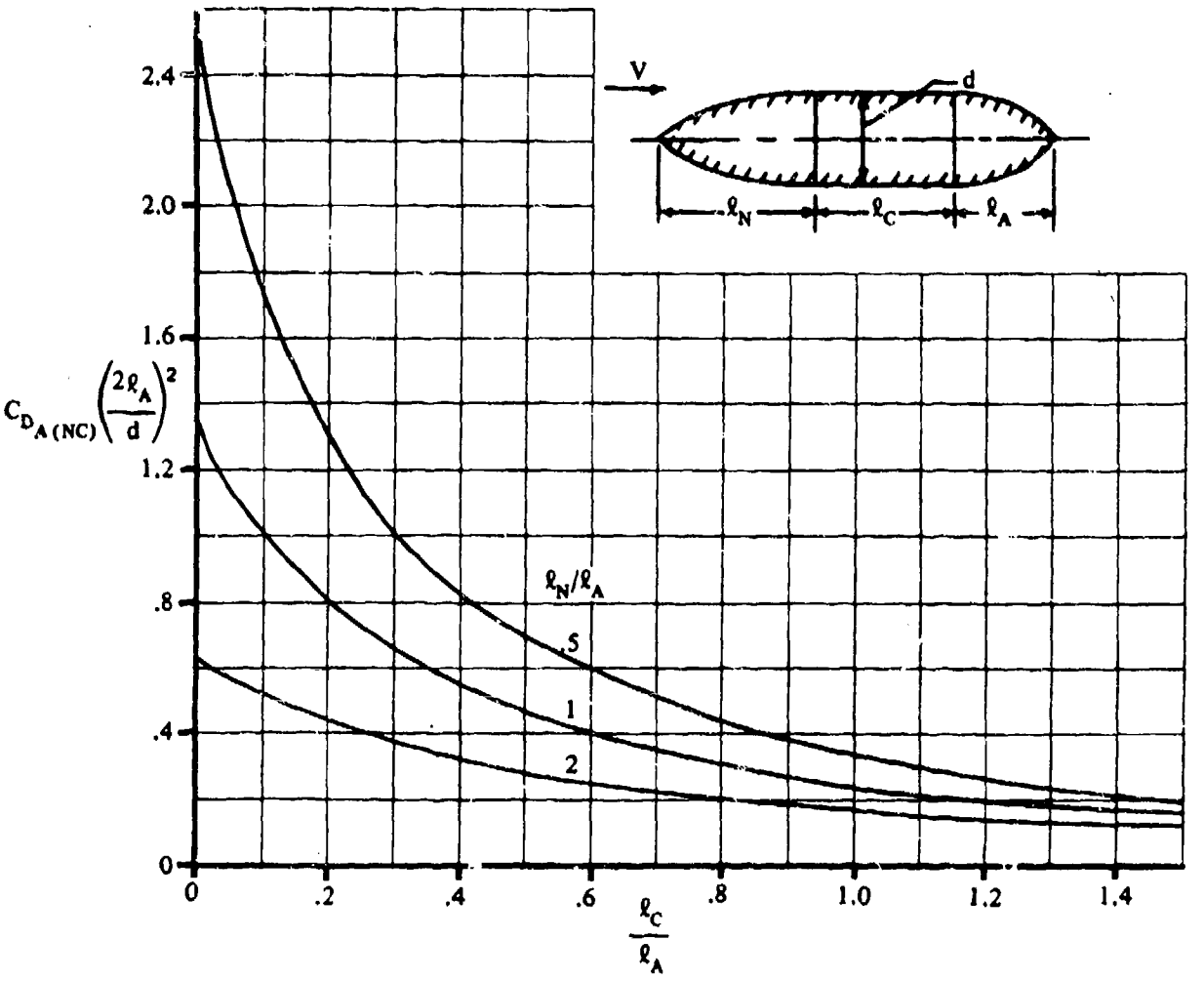

FIGURE 4.2.3.1-44b INTERFERENCE DRAG FOR POINTED BODIES OF PARABOLIC PROFILE

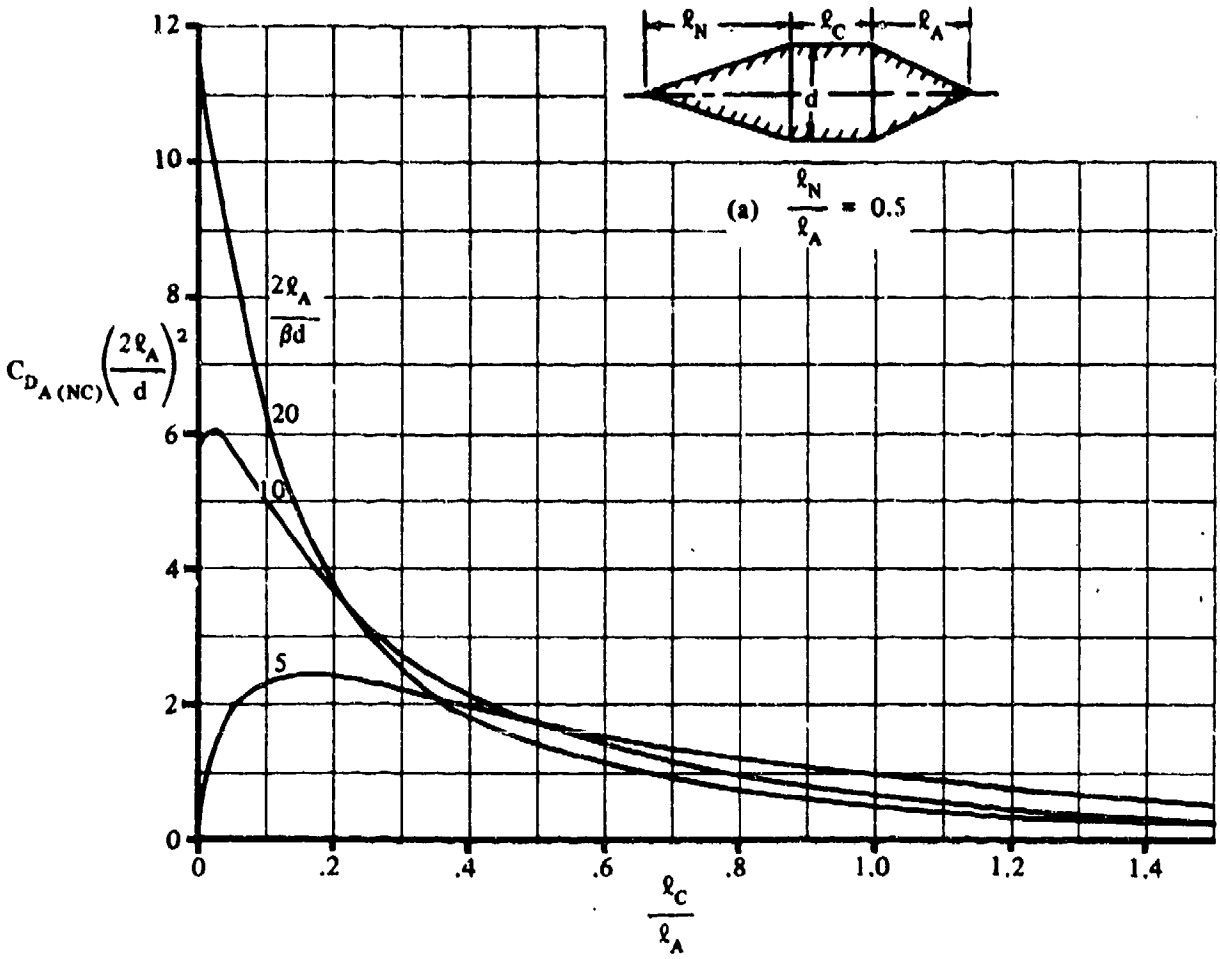

FIGURE 4.2.3.1-46 INTERFERENCE DRAG OF POINTED CONICAL BODIES

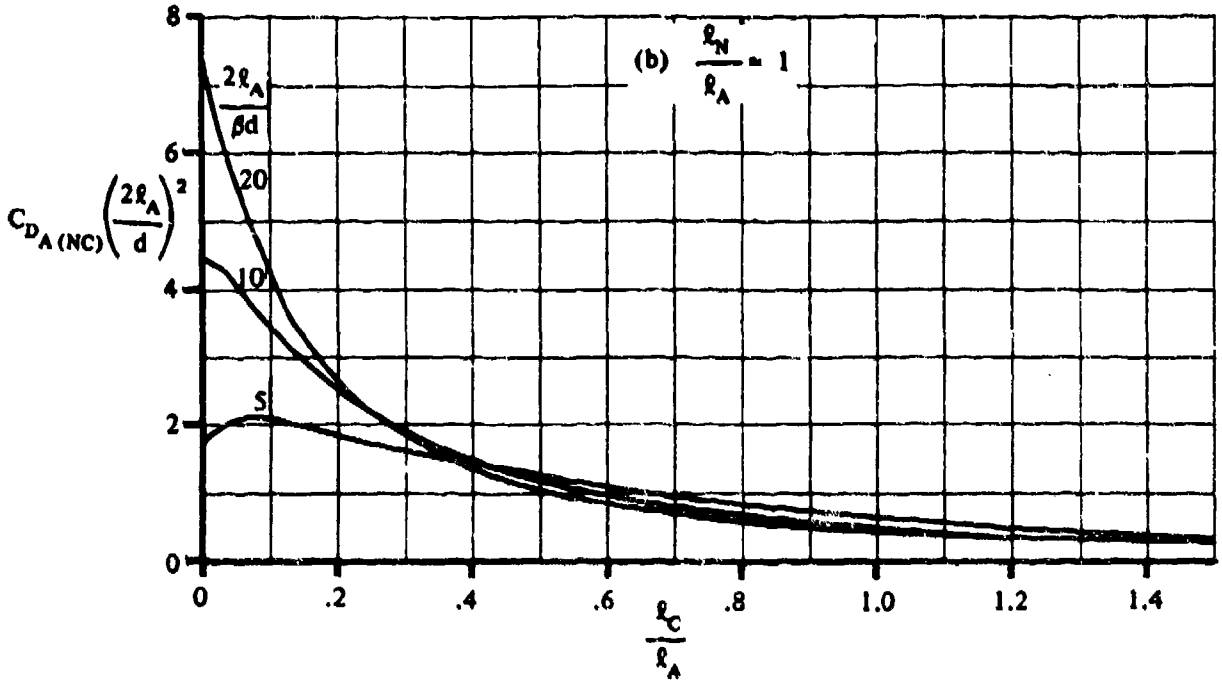

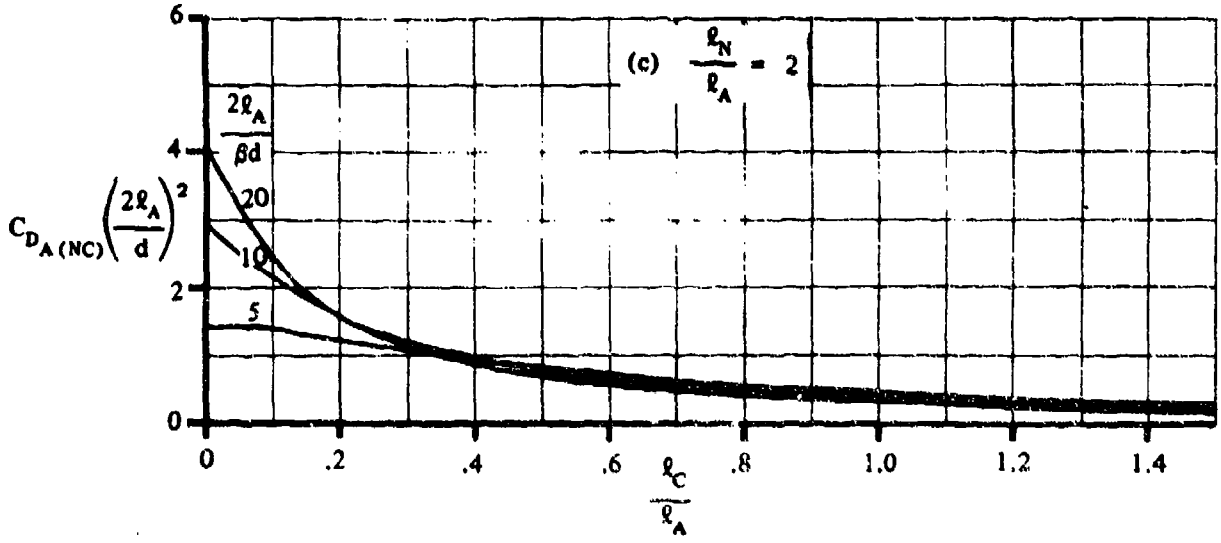

FIGURE 4.2.3.1-46 (CONTD)

S' is the nose area of forebody or base area of afterbody
S_B is the maximum frontal area of forebody or afterbody

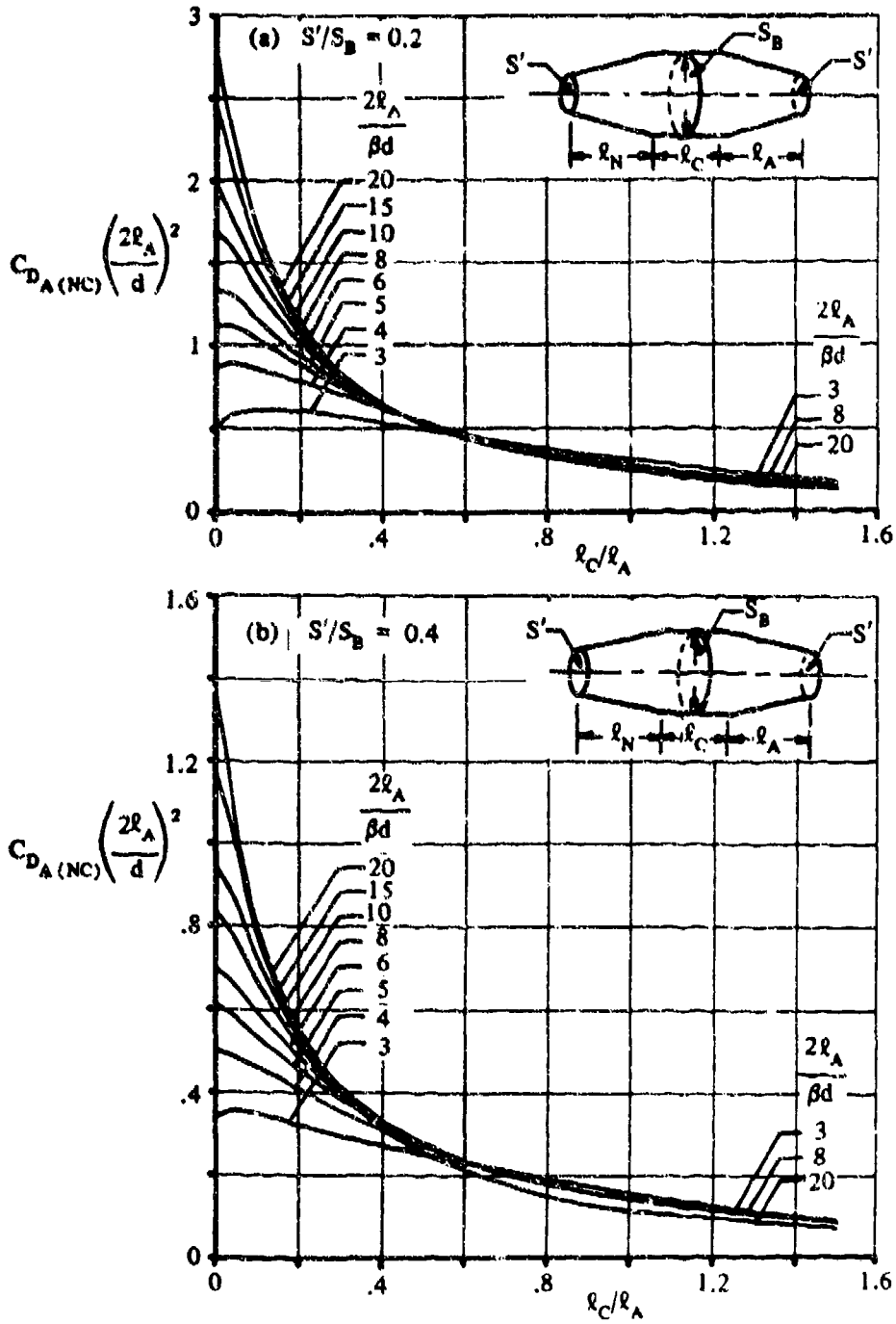

FIGURE 4.2.3.1-48 INTERFERENCE DRAG OF DUCTED CONICAL PROFILES

S′ is the nose area of forebody or base area of afterbody
S_B is the maximum frontal area of forebody or afterbody

(c) $S'/S_B = 0.6$

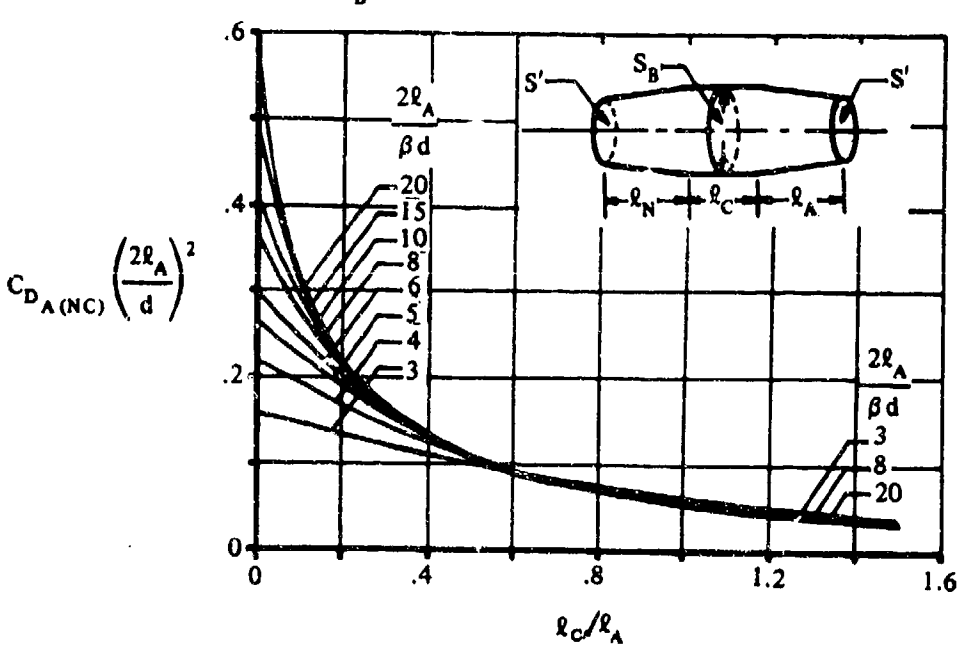

FIGURE 4.2.3.1-48 (CONTD)

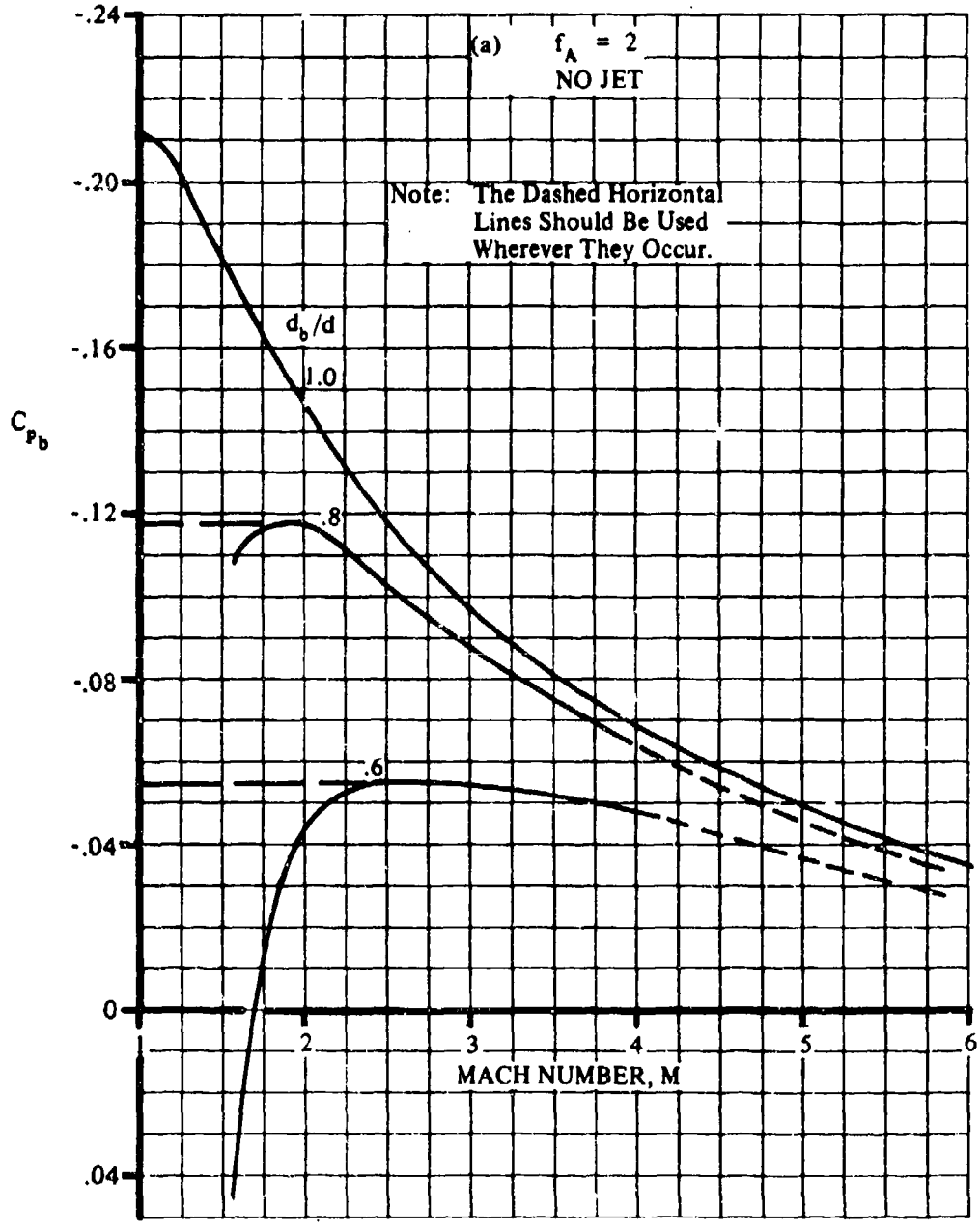

FIGURE 4.2.3.1-50 BASE-PRESSURE COEFFICIENT FOR OGIVE BOATTAILS

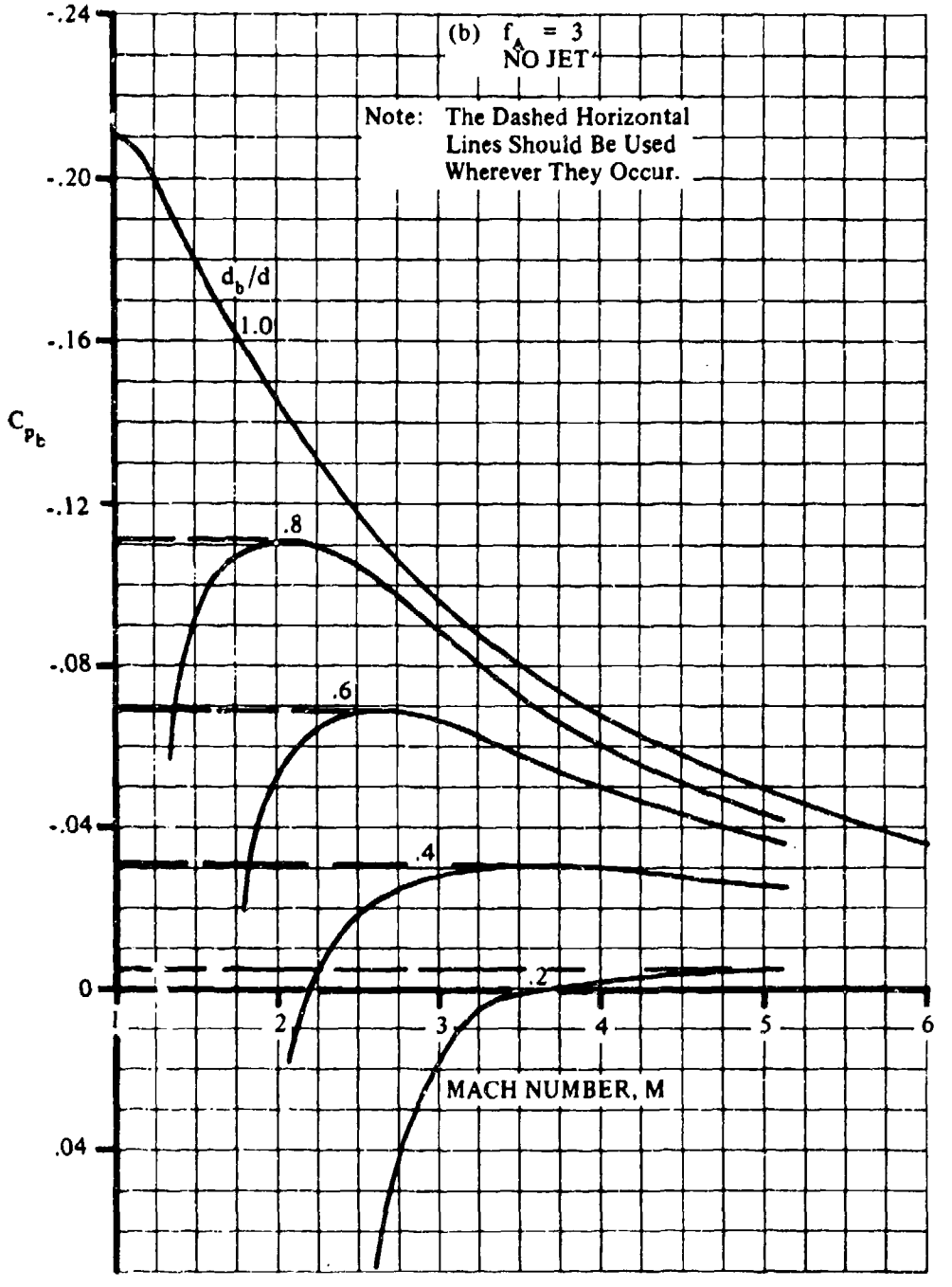

FIGURE 4.2.3.1-50 (CONTD)

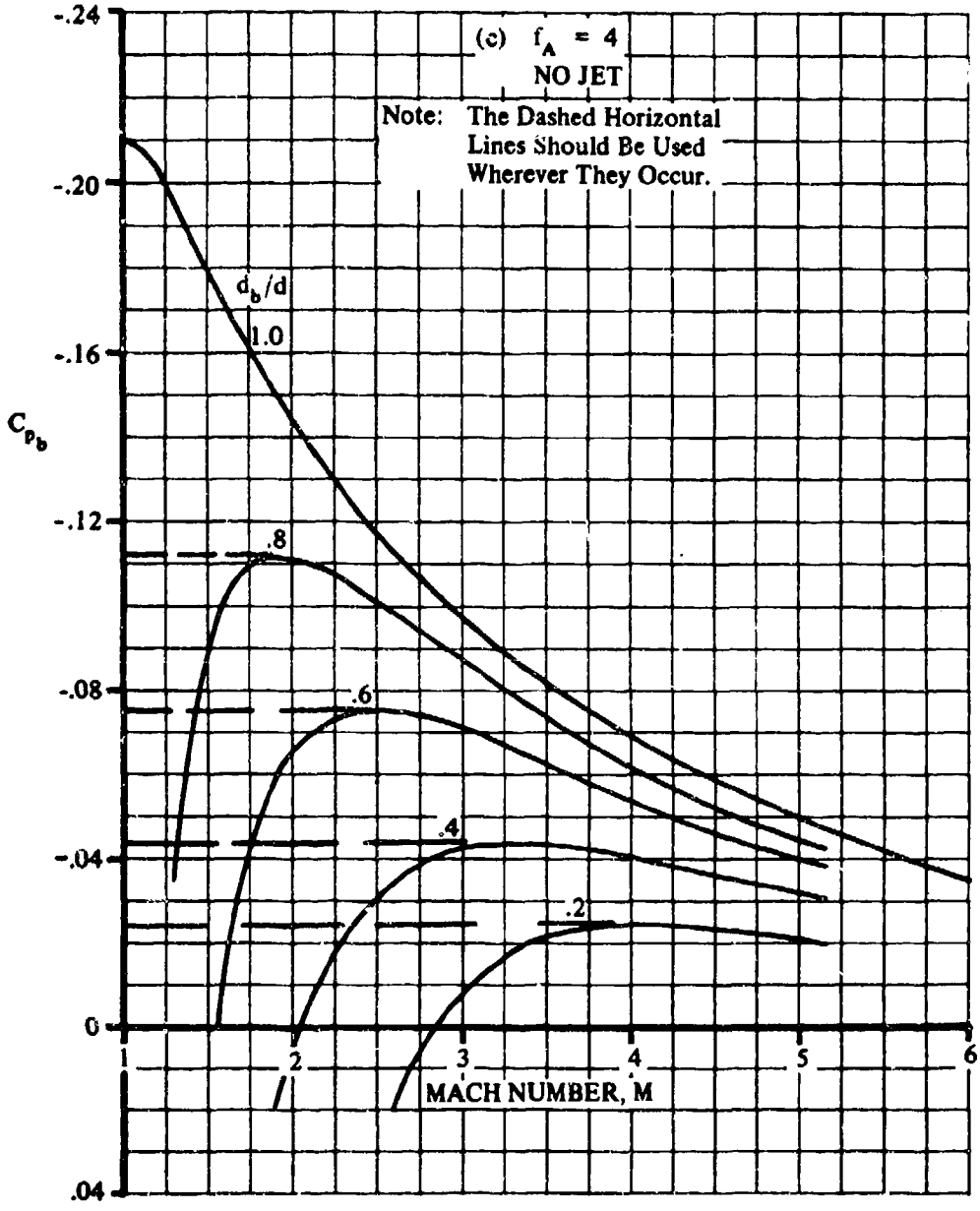

FIGURE 4.2.3.1-50 (CONTD)

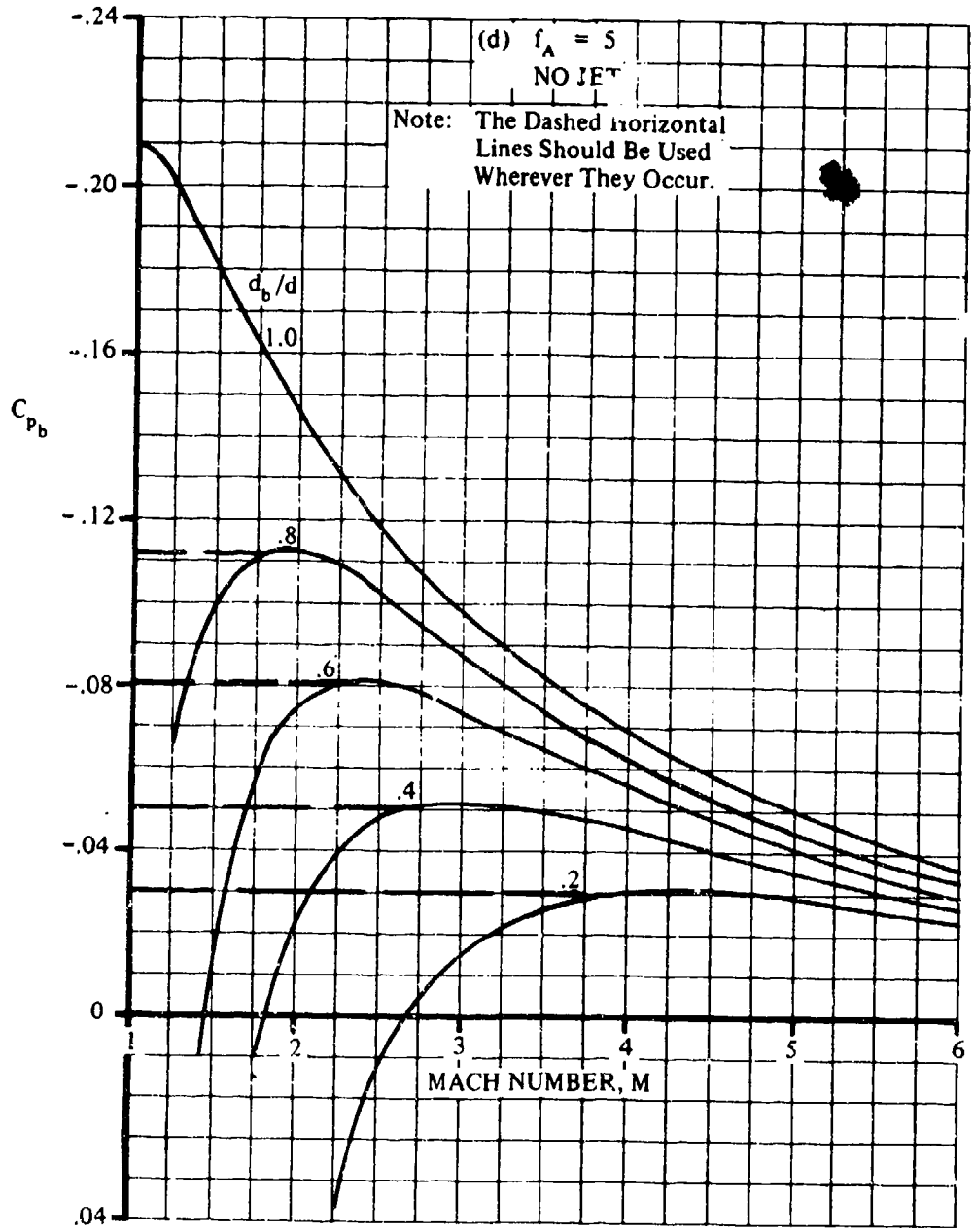

FIGURE 4.2.3.1-50 (CONTD)

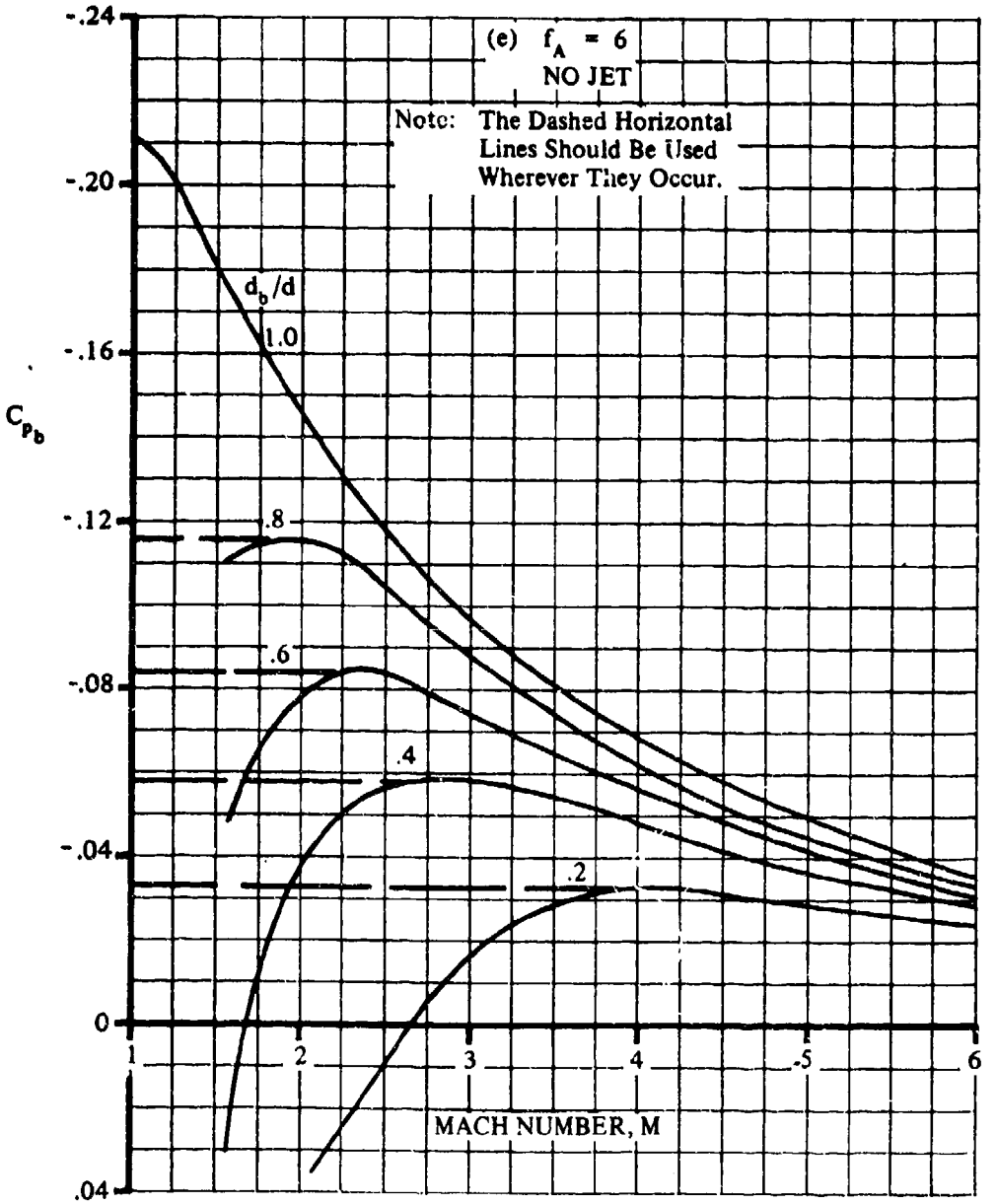

FIGURE 4.2.3.1-50 (CONTD)

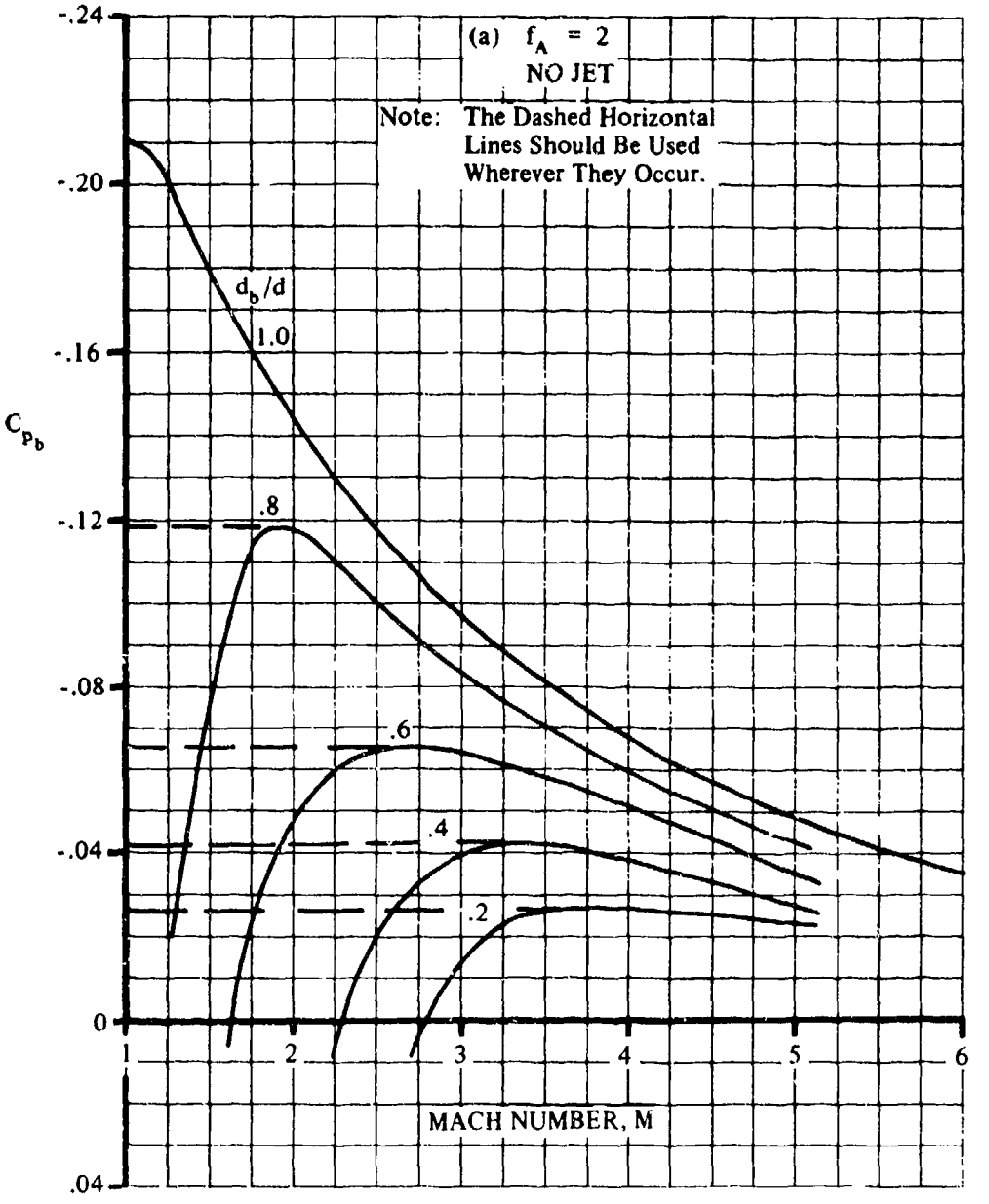

FIGURE 4.2.3.1-55 BASE-PRESSURE COEFFICIENT FOR CONICAL BOATTAILS

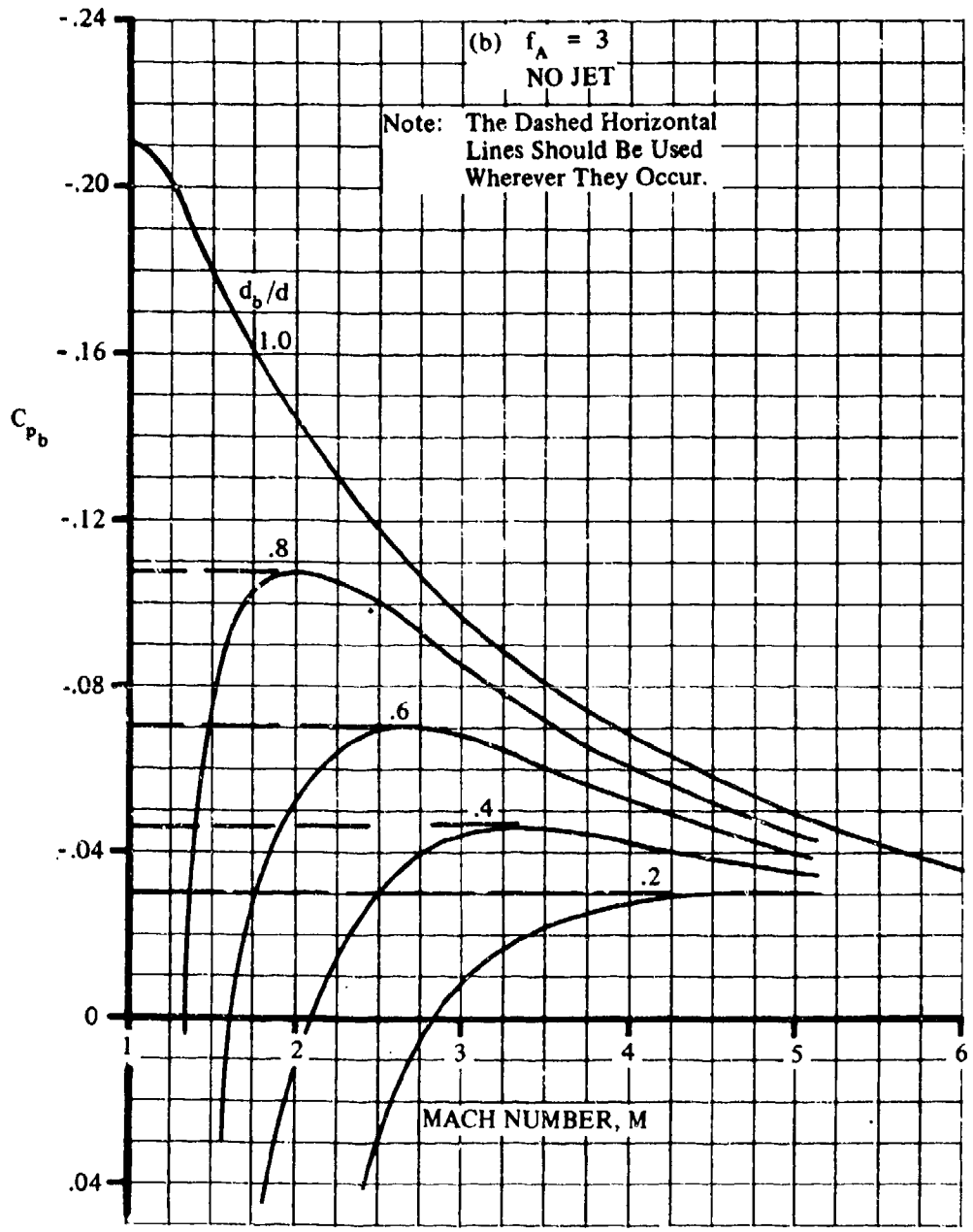

FIGURE 4.2.3.1-55 (CONTD)

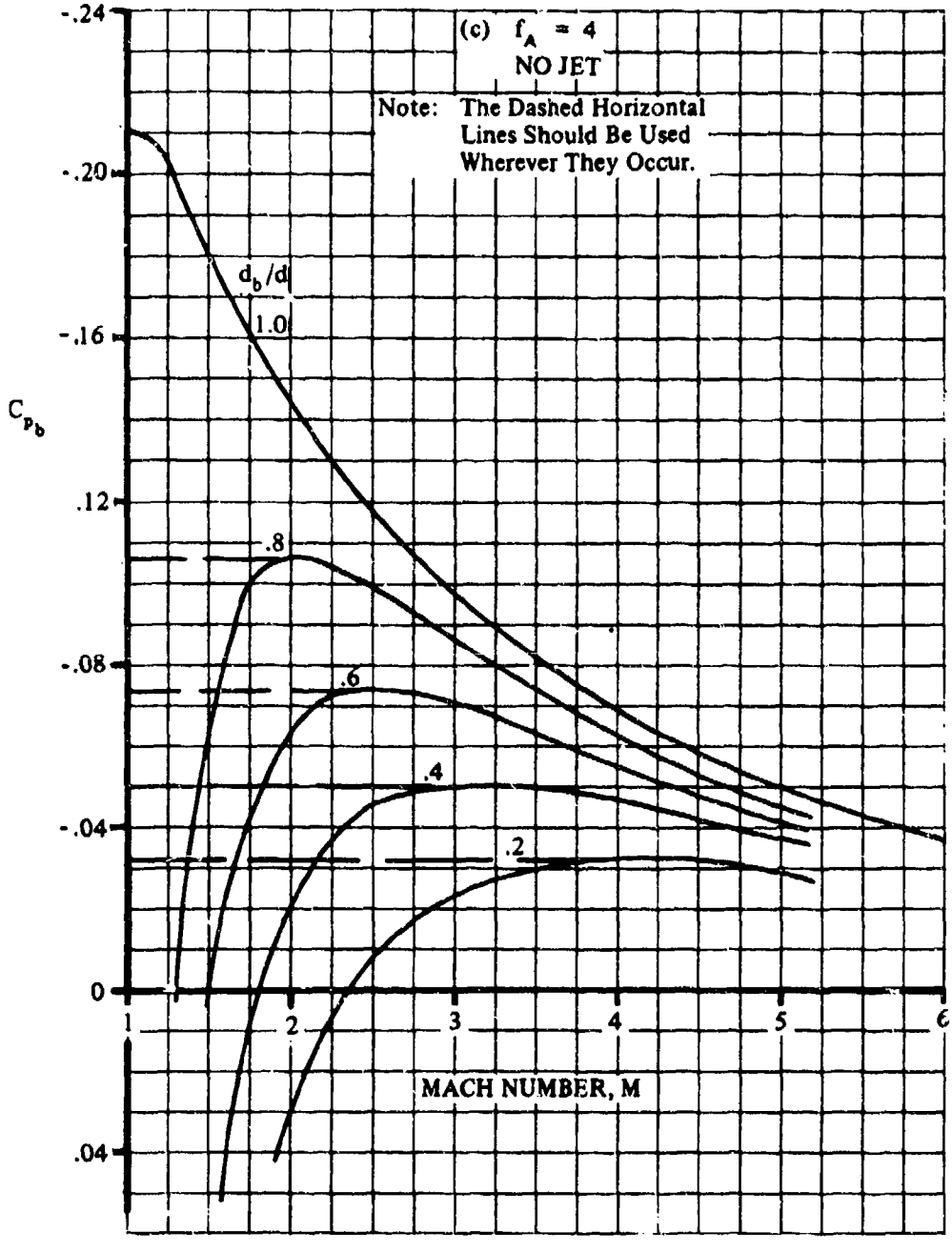

FIGURE 4.2.3.1-55 (CONTD)

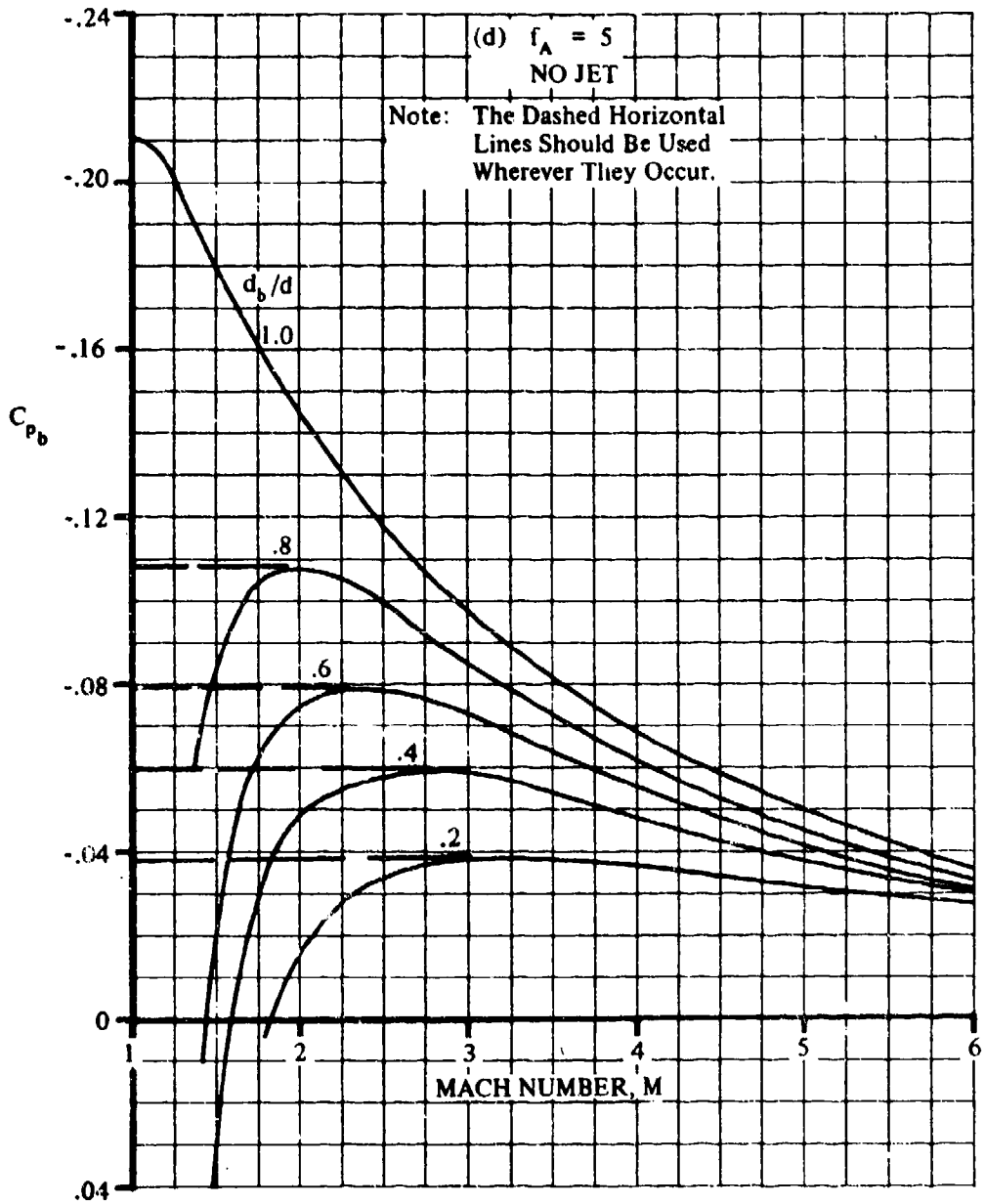

FIGURE 4.2.3.1-55 (CONTD)

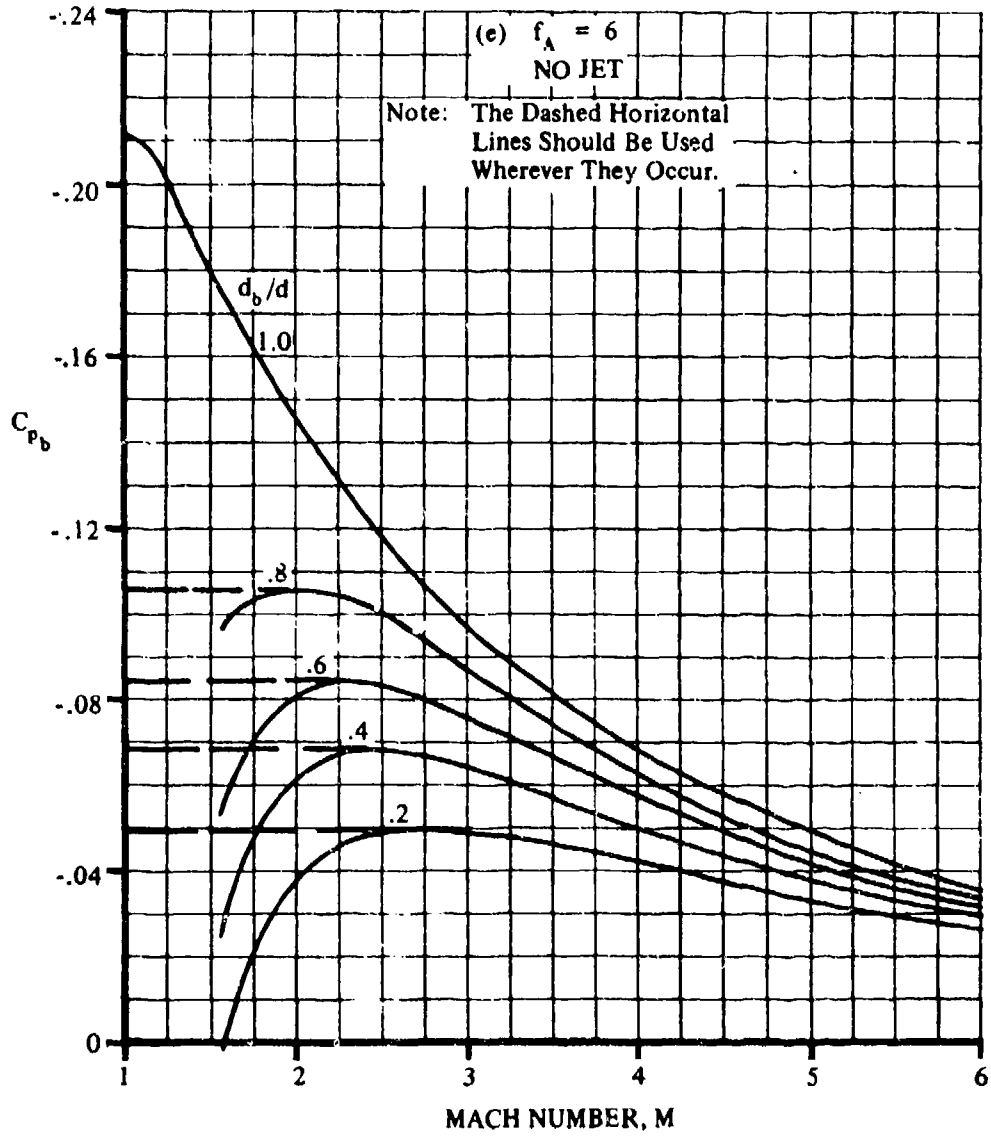

FIGURE 4.2.3.1-55 (CONTD)

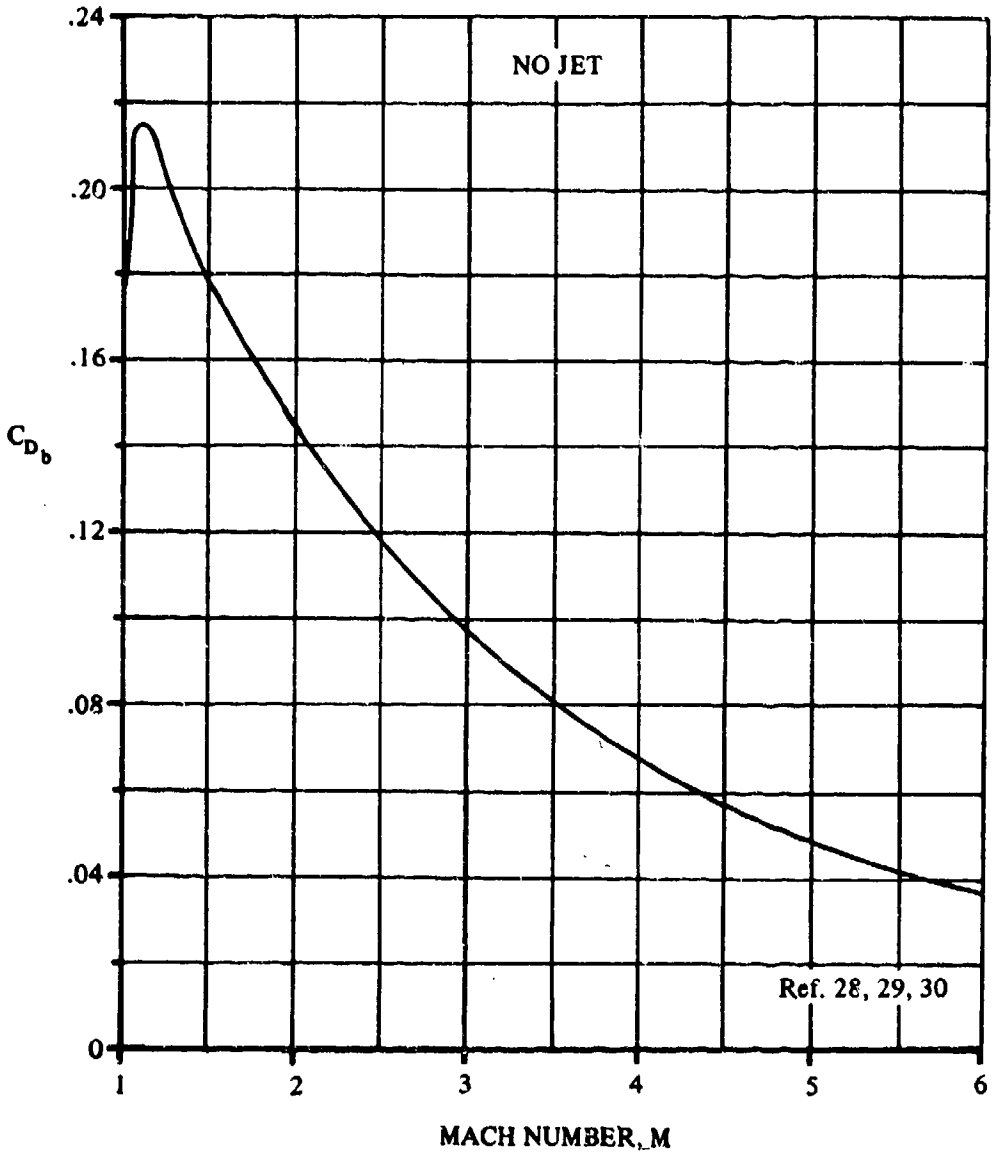

FIGURE 4.2.3.1-60 BASE DRAG COEFFICIENT FOR BODIES OF REVOLUTION WITH NO BOATTAIL

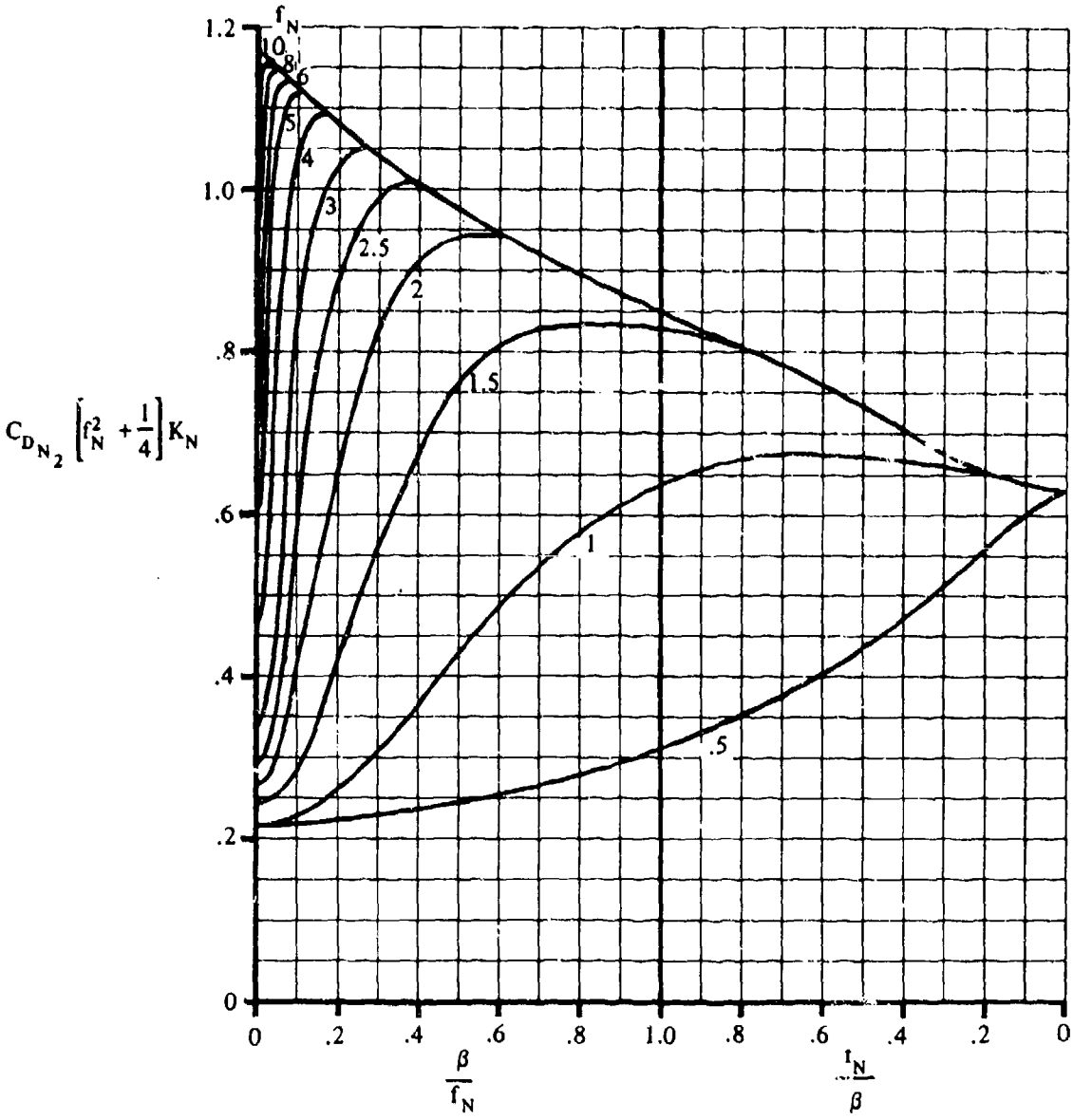

FIGURE 4.2.3.1-61 SUPERSONIC PRESSURE DRAG OF OGIVE NOSES

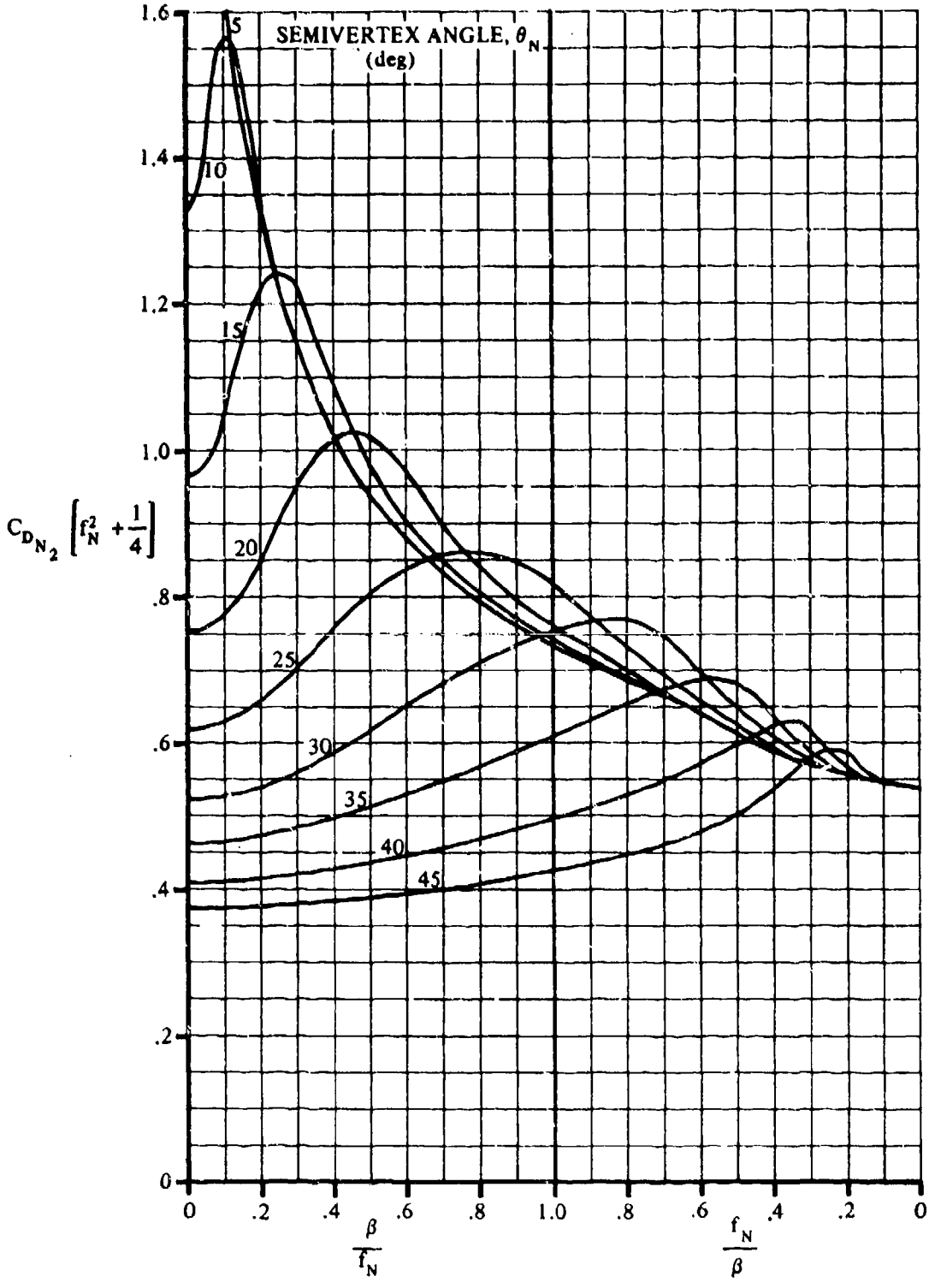

FIGURE 4.2.3.1-62 SUPERSONIC PRESSURE DRAG OF CONICAL NOSES

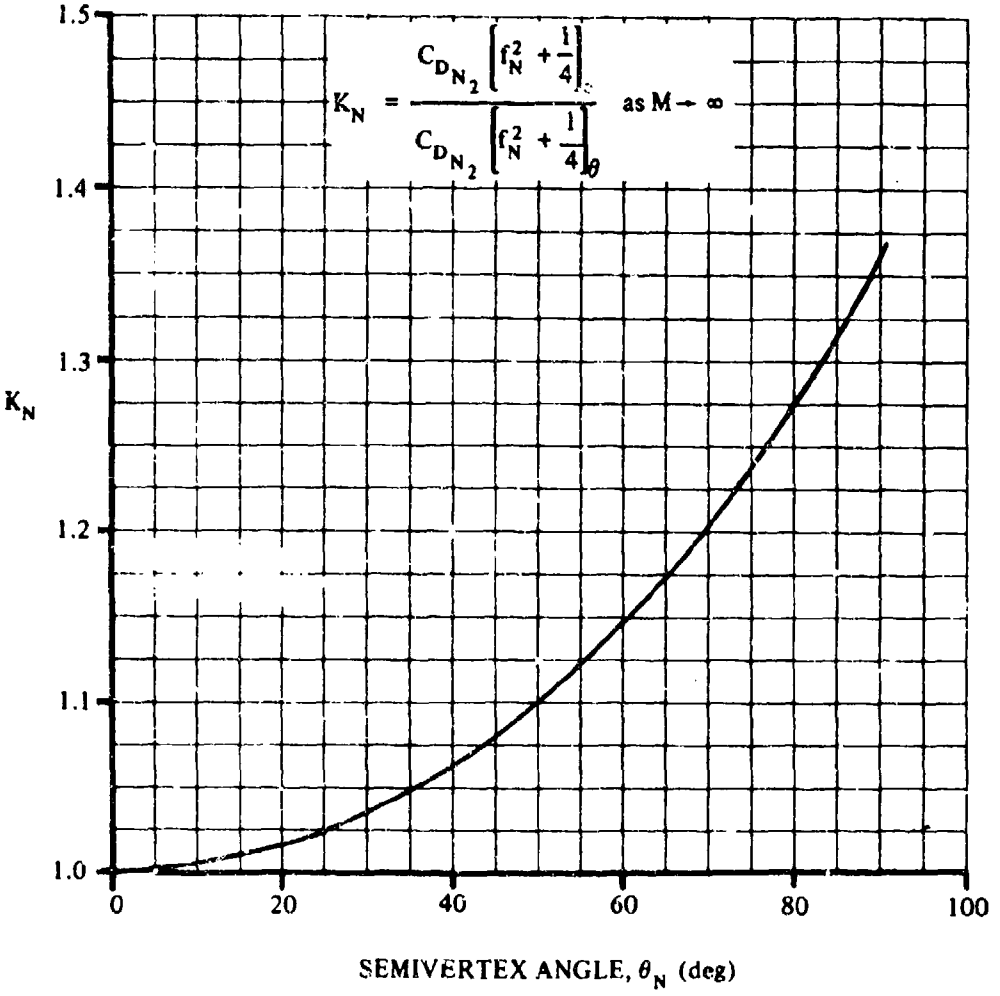

FIGURE 4.2.3.1-63 CORRELATION FACTOR FOR PRESSURE DRAG OF OGIVE NOSES

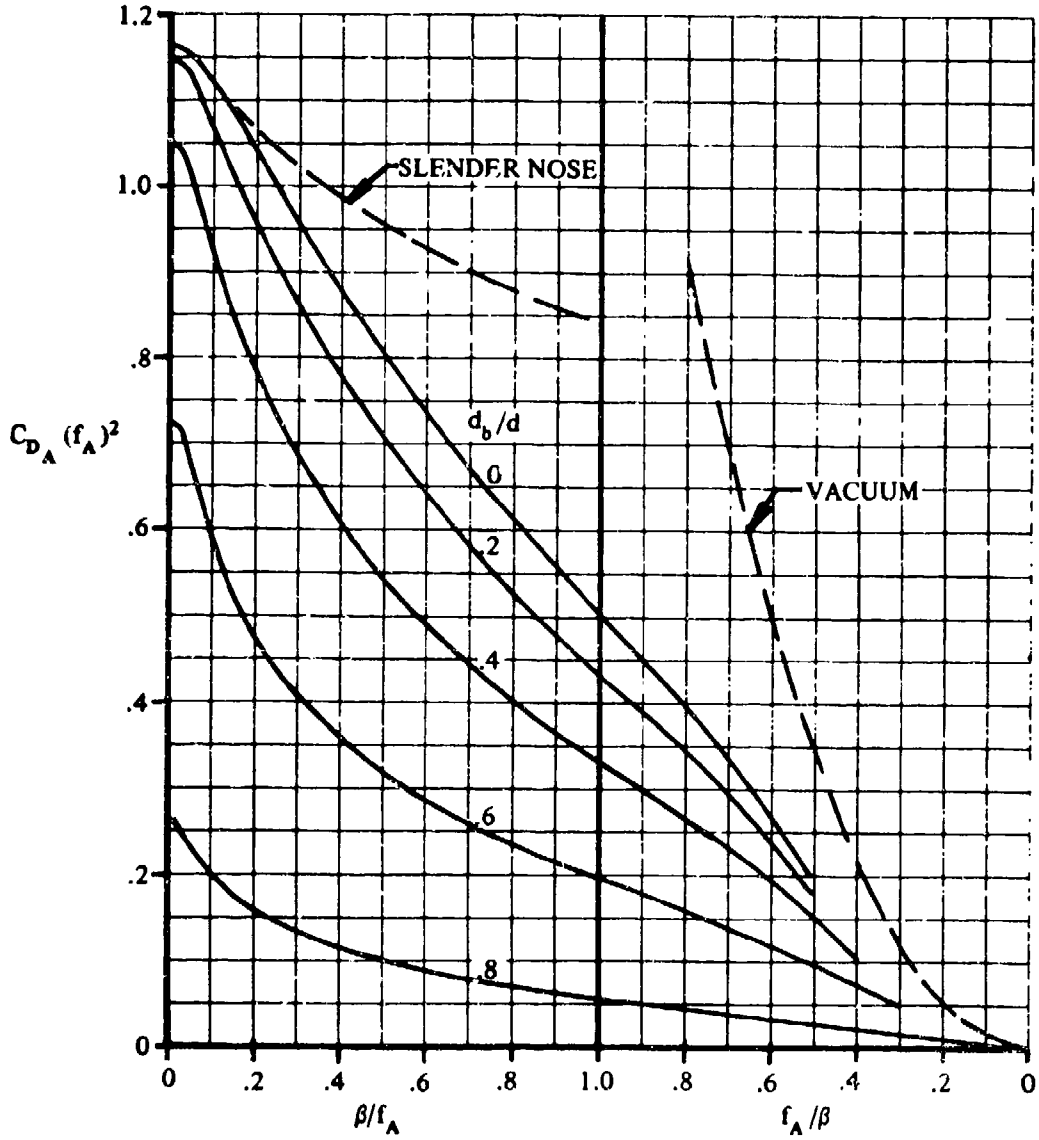

FIGURE 4.2.3.1-64 SUPERSONIC PRESSURE DRAG OF OGIVE BOATTAILS

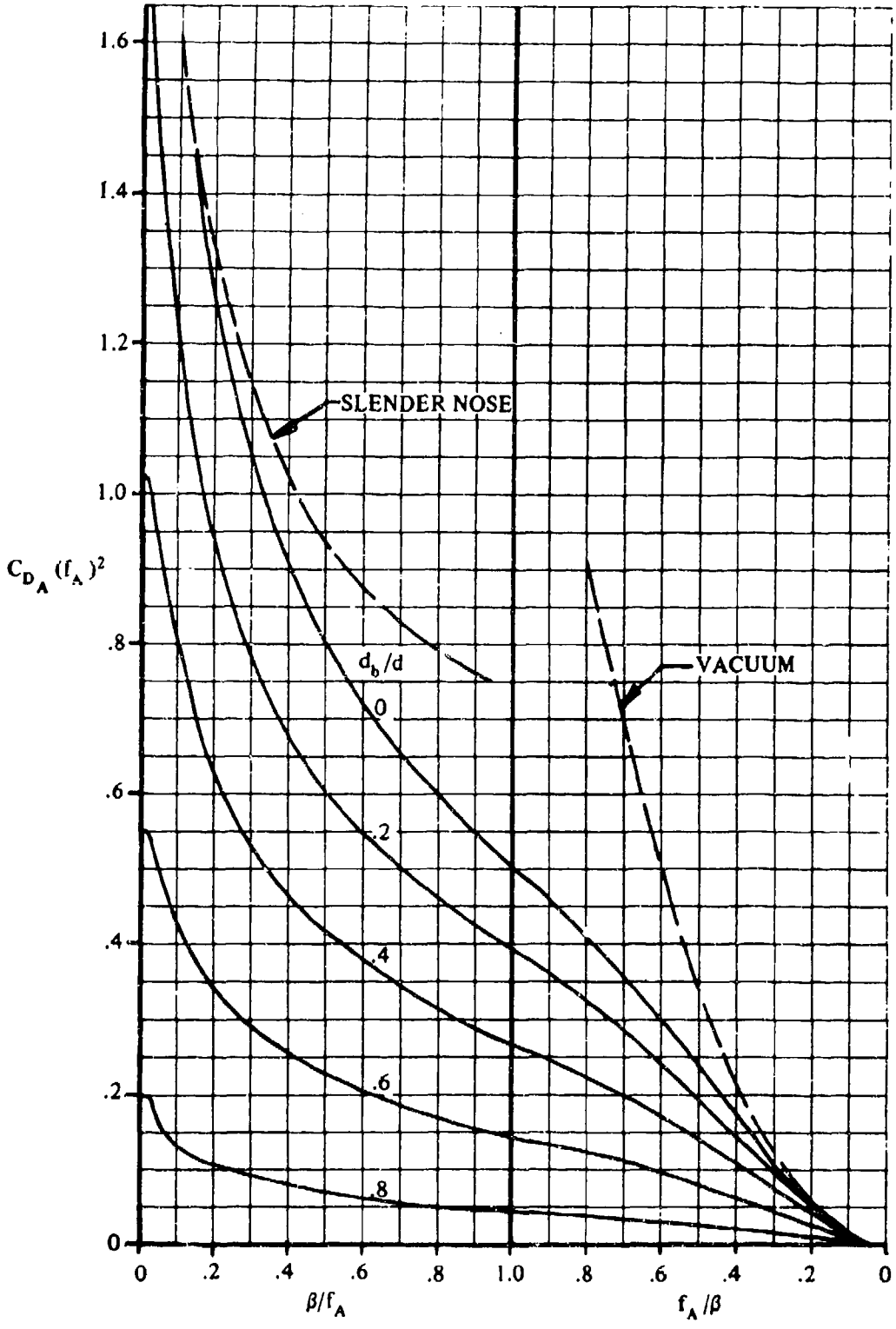

FIGURE 4.2.3.1-65 SUPERSONIC PRESSURE DRAG OF CONICAL BOATTAILS

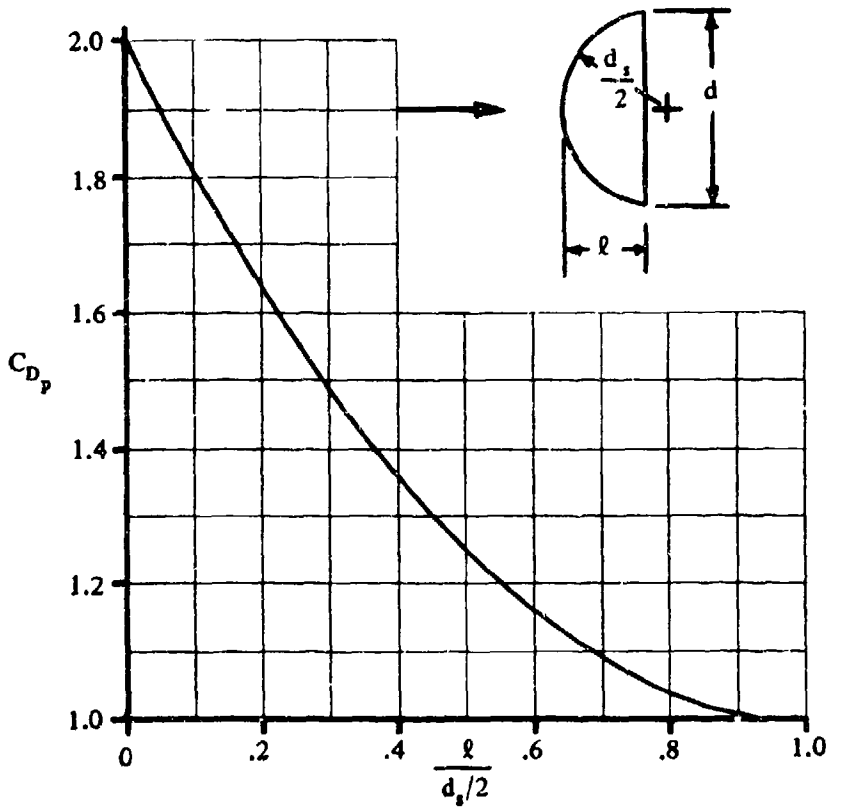

FIGURE 4.2.3.1-66 NEWTONIAN DRAG COEFFICIENT FOR SPHERICAL SEGMENTS REFERRED TO BASE AREA OF SEGMENT

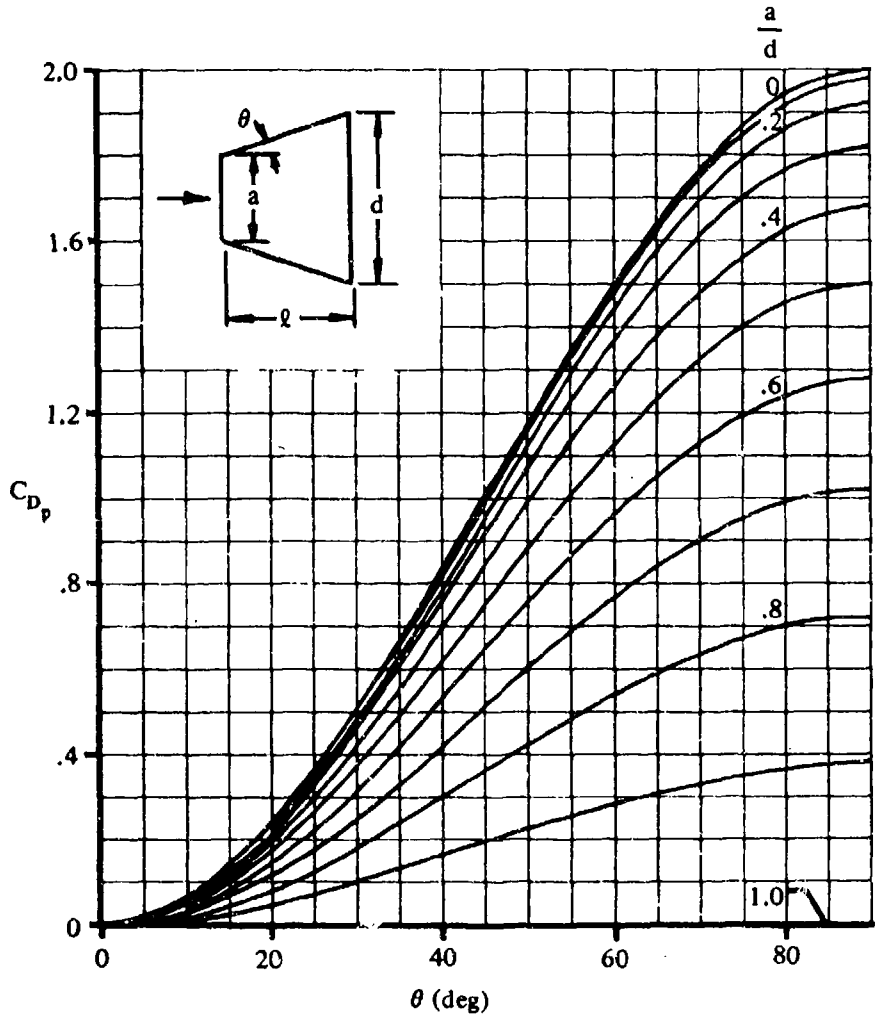

FIGURE 4.2.3.1-67 DRAG-FORCE COEFFICIENT DUE ONLY TO THE INCLINED SIDES OF A CONE FRUSTUM CALCULATED BY NEWTONIAN THEORY.
C_D IS BASED ON BODY BASE AREA S_b.

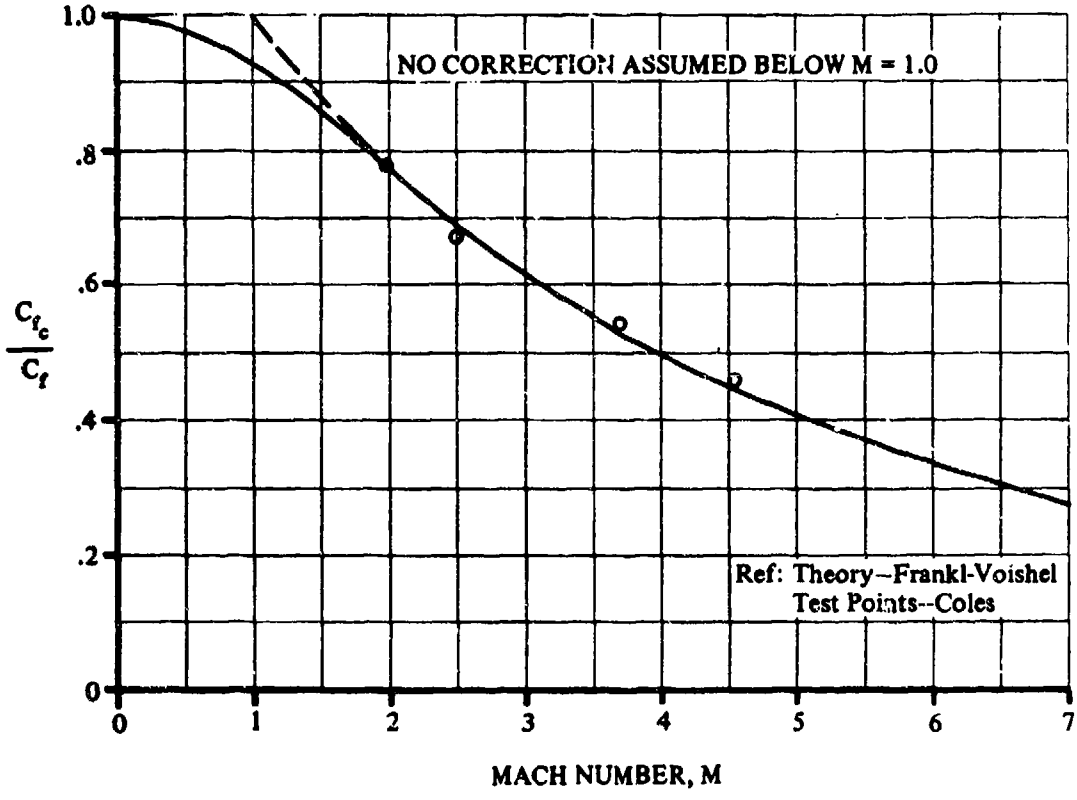

FIGURE 4.2.3.1-68 COMPRESSIBILITY EFFECT ON TURBULENT SKIN FRICTION (ZERO HEAT TRANSFER)

Reference Area:

Cylinder (axis normal to flow direction) – Cylindrical Surface Area

Sphere – Surface Area

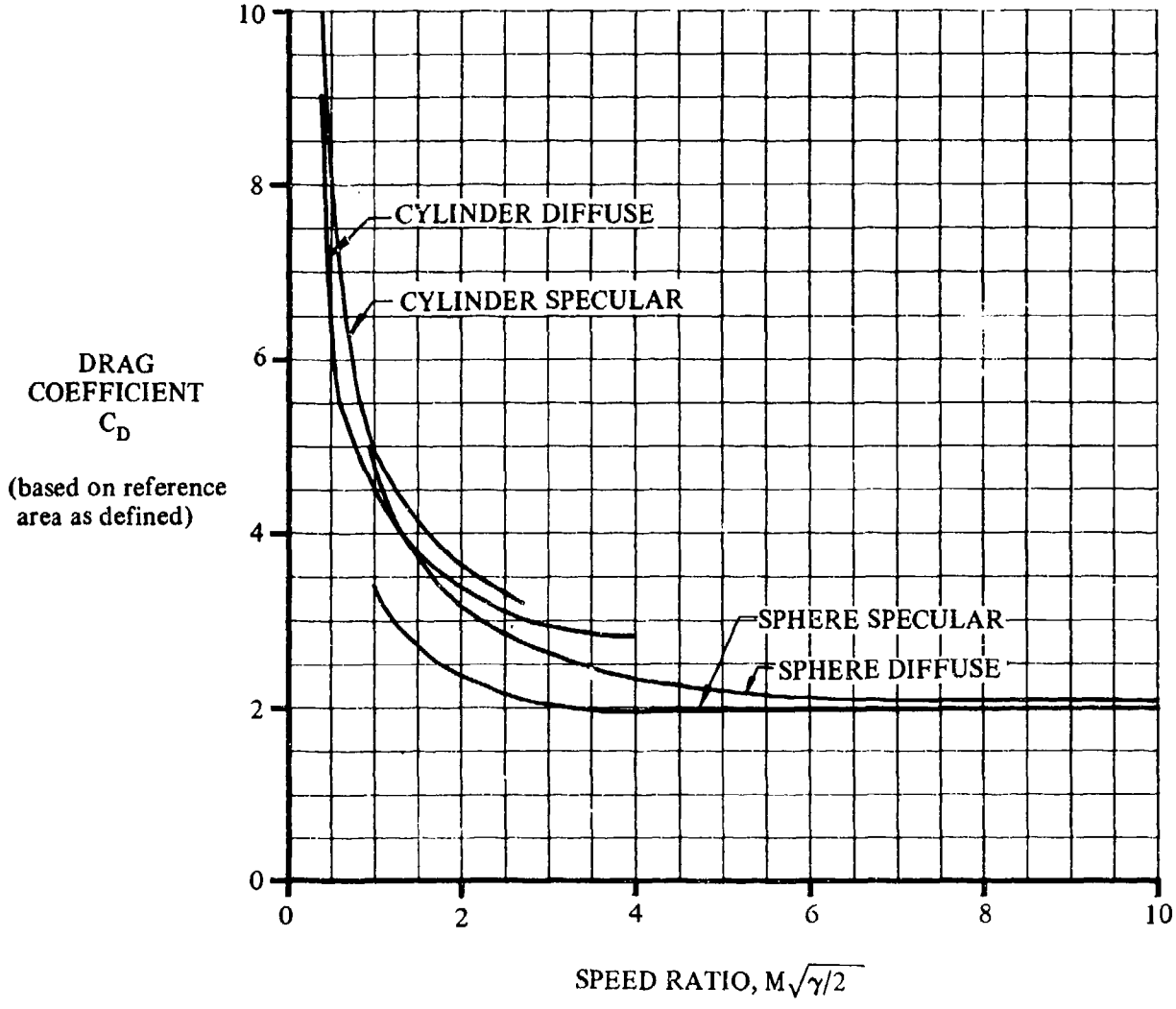

FIGURE 4.2.3.1-69 DRAG COEFFICIENTS FOR SPHERE AND CYLINDER IN FREE-MOLECULE FLOW

4.2.3.2 BODY DRAG AT ANGLE OF ATTACK

The drag of bodies at angle of attack is closely related to their lift and drag at zero angle of attack. The total drag of a body at angle of attack can be expressed as

$$C_D = C_{D_0} + C_D(\alpha) \qquad 4.2.3.2\text{-a}$$

where C_{D_0} is the body zero-lift drag, as developed in Section 4.2.3.1, and $C_D(\alpha)$ is the drag due to angle of attack as determined in this section. Discussions of the various applicable theories are given in Sections 4.2.1.1 and 4.2.1.2 and will not be repeated here.

A. SUBSONIC

Four methods are presented for estimating body drag due to angle of attack. The first method is taken from Reference 1 and is quite general since it applies to both short and long bodies of revolution. This method assumes that the flow is potential over the forward part of the body and has no viscous contribution in this region. On the aft part of the body, the flow is assumed to be entirely viscous, with lift arising solely from cross-flow drag. The second method, taken from Reference 2, is accurate to within ±10 percent for bodies of high fineness ratio but is not accurate for bodies of low fineness ratio. This method assumes that the viscous contribution at each station along the body is equal to the steady-state drag of a section of an infinite cylinder placed normal to a flow with velocity V sin α. This method is included for bodies of high fineness ratio because of its ease of application. The third method, taken from Reference 3, is also given because of its ease of application. This method is limited in application to small angles of attack and moderate fineness ratios. The fourth method, taken from Reference 4, presents a method of computing axial-force coefficient. This method (based on slender-body theory) applies to the angle-of-attack range of 0 to 180° for bodies with circular cross sections. It is recommended that one of the first three methods be used in the low-angle-of-attack range.

DATCOM METHODS

Method 1. General

The subsonic drag due to angle of attack of a body of revolution, based on $(V_B)^{2/3}$, is given in Reference 1 as

$$C_D(\alpha) = \frac{(k_2 - k_1)}{(V_B)^{2/3}} 2\alpha^2 S_o + \frac{2\alpha^3}{(V_B)^{2/3}} \int_{x_o}^{\ell_B} \eta\, r\, c_{d_c}\, dx \qquad 4.2.3.2\text{-b}$$

where

$\frac{(k_2 - k_1)}{(V_B)^{2/3}} 2\alpha^2 S_o$ is the potential-flow solution for C_{L_α} from Paragraph A of Section 4.2.1.1, multiplied by α^2

$\frac{2\alpha^3}{(V_B)^{2/3}} \int_{x_o}^{\ell_B} \eta\, r\, c_{d_c}\, dx$ is the viscous solution for C_L at angle of attack from Paragraph A of Section 4.2.1.2, multiplied by α.

α is the body angle of attack in radians.

All the parameters required to solve Equation 4.2.3.2-b are defined in Sections 4.2.1.1 and 4.2.1.2.

Method 2. Bodies of High Fineness Ratio

The subsonic drag due to angle of attack of a body of revolution, based on $(V_B)^{2/3}$, is given in Reference 2 as

$$C_D(\alpha) = 2\alpha^2 \frac{S_b}{(V_B)^{2/3}} + \eta c_{d_c} \frac{S_p}{(V_B)^{2/3}} \alpha^3 \qquad 4.2.3.2\text{-c}$$

where

S_b is the body base area.

V_B is the total body volume.

S_p is the body planform area.

α is the body angle of attack in radians.

η is the ratio of the drag on a finite cylinder to the drag on an infinite cylinder, obtained from Figure 4.2.1.2-35a as a function of the body fineness ratio ℓ_B/d.

c_{d_c} is the experimental steady-state cross-flow drag coefficient of a circular cylinder of infinite length, obtained from Figure 4.2.1.2-35b as a function of the cross-flow Mach number at a given angle of attack.

Comparisons between results obtained by this method and test results (Reference 2) show that the body drag due to angle of attack is, in general, fairly accurately predicted up to moderate angles of attack for bodies with fineness ratios as low as about 6. For bodies with fineness ratios of about 15 and greater, the method should predict the drag due to angle of attack quite accurately over the angle-of-attack range of practical interest.

Method 3. $\alpha < 10^o$ and $2f \tan\alpha < 5$

For the range of parameters $\alpha < 10^o$ and $2f \tan\alpha < 5$, the simplified method of Reference 3 indicates that the subsonic drag due to angle of attack of a body of revolution, based on body base area, may be given as

$$C_D(\alpha) = \alpha^2 + 0.49 f^2 \frac{c_{d_c}}{S_b} \alpha^4 \qquad 4.2.3.2\text{-d}$$

where α is the body angle of attack in radians, f is the body fineness ratio, and the remaining parameters are defined in Method 2 above.

The first three sample problems illustrate the accuracy of the above methods applied to the same configuration.

Method 4. High Angles of Attack

The method of Reference 4 is applicable to the angle-of-attack range of 0 to 180°. Due to the complexity of calculating drag for bodies with noncircular cross sections, the Datcom method is limited to bodies with circular cross sections. For noncircular cross-section bodies, the user is referred to the treatment presented in References 4 and 5. The Datcom method predicts axial-force coefficient C_X based on body base area. Sketch (a) shows how this term may be used in conjunction with the C_N calculated in Section 4.2.1.2 to obtain C_D ($C_D = C_N \sin\alpha - C_X \cos\alpha$).

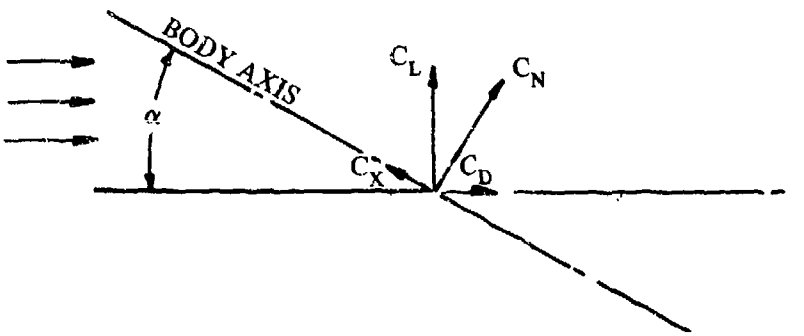

SKETCH (a)

The axial force C_X of a circular-cross-section body at an angle of attack, based on the body base area, is given by

$$C_X = C_{X_{\alpha=0}} \cos^2\alpha' \quad (\text{for } 0 \leqslant \alpha \leqslant 90^\circ) \qquad 4.2.3.2\text{-e}$$

$$C_X = C_{X_{\alpha=180^\circ}} \cos^2\alpha' \quad (\text{for } 90^\circ \leqslant \alpha \leqslant 180^\circ \qquad 4.2.3.2\text{-f}$$

and

$$C_{X_{\alpha=0}} = -(C_f + C_{D_b}) \qquad 4.2.3.2\text{-g}$$

$$C_{X_{\alpha=180^\circ}} = C_f + C_{D_b} \qquad 4.2.3.2\text{-h}$$

where

$C_{X_{\alpha=0}}$ is the axial-force coefficient at $\alpha = 0$.

α' is an incidence angle defined as $\alpha' = \alpha$ for $0 \leq \alpha \leq 90^{\circ}$ and $\alpha' = 180^{\circ} - \alpha$ for $90^{\circ} < \alpha < 180^{\circ}$.

$C_{X_{\alpha=180^{\circ}}}$ is the axial-force coefficient at $\alpha = 180^{\circ}$.

C_f is the turbulent flat-plate skin-friction coefficient based on the reference length. This value is obtained from Figure 4.2.3.2-27 as a function of Reynolds number (based on body length) and Mach number.

C_{D_b} is the base-drag coefficient based on the maximum body frontal area, given by Equation 4.2.3.1-b.

It is recommended that this method be used only in the high-angle-of-attack range where other Datcom methods are not applicable. No substantiating test data are available for this method in the subsonic speed range.

Sample Problems

1. Method 1

Given: The parabolic body of revolution of Reference 10.

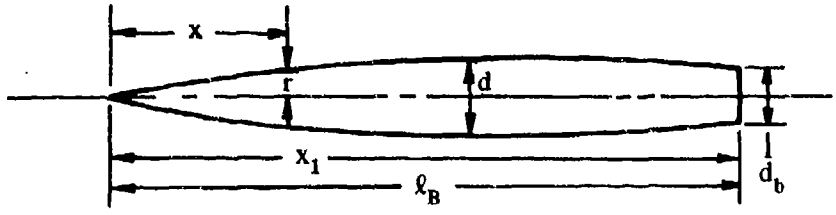

$\ell_B = 5.04$ ft d = 0.510 ft $d_b = 0.376$ ft f = 9.87

$V_B = 0.687$ cu ft; $(V_B)^{2/3} = 0.7786$ sq ft M = 0.40 $0 \leq \alpha \leq 18^{\circ}$

Body ordinates: $r = 0.255\left[1 - \left(1 - \frac{2x}{6.375}\right)^2\right]^{1/4}$

Compute:

Potential Flow Term (Section 4.2.1.1)

$x_1 = 5.04$ ft*

$x_1/\ell_B = 5.04/5.04 = 1.0$

* x_1 may be determined by inspection for this case

$x_o/\ell_B = 0.903$ (Figure 4.2.1.1-20b)

$x_o = (0.903)(5.04) = 4.55$ ft

$$S_o = \pi(r_o)^2 = \pi\left\{0.255\left[1-\left(1-\frac{2x_o}{6.375}\right)^2\right]^{3/4}\right\}^2 = \pi\left\{0.255\left[1-\left(1-\frac{(2)(4.55)}{6.375}\right)^2\right]^{3/4}\right\}^2$$

$= 0.151$ sq ft

$(k_2 - k_1) = 0.938$ (Figure 4.2.1.1-20a)

$$\frac{(k_2-k_1)}{(V_B)^{2/3}}\,2\alpha^2 S_o = \frac{(0.938)}{(0.7786)}\,2\alpha^2\,(0.151) = 0.364\,\alpha^2$$

Viscous Term (Section 4.2.1.2)

$\eta = 0.685$ (Figure 4.2.1.2-35a)

$c_{d_c} = f(M_c)$; $M_c = M \sin\alpha$

M_c varies between 0.40 sin (0) to 0.40 sin 18^o; $0 \le M_c \le 0.1236$

$c_{d_c} = 1.20$ (constant) (Figure 4.2.1.2-35b)

$$\int_{x_o}^{\ell_B} \eta\, r\, c_{d_c}\, dx = (0.685)(1.20)\int_{x_o}^{\ell_B} r\, dx = 0.822 \sum_{x_o}^{\ell_B} r\,\Delta x$$

x	r*	Δx	rΔx
$x_o = 4.55$	0.2136	0.20	0.043
4.75	0.2010	0.20	0.040
4.95	0.1906	0.09	0.017
$\ell_B = 5.04$			

$\Sigma r\Delta x = 0.100$

$$\int_{x_o}^{\ell_B} \eta\, r\, c_{d_c}\, dx = (0.822)(0.100) = 0.0822$$

* r is taken to be at the midpoint of each body segment.

$$\frac{2\alpha^3}{(V_B)^{2/3}} \int_{X_o}^{\ell_B} \eta \, r \, c_{d_c} \, dx = \frac{2\alpha^3}{(0.7786)} (0.0822) = 0.211 \, \alpha^3$$

Solution:

$$C_D(\alpha) = \frac{(k_2 - k_1)}{(V_B)^{2/3}} 2\alpha^2 S_o + \frac{2\alpha^3}{(V_B)^{2/3}} \int_{X_o}^{\ell_B} \eta \, r \, c_{d_c} \, dx \quad \text{(Equation 4.2.3.2-b)}$$

$$= 0.364 \, \alpha^2 + 0.211 \, \alpha^3$$

①	②	③	④	⑤
α (deg)	α (rad)	α^2 (rad^2)	α^3 (rad^3)	$C_D(\alpha)$ 0.364 ③ + 0.211 ④
0	0	0	0	0
2	0.0349	0.00122	0.00004	0.0005
4	0.0698	0.00487	0.00034	0.0018
6	0.1047	0.01096	0.00115	0.0042
8	0.1396	0.01949	0.00272	0.0077
10	0.1745	0.03045	0.00531	0.0122
12	0.2094	0.04385	0.00918	0.0179
14	0.2443	0.05968	0.01458	0.0248
16	0.2792	0.07795	0.02176	0.0330
18	0.3141	0.09866	0.03099	0.0425

The calculated results are compared with test values from Reference 10 in Sketch (b).

2. Method 2

Given: The same configuration as in Sample Problem 1.

Additional Characteristics:

$S_b = 0.111$ sq ft $\quad S_p = 2.016$ sq ft

Compute:

Potential Flow Term

$$2\alpha^2 \frac{S_b}{(V_B)^{2/3}} = 2\alpha^2 \left(\frac{0.111}{0.7786}\right) = 0.285 \, \alpha^2$$

Viscous Term

$$\left.\begin{aligned}\eta &= 0.685\\ c_{d_c} &= 1.20\end{aligned}\right\}\ \text{(Sample Problem 1)}$$

$$\eta\, c_{d_c} \frac{S_p}{(V_B)^{2/3}} \alpha^3 = (0.685)(1.20)\frac{2.016}{0.7786}\alpha^3 = 2.128\,\alpha^3$$

Solution:

$$C_D(\alpha) = 2\alpha^2 \frac{S_b}{(V_B)^{2/3}} + \eta\, c_{d_c} \frac{S_p}{(V_B)^{2/3}} \alpha^3 \quad \text{(Equation 4.2.3.2-c)}$$

$$= 0.285\,\alpha^2 + 2.128\,\alpha^3$$

①	②	③	④	⑤
α (deg)	α (rad)	α^2 (rad^2)	α^3 (rad^3)	$c_D(\alpha)$ 0.285 ③ + 2.128 ④
0	(See calculation table, Sample Problem 1)			0
2				0.0004
4				0.0021
6				0.0056
8				0.0113
10				0.0200
12				0.0320
14				0.0480
16				0.0685
18				0.0941

The calculated results are compared with test values from Reference 10 in Sketch (b).

3. Method 3

Given: The same configuration as in Sample Problems 1 and 2.

Compute:

$c_{d_c} = 1.20$ (Sample Problem 1)

2f $\tan\alpha > 5$ for $\alpha > 14.2^{\circ}$; therefore, the problem is limited to angles of attack $< 10^{\circ}$.

Solution:

$$C_D(\alpha) = \alpha^2 + 0.49\, f^2 \frac{c_{d_c}}{S_b}\, \alpha^4 \quad \text{(Equation 4.2.3.2-d)}$$

$$= \alpha^2 + (0.49)\,(9.87)^2\, \frac{1.20}{0.111}\, \alpha^4$$

$$= \alpha^2 + 516\, \alpha^4$$

①	②	③	④	⑤	⑥
α (deg)	α (rad)	α^2 (rad^2)	α^4 (rad^4)	$C_D(\alpha)$ (based on S_b) ③ + 516 ④	$C_D(\alpha)$ (based on $(V_B)^{2/3}$) ⑤ $S_b/(V_B)^{2/3}$
0	0	0	0	0	0
2	0.0349	0.00122	0.000001	0.00173	0.0002
4	0.0698	0.00487	0.000024	0.01725	0.0025
6	0.1047	0.01096	0.00012	0.07286	0.0104
8	0.1396	0.01949	0.00038	0.21549	0.0307

The calculated results from Column 6 are compared with test values from Reference 10 in Sketch (b)

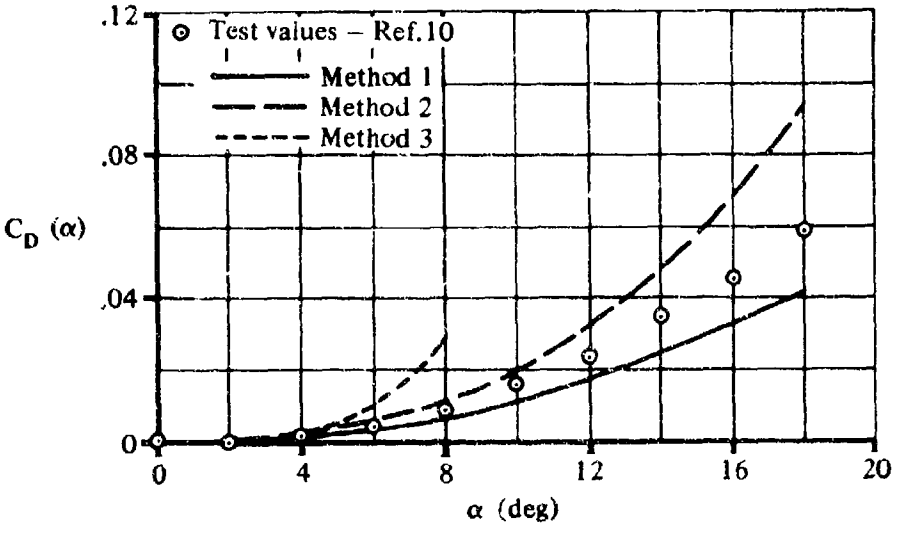

SKETCH (b)

4. Method 4

Given: The same configuration as in Sample Problems 1, 2, and 3.

Additional Characteristics:

$\alpha = 50^{o}$ $\qquad R_{\ell} = 10^{6}$

Compute:

$\alpha' = \alpha = 50^{o}$

$C_f = 0.0042$ (Figure 4.2.3.2-27)

$\ell_B/d = \dfrac{5.04}{0.510} = 9.88$ $\qquad \dfrac{d_b}{d} = \dfrac{0.376}{0.510} = 0.737$ (Sample Problem 1)

$\dfrac{S_S}{S_b} = 28.7$ (Figure 2.3-3)

$$(C_{D_f})_b = C_f \left[1 + \frac{60}{(\ell_B/d)^3} + 0.0025\left(\frac{\ell_B}{d}\right)\right] \frac{S_S}{S_B}$$ (first term in Equation 4.2.3.1-a)

$$= 0.0042 \left[1 + \frac{60}{(5.04/0.510)^3} + 0.0025\left(\frac{5.04}{0.510}\right)\right] 28.7$$

$$= 0.131$$

$$C_{D_b} = 0.029 \left(\frac{d_b}{d}\right)^3 \Big/ \sqrt{(C_{D_f})_b}$$ (Equation 4.2.3.1-b

$$= (0.029)\left(\frac{0.376}{0.510}\right)^3 \Big/ \sqrt{0.131}$$

$$= 0.0321$$

Solution:

$$C_{X_{\alpha=0}} = -(C_f + C_{D_b})$$ (Equation 4.2.3.2-g)

$$= -(0.0042 + 0.0321)$$

$$= -0.0363$$

$$C_X = C_{X_{\alpha=0}} \cos^2\alpha' \quad \text{(Equation 4.2.3.2-e)}$$

$$= -(0.0363)(0.6428)^2$$

$$= -0.0150 \text{ (based on body base area)}$$

No test data are available for a comparison.

B. TRANSONIC

Slender-body theory may be applied for a rapid but approximate estimate of body drag at angle of attack.

DATCOM METHOD

The drag coefficient due to angle of attack from slender-body theory is

$$C_D(\alpha) = \alpha^2 \text{ (based on } S_b) \qquad 4.2.3.2\text{-i}$$

where the drag coefficient is referred to body base area and α is the body angle of attack in radians.

C. SUPERSONIC

Three methods are given for estimating body drag due to angle of attack at supersonic speeds. The first two methods correspond to the first two methods of estimating body lift in Section 4.2.1.2. The general discussion of the methods used in Section 4.2.1.2 will not be repeated here. In addition, a third method is given for estimating the body axial-force coefficient (based on Reference 4 and similar to Method 4 of Paragraph A of this section). This method is applicable up to an angle of attack of 180° and is limited to bodies of revolution with blunt, conical, ogive, and 3/4-power noses.

DATCOM METHODS

Method 1

The supersonic body drag due to angle of attack, determined by the method of Reference 9 for moderate angles of attack, is

$$C_D(\alpha) = C_L\alpha \qquad 4.2.3.2\text{-j}$$

where C_L is given by Equation 4.2.1.2-g or Equation 4.2.1.2-h, depending on whether the body cross section is circular or elliptical, and α is the angle of attack in radians.

The supersonic drag due to angle of attack of a body of revolution, based on body base area, is then

$$C_D(\alpha) = 2\alpha^2 + c_{d_c}\frac{S_p}{S_b}\alpha^3 \qquad 4.2.3.2\text{-k}$$

where all the parameters are defined under Method 2 of Paragraph A.

The supersonic drag due to angle of attack of a body having an elliptical cross section, based on body base area, is

$$[C_D(\alpha)]_{a/b} = \left[\frac{a}{b}\cos^2\phi + \frac{b}{a}\sin^2\phi\right] C_D(\alpha) \qquad 4.2.3.2\text{-}l$$

where

a is the major axis of the elliptical cross section.

b is the minor axis of the elliptical cross section.

ϕ is the angle of bank of the body about its longitudinal axis; $\phi = 0$ with the major axis horizontal and $\phi = 90^o$ with the minor axis horizontal.

$C_D(\alpha)$ is the drag due to angle of attack of a body of revolution having the the same cross-sectional area distribution along its axis as the elliptical-cross-section body of interest. It is given by Equation 4.2.3.2-k.

Calculated results using this method have been compared with test data in Reference 9. The comparison included bodies of revolution and bodies of elliptical cross section, both having the same axial distribution of cross-sectional area. The tests included bodies of fineness ratios 6 and 10 at M = 1.98 and bodies of fineness ratio 6 at M = 3.88. The angle-of-attack range was from zero to approximately 20^o. For the cases considered, there is good agreement between results calculated by this method and test values.

Method 2

A method for predicting the normal force of bodies of revolution at supersonic speeds is given in Section 4.2.1.2. The drag due to angle of attack of a body of revolution can be expressed as

$$C_D(\alpha) = C_N \sin\alpha - C_X \cos\alpha \qquad 4.2.3.2\text{-m}$$

where C_N and C_X are defined in Sketch (a). For small angles of attack the resultant force vector is nearly normal to the body surface and the chordwise force component is neglected. Equation 4.2.3.2-m can then be approximated at small angles of attack as

$$C_D(\alpha) = C_N\alpha \qquad 4.2.3.2\text{-n}$$

where

α is the body angle of attack in radians.

C_N is the body normal-force coefficient at angle of attack, based on body base area, obtained from Figure 4.2.1.2-38.

The normal-force data of Figure 4.2.1.2-38 are for cone-cylinder configurations, but may be used for general pointed bodies without great loss of accuracy.

Method 3

The following method (Reference 4) predicts the axial-force coefficient C_X in the angle-of-attack range of 0 to 180°. The method is limited to bodies of revolution with blunt, conical, ogive, and 3/4-power nose shapes. Due to the complexity of calculating drag for bodies with noncircular cross sections, the Datcom method is limited to bodies with circular cross sections. For noncircular cross-section bodies, the user is referred to the treatment presented in References 4 and 5. This C_X term may be used in conjunction with the C_N calculated in Section 4.2.1.2 to obtain C_D; i.e., $C_D = C_N \sin\alpha - C_X \cos\alpha$.

The axial-force C_X of a circular-cross-section body at an angle of attack is given by

$$C_X = C_{X_{\alpha=0}} \cos^2\alpha' \quad (\text{for } 0 \leqslant \alpha \leqslant 90^\circ) \qquad 4.2.3.2\text{-o}$$

$$C_X = C_{X_{\alpha=180^\circ}} \cos^2\alpha' \quad (\text{for } 90^\circ \leqslant \alpha \leqslant 180^\circ) \qquad 4.2.3.2\text{-p}$$

and

$$C_{X_{\alpha=0}} = -(C_f + C_{D_b} + C_{D_w}) \qquad 4.2.3.2\text{-q}$$

$$C_{X_{\alpha=180^\circ}} = C_f + C_{D_b} + C_{D_w} \qquad 4.2.3.2\text{-r}$$

where

C_{D_b} is the base-drag coefficient for bodies of revolution, from Figure 4.2.3.1-60.

C_{D_w} is the wave-drag coefficient determined from Figure 4.2.3.2-28a for blunt nose or blunt base forward, or Figure 4.2.3.2-28b for other nose shapes.

The remaining terms are defined in Paragraph A of Section 4.2.3.2.

A comparison of test data taken from References 7 and 8 with results calculated by this method is presented in Table 4.2.3.2-A. It should be noted that very little reliable test data at high angles of attack were available, and much of that used to substantiate the method is suspected of being affected by model support interference. The method generally predicts a lower absolute value of C_X than evidenced by available test data; however, the user should be cautious in view of the uncertainty of the test data.

It is recommended that other Datcom methods be used whenever possible, especially at low angles of attack.

The method is applicable to $0 \leqslant M \leqslant 7$; however, caution should be used in the hypersonic range because of the lack of substantiating data.

Sample Problems

1. Method 1

Given: Three bodies of Reference 11, each having the same longitudinal area distribution.

Body 1. Ogive-cylinder

ℓ_B = 42.0 in. ℓ_N = 14.0 in. ℓ_A = 28.0 in. $d_b = d_{max}$ = 4.0 in.

f = 10.5 S_b = 12.57 sq in. S_p = 154.0 sq in.

Body 2. Horizontal ellipse

Same longitudinal area distribution as ogive-cylinder body.

a = 4.90 in. b = 3.26 in. $\phi = 0$

Body 3. Vertical ellipse

Same longitudinal area distribution as ogive-cylinder body.

a = 4.90 in. b = 3.26 in. $\phi = 90^o$

Additional Characteristics:

M = 2.01; β = 1.744 $0 \leq \alpha \leq 10^o$

Body 1. Ogive-cylinder

Compute:

S_p/S_b = 154.0/12.57 = 12.25

M_c = M sin α

c_{d_c} (Figure 4.2.1.2-35b)

} (See calculation table below.)

Solution:

$$C_D(\alpha) = 2\alpha^2 + c_{d_c} \frac{S_p}{S_b} \alpha^3$$ (Equation 4.2.3.2-k)

①	②	③	④	⑤	⑥	⑦	⑧
α (deg)	α (rad)	α^2 (rad^2)	α^3 (rad^3)	M_c M sin α	c_{d_c} (Fig. 4.2.1.2-35b)	$c_{d_c}\frac{S_p}{S_b}$ ⑥ 12.25	$C_D(\alpha)$ (Eq. 4.2.3.2-k) 2 ③ + ⑦④
0	0	0	0	0	1.20	14.70	0
2	0.0349	0.00122	0.00004	0.0701	1.20	14.70	0.00303
4	0.0698	0.00487	0.00034	0.1402	1.20	14.70	0.01474
6	0.1047	0.01096	0.00115	0.2101	1.20	14.70	0.03882
8	0.1396	0.01949	0.00272	0.2797	1.21	14.82	0.07929
10	0.1745	0.03045	0.00531	0.3489	1.233	15.10	0.1411

Bodies 2 and 3

Compute:

Horizontal ellipse

$$\left[\frac{a}{b}\cos^2\phi + \frac{b}{a}\sin^2\phi\right] = \left[1.5\cos^2(0) + 0.667\sin^2(0)\right] = 1.50$$

Vertical ellipse

$$\left[\frac{a}{b}\cos^2\phi + \frac{b}{a}\sin^2\phi\right] = \left[1.5\cos^2(90^o) + 0.667\sin^2(90^o)\right] = 0.667$$

Solution:

$$\left[C_D(\alpha)\right]_{a/b} = \left[\frac{a}{b}\cos^2\phi + \frac{b}{a}\sin^2\phi\right] C_D(\alpha) \quad \text{(Equation 4.2.3.2-}\ell\text{)}$$

$$= 1.50\, C_D(\alpha) \quad \text{Horizontal ellipse}$$

$$= 0.667\, C_D(\alpha) \quad \text{Vertical ellipse}$$

①	②	③	④
α (deg)	$C_D(\alpha)$ Ogive-Cyl.	$\left[C_D(\alpha)\right]_{a/b}$ Horiz. Ellipse 1.50 ②	$\left[C_D(\alpha)\right]_{a/b}$ Vert. Ellipse 0.667 ②
0	0	0	0
2	0.00303	0.00454	0.00202
4	0.01474	0.02211	0.00983
6	0.03882	0.05823	0.02589
8	0.07929	0.1189	0.0529
10	0.1411	0.2116	0.0941

The calculated results for the three bodies are compared with test values from Reference 11 in Sketch (c).

2. Method 2

Given: The ogive-cylinder body of Sample Problem 1.

Compute:

$$f_N = \frac{\ell_N}{d_{max}} = \frac{14.0}{4.0} = 3.50$$

$$f_A = \frac{\ell_A}{d_{max}} = \frac{28.0}{4.0} = 7.0$$

$f_A/f_N = 7.0/3.50 = 2.0$

$\beta/f_N = 1.744/3.50 = 0.498$

βC_N (Figure 4.2.1.2-38b) (See calculation table below.)

$C_N = \beta C_N/\beta$ (based on body base area) (See calculation table below.)

Solution:

$C_D(\alpha) = C_N \alpha$ (Equation 4.2.3.2-n)

①	②	③	④	⑤	⑥
α (deg)	α (rad)	$\beta\alpha$ (deg)	βC_N (Fig. 4.2.1.2-38b)	C_N ④ /β	$C_D(\alpha)$ (Eq. 4.2.3.2-n) ⑤ ②
0	0	0	0	0	0
2	0.0349	3.488	0.15	0.086	0.0030
4	0.0698	6.976	0.30	0.172	0.0120
6	0.1047	10.464	0.52	0.298	0.0312
8	0.1396	13.952	0.80	0.459	0.0641
10	0.1745	17.44	1.20	0.688	0.1201

The calculated results are compared with test values from Reference 11 in Sketch (c).

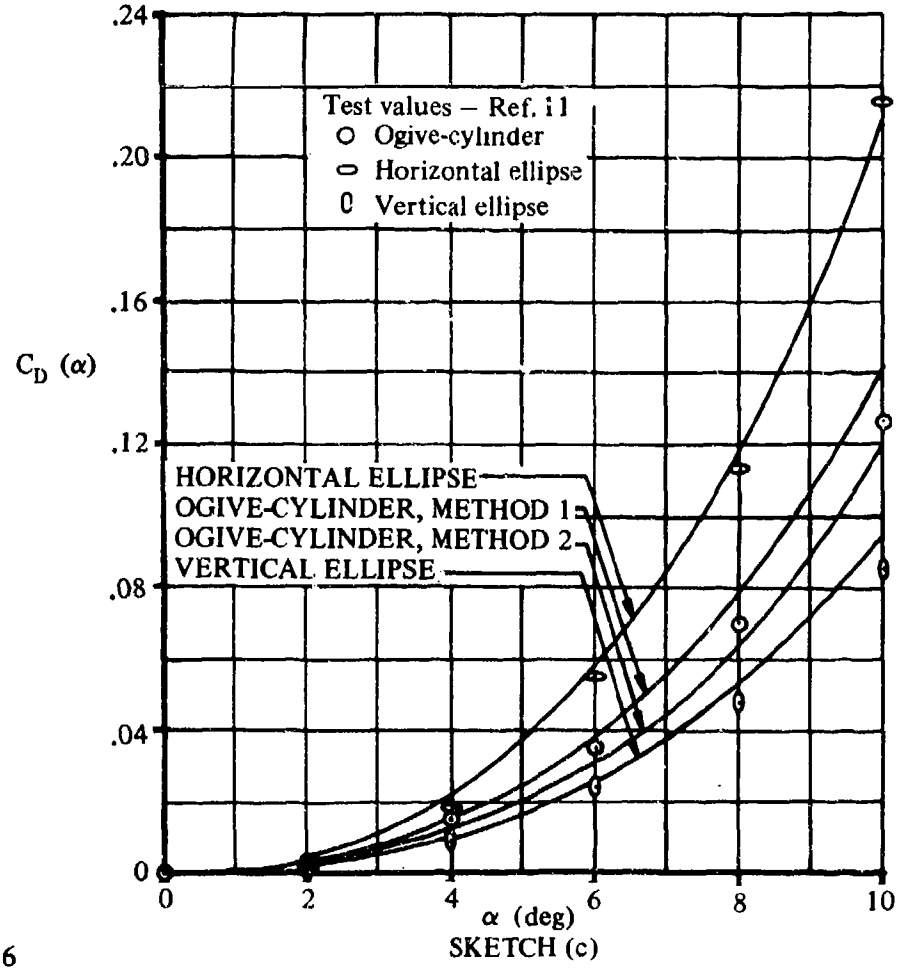

SKETCH (c)

3. Method 3

Given: An ogive-cylinder body of Reference 7.

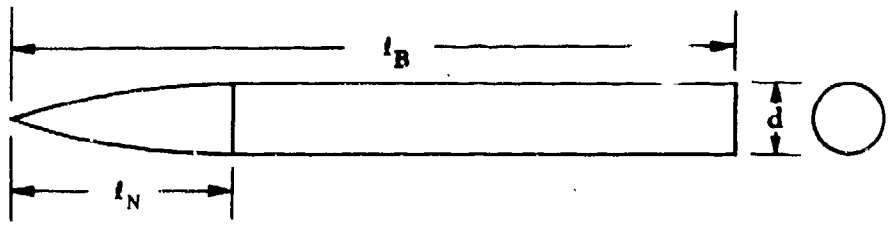

Body Characteristics:

$$\frac{\ell_B}{d} = 11 \qquad \frac{\ell_N}{d} = 5$$

Additional Characteristics:

$$\alpha = 40^o, 120^o \qquad M = 2.86 \qquad R_\ell = 1.375 \times 10^6$$

Compute:

C_X at $\alpha = 40^o$

$$\alpha' = \alpha = 40^o$$

$$C_f = 0.00287 \text{ (Figure 4.2.3.2-27)}$$

$$C_{D_b} = 0.103 \text{ (Figure 4.2.3.1-60)}$$

$$M\frac{d}{\ell_N} = (2.86)\left(\frac{1}{5}\right) = 0.572$$

$$0.7M^2 C_{D_w} = 0.215 \text{ (Figure 4.2.3.2-28b)}$$

$$C_{D_w} = \frac{0.215}{0.7M^2} = \frac{0.215}{0.7(2.86)^2} = 0.0375$$

$$C_{X_{\alpha=0}} = -(C_f + C_{D_b} + C_{D_w}) \text{ (Equation 4.2.3.2-q)}$$

$$= -(0.00287 + 0.103 + 0.0375)$$

$$= -0.143$$

$$C_X = C_{X_{\alpha=0}} \cos^2\alpha' \quad \text{(Equation 4.2.3.2-o)}$$

$$= -(0.143)(0.587)$$

$$= -0.084 \text{ (based on body base area)}$$

C_X at $\alpha = 120^o$

$$\alpha' = 180^o - \alpha = 60^o$$

$C_f = 0.00287$ (Figure 4.2.3.2-27)

$C_{D_b} = 0.103$ (Figure 4.2.3.1-60)

$C_{D_w} = 1.747$ (Figure 4.2.3.2-28a for blunt base forward)

$$C_{X_{\alpha=180^o}} = C_f + C_{D_b} + C_{D_w} \quad \text{(Equation 4.2.3.2-r)}$$

$$= 0.00287 + 0.103 + 1.747$$

$$= 1.85$$

$$C_X = C_{X_{\alpha=180^o}} \cos^2\alpha' \quad \text{(Equation 4.2.3.2-p)}$$

$$= (1.85)(0.25)$$

$$= 0.46 \text{ (based on body base area)}$$

Additional values have been calculated below:

M	α (deg)	C_X
2.86	0	−0.14
2.86	20	−0.126
2.86	40	−0.084
2.86	60	−0.036
2.86	80	−0.004
2.86	100	0.006
2.86	120	0.46
2.86	140	1.08
2.86	160	1.63
2.86	180	1.84

The calculated results of the sample problem are compared to test values from Reference 7 in Sketch (d).

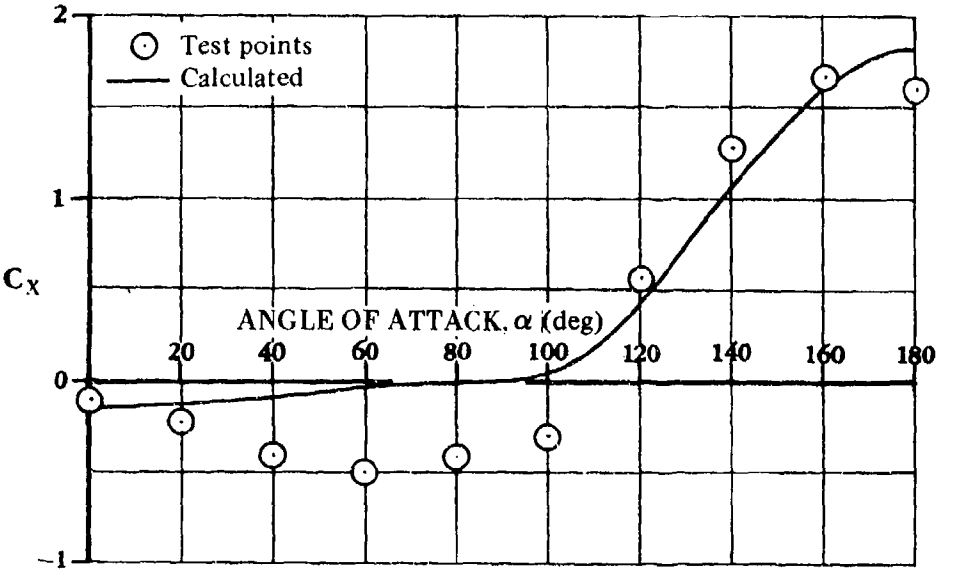

SKETCH (d)

D. HYPERSONIC

For small or moderate angles of attack the hypersonic drag of a body is given by Method 2 of Paragraph C. For large angles of attack the method of Reference 4 presented as Method 3 of Paragraph C of this section may be used.

DATCOM METHODS

Method 1

At small to moderate angles of attack, body drag due to angle of attack, based on base area, is given by Equation 4.2.3.2-n; i.e.,

$$C_D(\alpha) = C_N \alpha$$

where C_N is obtained from Paragraph D of Section 4.2.1.2 and α is the body angle of attack in radians. The design charts of Section 4.2.1.2 can be used to determine the normal-force coefficient at angles of attack for cone-cylinder-flare, cone-cylinder, or cone-flare bodies with pointed or spherically blunted noses, or for spherically blunted or pointed cones.

An approximate value of $C_D(\alpha)$ at small angles of attack for a spherically blunted ogive can be determined by

$$C_D(\alpha) = C_{N_\alpha} \alpha^2 \qquad 4.2.3.2\text{-s}$$

where C_{N_α} is obtained from Figure 4.2.1.1-25 and α is the body angle of attack in radians.

Method 2

This method is identical to Method 3 presented in Paragraph C of this section. The method is applicable to angles of attack from 0 to 180° and Mach numbers up to 7. Substantiating test data taken from Reference 8 for $\alpha \leq 25^{\circ}$ are presented in Table 4.2.3.2-A. The method has not been substantiated at higher angles of attack. It is recommended that the method be used cautiously and only when Method 1 cannot be used.

Sample Problems

1. Method 1

Given: A cone-cylinder body of Reference 12.

ℓ_B = 8.0 in. ℓ_A = 4.68 in. ℓ_N = 3.32 in. d = 1.17 in.

M = 6.86; β = 6.79 $0 \leq \alpha \leq 24^{\circ}$

Compute:

$$f_A = \frac{\ell_A}{d} = \frac{4.68}{1.17} = 4.0; \quad f_N = \frac{\ell_N}{d} = \frac{3.32}{1.17} = 2.84$$

f_A/f_N = 4.0/2.84 = 1.41

β/f_N = 6.79/2.84 = 2.39

βC_N (Figure 4.2.1.2-40a through -40d, interpolated) (See calculation table.)

C_N = $\beta C_N/\beta$ (based on body base area) (See calculation table.)

Solution:

$C_D(\alpha) = C_N \alpha$ (based on S_b) (Equation 4.2.3.2-n)

①	②	③	④	⑤	⑥
α (deg)	$\beta\alpha$ (deg)	βC_N (Fig. 4.2.1.2-40)	C_N ③ /6.79	α (rad)	$C_D(\alpha)$ (Eq. 4.2.3.2-n) ④⑤
0	0	0	0	0	0
4	27.2	1.4	0.206	0.0698	0.0144
8	54.3	3.0	0.442	0.1396	0.0617
12	81.5	5.2	0.766	0.2094	0.1604
16	108.6	7.7	1.134	0.2792	0.3166
20	135.8	10.4	1.53[illegible]	0.3490	0.5347
24	163.0	13.3	1.959	0.4188	0.8204

The calculated results are compared with test values from Reference 12 in Sketch (e)

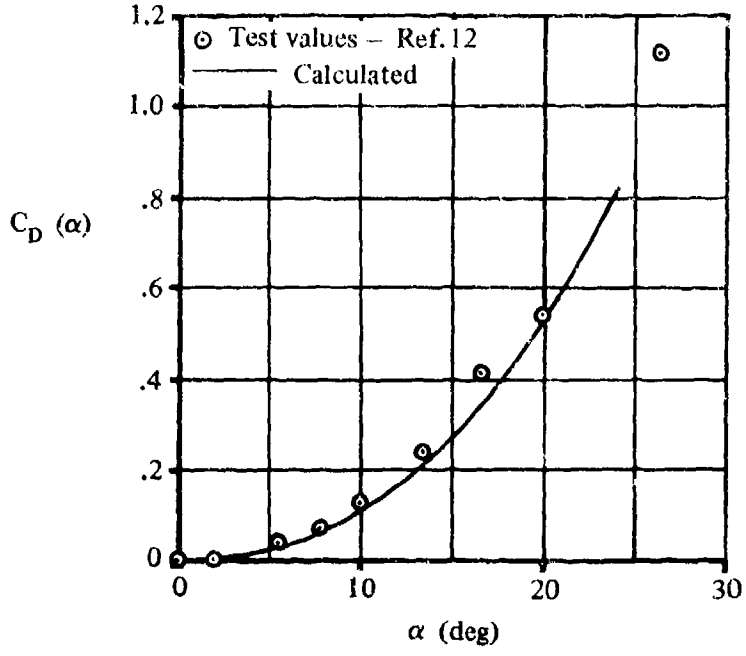

SKETCH (e)

2. Method 1

Given: A cone-cylinder-flare body of Reference 13.

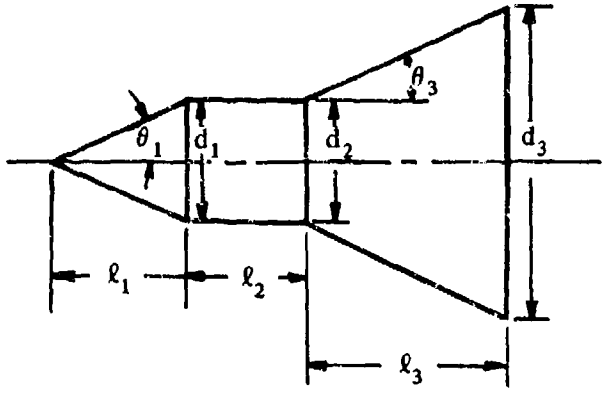

Cone:

$\ell_1 = \ell_N = 2.414$ in.

$d_1 = d_2 = 2.0$ in. $\theta_1 = 22.5^o$

Cylinder:

$\ell_2 = \ell_C = 2.0$ in. $d_2 = 2.0$ in.

Flare:

$\ell_3 = \ell_F = 3.29$ in.

$d_3 = 5.80$ in. $\theta_3 = 30^o$

Additional Characteristics:

$M = 6.0$; $\beta = 5.92$ $0 \leq \alpha \leq 16^o$

Compute:

In accordance with the method of Section 4.2.1.2, the increment of normal force due to the flare is added to the normal force of the cone-cylinder body.

$(C_N)_{cone\text{-}cylinder}$

$f_N = \ell_N/d = 2.414/2.0 = 1.207$

$f_A = f_C = \ell_C/d = 2.0/2.0 = 1.0$

$f_A/f_N = 1.0/1.207 = 0.829$

$\beta/f_N = 5.92/1.207 = 4.90$

βC_N (Figure 4.2.1.2-40d and -40e, interpolated) (See calculation table.)

$C_N = \beta C_N/\beta$ (based on cone-cylinder maximum frontal area) (See calculation table.)

$(C_N)_{flare}$

$$1 - \left(\frac{d_2}{d_3}\right)^2 = 1 - \left(\frac{2.0}{5.80}\right)^2 = 1 - 0.119 = 0.881$$

$$\frac{(\Delta C_N)_F}{1 - \left(\frac{d_2}{d_3}\right)^2}$$ (Figure 4.2.1.2-42b) (See calculation table.)

$$(\Delta C_N)_F = \frac{(\Delta C_N)_F}{1 - \left(\frac{d_2}{d_3}\right)^2}\left[1 - \left(\frac{d_2}{d_3}\right)^2\right] = 0.881 \frac{(\Delta C_N)_F}{1 - \left(\frac{d_2}{d_3}\right)^2}$$ (based on flare base area) (See calculation table.)

$(C_N)_{cone\text{-}cylinder\text{-}flare}$

$$C_N = (C_N)_{cone\text{-}cyl.} + (\Delta C_N)_F \left(\frac{d_3}{d_2}\right)^2$$ (based on cone-cylinder maximum frontal area) (See calculation table.)

Solution:

$C_D(\alpha) = C_N \alpha$ (Equation 4.2.3.2-n)

①	②	③	④	⑤	⑥	⑦	⑧	⑨	⑩
α (deg)	$\beta\alpha$ (deg)	$\beta C_{N_{cone\text{-}cyl.}}$ (Fig. 4.2.1.2-40)	$C_{N_{cone\text{-}cyl.}}$ ③ /5.92	$\frac{(\Delta C_N)_F}{1-\left(\frac{d_2}{d_3}\right)^2}$ (Fig. 4.2.1.2-42b)	$(\Delta C_N)_F$ ⑤ 0.881	$(\Delta C_N)_F \left(\frac{d_3}{d_2}\right)^2$ 8.41 ⑥	C_N ④ + ⑦	α (rad)	$C_D(\alpha)$ (Eq. 4.2.3.2-n) ⑧⑨
0	0	0	0	0	0	0	0	0	0
4	23.7	0.86	0.145	0.09	0.08	0.673	0.818	0.0698	0.0571
8	47.4	1.75	0.296	0.18	0.16	1.346	1.642	0.1396	0.2292
12	71.0	2.62	0.443	0.275	0.24	2.018	2.461	0.2094	0.5153
16	94.7	3.50	0.591	0.35	0.31	2.607	3.198	0.2792	0.8929

The calculated results are compared with test values from Reference 13 in Sketch (f).

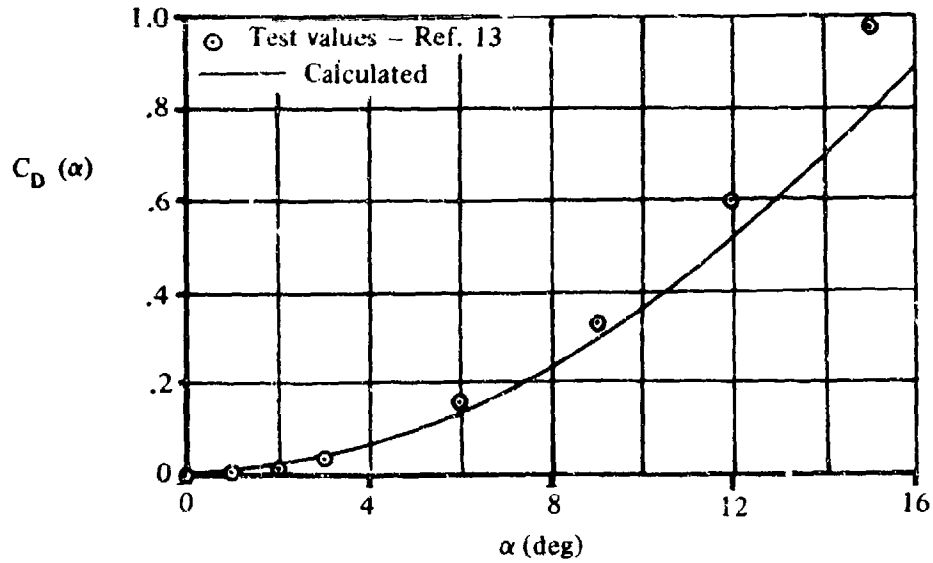

SKETCH (f)

3. Method 2

Refer to Sample Problem 3 in Paragraph C of this section for an example of the application of the method.

REFERENCES

1. Hopkins, E. J.: A Semiempirical Method for Calculating the Pitching Moment of Bodies of Revolution at Low Mach Number. NACA RM A51C14, 1951. (U)

2. Allen, H. J., and Perkins, E. W.: Characteristics of Flow Over Inclined Bodies of Revolution. NACA RM A50L07, 1951. (U)

3. Kelly, H. R.: The Estimation of Normal-Force, Drag, and Pitching-Moment Coefficients for Blunt-Based Bodies of Revolution at Large Angles of Attack. Jour. Aero. Sci., Aug. 1954. (U)

4. Jorgensen, L. H.: Prediction of Static Aerodynamic Characteristics for Space-Shuttle-Like and Other Bodies at Angles of Attack from 0° to 180°. NASA TN D-6996, 1973. (U)

5. Jorgensen, L. H.: A Method for Estimating Static Aerodynamic Characteristics for Slender Bodies of Circular and Noncircular Cross Section Alone and with Lifting Surfaces at Angles of Attack from 0° to 90°. NASA TN D-7228, 1973. (U)

6. Hopkins, E. J.: Charts for Predicting Turbulent Skin Friction from the Van Driest Method (II). NASA TN D-6945, 1972. (U)

7. Jernell, L. S.: Aerodynamic Characteristics of Bodies of Revolution at Mach Numbers from 1.50 to 2.86 and Angles of Attack to 180°. NASA TM X-1658, 1968. (U)

8. Dennis, D. H., and Cunningham, B. E.: Forces and Moments on Inclined Bodies at Mach Numbers from 3.0 to 6.3. NACA RM A54E03, 1954. (U)

9. Jorgensen, L. H.: Inclined Bodies of Various Cross Sections at Supersonic Speeds. NASA Memo 12-3-58A, 1958. (U)

10. Jones, J. L., and Demele, F. A.: Aerodynamic Study of a Wing-Fuselage Combination Employing a Wing Swept Back 63° – Characteristics Throughout the Subsonic Speed Range with the Wing Cambered and Twisted for a Uniform Load at a Lift Coefficient of 0.25. NACA RM A9D25, 1949. (U)

11. Carlson, H. W., and Gapcynski, J. P.: An Experimental Investigation at a Mach Number of 2.01 of the Effects of Body Cross-Section Shape on the Aerodynamic Characteristics of Bodies and Wing-Body Combinations. NACA RM L55E23, 1955. (U)

12. Cooper, R. D., and Robinson, R. A.: An Investigation of the Aerodynamic Characteristics of a Series of Cone-Cylinder Configurations at a Mach Number of 6.86. NACA RM L51J09, 1951. (U)

13. Ashby, G. C., Jr., and Cary, A. M., Jr.: A Parametric Study of the Aerodynamic Characteristics of Nose-Cylinder-Flare Bodies at a Mach Number of 6.0 NASA TN D-2854, 1965. (U)

TABLE 4.2.3.2-A
SUPERSONIC AXIAL FORCE COEFFICIENT FOR
CYLINDER-BODIES WITH VARIOUS NOSE SHAPES
METHOD 3
DATA SUMMARY AND SUBSTANTIATION

Ref	M	R_ℓ (based on diam)	$\frac{\ell_B}{d}$	$\frac{\ell_N}{d}$	Nose Shape	α (deg)	$C_{X_{calc}}$	$C_{X_{test}}$	ΔC_X
7	2.86	1.25×10^5	6	0	Blunt	0	−1.84	−1.70	−0.14
						20	−1.63	−1.69	0.06
						40	−1.08	−1.46	0.38
						60	−0.46	−0.84	0.38
						80	−0.56	−0.27	−0.29
						100	0.56	0	0.56
				3	Cone	0	−0.18	−0.22	0.04
						20	−0.16	−0.33	0.17
						40	−0.11	−0.44	0.33
						60	−0.05	−0.52	0.47
						80	−0.005	−0.50	0.49
						100	0.06	−0.21	0.27
						120	0.46	0.57	−0.11
						140	1.08	1.32	−0.24
						160	1.63	1.63	0
						180	1.84	1.64	0.20
				5	Ogive	0	−0.14	−0.11	−0.03
						20	−0.12	−0.22	0.10
						40	−0.08	−0.40	0.32
						60	−0.03	−0.50	0.47
						80	−0.004	−0.42	0.42
						100	0.06	−0.30	0.36
						120	0.46	0.57	−0.11
						140	1.08	1.30	−0.22
						160	1.63	1.68	−0.05
						180	1.84	1.62	0.22
8	4.24	5.4×10^5	7	3	Cone	0	−0.137	−0.105	−0.032
						5	−0.136	−0.096	−0.040
						10	−0.132	−0.107	−0.025
						15	−0.128	−0.121	−0.007
						20	−0.121	−0.171	0.050
						25	−0.112	−0.213	0.101
			10			0	−0.137	−0.125	−0.012
						5	−0.136	−0.128	−0.008
						10	−0.133	−0.124	−0.009
						15	−0.128	−0.120	−0.008
						20	−0.121	−0.122	0.001
						25	−0.113	−0.124	0.011
	5.04	2.6×10^5				0	−0.119	−0.151	0.032
						5	−0.118	−0.160	0.04

TABLE 4.2.3.2-A (CONTD)

Ref	M	R_ℓ (based on diam)	$\frac{\ell_B}{d}$	$\frac{\ell_N}{d}$	Nose Shape	α (deg)	$C_{X_{calc}}$	$C_{X_{test}}$	ΔC_X
8	5.04	2.6×10^5	10	3	Cone	10	−0.115	−0.177	0.062
						15	−0.111	−0.159	0.048
						20	−0.105	−0.159	0.054
						25	−0.098	−0.216	0.118
			7	5	Ogive	0	−0.082	−0.076	−0.006
						5	−0.081	−0.068	−0.013
						10	−0.0795	−0.0895	0.010
						15	−0.076	−0.120	0.044
	6.28	1.1×10^5		3	Cone	0	−0.096	−0.208	0.112
						5	−0.095	−0.195	0.100
						10	−0.093	−0.202	0.109
						15	−0.089	−0.236	0.147
						20	−0.084	−0.288	0.204
						25	−0.079	−0.320	0.241

Average Error = $\sum \frac{|\Delta C_x|}{n} = 0.149$

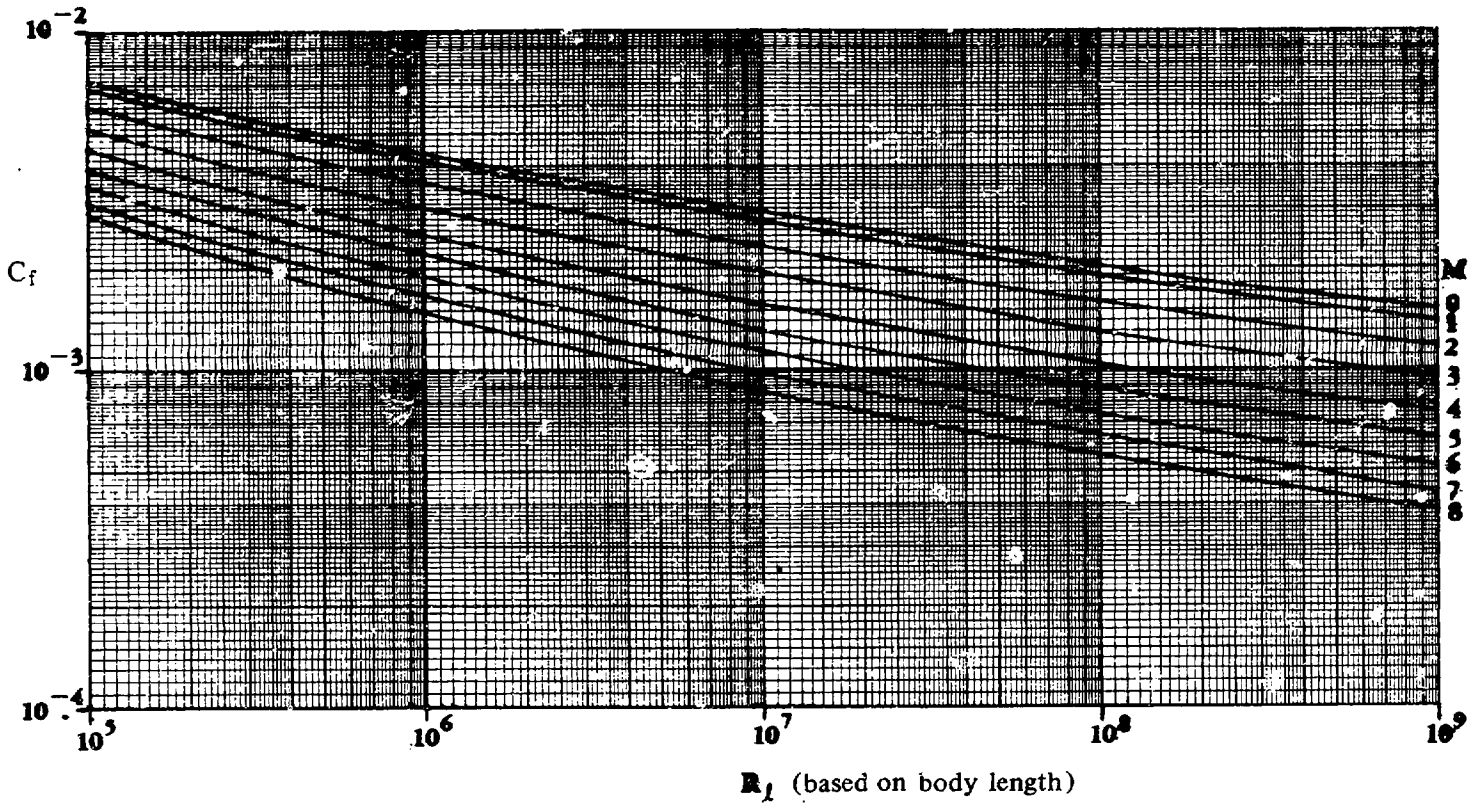

FIGURE 4.2.3.2 -27 TURBULENT FLAT-PLATE SKIN-FRICTION COEFFICIENT

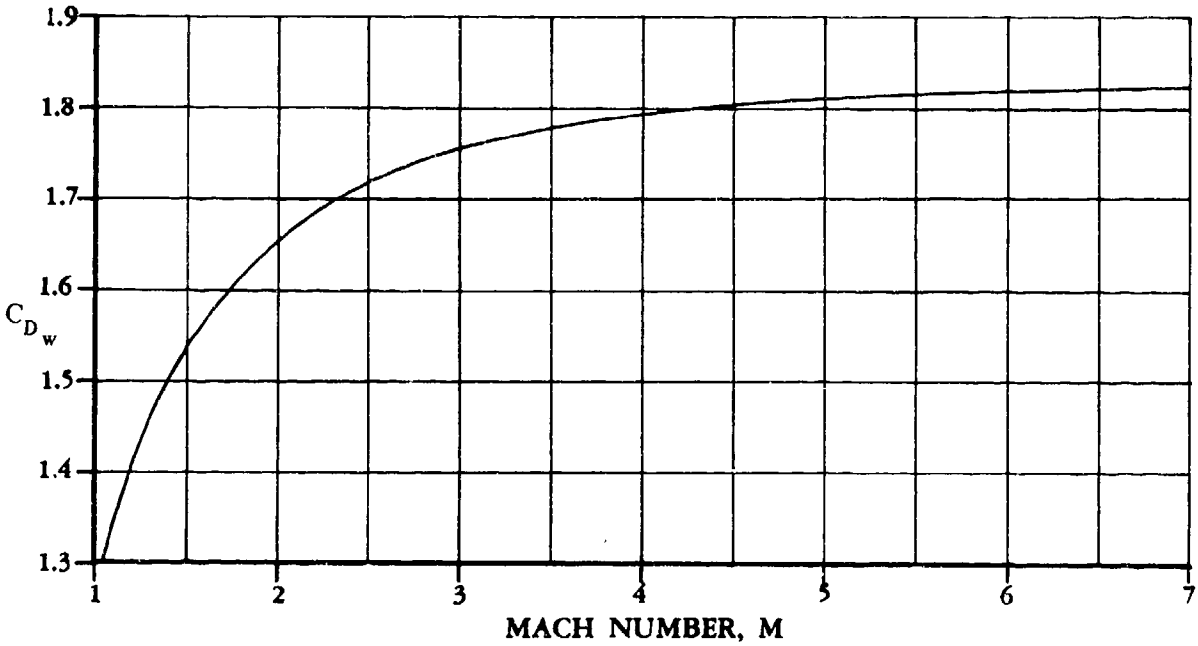

FIGURE 4.2.3.2 -28a BODY WAVE-DRAG COEFFICIENT FOR BLUNT NOSE

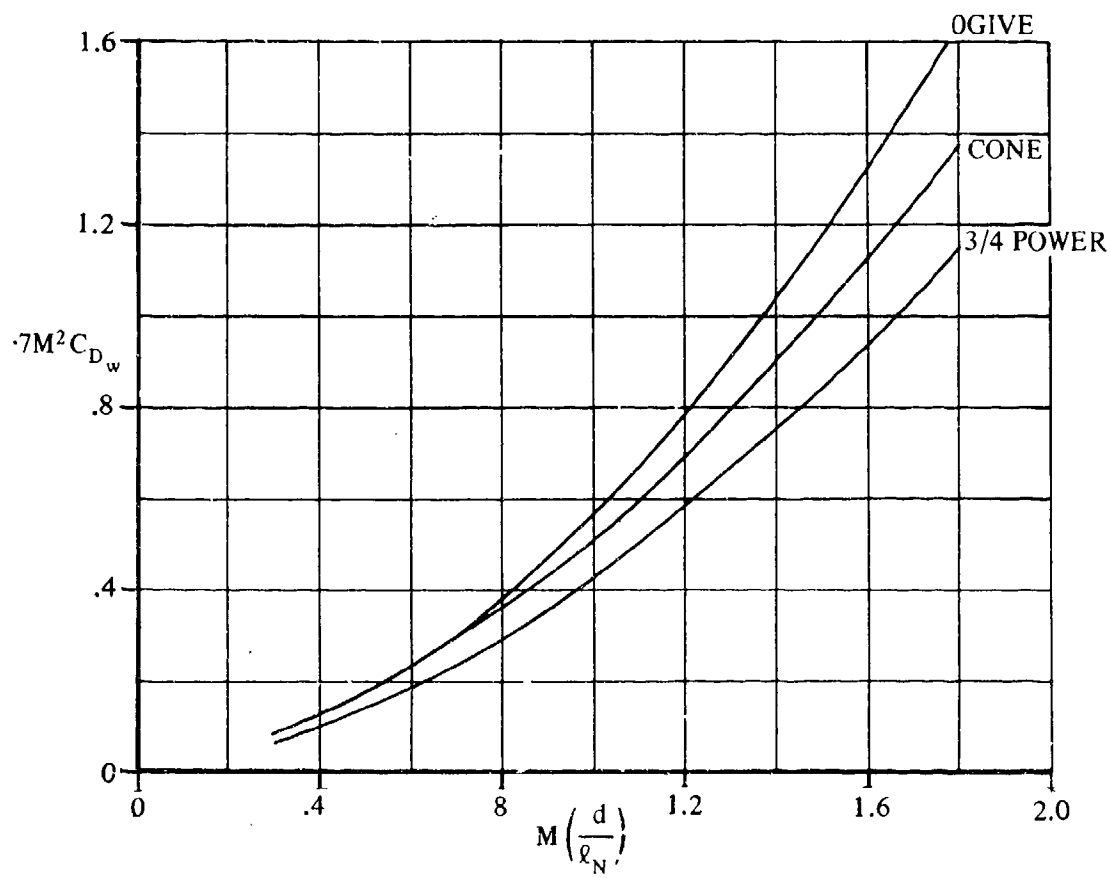

FIGURE 4.2.3.2 -28b VARIATION OF WAVE-DRAG COEFFICIENT WITH HYPERSONIC SIMILARITY PARAMETER FOR VARIOUS NOSE SHAPES

4.3 WING-BODY, TAIL-BODY COMBINATIONS AT ANGLE OF ATTACK

4.3.1 WING-BODY LIFT

4.3.1.2 WING-BODY LIFT-CURVE SLOPE

When a lifting panel is added to a body at low angles of attack, certain mutual interference effects may arise between the components. These can be classified as (a) the effect of body upwash or cross flow on the local angle of attack of the lifting panel, (b) the effect of local body-flow properties such as Mach number and dynamic pressure on the panel characteristics, (c) the effect of the lift carryover from the panel onto the body, (d) the effect of panel upwash on the body ahead of the panel (at subsonic speeds only), and (e) the effect of the panel lifting vortices on the body behind the wing. These interferences are generally small for configurations with large panel-span-to-body-diameter ratios typified by conventional, long-range subsonic aircraft. For these configurations the lift-curve slope of the combination is essentially the sum of the lift-curve slopes of the components. For configurations in which the panel-span-to-body-diameter ratio is small, such as conventional missiles or canard surfaces, these interference effects must usually be considered.

A. SUBSONIC

At subsonic speeds the wing-body (tail-body) interference effects are particularly difficult to estimate. Each of the interference effects discussed in the introduction is discussed below for this speed regime.

Body Upwash (Cross Flow)

In potential flow, a cylinder with the axis normal to the flow has a maximum velocity at the ends of the diameters normal to the flow equal to twice the free-stream velocity. An inclined cylinder can be treated by considering the cylinder to be in a combined axial and cross flow. The cross-flow velocity is thus equal to $2V\sin\alpha$ and serves to increase the local angle of attack of the lifting panel. In practice only about 40 percent of the full potential velocity is attained (see reference 1).

Body Flow Field (Axial Flow)

The perturbations in the potential flow field about a three-dimensional body are less than those for a corresponding two-dimensional body. For example, the local velocity about a three-dimensional body varies as $1/r^2$ and about a two-dimensional body as $1/r$, where r is the distance from the body centerline. Nevertheless, the effects of these perturbations can become significant and have sometimes been used in refined design analysis. However, for purposes of the Datcom, these effects are considered to be outside the scope of the book. Reference 2 contains a theoretical development that uses a distributed source-sink and doublet representation for elongated bodies. This method is best suited to machine computation.

Panel Lift Carryover

The carryover of the panel loading onto the body is calculated in reference 3 by means of a conformal mapping procedure. The lift that includes this carryover effect is always less than the lift of the gross panel. No method is included in the Datcom at the present time for estimating this effect.

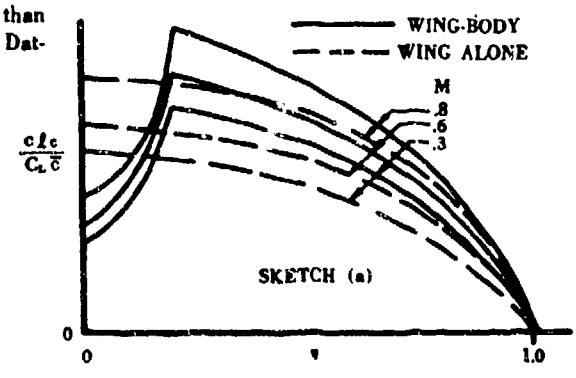

The combined effect of the lift carryover and the body upwash is shown for several Mach numbers in sketch (a) above. The comparison of the isolated panel and the combination indicates that these two effects tend to compensate for each other. The increment in lift-curve slope due to these effects is shown in sketch (b) as a function of body size and Mach number. The smaller bodies tend to increase the lift-curve slope and the larger bodies tend to decrease it.

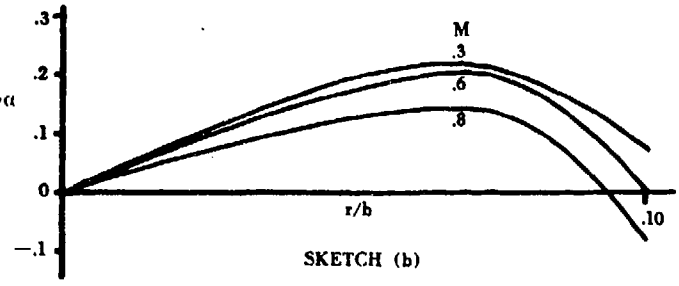

SKETCH (b)

Panel Upwash

The induced effects of the bound and trailing vortices of the panel are such as to cause an upwash ahead of the panel. The upwash is a maximum at the panel leading edge and rapidly decays with distance forward. These effects are more important for pitching-moment considerations than for lift.

Panel Vortices

The downwash behind the panel due to the bound and trailing vortices reduces the effective angle of attack on the aft portion of the body and hence reduces the body lift. Again the effect on the lift of the combination is invariably small; whereas the effect on pitching moment is more significant. These latter two effects have been successfully treated by Multhopp (reference 4).

A simple, yet relatively accurate, approach to the problem of wing-body interference is given in reference 5. In this reference a method based primarily on slender-body theory is presented for calculating the ratio of the lift of the wing-body combination to that of the wing alone. The derivation of the interference effects in terms of these ratios permits the extension of the method to nonslender configurations. The reason for this is that in certain instances slender-body theory accurately predicts the ratio of the wing-body lift to wing lift, even though it does not accurately predict the magnitudes of the individual lift-curve slopes.

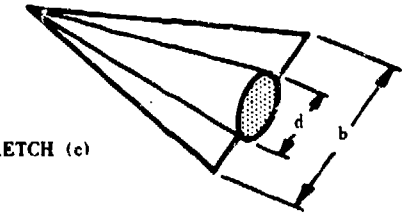

SKETCH (c)

The specific case of a conical body mounted on a delta wing (sketch (c)) has been solved by Spreiter in reference 6. Slender-body theory is used to obtain the ratio of the wing-body lift to that of the wing alone. Correlation with experimental data by this method is good throughout the speed range. In this Section, charts are presented for the determination of the appropriate wing-body interference ratios by means of the methods of references 5 and 6.

The methods are applicable to axisymmetric bodies in combination with straight-taper wings and are restricted to unbanked wings (zero roll angle). According to the limitations of slender-body theory, the methods of references 5 and 6 are not applicable to wings with sweptback trailing edges. Nevertheless, experimental data (see sample problems) indicate that good correlations can be obtained for these configurations.

The definition of exposed wing area depends upon the geometry of the wing-body combination. Two cases are illustrated in sketch (d) below. For a wing mounted on a cylindrical portion of a body the exposed wing is defined as the exposed half-wings joined together. For a wing mounted on an expanding section of a body the exposed wing is defined as the parts of the wing outboard of the largest body diameter at the wing-body intersection.

When the wing is mounted on a cylindrical body section, the nose of the body is defined as the section of the body ahead of the wing. When the wing is mounted on an expanding portion of the body, the nose is defined as the expanding portion of the body.

The latter definition is recommended in reference 5 for the case of a configuration with a small body-diameter-to-wing-

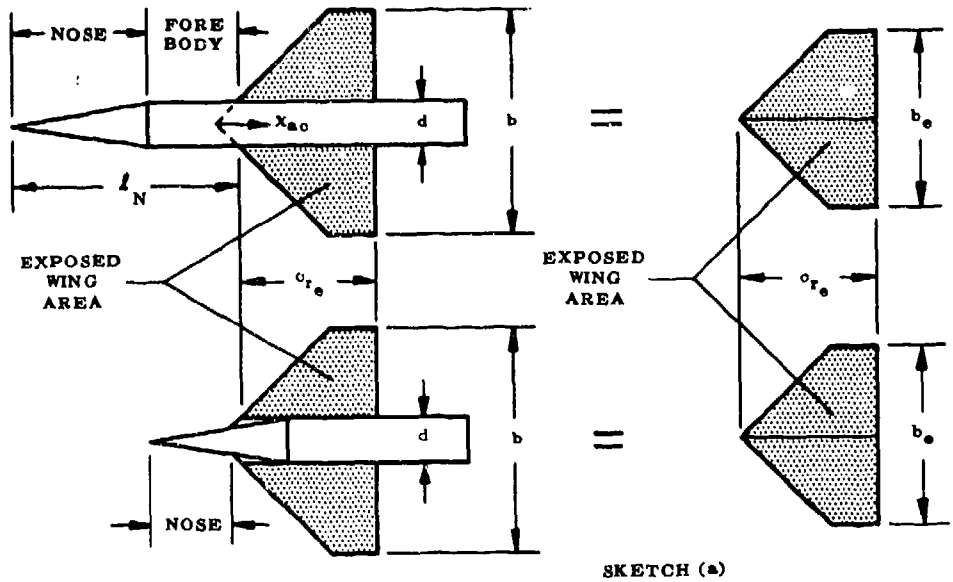

SKETCH (a)

span ratio; but for the case of a relatively large body-diameter-to-wing-span ratio with the wing extending the entire length of the body (see sketch (c)), the use of this definition can lead to substantial error.

DATCOM METHODS

Method 1 (reference 5)

This method is applicable to configurations such as those in sketch (d). The lift on a wing-body combination is taken to be the sum of three principal components:

1. Lift on nose including forebody (see sketch (d), upper configuration)
2. Lift on wing in presence of body
3. Lift on body due to the wing

Two cases of wing-body interference are considered. The first case is that in which the wing incidence is fixed relative to the body and the angle of attack is varied for the wing-body combination as a unit. The second case is that in which the body angle of attack remains fixed and the wing incidence varies relative to the body.

For the first case — wing fixed at zero incidence — the equation for wing-body lift-curve slope based on the total projected wing area, including that intercepted by the fuselage, is:

$$(C_{L_\alpha})_{WB} = \left[K_N + K_{W(B)} + K_{B(W)}\right](C_{L_\alpha})_e \frac{S_e}{S_W} \qquad 4.3.1.2\text{-a}$$

The quantities K_N, $K_{W(B)}$, and $K_{B(W)}$ represent the ratios of the nose lift, the wing lift in the presence of the body, and the body lift in the presence of the wing, respectively, to the wing-alone lift. For wings mounted on expanding bodies, the same procedure, with application of the definitions of sketch (d) in the discussion, usually yields satisfactory results. Configurations similar to that of sketch (c) are treated separately, in later paragraphs.

For the second case — fuselage fixed at zero angle of attack and wing incidence varying — the equation is:

$$(C_{L_i})_{WB} = \left[k_{W(B)} + k_{B(W)}\right](C_{L_\alpha})_e \frac{S_e}{S_W} \qquad 4.3.1.2\text{-b}$$

For both equations above, the best results are obtained for configurations in which the body radii do not exceed 80 percent of the total wing semispan. For larger ratios, the aerodynamic characteristics of the combination tend to be determined more by the body than by the wing.

The parameters common to equations 4.3.1.2-a and 4.3.1.2-b are determined as follows:

S_W = total projected wing area

S_e = exposed wing area. Exposed wing is defined as the exposed half-wings joined together for configurations in which the wing is mounted on a cylindrical section of the body (see sketch (d), upper configuration). For wings on expanding portions of bodies, the exposed wing area is the area outside of the maximum body diameter (see sketch (d), lower configuration).

$(C_{L_\alpha})_e$ = lift-curve slope of exposed wing based on exposed wing area and exposed aspect ratio. Determine from Section 4.1.3.2.

$$K_N = \frac{(C_{L_\alpha})_N S_{N_{ref}}}{(C_{L_\alpha})_e S_e}$$

$(C_{L_\alpha})_N$ = nose lift-curve slope. In most cases a value of 2 per radian (based on body frontal area) is sufficiently accurate. For cases where a higher degree of accuracy is required, use Section 4.2.1.1.

$S_{N_{ref}}$ = reference area for nose lift-curve slope, usually πr^2

$K_{W(B)}^*$ is obtained from figure 4.3.1.2-10

$K_{B(W)}^*$ is obtained from figure 4.3.1.2-10

$k_{W(B)}$ is obtained from figure 4.3.1.2-12a

$k_{B(W)}$ is obtained from figure 4.3.1.2-12a

Method 2 (reference 6)

This method is applicable to configurations similar to that of sketch (c).

The wing-body lift-curve slope is given by the following equation:

$$(C_{L_\alpha})_{WB} = K_{(WB)} (C_{L_\alpha})_W \qquad 4.3.1.2\text{-c}$$

where

$(C_{L_\alpha})_W$ is the wing lift-curve slope from section 4.1.3.2 (based on total wing area)

$K_{(WB)}$ is obtained from figure 4.3.1.2-12c

Comparison between experimental and calculated wing-body characteristics for a large number of cases (reference 5) shows that the lift of the wing-body combination is generally estimated by these methods to within ±10 percent.

Sample Problem

Given:

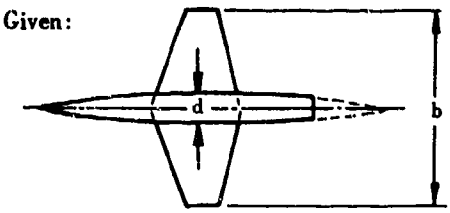

$A = 3$

$\Lambda_{LE} = 19.1°$

$\lambda = 0.4$

$\frac{d}{b} = 0.145$

Compute:

$\lambda_e = 0.438$

$A_e = 2.74$

$\frac{S_e}{S_w} = 0.802$

$\frac{S_{N_{ref}}}{S_e} = 0.0617$

$\Lambda_{c/2} = 0$

$(C_{L_\alpha})_e = 3.23$ (figure 4.1.3.2-49)

$$K_N = \frac{(C_{L_\alpha})_N \; S_{N_{ref}}}{(C_{L_\alpha})_e \quad S_e} = \frac{2}{3.23}(.0617) = 0.037$$

*The calculation (Reference 10) of the sum of $K_{W(B)}$ and $K_{B(W)}$ can be expressed in terms of the planform geometry as follows

$$K_{W(B)} + K_{B(W)} = \left(\frac{d}{b} + 1\right)^2.$$

$M = .25$ $K_{W(B)} = 1.12$ (figure 4.3.1.2-10)

$R_l = 2 \times 10^6$ to 8×10^6 (based on wing MAC) $K_{B(W)} = 0.20$ (figure 4.3.1.2-10)

Note: This is configuration 4 of reference 7

Solution:

$$(C_{L_\alpha})_{WB} = \left[K_N + K_{W(B)} + K_{B(W)} \right] (C_{L_\alpha})_e \frac{S_e}{S_w} = 3.51 \text{ per radian (equation 4.3.1.2-a)}$$

This compares with an experimental value of $(C_{N_\alpha})_{WB} = 3.33$ (figures 6 and 21 of reference 7).

B. TRANSONIC

For slender wing-body configurations, the aerodynamic interference effects are relatively insensitive to Mach number, and slender wing-body theory gives reasonable results. For nonslender configurations transonic interference effects can become quite large and sensitive to minor changes in local contour. At present, these effects cannot be predicted with any accuracy.

DATCOM METHOD

The method, which is based on slender-body theory, presented in Paragraph C below should be applied at transonic speeds.

C. SUPERSONIC

The mutual aerodynamic interference between a panel and a body at supersonic speeds at low angles of attack is due primarily to the upwash of the body and the lift carryover of the panel onto the body. The body upwash appears similar to its subsonic counterpart, that is, the upwash is a maximum at the body surface and decays with increasing distance from the surface. The integrated effect over the span of the panel at positive angles of attack increases the lift-curve slope of the panel.

The lift carryover on the body is displaced downstream parallel to the Mach lines, as illustrated in sketch (e) below. Important lift and moment differences can therefore exist between configurations in which the fuselage terminates at the wing trailing edge and those in which the fuselage extends beyond the wing trailing edge.

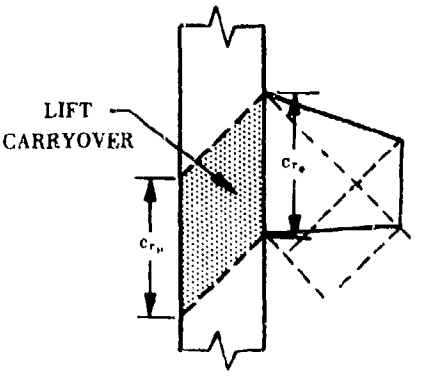

SKETCH (e)

These effects have been adequately predicted by slender-body theory in references 5 and 6 (see paragraph A above).

The local Mach-number and dynamic-pressure-ratio perturbations due to the axial flow component can also cause significant changes in the characteristics of the panels when the local body slopes in the vicinity of the panel become large. These perturbations decay with increasing distance from the body surface. This decay is more rapid than that in the corresponding two-dimensional case, because of the three-dimensional aspect of the body flow field. Sudden changes

in contour like flare or boattail corners, cause a two-dimensional Mach-number and dynamic-pressure-ratio change at the surface that then decays in a three-dimensional manner. Two-dimensional compression values for dynamic pressure and Mach number are given by equations 4.4.1-z and 4.4.1-aa, respectively, and corresponding expansion values are given in figure 4.4.1-74. The average values of these parameters acting on a panel are always less than the two-dimensional values.

DATCOM METHODS

Two methods are presented for estimating the lift-curve slope of wing-body or tail-body combinations. These methods, which are based on slender wing-body theory, are the same as those used in the subsonic paragraph.

Method 1:

Two cases are presented: (a) panel fixed at zero incidence to the body and angle of attack of the combination varied and (b) body kept at zero angle of attack and wing incidence varied. The lift is given by the following equations:

$$\text{(a)} \qquad (C_{L_\alpha})_{WB} = \left[K_N + K_{W(B)} + K_{B(W)}\right](C_{L_\alpha})_e \frac{S_e}{S_w} \tag{4.3.1.2-a}$$

$$\text{(b)} \qquad (C_{L_i})_{WB} = \left[k_{W(B)} + k_{B(W)}\right](C_{L_\alpha})_e \frac{S_e}{S_w} \tag{4.3.1.2-b}$$

The basic definitions and limitations for these equations are the same as those discussed in paragraph A above. However, special care must be used in specifying the "k" factors. These are summarized for the supersonic speed regime below.

$K_N = \dfrac{(C_{L_\alpha})_N S_{N_{ref}}}{(C_{L_\alpha})_e S_e}$

$K_{W(B)}$ all planforms use figure 4.3.1.2-10

$K_{B(W)}$

- triangular-type planforms
  - If $\beta A_e \leq 1$, use figure 4.3.1.2-10
  - If $\beta A_e > 1$,
    - and the fuselage extends beyond wing trailing edge, use figure 4.3.1.2-11a
    - and the fuselage does not extend beyond the wing trailing edge, use figure 4.3.1.2-11b
- nontriangular planforms
  - If $\beta A_e(1 + \lambda_e)\left(\dfrac{\tan \Lambda_{LE}}{\beta} + 1\right) \leq 4$, use figure 4.3.1.2-10
  - If $\beta A_e(1 + \lambda_e)\left(\dfrac{\tan \Lambda_{LE}}{\beta} + 1\right) > 4$,
    - and fuselage extends beyond wing trailing edge, use figure 4.3.1.2-11a
    - and fuselage does not extend beyond wing trailing edge, use figure 4.3.1.2-11b

$k_{W(B)}$ is obtained from figure 4.3.1.2-12b

$k_{B(W)}$ is obtained from figure 4.3.1.2-12a

Method 2:

This method is applicable to configurations similar ot that of sketch (c) and is identical to that presented as Method 2 of paragraph A.

1. Supersonic Lift-Curve Slope of Wing-Body Combination

Given:

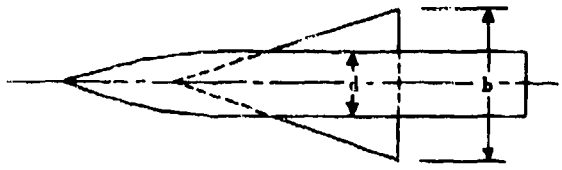

$A = 1.34$

$\Lambda_{LE} = 71.6°$

$\lambda = 0$

Airfoil: 8-percent-thick double wedge (free-stream direction)

$\frac{d}{b} = 0.428$

$M = 2.02$

$R = 2.6 \times 10^6$ (based on root chord)

Note: This is configuration 2 of reference 8.

Compute:

$\lambda_e = 0$

$A_e = 1.34$

$\frac{S_e}{S_W} = 0.328$

$\frac{S_{N\ ref}}{S_e} = 0.590$

$\beta = 1.75$

$A_e \tan \Lambda_{LE} = 4$

$\frac{\beta}{\tan \Lambda_{LE}} = 0.584$

$[(C_{N_\alpha})_e]_{theory} = 1.65$ (Section 4.1.3.2)

$\frac{(C_{N_\alpha})_e}{[(C_{N_\alpha})_e]_{theory}} = 0.94$ (Section 4.1.3.2) based on $\delta_\perp = 14.5°$

$(C_{N_\alpha})_e = 1.55$

$\frac{\beta}{f_N} = 0.526$

$(C_{N_\alpha})_N = 2.47$ (Section 4.2.1.1)

$K_{W(B)} = 1.38$ (figure 4.3.1.2-10)

$\frac{\beta d}{c_{r_e}} = 0.875$

$K_{B(W)}\, \beta\, (C_{L_\alpha})_e\, (\lambda_e + 1)\left(\frac{b}{d} - 1\right) = 2.1$ (figure 4.3.1.2-11a)

$\beta\, (\lambda_e + 1)\left(\frac{b}{d} - 1\right) = 2.35$

$K_{B(W)} = 0.576$

$K_N = \frac{(C_{N_\alpha})_N}{(C_{N_\alpha})_e} \quad \frac{S_{N\ ref}}{S_e} = 0.936$

Solution:

$$(C_{L_\alpha})_{WB} = [K_N + K_{W(B)} + K_{B(W)}]\,(C_{L_\alpha})_e\, \frac{S_e}{S_W} = 1.47 \text{ (equation 4.3.1.2-a)}$$

This compares with an experimental value of $(C_{L_\alpha})_{WB} = 1.57$ from reference 8.

2. Supersonic Lift-Curve Slope — Wing in Presence of Body

Case One: Wing incidence fixed at $i_w = 0$, fuselage rotating with wing

Given:

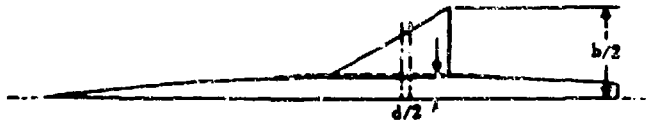

$A = 2.3$

$\Lambda_{LE} = 60°$

$\lambda = 0$

Airfoil: 9-percent-thick biconvex (free-stream direction)

$\frac{d}{b} = 0.23$

$M = 1.9$

$R_l = 1.9 \times 10^6$ (based on root chord)

Note: This is the delta-wing configuration in reference 9.

Compute:

$\lambda_e = 0$

$A_e = 2.31$

$\beta = 1.62$

$A_e \tan \Lambda_{LE} = 4$

$\frac{\beta}{\tan \Lambda_{LE}} = .935$

$[(C_{N_\alpha})_e]_{theory} = 2.38$ (Section 4.1.3.2)

$\frac{(C_{N_\alpha})_e}{[(C_{N_\alpha})_e]_{theory}} = .75$ (Section 4.1.3.2) based on $\delta_\perp = 20.7°$

$(C_{N_\alpha})_e = 1.79$

$K_{W(B)} = 1.2$ (figure 4.3.1.2-10)

Solution:

Since only the lift on the wing is of interest, the reference area is the exposed wing area, and equation 4.3.1.2-a reduces to

$$(C_{L_\alpha})_{w_e(B)} = K_{W(B)} (C_{L_\alpha})_e$$

Thus the wing lift in the presence of the body is $(C_{L_\alpha})_{w_e(B)} = 2.15$

The experimental value from reference 9 is $(C_{L_\alpha})_{w_e(B)} = 2.22$

Case Two: Body fixed at $\alpha = 0$, wing incidence variable

Given:

Same as Case One

Compute:

$k_{W(B)} = 0.96$ (figure 4.3.1.2-12b)
Other coefficients same as in Case One

Solution:

Again only the wing lift is of interest. Equation 4.3.1.2-b becomes

$$(C_{L_\alpha})_{w_e(B)} = k_{W(B)} (C_{L_\alpha})_e$$
$$= 1.72$$

The experimental value from reference 9 is 1.67.

REFERENCES

1. Zahm, A. F.: Flow and Drag Formulas for Simple Quadrics. NACA TR 253, 1926. (U)

2. Kaplan, C.: Potential Flow About Elongated Bodies of Revolution. NACA TR 516, 1935. (U)

3. Donovan, A. F., and Lawrence, H. R.: Aerodynamic Components of Aircraft at High Speeds. Princeton University Press, 1957. (U)

4. Multhopp, H.: Zur Aerodynamik des Flugzeugrumpfes (On the Aerodynamics of the Fuselage). Luftfahrtforschung 18, 52-66, 1941. (U)

5. Pitts, W., Nielsen, J., and Kaattari, G.: Lift and Center of Pressure of Wing-Body-Tail Combinations at Subsonic, Transonic, and Supersonic Speeds. NACA TR 1307, 1957. (U)

6. Spreiter, J.: The Aerodynamic Forces on Slender Plane and Cruciform-Wing and Body Combinations. NACA TR 962, 1950. (U)

7. Smith, D., Shibata, H., and Selan, R.: Lift, Drag, and Pitching Moment of Low-Aspect Ratio Wings at Subsonic and Supersonic Speeds – An Investigation at Large Reynolds Numbers of the Low-Speed Characteristics of Several Wing-Body Combinations. NACA RM A51K28, 1952. (U)

8. Nielsen, J., Katzen, E., and Tang, K.: Lift and Pitching-Moment Interference Between a Pointed Cylindrical Body and Triangular Wings of Various Aspect Ratios at Mach Numbers of 1.50 and 2.02. NACA TN 3795, 1956. (U)

9. Conner, D.: Aerodynamic Characteristics of Two All-Movable Wings Tested in the Presence of a Fuselage at a Mach Number of 1.9. NACA RM L8H04, 1948. (U)

10. Graham, R. E., and McDowell, J. L.: Simplification of the Wing-Body Interference Problem. Jour. of Aircraft Vol. 9 No. 10, Oct 1972. (U)

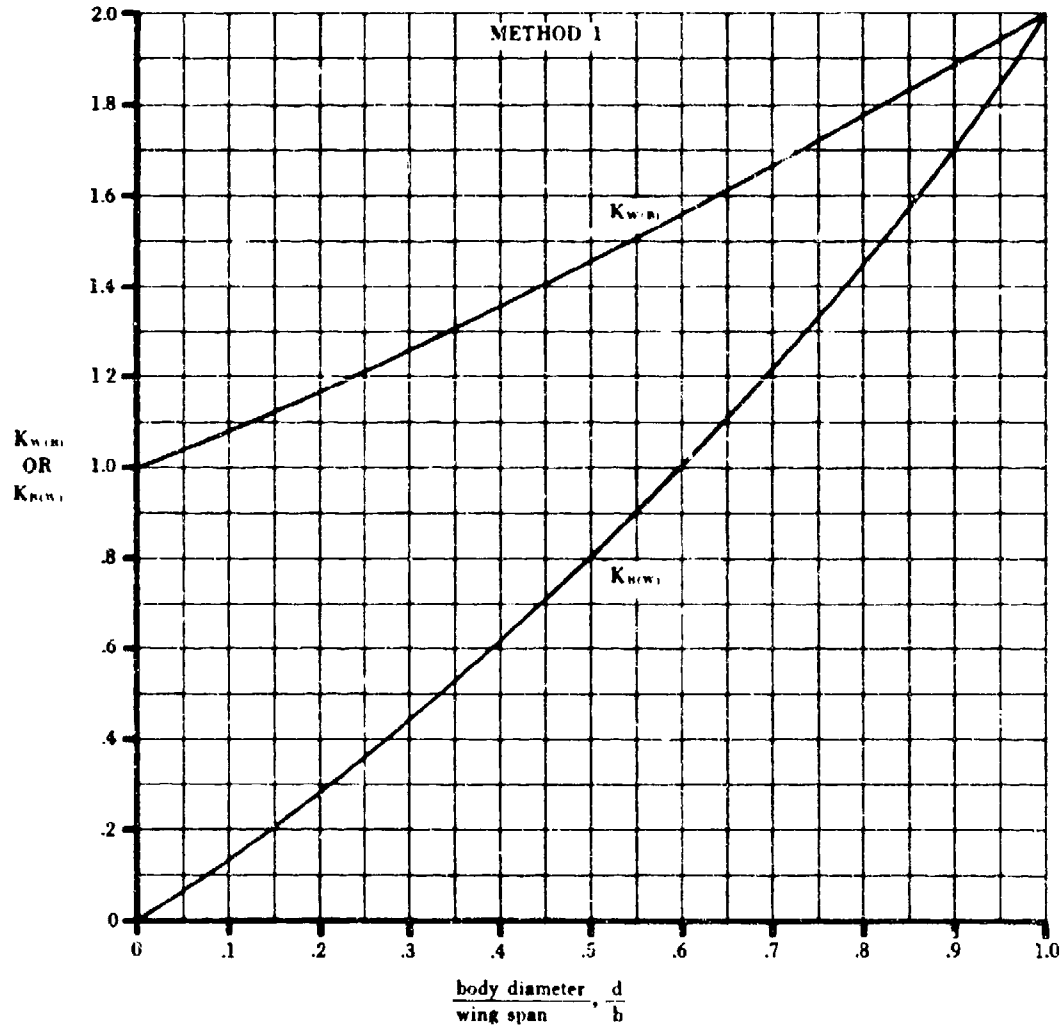

FIGURE 4.3.1.2-14 LIFT RATIOS $K_{W(B)}$ AND $K_{B(W)}$ —SLENDER-BODY THEORY— FIXED INCIDENCE—ALL SPEEDS

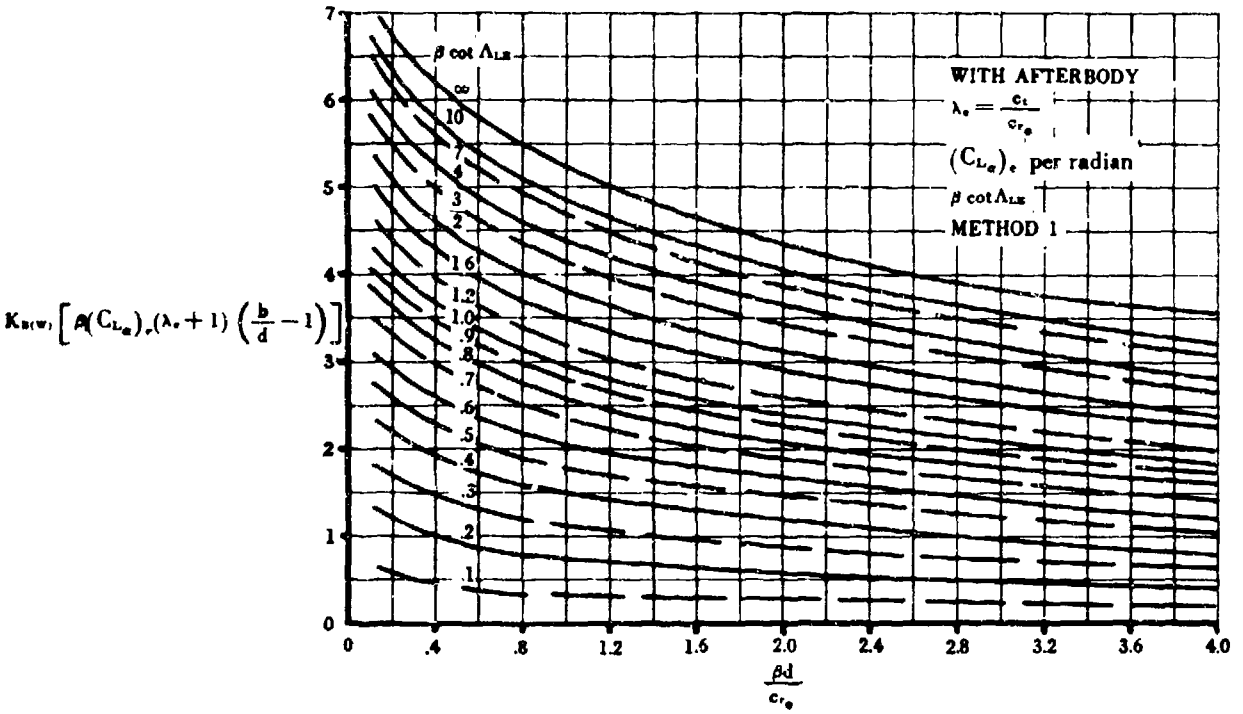

FIGURE 4.3.1.2-11a LIFT ON BODY IN PRESENCE OF WING—WITH AFTERBODY—FIXED WING INCIDENCE—SUPERSONIC SPEEDS

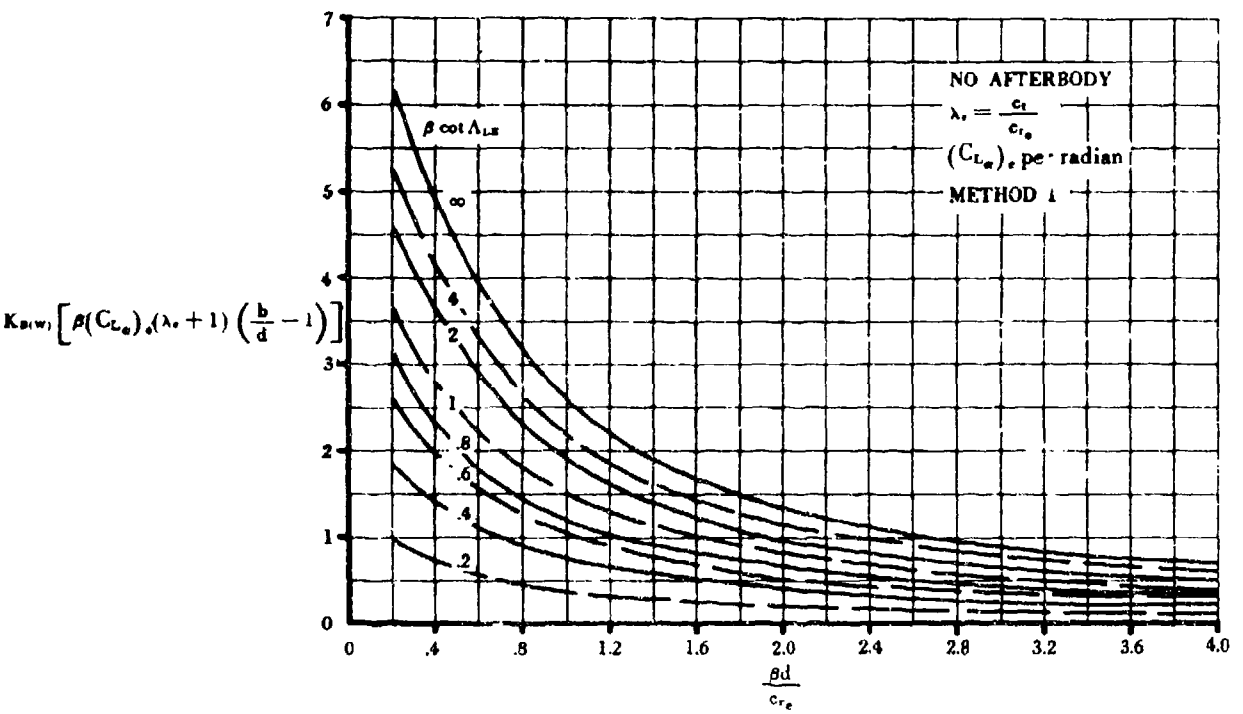

FIGURE 4.3.1.2-11b LIFT ON BODY IN PRESENCE OF WING—NO AFTERBODY—FIXED WING INCIDENCE—SUPERSONIC SPEEDS

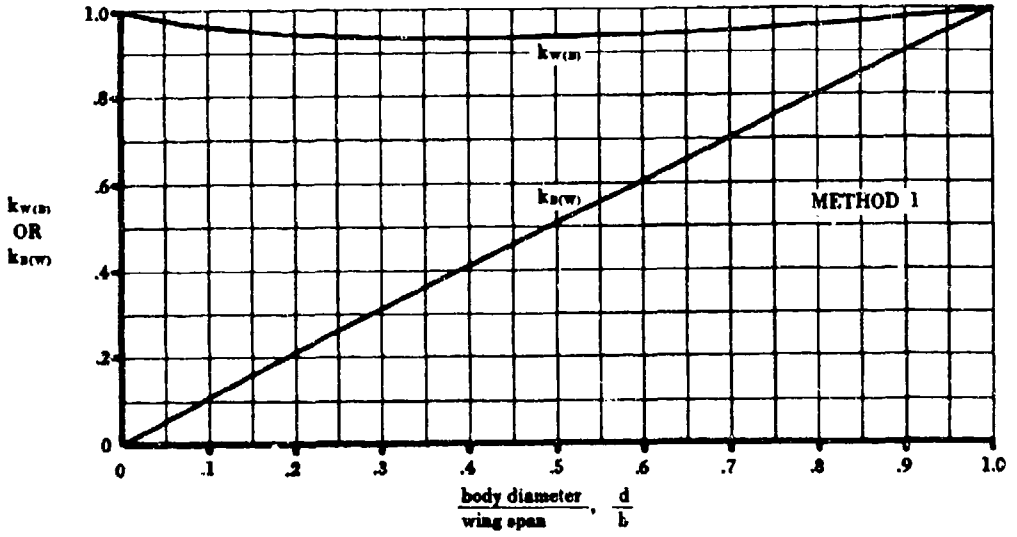

FIGURE 4.3.1.2-12a LIFT RATIOS $k_{w(B)}$ AND $k_{B(W)}$—SLENDER-BODY THEORY VARIABLE INCIDENCE—ALL SPEEDS

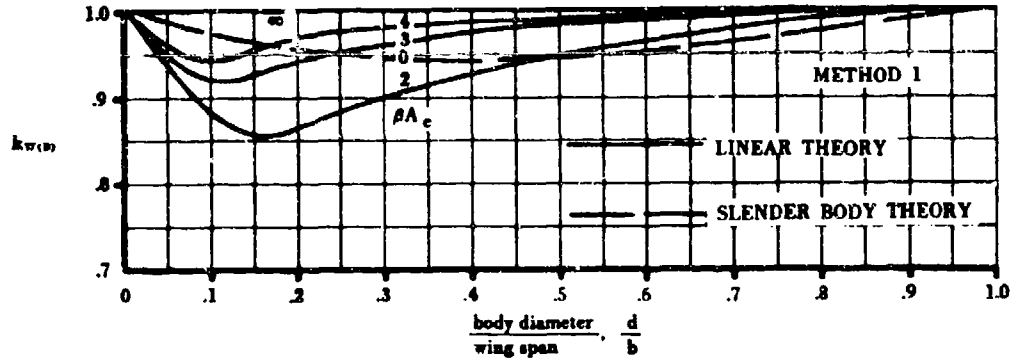

FIGURE 4.3.1.2-12b LIFT ON BODY IN PRESENCE OF WING--VARIABLE INCIDENCE SUPERSONIC SPEEDS

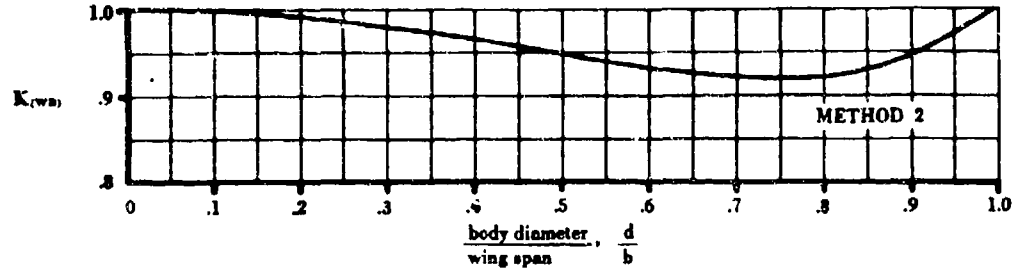

FIGURE 4.3.1.2-12c LIFT RATIO FOR METHOD 2

4.3.1.3 WING-BODY LIFT IN THE NONLINEAR ANGLE-OF-ATTACK RANGE

The mutual interference factors that influence the lift of a wing-body or a tail-body combination at low angles of attack (see Section 4.3.1.2) are also present at higher angles of attack. These include the nonlinear characteristics of the basic wing and body components (see Sections 4.1.3.3 and 4.2.1.2, respectively).

In addition, at angles of attack of approximately six degrees body vortices appear that can have strong influences on the loading on the lifting panels. The flow separates just behind or above the area of minimum pressure along the side of the body near the nose and wraps up into a pair of symmetrical vortices that proceed downstream in a nearly free-stream direction. The point at which separation first takes place depends upon the angle of attack (the higher the angle of attack, the nearer the nose separation occurs), the nose profile shape (the blunter the nose, the nearer the nose separation occurs), and body cross-sectional shape (sharply curving lateral contours promote early separation). The vortices increase in size and strength with increasing downstream distance. Since their strength also increases as the square of the angle of attack, they become quite significant at the higher angles of attack.

Quantitatively, these vortices do not change significantly between subsonic and supersonic speeds. This fact is substantiated by reference 1, which derives from supersonic data a method of estimating the cross-flow lift that gives equally reliable answers at subsonic and supersonic speeds. This is the method presented by the Datcom for handling the effects of these vortices on lifting surfaces at both subsonic and supersonic speeds.

A. SUBSONIC

Two methods of estimating the lift of wing-body configurations in the nonlinear angle-of-attack range are presented. The first uses the estimated nonlinear lift characteristics of isolated wings and bodies corrected by the slender-body interference factors used in Section 4.3.1.2. The effects of the body vortices are then added. This method is valid up to high angles of attack and is the more accurate of the two methods, though more laborious to use.

The second method simply uses the linear methods of Section 4.3.1.2 and adds the effects due to the body vortices. This method can be used with a minimum of effort but is less accurate than the first method because it does not include the nonlinearities of the basic components.

DATCOM METHODS

Method 1

The variation of lift with angle of attack is determined by the equation

$$C_N = \left\{(C_N)_N \frac{S_{N_{ref}}}{S_e} + \left[K_{W(B)} + K_{B(W)}\right](C_N)_e\right\}\frac{S_e}{S_W} + I_{v_{B(W)}}\left(\frac{\Gamma}{2\pi a V r}\right)\frac{r}{b_W/2}\frac{q}{q_\infty}\alpha\left(C_{L_\alpha}\right)_W \qquad 4.3.1.3\text{-a}$$

where

$(C_N)_N$ is the nose normal-force coefficient at a given angle of attack based on body frontal area $S_{N_{ref}}$ from Section 4.2.1.2

$K_{W(B)}$ and $K_{B(W)}$ are the mutual linear-theory interference values from figure 4.3.1.2-10

$(C_N)_e$ is the normal-force coefficient, at any given angle of attack, for the exposed wing (calculated by the method of Section 4.1.3.3 and based on exposed wing area)

$I_{v_{B(W)}}$ is the vortex interference factor for a lifting surface mounted on the body center line. This factor is given in figures 4.3.1.3-7a through 4.3.1.3-7ℓ for various wing taper ratios, relative wing sizes, and vortex-center line positions. In using these figures a possible problem can develop when interpolation must be made with respect to λ and $r/(b_W/2)$. For positions of the vortex near the body, the interpolation in $r/(b_W/2)$ can carry the vortex inside the body. Under these circumstances, it is recommended that the interpolation be made using $(y_o - r)/(b_W/2 - r)$ for the vortex lateral position in place of $y_o/(b_W/2)$, to avoid vortex positions inside the body. These figures are derived by means of strip theory in reference 2.

The vertical and lateral vortex positions at any given longitudinal station x can be determined from figures 4.3.1.3-13b and 4.3.1.3-14, respectively. These figures are based on the data of references 3, 4, and 5, for an ogive-cylinder, a cone-cylinder, and a modified cone-cylinder, respectively. The longitudinal position of vortex separation used in these figures is obtained from figure 4.3.1.3-13a, which is based on the ogive-cylinder test at a Mach number of 1.98 from reference 3.

$\frac{\Gamma}{2\pi a Vr}$ is the nondimensional vortex strength from figure 4.3.1.3-15, which is also based on the data of references 3, 4, and 5.

$\frac{r}{b_W/2}$ is the ratio of the radius of the body at the midpoint of the exposed root chord of the lifting panel to the semispan of the panel.

q/q_∞ is the dynamic pressure ratio acting on the panel. This value can either be assumed to be unity or can be estimated, with the information in Section 4.4.1 as a guide.

$(C_{L_\alpha})_W$ is the lift-curve slope of the isolated gross panel from Section 4.1.3.2.

Method 2

The variation of lift with angle of attack is given by the equation

$$C_L = \left[K_N + K_{W(B)} + K_{B(W)} \right] (C_{L_\alpha})_e \alpha \frac{S_e}{S_W} + I_{v_{B(W)}} \left(\frac{\Gamma}{2\pi a Vr} \right) \frac{r}{b_W/2} \frac{q}{q_\infty} \alpha \left(C_{L_\alpha} \right)_W \qquad 4.3.1.3\text{-b}$$

where the first term on the right-hand side is given by the method presented in Section 4.3.1.2 and the second term is determined as in Method 1.

The last terms of equations 4.3.1.3-a and -b, respectively, which represent the contributions of the body vortices, can normally be ignored for normal airplane-type wing-body combinations. For conventional missile configurations, these effects may become sizable.

Sample Problems

1. Method 1

Given:

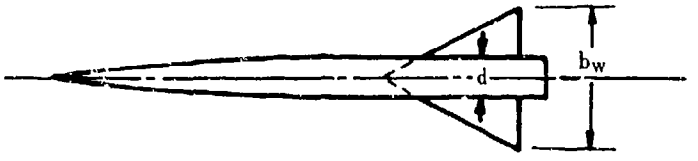

$A_W = A_e = 2$

$\Lambda_{c/2} = 45°$

$\lambda_W = \lambda_e = 0$

$\frac{S_e}{S_W} = 0.518$

$\frac{d}{b_W} = 0.280$

Airfoil: NACA 0005

$M = 0.2$

$q/q_\infty = 1.0$

$\frac{S_{N_{ref}}}{S_e} = 0.238$

$\frac{r}{b_W/2} = 0.280$

$\frac{x}{r} = 21.10$

where

x = distance from nose to c/4-point of the MAC of the exposed wing panel.

The following lift variation with angle of attack (from test data)

α(deg)	$(C_N)_N$	$(C_N)_e$
0	−.010	0
4	.035	.150
8	.175	.300
12	.430	.430
16	.810	.700

$(C_N)_N$ is based on $S_{N_{ref}}$

$(C_N)_e$ is based on S_e

The following lift-curve slopes

$(C_{L_\alpha})_e$ = 2.12 per radian (test data)

$(C_{L_\alpha})_W$ = 2.34 per radian (methods of Section 4.1.3.2)

$(C_{L_\alpha})_N$ = 2 per radian (slender-body theory)

$(C_{L_\alpha})_e$ based on S_e

$(C_{L_\alpha})_W$ based on S_W

$(C_{L_\alpha})_N$ based on $S_{N_{ref}}$

Compute:

$$\left.\begin{aligned} K_{W(B)} &= 1.240 \\ K_{B(W)} &= 0.420 \end{aligned}\right\} \text{(figure 4.3.1.2-10)}$$

The lift variation with angle of attack for the wing-body configuration, excluding the effect of body vortices, is calculated as follows:

$$\frac{C_L}{\cos\alpha} \approx C_N = \left\{(C_N)_N \frac{S_{N_{ref}}}{S_e} + \left[K_{W(B)} + K_{B(W)}\right](C_N)_e\right\}\frac{S_e}{S_W} \text{ (equation 4.3.1.3-a)}$$

α deg	C_N without vortices effect	$C_L = C_N \cos\alpha$
0	−.001	−.001
4	.133	.133
8	.280	.277
12	.423	.414
16	.701	.674

The calculation procedure for the effect of body vortices on lift variation with angle of attack is shown below.

$\frac{X_s}{r}$ (figure 4.3.1.3-13a)

$$\frac{X}{r} - \frac{X_s}{r} = 21.10 - \frac{X_s}{r}$$

$$\alpha\left(\frac{X}{r} - \frac{X_s}{r}\right) (\alpha \text{ in radians})$$

$\frac{x_o}{r}$ (figure 4.3.1.3-13b)

$\frac{y_o}{r}$ (figure 4.3.1.3-14)

$\frac{\Gamma}{2\pi a V_r}$ (figure 4.3.1.3-15)

$$\frac{y_o}{b_w/2} = \frac{y_o}{r}\frac{r}{b_w/2}$$

$$\frac{x_o}{b_w/2} = \frac{x_o}{r}\frac{r}{b_w/2}$$

$I_{v_{B(W)}}$ (figures 4.3.1.3-7a., 4.3.1.3-7b., and 4.3.1.3-7c, interpolated for $\frac{r}{b_w/2} = 0.280$)

$$\frac{r}{b_w/2}\frac{q}{q_\infty}(C_{L_\alpha})_W \alpha = 0.280\ (1.0)\ (.0408)\ \alpha^\circ = 0.0114\alpha^\circ$$

The solution for the vortices effect is

$$I_{v_{B(W)}}\left(\frac{\Gamma}{2\pi a V_r}\right)\frac{r}{b_w/2}\frac{q}{q_\infty}\alpha\left(C_{L_\alpha}\right)_W \quad (\alpha \text{ in degrees})$$

The details of the calculation for vortices effect are shown below.

① α deg	② $\frac{x_o}{r}$	③ $\alpha\left(\frac{x}{r} - \frac{x_o}{r}\right)$	④ $\frac{y_o}{r}$	⑤ $\frac{x_o}{r}$	⑥ $\frac{\Gamma}{2\pi a V_r}$
0	—	—	—	—	—
4	—	—	—	—	—
8	16.90	.58	.58	1.06	.51
12	11.25	2.05	.69	1.54	.82
16	8.55	3.50	.74	1.84	1.13

① α deg	⑦ $\frac{y_o}{b_w/2}$	⑧ $\frac{x_o}{b_w/2}$	⑨ $I_{v_{B(W)}}$	⑩ lift due to body vortices $= 0.0114$ ① ⑧ ⑨
0	—	—	—	—
4	—	—	—	—
8	.162	.297	−.22	−.0102
12	.193	.431	−.31	−.0348
16	.207	.515	−.38	−.0783

The solution for the lift variation with angle of attack of the wing-body configuration, including effect of body vortices, is shown below.

α deg	① C_L without vortices effect	② C_L due to body vortices	③ C_L = ① + ②
0	−.001	—	−.001
4	.133	—	.133
8	.277	−.0102	.267
12	.414	−.0348	.379
16	.674	−.0783	.596

2. Method 2

Given:

The same configuration and characteristics as in Method 1 above.

Compute:

$$K_N = \frac{(C_{L_\alpha})_N}{(C_{L_\alpha})_*} \frac{S_{N_{ref}}}{S_*} \quad \text{(Section 4.3.1.2)}$$

$$= \frac{2}{2.12} (.238)$$

$$= 0.225$$

$$\left.\begin{aligned} K_{W(B)} &= 1.240 \\ K_{B(W)} &= 0.420 \end{aligned}\right\} \text{ see Method 1 above}$$

The lift variation with angle of attack for the wing-body configuration, excluding the effect of body vortices, is calculated as follows:

$$C_L = [K_N + K_{W(B)} + K_{B(W)}] \frac{S_*}{S_W} (C_{L_\alpha})_* \alpha \ (\alpha \text{ in degrees})$$

$$= [.225 + 1.240 + .420] (.518) (.0370) \alpha$$

$$= 0.03613 \alpha \ (\alpha \text{ in degrees})$$

The lift due to body vortices is the same as that calculated in Method 1 above. The total lift variation is shown below.

α deg	① C_L without vortices effect	② C_L due to body vortices	③ C_L = ① + ②
0	0	—	0
4	.144	—	.144
8	.289	−.0102	.279
12	.434	−.0348	.399
16	.578	−.0783	.500

B. TRANSONIC

At transonic speeds compression and expansion waves interact at much greater distances from the body than at supersonic speeds. The disturbances in the flow field extend to greater distances from the body surface than at subsonic or supersonic speeds. With a knowledge of conditions at the surface of a body, the characteristics of a lifting surface mounted on the body can be approximated by assuming that the flow disturbances propagate undiminished in a direction normal to the free stream. An excellent discussion of methods of calculating surface pressures on bodies of revolution at zero angle of attack is given in reference 6. However, the corresponding problem at angle of attack is not well covered in the literature.

At angle of attack, the appearance of body vortices due to viscous separation effects is exactly analogous to that which occurs at subsonic or supersonic speeds.

DATCOM METHOD

No explicit method is presented in the Datcom at the present time, because of the complexity and uncertainty of estimating nonviscous transonic flow properties. It is recommended that the methods detailed in paragraph C be used at transonic speeds.

C. SUPERSONIC

The discussion of the potential flow field about a body at angle of attack, given in Section 4.2.1.2 is directly applicable to this Section, and therefore no new information is presented. Body vortices are also present at angles of attack in excess of approximately 6°. The physical mechanism of these vortices and their effect upon lifting panels are the same as at subsonic speeds; they are discussed in some detail in paragraph A.

DATCOM METHOD

Two methods are available for estimating the lift of wing-body configurations at supersonic speeds. These can be represented by equations 4.3.1.3-a and -b, respectively, of paragraph A. Because of the similarity of the application of these methods, the sample problem of paragraph A suffices to illustrate these methods.

REFERENCES

1. Kelly, H. R.: The Estimation of Normal-Force, Drag, and Pitching-Moment Coefficients for Blunt-Based Bodies of Revolution at Large Angles of Attack. Jour. Aero. Sci., Vol. 21, No. 8, August 1954. (U)
2. Pitts, W. C., Nielsen, J. N., and Kaattari, G. E.: Lift and Center of Pressure of Wing-Body-Tail Combinations at Subsonic, Transonic, and Supersonic Speeds. NACA TR 1307, 1959. (U)
3. Jorgensen, L. H. and Perkins, E. W.: Investigation of Some Wake Vortex Characteristics of an Inclined Ogive-Cylinder Body at Mach Number 1.98. NACA RM A55E31, August 1955. (U)
4. Mello, J. F.: Investigation of Normal-Force Distributions and Wake Vortex Characteristics of Bodies of Revolution at Supersonic Speeds. APL/JHU Rep. CM 867, Johns Hopkins Univ., April 1956. (U)
5. Raney, D. J.: Measurement of the Cross Flow Around an Inclined Body at a Mach Number of 1.91. British Repor. RAE TN Aero 2357 (ASTIA AD 82 343), January 1955. (U)
6. Spreiter, J. R.: Aerodynamics of Wings and Bodies at Transonic Speeds. Jour. Aero. Sci., Vol. 26, No. 8, August 1959. (U)

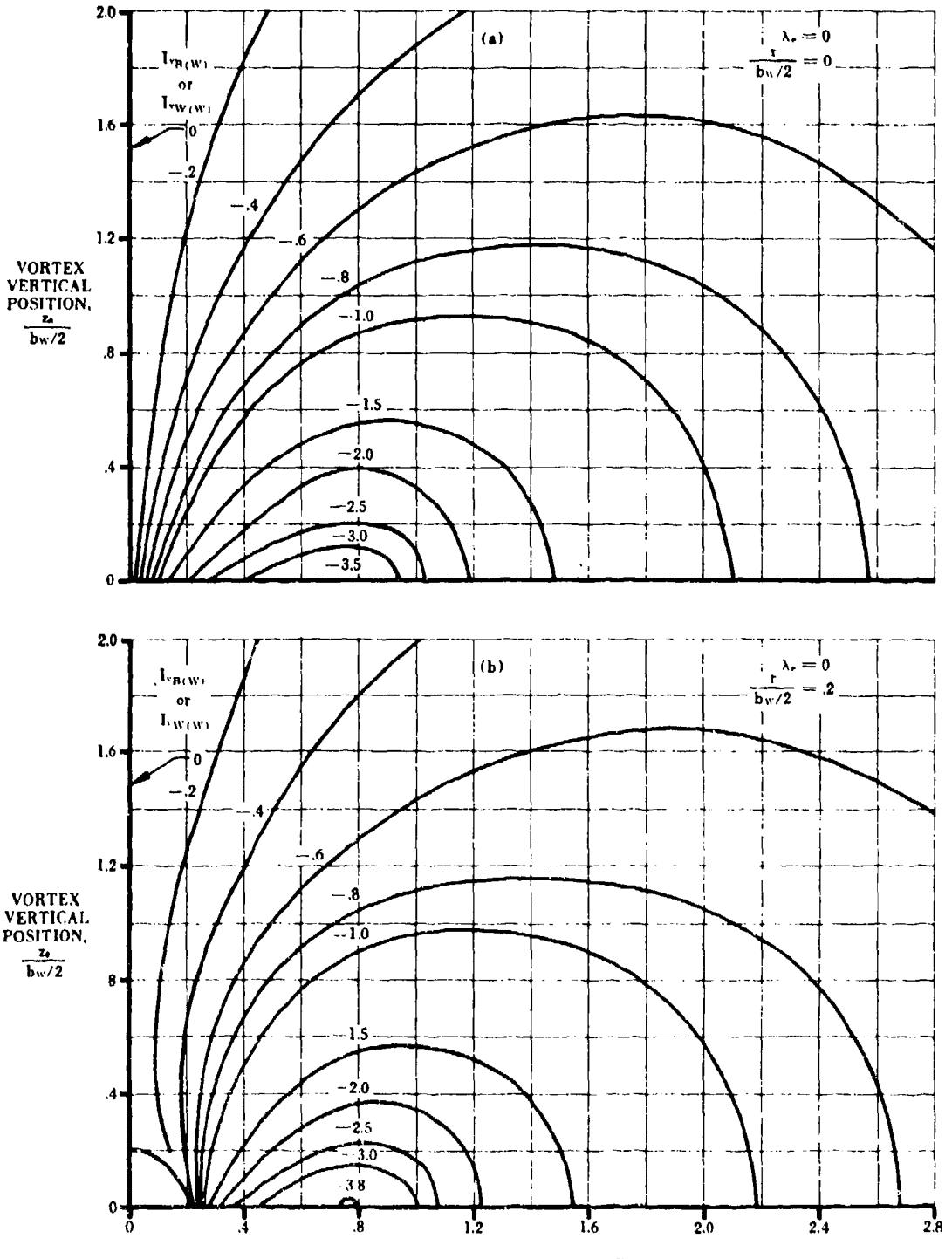

FIGURE 4.3.1.3-7 VORTEX INTERFERENCE FACTOR

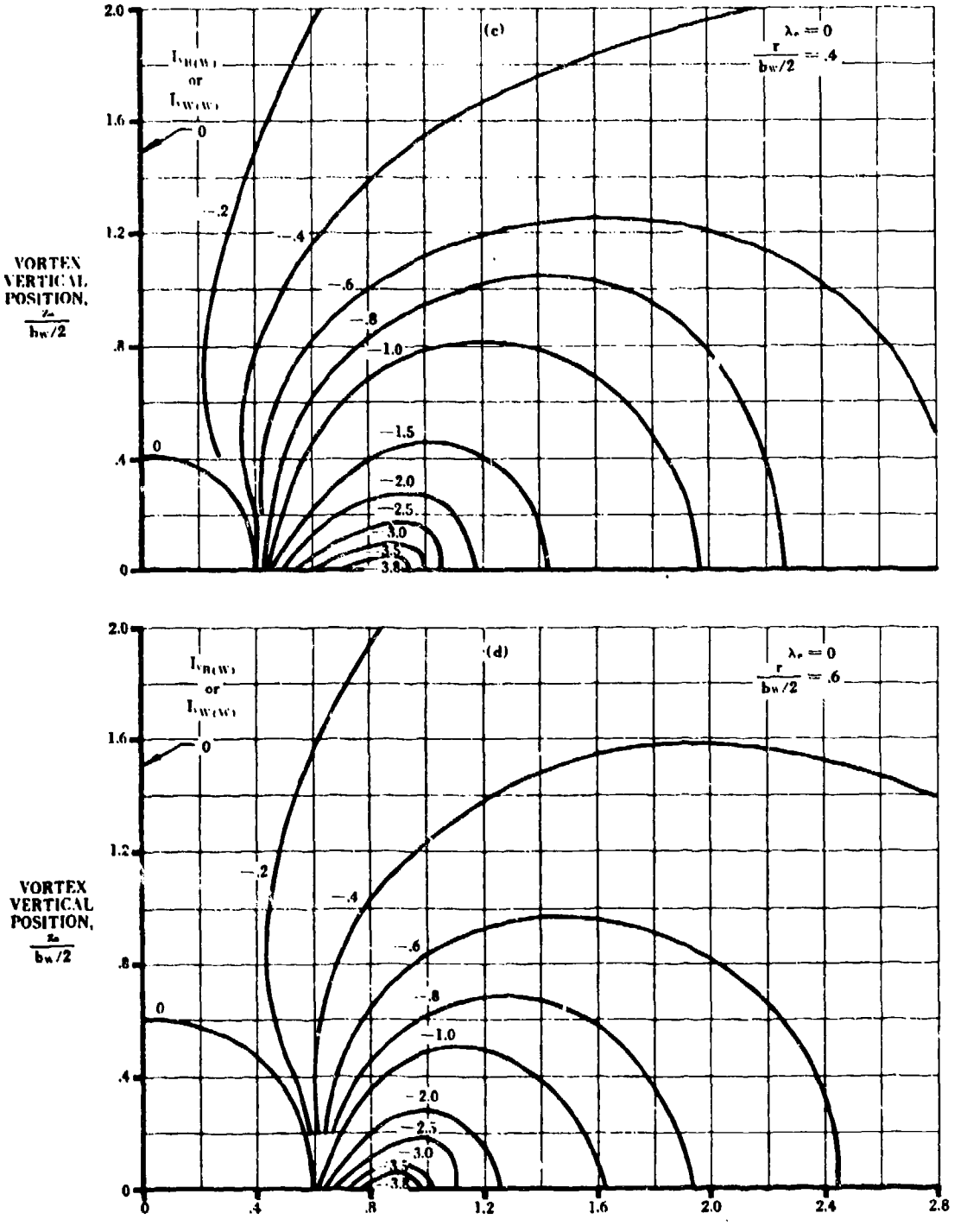

FIGURE 4.3.1.3-7 VORTEX INTERFERENCE FACTOR (CONT'D)

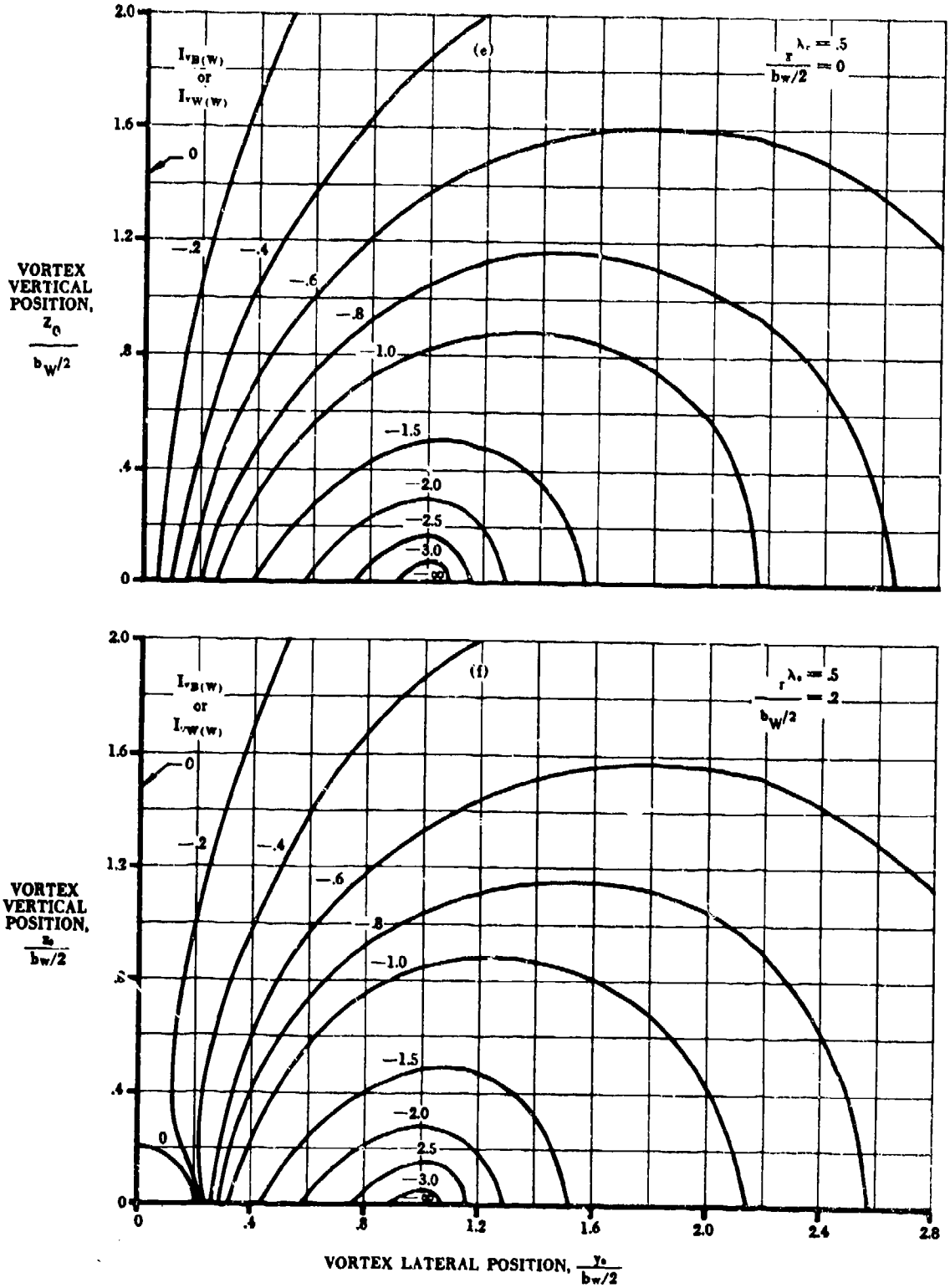

FIGURE 4.3.1.3-7 VORTEX INTERFERENCE FACTOR (CONT'D)

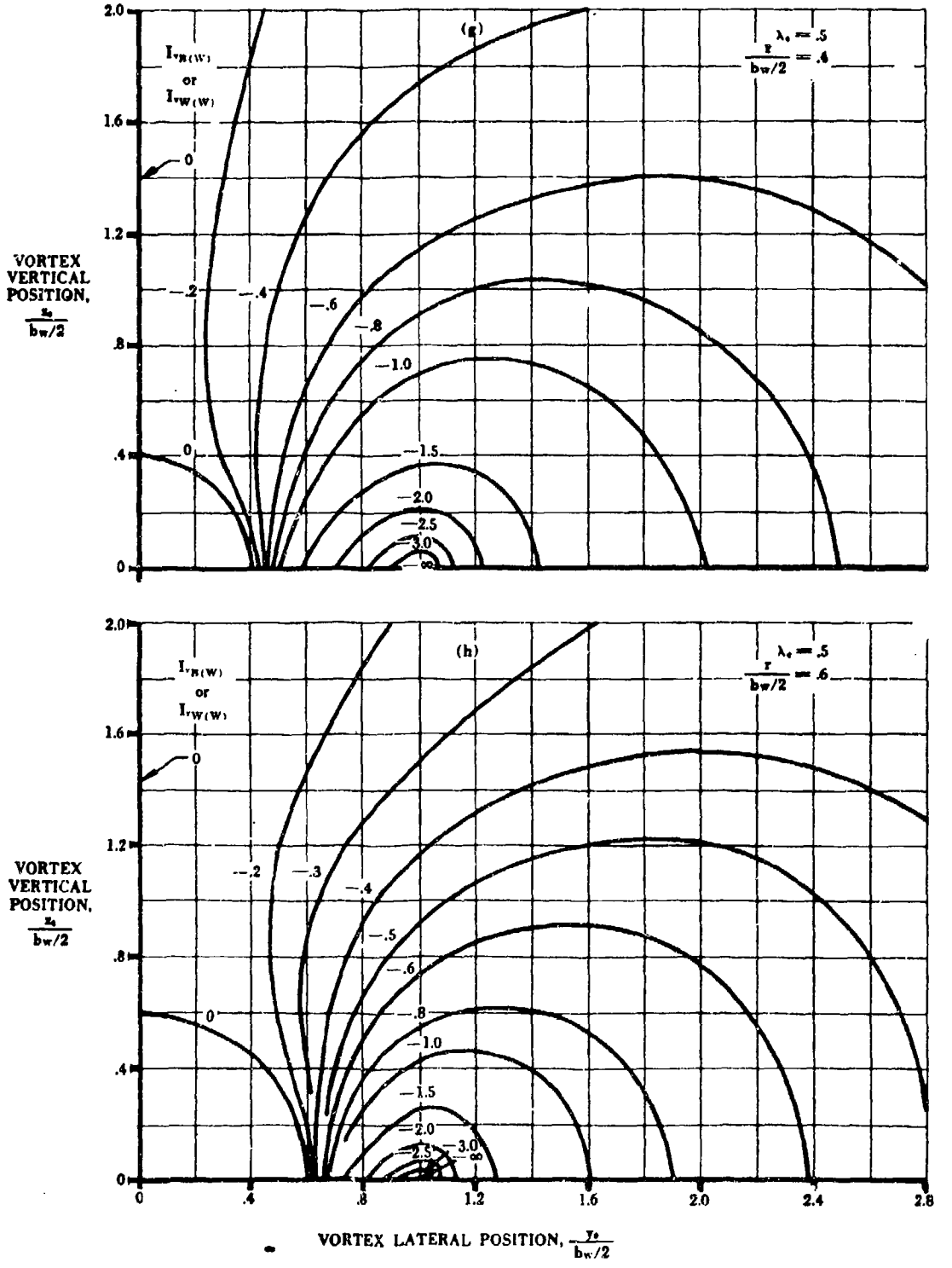

FIGURE 4.3.1.3-7 VORTEX INTERFERENCE FACTOR (CONT'D)

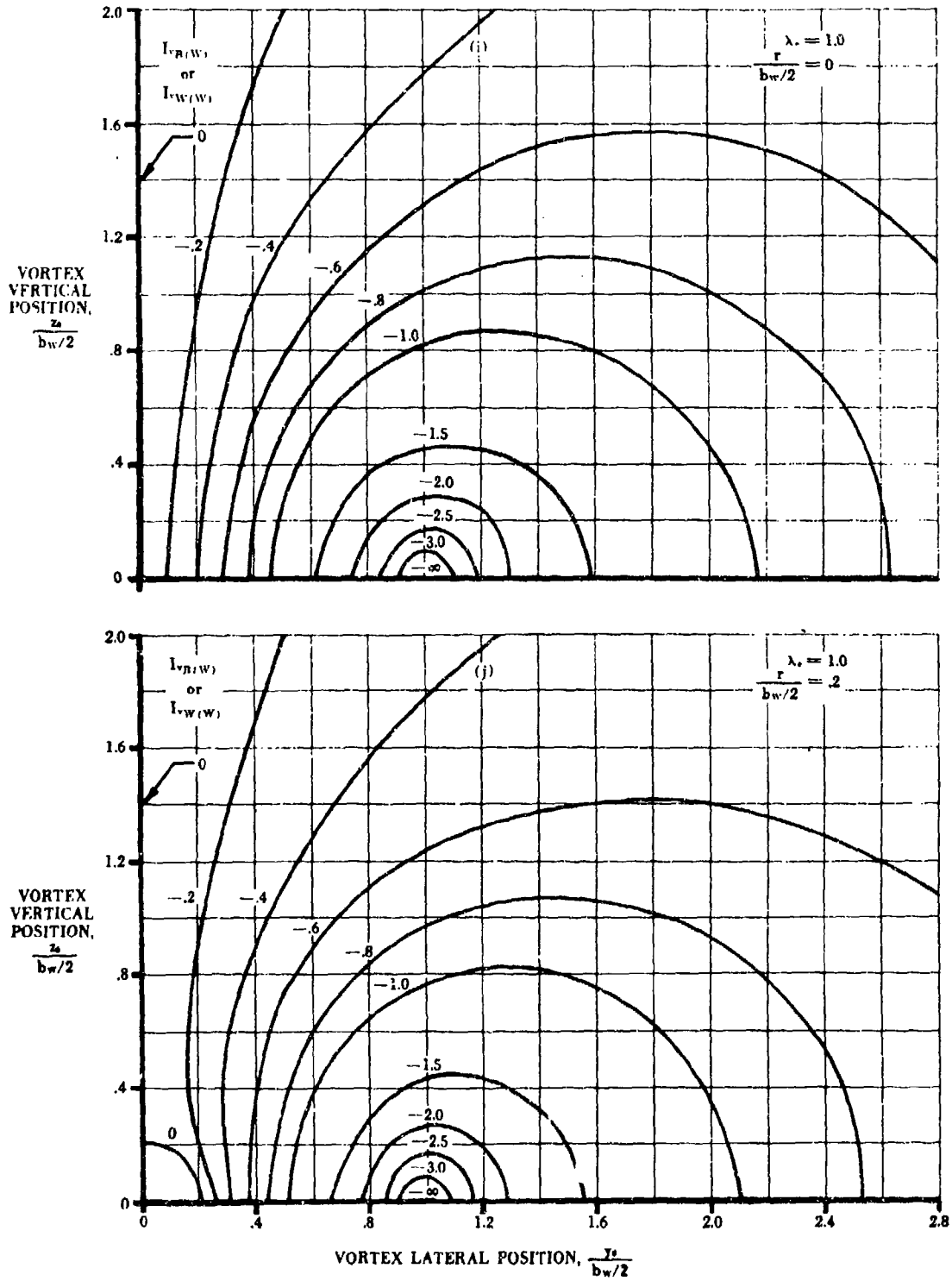

FIGURE 4.3.1.3-7 VORTEX INTERFERENCE FACTOR (CONT'D)

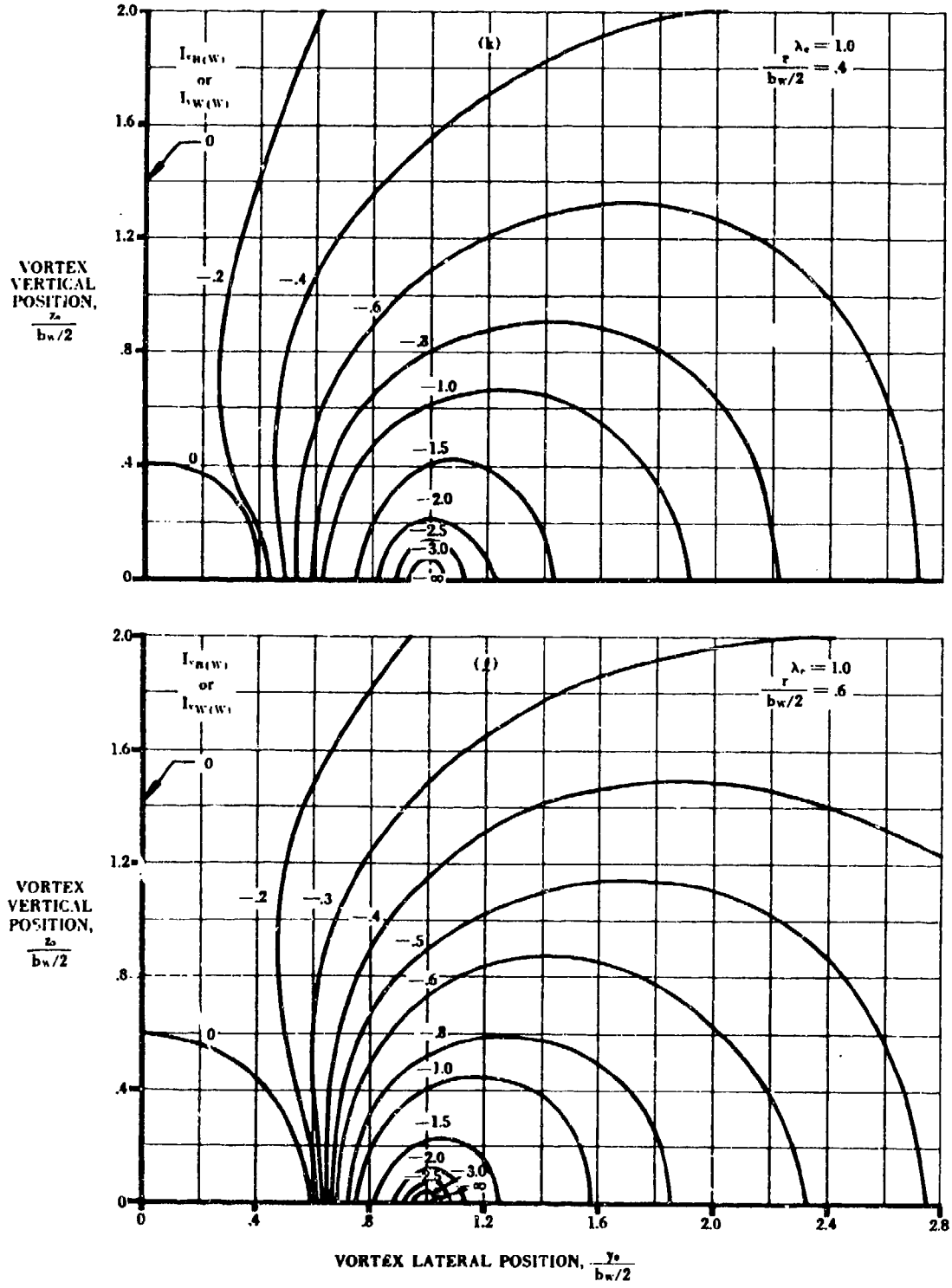

FIGURE 4.3.1.3-7 VORTEX INTERFERENCE FACTOR (CONT'D)

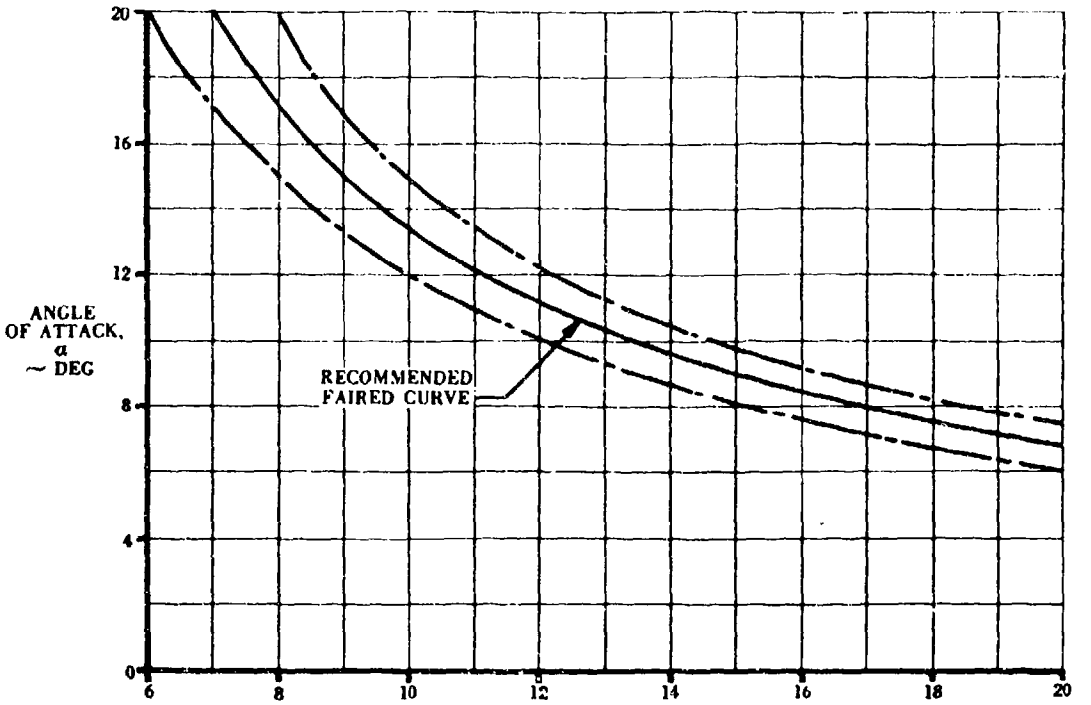

FIGURE 4.3.1.3-13a LONGITUDINAL POSITION OF VORTEX SEPARATION

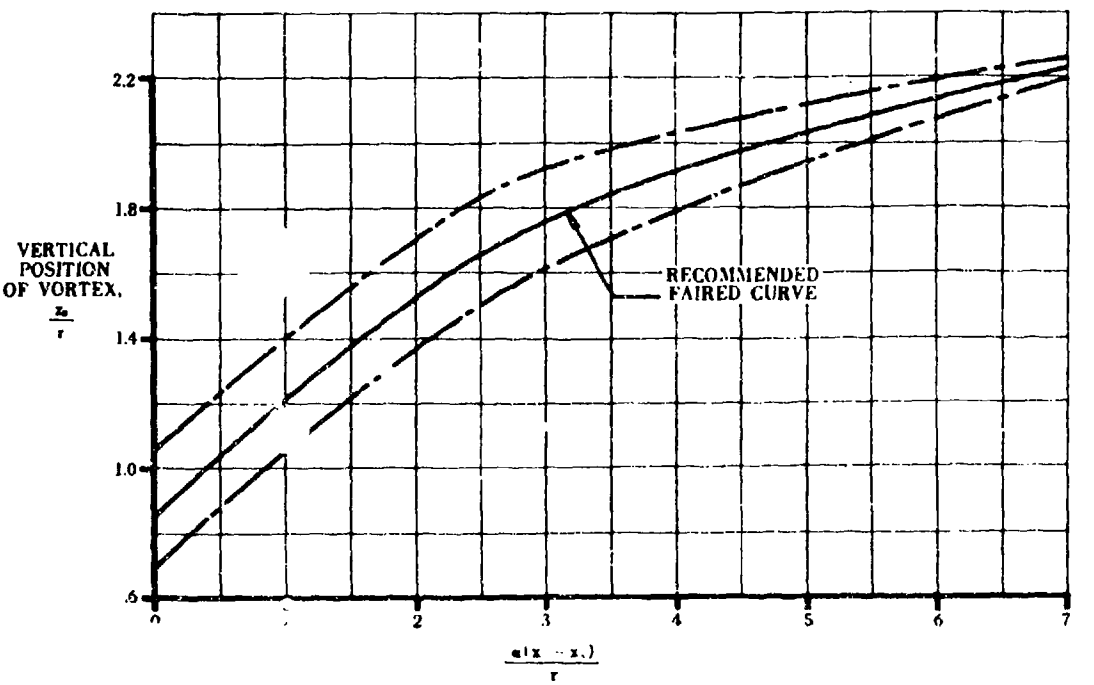

FIGURE 4.3.1.3-13b VERTICAL POSITION OF VORTEX

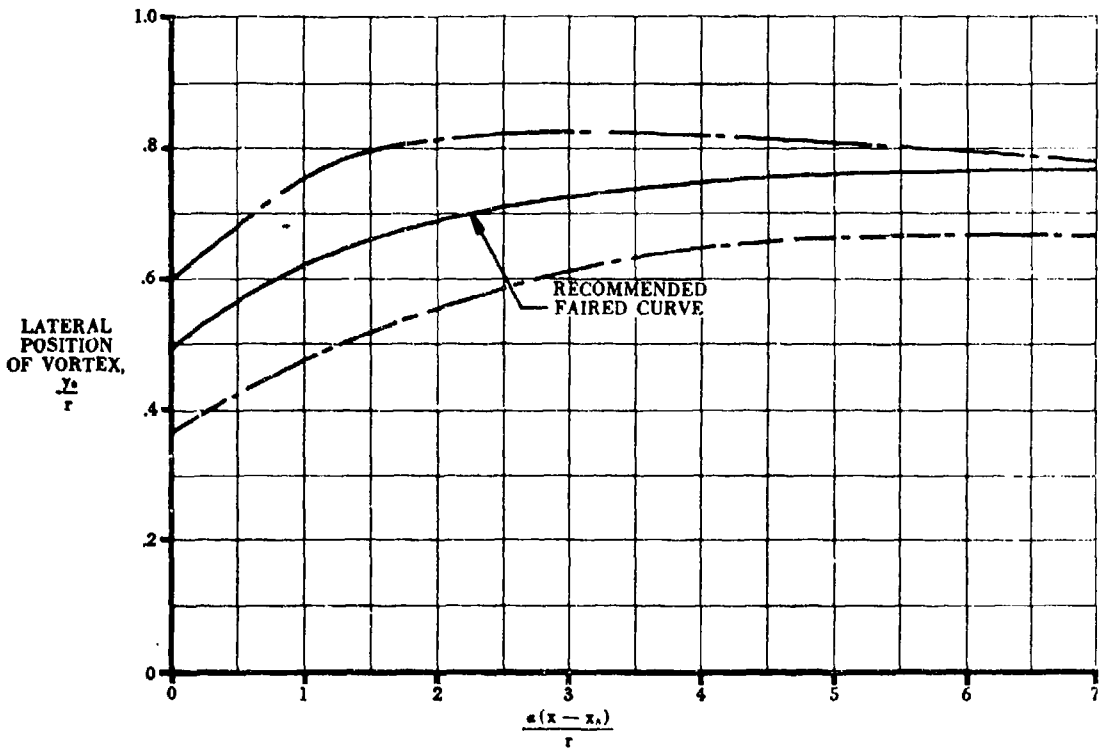

FIGURE 4.3.1.3-14 LATERAL POSITION OF VORTEX

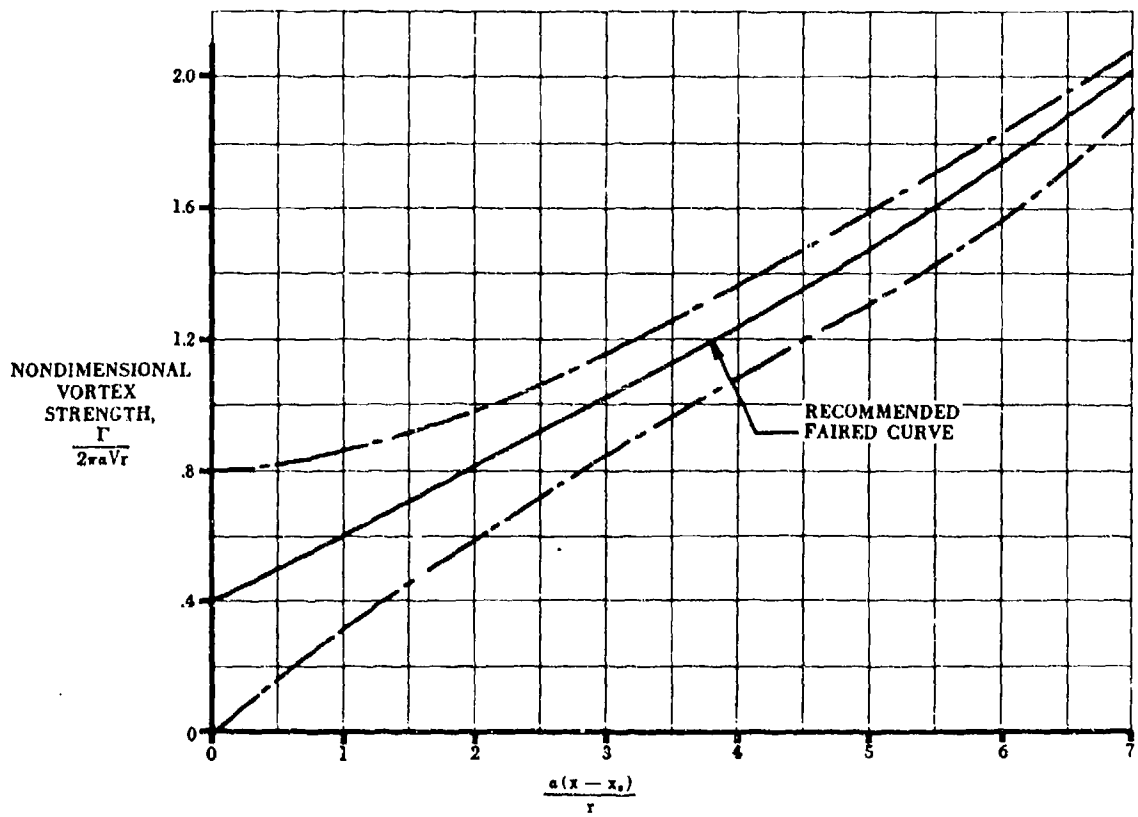

FIGURE 4.3.1.3-15 VORTEX STRENGTH

4.3.1.4 WING-BODY MAXIMUM LIFT

A. SUBSONIC

The addition of a body of revolution to a wing at high angles of attack increases the wing-induced angle of attack at all spanwise stations. The increase is greatest at the root and falls off in an exponential manner with increasing distance from the body.

This effective increase in angle of attack tends to make the wing in the presence of the body stall at a lower geometric angle of attack than that corresponding to the wing alone. However, this tendency to stall at a lower angle of attack may be modified or counteracted by changes in the wing stalling pattern. These changes are the result of the nonlinear spanwise variation of body-induced flow and also of the partial blanketing of the wing by the body. The relative magnitudes of these latter two effects are largely dependent on specific wing planform shape. This means that wing planform shape is a primary parameter in considering wing-body maximum lift.

Varying the wing height on the body, the body cross-section shape, or the body local area distribution (area rule) changes the body-induced effects on the wing and hence the maximum lift of the combination. Experimental data on variations of this type show small but generally consistent differences (see References 1, 2, 3, and 4).

The first method presented below is essentially that of Section 4.1.3.4, in that it requires the user to employ the most accurate wing-body spanwise-loading computer program available. In case no such program is available to the user, an alternate empirical method is presented as Method 2.

DATCOM METHODS

Method 1

This method requires that the user have at his disposal an accurate wing-body spanwise-loading computer program, e.g., a lifting-surface-theory computer program. Specific instructions for application of the program to obtain the wing-body maximum lift are identical to Steps 1 through 4 of Paragraph A in Section 4.1.3.4, which pertain to the wing-alone case.

No substantiation of this method is presented because of the variety of spanwise-loading programs that are available to different Datcom users.

Method 2

This method is based on empirical correlations and the wing-alone method of Section 4.1.3.4, and should be restricted to Mach numbers equal to or less than 0.60. The wing-body maximum lift coefficient and angle of attack at maximum lift are obtained using

$$\left(C_{L_{max}}\right)_{WB} = \frac{\left(C_{L_{max}}\right)_{WB}}{\left(C_{L_{max}}\right)_{W}} \left(C_{L_{max}}\right)_{W} \qquad 4.3.1.4\text{-a}$$

$$(\alpha_{C_{L_{max}}})_{WB} = \frac{(\alpha_{C_{L_{max}}})_{WB}}{(\alpha_{C_{L_{max}}})_{W}} (\alpha_{C_{L_{max}}})_{W} \qquad 4.3.1.4\text{-b}$$

where

$\frac{(C_{L_{max}})_{WB}}{(C_{L_{max}})_{W}}$ is the ratio of the wing-body maximum lift to wing maximum lift, obtained from Figure 4.3.1.4-12b as a function of wing-body geometry.

$(C_{L_{max}})_{W}$ is the wing maximum lift obtained from the appropriate method of Paragraph A in Section 4.1.3.4. The wing-alone value is based on the total wing, including that part covered by the body.

$\frac{(\alpha_{C_{L_{max}}})_{WB}}{(\alpha_{C_{L_{max}}})_{W}}$ is the ratio of the wing-body angle of attack at maximum lift to the wing angle of attack at maximum lift. This value is obtained from Figure 4.3.1.4-12c as a function of wing-body geometry.

$(\alpha_{C_{L_{max}}})_{W}$ is the wing-alone angle of attack at maximum lift obtained from the appropriate method of Paragraph A in Section 4.1.3.4. The wing-alone value is based on the total wing, including that part covered by the body.

A comparison of test data from References 5 through 17 with results calculated by this method is presented in Table 4.3.1.4-A.

Sample Problem

Given: Configuration 4 of Reference 14.

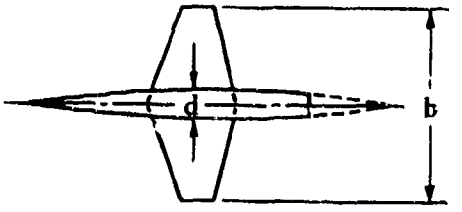

$A = 3.0$ $\Lambda_{LE} = 19.1^{o}$ $\lambda = 0.4$

Airfoil: 3-percent biconvex (free-stream direction)

$\frac{d}{b} = 0.145$ $M = 0.25$ $R_{\ell} = 8.8 \times 10^{6}$

$(C_{L_{max}})_{W} = 0.77$

$(\alpha_{C_{L_{max}}})_{W} = 15.9^{o}$

} Obtained using Section 4.1.3.4

Compute:

$C_2 = 1.10$ (Figure 4.3.1.4-12a)

$$(C_2 + 1) A \tan \Lambda_{LE} = (1.10 + 1)(3)(0.3463) = 2.18$$

$$\frac{\left(C_{L_{max}}\right)_{WB}}{\left(C_{L_{max}}\right)_{W}} = 0.98 \qquad \text{(Figure 4.3.1.4-12b)}$$

$$\frac{(\alpha_{C_{L_{max}}})_{WB}}{(\alpha_{C_{L_{max}}})_{W}} = 0.99 \qquad \text{(Figure 4.3.1.4-12c)}$$

Solution:

$$\left(C_{L_{max}}\right)_{WB} = \frac{\left(C_{L_{max}}\right)_{WB}}{\left(C_{L_{max}}\right)_{W}} \left(C_{L_{max}}\right)_{W} \qquad \text{(Equation 4.3.1.4-a)}$$

$$= (0.98)(0.77)$$

$$= 0.75$$

$$(\alpha_{C_{L_{max}}})_{WB} = \frac{(\alpha_{C_{L_{max}}})_{WB}}{(\alpha_{C_{L_{max}}})_{W}} (\alpha_{C_{L_{max}}})_{W} \qquad \text{(Equation 4.3.1.4-b)}$$

$$= (0.99)(15.9)$$

$$= 15.7^{o}$$

These compare with test-data values from Reference 14 of $\left(C_{L_{max}}\right)_{WB} = 0.71$ and $\left(\alpha_{C_{L_{max}}}\right)_{WB} = 14.3^{o}$

B. TRANSONIC

No method is presented in this speed regime. The lack of sufficient experimental data prevents the presentation of any empirical method. However, the trend of the limited data available (Reference 5) indicates that the wing-body maximum lift converges to the wing-alone value as the Mach number is increased above M = 0.6.

C. SUPERSONIC

Two separate methods are presented in this section for estimating the wing-body maximum lift at supersonic speeds. The first method is somewhat easier to apply than the second method. Both methods yield approximately the same degree of accuracy, based on the limited available test data (References 18, 19, and 20). Attempts to substantiate these methods completely have been impaired by lack of test data in the stall regime.

The first method is based on the application of the wing-body interference coefficients of Section 4.3.1.2 to the exposed-wing-alone maximum lift of Section 4.1.3.4. This approach is justified, since at supersonic and hypersonic speeds the wing lift is limited by geometric considerations rather than by flow separation on the wing. That is, maximum lift is reached when the component of the normal force in the lift direction ceases to increase with angle of attack. Therefore, the body-induced effects are felt mainly through their influence on the lift-curve slope, rather than on wing separation. This implies that the supersonic maximum lift of the wing-body combination may be obtained by applying wing-body interference coefficients to the wing-alone maximum lift value.

The second method uses the method of Section 4.3.1.3 to calculate the complete normal-force curve, from which the lift curve can easily be calculated.

Both methods assume that the angle of attack at wing-body maximum lift is the same as the angle of attack for wing maximum lift.

DATCOM METHODS

Method 1

This method applies the wing-body interference factors from Paragraph C of Section 4.3.1.2 to the wing-alone maximum lift coefficient. The limitations of the sections used in this method will also apply to this method. The wing-body maximum lift, based on S_W, is found by

$$\left(C_{L_{max}}\right)_{WB} = \left(C_{L_{max}}\right)_e \left[K_N + K_{W(B)} + K_{B(W)}\right] \frac{S_e}{S_W} \qquad 4.3.1.4\text{-a}$$

where

$\left(C_{L_{max}}\right)_e$ is the exposed-wing-alone maximum lift coefficient determined by Paragraph C of Section 4.1.3.4. (For the definition of exposed wing, see Section 4.3.1.2)

K_N, $K_{W(B)}$, and $K_{B(W)}$ are the wing-body interference factors from Method 1 of Paragraph C of Section 4.3.1.2.

$\frac{S_e}{S_W}$ is the ratio of the exposed wing area to the total wing area.

No substantiation of this method is presented; however, application of the method is illustrated in Sample Problem 1.

Method 2

Application of this method is restricted to straight-tapered planforms. The wing-body maximum lift is determined by using Equation 4.3.1.3-a to obtain the normal force C_N as a function of angle of attack. Then the lift curve is constructed by using the approximation $C_L \cong C_N \cos\alpha$, from which the $C_{L_{max}}$ value is obtained. The determination of the nose contribution term $(C_N)_N$ of Equation 4.3.1-3-a may present somewhat of a problem, since the supersonic design curves (Section 4.2.1.2) are inadequate at the higher angles of attack. Consequently, it is suggested that Method 2 of Paragraph D of Section 4.2.1.2 be used for determining $(C_N)_N$ in the high angle-of-attack regime.

No substantiation of this method is presented; however, application of the method is illustrated in Sample Problem 2.

Sample Problems

1. Method 1

Given: The wing-body configuration of Reference 19.

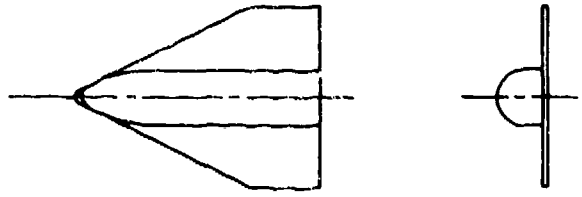

Total Wing:

$A = 1.15$ $\lambda = 0.3$ $b = 8.26$ in. $c_r = 11.0$ in.

$c_t = 3.30$ in. $\Lambda_{LE} = 63^{O}$ $S_W = 0.409$ sq ft Airfoil: flat plate

Exposed Wing:

$A_e = 0.97$ $\lambda_e = 0.354$ $b_e = 6.13$ in. $c_{r_e} = 9.31$ in.

$S_e = 0.268$ sq ft

Additional Characteristics:

$\ell_B = 10.65$ in. $d = 2.13$ in. LER = 0.125 in. $M = 1.97; \beta = 1.70$

Compute:

$\left(C_{L_{max}}\right)_e$

$A_e \tan \Lambda_{LE} = (0.97)(1.963) = 1.904$

$$\frac{\beta}{\tan \Lambda_{LE}} = \frac{1.70}{1.963} = 0.866$$

$\tan \Lambda_{LE} \left(C_{N_\alpha}\right)_{theory} = 3.175$ (Figure 4.1.3.2-56 interpolated)

$$\left(C_{N_\alpha}\right)_{theory} = \frac{3.175}{1.963} = 1.617 \text{ per rad}$$

$$\frac{C_{N_\alpha}}{\left(C_{N_\alpha}\right)_{theory}} = 1.0 \text{ for a flat plate} \qquad \text{(Figure 4.1.3.2-60)}$$

$$C_{N_\alpha} = 1.617 \text{ per rad}$$

$$\frac{\beta C_{N_\alpha}}{4} = \frac{(1.70)(1.617}{4} = 0.68?$$

$$\frac{1}{M} = \frac{1}{1.97} = 0.5076$$

$$\left(C_{L_{max}}\right)_e = 0.985 \qquad \text{(Figure 4.1.3.4-27a)}$$

$K_N = 0$, since nose does not extend ahead of wing apex

$K_{W(B)}$

$$\frac{d}{b} = \frac{2.13}{8.26} = 0.258$$

$K_{W(B)} = 1.22$ (Figure 4.3.1.2-10)

$K_{B(W)}$

$$\frac{\beta d}{c_{r_e}} = \frac{(1.70)(2.13)}{9.31} = 0.389$$

$$\beta \cot \Lambda_{LE} = (1.70)(0.5095) = 0.866$$

$$K_{B(W)}\left[\beta\left(C_{L_\alpha}\right)_e\left(\lambda_e + 1\right)\left(\frac{b}{d} - 1\right)\right] = 2.5 \qquad \text{(Figure 4.3.1.2-11b)}$$

$$K_{B(W)} = \frac{2.5}{(1.70)(1.617)(1.354)\left(\frac{8.26}{2.13} - 1\right)} = \frac{2.5}{10.71} = 0.233$$

Solution:

$$\left(C_{L_{max}}\right)_{WB} = \left(C_{L_{max}}\right)_e\left[K_N + K_{W(B)} + K_{B(W)}\right]\frac{S_e}{S_W} \qquad \text{(Equation 4.3.1.4-a)}$$

$$= (0.985)(0 + 1.22 + 0.233)\left(\frac{0.268}{0.409}\right) = 0.937$$

$\alpha_{C_{L_{max}}} = 44.2^{o}$ (Figure 4.1.3.4-27b)

This compares with a test value of $C_{L_{max}} = 0.94$ and $\alpha_{C_{L_{max}}} = 42^{o}$

2. Method 2

Given: Same configuration as Sample Problem 1.

$A = 1.15$ $\lambda = 0.3$ $\Lambda_{LE} = 63^{o}$ $S_W = 0.409$ sq ft

$S_e = 0.268$ sq ft Airfoil: flat plate

$K_{W(B)} = 1.22$

$K_{B(W)} = 0.233$ } (Sample Problem 1, above)

$\left(C_{N_\alpha}\right)_e = 1.617$ per rad

$M = 1.97$; $\beta = 1.70$

Compute:

$\left(C_N\right)_N = 0$, since nose does not extend ahead of wing apex

$\left(C_N\right)_e$

$$\frac{\beta}{\tan \Lambda_{LE}} = \frac{1.70}{1.963} < 1$$ (subsonic leading edge)

Step 1. $\left(C_{N_\alpha}\right)_e = 1.617$

Step 2. Empirical Parameter E (see Paragraph C of Section 4.1.3.3)

$\frac{\tan \Lambda_{LE}}{1.92} = \frac{1.963}{1.92} > 1$, therefore use equation:

$$E = \left(C_{N_\alpha}\right)_e \left[\frac{\tan \Lambda_{LE}}{1.92} + C\left(\frac{\tan \Lambda_{LE}}{1.92} - 1\right)\right]$$

$$\delta_{\perp} = \tan^{-1} \frac{\Delta y_{\perp}}{5.85} = 0 \text{ for flat plate} \qquad \text{(see sketch on Figure 2.2.1-8)}$$

$$C = 0 \qquad \text{(Figure 4.1.3.3-59a)}$$

$$E = (1.617)\left[\frac{1.963}{1.92} + (0)\left(\frac{1.963}{1.92} - 1\right)\right]$$

$$= 1.653 \text{ per rad}$$

Step 3.

$$E\,\frac{\beta}{\tan \Lambda_{LE}} = 1.653\ \frac{1.70}{1.963} = 1.432$$

$$\frac{C_{N_\alpha}}{\left(C_{N_\alpha}\right)_{theory}} = 1.0 \text{ for a flat plate} \qquad \text{(Figure 4.1.3.2-60)}$$

$$\frac{\left(C_{N_\alpha}\right)_{theory}}{C_{N_\alpha}}\ \beta \tan \alpha = \beta \tan \alpha;\ \frac{C_{N_\alpha}}{\left(C_{N_\alpha}\right)_{theory}}\ \frac{1}{\beta \tan \alpha} = \frac{1}{\beta \tan \alpha}$$

Step 4.

$$\left(C_N\right)_e = C_{N_\alpha}\ \frac{\sin 2\alpha}{2} + C_{N_{\alpha\alpha}} \sin \alpha |\sin \alpha| \qquad \text{(Equation 4.1.3.3-a)}$$

①	②	③	④	⑤	⑥	⑦	⑧	⑨	⑩
α (deg)	$\beta \tan \alpha$	$\frac{1}{\beta \tan \alpha}$	$C_{N_{\alpha\alpha}}$ (Fig. 4.1.3.3-69b)	$\sin \alpha$	$\sin^2 \alpha$ ⑤^2	$\sin 2\alpha$	$\left(C_{N_\alpha}\right)_e \frac{\sin 2\alpha}{2}$ (1.617)⑦/2	$C_{N_{\alpha\alpha}} \sin^2 \alpha$ ④⑥	$\left(C_N\right)_e$ ⑧ + ⑨
16	0.4874		1.58	0.2756	0.0760	0.5299	0.4284	0.1201	0.5485
20	0.6188		1.50	0.3420	0.1170	0.6428	0.5197	0.1755	0.6952
24	0.7568		1.42	0.4067	0.1654	0.7431	0.6008	0.2349	0.8357
28	0.9039		1.35	0.4695	0.2204	0.8290	0.6702	0.2975	0.9677
32		0.9413	1.29	0.5299	0.2808	0.8988	0.7267	0.3622	1.0889
36		0.8097	1.26	0.5878	0.3455	0.9511	0.7690	0.4353	1.2043
40		0.7010	1.25	0.6428	0.4132	0.9848	0.7962	0.5165	1.3127
44		0.6091	1.26	0.6947	0.4826	0.9994	0.8080	0.6081	1.4161
48		0.5297	1.27	0.7431	0.5522	0.9945	0.8041	0.7013	1.5054
52		0.4696	1.30	0.7880	0.6209	0.9703	0.7845	0.8072	1.5917

The contribution of body vortices (last term of Equation 4.3.1.3-a) can be neglected, since the configuration is more typical of an airplane configuration than of a missile.

Solution:

$$C_N = \left\{ \left(C_N\right)_N \frac{S_{N_{ref}}}{S_e} + \left[K_{W(B)} + K_{B(W)}\right] \left(C_N\right)_e \right\} \frac{S_e}{S_W} + I_{v_{B(W)}} \frac{\Gamma}{2\pi\alpha V r} \frac{r}{b_W/2} \frac{q}{q_\infty} \alpha \left(C_{L_\alpha}\right)_W$$

(Equation 4.3.1.3-a)

$$= \left\{0 + [1.22 + 0.233] \left(C_N\right)_e\right\} \left(\frac{0.268}{0.409}\right) + 0$$

$$= 0.952 \left(C_N\right)_e$$

① α (deg)	② $\left(C_N\right)_e$	③ C_N 0.952 ②	④ C_L cos α ③
16	0.5485	0.5222	0.502
20	0.6952	0.6618	0.622
24	0.8357	0.7956	0.727
28	0.9677	0.9213	0.813
32	1.0889	1.0366	0.879
36	1.2043	1.1465	0.928
40	1.3127	1.2497	0.957
44	1.4161	1.3481	0.970
48	1.5054	1.4331	0.959
52	1.5917	1.5153	0.933

These data are plotted in Sketch (a), where $C_{L_{max}} = 0.970$ and $\alpha_{C_{L_{max}}} = 44^o$. These compare with test values of $C_{L_{max}} = 0.94$ and $\alpha_{C_{L_{max}}} = 42^o$.

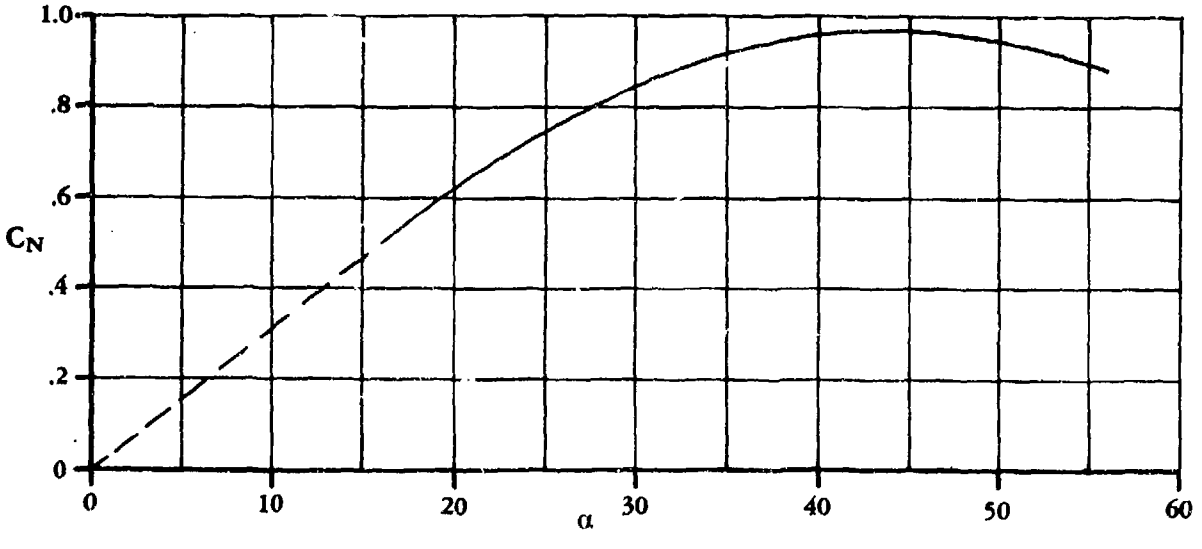

SKETCH (a)

REFERENCES

1. Letko, W., and Williams, J.: Experimental Investigation at Low Speed of Effects of Fuselage Cross Section on Static Longitudinal and Lateral Stability Characteristics of Models Having 0° and 45° Sweptback Surfaces. NACA TN 3551, 1955. (U)

2. Goodman, A., and Thomas, D.: Effects of Wing Position and Fuselage Size on the Low-Speed Static and Rolling Stability Characteristics of a Delta-Wing Model. NACA TR 1224, 1955. (U)

3. Fischetti, T.: Investigation of Mach Numbers from 0.80 to 1.43 of Pressure and Load Distributions over a Thin 45° Sweptback Highly Tapered Wing in Combination With Basic and Indented Bodies. NACA RM L57D29a, 1957. (U)

4. Sutton, F., and Lautenberger, W.: The Effect of Body Contouring on the Longitudinal Characteristics at Mach Numbers up to 0.92 of a Wing-Fuselage-Tail and Several Wing-Fuselage Combinations Having Sweptback Wings of Relatively High Aspect Ratio. NACA RM A56J08, 1957. (U)

5. Wiley, H.: Aerodynamic Characteristics Extended to High Angles of Attack at Transonic Speeds of Small-Scale 0° Sweep Wing, 45° Sweptback Wing, and 60° Delta Wing. NACA RM L52I30. (U)

6. Fischel, J., and Schneiter, L.: An Investigation at Low Speed of a 51.3° Sweptback Semispan Wing Equipped With 16.7-Percent-Chord Plain Flaps and Ailerons Having Various Spans and Three Trailing-Edge Angles. NACA RM L8H20, 1948. (U)

7. Foster, G., and Fitzpatrick, J.: Longitudinal-Stability Investigation of High-Lift and Stall-Control Devices on a 52° Sweptback Wing With and Without Fuselage and Horizontal Tail at a Reynolds Number of 6.8×10^{6}. NACA RM L8I08, 1948. (U)

8. Anderson, A.: An Investigation at Low Speed of a Large-Scale Triangular Wing of Aspect Ratio Two — III Characteristics of Wing With Body and Vertical Tail. NACA RM A9H04, 1949. (U)

9. Johnson, B., and Rollins, F.: Investigation of a Thin Wing of Aspect Ratio 4 in the Ames 12-Foot Pressure Wind Tunnel. V — Static Longitudinal Stability and Control Throughout the Subsonic Speed Range of a Semispan Model of a Supersonic Airplane. NACA RM A9I01, 1949. (U)

10. Griner, R., and Foster, G.: Low-Speed Longitudinal and Wake Air-Flow Characteristics at Reynolds Number of 6×10^{6} of a 52° Sweptback Wing Equipped With Various Spans of Leading-Edge and Trailing-Edge Flaps, a Fuselage, and a Horizontal Tail at Various Vertical Positions. NACA RM L50K29, 1951. (U)

11. Jaquet, B., and Queijo, M.: Low-Speed Static Longitudinal Stability and Control Characteristics of a 60° Triangular-Wing Model Having Half-Delta Tip Controls. NACA RM L51D20a, 1951. (U)

12. Johnson, B., and Shibata, H.: Characteristics Throughout the Subsonic Speed Range of a Plane Wing and of a Cambered and Twisted Wing, Both Having 45° of Sweepback. NACA RM A51D27, 1951. (U)

13. Hopkins, E., and Carel, H.: Experimental and Theoretical Study of the Effects of Body Size on the Aerodynamic Characteristics of an Aspect Ratio 3.0 Wing-Body Combination. NACA RM A51G24, 1951. (U)

14. Smith, D., Shibata, H., and Selan, R.: Lift, Drag, and Pitching Moment of Low-Aspect-Ratio Wings at Subsonic and Supersonic Speeds — An Investigation at Large Reynolds Numbers of the Low-Speed Characteristics of Several Wing-Body Combinations. NACA RM A51K28, 1952. (U)

15. Johnson, H.: Wind-Tunnel Investigation at Low Speed of the Effect of Varying the Ratio of Body Diameter to Wing Span From 0.1 to 0.8 on the Aerodynamic Characteristics in Pitch of a 45° Sweptback-Wing-Body Combination. NACA RM L53J09a, 1953. (U)

16. Wolhart, W., and Thomas, D., Jr.: Static Longitudinal and Lateral Stability Characteristics at Low Speed of Unswept-Midwing Models Having Wings With an Aspect Ratio of 2, 4, or 6. NACA TN 3649, 1956. (U)

17. Thomas, D., Jr., and Wolhart, W.: Static Longitudinal and Lateral Stability Characteristics at Low Speed of 45° Sweptback-Midwing Models Having Wings With an Aspect Ratio of 2, 4, or 6. NACA TN 4077, 1957. (U)

18. Foster, G. V.: Exploratory Investigation at Mach Number of 2.01 of the Longitudinal Stability and Control Characteristics of a Winged Reentry Configuration. NASA TM X-178, 1959. (U)

19. Foster, G. V.: Longitudinal Aerodynamic Characteristics at a Mach Number of 1.97 of a Series of Related Winged Reentry Configurations for Angles of Attack from 0° to 90°. NASA TM X-461, 1961. (U)

20. Stone, D. R.: Aerodynamic Characteristics of a Fixed-Wing Manned Space Shuttle Concept at a Mach Number of 6.0 NASA TM X-2049, 1970. (U)

TABLE 4.3.1.4-A
METHOD 2
SUBSONIC MAXIMUM LIFT COEFFICIENTS OF WING-BODY COMBINATIONS
DATA SUMMARY AND SUBSTANTIATION

Ref.	A	Λ_{LE} (deg)	$\frac{d}{b}$	Airfoil*	M	$\alpha C_{L_{max}}$ Calc.	$\alpha C_{L_{max}}$ Calc.	$C_{L_{max}}$ Test	$\alpha C_{L_{max}}$ Test	Percent Error, e	
										$C_{L_{max}}$	$\alpha C_{L_{max}}$
5	2.31	60	.18	65-006	.60	1.02	27.2°	.99	28°	3.0	−2.9
6	3.43	51.3	.065	65-012 (⊥ to .5c)	.12	1.04	26.8°	1.05	27°	−1.0	−0.7
7	2.88	52	.15	64$_1$-112 (⊥ to .25c)	.13	1.15	26.8°	1.17	26°	−1.7	3.1
8	2.04	63	.18	Double Wedge 5%	.13	1.32	31.5°	1.32	31.5°	0	0
9	4	10	.12	Double Wedge 4.2%	.20	.71	12.5°	.715	13.2°	−0.7	−3.0
10	2.88	52	.15	64$_1$-112 (⊥ to.28c)	.12	1.15	26.8°	1.18	30°	−2.5	−10.7
11	2.31	60	.18	65-006.5	.17	1.08	29.9°	1.08	33.2°	0	−10.0
12	5	46	.10	64A-010 (⊥ to.25c)	.25	1.09	22.9°	.955	23°	14.1	−0.4
	↓	↓	↓	↓	↓	.925	20.9°	.955	22°	−3.1	−5.0
13	3	23	.196	4.5% Hex.	.25	.795	15.1°	.82	14°	−3.0	7.9
	↓	↓	.259	↓	↓	.76	14.7°	.74	12.8°	2.7	14.8
	↓	↓	.343	↓	↓	.72	13.2°	.72	12.5°	0	5.6
14	3	19	.145	3% Bi-Convex	.25	.75	15.6°	.71	14.3°	+5.6	9.1
	↓	↓	↓	↓	.60	.75	14.9°	.70	15°	7.1	−0.7
	4	45	.127	↓	↓	.845	21.1°	.85	22°	−0.6	−4.1
	↓	↓	↓	↓	.25	.875	22.1°	.883	23°	−0.9	−3.9
	3	53.1	↓	↓	↓	1.00	25°	1.04	26°	−3.8	−3.8
15	3	45	.10	65A-006	.29	.93	24.8°	.94	22°	−1.1	12.7
	↓	↓	.20	↓	↓	.91	20°	.98	18.2°	−7.1	9.9
	↓	↓	.30	↓	↓	.95	16.4°	.96	16.6°	−1.0	−1.2
	↓	↓	.40	↓	↓	1.03	16.3°	1.00	16.0°	3.0	1.9
	↓	↓	.60	↓	↓	1.25	19.5°	1.24	18.3°	0.8	6.6
	↓	↓	.80	↓	↓	–	32°	2.24	31°	–	3.2
16	2	7.2	.23	65A-008	.13	.73	24°	.75	19°	−2.7	26.3
	4	3.6	.15	↓	↓	.75	14.4°	.76	16°	1.3	−10.0
	6	2.4	.135	↓	↓	.75	12.3°	.78	12°	−3.8	2.5
17	2	48	.23	65A-008	.13	.93	22.2°	.96	22.3°	−3.1	−0.4
	4	47	.15	↓	↓	.89	20.5°	.96	20°	−7.3	2.5
	6	46	.135	↓	↓	.89	18°	.96	20.4°	−7.3	−11.8

*Airfoil defined parallel to free stream unless stated otherwise.

Average Error in $C_{L_{max}} = \frac{\Sigma |e|}{n} = 3.2\%$

Average Error in $\alpha C_{L_{max}} = \frac{\Sigma |e|}{n} = 6.0\%$

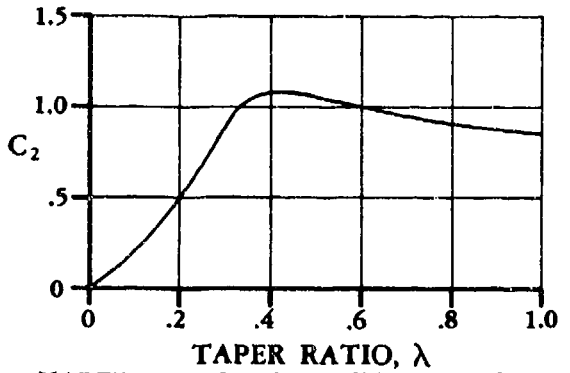

FIGURE 4.3.1.4-12a TAPER-RATIO CORRECTION FACTOR

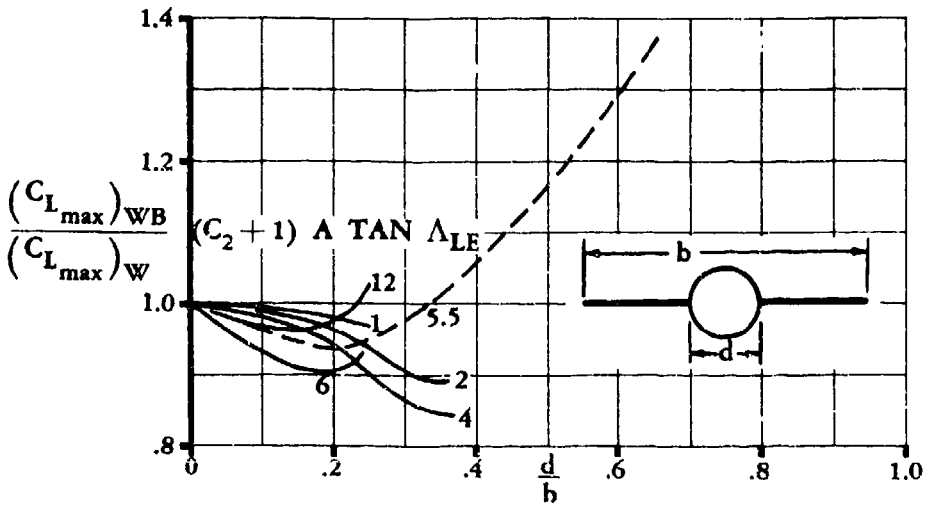

FIGURE 4.3.1.4-12b WING-BODY MAXIMUM LIFT

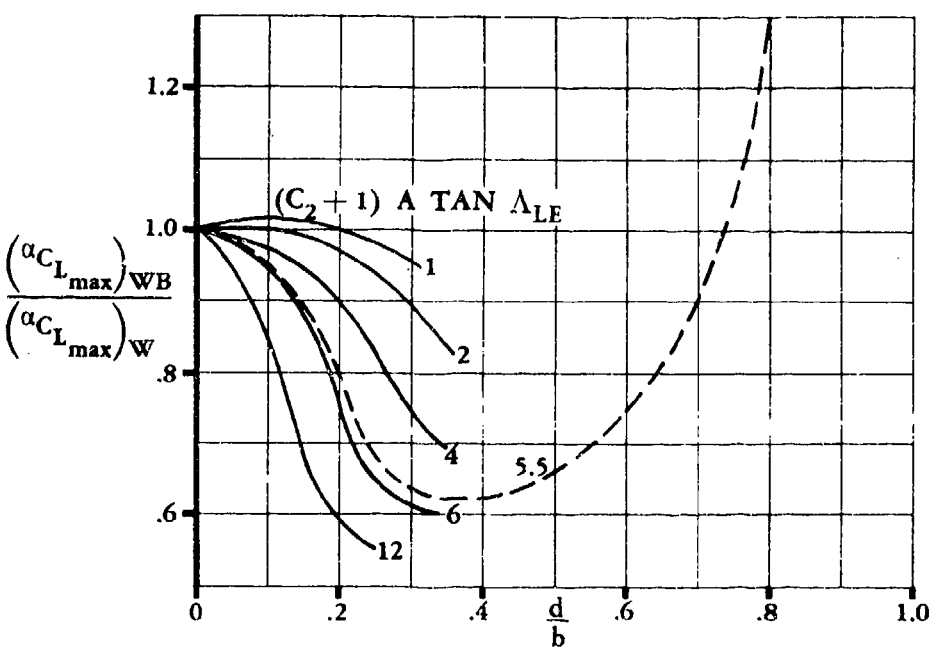

FIGURE 4.3.1.4-12c ANGLE OF ATTACK FOR MAXIMUM LIFT

4.3.2.1 WING-BODY ZERO-LIFT PITCHING MOMENT

Methods are presented for determining the wing-body zero-lift pitching-moment coefficient in the subsonic, transonic, and supersonic speed regimes. It is advisable to use experimental data whenever possible in each speed regime.

A. SUBSONIC

Two methods are presented for estimating the subsonic wing-body zero-lift pitching-moment coefficient for straight-tapered wings. Method 1 (Reference 1) was derived using the momentum considerations of H. Multhopp (Reference 2). Method 2 (Reference 3) has been empirically derived from fighter-type test data. Method 1 is considered to be more accurate than Method 2 because it includes the effects of fuselage width and fuselage camber distribution. Neither method is limited to bodies of revolution; however, only Method 1 accounts explicitly for noncircular bodies. If it becomes necessary to analyze a noncircular body in combination with a wing, the results of Method 2 should be used with caution.

DATCOM METHODS

Method 1

The wing-body zero-lift pitching-moment coefficient for straight-tapered wings* may be approximated by

$$\left(C_{m_0}\right)_{WB} = \left[\left(C_{m_0}\right)_W + \left(C_{m_0}\right)_B\right] \frac{\left(C_{m_0}\right)_M}{\left(C_{m_0}\right)_{M=0}} \qquad 4.3.2.1\text{-a}$$

where

$\left(C_{m_0}\right)_W$ is the wing zero-lift pitching-moment coefficient uncorrected for Mach-number effects, obtained from Section 4.1.4.1.

$\frac{\left(C_{m_0}\right)_M}{\left(C_{m_0}\right)_{M=0}}$ is the Mach-number correction factor obtained from Figure 4.1.4.1-6 as a function of Mach number. This chart gives the ratio of wing-body zero-lift pitching-moment coefficient in compressible flow to that in incompressible flow, based on test data.

$\left(C_{m_0}\right)_B$ is the body zero-lift pitching-moment coefficient, uncorrected for Mach-number effects. This parameter is approximated by using

$$\left(C_{m_0}\right)_B = \frac{(k_2 - k_1)}{36.5\, S_W \bar{c}} \sum_{x=0}^{x=\ell_B} w_f^2 \left[(\alpha_0)_W + (i_{CL})_B\right] \Delta x \qquad 4.3.2.1\text{-b}$$

*Method 1 should apply to non-straight-tapered planforms. However, the lack of a method for predicting the wing zero-lift pitching-moment contribution has prevented any substantiation of this method for non-straight-tapered planforms.

where

$(k_2 - k_1)$ is the apparent mass factor developed by Munk, obtained from Figure 4.2.1.1-20a as a function of the body fineness ratio

S_W is the wing reference area

$\bar{c}$ is the wing mean aerodynamic chord

w_f is the average width of a body increment (see Sketch (a))

$(\alpha_0)_W$ is the wing zero-lift angle relative to the fuselage reference plane, obtained from test data or estimated by using the wing zero-lift angle-of-attack method of Section 4.1.3.1 (the effects of wing incidence must be considered when using the method of this section).

$(i_{CL})_B$ is the incidence angle of the fuselage camber line relative to the fuselage reference plane at the increment center. The sign convention of $(i_{CL})_B$ is identical to that of horizontal-tail incidence, and is negative for both nose droop and upsweep as shown in Sketch (a). The fuselage camber line is defined by the vertical location of the fuselage-maximum-width line or the body mean line where the maximum-width line is not clearly defined (see Sketch (b)).

Δx is the length of the body increment (see Sketch (a)). Fuselage increment length should be chosen so that neither the change in average width nor the change in camber line incidence is too large between successive increments. The increments need not be of equal length.

ℓ_B is the body length.

Equation 4.3.2.1-b may be evaluated by dividing the fuselage into increments (see Sketch (a)), computing the value of each increment, and adding them up.

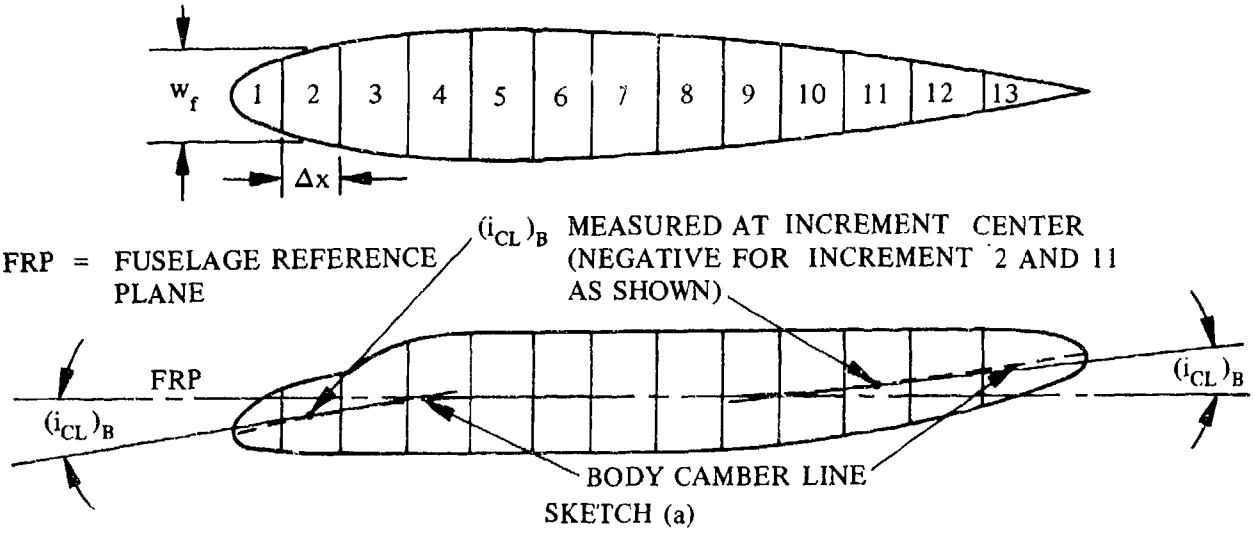

SKETCH (a)

SEVERAL FUSELAGE CROSS-SECTIONS
SHOWING CAMBER LINE VERTICAL LOCATION

SKETCH (b)

A comparison of test data with results calculated by this method is presented in Table 4.3.2.1-A. It should be noted that the test data are for configurations having cambered airfoils. For most configurations with symmetrical wings with no twist, the predicted values are zero or very small.

Method 2

This method was developed in Reference 3 for fighter-type aircraft by using the linear regression analysis of mathematical statistics. In general, a regression analysis involves the study of a group of variables to determine their effect on a given parameter. Because of the empirical nature of this method (values for the regression coefficients), exact solutions are available only at the following Mach numbers: 0.4, 0.6, 0.7, 0.8, 0.9, 0.95, 1.0, 1.1, 1.2, 1.3, 1.4, 1.5, 2.0, and 2.5. At other Mach numbers interpolation is necessary.

It is advisable to restrict the applicability of this method to the range of geometric parameters of the test data used in the formulation of the regression coefficients. The test data used in the formulation of the regression coefficients have geometric parameters within the following limits:

aspect ratio, A	1.6 to 6.0
taper ratio, λ	0 to 1
twist, θ	0 to -9.4^{o}
leading-edge radius, LER/$\bar{c}$	0 to 0.015
thickness, t/$\bar{c}$	0.025 to 0.10
NACA camber, $(y_c)_{max}/\bar{c}$	0 to 0.0263
conical-camber design lift coefficient, C_{L_d}	0 to 0.45
forebody fineness ratio, ℓ_N/d	2.2 to 8.4
afterbody fineness ratio, ℓ_A/d	0.3 to 5.6
leading-edge sweep, Λ_{LE}	0 to 70^{o}
Reynolds number, R_ℓ	0.8×10^6 to 8×10^6

This method is not limited to bodies of revolution; however, no attempt is made to account for the effects of noncircular bodies. If it becomes necessary to analyze a noncircular body in combination with a wing, it is suggested that an equivalent body of revolution be used, i.e., a body of revolution with the same cross-sectional area.

The wing-body zero-lift pitching-moment coefficient, based on the product of the wing area and mean aerodynamic chord $S_W \bar{c}_W$, is given at a specific Mach number by

$$\left(C_{m_0}\right)_{WB} = C_0 + C_1\left(\frac{1}{A}\right) + C_2\, A + C_3 \tan \Lambda_{LE} + C_4\left(\frac{t}{\bar{c}}\right) + C_5\left(\frac{\ell_N}{d}\right) + C_6\left(\frac{\ell_A}{d}\right) + C_7\, \lambda$$

$$+ C_8\, \lambda^2 + C_9\,(T_R) + C_{10}\left(\frac{LER}{\bar{c}}\right) + C_{11}\,\theta + C_{12}\left[\frac{\left(y_c\right)_{max}}{\bar{c}}\right] + C_{13}\, C_{L_d}$$

$$+ C_{14}\, W_L + C_{15}\, V_T + C_{16}\left(\frac{h}{d}\right) + C_{17}\left(\frac{\omega}{b}\right) + C_{18}\, R_\ell \qquad \text{4.3.2.1-c}$$

where

$C_0, C_1, \ldots C_{18}$ are the regression coefficients as a function of Mach number, obtained from Table 4.3.2.1-B.

A is the total wing aspect ratio.

Λ_{LE} is the sweep of the leading edge.

$\frac{t}{c}$ is the wing thickness ratio at the mean aerodynamic chord.

$\frac{\ell_N}{d}$ is the nose and forebody fineness ratio (see Sketch (b)).

$\frac{\ell_A}{d}$ is the afterbody fineness ratio taken at the afterbody wing-body juncture (see Sketch (b)).

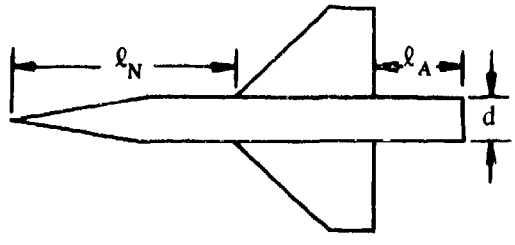

SKETCH (c)

λ	is the wing taper ratio.
T_R	is the transition indicator; 0 for no transition strips and 1 for transition strips or flight test.
$\frac{LER}{\bar{c}}$	is the ratio of the leading-edge radius to the mean aerodynamic chord taken at the mean aerodynamic chord.
θ	is the wing twist between the root and tip sections in radians, negative for washout (see Figure 5.1.2.1-30b).
$\frac{(y_c)_{max}}{\bar{c}}$	is the NACA camber in the form of a ratio of the maximum ordinate of the mean line to the airfoil chord taken at the mean aerodynamic chord.
C_{L_d}	is the conical-camber design lift coefficient for a M = 1.0 design with the designated camber ray line intersecting the wing trailing edge at 0.8 b/2. (For more details see Reference 4.) If the wing does not have a conical-camber design, the value of C_{L_d} is zero.
W_L	is the wing location index, with W_L = 1.0 for a high wing, W_L = 0.5 for a midwing, and W_L = 0 for a low wing.
V_T	is the vertical-tail indicator, with V_T = 1.0 for a vertical tail, and V_T = 0 for no vertical tail.
$\frac{h}{d}$	is the ratio of the maximum canopy height measured from the body center line to the body height at the point of maximum canopy height.
$\frac{d}{b}$	is the ratio of the maximum body width to wing span.
R_ℓ	is the Reynolds number based on the mean aerodynamic chord. For Reynolds numbers in excess of 8×10^6, the value of 8×10^6 should be used.

Sample Problems

1. Method 1

Given: The wing-body configuration of Reference 5 (Sketch (d))

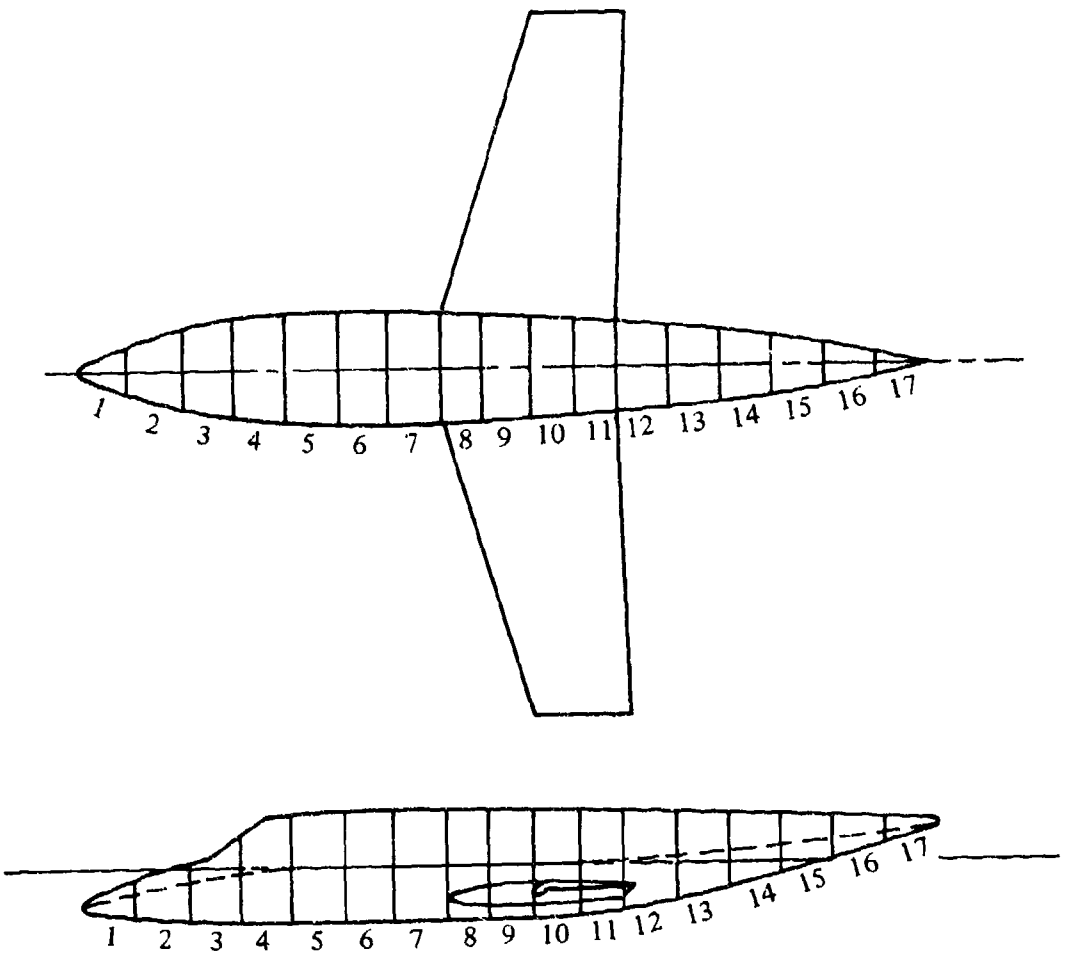

SKETCH (d)

Wing Characteristics:

S_W = 21.51 m^2 $\bar{c}$ = 2.14 m θ = 0^o

A = 5.02 λ = 0.507 $\Lambda_{c/4}$ = 13^o

$(\alpha_0)_W$ = -1.2^o (test data) M = 0.17

Root section airfoil is a NACA 64A-109

Tip section airfoil is a NACA 64A-109 modified by drooping the leading edge (Sketch (e)).

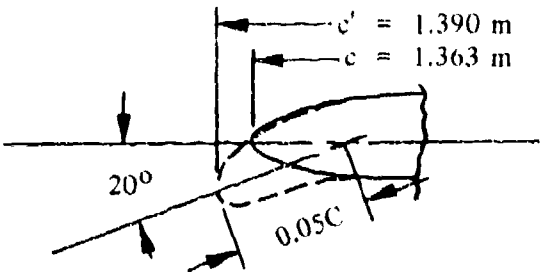

SKETCH (e)

For the Tip Section

$c' = 1.390$ m $c = 1.363$ m $\delta_{f_{LE}} = 20^{o}$ $c_{f_{LE}} = 0.05c$

The drooped leading edge varies linearly across the span from the tip section as shown in Sketch (e), to zero extension and deflection at the root section.

Fuselage Characteristics:

$\ell_B = 12.50$ m $d_{max} = 1.62$ m

Other fuselage dimensions are measured from the three view drawings in Reference 5 and are listed in tabular form when used.

Compute:

Determine wing section c_{m_0}

Root Section (64A-109) c_{m_0} is determined through use of data from Table 4.1.1-B

SECTION	c_{m_0}
64A-010	0
64A-210	−0.040
64-108	−0.015
64-110	−0.020

Note that the variation in c_{m_0} due to camber is identical for the "64" and "64A" series airfoils, i.e., the 64A-210 airfoil has twice the camber of the 64-110 airfoil and twice the c_{m_0}. Therefore, the "64" series airfoil c_{m_0} values can be used to determine the thickness effects.

$$c_{m_{0_{64A\text{-}109}}} = \frac{c_{m_{0\,64\text{-}108}} + c_{m_{0_{64\text{-}110}}}}{2} = \frac{-0.015 - 0.020}{2} = -0.0175$$

Tip section c_{m_0} can be determined by the method of Section 6.1.2.1.

$$\frac{c_{f_{LE}}}{c'} = \left(\frac{c_{f_{LE}}}{c}\right)\frac{c}{c'} = 0.05 \quad \frac{(1.363)}{(1.390)} = 0.049$$

$$c'_{m_{\delta_{LE}}} = -0.00024 \qquad \text{(Figure 6.1.2.1-36)}$$

Since the wing is assumed to be at zero-lift, and drooped leading edges contribute essentially zero incremental lift at constant angle of attack, assume: $\Delta c_\ell = c_\ell = 0$.

$$\Delta c_{m_{LE}} = c'_{m_{\delta_{LE}}}\left(\frac{c'}{c}\right)\delta_{f_{LE}} + \left(\frac{x_{ref}}{c} + \frac{c' - c}{c}\right)\Delta c_\ell + c_m\left[\left(\frac{c'}{c}\right)^2 - 1\right]$$

$$+ 0.075\, c_\ell\left(\frac{c'}{c}\right)\left(\frac{c'}{c} - 1\right) \qquad \text{(Equation 6.1.2.1-b)}$$

$$= -0.00024\left(\frac{1.390}{1.363}\right)20 + 0 - 0.0175\left[\left(\frac{1.390}{1.363}\right)^2 - 1\right] + 0$$

$$\Delta c_{m_{LE}} = -0.0056$$

$$c_{m_{0_{TIP}}} = c_{m_{0_{\substack{BASIC\\AIRFOIL}}}} + \Delta c_{m_{LE}}$$

$$= -0.0175 - 0.0056$$

$$= -0.0231$$

Determine wing zero-lift pitching-moment coefficient using Section 4.1.4.1.

$$\left(C_{m_0}\right)_{\theta=0} = \frac{A\cos^2\Lambda_{c/4}}{A + 2\cos\Lambda_{c/4}}\left(\frac{c_{m_{0_{ROOT}}} + c_{m_{0_{TIP}}}}{2}\right) \qquad \text{(Equation 4.1.4.1-b)}$$

$$= \frac{5.02\cos^2(13^O)}{5.02 + 2\cos(13^O)}\left(\frac{-0.0175 - 0.0231}{2}\right)$$

$$= -0.0139$$

Determine the fuselage $(C_{m_0})_B$ using Equation 4.3.2.1-b and the three-view drawing in Reference 5. Divide the fuselage into incremental parts and compute the value under the summation sign for each increment (Sketch (d)).

INCREMENT	w_f (m)	$(\alpha_0)_W$ (DEG)	$(i_{CL})_B$ (DEG)	Δx (m)	$w_f^2 [(\alpha_0)_W + (i_{CL})_B] \Delta x$
1	0.41	−1.2	−13.5	0.759	−1.376
2	0.95		−10.75		−8.186
3	1.32		−8.00		−12.167
4	1.50		−5.25		−11.015
5	1.58		−2.75		−7.484
6	1.61		−0.75		−3.836
7	1.59		0.0		−2.303
8	[illegible]		0.0	0.635	−1.795
9	1.460		0.0		−1.624
10	1.340		−0.500		−1.938
11	1.255		−2.000		−3.200
12	1.190		−3.750	0.758	−5.313
13	1.100		−4.750		−5.457
14	0.950		−5.375		−4.498
15	0.735		−6.250		−3.051
16	0.485		−6.875		−1.440
17	0.175		−7.000		−0.190

$$\sum_{x=0}^{\ell_B} w_f^2 [(\alpha_0)_W + (i_{CL})_B] \Delta x = -75.373$$

Determine the apparent mass factor

$$\frac{\ell_B}{d_{max}} = \frac{12.50}{1.62} = 7.7$$

$(k_2 - k_1) = 0.905$ (Figure 4.2.1.1-20a)

Determine $(C_{m_0})_B$

$$\left(C_{m_0}\right)_B = \frac{(k_2 - k_1)}{36.5\, S_W \bar{c}} \sum_{x=0}^{x=\ell_B} w_f^2 [(\alpha_0)_W + (i_{CL})_B] \Delta x \qquad \text{(Equation 4.3.2.1-b)}$$

$$= \frac{0.905}{(36.5)(21.51)(2.14)} = (-75.373)$$

$$= -0.0406$$

$$\frac{\left(C_{m_0}\right)_M}{\left(C_{m_0}\right)_{M=0}} = 1.0 \text{ at } M = 0.17 \qquad \text{(Figure 4.1.4.1-6)}$$

Solution:

$$\left(C_{m_0}\right)_{WB} = \left[\left(C_{m_0}\right)_W + \left(C_{m_0}\right)_B\right] \frac{\left(C_{m_0}\right)_M}{\left(C_{m_0}\right)_{M=0}} \qquad \text{(Equation 4.3.2.1-a)}$$

$$= (-0.0139 - 0.0406)\ 1.0$$

$$= -0.0545 \qquad \text{(based on } S_W \bar{c}\text{)}$$

This compares to a test value of −0.05 from Reference 5.

2. Method 2

Given: A wing-body configuration similar to that of Sample Problem 1 (See Sketch (f)).

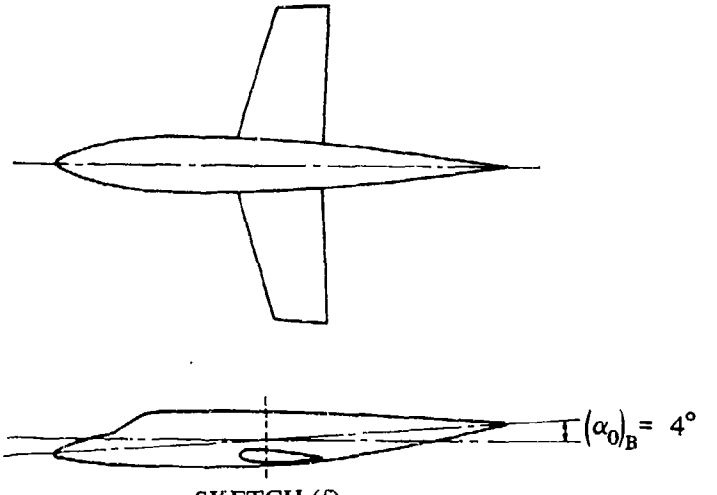

SKETCH (f)

Wing Characteristics:

A = 5.0 $\quad \Lambda_{LE} = 15.6°$ $\quad \lambda = 0.5$ $\quad \theta = 0$

NACA 65-209 airfoil $\quad \frac{LER}{\bar{c}} = 0.00552$

$\frac{(y_c)_{max}}{\bar{c}} = 0.01071$ $\quad C_{L_d} = 0$ $\quad$ Low wing

Body Characteristics:

$\frac{\ell_N}{d} = 3.32$ $\quad \frac{\ell_A}{d} = 2.99$ $\quad \frac{h}{d} = 0.50$ $\quad \frac{d}{b} = 0.152$

Additional Characteristics:

M = 0.4 $\quad R_\ell = 6 \times 10^6$ $\quad$ No vertical tail $\quad T_R = 1$

Compute:

The regression coefficients below are obtained from Table 4.3.2.1-B at M = 0.4.

Regression Coefficient	Value Table 4.3.2.1-B
C_0	−0.61496
C_1	0.034113
C_2	−0.0043111
C_3	−0.0067607
C_4	0.58626
C_5	−0.0021631
C_6	−0.0029718
C_7	−0.0013161
C_8	0.0034451
C_9	−0.0097535
C_{10}	−3.9389
C_{11}	−0.52560
C_{12}	−4.3982
C_{13}	0.036116
C_{14}	0.034068
C_{15}	−0.073114
C_{16}	1.2683
C_{17}	−0.16503
C_{18}	$-0.00077192 \times 10^{-6}$

Solution:

$$\left(C_{m_0}\right)_{WB} = C_0 + C_1\left(\frac{1}{A}\right) + C_2\, A + C_3 \tan \Lambda_{LE} + C_4\left(\frac{t}{\bar{c}}\right) + C_5\left(\frac{\ell_N}{d}\right) + C_6\left(\frac{\ell_A}{d}\right)$$

$$+ C_7\, \lambda + C_8\, \lambda^2 + C_9\, (T_R) + C_{10}\left(\frac{LER}{\bar{c}}\right) + C_{11}\, \theta + C_{12}\left[\frac{\left(y_c\right)_{max}}{\bar{c}}\right]$$

$$+ C_{13}\, C_{L_d} + C_{14}\, W_L + C_{15}\, V_T + C_{16}\left(\frac{h}{d}\right) + C_{17}\left(\frac{d}{b}\right) + C_{18}\, R_\ell$$

(Equation 4.3.2.1-c)

$$\left(C_{m_0}\right)_{WB} = -0.61496 + \frac{0.034113}{5} - 0.0043111\,(5) - 0.0067607\,(0.2793)$$

$$+ 0.58626\,(0.09) - 0.0021631\,(3.32) - 0.0029718\,(2.99)$$

$$- 0.0013161\,(0.5) + 0.0034451\,(0.25) - 0.0097535\,(1)$$

$$- 3.9389\,(0.00552) - 0.5256\,(0) - 4.3982\,(0.01071) + 0.036116\,(0)$$

$$+ 0.034068\,(0) - 0.073114\,(0) + (1.2683)\,(0.5) - 0.16503\,(0.152)$$

$$- 0.00077192 \times 10^{-6}\,(6 \times 10^{6})$$

$$= -0.61496 + 0.0068226 - 0.021555 - 0.0018882 + 0.052763$$

$$- 0.0071815 - 0.0088857 - 0.00065805 + 0.00086128 - 0.0097535$$

$$- 0.021743 - 0.047105 + 0.63415 - 0.0250846 - 0.0046315$$

$$= -0.0688 \text{ (based on } S_W \bar{c}\ )$$

B. TRANSONIC

The comments and methods of Paragraph A are applicable here. It should be noted that at near-sonic conditions or whenever shocks begin appearing on the wing, the value of $(C_{m_0})_{WB}$ may begin to change abruptly. For this reason Method 1 should not be used above M = 0.9 and should be used judiciously for $0.8 \leqslant M \leqslant 0.9$. Likewise, Method 2 should be applied with caution at near-sonic conditions.

DATCOM METHODS

At transonic speeds the methods described in Paragraph A may be applied. (It should be noted for Method 1 that the subsonic method of Section 4.1.4.1 must be used to evaluate the wing zero-lift pitching-moment contribution.) Both methods are restricted to straight-tapered-wing configurations.

Sample Problems

No sample problems are presented here because their solutions would be obtained in the same manner as in the subsonic speed regime.

C. SUPERSONIC

In the supersonic speed regime Method 2 of Paragraph A of this section may be used to estimate $(C_{m_0})_{WB}$ for fighter-type aircraft. The comments in Paragraph A pertaining to Method 2 are applicable here.

DATCOM METHOD

At supersonic speeds Method 2 described in Paragraph A may be applied to fighter-type straight-tapered-wing configurations.

Sample Problem

No sample problem is presented here because its solution would be obtained in the same manner as in the subsonic speed regime.

REFERENCES

1. Anderson, A. K., Jr.: Douglas Aircraft Company Memorandum C1-250-Aero-77-178, 7 March 1977. (U)
2. Multhopp, H.: Aerodynamics of the Fuselage. NACA TM-1036, 1942. (U)
3. Simon, W. E., et al.: Prediction of Aircraft Drag Due to Lift, AFFDL-TR-71-84, 1971. (U)
4. Boyd, J. W., Migotsky, E., and Wetzel, B. E.: A Study of Conical Camber for Triangular and Sweptback Wings, NACA RM A55G19, 1955. (U)
5. Soderman, P.T., and Aiken, T. N.: Full-Scale Wind-Tunnel Tests of a Small Unpowered Jet Aircraft with a T-Tail, NASA TN D-6573, 1971. (U)
6. Burrows, D. L., and Palmer, W. E.: A Transonic Wind-Tunnel Investigation of the Longitudinal Force and Moment Characteristics of a Plane and a Cambered 3-Percent-Thick Delta Wing of Aspect Ratio 3 on a Slender Body, NACA RM L54H25, 1954. (U)
7. Bielat, R. P.: A Transonic Wind-Tunnel Investigation of the Aerodynamic Characteristics of Three 4-Percent-Thick Wings of Sweepback Angles 10.8°, 35°, and 47°, Aspect Ratio 3.5, and Taper Ratio 0.2 in Combination with a Body, NACA RM L52B08, 1952. (U)
8. Bielat, R. P., Harrison, D. E., and Coppolino, D. A.: An Investigation at Transonic Speeds of the Effects of Thickness Ratio and of Thickened Root Sections on the Aerodynamic Characteristics of Wings with 47° Sweepback, Aspect Ratio 3.5, and Taper Ratio 0.2 in the Slotted Test Section of the Langley 8-Foot High-Speed Tunnel, NACA RM L51I04a, 1951. (U)
9. Loving, D. L.: A Transonic Investigation of Changing Indentation Design Mach Number on the Aerodynamic Characteristics of a 45° Sweptback-Wing-Body Combination Designed for High Performance, NACA RM L55J07, 1956. (U)
10. Munk, M. M.: The Aerodynamic Forces on Airship Hulls, NACA TR 184, 1924. (U)

TABLE 4.3.2.1-A

METHOD 1
DATA SUMMARY AND SUBSTANTIATION

Ref.	A	λ	$\Lambda_{c/4}$ (deg)	θ (deg)	M	$(C_{m_0})_{WB}$ Calc	$(C_{m_0})_{WB}$ Test	$\Delta\ (C_{m_0})_{WB}$ Calc-Test
5	5.02	0.507	13	0	0.08	−0.0543	−0.04	−0.0143
↓	↓	↓	↓	↓	0.17	−0.0545	−0.05	−0.0045
6	3	0	45	0	0.67	−0.00496	−0.008	+0.0030
↓	↓	↓	↓	↓	0.76	−0.00526	−0.005	−0.0003
↓	↓	↓	↓	↓	0.89	−0.00602	−0.004	−0.0020
7	3.5	0.20	10.8	0	0.7	−0.0234	−0.018	−0.0054
↓	↓	↓	↓	↓	0.85	−0.0266	−0.024	−0.0026
↓	↓	↓	↓	↓	0.9	−0.0282	−0.027	−0.0012
↓	↓	↓	35	↓	0.7	−0.0183	−0.018	−0.0003
↓	↓	↓	↓	↓	0.85	−0.0207	−0.022	0.0013
↓	↓	↓	↓	↓	0.9	−0.0220	−0.024	0.0020
↓	↓	↓	47	↓	0.696	−0.0137	−0.019	0.0053
↓	↓	↓	↓	↓	0.843	−0.0154	−0.023	0.0076
↓	↓	↓	↓	↓	0.892	−0.0164	−0.024	0.0076
8	3.5	0.20	47	0	0.696	−0.0137	−0.019	0.0053
↓	↓	↓	↓	↓	0.892	−0.0165	−0.024	0.0075
↓	↓	↓	↓	↓	0.7	−0.0149	−0.018	0.0031
↓	↓	↓	↓	↓	0.9	−0.0180	−0.022	0.0040
↓	↓	↓	↓	↓	0.696	−0.0139	−0.014	0.0001
↓	↓	↓	↓	↓	0.892	−0.0168	−0.019	0.0022
↓	↓	↓	↓	↓	0.7	−0.0145	−0.016	0.0015
↓	↓	↓	↓	↓	0.9	−0.0175	−0.017	−0.0005
9	4	0.15	45	0	0.8	−0.0219	−0.031	0.0091
↓	↓	↓	↓	↓	0.85	−0.0231	−0.033	0.0099
↓	↓	↓	↓	↓	0.9	−0.0246	−0.036	0.0114

TABLE 4.3.2.1-A (CONTD)

Ref.	A	λ	$\Lambda_{c/4}$ (deg)	θ (deg)	M	$(C_{m_0})_{WB}$ Calc	$(C_{m_0})_{WB}$ Test	$\Delta (C_{m_0})_{WB}$ Calc-Test
Unpub. data	7.028	0.230	30.61	−4.05	0.2	−0.0329	−0.040	0.0071
					0.4	−0.0339	−0.040	0.0061
					0.6	−0.0372	−0.040	0.0028
					0.7	−0.0393	−0.042	0.0027
					0.8	−0.0423	−0.046	0.0037
					0.825	−0.0436	−0.0455	0.0019
					0.85	−0.0444	−0.043	−0.0014
	8.71	0.2036	24.5	−4.7	0.2	−0.0760	−0.0830	0.0070
					0.3	−0.0761	−0.0830	0.0069
					0.4	−0.0783	−0.0835	0.0052
					0.5	−0.0813	−0.0845	0.0032
					0.6	−0.0859	−0.0860	0.0001
					0.7	−0.0908	−0.0890	−0.0018
					0.8	−0.0973	−0.0935	−0.0038
					0.85	−0.1026	−0.0950	−0.0076
	6.8	0.30	35	−7.1	0.2	−0.0223	−0.0220	−0.0003
					0.4	−0.0230	−0.0220	−0.0010
					0.6	−0.0252	−0.0245	−0.0007
					0.7	−0.0266	−0.0270	0.0004
					0.8	−0.0285	−0.0288	0.0003
					0.825	−0.0295	−0.0292	−0.0003
					0.85	−0.0302	−0.0300	−0.0002
					0.875	−0.0312	−0.0308	−0.0004
					0.9	−0.0321	−0.0315	−0.0006

Average $\Delta (C_{m_0})_{WB} = \dfrac{\Sigma |\Delta (C_{m_0})_{WB}|}{n} = 0.0036$

TABLE 4.3.2.1-8

METHOD 2
REGRESSION COEFFICIENTS

MACH NUMBER	C_0	C_1	C_2	C_3	C_4	C_5	C_6	C_7	C_8	C_9
0.4	−0.61496	0.034113	−0.0043111	−0.0057807	0.58626	−0.0021631	−0.0029718	−0.0013161	0.0034451	−0.0097535
0.6	0.030521	−0.026482	−0.0031117	0.00040854	0.043533	0.00010412	−0.0023971	0.010412	−0.0049864	−0.0023881
0.7	0.010449	0.0019975	−0.0011029	0.00019192	0.028208	0.00079415	−0.0012200	0.0051328	−0.0029594	0.00074312
0.8	0.024846	−0.0055509	−0.0024707	−0.0014904	0.031764	0.00036833	0.00037272	−0.0035006	0.00073299	0.0012306
0.9	0.023233	−0.00054868	−0.0027806	−0.0014790	0.024266	0.00040862	−0.00092113	0.00091995	−0.0010519	0.0021653
0.95	−0.029503	0.056041	0.0052306	−0.0021117	0.024656	0.00082755	−0.0016469	−0.0085456	0.0092825	0.0037542
1.0	−0.072908	0.11805	0.0091112	−0.0055601	0.016164	−0.0019504	0.0043904	−0.050916	0.039982	0.00011703
1.1	−0.047882	0.087861	0.012725	0.00058939	0.049004	−0.00018951	−0.0014263	−0.0073144	0.0025290	−0.00011616
1.2	−0.0077024	0.057409	0.0037585	−0.0020553	−0.013639	−0.00084471	−0.0027075	−0.00035333	−0.00030929	0.0017132
1.3	−0.0090333	0.061884	0.0029019	−0.0035078	−0.027873	−0.0016508	−0.00070990	−0.010550	0.0032408	0.00057507
1.4	−0.064029	0.11973	0.012987	0.0014900	−0.029892	−0.0013285	−0.0019031	0.0093873	−0.0049618	0.0011079
1.5	0.014988	0.066427	0.0007897	−0.0065439	−0.022854	−0.00098949	−0.0024785	−0.011328	0.0026880	−0.00002373
2.0	−0.10257	0.17653	0.022724	−0.0065667	0.0026084	−0.00036847	0.0015647	−0.026630	0.010089	−0.0018213
2.5	−0.097877	0.16776	0.028670	0.0043908	0.0020467	−0.0013417	−0.00077258	−0.023909	0.0094275	0.00057215

MACH NUMBER	C_{10}	C_{11}	C_{12}	C_{13}	C_{14}	C_{15}	C_{16}	C_{17}	C_{18} x 10^{+6}	
0.4	−3.9389	−0.52560	−4.3982	0.036116	0.034068	−0.073114	1.2683	−0.16603	−0.00077192	
0.6	0.56516	−0.51829	−4.0930	−0.0069271	0.011685	−0.0010598	−0.017713	−0.052268	0.00025439	
0.7	0.12045	−0.53503	−4.2059	−0.0013549	0.0053796	0.0020454	−0.0039115	−0.043905	−0.0012391	
0.8	−0.10408	−0.49728	−3.9483	0.0048901	0.0014643	0.0027298	−0.0092493	−0.051001	−0.0011483	
0.9	0.098669	−0.62200	−4.8034	0.0018263	0.0028848	0.00025683	0.0065923	−0.10221	−0.00078181	
0.95	−0.82906	−0.31518	−3.1686	0.0075362	−0.0038225	−0.0035619	0.0074832	−0.019949	−0.0010290	
1.0	1.0256	−0.39402	−3.4999	0.0035393	0.030079	0.0016422	0.025312	−0.053897	−0.0013250	
1.1	−0.62097	−0.36576	−3.1159	0.010248	0.0047945	−0.00065869	−0.037542	0.0063401	−0.00051180	
1.2	−1.5639	−0.21108	−2.5628	0.011013	0.0016835	0.0016923	0.017427	−0.13287	−0.0013416	
1.3	−0.43130	−0.10254	−2.0192	0.0067985	0.0083637	0.0013512	0.020635	−0.13673	−0.0023095	
1.4	−0.83720	−0.029314	−1.7911	0.0017144	0.0034691	0.0011693	0.018158	−0.080305	−0.0022940	
1.5	−0.16698	0.45021	0.13537	0.0022793	0.0040738	0.0032272	0.016570	−0.18294	−0.0014919	
2.0	0.97612	−4.7537	−15.553	−0.0010677	−0.0042213	0.0045941	−0.00063330	−0.11299	0.00094537	
2.5	1.3090	−5.3830	−16.996	0.014219	−0.0091883	0.0026961	−0.016885	−0.068530	−0.00099505	

4.3.2.2 WING-BODY PITCHING-MOMENT-CURVE SLOPE (AERODYNAMIC CENTER)

For wing-body configurations in which the body radii are large relative to the wing semispan, there exist mutual aerodynamic interferences between wing and body that can appreciably affect the aerodynamic center of the wing-body combination.

The body influences the wing lift primarily by inducing a change in the local angle of attack along the span. The wing influences the body by a lift carryover from the wing onto the body. For supersonic speeds the wing lift carryover on the body is displaced downstream parallel to the Mach lines, as illustrated in sketch (e) on page 4.3.1.2-5. Important moment differences can therefore exist between configurations in which the fuselage terminates at the wing trailing edge and those in which the fuselage extends beyond the wing trailing edge.

The aerodynamic-center location of a wing-body configuration is given in reference 1 as

$$\frac{x'_{a.c.}}{c_{r_e}} = \frac{\left(\frac{x'_{a.c.}}{c_{r_e}}\right)_N C_{L_{a_N}} + \left(\frac{x'_{a.c.}}{c_{r_e}}\right)_{W(B)} C_{L_{a_{W(B)}}} + \left(\frac{x'_{a.c.}}{c_{r_e}}\right)_{B(W)} C_{L_{a_{B(W)}}}}{C_{L_{a_N}} + C_{L_{a_{W(B)}}} + C_{L_{a_{B(W)}}}} \qquad 4.3.2.2\text{-a}$$

where the $x'_{a.c.}/c_{r_e}$ terms are the chordwise distances measured in exposed wing root chords from the apex of the exposed wing to the aerodynamic center, positive aft. The methods for calculating these terms are presented in this section and are based on exposed-wing geometry. The exposed wing is defined as the parts of the wing outboard of the largest body diameter at the wing-body intersection. Two cases are illustrated in sketch (a).

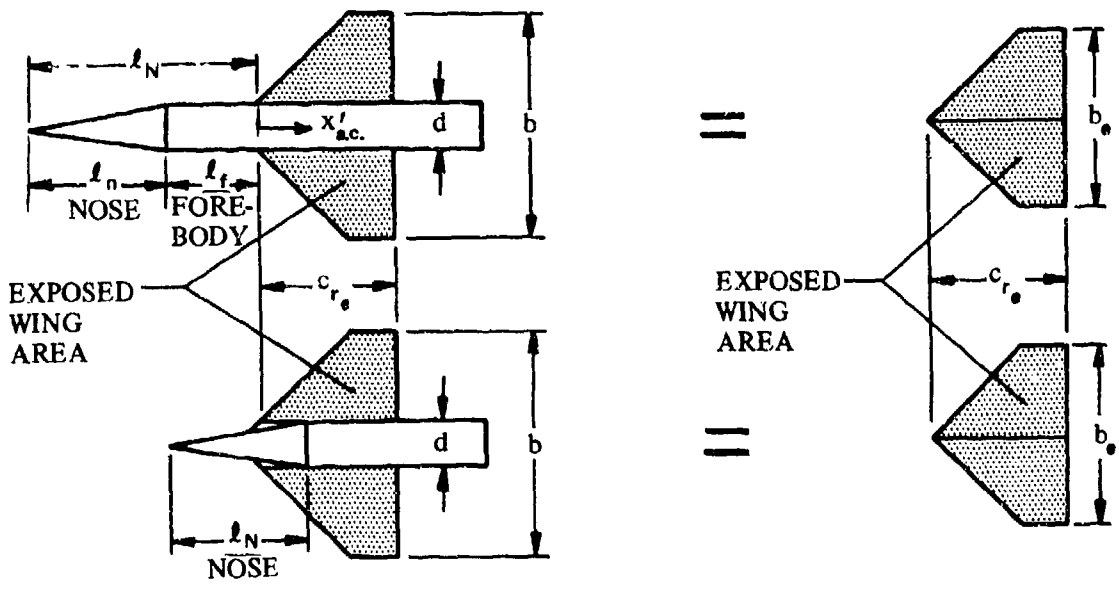

SKETCH (a)

The lift-curve slopes used in Equation 4.3.2.2-a are referred to the total wing area.

The aerodynamic-center location measured in wing root chords aft of the wing apex is given by

$$\frac{x_{a.c.}}{c_r} = \left(\frac{x'_{a.c.}}{c_{r_e}}\right) \frac{c_{r_e}}{c_r} + \frac{d}{2c_r} \tan \Lambda_{LE} \qquad 4.3.2.2\text{-b}$$

where $x'_{a.c.}/c_{r_e}$ is given by Equation 4.3.2.2-a.

The nose of the body is defined as the expanding portion of the body ahead of the wing. The forebody is the cylindrical portion of the body ahead of the wing. The base of the forebody is defined as the cross section at the wing-leading-edge – body intersection.

If the wing is at incidence relative to the body, the a.c. can be approximated by using the lift coefficient of each component – in the linear or near-linear range only – instead of the lift-curve slope. The angle of attack of the body relative to the free stream is used to calculate the body lift, and the angle of attack of the wing relative to the free stream is used to calculate the wing lift and lift carryover on the body.

The specific case of a conical body mounted on a delta wing (Sketch (c) on Page 4.3.1.2-2) has been solved by Spreiter in Reference 2. Slender-body theory is used to obtain the ratio of the wing-body lift to that of the wing alone. Correlation with experimental data by this method is good throughout the speed range. The method predicts that the aerodynamic center of the wing-body combination is the same as that of the wing alone.

Methods are presented in this section that are applicable to axisymmetric bodies in combination with straight-tapered wings throughout the subsonic, transonic, and supersonic speed ranges, and in combination with non-straight-tapered wings at subsonic and supersonic speeds. The methods are applicable only in the linear-lift range.

The effects of body cross-section shape and wing vertical position on wing-body lift-curve slope are not considered. (Some test data on these variables are given in References 3 and 4.) Therefore, the methods should not be construed as pertaining to generalized wing-body combinations with arbitrary body shapes.

The results of this section apply to single-wing-body configurations only; for cruciform and other multi-panel arrangements, interference effects may exist between the various panels.

The following general categories of non-straight-tapered wings are considered at subsonic and supersonic speeds:

Double-delta wings
Cranked wings
Curved (Gothic and ogee) wings

These wings are illustrated in Sketch (a) of Section 4.1.3.2. Their wing-geometry parameters are presented in Section 2.2.2.

A. SUBSONIC

DATCOM METHODS

Straight-Tapered Wing-Body Configurations

The subsonic aerodynamic-center location near zero lift of a wing-body configuration with a straight-tapered wing is obtained from the procedure outlined in the following steps:

Step 1. Divide the wing-body configuration into three components as follows and determine their pertinent geometric parameters (see Sketch (a)).

(1) The exposed wing in the presence of the body, denoted by the subscript W(B).

(2) The body in the presence of the wing, denoted by the subscript B(W).

(3) The body nose and forebody ahead of the wing-body juncture, denoted by the subscript N.

Step 2. Determine the lift-curve slope of the exposed wing $\left(C_{L_\alpha}\right)_e$ from the straight-tapered wing method of Paragraph A of Section 4.1.3.2, based on its exposed area S_e.

Step 3. Determine the lift-curve slope of the body nose by the method of paragraph A of Section 4.2.1.1. In most cases the slender-body-theory value of $\left(C_{N_\alpha}\right)_B = 2$ per radian (based on the nose frontal area) is sufficiently accurate.

Step 4. Using the lift-curve slopes determined in Steps 2 and 3, calculate $C_{L_{\alpha_{W(B)}}}$, $C_{L_{\alpha_{B(W)}}}$, and $C_{L_{\alpha_N}}$, referred to the total wing area, by

$$C_{L_{\alpha_{W(B)}}} = K_{W(B)} \left(C_{L_\alpha}\right)_e \frac{S_e}{S_W}$$

$$C_{L_{\alpha_{B(W)}}} = K_{B(W)} \left(C_{L_\alpha}\right)_e \frac{S_e}{S_W}$$

$$\left(C_{N_\alpha}\right)^*_N = \left(C_{N_\alpha}\right)_B \frac{\pi d^2}{4S_W}$$

where $K_{W(B)}$ and $K_{B(W)}$ are interference factors obtained from Figure 4.3.1.2-10.

Step 5. Determine the a.c. location of the exposed wing as a fraction of the root chord of the exposed wing $\frac{x'_{a.c.}}{c_{r_e}}$ from Figure 4.1.4.2-26. The interference effect of the body lift in the presence of the wing is neglected, and the a.c. location of the body-lift carryover on the wing is taken as the a.c. location for the exposed wing, i.e.,

$$\left(\frac{x'_{a.c.}}{c_{r_e}}\right)_{W(B)} = \frac{x'_{a.c.}}{c_{r_e}}$$

---

*The equation given for $\left(C_{N_\alpha}\right)_N$ is based on the slender-body-theory value for $\left(C_{N_\alpha}\right)_B$. If Equation 4.2.1.1-a is used to obtain $\left(C_{N_\alpha}\right)_B$, then $C_{N_{\alpha_N}} = \left(C_{N_\alpha}\right)_B \frac{(V_B)^{2/3}}{S_W}$

Step 6. Determine the a.c. location of the wing-lift carryover on the body $\left(\frac{x'_{a.c.}}{c_{r_e}}\right)_{B(W)}$

For $\beta A_e \geq 4.0$, the a.c. contribution due to the lift carryover of the wing on the body is obtained from the equation

$$\left(\frac{x'_{a.c.}}{c_{r_e}}\right)_{B(W)} = \frac{1}{4} + \frac{b-d}{2c_{r_e}} \tan \Lambda_{c/4} \left[- \frac{k}{1-k} + \frac{\sqrt{1-2k}\ \log_e\left(\frac{1-k}{k} + \frac{1}{k}\sqrt{1-2k}\right) - (1-k) + \frac{\pi}{2}\ k}{\frac{k(1-k)}{\sqrt{1-2k}}\ \log_e\left(\frac{1-k}{k} + \frac{1}{k}\sqrt{1-2k}\right) + \frac{(1-k)^2}{k} - \frac{\pi}{2}\ (1-k)} \right] \qquad 4.3.2.2\text{-c}$$

where $k = d/b$ and the term inside the brackets is plotted for various values of k in Figure 4.3.2.2-35.

Equation 4.3.2.2-c is developed from lifting-line theory applied to the portion of a fictitious wing inside the body, defined by the image of the actual wing at the intersection of the wing quarter-chord line with the body. Equation 4.3.2.2-c is mathematically limited to $\frac{d}{b} \leq 0.5$, but extrapolation to $\frac{d}{b} = 0.8$ gives accurate results.

For $\beta A_e < 4.0$ an interpolation procedure is required. The a.c. location at $\beta A_e = 0$, derived from slender-body theory, is given in Figure 4.3.2.2-36b. For βA_e between 0 and 4.0, the a.c. of the wing-lift carryover on the body is obtained by fairing values between those obtained from Figure 4.3.2.2-36b and Equation 4.3.2.2-c for $\beta A_e = 0$ and $\beta A_e \geq 4.0$, respectively. It is recommended in Reference 1 that the interpolation procedure for $\beta A_e < 4.0$ be performed using the calculated wing-alone values $\left(\frac{d}{b} = 0\right)$ as a guide. However, for the purpose of the Datcom this calculation is omitted, and the fairing is performed between $\beta A_e = 0$ and $\beta A_e = 4.0$ by a curve through the value at $\beta A_e = 0$ and tangent to the calculated line for $\beta A_e \geq 4$.

Step 7. Determine the a.c. location of the body nose and forebody as a fraction of the root chord of the exposed wing $\left(\frac{x'_{a.c.}}{c_{r_e}}\right)_N$, and referred to the exposed-wing apex.

Two methods are presented here for estimating the aerodynamic center of the nose and forebody (see Sketch (a)).

The first, which is based on the methods of Sections 4.2.1.1 and 4.2.2.1, is the more accurate of the two. It should be used when the nose lift is a significant fraction of the total lift of the vehicle. In Equation 4.2.2.1-b, ℓ_N should be substituted for x_m and dC_m/dC_L should be multiplied by the negative cube root of the nose volume and divided by c_{r_e}. This refers the moments to the apex of the exposed wing, i.e.,

$$\left(\frac{x'_{a.c.}}{c_{r_e}}\right)_N = \left(C_{m_\alpha}\right)_{4.2.2.1} \left[- \frac{V_B^{1/3}}{c_{r_e}\left(C_{L_\alpha}\right)_{4.2.1.1}} \right]$$

The second method presented in this section gives more approximate answers than the first method. Figure 4.3.2.2-36a gives the aerodynamic-center location for cones, ogives, and ellipsoids without forebodies. For ogives with forebodies an approximation can be made by defining an equivalent ogive to replace the actual ogive and forebody. Thus

$$(f)_{equiv} = (f)_{nose} + 1.6\,(f)_{forebody} \qquad 4.3.2.2\text{-d}$$

where $(f)_{nose}$, $(f)_{forebody}$, and $(f)_{equiv}$ are the fineness ratios of the actual nose, the forebody, and the equivalent nose, respectively. Figure 4.3.2.2-36a is entered with the actual nose fineness ratio to obtain the a.c. of the equivalent nose, referred to the apex of the exposed wing. Then

$$\left(\frac{x'_{a.c.}}{c_{r_e}}\right)_N = \left(\frac{x_{a.c.}}{\ell_{equiv}}\right)_N \left(\frac{\ell_{equiv}}{c_{r_e}}\right)$$

where ℓ_{equiv} is the length of the equivalent nose ($\ell_{equiv} = f_{equiv}\, d$).

Step 8. Using the results calculated in Steps 4 through 7, Equation 4.3.2.2-a gives the a.c. location of the wing-body configuration measured in exposed-wing root chords aft of the apex of the exposed wing. The a.c. location measured in wing root chords aft of the wing apex is given by Equation 4.3.2.2-b.

Application of this method is illustrated by the sample problem on Pages 4.3.2.2-7 through 4.3.2.2-10.

A comparison of test data with results calculated by using this method is presented as Table 4.3.2.2-A. The ranges of planform and flow parameters of the test data are:

$$2.88 \leq A \leq 4.0$$

$$7^\circ \leq \Lambda_{LE} \leq 60^\circ$$

$$0.143 \leq \lambda \leq 1.0$$

$$0.14 \leq d/b \leq 0.80$$

$$0.13 \leq M \leq 0.91$$

$$0.9 \times 10^6 \leq R_{\ell_{MAC}} \leq 6.8 \times 10^6$$

Although ranges of planform and flow parameters of the test data are in most cases quite broad, the limited number of test points makes it rather difficult to draw general conclusions regarding parameters not specifically noted in the prediction method. Within the linear-lift range, profile parameters such as camber, twist, and airfoil shape would be expected to have only a minor influence on the wing-body aerodynamic-center location. There are not enough data to allow a quantitative prediction of Reynolds-number effect, but it is reasonable to expect that Reynolds number will influence the wing-body aerodynamic-center location.

Non-Straight-Tapered Wing-Body Configuration

The method for determining the subsonic aerodynamic-center location near zero lift of wing-body configura-

tions with non-straight-tapered wings is taken fromReference 5. During the course of the study conducted in connection withReference 5, it was validated that the subsonic wing-body aerodynamic-center location of configurations with non-straight-tapered wings can be determined by using the wing-alone approach and neglecting the exposed-wing and body lift carryover and body-nose effects. Therefore, the method presented in paragraph A of Section 4.1.4.2 for determining the aerodynamic-center location of non-straight-tapered wings is directly applicable to the case of a body in combination with a non-straight-tapered wing.

Essentially, the method consists of dividing the complete theoretical wing planform (extended to the plane of symmetry) into two panels with each panel having conventional, straight-tapered geometry. Then for each of the constructed panels, the individual lift-curve slope and aerodynamic-center location are estimated by treating each constructed panel as a complete wing. The individual lift and aerodynamic-center location determined for each constructed panel are then mutually combined in accordance with an "inboard-outboard" weighted-area relationship to estimate the aerodynamic-center location for the basic wing-body configuration.

The sample problem of Paragraph A of Section 4.1.4.2 illustrates the use of the method.

Comparisons of test data with results calculated by using this wing-alone approach are presented as Tables 4.3.2.2-B and 4.3.2.2-C (both taken fromReference 5) for wing-body combinations with double-delta and cranked wings, respectively. Although the technique is applicable to wing-body combinations with curved wings, test data on such configurations are not available for substantiation purposes. Only two wing-body combinations with curved wings have been investigated. Since both of these configurations have very small bodies and the wing planform projection effectively blankets nearly all the body, they have been included in the curved wing-alone substantiation of Section 4.1.4.2 (Table 4.1.4.2-B). The ranges of planform parameters of the double-delta and cranked-wing configuration test data are:

Double-Delta Configurations	Cranked Configurations
$1.3 \leq A \leq 3.0$	$1.68 \leq A \leq 6.93$
$60^{\circ} \leq \Lambda_{LE_i} \leq 82.9^{\circ}$	$25^{\circ} \leq \Lambda_{LE_i} \leq 75^{\circ}$
$38.1^{\circ} \leq \Lambda_{LE_o} \leq 60^{\circ}$	$12^{\circ} \leq \Lambda_{LE_o} \leq 75^{\circ}$
$0.217 \leq \eta_B \leq 0.654$	$0.224 \leq \eta_B \leq 0.654$
$0 \leq \ell_N/\ell_B \leq 0.7$	$0 \leq \ell_N/\ell_B \leq 0.7$

The Mach-number range of the test data for the above configurations is $0.1 \leq M \leq 0.9$.

The test results indicate that airfoil shape, camber, and twist have only a minor influence on the wing-body aerodynamic-center location within the linear-lift range. There are not enough data to allow a quantitative prediction of Reynolds-number effect, but it is reasonable to expect that Reynolds number will influence the wing-body aerodynamic-center location.

Many double-delta and cranked wings have non-straight trailing edges with the trailing-edge break at a different span station from the leading-edge break. For such wings the irregular trailing-edge sweep angles of the subdivided panels are modified by using straight trailing-edge sweep angles for each panel, constructed so that the area moment about the respective wing-panel apex remains approximately the same

All the configurations listed inTables 4.3.2.2-B and 4.3.2.2-C have only one break in the wing leading edge. In certain cases, more than one wing leading-edge break can be handled provided the wing can be approximated by an equivalent two-panel planform. Such an approximation has been made for two cranked-wing

planforms included in the cranked-wing-alone data summary of Section 4.1.4.2 (Table 4.1.4.2-A). In both cases the inboard panel remains unchanged, and an outboard panel is approximated which has the same area moment about the wing-root apex as the original outer panels by adjusting and constructing straight leading and trailing edges.

Sample Problem

Straight-Tapered Wing Configuration

Given: A wing-body configuration ofReference 9.

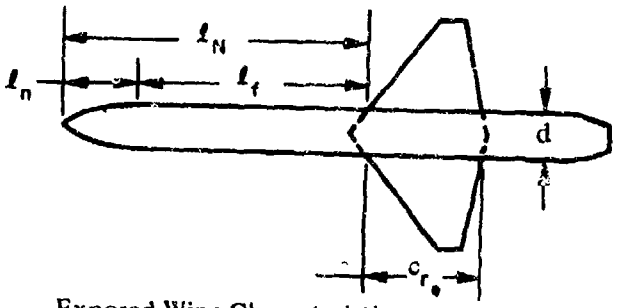

Total-Wing Characteristics:

$A_W = 3.0$ $S_W = 250.56$ sq in. $\lambda_W = 0.143$

$\Lambda_{LE_W} = 38.7^o$ $\Lambda_{c/4_W} = 28.8^o$

$b_W = 27.4$ in. $c_{r_W} = 16.0$ in.

Exposed-Wing Characteristics:

$$A_e = 2.84 \quad \lambda_e = 0.169 \quad \Lambda_{LE_e} = \Lambda_{LE_W} = 38.7^o \quad \Lambda_{c/2_e} = 16.7^o$$

$$c_{r_e} = 13.5 \text{ in.} \quad \frac{S_e}{S_W} = 0.705$$

Body-Nose Characteristics:

Ogive-cylinder $d = 5.0$ in. $\dfrac{d}{b_W} = 0.183$

$\ell_n = 8.75$ in. $f_{nose} = \dfrac{\ell_n}{d} = 1.75$

$\ell_f = \ell_{forebody} = 26.65$ in. $f_{forebody} = \dfrac{\ell_f}{d} = 5.33$

Additional Characteristics:

$M = 0.60$; $\beta = 0.80$ $\kappa = 1.0$ (assumed)

Compute:

$\left(C_{L_\alpha}\right)_e$ (Section 4.1.3.2)

$$\frac{A_e}{\kappa}\left[\beta^2 + \tan^2 \Lambda_{c/2_e}\right]^{1/2} = 2.43$$

$$\left(\frac{C_{L_\alpha}}{A}\right)_e = 1.22 \text{ per rad} \quad \text{(Figure 4.1.3.2-49)}$$

$$\left(C_{L_\alpha}\right)_e = 3.46 \text{ per rad}$$

$\left(C_{N_\alpha}\right)_B$

$$\left(C_{N_\alpha}\right)_B = 2 \text{ per rad (based on nose frontal area) (slender-body theory)}$$

Interference factors (Section 4.3.1.2)

$$\left.\begin{aligned} K_{W(B)} &= 1.153 \\ K_{B(W)} &= 0.255 \end{aligned}\right\} \quad \text{(Figure 4.3.1.2-10 at } \frac{d}{b_W} = 0.183\text{)}$$

Component lift-curve slopes, referred to S_W

$$C_{L_{\alpha_{W(B)}}} = K_{W(B)} \left(C_{L_\alpha}\right)_e \frac{S_e}{S_W} = (1.153)(3.46)(0.705) = 2.81 \text{ per rad}$$

$$C_{L_{\alpha_{B(W)}}} = K_{B(W)} \left(C_{L_\alpha}\right)_e \frac{S_e}{S_W} = (0.255)(3.46)(0.705) = 0.622 \text{ per rad}$$

$$C_{L_{\alpha_N}} = \left(C_{N_\alpha}\right)_B \frac{\pi d^2}{4S_W} = (2.0) \frac{\pi (5.0)^2}{(4)(250.56)} = 0.1567 \text{ per rad}$$

$\left(\frac{x'_{a.c.}}{c_{r_e}}\right)_{W(B)}$ (Section 4.1.4.2)

$$\frac{\beta}{\tan \Lambda_{LE_e}} = \frac{0.80}{\tan 38.7^\circ} = 1.00$$

$$(A \tan \Lambda_{LE})_e = (2.84)(\tan 38.7^\circ) = 2.28$$

$$\frac{x'_{a.c.}}{c_{r_e}} = 0.440 \text{ (Figure 4.1.4.2-26a through -26c, interpolated for } \lambda_e\text{)}$$

$$\left(\frac{x'_{a.c.}}{c_{r_e}}\right)_{W(B)} = \frac{x'_{a.c.}}{c_{r_e}} = 0.440$$

$\left(\frac{x'_{a.c.}}{c_{r_e}}\right)_{B(W)}$

$\beta A_e = (0.80)(2.84) = 2.28$. Since $\beta A_e < 4.0$, an interpolation between values of $\left(\frac{x'_{a.c.}}{c_{r_e}}\right)_{B(W)}$ at $\beta A_e = 0$ and $\beta A_e \geq 4.0$ must be performed. (See Step 6 of Datcom method.)

$\left(\frac{x'_{a.c.}}{c_{r_e}}\right)_{B(W)}$ at $\beta A_e = 0$

$$\frac{1}{4} A_e (1 + \lambda_e) \tan\Lambda_{LE} = \frac{1}{4} (2.84)(1.169)(\tan 38.7^{\circ}) = 0.665$$

$$\left(\frac{x'_{a.c.}}{c_{r_e}}\right)_{B(W)} = 0.330 \text{ (Figure 4.3.2.2-36b)}$$

$\left(\frac{x'_{a.c}}{c_{r_e}}\right)_{B(W)}$ at $\beta A_e \geq 4.0$

$$k = \frac{d}{b_W} = 0.183;\ 1 - k = 0.817;\ \sqrt{1 - 2k} = 0.796$$

$$\log_e \left(\frac{1-k}{k} + \frac{1}{k}\sqrt{1 - 2k}\right) = 2.176$$

Evaluate the term in brackets of Equation 4.3.2.2-c

$$\left[-\frac{k}{1-k} + \frac{\frac{b}{2}\sqrt{1-2k}\log_e\left(\frac{1-k}{k} + \frac{1}{k}\sqrt{1-2k}\right) - \frac{b}{2}(1-k) + \frac{\pi b}{4}k}{\frac{b}{2}\frac{k(1-k)}{\sqrt{1-2k}}\log_e\left(\frac{1-k}{k} + \frac{1}{k}\sqrt{1-2k}\right) + \frac{b}{2}\frac{(1-k)^2}{k} - \frac{\pi b}{4}(1-k)} \right] =$$

$$\left[-\frac{0.183}{0.817} + \frac{13.7\ (0.796)(2.176) - 13.7\ (0.817) + \frac{\pi}{2}(13.7)(0.133)}{\frac{13.7\ (0.183)(0.817)(2.176)}{0.796} + 13.7\ \frac{(0.817)^2}{0.183} - \frac{\pi}{2}(13.7)(0.817)} \right] = 0.210$$

$$\left(\frac{x'_{a.c.}}{c_{r_e}}\right)_{B(W)} = \frac{1}{4} + \frac{b - d}{2 c_{r_e}} \tan \Lambda_{c/4} \quad [0.210] \quad \text{(Equation 4.3.2.2-c)}$$

$$= \frac{1}{4} + \frac{27.4 - 5}{2(13.5)} (0.5498)\ [0.210]$$

$$= 0.346$$

$$\left(\frac{x'_{a.c.}}{c_{r_e}}\right)_{B(W)} = 0.345 \text{ (interpolated using values at } \beta A_e = 0 \text{ and } \beta A_e \geq 4.0)$$

(See Step 6 of the Datcom method for the interpolation procedure.)

$$\left(\frac{x'_{a.c.}}{c_{r_e}}\right)_N$$

$(f)_{equiv} = (f)_{nose} + 1.6\,(f)_{forebody}$ (Equation 4.3.2.2-d)

$= 1.75 + 1.6\,(5.33) = 10.28$

$\ell_{equiv} = (f_{equiv})\,(d) = (10.28)\,(5) = 51.4$

$\left(\frac{x_{a.c.}}{\ell_{equiv}}\right)_N = -0.545$ (Figure 4.3.2.2-36a at f_{nose})

$$\left(\frac{x'_{a.c.}}{c_{r_e}}\right)_N = \left(\frac{x_{a.c.}}{\ell_{equiv}}\right)\left(\frac{\ell_{equiv}}{c_{r_e}}\right) = (-0.545)\ \frac{51.4}{13.5} = -2.075$$

Solution:

$$\frac{x'_{a.c.}}{c_{r_e}} = \frac{\left(\frac{x'_{a.c.}}{c_{r_e}}\right)_N C_{L_{a_N}} + \left(\frac{x'_{a.c.}}{c_{r_e}}\right)_{W(B)} C_{L_{a_{W(B)}}} + \left(\frac{x'_{a.c.}}{c_{r_e}}\right)_{B(W)} C_{L_{a_{B(W)}}}}{C_{L_{a_N}} + C_{L_{a_{W(B)}}} + C_{L_{a_{B(W)}}}}$$ (Equation 4.3.2.2-a)

$$= \frac{(-2.075)\,(0.1567) + (0.440)\,(2.81) + (0.345)\,(0.622)}{0.1567 + 2.81 + 0.622}$$

$= 0.313$

$$\frac{x_{a.c.}}{c_r} = \left(\frac{x'_{a.c.}}{c_{r_e}}\right)\frac{c_{r_e}}{c_r} + \frac{d}{2\,c_r}\tan\Lambda_{LE}$$ (Equation 4.3.2.2-b)

$$= (0.313)\ \frac{13.5}{16.0} + \frac{5}{2\,(16)}\,(0.8012)$$

$= 0.389$

The calculated result compares with a test value of $\frac{x_{a.c.}}{c_r} = 0.35$ from Reference 9.

B. TRANSONIC

DATCOM METHOD

The transonic aerodynamic-center location near zero lift of a wing-body configuration with a straight-tapered wing may be approximated by the wing-body-combination approach presented in Paragraph A. In using this method at transonic speeds, care must be taken to evaluate the parameters by using the transonic methods presented in the applicable Datcom sections. The estimation of both the lift-curve slope and the aerodynamic-center location of the exposed wing at transonic speeds requires the use of data-fairing techniques outlined in Paragraphs B of Sections 4.1.3.2 and 4.1.4.2, respectively. It is suggested that the aerodynamic-center location of the wing lift carryover on the body $\left(x'_{a.c.}/c_{r_e}\right)_{B(W)}$ be estimated by the methods of Paragraphs A and C of this section, and any differences in the subsonic and supersonic values should be faired out smoothly in the transonic range. The two methods presented for estimating the aerodynamic-center location of the nose and forebody $\left(x'_{a.c.}/c_{r_e}\right)_N$ in Paragraph A of this section may be applied at transonic speeds.

The relatively simple application of the body effects on the aerodynamic-center location at transonic speeds is based on slender-body theory, which states that body force and moment characteristics are not functions of Mach number. On the other hand, the aerodynamic characteristics of wings in the transonic speed range are quite complex, and theoretical solutions are available for only a few specific planforms. Wing lift and pitching-moment characteristics at transonic speeds are discussed in Sections 4.1.3.2 and 4.1.4.2, respectively, and are not repeated here. The transonic methods of Sections 4.1.3.2 and 4.1.4.2 are applicable only to wings having symmetrical airfoils of conventional thickness distribution at low angles of attack.

C. SUPERSONIC

DATCOM METHODS

Straight-Tapered Wing-Body Configuration

The supersonic aerodynamic-center location near zero lift of a wing-body configuration with a straight-tapered wing is obtained by the wing-body-combination approach presented in Paragraph A. The procedure, applied at supersonic speeds, is outlined in the following steps:

Step 1. Divide the wing-body configuration into three components as in Step 1 of Paragraph A.

Step 2. Determine the normal-force-curve slope of the exposed wing $\left(C_{N_\alpha}\right)_e$ from the straight-tapered-wing method of Paragraph C of Section 4.1.3.2, based on its exposed area S_e.

Step 3. Determine the normal-force-curve slope of the body nose $\left(C_{N_\alpha}\right)_B$ by the method of Paragraph C of Section 4.2.1.1, based on the nose frontal area.

Step 4. Using the normal-force-curve slopes determined in Steps 2 and 3, calculate $C_{N_{\alpha_{W(B)}}}$, $C_{N_{\alpha_{B(W)}}}$, and $C_{N_{\alpha_N}}$, referred to the total wing area, by

$$C_{N_{\alpha_{W(B)}}} = K_{W(B)} \left(C_{N_\alpha}\right)_e \frac{S_e}{S_W}$$

$$C_{N_{\alpha_{B(W)}}} = K_{B(W)} \left(C_{N_\alpha}\right)_e \frac{S_e}{S_W}$$

$$C_{N_{\alpha_N}} = \left(C_{N_\alpha}\right)_B \frac{\pi d^2}{4S_W}$$

where $K_{W(B)}$ and $K_{B(W)}$ are interference factors obtained from Paragraph C of Section 4.3.1.2.

Step 5. Determine the a.c. location of the exposed wing as a fraction of the root chord of the exposed wing $\frac{x'_{a.c.}}{c_{r_e}}$ from Figure 4.1.4.2-26. The interference effect of the body-lift in the presence of the wing is neglected and the a.c. location of the body-lift carryover on the wing is taken as the a.c. location for the exposed wing, i.e.,

$$\left(\frac{x'_{a.c.}}{c_{r_e}}\right)_{W(B)} = \frac{x'_{a.c.}}{c_{r_e}}$$

Step 6. Determine the a.c. location of the wing-lift carryover on the body $\left(\frac{x'_{a.c.}}{c_{r_e}}\right)_{B(W)}$

Figure 4.3.2.2-37 is presented for estimating the a.c. of the lift carryover of the wing onto the body. The result is referred to the leading edge of the root chord of the exposed wing. Figure 4.3.2.2-37 is valid for

$$\beta A_e \ (1 + \lambda_e) \left(1 + \frac{1}{\beta \cot \Lambda_{LE}}\right) \geq 4.0$$

Figure 4.3.2.2-37 can be used for an approximation to $\left(\frac{x'_{a.c.}}{c_{r_e}}\right)_{B(W)}$ for the low-aspect-ratio range. However, if a more accurate result is desired, the low-aspect-ratio values may be found by cross-plotting these charts and extrapolating them to the slender-body-theory values at $\beta A_e = 0$ from Figure 4.3.2.2-36b.

Step 7. Determine the a.c. location of the body nose and forebody as a fraction of the root chord of the exposed wing $\left(\frac{x'_{a.c.}}{c_{r_e}}\right)_N$, and referred to the exposed-wing apex.

The center of pressure of the body nose and forebody as a fraction of body-nose length $\frac{x_{c.p.}}{\ell_N}$, and referred to the nose apex is obtained from Paragraph C of Section 4.2.2.1. Then

$$\left(\frac{x'_{a.c.}}{c_{r_e}}\right)_N = \frac{\ell_N}{c_{r_e}} \left(\frac{x_{c.p.}}{\ell_N} - 1\right)$$

Step 8. Using the results calculated in Steps 4 through 7, Equation 4.3.2.2-a gives the a.c. location of the wing-body configuration measured in exposed wing root chords and aft of the exposed wing apex. The a.c. location measured in wing root chords aft of the wing apex is given by Equation 4.3.2.2-b.

Sample Problem 1 on Pages 4.3.2.2-18 through 4.3.2.2-21 illustrates the use of this method.

A comparison of test data with results calculated by using this method is presented as Table 4.3.2.2-D. The limited number of test points presented precludes substantiation of this method over other than very limited ranges of planform and flow parameters. Within the linear-lift range, profile parameters such as camber, twist, and airfoil shape would be expected to have only a minor influence on the wing-body aerodynamic-center location.

It should be noted that the Datcom method for configurations with non-straight-tapered wings, which follows, uses essentially the same approach as that presented for configurations with straight-tapered wings. Therefore, substantiation of the method for non-straight-tapered wings serves to validate the method for straight-tapered wings.

Non-Straight-Tapered Wing-Body Configurations

The method for determining the supersonic aerodynamic-center location near zero lift of wing-body configurations with non-straight-tapered wings is taken from Reference 5. Both the wing-alone and the wing-body a.c.-prediction approaches are applied at supersonic speeds. Criteria have been established, during the course of the study conducted in connection with Reference 5, for determining which prediction approach is applicable to a given configuration.

The wing-body combinations are treated as wing-alone cases when the theoretical wing planform practically blankets the body. For such cases, the Datcom method for predicting the aerodynamic-center location of non-straight-tapered wings presented in Paragraph C of Section 4.1.4.2 is directly applicable. The method consists of dividing the complete theoretical planform (extended to the plane of symmetry) into two panels with each panel having conventional, straight-tapered geometry. Then for each of the constructed panels, the individual normal-force-curve slope and aerodynamic-center location are estimated by treating each constructed panel as a complete wing. The individual normal-force-curve slope and aerodynamic-center location determined for each constructed panel are then mutually combined in accordance with an "inboard-outboard" weighted-area relationship to estimate the aerodynamic-center location for the basic wing-body configuration.

The sample problem at the conclusion of Paragraph C of Section 4.1.4.2 illustrates the wing-alone approach.

The majority of the wing-body combinations investigated in Reference 5 required application of the wing-body approach to predict the linear aerodynamic-center location. This approach, introduced in this section, consists of breaking down the wing-body configuration into components and evaluating the exposed-wing lift in the presence of the body, the wing-lift carryover on the body, and the body nose effects. The basic approach is then essentially that presented for predicting the aerodynamic-center location of straight-tapered wing-body configurations at supersonic speeds. However, the method is more complex, since the exposed composite wing must be subdivided in order to estimate its normal-force-curve slope and aerodynamic-center location.

The procedure to be followed in using the wing-body approach to predict the supersonic linear aerodynamic-center location of a non-straight-tapered wing-body combination is outlined in the following steps:

Step 1. Divide the wing-body configuration into three components as follows (see Sketch (a)):

(1) The exposed composite wing in the presence of the body, denoted by the subscript W(B).

(2) The body in the presence of the wing, denoted by the subscript B(W).

(3) The body nose and forebody ahead of the wing-body juncture, denoted by the subscript N.

Step 2. Subdivide the exposed composite wing into inboard and outboard panels and determine their pertinent geometric parameters. The exposed wing is subdivided as discussed and illustrated in Paragraph A of Section 4.1.4.2 (see Pages 4.1.4.2-4 through 4.1.4.2-6). Application of that technique applied to a typical wing-body configuration is illustrated in Sketch (b).

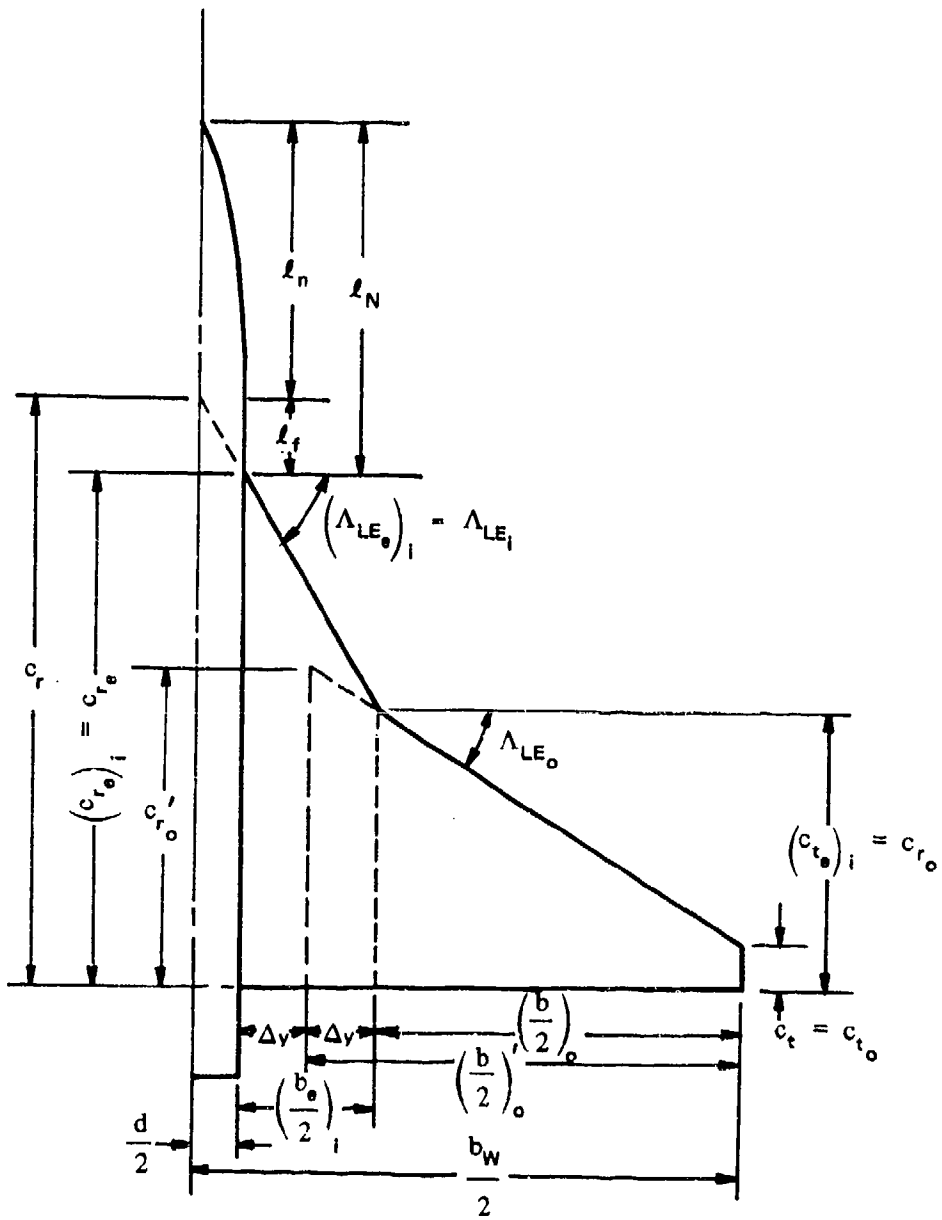

SKETCH (b)

Step 3. Determine the normal-force-curve slope $\left[\left(C_{N_\alpha}\right)_e\right]_i$ of the constructed inboard panel using the method for straight-tapered wings of Paragraph C, Section 4.1.3.2, based on the area $(S_e)_i$.

Step 4. Determine the a.c. location of the constructed inboard panel $\left(\frac{x'_{a.c.}}{c_{r_e}}\right)_i$ as a fraction of its root chord from Figure 4.1.4.2-26. This a.c. location is aft of the apex of the exposed constructed inboard panel.

Step 5. Determine the normal-force-curve slope $\left(C_{N_\alpha}\right)_o'$ of the constructed outboard panel using the method for the straight-tapered wings of Paragraph C of Section 4.1.3.2, based on the area S_o'.

Step 6. Determine the a.c. location of the constructed outboard panel $\left(\frac{x_{a.c.}}{c_r}\right)_o'$ as a fraction of its root chord from Figure 4.1.4.2-26. This a.c. location is aft of the apex of the constructed outboard panel.

Step 7. Convert the a.c. location determined in Step 6 to a fraction of the root chord of the exposed constructed inboard panel and aft of the apex of the exposed constructed inboard panel by

$$\frac{(x'_{a.c.})'_o}{(c_{r_e})_i} = \left(\frac{x_{a.c.}}{c_r}\right)'_o \frac{c'_{r_o}}{(c_{r_e})_i} - \frac{\Delta y}{(c_{r_e})_i} \tan \Lambda_{LE_o} + \frac{(b_e)_i}{2(c_{r_e})_i} \tan \Lambda_{LE_i} \qquad 4.3.2.2\text{-e}$$

Step 8. Calculate the a.c. location for the exposed composite wing, measured in root chords of the exposed inboard panel, aft of the exposed composite-wing apex by

$$\frac{x'_{a.c.}}{c_{r_e}} = \frac{\left[\left(C_{N_\alpha}\right)_e\right]_i (S_e)_i \left(\frac{x'_{a.c.}}{c_{r_e}}\right)_i + \left(C_{N_\alpha}\right)'_o S'_o \frac{(x'_{a.c.})'_o}{(c_{r_e})_i}}{\left[\left(C_{N_\alpha}\right)_e\right]_i (S_e)_i + \left(C_{N_\alpha}\right)'_o S'_o} \qquad 4.3.2.2\text{-f}$$

Step 9. Calculate the normal-force-curve slope for the exposed composite wing, based on the exposed wing area, by

$$\left(C_{N_\alpha}\right)_e = \frac{\left[\left(C_{N_\alpha}\right)_e\right]_i (S_e)_i + \left(C_{N_\alpha}\right)'_o S'_o}{(S_e)_i + S'_o} \qquad 4.3.2.2\text{-g}$$

Step 10. Determine the normal-force-curve slope of the body nose $\left(C_{N_\alpha}\right)_B$ by the method of Paragraph C of Section 4.2.1.1, based on the nose frontal area.

Step 11. Using the normal-force-curve slopes determined in Steps 9 and 10, calculate $C_{N_{\alpha_{W(B)}}}$, $C_{N_{\alpha_{B(W)}}}$, and $C_{N_{\alpha_N}}$, referred to the total wing area, by

$$C_{N_{a_{W(B)}}} = K_{W(B)} \left(C_{N_a}\right)_e \frac{(S_e)_i + S'_o}{S_W}$$

$$C_{N_{a_{B(W)}}} = K_{B(W)} \left(C_{N_a}\right)_e \frac{(S_e)_i + S'_o}{S_W}$$

$$C_{N_{a_N}} = \left(C_{N_a}\right)_B \frac{\pi d^2}{4S_W}$$

where $K_{W(B)}$ and $K_{B(W)}$ are interference factors obtained from Paragraph C of Section 4.3.1.2. The design charts of Section 4.3.1.2 are entered with the following geometric parameters:

A_e is the aspect ratio of the exposed composite wing.

λ_e is the taper ratio of the exposed composite wing $c_t/\left(c_{r_e}\right)_i$

Λ_{LE} is replaced by Λ_{LE_i}.

b is the total wing span (to body center line).

c_{r_e} is replaced by $\left(c_{r_e}\right)_i$.

Step 12. Determine the a.c. location of the exposed wing in the presence of the body $\left(\frac{x'_{a.c.}}{c_{r_e}}\right)_{W(B)}$. Th interference effect of the body lift in the presence of the wing is neglected and

$$\left(\frac{x'_{a.c.}}{c_{r_e}}\right)_{W(B)} = \frac{x'_{a.c.}}{c_{r_e}} \text{ (from Step 8)}$$

Step 13. Determine the a.c. location of the wing-lift carryover on the body $\left(\frac{x'_{a.c.}}{c_{r_e}}\right)_{B(W)}$ by the procedure outlined in Step 6 of the supersonic Datcom method for determining $\left(\frac{x'_{a.c.}}{c_{r_e}}\right)_{B(W)}$ for a straight-tapered wing-body configuration (Page 4.3.2.2-12). In applying that procedure the geometric parameters to be used are those defined in Step 11 of this method (see above).

Step 14. Determine the a.c. location of the body nose as a fraction of the root chord of the exposed wing $\left(\frac{x'_{a.c.}}{c_{r_e}}\right)_N$, and referred to the exposed-wing apex, by the procedure outlined in Step 7 of the Datcom method for a straight-tapered wing-body configuration (Page 4.3.2.2-12).

Step 15. Using the results calculated in Steps 11 through 14, Equation 4.3.2.2-a gives the a.c. location of the wing-body configuration measured in root chords of the exposed composite wing and aft of the apex of the exposed composite wing. The a.c. location, measured in root chords of the composite wing and aft of the wing apex, is given by Equation 4.3.2.2-b. In applying Equation 4.3.2.2-b the leading-edge sweep angle is that of the inboard panel Λ_{LE_i}.

This method is illustrated by Sample Problem 2 on Pages 4.3.2.2-21 through 4.3.2.2-26.

Comparisons of test data with results calculated by using this method are presented in Tables 4.3.2.2-E and 4.3.2.2-F (both taken from Reference 5) for configurations with double-delta and cranked wings, respectively The test data indicate that within the linear-lift range, profile parameters such as camber, twist, and airfoil shape have only a minor effect on the wing-body aerodynamic-center location. The ranges of planform parameters of the test data are:

Double-Delta Configurations	Cranked Configurations
$1.3 \leqslant A \leqslant 3.0$	$1.88 \leqslant A \leqslant 4.60$
$0 \leqslant \lambda \leqslant 0.143$	$0.086 \leqslant \lambda \leqslant 0.333$
$0.217 \leqslant \eta_B \leqslant 0.710$	$0.400 \leqslant \eta_B \leqslant 0.700$
$60^o \leqslant \Lambda_{LE_i} \leqslant 82.9^o$	$60^o \leqslant \Lambda_{LE_i} \leqslant 70.7^o$
$35^o \leqslant \Lambda_{LE_o} \leqslant 60^o$	$35^o \leqslant \Lambda_{LE_o} \leqslant 75^o$

The range of Mach number for both of these configurations is $1.0 \leqslant M \leqslant 3.0$.

The test configurations investigated have only one break in the leading-edge sweep, and for those configurations with both leading- and trailing-edge breaks, both breaks occur at the same span station.

Three double-delta configurations of Table 4.3.2.2-E meet the criteria established for the wing-alone prediction technique. Satisfactory results were obtained for each of these configurations by using the wing-alone approach. These cases are noted in Table 4.3.2.2-E. All the cranked-wing test configurations of Table 4.3.2.2-F were analyzed by using the wing-body approach.

It should be noted that several configurations which meet the prediction criteria for the wing- body approach have been evaluated by using the wing-alone approach, in which the wing-lift carryover and body-nose effects are neglected. The wing-alone approach did not yield satisfactory predictions for any of those configurations.

Although the techniques are applicable to wing-body combinations with curved wings, test data are not available for substantiation purposes. Only one wing-body combination with a curved wing has been investigated at supersonic speeds. Since this configuration has a very small body and the planform projection effectively blankets nearly all the body, it has been included in the curved wing alone substantiation of Section 4.1.4.2 (Table 4.1.4.2-C).

Sample Problems

1. Straight-Tapered Wing-Body Configuration

Given: A wing-body configuration of Reference 26.

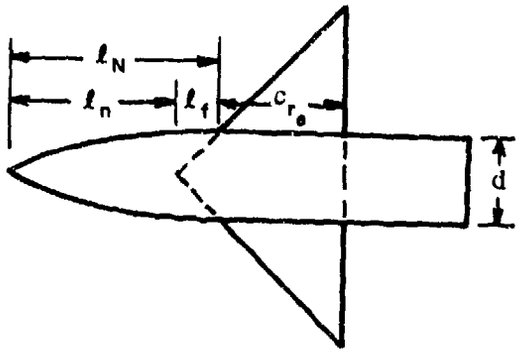

Total-Wing Characteristics:

$A_W = 4.0 \quad S_W = 13.99$ sq in. $\quad \lambda_W = 0$

$\Lambda_{LE_W} = 45^o \quad b_W = 7.48$ in.

$c_{r_W} = 3.74$ in.

Airfoil: 8-percent-thick double wedge (free-stream direction)

Exposed-Wing Characteristics:

$$A_e = 4.0 \quad \lambda_e = 0 \quad \Lambda_{LE_e} = \Lambda_{LE_W} = 45^o$$

$$c_{r_e} = 3.0 \text{ in.} \quad \frac{S_e}{S_W} = 0.64$$

Body-Nose Characteristics:

Ogive-cylinder $\quad d = 1.50$in. $\quad \dfrac{d}{b_W} = 0.20 \quad \ell_N = 5.0$ in.

$$\ell_n = 4.25 \text{ in.} \quad f_{nose} = \frac{\ell_n}{d} = 2.83$$

$$\ell_f = \ell_{forebody} = 0.75 \text{ in.} \quad f_{forebody} = \frac{\ell_f}{d} = 0.50$$

Additional Characteristics:

$M = 1.50$; $\beta = 1.12$

Compute:

$\left(C_{N_\alpha}\right)_e$ (Section 4.1.3.2)

$$\frac{\tan \Lambda_{LE}}{\beta} = \frac{1.00}{1.12} = 0.893 \text{ ; } A_e \tan \Lambda_{LE} = (4.0)(1.00) = 4.00$$

$$\beta \left[\left(C_{N_\alpha}\right)_{theory}\right]_e = 4.0 \text{ per rad (Figure 4.1.3.2-56a)}$$

$$\left[\left(C_{N_\alpha}\right)_{\text{theory}}\right]_e = 4.0/1.12 = 3.57 \text{ per rad}$$

$$\delta_\perp = \frac{\tan^{-1}\ \frac{0.04}{0.50}}{\cos \Lambda_{LE}} = 6.48^\circ$$

$$\left[\frac{C_{N_\alpha}}{\left(C_{N_\alpha}\right)_{\text{theory}}}\right]_e = 0.884 \text{ (Figure 4.1.3.2-60)}$$

$$\left(C_{N_\alpha}\right)_e = \left[\frac{C_{N_\alpha}}{\left(C_{N_\alpha}\right)_{\text{theory}}}\right]_e \left[\left(C_{N_\alpha}\right)_{\text{theory}}\right]_e = 0.884\ (3.57) = 3.16 \text{ per rad}$$

$\left(C_{N_\alpha}\right)_B$ (Section 4.2.1.1)

$$\frac{\beta}{f_n} = \frac{1.12}{2.83} = 0.396\ ;\ \frac{f_f}{f_n} = \frac{0.50}{2.83} = 0.177$$

$\left(C_{N_\alpha}\right)_B = 2.60$ per rad (based on nose frontal area) (Figure 4.2.1.1-21a)

Interference factors (Section 4.3.1.2)

$K_{W(B)} = 1.17$ (Figure 4.3.1.2-10 at $\frac{d}{b_W} = 0.20$)

$K_{B(W)}$ (Figure 4.3.1.2-11a)

$$\frac{\beta d}{c_{r_e}} = \frac{(1.12)\ (1.50)}{3.0} = 0.560\ ;\ \beta \cot \Lambda_{LE} = (1.12)\ (1.00) = 1.12$$

$$\left[\beta \left(C_{N_\alpha}\right)_e\ (\lambda_e + 1)\ \left(\frac{b}{d} - 1\right)\right] = 1.12\ (3.16)\ (1.0)\ (4.0) = 14.16$$

$$K_{B(W)} \left[\beta \left(C_{N_\alpha}\right)_e\ (\lambda_e + 1)\ \left(\frac{b}{d} - 1\right)\right] = 3.60 \text{ (Figure 4.3.1.2-11a)}$$

$$K_{B(W)} = 3.60/14.16 = 0.254$$

Component normal-force-curve slopes, referred to S_W

$$C_{N_{\alpha_{W(B)}}} = K_{W(B)}\ \left(C_{N_\alpha}\right)_e\ \frac{S_e}{S_W} = 1.17\ (3.16)\ (0.64) = 2.37 \text{ per rad}$$

$$C_{N_{\alpha_{B(W)}}} = K_{B(W)} \left(C_{N_\alpha}\right)_B \frac{S_e}{S_W} = 0.254\ (3.16)\ (0.64) = 0.514 \text{ per rad}$$

$$C_{N_{\alpha_N}} = \left(C_{N_\alpha}\right)_B \frac{\pi d^2}{4S_W} = 2.60\ \frac{\pi(1.5)^2}{4(13.99)} = 0.328 \text{ per rad}$$

$\left(\frac{X'_{a.c.}}{c_{r_e}}\right)_{W(B)}$ (Section 4.1.4.2)

$\frac{X'_{a.c.}}{c_{r_e}} = 0.670$ (Figure 4.1.4.2-26a)

$$\left(\frac{X'_{a.c.}}{c_{r_e}}\right)_{W(B)} = \frac{X'_{a.c.}}{c_{r_e}} = 0.670$$

$\left(\frac{X'_{a.c.}}{c_{r_e}}\right)_{B(W)}$

$$\beta A_e\ (1 + \lambda_e) \left(1 + \frac{1}{\beta \cot \Lambda_{LE}}\right) = (1.12)\ (4.0)\ (1.0) \left(1 + \frac{1}{1.12}\right) = 8.48;\ > 4.0.$$

$\left(\frac{X'_{a.c.}}{c_{r_e}}\right)_{B(W)} = 0.800$ (Figure 4.3.2.2-37a)

$\left(\frac{X'_{a.c.}}{c_{r_e}}\right)_N$

$\frac{X_{c.p.}}{\ell_N} = 0.488$ (Figure 4.2.2.1-18a)

$$\left(\frac{X'_{a.c.}}{c_{r_e}}\right)_N = \frac{\ell_N}{c_{r_e}} \left(\frac{X_{c.p.}}{\ell_N} - 1\right) = \frac{5}{3}\ (0.488 - 1) = -0.853$$

Solution:

$$\frac{X'_{a.c.}}{c_{r_e}} = \frac{\left(\frac{X'_{a.c.}}{c_{r_e}}\right)_N C_{N_{\alpha_N}} + \left(\frac{X'_{a.c.}}{c_{r_e}}\right)_{W(B)} C_{N_{\alpha_{W(B)}}} + \left(\frac{X'_{a.c.}}{c_{r_e}}\right)_{B(W)} C_{N_{\alpha_{B(W)}}}}{C_{N_{\alpha_N}} + C_{N_{\alpha_{W(B)}}} + C_{N_{\alpha_{B(W)}}}}$$ (equation 4.3.2.2-a)

$$= \frac{-0.853\,(0.328) + 0.670\,(2.37) + 0.800\,(0.514)}{0.328 + 2.37 + 0.514}$$

$$= 0.535$$

$$\frac{X_{a.c.}}{c_r} = \left(\frac{X'_{a.c.}}{c_{r_e}}\right)\left(\frac{c_{r_e}}{c_r}\right) + \frac{d}{2c_r}\tan\Lambda_{LE} \quad \text{(Equation 4.3.2.2-b)}$$

$$= 0.535\left(\frac{3}{3.74}\right) + \frac{1.5\,(1.0)}{2(3.74)} = 0.630$$

The calculated result compares with a test value of $\frac{X_{a.c.}}{c_r} = 0.62$ from Reference 26.

2. Non-Straight-Tapered Wing-Body Combination

Given: The wing-body combination of Reference 32 designated 6-67-67.

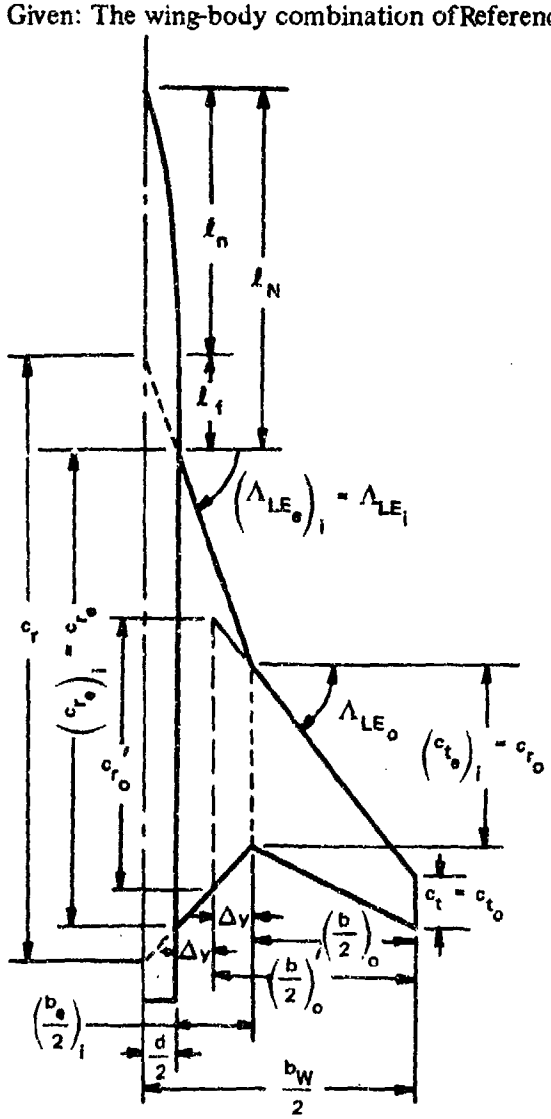

Total-Wing Characteristics:

$A_W = 2.42$ $S_W = 238.0$ sq in. $\lambda_W = 0.086$

$\Lambda_{LE_i} = 70.67^\circ$ $\Lambda_{LE_o} = 51.63^\circ$ $\eta_B = 0.40$

$\Lambda_{TE_i} = -47.37^\circ$ $\Lambda_{TE_o} = 26.62^\circ$ $c_t = 2.29$ in.

$c_r = 26.63$ in. $b_W = 24.0$ in.

Airfoil: 6% hexagonal with maximum thickness at c/3 (streamwise)

Exposed-Wing Characteristics:

$A_e = 1.82$ $\lambda_e = 0.110$ $c_{r_e} = 20.76$ in.

$b_e = 21.0$ in.

Body-Nose Characteristics:

Ogive-cylinder $d = 3.0$ in. $\frac{d}{b_W} = 0.125$

$\ell_n = 10.5$ in. $f_n = 3.50$

$\ell_f = \ell_{forebody} = 5.33$ in. $f_f = 1.78$

$\ell_N = 15.83$ in.

Constructed-Exposed-Inboard-Panel Characteristics:

$(A_e)_i = 0.463 \quad (\lambda_e)_i = 0.374 \quad \left(c_{r_e}\right)_i = 20.76 \text{ in.} \quad \left(\Lambda_{LE_e}\right)_i = \Lambda_{LE_i} = 70.67^o$

$\left(\frac{b_e}{2}\right)_i = 3.30 \text{ in.} \quad \Delta y = 1.65 \text{ in.} \quad (S_e)_i = 94.15 \text{ sq in.}$

Constructed-Exposed-Outboard-Panel Characteristics:

$A'_o = 3.13 \quad \lambda'_o = 0.254 \quad c'_{r_o} = 9.03 \text{ in.} \quad \Lambda'_{LE_o} = \Lambda_{LE_o} = 51.63^o$

$\left(\frac{b}{2}\right)'_o = 8.85 \text{ in.} \quad S'_o = 100.2 \text{ sq in.}$

Additional Characteristics:

$M = 2.01 \; ; \; \beta = 1.744$

Compute:

$\left[\left(C_{N_\alpha}\right)_e\right]_i$ (Section 4.1.3.2)

$\frac{\beta}{\tan \Lambda_{LE_i}} = \frac{1.744}{\tan 70.67^o} = 0.6117; \quad \left[(A \tan \Lambda_{LE})_e\right]_i = (0.463)(\tan 70.67^o) = 1.32$

$\tan \Lambda_{LE_i} \left[\left(C_{N_\alpha}\right)_{e_{theory}}\right]_i = 2.30 \text{ per rad}$ (Figures 4.1.3.2-56c through -56e, interpolated)

$\left[\left(C_{N_\alpha}\right)_{e_{theory}}\right]_i = 0.807 \text{ per rad}$

$\delta_\perp = \frac{\tan^{-1} \frac{0.03}{0.333}}{\cos \Lambda_{LE_i}} = 15.63^o \; ; \; \Delta y_\perp = 5.85 \tan \delta_\perp = 1.638$

$\left[\frac{\left(C_{N_\alpha}\right)_e}{\left(C_{N_\alpha}\right)_{e_{theory}}}\right]_i = 0.920$ (Figure 4.1.3.2-60)

$\left[\left(C_{N_\alpha}\right)_e\right]_i = \left[\frac{\left(C_{N_\alpha}\right)_e}{\left(C_{N_\alpha}\right)_{e_{theory}}}\right]_i \left[\left(C_{N_\alpha}\right)_{e_{theory}}\right]_i = 0.742 \text{ per rad}$

$\left(\frac{x'_{a.c.}}{c_{r_e}}\right)_i$ (Section 4.1.4.2)

$\left(\frac{x'_{a.c.}}{c_{r_e}}\right)_i = 0.430$ (Figures 4.1.4.2-26c through -26e, interpolated)

$\left(C_{N_\alpha}\right)'_o$ (Section 4.1.3.2)

$\frac{\tan \Lambda_{LE_o}}{\beta} = \frac{\tan 51.63^o}{1.744} = 0.724$; $(A \tan \Lambda_{LE})'_o \doteq (3.13)(\tan 51.63^o) = 3.95$

$\beta \left[\left(C_{N_\alpha}\right)_{theory}\right]'_o = 4.18$ per rad (Figures 4.1.3.2-56b through -56d, interpolated)

$\left[\left(C_{N_\alpha}\right)_{theory}\right]'_o \doteq 2.40$ per rad

$\delta_\perp = \frac{\tan^{-1} \frac{0.03}{0.333}}{\cos \Lambda_{LE_o}} = 8.30^o$

$\left[\frac{C_{N_\alpha}}{\left(C_{N_\alpha}\right)_{theory}}\right]'_o = 0.896$ (Figure 4.1.3.2-60)

$\left(C_{N_\alpha}\right)'_o = \left[\frac{C_{N_\alpha}}{\left(C_{N_\alpha}\right)_{theory}}\right]'_o \left[\left(C_{N_\alpha}\right)_{theory}\right]'_o \doteq 2.15$ per rad

$\left(\frac{x_{a.c.}}{c_r}\right)'_i$ (Section 4.1.4.2)

$\left(\frac{x_{a.c.}}{c_r}\right)'_o = 0.863$ (Figures 4.1.4.2-26b through -26d, interpolated)

$\frac{(x'_{a.c.})'_o}{\left(c_{r_e}\right)_i} = \left(\frac{x_{a.c.}}{c_r}\right)'_o \frac{c_{r_o}}{\left(c_{r_e}\right)_i} - \frac{\Delta y}{\left(c_{r_e}\right)_i} \tan \Lambda_{LE_o} + \frac{(b_e)_i}{2\left(c_{r_e}\right)_i} \tan \Lambda_{LE_i}$ (Equation 4.3.2.2-e)

$= 0.863 \frac{9.03}{20.76} - \frac{1.65}{20.76}(1.2631) + \frac{3.30}{20.76}(2.851) = 0.728$

Determine the a.c. location of the exposed composite wing $\frac{x'_{a.c.}}{c_{r_e}}$

$$\frac{x'_{a.c.}}{c_{r_e}} = \frac{\left[\left(C_{N_\alpha}\right)_e\right]_i (S_e)_i \left(\frac{x'_{a.c.}}{c_{r_e}}\right)_i + \left(C_{N_\alpha}\right)'_o S'_o \frac{(x'_{a.c.})'_o}{\left(c_{r_e}\right)_i}}{\left[\left(C_{N_\alpha}\right)_e\right]_i (S_e)_i + \left(C_{N_\alpha}\right)'_o S'_o} \quad \text{(Equation 4.3.2.2-f)}$$

$$= \frac{0.742\,(94.15)\,(0.430) + 2.15\,(100.2)\,(0.728)}{0.742\,(94.15) + 2.15\,(100.2)}$$

$$= 0.655$$

Determine the normal-force-curve slope of the exposed composite wing $\left(C_{N_\alpha}\right)_e$

$$\left(C_{N_\alpha}\right)_e = \frac{\left[\left(C_{N_\alpha}\right)_e\right]_i (S_e)_i + \left(C_{N_\alpha}\right)'_o S'_o}{(S_e)_i + S'_o} \quad \text{(Equation 4.3.2.2-g)}$$

$$= \frac{0.742\,(94.15) + 2.15\,(100.2)}{94.15 + 100.2}$$

$$= 1.468 \text{ per rad}$$

$\left(C_{N_\alpha}\right)_B$ (Section 4.2.1.1)

$$\frac{\beta}{f_n} = \frac{1.744}{3.50} = 0.50 \; ; \frac{f_f}{f_n} = \frac{1.78}{3.50} = 0.51$$

$\left(C_{N_\alpha}\right)_B = 2.78$ per rad (Figure 4.2.1.1-21a)

Interference factors (Section 4.3.1.2) (See Step 11 of Datcom method for correct geometric parameters, Page 4.3.2.2-16.)

$K_{W(B)} = 1.10$ (figure 4.3.1.2-10 at $\frac{d}{b_W} = 0.125$)

$K_{B(W)}$

$$\beta A_c (1 + \lambda_e)\left(\frac{\tan \Lambda_{LE_i}}{\beta} + 1\right) = (1.744)\,(1.82)\,(1.110)\left(\frac{2.851}{1.744} + 1\right) = 9.28;$$

therefore, use Figure 4.3.1.2-11a.

$$\left[\beta \left(C_{N_\alpha}\right)_e (\lambda_e + 1)\left(\frac{b}{d} - 1\right)\right] = 1.744\,(1.468)\,(1.110)\,(7.0) = 19.89$$

$$\beta \cot \Lambda_{LE_i} = (1.744)(0.3508) = 0.612; \quad \frac{\beta d}{\left(c_{r_e}\right)_i} = \frac{(1.744)(3.0)}{20.76} = 0.252$$

$$K_{B(W)}\left[\beta\left(C_{N_\alpha}\right)_e (\lambda_e + 1)\left(\frac{b}{d} - 1\right)\right] = 2.90 \quad \text{(Figure 4.3.1.2-11a)}$$

$$K_{B(W)} = 0.147$$

Component normal-force-curve slopes, referred to S_W

$$C_{N_{\alpha_{W(B)}}} = K_{W(B)}\left(C_{N_\alpha}\right)_e \frac{(S_e)_i + S'_c}{S_W} = 1.10\,(1.468)\frac{94.15 + 100.2}{238.0} = 1.32 \text{ per rad}$$

$$C_{N_{\alpha_{B(W)}}} = K_{B(W)}\left(C_{N_\alpha}\right)_e \frac{(S_e)_i + S'_o}{S_W} = 0.147\,(1.468)\frac{94.15 + 100.2}{238.0} = 0.176 \text{ per rad}$$

$$C_{N_{\alpha_N}} = \left(C_{N_\alpha}\right)_B \frac{\pi d^2}{4S_W} = (2.78)\frac{\pi 9}{4(238)} = 0.0826 \text{ per rad}$$

$\left(\frac{x'_{a.c.}}{c_{r_e}}\right)_{W(B)}$ The interference effect of the body is neglected.

$$\left(\frac{x'_{a.c.}}{c_{r_e}}\right)_{W(B)} = \frac{x'_{a.c.}}{c_{r_e}} = 0.655 \text{ (calculated on Page 4.3.2.2-24)}$$

$\left(\frac{x'_{a.c.}}{c_{r_e}}\right)_{B(W)}$ (See Step 11 of Datcom method for correct geometric parameters, Page 4.3.2.2-16.)

$$\left(\frac{x'_{a.c.}}{c_{r_e}}\right)_{B(W)} = 0.640 \text{ (Figure 4.3.2.2-37a)}$$

$\left(\frac{x'_{a.c.}}{c_{r_e}}\right)_N$

$$\frac{x_{c.p.}}{\ell_N} = 0.405 \text{ (Figure 4.2.2.1-18a)}$$

$$\left(\frac{x'_{a.c.}}{c_{r_e}}\right)_N = \frac{\ell_N}{c_{r_e}}\left(\frac{x_{c.p.}}{\ell_N} - 1\right) = \frac{15.83}{20.76}(0.405 - 1) = -0.454$$

Solution:

$$\frac{x'_{a.c.}}{c_{r_e}} = \frac{\left(\frac{x'_{a.c.}}{c_{r_e}}\right)_N C_{N_{a_N}} + \left(\frac{x'_{a.c.}}{c_{r_e}}\right)_{W(B)} C_{N_{a_{W(B)}}} + \left(\frac{x'_{a.c.}}{c_{r_e}}\right)_{B(W)} C_{N_{a_{B(W)}}}}{C_{N_{a_N}} + C_{N_{a_{W(B)}}} + C_{N_{a_{B(W)}}}} \quad \text{(Equation 4.3.2.2-a)}$$

$$= \frac{-0.454\,(0.0826) + 0.655\,(1.32) + 0.640\,(0.176)}{0.0826 + 1.32 + 0.176}$$

$$= 0.595$$

$$\frac{x_{a.c.}}{c_r} = \left(\frac{x'_{a.c.}}{c_{r_e}}\right)\left(\frac{c_{r_e}}{c_r}\right) + \frac{d}{2c_r} \tan \Lambda_{LE_i} \quad \text{(Equation 4.3.2.2-b)}$$

$$= 0.595 \quad \frac{20.76}{26.63} + \frac{3}{2(26.63)} \quad (2.851)$$

$$= 0.624$$

The calculated result compares with a test value of $\frac{x_{a.c.}}{c_r} = 0.626$ from Reference 32.

REFERENCES

1. Pitts, W., Nielsen, J., and Kaattari, G.: Lift and Center of Pressure of Wing-Body-Tail Combinations at Subsonic, Transonic, and Supersonic Speeds. NACA TR 1307, 1957. (U)

2. Spreiter, J.: The Aerodynamic Forces on Slender Plane- and Cruciform-Wing and Body Combinations. NACA TR 962, 1950. (U)

3. Letko, W., and Williams, J.: Experimental Investigation at Low Speed of Effects of Fuselage Cross Section on Static Longitudinal and Lateral Stability Characteristics of Models Having 0° and 45° Sweptback Surfaces. NACA TN 3551, 1955. (U)

4. Spearman, L.: Investigation of the Aerodynamic Characteristics in Pitch and Sideslip of a 45° Sweptback-Wing Airplane Model With Various Vertical Locations of the Wing and Horizontal Tail. NACA RM L55B18, 1955. (U)

5. Benepe, D. B., Kouri, B. G., Webb, J. B., et al: Aerodynamic Characteristics of Non-Straight-Taper Wings. AFFDL-TR-66-73, 1966. (U)

6. Foster, G., and Fitzpatrick, J.: Longitudinal-Stability Investigation of High-Lift and Stall-Control Devices on a 52° Sweptback Wing with and Without Fuselage and Horizontal Tail at a Reynolds Number of 6.8 x 10^6. NACA RM L8I08, 1948. (U)

7. Wiggins, J., and Kuhn, R. E.: Wind-Tunnel Investigation of the Aerodynamic Characteristics in Pitch of Wing-Fuselage Combinations at High-Subsonic Speeds – Sweep Series. NACA RM L52D18, 1952. (U)

8. Johnson, H.: Wind-Tunnel Investigation at Low Speed of the Effect of Varying the Ratio of Body Diameter to Wing Span from 0.1 to 0.8 on the Aerodynamic Characteristics in Pitch of a 45° Sweptback-Wing-Body Combination. NACA RM L53J09a, 1953. (U)

9. Goodson, K.: Effect of Nose Length, Fuselage Length, and Nose Fineness Ratio on the Longitudinal Aerodynamic Characteristics of Two Complete Models at High Subsonic Speeds. NASA Memo 10-10-58L, 1958. (U)

10. Anon: Small-Scale Wing-Body Planform Investigation at Mach Numbers from 0.40 to 2.94. Unpublished Data. (U)

11. Kuhns, R. M.: HSWT-083-0 Analysis Report, Supersonic Transport Lifting Fuselage Investigation. Convair, General Dynamics, San Diego Report AD-SST-012, 1961. (U)

12. Anon: Large-Scale Double-Delta Wing-Body Planform Investigation at Low Speed. Unpublished Data. (U)

13. Kuhns, R. M.: LSWT-322 Analysis Report, Supersonic Transport Low-Speed Investigation. Convair, General Dynamics, San Diego Report AD-SST-016, 1961. (U)

14. Anon: System 125A, Convair Model 25, Summary Data Report, Subsonic Tests of a Preliminary 1/27-Scale Force Model (CVAL 201). Convair, General Dynamics, F/W Report FZT-25-004, 1956. (C) Title Unclassified

15. Anon: System 125A, Convair Model 25 Preliminary Design Proposal, Summary of Wind-Tunnel Results on Wing-Flap Configurations. Convair, General Dynamics, F/W Report FZA-25-017, 1956. (C) Title Unclassified

16. Koenig, D. G., and Corsiglia, V. R.: Large-Scale Low-Speed Wind-Tunnel Tests of a Delta-Wing Supersonic-Transport Model With Various Canard, Horizontal-Tail, and Wing Modifications. NASA TM X-857, 1964. (C) Title Unclassified

17. Grant, F. C., and Sevier, J. R., Jr.: Transonic and Supersonic Wind-Tunnel Tests of Wing-Body Combinations Designed for High Efficiency at a Mach Number of 1.41. NASA TN D-435, 1960. (U)

18. Mansell, C. J.: Low-Speed Wind-Tunnel Tests on Two Thin Cranked Wings With 60-Degree Sweepback Inboard. ARC R&M 2995, 1957. (U)

19. Jernell, L. S.: The Effects of Conical Camber on the Longitudinal Aerodynamic Characteristics of a Variable-Sweep Wing-Fuselage Configuration at Mach Numbers From 0.50 to 3.50. NASA TM X-804, 1964. (C) Title Unclassified

20. Trescot, C. D., and Spencer, B., Jr.: Effect of Reynolds Number on the Low-Speed Longitudinal Aerodynamic Characteristics of Two Variable-Wing-Sweep Airplane Configurations. NASA TM X-434, 1961. (C) Title Unclassified

21. Spencer, B., Jr.: Low-Speed Longitudinal Aerodynamic Characteristics Associated With Variations in the Geometry of the Fixed Portion of a Variable-Wing-Sweep Airplane Configuration Having an Outboard Pivot. NASA TM X-625, 1962. (C) Title Unclassified

22. Spencer, B., Jr.: Stability and Control Characteristics at Low Subsonic Speeds of an Airplane Configuration Having Two Types of Variable-Sweep Wings. NASA TM X-303, 1960. (U)

23. Spearman, M. L.: Longitudinal and Lateral Aerodynamic Characteristics at Mach Numbers From 0.60 to 2.20 of a Variable-Sweep Fighter Model With Sweep Angles From 25° to 75°. NASA TM X-710, 1962. (C) Title Unclassified

24. Sleeman, W. C., Jr., and Robins, A. W.: Low-Speed Investigation of the Aerodynamic Characteristics of a Variable-Sweep Supersonic Transport Configuration Having a Blended Wing and Body. NASA TM X-619, 1961. (C) Title Unclassified

25. Henderson, W. P.: Low-Speed Longitudinal Stability Characteristics of a Supersonic Transport Configuration With Variable-Sweep Wings Employing a Double Inboard Pivot. NASA TM X-744, 1963. (C) Title Unclassified

26. Nielsen, J., Katzen, E., and Tang, K.: Lift and Pitching-Moment Interference Between a Pointed Cylindrical Body and Triangular Wings of Various Aspect Ratios at Mach Numbers of 1.50 and 2.02. NACA TN 3795, 1956. (U)

27. Robinson, R.: Aerodynamic Characteristics at Supersonic Speeds of a Series of Wing-Body Combinations Having Cambered Wings With an Aspect Ratio of 3.5 and a Taper Ratio of 0.2. Effects of Sweep Angle and Thickness Ratio on the Aerodynamic Characteristics in Pitch at M = 2.01. NACA RM L52E09, 1952. (U)

28. Sevier, J. R., Jr.: Aerodynamic Characteristics at Mach Numbers of 1.41 and 2.01 of a Series of Cranked Wings Ranging in Aspect Ratio From 4.0 to 1.74 in Combination With a Body. NASA TM X-172, 1960. (U)

29. Bryson, R. B.: Project MX-1964, Summary Data Report of Force Tests of B-58 Airplane Models With a Linearizer. CVAL 269, ARC 9 x 7 Test 43, Convair, General Dynamics, F/W Report FZT-4-206, 1959. (U)

30. Foster, G. V.: Exploratory Investigation at Mach Number of 2.01 of the Longitudinal Stability and Control Characteristics of a Winged Reentry Configuration. NASA TM X-176, 1959. (U)

31. Pierce, S. R.: System 126A, Convair Model 25 Summary Data Report, Wind-Tunnel Tests of a 1/125-Scale Model. JPL 20-202, Convair, General Dynamics, F/W Report FZT-25-006, 1956. (C) Title Unclassified

32. Cooper, M. and Sevier, J. R., Jr.: Effects of a Series of Inboard Plan-Form Modifications on the Longitudinal Characteristics of Two 47° Sweptback Wings of Aspect Ratio 3.5, Taper Ratio 0.2, and Different Thickness Distributions at Mach Numbers of 1.61 and 2.01. NACA RM L53E07a, 1953. (U)

33. Sevier, J. R., Jr.: Investigation of the Effects of Body Indentation and Wing-Plan-Form Modification on the Longitudinal Characteristics of a 60° Swept-Wing-Body Combination at Mach Numbers of 1.41, 1.61, and 2.01. NACA RM L55E17, 1955. (U)

34. Foster, G. V.: Stability and Control Characteristics at Mach Numbers of 2.50, 3.00, and 3.71 of a Variable-Wing-Sweep Configuration With Outboard Wing Panels Swept Back 75°. NASA TM X-267, 1960. (U)

35. Alford, W. J., Jr., Luoma, A. A., and Henderson, W. P.: Wind-Tunnel Studies at Subsonic and Transonic Speeds of a Multiple-Mission Variable-Wing-Sweep Airplane Configuration. NASA TM X-206, 1959. (U)

36. Jones, R. T.: Properties of Low-Aspect-Ratio Pointed Wings at Speeds Below and Above the Speed of Sound. NACA TR 835, 1946. (U)

37. Lawrence, H. R.: The Lift Distribution on Low Aspect Ratio Wings at Subsonic Speeds. Jour. Aero. Sci., Vol. 18, No. 10, October, 1951. (U)

TABLE 4.3.2.2-A

SUBSONIC AERODYNAMIC-CENTER LOCATIONS OF WING-BODY COMBINATIONS WITH STRAIGHT-TAPERED WINGS

DATA SUMMARY AND SUBSTANTIATION

Ref.	$\frac{d}{b}$	λ_e	$\frac{S_e}{S_W}$	A_e	Λ_{LE} (deg)	f_N	f_f	M	$R\ell_{MAC} \times 10^{-6}$	$\frac{x_{a.c.}}{c_r}$ Calc.	$\frac{x_{a.c.}}{c_r}$ Test	e Percent Error
6	.15	.67	.82	2.54	52	2.75	.80	.13	6.8	.910	.900	1.1
7	.14	.62	.83	3.58	60	4.00	0	.40	2.0	1.510	1.520	-0.7
								.70	3.1	1.520	1.520	0
								.91	3.5	1.530	1.540	-0.6
	.14	.62	.83	3.58	35	5.00	0	.40	2.0	.690	.690	0
								.70	3.1	.690	.690	0
								.91	3.5	.750	.770	-2.6
	.14	.62	.83	3.58	7	5.50	0	.40	2.0	.220	.230	-4.3
								.70	3.1	.220	.230	-4.3
								.91	3.5	.300	.330	-9.1
8	.20	1.00	.80	2.40	45	1.50	1.0	.29	.9	.960	.950	1.1
	.40		.60	1.80						.640	.650	-1.5
	.80		.20	.60						-2.180	-2.200	-0.9
9	.18	.17	.70	2.84	38.7	1.75	5.33	.60	3.0	.389	.350	11.1

Average Error = $\frac{\Sigma |e|}{n}$ = 2.7%

TABLE 4.3.2.2-B

SUBSONIC AERODYNAMIC-CENTER LOCATIONS OF WING-BODY COMBINATIONS WITH DOUBLE-DELTA WINGS

DATA SUMMARY AND SUBSTANTIATION

Ref.	Config.	A	λ	η_B	Λ_{LE_i} (deg)	Λ_{LE_o} (deg)	M	$\frac{x_{a.c.}}{c_r}$ Calc.	$\frac{x_{a.c.}}{c_r}$ Test	e Percent Error
10	WB	2.01	0.067	0.313	78.0	53.3	0.40	0.689	0.714	− 3.5
							0.70	0.697	0.724	− 3.7
							0.90	0.705	0.738	− 4.5
		1.96	0.062	0.405		48.5	0.40	0.702	0.728	− 3.6
							0.70	0.710	0.738	− 3.8
							0.90	0.722	0.756	− 4.5
		1.93	0.069	0.498		38.1	0.40	0.714	0.738	− 3.3
							0.70	0.726	0.746	− 2.7
							0.90	0.739	0.772	− 4.3
		1.30	0	0.500	82.0	60.0	0.40	0.737	0.777	− 5.1
							0.70	0.760	0.785	− 4.5
							0.90	0.765	0.798	− 4.1
		1.33	0.049	0.403			0.40	0.737	0.770	− 4.3
							0.70	0.741	0.744	− 0.4
							0.90	0.749	0.788	− 4.9
		1.55	0	0.400		59.0	0.40	0.730	0.743	− 1.7
							0.70	0.737	0.755	− 2.4
							0.90	0.748	0.768	− 2.6
		1.72		0.414	77.4		0.40	0.668	0.700	− 4.6
							0.70	0.676	0.707	− 4.4
							0.90	0.688	0.727	− 5.4
11	WB	2.39	0	0.217	82.9	60.0	0.70	0.757	0.748	1.2
							0.90	0.764	0.761	0.4
12	WB	1.87	0	0.424	72.6	59.0	0.10	0.685	0.710	− 3.5
		1.73		0.551	73.0			0.681	0.721	− 5.5
				0.414	77.4			0.663	0.676	− 1.9

TABLE 4.3.2.2-B (CONTD)

Ref.	Config.	A	λ	η_B	Λ_{LE_i} (deg)	Λ_{LE_o} (deg)	M	$\frac{x_{a.c.}}{c_r}$ Calc.	$\frac{x_{a.c.}}{c_r}$ Test	e Percent Error
12	WB	1.87	0	0.332	77.2	59.0	0.10	0.662	0.660	0.3
↓	↓	1.46	0.091	0.484	72.6	↓	↓	0.644	0.683	− 5.7
↓	↓	1.34	0.083	0.628	73.0	↓	↓	0.643	0.706	− 8.9
↓	↓	↓	0.075	0.473	77.4	↓	↓	0.633	0.666	− 5.0
↓	↓	1.46	0.082	0.379	77.2	↓	↓	0.628	0.659	− 4.7
13	WB	2.39	0	0.217	82.9	50.0	0.30	0.753	0.750	0.4
14	WBV	3.00	0	0.654	60.0	42.1	0.20	0.576	(a)	
15	WB	3.00	0	0.654	60.0	42.1	0.70	0.589		
↓	↓	↓	↓	↓	↓	↓	0.80	0.595		
↓	↓	↓	↓	↓	↓	↓	0.90	0.604		
16	WBV	1.89	0	0.400	73.4	59.0	0.10	0.624		

(a) This information is classified CONFIDENTIAL.

Average Error = $\frac{\Sigma |e|}{n}$ = 3.4%

TABLE 4.3.2.2-C

SUBSONIC AERODYNAMIC-CENTER LOCATIONS OF WING-BODY COMBINATIONS WITH CRANKED WINGS

DATA SUMMARY AND SUBSTANTIATION

Ref.	Config.	A	λ	η_B	Λ_{LE_i} (deg)	Λ_{LE_o} (deg)	M	$\frac{x_{a.c.}}{c_r}$ Calc.	$\frac{x_{a.c.}}{c_r}$ Test	e Percent Error
17	WB	2.91	.167	.500	67.0	61.7	.60	.770	.797	− 3.4
↓	↓	↓	↓	↓	↓	↓	.30	.780	.802	− 2.7
↓	↓	↓	↓	↓	↓	↓	.90	.784	.804	− 2.5
18	WB	3.00	.455	.584	59.0	48.5	.18	1.038	.997	4.1
19	WB	6.18	.136	.308	65.0	12.0	.50	.739	(a)	
↓	↓	↓	↓	↓	↓	↓	.80	.750		
↓	↓	↓	↓	↓	↓	↓	.90	.757		

TABLE 4.3.2.2-C (CONTD)

Ref.	Config.	A	λ	η_B	Λ_{LE_i} (deg)	Λ_{LE_o} (deg)	M	$\frac{x_{a.c.}}{c_r}$ Calc.	$\frac{x_{a.c.}}{c_r}$ Test	% Percent Error
19	WB	4.60	Raked	.404		45.0	.50	.928		
							.80	.943		
							.90	.954		
20	WBV	5.95	0	.345	60.0	25.0	.30	.771		
		5.15	.090	.379				.689	(a)	
21	WBV	2.49	.280	.654	25.0	75.0	.25	.610		
		2.18	.187		45.0			.672		
		1.86	.129		60.0			.707		
		1.68	.104		66.3			.726		
22	WBVN	5.15	.089	.371	60.0	25.0	.23	.679	.683	− 0.6
		1.89	Raked	.640		75.0		.845	.900	− 6.1
		4.49	.129	.269		30.0	.21	.654	.660	− 0.9
		4.00	.152	.302		43.0		.714	.725	− 1.5
		1.75	Raked	.463		70.5		.690	.749	− 7.9
23	WBVN	5.15	.090	.379	60.0	25.0	.60	.693		
							.80	.704		
							.90	.716		
		3.44	Raked	.475		55.0	.60	.802		
							.80	.814		
							.90	.832	(a)	
23	WBVN	1.88	Raked	.654	60.0	75.0	.60	.831		
							.80	.835		
							.90	.833		
24	WBV	3.63	.075	.413	72.0	25.0	.19	.720		
25	WB	6.93	.116	.224	75.0	35.0	.27	.964		
		6.40	.102	.270				.823		

(a) This information is classified CONFIDENTIAL.

Average Error = $\frac{\Sigma |e|}{n}$ = 3.0%

TABLE 4.3.2.2-D

SUPERSONIC AERODYNAMIC-CENTER LOCATIONS OF WING-BODY COMBINATIONS WITH STRAIGHT-TAPERED WINGS

DATA SUMMARY

Ref.	$\frac{d}{b}$	λ_e	$\frac{S_e}{S_W}$	A_e	Λ_{LE} (deg)	f_N	f_f	M	$R_{\ell_{MAC}} \times 10^{-6}$	$\frac{x_{a.c.}}{c_r}$ Calc.	$\frac{x_{a.c.}}{c_r}$ Test	e Percent Error
26	.60	0	.16	.67	80.4	2.85	.50	1.50	5.5	.570	.580	−1.7
								2.02		.580	.560	3.6
	.20	0	.64	4.0	45.0	2.85	.50	1.50	5.5	.630	.620	1.6
								2.02		.620	.620	0
27	.09	.21	.85	3.4	51.5	2.9	1.6	2.01	2.2	.860	.848	1.4
										.860	.844	1.9
										.850	.828	2.7
	.09	.21	.85	3.4	21.5	2.9	3.3	1.60	2.2	.460	.463	−0.6
								2.01		.470	.450	4.4

Average Error = $\frac{\Sigma |e|}{n}$ = 2.0%

TABLE 4.3.2.2-E

SUPERSONIC AERODYNAMIC-CENTER LOCATIONS OF WING-BODY COMBINATIONS WITH DOUBLE-DELTA WINGS

DATA SUMMARY AND SUBSTANTIATION

Ref.	Config.	A	λ	η_B	Λ_{LE_i} (deg)	Λ_{LE_o} (deg)	M	$\frac{x_{a.c.}}{c_r}$ Calc.	$\frac{x_{a.c.}}{c_r}$ Test	e Percent Error
10	WB	1.30	0	.500	82.0	60.0	1.00	.795	.821	−3.2
							1.10	.790	.821	−3.8
							1.40	.787	.805	−2.2
							1.98	.775	.785	−1.3
							2.94	.754	.760	−0.8
	WB	1.33	.049	.403	82.0	60.0	1.00	.766	.861	−11.0
							1.10	.790	.813	−2.8
							1.40	.786	.808	−2.7
							1.98	.775	.791	−2.0
							2.94	.762	.771	−1.2

TABLE 4.3.2.2-E (CONTD)

Ref.	Config.	A	λ	η_B	Λ_{LE_i} (deg)	Λ_{LE_o} (deg)	M	$\frac{x_{a.c.}}{c_r}$ Calc.	$\frac{x_{a.c.}}{c_r}$ Test	ε Percent Error
10	WB[a]	1.55	0	.400	82.0	59.0	1.00	.769	.790	− 2.7
							1.10	.774	.790	− 2.0
							1.40	.765	.781	− 2.0
							1.98	.753	.768	− 2.0
							2.94	.738	.749	− 1.5
	WB	1.72	0	.414	82.0	59.0	1.00	.725	.751	−3.5
							1.10	.737	.750	− 1.7
							1.39	.732	.748	− 2.1
11	WB[a]	2.39	0	.217	82.9	50.0	1.20	.800	.800	0
							2.00	.785	.790	− 0.6
							3.00	.700	.778	− 1.0
							4.00	.759	.771	− 1.6
28	WB	2.35	.143	.700	61.7	35.0	1.41	.670	.680	− 1.5
							2.01	.660	.640	3.1
		1.95	.111				1.41	.544	.569	− 4.4
							2.01	.546	.531	2.8
29	WBVN	1.95	0	.215	74.7	60.0	1.70	.669	.697	− 4.0
							2.00	.671	.694	− 3.3
							2.20	.673	.688	− 2.2
30	WB[a]	1.79	.104	.556	73.0	47.2	2.01	.724	.706	2.7
15	WB	3.00	0	.654	60.0	42.1	1.00	.656	(b)	
							1.05	.654		
							1.25	.655		
							1.30	.656		
31	WB	2.60	0	.710	60.0	49.3	1.80	.645		
							2.16	.647		
							2.56	.650		
							3.07	.652		

(a) Predicted using wing-alone approach

(b) This information is classified CONFIDENTIAL.

Average Error = $\frac{\Sigma\ |\varepsilon|}{n}$ = 2.6%

TABLE 4.3.2.2-F

SUPERSONIC AERODYNAMIC-CENTER LOCATIONS OF WING-BODY COMBINATIONS WITH CRANKED WINGS

DATA SUMMARY AND SUBSTANTIATION

Ref.	Config.	A	λ	η_b	Λ_{LE_i} (deg)	Λ_{LE_o} (deg)	M	$\frac{x_{a.c.}}{c_r}$ Calc	$\frac{x_{a.c.}}{c_r}$ Test	Percent Error
32	WB	3.15	.150	.400	64.1	51.6	1.61	.845	.845	0
		2.86	.120					.691	.688	0.4
		2.62	.100					.584	.586	– 0.3
		2.86	.120		70.7	51.6		.859	.863	– 0.5
		2.62	.100					.724	.727	– 0.4
		2.42	.086					.631	.635	– 0.6
		2.86	.120				2.01	.853	.846	0.8
		2.42	.086					.624	.626	– 0.3
28	WB	4.00	.333	.700	61.7	35.0	1.41	1.433	1.420	0.9
							2.01	1.391	1.364	2.0
		2.97	.200	.700	61.7	35.0	1.41	.891	.903	– 1.3
							2.01	.876	.864	1.4
17	WB	2.91	.167	.500	67.0	61.7	1.41	.843	.872	– 3.3
							2.01	.853	.863	– 1.2
33	WB	2.91	.167	.500	67.0	61.7	1.41	.859	.899	– 4.4
							1.61	.865	.899	– 3.9
							2.01	.852	.879	– 3.1
34	WBV	1.88	.130	.654	60.0	75.0	2.50	.896	.875	2.4
							3.00	.903	.862	4.6
35							1.00	.776	.790	– 1.8
							1.13	.810	.821	– 1.3
							1.20	.821	.824	– 0.4
							1.30	.828	.827	0.1
19	WB	4.60	Raked tip	.404	65.0	45.0	1.03	1.008	.990	1.8
							1.20	1.012	1.010	0.2
							2.30	.977	.946	3.3
							2.60	.970	.926	4.8
							3.00	.962	.910	5.7

TABLE 4.3.2.2-F (CONTD)

Ref.	Config.	A	λ	η_B	Λ_{LE_i} (deg)	Λ_{LE_o} (deg)	M	$\frac{x_{a.c.}}{c_r}$ Calc.	$\frac{x_{a.c.}}{c_r}$ Test	e Percent Error
23	WBVN	3.44	Raked tip	.475	60.0	55.0	1.00	.935	(a)	
							1.20	.956		
							1.40	.962		
							2.20	.979		
		1.88	Raked tip	.675	60.0	75.0	1.00	.949		
							1.20	1.004		
							1.40	1.002		
							2.20	1.100		

(a) This information is classified CONFIDENTIAL.

Average Error = $\frac{\Sigma |e|}{n}$ = 2.6%

$$\frac{k}{1-k} + \frac{\frac{k(1-k)}{\sqrt{1-2k}}\log_e\left(\frac{1-k}{k}+\frac{1}{k}\sqrt{1-2k}\right) - (1-k) + \frac{\pi}{2}k}{\frac{(1-k)^2}{k}\left(\frac{1-k}{k}+\frac{1}{k}\sqrt{1-2k}\right) + \frac{\pi}{2}(1-k)}$$

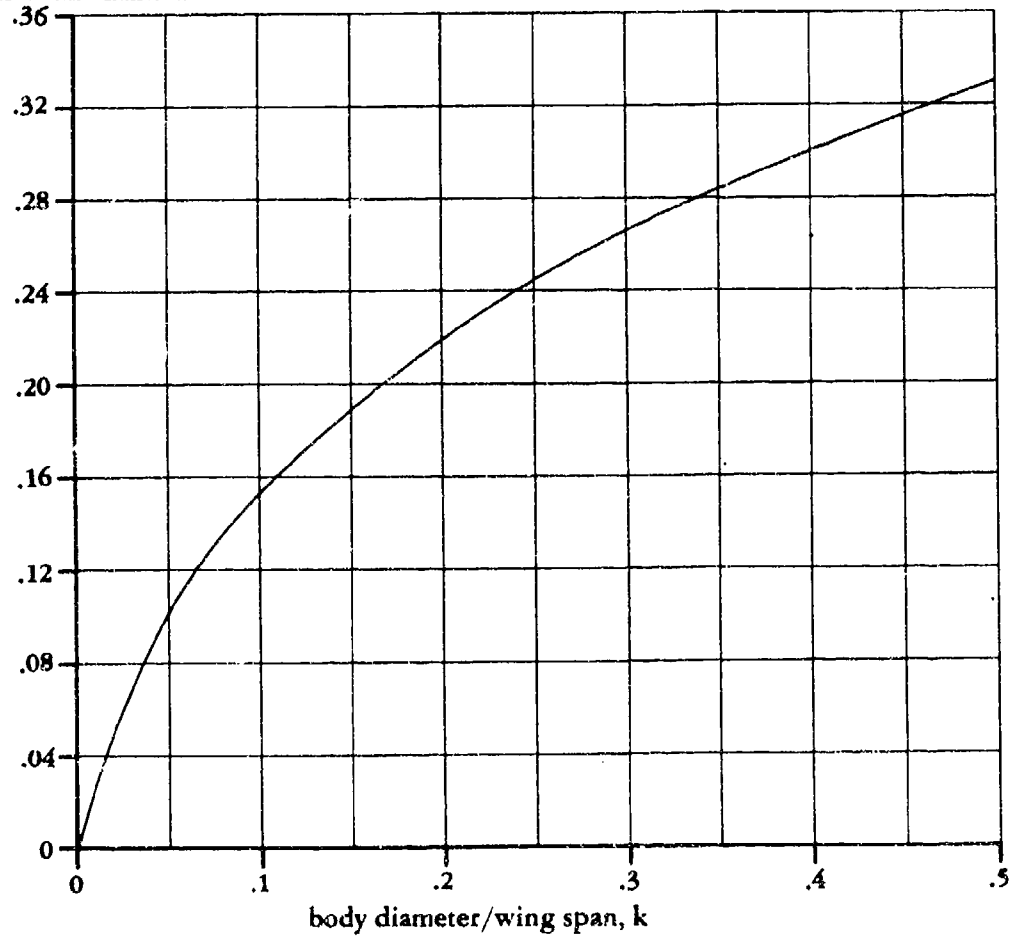

FIGURE 4.3.2.2-35 PARAMETER USED IN ACCOUNTING FOR WING-LIFT CARRYOVER ON THE BODY

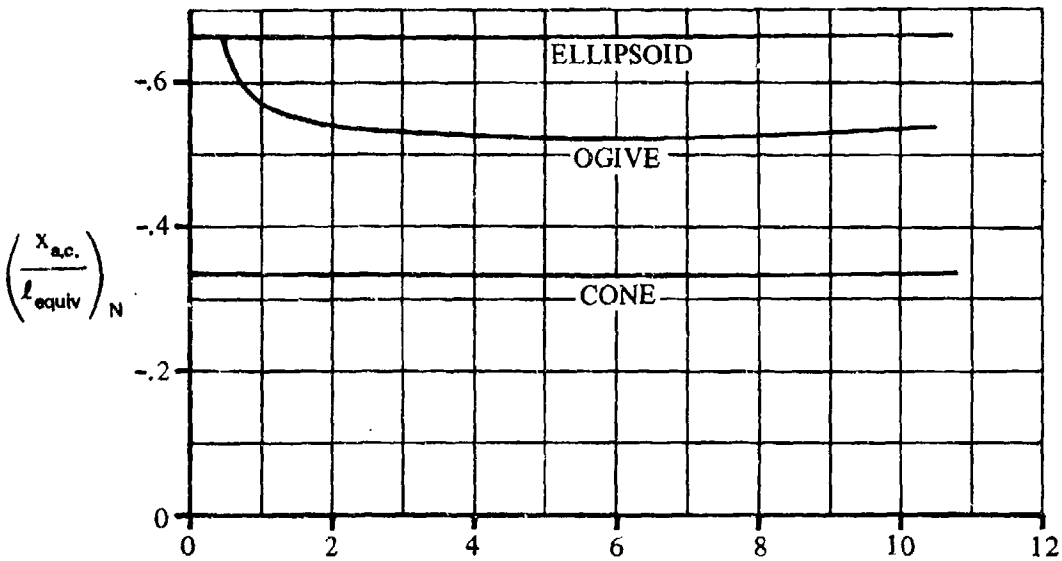

FIGURE 4.3.2.2-36a AERODYNAMIC-CENTER LOCATIONS OF VARIOUS NOSES (SLENDER-BODY THEORY)

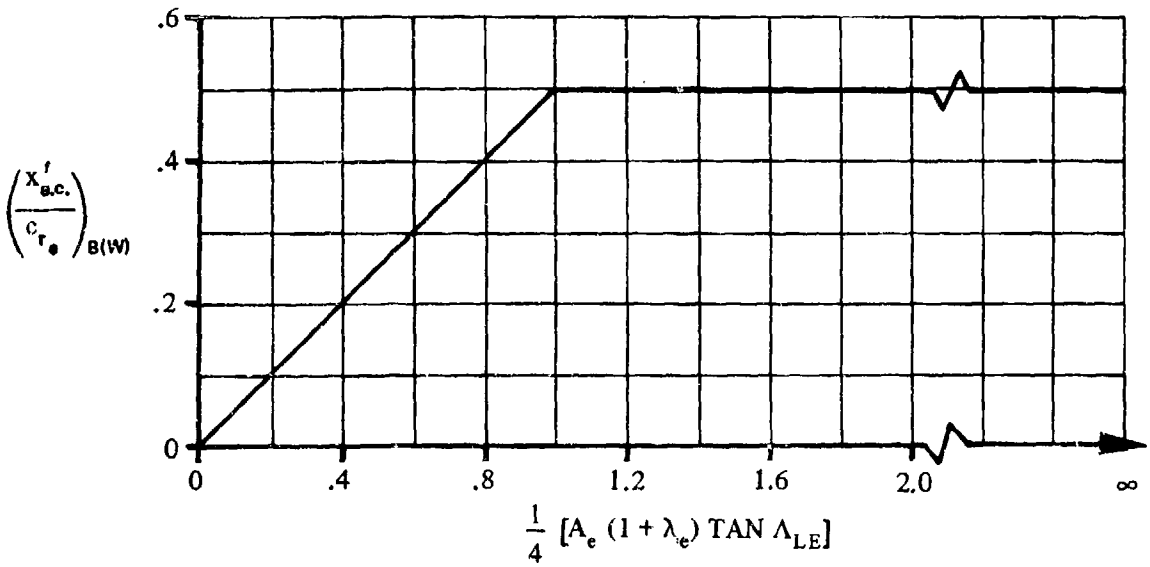

FIGURE 4.3.2.2-36b THEORETICAL AERODYNAMIC-CENTER LOCATIONS FOR βA_e =

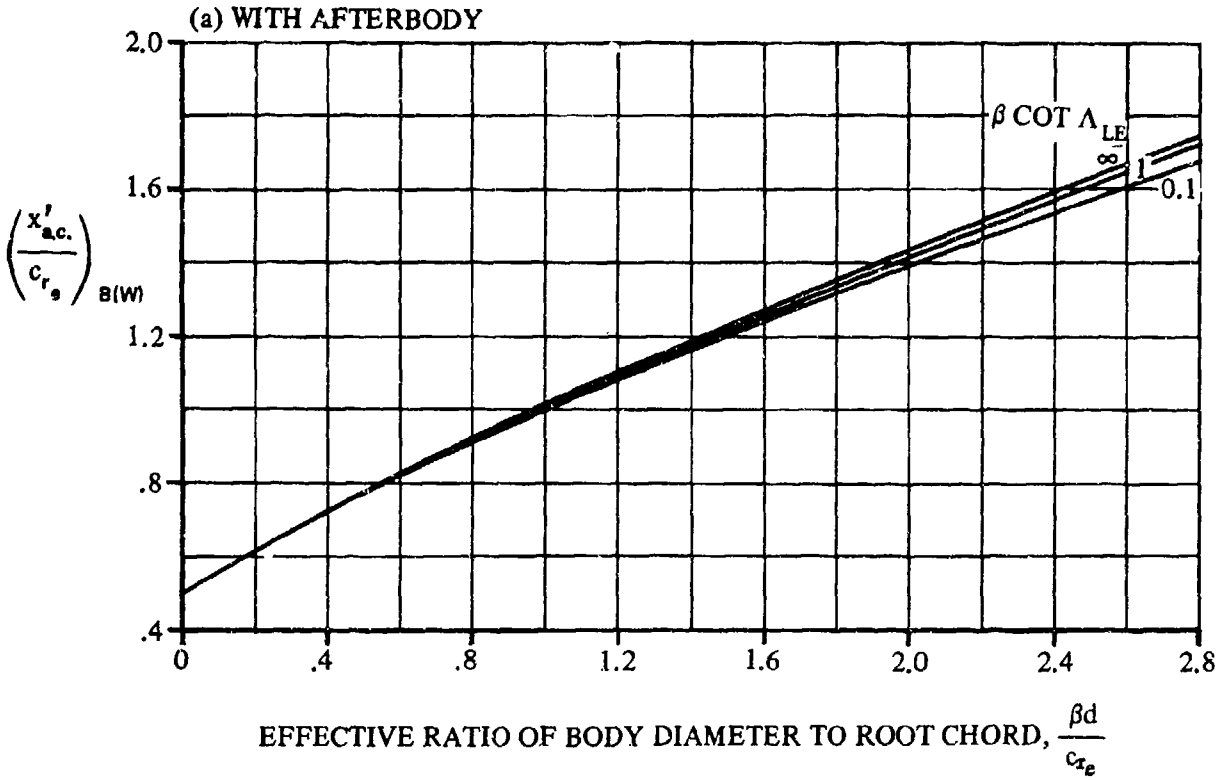

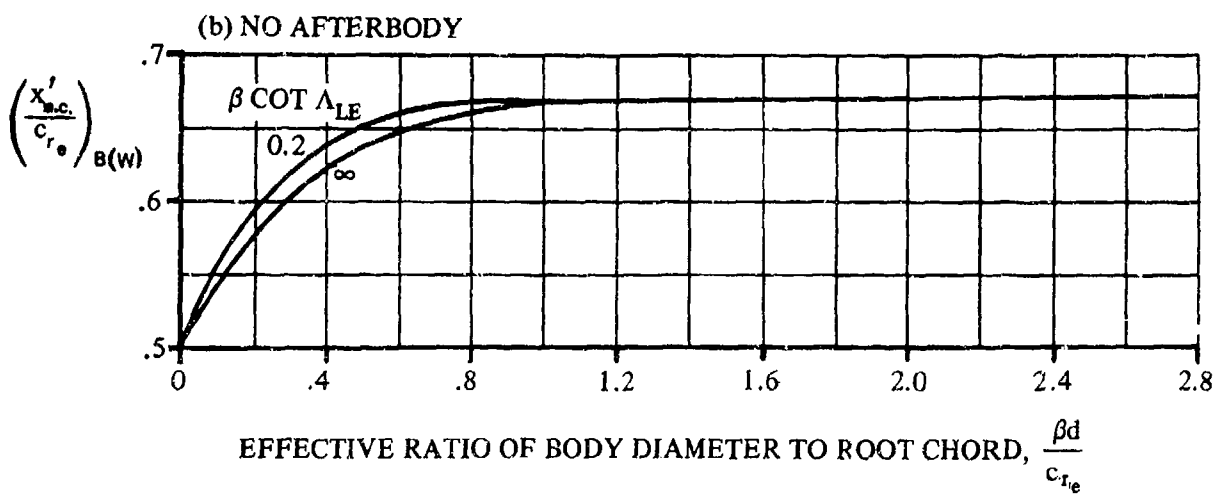

FIGURE 4.3.2.2-37 AERODYNAMIC-CENTER LOCATIONS FOR LIFT CARRYOVER OF WING ONTO BODY AT SUPERSONIC SPEEDS WHEN $\beta A_e (1 + \lambda_e) \left(1 + \frac{1}{\beta \text{ COT } \Lambda_{LE}}\right) \geq 4.0$

4.3.3 WING-BODY DRAG

4.3.3.1 WING-BODY ZERO-LIFT DRAG

The problem of estimating the zero-lift drag of a wing-body combination is one of properly accounting for the mutual interferences that exist between its components. There are two principal approaches to the problem. One attempts to isolate the individual interferences, and the other combines the drag of components with the interference drag and analyzes the total configuration. The Datcom method for subsonic speeds consists of applying an interference correction factor to the skin-friction and pressure-drag contributions of the exposed components. The method presented for transonic speeds treats the configuration as a unit by simply adding the drag contributions of the gross components. At supersonic speeds the wing-body zero-lift drag is obtained by summing the drag contributions of the exposed wing and the isolated body. The methods presented for the subsonic-, transonic-, and supersonic-speed regimes are for a fully turbulent boundary layer over the body and the wing.

A. SUBSONIC

Subsonic wing-body interference is caused by several phenomena, of which two are especially important. First, the wing and body produce supervelocities due to thickness that increase the skin friction in the vicinity of the wing-body junction. Second, the confluence of boundary layers at the junction can cause premature boundary-layer separation, which, however, can sometimes be prevented or at least postponed by proper fillet design. It has not been possible to establish a general method for estimating interference drag. Although the Datcom method uses interference correction factors based on experimental results for wing-body combinations, it should be pointed out that most of the bodies were conventional, ogive-cylinder combinations of high fineness ratio, and no detailed investigation has been made to evaluate body effects. Therefore, the method should not be construed as pertaining to generalized wing-body combinations with arbitrary body shapes.

The Datcom method is that of reference 1 and is applicable to wing-body configurations consisting of a body of revolution in combination with the following two classes of wing planforms:

Straight-Tapered Wings (conventional, trapezoidal planforms)

Non-Straight-Tapered Wings

- Double-delta wings
- Cranked wings
- Curved (Gothic and ogee) wings

DATCOM METHOD

The subsonic zero-lift drag coefficient of a wing-body combination, based on the reference area, is determined by adding the drag coefficients of the exposed components and applying an interference correction factor to the skin-friction and pressure-drag contributions. The component contributions of the wing and body are determined by the methods of Sections 4.1.5.1 and 4.2.3.1, respectively. This approach is summarized by

$$\left(C_{D_0}\right)_{WB} = \left\{ C_{f_W} \left[1 + L\left(\frac{t}{c}\right) + 100\left(\frac{t}{c}\right)^4 \right] R_{L.S.} \frac{(S_{wet})_e}{S_{ref}} + C_{f_B} \left[1 + \frac{60}{(\ell_B/d)^3} + 0.0025\frac{\ell_B}{d} \right] \frac{(S_B)_e}{S_{ref}} \right\} R_{WB} + C_{D_b} \frac{S_B}{S_{ref}} \qquad 4.3.3.1\text{-a}$$

where

C_{f_W} is the turbulent flat-plate skin-friction coefficient of the wing (or wing panel in the case of composite wings), including roughness effects, as a function of Mach number and the Reynolds number based on the reference length ℓ. This value is determined as discussed in paragraph A of Section 4.1.5.1. The reference length ℓ is the mean aerodynamic chord $\bar{c}_e$ of the exposed wing (or exposed wing panels in the case of composite wings).

C_{f_B} is the turbulent flat-plate skin-friction coefficient of the body, including roughness effects, as a function of Mach number and the Reynolds number based on the reference length ℓ. This value is determined as discussed in paragraph A of Section 4.1.5.1. The reference length ℓ is the actual body length ℓ_B.

$(S_{wet})_e$ is the wetted area of the exposed wing (or exposed wing panels in the case of composite wings).

$(S_S)_e$ is the exposed wetted area of the body (the wetted area of the isolated body minus the surface area covered by the wing at the wing-body juncture).

S_{ref} is the reference area.

R_{WB} is the wing-body interference correlation factor obtained from figure 4.3.3.1-37 as a function of Mach number and the fuselage Reynolds number based on the actual body length ℓ_B.

The remaining parameters in equation 4.3.3.1-a are presented in either Section 4.1.5.1 or Section 4.2.3.1.

In treating non-straight-tapered wings the wing zero-lift drag contribution is obtained for the exposed inboard and the outboard panels separately (based on the reference area) and then added. Curved planforms are approximated by combinations of trapezoidal panels, in which case two such panels are usually sufficient to give a satisfactory result. An ogee planform has been chosen for the sample problem to illustrate how the method is applied to curved planforms, as well as to show the general application of the method to double-delta and cranked planforms.

Non-straight-tapered wing geometric parameters are presented in Section 2.2.2.

The wing-body interference correlation factor R_{WB} was developed in reference 1 by determining the ratio of test values of C_{D_0} to values predicted on the basis of $R_{WB} = 1.0$ for several wing-body combinations. Both conventional, trapezoidal planforms and composite planforms have been used in the correlation; however, most of the bodies were conventional ogive-cylinders of high fineness ratio. Composite planform data are limited to values of fuselage Reynolds number below 2.4×10^7. The curves for values of $R_{\ell_{fus}} > 2.4 \times 10^7$ were generated using the basic prediction method of reference 2, which has been correlated with flight-test data. It should also be noted that the correlation does not include data below $M = 0.25$.

A comparison of test data for 15 configurations with $\left(C_{D_0}\right)_{WB}$ calculated by this method is presented as table 4.3.3.1-A (taken from reference 1). The results are indicative of the accuracy that can be expected when applying the method to configurations with $R_{\ell_{fus}} \leq 2.4 \times 10^7$. The validity of the method for configurations with non-straight-tapered wings has not been verified above $R_{\ell_{fus}} > 2.4 \times 10^7$; however, the accuracy of the basic prediction method as applied to configurations consisting of conventional, trapezoidal wings mounted on ogive-cylinders of high fineness ratio indicates that accuracy to within ±10 percent can be expected. It should be noted that the test values in table 4.3.3.1-A have been corrected to remove base drag and that the calculated values do not include the base-drag term of equation 4.3.3.1-a.

Sample Problem

Given: A wing-body configuration of reference 14. The ogee planform is approximated by a double-delta planform with a streamwise tip. The inboard and outboard panels of the double-delta wing have been selected to have leading and trailing edges which closely approximate the sweeps of the curved edges. The sweeps of the maximum thickness lines of the inboard and outboard panels closely approximate the sweep of the maximum thickness line of the ogee planform within the boundaries of each panel.

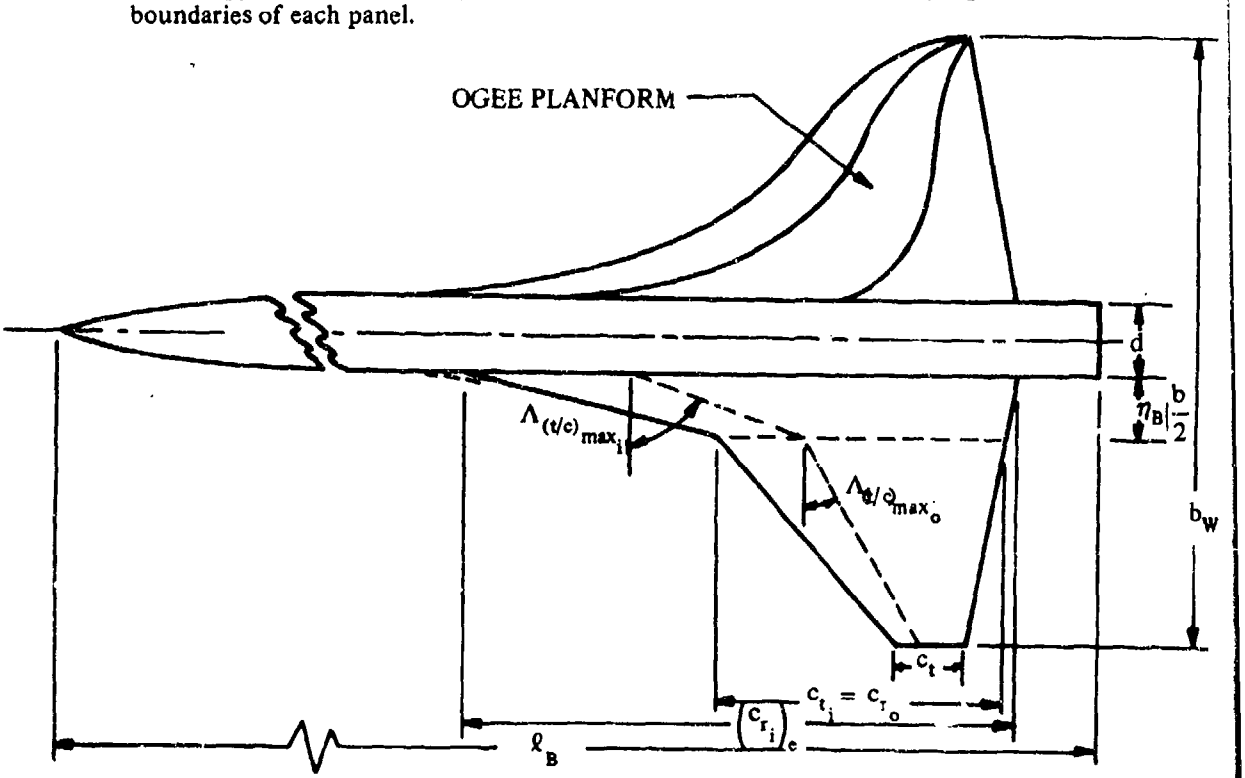

SKETCH (a)

Ogee Planform:

$S_W = S_{ref} = 21.75$ sq in. $\quad S_{W_e} = 16.57$ sq in. $\quad t/c = 0.02$

Airfoil section: Hexagonal with ridge lines at 0.30c and 0.70c (x_t @ 0.30c)

Body:

Ogive-cylinder $\quad \ell_B = 14.216$ in. $\quad d = 0.875$ in. $\quad f_{fus} = 16.25$

$(S_S)_e = 33.70$ sq in. (fuselage area covered by wing at wing-body juncture is removed from isolated body wetted area).

$\frac{(S_S)_e}{S_{ref}} = 1.550 \quad \frac{d_b}{d} = 1.0 \quad \frac{S_B}{S_{ref}} = 0.0276 \quad \frac{(S_S)_e}{S_B} = 56.04$

Double-Delta Approximation:

Inboard panel:

$(S_i)_e$ = 7.21 sq in. $\left(S_{wet_i}\right)_e$ = 14.42 sq in. $\left(S_{wet_i}\right)_e / S_{ref}$ = 0.663

$(\bar{c}_i)_e$ = 5.11 in. $\Lambda_{(t/c)_{max_i}} = 70^o$ $(t/c)_i$ = 0.02

Outboard panel:

$(S_o)_e$ = 9.67 sq in. $\left(S_{wet_o}\right)_e$ = 19.34 sq in. $\left(S_{wet_o}\right)_e / S_{ref}$ = 0.889

$(\bar{c}_o)_e$ = 2.375 in. $\Lambda_{(t/c)_{max_o}} = 31^o$ $(t/c)_o$ = 0.02

Additional Characteristics:

M = 0.70 R_ℓ = 2.5×10^6 per ft

Polished metal surface (assume k = 0.03×10^{-3} in.)

Compute:

Determine C_f for each component (Section 4.1.5.1)

Body

$R_\ell = (2.50 \times 10^6)(\ell_B) = (2.5 \times 10^6)(14.216/12) = 2.96 \times 10^6$

$\ell/k = 14.216/(.03 \times 10^{-3}) = 4.74 \times 10^5$; cutoff $R_\ell \simeq 4.5 \times 10^7$ (figure 4.1.5.1-27)

Since cutoff R_ℓ > calculated R_ℓ, read C_{f_B} at calculated R_ℓ.

C_{f_B} = 0.00354 (figure 4.1.5.1-26)

Inboard Panel

$R_\ell = (2.5 \times 10^6)(\bar{c}_i)_e = (2.5 \times 10^6)(5.11/12) = 1.065 \times 10^6$

$\ell/k = 5.11/(.03 \times 10^{-3}) = 1.70 \times 10^5$; cutoff $R_\ell \simeq 1.4 \times 10^7$ (figure 4.1.5.1-27)

Since cutoff $R_\ell \simeq$ calculated R_ℓ, read $\left(C_{f_W}\right)_i$ at calculated R_ℓ.

$\left(C_{f_W}\right)_i$ = 0.00425 (figure 4.1.5.1-26)

Outboard Panel

$R_\ell = (2.5 \times 10^6)(\bar{c}_o)_e = (2.5 \times 10^6)(2.375/12) = 4.95 \times 10^5$

$\ell/k = 2.375/(.03 \times 10^{-3}) = 7.92 \times 10^4$; cutoff $R_\ell \simeq 6.5 \times 10^6$ (figure 4.1.5.1-27)

Since cutoff R_ℓ > calculated R_ℓ, read $\left(C_{f_W}\right)_o$ at calculated R_ℓ.

$\left(C_{f_W}\right)_o = 0.00488$ (figure 4.1.5.1-26)

Determine the zero-lift drag contribution of the exposed inboard and outboard panels (Section 4.1.5.1).

Inboard panel

$\left[1 + L\left(\frac{t}{c}\right) + 100\left(\frac{t}{c}\right)^4\right] = 1.021$ (figure 4.1.5.1-28a, for L = 1.2)

$\cos \Lambda_{(t/c)_{max_i}} = \cos 70^o = 0.342$

$(R_{L.S.})_i = 1.055$ (figure 4.1.5.1-28b, interpolated using dashed lines)

$$\left(C_{D_0}\right)_i = \left(C_{f_W}\right)_i \left[1 + L\left(\frac{t}{c}\right) + 100\left(\frac{t}{c}\right)^4\right] R_{L.S.} \frac{\left(S_{wet_i}\right)_e}{S_{ref}} = (0.00425)(1.021)(1.055)(0.663)$$

$= 0.003035$ (based on S_{ref})

Outboard panel

$\left[1 + L\left(\frac{t}{c}\right) + 100\left(\frac{t}{c}\right)^4\right] = 1.021$ (figure 4.1.5.1-28a, for L = 1.2)

$\cos \Lambda_{(t/c)_{max_o}} = \cos 31^o = 0.8572$

$(R_{L.S.})_o = 1.180$ (figure 4.1.5.1-28b, interpolated using solid lines)

$$\left(C_{D_0}\right)_o = \left(C_{f_W}\right)_o \left[1 + L\left(\frac{t}{c}\right) + 100\left(\frac{t}{c}\right)^4\right] R_{L.S.} \frac{\left(S_{wet_o}\right)_e}{S_{ref}}$$

$= (0.00488)(1.021)(1.180)(0.889) = 0.00523$ (based on S_{ref})

Determine the zero-lift drag contribution of the isolated body (Section 4.2.3.1)

Zero-lift drag exclusive of base drag

$$\left[1 + \frac{60}{(\ell_B/d)^3} + 0.0025\,\frac{\ell_B}{d}\right] = 1.054$$

$$C_{f_B}\left[1 + \frac{60}{(\ell_B/d)^3} + 0.0025\frac{\ell_B}{d}\right]\frac{(S_S)_e}{S_{ref}} = (0.00354)\,(1.054)\,(1.550) = 0.00578 \text{ (based on } S_{ref})$$

Base-drag coefficient

$$C_{D_b} = 0.029\left(\frac{d_b}{d}\right)^3 \Big/ \sqrt{\left(C_{D_f}\right)_b} \quad \text{(equation 4.2.3.1-b)}$$

where $\left(C_{D_f}\right)_b$ is the zero-lift drag coefficient exclusive of the base drag,

based on body base area; i.e.,

$$\left(C_{D_f}\right)_b = C_{f_B}\left[1 + \frac{60}{(\ell_B/d)^3} + 0.0025\,\frac{\ell_B}{d}\right]\frac{(S_S)_e}{S_B}$$

$$= (0.00354)\,(1.054)\,(56.04) = 0.209$$

$$C_{D_b} = (0.029)\,(1.0)^3 / \sqrt{0.209} = 0.0634 \quad \text{(based on } S_B)$$

Determine the wing-body correlation factor R_{WB}

$$R_{WB} = 0.955 \quad \text{(figure 4.3.3.1-37)}$$

Solution:

$$\left(C_{D_0}\right)_{WB} = \left\{C_{f_W}\left[1 + L\left(\frac{t}{c}\right) + 100\left(\frac{t}{c}\right)^4\right] R_{L.S.}\frac{(S_{wet})_e}{S_{ref}} + C_{f_B}\left[1 + \frac{60}{(\ell_B/d)^3} + 0.0025\,\frac{\ell_B}{d}\right]\frac{(S_S)_e}{S_{ref}}\right\} R_{WB}$$

$$+ C_{D_b}\,\frac{S_B}{S_{ref}} \quad \text{(equation 4.3.3.1-a)}$$

$$= \left\{\left[(0.003035) + (0.00523)\right] + (0.00578)\right\}(0.955) + (0.0634)\,(0.0276)$$

$$= 0.0152 \text{ (based on } S_{ref})$$

The test value from reference 14, corrected to remove base drag, is 0.0131. The corresponding calculated value is 0.0152 - 0.00175 = 0.01345

B. TRANSONIC

Interference effects in the transonic range are generally greater than those in the subsonic region, because of the higher local velocities of the individual components and the greater propagation of these perturbations from their source. There often exist large supersonic regions that contribute substantially to the wave drag Many theoretical attempts have been made to correlate these effects in the transonic range, but until the advent of the area-rule concept, none of them proved very satisfactory.

The area-rule method is based on supersonic linear theory, which assumes that pressure disturbances are propagated in the direction of the Mach lines and do not diminish with distance. If it is assumed that these concepts can be applied in a limiting case at a Mach number of one, where Mach lines are normal to the flow direction, it can also be assumed that at large distances from the body the disturbances are independent of the arrangement of the components and only a function of the cross-sectional-area distribution. This means that the drag of a wing-body combination can be calculated as though the combination were a body of revolution with equivalent-area cross sections.

In addition to affording a means of estimating drag by calculation or by testing a simplified model (body of revolution) in the transonic range, the area rule is extremely useful as a design tool, since it indicates the most desirable way to arrange the vehicle components for minimum wave drag. The most common example of this is to indent, or "coke-bottle," a fuselage enough to permit the wing to be added without a marked increase in the over-all area distribution. As is obvious from the body-of-revolution wave-drag curves, it is always desirable from the wave-drag point of view to have a body of as high a fineness ratio as possible. However, it should be remembered that "coke-bottling" should be used judiciously, to avoid undesirable local effects.

The linear-theory wave drag of a smooth, pointed, closed body of revolution was first given by von Kármán (reference 3) as

$$C_D = \frac{1}{2\pi S_{ref}} \int_0^{\ell_B} \int_0^{\ell_B} \frac{d^2S}{dx^2} \frac{d^2S}{d\xi^2} \ell n (x - \xi) \, dx d\xi \qquad 4.3.3.1\text{-b}$$

where

ℓ_B is the body length.

x is any point on the longitudinal axis; $x = 0$ at the nose and $x = \ell_B$ at the aft end.

ξ is any point on the longitudinal axis; $\xi = 0$ at the nose and $\xi = \ell_B$ at the aft end (not necessarily the same point as x).

S is the cross-sectional area of the body at any point x.

$\frac{d^2S}{dx^2}$ and $\frac{d^2S}{d\xi^2}$ are obtained from the area distribution determined in step 1 of paragraph C below.

S_{ref} is the reference area, usually the total wing area.

This equation is subject to the conditions:

1. $\left(\frac{dS}{dx}\right)_{x=0} = \left(\frac{dS}{dx}\right)_{x=\ell_B} = 0$

2. The body is slender, in accordance with the usual slender-body restrictions (reference 3).

3. No discontinuities in dS/dx occur anywhere along the body.

Additional terms have been derived that account for the condition $(dS/dx)_{x=\ell_B} \neq 0$ and for finite discontinuities in dS/dx along the body. References 3, 4, 5, and 6 pertain to these conditions.

References 7 and 8 contain numerical methods of evaluating equation 4.3.3.1-b. However, the solution of this equation by hand is tedious, and automatic computing equipment is invariably used. The preparation of the area-distribution plot for a given configuration is usually performed manually.

The accuracy of this method varies with the smoothness and fineness ratio of the equivalent body. Studies of the accuracy of the area rule are given in references 8, 9, 10, and 11.

The Datcom method is at best approximate and consists of simply adding the zero-lift drag coefficients of the individual isolated components. Since the exposed wetted area of a wing-body combination is less than the sum of the wing-alone and body-alone wetted areas, this amounts to adding an increment to the wing-body drag of the combination to account for interference effects.

The interference drag is usually positive for configurations not specifically contoured to reduce this drag component. However, for area-ruled configurations, this interference drag can become negative.

The Datcom method is applicable only to configurations with conventional, trapezoidal wings.

DATCOM METHOD

At the present it is recommended that the transonic zero-lift drag coefficient of a wing-body combination be approximated by adding the drag coefficients based on the total wetted area of each individual component and referred to a common reference area. This approach is summarized by

$$\left(C_{D_0}\right)_{WB} = \left(C_{D_0}\right)_W + \left(C_{D_0}\right)_B \frac{S_B}{S_{ref}} \qquad 4.3.3.1\text{-c}$$

where

$\left(C_{D_0}\right)_W$ is the zero-lift drag coefficient of the wing, based on the reference area, obtained from paragraph B of Section 4.1.5.1; i.e.,

$$\left(C_{D_0}\right)_W = \left(C_{D_f} + C_{D_w}\right)_W \quad \text{(equation 4.1.5.1-g)}$$

$\left(C_{D_0}\right)_B$ is the zero-lift drag coefficient of the body, based on body base area, obtained from paragraph B of Section 4.2.3.1; i.e.,

$$\left(C_{D_0}\right)_B = \left(C_{D_f}\right)_B + C_{D_P} + C_{D_b} + \left(C_{D_w}\right)_B \quad \text{(equation 4.2.3.1-e)}$$

S_B/S_{ref} is the ratio of the body base area to the reference area.

Sample Problem

Given: The swept-wing cylindrical-body configuration of reference 19.

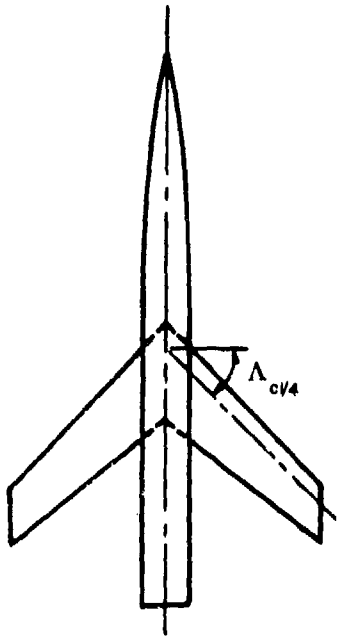

Body Characteristics:

Ogive-cylinder $\ell_B = 43.0$ in. $d_{max} = d_b = 3.75$ in.

$\ell_B/d = 11.47$ $S_B = 11.05$ sq in. $\frac{S_S}{S_B} = 40.19$

Wing Characteristics:

$A = 4.0$ $\Lambda_{c/4} = 45^o$ $\lambda = 0.60$ $\bar{c} = 6.125$ in.

$S_W = S_{ref} = 144$ sq in. $S_{wet} = 288$ sq in.

NACA 65A006 airfoil (x_t @ 0.50c) $t/c = 0.06$

Additional Characteristics:

$R_{\ell_{M=0.6}} = 2.50 \times 10^5$ per in. $0.80 \le M \le 1.2$

Polished metal surface (assume $k = 0.03 \times 10^{-3}$ in.)

Compute:

The final calculations are presented in table form on page 4.3.3.1-13. Many of the quantities listed below appear as columns in the table.

Wing zero-lift drag coefficient $\left(C_{D_0}\right)_W$ (Section 4.1.5.1)

Determine the skin-friction drag coefficient.

$R_\ell = (2.50 \times 10^5)(\bar{c}) = (2.50 \times 10^5)(6.125) = 1.53 \times 10^6$

$\ell/k = 6.125/(0.03 \times 10^{-3}) = 2.04 \times 10^5$; cutoff $R_{\ell_{M=0.6}} \simeq 1.6 \times 10^7$ (figure 4.1.5.1-27)

Since cutoff $R_\ell >$ calculated R_ℓ, read $(C_f)_W$ at calculated R_ℓ.

$(C_f)_W = 0.0040$ (figure 4.1.5.1-26 @ M = 0.60)

$$\left(C_{D_f}\right)_W = (C_f)_W \left[1 + L\left(\frac{t}{c}\right)\right] \frac{S_{wet}}{S_{ref}}$$ (equation 4.1.5.1-c)

$$= (0.0040)\,[1 + 1.2(0.06)]\,\frac{288}{144}$$ ($L = 1.2$ for $x_t > 0.30c$) $= 0.00858$

Determine and construct the variation of $\left(C_{D_w}\right)_W$ with Mach number for an unswept wing.

$$A\left(\frac{t}{c}\right)^{1/3} = (4.0)(0.392) = 1.568$$

① M	② $\frac{\sqrt{\lvert M^2-1\rvert}}{(t/c)^{1/3}}$	③ $\frac{\left(C_{D_w}\right)_W}{(t/c)^{5/3}}$ fig 4.1.5.1-29	④ $\left(C_{D_w}\right)_W$ ③ (0.0092)
0.80	1.53	0	0
0.85	1.34	0.10	0.0009
0.90	1.11	0.58	0.0053
0.95	0.80	1.95	0.0179
1.00	0	3.02	0.0278
1.025	0.57	3.08	0.0283
1.05	0.82	3.10	0.0285
1.10	1.17	3.12	0.0287
1.15	1.45	3.13	0.0288

Plot $\left(C_{D_w}\right)_W$ vs M for the unswept wing (sketch (a))

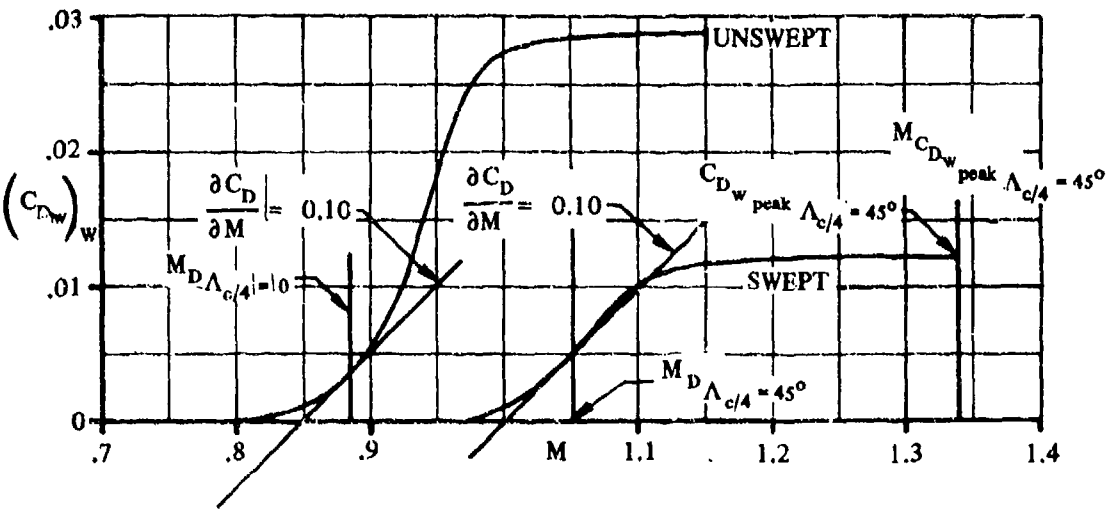

SKETCH (a)

Read the following values from the curve of $\left(C_{D_w}\right)_W$ vs M for the unswept wing:

$$M_{D_{\Lambda_{c/4}=0}} = 0.885$$

$$C_{D_{w_{peak}\Lambda_{c/4}=0}} = 0.0288$$

$$M_{C_{D_{w_{peak}}\Lambda_{c/4}=0}} = 1.125$$

Apply sweep corrections:

$$M_{D_{\Lambda_{c/4}=45^o}} = \frac{M_{D_{\Lambda_{c/4}=0}}}{(\cos 45^o)^{1/2}} = 1.05 \quad \text{(equation 4.1.5.1-d)}$$

$$C_{D_{w_{peak}\Lambda_{c/4}=45^o}} = C_{D_{w_{peak}\Lambda_{c/4}=0}} (\cos 45^o)^{2.5} = 0.0121 \quad \text{(equation 4.1.5.1-e)}$$

$$M_{C_{D_{w_{peak}\Lambda_{c/4}=45^o}}} = \frac{M_{C_{D_{w_{peak}\Lambda_{c/4}=0}}}}{(\cos 45^o)^{1/2}} = 1.34 \quad \text{(equation 4.1.5.1-f)}$$

Construct the curve of $\left(C_{D_w}\right)_W$ vs M for the swept wing using the straight-wing curve to aid in fairing (see sketch (a)). List the swept-wing values in column (3) of the calculation table on page 4.3.3.1-13.

The wing zero-lift drag coefficient is tabulated in column (4) of the calculation table on page 4.3.3.1-13 as

$$\left(C_{D_0}\right)_W = \left(C_{D_f} + C_{D_w}\right)_W \quad \text{(equation 4.1.5.1-g)}$$

Body zero-lift drag coefficient $\left(C_{D_0}\right)_B$ (Section 4.2.3.1)

Determine the skin-friction drag coefficient.

$$R_\ell = (2.50 \times 10^5)(\ell_B) = (2.50 \times 10^5)(43.0) = 1.075 \times 10^7$$

$$\ell/k = 43.0/(0.03 \times 10^{-3}) = 1.433 \times 10^6; \text{ cutoff } R_{\ell_{M=0.6}} \approx 1.3 \times 10^8 \quad \text{(figure 4.1.5.1-27)}$$

Since cutoff R_ℓ > calculated R_ℓ, read $(C_f)_B$ at calculated R_ℓ.

$(C_f)_B = 0.00288$ (figure 4.1.5.1-26 @ M = 0.60)

$$\left(C_{D_f}\right)_B = (C_f)_B \frac{S_S}{S_B} \quad \text{(equation 4.2.3.1-c)}$$

$$= (0.00288)(40.19) = 0.1157$$

Determine the pressure-drag coefficient.

$$C_{D_P} = (C_f)_{B_{M=0.6}} \left[\frac{60}{(\ell_B/d)^3} + 0.0025 \frac{\ell_B}{d} \right] \frac{S_S}{S_B} \quad \text{(equation 4.2.3.1-d)}$$

$$= 0.00288 \left[\frac{60}{(11.47)^3} + 0.0025\,(11.47) \right] 40.19$$

$$= 0.00792 \text{ (based on } S_B)$$

This value of C_{D_P} is taken to be constant for $0 < M < 1.0$, then reduced linearly to zero at M = 1.2 (see column (6) of calculation table, page 4.3.3.1-13).

Determine the base-drag coefficient.

$$C_{D_b} = 0.029 \left(\frac{d_b}{d}\right)^3 \Big/ \sqrt{\left(C_{D_f}\right)_b} \quad \text{(equation 4.2.3.1-b)}$$

$$\left(C_{D_f}\right)_b = (C_f)_{B_{M=0.6}} \left[1 + \frac{60}{(\ell_B/d)^3} + 0.0025 \frac{\ell_B}{d} \right] \frac{S_S}{S_B} \quad \text{(first term, eq. 4.2.3.1-a)}$$

$$= (C_f)_{B_{M=0.6}} \frac{S_S}{S_B} + C_{D_P} = (0.00288)(40.19) + 0.00792$$

$$= 0.124$$

$$C_{D_b} = (0.029)(1.0)^3 / \sqrt{0.124} = 0.0824 \text{ (at M = 0.6)}$$

$$\left[\frac{C_{D_b}}{\left(\frac{d_b}{d}\right)^2} \right]_{M=0.6} = \frac{0.0824}{(1)^2} = 0.0824$$

With this value and by using the curves of figure 4.2.3.1-24 as guide lines, obtain values of $C_{D_b}/(d_b/d)^2$ for $0.8 < M < 1.2$.

Then $C_{D_b} = \left[C_{D_b}/(d_b/d)^2\right]_{M=0.6}(d_b/d)^2$ (see column ⑦ of calculation table, page 4.3.3.1-13).

Determine the drag-divergence Mach number.

$M_D = 0.98$ (figure 4.2.3.1-25)

Determine the wave-drag coefficient.

The wave-drag coefficient as a f(M) is obtained from figure 4.2.3.1-26 (see column ⑧ of the calculation table, page 4.3.3.1-13).

The body zero-lift drag coefficient is tabulated in column ⑨ of the calculation table on page 4.3.3.1-13 as

$$\left(C_{D_0}\right)_B = \left(C_{D_f}\right)_B + C_{D_P} + C_{D_b} + \left(C_{D_w}\right)_B \quad \text{(equation 4.2.3.1-e)}$$

Solution:

$$\left(C_{D_0}\right)_{WB} = \left(C_{D_0}\right)_W + \left(C_{D_0}\right)_B \frac{S_B}{S_{ref}} \quad \text{(equation 4.3.3.1-c)}$$

$$= \left(C_{D_f} + C_{D_w}\right)_W + \left(C_{D_f} + C_{D_P} + C_{D_b} + C_{D_w}\right)_B \frac{S_B}{S_{ref}}$$

Zero-Lift Drag-Coefficient Calculation Table

	Wing C_{D_0}			Body C_{D_0}						
①	②	③	④	⑤	⑥	⑦	⑧	⑨	⑩	⑪
M	$\left(C_{D_f}\right)_W$ eq. 4.1.5.1-c	$\left(C_{D_w}\right)_W$ sketch (a)	$\left(C_{D_0}\right)_W$ eq. 4.1.5.1-e ② + ③	$\left(C_{D_f}\right)_B$ eq. 4.2.3.1-c	C_{D_P} eq. 4.2.3.1-d	C_{D_b} fig. 4.2.3.1-24	$\left(C_{D_w}\right)_B$ fig. 4.2.3.1-26	$\left(C_{D_0}\right)_B$ eq. 4.2.3.1-e ⑤ + ⑥ + ⑦ + ⑧	$\left(C_{D_0}\right)_B S_B/S_{ref}$ ⑨ S_B/S_{ref}	$\left(C_{D_0}\right)_{WB}$ eq. 4.3.3.1-c ④ + ⑩
0,80	0,00858	...	0,00858	0,1157	0,00792	0,083	...	0,2066	0,01586	0,0244
0,90		...	0,00858		0,00792	0,096	...	0,2188	0,01677	0,0254
0,95		...	0,00858		0,00792	0,112	...	0,2356	0,01808	0,0267
1,00		0,0010	0,00868		0,00792	0,160	0,031	0,3146	0,02414	0,0337
1,025		0,0026	0,01108		0,00893	0,163	0,046	0,3316	0,02544	0,0366
1,05		0,00475	0,01333		0,00894	0,1026	0,054	0,2781	0,02134	0,0347
1,10		0,0101	0,01868		0,00386	0,077	0,061	0,2677	0,01977	0,0395
1,20		0,0121	0,02068		0	0,081	0,064	0,2407	0,01847	0,0382

The calculated values of the wing-body zero-lift drag coefficient are compared with modified test results from reference 19 in sketch (b). The drag-divergence Mach number of the isolated body has been used to aid in fairing the curve through the calculated points. The test results presented in reference 19 were corrected to a condition at which the base pressure is equal to the stream static pressure. The test points plotted on sketch (b) have been modified by addition of the calculated base-drag coefficient.

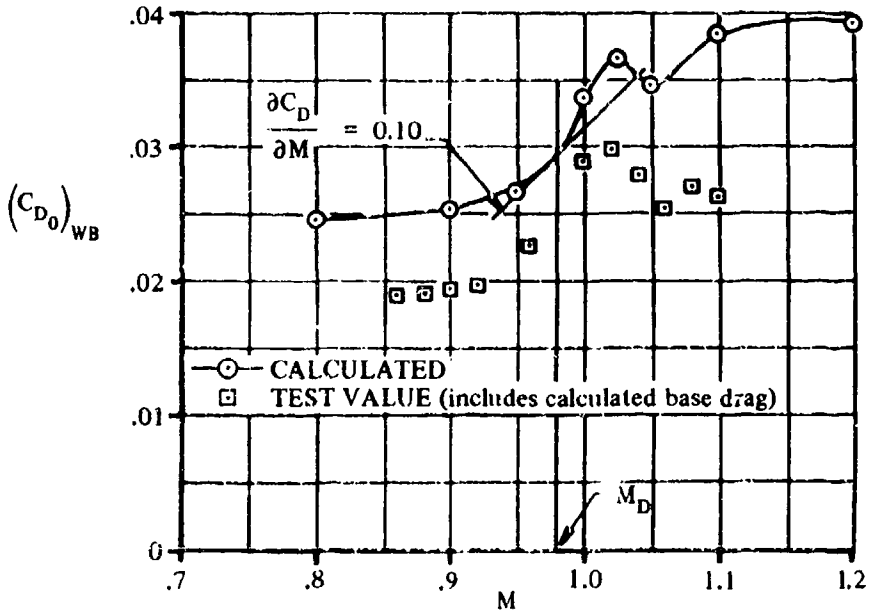

SKETCH (b)

C. SUPERSONIC

The estimation of wing-body drag at supersonic speeds also involves the calculation of interference effects. It is possible by using linear or higher-order theories to calculate some of these effects. However, the calculations require considerable effort and must be tailored carefully to the geometry of the configuration. The equivalent-body technique discussed in paragraph B above has been adapted to supersonic speeds, but with considerable complication. The resulting method, termed the "supersonic area-rule," gives the wave drag, including aerodynamic interferences, at a given Mach number.

Application of the supersonic area-rule requires automatic computing equipment. If such a computer is to be used, the following steps are required to prepare the machine input information and to interpret the computed drag values obtained.

Step 1. At a series of longitudinal stations compute the cross-sectional area intercepted by planes inclined at the angle $\mu = \sin^{-1}(1/M)$ to the x-axis (see sketch (c)). The areas so determined at each station are then projected on the plane normal to the longitudinal axis. The values of these projected areas are plotted at the intersection of the inclined plane and the longitudinal axis. This plot is the area distribution of the equivalent body of revolution.

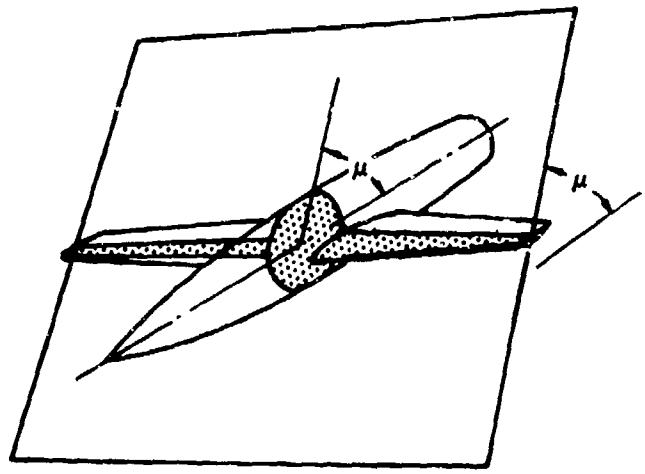

SKETCH (c)

This step can be simplified by using the following graphical procedure. First, construct cross sections normal to the longitudinal axis at an evenly-spaced number of longitudinal stations, say, spaced at Δx. Prepare a set of parallel lines on transparent paper with a spacing equal to $\Delta x \tan \mu$. Each one of these lines corresponds to one of the downstream stations intercepted by the inclined plane. The required projected cross section at a given station x is then determined by overlaying the transparent paper on the given normal cross sections and plotting the intersection of each of the parallel lines with its corresponding given normal-cross-section contour. The curve formed on the transparent paper by connecting the above intersections encloses the required projected area that when integrated is to be plotted at station x. This procedure is illustrated in sketch (d).

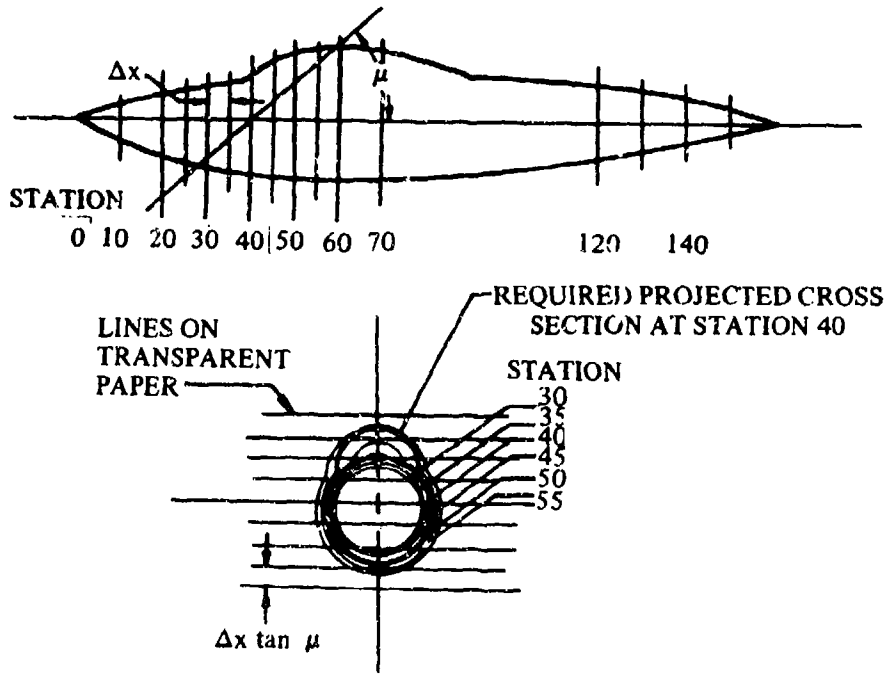

SKETCH (d)

Step 2. The procedure of step 1 is repeated for additional cases, where the inclined plane is fixed and the vehicle is rolled at a specified number of roll angles, as shown in sketch (e). For a configuration with four planes of symmetry, such as a symmetrical cruciform missile, only roll angles between 0 and 45^{o} must be considered. For cruciform configurations with two planes of symmetry, roll angles between 0 and 90^{o} should be considered. If there is just one plane of symmetry, roll angles between 0 and 180^{o} need to be considered.

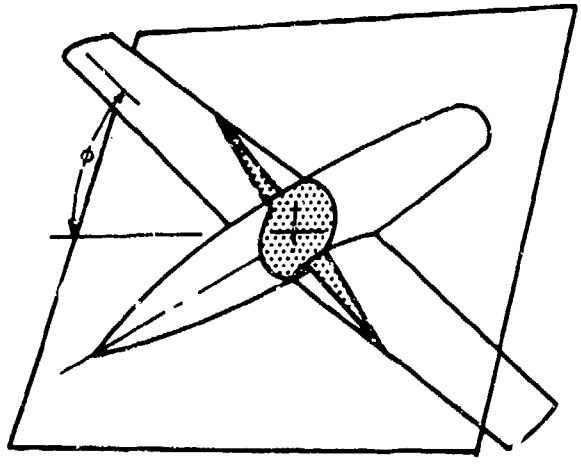

SKETCH (e)

Step 3. The drag for the equivalent body of revolution at each roll angle is then calculated by means of equation 4.3.3.1-b, or by the equation given in, for example, reference 4. These drag values are plotted as a function of roll angle and integrated to determine an average value of C_D. This average drag coefficient is taken to be the wave drag of the configuration at the chosen Mach number.

The number of roll angles required to achieve an accurate value of C_D varies with the configuration. If the C_D vs ϕ plot can be constructed without ambiguity with the number of roll angles chosen, then that number is sufficient. One should be particularly careful of conditions where the Mach angle lies along or very close to the leading edge of a wing, since this condition causes "spikes" in the C_D vs ϕ plot.

If automatic computing equipment is available, the supersonic-area-rule method should be used. Otherwise the Datcom method outlined below may be used.

The Datcom method is taken from reference 1 and is applicable to the following two classes of wing planforms:

Straight-Tapered Wings (conventional, trapezoidal planforms)

Non-Straight-Tapered Wings

- Double-delta wings
- Cranked wings
- Curved (Gothic and ogee) wings

DATCOM METHOD

The supersonic zero-lift drag coefficient of a wing-body combination, based on the reference area, is determined by adding the drag coefficients of the exposed components. The component contributions of the wing and body are determined by the methods of Sections 4.1.5.1 and 4.2.3.1, respectively. This approach is summarized by

$$\left(C_{D_0}\right)_{WB} = \left(C_{D_0}\right)_W + \left(C_{D_0}\right)_B \frac{S_B}{S_{ref}} \qquad 4.3.3.1\text{-d}$$

where

$\left(C_{D_0}\right)_W$ is the wing zero-lift drag coefficient at supersonic speeds determined as outlined below.

$\left(C_{D_0}\right)_B$ is the body zero-lift drag coefficient at supersonic speeds based on the body base area. This value is obtained from paragraph C of Section 4.2.3.1.

$\frac{S_B}{S_{ref}}$ is the ratio of the body base area to the reference area.

The method of determining the wing zero-lift drag coefficient is essentially that of paragraph C of Section 4.1.5.1, but with the parameters of the exposed wing (or wing panels in the case of composite wings) used to determine the skin-friction and wave-drag contributions. In order to present a more comprehensive method, the procedure of Section 4.1.5.1 as applied to the exposed panel(s) is fully outlined below.

The wing zero-lift drag coefficient is given by

$$\left(C_{D_0}\right)_W = \left(C_{D_f} + C_{D_w}\right)_W \qquad 4.3.3.1\text{-e}$$

where C_{D_f} and C_{D_w} are the supersonic skin-friction drag coefficient and the supersonic wave-drag coefficient, respectively, both based on a common reference area and outlined in the following paragraphs.

Skin-Friction Drag Coefficient

The supersonic skin-friction drag coefficient is given by

$$\left(C_{D_f}\right)_W = \left(C_f\right)_W \frac{\left(S_{wet}\right)_e}{S_{ref}} \qquad 4.3.3.1\text{-f}$$

for a conventional, trapezoidal planform, and

$$\left(C_{D_f}\right)_W = \left(C_{f_W}\right)_i \frac{\left(S_{wet_i}\right)_e}{S_{ref}} + \left(C_{f_W}\right)_o \frac{S_{wet_o}}{S_{ref}} \qquad 4.3.3.1\text{-g}$$

for a non-straight-tapered planform;

where

C_{f_W} is the turbulent flat-plate skin-friction coefficient of the wing (or wing panel in the case of composite wings), including roughness effects, as a function of Mach number and the Reynolds number based on the reference length ℓ. This value is determined as discussed in paragraph A of Section 4.1.5.1. The reference length ℓ is the mean aerodynamic chord $\bar{c}_e$ of the expose wing (or exposed wing panel in the case of composite wings).

$\frac{(S_{wet})_e}{S_{ref}}$ is the ratio of the wetted area of the exposed wing (or exposed wing panel in the case of composite wings) to the reference area.

The subscripts i and o refer to the inboard and outboard panels, respectively, of composite planforms.

Curved planforms are approximated by combinations of trapezoidal panels, in which case two such panels are usually sufficient to give a satisfactory result.

Non-straight-tapered wing geometric parameters are presented in Section 2.2.2.

Wave-Drag Coefficient

The form of the supersonic wave-drag-coefficient equation is in accordance with the results that have been arrived at in linear supersonic theory for the two-dimensional case. The effects of changes in wing planform and variable thickness ratio are accounted for by defining an effective thickness ratio and computing the wave-drag coefficient on a basic planform shape. A distinction is made between wings with sharp-nosed airfoil sections and wings with round-nosed airfoil sections.

Wings With Sharp-Nosed Airfoil Sections

For wings with sharp-nosed airfoil sections

$$\left(C_{D_w}\right)_W = \frac{K}{\beta}\left(\frac{t}{c}\right)^2_{eff} \frac{(S_{bw})_e}{S_{ref}} \qquad 4.3.3.1\text{-h}$$

when the leading edge of the basic wing is supersonic ($\beta \cot \Lambda_{LE_{bw}} \geq 1$), and

$$\left(C_{D_w}\right)_W = K \cot \Lambda_{LE_{bw}} \left(\frac{t}{c}\right)^2_{eff} \frac{(S_{bw})_e}{S_{ref}} \qquad 4.3.3.1\text{-i}$$

when the leading edge of the basic wing is subsonic ($\beta \cot \Lambda_{LE_{bw}} < 1$). The subscript bw refers to the basic wing (straight leading and trailing edges), and

$(S_{bw})_e$ is the area of the exposed basic wing. The selection of the basic planform for composite wings is discussed and illustrated schematically in paragraph C of Section 4.1.5.1.

$\left(\frac{t}{c}\right)_{eff}$ is the effective thickness ratio (for a conventional, trapezoidal planform, use the average thickness ratio of the exposed planform $(t/c)_{av}$). For a nonstraight-tapered planform

the effective thickness ratio is defined in terms of the basic planform and is given by

$$\left(\frac{t}{c}\right)_{eff} = \left[\frac{\int_{r_b}^{b/2}\left(\frac{t}{c}\right)^2 c_{bw}\, dy}{\int_{r_b}^{b/2} c_{bw_l}\, dy}\right]^{1/2} \qquad 4.3.3.1\text{-j}$$

where c_{bw} is the chord of the basic wing and r_b is the average radius of the body at the wing-body juncture. Note that both the chord of the actual wing and the chord of the basic wing appear in the numerator. The denominator is one-half the planform area of the exposed basic wing, so that

$$\left(\frac{t}{c}\right)_{eff} = \frac{\left[\int_{r_b}^{b/2}\left(\frac{t}{c}\right)^2 c_{bw}\, dy\right]^{1/2}}{\left[\frac{(S_{bw})_e}{2}\right]^{1/2}} \qquad 4.3.3.1\text{-j}'$$

Numerical integration of the integrand in the numerator is illustrated in the sample problem.

$\Lambda_{LE_{bw}}$ is the leading-edge sweep of the basic wing.

K is a constant factor for a given sharp-nosed airfoil section. K factors for sharp-nosed airfoils are presented in paragraph C of Section 4.1.5.1. For basic wings with variable thickness ratios the K factor is based on the airfoil section at the average chord of the exposed planform.

Wings With Round-Nosed Airfoil Sections

Wings with round-nosed airfoil sections exhibit a detached bow wave and a stagnation point, and the pressure-drag coefficient increases as a function of Mach number in a manner similar to the stagnation pressure. Consequently, a constant value of K cannot be used for basic wings with round-nosed airfoils.

The wave-drag coefficient of wings with round-nosed airfoil sections is approximated by adding the pressure drag of a blunt leading edge to the wave drag of tne basic wing with an assumed sharp leading edge. By assuming a biconvex shape aft of the leading edge, the wave drag of a wing with a round-nosed leading edge is given by

$$\left(C_{D_w}\right)_w = C_{D_{LE}} + \frac{16}{3\beta}\left(\frac{t}{c}\right)^2_{eff}\frac{(S_{bw})_e}{S_{ref}} \qquad 4.3.3.1\text{-k}$$

when the leading edge of the basic wing is supersonic ($\beta \cot \Lambda_{LE} \geq 1$), and

$$\left(C_{D_w}\right)_w = C_{D_{LE}} + \frac{16}{3}\cot \Lambda_{LE_{bw}}\left(\frac{t}{c}\right)^2_{eff}\frac{(S_{bw})_e}{S_{ref}} \qquad 4.3.3.1\text{-}\ell$$

when the leading edge of the basic wing is subsonic ($\beta \cot \Lambda_{LE_{bw}} < 1$).

The second terms on the right-hand side of equations 4.3.3.1-k and 4.3.3.1-ℓ are the wing wave-drag coefficients of the basic wing with sharp-nosed, biconvex airfoils at the appropriate leading-edge condition, and

$C_{D_{LE}}$ is the pressure-drag coefficient on a swept, cylindrical leading edge obtained as a function of the Mach number and the leading-edge sweep of the basic wing from figure 4.3.3.1-38. The term $2r_{LE_{bw}} \dfrac{b_{bw} - 2r_b}{\cos \Lambda_{LE_{bw}}}$ is the frontal area of the leading edge of the exposed planform. For basic wings with variable thickness ratios the leading-edge radius $r_{LE_{bw}}$ is the radius of the section at the average chord of the exposed planform.

The correlation of cylindrical leading-edge pressure-drag coefficients is derived in reference 12 and has been substantiated over the Mach number range from 0.5 to 8.0 and for sweep angles from 0 to 75°.

A comparison of test data for 52 configurations with $\left(C_{D_0}\right)_{WB}$ calculated by this method is presented as table 4.3.3.1-B (taken from reference 1). The test configurations consisted of conventional and composite wings with sharp-nosed airfoil sections mounted on ogive-cylinder bodies of high fineness ratio. No detailed investigation has been made to evaluate body effects; therefore, the method should not be construed as pertaining to generalized wing-body combinations with arbitrary body shapes.

Within the limitations of the body shapes investigated, the method shows good agreement with the test results of reference 15. This can be attributed largely to low-thickness-ratio airfoils and small planform modifications – the conditions for which the wing-wave drag method of reference 1 is primarily intended. Predictions for the configurations of the remaining references are generally lower than the test results. This should be expected since the supersonic linear theory used as the basis for the wave-drag prediction is expected to underpredict this contribution for the thicker wing sections and the more extensive planform modifications.

The authors of reference 1 point out that some of the error is quite possibly associated with the manner in which the test data were analyzed. The test results presented in reference 14 were obtained on wing-body configurations without boundary-layer trips and with slightly blunted leading edges. Corrections were applied by the authors of reference 1 to obtain drag values corresponding to fully turbulent flow and sharp leading edges. References 20 and 21 present test results with natural transition. The skin-friction drag for these configurations was predicted by assuming fully turbulent flow over the body and laminar flow over the wing as suggested in the references.

It should be noted that the test values in table 4.3.3.1-B have been corrected to remove base drag, and that the calculated values do not include the base-drag term.

Perhaps the greatest value of the method is that it can be used to predict the supersonic wave-drag increments due to planform modifications and thickness variations. If test data are available for a configuration, the wave drag for a similar configuration can be estimated by predicting the wave drag for both configurations using the Datcom technique, and then applying the increment between the predictions to the test data. Sketches (f) and (g), both taken from reference 1, illustrate the application of this technique to predict the wave-drag variation as a function of planform modification and thickness variation, respectively. Note that although the absolute value of wave drag is not accurately predicted, the trends due to planform modifications and thickness variations are predicted quite well, even for thick, highly modified planforms.

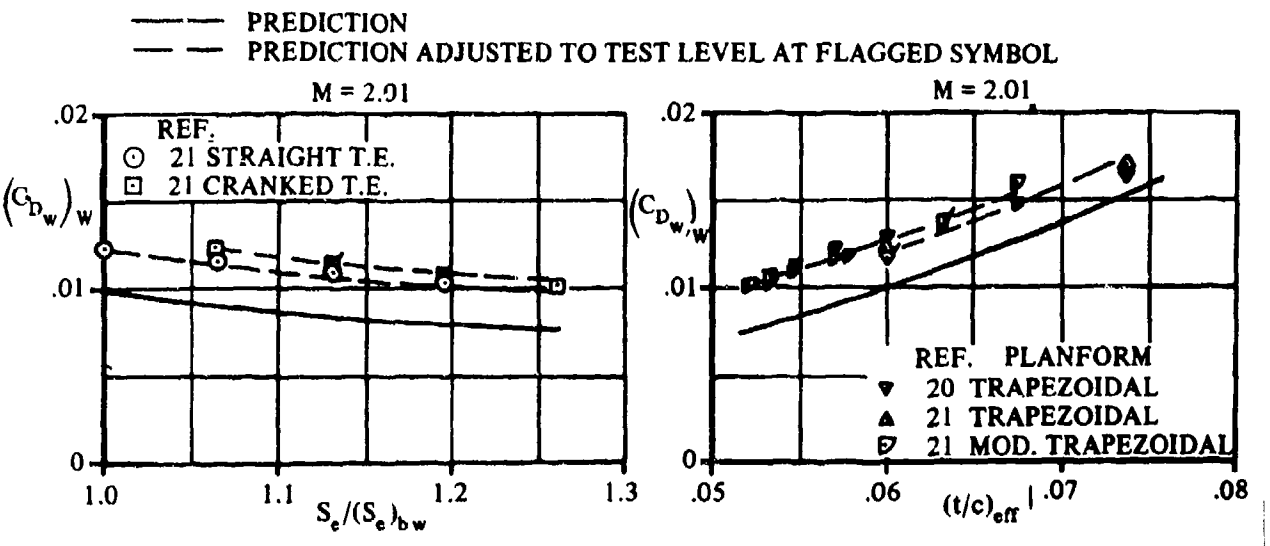

EFFECT OF PLANFORM MODIFICATIONS ON WING WAVE DRAG

SKETCH (f)

EFFECT OF THICKNESS DISTRIBUTION ON WING WAVE DRAG

SKETCH (g)

The limited availability of test data precludes substantiation of the supersonic zero-lift-drag method over wide ranges of planform and flow parameters for configurations having wings with blunt leading edges. A brief statement of an analysis conducted on the blunt-leading-edge planforms of references 23 and 24 is reported in reference 1. It is indicated therein that the method will give satisfactory results for bluntness drag for thin wings.

Sample Problem

Given: The wing-body configuration of reference 15. The configuration consists of a double-delta wing mounted on a cylindrical-ogive body.

Actual Wing Characteristics:

Double-delta planform $A = 1.25$ $\lambda = 0$ $\Lambda_{LE_i} = 83^o$ $\Lambda_{LE_o} = 70^o$

$\Lambda_{TE} = -15^o$ $b/2 = 10.0$ in. $\eta_B = 0.181$ $c_r = 40.0$ in.

$S_W = 319.32$ sq in. t/c (varies, see sketch (h))

Body Characteristics:

Ogive-cylinder $\ell_B = 40.0$ in. $d_{max} = 2.0$ in. $d_b = 2.0$ in. $\ell_B/d = 20.0$

$\ell_N = 12.0$ in. $f_N = \ell_N/d = 6.0$ $\ell_A = 28.0$ in. $f_A = \ell_A/d = 14.0$

$S_B = 3.14$ sq in. $S_S/S_B = 72.0$ $\theta_N = 8.5^o$

Basic Wing Characteristics (Wave-drag calculations):

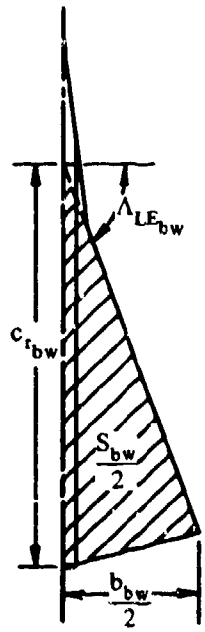

Delta planform $A_{bw} = 1.33$ $\lambda_{bw} = 0$ $\Lambda_{LE_{bw}} = 70^{o}$

$\Lambda_{TE_{bw}} = -15^{o}$ $(b/2)_{bw} = 10.0$ in. $c_{r_{bw}} = 30.16$ in.

$(S_{bw})_e = 244.26$ sq in.

Airfoil: hexagonal, sharp leading edge

$\frac{x_1}{c} = 0.4$ $\frac{x_2}{c} = 0.3$ $\frac{x_3}{c} = 0.3$ $(t/c)_{bw} = 0.02$

Inboard and Outboard Panel Characteristics (Skin-friction drag calculations):

Inboard panel (exposed)

$\left(c_{r_i}\right)_e = 31.165$ in. $(\lambda_i)_e = 0.794$

$(\bar{c}_i)_e = 28.25$ in. $(S_i)_e = 45.275$ sq in.

$\left(S_{wet_i}\right)_e = 90.55$ sq in. $(b_i/2)_e = 0.81$ in.

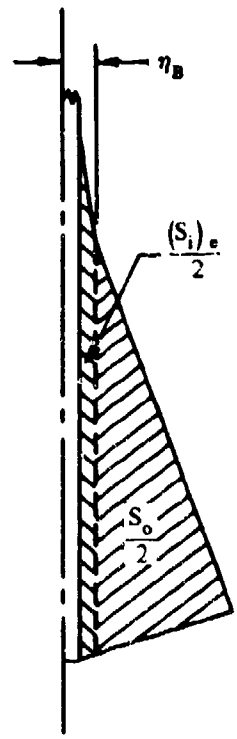

Outboard panel

$c_{r_o} = 24.73$ in. $\lambda_o = 0$ $\bar{c}_o = 16.5$ in.

$S_o = 202.52$ sq in. $(S_{wet})_o = 405.04$ sq in.

$b_o/2 = 8.19$ in.

Additional Characteristics:

$M = 2.98$; $\beta = 2.807$ Smooth surfaces (assume $k = 0$)

$S_{ref} = S_{bw} = 301.55$ sq in. $R_\ell = 1.741 \times 10^6$ per in.

Compute:

Determine the wing skin-friction-drag contribution

Inboard panel (exposed)

$$R_\ell = (1.741 \times 10^6)(\bar{c}_i)_e = (1.741 \times 10^6)(28.25) = 4.92 \times 10^7$$

$\ell/k = \infty$, read $\left(C_{f_W}\right)_i$ at calculated R_ℓ

$\left(C_{f_W}\right)_i = 0.00146$ (figure 4.1.5.1-26)

Outboard panel

$$R_\ell = (1.741 \times 10^6)(\bar{c}_o) = (1.741 \times 10^6)(16.5) = 2.87 \times 10^7$$

$\ell/k = \infty$, read $\left(C_{f_W}\right)_o$ at calculated R_ℓ

$\left(C_{f_W}\right)_o = 0.00158$ (figure 4.1.5.1-26)

$$\left(C_{D_f}\right)_W = \left(C_{f_W}\right)_i \frac{\left(S_{wet_i}\right)_e}{S_{ref}} + \left(C_{f_W}\right)_o \frac{S_{wet_o}}{S_{ref}} \quad \text{(equation 4.3.3.1-g)}$$

$$= (0.00146)\frac{90.55}{301.55} + (0.00158)\frac{405.04}{301.55}$$

$$= 0.00256 \text{ (based on } S_{ref})$$

Determine the wing wave-drag coefficient.

$$K = \frac{c(c - x_2)}{x_1 x_3} = \frac{1\,(1 - 0.3)}{(0.4)\,(0.3)} = 5.833$$

$(t/c)_{eff}$

The thickness distribution of the actual wing and the chord distribution of the basic wing are shown in sketch (h).

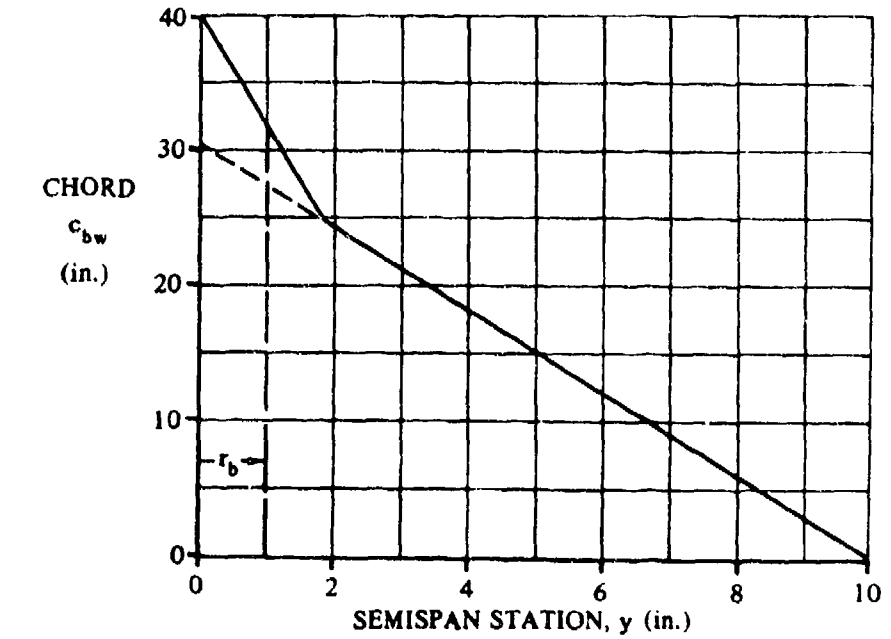

CHORD DISTRIBUTION (BASIC WING)

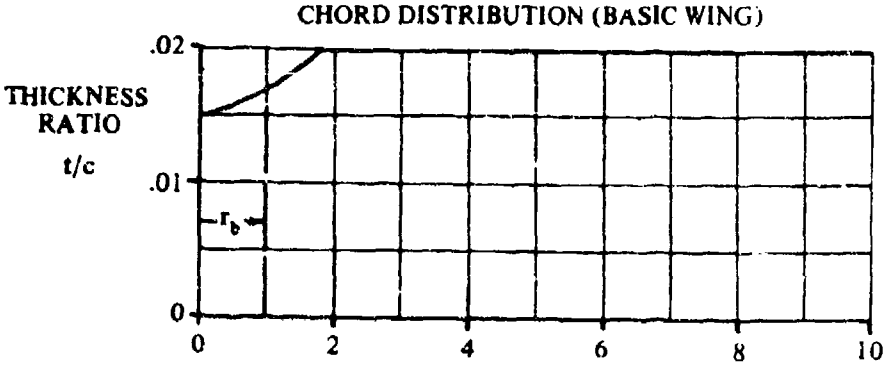

SEMISPAN STATION, y (in.)

THICKNESS DISTRIBUTION (ACTUAL PLANFORM)

SKETCH (h)

Sketch (i) shows $(t/c)^2\ c_{bw}$ versus spanwise position. Graphical integration of this curve gives

$$\int_{r_b}^{b/2} \left(\frac{t}{c}\right)^2 c_{bw}\ dy = 0.0474 \text{ sq in.}$$

$$\left(\frac{t}{c}\right)^2_{eff} = \frac{\int_{r_b}^{b/2} \left(\frac{t}{c}\right)^2 c_{bw}\ dy}{1/2\ (S_{bw})_e} \quad \text{(equation 4.3.3.1-j')}$$

$$= \frac{0.0474}{1/2\,(244.26)} = 0.000388$$

$$\left(\frac{t}{c}\right)_{eff} = 0.0197$$

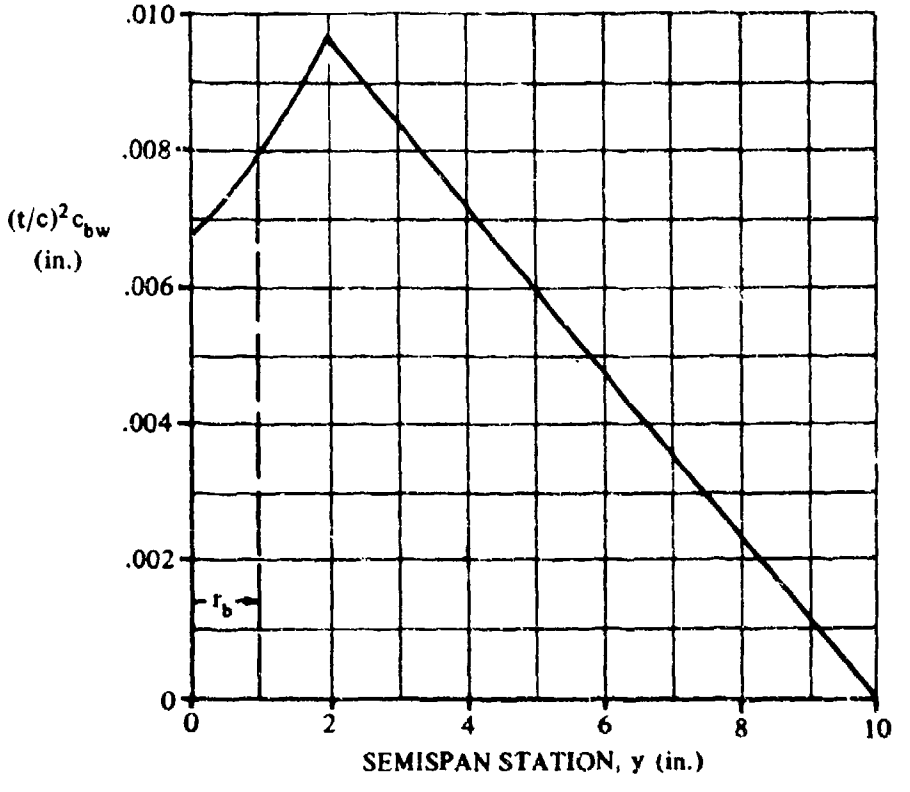

INTEGRAND FOR DETERMINING $(t/c)_{eff}$ FOR WING OF SAMPLE WAVE-DRAG CALCULATION

SKETCH (i)

$\beta \cot \Lambda_{LE} = (2.807)\,(\cot 70^{o}) = 1.022$ (supersonic leading edge)

$$\left(C_{D_w}\right)_w = \frac{K}{\beta}\left(\frac{t}{c}\right)^2_{eff} \frac{(S_{bw})_e}{S_{ref}} \quad \text{(equation 4.3.3.1-h)}$$

$$= \left(\frac{5.833}{2.807}\right)(0.0197)^2 \frac{244.26}{301.55}$$

$$= 0.00065 \quad \text{(based on } S_{ref})$$

Determine the body contribution.

Skin-friction-drag coefficient

$R_\ell = (1.741 \times 10^6)(\ell_B) = (1.741 \times 10^6)(40) = 6.964 \times 10^7$

$\ell/k = \infty$, read $(C_f)_B$ at calculated R_ℓ

$(C_f)_B = 0.00139$ (figure 4.1.5.1-26)

Wave-drag coefficients (method 2, paragraph C, Section 4.2.3.1)

Forebody

$\beta/f_N = \dfrac{2.807}{6.0} = 0.468$; $K_N = 1.005$ (figure 4.2.3.1-63)

$C_{D_{N_2}} \left[f_N^2 + \dfrac{1}{4}\right] K_N = 0.985$ (figure 4.2.3.1-61)

$C_{D_{N_2}} = \dfrac{0.985}{(36 + 0.25)(1.005)} = 0.0270$ (based on S_B)

Afterbody

$\dfrac{d_b}{d} = 1.0$; $C_{D_A} = 0$ (figure 4.2.3.1-64)

Nose bluntness

$C_{D_{N_1}} = 0$ (no bluntness)

Afterbody interference-drag coefficient

$\dfrac{d_b}{d} = 1.0$; $C_{D_{A(NC)}} = 0$ (figure 4.2.3.1-44a)

Base-drag coefficient

$C_{D_b} = 0.098$ (figure 4.2.3.1-60) (based on S_B)

$\left(C_{D_0}\right)_B = (C_f)_B \dfrac{S_S}{S_B} + C_{D_{N_2}} + C_{D_A} + C_{D_{A(NC)}} + C_{D_{N_1}} + C_{D_b}$ (equation 4.2.3.1-h)

$= (0.00139)(72.0) + 0.0270 + 0 + 0 + 0 + 0.098$

$= 0.225$ (based on S_B)

Solution:

$$C_{D_0} = \left(C_{D_0}\right)_W + \left(C_{D_0}\right)_B \frac{S_B}{S_{ref}} \quad \text{(equation 4.3.3.1-d)}$$

$$= \left(C_{D_f} + C_{D_w}\right)_W + \left(C_{D_0}\right)_B \frac{S_B}{S_{ref}}$$

$$= 0.00256 + 0.00065 + (0.225)\ \frac{3.14}{301.55}$$

$$= 0.00555 \text{ (based on } S_{ref})$$

The test value from reference 15, corrected to remove base drag, is $C_{D_0} = 0.0046$. The corresponding calculated value is given by

$$C_{D_0} = 0.00555 - C_{D_b} \frac{S_B}{S_{ref}}$$

$$= 0.00555 - 0.00102$$

$$= 0.00453 \text{ (based on } S_{ref})$$

REFERENCES

1. Benepe, D.B., Kouri, B.G., Webb, J.B., et al: Aerodynamic Characteristics of Non-Straight-Taper Wings. AFFDL-TR-66-73, 1966. (U)
2. Marquardt, R.F.: A General Method for Predicting Subsonic Minimum Drag of an Arbitrary Aircraft Configuration. General Dynamics, F/W MR-A-1261, 1961. (C) Title Unclassified
3. Ward, G.N.: Supersonic Flow Past Slender Pointed Bodies. Quart. Jour. Mech. and Appl. Math., Vol. II, Pt. I, 1949. (U)
4. Fraenkel, L.E.: The Theoretical Wave Drag of Some Bodies of Revolution. RAE Aero 2420, 1951. (U)
5. Eminton, E.: On the Minimisation and Numerical Evaluation of Wave Drag. RAE Aero 2564, 1955. (U)
6. Weber, J.: Numerical Methods for Calculating the Zero-Lift Wave-Drag and the Lift-Dependent Wave-Drag of Slender Wings. RAE Aero 2629, 1959. (U)
7. Cahn, M.S., and Olstad, W.B.: A Numerical Method for Evaluating Wave Drag. NACA TN 4258, 1958. (U)
8. Holdaway, G.H.: Comparison of Theoretical and Experimental Zero-Lift Drag-Rise Characteristics of Wing-Body-Tail Combinations Near the Speed of Sound. NACA RM A53H17, 1953. (U)
9. Whitcomb, R.T.: Recent Results Pertaining to the Application of the "Area Rule." NACA RM L53I15a, 1953. (U)
10. Spreiter, J.R.: On the Range of Applicability of the Transonic Area Rule. NACA RM A54F28, 1954. (U)
11. Nelson, R.L., and Welsh, C.J.: Some Examples of the Applications of the Transonic and Supersonic Area Rules to the Prediction of Wave Drag. NASA TN D-446, 1960. (U)
12. Crosthwait, E.L.: Drag of Two-Dimensional Cylindrical Leading Edges. General Dynamics, F/W rpt. AIM No. 50, 1966. (U)
13. Holdaway, G.H., and Mellenthin, J.A.: Evaluation of Blended Wing-Body Combinations with Curved Planforms at Mach Numbers up to 3.0. NASA TM X-379, 1960. (U)
14. Hicks, R.M., and Hopkins, E.J.: Effects of Spanwise Variation of Leading-Edge Sweep on the Lift, Drag, and Pitching Moment of a Wing-Body Combination at Mach Numbers from 0.7 to 2.94. NASA TN D-2236, 1964. (U)

15. Anon: Wind-Tunnel Tests of a Series of . . . Wing-Body Configurations for Investigation of Supersonic Lift/Drag Ratios. Unpublished Data. (U)

16. Anon: Unpublished Data on a Wing-Body-Glove Model Tested at Subsonic Speeds. (U)

17. Alford, W.J., and Ward, R.J.: Low-Speed Wind-Tunnel Investigation of the Aerodynamic Characteristics of a Hypersonic Airplane Model With Variable Wing Geometry. NASA TM X-663, 1962. (C) Title Unclassified

18. Jernell, L.S.: The Effects of Conical Camber on the Longitudinal Aerodynamic Characteristics of a Variable-Sweep Wing-Fuselage Configuration at Mach Numbers from 0.50 to 3.50. NASA TM X-804, 1963. (C) Title Unclassified

19. Whitcomb, R.T.: A Study of the Zero-Lift Drag Rise Characteristics of Wing-Body Combinations Near the Speed of Sound. NACA TR 1273, 1956. (U)

20. Cooper, M., and Sevier, J.R., Jr.: Effects of a Series of Inboard Planform Modifications on the Longitudinal Characteristics of Two 47° Sweptback Wings of Aspect Ratio 3.5, Taper Ratio 0.2, and Different Thickness Distributions at Mach Numbers of 1.61 and 2.01. NACA RM L53E07a, 1953. (U)

21. Sevier, J.R., Jr.: Effects of a Series of Inboard Plan-form Modifications on the Longitudinal Characteristics of Two Unswept Wings of Aspect Ratio 3.5, Taper Ratio 0.2, and Different Thickness Distributions at Mach Numbers of 1.61 and 2.01. NACA RM L53K11, 1954. (U)

22. Robins, A.W., Harris, R.V., Jr., and Jackson, C.M., Jr.: Characteristics at Mach Number of 2.03 of a Series of Wings Having Various Spanwise Distributions of Thickness Ratio and Chord. NASA TN D-631, 1960. (U)

23. Durgin, F.A.: A Study of Twist and Camber on Wings in Supersonic Flow. FDL-TDR-64-109, 1964. (U)

24. Anon: System 125A Design Study—Summary and Analysis of Wind-Tunnel Test Results from 1/125-Scale Model. General Dynamics, F/W Rpt. FZA-105, 1955. (C) Title Unclassified

TABLE 4.3.3.1-A
SUBSONIC WING-BODY ZERO-LIFT DRAG
DATA SUMMARY AND SUBSTANTIATION

Ref.	Config.	Planform	S_{ref} (ft^2)	ℓ_B (ft)	f_{fus}	$(S_S)_e$ (ft^2)	$\bar{c}_e$ (ft)	$\frac{t}{c}$	$\Lambda_{(t/c)_{max}}$ (deg)	$(S_{wet})_e$ (ft^2)	M	$R\ell/ft$ x 10^{-6}	$\left(C_{D_0}\right)_{WB}$ Calc.	$\left(C_{D_0}\right)_{WB}$ Test	e Percent Error
13	WB	Ogee	5.55	5.0	18.75	3.55	$(2.58)_i$ $(1.47)_o$	$(0.050)_i$ $(0.025)_o$	$(74)_i$ $(20)_o$	$(3.28)_i$ $(6.68)_o$	0.6	3.50	0.00844	0.0083	1.7
											0.7	3.75	0.00834	0.0081	3.0
											0.8	4.00	0.00836	0.0081	3.1
											0.9		0.00811	0.0079	2.7
14	WB	Ogee	0.151	1.186	16.25	0.234	$(0.426)_i$ $(0.198)_o$	$(0.020)_i$ $(0.020)_o$	$(70)_i$ $(31)_o$	$(0.100)_i$ $(0.134)_o$	0.7	2.50	0.01345	0.0131	2.7
											0.9		0.01307	0.0128	2.1
	WB	Delta	0.151	1.186	16.25	0.234	0.231	0.020	47.5	0.230	0.7	2.50	0.01332	0.0131	1.7
											0.9		0.01279	0.0130	-1.6
	WB	Modified Trapezoidal	0.151	1.186	16.25	0.234	$(0.636)_i$ $(0.209)_o$	$(0.020)_i$ $(0.020)_o$	$(77.5)_i$ $(21.5)_o$	$(0.079)_i$ $(0.122)_o$	0.7	2.50	0.01362	0.0138	-1.3
											0.9		0.01381	0.0134	3.1
	WB	Trapezoidal	0.151	1.186	16.25	0.234	0.230	0.020	10	0.230	0.7	2.50	0.01427	0.0147	-2.9
15	WB	Double-Delta	2.44	3.466	18.9	1.788	$(2.23)_i$ $(1.13)_o$	$(0.028)_i$ $(0.027)_o$	$(75)_i$ $(47.5)_o$	$(0.803)_i$ $(2.93)_o$	0.4	6.2	0.00740	0.0074	0
											0.72	6.8	0.00699	0.0073	-4.2
											0.89	6.1	0.00694	0.0070	-0.9
			2.46	3.466	18.9	1.788	$(2.20)_i$ $(1.12)_o$	$(0.028)_i$ $(0.026)_o$	$(75)_i$ $(47.5)_o$	$(1.01)_i$ $(2.78)_o$	0.41	3.7	0.00746	0.0076	-2.0
											0.72	5.5	0.00706	0.0071	-0.3
											0.88	6.3	0.00683	0.0065	5.1

TABLE 4.3.3.1-A (CONTD)

Ref.	Config.	Planform	S_{ref} (ft^2)	ℓ_B (ft)	f_{fus}	$(S_S)_e$ (ft^2)	$\bar{c}_e$ (ft)	$\frac{t}{c}$	$\Lambda_{(t/c)_{max}}$ (deg)	$(S_{wet})_e$ (ft^2)	M	R /ft $\times 10^{-6}$	$(C_{D_0})_{WB}$ Calc.	$(C_{D_0})_{WB}$ Test	e Percent Error
16	WB	Cranked	0.913	3.33	10	2.66	$(0.615)_i$ $(0.334)_o$	$(0.118)_i$ $(0.102)_o$	$(8.5)_i$ $(12.5)_o$	$(0.326)_i$ $(1.330)_o$	0.7	7.0	0.0220	0.0210	4.8
			0.913	3.33	10	2.66	$(0.794)_i$ $(0.334)_o$	$(0.091)_i$ $(0.102)_o$	$(30.5)_i$ $(12.5)_o$	$(0.868)_i$ $(1.330)_o$	0.7	7.0	0.0254	0.0251	1.2
			0.913	3.33	10	2.66	$(0.997)_i$ $(0.334)_o$	$(0.073)_i$ $(0.102)_o$	$(41)_i$ $(12.5)_o$	$(1.520)_i$ $(1.330)_o$	0.7	7.0	0.0274	0.0282	-2.8
17	WBNHV	Cranked	4.67	5.34	17.8	2.81	$(1.69)_i$ $(0.682)_o$	$(0.0123)_i$ $(0.0372)_o$	$(70)_i$ $(25)_o$	$(4.28)_i$ $(3.58)_o$	0.25	1.31	0.0175	(a)	
			4.58	5.34	17.8	2.81	$(1.87)_i$ $(0.813)_o$	$(0.0115)_i$ $(0.0328)_o$	$(70)_i$ $(47.5)_o$	$(4.42)_i$ $(3.31)_o$	0.25	1.31	0.01695		
18	WB	Cranked	1.30	3.70	18.2	1.984	$(0.844)_i$ $(0.306)_o$	$(0.032)_i$ $(0.060)_o$	$(52)_i$ $(7.4)_o$	$(1.120)_i$ $(1.186)_o$	0.5	1.042	0.01538		
			1.30	3.70	18.2	1.984	$(0.806)_i$ $(0.367)_o$	$(0.032)_i$ $(0.040)_o$	$(54.6)_i$ $(40)_o$	$(1.508)_i$ $(0.934)_o$	0.5	1.042	0.01394		
											0.8	1.414	0.01298		
			1.30	3.70	18.2	1.984	$(1.008)_i$ $(0.378)_o$	$(0.032)_i$ $(0.021)_o$	$(64.5)_i$ $(70)_o$	$(1.412)_i$ $(0.704)_o$	0.5	1.042	0.01227		
											0.8	1.414	0.01150		
											0.9	1.498	0.01115		

(a) This information is classified CONFIDENTIAL.

Average Error = $\frac{\Sigma|e|}{n}$ = 2.8%

TABLE 4.3.3.1-8
SUPERSONIC WING-BODY ZERO-LIFT DRAG
DATA SUMMARY AND SUBSTANTIATION

Ref.	Config.	Planform	Airfoil	f_N	S_{ref} (ft^2)	A	Λ_{LE_i} (deg)	Λ_{LE_o} (deg)	η_B	$\left(\frac{t}{c}\right)_{eff}$	M	$R\varrho$/ft x 10^{-6}	$\left(C_{D_0}\right)_{WB}$ Calc.	$\left(C_{D_0}\right)_{WB}$ Test	e Percent Error
20	WB	Trapezoidal	Hexagonal	3.5	1.14	3.50	—	51.6	—	0.06	1.61	4.1	0.0235	0.0238	-1.3
							—		—		2.01	3.4	0.0194	0.0215	-9.8
		Modified Trapezoidal	Hexagonal	3.5	1.14	3.15	—	51.6	—	0.0569	1.61	4.1	0.0221	0.0235	-6.0
						2.86	—	51.6	—	0.0547	1.61	4.1	0.0211	0.0233	-9.4
							—		—		2.01	3.4	0.0177	0.0208	-14.9
						3.15	64.1	51.6	0.40	0.0569	1.61	4.1	0.0221	0.0228	-3.1
						2.86	64.1	51.6	0.40	0.0547	1.61	4.1	0.0211	0.0225	-6.2
						2.62	64.1	51.6	0.40	0.0532	1.61	3.4	0.0207	0.0221	-6.3
						2.86	70.7	51.6	0.40	0.0547	1.61	4.1	0.0211	0.0227	-7.0
											2.01	3.4	0.0177	0.0202	-12.4
						2.62	70.7	51.6	0.40	0.0532	1.61	4.1	0.0207	0.0225	-8.0
						2.42	70.7	51.6	0.40	0.0519	1.61	3.4	0.0202	0.0221	-8.6
											2.01	3.4	0.0168	0.0207	-18.9
		Trapezoidal	Hexagonal	3.5	1.14	3.50	—	51.6	—	0.0737	1.61	4.1	0.0304	0.0296	2.7
							—	51.6	—		2.01	3.4	0.0245	0.0265	-7.5
		Modified Trapezoidal	Hexagonal	3.5	1.14	3.15	—	51.6	—	0.0674	1.61	4.1	0.0270	0.0280	-3.6
						2.86	—	51.6	—	0.0632	1.61	4.1	0.0249	0.0273	-8.8
							—		—		2.01	3.4	0.0205	0.0252	-18.7
						3.15	64.1	51.6	0.40	0.0674	1.61	4.1	0.0270	0.0279	-3.2

TABLE 4.3.3.1-B (CONTD)

Ref.	Config.	Planform	Airfoil	f_N	S_{ref} (ft^2)	A	Λ_{LE_i} (deg)	Λ_{LE_o} (deg)	η_B	$\left(\frac{t}{c}\right)_{eff}$	M	Rℓ/ft x 10^{-6}	$\left(C_{D_0}\right)_{WB}$ Calc.	$\left(C_{D_0}\right)_{WB}$ Test	e Percent Error
20	WB	Trapezoidal	Hexagonal	3.5	1.14	2.86	64.1	51.6	0.40	0.0632	1.61	4.1	0.0249	0.0258	-3.5
						2.62	64.1	51.6	0.40	0.0600	1.61	3.4	0.0237	0.0248	-4.4
						2.86	70.7	51.6	0.40	0.0632	1.61	4.1	0.0249	0.0265	-6.0
											2.01	3.4	0.0205	0.0235	-12.8
						2.62	70.7	51.6	0.40	0.0600	1.61	3.4	0.0237	0.0249	-4.8
						2.42	70.7	51.6	0.40	0.0577	1.61	3.4	0.0266	0.0238	11.8
											2.01	3.4	0.0186	0.0218	-14.7
21	WB	Trapezoidal	Hexagonal	3.5	1.14	3.50	—	20.9	—	0.060	1.61	4.1	0.0235	0.0270	-13.0
							—		—		2.01	3.4	0.0194	0.0218	-11.0
		Modified Trapezoidal	Hexagonal	3.5	1.14	3.15	49.6	20.9	0.40	0.0569	2.01	3.4	0.0184	0.0210	-12.4
						2.86	63.1	20.9	0.40	0.0547	2.01	3.4	0.0177	0.0203	-12.8
						2.62	70.1	20.9	0.40	0.0532	1.61	2.2	0.0217	0.0241	-10.0
						2.62	70.1	20.9	0.40	0.0532	2.01	2.5	0.0179	0.0204	-12.3
						3.15	—	20.9	—	0.0569	1.61	4.1	0.0221	0.0266	-16.9
							—		—		2.01	3.4	0.0184	0.0217	-19.8
						2.86	49.6	20.9	0.40	0.0547	2.01	3.4	0.0177	0.0208	-14.9
						2.62	63.1	20.9	0.40	0.0532	2.01	3.4	0.0172	0.0201	-14.4
						2.42	70.1	20.9	0.40	0.0519	1.61	2.2	0.0213	0.0240	-11.3
											2.01	2.5	0.0176	0.0202	-12.9
		Trapezoidal	Hexagonal	3.5	1.14	3.50	—	20.9	—	0.0737	1.61	4.1	0.0304	0.0323	-5.9
							—		—		2.01	3.4	0.0245	0.0260	-5.8

TABLE 4.3.3.1-B (CONTD)

Ref.	Config.	Planform	Airfoil	f_N	S_{ref} (ft^2)	A	Λ_{LE_i} (deg)	Λ_{LE_o} (deg)	η_B	$\left(\frac{t}{c}\right)_{eff}$	M	R_Q/ft $\times 10^{-6}$	$\left(C_{D_0}\right)_{WB}$ Calc.	$\left(C_{D_0}\right)_{WB}$ Test	e Percent Error
21	WB	Modified Trapezoidal	Hexagonal	3.5	1.14	3.15	49.6	20.9	0.40	0.0674	2.01	3.4	0.0220	0.0242	-9.1
						2.86	63.1	20.9	0.40	0.0632	2.01	3.4	0.0205	0.0230	-10.9
						2.62	70.1	20.9	0.40	0.0600	1.61	2.2	0.0247	0.0272	-9.2
											2.01	2.5	0.0200	0.0224	-10.7
						3.15	—	20.9	—	0.0674	1.61	4.1	0.0207	0.0311	-13.2
							—		—		2.01	3.4	0.0220	0.0255	-13.7
						2.86	49.6	20.9	0.40	0.0632	2.01	3.4	0.0205	0.0232	-11.6
						2.62	63.1	20.9	0.40	0.0600	2.01	3.4	0.0193	0.0223	-13.5
						2.42	70.1	20.9	0.40	0.0577	1.61	2.2	0.0237	0.0266	-10.9
											2.01	2.5	0.0193	0.0218	-11.5
		Delta	Hexagonal	6.0	2.09	1.33	—	70	—	0.02	2.98	10.8	0.0048	0.0046	4.3
							—		—			20.5	0.0044	0.0044	0
15	WB	Double-Delta	Hexagonal	6.0	1.94	1.57	80	60	0.322	0.0258	3.01	10.8	0.0060	0.0060	0
											2.98	20.8	0.0056	0.0048	16.7
											2.50	10.0	0.0067	0.0063	6.3
												22.8	0.0061	0.0062	-1.6
			Parabolic	6.0	1.91	1.60	80	60	0.330	0.0253	2.98	10.9	0.0059	0.0068	-13.2
												20.8	0.0054	0.0067	-19.4
			Hexagonal	6.0	2.09	1.25	83	70	0.181	0.0199	2.98	11.1	0.0049	0.0049	0
												20.9	0.0045	0.0046	-2.2

TABLE 4.3.3.1-B (CONTD)

Ref.	Config.	Planform	Airfoil	f_N	S_{ref} (ft^2)	A	Λ_{LE_i} (deg)	Λ_{LE_o} (deg)	η_B	$\left(\frac{t}{c}\right)_{eff}$	M	Rℓ/ft x 10^{-6}	$\left(C_{D_0}\right)_{WB}$ Calc.	$\left(C_{D_0}\right)_{WB}$ Test	e Percent Error
15	WB	Double Delta	Hexagonal	6.0	2.08	1.06	83	70	0.197	0.0198	2.98	11.0	0.0051	0.0048	6.3
											↓	20.7	0.0047	0.0045	4.4
											2.59	10.0	0.0056	0.0054	3.7
											↓	22.8	0.0051	0.0051	0
			Hexagonal	6.0	2.02	1.64	82	60	0.215	0.0185	2.98	10.9	0.0062	0.0062	0
											2.59	9.9	0.0070	0.0071	-1.4
			Hexagonal	6.0	2.28	1.53	81	63	0.215	0.0171	2.98	11.5	0.0058	0.0058	0
											2.59	10.6	0.0063	0.0064	-1.6
					2.51	1.41	80	66	0.215	0.0155	2.98	11.0	0.0053	0.0054	-1.9
			Double-Wedge	6.2	2.16	1.52	83	62	0.215	0.0218	2.98	11.3	0.0052	0.0051	2.0
											↓	21.9	0.0048	0.0048	0
											2.59	10.2	0.0057	0.0057	0
											↓	22.2	0.0053	0.0054	-1.9
											2.20	10.5	0.0053	0.0054	-1.6
											1.59	10.6	0.0070	0.0070	0
			Parabolic	6.0	2.16	1.52	83	62	0.215	0.0214	2.98	11.5	0.0054	0.0051	5.9
											↓	22.4	0.0049	0.0048	2.1
											2.81	10.8	0.0057	0.0057	0
											↓	22.6	0.0052	0.0054	-3.7
											2.59	10.3	0.0060	0.0059	1.7
											↓	22.3	0.0055	0.0054	1.9

TABLE 4.3.3.1-B (CONTD)

Ref.	Config.	Planform	Airfoil	f_N	S_{ref} (ft^2)	A	Λ_{LE_i} (deg)	Λ_{LE_o} (deg)	η_B	$\left(\frac{t}{c}\right)_{eff}$	M	R_Q/ft x 10^{-6}	$\left(C_{D_0}\right)_{WB}$ Calc.	$\left(C_{D_0}\right)_{WB}$ Test	• Percent Error
15	WB	Double-Delta	Parabolic	6.0	2.16	1.52	83	32	0.215	0.0214	2.20	10.4	0.0066	0.0062	6.5
											1.59	10.5	0.0073	0.0067	9.0
											1.08	6.6	0.0084	0.0085	-1.2
			Hexagonal	6.0	2.25	1.48	83	62	0.215	0.0168	2.98	11.8	0.0057	0.0057	0
											2.81	10.9	0.0060	0.0061	-1.6
											2.59	10.6	0.0064	0.0063	1.6
											2.20	10.6	0.0071	0.0071	0
											1.59	13.2	0.0076	0.0076	0
											1.17	6.5	0.0087	0.0096	-9.4
14	WB	Delta	Hexagonal	6.5	0.15	2.17	—	59	—	0.02	1.40	2.5	0.0131	0.0159	-17.6
							—		—		1.98	2.5	0.0118	0.0125	-5.6
							—		—		2.94	2.5	0.0095	0.0114	-16.7
		Ogee	Hexagonal	6.5	0.15	2.17	—	—	—	0.02	1.40	2.5	0.0131	0.0150	-12.7
							—	—	—		1.98	2.5	0.0118	0.0116	1.7
							—	—	—		2.94	2.5	0.0096	0.0100	-5.0
		Trapezoidal	Hexagonal	6.5	0.15	1.9	—	10	—	0.02	1.40	2.5	0.0143	0.0160	-10.6
							—		—		1.98	2.5	0.0122	0.0125	-2.4
							—		—		2.94	2.5	0.0098	0.0114	-14.0
		Modified Trapezoidal	Hexagonal	6.5	0.15	1.9	—	—	—	0.02	1.40	2.5	0.0141	0.0152	-7.2
							—	—	—		1.98	2.5	0.0119	0.0129	-7.8
							—	—	—		2.94	2.5	0.0096	0.0108	-11.1

TABLE 4.3.3.1-B (CONTD)

Ref.	Config.	Planform	Airfoil	f_N	S_{ref} (ft^2)	A	Λ_{LE_i} (deg)	Λ_{LE_o} (deg)	η_B	$\left(\frac{t}{c}\right)_{eff}$	M	R_Q/ft $\times 10^{-6}$	$\left(C_{D_0}\right)_{WB}$ Calc.	$\left(C_{D_0}\right)_{WB}$ Test	e Percent Error
22	W	Trapezoidal	Biconvex	—	1.60	2.5	—	63.4	—	0.04	2.03	4.3	0.0097	0.0110	-11.8
				—			—		—			2.1	0.0104	0.0112	-7.1
				—			—		—			4.3	0.0097	0.0109	-11.0
				—			—		—			2.1	0.0104	0.0114	-8.8
				—	0.96	1.5	—	63.4	—	0.04	2.03	5.5	0.0094	0.0106	-11.3
				—			—		—			6.8	0.0101	0.0113	-10.6

Average Error = $\frac{\Sigma|e|}{n}$ = 7.5%

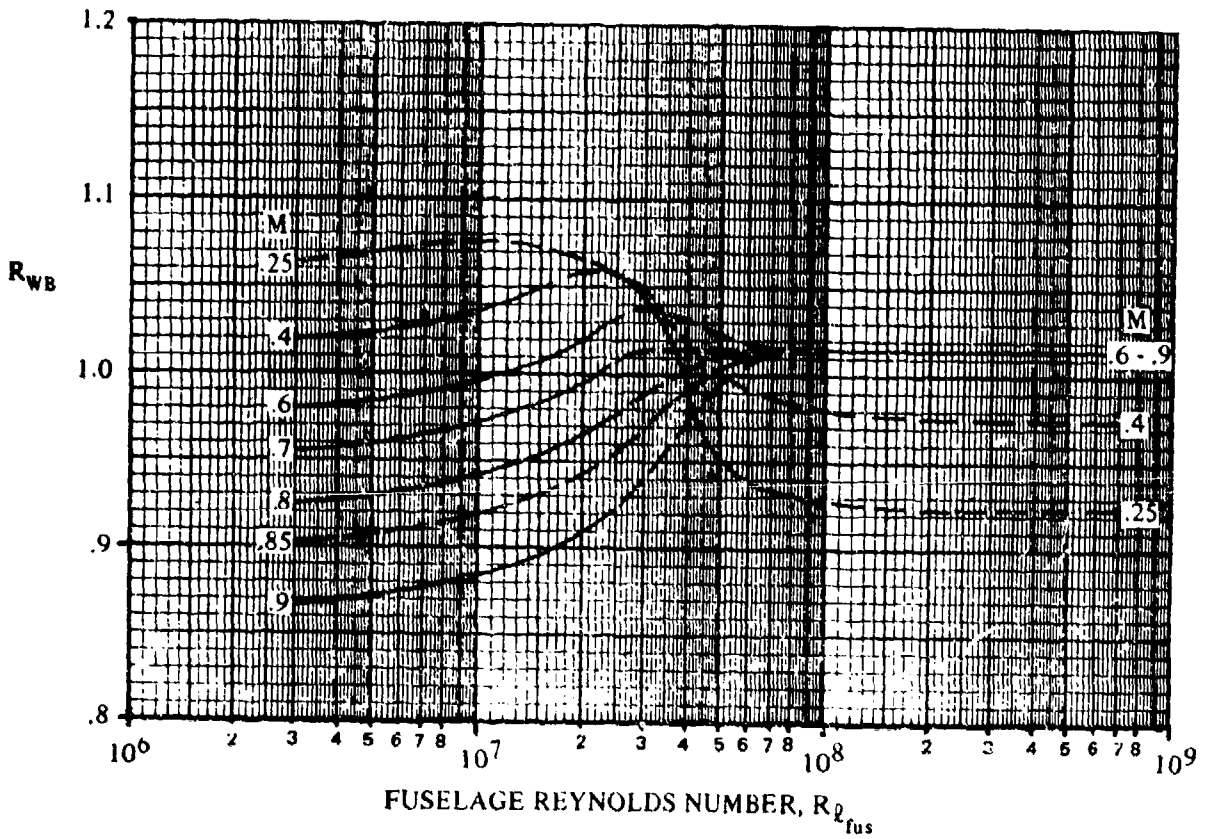

FIGURE 4.3.3.1-37 WING-BODY INTERFERENCE CORRELATION FACTOR – SUBSONIC SPEEDS

$$C_{D_{LE}}\left[\frac{S_{ref}}{2r_{LE_{bw}}\left(\frac{b_{bw}-2r_b}{\cos\Lambda_{LE_{bw}}}\right)}\right] = 1.28\,\frac{M^3\cos^6\Lambda_{LE_{bw}}}{1+M^3\cos^3\Lambda_{LE_{bw}}} \quad \text{(Ref. 12)}$$

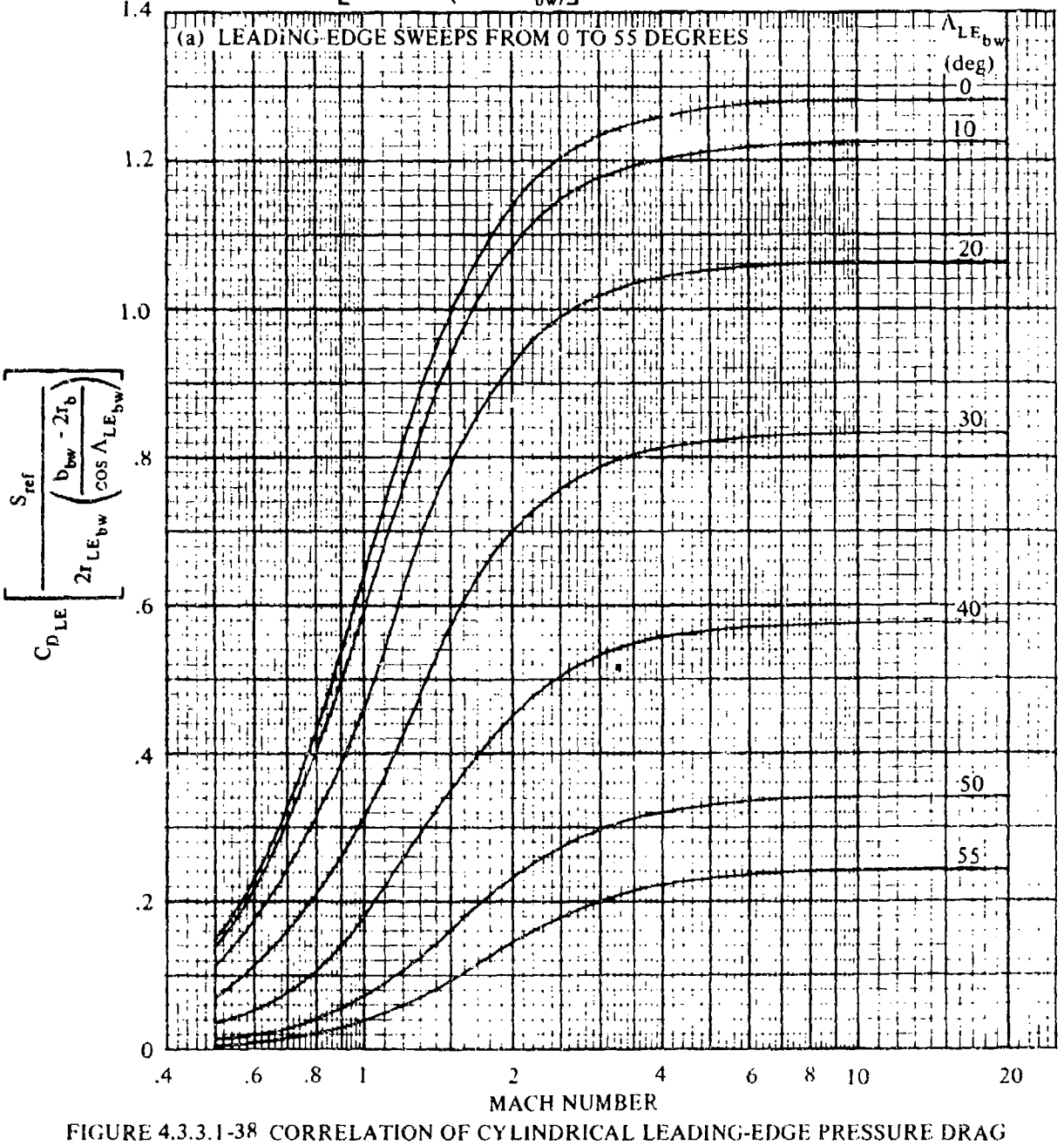

FIGURE 4.3.3.1-38 CORRELATION OF CYLINDRICAL LEADING-EDGE PRESSURE DRAG COEFFICIENTS

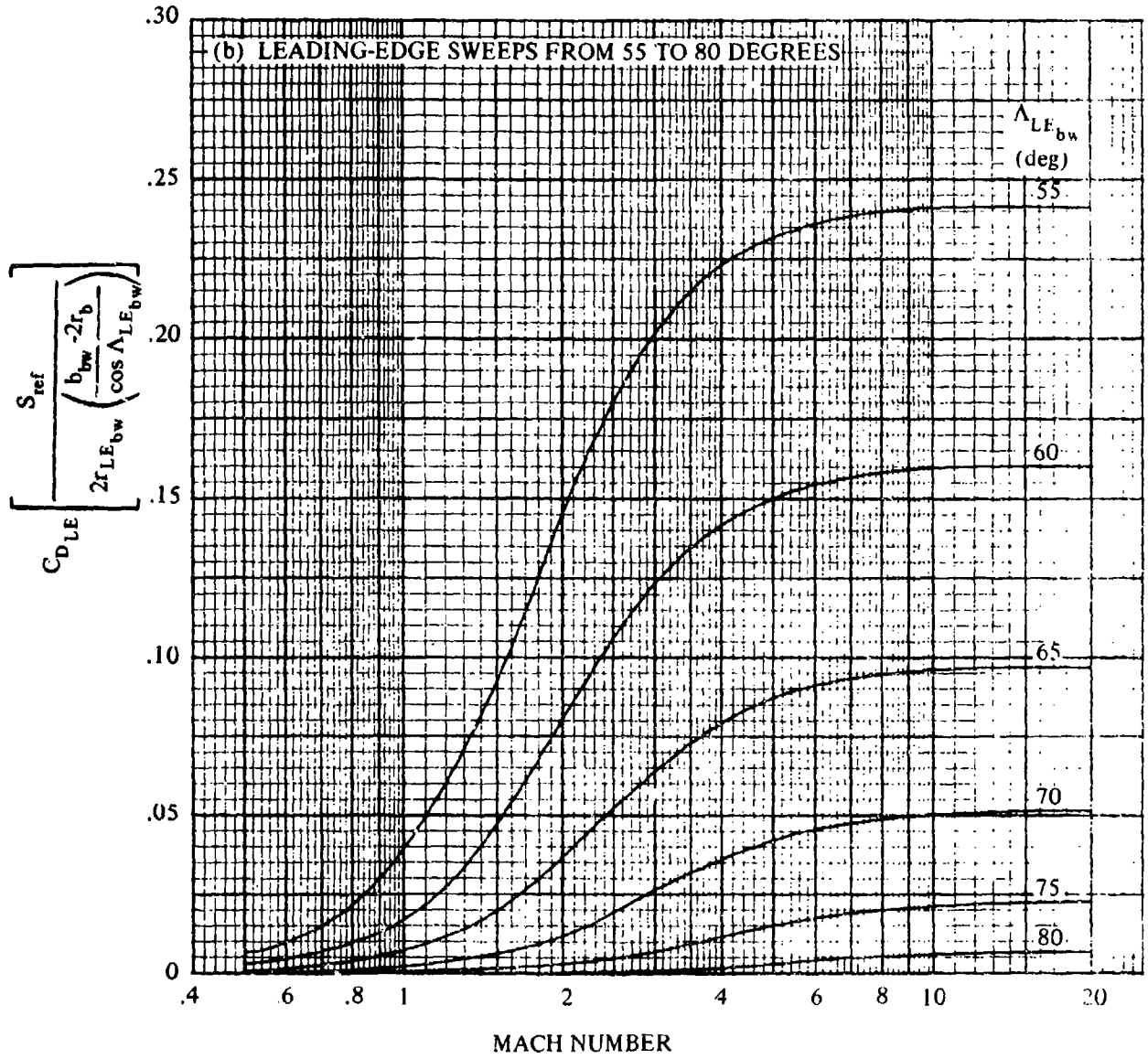

FIGURE 4.3.3.1-38 (CONTD)

4.3.3.2 WING-BODY DRAG AT ANGLE OF ATTACK

Determination of wing-body or tail-body drag at angle of attack is more an art than a science. Little is known concerning the wing-body aerodynamic interferences that occur at angle of attack. These interferences are usually significant only during the detailed design of a configuration or for a configuration especially designed for minimum interference at a particular flight condition. The total drag of a wing-body configuration at angle of attack may be expressed in the form

$$(C_D)_{WB} = (C_{D0})_{WB} + (C_{DL})_{WB} \qquad 4.3.3.2\text{-a}$$

where $(C_{D0})_{WB}$ is the zero-lift drag and $(C_{DL})_{WB}$ represents the drag due to lift. The zero-lift drag of the wing-body configuration may be obtained by using the methods of Section 4.3.3.1. The same two methods for estimating the wing-body drag-due-to-lift term are presented in each speed regime of this section. The first method, taken from Reference 1, evaluates the wing-body configuration as a unit. The second method evaluates and combines the isolated drag due to lift of the wing and of the body.

The primary advantage of Method 1 is its consideration of camber effects and its applicability to the high-lift region, i.e., beyond the parabolic drag region. However, its application is restricted to fighter-type aircraft with straight-tapered planforms.

Because of the empirical nature of Method 1 (values for the regression coefficients), exact solutions are available only at the following Mach numbers: 0.6, 0.7, 0.8, 0.9, 0.95, 1.0, 1.1, 1.2, 1.3, 1.4, 1.5, 2.0, and 2.5. At other Mach numbers interpolation is necessary. For the low-speed regime, the M = 0.6 values can be used, but only as an approximation. The solutions at Mach numbers 1.0 and 2.5 should be used cautiously, because of the somewhat limited amount of test data used in the determination of the regression coefficients.

A. SUBSONIC

Two different methods are presented for evaluating the total drag of a wing-body configuration. The first method is restricted to fighter-type aircraft with straight-tapered planforms. The second method is general and may be applied to both straight-tapered planforms and non-straight-tapered planforms, including double-delta, cranked, and curved wings.

The general categories of non-straight-tapered wings are illustrated in Sketch (a) of Section 4.1.3.2, while the wing-geometry parameters are presented in Section 2.2.2.

For Mach numbers less than 0.6 and values within the parabolic drag region (generally for $C_L < 0.4$ or 0.5), Method 2 should be used because of the limitation of Method 1 for Mach numbers below 0.6.

DATCOM METHOD

Method 1

This method was developed in Reference 1 for fighter-type aircraft by using the linear regression analysis of mathematical statistics. In general, a regression analysis involves the study of a group of variables to determine their effect on a given parameter. In this case, multidimensional least-squares curve fits were used to relate linearly the incremental drag due to lift of a wing-body configuration

to certain nondimensional geometric parameters. The result of this work is presented below in Equation 4.3.3.2-b, a purely empirical equation based on the various total-wing-planform geometric parameters and Reynolds number. For more detailed information regarding the analysis, the reader is referred to Reference 1.

The regression coefficients given in Table 4.3.3.2-D, as a function of Mach number and angle of attack, are not those presented in Reference 1. Those in Table 4.3.3.2-D are a more recent and improved version obtained from the authors of Reference 1.

An unfortunate feature of this method is the lack of physical appreciation of where the parabolic drag region ends; i.e., where separation effects become prominent. A second method, called the semiempirical method, which provides a physical appreciation of the flow conditions, is also presented in Reference 1. The semiempirical method is structured to consider the following various flow conditions: attached flow, initially contained separated or mixed flow, and major flow separation occurring after the initially contained separated or mixed flow. The semiempirical method is somewhat more difficult to apply, while its accuracy is approximately the same as that of Method 1 presented herein. For the details regarding the application of the semiempirical method, the reader is referred to Reference 1.

It is advisable to restrict the applicability of Method 1 to the range of geometric parameters of the test data used in the formulation of the regression coefficients. If the method is used for configurations that exceed the range of test data, the results should be applied with caution. The test data used in the formulation of the regression coefficients have geometric parameters within the following limits:

aspect ratio, A	1.6 to 6.0
taper ratio, λ	0 to 1
twist, θ	0 to -9.4^{o}
leading-edge radius, LER/$\bar{c}$	0 to 0.015
thickness, t/$\bar{c}$	0.025 to 0.10
NACA camber, $(y_c)_{max}/\bar{c}$	0 to 0.0263
conical-camber design lift coefficient, C_{L_d}	0 to 0.45
forebody fineness ratio, ℓ_N/d	2.2 to 8.4
afterbody fineness ratio, ℓ_A/d	0.3 to 5.6
leading-edge sweep, Λ_{LE}	0 to 70^{o}
Reynolds number, R_ℓ	0.8×10^6 to 8×10^6

Equation 4.3.3.2-b below enables the user to calculate the drag due to lift as a function of angle of attack and Mach number. When a series of points are calculated to define the drag due to lift versus angle of attack, it becomes necessary to use discretion and fair the best possible curve through the points. This is necessary since some values at high angles of attack do not describe a smooth continuous curve.

This method is not limited to bodies of revolution; however, no attempt is made to account for the effects of noncircular bodies. If it becomes necessary to analyze a noncircular body in combination with a wing, it is suggested that an equivalent body of revolution be used, i.e., a body of revolution with the same cross-sectional area.

The drag due to lift at a given angle of attack of a wing-body configuration, based on the area of the basic straight-tapered wing, is given by

$$(C_{D_L})_{WB} = B_0 + B_1\left(\frac{1}{A}\right) + B_2 A + B_3(\tan \Lambda_{LE})^{1/2} + B_4(t/\bar{c}) + B_5\left(\frac{\ell_N}{d}\right) + B_6\left(\frac{\ell_A}{d}\right) + B_7 \lambda$$

$$+ B_8\lambda^2 + B_9\lambda^3 + B_{10}(T_R) + B_{11}\left(\frac{LER}{\bar{c}}\right) + B_{12}\theta + B_{13}\left[\frac{(y_c)_{max}}{\bar{c}}\right] + B_{14}\, C_{L_d}$$

$$+ B_{15} R_\ell \qquad \text{4.3.3.2-b}$$

where

$B_0, B_1, \ldots B_{15}$ are the regression coefficients as a function of Mach number and angle of attack obtained from Table 4.3.3.2-D.

A is the total wing aspect ratio.

Λ_{LE} is the sweep of the leading edge.

$t/\bar{c}$ is the wing thickness ratio at the mean aerodynamic chord.

$\frac{\ell_N}{d}$ is the nose and forebody fineness ratio (see Sketch (a)).

$\frac{\ell_A}{d}$ is the afterbody fineness ratio taken at the afterbody wing-body juncture (see Sketch (a)).

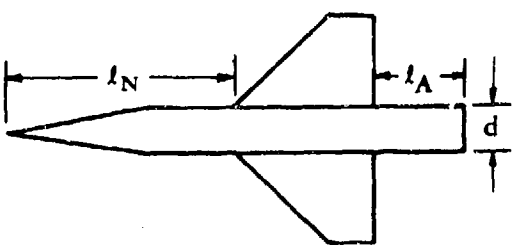

SKETCH (a)

λ is the wing taper ratio.

T_R is the transition indicator; 0 for no transition strips and 1 for transition strips or flight test.

$\frac{LER}{\bar{c}}$ is the ratio of the leading-edge radius to the mean aerodynamic chord taken at the mean aerodynamic chord.

θ is the wing twist between the root and tip sections in radians, negative for washout (see Figure 5.1.2.1-30b).

$\frac{(y_c)_{max}}{\bar{c}}$ is the NACA camber in the form of a ratio of the maximum ordinate of the mean line to the airfoil chord taken at the mean aerodynamic chord.

C_{L_d} is the conical camber design lift coefficient for a M = 1.0 design with the designated camber ray line intersecting the wing trailing edge at 0.8 b/2. (For more details see Reference 2.) If the wing does not have a conical-camber design, the value of C_{L_d} is zero.

R_ℓ is the Reynolds number based on the mean aerodynamic chord. For Reynolds numbers in excess of 8×10^6, the value of 8×10^6 should be used.

An indication of the accuracy of Method 1 can be obtained from Table 4.3.3.2-A. This table contains a comparison of test values with results calculated by using this method for wing-body configurations without camber. The test data used in this comparison are taken from Table 4.1.5.2-A and some have been used in the determination of the regression coefficients.

Method 2

This method evaluates and combines the isolated drag due to lift of the wing and of the body. The limitations of the method are those of Sections 4.1.5.2 and 4.2.3.2. The method is not applicable to generalized wing-body configurations with arbitrary body shapes. If it becomes necessary to analyze a noncircular body in combination with a wing, it is suggested that an equivalent body of revolution be used, i.e., a body of revolution with the same cross-sectional area. The method is applicable only for wing lift coefficients up to the critical lift coefficients for configurations having straight-tapered wings; whereas, for non-straight-tapered wings the method may be applied to configurations over a wide range of lift coefficients (see Paragraph A, Section 4.1.5.2).

The drag due to lift of a wing-body configuration is given by

$$(C_{D_L})_{WB} = (C_{D_L})_W + [C_D(\alpha)]_B \frac{(S_B)_{ref}}{S_W} \qquad 4.3.3.2\text{-c}$$

where

$(C_{D_L})_W$ is the drag due to lift of the wing, obtained from Paragraph A of Section 4.1.5.2 and based on the total wing area.

$[C_D(\alpha)]_B$ is the body drag due to angle of attack, obtained from Paragraph A of Section 4.2.3.2 and based on the maximum body frontal area.

$\frac{(S_B)_{ref}}{S_W}$ is the ratio of the body reference area (maximum body frontal area) to the total wing area.

No substantiation is presented for this method. However, substantiation tables for the wing contribution are presented in Section 4.1.5.2 for straight-tapered and non-straight-tapered planforms.

Sample Problems

The same wing-body configurations will be evaluated for both Methods 1 and 2 to enable a comparison of their application to be made.

1. Method 1

Given: The straight-tapered wing-body configuration of Reference 3.

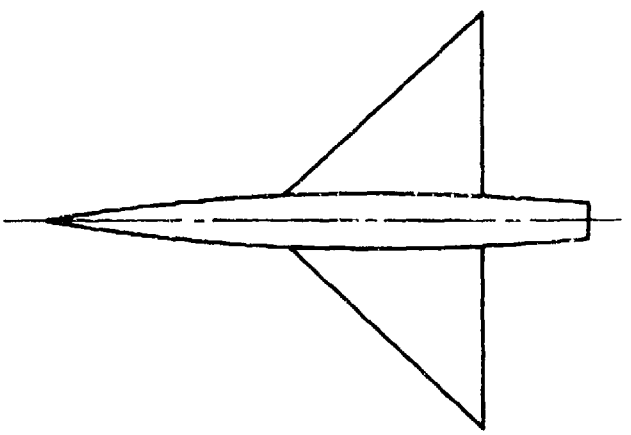

Wing Characteristics:

$A = 4.0$ $\quad \lambda = 0$ $\quad t/c = 0.03$ $\quad \Lambda_{LE} = 45^{o}$

$\theta = 0$ $\quad$ No camber, $\dfrac{(y_c)_{max}}{\bar{c}} = 0$ $\quad C_{L_d} = 0$

3-percent-thick biconvex airfoil with elliptic nose

$$\frac{LER}{\bar{c}} = 0.00045$$

Body Characteristics:

$$\frac{\ell_N}{d} = 4.28 \qquad \frac{\ell_A}{d} = 2.141$$

Additional Characteristics:

$M = 0.61$ $\quad R_{\ell} = 4.20 \times 10^{6}$ $\quad$ No transition strips, $T_R = 0$

Compute the drag due to lift for the above configuration at an angle of attack of 10^{o}.

The regression coefficients below are obtained from Table 4.3.3.2-D at M = 0.6.

Regression Coefficient	Value Table 4.3.3.2-D
B_0	0.12873
B_1	–0.05227
B_2	0.00855
B_3	–0.00826
B_4	–0.69952
B_5	–0.00295
B_6	–0.00487
B_7	0.14051
B_8	–0.28982
B_9	0.16952
B_{10}	–0.00215
B_{11}	2.27613
B_{12}	–0.34643
B_{13}	–0.52607
B_{14}	–0.09097
B_{15}	-0.00076×10^{-6}

Solution:

$$(C_{D_L})_{WB} = B_0 + B_1\left(\frac{1}{A}\right) + B_2 A + B_3(\tan \Lambda_{LE})^{1/2} + B_4(t/\bar{c}) + B_5\left(\frac{\ell_N}{d}\right) + B_6\left(\frac{\ell_A}{d}\right) + B_7\lambda$$

$$+ B_8\lambda^2 + B_9\lambda^3 + B_{10}T_R + B_{11}\left(\frac{LER}{\bar{c}}\right) + B_{12}\theta + B_{13}\left[\frac{(y_c)_{max}}{\bar{c}}\right]$$

$$+ B_{14}C_{L_d} + B_{15}R_\ell \qquad \text{(Equation 4.3.3.2-5)}$$

$$C_{D_L} = 0.12873 - 0.05227\left(\frac{1}{4}\right) + 0.00855(4) - 0.00826(1)^{1/2} - 0.69952(0.03)$$

$$- 0.00295(4.28) - 0.00487(2.141) + 0.14051(0) - 0.28982(0)^2 + 0.16952(0)^3$$

$$- 0.00215(0) + 2.27613(0.00045) - 0.34643(0) - 0.52607(0) - 0.09097(0)$$

$$- 0.00076 \times 10^{-6}(4.20 \times 10^6)$$

$$= 0.12873 - 0.01307 + 0.03420 - 0.00826 - 0.02099 - 0.01263 - 0.01043$$

$$+ 0.00102 - 0.00319$$

$$= 0.0954$$

The above procedure is used to generate the complete variation of C_{D_L} given below as a function of angle of attack. The comparison of test data with these predicted values and the predicted values from Method 2 are presented in Sketch (b), which follows the next sample problem.

α (deg)	$(C_{D_L})_{WB}$
0	0
1	0.00059
2	0.00196
3	0.00568
4	0.0115
6	0.0306
8	0.0598
10	0.0954
12	0.1356
14	0.1769
16	0.2196
18	0.2644

2. Method 2

Given: The same wing-body configuration used in Sample Problem 1, i.e., from Reference 3.

Wing Characteristics:

$A = 4.0$ $\quad \lambda = 0$ $\quad t/c = 0.03$ $\quad \Lambda_{LE} = 45^{o}$

$S_W = 2.425\ ft^2$ $\quad \bar{c} = 1.038\ ft$

$\theta = 0$ $\quad$ No camber $\quad \frac{LER}{\bar{c}} = 0.00045$

Body Characteristics:

$\ell_B = 46.93$ in. $\quad d = 4.76$ in. $\quad d_b = 2.589$ in.

$V_B = 0.2687\ ft^3$ $\quad V_B^{2/3} = 0.4164\ ft^2$

$f = \frac{\ell_B}{d} = 9.86$ $\quad r = 2.38 \left[1 - \left(1 - \frac{2x}{59.5} \right)^2 \right]^{3/2}$

Additional Characteristics:

$M = 0.61, \beta^2 = 0.6279$ $\quad R_{\ell_{MAC}} = 4.20 \times 10^6$ $\quad \kappa = 1.0$ (assumed)

Compute:

Wing Drag Due to Lift (Section 4.1.5.2)

$$\tan \Lambda_{c/2} = \tan \Lambda_{LE} - \frac{4}{A}\left[\frac{1}{2}\left(\frac{1-\lambda}{1+\lambda}\right)\right]$$

$$= 1.0 - \frac{4}{4}\left[\frac{1}{2}\left(\frac{1.0}{1.0}\right)\right]$$

$$= 0.5$$

$$\frac{A}{\kappa}[\beta^2 + \tan^2 \Lambda_{c/2}]^{1/2} = \frac{4}{1.0}[0.6279 + (0.5)^2]^{1/2} = 3.748$$

$$\frac{C_{L_\alpha}}{A} = 1.0 \text{ per rad} \qquad \text{(Figure 4.1.3.2-49)}$$

$$R_{\ell_{LER}} = 4.20 \times 10^6 \frac{0.00045\ \bar{c}}{\bar{c}} = 1.89 \times 10^3$$

$$R_{\ell_{LER}} \cot \Lambda_{LE} \sqrt{1 - M^2 \cos^2 \Lambda_{LE}} = (1.89 \times 10^3)(1.0)\sqrt{1 - (0.372)(0.7071)^2}$$

$$= 1.705 \times 10^3$$

$$\frac{A\lambda}{\cos \Lambda_{LE}} = \frac{(4.0)(0)}{(0.7071)} = 0$$

$R = 0.120$ (Figure 4.1.5.2-53a)

$$e = \frac{1.1\,(C_{L_\alpha}/A)}{R(C_{L_\alpha}/A) + (1-R)\pi} \qquad \text{(Equation 4.1.5.2-i)}$$

$$= \frac{1.1(1.0)}{0.120(1.0) + (1-0.120)\pi}$$

$$= 0.382$$

$$(C_{D_L})_W = \frac{C_L^{\,2}}{\pi Ae} + C_L \theta c_{\ell_\alpha} v + (\theta c_{\ell_\alpha})^2 w \qquad \text{(Equation 4.1.5.2-h)}$$

$$= \frac{C_L^{\,2}}{\pi(4.0)(0.382)}$$

C_L	$C_{D_L} = 0.209\ C_L^2$
0	0
0.05	0.00052
0.10	0.00209
0.15	0.00470
0.20	0.00836
0.25	0.01306
0.30	0.01881
0.35	0.02560
0.40	0.03344
0.50	0.05225

Body Drag Due to Lift (Section 4.2.3.2)

$k_2 - k_1 = 0.94$ (Figure 4.2.1.1-20a)

$x_1 = 46.93$ (by inspection)

$$\frac{x_1}{\ell_B} = 1.0$$

$$\frac{x_o}{\ell_B} = 0.905 \qquad \text{(Figure 4.2.1.1-20b)}$$

$x_o = 42.47$ in.

$$(r)_{x_o} = 2.38 \left[1 - \left(1 - \frac{2(42.4)}{59.5}\right)^2\right]^{3/2} = 1.765 \text{ in.}$$

$S_o = \pi r^2 = \pi(1.765)^2 = 9.79$ in.^{2}

$$C_{L_\alpha} = \frac{2(k_2 - k_1)\, S_o}{V_B^{2/3}} \qquad \text{(Equation 4.2.1.1-a)}$$

$$= \frac{2(0.94)(9.79)}{(0.4164)144}$$

$= 0.307$ per rad

$\eta = 0.686$ (Figure 4.2.1.2-23a)

$M_c = M \sin \alpha$

The α range is approximately $0 \leqslant \alpha \leqslant 10^o$

M_c varies from 0.6(0) to 0.6(0.1736)

$0 \leqslant M_c \leqslant 0.104$

$c_{d_c} = 1.20$ (constant) (Figure 4.2.1.2-23b)

$$\int_{X_o}^{\ell_B} \eta \, r \, c_{d_c} \, dx = \int_{42.47}^{46.93} (0.686) \, r \, (1.20) \, dx$$

Assuming r varies linearly from x_o to ℓ_B

$$\int_{X_o}^{\ell_B} \eta \, r \, c_{d_c} \, dx = \int_{42.47}^{46.93} (0.686) \left(\frac{1.765 + 1.295}{2} \right) (1.20) dx$$

$$= 1.26(46.93 - 42.47)$$

$$= 5.62 \text{ sq in.} = 0.0390 \text{ sq ft}$$

$$C_D(\alpha) = \frac{k_2 - k_1}{V_B^{2/3}} 2 \alpha^2 S_o + \frac{2 \alpha^3}{V_B^{2/3}} \int_{x_o}^{\ell_B} \eta \, r \, c_{d_c} \, dx \qquad \text{(Equation 4.2.3.2-b)}$$

$$= 0.307 \alpha^2 + \frac{2 \alpha^3}{0.4164} (0.0390)$$

$$= 0.307 \alpha^2 + 0.187 \alpha^3$$

Equation 4.2.3.2-b becomes

$$[C_D(\alpha)]_B \frac{S_{B_{ref}}}{S_W} = (0.307 \alpha^2 + 0.187 \alpha^3) \frac{V_B^{2/3}}{S_W}$$

$$= (0.307 \alpha^2 + 0.187 \alpha^3) \frac{0.4164}{2.425}$$

$$= 0.0527 \alpha^2 + 0.0321 \alpha^3$$

$(C_{L_\alpha})_W = (C_{L_\alpha}/A) \, A = (1.0)(4.0) = 4.0$ per rad

(1)	(2)	(3)	(4)	(5)
C_L	$\alpha = \frac{C_L^*}{(C_{L_\alpha})_W}$ (rad)	$0.0527\,\alpha^2$	$0.0321\,\alpha^3$	$[C_D(\alpha)]_B \frac{S_{B_{ref}}}{S_W}$ (3) + (4)
0	0	0	0	0
0.05	0.0125	0.000008	0	0.000008
0.10	0.0250	0.000033	0.000001	0.000034
0.15	0.0375	0.000074	0.000002	0.000076
0.20	0.0500	0.000132	0.000004	0.000136
0.25	0.0625	0.000206	0.000008	0.000214
0.30	0.0750	0.000296	0.000014	0.000310
0.35	0.0875	0.000403	0.000022	0.000425
0.40	0.1000	0.000527	0.000032	0.000559
0.50	0.1250	0.000823	0.000063	0.000886

Solution:

$$(C_{D_L})_{WB} = (C_{D_L})_W + [C_D(\alpha)]_B \frac{S_{B_{ref}}}{S_W} \qquad \text{(Equation 4.3.3.2-a)}$$

(1)	(2)	(3)	(4)
C_L	$(C_{D_L})_W$	$[C_D(\alpha)]_B \frac{S_{B_{ref}}}{S_W}$	$(C_{D_L})_{WB}$ (2) + (3)
0	0	0	0
0.05	0.00052	0.000008	0.00053
0.10	0.00209	0.000034	0.00212
0.15	0.00470	0.000076	0.00478
0.20	0.00836	0.000136	0.00850
0.25	0.01306	0.000214	0.01327
0.30	0.01881	0.000310	0.01912
0.35	0.02560	0.000425	0.02603
0.40	0.03344	0.000559	0.03400
0.50	0.05225	0.000886	0.05314

These calculated results are compared with the calculated results from Method 1 and the test values from Reference 3 in Sketch (b).

*This approximation assumes a zero lift value of zero.

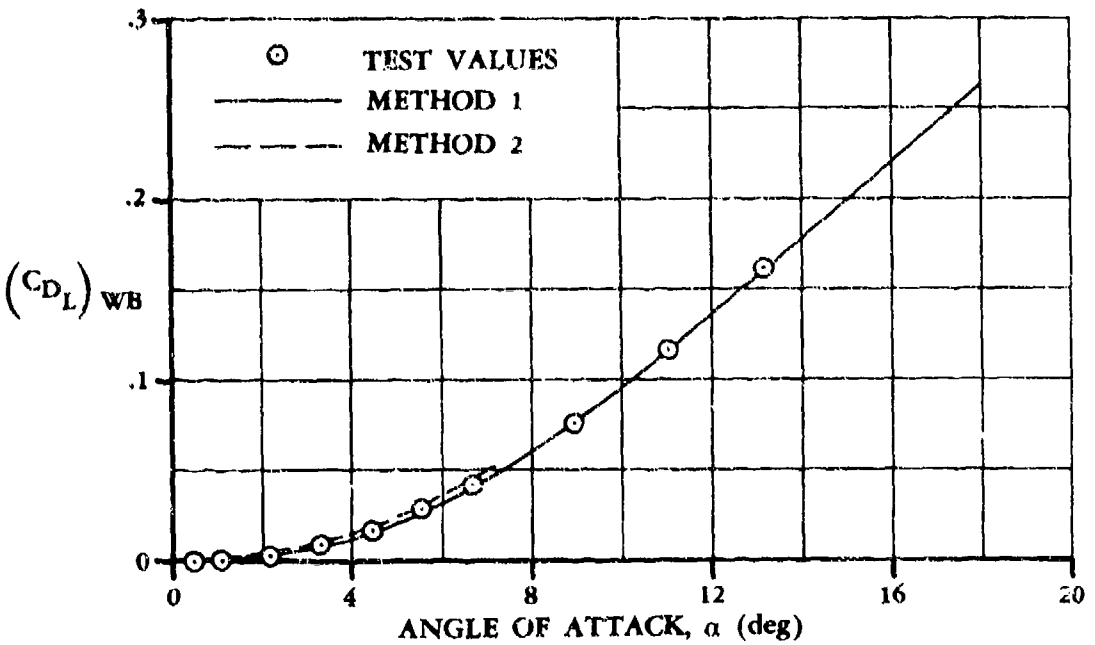

SKETCH (b)

B. TRANSONIC

The comments presented in the discussion preceding Paragraph A are applicable here.

DATCOM METHODS

At transonic speeds the methods described in Paragraph A may be applied. Both methods are restricted to straight-tapered-wing configurations. Method 1 may be applied in the high-lift region; while Method 2 is restricted to the parabolic-drag region.

An indication of the accuracy of Method 1 can be obtained from Table 4.3.3.2-B. This table contains a comparison of test values with results calculated by using this method for wing-body configurations without camber.

Sample Problem

No sample problem is presented for Method 1 because its application is identical to that in the subsonic speed regime.

Method 2

Given: A wing-body configuration of Reference 2 designated 45-series.

Wing Characteristics:

$A = 3.0$ $\quad \lambda = 0.40$ $\quad b_W = 10.8$ in. $\quad \Lambda_{LE} = 45^o$

$\Lambda_{c/2} = 35.54^o$ $\quad (t/c)_{av} = 0.045$ $\quad S_W = 38.889$ sq in. $\quad$ Round-nosed airfoil

Additional Characteristics:

$\frac{S_b}{S_W} = 0.0278$ $\quad 0 \le C_L \le 0.50$ $\quad M = 1.02;\ \beta = 0.20$ $\quad \kappa = 1.0$ (assumed)

Compute:

Wing Drag Due to Lift (Section 4.1.5.2)

$$\left(t/c\right)^{1/3} = 0.3557$$

$$\left(t/c\right)^{2/3} = 0.1265$$

$$A\left(t/c\right)^{1/3} = 3(0.3557) = 1.067$$

$$A \tan \Lambda_{LE} = 3.0$$

$$\frac{M^2 - 1}{(t/c)^{2/3}} = \frac{0.0404}{0.1265} = 0.319$$

$$\left(\frac{t}{c}\right)^{-1/3} \frac{C_{D_L}}{C_L{}^2} = 0.590 \quad \text{(Figure 4.1.5.2-55b, interpolated)}$$

$$\frac{C_{D_L}}{C_L{}^2} = 0.590\,(0.3557) = 0.210$$

① C_L	② $C_L{}^2$	③ $\left(C_{D_L}\right)_W$ 0.210 ②
0	0	0
.05	.0025	.00053
.10	.0100	.00210
.15	.0225	.00473
.20	.0400	.00840
.25	.0625	.01313
.30	.0900	.01890
.35	.1225	.02573
.40	.1600	.03360
.45	.2025	.04253
.50	.2500	.05250

Body Drag Due to Lift (Section 4.2.3.2)

$$\left[\left(C_{L_\alpha}\right)_W\right]_{M\,=\,1.02} = 4.0 \text{ per rad} \quad \text{(method of Paragraph B, Section 4.1.3.2)}$$

Equation 4.2.3.2-e becomes $\left[C_D(\alpha)\right]_B \frac{S_b}{S_W} = \alpha^2 \frac{S_b}{S_W}$

①	②	③	④
C_L	$C_L / \left(C_{L_\alpha}\right)_W$ ① /4.0 (rad)	α^2 (rad^2)	$\left[C_D(\alpha)\right]_B \frac{S_b}{S_W}$ ③ (0.0278)
0	0	0	0
.05	.0125	.00016	0
.10	.0250	.00063	.00002
.15	.0375	.00141	.00004
.20	.0500	.00250	.00007
.25	.0625	.00391	.00011
.30	.0750	.00563	.00016
.35	.0875	.00766	.00021
.40	.1000	.01000	.00028
.45	.1125	.01266	.00035
.50	.1250	.01563	.00043

Solution:

$$\left(C_{D_L}\right)_{WB} = \left(C_{D_L}\right)_W + \left[C_D(\alpha)\right]_B \frac{S_b}{S_W} \quad \text{(Equation 4.3.3.2-a)}$$

①	②	③	④
C_L	$\left(C_{D_L}\right)_W$	$\left[C_D(\alpha)\right]_B \frac{S_b}{S_W}$	$\left(C_{D_L}\right)_{WB}$ ② + ③
0	0	0	0
.05	.00053	0	.00053
.10	.00210	.00002	.00212
.15	.00473	.00004	.00477
.20	.00840	.00007	.00847
.25	.01313	.00011	.01324
.30	.01890	.00016	.01906
.35	.02573	.00021	.02594
.40	.03360	.00028	.03388
.45	.04253	.00035	.04288
.50	.05250	.00043	.05293

The calculated results are compared with test values from Reference 4 in Sketch (c).

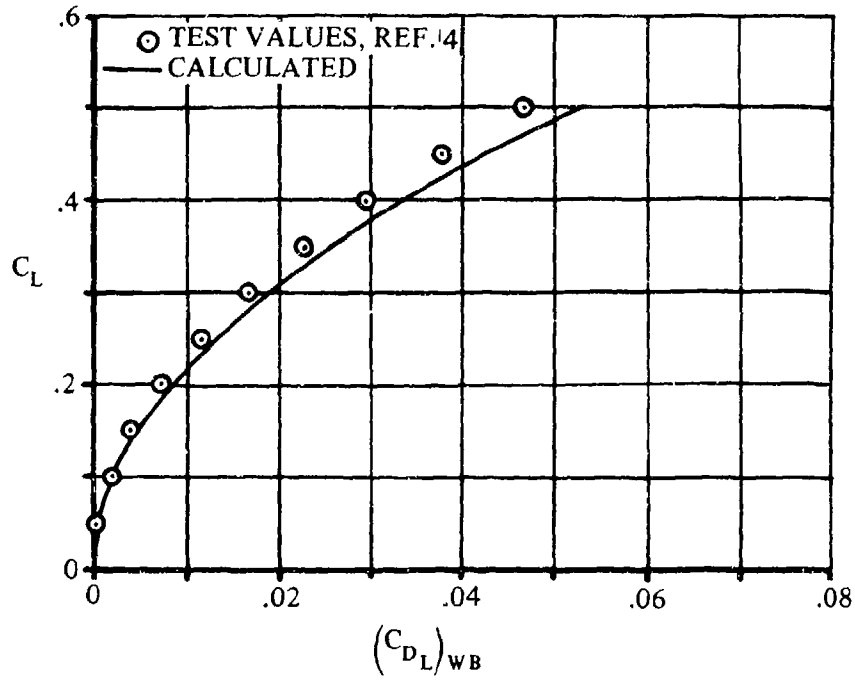

SKETCH (c)

C. SUPERSONIC

The comments presented in the discussion preceding Paragraph A are applicable here.

DATCOM METHODS

At supersonic speeds the methods described in Paragraph A may be applied. Method 1 is restricted to straight-tapered planforms; while Method 2 may be applied to either straight-tapered or non-straight-tapered wings. An indication of the accuracy of Method 1 can be obtained from Table 4.3.3.2-C. This table contains a comparison of test values with results calculated by using this method for wing-body configurations without camber.

Sample Problem

No sample problem is presented for Method 1 because its application is identical to that in the subsonic speed regime.

Method 2

Given: The wing-body configuration of Reference 5.

Wing Characteristics:

$A = 3.50$ $b_W = 24$ in. $\lambda = 0.20$ $\Lambda_{LE} = 51.6^o$

$\ell = 17.44$ in. $S_W = 164.64$ sq in. $\delta_\perp = 8.4^o$

Airfoil: 6-percent-thick hexagonal section with maximum thickness at c/3 (sharp-nosed airfoil)

Additional Characteristics:

$M = 2.01$; $\beta = 1.744$ $\qquad S_b = 12.57$ sq in.

$0 \leq C_L \leq 0.40$ $\qquad S_p = 154$ sq in.

Compute:

Wing Drag Due to Lift (Section 4.1.5.2)

$$\frac{\beta b_W}{2\ell} = \frac{1.744\,(24)}{2\,(17.44)} = 1.20$$

$$p = \frac{S_W}{b_W \ell} = \frac{164.64}{24\,(17.44)} = 0.393$$

$$\pi A \frac{C_{D_L}}{C_L^2} \frac{p}{1+p} = 1.29 \qquad \text{(Figure 4.1.5.2-58)}$$

$$\frac{C_{D_L}}{C_L^2} = \left[\pi A \frac{C_{D_L}}{C_L^2} \frac{p}{1+p}\right] \frac{1}{\pi A} \frac{1+p}{p} \qquad \text{(Equation 4.1.5.2-n)}$$

$$= 1.29 \left(\frac{1}{\pi(3.5)}\right)\left(\frac{1.393}{0.393}\right)$$

$$= 0.416$$

①	②	③
C_L	C_L^2	$\frac{C_{D_L}}{0.416}$ ②
0	0	0
0.05	0.0025	0.00104
0.10	0.0100	0.00416
0.15	0.0225	0.00936
0.20	0.0400	0.01664
0.25	0.0625	0.02600
0.30	0.0900	0.03744
0.35	0.1225	0.05096
0.40	0.1600	0.06656

Body Drag Due to Lift (Section 4.2.3.2)

Wing C_{N_α} (Section 4.1.3.2)

$$\frac{\tan \Lambda_{LE}}{\beta} = \frac{1.262}{1.744} = 0.724$$

$$A \tan \Lambda_{LE} = 3.5\,(1.262) = 4.42$$

$$\beta\left(C_{N_\alpha}\right)_{theory} = 4.24 \text{ per rad} \quad \text{(Figure 4.1.3.2-56b)}$$

$$\left(C_{N_\alpha}\right)_{theory} = 4.24/1.744 = 2.\ldots \text{ per rad}$$

$$\frac{C_{N_\alpha}}{\left(C_{N_\alpha}\right)_{theory}} = 0.895 \quad \text{(Figure 4.1.3.2-60)}$$

$$C_{N_\alpha} = (2.43)\,(0.895) = 2.17 \text{ per rad}$$

$\left[C_D(\alpha)\right]_B$ (based on body base area)

$$\left[C_D(\alpha)\right]_B = 2\alpha^2 + c_{d_c}\frac{S_p}{S_b}\alpha^3 \quad \text{(Equation 4.2.3.2-g)}$$

$$\frac{S_p}{S_b} = \frac{154}{12.57} = 12.25$$

①	②	③	④	⑤	⑥	⑦	⑧	⑨
C_L	$\alpha_{C_L/(C_{N_\alpha})_W}$ ①/2.17 (rad)	α^2 (rad^2)	α^3 (rad^3)	α (deg)	M_c M sin α	c_{d_c} Fig. 4.2.1.2-23b	$c_{d_c}\frac{S_p}{S_b}$ ⑦ 12.25	$\left[C_D(\alpha)\right]_B$ 2③+④⑧
0	0	0	0	0	0	1.20	14.70	0
0.05	0.0230	0.00053	0.00001	1.32	0.0463	1.20	14.70	0.00121
0.10	0.0461	0.00213	0.00010	2.64	0.0926	1.20	14.70	0.00573
0.15	0.0691	0.00477	0.00033	3.96	0.1388	1.20	14.70	0.01439
0.20	0.0922	0.00850	0.00078	5.28	0.1850	1.20	14.70	0.02847
0.25	0.1152	0.01327	0.00153	6.60	0.2310	1.20	14.70	0.04903
0.30	0.1382	0.01910	0.00264	7.92	0.2770	1.21	14.82	0.07732
0.35	0.1613	0.02602	0.00420	9.24	0.3227	1.213	14.98	0.11495
0.40	0.1843	0.03397	0.00626	10.56	0.3684	1.244	15.24	0.16334

Solution:

Equation 4.3.3.2-a becomes

$$\left(C_{D_L}\right)_{WB} = \left(C_{D_L}\right)_W + \left[C_D(\alpha)\right]_B \frac{S_b}{S_W}$$

$$\frac{S_b}{S_W} = \frac{12.57}{164.64} = 0.0763$$

(1)	(2)	(3)	(4)
C_L	C_{D_L}	$[C_D(\alpha)]_B$ (based on S_b)	$(C_{D_L})_{WB}$ (2) + 0.0763 (3)
0.05	0.00104	0.00121	0.0011
0.10	0.00416	0.00573	0.0046
0.15	0.00936	0.01439	0.0105
0.20	0.01664	0.02847	0.0188
0.25	0.02600	0.04903	0.0297
0.30	0.03744	0.07732	0.0433
0.35	0.05096	0.11495	0.0597
0.40	0.06656	0.16334	0.0790

The calculated results are compared with test values from Reference 5 in Sketch (d).

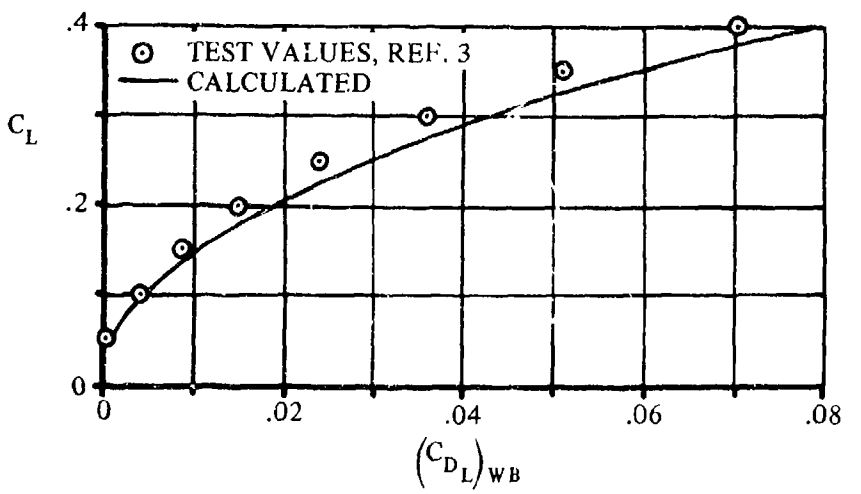

SKETCH (d)

REFERENCES

1. Simon, W. E., et al.: Prediction of Aircraft Drag Due to Lift. AFFDL-TR-71-84, 1971. (U)

2. Boyd, J. W., Migotsky, E., and Wetzel, B. E.: A Study of Conical Camber for Triangular and Sweptback Wings. NACA RM A55G19, 1955. (U)

3. Hall, C. F.: Lift, Drag, and Pitching Moment of Low-Aspect-Ratio Wings at Subsonic and Supersonic Speeds. NACA RM A53A30, 1953. (U)

4. Wakefield, R. M.: Effects of Wing-Crank, Leading-Edge Chord Extensions and Horizontal-Tail Height on the Longitudinal Stability of Swept-Wing Models at Mach Numbers from 0.6 to 1.4. NASA TM X-92, 1959. (U)

5. Carlson, H. W., and Gapcynski, J. P.: An Experimental Investigation at a Mach Number of 2.01 of the Effects of Body Cross-Section Shape on the Aerodynamic Characteristics of Bodies and Wing-Body Combinations. NACA RM L55E23, 1955. (U)

6. Kuhn, R. E., and Wiggins, J. W.: Wind-Tunnel Investigation of the Aerodynamic Characteristics in Pitch of Wing-Fuselage Combinations at High Subsonic Speeds — Aspect-Ratio Series. NACA RM L52A29, 1952. (U)

7. Tinling, B. E., and Kolk, W. R.: The Effects of Mach Number and Reynolds Number on the Aerodynamic Characteristics of Several 12-Percent-Thick Wings Having 35° of Sweepback and Various Amounts of Camber. NACA RM A50K27, 1951. (U)

8. Boyd, J. W., and Peterson, V. L.: Static Stability and Control of Canard Configurations at Mach Numbers from 0.7 to 2.22 — Longitudinal Characteristics of a Triangular Wing and Canard. NACA RM A57J15, 1958. (U)

9. Palazzo, E. B., and Spearman, M. L.: Static Longitudinal and Lateral Stability and Control Characteristics of a Model of a 35° Swept-Wing Airplane at a Mach Number of 1.41. NACA RM L54G08, 1955. (U)

10. Cooper, M., and Sevier, J. R., Jr.: Effects of a Series of Inboard Plan-Form Modifications on the Longitudinal Characteristics of Two 47° Sweptback Wings of Aspect Ratio 3.5, Taper Ratio 0.2, and Different Thickness Distributions at Mach Numbers of 1.61 and 2.01. NACA RM L53E07a, 1953. (U)

11. Wetzel, B. E.: Effect of Taper Ratio on Lift, Drag, and Pitching-Moment Characteristics of Thin Wings of Aspect Ratio 3 with 53.1° Sweepback of Leading Edge at Subsonic and Supersonic Speeds. NACA RM A54J20, 1955. (U)

TABLE 4.3.3.2-A
SUBSONIC WING-BODY DRAG DUE TO LIFT OF STRAIGHT-TAPERED WINGS
METHOD 1
DATA SUMMARY AND SUBSTANTIATION
NO TWIST OR CAMBER

Ref	A	λ	Λ_{LE} (deg)	NACA Airfoil	$Rg_{MAC} \times 10^{-6}$	M	α	C_{D_L} Calc.	C_{D_L} Test	ΔC_{D_L}
3	3.0	0	53.1	0003-63	5.9	0.25	4	0.010	0.010	0
							8	0.052	0.045	0.007
							12	0.124	0.114	0.010
							14	0.164	0.156	0.008
							16	0.213	0.203	0.010
					4.8	0.61	4	0.011	0.012	−0.001
							8	0.053	0.052	0.001
							10	0.084	0.084	0
							12	0.125	0.125	0
	2.0	0	63.4	0003-63	3.0	0.81	4	0.009	0.012	−0.003
							8	0.050	0.060	−0.010
							12	0.116	0.130	−0.014
							14	0.168	0.184	−0.016
							16	0.224	0.243	−0.019
	4.0	0	45.0	biconvex t/c=0.03	9.1	0.25	4	0.010	0.010	0
							8	0.057	0.053	0.004
							12	0.128	0.121	0.007
							14	0.177	0.170	0.007
					4.2	0.61	4	0.012	0.015	−0.003
							8	0.061	0.061	0
							10	0.097	0.097	0
							12	0.136	0.139	−0.003
	2.0	0	63.4	0005-63	3.0	0.40	4	0.008	0.008	0
							8	0.038	0.038	0
							12	0.093	0.089	0.004
							14	0.130	0.127	0.003
							16	0.182	0.178	0.004
					8.0	0.25	4	0.006	0.006	0
							8	0.034	0.025	0.009
							12	0.095	0.080	0.015
							14	0.135	0.117	0.018
							16	0.186	0.166	0.020
				0008-63	3.0	0.40	4	0.006	0.008	−0.002
							8	0.028	0.026	0.002
							12	0.084	0.066	0.018
							14	0.130	0.100	0.030
							16	0.181	0.139	0.042
						0.60	4	0.006	0.006	0
							8	0.028	0.028	0
							12	0.084	0.080	0.004
							14	0.129	0.120	0.009
							16	0.182	0.170	0.012
						0.80	4	0.006	0.008	−0.002
							8	0.036	0.036	0
							12	0.108	0.102	0.006
							14	0.149	0.142	0.007
							16	0.198	0.190	0.008
		0.333	45.0	biconvex t/c=0.03	4.8	0.61	4	0.012	0.012	0
							8	0.056	0.055	0.001
							10	0.088	0.088	0
							12	0.129	0.132	−0.003
							14	0.169	0.171	−0.002

TABLE 4.3.3.2-A (CONTD)

Ref	A	λ	Λ_{LE} (deg)	NACA Airfoil	$R_{\ell_{MAC}} \times 10^{-6}$	M	α	C_{D_L} Calc.	C_{D_L} Test	ΔC_{D_L}
3	3.08	0.388	19.1	biconvex t/c=0.03	3.8	0.61	4	0.014	0.013	0.001
							8	0.066	0.066	0
							12	0.153	0.153	0
							14	0.196	0.196	0
							16	0.231	0.217	0.014
						0.71	4	0.014	0.014	0
							8	0.068	0.068	0
							12	0.150	0.152	−0.002
							14	0.179	0.183	−0.004
							16	0.213	0.223	−0.010
6	2.0	0.600	48.4	65A006	4.53	0.60	4	0.006	0.006	0
							8	0.035	0.039	−0.004
							12	0.099	0.114	−0.015
							14	0.141	0.166	−0.025
							16	0.190	0.220	−0.030
					5.46	0.80	4	0.009	0.008	0.001
							8	0.043	0.045	−0.002
							12	0.122	0.129	−0.007
							14	0.162	0.167	−0.005
							16	0.198	0.202	−0.004
	4.0	0.600	46.7	65A006	2.78	0.60	4	0.007	0.007	0
							8	0.047	0.043	0.004
							12	0.128	0.138	−0.010
							14	0.171	0.182	−0.011
							16	0.222	0.234	−0.012
					3.35	0.80	4	0.010	0.010	0
							8	0.061	0.059	0.002
							12	0.145	0.133	0.012
							14	0.191	0.176	0.015
							16	0.221	0.214	0.007
	.0	0.600	46.2	65A006	2.39	0.70	4	0.007	0.007	0
							8	0.058	0.045	0.013
							12	0.129	0.118	0.011
							14	0.159	0.167	−0.008
							16	0.177	0.215	−0.038
7	5.14	0.713	36.2	65_1A012	2.0	0.40	4	0.004	0.005	−0.001
							8	0.040	0.019	0.021
							12	0.121	0.090	0.031
							14	0.170	0.148	0.022
							16	0.240	0.194	0.046
						0.80	4	0.008	0.007	0.001
							8	0.060	0.051	0.009
							10	0.106	0.100	0.006
							12	0.150	0.150	0
							14	0.175	0.175	0
									$\lvert\Delta C_{D_L}\rvert_{av}$ =	0.008

TABLE 4.3.3.2-B
TRANSONIC WING-BODY DRAG DUE TO LIFT OF STRAIGHT-TAPERED WINGS
METHOD 1
DATA SUMMARY AND SUBSTANTIATION
NO TWIST OR CAMBER

Ref	A	λ	Λ_{LE} (deg)	NACA Airfoil	$R_{\ell_{MAC}} \times 10^{-6}$	M	α	C_{D_L} Calc.	C_{D_L} Test	ΔC_{D_L}
3	3.0	0	53.1	0003-63	1.9	0.92	4	0.013	0.017	−0.004
							6	0.036	0.041	−0.005
							8	0.066	0.070	−0.004
						1.2	4	0.010	0.015	−0.005
							8	0.055	0.067	−0.012
							12	0.128	0.150	−0.022
							14	0.177	0.199	−0.022
	3.08	0.388	19.1	biconvex t/c=0.03	1.4	1.2	4	0.020	0.019	0.001
							8	0.085	0.086	−0.001
							10	0.129	0.135	−0.006
							12	0.180	0.191	−0.011
							14	0.241	0.249	−0.008
	3.0	0.4	45.0	biconvex t/c=0.03	3.8	0.91	4	0.015	0.017	−0.002
							6	0.041	0.043	−0.002
							7	0.060	0.060	0
	2.0	0.333	45.0	biconvex t/c=0.03	1.9	0.93	4	0.017	0.014	0.003
							6	0.042	0.039	0.003
							8	0.073	0.071	0.002
						1.2	4	0.015	0.015	0
							6	0.036	0.037	−0.001
							8	0.067	0.069	−0.002
							10	0.103	0.109	−0.006
8	2.0	0	63.3	0003-63	1.84	1.0	4	0.012	0.017	−0.005
							6	0.027	0.032	−0.005
							8	0.061	0.063	−0.002
							10	0.103	0.098	0.005
						1.1	4	0.011	0.013	−0.002
							8	0.053	0.056	−0.003
							10	0.087	0.090	−0.003
							12	0.129	0.127	0.002
							14	0.184	0.180	0.004

$|\Delta C_{D_L}|_{av} = 0.005$

TABLE 4.3.3.2-C
SUPERSONIC WING-BODY DRAG DUE TO LIFT OF STRAIGHT-TAPERED WINGS
METHOD 1
DATA SUMMARY AND SUBSTANTIATION
NO TWIST OR CAMBER

Ref	A	λ	Λ_{LE} (deg)	NACA Airfoil	$R_{\ell_{MAC}} \times 10^{-6}$	M	α	C_{D_L} Calc.	C_{D_L} Test	ΔC_{D_L}
2	3.0	0.40	45.0	64A005	2.9	1.50	4	0.015	0.013	0.002
							8	0.058	0.053	0.005
							10	0.089	0.087	0.002
							12	0.126	0.120	0.006
							14	0.175	0.160	0.015
						1.90	4	0.018	0.011	0.007
							8	0.050	0.043	0.007
							10	0.075	0.065	0.010
							12	0.103	0.094	0.009
							14	0.138	0.128	0.010

TABLE 4.3.3.2-C (CONTD)

Ref	A	λ	Λ_{LE} (deg)	NACA Airfoil	$R\varrho_{MAC} \times 10^{-6}$	M	α	C_{D_L} Calc.	C_{D_L} Test	ΔC_{D_L}
9	4.0	0.50	38.1	65A006	1.96	1.41	4	0.018	0.016	0.002
				65A004			6	0.039	0.037	0.002
							8	0.066	0.064	0.002
							10	0.105	0.101	0.004
10	3.5	0.20	51.6	hexagonal	2.68	1.61	4	0.022	0.013	0.009
				t/c=0.06			6	0.044	0.029	0.015
							8	0.076	0.052	0.024
							10	0.119	0.081	0.038
						2.01	4	0.010	0.012	−0.002
							6	0.025	0.024	0.001
							8	0.050	0.048	0.002
11	3.0	0	53.1	0003-63	3.6	1.5	4	0.014	0.013	0.001
							8	0.053	0.055	−0.002
							10	0.081	0.082	−0.001
							12	0.113	0.120	−0.007
							14	0.160	0.157	0.003
						1.9	4	0.009	0.011	−0.002
							8	0.037	0.041	−0.004
							10	0.060	0.063	−0.003
							12	0.089	0.091	−0.002
							14	0.125	0.123	0.002
		0.20			3.1	1.5	4	0.017	0.015	0.002
							8	0.063	0.055	0.008
							10	0.096	0.088	0.008
							12	0.133	0.126	0.007
							14	0.180	0.157	0.023
						1.9	4	0.014	0.011	0.003
							8	0.048	0.043	0.005
							10	0.074	0.067	0.007
							12	0.105	0.093	0.012
							14	0.146	0.125	0.021
		0.40			2.9	1.5	4	0.016	0.014	0.002
							8	0.055	0.053	0.002
							10	0.083	0.080	0.003
							12	0.122	0.114	0.008
							14	0.178	0.153	0.025
						1.9	4	0.020	0.011	0.009
							8	0.055	0.043	0.012
							10	0.078	0.067	0.011
							12	0.108	0.092	0.016
							14	0.150	0.122	0.028
8	2.0	0	63.26	0003-63	1.84	1.3	4	0.008	0.010	−0.002
							8	0.044	0.046	−0.002
							10	0.072	0.078	−0.006
							12	0.104	0.109	−0.005
							14	0.150	0.153	−0.003
						1.9	4	0.007	0.008	−0.001
							8	0.030	0.034	−0.004
							10	0.050	0.052	−0.002
							12	0.073	0.072	0.001
							14	0.103	0.097	0.006
									$\lvert\Delta C_{D_L}\rvert_{av}$ =	0.007

TABLE 4.3.3.2-D
METHOD 1
REGRESSION COEFFICIENTS
M = 0.600

α	B_0	B_1	B_2	B_3	B_4	B_5
1	0.00045	0.00165	0.00026	−0.00069	0.00192	−0.00004
2	0.00353	0.00445	0.00042	−0.00109	−0.01622	−0.00029
3	0.01317	−0.00024	0.00013	−0.00266	−0.03562	−0.00043
4	0.02608	−0.00589	−0.00014	−0.00588	−0.05901	−0.00043
5	0.04109	−0.01099	0.00023	−0.00694	−0.14925	−0.00082
6	0.05140	−0.00482	0.00223	−0.01028	−0.24447	−0.00112
7	0.05749	0.00003	0.00539	−0.01129	−0.33547	−0.00137
8	0.07379	−0.00890	0.00734	−0.01049	−0.44144	−0.00175
9	0.09548	−0.03037	0.00885	−0.00781	−0.58794	−0.00170
10	0.12873	−0.05227	0.00855	−0.00826	−0.69952	−0.00295
11	0.15889	−0.07595	0.00833	−0.01261	−0.82886	−0.00220
12	0.18028	−0.07664	0.00745	−0.01593	−0.90625	−0.00181
13	0.21132	−0.11041	0.00433	−0.01859	−0.70087	−0.00001
14	0.25119	−0.14562	0.00092	−0.01361	−0.66342	0.00038
15	0.25845	−0.15418	0.00148	−0.00483	−0.69530	0.00152
16	0.28929	−0.18997	0.00143	−0.00886	−0.85331	0.00161
17	0.30498	−0.20240	−0.00196	0.02569	−0.65569	0.00096
18	0.31398	−0.22017	−0.00140	0.04032	−0.51782	0.00025

α	B_6	B_7	B_8	B_9	B_{10}	B_{11}
1	−0.00017	0.00079	−0.00243	0.00100	−0.00003	−0.00127
2	−0.00030	0.00434	−0.00817	0.00277	0.00001	−0.01298
3	−0.00047	0.00775	−0.02023	0.01039	−0.00038	−0.05350
4	−0.00068	0.01653	−0.04953	0.02785	−0.00165	−0.10679
5	−0.00121	0.02395	−0.05927	0.03084	−0.00222	−0.02883
6	−0.00168	0.04265	−0.11424	0.06512	−0.00275	0.19133
7	−0.00261	0.06777	−0.16815	0.09609	−0.00309	0.32420
8	−0.00330	0.09456	−0.23327	0.14239	−0.00204	0.77765
9	−0.00486	0.11723	−0.25173	0.14974	−0.00243	1.51741
10	−0.00487	0.14051	−0.28982	0.16952	−0.00215	2.27613
11	−0.00595	0.16340	−0.32756	0.18710	−0.00370	3.88429
12	−0.00386	0.19145	−0.42892	0.26626	−0.00202	4.34530
13	−0.00504	0.21710	−0.50195	0.30725	−0.00346	3.76319
14	−0.00566	0.22051	−0.50067	0.30752	−0.00086	3.48312
15	−0.00791	0.22128	−0.45958	0.28357	0.00040	4.43698
16	−0.01134	0.20554	−0.39035	0.25450	0.00294	6.01805
17	−0.00901	0.23888	−0.50267	0.32743	0.00370	4.60500
18	−0.00926	0.29613	−0.70455	0.49100	0.00020	4.00069

α	B_{12}	B_{13}	B_{14}	$B_{15} \times 10^{+6}$
1	0.02836	0.00293	−0.00471	−0.00004
2	0.05179	0.03795	−0.00819	−0.00022
3	0.07105	0.05725	−0.01192	−0.00033
4	0.08494	0.07442	−0.01580	−0.00036
5	0.09681	0.02204	−0.02255	−0.00049
6	0.11610	−0.10824	−0.03253	−0.00061
7	0.14943	−0.35912	−0.04761	−0.00049
8	0.19746	−0.49931	−0.06384	−0.00077
9	0.29222	−0.47586	−0.07863	−0.00067
10	0.34643	−0.52607	−0.09097	−0.00076
11	0.39755	−0.49629	−0.10051	0.00002
12	0.43743	−0.48216	−0.10223	0.00044
13	0.49084	−0.30237	−0.10159	0.00092
14	0.51916	−0.11923	−0.09866	0.00021
15	0.50871	−0.06195	−0.09704	0.00095
16	0.49258	0.00176	−0.10124	0.00083
17	0.49678	0.00645	−0.09760	0.00009
18	0.52715	−0.01712	−0.09182	0.00077

TABLE 4.3.3.2-D (CONTD)
METHOD 1
REGRESSION COEFFICIENTS
M = 0.700

α	B_0	B_1	B_2	B_3	B_4	B_5
1	−0.00007	0.00201	0.00022	−0.00135	−0.00725	0.00007
2	−0.00033	0.00463	0.00074	−0.00148	−0.03061	0.00012
3	0.00298	0.00816	0.00104	−0.00409	−0.05738	0.00022
4	0.00952	0.00977	0.00158	−0.00596	−0.10542	0.00024
5	0.01365	0.01690	0.00255	−0.00959	−0.16575	0.00060
6	0.02140	0.02569	0.00468	−0.01204	−0.21467	−0.00007
7	0.03280	0.03299	0.00753	−0.01552	−0.31023	−0.00068
8	0.04427	0.02903	0.01022	−0.01617	−0.41625	−0.00056
9	0.07156	0.01444	0.01163	−0.01605	−0.53882	−0.00079
10	0.11009	−0.02070	0.00879	−0.01748	−0.57938	−0.00131
11	0.13603	−0.04580	0.00794	−0.01852	−0.65951	−0.00053
12	0.09477	0.06299	0.01071	−0.01897	−0.54804	−0.00173
13	0.13093	0.02476	0.00847	−0.00460	−0.61551	−0.00301
14	0.15005	0.07016	0.00453	−0.02278	−0.26831	−0.00323
15	0.11178	0.13769	0.00500	0.00024	−0.01360	−0.00467
16	0.16474	0.10007	0.00168	−0.02076	0.23531	0.00169
17	0.27867	−0.01521	−0.00150	−0.03375	0.53500	0.00416
18	0.35631	−0.05496	−0.00269	−0.04285	0.32793	0.00590

α	B_6	B_7	B_8	B_9	B_{10}	B_{11}
1	−0.00001	0.00605	−0.01896	0.01137	0.00007	0.05663
2	−0.00038	0.01304	−0.03081	0.01730	−0.00037	0.17544
3	−0.00024	0.02194	−0.05995	0.03480	−0.00051	0.27522
4	−0.00071	0.03369	−0.08731	0.04965	−0.00072	0.35126
5	−0.00042	0.05308	−0.14787	0.08719	−0.00078	0.41736
6	−0.00069	0.07008	−0.19058	0.11191	−0.00074	0.21681
7	−0.00097	0.08932	−0.23841	0.13886	−0.00121	0.56157
8	−0.00254	0.13154	−0.33205	0.19557	0.00003	1.08763
9	−0.00512	0.16180	−0.37175	0.21318	0.00190	1.52565
10	−0.00517	0.19468	−0.43251	0.24542	0.00542	2.11903
11	−0.00530	0.19852	−0.43424	0.24919	0.00584	3.19374
12	0.00049	0.30677	−0.81576	0.52282	0.01558	2.42095
13	−0.00132	0.29722	−0.71510	0.45468	0.01598	2.83715
14	0.00483	0.22818	−0.52780	0.28270	0.02293	−0.19638
15	0.01013	0.30323	−0.81142	0.50265	0.02790	−2.43719
16	−0.00023	0.28821	−0.68001	0.35785	0.03395	−2.90182
17	−0.00071	0.26551	−1.03124	0.70318	0.02908	−7.14091
18	−0.00632	0.22175	−0.87165	0.58893	0.02677	−6.40790

α	B_{12}	B_{13}	B_{14}	$B_{15} \times 10^{+6}$
1	0.03248	0.02814	−0.00546	0.00012
2	0.04260	0.04867	−0.00974	0.00021
3	0.06622	0.06841	−0.01333	0.00028
4	0.09946	0.10427	−0.01888	0.00024
5	0.10760	0.01684	−0.02734	0.00043
6	0.14430	−0.12045	−0.04174	0.00035
7	0.18066	−0.27628	−0.05621	0.00015
8	0.24523	−0.46906	−0.07745	0.00034
9	0.33416	−0.43756	−0.09118	−0.00040
10	0.41420	−0.36868	−0.09857	−0.00051
11	0.45796	−0.33092	−0.10509	0.00037
12	0.45075	−0.14214	−0.08911	−0.00146
13	0.50671	−0.05438	−0.08978	−0.00174
14	0.28798	0.22777	−0.06876	−0.00277
15	0.26261	0.25419	−0.05078	−0.00464
16	0.31661	0.21182	−0.07109	−0.00514
17	0.20470	0.24062	−0.06928	−0.00801
18	0.27279	0.36714	−0.06778	−0.00899

TABLE 4.3.3.2-D (CONTD)
METHOD 1
REGRESSION COEFFICIENTS
M = 0.800

α	B_0	B_1	B_2	B_3	B_4	B_5
1	0.00221	−0.00144	−0.00009	−0.00073	−0.00797	0.00001
2	0.00338	−0.00302	0.00036	−0.00054	−0.04293	0.00016
3	0.01022	−0.00891	0.00044	−0.00118	−0.09171	0.00029
4	0.02014	−0.01193	0.00101	−0.00320	−0.16796	0.00031
5	0.03137	−0.01895	0.00175	−0.00608	−0.26045	0.00073
6	0.04483	−0.02209	0.00408	−0.00776	−0.38466	0.00035
7	0.06954	−0.02427	0.00622	−0.01036	−0.46785	−0.00004
8	0.08586	−0.04047	0.00675	−0.01503	−0.53205	0.00026
9	0.12288	−0.06032	0.00656	−0.01914	−0.61233	−0.00006
10	0.15902	−0.09484	0.00500	−0.01786	−0.67543	0.00000
11	0.19087	−0.12050	0.00376	−0.01996	−0.70864	0.00052
12	0.19993	−0.10093	0.00286	−0.00038	−0.80847	−0.00080
13	0.21762	−0.05886	0.00378	−0.01095	−0.87035	−0.00312
14	0.22825	−0.06174	0.00297	−0.00059	−0.75253	−0.00286
15	0.26345	−0.08437	−0.00007	0.01070	−0.72073	−0.00351
16	0.26728	−0.04519	0.00045	0.01068	−0.81612	−0.00314
17	0.26672	0.03024	0.00162	0.00616	−0.73124	−0.00435
18	0.38780	−0.06958	−0.00033	−0.04003	−0.00836	0.00680

α	B_6	B_7	B_8	B_9	B_{10}	B_{11}
1	−0.00011	0.00404	−0.00852	0.00366	−0.00020	0.04986
2	−0.00059	0.01149	−0.02119	0.01016	−0.00084	0.27904
3	−0.00081	0.01741	−0.03594	0.01916	−0.00120	0.48014
4	−0.00136	0.02455	−0.05123	0.02690	−0.00164	0.88190
5	−0.00160	0.03701	−0.08555	0.04712	−0.00185	1.46725
6	−0.00268	0.04932	−0.10395	0.05655	−0.00274	2.24272
7	−0.00275	0.06720	−0.13865	0.07161	−0.00361	2.52398
8	−0.00385	0.09758	−0.19441	0.09494	−0.00314	2.78528
9	−0.00533	0.13366	−0.27088	0.13617	−0.00244	3.34227
10	−0.00651	0.14191	−0.25370	0.11523	−0.00263	4.11935
11	−0.00645	0.12269	−0.19227	0.07658	−0.00338	4.86755
12	−0.00359	0.12092	−0.17696	0.07638	0.00149	5.29550
13	−0.00071	0.12946	−0.23012	0.11647	0.00542	4.41136
14	0.00082	0.11291	−0.19585	0.10526	0.00530	2.93353
15	0.00351	0.12110	−0.33286	0.23396	0.01239	1.94911
16	0.00615	0.17305	−0.52066	0.36192	0.01483	2.44009
17	0.00963	0.20127	−0.66993	0.46675	0.02226	1.45434
18	−0.01148	0.23079	−0.81556	0.53140	0.01939	−4.53597

α	B_{12}	B_{13}	B_{14}	$B_{15} \times 10^{+6}$
1	0.03464	0.03796	−0.00568	0.00011
2	0.05100	0.05301	−0.01138	0.00034
3	0.07937	0.08300	−0.01716	0.00055
4	0.10986	0.11608	−0.02432	0.00065
5	0.12995	0.04853	−0.03608	0.00101
6	0.17974	0.01871	−0.05082	0.00108
7	0.23537	−0.06230	−0.06341	0.00109
8	0.28989	−0.20397	−0.08082	0.00119
9	0.34386	−0.16500	−0.08837	0.00023
10	0.40218	−0.06673	−0.09428	0.00021
11	0.43511	0.01019	−0.09377	0.00072
12	0.44284	0.01175	−0.08753	−0.00022
13	0.39269	−0.55132	−0.08675	−0.00105
14	0.24896	0.03958	−0.07231	−0.00175
15	0.23602	−0.13912	−0.07000	−0.00357
16	0.21889	−0.40147	−0.08010	−0.00315
17	0.17675	−0.44420	−0.07856	−0.00488
18	0.35079	0.06490	−0.07221	−0.00986

TABLE 4.3.3.2-D (CONTD)
METHOD 1
REGRESSION COEFFICIENTS
M = 0.900

α	B_0	B_1	B_2	B_3	B_4	B_5
1	−0.00018	0.00149	0.00049	−0.00073	−0.01288	0.00002
2	0.00085	0.00228	0.00121	−0.00194	−0.03023	0.00020
3	0.00686	0.00006	0.00220	−0.00452	−0.09050	0.00033
4	0.01655	0.00152	0.00381	−0.00939	−0.16820	0.00044
5	0.03421	0.00025	0.00585	−0.01606	−0.31665	0.00011
6	0.05013	0.00707	0.00817	−0.02058	−0.40391	−0.00009
7	0.07780	−0.00719	0.00818	−0.02851	−0.48392	−0.00013
8	0.10210	−0.03657	0.00766	−0.02671	−0.49372	0.00080
9	0.14499	−0.06085	0.00615	−0.03327	−0.58207	0.00055
10	0.16459	−0.05228	0.00708	−0.03939	−0.57416	0.00041
11	0.17308	−0.01765	0.00635	−0.03038	−0.60311	−0.00147
12	0.24567	−0.01323	−0.00076	−0.04699	−0.52503	−0.00381
13	0.25980	−0.02503	−0.01431	−0.03221	0.02489	−0.00265
14	0.28659	−0.02031	−0.01516	−0.03412	−0.24196	−0.00242
15	0.35500	−0.10280	−0.03013	−0.00726	−0.15999	−0.00365
16	−0.02321	0.50911	0.05826	−0.07837	0.10819	0.00110
17	0.00224	0.41838	0.05118	−0.02457	−0.19688	−0.00106
18	−0.30160	0.86541	0.12481	−0.02627	−0.15727	−0.00442

α	B_6	B_7	B_8	B_9	B_{10}	B_{11}
1	−0.00029	0.00368	−0.00564	0.00171	−0.00034	0.15304
2	−0.00072	0.01144	−0.02520	0.01329	−0.00058	0.46101
3	−0.00119	0.01294	−0.02237	0.00728	−0.00094	1.09961
4	−0.00198	0.01829	−0.02715	0.00412	−0.00092	1.81146
5	−0.00250	0.03007	−0.05654	0.01904	−0.00117	3.06166
6	−0.00294	0.04804	−0.08597	0.02708	−0.00198	3.45630
7	−0.00267	0.07875	−0.15670	0.06535	−0.00157	3.48608
8	−0.00470	0.10510	−0.17727	0.06858	−0.00079	3.23396
9	−0.00499	0.12259	−0.20621	0.07849	−0.00095	3.85120
10	−0.00507	0.13288	−0.21749	0.07251	0.00073	3.69670
11	−0.00161	0.16048	−0.22384	0.05180	−0.00034	2.96357
12	0.00356	0.13104	−0.17885	−0.00130	0.00693	1.11615
13	0.00890	0.11813	−0.20085	0.01759	0.01678	−1.67578
14	0.00994	0.08659	−0.07871	−0.08308	0.02128	−0.12470
15	0.01574	0.11651	−0.16128	−0.00975	0.02559	−2.81231
16	0.00687	0.02378	0.11590	−0.29281	0.04029	−3.95931
17	0.00761	−0.07051	0.08506	1.29494	0.05010	−1.21388
18	0.00782	−0.17396	0.57898	0.55814	0.05542	−3.35470

α	B_{12}	B_{13}	B_{14}	$B_{15} \times 10^{+6}$
1	0.03891	0.09467	−0.00564	0.00009
2	0.07985	0.20140	−0.01169	0.00016
3	0.10833	0.27199	−0.01904	0.00040
4	0.14272	0.28821	−0.02860	0.00040
5	0.16786	0.18235	−0.04081	0.00046
6	0.19252	0.03040	−0.05024	0.00032
7	0.26545	0.11939	−0.05983	0.00022
8	0.31886	−0.00803	−0.06984	0.00025
9	0.35199	−0.03479	−0.07633	−0.00009
10	0.38080	−0.13176	−0.08018	−0.00031
11	0.40789	−0.30354	−0.07411	−0.00174
12	0.38815	−0.39060	−0.06307	−0.00512
13	0.30251	−0.36091	−0.04905	−0.00682
14	0.28643	−0.42389	−0.05155	−0.00616
15	0.25151	−0.54633	−0.03975	−0.00792
16	0.28255	−0.09940	−0.05434	−0.00883
17	0.27277	0.21319	−0.05330	−0.00839
18	0.32974	0.55880	−0.04722	−0.01182

TABLE 4.3.3.2-D (CONTD)
METHOD 1
REGRESSION COEFFICIENTS
M = 0.950

α	B_0	B_1	B_2	B_3	B_4	B_5
1	−0.00838	0.01178	0.00121	0.00009	0.00809	−0.00005
2	−0.00357	0.00752	0.00193	−0.00002	−0.05533	0.00001
3	0.00810	0.00508	0.00244	−0.00514	−0.09663	0.00006
4	0.03190	−0.00520	0.00165	−0.01368	−0.15750	0.00036
5	0.05470	−0.00974	0.00215	−0.02267	−0.22959	0.00049
6	0.08580	−0.02069	0.00170	−0.03115	−0.37571	0.00084
7	0.11675	−0.03737	0.00250	−0.03773	−0.50555	0.00100
8	0.14670	−0.04756	0.00030	−0.04832	−0.40434	0.00248
9	0.18449	−0.07402	−0.00266	−0.05180	−0.01091	0.00153
10	0.19113	−0.02070	0.00791	−0.06569	−0.60252	0.00152
11	0.22544	0.02716	0.01117	−0.09426	−0.87604	0.00286

α	B_6	B_7	B_8	B_9	B_{10}	B_{11}
1	−0.00025	−0.00078	0.01625	−0.01505	0.00018	0.12846
2	−0.00070	0.00316	0.02724	−0.02814	−0.00030	0.98002
3	0.00008	0.00303	0.01796	−0.02569	−0.00131	1.49493
4	0.00201	0.01412	−0.04312	0.01461	−0.00291	2.11918
5	0.00291	0.01358	−0.04992	0.01207	−0.00344	2.24598
6	0.00382	0.02640	−0.08947	0.03485	−0.00382	3.11378
7	0.00222	0.02453	−0.04389	−0.01608	−0.00198	4.23658
8	0.00404	0.01225	−0.04267	−0.01428	−0.00337	3.55768
9	0.00426	−0.00656	0.03526	−0.08574	−0.00147	−0.81326
10	0.00052	0.02266	0.03270	−0.11326	−0.00128	3.94893
11	0.00030	0.00033	0.12082	−0.20285	−0.00459	7.53037

α	B_{12}	B_{13}	B_{14}	$B_{15} \times 10^{+6}$
1	0.11372	0.26412	−0.00790	0.00011
2	0.12969	0.38083	−0.01354	−0.00028
3	0.16049	0.36673	−0.02110	−0.00072
4	0.13857	0.14239	−0.03305	−0.00143
5	0.13531	0.05344	−0.04690	−0.00172
6	0.28422	0.62238	−0.06146	−0.00241
7	0.33755	0.64386	−0.07750	−0.00263
8	0.46401	1.49135	−0.08695	−0.00337
9	0.78061	2.53411	−0.10360	−0.00386
10	0.48502	0.10404	−0.09913	−0.00361
11	0.43784	0.31377	−0.10616	−0.00522

TABLE 4.3.3.2-D (CONTD)
METHOD 1
REGRESSION COEFFICIENTS
M = 1.000

α	B_0	B_1	B_2	B_3	B_4	B_5
1	−0.00184	−0.00510	−0.00023	0.00191	0.03683	0.00037
2	0.00039	0.00326	0.00184	−0.00236	−0.11220	0.00046
3	−0.05094	0.09969	0.01520	−0.01431	−0.17369	0.00029
4	−0.11879	0.29136	0.04005	−0.05546	−0.94287	0.00031
5	−0.02635	0.14202	0.02414	−0.04156	−0.84098	0.00055
6	−0.06161	0.24704	0.03977	−0.06338	−1.21329	0.00049
7	−0.51857	1.09040	0.14419	−0.15946	−1.51798	−0.00163
8	−0.41208	0.95781	0.12733	−0.15441	−1.45667	−0.00103
9	−0.54877	1.19553	0.15925	−0.17971	−1.07918	−0.00208
10	−1.12307	2.34028	0.28663	−0.32300	−1.47035	−0.00457
11	−1.88393	2.80793	0.39284	−0.17471	4.11060	0.00066
12	−3.71327	6.39571	0.88455	−0.64685	−7.92697	0.00000

α	B_6	B_7	B_8	B_9	B_{10}	B_{11}
1	−0.00042	−0.00431	0.03435	−0.03837	0.00017	−0.32067
2	−0.00063	0.02795	−0.10548	0.11581	−0.00009	1.43644
3	−0.00086	0.05446	−0.23999	0.24547	−0.00045	1.83557
4	−0.00097	0.16868	−0.87339	0.95296	−0.00023	12.40156
5	−0.00112	0.13169	−0.61505	0.66843	0.00069	9.69120
6	−0.00123	0.18757	−0.91157	0.99576	−0.00101	13.90155
7	0.00503	0.48849	−2.82813	3.13791	−0.00809	14.80998
8	0.00425	0.48904	−2.79021	3.11841	−0.00832	13.65930
9	0.00586	0.47045	−2.83951	3.18905	−0.00556	8.54019
10	0.01387	1.11512	−6.47644	7.23240	−0.02132	14.09991
11	−0.00727	−1.38447	5.79307	−6.58945	−0.00979	−49.73547
12	−0.00495	1.72879	−7.81054	8.85635	−0.08292	43.19402

α	B_{12}	B_{13}	B_{14}	$B_{15} \times 10^{+6}$
1	−0.02364	0.11396	−0.00713	0.00017
2	0.12498	−0.00827	−0.01494	−0.00004
3	0.14708	−0.41706	−0.02709	0.00015
4	1.05810	−1.47681	−0.04821	−0.00010
5	0.76958	−1.14098	−0.06112	−0.00073
6	0.94294	−1.81063	−0.07002	−0.00083
7	3.24042	3.22464	−0.05688	−0.00211
8	2.89318	2.79437	−0.07367	−0.00250
9	4.30224	6.63418	−0.07343	−0.00203
10	8.16605	12.54916	−0.04314	−0.00417
11	−6.18641	15.14346	0.00058	−0.00022
12	6.25554	16.75446	0.35531	0.00127

TABLE 4.3.3.2-D (CONTD)
METHOD 1
REGRESSION COEFFICIENTS
M = 1.100

α	B_0	B_1	B_2	B_3	B_4	B_5
1	−0.04484	0.08372	0.00940	−0.00817	−0.04487	−0.00010
2	−0.04355	0.09444	0.01029	−0.01400	−0.03926	−0.00005
3	−0.03818	0.10749	0.01176	−0.01903	−0.13134	−0.00036
4	−0.06102	0.16158	0.01869	−0.02982	−0.14335	−0.00010
5	−0.04984	0.18025	0.02032	−0.03960	−0.21009	−0.00026
6	−0.03717	0.20704	0.02251	−0.05545	−0.36705	0.00009
7	−0.08362	0.32672	0.03894	−0.07228	−0.58530	−0.00065
8	−0.18809	0.43881	0.05636	−0.06272	−0.54914	0.00034
9	−0.16553	0.43886	0.05666	−0.07680	−0.46356	0.00229
10	−0.27549	0.59413	0.08484	−0.07664	−0.30332	−0.00097
11	−0.29751	0.66053	0.09320	−0.07554	−0.40645	−0.00235
12	−0.29560	0.73732	0.10393	−0.09837	−0.59564	−0.00164
13	−0.34429	0.87460	0.12440	−0.12202	−0.66147	−0.00237
14	0.17848	0.28522	0.02090	−0.14298	0.56890	−0.00414
15	0.53359	−0.32241	−0.06227	−0.07706	1.53930	−0.00261

α	B_6	B_7	B_8	B_9	B_{10}	B_{11}
1	−0.00083	0.03295	−0.15500	0.16983	−0.00164	0.82746
2	−0.00051	0.02717	−0.11801	0.12194	−0.00174	0.88339
3	−0.00098	0.04605	−0.19072	0.21743	−0.00164	1.67764
4	−0.00129	0.04320	−0.18755	0.22187	−0.00101	2.18522
5	−0.00125	0.09835	−0.42457	0.47771	−0.00091	2.80951
6	−0.00171	0.09902	−0.45321	0.55087	0.00099	4.98784
7	−0.00311	0.17055	−0.79734	0.96443	0.00293	6.25124
8	0.00056	0.10552	−0.29838	0.25776	0.00349	5.58307
9	−0.00065	0.12365	−0.35773	0.28341	0.00473	5.89547
10	−0.00037	0.04642	0.05276	−0.21425	0.01034	2.61690
11	−0.00004	0.06654	0.09562	−0.29549	0.00938	2.41419
12	−0.00302	0.18490	−0.45240	0.26825	0.00698	3.69788
13	−0.00304	0.18917	−0.50258	0.27871	0.00968	3.72855
14	0.01223	−0.01709	0.42603	−1.46168	0.01947	−4.76428
15	0.02637	−0.26299	2.21540	−4.14095	0.02659	−14.41504

α	B_{12}	B_{13}	B_{14}	$B_{15} \times 10^{+6}$
1	0.02607	−0.02705	−0.01003	−0.00003
2	0.05290	0.00332	−0.01502	0.00010
3	0.08191	0.05082	−0.02014	−0.00013
4	0.10961	0.04423	−0.02851	0.00019
5	0.13773	0.03226	−0.03272	−0.00033
6	0.15323	−0.07582	−0.04362	−0.00004
7	0.18095	−0.05587	−0.05040	−0.00065
8	0.20404	−0.22864	−0.05851	0.00162
9	0.22347	−0.35035	−0.07051	0.00174
10	0.26634	−0.28720	−0.07333	0.00219
11	0.26552	−0.32247	−0.07404	0.00224
12	0.26718	−0.38297	−0.07983	0.00126
13	0.27717	−0.32919	−0.08411	0.00081
14	0.18642	−0.06096	−0.04441	−0.00357
15	0.23323	0.06531	0.01127	−0.00447

TABLE 4.3.3.2-D (CONTD)
METHOD 1
REGRESSION COEFFICIENTS
M = 1.200

α	B_0	B_1	B_2	B_3	B_4	B_5
1	−0.00629	−0.00384	0.00036	0.00199	0.08753	0.00062
2	−0.01132	0.01013	0.00209	−0.00207	0.11552	0.00063
3	−0.01203	0.02211	0.00350	−0.00806	0.16420	0.00065
4	−0.01206	0.03319	0.00473	−0.01526	0.25095	0.00110
5	−0.02330	0.07276	0.01135	−0.02196	0.14635	0.00072
6	−0.01091	0.07268	0.01255	−0.02780	0.13904	0.00107
7	−0.01717	0.12154	0.02004	−0.03729	−0.00996	0.00014
8	−0.00842	0.15381	0.02466	−0.05047	−0.15838	−0.00012
9	−0.03652	0.22732	0.03691	−0.06119	−0.19927	−0.00114
10	0.09571	0.07832	0.01571	−0.06356	−0.23286	−0.00067
11	0.15972	0.01584	0.01023	−0.06640	−0.28670	−0.00091
12	0.12048	0.13091	0.02415	−0.07384	−0.18197	−0.00249
13	−0.03809	0.43572	0.06381	−0.10453	−0.43468	−0.00246
14	−0.11557	0.63985	0.08428	−0.12262	−0.48088	−0.00327
15	−1.28236	2.60841	0.32970	−0.29107	−0.11267	−0.00158

α	B_6	B_7	B_8	B_9	B_{10}	B_{11}
1	−0.00080	0.00609	0.00409	−0.00586	−0.00122	−0.11648
2	−0.00049	0.00324	0.01675	−0.02070	−0.00128	−0.20069
3	0.00031	−0.00122	0.02598	−0.03330	−0.00115	−0.40599
4	0.00101	0.00664	−0.00919	−0.01439	−0.00104	−0.49071
5	0.00005	0.01615	−0.02405	−0.01345	−0.00075	0.03910
6	−0.00012	0.02910	−0.06189	0.00746	−0.00100	0.24032
7	−0.00057	0.04242	−0.10277	0.02792	0.00014	0.92401
8	−0.00203	−0.02183	0.29348	−0.51237	0.00193	2.70883
9	−0.00289	−0.06161	0.56545	−0.91636	0.00456	3.31566
10	−0.00229	−0.06868	0.70933	−1.18044	0.00520	3.65242
11	−0.00206	−0.11603	1.05318	−1.75138	0.00531	4.08376
12	−0.00695	0.04728	0.18852	−0.46850	0.00759	2.22800
13	−0.00794	0.03489	0.17526	−0.50592	0.00558	6.71935
14	−0.00674	0.14918	−0.57903	0.61631	0.00038	5.64320
15	−0.01478	2.42693	−17.16211	27.39923	−0.01586	1.34910

α	B_{12}	B_{13}	B_{14}	$B_{15} \times 10^{+6}$
1	0.06357	0.06844	−0.00754	0.00020
2	0.07738	0.04564	−0.01260	0.00037
3	0.06695	−0.04451	−0.01749	0.00060
4	0.06682	−0.15000	−0.02362	0.00084
5	0.05120	−0.29811	−0.02926	0.00082
6	0.05617	−0.41686	−0.03565	0.00098
7	0.06405	−0.48130	−0.04083	0.00076
8	0.00266	−0.71579	−0.05045	0.00109
9	−0.04614	−0.98680	−0.05984	0.00117
10	−0.11013	−1.29176	−0.06452	0.00122
11	−0.16349	−1.54903	−0.07158	0.00157
12	−0.07644	−1.77188	−0.08773	0.00029
13	−0.25184	−2.00624	−0.10028	0.00047
14	−0.23828	−2.04665	−0.10330	0.00022
15	0.51026	3.57818	−0.12676	−0.00872

TABLE 4.3.3.2-D (CONTD)
METHOD 1
REGRESSION COEFFICIENTS
M = 1.300

α	B_0	B_1	B_2	B_3	B_4	B_5
1	0.01073	−0.01651	−0.00239	−0.00130	0.03077	0.00032
2	0.01124	−0.01236	−0.00186	−0.00349	0.06002	0.00025
3	0.01222	−0.00992	−0.00090	−0.00610	0.09056	0.00054
4	0.01289	0.00091	0.00109	−0.00977	0.13145	0.00014
5	0.01732	0.00436	0.00258	−0.01275	0.18255	0.00037
6	0.04046	−0.00836	0.00183	−0.01702	0.20021	0.00010
7	0.03964	0.01740	0.00620	−0.02283	0.22781	−0.00059
8	0.03812	0.04382	0.01016	−0.03103	0.25309	0.00026
9	0.12317	−0.00959	0.00143	−0.04214	0.14197	−0.00374
10	0.14136	−0.00742	0.00110	−0.05227	0.27808	−0.00146
11	0.07022	0.06183	0.01130	−0.04890	0.50921	0.00200
12	0.08746	0.09711	0.01424	−0.05404	0.28856	−0.00129
13	0.37881	−0.20159	−0.03400	−0.07169	−0.38882	−0.00079
14	0.35522	−0.11761	−0.03078	−0.07623	0.13295	0.00246
15	−0.71802	1.47949	0.21882	−0.13860	0.37682	0.00262

α	B_6	B_7	B_8	B_9	B_{10}	B_{11}
1	0.00074	0.00224	−0.01367	0.00902	−0.00037	−0.08973
2	0.00113	0.01025	−0.04063	0.02565	−0.00071	−0.17503
3	0.00111	0.02331	−0.08208	0.05267	−0.00086	−0.26347
4	0.00155	0.03354	−0.11671	0.07414	−0.00092	−0.33645
5	0.00126	0.07141	−0.24091	0.15987	−0.00110	−0.60188
6	0.00147	0.09155	−0.31135	0.20772	−0.00097	−0.71345
7	0.00216	0.11071	−0.38611	0.25792	−0.00076	−1.05681
8	0.00142	0.18615	−0.76108	0.74001	−0.00013	−1.35729
9	0.00681	0.09964	−0.30165	−0.00252	0.00032	0.05106
10	0.00536	0.16930	−0.54852	0.20149	0.00133	−1.39210
11	0.00871	0.21573	−0.34730	−0.55274	0.00252	−3.93809
12	0.01268	0.19176	−0.22055	−0.71886	0.00238	−2.50095
13	0.01891	0.25610	−0.61300	−0.34549	0.00206	4.39566
14	0.01283	0.57924	−2.91125	3.62863	−0.00003	−3 12316
15	−0.05784	1.30330	−9.95914	18.12476	0.00216	−0.97701

α	B_{12}	B_{13}	B_{14}	$B_{15} \times 10^{+6}$
1	0.01334	−0.06052	−0.00463	0.00028
2	0.02758	−0.12623	−0.00965	0.00034
3	0.02390	−0.25254	−0.01479	0.00045
4	0.00935	−0.41783	−0.02001	0.00036
5	−0.00116	−0.68714	−0.02647	0.00021
6	−0.00696	−0.90402	−0.03292	0.00002
7	0.13956	−0.51697	−0.03541	−0.00031
8	0.17097	−0.59970	−0.04157	−0 00041
9	0.17897	−0.58601	−0.04958	−0.00024
10	0.20709	−0.69765	−0.05311	−0.00056
11	0.23022	−1.12538	−0.05796	0.00077
12	0.22683	−1.17960	−0.06484	0.00127
13	0.08343	−1.80161	−0.08567	0.00253
14	0.33804	−0.57097	−0.06865	0.00025
15	0.35827	2.28471	−0.09056	−0.01175

TABLE 4.3.3.2-D (CONTD)
METHOD 1
REGRESSION COEFFICIENTS
M = 1.400

α	B_0	B_1	B_2	B_3	B_4	B_5
1	0.00157	−0.00557	−0.00067	−0.00067	0.04543	0.00020
2	0.00283	−0.00385	−0.00035	−0.00231	0.08027	0.00020
3	0.00580	−0.00543	0.00011	−0.00436	0.13016	0.00044
4	0.01126	−0.00755	0.00060	−0.00607	0.16445	0.00036
5	0.01710	−0.00602	0.00147	−0.00887	0.21080	0.00052
6	0.03541	−0.01819	0.00101	−0.01140	0.22765	0.00043
7	0.04051	−0.00700	0.00376	−0.01602	0.24154	0.00042
8	0.04478	−0.00232	0.00583	−0.01817	0.34976	0.00084
9	0.07564	−0.00509	0.00509	−0.02763	0.20858	0.00099
10	0.08951	0.00473	0.00632	−0.03430	0.16744	0.00120
11	0.11793	−0.00028	0.00502	−0.04128	0.18050	0.00162
12	0.08874	0.08143	0.01520	−0.04933	0.21049	0.00090
13	0.26017	−0.12899	−0.01372	−0.04668	0.12047	0.00000
14	0.06149	0.12399	0.01598	−0.02868	0.40721	−0.00173
15	0.32684	−0.00669	−0.00231	−0.09153	0.13368	−0.00016

α	B_6	B_7	B_8	B_9	B_{10}	B_{11}
1	0.00049	−0.00040	0.00088	−0.00206	−0.00018	−0.21101
2	0.00065	0.00556	−0.01723	0.00889	−0.00065	−0.31472
3	0.00066	0.01074	−0.03276	0.01790	−0.00112	−0.52483
4	0.00095	0.01416	−0.04143	0.02282	−0.00151	−0.61570
5	0.00092	0.03055	−0.09043	0.05429	−0.00172	−0.91572
6	0.00083	0.04136	−0.12409	0.07650	−0.00188	−1.06178
7	0.00059	0.06188	−0.19356	0.12308	−0.00183	−1.29615
8	0.00034	0.09682	−0.30521	0.20225	−0.00202	−2.30528
9	0.00104	0.19819	−0.85614	0.92464	−0.00193	−1.16990
10	0.00204	0.22722	−0.95835	1.01882	−0.00219	−0.83807
11	0.00182	0.27365	−1.15352	1.24001	−0.00241	−0.99790
12	0.00170	0.32167	−1.34443	1.47775	−0.00156	−1.42727
13	0.00886	0.13442	0.06467	−1.04149	−0.00131	−0.91704
14	0.01785	−0.02692	0.81494	−1.76098	−0.00915	−5.61367
15	−0.01151	0.26982	−1.48732	2.19990	0.00757	0.06241

α	B_{12}	B_{13}	B_{14}	$B_{15} \times 10^{+6}$
1	0.01591	−0.05851	−0.00435	0.00024
2	0.02992	−0.13305	−0.00929	0.00030
3	0.04719	−0.17722	−0.01392	0.00043
4	0.04159	−0.29398	−0.01873	0.00062
5	0.04397	−0.43206	−0.02376	0.00065
6	0.06035	−0.53017	−0.02925	0.00071
7	0.16772	−0.29734	−0.03314	0.00062
8	0.21498	−0.26741	−0.03588	0.00037
9	0.24629	−0.29801	−0.04400	0.00029
10	0.25079	−0.45710	−0.05218	0.00082
11	0.23820	−0.66717	−0.05883	0.00091
12	0.22909	−0.91669	−0.06660	0.00074
13	0.16346	−1.43306	−0.07209	0.00208
14	0.22960	−0.52901	−0.04924	0.00550
15	0.14657	−0.55797	−0.06595	−0.00540

TABLE 4.3.3.2-D (CONTD)
METHOD 1
REGRESSION COEFFICIENTS
M = 1.500

α	B_0	B_1	B_2	B_3	B_4	B_5
1	0.00028	−0.00531	−0.00047	0.00083	0.01860	0.00016
2	0.00572	−0.01091	−0.00099	0.00044	0.04745	0.00011
3	0.00691	−0.00879	−0.00019	−0.00178	0.10149	0.00033
4	0.02023	−0.02725	−0.00172	−0.00011	0.10141	0.00023
5	0.02641	−0.01846	−0.00020	−0.00592	0.18507	0.00036
6	0.04958	−0.05108	−0.00283	−0.00226	0.13830	0.00036
7	0.06259	−0.04729	−0.00172	−0.00838	0.16567	0.00038
8	0.07827	−0.04638	−0.00111	−0.01498	0.25049	0.00072
9	0.09523	−0.04553	−0.00034	−0.02197	0.31504	0.00126
10	0.10838	−0.04623	0.00092	−0.02505	0.38815	0.00207
11	0.11457	−0.02888	0.00335	−0.03059	0.48120	0.00267
12	0.15792	−0.05294	−0.00049	−0.03716	0.53228	0.00291
13	0.21437	−0.12313	−0.00797	−0.02976	0.59260	0.00220
14	0.06391	0.09522	0.01730	−0.03031	0.62570	0.00079
15	0.32106	−0.07231	−0.00820	−0.07269	0.22147	0.00030
16	103.09483	−130.05203	−23.01212	−0.12115	1.41383	−0.26344
17	75.90837	−96.81050	−17.28999	0.43793	2.46481	−0.20733

α	B_6	B_7	B_8	B_9	B_{10}	B_{11}
1	0.00041	0.00447	−0.01491	0.01125	−0.00042	−0.04700
2	0.00054	0.00779	−0.02110	0.01391	−0.00111	−0.12996
3	0.00058	0.01793	−0.05555	0.03640	−0.00135	−0.44197
4	0.00112	0.02610	−0.08192	0.05726	−0.00260	−0.28129
5	0.00045	0.04744	−0.14930	0.09895	−0.00205	−1.02289
6	0.00102	0.05170	−0.19775	0.13913	−0.00390	−0.58817
7	0.00070	0.07877	−0.25819	0.17831	−0.00358	−0.77266
8	0.00035	0.11264	−0.37444	0.25663	−0.00328	−1.41942
9	−0.00007	0.15081	−0.50534	0.34530	−0.00271	−2.00938
10	−0.00133	0.23586	−0.98431	1.05085	−0.00333	−3.04438
11	−0.00223	0.26174	−1.02835	1.04236	−0.00439	−4.08522
12	−0.00240	0.24543	−0.82995	0.65777	−0.00453	−4.59546
13	−0.00054	0.18633	−0.30029	−0.24104	−0.00544	−5.99071
14	0.01018	0.00306	0.60273	−1.42956	−0.01247	−7.48227
15	−0.00483	0.16214	−0.49650	0.31938	0.00032	−2.96651
16	5.07326	−141.25533	589.65942	−677.16602	−1.35118	−13.47584
17	3.99498	−108.87743	472.99951	−562.11035	−1.13367	−21.36497

α	B_{12}	B_{13}	B_{14}	$B_{15} \times 10^{+6}$
1	0.02767	−0.03146	−0.00443	0.00025
2	0.03932	−0.12355	−0.00939	0.00033
3	0.07609	−0.12497	−0.01370	0.00032
4	0.06646	−0.26070	−0.01820	0.00072
5	0.08017	−0.40137	−0.02307	0.00033
6	0.10356	−0.43001	−0.02758	0.00091
7	0.15294	−0.41352	−0.03275	0.00083
8	0.18420	−0.45614	−0.03651	0.00041
9	0.22163	−0.48580	−0.04082	0.00006
10	0.28647	−0.43662	−0.04560	−0.00007
11	0.30032	−0.57579	−0.04976	−0.00002
12	0.30269	−0.67818	−0.05251	−0.00015
13	0.30106	−0.96184	−0.05740	0.00054
14	0.31863	−0.32660	−0.04391	0.00445
15	0.26122	−0.41801	−0.05250	−0.00274
16	144.72121	390.29077	0.37379	1.40259
17	121.12621	271.07422	0.28761	1.14584

TABLE 4.3.3.2-D (CONTD)
METHOD 1
REGRESSION COEFFICIENTS
M = 2.000

α	B_0	B_1	B_2	B_3	B_4	B_5
1	0.02739	−0.04233	−0.00606	0.00381	−0.02875	0.00029
2	0.07553	−0.11930	−0.01586	0.01171	−0.07630	0.00056
3	0.07364	−0.11607	−0.01476	0.01119	−0.05201	0.00056
4	0.08820	−0.13065	−0.01690	0.01067	−0.04046	0.00073
5	0.10524	−0.15034	−0.01915	0.01121	−0.00600	0.00085
6	0.11737	−0.15989	−0.02016	0.01074	0.00851	0.00097
7	0.13005	−0.16403	−0.02019	0.00823	0.01741	0.00097
8	0.15887	−0.19848	−0.02321	0.00928	0.01671	0.00114
9	0.19314	−0.22421	−0.02756	0.00788	0.04264	0.00100
10	0.21766	−0.23029	−0.02967	0.00394	0.06635	0.00087
11	0.22138	−0.22948	−0.02480	0.00030	0.03912	0.00094
12	0.27413	−0.27002	−0.03168	−0.00152	−0.02566	0.00089
13	0.29047	−0.25721	−0.03340	−0.00232	0.04553	0.00036
14	0.37017	−0.34377	−0.04454	0.00100	0.04507	0.00075
15	0.56237	−0.47765	−0.06868	−0.02981	−0.19184	−0.00103

α	B_6	B_7	B_8	B_9	B_{10}	B_{11}
1	−0.00045	0.04098	−0.23030	0.38557	−0.00046	0.26480
2	−0.00166	0.09261	−0.56299	1.03211	−0.00012	1.13879
3	−0.00137	0.09665	−0.57350	1.02931	−0.00037	1.01436
4	−0.00139	0.11595	−0.64778	1.10953	−0.00082	0.92580
5	−0.00176	0.13154	−0.70979	1.19218	−0.00132	0.78751
6	−0.00200	0.15482	−0.81082	1.31452	−0.00148	0.65558
7	−0.00212	0.17280	−0.89271	1.41543	−0.00208	0.51476
8	−0.00186	0.17449	−0.83012	1.25395	−0.00413	0.17723
9	−0.00236	0.21284	−0.99934	1.47842	−0.00507	−0.04647
10	−0.00321	0.25793	−1.23851	1.83802	−0.00493	0.08167
11	−0.00250	0.22251	−1.00127	1.40514	−0.00436	−0.00866
12	−0.00398	0.28785	−1.30884	1.95827	−0.00494	0.42450
13	−0.00477	0.36357	−1.63001	2.31215	−0.00656	−0.45700
14	−0.00421	0.28733	−1.07968	1.39936	−0.01287	−0.91426
15	−0.00647	0.13657	−0.18101	−0.06424	−0.00363	2.27686

α	B_{12}	B_{13}	B_{14}	$B_{15} \times 10^{+6}$
1	0.01276	−0.14413	−0.00677	0.00026
2	−0.00739	−0.45431	−0.01837	0.00048
3	0.01489	−0.45917	−0.02103	0.00058
4	0.03859	−0.56613	−0.02521	0.00076
5	0.04974	−0.57770	−0.02809	0.00079
6	0.05515	−0.65604	−0.03121	0.00090
7	0.08463	−0.64573	−0.03368	0.00094
8	0.11120	−0.74441	−0.03771	0.00152
9	0.13302	−0.83799	−0.04221	0.00141
10	0.14411	−0.94664	−0.04835	0.00113
11	0.17336	−0.91347	−0.05040	0.00154
12	0.17794	−1.16748	−0.06059	0.00159
13	0.19870	−1.30091	−0.06413	0.00117
14	0.21462	−1.31872	−0.06397	0.00160
15	0.10918	−1.62533	−0.06664	−0.00145

TABLE 4.3.3.2-D (CONTD)
METHOD 1
REGRESSION COEFFICIENTS
M = 2.500

α	B_0	B_1	B_2	B_3	B_4	B_5
1	0.00478	−0.01228	−0.00200	0.00178	0.02268	0.00042
2	−0.00290	0.00255	0.00032	−0.00094	0.00174	0.00052
3	−0.00643	0.01813	0.00254	−0.00548	−0.04823	0.00057
4	0.03039	−0.01018	−0.00289	−0.00806	−0.06663	0.00035
5	0.18151	−0.13661	−0.02839	−0.01167	−0.17355	−0.00194
6	0.10365	−0.04753	−0.01221	−0.01596	−0.10382	−0.00109
7	0.05376	−0.01156	−0.00259	−0.01308	−0.03618	0.00015
8	0.09862	−0.04772	−0.00967	−0.01519	−0.07924	0.00002
9	0.15347	−0.09079	−0.01754	−0.01811	−0.11204	−0.00043
10	0.23161	−0.14988	−0.02798	−0.02334	−0.18635	−0.00097
11	0.21702	−0.12739	−0.02026	−0.03322	−0.19810	−0.00056
12	0.24585	−0.14100	−0.02160	−0.03754	−0.15242	−0.00033
13	0.36687	−0.35416	−0.04882	−0.00576	0.35932	0.00081
14	0.20578	−0.24662	−0.02417	0.02798	0.06527	0.00130
15	0.38159	−0.28580	−0.03447	−0.03879	0.01325	−0.00040

α	B_6	B_7	B_8	B_9	B_{10}	B_{11}
1	0.00046	0.03499	−0.19529	0.30678	−0.00252	−0.31168
2	0.00030	0.01727	−0.04537	−0.01635	−0.00044	−0.44534
3	−0.00034	0.00483	0.08492	−0.31595	0.00307	−0.62776
4	−0.00130	0.01234	0.06025	−0.23702	0.00223	−0.95984
5	−0.00438	0.03798	−0.18556	0.57011	−0.00334	−0.15262
6	−0.00305	0.01707	0.04987	−0.11416	−0.00016	−1.03480
7	−0.00178	0.04656	−0.03574	−0.22868	0.00149	−1.98522
8	−0.00242	0.06384	−0.12008	−0.03324	0.00061	−1.46935
9	−0.00345	0.08977	−0.20825	0.09932	−0.00032	−2.02305
10	−0.00545	0.11321	−0.25012	0.18655	−0.00271	−2.29838
11	−0.00359	−0.02825	0.54326	−1.28762	0.00672	−0.67739
12	−0.00346	−0.02755	0.58868	−1.43130	0.00327	−0.88390
13	0.00062	−0.00716	0.50164	−1.02755	−0.01386	−4.00934
14	0.00750	−0.02177	0.82050	−1.68213	−0.01220	−7.39198
15	−0.00074	−0.32694	2.67639	−4.90278	0.00633	−2.65221

α	B_{12}	B_{13}	B_{14}	$B_{15} \times 10^{+6}$
1	0.04574	0.10784	−0.00198	0.00046
2	0.06010	0.09237	−0.00325	0.00042
3	0.06792	0.01173	−0.00551	0.00035
4	0.08604	−0.08550	−0.00935	0.00010
5	0.01677	−0.58262	−0.01818	−0.00145
6	0.09659	−0.35116	−0.01834	−0.00077
7	0.15009	−0.24464	−0.01898	0.00026
8	0.12706	−0.38722	−0.02282	0.00019
9	0.18927	−0.41734	−0.02724	0.00013
10	0.19130	−0.72356	−0.03387	−0.00038
11	0.14314	−0.66563	−0.03354	−0.00065
12	0.14943	−0.75084	−0.03504	−0.00105
13	0.14865	−0.84247	−0.02897	−0.00132
14	0.16566	−0.72137	−0.01595	0.00093
15	0.11597	−1.18691	−0.03044	−0.00194

4.4 WING-WING COMBINATIONS AT ANGLE OF ATTACK (WING FLOW FIELDS)

4.4.1 WING-WING COMBINATIONS AT ANGLE OF ATTACK

This section presents methods of estimating the properties of wing flow fields. The subsonic methods include the effects of flow direction (downwash) and dynamic-pressure ratio. The supersonic methods include the effects of downwash, dynamic-pressure ratio, and Mach number.

A. SUBSONIC

Downwash*

The downwash behind a wing in subsonic flow is a consequence of the wing-trailing-vortex system. The trailing-vortex system behind a swept wing is shown in Sketch (a). A vortex sheet is shed by the lifting wing, and the sheet is deflected downward by the bound or lifting vortex and the tip vortices, which comprise the vortex system. In general, the sheet is not flat, but the curvature near the wing midspan is usually relatively small. This is particularly true of straight wings of reasonably large aspect ratio, for which the central portion of the vortex sheet is extremely flat. Wings with considerable trailing-edge sweepback produce a vortex sheet that is bowed upward near the plane of symmetry.

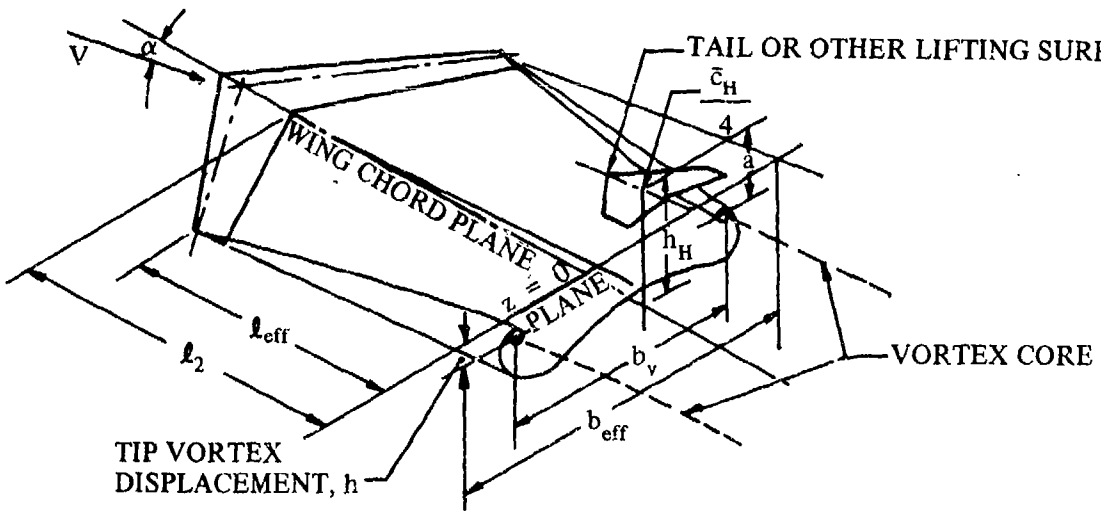

SKETCH (a)

The tip vortices do not experience a vertical displacement as great as the displacement of the central portion of the vortex sheet. In general, they trail back comparatively close to the streamwise direction.

*This general discussion is essentially quoted from Reference 1.

Furthermore, as the vortex system proceeds downstream, the tip vortices tend to move inboard. Also, with increasing distance behind the wing, the trailing-sheet vorticity tends to be transferred to the tip vortices. The transfer of vorticity and inboard movement of the tip vortices takes place in such a fashion that the lateral center of gravity of the vorticity remains at a fixed spanwise location. When all of the vorticity is transferred from the sheet to the trailing vortices, the vortex system is considered to be fully rolled up, and, in a nonviscous fluid, the vortex system then extends unchanged to infinity.

Ahead of the longitudinal station for complete rollup, the spanwise downwash distribution is dependent upon the spanwise lift distribution of the wing. However, when the rollup is complete, the downwash angles for all wings of equal lift and equal effective span are identical. It is evident that the shape of the vortex sheet has a significant influence on the downwash experienced by a tail located in the flow field of a wing and that the tail location relative to the trailing vortices is very important. Since the tip vortices are somewhat above the vortex sheet, the downwash above the sheet is somewhat greater than the downwash beneath the sheet.

The tip vortices spring from the wing tips at angles of attack for which the flow is unseparated. However, wings with high sweepback angles tend to stall at the tips, and in many instances the tip vortices originate well inboard of the wing tip at high angles of attack. This phenomenon has a significant influence on the downwash.

The previous discussion has been concerned with wings that behave in a somewhat conventional manner at high angles of attack. Certain thin, highly swept wings have a significantly different flow pattern in the higher angle-of-attack range. These wings are characterized by a leading-edge separation vortex that lies above the surface of the wing. From its inception near the plane of symmetry, it moves outboard in the approximate direction of the wing leading edge and is finally shed in a streamwise direction near the wing tip. Reference 2 shows some interesting studies of the separation vortex. It is clear that the existence of this vortex has an important influence on the downwash.

For very low-aspect-ratio configurations or for canard configurations, the tip vortex from the forward panel may impinge directly on the aft surface. Reference 3 contains a method (presented as Method 3 herein) of estimating the lift acting on the aft panel for this type of configuration. The method assumes that the trailing vortices are shed at a spanwise station corresponding to the center of vorticity of the isolated panel. The vortex pair is then assumed to remain at this spacing for longitudinal distances at least beyond the aft panel. This spacing is also assumed to be constant as a function of angle of attack. In the vertical plane the vortex pair is assumed to trail in the free-stream direction. These assumptions are shown in Reference 3 to be not only convenient, but reasonable in the light of experimental data. With the position of the vortices determined and their strength calculated from the lift of the forward panel, the integrated lift on the aft panel can be computed by means of strip theory. Because the theoretical vortex contains infinite velocities at its center, the method gives erroneous answers where the vortices trail very close to the aft panel. In reality the cores of the vortices revolve as solid bodies with zero tangential velocity at their centers.

Downwash Due to Flap Deflection

The downwash behind a wing is substantially modified by the deflection of trailing-edge flaps. This deflection creates an increase in the spanwise loading on the wing that increases the strength of the wing-trailing-vortex system. Consequently, the increased strength of the wing-trailing vortex produces an increase in the downwash angle.

At present, no theoretical methods exist that lend themselves to hand calculation for predicting the variation in downwash angle due to flap deflection. However, empirical curves are presented for estimating the variation in downwash angle due to deflection of plain or slotted flaps at small angles of attack at low subsonic speeds. The correlation parameters used to generate these curves are presented in Reference 4. The curve for slotted flaps is based on data from single- and double-slotted flap data.

Upwash

Upwash ahead of the wing is induced by the wing vortex system in a manner similar to that for downwash. A knowledge of flow fields beneath and ahead of a wing is sometimes required for the determination of forces and moments on nacelles or external stores or for the determination of inflow velocities into propellers of jet-engine intakes. Reference 3 contains charts for determining upwash about any straight-tapered swept or unswept wing. Because of their volume, these charts have not been included in the Datcom. Reference 5 contains a limited treatment for unswept wings only.

Dynamic-Pressure Ratio

The effectiveness of a lifting surface is directly proportional to the average dynamic pressure acting over that surface. A surface operating in the wake of an upstream surface therefore experiences a loss in effectiveness because of the reduced dynamic pressure. The decrease in dynamic pressure is caused by the loss of flow energy in the form of friction and separation drag of the forward surface; the greater the drag, the greater the pressure loss.

The wake, usually thin and intense at or near the trailing edge, spreads and decays with increasing distance downstream in such a manner that the integrated momentum across the wake at any station is constant. This type of wake, which is due to viscous effects, occurs at all speeds.

DATCOM METHODS

Subsonic Downwash

Three methods are presented below for estimating downwash characteristics. The first method is somewhat laborious, but enables the complete downwash curve to be estimated. The second method is accurate and expedient to use, but predicts only the downwash gradient. The third method is applicable only for configurations where the span of the forward surface is approximately equal to or less than that of the aft surface. Tables 4.4.1-A and -B present a data summary and substantiation for Methods 1 and 2,respectively, using the same test data.

Method 1

This method for estimating the downwash behind straight-tapered lifting wings at subsonic speeds is taken from Reference 1. The method is applicable to configurations in which the span of the wing is at least 1.5 times as large as that of the horizontal tail ($b/b_H \geq 1.5$). The basic approach is as follows (see Sketch(a)):

1. Determine the downwash in the plane of symmetry at the height of the vortex cores and at the longitudinal station of the quarter-chord point of the horizontal-tail mean aerodynamic chord.

2. Correct this value for the horizontal-tail height above or below the trailing vortices.

3. Evaluate the effect of horizontal-tail span by relating the average downwash at the tail to the downwash determined in the second step.

The downwash gradient $\frac{\partial \epsilon}{\partial \alpha}$ at the trailing edge of a wing is unity. The value at a distance infinitely far downstream is given by (Reference 6) as

$$\left(\frac{\partial \epsilon}{\partial \alpha}\right)_{\infty} = \frac{2\ (57.3)}{\pi A}\ C_{L_\alpha} \qquad 4.4.1\text{-a}$$

If these two values are known, the downwash gradient for any intermediate longitudinal position can be found by means of lifting-line theory.

For straight wings that have tip stall or thin swept wings that shed the leading-edge vortices inboard of the wing tips, the effective wing aspect ratio is considerably less than the geometric aspect ratio. An effective aspect ratio based on induced-drag considerations has been determined for these wings.

The maximum downwash at the plane of symmetry occurs at the intersection of the plane of symmetry with the plane containing the tip vortices. The ratio of the downwash at the plane of symmetry at a height a above or below this intersection to the downwash at the height of the vortex cores $\frac{\epsilon}{\epsilon_v}$ is given by

$$\frac{\epsilon}{\epsilon_v} = \frac{1}{1 + \left(\frac{2a}{b_v}\right)^2} \qquad 4.4.1\text{-b}$$

where b_v is the span of the wing-tip vortices at the quarter-chord point of the horizontal-tail MAC, and a is the height determined by means of Equation 4.4.1-c or 4.4.1-d (see Sketch (a)).

Because of the spanwise variation of downwash, the effective downwash acting on a horizontal tail is different from that at the plane of symmetry. A correction for tail-span effect is presented from Reference 1; it is based on the assumption that the vortices are essentially rolled up at the longitudinal tail station. This is a valid assumption except for cases where the core of the vortex approaches the surface of the tail. It should be noted that the vortex rolls up in a shorter distance as the angle of attack is increased. This is fortunate, because downwash effects become increasingly important at the higher angles of attack.

The subsonic downwash is obtained from the procedure outlined in the following steps:

Step 1. The effective wing aspect ratio A_{eff} and the effective wing span b_{eff} are obtained from Figure 4.4.1-66 as a function of the wing angle-of-attack parameter $\frac{\alpha - \alpha_0}{\alpha_{C_{L_{max}}} - \alpha_0}$. α is the selected wing angle of attack and α_0 and $\alpha_{C_{L_{max}}}$ may be estimated from Sections 4.1.3.1 and 4.1.3.4, respectively.

Step 2. The downwash gradient $\left(\frac{\partial \epsilon}{\partial \alpha}\right)_v$ in the plane of symmetry at the height of the vortex core is obtained for any longitudinal station, e.g., the quarter-chord point of the MAC of the horizontal tail, from Figure 4.4.1-67. This figure is entered with $2\frac{\ell_2}{b}$ and A_{eff}, where ℓ_2 is the distance measured parallel to the wing root chord, between the aft end of the wing root chord and the quarter-chord point of the MAC of the horizontal tail (see Sketch (a)).

Step 3. Determine the vertical position of the vortex core (see Sketch (a)). This depends upon the type of wing flow separation as determined from Figure 4.4.1-68a.

For trailing-edge separation

$$a = h_H - \ell_{eff}\left(\alpha - \frac{0.41\,C_L}{\pi A_{eff}}\right) - \frac{b_{eff}}{2}\tan\Gamma \qquad 4.4.1\text{-c}$$

For leading-edge separation

$$a = h_H - (\ell_2 + \ell_3)\left(\alpha - \frac{0.41\,C_L}{\pi A_{eff}}\right) - \frac{b_{eff}}{2}\tan\Gamma \qquad 4.4.1\text{-d}$$

where

C_L is the wing-alone lift coefficient obtained from test data or estimated by using the straight-tapered-wing method of Paragraph A of Section 4.1.3.3.

a is the distance from the quarter-chord point of the MAC of the horizontal tail to the plane of the tip vortex cores, positive for the horizontal tail MAC above the plane of the tip vortex cores.

h_H is the height of the horizontal-tail MAC quarter-chord point above or below the plane of the wing root chord, measured in the plane of symmetry and normal to the extended wing root chord, positive for the horizontal tail MAC above the plane of the wing root chord.

ℓ_{eff} is the distance measured parallel to the wing root chord, between the effective wing-tip quarter-chord point and the horizontal-tail MAC quarter-chord point.

ℓ_3 is the distance measured parallel to the plane of symmetry, between the forward end of the wing MAC and the aft end of the wing root chord, and ℓ_2 is defined in Step 2. In both Equations 4.4.1-c and 4.4.1-d, α is in radians, and the values of ℓ_{eff}, ℓ_2, and ℓ_3 are positive.

Step 4. Determine the span of the vortices at the longitudinal location of the quarter-chord point of the horizontal-tail MAC by

$$b_v = b_{eff} - \left(b_{eff} - b_{v_{ru}}\right)\left(\frac{2\ell_{eff}}{b\xi_{ru}}\right)^{1/2} \qquad 4.4.1\text{-e}$$

where

$$b_{v_{ru}} = [0.78 + 0.10\,(\lambda - 0.4) + 0.003\,\Lambda_{c/4}]\,b_{eff} \quad (\Lambda_{c/4} \text{ in degrees}) \qquad 4.4.1\text{-f}$$

$$\xi_{ru} = \frac{0.56\,A}{C_L}$$

Step 5. By using the parameters calculated in the above steps, obtain the average downwash gradient acting on the tail $\left(\frac{\partial \bar{\epsilon}}{\partial \alpha}\right)$ from Figure 4.4.1-68b.

Step 6. The procedures of Steps 1 through 5 are for low speeds. For higher subsonic Mach numbers the downwash gradient is given by

$$\left(\frac{\partial \bar{\epsilon}}{\partial \alpha}\right)_M = \left(\frac{\partial \bar{\epsilon}}{\partial \alpha}\right)_{\substack{\text{low} \\ \text{speed}}} \frac{\left(\frac{dC_L}{d\alpha}\right)_M}{\left(\frac{dC_L}{d\alpha}\right)_{\substack{\text{low} \\ \text{speed}}}} \qquad 4.4.1\text{-g}$$

where

$\left(\frac{\partial \bar{\epsilon}}{\partial \alpha}\right)_{\substack{\text{low} \\ \text{speed}}}$ is obtained by using Steps 1 through 5.

$\left(\frac{dC_L}{d\alpha}\right)_M$ and $\left(\frac{dC_L}{d\alpha}\right)_{\substack{\text{low} \\ \text{speed}}}$ are given by the straight-tapered wing methods of Paragraph A of Sections 4.1.3.2 or 4.1.3.3, depending upon the Mach number and angle of attack.

Step 7. Determine the average downwash acting on the horizontal tail by integrating the average downwash gradient from Step 5 or 6, i.e.,

$$\bar{\epsilon} = \int_{\alpha_0}^{\alpha} \frac{\partial \bar{\epsilon}}{\partial \alpha}\, d\alpha$$

A sample problem illustrating the use of this method is presented on Pages 4.4.1-12 through 4.4.1-16. The method will predict the downwash angles at the horizontal tail with accuracy acceptable for preliminary-design purposes for most configurations. However, since the effect of tail span has been determined under the assumption that the vortices are essentially rolled up at the tail location, caution should be used in applying the method if the tail length is short and the tail plane is near the location of the vortex core height.

Not enough test data are available to substantiate the validity of the compressibility correction given by Equation 4.4.1-g.

Method 2

An empirical method for estimating the downwash gradient behind straight-tapered wings at subsonic speeds is taken from Reference 7. The method is restricted to the angle-of-attack range over which the variation of downwash angle is a linear function of angle of attack.

The average low-speed downwash gradient at the horizontal tail is given by

$$\frac{\partial \bar{\epsilon}}{\partial \alpha} = 4.44 \left[K_A K_\lambda K_H (\cos \Lambda_{c/4})^{1/2} \right]^{1.19} \qquad 4.4.1\text{-h}$$

where K_A, K_λ, and K_H are wing-aspect-ratio, wing-taper-ratio, and horizontal-tail-location factors obtained from Figures 4.4.1-69a, 4.4.1-69b, and 4.4.1-70, respectively. In Figure 4.4.1-70, ℓ_H is the distance measured parallel to the wing root chord, between the wing MAC quarter-chord point and the quarter-chord point of the MAC of the horizontal tail, and h_H is the position of the quarter-chord point of the horizontal tail MAC relative to the plane of the wing root chord as defined in Method 1.

At higher subsonic speeds the effect of compressibility is approximated by

$$\left(\frac{\partial \bar{\epsilon}}{\partial \alpha}\right)_M = \left(\frac{\partial \bar{\epsilon}}{\partial \alpha}\right)_{\substack{\text{low} \\ \text{speed}}} \frac{\left(C_{L_\alpha}\right)_M}{\left(C_{L_\alpha}\right)_{\substack{\text{low} \\ \text{speed}}}} \qquad 4.4.1\text{-i}$$

where

$\left(\frac{\partial \bar{\epsilon}}{\partial \alpha}\right)_{\substack{\text{low} \\ \text{speed}}}$ is obtained using Equation 4.4.1-h.

$\left(C_{L_\alpha}\right)_{\substack{\text{low} \\ \text{speed}}}$ and $\left(C_{L_\alpha}\right)_M$ are the wing lift-curve slopes at the appropriate Mach numbers, obtained by using the straight-tapered-wing method of Paragraph A of Section 4.1.3.2.

A comparison of low-speed test data with $\partial\epsilon/\partial\alpha$ calculated by this method is presented as Table 4.4.1-B. The ranges of geometric parameters of the test data are:

$$2.00 \leq A \leq 8.00$$

$$0 \leq \lambda \leq 1.625$$

$$3.4 \leq \Lambda_{c/4} \leq 56.5$$

$$-0.177 \leq \frac{2 h_H}{b} \leq 0.537$$

$$0.78 \leq \frac{2 \ell_H}{b} \leq 2.44$$

$$0.280 \leq \frac{b_H}{b} \leq 0.800$$

Since the tail-span effect has not been explicitly included in this method, the authority of the method outside the limits $0.280 \leq \frac{b_H}{b} \leq 0.800$ is unknown.

Not enough test data are available to substantiate the validity of the compressibility correction given by Equation 4.4.1-i.

Method 3

For configurations in which the span of the forward surface is approximately equal to or less than that of the aft surface, the following method, taken from Reference 3, is recommended.

Step 1. The spatial position of the trailing vortices is first determined relative to the aft surface. The lateral spacing is determined from Figure 4.4.1-71 as a function of the exposed forward-surface planform geometry. This spacing is invariant with longitudinal distance and angle of attack. The vertical position is determined by assuming that the vortex springs from the trailing edge at the previously determined lateral position and trails in the free-stream direction. The pertinent vertical dimension is the distance between the quarter-chord point of the MAC of the aft surface and the vortex as determined above.

Step 2. The vortex interference factor $I_{v_{W'(W'')}}$ is obtained from Figures 4.3.1.3-7a through 4.3.1.3-7ℓ as a function of the lateral and vertical vortex positions, determined in Step 1 above, and the geometry of the aft panel. (The primed notation refers to the forward panel and the double-primed notation refers to the aft panel.)

Step 3. The vortex interference factor so determined is used in Sections 4.5.1.1 and 4.5.1.2 to obtain the lift generated on the aft surface for complete wing-body-tail combinations.

The use of the sample problem on Page 4.4.1-16 as a guide is essential in applying this method.

Subsonic Downwash Due to Flap Deflection

The method for estimating the change in downwash due to deflection of plain or slotted flaps is based on the empirical curves presented in Figure 4.4.1-72. Tables 4.4.1-C and -D present a data summary and substantiation of the test data used to generate these empirical curves. The user is advised to exercise caution when evaluating a configuration with different geometric parameters from those appearing in Table 4.4.1-C.

To utilize Figure 4.4.1-72, the user obtains a value for $\frac{\Delta\epsilon\, A\lceil b_f/(b/2)\rceil}{\Delta C_L}$ based on the flap type and the ratio of tail height above the wing-chord plane to wing semispan $\frac{h_H}{b/2}$. The change in downwash angle $\Delta\epsilon$ is then

obtained by

$$\Delta\epsilon = \left\{\frac{\Delta\epsilon\, A[b_f/(b/2)]}{\Delta C_L}\right\} \frac{\Delta C_L}{A[b_f/(b/2)]}$$

where

A	is the wing aspect ratio.
$\frac{b_f}{b/2}$	is the ratio of flap span of one wing to wing semispan.
ΔC_L	is the lift increment due to flap deflection obtained from test data or Section 6.1.4.1.
b/2	is the wing semispan.
h_H	is the tail height above the wing-chord plane, positive up.

Subsonic Upwash

The upwash gradient $\frac{\partial \epsilon_u}{\partial \alpha}$ in the plane of symmetry of an unswept wing is presented as a function of the wing aspect ratio in Figure 4.4.1-73. This chart is from Reference 5.

In Reference 3, the flow characteristics beneath a wing are calculated by assuming the wing to be represented by a multiple arrangement (both chordwise and spanwise) of horseshoe vortices and accounting for the effects of wing thickness distribution by using the appropriate singularity distribution in conjunction with simple sweep theory. The calculative procedures, together with the required design charts, are presented in Reference 3. Also presented are comparisons between detailed experimental flow fields around swept and unswept wing-fuselage combinations and wing-alone flow fields calculated by this method. The calculated results are qualitatively correct in all cases investigated.

Subsonic Dynamic-Pressure Ratio

This method for estimating the dynamic-pressure q/q_∞ at subsonic speeds and in the linear angle-of-attack range is based on the method presented in Reference 8, which relates the dynamic-pressure ratio to the drag coefficient of the wing. The method gives values of q/q_∞ at the plane of symmetry only. Actually, considerable variations in q/q_∞ can occur in both the spanwise and longitudinal directions. Sketches (b) and (c) show typical spanwise and longitudinal variations, respectively, of dynamic-pressure ratio for a straight wing and a 60° sweptback wing (from Reference 9). In general these data indicate that stronger spanwise deviations result when the wing is swept back, and stronger longitudinal deviations result when the wing is unswept.

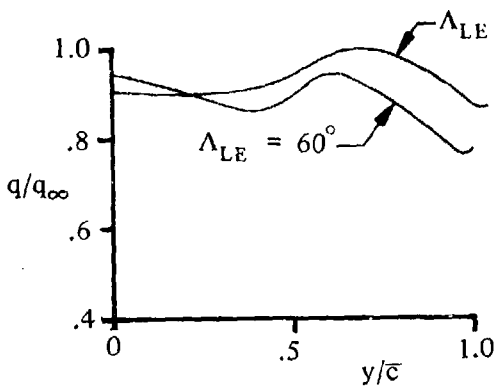

SKETCH (b)

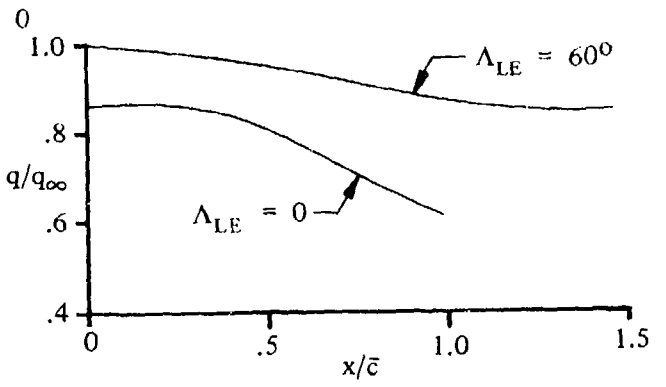

SKETCH (c)

In the linear angle-of-attack range, the ratio of the dynamic pressure in the plane of symmetry at some distance x aft of the wing-root-chord trailing edge to the free-stream dynamic pressure q/q_∞ is obtained from the procedure outlined in the following steps:

Step 1. Calculate the half-width of the wing wake by

$$\frac{z_w}{\bar{c}} = 0.68 \sqrt{C_{D_0}\left(\frac{x}{\bar{c}} + 0.15\right)} \qquad 4.4.1\text{-j}$$

where

x is the longitudinal distance measured along the wake center line from the wing-root-chord trailing edge, positive aft.

z_w is the half-width of the wake at any position x.

C_{D_0} is the wing zero-lift drag coefficient obtained from Paragraph A of Section 4.1.5.1.

Step 2. Calculate the downwash in the plane of symmetry at the vortex sheet (assumed to be the same location as the wake center line) by

$$\epsilon = \frac{1.62\, C_L}{\pi A} \text{ (radians)} \qquad 4.4.1\text{-k}$$

Step 3. Determine the vertical distance z from the vortex sheet to the point of interest (usually the quarter-chord point of the MAC of the horizontal tail) by

$$z = x \tan(\gamma + \epsilon - \alpha) \qquad 4.4.1\text{-}\ell$$

where γ is defined in Sketch (d).

Step 4. Determine the dynamic-pressure-loss ratio at the wake center $\left(\frac{\Delta q}{q}\right)_o$ by the empirical relation

$$\left(\frac{\Delta q}{q}\right)_o = \frac{2.42\,(C_{D_0})^{1/2}}{\frac{x}{\bar{c}} + 0.30} \qquad 4.4.1\text{-m}$$

Step 5. Determine the dynamic-pressure-loss ratio for points not on the wake center line by

$$\frac{\Delta q}{q} = \left(\frac{\Delta q}{q}\right)_o \cos^2\left(\frac{\pi}{2}\,\frac{z}{z_w}\right) \qquad 4.4.1\text{-n}$$

where $\left(\frac{\pi}{2}\,\frac{z}{z_w}\right)$ is expressed in radians.

Step 6. Determine the dynamic-pressure ratio in the plane of symmetry at an arbitrary distance x aft of the wing-root-chord trailing edge by

$$\frac{q}{q_\infty} = 1 - \frac{\Delta q}{q} \qquad 4.4.1\text{-o}$$

Note, that if the distance from the vortex sheet to the point of interest is equal to or greater than the wing wake half-width, the dynamic-pressure ratio at the point of interest is unity, i.e., $q/q_\infty = 1.0$ for $z/z_w \geq 1.0$.

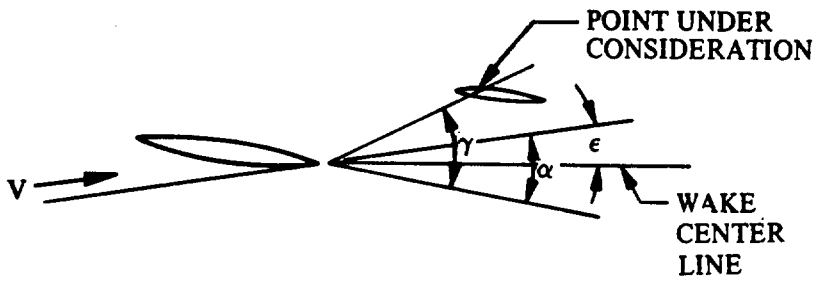

SKETCH (d)

A comparison of test data with dynamic-pressure ratios calculated by this method is given in Table 4.4.1-E.

Sample Problems

1. Subsonic Downwash (Method 1)

Given: The wing-body-tail configuration of Reference 20.

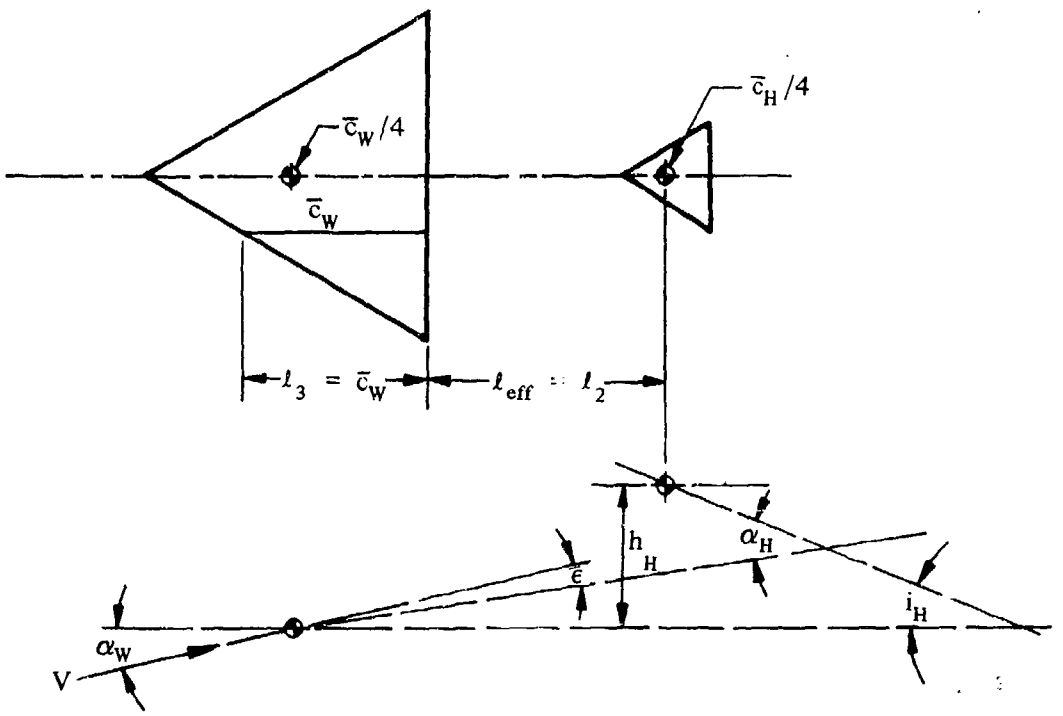

Wing Characteristics:

$A = 2.31 \quad \lambda = 0$

$\Lambda_{c/4} = 52.4^o \quad i_W = 0$

$\Gamma = 0 \quad b = 36.5$ in.

$\bar{c} = 21.1$ in.

NACA $65_{(06)}$–006.5 (free-stream direction)

Horizontal-Tail Characteristics:

$b_H = 11.53$ in. $\qquad h_H = 15.88$ in.

Additional Characteristics:

$\ell_3 = \bar{c}_w$ (delta wing) $\quad \ell_2 = 26.28$ in. $\quad \ell_{eff} = \ell_2$ (delta wing)

Low speed (M = 0.17)

$(\alpha_0)_w = 0 \qquad \left(\alpha_{C_{L_{max}}}\right)_w = 33^o$

α	4^o	8^o	12^o	16^o	20^o	24^o	28^o
C_L	0.15	0.315	0.48	0.655	0.825	0.975	1.115

(wing-alone test data from Reference 20)

Compute:

The final calculations are presented in table form on Page 4.4.1-15. Many of the quantities listed below appear as columns in the table.

Determine the effective wing aspect ratio and the effective wing span.

$$\frac{\alpha - \alpha_0}{\alpha_{C_{L_{max}}} - \alpha_0} = \frac{\alpha - 0}{33.0 - 0} = \frac{\alpha}{33.0}$$

$\frac{A_{eff}}{A}$, $\frac{b_{eff}}{b}$ (Figure 4.4.1-66)

Determine the downwash gradient in the plane of symmetry at the height of the vortex core.

$$\frac{2\ell_2}{b} = \frac{2(26.28)}{36.5} = 1.44$$

$\left(\frac{\partial \epsilon}{\partial \alpha}\right)_v$ (Figure 4.4.1-67)

Determine the vertical position of the vortex core.

$\Delta y = 1.28\%\ c$ (Figure 2.2.1-8)

Leading-edge separation is predominant (Figure 4.4.1-68a); therefore

$$a = h_H - (\ell_2 + \ell_3)\left(\alpha - \frac{0.41\,C_L}{\pi\,A_{eff}}\right) - \frac{b_{eff}}{2}\tan\Gamma \quad \text{(Equation 4.4.1-d)}$$

$$= 15.88 - (26.28 + 21.10)\left(\alpha - \frac{0.41\,C_L}{\pi\,A_{eff}}\right) - 0$$

$$= 15.88 - 47.38\left(\alpha - \frac{0.41\,C_L}{\pi\,A_{eff}}\right)$$

Determine the span of the vortices at the longitudinal location of the quarter-chord point of the tail MAC.

$$b_{v_{ru}} = [0.78 + 0.10\,(\lambda - 0.4) + 0.003\,\Lambda_{c/4}]\;b_{eff} \quad \text{(Equation 4.4.1-f)}$$

$$= [0.78 + 0.10\,(0 - 0.4) + 0.003\,(52.4)]\;b_{eff}$$

$$= 0.897\,b_{eff}$$

$$\xi_{ru} = \frac{0.56\,A}{C_L} = \frac{(0.56)\,(2.31)}{C_L} = \frac{1.294}{C_L}$$

$$b_v = b_{eff} - (b_{eff} - b_{v_{ru}})\left(\frac{2\ell_{eff}}{b\,\xi_{ru}}\right)^{1/2} \quad \text{(Equation 4.4.1-e)}$$

$$= b_{eff} - (b_{eff} - b_{v_{ru}})\left(\frac{1.44}{\xi_{ru}}\right)^{1/2}$$

Determine the average downwash gradient acting on the tail.

$$\left(\frac{\partial\bar{\epsilon}}{\partial\alpha}\right)\Big/\left(\frac{\partial\epsilon}{\partial\alpha}\right)_v = f\left(\frac{2a}{b_v}, \frac{b_H}{b_v}\right) \quad \text{(Figure 4.4.1-68b)}$$

Solution:

(1) α (deg)	(2) $\frac{\alpha-\alpha_0}{\alpha_{C_{L_{max}}}-\alpha_0}$ (1)/33.0	(3) $\frac{A_{eff}}{A}$ (Fig. 4.4.1-66)	(4) $\frac{b_{eff}}{b}$ (Fig. 4.4.1-66)	(5) A_{eff} 2.31(3)	(6) b_{eff} (in.) 36.5(4)	(7) $(\partial\epsilon/\partial\alpha)_v$ (Fig. 4.4.1-67)	(8) C_L Test Values
4	0.121	1.00	1.00	2.31	36.5	0.590	0.150
8	0.242	↓	↓	↓	↓	↓	0.315
12	0.364	↓	↓	↓	↓	↓	0.480
16	0.485	0.975	0.988	2.25	36.1	0.600	0.655
20	0.606	0.875	0.933	2.02	34.1	0.640	0.825
24	0.727	0.780	0.877	1.80	32.0	0.670	0.975
28	0.848	0.680	0.809	1.57	29.5	0.730	1.115

(9) α (deg) $\frac{0.41\,C_L}{\pi A_{eff}}$ $\frac{0.41\,(8)}{\pi\,(5)}$	(10) a (Eq. 4.4.1-d) $15.88-47.38\left(\frac{(1)}{57.3}-(9)\right)$	(11) ξ_{ru} $\frac{1.294}{(8)}$	(12) $b_{v_{ru}}$ (Eq. 4.4.1-f) 0.897(6)	(13) b_v (Eq. 4.4.1-e) $(6)-[(6)-(12)]\left(\frac{1.44}{(11)}\right)^{1/2}$
4	0.0085	12.97	8.627	32.7	34.9
8	0.0178	10.11	4.108	↓	34.3
12	0.0271	7.24	2.696	↓	33.7
16	0.0380	4.45	1.976	32.4	32.9
20	0.0533	1.87	1.568	30.6	30.7
24	0.0707	− 0.61	1.327	28.7	28.6
28	0.0927	− 2.88	1.161	26.5	26.2

(14) α (deg) $\frac{2a}{b_v}$ 2(10)/(13)	(15) $\frac{b_H}{b_v}$ 11.53/(13)	(16) $\left(\frac{\partial\bar{\epsilon}}{\partial\alpha}\right)\Big/\left(\frac{\partial\epsilon}{\partial\alpha}\right)_v$ (Fig. 4.4.1-68b)	(17) $\frac{\partial\bar{\epsilon}}{\partial\alpha}$ (7)(16)	(18) $\int_0^{\alpha}(17)\,d\alpha$
4	0.743	0.330	0.65	0.3835	1.44
8	0.590	0.336	0.73	0.4307	3.06
12	0.430	0.342	0.82	0.4838	4.88
16	0.271	0.350	0.92	0.552	6.92
20	0.122	0.376	0.99	0.6336	9.28
24	−0.043	0.403	1.04	0.6935	11.96
28	−0.220	0.440	0.95	0.6968	14.76

The calculated results are compared with test values from Reference 20 in Sketch(e).

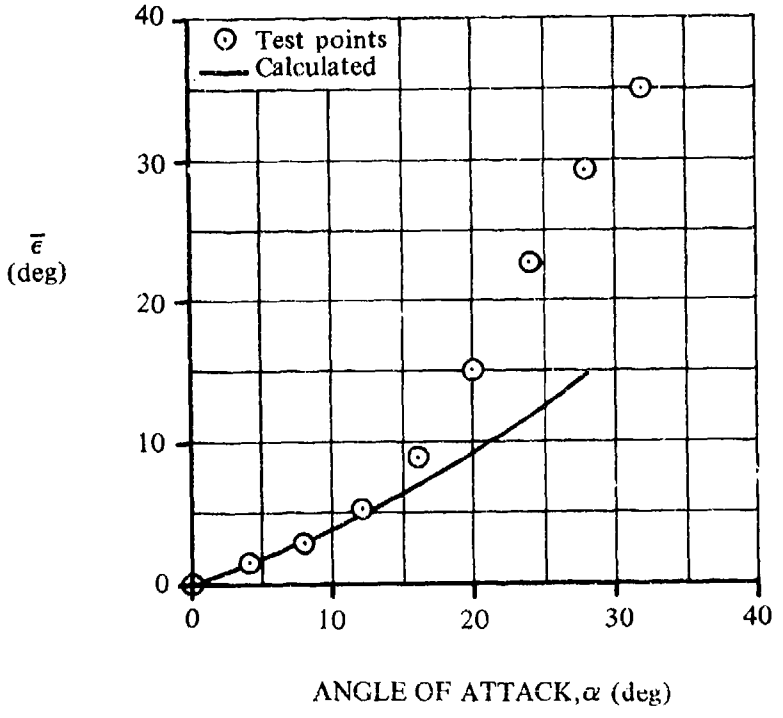

SKETCH (e)

2. Subsonic Downwash (Method 2)

Given: The wing-body-tail configuration of Reference 20. This is the same configuration as Sample Problem 1 above.

Wing Characteristics:

$A = 2.31$ $\lambda = 0$ $\Lambda_{c/4} = 52.4^{o}$ $i_W = 0$ $\Gamma = 0$

$b = 36.5$ in. NACA $65_{(06)}$-006.5 (free-stream direction)

Horizontal-Tail Characteristics:

$h_H = 15.88$ in.

Additional Characteristics:

$\ell_H = 31.57$ in. Low speed (M = 0.17)

Compute:

$$\frac{2h_H}{b} = \frac{2(15.88)}{36.5} = 0.870$$

$$\frac{2\ell_H}{b} = \frac{2(31.57)}{36.5} = 1.73$$

$K_A = 0.240$ (Figure 4.4.1-69a)

$K_\lambda = 1.43$ (Figure 4.4.1-69b)

$K_H = 0.470$ (Figure 4.4.1-70)

Solution:

$$\frac{\partial \bar{\epsilon}}{\partial \alpha} = 4.44 \left[K_A \, K_\lambda \, K_H \, (\cos \Lambda_{c/4})^{1/2} \right]^{1.19} \quad \text{(Equation 4.4.1-h)}$$

$$= 4.44 \left[(0.240)\,(1.43)\,(0.470)\,(\cos 52.4^o)^{1/2} \right]^{1.19}$$

$$= 4.44\,(0.126)^{1.19}$$

$$= 0.377$$

The calculated value compares with a test value of 0.330 from Reference 20.

3. Subsonic Downwash (Method 3)

Given: The same configuration as that of Sample Problem 2 of Paragraph A of Section 4.5.1.1.

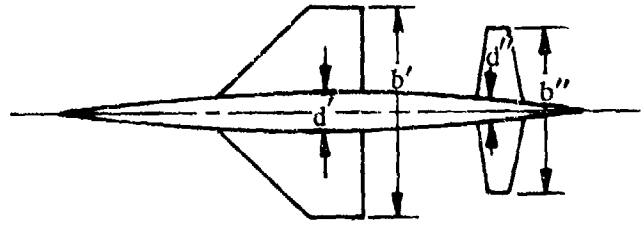

Wing Characteristics:

$A_e' = 1.80$ $\lambda_e' = 0.378$ $b'/2 = 141.42$ in. $d'/2 = 26.94$ in.

$\Lambda_{TE} = 0$

Horizontal-Tail Characteristics:

λ_e'' = 0.515 $\quad b''/2$ = 110.64 in. $\quad d''/2$ = 22.08 in.

Additional Characteristics:

Low speed (M = 0.13); β = 0.9915

x = 165.6 in. (distance from the wing trailing edge to the quarter-chord point of the horizontal-tail MAC)

Compute:

Determine the lateral spacing of the trailing vortices at station x.

$\beta A_e'$ = (0.9915) (1.80) = 1.785

$\frac{b_v'/2 - d'/2}{b'/2 - d'/2}$ = 0.785 (Figure 4.4.1-71c)

$b'/2 - d'/2$ = 141.42 – 26.94 = 114.48 in.

$b_v'/2 - d'/2$ = (0.785) (114.48) = 89.87 in.

$b_v'/2$ = 89.87 in. + $d'/2$ = 116.81 in.

$b_v''/2 = b_v'/2$ = 116.81 in. (The method assumes that the lateral spacing of trailing vortices is invariant with longitudinal distance and angle of attack.)

$\frac{b_v''/2}{b''/2} = \frac{116.81}{110.64}$ = 1.056 (This value is used in place of $\frac{y_o}{b_w/2}$ in Figure 4.3.1.3-7.)

Determine the vertical position of the trailing vortices.

$h_v = x \tan\alpha = 165.6 \tan\alpha$ (see table below) (The method assumes the vortex springs from the wing trailing edge and trails in the free-stream direction.)

The ratio $\frac{h_v}{b''/2}$ is used in place of $\frac{z_o}{b_w/2}$ in Figure 4.3.1.3-7.

$\frac{d''/2}{b''/2} = \frac{22.08}{110.64}$ = 0.200 (This value is used in place of $\frac{r}{b_w/2}$ in Figure 4.3.1.3-7.)

Solution:

α (deg)	h_v / 165.6 tan α (in.)	$\frac{h_v}{b''/2}$	$I_{v_{W''(W'')}}$ Fig. 4.3.1.3-7 @ λ_e'', $\frac{b_v''/2}{b''/2}$ and $\frac{h_v}{b''/2}$
0	0	0	−3.0
5	14.49	0.131	−2.5
10	29.20	0.264	−2.0
15	44.37	0.401	−1.68
20	60.27	0.545	−1.40
23	70.29	0.635	−1.27
26	80.77	0.730	−1.15

The interference factor $I_{v_{W''(W'')}}$ at $\alpha = 0$ is used in Sample Problem 2 of Paragraph A of Section 4.5.1.1 to obtain the effect on total airplane lift, of the wing trailing vortices on the horizontal tail.

4. Subsonic Downwash Due to Flap Deflection

Given: The wing-body-tail configuration of Reference 31

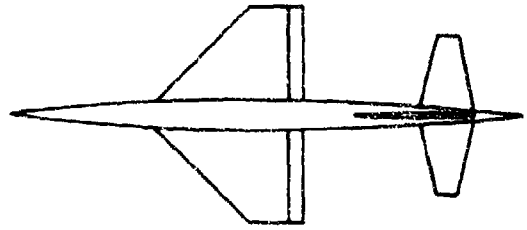

Wing Characteristics:

$A = 2.0$ $b = 23.56$ ft $\Delta C_L = 0.57$ (test data)

Inboard flap station $\eta_i = 0.191$ Outboard flap station $\eta_o = 1.00$

Slotted trailing-edge flaps $\delta_f = 40°$

Tail Characteristic:

$h_H = 0$

Compute:

$$\frac{h_H}{b/2} = \frac{0}{(23.56/2)} = 0$$

$$\frac{b_f}{b/2} = \eta_o - \eta_i$$

$$= 1.00 - 0.191 = 0.809$$

$$\left\{\frac{\Delta\epsilon\, A[b_f/(b/2)]}{\Delta C_L}\right\} = 28.5 \quad \text{(Figure 4.4.1-72)}$$

Solution:

$$\Delta\epsilon = \left\{\frac{\Delta\epsilon\, A[b_f/(b/2)]}{\Delta C_L}\right\} \frac{\Delta C_L}{A[b_f/(b/2)]}$$

$$= (28.5)\,\frac{0.57}{(2.0)\,(0.809)}$$

$$= 10.04^\circ$$

This compares with a test value of 8.8° from Reference 31.

5. Subsonic Dynamic-Pressure Ratio

Given: A wing-tail configuration of Reference 9

Wing Characteristics:

$A = 6.0$ $\lambda = 1.0$ $\bar{c} = 10.0$ in. $S_W = 600$ sq in. $S_{wet} = 1200$ sq in.

NACA 0015 airfoil (x_t @ 0.30c)

Additional Characteristics:

$x = 20.0$ in. (survey station location, aft of wing trailing edge)

Low speed $R_\ell = 0.62 \times 10^6$ (based on $\bar{c}$) $\gamma = 0$

Smooth surface (assume $k = 0$) $S_{ref} = S_W = 600$ sq in.

α	0	1°	2°	3°	4°	6°	8°
C_L	−.01	.055	.115	.175	.240	.360	.485

(test data from Reference 9)

Compute:

Determine the half-width of the wake.

$\ell/k = \infty$; read C_f at given R_ℓ

$C_f = 0.00487$ (Figure 4.1.5.1-26)

$\left[1 + L\left(\frac{t}{c}\right) + 100\left(\frac{t}{c}\right)^4\right] = 1.225$ (figure 4.1.5.1-28a, for L = 1.2)

$\cos \Lambda_{(t/c)_{max}} = \cos 0 = 1.0$

$R_{L.S.} = 1.07$ (Figure 4.1.5.1-28b)

$\frac{S_{wet}}{S_{ref}} = \frac{1200}{600} = 2.0$

$C_{D_0} = C_f \left[1 + L\left(\frac{t}{c}\right) + 100\left(\frac{t}{c}\right)^4\right] R_{L.S.} \frac{S_{wet}}{S_{ref}}$ (Equation 4.1.5.1-a)

$= (0.00487)(1.225)(1.07)(2.0)$

$= 0.0128$

$x/\bar{c} = 20.0/10.0 = 2.0$

$\frac{z_w}{\bar{c}} = 0.68 \sqrt{C_{D_0}\left(\frac{x}{\bar{c}} + 0.15\right)}$ (Equation 4.4.1-j)

$= 0.68 \sqrt{(0.0128)(2.15)}$

$= 0.113$

Determine the downwash in the plane of symmetry at the vortex sheet.

$\epsilon = \frac{1.62\, C_L}{\pi A}$ (Equation 4.4.1-k)

$= \frac{1.62\, C_L}{\pi\, 6.0} = 0.0859\, C_L$ (radians)

$= 4.92\, C_L$ (degrees) (see calculation table below)

Determine the vertical distance z from the vortex sheet to the point of interest.

$z = x \tan (\gamma + \epsilon - \alpha)$ (Equation 4.4.1-ℓ)

$= 20.0 \tan (0 + \epsilon - \alpha) = 20.0 \tan (\epsilon - \alpha)$ (see calculation table below)

Determine the dynamic-pressure-loss ratio at the wake center.

$$\left(\frac{\Delta q}{q}\right)_o = \frac{2.42\left(C_{D_0}\right)^{1/2}}{\frac{x}{\bar{c}} + 0.30} \qquad \text{(Equation 4.4.1-m)}$$

$$= \frac{2.42(0.0128)^{1/2}}{2.0 + 0.30} = 0.119$$

Determine the dynamic-pressure-loss ratio for points not on the wake center line.

$$\frac{\Delta q}{q} = \left(\frac{\Delta q}{q}\right)_o \cos^2\left(\frac{\pi}{2}\,\frac{z}{z_w}\right) \qquad \text{(Equation 4.4.1-n)}$$

$$= 0.119\ \cos^2\left(\frac{\pi}{2}\,\frac{z}{1.13}\,\frac{57.3}{1}\right)$$

$$= 0.119\ \cos^2\ (79.65\ z) \qquad \text{(see calculation table below)}$$

Solution:

The dynamic-pressure ratio in the plane of symmetry at a distance x = 20.0 in. aft of the wing-root-chord trailing edge is

$$\frac{q}{q_\infty} = 1 - \frac{\Delta q}{q} \qquad \text{(Equation 4.4.1-o)} \qquad \text{(see calculation table below)}$$

①	②	③	④	⑤	⑥	⑦
α (deg)	C_L test values	ϵ (deg) (Eq. 4.4.1-k) 4.92 ②	$\frac{z}{z_w}$ (Eq. 4.4.1-l) 20 tan (③ − ①)	$\cos^2\left(\frac{\pi}{2}\,\frac{z}{z_w}\right)$ ($\cos^2$ (79.65 ④)	$\frac{\Delta q}{q}$ (Eq. 4.4.1-n) 0.119 ⑤	$\frac{q}{q_\infty}$ (Eq.4.4.1-o) 1 − ⑥
0	−0.01	−0.049	−0.0172	0.9994	0.119	0.881
1	0.055	0.271	−0.2544	0.8800	0.105	0.895
2	0.115	0.566	−0.5008	0.5887	0.0701	0.930
3	0.175	0.861	−0.7470	0.1576	0.0307	0.969
4	0.240	1.181	−0.9848	0.0402	0.0048	0.995
6	0.360	1.771	−1.4790	–	–	1.00*
8	0.485	2.386	−1.9660	–	–	1.00*

* $q/q_\infty = 1.0$ when $z/z_w \geq 1.0$.

The calculated results are compared with test values from Reference 9 in Table 4.4.1-E. (This is the second configuration given in Table 4.4.1-E.)

B. TRANSONIC

Downwash

In general, the downwash gradient is proportional to the lift-curve slope. The transonic lift-curve-slope characteristics are discussed in detail in Section 4.1.3.2. The following discussion summarizes these transonic characteristics.

For thin, low-aspect-ratio wings the downwash gradient varies smoothly with Mach number. The typical variation is similar to the lift-curve-slope variation for Type "B" wings shown on Page 4.1.3.2-13. For thick, high-aspect-ratio wings at low angles of attack the variation is like that of Type "A" wings (shown on the same page), but at high angles of attack the downwash-gradient variation of these wings is smooth.

The erratic behavior of the thicker wings at low angles of attack is frequently accentuated by shock-induced boundary-layer separation, which can cause significant changes in the span-load characteristics and hence in the downwash distribution behind a wing.

No design charts for the transonic range are presented, because so few flow surveys are available.

Dynamic-Pressure Ratio

No method has been suggested in the literature for estimating the dynamic-pressure ratio at transonic speeds. Furthermore, few data measuring this parameter are known to exist. The method suggested herein is therefore tentative.

DATCOM METHODS

Transonic Downwash

No accurate method is available for the prediction of transonic downwash characteristics. It is suggested that values be approximated by assuming that the downwash gradient is proportional to the lift-curve slope as given in Section 4.1.3.2 for low angles of attack and in Section 4.1.3.3 for high angles of attack.

Transonic Dynamic-Pressure Ratio

For estimating the transonic dynamic-pressure ratio, it is suggested that the method presented in Paragraph A above be applied, with the appropriate zero-lift drag values from Section 4.1.5.1 (excluding wave drag).

C. SUPERSONIC

Downwash

At supersonic speeds downwash is caused by two factors. First, the region behind the trailing-edge shock or expansion wave is distorted by the wing vortex system in a manner similar to that which occurs at subsonic speeds. Because of the variation in span load, a vortex sheet is shed that rolls up with increasing downstream distance from the surface. Tip vortices similar to their subsonic counterparts are also present. At the supersonic Mach numbers, however, the entire flow field is swept back and isolated regions of

influence may exist over certain portions of the wing surface and in the flow field behind it. For instance, regions not affected by the wing tip are generally present. For a rectangular wing such a region can be treated in a two-dimensional manner, i.e., no lateral variation of downwash exists.

Secondly, a change in flow direction occurs in the flow region between the leading- and trailing-edge shock or expansion waves. Since this region of the flow field does not "see" the wing vortex system, numerical values of downwash can be calculated by applying shock-expansion theory. In order to simplify the calculations, it is standard practice to perform the calculations with wing-root geometry and to assume two-dimensional flow. For cases in which the vehicle component (i.e., horizontal tail) immersed in the wing flow field has less span than the wing, this latter assumption is justified. For cases in which the aft component is large compared to the forward component (i.e., a wing following a canard surface), this assumption is not justified, because of the significant spanwise downwash variations associated with the wing tips. Behind the trailing-edge shock or expansion wave the downwash due to these compressibility effects is zero.

Dynamic-Pressure Ratio

Variations in the dynamic-pressure ratio exist throughout the field of influence of a wing in supersonic flight. A thin viscous wake exists behind the wing, with characteristics quite similar to its subsonic counterpart (see Paragraph A above). In addition, the nonviscous flow region behind the leading-edge shock or expansion wave also exhibits dynamic-pressure-ratio variations due to compressibility effects. The application of shock-expansion theory has been shown to yield a reasonable approximation for the dynamic-pressure ratio in the nonviscous portion of the flow field.

The existence of the trailing-edge shock wave on the upper surface can cause a significant boundary-layer-separation region under conditions of low Reynolds number and/or large angles of attack (see Sketch (f)). This region of separation creates a wide wake near the trailing edge that is not predicted by the method presented herein.

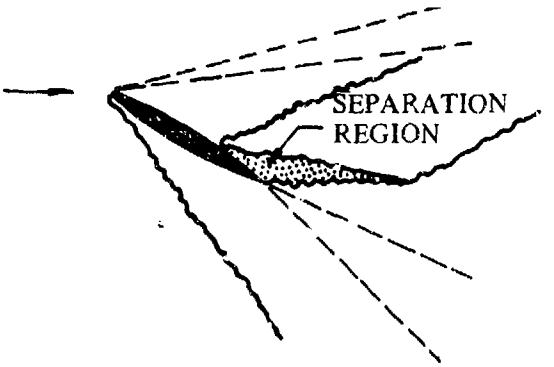

SKETCH (f)

Mach Number Effects

The local Mach number between the leading- and trailing-edge shock or expansion waves can vary significantly from the free-stream value. Expansion fields increase the Mach number, and compression fields decrease the Mach number. Vehicle components immersed in these flow fields exhibit different aerodynamic characteristics because of the varying Mach number. This is illustrated in Sketch (g) for a double wedge airfoil.

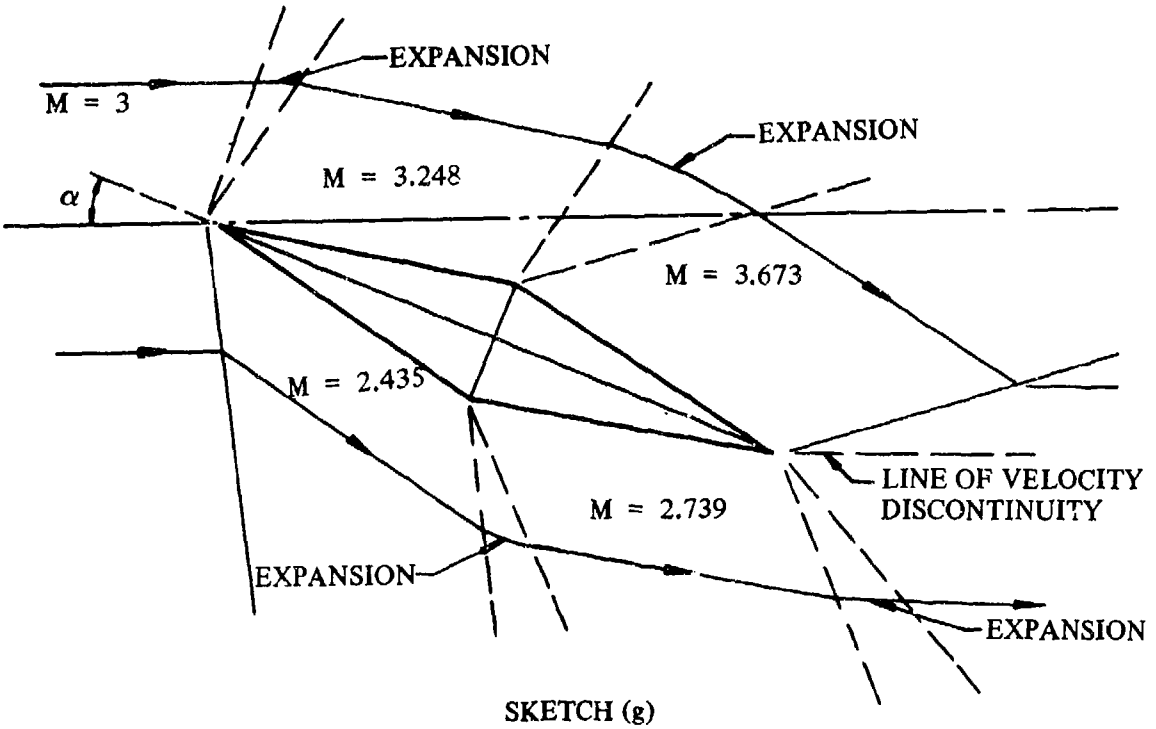

SKETCH (g)

Lumped Parameter

At least one author(Reference10) has treated the flow field at supersonic speeds by combining the effects of downwash, dynamic-pressure ratio, and Mach number into a single lumped parameter. This approach gives valid values for determining the effect of the wing shock-expansion field on stabilizer effectiveness but cannot give the isolated effects. In the Datcom, this analysis is presented in Section 4.5.1.2.

DATCOM METHODS

Supersonic Downwash

Method 1

The downwash behind a straight-tapered wing for either subsonic or supersonic leading and trailing edges can be approximated by the theoretical method presented in Reference 11. The basic theory uses a system of 20 swept unit horseshoe vortices placed along the load line of the wing (assumed to be the midchord line in the Datcom). The vortices are then weighted by the span-load variation. The integrated contribution of each bound and each trailing vortex is then determined as a function of the spatial coordinates and presented in either table or chart form.

For computing downwash in the plane of symmetry, tables have been prepared based on the downwash due to the system of swept unit horseshoe vortices.

For computing the spanwise variation of downwash, design charts have been prepared based on an approximation of the downwash due to the system of swept unit horseshoe vortices. The swept lifting line

has been approximated with semi-infinite unswept horseshoe vortices. Although this approximation does not predict the exact magnitude of the spanwise variation in downwash, it has been applied in an effort to simplify the final solution and to allow design charts to be presented in lieu of lengthy calculation tables. By using this approach, the calculated level of the spanwise downwash variation is adjusted, if necessary, to the value at the plane of symmetry obtained using the tables.

This method is presented in the Datcom because of its wide range of applicability, even though the tables and design charts of Reference 11 have not been reproduced. However, the basic equations are presented for use in the event that the reference is not available to the user. The span loading of the particular wing being considered must be known. At the present time this information must be obtained from sources other than the Datcom, for instance Reference 12.

The derivative $\frac{\partial \epsilon}{\partial \alpha}$ at a particular point (x, y, z) in the flow field not close to the trailing edge of the wing is obtained by means of the equation

$$\frac{\partial \epsilon}{\partial \alpha} = -\frac{w}{V_\infty \alpha} \qquad 4.4.1\text{-p}$$

For points on the plane of symmetry

$$-w = 2\sum_{i=o}^{n_2} \frac{\Gamma_{y_{i+1}} - \Gamma_{y_{i-1}}}{b/2} F_w(|y_{i,o}|) + \frac{\Gamma_o}{b/2} F_{w,o} \qquad 4.4.1\text{-q}$$

For points not on the plane of symmetry (spanwise downwash)

$$-w = -\sum_{i=n_1}^{o} \frac{\Gamma_{y_{i+1}} - \Gamma_{y_{i-1}}}{b/2} F_w(Y_{i,o}) + \sum_{i=o}^{i=n_2} \frac{\Gamma_{y_{i+1}} - \Gamma_{y_{i-1}}}{b/2} F_w(Y_{i,o}) \qquad 4.4.1\text{-r}$$

The functions $F_w(|y_{i,o}|)$, $F_w(Y_{i,o})$, and $F_{w,o}$ are presented in Reference 11 as Table II, Figure 6, and Table III, respectively, and are expressed mathematically by

$$F_w(|y_{i,o}|) = \frac{-|y_{i,o}|X_{i,o}^3 + X_{i,o}(z_o^2 - y_{i,o}^2) + \beta m^2 |y_{i,o}|X_{i,o}(|y_{i,o}|^2 + 2z_o^2) + \beta m^2 |y_{i,o}|(z_o^2 + |y_{i,o}|^2)}{4\pi\sqrt{X_{i,o}^2 - \beta^2 m^2 (|y_{i,o}|^2 + z_o^2)}\,[(|y_{i,o}|X_{i,o} + z_o^2 + |y_{i,o}|^2)^2 + z_o^2(X_{i,o}^2 - \beta^2 m^2 |y_{i,o}|^2 - \beta^2 m^2 z_o^2)]} \qquad 4.4.1\text{-s}$$

$$F_w(Y_{i,o}) = \frac{Y_{i,o}\bar{X}_i^3 - Y_{i,o}\bar{X}_i(Y_{i,o}^2 + 2z_o^2)}{4\pi\sqrt{\bar{X}_i^2 - Y_{i,o}^2 - z_o^2}\,(\bar{X}_i^2 - z_o^2)(Y_{i,o}^2 + z_o^2)} \qquad 4.4.1\text{-t}$$

$$F_{w,o} = \frac{x_o}{\pi\sqrt{x_o^2 - \beta^2 m^2 z_o^2}\,[x_o^2 + z_o^2(1 - \beta^2 m^2)]} \qquad 4.4.1\text{-u}$$

Definitions applying to this method are given as follows (symbolism used for this method is identical with that of Reference 11).

V_∞ = free-stream velocity.

α = angle of attack in radians.

x,y,z = standard rectangular Cartesian coordinates with the origin at the 50-percent-chord point of the root section.

x_i, y_i = standard rectangular Cartesian coordinates of the inboard corners of the horseshoe vortices.

$$x_o = \frac{mx}{b/2}$$

$$x_{i,o} = \pm \frac{mx_i}{b/2} = \pm y_{i,o}$$

$$X_{i,o} = x_o - x_{i,o} = x_o \pm y_{i,o} = \frac{mX_i}{b/2}$$

$$\bar{X}_i = \bar{x} \pm \frac{y_{i,o}}{\beta m}$$

$$\bar{x} = \frac{x}{\beta b/2} \left(= \frac{x_o}{\beta m} \text{ for swept lifting line} \right)$$

$$y_o = \frac{y}{b/2}$$

$$y_{i,o} = \frac{y_i}{b/2}$$

$$Y_{i,o} = y_o - y_{i,o} = \frac{Y_i}{b/2}$$

$$z_o = \frac{z}{b/2}$$

i = variable index used in summation, designating a particular horseshoe vortex. Values of i from o to n_1 are associated with negative values of y_i and values from o to n_2 with positive values of y_i.

m = slope of lifting line ($\cot|\Lambda_{c/2}|$)

n_1, n_2 = value of i at left- and right-hand wing tips of a swept wing, looking from trailing edge to leading edge.

Γ_y = value of circulation at any spanwise station. If the load distribution is given in terms of the section lift coefficient, the circulation is determined by the equation

$$\Gamma_y = 1/2\, c_\ell Vc$$

where c is the local chord.

Γ_o = circulation at $y_i = 0$

The suggested method of adjusting the calculated spanwise downwash given by Equation 4.4.1-r is to translate the curve of calculated spanwise downwash so that the value at the plane of symmetry ($y_o = 0$) is made to coincide with that computed by using Equation 4.4.1-q. This approach is illustrated in the sample problem on Page 4.4.1-35.

For locations near the wing trailing edge, lifting-line theory does not give adequate answers and a more precise determination must be made. An exact equation is given in Reference 13 for determining this value, which involves the local angle of attack and the perturbation velocity at the trailing edge.

The effects of vortex-sheet displacement and distortion have not been included in this method, although this effect may be approximated by the theory of Reference 14. (See Steps 1 and 2 of Method 2 that follows.) The displacement of the vortex sheet at the center line is determined, and it is assumed that this displacement is constant for all lateral stations. Therefore, the effects of vortex-sheet displacement and distortion are approximated by calculating a new z_o value to be used in this method. In using the design charts associated with Method 2, it should be noted that the origin of the spatial coordinates is located at the wing apex rather than at the 50-percent-chord point of the root section as for this method.

Method 2

Supersonic downwash for straight-tapered wings with supersonic leading edges ($\beta \cot \Lambda_{LE} > 1$) and supersonic trailing edges ($\beta \cot \Lambda_{TE} > 1$) may be computed by means of the charts presented in Reference 14. (It should be noted that Figures 4.4.1-76a and -76d from Reference 14 have been expanded somewhat, based on available test data. In addition, Figure 4.4.1-76e has been obtained semiempirically by using Figure 4.4.1-76d as a basis and should be applied with caution.) The charts, based on lifting-line theory, are derived for flat-plate wings and include a correction for the displacement and distortion of the trailing vortex sheet. The lifting line is assumed to be at $\Lambda_{c/2}$ for the rectangular and trapezoidal wings and at $\Lambda_{3c/4}$ for the triangular wings. Near the sonic-leading-edge condition, the lift of a finite-thickness wing is significantly less than the values for flat-plate wings (see Section 4.1.3.2). The downwash gradient $\partial\bar{\epsilon}/\partial\alpha$ may be corrected to account for wing thickness effects as indicated in the procedure below. Table 4.4.1-F presents a data summary and substantiation. The limited number of test points presented precludes substantiation of this method over other than very limited ranges of planform and flow parameters.

The derivative $\dfrac{\partial\bar{\epsilon}}{\partial\alpha}$ for wings with supersonic leading and trailing edges is obtained by the following procedure:

Step 1. For the Mach number under consideration, the coordinates of the point where the downwash is desired are reduced to the parameters $\frac{2x}{\beta b}$, $\frac{2y}{b}$, and $\frac{2z}{b}$ measured from an origin at the apex of the wing (x, y, and z are positive in the conventional sense and refer to wind axes).

Step 2. The effects of displacement and distortion of the vortex sheet are accounted for by determining the displacement of the sheet at the center line and assuming that this displacement is constant for all lateral stations (see Reference 14). The vertical displacement 2h/b of the vortex sheet at the center line is obtained from Figure 4.4.1-74 (derived from Reference 8). This value is added to the parameter $\frac{2z}{b}$ from Step 1 to obtain the effective value of the height parameter relative to the displaced vortex. This effective parameter is designated $\left(\frac{2z}{b}\right)_{eff}$

Step 3. For the values of $\frac{2x}{\beta b}$, $\frac{2y}{b}$, and $\left(\frac{2z}{b}\right)_{eff}$, the derivative $\frac{\partial \bar{\epsilon}}{\partial \alpha}$ is obtained from Figures 4.4.1-76a through 4.4.1-76e, depending upon the appropriate wing planform geometry. This value is valid for finite-thickness wings except near the sonic-leading-edge condition, where an additional correction is required.

Step 4. For near-sonic-leading-edge conditions, the value of $\frac{\partial \bar{\epsilon}}{\partial \alpha}$ obtained from Step 3 is multiplied by the thickness correction factor from Figure 4.1.3.2-60.

Step 5. For moderate angles of attack below wing stall, where the nonlinear lift becomes important, the downwash gradient determined from Step 3 can be approximately corrected by the equation

$$\frac{\partial \bar{\epsilon}}{\partial \alpha} = \frac{(C_{N_\alpha})_{4.1.3.3}}{(C_{N_\alpha})_{4.1.3.2}} \left(\frac{\partial \bar{\epsilon}}{\partial \alpha}\right)_{step\ 3} \qquad 4.4.1\text{-v}$$

where

$(C_{N_\alpha})_{4.1.3.3}$ is the local normal-force-curve slope from Paragraph C of Section 4.1.3.3 for the angle of attack under consideration. It is $(C_{N_\alpha})_{4.1.3.2}$ corrected for thickness effects.

$(C_{N_\alpha})_{4.1.3.2}$ is the normal-force-curve slope at zero angle of attack from the straight-tapered-wing method of Paragraph C of Section 4.1.3.2, excluding the thickness correction factor of Figure 4.1.3.2-60.

$\left(\frac{\partial \epsilon}{\partial \alpha}\right)_{step\ 3}$ is the downwash gradient from Step 3.

Step 6. The average downwash over the span of a horizontal tail is obtained by computing the downwash at several spanwise locations and computing an average value.

Step 5 should be used with caution. Nonlinear lift (which is characteristic of low-aspect-ratio configurations) is caused by strong vortices that generally move inboard with increasing angle of attack and may have a spanwise spacing comparable to that of the downstream surfaces.

For those configurations that do not satisfy the supersonic leading- and trailing-edge condition, an approximation (used in Digital Datcom) for the downwash gradient may be obtained by using Equation 4.4.1-k, i.e.,

$$\epsilon = \frac{1.62\, C_L}{\pi A} \quad \text{(radians)}$$

From this equation a relationship is obtained for ϵ as a function of angle of attack. Plotting the curve from this relationship enables the user to obtain a value for $\partial\epsilon/\partial\alpha$ at a specific angle of attack. However, this approximation should be used with caution since it has not been substantiated in the supersonic speed regime.

Method 3

For low-aspect-ratio or canard configurations the vortex pair from the forward surface interacts more directly with the aft surface and the following method from Reference3 is applicable.

Step 1. The spatial position of the trailing vortices is first determined relative to the aft surface. The lateral spacing is determined from Figure 4.4.1-80 as a function of the exposed forward-surface planform geometry. This spacing is invariant with longitudinal distance and angle of attack. The vertical position is determined by assuming that the vortex springs from the trailing edge at the previously determined lateral position and trails in the free-stream direction. The pertinent vertical dimension is the distance between the quarter-chord point of the MAC of the aft surface and the vortex as determined above.

Step 2. The vortex interference factor $I_{v\bar{W}'(W'')}$ is obtained from Figures 4.3.1.3-7a through 4.3.1.3-7ℓ as a function of the lateral and vertical vortex positions, determined in Step 1, and the geometry of the aft panel. (The primed notation refers to the forward panel and the double-primed notation refers to the aft panel.)

Step 3. The vortex interference factor so determined is used in Sections 4.5.1.1 and 4.5.1.2 to obtain the lift generated on the aft surface for complete wing-body-tail combinations.

This method is similar to Method 3 for estimating subsonic downwash in paragraph A. The use of the subsonic sample problem on Page 4.4.1-17 as a guide is essential in applying this method.

Supersonic Dynamic-Pressure Ratio

The dynamic-pressure ratio at supersonic speeds is estimated separately for the nonviscous and viscous flow regions. The nonviscous flow region is approximated by the flow emanating from the wing in the absence of separation, and bound by shock or expansion waves. The viscous flow region is considered to be the viscous wake behind a wing, with attached flow in the vicinity of the trailing edge.

Nonviscous Flow Field

The dynamic-pressure ratio in the nonviscous flow field of a wing is estimated by means of shock-expansion theory. Application of this technique assumes that the flow field is two-dimensional. For a rectangular wing, the region outside the influence of the tips is two-dimensional. Therefore, the method applied to rectangular wings will, in general, predict the experimental trends and even the magnitude of the flow-field quantities with fair accuracy, except in the region influenced by the tip or in the viscous wake. For some rectangular wings of high effective aspect ratio (βA), the greater portion of the flow field can be predicted reasonably well by shock-expansion theory.

Strictly speaking, this method can not be applied to sweptback wings, since the large portion of the flow field of such wings will not be two-dimensional. However, the method might furnish a good approximation to the dynamic-pressure-ratio variations, because the theory does account for the presence of shock and expansion waves. In Reference 15 the method has been applied to a triangular wing with supersonic leading edges, and the dynamic-pressure ratio was predicted fairly accurately except in the viscous flow region. No comparison of calculated results with experimental data has been made for wings with subsonic leading edges.

The theory as applied herein allows calculation of the dynamic-pressure ratio on an arbitrarily selected survey plane located downstream from the wing. The geometric relationship between points on this plane and points on the airfoil from which the disturbance originates is illustrated in Sketch (h). It is assumed that disturbances emanating from a point on the wing (x '– z 'plane)

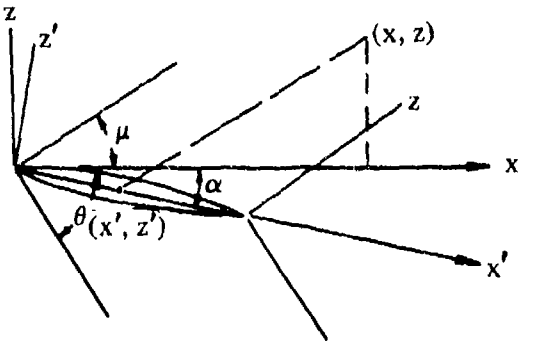

SKETCH (h)

proceed downstream at the theoretical Mach angle μ for surfaces with an initial expansion angle, and at the shock angle θ for surfaces with an initial compression angle. It is further assumed that the dynamic-pressure ratio at some point (x, y) on the survey plane is the same as that at the corresponding point (x', y') on the airfoil surface.

The basic approach is as follows:

1. For a given airfoil and flow condition determine the points (x, y) in the flow field at the survey plane corresponding to the points (x', y') on the airfoil from which the disturbance is assumed to originate.

2. By using shock-expansion theory, determine the dynamic-pressure ratio at point (x, y) in the flow field – which is assumed to be the same as that at corresponding point (x', y').

In applying shock-expansion theory the flows on the upper and lower airfoil surfaces can be treated separately. The type of flow (either expansion or compression) at a given point is governed by the sign of the flow-deflection angle at that point.

If the flow-deflection angle is positive, the flow expands isentropically and the characteristics of the flow are given by Prandtl-Meyer expansion relations. If the flow quantities are known at one point, the values at any second point can be calculated by identifying the change in the flow angle between the two points.

If the flow-deflection angle is negative, the flow is compressed and the flow characteristics are given by oblique-shock-wave relations. The Datcom presents a design chart showing the variation of shock angle with flow-deflection angle for various upstream Mach numbers. In addition, since flow through weak shock waves is nearly isentropic, compressions through small angles may also be calculated by regarding them as reversed Prandtl-Meyer expansions.

Although expansion and compression waves proceed at different angles and therefore interact, this simplified method does in some cases give a good approximation of the dynamic-pressure ratio. The accuracy of the method deteriorates as the wing thickness and/or distance of the survey plane aft of the wing increase.

The following steps outline the procedure to be followed for determining the supersonic dynamic-pressure ratio in the nonviscous flow field. The use of the sample problem on Page 4.4.1-41 as a guide is essential in applying this procedure.

Step 1. For a given airfoil and flow condition, determine the flow-deflection angles on the upper and lower airfoil surfaces at the leading edge.

For an airfoil at a positive angle of attack the flow-deflection angle at the leading edge is given by:

For the upper airfoil surface

$$\delta'_{LE} = \alpha - \delta_{LE_{upper}}$$

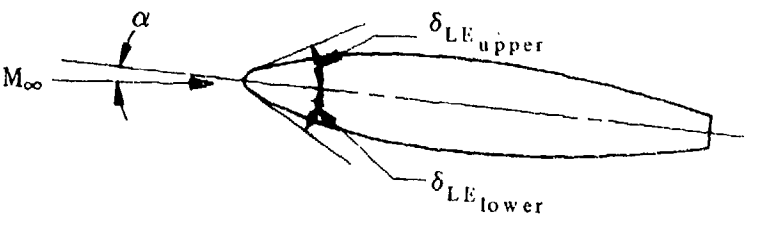

For the lower airfoil surface

$$\delta'_{LE} = -\alpha - \delta_{LE_{lower}}$$

where the δ' values are the flow-deflection angles and the δ values are the slopes of the airfoil surface with respect to the chord plane x'.

If δ'_{LE} is positive the surface has an initial expansion angle. If δ'_{LE} is negative the surface has an initial compression angle.

Step 2. Determine the points (x , z) in the flow field corresponding to the points (x' , z') on the airfoil from which the disturbance is assumed to have originated.

For surfaces with an initial expansion angle

$$z = \frac{-x' + x\cos\alpha - \dfrac{x\sin\alpha}{\tan(\mu+\alpha)}}{\sin\alpha + \dfrac{\cos\alpha}{\tan(\mu+\alpha)}} \qquad \text{4.4.1-w}$$

where

x' is an arbitrarily chosen point on the airfoil chord plane, positive aft of the leading edge.

x is the location of the arbitrarily chosen survey plane on the x-axis, positive aft of the leading edge.

α is the angle of attack in degrees.

μ is the Mach angle, $\mu = \sin^{-1}\dfrac{1}{M_\infty}$.

For surfaces with initial compression angles

$$z = \frac{-x' + x\cos\alpha - \dfrac{x\sin\alpha}{\tan(\alpha-\theta)}}{\sin\alpha + \dfrac{\cos\alpha}{\tan(\alpha-\theta)}} \qquad \text{4.4.1-x}$$

where x', x, and α are defined above and θ is the shock-wave angle obtained as a function of the free-stream Mach number and the flow-deflection angle from Figure 4.4.1-81.

Equations 4.4.1-w and 4.4.1-x are based on the assumption that the disturbance originates from a point located on the airfoil chord. Therefore, $z' = 0$.

Step 3. Determine the dynamic-pressure ratio at point (x , z) – which is assumed to be the same as that at corresponding point (x', z').

For expansion fields (positive flow-deflection angles) the procedure is as follows:

a. Using the Mach number upstream of a point M_{n-1}, enter Figure 4.4.1-82 and obtain ν_{n-1}, the Prandtl-Meyer angle (angle through which the supersonic stream is turned to expand from M = 1 to M > 1). n refers to an individual point.

b. Determine $\Delta\nu_n$, the change in flow-deflection angle between two points. In expanding from the free stream to a point downstream of the leading edge, $\Delta\nu_n = \alpha - \delta_{LE}$. On the airfoil surface $\Delta\nu_n$ is simply the change in surface slope between two points; i.e., $\Delta\nu_n = \delta_{n-1} - \delta_n$.

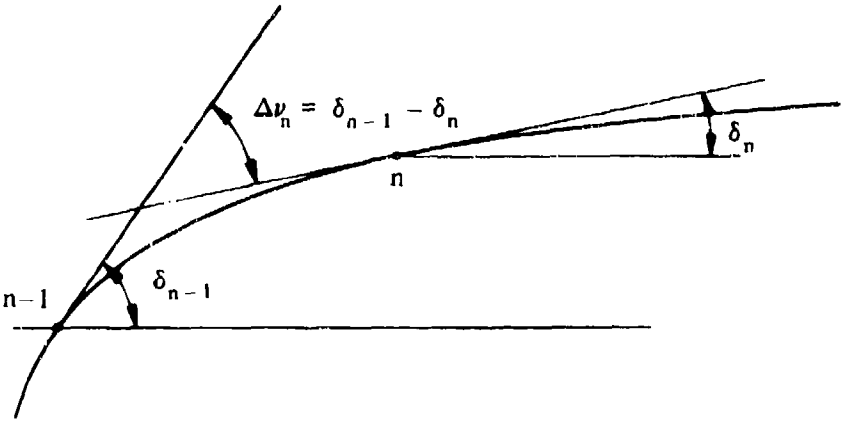

c. Determine the new Prandtl-Meyer angle at point n by $\nu_n = \nu_{n-1} + \Delta\nu_n$

d. Enter Figure 4.4.1-82 with ν_n and read M_n.

e. Using M_{n-1} (upstream Mach number) and M_n (Mach number at point in question), enter Figure 4.4.1-82 and read the ratio of dynamic pressure to total pressure q/p_t at the respective Mach numbers. Then

$$\frac{q_n}{q_\infty} = \frac{(q/p_t)_n}{(q/p_t)_{n-1}} \frac{q_{n-1}}{q_\infty} \qquad 4.4.1\text{-y}$$

For compression fields (negative flow-deflection angles) the procedure is as follows:

The dynamic-pressure ratio following an oblique shock is given by

$$\frac{q_n}{q_{n-1}} = \frac{60}{M_{n-1}^2} \frac{(1 + 0.2\, M_{n-1}^2)^{7/2}}{(5 + M_{n-1}^2 \sin^2\theta)^{5/2}} \qquad 4.4.1\text{-z}$$

where n refers to an individual point and

M_{n-1} is the Mach number upstream of the shock.

θ is the shock-wave angle obtained as a function of the upstream Mach number M_{n-1} and the flow-deflection angle δ' at the point in question.

The Mach number behind an oblique shock is given by

$$M_n = \left[\frac{M_{n-1}^2 \sin^2\theta + 5}{7\, M_{n-1}^2 \sin^2\theta - 1}\right]^{1/2} \frac{1}{\sin(\theta + \delta')} \qquad 4.4.1\text{-aa}$$

where M_{n-1}, θ, and δ are defined under Equation 4.4.1-z.

At the airfoil trailing edge the flow over both the upper and lower surfaces of the airfoil returns to nearly free-stream flow. If the Mach number at the trailing edge is greater than the free-stream Mach number, the flow is compressed through a shock wave θ_{TE} corresponding to the Mach number at the trailing edge, and the flow-deflection angle $\delta' = -\alpha + \delta_{TE}$. If the Mach number at the trailing edge is less than the free-stream Mach number, the flow is expanded through the angle $\Delta\nu_{TE} = \alpha + \delta_{TE}$.

This procedure is best applied by starting with the leading edge. The sample problem on Page 4.4.1-41 illustrates the procedure.

Viscous Flow Field

No known method exists in the literature for estimating the dynamic-pressure ratio in the viscous wake of a wing at supersonic speeds. Because of the similarity of this part of the flow field to the corresponding viscous wake at subsonic speeds, it is recommended that the method presented for determining the subsonic dynamic-pressure ratio in Paragraph A be applied at supersonic Mach numbers. In using this method the appropriate value of C_{D_0} must be obtained from Paragraph C of Section 4.1.5.1.

It should be noted that the x- and z-distances used in this method are measured from different origins from those used in the method for the nonviscous flow field. In this method x is measured from the wing-root trailing edge and z is measured from the wake center line.

Mach Number Effects

No explicit method is presented in the Datcom for determining the Mach number field about an airfoil. However Reference 16 explains and illustrates a calculation process. Compressibility tables such as those of Reference 17 can be of great help in estimating compressible-flow properties

Sample Problems

1. Supersonic Downwash (Method 1)

Given:

The sample problem presented in Reference 11. The calculation procedure is illustrated by showing calculations for one Mach number and two points in the flow field, one in the plane of symmetry ($y_o = 0$) and one outside the plane of symmetry at $y_o = 0.15$. The points for which the downwash calculations are given are both located at longitudinal position $x_o = 2.2$ and vertical position $z_o = 0$.

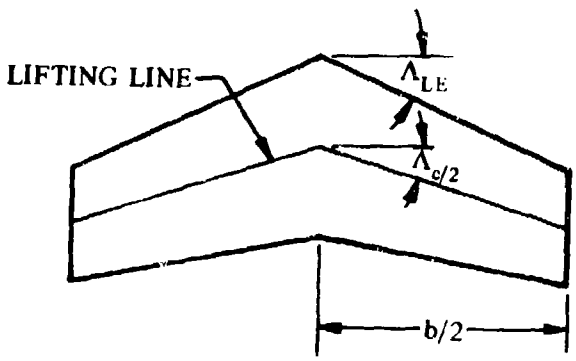

A = 3.57 $\quad\quad$ λ = 0.565

Λ_{LE} = 38.8° $\quad\quad$ $\Lambda_{c/2} = \Lambda_{\text{lifting line}}$ = 33°

m_o = cot Λ_{LE} = 1.244

m = cot $\Lambda_{c/2}$ = 1.54

M = 1.64; β = 1.30

The following span-load distribution from Reference 12 at a constant angle of attack as f(A, λ, M, Λ_{LE}).

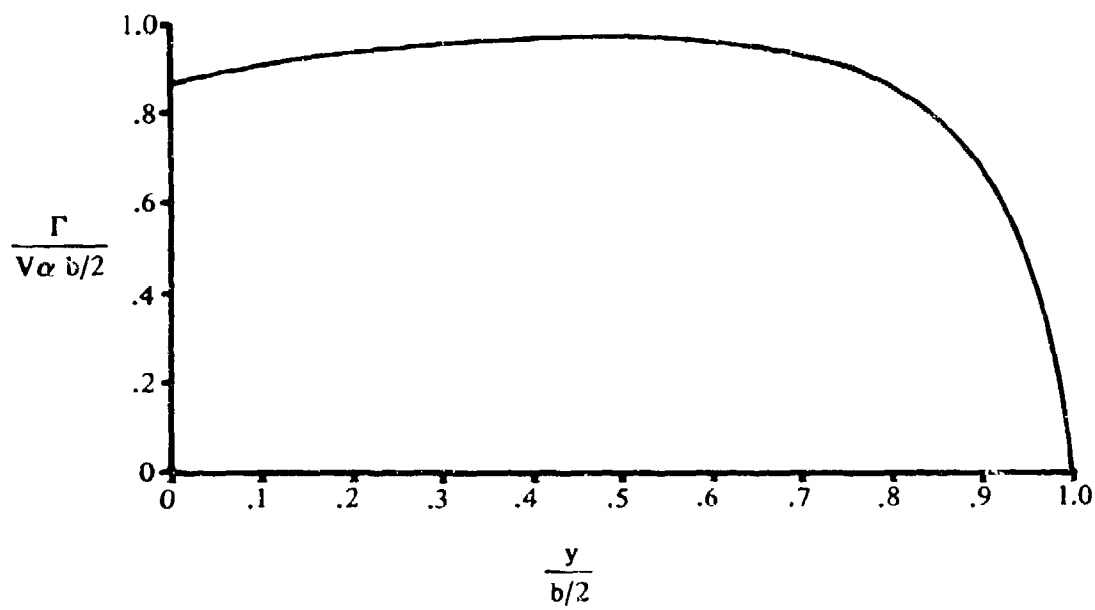

Compute: Plane of Symmetry

Determine the downwash gradient in the plane of symmetry (y_o = 0) at z_o = 0, x_o = 2.2.

$$-w = 2\sum_{i=o}^{n_2} \frac{\Gamma_{y_{i+1}} - \Gamma_{y_{i-1}}}{b/2} F_w\ (|y_{i,o}|) + \frac{\Gamma_o}{b/2} F_{w,o}$$

(Equation 4.4.1-q)

(see calculation table below)

Solution: Plane of Symmetry

$$\frac{\partial \epsilon}{\partial \alpha} = -\frac{w}{V_\infty \alpha} \quad \text{(Equation 4.4.1-p)}$$

①	②	③	④	⑤	⑥	⑦
$y_{i,o}$ Spanwise location of trailing vortices	$\frac{\Gamma y_i}{V\alpha b/2}$ Circulation strength at $y_{i,o}$ (given)	$\frac{\Gamma y_{i+1} - \Gamma y_{i-1}}{V\alpha b/2}$ Incremental circulation strength	$F_w\ (\lvert y_{i,o} \rvert)$ From Equation 4.4.1-s or Table II of Reference 11	③ × ④	$F_{w,o}$ From Equation 4.4.1-u or Table III of Reference 11	$\frac{\partial \epsilon}{\partial \alpha} = 2\Sigma ⑤ + ⑥ \frac{\Gamma_o}{V\alpha b/2}$
0	0.868	0	....	....	0.144686	−0.11184
0.05	0.890	0.043	−1.553695	−0.0668089		
0.10	0.911	0.034	−0.756150	−0.0257091		
0.15	0.924	0.023	−0.489023	−0.0112475		
0.20	0.934	0.018	−0.354408	−0.0063793		
0.25	0.942	0.020	−0.272706	−0.0054541		
0.30	0.954	0.018	−0.217364	−0.0039126		
0.35	0.960	0.012	−0.176978	−0.0021237		
0.40	0.966	0.010	−0.145812	−0.0014581		
0.45	0.970	0.003	−0.120639	−0.0003619		
0.50	0.969	−0.002	−0.099455	+0.0001989		
0.55	0.968	−0.012	−0.080882	0.0009706		
0.60	0.957	−0.018	−0.063801	0.0011484		
0.65	0.950	−0.020	−0.046973	0.0009395		
0.70	0.937	−0.048	−0.027827	0.0013357		
0.75	0.902	−0.075	0	0		
0.80	0.862	−0.102	0	0		
0.85	0.800	−0.179	0	0		
0.90	0.682	−0.345	0	0		
0.95	0.455	−0.683	0	0		
1.00	0	−0.455	0	0		

$\Sigma = -0.1188621$

Compute: Outside the Plane of Symmetry

Determine the downwash gradient outside the plane of symmetry at $y_o = 0.15$, $z_o = 0$, $x_o = 2.2$

$$-w = -\sum_{i=n_1}^{o} \frac{\Gamma_{y_{i+1}} - \Gamma_{y_{i-1}}}{b/2} F_w\ (Y_{i,o}) + \sum_{i=o}^{i=n_2} \frac{\Gamma_{y_{i+1}} - \Gamma_{y_{i-1}}}{b/2} F_w\ (Y_{i,o}) \quad \text{(Equation 4.4.1-r)}$$

(see calculation table below)

Solution: Outside the Plane of Symmetry

$$\frac{\partial \epsilon}{\partial \alpha} = -\frac{w}{V_\infty \alpha} \quad \text{(Equation 4.4.1-p)}$$

①	②	③	④	⑤	⑥	⑦	⑧	⑨	⑩	⑪
$y_{i,o}$ Spanwise location of trailing vortices (L.H. panel)	$Y_{i,o} = y_o - y_{i,o} = 0.15 - ①$ (L.H. panel)	$\overline{X}_i = \frac{x_o}{\beta m} + \frac{y_{i,o}}{\beta m} = 1.1 + \frac{①}{2}$	$F_w(Y_{i,o})$ From Equation 4.4.1-t or Fig. 6 of Ref. 11	$\frac{\Gamma y_{i+1} + \Gamma y_{i-1}}{V \alpha b/2}$ Incremental circulation strength	④ × ⑤	$y_{i,o}$ Spanwise location of trailing vortices (R.H. panel)	$Y_{i,o} = y_o - y_{i,o} = 0.15 - ⑦$ (R.H. panel)	$F_w(Y_{i,o})$ From Equation 4.4.1-t or Fig. 6 of Ref. 11	⑤ × ⑨	$\frac{\partial \epsilon}{\partial \alpha} = \Sigma ⑩ - \Sigma ⑥$
−1.0	1.15	0.6	0	−0.455	0	1.0	−0.85	0	0	0.003
−0.95	1.10	0.625	0	−0.683	0	0.95	−0.80	0	0	
−0.90	1.05	0.650	0	−0.345	0	0.90	−0.75	0	0	
−0.85	1.00	0.675	0	−0.179	0	0.85	−0.70	0	0	
−0.80	0.95	0.700	0	−0.102	0	0.80	−0.65	−0.045	0.004590	
−0.75	0.90	0.725	0	−0.075	0	0.75	−0.60	−0.074	0.005550	
−0.70	0.85	0.750	0	−0.048	0	0.70	−0.55	−0.098	0.004704	
−0.65	0.80	0.775	0	−0.020	0	0.65	−0.50	−0.118	0.002360	
−0.60	0.75	0.800	0.036	−0.018	−0.000648	0.60	−0.45	−0.146	0.002628	
−0.55	0.70	0.825	0.060	−0.012	−0.000720	0.55	−0.40	−0.173	0.002076	
−0.50	0.65	0.850	0.078	−0.002	−0.000156	0.50	−0.35	−0.207	0.000414	
−0.45	0.60	0.875	0.097	0.003	0.000291	0.45	−0.30	−0.248	−0.000744	
−0.40	0.55	0.900	0.114	0.010	0.001140	0.40	−0.25	−0.307	−0.003070	
−0.35	0.50	0.925	0.133	0.012	0.001596	0.35	−0.20	−0.388	−0.004656	
−0.30	0.45	0.950	0.156	0.018	0.002808	0.30	−0.15	−0.523	−0.009414	
−0.25	0.40	0.975	0.181	0.020	0.003620	0.25	−0.10	−0.793	−0.015860	
−0.20	0.35	1.000	0.213	0.018	0.003834	0.20	−0.05	−1.590	−0.028620	
−0.15	0.30	1.025	0.254	0.023	0.005842	0.15	0	....	....	
−0.10	0.25	1.050	0.312	0.034	0.010608	0.10	0.05	1.591	0.054094	
−0.05	0.20	1.075	0.391	0.043	0.016813	0.05	0.10	0.794	0.034142	
0	0.15	1.100	0.526	0	0	0	0.15	0.526	0	
					$\Sigma = 0.04503$				$\Sigma = 0.04819$	

Additional results are presented in Reference 11 for the variation of $\partial\epsilon/\partial\alpha$ in the plane of symmetry with Mach number and longitudinal position. These results are shown in Sketch(i).

SKETCH (i)

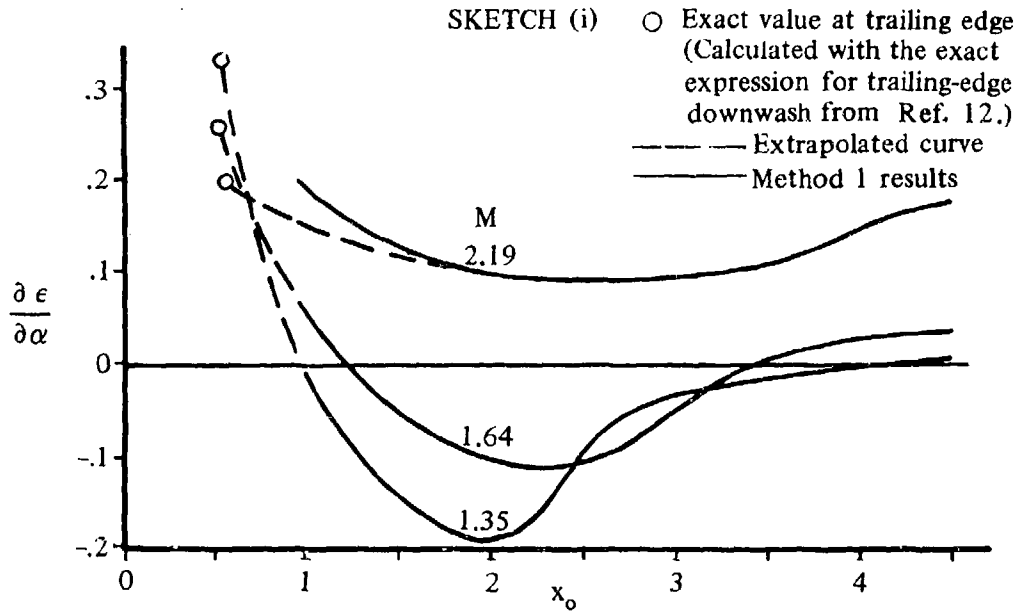

The inaccuracies in Method 1 near the trailing edge are not too apparent except for the M = 2.19 curve. As was pointed out previously (Page 4.4.1-28), these inaccuracies may be minimized by determining the exact value at the trailing edge.

Additional results from Reference 11 for the spanwise variation of downwash are shown in Sketch(j). The spanwise variation of downwash at $x_o = 2.2$ and $z_o = 0$, calculated by Equation 4.4.1-r, is shown by the solid curve. This curve is then translated so that the value at $y_o = 0$ coincides with that calculated using Equation 4.4.1-q. The translated values shown by the dashed curve agree reasonably well with values calculated by the more exact method, which uses the swept vortex equation of Reference 11.

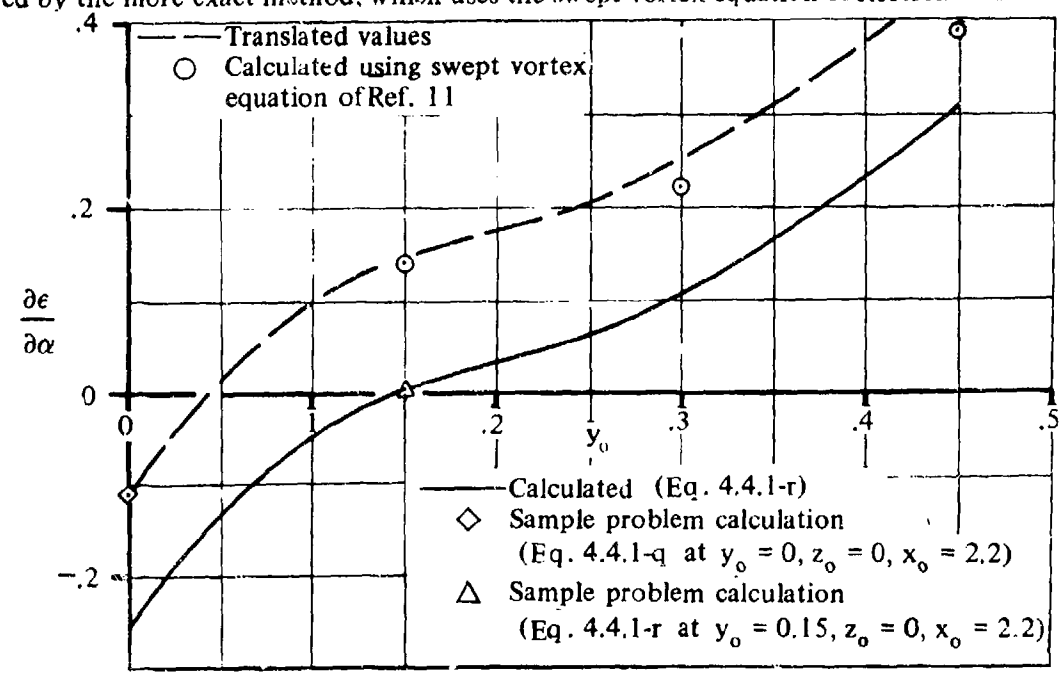

SKETCH (j)

2. Supersonic Downwash (Method 2)

Given: A rectangular wing.

Wing Characteristics:

A = 2.31 b = 10.0 ft λ = 1.0 c = 4.33 ft

Coordinates of Quarter-Chord of Tail MAC:

x = 15.0 ft y = 1.50 ft z = 1.0 ft

Additional Characteristics:

M = 2.0; β = 1.732 α = 4° = 0.07 rad

QUARTER-CHORD OF THE HORIZONTAL-TAIL MAC

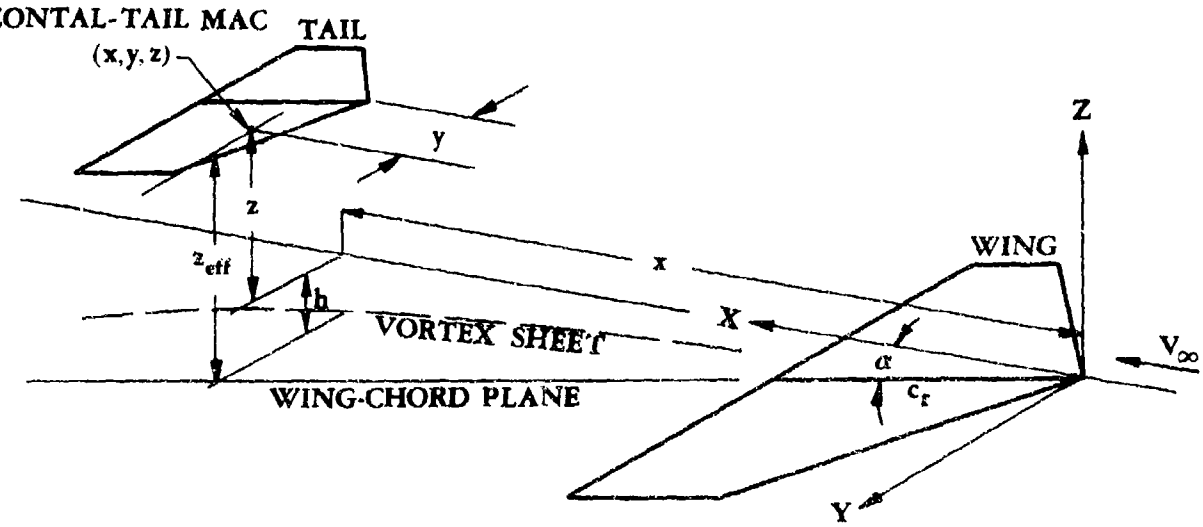

Compute:

$$\frac{2x}{\beta b} = \frac{(2)\,(15)}{(1.732)\,(10)} = 1.73$$

$$\frac{2y}{b} = \frac{(2)\,(1.5)}{10} = 0.30$$

$$\frac{2z}{b} = \frac{(2)\,(1)}{10} = 0.20$$

$$\beta A = (1.732)\,(2.31) = 4.0$$

$$\frac{2h}{\alpha \beta b} = 0.64 \quad \text{(Figure 4.4.1-74d)}$$

$$\left(\frac{2z}{b}\right)_{eff} = \left(\frac{2z}{b}\right) + \left(\frac{2h}{\alpha\beta b}\right)\alpha\beta$$

$$= 0.20 + (0.64)\,(0.07)\,(1.732)$$

$$= 0.28$$

Solution:

$\frac{\partial \bar{\epsilon}}{\partial \alpha}$ is obtained from Figure 4.4.1-76 as $f\left[\frac{2x}{\beta b}, \left(\frac{2z}{b}\right)_{eff}, \frac{2y}{b}, \beta A\right]$

$$\frac{\partial \bar{\epsilon}}{\partial \alpha} = 0.270$$

3. Supersonic Dynamic-Pressure Ratio

Given: The rectangular wing of Reference 15

Wing Characteristics:

$A = 2.0$ $\quad b_W = 8.0$ in. $\quad c_r = \bar{c} = 4.0$ in.

$\Lambda_{c/4} = 0$ $\quad S_W = S_{ref} = 32.0$ in.

Additional Characteristics:

$M_\infty = 2.46;\ \beta = 2.25$ $\quad R_\ell = 1.04 \times 10^6$ (based on $\bar{c}$)

Smooth surface (assume $k = 0$) $\quad$ Survey plane at $x = 6.4$ in.

$\alpha = 6^o$ $\quad C_L = 0.159$ (test value)

Symmetrical airfoil with following characteristics:

Point	x' (in.)	δ (surface slope) (deg)
1 (LE)	0	5.1
2	0.80	3.4
3	1.60	1.0
4	2.40	−0.5
5	3.20	−1.7
6 (TE)	4.00	−2.6

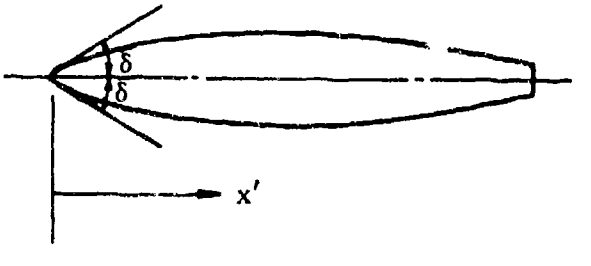

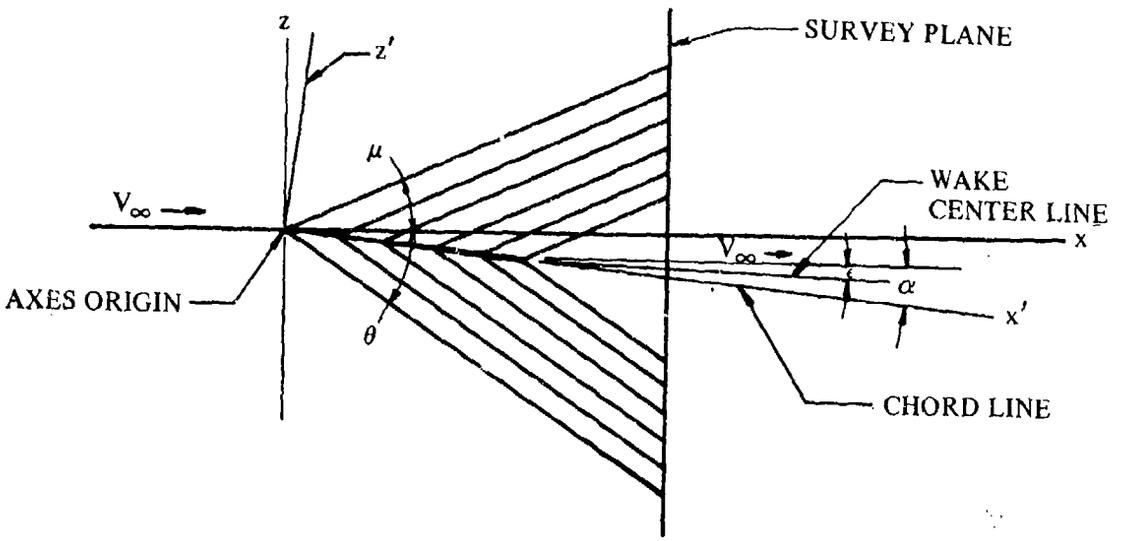

Outside Wake Portion (nonviscous flow field)

Compute:

Determine the flow-deflection angles at the leading edge.

Upper surface

$$\delta'_{LE} = \alpha - \delta_{LE_{upper}} = 6^{o} - 5.1^{o} = 0.9^{o} \text{ (expansion)}$$

Lower surface

$$\delta'_{LE} = -\alpha - \delta_{LE_{lower}} = -6^{o} - 5.1^{o} = -11.1^{o} \text{ (compression)}$$

Determine the values of z on the survey plane (located at $x = 6.4$ in. from the airfoil leading edge) corresponding to x' values of 0, 0.8, 1.6, 2.4, 3.2, and 4.0 (points 1 - 6).

Upper surface (initial expansion angle)

$$\mu = \sin^{-1}\frac{1}{M_{\infty}} = \sin^{-1}\frac{1}{2.46} = 24^{o}$$

$$z = \frac{-x' + x\cos\alpha - \dfrac{x\sin\alpha}{\tan(\mu+\alpha)}}{\sin\alpha + \dfrac{\cos\alpha}{\tan(\mu+\alpha)}} \quad \text{(Equation 4.4.1-w)}$$

$$= \frac{-x' + (6.4)\cos 6^o - \dfrac{(6.4)\sin 6^o}{\tan (24^o + 6^o)}}{\sin 6^o + \dfrac{\cos 6^o}{\tan (24^o + 6^o)}} = \frac{-x'(6.4)(0.9945) - \dfrac{(6.4)(0.1045)}{0.5774}}{0.1045 + \dfrac{0.9945}{0.5774}}$$

$$= 0.5473\,x' + 2.85$$

	x' (in.)	z (in.)	$\frac{z}{b_W/2}$
LE	0	2.850	0.713
	0.8	2.412	0.603
	1.6	1.974	0.494
	2.4	1.536	0.384
	3.2	1.098	0.275
TE	4.0	0.660	0.165

Lower surface (initial compression angle)

θ = 33.5° (Figure 4.4.1-81 at M_∞ = 2.46 and δ' = −11.1°)

$$z = \frac{-x' + x\cos\alpha - \dfrac{x\sin\alpha}{\tan(\alpha - \theta)}}{\sin\alpha + \dfrac{\cos\alpha}{\tan(\alpha - \theta)}} \qquad \text{(Equation 4.4.1-x)}$$

$$= \frac{-x' + (6.4)\cos 6^o - \dfrac{(6.4)\sin 6^o}{\tan (6^o - 33.5^o)}}{\sin 6^o + \dfrac{\cos 6^o}{\tan (6^o - 33.5^o)}} = \frac{-x' + (6.4)(0.9945) - \dfrac{(6.4)(0.1045)}{-0.5206}}{0.1045 + \dfrac{0.9945}{-0.5206}}$$

$$= 0.554\,x' - 4.236$$

	x' (in.)	z (in.)	$\frac{z}{b_W/2}$
LE	0	−4.236	−1.059
	0.8	−3.793	−0.948
	1.6	−3.350	−0.838
	2.4	−2.906	−0.727
	3.2	−2.463	−0.616
TE	4.0	−2.020	−0.505

Determine q/q_∞ at points (x,z) on the survey plane corresponding to points (x',z') on the airfoil.

Upper surface

Point 1 (x' = 0)

$M_\infty = 2.46$

$\Delta\nu_1 = \alpha - \delta_1 = 6^o - 5.1^o = 0.9^o$ (expansion)

$\nu_\infty = 38.2^o$ (Figure 4.4.1-82 at M_∞)

$\nu_1 = \nu_\infty + \Delta\nu_1 = 38.2^o + 0.9^o = 39.1^o$

$M_1 = 2.50$ (Figure 4.4.1-82 at ν_1)

$\left(q/p_t\right)_\infty = 0.264$ (Figure 4.4.1-82 at M_∞)

$\left(q/p_t\right)_1 = 0.256$ (Figure 4.4.1-82 at M_1)

$q_1/q_\infty = \left(q/p_t\right)_1 / \left(q/p_t\right)_\infty = 0.256/0.264 = 0.970$

Point 2 (x' = 0.8 in.)

$\Delta\nu_2 = \delta_1 - \delta_2 = 5.1^o - 3.4^o = 1.7^o$ (expansion)

$\nu_2 = \nu_1 + \Delta\nu_2 = 39.1^o + 1.7^o = 40.8^o$

$M_2 = 2.57$ (Figure 4.4.1-82 at ν_2)

$\left(q/p_t\right)_2 = 0.243$ (Figure 4.4.1-82 at M_2)

$$\frac{q_n}{q_\infty} = \frac{\left(q/p_t\right)_n}{\left(q/p_t\right)_{n-1}} \frac{q_{n-1}}{q_\infty}$$ (Equation 4.4.1-y)

$$\frac{q_2}{q_\infty} = \frac{\left(q/p_t\right)_2}{\left(q/p_t\right)_1} \frac{q_1}{q_\infty} = \frac{0.243}{0.256}(0.970) = 0.921$$

Point 3 ($x' = 1.6$ in.)

$$\Delta\nu_3 = \delta_2 - \delta_3 = 3.4^o - 1.0^o = 2.4^o \text{ (expansion)}$$

$$\nu_3 = \nu_2 + \Delta\nu_3 = 40.8^o + 2.4^o = 43.2^o$$

$$M_3 = 2.68 \quad \text{(Figure 4.4.1-82 at } \nu_3\text{)}$$

$$\left(q/p_t\right)_3 = 0.223 \quad \text{(Figure 4.4.1-82 at } M_3\text{)}$$

$$\frac{q_3}{q_\infty} = \frac{\left(q/p_t\right)_3}{\left(q/p_t\right)_2} \quad \frac{q_2}{q_\infty} = \frac{0.223}{0.243}(0.921) = 0.845 \quad \text{(Equation 4.4.1-y)}$$

Point 4 ($x' = 2.4$ in.)

$$\Delta\nu_4 = \delta_3 - \delta_4 = 1.0^o - (-0.5^o) = 1.5^o \text{ (expansion)}$$

$$\nu_4 = \nu_3 + \Delta\nu_4 = 43.2^o + 1.5^o = 44.7^o$$

$$M_4 = 2.75 \quad \text{(Figure 4.4.1-82 at } \nu_4\text{)}$$

$$\left(q/p_t\right)_4 = 0.211 \quad \text{(Figure 4.4.1-82 at } M_4\text{)}$$

$$\frac{q_4}{q_\infty} = \frac{\left(q/p_t\right)_4}{\left(q/p_t\right)_3} \quad \frac{q_3}{q_\infty} = \frac{0.211}{0.223}(0.845) = 0.800 \quad \text{(Equation 4.4.1-y)}$$

Point 5 ($x' = 3.2$ in.)

$$\Delta\nu_5 = \delta_4 - \delta_5 = -0.5^o - (-1.7^o) = 1.2^o \text{ (expansion)}$$

$$\nu_5 = \nu_4 + \Delta\nu_5 = 44.7^o + 1.2^o = 45.9^o$$

$$M_5 = 2.81 \quad \text{(Figure 4.4.1-82 at } \nu_5\text{)}$$

$$\left(q/p_t\right)_5 = 0.201 \quad \text{(Figure 4.4.1-82 at } M_5\text{)}$$

$$\frac{q_5}{q_\infty} = \frac{\left(q/p_t\right)_5}{\left(q/p_t\right)_4} \quad \frac{q_4}{q_\infty} = \frac{0.201}{0.211}(0.800) = 0.762 \quad \text{(Equation 4.4.1-y)}$$

Point 6 (x' = 4.0 in.)

$$\Delta\nu_6 = \delta_5 - \delta_6 = -1.7^{\circ} - (-2.6^{\circ}) = 0.9^{\circ} \quad \text{(expansion)}$$

$$\nu_6 = \nu_5 + \Delta\nu_6 = 45.9^{\circ} + 0.9^{\circ} = 46.8^{\circ}$$

$$M_6 = 2.85 \quad \text{(Figure 4.4.1-82 at } \nu_6\text{)}$$

$$\left(q/p_t\right)_6 = 0.194 \quad \text{(Figure 4.4.1-82 at } M_6\text{)}$$

$$\frac{q_6}{q_\infty} = \frac{\left(q/p_t\right)_6}{\left(q/p_t\right)_5} \frac{q_5}{q_\infty} = \frac{0.194}{0.201}(0.762) = 0.735 \quad \text{(Equation 4.4.1-y)}$$

Return to free-stream flow at TE (x = 4.0 in.)

Since $M_6 > M_\infty$, the flow is compressed by turning through an oblique shock at the upper surface trailing edge.

$$\delta' = -\alpha + \delta_{TE} = -6^{\circ} + (-2.6^{\circ}) = -8.6^{\circ}$$

$$\theta = 27.2^{\circ} \quad \text{(Figure 4.4.1-81 at } M_6 = 2.85 \text{ and } \delta' = -8.6^{\circ}\text{)}$$

$$\theta + \delta = 27.2^{\circ} - 8.6^{\circ} = 18.6^{\circ}$$

$$M_n = \left[\frac{M_{n-1}^2 \sin^2\theta + 5}{7 M_{n-1}^2 \sin^2\theta - 1}\right]^{1/2} \frac{1}{\sin(\theta + \delta')} \quad \text{(Equation 4.4.1-aa)}$$

$$M_7 = \left[\frac{M_6^2 \sin^2\theta + 5}{7 M_6^2 \sin^2\theta - 1}\right]^{1/2} \frac{1}{\sin(\theta + \delta')}$$

$$= \left[\frac{(2.85)^2 (\sin^2 27.2^{\circ}) + 5}{7(2.85)^2 (\sin^2 27.2^{\circ}) - 1}\right] \frac{1}{\sin(18.6^{\circ})} = 2.46$$

$$\frac{q_n}{q_{n-1}} = \frac{60}{M_{n-1}^2} \frac{\left(1 + 0.2 M_{n-1}^2\right)^{7/2}}{\left(5 + M_{n-1}^2 \sin^2\theta\right)^{5/2}} \quad \text{(Equation 4.4.1-z)}$$

$$\frac{q_7}{q_6} = \frac{60}{M_6^2} \frac{\left(1 + 0.2\, M_6^2\right)^{7/2}}{\left(5 + M_6^2 \sin^2 \theta\right)^{5/2}} = \frac{60}{(2.85)^2} \frac{\left[1 + 0.2(2.85)^2\right]^{7/2}}{\left[5 + (2.85)^2 \left(\sin^2 27.2\right)\right]^{5/2}}$$

$$= \frac{60}{(2.85)^2} \frac{29.28}{116.0} = 1.86$$

$$\frac{q_7}{q_\infty} = \frac{q_7}{q_6} \frac{q_6}{q_\infty} = (1.86)\,(0.735) = 1.367$$

Lower surface

Point 1 ($x' = 0$)

$\Delta\nu_1 = \delta' = -\alpha - \delta_{LE} = -6^\circ - 5.1^\circ = -11.1^\circ$ (compression)

$\theta = 33.5^\circ$ (Figure 4.4.1-81 at $M_\infty = 2.46$ and $\delta' = -11.1^\circ$)

$$\frac{q_n}{q_{n-1}} = \frac{60}{M_{n-1}^2} \frac{\left(1 + 0.2\, M_{n-1}^2\right)^{7/2}}{\left(5 + M_{n-1}^2 \sin^2 \theta\right)^{5/2}}$$ (Equation 4.4.1-z)

$$\frac{q_1}{q_\infty} = \frac{60}{M_\infty^2} \frac{\left(1 + 0.2\, M_\infty^2\right)^{7/2}}{\left(5 + M_\infty^2 \sin^2 \theta\right)^{5/2}} = \frac{60}{(2.46)^2} \frac{\left[1 + 0.2(2.46)^2\right]^{7/2}}{\left[5 + (2.46)^2 (\sin^2 33.5^\circ)\right]^{5/2}}$$

$$= \frac{60}{(2.46)^2} \frac{16.06}{122.5} = 1.300$$

$$M_n = \left[\frac{M_{n-1}^2 \sin^2 \theta + 5}{7\, M_{n-1}^2 \sin^2 \theta - 1}\right]^{1/2} \frac{1}{\sin(\theta + \delta')}$$ (Equation 4.4.1-aa)

$$M_1 = \left[\frac{M_\infty^2 \sin^2 \theta + 5}{7\, M_\infty^2 \sin^2 \theta - 1}\right]^{1/2} \frac{1}{\sin(\theta + \delta')}$$

$$= \left[\frac{(2.46)^2 (\sin^2 33.5^\circ) + 5}{7(2.46)^2 (\sin^2 33.5^\circ) - 1}\right]^{1/2} \frac{1}{\sin[33.5^\circ + (-11.1^\circ)]}$$

$$= (0.758)\,(2.621) = 1.987$$

$\nu_1 = 26.0^\circ$ (Figure 4.4.1-82 at M_1)

$\left(q/p_t\right)_1 = 0.360$ (Figure 4.4.1-82 at M_1)

Point 2 ($x' = 0.8$ in.)

$\Delta\nu_2 = \delta_1 - \delta_2 = 5.1^o - 3.4^o = 1.7^o$ (expansion)

$\nu_2 = \nu_1 + \Delta\nu_2 = 26.0^o + 1.7^o = 27.7^o$

$M_2 = 2.05$ (Figure 4.4.1-82 at ν_2)

$\left(q/p_t\right)_2 = 0.348$ (Figure 4.4.1-82 at M_2)

$$\frac{q_2}{q_\infty} = \frac{\left(q/p_t\right)_2}{\left(q/p_t\right)_1}\frac{q_1}{q_\infty} = \frac{0.348}{0.360}(1.300) = 1.256 \quad \text{(Equation 4.4.1-y)}$$

Point 3 ($x' = 1.6$ in.)

$\Delta\nu_3 = \delta_2 - \delta_3 = 3.4^o - 1.0^o = 2.4^o$ (expansion)

$\nu_3 = \nu_2 + \Delta\nu_3 = 27.7^o + 2.4^o = 30.1^o$

$M_3 = 2.14$ (Figure 4.4.1-82 at ν_3)

$\left(q/p_t\right)_3 = 0.329$ (Figure 4.4.1-82 at M_3)

$$\frac{q_3}{q_\infty} = \frac{\left(q/p_t\right)_3}{\left(q/p_t\right)_2}\frac{q_2}{q_\infty} = \frac{0.329}{0.348}(1.256) = 1.187 \quad \text{(Equation 4.4.1-y)}$$

Point 4 ($x' = 2.4$ in.)

$\Delta\nu_4 = \delta_3 - \delta_4 = 1.0^o - (-0.5^o) = 1.5^o$ (expansion)

$\nu_4 = \nu_3 + \Delta\nu_4 = 30.1^o + 1.5^o = 31.6^o$

$M_4 = 2.20$ (Figure 4.4.1-82 at ν_4)

$\left(q/p_t\right)_4 = 0.317$ (Figure 4.4.1-82 at M_4)

$$\frac{q_4}{q_\infty} = \frac{\left(q/p_t\right)_4}{\left(q/p_t\right)_3}\frac{q_3}{q_\infty} = \frac{0.317}{0.329}(1.187) = 1.141 \quad \text{(Equation 4.4.1-y)}$$

Point 5 ($x' = 3.2$ in.)

$$\Delta\nu_5 = \delta_4 - \delta_5 = -0.5^\circ - (-1.7)^\circ = 1.2^\circ \text{ (expansion)}$$

$$\nu_5 = \nu_4 + \Delta\nu_5 = 31.6^\circ + 1.2^\circ = 32.8^\circ$$

$$M_5 = 2.24 \quad \text{(Figure 4.4.1-82 at } \nu_5\text{)}$$

$$\left(q/p_t\right)_5 = 0.308 \quad \text{(Figure 4.4.1-82 at } M_5\text{)}$$

$$\frac{q_5}{q_\infty} = \frac{\left(q/p_t\right)_5}{\left(q/p_t\right)_4}\frac{q_4}{q_\infty} = \frac{0.308}{0.317}(1.141) = 1.109 \quad \text{(Equation 4.4.1-y)}$$

Point 6 ($x' = 4.0$ in.)

$$\Delta\nu_6 = \delta_5 - \delta_6 = -1.7^\circ - (-2.6)^\circ = 0.9^\circ \text{ (expansion)}$$

$$\nu_6 = \nu_5 + \Delta\nu_6 = 32.8^\circ + 0.9^\circ = 33.7^\circ$$

$$M_6 = 2.28 \quad \text{(Figure 4.4.1-82 at } \nu_6\text{)}$$

$$\left(q/p_t\right)_6 = 0.300 \quad \text{(Figure 4.4.1-82 at } M_6\text{)}$$

$$\frac{q_6}{q_\infty} = \frac{\left(q/p_t\right)_6}{\left(q/p_t\right)_5}\frac{q_5}{q_\infty} = \frac{0.300}{0.308}(1.109) = 1.080 \quad \text{(Equation 4.4.1-y)}$$

Return to free-stream flow at TE ($x = 4.0$ in.)

Since $M_6 < M_\infty$, the flow is expanded at the lower surface trailing edge

$$\Delta\nu_7 = \Delta\nu_{TE} = \alpha + \delta_{TE} = 6^\circ + (-2.6^\circ) = 3.4^\circ$$

$$\nu_7 = \nu_6 + \Delta\nu_7 = 33.7^\circ + 3.4^\circ = 37.1^\circ$$

$$M_7 = 2.41 \quad \text{(Figure 4.4.1-82 at } \nu_7\text{)}$$

$$\left(q/p_t\right)_7 = 0.274 \quad \text{(Figure 4.4.1-82 at } M_7\text{)}$$

$$\frac{q_7}{q_\infty} = \frac{\left(q/p_t\right)_7}{\left(q/p_t\right)_6}\frac{q_6}{q_\infty} = \frac{0.274}{0.300}(1.080) = 0.986 \quad \text{(Equation 4.4.1-y)}$$

The results for q/q_∞ calculated above for the nonviscous flow field are compared with test data in Figure 4.4.1-83. A summary of the above calculations is presented in the following table.

	①	②	③	④	⑤	⑥	⑦	⑧	⑨	⑩
Surface	Point	x' (in.)	$\frac{z}{b_W/2}$	δ (deg)	$\frac{\Delta\nu}{④_{n-1}} - ④$ (deg)	⑤ + ν ⑥$_{n-1}$ (deg)	M (Fig 4.4.1-82)	q/p_t (Fig 4.4.1-82)	$\frac{(q/p_t)_n}{(q/p_t)_{n-1}}$ ⑧/⑧$_{n-1}$	$\frac{q}{q_\infty}$ ⑨ ⑩$_{n-1}$
Upper	∞	0	0.713			38.2	2.46	0.264		1.0
	1(LE)	0	0.713	5.1	0.9	39.1	2.50	0.256	0.970	0.970
	2	0.8	0.603	3.4	1.7	40.8	2.57	0.243	0.949	0.921
	3	1.6	0.494	1.0	2.4	43.2	2.68	0.223	0.918	0.845
	4	2.4	0.384	−0.5	1.5	44.7	2.75	0.211	0.946	0.800
	5	3.2	0.275	−1.7	1.2	45.9	2.81	0.201	0.953	0.762
	6(TE)	4.0	0.165	−2.6	0.9	46.8	2.85	0.194	0.965	0.735
	7	4.0	0.165		−8.6		2.46			1.367
Lower	∞	0	−1.059				2.46			1.0
	1(LE)	0	−1.059	5.1		26.0	1.987	0.360		1.300
	2	0.8	−0.948	3.4	1.7	27.7	2.95	0.348	0.966	1.256
	3	1.6	−0.838	1.0	2.4	30.1	2.14	0.329	0.946	1.187
	4	2.4	−0.727	−0.5	1.5	31.6	2.20	0.317	0.963	1.141
	5	3.2	−0.616	−1.7	1.2	32.8	2.24	0.308	0.972	1.109
	6(TE)	4.0	−0.505	−2.6	0.9	33.7	2.28	0.300	0.974	1.080
	7	4.0	−0.505		3.4	37.1	2.41	0.274	0.913	0.986

Inside-Wake Portion (viscous flow field)

Compute:

Determine the half-width of the viscous wake at the survey plane.

Skin-friction drag coefficient

$\ell/k = \infty$; read C_f at give R_ℓ

$C_f = 0.00305$ (Figure 4.1.5.1-26)

Wave-drag coefficient

$\beta \cot \Lambda_{LE_{bw}} = 2.25 \cot (0) > 1$; leading edge is supersonic

$K = 16/3$ (Table, Page 4.1.5.1-16)

$$C_{D_w} = \frac{K}{\beta} \left(\frac{t}{c}\right)^2_{eff} \frac{S_{bw}}{S_{ref}}$$ (Equation 4.1.5.1-k)

$$= \frac{16}{3(2.25)} (0.05)^2 \frac{32.0}{32.0} = 0.00593$$

Zero-lift drag coefficient

$$C_{D_0} = C_{D_f} + C_{D_w} \quad \text{(Equation 4.1.5.1-h)}$$

$$= 0.00305 + 0.00593$$

$$= 0.00898$$

$$\frac{x}{\bar{c}} = \frac{6.4 - 4.0}{4.0} = 0.60 \quad \text{(x measured from wing-root-chord trailing edge)}$$

$$\frac{z_w}{\bar{c}} = 0.68 \sqrt{C_{D_0}\left(\frac{x}{\bar{c}} + 0.15\right)} \quad \text{(Equation 4.4.1-j)}$$

$$= 0.68 \sqrt{0.00898\ (0.60 + 0.15)}$$

$$= 0.0558$$

$$z_w = (0.0558)(\bar{c}) = (0.0558)(4) = 0.223 \text{ in.}$$

Determine the downwash in the plane of symmetry at the vortex sheet (wake center line).

$$\epsilon = \frac{1.62\, C_L}{\pi A} \quad \text{(Equation 4.4.1-k)}$$

$$= \frac{(1.62)(0.159)}{\pi\ 2.0}$$

$$= 0.041 \text{ rad} = 2.35 \text{ deg}$$

Calculate the vertical location, measured from the x-axis, of the intersection of the wake center line and the survey plane.

Distance of origin O below x-axis = $-[4 \sin\alpha + (6.4 - 3.97) \sin\epsilon] = -0.518$ in. In determining the dynamic-pressure ratio in the viscous region, this location is taken as the origin of the vertical distance from the wake center line to the points of interest on the survey plane.

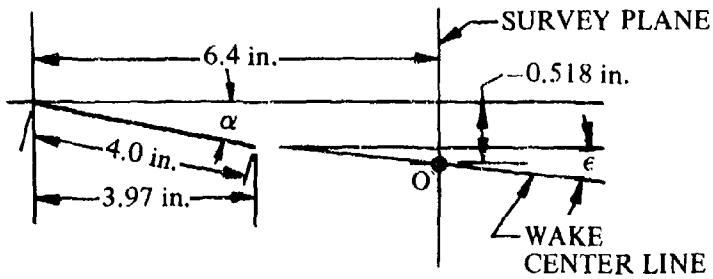

The points in the viscous wake at which the dynamic-pressure ratios are to be calculated are arbitrarily selected. For this example the following points are selected:

$z = 0$	wake center line
$z = \pm 0.08$	within the wake
$z = \pm 0.16$	within the wake
$z = \pm 0.223$	at the edges of the wake

Determine the dynamic-pressure-loss ratio at the wake center.

$$\left(\frac{\Delta q}{q}\right)_o = \frac{2.42\,(C_{D_0})^{1/2}}{\frac{x}{c} + 0.30} \quad \text{(Equation 4.4.1-m)}$$

$$= \frac{(2.42)\,(0.00898)^{1/2}}{0.60 + 0.30} = 0.255$$

Determine the dynamic-pressure-loss ratio for points not on the wake center line.

$$\frac{\Delta q}{q} = \left(\frac{\Delta q}{q}\right)_o \cos^2\left(\frac{\pi}{2}\,\frac{z}{z_w}\right) \quad \text{(Equation 4.4.1-n)}$$

$$= 0.255 \cos^2\left(\frac{\pi}{2}\,\frac{z}{z_w}\right) \text{ (see calculation table below)}$$

Solution: Viscous flow field

$$\frac{q}{q_\infty} = 1 - \frac{\Delta q}{q} \quad \text{(Equation 4.4.1-o)} \quad \text{(see calculation table below)}$$

①	②	③	④	⑤
z (in.) (measured from origin O)	$\frac{z}{z_W}$ ① /0.223	$\frac{\pi}{2}\frac{z}{z_W}$ (rad)	$\Delta q/q$ (Eq. 4.4.1-n) $0.255\cos^2$ ③	q/q_∞ (Eq. 4.4.1-o) 1 - ④
− 0.223	− 1.0	$-\pi/2$	0	1.00
− 0.160	− 0.717	−1.127	0.047	0.953
− 0.080	− 0.359	−0.564	0.182	0.818
0	0	0	0.255	0.745
0.080	0.359	0.564	0.182	0.818
0.160	0.717	1.127	0.047	0.953
0.223	1.0	$\pi/2$	0	1.00

The calculated results for both the nonviscous and viscous flow fields are compared with test data in Figure 4.4.1-83. The results are plotted as a function of $\frac{z}{b_W/2}$, where z is measured from the x-axis. The wake center is at $\frac{z}{b_W/2} = \frac{-0.518}{4.0} = -0.1295$.

REFERENCES

1. Decker, J. L.: Prediction of Downwash at Various Angles of Attack for Arbitrary Tail Locations. Aeronautical Engineering Review, Vol. 15, No. 8, 1956. (U)

2. Lange, R. H., and Fink, M. P.: Studies of the Flow Field Behind a Large Scale 47.5° Sweptback Wing Having Circular-Arc Airfoil Sections and Equipped With Drooped-Nose and Plain Flaps. NACA RM L51L12, 1952. (U)

3. Pitts, W., Nielsen, J., and Kaattari, G.: Lift and Center of Pressure of Wing-Body-Tail Combinations at Subsonic, Transonic, and Supersonic Speeds. NACA TR1307, 1957. (U)

4. Neely, R. H., and Griner, R. F.: Summary and Analysis of Horizontal-Tail Contribution to Longitudinal Stability of Swept-Wing Airplanes at Low Speeds. NASA TR R-49, 1959. (U)

5. Ribner, H. S.: Notes on the Propeller Slipstream in Relation to Stability. NACA WR L-25, 1944. (U)

6. Glauert, H.: The Elements of Airfoil and Airscrew Theory. Cambridge University Press, Cambridge, Great Britain, 1948. (U)

7. Sanders, K. L.: An Empirical Method for the Estimation of Downwash. Ryan Rpt. No. 29264-2A, 1967. (U)

8. Silverstein, A., and Katzoff, S.: Design Charts for Predicting Downwash Angles and Wake Characteristics Behind Plain and Flapped Wings. NACA TR 648, 1939. (U)

9. Hoggard, H. P., Jr., and Hagerman, J. R.: Downwash and Wake Behind Untapered Wings of Various Aspect Ratios and Angles of Sweep. NACA TN 1703, 1948. (U)

10. Nielsen, J. N.: The Effects of Body Vortices and the Wing Shock-Expansion Field on the Pitch-Up Characteristics of Supersonic Airplanes. NACA RM A57L23, 1958. (U)

11. Bobbitt, P. J.: Tables for the Rapid Estimation of Downwash and Sidewash Behind Wings Performing Various Motions at Supersonic Speeds. NASA Memo 2-20-59L, 1959. (U)

12. Martin, J. C., and Jeffreys, I.: Span Load Distributions Resulting from Angle of Attack, Rolling, and Pitching for Tapered Sweptback Wings with Streamwise Tips – Supersonic Leading and Trailing Edges. NACA TN 2643, 1952. (U)

13. Martin, J. C.: The Calculation of Downwash Behind Wings of Arbitrary Plan Form at Supersonic Speeds. NACA TN 2135, 1950. (U)

14. Haefeli, R. C., Mirels, H., and Cummings, J. L.: Charts for Estimating Downwash Behind Rectangular, Trapezoidal, and Triangular Wings at Supersonic Speeds. NACA TN 2141, 1950. (U)

15. Centolanzi, F. J.: Measured and Theoretical Flow Fields Behind a Rectangular and a Triangular Wing Up to High Angles of Attack at a Mach Number of 2.46. NASA TN D-92, 1959. (U)

16. Schaef, S. A., and Talbot, L.: Handbook of Supersonic Aerodynamics, Section 6, Two-Dimensional Airfoils. NAVORD Report 1488 (Vol. 3), June 1957. (U)

17. Ames Research Staff: Equations, Tables, and Charts for Compressible Flow. NACA TR 1135, 1953. (U)

18. Purser, P. E., Spearman, M. L., and Bates, W. R.: Preliminary Investigation at Low Speed of Downwash Characteristics of Small-Scale Sweptback Wings. NACA TN 1378, 1947. (U)

19. Anderson, A. E.: An Investigation at Low Speed of a Large-Scale Triangular Wing of Aspect Ratio Two. – The Effect of Airfoil Section Modifications and the Determination of the Wake Downwash. NACA RM A7H28, 1947. (U)

20. Jaquet, B. M.: Effects of Horizontal Tail Position, Area, and Aspect Ratio on Low-Speed Static Longitudinal Stability and Control Characteristics of a 60° Triangular-Wing Model Having Various Triangular All-Movable Horizontal Tails. NACA RM L51I06, 1951. (U)

21. Griner, R. F., and Foster, G. V.: Low-Speed Longitudinal and Wake Air-Flow Characteristics at a Reynolds Number of 6.0×10^6 of a 52° Sweptback Wing Equipped With Various Spans of Leading-Edge and Trailing-Edge Flaps, a Fuselage, and a Horizontal Tail at Various Vertical Positions. NACA RM L50K29, 1951. (U)

22. Salmi, R. J., and Jacques, W. A.: Effect of Vertical Location of a Horizontal Tail on the Static Longitudinal Stability Characteristics of a 45° Sweptback-Wing-Fuselage Combination of Aspect Ratio 8 at a Reynolds Number of 4.0×10^6. NACA RM L51J08, 1952. (U)

23. Hadaway, W. M., and Cancro, P. A.: Low-Speed Longitudinal Characteristics of Two Unswept Wings of Hexagonal Airfoil Sections Having Aspect Ratios of 2.5 and 4.0 With Fuselage and Horizontal Tail Located at Various Vertical Positions. NACA RM L53H14a, 1953. (U)

24. Foster, G. V., Mollenberg, E. F., and Woods, R. L.: Low-Speed Longitudinal Characteristics of an Unswept Hexagonal Wing With and Without a Fuselage and a Horizontal Tail Located at Various Positions at Reynolds Numbers From 2.8×10^6 to 7.6×10^6. NACA RM L52L11b, 1953. (U)

25. Ross, J. G., et al: Wind-Tunnel Tests on a 90° Apex Delta Wing of Variable Aspect Ratio (Sweepback 36.8°). ARC CP 83, 1952. (U)

26. Foster, G. V.: Longitudinal Stability and Wake-Flow Characteristics of a Twisted and Cambered Wing-Fuselage Combination of 45° Sweepback and Aspect Ratio 8 With a Horizontal Tail and Stall-Control Devices at a Reynolds Number of 4.0×10^6. NACA RM L53D08, 1953. (U)

27. Foster, G. V., and Griner, R. F.: Low-Speed Longitudinal and Wake Air-Flow Characteristics at a Reynolds Number of 5.5×10^6 of a Circular-Arc 52° Sweptback Wing With a Fuselage and a Horizontal Tail at Various Vertical Positions. NACA RM L51C30, 1951. (U)

28. Spooner, S. H., and Martina, A. P.: Longitudinal Stability Characteristics of a 42° Sweptback Wing and Tail Combination at a Reynolds Number of 6.8×10^6. NACA RM L8E12, 1948. (U)

29. Woods, R. L., and Spooner, S. H.: Effects of High-Lift and Stall-Control Devices, Fuselage, and Horizontal Tail on a Wing Swept Back 42° at the Leading Edge and Having Symmetrical Circular-Arc Airfoil Sections at a Reynolds Number of 6.9×10^6. NACA RM L9B11, 1949. (U)

30. Graham, D., and Koenig, D. G.: Tests in the Ames 40- by 80-Foot Wind Tunnel of an Airplane Configuration With an Aspect Ratio 4 Triangular Wing and an All-Movable Horizontal Tail – Longitudinal Characteristics. NACA RM A51H10a, 1951. (U)

31. Franks, R. W.: Tests in the Ames 40- by 80-Foot Wind Tunnel of Two Airplane Models Having Aspect Ratio 2 Trapezoidal Wings of Taper Ratios 0.33 and 0.20. NACA RM A52L16, 1953. (U)

32. Graham, D., and Koenig, D. B.: Tests in the Ames 40- by 80-Foot Wind Tunnel of an Airplane Configuration With an Aspect Ratio 2 Triangular Wing and an All-Movable Horizontal Tail – Longitudinal Characteristics. NACA RM A51B21, 1951. (U)

33. Salmi, R. J.: Horizontal-Tail Effectiveness and Downwash Surveys for Two 47.7° Sweptback Wing-Fuselage Combinations With Aspect Ratios of 5.1 and 6.0 at a Reynolds Number of 6.0×10^6. NACA RM L50K06, 1951. (U)

34. Franks, R. W.: Tests in the Ames 40- by 80-Foot Wind Tunnel of an Airplane Model With an Aspect Ratio 4 Triangular Wing and an All-Movable Horizontal Tail – High-Lift Devices and Lateral Controls. NACA RM A52K13, 1953. (U)

35. Goodson, K. W., and Few, A. G., Jr.: Low-Speed Static Longitudinal and Lateral Stability Characteristics of a Model with Leading-Edge Chord-Extensions Incorporated on a 40° Sweptback Circular-Arc Wing of Aspect Ratio 4 and Taper Ratio 0.50. NACA RM L52I18, 1952. (U)

36. Schuldenfrei, M., Comisarow, P., and Goodson, K. W.: Stability and Control Characteristics of a Complete Airplane Model Having a Wing With Quarter-Chord Line Swept Back 40°, Aspect Ratio 2.50, and Taper Ratio 0.42. NACA TN 2482, 1951. (U)

37. Weil, J., Sleeman, W. C., and Byrnes, A. L., Jr.: Investigation of the Effects of Wing and Tail Modifications on the Low-Speed Stability Characteristics of a Model Having a Thin 40° Swept Wing of Aspect Ratio 3.5. NACA RM L53C09, 1953. (U)

38. Perkins, E. W., and Canning, T. N.: Investigation of Downwash and Wake Characteristics at a Mach Number of 1.53. I – Rectangular Wing. NACA RM A8L16, 1949. (U)

39. Spearman, M. L., and Hilton, J. H., Jr.: An Investigation of a Supersonic Aircraft Configuration Having a Tapered Wing with Circular-Arc Sections and 40° Sweepback. Static Longitudinal Stability and Control Characteristics at a Mach Number of 1.59. NACA RM L50E12, 1950. (U)

40. Spearman, M. L.: An Investigation of a Supersonic Aircraft Configuration Having a Tapered Wing with Circular-Arc Sections and 40° Sweepback. Static Longitudinal Stability and Control Characteristics at a Mach Number of 1.40. NACA RM L9L08, 1950. (U)

41. Grant, F. C., and Gapcynski, J. P.: An Investigation of a Supersonic Aircraft Configuration Having a Tapered Wing with Circular-Arc Sections and 40° Sweepback. Estimated Downwash Angles Derived from Pressure Measurements on the Tail at Mach Numbers of 1.40 and 1.59. NACA RM L51L17, 1952. (U)

42. Ellis, M. C., Jr., and Grigsby, C. E.: Aerodynamic Investigation at Mach Number of 1.92 of a Rectangular Wing and Tail and Body Configuration and Its Components. NACA RM L9L28a, 1950. (U)

43. Grigsby, C. E.: An Investigation at Mach Numbers of 1.62 and 1.93 of the Lift Effectiveness and Integrated Downwash Characteristics of Several In-Line Missile Configurations Having Equal-Span Wings and Tails. NACA RM L52A02, 1952. (U)

44. Adamson, D., and Boatright, W. B.: Investigation of Downwash, Sidewash, and Mach Number Distribution Behind a Rectangular Wing at a Mach Number of 2.41. NACA RM L50G12, 1950. (U)

45. Boatright, W. B.: An Analysis of Pressure Studies and Experimental and Theoretical Downwash and Sidewash Behind Five Pointed-Tip Wings at Supersonic Speeds. NACA RM L54B10, 1954. (U)

TABLE 4.4.1-A

SUBSONIC DOWNWASH GRADIENT BEHIND STRAIGHT-TAPERED WINGS
METHOD 1

DATA SUMMARY AND SUBSTANTIATION

Ref.	A	λ	$\Lambda_{c/4}$ (deg)	$\frac{b_H}{b}$	$\frac{2\ell_H}{b}$	$\frac{2h_H}{b}$	$\partial\bar{\epsilon}/\partial\alpha$ Calc. ($\alpha = 0$)	$\partial\bar{\epsilon}/\partial\alpha$ Test	$\lvert\Delta\bar{\epsilon}\rvert$ Average Error (deg)
18	4.00	1.00	40.0	0.50	1.00	0.18	0.518	0.400	0.8
					1.50		0.491	0.335	0.6
	2.50	1.00	40.0	0.80	1.60	0.29	0.619	0.520	1.0
					2.40		0.600	0.465	1.0
				0.50	1.50		0.600	0.440	1.8
						0.03	0.720	0.510	1.0
					2.30	0.29	0.583	0.360	2.1
						0.03	0.695	0.400	0.8
	3.00	1.625	37.5	0.50	1.36	0.43	0.465	0.300	0.9
						0.21	0.560	0.400	0.6
						0.03	0.620	0.420	0.7
					1.91	0.43	0.451	0.270	0.7
						0.22	0.528	0.320	1.1
						0.04	0.596	0.400	0.3
19	2.00	0	56.5	0.378	1.64	0	0.730	0.710	1.0
					1.96		0.686	0.660	0.5
					2.28		0.658	0.630	0.7
20	2.31	0	52.4	0.316	1.73	0.870	0.363	0.330	0.6
						0.290	0.586	0.570	0.1
						−0.060	0.657	0.720	0.6
21	2.88	0.625	50.0	0.48	1.229	0.504	0.446	0.390	0.7
						0.196	0.554	0.500	0.8
						−0.074	0.588	0.500	4.3
22	8.0	0.45	45.0	0.282	0.785	−0.060	0.317	0.375	1.3
						0.140	0.310	0.310	2.4
						0.300	0.284	0.238	1.9
23	4.00	0.625	3.4	0.50	1.66	−0.177	0.472	0.390	2.5
						0.177	0.558	0.490	2.1
						0.400	0.472	0.380	1.0
24	2.50	0.625	5.3	0.50	1.63	−0.177	0.839	0.600	3.9
						0.177	0.831	0.600	2.2
						0.400	0.646	0.550	1.0
					2.44	0.177	0.730	0.600	0.8
						0.400	0.620	0.440	2.7

TABLE 4.4.1-A (CONTD)

Ref.	A	λ	$\Lambda_{c/4}$ (deg)	$\frac{b_H}{b}$	$\frac{2\ell_H}{b}$	$\frac{2h_H}{b}$	$\partial\bar{\epsilon}/\partial\alpha$ Calc. ($\alpha = 0$)	$\partial\bar{\epsilon}/\partial\alpha$ Test	$\lvert\Delta\bar{\epsilon}\rvert$ Average Error (deg)
25	2.30	0.25	36.8	0.35	1.37	0	0.800	0.770	0.3
						0.223	0.720	0.645	0.4
						0.450	0.614	0.500	0.5
	3.00	0.14	36.8	0.30	1.17	0.200	0.663	0.615	0.3
					0.78	0.388	0.840	0.560	1.2
						0.200	0.786	0.660	0.7
26	8.00	0.45	45.0	0.28	0.767	0.300	0.285	0.310	2.1
						0.140	0.308	0.285	4.3
						−0.060	0.516	0.320	1.7
27	2.84	0.616	50.0	0.48	1.229	0.442	0.453	0.380	1.9
						0.136	0.570	0.500	2.1
						−0.132	0.580	0.500	3.1
28	4.00	0.625	40.0	0.40	1.018	−0.060	0.520	0.500	3.8
						0.160	0.525	0.500	3.7
						0.420	0.443	0.410	4.0
29	3.94	0.625	40.0	0.40	1.033	−0.011	0.512	0.475	1.7
						0.211	0.560	0.400	2.0
						0.339	0.525	0.410	2.2
30	4.00	0	36.9	0.52	1.275	0	0.640	0.560	0.3
						0.360	0.551	0.430	1.3
31	2.00	0.33	36.9	0.78	1.95	0	1.034	0.760	1.4
				0.67		0.537	0.727	0.510	0.5
32	2.00	0	56.3	0.74	1.80	0	0.870	0.660	0.7
				0.63		0.254	0.635	0.660	0.7
						0.506	0.500	0.500	0.7
33	5.10	0.383	45.0	0.366	0.928	0.382	0.379	0.331	0.2
						−0.053	0.455	0.437	2.8
	6.00	0.313		0.328	0.800	0.343	0.353	0.312	0.7
						−0.048	0.355	0.410	1.6
								Average $\lvert\Delta\bar{\epsilon}\rvert$ =	1.45

TABLE 4.4.1-8

SUBSONIC DOWNWASH GRADIENT BEHIND STRAIGHT-TAPERED WINGS
METHOD 2

DATA SUMMARY AND SUBSTANTIATION

Ref.	A	λ	$\Lambda_{c/4}$ (deg)	$\frac{b_H}{b}$	$\frac{2\ell_H}{b}$	$\frac{2h_H}{b}$	$\partial\bar{\epsilon}/\partial\alpha$ Calc.	$\partial\bar{\epsilon}/\partial\alpha$ Test	e Percent Error
18	4.00	1.00	40.0	0.50	1.00	0.18	0.386	0.400	− 3.5
					1.50		0.326	0.335	− 2.7
	2.50	1.00	40.0	0.80	1.30	0.29	0.439	0.520	−15.6
					2.40		0.377	0.465	−18.9
				0.50	1.50		0.451	0.440	2.5
						0.03	0.537	0.510	5.3
					2.30	0.29	0.382	0.360	6.1
						0.03	0.451	0.400	12.8
	3.00	1.625	37.5	0.50	1.36	0.43	0.263	0.300	−12.3
						0.21	0.338	0.400	−15.5
						0.03	0.377	0.420	−10.2
					1.91	0.43	0.229	0.270	−15.2
						0.22	0.266	0.320	−16.9
						0.04	0.297	0.400	−25.8
19	2.00	0	56.5	0.378	1.64	0	0.790	0.710	11.3
					1.96		0.737	0.660	11.7
					2.28		0.693	0.630	10.0
20	2.31	0	52.4	0.316	1.73	0.870	0.377	0.330	12.5
						0.290	0.595	0.570	4.4
						−0.060	0.702	0.720	− 2.5
21	2.88	0.625	50.0	0.48	1.229	0.504	0.400	0.390	2.6
						0.196	0.497	0.500	− 0.6
						−0.074	0.539	0.500	7.8
22	8.0	0.45	45.0	0.282	0.785	−0.060	0.324	0.375	−13.6
						0.140	0.310	0.310	0
						0.300	0.275	0.238	15.5
23	4.00	0.625	3.4	0.50	1.66	−0.177	0.446	0.390	14.3
						0.177	0.446	0.490	− 9.0
						0.400	0.382	0.380	0.5
24	2.50	0.625	5.3	0.50	1.63	−0.177	0.664	0.600	10.7
						0.177	0.664	0.600	10.7
						0.400	0.566	0.550	2.9
					2.44	0.177	0.559	0.600	− 6.8
						0.400	0.482	0.440	9.5

TABLE 4.4.1-8 (CONTD)

Ref.	A	λ	$\Lambda_{c/4}$ (deg)	$\frac{b_H}{b}$	$\frac{2\ell_H}{b}$	$\frac{2h_H}{b}$	$\partial\bar{\epsilon}/\partial\alpha$ Calc.	$\partial\bar{\epsilon}/\partial\alpha$ Test	e Percent Error
25	2.30	0.25	36.8	0.35	1.37	0	0.875	0.770	13.6
						0.223	0.764	0.645	18.4
						0.450	0.648	0.500	29.6
	3.00	0.14	36.8	0.30	1.17	0.200	0.693	0.615	12.7
					0.78	0.388	0.710	0.560	26.8
						0.200	0.813	0.660	23.2
26	8.00	0.45	45.0	0.28	0.767	0.300	0.280	0.310	− 9.7
						0.140	0.313	0.285	9.8
						−0.060	0.329	0.320	2.8
27	2.84	0.616	50.0	0.48	1.229	0.442	0.417	0.380	9.7
						0.136	0.515	0.500	3.0
						−0.132	0.515	0.500	3.0
28	4.00	0.625	40.0	0.40	1.018	−0.060	0.497	0.500	− 0.6
						0.160	0.470	0.500	− 6.0
						0.420	0.389	0.410	− 5.1
29	3.94	0.625	40.0	0.40	1.033	−0.011	0.526	0.475	10.7
						0.211	0.463	0.400	15.8
						0.339	0.429	0.410	4.6
30	4.00	0	36.9	0.52	1.275	0	0.622	0.560	11.1
						0.360	0.488	0.430	13.5
31	2.00	0.33	36.9	0.78	1.95	0	0.804	0.760	5.8
				0.67		0.537	0.559	0.510	9.6
32	2.00	0	56.3	0.74	1.80	0	0.764	0.660	13.0
				0.63		0.254	0.648	0.660	− 1.8
						0.506	0.539	0.500	7.8
33	5.10	0.383	45.0	0.366	0.928	0.382	0.335	0.331	7.3
						−0.053	0.439	0.437	0.5
	6.00	0.313		0.328	0.800	0.343	0.346	0.312	10.9
						−0.048	0.417	0.410	1.7

Average Error = $\frac{\Sigma \mid e \mid}{n}$ = 9.7%

TABLE 4.4.1-C
SUBSONIC CHANGE IN DOWNWASH ANGLE DUE TO SLOTTED-FLAP DEFLECTION
DATA SUMMARY AND SUBSTANTIATION

Ref.	A	$\Lambda_{c/4}$ (deg)	b_f/b	$\frac{h_H}{b/2}$	ΔC_L	δ_f (deg)	$\Delta\epsilon_{calc.}$	$\Delta\epsilon_{test}$	$\Delta\epsilon_{test} - \Delta\epsilon_{calc.}$
31	2.0	36.9	0.809	0	0.57	40	9.93	8.8	−1.13
↓	2.0	45.0	0.778	0	0.55	40	9.97	8.7	−1.27
33	5.1	45.4	0.288	0.382	0.44	40	3.55	2.5	−1.05
↓	5.1	45.4	0.288	−0.053	0.42	40	9.49	6.5	−3.0
↓	6.0	45.4	0.35	0.343	0.55	40	3.30	3.3	0
↓	6.0	45.4	0.35	−0.048	0.57	40	8.88	5.5	−3.38
34	4.0	36.9	0.539	0	0.61	40	7.98	8.4	0.42
Unpub. data	6.8	35.0	0.524	0.0862	1.01	50	6.22	3.6	−2.62
↓	6.8	35.0	0.524	0.0862	0.63	25	3.88	2.3	−1.58
↓	8.5	24.0	0.547	0.466	1.23	50	2.80	2.8	0
↓	8.7	24.5	0.522	0.441	1.08	50	2.59	3.3	0.71
↓	7.0	30.6	0.475	0.093	0.84	50	5.46	5.3	−0.16
↓	7.5	30.6	0.456	0.089	0.84	50	5.34	6.0	0.66
↓	7.8	−0.5	0.467	0.071	0.96	40	6.06	4.9	−1.16
↓	6.2	2.7	0.403	0.157	0.67	40	4.88	5.1	0.22
↓	9.4	2.0	0.503	0.085	0.62	30	2.89	2.9	0.01
↓	9.4	2.0	0.503	0.088	1.16	50	5.35	4.9	−0.45
↓	12.1	−0.6	0.517	0.033	0.73	25	2.88	3.2	0.32
↓	12.1	−0.6	0.517	0.033	1.50	50	5.92	6.3	0.38
↓	6.25	2.0	0.529	0.28	0.39	20	1.66	2.2	0.54
↓	6.25	2.0	0.529	0.28	0.71	40	3.03	4.0	0.97

TABLE 4.4.1-D
SUBSONIC CHANGE IN DOWNWASH ANGLE DUE TO PLANE FLAP DEFLECTION
DATA SUMMARY AND SUBSTANTIATION

Ref.	A	$\Lambda_{c/4}$ (deg)	b_f/b	$\frac{h_H}{b/2}$	ΔC_L	δ_f (deg)	$\Delta\epsilon_{calc.}$	$\Delta\epsilon_{test}$	$\Delta\epsilon_{test} - \Delta\epsilon_{calc.}$
23	4.0	3.4	0.393	0.40	0.33	50	1.89	3.0	1.11
↓	↓	↓	↓	0.177	↓	↓	2.85	3.1	0.25
↓	↓	↓	↓	−0.177	↓	↓	6.02	6.3	0.28
↓	2.5	5.3	0.35	0.40	0.26	↓	2.67	2.6	−0.07
↓	↓	↓	↓	0.177	↓	↓	4.04	3.9	−0.14
↓	↓	↓	↓	−0.177	↓	↓	8.53	8.3	−0.23
35	4.0	40	0.496	0.246	0.39	50	2.29	2.4	0.11
24	2.5	6.4	0.35	0.4	0.28	50	2.88	2.9	0.02
↓	↓	↓	0.75	0.4	0.47	↓	2.26	3.5	1.24
36	2.5	40	0.814	0.322	0.28	50	1.37	1.2	−0.17
↓	↓	↓	↓	↓	0.25	↓	1.22	1.2	−0.02
37	3.5	40	0.363	0.36	0.315	40	2.33	2.4	0.07

TABLE 4.4.1-E

SUBSONIC DYNAMIC-PRESSURE RATIO

DATA SUMMARY AND SUBSTANTIATION

Ref.	A	Λ_{LE} (deg)	λ	$\frac{x}{c}$	$\frac{z}{c}$	α (deg)	q/q_∞ Calc.	q/q_∞ Test	e Percent Error
9	3.0	0	1.0	2.0	0	0	0.88	0.90	−2.2
						1	0.89	0.92	−3.3
						2	0.92	0.94	−2.1
						3	0.95	0.95	0
						4	0.98	0.96	2.1
						6	1.00	0.96	4.2
	6.0	0	1.0	2.0	0	0	0.88	0.87	1.1
						1	0.89	0.89	0
						2	0.93	0.92	1.1
						3	0.97	0.93	4.3
						4	0.99	0.95	4.2
						6	1.00	0.97	3.1
	6.0	0	1.0	2.0	0.28	6	1.00	0.97	3.1
						8	0.98	0.96	2.1
						10	0.91	0.93	−2.2
	4.5	30.0	1.0	2.0	0	0	0.88	0.96	−8.3
						1	0.89	0.96	−7.3
						2	0.92	0.95	−3.2
						3	0.95	0.95	0
						4	0.98	0.94	4.3
						6	1.00	0.98	2.0
	5.2	30.0	1.0	2.0	0	0	0.88	0.95	−7.4
						1	0.89	0.94	−5.3
						2	0.92	0.94	−2.1
						3	0.96	0.94	2.1
						4	0.99	0.94	5.3
						6	1.00	0.96	4.2
					0.28	6	1.00	1.01	−1.0
						8	0.996	1.02	−2.4
						10	0.94	1.02	−7.8
						12	0.88	1.01	−13.0

TABLE 4.4.1-E (CONTD)

Ref.	A	Λ_{LE} (deg)	λ	$\frac{x}{\bar{c}}$	$\frac{z}{\bar{c}}$	α (deg)	q/q_∞ Calc.	q/q_∞ Test	e Percent Error
9	1.5	60.0	1.0	2.0	0	0	0.89	0.95	−6.3
						1	0.895	0.95	−5.8
						2	0.91	0.95	−4.2
						3	0.93	0.94	−1.1
						4	0.96	0.94	2.1
						6	0.99	0.97	2.1
						8	1.00	1.00	0
	3.0	60.0	1.0	3.0	0	0	0.92	0.92	0
						1	0.93	0.93	0
						2	0.96	0.95	1.1
						3	0.99	0.97	2.1
						4	1.00	0.99	1.0
2	3.5	47.5	0.5	1.213	0	0	0.85	–	–
						1	0.86	–	–
						2	0.89	–	–
						3	0.93	0.86	8.1
						4	0.96	0.88	9.1
						6	1.00	0.92	8.7
5	4.01	42.0	0.625	1.814	0.25	8	1.00	1.00	0
						10	0.98	1.00	−2.0
						12	0.95	1.00	−5.0
						13.1	0.91	1.00	−9.0
						14	0.90	0.98	−8.2
6	4.00	42.0	0.5	2.504	0	0	0.93	0.94	−1.1
						1	0.94	0.95	−1.1
						2	0.97	0.96	1.0
						3	0.98	0.96	2.1
						4	1.00	0.97	3.1

$$\text{Average Error} = \frac{\Sigma|e|}{n} = 3.5\%$$

TABLE 4.4.1-F
SUPERSONIC DOWNWASH GRADIENT BEHIND STRAIGHT-TAPERED WINGS
METHOD 2
DATA SUMMARY AND SUBSTANTIATION

Ref.	A	λ	Λ_{LE} (deg)	$\frac{2x}{b}$	$\frac{2y}{b}$	$\frac{2z}{b}$	$\partial\bar{\epsilon}/\partial\alpha$ Calc.	$\partial\bar{\epsilon}/\partial\alpha$ Test	$\Delta\partial\bar{\epsilon}/\partial\alpha$
38	3.5	1.0	0	1.72	0.10	0.20	0.23	0.26	−0.03
↓	↓	↓	↓	↓	0.30	↓	0.26	0.38	−0.12
				1.72	0.10	0.40	0.14	0.14	0
				↓	0.30	↓	0.16	0.12	0.04
				2.52	0.10	0.20	0.31	0.35	−0.04
↓	↓	↓	↓	↓	0.30	↓	0.35	0.39	−0.04
39	4.0	0.5	42.7	1.39	0.176	0.22	0.20	0.18	0.02
40	4.0	0.5	42.7	1.39	0.176	0.22	0.18	0.214	−0.034
41	4.0	0.5	42.7	1.39	0.176	0.206	0.20	0.244	−0.044
↓	↓	↓	↓	1.38	↓	0.013	0.24	0.325	−0.085
	4.0	0.5	42.7	1.39	0.176	0.206	0.24	0.21	0.03
↓	↓	↓	↓	↓	↓	0.11	0.28	0.32	−0.04
42	4.0	1.0	0	1.85	0.25	0.35	0	0.06	−0.06
↓	↓	↓	↓	↓	↓	0.175	0.04	0	0.04
↓	↓	↓	↓	1.55	↓	↓	0	−0.02	0.02
43	3.11	1.0	0	2.73	0.333	0	0.28	0.14	0.14
↓	↓	↓	↓	↓	↓	↓	0.38	0.30	0.08
44	2.34	1.0	0	2.13	0.286	0	0.06	0.08	−0.02
↓	↓	↓	↓	↓	↓	↓	0.03	0.07	−0.04
				2.98	↓	0.309	0.14	0.12	0.02
				↓	↓	0	0.22	0.14	0.08
				↓	↓	−0.309	0.14	0.13	0.01
				↓	↓	0.309	0.17	0.085	0.085
				↓	↓	0	0.21	0.145	0.065
				↓	↓	−0.309	0.17	0.14	0.03
↓	↓	↓	↓	↓	↓	−0.10	0.215	0.145	0.07
45	3.36	0	50	3.0	0.4	0.134	0.40	0.40	0
↓	↓	↓	↓	↓	0.6	↓	0.32	0.32	0
					0.8		0.22	0.14	0.08
					0.4	−0.089	0.43	0.32	0.11
					↓	−0.315	0.29	0.24	0.05
					0.6	↓	0.21	0.17	0.04
↓	↓	↓	↓	↓	0.8	↓	0.10	−0.07	0.17

TABLE 4.4.1-F (CONTD)

Ref.	A	λ	$\Lambda_{L.E.}$ (deg)	$\frac{2x}{b}$	$\frac{2y}{b}$	$\frac{2z}{b}$	$\partial\bar{\epsilon}/\partial\alpha$ Calc.	$\partial\bar{\epsilon}/\partial\alpha$ Test	$\Delta\partial\bar{\epsilon}/\partial\alpha$
45	3.36	0	50	3.0	0.4	0.346	0.26	0.29	−0.03
↓	↓	↓	↓	↓	↓	0.130	0.40	0.39	0.01
						−0.093	0.44	0.40	0.04
						−0.317	0.27	0.29	−0.02
					0.35	0.394	0.03	0.08	−0.05
					0.4	↓	0	0.08	−0.08
					0.35	−0.049	0.27	0.29	−0.02
					0.4	↓	0.24	0.24	0
					0.6		0.14	0.13	0.01
					0.8		0.05	0	0.05
					0.35	−0.345	0.05	0.10	−0.05
	2.04	0	63	3.0	0.4	0.386	0.23	0.22	0.01
	↓	↓	↓	↓	0.6	↓	0.14	0.10	0.04
					0.8		0.03	−0.02	0.05
					0.4	−0.049	0.46	0.52	−0.06
					0.6	↓	0.36	0.36	0
					0.8		0.26	0.25	0.01
				4.9	0.275	0.386	0.33	0.28	0.05
				↓	↓	−0.103	0.52	0.42	0.10
						−0.348	0.35	0.28	0.07
							Average $\lvert\Delta\partial\bar{\epsilon}/\partial\alpha\rvert$ = 0.045		

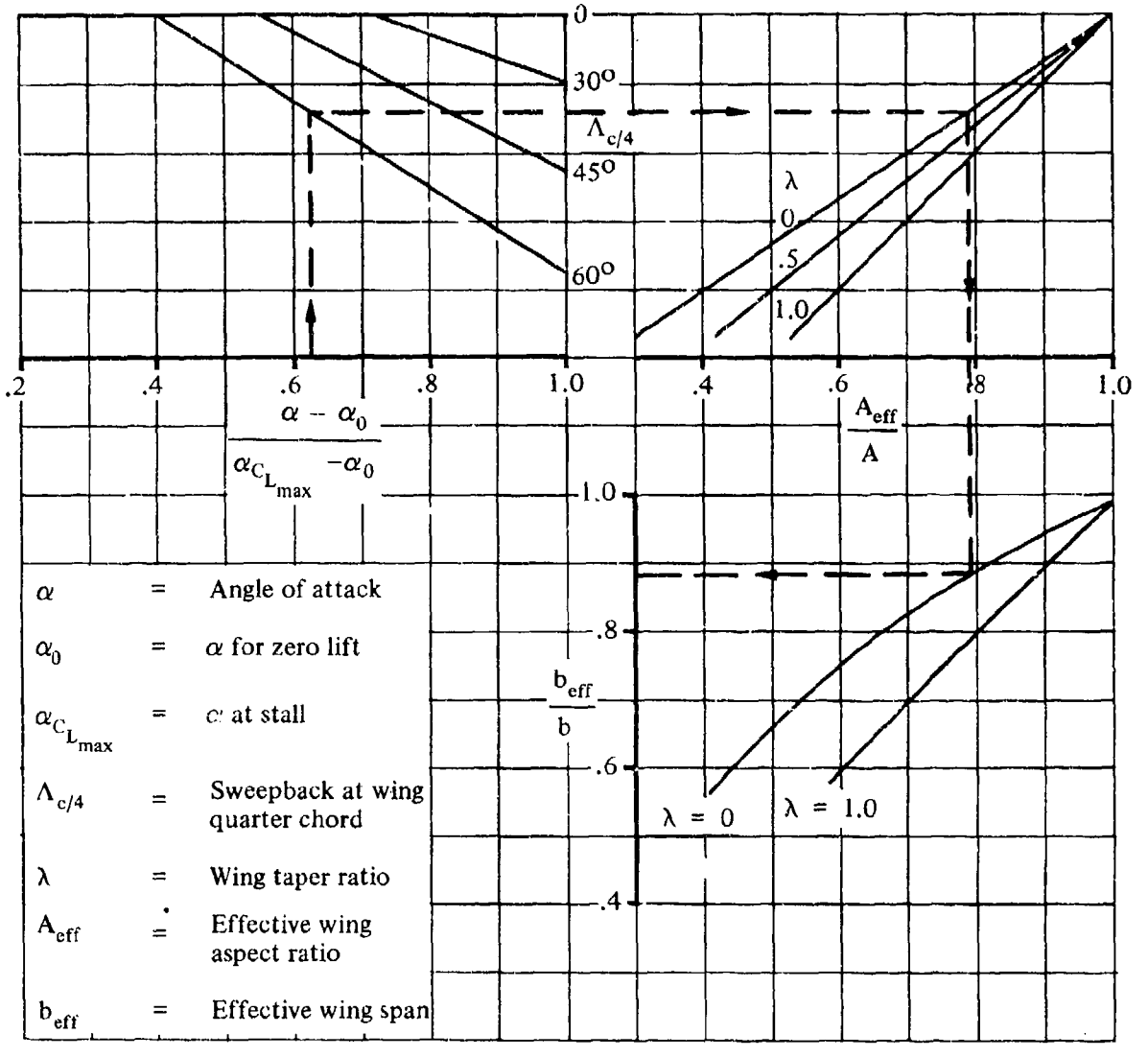

FIGURE 4.4.1-66 EFFECTIVE WING ASPECT RATIO AND SPAN – LOW SPEEDS

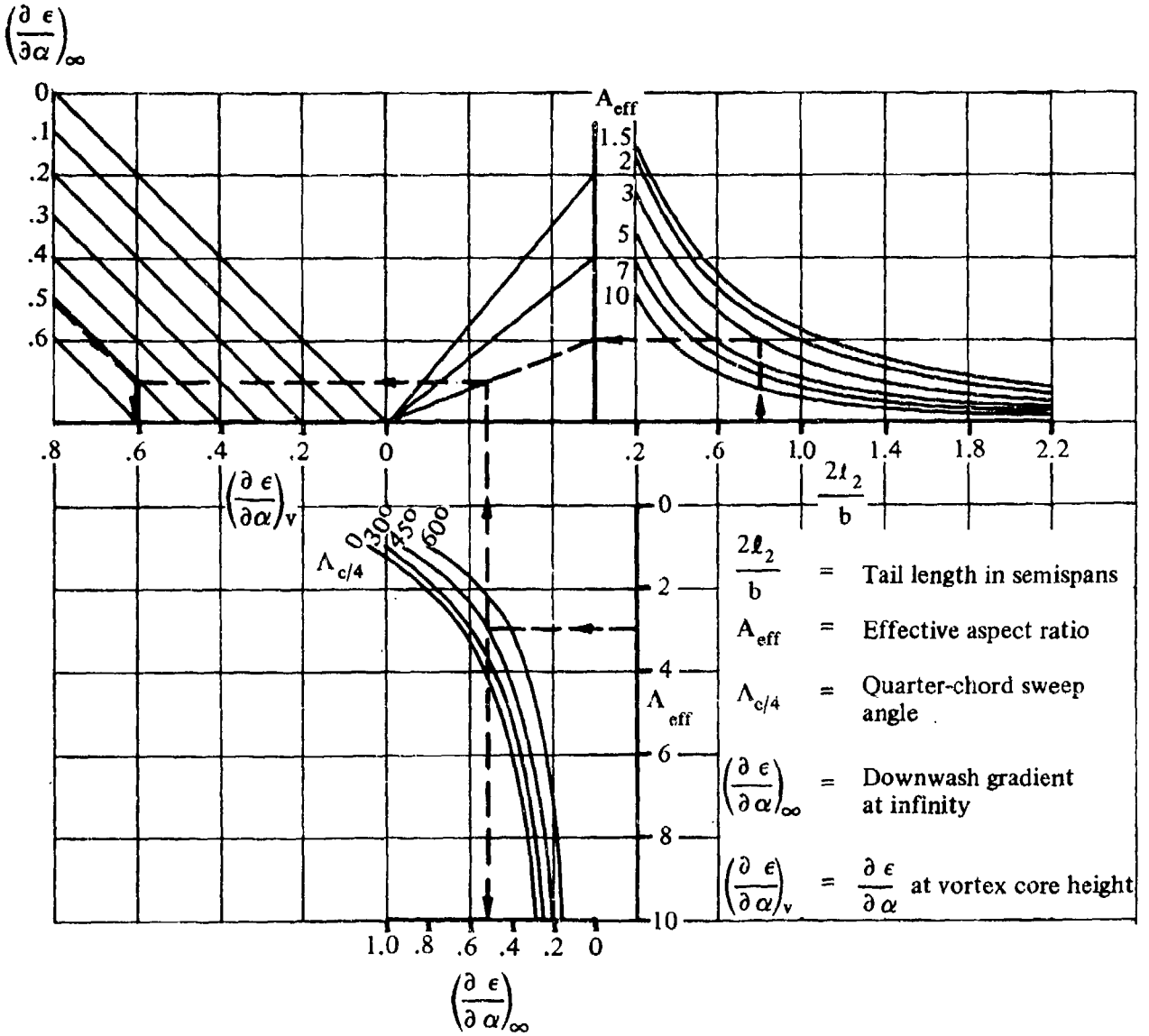

FIGURE 4.4.1-67 DOWNWASH AT THE PLANE OF SYMMETRY AND HEIGHT OF VORTEX CORE – LOW SPEEDS

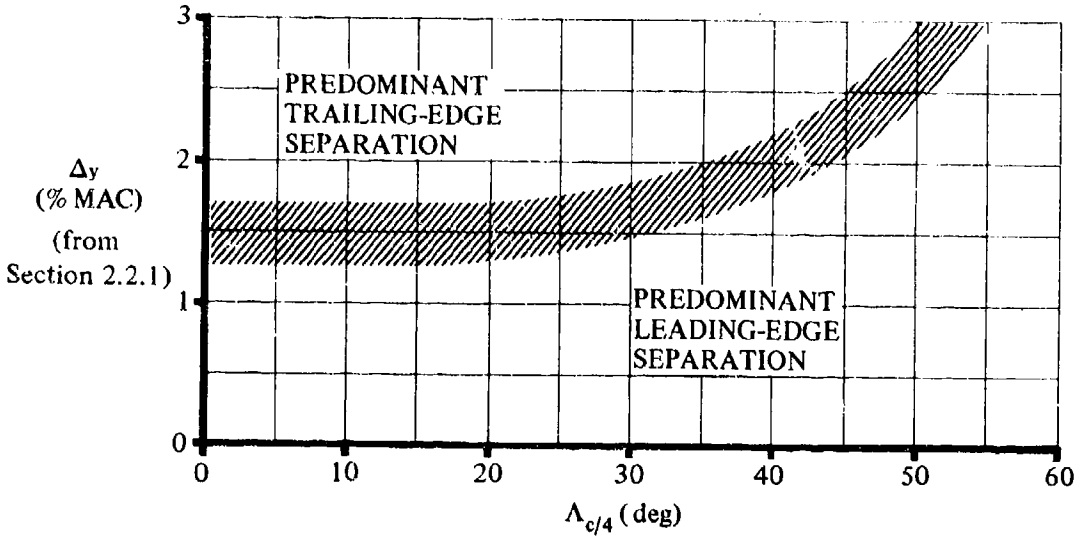

FIGURE 4.4.1-68a TYPE OF FLOW SEPARATION AS A FUNCTION OF AIRFOIL AND WING SWEEP – SUBSONIC SPEEDS

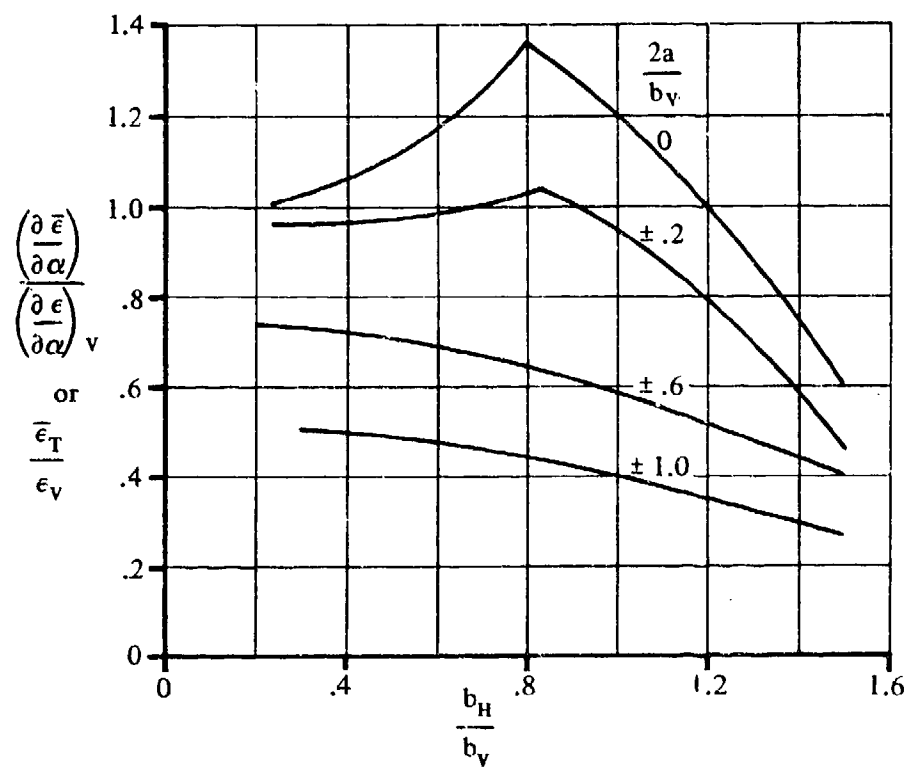

FIGURE 4.4.1-68b AVERAGE DOWNWASH ACTING ON AFT LIFTING SURFACE – LOW SPEEDS

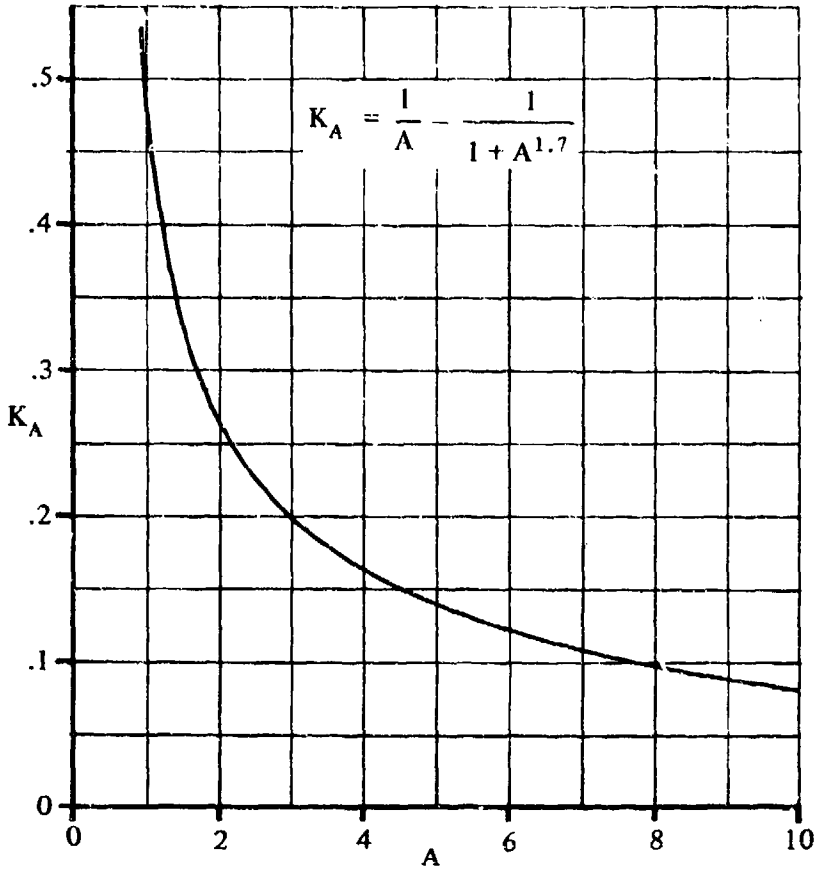

FIGURE 4.4.1-69a WING ASPECT-RATIO FACTOR – METHOD 2

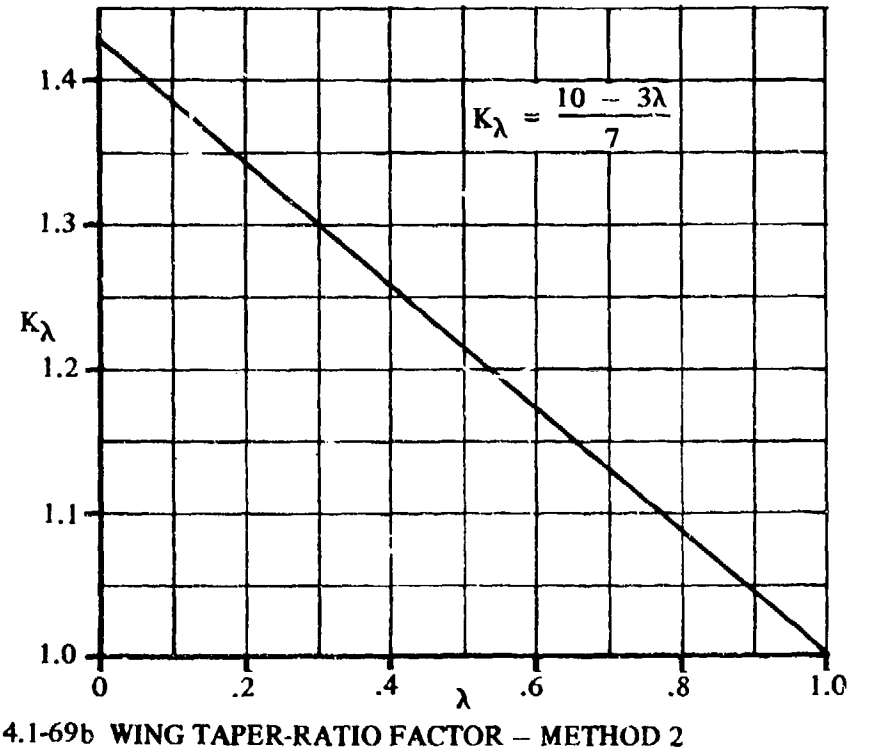

FIGURE 4.4.1-69b WING TAPER-RATIO FACTOR – METHOD 2

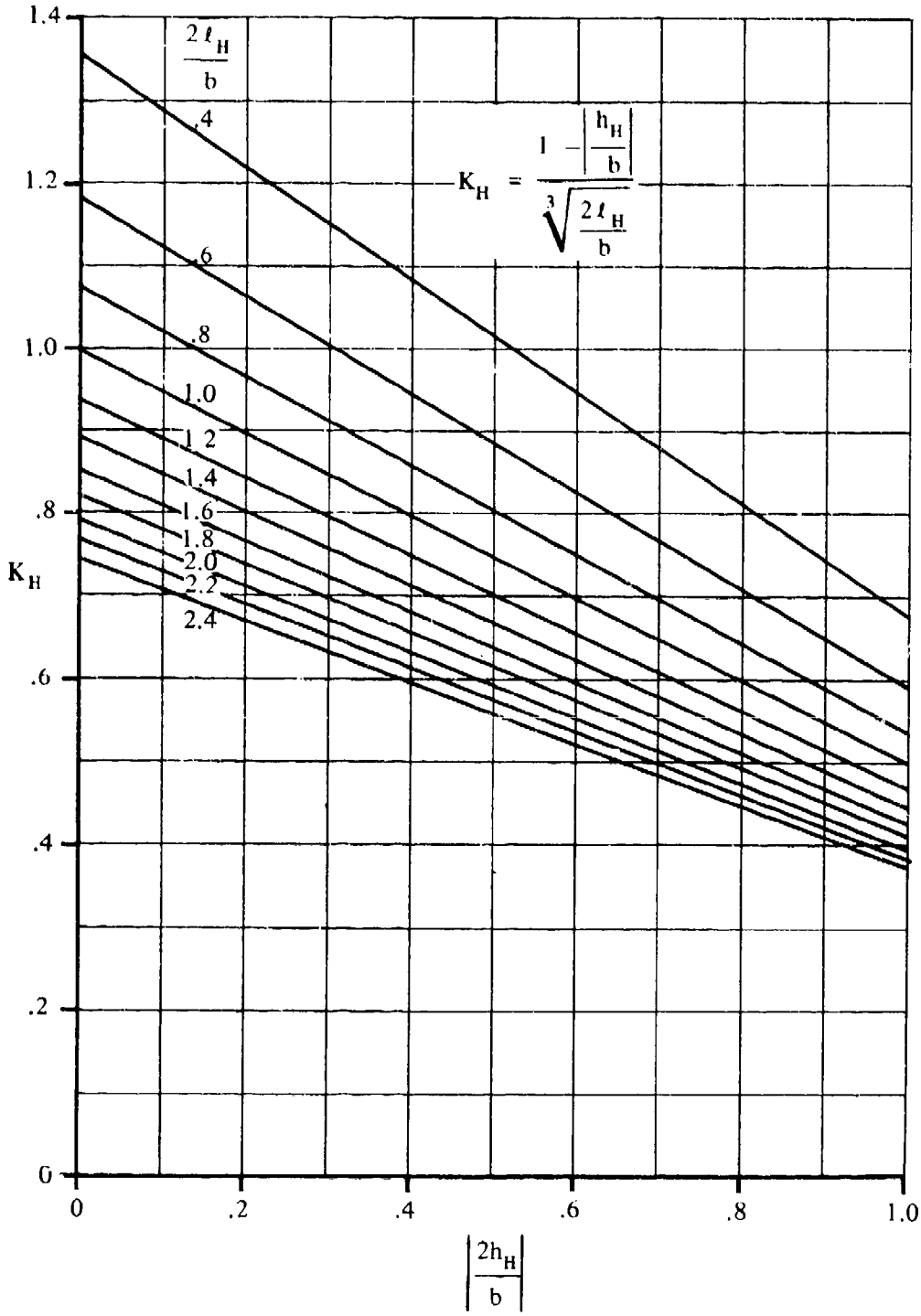

FIGURE 4.4.1-70 HORIZONTAL-TAIL-LOCATION FACTOR – METHOD 2

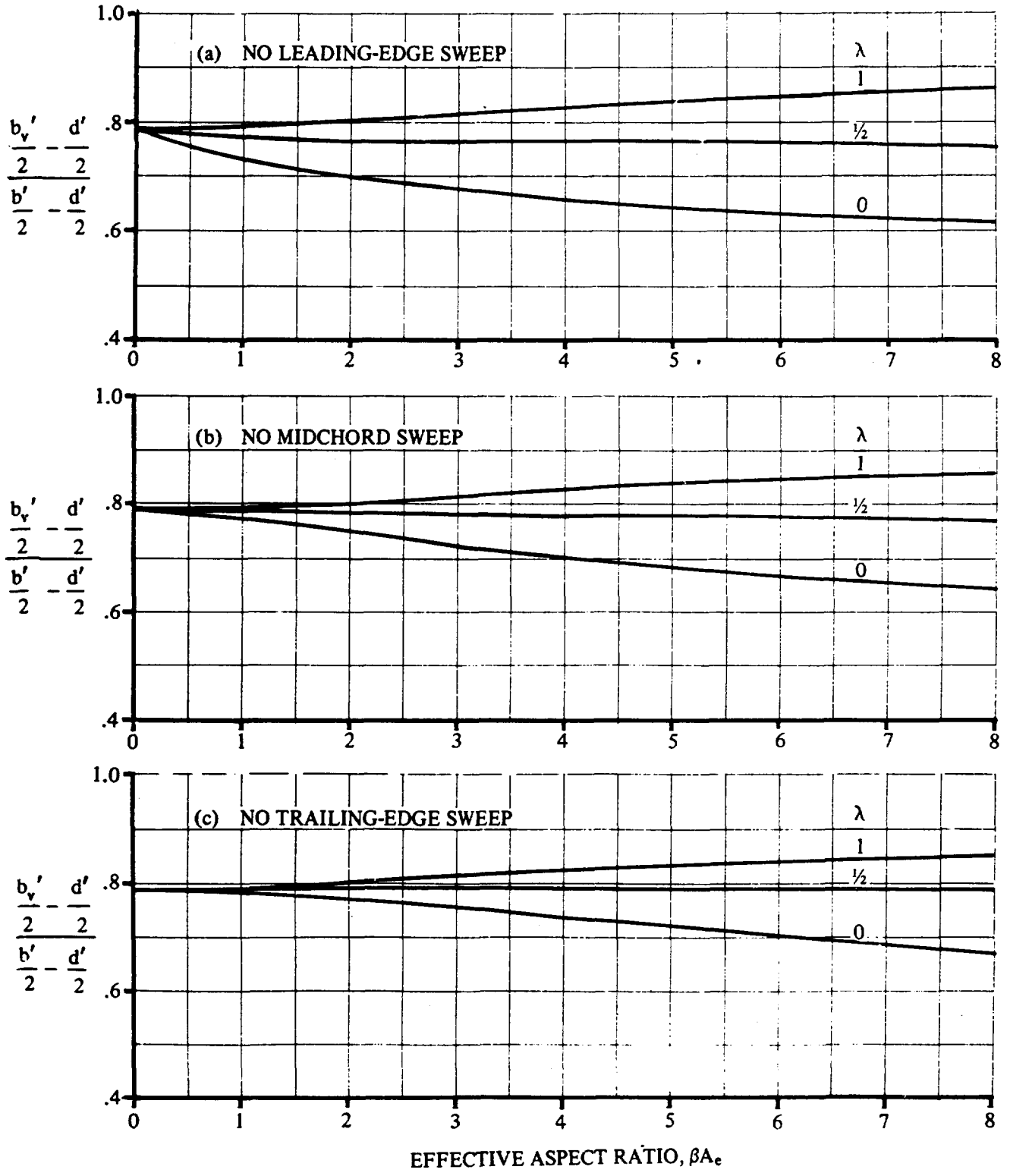

FIGURE 4.4.1-71 WING-VORTEX LATERAL POSITIONS AT SUBSONIC SPEEDS

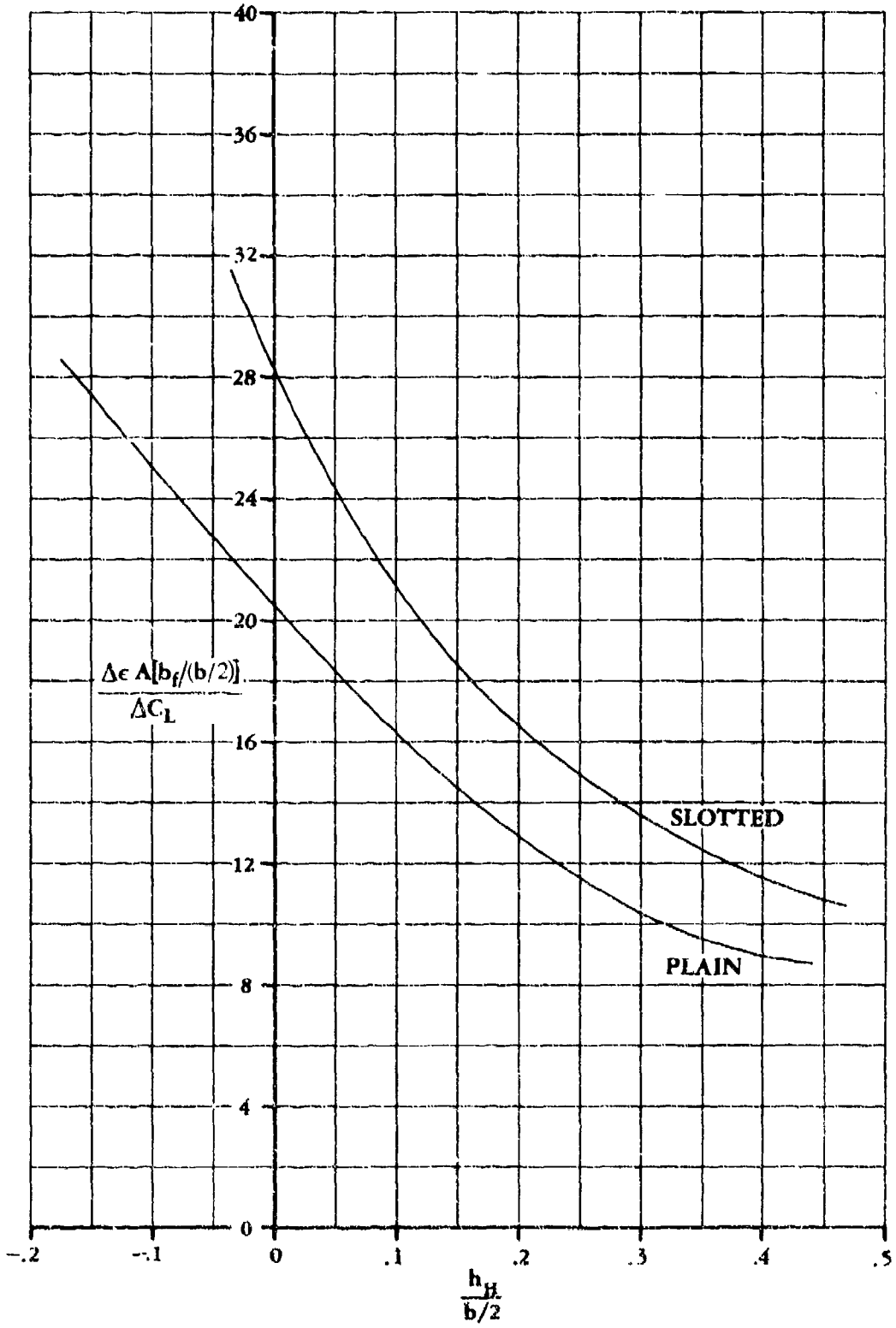

FIGURE 4.4.1-72 DOWNWASH INCREMENT DUE TO FLAPS

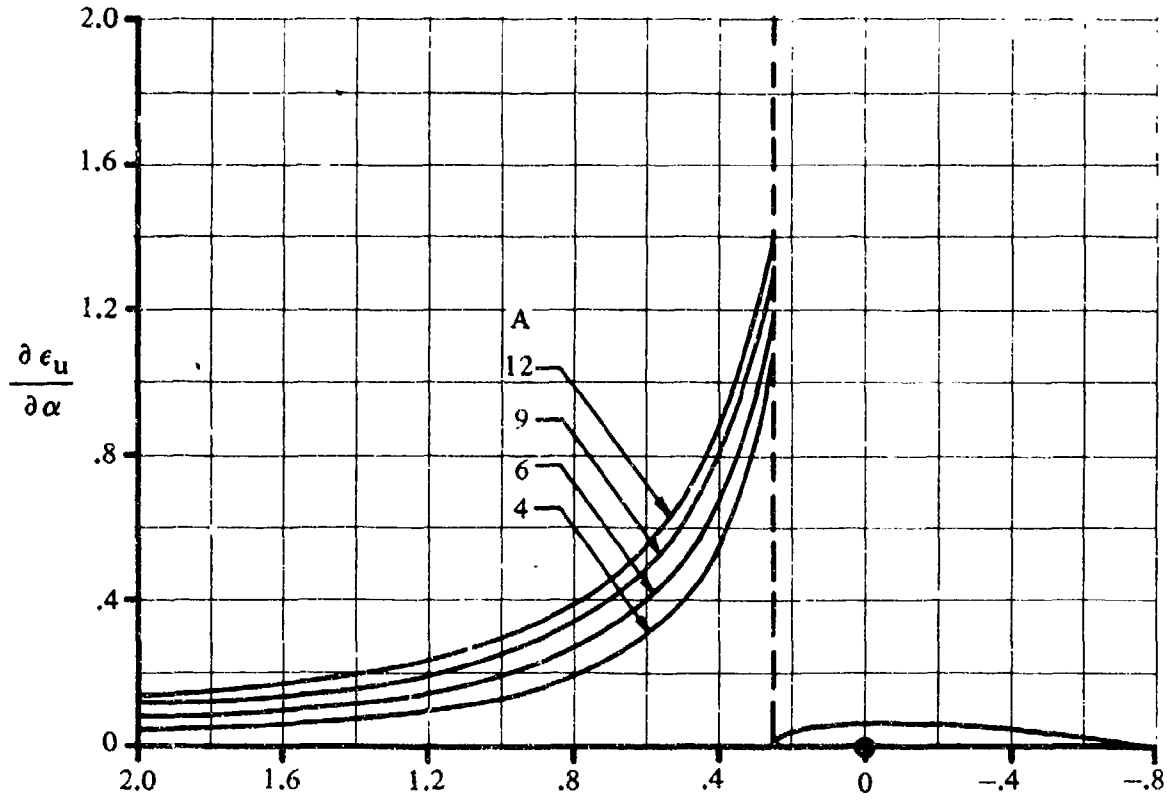

FIGURE 4.4.1-73 UPWASH GRADIENT AT PLANE OF SYMMETRY FOR UNSWEPT WINGS

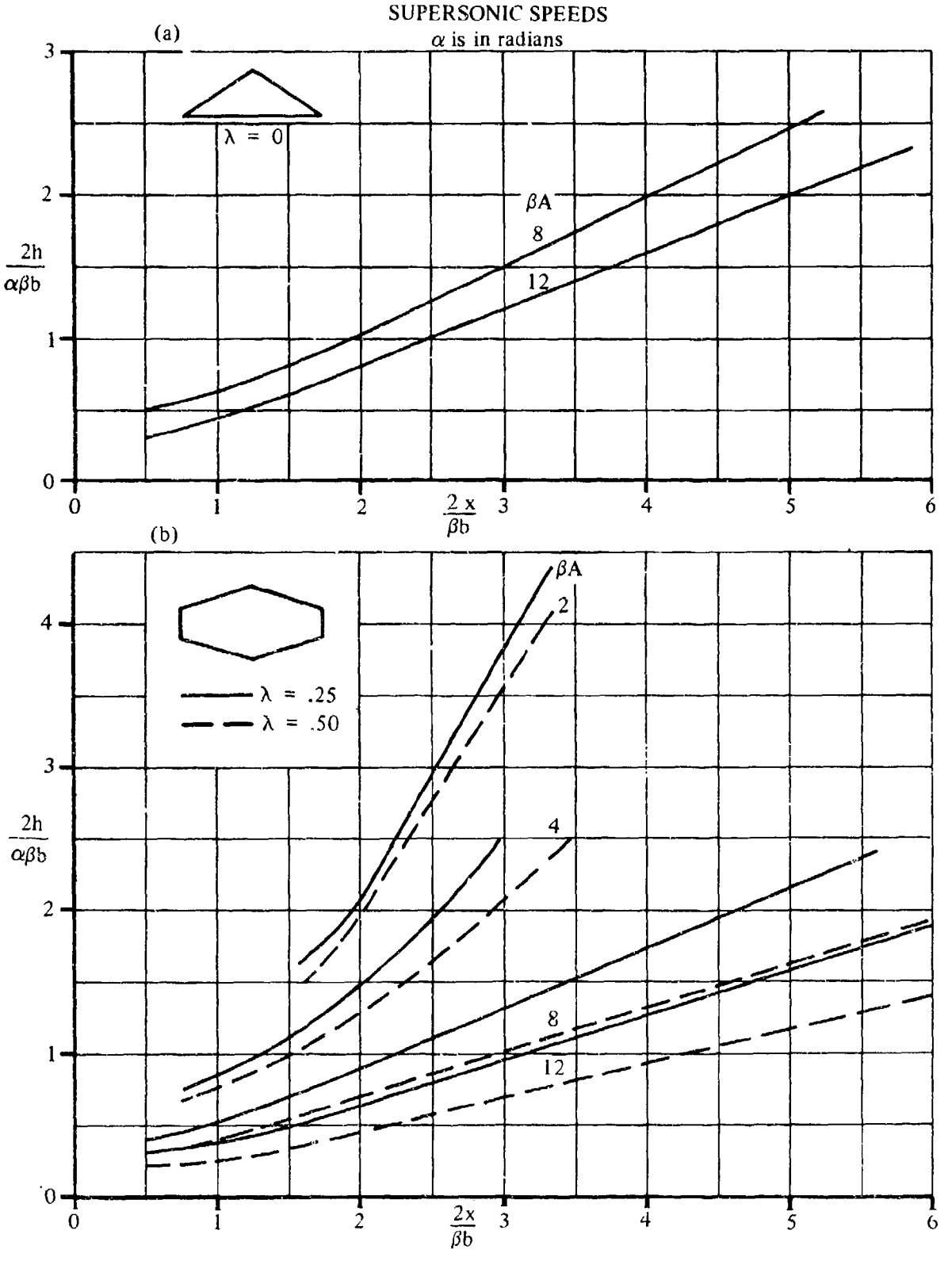

FIGURE 4.4.1-74 DOWNWARD DISPLACEMENT OF VORTEX CORE BELOW Z = 0 PLANE

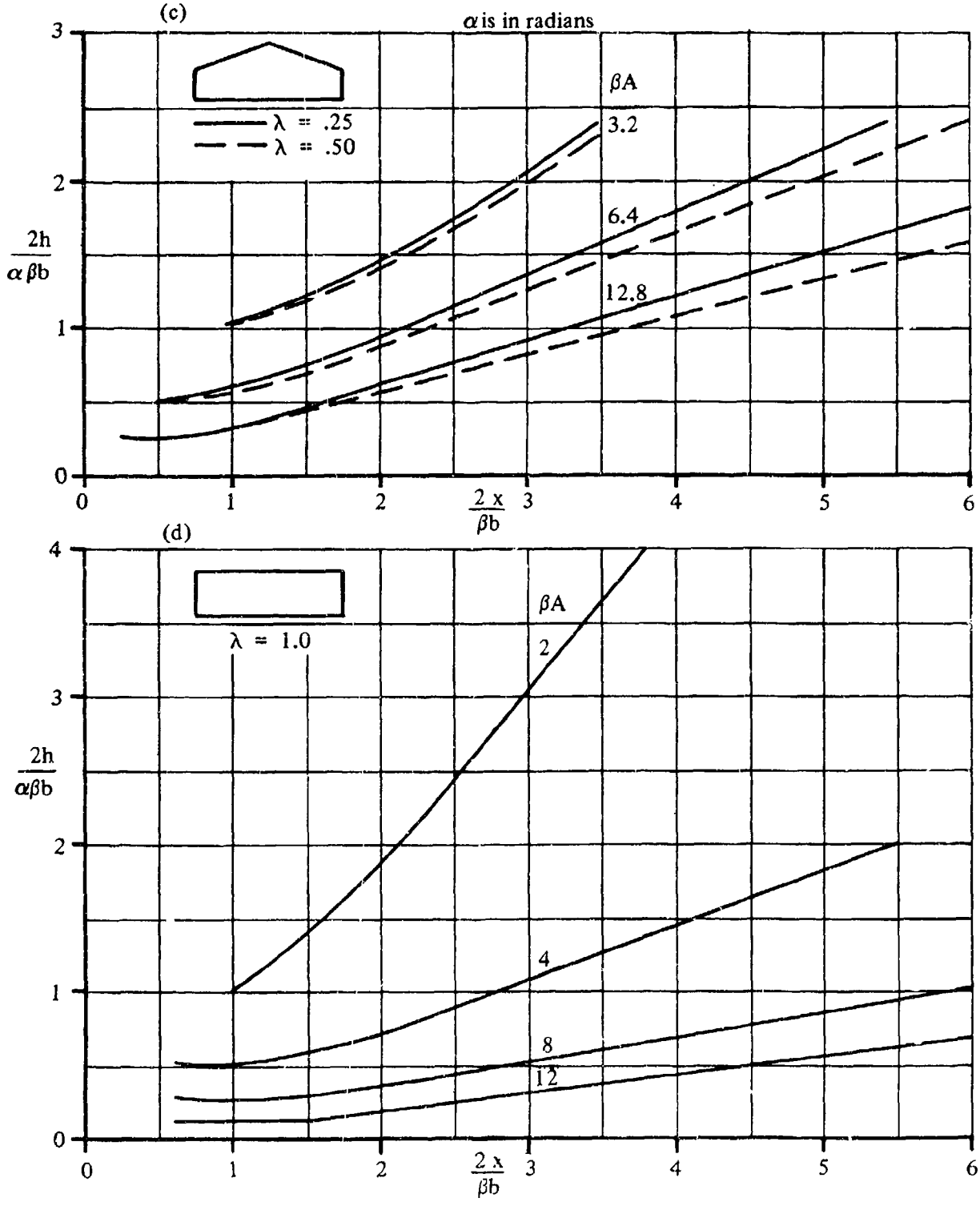

FIGURE 4.4.1-74 (CONTD)

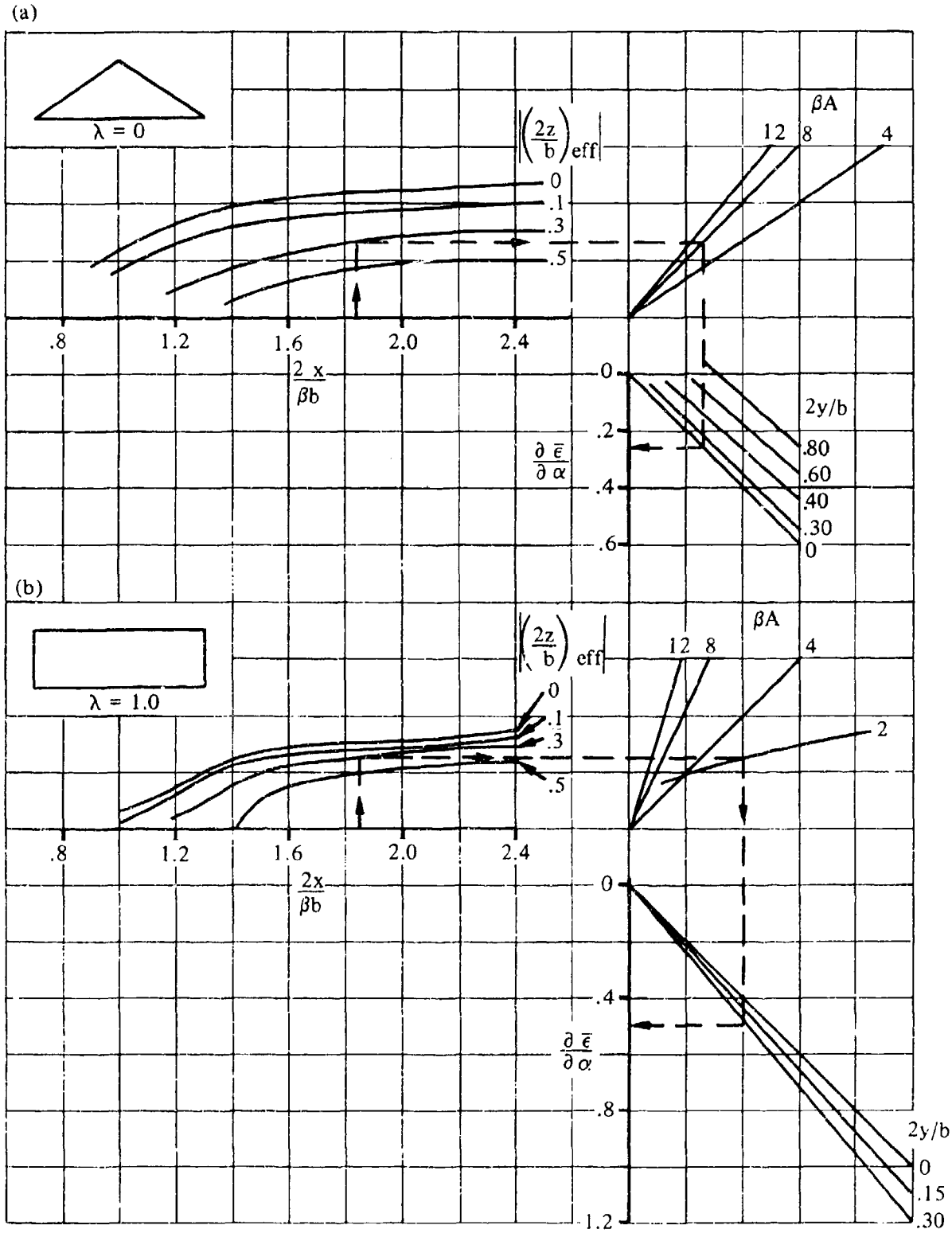

FIGURE 4.4.1-76 DOWNWASH AT SUPERSONIC SPEEDS

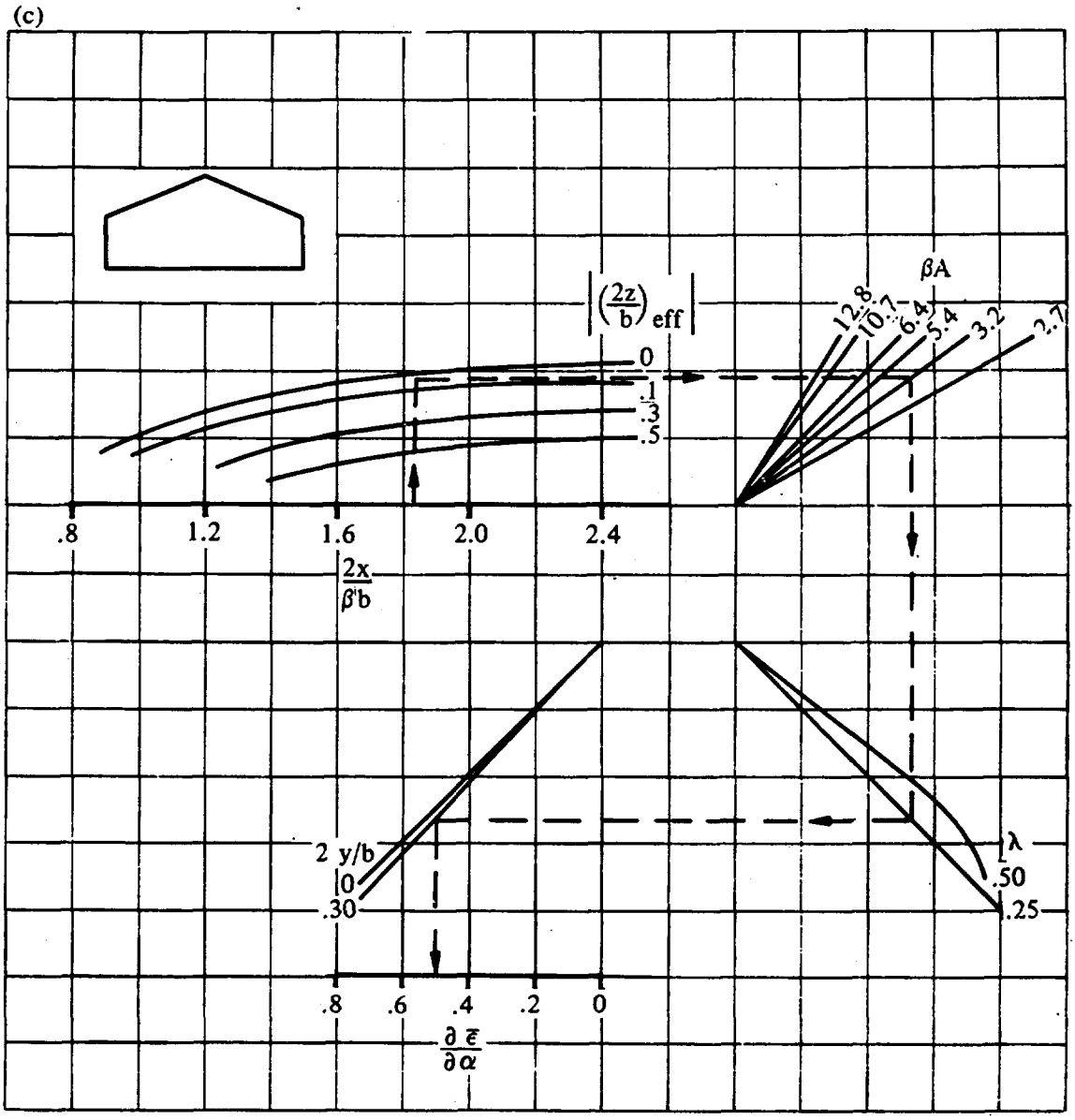

FIGURE 4.4.1-76 (CONTD)

(d)

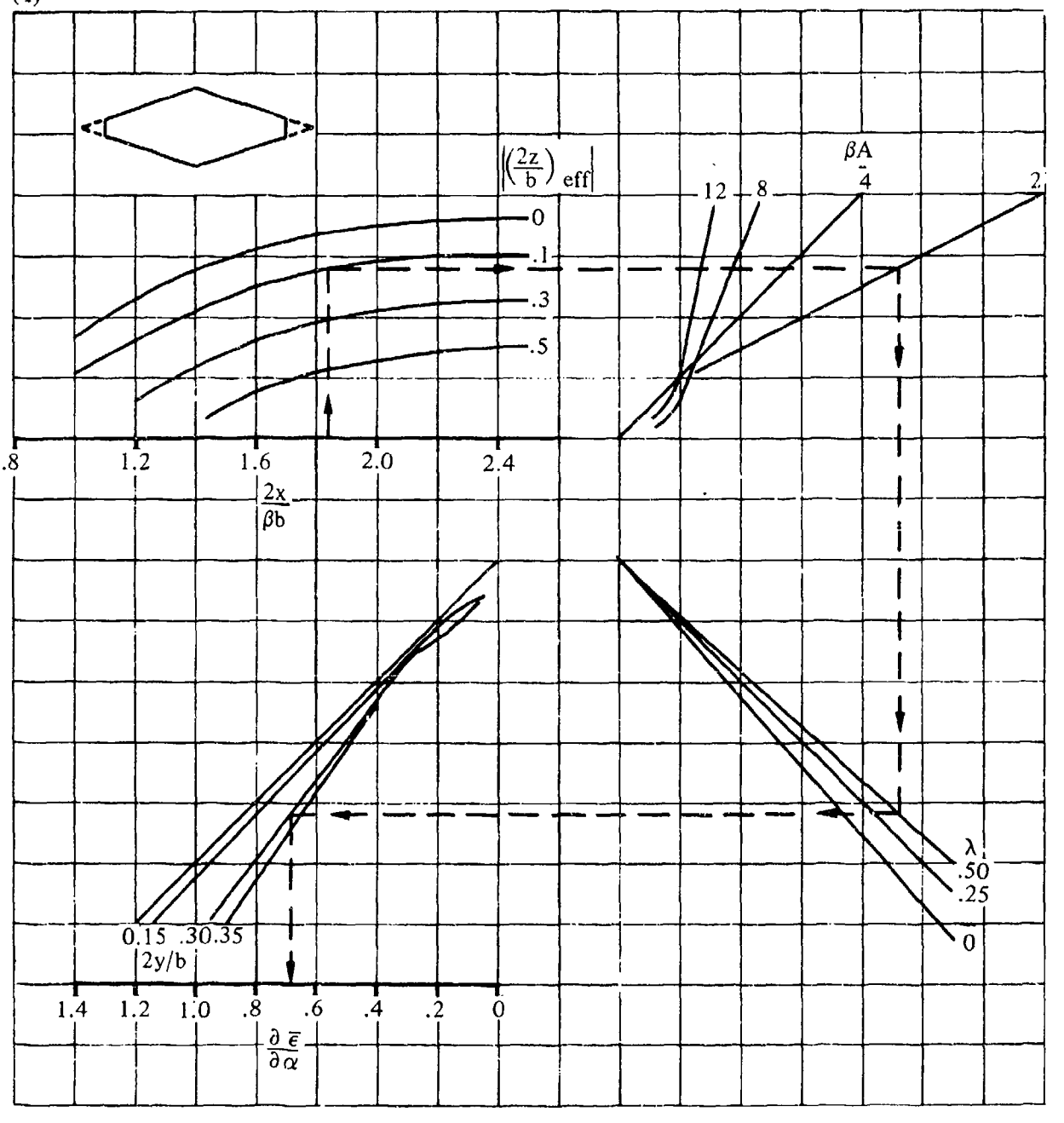

FIGURE 4.4.1-76 (CONTD)

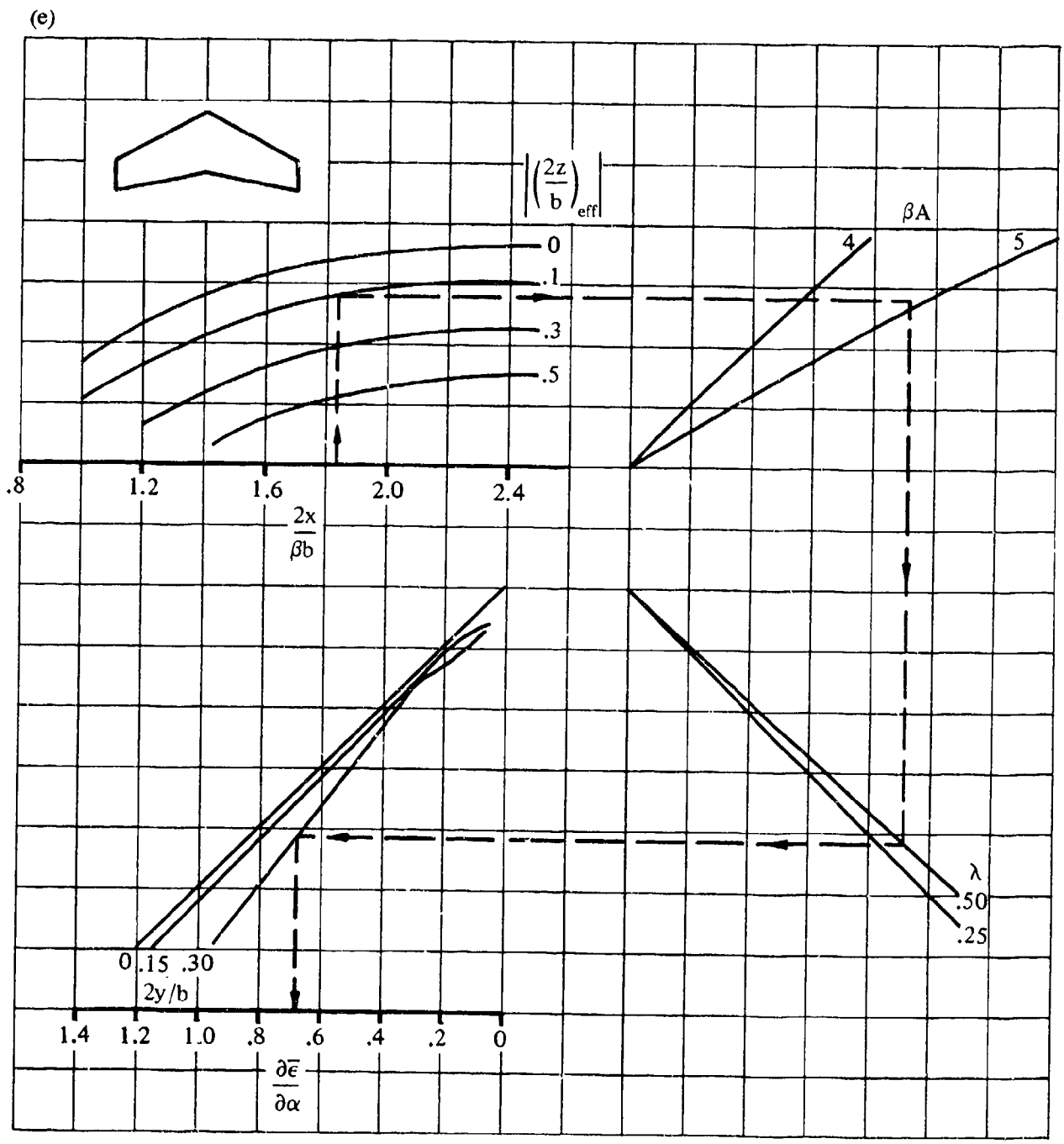

FIGURE 4.4.1-76 (CONTD)

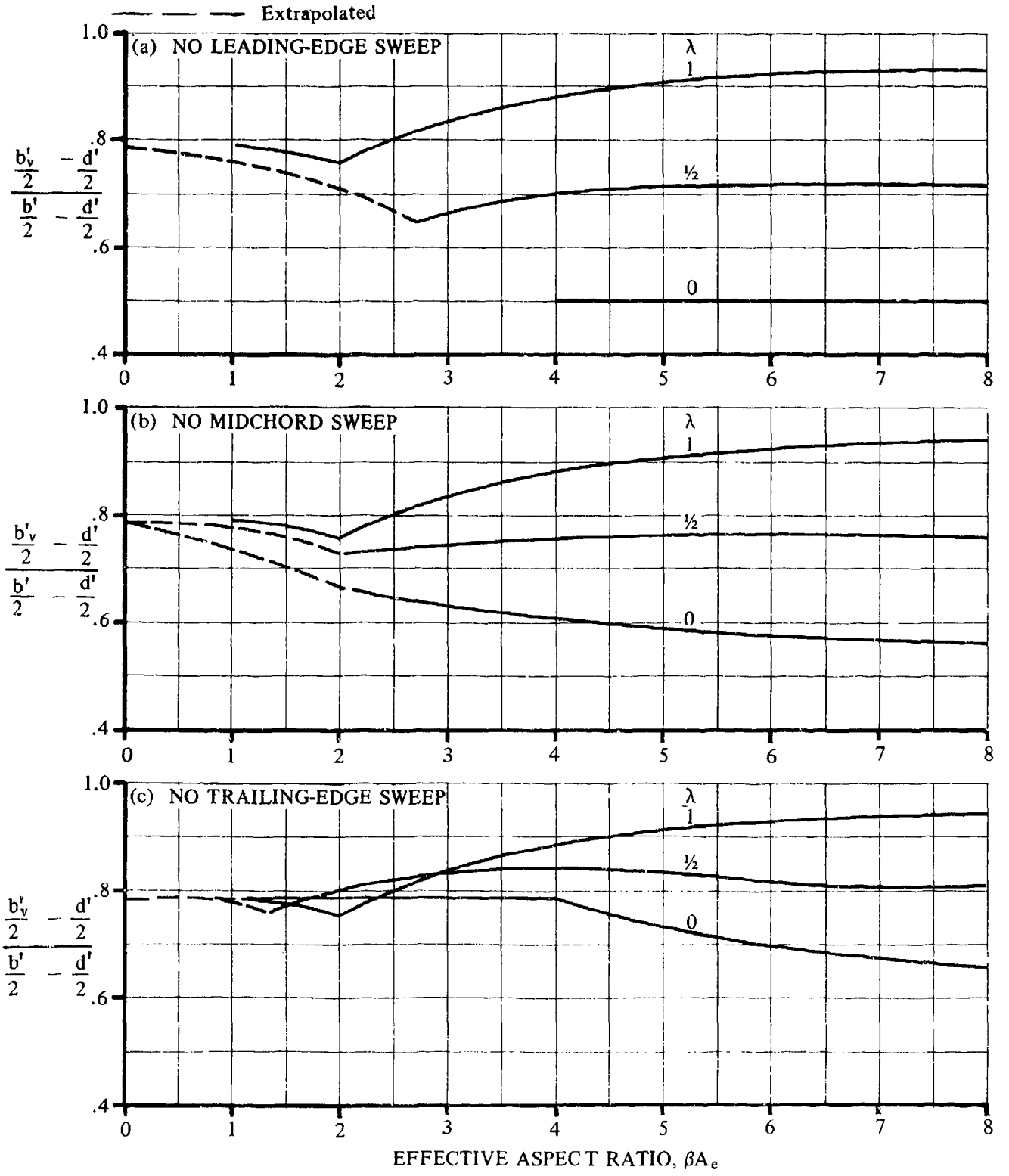

FIGURE 4.4.1-80 WING VORTEX LATERAL POSITION AT SUPERSONIC SPEEDS

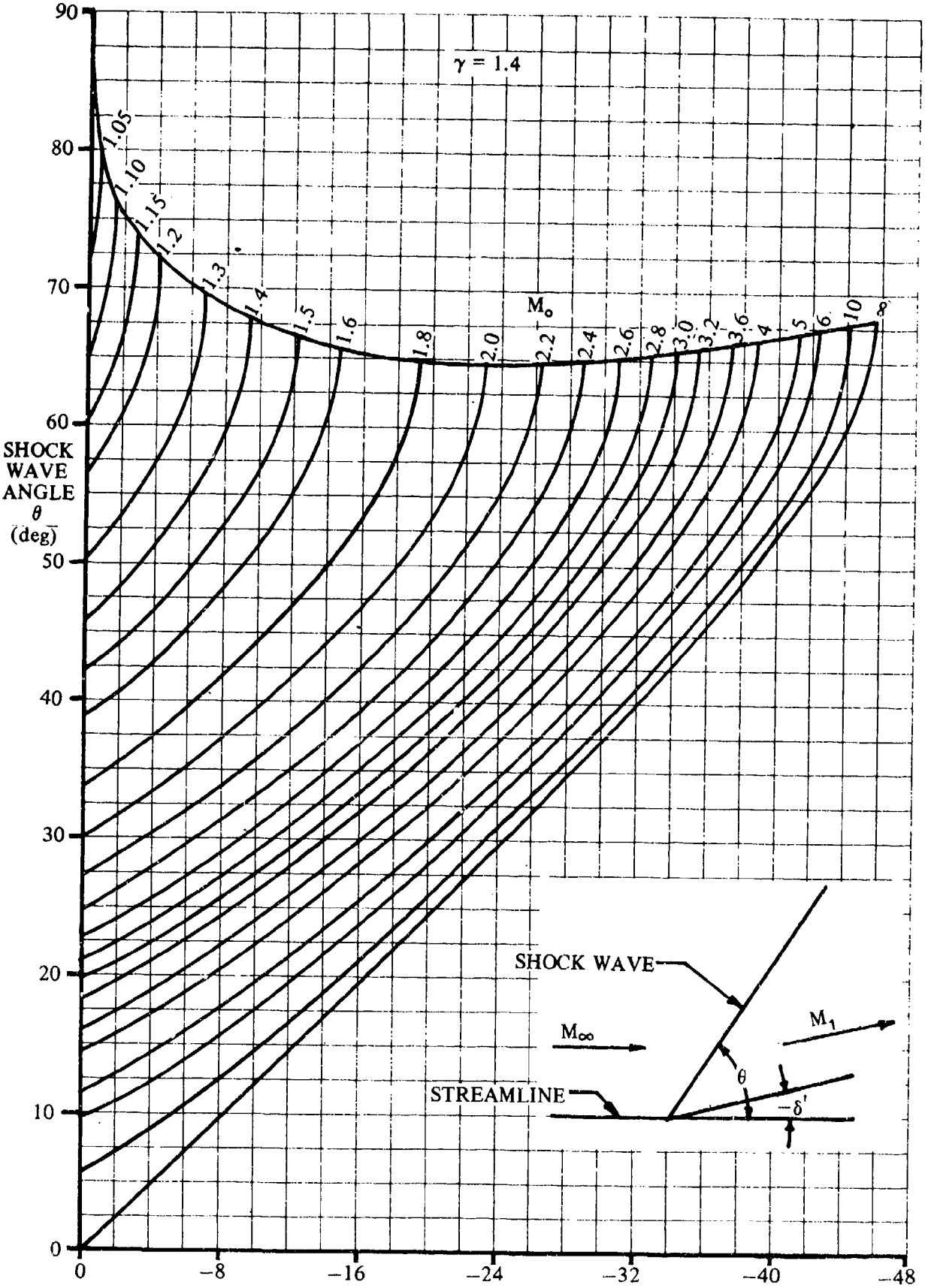

FIGURE 4.4.1-81 SHOCK ANGLE FOR TWO-DIMENSIONAL WEDGE

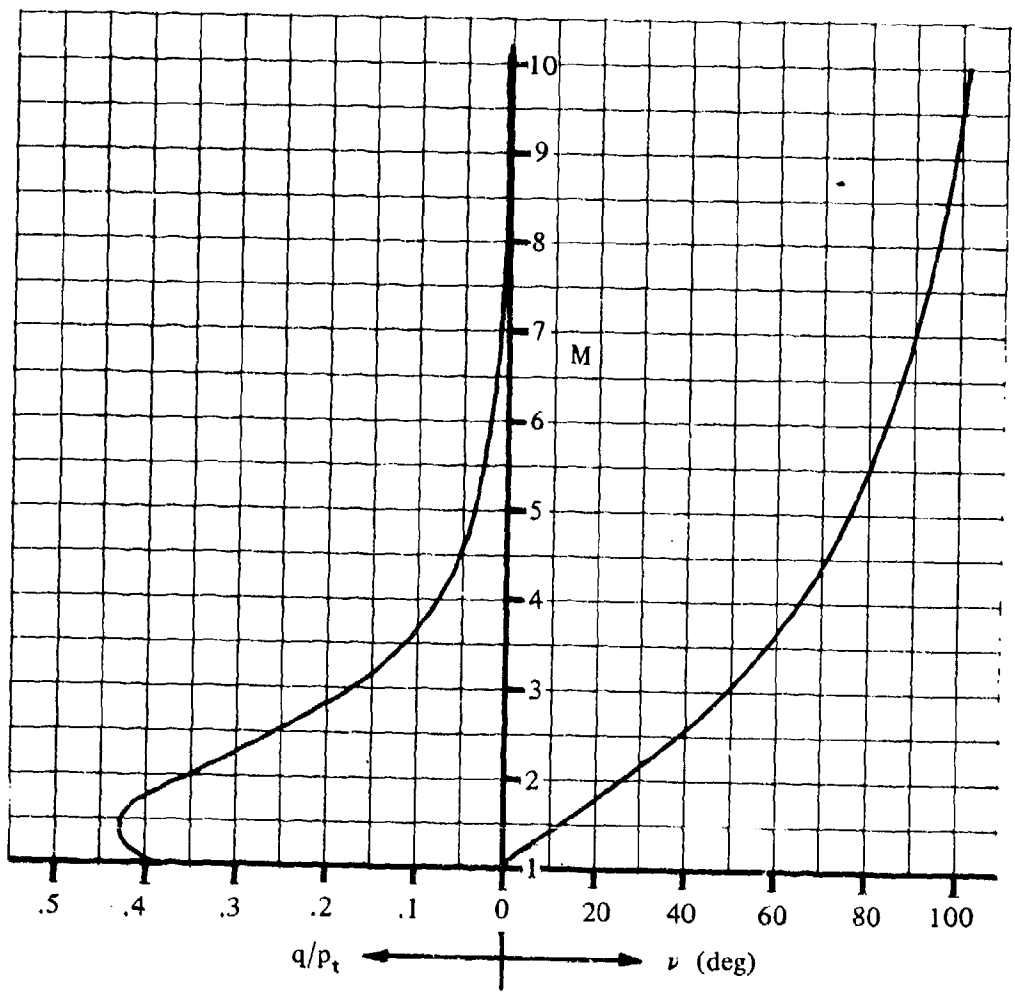

FIGURE 4.4.1-82 DYNAMIC-PRESSURE RATIO AND MACH NUMBER FOR PRANDTL-MEYER EXPANSION

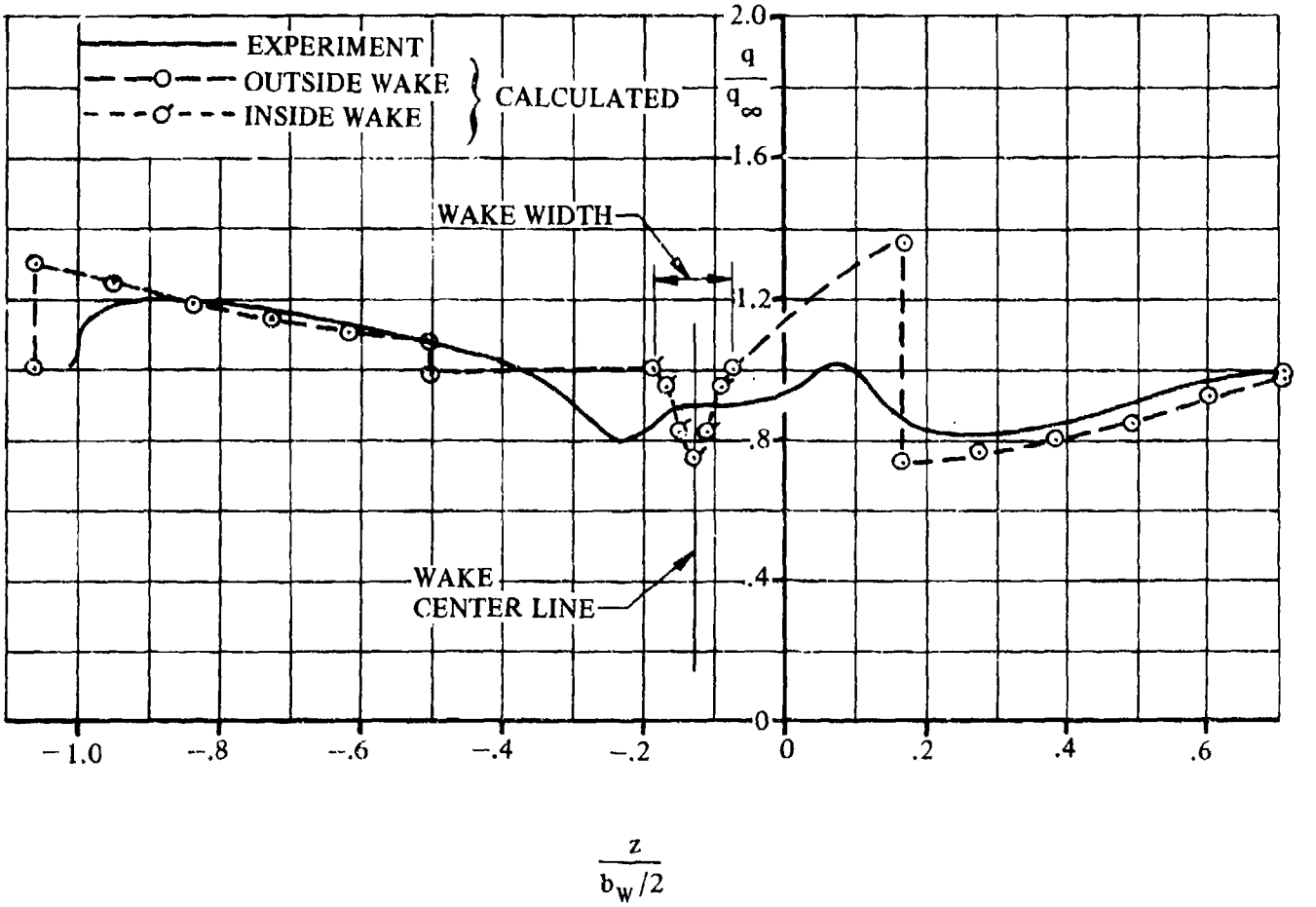

FIGURE 4.4.1-83 SUPERSONIC SAMPLE PROBLEM RESULTS

4.5 WING-BODY-TAIL COMBINATIONS AT ANGLE OF ATTACK
4.5.1 WING-BODY-TAIL LIFT

4.5.1.1 WING-BODY-TAIL LIFT-CURVE SLOPE

The information contained in this section is for the estimation of the lift-curve slope of wing-body-tail combinations at low angles of attack. In general, it consists of a synthesis of material presented in other sections, although some new information is presented.

The lift-curve slope of typical high-aspect-ratio subsonic aircraft is quite linear up to angles of attack approaching the stall. The lift of the panels is actually linear with angle of attack while the body lift varies as the square of the angle of attack. However, for angles of attack below the stall, the body contribution is small enough so that the lift characteristic of the combination is still sensibly linear. In fact, first-order estimates of lift-curve slope frequently neglect the lift of the body.

When the forward surface has a considerably larger span than the aft surface, the tip vortices shed from the forward panels lie outboard of the aft panels. As a consequence, the integrated effect of the downwash over the aft panel decreases the effectiveness of the aft panel in a linear fashion, and hence the lift-curve slope of the combination still remains linear. This effect is quite constant until the forward panel begins to exhibit flow separation, which distorts the span loading and/or the effective planform. For these types of configurations it is also necessary to assume that the vortex is not fully rolled up (see Paragraph A of Section 4.4.1), and the actual distance between the two surfaces must be taken into account.

When the span of the forward surface is approximately equal to or less than that of the aft surface, the vortex shed from the forward surface interacts directly with the aft surface, generally causing nonlinear lift characteristics at relatively low angle of attack.

A. SUBSONIC

Several methods of estimating the subsonic lift-curve slope of a wing-body-tail combination are available in the Datcom. Two of these methods are presented, differing only in their treatment of the effect of the flow field of the forward surface on the aft surface.

DATCOM METHODS

Method 1

For configurations in which the span of the forward surface is large compared to that of the aft surface, the following approach can be used. For purposes of the Datcom this method is to be used when the ratio of forward- to aft-surface span is 1.5 or greater. The lift-curve slope is given by the equation

$$C_{L_\alpha} = (C_{L_\alpha})'_e [K_N + K_{W(B)} + K_{B(W)}]' \frac{S_e'}{S'} + (C_{L_\alpha})''_e [K_{W(B)} + K_{B(W)}]'' \left(1 - \frac{\partial \bar{\epsilon}}{\partial \alpha}\right) \frac{q''}{q_\infty} \frac{S''}{S'} \frac{S_e''}{S''} \qquad \text{4.5.1.1-a}$$

where

C_{L_α} is the desired lift-curve slope of the wing-body-tail combination.

$(C_{L_\alpha})'_e$ and $(C_{L_\alpha})''_e$ are the lift-curve slopes of the exposed forward and aft surfaces, respectively, from Section 4.1.3.2. (See Section 4.3.1.2 for the definition of exposed surfaces.)

$[K_N + K_{W(B)} + K_{B(W)}]'$ and $[K_{W(B)} + K_{B(W)}]''$ are the appropriate wing-body interference factors from Section 4.3.1.2 for the forward and aft surfaces, respectively.

$\frac{\partial \bar{\epsilon}}{\partial \alpha}$ is the downwash gradient averaged over the aft surface, from Section 4.4.1.

$\frac{q''}{q_\infty}$ is the average dynamic-pressure ratio acting on the aft surface, from Section 4.4.1.

$\frac{S_e'}{S'}$ and $\frac{S_e''}{S''}$ are the ratios of the exposed to gross planform areas of the fore and aft surfaces, respectively.

$\frac{S''}{S'}$ is the ratio of aft to forward gross planform areas.

Equation 4.5.1.1-a is valid only where the aerodynamic parameters are linear. Specifically, the equation is valid for high-aspect-ratio, unswept configurations up to angles of attack approaching the stall. For low-aspect-ratio or swept wings, the applicable angle-of-attack range is considerably less, depending upon the degree of accuracy desired.

Method 2

For configurations in which the spans of the forward and aft surfaces are approximately equal or in which the span of the forward surface is less than that of the aft surface, the following procedure is recommended. The lift-curve slope of the combination is given by the equation

$$C_{L_\alpha} = (C_{L_\alpha})'_e [K_N + K_{W(B)} + K_{B(W)}]' \frac{S_e'}{S'}$$

$$+ (C_{L_\alpha})''_e [K_{W(B)} + K_{B(W)}]'' \frac{q''}{q_\infty} \frac{S''}{S'} \frac{S_e''}{S''} + (C_{L_\alpha})_{W''(V)} \qquad 4.5.1.1\text{-b}$$

where

$$(C_{L_\alpha})_{W''(V)} = \frac{(C_{L_\alpha})'_e \frac{S_e'}{S'} (C_{L_\alpha})''_e \frac{q''}{q_\infty} K_{W(B)}' I_{v_{W'(W'')}} \left(\frac{b''}{2} - \frac{d''}{2}\right)}{2\pi A''_e \left(\frac{b_e'}{2} - \frac{d'}{2}\right)}$$

The parameters in the first two terms on the right-hand side are the same as in equation 4.5.1.1-a. The last term represents the effect of the forward-surface vortices on the aft surface. To obtain the contribution of the last term to the lift-curve slope, refer to Method 3 of Paragraph A in Section 4.4.1. The quantities $(C_{L_\alpha})'_e$ and $(C_{L_\alpha})''_e$ of the last term must be expressed in radians. If the result of this term is desired per degree, the conversion must be applied after the term is evaluated.

Sample Problems

1. Method 1

Given:

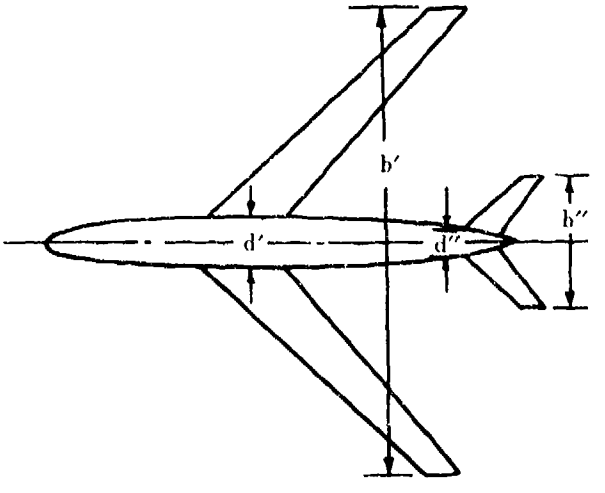

Wing Characteristics:

Total Panel			Exposed Panel
$A' = 8$	$\lambda' = 0.45$		$A'_e = 7.61$
$\Lambda'_{LE} = 46.3°$	$\Lambda'_{c/4} = 45°$	$\Lambda'_{c/2} = 43.6°$	$\lambda'_e = 0.470$
$i' = 0$	$I'' = 0$		

NACA 63A012 airfoil section

$\alpha'_0 = 0$

Horizontal-Tail Characteristics:

Total Panel			Exposed Panel
$A'' = 4$	$\lambda'' = 0.45$		$A''_e = 3.45$
$\Lambda''_{LE} = 47.6°$	$\Lambda''_{c/4} = 45°$	$\Lambda''_{c/2} = 42.2°$	$\lambda''_e = 0.507$
$i'' = 0$	$\gamma = -3.6°$		

NACA 63A012 airfoil section

The following ratios, based on total panel dimensions:

$\frac{b'}{b''} = 3.536$	$\frac{b'}{d'} = 10.0$	$\frac{b''}{d''} = 4.9$
$\frac{2\ell_a}{b'} = 0.954$	$\frac{\ell_a}{b'} = -0.054$	$\frac{\ell_{eff}}{b'} = 0.120$
$\frac{h_H}{b'} = -0.03$	$\frac{x}{c'} = 3.64$	

The following area ratios:

$\frac{S'_e}{S'} = 0.896$	$\frac{S''_e}{S''} = 0.735$	$\frac{S''}{S'} = 0.160$
$\frac{S_{N_{ref}}}{S'_e} = 0.0701$		

Additional characteristics:

$M = 0.19$	$R = 4 \times 10^6$
$\beta = 0.9818$	smooth surfaces

Note: The above parameters are defined in the sections used to calculate C_{L_α}.

Compute:

Step 1. Lift-curve slopes for the exposed wing and exposed horizontal-tail panels

Exposed wing panel (Section 4.1.3.2)

$c_a = 6.30$ per rad (Section 4.1.1.2) $\qquad \kappa = \frac{c_{\ell_\alpha}}{2\pi} = 1.0$

$\frac{\Lambda'_e}{K}\left[\beta^2 + \tan^2 \Lambda'_{c/2}\right]^{1/2} = 10.41$

$\frac{(C_{L_\alpha})'_e}{A'_e} = 0.500$ per rad (Figure 4.1.3.2-49)

$(C_{L_\alpha})'_e = 0.0664$ per deg

Exposed horizontal-tail panel (Section 4.1.3.2)

$c\ell_\alpha = 6.30$ per rad (Section 4.1.1.2) $\qquad \kappa = \frac{c\ell_\alpha}{2\pi} = 1.0$

$\frac{A''_e}{\kappa}[\beta^2 + \tan^2 \Lambda''_{c/2}]^{1/2} = 4.610$

$\frac{(C_{L_\alpha})''_e}{A''_e} = 0.900$ per rad (Figure 4.1.3.2-49)

$(C_{L_\alpha})''_e = 0.0542$ per deg

Step 2. Wing-body and tail-body interference factors (Section 4.3.1.2)

Wing-body

$(C_{L_\alpha})_N = 2.0$ per rad

$K'_N = \frac{(C_{L_\alpha})_N}{(C_{L_\alpha})'_e}\frac{S_{N_{ref}}}{S'_e} = .037$

$K_{W(B)}' = 1.08$

$K_{B(W)}' = .14$ } Figure 4.3.1.2-10 for $\frac{d'}{b'} = .10$

$[K_N + K_{W(B)} + K_{B(W)}]' = 1.257$

Horizontal-tail-body

$K_{W(B)}'' = 1.170$

$K_{B(W)}'' = .290$ } Figure 4.3.1.2-10 for $\frac{d''}{b''} = .204$

$[K_{W(B)} + K_{B(W)}]'' = 1.460$

Step 3. Downwash parameter (Section 4.4.1)

Obtain value at $\alpha = 0°$

$C_L = 0$ $\qquad \frac{\alpha - \alpha_o}{\alpha_{C_{L_{max}}} - \alpha_o} = 0$

$\frac{A'_{eff}}{A'} = 1.0$

$\frac{b'_{eff}}{b'} = 1.0$ } Figure 4.4.1-66

$A'_{eff} = 8$ $\qquad \left(\frac{\partial \epsilon}{\partial \alpha}\right)_\infty = .23$

$\left(\frac{\partial \epsilon}{\partial \alpha}\right)_{\ell} = .3$ } Figure 4.4.1-67

$\Delta y = 2.65$ (Section 2.2.1)

Type of flow separation: trailing-edge separation is predominant (Figure 4.4.1-68a)

$$\frac{a}{b'} = \frac{h_H}{b'} - \frac{\ell_{eff}}{b'}\left(\alpha - \frac{0.41\,C_L}{\pi A'_{eff}}\right) - \frac{b'_{eff}}{2b'}\tan\Gamma^{v} \quad \text{(Equation 4.4.1-c)}$$

$$\frac{a}{b'} = -0.03$$

$$\frac{b_v}{b'} = \frac{b'_{eff}}{b'} \text{ (at } C_L = 0)$$

$$\frac{b_H}{b_v} = \frac{b''}{b_v} = \frac{b''}{b'}\frac{b'}{b_v} = 0.283$$

$$\frac{2a}{b_v} = 2\frac{a}{b'}\frac{b'}{b_v} = -0.06$$

$$\frac{\left(\frac{\partial \bar{\epsilon}}{\partial \alpha}\right)}{\left(\frac{\partial \epsilon}{\partial \alpha}\right)_v} = 1.0 \text{ (Figure 4.4.1-68b)}$$

$$\frac{\partial \bar{\epsilon}}{\partial \alpha} = \frac{\left(\frac{\partial \bar{\epsilon}}{\partial \alpha}\right)}{\left(\frac{\partial \epsilon}{\partial \alpha}\right)_v}\left(\frac{\partial \epsilon}{\partial \alpha}\right)_v = 0.30$$

$$\left(1 - \frac{\partial \epsilon}{\partial \alpha}\right) = 0.70$$

Step 4. Dynamic-pressure ratio at the horizontal tail (Section 4.4.1)

Obtain value at $\alpha = 0°$

$$\epsilon = 0$$

$$(\gamma + \epsilon - \alpha) = -3.6°$$

$$\frac{z}{\bar{c}'} = \frac{x}{\bar{c}'}\tan(\gamma + \epsilon - \alpha) = -0.229 \text{ (Equation 4.4.1-l)}$$

$C_f = 0.00350$ (Figure 4.1.5.1-26)

$$C_{D_0} = C_f\left[1 + L\left(\frac{t}{c}\right) + 100\left(\frac{t}{c}\right)^4\right]R_{L.S.}\frac{S_{wet}}{S_{ref}} \text{ (Equation 4.1.5.1-a)}$$

$$= 0.0088$$

$$\frac{z_w}{\bar{c}'} = .68\sqrt{C_{D_0}\left(\frac{x}{\bar{c}'} + .15\right)} = .124 \text{ (Equation 4.4.1-j)}$$

$$\frac{z}{z_w} = \frac{z/\bar{c}'}{z_w/\bar{c}'} = -1.85$$

Since $\left|\frac{z}{z_w}\right| \geq 1.0$, $\frac{q''}{q_\infty} = 1.0$

Step 5. Solution for C_{L_α} of wing-body-tail combination

$$C_{L_\alpha} = (C_{L_\alpha})'_e\,[K_N + K_{W(B)} + K_{B(W)}]'\frac{S'_e}{S'} + (C_{L_\alpha})''_e\,[K_{W(B)} + K_{B(W)}]''\left(1 - \frac{\partial \epsilon}{\partial \alpha}\right)\frac{q''}{q_\infty}\frac{S''}{S'}\frac{S_e''}{S''}$$

(Equation 4.5.1.1-a)

$C_{L_\alpha} = 0.0748 + 0.0065$

$C_{L_\alpha} = 0.0813$ per deg

2. Method 2

Given:

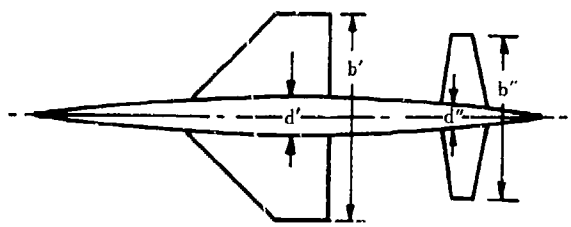

Wing Characteristics:

	Total Panel		Exposed Panel
$A' = 2$	$\lambda' = 0.33$		$A'_e = 1.80$
$\Lambda'_{LE} = 45°$	$\Lambda'_{c/4} = 36.8°$	$\Lambda'_{c/2} = 26.45°$	$\lambda'_e = 0.378$
$i' = 0$	$\Gamma' = 0$		
NACA 0005 airfoil section			
$\alpha_0 = 0$			

Horizontal-Tail Characteristics:

	Total Panel		Exposed Panel
$A'' = 4.4$	$\lambda'' = 0.46$		$A''_e = 3.82$
$\Lambda''_{LE} = 9.46°$	$\Lambda''_{c/4} = 4.74°$	$\Lambda''_{c/2} = 0$	$\lambda''_e = 0.515$
$i'' = 0$	$\gamma = 0$		
NACA 0005 airfoil section			

The following ratios, based on total panel dimensions:

$\frac{b'}{b''} = 1.278$ $\quad \frac{b'}{d'} = 5.25$ $\quad \frac{b''}{d''} = 5.01$

$\frac{x}{c'} = 1.080$

The following area ratios:

$\frac{S'_e}{S'} = 0.730$ $\quad \frac{S''_e}{S''} = 0.741$ $\quad \frac{S''}{S'} = 0.277$

$\frac{S_{N_{ref}}}{S'_e} = 0.0781$

Additional characteristics:

$M = 0.13$	$R_l = 11.4 \times 10^6$
$\beta = 0.9915$	smooth surface

Compute:

The calculation procedures of Method 2 that are similar to those of Method 1 are not listed in detail here. See sample problem 1 for a detailed presentation.

Step 1. Lift-curve slopes for the exposed wing and exposed horizontal-tail panels (Section 4.1.3.2)

$(C_{L_\alpha})_e' = 0.0405$ per deg

$(C_{L_\alpha})_e'' = 0.0667$ per deg

Step 2. Wing-body and tail-body interference factors (Section 4.3.1.2)

Wing-body

$K_N' = 0.067$ $\quad K_{W(B)}' = 1.16$ $\quad K_{B(W)}' = 0.27$

Tail-body

$K_{W(B)}'' = 1.17$ $\quad K_{B(W)}'' = 0.28$

Step 3. Dynamic-pressure ratio at the horizontal tail (Section 4.4.1)

Obtain at $\alpha = 0$

$$\frac{q''}{q_\infty} = 0.859$$

Step 4. Lift-curve slope of tail section due to wing vortices

$$(C_{L_\alpha})_e' \frac{S_e'}{S'} = .0405\ (.730) = 0.0296 \text{ per deg}$$

$$= 1.696 \text{ per rad}$$

$$(C_{L_\alpha})_e'' \frac{q''}{q_\infty} = .0667\ (.859) = 0.0574 \text{ per deg}$$

$$= 3.28 \text{ per rad}$$

$K_{W(B)}' = 1.16$ $\quad A_e'' = 3.82$

Tail interference factor, $I_{v_{W'(W'')}}$, at $\alpha = 0$

$I_{v_{W'(W'')}} = -3.0$ (sample problem 3, paragraph A, Section 4.4.1)

$\left.\begin{aligned} \frac{b''}{2} - \frac{d''}{2} &= 88.56 \text{ in.} \\ \frac{b_v'}{2} - \frac{d'}{2} &= 89.87 \text{ in.} \end{aligned}\right\}$ also from above sample problem

$$(C_{L_\alpha})_{W''(v)} = \frac{(C_{L_\alpha})_e' \frac{S_e'}{S'} (C_{L_\alpha})_e'' \frac{q''}{q_\infty} K_{W(B)}' I_{v_{W'(W'')}} \left(\frac{b''}{2} - \frac{d''}{2}\right)}{2\pi A_e'' \left(\frac{b_v'}{2} - \frac{d'}{2}\right)}$$

$$= \frac{1.696\ (3.280)\ (1.16)\ (-3.0)\ (88.56)}{2\pi\ (3.82)\ (89.87)}$$

$$= -0.794 \text{ per rad}$$

$$= -0.0139 \text{ per deg}$$

Step 5. Solution for C_{L_α} of wing-body-tail combination

$$C_{L_\alpha} = (C_{L_\alpha})_e' [K_N + K_{W(B)} + K_{B(W)}]' \frac{S_e'}{S'}$$

$$+ (C_{L_\alpha})_e'' [K_{W(B)} + K_{B(W)}]'' \frac{q''}{q_\infty} \frac{S''}{S'} \frac{S_e''}{S''}$$

$$+ (C_{L_\alpha})_{W''(V)}$$

In the above equation the first term represents the wing contribution, including interference effects, and the last two terms represent the tail contribution, including interference effects.

$$C_{L_\alpha} = .0405\ (1.497)\ (.730) + .0667\ (1.450)\ (.859)\ (.277)\ (.741) + (-.0139)$$

$$= 0.0443 + 0.0171 - 0.0139$$

$$= 0.0443 + 0.0032$$

(wing) (tail)

$$C_{L_\alpha} = 0.0475 \text{ per deg}$$

B. TRANSONIC

The estimation of transonic characteristics is one of the nebulous topics of aerodynamics. Variations in the lift-curve slope with Mach number for wing-body-tail configurations at transonic speeds are determined primarily by the wing characteristics, since body characteristics do not change significantly with Mach number. Also the lift-curve slope (at low angles of attack) of the body is generally small compared to that of the lifting surfaces, so that again the low-angle-of-attack lift characteristics can be approximated by the lift of the panels alone. Refinements can be made by applying theoretically derived wing-body interference parameters such as those presented in Section 4.3.1.2, but the improvement in accuracy is questionable.

DATCOM METHOD

It is recommended that the methods presented in Paragraph A above be applied directly to the transonic speed regime. Care should be taken to estimate the lift-curve slope of the isolated lifting panels at the proper Mach number. The interference factors should be obtained from Paragraph C, Section 4.3.1.2.

C. SUPERSONIC

The procedure for estimating the supersonic lift-curve slope of a wing-body-tail combination is essentially identical to that at subsonic speeds. Several methods are presented that depend upon the general arrangement of the configuration.

DATCOM METHODS

Method 1

For configuration in which the forward surface has a span at least 1.5 times the aft-surface span, the lift-curve slope of the configuration can be estimated by using equation 4.5.1.1-a of paragraph A above. Two methods of estimating the interference "K" factors in this equation are presented in Section 4.3.1.2. Two methods of determining the downwash gradient for this type of configuration at supersonic speeds are presented as Methods 1 and 2 in Section 4.4.1.

Method 2

For configurations in which the span of the forward surface is approximately equal to or less than that of the aft surface, equation 4.5.1.1-b of paragraph A is used. For this type of configuration, the trailing vortices of the forward surface strongly interact with the aft surface, and a special accounting must be taken of this situation. Method 3 of Section 4.4.1, which estimates the contribution of this interaction to aft-panel lift, should therefore be used to evaluate the last term of equation 4.5.1.1-b.

4.5.1.2 WING-BODY-TAIL LIFT IN THE NONLINEAR ANGLE-OF-ATTACK RANGE

The lift of wing-body-tail combinations in the nonlinear angle-of-attack range depends primarily on the characteristics of the isolated components. Although little is known about the mutual aerodynamic interference effects in this range, certain reasonable assumptions can be made. First, the wing lift carryover onto the body and the effect of the body upwash on the wing lift are similar in nature to those of the low-angle-of-attack case. These effects, calculated for low angles of attack by slender-body theory, are presented in Section 4.3.1.2.

The effects of the shed vortices are somewhat more involved. For high-aspect-ratio, unswept subsonic configurations, the flow remains attached over the lifting panels up to angles of attack approaching the stall. For this angle-of-attack range, the aerodynamic lift characteristics are linear and the methods of the previous section are adequate. During the stalling process the flow may separate in an infinite variety of ways – depending upon the details of the wing design – each producing a different flow behind the surface and hence a different lift contribution from the aft panel. At present the stalling range of angles of attack is not covered in the Datcom. It can be assumed that above the stall angle of the forward panel the flow from the forward surface does not interact with the aft surface if the aft surface is not directly in the wake, i.e., $\frac{\partial \epsilon}{\partial \alpha} = 0$. For the purposes of the Datcom the wake of a stalled wing can be taken to be bounded by the lines emanating from the leading and trailing edges of the forward surface in the streamwise direction. For aft panels lying within this stall region, the aft-panel contribution to lift is taken to be zero.

For swept and/or low-aspect-ratio configurations, the trailing vortices are shed at progressively more inboard stations as the angle of attack is increased. The effect appears in the downwash field and hence in the lift generated by the aft panel.

The bodies of these configurations lift in a continuous fashion as a function of angle of attack and do not stall in the normal sense. The nonlinear cross-flow contribution to body lift is sizable at the higher angles (near and beyond stall) and should not be neglected. This cross-flow lift is caused by a pair of body vortices that can also strongly affect the lift contributions from the panels. These effects have been accounted for in the Datcom.

A. SUBSONIC

DATCOM METHOD

The lift of a wing-body-tail combination can be estimated at subsonic speeds by using the following equations*:

$$\text{For } \frac{b'}{b''} \geqq 1.5: \quad C_N = \left\{ (C_{N_1}')_o' [K_N + K_{W(B)} + K_{B(W)}]' + (C_{N_2}')_o' [k_{W(B)} + k_{B(W)}]' \right\} \frac{S_o'}{S'}$$

$$+ \left\{ (C_{N_1}')_o'' [K_{W(B)} + K_{B(W)}]'' + (C_{N_2}')_o'' [k_{W(B)} + k_{(B)W}]'' \right\} \frac{q''}{q_\infty} \frac{S_o''}{S'}$$

$$+ I_{r_{B(W')}} \left(\frac{\Gamma}{2\pi a V_r} \right)' \frac{r'}{b_W'/2} \left| \frac{q'}{q_\infty} (C_{L_\alpha})' \alpha' + I_{r_{B(W'')}} \left(\frac{\Gamma}{2\pi a V_r} \right)'' \frac{r''}{b_W''/2} \frac{S''}{S'} \frac{q''}{q_\infty} (C_{L_\alpha})'' \alpha'' \right.$$

4.5.1.2-a

*Note: The limits suggested for b'/b" are quite flexible, depending upon the configuration details and the degree of accuracy desired.

For $\frac{b'}{b''} < 1.5$:

$$C_N = \left\{(C'_{N_1})'_e [K_N + K_{W(B)} + K_{B(W)}]' + (C'_{N_2})'_e [k_{W(B)} + k_{B(W)}]'\right\} \frac{S'_e}{S'}$$

$$+ \left\{(C'_{N_1})''_e [K_{W(B)} + K_{B(W)}]'' + (C'_{N_2})''_e [k_{W(B)} + k_{B(W)}]''\right\} \frac{q''}{q_\infty} \frac{S''_e}{S'}$$

$$+ \frac{(C_{L_\alpha})'_e \frac{S'_e}{S'} (C_{L_\alpha})''_e \frac{q''}{q_\infty} K_{W(B)'} \alpha I_{v_{W'(W'')}} \left(\frac{b''}{2} - \frac{d''}{2}\right)}{2\pi A''_e \left(\frac{b'_v}{2} - \frac{d'}{2}\right) \cos \alpha}$$

$$+ I_{v_{B(W'')}} \left(\frac{\Gamma}{2\pi \alpha Vr}\right)' \frac{r'}{b_{W'}/2} \left| \frac{q'}{q_\infty} (C_{L_\alpha})' \alpha' + I_{vB(W'')} \left(\frac{\Gamma}{2\pi \alpha Vr}\right)'' \frac{r''}{b_{W''}/2} \frac{S''}{S'} \frac{q''}{q_\infty} (C_{L_\alpha})'' \alpha'' \right.$$

4.5.1.2-b

where the primed quantities refer to the forward panel, the double-primed quantities refer to the aft panel, and the subscript e refers to the exposed panel.

$(C'_{N_1})'_e$ is the pseudonormal-force coefficient of the exposed forward panel calculated at the wing angle $\alpha - \alpha'_0$ where α is the angle of attack of the body reference line and α'_0 is the angle, negative in sign, measured from the wing chord line at the MAC to the wing zero-lift line. The value of $(C'_{N_1})'_e$ is obtained from Section 4.1.3.3. (See Section 4.3.1.2 for the definition of exposed panels.)

$(C'_{N_2})'_e$ is the pseudonormal-force coefficient of the exposed forward panel calculated at the wing angle of incidence i' from Section 4.1.3.3. $\left[(C'_{N_2})'_e = 0 \text{ for } i' = 0.\right]$

$(C'_{N_1})''_e$ is the pseudonormal-force coefficient of the exposed aft panel calculated from Section 4.1.3.3 at the angle $\alpha - \epsilon$ for $\frac{b'}{b''} \geq 1.5$ and at α for $\frac{b'}{b''} < 1.5$. The downwash angle ϵ is obtained from Section 4.4.1.

$(C'_{N_2})''_e$ is the pseudonormal-force coefficient of the exposed aft panel calculated from Section 4.1.3.3 at the aft-surface incidence angle i''. $\left[(C'_{N_2})''_e = 0 \text{ for } i'' = 0.\right]$

$(C_{L_\alpha})'_e$ and $(C_{L_\alpha})''_e$ are the lift-curve slopes of the exposed forward and aft panels, respectively, from Section 4.1.3.2.

$(C_{L_\alpha})'$ and $(C_{L_\alpha})''$ are the lift-curve slopes of the forward and aft panels, respectively, from Section 4.1.3.2.

K_N, $K_{W(B)}$, $K_{B(W)}$, $k_{W(B)}$, and $k_{B(W)}$ are the aerodynamic interference factors from Section 4.3.1.2.

$\left[\frac{\Gamma_B}{2\pi Vr\alpha}\right]'$ and $\left[\frac{\Gamma_B}{2\pi Vr\alpha}\right]''$ are nondimensional vortex strenths obtained from Section 4.3.1.3.

$I_{v_{B(W')}}$, $I_{v_{B(W'')}}$, and $I_{v_{W'(W'')}}$ are the vortex interference factors between vehicle components. The values

$I_{v_{B(W')}}$ and $I_{v_{B(W'')}}$ are obtained from Section 4.3.1.3 and $I_{v_{W'(W'')}}$ is obtained from Section 4.4.1.

$\frac{r'}{b'}$ and $\frac{r''}{b''}$ are the ratios of the body radii at the midpoint of the exposed root chord to the total spans of the forward and aft panels, respectively.

α'' is the angle of attack of the aft panel, $\alpha - \epsilon + i''$, where ϵ is obtained from Section 4.4.1.

b'_v is the lateral position of the forward-surface vortex from Section 4.4.1.

$\frac{q''}{q_\infty}$ is the dynamic-pressure ratio due to the forward panel acting on the aft panel. This value is obtained from Section 4.4.1. The value of $\frac{q}{q_\infty}$ is almost always taken to be 1.0.

For configurations in which the body is relatively small compared to the span of the panels, the terms involving $I_{v_{B(W')}}$ and $I_{v_{B(W'')}}$ in equations 4.5.1.2-a and 4.5.1.2-b can be neglected. For purposes of the Datcom these terms are neglected when $b'/(2r)$ or $b''/(2r) \geq 3.0$ (care should be taken to evaluate the coefficients at the proper angles of attack and incidence).

Sample Problems

1. The span of the forward panel is large compared to that of the aft panel ($b'/b'' \geq 1.5$).

Given: Configuration of sample problem 1, paragraph A, Section 4.5.1.1.

Compute:

Step 1. $(C'_{N_1})'_e$ and $(C'_{N_2})'_e$ (Section 4.1.3.3)

From sample problem 1, paragraph A, Section 4.5.1.1

$\alpha'_0 = 0$ $\qquad (C_{L_\alpha})'_e = 0.0664$ per deg $= 3.805$ per rad

$\Delta y = 2.65$

Obtain $(C_{L_{max}})'_e$ and $(\alpha_{C_{L_{max}}})'_e$ (Section 4.1.3.4)

Test for method most applicable

$C_1 = 0.32$ (figure 4.1.3.4-24b)

$$\frac{4}{(C_1 + 1)\cos \Lambda'_{LE}} = 4.386$$

Since $A'_e = 7.61 > 4.386$, use high-aspect-ratio method

$\left(\frac{C_{L_{max}}}{c\ell_{max}}\right)'_e = 0.68$ (figure 4.1.3.4-21a)

$(c\ell_{max})'_e = 1.45$ (Section 4.1.1.4)

$(\Delta C_{L_{max}})'_e = 0$ (figure 4.1.3.4-22)

$(\Delta\alpha_{C_{L_{max}}})'_e = 5.7°$ (figure 4.1.3.4-21b)

$$(C_{L_{max}})'_e = \left[\left(\frac{C_{L_{max}}}{c\ell_{max}}\right) c\ell_{max} + \Delta C_{L_{max}}\right]'_e = 0.986 \quad \text{(equation 4.1.3.4-d)}$$

$$(\alpha_{C_{L_{max}}})'_e = \left[\frac{C_{L_{max}}}{C_{L_\alpha}} + \alpha_0 + \Delta\alpha_{C_{L_{max}}}\right]'_e = 20.5° \quad \text{(equation 4.1.3.4-e)}$$

Obtain $(\alpha^*)'$ (Section 4.1.1)

$(\alpha^*)' = 10°$

Construct curve of $(C_L)'_e$ vs α

$(C_L)'_e = (C_{L_\alpha})'_e \alpha$ for α's below $(\alpha^*)'$

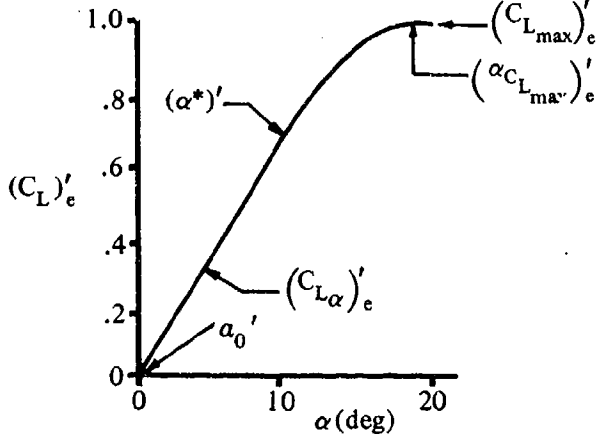

From constructed curve, obtain $(C_{N_1})'_e$, substituting the wing angle $\alpha - \alpha_0'$ for α.

$\alpha - \alpha_0' = \alpha - 0 = \alpha$

① α deg	② $\alpha - \alpha_0'$ deg	③ $(C_L)'_e$ at ②	④ $(C_{N_1})'_e = (C_L)'_e/\cos$ ②
0	0	0	0
5	5	.332	.333
10	10	.664	.674
15	15	.915	.947
20.5	20.5	.986	1.053

$(C_{N_2})'_e = 0$, since $i' = 0$

Step 2. Downwash angle at horizontal tail (Section 4.4.1). Sample problem 1, paragraph A, Section 4.5.1.1, has the procedure briefly outlined and sample problem 1, paragraph A, Section 4.4.1, is a detailed example.

The final result is shown below.

α deg	ϵ deg	$\alpha - \epsilon$ deg
0	0	0
5	1.5	3.5
10	2.9	7.1
15	4.9	10.1
20.5	8.0	12.5

Step 3. $(C'_{N_1})''_e$ and $(C'_{N_2})''_e$ (Section 4.1.3.3)

Test for method most applicable (Section 4.1.3.4)

$C_1 = 0.32$ (figure 4.1.3.4-24b)

$$\frac{4}{(C_1 + 1)\cos \Lambda''_{LE}} = 4.494; \quad \frac{3}{(C_1 + 1)\cos \Lambda''_{LE}} = 3.370$$

$A''_e = 3.45$, which lies between the above limits.

Borderline case: use low-aspect-ratio method

$(C_{N_\alpha})''_e = (C_{L_\alpha})''_e = 0.0542$ per deg $= 3.106$ per rad (sample problem 1, paragraph A, Section 4.5.1.1)

Obtain $(C_{L_{max}})''_e$ and $(\alpha_{C_{L_{max}}})''_e$

$$(C_1 + 1)\frac{A''_e}{\beta}\cos \Lambda''_{LE} = 3.13$$

$$\left[(C_{L_{max}})_{base}\right]''_e = 0.80 \text{ (figure 4.1.3.4-23a)}$$

$C_2 = 1.05$ (figure 4.1.3.4-24b)

$(C_2 + 1)\, A''_e \tan \Lambda''_{LE} = 7.75$

$(\Delta C_{L_{max}})''_e = 0.22$ (figure 4.1.3.4-25a)

$$\left[(\alpha_{C_{L_{max}}})_{base}\right]''_e = 22° \text{ (figure 4.1.3.4-25a)}$$

$(\Delta\alpha_{C_{L_{max}}})''_e = 4°$ (figure 4.1.3.4-25b)

$(C_{L_{max}})''_e = [(C_{L_{max}})_{base} + \Delta C_{L_{max}}]''_e = 1.02$ (equation 4.1.3.4-g)

$(\alpha_{C_{L_{max}}})''_e = [(\alpha_{C_{L_{max}}})_{base} + \Delta\alpha_{C_{L_{max}}}]''_e = 26°$ (equation 4.1.3.4-h)

Obtain $[(C_{N_{\alpha\alpha}})_{ref}]''_e$

$$\left[C_{N'} @ C_{L_{max}}\right]''_e = \left(\frac{C_{L_{max}}}{\cos \alpha_{C_{L_{max}}}}\right)''_e = 1.13$$

$$[(C_{N_{\alpha\alpha}})_{ref}]''_e = \frac{\left[C_{N'} @ C_{L_{max}}\right]''_e - (C_{N_\alpha})''_e \frac{\sin 2\alpha}{2}}{\sin \alpha \,|\sin \alpha|} = -0.292 \text{ (equation 4.1.3.3-b, } (C_{N_\alpha})''_e \text{ in rad)}$$

where $\alpha = (\alpha_{C_{L_{max}}})''_e$

Obtain J

$$J = 0.3\,(C_1 + 1)\frac{A''_e}{\beta}\cos \Lambda''_{LE}\left\{(C_1 + 1)\,(C_2 + 1) - \left[\frac{(C_2 + 1)\, A''_e \tan \Lambda''_{LE}}{7}\right]^3\right\} = 1.27$$

Calculate $(C'_{N_1})''_e$ vs α'' (equation 4.1.3.3-a)

① α'' deg	③ $\frac{\tan \alpha''}{\tan (\alpha_{C_{L_{max}}})''_e}$	⑧ $(\Delta C_{N_{\alpha\alpha}})''_e$ figure 4.1.3.3-55a	④ $(C_{N_{\alpha\alpha}})''_e$ $= [(C_{N_{\alpha\alpha}})_{ref} + \Delta C_{N_{\alpha\alpha}}]''_e$	⑤ $(C_{N_{\alpha\alpha}})''_e \sin^2\alpha''$ $= ④ \sin^2\alpha''$	⑥ $(C_{N_\alpha})''_e \frac{\sin 2\alpha''}{2}$ $= 3.106 \frac{\sin 2\alpha''}{2}$	⑦ $(C'_{N_1})''_e$ $= ⑤ + ⑥$
5	.179	1.85	1.558	0.0118	.269	0.281
10	.361	1.85	1.558	0.0468	.531	0.578
15	.550	1.50	1.208	0.081	.777	0.858
20.5	.767	0.75	0.458	0.056	1.019	1.075

Plot $(C'_{N_1})''_e$ vs α and read values at $\alpha - \epsilon$ (since $b'/b'' > 1.5$)

α deg	α'' $(\alpha - \epsilon)$	$(C'_{N_1})''_e$
5	3.5	0.195
10	7.1	0.408
15	10.1	0.583
20.5	12.5	0.720

$(C'_{N_2})''_e = 0$, since $i'' = 0$

Step 4. Wing-body and tail-body interference factors (Section 4.3.1.2)

From sample problem 1, paragraph A, Section 4.5.1.1

$[K_N + K_{W(B)} + K_{B(W)}]' = 1.257$

$[K_{W(B)} + K_{B(W)}]'' = 1.460$

Step 5. Dynamic pressure at horizontal tail (Section 4.4.1)

Sample problem 1, paragraph A, Section 4.5.1.1, has the procedure briefly outlined and sample problem 4, paragraph A, Section 4.4.1, is a detailed example.

The final result is shown below.

$\frac{q''}{q_\infty} = 1.0$ for all α's

(since $\left|\frac{z}{z_W}\right| > 1.0$ for all α's)

Step 6. Vortices effect (Section 4.3.1.3)

$$\frac{b'}{d'} = 10 \qquad \frac{b''}{d''} = 4.9$$

Since these ratios are both greater than 3.0, the vortices effect can be neglected.

$I_{v_{B(W')}} = I_{v_{B(W'')}} = 0$

Step 7. Solution for C_N vs α

$$C_N = \left\{(C'_{N_1})'_e [K_N + K_{W(B)} + K_{B(W)}]' + (C'_{N_2})'_e [k_{W(B)} + k_{B(W)}]'\right\} \frac{S_e'}{S'}$$
$$+ \left\{(C'_{N_1})''_e [K_{W(B)} + K_{B(W)}]'' + (C_{N_2})''_e [k_{W(B)} + k_{B(W)}]''\right\} \frac{q''}{q_\infty} \frac{S_e''}{S'}$$

(equation 4.5.1.2-a simplified)

$C_N = (C'_{N_1})'_e (1.257)(.896) + (C'_{N_1})''_e (1.460)(1.0)(.118)$

$= 1.126 (C'_{N_1})'_e + .1723 (C'_{N_1})''_e$

①	②	③	④	⑤	⑥
α deg	$(C'_{N_1})'_e$	$(C'_{N_1})''_e$	$1.126 (C'_{N_1})'_e$	$.1723 (C'_{N_1})''_e$	$C_N = ④ + ⑤$
0	0	0	0	0	0
5	0.333	0.195	0.375	0.0336	0.4086
10	0.674	0.408	0.759	0.0705	0.8295
15	0.947	0.583	1.066	0.1000	1.166
20.5	1.053	0.720	1.186	0.1240	1.310

2. The span of the forward panel is approximately equal to or less than the span of the aft panel ($b'/b'' < 1.5$).

Given: Configuration of sample problem 2, paragraph A, Section 4.5.1.1.

Compute:

The calculation procedures of sample problem 2 that are similar to those of sample problem 1 are not listed in detail here.

Step 1. $(C'_{N_1})'_\ell$ and $(C'_{N_2})'_\ell$ (Section 4.1.3.3)

The low-aspect-ratio method is used to calculate $(C'_{N_1})'_\ell$.

$(C_{L_{max}})'_\ell = 0.935$ $\qquad$ $(\alpha_{C_{L_{max}}})'_\ell = 26.0°$

$(C_{N_\alpha})'_\ell = 0.0405$ per deg $= 2.32$ per rad $\qquad$ $[(C_{N_{\alpha\alpha}})_{ref}]'_\ell = 0.655$ per rad

$J = 1.60$ $\qquad$ $[C'_N @ C_{L_{max}}]'_\ell = 1.04$

$$(C'_{N_1})'_\ell = (C_{N_\alpha})'_\ell \frac{\sin 2\alpha}{2} + (C_{N_{\alpha\alpha}})'_\ell \sin\alpha \,|\sin\alpha| \quad \text{(equation 4.1.3.3-a)}$$

①	②	③	④	⑤	⑥	⑦
α deg	$\frac{\tan\alpha}{\tan(\alpha_{C_{L_{max}}})'_\ell}$	$(\Delta C_{N_{\alpha\alpha}})'_\ell$ figure 4.1.3.3-55a	$(C_{N_{\alpha\alpha}})'_\ell = [(C_{N_{\alpha\alpha}})_{ref} + \Delta C_{N_{\alpha\alpha}}]'_\ell$	$(C_{N_{\alpha\alpha}})'_\ell \sin^2\alpha$	$(C_{N_\alpha})'_\ell \frac{\sin 2\alpha}{2}$	$(C'_{N_1})'_\ell = ⑤ + ⑥$
5	.179	2.10	2.755	.021	.202	.223
10	.361	2.10	2.755	.083	.397	.480
15	.549	1.80	2.455	.164	.580	.744
20	.746	1.00	1.655	.194	.746	.940
23	.870	.50	1.155	.176	.835	1.011
26	1.0	0	.655	.126	.914	1.040

$(C'_{N_2})'_\ell = 0$, since $i' = 0$

Step 2. $(C'_{N_1})''_\ell$ and $(C'_{N_2})''_\ell$ (Section 4.1.3.4)

Since $\frac{b'}{b''} < 1.5$, evaluate $(C'_{N_1})''_\ell$ at α.

From low-aspect-ratio method, the following is obtained.

$(C_{L_{max}})''_\ell = 0.705$ $\qquad$ $(\alpha_{C_{L_{max}}})''_\ell = 14.5°$

Since $(\alpha_{C_{L_{max}}})''_\ell$ is considerably lower than $(\alpha_{C_{L_{max}}})'_\ell$, the solution for $(C'_{N_1})''_\ell$ must include both below-stall and above-stall calculations. The final result is listed below.

α deg	$(C'_{N_1})''_\ell$
5	.330
10	.625
15	.749
20	.738
23	.767
26	.824

Because of the limitation of the method, the accuracy deteriorates at high angles of attack. Calculate the remaining portion of the solution at $\alpha \leqq 20°$.

$$(C'_{N_2})''_e = 0, \text{ since } i'' = 0$$

Step 3. Wing-body and tail-body interference factors (Section 4.3.1.2)

From sample problem 2, paragraph A, Section 4.5.1.1

$$[K_N + K_{W(B)} + K_{B(W)}]' = 1.497$$

$$[K_{W(B)} + K_{(B)W}]'' = 1.450$$

Step 4. Dynamic pressures at horizontal tail

From the methods of Section 4.4.1 the following is obtained.

α deg	$\frac{q''}{q_\infty}$
0	.859
5	.937
10	.999
15	1.0
20	1.0

Step 5. Vortices effect

$$\frac{b'}{d'} = 5.25 \qquad \frac{b''}{d''} = 5.01$$

Since these ratios are both greater than 3.0, the terms involving $I_{v_{B(W')}}$ and $I_{v_{B(W'')}}$ can be neglected.

Calculate lift of tail due to wing vortices.

From sample problem 2, paragraph A, Section 4.5.1.1

$$(C_{L_\alpha})'_e \frac{S_e'}{S'} = 1.696 \text{ per rad}$$

$$(C_{L_\alpha})''_e \frac{q''}{q_\infty} = 3.28 \text{ per rad (at } \alpha = 0)$$

$$\text{Therefore } (C_{L_\alpha})''_e \frac{q''}{q_\infty} = 3.82 \frac{q''}{q_\infty} \text{ per rad}$$

$$K_{W(B)'} = 1.16$$

$$\frac{\frac{b''}{2} - \frac{d''}{2}}{2\pi A''_e \left(\frac{b_v'}{2} - \frac{d'}{2}\right)} = 0.04106$$

$$C_{L_{W''(v)}} = \frac{(C_{L_\alpha})'_e \frac{S_e'}{S'} (C_{L_\alpha})''_e \frac{q''}{q_\infty} K_{W(B)'} \alpha I_{v_{W'(W'')}} \left(\frac{b''}{2} - \frac{d''}{2}\right)}{2\pi A''_e \left(\frac{b_v'}{2} - \frac{d'}{2}\right)}$$

$$= 1.696 \left(3.82 \frac{q''}{q_\infty}\right) (1.16)\ (0.04106)\ \alpha I_{v_{W'(W'')}}$$

$$= 0.308 \frac{q''}{q_\infty} \alpha I_{v_{W'(W'')}} \ (\alpha \text{ in radians})$$

The variation of $I_{v_{W'(W'')}}$ with α has been calculated in sample problem 3, paragraph A, Section 4.4.1 and is not repeated here.

① α deg	② α rad	③ $I_{v_{W'(W'')}}$	④ $C_{L_{W''(v)}} = 0.308 \frac{q''}{q_\infty}$ ② ③	⑤ $C_{N_{W''(v)}} =$ ④/cos α
0	0	--3.0	0	0
5	0.08725	−2.5	−0.063	−0.063
10	0.1745	−2.0	−0.108	−0.110
15	0.2618	−1.68	−0.135	−0.140
20	0.3490	−1.40	−0.150	−0.160

Step 6. Solution for C_N vs α

$$C_N = \left\{(C_{N_1})'_e [K_N + K_{W(B)} + K_{B(W)}]' + (C'_{N_2})'_e [k_{W(B)} + k_{B(W)}]'\right\} \frac{S'_e}{S'}$$

$$+ \left\{(C'_{N_1})''_e [K_{W(B)} + K_{B(W)}]'' + (C'_{N_2})''_e [k_{W(B)} + k_{B(W)}]''\right\} \frac{q''}{q_\infty} \frac{S''_e}{S'}$$

$$+ C_{N_{W''(v)}} \quad \text{(equation 4.5.1.2-b simplified)}$$

Substituting the constants gives

$$C_N = (C'_{N_1})'_e (1.497)\ (.730) + (C'_{N_1})''_e (1.450) \frac{q''}{q_\infty} (.205) + C_{N_{W''(v)}}$$

$$= 1.093\ (C'_{N_1})'_e + .2973\ (C'_{N_1})''_e \frac{q''}{q_\infty} + C_{N_{W''(v)}}$$

① α deg	② $(C'_{N_1})'_e$	③ $(C'_{N_1})''_e$	④ $\frac{q''}{q_\infty}$	⑤ 1.093 $(C'_{N_1})'_e$	⑥ .2973 $(C'_{N_1})''_e \frac{q''}{q_\infty}$	⑦ $C_{N_{W''(v)}}$	⑧ C_N ⑤ + ⑥ + ⑦
0	0	0	.859	0	0	0	0
5	.223	.330	.937	.244	.092	−0.063	0.265
10	.480	.625	.999	.525	.186	−0.110	0.601
15	.744	.749	1.0	.813	.223	−0.140	0.896
20	.940	.738	1.0	1.027	.219	−0.160	1.086

B. TRANSONIC

At present it is not possible to predict the aerodynamic characteristics of wing-body-tail combinations in the nonlinear angle-of-attack range. However, it is anticipated that the interference effects can be large.

DATCOM METHOD

It is recommended that the equations presented in paragraph A above be applied throughout the transonic speed range. Care should be exercised to evaluate the various terms of these equations at the proper Mach number. The interference k factors are most accurate for slender configurations. The 'vortex

terms $I_{v_{B(W')}}$, etc., are thought to be quite valid. But the characteristics of the isolated panels and the downwash cannot be determined as accurately.

C. SUPERSONIC

At supersonic speeds the direct influence of the wing shock-expansion field on the horizontal tail must be considered, as well as the effects of wing vortices and body vortices considered in the subsonic method of paragraph A. The introductory discussion pertaining to body-vortex and wing-vortex effects applies equally as well at subsonic and supersonic speeds.

In cases for which the wing shock-expansion effects are important, account can be taken of the downwash angle, dynamic pressure, and Mach number at the tail by direct application of shock-expansion theory. It is assumed that the flow in the region of the horizontal tail is the two-dimensional shock-expansion field radiating from the exposed root chord of the wing (see sketch (a)). Any effects of wing-body interference or wing section in distorting the shock-expansion field are neglected. This assumption is valid only if the span of the forward surface is greater than the span of the aft surface; i.e., $b' > b''$.

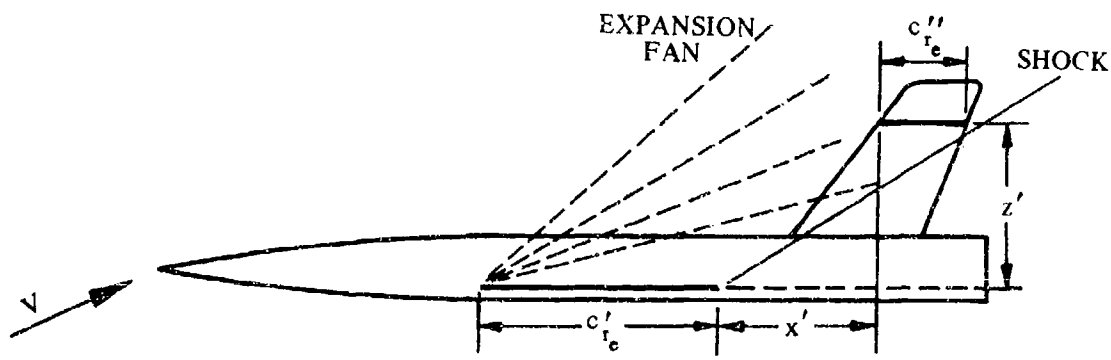

SKETCH (a)

The tail in sketch (a) is in a high downwash field so that the flow at the tail is nearly parallel to the tail chord. As the angle of attack is increased, the tail will move downward with respect to the trailing-edge shock wave, out of the shock-expansion field and into a region of lower downwash. If the tail were initially above the expansion fan from the wing leading edge, an increase in angle of attack would move the tail into the shock-expansion field and, consequently, into a region of increased downwash. It is seen then that the wing shock-expansion field can cause either an increase or a decrease in the tail download in contrast to body vortices and wing vortices, which cause only an increase in tail download.

DATCOM METHOD

The lift of a wing-body-tail combination in the nonlinear angle-of-attack range at supersonic speeds is approximated by using the subsonic method (paragraph A) minus the second term on the right-hand side of the equation,which accounts for the horizontal tail effects, plus an additional term to account for the direct influence of the wing shock-expansion field on the horizontal tail. The influence of the shock-expansion field may be evaluated only for configurations with $b' > b''$. Furthermore, the shock-expansion term presented in the Datcom is applicable only to configurations with neither wing nor tail incidence. In using the method of paragraph A, care should be taken to evaluate all parameters at the proper Mach number.

It should be noted that if the tail is in the wing shock-expansion field, it cannot "see" the wing trailing vortices. In this case, the contribution of the wing-vortex interference (third term of equation 4.5.1.2-b) is

neglected. If, however, the tail is behind the wing shock-expansion field, it can "see" the wing trailing vortices and the wing-vortex interference should be considered rather than the shock-expansion field.

The shock-expansion term for configurations with neither wing nor tail incidence, taken from reference 1*, is

$$\left(\Delta C_L\right)_{SE} = \eta_\alpha \frac{S''}{S'} \alpha C''_{L_\alpha} \qquad 4.5.1.2\text{-c}$$

where all terms except η_α are defined in the subsonic paragraph.

η_α is a "lumped" angle-of-attack effectiveness parameter obtained from figures 4.5.1.2-13a through 4.5.1.2-13p for combinations of angle of attack of 5°, 10°, 15°, and 20° and Mach numbers of 2, 3, 4, and 5. η_α accounts for the change in dynamic pressure at the tail, the change in the tail lift-curve slope, and the downwash at the tail, and is defined as

$$\eta_\alpha = \frac{q''}{q_\infty}\left(1 - \frac{\epsilon}{\alpha}\right)\frac{\left(C''_{L_\alpha}\right)_{M_H}}{\left(C''_{L_\alpha}\right)_{M_\infty}}$$

where

$\left(C''_{L_\alpha}\right)_{M_H}$ is the lift-curve slope of the horizontal tail operating at the local Mach number of the flow in the region of the horizontal tail.

$\left(C''_{L_\alpha}\right)_{M_\infty}$ is the lift-curve slope of the isolated horizontal tail at the free-stream Mach number.

The procedure for using figure 4.5.1.2-13 is as follows:

Step 1. Determine the exposed-wing root chord c_{r_e}' and the exposed-tail root chord c_{r_e}''.

Step 2. Determine the longitudinal distance x' from the trailing edge of the exposed-wing root chord to the leading edge of the exposed-tail root chord, positive for the leading edge of the exposed-tail root chord aft of the trailing edge of the exposed-wing root chord (see sketch (a)).

Step 3. Determine the vertical distance z', measured normal to the longitudinal axis, between the exposed-wing root chord and the exposed-tail root chord, positive for the tail plane above the wing plane (see sketch (a)).

Step 4. Calculate x'/c_{r_e}' and z'/c_{r_e}', and by using these parameters locate the exposed-tail root chord c_{r_e}'' in the proper influence zone of the shock-expansion field of figure 4.5.1.2-13.

*In reference 1, the case of a configuration with tail incidence is analyzed. The shock-expansion term is given by

$$(\Delta C_L)_{SE} = C''_{L_\alpha}\alpha \frac{S''}{S'}\left(\eta_\alpha + \frac{i_W}{\alpha_W}\eta_\delta\right)$$

where η_δ is the tail-incidence effectiveness parameter. Unfortunately, no design charts are available for determining η_δ.

Step 5. The exposed-tail root chord will be divided into several segments by the shock-expansion field. It is assumed that the average value of η_α in the various influence zones is uniform over the tail area within that zone. The average value of η_α in each zone is then multiplied by the ratio of the tail area in that zone to the total exposed tail area S_e' to obtain a weighted value in each zone.

Step 6. Sum the weighted values of η_{l_α} to obtain the total "lumped" effectiveness parameter η_α.

Step 7. Interpolation for angle of attack and/or Mach number may be necessary. If so, a three-point interpolation for α should be made using weighted values of η_α. Two points are sufficient for Mach number interpolation.

For a specified initial Mach number there is a maximum value of the angle of attack for which there exists an oblique-shock solution. Or, conversely, for a specified angle of attack there is a minimum initial Mach number for which there is an oblique-shock solution. The relation between Mach number and angle of attack, below which no solutions for η_α may be obtained, is indicated in sketch (b).

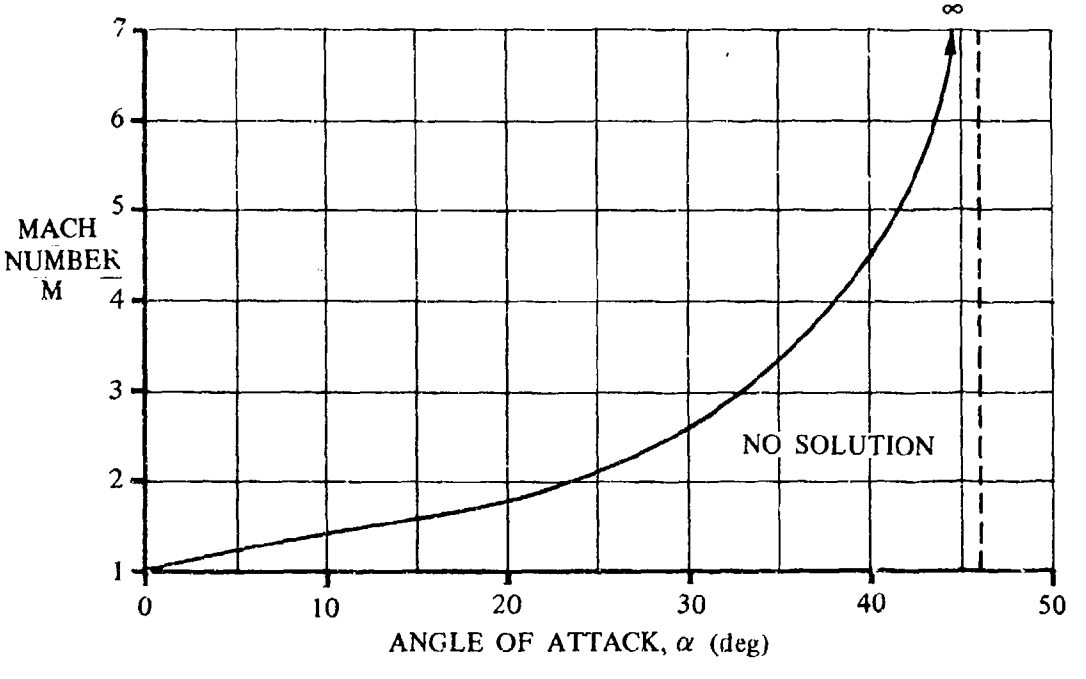

SKETCH (b)

REFERENCES

1. Nielsen, J. N.: The Effect of Body Vortices and the Wing Shock-Expansion Field on the Pitch-Up Characteristics of Supersonic Airplanes. NACA RM A57L23, 1958. (U)

2. Ames Research Staff: Equations, Tables, and Charts for Compressible Flow. NACA TR 1135, 1953. (U)

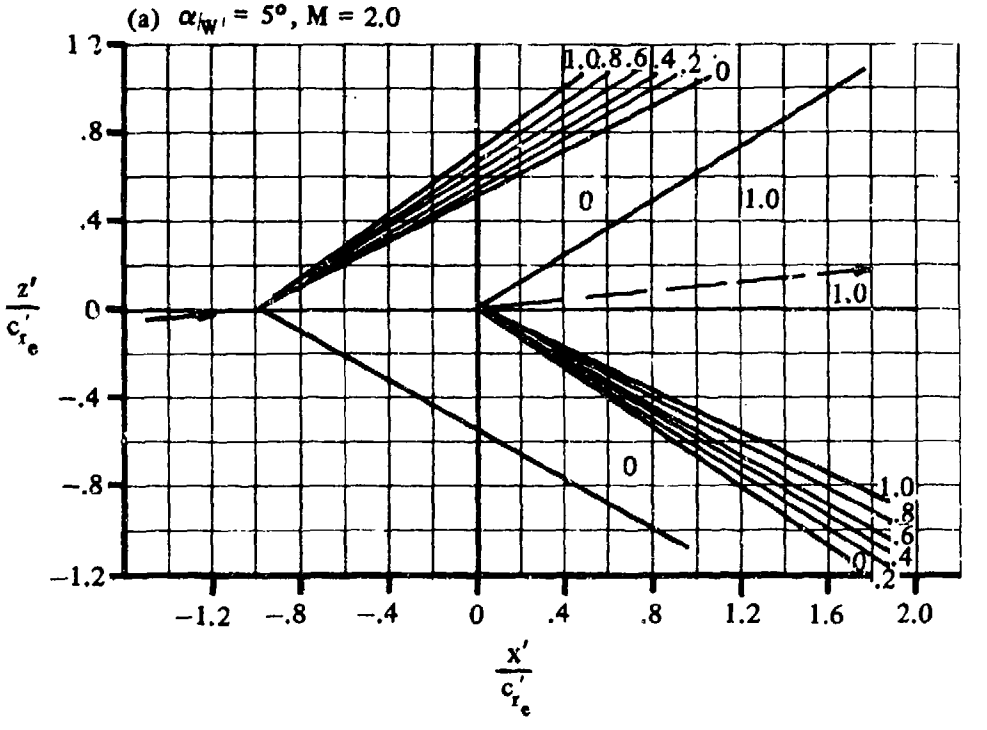

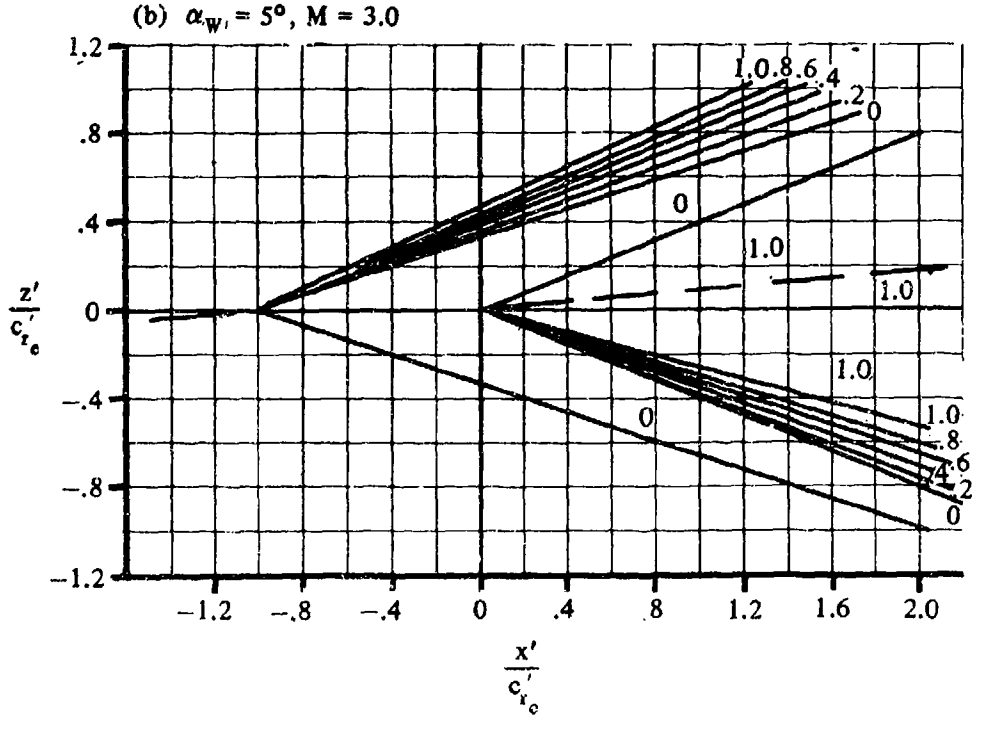

FIGURE 4.5.1.2-13 TAIL-EFFECTIVENESS PARAMETER, η_α

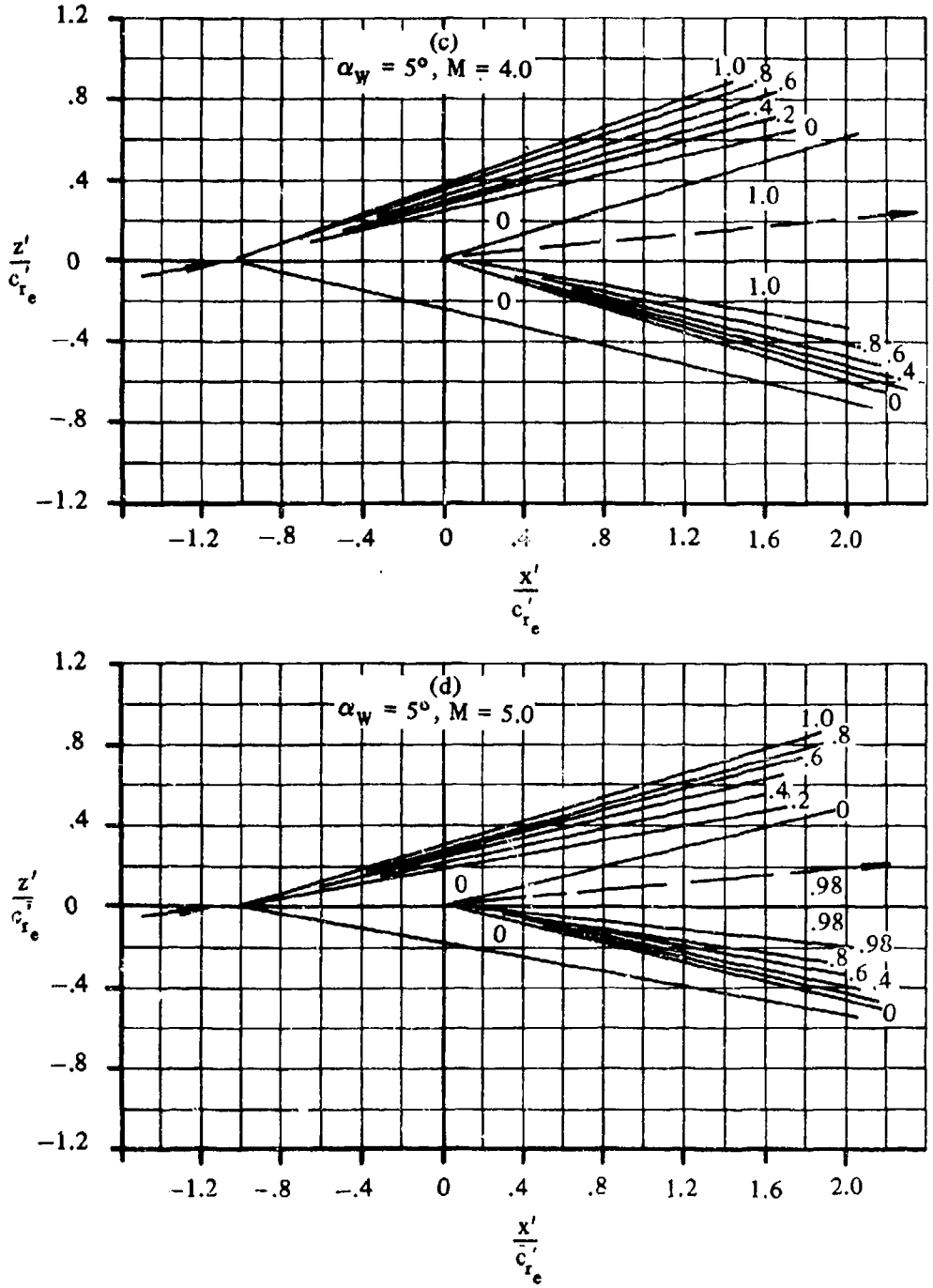

FIGURE 4.5.1.2-13 TAIL-EFFECTIVENESS PARAMETER, η_α (CONTD)

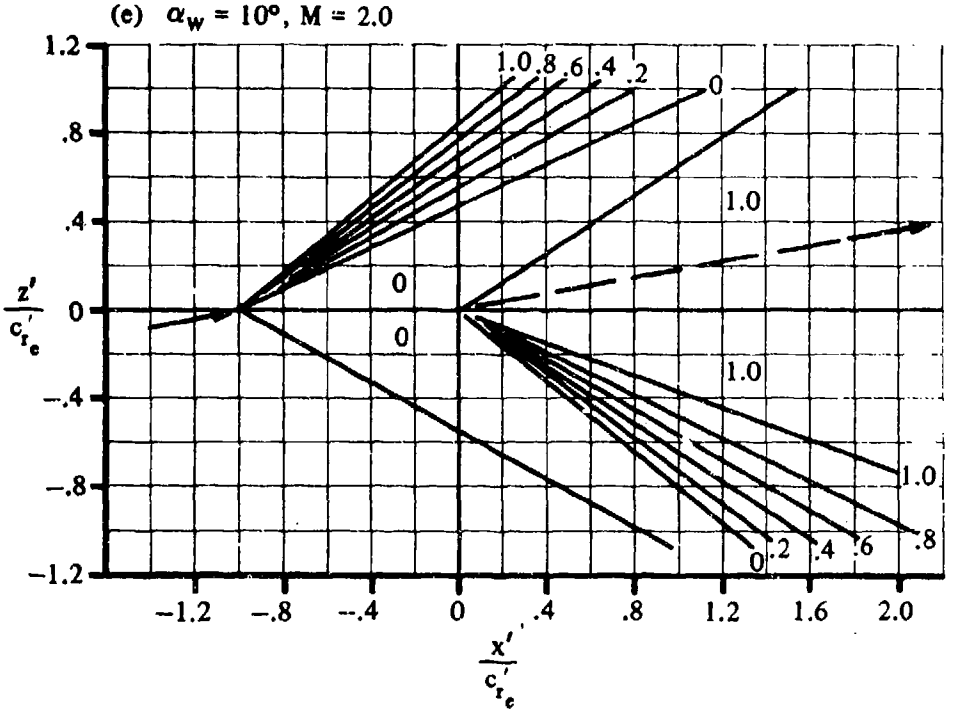

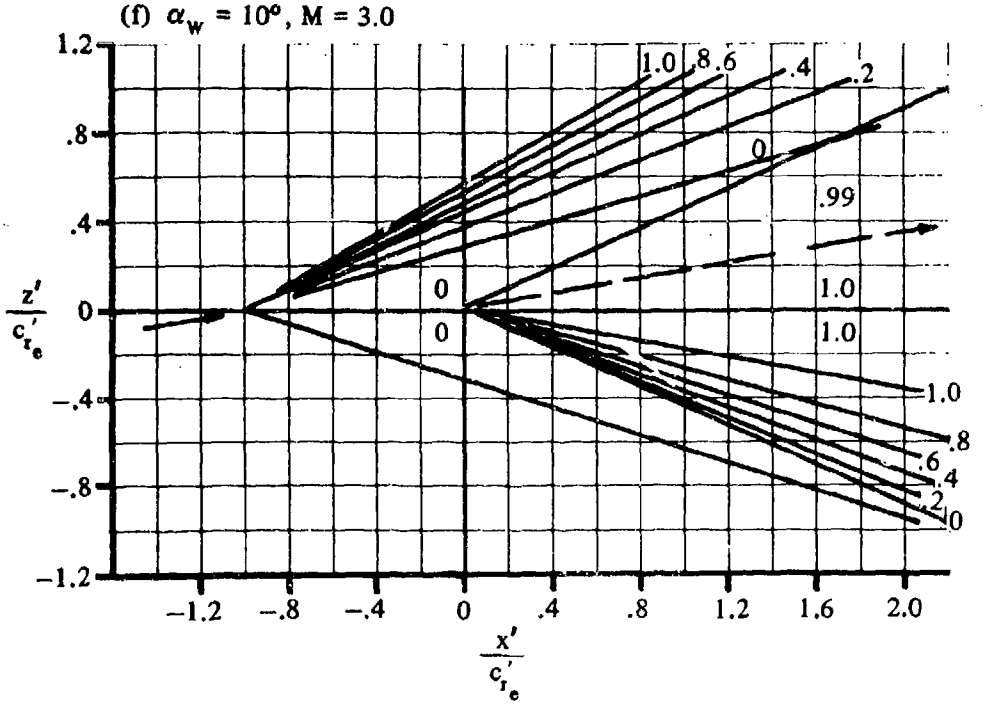

FIGURE 4.5.1.2-13 (CONTD)

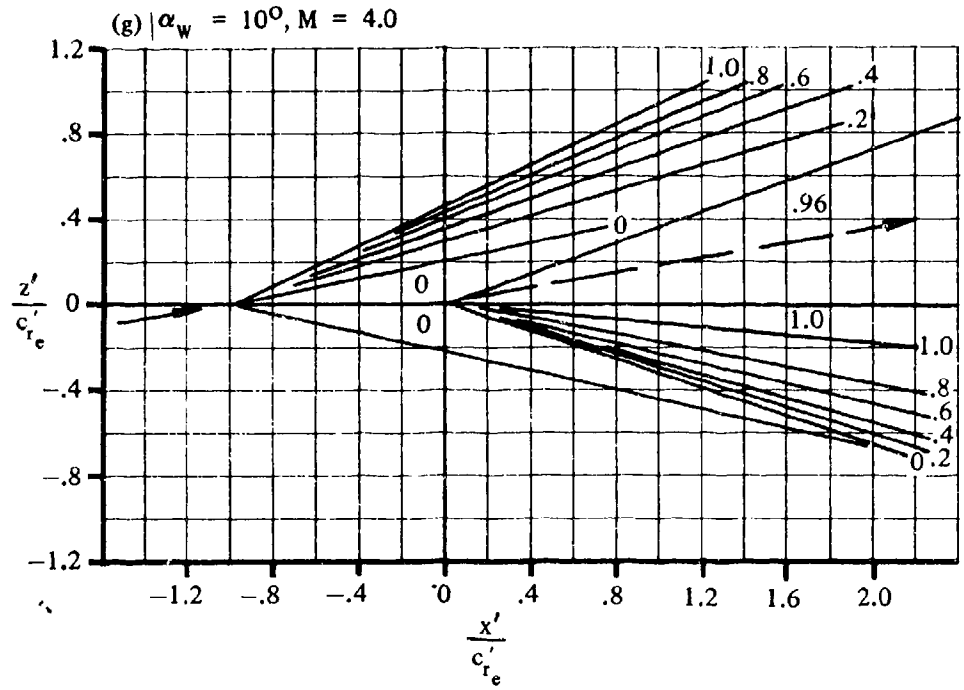

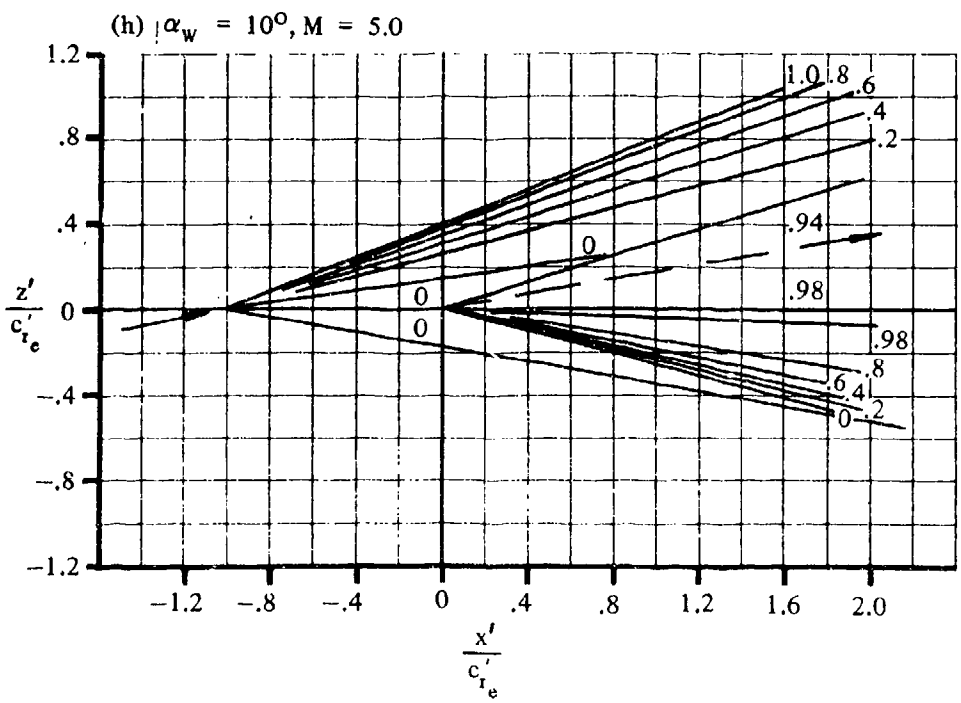

FIGURE 4.5.1.2-13 (CONTD)

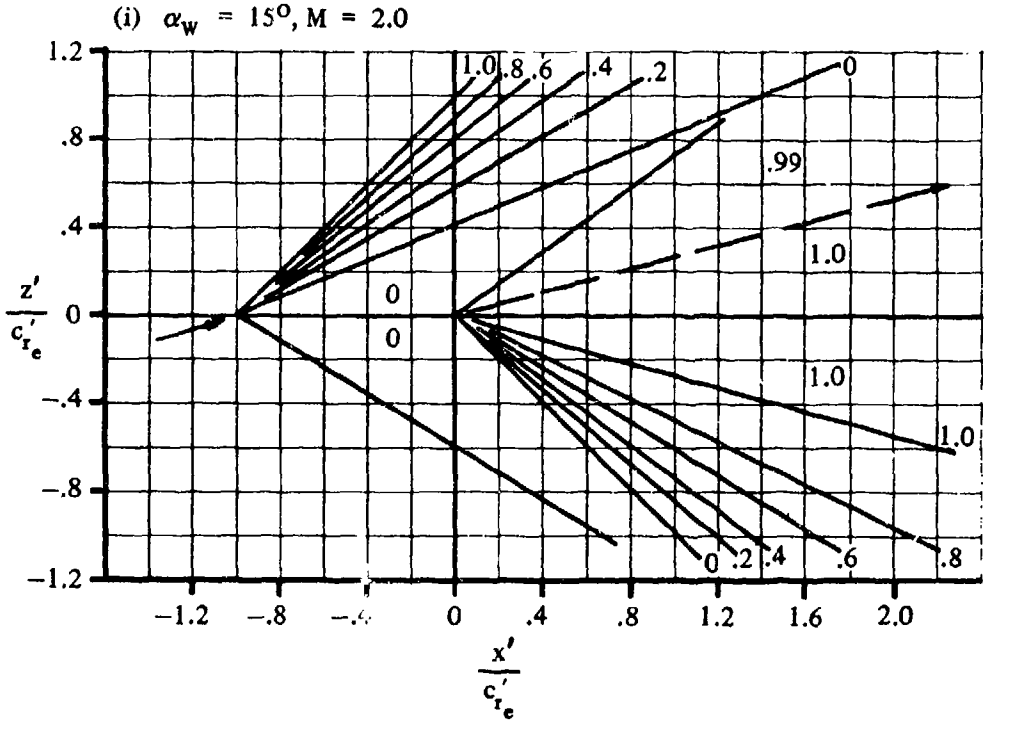

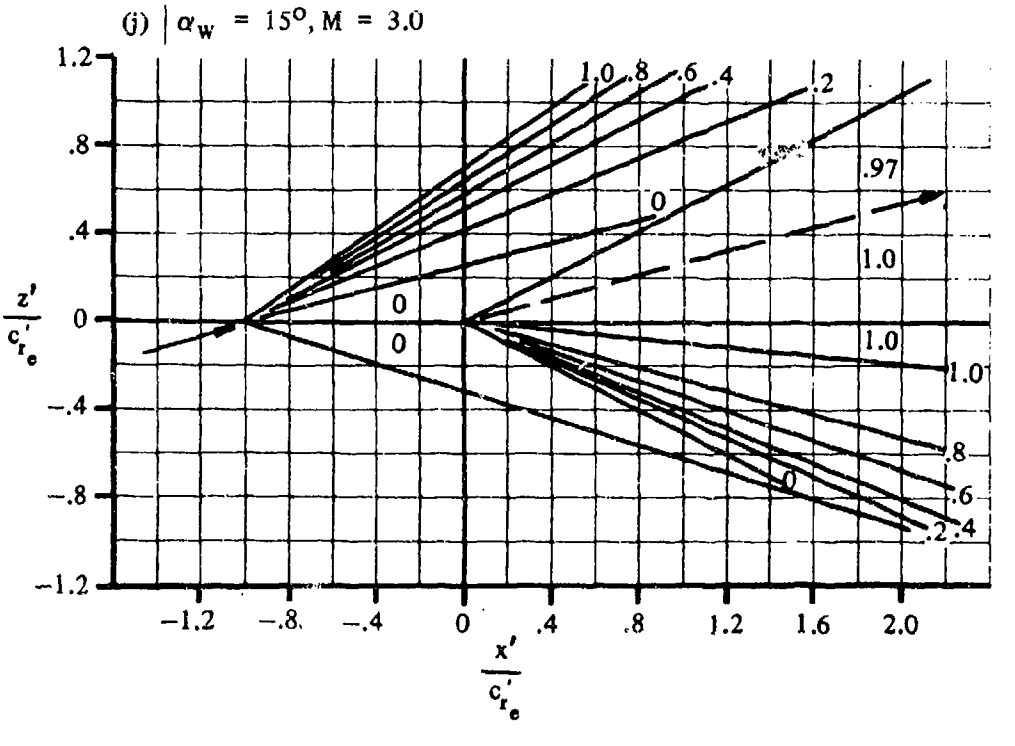

FIGURE 4.5.1.2-13 (CONTD)

(k) $\alpha_W = 15^o$, M = 4.0

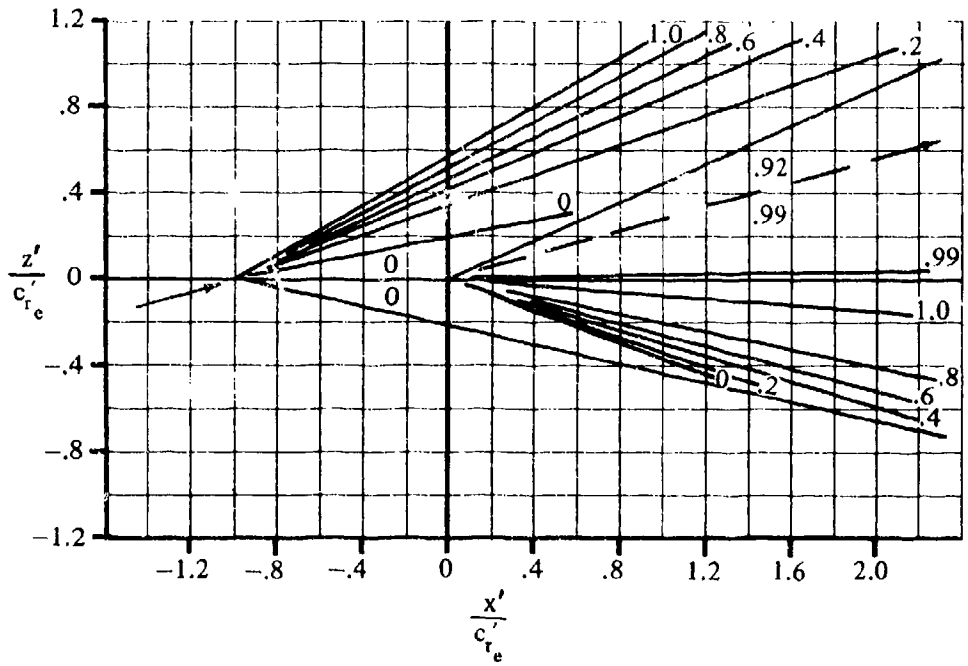

(ℓ) $\alpha_W = 15^o$, M = 5.0

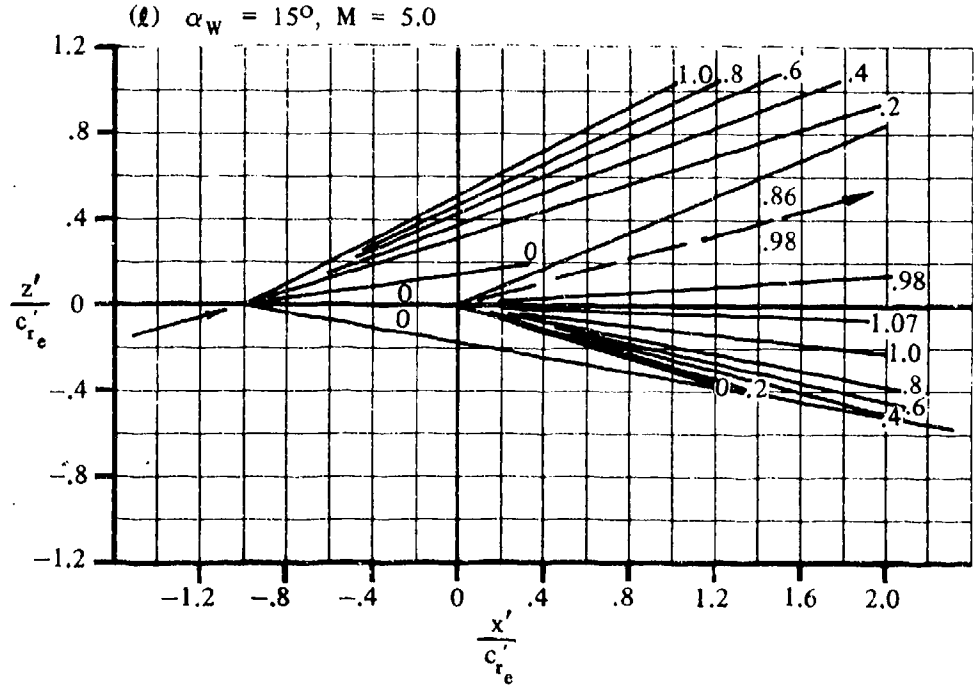

FIGURE 4.5.1.2-13 (CONTD)

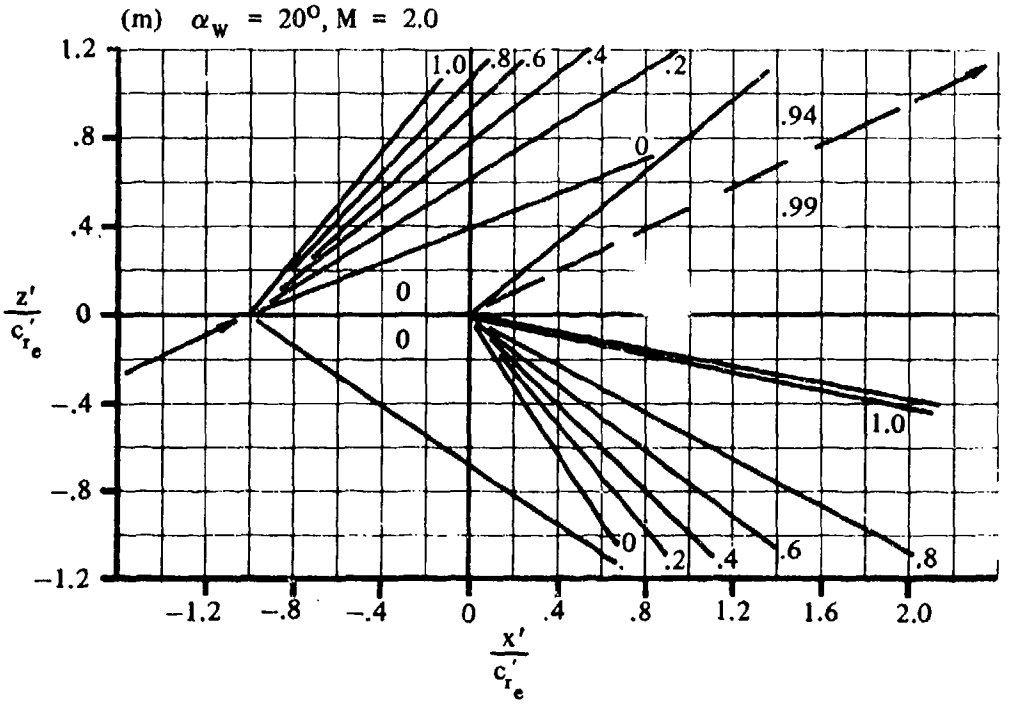

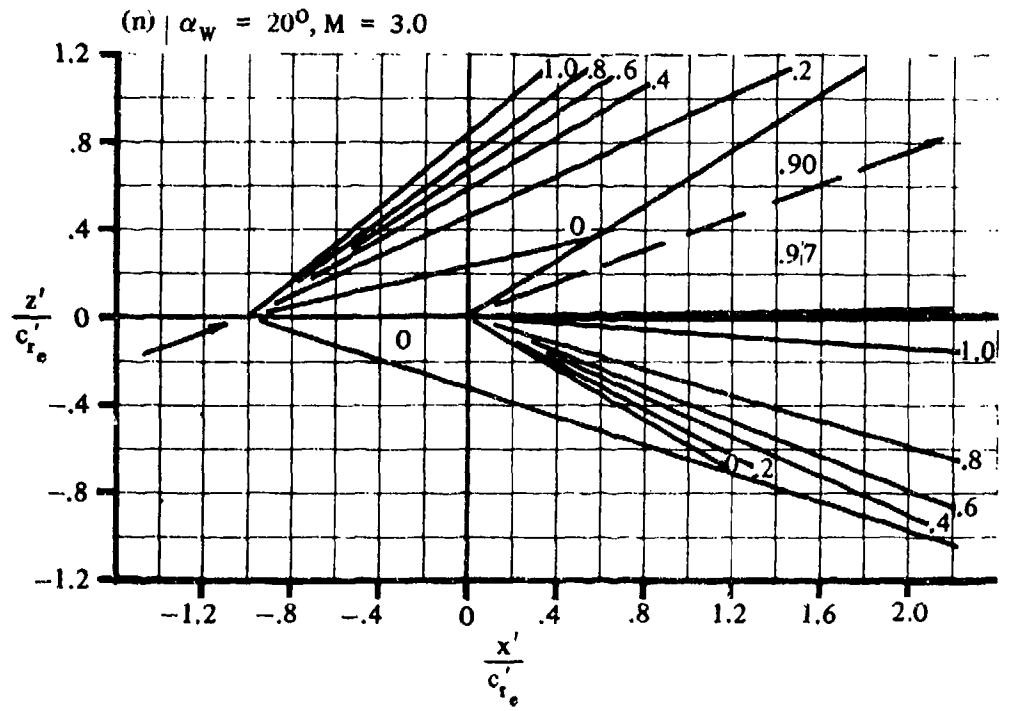

FIGURE 4.5.1.2-13 (CONTD)

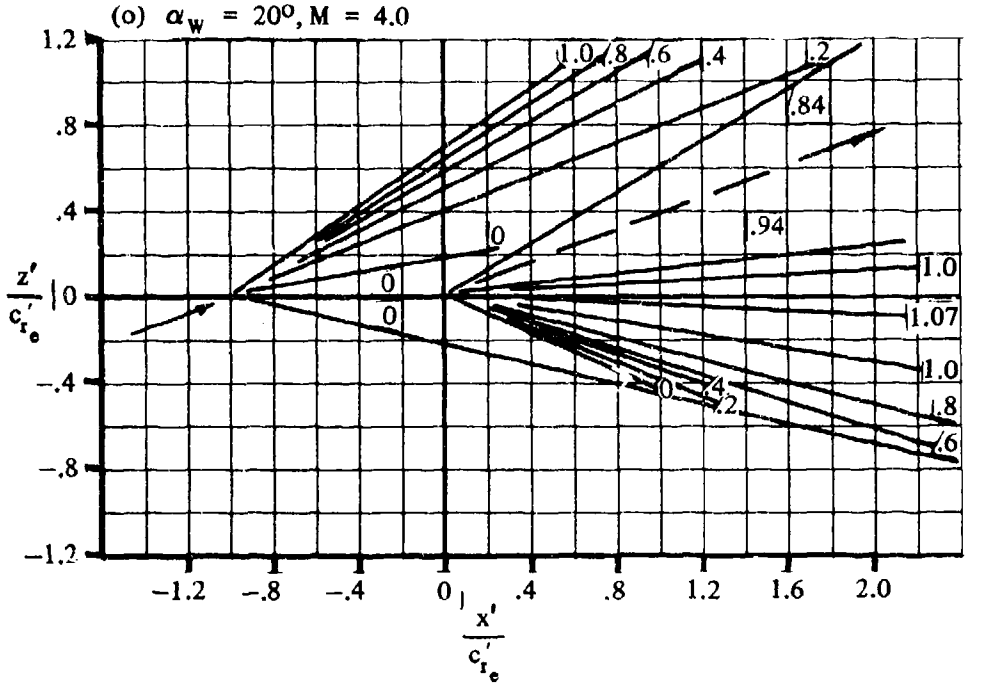

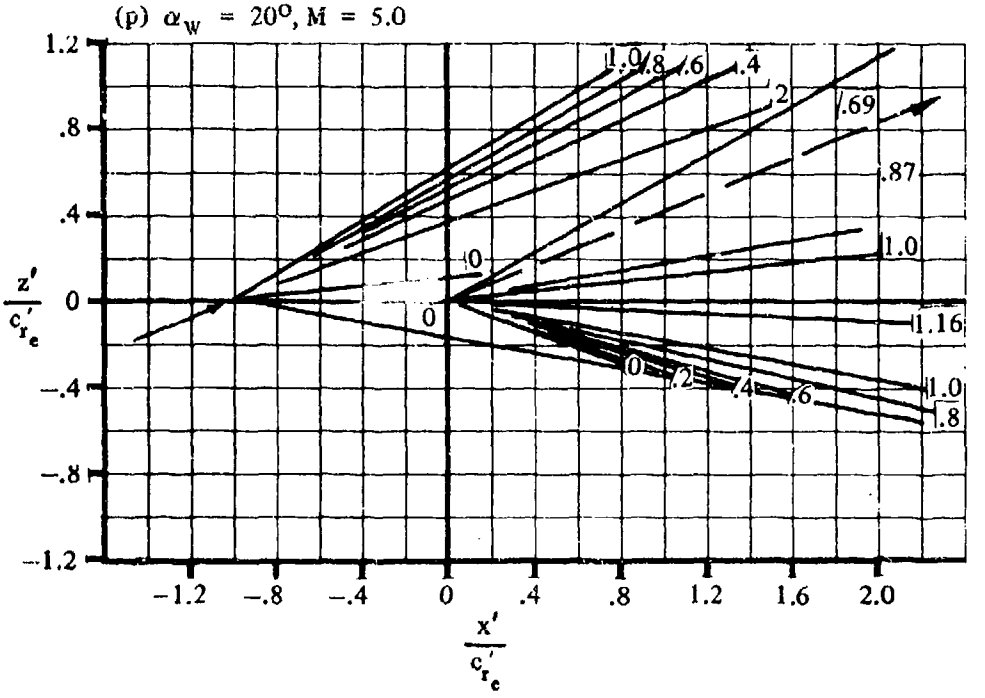

FIGURE 4.5.1.2-13 (CONTD)

4.5.1.3 WING-BODY-TAIL MAXIMUM LIFT

In this section a general method applicable to all speed regimes is presented for estimating the usable or trimmed maximum lift coefficient for a wing-body-tail configuration with no high-lift devices. The wing-body-tail maximum lift is assumed to occur at the wing-body angle of attack for maximum lift.

The effective tail-body lift component is a direct result of the wing-body pitching moment that must be trimmed. Most conventional clean-wing tail-off configurations exhibit a positive pitching moment at stall, therefore requiring a positive tail lift, which generates a balancing negative pitching moment.

The contribution of the tail lift is only as accurate as the wing-body pitching-moment estimate at stall. Unfortunately, many configurations exhibit nonlinear pitching-moment characteristics at or before stall that effectively prohibit an accurate analytical estimate of the pitching moment at stall. For this reason, it is highly desirable to have pitching-moment test data for the particular configuration or for a similar configuration.

DATCOM METHOD

The wing-body-tail angle of attack at maximum lift is assumed to be identical to the wing-body angle of attack at maximum lift from Section 4.3.1.4.

The following method is based on the wing-body maximum lift plus the tail-body lift that is required to trim the vehicle at $(\alpha_{C_{L_{max}}})_{WB}$. The wing-body-tail maximum lift, based on the wing area S_W and neglecting the vertical-tail drag, is determined by

$$C_{L_{max}} = (C_{L_{max}})_{WB} + C_{L_{H(WBV)}} \qquad 4.5.1.3\text{-a}$$

where

$(C_{L_{max}})_{WB}$ is the wing-body maximum lift from test data or Section 4.3.1.4 at the appropriate speed, based on S_W.

$C_{L_{H(WBV)}}$ is the horizontal-tail lift at $(\alpha_{C_{L_{max}}} - \epsilon)$ in the presence of the wing-body, and vertical tail, based on the wing area S_W. The value of this term is determined from considering the horizontal-tail forces that affect the vehicle pitching moment.

The tail lift can be evaluated using one of the three equations that are presented below. The first equation is complete; whereas, the second and third equations are simplifications of the first equation.

$$C_{L_{H(WBV)}} = \frac{\left(C_{m_{WB}}\right)_{\alpha_{C_{L_{max}}}} + C_{D_H} \cos\left(\alpha_{C_{L_{max}}} - \epsilon\right) \frac{z_H}{\bar{c}} - C_{D_H} \sin\left(\alpha_{C_{L_{max}}} - \epsilon\right) \frac{\ell''}{\bar{c}} + C_{m_{H(WBV)}}}{\cos\left(\alpha_{C_{L_{max}}} - \epsilon\right) \frac{\ell''}{\bar{c}} + \sin\left(\alpha_{C_{L_{max}}} - \epsilon\right) \frac{z_H}{\bar{c}}}$$

4.5.1.3-b

where

$\left(C_{m_{WB}}\right)_{\alpha_{C_{L_{max}}}}$ is the wing-body pitching moment at the stall angle of attack based on $S_W \bar{c}_W$ with respect to $\bar{c}_W/4$, obtained from test data for the particular configuration. If no test data are available, it is suggested that an approximation be made by using the methods of Sections 4.1.4.2, 4.1.4.3, and 4.3.2.2 in conjunction with test data on a similar configuration.

C_{D_H} is the horizontal-tail-body drag at $\left(\alpha_{C_{L_{max}}} - \epsilon\right)$ based on S_W, obtained from test data or the appropriate methods of Sections 4.3.3.1 and 4.3.3.2.

$\alpha_{C_{L_{max}}}$ is the wing-body angle of attack at stall, obtained from test data or from the appropriate method of Section 4.3.1.4.

ϵ is the wing downwash at the horizontal tail, obtained from test data or the appropriate method of Section 4.4.1.

$\frac{z_H}{\bar{c}}$ is the ratio of the height of the quarter-chord point of the horizontal-tail MAC above the quarter-chord point of the wing MAC, to the wing MAC. The height is measured perpendicular to the longitudinal axis and is positive for the horizontal tail above the wing (see Sketch (a)).

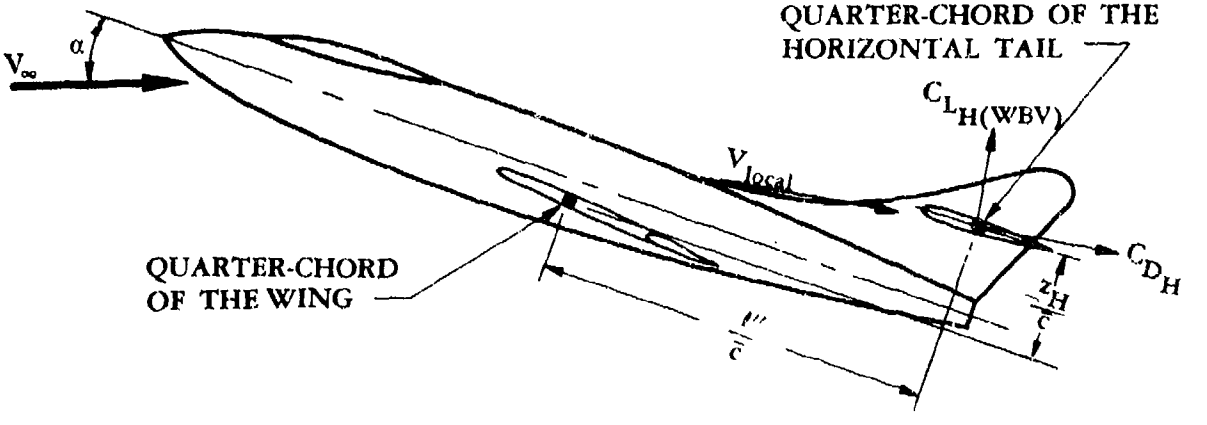

SKETCH (a)

$\frac{\ell''}{\bar{c}}$ is the ratio of the distance from the quarter-chord point of the wing MAC to the quarter-chord point of the horizontal panel MAC (measured parallel to the longitudinal axis), to the wing MAC (see Sketch (a)).

$C_{m_{H(WBV)}}$ is the horizontal-tail pitching moment at $\left(\alpha_{C_{L_{max}}} - \epsilon\right)$ based on $S_W \bar{c}_W$ with respect to the quarter-chord point of the horizontal-tail MAC obtained from test data. If no test data are available, it is suggested that an approximation be made by using the methods from Sections 4.1.4.2, 4.1.4.3, and 4.3.2.2 in conjunction with test data on a similar configuration. However, for horizontal tails with symmetrical airfoil sections, this term can be neglected.

For those configurations where the horizontal-tail drag is very small in comparison with the wing-body pitching moment, the drag terms of Equation 4.5.1.3-b can be omitted. In addition, since most horizontal tails have symmetrical airfoil sections, the $C_{m_{H(WBV)}}$ term can also be omitted. Thus Equation 4.5.1.3-b can be written as

$$C_{L_{H(WBV)}} = \frac{\left(C_{m_{WB}}\right)_{\alpha_{C_{L_{max}}}}}{\cos\left(\alpha_{C_{L_{max}}} - \epsilon\right)\frac{\ell''}{\bar{c}} + \sin\left(\alpha_{C_{L_{max}}} - \epsilon\right)\frac{z_H}{\bar{c}}} \qquad 4.5.1.3\text{-c}$$

If the small-angle approximation can be justified for $\left(\alpha_{C_{L_{max}}} - \epsilon\right)$, the above can be further simplified to yield

$$C_{L_{H(WBV)}} = \frac{\left(C_{m_{WB}}\right)_{\alpha_{C_{L_{max}}}}}{\frac{\ell''}{\bar{c}}} \qquad 4.5.1.3\text{-d}$$

No substantiation is presented because of the lack of test data on wing-body-tail configurations.

Sample Problem

Given:

$\left(C_{L_{max}}\right)_{WB} = 1.0$ $\quad \alpha_{C_{L_{max}}} = 16.5^{o}$ $\quad \epsilon = 9.2^{o}$ $\quad \left(C_{m_{WB}}\right)_{\alpha_{C_{L_{max}}}} = 0.10$

$C_{D_H} = 0.02$ $\quad C_{m_{H(WBV)}} = 0$ $\quad \frac{\ell''}{\bar{c}} = 2.75$ $\quad \frac{z_H}{\bar{c}} = 1.23$

Compute:

$$C_{L_{H(WBV)}} = \frac{\left(C_{m_{WB}}\right)_{\alpha_{C_{L_{max}}}} + C_{D_H} \cos\left(\alpha_{C_{L_{max}}} - \epsilon\right) \frac{z_H}{\bar{c}} - C_{D_H} \sin\left(\alpha_{C_{L_{max}}} - \epsilon\right) \frac{\ell''}{\bar{c}} + C_{m_{H(WBV)}}}{\cos\left(\alpha_{C_{L_{max}}} - \epsilon\right) \frac{\ell''}{\bar{c}} + \sin\left(\alpha_{C_{L_{max}}} - \epsilon\right) \frac{z_H}{\bar{c}}}$$

(Equation 4.5.1.3-b)

$$= \frac{0.10 + 0.02 \cos (16.5^\circ - 9.2^\circ) (1.23) - 0.06 \sin (16.5^\circ - 9.2^\circ) (2.75) + 0}{\cos (16.5^\circ - 9.2^\circ) (2.75) + \sin (16.5^\circ - 9.2^\circ) (1.23)}$$

$$= \frac{0.10 + (0.02) (0.9919) (1.23) - (0.06) (0.1271) (2.75)}{(0.9919) (2.75) + (0.1271) (1.23)}$$

$$= \frac{0.1034}{2.884}$$

$$= 0.0359$$

Solution:

$$C_{L_{max}} = (C_{L_{max}})_{WB} + C_{L_{H(WBV)}} \quad \text{(Equation 4.5.1.3-a)}$$

$$= 1.0 + 0.036$$

$$= 1.036$$

4.5.2 WING-BODY-TAIL PITCHING MOMENT

4.5.2.1 WING-BODY-TAIL PITCHING-MOMENT-CURVE SLOPE

Pitching-moment-estimation methods are inherently less accurate than those for lift, since pitching moment is dependent primarily on load distribution, while lift depends primarily on gross forces. Many of the comments on lift given in Section 4.5.1.1 are also applicable to this Section.

A. SUBSONIC

DATCOM METHODS

Two methods are presented, differing in their treatment of the effect of the forward-surface flow field on the aft surface.

Method 1 ($b'/b'' \geq 1.5$)

For configurations in which the span of the forward surface is large compared to that of the aft surface, the following approach can be used. This method is to be used when the ratio of the forward- to the aft-surface span is 1.5 or greater. The complete equation for the pitching-moment-curve slope C_{m_α} of a wing-body-tail configuration based on the gross area and MAC of the forward panel and an arbitrary center-of-gravity position is given by

$$C_{m_\alpha} = -\frac{x_{cg} - x'}{\bar{c}'}\left[\left\{-(C_L)' + (C_{D_\alpha})'\right\}\sin\alpha + \left\{(C_{L_\alpha})' + (C_D)'\right\}\cos\alpha\right]$$

$$-\frac{z_{cg} - z'}{\bar{c}'}\left[\left\{(C_{L_\alpha})' + (C_D)'\right\}\sin\alpha + \left\{(C_L)' - (C_{D_\alpha})'\right\}\cos\alpha\right]$$

$$-\frac{x_{cg} - x''}{\bar{c}''}\left[\left\{-(C_L)'' + (C_{D_\alpha})''\right\}\sin(\alpha-\epsilon) + \left\{(C_{L_\alpha})'' + (C_D)''\right\}\cos(\alpha-\epsilon)\right]\frac{q''}{q_\infty}\frac{S''}{S'}\frac{\bar{c}''}{\bar{c}'}\left(1 - \frac{\partial\epsilon}{\partial\alpha}\right)$$

$$-\frac{z_{cg} - z''}{\bar{c}''}\left[\left\{(C_{L_\alpha})'' + (C_D)''\right\}\sin(\alpha-\epsilon) + \left\{(C_L)'' - (C_{D_\alpha})''\right\}\cos(\alpha-\epsilon)\right]\frac{q''}{q_\infty}\frac{S''}{S'}\frac{\bar{c}''}{\bar{c}'}\left(1 - \frac{\partial\epsilon}{\partial\alpha}\right)$$

where

geometric parameters are defined in figure 4.5.2.1-7 (note that g', g'', and ℓ'' are always positive)

primed quantities pertain to the forward panel

double-primed quantities pertain to the aft panel

the lift and drag terms below are calculated by the methods of Sections 4.3.1.2 and 4.3.3.2, respectively

$(C_L)'$ and $(C_D)'$ are the complete lift and drag coefficients of the forward panel and body, including wing-body interference. The coefficients are evaluated at the angle $\alpha - \alpha_0 + i'$.

$(C_{L_\alpha})'$ and $(C_{D_\alpha})'$ are the complete lift-curve and drag-curve slopes of the forward panel and body including interferences.

$(C_L)''$ and $(C_D)''$ are the lift and drag coefficients of the aft panel evaluated at the tail angle of attack $\alpha'' = \alpha - \epsilon + i''$. These coefficients include wing-body interferences.

$(C_{L_\alpha})''$ and $(C_{D_\alpha})''$ are the lift-curve and drag-curve slopes of the aft panel including wing-body interference effects.

ϵ and $\frac{\partial\epsilon}{\partial\alpha}$ are the downwash angle and downwash gradient, respectively, from Section 4.4.1

α'' is the angle of attack of the aft panel, $\alpha - \epsilon + i''$, where ϵ is the average downwash angle (Section 4.4.1) acting on the aft panel evaluated at the forward-panel angle of attack $\alpha - \alpha_0 + i'$

$$\frac{x_{cg} - x'}{\bar{c}'} = \frac{x_{cg}}{\bar{c}'} + \left(\frac{x_{ac}'}{c_r'}\right)\left(\frac{c_r'}{\bar{c}'}\right) - \frac{g'}{\bar{c}'} - .25 \qquad 4.5.2.1\text{-b}$$

$$\frac{x_{cg} - x''}{\bar{c}''} = \frac{\ell''}{\bar{c}''} + \frac{x_{cg}}{\bar{c}''} + \left(\frac{x_{ac}''}{c_r''}\right)\left(\frac{c_r''}{\bar{c}''}\right) - \frac{g''}{\bar{c}''} - .25 \qquad 4.5.2.1\text{-c}$$

$x'_{a.c.}$ is the aerodynamic center of the forward panel obtained from Section 4.3.2.2 (referred to the forward-panel apex and based on exposed panel geometry)

$x''_{a.c.}$ is the aerodynamic center of the aft panel obtained from Section 4.3.2.2 (referred to the aft-panel apex and based on exposed panel geometry)

For most configurations the terms involving z_{cg} are negligible, and frequently the drag terms are small enough to be negligible. If, in addition, the usual approximations for small angle of attack are made, equation 4.5.2.1-a can be simplified to give

$$C_{m_\alpha} = -\frac{x_{cg} - x'}{\bar{c}'}(C_{L_\alpha})' - \frac{x_{cg} - x''}{\bar{c}''}(C_{L_\alpha})''\frac{q''}{q_\infty}\frac{S''}{S'}\frac{\bar{c}''}{\bar{c}'}\left(1 - \frac{\partial \epsilon}{\partial \alpha}\right) \qquad 4.5.2.1\text{-d}$$

which can be written as

$$C_{m_\alpha} = -\frac{x_{cg} - x'}{\bar{c}'}[K_N + K_{B(W)} + K_{W(B)}]'\,(C_{L_\alpha})'_e\frac{S_e'}{S'}$$

$$-\frac{x_{cg} - x''}{\bar{c}''}[K_{B(W)} + K_{W(B)}]''\,(C_{L_\alpha})''_e\left(1 - \frac{\partial \epsilon}{\partial \alpha}\right)\frac{q''}{q_\infty}\frac{S_e''}{S''}\frac{S''}{S'}\frac{\bar{c}''}{\bar{c}'} \qquad 4.5.2.1\text{-d}'$$

where

$$\frac{x_{cg} - x'}{\bar{c}'} = \frac{x_{cr}}{\bar{c}'} + \left(\frac{x_{ac}'}{c_r'}\right)\left(\frac{c_r'}{\bar{c}'}\right) - \frac{g'}{\bar{c}'} - .25 \quad \text{(equation 4.5.2.1-b)}$$

$$\frac{x_{cg} - x''}{\bar{c}''} = \frac{l''}{\bar{c}''} + \frac{x_{cg}}{\bar{c}''} \qquad 4.5.2.1\text{-e}$$

and the remaining terms are defined in Section 4.5.1.1.

Method 2 $(b'/b'') < 1.5$

For configurations in which the span of the forward surface is approximately equal to or less than that of the aft surface, the vortex shed from the forward surface interacts directly with the aft surface and the resulting interference effects must be accounted for in the tail terms. This method is to be used when the ratio of the forward- to the aft-surface span is less than 1.5. The contribution of this interference effect to the drag coefficient is not given in literature. However, by making the assumptions that led to equation 4.5.2.1-d, a simplified expression for the pitching-moment-curve slope of a complete wing-body-tail configuration based on the gross area and MAC of the forward panel and an arbitrary center-of-gravity position is:

$$C_{m_\alpha} = -\frac{x_{cg} - x'}{\bar{c}'}(C_{L_\alpha})' - \frac{x_{cg} - x''}{\bar{c}''}\left(\frac{\bar{c}''}{\bar{c}'}\right)\left[(C_{L_\alpha})''\frac{S''}{S'}\frac{q''}{q_\infty} + (C_{L_\alpha})_{W''(v)}\right] \qquad 4.5.2.1\text{-f}$$

Equation 4.5.2.1-f can be written as

$$C_{m_\alpha} = -\frac{x_{cg} - x'}{\bar{c}'}[K_N + K_{(B)W} + K_{W(B)}]'\,(C_{L_\alpha})'_e\frac{S_e'}{S'}$$

$$-\frac{x_{cg} - x''}{\bar{c}''}\left(\frac{\bar{c}''}{\bar{c}'}\right)\left\{[K_{W(B)} + K_{B(W)}]''\,(C_{L_\alpha})''_e\frac{S_e''}{S''}\frac{S''}{S'}\frac{q''}{q_\infty} + (C_{L_\alpha})_{W''(v)}\right\} \qquad 4.5.2.1\text{-f}'$$

where

$\frac{x_{cg} - x'}{\bar{c}'}$ is given by equation 4.5.2.1-b

$\frac{x_{cg} - x''}{\bar{c}''}$ is given by equation 4.5.2.1-e

$(C_{L_\alpha})_{W''(v)}$ is the effect of the forward-surface vortices on the aft surface as defined in Section 4.5.1.1 and the remaining terms are defined in Section 4.5.1.1.

Sample Problems

1. Method 1 ($b'/b'' \geq 1.5$)

Given:

Configuration of sample problem 1, paragraph A, Section 4.5.1.1. Additional characteristics are based on total-panel dimensions.

c.g. at $\frac{\bar{c}'}{4}$

$\frac{c_r'}{\bar{c}'} = 1.316$ $\qquad$ $\frac{\bar{c}''}{\bar{c}'} = 0.566$

$\frac{g'}{\bar{c}'} = 1.745$ $\qquad$ $\frac{\ell''}{\bar{c}''} = 5.30$

$\left(\frac{x_{ac}}{c_r}\right)_N = -0.783$

$\left(\frac{x_{ac}}{c_r}\right)_{W(B)} = 1.650$ } From Section 4.3.2.2; functions of wing-body geometry

$\left(\frac{x_{ac}}{c_r}\right)_{B(W)} = 0.822$

Compute:

Step 1. $\frac{x_{ac}'}{c_r'}$

From Section 4.3.1.2:

$$(C_{L_\alpha})_N = K_N' (C_{L_\alpha})_e' \frac{S_e'}{S'}$$

$$(C_{L_\alpha})_{W(B)} = K_{W(B)}' (C_{L_\alpha})_e' \frac{S_e'}{S'}$$

$$(C_{L_\alpha})_{B(W)} = K_{B(W)}' (C_{L_\alpha})_e' \frac{S_e'}{S'}$$

The above parameters have been calculated in sample problem 1, paragraph A, Section 4.5.1.1.

$(C_{L_\alpha})_e' \frac{S_e'}{S'} = .0664\ (.896) = .0595$ per deg

$(C_{L_\alpha})_N = 0.037\ (.0595) = 0.0022$ per deg

$(C_{L_\alpha})_{W(B)} = 1.08\ (.0595) = 0.0643$ per deg

$(C_{L_\alpha})_{B(W)} = 0.14\ (.0595) = 0.0083$ per deg

From Section 4.3.2.2:

$$\frac{x_{ac}'}{c_r'} = \frac{\left(\frac{x_{ac}}{c_r}\right)_N (C_{L_\alpha})_N + \left(\frac{x_{ac}}{c_r}\right)_{W(B)} (C_{L_\alpha})_{W(B)} + \left(\frac{x_{ac}}{c_r}\right)_{B(W)} (C_{L_\alpha})_{B(W)}}{(C_{L_\alpha})_N + (C_{L_\alpha})_{W(B)} + (C_{L_\alpha})_{B(W)}} \quad \text{(equation 4.3.2.2-a)}$$

$$= \frac{-.783\ (.0022) + 1.650\ (.0643) + .822\ (.0083)}{0.0022 + 0.0643 + 0.0083}$$

$$= 1.49$$

Step 2. $\frac{x_{cg} - x'}{\bar{c}'}$ and $\frac{x_{cg} - x''}{\bar{c}''}$

$$\frac{x_{cg}}{\bar{c}'} = 0$$

$$\frac{x_{cg} - x'}{\bar{c}'} = \frac{x_{cg}}{\bar{c}'} + \left(\frac{x_{ac}'}{c_r'}\right)\left(\frac{c_r'}{\bar{c}'}\right) - \frac{g'}{\bar{c}'} - .25 \quad \text{(equation 4.5.2.1-b)}$$

$$= 0 + 1.49\ (1.316) - 1.745 - .25$$

$$= -0.034$$

$$\frac{x_{cg} - x''}{\bar{c}''} = \frac{l''}{\bar{c}''} + \frac{x_{cg}}{\bar{c}''} = 5.30 \quad \text{(equation 4.5.2.1-e)}$$

Step 3. Solution for C_{m_α}

$(C_{L_\alpha})'$ and $(C_{L_\alpha})''$ have been calculated in sample problem 1, paragraph A, Section 4.5.1.1.

$(C_{L_\alpha})' = 0.0748$ per deg

$(C_{L_\alpha})'' \frac{q''}{q_\infty} \frac{S''}{S'}\left(1 - \frac{\partial \epsilon}{\partial \alpha}\right) = 0.0065$ per deg (this value includes wake and wash effects calculated in referenced problem)

$$C_{m_\alpha} = -\frac{x_{cg} - x'}{\bar{c}'}(C_{L_\alpha})' - \frac{x_{cg} - x''}{\bar{c}''}(C_{L_\alpha})'' \frac{q''}{q_\infty} \frac{S''}{S'} \frac{\bar{c}''}{\bar{c}'}\left(1 - \frac{\partial \epsilon}{\partial \alpha}\right) \quad \text{(equation 4.5.2.1-d)}$$

$$= -(-.034)\ (.0748) - (5.30)\ (.566)\ (.0065)$$

$$= 0.0025 - 0.0195$$

$$= -0.0170 \text{ per deg}$$

2. Method 2 ($b'/b'' < 1.5$)

Given:

Configuration of sample problem 2, paragraph A, Section 4.5.1.1. Additional characteristics are based on total panel dimensions.

e.g. at $\frac{\bar{c}'}{4}$

$$\frac{c_r'}{\bar{c}'} = 1.38 \qquad \frac{\bar{c}''}{\bar{c}'} = 0.343 \qquad \frac{g'}{\bar{c}'} = 0.389 \qquad \frac{l''}{\bar{c}''} = 5.32$$

$\left(\frac{x_{ac}}{c_r}\right)_N = -0.333$

$\left(\frac{x_{ac}}{c_r}\right)_{W(B)} = 0.526$

$\left(\frac{x_{ac}}{c_r}\right)_{B(W)} = 0.356$

} From Section 4.3.2.2; functions of wing-body geometry

Compute:

Step 1. $\frac{x_{ac}'}{c_r'}$:

From Section 4.3.1.2:

$$(C_{L_\alpha})_N = K_N' (C_{L_\alpha})_e' \frac{S_e'}{S'}$$

$$(C_{L_\alpha})_{W(B)} = K_{W(B)}' (C_{L_\alpha})_e' \frac{S_e'}{S'}$$

$$(C_{L_\alpha})_{B(W)} = K_{B(W)}' (C_{L_\alpha})_e' \frac{S_e'}{S'}$$

The above parameters have been calculated in sample problem 2, paragraph A, Section 4.5.1.1.

$$(C_{L_\alpha})_e' \frac{S_e'}{S'} = (0.0405)\ (0.730) = 0.0296 \text{ per deg}$$

$$(C_{L_\alpha})_N = (0.67)\ (0.0296) = 0.0198 \text{ per deg}$$

$$(C_{L_\alpha})_{W(B)} = (1.16)\ (0.0296) = 0.0343 \text{ per deg}$$

$$(C_{L_\alpha})_{B(W)} = (0.27)\ (0.0296) = 0.0080 \text{ per deg}$$

$$\frac{x_{ac}'}{c_r'} = \frac{\left(\frac{x_{ac}}{c_r}\right)_N (C_{L_\alpha})_N + \left(\frac{x_{ac}}{c_r}\right)_{W(B)} (C_{L_\alpha})_{W(B)} + \left(\frac{x_{ac}}{c_r}\right)_{B(W)} (C_{L_\alpha})_{B(W)}}{(C_{L_\alpha})_N + (C_{L_\alpha})_{W(B)} + (C_{L_\alpha})_{B(W)}} \quad \text{(equation 4.3.2.2-a)}$$

$$= \frac{(-0.333).\ (0.0198) + (0.526)\ (0.0343) + (0.356)\ (0.0080)}{0.0198 + 0.0343 + 0.008}$$

$$= 0.230$$

Step 2. $\frac{x_{cg} - x'}{\bar{c}'}$ and $\frac{x_{cg} - x''}{\bar{c}''}$:

$$\frac{x_{cg}}{\bar{c}'} = 0$$

$$\frac{x_{cg} - x'}{\bar{c}'} = \frac{x_{cg}}{\bar{c}'} + \left(\frac{x_{ac}'}{c_r'}\right)\left(\frac{c_r'}{\bar{c}'}\right) - \frac{g'}{\bar{c}'} - .25 \quad \text{(equation 4.5.2.1-b)}$$

$$= 0 + (0.230)\ (1.38) - 0.389 - .25$$

$$= -0.3216$$

$$\frac{x_{cg} - x''}{\bar{c}''} = \frac{l''}{\bar{c}''} + \frac{x_{cg}}{\bar{c}''} \quad \text{(equation 4.5.2.1-e)}$$

$$= 5.32$$

Step 3. Solution for C_{m_α}:

$$C_{m_\alpha} = \frac{x_{cg} - x'}{\bar{c}'} [K_N + K_{W(B)} + K_{B(W)}]' (C_{L_\alpha})_e' \frac{S_e'}{S'}$$

$$- \frac{x_{cg} - x''}{\bar{c}''} \left(\frac{\bar{c}''}{\bar{c}'}\right) \left\{ [K_{W(B)} + K_{B(W)}]'' (C_{L_\alpha})_e'' \frac{S_e''}{S''} \frac{S''}{S'} \frac{q''}{q_\infty} + (C_{L_\alpha})_{W''(V)} \right\} \quad \text{(equation 4.5.2.1-f')}$$

Using the above results and the parameters calculated in sample problem 2, par graph A, Section 4.5.1.1 gives

$$C_{m_\alpha} = -(-0.3216)\ (1.497)\ (0.0405)\ (0.730)$$
$$-\ (5.32)\ (0.343)\ [(1.45)\ (0.0667)\ (0.741)\ (0.277)\ (0.859) + (-0.0139)]$$
$$= 0.0085 \text{ per deg}$$

B. TRANSONIC

At transonic speeds the mutual interferences that exist between components can have pronounced effects upon the pitching-moment characteristics of wing-body-tail combinations. The sensitivity of shock-wave position and strength to minor configuration changes and the common occurrence of shock-induced boundary-layer separation have significant effects on the pressure-loading variations and hence the pitching characteristics. At present the methods of predicting these effects are either nonexistent or oversimplified. The downwash from the forward panel is also difficult to evaluate for cases of mixed flow and/or separation over the forward panel.

DATCOM METHOD

It is recommended that the procedure outlined in paragraph A above be applied at transonic speeds.

C. SUPERSONIC

The information included in the Datcom accounts for most of the mutual interferences that occur between components at supersonic speeds. In particular, the wing-body interferences have been accounted for by the slender-body interference factors of Section 4.3.1.2. The wing-wing interference methods include the effects of the downwash field due to lift, the downwash due to the local compressible flow field, Mach number, and the local dynamic pressure.

DATCOM METHOD

The equations presented in paragraph A for estimating the pitching-moment-curve slope of wing-body-tail combinations are applicable to the supersonic speed regime.

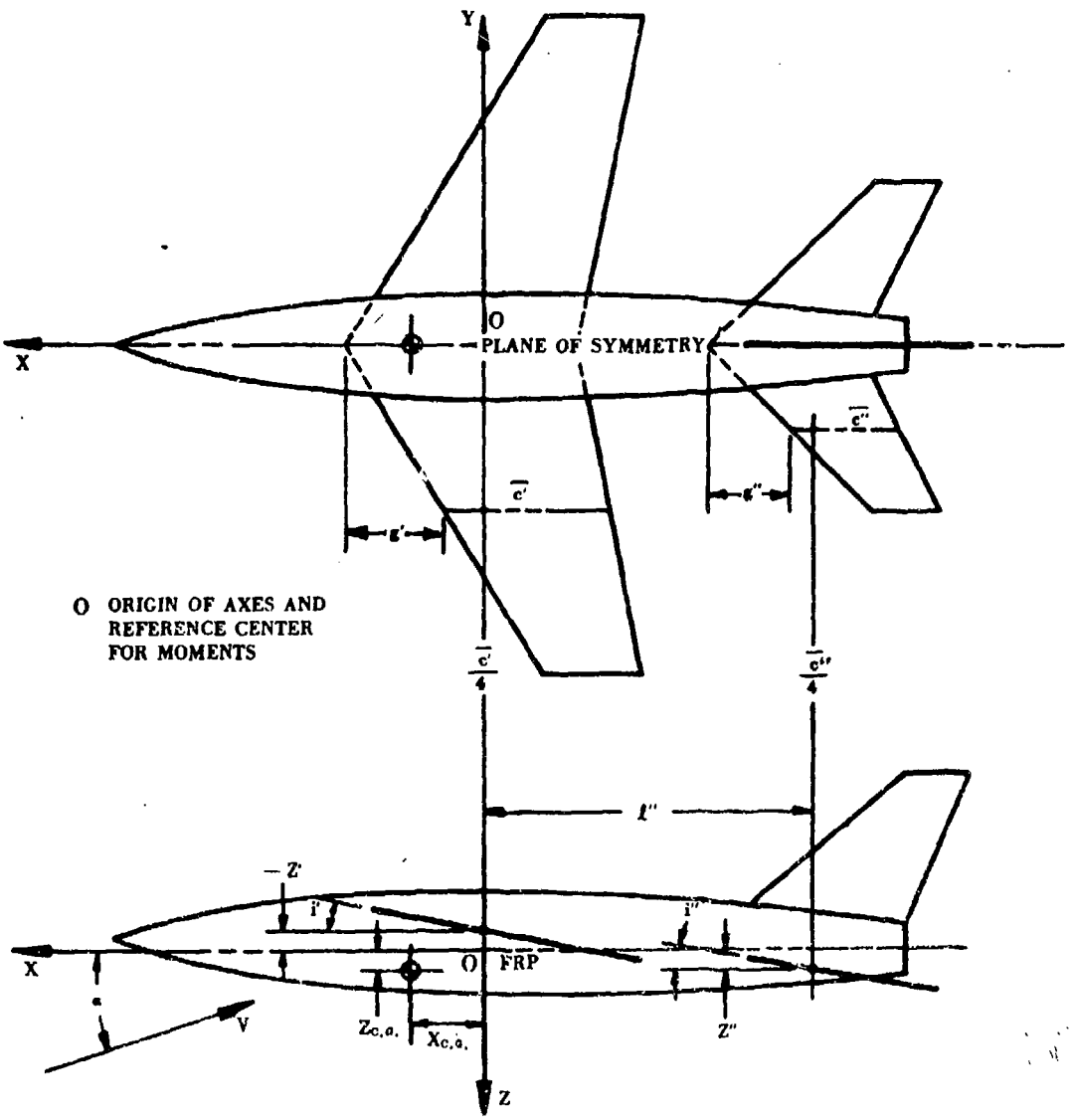

VEHICLE GEOMETRY FOR TAIL-LAST CONFIGURATIONS

Figure 4.5.2.1-7a VEHICLE GEOMETRIC PARAMETERS

Note: Z' and Z'' are measured from the FRP to the aerodynamic centers of the forward and aft surfaces, respectively.

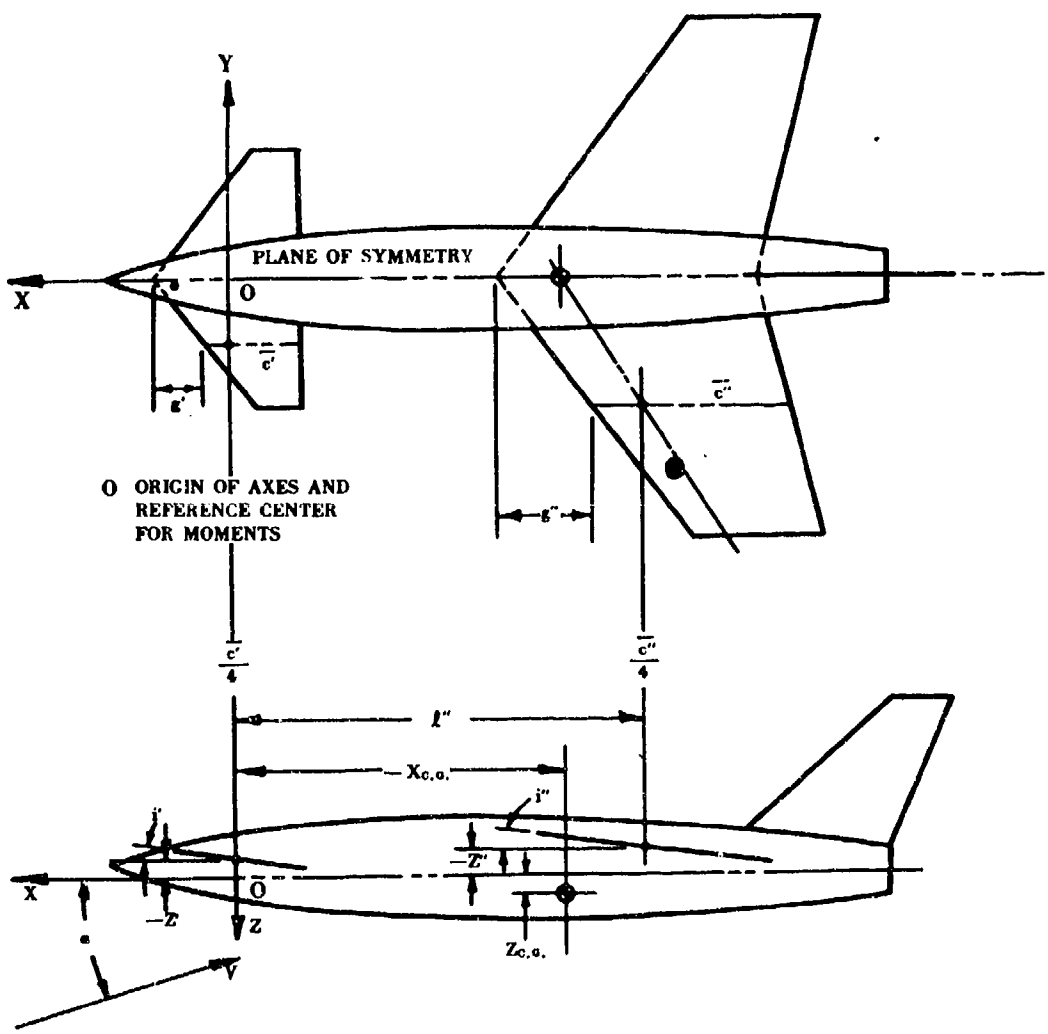

GEOMETRY FOR TAIL-FIRST CONFIGURATIONS

Figure 4.5.2.1-7b VEHICLE GEOMETRIC PARAMETERS (CONTD)

Note: Z' and Z'' are measured from the FRP to the aerodynamic centers of the forward and aft surfaces, respectively.

4.5.3 WING-BODY-TAIL DRAG

4.5.3.1 WING-BODY-TAIL ZERO-LIFT DRAG

The information presented in this section is for estimating the zero-lift drag coefficient of complete configurations in the aerodynamically clean condition. In general it consists of a synthesis of material presented in other sections. The methods are presented for a tail-aft configuration. The procedures to be applied in treating canard configurations in the various speed regimes are noted.

The problem of estimating the zero-lift drag is one of accounting for the mutual interferences between components. The methods use basically the same approaches to account for mutual interferences at subsonic and supersonic speeds as those of paragraphs A and C, respectively, of Section 4.3.3.1 for determining wing-body zero-lift drag. The Datcom method at subsonic speeds consists of applying an interference correction factor to the skin-friction and pressure-drag contributions of the exposed wing and body, and treating the tail panels as exposed components. At supersonic speeds the zero-lift drag of the configuration is obtained by adding the drag contributions of the exposed lifting surfaces and the isolated body. A simple fairing technique is used to approximate the zero-lift drag rise through the transonic speed regime.

Discussions of the various applicable theories are given in Sections 4.1.5.1, 4.2.3.1, and 4.3.3.1 and are not repeated here.

It should be pointed out that the basic approach taken here is satisfactory for preliminary design stability studies and that no attempt is made to provide methods suitable for performance estimates.

A. SUBSONIC ($M \leq 0.70$)

The zero-lift drag of a wing-body-tail configuration is approximated by adding the wing-body zero-lift drag determined by the method of Section 4.3.3.1 and the drag contributions of the isolated tail panels determined by the method of Section 4.1.5.1. Although the method for determining the wing-body contribution includes interference correction factors based on experimental results for wing-body combinations, it should be pointed out that most of the bodies were conventional, ogive-cylinder combinations of high fineness ratio, and no detailed investigation has been made to evaluate body effects. The tail-body combination also produces interference drag, but no explicit correction factors are presented for this effect. Chapter VII of reference 1 discusses the interference drag produced by tail configurations at their junctions with the fuselage as well as in the corners formed by the intersection of horizontal and vertical tails. Tail-body interference is compensated for to some extent in the Datcom by assuming that the average dynamic-pressure ratio at the tail panels is unity.

The Datcom method is applicable to configurations employing the following two classes of wing planforms:

Straight-Tapered Wings (conventional, trapezoidal planforms)

Non-Straight-Tapered Wings

- Double-delta wings
- Cranked wings
- Curved (Gothic and ogee) wings

Non-straight-tapered wing geometric parameters are presented in Section 2.2.2.

DATCOM METHOD

The subsonic zero-lift drag coefficient of a complete configuration is approximated by

$$C_{D_0} = \left(C_{D_0}\right)_{WB} + \Sigma_p \left(C_{D_0}\right)_p \qquad 4.5.3.1\text{-a}$$

where the subscript p refers to the tail panels, and

$\left(C_{D_0}\right)_{WB}$ is the zero-lift drag coefficient of the wing-body configuration, based on the reference area, obtained from paragraph A of Section 4.3.3.1.

$\left(C_{D_0}\right)_p$ is the zero-lift drag coefficient of a tail panel, based on the exposed panel geometry and referred to the reference area, obtained from paragraph A of Section 4.1.5.1. Applied in this manner, equation 4.1.5.1-a is expressed as

$$\left(C_{D_0}\right)_p = (C_f)_p \left[1 + L\left(\frac{t}{c}\right) + 100\left(\frac{t}{c}\right)^4\right]_p (R_{L.S.})_p \frac{\left[(S_{wet})_p\right]_e}{S_{ref}}$$

where $\left[(S_{wet})_p\right]_e$ is the wetted area of the exposed panel. The Reynolds number used in determining the turbulent flat-plate skin-friction coefficient is based on the mean aerodynamic chord $(\bar{c}_p)_e$ of the exposed panel.

The method is applied to tail-forward configurations by applying the wing-body method of Section 4.3.3.1 to the primary lifting-surface-body combination and the method of Section 4.1.5.1 to the exposed forward panel.

Sample Problem

Given: A wing-body-tail configuration of reference 2, designated 53-series.

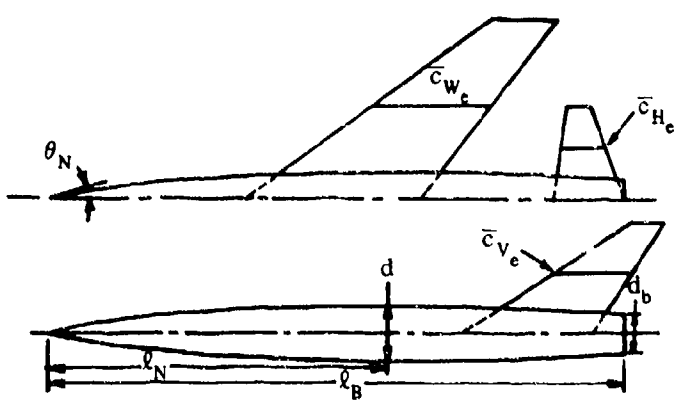

Wing Characteristics:

$A_W = 3.0$ $b_W = 10.80$ in. $\lambda_W = 0.40$ $S_W = S_{ref} = 38.89$ sq in.

$\Lambda_{LE_W} = 53.13^o$ $(\bar{c}_W)_e = 3.55$ in. $\left[(S_{wet})_W\right]_e = 62.86$ sq in.

$(t/c)_{av} = 0.044$ $(t/c)_{max}$ @ 0.30c $\Lambda_{(t/c)_{max}} = 49.3^o$

$$\frac{\left[(S_{wet})_W\right]_e}{S_{ref}} = 1.616$$

Horizontal-Tail Characteristics:

$A_H = 3.994$ $b_H = 5.56$ in. $\lambda_H = 0.334$ $\Lambda_{LE_H} = 8.53^o$

$(\bar{c}_H)_e = 1.296$ in. $\left[(S_{wet})_H\right]_e = 10.372$ sq in. $t/c = 0.03$

$(t/c)_{max}$ @ 0.30c $\Lambda_{(t/c)_{max}} = 0$ $\dfrac{\left[(S_{wet})_H\right]_e}{S_{ref}} = 0.2667$

Vertical-Tail Characteristics:

$A_V = 1.356$ $b_V = 3.294$ in. $\lambda_V = 0.275$ $\Lambda_{LE_V} = 56.55^o$

$(\bar{c}_V)_e = 2.305$ in. $\left[(S_{wet})_V\right]_e = 11.01$ sq in. $t/c = 0.03$

$(t/c)_{max}$ @ 0.30c $\Lambda_{(t/c)_{max}} = 45.3^o$ $\dfrac{\left[(S_{wet})_V\right]_e}{S_{ref}} = 0.2832$

Body Characteristics:

$\ell_B = 17.0$ in. $d = d_{max} = 1.588$ in. $d_b = 1.174$ in. $S_B = 1.083$ sq in.

$f = \ell_B/d = 10.70$ $d_b/d = 0.739$ $(S_S)_e = 23.63$ sq in. $\dfrac{(S_S)_e}{S_B} = 21.82$

$\dfrac{(S_S)_e}{S_{ref}} = 0.6076$ $\dfrac{S_B}{S_{ref}} = 0.0278$ Body ordinates: $r = 0.794\left[1 - \left(1 - \dfrac{2x}{19.833}\right)^2\right]^{3/4}$

The body is modified by a 1.369-inch cylindrical extension at $x = 12$.

Additional Characteristics:

$R_\ell = 0.393 \times 10^6$ per in. Polished metal surfaces (assume k = 0)

M = 0.4, 0.6, 0.7

Compute:

Step 1. Determine C_f for each component (Section 4.1.5.1) (For all components the admissible roughness $\ell/k = \infty$, and the skin-friction coefficient is obtained at the calculated R_ℓ)

Reynolds numbers

Wing: $R_\ell = (0.393 \times 10^6)(\bar{c}_W)_e = (0.393 \times 10^6)(3.55) = 1.395 \times 10^6$

Horizontal: $R_\ell = (0.393 \times 10^6)(\bar{c}_H)_e = (0.393 \times 10^6)(1.296) = 5.09 \times 10^5$

Vertical: $R_\ell = (0.393 \times 10^6)(\bar{c}_V)_e = (0.393 \times 10^6)(2.305) = 9.06 \times 10^5$

Body: $R_\ell = (0.393 \times 10^6)(\ell_B) = (0.393 \times 10^6)(17.0) = 6.68 \times 10^6$

Skin-friction coefficients as f(M) (figure 4.1.5.1-26)

M	$(C_f)_W$	$(C_f)_H$	$(C_f)_V$	$(C_f)_B$
0.4	0.00413	0.00495	0.00444	0.00315
0.6	0.00407	0.00488	0.00440	0.00310
0.7	0.00404	0.00484	0.00436	0.00308

Step 2. Determine the skin-friction and pressure-drag contributions of the components. (Sections 4.1.5.1 and 4.2.3.1)

Wing: $\left[1 + L\left(\frac{t}{c}\right) + 100\left(\frac{t}{c}\right)^4\right]_W = 1.05$ (figure 4.1.5.1-26a, for L = 1.2)

Horizontal: $\left[1 + L\left(\frac{t}{c}\right) + 100\left(\frac{t}{c}\right)^4\right]_H = 1.02$ (figure 4.1.5.1-26a, for L = 1.2)

Vertical: $\left[1 + L\left(\frac{t}{c}\right) + 100\left(\frac{t}{c}\right)^4\right]_V = 1.02$ (figure 4.1.5.1-26a, for L = 1.2)

Body: $$\left[1 + \frac{60}{(\ell_B/d)^3} + 0.0025\,\frac{\ell_B}{d}\right] = \left[1 + \frac{60}{(10.7)^3} + 0.0025\,(10.7)\right] = 1.0757$$

Step 3. Determine the lifting-surface correction factors. (Section 4.1.5.1)

Wing: $\cos \Lambda_{(t/c)_{max}} = 49.3^{o} = 0.6521$

Horizontal: $\cos \Lambda_{(t/c)_{max}} = \cos(0) = 1.00$

Vertical: $\cos \Lambda_{(t/c)_{max}} = \cos 45.3^{o} = 0.7034$

Lifting-surface correction factors as f(M) (figure 4.1.5.1-28b)

M	$(R_{L.S.})_W$	$(R_{L.S.})_H$	$(R_{L.S.})_V$
0.4	0.960	1.105	1.000
0.6	1.002	1.150	1.044
0.7	1.058	1.205	1.098

Step 4. Determine the wing-body interference correlation factor (figure 4.3.3.1-37

$R_{\ell_{fus}} = 6.68 \times 10^{6}$ (calculated above)

M	R_{WB}
0.40	1.028
0.60	0.988
0.70	0.963

Step 5. Determine the wing-body zero-lift drag exclusive of base drag. (Section 4.3.3.1)

$$\left(C_{D_0}\right)_{WB} - C_{D_b}\,\frac{S_B}{S_{ref}} = \left\{(C_f)_W \left[1 + L\left(\frac{t}{c}\right) + 100\left(\frac{t}{c}\right)^4\right]_W (R_{L.S.})_W \frac{\left[(S_{wet})_W\right]_e}{S_{ref}} + (C_f)_B \left[1 + \frac{60}{(\ell_B/d)^3} + 0.0025\,\frac{\ell_B}{d}\right] \frac{(S_S)_e}{S_{ref}}\right\} R_{WB} \quad \text{(equation 4.3.3.1-a)}$$

$$= \left\{(C_f)_W\,(1.05)\,(R_{L.S.})_W\,(1.616) + (C_f)_B\,(1.0757)\,(0.6076)\right\} R_{WB}$$

$$= \left\{(1.697)\,(C_f)_W\,(R_{L.S.})_W + (0.6536)\,(C_f)_B\right\} R_{WB}$$

①	②	③	④	⑤	⑥	⑦	⑧
M	$(C_f)_W$ step 1	$(R_{L.S.})_W$ step 3	(1.697) ② ③	$(C_f)_B$ step 1	(0.6536) ⑤	R_{WB} step 4	$(C_{D_0})_{WB} - C_{D_b}\frac{S_B}{S_{ref}}$ eq. 4.3.3.1-a (④ + ⑥) ⑦
0.4	0.00413	0.960	0.00673	0.00315	0.00206	1.028	0.00904
0.6	0.00407	1.002	0.00692	0.00310	0.00203	0.988	0.00884
0.7	0.00404	1.058	0.00725	0.00308	0.00201	0.967	0.00892

Step 6. Determine the base drag (based on S_B) (Section 4.2.3.1)

$$C_{D_b} = 0.029 \left(\frac{d_b}{d}\right)^3 \Big/ \sqrt{\left(C_{D_f}\right)_b} = 0.0117 \Big/ \sqrt{\left(C_{D_f}\right)_b} \text{ (equation 4.2.3.1-b)}$$

$$\left(C_{D_f}\right)_b = (C_f)_B \left[1 + \frac{60}{(\ell_B/d)^3} + 0.0025\,\frac{\ell_B}{d}\right]\frac{(S_S)_e}{S_B} = (C_f)_B\,(1.0757)\,(21.82) = (23.47)\,(C_f)_B$$

①	②	③	④	⑤
M	$(C_f)_B$ step 1	$(23.47)\,(C_f)_B$	$\sqrt{③}$	C_{D_b} eq. 4.2.3.1-b 0.0117/ ④
0.4	0.00315	0.0739	0.272	0.0430
0.6	0.00310	0.0728	0.270	0.0433
0.7	0.00308	0.0723	0.269	0.0435

Step 7. Determine the total wing-body zero-lift drag using equation 4.3.3.1-a.

①	②	③	④	⑤
M	$\left(C_{D_0}\right)_{WB} - C_{D_b}\frac{S_B}{S_{ref}}$ step 5, col. ⑧	C_{D_b} (based on S_B) step 6, col. ⑤	$C_{D_b}\frac{S_B}{S_{ref}}$ ③ (0.0278)	$\left(C_{D_0}\right)_{WB}$ (based on S_{ref}) ② + ④
0.4	0.00904	0.0430	0.00120	0.01024
0.6	0.00884	0.0433	0.00120	0.01004
0.7	0.00892	0.0435	0.00121	0.01013

Step 8. Determine the horizontal- and vertical-tail zero-lift drag contributions.

$$\left(C_{D_0}\right)_H = (C_f)_H \left[1 + L\left(\frac{t}{c}\right) + 100\left(\frac{t}{c}\right)^4\right]_H (R_{L.S.})_H \frac{\left[(S_{wet})_H\right]_e}{S_{ref}} \quad \text{(equation 4.1.5.1-a)}$$

$$= (C_f)_H\,(1.02)\,(R_{L.S.})_H\,(0.2667)$$

$$= (0.2720)\,(C_f)_H\,(R_{L.S.})_H$$

$$\left(C_{D_0}\right)_V = (C_f)_V \left[1 + L\left(\frac{t}{c}\right) + 100\left(\frac{t}{c}\right)^4\right]_V (R_{L.S.})_V \frac{\left[(S_{wet})_V\right]_e}{S_{ref}} \quad \text{(equation 4.1.5.1-a)}$$

$$= (C_f)_V\,(1.02)\,(R_{L.S.})_V\,(0.2832)$$

$$= (0.2889)\,(C_f)_V\,(R_{L.S.})_V$$

①	②	③	④	⑤	⑥	⑦
M	$(C_f)_H$ step 1	$(R_{L.S.})_H$ step 3	$\left(C_{D_0}\right)_H$ (based on S_{ref}) (0.2720) ② ③	$(C_f)_V$ step 1	$(R_{L.S.})_V$ step 3	$\left(C_{D_0}\right)_V$ (based on S_{ref}) (0.2889) ⑤ ⑥
0.4	0.00495	1.105	0.00149	0.00444	1.000	0.00128
0.6	0.00488	1.150	0.00153	0.00440	1.044	0.00133
0.7	0.00484	1.205	0.00159	0.00436	1.098	0.00138

Solution:

$$C_{D_0} = \left(C_{D_0}\right)_{WB} + \Sigma_p \left(C_{D_0}\right)_p \qquad \text{(equation 4.5.3.1-a)}$$

$$= \left(C_{D_0}\right)_{WB} + \left(C_{D_0}\right)_H + \left(C_{D_0}\right)_V$$

①	②	③	④	⑤
M	$\left(C_{D_0}\right)_{WB}$ step 7, col ⑤	$\left(C_{D_0}\right)_H$ step 8, col ④	$\left(C_{D_0}\right)_V$ step 8, col ⑦	C_{D_0} (based on S_{ref}) ② + ③ + ④
0.4	0.01024	0.00149	0.00128	0.0130
0.6	0.01004	0.00153	0.00133	0.0129
0.7	0.01013	0.00159	0.00138	0.0131

The calculated results are compared with test values from reference 2 in figure 4.5.3.1-18.

B. TRANSONIC ($0.7 \leq M \leq 1.1$)

Interference effects in the transonic range are generally greater than those in the subsonic range. This is due to the higher local velocities over the individual components and the greater propagation of the associated perturbations from their source. Furthermore, large supersonic flow regions often exist that contribute substantially to the wave drag. These effects may be accounted for by the application of the area-rule method, whereby the zero-lift drag of a wing-body-tail combination can be calculated as though the combination were a body of revolution with equivalent-area cross sections.

Application of the area-rule method for computation of transonic zero-lift drag is discussed in paragraph B of Section 4.3.3.1 and will not be repeated here. Since the method is quite tedious to compute by hand, automatic computing equipment is invariably used.

There is no general method available for determining the interference drag between components at transonic speeds. The method of approach used in Section 4.3.3.1 to determine transonic wing-body zero-lift drag could be extended to include the contributions of the tail panels in a manner similar to that used in paragraph A. However, such a method is considered to be unwarranted in view of the approximate nature of the results in conjunction with the labor required to apply the method.

The Datcom method has been selected for its ease of application. The degree of accuracy of the Datcom method should be equivalent to that using the build-up procedure discussed above.

DATCOM METHOD

An indication of the wing-body-tail zero-lift drag coefficient at transonic speeds may be obtained by the following procedure:

Step 1. Calculate the zero-lift drag coefficient over the subsonic and supersonic speed regimes by the methods of paragraphs A and C, respectively.

Step 2. Obtain the drag-divergence Mach number M_D from figure 4.5.3.1-19 as a function of wing geometry and general wing-body configuration.

Step 3. Obtain the zero-lift drag coefficient at M_D by

$$\left(C_{D_0}\right)_{M_D} = \left(C_{D_0}\right)_{M=0.7} + 0.002 \qquad 4.5.3.1\text{-b}$$

Step 4. Using the information determined in steps 1 through 3 as a guide, construct the approximate zero-lift drag coefficient for the range of Mach numbers between 0.7 and 1.1. The C_{D_0} vs M curve is faired tangent to a line whose slope is $\partial C_D/\partial M = 0.10$ passing through $\left(C_{D_0}\right)_{M_D}$

Equation 4.5.3.1-b for determining $\left(C_{D_0}\right)_{M_D}$ is arbitrary, since for all configurations an initial drag rise at $M_I = 0.7$ is assumed, and the drag-rise increment $\Delta C_{D_0} = \left[\left(C_{D_0}\right)_{M_D} - \left(C_{D_0}\right)_{M_I}\right]$ is assumed to be 0.002. (See sketch (a)).

The method is applicable only to tail-aft configurations with straight-tapered wings.

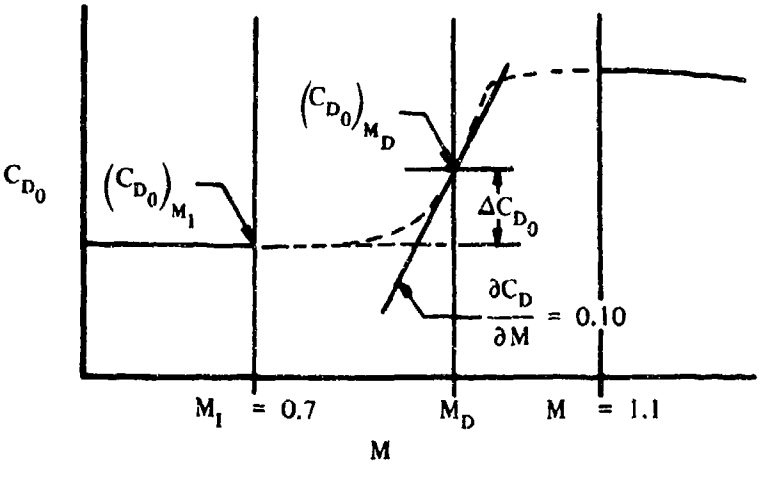

SKETCH (a)

Sample Problem

Given: The configuration of the sample problem of paragraph A. Some of the characteristics are repeated.

$A_W = 3.0 \quad \lambda_W = 0.40 \quad (\Lambda_{c/4})_W = 49.8^\circ$

$(t/c)_{av}$ = 0.044 Swept wing design without area rule

Compute:

M_D = 0.96 (figure 4.5.3.1-19)

$\left(C_{D_0}\right)_{M=0.7}$ = 0.0131 (sample problem, paragraph A)

$\left(C_{D_0}\right)_{M_D} = \left(C_{D_0}\right)_{M=0.7} + 0.002$ (equation 4.5.3.1-b)

$= 0.0131 + 0.002$

$= 0.0151$

The zero-lift drag coefficient is constructed for the range of Mach numbers between 0.7 and 1.1 in figure 4.5.3.1-18.

C. SUPERSONIC ($M \geq 1.1$)

The area-rule method, discussed in paragraph B of Section 4.3.3.1, has been adapted to supersonic speeds to allow the computation of the zero-lift drag of complete configurations at supersonic speeds. The resulting method, termed the "supersonic area rule" gives wave drag, including aerodynamic interferences, at a given Mach number.

Application of the "supersonic area rule" requires automatic computing equipment. A general discussion of the method and the steps required to prepare the machine input and to interpret the computed drag values are given in paragraph C of Section 4.3.3.1.

The method presented is essentially the same as that of paragraph A of this section. The zero-lift drag of exposed tail panels determined by the method of Section 4.1.5.1 is added to the wing-body zero-lift drag determined by the method of Section 4.3.3.1.

The Datcom method may be applied to configurations having the following classes of wing planforms:

Straight-Tapered Wings (conventional, trapezoidal planforms)

Non-Straight-Tapered Wings

- Double-delta wings
- Cranked wings
- Curved (Gothic and ogee) wings

Non-straight-tapered wing geometric parameters are presented in Section 2.2.2.

It is assumed that the average dynamic-pressure ratio at the tail panels is unity.

DATCOM METHOD

The supersonic zero-lift drag coefficient of a complete configuration is approximated by equation 4.5.3.1-a; i.e.,

$$C_{D_0} = \left(C_{D_0}\right)_{WB} + \Sigma_p \left(C_{D_0}\right)_p$$

where the subscript p refers to the tail panels, and

$\left(C_{D_0}\right)_{WB}$ is the zero-lift drag of the wing-body configuration, based on the reference area, obtained from paragraph C of Section 4.3.3.1.

$\left(C_{D_0}\right)_p$ is the zero-lift drag coefficient of a tail panel, based on the exposed panel geometry and referred to the reference area, obtained from paragraph C of Section 4.1.5.1. In applying this method the Reynolds numbers used in determining the turbulent flat-plate skin-friction coefficients are based on the mean aerodynamic chord $(\bar{c}_p)_e$ of the exposed panels, and the wetted areas are the exposed wetted areas of the panels $\left[(S_{wet})_p\right]_e$.

The method is applied to tail-forward configurations in the same manner as noted at the conclusion of paragraph A.

Sample Problem

Given: The configuration of the sample problem of paragraph A. Some of the characteristics are repeated.

Wing Characteristics:

$S_W = S_{ref} = 38.89$ sq in. $\quad (S_W)_e = 31.43$ sq in.

$\Lambda_{LE} = 53.13^o \quad (\bar{c}_W)_e = 3.55$ in. $\quad \left[(S_{wet})_W\right]_e = 62.86$ sq in.

$(t/c)_{av} = (t/c)_{eff} = 0.044 \quad \dfrac{(S_W)_e}{S_{ref}} = 0.808 \quad \dfrac{\left[(S_{wet})_W\right]_e}{S_{ref}} = 1.616$

Horizontal-Tail Characteristics:

$(S_H)_e = 5.186$ sq in. $\quad \left[(S_{wet})_H\right]_e = 10.372$ sq in.

$\Lambda_{LE_H} = 8.53^o \quad (\bar{c}_H)_e = 1.296$ in. $\quad t/c = (t/c)_{eff} = 0.03$

$\dfrac{(S_H)_e}{S_{ref}} = 0.1333 \quad \dfrac{\left[(S_{wet})_H\right]_e}{S_{ref}} = 0.2667$

Vertical-Tail Characteristics:

$(S_V)_e = 5.507$ sq in. $\quad \left[(S_{wet})_V\right]_e = 11.014$ sq in.

$\Lambda_{LE_V} = 56.55^o \quad (\bar{c}_V)_e = 2.305$ in. $\quad t/c = (t/c)_{eff} = 0.03$

$\dfrac{(S_V)_e}{S_{ref}} = 0.1416 \quad \dfrac{\left[(S_{wet})_V\right]_e}{S_{ref}} = 0.2832$

Body Characteristics:

$\ell_B = 17.0$ in. $\quad d = d_{max} = 1.588$ in. $\quad d_b = 1.174$ in. $\quad S_B = 1.083$ sq in.

$\ell_A = 7.0$ in. $\quad \ell_N = 10.0$ in. $\quad f_A = \ell_A/d = 4.408 \quad f_N = \ell_N/d = 6.297$

$\theta_N = 17^o \quad (S_S)_e = 23.63$ sq in. $\quad \dfrac{(S_S)_e}{S_{ref}} = 0.6076 \quad \dfrac{S_B}{S_{ref}} = 0.0278$

$\dfrac{(S_S)_e}{S_B} = 21.82$

Additional Characteristics:

$R_\ell \simeq 0.250 \times 10^6$ per in. Polished metal surface (assume $k = 0$)

M	1.10	1.20	1.30	1.40	Biconvex airfoils
β	0.458	0.663	0.831	0.980	

Compute:

Step 1. Determine C_f for each component (Section 4.1.5.1) (For all components the admissible roughness $\ell/k = \infty$, and the skin-friction coefficient is obtained at the calculated R_ℓ.)

Reynolds number

Wing: $R_\ell = (0.250 \times 10^6)(\bar{c}_W)_e = (0.250 \times 10^6)(3.55) = 8.875 \times 10^5$

Horizontal: $R_\ell = (0.250 \times 10^6)(\bar{c}_H)_e = (0.250 \times 10^6)(1.296) = 3.24 \times 10^5$

Vertical: $R_\ell = (0.250 \times 10^6)(\bar{c}_V)_e = (0.250 \times 10^6)(2.305) = 5.76 \times 10^5$

Body: $R_\ell = (0.250 \times 10^6)(\ell_B) = (0.250 \times 10^6)(17.0) = 4.25 \times 10^6$

Skin-friction coefficients (figure 4.1.5.1-26)

M	$(C_f)_W$	$(C_f)_H$	$(C_f)_V$	$(C_f)_B$
1.10	0.00417	0.00503	0.00450	0.00317
1.20	0.00411	0.00498	0.00443	0.00312
1.30	0.00404	0.00490	0.00436	0.00307
1.40	0.00397	0.00482	0.00429	0.00302

Step 2. Determine the skin-friction drag coefficients of the lifting surfaces, based on S_{ref}. (Section 4.3.3.1)

$$C_{D_f} = C_f \frac{(S_{wet})_e}{S_{ref}} \quad \text{(equation 4.3.3.1-f)}$$

Wing: $$\left(C_{D_f}\right)_W = (C_f)_W \frac{\left[(S_{wet})_W\right]_e}{S_{ref}} = 1.616\,(C_f)_W$$

Horizontal: $$\left(C_{D_f}\right)_H = (C_f)_H \frac{\left[(S_{wet})_H\right]_e}{S_{ref}} = 0.2667\,(C_f)_H$$

Vertical: $$\left(C_{D_f}\right)_V = (C_f)_V \frac{\left[(S_{wet})_V\right]_e}{S_{ref}} = 0.2832\,(C_f)_V$$

M	$\left(C_{D_f}\right)_W$	$\left(C_{D_f}\right)_H$	$\left(C_{D_f}\right)_V$
1.10	0.00674	0.00134	0.00127
1.20	0.00664	0.00133	0.00125
1.30	0.00653	0.00131	0.00123
1.40	0.00642	0.00129	0.00121

Step 3. Determine the wave-drag coefficients of the lifting surfaces, based on S_{ref}. (Section 4.3.3.1) (Since all lifting surfaces are conventional, straight-tapered planforms, the subscript bw used in Section 4.3.3.1 has been dropped.)

Wing:

$K = \frac{16}{3}$ (biconvex airfoil. See table, paragraph C, Section 4.1.5.1.)

$\beta \cot \Lambda_{LE_W} < 1.0$ for all M

$$\left(C_{D_w}\right)_W = K \cot \Lambda_{LE_W} \left(\frac{t}{c}\right)^2_{eff} \frac{(S_W)_e}{S_{ref}} \text{ (equation 4.3.3.1-i)}$$

$$= \frac{16}{3} \cot 53.13^o (0.044)^2 (0.808) = 0.00626$$

Horizontal:

$$K = \frac{16}{3} \text{ (biconvex airfoil)}$$

$\beta \cot \Lambda_{LE_H} > 1.0$ for all M

$$\left(C_{D_w}\right)_H = \frac{K}{\beta} \left(\frac{t}{c}\right)^2_{eff} \frac{(S_H)_e}{S_{ref}} \text{ (equation 4.3.3.1-h)}$$

$$= \frac{16}{3\beta} (0.03)^2 (0.1333) = \frac{0.000640}{\beta}$$

M	1.10	1.20	1.30	1.40
β	0.458	0.663	0.831	0.980
$\left(C_{D_w}\right)_H$	0.00140	0.000965	0.000770	0.000653

Vertical:

$$K = \frac{16}{3} \text{ (biconvex airfoil)}$$

$\beta \cot \Lambda_{LE_V} < 1.0$ for all M

$$\left(C_{D_w}\right)_V = K \cot \Lambda_{LE_V} \left(\frac{t}{c}\right)^2_{eff} \frac{(S_V)_e}{S_{ref}} \text{ (equation 4.3.3.1-i)}$$

$$= \frac{16}{3} \cot 56.55^o (0.03)^2 (0.1416) = 0.000449$$

Step 4. Determine the zero-lift drag of the lifting surfaces by combining the results of steps 2 and 3.

$$\left(C_{D_0}\right)_{\substack{\text{lifting} \\ \text{surface}}} = \left(C_{D_f} + C_{D_w}\right)_{\substack{\text{lifting} \\ \text{surface}}} \text{ (based on } S_{ref}\text{) (equation 4.3.3.1-e)}$$

	WING			HORIZONTAL			VERTICAL		
①	②	③	④	⑤	⑥	⑦	⑧	⑨	⑩
M	$(C_{D_f})_W$ step 2	$(C_{D_w})_W$ step 3	$(C_{D_0})_W$ ②+③	$(C_{D_f})_H$ step 2	$(C_{D_w})_H$ step 3	$(C_{D_0})_H$ ⑤+⑥	$(C_{D_f})_V$ step 2	$(C_{D_w})_V$ step 3	$(C_{D_0})_V$ ⑧+⑨
1.10	0.00674	0.00626	0.01300	0.00134	0.00140	0.00274	0.00127	0.000449	0.00172
1.20	0.00664	↓	0.01290	0.00133	0.000965	0.00230	0.00125	↓	0.00170
1.30	0.00653	↓	0.01279	0.00131	0.000770	0.00208	0.00123	↓	0.00168
1.40	0.00642	↓	0.01268	0.00129	0.000653	0.00194	0.00121	↓	0.00166

Step 5. Determine the body zero-lift drag coefficient.

Skin-friction coefficient (see step 1)

Wave-drag coefficients (method 2, paragraph C, Section 4.2.3.1)

Forebody

$$f_N = 6.297$$

$$K_N = 1.012 \text{ (figure 4.2.3.1-63)}$$

$$\left[f_N^2 + \frac{1}{4}\right] K_N = \left[(6.297)^2 + \frac{1}{4}\right] (1.012) = 40.38$$

①	②	③	④	⑤
M	β	β/f_N ② /6.297	$C_{D_{N_2}}\left[f_N^2 + \frac{1}{4}\right]K_N$ fig. 4.2.3.1-61	$C_{D_{N_2}}$ ④ /40.38
1.10	0.458	0.073	1.130	0.0280
1.20	0.663	0.105	1.124	0.0278
1.30	0.831	0.132	1.112	0.0275
1.40	0.980	0.156	1.100	0.0272

Afterbody

$d_b/d = 0.739$; $f_A = 4.408$

①	②	③	④	⑤
M	β	β/f_A ② /4.408	$C_{D_A}(f_A)^2$ fig. 4.2.3.1-64	C_{D_A} ④ /19.43
1.10	0.458	0.104	0.297	0.0153
1.20	0.663	0.150	0.290	0.0149
1.30	0.831	0.189	0.265	0.0136
1.40	0.980	0.222	0.248	0.0128

Nose bluntness

$C_{D_{N_1}} = 0$ (no bluntness)

Afterbody interference-drag coefficient

$$\left(\frac{2\ell_A}{d}\right)^2 = \left[\frac{(2)\ (7.0)}{1.588}\right]^2 = 77.72; \frac{\ell_N}{\ell_A} = \frac{10.0}{7.0} = 1.429; \left(\frac{d_b}{d}\right)^2 = (0.739)^2 = 0.546$$

$C_{D_{A(NC)}}\left(\frac{2\ell_A}{d}\right)^2 = 0.350$ (figure 4.2.3.1-44a)

$C_{D_{A(NC)}} = (0.350)/(77.72) = 0.00450$

Base-drag coefficient

$f_A = 4.408$; $(d_b/d)^2 = (0.739)^2 = 0.546$

$C_{D_b} = -C_{p_b}\left(\frac{d_b}{d}\right)^2$ (equation 4.2.3.1-g)

① M	② C_{p_b} fig. 4.2.3.1-50, interpolated	③ C_{D_b} eq. 4.2.3.1-g ② (0.546)
1.10	-0.101	0.0551
1.20	-0.101	0.0551
1.30	-0.101	0.0551
1.40	-0.101	0.0551

$$\left(C_{D_0}\right)_B = (C_f)_B \frac{(S_S)_e}{S_B} + C_{D_{N_2}} + C_{D_A} + C_{D_{A(NC)}} + C_{D_{N_1}} + C_{D_b} \quad \text{(based on } S_B\text{)}$$

(equation 4.2.3.1-h)

① M	② $(C_f)_B$ step1	③ $(C_f)_B \frac{(S_S)_e}{S_B}$ ② (21.82)	④ $C_{D_{N_2}}$	⑤ C_{D_A}	⑥ $C_{D_{A(NC)}}$	⑦ $C_{D_{N_1}}$	⑧ C_{D_b}	⑨ $\left(C_{D_0}\right)_B$ eq. 4.2.3.1-h ③ + ④ + ⑤ + ⑥ + ⑦ + ⑧
1.1	0.00317	0.0692	0.0280	0.0153	0.00450	0	0.0551	0.1721
1.2	0.00312	0.0681	0.0278	0.0149	↓	0	↓	0.1704
1.3	0.00307	0.0670	0.0275	0.0136		0		0.1677
1.4	0.00302	0.0659	0.0272	0.0128		0		0.1655

Solution:

$$C_{D_0} = \left(C_{D_0}\right)_{WB} + \Sigma_p \left(C_{D_0}\right)_p \quad \text{(based on } S_{ref}\text{)} \quad \text{(equation 4.5.3.1-a)}$$

$$= \left(C_{D_0}\right)_W + \left(C_{D_0}\right)_B \frac{S_g}{S_{ref}} + \left(C_{D_0}\right)_H + \left(C_{D_0}\right)_V$$

①	②	③	④	⑤	⑥	⑦
M	$(C_{D_0})_W$ step 4	$(C_{D_0})_H$ step 4	$(C_{D_0})_V$ step 4	$(C_{D_0})_B$ step 5	$(C_{D_0})_B \frac{S_B}{S_{ref}}$ ⑤ (0.0278)	C_{D_0} eq. 4.5.3.1-a ② + ③ + ④ + ⑥
1.10	0.01300	0.00274	0.00172	0.1721	0.00478	0.02224
1.20	0.01290	0.00230	0.00170	0.1704	0.00474	0.02164
1.30	0.01279	0.00208	0.00168	0.1677	0.00466	0.02121
1.40	0.01268	0.00194	0.00166	0.1655	0.00460	0.02088

The calculated results are compared with test values from reference 2 in figure 4.5.3.1-18.

REFERENCES

1. Hoerner, S.F.: Fluid-Dynamic Drag. Published by Author, 1958. (U)

2. Wakefield, R.M.: Effects of Wing-Crank, Leading Edge Chord Extensions and Horizontal-Tail Height on the Longitudinal Stability of Swept-Wing Models at Mach Numbers From 0.6 to 1.4. NASA TM X-92, 1959. (U)

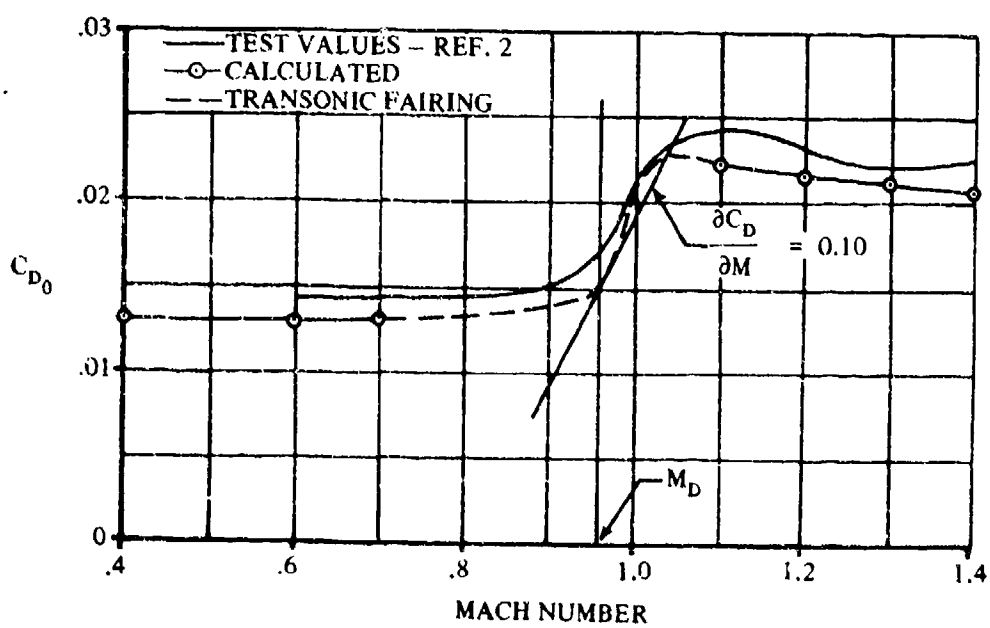

FIGURE 4.5.3.1-18 WING-BODY-TAIL ZERO-LIFT DRAG SUMMARY

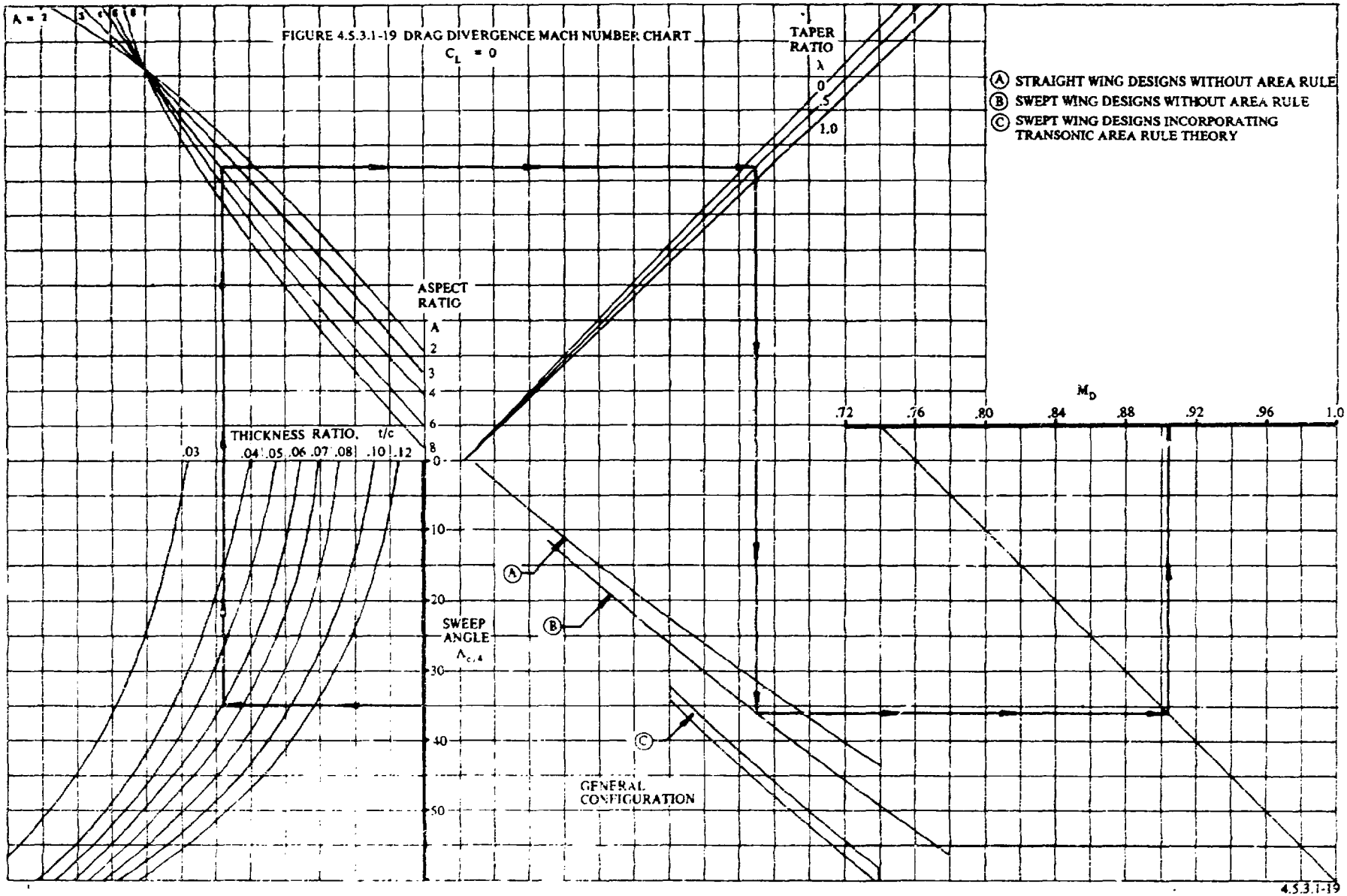
FIGURE 4.5.3.1-19 DRAG DIVERGENCE MACH NUMBER CHART
$C_L = 0$
TAPER RATIO λ
0
.5
1.0
Ⓐ STRAIGHT WING DESIGNS WITHOUT AREA RULE
Ⓑ SWEPT WING DESIGNS WITHOUT AREA RULE
Ⓒ SWEPT WING DESIGNS INCORPORATING TRANSONIC AREA RULE THEORY
ASPECT RATIO
A
2
3
4
6
8
THICKNESS RATIO, t/c
.03
.04
.05
.06
.07
.08
.10
.12
0
10
20
30
40
50
SWEEP ANGLE
$\Lambda_{c/4}$
M_D
.72
.76
.80
.84
.88
.92
.96
1.0
GENERAL CONFIGURATION
4.5.3.1-19

4.5.3.2 WING-BODY-TAIL DRAG AT ANGLE OF ATTACK

The information contained in this section is for estimating the drag coefficient of complete vehicle configurations at angle of attack.

The total vehicle drag at angle of attack consists of the following items:

1. wing-body zero-lift drag
2. wing-body induced drag
3. vertical stabilizer zero-lift drag
4. horizontal-stabilizer zero-lift drag
5. horizontal-stabilizer induced drag

The aerodynamic phenomena associated with, and methods for estimating Items 1-3 are presented in Sections 4.1.5.1, 4.3.3.1, 4.3.3.2, and 4.5.3.1 and are not repeated here.

A vehicle in non-maneuvering flight has the horizontal stabilizer or elevator deflected such that the sum of all moments about the vehicle center of gravity is zero. The pitching moment required to trim arises from the tail-lift and drag vectors and the position of these vectors with respect to the vehicle center of gravity. The method presented in this section is concerned primarily with the estimation of the drag increment resulting from the horizontal-stabilizer contribution required to trim the vehicle ($C_{m_{cg}} = 0$) at usable lift coefficients. A tail-aft configuration is assumed.

The equations pertinent to trim drag presented herein are applicable at all speeds. The method is restricted only by the limitations imposed upon the parameters in other sections of the Datcom. Of course, wing-body test values at the appropriate angle of attack are preferred.

DATCOM METHOD

All Speeds

The drag coefficient of a wing-body-tail configuration at angle of attack is given by

$$C_D = \left(C_{D_0}\right)_{WB} + \left(C_{D_0}\right)_V + \left(C_{D_i}\right)_{WB} + \Delta C_{D_{trim}} \qquad 4.5.3.2\text{-a}$$

where all coefficients are based on total wing area, and

$\left(C_{D_0}\right)_{WB}$ is the wing-body zero-lift drag coefficient obtained from Section 4.3.3.1.

$\left(C_{D_0}\right)_V$ is the vertical-stabilizer zero-lift drag coefficient obtained from Section 4.1.5.1 (see Section 4.5.3.1 for proper treatment of this term).

$\left(C_{D_i}\right)_{WB}$ is the induced drag coefficient of the wing-body combination obtained from Section 4.3.3.2.

$\Delta C_{D_{trim}}$ is the drag-coefficient increment between the drag coefficient of the complete vehicle in pitch equilibrium and the drag coefficient of the wing-body-vertical-tail configuration.

The trim-drag coefficient is given by

$$\Delta C_{D_{trim}} = \left(C_{D_H} \cos \epsilon_H + C_{L_H} \sin \epsilon_H\right) \frac{S_H}{S_W} \frac{q_H}{q_\infty} \qquad 4.5.3.2\text{-b}$$

where

C_{D_H} is the horizontal-stabilizer drag coefficient, based on total horizontal-stabilizer area and taken relative to the local-flow direction at the horizontal stabilizer.

C_{L_H} is the horizontal-stabilizer lift coefficient required to trim, based on total horizontal-stabilizer area and taken relative to the local-flow direction at the horizontal stabilizer.

ϵ_H is the average downwash angle at the horizontal stabilizer, obtained from Section 4.4.1.

S_H/S_W is the ratio of total horizontal-stabilizer area to total wing area.

q_H/q_∞ is the average dynamic-pressure ratio at the horizontal tail, obtained from Section 4.4.1.

The horizontal-stabilizer drag coefficient is given by

$$C_{D_H} = \left(C_{D_0}\right)_H + \left(C_{D_i}\right)_H \qquad 4.5.3.2\text{-c}$$

where

$\left(C_{D_0}\right)_H$ is the horizontal-stabilizer zero-lift drag coefficient obtained from Section 4.1.5.1 (see Section 4.5.3.1 for proper treatment of this term).

$\left(C_{D_i}\right)_H$ is the horizontal-stabilizer induced-drag coefficient given by

$$\left(C_{D_i}\right)_H = \frac{\left(C_{L_H}\right)^2}{\pi A_H e_H} \qquad 4.5.3.2\text{-d}$$

where

A_H is the geometric aspect ratio of the horizontal stabilizer.

e_H is Oswald's efficiency factor for induced drag of the horizontal tail. No method presently exists for determining this parameter. For purposes of the Datcom $e_H = 0.50$ for a horizontal stabilizer mounted on a body, and 0.70 for a horizontal stabilizer mounted on the vertical stabilizer.

The horizontal-stabilizer lift coefficient required to trim is given by

$$C_{L_H} = \frac{2\left[\dfrac{C_{m_{WB}}}{\cos(\Omega - \alpha + \epsilon_H)\ \dfrac{S_H}{S_W}\ \dfrac{q_H}{q_\infty}\ \dfrac{x_H}{\bar{c}_W}} + C_{D_{0_H}} \tan(\Omega - \alpha + \epsilon_H)\right]}{1 + \sqrt{1 - 4\left[\dfrac{\tan(\Omega - \alpha + \epsilon_H)}{\pi A_H e_H}\right]\left[\dfrac{C_{m_{WB}}}{\cos(\Omega - \alpha + \epsilon_H)\ \dfrac{S_H}{S_W}\ \dfrac{q_H}{q_\infty}\ \dfrac{x_H}{\bar{c}_W}} + C_{D_{0_H}} \tan(\Omega - \alpha + \epsilon_H)\right]}}$$

4.5.3.2-e

where

$(C_m)_{WB}$ is the wing-body pitching-moment coefficient given by

$$(C_m)_{WB} = (C_L)_{WB}\left(\frac{dC_m}{dC_L}\right)_{WB} + (C_{m_0})_{WB} \qquad 4.5.3.2\text{-f}$$

where

$\left(\dfrac{dC_m}{dC_L}\right)_{WB}$ is the wing-body pitching-moment-curve slope obtained from Section 4.3.2.2.

$(C_{m_0})_{WB}$ is the wing-body zero-lift pitching-moment coefficient. This parameter must be obtained from test data on a similar configuration or from Section 4.3.2.1.

$(C_L)_{WB}$ is the wing-body lift coefficient given by

$$(C_L)_{WB} = (C_{L_\alpha})_{WB}(\alpha - \alpha_0)_{WB} \qquad 4.5.3.2\text{-g}$$

where

$(C_{L_\alpha})_{WB}$ is the wing-body lift-curve slope, obtained from Section 4.3.1.2.

$(\alpha_0)_{WB}$ is the wing-body zero-lift angle of attack obtained from the wing-alone data of Section 4.1.3.1*.

α_{WB} is the wing-body angle of attack.

*Test data from a similar configuration should be used if available. Wing surface velocity is increased by the presence of the fuselage; therefore, when the fuselage is below the wing the lift is reduced and with the fuselage above the wing the lift will be increased. This effect is generally small unless wing-mounted bodies such as stores or nacelles are close to the fuselage or to each other.

x_H is the distance between the vehicle center of gravity and the quarter-chord point of the horizontal-stabilizer MAC (see Figure 4.5.3.2-4).

Ω is the angle defined by the intersection of x_H with the FRP (see Figure 4.5.3.2-4).

The drag increment due to longitudinally trimming a vehicle is used in conjunction with the lift increment required for trim to obtain points on the trimmed drag polar. The procedure used to obtain points on the trimmed drag polar is illustrated in Sketch (a).

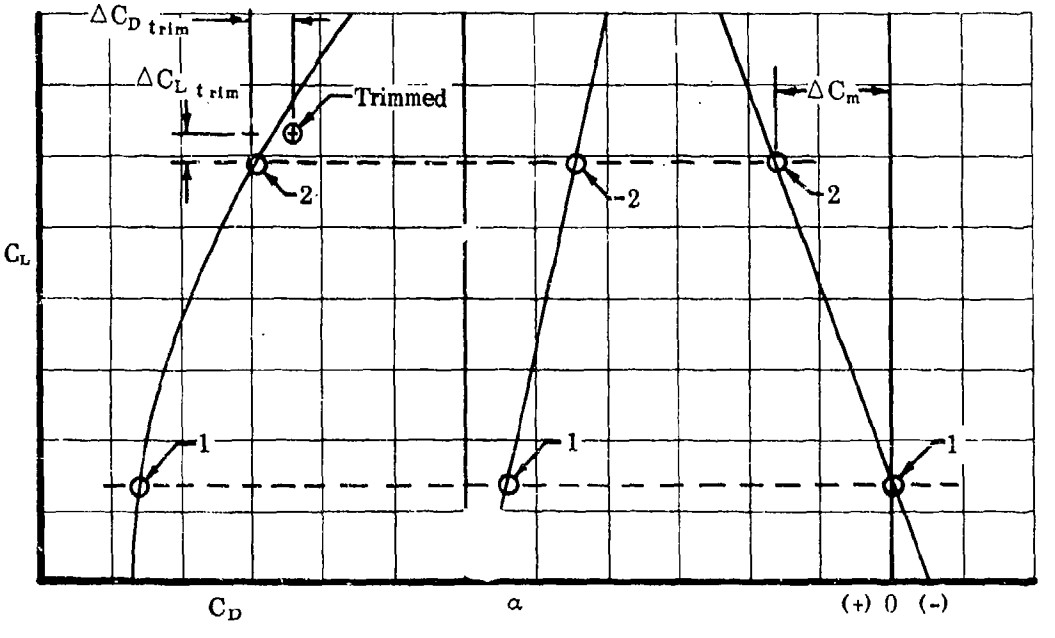

SKETCH (a)

Point 1 represents the horizontal tail-off trimmed condition ($C_{m_{WB}} = 0$). To trim the vehicle at Point 2 the drag polar is corrected for the horizontal-tail load required to apply ΔC_m. This tail load is (see Figure 4.5.3.2-5)

$$-\Delta C_m = -\Delta C_{D_{trim}} \frac{x_H}{\bar{c}_W} \sin(\Omega - \alpha) + \Delta C_{L_{trim}} \frac{x_H}{\bar{c}_W} \cos(\Omega - \alpha)$$

where the lift increment required to trim is

$$\Delta C_{L_{trim}} = \left(C_{L_H} \cos \epsilon_H - C_{D_H} \sin \epsilon_H\right) \frac{S_H}{S_W} \frac{q_H}{q_\infty}$$

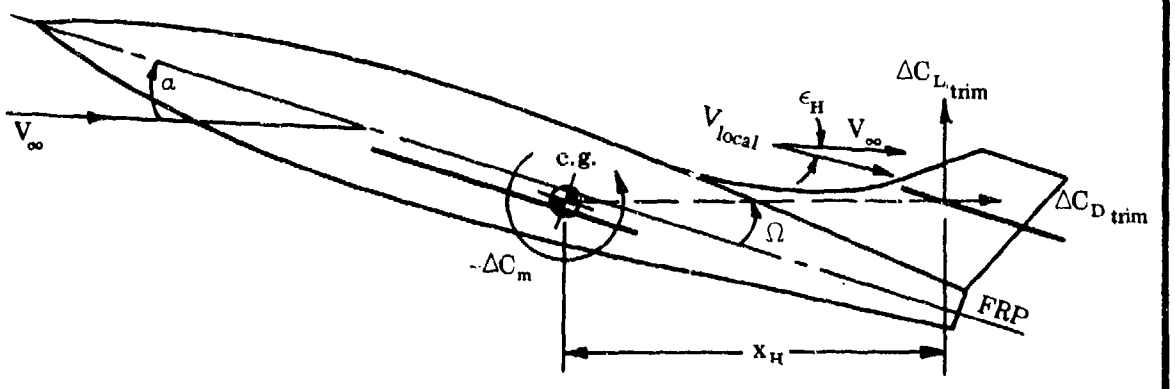

VIEW IN PLANE OF SYMMETRY

α = Airplane angle of attack (positive as shown)

x_H = Distance from c.g. to quarter-chord point of horizontal-stabilizer MAC

Ω = Angle defined by intersection of x_H with FRP (positive as shown with horizontal stabilizer above c.g.)

FIGURE 4.5.3.2-5 DEFINITION SKETCH FOR TRIM DRAG CALCULATIONS

4.6 POWER EFFECTS AT ANGLE OF ATTACK

The propulsion unit has many important influences upon the aerodynamic parameters of a vehicle, other than its main function of overcoming drag. The stability and control characteristics in particular can often be affected significantly by the effects of power.

This section presents methods for analyzing the power effects of jet- and propeller-propulsion units. In order to apply the Datcom methods, it is necessary to have experimental results for or to be able to estimate power-off lift and drag-force characteristics of the wing.

The power effects arising from propeller operation are frequently large enough to warrant consideration in preliminary analysis, especially in take-off and landing configurations. The propeller wash usually interacts with the flow around several of the airplane components, creating numerous separate effects that must be evaluated.

Propeller and propeller-wash characteristics are dependent upon several factors, such as blade shapes, fin effects, flow entrainment, and propeller rotating properties (dual rotating, counter rotating, etc.). These factors have prevented the formulation of a complete and accurate theoretical analysis. Consequently, propeller and propeller-wash effects are usually estimated by empirical methods.

The majority of the experimental data used to formulate the methods and design charts for propeller effects in this section were based on single-engine flaps-up configurations, because of a scarcity of adequate flaps-down data on single- or multiple-engine configurations. Consequently, the accuracy of the method for evaluating the power effects for flaps-down configurations is unknown. Methods are presented in Section 9.2 for evaluating the power effects of V/STOL-type aircraft configurations. For flaps-down configurations the methods of Section 9.2 should be used, since they will probably give a more accurate evaluation of the propeller power effects.

Although many of the power effects arising from propellers are undesirable, i.e., destabilizing, some are advantageous. For instance, large increases in maximum lift can be obtained from wing sections immersed in the propeller slipstream with the propeller operating at high-power conditions.

The power effects from jet-propelled aircraft are generally easy to analyze and have relatively minor effects on the stability and control characteristics of a vehicle. The increased simplicity is due to the elimination of the propeller and of the complex flow region of its slipstream on the wing, tail, and other surfaces. Jet-propelled aircraft are designed to keep the jet exhaust at a safe distance from the horizontal tail because of its extreme heat. Therefore, slipstream problems are minimized.

The Datcom methods presented in the following sections estimate the propeller effects at subsonic speeds and the jet effects at subsonic and supersonic speeds on the lift, drag, and pitching moments of a vehicle. By using the methods presented, a variety of vehicle and

power-plant configurations can be evaluated. These include conventional tail-aft aircraft and canard aircraft, having tractor, pusher, and single- and multiple-power plants. Positive- and negative-thrust and windmilling conditions for propellers are included. Reverse-thrust conditions that cause large interferences and flow separation cannot be evaluated by the methods presented in the following sections.

A general notation list and reference list are included in this section for all power-effects sections. Figures 4.6-12 and 4.6-13 indicate the geometric data required by the methods of these sections. Figure 4.6-12 specifically illustrates the geometric data required for calculating the wing area immersed in the slipstream.

NOTATION

SYMBOL	DEFINITION
A	aspect ratio
A_H	aspect ratio of horizontal tail
A_I	engine inlet duct area
A_i	effective aspect ratio of the immersed wing
a	inflow factor
b_H	span of horizontal tail, ft
b_i	span of immersed wing, ft
b_p	blade width, ft
C_1, C_2	constants for determining downwash
C_D	drag coefficient
C_{D_b}	base drag coefficient
C_{D_L}	drag-coefficient due to lift
C_{D_0}	zero-lift drag coefficient

SYMBOL	DEFINITION
ΔC_{D_0}	increment in zero-lift drag coefficient
$\left(\Delta C_{D_0}\right)_s$	increment in skin-friction drag caused by change in dynamic pressure
C_f	local skin-friction drag coefficient
C_L	lift coefficient
C_{L_P}	propeller lift coefficient
C_{L_W}	wing lift coefficient
$\left(\Delta C_L\right)_H$	change in lift coefficient due to horizontal tail
$\Delta C_{L_{max}}$	increment of maximum lift due to power effects
$\left(\Delta C_L\right)_{N_j}$	increment in lift due to the turning of the free-stream flow at the engine inlet
$\left(\Delta C_l\right)_{N_p}$	increment in lift due to propeller normal force
$\left(\Delta C_L\right)_q$	change in lift coefficient due to the change in slipstream dynamic pressure
$\left(\Delta C_L\right)_T$	increment in lift due to thrust
C_{L_α}	lift-curve slope of the power-off lift curve
$C_{L_{\alpha_H}}$	lift-curve slope of the horizontal tail
$\left(\Delta C_L\right)_{\Delta\alpha_w}$	increment in lift due to the upwash or downwash of the propeller flow field
$\left(\Delta C_L\right)_e$	increment in lift due to jet interference effects
C_m	pitching-moment coefficient

SYMBOL	DEFINITION
$\left(C_{m_0}\right)_i$	zero-lift pitching-moment coefficient of the components immersed in the slipstream
$\left(C_{m_0}\right)_{\text{area not immersed}}$	zero-lift pitching-moment coefficient of the area not immersed in the slipstream
$\left(C_{m_0}\right)_{\text{wing-body}}$	zero-lift pitching-moment coefficient of the wing-body combination
$\left(\Delta C_m\right)_H$	total change in pitching-moment coefficient of the horizontal tail
$\left(\Delta C_m\right)_L$	increment in pitching-moment coefficient due to the immersed-wing lift increments
$\left(\Delta C_m\right)_{N_p}$	increment in pitching-moment coefficient due to propeller normal force
$\left(\Delta C_m\right)_q$	increment in pitching-moment coefficient due to the change in slipstream dynamic pressure
$\left(\Delta C_m\right)_T$	increment in pitching-moment coefficient due to the offset of the thrust axis from the origin of the axes
$\left(\Delta C_{m_H}\right)_q$	increment in pitching-moment coefficient due to a change in the dynamic pressure on the horizontal tail
$\left(\Delta C_{m_H}\right)_\epsilon$	increment in pitching-moment coefficient due to a change in the downwash at the horizontal tail
C_{N_p}	propeller normal-force coefficient
$\left(C_{N_\alpha}\right)_p$	propeller normal-force derivative
$\left[\left(C_{N_\alpha}\right)_p\right]_{K_N=80.7}$	propeller normal-force derivative based on $K_N = 80.7$
c_i	average chord of immersed wing section
$\bar{c}$	mean aerodynamic chord, MAC

SYMBOL	DEFINITION
$\bar{c}_H$	mean aerodynamic chord of the horizontal tail
$\bar{c}_{\text{area not immersed}}$	mean aerodynamic chord of the wing area not immersed in the slipstream
f	propeller-inflow factor
h	altitude
i_H	incidence of the horizontal tail
i_T	incidence of the thrust axis
i_W	incidence of the wing
K	maximum-lift empirical constant
K_1	nacelle or fuselage empirical constant
K_D	propeller drag factor
K_N	empirical normal-force factor
ℓ_H	distance from axes origin to quarter-chord point on the mean aerodynamic chord of the horizontal tail
M_∞	free-stream Mach number
n	number of engines
n'	load factor
p	pressure
Δp	change in pressure
q	dynamic pressure
Δq	change in dynamic pressure

SYMBOL	DEFINITION
R_j	radius of jet orifice
R'_j	radius of equivalent jet orifice
R_p	propeller radius
S	reference area
S_{H_i}	area of portion of horizontal tail immersed in propeller slipstream
S_I	total surface area immersed in the slipstream
S_p	propeller disk area
S_W	wing area
S_{W_f}	wing planform area including and directly forward of flap area
T	thrust per engine
T'_c	thrust coefficient per engine
V	velocity
V_j	actual jet velocity
V'_j	equivalent jet velocity
W	weight
x'_e	longitudinal distance from the jet exit to the quarter-chord point of horizontal-tail mean aerodynamic chord
x'_H	longitudinal distance from jet-wake origin to quarter-chord point of horizontal-tail mean aerodynamic chord
x_I	longitudinal distance from quarter-chord point of wing mean aerodynamic chord to leading edge of engine inlet
x'_j	longitudinal distance from jet-wake origin to jet exit, usually considered to be 4.6 times the orifice exhaust radius

SYMBOL	DEFINITION
x_p	longitudinal distance from intersection of propeller plane with thrust axis and the quarter-chord point of the wing mean aerodynamic chord
x_W	longitudinal distance from moment-reference-center location to the aerodynamic center of the wing area immersed in the slipstream, positive for the aerodynamic center forward of the moment reference center.
y_T	spanwise distance from thrust axis to fuselage center line
z_H	vertical distance from X-axis to quarter-chord point of horizontal-tail mean aerodynamic chord
$z_{H_{eff}}$	vertical distance from quarter-chord point of horizontal-tail mean aerodynamic chord to the slipstream center line
z_{H_T}	vertical distance from propeller thrust axis to quarter-chord point of horizontal-tail mean aerodynamic chord
z_j'	vertical distance from jet thrust axis to quarter-chord point of horizontal-tail mean aerodynamic chord
z_s	vertical distance from X-axis to propeller-slipstream center line at the quarter-chord point of the wing mean aerodynamic chord
z_T	vertical distance from propeller thrust axis to coordinate origin
z_W	vertical distance from the quarter-chord point of the wing mean aerodynamic chord to the coordinate origin
α	angle of attack
α_0	angle of attack at zero lift
α_j	angle between thrust axis and direction of local velocity
α_p	angle between direction of local airstream and thrust axis
α_T	angle between thrust axis and direction of free stream
α_W	wing angle of attack
$\alpha_{C_{L_{max}}}$	angle of attack at maximum lift

SYMBOL	DEFINITION
β	propeller blade angle at 0.75 radius
ϵ_H	downwash at the quarter-chord point of the horizontal-tail mean aerodynamic chord
ϵ_p	downwash angle behind the propeller
ϵ_u	upwash angle ahead of wing
$\bar{\epsilon}$	effective downwash over the wing span
$\Delta\epsilon$	downwash increment
$\Delta\bar{\epsilon}$	mean-effective-downwash increment
$\frac{\Delta\bar{\epsilon}}{\Delta\epsilon}$	mean-effective-downwash ratio
$\frac{\partial\epsilon_p}{\partial\alpha_p}$	propeller-downwash gradient
$\frac{\partial\epsilon_u}{\partial\alpha}$	upwash gradient
λ_H	taper ratio of the horizontal tail
$\Lambda_{c/4}$	sweep angle of the wing quarter-chord
$\Lambda_{H_{c/4}}$	sweep angle of the horizontal-tail quarter-chord

SUBSCRIPTS

b	base conditions
H	horizontal tail
i	immersed in slipstream
L	lift
N	normal force

SYMBOL	DEFINITION
N_p	propeller normal force
s	slipstream conditions
T	thrust
W	wing
α	angle of attack
∞	free-stream conditions

REFERENCES

1. Abzug, M. J.: Effect of Jet and Rocket Operation on Static Longitudinal and Directional Stability. BuAer ADR Report M-35, 1945. (U)
2. Anon.: Flow Fields of Free Air Jets – A Report Bibliography. Defense Doc Center, DDC-ARB-41,247, 1965. (SRD) Title Unclassified
3. Anon.: Model C-133A Estimated Basic Stability and Control Data. Douglas Aircraft Co. Report LB-21984, 1956. (U)
4. Anon.: Preliminary Description of Method Used to Determine Slipstream Power Reduction Factor. Douglas Aircraft Co. Report DAC RR-1104, 1952. (U)
5. Anon.: Velocity Correlation Measurements in the Mixing Region of a Jet. AGARD 452, 1963. (U)
6. Bradbury, L. J. S., and Wood, M. N.: Static Pressure Distribution Around a Circular Jet Exhausting Normally From a Plane Wall Into an Airstream. ARC CP-822, 1964. (U)
7. Bressette, W. E.: Investigation of the Jet Effects on a Flat Surface Downstream of the Exit of a Simulated Turbojet Nacelle at a Free-Stream Mach Number of 2.02. NACA RM L54E05a, 1954. (U)
8. Carroll, R. L.: Aerodynamics of Powered Flight. John Wiley and Sons, New York, 1960. (U)
9. Cherwat, A. F.: Investigation of the Flow and Drag Due to Supersonic Jets Discharging Upstream Into a Supersonic Flow. Rand Corp., P-2943, 1964. (U)
10. Church, R. M. W.: A Method for the Calculation of Force, Moment and Power Coefficients of Propellers in Forward Flight of Tilt Angles From 0 to 90 Degrees. Naval Ship Research and Development Center, TN AL-119, 1969. (U)
11. Cubbage, J. M., Jr.: Jet Effects on Base and Afterbody Pressures of a Cylindrical Afterbody at Transonic Speeds. NACA RM L56C21, 1956. (U)
12. Curry, T. B., Jr., and Crabill, N. L.: Rocket-Model Investigation of Lateral Stability Characteristics and Power Effects of a Jet-Engine Airplane Configuration with Tail Boom at Mach Numbers From 1.15 to 1.37. NASA TN D-638, 1961. (U)
13. Decker, J., et al: USAF Stability and Control Handbook. M-3671, 1956. (U)
14. Draper, J. W., and Kuhn, R. E.: Investigation of the Aerodynamic Characteristics of a Model Wing-Propeller Combination and of the Wing and Propeller Separately at Angles of Attack up to 90°. NACA TN 3304, 1954. (U)
15. Fulenga, R. A., and Judd, J. H.: Flight Investigation of the Effect of Underwing Propulsive Jets on the Lift, Drag, and Longitudinal Stability of a Delta-Wing Configuration at Mach Numbers from 1.23 to 1.62. NACA RM L55I13, 1955. (U)

16. Falanga, R. A., and Judd, J. H.: Low-Lift Flight Tests of Four-Engine Delta-Wing Configurations to Obtain Wing Pressure and Aerodynamic Coefficients Including Some Jet Effects From Mach Numbers 0.5 to 1.5. NASA TM X-282, 1960. (C) Title Unclassified

17. Faris, G.N.: Some Entrainment Properties of a Turbulent Axi-Symmetric Jet. Mississippi Univ. RR 39, 1963. (U)

18. Ferrari, C.: Interference Between a Jet Issuing Laterally From a Body and the Enveloping Supersonic Stream. Johns Hopkins Univ., Bumblebee Report 286, 1959. (U)

19. Fink, M. P., Cocke, B. W., and Lipson, S.: A Wind-Tunnel Investigation of a 0.4-Scale Model of an Assault-Transport Airplane With Boundary-Layer Control Applied. NACA RM L55G26a, 1956. (U)

20. George, M., and Kisielowski, E.: Investigation of Propeller Slipstream Effects on Wing Performance. USAAVLABS TR-67-67, 1967. (U)

21. Goett, H. J., and Delaney, N. K.: Effect of Tilt of the Propeller Axis on the Longitudinal-Stability Characteristics of Single-Engine Airplanes. NACA A-59, 1944. (U)

22. Graham, E. W., et al: A Preliminary Theoretical Investigation of the Effects of Propeller Slipstream on Wing Lift. Douglas Aircraft Co. Report SM-14991, 1953. (U)

23. Greenwood, G. H.: An Investigation Into a Technique for Measuring Jet Interference Effects Using Free-Flight Models. ARC CP-969, 1966. (U)

24. Harries, M. H.: Pressure on Axisymmetric Base in Transonic or Supersonic Free Stream in the Presence of a Jet. Aero. Res. Inst. of Sweden FFA R-111, 1967. (U)

25. Jackson, B. G., and Crabill, N. L.: Free-Flight Investigation of Jet Effects at Low Supersonic Mach Numbers on a Fighter-Type Configuration Employing a Tail-Boom Assembly – Longitudinal Stability and Trim. NACA RM L57F19, 1957. (U)

26. Johnson, H. S.: Wind-Tunnel Investigation of Effects of Tail Length on the Longitudinal and Lateral Stability Characteristics of a Single-Propeller Airplane Model. NACA TN 1766, 1948. (U)

27. Korst, H. H., Chow, W. L., and Zumwalt, G. W.: Research on Transonic and Supersonic Flow of a Real Fluid at Abrupt Increases in Cross Section. Univ. of Ill. ME Tech Report 39-2-5, 1959. (U)

28. Krase, W. H.: Thrust Deflection for Cruise. Rand Corp. Paper 3450, 1966. (U)

29. Lees, J. H., Davies, H., and Callen, C.: Wind Tunnel Tests on the Effect of Extreme Slipstream on Single and Twin-Engine Monoplanes with Split or Slotted Flaps. ARC R&M 1797, 1937. (U)

30. Peake, D. J.: The Pressures on a Surface Surrounding a Jet Issuing Normal to a Mainstream. NRCC Aero Report LR-410, 1964. (U)

31. Pitts, W. C., and Wiggins, L. E.: Axial-Force Reduction by Interference Between Jet and Neighboring Afterbody. NASA TN D-332, 1960. (U)

32. Ribner, H. S.: Field of Flow About a Jet and Effects of Jets on Stability of Jet-Propelled Airplanes. NACA WR L-213, 1946. (U)

33. Ribner, H. S.: Formulas for Propellers in Yaw and Charts of the Side-Force Derivative. NACA WR L-217, 1943. (U)

34. Ribner, H. S.: Notes on the Propeller and Slipstream in Relation to Stability. NACA WR L-25, 1944. (U)

35. Ribner, H. S.: Propellers in Yaw. NACA WR L-219, 1943. (U)

36. Ribner, H. S.: Proposal for a Propeller Side-Force Factor. NACA WR L-336, 1943. (U)

37. Ribner, H. S.,: A Transonic Propeller of Triangular Platform. NACA TN 1303, 1947. (U)

38. Rossiter, J. E., and Kurn, A. G.: Wind Tunnel Measurements of the Effect of a Jet on the Time Average and Unsteady Pressures on the Base of a Bluff Afterbody. ARC CP-903, 1965. (U)

39. Rylands, H. D.: Some Data on the Effects of Thrust on Drag at Subsonic Speeds. Aeroplane and Armament Experimental Estab., Gr. Brit. AAEE/Res/309, 1962. (U)

40. Salmi, R. J.: Effects of Jet Billowing on Stability of Missile-Type Bodies at Mach 3.85. NASA TN D-284, 1960. (U)

41 Salmi, R. J., and Klann, J. L.: Interference Effects at Mach 1.9 on a Horizontal Tail Due to Trailing Shock Waves From an Axisymmetric Body With an Exiting Jet. NACA RM E55J13e, 1956. (U)

42. Smelt, R., and Davies, H.: Estimation of Increase in Lift Due to Slipstream. ARC R&M 1788, 1937. (U)

43. Smith, R. D.: The Effect of Free Stream Turbulence and Vorticity on the Field of a Free Jet. MIT ASRL TR 1013, 1963. (U)

44. Squire, H. B., and Trouncer, J.: Round Jets in a General Stream. ARC R&M 1974, 1944. (U)

45. Sweberg, H. H., and Dingeldein, R. C.: Summary of Measurements in Langley Full-Scale Tunnel of Maximum Lift Coefficients and Stalling Characteristics of Airplanes. NACA WR L-145, 1945. (U)

46. Swihart, J. M., and Crabill, N. L.: Steady Loads Due to Jet Interference on Wings, Tails, and Fuselages at Transonic Speeds. NACA RM L57D24b, 1957. (U)

47. Tomlinson, B. N.: A Brief Note on the Effect of an Offset Thrust Line on the Longitudinal Static Stability of an Aeroplane. Jour. Royal Aeron. Soc., Vol. 59, Aug. 1955. (U)

48. Vidal, R. J., Curtis, J. T., and Hilton, J. H.: The Influence of Two-Dimensional Stream Shear on Airfoil Maximum Lift. Cornell Aeron. Lab., Report A1-1190-A-7, 1961. (U)

49. Vidal, R. J., Hilton, J. H., and Curtis, J. T.: The Two-Dimensional Effects of Slipstream Shear on Airfoil Characteristics. Cornell Aeron. Lab., Report A1-1109-A-5, 1960. (U)

50. Weiberg, J. A., Griffin, R. N., Jr., and Florman, G. L.: Large-Scale Wind-Tunnel Tests of an Airplane Model With an Unswept, Aspect-Ratio-10 Wing, Two Propellers, and Area-Suction Flaps. NACA TN 4365, 1958. (U)

51. Weil, J., and Sleeman, W. C., Jr.: Prediction of the Effects of Propeller Operation on the Static Longitudinal Stability of Single-Engine Tractor Monoplanes With Flaps Retracted. NACA TN 1722, 1948. (U)

52. Weil, J., and Wells, E. G.: Wind-Tunnel Tests of the 1/8-Scale Powered Model of the Curtiss XBTC-2 Airplane. I-Preliminary Investigation of Longitudinal Stability. NACA WR L-667, 1944. (U)

53. Weil, J., and Boykin, R. I.: Wind-Tunnel Tests of the 0.15-Scale Powered Model of the Fleetwings XBTK-1 Airplane Longitudinal Stability and Control. NACA WR L-785, 1945. (U)

54. Wu, J. C., Mosher, D. K., and Wright, M. A.: Experimental and Analytical Investigations of Jets Exhausting Into a Deflecting Stream. AIAA P-69-0223, 1969. (U)

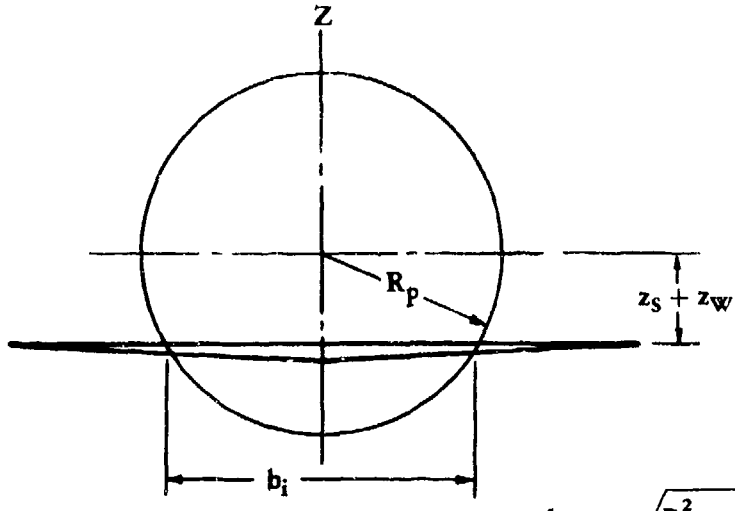

$$b_i = 2\sqrt{R_p^2 - (z_s + z_w)^2}$$

Cross section taken at quarter-chord of wing MAC for S_i (S_{H_i} is found in an identical manner as S_i with the cross section taken at the quarter-chord of the tail MAC.)

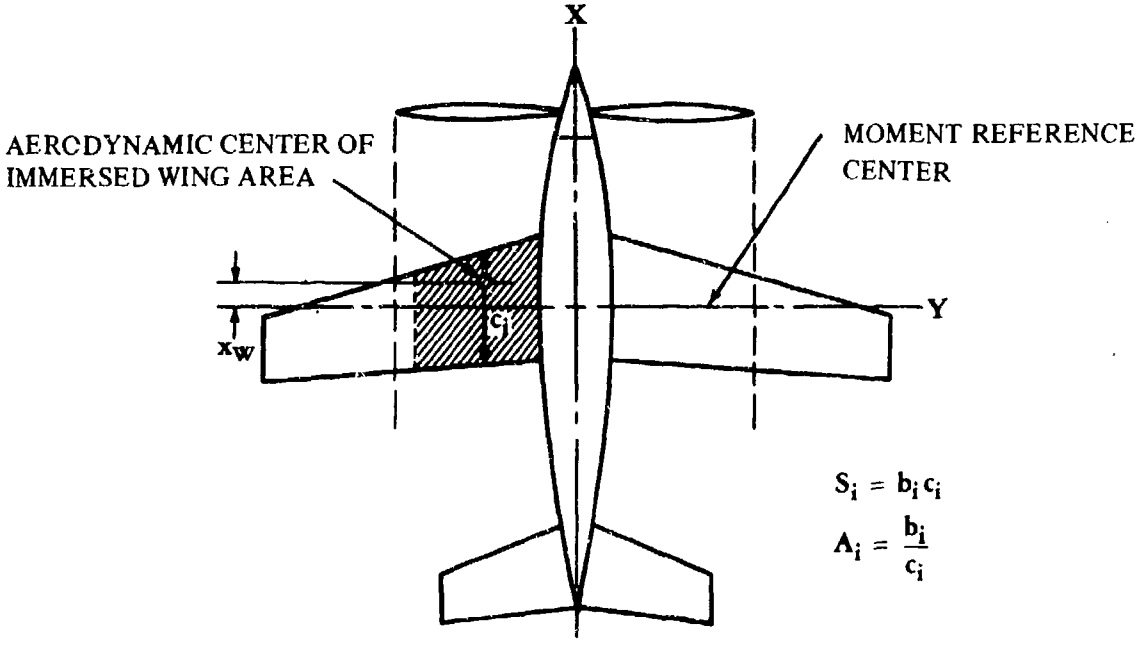

$$S_i = b_i c_i$$

$$A_i = \frac{b_i}{c_i}$$

FIGURE 4.6-12 DEFINITION SKETCH FOR CALCULATION OF IMMERSED WING AREA

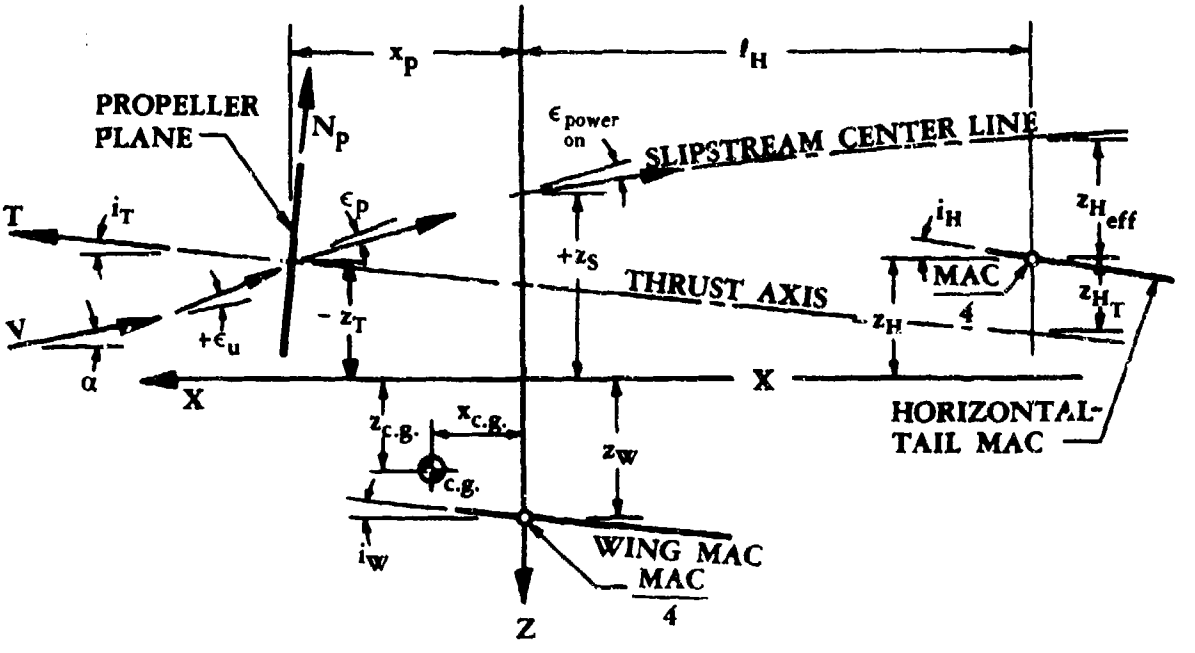

FIGURE 4.6-13a DEFINITION SKETCH FOR PROPELLER POWER EFFECTS CALCULATIONS

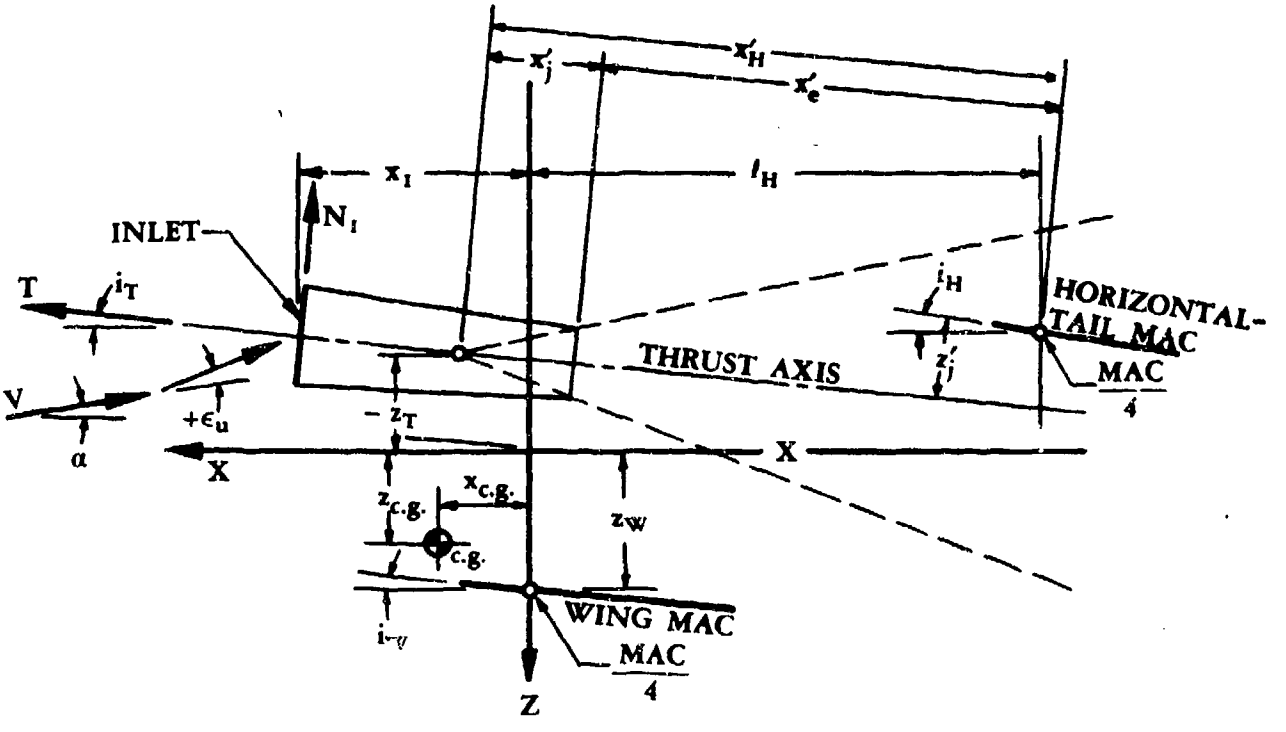

FIGURE 4.6-13b DEFINITION SKETCH FOR JET POWER EFFECTS CALCULATIONS

4.6.1 POWER EFFECTS ON LIFT VARIATION WITH ANGLE OF ATTACK

A. PROPELLER POWER EFFECTS ON LIFT

The primary purpose of a propeller is to develop thrust. In performing this function, the propeller often causes pronounced changes in the aerodynamic characteristics of a vehicle.

The effects of a propeller on the forces and moments acting on a vehicle may be divided into two groups, those due to the direct action of the propeller forces and those due to the propeller slipstream.

The first group includes the forces and moments due to the thrust vector and the forces and moments acting on the propeller as a result of its inclination to the oncoming stream. When a propeller is placed at an angle of attack, a force results normal to the thrust axis in the vertical plane. A pitching moment and a yawing moment also result. These forces and moments act on the propeller because of the unsymmetrical loading on the blades as a function of their rotational position. For counterrotating propellers the normal forces and pitching moments are additive, but the yawing moments cancel. These forces and moments are generally functions of propeller geometry.

The second group, those due to slipstream effects, depends greatly upon the component arrangement of the vehicle. However, the following generalizations can be made.

The dynamic pressure behind the propeller may be greater or less than the free-stream dynamic pressure, depending upon whether the propeller is delivering positive or negative thrust, respectively. The forces and moments acting on airframe components immersed in the slipstream are directly proportional to the slipstream dynamic pressure.

Because of the normal force acting on a propeller at angle of attack, a downwash field is generated behind the propeller plane. This downwash field changes the angle of attack of the airframe components operating in the propeller slipstream.

The method presented in this section for estimating propeller power effects on lift is based on a tail-last configuration. The method was taken from reference 1, which was developed from reference 2. The method predicts increments of lift for given values of thrust coefficient and angle of attack in the linear range. The effect of power on maximum lift is given in Section 4.6.2.

DATCOM METHOD

The Datcom method estimates the power-on lift curves based on power-off lift curves as a function of angle of attack, thrust coefficient, and lift coefficient.

This method analyzes the increments of lift coefficient due to propeller power effects in the following order:

1. Lift component of the thrust
2. Lift component of the propeller normal force
3. Change in angle of attack of the section of the wing in the propeller slipstream, due to the downwash flow field behind the propeller
4. Change in dynamic pressure over the section of the wing in the propeller slipstream
5. Change in lift due to downwash and changes in dynamic pressure acting on the horizontal tail

After the above lift increments for a given angle of attack have been calculated, the accumulated total is then applied to the power-off lift curve to obtain a point on the power-on lift curve. After several points have been generated (by considering several angles of attack), the linear section of the power-on lift curve is obtained for a given thrust coefficient.

The above increments in lift can be determined by the following steps. (Reference should be made to figure 4.6-13a for geometric definitions. In all cases the lift increments are based on the wing reference area.)

Step 1. Calculate the lift component of thrust as follows:

a. Calculate the angle of attack of the thrust axis α_T measured from the free-stream direction by

$$\alpha_T = i_T + \alpha \qquad 4.6.1\text{-a}$$

b. Calculate the thrust coefficient per engine T_c' (if not given or assumed) by

$$T_c' = \frac{T}{q_\infty S_W} \qquad 4.6.1\text{-b}$$

where the thrust per engine T is a given or chosen quantity.

c. Calculate the lift component of thrust by

$$\left(\Delta C_L\right)_T = nT_c' \sin \alpha_T \qquad 4.6.1\text{-c}$$

where n is the number of engines. This equation is valid only when the thrust coefficients and the angles of attack of the thrust axis to the free stream are equal for all n engines.

Step 2. Calculate the lift component of propeller normal force per engine as follows:

a. Calculate the empirical normal-force factor K_N per blade (usually supplied by the propeller manufacturer) by

$$K_N = 262\left(\frac{b_p}{R_p}\right)_{.3R_p} + 262\left(\frac{b_p}{R_p}\right)_{.6R_p} + 135\left(\frac{b_p}{R_p}\right)_{.9R_p} \qquad 4.6.1\text{-d}$$

where the subscript indicates the radial position from the center of the propeller where the blade width b_p is to be evaluated.

b. From figure 4.6.1-25a (taken from reference 3) obtain a value for the propeller normal-force coefficient $\left[\left(C_{N_\alpha}\right)_p\right]_{K_N = 80.7}$, based on $K_N = 80.7$, as a function of propeller blade angle and type of propeller.

c. Calculate the true propeller normal-force coefficient $\left(C_{N_\alpha}\right)_p$ by

$$\left(C_{N_\alpha}\right)_p = \left[\left(C_{N_\alpha}\right)_p\right]_{K_N = 80.7}\left[1 + 0.8\left(\frac{K_N}{80.7} - 1\right)\right] \text{ (per radian)} \qquad 4.6.1\text{-e}$$

d. Evaluate the propeller correlation parameter defined as

$$\frac{S_W T_c'}{8R_p^2}$$

e. From figure 4.6.1-25b (taken from reference 3) obtain a value for the propeller-inflow factor f as a function of the propeller correlation parameter evaluated above (step 2.d).

f. Calculate the propeller disk area S_p by

$$S_p = \pi R_p^2 \qquad 4.6.1\text{-f}$$

g. Calculate the angle of attack of the propeller plane (local airstream to thrust axis) α_p by

$$\alpha_p = \alpha_T + \frac{\partial \epsilon_u}{\partial \alpha}(\alpha_W - \alpha_0) \qquad 4.6.1\text{-g}$$

where the upwash gradient $\partial\epsilon_u/\partial\alpha$ at the propeller may be obtained in Section 4.4.1 and

$$\alpha_W = \alpha + i_W \qquad \text{4.6.1-h}$$

h. Calculate the lift component of the propeller normal force by

$$\left(\Delta C_L\right)_{N_p} = f\left(C_{N_\alpha}\right)_p \frac{\alpha_p}{57.3} \frac{S_p}{S_W} \cos\alpha_T \qquad \text{4.6.1-i}$$

For multiple-engine configurations the total lift component of the propeller normal force is found by summing the single components due to each engine.

Step 3. Calculate the increment of lift due to the change in angle of attack on the wing induced by the propeller flow field per engine as follows:

a. Calculate the upwash gradient $\partial\epsilon_p/\partial\alpha_p$ by

$$\frac{\partial\epsilon_p}{\partial\alpha_p} = C_1 + C_2\left(C_{N_\alpha}\right)_p \qquad \text{4.6.1-j}$$

where the constants C_1 and C_2 are obtained from figure 4.6.1-26 as a function of the propeller correlation parameter. The parameter $\left(C_{N_\alpha}\right)_p$ is obtained from step 2.c.

b. Calculate the downwash ϵ_p behind the propeller by

$$\epsilon_p = \frac{\partial\epsilon_p}{\partial\alpha_p}\alpha_p \qquad \text{4.6.1-k}$$

where the angle of attack of the propeller plane α_p is determined in step 2.g.

c. Calculate the change in the wing angle of attack $\Delta\alpha_W$ ahead of or behind the propeller by

$$\Delta\alpha_W = \frac{-\epsilon_p}{1 + \partial\epsilon_u/\partial\alpha} \qquad \text{4.6.1-l}$$

d. Calculate the angle of upwash ϵ_u at the propeller by

$$\epsilon_u = \frac{\partial\epsilon_u}{\partial\alpha}\left(\alpha_W - \alpha_0\right) \qquad \text{4.6.1-m}$$

e. Calculate the vertical distance from the X-axis to the propeller slipstream center line at the quarter-chord of the wing MAC by

$$z_s = x_p \tan(\alpha_T + \epsilon_u - \epsilon_p) - z_T \qquad 4.6.1\text{-n}$$

It should be noted that this equation is based on the assumption that the upwash and downwash are constant from the propeller to the quarter-chord of the MAC.

f. Calculate the span of the immersed wing b_i by

$$b_i = 2\left[R_p^2 - (z_s + z_w)^2\right]^{1/2} \qquad 4.6.1\text{-o}$$

g. Calculate the immersed wing area S_i by

$$S_i = b_i c_i \qquad 4.6.1\text{-p}$$

h. Calculate the effective aspect ratio A_i of the wing immersed in the slipstream (see figure 4.6-12) by

$$A_i = \frac{b_i}{c_i} \qquad 4.6.1\text{-q}$$

i. From figure 4.6.1-27 obtain a value for the empirical constant K_1 accounting for a nacelle or fuselage as a function of the wing and immersed-wing aspect ratio and the propeller correlation parameter (step 2.d).

j. Calculate the gain or loss in slipstream dynamic pressure $\Delta q_s/q_\infty$ by

$$\frac{\Delta q_s}{q_\infty} = \frac{S_W T_c'}{\pi R_p^2} \text{ (per engine)} \qquad 4.6.1\text{-r}$$

k. Calculate the change in wing lift due to the upwash or downwash of the propeller flow field per engine by

$$\left(\Delta C_L\right)_{\Delta\alpha_W} = \left(1 + \frac{\Delta q_s}{q_\infty}\right) \frac{S_i}{S_W} C_{L_\alpha} \Delta\alpha_W K_1 \qquad 4.6.1\text{-s}$$

where C_{L_α} is the lift-curve slope of the power-off lift curve, obtained by using the method of Section 4.1.3.2.

For multiple-engine configurations, the total lift component due to the change in angle of attack on the wing is found by summing the single components due to each engine.

Step 4. Calculate the increment of lift per engine due to the change in slipstream dynamic pressure on the wing by

$$\left(\Delta C_L\right)_q = K_1 \frac{\Delta q_s}{q_\infty} \frac{S_i}{S_W} \left(C_L\right)_{\substack{\text{power} \\ \text{off}}} \qquad 4.6.1\text{-t}$$

where $\left(C_L\right)_{\substack{\text{power} \\ \text{off}}}$ must be obtained from the power-off lift curve at the given angle of attack. For multiple-engine configurations, the total lift component due to the change in slipstream dynamic pressure acting on the wing is found by summing the single components due to each engine.

Step 5. Calculate the increment of lift on the horizontal tail due to the change in dynamic pressure and angle of attack as follows:

a. Calculate the total change in pitching-moment coefficient of the horizontal tail $\left(\Delta C_m\right)_H$ by

$$\left(\Delta C_m\right)_H = \left(\Delta C_{m_H}\right)_e + \left(\Delta C_{m_H}\right)_q \qquad 4.6.1\text{-u}$$

where $\left(\Delta C_{m_H}\right)_e$ and $\left(\Delta C_{m_H}\right)_q$ are calculated in Section 4.6.3.

b. Calculate the lift due to the horizontal tail by

$$\left(\Delta C_L\right)_H = -\left(\Delta C_m\right)_H \frac{\bar{c}}{\ell_H} \qquad 4.6.1\text{-v}$$

Step 6. Calculate the total change of lift due to the propeller power effects by summing the previously calculated elements as follows:

$$\left(\Delta C_L\right)_{\substack{\text{power} \\ \text{on}}} = \left(\Delta C_L\right)_T + \left(\Delta C_L\right)_{N_p} + \left(\Delta C_L\right)_{\Delta\alpha_W} + \left(\Delta C_L\right)_q + \left(\Delta C_L\right)_H \qquad 4.6.1\text{-w}$$

This equation is computed for a range of angles of attack and thrust coefficients, and the lift curves are constructed. These curves are valid only in the linear-lift range.

Sample Problem

The following example is based on the single-engine test configuration of reference 3. The example is presented for one value of α and one value of T_c'.

Given:

Wing Parameters:

$S_W = 380\ ft^2$ $\quad A = 6.23$ $\quad i_W = 2.0°$ $\quad \bar{c} = 8.17\ ft$

$c_l = 9.17\ ft$ $\quad z_W = 1.4\ ft$ $\quad$ Wing root section: NACA 2416

Wing tip section: NACA 4412 $\quad C_{L_\alpha} = 0.08$ per deg $\quad C_{L_{\substack{power\\off}}} = 0.50$ $\quad$ use test data or Sections 4.1.3.2 and 4.1.3.3

Angles:

$\alpha = 4.0°$ (assumed) $\quad \alpha_0 = -2.8°$ $\quad \partial\epsilon_u/\partial\alpha = 0.13$ (Section 4.4.1)

Propeller Parameters:

Four-bladed propeller $\quad R_p = 6.79\ ft$ $\quad \beta = 18°$ (at $0.75\ R_p$) $\quad K_N = 65.8$

Engine Parameters:

$T_c' = 0.150$ per engine (assumed)

$n = 1$ $\quad i_T = 0$ $\quad z_T = 0$ $\quad x_p = 10.9\ ft$

Horizontal-Tail Parameters:

$S_H = 80\ ft^2$ $\quad \ell_H = 20.4\ ft$ $\quad (\Delta C_{n_H}) = 0.0218$ (Section 4.6.3)

Compute:

Determine the lift component of thrust

$\alpha_T = i_T + \alpha$ (equation 4.6.1-a)

$= 0 + 4 = 4°$

$T_c' = 0.150$ (given)

$$\left(\Delta C_L\right)_T = n\, T_c'\, \sin \alpha_T \qquad \text{(equation 4.6.1-c)}$$

$$= (1)\,(0.15)\,(0.0698) = 0.0105$$

Determine the lift component of propeller normal force

$$K_N = 65.8 \text{ (given)}$$

$$\left[\left(C_{N_\alpha}\right)_p\right]_{K_N = 80.7} = 0.165 \qquad \text{(figure 4.6.1-25a)}$$

$$\left(C_{N_\alpha}\right)_p = \left[\left(C_{N_\alpha}\right)_p\right]_{K_N = 80.7} \left[1 + 0.8\left(\frac{K_N}{80.7} - 1\right)\right] \qquad \text{(equation 4.6.1-e)}$$

$$= 0.165 \left[1 + 0.8\left(\frac{65.8}{80.7} - 1\right)\right]$$

$$= 0.141$$

The propeller correlation parameter is

$$\frac{S_W T_c'}{8R_p^2} = \frac{(380)\,(0.15)}{(8)\,(6.79)^2} = 0.155$$

$$f = 1.1 \qquad \text{(figure 4.6.1-25b)}$$

$$S_p = \pi R_p^2 \qquad \text{(equation 4.6.1-f)}$$

$$= (3.14)\,(6.79)^2 = 144.8 \text{ ft}^2$$

$$\frac{\partial \epsilon_u}{\partial \alpha} = 0.13 \text{ (given)}$$

$$\alpha_W = \alpha + i_W \qquad \text{(equation 4.6.1-h)}$$

$$= 4.0 + 2.0 = 6.0^\circ$$

$$\alpha_p = \alpha_T + \frac{\partial \epsilon_u}{\partial \alpha}\left(\alpha_W - \alpha_0\right) \qquad \text{(equation 4.6.1-g)}$$

$$= 4.0 + 0.13\,(6.0 + 2.8)$$

$$= 5.14^\circ$$

$$\left(\Delta C_L\right)_{N_p} = f\left(C_{N_\alpha}\right)_p \frac{\alpha_p}{57.3} \frac{S_p}{S_W} \cos \alpha_T \quad \text{(equation 4.6.1-i)}$$

$$= (1.1)(0.141)\frac{5.14}{57.3}\frac{144.8}{380}(0.998)$$

$$= 0.00529$$

Determine the increment of lift due to the change in angle of attack on the wing induced by the propeller flow field

$$\frac{\partial \epsilon_p}{\partial \alpha_p} = C_1 + C_2 \left(C_{N_\alpha}\right)_p \quad \text{(equation 4.6.1-j)}$$

$$\left.\begin{aligned} C_1 &= 0.08 \\ C_2 &= 0.25 \end{aligned}\right\} \text{(figure 4.6.1-26)}$$

$$\frac{\partial \epsilon_p}{\partial \alpha_p} = 0.08 + (0.25)(0.141) = 0.115$$

$$\epsilon_p = \frac{\partial \epsilon_p}{\partial \alpha_p} \alpha_p \quad \text{(equation 4.6.1-k)}$$

$$= (0.115)(5.14) = 0.59^\circ$$

$$\Delta \alpha_W = \frac{-\epsilon_p}{1 + \partial \epsilon_u / \partial \alpha} \quad \text{(equation 4.6.1-ℓ)}$$

$$= \frac{-0.59}{1 + 0.13} = -0.522^\circ$$

$$\epsilon_u = \frac{\partial \epsilon_u}{\partial \alpha} (\alpha_W - \alpha_0) \quad \text{(equation 4.6.1-m)}$$

$$= 0.13\,(6.0 + 2.8) = 1.14^\circ$$

$$z_s = x_p \tan(\alpha_T + \epsilon_u - \epsilon_p) - z_T \quad \text{(equation 4.6.1-n)}$$

Using the small-angle approximation,

$$z_s = \frac{x_p}{57.3}(\alpha_T + \epsilon_u - \epsilon_p) + 0$$

$$= \frac{10.9}{57.3}(4.0 + 1.14 - 0.59) = 0.866 \text{ ft}$$

$$b_i = 2\left[R_p^2 - (z_s + z_w)^2\right]^{1/2} \quad \text{(equation 4.6.1-o)}$$

$$= 2\left[(6.79)^2 - (0.866 + 1.4)^2\right]^{1/2}$$

$$= 12.8 \text{ ft}$$

$$S_i = b_i c_i \quad \text{(equation 4.6.1-p)}$$

$$= (12.8)(9.17) = 117.4 \text{ ft}^2$$

$$A_i = \frac{b_i}{c_i} \quad \text{(equation 4.6.1-q)}$$

$$= \frac{12.8}{9.17} = 1.40$$

$$K_1 = 0.96 \quad \text{(figure 4.6.1-27)}$$

$$\frac{\Delta q_s}{q_\infty} = \frac{S_w T_c'}{\pi R_p^2} \quad \text{(equation 4.6.1-r)}$$

$$= \frac{(380)(0.15)}{(3.14)(6.79)^2}$$

$$= 0.394$$

$$\left(\Delta C_L\right)_{\Delta\alpha_w} = \left(1 + \frac{\Delta q_s}{q_\infty}\right)\frac{S_i}{S_w} C_{L_\alpha} \Delta\alpha_w K_1 \quad \text{(equation 4.6.1-s)}$$

$$= (1 + 0.394)\ \frac{117.4}{380}\ (0.08)(-0.522)(0.96)$$

$$= -0.0173$$

Determine the increment of lift due to the change in slipstream dynamic pressure

$$\left(\Delta C_L\right)_q = K_1 \frac{\Delta q_s}{q_\infty} \frac{S_i}{S_W} \left(C_L\right)_{\substack{\text{power} \\ \text{off}}} \qquad \text{(equation 4.6.1-t)}$$

$$= (0.96)\,(0.394)\ \frac{117.4}{380}\ (0.50)$$

$$= 0.0584$$

Determine the increment of lift on the horizontal tail due to the change in dynamic pressure and angle of attack

$$\left(\Delta C_m\right)_H = \left(\Delta C_{m_H}\right)_e + \left(\Delta C_{m_H}\right)_q \qquad \text{(equation 4.6.1-u)}$$

$$\left.\begin{aligned} \left(\Delta C_{m_H}\right)_e &= 0.0218 \\ \left(\Delta C_{m_H}\right)_q &= 0 \end{aligned}\right\} \text{(sample problem, Section 4.6.3)}$$

$$\left(\Delta C_m\right)_H = 0.0218$$

$$\left(\Delta C_L\right)_H = -\left(\Delta C_m\right)_H \frac{\bar{c}}{\ell_H} \qquad \text{(equation 4.6.1-v)}$$

$$= -(0.0218)\left(\frac{8.17}{20.4}\right)$$

$$= -0.00873$$

Determine the total change of lift due to the propeller power effects

$$\left(\Delta C_L\right)_{\substack{\text{power} \\ \text{on}}} = \left(\Delta C_L\right)_T + \left(\Delta C_L\right)_{N_p} + \left(\Delta C_L\right)_{\Delta\alpha_W} + \left(\Delta C_L\right)_q + \left(\Delta C_L\right)_H$$

(equation 4.6.1-w)

$$= 0.0105 + 0.00529 - 0.0173 + 0.0584 - 0.00873$$

$$= 0.0482$$

The value of $\left(\Delta C_L\right)_{\substack{\text{power} \\ \text{on}}}$ from reference 4 at $\alpha = 4.0^\circ$ and $T_c' = 0.15$ is 0.080.

B. JET POWER EFFECTS ON LIFT

The effects of jets on the aerodynamic characteristics of vehicles are generally of smaller magnitude than the effects of propellers. There are three effects of jets on the lift of a vehicle. The first is a contribution to the lift due to the thrust component. The second is a force acting at the engine inlet duct in a direction normal to the thrust axis. This force is due to the turning of the free stream in a direction parallel to the thrust axis. The third is the induced effect of the jet on wing or tail surfaces, i.e., that caused by the jets on the surrounding flow.

The first two effects are analyzed by the methods of reference 1 at both subsonic and supersonic speeds. The third effect requires special treatment.

The following discussion on jet flow fields will help clarify some of the important distinctions between subsonic and supersonic jets operating in subsonic and supersonic flows.

Subsonic Jets in Subsonic Flow

The velocity profile across a jet exit is nearly uniform. Mixing of the jet flow and the local free-stream flow starts at the lip of the jet and propagates laterally in the downstream direction. The velocity profile is modified by this viscous mixing action, and at some distance downstream of the apex of the core the velocity profiles become similar. This usually occurs at approximately eight exit-diameters from the nozzle. The region of flow less than approximately eight exit-diameters downstream is referred to as the transition region, and the region beyond this point is referred to as the fully developed region (see sketch (a)).

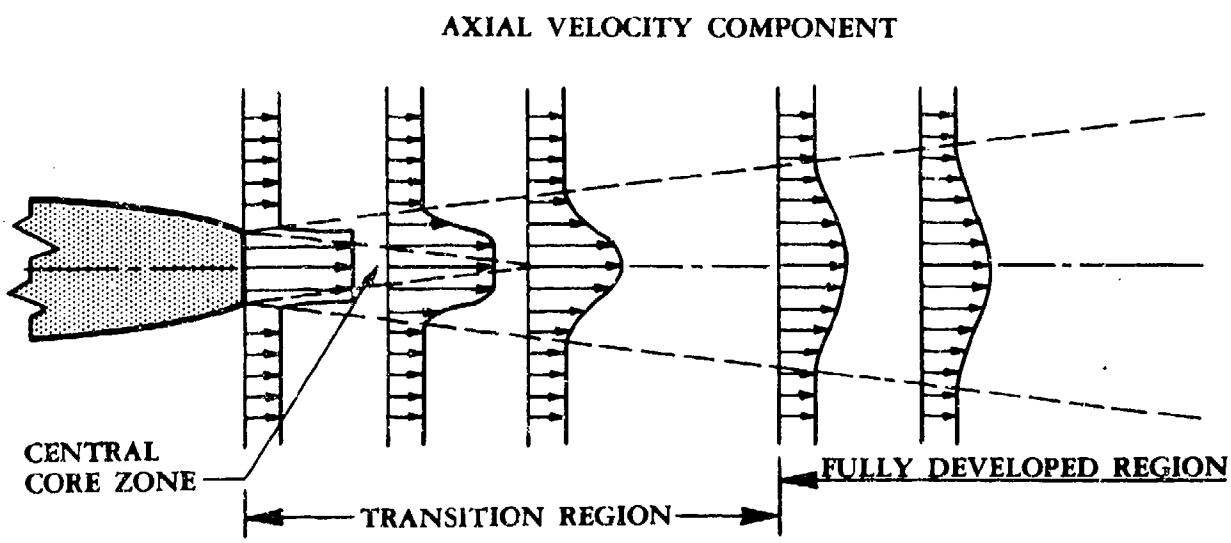

SKETCH (a)

Existing within the transition region is the central core zone of uniform flow, which dissipates downstream. The remaining segment of the two regions is made up of the mixing zone, which lies between the central core and the external flow.

The external flow is entrained by the jet, causing a radial inflow velocity component in the external flow as shown in sketch (b).

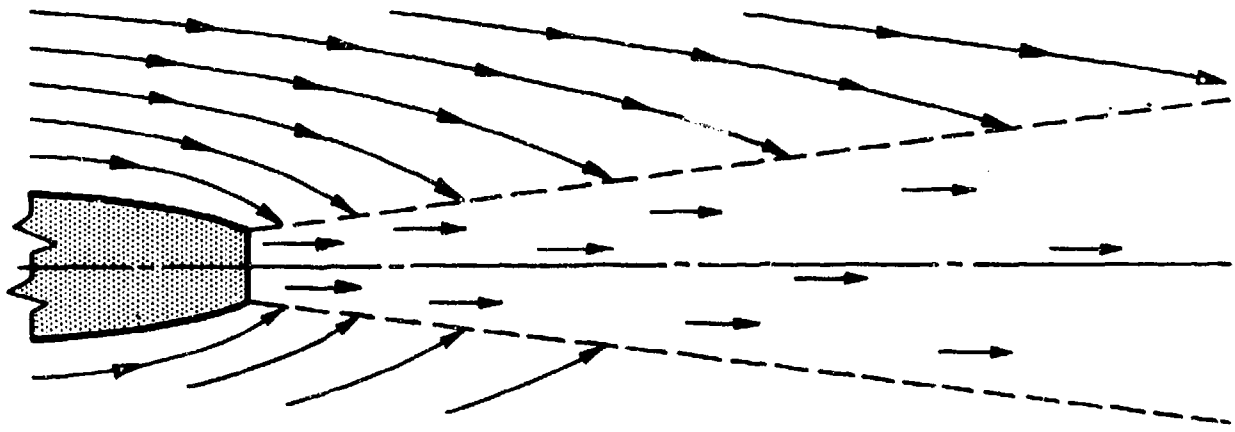

SKETCH (b)

Airframe components immersed in this external flow field experience changes in forces and moments due to these induced angle-of-attack changes.

Two methods are presented for calculating the interference effects of subsonic jets in a subsonic free stream. The first method is valid for downstream distances less than eight exit-diameters. This method incorporates a technique presented in reference 5 with a temperature-ratio correction from reference 6 and a span correction factor from reference 7.

The second method is valid for downstream distances greater than eight exit-diameters. This method is based on a technique from reference 7.

Supersonic Jet in Subsonic Flow

If the jet pressure ratio becomes sufficiently large, the jet expands supersonically beyond the exit. The jet will "plume" or bulge, as shown in sketch (c).

At some station downstream, the jet reaches a condition where it is expanded to atmospheric pressure. This station is termed the equivalent jet exit station. The external flow in the region of the jet plume can cause either inflow- or outflow-radial-velocity components. In general, large jet-pressure ratios and high free-stream velocities cause outflow velocities, and lower jet-pressure ratios and low free-stream velocities cause inflow velocities resulting from the entrainment of the external flow. A quantitative evaluation of these effects is not available. The external flow downstream of the equivalent jet exit station always has an inflow velocity component and is similar in this respect to subsonic jets.

Flow depends upon jet pressure ratio, free-stream velocity, and boattail geometry

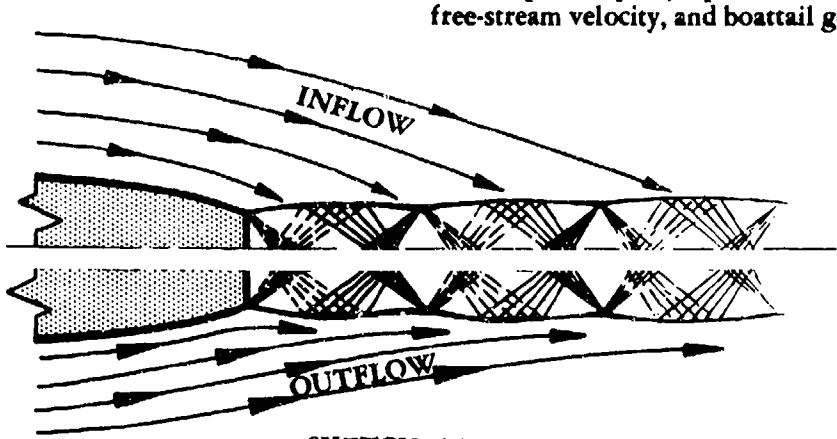

SKETCH (c)

No accurate flow model is available for predicting the jet interference effects of a supersonic jet exhausting into a subsonic flow. However, an approximate method is presented that is based on the method for analyzing subsonic jets in subsonic flow. The accuracy of this method has not been established.

Supersonic Jets in Supersonic Flow

At supersonic speeds the exhaust from supersonic jets causes strong disturbances in the external flow field in the form of shock and expansion waves. A typical flow pattern is shown in sketch (d).

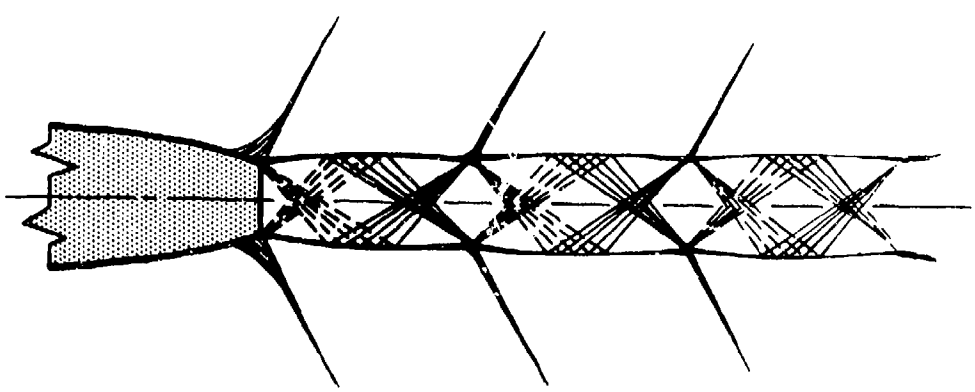

SKETCH (d)

Jets become greatly underexpanded at extreme altitudes, a phenomenon that results in strong effects on the flow upstream of the jet exit. Some limited data on this problem are available in reference 8.

The correct approach for analyzing the lift increment should consider the change in pressure distribution on the wing or tail due to the presence of the jet. The surface pressure distribution is a function of the free-stream Mach number and jet pressure ratio. Unfortunately, insufficient test data are available to provide complete charts for this estimation procedure. Test data at $M_\infty = 2.0$ and a jet pressure ratio of 7.0 from reference 9 are presented in figure 4.6.1-33 as representative data. The chart shows pressure contours at the vertical plane of symmetry of the jet. It is intended that these limited data, together with a description of the procedure, will provide some feeling for the problem.

DATCOM METHOD

The Datcom method estimates the power-on lift curves, based on power-off lift curves, as a function of angle of attack, thrust coefficient, engine-inlet area, and horizontal-tail parameters.

This method analyzes the increments of lift coefficient due to jet power effects in the following order:

1. Lift component of thrust
2. Lift component due to the turning of the free-stream flow parallel to the thrust axis
3. Lift component due to jet interference effects

After the above lift increments for a given angle of attack have been calculated, the accumulated total is then applied to the power-off lift curve to obtain a point on the power-on lift curve. After several points have been generated (by considering several angles of attack), the linear section of the power-on lift curve is obtained for a given thrust coefficient.

The above increments in lift can be determined by the following steps. (Reference should be made to figure 4.6-13b for geometric definitions. In all cases the lift increments are based on the wing reference area.)

Step 1. Calculate the lift component of thrust as follows:

a. Calculate the angle of attack of the thrust axis to the free stream α_T by

$$\alpha_T = i_T + \alpha \qquad 4.6.1\text{-a}$$

b. Calculate the thrust coefficient per engine T_c' (if not given or assumed) by

$$T_c' = \frac{T}{q_\infty S_W} \qquad 4.6.1\text{-b}$$

where the thrust per engine T is a given or chosen quantity.

c. Calculate the lift component of thrust by

$$\left(\Delta C_L\right)_T = n\, T_c' \sin \alpha_T \qquad 4.6.1\text{-c}$$

where n is the number of engines. This equation is valid only when the thrust coefficients and the angles of attack of the thrust axis to the free stream are equal for all n engines.

Step 2. Calculate the lift component per engine due to the turning of the free-stream flow in a direction parallel to the thrust axis as follows:

a. Calculate the angle between the thrust axis and the local velocity α_j at the engine inlet by

$$\alpha_j = \alpha_T + \epsilon_u \qquad 4.6.1\text{-x}$$

where the upwash ahead of the wing ϵ_u is obtained by

$$\epsilon_u = \frac{\partial \epsilon_u}{\partial \alpha} (\alpha_W - \alpha_0) \qquad 4.6.1\text{-m}$$

and the downwash gradient $\frac{\partial \epsilon_u}{\partial \alpha}$ is obtained from Section 4.4.1.

b. Calculate the turning component of lift by

$$\left(\Delta C_L\right)_{N_j} = \frac{2A_1 \sin \alpha_j}{S_W} \qquad 4.6.1\text{-y}$$

For multiple-engine configurations, the total lift component due to the turning of the free-stream flow is found by summing the individual lift increments due to each engine.

Step 3. Calculate the lift component per engine due to the jet interference effects.

The various possible combinations of Mach number for the free-stream and nozzle exit conditions require different combinations to be analyzed separately. Methods for calculating four different jet interaction cases are presented. The surface affected is assumed to be a horizontal tail. Application to other lifting surfaces and to other bodies is similar.

Case 1. Subsonic Free Stream – Subsonic Jet – Downstream Distance Less than Eight Exit-Diameters

a. Obtain the lift-curve slope of the horizontal tail $C_{L_{\alpha_H}}$ from Section 4.1.3.2.

b. Obtain the ratio of the horizontal-tail to free-stream dynamic pressure q_H/q_∞ at the quarter-chord of the horizontal-tail MAC from wind-tunnel-test data or Section 4.4.1.

c. From figure 4.6.1-28 obtain a value for the mean-effective-downwash ratio $\Delta\bar{\epsilon}/\Delta\epsilon$ as a function of aircraft geometry.

d. From figure 4.6.1-29 obtain the equivalent-jet-velocity ratio V_j'/V_∞ as a function of the actual-jet-velocity ratio V_j/V_∞ and the ratio of ambient temperature to jet static temperature.

e. From figures 4.6.1-30a through -30c obtain a value for the downwash increment $\Delta\epsilon$ as a function of aircraft geometry and equivalent-jet-velocity ratio.

f. Calculate the mean-effective-downwash increment $\Delta\bar{\epsilon}$ by

$$\Delta\bar{\epsilon} = \left(\frac{\Delta\bar{\epsilon}}{\Delta\epsilon}\right) \Delta\epsilon \qquad 4.6.1\text{-z}$$

g. Calculate the increment in lift per engine due to jet interference effects by

$$\left(\Delta C_L\right)_\epsilon = -C_{L_{\alpha_H}} \frac{S_H}{S_W} \frac{q_H}{q_\infty} \Delta\bar{\epsilon} \qquad 4.6.1\text{-aa}$$

For multiple-engine configurations, the total lift component due to jet interference effects is found by summing the individual lift increments due to each engine.

Case II. Subsonic Free Stream – Subsonic Jet – Downstream Distances Greater than Eight Exit-Diameters

a. Obtain the lift-curve slope of the horizontal tail $C_{L_{\alpha_H}}$ from Section 4.1.3.2.

b. Obtain the ratio of the horizontal-tail to free-stream dynamic pressure q_H/q_∞ at the quarter-chord of the horizontal-tail MAC from wind-tunnel-test data or Section 4.4.1.

c. From figure 4.6.1-28 obtain a value for the mean-effective-downwash ratio $\Delta\bar{\epsilon}/\Delta\epsilon$ as a function of aircraft geometry.

d. From figure 4.6.1-31 obtain a value for $z_j'\Delta\epsilon/x_H$ as a function of aircraft geometry and thrust coefficient.

e. Calculate the jet-induced downwash angle $\Delta\epsilon$ by

$$\Delta\epsilon = \frac{z_j'\Delta\epsilon}{x_H'}\frac{x_H'}{z_j'} \qquad \text{4.6.1-bb}$$

$$\text{where } x_H' = x_j' + x_e' \qquad \text{4.6.1-cc}$$

and x_j' is usually expressed as

$$x_j' = 4.6\ R_j \qquad \text{4.6.1-dd}$$

f. Calculate the mean-effective-downwash increment $\Delta\bar{\epsilon}$ by

$$\Delta\bar{\epsilon} = \left(\frac{\Delta\bar{\epsilon}}{\Delta\epsilon}\right)\Delta\epsilon \qquad \text{4.6.1-z}$$

g. Calculate the increment in lift per engine due to jet interference effects by

$$\left(\Delta C_L\right)_\epsilon = -C_{L_{\alpha_H}}\frac{S_H}{S_W}\frac{q_H}{q_\infty}\Delta\bar{\epsilon} \qquad \text{4.6.1-aa}$$

For multiple-engine configurations, the total lift component due to jet interference effects is found by summing the individual lift increments due to each engine.

Case III. Subsonic Free Stream – Supersonic Jet – Distances Downstream of the Fully Expanded Flow

a. From figure 4.6.1-32a obtain a value for the equivalent-jet orifice radius ratio R_j'/R_j as a function of the jet-exit total-pressure ratio.

b. From figure 4.6.1-32b obtain a value for the downstream displacement of the equivalent-jet orifice as a function of the equivalent-jet orifice radius.

The downstream displacement distance corresponds to the point at which the supersonic-jet flow has expanded to ambient pressure. The corresponding jet ratio at this station is the equivalent radius R_j'. These values are used in lieu of the actual jet radius and jet location in approximating the inflow velocities of the surrounding flow downstream of this equivalent jet-exit station.

Depending on the location of the surface of interest, the remaining steps are identical to those of case I (less than eight exit-diameters downstream) or case II (greater than eight exit-diameters downstream). For locations upstream of the fully expanded flow no method is available.

As pointed out in the discussion, the accuracy of this method is not known.

Case IV. Supersonic Free Stream – Supersonic Jet

A complete method is not presented because of a lack of wind-tunnel test data required for the formulation of design charts. However, if wind-tunnel data are available the following procedure is suggested:

a. Divide the surface under consideration into incremental areas ΔS_H.

b. Calculate the respective axial and radial locations of the incremental areas relative to the jet exit.

c. Construct a pressure-coefficient-contour chart from available data (see figure 4.6.1-33).

d. Obtain values of $\Delta p/q_\infty$ for each incremental area from the pressure-coefficient-contour chart as a function of their relative locations.

e. Sum the incremental forces acting over the surfaces to obtain the total change in lift coefficient by

$$\Delta C_L = \frac{1}{S_W} \Sigma \left[\Delta S_H \frac{\Delta p}{q_\infty} \right] \qquad 4.6.1\text{-ee}$$

By using the above procedure, several increments in horizontal-tail lift coefficient were calculated for the configuration tested in reference 10. The calculations were computed from the data of figure 4.6.1-33 for a variety of tail positions at Mach number of 1.9 and a jet pressure ratio of 6.66. The results of the calculations revealed errors ranging from 15 to 133 percent.

The total change in aircraft lift due to jet power effects is obtained by summing all lift components, i.e.,

$$\left(\Delta C_L\right)_{\substack{\text{power} \\ \text{on}}} = \left(\Delta C_L\right)_T + \left(\Delta C_L\right)_{N_j} + \left(\Delta C_L\right)_e \qquad 4.6.1\text{-ff}$$

Sample Problem

The following example is based on the four-engine DC-8 configuration. The example is presented for one value of α and one value of T_c'. The lift due to jet-interference effects is calculated by using the methods of case II, since the downstream distance of the horizontal tail is greater than eight engine exit-diameters.

Given:

Wing Parameters:

$S_W = 2930\ ft^2$ $\quad \bar{c} = 272.8$ in. $\quad A = 7.52$

$i_W = 0$ $\quad \alpha = 5°$ $\quad \alpha_0 = -2.5°$ (flaps up)

Horizontal-Tail Parameters:

$S_H = 560\ ft^2$ $\quad \bar{c}_H$ 153.2 in. $\quad C_{L_{\alpha_H}} = 0.0627$/deg (Section 4.1.3.2)

$q_H/q_\infty = 0.968$ (Section 4.4.1) $\quad \ell_H = 855.0$ in. $\quad b_H = 570.0$ in.

Engine Parameters:

Outboard Engines (2) $\quad z_T = 53.0$ in. $\quad z_j' = 175.7$ in.

$x_I = 145.2$ in. $\quad x_e' = 788.0$ in. $\quad y_T = 44.6$ ft

$\partial\epsilon_u/\partial\alpha = 0.17$ (Section 4.4.1) $\quad R_j = 20$ in. $\quad A_I = 13.64\ ft^2$

$i_T = 3.6°$ $\quad T = 12{,}500$ lb

Inboard Engines (2) $\quad z_T = 70.8$ in. $\quad z_j' = 201.7$ in.

$x_I = 283.8$ in. $\quad x_e' = 927.0$ in. $\quad y_T = 25.7$ ft

$\partial\epsilon_u/\partial\alpha = 0.24$ (Section 4.4.1) $\quad R_j = 20$ in. $\quad A_I = 13.64\ ft^2$

$i_T = 3.6°$ $\quad T = 12{,}500$ lb

Additional Parameters:

$M = 0.2$ $\quad q_\infty = 57.2$ psf $\quad h = 1000$ ft

Compute:

Determine the lift component of thrust

$$\alpha_T = i_T + \alpha \qquad \text{(equation 4.6.1-a)}$$

$$= 3.6 + 5 = 8.6°$$

$$T_c' = \frac{T}{q_\infty S_W} \qquad \text{(equation 4.6.1-b)}$$

$$= \frac{12{,}500}{(57.2)\,(2930)} = 0.0746 \text{ (per engine)}$$

$$\left(\Delta C_L\right)_T = n\, T_c' \sin \alpha_T \qquad \text{(equation 4.6.1-c)}$$

$$= (4)\,(0.0746)\,(0.1495)$$

$$= 0.0446$$

Determine the lift component due to the turning of the free stream

$$\alpha_W = \alpha + i_W \qquad \text{(equation 4.6.1-h)}$$

$$= 5 + 0 = 5°$$

$$\epsilon_u = \frac{\partial \epsilon_u}{\partial \alpha} (\alpha_W - \alpha_0) \qquad \text{(equation 4.6.1-m)}$$

$$\left(\epsilon_u\right)_{\substack{\text{outboard}\\ \text{engine}}} = (0.17)\,(5 + 2.5) = 1.27°$$

$$\left(\epsilon_u\right)_{\substack{\text{inboard}\\ \text{engine}}} = (0.24)\,(5 + 2.5) = 1.80°$$

$$\alpha_j = \alpha_T + \epsilon_u \qquad \text{(equation 4.6.1-x)}$$

$$\left(\alpha_j\right)_{\substack{\text{outboard}\\ \text{engine}}} = 8.6 + 1.27 = 9.87°$$

$$\left(\alpha_j\right)_{\substack{\text{inboard}\\ \text{engine}}} = 8.6 + 1.80 = 10.4°$$

$$\left(\Delta C_L\right)_{N_j} = \frac{2A_1 \sin \alpha_j}{S_W} \qquad \text{(equation 4.6.1-y)}$$

Considering the lift increment due to both outboard engines

$$\left[\left(\Delta C_L\right)_{N_j}\right]_{\substack{\text{outboard}\\\text{engines}}} = \frac{(2)\,(13.64)\,(0.1714)\,(2)}{2930} = 0.00319$$

Considering the lift increment due to both inboard engines

$$\left[\left(\Delta C_L\right)_{N_j}\right]_{\substack{\text{inboard}\\\text{engines}}} = \frac{(2)\,(13.64)\,(0.1805)\,(2)}{2930} = 0.00336$$

The total lift component due to the turning of the free stream is

$$\left(\Delta C_L\right)_{N_j} = \left[\left(\Delta C_L\right)_{N_j}\right]_{\substack{\text{outboard}\\\text{engines}}} + \left[\left(\Delta C_L\right)_{N_j}\right]_{\substack{\text{inboard}\\\text{engines}}}$$

$$= 0.00319 + 0.00336$$

$$= 0.00655$$

Determine the lift component due to jet interference effects on the horizontal tail. The method of case II will be used to evaluate the jet interference effects, since $(\ell_H/R_j) > 8$.

$$\left.\frac{\Delta\bar{\epsilon}}{\Delta\epsilon}\right|_{\substack{\text{inboard}\\\text{engines}}} = 0.37 \qquad \text{(figure 4.6.1-28)}$$

$$\left.\frac{\Delta\bar{\epsilon}}{\Delta\epsilon}\right|_{\substack{\text{outboard}\\\text{engines}}} = 0.10 \qquad \text{(figure 4.6.1-28)}$$

$$\left.\frac{z_j'\Delta\epsilon}{x_H'}\right|_{\substack{\text{inboard}\\\text{engines}}} = 0.07 \qquad \text{(figure 4.6.1-31)}$$

$$\left.\frac{z_j'\Delta\epsilon}{x_H'}\right|_{\substack{\text{outboard}\\\text{engine}}} = 0.08 \qquad \text{(figure 4.6.1-31)}$$

$$x'_H = x'_j + x'_e \qquad \text{(equation 4.6.1-cc)}$$

$$x'_j = 4.6\ R_j \qquad \text{(equation 4.6.1-dd)}$$

$$\left(x'_H\right)_{\substack{\text{inboard}\\ \text{engine}}} = (4.6)\ (20) + 927$$

$$= 1019 \text{ in.}$$

$$\left(x'_H\right)_{\substack{\text{outboard}\\ \text{engine}}} = (4.6)\ (20) + 788$$

$$= 880 \text{ in.}$$

$$\Delta\epsilon = \frac{z'_j \Delta\epsilon}{x'_H} \frac{x'_H}{z'_j} \qquad \text{(equation 4.6.1-bb)}$$

$$\left(\Delta\epsilon\right)_{\substack{\text{inboard}\\ \text{engine}}} = (0.07)\ \frac{(1019)}{(201.7)}$$

$$= 0.354$$

$$\left(\Delta\epsilon\right)_{\substack{\text{outboard}\\ \text{engine}}} = (0.08)\ \frac{(880)}{175.7}$$

$$= 0.40$$

$$\Delta\bar{\epsilon} = \left(\frac{\Delta\bar{\epsilon}}{\Delta\epsilon}\right)_i \Delta\epsilon \qquad \text{(equation 4.6.1-z)}$$

$$\left(\Delta\bar{\epsilon}\right)_{\substack{\text{inboard}\\ \text{engines}}} = (0.37)\ (0.354)$$

$$= 0.131$$

$$\left(\Delta\bar{\epsilon}\right)_{\substack{\text{outboard}\\ \text{engines}}} = (0.10)\ (0.40)$$

$$= 0.04$$

$$\left(\Delta C_L\right)_\epsilon = -C_{L_{\alpha_H}} \frac{S_H}{S_W} \frac{q_H}{q_\infty} \Delta\bar{\epsilon} \qquad \text{(equation 4.6.1-aa)}$$

$$\left[\left(\Delta C_L\right)_\epsilon\right]_{\substack{\text{inboard}\\\text{engines}}} = -(0.0627)\ \frac{560}{2930}\ (0.968)\ (0.131)$$

$$= -0.00152$$

$$\left[\left(\Delta C_L\right)_\epsilon\right]_{\substack{\text{outboard}\\\text{engines}}} = -(0.0627)\ \frac{560}{2930}\ (0.968)\ (0.04)$$

$$= 0.00046$$

The total lift component due to jet interference effects on the horizontal tail is

$$\left(\Delta C_L\right)_\epsilon = -0.00152 - 0.00046$$

$$= -0.0020$$

$$\left(\Delta C_L\right)_{\substack{\text{power}\\\text{on}}} = \left(\Delta C_L\right)_T + \left(\Delta C_L\right)_{N_j} + \left(\Delta C_L\right)_\epsilon \qquad \text{(equation 4.6.1-ff)}$$

$$= (0.0446) + (0.00655) + (-0.0020)$$

$$= 0.049$$

REFERENCES

1. Decker, J., et al: USAF Stability and Control Handbook. M-3671, 1956. (U)
2. Ribner, H. S.: Notes on the Propeller and Slipstream in Relation to Stability. NACA WR L-25, 1944. (U)
3. Weil, J., and Sleeman, W. C., Jr.: Prediction of the Effects of Propeller Operation on the Static Longitudinal Stability of Single-Engine Tractor Monoplanes With Flaps Retracted. NACA TN 1722, 1948. (U)
4. Weil, J., and Boykin, R. I.: Wind-Tunnel Tests of the 0.15-Scale Powered Model of the Fleetwings XBTK-1 Airplane Longitudinal Stability and Control. NACA WR L-785, 1945. (U)
5. Squire, H. B., and Trouncer, J.: Round Jets in a General Stream. RAE Report Aero 1974, 1944. (U)
6. Abzug, M. J.: Effect of Jet and Rocket Operation on Static Longitudinal and Directional Stability. BuAer ADR Report M-35, 1945. (U)
7. Ribner, H. S.: Field of Flow About a Jet and Effect of Jets on Stability of Jet-Propelled Airplanes. NACA WR L-213, 1946. (U)
8. Salmi, R. J.: Effects of Jet Billowing on Missile-Type Bodies at Mach 3.85. NASA TN D-284, 1960. (U)
9. Bressette, W. E.: Investigation of the Jet Effects on a Flat Surface Downstream of the Exit of a Simulated Turbojet Nacelle at a Free-Stream Mach Number of 2.02. NACA RM L54E05a, 1954. (U)
10. Salmi, R. J., and Klann, J. L.: Interference Effects at Mach 1.9 on a Horizontal Tail Due to Trailing Shock Waves From an Axisymmetric Body With an Exiting Jet. NACA RM E55J13a, 1956. (U)

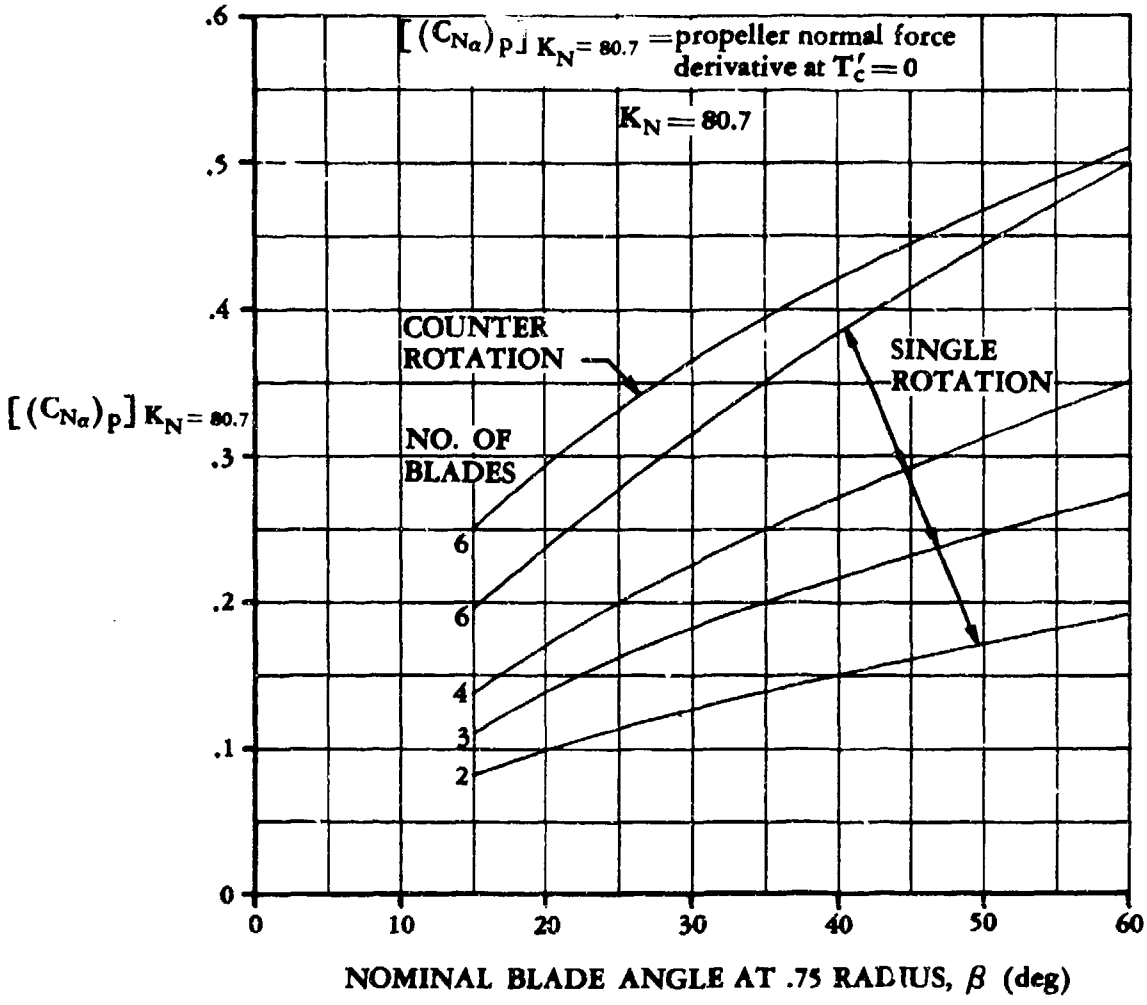

FIGURE 4.6.1-25a **PROPELLER NORMAL-FORCE PARAMETER**

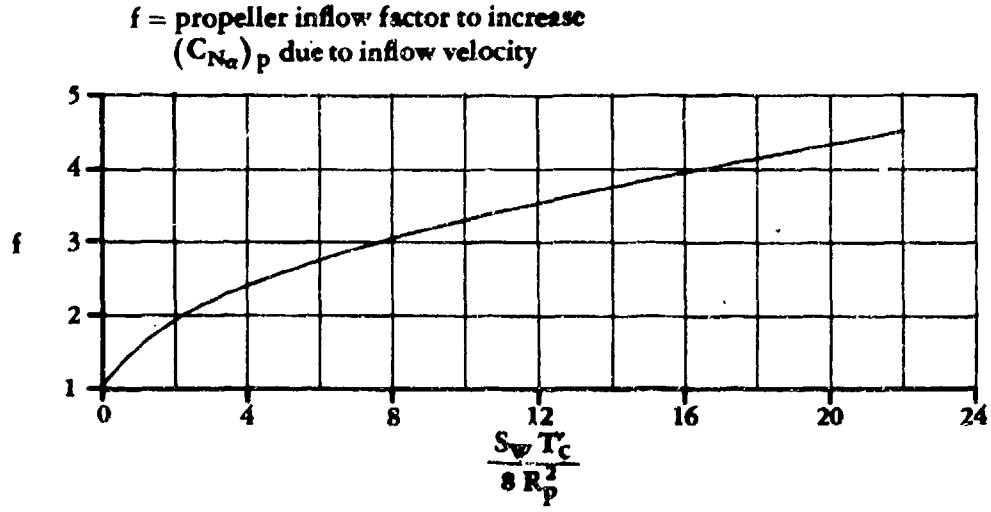

FIGURE 4.6.1-25b **PROPELLER INFLOW FACTOR**

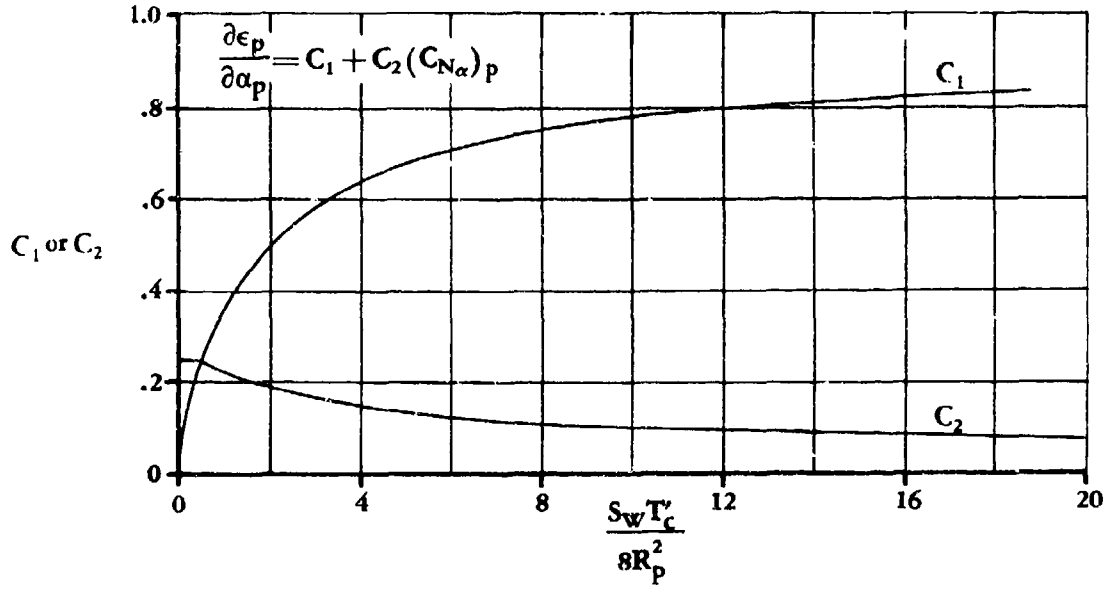

FIGURE 4.6.1-26 FACTORS FOR DETERMINING DOWNWASH DUE TO PROPELLERS

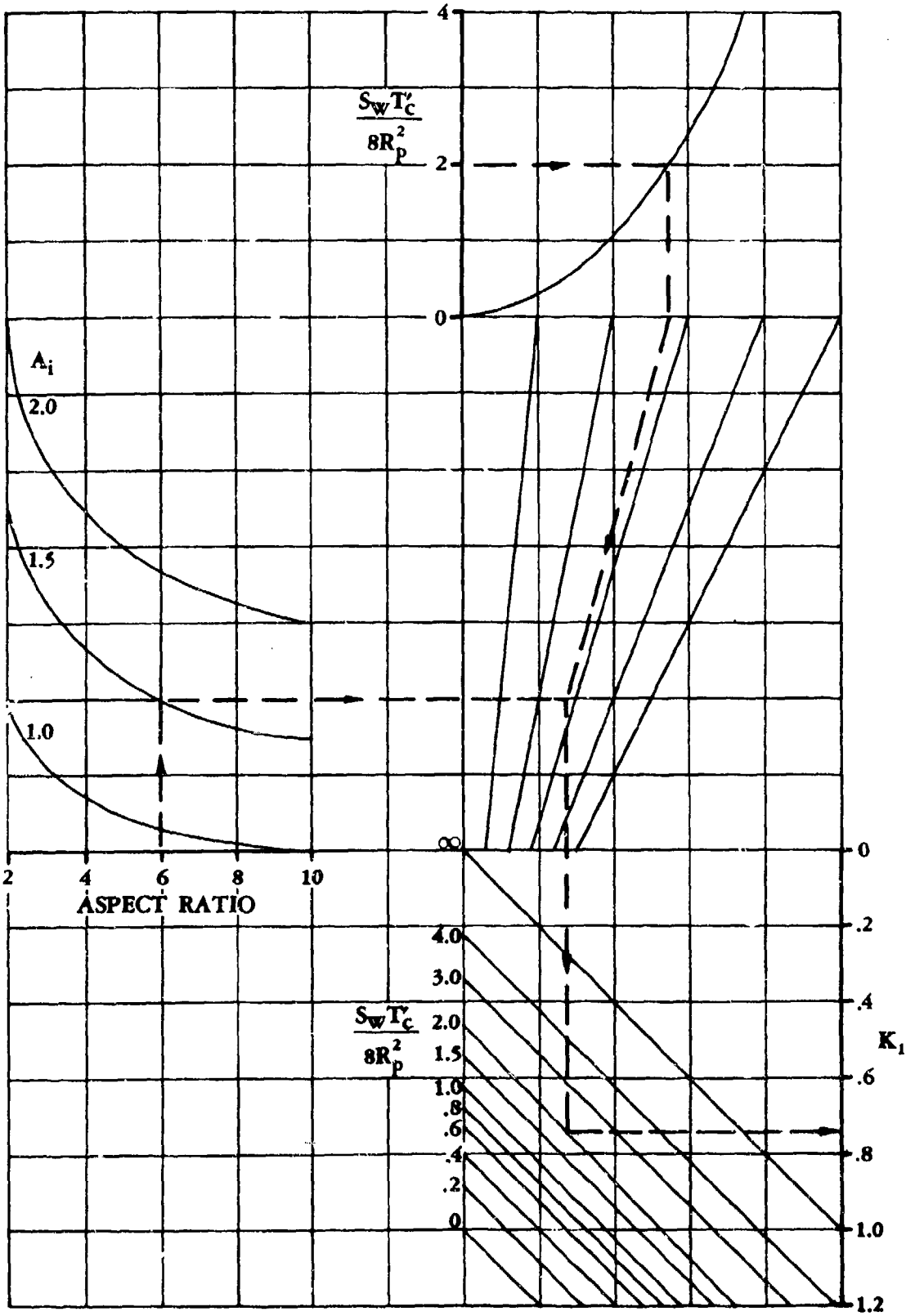

FIGURE 4.6.1-27 CORRELATION PARAMETER FOR ADDITIONAL WING LIFT DUE TO PROPELLER POWER

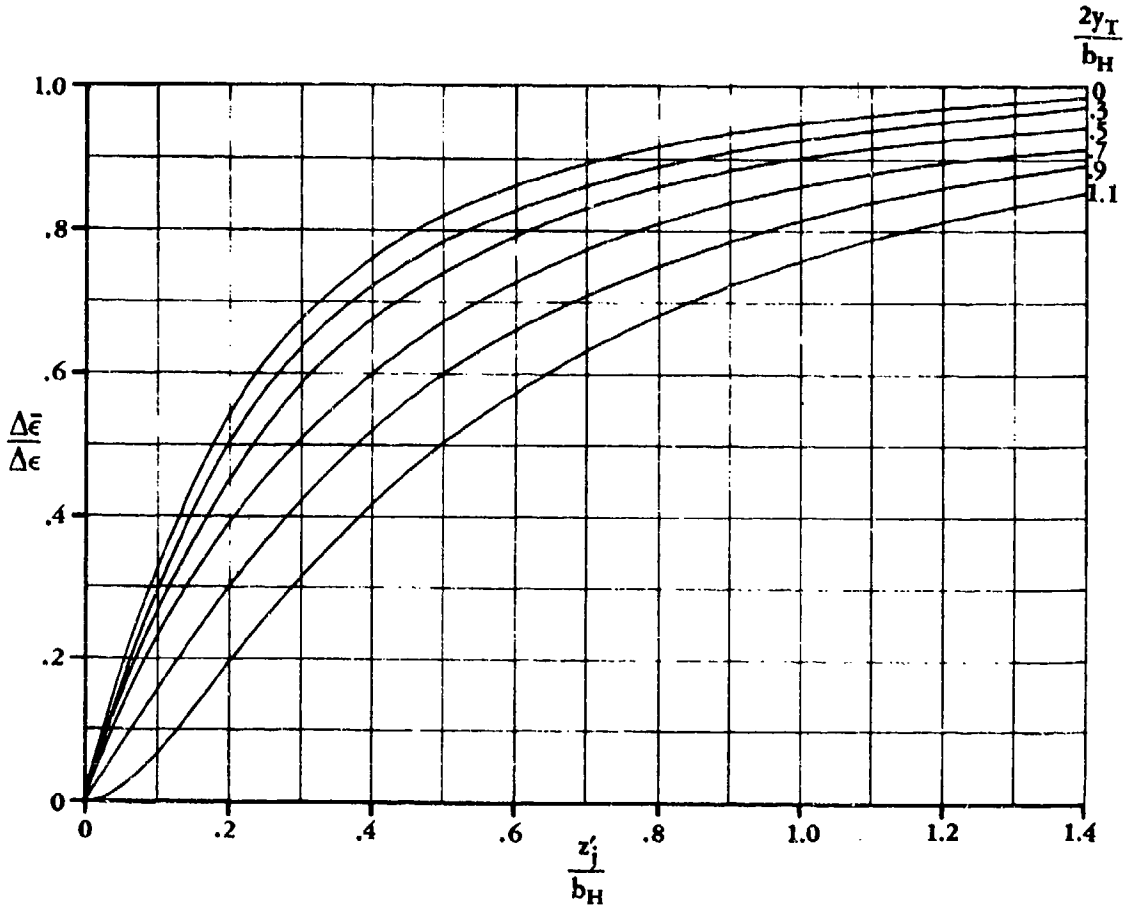

FIGURE 4.6.1-28 MEAN EFFECTIVE DOWNWASH ACTING ON HORIZONTAL TAIL

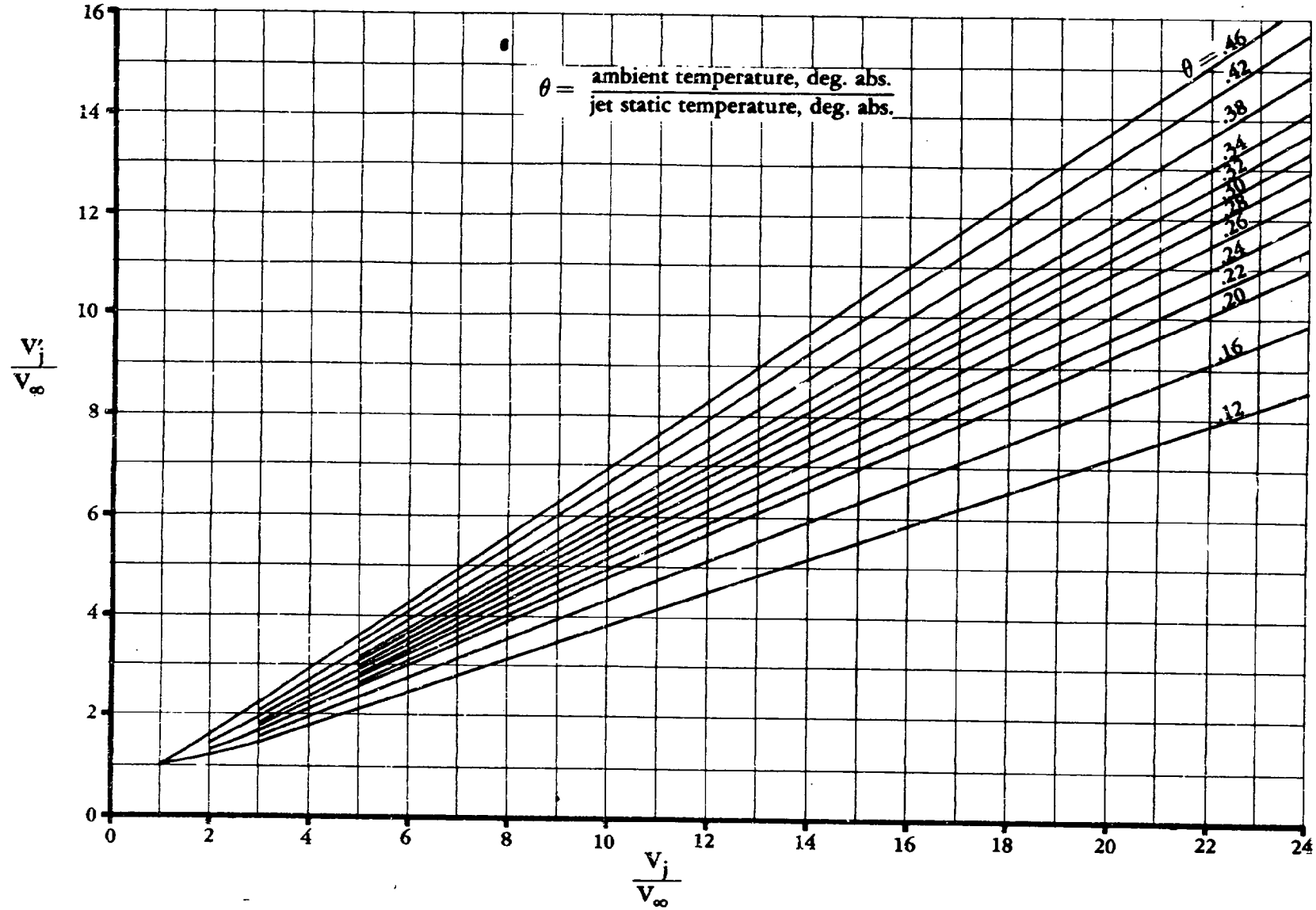

FIGURE 4.6.1-29 VARIATION OF EQUIVALENT VELOCITY RATIO, $\frac{V'_j}{V_\infty}$, WITH VELOCITY RATIO, $\frac{V_j}{V_\infty}$

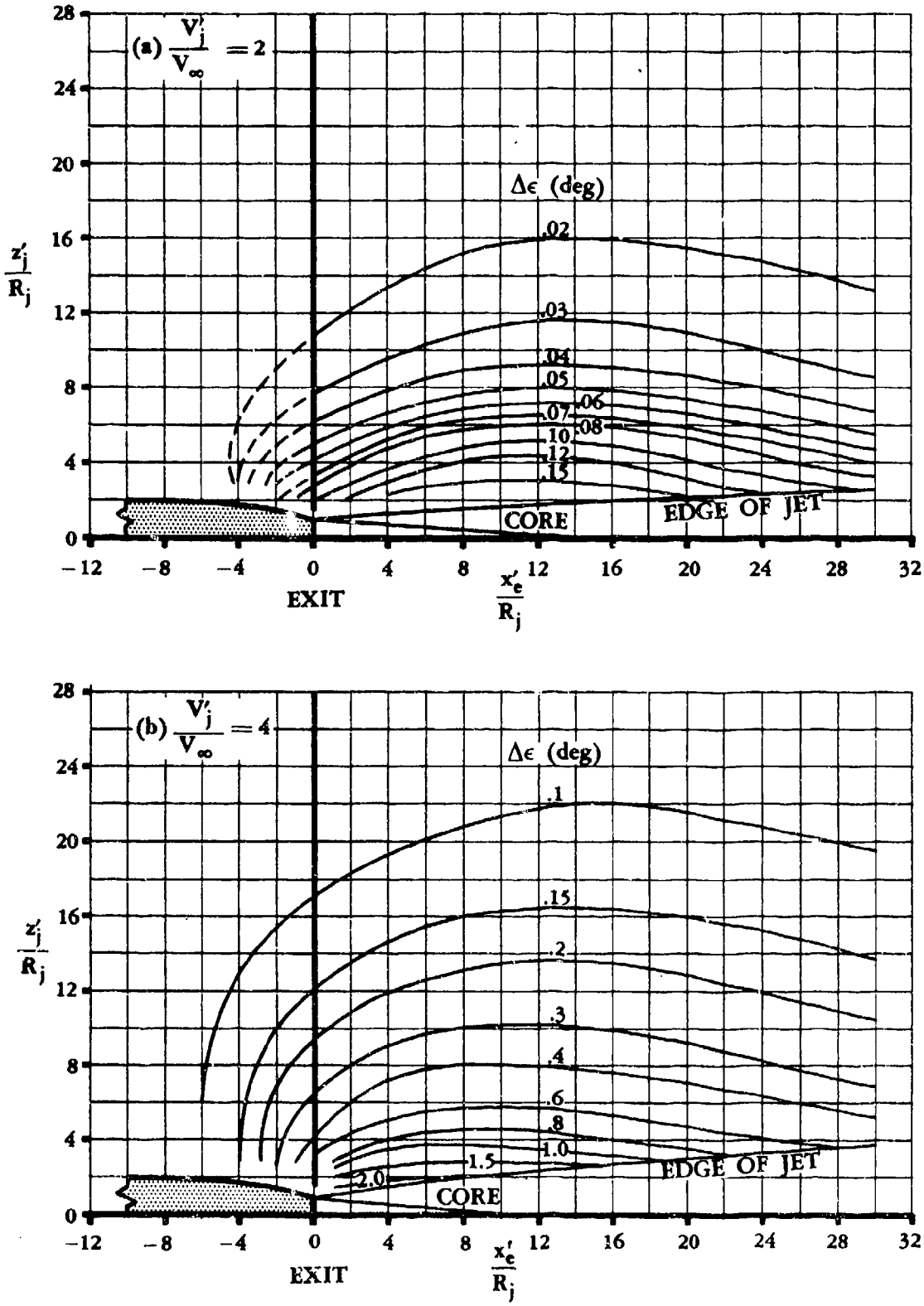

FIGURE 4.6.1-30 DOWNWASH INCREMENT DUE TO SUBSONIC JET IN A SUBSONIC STREAM

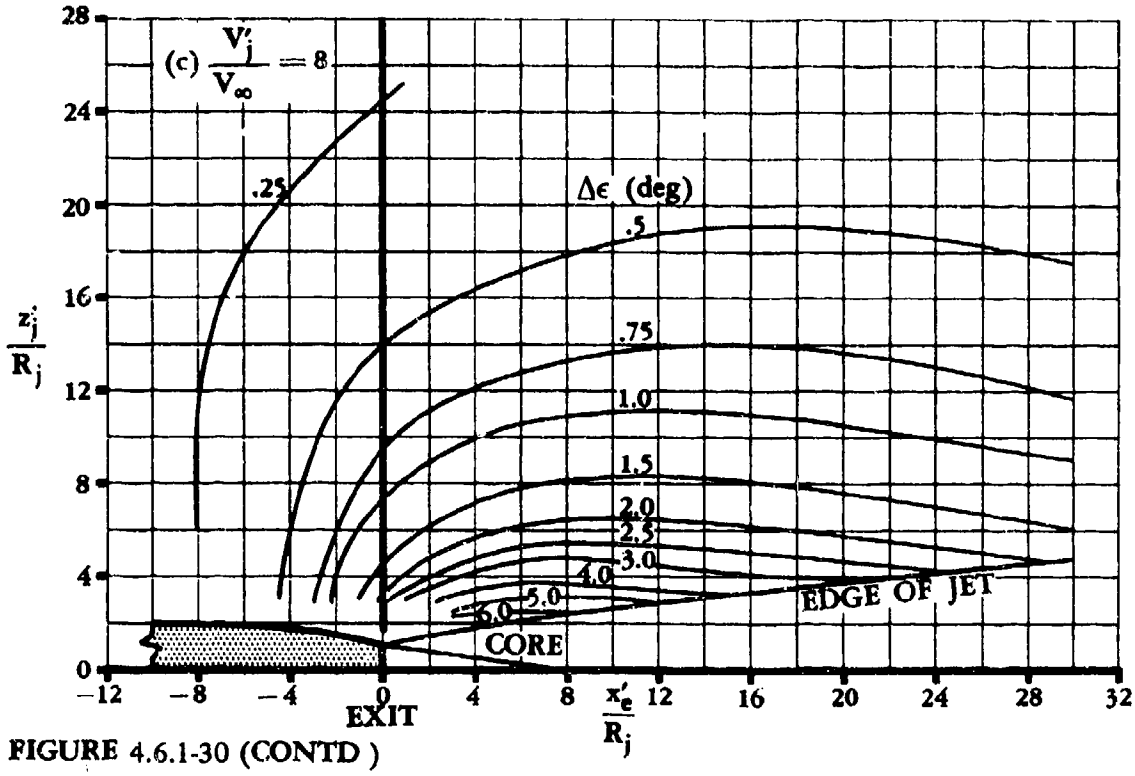

FIGURE 4.6.1-30 (CONTD)

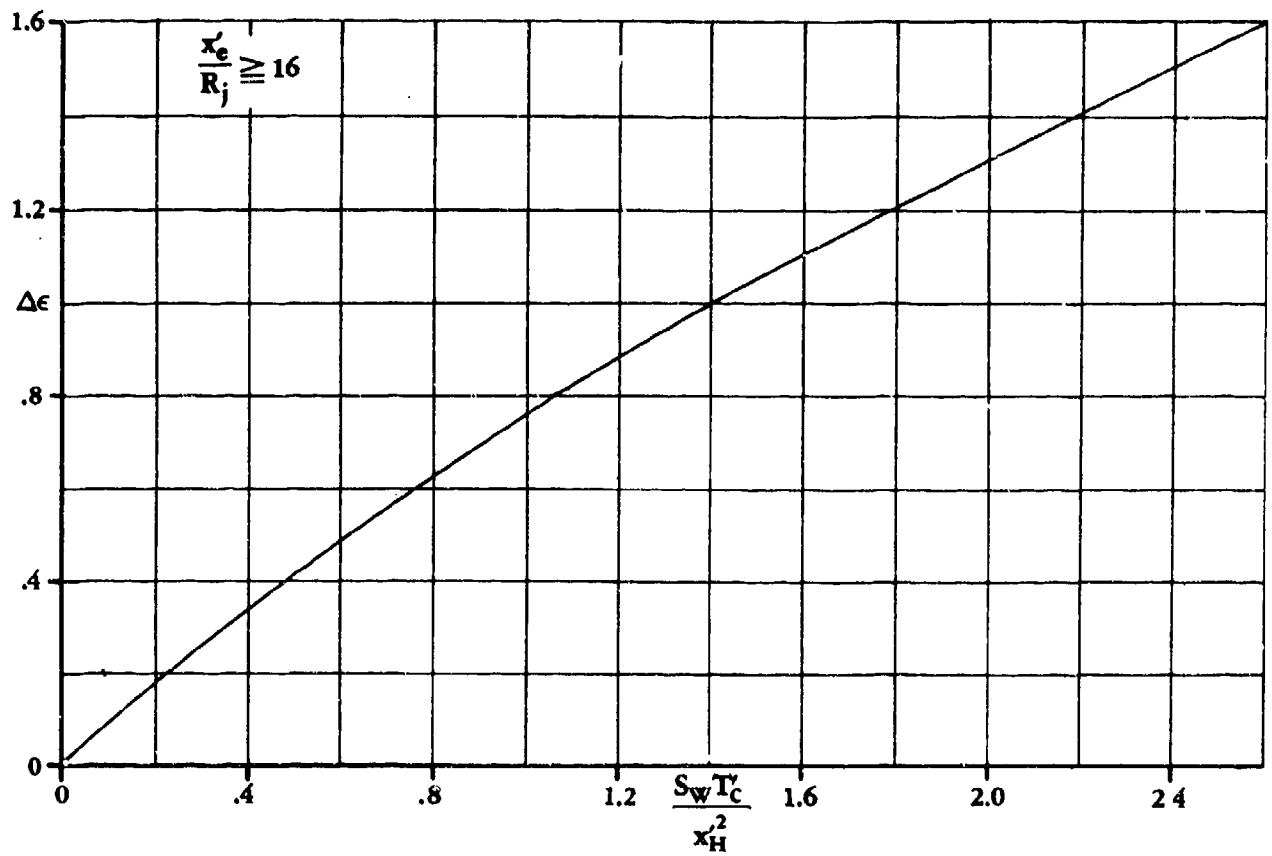

FIGURE 4.6.1-31 DOWNWASH INCREMENT DUE TO A SUBSONIC JET IN A SUBSONIC STREAM

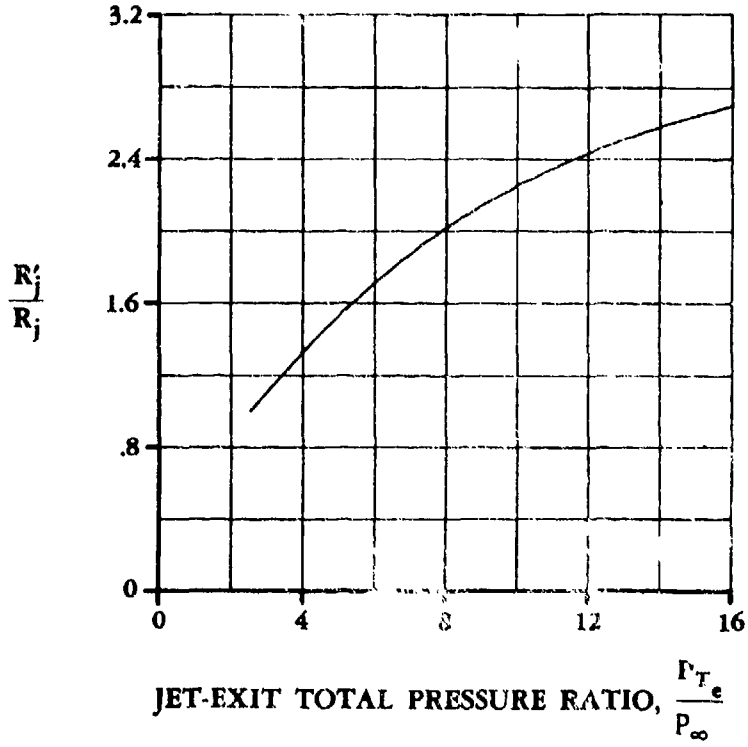

FIGURE 4.6.1-32a EQUIVALENT JET ORIFICE RADIUS FOR SUPERSONIC JET IN A SUBSONIC STREAM

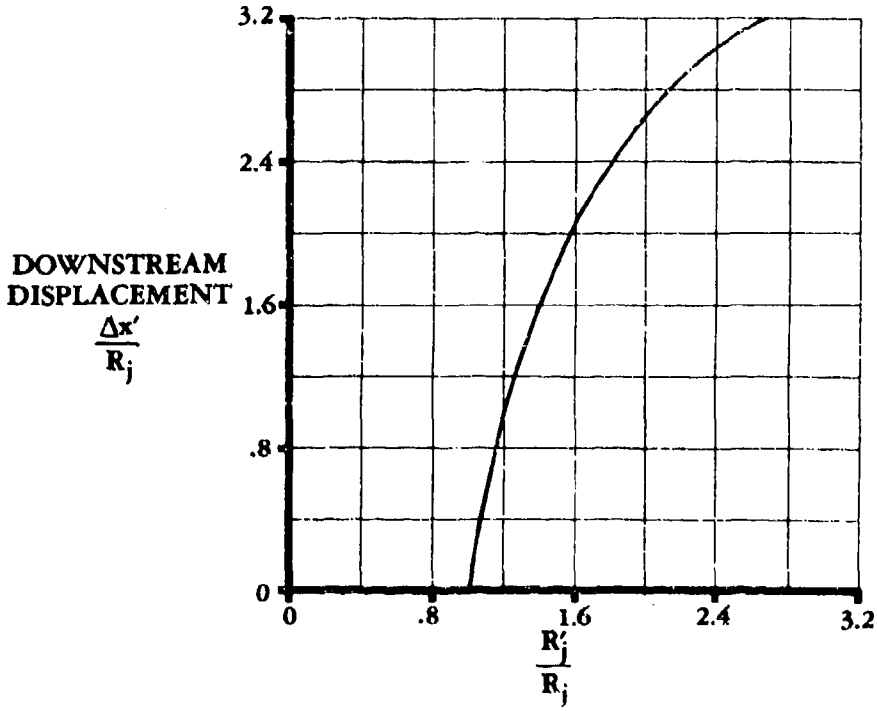

FIGURE 4.6.1-32b DOWNSTREAM DISPLACEMENT OF EQUIVALENT JET ORIFICE LOCATION FOR A SUPERSONIC JET IN A SUBSONIC STREAM

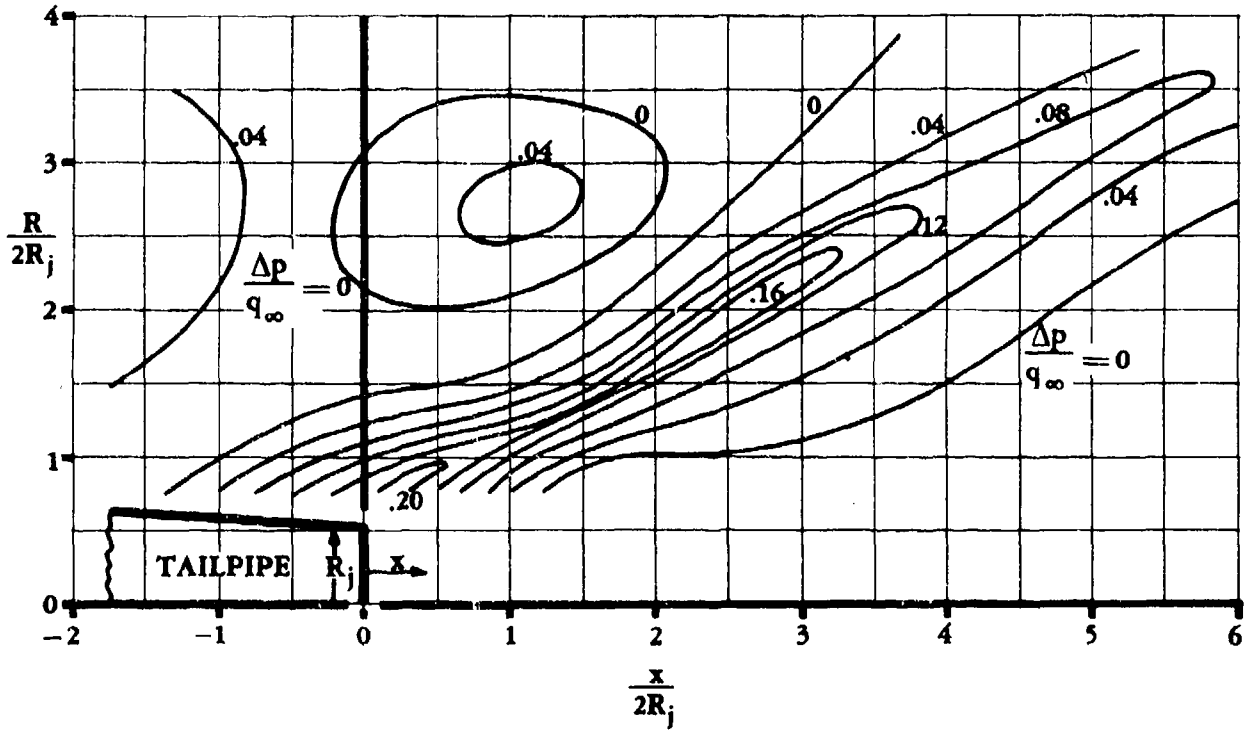

FIGURE 4.6.1-33 PRESSURE FIELD DUE TO JET EXHAUST — M = 2.0 AND P_{T_e}/P_∞ = 7.0 (FROM REFERENCE 9)

4.6.2 POWER EFFECTS ON MAXIMUM LIFT

A. PROPELLER POWER EFFECTS ON MAXIMUM LIFT

Over the linear lift-curve-slope range, increases in lift due to propeller power result from the factors discussed in Section 4.6.1, paragraph A. However, near or at maximum lift an additional increase in lift coefficient occurs because the angle of attack for stall increases with power. This effect depends primarily upon the ratio of the immersed wing area to the total wing area. An empirical method, based on data from references 1 and 2, is presented in this section for estimating the maximum lift increase due to power.

DATCOM METHOD

Step 1. From figure 4.6.2-3 obtain a value for the empirical constant K as a function of the ratio of immersed wing area to total wing area S_i/S_W. (The immersed wing area S_i is calculated in Section 4.6.1.)

Step 2. Calculate the increment in lift due to power $(\Delta C_L)_{\substack{power\\on}}$ at the angle of attack for maximum lift, power off. This value is obtained from equation 4.6.1-w of Section 4.6.1.

Step 3. Calculate the increment of maximum lift due to propeller power by

$$\Delta C_{L_{max}} = K\left(\Delta C_L\right)_{\substack{power\\on}} \qquad 4.6.2\text{-a}$$

The shift in $\alpha_{C_{L_{max}}}$ for the power-on lift curve can only be approximated, based on the shape of the power-off curve. Based on this geometrical approximation, the complete lift curve can then be constructed as shown in sketch (a).

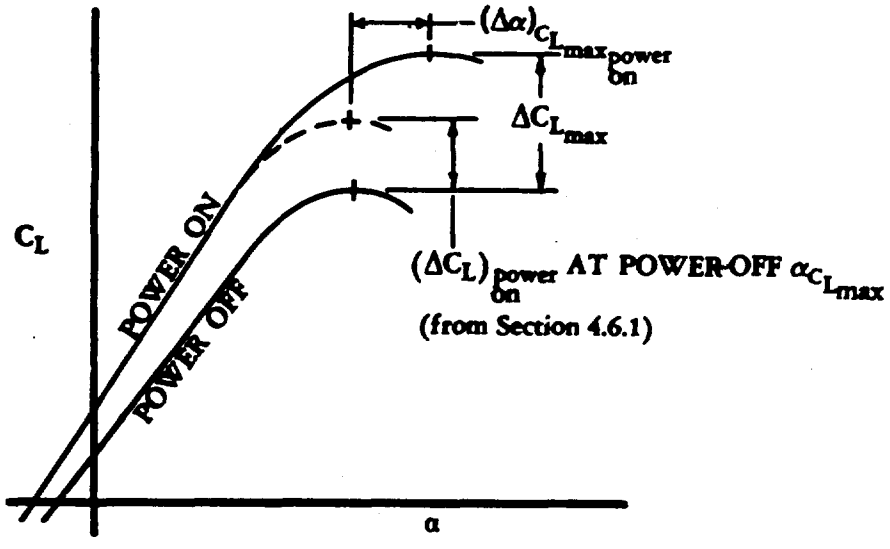

SKETCH (a)

Table 4.6.2-A compares the results obtained by this method with test data.

Sample Problem

Given:

$S_W = 314\ ft^2$ $\quad T_c' = 0.20$ $\quad \left(\alpha_{stall}\right)_{\substack{power \\ off}} = 16°$ (wind-tunnel data)

$\left(\Delta C_L\right)_{\substack{power \\ on}} = 0.438$ (Section 4.6.1) $\quad S_i = 114\ ft^2$ (Section 4.6.1)

Compute:

$$\frac{S_i}{S_W} = \frac{114}{314} = 0.364$$

$K = 1.38$ (figure 4.6.2-3)

$$\Delta C_{L_{max}} = K\left(\Delta C_L\right)_{\substack{power \\ on}} \quad \text{(equation 4.6.2-a)}$$

$$= (1.38)(0.438)$$

$$= 0.604$$

B. JET POWER EFFECTS ON MAXIMUM LIFT

The maximum lift due to jet power is described in Section 4.6.1, paragraph B, since the angle of attack for stall does not exhibit an increase with power as in the case for propellers. The increment in maximum lift is therefore found by calculating the lift increment at the angle of attack for maximum lift, power off, by using the method of Section 4.6.1. The shape of the power-on lift curve near stall is similar to that of the power-off curve determined by using other sections of the Datcom.

REFERENCES

1. Sweberg, H. H., and Dingeldein, R. C.: Summary of Measurements in Langley Full-Scale Tunnel of Maximum Lift Coefficients and Stalling Characteristics of Airplanes. NACA WR L-145, 1945. (U)

2. Anon.: Model C-133A Estimated Basic Stability and Control Data. Douglas Aircraft Company Report LB-21984, 1956. (U)

TABLE 4.8.2-A

LOW-SPEED MAXIMUM-LIFT INCREMENT DUE TO POWER

DATA SUMMARY

Reference	Airplane	T_c	$\frac{S_i}{S_W}$	K	$\left(\Delta C_L\right)_{power\ on}$	$\Delta C_{L_{max}}$ Calc	$\Delta C_{L_{max}}$ Test
1	F4U	0.20	0.364	1.38	0.438	0.60	0.64
	Mars	0.13	0.405	1.55	0.123	0.19	0.20
	B-15	0.31	0.500	2.06	0.160	0.33	0.30
	F6F	idle	0.360	1.36	0.101	0.14	0.14
	P-63	idle	0.360	1.36	0.072	0.10	0.08
2	C-133	0.60	0.486	1.97	0.241	0.48	0.56

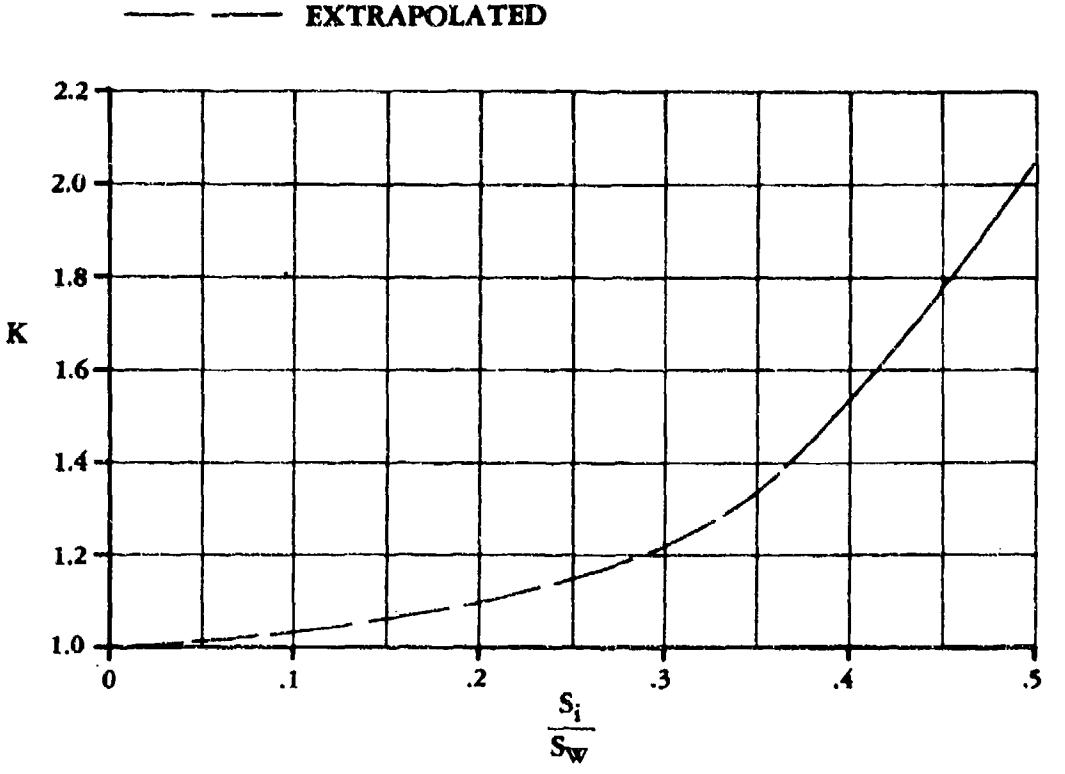

FIGURE 4.6.2-3 CORRECTION FACTOR FOR MAXIMUM LIFT DUE TO POWER

4.6.3 POWER EFFECTS ON PITCHING-MOMENT VARIATION WITH ANGLE OF ATTACK

A. PROPELLER POWER EFFECTS ON PITCHING MOMENT

This section presents a method from references 1 and 2 for estimating the power effects of propellers on the pitching-moment characteristics of a vehicle. Since power effects on pitching-moment characteristics are primarily a result of the increments in lift due to propellers, part A of Section 4.6.1 is directly applicable to this section, and the reader is referred to that discussion for a general description of the fundamental phenomena.

DATCOM METHOD

The Datcom method estimates the power-on pitching-moment curves based on power-off curves, as a function of angle of attack, thrust coefficient, and lift coefficient.

This method analyzes the increments of pitching-moment coefficient due to propeller-power effects in the following order:

1. Offset of the thrust axis from the origin of the axes
2. Propeller normal force due to angle of attack
3. Change in dynamic pressure over the section of the wing in the propeller slipstream
4. Change in lift of the wing caused by power effects
5. Change in dynamic pressure acting on the horizontal tail
6. Change in angle of attack at the horizontal tail

After the above pitching-moment increments for a given angle of attack have been calculated, the accumulated total is then applied to the power-off pitching-moment curve to obtain a point on the power-on pitching-moment curve. After several points have been generated (by considering several angles of attack), the linear section of the power-on pitching-moment curve is obtained for a given thrust coefficient.

All increments of pitching-moment coefficients are nondimensionalized with respect to the product of wing area and wing MAC. Their moment center is at the quarter-chord point of the wing MAC.

Step 1. Calculate the increment in pitching-moment coefficient per engine due to an offset of the thrust axis from the origin of the axes by

$$\left(\Delta C_m\right)_T = T_c' \frac{z_T}{\bar{c}} \qquad 4.6.3\text{-a}$$

where the thrust coefficient is a given or chosen quantity. For multiple-engine configurations the total pitching-moment component is found by summing the component due to each engine.

Step 2. Calculate the increment in pitching-moment coefficient due to the propeller normal force by

$$\left(\Delta C_m\right)_{N_p} = \left(\Delta C_L\right)_{N_p} \frac{x_p}{\bar{c}} \frac{\cos i_T}{\cos \alpha_T} \qquad 4.6.3\text{-b}$$

where $(\Delta C_L)_{N_p}$ is obtained from Section 4.6.1 and α_T is given by equation 4.6.1-a, i.e.,

$$\alpha_T = \alpha + i_T$$

Step 3. Calculate the increment in pitching-moment coefficient due to the change in slipstream dynamic pressure acting on the wing as follows:

a. Calculate the zero-lift pitching-moment coefficient $(C_{m_0})_i$ of those components of the tail-off configuration that are immersed in the slipstream by

$$\left(C_{m_0}\right)_i = \left(C_{m_0}\right)_{\text{wing-body}} - \left(C_{m_0}\right)_{\substack{\text{area not} \\ \text{immersed}}} \qquad 4.6.3\text{-c}$$

where $(C_{m_0})_{\text{wing-body}}$ must be obtained from wind-tunnel tests and $(C_{m_0})_{\substack{\text{area not} \\ \text{immersed}}}$ may be obtained from Section 4.1.4.1 and is based on the combined planform area of the wing not immersed in the propeller slipstream.

b. Calculate the change in slipstream dynamic pressure given by equation 4.6.1-r, i.e.,

$$\frac{\Delta q_s}{q_\infty} = \frac{S_W T_c'}{\pi R_p^2}$$

c. Calculate the pitching-moment increment due to the change in slipstream dynamic pressure by

$$\left(\Delta C_m\right)_q = \frac{\Delta q_s}{q_\infty} \left(C_{m_0}\right)_i \qquad 4.6.3\text{-d}$$

Step 4. Calculate the increment in pitching-moment coefficient due to the change in lift of the wing caused by power effects as follows:

a. Calculate the lift increments $(\Delta C_L)_q$ and $(\Delta C_L)_{\Delta\alpha_W}$ by the method in Section 4.6.1.

b. Calculate the pitching-moment increment due to the immersed wing lift increments by

$$\left(\Delta C_m\right)_L = \left[\left(\Delta C_L\right)_q + \left(\Delta C_L\right)_{\Delta\alpha_W}\right] \frac{x_W}{\bar{c}} \qquad 4.6.3\text{-e}$$

where x_W is the longitudinal distance from the aerodynamic center of that portion of the wing immersed in the propeller slipstream to the moment-reference-center location, positive for the aerodynamic center forward of the moment reference center (see Figure 4.6-12).

Step 5. Calculate the increment in pitching-moment coefficient due to the change in dynamic pressure acting on the horizontal tail as follows:

a. Calculate the angle of attack at the horizontal tail α_H by

$$\alpha_H = \alpha + i_H - \left(\epsilon_H\right)_{\substack{\text{power}\\\text{off}}} \qquad 4.6.3\text{-f}$$

where $(\epsilon_H)_{\substack{\text{power}\\\text{off}}}$ is obtained in Section 4.4.1.

b. Obtain a value for the lift-curve slope of the horizontal tail $(C_{L_{\alpha_H}})_{\substack{\text{power}\\\text{off}}}$ from Section 4.1.3.2.

c. Calculate the lift coefficient of the horizontal tail by

$$C_{L_H} = \left(C_{L_{\alpha_H}}\right)_{\substack{\text{power}\\\text{off}}} \alpha_H \qquad 4.6.3\text{-g}$$

d. From figure 4.6.3-14 or 4.6.3-15 obtain a value for the change in downwash at the horizontal tail $\Delta\epsilon_H$ as a function of geometric characteristics, thrust coefficient, and the power-off downwash angle.

e. Calculate the power-on downwash angle at the horizontal tail by

$$\left(\epsilon_H\right)_{\substack{\text{power}\\\text{on}}} = \left(\epsilon_H\right)_{\substack{\text{power}\\\text{off}}} + \Delta\epsilon_H \qquad 4.6.3\text{-h}$$

f. Calculate the geometric distance z_s by equation 4.6.1-n, i.e.

$$z_s = x_p \tan\left(\alpha_T + \epsilon_u - \epsilon_p\right) - z_T$$

g. Calculate the geometric distance $z_{H_{eff}}$ by

$$z_{H_{eff}} = z_s + z_H + \ell_H \tan\left[\alpha_T + \epsilon_u - \epsilon_p - \left(\epsilon_H\right)_{\substack{\text{power}\\\text{on}}}\right] \qquad 4.6.3\text{-i}$$

h. From figure 4.6.3-16 obtain a value for the change in dynamic pressure $\Delta q_H/q_\infty$ as a function of geometric characteristics and thrust coefficient.

i. Calculate the change in pitching-moment coefficient due to the incremental change in dynamic pressure at the horizontal tail by

$$\left(\Delta C_{m_H}\right)_q = -C_{L_H} \frac{\Delta q_H}{q_\infty} \frac{S_H}{S_W} \frac{\ell_H}{\bar{c}} \qquad 4.6.3\text{-j}$$

Step 6. Calculate the increment in pitching-moment coefficient due to the change in angle of attack of the horizontal tail as follows:

a. Calculate the power-on dynamic-pressure ratio at the horizontal tail by

$$\left(\frac{q_H}{q_\infty}\right)_{\substack{\text{power}\\\text{on}}} = \left(\frac{q_H}{q_\infty}\right)_{\substack{\text{power}\\\text{off}}} + \frac{\Delta q_H}{q_\infty} \qquad 4.6.3\text{-k}$$

where $\Delta q_H/q_\infty$ is found in step 5.h and $(q_H/q_\infty)_{\substack{\text{power}\\\text{off}}}$ is obtained in Section 4.4.1.

b. Calculate the change in pitching-moment coefficient due to the change in angle of attack at the horizontal tail by

$$\left(\Delta C_{m_H}\right)_\epsilon = C_{L_{\alpha_H}} \Delta\epsilon_H \frac{S_H}{S_W} \frac{\ell_H}{\bar{c}} \left(\frac{q_H}{q_\infty}\right)_{\substack{\text{power}\\\text{on}}} \qquad 4.6.3\text{-}\ell$$

where $\Delta\epsilon_H$ is found in Step 5.d.

Step 7. Calculate the total incremental change in pitching-moment coefficient due to propeller power effects by

$$\left(\Delta C_m\right)_{\substack{\text{power}\\\text{on}}} = \left(\Delta C_m\right)_T + \left(\Delta C_m\right)_{N_p} + \left(\Delta C_m\right)_q + \left(\Delta C_m\right)_L + \left(\Delta C_{m_H}\right)_q + \left(\Delta C_{m_H}\right)_\epsilon \qquad 4.6.3\text{-m}$$

Sample Problem

The configuration used in this sample problem is the same as that used in the sample problem for propeller effects on lift in Section 4.6.1.

Given:

Wing Parameters:

$S_W = 380\ ft^2 \qquad S_i = 117.4\ ft^2 \qquad b_i = 12.8\ ft$ } (calculated in Section 4.6.1)

$\left(\Delta C_L\right)_{N_p} = 0.00529$

$\left(\Delta C_L\right)_{\Delta\alpha_W} = -0.0173$ } (calculated in Section 4.6.1)

$\left(\Delta C_L\right)_q = 0.0584$

$\bar{c} = 8.17\ ft \qquad \Lambda_{c/4} = 0 \qquad c_i = 9.17\ ft \qquad \bar{c}_{\substack{\text{area not}\\ \text{immersed}}} = 7.50\ ft$

$A_{\substack{\text{area not}\\ \text{immersed}}} = 4.90 \qquad \left(c_{m_0}\right)_{\substack{\text{area not}\\ \text{immersed}}} = -0.07$ (average value for wing sections not immersed in the slipstream)

$\left(C_{m_0}\right)_{\text{wing-body}} = -0.080$ (tail-off wind-tunnel data) $\qquad x_W = 0$

$\alpha = 4.0° \qquad \alpha_T = 4.0° \qquad \epsilon_u = 1.14° \qquad \epsilon_p = 0.59°$

$\epsilon_{\substack{\text{power}\\ \text{off}}} = 4.0°$ (wind-tunnel data or Section 4.4.1)

Horizontal-Tail Parameters:

$S_H = 80\ ft^2 \qquad \frac{S_{H_i}}{S_H} = \frac{59}{80} = 0.738 \qquad i_H = 0 \qquad A_H = 4.26$

$\lambda_H = 0.59 \qquad \Lambda_{H_{c/4}} = 0 \qquad \left(\frac{q_H}{q_\infty}\right)_{\substack{\text{power}\\ \text{off}}} = 0.9$ (Section 4.4.1)

$C_{L_{\alpha_H}} = 0.057 \quad z_H = -4.10 \text{ ft} \quad z_{H_T} = 3.0 \text{ ft} \quad \ell_H = 20.4 \text{ ft}$

Engine Parameters:

$T_c' = 0.15 \quad R_p = 6.79 \text{ ft} \quad x_p = 10.9 \text{ ft} \quad z_T = -1.10 \text{ ft}$

Compute:

Determine the increment of pitching moment due to an offset of the thrust axis from the origin of the axes

$$\left(\Delta C_m\right)_T = T_c' \frac{z_T}{\bar{c}} \qquad \text{(equation 4.6.3-a)}$$

$$= (0.15) \frac{(-1.10)}{(8.17)} = -0.0202$$

Determine the increment of pitching moment due to the propeller normal force

$$\left(\Delta C_m\right)_{N_p} = \left(\Delta C_L\right)_{N_p} \frac{x_p}{\bar{c}} \frac{1}{\cos \alpha_T} \qquad \text{(equation 4.6.3-b)}$$

$$= (0.00529) \frac{10.9}{8.17} \frac{1}{\cos 4.0^\circ} = 0.00707$$

Determine the increment of pitching moment due to the change in dynamic pressure

$$C_{m_0} = \frac{A \cos \Lambda_{c/4}}{A + 2 \cos \Lambda_{c/4}} \cos \Lambda_{c/4} \, c_{m_0} \qquad \text{(equation 4.1.4.1-a)}$$

where A is the aspect ratio of the combined wing not immersed in the slipstream.

$$C_{m_0} = \frac{4.90}{4.90 + 2} (-0.07)$$

$= -0.05$ (Note: this is based on the wing area not immersed in the slipstream)

$$\left(C_{m_0}\right)_{\substack{\text{area not} \\ \text{immersed}}} = C_{m_0} \left(\frac{S_W - S_i}{S_W}\right) \bar{c}_{\substack{\text{area} \\ \text{immersed}}} \frac{1}{\bar{c}} \qquad \text{(based on } S_W \text{ and } \bar{c}\text{)}$$

$$= (-0.05) \frac{(380 - 117.4)}{380} \frac{(7.50)}{(8.17)} = -0.0317$$

$$\left(C_{m_0}\right)_i = \left(C_{m_0}\right)_{\text{wing-body}} - \left(C_{m_0}\right)_{\substack{\text{area not} \\ \text{immersed}}} \qquad \text{(equation 4.6.3-c)}$$

$$= -0.080 + 0.0317$$

$$= -0.0483$$

$$\frac{\Delta q_s}{q_\infty} = \frac{S_W T_c'}{\pi R_p^2} \qquad \text{(equation 4.6.1-r)}$$

$$= \frac{(380)\,(0.15)}{(3.14)\,(6.79)^2} = 0.394$$

$$\left(\Delta C_m\right)_q = \frac{\Delta q_s}{q_\infty}\left(C_{m_0}\right)_i \qquad \text{(equation 4.6.3-d)}$$

$$= (0.394)\,(-0.0483)$$

$$= -0.019$$

Determine the increment of pitching moment due to the change in lift of the wing

$$\left(\Delta C_m\right)_L = -\left[\left(\Delta C_L\right)_q + \left(\Delta C_L\right)_{\Delta\alpha_W}\right]\frac{x_W}{\bar{c}} \qquad \text{(equation 4.6.3-e)}$$

$$= -\,[0.0584 - 0.0173]\,\frac{0}{8.17}$$

$$= 0$$

Determine the increment of pitching moment due to the change in dynamic pressure on the horizontal tail

$$\alpha_H = \alpha + i_H - \left(\epsilon_H\right)_{\substack{\text{power} \\ \text{off}}} \qquad \text{(equation 4.6.3-f)}$$

$$= 4 + 0 - 4 = 0$$

$$C_{L_H} = \left(C_{L_{\alpha_H}}\right)_{\substack{\text{power} \\ \text{off}}} \alpha_H \qquad \text{(equation 4.6.3-g)}$$

$$= (0.057)\,(0) = 0$$

$\Delta\epsilon_H = 0.7$ (figure 4.6.3-14)

$\left(\epsilon_H\right)_{\substack{\text{power}\\\text{on}}} = \left(\epsilon_H\right)_{\substack{\text{power}\\\text{off}}} + \Delta\epsilon_H$ (equation 4.6.3-h)

$= 4.0 + 0.7$

$= 4.7°$

$z_s = x_p \tan(\alpha_T + \epsilon_u - \epsilon_p) - z_T$ (equation 4.6.1-n)

$= 10.9 \tan(4.0 + 1.14 - 0.59) + 1.10$

$= 1.96$ ft

$z_{H_{eff}} = z_s + z_H + \ell_H \tan\left[\alpha_T + \epsilon_u - \epsilon_p - \left(\epsilon_H\right)_{\substack{\text{power}\\\text{on}}}\right]$ (equation 4.6.3-i)

$= 1.96 - 4.10 + 20.4 \tan(4 + 1.14 - 0.59 - 4.7)$

$= -2.14 + 20.4\,(-0.00262)$

$= -2.19$ ft

$\frac{\Delta q_H}{q_\infty} = 0.14$ (figure 4.6.3-16)

$\left(\Delta C_{m_H}\right)_q = -C_{L_H} \frac{\Delta q_H}{q_\infty} \frac{S_H}{S_W} \frac{\ell_H}{\bar{c}}$ (equation 4.6.3-j)

$= -(0)\,(0.14)\,\frac{80}{380}\,\frac{20.4}{8.17}$

$= 0$

Determine the increment of pitching moment due to the change in angle of attack at the horizontal tail

$\left(\frac{q_H}{q_\infty}\right)_{\substack{\text{power}\\\text{on}}} = \left(\frac{q_H}{q_\infty}\right)_{\substack{\text{power}\\\text{off}}} + \frac{\Delta q_H}{q_\infty}$ (equation 4.6.3-k)

$= 0.90 + 0.14 = 1.04$

$$\left(\Delta C_{m_H}\right)_\epsilon = C_{L_{\alpha_H}} \Delta\epsilon_H \frac{S_H}{S_W} \frac{\ell_H}{\bar{c}} \left(\frac{q_H}{q_\infty}\right)_{\substack{\text{power} \\ \text{on}}} \qquad \text{(equation 4.6.3-}\ell\text{)}$$

$$= (0.057)(0.7)\left(\frac{80}{380}\right)\left(\frac{20.4}{8.17}\right)(1.04)$$

$$= 0.0218$$

Determine the total change in pitching moment due to propeller power effects

$$\left(\Delta C_m\right)_{\substack{\text{power} \\ \text{on}}} = \left(\Delta C_m\right)_T + \left(\Delta C_m\right)_{N_p} + \left(\Delta C_m\right)_q + \left(\Delta C_m\right)_L$$

$$\left(\Delta C_{m_H}\right)_q + \left(\Delta C_{m_H}\right)_\epsilon \qquad \text{(equation 4.6.3-m)}$$

$$= -0.0202 + 0.00707 - 0.019 + 0 + 0 + 0.0218$$

$$= -0.0103$$

B. JET POWER EFFECTS ON PITCHING MOMENT

This section presents a method from references 1, 3, and 4 for estimating the subsonic jet power effects on pitching moment. The method presented here for estimating the supersonic jet power effects is based on approximate methods developed for the Datcom. Since the power effects on pitching-moment characteristics are primarily a result of the increments in lift due to jet effects, part B of Section 4.6.1 is directly applicable to this section, and the reader is referred to that discussion for a general description of the fundamental phenomena.

DATCOM METHOD

The Datcom method estimates the power-on pitching-moment curves, based on power-off pitching-moment curves, as a function of angle of attack, thrust coefficient, and lift coefficient.

This method analyzes the increments of pitching-moment coefficient due to jet power effects in the following order:

1. Offset of the thrust axis from the origin of the axes
2. Normal force acting at the engine inlet
3. Interference effects

After the above lift increments for a given angle of attack have been calculated, the accumulated total is then applied to the power-off pitching-moment curve to obtain a point on the power-on pitching-moment curve. After several points have been generated (by considering several angles of

attack), the linear section of the power-on pitching-moment curve is obtained for a given thrust coefficient. (Refer to figure 4.6-13b for geometrical definitions.)

All increments of pitching-moment coefficients are nondimensionalized with respect to the product of wing area and wing MAC. Their moment center is at the quarter-chord of the wing MAC.

Step 1. Calculate the increment in pitching-moment coefficient for each engine due to an offset of the thrust axis from the origin of the axes by

$$\left(\Delta C_m\right)_T = \frac{T_c' z_T}{\bar{c}} \qquad 4.6.3\text{-a}$$

where the thrust coefficient is a given or chosen quantity. For multiple-engine configurations the total pitching-moment component is found by summing the single components due to each engine.

Step 2. Calculate the increment in pitching-moment coefficient due to the normal force at the engine inlet as follows:

a. Calculate the inclination of the thrust axis to the oncoming stream α_j at the engine inlet, given by equation 4.6.1-x, i.e.,

$$\alpha_j = \alpha_T + \epsilon_u$$

where the upwash ahead of the wing ϵ_u is obtained from equation 4.6.1-m, i.e.,

$$\epsilon_u = \frac{\partial \epsilon_u}{\partial \alpha} \left(\alpha_W - \alpha_0\right)$$

and the upwash gradient $\partial \epsilon_u / \partial \alpha$ at the engine inlet may be obtained in Section 4.4.1.

b. Calculate the incremental pitching-moment coefficient per engine by

$$\left(\Delta C_m\right)_{N_j} = \frac{2 A_I x_I \sin \alpha_j}{S_W \bar{c}} \qquad 4.6.3\text{-n}$$

where A_I is the inlet duct area. For multiple-engine configurations the total pitching-moment component is found by summing the single components due to each engine.

Step 3. Calculate the increment in pitching-moment coefficient due to the jet interference effects at the horizontal tail or other surface by

$$\left(\Delta C_m\right)_\epsilon = \left(\Delta C_L\right)_\epsilon \frac{x}{\bar{c}} \qquad 4.6.3\text{-o}$$

where $\left(\Delta C_L\right)_\epsilon$ is calculated in Section 4.6.1 and where x is the distance from the moment center to the centroid of the affected area, positive ahead of the moment center (in the case of tail-last configurations x corresponds to the negative value of the tail length ℓ_H).

Step 4. Calculate the total incremental change in pitching-moment coefficient due to jet effects by

$$\left(\Delta C_m\right)_{\substack{\text{power}\\ \text{on}}} = \left(\Delta C_m\right)_T + \left(\Delta C_m\right)_{N_j} + \left(\Delta C_m\right)_\epsilon \qquad 4.6.3\text{-p}$$

Sample Problem

The configuration used in this sample problem is the same as that used in the sample problem of Section 4.6.1, paragraph B.

Given:

Engine Parameters:

Outboard Engines (2)

$T_c' = 0.0746$ (per engine) $\quad A_I = 13.64\ ft^2 \quad x_I = 145.2$ in.

$z_T = 53.0$ in. $\quad \alpha_j = 9.87°$ (Section 4.6.1)

Inboard Engines (2)

$T_c' = 0.0746$ (per engine) $\quad A_I = 13.64\ ft^2 \quad x_I = 283.8$ in.

$z_T = 70.8$ in. $\quad \alpha_j = -10.4°$ (Section 4.6.1)

Horizontal-Tail Parameters:

$\left(\Delta C_L\right)_\epsilon = -0.002$ (Section 4.6.1) $\quad \ell_H = 855.0$ in.

Wing Parameters:

$\bar{c} = 272.8$ in. $\quad S_W = 2930\ ft^2$

Compute:

Determine the increment in pitching-moment coefficient due to an offset of the thrust axis from the origin of the axes by

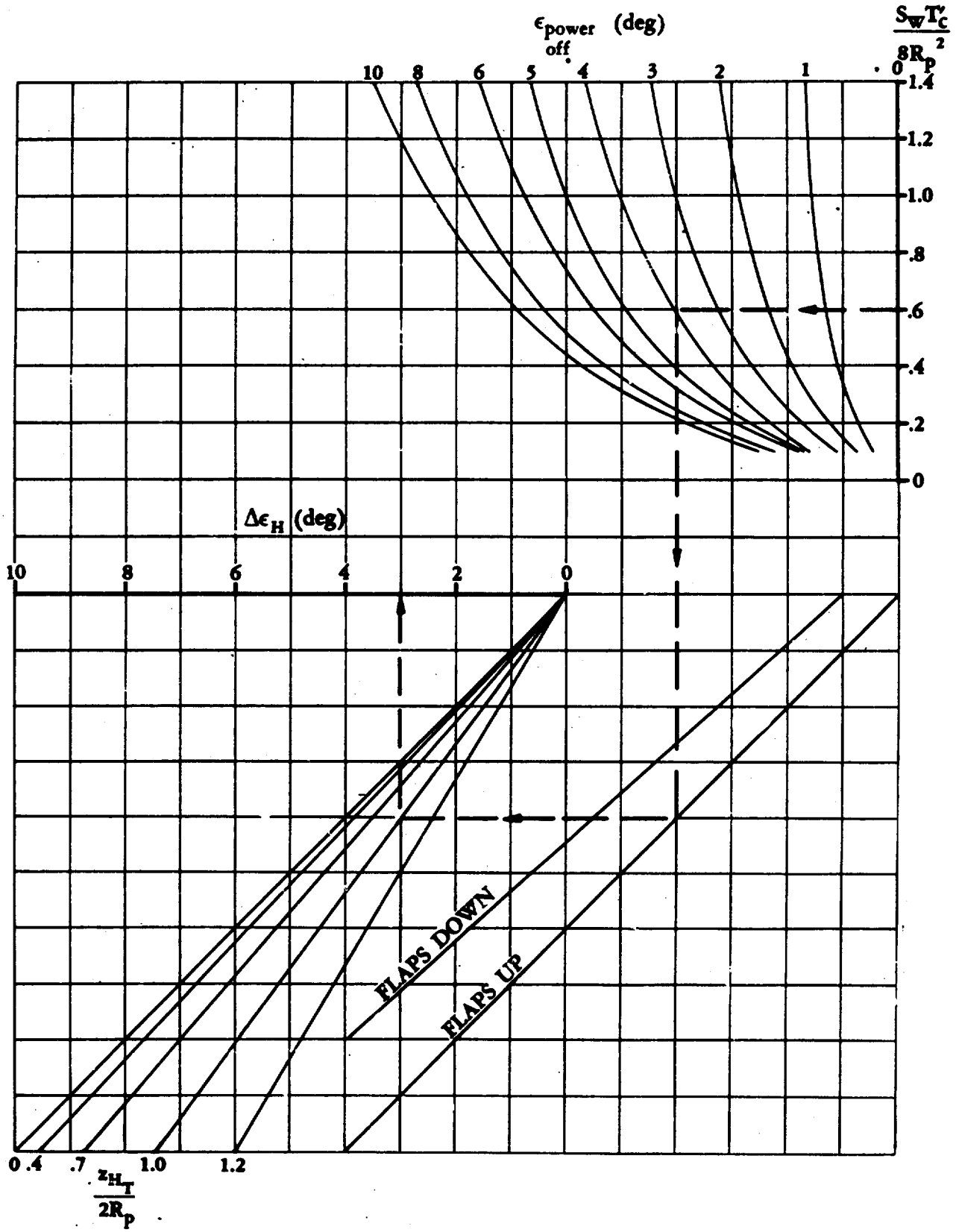

FIGURE 4.6.3-15 INCREMENT IN DOWNWASH DUE TO PROPELLER POWER FOR MULTIENGINE AIRPLANES

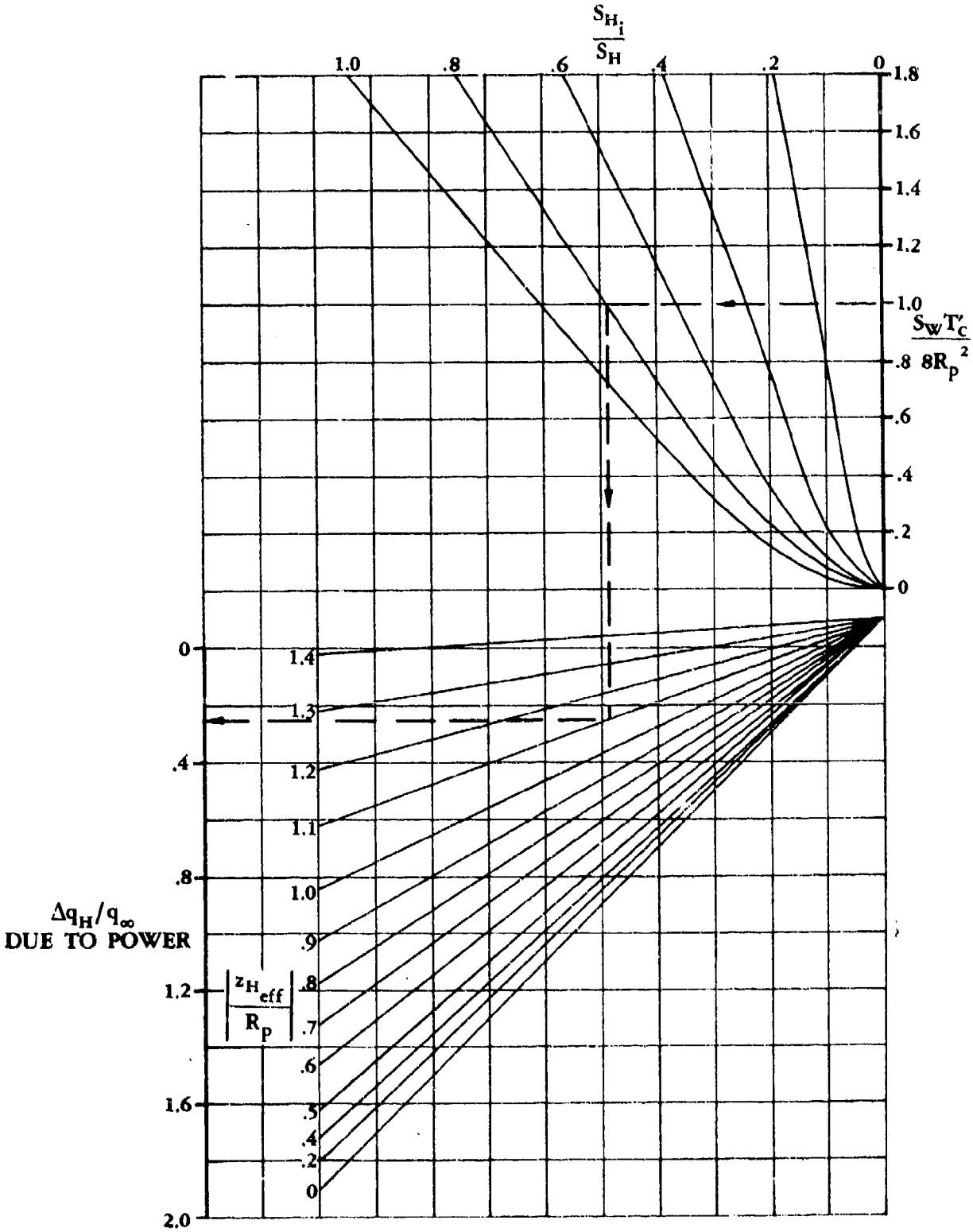

FIGURE 4.6.3-16 EFFECT OF PROPELLER POWER ON DYNAMIC PRESSURE RATIO AT THE HORIZONTAL TAIL

4.6.4 POWER EFFECTS ON DRAG AT ANGLE OF ATTACK

This section presents methods for estimating jet and propeller power effects on the drag of an aircraft. Many of the basic phenomena associated with changes in the drag are discussed in Section 4.6.1, and the reader is referred to that discussion for a more complete description of the fundamental phenomena.

A. PROPELLER POWER EFFECTS ON DRAG

The effects of propeller power on the drag of an airplane require corrections to the zero-lift drag and the lift-dependent drag.

The zero-lift drag is corrected to account for the change in dynamic pressure caused by the propeller slipstream.

The lift-dependent drag of an airplane is affected by propeller power in the following ways:

1. The components of propeller thrust and normal force that are parallel to and have the same direction as the wing lift reduce the wing lift required, thereby reducing the wing drag due to lift.

2. The propeller slipstream modifies the downwash over portions of the wing, thus changing the wing drag due to lift.

3. Propeller thrust is usually assumed to act parallel to the free stream. However, the free-stream component of thrust is really T cos α_T. Therefore, the drag component must include this differential thrust and the propeller normal-force component parallel to the free stream.

DATCOM METHOD

The Datcom method (reference 1) estimates the drag increment due to propeller-thrust effects as a function of angle of attack, thrust coefficient, and propeller normal force.

This method analyzes the increments of drag coefficient due to propeller power effects in the following order:

1. Change in zero-lift drag due to the slipstream dynamic pressure of that portion of the vehicle immersed in the propeller slipstream

2. Change in vehicle drag due to lift as a result of the lift components of propeller thrust and propeller normal force

3. Change in drag due to lift as a result of the change in angle of attack of the wing section immersed in the propeller slipstream

After the above drag increments for a given lift coefficient have been calculated, the accumulated total is then applied to the power-off drag curve to obtain a point on the power-on drag polar. After several points have been generated (by considering several lift coefficients), the power-on drag polar is obtained for a given thrust coefficient.

The above increments in drag can be determined by the following steps. (Reference should be made to figure 4.6-13a for geometric definitions. In all cases the drag increments are based on the wing reference area)

Step 1. Calculate the zero-lift increment of change in drag coefficient due to propeller-power effects as follows:

a. Calculate the increment of skin-friction drag caused by a higher local dynamic pressure on all surface area immersed in the propeller slipstream S_I by

$$\left(\Delta C_{D_0}\right)_s = \frac{1}{S\, q_\infty} \int_{S_I} C_f\, \Delta q_s\, ds \qquad 4.6.4\text{-a}$$

where C_f is the local skin-friction drag coefficient determined by the methods of Sections 4.1.5.1 and 4.2.3.1. By assuming that q_s and C_f are constant over the area wetted by the slipstream, equation 4.6.4-a may be simplified to

$$\left(\Delta C_{D_0}\right)_s = C_f\, \frac{S_I}{S}\, \frac{\Delta q_s}{q_\infty} \qquad 4.6.4\text{-b}$$

where $\Delta q_s/q_\infty$ is determined in Section 4.6.1.

b. Calculate the flap increment of zero-lift drag due to propeller power effects when the wing flaps are extended and are partially or entirely immersed in the propeller slipstream, as follows:

(1) Evaluate the propeller correlation parameter defined as

$$\frac{S_W T_c'}{R_p^2}$$

(2) From figure 4.6.4-12 obtain a value for $T_c' \sqrt{\frac{1+a}{1+2a}}\, \frac{S_W}{S_p}$ as a function of of the propeller correlation parameter.

(3) Obtain a value for the power-off drag increment of the deflected flap $\left(\Delta C_{D_0}\right)_{flap}$ from test data if available or from Section 6.1.7.

(4) Calculate the wing planform area S_{W_f} including and directly forward of the flap area.

(5) Calculate the part of S_{W_f} immersed in the propeller slipstream S_i.

(6) Calculate the flap increment of zero-lift drag by

$$\left[\left(\Delta C_{D_0}\right)_{flaps}\right]_{\substack{power\\on}} = \left(\Delta C_{D_0}\right)^{*}_{flaps}\left(T_c' \sqrt{\frac{1+a}{1+2a}}\ \frac{S_W}{S_p}\right)\left(\frac{S_i}{S_{W_f}}\right) \qquad 4.6.4\text{-c}$$

c. Calculate the total zero-lift increment of drag due to propeller power effects by

$$\left(\Delta C_{D_0}\right)_{\substack{power\\on}} = \left(\Delta C_{D_0}\right)_s + \left[\left(\Delta C_{D_0}\right)_{flaps}\right]_{\substack{power\\on}} \qquad 4.6.4\text{-d}$$

When the flaps are retracted the total zero-lift increment is given by equation 4.6.4-b.

Step 2. Calculate the propeller power effects on drag due to lift as follows:

a. Calculate the propeller normal-force coefficient per engine by

$$C_{N_p} = \left(C_{N_\alpha}\right)_p \frac{\alpha_p}{57.3}\ \frac{S_p}{S_W} \qquad 4.6.4\text{-e}$$

where $\left(C_{N_\alpha}\right)_p$ is obtained from Section 4.6.1.

b. Calculate the angle of attack of the thrust axis α_T measured from the free-stream direction and given by equation 4.6.1-a, i.e.,

$$\alpha_T = \alpha + i_T$$

c. Calculate the thrust coefficient T_c' per engine given by equation 4.6.1-b, i.e.,

$$T_c' = \frac{T}{q_\infty S_W}$$

where the thrust is a given or chosen quantity.

d. Calculate the sum of the propeller lift components by

$$C_{L_p} = T'_c \sin \alpha_T + C_{N_p} \cos \alpha_T \qquad 4.6.4\text{-f}$$

For multiple-engine configurations the total lift component due to propeller forces is found by summing the components due to each engine.

e. Calculate the wing lift coefficient C_L by

$$C_L = \frac{n'W}{q_\infty S_W} \qquad 4.6.4\text{-g}$$

where $n'W$ is the product of load factor and weight.

f. From figure 4.6.4-13a obtain a value for the empirical drag factor K_D as a function of geometry and thrust coefficient.

g. Calculate the wing lift coefficient with power effects C_{L_W} by

$$C_{L_W} = C_L - C_{L_p} \qquad 4.6.4\text{-h}$$

where C_{L_p} is the total lift component due to propeller forces.

h. From figure 4.6.4-13b obtain a value for the ratio of effective downwash to propeller downwash $\bar{\epsilon}/\epsilon_p$ as a function of the propeller correlation parameter and aircraft geometry.

i. Calculate the upwash gradient $\partial\epsilon_p/\partial\alpha_p$ given by equation 4.6.1-j, i.e.,

$$\frac{\partial \epsilon_p}{\partial \alpha_p} = C_1 + C_2 \left(C_{N_\alpha}\right)_p$$

where the constants C_1 and C_2 are obtained from figure 4.6.1-26 as a function of the propeller correlation parameter, and $\left(C_{N_\alpha}\right)_p$ is obtained from Section 4.6.1.

j. Calculate the angle of attack of the propeller plane α_p given by equation 4.6.1-g, i.e.,

$$\alpha_p = \alpha_T + \frac{\partial \epsilon_u}{\partial \alpha} (\alpha_W - \alpha_0)$$

where the upwash gradient $\partial\epsilon_u/\partial\alpha$ at the propeller may be obtained in Section 4.4.1.

k. Calculate the effective downwash over the wing span $\bar{\epsilon}$ by

$$\bar{\epsilon} = \frac{\bar{\epsilon}}{\epsilon_p} \left(\frac{\partial \epsilon_p}{\partial \alpha_p} \right) \alpha_p \qquad 4.6.4\text{-i}$$

l. Calculate the ratio of the power-on induced drag to the power-off induced drag by

$$\frac{\left(C_{D_L}\right)_{\substack{\text{power} \\ \text{on}}}}{\left(C_{D_L}\right)_{\substack{\text{power} \\ \text{off}}}} = \left(\frac{C_{L_W}}{C_L} \right)^2 \left[1 + \frac{\pi^2 A \bar{\epsilon}}{180\, C_{L_W}} \right] + K_D \left[\left(\frac{b}{2R_p} \right) \left(\frac{C_{L_p}}{C_L} \right) \right]^2 \qquad 4.6.4\text{-j}$$

The contribution from the last term in the above equation is generally less than ten percent.

The value for $\left(C_{D_L}\right)_{\substack{\text{power} \\ \text{off}}}$ must be available from wind-tunnel data or may be approximated by the wing-alone value of C_{D_L} obtained by using the method of Section 4.1.5.2.

Step 3. Calculate the total drag of an aircraft including power effects by

$$\left(C_D\right)_{\substack{\text{power} \\ \text{on}}} = \left(C_{D_0}\right)_{\substack{\text{power} \\ \text{on}}} + \left(\Delta C_{D_0}\right)_{\substack{\text{power} \\ \text{on}}} + \left(C_{D_L}\right)_{\substack{\text{power} \\ \text{on}}} \qquad 4.6.4\text{-k}$$

This equation is computed for a range of lift coefficients and thrust coefficients, and the drag-polar curves are constructed. These curves are valid only in the linear-lift region.

Sample Problem

The configuration used in this sample problem is the same as that used in the sample problem for propeller power effects on lift in Section 4.6.1. The quantities listed below are either given or calculated in the sample problem of paragraph A, Section 4.6.1, or assumed.

Given:

Wing Parameters:

$S_W = 380\ ft^2$ $\quad \frac{S_I}{S_W} = 0.309$ $\quad A = 6.23$ $\quad \frac{\Delta q_s}{q_\infty} = 0.394$ $\quad \frac{\partial \epsilon_p}{\partial \alpha_p} = 0.115$

$C_L = 0.523$ $\quad \frac{c_f}{c} = 0.20$ $\quad \delta_f = 30^\circ$ $\quad \frac{S_i}{S_{W_f}} = 0.80$ $\quad b = 48.65\ ft$

Engine Parameters:

$\left(C_{N_\alpha}\right)_p = 0.141$ $\quad i_T = 0$ $\quad \alpha_T = 4°$ $\quad R_p = 6.79$ ft $\quad T_c' = 0.150$

$\alpha_p = 5.14°$ $\quad n = 1$

Additional Parameters:

$\alpha = 4.0°$ $\quad n' = 1.0$ $\quad C_f = 0.0040$ $\quad \left(\Delta C_{D_0}\right)_{flap} = 0.040$

$\left(C_{D_L}\right)_{\substack{power \\ off}} = 0.0160$ $\quad \left(C_{D_0}\right)_{\substack{power \\ off}} = 0.10$

Compute:

Determine the zero-lift increment in drag

$$\left(\Delta C_{D_0}\right)_s = C_f \frac{S_l}{S} \frac{\Delta q_s}{q_\infty} \qquad \text{(equation 4.6.4-b)}$$

$$= (0.0040)\ (0.309)\ (0.394)$$

$$= 0.0005$$

$$\frac{S_W T_c'}{R_p^2} = \frac{(380)\ (0.15)}{(6.79)^2} = 1.236$$

$$T_c' \sqrt{\frac{1+a}{1+2a}} \frac{S_W}{S_p} = 0.25 \qquad \text{(figure 4.6.4-12)}$$

$$\left[\left(\Delta C_{D_0}\right)_{flaps}\right]_{\substack{power \\ on}} = \left(\Delta C_{D_0}\right)_{flaps} \left(T_c' \sqrt{\frac{1+a}{1+2a}} \frac{S_W}{S_p}\right) \left(\frac{S_i}{S_{W_f}}\right)$$

(equation 4.6.4-c)

$$= (0.040)\ (0.25)\ (0.80)$$

$$= 0.0080$$

$$\left(\Delta C_{D_0}\right)_{\substack{\text{power}\\\text{on}}} = \left(\Delta C_{D_0}\right)_s + \left[\left(\Delta C_{D_0}\right)_{\text{flaps}}\right]_{\substack{\text{power}\\\text{on}}} \qquad \text{(equation 4.6.4-d)}$$

$$= 0.0005 + 0.0080$$

$$= 0.0085$$

Determine the effects on drag due to lift

$$C_{N_p} = \left(C_{N_\alpha}\right)_p \frac{\alpha_p}{57.3} \frac{S_p}{S_W} \qquad \text{(equation 4.6.4-e)}$$

$$= (0.141) \left(\frac{5.14}{57.3}\right) \frac{(3.14)\,(6.79)^2}{380}$$

$$= 0.0048$$

$$C_{L_p} = T_c' \sin \alpha_T + C_{N_p} \cos \alpha_T \qquad \text{(equation 4.6.4-f)}$$

$$= (0.150)\,(0.0698) + (0.0048)\,(0.998)$$

$$= 0.0105 + 0.0048$$

$$= 0.0153$$

$K_D = 3.75$ (figure 4.6.4-13a)

$$C_{L_W} = C_L - C_{L_p} \qquad \text{(equation 4.6.4-h)}$$

$$= 0.523 - 0.0153$$

$$= 0.508$$

$$\frac{\bar{\epsilon}}{\epsilon_p} = 0.24 \qquad \text{(figure 4.6.4-13b)}$$

$$\bar{\epsilon} = \frac{\bar{\epsilon}}{\epsilon_p} \left(\frac{\partial \epsilon_p}{\partial \alpha_p}\right) \alpha_p \qquad \text{(equation 4.6.4-i)}$$

$$= (0.24)\,(0.115)\,(5.14^\circ)$$

$$= 0.142^\circ$$

$$\frac{\left(C_{D_L}\right)_{\substack{\text{power}\\ \text{on}}}}{\left(C_{D_L}\right)_{\substack{\text{power}\\ \text{off}}}} = \left(\frac{C_{L_W}}{C_L}\right)^2 \left[1 + \frac{\pi^2 A\bar{\epsilon}}{180\, C_{L_W}}\right] + K_D \left[\left(\frac{b}{2R_p}\right)\left(\frac{C_{L_p}}{C_L}\right)\right]^2$$

(equation 4.6.4-j)

$$= \left(\frac{0.508}{0.523}\right)^2 \left[1 + \frac{(3.14)^2\ (6.23)\ (0.142)}{(180)\ (0.508)}\right] + 3.75 \left[\left(\frac{48.65}{13.58}\right)\ \frac{0.0153}{0.523}\right)\right]^2$$

$$= 0.943\ [1.0954] + 3.75\ [0.01098]$$

$$= 1.074$$

$$\left(C_{D_L}\right)_{\substack{\text{power}\\ \text{on}}} = (1.074)\ (0.016)$$

$$= 0.0172$$

Determine the total drag

$$\left(C_D\right)_{\substack{\text{power}\\ \text{on}}} = \left(C_{D_0}\right)_{\substack{\text{power}\\ \text{off}}} + \left(\Delta C_{D_0}\right)_{\substack{\text{power}\\ \text{on}}} + \left(C_{D_L}\right)_{\substack{\text{power}\\ \text{on}}} \qquad \text{(equation 4.6.4-k)}$$

$$= 0.10 + 0.0085 + 0.0172$$

$$= 0.126$$

B. JET POWER EFFECTS ON DRAG

There are three jet power effects on the drag of an airplane. A jet emanating from the rear of a fuselage or nacelle has large effects on both the afterbody drag and the base drag of the fuselage or nacelle. The remaining two jet power effects on drag can be attributed to the lift force of the jet (the vertical component of the thrust) and the inlet normal force. (See Section 4.6.1, paragraph B, for additional discussion.) These lift forces reduce the wing lift and therefore reduce the wing drag due to lift.

Accurate and rapid procedures for estimating the effects of jets on base and afterbody drag are not available. The large number of internal- and external-flow variables and the large number of geometric variables pertaining to the nozzle and the afterbody prevent the prediction of these effects by the use of either simplified theory or empirical correlation of the available test data. Therefore, no Datcom method for treating jet power effects on base and afterbody drag is given. However, a brief discussion is given from references 2 and 3 presenting the salient aspects of the flow elements. The major portion of the discussion is taken from a method for treating transonic

and supersonic base drag due to jets from reference 3. (The complexity of the method prevents its formulation into a Datcom method.) Curves are presented that indicate the trends of base pressure with some of the significant variables.

DATCOM METHOD

The Datcom method is composed of two parts. The first part presents a discussion of the jet power effects on base and afterbody drag. The second part presents a method for estimating the jet power effects due to the vertical component of thrust and the inlet normal force.

Jet Power Effects on Base and Afterbody Drag

The mathematical expression for base drag in terms of base pressure may be expressed as

$$C_{D_b} = \frac{1}{q_\infty S} \int_{S_b} \int [p_\infty - p_b\,(x, y)]\, dxdy \qquad 4.6.4\text{-}\ell$$

where S_b is the base area and S is the reference area. The base lies in the XY-plane, and the base pressure p_b may vary over the base. For most cases, p_b is almost constant and equation 4.6.4-ℓ reduces to

$$C_{D_b} = \frac{(p_\infty - p_b)\, S_b}{q_\infty S} \qquad 4.6.4\text{-}m$$

A plot of some of the data of reference 2 is given in figure 4.6.4-14 for the model geometry sketched in the upper part of the figure. The base-pressure coefficient is presented as a function of Mach number for three ratios of jet total pressure to ambient pressure. From figure 4.6.4-14 it can be seen that the highest base-drag conditions occur in the transonic regime.

The geometry and initial-flow parameters for an axially symmetric boattailed afterbody with a nozzle are presented in figure 4.6.4-15. Directly behind the base area is a region of low-velocity air at pressure p_b. The free-stream flow expands to this pressure p_b as it passes the end of the afterbody. The expanded free-stream flow mixes with the low-velocity air along a boundary until it encounters flow from the jet. In similar fashion, flow from the jet expands as it passes through the nozzle exit plane. The flow mixes with the low-velocity air at the base along some boundary. When the external and internal flows meet, each must go through a shock wave that (1) turns the flows until they are parallel, and (2) equalizes the pressures of the two flows. The external flow and the flow from the jet then proceed downstream with a mixing zone lying between them. A flow pattern for the above geometrical description is indicated in figure 4.6.4-16 for a supersonic jet and free stream at a ratio of total pressure to ambient pressure greater than 2.35.

The influence of major design parameters on the base-pressure ratio of axially symmetric afterbodies with jets is presented in figures 4.6.4-17 through 4.6.4-21. The influence of free-stream Mach number on afterbody pressure is given in figure 4.6.4-17 for a convergent nozzle with the indicated geometry and pressure conditions. Figures 4.6.4-18a and 4.6.4-18b present the

effects of the ratios of jet total pressure to ambient pressure and of jet diameter to body diameter, respectively, on base pressure. In these two figures the free-stream and exit Mach numbers are constant. For the given free-stream and geometric parameters, divergence of the nozzle significantly increases the base pressure, causing a decrease in base drag. The importance of nozzle divergence angle is shown in figure 4.6.4-19.

The low-speed air at the base of a boattailed afterbody can interact with the boundary layer of the exterior flow. If the jet pressure is sufficiently high, the interaction will increase the pressure in the boundary layer on the rear of the afterbody, decreasing the afterbody drag. Figure 4.6.4-20 presents the probably favorable effects of boattail angle and nozzle divergence angle on both the base pressure and afterbody drag.

The unfavorable effects on base pressure caused by the flaring of an afterbody are presented in figure 4.6.4-21. The flared afterbody is also likely to have more afterbody drag because of its forward-facing slopes.

Jet Power Lift Effects on Drag Due to Lift

The power-on drag due to lift is obtained from the following equation:

$$\left(C_{D_L}\right)_{\substack{\text{power}\\\text{on}}} = \left(C_{D_L}\right)_{\substack{\text{power}\\\text{off}}} \left[\frac{C_L - \left(\Delta C_L\right)_T - \left(\Delta C_L\right)_{N_j}}{C_L}\right]^2 \qquad 4.6.4\text{-n}$$

where C_L is the power-off lift coefficient required for the given flight condition, $\left(C_{D_L}\right)_{\substack{\text{power}\\\text{off}}}$ is the drag due to lift corresponding to C_L obtained by the method of Section 4.1.5.2, $\left(\Delta C_L\right)_T$ and $\left(\Delta C_L\right)_{N_j}$ are found in Section 4.6.1.

Sample Problem

The configuration used in this sample problem is the same as that used in the sample problem of Section 4.6.1, paragraph B.

Given:

$$\left.\begin{array}{ll} C_L = 0.75 & \left(\Delta C_L\right)_T = 0.0446 \\ & \left(\Delta C_L\right)_{N_j} = 0.00655 \end{array}\right\} \text{(Section 4.6.1)}$$

$$\left(C_{D_L}\right)_{\substack{\text{power}\\\text{off}}} = 0.16 \qquad \text{(Section 4.1.5.2)}$$

Compute:

Determine the power-on drag due to lift

$$\left(C_{D_L}\right)_{\substack{\text{power}\\\text{on}}} = \left(C_{D_L}\right)_{\substack{\text{power}\\\text{off}}} \left[\frac{C_L - \left(\Delta C_L\right)_T - \left(\Delta C_L\right)_{N_j}}{C_L}\right]^2 \qquad \text{(equation 4.6.4-n)}$$

$$= 0.16 \left[\frac{0.75 - 0.0446 - 0.00655}{0.75}\right]^2$$

$$= (0.16)\ (0.868)$$

$$= 0.139$$

REFERENCES

1. Decker, J., et al: USAF Stability and Control Handbook. M-3671, 1956. (U)

2. Cubbage, J. M., Jr.: Jet Effects on Base and Afterbody Pressures of a Cylindrical Afterbody at Transonic Speeds. NACA RM L56C21, 1956. (U)

3. Korst, H. H., Chow, W. L., and Zumwalt, G. W.: Research on Transonic and Supersonic Flow of a Real Fluid at Abrupt Increases in Cross Section. Univ. of Ill., Tech. Report. 392-5, 1959. (U)

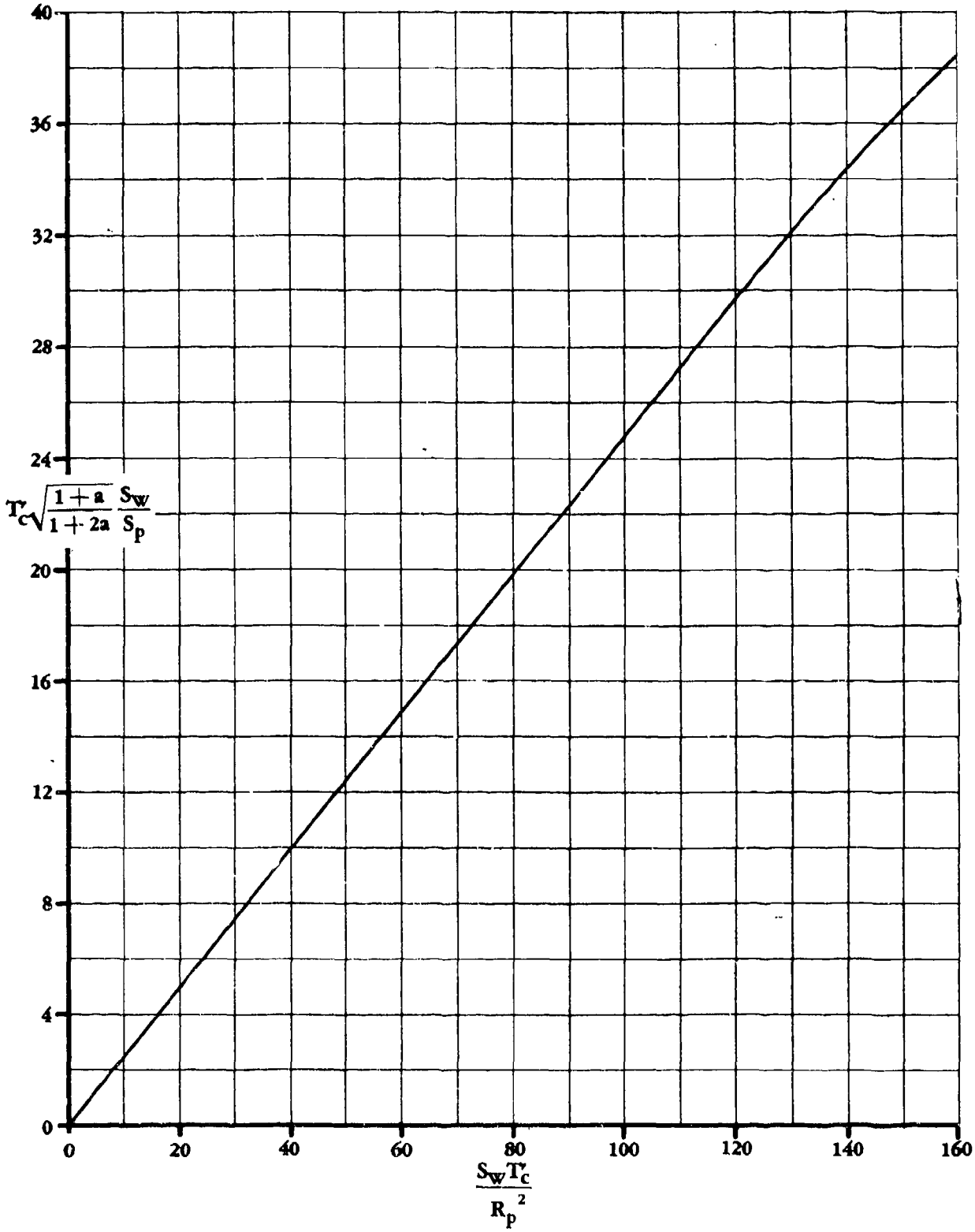

FIGURE 4.6.4-12 THRUST-COEFFICIENT FUNCTION

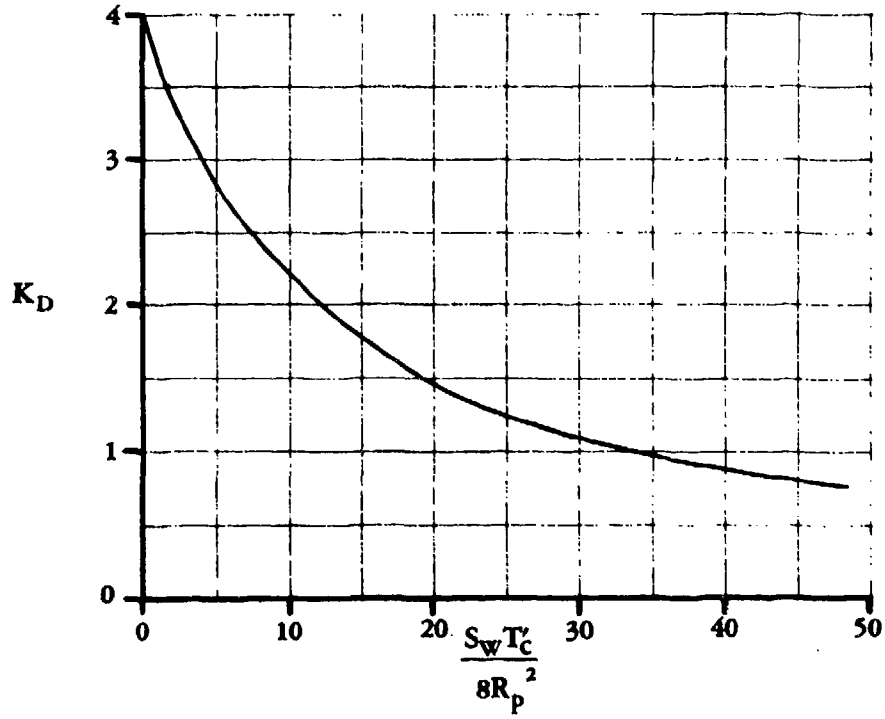

FIGURE 4.6.4-13a PROPELLER DRAG FACTOR

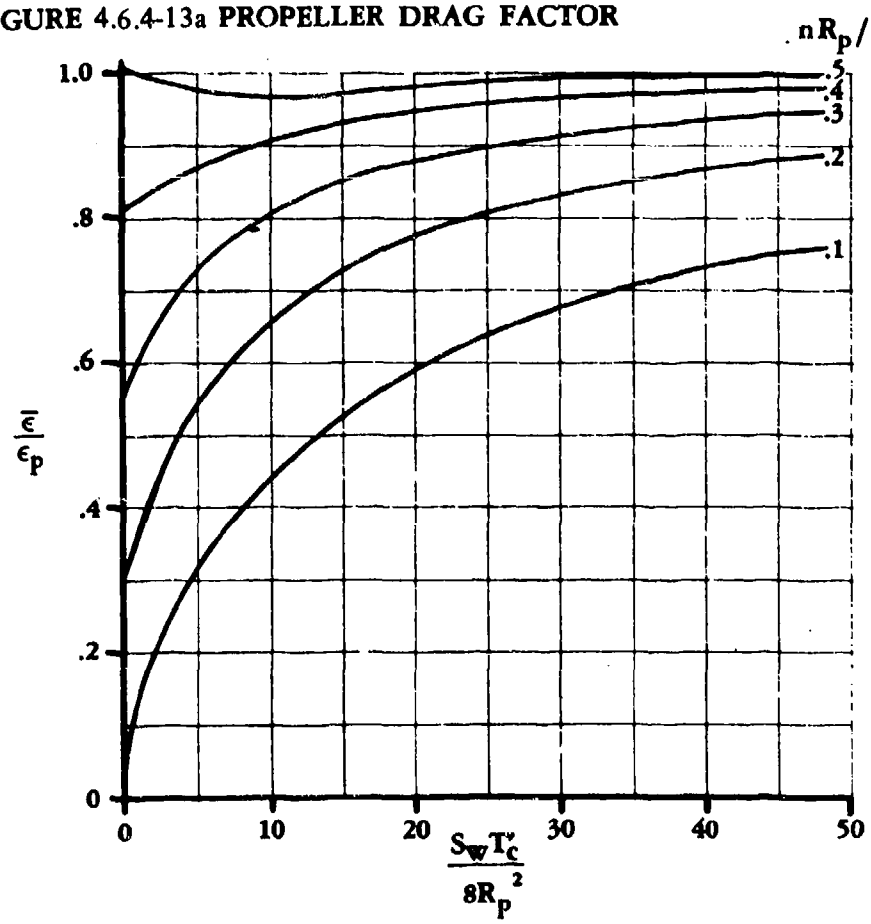

FIGURE 4.6.4-13b AVERAGE PROPELLER DOWNWASH

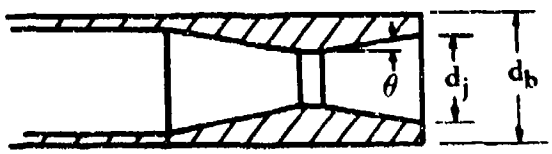

SUPERSONIC NOZZLE
$d_j/d_b = 0.75$
$\theta = 10°$

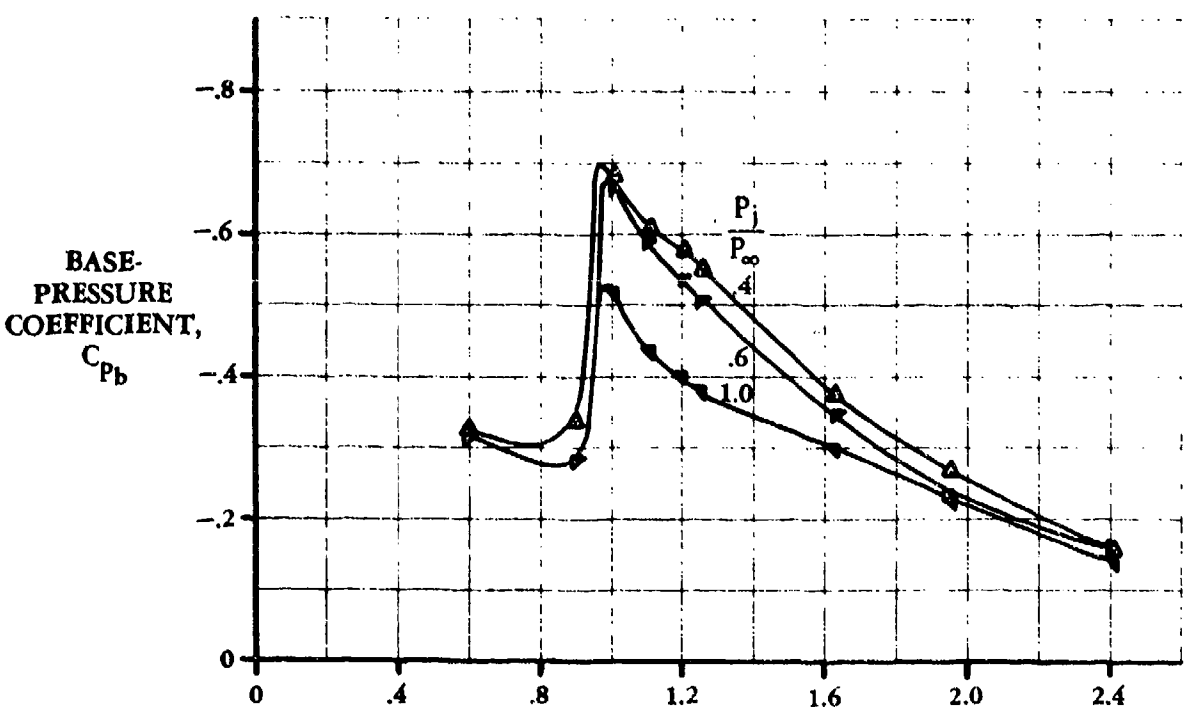

FIGURE 4.6.4-14 EXPERIMENTAL EFFECT OF FREE-STREAM MACH NUMBER ON BASE PRESSURE

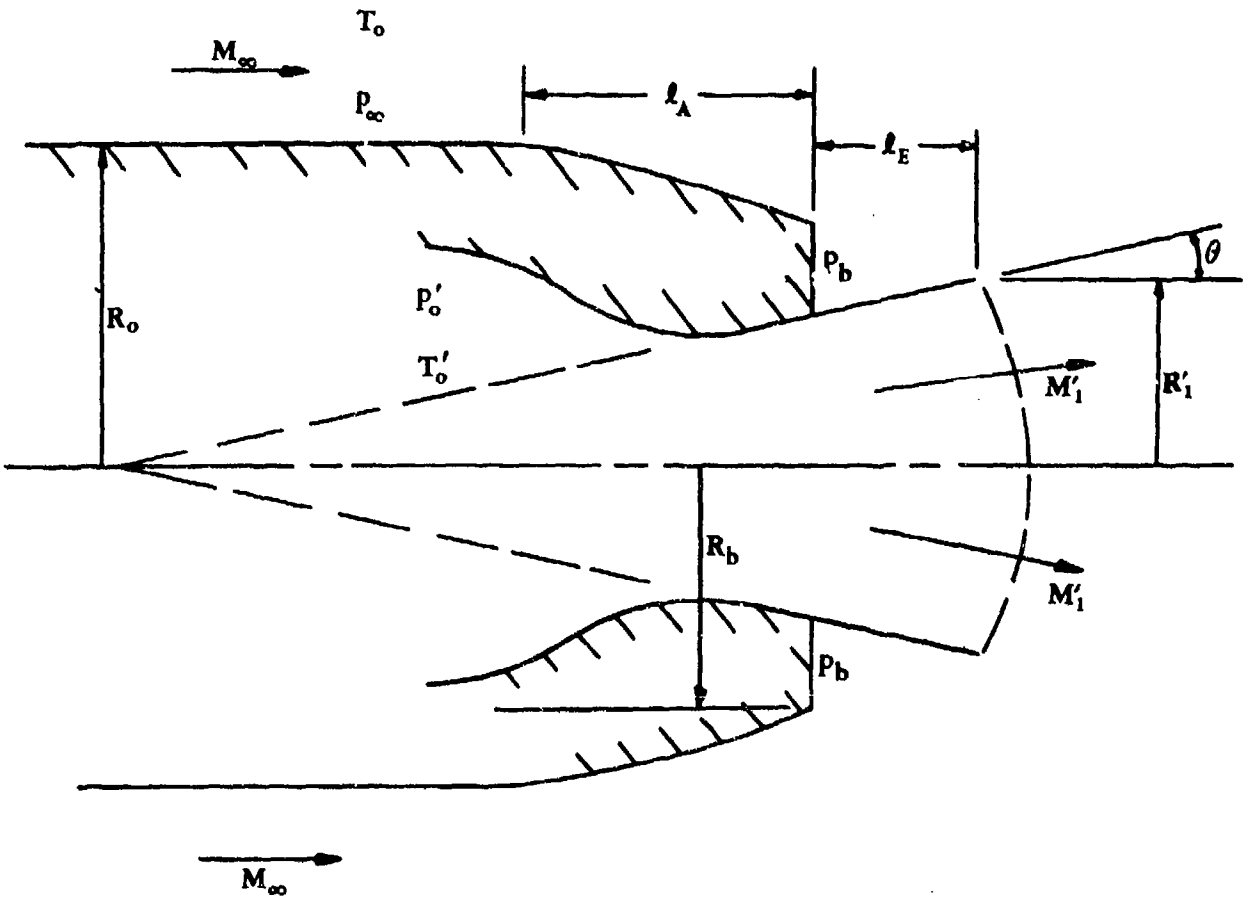

FIGURE 4.6.4-15 GEOMETRY AND INITIAL FLOW PARAMETERS FOR A AXIALLY SYMMETRIC BOATTAILED AFTERBODY WITH A NOZZLE

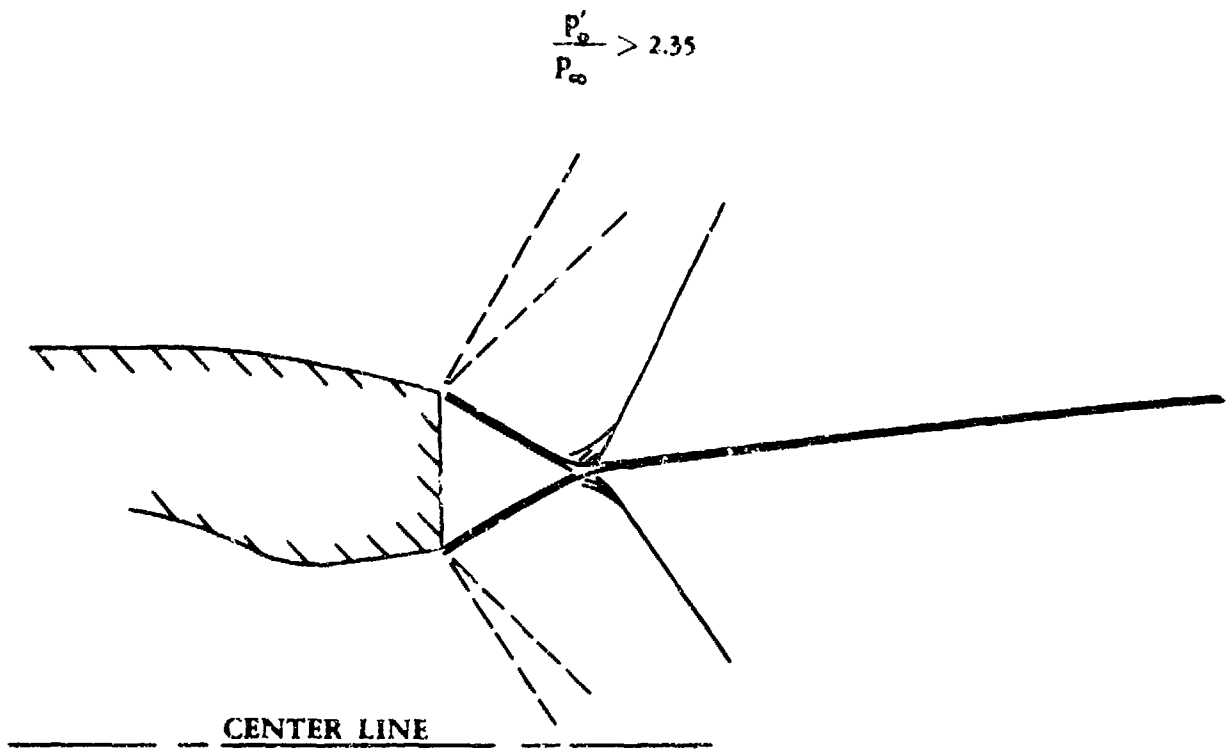

FIGURE 4.6.4-16 TYPICAL FLOW PATTERN

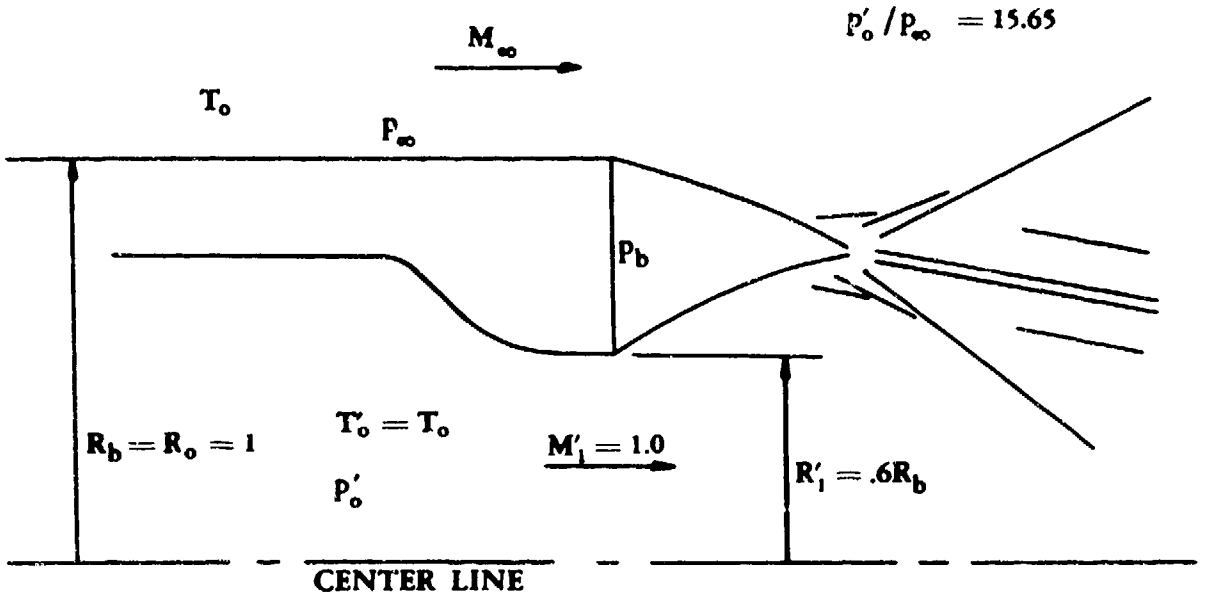

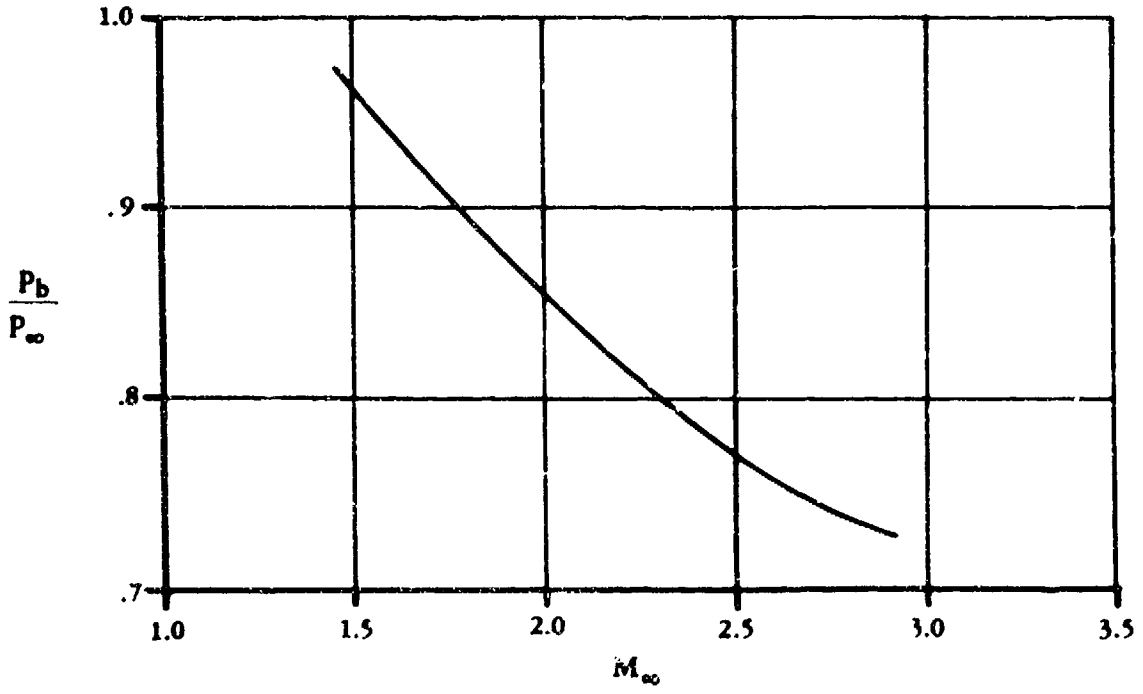

FIGURE 4.6.4-17 INFLUENCE OF FREE-STREAM MACH NUMBER ON BASE-PRESSURE RATIO

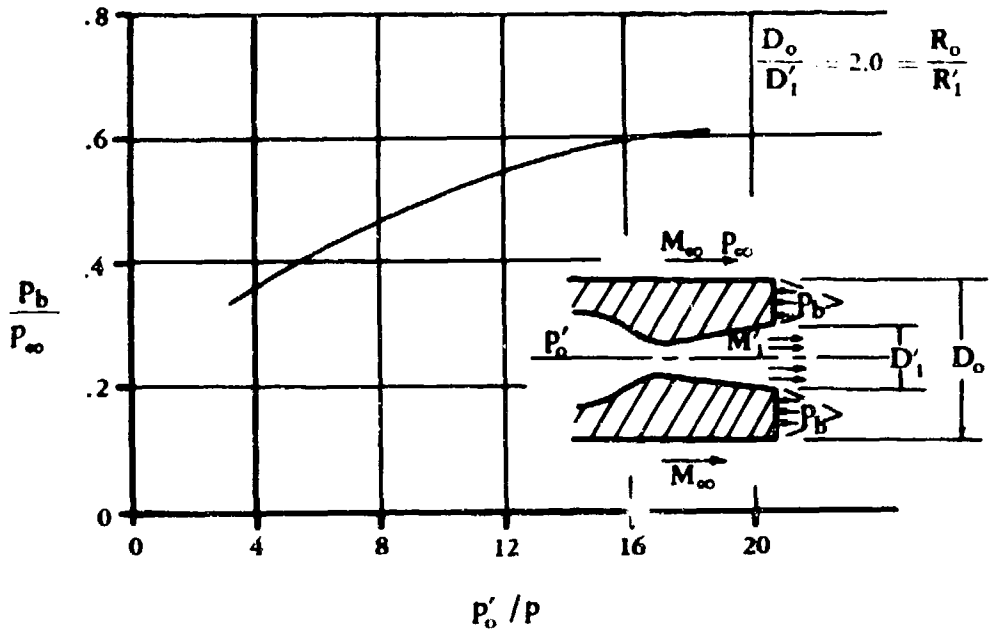

FIGURE 4.6.4-18a EFFECT OF JET-PRESSURE RATIO ON BASE-PRESSURE RATIO

$M_\infty = 2.0$ $M'_1 = 1.5$

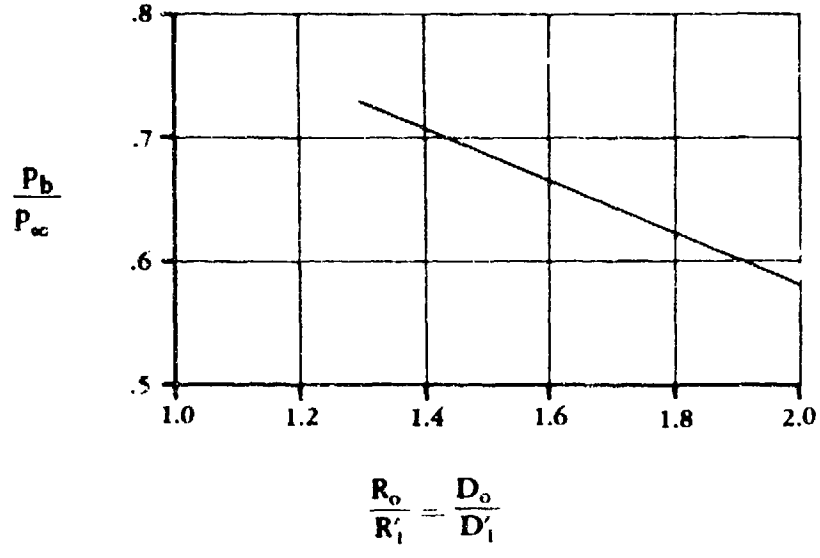

FIGURE 4.6.4-18b EFFECT OF JET-DIAMETER-BODY-DIAMETER RATIO ON BASE-PRESSURE RATIO

$M_\infty = 2.0$ $M'_1 = 1.5$ $p_o / p_\infty = 16$

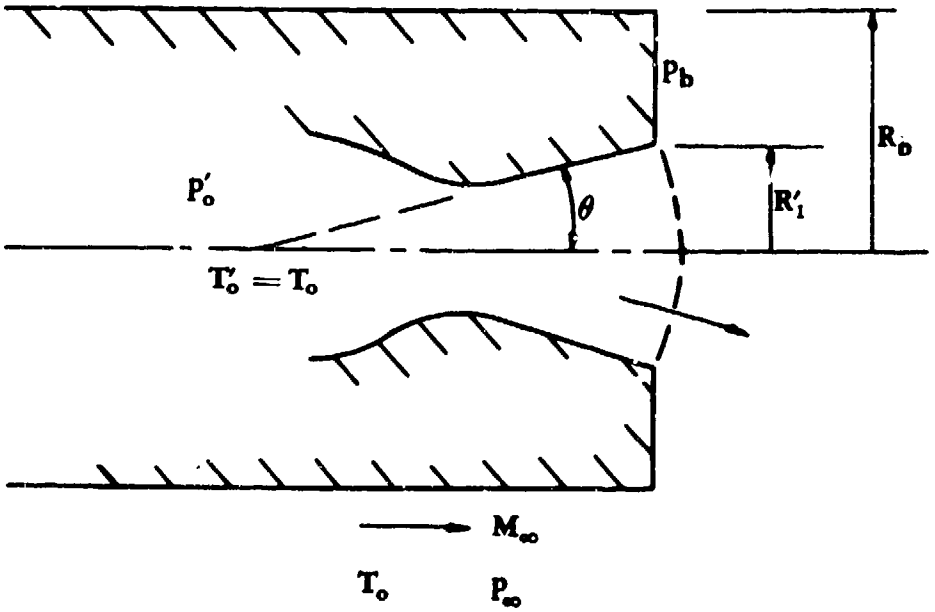

$R'_1/R_1 = .82$

$M_\infty = 2.00$

$M'_1 = 2.54$

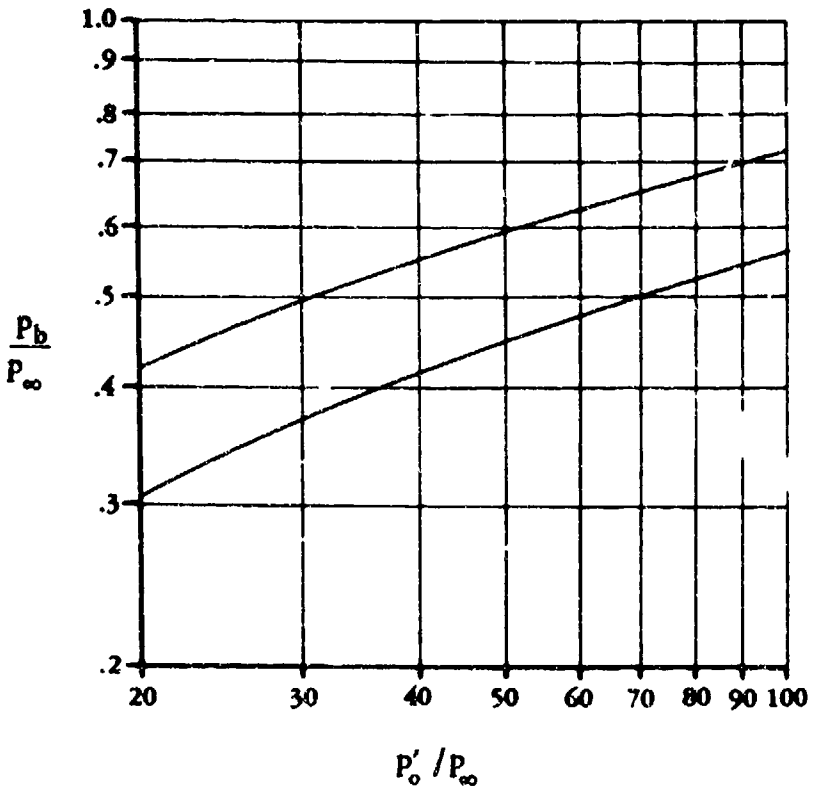

FIGURE 4.6.4-19 EFFECT OF NOZZLE DIVERGENCE ON THE BASE-PRESSURE RATIO

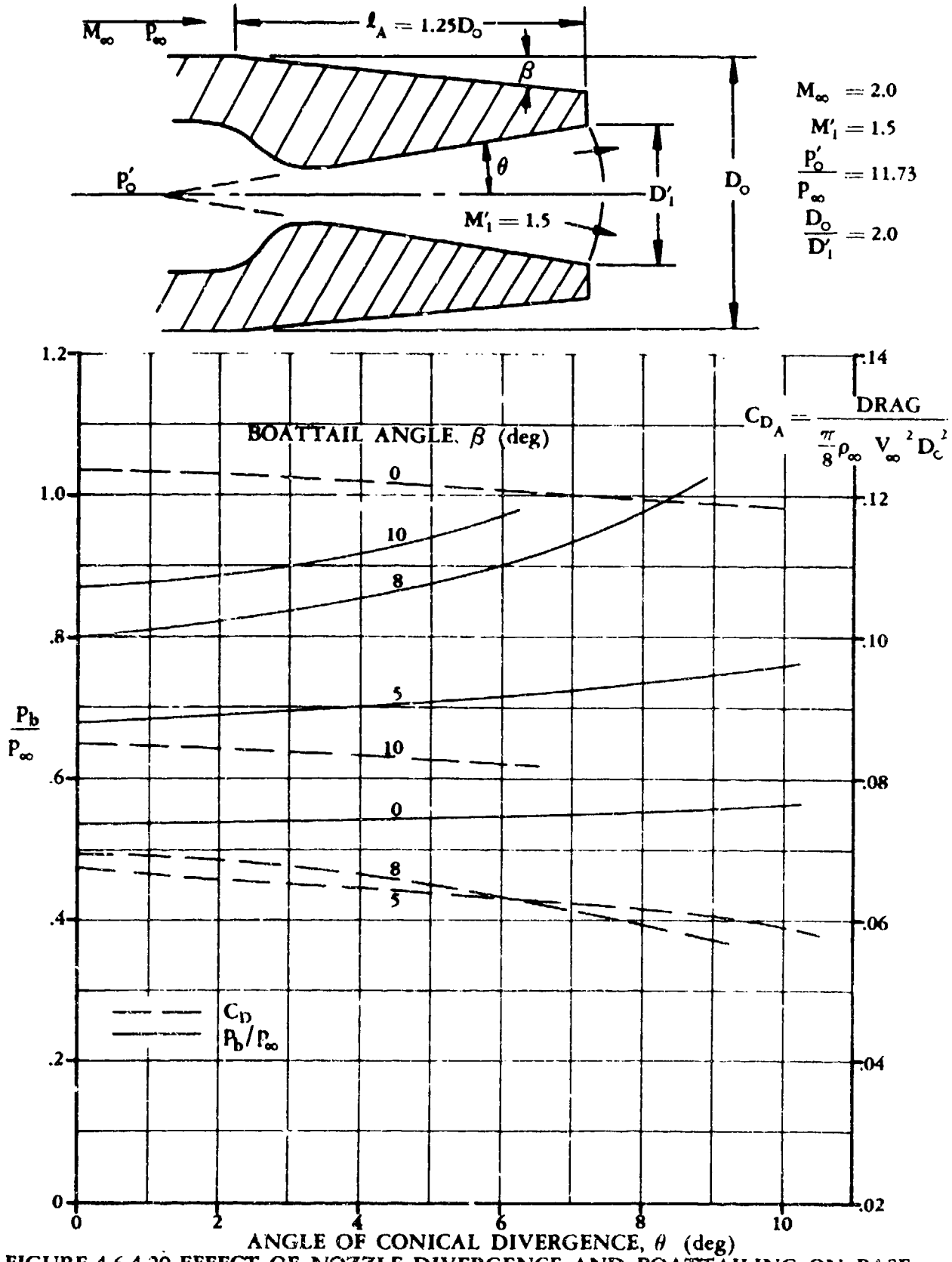

FIGURE 4.6.4-20 EFFECT OF NOZZLE DIVERGENCE AND BOATTAILING ON BASE-PRESSURE RATIO AND AFTERBODY DRAG OF A JET ENGINE

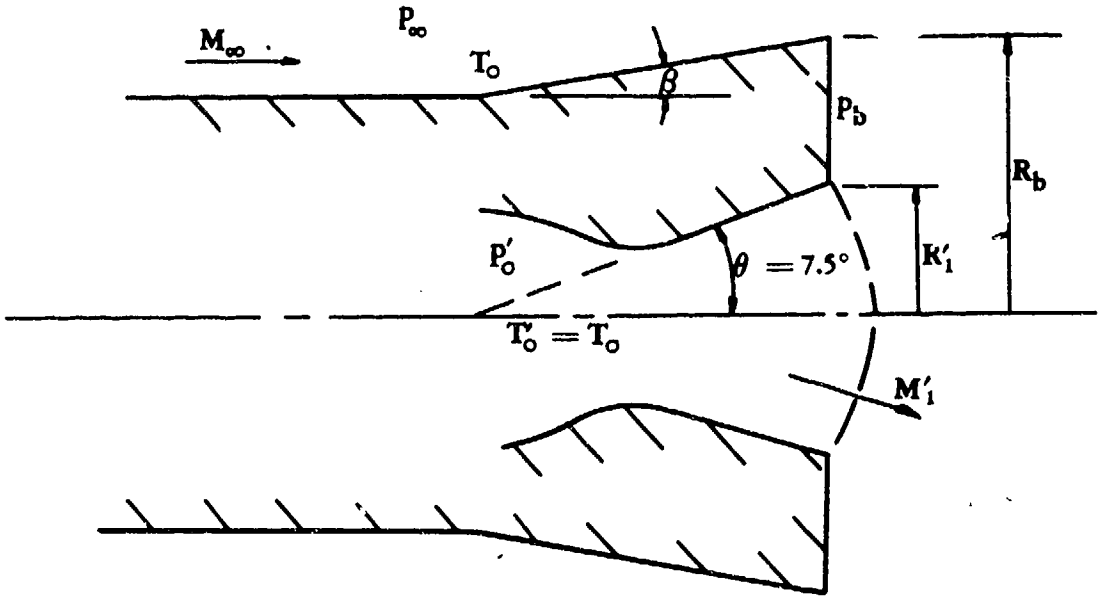

$R'_1/R_1 = .82$

$M_\infty = 2.00$

$M'_1 = 2.54$

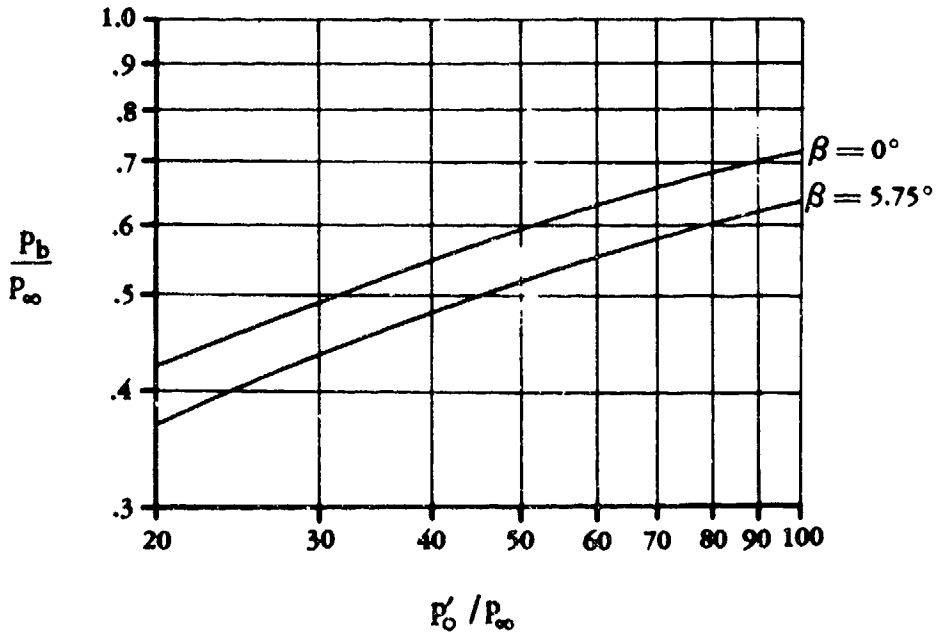

FIGURE 4.6.4-21 EFFECT OF CONICAL FLARING ON THE BASE-PRESSURE RATIO

4.7 GROUND EFFECTS AT ANGLE OF ATTACK

Methods are presented in subsequent sections for estimating ground effects in the linear-lift range on lift, pitching moment, and drag.

In order that the Datcom user may better understand ground effects, a qualitative discussion regarding various aspects of ground effects is presented.

Because of the obvious influence of ground proximity during the takeoff and landing phases, it has been the subject of considerable investigation. However, despite this consideration, an adequate amount of reliable ground-effects data does not appear in the literature. In particular, the prediction of $C_{L_{max}}$, $\alpha_{C_{L_{max}}}$ and pitching moment need additional investigation in ground effects.

The effects of ground proximity generally become measurable at a height above the ground of one wing-[illegible] and increase in magnitude as the height above the ground decreases. Both theoretical and experimental investigations indicate that ground proximity produces an increase in the lift-curve slope, a decrease in drag, and a reduction of nose-up pitching moment for most aircraft planforms in the clean configuration. However, high-lift configurations deviate from this trend in that the ground effect tends to reduce the lift-curve slope (Reference 1).

Wind-tunnel investigation of ground effects has been approached by using the following testing techniques: (1) fixed ground plane, (2) moving-belt ground plane, and (3) an image-model aircraft with respect to a fictitious ground. The fixed ground-plane technique provides the most straightforward approach to simulation. However, this approach does not give a true representation of the phenomena because of the lack of relative motion between the ground plane and the model. This lack of motion permits a boundary-layer build-up on the ground plane that introduces an objectionable component into the simulation. Moving-belt ground-plane simulations eliminate this undesirable feature; however, not all wind tunnels offer this capability. The third testing technique, the image-model approach, has the disadvantage of added cost and complexity of constructing and installing a second model in the tunnel to simulate the mirror image of the test model. Most authorities tend to agree on the relative advantages of these different approaches. As might be expected, results from these different testing techniques do not predict identical results for the same configuration. The lack of agreement between various wind-tunnel results is exemplified in the comparisons presented in References 3 and 4. In addition, these wind-tunnel predictions do not compare favorably with the limited flight-test results of References 3 and 4.

The majority of the theoretical approaches analyzing ground effects employ an image-vortex theory to represent the ground plane. The salient aspects of this theory are discussed below.

The lifting wing is represented theoretically by a bound vortex and two trailing vortices. The effect of a ground plane on this "horseshoe" vortex system is represented by placing a mirror image of the vortex system two ground-plane heights below the vortex system representing the wing. The resulting plane of symmetry satisfies the boundary condition of zero vertical velocity at the ground plane. The two vortex systems (the wing-vortex system and the image-vortex system) and the ground plane are illustrated in Sketches (a), (b), and (c).

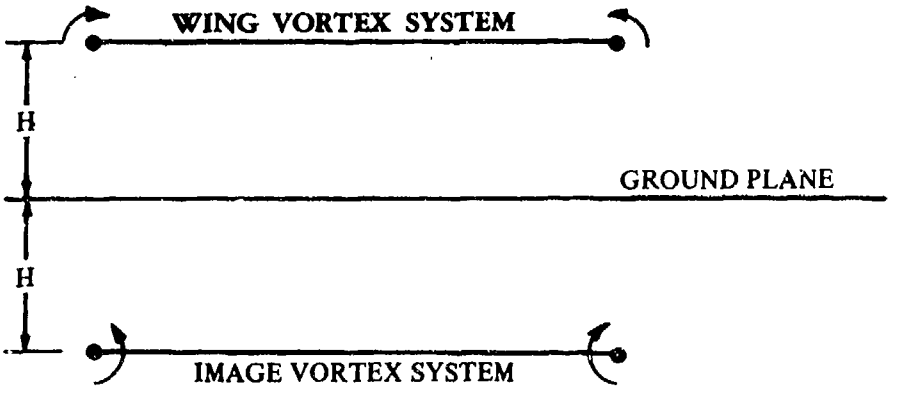

Bound vortices

● End view of trailing vortices

(Arrows indicate direction of circulation)

SKETCH (a)

THEORETICAL WING VORTEX SYSTEM, FRONT VIEW

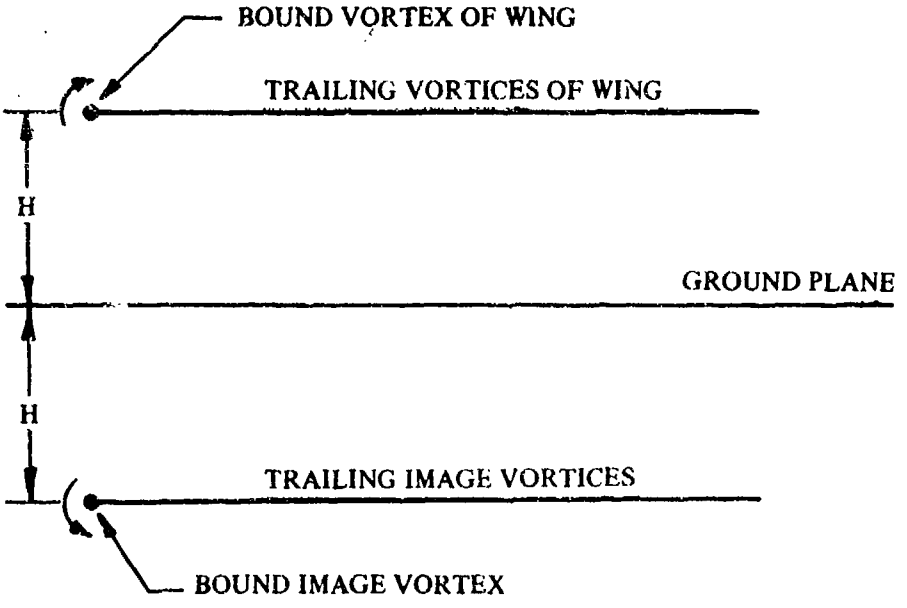

● End view of bound vortices

Trailing vortices

(Arrows indicate direction of circulation)

SKETCH (b)

THEORETICAL WING VORTEX SYSTEM, SIDE VIEW

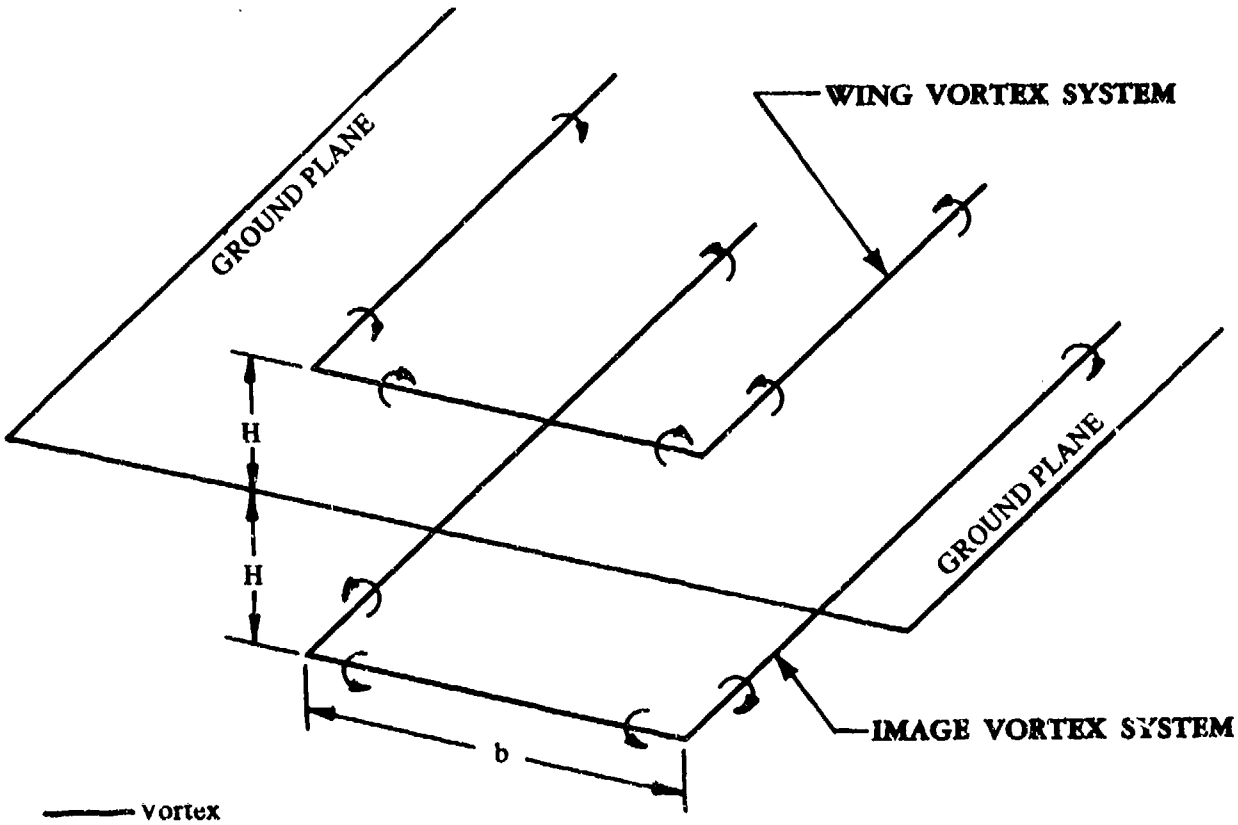

SKETCH (c)

Away from the ground plane, the downwash of the two trailing vortices contributes to the wing drag due to lift by rotating the force vector rearward, as shown in Sketch (d). However, near the ground plane, the trailing vortices of the image vortex system have an upwash component, as shown in Sketch (c) and Sketch (e) (Reference 5). This upwash velocity component reduces the downward rotation of the flow direction caused by the wing trailing vortices, thus decreasing the wing drag due

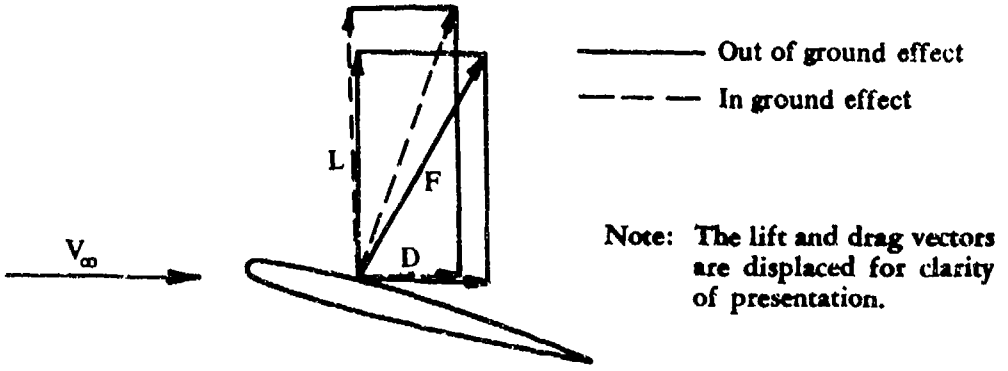

SKETCH (d)

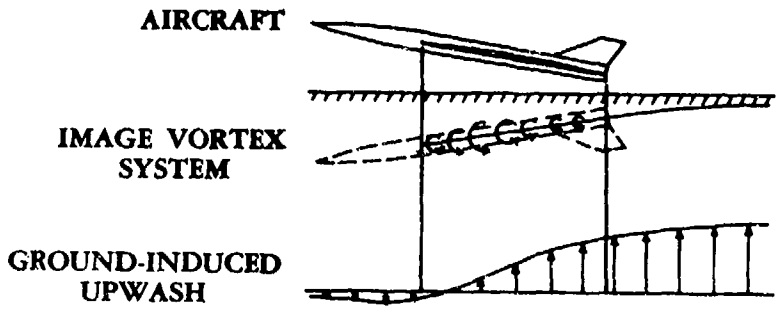

SKETCH (e)
GROUND-INDUCED UPWASH

to lift. The classical treatment of this effect is given by Wieselsberger in Reference 6. Wieselsberger's approach has been extended in Reference 7 by Tani, Taima, and Simidu to consider the induced effects of the image bound vortex. Both of these approaches are summarized in Reference 8. As indicated in the side view of the vortex system presented as Sketch (b), the bound vortex of the image-vortex system will reduce the longitudinal velocity component at the wing bound vortex, thus modifying the circulation of the wing bound vortex. These effects of the image bound-vortex system become more predominant as the height above the ground is reduced.

Improved theoretical analyses of the effects of ground proximity have been formulated using lifting-surface theory. Because of the general nature of lifting-surface theory, computer programs have been generated to facilitate the computations. Reference 9 presents an example of an image-vortex representation using lifting-surface theory, generalized to apply to a straight-tapered wing in nonviscous flow.

The influence of ground effects on the lateral-control characteristics of aircraft has received consideration in References 10 through 12. Results of Reference 10 suggest that ground effects completely alter the basic lateral characteristics of slender aircraft during the period immediately preceding touchdown. As a result, disturbances in bank angle are drastically attenuated just prior to aircraft touchdown.

The influence of wing-tip fairings and wing-tip end plates is examined in References 13 through 15. The general effect of these wing-tip devices is an increase in lift-curve slope and a reduction in induced drag, which generally results in a significant increase in the lift-drag ratio.

The reader is referred to Reference 16 for a comprehensive literature search and survey of the literature available prior to 1966 in the general field of wings operating in ground effect and related phenomena. Comments are included in this reference regarding some of the papers published, along with sketches of the methods of approach taken by the authors. The bibliography presents sources that consider the problem from the theoretical, experimental, and/or applications points of view. Tables are included that provide a convenient breakdown of the various sources, for a quicker method of locating specific references dealing with an area of special interest to the reader.

A list of pertinent references is included at the end of this section, following a list of notation used in subsequent sections.

NOTATION

A	wing aspect ratio
B	parameter accounting for change in circulation
b_{eff}	effective wing span
b'_f	effective span for increment in load due to flaps
b'_W	effective span for unflapped wing
$\bar{c}$	wing mean aerodynamic chord
C_D	wing drag coefficient, $\frac{\text{drag}}{qS}$
C_{D_L}	drag coefficient due to lift
$\left(\Delta C_{D_L}\right)_G$	increment in drag due to lift in the presence of the ground
$C_{D_{WB}}$	wing-body drag coefficient in absence of ground plane
$\left(C_{D_{WB}}\right)_G$	wing-body drag coefficient in the presence of the ground
C_{D_0}	zero-lift drag coefficient
C_L	wing lift coefficient in absence of ground plane
ΔC_{L_f}	increment in lift coefficient due to flaps in absence of ground plane
$\left(C_{L_f}\right)_{WB}$	wing-body lift coefficient including flap effects, out of ground effect
$\Delta\left(\Delta C_L\right)_{flap}$	empirical factor accounting for flap effects in the presence of the ground
$\left(\Delta C_L\right)_G$	increment in lift coefficient in the presence of the ground
$\left(\Delta C_{L_H}\right)_G$	increment in horizontal-tail lift coefficient in the presence of the ground
$C_{L_{max}}$	maximum lift coefficient, $\frac{\text{maximum lift}}{qS}$

$C_{L_{WB}}$	wing-body lift coefficient in absence of ground plane
$\left(\Delta C_{L_{WB}}\right)_G$	increment in wing-body lift coefficient in the presence of the ground
$\left(C_{L_\alpha}\right)_{WB}$	wing-body lift-curve slope
$\left(\Delta C_m\right)_G$	increase in pitching moment in the presence of the ground
$\left(\Delta C_{m_H}\right)_G$	increase in horizontal-tail pitching moment in the presence of the ground
$\left(\Delta C_{m_{WB}}\right)_G$	increase in wing-body pitching moment in the presence of the ground
$\frac{c_r}{b}$	ratio of wing root chord to wing span
H	height of quarter-chord point of wing mean aerodynamic chord above the ground
H_H	height of quarter-chord point of horizontal-tail mean aerodynamic chord above the ground
h	average height above the ground of the quarter-chord point of wing chord at 75-percent semispan and the three-quarter-chord point of the wing root chord (see sketch on Figure 4.7.1-14)
$h_{c_r/4}$	height of the quarter-chord point of the wing root chord above the ground
K	parameter accounting for effective wing thickness
ℓ_H	distance from moment reference center to the quarter-chord point of horizontal-tail MAC, measured parallel to body center line
$\frac{L}{L_o} - 1$	parameter accounting for effect of image bound vortex on lift
n	distance from wing apex to moment reference center measured in wing mean aerodynamic chords, positive aft
$\frac{q_H}{q_\infty}$	effective dynamic-pressure ratio at horizontal tail
r	parameter accounting for effect of finite span
$\frac{S_H}{S_W}$	ratio of area of horizontal tail to wing area

T	parameter accounting for reduction in longitudinal velocity
$\left(\frac{t}{c}\right)_{max}$	ratio of maximum wing thickness to wing chord
x	parameter accounting for effect of image trailing vortex on lift
Δx	the chordwise distance from the quarter-chord point of the 75-percent-semispan chord to the three-quarter-chord point of the wing root chord, positive when the latter is aft of the former (see Figure 4.7.1-14)
$x_{a.c.}$	distance from the wing apex to the wing-body aerodynamic center, positive for a.c. aft of wing apex
$\Delta\alpha$	increment in angle of attack
$\alpha_{C_{L_{max}}}$	wing angle of attack at maximum lift coefficient
$(\Delta\alpha)_G$	increment in angle of attack at a constant lift coefficient in the presence of the ground
$(\Delta\alpha_H)_G$	increment in angle of attack of the horizontal tail in the presence of the ground
ϵ	downwash angle out of ground effect
$(\Delta\epsilon)_G$	increment in downwash due to ground effect in linear-lift range
$\Lambda_{c/4}$	sweep angle of the wing quarter-chord
σ	Prandtl interference coefficient

REFERENCES

1. Recant, I. G.: Wind-Tunnel Investigation of Ground Effect on Wings with Flaps. NACA TN 705, 1939. (U)
2. de Sievers, A.: Wind-Tunnel Tests on the Ground Effect. NASA TT F-11059, 1967. (U)
3. Baker, P. A., Schweikhard, W. G., and Young, W. R.: Flight Evaluation of Ground Effect on Several Low-Aspect-Ratio Airplanes. NASA TN D-6053, 1970. (U)
4. Rolls, L. S., and Koenig, D. G.: Flight-Measured Ground Effect on a Low-Aspect-Ratio Ogee Wing Including a Comparison with Wind-Tunnel Results. NASA TN D-3431, 1966. (U)
5. Kemp, W. B., Jr., Lockwood, V. E., and Phillips, W. P.: Ground Effects Related to Landing of Airplanes with Low-Aspect-Ratio Wings. NASA TN D-3583, 1966. (U)
6. Wieselsberger, C.: Wing Resistance Near the Ground. NACA TM 77, 1922. (U)

7. Tani, I., Taima, M., and Simidu, S.: The Effect of Ground on the Aerodynamic Characteristics of a Monoplane Wing. Tokyo Univ. Aeronautical Research Inst. Report 156, 1937. (U)

8. Wetmore, J. W., and Turner, L. I., Jr.: Determination of Ground Effect from Tests of a Glider in Towed Flight. NACA TR 695, 1940. (U)

9. Kohlman, D. L., and Glatt, C.: A Theoretical Method of Determining the Ground Effect on Lift and Pitching Moment for Wings of Arbitrary Planform. Boeing Airplane Co., D 3-1861, 1958. (U)

10. Pinsker, W. J. G.: The Aerodynamic Effect of Ground Proximity on Lateral Control of Slender Aircraft in the Landing Approach. RAE TR 70079, 1970. (U)

11. Kumar, P. E.: The Lateral Dynamic Stability of a Ground Effect Wing. College of Aeronautics, Cranfield, Gr. Brit., CoA Report Aero 207, 1968. (U)

12. Kumar, P. E.: An Experimental Investigation Into the Aerodynamic Characteristics of a Wing with and without Endplates, in Ground Effect. College of Aeronautics, Cranfield, Gr. Brit., CoA Report Aero 201, 1968. (U)

13. Carter, A. W.: Effect of Ground Proximity on the Aerodynamic Characteristics of Aspect-Ratio-1 Airfoils with and without End Plates. NASA TN D-970, 1961. (U)

14. White, H. E.: Wind-Tunnel Tests of a Low-Aspect-Ratio Wing in Close Proximity to the Ground. DTMB Aero 1056, 1963. (U)

15. Fink, M. P., and Lastinger, J. L.: Aerodynamic Characteristics of Low-Aspect-Ratio Wings in Close Proximity to the Ground. NASA TN D-926, 1961. (U)

16. Foschag, W. F.: Literature Search and Comprehensive Bibliography of Wings in Ground Effect and Related Phenomena. DTMB Aero 1088, 1966. (U)

17. Tani, I., Itokawa, H., and Taima, M.: Further Studies of the Ground Effect on the Aerodynamic Characteristics of an Aeroplane, with Special Reference to Tail Moment. Tokyo Univ. Aeronautical Research Inst. Report 158, 1937. (U)

18. Gersten, K.: Calculation of the Aerodynamic Characteristics of Wings of Finite Span Near the Ground. Abhandlungen der Braunschweigischen Wissenschaftlichen Gesellschaft, XII, 1960, pp. 95-115. (U)

19. Kirkpatrick, D. L. I.: A Method of Correlating the Ground Effects on the Longitudinal Characteristics of Slender Wings. RAE TR 69190, 1969. (U)

20. Thomas, F.: Aerodynamic Properties of Sweptback and Delta Wings Near the Ground. Jahrbuch der Wissenschaftlichen Gesellschaft fur Luftfahrt, E. V., pp. 53-61, 1958. (U)

21. Shan, Y. C.: Theoretical Analysis of Jet-Ground Plane Interaction. IAS Paper 62-144, 1962. (U)

22. Owen, P. R., and Hogg, H.: Ground Effect on Downwash with Slipstream. ARC R&M 2449, 1952. (U)

23. Schweikhard, W.: A Method for In-Flight Measurement of Ground Effect on Fixed-Wing Aircraft. AIAA Paper 66-468 1966. (U)

24. de Sievers, A.: Wind-Tunnel Tests of the Ground Effect on Aircraft Models. NASA TT F-9709, 1965. (U)

25. O'Leary, C. O.: Flight Measurements of Ground Effect on the Lift and Pitching Moment of a Large Transport Aircraft (Comet 3B) and Comparison with Wind Tunnel and Other Data. RAE TR 68158, 1968. (U)

26. Buell, D. A., and Tinling, B. E.: Ground Effects on the Longitudinal Characteristics of Two Models with Wings Having Low Aspect Ratio and Pointed Tips. NACA TN 4044, 1957. (U)

27. Wood, M. N., and Trebble, W. J. G.: Low Speed Tunnel Measurements of the Ground Effect on a 1/5th Scale Model of the Swift. ARC CP 458, 1959. (U)

28. Fliebe, J. M., and Graven, J. C., Jr.: Low-Speed Investigation of the Effects of Location of a Delta Horizontal Tail on the Longitudinal Stability and Control of a Fuselage and Thin Delta Wing with Double Slotted Flaps Including the Effects of a Ground Board. NACA RM L53H19a, 1953. (U)

29. Buell, D. A., and Tinling, B. E.: The Static Longitudinal Stability and Control Characteristics in the Presence of the Ground of a Model Having a Triangular Wing and Canard. NASA Memo 3-4-59A, 1959. (U)

30. Bagley, J. A.: Low-Speed Wind Tunnel Tests on a Two-Dimensional Aerofoil with Split Flap Near the Ground. RAE TN Aero 2636, 1961. (U)

31. Bagley, J. A.: The Pressure Distribution on Two-Dimensional Wings Near the Ground. ARC R&M 3238, 1961. (U)

32. Colin, P. E.: Powered Lift Model Testing for Ground Proximity Effects. Training Center for Experimental Aerodynamics, Rhode-Saint-Genese, Belgium, TN 14, 1963. (U)

33. Furlong, G. C., and Bollech, T. V.: Effect of Ground Interference on the Aerodynamic and Flow Characteristics of a 42° Sweptback Wing at Reynolds Numbers up to .8 x 10^6. NACA TR 1218, 1955. (U)

34. Butler, S. F. J., Moy, B. A., and Hutchins, G. D.: Low-Speed Tunnel Tests of an Aspect-Ratio 9 Jet-Flap Model, with Ground Simulation by Moving-Belt Rig. ARC CP 849, 1966. (U)

35. Alexander, A. J.: Experiments on a Jet-Flap Delta Wing in Ground Effect. College of Aeronautics, Cranfield, Gr. Brit., CoA Report Aero 164, 1963. (U)

36. Kumar, P. E.: An Analogue Simulation of the Longitudinal Motion of a Ground Effect Wing. College of Aeronautics, Cranfield, Gr. Brit., CoA Report Aero 208, 1968. (U)

37. Piper, R. W., and Davies, H.: Note on Factors Affecting Trim at Take-off and Landing. Aero. Departmental Note — Wind Tunnel No. 540, 1941. (Unpublished British Paper). (U)

4.7.1 GROUND EFFECTS ON LIFT VARIATION WITH ANGLE OF ATTACK

Methods are presented in this section for estimating the ground effects on lift in the linear-lift region. The reader is referred to Section 4.7 for a basic discussion of various aspects of ground effects.

Representation of the ground plane by an image-vortex system (see Sketches (a), (b), and (c) in Section 4.7) enables the ground effects on lift to be identified (Reference 1) as follows: (1) the decrease in longitudinal velocity at the real wing due to the reflected bound vortex, (2) the change in circulation about the real wing due to the reflected bound vortex, (3) the increase in induced upwash at the real wing due to the reflected trailing vortices, and (4) the change in the flow pattern due to the finite thickness of the wing. The first two effects are opposite and approximately equal, while the effects of wing thickness are generally small. As a result, the ground effects on lift can be approximated by considering only the increase in the upwash. This is the approach taken in the classical theoretical treatment of ground effects by Wieselsberger in Reference 2. Wieselsberger's method of approach has been extended in Reference 3 by Tani, Taima, and Simidu to include the induced effects of the reflected bound vortex and of wing thickness.

The increase in aircraft lift due to ground proximity decreases in magnitude as the height above the ground increases. Flight-test data from Reference 4, showing the increase in lift due to ground effects at a constant angle of attack as a function of ground height, are presented in Sketches (a) and (b) for the F5D-1 and XB-70 airplanes, respectively. These trends are representative of the variation of lift due to ground effects that might be expected from similar aircraft.

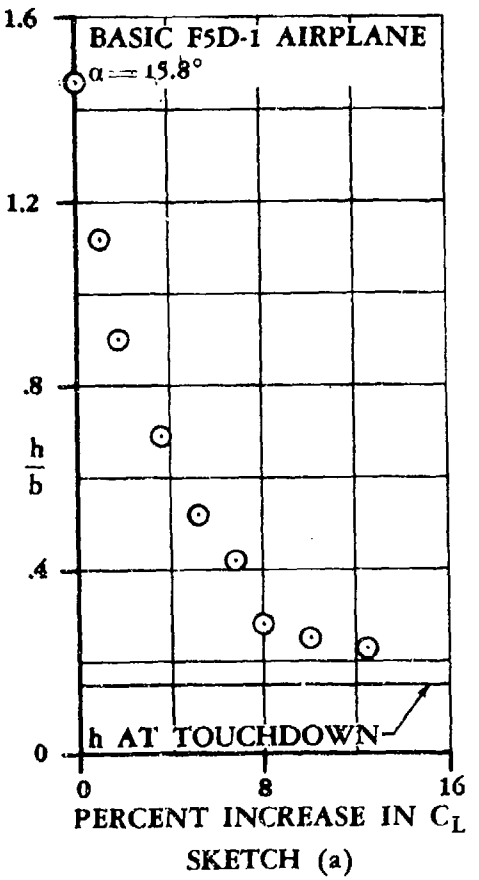

SKETCH (a)

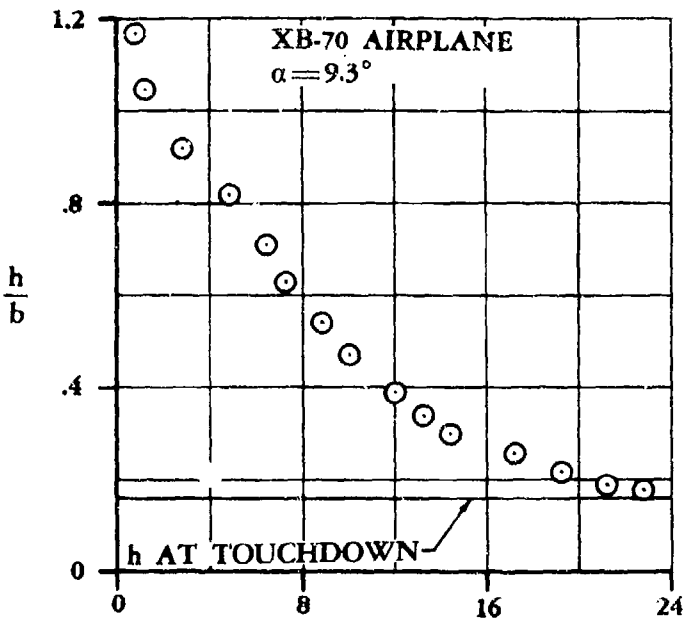

SKETCH (b)

FLIGHT-TEST GROUND-EFFECT DATA AT A CONSTANT-ANGLE-OF-ATTACK APPROACH

Empirical prediction methods have been formulated for low-aspect-ratio delta configurations in References 5, 6, and 7. However, calculated ground effects using these methods do not compare favorably with the flight-test data of Reference 4. The comparisons indicate an inability to predict accurately the variation of ground effect on lift as the height above the ground is varied.

The ground effects on lift are determined somewhat by the planform of the configuration. For low-aspect-ratio delta configurations, the general trend is a constant increase in C_L due to ground effect, as shown in Sketch (c) (Reference 8). However, transport-type configurations show quite a different trend, as presented in Sketch (d) (Reference 8). This trend is dependent upon the type of high-lift system employed. Computer programs utilizing lifting-surface theory are currently the most favorable means of evaluating the effects of various components of high-lift systems on ground effects.

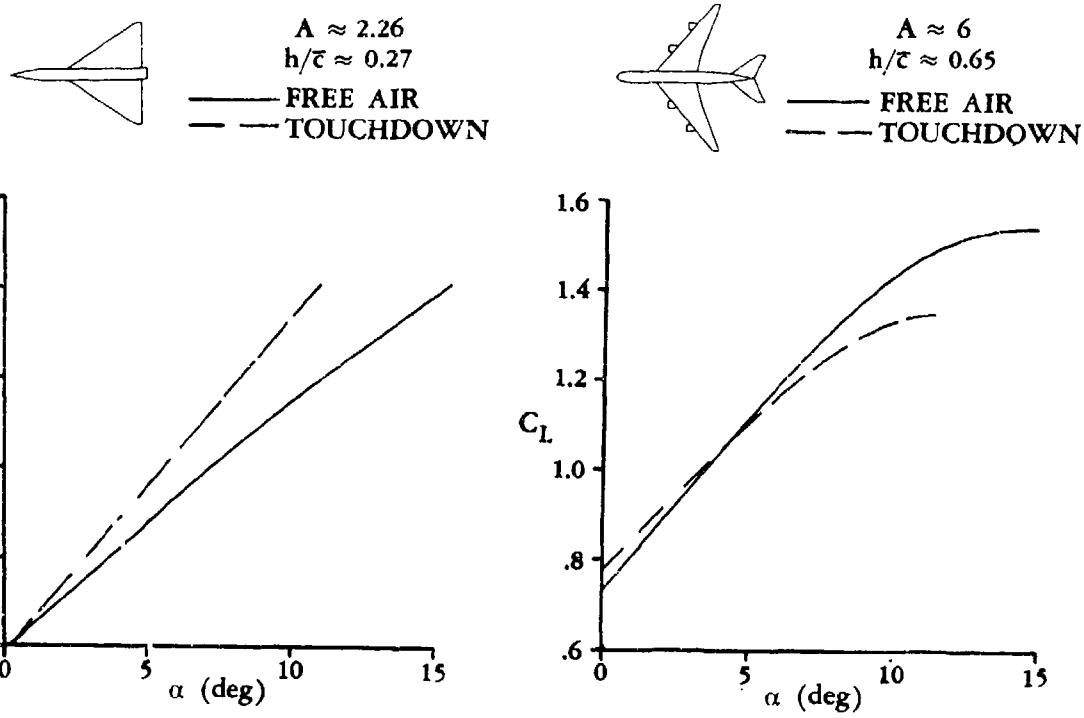

SKETCH (c)
GROUND EFECT ON 55°
DELTA CONFIGURATION

SKETCH (d)
GROUND EFFECT ON A JET
TRANSPORT CONFIGURATION

DATCOM METHODS

For most vehicles, calculating the change in lift due to ground effects consists of evaluating two components:

1. the change in wing-body lift
2. the change in tail-body lift due to the effects of downwash

The change in tail-body lift due to the presence of the ground is generally small in comparison to the downwash effects and is neglected in the Datcom methods. For canard-type configurations the change in downwash due to ground effect should be accounted for in the wing contribution.

Both of the Datcom methods presented require the user to construct wing-body and tail-body lift curves in ground effect based on their corresponding free-air lift curves. Equations are given that calculate the change in angle of attack due to ground effect at a constant lift coefficient. The ground-effect lift curves are then constructed by shifting the free-air lift curves at every C_L by the corresponding increment in angle of attack due to ground effect at constant lift coefficients (see Sketch (e)).

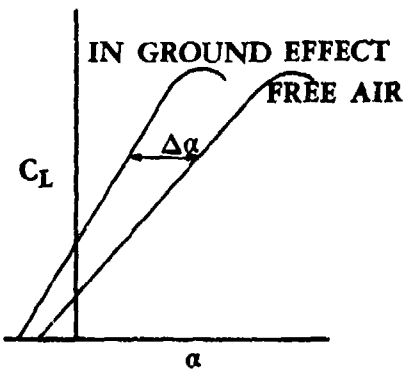

SKETCH (e)

Method 1

This method estimates the ground effects on lift in the linear-lift range for a subsonic transport configuration. The method is an extension of the Tani method of References 3 and 4 and includes the effects of taper ratio, sweep-back, dihedral, and flap deflection, while neglecting the effects of wing thickness since they are generally small. The wing-flap effects are valid only for split and slotted flaps as they are accounted for by empirical curves. The first term in Equation 4.7.1-a accounts for the effects of the trailing vortex, the second term for the effects of the bound vortex, and the third term for wing-flap effects. The method does not account for the effects of wing-leading-edge devices.

The change in wing-body angle of attack at a constant lift coefficient due to ground effect with respect to the out-of-ground-effect lift curve is given by

$$(\Delta\alpha)_G = -\left[\frac{9.12}{A} + 7.16\left(\frac{c_r}{b}\right)\right]\left(C_{L_f}\right)_{WB} x - \frac{A}{2\left(C_{L_\alpha}\right)_{WB}}\left(\frac{c_r}{b}\right)\left(\frac{L}{L_o} - 1\right)\left(C_{L_f}\right)_{WB} r$$

$$- \frac{\left(\delta_f/50\right)^2}{\left(C_{L_\alpha}\right)_{WB}} \Delta\left(\Delta C_L\right)_{flap} \quad \text{(per deg)} \qquad 4.7.1\text{-a}$$

where

A	is the wing aspect ratio.
$\frac{c_r}{b}$	is the ratio of wing root chord to wing span.
$\left(C_{L_f}\right)_{WB}$	is the wing-body lift coefficient including flap effects, out of ground effect, obtained from test data or Section 4.3.1 and Section 6.1.4.1.
x	accounts for the effects on lift due to the image trailing vortex and is obtained from Figure 4.7.1-14 as a function of wing geometry and the wing height above the ground.
$\left(C_{L_\alpha}\right)_{WB}$	is the wing-body lift-curve slope, per degree, out of ground effect, obtained from test data or Section 4.3.1.2.
$\frac{L}{L_o} - 1$	accounts for the effects on lift due to the image bound vortex and is obtained from Figure 4.7.1-15 as a function of wing geometry, lift coefficient, and the height of the quarter-chord point of the wing root chord above the ground.
r	accounts for the effect of finite span and is obtained from Figure 4.7.1-16 as a function of wing height above the ground.
$\Delta\left(\Delta C_L\right)_{flap}$	is an empirical factor to account for the effect of flaps and is obtained from Figure 4.7.1-17 as a function of the height of the quarter-chord point of the wing root chord above the ground.

In the linear-lift region, the change in downwash (a decrease) on the tail-body due to ground effects is derived theoretically by representing the ground plane as an image-vortex system. A modification to the method of Reference 9 is given in Reference 10, wherein certain geometric terms are redefined. This modified method is the method presented in the Datcom. The change (a decrease) in tail-body downwash due to ground effects in the linear-lift range is given by

$$(\Delta\epsilon)_G = \epsilon\left[\frac{b_{eff}^2 + 4(H_H - H)^2}{b_{eff}^2 + 4(H_H + H)^2}\right] \qquad 4.7.1\text{-b}$$

where

$(\Delta\epsilon)_G$	is the difference between the downwash in free air and the downwash in ground effect.
ϵ	is the downwash out of ground effect.
H	is the height of $\bar{c}/4$ of the wing above the ground.
H_H	is the height of $\bar{c}/4$ of the horizontal tail above the ground.

b_{eff} is the effective wing span defined as

$$b_{eff} = \frac{C_{L_{WB}} + \Delta C_{L_f}}{\frac{C_{L_{WB}}}{b'_W} + \frac{\Delta C_{L_f}}{b'_f}} \qquad 4.7.1\text{-c}$$

where

$C_{L_{WB}}$ is the wing-body lift coefficient, flaps retracted, out of ground effect, obtained from test data or Section 4.3.1.

ΔC_{L_f} is the change in lift coefficient due to flaps, out of ground effect, obtained from test data or Section 6.1.4.1.

$$b'_W = \left(\frac{b'_W}{b}\right) b \qquad 4.7.1\text{-d}$$

$$b'_f = \left(\frac{b'_f}{b'_W}\right)\left(\frac{b'_W}{b}\right) b \qquad 4.7.1\text{-e}$$

The ratio $\frac{b'_W}{b}$ is given in Figure 4.7.1-18a as a function of taper ratio and aspect ratio, and $\frac{b'_f}{b'_W}$ is given in Figure 4.7.1-18b as a function of the ratio of flap span to wing span.

The horizontal-tail lift curve in ground effect is constructed by shifting the free-air lift curve at every C_L by the corresponding $-(\Delta\epsilon)_G$, i.e.,

$$(\Delta\alpha_H)_G = -(\Delta\epsilon)_G \qquad 4.7.1\text{-f}$$

Method 2

This method estimates the ground effects on wing-body lift in the linear-lift range for all configurations not included in Method 1. The method is Tani's method from References 3 and 11, modified to include the effects of dihedral. The change in wing-body angle of attack due to ground effects with respect to the out-of-ground-effect lift curve is given by

$$(\Delta\alpha)_G = -18.24 \frac{\left(C_{L_f}\right)_{WB}\sigma}{A} + rT \frac{\left(C_{L_f}\right)^2_{WB}}{57.3\left(C_{L_\alpha}\right)_{WB}} - rB + K\left(\frac{t}{c}\right)_{max} \text{(per deg)} \qquad 4.7.1\text{-g}$$

where

σ is Prandtl's interference coefficient from multiplane theory and is obtained from Figure 4.7.1-19 as a function of wing height above the ground.

r accounts for the effect of finite span and is obtained from Figure 4.7.1-16 as a function of wing height above the ground.

T accounts for the reduction of the longitudinal velocity and is obtained from Figure 4.7.1-20 as a function of wing height above the ground.

B accounts for the change in circulation and is obtained from Figure 4.7.1-21 as a function of wing height above the ground.

K accounts for the effective wing thickness and is obtained from Figure 4.7.1-22 as a function of wing height above the ground.

$\left(C_{L_\alpha}\right)_{WB}$ is the wing-body lift-curve slope, per degree, out of ground effect, obtained from test data or Section 4.3.1.2.

$\left(\frac{t}{c}\right)_{max}$ is the ratio of maximum wing thickness to wing chord.

$\left(C_{L_f}\right)_{WB}$ is the wing-body lift coefficient including flap effects, out of ground effect, obtained from test data or Section 4.3.1 and Section 6.1.4.1.

The change in lift on the horizontal tail due to ground effect is accounted for in the same manner as in Method 1 above.

Sample Problems

1. Method 1

Given: a jet-transport configuration

Wing Characteristics:

$A = 6.8$ $\quad \frac{c_r}{b} = 0.291$ $\quad \frac{h_{c_r/4}}{c_r} = 0.29$ $\quad \Lambda_{c/4} = 35^\circ$

$\lambda = 0.30$ $\quad b = 1864.4$ in. $\quad \frac{b_f}{b} = 0.54$ $\quad \delta_f = 50^\circ$

$H = 158$ in. $\quad \left(C_{L_\alpha}\right)_{WB} = 0.078$ per deg (test data) $\quad \frac{h}{b/2} = 0.168$

$\frac{\Delta x}{b/2} = 0.04$ Slotted flaps

From wind-tunnel-test data (out of ground effect):

α (deg)	0	2	4	6	8	10
$(C_{L_f})_{WB}$ (with flaps)	1.19	1.35	1.50	1.66	1.82	1.96
$C_{L_{WB}}$ (without flaps)	0.18	0.34	0.49	0.65	0.81	0.97
ΔC_{L_f}	1.01	1.01	1.01	1.01	1.01	0.99

Tail Characteristics:

$A = 3.79$ $\frac{c_t}{b} = 0.386$ $\Lambda_{c/4} = 35°$ $\frac{S_H}{S_W} = 0.377$

$i_H = -6°$ $H_H = 233.7 \cos\alpha - 664.1 \sin\alpha$

From wind-tunnel-test data (out of ground effect):

α (deg)	0	2	4	6	8	10
C_{L_H}	−0.606	−0.535	−0.475	−0.415	−0.360	−0.300
ϵ (deg)	5.1	6.0	6.9	7.8	8.8	9.7

Compute: The change in wing-body lift due to ground effect

$x = 0.56$ (Figure 4.7.1-14)

$$\frac{57.3\, C_L}{2\pi \cos^2 \Lambda_{c/4}} = \frac{57.3\, C_L}{(6.28)(0.671)} = 13.6\, C_L$$

α (deg)	$\left(C_{L_f}\right)_{WB}$ (test)	13.6 C_L	$\frac{L}{L_o} - 1$ (Fig. 4.7.1-16)
0	1.19	16.2	–0.04
2	1.35	18.4	–0.09
4	1.50	20.4	–0.13
6	1.66	22.6	–0.175
8	1.82	24.8	–0.205
10	1.96	26.7	–0.212

r = 0.845 (Figure 4.7.1-16)

$\Delta\left(\Delta C_L\right)_{flap} = -0.083$ (Figure 4.7.1-17)

Solution:

$$(\Delta\alpha)_G = -\left[\frac{9.12}{A} + 7.16\,\frac{c_f}{b}\right]\left(C_{L_f}\right)_{WB} x - \frac{A}{2\left(C_{L_\alpha}\right)_{WB}}\left(\frac{c_f}{b}\right)\left(\frac{L}{L_o} - 1\right)\left(C_{L_f}\right)_{WB} r$$

$$- \frac{\left(\delta_f/50\right)^2}{\left(C_{L_\alpha}\right)_{WB}}\,\Delta\left(\Delta C_L\right)_{flap} \quad \text{(Equation 4.7.1-a)}$$

$$= -\left[\frac{9.12}{6.8} + 7.16(0.291)\right](0.56)\left(C_{L_f}\right)_{WB} - \frac{(6.8)(0.291)(0.845)}{2(0.078)}\left(\frac{L}{L_o} - 1\right)\left(C_{L_f}\right)_{WB}$$

$$- \frac{(50/50)^2}{0.078}\,(-0.083)$$

$$= -1.92\left(C_{L_f}\right)_{WB} - 10.7\left(\frac{L}{L_o} - 1\right)\left(C_{L_f}\right)_{WB} + 1.064$$

α (deg)	$\left(C_{L_f}\right)_{WB}$ (test)	$\frac{L}{L_o} - 1$	$(\Delta\alpha)_G$ (deg)
0	1.19	–0.04	–0.71
2	1.35	–0.09	–0.23
4	1.50	–0.13	0.27
6	1.66	–0.175	0.99
8	1.82	–0.205	1.57
10	1.96	–0.212	1.76

The in-ground-effect lift curve can be constructed and is shown in Sketch (f). A comparison of the predicted lift curve to wind-tunnel-test data is shown in Sketch (g).

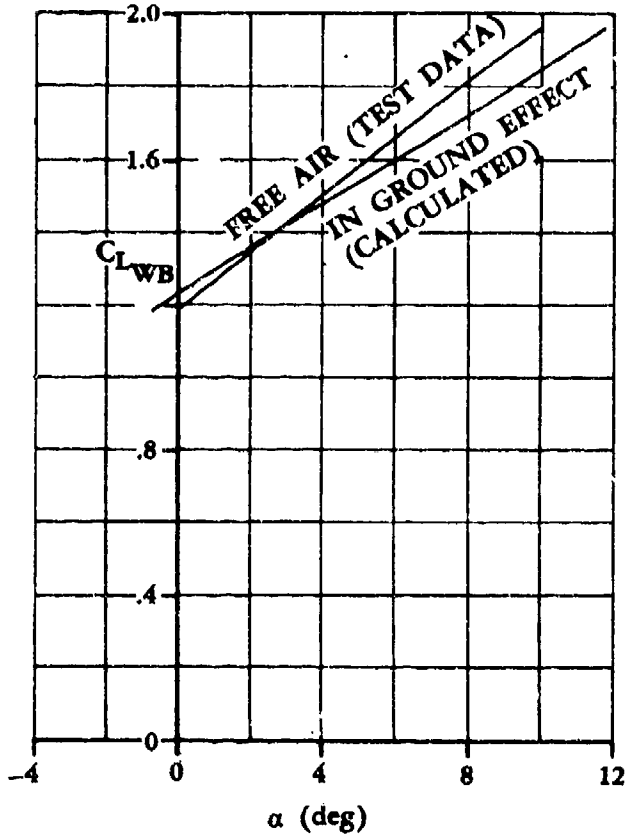

SKETCH (f)

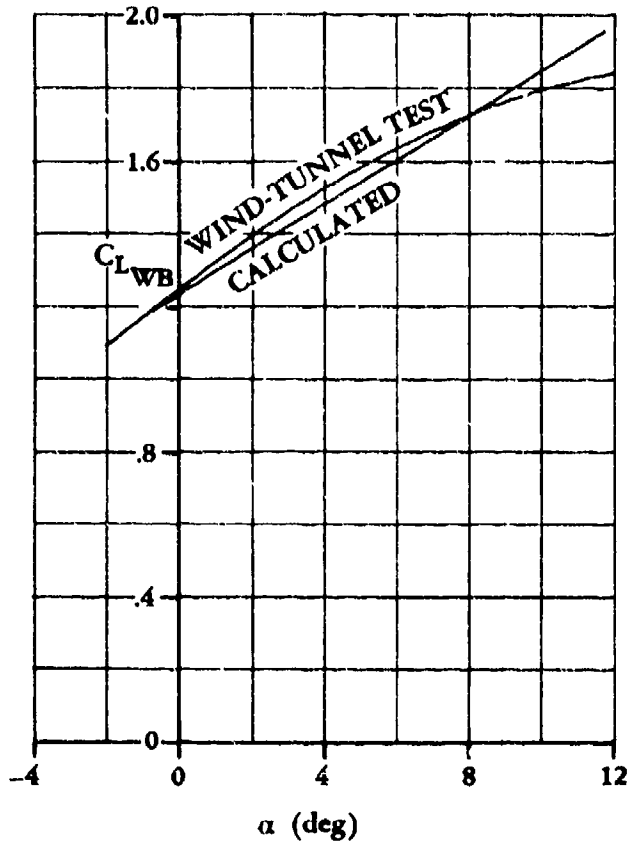

SKETCH (g)

Compute the change in downwash at the horizontal tail due to ground effect

$$\frac{b'_W}{b} = 0.725 \quad \text{(Figure 4.7.1-18a)}$$

$$\frac{b'_f}{b'_W} = 0.70 \quad \text{(Figure 4.7.1-18b)}$$

$$b'_W = \left(\frac{b'_W}{b}\right) b \quad \text{(Equation 4.7.1-d)}$$

$$= (0.725)\,(1864.4)$$

$$= 1352 \text{ in.}$$

$$b_f = \left(\frac{b'_f}{b'_W}\right)\left(\frac{b'_W}{b}\right) b \quad \text{(Equation 4.7.1-e)}$$

$$= (0.70)\,(0.725)\,(1864.4)$$

$$= 946 \text{ in.}$$

$$b_{eff} = \frac{C_{L_{WB}} + \Delta C_{L_f}}{\frac{C_{L_{WB}}}{b'_W} + \frac{\Delta C_{L_f}}{b'_f}} \quad \text{(Equation 4.7.1-c)}$$

α (deg)	$C_{L_{WB}}$ (test)	ΔC_{L_f} (test)	b_{eff} (in.)
0	0.18	1.01	991
2	0.34	1.01	1023
4	0.49	1.01	1049
6	0.65	1.01	1072
8	0.81	1.01	1092
10	0.97	0.99	1111

The height of the quarter-chord of the horizontal-tail MAC above the ground is calculated by

$$H_H = 233.7 \cos\alpha - 664.1 \sin\alpha$$

α	0	2	4	6	8	10
H_H (in.)	233.7	210.3	186.6	163.1	138.7	114.8

$$(\Delta\epsilon)_G = \epsilon\left[\frac{b_{eff}^2 + 4(H_H - H)^2}{b_{eff}^2 + 4(H_H + H)^2}\right] \quad \text{(Equation 4.7.1-b)}$$

$$(\Delta\alpha_H)_G = -(\Delta\epsilon)_G \quad \text{(Equation 4.7.1-f)}$$

α (deg)	b_{eff} (in.)	H (in.)	H_H (in.)	ϵ (deg)	$(\Delta\epsilon)_G$ (deg)	$(\Delta\alpha_H)_G$ (deg)
0	991	158.0	233.7	5.1	3.21	−3.21
2	1023	158.0	210.3	6.0	3.99	−3.99
4	1049	158.0	186.6	6.9	4.83	−4.83
6	1072	158.0	163.1	7.8	5.74	−5.74
8	1092	158.0	138.7	8.8	6.80	−6.80
10	1111	158.0	114.8	9.7	7.86	−7.86

The in-ground-effect lift curve can be constructed for $i_H = -6°$ and is shown in Sketch (h). No test data are available for comparison.

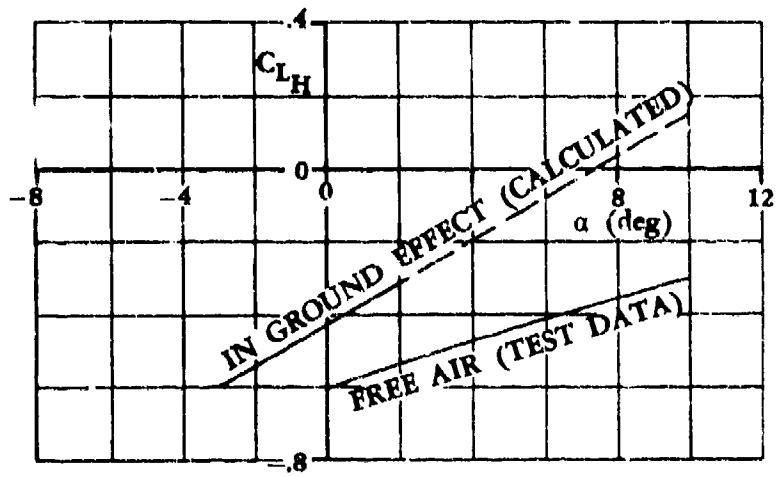

SKETCH (h)

2. Method 2

Given: the F5D-1 aircraft

Wing Characteristics:

$A = 2.02$ $\quad \frac{h}{\bar{c}} = 0.329$ $\quad \frac{h}{b/2} = 0.36$ $\quad \left(C_{L_\alpha}\right)_{WB} = 0.0363$ per degree (test data)

$\left(\frac{t}{c}\right)_{max} = 0.05$

From wind-tunnel-test data:

α (deg)	0	2	4	6	8	10	12	14	16
$C_{L_{WB}}$ (free air)	-0.023	0.048	0.12	0.194	0.267	0.34	0.418	0.495	0.572

Compute:

σ = 0.322 (Figure 4.7.1-19)

r = 0.703 (Figure 4.7.1-16)

K = 4.6 (Figure 4.7.1-22)

T = 6.06 (Figure 4.7.1-20)

$C_{L_{WB}}$ (test)	−0.023	0.048	0.12	0.194	0.267	0.34	0.418	0.495	0.572
B (deg) (Fig. 4.7.1-21)	–	0.17	0.30	0.50	0.68	0.86	1.04	1.21	1.41

Solution:

$$(\Delta\alpha)_G = -18.24\,\frac{\left(C_{L_f}\right)_{WB}\,\sigma}{A} + \frac{rT\left(C_{L_f}\right)_{WB}^{2}}{57.3\left(C_{L_\alpha}\right)_{WB}} - rB + K\left(\frac{t}{c}\right)_{max} \qquad \text{(Equation 4.7.1-g)}$$

① α (deg)	② $C_{L_{WB}}$ (test)	③ $-18.24\,\frac{\left(C_{L_f}\right)_{WB}\,\sigma}{A}$	④ $\frac{rT\left(C_{L_f}\right)^2_{WB}}{57.3\left(C_{L_\alpha}\right)_{WB}}$	⑤ $-rB$	⑥ $K\left(\frac{t}{c}\right)_{max}$	⑦ $(\Delta\alpha)_G$ (deg) (Eq. 4.7.1-g) ③+④+⑤+⑥
0	−0.023	0.067	0.0011	–	0.23	0.298
2	0.048	−0.140	0.0047	−0.0844	0.23	0.010
4	0.12	−0.349	0.0295	−0.211	0.23	−0.300
6	0.194	−0.564	0.0771	−0.352	0.23	−0.609
8	0.267	−0.776	0.146	−0.478	0.23	−0.878
10	0.34	−0.989	0.237	−0.605	0.23	−1.127
12	0.418	−1.216	0.358	−0.731	0.23	−1.359
14	0.495	−1.440	0.502	−0.851	0.23	−1.559
16	0.572	−1.663	0.670	−0.991	0.23	−1.754

The calculated F5D-1 lift curve in ground effect is now constructed in Sketch (i) by shifting the free-air lift curve at every C_L by the corresponding $(\Delta\alpha)_G$. A comparison of the predicted lift curve to wind-tunnel-test data is shown in Sketch (j).

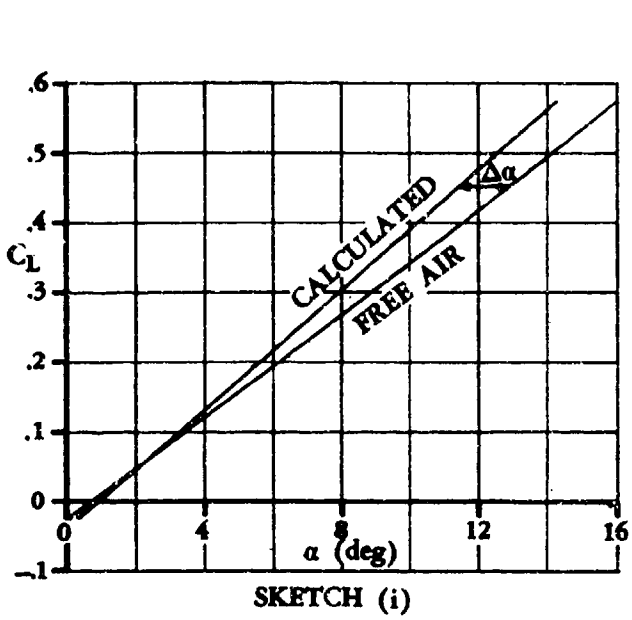

SKETCH (i)

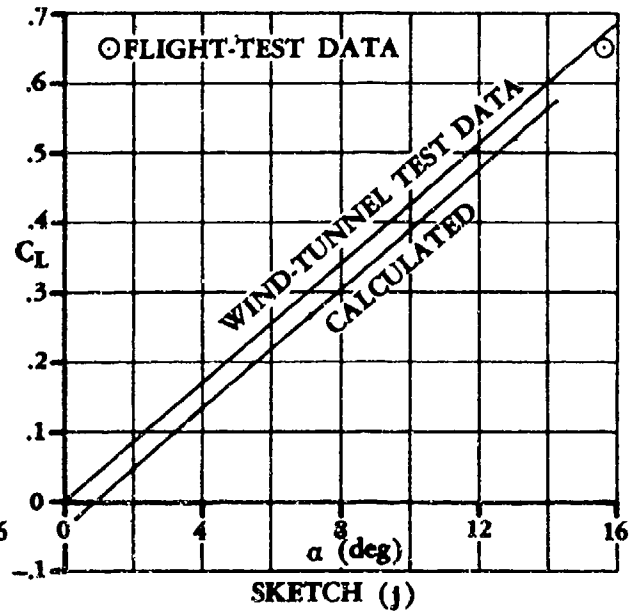

SKETCH (j)

REFERENCES

1. Wetmore, J. W., and Turner, L. I., Jr.: Determination of Ground Effect from Tests of a Glider in Towed Flight. NACA TR 696, 1940. (U)

2. Wieselsberger, C.: Wing Resistance Near the Ground. NACA TM 77, 1922. (U)

3. Tani, I., Taima, M., and Simidu, S.: The Effect of Ground on the Aerodynamic Characteristics of a Monoplane Wing. Tokyo Univ. Aeronautical Research Inst. Report 156, 1937. (U)

4. Baker, P. A., Schweikhard, W. G., and Young, W. R.: Flight Evaluation of Ground Effect on Several Low-Aspect-Ratio Airplanes. NASA TN D-6053, 1970. (U)

5. de Sievers, A.: Wind-Tunnel Tests on the Ground Effect. NASA TT F-11059, 1967. (U)

6. Gersten, K.: Calculation of the Aerodynamic Characteristics of Wings of Finite Span Near the Ground. Abhandlungen der Braunschweigischen Wissenschaftlichen Gesellschaft, XII, 1960, pp. 95-115. (U)

7. Kirkpatrick, D. L. I.: A Method of Correlating the Ground Effects on the Longitudinal Characteristics of Slender Wings. RAE TR 69190, 1969. (U)

8. Kemp, W. B., Jr., Lockwood, V. E., and Phillips, W. P.: Ground Effects Related to Landing of Airplanes with Low-Aspect-Ratio Wings. NASA TN D-3683, 1966. (U)

9. Piper, R. W., and Davies, H.: Note on Factors Affecting Trim at Take-off and Landing. Aero. Departmental Note – Wind Tunnel No. 540, 1941. (Unpublished British Paper). (U)

10. Owen, P. R., and Hugg, H.: Ground Effect on Downwash with Slipstream. ARC R&M 2449, 1952. (U)

11. Tani, I., Itokawa, H., and Taima, M.: Further Studies of the Ground Effect on the Aerodynamic Characteristics of an Aeroplane, with Special Reference to Tail Moment. Tokyo Univ. Aeronautical Research Inst. Report 158, 1937. (U)

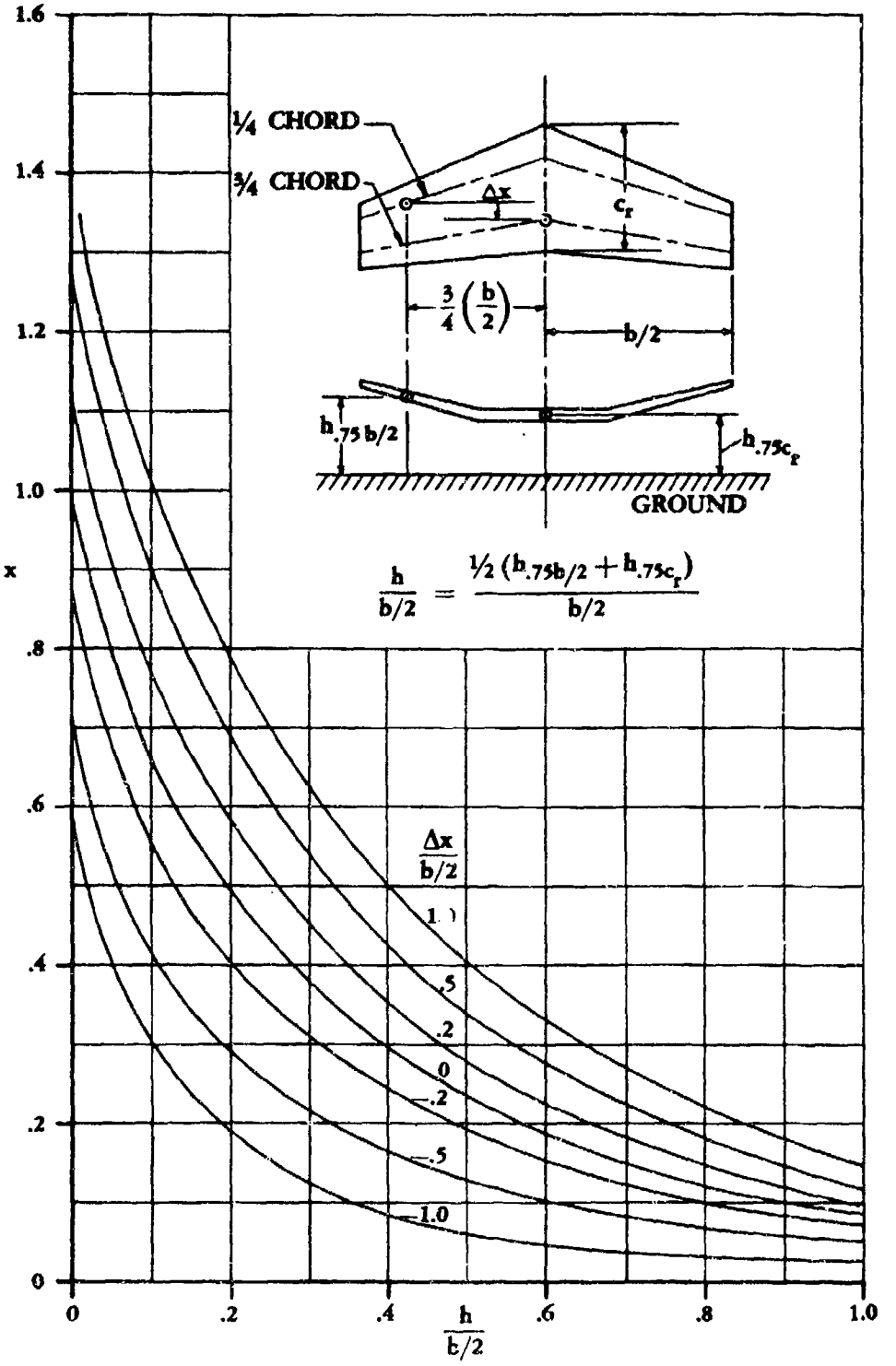

FIGURE 4.7.1-14 PARAMETER ACCOUNTING FOR GROUND EFFECT ON LIFT DUE TO TRAILING VORTICES

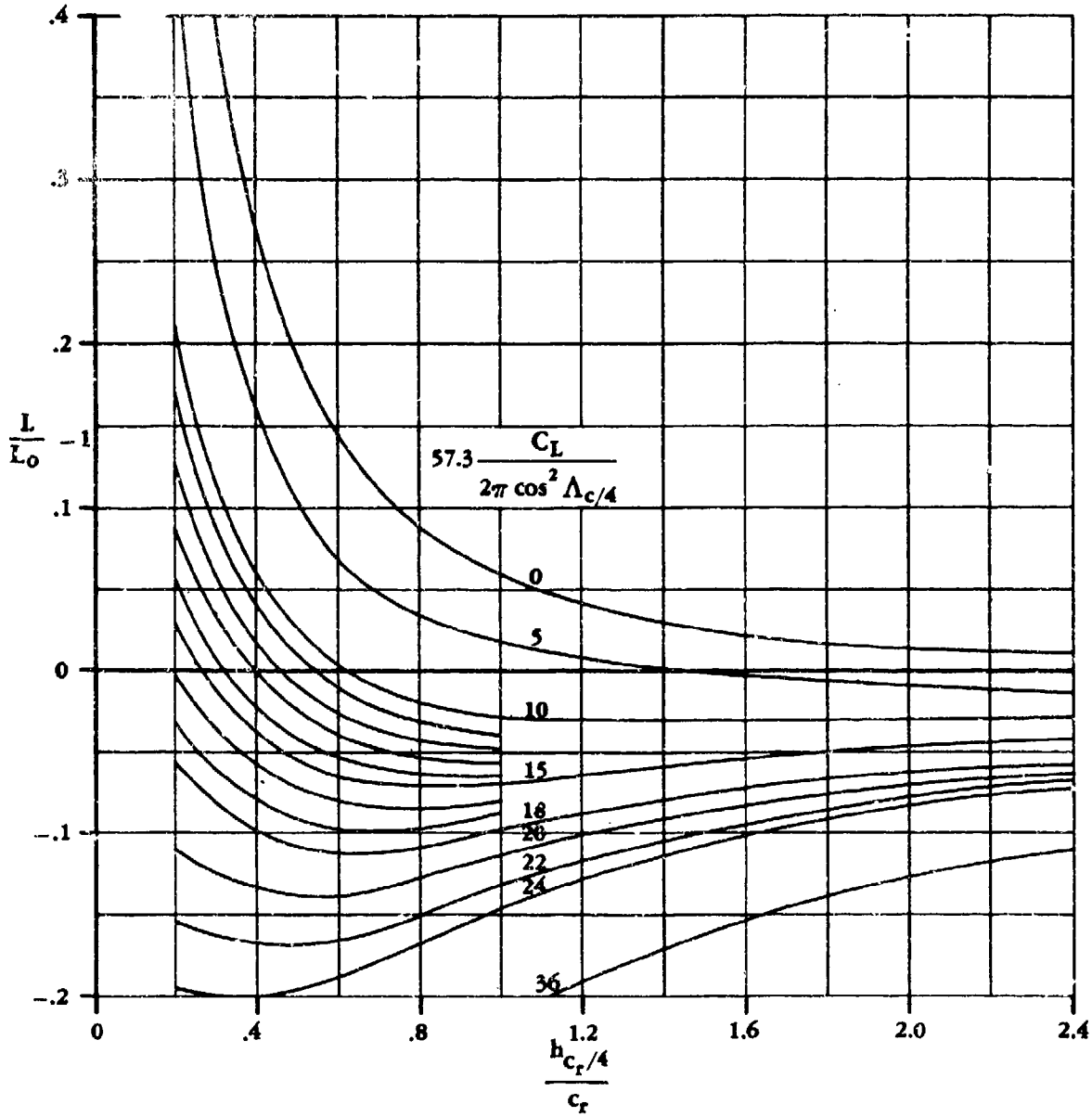

FIGURE 4.7.1-15 PARAMETER ACCOUNTING FOR GROUND EFFECT ON LIFT DUE TO BOUND VORTICES

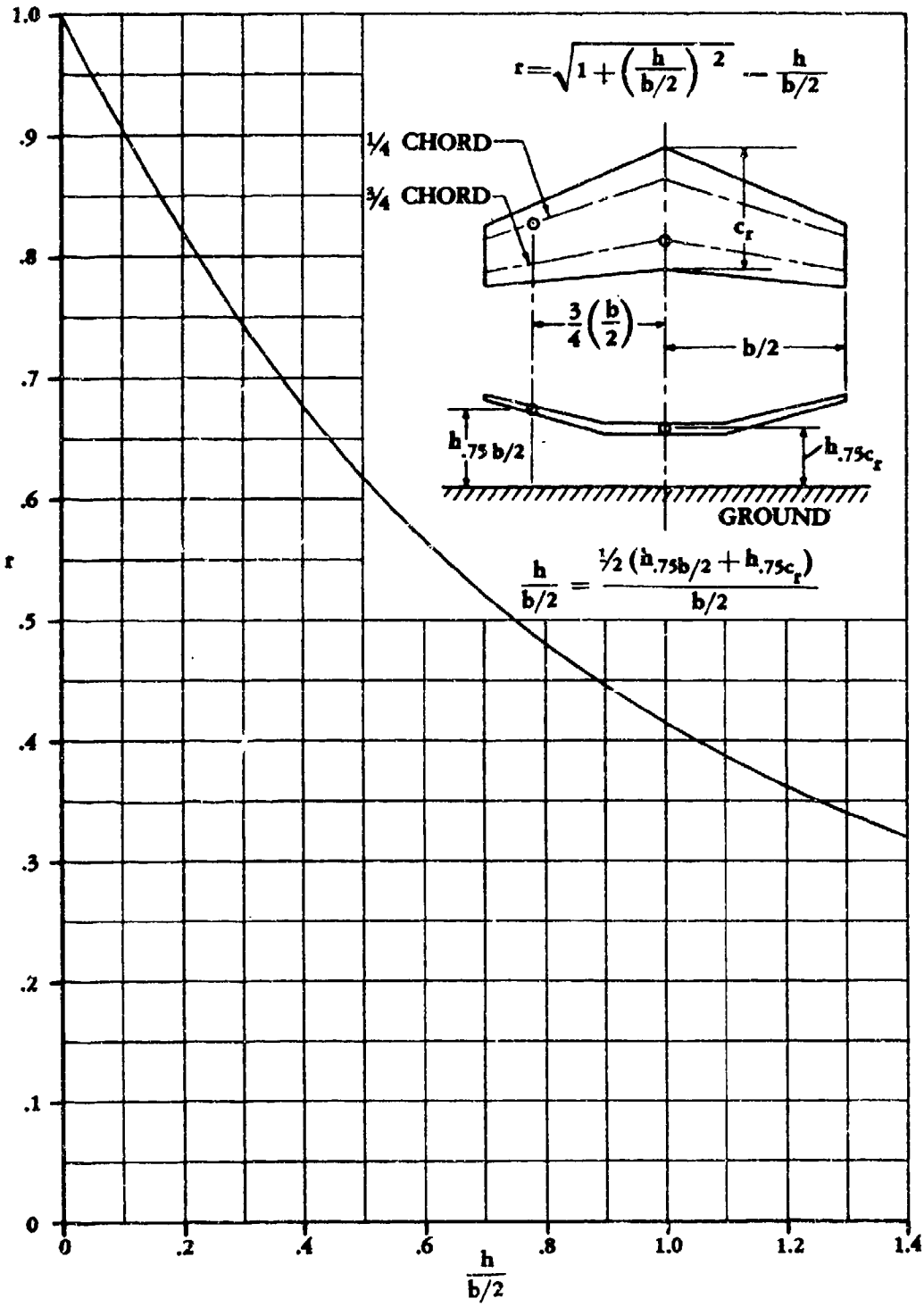

FIGURE 4.7.1-16 FACTOR ACCOUNTING FOR FINITE SPAN IN GROUND EFFECT

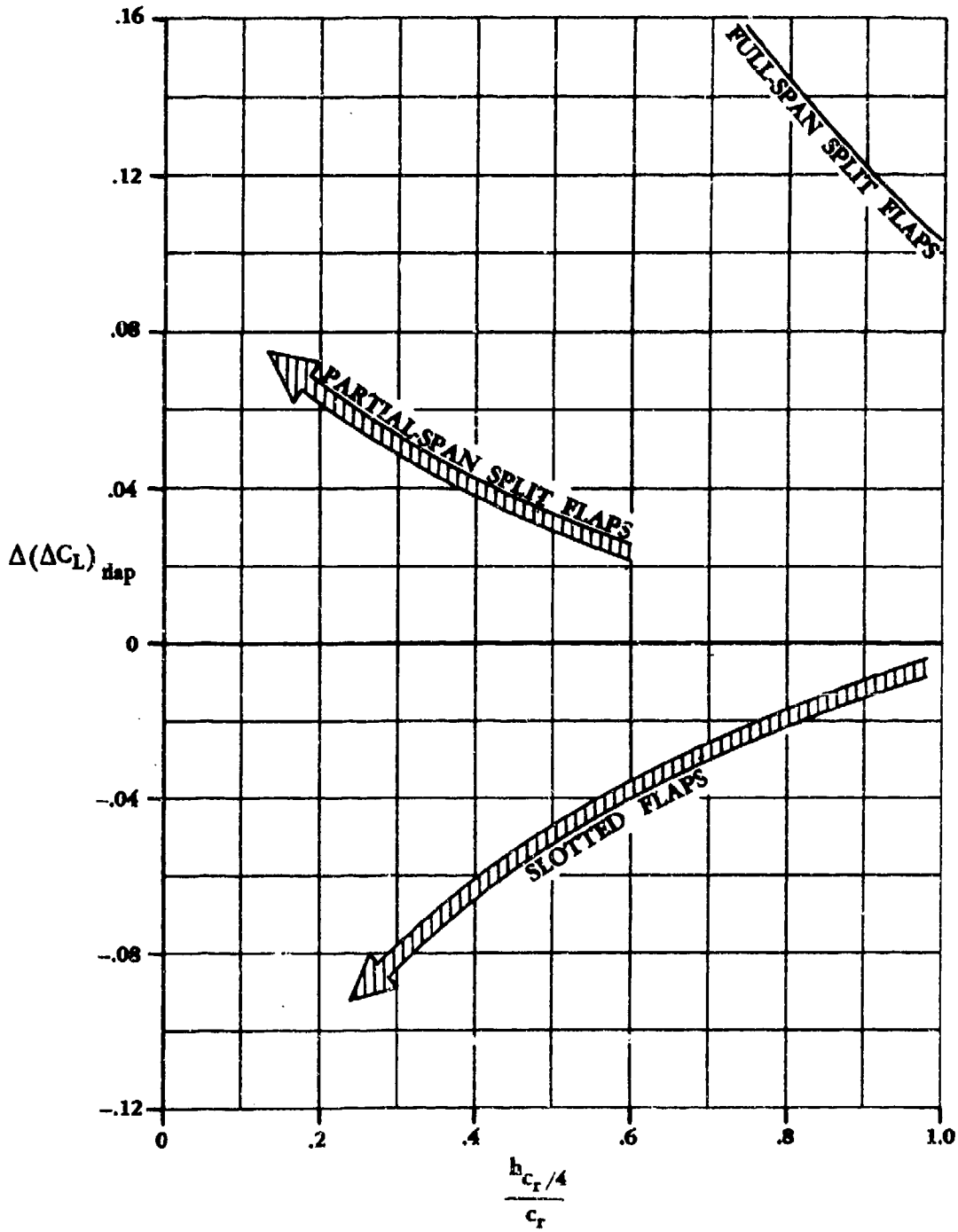

FIGURE 4.7.1-17 EFFECT OF FLAP DEFLECTION ON THE GROUND INFLUENCE ON LIFT

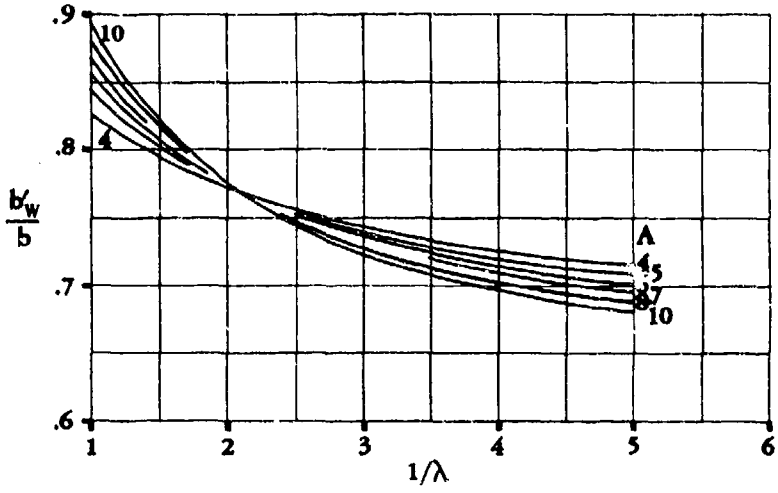

FIGURE 4.7.1-18a EFFECTIVE WING SPAN IN THE PRESENCE OF THE GROUND

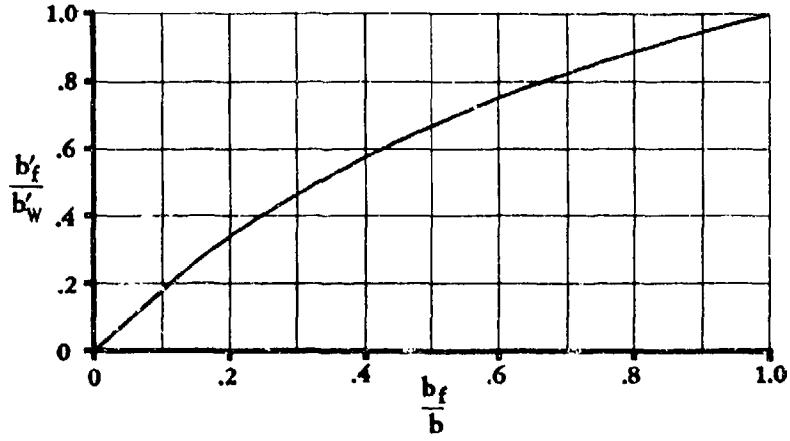

FIGURE 4.7.1-18b EFFECTIVE FLAP SPAN IN THE PRESENCE OF THE GROUND

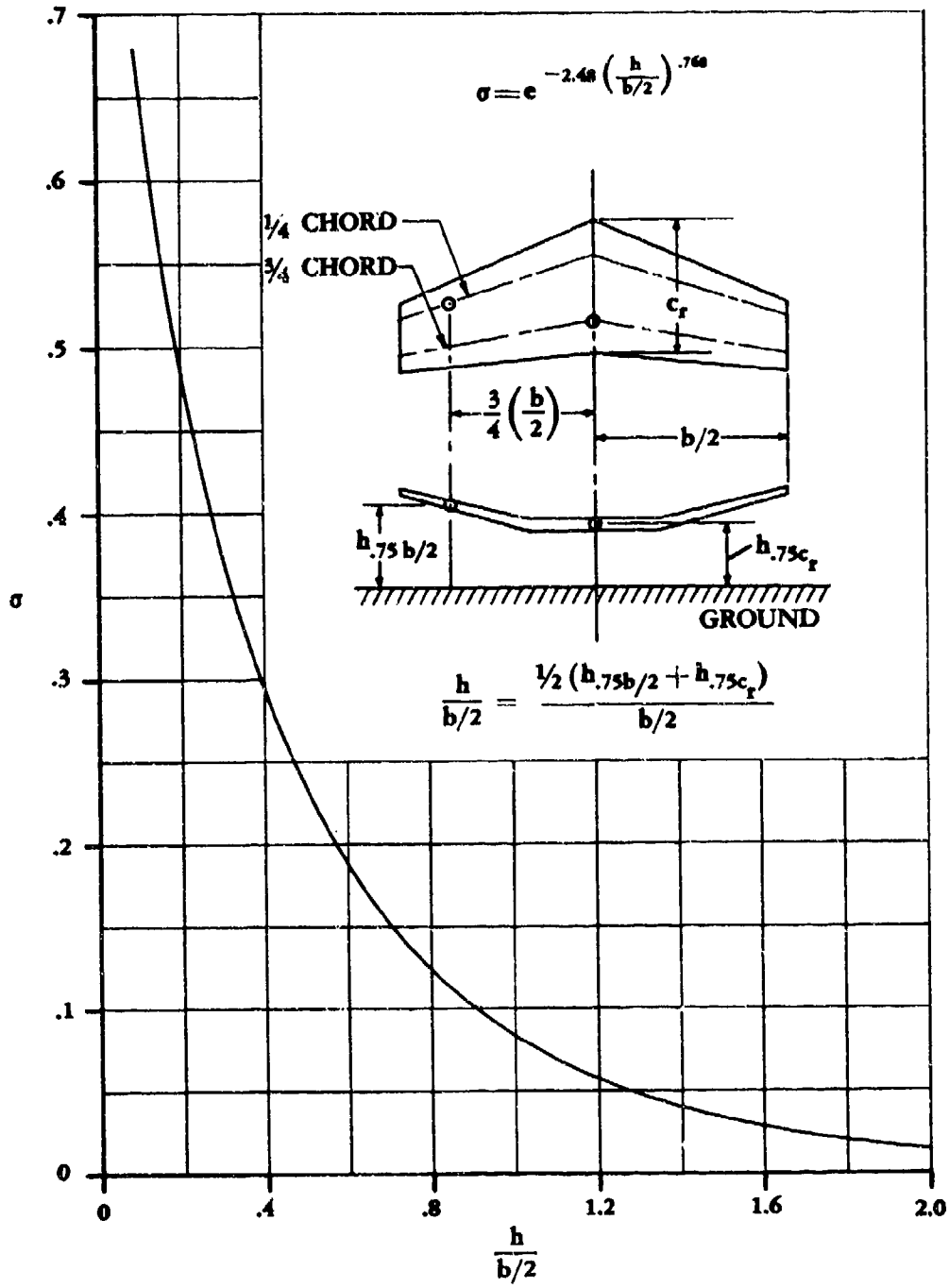

FIGURE 4.7.1-19 PRANDTL'S INTERFERENCE COEFFICIENT — INDICATIVE OF VARIATION IN INDUCED VERTICAL VELOCITY WITH GROUND HEIGHT

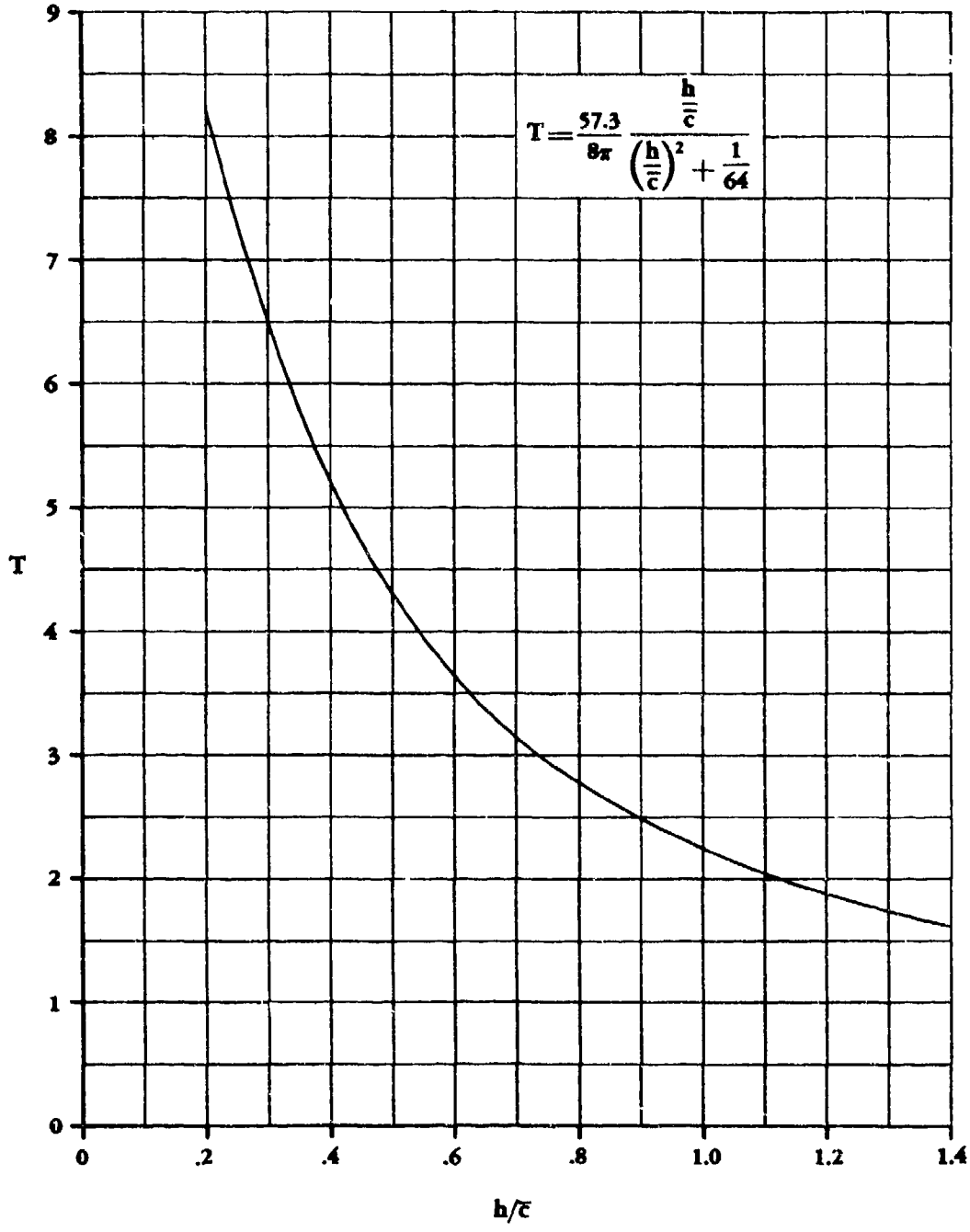

FIGURE 4.7.1-20 PARAMETER ACCOUNTING FOR VARIATION IN LONGITUDINAL VELOCITY WITH GROUND HEIGHT

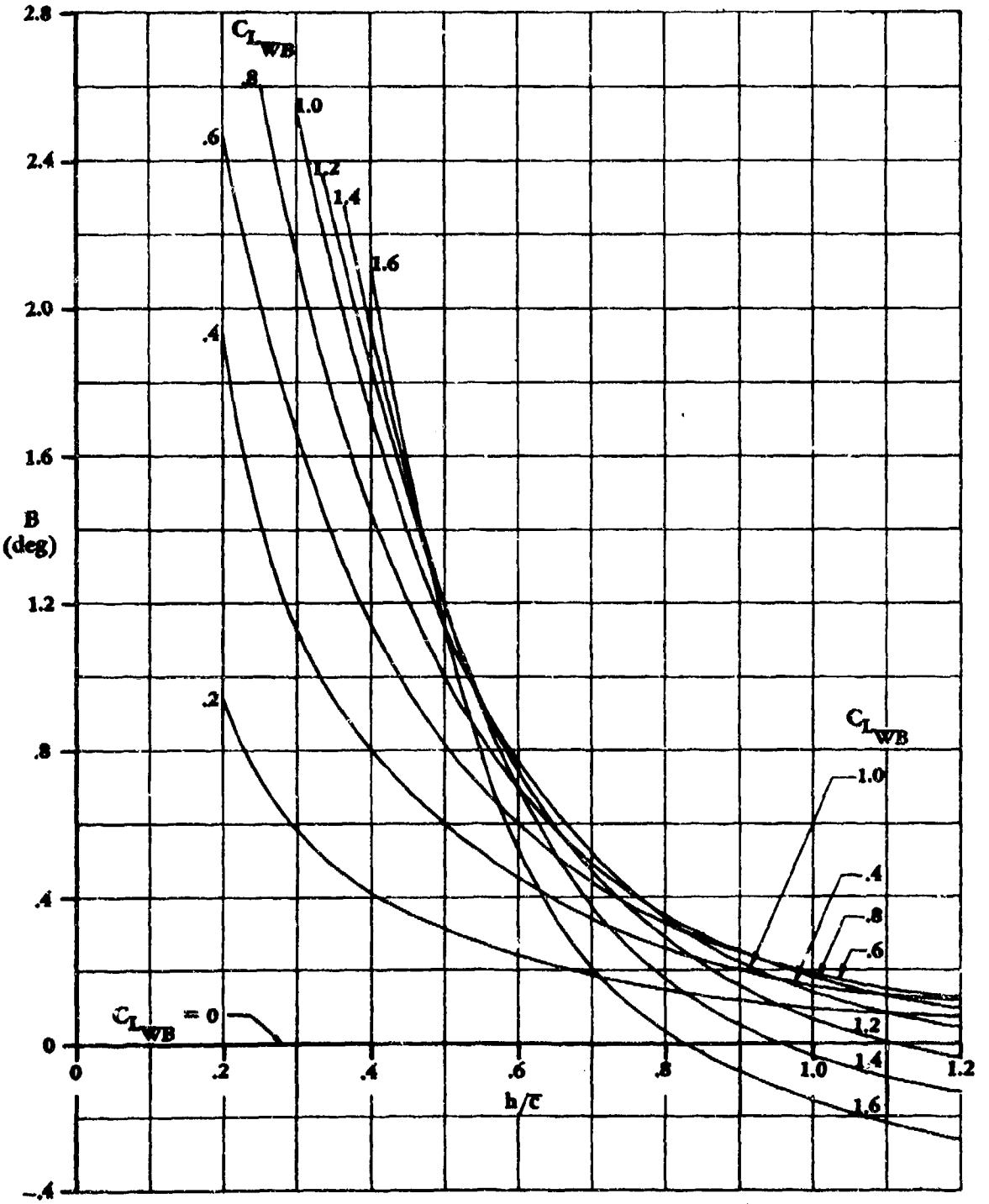

FIGURE 4.7.1-21 PARAMETER ACCOUNTING FOR VARIATION IN CIRCULATION WITH LIFT AND HEIGHT ABOVE GROUND

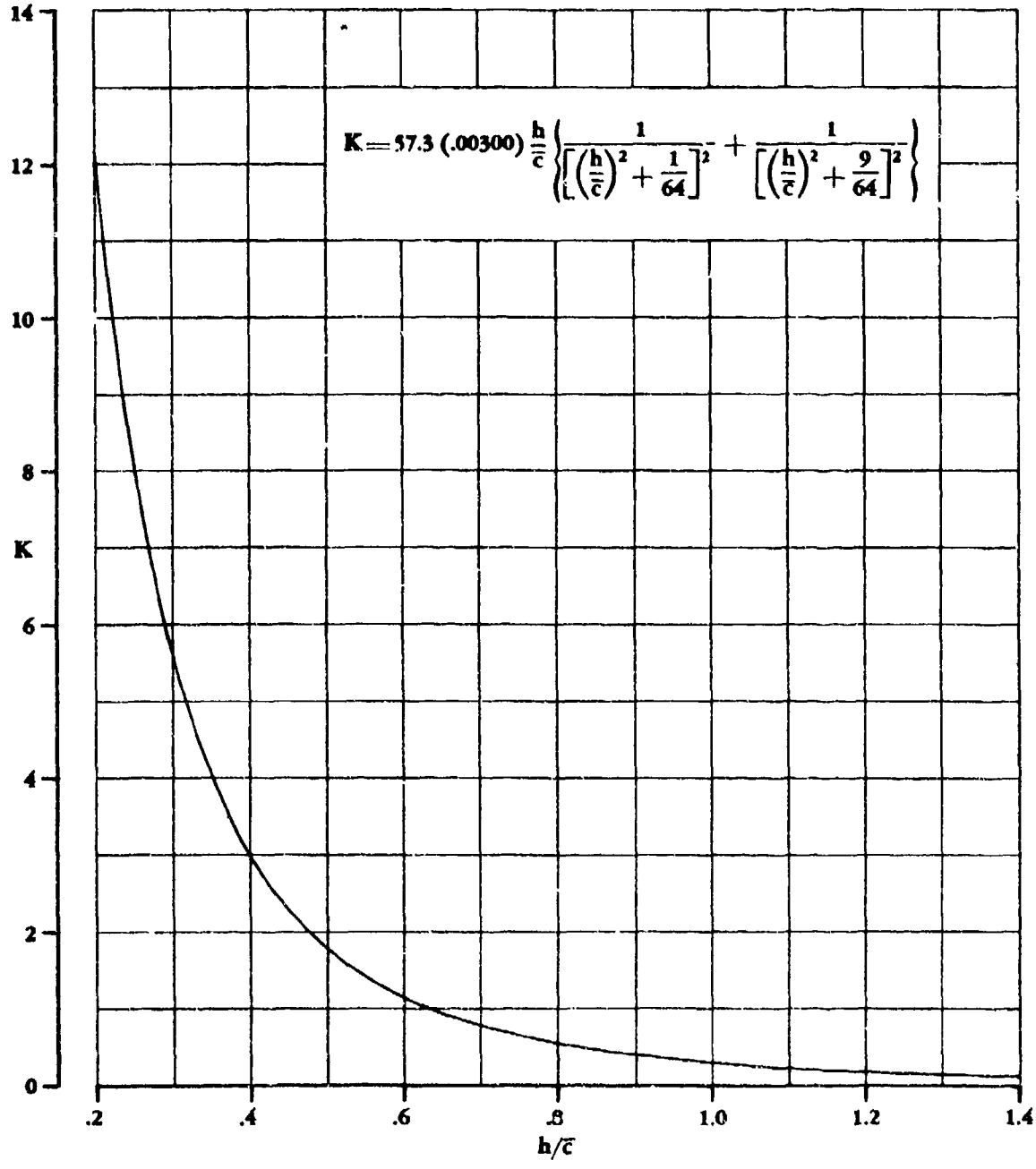

FIGURE 4.7.1-22 PARAMETER ACCOUNTING FOR INFLUENCE OF WING THICKNESS DUE TO HEIGHT ABOVE GROUND

4.7.3 GROUND EFFECTS ON PITCHING-MOMENT VARIATION WITH ANGLE OF ATTACK

A method is presented in this section for estimating the ground effects on pitching moment in the linear-lift region. The reader is referred to Section 4.7 for a basic discussion of various aspects of ground effects.

The change in pitching moment due to ground effects is due primarily to the change in lift on the horizontal tail, which in most cases can be attributed to the change in downwash. An additional pitching-moment increment is produced by the increased lift on the wing and any possible shift in the aerodynamic center due to ground effect.

DATCOM METHOD

The method presented herein is based upon the lift estimates of Section 4.7.1. The method assumes no change in the location of the wing aerodynamic center due to ground effects. The total change in pitching-moment coefficient due to ground effects is the sum of the changes of the horizontal-tail-body and wing-body pitching-moment components, based on the product of wing area and wing MAC, and is expressed as

$$\left(\Delta C_m\right)_G = \left(\Delta C_{m_H}\right)_G + \left(\Delta C_{m_{WB}}\right)_G \qquad 4.7.3\text{-a}$$

The change in pitching-moment coefficient of the horizontal-tail-body due to ground effects may be expressed as

$$\left(\Delta C_{m_H}\right)_G = -\left(\Delta C_{L_H}\right)_G \frac{\ell_H}{\bar{c}} \frac{S_H}{S_W} \frac{q_H}{q_\infty} \qquad 4.7.3\text{-b}$$

where

$\left(\Delta C_{L_H}\right)_G$ is the change in lift on the horizontal-tail-body at a given angle of attack due to ground effect, based on the horizontal-tail area, and is found from the tail-body lift curves constructed by using Section 4.7.1.

ℓ_H is the distance from the quarter-chord point of the horizontal-tail MAC to the moment reference center, measured parallel to the body center line.

$\bar{c}$ is the wing mean aerodynamic chord.

$\frac{S_H}{S_W}$ is the ratio of horizontal-tail area to wing area.

$\frac{q_H}{q_\infty}$ is the effective dynamic-pressure ratio at the horizontal tail, obtained from Section 4.4.1.

The change in pitching-moment coefficient of the wing-body due to ground effects may be expressed as

$$\left(\Delta C_{m_{WB}}\right)_G = \left(n - \frac{x_{a.c.}}{\bar{c}}\right)\left(\Delta C_{L_{WB}}\right)_G \qquad 4.7.3\text{-c}$$

where

n is the distance from the wing apex to the desired moment reference center measured in wing mean aerodynamic chords, positive aft.

$x_{a.c.}$ is the wing-body aerodynamic-center location measured from the wing apex, positive for a.c. aft of wing apex, obtained from Section 4.3.2.2.

$\bar{c}$ is the wing mean aerodynamic chord.

$\left(\Delta C_{L_{WB}}\right)_G$ is the change in lift due to ground effect on the wing-body and is found from the wing-body lift curves constructed by using Section 4.7.1.

Sample Problem

Given: Same jet-transport configuration as Sample Problem 1 of Section 4.7.1.

Wing-Body Characteristics:

$$\frac{x_{a.c.}}{\bar{c}} = 1.182 \qquad n = 1.242$$

From Sample Problem 1 of Section 4.7.1:

α (deg)	0	2	4	6	8	10
$\left(\Delta C_{L_{WB}}\right)_G$	0.04	0.01	−0.025	−0.06	−0.09	−0.11

Tail Characteristics:

$$\frac{\ell_H}{\bar{c}} = 2.43 \qquad \frac{S_H}{S_W} = 0.377 \qquad \frac{q_H}{q_\infty} = 0.95$$

From Sample Problem 1 of Section 4.7.1:

α (deg)	0	2	4	6	8	10
$\left(\Delta C_{L_H}\right)_G$	0.255	0.305	0.355	0.415	0.470	0.530

Compute:

$$\left(\Delta C_{m_H}\right)_G = -\left(\Delta C_{L_H}\right)_G \frac{\ell_H}{\bar{c}} \frac{S_H}{S_W} \frac{q_H}{q_\infty} \qquad \text{(Equation 4.7.3-b)}$$

$$= -\left(\Delta C_{L_H}\right)_G (2.43)(0.377)(0.95)$$

$$= -0.870 \left(\Delta C_{L_H}\right)_G$$

α (deg)	0	2	4	6	8	10
$\left(\Delta C_{m_H}\right)_G$	−0.222	−0.265	−0.309	−0.361	−0.409	−0.461

$$\left(\Delta C_{m_{WB}}\right)_G = \left(n - \frac{X_{a.c.}}{\bar{c}}\right)\left(\Delta C_{L_{WB}}\right)_G \qquad \text{(Equation 4.7.3-c)}$$

$$= (1.242 - 1.182)\left(\Delta C_{L_{WB}}\right)_G$$

$$= (0.06)\left(\Delta C_{L_{WB}}\right)_G$$

α (deg)	0	2	4	6	8	10
$\left(\Delta C_{m_{WB}}\right)_G$	0.0024	0.0006	−0.0016	−0.0036	−0.0054	−0.0066

Solution:

$$\left(\Delta C_m\right)_G = \left(\Delta C_{m_H}\right)_G + \left(\Delta C_{m_{WB}}\right)_G \qquad \text{(Equation 4.7.3-a)}$$

α (deg)	0	2	4	6	8	10
$\left(\Delta C_m\right)_G$	−0.220	−0.264	−0.311	−0.365	−0.414	−0.468

No test data are available for comparison.

4.7.4 GROUND EFFECTS ON DRAG AT ANGLE OF ATTACK

In this section, methods are presented for estimating the ground effects on drag in the linear-lift region. The reader is referred to Section 4.7 for a basic discussion of various aspects of ground effects.

The drag of a vehicle in the presence of a ground plane is affected in three ways.

1. The drag due to lift is decreased.

2. A change in the drag at zero lift is also experienced, but is small relative to the change in drag due to lift.

3. The presence of a ground plane introduces a pitching-moment increment (Section 4.7.3), which changes the drag due to lift of the trimmed vehicle.

The second effect is ignored in most calculations and is not presented in the Datcom.

Two methods are presented to determine the reduction in drag due to lift in the presence of the ground. Both methods are based on an image-vortex representation of the ground plane (see Sketches (a), (b), (c), and (d) in Section 4.7). The method of Wieselsberger from Reference 1 considers only the effects of the bound image vortex. However, the method of Tani (References 2 and 3) considers the effects of both the bound and trailing image vortices.

The change in drag due to lift resulting from trimming the pitching-moment increment due to ground effect consists of a synthesis of material presented in other sections.

DATCOM METHODS

Change in Trim Drag Due to Ground Plane

Procedures for calculating the drag increment due to longitudinally trimming a vehicle are presented in Section 4.5.3.2. To determine trim drag in ground effect, the pitching-moment increment due to ground effect $(\Delta C_m)_G$ of Equation 4.7.3-a is added to the vehicle pitching moment out of ground effect. The combined pitching moment is then used in the standard procedure for determining trim drag out of ground effect (Section 4.5.3.2).

Change, Due to Ground Effect, of Drag Due to Lift of the Wing

According to Reference 3, the two methods presented herein for predicting ground effects on drag due to lift give nearly identical results at moderate to large ground heights. Therefore, Method 1 is preferred for its simplicity. At ground heights within the approximate range $0.3 \geq h/b > 0$ however, Method 2 should be used, since its accuracy is significantly better than that of Method 1 in this range. Both methods have been modified slightly to include the effects of wing dihedral.

Neither Method 1 nor Method 2 is very successful in estimating ground effects on drag with flaps down. At low heights above the ground, Method 2 gives results closer to experimental data than does Method 1. although both methods underestimate the reduction of drag in ground effect. At intermediate heights above the ground, the two methods yield nearly equivalent results.

Method 1

The change in wing drag due to lift caused by ground effect as determined by Wieselsberger (Reference 1) is given by

$$\left(\Delta C_{D_L}\right)_G = -\frac{\sigma C_L^2}{\pi A} \qquad 4.7.4\text{-a}$$

where

- σ is Prandtl's interference coefficient from multiplane theory and is obtained from Figure 4.7.1-19 as a function of wing height above the ground.
- C_L is the lift coefficient of the wing out of ground effect, obtained from test data or estimated by using the method of Section 4.1.3.3.
- A is the wing aspect ratio.

The total drag of a wing-body configuration in ground effect is then given by

$$\left(C_{D_{WB}}\right)_G = C_{D_{WB}} + \left(\Delta C_{D_L}\right)_G \qquad 4.7.4\text{-b}$$

where $C_{D_{WB}}$ is the total drag coefficient of the wing-body configuration out of ground effect obtained from test data or Section 4.3.3.2, and $\left(\Delta C_{D_L}\right)_G$ is obtained by using either Method 1 or 2.

Method 2

The reduction in drag due to lift as determined by the method of Tani (References 2 and 3) is given by

$$\left(\Delta C_{D_L}\right)_G = -\frac{\sigma C_L^2}{\pi A} - \left(C_D - \frac{\sigma C_L^2}{\pi A}\right)\frac{\tau T C_L}{57.3} \qquad 4.7.4\text{-c}$$

where

- C_D is the wing-alone drag coefficient corresponding to C_L out of ground effect, obtained from test data or estimated by the method of Section 4.1.5.2, i.e., $\left(C_{D_0} + C_{D_L}\right)$.
- τ accounts for the condition of finite span and is obtained from Figure 4.7.1-16 as a function of wing height above the ground.

T accounts for the reduction of the longitudinal velocity and is obtained from Figure 4.7.1-20 as a function of wing height above the ground.

All remaining parameters have been defined in Method 1 above.

The total drag of a wing-body configuration in ground effect is calculated by using the procedure in Method 1 above; i.e.,

$$\left(C_{D_{WB}}\right)_G = C_{D_{WB}} + \left(\Delta C_{D_L}\right)_G \qquad 4.7.4\text{-b}$$

The sample problems presented below illustrate the use of both Methods 1 and 2 applied to a wing-alone configuration. It should be noted that, in applying Method 2 to a wing-body configuration, the value of C_D in Equation 4.7.4-c is that of the wing alone. If no test data are available for the particular configuration, the wing drag may be estimated by using the method of Section 4.1.5.2, as noted previously. On the other hand, if only wing-body test data are available, it is suggested that the wing-body result be used instead of attempting to estimate a wing-alone value.

Sample Problems

1. Method 1

Given: The sweptback wing of Reference 4

Wing Characteristics:

$A = 4.01$ $\quad b = 11.375$ ft $\quad \bar{c} = 2.89$ ft $\quad \Lambda_{c/4} = 40^o$

Additional Characteristics:

$h = 1.97$ ft

The following drag variation with lift (out of ground effect) from Reference 4:

C_L	0.10	0.20	0.40	0.60	0.70	0.80
C_D Wing Alone	0.0063	0.0093	0.0220	0.0400	0.0500	0.0660

Compute:

$h/(b/2) = (2)(1.97)/11.375 = 0.346$

$\sigma = 0.33$ (Figure 4.7.1-19)

Solution:

$$\left(\Delta C_{D_L}\right)_G = -\frac{\sigma C_L^2}{\pi A} \quad \text{(Equation 4.7.4-a)}$$

$$= -\frac{0.33\, C_L^2}{(3.14)(4.01)}$$

$$= -0.0262\, C_L^2$$

① C_L	② C_L^2	③ $\left(\Delta C_{D_L}\right)_G$ (Eq. 4.7.4-a) -0.0262 ②
0.10	0.01	−0.0003
0.20	0.04	−0.0010
0.40	0.16	−0.0042
0.60	0.36	−0.0094
0.70	0.49	−0.0128
0.80	0.64	−0.0168

The calculated results are compared with test values from Reference 4 in Sketch (a).

2. Method 2

Given: The same configuration as that of Sample Problem 1

Compute:

$$\frac{\sigma C_L^2}{\pi A} = 0.0262\, C_L^2 \quad \text{(see Sample Problem 1)}$$

$r = 0.712$ (Figure 4.7.1-16)

$T = 3.24$ (Figure 4.7.1-20)

$rT = (0.712)(3.24) = 2.31$

Solution.

$$\left(\Delta C_{D_L}\right)_G = -\frac{\sigma C_L^2}{\pi A} - \left(C_D - \frac{\sigma C_L^2}{\pi A}\right)\frac{rTC_L}{57.3} \quad \text{(Equation 4.7.4-c)}$$

$$= -0.0262\,C_L^2 - \left(C_D - 0.0262\,C_L^2\right)(0.0403)\,C_L$$

① C_L	② C_D Wing Alone	③ C_L^2	④ $\frac{\sigma C_L^2}{\pi A}$ 0.0262 ③	⑤ $\left(C_D - \frac{\sigma C_L^2}{\pi A}\right)$ ② − ④	⑥ $\left(C_D - \frac{\sigma C_L^2}{\pi A}\right)\frac{rTC_L}{57.3}$ 0.0403 ⑤ ①	⑦ $\left(\Delta C_{D_L}\right)_G$ (Eq. 4.7.4-c) − ④ − ⑥
0.10	0.0053	0.01	0.0003	0.0050	0.00002	−0.0003
0.20	0.0093	0.04	0.0010	0.0083	0.0001	−0.0011
0.40	0.0220	0.16	0.0042	0.0178	0.0003	−0.0045
0.60	0.0400	0.36	0.0094	0.0306	0.0007	−0.0101
0.70	0.0500	0.49	0.0128	0.0372	0.0011	−0.0139
0.80	0.0650	0.64	0.0168	0.0482	0.0016	−0.0184

The calculated results are compared with test values from Reference 4 in Sketch (a).

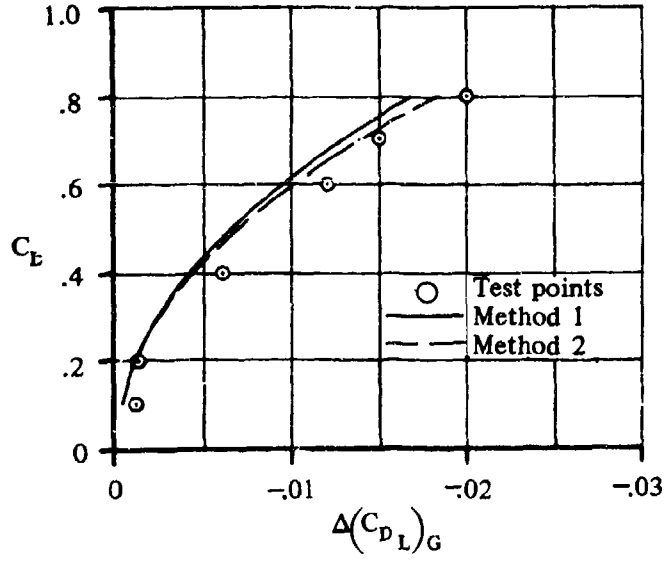

SKETCH (a)

REFERENCES

1. Wieselsberger, C.: Wing Resistance Near the Ground. NACA TM 77, 1922. (U)

2. Tani, I., Taima, M., and Simidu, S.: The Effect of Ground on the Aerodynamic Characteristics of a Monoplane Wing. Tokyo Univ. Aeronautical Research Inst. Report 156, 1937. (U)

3. Tani, I., Itokawa, H., and Taima, M.: Further Studies of the Ground Effect on the Aerodynamic Characteristics of an Aeroplane, with Special Reference to Tail Moment. Tokyo Univ. Aeronautical Research Inst. Report 158, 1937. (U)

4. Furlong, G. C., and Bollech, T. V.: Effect of Ground Interference on the Aerodynamic and Flow Characteristics of a 42° Sweptback Wing at Reynolds Numbers Up to 6.8×10^6. NACA TR 1218, 1955. (U)

4.8 LOW-ASPECT-RATIO WINGS AND WING-BODY COMBINATIONS AT ANGLE OF ATTACK

During recent years much work has been done on problems associated with the design and operation of advanced flight vehicles. These vehicles include re-entry configurations and those designed for hypersonic cruise. The requirement that these vehicles operate within the atmosphere at hypersonic speeds necessitates the use of configurations that are not well suited for subsonic flight at low altitudes. The configurations proposed for this type of mission feature, for the most part, extremely low aspect ratios of the order of two or less, and thick, generously-rounded lifting surfaces. These configurations also often have large blunt bases.

The subsonic flow about these vehicles is extremely complex, so much so that in most cases the use of available theoretical methods does not result in satisfactory estimates of the aerodynamic characteristics for this type of vehicle. The methods presented in this section for estimating the aerodynamic characteristics of advanced flight vehicles at subsonic speeds are necessarily semiempirical in nature. The methods are based on test data, which have been correlated with the aid of the extension of available theory. A large portion of the material is related to delta and modified-delta configurations, since a major portion of the pertinent theory and test results relate to these planforms.

In the following group of sections (4.8.1, 4.8.2, and 4.8.3) methods are presented for estimating the normal force, axial force, and pitching moment on specific types of advanced flight vehicles at angles of attack up to 20°.

The aerodynamic forces acting on the vehicle are illustrated in figure 4.8-12. In the lift axis system, the force is resolved into components perpendicular to and parallel to the free stream, called the lift and drag, respectively. In the normal-force axis system, the force is resolved into components perpendicular to and parallel to the zero-normal-force reference plane, called the normal force and axial force, respectively. For unsymmetrical configurations the zero-normal-force reference plane is inclined at some angle α_{N_0} to the body horizontal plane. The body horizontal plane passes through the most forward point on the vehicle nose and its inclination to the free stream defines the angle of attack α in the familiar lift axis system (see figure 4.8-12). The normal-force and axial-force coefficients and the angle of attack of unsymmetrical configurations are designated as $C_{N'}$, $C_{X'}$, and α', respectively. For symmetrical configurations $\alpha_{N_0} = 0$ and $\alpha' = \alpha$, and the zero-normal-force reference plane coincides with the body horizontal plane of symmetry. For symmetrical configurations the normal-force and axial-force ceofficients are designated as C_N and C_X, respectively.

The equations relating lift, drag, normal force, and axial force are as follows:

For unsymmetrical configurations

$$C_{N'} = C_L \cos \alpha' + C_D \sin \alpha'$$

$$C_{X'} = -C_D \cos \alpha' + C_L \sin \alpha'$$

$$C_L = C_{N'} \cos \alpha' + C_{X'} \sin \alpha'$$

$$C_D = -C_{X'} \cos \alpha' + C_{N'} \sin \alpha'$$

For symmetrical configurations (symmetry about the Z = 0 plane)

$$C_N = C_L \cos\alpha + C_D \sin\alpha$$

$$C_X = -C_D \cos\alpha + C_L \sin\alpha$$

$$C_L = C_N \cos\alpha + C_X \sin\alpha$$

$$C_D = -C_X \cos\alpha + C_N \sin\alpha$$

The pitching-moment coefficient at a specified angle is independent of the axis system.

The normal-force axis system is used throughout the following group of sections, since it was found to be more convenient in the correlation of the available test data.

Many of the available test results do not separate the base pressure from other aerodynamic forces. Therefore, the total axial force is analyzed in Section 4.8.2 by separating it into a component produced by base pressure plus a component related to the viscous forces acting on areas other than the base.

A general notation list is included in this section for all sections included under Section 4.8.

Sketches showing planform geometry for nearly all the configurations analyzed in Sections 4.8.1.1 through 4.8.3.2 are presented in table 4.8-A.

NOTATION

SYMBOL	DEFINITION	SECTION
A	aspect ratio of surface	4.8.1.2 4.8.2.2 4.8.3.2
B	blunting parameter, $\frac{\tan\theta}{\sqrt{\tan^2\theta + 2}}$	4.8.3.2
b	surface span	4.8.1.2 4.8.2.2 4.8.3.2
b_b	maximum span of base	4.8.2.1 4.8.2.2
c_r	surface root chord	4.8.1.2 4.8.3.2
h_b	maximum height of base	4.8.1.1 4.8.2.1 4.8.2.2

SYMBOL	DEFINITION	SECTION
ℓ_B	total length of body	4.8.1.1 4.8.2.1
M	Mach number	4.8.1.2 4.8.2.2 4.8.3.2
N'	normal force, perpendicular to zero-normal-force reference plane (unsymmetrical configuration)	4.8.2.2
P	perimeter of base (see figure 4.8.2.1-7a)	4.8.2.1
q_∞	free-stream dynamic pressure	4.8.2.2
R_ℓ	Reynolds number	4.8.1.2 4.8.2.2 4.8.3.2
$R_{\frac{1}{3}LE}$	effective radius of round leading-edged wing, perpendicular to leading edge at $c_r/3$ from the nose (see figure 4.8.1.2-11b)	4.8.1.2 4.8.2.2
S	planform area	4.8.1.2 4.8.2.1 4.8.2.2 4.8.3.2
S_b	base area	4.8.2.1 4.8.2.2
S_F	projected frontal area perpendicular to zero-normal-force reference plane	4.8.1.2 4.8.2.2 4.8.3.2
S_{ref}	reference area	4.8.1.2 4.8.2.1 4.8.2.2
S_{wet}	wetted area, excluding base area	4.8.2.1
V_∞	free-stream velocity	4.8.1.1
v	blunting parameter, $\sqrt{1 - \frac{4 \tan \theta}{A}}$	4.8.3.2
X	axial force parallel to zero-normal-force reference plane (unsymmetrical configuration)	4.8.2.2

SYMBOL	DEFINITION	SECTION
$\left[\left(\frac{X'}{N'}\right)_{calc}\right]_{20}$	calculated value of parameter at $\alpha' = 20^{\circ}$	4.8.2.2
$x_{c.p.}$	chordwise distance from the wing apex to the wing center of pressure, positive for c.p. aft of apex	4.8.3.2
$(x_{c.p.})_{\Delta}$	value of parameter for thin, pointed-nose delta wing	4.8.3.2
$\Delta(x_{c.p.})_{B}$	shift in thin delta wing c.p. due to nose blunting	4.8.3.2
$\Delta(x_{c.p.})_{t}$	shift in pointed-nose delta wing c.p. due to wing thickness	4.8.3.2
x_m	axial distance from the body nose to the chosen moment center	4.8.3.2
$\bar{z}_{base}$	vertical distance, measured normal to the body horizontal plane, between the centroid of the base area and the body horizontal plane, positive as shown in figure 4.8-12	4.8.1.1
Z	normal-force non-linearity parameter	4.8.1.2
α	angle of attack, positive nose up	4.8.1.1
α_{N_0}	angle of attack at zero normal force	4.8.1.1 4.8.3.1
α'	angle of attack measured from zero-normal-force reference plane, $\alpha - \alpha_{N_0}$ (see figure 4.8-12)	4.8.1.1 4.8.2.2 4.8.3.2
α_0	angle of attack at zero lift	4.8.1.1
$\delta_{\perp}$	total wedge angle of sharp-leading-edged wing, perpendicular to leading edge at $c_r/3$ from nose (see figure 4.8.1.2-11a)	4.8.1.2
$\delta_{e_{\perp}}$	effective wedge angle of sharp-leading-edged wing, perpendicular to leading edge at $c_r/3$ from nose (see figure 4.8.1.2-11a)	4.8.1.2
$\delta_{L_{\perp}}$	average lower-surface angle of sharp leading-edged wing, perpendicular to wing leading edge at $c_r/3$ from nose (see figure 4.8.1.2-11a)	4.8.1.2
δ_L	lower-surface angle of round-leading-edged wing, perpendicular to wing leading edge at $c_r/3$ from nose (see figure 4.8.1.2-11b)	4.8.1.2
θ	wing semiapex angle	4.8.3.2

SYMBOL	DEFINITION	SECTION
Λ_{LE}	sweepback angle of wing leading edge	4.8.1.2 4.8.2.2 4.8.3.2
λ	taper ratio, $\frac{\text{tip chord}}{\text{root chord}}$	4.8.1.2 4.8.2.2 4.8.3.2
C_D	drag coefficient, $\frac{\text{drag}}{qS}$	4.8.1.1
C_f	skin-friction coefficient for incompressible flow	4.8.2.1
ΔC_f	increment in skin-friction coefficient for incompressible flow	4.8.2.1
C_L	lift coefficient, $\frac{\text{lift}}{qS}$	4.8.1.1
C_m	pitching-moment coefficient, $\frac{\text{pitching moment}}{qS\,c_r}$	4.8.3.2
$C_{m_{N_0}}$	pitching-moment coefficient at zero normal force	4.8.3.1 4.8.3.2
C_N	normal-force coefficient, $\frac{N}{qS}$, for a symmetrical configuration	4.8.1.1
$C_{N'}$	normal-force coefficient, $\frac{N'}{qS}$, for an unsymmetrical configuration	4.8.1.1 4.8.1.2 4.8.2.2 4.8.3.2
$(C_{N'})_{20}$	value of coefficient at $\alpha' = 20^\circ$	4.8.1.2
$(C_{N'_{calc}})_{20}$	calculated value of coefficient at $\alpha' = 20^\circ$	4.8.1.2
$\left[\frac{C_{N'}}{C_{N'_{calc}}}\right]_{20}$	normal-force-coefficient correlation factor	4.8.1.2
$\left[(C_{N'})_{20}\right]_t$	value of $(C_{N'})_{20}$ corrected for rounded leading edges	4.8.1.2
$(C_{N_\alpha})'$	rate of change of normal-force coefficient with angle of attack $\frac{dC_{N'}}{d\alpha'}$	4.8.1.2

SYMBOL	DEFINITION	SECTION
$\left(C_{N\alpha}\right)'_{N_0}$	value of derivative at zero normal force	4.8.1.2
$\left(C_{N\alpha_{calc}}\right)'_{N_0}$	calculated value of the derivative	4.8.1.2
$\left[\frac{C_{N\alpha}}{C_{N\alpha_{calc}}}\right]'_{N_0}$	normal-force-curve-slope correlation factor	4.8.1.2
C_{p_b}	base pressure coefficient, $\frac{p_b - p_\infty}{q_\infty}$	4.8.2.1 4.8.2.2
$C_{p_{b_{N_0}}}$	value of coefficient at zero normal force	4.8.2.1 4.8.2.2
$\left(C_{p_b}\right)_{\alpha'}$	value of coefficient at given angle of attack, α'	4.8.2.2
$C_{p_{b_{20}}}$	value of coefficient at $\alpha' = 20^o$	4.8.2.2
$\frac{C_{p_{b_{20}}}}{C_{p_{b_{N_0}}}}$	pressure-coefficient-ratio correlation factor	4.8.2.2
C_X	axial-force coefficient, $\frac{X}{qS}$, for a symmetrical configuration	4.8.1.1
$C_{X'}$	axial-force coefficient, $\frac{X'}{qS}$, for an unsymmetrical configuration	4.8.2.2
$\left(C_{X'}\right)_{N_0}$	value of coefficient at zero normal force	4.8.2.1 4.8.2.2
$\Delta C_{X'}$	increment in coefficient due to angle of attack	4.8.2.2
$\Delta C'_{X_{calc}}$	calculated value of the increment	4.8.2.2
$\left[\frac{\Delta C_{X'}}{\Delta C'_{X_{calc}}}\right]_{20}$	axial-force correlation factor at $\alpha' = 20^o$	4.8.2.2

SYMBOL	DEFINITION	SECTION
$\Delta C_{X_b'}$	increment in coefficient due to base pressure	4.8.2.1 4.8.2.2
$\Delta C_{X_{b_{N_0}}'}$	value of increment at zero normal force	4.8.2.1
$\left(\Delta C_{X_{b_\alpha}}\right)'$	value of increment at a given angle of attack, α'	4.8.2.2
$\Delta C_{X_f'}$	increment in coefficient due to skin friction	4.8.2.1
$\Delta C_{X_{f_{N_0}}'}$	value of increment at zero normal force	4.8.2.1

REFERENCES

1. Mantz, K., Seeger, D. B., and Ross, R.: Tests to Determine Subsonic Aerodynamic Characteristics of Hypersonic Re-Entry Configurations. ASD-TR-61-485, Supplement 1, 1963. (U)

2. Mantz, K., Seeger, D. B., and Ross, R.: Tests to Determine Subsonic Pressures, Forces and Moments Acting on a Hypersonic Re-Entry Configuration. ASD-TDR-62-270, Supplement 1, 1963. (U)

3. Mugler, J. P., Jr., and Olstad, W. B.: Static Longitudinal Aerodynamic Characteristics at Transonic Speeds of a Blunted Right Triangular Pyramidal Lifting Re-Entry Configuration for Angles of Attack up to 110°. NASA TN D-797, 1961. (U)

4. Ware, G. M.: Low-Subsonic-Speed Static Stability of Right-Triangular-Pyramid and Half-Cone Lifting Re-Entry Configurations. NASA TN D-646, 1961. (U)

5. Paulson, J. W.: Low-Speed Static Stability and Control Characteristics of a Model of a Right Triangular Pyramid Re-Entry Configuration. NASA Memo 4-11-59L, 1959. (U)

6. Olstad, W. B., Mugler, J. P., Jr., and Cahn, M. S.: Static Longitudinal and Lateral Stability Characteristics of a Right Triangular Pyramidal Lifting Re-Entry Configuration at Transonic Speeds. NASA TN D-655, 1961. (U)

7. Paulson, J. W., and Shanks, R. E.: Investigation of Low-Subsonic Flight Characteristics of a Model of a Hypersonic Boost-Glide Configuration Having a 78° Delta Wing. NASA TN D-894, 1961. (U)

8. Boisseau, P. C.: Investigation of the Low-Subsonic Flight Characteristics of a Model of a Re-Entry Vehicle with a Thick Flat 75° Swept Delta Wing and a Half-Cone Fuselage. NASA TN D-1007, 1962. (U)

9. Shanks, R. E.: Investigation of the Low-Subsonic Flight Characteristics of a Model of an All-Wing Hypersonic Boost-Glide Configuration Having Very High Sweep. NASA TN D-369, 1960. (U)

TABLE 4.8-A
CONFIGURATION SKETCHES

Ref.	Configuration	Sketch
1	D-1	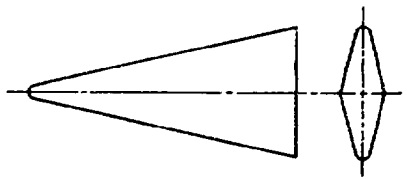
1	D-2	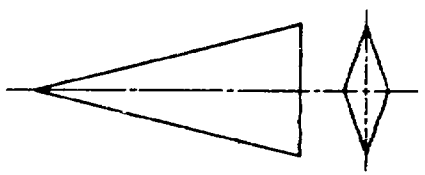
1	D-3	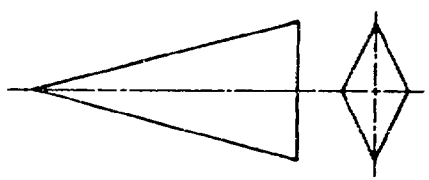
1	D-4	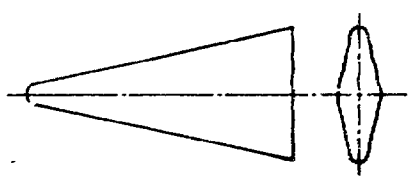

Ref.	Configuration	Sketch
1	D-5	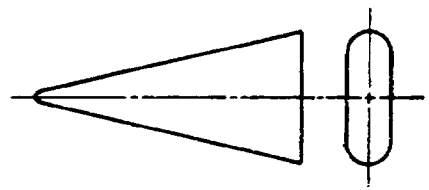
1	D-6	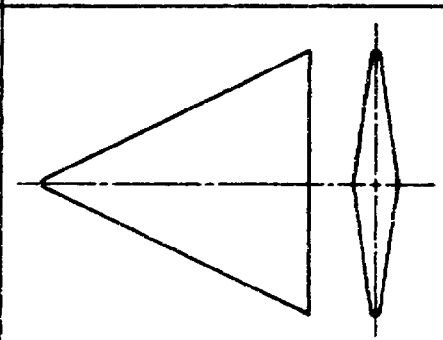
1	D-7	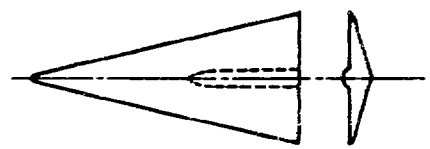
1	D-8	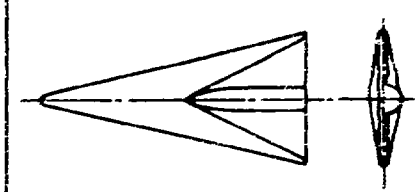

TABLE 4.8-A (CONTD)

Ref.	Configuration	Sketch
1	D-9	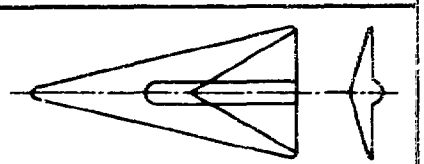
1	D-10	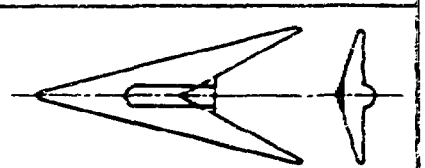
2	D-50	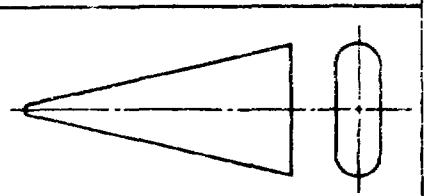
3	Blunted Right Triangular Pyramid	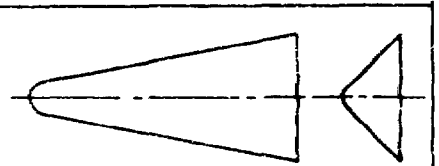
4	a	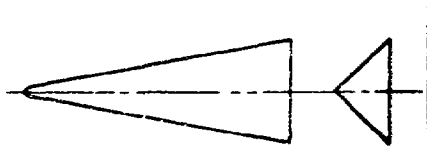

Ref.	Configuration	Sketch
4	b (basic)	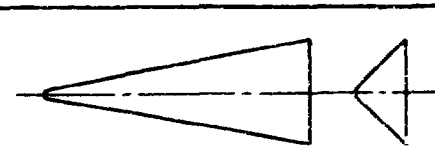
4	c (basic)	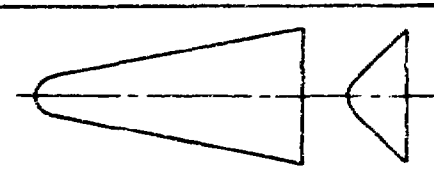
4	c (extended nose)	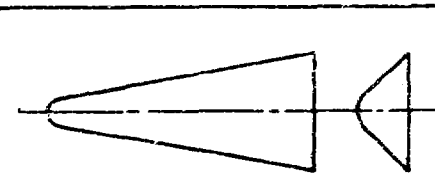
4	d	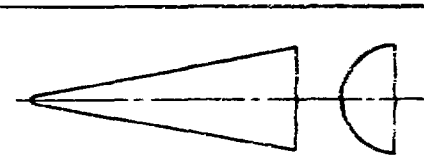
5	Right Triangular Pyramid	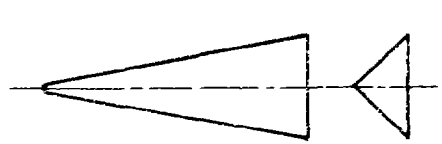

TABLE 4.8-A (CONTD)

Ref.	Configuration	Sketch
6	1	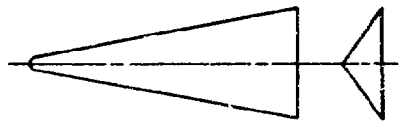
1	WB-1	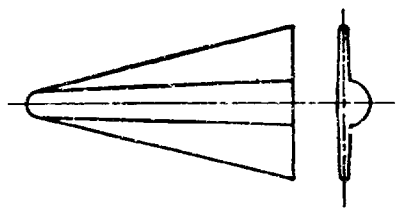
1	WB-2	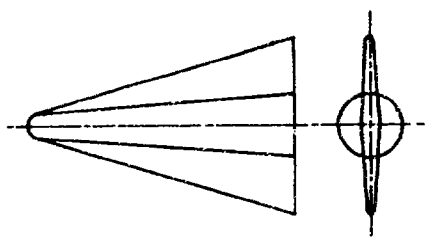
1	WB-3	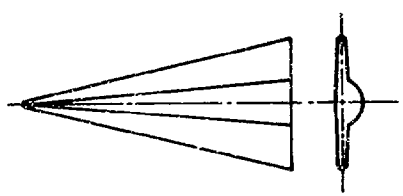

Ref.	Configuration	Sketch
1	WB-4	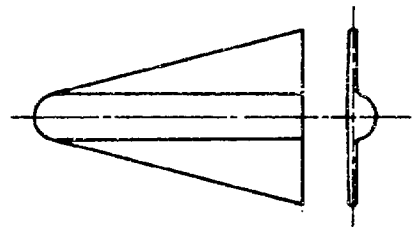
1	WB-5	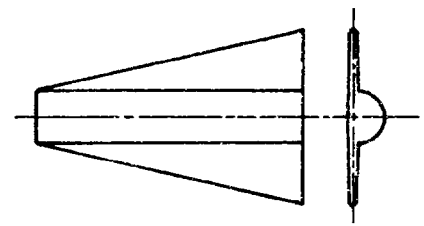
1	WB-6	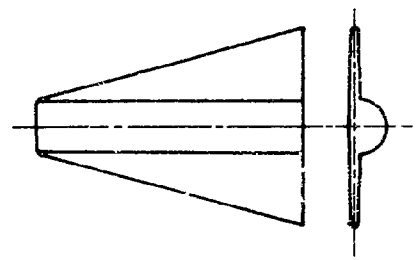
1	WB-7	

TABLE 4.8-A (CONTD)

Ref.	Configuration	Sketch
1	WB-8	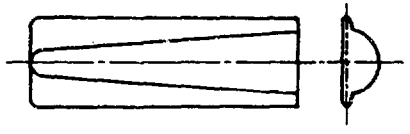
1	WB-9	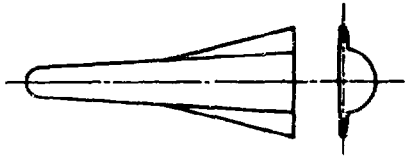
1	WB-10 (0)	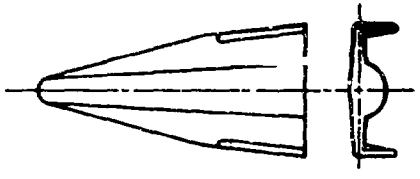
1	R-2	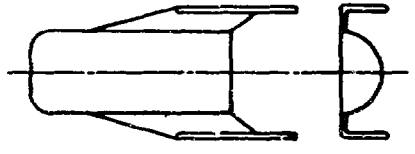

Ref.	Configuration	Sketch
1	R-3	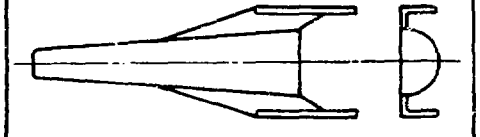
7	Delta Wing Boost-Glide	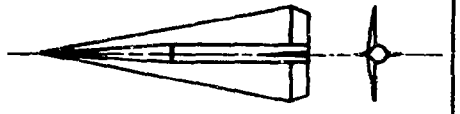
8	Delta Wing With Half-Cone Fuselage	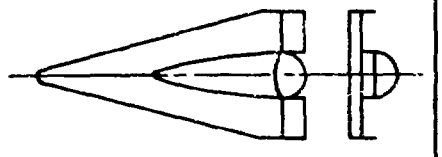
9	All-Wing Boost-Glide	

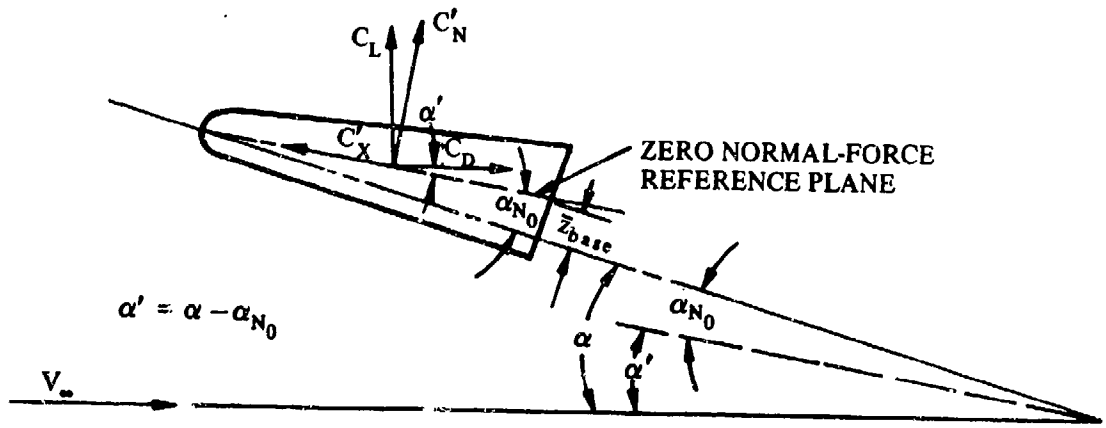

FIGURE 4.8-12 DEFINITION OF REFERENCE-AXIS SYSTEM

4.8.1 WING, WING-BODY NORMAL FORCE

4.8.1.1 WING, WING-BODY ZERO-NORMAL-FORCE ANGLE OF ATTACK

The longitudinal data for the low-aspect-ratio configurations are presented in terms of the normal-force and axial-force coefficients of a normal-force axis system rather than the more common lift and drag coefficients of the lift axis system. The problem arising with the normal-force axis system is that of defining a reference plane for the nonsymmetrical configurations which specifies the direction of the normal force and axial force. This is accomplished by defining a reference axis system which is oriented with respect to the particular configuration so that the normal force is zero at zero angle of attack.

The defined normal-force axis system is illustrated in figure 4.8-12. The normal-force coefficient $C_{N'}$ is perpendicular to and the axial-force coefficient $C_{X'}$ is parallel to a reference plane which passes through the centroid of the base area and the most forward point on the vehicle nose. For symmetrical configurations this is the plane of symmetry.

The zero-normal-force angle of attack α_{N_0} is defined as the angle of attack at which the normal force acting on the body is zero. For a symmetrical configuration, the normal force is zero when the plane of symmetry is parallel to the free stream. Therefore, for symmetrical configurations $\alpha_{N_0} = 0$. For unsymmetrical configurations, α_{N_0} may be related to an arbitrary plane as shown in figure 4.8-12. This arbitrary reference plane is chosen so that its inclination to the free stream defines the angle of attack in the familiar lift axis system. It is referred to as the body horizontal plane.

From the geometry of figure 4.8-12, the angle of attack α' in the defined normal-force axis system is

$$\alpha' = \alpha - \alpha_{N_0} \qquad 4.8.1.1\text{-a}$$

where

α is the angle of attack, positive nose-up, measured from the free stream to the body horizontal axis.

α_{N_0} is the zero-normal-force angle of attack, measured between the reference plane and the body horizontal plane, positive as shown in figure 4.8-12.

DATCOM METHOD

The zero-normal-force angle of attack is determined from the configuration geometry as follows:

Step 1. Determine the location of the centroid of the base area and the location of the most forward point on the vehicle nose.

Step 2. Determine α_{N_0} as the angle between the line connecting the centroid of the base and the most forward point on the nose, and the horizontal plane of the body.

Values of the zero-normal-force angle of attack calculated by using this method are compared with test results in table 4.8.1.1-A. Many of the configurations tested were complex re-entry shapes, and the reader should refer to table 4.8-A for a more complete description of the model. Unfortunately, there are not enough data available to illustrate a consistent effect of planform geometry on the zero-normal-force angle of attack.

Sample Problems

1. Given: The right-triangular pyramidal body designated as configuration 1 of reference 6.

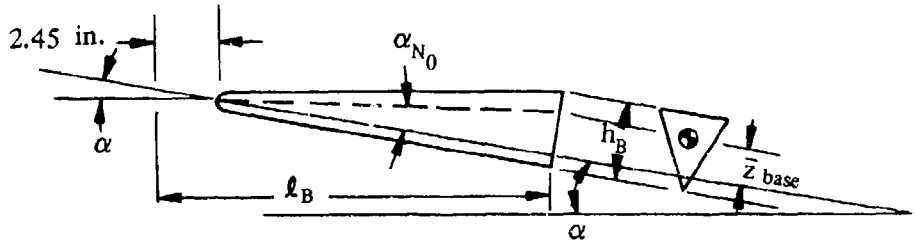

ℓ_B = 31.55 in. Nose radius = 0.1875 in. h_b = 6.44 in.

Compute:

Centroid of base

$$\bar{z}_{base} = \frac{2}{3} h_b - \text{nose radius} = \frac{2}{3}(5.44) - 0.1875 = 4.106 \text{ in.}$$

Solution:

$$\alpha_{N_0} = \tan^{-1} \frac{\bar{z}_{base}}{\ell_B - 2.45} = \tan^{-1} \frac{4.106}{31.55 - 2.45} = \tan^{-1} 0.1412$$

$$= 8.04^{\circ}$$

This compares with a test value of $\alpha_{N_0} = 8.6^{\circ}$ from reference 6.

2. Given: A re-entry configuration of the wing-body group of reference 1 designated WB-10(0). This is a round-nosed, wing-body model of 75° sweep back with a semicircular-body cross section at the point of maximum thickness and with twin vertical tails.

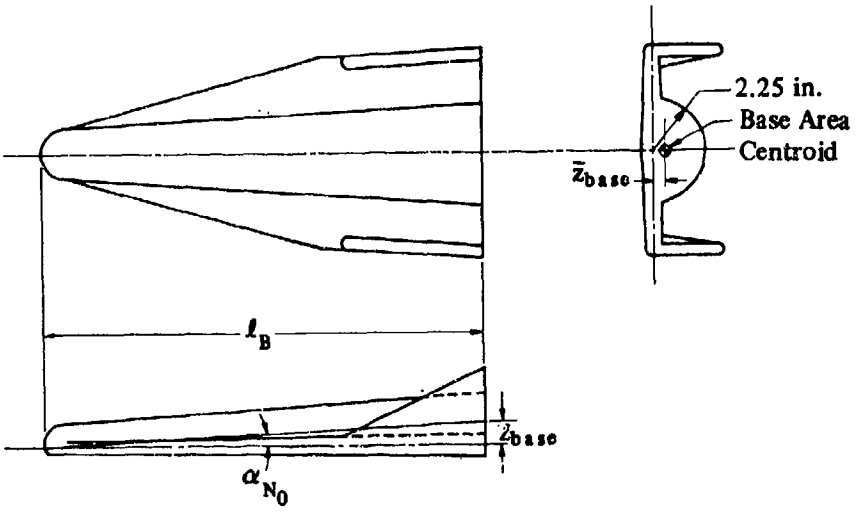

ℓ_B = 20.0 in. $\quad\quad$ $\bar{z}_{base}$ = 0.68 in.

Solution:

$$\alpha_{N_0} = \tan^{-1} \frac{\bar{z}_{base}}{\ell_B} = \tan^{-1} \frac{0.68}{20.0} = \tan^{-1} 0.0340$$

$$= 1.95^{o}$$

This compares with a test value of $\alpha_{N_0} = 0.30^{o}$ from reference 1.

REFERENCES

1. Mantz, K., Seager, D. B., and Ross, R.: Tests to Determine Subsonic Aerodynamic Characteristics of Hypersonic Re-Entry Configurations. ASD-TR-61-485, Supplement 1, 1963. (U)

2. Mantz, K., Seager, D. B., and Ross, R.: Tests to Determine Subsonic Pressures, Forces and Moments Acting on a Hypersonic Re-Entry Configuration. ASD:—TDR-62-270, Supplement 1, 1963. (U)

3. Paulson, J. W.: Low-Speed Static Stability and Control Characteristics of a Right Triangular Pyramid Re-Entry Configuration. NASA Memo 4-11-59L, 1959. (U)

4. Boisseau, P. C.: Investigation of the Low-Subsonic Flight Characteristics of a Model of a Re-Entry Vehicle with a Thick Flat 75° Swept Delta Wing and a Half-Cone Fuselage. NASA TN D-1007, 1962. (U)

5. Ware, G. M.: Low-Subsonic-Speed Static Stability of Right-Triangular-Pyramid and Half-Cone Lifting Re-Entry Configurations. NASA TN D-646, 1961. (U)

6. Olstad, W. B., Mugler, J. P., Jr., and Cahn, M. S.: Static Longitudinal and Lateral Stability Characteristics of a Right Triangular Pyramidal Lifting Re-Entry Configuration at Transonic Speeds. NASA TN D-655, 1961. (U)

7. Mugler, J. P., Jr., and Olstad, W. B.: Static Longitudinal Aerodynamic Characteristics at Transonic Speeds of a Blunted Right Triangular Pyramidal Lifting Re-Entry Configuration for Angles of Attack up to 110°. NASA TN D-797, 1961. (U)

8. Paulson, J. W., and Shanks, R. E.: Investigation of Low-Subsonic Flight Characteristics of a Model of a Hypersonic Boost-Glide Configuration Having a 78° Delta Wing. NASA TN D-894, 1961. (U)

9. Wright Air Development Division: Unpublished data from the 5-foot wind tunnel, 1961. (U)

10. Seeger, D. B., and Meyer, J. E.: An Investigation of the Subsonic Aerodynamic Characteristics and the Landing Flare Maneuver for Hypersonic Re-Entry Configurations. ASD-TDR-62-271, 1962. (C) Title Unclassified

11. Shanks, R. E.: Investigation of the Low-Subsonic Flight Characteristics of a Model of an All-Wing Hypersonic Boost-Glide Configuration Having Very High Sweep. NASA TN D-369, 1960. (U)

TABLE 4.8.1.1-A

SUBSONIC ZERO-NORMAL-FORCE ANGLE OF ATTACK

DATA SUMMARY

Ref.	Configuration	α_{N_0} (deg) Calc.	α_{N_0} (deg) Test	$\Delta\alpha_{N_0}$ (deg) Calc.-Test
1	D-7	− 2.15	− 2.5	0.35
	D-8	0.20	− 0.20	0.40
	D-9	0	2.50	− 2.50
	D-10	− 1.45	− 1.60	0.15
	WB-1	1.35	1.00	0.35
	WB-3	1.46	1.70	− 0.24
	WB-4	1.35	− 0.30	1.65
	WB-5	1.21	0.70	0.51
	WB-6	1.21	0.70	0.51
	WB-7	1.63	1.20	0.43
	WB-8	1.57	0.90	0.67
	WB-9	2.12	1.90	0.32
	WB-10(0)	1.95	0.30	1.65
	R-2	3.79	2.30	1.49
	R-3	2.62	2.00	0.62
3	Rt. triangular pyramid	7.40	5.20	2.20
4	Delta wing w/half-cone fuselage	0.66	0.40	0.26
5	a	7.23	5.50	1.73
	b (basic)	6.44	6.50	− 0.06
	c (basic)	7.15	10.20	− 3.05
	d	4.40	4.60	− 0.20
6	Rt. triangular pyramid	8.04	8.60	− 0.56
7	Blunted right triangular pyramid	6.91	6.30	0.61
8	Delta-wing boost-glide	− 0.20	0.60	− 0.80
9	W-II E-3	− 1.80	− 2.00	0.20
	W-III E-3	2.40	1.80	0.60

4.8.1.2 WING, WING-BODY NORMAL-FORCE VARIATION WITH ANGLE OF ATTACK

A. SUBSONIC

This section presents a method for estimating the normal-force variation with angle of attack for a delta- or modified-delta-planform re-entry configuration at subsonic speeds.

The subsonic normal-force characteristics of thin delta wings at small angles of attack can be satisfactorily predicted through the use of linearized theory, which assumes that the flow is unseparated and that the cross-flow components are negligible. At higher angles ($\alpha \geq 5^{o}$, approximately) both cross-flow and separation phenomena become important and these assumptions are no longer valid. The normal force tends to increase more rapidly with angle of attack as the angle is increased.

A major factor influencing the normal-force characteristics of delta wings is leading-edge geometry. Sharp leading edges influence relatively large amounts of air and the corresponding variation of the normal force with angle of attack tends to be high. Rounded leading edges affect a smaller amount of air and the normal-force-curve slope is consequently less.

The method presented herein is taken from reference 1, and is based on a study of test data on low-aspect-ratio delta wings with thick and thin surfaces, with sharp and rounded leading edges, and with varying degrees of nose bluntness. Thin, sharp-leading-edged delta wings were selected as "reference wings," and theoretical relationships were written for the normal-force characteristics of these planforms. The normal-force characteristics of all the test configurations were then calculated by using these "reference wing" relationships, and any deviation between the calculated and the test values was related to the geometry of the wing leading edge. It was found that satisfactory correlation could be obtained by relating the deviation in normal-force characteristics to the leading-edge geometry in a plane normal to the wing leading edge and located one-third the length of the root chord aft of the nose.

Design charts are presented for estimating the normal-force-curve slope at $C_N' = 0$, the value of C_N' at $\alpha' = 20^{o}$, and the characteristics of the normal-force variation with angle of attack. The correlation parameters used to develop these charts are leading-edge radius and leading-edge angle for round and sharp leading edges, respectively. It should be noted that as the leading-edge radius approaches zero, the normal-force-curve slope at $C_N' = 0$, the normal force at $\alpha' = 20^{o}$, and the normal-force-variation parameter all approach the respective values for a sharp leading edge. Therefore, a configuration with a small leading-edge radius can be analyzed as one having a sharp leading edge.

For configurations with round leading edges, an empirical correction factor is presented to account for the reduction in normal force at higher angles of attack as the wing thickness is increased. This separate correlation is required, since the limited number of test data for very thick delta wings does not correlate well with the thin wing results.

DATCOM METHOD

The normal-force variation with angle of attack for a delta or modified-delta configuration at low speeds, based on the reference area (usually the planform area), is obtained from the procedure outlined in the following steps:

Step 1. Determine the effective leading edge angle. δ_{e_1} for sharp leading edges or the effective

leading-edge radius $R_{\frac{1}{3}LE}$ and lower surface angle δ_L for round leading edges. These parameters are functions of the configuration geometry in a plane normal to the leading edge at $\frac{1}{3} c_r$ from the nose. The applicable configuration geometry is illustrated on figures 4.8.1.2-11a and 4.8.1.2-11b.

Step 2. Determine the normal-force-curve slope at zero normal force ($C_{N'} = 0$) by

$$\left(C_{N_\alpha}\right)'_{N_0} = \left(\frac{C_{N_\alpha}}{C_{N_{\alpha_{calc}}}}\right)'_{N_0} \left(C_{N_{\alpha_{calc}}}\right)'_{N_0} \quad \text{(per radian)} \qquad 4.8.1.2\text{-a}$$

where

$\left(C_{N_\alpha}\right)'_{N_0}$ is the normal-force-curve slope at zero normal force $\left(\frac{\partial C_{N'}}{\partial \alpha'}\right)_{N_0}$

$\left[\frac{C_{N_\alpha}}{C_{N_{\alpha_{calc}}}}\right]'_{N_0}$ is the empirical correlation factor of normal-force-curve slope for delta or modified-delta configurations. It is presented as a function of the effective leading-edge angle for configurations with sharp leading edges in figure 4.8.1.2-12a, and as a function of the effective leading-edge radius for configurations with round leading edges in figure 4.8.1.2-12b.

$\left(C_{N_{\alpha_{calc}}}\right)'_{N_0}$ is the calculated normal-force-curve slope at zero normal force, given by

$$\left(C_{N_{\alpha_{calc}}}\right)'_{N_0} = \left(\frac{\pi A}{2} + 2\frac{S_F}{S_{ref}}\right)\frac{4}{4+A} \quad \text{(per radian)} \qquad 4.8.1.2\text{-b}$$

where

S_{ref} is the reference area.

S_F is the projected frontal area perpendicular to the zero-normal-force reference plane (projected frontal area at $C_{N'} = 0$).

A is the aspect ratio of the surface.

Step 3. Determine the normal-force coefficient at $\alpha' = 20^{o}$ by

$$\left(C_{N'}\right)_{20} = \left[\frac{C_{N'}}{C_{N'_{calc}}}\right]_{20} \left(C_{N'_{calc}}\right)_{20} \qquad 4.8.1.2\text{-c}$$

where

$\left(C_{N'}\right)_{20}$ is the normal-force coefficient at $\alpha' = 20^{o}$.

$\left[\frac{C_{N'}}{C_{N'_{calc}}}\right]_{20}$ is the empirical correlation factor of the normal force for delta and modified-delta configurations. It is presented as a function of the effective leading-edge angle for configurations with sharp leading edges in figure 4.8.1.2-13a, and as a function of the effective leading-edge radius for configurations with round leading edges in figure 4.8.1.2-13b.

$\left(C_{N'_{calc}}\right)_{20}$ is the calculated normal force at $\alpha' = 20^{o}$, given by

$$\left(C_{N'_{calc}}\right)_{20} = 2.195\left(\frac{A + 0.61}{A + 4.0}\right) \qquad 4.8.1.2\text{-d}$$

Step 4.* Determine the thickness correction to the normal force at $\alpha' = 20^{o}$ for configurations with round leading edges by

$$\left[\left(C_{N'}\right)_{20}\right]_{t} = \left(\frac{1 + \cos\delta_{L}}{2}\right)\left(C_{N'}\right)_{20} \qquad 4.8.1.2\text{-e}$$

where δ_{L} is the lower surface angle from step 1 and $\left(C_{N'}\right)_{20}$ is obtained from step 3.

Step 5. Determine Z, the empirical, nonlinear-normal-force correction factor. This parameter is obtained as a function of the effective leading-edge angle or the effective leading-edge radius for configurations with sharp leading edges or round leading edges, respectively, from figure 4.8.1.2-14.

Step 6. The variation of the normal force with angle of attack is given by:

For round-leading-edged configurations

$$C_{N'} = \left(C_{N_{\alpha}}\right)'_{N_0}\alpha' + 8.21\left\{\left[\left(C_{N'}\right)_{20}\right]_{t} - 0.349\left(C_{N_{\alpha}}\right)'_{N_0}\right\}\left[Z + 2.81(1 - Z)\alpha'\right]\alpha'^{2} \qquad 4.8.1.2\text{-f}$$

*Step 4 is required only for configurations with round leading edges. For sharp-leading-edged configurations, go to step 5.

For sharp-leading-edged configurations the normal-force coefficient at $\alpha' = 20^{\circ}$ from step 3 $\left(C_{N'}\right)_{20}$ is used instead of the term $\left[\left(C_{N'}\right)_{20}\right]_t$ in the above equation.

α' in the above relation is in radians.

A comparison of the normal-force variation with angle of attack calculated by this method with test results is presented as table 4.8.1.2-A. The Reynolds-number range of the test data is not sufficient to allow analysis of the effect of Reynolds number on the normal force. However, over the angle-of-attack range of this method ($\alpha' \leq 20^{\circ}$), Reynolds-number effects should be negligible even for the thicker configurations.

Sample Problems

1. Round Leading Edge

Given: A delta model with a symmetrical diamond cross section and a blunt trailing edge. This is model D-6 of reference 6.

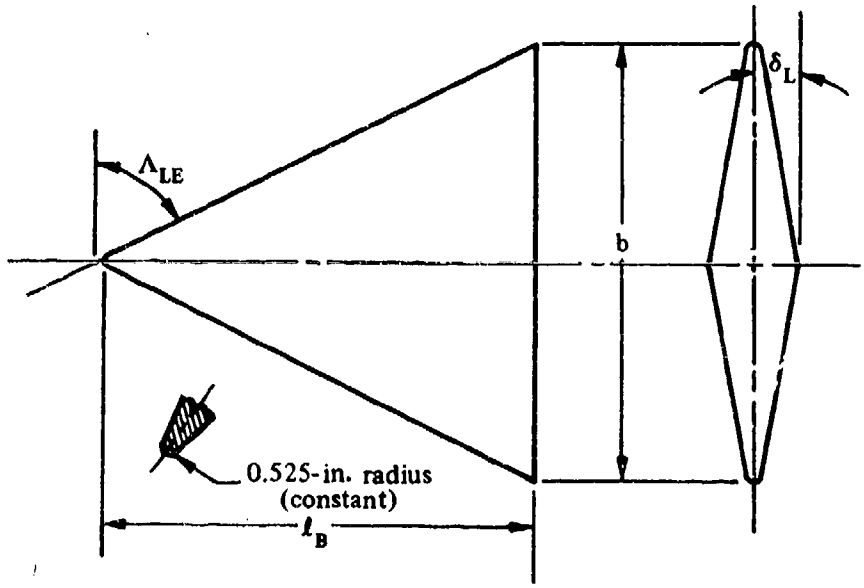

$A = 1.868$ $b = 22.116$ in. $S_{ref} = S = 261.95$ sq in. $\Lambda_{LE} = 65^{\circ}$

$S_F = 57.42$ sq in. (base area) $\delta_L = 9^{\circ}$ $R_{\frac{1}{3}\,LE} = 0.525$ in.

Compute:

Determine the normal-force-curve slope at $C_{N'} = 0$

$$R_{\frac{1}{3}\,LE}/b = 0.525/22.116 = 0.0237$$

$$\left[\frac{C_{N_\alpha}}{C_{N_{\alpha_{calc}}}}\right]'_{N_0} = 0.982 \quad \text{(figure 4.8.1.2-12b)}$$

$$\left(C_{N_{\alpha_{calc}}}\right)'_{N_0} = \left(\frac{\pi A}{2} + 2\frac{S_F}{S_{ref}}\right)\frac{4}{4+A} \qquad \text{(equation 4.8.1.2-b)}$$

$$= \left[\frac{\pi(1.868)}{2} + 2\,\frac{57.42}{261.95}\right]\frac{4}{4+1.868}$$

$$= 2.30 \text{ per rad}$$

$$(C_N)'_{N_0} = \left[\frac{C_{N_\alpha}}{C_{N_{\alpha_{calc}}}}\right]_{N_0} \left(C_{N_{\alpha_{calc}}}\right)'_{N_0} \qquad \text{(equation 4.8.1.2-a)}$$

$$= (0.982)\,(2.30)$$

$$= 2.26 \text{ per rad}$$

Determine the normal-force coefficient at $\alpha' = 20^o$

$$\left[\frac{C_{N'}}{C_{N'_{calc}}}\right]_{20} = 0.935 \quad \text{(figure 4.8.1.2-13b)}$$

$$\left(C_{N'_{calc}}\right)_{20} = 2.195\left(\frac{A + 0.61}{A + 4.0}\right) \qquad \text{(equation 4.8.1.2-d)}$$

$$= 2.195\left(\frac{1.868 + 0.61}{1.868 + 4.0}\right)$$

$$= 0.927$$

$$(C_{N'})_{20} = \left[\frac{C_{N'}}{C_{N'_{calc}}}\right]_{20} \left(C_{N'_{calc}}\right)_{20} \qquad \text{(equation 4.8.1.2-c)}$$

$$= (0.935)\,(0.927)$$

$$= 0.867$$

Determine the thickness correction factor to the normal force at $\alpha' = 20^{o}$ (round leading edge)

$$\left[(C_{N'})_{20}\right]_t = \left(\frac{1 + \cos \delta_L}{2}\right) (C_{N'})_{20} \quad \text{(equation 4.8.1.2-e)}$$

$$= \left(\frac{1 + \cos 9^{o}}{2}\right) (0.867)$$

$$= 0.862$$

Determine the empirical, nonlinear-normal-force correction factor

$Z = 0.945$ (figure 4.8.1.2-14)

Solution:

$$C_{N'} = \left(C_{N_\alpha}\right)'_{N_0} \alpha' + 8.21 \left\{\left[(C_{N'})_{20}\right]_t - 0.349 \left(C_{N_\alpha}\right)'_{N_0}\right\} \left[Z + 2.81(1 - Z)\alpha'\right] \alpha'^2$$

(equation 4.8.1.2-f)

$$= 2.26\ \alpha' + 8.21 \left\{0.862 - 0.349(2.26)\right\} \left[0.945 + 2.81(1 - 0.945)\alpha'\right] \alpha'^2$$

$$= 2.26\ \alpha' + 0.568\ \alpha'^2 + 0.0930\ \alpha'^3$$

①	②	③	④	⑤	⑥	⑦	⑧
α' (deg)	α' (rad)	α'^2 (rad^2)	α'^3 (rad^3)	$2.26\,\alpha'$ 2.26 ②	$0.568\,\alpha'^2$ 0.568 ③	$0.0930\,\alpha'^3$ 0.0930 ④	$C_{N'}$ (based on S) (eq. 4.8.1.2-f) ⑤ + ⑥ + ⑦
0	0	0	0	0	0	0	0
5	0.0873	0.00762	0.000665	0.1973	0.00433	0.00006	0.2017
10	0.1745	0.03045	0.005314	0.3944	0.01730	0.00049	0.4122
15	0.2618	0.06854	0.01794	0.5917	0.03893	0.001668	0.6323
20	0.3490	0.12180	0.04261	0.7887	0.06918	0.003953	0.8618

The calculated results are compared with test values from reference 6 in sketch (a) and in table 4.8.1.2-A.

2. Sharp Leading Edge

Given: A delta model with a symmetrical diamond cross section and a blunt trailing edge. This is model D-3 of reference 6.*

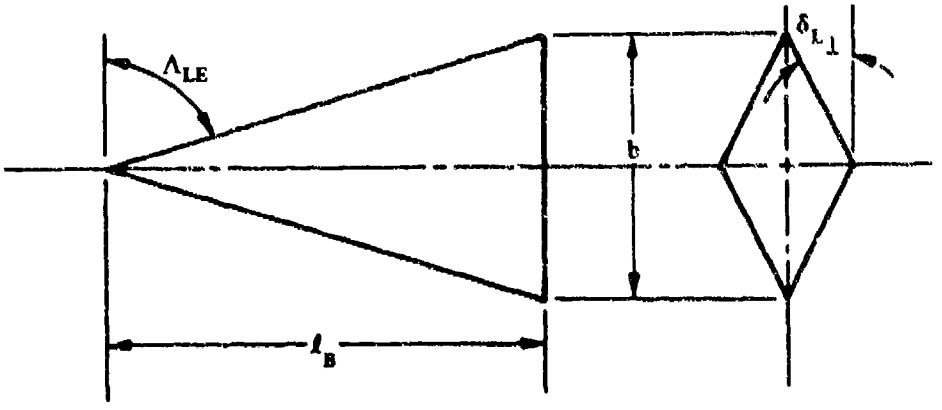

$A = 1.076$ $\quad b = 12.374$ in. $\quad S_{ref} = S = 142.30$ sq in. $\quad \Lambda_{LE} = 75^o$

$S_F = 44.20$ sq in. (base area) $\quad \delta_{L\perp} = 30^o \quad \delta_{\perp} = 60^o \quad \delta_{e\perp} = 90^o$

Compute:

Determine the normal-force-curve slope at $C_N' = 0$

$$\left[\frac{C_{N_\alpha}}{C_{N_{\alpha_{calc}}}}\right]_{N_0} = 0.775 \quad \text{(figure 4.8.1.2-12a)}$$

$$\left(C_{N_{\alpha_{calc}}}\right)'_{N_0} = \left(\frac{\pi A}{2} + 2\frac{S_F}{S_{ref}}\right)\frac{4}{4+A} \quad \text{(equation 4.8.1.2-b)}$$

$$= \left[\frac{\pi(1.076)}{2} + 2\frac{44.20}{142.30}\right]\frac{4}{4+1.076}$$

$$= 1.821 \text{ per rad}$$

$$\left(C_{N_\alpha}\right)'_{N_0} = \left[\frac{C_{N_\alpha}}{C_{N_{\alpha_{calc}}}}\right]_{N_0}\left(C_{N_{\alpha_{calc}}}\right)'_{N_0} \quad \text{(equation 4.8.1.2-a)}$$

$$= (0.775)(1.821)$$

$$= 1.411 \text{ per rad}$$

*Although this model has a very small nose radius (0.032 in.), it is analyzed as having a sharp leading edge.

Determine the normal-force coefficient at $\alpha' = 20^{o}$

$$\left[\frac{C_{N'}}{C_{N'_{calc}}}\right]_{20} = 0.960 \quad \text{(figure 4.8.1.2-13a)}$$

$$\left(C_{N'_{calc}}\right)_{20} = 2.195\left(\frac{A + 0.61}{A + 4.0}\right) \quad \text{(equation 4.8.1.2-d)}$$

$$= 2.195\left(\frac{1.076 + 0.61}{1.076 + 4.0}\right)$$

$$= 0.7291$$

$$(C_{N'})_{20} = \left[\frac{C_{N'}}{C_{N'_{calc}}}\right]_{20}\left(C_{N'_{calc}}\right)_{20} \quad \text{(equation 4.8.1.2-c)}$$

$$= (0.960)(0.7291) = 0.700$$

Determine the empirical, nonlinear-normal-force correction factor

$Z = 0.972$ (figure 4.8.1.2-14)

Solution:

$$C_{N'} = \left(C_{N_\alpha}\right)'_{N_0}\alpha' + 8.21\left\{(C_{N'})_{20} - 0.349\left(C_{N_\alpha}\right)'_{N_0}\right\}[Z + 2.81(1 - Z)\alpha']\alpha'^{2}$$

(equation 4.8.1.2-f, sharp leading edge)

$$= 1.411\alpha' + 8.21\left\{(0.700) - 0.349(1.411)\right\}[0.972 + 2.81(1 - 0.972)\alpha']\alpha'^{2}$$

$$= 1.411\alpha' + 1.656\alpha'^{2} + 0.134\alpha'^{3}$$

①	②	③	④	⑤	⑥	⑦	⑧
α' (deg)	α' (rad)	α'^2 (rad^2)	α'^3 (rad^3)	$1.411\alpha'$ 1.411 ②	$1.656\alpha'^2$ 1.656 ③	$0.134\alpha'^3$ 0.134 ④	$C_{N'}$ (based on S) (eq. 4.8.1.2-f) ⑤ + ⑥ + ⑦
0	0	0	0	0	0	0	0
5	0.0873	0.00762	0.000665	0.1232	0.0126	0.00009	0.1359
10	0.1745	0.03045	0.005314	0.2462	0.0504	0.00071	0.2973
15	0.2618	0.06854	0.01794	0.3694	0.1135	0.00240	0.4853
20	0.3490	0.12180	0.04251	0.4924	0.2017	0.00570	0.6998

The calculated results are compared with test values from reference 6 in sketch (a) and in table 4.8.1.2-A.

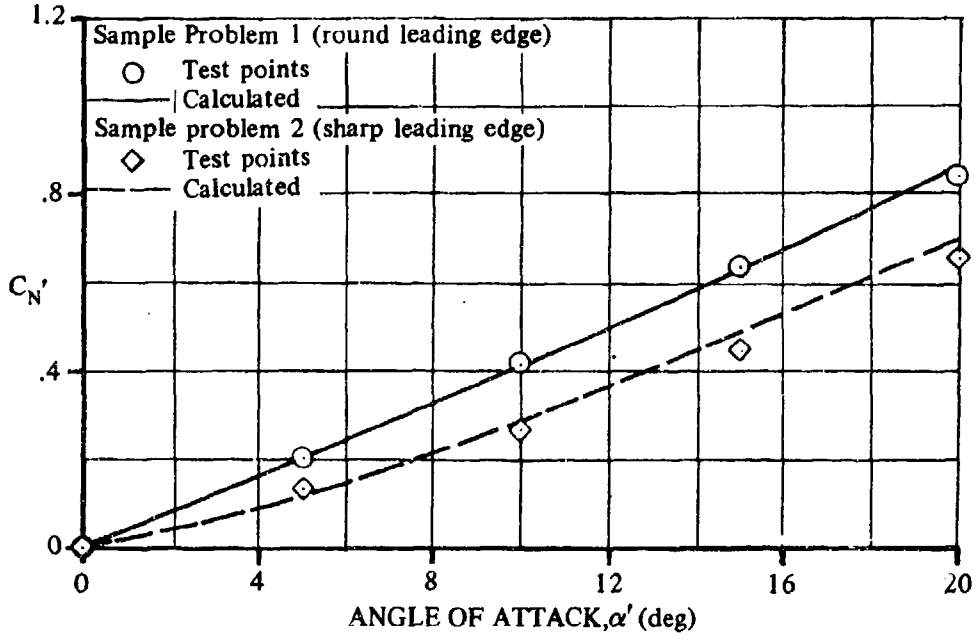

SKETCH (a)

REFERENCES

1. Seeger, D. B., and Meyer, J. E.: An Investigation of the Subsonic Aerodynamic Characteristics and the Landing Flare Maneuver for Hypersonic Re-Entry Configurations. ASD-TDR-62-271, 1962. (C) Title Unclassified

2. Jaquet, B. M., and Brewer, J. D.: Low-Speed Static-Stability and Rolling Characteristics of Low-Aspect-Ratio Wings of Triangular and Modified Triangular Planforms. NACA RM L9L29, 1949. (U)

3. Mugler, J. P., Jr., and Olstad, W. B.: Static Longitudinal Aerodynamic Characteristics at Transonic Speeds of a Blunted Right Triangular Pyramidal Lifting Re-Entry Configuration for Angles of Attack up to 110°. NASA TN D-797, 1961. (U)

4. Paulson, J. W., and Shanks, R. E.: Investigation of Low-Subsonic Flight Characteristics of a Model of a Hypersonic Boost-Glide Configuration Having a 78° Delta Wing. NASA TN D-894, 1961. (U)

5. Ware, G. M.: Low-Subsonic-Speed Static Stability of Right-Triangular-Pyramid and Half-Cone Lifting Re-Entry Configurations. NASA TN D-646, 1961. (U)

6. Mantz, K., Seeger, D. B., and Ross, R.: Tests to Determine Subsonic Aerodynamic Characteristics of Hypersonic Re-Entry Configurations. ASD-TR-61-485, Supplement 1, 1963. (U)

7. Mantz, K., Seager, D. B., and Ross, R.: Tests to Determine Subsonic Pressures, Forces and Moments Acting on a Hypersonic Re-Entry Configuration. ASD-TDR-62-270, Supplement 1, 1963. (U)

8. Olstad, W. B., Mugler, J. P., Jr., and Cahn, M. S.: Static Longitudinal and Lateral Stability Characteristics of a Right Triangular Pyramidal Lifting Re-Entry Configuration at Transonic Speeds. NASA TN D-655, 1961. (U)

TABLE 4.8.1.2-A

SUBSONIC NORMAL-FORCE VARIATION WITH ANGLE OF ATTACK
DELTA PLANFORM CONFIGURATIONS

Ref.	Configuration	A	Λ_{LE} (deg)	b (in.)	$\frac{S_F}{S_{ref}}$	Leading Edge	α' (deg)	C_N' Calc.	C_N' Test	e Percent Error
4	Hypersonic-boost-glide w/out tip cones	0.74	78.0	35.40	0.0497	Sharp $\delta_{e_L} = 26.4°$	0 5 10 15 20	0 0.119 0.276 0.471 0.704	0 0.118 0.290 0.500 0.707	0 0.8 – 4.8 – 5.8 – 0.4
5	Half-cone cross section	0.783	79.50	21.10	0.307	Round $R_1 = 0.05$ in. $\frac{-LE}{3}$ $\delta_L = 0$	0 5 10 15 20	0 0.111 0.226 0.347 0.476	0 0.098 0.214 0.357 0.512	0 13.3 5.6 – 2.8 – 7.0
6	D-2	1.076	75.0	12.374	0.188	Sharp* $\delta_{e_L} = 58°$	0 5 10 15 20	0 0.132 0.319 0.522 0.774	0 0.124 0.303 0.525 0.778	0 6.5 5.3 – 0.6 – 0.5
	D-3	1.076	75.0	12.374	0.311	Sharp* $\delta_{e_L} = 90°$	0 5 10 15 20	0 0.133 0.293 0.481 0.696	0 0.116 0.267 0.445 0.700	0 14.6 9.7 8.1 5.7
	D-6	1.868	65.0	22.116	0.219	Round $R_1 = 0.525$ in. $\frac{-LE}{3}$ $\delta_L = 9°$	0 5 10 15 20	0 0.202 0.412 0.630 0.860	0 0.202 0.418 0.635 0.835	0 0 – 1.4 – 0.8 3.0
	D-5	1.076	75.0	13.13	0.329	Round $R_1 = 1.05$ in. $\frac{-LE}{3}$ $\delta_L = 0$	0 5 10 15 20	0 0.128 0.258 0.390 0.526	0 0.135 0.263 0.396 0.535	0 – 5.2 – 1.9 – 1.5 – 1.7

*Model analyzed as having a sharp leading edge, although LER = 0.032 in.

Average Error = $\frac{\Sigma|e|}{n}$ = 3.4%

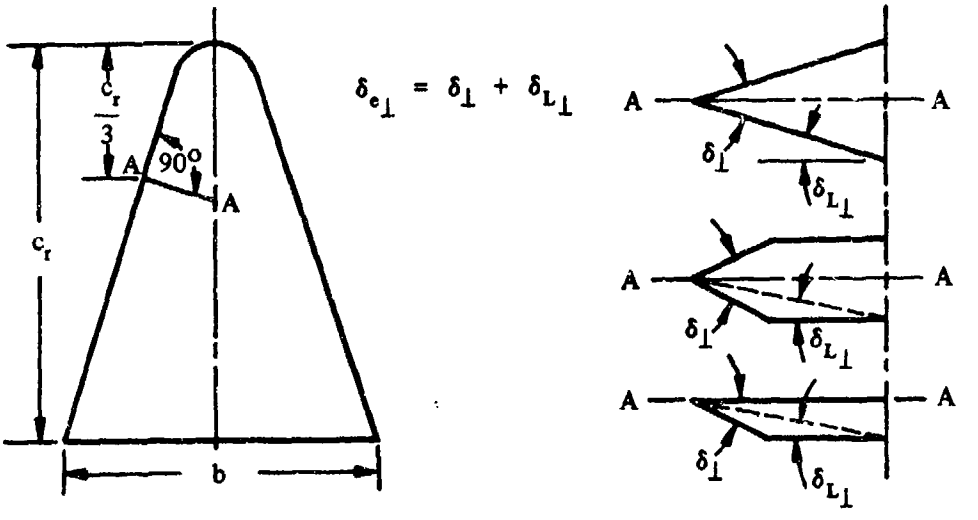

FIGURE 4.8.1.2-11a DEFINITION OF THE EFFECTIVE LEADING-EDGE ANGLE FOR DELTA AND MODIFIED-DELTA CONFIGURATIONS WITH SHARP LEADING EDGES

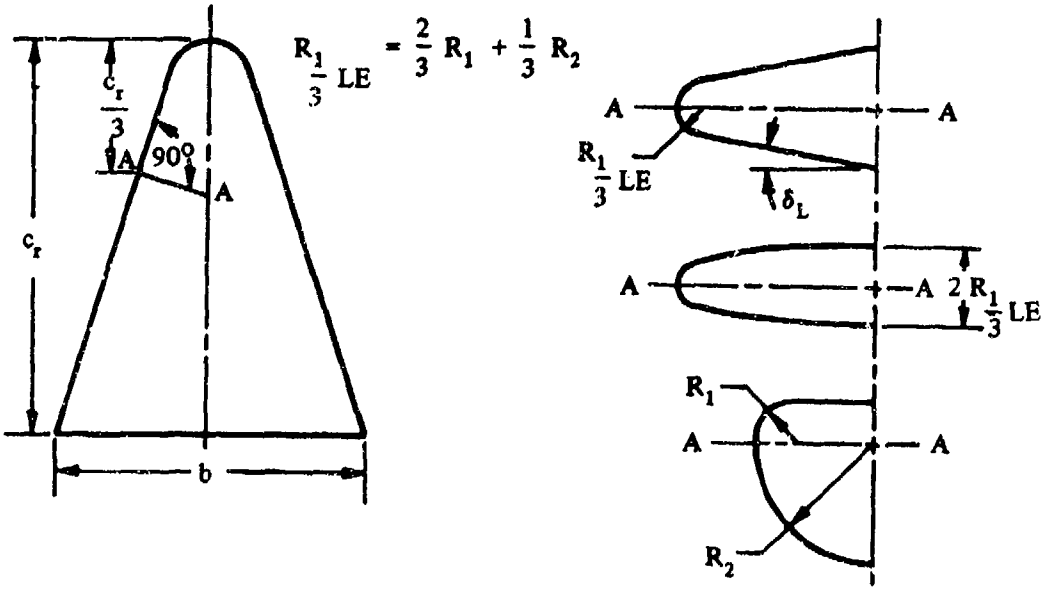

FIGURE 4.8.1.2-11b DEFINITION OF THE EFFECTIVE LEADING-EDGE RADIUS FOR DELTA AND MODIFIED-DELTA CONFIGURATIONS WITH ROUND LEADING EDGES

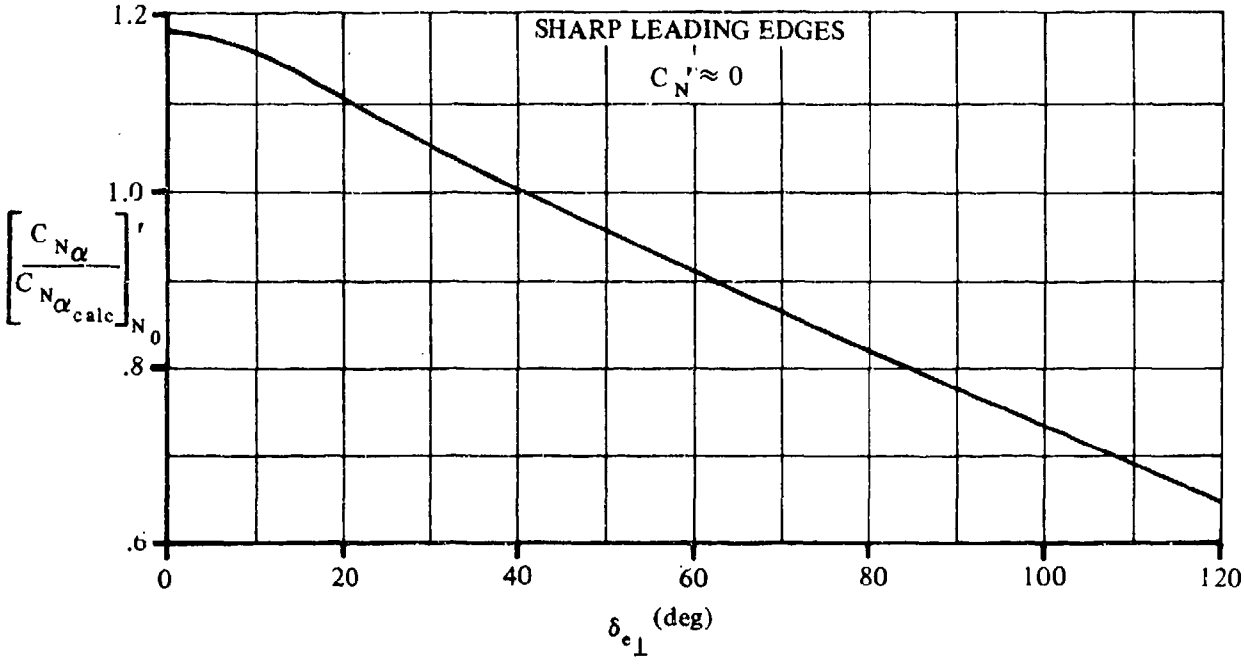

FIGURE 4.8.1.2-12a NORMAL-FORCE-CURVE-SLOPE CORRELATION FACTOR – DELTA AND MODIFIED-DELTA CONFIGURATIONS WITH SHARP LEADING EDGES

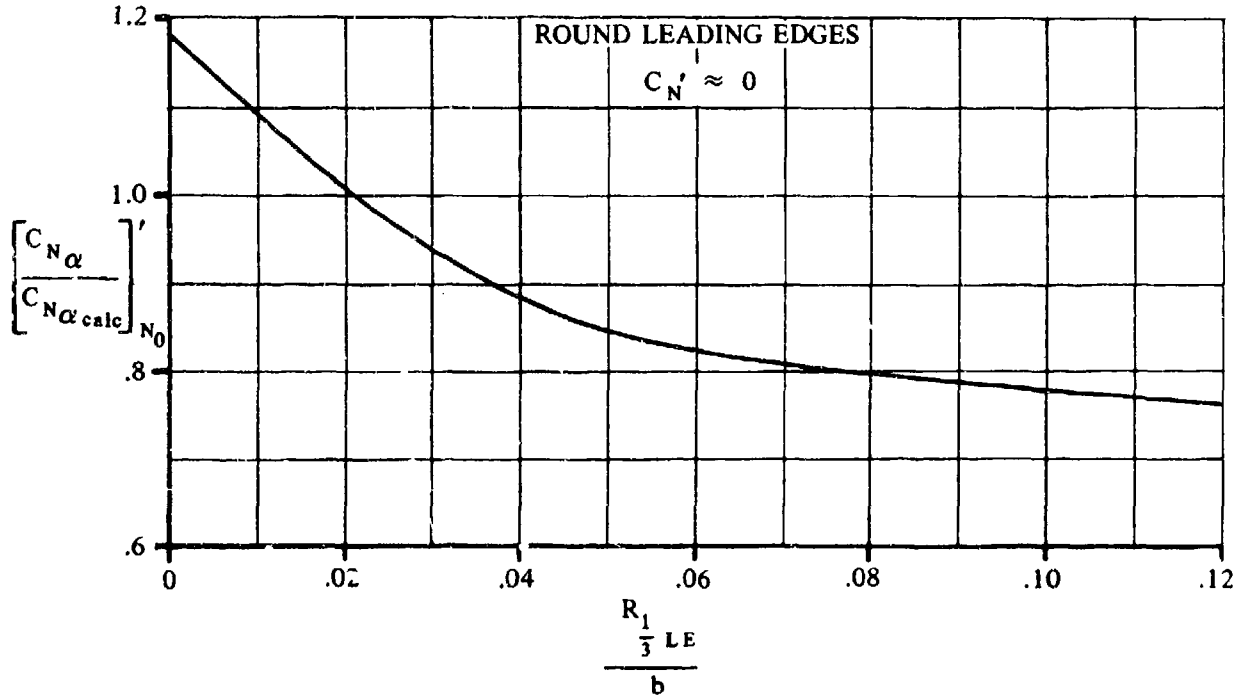

FIGURE 4.8.1.2-12b NORMAL-FORCE-CURVE-SLOPE CORRELATION FACTOR – DELTA AND MODIFIED-DELTA CONFIGURATIONS WITH ROUND LEADING EDGES

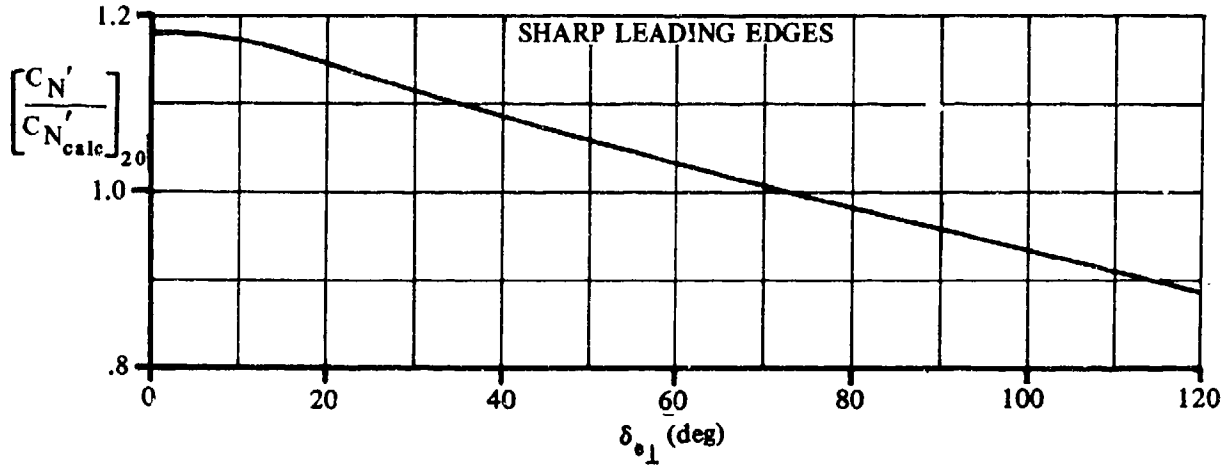

FIGURE 4.8.1.2-13a NORMAL-FORCE-COEFFICIENT CORRELATION FACTOR AT $\alpha' = 20^\circ$ – DELTA AND MODIFIED-DELTA CONFIGURATIONS WITH SHARP LEADING EDGES

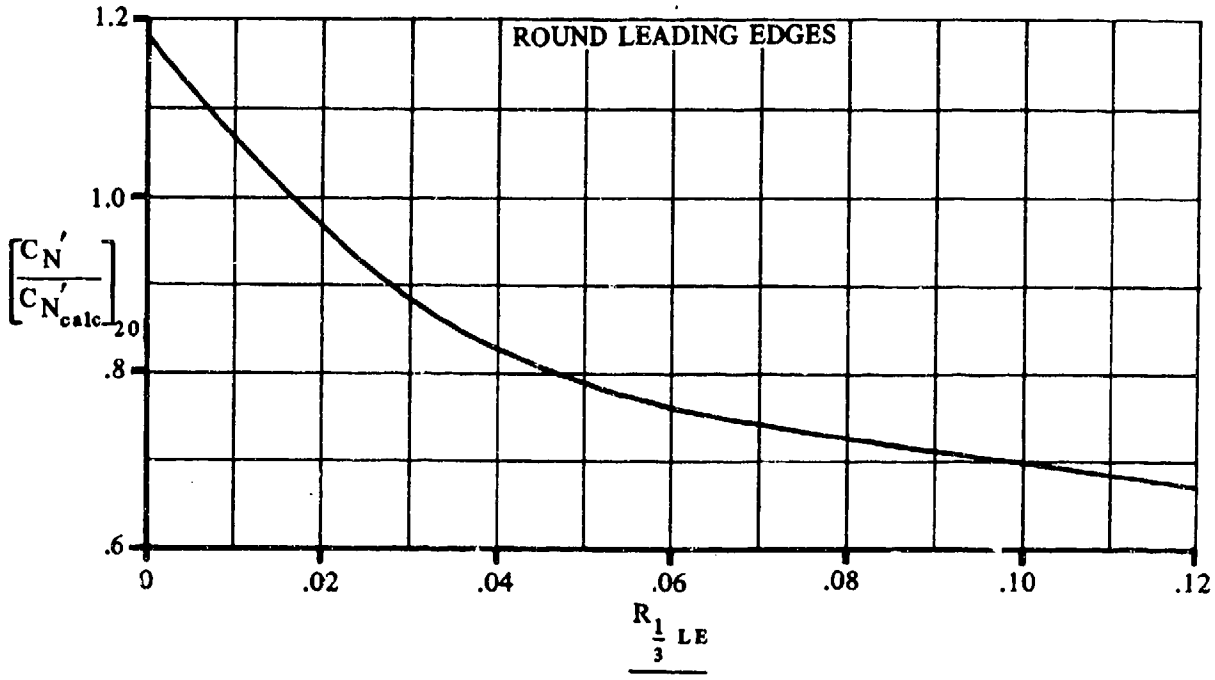

FIGURE 4.8.1.2-13b NORMAL-FORCE-COEFFICIENT CORRELATION FACTOR AT $\alpha' = 20^\circ$ – DELTA AND MODIFIED-DELTA CONFIGURATIONS WITH ROUND LEADING EDGES

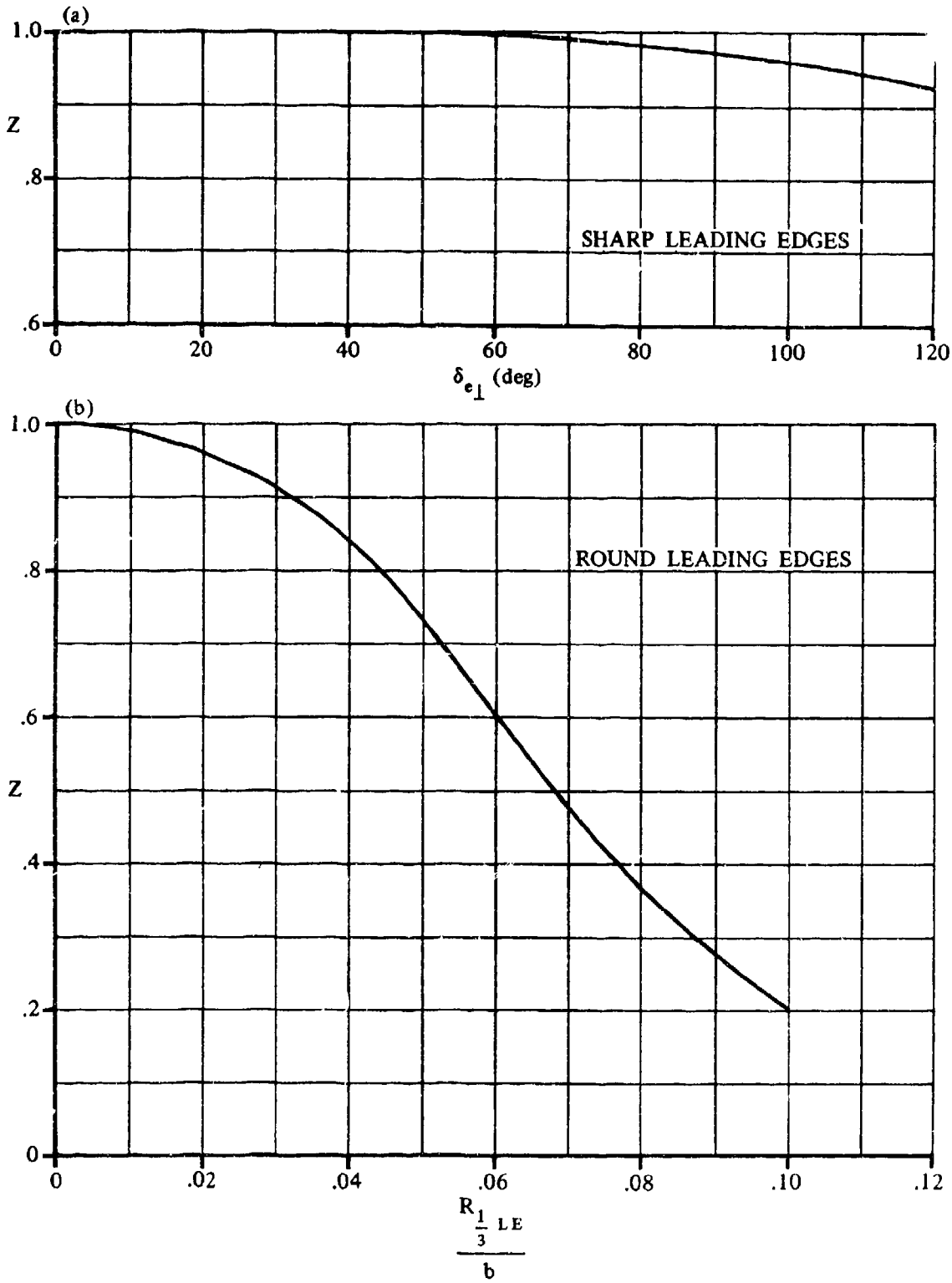

FIGURE 4.8.1.2-14 EFFECT OF LEADING-EDGE GEOMETRY ON THE NORMAL-FORCE COEFFICIENT – DELTA AND MODIFIED DELTA CONFIGURATIONS

4.8.2 WING, WING-BODY AXIAL FORCE

4.8.2.1 WING, WING-BODY ZERO-NORMAL-FORCE AXIAL FORCE

A. SUBSONIC

This section presents a method, taken from reference 1, for estimating the zero-normal-force axial force of advanced flight vehicles at subsonic speeds.

The drag at zero normal force is assumed to be composed of skin-friction drag, base drag, and the pressure drag acting on portions of the configuration other than the base. For most advanced flight vehicles at subsonic speeds, the component of pressure drag acting on portions of the vehicle other than the base is relatively small compared to the sum of the base drag and the skin-friction drag, and it is difficult to isolate. Consequently, in this section it is included as part of an "effective" friction drag.

The "effective" friction drag is determined by multiplying the total wetted area, excluding the base area, by some friction coefficient. For configurations having an average aerodynamic cleanliness, and for thickness ratios not exceeding approximately fifteen to twenty percent, the equivalent friction drag coefficient, based on wetted area, can be assumed to be $C_f = 0.0040$. Of course, this quantity will depend upon such items as surface condition and Reynolds number. Heat and drag loads during re-entry could be such as to roughen the surface and increase surface drag significantly. However, for most configurations of this class, surface drag is a relatively small part of the total drag at most speeds and angles of attack, and it is not considered necessary to go into these effects in greater detail.

Advanced flight vehicles are frequently characterized by large surface areas approximately normal to the direction of flight and facing aft. The "base pressures" acting upon these areas can significantly increase the drag and reduce the maximum lift-drag ratio of these aircraft. For the purpose of definition, "bases" are considered to be those external surface areas which face aft and are approximately perpendicular to the direction of flight; they are formed by the "cutting-off" of some component. The flow ahead of the base should be unseparated and approximately parallel to the free stream, at least near zero lift. In keeping with this definition, bases include the aft facing areas produced by blunting wing trailing edges and by the jet exits of inoperative rocket engines.

The manner in which base drag arises can be visualized by considering the viscous pumping action of the air flowing around the periphery of the base. The viscous forces produced by the external flow tend to drag the air away from the base and consequently reduce the base pressure. In addition, the base pressure would be other than ambient even for a nonviscous flow, since the base would be influenced by the static pressures in the external flow, which are, in general, other than ambient. Consequently, the base pressure would depend both on the magnitude of the pumping, which is related to the ratio of the viscous mixing area to the total base area, and on the shape of the body ahead of the base, which determines the static pressures in the external flow at the boundary of the base.

Because of the complexity of base pressure phenomena at subsonic speeds, it has not been possible theoretically to predict base pressures for even the most simple configurations without entailing complex computational techniques, which nevertheless produce results of doubtful accuracy. Hence, the approach presented in this section is based on semiempirical techniques aimed at isolating the parameters known to be of primary importance.

Factors that might be expected to influence base pressure but which were not isolated in the analysis reported in reference 1 include scale effect and Reynolds number. Available test data show that the variation in Reynolds number produces little effect in base pressure when the flow is turbulent at the base.

DATCOM METHOD

The subsonic axial-force coefficient at zero normal force, based on the reference area (usually the planform area), is obtained from the procedure outlined in the following steps:

Step 1. Determine the increment in axial-force coefficient due to skin friction at zero normal force by

$$\Delta C_{X'_{f_{N_0}}} = -C_f \frac{S_{wet}}{S_{ref}} \qquad 4.8.2.1\text{-a}$$

where

C_f is the turbulent flat-plate skin-friction coefficient based on the wetted area. It is recommended that a value of $C_f = 0.0040$ be used unless detailed data on surface condition are available. In that case the method of paragraph A of of Section 4.1.5.1 should be used to obtain C_f.

S_{wet} is the wetted area or surface area of the configuration excluding the base area.

S_{ref} is the reference area (usually the configuration planform area).

Step 2. Determine the base-pressure coefficient at zero normal force, based on the base area, by

$$C_{p_{b_{N_0}}} = \frac{C_{p_{b_{N_0}}}}{\frac{P}{2\sqrt{\pi S_b}}} \frac{P}{2\sqrt{\pi S_b}} \qquad 4.8.2.1\text{-b}$$

where

P is the perimeter of the base of the configuration (see figure 4.8.2.1-7a).

S_b is the base area of the configuration.

$\frac{C_{p_{b_{N_0}}}}{\frac{P}{2\sqrt{\pi S_b}}}$ is obtained from figure 4.8.2.1-7b as a function of the shape parameter $\frac{2 S_b}{\pi \ell_B (h_b + b_b)}$.

where

ℓ_B is the total length of the body.

h_b is the maximum height of the base of the configuration (see figure 4.8.2.1-7a).

b_b is the maximum span of the base of the configuration.

Step 3. Determine the increment in axial-force coefficient at zero normal force due to base pressure by

$$\Delta C_{X'_{b_{N_0}}} = C_{p_{b_{N_0}}} \frac{S_b}{S_{ref}} \qquad 4.8.2.1\text{-c}$$

where $C_{p_{b_{N_0}}}$ is obtained from step 2.

Step 4. Determine the axial-force coefficient at zero normal force, based on the reference area, by

$$C_{X'_{N_0}} = \Delta C_{X'_{f_{N_0}}} + \Delta C_{X'_{b_{N_0}}} \qquad 4.8.2.1\text{-d}$$

where $\Delta C_{X'_{f_{N_0}}}$ and $\Delta C_{X'_{b_{N_0}}}$ are obtained from steps 1 and 3, respectively.

Figure 4.8.2.1-7b presents a semiempirical correlation of the base-pressure coefficient at zero normal force. This correlation comprises both a measure of the ratio of the viscous pumping area to the base area, and the effect of the shape of the configuration ahead of the base on the pressures in the external flow.

A comparison of the zero-normal-force axial force calculated by this method with test values is presented as table 4.8.2.1-A.

Sample Problem

Given: The blunted, right-triangular pyramidal lifting body of reference 2.

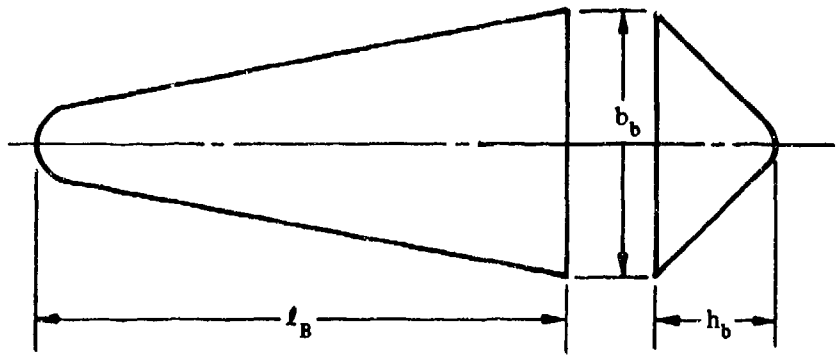

ℓ_B = 19.125 in. S_{ref} = S = 104.98 sq in. S_b = 21.96 sq in.

S_{wet} = 248.83 sq in. P = 22.16 in. h_b = 4.12 in. b_b = 9.08 in.

Compute:

Determine the increment in axial-force coefficient due to skin friction at zero normal force.

C_f = 0.0040

$$\Delta C_{X'_{f_{N_0}}} = -C_f \frac{S_{wet}}{S_{ref}} \quad \text{(equation 4.8.2.1-a)}$$

$$= -(0.0040)\left(\frac{248.83}{104.98}\right)$$

$$= -0.00948$$

Determine the base-pressure coefficient at zero normal force

$$\frac{P}{2\sqrt{\pi S_b}} = \frac{22.16}{2\sqrt{\pi (21.96)}} = 1.333$$

$$\frac{2 S_b}{\pi \ell_B (h_b + b_b)} = \frac{2 (21.96)}{\pi (19.125) (4.12 + 9.08)} = 0.0554$$

$$\frac{C_{p_{b_{N_0}}}}{\frac{P}{2\sqrt{\pi S_b}}} = -0.181 \quad \text{(figure 4.8.2.1-7b)}$$

$$C_{p_{b_{N_0}}} = \frac{C_{p_{b_{N_0}}}}{\frac{P}{2\sqrt{\pi S_b}}} \frac{P}{2\sqrt{\pi S_b}} \quad \text{(equation 4.8.2.1-b)}$$

$$= (-0.181)(1.333)$$

$$= -0.241 \text{ (based on } S_b)$$

Determine the increment in axial-force coefficient at zero normal force.

$$\Delta C_{X'_{b_{N_0}}} = C_{p_{b_{N_0}}} \frac{S_b}{S_{ref}} \quad \text{(equation 4.8.2.1-c)}$$

$$= (-0.241)\left(\frac{21.96}{104.98}\right)$$

$$= -0.0504 \text{ (based on } S_{ref})$$

Solution:

$$C_{X'_{N_0}} = \Delta C_{X'_{f_{N_0}}} + \Delta C_{X'_{b_{N_0}}} \quad \text{(equation 4.8.2.1-d)}$$

$$= -0.00948 - 0.0504$$

$$= -0.0599 \text{ (based on S)}$$

This compares with a test value of −0.0582 from reference 2.

REFERENCES

1. Seeger, D. B., and Meyer, J. E.: An Investigation of the Subsonic Aerodynamic Characteristics and the Landing Flare Maneuver for Hypersonic Re-Entry Configurations. ASD-TDR-62-271, 1962. (C) Title Unclassified

2. Mugler, J. P., Jr., and Olstad, W. B.: Static Longitudinal Aerodynamic Characteristics at Transonic Speeds of a Blunted Right Triangular Pyramidal Lifting Re-Entry Configuration for Angles of Attack up to 110°. NASA TN D-797, 1961. (U)

3. Mantz, K., Seeger, D. B., and Ross, R.: Tests to Determine Subsonic Aerodynamic Characteristics of Hypersonic Re-Entry Configurations. ASD-TR-61-485, Supplement 1, 1963. (U)

4. Mantz, K., Seeger, D. B., and Ross, R.: Tests to Determine Subsonic Pressures, Forces and Moments Acting on a Hypersonic Re-Entry Configuration. ASD-TDR-62-270, Supplement 1, 1963. (U)

5. Paulson, J. W., and Shanks, R. E.: Investigation of Low-Subsonic Flight Characteristics of a Model of a Hypersonic Boost-Glide Configuration Having a 78° Delta Wing. NASA TN D-894, 1961. (U)

6. Hoerner, S. F.: Fluid Dynamic Drag. Published by author, 1958. (U)

7. Ware, G. M.: Low-Subsonic-Speed Static Stability of Right-Triangular-Pyramid and Half-Cone Lifting Re-Entry Configurations. NASA TN D-646, 1961. (U)

8. Olstad, W. B., Mugler, Jr., J. P., and Cahn, M. S.: Static Longitudinal and Lateral Stability Characteristics of a Right Triangular Pyramidal Lifting Re-Entry Configuration at Transonic Speeds. NASA TN D-655, 1961. (U)

9. Paulson, J. W.: Low-Speed Static Stability and Control Characteristics of a Right Triangular Pyramid Re-Entry Configuration. NASA Memo 4-11-59L, 1959. (U)

10. Boisseau, P. C.: Investigation of the Low-Subsonic Flight Characteristics of a Model of a Re-Entry Vehicle with a Thick Flat 75° Swept Delta Wing and a Half-Cone Fuselage. NASA TN D-1007, 1962. (U)

11. Shanks, R. E.: Investigation of the Low-Subsonic Flight Characteristics of a Model of an All-Wing Hypersonic Boost-Glide Configuration Having Very High Sweep. NASA TN D-389, 1960. (U)

12. Peckham, D. H.: Low-Speed Wind Tunnel Tests on a Series of Uncambered Slender Pointed Wings with Sharp Edges. ARC R&M 3186, 1958. (U)

13. Paulson, J. W., and Shanks, R. E.: Investigation of the Low-Subsonic Stability and Control Characteristics of a Free-Flying Model of a Thick 70° Delta Re-Entry Configuration. NASA TN D-913, 1961. (U)

TABLE 4.8.2.1-A

SUBSONIC ZERO-NORMAL-FORCE AXIAL FORCE

DATA SUMMARY

Ref.	Configuration	S_{ref} (sq in.)	S_b (sq in.)	S_{wet} (sq in.)	ℓ_B (in.)	P (in.)	h_b (in.)	b_b (in.)	$C_{X'_{N_0}}$ Calc.	$C_{X'_{N_0}}$ Test	e Percent Error
2	Blunted right triangular pyramid	104.98	21.96	246.83	19.13	22.16	4.12	9.08	−0.0599	−0.0582	2.9
3	D-1	160.19	33.29	361.73	23.00	28.40	4.32	13.13	−0.0587	−0.0550	6.7
	D-2	142.30	26.98	305.00	23.00	26.54	4.32	12.37	−0.0498	−0.0520	− 4.2
	D-3	142.30	44.36	329.00	23.00	28.58	7.14	12.37	−0.0832	−0.0830	0.2
7	a	570.00	111.30	1251.30	54.00	51.94	10.55	21.10	−0.0480	−0.0480	0
	b (basic)	570.00	109.40	1281.00	54.00	49.65	9.35	21.10	−0.0528	−0.0480	10.0
	c (basic)	1110.00	215.45	2158.00	62.50	70.00	13.50	29.50	−0.0417	−0.0450	− 7.3
	c (extended nose)	1152.00	215.45	2313.00	70.10	70.00	13.50	29.50	−0.0377	−0.0360	4.7
8	1	204.00	41.50	448.50	31.59	31.11	12.89	6.44	−0.0495	−0.0500	− 1.0

Average Error = $\frac{\Sigma|e|}{n}$ = 3.8%

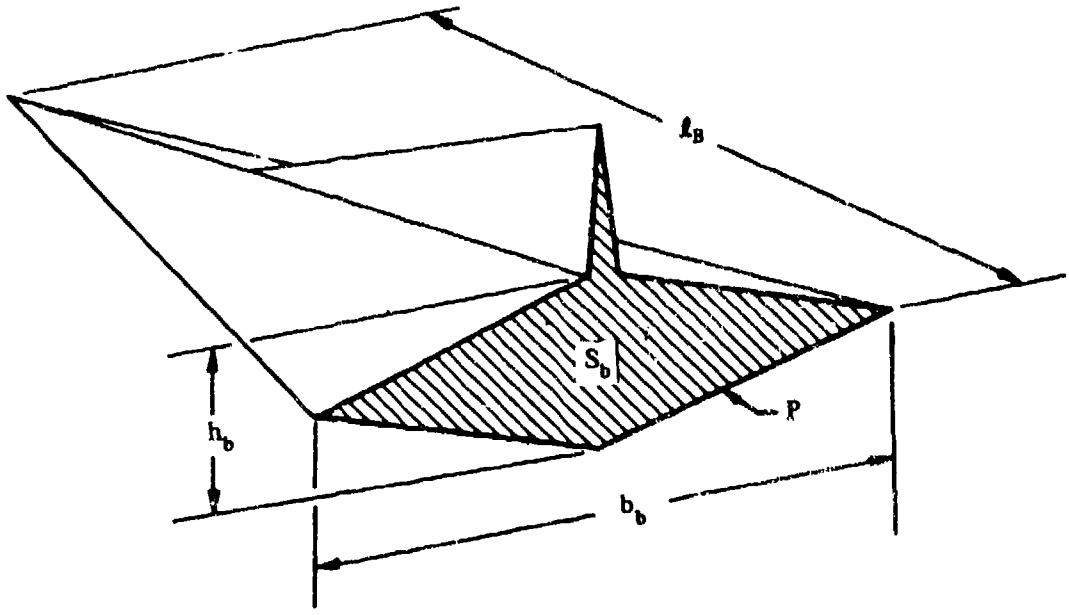

FIGURE 4.8.2.1-7a CONFIGURATION GEOMETRY

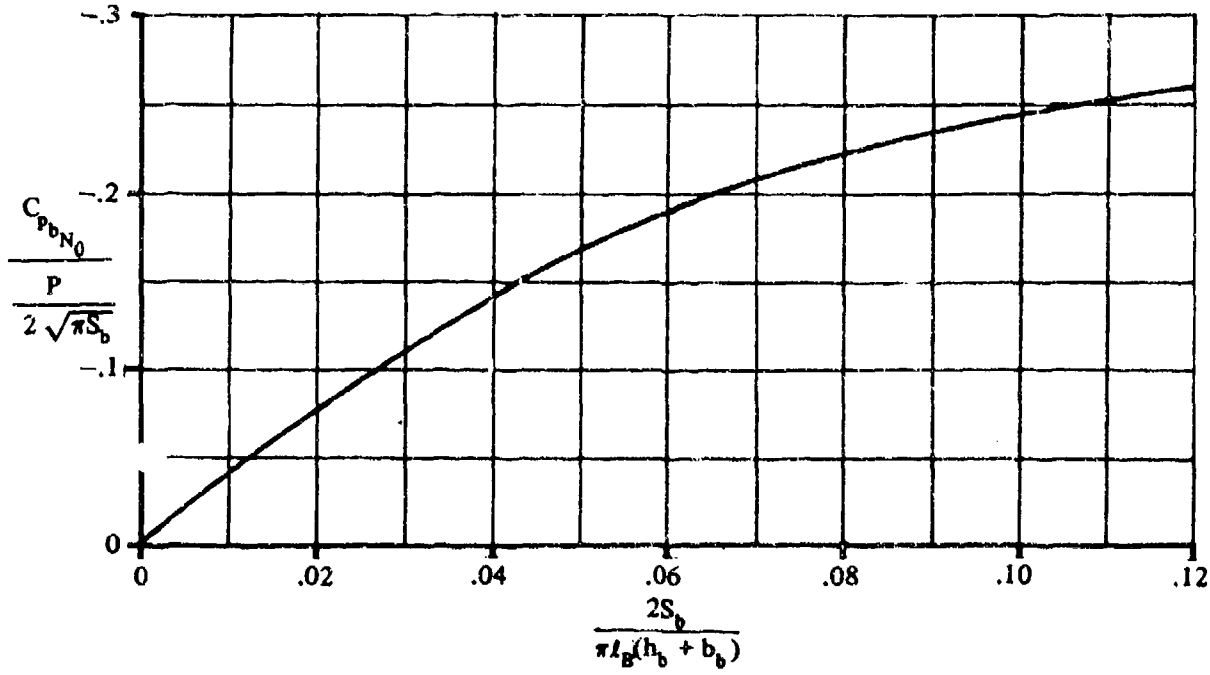

FIGURE 4.8.2.1-7b ZERO-NORMAL-FORCE BASE-PRESSURE COEFFICIENT

4.8.2.2 WING, WING-BODY AXIAL-FORCE VARIATION WITH ANGLE OF ATTACK

A. SUBSONIC

This section presents a method for estimating the axial-force variation with angle of attack for a delta or modified-delta planform re-entry configuration at subsonic speeds.

The method presented herein is taken from reference 1. The total axial force at angle of attack is taken as the sum of that at zero normal force, the increment due to angle of attack, and an increment due to the base pressure at angle of attack.

The axial force at zero normal force is given by the method of Section 4.8.2.1.

The increment of axial force due to angle of attack is obtained by a procedure that closely parallels the one used to obtain the normal-force variation with angle of attack as discussed in Section 4.8.1.2. The method is based on a study of test data on low-aspect-ratio delta wings with thick and thin surfaces, with sharp and rounded leading edges, and with varying degrees of nose bluntness. Thin, sharp-leading-edge delta wings were selected as "reference wings," and theoretical relationships were written for the axial-force characteristics of these planforms. The axial-force characteristics of all the test configurations were then calculated at $\alpha' = 20^{\circ}$ by using these "reference wing" relationships, and any deviation between the calculated and test values was related to aspect ratio, frontal area, and leading-edge characteristics. The variation of this component of axial force between that at zero normal force and that at $\alpha' = 20^{\circ}$ is then approximated as a function of the normal-force variation with angle of attack.

In general, the base pressures acting on advanced flight vehicles become less as the angle of attack increases and, consequently, the component of axial force due to base pressure increases negatively as the angle of attack increases. In reference 1 the change in base pressures of the test configurations are correlated with changes in angle of attack by using the base pressures at $\alpha' = 20^{\circ}$ and at zero normal force as the basis for the correlation.

DATCOM METHOD

The axial-force variation with angle of attack for a delta or modified-delta configuration at low speeds, based on the reference area (usually the planform area), is obtained from the procedure outlined in the following steps:

Step 1. Determine the increment of axial-force coefficient due to angle of attack by

$$\Delta C_{X'} = \left[\left(\frac{X'}{N'}\right)_{calc}\right]_{20} \left[\frac{\Delta C_{X'}}{\Delta C_{X'_{calc}}}\right]_{20} \sqrt{\frac{\alpha'}{20}} \quad C_{N'} \qquad 4.8.2.2\text{-a}$$

where

$\left[\left(\frac{X'}{N'}\right)_{calc}\right]_{20}$ is the calculated ratio of the axial force to the normal force at $\alpha' = 20^{o}$, given by

$$\left[\left(\frac{X'}{N'}\right)_{calc}\right]_{20} = -0.349\left(\frac{A+2}{A+4}\right) \qquad 4.8.2.2\text{-b}$$

$\left[\frac{\Delta C_{X'}}{\Delta C_{X'_{calc}}}\right]_{20}$ is the empirical correlation factor of the axial-force coefficient at $\alpha' = 20^{o}$ for delta or modified-delta configurations. This parameter is presented as a function of configuration geometry in figure 4.8.2.2-10. Figure 4.8.2.2-10 is entered with the following geometric parameters:

A	the aspect ratio of the surface
S_F	the projected frontal area perpendicular to the zero-normal-force reference plane (projected frontal area at $C_{N'} = 0$)
S_{ref}	the reference area (usually the configuration planform area)
b	the surface span
$R_{\frac{1}{3}\ LE}$	the leading-edge radius in a plane normal to the leading edge at $\frac{1}{3}$ c_r from the nose

α' is the angle of attack in degrees.

$$\alpha' = \alpha - \alpha_{N_0}$$

$C_{N'}$ is the normal-force variation with angle of attack obtained by using the method of Section 4.8.1.2.

Step 2. Determine the variation of base pressure with angle of attack by

$$\left(C_{p_b}\right)_{\alpha'} = \left(\frac{C_{p_{b_{20}}}}{C_{p_{b_{N_0}}}} - 1\right)\left(\frac{\alpha}{20}\right)^2 C_{p_{b_{N_0}}} \qquad 4.8.2.2\text{-c}$$

where α' is defined above, and

$\frac{C_{p_{b_{20}}}}{C_{p_{b_{N_0}}}}$ is the empirical correlation of the ratio of the pressure coefficient at $\alpha' = 20^o$ to that at zero normal force. This parameter is obtained from figure 4.8.2.2-11 as a function of the shape parameter

$$\frac{b_b^2}{h_b\sqrt{S_b}}$$

where

b_b is the maximum span of the base of the configuration.

h_b is the maximum height of the base of the configuration (see figure 4.8.2.1-7a).

S_b is the base area of the configuration.

The two curves on figure 4.8.2.2-11 refer to two types of re-entry configurations. The upper curve is to be applied to configurations for which the entire base is influenced directly by the primary lifting surface. The lower curve is to be applied to configurations for which portions of the base are aft of nonlifting components, e.g., bodies and vertical surfaces.

$C_{p_{b_{N_0}}}$ is the base pressure coefficient at zero normal force obtained as outlined in step 2 of the Datcom method of Section 4.8.2.1.

Step 3. Determine the variation of the increment of axial-force coefficient due to the base pressure with angle of attack by

$$\left(\Delta C_{X_{b_\alpha}}\right) = \left(C_{p_b}\right)_{\alpha'} \frac{S_b}{S_{ref}} \qquad 4.8.2.2\text{-d}$$

where

$\left(C_{p_b}\right)_{\alpha'}$ is the variation of base pressure with angle of attack from step 2.

S_{ref} is the reference area (usually the configuration planform area).

Step 4. Determine the zero-normal-force axial force $C_{X'_{N_0}}$ by using the method of Section 4.8.2.1.

Step 5. The variation of axial force with angle of attack, based on the reference area, is given by

$$C_{X'} = -\Delta C_{X'} + \left(\Delta C_{X_{b_\alpha}}\right)' + C_{X'_{N_0}} \qquad 4.8.2.2\text{-e}$$

where $\Delta C_{X'}$, $\left(\Delta C_{X_{b_\alpha}}\right)'$, and $C_{X'_{N_0}}$ are from steps 1, 3, and 4, respectively.

A comparison of the axial-force variation with angle of attack calculated by this method with test results is presented as table 4.8.2.2-A.

While it is considered that the results presented are satisfactory for use in preliminary design, it should be noted that scale effect and Reynolds number, which might be expected to influence the base pressure, were not isolated in the data correlation reported in reference 1. (Available test data showed, however, that the variation in Reynolds number produced little effect in base pressure when the flow was turbulent at the base.) Furthermore, in many cases the data were not sufficient to accurately define the variation of base pressure over the surface of the base. Consequently, much of the data included in the empirical correlation for axial-force coefficient at $\alpha' = 20^{\circ}$ (figure 4.8.2.2-10) and in the empirical correlation for the ratio of the pressure coefficient at $\alpha' = 20^{\circ}$ to that at zero normal force (figure 4.8.2.2-11), are known to be in error.

Sample Problem

Given: A delta model with a symmetrical diamond cross section and a blunt trailing edge. This is model D-3 of reference 3 and is the same configuration as sample problem 2 of Section 4.8.1.2.

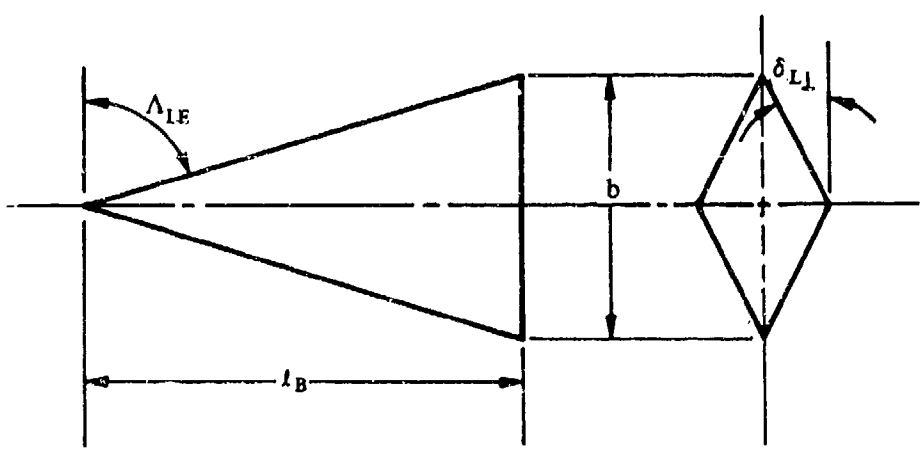

$A = 1.076$ $b = b_b = 12.374$ in. $S_{ref} = S = 142.30$ sq in.

$S_F = S_b = 44.20$ sq in. $S_{wet} = 329.0$ sq in. $h_b = 7.14$ in.

$\ell_B = 23.0$ in. $P = 28.58$ in.

The following variation of C_N' with α' from sample problem 2 of Section 4.8.1.2:

α'	0	5	10	15	20
C_N'	0	0.1359	0.2573	0.4853	0.6998

Compute:

Determine the increment in axial-force coefficient due to angle of attack.

$$\left[\left(\frac{X'}{N'}\right)_{calc}\right]_{20} = -0.349\left(\frac{A+2}{A+4}\right) \quad \text{(equation 4.8.2.2-b)}$$

$$= -0.349\left(\frac{1.076+2}{1.076+4}\right) = -0.2115$$

$$S_F/S_{ref} = 44.20/142.30 = 0.311$$

$$\left[\frac{\Delta C_{X'}}{\Delta C_{X'_{calc}}}\right]_{20} = 0.389 \quad \text{(figure 4.8.2.2-10, sharp leading edge)}$$

$$\Delta C_{X'} = \left[\frac{X'}{N'_{calc}}\right]_{20}\left(\frac{\Delta C_{X'}}{\Delta C_{X'_{calc}}}\right)_{20}\sqrt{\frac{\alpha'}{20}}\ C_{N'} \quad \text{(equation 4.8.2.2-a)}$$

$$= (-0.2115)(0.389)\sqrt{\frac{\alpha'}{20}}\ C_{N'}$$

$$= -0.0823\sqrt{\frac{\alpha'}{20}}\ C_{N'} \quad \text{(see calculation table below)}$$

Determine the variation of base pressure with angle of attack.

$$\frac{b_b^{\,2}}{h_b\sqrt{S_b}} = \frac{(12.374)^2}{7.14\sqrt{44.20}} = 3.226$$

$$\frac{C_{P_{b_{20}}}}{C_{P_{b_{N_0}}}} = 1.42 \quad \text{(figure 4.8.2.2-11, upper curve)}$$

$$\frac{P}{2\sqrt{\pi S_b}} = \frac{28.58}{2\sqrt{\pi(44.2)}} = 1.213$$

$$\frac{2S_b}{\pi \ell_B (h_b + b_b)} = \frac{2(44.2)}{\pi(23.0)(7.14+12.37)} = 0.0627$$

$$\frac{C_{p_{b_{N_0}}}}{\frac{P}{2\sqrt{\pi S_b}}} = -0.196 \quad \text{(figure 4.8.2.1-7b)}$$

$$C_{p_{b_{N_0}}} = \frac{C_{p_{b_{N_0}}}}{\frac{P}{2\sqrt{\pi S_b}}} \cdot \frac{P}{2\sqrt{\pi S_b}} \quad \text{(equation 4.8.2.1-b)}$$

$$= (-0.196)\,(1.213)$$

$$= -0.238 \left(\text{This result is also used below in calculating } C_{X'_{N_0}}\right)$$

$$\left(C_{p_b}\right)_{\alpha'} = \left(\frac{C_{p_{b_{20}}}}{C_{p_{b_{N_0}}}} - 1\right)\left(\frac{\alpha'}{20}\right)^2 C_{p_{b_{N_0}}} \quad \text{(equation 4.8.2.2-c)}$$

$$= (1.42 - 1)\left(\frac{\alpha'}{20}\right)^2 (-0.238)$$

$$= -0.100\left(\frac{\alpha'}{20}\right)^2$$

Determine the variation of the increment of axial-force coefficient due to the base pressure with angle of attack.

$$\left(\Delta C_{X_{b_\alpha}}\right)' = \left(C_{p_b}\right)_{\alpha'} \frac{S_b}{S_{ref}} \quad \text{(equation 4.8.2.2-d)}$$

$$= \left[-0.100\left(\frac{\alpha'}{20}\right)^2\right]\left(\frac{44.20}{142.3}\right)$$

$$= -0.0311\left(\frac{\alpha'}{20}\right)^2 \quad \text{(see calculation table below)}$$

Determine the zero-normal-force axial force by the method of Section 4.8.2.1.

$$C_f = 0.0040$$

$$\Delta C_{X'_{f_{N_0}}} = -C_f \frac{S_{wet}}{S_{ref}} \quad \text{(equation 4.8.2.1-a)}$$

$$= (-0.0040)\left(\frac{329.0}{142.3}\right)$$

$$= -0.00925$$

$$C_{p_{b_{N_0}}} = -0.238 \text{ (calculated in determining } \left(C_{p_b}\right)_{\alpha'} \text{ above)}$$

$$\Delta C_{X'_{b_{N_0}}} = C_{p_{b_{N_0}}} \frac{S_b}{S_{ref}} \quad \text{(equation 4.8.2.1-c)}$$

$$= (-0.238)\left(\frac{44.2}{142.3}\right)$$

$$= -0.0739$$

$$C_{X'_{N_0}} = \Delta C_{X'_{f_{N_0}}} + \Delta C_{X'_{b_{N_0}}} \quad \text{(equation 4.8.2.1-d)}$$

$$= -0.00925 + (-0.0739)$$

$$= -0.0832$$

Solution:

$$C_{X'} = -\Delta C_{X'} + \left(\Delta C_{X_{b_\alpha}}\right) + C_{X'_{N_0}} \quad \text{(equation 4.8.2.2-e)}$$

$$= -(-0.0823)\sqrt{\frac{\alpha'}{20}}\, C_{N'} + (-0.0311)\left(\frac{\alpha'}{20}\right)^2 + (-0.0832)$$

① α' (deg)	② C'_N (given)	③ $-0.0823\sqrt{\frac{\alpha'}{20}}\, C'_N$ $-0.0823\sqrt{\frac{①}{20}}$ ②	④ $-0.0311\left(\frac{\alpha'}{20}\right)^2$ $-0.0311\left(\frac{①}{20}\right)^2$	⑤ C'_X (based on S) (eq. 4.8.2.2-e) − ③ + ④ − 0.0832
0	0	0	0	−0.0832
5	0.1359	−0.00559	−0.00194	−0.0796
10	0.2973	−0.01727	−0.00776	−0.0737
15	0.4653	−0.0346	−0.0175	−0.0961
20	0.6906	−0.0576	−0.0311	−0.0567

The calculated results are compared with test values from reference 3 in sketch (a) and in table 4.8.2.2-A.

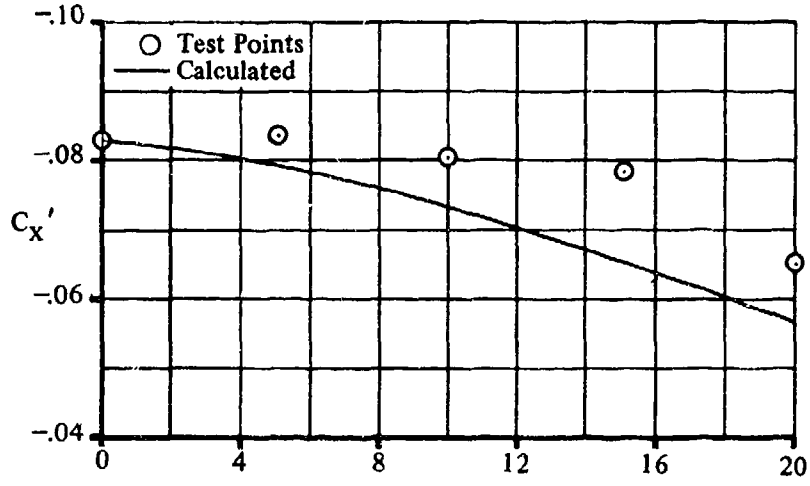

SKETCH (a)

REFERENCES

1. Seeger, D. B., and Meyer, J. E.: An Investigation of the Subsonic Aerodynamic Characteristics and the Landing Flare Maneuver for Hypersonic Re-Entry Configurations. ASD-TDR-62-271, 1962. (C) Title Unclassified

2. Mugler, J. P., Jr., and Olstad, W. B.: Static Longitudinal Aerodynamic Characteristics at Transonic Speeds of a Blunted Right Triangular Pyramidal Lifting Re-Entry Configuration for Angles of Attack up to 110°. NASA TN D-797, 1961. (U)

3. Mantz, K., Seeger, D. B., and Ross, R.: Tests to Determine Subsonic Aerodynamic Characteristics of Hypersonic Re-Entry Configurations. ASD-TR-61-485, Supplement 1, 1963. (U)

4. Mantz, K., Seeger, D. B., and Ross, R.: Tests to Determine Subsonic Pressures, Forces and Moments Acting on a Hypersonic Re-Entry Configuration. ASD-TDR-62-270, Supplement 1, 1963. (U)

5. Paulson, J. W., and Shanks, R. E.: Investigation of Low-Subsonic Flight Characteristics of a Model of a Hypersonic Boost-Glide Configuration Having a 78° Delta Wing. NASA TN D-894, 1961. (U)

6. Jaquet, B. M., and Brewer, J. D.: Low-Speed Static-Stability and Rolling Characteristics of Low-Aspect-Ratio Wings of Triangular and Modified Triangular Planforms. NACA RM L8L29, 1949. (U)

7. Ware, G. M.: Low-Subsonic-Speed Static Stability of Right-Triangular-Pyramid and Half-Cone Lifting Re-Entry Configurations. NASA TN D-646, 1961. (U)

8. Olstad, W. B., Mugler, J. P., Jr., and Cahn, M. S.: Static Longitudinal and Lateral Stability Characteristics of a Right Triangular Pyramidal Lifting Re-Entry Configuration at Transonic Speeds. NASA TN D-655, 1961. (U)

9. Paulson, J. W.: Low-Speed Static Stability and Control Characteristics of a Right Triangular Pyramid Re-Entry Configuration. NASA Memo 4-11-59L, 1959. (U)

10. Boisseau, P. C.: Investigation of the Low-Subsonic Flight Characteristics of a Model of a Re-Entry Vehicle with a Thick Flat 75° Swept Delta Wing and a Half-Cone Fuselage. NASA TN D-1007, 1962. (U)

11. Shanks, R. E.: Investigation of the Low-Subsonic Flight Characteristics of a Model of an All-Wing Hypersonic Boost-Glide Configuration Having Very High Sweep. NASA TN D-369, 1960. (U)

12. Peckham, D. H.: Low-Speed Wind Tunnel Tests on a Series of Uncambered Slender Pointed Wings with Sharp Edges. ARC R&M 3186, 1958. (U)

TABLE 4.8.2.2-A

SUBSONIC AXIAL-FORCE VARIATION WITH ANGLE OF ATTACK
DELTA PLANFORM CONFIGURATIONS

Ref.	Configuration	A	b (in.)	b_b (in.)	h_b (in.)	S_F (sq in.)	S_{ref} (sq in.)	S_b (sq in.)	Leading Edge	α (deg)	C_X' Calc.	C_X' Test	* Percent Error
2	Blunted right triangular pyramid	0.788	9.08	9.08	4.12	21.96	104.98	21.96	Round	0	−0.0599	−0.0582	2.9
									$R_{\frac{1}{3}LE}$ = .14 in.	5	−0.0564	−0.0575	− 1.9
									$\delta_L = 45^o$	10	−0.0517	−0.0540	− 4.3
										15	−0.0471	−0.0470	0.2
										20	−0.0427	−0.0440	− 3.0
3	D-1	1.076	13.13	13.13	4.32	33.29	160.19	33.29	Round	0	−0.0587	−0.0550	6.7
									$R_{\frac{1}{3}LE}$ = .525 in.	5	−0.0535	−0.0564	− 5.1
									$\delta_L = 15^o$	10	−0.0461	−0.0530	−13.0
										15	−0.0375	−0.0486	−22.8
										20	−0.0270	−0.0338	−20.1
	D-2	1.076	12.374	12.374	4.32	26.98	142.30	26.98	Sharp*	0	−0.0498	−0.0520	− 4.2
									$\delta_{e_\perp} = 58^o$	5	−0.0475	−0.0544	−12.7
										10	−0.0431	−0.0524	−17.7
										15	−0.0382	−0.0476	−19.7
	D-3	1.076	12.374	12.374	7.14	44.20	142.30	44.20	Sharp*	0	−0.0832	−0.0830	0.2
									$\delta_{e_\perp} = 90^o$	5	−0.0814	−0.0834	− 2.4
										10	−0.0795	−0.0802	− 0.9
										15	−0.0776	−0.0785	− 1.1
										20	−0.0756	−0.0655	15.4
	D-4	1.078	13.934	13.934	4.32	41.44	178.56	41.44	Round	0	−0.0695	−0.0620	12.1
									$R_{\frac{1}{3}LE}$ = 1.05 in.	5	−0.0598	−0.0545	9.7
									$\delta_L = 10.5^o$	10	−0.0445	−0.0446	− 0.2
										15	−0.0262	−0.0323	−18.9
8	Right triangular pyramid	0.742	12.89	12.89	6.44	41.40	222.0	41.40	Round	0	−0.0495	−0.0500	− 1.0
									$R_{\frac{1}{3}LE}$ = .187 in.	5	−0.0461	−0.0570	−19.1
									$\delta_L = 45^o$	10	−0.0410	−0.0540	−24.1
										15	−0.0362	−0.0430	−18.1

*Model analyzed as having sharp leading edge, although LER = 0.032 in.

Average error = $\frac{\Sigma |e|}{n}$ = 9.5%

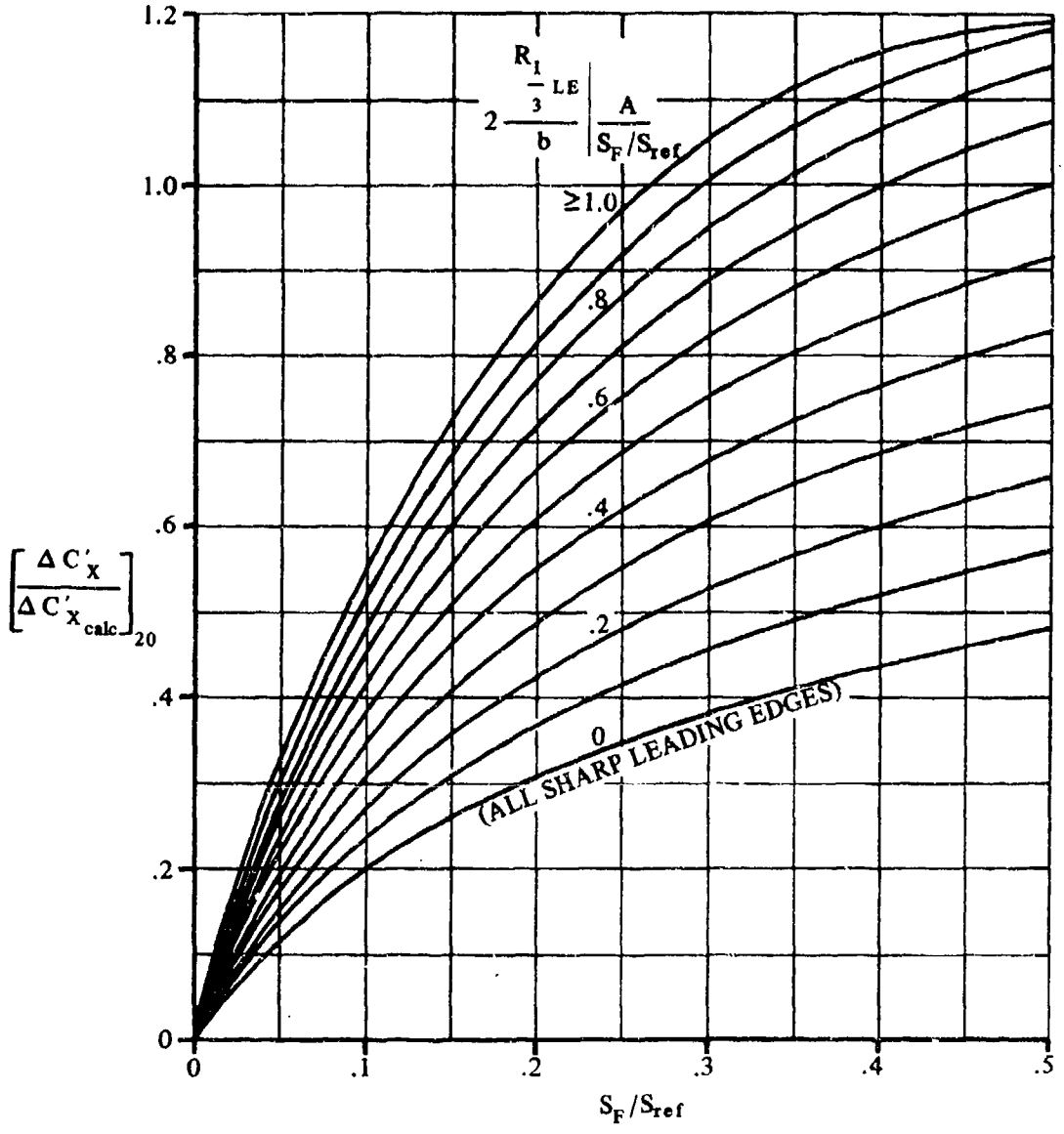

FIGURE 4.8.2.2-10 BASE-PRESSURE-COEFFICIENT CORRELATION FACTOR AT $\alpha' = 20^o$ DELTA AND MODIFIED-DELTA CONFIGURATIONS

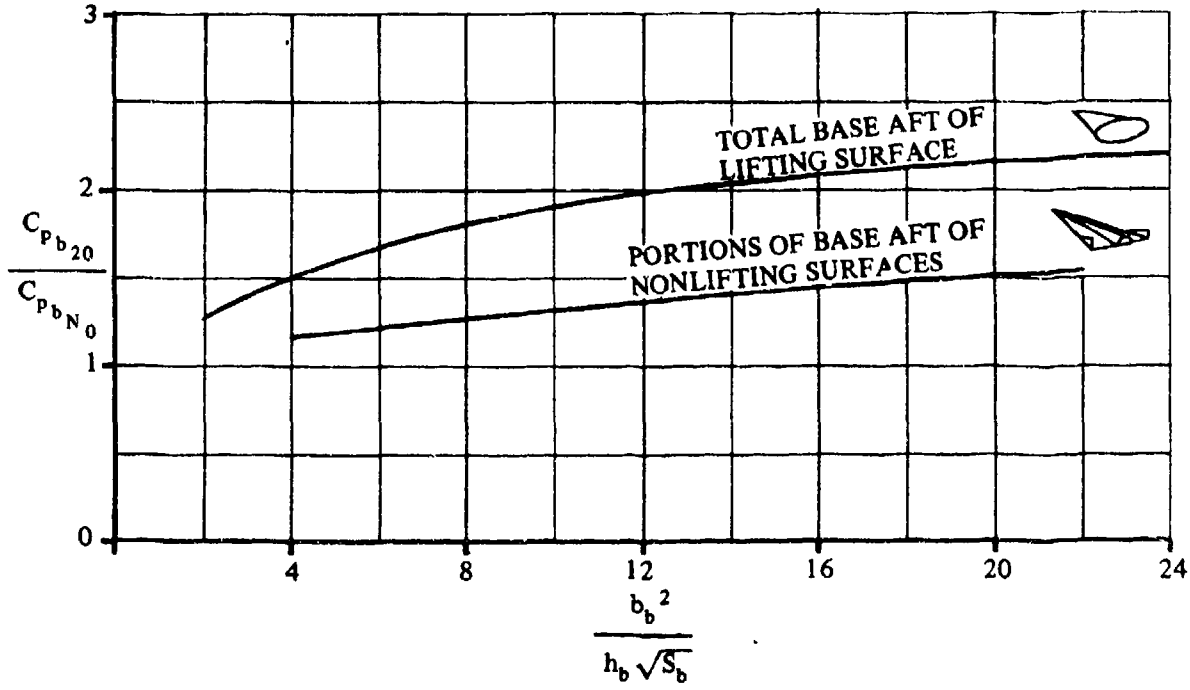

FIGURE 4.8.2.2-11 AXIAL-FORCE-COEFFICIENT CORRELATION FACTOR AT $\alpha' = 20^{\circ}$ --

4.8.3 WING, WING-BODY PITCHING MOMENT

4.8.3.1 WING, WING-BODY ZERO-NORMAL-FORCE PITCHING MOMENT

A. SUBSONIC

This section presents a design chart, taken from reference 1, to be used in approximating the zero-normal-force pitching-moment coefficient of nonsymmetrical delta-planform configurations with rounded leading edges at low speeds.

The design chart is based on a limited amount of experimental data and, furthermore, does not represent an extensive analysis of the zero-normal-force pitching moment. It is considered to provide only a first-order approximation of $C_{m_{N_0}}$.

DATCOM METHOD

The low-speed zero-normal-force pitching-moment coefficient of a nonsymmetrical delta-planform configuration with rounded leading edges, based on the product of the planform area and root chord Sc_r, is approximated from the procedure outlined in the following steps:

Step 1. Determine the zero-normal-force angle of attack α_{N_0} by using the method of Section 4.8.1.1.

Step 2. Obtain the zero-normal-force pitching-moment coefficient $C_{m_{N_0}}$ from figure 4.8.3.1-4 as a function of α_{N_0} determined in step 1.

Figure 4.8.3.1-4 is not applicable to configurations with sharp leading edges.

A comparison of the zero-normal-force pitching-moment coefficient of unsymmetrical delta-planform configurations calculated by this method with test results is presented as table 4.8.3.1-A. The values of α_{N_0} used in this data summary were calculated by using the method of Section 4.8.1.1.

Sample Problem

Given: The right-triangular pyramidal body designated configuration 1 in reference 7. This is the configuration of sample problem 1 of Section 4.8.1.1.

ℓ_B = 31.55 in. Nose radius = 0.1875 in. h_b = 6.44 in.

$\bar{z}_{base}$ = 4.105 in.

Compute:

Determine α_{N_0}

α_{N_0} = 8.04° (sample problem 1, Section 4.8.1.1)

Solution:

$$C_{m_{N_0}} = 0.00\,?7 \quad \text{(based on } Sc_r\text{)} \quad \text{(figure 4.8.3.1-4, extrapolated)}$$

The calculated result compares with a test value of 0.0028 from reference 7.

REFERENCES

1. Seeger, D. B., and Meyer, J. E.: An Investigation of the Subsonic Aerodynamic Characteristics and the Landing Flare Maneuver for Hypersonic Re-Entry Configurations. ASD-TDR-62-271, 1962. (C) Title Unclassified

2. Mantz, K., Seeger, D. B., and Ross, R.: Tests to Determine Subsonic Aerodynamic Characteristics of Hypersonic Re-Entry Configurations. ASD-TR-61-485, Supplement 1, 1963. (U)

3. Mantz, K., Seeger, D. B., and Ross, R.: Tests to Determine Subsonic Pressures, Forces and Moments Acting on a Hypersonic Re-Entry Configuration. ASD-TDR-62-270, Supplement 1, 1963. (U)

4. Paulson, J. W.: Low-Speed Static Stability and Control Characteristics of a Right Triangular Pyramid Re-Entry Configuration. NASA Memo 4-11-59L, 1959. (U)

5. Boisseau, P. C.: Investigation of the Low-Subsonic Flight Characteristics of a Model of a Re-Entry Vehicle with a Thick Flat 75° Swept Delta Wing and a Half-Cone Fuselage. NASA TN D-1007, 1962. (U)

6. Ware, G. M : Low-Subsonic-Speed Static Stability of Right-Triangular-Pyramid and Half-Cone Lifting Re-Entry Configurations. NASA TN D-646, 1961. (U)

7. Olstad, W. B., Mugler, J. P., Jr., and Cahn, M. S.: Static Longitudinal and Lateral Stability Characteristics of a Right Triangular Pyramidal Lifting Re-Entry Configuration at Transonic Speeds. NASA TN D-655, 1961. (U)

8. Mugler, J. P., Jr., and Olstad, W. B.: Static Longitudinal Aerodynamic Characteristics at Transonic Speeds of a Blunted Right Triangular Pyramidal Lifting Re-Entry Configuration for Angles of Attack up to 110°. NASA TN D-797, 1961. (U)

9. Paulson, J. W., and Shanks, R. E.: Investigation of Low-Subsonic Flight Characteristics of a Model of a Hypersonic Boost-Glide Configuration Having a 78° Delta Wing. NASA TN D-294, 1961. (U)

10. Wright Air Development Division: Unpublished data from the 5-foot wind tunnel, 1961. (U)

11. Shanks, R. E.: Investigation of the Low-Subsonic Flight Characteristics of a Model of an All-Wing Hypersonic Boost-Glide Configuration Having Very High Sweep. NASA TN D-369, 1960. (U)

TABLE 4.8.3.1-A

SUBSONIC ZERO-NORMAL-FORCE PITCHING MOMENT
DELTA PLANFORM CONFIGURATIONS
ROUND LEADING EDGES

DATA SUMMARY

Ref.	Configuration	$\alpha_{N_{0_{calc.}}}$ (Sect 4.8.1.1)	$C_{m_{N_0}}$ Calc.	$C_{m_{N_0}}$ Test
2	D-7	−2.15	−0.0007	−0.002
	D-8	0.20	0.0001	−0.0008
	D-9	0	0	0.0315
	WB-1	1.35	0.00045	0
	WB-3	1.46	0.00048	0
	WB-4	1.35	0.00045	−0.002
	WB-5	1.21	0.0004	−0.004
	WB-6	1.21	0.0004	−0.001
	WB-7	1.63	0.00054	−0.002
	WB-8	1.57	0.00052	0.0015
	WB-9	2.12	0.0007	0.001
	WB-10(0)	1.95	0.00065	−0.004
	R-2	3.79	0.00126	−0.009
	R-3	2.62	0.00087	−0.001
4	Right triangular pyramid	7.40	0.00246	0.002
5	Delta wing with half-cone fuselage	0.66	0.00022	−0.0123
6	a	7.23	0.00244	0.00133
	b(basic)	6.44	0.00214	−0.00133
	c(basic)	7.15	0.00214	0.00622
	d	4.40	0.0015	0
7	1	8.04	0.0027	0.0028
8	Blunted right triangular pyramid	6.91	0.0023	0.0023
9	Delta-wing boost-glide	−0.20	−0.0001	−0.0067
10	W-II E-3	−1.80	−0.0006	0.0100
11	All-wing boost-glide	−2.1	−0.0007	−0.00146

ROUND LEADING EDGES

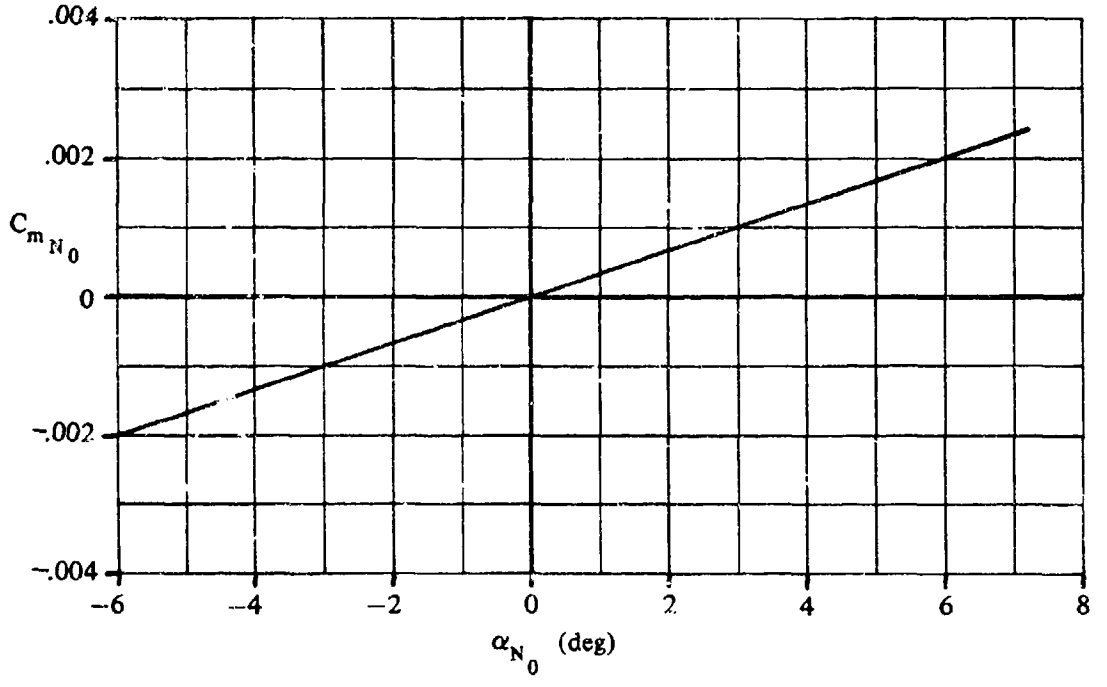

FICURE 4.8.3.1-4 VARIATION OF ZERO-NORMAL-FORCE PITCHING-MOMENT COEFFICIENT WITH CAMBER – DELTA AND MODIFIED DELTA CONFIGURATIONS

4.8.3.2 WING, WING-BODY PITCHING-MOMENT VARIATION WITH ANGLE OF ATTACK

A. SUBSONIC

This section presents a method for estimating the variation of pitching-moment coefficient with angle of attack for delta or modified-delta planform re-entry configurations at subsonic speeds.

The design charts are given in terms of the center-of-pressure location. The following equation is used to find the pitching-moment coefficient, based on the product of the planform area and root chord Sc_r:

$$C_m = C_{m_{N_0}} + \left(\frac{x_m}{c_r} - \frac{x_{c.p.}}{c_r}\right) C_{N'} \qquad 4.8.3.2\text{-a}$$

where

$\left(\frac{x_m}{c_r}\right)$ is the distance from the nose of the configuration to the desired moment reference center measured in root chords, positive aft.

$\left(\frac{x_{c.p.}}{c_r}\right)$ is the distance from the nose of the configuration to the center of pressure measured in root chords, positive aft.

$C_{N'}$ is the normal-force variation with angle of attack obtained by using the method of Section 4.8.1.2.

$C_{m_{N_0}}$ is the zero-normal-force pitching-moment coefficient obtained by using the method of Section 4.8.3.1. For symmetrical configurations $C_{m_{N_0}} = 0$.

The method for estimating the center-of-pressure location is taken from reference 1. A theoretical variation of center-of-pressure location with aspect ratio (or semiapex angle) from reference 2 was corrected to provide center-of-pressure estimates for thin, pointed-nose, symmetrical delta configurations. This result was then corrected to account for the effects of nose blunting and finite thickness.

The effect of nose blunting on delta wings was evaluated by assuming that the normal force acting on a pure delta wing can be divided into two components. One of these components is distributed uniformly over the planform and the other is concentrated at the leading edge. The strength of the concentrated component has a magnitude at any spanwise station proportional to the local chord. In accordance with this concept, the resultant of the uniform load acts 1/3 of the root chord forward of the trailing edge and the resultant of the leading-edge component acts 2/3 of the root chord forward of the trailing edge for a pure delta wing. The nose-blunting effects were then determined by assuming that the pitching moment depends only on normal force and by analyzing a simplified situation where a part of the nose of a pure delta wing is removed by a straight cut normal to the root chord. The center-of-pressure movement predicted in this manner is different from experimental results, since actual nose blunting usually consists of a rounding of the forward part of the wing rather than a sharp cut-off. Therefore, an empirical factor was applied, based on the results of reference 3, to compensate for this difference.

Finite thickness modifies the center-of-pressure location because of the contribution of axial force to pitching moment. The axial force produces a nose-down pitching moment at positive lifts as a result of the negative pressures on the upper surface of the wing and the positive pressures on the lower surface. An empirical correction for this effect, taken from reference 1, is presented in the Datcom method.

The Datcom method is applicable for angles of attack up to 20°.

DATCOM METHOD

The center-of-pressure location of delta or modified-delta configurations is given by

$$\frac{X_{c.p.}}{c_r} = \left(\frac{X_{c.p.}}{c_r}\right)_{\Delta} + \Delta\left(\frac{X_{c.p.}}{c_r}\right)_{B} + \Delta\left(\frac{X_{c.p.}}{c_r}\right)_{t} \qquad 4.8.3.2\text{-}b$$

where

$\left(\frac{X_{c.p.}}{c_r}\right)_{\Delta}$ is the distance from the wing apex to the center-of-pressure location, measured in root chords, of thin, pointed-nose, symmetrical delta configurations. This parameter is obtained from figure 4.8.3.2-6b as a function of the wing semiapex angle θ. The semiapex angle is measured as illustrated on figure 4.8.3.2-6a.

$\Delta\left(\frac{X_{c.p.}}{c_r}\right)_{B}$ is the increment in the center-of-pressure location, measured in root chords, due to nose blunting. This parameter is obtained from figure 4.8.3.2-7a as a function of the configuration semiapex angle θ and aspect ratio. The aspect ratio is that of the blunt-nose configuration.

$\Delta\left(\frac{X_{c.p.}}{c_r}\right)_{t}$ is the increment in the center-of-pressure location, measured in root chords, due to finite thickness. This parameter is obtained from figure 4.8.3.2-7b as a function of the ratio of the projected frontal area to the planform area S_F/S.

Figure 4.8.3.2-6a illustrates the configuration geometry used in this method.

A comparison of the center-of-pressure location calculated by this method with test results is presented as table 4.8.3.2-A. It should be noted that Reynolds-number effects might be expected to influence the pitching-moment characteristics of these configurations as the angle of attack and normal-force coefficients increase. However, the limited Reynolds-number range of the test data precluded isolation of Reynolds-number effects during the data correlation reported in reference 1.

Sample Problem

Given: A blunt-nose delta-wing model with a symmetrical diamond cross section and a blunt trailing edge. This is model D-4 of reference 5.

$A = 1.087$ $b = 13.934$ in. $S = 178.56$ sq in. $S_F = 41.44$ in.

$\theta = 15^{\circ}$ $c_r = 23.0$ in.

Compute:

$$\left(\frac{X_{c.p.}}{c_r}\right)_{\Delta} = 0.60 \quad \text{(figure 4.8.3.2-6b)}$$

$$1 - \frac{4 \tan \theta}{A} = 1 - \frac{4 \tan 15^{o}}{1.087} = 0.0140$$

$$\Delta\left(\frac{X_{c.p.}}{c_r}\right)_{B} = -0.049 \quad \text{(figure 4.8.3.2-7a)}$$

$$S_F/S = 41.44/178.56 = 0.232$$

$$\Delta\left(\frac{X_{c.p.}}{c_r}\right)_{t} = 0.0238 \quad \text{(figure 4.8.3.2-7b)}$$

Solution:

$$\frac{X_{c.p.}}{c_r} = \left(\frac{X_{c.p.}}{c_r}\right)_{\Delta} + \Delta\left(\frac{X_{c.p.}}{c_r}\right)_{B} + \Delta\left(\frac{X_{c.p.}}{c_r}\right)_{t} \quad \text{(equation 4.8.3.2-b)}$$

$$= 0.600 - 0.049 + 0.0238$$

$$= 0.5748$$

This compares with a test value of 0.582 from reference 5.

REFERENCES

1. Seeger, D. B., and Meyer, J. E.: An Investigation of the Subsonic Aerodynamic Characteristics and the Landing Flare Maneuver for Hypersonic Re-Entry Configurations. ASD-TDR-62-271, 1962. (C) Title Unclassified

2. Holmboe, V.: The Center of Pressure Position at Low Speeds and Small Angles of Attack for a Certain Type of Delta Wings. SAAB TN 13, 1952. (U)

3. Edwards, G. G., and Savage, H. F.: The Subsonic Aerodynamic Characteristics of Some Blunt Delta Configurations with 75° Sweepback. NASA TM X-581, 1961. (C) Title Unclassified

4. Mugler, J. P., Jr., and Olstad, W. B.: Static Longitudinal Aerodynamic Characteristics at Transonic Speeds of a Blunted Right Triangular Pyramidal Lifting Re-Entry Configuration for Angles of Attack up to 110°. NASA TN D-797, 1961. (U)

5. Mantz, K., Seeger, D. B., and Ross, R.: Tests to Determine Subsonic Aerodynamic Characteristics of Hypersonic Re-Entry Configurations. ASD-TR-61-485, Supplement 1, 1963. (U)

6. Mantz, K., Seeger, D. B., and Ross, R.: Tests to Determine Subsonic Pressures, Forces and Moments Acting on a Hypersonic Re-Entry Configuration. ASD-TDR-62-270, Supplement 1, 1963. (U)

7. De Young, J., and Harper, C. W.: Theoretical Span Loading at Subsonic Speeds for Wings Having Arbitrary Planform. NACA TR 921, 1948. (U)

8. Paulson, J. W., and Shanks, R. E.: Investigation of Low-Subsonic Flight Characteristics of a Model of a Hypersonic Boost-Glide Configuration Having a 78° Delta Wing. NASA TN D-894, 1961. (U)

9. Wright Air Development Division: Unpublished data from the 5-foot wind tunnel, 1961. (U)

10. Shanks, R. E.: Investigation of the Low-Subsonic Flight Characteristics of a Model of an All-Wing Hypersonic Boost-Glide Configuration Having Very High Sweep. NASA TN D-369, 1960. (U)

11. Paulson, J. W.: Low-Speed Static Stability and Control Characteristics of a Right Triangular Pyramid Re-Entry Configuration. NASA Memo 4-11-59L, 1959. (U)

12. Boisseau, P. C.: Investigation of the Low-Subsonic Flight Characteristics of a Model of a Re-Entry Vehicle with a Thick Flat 75° Swept Delta Wing and a Half-Cone Fuselage. NASA TN D-1007, 1962. (U)

13. Ware, G. M.: Low-Subsonic-Speed Static Stability of Right-Triangular-Pyramid and Half-Cone Lifting Re-Entry Configurations. NASA TN D-646, 1961. (U)

14. Olstad, W. B., Mugler, J. P., Jr., and Cahn, M. S.: Static Longitudinal and Lateral Stability Characteristics of a Right Triangular Pyramidal Lifting Re-Entry Configuration at Transonic Speeds. NASA TN D-655, 1961. (U)

15. Jaquet, B. M., and Brewer, J. D.: Low-Speed Static-Stability and Rolling Characteristics of Low-Aspect-Ratio Wings of Triangular and Modified Triangular Planforms. NACA RM L8L29, 1949. (U)

TABLE 4.8.3.2-A

SUBSONIC CENTER-OF-PRESSURE LOCATION
DELTA PLANFORM CONFIGURATIONS

DATA SUMMARY

Ref.	Configuration	A	θ (deg)	$\frac{S_F}{S}$	Nose Configuration	$\frac{x_{c.p.}}{c_r}$ Calc.	$\frac{x_{c.p.}}{c_r}$ Test	e Percent Error
4	Blunted right triangular pyramid	0.788	10.5	0.208	blunt	0.548	0.529	3.6
5	D-1	1.076	15.0	0.208	blunt	0.594	0.596	−0.2
	D-2	1.075		0.190	sharp	0.619	0.612	1.1
	D-3	1.076		0.312	sharp	0.631	0.626	0.8
	D-4	1.087		0.232	blunt	0.575	0.582	−1.2
	D-5	1.076		0.329	blunt	0.607	0.608	−0.2
	D-6	1.868	25.0	0.219	blunt	0.586	0.594	−1.3
	WB-2	1.094	15.0	0.161	blunt	0.560	0.577	−2.9
	WB-3	1.074		0.150	blunt	0.601	0.582	3.3
6	D-60	1.076	15.0	0.329	blunt	0.607	0.609	−0.3
8	Delta-wing boost-glide	0.74	12.0	0.050	sharp	0.613	0.625	−1.9
9	W-III E-3	1.07	15.0	0.029	blunt	0.583	0.578	0.9
11	Rt. triangular pyramid	0.78	10.6	0.203	blunt	0.547	0.618	−11.5
12	Delta wing with half-cone fuselage	0.77	15.0	0.484	blunt	0.598	0.568	5.3
13	b(basic)	0.783	10.5	0.201	blunt	0.551	0.575	−4.2
	c(basic)	0.787		0.371	blunt	0.566	0.591	−4.2
	d	0.783		0.291	blunt	0.560	0.553	1.3
14	1	0.742	10.5	0.186	blunt	0.632	0.560	12.9
15	2	2.31	30.0	0.120	sharp	0.583	0.539	8.2
	4	1.07	15.0		sharp	0.613	0.534	14.8
	7	4.00	45.0		sharp	0.559	0.548	2.0

Average Error = $\frac{\Sigma|e|}{n}$ = 3.9%

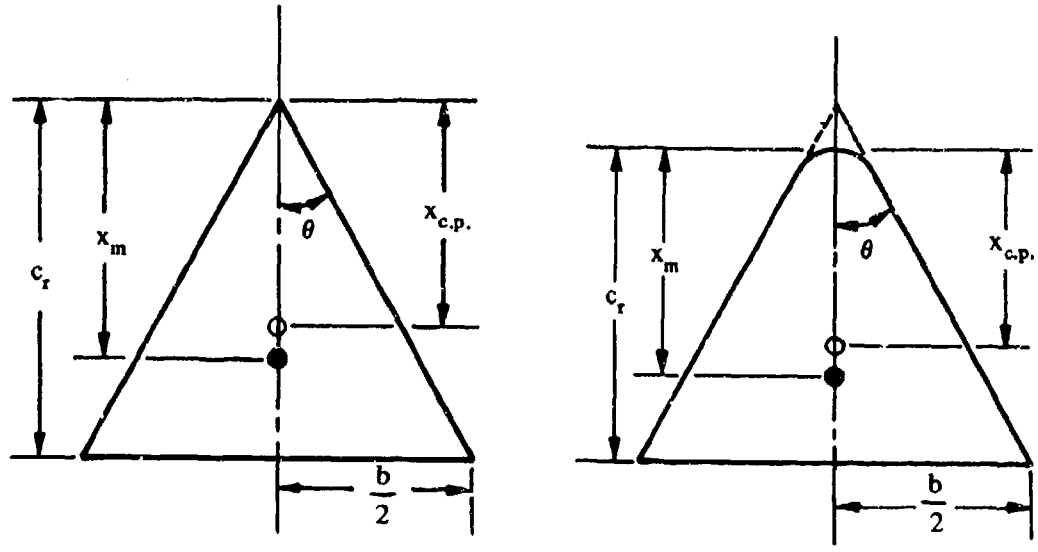

FIGURE 4.8.3.2- 6a CONFIGURATION GEOMETRY

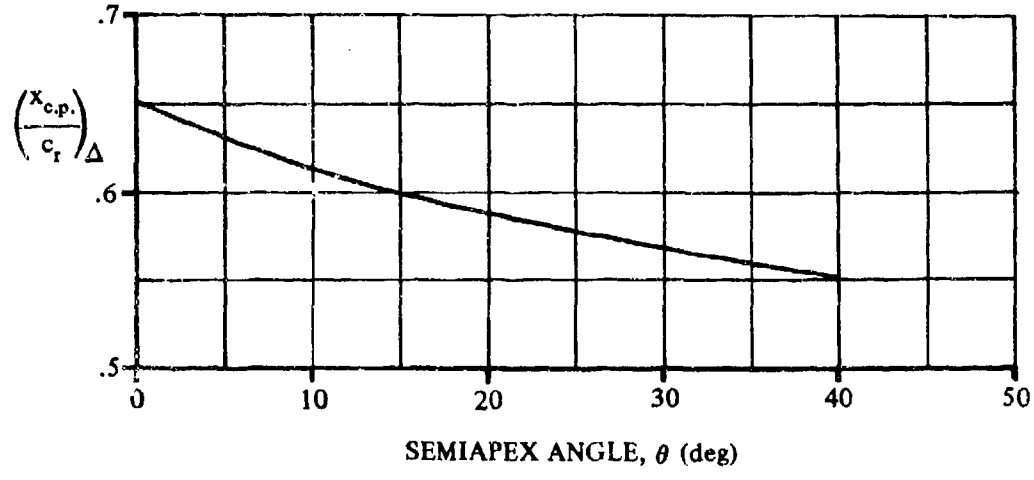

FIGURE 4.8.3.2- 6b CENTER OF PRESSURE FOR THIN, POINTED-NOSED, SYMMETRICAL DELTA CONFIGURATIONS

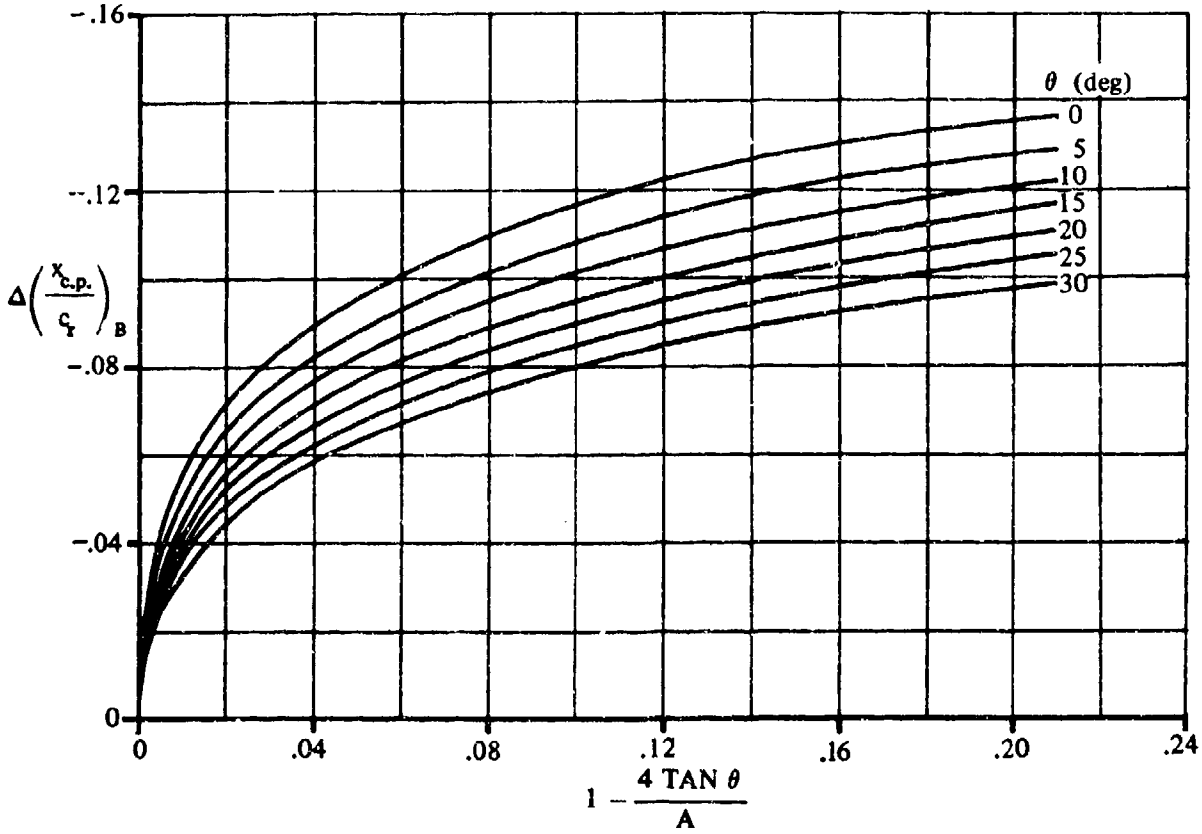

FIGURE 4.8.3.2-7a EFFECTS OF NOSE BLUNTING ON CENTER OF PRESSURE FOR DELTA AND MODIFIED-DELTA CONFIGURATIONS

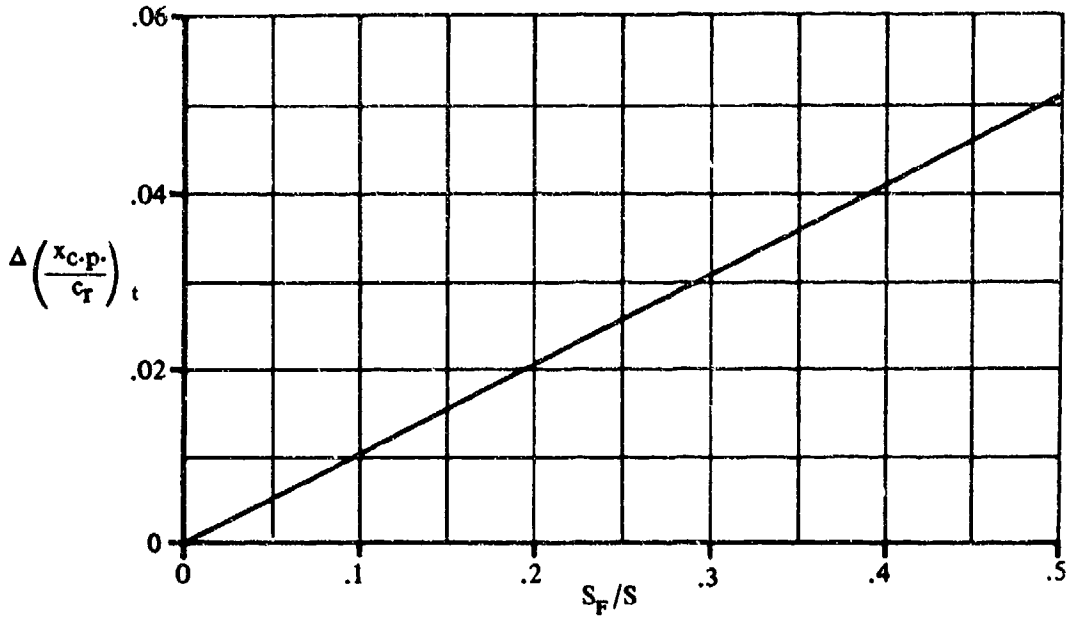

FIGURE 4.8.3.2-7b EFFECTS OF CONFIGURATION THICKNESS ON CENTER OF PRESSURE FOR DELTA AND MODIFIED-DELTA CONFIGURATIONS

5.1 WINGS IN SIDESLIP

5.1.1 WING SIDESLIP DERIVATIVE C_{Y_β}

5.1.1.1 WING SIDESLIP DERIVATIVE C_{Y_β} IN THE LINEAR ANGLE-OF-ATTACK RANGE

The wing contribution to the derivative C_{Y_β} is small, of the order α^2, and its accurate estimation is not vital.

Methods are presented in this section for estimation of wing side force due to sideslip in the subsonic and supersonic speed regimes. Methods for the estimation of this derivative in the transonic speed regime are not available.

A. SUBSONIC

InReference 1 a simplified theory consisting of an application of strip theory and lifting-line theory is applied to constant-chord swept wings in sideslip to determine approximate relations for the low-speed sideslip derivatives. The method presented in this section for estimating the wing side force due to sideslip at low subsonic speeds is taken from Reference 1. It is valid in the linear-lift region.

DATCOM METHOD

The wing sideslip derivative C_{Y_β} at low speeds neglecting the effect of dihedral is given inReference 1 as

$$C_{Y_\beta} = C_L^2 \left[\frac{6 \tan \Lambda_{c/4} \sin \Lambda_{c/4}}{\pi A (A + 4 \cos \Lambda_{c/4})} \right] \frac{1}{57.3} \text{ (per deg)} \qquad 5.1.1.1\text{-a}$$

The increment in side force due to dihedral at low subsonic speeds can be approximated by

$$\frac{\Delta C_{Y_\beta}}{|\Gamma|} = -0.0001 \ (\beta \text{ and } \Gamma \text{ in degrees}) \qquad 5.1.1.1\text{-b}$$

For subcritical speeds, the low-speed derivative can be modified by the Prandtl-Glauert rule to yield approximate corrections for the first-order three-dimensional effects of compressibility. The resulting expression fromReference 2 is

$$\left(\frac{C_{Y_\beta}}{C_L} \right)_M = \frac{A + 4 \cos \Lambda_{c/4}}{AB + 4 \cos \Lambda_{c/4}} \left(\frac{C_{Y_\beta}}{C_L} \right)_{\substack{\text{low} \\ \text{speed}}} \qquad 5.1.1.1\text{-c}$$

where

$$B = \sqrt{1 - M^2 \cos^2 \Lambda_{c/4}}$$

Calculated values for the wing side force due to sideslip obtained by the Datcom method for the wing configurations of References 3, 4, and 5 are compared with experimental data in Figure 5.1.1.1-5. The comparison indicates that the calculated values are fairly reliable over a range of lift coefficient (starting from zero) that decreases as wing sweep increases. Large discrepancies are noted for highly swept wings at lift coefficients for which the flow is believed to be partially separated.

Sample Problem

Given: The wing of Reference 5

$A = 4.0 \qquad \Lambda_{c/4} = 60^{\circ} \qquad \lambda = 0.6 \qquad \Gamma = 0.6 \qquad M = 0.13$

Compute:

$\sin \Lambda_{c/4} = 0.866$
$\cos \Lambda_{c/4} = 0.500$
$\tan \Lambda_{c/4} = 1.732$

Solution:

$$\frac{C_{Y_\beta}}{C_L^2} = \left[\frac{6 \tan \Lambda_{c/4} \sin \Lambda_{c/4}}{\pi A (A + 4 \cos \Lambda_{c/4})}\right] \frac{1}{57.3} \text{ (per deg)} \qquad \text{(Equation 5.1.1.1-a)}$$

$$= \frac{(6)(1.732)(0.866)}{\pi(4)\,[4 + 4(0.500)]} \frac{1}{57.3}$$

$$= \frac{9}{24\pi} \frac{1}{57.3}$$

$$= 0.00208 \text{ per deg}$$

C_L	C_L^2	$C_{Y_\beta} \times 10^3$ (per deg)
0.05	0.0025	0.0052
0.10	0.010	0.0208
0.20	0.040	0.0832
0.30	0.090	0.1872
0.40	0.160	0.3328
0.50	0.250	0.5200
0.60	0.360	0.7488

These results are compared with experimental values in Figure 5.1.1.1-5.

B. TRANSONIC

No method is available in the literature for estimation of the wing contribution to the derivative C_{Y_β} in the transonic speed regime and none is presented in the Datcom. Furthermore, no experimental data are available in this speed regime.

C. SUPERSONIC

No general method has been developed for estimating the wing side force due to sideslip at supersonic speeds. However, theoretical methc is are available for discrete planforms over certain speed ranges. A comprehensive summary of the available theoretical methods for calculating the wing side force due to sideslip is presented in Reference 6. The expressions for the derivatives for each planform have been obtained from application of the linearized theory for compressible flow as applied to thin airfoils. The linearized theory is directly applicable for the lateral motion of sideslip and the results are limited only by the complexity of the calculations required to determine the load distributions for certain planforms under certain conditions. Calculation complexities arise as a result of the existence of regions of interacting or mutually subsonic edges (a subsonic edge lying within the region of influence of another). Consequently, the theoretical calculations available are limited primarily to combinations of planforms and Mach lines that do not have interacting or mutually subsonic edges.

No experimental data are available in the supersonic speed regime; consequently, the quantitative accuracy of the estimation methods cannot readily be assessed. However, a review of the application of linearized theory for the prediction of wing lift-curve slope at supersonic speeds can at least lead to a qualitative conclusion of the theory's accuracy when applied to lateral derivatives. Comparison has shown that the agreement between experiment and linear compressible-flow theory with regard to wing lift-curve slope is satisfactory for most practical purposes. To conclude that linearized theory is therefore adequate for lateral derivative prediction seems somewhat questionable in that the lift-curve slope is dependent on the integrated pressure; whereas the lateral derivatives are dependent on pressure distribution. However, when coupled with the fact that the lateral derivatives are relatively insensitive to small shifts in spanwise center of pressure, the indication is that application of the linearized compressible-flow theory should give fairly good results at least insofar as general trends and orders of magnitude are concerned.

DATCOM METHODS

The Datcom methods are taken from References 7, 8, and 9 and present the wing side force due to sideslip over limited Mach number ranges for rectangular planforms, triangular planforms, and fully tapered sweptback planforms with swept forward or sweptback trailing edges. The results are mainly functions of planform geometry and Mach number.

Rectangular Planform: $A\beta \geq 1.0$

The wing side force due to sideslip for rectangular planforms (neglecting the effect of dihedral) is derived in Reference 7 as

$$\frac{C_{Y_\beta}}{\alpha^2} = -\frac{8M^2}{\pi A\beta^2}\,\frac{1}{57.3} \text{ (per deg)} \qquad 5.1.1.1\text{-d}$$

where α is in radians and $\beta = \sqrt{M^2 - 1}$.

Equation 5.1.1.1-d is valid for Mach number and aspect ratio greater than that for which the Mach line from the leading edge of the tip section intersects the trailing edge of the opposite tip section ($A\beta \geq 1.0$).

Sweptback Planform ($\lambda = 0$): $\beta \cot \Lambda_{LE} \leq 1.0$

The wing side force due to sideslip for fully tapered sweptback planforms (neglecting the effect of dihedral) is derived in Reference 8 for triangular planforms and in Reference 9 for planforms with sweptforward or sweptback trailing edges as

$$\frac{C_{Y_\beta}}{\alpha^2} = -\frac{\pi}{4} AM^2 Q(\beta C) \frac{1}{57.3} \text{ (per deg)} \qquad 5.1.1.1\text{-e}$$

where α is in radians and $Q(\beta C)$ is obtained from figure 5.1.1.1-6.

Equation 5.1.1.1-e is valid for Mach number and aspect ratio for which the wing is contained within the Mach cones springing from the apex and the trailing edge at the center of the wing.

The increment in side force due to dihedral given by Equation 5.1.1.1-b is also applicable at supersonic speeds.

REFERENCES

1. Toll, T. A., and Queijo, M. J.: Approximate Relations and Charts for Low-Speed Stability Derivatives of Swept Wings. NACA TN 1581, 1948. (U)

2. Fisher, L.: Approximate Corrections for the Effects of Compressibility on the Subsonic Stability Derivatives of Swept Wings. NACA TN 1854, 1949. (U)

3. Wolhart, W. D., and Thomas, D. F., Jr.: Static Longitudinal and Lateral Stability Characteristics at Low Speed of Unswept-Midwing Models Having Wings with an Aspect Ratio of 2, 4, or 6. NACA TN 3649, 1956. (U)

4. Thomas, D. F., Jr., and Wolhart, W. D.: Static Longitudinal and Lateral Stability Characteristics at Low Speed of 45° Sweptback-Midwing Models Having Wings with an Aspect Ratio of 2, 4, or 6. NACA TN 4077, 1957. (U)

5. Wolhart, W. D., and Thomas, D. F., Jr.: Static Longitudinal and Lateral Stability Characteristics at Low Speed of 60° Sweptback-Midwing Models Having Wings with an Aspect Ratio of 2, 4, or 6. NACA TN 4397, 1958. (U)

6. Jones, A. L., and Alksne, A.: A Summary of Lateral-Stability Derivatives Calculated for Wing Planforms in Supersonic Flow. NACA TR 1052, 1951. (U)

7. Harmon, S. M.: Stability Derivatives at Supersonic Speeds of Thin Rectangular Wings with Diagonals Ahead of Tip Mach Lines. NACA TR 925, 1949. (U)

8. Ribner, H. S., and Malvestuto, F. S., Jr.: Stability Derivatives of Triangular Wings at Supersonic Speeds. NACA TR 903, 1948. (U)

9. Malvestuto, F. S., Jr., and Margolis, K.: Theoretical Stability Derivatives of Thin Sweptback Wings Tapered to a Point with Sweptback or Sweptforward Trailing Edges for a Limited Range of Supersonic Speeds. NACA TR 971, 1950. (U)

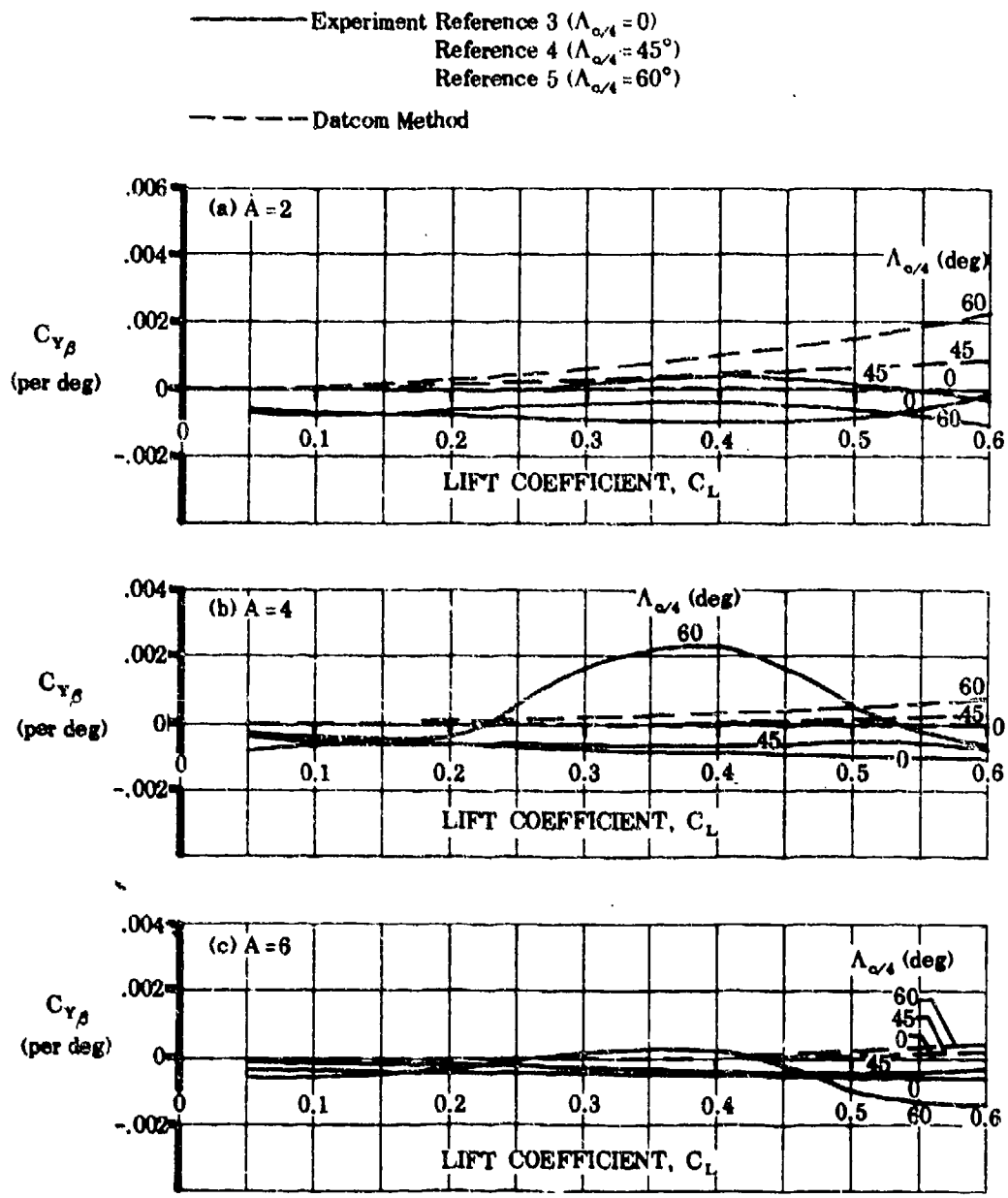

FIGURE 5.1.1.1-5 COMPARISON OF CALCULATED AND EXPERIMENTAL VALUES OF WING SIDE FORCE DUE TO SIDESLIP FOR THE WING CONFIGURATIONS OF REFERENCES 3, 4, AND 5

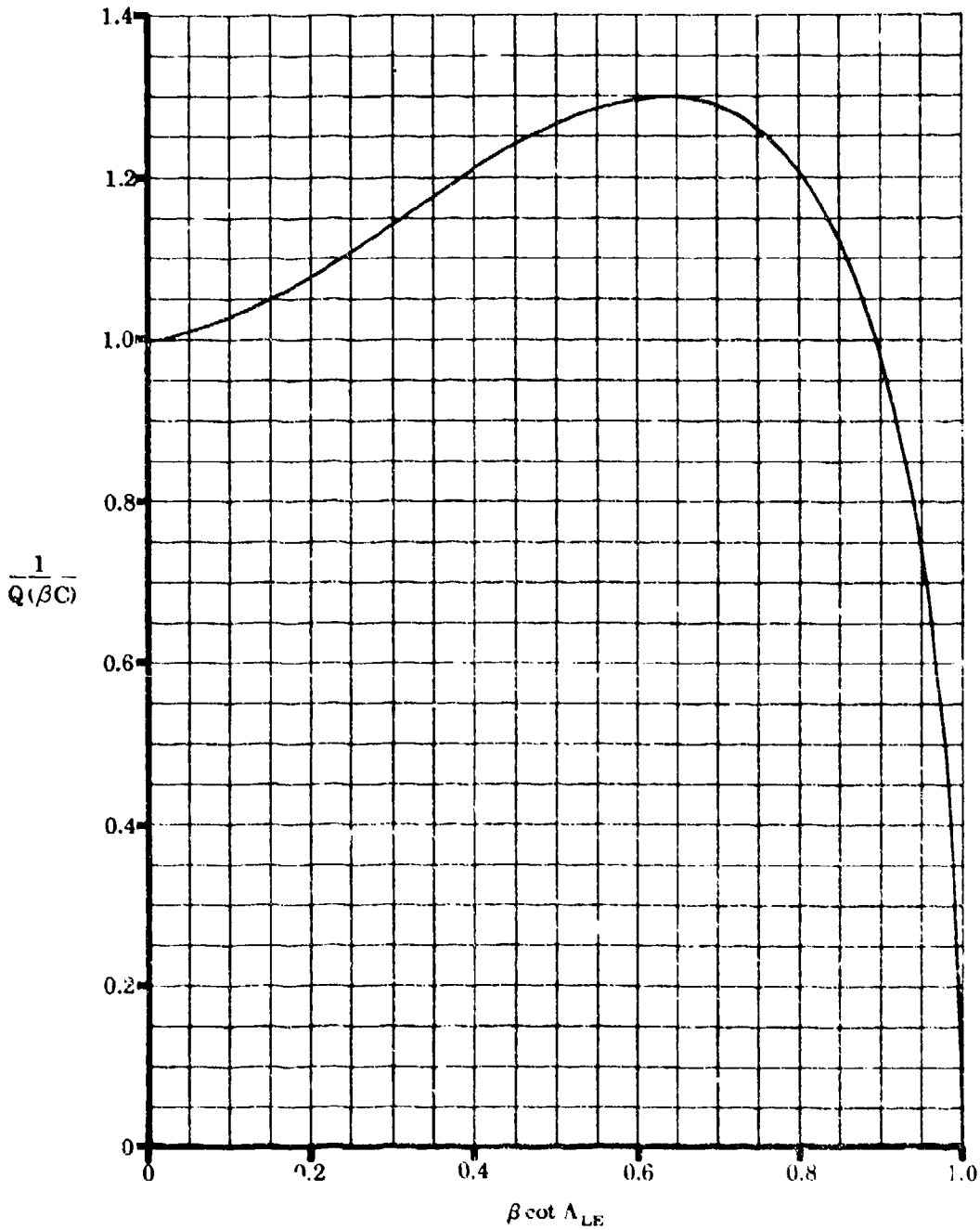

FIGURE 5.1.1.1-6 ELLIPTIC INTEGRAL FACTOR OF THE STABILITY DERIVATIVE

5.1.2 WING SIDESLIP DERIVATIVE C_{l_β}

5.1.2.1 WING SIDESLIP DERIVATIVE C_{l_β} IN THE LINEAR ANGLE-OF-ATTACK RANGE

A. SUBSONIC

For wings at low angles of attack and subsonic speeds, the rolling moment due to sideslip is principally a function of wing aspect ratio, taper ratio, dihedral angle, and sweep.

The effect of aspect ratio on the rolling moment of unswept wings is treated theoretically in reference 1. In this reference, a wing in sideslip is represented by a suitably restricted system of vortices. The span loading is calculated and then integrated to obtain the rolling moment. The results show that C_{l_β} for three-dimensional unswept wings increases approximately linearly with $1/A$ and decreases slightly with taper ratio.

The vortex representation used in reference 1 for unswept wings is applied to swept straight-tapered planforms in reference 2. Here, the rolling moment is found to be a strong function of sweep, but the increment provided by sweep is relatively insensitive to variations of aspect ratio and taper ratio.

A rather different approach to the straight-tapered-wing rolling-moment problem is taken in reference 3. Here, the effects of sweep on C_{l_β} are calculated as the difference between the effective lift-curve slopes for the upwind and downwind wing panels. Panel lift-curve slope is assumed to be a function of effective sweep angle $(\Lambda \pm \beta)$ and effective geometric aspect ratio. Aspect-ratio effects are then taken to be the difference between the experimental and the calculated values for swept wings.

In spite of their widely differing approaches, references 2 and 3 give similar results. For very low aspect ratios, slender-body theory, as applied in reference 4, shows that $C_{l_\beta} = -2/3\ A$ (per radian). This value compares well with experimental data for low-aspect-ratio delta wings.

Neither reference 2 nor reference 3 defines a lower aspect-ratio limit, below which the respective theories are invalid. However, since neither theory converges to the slender-body value at low aspect ratios, there must be a transition region between the high-aspect-ratio values of references 2 and 3 and the slender-body value of reference 4.

At subsonic speeds methods are presented for determining the rolling moment due to sideslip for the following classes of wing planforms:

Straight-Tapered Wings (conventional, trapezoidal wings)

Non-Straight-Tapered Wings

- Double-delta wings
- Cranked wings

These two general categories of non-straight-tapered wings are illustrated in sketch (a) of Section 4.1.3.2. Their wing-geometry parameters are presented in Section 2.2.2.

The Datcom method for straight-tapered wings is a combination of the methods of references 1, 2, 3, and 4. Reference 4 is used for low-aspect-ratio wings. References 1, 2, and 3 are used for high aspect ratios, with experimental data serving as a guide as to which theory is most applicable. For intermediate aspect ratios the experimental data of references 8 through 13 are used as a guide in constructing a faired curve between the slender-body values of reference 4 and the high-aspect-ratio values of references 1, 2, and 3. Mach number effects are calculated by the method of reference 3. The effect of uniform geometric dihedral is accounted for by the method of references 5 and 6, that of nonuniform geometric dihedral by the method of reference 6, and that of wing twist by the method of reference 7.

The Datcom method for double-delta and cranked wings is taken from reference 14. In addition to wing aspect ratio, taper ratio, dihedral angle, and sweep, the location of the leading-edge or trailing-edge sweep break is an important factor in determining the rolling moment due to sideslip of these non-straight-tapered wings. The method is based on the results presented for straight-tapered wings. The composite wing is divided into two individual panels and a "weighted-lift" relationship is applied to the rolling moment due to sideslip of each panel calculated using the straight-tapered wing method.

The subsonic methods presented in this section are valid for sideslip angles between -5^{o} and $+5^{o}$ at speeds up to $M = 0.60$ and low angles of attack.

No provision is made for the effective-dihedral contribution of the wing tip shape. This contribution is important only for thick wings and taper ratios near 1.0.

DATCOM METHODS

Straight-Tapered Wings

The subsonic rolling moment due to sideslip of a straight-tapered wing with uniform geometric dihedral at low angles of attack is given by the following equations:

For $A \geq 1.0$:

$$C_{l_\beta} = C_L \left[\left(\frac{C_{l_\beta}}{C_L} \right)_{\Lambda_{c/2}} K_{M_\Lambda} + \left(\frac{C_{l_\beta}}{C_L} \right)_{A} \right] + \Gamma \left(\frac{C_{l_\beta}}{\Gamma} K_{M_\Gamma} \right) + \theta \tan \Lambda_{c/4} \frac{\Delta C_{l_\beta}}{\theta \tan \Lambda_{c/4}} \text{ (per degree)} \qquad 5.1.2.1\text{-a}$$

For $A < 1.0$:

$$C_{l_\beta} = C_L \left[-\frac{1}{57.3} \frac{2}{3} \frac{1}{A} \right] - \Gamma \left(\frac{A}{6} \right) \text{ (per degree)} \qquad 5.1.2.1\text{-a}'$$

where

$\left(\frac{C_{l_\beta}}{C_L} \right)_{\Lambda_{c/2}}$ is the wing-sweep contribution obtained from figure 5.1.2.1-27.

K_{M_Λ} is the compressibility correction to the sweep contribution, obtained from figure 5.1.2.1-28a.

$\left(\frac{C_{l_\beta}}{C_L}\right)_A$ is the aspect-ratio contribution, including taper-ratio effects, obtained from figure 5.1.2.1-28b.

$\frac{C_{l_\beta}}{\Gamma}$ is the dihedral effect for uniform geometric dihedral, obtained from figure 5.1.2.1-29.

Γ is the dihedral angle in degrees.

$K_{M\Gamma}$ is the compressibility correction factor to the uniform-geometric-dihedral effect, obtained from figure 5.1.2.1-30a.

$\frac{\Delta C_{l_\beta}}{\theta \tan \Lambda_{c/4}}$ is the wing-twist correction factor, obtained from figure 5.1.2.1-30b.

θ is the wing-twist between the root and tip stations, negative for washout (see figure 5.1.2.1-30b).

For wings with nonuniform dihedral, the dihedral term of equation 5.1.2.1-a; i.e., $\Gamma\left(\frac{C_{l_\beta}}{\Gamma} K_{M\Gamma}\right)$, is replaced by $\left(\frac{\beta C_{l_\beta}}{\kappa\Gamma}\right)\left(\frac{\kappa\Gamma}{\beta}\right)$ (per degree).

where

$\frac{\beta C_{l_\beta}}{\kappa\Gamma}$ is the rolling-moment-due-to-sideslip parameter for any symmetric, spanwise distribution of dihedral angle, obtained from figure 5.1.2.1-31 as a function of Λ_β and $\beta A/\kappa$.

The parameter κ is the ratio of the two-dimensional lift-curve slope at the appropriate Mach number to 2π; i.e., $\left(c_{\ell_\alpha}\right)_M / 2\pi$. The two-dimensional lift-curve slope is obtained from Section 4.1.1.2. For wings with airfoil sections varying in a reasonably linear manner with span, the average value of the lift-curve slopes of the root and tip sections is adequate.

The parameter Λ_β is the compressible sweep parameter given as $\Lambda_\beta = \tan^{-1}(\tan \Lambda_{c/4}/\beta)$.

Γ is the geometric dihedral in degrees.

Figure 5.1.2.1-31 applies directly to a gull-wing arrangement with the dihedral starting at the wing root and extending outboard to some spanwise station. For partial-span dihedral starting at some spanwise station η_i and extending outboard to some spanwise station η_o, the value of $\frac{\beta C_{l_\beta}}{\kappa\Gamma}$ is obtained as illustrated in sketch (a).

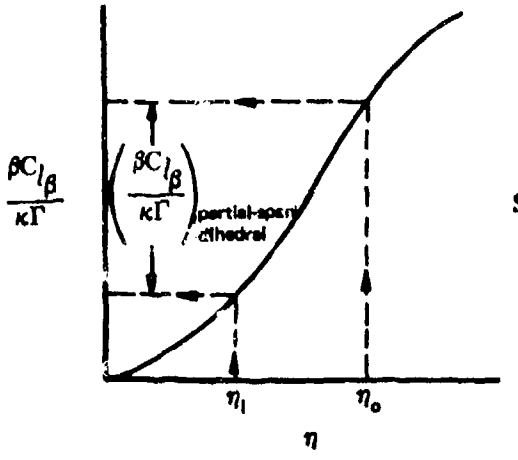

SKETCH (a)

Lifting-surface theory has been used in reference 6 to obtain the rolling moment due to sideslip for any symmetric, spanwise distribution of dihedral. The theory is applicable only to wings for which $\beta A \geq 2$ and $\Lambda_\beta \leq 60^\circ$.

It should be noted that at $\eta = 1.0$ figure 5.1.2.1-31 gives the dihedral effect due to uniform dihedral. However, the uniform-dihedral term of equation 5.1.2.1-a has been retained because of the ease with which figure 5.1.2.1-29 can be applied.

Sample problem 1 at the conclusion of this paragraph (page 5.1.2.1-5) illustrates the use of this method applied to a straight-tapered, untwisted wing with no dihedral. A sample problem including the effect of uniform dihedral is presented in paragraph A of Section 5.2.2.1.

A comparison of low-speed test values with results calculated by using this method for straight-tapered wings is presented as table 5.1.2.1-A. The ranges of geometric parameters of the test data are:

$$0.25 \leq A \leq 6.93$$

$$\leq \Lambda_{c/2} \leq 75.3^\circ$$

$$0 \leq \lambda \leq 1.0$$

$$\Gamma = 0$$

$$\theta = 0$$

Test data are not available to permit substantiation of the effects of either wing-twist or dihedral on the wing rolling moment due to sideslip.

Non-Straight-Tapered Wings

The method for determining the rolling moment due to sideslip of double-delta and cranked wings is taken from reference 14. The non-straight-tapered wing is divided into two panels, with each panel having conventional straight-tapered geometry. Then for each of the constructed panels, the individual rolling moment due to sideslip is estimated by the method presented above for straight-tapered wings. The individual rolling-moment coefficients derived for each constructed panel are then weighted according to the proportion of the total lift that those panels produce. In order to maintain the proper span reference, the rolling-moment coefficient of the constructed inboard set of panels is further modified by multiplying its contribution by the ratio of the inboard span to the reference span (total wing span).

The method is applicable only to untwisted wings with zero degrees dihedral at low angles of attack.

The rolling moment due to sideslip of double-delta and cranked wings is obtained from the procedure outlined in the following steps:

Step 1. Divide the composite wing into constructed inboard and outboard panels as discussed in paragraph A of Section 4.1.4.2 (see pages 4.1.4.2-5, -6), and determine their pertinent geometric parameters.

Step 2. Determine the lift-curve slopes of the constructed inboard and outboard panels from figure 4.1.3.2-49, based on their respective areas S_i and S_o'.

Step 3. Determine the rolling moment due to sideslip, based on the total wing area and span, by

$$\frac{C_{l_\beta}}{C_L} = \frac{1}{(C_{L_\alpha})_{total}} \left\{ (C_{L_\alpha})_i \frac{S_i}{S_W} \left[\left(\frac{C_{l_\beta}}{C_L} \right)_{\Lambda_{c/2_i}} K_{M_{\Lambda_i}} + \left(\frac{C_{l_\beta}}{C_L} \right)_{A_i} \right] \frac{b_i}{b_W} \right.$$
$$\left. + (C_{L_\alpha})_o' \frac{S_o'}{S_W} \left[\left(\frac{C_{l_\beta}}{C_L} \right)_{\Lambda_{c/2_o}'} K_{M_{\Lambda_o'}} + \left(\frac{C_{l_\beta}}{C_L} \right)_{A_o'} \right] \right\} \text{(per degree)} \qquad 5.1.2.1\text{-b}$$

where the subscript i and the prime and subscript o denote the constructed inboard and outboard panels, respectively.

The parameters $(C_{l_\beta}/C_L)_{\Lambda_{c/2}}$, K_{M_Λ}, and $(C_{l_\beta}/C_L)_A$ are obtained from figures 5.1.2.1-27, 5.1.2.1-28a, and 5.1.2.1-28b, respectively, by using the geometry of the constructed inboard and outboard panels.

$$(C_{L_\alpha})_{total} = (C_{L_\alpha})_i \frac{S_i}{S_W} + (C_{L_\alpha})_o' \frac{S_o'}{S_W}$$

If the aspect ratio of an individual set of constructed wing panels is less than one, C_{l_β}/C_L for that set of panels is calculated by equation 5.1.2.1-a'. For example, if the aspect ratio of the constructed inboard panel is less than one, then equation 5.1.2.1-b would be expressed as

$$\frac{C_{l_\beta}}{C_L} = \left(\frac{1}{C_{L_\alpha}} \right)_{total} \left\{ (C_{L_\alpha})_i \frac{S_i}{S_W} \left[\frac{1}{57.3} \frac{2}{3} \frac{1}{A_i} \right] \frac{b_i}{b_W} + (C_{L_\alpha})_o' \frac{S_o'}{S_W} \left[\left(\frac{C_{l_\beta}}{C_L} \right)_{\Lambda_{c/2_o}'} K_{M_{\Lambda_o'}} + \left(\frac{C_{l_\beta}}{C_L} \right)_{A_o'} \right] \right\}$$

Sample problem 2 on page 5.1.2.1-6 illustrates the use of this method.

A comparison of low-speed test values with results calculated by this method is presented as table 5.1.2.1-B (taken from reference 14). The limited availability of experimental data precludes substantiation of this method.

Sample Problems

1. Straight-Tapered Wing

Given: A sweptback wing of reference 29.

$A = 4.0$ $\lambda = 0.60$ $\Lambda_{c/2} = 59.2^{o}$ $\Gamma = 0$ $\theta = 0$ $M = 0.13$

Compute:

$$\left(\frac{C_{l_\beta}}{C_L}\right)_{\Lambda_{c/2}} = \text{-0.0072 per deg (figure 5.1.2.1-27, interpolated)}$$

$$\frac{A}{\cos \Lambda_{c/2}} = \frac{4.0}{\cos 59.2^{o}} = 7.81$$

$$M \cos \Lambda_{c/2} = 0.13 \cos \Lambda_{c/2} = 0.067$$

$K_{M_\Lambda} = 1.00$ (figure 5.1.2.1-28a)

$$\left(\frac{C_{l_\beta}}{C_L}\right)_{A} = \text{-0.0016 per deg (figure 5.1.2.1-28b)}$$

Solution:

$$\frac{C_{l_\beta}}{C_L} = \left[\left(\frac{C_{l_\beta}}{C_L}\right)_{\Lambda_{c/2}} K_{M_\Lambda} + \left(\frac{C_{l_\beta}}{C_L}\right)_{A}\right] \text{(equation 5.1.2.1-a with } \Gamma = 0,\ \theta = 0)$$

$$= \left[-(0.0072)\,(1.0) + (-0.0016)\right]$$

$$= \text{-0.0088 per deg (based on } S_W\, b_W)$$

This result compares with a test value of -0.0094 from reference 29.

2. Non-Straight-Tapered Wing

Given: A cranked wing of reference 30.

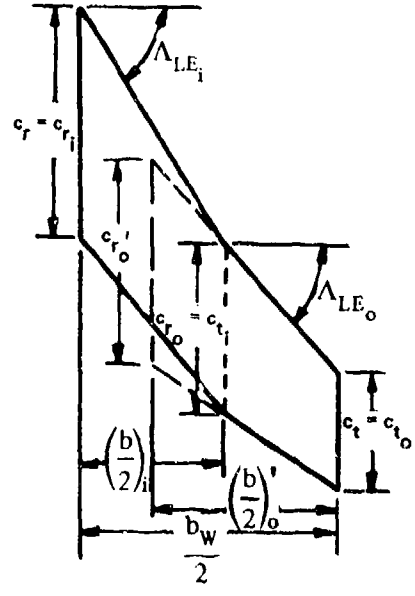

Total-Wing Characteristics:

$S_W = 12.10$ sq ft $\quad \frac{b_W}{2} = 3.0$ ft $\quad \lambda_W = 0.470$

$\eta_B = 0.583$ $\quad c_{r_W} = 2.75$ ft $\quad A_W = 2.975$

$\Lambda_{LE_i} = 59.0^{o}$ $\quad \Lambda_{LE_o} = 48.5^{o}$ $\quad \Lambda_{c/2_i} = 55.0^{o}$

$\Lambda_{c/2_o} = 41.0^{o}$ $\quad \Gamma = 0$ $\quad \theta = 0$

Constructed-Inboard-Panel Characteristics:

$S_i = 8.18$ sq ft $\quad A_i = 1.50$ $\quad \lambda_i = 0.70$

$\left(\frac{b}{2}\right)_i = 1.75$ ft $\quad \Lambda_{c/2_i} = 55.0^{o}$ $\quad \Lambda_{LE_i} = 59.0^{o}$

$$\frac{S_i}{S_W} = 0.676$$

Constructed-Outboard-Panel Characteristics:

$S'_o = 7.72$ sq ft $\quad A'_o = 2.34 \quad \lambda'_o = 0.55 \quad \left(\frac{b}{2}\right)'_o = 2.125$ ft

$\left(\Lambda_{LE}\right)'_o = \Lambda_{LE_o} = 48.5^o \quad \left(\Lambda_{c/2}\right)'_o = \Lambda_{c/2_o} = 41.0^o \quad \frac{S'_o}{S_W} = 0.638$

Additional Characteristics:

$M = 0.18; \quad \beta = 0.984 \qquad \kappa = 1.0$ (assumed)

Compute

$\left(C_{L_\alpha}\right)_i$ and $\left(C_{L_\alpha}\right)'_o$ (Section 4.1.3.2)

$$\frac{A_i}{\kappa}\left[\beta^2 + \tan^2 \Lambda_{c/2_i}\right]^{1/2} = \frac{1.50}{1.0}\left[0.9676 + (1.4281)^2\right]^{1/2} = 2.60$$

$$\left(\frac{C_{L_\alpha}}{A}\right)_i = 1.19 \text{ per rad (figure 4.1.3.2-49)}$$

$$\left(C_{L_\alpha}\right)_i = \left(\frac{C_{L_\alpha}}{A}\right)_i A_i = (1.19)(1.5) = 1.785 \text{ per rad}$$

$$\frac{A'_o}{\kappa}\left[\beta^2 + \tan^2 \Lambda_{c/2'_o}\right]^{1/2} = \frac{2.34}{1.0}\left[0.9676 + (0.8693)^2\right]^{1/2} = 3.07$$

$$\left(\frac{C_{L_\alpha}}{A}\right)'_o = 1.11 \text{ per rad (figure 4.1.3.2-49)}$$

$$\left(C_{L_\alpha}\right)'_o = \left(\frac{C_{L_\alpha}}{A}\right)'_o A'_o = (1.11)(2.34) = 2.60 \text{ per rad}$$

$$\left(C_{L_\alpha}\right)_{total} = \left(C_{L_\alpha}\right)_i \frac{S_i}{S_W} + \left(C_{L_\alpha}\right)'_o \frac{S'_o}{S_W}$$

$$= 1.785\,(0.676) + 2.60\,(0.638) = 2.865$$

$\left(\frac{C_{l_\beta}}{C_L}\right)_{\Lambda_{c/2_i}}$ and $\left(\frac{C_{l_\beta}}{C_L}\right)_{\Lambda_{c/2_o}'}$

$\left(\frac{C_{l_\beta}}{C_L}\right)_{\Lambda_{c/2_i}}$ = -0.0045 per deg (figure 5.1.2.1-27, interpolated for A_i, λ_i, and $\Lambda_{c/2_i}$)

$\left(\frac{C_{l_\beta}}{C_L}\right)_{\Lambda_{c/2_o}'}$ = -0.0032 per deg (figure 5.1.2.1-27, interpolated for A_o', λ_o', and $\Lambda_{c/2_o}'$)

$K_{M\Lambda_i}$ and $K_{M\Lambda_o'}$

$$\frac{A_i}{\cos \Lambda_{c/2_i}} = \frac{1.50}{0.5736} = 2.615$$

$$M \cos \Lambda_{c/2_i} = (0.18)(0.5736) = 0.103$$

$K_{M\Lambda_i}$ = 1.0 (figure 5.1.2.1-28a)

$$\frac{A_o'}{\cos \Lambda_{c/2_o}'} = \frac{2.34}{0.7547} = 3.10$$

$$M \cos \Lambda_{c/2_o}' = (0.18)(0.7547) = 0.136$$

$K_{M\Lambda_o'}$ = 1.0 (figure 5.1.2.1-28a)

$\left(\frac{C_{l_\beta}}{C_L}\right)_{A_i}$ and $\left(\frac{C_{l_\beta}}{C_L}\right)_{A_o'}$

$\left(\frac{C_{L_\beta}}{C_L}\right)_{A_i}$ = -0.0065 per deg (figure 5.1.2.1-28b at A_i and λ_i)

$\left(\frac{C_{L_\beta}}{C_L}\right)_{A_o'}$ = -0.0034 per deg (figure 5.1.2.1-28b at A_o' and λ_o')

Solution:

$$\frac{C_{l_\beta}}{C_L} = \frac{1}{\left(C_{L_\alpha}\right)_{total}}\left\{\left(C_{L_\alpha}\right)_i \frac{S_i}{S_W}\left[\left(\frac{C_{l_\beta}}{C_L}\right)_{\Lambda_{c/2_i}} K_M \Lambda_i + \left(\frac{C_{l_\beta}}{C_L}\right)_{A_i}\right]\frac{b_i}{b_W}\right.$$

$$\left. + \left(C_{L_\alpha}\right)_o' \frac{S_o'}{S_W}\left[\left(\frac{C_{l_\beta}}{C_L}\right)_{\Lambda_{c/2_o}'} K_M \Lambda_o' + \left(\frac{C_{l_\beta}}{C_L}\right)_{A_o'}\right]\right\} \quad \text{(equation 5.1.2.1-b)}$$

$$= \frac{1}{2.865}\left\{1.785\,(0.676)\left[-0.0045\,(1.0) + (-0.0065)\right]\frac{3.5}{6.0} + 2.60\,(0.638)\left[-0.0032\,(1.0) + (-0.0034)\right]\right\}$$

$$= \frac{1}{2.865}\left\{-0.00774 - 0.01095\right\} = -0.00652 \text{ per deg (based on } S_W b_W)$$

This result compares with a test value of -0.00628 from reference 30.

B. TRANSONIC

As the Mach number increases above M = 0.6, the rolling-moment derivative C_{l_β} of straight-tapered wings also increases, up to the force-break Mach number. The increase is nonlinear, with the largest gradient occurring just below the force-break Mach number. Beyond the force-break Mach number the value of the rolling-moment derivative falls off abruptly.

This variation with Mach number is quite similar to that of the wing lift-curve slope, as discussed in paragraph B of Section 4.1.3.2. This correspondence should perhaps be expected, since C_{l_β} has been successfully treated by using the effective lift-curve slopes of the upwind and downwind panels (reference 3).

The similarity in Mach number characteristics between rolling moment and lift-curve slope suggests a transonic interpolation method based on lift-curve slope, for calculating rolling moment. An interpolation equation is presented that is based on the square of the lift-curve slope values at M = 0.6 and at M = 1.4.

Although this interpolation method gives good results in most cases, it must be recognized that it is an interpolation technique and should be replaced by more accurate methods or data if they are available.

The Datcom method is limited to straight-tapered wings and is valid for sideslip angles between -5° and +5° and low angles of attack.

DATCOM METHOD

The wing rolling moment due to sideslip of straight-tapered wings may be approximated through the transonic region by means of the interpolation formula

$$\frac{C_{l_\beta}}{C_L} = \left\{\left[\frac{\left(\frac{C_{l_\beta}}{C_N}\right)_{M=1.4}}{\left(C_{N_\alpha}^2\right)_{M=1.4}} - \frac{\left(\frac{C_{l_\beta}}{C_L}\right)_{M=0.6}}{\left(C_{L_\alpha}^2\right)_{M=0.6}}\right]\left(\frac{M-0.6}{0.8}\right) + \frac{\left(\frac{C_{l_\beta}}{C_L}\right)_{M=0.6}}{\left(C_{L_\alpha}^2\right)_{M=0.6}}\right\}\left(C_{L_\alpha}^2\right) \quad \text{(per degree)} \qquad 5.1.2.1\text{-c}$$

where

$\left(\frac{C_{l_\beta}}{C_L}\right)_{M=0.6}$ is the sideslip derivative at M = 0.6 from the straight-tapered wing method of paragraph A.

$\left(\frac{C_{l_\beta}}{C_N}\right)_{M=1.4}$ is the sideslip derivative at M = 1.4 from the straight-tapered-wing method of paragraph C.

$\left(C_{L_\alpha}{}^2\right)_{M=0.6}$ is the square of the lift-curve slope at M = 0.6 from the straight-tapered-wing method of paragraph A of Section 4.1.3.2 (figure 4.1.3.2-49).

$\left(C_{N_\alpha}{}^2\right)_{M=1.4}$ is the square of the normal-force-curve slope at M = 1.4 from the straight-tapered-wing method of paragraph C of Section 4.1.3.2.

The transonic interpolation procedure is the same for wing-alone and wing-body configurations. Since the only available experimental data are for wing-body configurations, the sample problem of paragraph B of Section 5.2.2.1 can be taken as an example of the application of this method.

C. SUPERSONIC

The rolling moment due to sideslip for a wing at supersonic speeds is mainly a function of planform, Mach number, and dihedral angle.

A comprehensive summary of theoretical methods for calculating the effect of planform on rolling moment is given in reference 15. The information presented in this reference is not generalized, but is presented for discrete straight-tapered planforms over certain speed ranges. This is done because the theoretical calculations available are limited primarily to combinations of planforms and Mach lines that do not have mutually interacting subsonic edges. Techniques for handling mutually interacting subsonic edges are lengthy and involved. Consequently, numerical results are available for only a relatively few planforms that require such methods. Even when the boundary conditions can be specified and a linear-theory analysis carried out, the rolling moment cannot be generally expressed as a linear function of sideslip angle (see reference 16). To obtain the derivative C_{l_β}, it is necessary to plot C_l against β and measure the slope.

For planforms having streamwise tips there are additional questions concerning whether or not the Kutta condition applies at the trailing tip. In reference 6 it is assumed that it does. In reference 8 it is assumed that it does not, and values of opposite (negative) sign are obtained. In very few cases should any significant contribution be expected from the trailing tip. Nevertheless, most experimental measurements made to date give negative values of C_{l_β}.

Reference 17 indicates that agreement between experiment and theory for straight-tapered swept wings with streamwise tips may be obtained by integrating the span loading at combined angles of attack and sideslip; references 7 and 18 show calculations for such span loadings. However, there is no simple analytic expression for calculating C_{l_β}/α, and general digital computer solutions are not yet available.

For delta wings, the theory of reference 16 predicts a discontinuity and change in sign for C_{l_β} at the Mach number at which the leading edge is sonic. Since discontinuities of this type do not occur physically, there is some question as to what shape the C_{l_β} curve should have in the sonic-leading-edge region.

The above discussions indicate the present uncertain status of supersonic rolling-moment theory.

None of the previously mentioned theoretical methods are used in the Datcom. However, the discussion is included because no method yet developed is entirely satisfactory for all configurations over the entire speed range. It is felt that the Datcom does give best results for the widest range of configurations and speeds, but it must be recognized that there may be regions where one of the references mentioned gives better results.

Methods are presented for determining the rolling moment due to sideslip for the following classes of wing planforms:

Straight-Tapered Wings (conventional, trapezoidal wings)

Non-Straight-Tapered Wings

Double-delta wings
Cranked wings

These two general categories of non-straight-tapered wings are illustrated in sketch (a) of Section 4.1.3.2. Their wing-geometry parameters are presented in Section 2.2.2.

The straight-tapered-wing method is essentially that of reference 19, with the nomograph of page J.2-1.10 represented by an equation. This is done because of the inaccuracy of the nomograph at the higher Mach numbers, where the rolling moments are small. The nomograph of reference 19 was derived by writing the effective lift-curve slope for each wing panel as a function of sweepback and sideslip, multiplying this effective lift-curve slope by the spanwise center-of-pressure location, and taking the derivative of this product with respect to sideslip angle. One characteristic of this method is that it does not give positive rolling moments with positive sideslip angles (negative dihedral effect) for any speed range or planform. This is in direct opposition to certain other theories (reference 16) but is in qualitative agreement with experimental data. (References 20 through 27).

Another characteristic of the straight-tapered-wing method is that it predicts a linear variation of C_{l_β} with C_L. This, however, is not in agreement with the experimental data of references 20 through 27. In these tests, C_{l_β} is nonlinear with both angle of attack and sideslip. Since all these experimental tests are on wing-body combinations, it is not known to what extent the experimental nonlinearities may be caused by the body or by wing-body interference effects.

Geometric-dihedral effects are accounted for by the method of reference 28. This reference bases the dihedral parameter C_{l_β}/Γ on the damping-in-roll parameter C_{l_p}, by means of the following equation:

$$\frac{C_{l_\beta}}{\Gamma} = \frac{2}{(57.3)^2}\left(\frac{1+2\lambda}{1+3\lambda}\right)C_{l_p} \quad \text{(per degree}^2\text{)} \qquad 5.1.2.1\text{-d}$$

Although this equation is strictly an approximation, comparison of experimental data with values calculated from it shows that it gives good results. This success is largely due to the use of C_{l_p} as a base, since this latter derivative is one for which supersonic theory has given best results.

The Datcom method for double-delta and cranked wings is taken from reference 14. The supersonic prediction method has resulted from an analysis based on the same guide lines as the subsonic analysis. The straight-tapered-wing method is used as a base and a wing-lift prediction technique is used to weight the rolling-moment contributions of the various portions of the wing.

The nonlinearities of C_{l_β} with both angle of attack and sideslip, discussed above in connection with straight-tapered wings, also exist for the double-delta and cranked wings investigated during the course of the study conducted in connection with reference 11.

DATCOM METHODS

Straight-Tapered Wings

The rolling moment at Mach numbers above 1.4 for conventional, untwisted wings with uniform geometric dihedral in the linear angle-of-attack and sideslip ranges is given by

$$C_{l_\beta} = -0.061\, C_N \frac{C_{N_\alpha}}{57.3}\left[1 + \lambda\,(1 + \Lambda_{LE})\right]\left(1 + \frac{\Lambda_{LE}}{2}\right)\frac{\tan \Lambda_{LE}}{\beta}\left[\frac{M^2 \cos^2 \Lambda_{LE}}{A} + \left(\frac{\tan \Lambda_{LE}}{4}\right)^{4/3}\right] + \Gamma\left(\frac{C_{l_\beta}}{\Gamma}\right) \quad \text{(per degree)} \qquad 5.1.2.1\text{-e}$$

where

Λ_{LE} is the wing leading-edge sweep in radians.

C_{N_α} is the wing normal-force-curve slope per radian, obtained from the straight-tapered-wing method of paragraph C of Section 4.1.3.2.

$\frac{C_{l_\beta}}{\Gamma}$ is the dihedral parameter calculated by using equation 5.1.2.1-d with C_{l_p} (per radian) obtained from paragraph C of Section 7.1.2.2.

Γ is the dihedral angle in degrees (uniform dihedral).

Sample problem 1 on page 5.1.2.1-16 illustrates the use of this method applied to a straight-tapered wing with zero degrees dihedral.

A sample problem including the effect of uniform dihedral is presented in paragraph C of Section 5.2.2.1.

A comparison of test values of supersonic wing rolling moments due to sideslip with results calculated by using this method is presented as table 5.1.2.1-C. The ranges of Mach number and geometric parameters of the data are:

$$3.0 \le A \le 4.0$$

$$20.9^o \le \Lambda_{LE} \le 62.9^o$$

$$0.140 \le \lambda \le 0.250$$

$$\Gamma = 0$$

$$1.62 \le M \le 4.65$$

A data summary of calculated versus test values of the dihedral parameter $(\Delta C_{l_\beta})_\Gamma$ (including fuselage effects) is presented for wing-body configurations at supersonic speeds in Section 5.2.2.1 (table 5.2.2.1-E).

Non-Straight-Tapered Wings

The method for determining the rolling moment due to sideslip of double-delta and cranked wings is taken from reference 14. The composite wing is divided into two panels with each panel having conventional straight-tapered geometry. Then the lift-curve slopes and geometric characteristics of the two panels are substituted into the straight-tapered-wing method (equation 5.1.2.1-e). In order to maintain the proper span reference the rolling-moment contribution of the innermost panel is further modified by multiplying its contribution by the ratio of its span to the reference span (total wing span).

The method is applicable only to untwisted wings with zero degrees dihedral at low angles of attack and sideslip. A further restriction is that the composite-wing trailing edge must be unbroken (straight trailing edge from root to tip).

The rolling-moment derivative C_{l_β} of double-delta and cranked wings is obtained from the procedure outlined in the following steps:

Step 1. Divide the composite wing into two panels as follows (see sketch (b)), and determine their pertinent geometric characteristics.

Basic Wing – the outboard leading and trailing edges extended to the center line. This constructed panel is denoted by the subscript bw.

Glove – a delta wing superimposed over the basic wing. The glove leading edge is that of the inboard panel. This zero-taper wing is denoted by the subscript g.

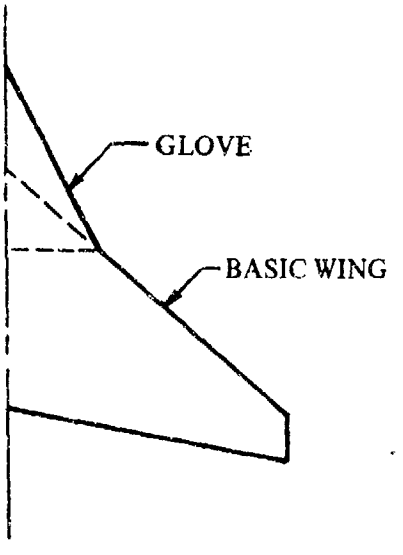

SKETCH (b)

Step 2. Determine the normal-force-curve slopes of the glove and basic wing (per radian) by using the supersonic design charts of Section 4.1.3.2. $\left(C_{N_\alpha}\right)_{bw}$ is obtained from figure 4.1.3.2-56 and $\left(C_{N_\alpha}\right)_g$ from figure 4.1.3.2-63.

Step 3. Determine the "lift-interference factor" K_L from figure 4.1.3.2-61 as a function of the glove normal-force-curve slope.

Step 4. Determine the rolling moment due to sideslip, based on the total wing area and span, by

$$\frac{C_{l_\beta}}{C_N} = -0.061 \left[\frac{K_L \left(C_{N_\alpha}\right)_g \frac{S_g}{S_W}}{57.3}\right]\left(1 + \frac{\Lambda_{LE_g}}{2}\right)\left(\frac{\tan \Lambda_{LE_g}}{\beta}\right)\left[\frac{M^2 \cos^2 \Lambda_{LE_g}}{A_g} + \left(\frac{\tan \Lambda_{LE_g}}{4}\right)^{4/3}\right]\frac{b_g}{b_W}$$

$$-0.061 \left[\frac{K_L \left(C_{N_\alpha}\right)_{bw} \frac{S_{bw}}{S_W}}{57.3}\right]\left[1 + \lambda_{bw}\left(1 + \Lambda_{LE_{bw}}\right)\right]\left(1 + \frac{\Lambda_{LE_{bw}}}{2}\right) \cdot$$

$$\left(\frac{\tan \Lambda_{LE_{bw}}}{\beta}\right)\left[\frac{M^2 \cos^2 \Lambda_{LE_{bw}}}{A_{bw}} + \left(\frac{\tan \Lambda_{LE_{bw}}}{4}\right)^{4/3}\right] \text{ (per degree)} \qquad 5.1.2.1\text{-f}$$

where the subscripts g and bw denote the glove and basic wing, respectively. The leading-edge sweep of the panels, Λ_{LE_g} and $\Lambda_{LE_{bw}}$, are in radians.

Another class of composite wings of practical interest are those with the outboard wing sweep greater than the inboard wing sweep. In treating such wings, if the basic wing breakdown is defined as in sketch (b), some additional wing area is created forward of the wing sweep break as illustrated in sketch (c).

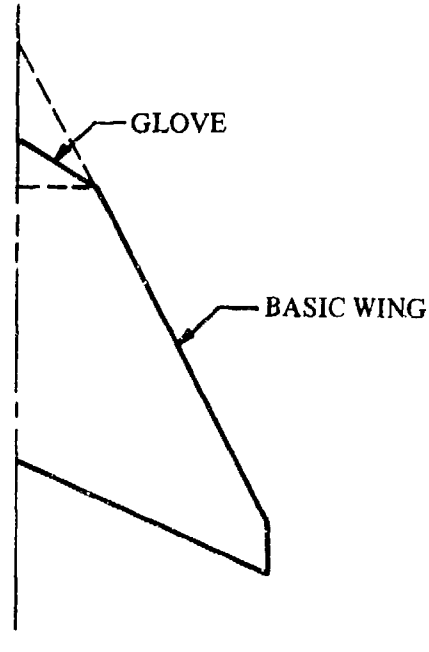

SKETCH (c)

For this class of composite wings the normal-force-curve slope of the basic wing $\left(C_{N_\alpha}\right)_{bw}$ is determined by extending the basic-wing leading edge to the center line, calculating the normal-force-curve slope of the extended basic wing panel, and calculating and subtracting the normal-force-curve slope of the section of the basic-wing panel forward of the wing sweep break. This is shown schematically in sketch (d).

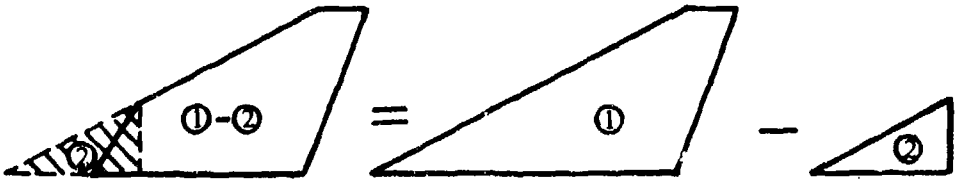

$$\left(C_{N_\alpha}\right)_{bw} \frac{S_{bw}}{S_w} = \left(C_{N_\alpha}\right)_1 \frac{S_1}{S_w} - \left(C_{N_\alpha}\right)_2 \frac{S_2}{S_w}$$

SKETCH (d)

During the course of study conducted in connection with reference 14, the normal-force-curve slopes of the basic wing and glove were correlated with test data for configurations with the outboard wing sweep greater than the inboard wing sweep through the use of an empirical correlation factor K, which corresponds to the "lift-interference factor" K_L. A complete analysis was not accomplished; however, based on a limited amount of rolling-moment data, K appears to be approximately one.

The rolling moment due to sideslip for this class of composite wings is obtained using equation 5.1.2.1-f in the following manner:

1. The term K_L is replaced by the term K, where K = 1.0.
2. The product of the normal-force-curve slope and the ratio of basic-wing area to total-wing area is replaced by the expression shown in sketch (d).
3. The aspect ratio, taper ratio, and sweepback of the basic wing are considered to be those of the extended basic wing, which corresponds to panel (i) in sketch (d).
4. The glove has the same geometry as in cases where the glove sweep is greater than the outboard wing sweep.

Sample problem 2 on page 5.1.2.1-18 illustrates the use of the non-straight-tapered-wing method.

A comparison of test values of supersonic wing rolling moments due to sideslip with results calculated by using this method is presented as table 5.1.2.1-D (taken from reference 14). A specific comparison of test values with calculated results for a cranked wing is shown in sketch (e). Also shown is a comparison of test values and results calculated by using the straight-tapered-wing method for the case where the basic-wing and the glove sweep angles are the same.

It is suggested that this method be restricted to Mach numbers above 1.4 and to glove leading-edge sweep angles less than 80°. At high leading-edge sweep angles the terms $\tan\Lambda_{LE_g}/\beta$ and $\left(\tan\Lambda_{LE_g}/4\right)^{4/3}$ become excessively large and equation 5.1.2.1-f overpredicts C_{l_β}.

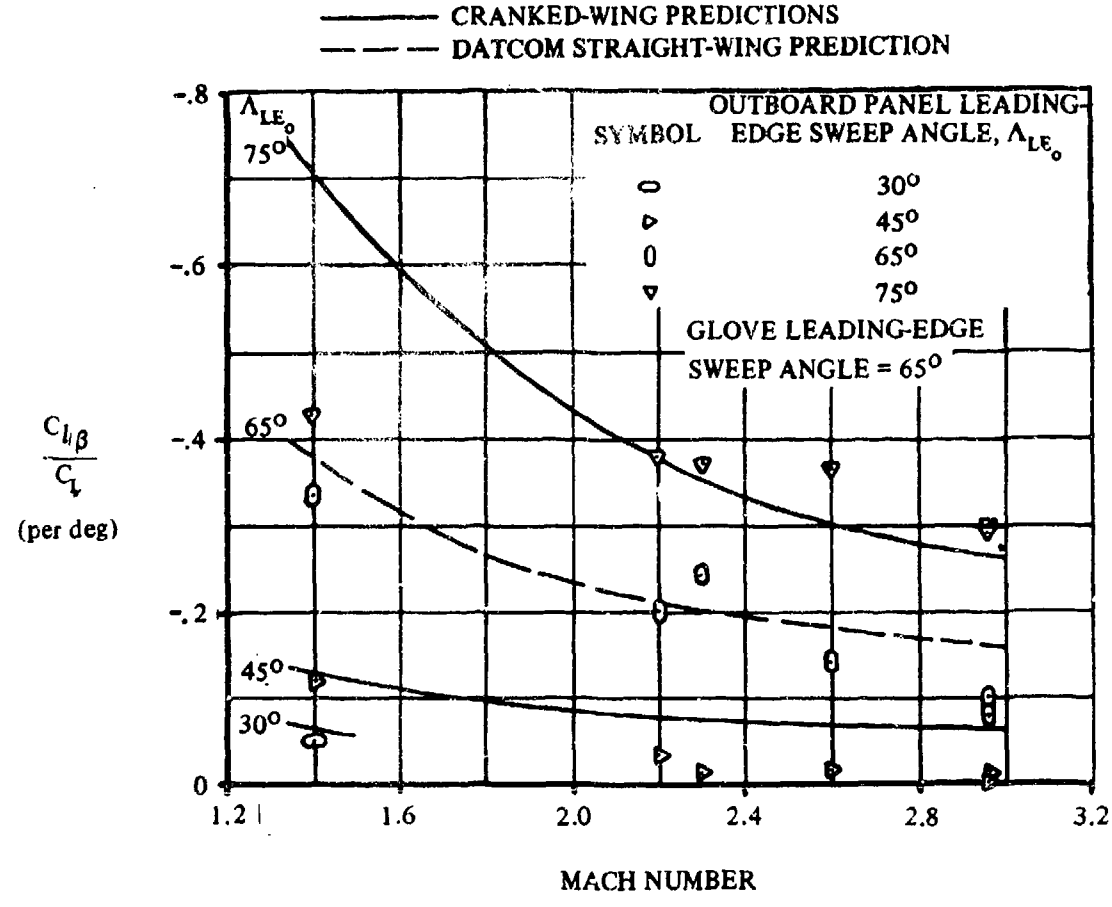

COMPARISON OF CRANKED-WING ROLLING-MOMENT-COEFFICIENT PREDICTIONS WITH TEST DATA

SKETCH (e)

Sample Problems

1. Straight-Tapered Wing

Given: A wing-body configuration with a midwing location from reference 25.

$A = 3.0$ $\lambda = 0.250$ $\Lambda_{LE} = 30.97^\circ = 0.540$ rad $\Gamma = 0$

$M = 2.01$; $\beta = 1.744$ Airfoil section: 4-percent circular arc

Compute:

$\Delta y = 0.47$ (figure 2.2.1-8)

$$\Delta y_{\perp} = \frac{\Delta y}{\cos \Lambda_{LE}} = \frac{0.47}{0.8575} = 0.548 \qquad \text{(Section 4.1.3.2)}$$

$$\delta_{\perp} = \tan^{-1} \frac{\Delta y_{\perp}}{5.85} = \tan^{-1} 0.09368 = 5.35^{o}$$

$$\frac{\tan \Lambda_{LE}}{\beta} = \frac{0.6002}{1.744} = 0.3442$$

$$\frac{M^2 \cos^2 \Lambda_{LE}}{A} = \frac{(2.01)^2 \ (0.8575)^2}{3.0} = 0.990$$

$$\left(\frac{\tan \Lambda_{LE}}{4}\right)^{4/3} = \left(\frac{0.6002}{4.0}\right)^{4/3} = 0.0797$$

C_{N_α} (Section 4.1.3.2)

$$A \tan \Lambda_{LE} = (3.0)\ (0.6002) = 1.80$$

$$\beta \left(C_{N_\alpha}\right)_{theory} = 3.83 \text{ per rad (figure 4.1.3.2-56c)}$$

$$\left(C_{N_\alpha}\right)_{theory} = 2.20 \text{ per rad}$$

$$\frac{C_{N_\alpha}}{\left(C_{N_\alpha}\right)_{theory}} = 1.0 \qquad \text{(figure 4.1.3.2-60)}$$

$$C_{N_\alpha} = \frac{C_{N_\alpha}}{\left(C_{N_\alpha}\right)_{theory}} \left(C_{N_\alpha}\right)_{theory} = (1.0)\ (2.20) = 2.20 \text{ per rad}$$

Solution:

$$\frac{C_{l_\beta}}{C_N} = -0.061 \frac{C_{N_\alpha}}{57.3} \left[1 + \lambda\ (1 + \Lambda_{LE})\right] \left(1 + \frac{\Lambda_{LE}}{2}\right) \frac{\tan \Lambda_{LE}}{\beta} \left[\frac{M^2 \cos^2 \Lambda_{LE}}{A} + \left(\frac{\tan \Lambda_{LE}}{4}\right)^{4/3}\right]$$

(equation 5.1.2.1-e with $\Gamma = 0$)

$$= -0.061 \frac{2.20}{57.3} \left[1 + 0.25\ (1 + 0.540)\right] \left(1 + \frac{0.540}{2}\right) (0.3442) \left[0.990 + 0.0797\right]$$

$$= -0.00152 \text{ per deg (based on } S_w b_w)$$

This result compares with a test value of -0.00143 from reference 25.

2. Non-Straight-Tapered Wing

Given: A hypothetical cranked wing

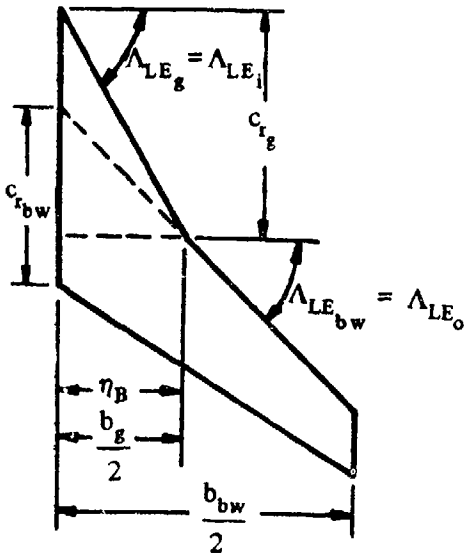

Total Wing Characteristics:

$S_W = 7.05$ sq ft $\quad \frac{b_W}{2} = 2.50$ ft

$c_{t_W} = 0.608$ ft $\quad \eta_B = 0.400 \quad \Lambda_{LE_i} = 60^o$

$\Lambda_{LE_o} = 45^o$

Glove Characteristics:

$A_g = 2.31 \quad \lambda_g = 0 \quad S_g = 1.732$ sq ft

$\frac{S_g}{S_W} = 0.246 \quad \frac{b_g}{2} = 1.0$ ft

$\Lambda_{LE_g} = \Lambda_{LE_i} = 60^o = 1.047$ rad

Basic Wing Characteristics:

$A_{bw} = 3.97 \quad \lambda_{bw} = 0.407 \quad S_{bw} = 6.30$ sq ft $\quad \frac{b_{bw}}{2} = \frac{b_W}{2} = 2.50$ ft

$\Lambda_{LE_{bw}} = \Lambda_{LE_o} = 45^o = 0.785$ rad $\quad \frac{S_{bw}}{S_W} = 0.894$

Additional Characteristics:

$M = 2.96; \ \beta = 2.79$

Compute:

$$1 + \frac{\Lambda_{LE_g}}{2} = 1.524$$

$$\frac{\tan \Lambda_{LE_g}}{\beta} = \frac{1.732}{2.79} = 0.621$$

$$\frac{M^2 \cos^2 \Lambda_{LE_g}}{A_g} = \frac{(2.96)^2 (0.50)^2}{2.31} = 0.948$$

$$\left(\frac{\tan \Lambda_{LE_g}}{4}\right)^{4/3} = \left(\frac{1.732}{4}\right)^{4/3} = 0.3276$$

$\left(C_{N_\alpha}\right)_g$ (Section 4.1.3.2)

$$\frac{\beta}{\tan \Lambda_{LE_g}} = \frac{2.79}{1.732} = 1.611$$

$$\frac{\left(C_{N_\alpha}\right)_g}{A_g} = 0.624 \text{ per rad (figure 4.1.3.2-63)}$$

$$\left(C_{N_\alpha}\right)_g = 1.44 \text{ per rad}$$

K_L (Section 4.1.3.2)

$$\frac{1}{\beta}\left(C_{N_\alpha}\right)_g \frac{S_g}{S_W} = \frac{1}{2.79}(1.44)(0.246) = 0.127 \text{ per rad}$$

$K_L = 0.873$ (figure 4.1.3.2-61)

$$1 + \lambda_{LE_{bw}} = 1.785;\ 1 + \frac{\Lambda_{LE_{bw}}}{2} = 1.393$$

$$\frac{\tan \Lambda_{LE_{bw}}}{\beta} = \frac{1.00}{2.79} = 0.358$$

$$\frac{M^2 \cos^2 \Lambda_{bw}}{A_{bw}} = \frac{(2.96)^2 (0.7071)^2}{3.97} = 1.103$$

$$\left(\frac{\tan \Lambda_{LE_{bw}}}{4}\right)^{4/3} = \left(\frac{1.00}{4.0}\right)^{4/3} = 0.1575$$

$\left(C_{N_\alpha}\right)_{bw}$ (Section 4.1.3.2)

$$\frac{\tan \Lambda_{LE_{bw}}}{\beta} = 0.358;\ A \tan \Lambda_{LE_{bw}} = 3.97$$

$\beta C_{N_\alpha} = 4.07$ per rad (figures 4.1.3.2-56c through -56e, interpolated)

$$\left(C_{N_\alpha}\right)_{bw} = 1.46 \text{ per rad}$$

Solution:

$$\frac{C_{l_\beta}}{C_L} = -0.061 \left[\frac{K_L \left(C_{N_\alpha}\right)_g \frac{S_g}{S_W}}{57.3}\right]\left(1 + \frac{\Lambda_{LE_g}}{2}\right)\left(\frac{\tan \Lambda_{LE_g}}{\beta}\right)\left[\frac{M^2 \cos^2 \Lambda_{LE_g}}{A_g} + \left(\frac{\tan \Lambda_{LE_g}}{4}\right)^{4/3}\right]\frac{b_g}{b_W}$$

$$-0.061 \left[\frac{K_L \left(C_{N_\alpha}\right)_{bw} \frac{S_{bw}}{S_W}}{57.3}\right]\left[1 + \lambda_{bw}\left(1 + \Lambda_{LE_{bw}}\right)\right]\left(1 + \frac{\Lambda_{LE_{bw}}}{2}\right)$$

$$\left(\frac{\tan \Lambda_{LE_{bw}}}{\beta}\right)\left[\frac{M^2 \cos^2 \Lambda_{LE_{bw}}}{A_{bw}} + \left(\frac{\tan \Lambda_{LE_{bw}}}{4}\right)^{4/3}\right] \qquad \text{(equation 5.1.2.1-f)}$$

$$= -0.061 \left[\frac{0.873\ (1.44)\ (0.246)}{57.3}\right](1.524)\ (0.621)\left[0.948 + 0.3276\right]\frac{2.0}{5.0}$$

$$-0.061 \left[\frac{0.873\ (1.46)\ (0.894)}{57.3}\right]\left[1 + 0.407\ (1.785)\right](1.393)\ (0.358)\left[1.103 + 0.1575\right]$$

$$= -0.061 \left[0.00261\right] - 0.061 \left[0.0216\right]$$

$$= -0.00148 \text{ per deg}$$

REFERENCES

1. Weissinger, J.: Der schiebende Tragfluegel bei gesunder Stroemung. Bericht S 2 der Lilienthal-Gesellschaft fuer Luftfahrtforschung, 1938-39. (U)

2. Queijo, M.: Theoretical Span Load Distributions and Rolling Moments for Sideslipping Wings of Arbitrary Planform in Incompressible Flow. NACA TR 1269, 1956. (U)

3. Polhamus, E., and Sleeman, W., Jr.: The Rolling Moment Due to Sideslip of Swept Wings at Subsonic and Transonic Speeds. NASA TN D-208, 1960. (U)

4. Ribner, H.: The Stability Derivatives of Low-Aspect Ratio Triangular Wings at Subsonic and Supersonic Speeds. NACA TN 1423, 1947. (U)

5. Bird, J.: Some Theoretical Low-Speed Span Loading Characteristics of Swept Wings in Roll and Sideslip. NACA TR 969, 1950. (U)

6. DeYoung, J.: Theoretical Antisymmetric Span Loading for Wings of Arbitrary Plan Form at Subsonic Speeds. NACA TR 1056, 1951. (U)

7. Sherman, W., and Margolis, K.: Theoretical Calculations of the Effects of Finite Sideslip at Supersonic Speeds on the Span Loading and Rolling Moment for Families of Thin Sweptback Tapered Wings at Angle of Attack. NACA TN 3046, 1953. (U)

8. Goodman, A., and Brewer, J.: Investigation at Low Speeds of the Effect of Aspect Ratio and Sweep on Static and Yawing Stability Derivatives of Untapered Wings. NACA TN 1669, 1948. (U)

9. McCormack, G., and Walling, W.: Aerodynamic Study of a Wing-Fuselage Combination Employing a Wing Swept Back 63°—Investigation of a Large-Scale Model at Low Speed. NACA RM A8D02, 1949. (U)

10. Goodman, A., and Thomas, D.: Effects of Wing Position and Fuselage Size on the Low-Speed Static and Rolling Stability Characteristics of a Delta-Wing Model. NACA TR 1224, 1955. (U)

11. Wolhart, W., and Thomas, D.: Static Longitudinal and Lateral Stability Characteristics at Low Speeds of Unswept-Midwing Models Having Wings with an Aspect Ratio of 2, 4, or 6. NACA TN 3649, 1956. (U)

12. Thomas, D., and Wolhart, W.: Static Longitudinal and Lateral Stability Characteristics at Low Speed of 45° Sweptback-Midwing Models Having Wings with an Aspect Ratio of 2, 4, or 6. NACA TN 4077, 1957. (U)

13. Letko, W.: Experimental Determination at Subsonic Speeds of the Oscillatory and Static Lateral Stability Derivatives of a Series of Delta Wings with Leading-Edge Sweep from 30° to 86.5°. NACA RM L57A30, 1957. (U)

14. Benepe, D.B., Kouri, B.G., Webb, J.B., et al: Aerodynamic Characteristics of Non-Straight-Taper Wings. AFFDL-TR-66-73, 1966. (U)

15. Jones, A., and Alksne, A.: A Summary of Lateral-Stability Derivatives Calculated for Wing Plan Forms in Supersonic Flow. NACA TN 1052, 1951. (U)

16. Jones, A., and Spreiter, J.: The Rolling Moment Due to Sideslip of Triangular, Trapezoidal, and Related Plan Forms in Supersonic Flow. NACA TN 1700, 1948. (U)

17. Harmon, S.: Stability Derivatives at Supersonic Speeds of Thin Rectangular Wings with Diagonals Ahead of Tip Mach Lines. NACA TR 925, 1949. (U)

18. Margolis, K., Sherman, W., and Hannah, M.: Theoretical Calculation of the Pressure Distribution, Span Loading, and Rolling Moment due to Sideslip at Supersonic Speeds for Thin Sweptback Tapered Wings with Supersonic Trailing Edges and Wing Tips Parallel to the Axis of Wing Symmetry. NACA TN 2898, 1953. (U)

19. Decker, J., et al: USAF Stability and Control Handbook. M-03671, 1956. (C) Title Unclassified

20. Lessing, H.: Aerodynamic Study of a Wing-Fuselage Combination Employing a Wing Swept Back 63°—Effect of Sideslip on Aerodynamic Characteristics at a Mach Number of 1.4 with the Wing Twisted and Cambered. NACA RM A50F09, 1950. (U)

21. Hamilton, C.: Aerodynamic Characteristics at Supersonic Speeds of a Series of Wing-Body Combinations Having Cambered Wings With an Aspect Ratio of 3.5 and a Taper Ratio of 0.2. Effects of Sweep Angle and Thickness Ratio on the Static Lateral Stability Characteristics at M = 2.01. NACA RM L52E23, 1952. (U)

22. Christensen, F.: An Experimental Investigation of Four Triangular-Wing--Body Combinations in Sideslip at Mach Numbers 0.6, 0.9, 1.4, and 1.7. NACA RM A53L22, 1954. (U)

23. Dunning, R., and Ulman, E.: Static Longitudinal and Lateral Stability Data From an Exploratory Investigation at Mach Number 4.06 of an Airplane Configuration Having a Wing of Trapezoidal Plan Form. NACA RM L55A21, 1955. (U)

24. Spearman, M.: Investigation of the Aerodynamic Characteristics in Pitch and Sideslip of a 45° Sweptback-Wing Airplane Model With Various Vertical Locations of the Wing and Horizontal Tail. NACA RM L55B18, 1955. (U)

25. Robinson, R.: Effects of Vertical Location of the Wing and Horizontal Tail on the Static Lateral and Directional Stability of a Trapezoidal-Wing Airplane Model at Mach Numbers of 1.41 and 2.01. NACA RM L58C18, 1958. (U)

26. Jaquet, B.M., and Fournier, R.: Effects of Wing Sweep, Horizontal-Tail Configuration, and a Ventral Fin on Static Stability Characteristics of a Model with Wing of Aspect Ratio 3 at Mach Numbers from 2.29 to 4.65. NACA RM L58E06, 1958. (U)

27. Boatright, W.: Experimental Investigation of Effects of Wing Plan Form and Dihedral Angle on Sideslip Derivatives of Sweptback-Wing—Body Combinations at Supersonic Speeds. NACA RM L58E08, 1958. (U)

28. Purser, P.: An Approximation to the Effect of Geometric Dihedral on the Rolling Moment due to Sideslip for Wings at Transonic and Supersonic Speeds. NACA RM L52B01, 1952. (U)

29. Wolhart, W., and Thomas, D.: Static Longitudinal and Lateral Stability Characteristics at Low Speed of 60° Sweptback-Midwing Models Having Wings With an Aspect Ratio of 2, 4, or 6. NACA TN 4397, 1958. (U)

30. Mansell, C.J.: Low-Speed Wind-Tunnel Tests on Two Thin Cranked Wings with 60-Degree Sweepback Inboard. ARC R&M 2995, 1957. (U)

31. Kruger, W.: Six-Component Measurements on a Cranked Swept-Back Wing. Great Britain Ministry of Supply Translation 816, 1947. (U)

32. Lange, R.H., and McLemore, H.C.: Low-Speed Lateral Stability and Aileron Effectiveness Characteristics at a Reynolds Number of 3.6×10^6 of a Wing With Leading Edge Sweepback Decreasing From 45° at the Root to 20° at the Tip. NACA RM L50D14, 1950. (U)

33. Jornell, L.S.: Aerodynamic Cha ristics at Mach Numbers from 2.50 to 4.63 of a Variable-Sweep Model at Sweep Angles from 55° to 75°. NASA TM X-959, 1964. (C) Title Unclassified

34. Landrum, E.J.: Effect of Skewed Wing-Tip Controls on a Variable-Sweep Wing-Fuselage Configuration at Mach Numbers of 1.41 and 2.20. NASA TM X-951, 1964. (C) Title Unclassified

35. Landrum, E.J., and Babb, C.D.: Effect of Skewed Wing-Tip Controls on a Variable-Sweep Wing-Fuselage Configuration at Mach Numbers from 2.60 to 4.62. NASA TM X-1031, 1964. (C) Title Unclassified

36. Spearman, M.L., and Foster, G.V.: Static Longitudinal and Lateral Aerodynamic Characteristics at Mach Number of 2.01 of a Tailless Delta V/STOL Configuration Having Variable-Sweep Wing Panels. NASA TM X-634, 1961. (C) Title Unclassified

37. Spearman, M.L.: Static Longitudinal and Lateral Aerodynamic Characteristics at Mach Numbers of 1.41 and 2.20 of a Model of a Low Aspect Ratio 83.5° Delta-Wing Airplane Having Auxiliary Variable-Sweep Wing Panels. NASA TM X-708, 1963. (C) Title Unclassified

38. Campbell, J.P., and McKinney, M.O.: Summary of Methods for Calculating Dynamic Lateral Stability and Response and for Estimating Lateral Stability Derivatives. NACA TR 1098, 1952. (U)

TABLE 5.1.2.1-A

LOW-SPEED ROLLING MOMENT DUE TO SIDESLIP

DATA SUMMARY AND SUBSTANTIATION

Ref.	A	$\Lambda_{c/2}$ (deg)	λ	M	$R\ell \times 10^{-6}$	$\left(\frac{c_{l_\beta}}{c_L}\right)_{calc} \times 10^3$ (per deg)	$\left(\frac{c_{l_\beta}}{c_L}\right)_{test} \times 10^3$ (per deg)	$\Delta c_{l_\beta} \times 10^3$ (per deg) (Calc–Test)
8	1.34	0	1.0	0.13	1.6	– 8.8	– 8.0	–0.8
↓	↓	45	↓	↓	↓	–11.8	–11.6	–0.2
↓	↓	60	↓	↓	↓	–13.5	–14.6	1.1
↓	2.61	0	↓	↓	1.1	– 4.3	– 4.4	0.1
↓	↓	45	↓	↓	↓	– 8.0	– 8.0	0
↓	↓	60	↓	↓	↓	–11.0	–11.3	0.3
↓	5.16	0	↓	↓	0.8	– 1.8	– 1.2	–0.6
↓	↓	45	↓	↓	↓	– 6.3	– 5.6	–0.7
↓	↓	60	↓	↓	↓	–10.2	–10.0	–0.2
9	3.5	58.3	0.25	0.13	8.0	– 7.8	– 8.2	0.4
10	2.31	40.9	0	0.17	2.1	– 5.0	– 4.5	–0.5
11	2	–7.1	0.6	0.13	1.0	– 4.0	– 4.2	0.2
↓	4	–3.6	↓	↓	0.7	– 1.4	– 1.4	0
↓	6	–2.4	↓	↓	0.6	– 0.5	– 0.7	0.2
12	2	41.2	0.6	0.13	1.0	– 7.5	– 7.5	0
↓	4	43.0	↓	↓	0.7	– 5.5	– 5.5	0
↓	6	43.8	↓	↓	0.6	– 5.0	– 4.5	–0.5
13	0.25	83.2	0	0.13	1.0	–46.5	–40.0	–6.5
↓	0.53	75.3	↓	↓	↓	–22.0	–20.0	–2.0
↓	1.07	61.7	↓	↓	↓	– 9.9	–11.6	1.7
↓	2.31	40.9	↓	↓	↓	– 5.0	– 4.1	–0.9
↓	4.0	26.6	↓	↓	↓	– 2.3	– 2.0	–0.3
↓	6.93	16.1	↓	↓	↓	– 1.0	– 1.0	0
29	2	58.0	0.6	0.13	1.0	–10.1	–10.6	0.5
↓	4	59.2	↓	↓	0.7	– 8.8	– 9.4	0.6
↓	6	59.4	↓	↓	0.6	– 8.7	– 9.4	0.7

$$\text{Average Error} = \frac{\Sigma \left| \Delta c_{l_\beta} \times 10^3 \right|}{n} = 0.7 \times 10^{-3} \text{ per deg}$$

TABLE 5.1.2.1-8
LOW-SPEED ROLLING MOMENT DUE TO SIDESLIP
OF NON-STRAIGHT-TAPERED WINGS

DATA SUMMARY

Ref.	Config.	Planform	Λ_{LE_i} (deg)	Λ_{LE_o} (deg)	M	$R\ell_{MAC}$ $\times 10^{-6}$	$\left(\frac{C_{l_\beta}}{C_L}\right)_{calc} \times 10^3$ (per deg)	$\left(\frac{C_{l_\beta}}{C_L}\right)_{test} \times 10^3$ (per deg)	$\Delta\frac{C_{l_\beta}}{C_L} \times 10^3$ (per deg)
30	WB	Cranked TE	60	60	0.18	1.26	-5.68	-5.03	-0.65
↓	↓	Cranked LE	59	48.5	0.18	↓	-6.52	-6.28	-0.24
31	W	Cranked[a]	45	30.25	0.132	0.84	-2.45	-2.97	0.52
32	W	Cranked[a]	45	30.20	0.07	0.48	-2.97	-2.20	-0.77

(a) Two breaks in leading-edge sweep

$$\text{Average Error} = \frac{\sum\left|\Delta\frac{C_{l_\beta}}{C_L} \times 10^3\right|}{n} = 0.65 \times 10^{-3} \text{ per deg}$$

TABLE 5.1.2.1-C

SUPERSONIC WING ROLLING MOMENT DUE TO SIDESLIP

DATA SUMMARY AND SUBSTANTIATION

Ref.	A	Λ_{LE} (deg)	λ	M	$R_\ell \times 10^{-6}$	$\left(\frac{C_{l_\beta}}{C_N}\right)_{calc} \times 10^3$ (per deg)	$\left(\frac{C_{l_\beta}}{C_N}\right)_{test} \times 10^3$ (per deg)	$\Delta C_{l_\beta} \times 10^3$ (per deg) (Calc.-Test)
21	3.5	20.9	0.200	2.01	2.20	-0.85	-0.80	-0.05
		41.7				-1.78	-1.00	-0.78
		51.6				-2.34	-1.80	-0.54
23	3.0	38.3	0.140	4.06	2.7	-1.50	-1.00	-0.50
24	4.0	49.4	0.200	2.01	1.84	-1.84	-2.02	0.18
25	3.0	31.0	0.250	2.01	1.84	-1.66	-1.43	-0.23
26	3.0	38.7	0.143	2.29	2.10	-1.75	-1.33	-0.42
				2.98		-1.66	-1.66	0
				3.96		-1.57	-1.77	0.20
				4.65		-1.73	-1.86	0.13
27	3.0	50.7	0.200	1.62	0.64	-3.06	-1.49	-1.56
				2.62	0.72	-2.20	-1.56	-0.64
	4.0	49.4		1.62	0.64	-2.43	-1.27	-1.16
				2.62	0.72	-1.70	-1.87	0.17
	3.0	62.9		1.62	0.64	-4.90	-3.10	-1.80
				2.62	0.72	-2.70	-2.41	-0.29

Note: In calculating C_{l_β}/C_N for this table, experimental values of C_{N_α} were used.

Average Error $= \frac{\sum_i \left| \Delta C_{l_\beta} \times 10^3 \right|}{n} = 0.54 \times 10^{-3}$ per deg

TABLE 5.1.2.1-D

SUPERSONIC ROLLING MOMENT DUE TO SIDESLIP OF NON-STRAIGHT-TAPERED WINGS

DATA SUMMARY

Ref.	Config.	Planform	Λ_{LE_i} (deg)	Λ_{LE_o} (deg)	M	Rℓ/ft $\times 10^{-6}$	$\left(\frac{C_{l_\beta}}{C_L}\right)_{calc} \times 10^3$ (per deg)	$\left(\frac{C_{l_\beta}}{C_L}\right)_{test} \times 10^3$ (per deg)	$\Delta\frac{C_{l_\beta}}{C_L} \times 10^3$ (per deg)
33	WB	Cranked	60	75	2.50	3.0	-5.38		
					2.96		-4.40		
					3.95		-3.37		
34	WB	Cranked	65	30	1.41	3.0	-1.19		
				45			-2.27		
35					2.20		-1.31		
					2.60		-1.14		
					2.96		-1.08		
					3.95		-0.99	(a)	
34				75	1.41		-12.60		
					2.20		-6.61		
35					2.60		-5.41		
					2.96		-4.79		
					3.95		-3.68		
36	WBN	Double Delta	81	50	2.01	1.10	-8.74		
			73	50	2.01		-3.68		
37	WBN		83.5	50	1.41	1.45	-17.90		
					2.20	2.26	-10.30		

(a) This information is classified CONFIDENTIAL.

Average Error = $\dfrac{\sum\left|\Delta\frac{C_{l_\beta}}{C_L} \times 10^3\right|}{n}$ = 1.61 x 10^{-3} per deg

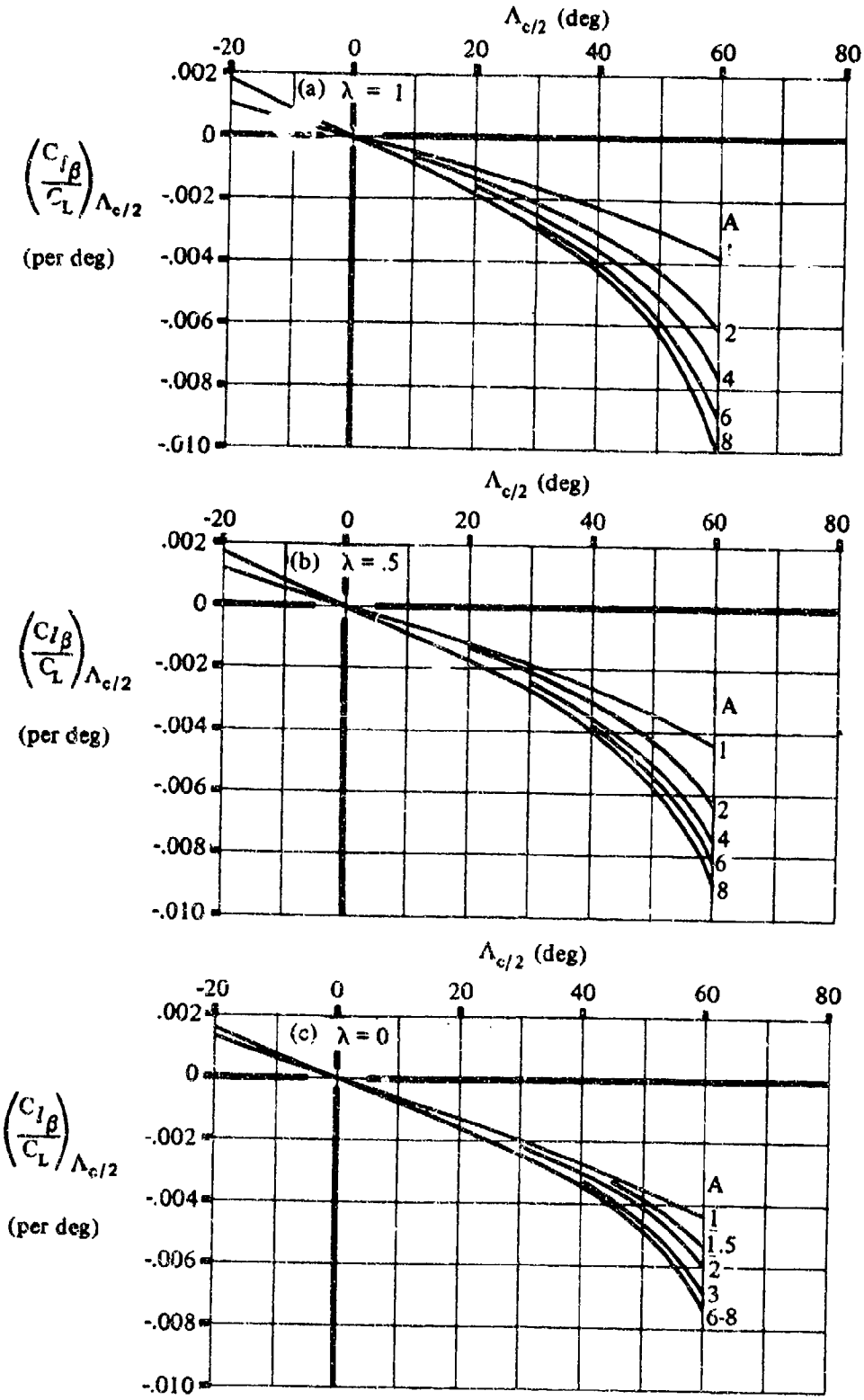

FIGURE 5.1.2.1-27 WING SWEEP CONTRIBUTION TO C_{l_β}

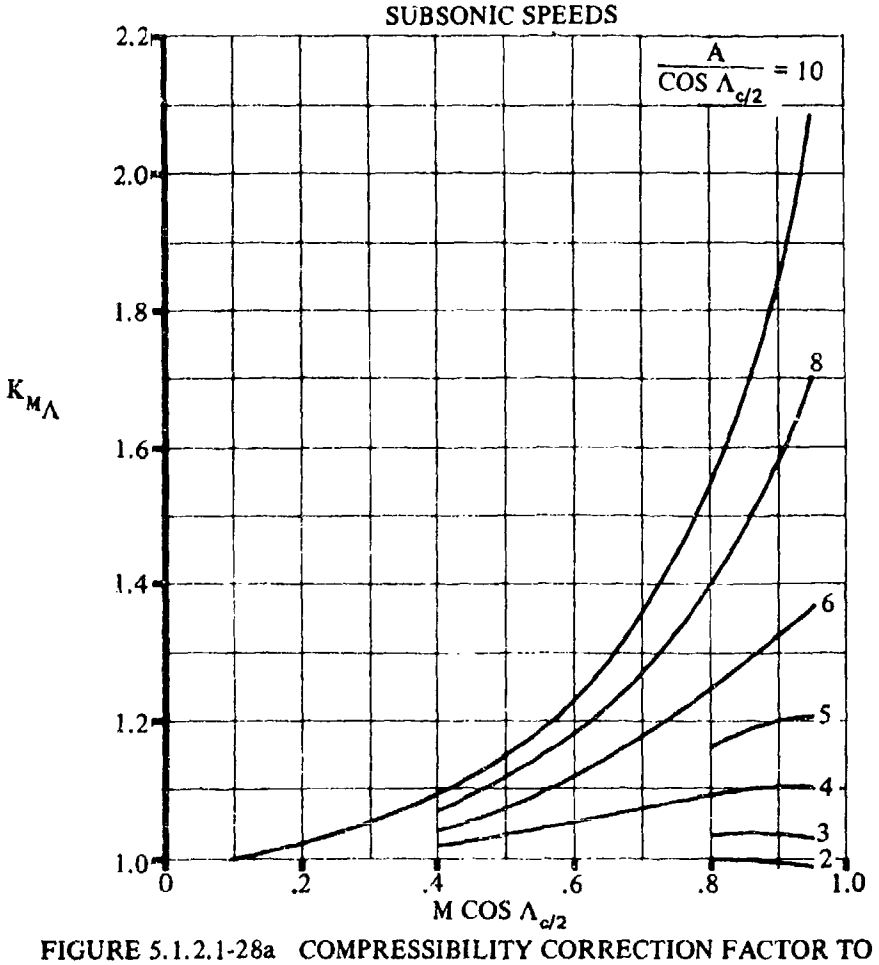

FIGURE 5.1.2.1-28a COMPRESSIBILITY CORRECTION FACTOR TO SWEEP CONTRIBUTION TO WING C_{l_β}

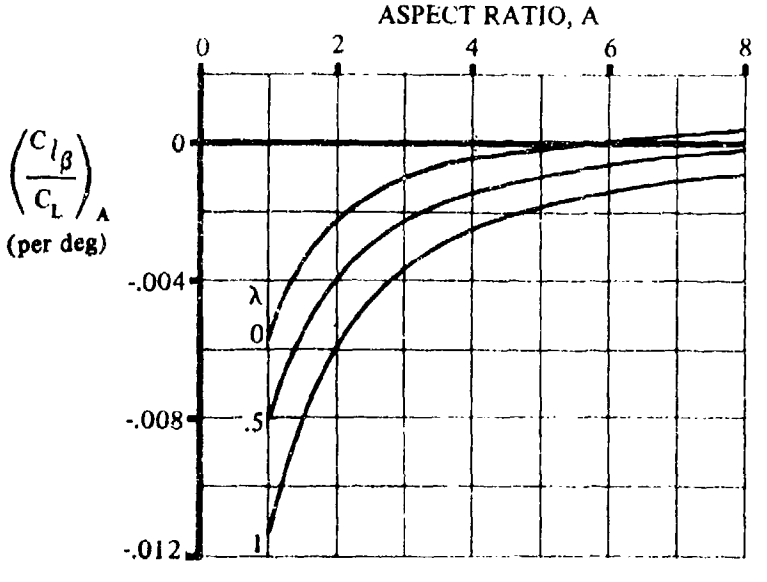

FIGURE 5.1.2.1-28b ASPECT RATIO CONTRIBUTION TO WING C_{l_β}

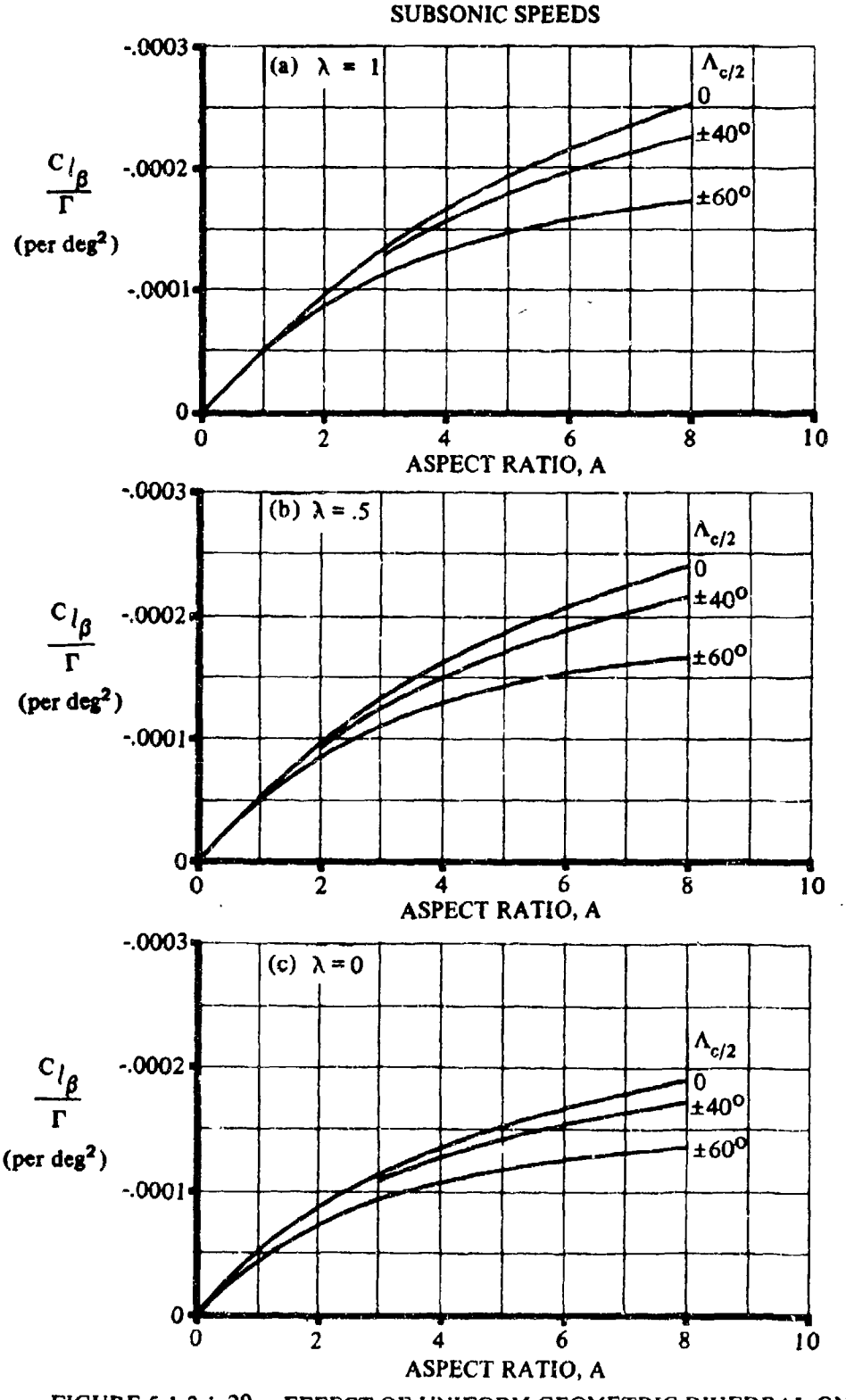

FIGURE 5.1.2.1-29 EFFECT OF UNIFORM GEOMETRIC DIHEDRAL ON WING C_{l_β}

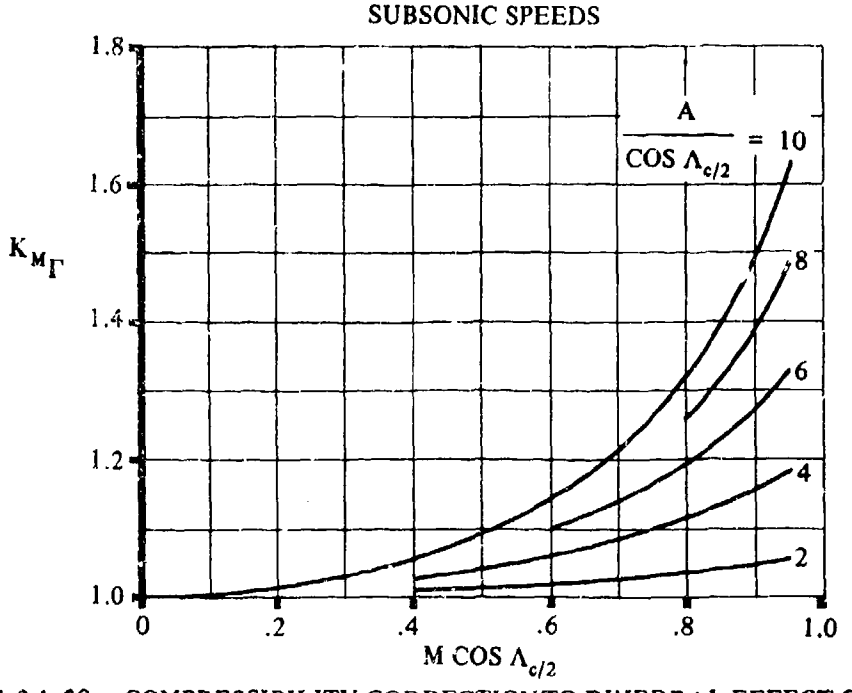

FIGURE 5.1.2.1-30a COMPRESSIBILITY CORRECTION TO DIHEDRAL EFFECT ON WING C_{l_β}

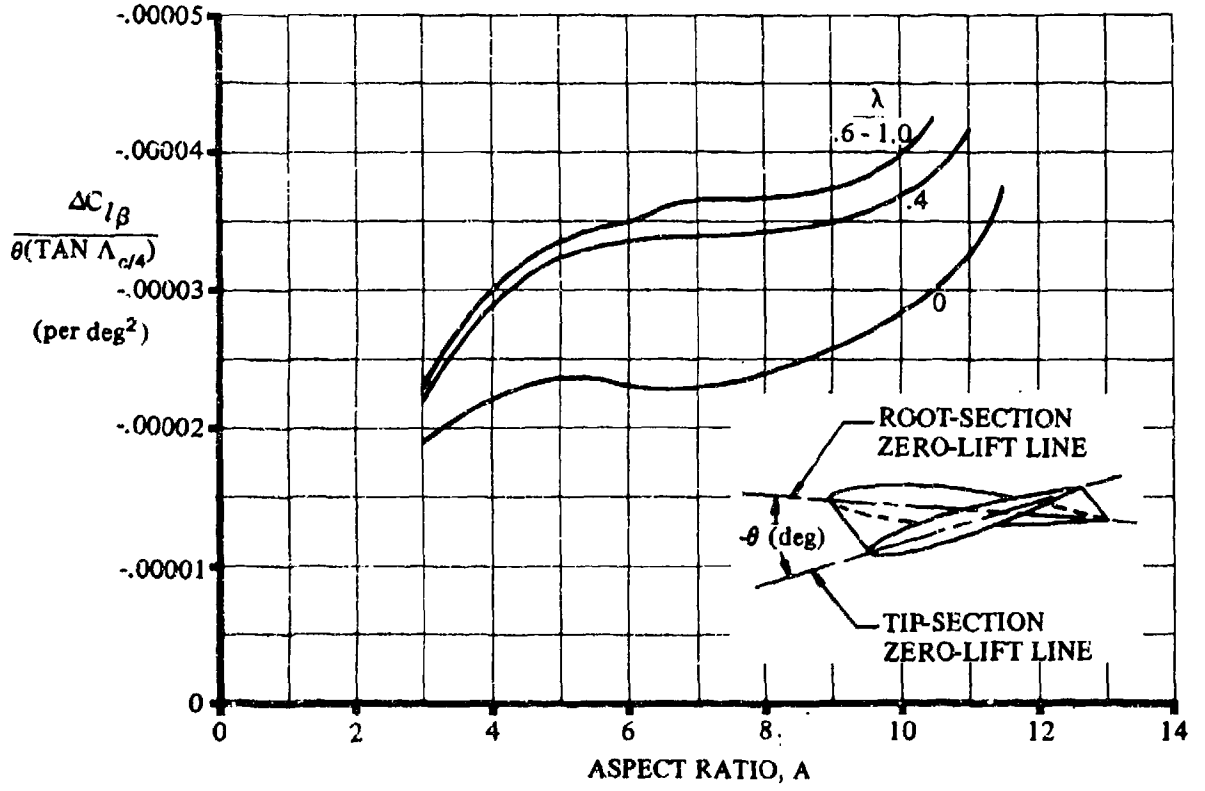

FIGURE 5.1.2.1-30b EFFECT OF WING TWIST ON WING C_{l_β}

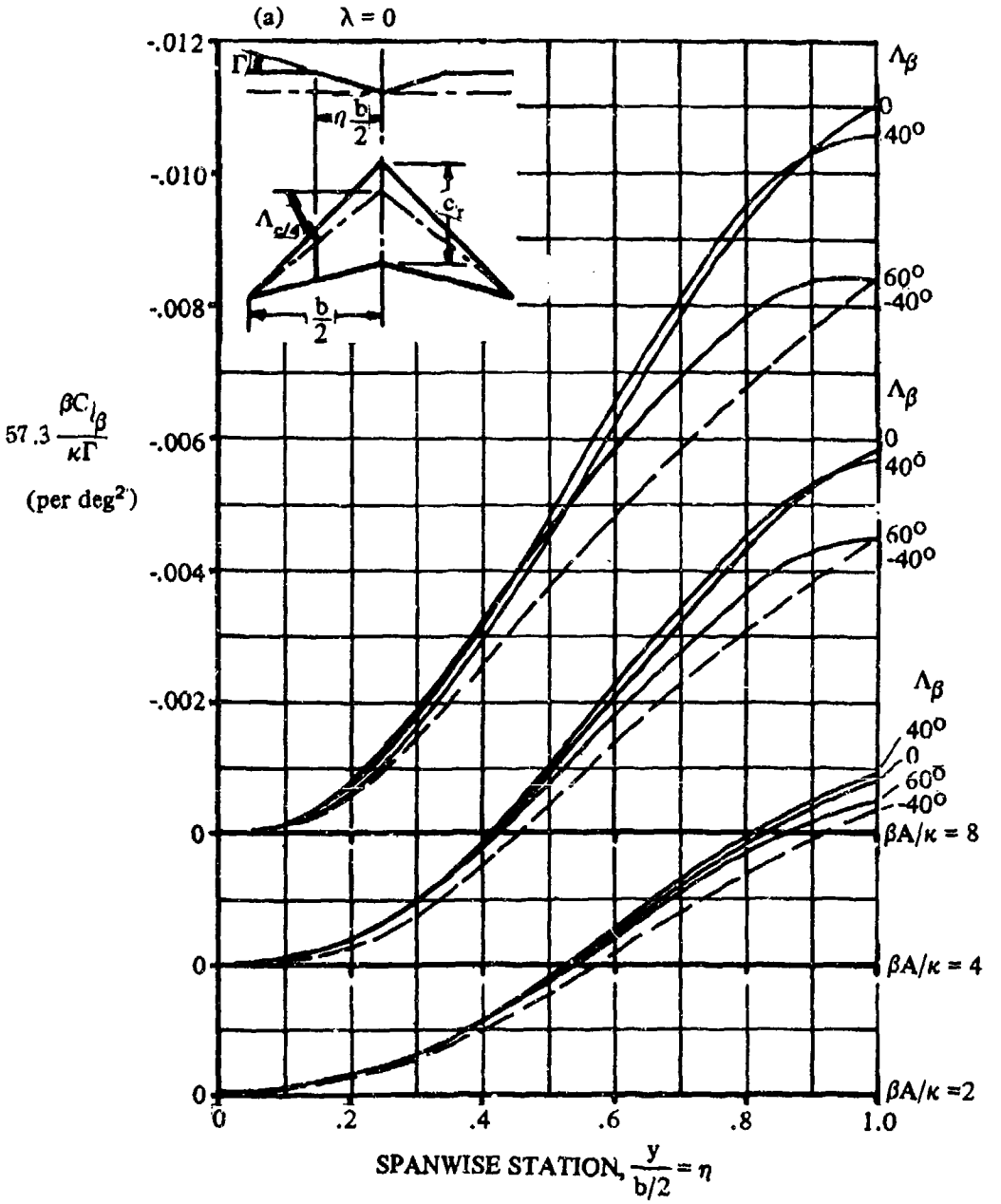

FIGURE 5.1.2.1-31 ROLLING MOMENT DUE TO SIDESLIP FOR SYMMETRIC SPANWISE DISTRIBUTION OF DIHEDRAL ANGLE

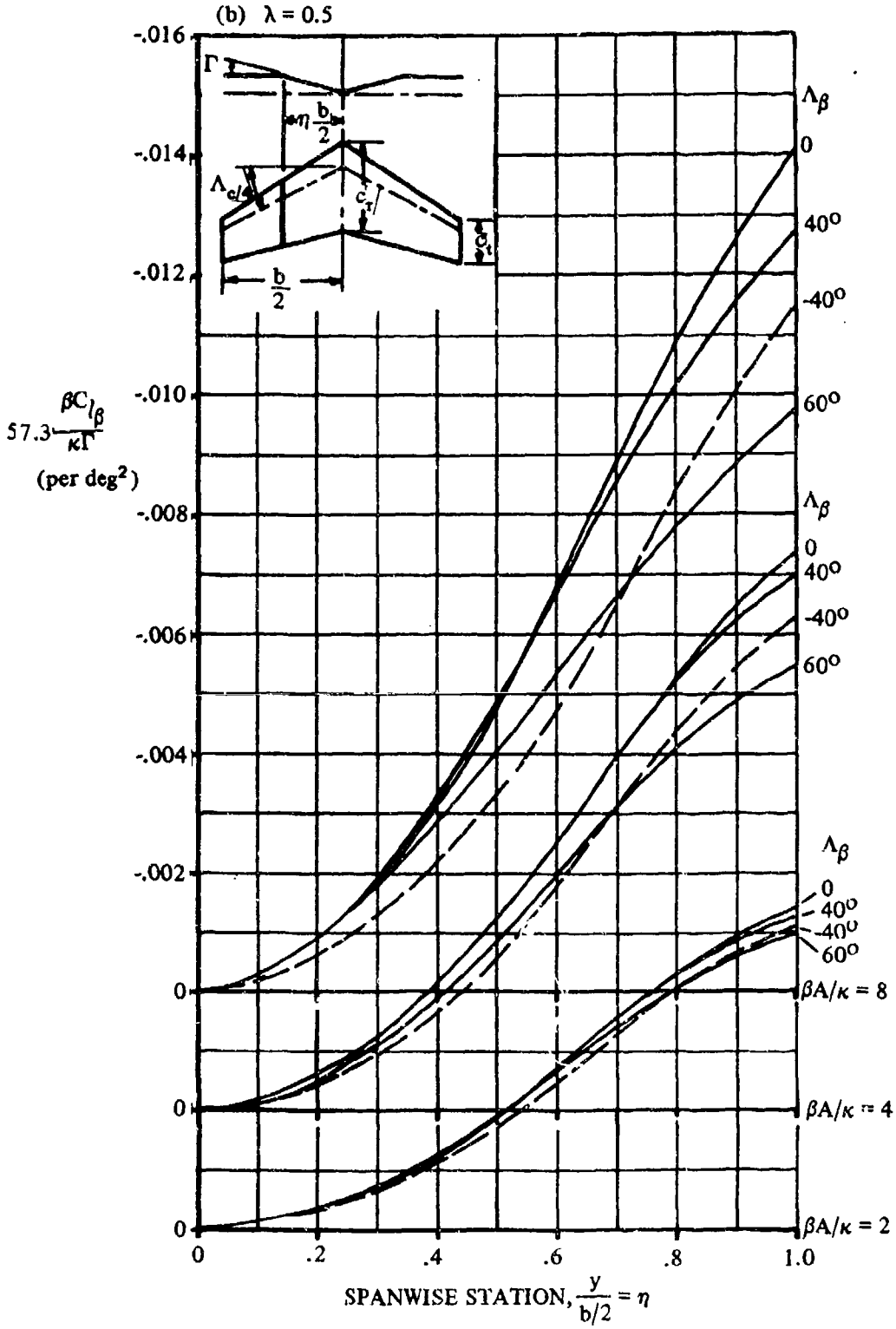

FIGURE 5.1.2.1 -31 (CONTD)

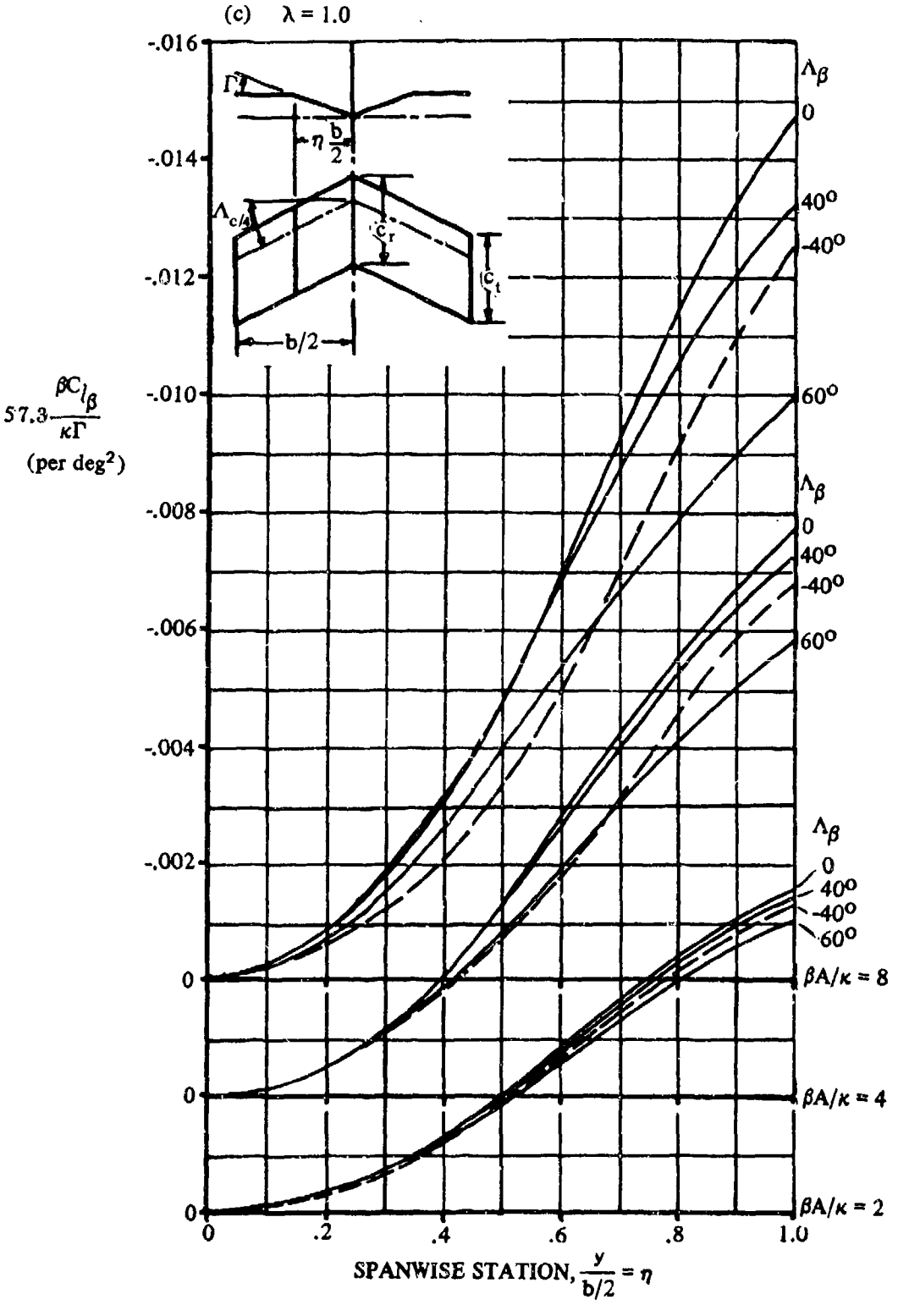

FIGURE 5.1.2.1-31 (CONTD)

5.1.2.2 WING ROLLING-MOMENT COEFFICIENT C_l AT ANGLE OF ATTACK

A. SUBSONIC

In Section 5.1.2.1, the wing rolling moments due to sideslip were discussed in terms of the parameters $\frac{C_{l_\beta}}{C_L}$ and $\frac{C_{l_\beta}}{\Gamma}$. These parameters imply that the rolling moment is a linear function of both lift coefficient and dihedral angle. This linearity holds true only if the flow is everywhere attached. Once separation takes place, the rolling-moment derivatives may vary considerably from the linear-range value, even changing sign in certain cases.

Because of the nonlinear nature of the separation effects governing C_{l_β}, no theoretical analysis of this parameter at the higher angles of attack has been successful. An empirical approach along the lines of Section 4.1.3.4 appears to be feasible. However, until a systematic method is developed, the presentation of this Handbook will be limited to a qualitative discussion of the important parameters governing C_{l_β} at high angles of attack, including certain representative examples.

Effect of Planform

As was mentioned in Section 4.1.3.4, planform shape plays an important part in determining the place at which separation first appears on a wing and how it subsequently progresses with increasing angle of attack. The manner in which the various separation patterns influence the rolling-moment characteristics is illustrated in figure 5.1.2.2-4.

For the unswept wing of figure 5.1.2.2-4 , separation occurs first at the wing trailing edge and then progresses forward with increasing angle of attack. When this wing is yawed, the separated area is displaced toward the downwind wing tip (presumably the result of spanwise boundary-layer flow). The size of the separated area on the downwind panel also increases with increasing angle of attack. The resulting lift differential between the upwind and downwind panels then gives rise to a powerful negative rolling moment (positive dihedral effect).

For swept and delta wings, separation occurs first at the wing leading edge. The separated flow rolls into two strong vortices lying along the wing leading edges. Changes in magnitude and distribution of the lift force on the wing are associated with these vortices. When these wings are yawed, the decrease in sweep angle of the upwind wing panel causes the leading-edge vortex on this panel to lose strength and to turn away from the leading edge farther inboard than the corresponding vortex on the downwind panel (see figure 5.1.2.2-4). This asymmetry results in a relative loss in lift on the upwind wing panel, even though there is a partially compensating effective increase in angle of attack due to the geometry of combined sweep and yaw. At angles of attack beyond the stall, flow over the wing is completely separated and all wing planforms have basically similar rolling-moment characteristics.

The trends presented in figure 5.1.2.2-4 are valid only for small sideslip angles ($\pm 5°$). At larger angles of sideslip, the curves of C_l as a function of β for the swept and delta wings reverse, and these wings then show positive-dihedral characteristics, as shown in figure 5.1.2.2-5.

Effect of Leading-Edge Shape

Since leading-edge shape is shown to have an important effect on the strength of the wing leading-edge vortex, and hence on the wing lift (Section 4.1.3.4), it is to be expected that wing rolling moments that also depend on vortex characteristics are influenced by wing leading-edge shape.

The effect of wing airfoil section (leading-edge shape) on C_{l_β} is illustrated in figure 5.1.2.2-6.

Briefly summarised, this figure shows that the sharper the wing leading edge, the lower the lift coefficient at which C_{l_β} deviates from the linear-theory value (figures 5.1.2.2-6a and 5.1.2.2-6b). Reducing the Reynolds number tends to promote leading-edge separation and thus produces the same effects as sharpening the leading edge (figure 5.1.2.2-6c).

Under certain circumstances, introduction of leading-edge roughness also triggers leading-edge separation and therefore causes the rolling-moment characteristics to deviate from linear values.

Very Low Aspect Ratios

For very low-aspect-ratio wings, C_{l_β} at high angles of attack is not only highly nonlinear but may also be non-symmetrical with respect to sideslip. Experimental data showing this effect for low-aspect-ratio triangular wings is given in reference 3. This unusual characteristic may be related to the formation of unsymmetrical leading-edge vortices similar to those observed for bodies of revolution at high angles of attack in references 4 and 5. In these two references it is shown that as the angle of attack is increased for bodies of revolution, the vortex system changes from a steady symmetric pair to a steady asymmetric configuration of two or more vortices and, finally, at large angles of attack, to an unsteady asymmetric arrangement. Experimental tests with free flying low-aspect-ratio-wing models have shown that undesirable lateral characteristics are present for aspect ratios considerably larger than those at which static asymmetric rolling moments cease to be apparent (reference 6). However, in this test the static rolling-moment characteristics may be obscured by the dynamic coupling effects of free flight.

Geometric Dihedral

The effects of geometric dihedral on wings at high angles of attack are directly related to the lift-curve slope at the same angle of attack. This relationship is

$$\left(\frac{C_{l_\beta}}{\Gamma}\right)_{C_L} = \left(\frac{C_{l_\beta}}{\Gamma}\right)_{C_L=0} \frac{(C_{L_\alpha})_{C_L}}{(C_{L_\alpha})_{C_L=0}} \qquad 5.1.2.2\text{-a}$$

It is evident that near maximum lift, where the lift-curve slope is small, a variation in geometric dihedral is not an effective way to change the wing rolling-moment characteristics.

B. TRANSONIC

The transonic rolling-moment characteristics of wings at high angles of attack generally show considerable variation with Mach number. (reference 2).

The changes in rolling-moment characteristics are roughly related to changes in panel lift characteristics. At transonic Mach numbers ($M > .9$) the wing lift-curve slope and maximum-lift characteristics undergo marked changes (see Sections 4.1.3.2 and 4.1.3.4), which are reflected in changes in the wing rolling moments.

For swept wings, the negative-dihedral effects at high angles of attack are reduced or eliminated with increasing Mach number. This is due to changes in the leading-edge vortex characteristics with Mach number that permit the leading wing panel to carry more lift.

For unswept wings, the increased compressibility effects on the force-break characteristics of the more highly loaded leading wing tend to reduce or even reverse the positive-dihedral characteristics in evidence at lower speeds. Mach number effects on the rolling moment due to geometric dihedral of any wing at high angles of attack are small.

C. SUPERSONIC

Experimental data on wing rolling moments due to sideslip at supersonic speeds and high angles of attack are relatively scarce, but the following general trends are observed.

Effect of Planform

For swept wings, the positive-dihedral effects that are in evidence at low angles of attack increase in magnitude with increasing angle of attack. This characteristic is relatively insensitive to Mach number variations (reference 7).

For unswept wings at Mach numbers below 2 the value of C_{l_β} tends toward zero with increasing angle of attack. This is true for the high-wing, midwing, and low-wing configurations tested in reference 8. At Mach numbers above 2 the same configurations show a trend toward increasingly positive dihedral effects with increasing angle of attack. At the higher Mach numbers the unswept-wing characteristics are similar to the swept-wing characteristics.

Geometric Dihedral

The experimental data of reference 7 show that up to 12° angle of attack the rolling-moment increment due to dihedral is essentially the same as at zero angle of attack. This result is somewhat unexpected, since a calculation of the local angles of attack of the left and right wing panels individually would predict a variation in dihedral effect (see reference 7). Possibly the discrepancy is due to sweep and/or wing-body interference effects.

If the geometric dihedral effects are assumed to be independent of angle of attack for all configurations at supersonic speeds, then the methods of Section 5.1.2.1 intended for low angles of attack are also applicable at the higher angles of attack.

REFERENCES

1. Johnson, J., Jr.: Low-Speed Measurements of Static Stability, Damping in Yaw, and Damping in Roll of a Delta, a Swept, and an Unswept Wing for Angles of Attack from 0° to 90°. NACA RM L56B01, 1956. (U)

2. Polhamus, E., and Sleeman, W., Jr.: The Rolling Moment Due to Sideslip of Swept Wings at Subsonic and Transonic Speeds. NASA TN D-309, 1960. (U)

3. Letko, W.: Experimental Determination at Subsonic Speeds of the Oscillatory and Static Lateral Stability Derivatives of a Series of Delta Wings with Leading-Edge Sweep from 30° to 86.5°. NACA RM L57A30, 1957. (U)

4. Allen, H. J., and Perkins, E.: Characteristics of Flow Over Inclined Bodies of Revolution. NACA RM A50L07, 1951. (U)

5. Gowen, F., and Perkins, E.: A Study of the Effects of Body Shape on the Vortex Wakes of Inclined Bodies at a Mach Number of 2. NACA RM A53I17, 1953. (U)

6. Toll, L.: Low-Speed Static Stability and Damping-in-Roll Characteristics of Some Swept and Unswept Low-Aspect-Ratio Wings. NACA TN 1468, 1947. (U)

7. Boatright, W.: Experimental Investigation of Effects of Wing Plan Form and Dihedral Angle on Sideslip Derivatives of Sweptback-Wing--Body Combinations at Supersonic Speeds. NACA RM L58E08, 1958. (C) Title Unclassified

8. Robinson, E.: Effects of Vertical Location of the Wing and Horizontal Tail on the Static Lateral and Directional Stability of a Trapezoidal-Wing Airplane Model at Mach Numbers of 1.41 and 2.01. NACA RM L58C18, 1958. (U)

9. Jaquet, B., and Fournier, R.: Effects of Wing Sweep, Horizontal-Tail Configuration, and a Ventral Fin on Static Stability Characteristics of a Model with a Wing of Aspect Ratio 4 at Mach Numbers From 2.39 to 4.65. NACA RM L58E06, 1958. (C) Title Unclassified

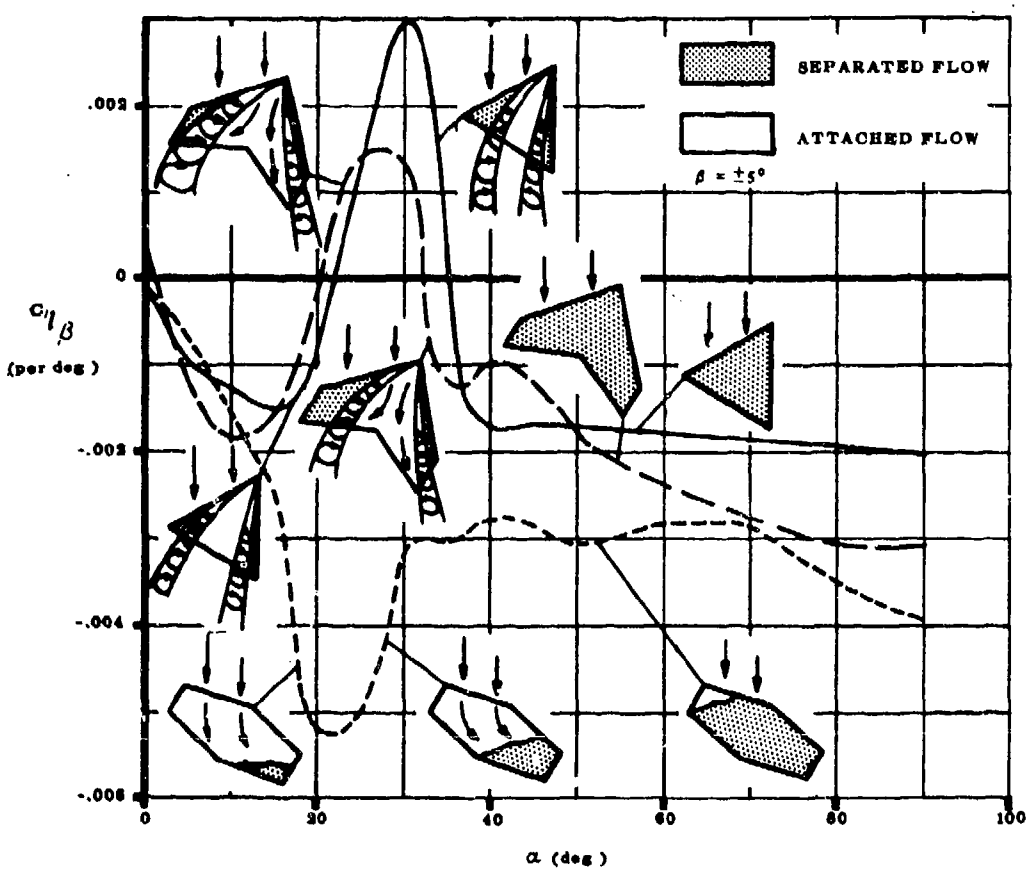

FIGURE 5.1.2.2-4 EFFECT OF PLANFORM ON THE VARIATION OF C_{l_β} WITH ANGLE OF ATTACK, ZERO DIHEDRAL, LOW SPEEDS (FROM REF. 1).

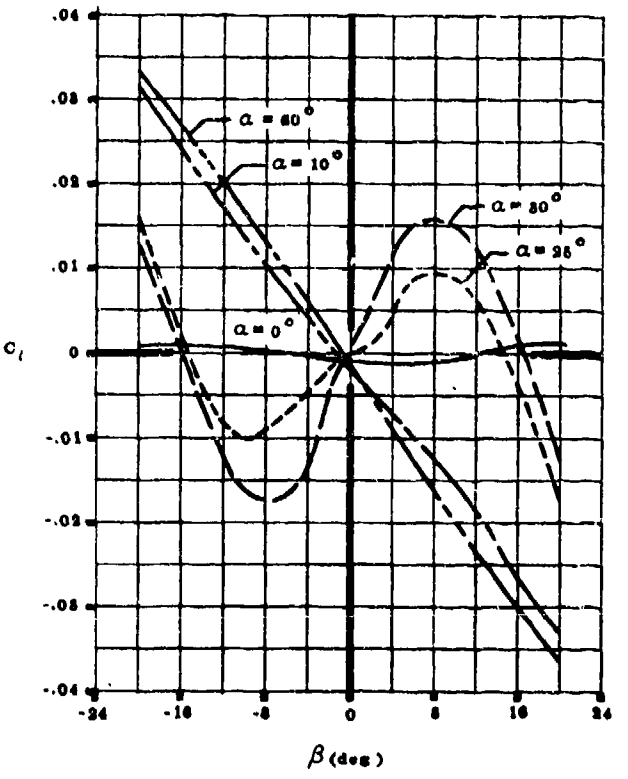

FIGURE 5.1.2.2-5 VARIATIONS OF ROLLING MOMENT WITH SIDESLIP FOR A DELTA WING AT LOW SPEEDS, ZERO DIHEDRAL, (REF. 1).

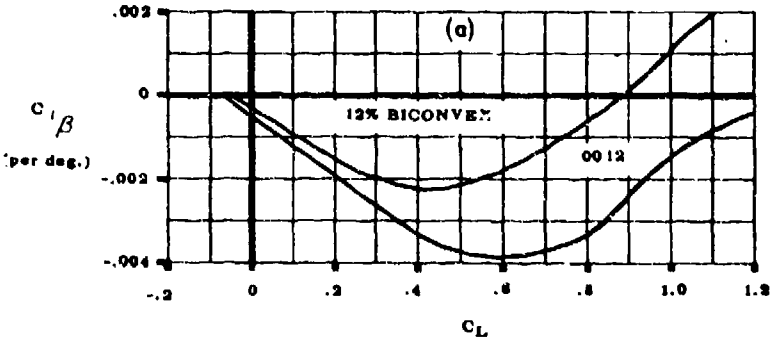

A = 60°
A = 2.31
R = 1.6 X 10^6

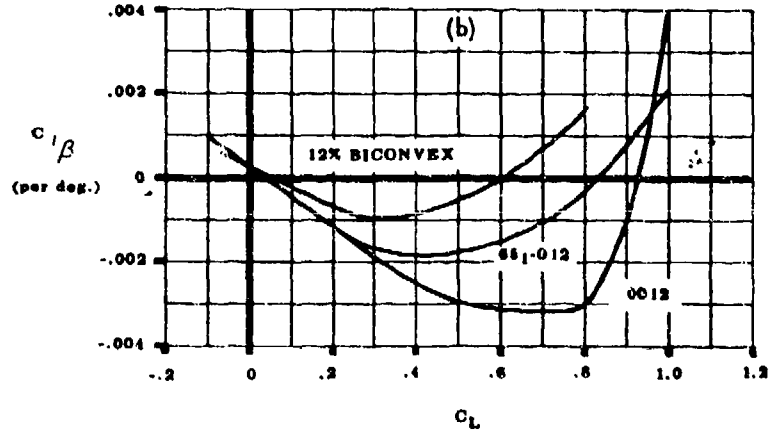

A = 45°
A = 2.61
R = 1.1 X 10^6

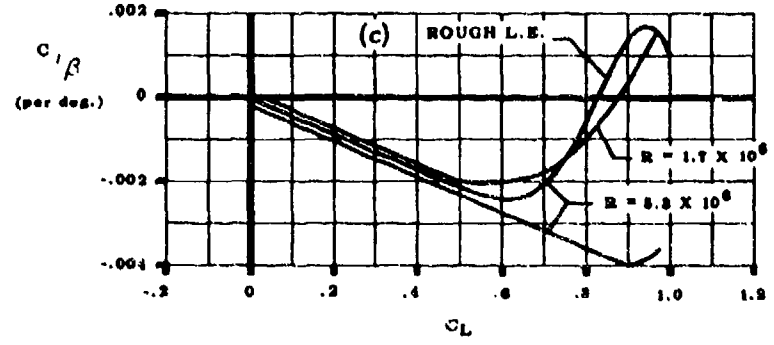

A = 40°
A = 4
λ = .625

FIGURE 5.1.2.2-6 EFFECT OF ANGLE OF ATTACK ON C_{l_β} AT LOW SPEEDS

5.1.3 WING SIDESLIP DERIVATIVE C_{n_β}

5.1.3.1 WING SIDESLIP DERIVATIVE C_{n_β} IN THE LINEAR ANGLE-OF-ATTACK RANGE

The yawing moment of a wing in sideslip is primarily caused by the asymmetrical induced-drag distribution associated with the asymmetrical lift distribution. The wing contribution to the derivative C_{n_β} is important only at large incidences.

Methods are presented in this section for estimating the wing yawing moment due to sideslip in the subsonic and supersonic speed regimes. Methods for estimating this derivative in the transonic speed regime are not available.

A. SUBSONIC

The Datcom method presented herein is based on the same theory as that used to determine wing side force due to sideslip, and the general discussion of Paragraph A of Section 5.1.1.1 is directly applicable here. The method is valid in the linear angle-of-attack region.

DATCOM METHOD

The yawing moment derivative at low speeds is given in Reference 1 as

$$\frac{C_{n_\beta}}{C_L^2} = \frac{1}{57.3}\left[\frac{1}{4\pi A} - \frac{\tan \Lambda_{c/4}}{\pi A(A + 4\cos \Lambda_{c/4})}\left(\cos \Lambda_{c/4} - \frac{A}{2} - \frac{A^2}{8\cos \Lambda_{c/4}} + 6\frac{\bar{x}}{\bar{c}}\frac{\sin \Lambda_{c/4}}{A}\right)\right]$$

(per deg) 5.1.3.1-a

where $\bar{x}$ is the longitudinal distance (positive rearward) from the coordinate origin (usually the center of gravity) to the wing aerodynamic center.

The wing contribution to the yawing moment due to sideslip at low speeds is shown to be independent of both taper ratio and dihedral in References 2 and 3, respectively.

For subcritical speeds, the low-speed derivative can be modified by the Prandtl-Glauert rule to yield approximate corrections for the first-order three-dimensional effects of compressibility. The resulting expression from Reference 4 is

$$\left(\frac{C_{n_\beta}}{C_L^2}\right)_M = \left(\frac{A + 4\cos \Lambda_{c/4}}{AB + 4\cos \Lambda_{c/4}}\right)\left(\frac{A^2B^2 + 4AB\cos \Lambda_{c/4} - 8\cos^2 \Lambda_{c/4}}{A^2 + 4A\cos \Lambda_{c/4} - 8\cos^2 \Lambda_{c/4}}\right)\left(\frac{C_{n_\beta}}{C_L^2}\right)_{\substack{\text{low}\\\text{speed}}}$$

5.1.3.1-b

where

$$B = \sqrt{1 - M^2\cos^2 \Lambda_{c/4}}.$$

5.1.3.1-1

Calculated values for the wing yawing moment due to sideslip at low subsonic speeds obtained by the Datcom method for the wing configurations of References 5, 6, and 7 are compared with experimental data in Figure 5.1.3.1-5. The comparison indicates that the calculated values are fairly reliable over a range of lift coefficient (starting from zero) that decreases as wing sweep increases. Large discrepancies are noted for highly swept wings at lift coefficients for which the flow is believed to be partially separated.

Sample Problem

Given: The wing of Reference 5

$$A = 4.0 \qquad \Lambda_{c/4} = 60^\circ \qquad \frac{\bar{x}}{\bar{c}} = 0.037 \qquad M = 0.13$$

Compute:

$$\sin \Lambda_{c/4} = 0.866$$
$$\cos \Lambda_{c/4} = 0.500$$
$$\tan \Lambda_{c/4} = 1.732$$

Solution:

$$\frac{C_{n_\beta}}{C_L^2} = \frac{1}{57.3}\left[\frac{1}{4\pi A} - \frac{\tan \Lambda_{c/4}}{\pi A(A + 4 \cos \Lambda_{c/4})}\left(\cos \Lambda_{c/4} - \frac{A}{2} - \frac{A^2}{8 \cos \Lambda_{c/4}} + 6\,\frac{\bar{x}}{\bar{c}}\,\frac{\sin \Lambda_{c/4}}{A}\right)\right]$$

(per deg) (equation 5.1.3.1-a)

$$= \frac{1}{57.3}\left[\frac{1}{16\pi} - \frac{1.732}{4\pi\,[4 + (4)\,(0.50)]}\left(0.50 - \frac{4}{2} - \frac{(4)^2}{(8)\,(0.50)} + (6)\,(0.037)\,\frac{0.866}{4}\right)\right]$$

$$= \frac{1}{57.3}\,[(0.01989) - (0.02297)\,(-5.452)]$$

$$= \frac{1}{57.3}\,[(0.01989) + (0.1252)]$$

$$= 0.00253 \text{ per deg}$$

C_L	C_L^2	$C_{n_\beta} \times 10^3$ (per deg)
0.05	0.0025	0.00633
0.10	0.010	0.0253
0.20	0.040	0.1012
0.30	0.090	0.2277
0.40	0.160	0.4048
0.50	0.250	0.6325
0.60	0.360	0.9108

These results are compared with experimental values in Figure 5.1.3.1-5.

B. TRANSONIC

There are no methods available for estimating the wing yawing moment due to sideslip in the transonic regime and none are presented in the Datcom. Furthermore, there are no experimental data available in the transonic speed regime.

C. SUPERSONIC

No general method has been developed for estimating the wing yawing moment due to sideslip at supersonic speeds. However, theoretical methods are available for discrete planforms over certain speed ranges. A comprehensive summary of the available theoretical methods for calculating the wing yawing moment due to sideslip is presented in Reference 9. Datcom methods are based on the same theory as that used to determine wing side force due to sideslip, and the general discussion of Paragraph C of Section 5.1.1.1 is directly applicable here.

DATCOM METHODS

The Datcom methods are taken from References 10, 11, and 12 and present the wing yawing moment due to sideslip for rectangular planforms, triangular planforms, and fully tapered sweptback planforms with sweptforward or sweptback trailing edges. The results are mainly functions of planform geometry and Mach number. The general trend of the variation of C_{n_β} with Mach number and aspect ratio is a reduction in the magnitude of the derivative with an increase in these parameters.

Rectangular Planform: $A\beta \geq 1.0$

The wing yawing moment due to sideslip for rectangular planforms referred to an arbitrary moment center is given in Reference10 as

$$\frac{C_{n_\beta}}{\alpha^2} = \frac{1}{\pi A^2 \beta^2}\left[\frac{4M^2}{3} + 8M^2\frac{x}{\bar{c}} - \pi\left\{\frac{A(1-\beta^2)}{\beta}\frac{3+\beta^2}{3\beta^2}\right\}\right]\frac{1}{57.3} \text{ (per deg)} \qquad 5.1.3.1\text{-c}$$

where α is in radians, $\beta = \sqrt{M^2 - 1}$ and x is the distance of the origin of moments from the midchord point, measured along the longitudinal axis, positive ahead of midchord point.

Equation 5.1.3.1-c is valid for Mach number and aspect ratio greater than that for which the Mach line from the leading edge of the tip section intersects the trailing edge of the opposite tip section ($A\beta \geq 1.0$).

Sweptback Planform ($\lambda = 0$): $\beta \cot \Lambda_{LE} \leq 1.0$

The wing yawing moment due to sideslip for fully tapered sweptback planforms is derived in Reference 11 for triangular planforms and in Reference 12 for planforms with sweptforward or sweptback trailing edges as

$$\frac{C_{n_\beta}}{\alpha^2} = \frac{\pi}{3}\left[E''(\beta C)F_9(N) + \left(\frac{A^2}{16}F_{11}(N) + \frac{x}{\bar{c}}\right)M^2 Q(\beta C)\right]\frac{1}{57.3} \text{ (per deg)} \qquad 5.1.3.1\text{-d}$$

where α is in radians and

$Q(\beta C)$ is obtained from Figure 5.1.1.1-6
$E''(\beta C)$ is obtained from Figure 7.1.1.1-8
$F_{11}(N)$ is obtained from Figure 7.1.1.2-8
$F_9(N)$ is obtained from Figure 5.1.3.1-6

x is the distance of the origin of moments from the 2/3 c_{r_B} point of the basic triangular wing, measured along the longitudinal axis, positive ahead of the 2/3 c_{r_B} point. (See Sketch (a) of Section 7.1.1.1 for definition of basic triangular wing.)

For a triangular planform the factors $F_9(N)$ and $F_{11}(N)$ are equal to 1.0.

Equation 5.1.3.1-d is valid for Mach number and aspect ratio for which the wing is contained within the Mach cones springing from the apex and the trailing edge at the center of the wing.

REFERENCES

1. Toll, T.A., and Queijo, M. J.: Approximate Relations and Charts for Low-Speed Stability Derivatives of Swept Wings. NACA TN 1581, 1948. (U)

2. Letko, W., and Cowan, J. W.: Effect of Taper Ratio on Low-Speed Static and Yawing Stability Derivatives of 45° Sweptback Wings with Aspect Ratio of 2.61. NACA TN 1671, 1948. (U)

3. Queijo, M. J., and Jaquet, B.: Investigation of Effects of Geometric Dihedral on Low-Speed Static Stability and Yawing Characteristics of an Untapered 45° Sweptback-Wing Model of Aspect Ratio 2.61. NACA TN 1668, 1948. (U)

4. Fisher, L.: Approximate Corrections for the Effects of Compressibility on the Subsonic Stability Derivatives of Swept Wings. NACA TN 1854, 1949. (U)

5. Wolhart, W. D., and Thomas, D. F., Jr.: Static Longitudinal and Lateral Stability Characteristics at Low Speed of Unswept-Midwing Models Having Wings with an Aspect Ratio of 2, 4, or 6. NACA TN 3649, 1956. (U)

6. Thomas, D. F., Jr., and Wolhart, W.D.: Static Longitudinal and Lateral Stability Characteristics at Low Speed of 45° Sweptback-Midwing Models Having Wings with an Aspect Ratio of 2, 4, or 6. NACA TN 4077, 1957. (U)

7. Wolhart, W. D., and Thomas, D. F., Jr.: Static Longitudinal and Lateral Stability Characteristics at Low Speed of 60° Sweptback-Midwing Models Having Wings with an Aspect Ratio of 2, 4, or 6. NACA TN 4397, 1958. (U)

8. Jones, A.L.: The Theoretical Lateral-Stability Derivatives for Wings at Supersonic Speeds. Jour. Aero. Sci., Vol. 17, No. 1, January 1950. (U)

9. Jones, A. L., and Alksne, A.: A Summary of Lateral-Stability Derivatives Calculated for Wing Planforms in Supersonic Flow. NACA TR 1052, 1951. (U)

10. Harmon, S. M.: Stability Derivatives at Supersonic Speeds of Thin Rectangular Wings with Diagonals Ahead of Tip Mach Lines. NACA TR 925, 1949. (U)

11. Ribner, H.S., and Malvestuto, F.S., Jr.: Stability Derivatives of Triangular Wings at Supersonic Speeds. NACA TR 908, 1948. (U)

12. Malvestuto, F. S., Jr., and Margolis, K.: Theoretical Stability Derivatives of Thin Sweptback Wings Tapered to a Point with Sweptback or Sweptforward Trailing Edges for a Limited Range of Supersonic Speeds. NACA TR 971, 1950. (U)

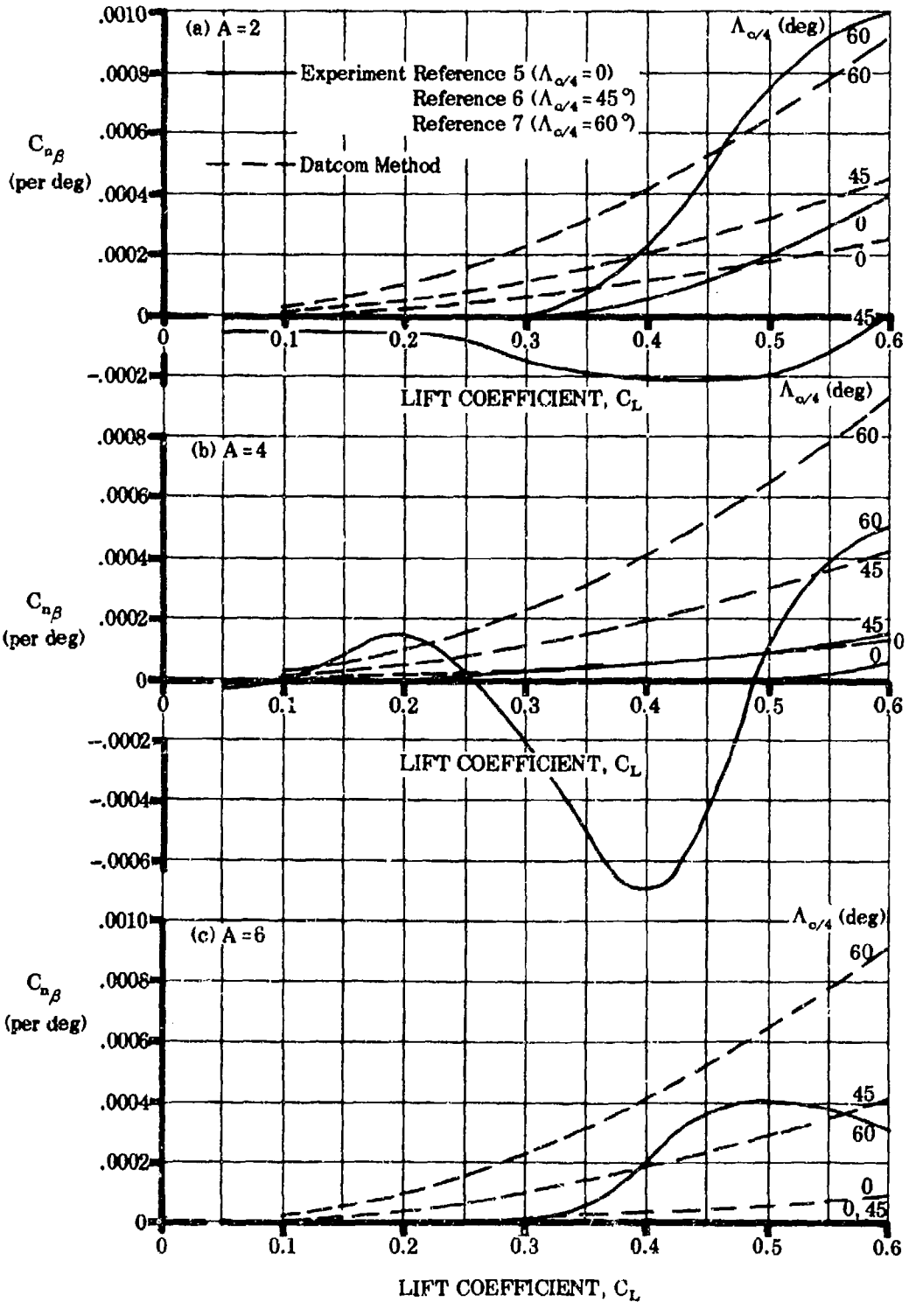

FIGURE 5.1.3.1-5 COMPARISON OF CALCULATED AND EXPERIMENTAL VALUES OF WING YAWING MOMENT DUE TO SIDESLIP FOR THE WING CONFIGURATIONS OF REFERENCES 5, 6, AND 7.

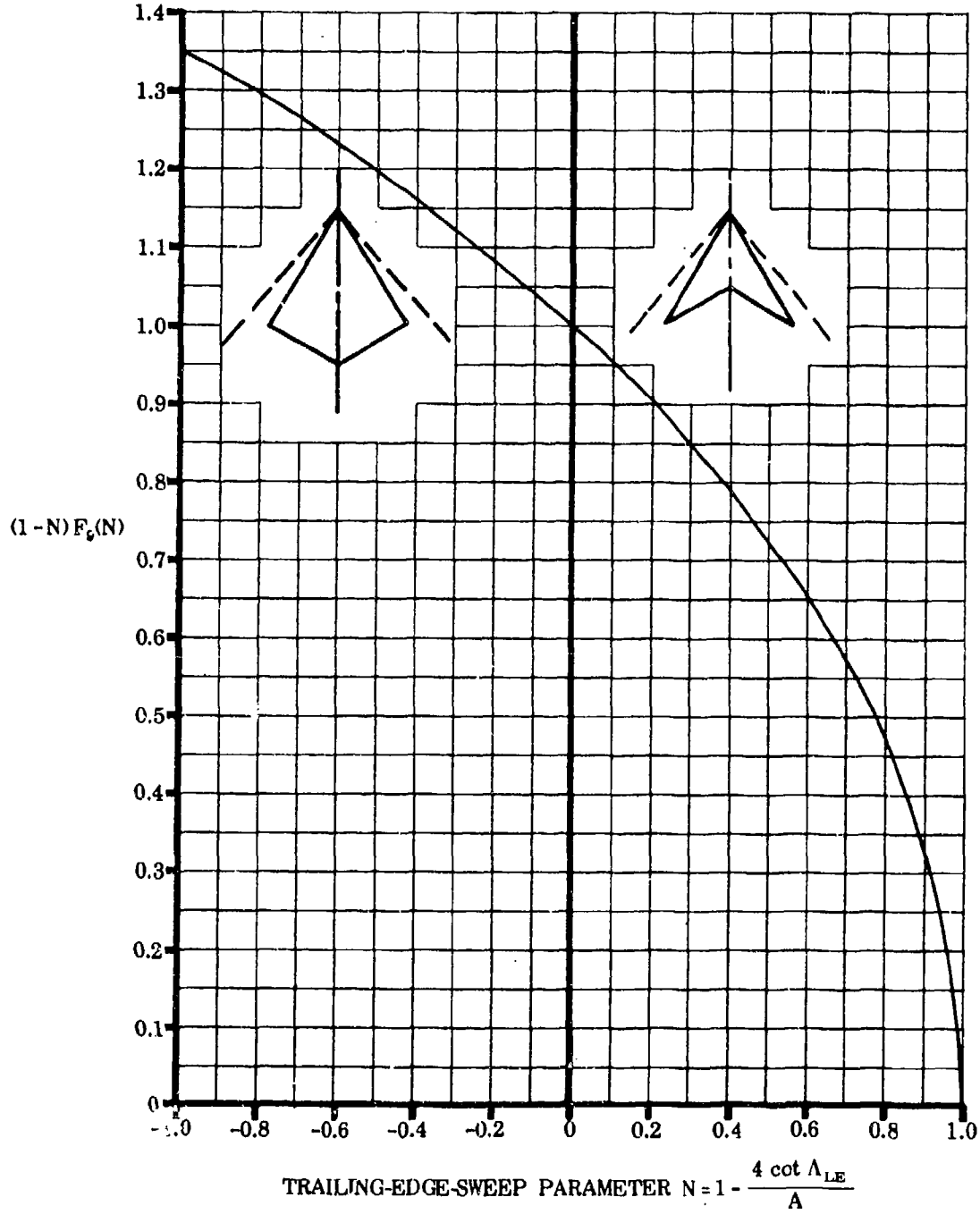

FIGURE 5.1.3.1-6 $F_0(N)$ FACTOR OF THE STABILITY DERIVATIVE

5.2 WING-BODY COMBINATIONS IN SIDESLIP
5.2.1 WING-BODY SIDESLIP DERIVATIVE C_{Y_β}

5.2.1.1 WING-BODY SIDESLIP DERIVATIVE C_{Y_β} IN THE LINEAR ANGLE-OF-ATTACK RANGE

The wing-body side force due to sideslip can be considered as the sum of the side forces of the body, the wing, the wing-body interference, and the wing dihedral effect. The wing side force due to sideslip at low lift coefficient is small in comparison to that due to the body and is neglected in the Datcom methods of this Section.

Wing-body interference, which is primarily a function of wing vertical position on the body, is presented as a fraction of the body contribution. Experimental investigations show that the contribution of wing-body interference to the sideslip derivative C_{Y_β} is essentially independent of sweep, wing planform, taper ratio, and Mach number.

The body is the chief contributor to the side force of a wing-body combination. Experimental results for the body alone show a negative lateral force which increases as the body fineness ratio is decreased.

The range of applicability of the method is limited to the linear angle-of-attack range.

A. SUBSONIC

The wing-body side force due to sideslip is estimated by the following method.

DATCOM METHOD

The wing-body side force due to sideslip, based on wing area, is given by

$$(C_{Y_\beta})_{WB} = K_i\,(C_{Y_\beta})_B \left(\frac{\text{Body Reference Area}}{S_W}\right) + (\Delta C_{Y_\beta})_\Gamma \qquad \text{5.2.1.1-a}$$

where

K_i is the wing-body interference factor obtained from figure 5.2.1.1-7

$(C_{Y_\beta})_B$ is the body side force due to sideslip obtained from paragraph A of Section 4.2.1.1 as

$$(C_{Y_\beta})_B = -\,(C_{L_\alpha})_B$$

$(\Delta C_{Y_\beta})_\Gamma$ is the increment in side force due to wing dihedral and is approximated by $(\Delta C_{Y_\beta})_\Gamma = -0.0001\,|\Gamma|$ (Γ and β in degrees) (equation 5.1.1.1-b)

For a rapid but approximate estimation of the body side force due to sideslip, slender-body theory can be used, which gives $(C_{Y_\beta})_B = -2$ (per rad), where $(C_{Y_\beta})_B$ is based on the body cross-sectional area at x_0 (see page 4.2.1.1-1 for definition of x_0).

A comparison of experimental data and values of wing-body side force due to sideslip at subsonic speeds calculated by equation 5.2.1.1-a is presented as table 5.2.1.1-A.

Sample Problem

Given: The wing body configuration of reference 3.

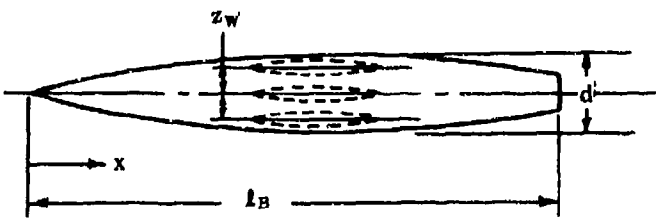

ℓ_B = 3.45 ft d = 0.5 ft f = 6.90 z_W = 0, ±0.1667 ft S_W = 2.25 sq ft

$\frac{x_1}{\ell_B}$ = 0.50 $V_B^{2/3}$ = 0.542 sq ft Γ = 0

S_0 = 0.175 sq ft (area distribution curve at $\frac{x_0}{\ell_B}$)

Compute:

$z_W/\frac{d}{2}$ = 0, ±0.667

$K_{l\ High}$ = 1.57
$K_{l\ Mid}$ = 1.0
$K_{l\ Low}$ = 1.33
} (figure 5.2.1.1-7)

$(k_2 - k_1)$ = 0.890 (figure 4.2.1.1-20a)

$\frac{x_0}{\ell_B}$ = 0.640 (figure 4.2.1.1-20b)

$$(C_{Y_\beta})_B = -\left[\frac{2(k_2 - k_1)\,S_0}{V_B^{2/3}}\right] \text{ (per rad)} \quad \text{(equation 4.2.1.1-a)}$$

$$= -\frac{(2)(0.89)(0.175)}{0.542} = -0.575 \text{ per rad (based on } V_B^{2/3})$$

Solution:

$$(C_{Y_\beta})_{WB} = K_l\,(C_{Y_\beta})_B\left(\frac{\text{Body Reference Area}}{S_W}\right) + (\Delta\, C_{Y_\beta})_\Gamma \quad \text{(equation 5.2.1.1-a)}$$

$$= K_l(-0.575)\left(\frac{0.542}{2.25}\right) + 0$$

$$= -0.1385\, K_l \text{ per rad}$$

$$= -0.00242\, K_l \text{ per deg}$$

Wing Position	K_l	$(C_{Y_\beta})_{WB}$ (per deg)
High	1.57	-0.00380
Mid	1.0	-0.00242
Low	1.33	-0.00322

These results compare with experimental values of -0.004 per deg, -0.0024 per deg, and -0.0034 per deg for the high-, mid-, and low-wing configurations, respectively, obtained from reference 3.

B. TRANSONIC

The contribution of wing-body interference to the side force derivative is essentially independent of Mach number. Furthermore, slender-body theory states that body force characteristics are not functions of Mach number.

DATCOM METHOD

The method presented in paragraph A is applicable throughout the transonic speed regime.

C. SUPERSONIC

The contribution of wing-body interference to the side force derivative is essentially independent of Mach number. Several of the theoretical methods that have been developed for estimating body force characteristics at supersonic speeds are discussed in paragraph C of Section 4.2.1.1.

The experimental results of reference 6 indicate a negative lateral force increment due to wing camber at supersonic speeds; however, no method is available to predict this effect.

DATCOM METHOD

The method presented in paragraph A is applicable throughout the supersonic speed range. The body side force due to sideslip is obtained by conversion of the body lift-curve slope of paragraph C of Section 4.2.1.1.

A comparison of experimental data and values of wing-body side force due to sideslip at supersonic speeds calculated by the Datcom method is presented as table 5.2.1.1-B.

Sample Problem

Given: The midwing-ogive-cylinder body configuration of reference 12.

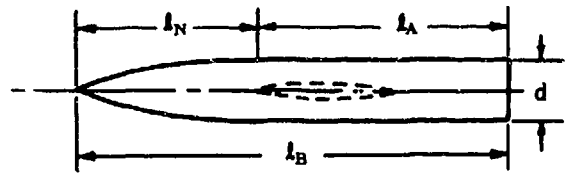

$d = 0.0625$ ft $\quad l_N = 0.2188$ ft $\quad l_A = 0.4062$ ft $\quad S_W = 0.0506$ sq ft $\quad S_b = 0.00307$ sq ft

$\Gamma = 10°$ $\quad M = 1.62, 2.62$

Compute:

$$f_N = \frac{l_N}{d} = 3.5$$

$$f_A = \frac{l_A}{d} = 6.5$$

$$\frac{f_A}{f_N} = \frac{6.5}{3.5} = 1.857$$

$$\beta_{M = 1.62} = \sqrt{M^2 - 1} = 1.275$$

$$\beta_{M = 2.62} = \sqrt{M^2 - 1} = 2.42$$

$$(\beta/f_N)_{M = 1.62} = \frac{1.275}{3.5} = 0.364$$

$$(\beta/f_N)_{M = 2.62} = \frac{2.42}{3.5} = 0.691$$

$[(C_{Y_\beta})_B]_{M = 1.62} = -2.78$ per rad (based on S_b)

$[(C_{Y_\beta})_B]_{M = 2.62} = -3.06$ per rad (based on S_b)

(figure 4.2.1.1-21a; $(C_{Y_\beta})_B = -(C_{N_\alpha})_B$)

$K_1 = 1.0$ (figure 5.2.1.1-7; mid-wing configuration)

$(\Delta C_{Y_\beta})_\Gamma = (-0.0001)(10) = -0.0010$ per deg (equation 5.1.1.1-b)

Solution:

$$(C_{Y\beta})_{WB} = K_I (C_{Y\beta})_B \left(\frac{\text{Body Reference Area}}{S_W} \right) + (\Delta C_{Y\beta})_\Gamma \qquad \text{(equation 5.2.1.1-a)}$$

$$= 1.0 (C_{Y\beta})_B \left(\frac{0.00307}{0.0506} \right) + (-0.0010)$$

$$= 0.0607 (C_{Y\beta})_B - 0.0010$$

M	$(C_{Y\beta})_B$ (per rad)	$(C_{Y\beta})_B$ (per deg)	$0.0607 (C_{Y\beta})_B$ (per deg)	$(C_{Y\beta})_{WB}$ (per deg)
1.62	-2.78	-0.0485	-0.00294	-0.00394
2.62	-3.06	-0.0534	-0.00324	-0.00424

These results compare with experimental values of -0.0038 per degree and -0.0042 per degree at Mach numbers 1.62 and 2.62, respectively, obtained from reference 12.

REFERENCES

1. Queijo, M., and Wolhart, W.: Experimental Investigation of the Effect of Vertical-Tail Size and Length and of Fuselage Shape and Length on the Static Lateral Stability Characteristics of a Model with 45° Sweptback Wing and Tail Surfaces. NACA TR 1049, 1951. (U)
2. Goodman, A., and Thomas, D., Jr.: Effects of Wing Position and Fuselage Size on the Low-Speed Static and Rolling Stability Characteristics of a Delta-Wing Model. NACA TR 1224, 1955. (U)
3. Goodman, A.: Effects of Wing Position and Horizontal-Tail Position on the Static Stability Characteristics of Model with Unswept and 45° Sweptback Surfaces with some Reference to Mutual Interference. NACA TN 2504, 1951. (U)
4. Savage, H. F., and Tinling, B. E.: The Subsonic Static Aerodynamic Characteristics of an Airplane Model having a Triangular Wing of Aspect Ratio 3. II- Lateral and Directional Characteristics. NACA TN 4042, 1957. (U)
5. Kuhn, R. E., and Draper, J. W.: Wind-Tunnel Investigation of the Effects of Geometric Dihedral on the Aerodynamic Characteristics in Pitch and Sideslip of an Unswept- and a 45° Sweptback-Wing-Fuselage Combination at High Subsonic Speeds. NACA RM L53F09, 1953. (U)
6. Christensen, F. B.: An Experimental Investigation of Four Triangular-Wing-Body Combinations in Sideslip at Mach Numbers 0.6, 0.9, 1.4 and 1.7. NACA RM A53L22, 1954. (U)
7. Jaquet, B. J., and Williams, J. L.: Wind-Tunnel Investigation at Low Speeds of Effect of Size and Position of Closed Air Ducts on Static Longitudinal and Static Lateral Stability Characteristics of Unswept-Midwing Models having Wings of Aspect Ratio 2, 4, and 6. NACA TN 3451, 1955. (U)
8. Kuhn, R. E., and Fournier, P. G.: Wind-Tunnel Investigation of the Static Lateral Stability Characteristics of Wing-Fuselage Combinations at High Subsonic Speeds. NACA RM L52G11a, 1952. (U)
9. Wiggins, J. W., Kuhn, R. E., and Fournier, P. G.: Wind-Tunnel Investigation to Determine the Horizontal- and Vertical-Tail Contributions to the Static Lateral Stability Characteristics of a Complete-Model Swept-Wing Configuration at High Subsonic Speeds. NACA TN 3818, 1956. (U)
10. Letko, W., and Williams, J. L.: Experimental Investigation at Low Speed of Effects of Fuselage Cross Section on Static Longitudinal and Lateral Stability Characteristics of Model Having 0° and 45° Sweptback Surfaces. NACA TN 3551, 1955. (U)
11. Robinson, R. B.: Effects of Vertical Location of the Wing and Horizontal Tail on the Static Lateral and Directional Stability of a Trapezoidal-Wing Airplane Model at Mach Numbers of 1.41 and 2.01. NACA RM L58C18, 1958. (U)
12. Boatright, W. B.: Experimental Investigation of Effects of Wing Planform and Dihedral Angle on Sideslip Derivatives of Sweptback-Wing-Body Combinations at Supersonic Speeds. NACA RM L58E08, 1958. (U)
13. Spearman, M. L., Driver, C., and Hughes, W. C.: Investigation of Aerodynamic Characteristics in Pitch and Sideslip of a 45° Sweptback-Wing Airplane Model with Various Vertical Locations of Wing and Horizontal Tail. Basic-Data Presentation, M = 2.01. NACA RM L54L06, 1955. (U)

TABLE 5.2.1.1-A

LOW SPEED WING-BODY SIDE FORCE DUE TO SIDESLIP

DATA SUMMARY

Ref	M	f	Wing Position	Γ (deg)	$\frac{x_1}{l_n}$	$\frac{x_0}{l_n}$	$(k_2 - k_1)$	S_0 sq ft	$V_\beta^{2/3}$ sq ft	S_w sq ft	K_1	$C_{Y_{\beta\,calc}} \times 10^3$ per deg	* $C_{Y_{\beta\,test}} \times 10^3$ per deg	$\Delta C_{Y_\beta} \times 10^3$ per deg (Calc - Test)
1	0.13	5.00	Mid	0	0.50	0.64	0.825	0.363	0.415	2.25	1.00	-2.090	-2.20	0.11
		6.67					0.880	0.362	0.496			-2.200	-2.21	0.01
		10.00					0.940	0.166	0.652			-2.240	-2.25	0.01
		6.67					0.880	0.162	0.586			-2.210	-2.28	0.07
		6.67					0.880	0.181	0.530			-2.470	-2.28	-0.19
2	0.17	12.0	High	0	0.40	0.595	0.955	0.110	0.464	4.00	1.57	-1.445	-2.00	0.555
			Mid								1.00	-0.920	-1.20	0.28
			Low								1.33	-1.220	-1.60	0.38
		9.00	High				0.925	0.198	0.690		1.57	-2.510	-3.00	0.49
			Mid								1.00	-1.600	-2.00	0.40
			Low								1.33	-2.125	-2.00	-0.125
		6.00	High				0.860	0.440	1.174		1.57	-5.180	-5.60	0.42
			Mid								1.00	-3.300	-2.40	-0.90
			Low								1.33	-4.390	-4.60	0.21
3	0.17	6.90	High	0	0.50	0.64	0.888	0.175	0.542	2.25	1.57	-3.760	-4.00	0.24
			Mid								1.00	-2.400	-2.40	0
			Low								1.33	-3.190	-3.40	0.21
4	0.25	12.0	High	0	0.75	0.765	0.955	0.195	0.924	4.00	1.58	-2.560	-2.60	0.04
5	0.50	9.84	Mid	10	0.61	0.70	0.937	0.136	0.522	2.25	1.00	-2.980	-3.100	0.12
				5								-2.480	-2.000	-0.48
				-5								-2.480	-2.000	-0.48
				-10								-2.980	-3.000	0.02
6	0.60	9.87	Mid	0	0.50	0.645	0.94	0.180	0.798	4.014	1.0	-1.470	-1.40	-0.07
	0.90												-1.40	-0.07
	0.60	10.45					0.95	0.090	0.410	2.007		-1.490	-1.40	-0.09
	0.90												-1.40	-0.09
9	0.40	9.84	Mid	0	0.61	0.70	0.937	0.136	0.522	2.25	1.0	-1.980	-1.90	-0.08
10	0.13	7.50	Mid	0	0.40	0.59	0.900	0.196	0.609	2.25	1.0	-2.254	-2.20	-0.054

*Test result at $\alpha = 0$

$$\text{Average Error} = \frac{\Sigma\,|\Delta C_{Y_\beta}|}{n} = 0.217 \times 10^{-3}\ \text{(per deg)}$$

TABLE 5.2.1.1-B

SUPERSONIC WING-BODY SIDE FORCE DUE TO SIDESLIP

DATA SUMMARY

Ref	M	Wing Position	K_i	Γ (deg)	f_N	f_A	S_b sq ft	S_W sq ft	$C_{Y_\beta\ calc} \times 10^3$ per deg	* $C_{Y_\beta\ test} \times 10^3$ per deg	$\Delta C_{Y_\beta} \times 10^3$ per deg (Calc-Test)
11	1.41	High	1.72	0	7.00	15.00	.0605	1.33	-3.54	-3.00	-0.54
		Mid	1.00						-2.06	-1.60	-0.46
		Low	1.42						-2.93	-3.50	0.57
	2.01	High	1.72						-3.68	-3.50	-0.18
		Mid	1.00						-2.14	-1.80	-0.34
		Low	1.42						-3.04	-3.50	0.46
12	1.72	Mid	1.00	0	3.50	6.50	.00307	0.0506	-2.94	-2.80	-0.14
				-5					-3.44	-3.20	-0.24
				-10					-3.94	-3.80	-0.14
	2.02			0					-3.24	-3.20	-0.04
				-5					-3.70	-3.70	0
				-10					-4.20	-4.20	0
13	2.01	High	1.73	0	4.30	6.67	.0605	1.00	-4.90	-4.60	-0.30
		Mid	1.00						-2.85	-2.90	0.05
		Low	1.43						-4.08	-5.00	0.92
		Mid	1.00	3					-3.15	-3.00	-0.15
				3					-3.15	-3.00	-0.15

*Test result at $\alpha = 0$.

$$\text{Average Error} = \frac{\Sigma \left| \Delta C_{Y_\beta} \right|}{n} = 0.275 \times 10^{-3} \text{ (per deg)}$$

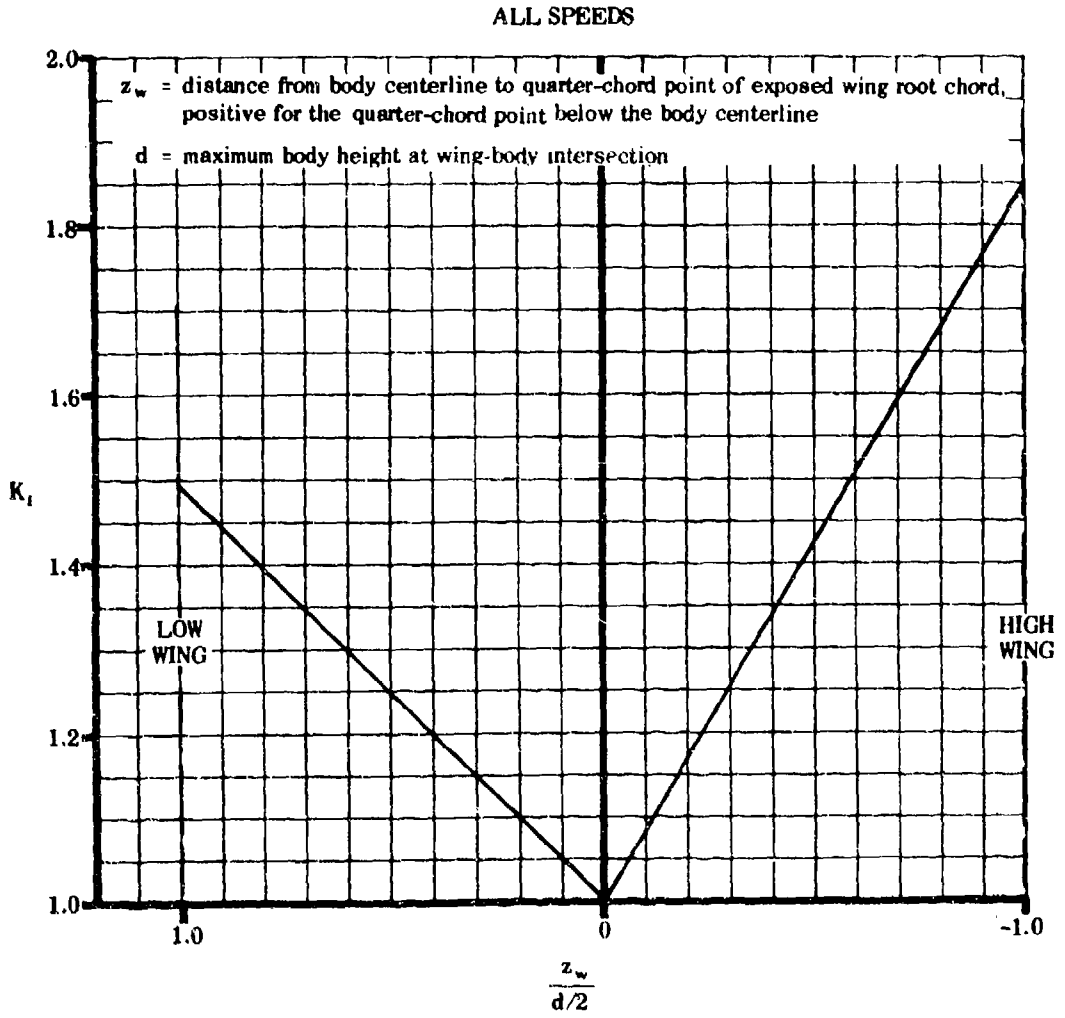

FIGURE 5.2.1.1-7 WING-BODY INTERFERENCE FACTOR FOR WING-BODY SIDESLIP DERIVATIVE C_{Y_β}

5.2.1.2 WING-BODY SIDE-FORCE COEFFICIENT C_Y AT ANGLE OF ATTACK

The wing-body side force developed at combined angles is nonlinear with respect to both sideslip and angle of attack due to viscous cross-flow effects and cross-coupling of upwash and sidewash velocities. To obtain the sideslip derivative $C_{Y_{\beta_{WB}}}$ it is recommended that $C_{Y_{WB}}$ be calculated at several angles of attack for a small sideslip angle ($\beta \leq 4^\circ$). Then at each angle of attack the side force is assumed linear with sideslip for small values of β so that

$$C_{Y_{\beta_{WB}}} \approx \frac{C_{Y_{WB}}}{\beta} .$$

A. SUBSONIC

No method is presently available for determining the viscous cross-flow effects and cross-coupling of upwash and sidewash velocities at angles of attack and subsonic speeds.

The method presented herein is restricted to first-order approximations at relatively low angles of attack.

DATCOM METHOD

It is recommended that the method of paragraph A of Section 5.2.1.1 be used in the linear-lift angle-of-attack region.

B. TRANSONIC

The comments of paragraph A for the subsonic case also apply to wing-body combinations at combined angles and transonic speeds.

DATCOM METHOD

It is recommended that the method of paragraph B of Section 5.2.1.1 be used in the linear-lift angle-of-attack region.

C. SUPERSONIC

Although higher order slender-body solutions which account for cross-coupling of upwash and sidewash velocities at supersonic speeds are presently unavailable, an approximate method is developed in reference 1 which accounts for the effects of angle of attack on wing-body interference.

Two types of interference forces are considered significant at combined sideslip and angle of attack. One effect is due to the influence of the forebody on cross flow. The resulting asymmetric wing loading causes interference pressures on the sides of the body that increase the body side force. The other effect is produced by the wing inhibiting the viscous cross flow occuring along the body at large angles of attack. This phenomenon is termed "viscous cross-flow suppression" in that it reduces the body side force. No attempt is made to estimate the magnitude of wing sweepback effects on wing-body interference and the effect of body vortices on wing-body interference is considered negligible.

DATCOM METHOD

The method presented in this Section for estimating the wing-body side-force coefficient is that of reference 1. The determination of the body-alone contribution is adapted from the method of reference 2 which is discussed in Section 4.2.1.2. For combined angles the method is valid only for circular bodies. In addition reference 1 specifies that the wing leading edge be supersonic. But fair accuracy is obtained for configurations with subsonic leading edges when the aspect ratio is not too low. The wing-alone contribution to side force is usually very small and is therefore neglected.

Reference 1 gives two expressions for wing-body interference effects, one for midwing and one for tangent-wing configurations. The forebody cross-flow effect is zero for the midwing case since the wing plane then coincides with a body-alone cross-flow streamline and no change in cross flow takes place. Therefore, the midwing case is based on the premise that the sole effect of the wing is to inhibit the nonlinear effects of the viscous body cross flow.

The wing-body contribution to the side-force coefficient at combined sideslip and angle of attack is given by

$$C_{Y_{WB}} = C_{Y_B} + C_{Y_{W(B)}} \qquad 5.2.1.2\text{-a}$$

where C_{Y_B} is the body-alone side-force contribution given by

$$C_{Y_B} = -\frac{S_B}{S_W} 2\beta - c_{d_c} \frac{S_{B_S}}{S_W} \beta\alpha' \qquad 5.2.1.2\text{-b}$$

where

$\frac{S_B}{S_W}$ is the ratio of the body frontal area to the total wing area

β is the sideslip angle in radians

c_{d_c} is the cross-flow drag coefficient, obtained from figure 4.2.1.2-23b, with $M_c = M_\infty \sin \alpha'$

$\frac{S_{B_S}}{S_W}$ is the ratio of the body side area to the total wing area

α' is the angle of inclination, $\alpha' = \sqrt{\alpha^2 + \beta^2}$, in radians

$C_{Y_{W(B)}}$ is the side-force contribution of the wing due to the presence of the body, given by

$$C_{Y_{W(B)}} = -2\eta_B K_{W(B)} k(\alpha) \frac{S_B}{S_W} \beta - \frac{c_{d_c} c_{r_e} d}{S_W} \beta(\beta - \alpha') \qquad 5.2.1.2\text{-c}$$

where the first term on the right-hand side is the forebody cross-flow effect and is taken as zero for the midwing case, and the second term on the right-hand side is an approximate effect of the wing inhibiting the viscous cross flow occuring along the body at large angles of attack.

η_B is the Mach number correction to the wing-body interference coefficient, from figure 5.2.1.2-7

$K_{W(B)}$ is the wing-body interference coefficient, or apparent-mass ratio, from figure 5.3.1.1-25oo. For wing positions other than midwing ($K_{W(B)} = 0$) or tangent, a nonlinear interpolation is described in Method 3, paragraph A, Section 5.3.1.1.

$k(\alpha)$ is the angle-of-attack correction to the wing-body interference coefficient. Values of this parameter for high- and low-tangent wings are presented in figure 5.2.1.2-8. For wing positions other than midwing ($k(\alpha) = 0$) or tangent, a nonlinear interpolation is described in Method 3, paragraph A, Section 5.3.1.1.

d is the average body diameter at the exposed wing root

c_{r_e} is the exposed root chord of the wing

Values for the incremental coefficient resulting from the addition of wings in the mid- and high- and low-tangent positions on circular bodies, calculated using equation 5.2.1.2-c, are compared with experimental results in figure 5.2.1.2-5.

The incremental coefficient resulting from the addition of a wing in the midbody position is presented in figure 5.2.1.2-5a. The Datcom method does not account for additional differential load on the body resulting from unequal panel loading occuring with yawed sweptback wings. This neglected effect, in conjunction with the approximate account of viscous cross-flow suppression may account for the lack of better agreement between experimental and calculated results at higher angles of attack.

The incremental coefficient resulting from the addition of sweptback wings in the high- and low-tangent positions on a body are presented in figure 5.2.1.2-5b through -5d. The agreement between experimental and calculated values is surprisingly good in view of the fact that the angle-of-attack correction to the wing-body interference coefficient, $k(\alpha)$, applies strictly to unswept two-dimensional wings. The additional differential load on the body occuring with yawed sweptback wings tends to compensate for the reduction in $k(\alpha)$ resulting from wing sweepback.

Sample Problem

Given: The wing-body configuration of reference 3. Find the side-force coefficient developed by the wing-body combination at $\alpha = 12^\circ$ and $\beta = 4^\circ$.

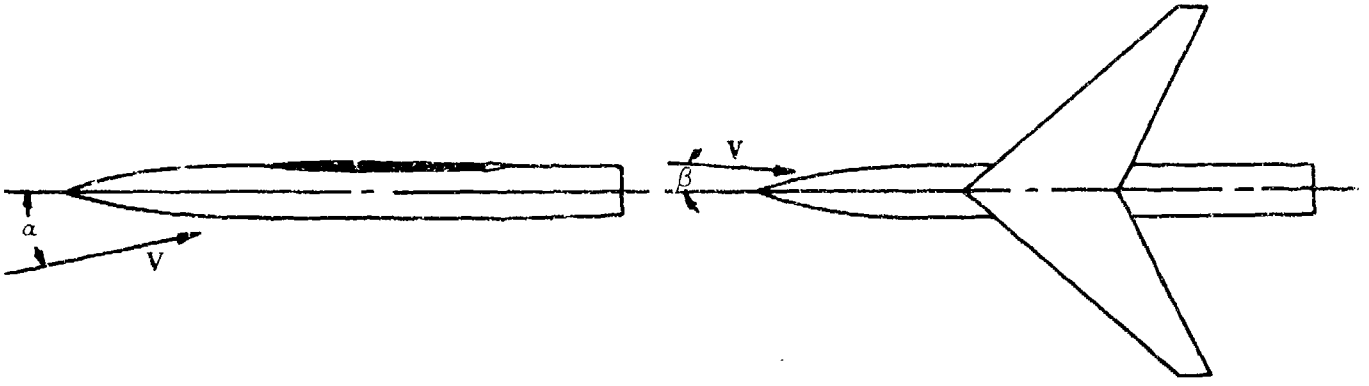

Wing Characteristics

High-tangent wing	$S_W = 144.0$ sq in.	$b_W = 24.0$ sq in.	$c_{r_e} = 8.90$ in.

Body Characteristics

Ogive-cylinder body	$d = 3.33$ in.	$S_B = 8.70$ sq in.	$S_{B_S} = 110.0$ sq in.

Additional Characteristics

$M_\infty = 2.01$	$\alpha = 12^\circ = 0.209$ rad	$\beta = 4^\circ = 0.070$ rad

$\alpha' = \sqrt{\alpha^2 + \beta^2} = 12.65$ deg $= 0.221$ rad

Compute:

Body-along contribution

$M_c = M_\infty \sin \alpha' = 2.01 \sin 12.56^\circ = 0.440$

$c_{d_c} = 1.30$ (figure 4.2.1.2-23b)

$$C_{Y_B} = -\frac{S_B}{S_W} 2\beta - c_{d_c} \frac{S_{B_S}}{S_W} \beta\alpha' \qquad \text{(equation 5.2.1.2-b)}$$

$$= -\frac{8.70}{144.0} (2)(0.070) - (1.30) \frac{110.0}{144.0} (0.070)(0.221)$$

$= -0.0238$ (based on S_W)

Wing interference contribution

$$\sqrt{M^2 - 1} \frac{d}{c_{r_e}} = \sqrt{(2.01)^2 - 1} \left(\frac{3.33}{8.90}\right) = 0.651$$

$\eta_B = 0.81$ (figure 5.2.1.2-7)

$$\frac{d}{b_W} = \frac{3.33}{24.0} = 0.139$$

$K_{W(B)}$ = 1.22 (figure 5.3.1.1-25oo)

$$\frac{c_{r_e}}{d} = \frac{8.90}{3.33} = 2.67$$

$k(\alpha)$ = 2.27 (figures 5.2.1.2-8d, 5.2.1.2-8e, and 5.2.1.2-8f by interpolation)

$$C_{Y_{W(B)}} = -2\eta_B K_{W(B)} k(\alpha) \frac{S_B}{S_W}\beta - \frac{c_{d_c} c_{r_e} d}{S_W}\beta(\beta - \alpha') \qquad \text{(equation 5.2.1.2-c)}$$

$$= -2(0.81)(1.22)(2.27)\frac{8.70}{144.0}(0.070) - \frac{(1.30)(8.90)(3.33)(0.70)(0.070 - 0.221)}{144.0}$$

$$= -0.0162 \text{ (based on } S_W)$$

Solution:

$$C_{Y_{WB}} = C_{Y_B} + C_{Y_{W(B)}} \qquad \text{(equation 5.2.1.2-a)}$$

$$= -0.0238 - 0.0162$$

$$= -0.0400 \text{ (based on } S_W)$$

This compares with an experimental value (based on S_W) of $C_{Y_{WB}} = -0.0480$ from reference 3.

A comparison between calculated and experimental results for this configuration at sideslip angles of 2, 4, and 8 degrees and over an angle-of-attack range to 16 degrees is presented in figure 5.2.1.2-6.

REFERENCES

1. Kaattari, G. E.: Estimation of Directional Stability Derivatives at Moderate Angles and Supersonic Speeds. NASA Memo 12-1-58A, 1959. (U)

2. Allen, H., and Perkins, E. W.: Characteristics of Flow Over Inclined Bodies of Revolution. NACA RM A50L07, 1951. (U)

3. Spearman, M. L.: Effect of Wing Location and Geometric Dihedral for the Wing-Body Combination, M = 2.01. NACA RM L55B18, 1955. (U)

4. Spearman, M. L., Driver, C., and Hughes, W. C.: Investigation of Aerodynamic Characteristics in Pitch and Sideslip of a 45° Sweptback-Wing Airplane Model with Various Vertical Locations of Wing and Horizontal Tail – Basic-Data Presentation, M = 2.01. NACA RM L54L06, 1955. (U)

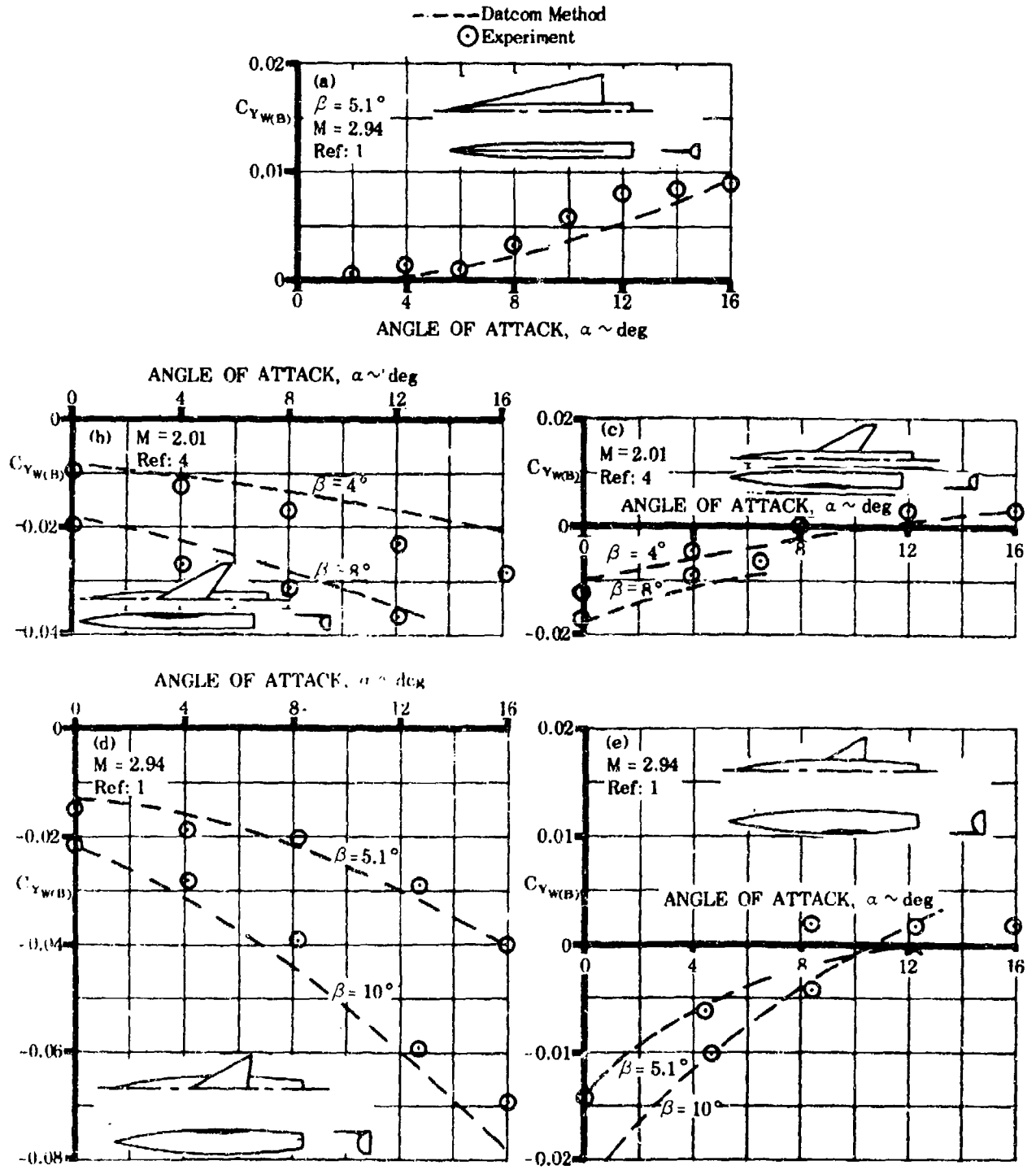

FIGURE 5.2.1.2-5 COMPARISON OF EXPERIMENTAL AND CALCULATED SIDE-FORCE COEFFICIENT INCREMENTS DUE TO ADDING A WING TO A BODY

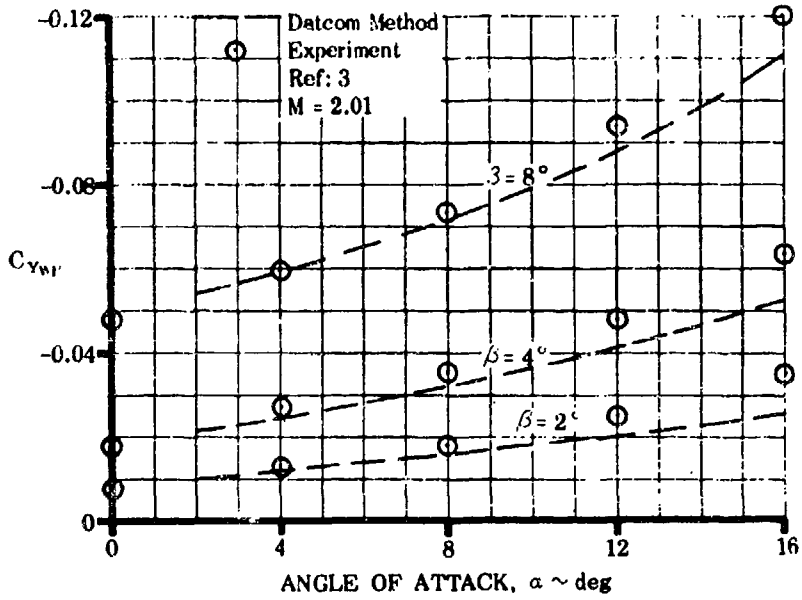

FIGURE 5.2.1.2-6 COMPARISON OF EXPERIMENTAL AND CALCULATED VALUES OF WING-BODY SIDE-FORCE COEFFICIENT FOR THE SAMPLE PROBLEM CONFIGURATION

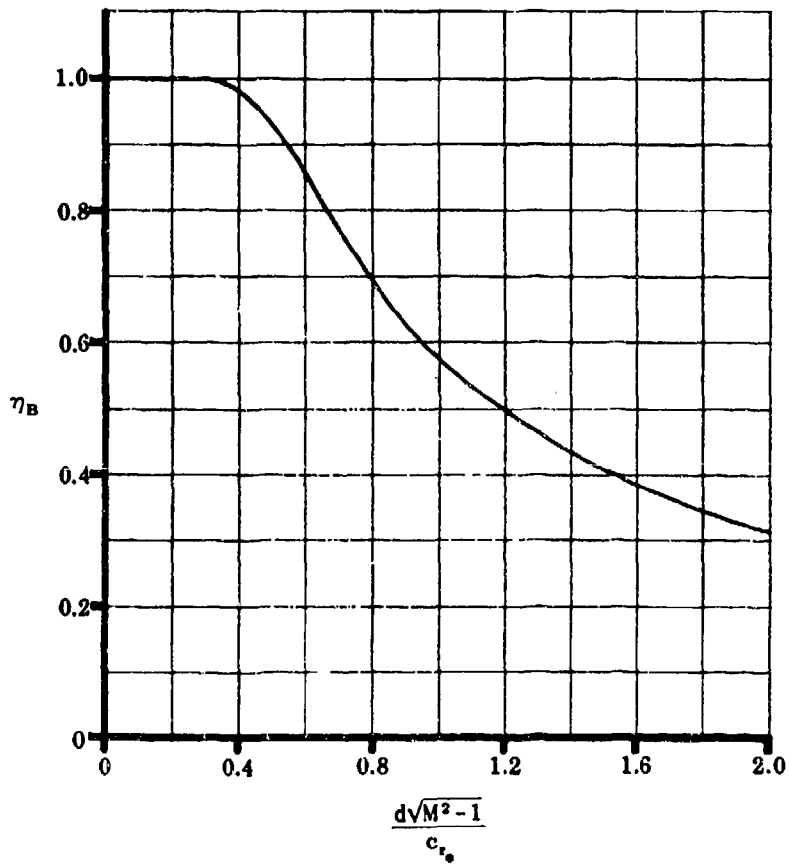

FIGURE 5.2.1.2-7 MACH NUMBER CORRECTION TO WING-BODY INTERFERENCE COEFFICIENT

LOW WING

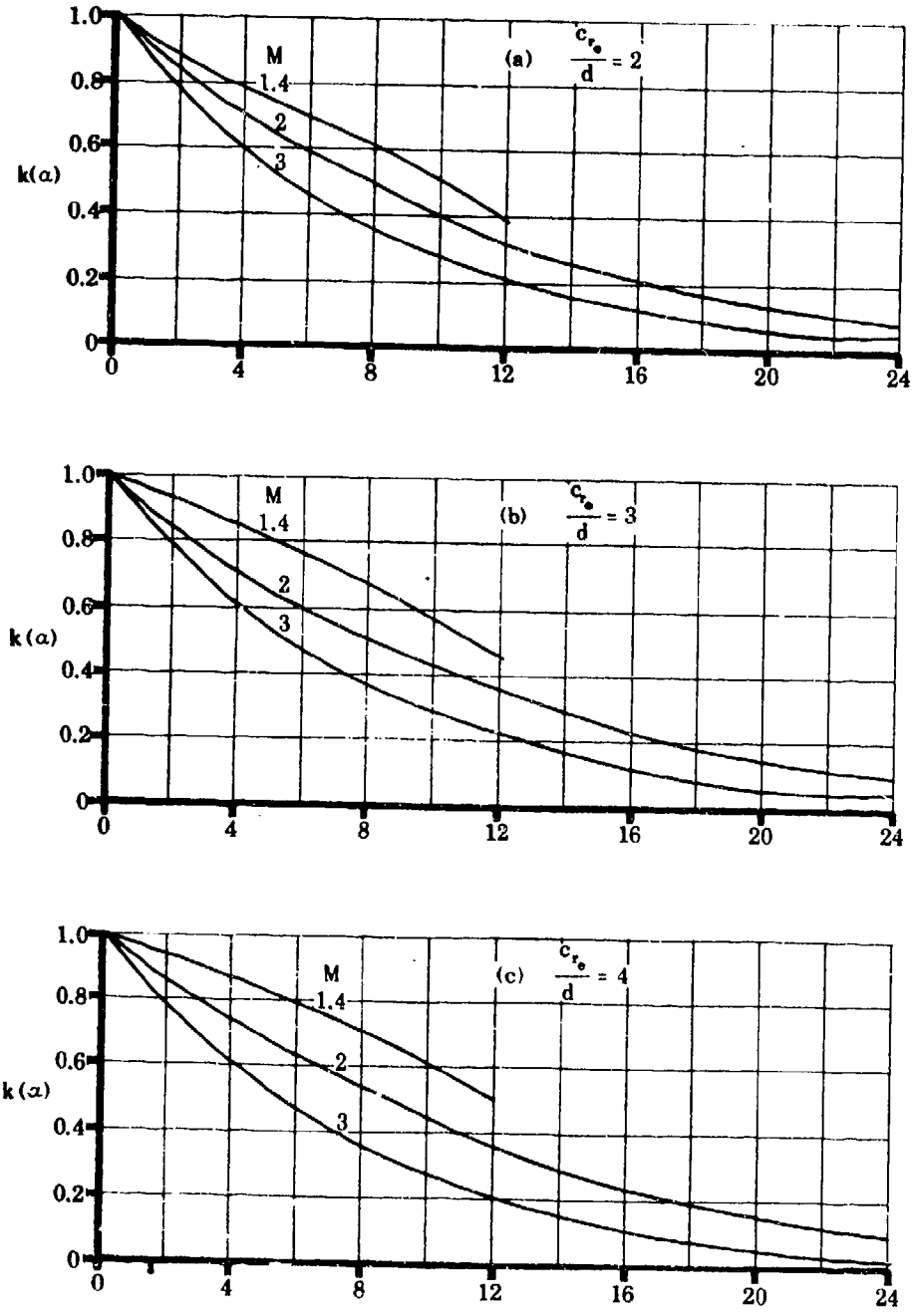

FIGURE 5.2.1.2-8 ANGLE-OF-ATTACK CORRECTION TO WING-BODY INTERFERENCE COEFFICIENT

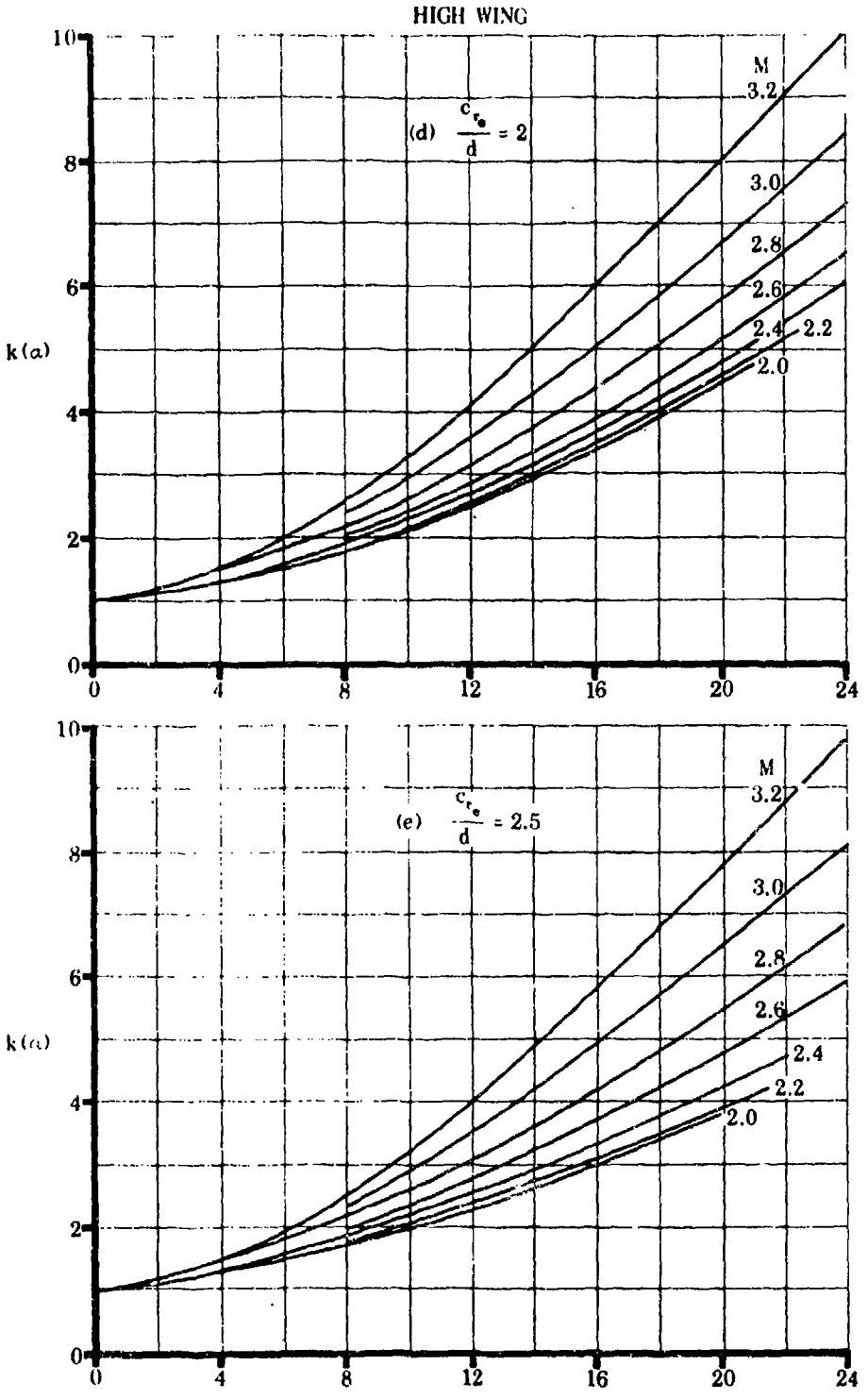

FIGURE 5.2.1.2-8 ANGLE-OF-ATTACK CORRECTION TO WING-BODY INTERFERENCE COEFFICIENT (contd)

HIGH WING

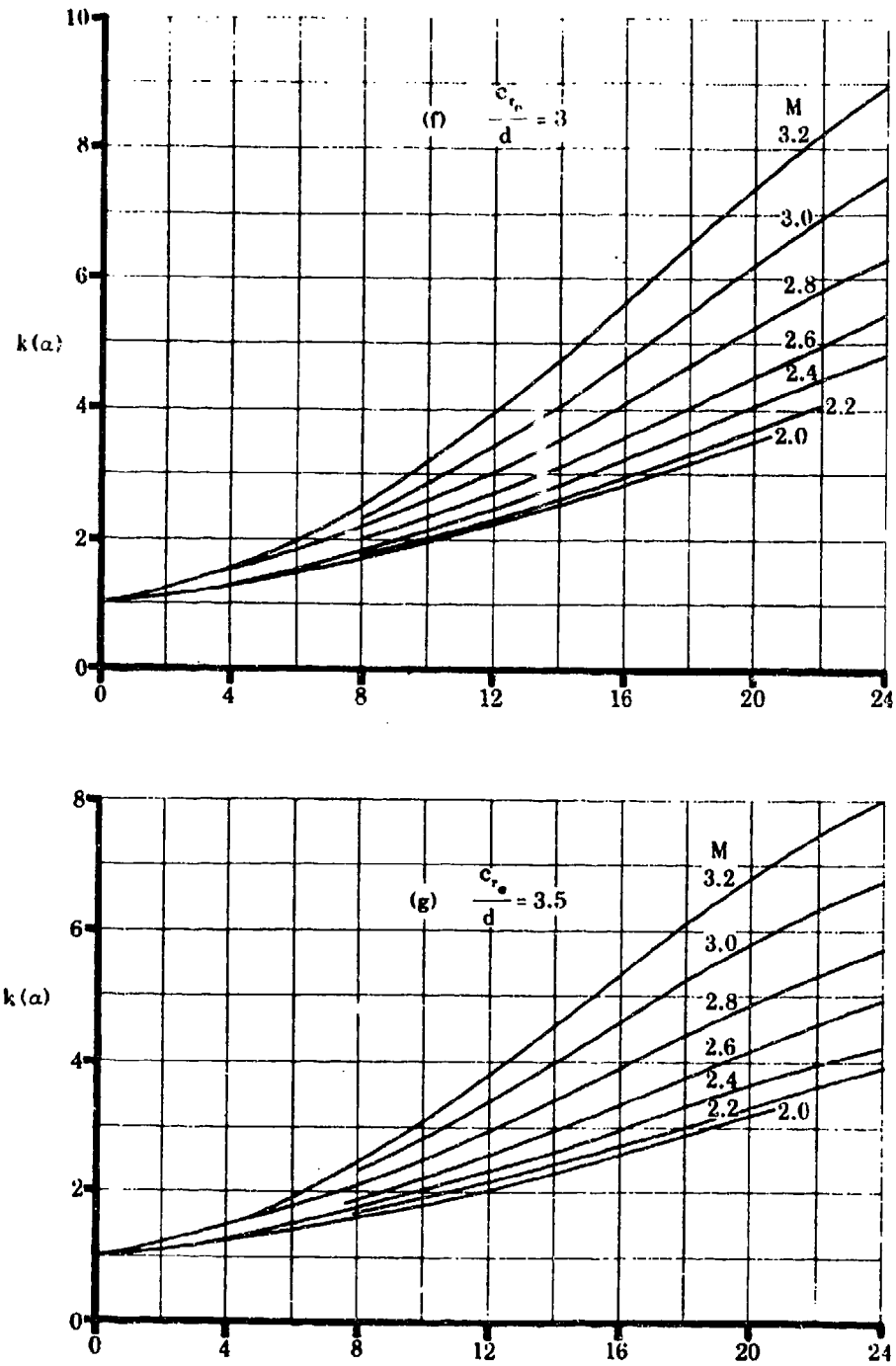

ANGLE OF ATTACK, $\alpha \sim$ DEGREES

FIGURE 5.2.1.2-8 ANGLE-OF-ATTACK CORRECTION TO WING-BODY INTERFERENCE COEFFICIENT (contd)

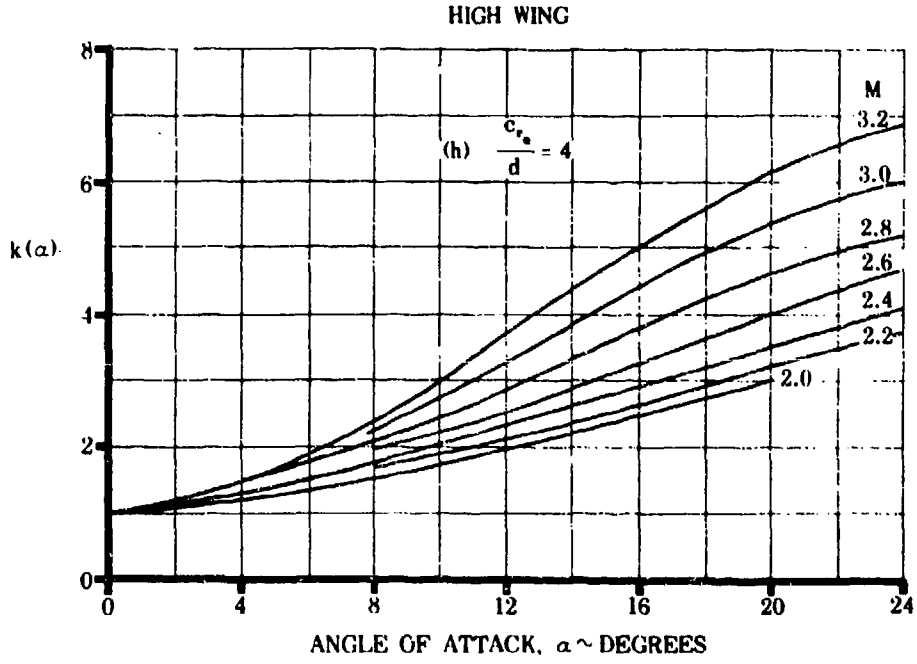

FIGURE 5.2.1.2-8 ANGLE-OF-ATTACK CORRECTION TO WING-BODY INTERFERENCE COEFFICIENT (contd)

5.2.2 WING-BODY SIDESLIP DERIVATIVE C_{l_β}

5.2.2.1 WING-BODY SIDESLIP DERIVATIVE C_{l_β} IN THE LINEAR ANGLE-OF-ATTACK RANGE

A. SUBSONIC

The addition of a body to a wing in sideslip is shown experimentally to change the wing rolling moment in two ways. First, there is the well known change in effective dihedral as a function of wing height on the body. This occurs because the cross flow around the body induces changes in the local angle of attack of the wing (see sketch (a)). The resulting change in lift distribution has a significant influence on C_{l_β}. The simplified expression presented in the Datcom for determining the body-induced effect on wing height is based on a fuselage of circular cross section, and is presented in such sources as references 1 and 2. The sign of the value of this effect is dependent upon whether the wing is located above or below the center line of the fuselage. A high location of the wing results in more positive effective dihedral and a low location results in less positive effective dihedral than a midwing location.

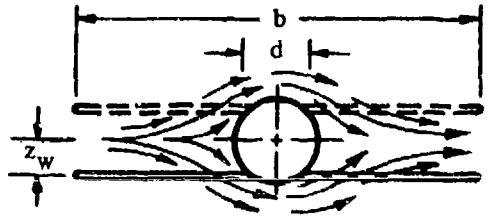

SKETCH (a)

For wings with geometric dihedral, the body-induced effect on wing height must be modified, since the vertical position of the wing relative to the fuselage varies along the span (see sketch (b)). The method presented in the Datcom to account for this modification is taken from reference 3. The method is applicable only for wings with dihedral that intersect the vertical plane of symmetry of a body of circular cross section at or near the midfuselage height. In reference 3 the wing with dihedral is replaced with a wing without dihedral at some effective height relative to the fuselage, and the fuselage flow effect for the equivalent wing is then evaluated. The vertical position of the equivalent wing was taken to coincide with the wing with dihedral at the spanwise position equal to 0.7d.

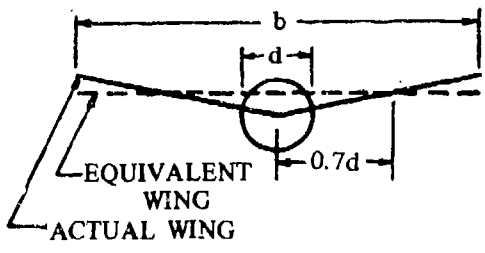

SKETCH (b)

The second fuselage effect on rolling moment is a decrease in wing-body positive effective dihedral with increasing fuselage length. This effect is discussed in reference 3, where it is suggested that this may be the result of the fuselage reducing the wing effective sideslip angle (see sketch (c)).

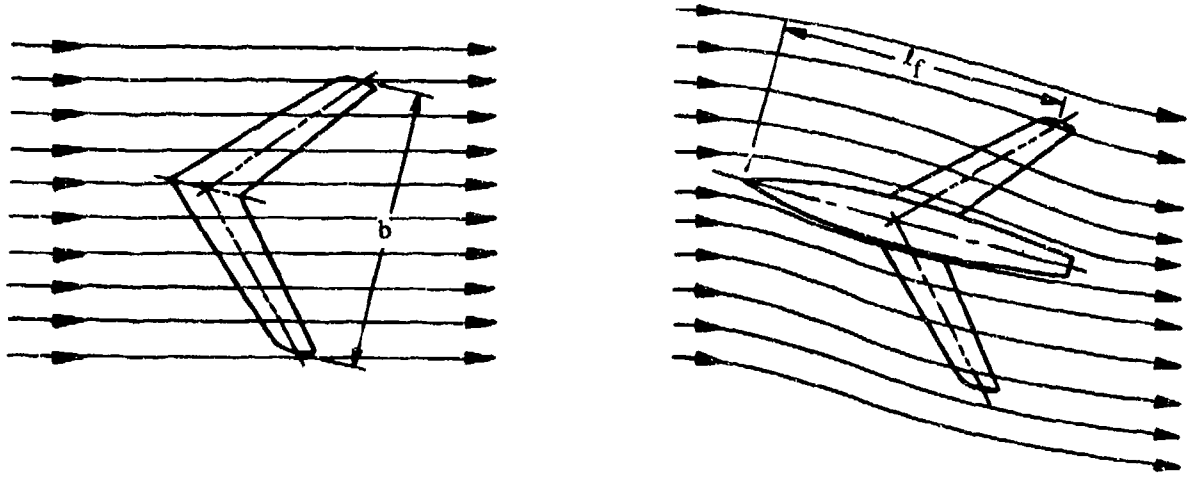

SKETCH (c)

In reference 3 an empirical study of limited scope shows that the fuselage effects may be correlated as a function of the ratio of fuselage length ahead of the wing-tip half-chord point and the wing span $\frac{l_f}{b}$

More extensive studies indicate that the parameter $\frac{A}{\cos \Lambda_{c/2}}$ is also important. There may be additional parameters, such as the ratio of the body diameter to wing span and fuselage cross-sectional shape that also exert an influence. The design chart presented herein is limited to the parameters $\frac{l_f}{b}$ and $\frac{A}{\cos \Lambda_{c/2}}$, and is based on experimental data from configurations employing fuselages of circular cross section.

The increments in C_{l_β} due to the body-induced effects on wing height and the effect of fuselage length have been derived for configurations with fuselages of circular cross section. Not enough test data exist to determine any effect the fuselage cross-sectional shape may have on the fuselage-length parameter. On the other hand, both theory and experiment indicate that the body-induced effects on wing height are strongly influenced by the cross-sectional shape of the fuselage.

It is suggested that for non-body-of-revolution configurations the equivalent diameter be used in determining the increments in C_{l_β} due to the body induced effects on wing height.

The subsonic method is valid for configurations with straight-tapered wings for sideslip angles between -5^o and $+5^o$ at speeds up to the force-break Mach number and at low angles of attack. The

fuselage-effect parameters do not include the effect of either nonuniform geometric dihedral or non-straight-tapered planforms.

DATCOM METHOD

The rolling moment due to sideslip, based on the product of the wing area and span Sb, for straight-tapered wing-body combinations at low angles of attack is given by

$$C_{l_\beta} = C_L \left[\left(\frac{C_{l_\beta}}{C_L} \right)_{\Lambda_{c/2}} K_{M_\Lambda} K_f + \left(\frac{C_{l_\beta}}{C_L} \right)_A \right] + \Gamma \left[\frac{C_{l_\beta}}{\Gamma} K_{M_\Gamma} + \frac{\Delta C_{l_\beta}}{\Gamma} \right]$$

$$+ \left(\Delta C_{l_\beta} \right)_{z_W} + \theta \tan \Lambda_{c/4} \left(\frac{\Delta C_{l_\beta}}{\theta \tan \Lambda_{c/4}} \right) \text{ (per degree)} \qquad 5.2.2.1\text{-a}$$

where

C_L is the wing-body lift coefficient.

$\left(\frac{C_{l_\beta}}{C_L} \right)_{\Lambda_{c/2}}$ is the wing-sweep contribution obtained from paragraph A of Section 5.1.2.1 (figure 5.1.2.1-27)

K_{M_Λ} is the compressibility correction to the sweep contribution obtained from paragraph A of Section 5.1.2.1 (figure 5.1.2.1-28a)

K_f is the empirical fuselage-length-effect correction factor obtained from figure 5.2.2.1-26.

$\left(\frac{C_{l_\beta}}{C_L} \right)_A$ is the aspect ratio contribution obtained from paragraph A of Section 5.1.2.1 (figure 5.1.2.1-28b)

Γ is the geometric dihedral angle in degrees, positive for the wing tip above the plane of the root chord.

$\frac{C_{l_\beta}}{\Gamma}$ is the wing dihedral effect for uniform geometric dihedral obtained from paragraph A of Section 5.1.2.1 (figure 5.1.2.1-29).

K_{M_Γ} is the compressibility correction factor to the dihedral effect obtained from paragraph A of Section 5.1.2.1 (figure 5.1.2.1-30a).

$\frac{\Delta C_{l_\beta}}{\Gamma}$ is the body-induced effect on wing height due to uniform geometric dihedral given by*

$$\frac{\Delta C_{l_\beta}}{\Gamma} = -0.0005 \sqrt{A} \left(\frac{d}{b}\right)^2 \quad \text{(per degree}^2\text{)} \qquad 5.2.2.1\text{-b}$$

where d/b is the average fuselage diameter at the wing root divided by the wing span. For non-body-of-revolution configurations, the average equivalent diameter at the wing root should be used, where $(d_{equiv})_{av} = \sqrt{\frac{\text{average cross-sectional area}}{0.7854}}$

$\left(\Delta C_{l_\beta}\right)_{z_W}$ is the increment in C_{l_β} due to the body-induced effect on wing height for configurations with wings located above or below the midfuselage height. This increment is given by

$$\left(\Delta C_{l_\beta}\right)_{z_W} = \frac{1.2\sqrt{A}}{57.3}\left(\frac{z_W}{b}\right)\left(\frac{2d}{b}\right) \quad \text{(per degree)} \qquad 5.2.2.1\text{-c}$$

where

$\frac{z_W}{b}$ is the vertical distance from the center line of the fuselage to the quarter-chord point of the root chord divided by the wing span, positive for the wing located below the center line of the fuselage.

$\frac{d}{b}$ is defined under equation 5.2.2.1-b

$\frac{\Delta C_{l_\beta}}{\theta \tan \Lambda_{c/4}}$ is the wing-twist correction factor obtained from paragraph A of Section 5.1.2.1 (figure 5.1.2.1-30b).

θ is the wing twist between the root and tip sections in degrees, negative for washout (see figure 5.1.2.1-30b).

For the case of a wing with dihedral mounted on a body at a location other than at or near the midfuselage height, both the modification of the body-induced effect on wing height due to dihedral (equation 5.2.2.1-b) and the body-induced effect on wing height (equation 5.2.2.1-c) should be considered.

A comparison of test values with results calculated by using the Datcom method for wing-body configurations without dihedral and with the wings mounted at the midufselage location is presented as table 5.2.2.1-A. Comparisons of test values with results calculated by using the Datcom method for the effects of dihedral and wing height are presented in tables 5.2.2.1-B and 5.2.2.1-C, respectively.

*Equation 5.2.2.1-b is derived by replacing z_W in equation 5.2.2.1-c with the expression for the height above the fuselage center line of an equivalent wing at a height corresponding to the height of the .0.7d spanwise station of a wing with dihedral (see sketch (b)).

Test data are not available to permit substantiation of the effect of wing twist on the wing-body rolling moment due to sideslip.

Sample Problem

1. Midwing, no dihedral, no twist

Given: The wing-body configuration of reference 8 designated 60-4-0.6-006.

$A = 4.0$ $\quad \lambda = 0.6$ $\quad \Lambda_{c/2} = 59.08^{o}$ $\quad b = 36.0$ in. $\quad \ell_f = 49.58$ in.

$z_w = 0$ (midwing) $\quad \Gamma = 0$ $\quad \theta = 0$ $\quad M = 0.60$

Body of revolution

Compute:

$$\left(\frac{C_{l_\beta}}{C_L}\right)_{\Lambda_{c/2}} = -0.00723 \text{ per deg} \quad \text{(figure 5.1.2.1-27)}$$

$$\left(\frac{C_{l_\beta}}{C_L}\right)_{A} = -0.00180 \text{ per deg} \quad \text{(figure 5.1.2.1-28b)}$$

$M \cos \Lambda_{c/2} = (0.60) \cos 59.08^{o} = 0.308$

$A/\cos \Lambda_{c/2} = 4.0/\cos 59.08^{o} = 7.785$

$K_{M_\Lambda} = 1.02$ (figure 5.1.2.1-28a)

$\ell_f/b = 49.58/36.0 = 1.377$

$K_f = 0.685$ (figure 5.2.2.1-26)

Solution:

$$C_{l_\beta} = C_L \left[\left(\frac{C_{l_\beta}}{C_L}\right)_{\Lambda_{c/2}} K_{M_\Lambda} K_f + \left(\frac{C_{l_\beta}}{C_L}\right)_{A}\right] \text{(equation 5.2.2.1-a)}$$

$$= C_L \left[(-0.00723)(1.02)(0.685) + (-0.00180)\right]$$

$$= C_L \left[-0.00505 - 0.00180\right]$$

$$\frac{C_{l_\beta}}{C_L} = -0.00685 \text{ per deg}$$

This result compares with a test value of −0.0074 per degree from reference 8.

2. High wing, dihedral, no twist

Given: A wing-body configuration of reference 16.

$A = 6.383$ $\lambda = 1.0$ $\Lambda_{c/2} = 0$ $b = 60.0$ in. $\ell_f = 15.7$ in.

$d = 6.70$ in. (average over root chord) $z_W = -2.66$ in. (high wing)

$\Gamma = 5^o$ $\theta = 0$ $M = 0.105$ Body of revolution

Compute:

$$\left(\frac{C_{l_\beta}}{C_L}\right)_{\Lambda_{c/2}} = 0 \quad \text{(figure 5.1.2.1-27)}$$

$$\left(\frac{C_{l_\beta}}{C_L}\right)_{M} = -0.0013 \text{ per deg} \quad \text{(figure 5.1.2.1-28b)}$$

$M \cos \Lambda_{c/2} = (0.105)(\cos 0) = 0.105$

$A/\cos \Lambda_{c/2} = 6.383/(\cos 0) = 6.383$

$K_{M_A} = 1.0$ (figure 5.1.2.1-28a)

$\ell_f/b = 15.7/60.0 = 0.262$

$K_f = 1.0$ (figure 5.2.2.1-26)

Determine dihedral-effect parameters

Geometric dihedral

$$\frac{C_{l_\beta}}{\Gamma} = -0.000224 \text{ per deg}^2 \quad \text{(figure 5.1.2.1-29)}$$

$$K_{M_\Gamma} = 1.0 \quad \text{(figure 5.1.2.1-30a)}$$

Body-induced effect on wing height due to dihedral

$$\frac{\Delta C_{l_\beta}}{\Gamma} = -0.0005 \sqrt{A} \left(\frac{d}{b}\right)^2 \qquad \text{(equation 5.2.2.1-b)}$$

$$= -0.0005 \sqrt{6.383} \left(\frac{6.7}{60}\right)^2$$

$$= -0.000016 \quad \text{per deg}^2$$

Determine the effect of wing height

$$z_w/b = -2.66/60.0 = -0.0443$$

$$2d/b = 2(6.70)/60.0 = 0.223$$

$$\Delta C_{l_{\beta_{z_w}}} = \frac{1.2\sqrt{A}}{57.3} \left(\frac{z_w}{b}\right)\left(\frac{2d}{b}\right) \qquad \text{(equation 5.2.2.1-c)}$$

$$= \frac{1.2\sqrt{6.383}}{57.3} (-0.0443)(0.233)$$

$$= -0.000547 \quad \text{per deg}$$

Solution:

$$C_{l_\beta} = C_L \left[\left(\frac{C_{l_\beta}}{C_L}\right)_{\Lambda_{c/2}} K_{M_\Lambda} K_f + \left(\frac{C_{l_\beta}}{C_L}\right)_A\right] + \Gamma\left[\frac{C_{l_\beta}}{\Gamma} K_{M_\Gamma} + \frac{\Delta C_{l_\beta}}{\Gamma}\right]$$

$$+ \Delta C_{l_{\beta_{z_w}}} \qquad \text{(equation 5.2.2.1-a)}$$

Midwing, no dihedral

$$\frac{C_{l_\beta}}{C_L} = \left[\left(\frac{C_{l_\beta}}{C_L}\right)_{\Lambda_{c/2}} K_{M_\Lambda} K_f + \left(\frac{C_{l_\beta}}{C_L}\right)_A\right]$$

$$= [(0)(1.0)(1.0) + (-0.0013)]$$

$$= -0.0013 \text{ per deg}$$

Dihedral effect

$$\Gamma\left[\frac{C_{l_\beta}}{\Gamma}\ K_{M_\Gamma} + \frac{\Delta C_{l_\beta}}{\Gamma}\right] = (5.0)\,[(-0.000224)\,(1.0) + (-0.000016)] = -0.0012 \text{ per deg}$$

This compares with a test value of −0.00115 per degree from reference 16.

Wing-height effect

$$\left(\Delta C_{l_\beta}\right)_{z_W} = -0.000547 \text{ per deg}$$

This compares with a test value of −0.00053 per degree from reference 16.

B. TRANSONIC

Test data show that the variation of wing-body rolling moment due to sideslip is similar to that of the lift-curve slope. This correspondence should be expected, since C_{l_β} has been treated by using effective lift-curve slopes in reference 3.

The similarity in Mach number characteristics between rolling moment and lift-curve slope suggests a transonic interpolation method, based on lift-curve slope, for calculating rolling moment. An interpolation equation is presented that is based on the square of the lift-curve-slope values at the force-break Mach number M_{fb} and at M = 1.4.

Since no reliable method exists for predicting the variation of the wing-body lift-curve slope with Mach number over the transonic speed range, wing-alone lift-curve slopes are used in the Datcom method. For slender wing-body configurations, the aerodynamic interference effects are relatively insensitive to Mach number, and the use of the wing-alone lift-curve-slope values in the interpolation method should give satisfactory results. However, for nonslender configurations transonic interference effects can become quite large and sensitive to minor changes in local contour. For these configurations the interpolation method cannot be expected to provide satisfactory results unless wing-body test values of the lift-curve slope are used.

The method is limited to configurations with straight-tapered wings and is applicable over the sideslip-angle range of $\beta = \pm 5^o$.

DATCOM METHOD

The wing-body rolling moment due to sideslip of straight-tapered wing-body configurations, based on the product of the wing area and span Sb, may be approximated through the transonic region from M_{fb} to M = 1.4 by means of the interpolation formula

$$\frac{C_{l_\beta}}{C_L} = \left\{ \left[\frac{\left(\frac{C_{l_\beta}}{C_N}\right)_{M=1.4} - \left(\frac{C_{l_\beta}}{C_L}\right)_{M_{fb}}}{\left(C_{N_\alpha}{}^2\right)_{M=1.4} \left(C_{L_\alpha}{}^2\right)_{M_{fb}}} \right] \left(\frac{M - M_{fb}}{1.4 - M_{fb}}\right) + \frac{\left(\frac{C_{l_\beta}}{C_L}\right)_{M_{fb}}}{\left(C_{L_\alpha}{}^2\right)_{M_{fb}}} \right\} \left(C_{L_\alpha}{}^2\right)_M \quad \text{(per degree)} \qquad 5.2.2.1\text{-d}$$

where

$\left(\frac{C_{l_\beta}}{C_L}\right)_{M_{fb}}$ is the wing-body sideslip-derivative slope at the force-break Mach number M_{fb}, obtained by using the method of paragraph A. The force-break Mach number is defined in paragraph B of Section 4.1.3.2.

$\left(\frac{C_{l_\beta}}{C_N}\right)_{M=1.4}$ is the wing-body sideslip-derivative slope $M = 1.4$, obtained by using the method of paragraph C.

$\left(C_{L_\alpha}{}^2\right)_{M_{fb}}$ is the square of the wing-alone lift-curve slope at M_{fb}, obtained by using the method of paragraph B of Section 4.1.3.2.

$\left(C_{N_\alpha}{}^2\right)_{M=1.4}$ is the square of the wing-alone normal-force-curve slope at $M = 1.4$, obtained by using the straight-tapered-wing method of paragraph C of Section 4.1.3.2.

$\left(C_{L_\alpha}{}^2\right)_M$ is the square of the wing-alone lift-curve slope at pre-determined Mach numbers, obtained by using the methods of paragraphs B and C of Section 4.1.3.2. The pre-determined Mach numbers consist of those at the end points of the method ($M = M_{fb}$ and $M = 1.4$) and two intermediate Mach numbers defined in paragraph B of Section 4.1.3.2 as $M_a = M_{fb} + 0.007$ and $M_b = M_{fb} + 0.14$.

The increments in C_{l_β} due to fuselage transverse flow and wing height may be approximated by equations 5.2.2.1-b and 5.2.2.1-c, respectively.

Equation 5.1.2.1-d for determining the effect of geometric dihedral at supersonic speeds is also applicable at transonic speeds. However, no known method exists for determining transonic values of C_{l_p} required for this method. It is suggested that reference be made to table 7-A for transonic C_{l_p} test data.

If test data are not available the supersonic method of paragraph C of Section 7.1.2.2 should be used to approximate C_{l_p}.

Sample Problem

Given: A wing-body configuration of reference 6.

Wing Characteristics:

$A = 2.0$ $\lambda = 0$ $\Lambda_{LE} = 63.4^{o}$ $\Lambda_{TE} = 0$ $\Lambda_{c/2} = 45^{o}$

$b = 34.0$ in. $S_W = 578.0$ sq in. $z_W = 0$ (midwing)

NACA 0005-63 airfoil $\theta = 0$ $\Gamma = 0$ $t/c = 0.05$

Body of revolution

Body Characteristics:

$d = 6.12$ in. $\ell_f = 55.12$ in.

Additional Characteristics:

$\kappa = 1.0$ (assumed) $M_{fb} < M < 1.4$

Compute:

Determine M_{fb}, M_a, M_b, $(C_{L_\alpha})_{M_{fb}}$, $(C_{L_\alpha})_{M_a}$, and $(C_{L_\alpha})_{M_b}$ (paragraph B, Section 4.1.3.2).

$(M_{fb})_{\Lambda=0} = 1.0$ (figure 4.1.3.2-53a)

$(M_{fb})_{\Lambda} = 1.0$ (figure 4.1.3.2-53b)

$(C_{L_\alpha})_{fb}$

$$\beta_{fb} = \sqrt{M_{fb}^{\ 2} - 1} = 0$$

$$\frac{A}{\kappa}\left[(\beta_{fb})^2 + \tan^2 \Lambda_{c/2}\right]^{1/2} = \frac{2.0}{1.0}\left[(0) + (1)\right]^{1/2} = 2.0$$

$$\frac{\left[(C_{L_\alpha})_{M_{fb}}\right]_{theory}}{A} = 1.30 \text{ per rad} \quad \text{(figure 4.1.3.2-49)}$$

$$\left[(C_{L_\alpha})_{M_{fb}}\right]_{theory} = (1.30)(2) = 2.60 \text{ per rad}$$

$$\frac{\left(C_{L_\alpha}\right)_{M_{fb}}}{\left[\left(C_{L_\alpha}\right)_{M_{fb}}\right]_{theory}} = 1.08 \quad \text{(figure 4.1.3.2-54a)}$$

$$\left(C_{L_\alpha}\right)_{M_{fb}} = (2.60)\,(1.08) = 2.81 \text{ per rad} = 0.049 \text{ per deg}$$

$$M_a = M_{fb} + 0.07 = 1.07$$

$$\left(C_{L_\alpha}\right)_{M_a}$$

$$\frac{a}{c} = -0.07 \quad \text{(figure 4.1.3.2-54b)}$$

$$\left(C_{L_\alpha}\right)_{M_a} = \left(1 - \frac{a}{c}\right)\left(C_{L_\alpha}\right)_{M_{fb}}$$

$$= [1 - (-0.07)]\,(2.81) = 3.00 \text{ per rad} = 0.0524 \text{ per deg}$$

$$M_b = M_{fb} + 0.14 = 1.14$$

$$\left(C_{L_\alpha}\right)_{M_b}$$

$$\frac{b}{c} = 0.11 \quad \text{(figure 4.1.3.2-54c)}$$

$$\left(C_{L_\alpha}\right)_{M_b} = \left(1 - \frac{b}{c}\right)\left(C_{L_\alpha}\right)_{M_{fb}}$$

$$= [1 - (0.11)]\,(2.86) = 2.55 \text{ per rad} = 0.0444 \text{ per deg}$$

Determine $\left(C_{N_\alpha}\right)_{M=1.4}$ (paragraph C, Section 4.1.3.2)

$$\beta = \sqrt{M^2 - 1} = 0.98$$

$$\beta/\tan \Lambda_{LE} = 0.98/\tan 63.4^\circ = 0.491$$

$$\tan \Lambda_{TE}/\tan \Lambda_{LE} = 0$$

$$\frac{\left(C_{N_\alpha}\right)_{theory}}{A} = 1.31 \text{ per rad} \quad \text{(figure 4.1.3.2-63)}$$

$$\left(C_{N_\alpha}\right)_{\text{theory}} = (1.31)\,(2) = 2.62 \text{ per rad}$$

$\Delta y_\perp = 1.37$ (figure 2.2.1-8)

$$\frac{C_{N_\alpha}}{\left(C_{N_\alpha}\right)_{\text{theory}}} = 1.0 \quad \text{(figure 4.1.3.2-60)}$$

$$\left(C_{N_\alpha}\right)_{M=1.4} = (1.0)\,(2.62) = 2.62 \text{ per rad} = 0.0457 \text{ per deg}$$

Determine $\left(\frac{C_{l_\beta}}{C_L}\right)_{M_{fb}}$ and $\left(\frac{C_{l_\beta}}{C_L}\right)_{M=1.4}$

$$\left(\frac{C_{l_\beta}}{C_L}\right)_{M_{fb}}$$

$\left(\frac{C_{l_\beta}}{C_L}\right)_{\Lambda_{c/2}} = -0.0035$ per deg (figure 5.1.2.1-27)

$\left(\frac{C_{l_\beta}}{C_L}\right)_{A} = -0.0022$ per deg (figure 5.1.2.1-28b)

$M_{fb} \cos \Lambda_{c/2} = (1.0)\,(\cos 45^{O}) = 0.7071$

$$\frac{A}{\cos \Lambda_{c/4}} = \frac{2}{0.7071} = 2.83$$

$K_{M_\Lambda} = 1.015$ (figure 5.1.2.1-28a)

$\ell_f/b = 55.12/34.0 = 1.62$

$K_f = 1.0$ (figure 5.2.2.1-26)

$$\left(\frac{C_{l_\beta}}{C_L}\right)_{M_{fb}} = \left[\left(\frac{C_{l_\beta}}{C_L}\right)_{\Lambda_{c/2}} K_{M_\Lambda}\, K_f + \left(\frac{C_{l_\beta}}{C_L}\right)_{A}\right] \quad \text{(equation 5.2.2.1-a)}$$

$$= [(-0.0035)\ (1.015)\ (1.0) + (-0.0022)]$$

$$= -0.00575 \text{ per deg}$$

$$\left(\frac{C_{l_\beta}}{C_N}\right)_{M=1.4}$$

$$\left(\frac{C_{l_\beta}}{C_N}\right)_{M=1.4} = -0.061\ \frac{C_{N_\alpha}}{57.3}\left[1 + \lambda(1 + \Lambda_{LE})\right]\left(1 + \frac{\Lambda_{LE}}{2}\right)\left(\frac{\tan \Lambda_{LE}}{\beta}\right) \cdot$$

$$\left[\frac{M^2 \cos^2 \Lambda_{LE}}{A} + \left(\frac{\tan \Lambda_{LE}}{4}\right)^{4/3}\right] \quad \text{(equation 5.2.2.1-e)}$$

$$= -0.061\ \frac{2.62}{57.3}\ [1 + 0]\left(1 + \frac{63.4/57.3}{2}\right)\left(\frac{\tan 63.4^\circ}{0.98}\right) \cdot$$

$$\left[\frac{(1.4)^2 \cos^2 63.4^\circ}{2.0} + \left(\frac{\tan 63.4^\circ}{4}\right)^{4/3}\right]$$

$$= -0.061\ (0.0457)[1](1 + 0.5532)\ (2.038)[0.1965 + (0.3965)]$$

$$= -0.00523 \text{ per deg}$$

Solution:

$$\frac{C_{l_\beta}}{C_L} = \left\{\left[\frac{\left(\frac{C_{l_\beta}}{C_N}\right)_{M=1.4}}{\left(C_{N_\alpha}{}^2\right)_{M=1.4}} - \frac{\left(\frac{C_{l_\beta}}{C_L}\right)_{M_{fb}}}{\left(C_{L_\alpha}{}^2\right)_{M_{fb}}}\right]\left(\frac{M - M_{fb}}{1.4 - M_{fb}}\right) + \frac{\left(\frac{C_{l_\beta}}{C_L}\right)_{M_{fb}}}{\left(C_{L_\alpha}{}^2\right)_{M_{fb}}}\right\}\left(C_{L_\alpha}{}^2\right)_M$$

(equation 5.2.2.1-d)

$$= \left\{\left[\frac{(-0.00523)}{(0.0457)^2} - \frac{(-0.00575)}{(0.049)^2}\right]\left(\frac{M - 1.0}{1.4 - 1.0}\right) + \frac{(-0.00575)}{(0.049)^2}\right\}\left(C_{L_\alpha}{}^2\right)_M$$

$$= \left\{[-0.10]\left(\frac{M - 1.0}{0.4}\right) - 2.309\right\}\left(C_{L_\alpha}{}^2\right)_M$$

$$\left(\frac{C_{l_\beta}}{C_L}\right)_{M_a=1.07}$$

$$\left(\frac{C_{l_\beta}}{C_L}\right)_{M_a=1.07} = \left\{[-0.100]\left(\frac{1.07-1.0}{0.4}\right) - 2.309\right\}(0.0524)^2$$

$$= \left\{[-0.100]\ (0.175)\ -2.309\right\}(0.002745)$$

$$= -0.00639 \text{ per deg}$$

$$\left(\frac{C_{l_\beta}}{C_L}\right)_{M_b=1.14}$$

$$\left(\frac{C_{l_\beta}}{C_L}\right)_{M_b=1.14} = \left\{[-0.100]\left(\frac{1.14-1.0}{0.4}\right) - 2.309\right\}(0.0444)^2$$

$$= \left\{[-0.100]\ (0.350) - 2.309\right\}(0.00197)$$

$$= -0.00462 \text{ per deg}$$

The calculated results are compared with test values in sketch (d). Additional points have been calculated at M = 0.6, 0.9, and 1.7.

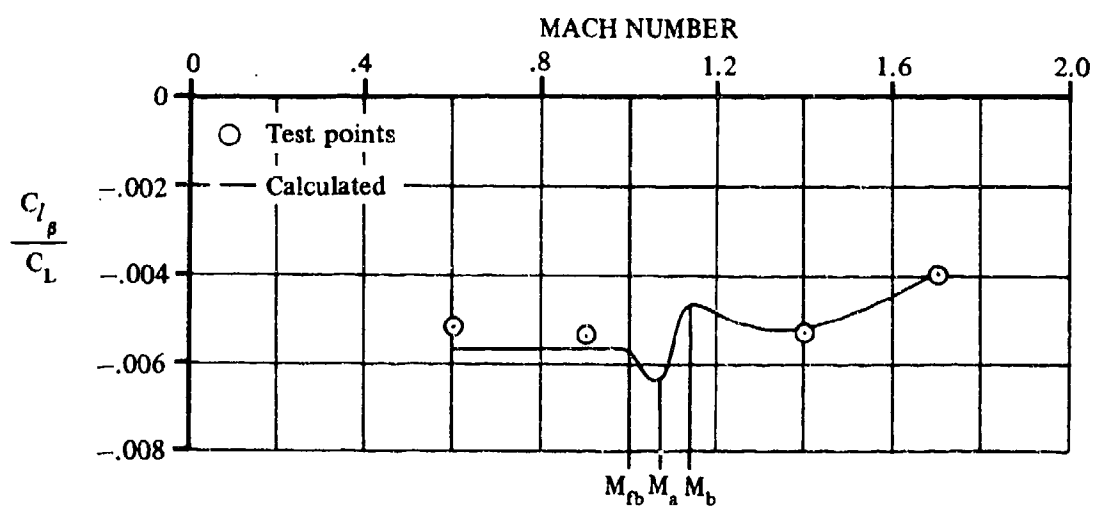

SKETCH (d)

C. SUPERSONIC

The present status of supersonic rolling-moment theory is discussed in paragraph C of Section 5.1.2.1. As indicated therein, insufficient experimental data exist at the present time to distinguish between the supersonic rolling moments for wing-alone and for wing-body configurations where the wing is mounted on the fuselage center line. Therefore, for configurations with the wing mounted on the fuselage center line the supersonic wing-alone method of paragraph C is employed.

Experimental data indicate that for wings located at positions other than on the fuselage center line there is a considerable variation in effective dihedral with wing height on the body. Furthermore, the effect of geometric dihedral on the body-induced effect due to wing height, discussed in paragraph A, must also be considered at supersonic speeds. No methods have been developed to account for the body-induced effects on wing height at supersonic speeds. The subsonic methods of paragraph A (equations 5.2.2.1-b and 5.2.2.1-c) are applied at supersonic speeds.

DATCOM METHOD

The supersonic rolling moment due to sideslip for wing-body configurations with straight-tapered wings at low angles of attack and at $M = 1.4$ and higher speeds is approximated by

$$C_{l_\beta} = -0.061\, C_N \frac{C_{N_\alpha}}{57.3}\left[1 + \lambda(1 + \Lambda_{LE})\right]\left(1 + \frac{\Lambda_{LE}}{2}\right)\left(\frac{\tan \Lambda_{LE}}{\beta}\right)\left[\frac{M^2 \cos^2 \Lambda_{LE}}{A} + \left(\frac{\tan \Lambda_{LE}}{4}\right)^{4/3}\right]$$
$$+ \Gamma\left[\frac{C_{l_\beta}}{\Gamma} + \frac{\Delta C_{l_\beta}}{\Gamma}\right] + \Delta C_{l_{\beta_{z_W}}} \quad \text{(per degree)} \qquad 5.2.2.1\text{-e}$$

where

Λ_{LE} is the wing leading-edge sweep in radians.

C_{N_α} is the wing normal-force-curve slope per radian, obtained by using the straight-tapered-wing method of paragraph C of Section 4.1.3.2.

$\frac{C_{l_\beta}}{\Gamma}$ is the wing dihedral effect for uniform geometric dihedral, calculated by using equation 5.1.2.1-d with C_{l_p} (per radian) obtained by using the method of paragraph C of Section 7.1.2.2.

$\frac{\Delta C_{l_\beta}}{\Gamma}$ is the body-induced effect on wing height due to uniform geometric dihedral obtained by using equation 5.2.2.1-b.

$\left(\Delta C_{l_\beta}\right)_{z_W}$ is the increment in C_{l_β} due to the body-induced effect on wing height for configurations with wings located above or below the fuselage center line, obtained by using equation 5.2.2.1-c.

A comparison of test values with results calculated by using the Datcom method for wing-body configurations without dihedral and with wings mounted at the midfuselage location is presented as table 5.2.2.1-D. A comparison of test values with results calculated by using the Datcom method for the effects of dihedral is presented as table 5.2.2.1-E.

It is difficult to assess the validity of the Datcom method for establishing the value of C_{l_β}/C_L, even at small lift coefficients. Test data show that for many configurations the variation of C_{l_β} with C_L at supersonic speeds is nonlinear throughout the lift-coefficient range. Some of the test values listed in table 5.2.2.1-D are questionable, and those configurations for which no test values are listed exhibit nonlinear rolling moment due to sideslip throughout the lift-coefficient range.

Although the data of table 5.2.2.1-E are limited, it appears that the method provides relatively good results for the effect of dihedral on C_{l_β} at supersonic speeds.

Not enough experimental data are available to assess the validity of equation 5.2.2.1-c applied at supersonic speeds for determining the effect of wing vertical location. Equation 5.2.2.1-c has been applied to the configurations of references 19 and 20; the results of these calculations are compared with test values in table 5.2.2.1-F. The calculated values are somewhat less than the test values in all cases.

Sample Problem

Given: The wing-body configuration of reference 19.

Wing Characteristics:

$A = 4.0$ $\quad \lambda = 0.2$ $\quad \Lambda_{LE} = 49.4^\circ$ $\quad \Lambda_{c/2} = 42.5^\circ$

$b = 24.0$ in. $\quad \Gamma = 3^\circ$ $\quad z_w = 0$ (midwing) $\quad$ NASA 65A004 airfoil

Body Characteristics:

$d = 3.33$ in. $\quad d/b = 0.139$ $\quad$ Body of revolution

Additional Characteristics:

$M = 2.01$; $\beta = 1.74$ $\quad C_{N_\alpha} = 2.235$ per rad (test value)

Midwing, no dihedral

Compute:

$$\left(1 + \Lambda_{LE}\right) = 1 + \frac{49.4}{57.3} = 1.862$$

$$[1 + \lambda(1 + \Lambda_{LE})] = [1 + 0.2\,(1.862)] = 1.372$$

$$\left(1 + \frac{\Lambda_{LE}}{2}\right) = \left[1 + \frac{49.4}{2(57.3)}\right] = 1.431$$

$$(\tan \Lambda_{LE}/\beta) = \tan 49.4^{o}/1.74 = 0.6705$$

$$\left[\frac{M^2 \cos^2 \Lambda_{LE}}{A} + \left(\frac{\tan \Lambda_{LE}}{4}\right)^{4/3}\right] = \left[\frac{(2.01)^2 \cos^2 49.4^{o}}{4.0} + \left(\frac{\tan 49.4^{o}}{4}\right)^{4/3}\right] = 0.621$$

Solution:

$$\frac{C_{l_\beta}}{C_N} = -0.061 \frac{C_{N_\alpha}}{57.3} [1 + \lambda(1 + \Lambda_{LE})] \left(1 + \frac{\Lambda_{LE}}{2}\right)\left(\frac{\tan \Lambda_{LE}}{\beta}\right)\left[\frac{M^2 \cos^2 \Lambda_{LE}}{A} + \left(\frac{\tan \Lambda_{LE}}{4}\right)^{4/3}\right]$$

(equation 5.2.2.1-e with $\Gamma = 0$, $z_w = 0$)

$$= -0.061 \frac{2.235}{57.3} [1.372](1.431)(0.6705)[0.621]$$

$$= -0.00195 \text{ per deg}$$

This compares with a test value of −0.0019 per degree from reference 19.

Dihedral effect

Compute:

$$\beta A = (1.74)(4.0) = 6.96$$

$$A \tan \Lambda_{c/2} = (4.0)(\tan 42.5^{o}) = 3.67$$

$$\frac{C_{l_{p\ \text{theory}}}}{A} = -0.0665 \text{ per rad} \quad \text{(figure 7.1.2.2-38, interpolated)}$$

$$\Delta y_\perp = 0.80 \quad \text{(figure 2.2.1-8)}$$

$$\delta_\perp = \tan^{-1} \frac{\Delta y_\perp}{5.85} = \tan^{-1} \frac{0.80}{5.85} = 7.8^{o}$$

$$\frac{C_{l_p}}{(C_{l_p})_{\text{theory}}} = 0.918 \quad \text{(figure 7.1.2.2-40)}$$

$$C_{l_p} = \left[\frac{(C_{l_p})_{\text{theory}}}{A}\right] A \frac{C_{l_p}}{(C_{l_p})_{\text{theory}}} \quad \text{(equation 7.1.2.2-d)}$$

$$= [-0.0665](4.0)(0.918) = -0.244 \text{ per rad}$$

$$\frac{C_{l_\beta}}{\Gamma} = \frac{2}{(57.3)^2}\left(\frac{1+2\lambda}{1+3\lambda}\right)C_{l_p} \quad \text{(equation 5.1.2.1-d)}$$

$$= \frac{2}{(57.3)^2}\left(\frac{1.4}{1.6}\right)(-0.244) = -0.000130 \text{ per deg}^2$$

$$\frac{\Delta C_{l_\beta}}{\Gamma} = -0.0005\sqrt{A}\left(\frac{d}{b}\right)^2 \quad \text{(equation 5.2.2.1-b)}$$

$$= -0.0010\sqrt{4.0}\left(\frac{3.33}{24}\right)^2$$

$$= -0.0000193 \text{ per deg}^2$$

Solution:

$$\Gamma\left(\frac{C_{l_\beta}}{\Gamma} + \frac{\Delta C_{l_\beta}}{\Gamma}\right) \quad \text{(dihedral effect term of equation 5.2.2.1-e)}$$

$$3.0\,[-0.000130 + (-0.0000193)] = -0.000448 \text{ per deg}$$

This compares with a test value of −0.00046 per degree from reference 19.

REFERENCES

1. Campbell, J. P., and McKinney, M. O.: Summary of Methods for Calculating Dynamic Lateral Stability and Response and for Estimating Lateral Stability Derivatives. NACA TR 1098, 1952. (U)

2. Levacic, I.: Rolling Moment Due to Sideslip. Part III. RAE Aero Rep. No. 2139, 1946. (U)

3. Polhamus, E. C., and Sleeman, W. C., Jr.: The Rolling Moment Due to Sideslip of Swept Wings at Subsonic Speeds. NASA TN D-209, 1960. (U)

4. Wolhart, W. D., and Thomas, D. F., Jr.: Static Longitudinal and Lateral Stability Characteristics at Low Speed of 60° Sweptback-Midwing Models Having Wings With an Aspect Ratio of 2, 4, or 6. NACA TN 4397, 1958. (U)

5. Kuhn, R. E., and Draper, J. W.: Wind-Tunnel Investigation of the Effects of Geometric Dihedral on the Aerodynamic Characteristics in Pitch and in Sideslip of an Unswept and a 45° Sweptback-Wing-Fuselage Combination at High Subsonic Speeds. NACA RM L53F09, 1953. (U)

6. Christensen, F. B.: An Experimental Investigation of Four Tirangular-Wing-Body Combinations in Sideslip at Mach Numbers 0.6, 0.9, 1.4, and 1.7. NACA RM A53L22, 1954. (U)

7. Letko, W., and Williams, J. L.: Experimental Investigation at Low Speed of Effects of Fuselage Cross Section on Static Longitudinal and Lateral Stability Characteristics of Models Having 0° and 45° Sweptback Surfaces. NACA TN 3551 1955. (U)

8. Kuhn, R. E., and Fournier, P. G.: Wind-Tunnel Investigation of the Static Lateral Stability Characteristics of Wing-Fuselage Combinations at High Subsonic Speeds – Sweep Series. NACA RM L52G11a, 1952. (U)

9. Sleeman, W. C., Jr.: An Experimental Study at High Subsonic Speeds of Several Tail Configurations on a Model Having a 45° Sweptback Wing. NACA RM L57C08, 1957. (U)

10. Goodson, K. W., and Becht, R. E.: Wind-Tunnel Investigation at High Subsonic Speeds of the Stability Characteristics of a Complete Model Having Sweptback-, M-, W-, and Cranked-Wing Plan Forms and Several Horizontal-Tail Locations. NACA RM L54C29, 1954. (U)

11. Brewer, J. D., and Lichtenstein, J. H.: Effect of Horizontal Tail on Low-Speed Static Lateral Stability Characteristics of a Model Having 45° Sweptback Wing and Tail Surfaces. NACA TN 2010, 1950. (U)

12. Fournier, P. G.: Wind-Tunnel Investigation of the Aerodynamic Characteristics in Pitch and Sideslip at High Subsonic Speeds of a Wing-Fuselage Combination Having a Triangular Wing of Aspect Ratio 4. NACA RM L53G14a, 1953. (U)

13. Wiggins, J. W.: Wind-Tunnel Investigation at High Subsonic Speeds of the Static Longitudinal and Static Lateral Stability Characteristics of a Wing-Fuselage Combination Having a Triangular Wing of Aspect Ratio 2.31 and an NACA 65A003 Airfoil. NACA RM L53G09a, 1953. (U)

14. Fournier, P. G., and Byrnes, A. L., Jr.: Wind-Tunnel Investigation of the Static Lateral Stability Characteristics of Wing-Fuselage Combinations at High Subsonic Speeds. NACA RM L52L18, 1953. (U)

15. Wiggins, J. W., and Fournier, P. G.: Wind-Tunnel Investigation of the Static Lateral Stability Characteristics of Wing-Fuselage Combinations at High Subsonic Speeds – Taper Ratio Series. NACA TN 4174, 1957. (U)

16. House, R. O., and Wallace, A. R.: Wind-Tunnel Investigation of Effect of Interference on Lateral-Stability Characteristics of Four NACA 23012 Wings, an Elliptical and a Circular Fuselage, and Vertical Fins. NACA TR 705, 1941. (U)

17. Savage, H. F., and Tinling, B. E.: The Subsonic Static Aerodynamic Characteristics of an Airplane Model Having a Triangular Wing of Aspect Ratio 3. II—Lateral and Directional Characteristics. NACA TN 4042, 1957. (U)

18. Goodman, A., and Thomas, D. F., Jr.: Effects of Wing Position and Fuselage Size on the Low-Speed Static and Rolling Stability Characteristics of a Delta-Wing Model. NACA TR 1224, 1955. (U)

19. Spearman, M. L.: Investigation of the Aerodynamic Characteristics in Pitch and Sideslip of a 45° Sweptback-Wing Airplane Model With Various Vertical Locations of the Wing and Horizontal Tail. – Effect of Wing Location and Geometric Dihedral for the Wing-Body Combination, M = 2.01. NACA RM L55B18, 1955. (U)

20. Robinson, R. B.: Effects of Vertical Location of the Wing and Horizontal Tail on the Static Lateral and Directional Stability of a Trapezoidal-Wing Airplane Model at Mach Numbers of 1.41 and 2.01. NACA RM L58C18, 1958. (U)

21. Boatright, W. B.: Experimental Investigation of Effects of Wing Plan Form and Dihedral Angle on Sideslip Derivatives of Sweptback-Wing-Body Combinations at Supersonic Speeds. NACA RM L58E08, 1958. (U)

22. Feryn, M. O., and Campbell, J. F.: Effects of Wing Dihedral and Planform on Stability Characteristics of a Research Model at Mach Numbers From 1.80 to 4.63. NASA TN D-2914, 1965. (U)

23. Jernell, L. S.: Effects of Wing Planform on the Aerodynamic Characteristics of a Wing-Body-Tail Model at Mach Number From 1.70 to 4.63. NASA TN D-3105, 1965. (U)

TABLE 5.2.2.1-A

SUBSONIC WING-BODY ROLLING MOMENT DUE TO SIDESLIP

Midwing Configurations
No Dihedral

DATA SUMMARY

Ref.	A	λ	$\Lambda_{c/2}$ (deg)	$\frac{\ell_f}{b}$	M	C_{l_β}/C_L Calc. (per deg)	C_{l_β}/C_L Test (per deg)	$\Delta\left(\frac{C_{l_\beta}}{C_L}\right)$ Calc.-Test (per deg)	e Percent Error
4	2.0	0.6	58.1	0.962	0.13	−0.0102	−0.0092	−0.0010	10.9
↓	4.0	↓	59.1	0.680	↓	−0.0083	−0.0089	0.0006	− 6.7
↓	6.0	↓	59.4	0.555	↓	−0.0079	−0.0083	0.0004	− 4.8

TABLE 5.2.2.1-A (CONTD)

Ref.	A	λ	$\Lambda_{c/2}$ (deg)	$\frac{\ell_f}{b}$	M	C_{l_β}/C_L Calc. (per deg)	C_{l_β}/C_L Test (per deg)	$\Delta\left(\frac{C_{l_\beta}}{C_L}\right)$ Calc.-Test (per deg)	e Percent Error
5	4.0	0.6	0	0.833	0.60	−0.0018	−0.0016	−0.0002	12.5
					0.80	−0.0018	−0.0020	0.0002	−10.0
					0.93	−0.0018	−0.0020	0.0002	−10.0
			43.2		0.60	−0.0056	−0.0053	−0.0003	5.7
					0.80	−0.0059	−0.0057	−0.0002	3.5
					0.93	−0.0061	−0.0060	−0.0001	1.7
6	2.0	0	45.0	1.62	0.80	−0.0057	−0.0052	−0.0005	9.6
					0.90	−0.0057	−0.0054	−0.0003	5.6
7	4.0	0.6	− 3.58	0.713	0.13	−0.00155	−0.0020	0.00045	−22.5
			43.5	1.02		−0.0054	−0.0052	−0.0002	3.8
8	4.0	0.6	0	0.897	.60	−0.0018	−0.0014	−0.0004	28.6
					0.93	−0.0018	−0.00188	0.00008	− 4.3
			30.0	1.05	0.60	−0.0043	−0.0039	−0.0004	10.3
					0.93	−0.0045	−0.0042	−0.0003	7.1
			59.1	1.38	0.60	−0.0069	−0.0074	0.0005	− 6.8
					0.93	−0.0072	−0.0078	0.0006	− 7.7
9	4.0	0.3	40.9	1.19	0.80	−0.00467	−0.00344	−0.00113	32.8
10	4.0	0.3	40.9	1.19	0.80	−0.00467	−0.00606	0.00039	− 7.7
11	4.0	0.6	43.16	0.873	0.13	−0.00555	−0.00508	−0.00047	9.3
12	4.0	0	26.6	1.08	0.40	−0.0024	−0.0029	0.00050	−17.2
13	2.31	0	40.9	1.53	0.40	−0.0049	−0.0049	0	0
14	2.0	0.6	41.2	1.33	0.60	−0.0076	−0.0079	0.0003	− 3.8
					0.93	−0.0076	−0.0080	0.0004	− 5.0
	6.0	0.6	43.8	1.02	0.60	−0.0046	−0.00604	0.00044	− 8.7
					0.93	−0.0052	−0.0064	0.0012	−18.8
15	4.0	0.3	40.9	1.157	0.40	−0.0044	−0.0047	0.0003	− 6.4
					0.80	−0.0047	−0.0052	0.0005	− 9.6
					0.95	−0.0048	−0.0046	−0.0002	4.3
	4.0	1.0	45.0	1.146	0.40	−0.0062	−0.0060	−0.0002	3.3
					0.80	−0.0065	−0.0066	0.0001	− 1.5
					0.95	−0.0067	−0.0068	0.0001	− 1.5

Average Error = $\frac{\Sigma|e|}{n}$ = 8.9%

TABLE 5.2.2.1-8

EFFECT OF DIHEDRAL ON SUBSONIC ROLLING MOMENT DUE TO SIDESLIP
$\alpha = 0$

DATA SUMMARY

Ref.	A	λ	$\Lambda_{c/2}$ (deg)	$\frac{d}{b}$	Γ (deg)	M	$(\Delta C_{l_\beta})_\Gamma$ Calc. (per deg)	$(\Delta C_{l_\beta})_\Gamma$ Test (per deg)	$\Delta\left[(\Delta C_{l_\beta})_\Gamma\right]$ Calc.-Test (per deg)	e Percent Error
5	4.0	0.6	0	0.139	5.0	0.13	−0.00095	−0.00117	0.00022	−18.8
					− 5.0		0.00095	0.00104	−0.00009	− 8.7
					10.0		−0.0019	−0.0022	0.0003	−13.6
					−10.0		0.0019	0.0022	−0.0003	−13.6
					10.0	0.80	−0.0020	−0.0025	0.0005	−20.0
					−10.0		0.0020	0.0023	−0.0003	−13.0
					10.0	0.93	−0.0021	−0.0028	0.0007	−25.0
					−10.0		0.0021	0.0026	−0.0005	−19.2
			43.2		5.0	0.50	−0.00086	−0.00097	0.00011	−11.3
					− 5.0		0.00086	0.00097	−0.00011	−11.3
					10.0		−0.00173	−0.00195	0.00022	−11.3
					−10.0		0.00173	0.00187	−0.00014	− 7.5
					10.0	0.80	−0.0016	−0.00214	0.00034	−15.9
					−10.0		0.0016	0.0019	−0.0001	− 5.3
					10.0	0.93	−0.0019	−0.00235	0.00045	−19.1
					−10.0		0.0019	0.00204	−0.00014	− 6.9
18	6.38	1.0	0	0.112	5.0	0.105	−0.0012	−0.00115	−0.00005	− 4.3

Average Error = $\frac{\Sigma|e|}{n}$ = 13.2%

TABLE 5.2.2.1-C

EFFECT OF WING HEIGHT ON SUBSONIC
ROLLING MOMENT DUE TO SIDESLIP
α = 0

DATA SUMMARY

Ref.	A	λ	$\Lambda_{c/2}$ (deg)	$\frac{d}{b}$	$\frac{z_W}{b}$	M	$(\Delta C_{l_\beta})_{z_W}$ Calc (per deg)	$(\Delta C_{l_\beta})_{z_W}$ Test (per deg)	$\Delta\left[(\Delta C_{l_\beta})_{z_W}\right]$ Calc.-Test (per deg)	e Percent Error
17	3.0	0	33.6	0.144	−0.0501	0.25	−0.00052	−0.0005	−0.00002	4.0
						0.80	−0.00052	−0.0006	0.00008	−13.3
						0.90	−0.00052	−0.00066	0.00014	−21.2
18	2.31	0	56.6	0.115	−0.0411	0.17	−0.0003	−0.00035	0.00005	−14.3
				0.229	−0.0822		−0.0012	−0.0011	−0.0001	9.1
					0.0822		0.0012	0.00095	0.00025	26.3
				0.153	−0.0548		−0.00053	−0.00045	−0.00008	17.8
					0.0548		0.00053	0.00065	−0.00012	−18.5
16	6.10	0.333	0	0.112*	−0.0559	0.105	−0.000645	−0.00070	0.000055	− 7.9
					0.0622		0.00072	0.00073	−0.00001	− 1.4
	6.38	1.0		0.112*	−0.0628		−0.00074	−0.00108	0.00034	−31.5
					0.0664		0.00078	0.00070	0.00008	11.4
				0.112	−0.0443		−0.000547	−0.00053	−0.000017	3.2
					0.0496		0.00059	0.00064	−0.00005	− 7.8
	6.10	0.333			−0.0375		−0.00044	−0.00062	0.00018	−29.0
					0.0447		0.00052	0.00055	−0.00003	− 5.5
			−0.4		−0.0382		−0.00044	−0.00055	0.00011	−20.0
					0.0443		0.00051	0.00040	0.00011	27.5

*Elliptical cross section, $d = d_{equiv}$

Average Error = $\frac{\Sigma|e_i|}{n}$ = 15.0%

TABLE 5.2.2.1-D

SUPERSONIC WING-BODY ROLLING MOMENT DUE TC SIDESLIP

Midwing Configurations
No Dihedral

DATA SUMMARY

Ref.	A	λ	Λ_{LE} (deg)	M	$^{*}C_{l_\beta}/C_L$ Calc. (per deg)	C_{l_β}/C_L Test (per deg)	$\Delta\left(C_{l_\beta}/C_L\right)$ Calc.-Test (per deg)	e Percent Error
19	4.0	0.2	49.4	2.01	−0.00161	−0.0019	0.00029	−15.3
20	3.0	0.26	30.97	1.41	−0.00231	−0.0023	−0.00001	0.4
↓	↓	↓	↓	2.01	−0.0017	−0.0019	0.0002	−10.5
16	4.0	0	45.0	1.40	−0.00246	—	—	—
↓	2.0	0	63.43	↓	−0.00524	−0.00530	0.00006	− 1.1
↓	↓	↓	↓	1.70	−0.00304	−0.0040	0.00096	− 1.5
21	3.0	0.2	50.71	1.62	−0.0030	−0.0030	0	0
↓	↓	↓	↓	2.62	−0.0022	—	—	—
↓	4.0	0.2	49.4	1.62	−0.0024	—	—	—
↓	↓	↓	↓	2.62	−0.0017	—	—	—
↓	3.0	0.2	62.9	1.62	−0.00495	—	—	—
↓	↓	↓	↓	2.62	−0.00270	−0.00207	−0.00063	30.4
22	3.0	0.26	31.0	2.50	−0.00179	−0.0012	−0.00059	49.2
↓	↓	↓	↓	2.86	−0.0017	−0.00122	−0.00048	39.3
↓	↓	↓	↓	3.95	−0.00164	−0.0014	−0.00024	17.1
↓	↓	↓	↓	4.83	−0.00163	−0.00144	−0.00019	13.2
↓	1.313	0.15	73.0	1.80	−0.00883	−0.00831	−0.00052	6.3
↓	↓	↓	↓	2.16	−0.00709	−0.00690	−0.00019	2.8
↓	↓	↓	↓	2.50	−0.00576	−0.00562	−0.00014	2.5
↓	↓	↓	↓	2.86	−0.00494	−0.00464	−0.00030	6.5

*Test values of C_{N_α} were used in calculating C_{l_β}/C_L.

Average Error = $\frac{\Sigma|e|}{n}$ = 12.7%

TABLE 5.2.2.1-E

EFFECT OF DIHEDRAL ON SUPERSONIC ROLLING MOMENT DUE TO SIDESLIP

Midwing Configurations
$\alpha = 0$

DATA SUMMARY

Ref.	A	λ	Λ_{LE} (deg)	$\frac{d}{b}$	Γ (deg)	M	$(\Delta C_{l_\beta})_\Gamma$ Calc. (per deg)	$(\Delta C_{l_\beta})_\Gamma$ Test (per deg)	$\Delta\left[(\Delta C_{l_\beta})_\Gamma\right]$ Calc.-Test (per deg)	e Percent Error
19	4.0	0.2	49.4	0.139	3.0	2.01	−0.00045	−0.00046	0.00001	− 2.2
↓	↓	↓	↓	↓	− 3.0	↓	0.00045	0.00046	−0.00001	− 2.2
21	3.0	0.2	60.71	0.160	− 5.0	1.62	0.00086	0.00091	−0.00005	− 5.5
↓	↓	↓	↓	↓	−10.0	↓	0.00173	0.0015	0.00023	15.3
↓	↓	↓	↓	↓	− 5.0	2.62	0.00069	0.0008	−0.00001	− 1.7
↓	↓	↓	↓	↓	−10.0	↓	0.00119	0.00116	0.00303	2.6
↓	4.0	0.2	49.4	0.139	− 5.0	1.62	0.00092	0.0009	0.00002	2.2
↓	↓	↓	↓	↓	−10.0	↓	0.00185	0.0016	0.00025	15.6
↓	↓	↓	↓	↓	− 5.0	2.62	0.00060	0.00055	0.00005	9.1
↓	↓	↓	↓	↓	−10.0	↓	0.00120	0.00105	0.00015	14.3
↓	3.0	0.2	62.9	0.160	− 5.0	1.62	0.00071	0.00085	−0.00014	−16.5
↓	↓	↓	↓	↓	−10.0	↓	0.00143	0.0018	−0.00037	−20.6
↓	↓	↓	↓	↓	− 5.0	2.62	0.00061	0.0006	0.00001	1.7
↓	↓	↓	↓	↓	−10.0	↓	0.00123	0.0011	0.00013	11.8
22	3.0	0.25	31.0	0.146	3.0	2.50	−0.00035	−0.00041	0.00006	−14.6
↓	↓	↓	↓	↓	3.0	2.86	−0.000327	−0.00036	0.000033	− 9.2
↓	↓	↓	↓	↓	3.0	4.63	−0.00018	−0.00019	0.00001	− 5.3
↓	1.313	0.15	73.0	0.233	3.0	1.80	−0.00027	−0.00025	−0.00002	8.0
↓	↓	↓	↓	↓	− 3.0	↓	0.00027	0.00023	0.00004	17.4
↓	↓	↓	↓	↓	3.0	2.16	−0.000282	−0.00026	−0.000022	8.5
↓	↓	↓	↓	↓	− 3.0	↓	0.000282	0.00030	−0.000018	− 6.0
↓	↓	↓	↓	↓	3.0	2.50	−0.000273	−0.00022	−0.000063	24.1
↓	↓	↓	↓	↓	− 3.0	↓	0.000273	0.00025	0.000023	9.2
↓	↓	↓	↓	↓	3.0	2.86	−0.00024	−0.00019	−0.00005	26.3
↓	↓	↓	↓	↓	− 3.0	↓	0.00021	0.00024	−0.00003	−12.5

Average Error = $\frac{\Sigma|e|}{n}$ = 10.5%

TABLE 5.2.2.1-F

EFFECT OF WING HEIGHT ON SUPERSONIC ROLLING

MOMENT DUE TO SIDESLIP

$\alpha = 0$

DATA SUMMARY

Ref.	A	λ	Λ_{LE} (deg)	$\frac{d}{b}$	$\frac{z_W}{b}$	M	$\left(\Delta C_{l_\beta}\right)_{z_W}$ Calc. (per deg)	$\left(\Delta C_{l_\beta}\right)_{z_W}$ Test (per deg)
19	4.0	0.2	49.4	0.139	−0.588	2.01	−0.00068	−0.00103
↓	↓	↓	↓	↓	0.588	↓	0.00068	0.00103
20	3.0	0.25	30.97	0.139	−0.588	1.41	−0.00059	−0.00110
↓	↓	↓	↓	↓	0.588	↓	0.00059	0.00120
↓	↓	↓	↓	↓	−0.588	2.01	−0.00059	−0.00085
↓	↓	↓	↓	↓	0.588	↓	0.00059	0.00080

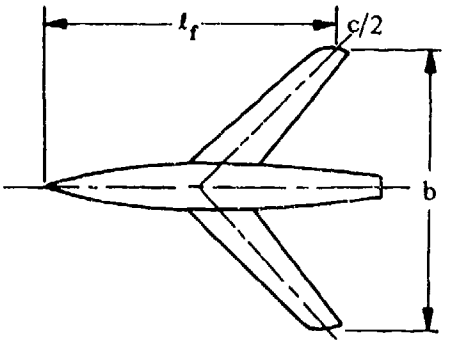

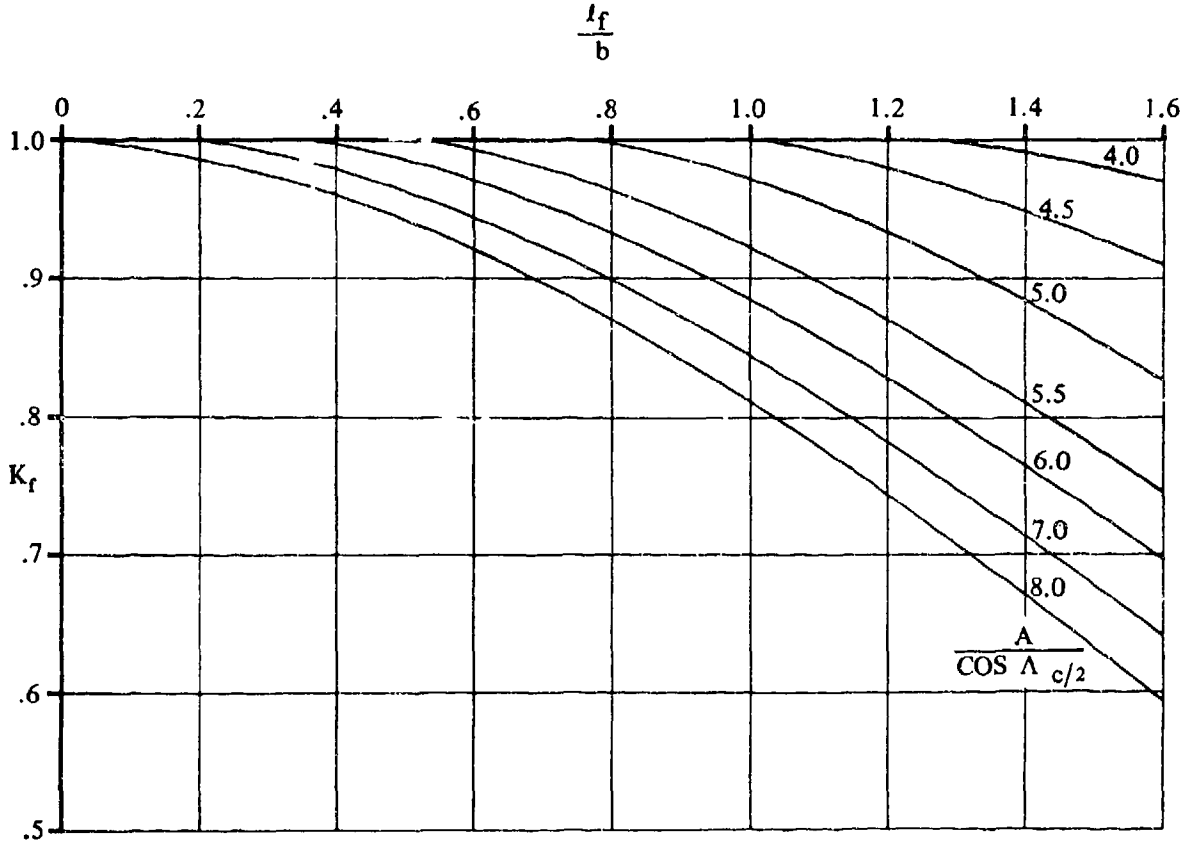

FIGURE 5.2.2.1-26 FUSELAGE CORRECTION FACTOR

5.2.3 WING-BODY SIDESLIP DERIVATIVE C_{n_β}

5.2.3.1 WING-BODY SIDESLIP DERIVATIVE C_{n_β} IN THE LINEAR ANGLE-OF-ATTACK RANGE

The wing-body yawing moment due to sideslip can be considered as the sum of the yawing moments of the body, the wing, and the wing-body interference. The wing contribution is important only at large incidences and is deleted from the solution of wing-body yawing moment due to sideslip. The method provided herein gives the total wing-body sideslip derivative C_{n_β} as the sum of the body and wing-body interference contributions.

The unstable directional stability contribution of the fuselage is dominant in this analysis, and since slender-body theory predicts the body contribution to be essentially independent of Mach number, the method presented is considered to be valid for all speeds.

Experimental investigations have shown that the wing-body interference contribution to the yawing-moment derivative is essentially independent of sweep, taper ratio, and Mach number. Furthermore, the evidence of references 1, 2, and 3 is that the effect of wing vertical position on wing-body yawing moment is small.

The maximum angle of applicability is limited to the linear-lift region. Above this angle-of-attack limitation, separation occurs and both the wing and wing-fuselage interference have an appreciable effect on the wing-body sideslip derivative C_{n_β} as a result of the changes in the magnitude and orientation of the resultant force on the two wing semispans.

DATCOM METHOD

All Speeds

The total wing-body sideslip derivative C_{n_β}, based on the product of total wing area and wing span Sb, and referred to an arbitrary moment center, is given by

$$\left(C_{n_\beta}\right)_{WB} = -K_N K_{R_\ell} \frac{S_{B_S}}{S_W} \frac{\ell_B}{b} \quad \text{(per degree)} \qquad 5.2.3.1\text{-a}$$

where

K_N is an empirical factor related to the sideslip derivative for body plus wing-body interference, obtained from figure 5.2.3.1 -8 as a function of the body geometry.

K_{R_ℓ} is an empirical Reynolds-number factor obtained from figure 5.2.3.1 -9 as a function of the fuselage Reynolds number.

S_{B_S} is the projected side area of the body.

ℓ_B is the length of the body.

A comparison of results calculated by using this method with test data is presented as table 5.2.3.1-A.

It should be noted that the upper limit of the fuselage Reynolds number of the test data is 49.2 million. For configurations at higher full-scale Reynolds numbers the method is expected to give results that are satisfactory for preliminary design.

Sample Problem

1. Given: The wing-body configuration of reference 12.

Body Characteristics:

$\ell_B = 4.1$ ft $\quad S_{B_S} = 1.35$ sq ft $\quad x_m = 2.5$ ft $\quad h = 0.416$ ft

$w = 0.416$ ft $\quad h_1 = 0.315$ ft $\quad h_2 = 0.388$ ft

Wing Characteristics:

$S_W = 2.25$ sq ft $\quad b = 3.0$ ft

Additional Characteristics:

$M = 0.91$ $\quad R_\ell = 3.87 \times 10^6$ per ft

Compute:

$$\frac{x_m}{\ell_B} = \frac{2.5}{4.1} = 0.610$$

$$\frac{\ell_B{}^2}{S_{B_S}} = \frac{(4.1)^2}{1.35} = 12.45$$

$$\sqrt{\frac{h_1}{h_2}} = \sqrt{\frac{0.315}{0.388}} = 0.902$$

$$\frac{h}{w} = \frac{0.416}{0.416} = 1.00$$

K_N = 0.00105 per deg (figure 5.2.3.1-8)

$R_{\ell_{fuselage}} = (3.87 \times 10^6)\,\ell_B = (3.87 \times 10^6)(4.1) = 15.87 \times 10^6$

K_{R_ℓ} = 1.567 (figure 5.2.3.1-9)

Solution:

$$\left(C_{n_\beta}\right)_{WB} = -K_N K_{R_\ell} \frac{S_{B_S}}{S_W} \frac{\ell_B}{b} \quad \text{(equation 5.3.2.1-a)}$$

$$= -(0.00105)(1.567) \frac{1.35}{2.25} \frac{4.1}{3.0}$$

$$= -0.00135 \text{ per deg} \quad \text{(based on } S_W b\text{)}$$

This compares with a test value of −0.00130 per degree from reference 12.

REFERENCES

1. Goodman, A., and Thomas, D. F., Jr.: Effects of Wing Position and Fuselage Size on the Low-Speed Static and Rolling Stability Characteristics of a Delta-Wing Model. NACA TR 1224, 1955. (U)

2. Goodman, A.: Effects of Wing Position and Horizontal-Tail Position on the Static Stability Characteristics of Models With Unswept and 45° Sweptback Surfaces With Some Reference to Mutual Interference. NACA TN 2304, 1951. (U)

3. Spearman, M. L., Driver, C., and Hughes, W. C.: Investigation of Aerodynamic Characteristics in Pitch and Sideslip of a 45° Sweptback-Wing Airplane Model With Various Vertical Locations of Wing and Horizontal Tail. Basic-Data Presentation, M = 2.01. NACA RM L54L06, 1955. (U)

4. Jaquet, B. M., and Brewer, J. D.: Effects of Various Outboard and Central Fins on Low-Speed Static-Stability and Rolling Characteristics of a Triangular-Wing Model. NACA RM L9E18, 1949. (U)

5. Queijo, M. J., and Wolhart, W. D.: Experimental Investigation of the Effect of Vertical-Tail Size and Length and of Fuselage Shape and Length on the Static Lateral Stability Characteristics of a Model with 45° Sweptback Wing and Tail Surfaces. NACA TR 1049, 1951. (U)

6. Brewer, J. D., and Lichtenstein, J. H.: Effect of Horizontal Tail on Low-Speed Static Lateral Stability Characteristics of a Model Having 45° Sweptback Wing and Tail Surfaces. NACA TN 2010, 1950. (U)

7. Letko, W., and Williams, J. L.: Experimental Investigation at Low Speed of Effects of Fuselage Cross Section on Static Longitudinal and Lateral Stability Characteristics of Models Having 0° and 45° Sweptback Surfaces. NACA TN 3551, 1955. (U)

8. Graham, D., and Koenig, D. G.: Tests in the Ames 40- by 80-Foot Wind Tunnel of an Airplane Configuration With an Aspect Ratio 2 Triangular Wing and an All-Movable Horizontal Tail — Lateral Characteristics. NACA RM A51L03, 1952. (U)

9. Bird, J. D., Lichtenstein, J. H., and Jaquet, B. M.: Investigation of the Influence of Fuselage and Tail Surfaces on Low-Speed Static Stability and Rolling Characteristics of a Swept-Wing Model. NACA TN 2741, 1952. (U)

10. Fournier, P. G.: Low-Speed Static Stability Characteristics of a Complete Model With an M-Wing in Mid and High Positions and With Three Horizontal-Tail Heights. NACA RM L55J06, 1956. (U)

11. Anon: Unpublished preliminary wind-tunnel tests of the Model DC-10. McDonnell Douglas Company, 1968. (U)

12. Merritt, F. D., Roensch, R. L., and Weiner, A. H.: Results of a DC-8-AWACS Test in the Galcit 10-Foot Low-Speed Wind Tunnel. McDonnell Douglas Company Report DAC 67253, 1967. (U)

13. Savage, H. F., and Tinling, B. E.: The Subsonic Static Aerodynamic Characteristics of an Airplane Model Having a Triangular Wing of Aspect Ratio 3. II – Lateral and Directional Characteristics. NACA TN 4042, 1957. (U)

14. Wiggins, J. W., Kuhn, R. E., and Fournier, P. G.: Wind-Tunnel Investigation to Determine the Horizontal- and Vertical-Tail Contributions to the Static Lateral Stability Characteristics of a Complete-Model Swept-Wing Configuration at High Subsonic Speeds. NACA TN 3818, 1956. (U)

15. Kuhn, R. E., and Draper, J. W.: Wind-Tunnel Investigation of the Effects of Geometric Dihedral on the Aerodynamic Characteristics in Pitch and Sideslip of an Unswept- and a 45° Sweptback-Wing-Fuselage Combination at High Subsonic Speeds. NACA RM L53F09, 1953. (U)

16. Christensen, F. B.: An Experimental Investigation of Four Triangular-Wing-Body Combinations in Sideslip at Mach Numbers 0.6, 0.9, 1.4, and 1.7. NACA RM A53L22, 1954. (U)

17. Sleeman, W. C., Jr.: An Experimental Study at High Subsonic Speeds of Several Tail Configurations on a Model Having a 45° Sweptback Wing. NACA RM L57C08, 1957. (U)

18. Goodson, K. W., and Becht, R. E.: Wind-Tunnel Investigation at High Subsonic Speeds of the Stability Characteristics of a Complete Model Having Sweptback, M-, W-, and Cranked-Wing Plan Forms and Several Horizontal-Tail Locations. NACA RM L54C29, 1954. (U)

19. Spearman, M. L., and Robinson, R. B.: Static Lateral Stability and Control Characteristics of a Model of a 45° Swept-Wing Fighter Airplane With Various Vertical Tails at Mach Numbers of 1.41, 1.61, and 2.01. NACA RM L56D05, 1956. (U)

20. Spearman, M. L., and Robinson, R. B.: Investigation of the Aerodynamic Characteristics in Pitch and Sideslip of a 45° Swept-Wing Airplane Configuration With Various Vertical Locations of the Wing and Horizontal Tail. Static Lateral and Directional Stability; Mach Numbers of 1.41 and 2.01. NACA RM L57J25a, 1957. (U)

21. Spearman, M. L.: Static Lateral and Directional Stability and Effective Sidewash Characteristics of a Model of a 35° Swept-Wing Airplane at a Mach Number of 1.61. NACA RM L56E23, 1956. (U)

22. Boatright, W. B.: Experimental Investigation of Effects of Wing Plan Form and Dihedral Angle on Sideslip Derivatives of Sweptback-Wing-Body Combinations at Supersonic Speeds. NACA RM L58E08, 1958. (U)

23. Robinson, R. B.: Effects of Canopy, Revised Vertical Tail, and a Yaw-Damper Vane on the Aerodynamic Characteristics of a 1/16-Scale Model of the Douglas D-558-II Research Airplane at a Mach Number of 2.01. NACA RM L54F25, 1954. (U)

24. Spearman, M. L., Robinson, R. B., and Driver, C.: The Effects of the Addition of Small Fuselage-Mounted Fins on the Static Directional Stability Characteristics of a Model of a 45° Swept-Wing Airplane at Angles of Attack up to 15.3° at a Mach Number of 2.01. NACA RM L56D16a, 1956. (U)

25. Spearman, M. L.: Investigation of the Aerodynamic Characteristics in Pitch and Sideslip of a 45° Sweptback-Wing Airplane Model With Various Vertical Locations of the Wing and Horizontal Tail. Effect of Wing Location and Geometric Dihedral for the Wing-Body Combination, M = 2.01. NACA RM L55B18, 1955. (U)

26. Hamilton, C. V.: Aerodynamic Characteristics at Supersonic Speeds of a Series of Wing-Body Combinations Having Cambered Wings With an Aspect Ratio of 3.5 and . Taper Ratio of 0.2. Effects of Sweep Angle and Thickness Ratio on the Static Lateral Stability Characteristics at M = 2.01. NACA RM L52E23, 1952. (U)

27. Jaquet, B. M., and Fournier, R. H.: Effects of Wing Sweep, Horizontal-Tail Configuration, and a Ventral Fin on Static Stability Characteristics of a Model With a Wing of Aspect Ratio 3 at Mach Numbers From 2.29 to 4.65. NACA RM L58E06, 1958. (U)

TABLE 5.2.3.1-A

WING-BODY YAWING MOMENT DUE TO SIDESLIP

DATA SUMMARY – ALL SPEEDS

Ref	M	$R_{\ell_{fus}}$ x 10^{-6}	x_m (ft)	ℓ_B (ft)	S_{B_S} (sq ft)	$\sqrt{\frac{h_1}{h_2}}$	$\frac{h}{w}$	K_N (per deg)	$S_w b$ (cu ft)	K_{R_ℓ}	$(C_{n_\beta})_{WB}$ Calc. (per deg)	$(C_{n_\beta})_{WB}$ Test (per deg)	e Percent Error
4	0.13	3.69	1.93	4.0	1.76	1.008	1.0	0.0012	12.18	1.27	–0.00088	–0.00090	– 2.2
↓	↓	↓	↓	↓	1.77	1.01	↓	0.0012	↓	1.27	–0.00090	–0.00090	0
5	0.13	2.32	1.25	2.5	0.833	1.0	1.0	0.00155	6.75	1.172	–0.00056	–0.00053	5.7
↓	↓	3.10	1.67	3.34	1.11	↓	↓	0.00145	↓	1.232	–0.00099	–0.00090	10.0
		4.64	2.5	5.0	1.67			0.00080		1.316	–0.00130	–0.00170	–23.5
		3.10	1.67	3.34	1.30	1.147		0.0016		1.232	–0.00127	–0.00140	– 9.3
↓	↓	↓	↓	↓	1.25	0.93	↓	0.00113	↓	1.232	–0.0010	–0.0010	0
6	0.13	3.09	1.67	3.33	1.117	1.0	1.0	0.00120	6.75	1.232	–0.00081	–0.00090	–10.0
7	0.13	3.48	2.00	3.75	1.43	1.02	1.0	0.00130	6.75	1.257	–0.00129	–0.00133	– 3.0
↓	↓	↓	2.12	↓	↓	↓	↓	0.00138	↓	1.257	–0.00138	–0.00150	– 8.0
			2.00		1.29			0.00115		1.257	–0.00104	–0.00150	–30.7
			2.12		↓			0.00130		1.257	–0.00117	–0.00145	–19.3
			2.00		1.736		2.213	0.00190		1.257	–0.00230	–0.00260	–11.5
↓	↓	↓	2.12	↓	↓	↓	↓	0.00210	↓	1.257	–0.00256	–0.00270	– 5.6
8	0.13	49.2	23.91	56.16	181.33	1.0	1.0	0.00045	7812.5	1.80	–0.00106	–0.00120	–11.7
1	0.17	5.27	2.25	4.5	1.29	1.02	1.0	0.00095	12.18	1.343	–0.00080	–0.00060	0
↓	↓	↓	↓	↓	1.75	↓	↓	0.00110	↓	1.343	–0.00095	–0.00095	0
↓	↓	↓	↓	↓	2.57	↓	↓	0.00140	↓	1.343	–0.00179	–0.00200	–10.5
2	0.17	3.96	1.67	3.45	1.25	0.96	1.0	0.00105	6.75	1.283	–0.00086	–0.00090	– 4.4
9	0.17	5.36	2.25	4.5	1.63	1.0	1.0	0.00100	10.94	1.345	–0.00090	–0.00100	–10.0
10	0.17	9.20	3.97	7.39	3.75	0.946	1.0	0.00073	36.00	1.456	–0.00082	–0.00100	–18.0
11	0.20	10.8	72.0	152.9	1730.0	1.05	1.10	0.00085	434,337	1.49	–0.00071	–0.00085	– 9.4
12	0.20	21.2	83.08	163.0	2800.0	1.03	1.0	0.00137	547,866	1.625	–0.00185	–0.00190	– 2.6
↓	↓	32.0	↓	↓	↓	↓	↓	↓	↓	1.71	–0.00195	–0.00170	14.7
↓	↓	46.0	↓	↓	↓	↓	↓	↓	↓	1.79	–0.00204	–0.00187	9.1
13	0.25	9.74	3.30	6.0	2.44	0.86	1.0	0.00092	13.86	1.468	–0.00142	–0.00120	18.3
↓	↓	8.80	↓	5.42	2.17	0.83	↓	0.00090	↓	1.447	–0.00110	–0.00100	10.0
14	0.40	9.66	2.5	4.1	1.36	0.89	1.0	0.00105	6.75	1.464	–0.00126	–0.00130	– 3.1

TABLE 5.2.3.1-A (CONTD)

Ref	M	$R_{\ell_{fus}}$ x 10^{-6}	x_m (ft)	ℓ_B (ft)	S_{B_S} (sq ft)	$\sqrt{\frac{h_1}{h_2}}$	$\frac{h}{w}$	K_N (per deg)	$S_w b$ (cu ft)	K_{R_ℓ}	$(C_{n_\beta})_{WB}$ Calc. (per deg)	$(C_{n_\beta})_{WB}$ Test (per deg)	e Percent Error
15	0.60	11.4	2.5	4.1	1.35	0.89	1.0	0.00105	6.75	1.498	−0.00129	−0.00130	− 0.8
↓	0.70	14.42	↓	↓	↓	↓	↓	0.00105	↓	1.548	−0.00133	−0.00130	2.3
	0.80	15.38						0.00105		1.558	−0.00134	−0.00130	3.1
	0.91	15.87						0.00105		1.567	−0.00135	−0.00130	3.8
↓	0.93	15.92	↓	↓	↓	↓	↓	0.00105	↓	1.567	−0.00135	−0.00130	3.8
16	0.60	8.0	3.18	5.04	2.03	0.85	1.0	0.00110	11.36	1.427	−0.00140	−0.00130	7.7
↓	0.90	10.6	↓	↓	↓	↓	↓	0.00110	↓	1.483	−0.00147	−0.00135	8.9
17	0.60	5.11	0.87	1.52	0.189	0.95	1.0	0.00110	0.26	1.336	−0.00168	−0.00110	52.7
↓	0.94	6.38	↓	↓	↓	↓	↓	0.00110	↓	1.380	−0.00174	−0.00160	8.7
	0.60	5.11			0.181			0.00098		1.336	−0.00144	−0.00150	− 4.0
↓	0.94	6.38	↓	↓	↓	↓	↓	0.0009	↓	1.380	−0.00149	−0.00180	−17.2
18	0.80	13.86	2.60	4.56	1.64	0.98	1.0	0.00110	6.75	1.537	−0.00188	−0.00170	10.6
↓	0.92	16.63	↓	↓	↓	↓	↓	0.00110	↓	1.576	−0.00192	−0.00180	6.7
18	1.4	7.61	2.265	3.78	1.07	0.87	1.0	0.00095	5.69	1.417	−0.00096	−0.00097	− 1.0
↓	1.4	16.50	3.18	5.04	2.03	0.85	1.0	0.00110	11.36	1.573	−0.00156	−0.00130	20.0
↓	1.7	20.00	↓	↓	↓	↓	↓	0.00110	↓	1.62	−0.00160	−0.00140	14.3
20	1.41	5.12	1.56	3.05	0.74	0.98	1.0	0.001	2.67	1.462	−0.00123	−0.00115	6.9
↓	2.01	7.52	↓	↓	↓	↓	↓	0.001	↓	1.413	−0.00120	−0.00094	27.7
19	1.41	6.04	2.08	3.37	1.118	0.98	1.08	0.0015	5.10	1.37	−0.00152	−0.00150	1.3
↓	1.61	5.76	↓	↓	↓	↓	↓	0.0015	↓	1.36	−0.00151	−0.00165	− 8.5
↓	2.01	5.00	↓	↓	↓	↓	↓	0.0015	↓	1.331	−0.00148	−0.00160	− 7.5
20	1.41	9.11	1.73	3.04	0.738	0.97	1.0	0.00115	2.0	1.452	−0.00189	−0.00150	26.0
↓	2.01	8.79	↓	↓	↓	↓	↓	0.00115	↓	1.447	−0.00188	−0.00170	10.6
21	1.61	7.64	1.59	2.69	0.820	1.04	1.0	0.00170	2.35	1.416	−0.00227	−0.00253	−10.3
22	1.62	2.69	0.39	0.625	0.032	0.97	1.0	0.00122	0.023	1.204	−0.00130	−0.00095	36.8
↓	2.62	3.015	↓	↓	↓	↓	↓	0.00122	0.020	1.228	−0.00152	−0.00145	4.8
↓	↓	↓	↓	↓	↓	↓	↓	0.00122	↓	1.228	−0.00152	−0.00152	0
↓	↓	↓	↓	↓	↓	↓	↓	0.00122	0.023	1.228	−0.00132	−0.00127	3.9
3	2.01	9.747	1.734	3.04	0.717	0.95	1.0	0.00106	2.0	1.468	−0.00170	−0.00170	0
23	2.01	8.42	1.357	2.625	0.66	1.07	1.0	0.00130	1.07	1.437	−0.00297	−0.00345	−13.9
24	2.01	3.38	1.50	2.74	0.71	1.06	1.34	0.00150	1.26	1.25	−0.00298	−0.00296	2.4
25	2.01	9.75	1.73	3.04	0.736	0.98	1.0	0.00115	2.0	1.468	−0.00189	−0.00175	8.0

TABLE 5.2.3.1-A (CONTD)

Ref	M	$R_{\ell_{fus}}$ x 10^{-6}	x_m (ft)	ℓ_B (ft)	S_{B_S} (sq ft)	$\sqrt{\frac{h_1}{h_2}}$	$\frac{h}{w}$	K_N (per deg)	$S_w b$ (cu ft)	K_{R_ℓ}	$(C_{n_\beta})_{WB}$ Calc. (per deg)	$(C_{n_\beta})_{WB}$ Test (per deg)	e Percent Error
26	2.01	7.02	1.385	2.09	0.358	0.99	1.0	0.00150	3.43	1.40	−0.00686	−0.00625	9.8
27	2.29	10.6	1.958	3.43	0.962	0.965	1.0	0.00115	1.68	1.485	−0.00255	−0.00273	− 6.6
↓	2.98	↓	↓	↓	↓	↓	↓	↓	↓	↓	↓	−0.00280	− 8.9
↓	3.96	↓	↓	↓	↓	↓	↓	↓	↓	↓	↓	−0.00262	− 2.7
↓	4.65	↓	↓	↓	↓	↓	↓	↓	↓	↓	↓	−0.00275	− 7.3
Average Error = $\frac{\Sigma\lvert e\rvert}{n}$ = 9.7%													

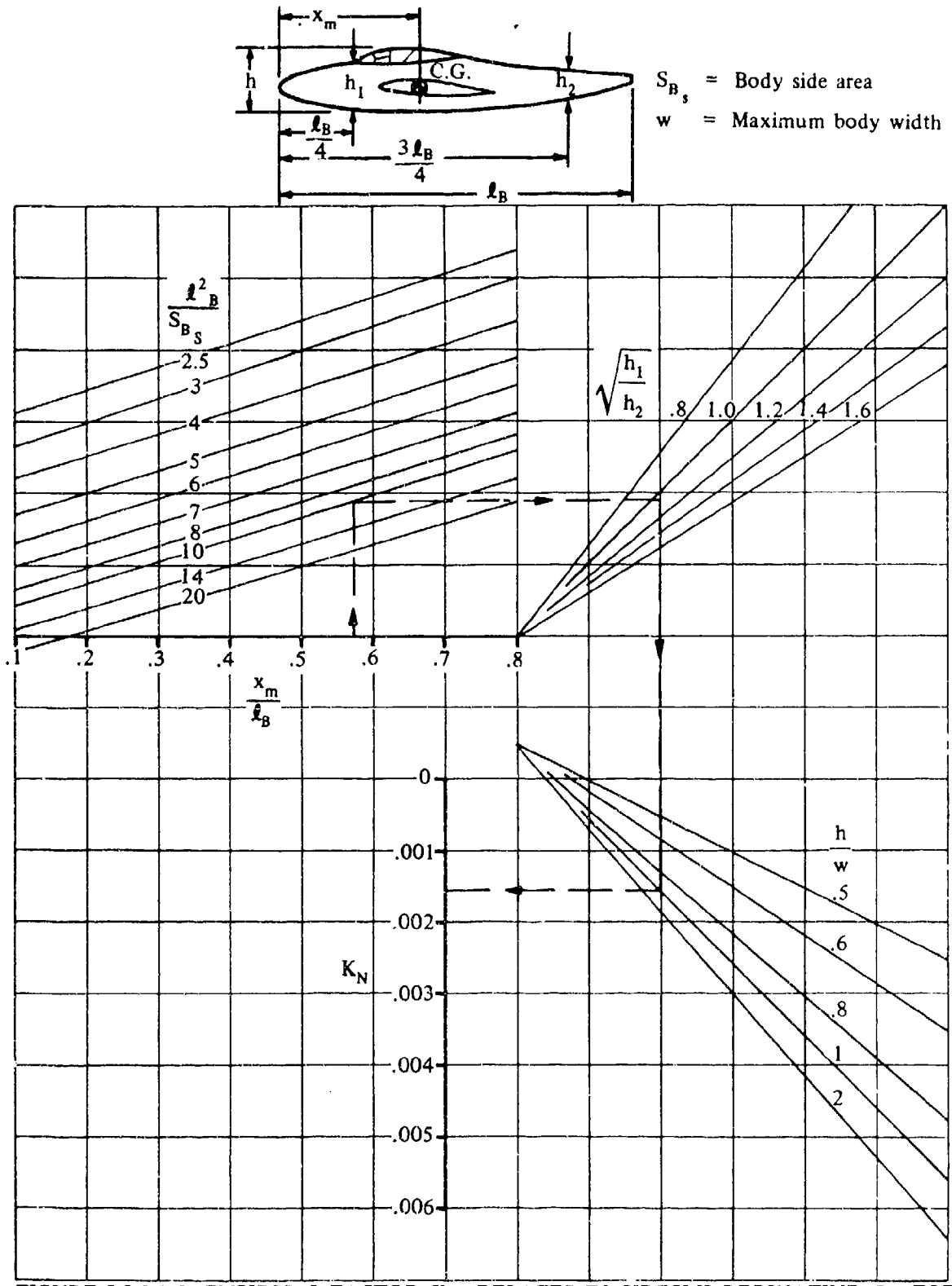

FIGURE 5.2.3.1-8 EMPIRICAL FACTOR K_N RELATED TO SIDESLIP DERIVATIVE C_{n_β} FOR BODY + WING-BODY INTERFERENCE

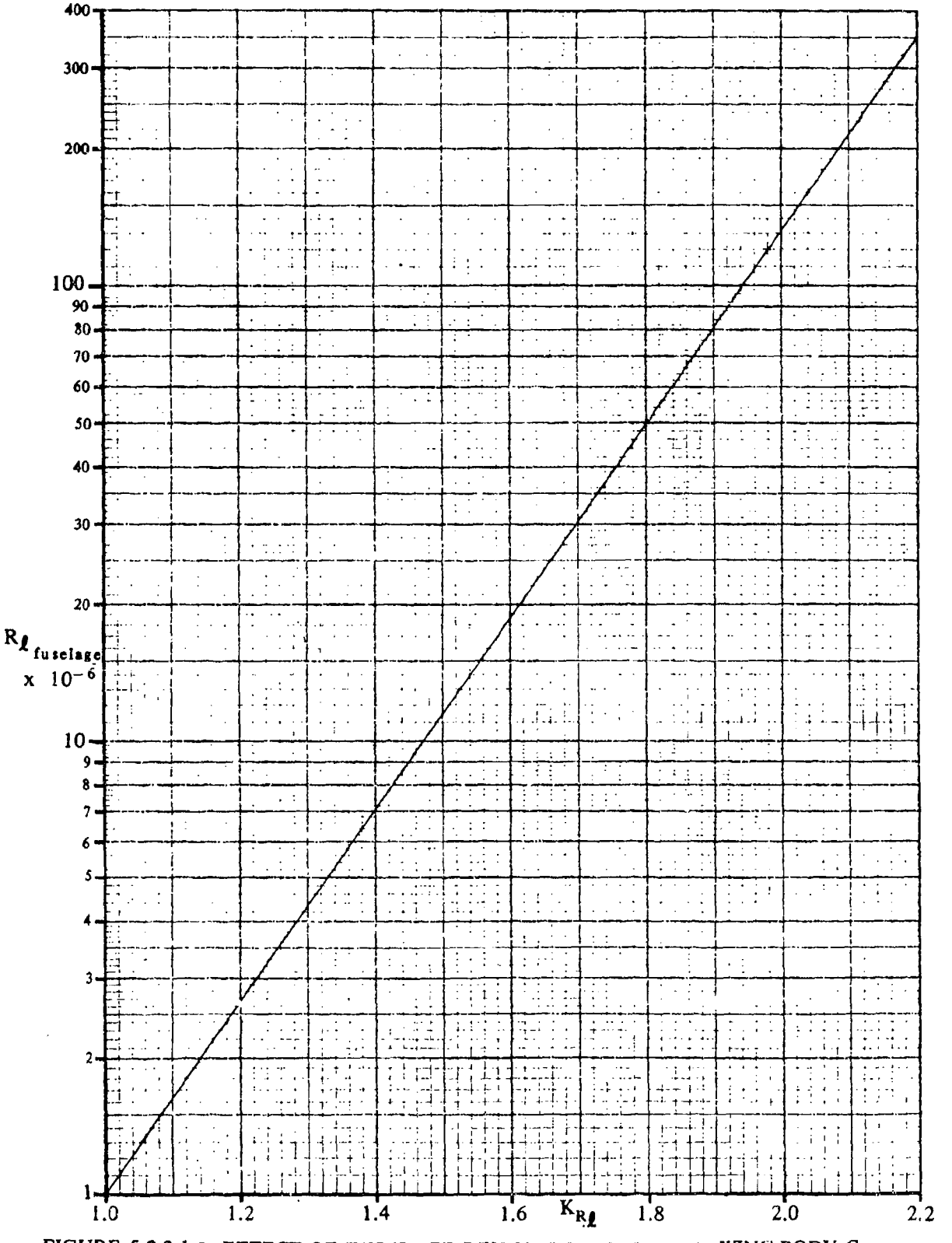

FIGURE 5.2.3.1-9 EFFECT OF FUSELAGE REYNOLDS NUMBER ON WING-BODY C_{n_β}

5.2.3.2 WING-BODY YAWING-MOMENT COEFFICIENT C_n AT ANGLE OF ATTACK

The wing-body yawing moment developed at combined angles is nonlinear with respect to both sideslip and angle of attack because of viscous cross-flow effects and cross-coupling of upwash and sidewash velocities. To obtain the sideslip derivative $C_{n_{\beta_{WB}}}$ it is recommended that $C_{n_{WB}}$ be calculated at several angles of attack for a small sideslip angle ($\beta \leq 4^\circ$). Then at each angle of attack the yawing moment is assumed linear with sideslip for small values of β so that

$$C_{n_{\beta_{WB}}} = \frac{C_{n_{WB}}}{\beta} .$$

A. SUBSONIC

No method is presently available for determining the wing-body yawing moment at large angles of attack and subsonic speeds. The method presented herein is restricted to first-order approximations at relatively low angles of attack.

DATCOM METHOD

It is recommended that the method of Section 5.2.3.1 be used in the linear-lift angle-of-attack range.

B. TRANSONIC

No method is presently available for determining the wing-body yawing moment at large angles of attack and transonic speeds. The method presented herein is restricted to first-order approximations at relatively low angles of attack.

DATCOM METHOD

It is recommended that the method of Section 5.2.3.1 be used in the linear-lift angle-of-attack range.

C. SUPERSONIC

The method for estimating the wing-body yawing-moment coefficient $C_{n_{WB}}$ is based on the theory involved in estimating $C_{Y_{WB}}$ presented in Section 5.2.1.2. Therefore, the comments in that Section applying to the aerodynamics of wing-body interference also apply to this Section but are not repeated here.

To obtain the wing-body yawing-moment coefficient it is necessary to apply the appropriate moment arm to the side-force coefficient of Section 5.2.1.2. The center of pressure of the aerodynamic forces on the body at angle of attack establishes one moment arm. No simple method is available for estimating the body-alone center of pressure. The method suggested herein is necessarily tentative and will be updated as information becomes available. Of course, test values at the appropriate angle of attack are to be preferred. The position at which the wing-body interference side force acts on the body establishes a second moment arm. In the method that follows, this position is expressed as a function of the vertical location of the wing on the body and is based on the assumption that both the pressure and viscous force components of interference act at the same location.

The same limitations apply to the estimation of the yawing moments as to the estimation of the side force: although the wing leading edge should be supersonic, fair results are obtained for subsonic leading edges if the aspect ratio is not too low. Furthermore, correlation of experimental and estimated values of the wing-body interference moment indicates that the Datcom method is in actuality only warranted for cases in which the mid-point of the wing root chord is substantially displaced from the moment reference point.

DATCOM METHOD

The yawing-moment coefficient for wing-body combinations at supersonic speeds is given by the equation

$$C_{n_{WB}} = C_{n_B} + \left[\frac{x_m - \bar{l}_{W(B)}}{b_W}\right] C_{Y_{W(B)}} \qquad 5.2.3.2\text{-a}$$

where

C_{n_B} is the body-alone contribution given by

$$C_{n_B} = \left[\frac{x_m}{l_B} - x_{c.p.}\right] \frac{l_B}{b_W} C_{Y_B} \qquad 5.2.3.2\text{-b}$$

where

x_m is the distance from the body nose to the moment center

l_B is the body length

$x_{c.p.}$ is the distance from the body nose to the body center of pressure, measured in body lengths. This parameter is approximated by $x_{c.p.} = \frac{C_m}{C_L}$

where C_m and C_L are obtained from paragraph C of Sections 4.2.2.2 and 4.2.1.2, respectively, at $\alpha = \alpha'$. The pitching-moment coefficient from Section 4.2.2.2 is referred to the body nose ($x_m = 0$).

b_W is the wing span

C_{Y_B} is the body-alone side-force coefficient obtained from Section 5.2.1.2

$C_{Y_{W(B)}}$ is the side-force interference contribution obtained from Section 5.2.1.2

$\bar{l}_{W(B)}$ is the distance from the body nose to the center of pressure of the wing-induced body side force

For midwing configurations

$$\bar{l}_{W(B)} = l_n + \tfrac{1}{2} c_{r_e} \qquad 5.2.3.2\text{-c}$$

where

l_n is the distance from the body nose to the juncture of the wing leading edge and body

For tangent wing configurations

$$\bar{l}_{W(B)} = l_n + c_{r_e}\left[\frac{x_{l_{(\alpha)}}}{x_{l_{(\alpha=0)}}}\right]\left[\frac{x_{l_{(\alpha=0)}}}{c_{r_e}}\right] \qquad 5.2.3.2\text{-d}$$

where

$x_{l_{(\alpha)}}$ is the distance to the center of pressure of the wing-induced body side force from the juncture of the wing leading edge and the body at the prop- angle of attack

$x_{l_{(\alpha=0)}}$ is the distance to the center of pressure of the wing-induced body side force from the juncture of the wing leading edge and the body at zero angle of attack

$\frac{x_{l_{(\alpha)}}}{x_{l_{(\alpha=0)}}}$ is obtained from figure 5.2.3.2-6

$\frac{x_{l_{(\alpha=0)}}}{c_{r_e}}$ is obtained from figure 5.2.3.2-8

Values for the incremental coefficient resulting from the addition of wings in the mid and high- and low-tangent positions on circular bodies, calculated using the second term on the right-hand side of equation 5.2.3.2-a, are compared with experimental results in figure 5.2.3.2-5. This correlation is somewhat inconclusive in that for the conventional wing locations considered the centers of pressure of the wing-body interference side forces are close to the moment reference point. The resulting small yawing moments are likely no larger than the yawing moments of the wing alone which are neglected in the method. Furthermore, exact knowledge of the wing effects on the body cross-flow load distribution is precluded since the center of pressure of the body cross-flow loading is not accurately known.

Sample Problem

Given: Configuration of the sample problem, paragraph C, Section 5.2.1.2. This configuration is also tested in reference 1 of this Section. Some of the characteristics are repeated. Find the yawing-moment coefficient developed by the wing-body combination at $\alpha = 12^\circ$ and $\beta = 4^\circ$.

Characteristics

$\ell_B = 36.5$ in. $\quad \ell_n = 15.62$ in. $\quad x_m = 20.81$ in. $\quad c_{r_e} = 8.90$ in. $\quad c_{r_e}/d = 2.67$

$b_W = 24.0$ in. $\quad x_{c.p.} = 0.36$ at $\alpha' = 12.65^\circ$ (test results) $\quad M = 2.01$ $\quad \alpha' = 12.65^\circ$

Compute:

Body-alone yawing-moment coefficient C_{n_B}

$C_{Y_B} = -0.0238$ (based on S_W) (sample problem, paragraph C, Section 5.2.1.2)

$$C_{n_B} = \left[\frac{x_m}{\ell_B} - x_{c.p.}\right] \frac{\ell_B}{b_W} C_{Y_B} \qquad \text{(equation 5.2.3.2-b)}$$

$$= (0.57 - 0.36)\ \frac{36.5}{24.0}\ (-0.0238)$$

$$= -0.0076 \text{ (based on } S_W b_W)$$

Wing interference yawing-moment coefficient

$$\frac{x_{l_{(\alpha)}}}{x_{l_{(\alpha=0)}}} = 0.77 \text{ (figure 5.2.3.2-6)}$$

$$\sqrt{M^2 - 1}\left[\frac{d}{c_{r_e}}\right] = \sqrt{(2.01)^2 - 1}\left[\frac{3.33}{8.90}\right] = 0.651$$

$$\frac{x_{l_{(\alpha=0)}}}{c_{r_e}} = 0.90 \text{ (figure 5.2.3.2-8)}$$

$$\bar{\ell}_{W(B)} = \ell_n + c_{r_e}\left[\frac{x_{l_{(\alpha)}}}{x_{l_{(\alpha=0)}}}\right]\left[\frac{x_{l_{(\alpha=0)}}}{c_{r_e}}\right] \qquad \text{(equation 5.2.3.2-d)}$$

$$= 15.62 + 8.90\ (0.77)\ (0.90)$$

$$= 21.78$$

$C_{Y_{W(B)}} = -0.0162$ (based on S_W) (sample problem, paragraph C, Section 5.2.1.2)

Solution:

$$C_{n_{WB}} = C_{n_B} + \left[\frac{x_m - \bar{l}_{W(B)}}{b_W}\right] C_{Y_{W(B)}} \qquad \text{(equation 5.2.3.2-a)}$$

$$= -0.0076 + \frac{20.81 - 21.78}{24.0} (-0.0162)$$

$$= -0.00695 \text{ (based on } S_W b_W)$$

This compares with an experimental value (based on $S_W b_W$) of $C_{n_{WB}} = -0.0070$ from reference 1.

A comparison between calculated and experimental results for this configuration at sideslip angles of 2, 4, and 8 degrees and over an angle-of-attack range to 16 degrees is presented in figure 5.2.3.2 -4.

REFERENCES

1. Spearman, M. L., Driver, C., and Hughes, W. C.: Investigation of Aerodynamic Characteristics in Pitch and Sideslip of a 45° Sweptback-Wing Airplane Model with Various Vertical Locations of Wing and Horizontal Tail – Basic-Data Presentation, M = 2.01. NACA RM L54L06, 1955. (U)

2. Kasttari, G. E.: Estimation of Directional Stability Derivatives at Moderate Angles and Supersonic Speeds. NASA Memo 12-1-58A, 1959. (U)

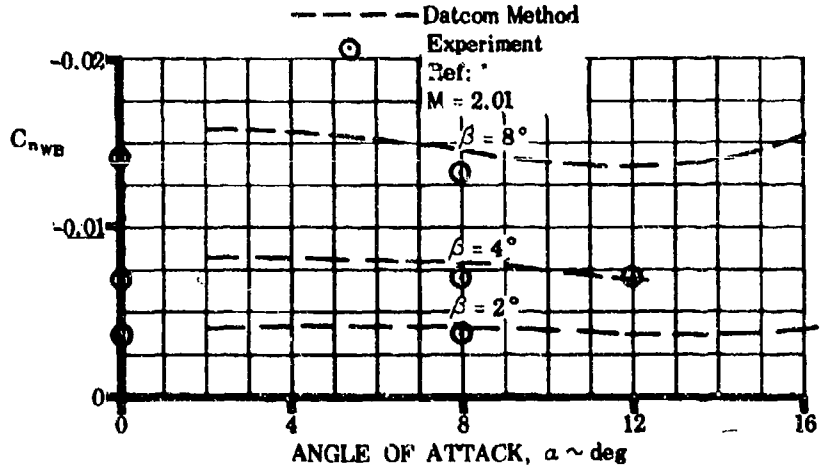

FIGURE 5.2.3.2-4 COMPARISON OF EXPERIMENTAL AND CALCULATED VALUES OF WING-BODY YAWING-MOMENT COEFFICIENT FOR THE SAMPLE PROBLEM CONFIGURATION

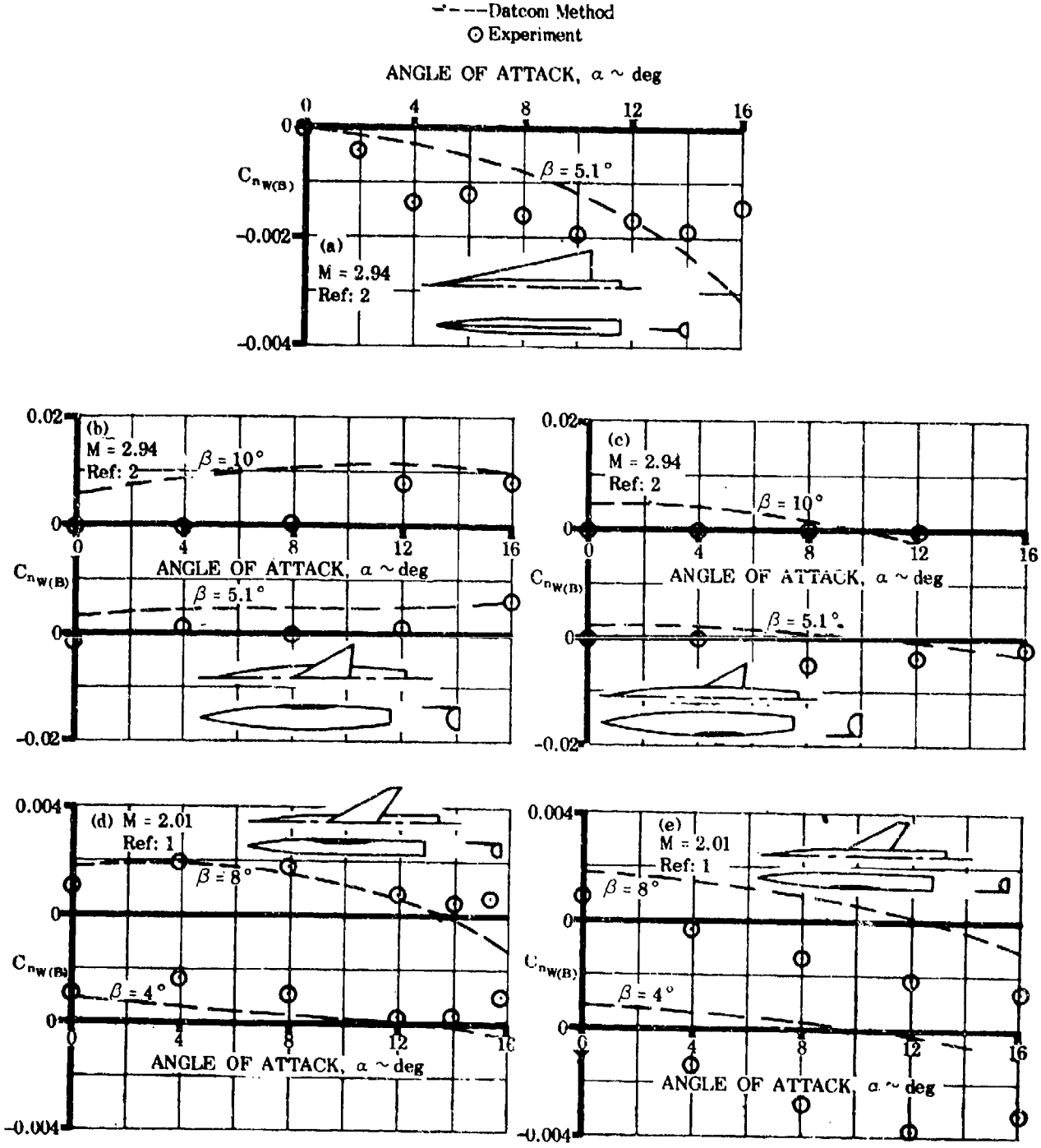

FIGURE 5.2.3.2-5 COMPARISON OF EXPERIMENTAL AND CALCULATED YAWING-MOMENT COEFFICIENT INCREMENTS DUE TO ADDING A WING TO A BODY

(a) LOW WING

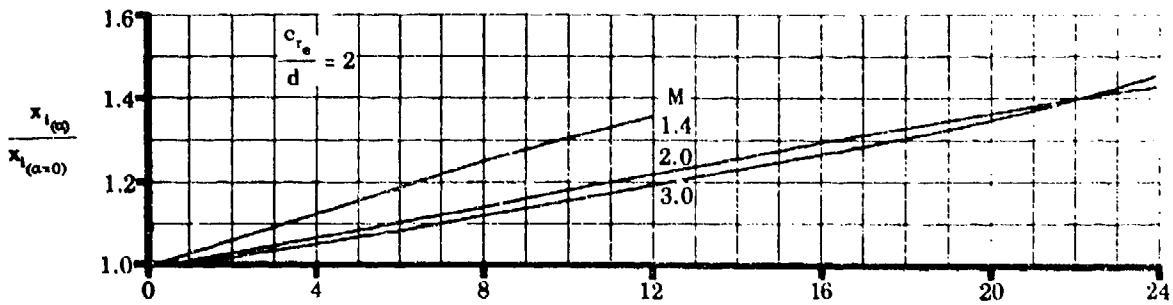

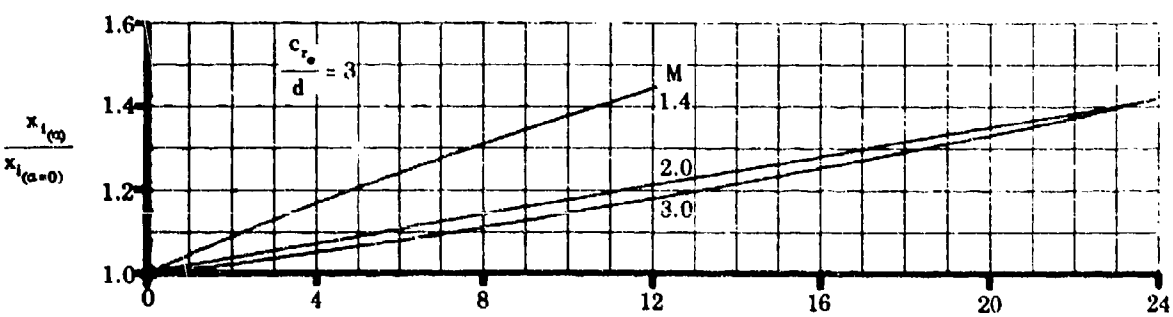

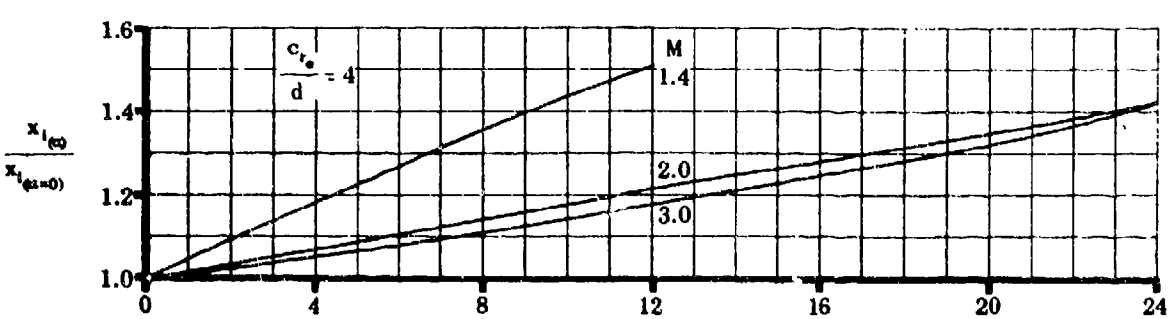

FIGURE 5.2.3.2-6 EFFECT OF ANGLE OF ATTACK ON CENTER-OF-PRESSURE LOCATION OF WING-INDUCED BODY SIDE FORCE

(b) HIGH WING

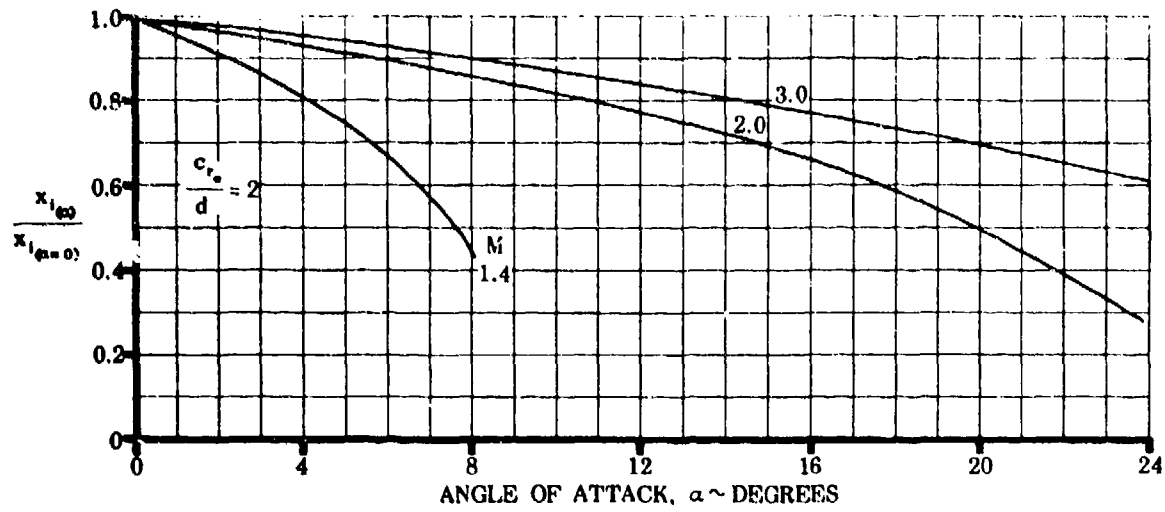

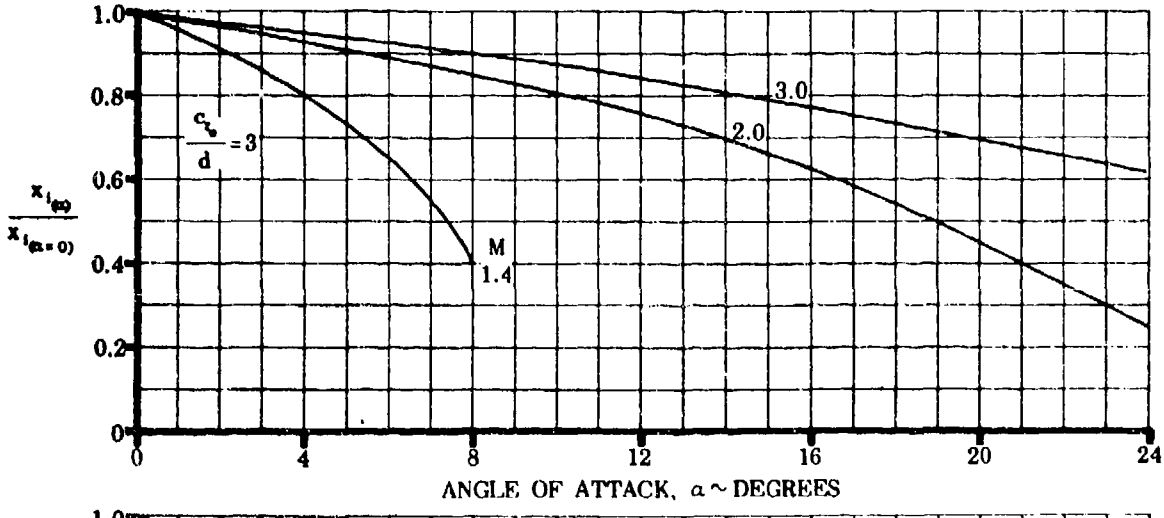

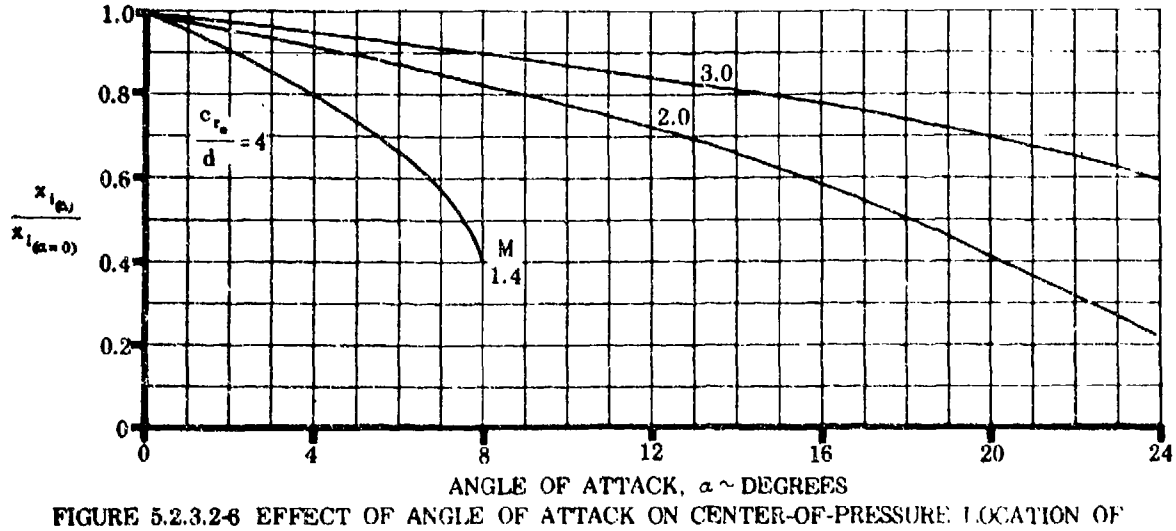

FIGURE 5.2.3.2-6 EFFECT OF ANGLE OF ATTACK ON CENTER-OF-PRESSURE LOCATION OF WING-INDUCED BODY SIDE FORCE (contd)

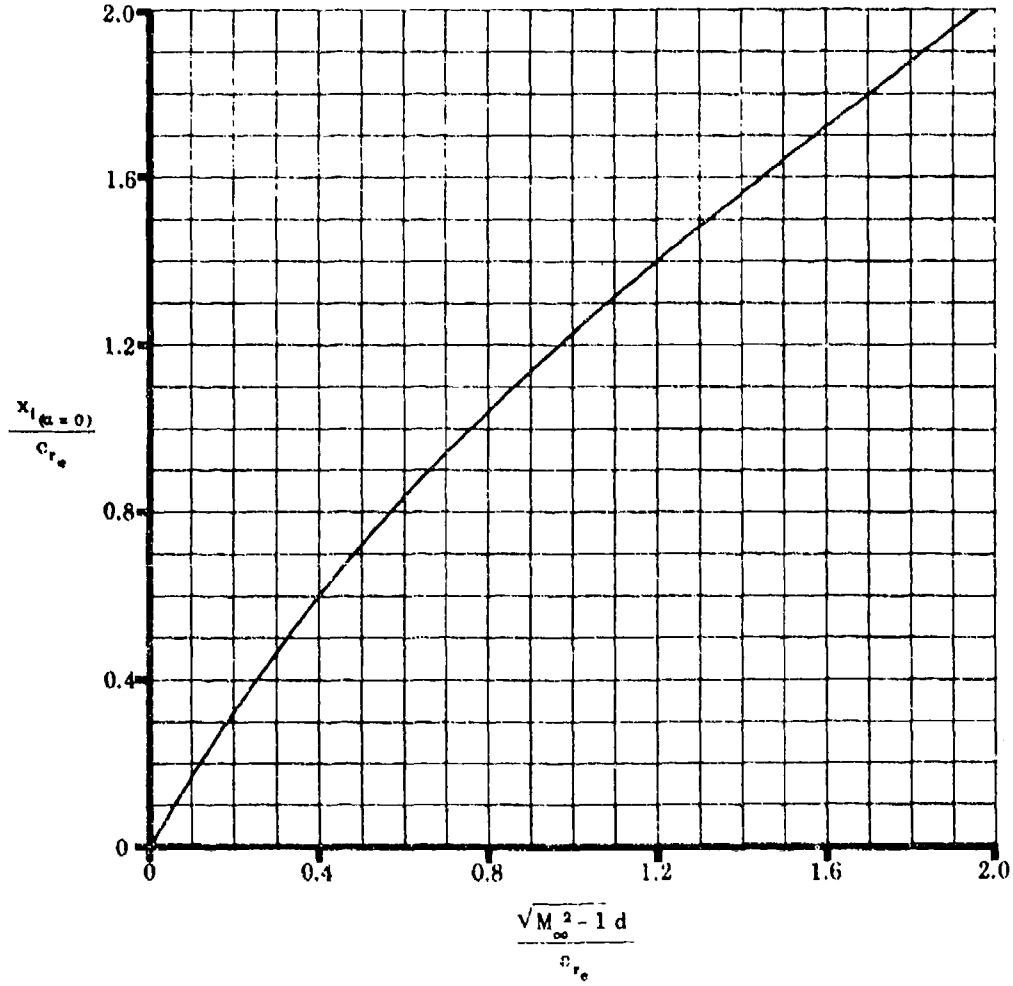

FIGURE 5.2.3.2-8 CENTER-OF-PRESSURE LOCATION OF WING-INDUCED BODY SIDE FORCE AT ZERO ANGLE OF ATTACK

5.3 TAIL-BODY COMBINATIONS IN SIDESLIP

5.3.1 TAIL-BODY SIDESLIP DERIVATIVE C_{Y_β}

5.3.1.1 TAIL-BODY SIDESLIP DERIVATIVE C_{Y_β} IN THE LINEAR ANGLE-OF-ATTACK RANGE

The contributions of panels present in the empennage to the vehicle sideslip derivative C_{Y_β} are presented in this section for speeds ranging from low subsonic to hypersonic. The methods presented include the mutual interference effects of the wing, body, and the horizontal panels.

A. SUBSONIC

At subsonic speeds the vehicle body and horizontal tail affect the flow on the vertical tail in such a way as to increase the effectiveness of the vertical tail. This phenomenon, known as the "end-plate effect," is frequently represented by an effective change in panel aspect ratio required to give the same lift effectiveness as the actual panel in the presence of the other vehicle components. Interferences also exist between the vertical tail, the body, and any forward lifting surface.

In the literature, these mutual interference effects are treated in various ways. In some cases, the wing-body wake and sidewash effects are treated independently of the body and horizontal-tail end-plate effects. The British are notable for this approach. In other cases, all the interference effects are lumped into a single vertical-tail effectiveness parameter. One of the methods presented herein uses this latter approach.

The effect of each of the vehicle components on the subsonic vertical-tail effectiveness is discussed in the following paragraphs.

Effect of Body Cross Flow

A body in sideslip exhibits a flow characteristic similar to a cylinder in cross flow. For potential flow the peak local velocity occurs at the top of the cylinder and is equal to twice the free-stream cross-flow velocity. Actually, separation exists on the leeward side, reducing the peak velocity from the potential-flow value. In either case, the velocity decays to the free-stream cross-flow value with distance from the body surface. Thus, it is to be expected that tail-body combinations with large bodies and small tails have a greater effectiveness per unit area than combinations with large tails and small bodies. This trend is exhibited by test data. The vertical panel itself causes a load carry-over from the panel onto the body. This carry-over increases the effectiveness of the vertical panel and is included in the methods presented.

Effect of Horizontal Surface

The presence of a horizontal panel in the vicinity of a vertical panel causes a change in the pressure loading of the latter if the horizontal panel is at a height where the vertical panel has an appreciable gradient, i.e., at a relatively high or low position. Test data substantiate the greater effectiveness of horizontal panels in these positions and the relative ineffectiveness of a horizontal panel at the midspan position on the vertical panel.

Effect of Wing-Body Wake and Sidewash

The effect of wing-body wake and sidewash on the effectiveness of the vertical panel is discussed in detail in Section 5.4.1. This effect is implicitly included in only one of the methods presented herein (Method 3).

Several approaches to this problem have been taken in the literature. Reference 1 presents a method accounting for the effects of body size relative to vertical-panel size, and dealing with horizontal-tail height ranging from positions on the body to the top of the vertical. This method appears to be the most accurate one available. It is presented in this Section as Method 1.

Reference 2 contains a method which is also widely used. Included in this method is a chart for twin tails that is presented in this section. The charts give the average lift-curve slope of the two panels. (The interferences and hence the individual lift-curve slope of the panels differ somewhat.)

A different approach is given in reference 3. This method is based on the assumption that the ratio of the increment in side force due to the addition of a vertical panel to the side force developed by the panel alone is the same as the ratio of the increment in apparent mass of the cross section at the base of the empennage with panel added to the apparent mass of the panel alone. The development of the apparent-mass concept is

given in many places in the literature, e.g., reference 4. The panel alone is taken to be the actual panel reflected about a reflection plane. This assumption implies two-dimensional flow and a slender configuration with all surfaces of the empennage lying in the base plane of the configuration. It is shown in reference 3, however, that good accuracy is obtained for nonslender configurations where the longitudinal locations of the separate surfaces are not in the base plane. This method is limited to configurations in which the horizontal surfaces are mounted on the body or configurations with no horizontal surface. The charts for this method are also used for the supersonic method.

There are some additional effects that are not accounted for by these methods. For instance, dorsal fins may cause a considerable error in the values obtained, although the effect of dorsal fins is more pronounced at the higher angles of sideslip. The use of lift-curve slopes for double-delta wings may decrease this error. A method for calculating the lift-curve slope of double-delta wings is presented in Section 4.1.3.2 under the nonstraight-tapered-wing methods. Dihedral in the horizontal surfaces is known to change the pressure loading on the vertical panel and hence its effectiveness. For rapidly converging bodies, flow separation frequently exists at the juncture of the vertical panel with the body. This effect generally decreases the effectiveness of the vertical tail and is not accounted for by the methods included herein. Similar effects can result when the maximum thickness of two orthogonal panels are made to coincide.

DATCOM METHODS

Method 1

Vertical Panels on Plane of Symmetry

The contribution of the vertical panel to the sideslip derivative C_{Y_β} is determined by the following steps (reference 1).

Step 1. The effective aspect ratio of the vertical panel is determined by means of the equation

$$A_{eff} = \frac{(A)_{V(B)}}{(A)_V} (A)_V \left\{ 1 + K_H \left[\frac{(A)_{V(HB)}}{(A)_{V(B)}} - 1 \right] \right\} \qquad 5.3.1.1\text{-a}$$

where

$\frac{(A)_{V(B)}}{(A)_V}$ is the ratio of the aspect ratio of the vertical panel in the presence of the body to that of the isolated panel. This ratio is given in figure 5.3.1.1-22a as a function of span-to-body-diameter ratio and tail taper ratio.

$(A)_V$ is the geometric aspect ratio of the isolated panel with the span and area of the panel measured to the body center line.

$\frac{(A)_{V(HB)}}{(A)_{V(B)}} = \frac{(A)_{V(HB)}}{\frac{(A)_{V(B)}}{(A)_V} (A)_V}$ is the ratio of the vertical-panel aspect ratio in the presence of the horizontal tail and body to that of the panel in the presence of the body alone. This ratio is given in figure 5.3.1.1-22b as a function of the horizontal and vertical position of the horizontal tail on the vertical panel.

K_H is a factor accounting for the relative size of the horizontal and vertical tails, obtained from figure 5.3.1.1-22c.

Step 2. The lift-curve slope of the vertical panel is determined from paragraph A of Section 4.1.3.2, with the effective aspect ratio of the vertical panel determined from equation 5.3.1.1-a.

Step 3. The wake and sidewash effects as represented by the parameter $\left(1 + \frac{\partial\sigma}{\partial\beta}\right) \frac{q_V}{q_\infty}$ are presented in Section 5.4.1 for the appropriate Mach number and vehicle geometry.

Step 4. The increment in C_{Y_β} due to the vertical panel is given by the equation (based on wing area)

$$(\Delta C_{Y_\beta})_{V(WBH)} = -k(C_{L_\alpha})_V \left(1 + \frac{\partial \sigma}{\partial \beta}\right) \frac{q_V}{q_\infty} \frac{S_v}{S_w} \qquad 5.3.1.1\text{-b}$$

where $(C_{L_\alpha})_V$ is obtained from Step 2

$\left(1 + \frac{\partial \sigma}{\partial \beta}\right)\frac{q_V}{q_\infty}$ is obtained from Step 3

k is an empirical factor obtained from figure 5.3.1.1-22d

$\frac{S_v}{S_w}$ is the ratio of the vertical panel area (measured to the body centerline) to the total wing area

This method is substantiated by test data in table 5.3.1.1-B.

Method 2

Twin Vertical Panels

The contribution of twin vertical panels mounted on the tips of a horizontal tail or wing is given by the following steps. This method (from reference 2) includes the effects of the wing-body wake and sidewash.

Step 1. Determine the ratio of the effective to actual aspect ratio, $\frac{A_{eff}}{A}$, from figure 5.3.1.1-24a as a function of the geometric variable shown.

Step 2. Determine the lift-curve slope of the equivalent rectangular vertical panel $(C_{Y_\beta})_{V_{eff}}$ from figure 5.3.1.1-24b; use the effective aspect ratio found in Step 1 and the total trailing-edge angle of the airfoil section.

Step 3. The increment in vehicle sideslip derivative C_{Y_β} due to the twin panels (based on total wing area) is given by the equation

$$(\Delta C_{Y_\beta})_{V(WBH)} = -\frac{(C_{Y_\beta})_{V(WBH)}}{(C_{Y_\beta})_{V_{eff}}} (C_{Y_\beta})_{V_{eff}} \frac{2S_v}{S_w} \qquad 5.3.1.1\text{-c}$$

where $\frac{(C_{Y_\beta})_{V(WBH)}}{(C_{Y_\beta})_{V_{eff}}}$ is obtained from figure 5.3.1.1-24c for the appropriate geometry shown

$(C_{Y_\beta})_{V_{eff}}$ is obtained from Step 2 above

S_v is the area of a single vertical panel

There are not sufficient data existing to substantiate the accuracy of this method, although reference 2 indicates that the method is accurate to within ±10 percent.

Method 3

A third general method is based on the work in reference 3. This method is limited to configurations in which the horizontal tail is mounted on the body or configurations with no horizontal tail. It is discussed in the introduction to this Section. The charts of this method are also used in the supersonic method of paragraph C.

The method as presented for the vertical panel estimates the increment in C_{Y_β} due to the addition of one panel in the empennage and includes the effects of all existing panels on the added panel. An extension of the method to determine the total empennage side force due to sideslip at subsonic speeds which results from the addition of all panels present in the empennage is presented in paragraph A of Section 5.6.1.1.

Contribution of Vertical Panel

The side force-curve slope (based on total wing area) of a vertical panel added to an empennage is given by the equation

$$(\Delta C_{Y_\beta})_p = -K(C_{L_\alpha})_p \frac{S_{p_e}}{S_w} \qquad 5.3.1.1\text{-d}$$

where the subscript $_p$ refers to the added vertical panel (either an upper vertical stabilizing surface V or a lower vertical stabilizing surface U)

$(C_{L_\alpha})_p$ is the lift-curve slope of the isolated vertical panel mounted on a reflection plane from paragraph A of Section 4.1.3.2. For this calculation the aspect ratio must be taken as twice the aspect ratio defined by the average exposed span and exposed area.

S_{p_e} is the area of the exposed vertical panel

K is the apparent mass factor from figures 5.3.1.1-25a through 5.3.1.1-25nn. When using these figures the vertical panel for which the contribution to C_{Y_β} is desired is termed the "added panel" and other panels existing in the empennage are termed the "existing panels" as shown schematically in sketch (a).

The body radii dimensions r_1 and r_2 are defined in the region of the tail panels. If these dimensions change in this region the average values should be used. In general interpolation procedures must be used since the geometry rarely coincides with that of a specific figure. Since the variation of parameters between figures is generally non-linear, graphical interpolation using at least three points is recommended. An index of the K charts and the range of variables covered by each is presented as table 5.3.1.1-A.

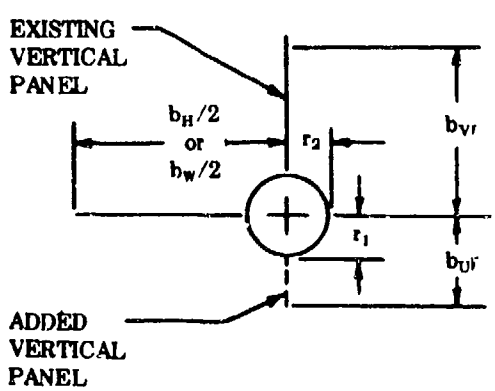

SKETCH (a)

Although the sketches on the figures show only the upper vertical panel as the added panel, the added panel can be either the upper or lower vertical panel. Special mention is made of figures 5.3.1.1-25g through 5.3.1.1-25p. Figures 5.3.1.1-25g through 5.3.1.1-25k are used to estimate the K value due to adding an upper vertical stabilizing surface to a body with the horizontal surface in the high tangent position. These figures also apply in estimating the K value due to adding a lower vertical stabilizing surface to a body with a horizontal surface located in the low tangent position. Figures 5.3.1.1-25l through 5.3.1.1-25p are used in the same manner as figures 5.3.1.1-25g through 5.3.1.1-25k except that the horizontal surface is tangent to the body on the side opposite to which the panel is added.

Apparent mass factor solutions for bodies other than circular or elliptic cross sections are not available. In treating bodies of other cross-sectional shapes the assumption is made that the ratio of height to width, r_1/r_2, is the important parameter and that details of the body contour are of secondary importance. This assumption has been used in reference 3, where the body was other than circular or elliptic, and the resulting correlation with experiment was as good as for the cases to which the figures apply directly.

The case of a vertical tail added to an empennage consisting of a horizontal panel located at other than the mid-position on the elliptical body is not covered by the K charts (see table 5.3.1.1-A). To handle such a case, either the body must be considered circular and an interpolation made for horizontal panel height, or the horizontal panel must be assumed located at the mid-position and an interpolation performed between r_1/r_2 ratios. A comparison of the effect of both horizontal panel location and body shape on the K factor should be made in determining the proper approach to the K factor solution.

Contribution of Horizontal Tail

In determining the total empennage side force due to sideslip which results from the addition of all panels present in the empennage the horizontal tail must be added first (see method 3, paragraph A, Section 5.6.1.1). Although the horizontal tail contribution to C_{Y_β} is usually small and for most calculations can be neglected; it can provide a significant contribution to the sideslip derivative C_{l_β}.

The contribution to the sideslip derivative C_{Y_β} (based on total wing area) of a horizontal tail added to a body is given by

$$(\Delta C_{Y_\beta})_{H(B)} = K_{H(B)} (C_{Y_\beta})_B \frac{S_{B_{Ref}}}{S_W} \qquad 5.3.1.1\text{-e}$$

where

$(C_{Y_\beta})_B$ is the side force due to sideslip (based on body reference area, $S_{B_{Ref}}$) obtained from Section 4.2.1.1 by conversion of the body lift-curve slope i.e.; $(C_{Y_\beta})_B = -(C_{L_\alpha})_B$

$K_{H(B)}$ is the apparent mass factor due to the addition of a horizontal tail in the presence of a body for the appropriate tail span and vertical position from figure 5.3.1.1-25oo.

For a horizontal tail mounted at an intermediate position on the body (between mid- and high- or low-tangent position), the following second order interpolation using the equation of an ellipse should be applied

$$K_{H(B)} = K_{\text{High or Low}} \left\{ 1 - \left[1 - \left(\frac{Z_H}{r_1} \right)^2 \right]^{1/2} \right\}$$

A substantiation table comparing experimental data with results calculated by this method is shown in table 5.3.1.1-B. A comparison is made in this table of the relative accuracy of Method 1 and Method 3.

Sample Problems

1. Method 1

Given: The configuration of reference 6 consisting of wing, body, horizontal tail, and vertical tail. Find the effect of adding the vertical tail to the wing-body-horizontal tail combination.

Wing Characteristics

$A_W = 3.0$ $S_W = 576.0$ sq in. $b_W = 41.56$ in. $z_W = 0$ $\Lambda_{c/4_W} = 45^\circ$

Horizontal Tail Characteristics

$A_H = 4.0$ $S_H = 121.6$ sq in. $b_H = 22.42$ in. $z_H = 0$

Vertical Tail Characteristics

$A_V = 1.50$ $S_V = 153.7$ sq in. $b_V = 15.23$ in. $c_{r_V} = 17.40$ in. $\lambda_V = 0.160$

$\Lambda_{c/2_V} = 41.9^\circ$ Airfoil: NACA 0003.5-64

Additional Characteristics

$M = 0.25$ $r_1 = 2.8$ in. $d = 6.0$ in. $x/c_V = 0.55$

Compute:

$(c\ell_\alpha)_V = 6.18$ per rad (Section 4.1.1.2)

$K = \dfrac{c\ell_\alpha}{2\pi} = 0.984$

$b_V/2r_1 = 2.72$

$\dfrac{(A)_{V(B)}}{(A)_V} = 1.47$ (figure 5.3.1.1-22a)

$(A)_{V(B)} = \dfrac{(A)_{V(B)}}{(A)_V}(A)_V = 2.20$

$S_H/S_V = 0.820$

$K_H = 0.83$ (figure 5.3.1.1-22c)

$z_H/b_V = 0$

$\dfrac{(A)_{V(HB)}}{(A)_{V(B)}} = 1.10$ (figure 5.3.1.1-22b)

$S_V/S_W = 0.267$

$z_W/d = 0$

$A_{eff} = (A)_{V(B)}\left\{1 + K_H\left[\dfrac{(A)_{V(HB)}}{(A)_{V(B)}} - 1\right]\right\} = 2.38$ (equation 5.3.1.1-a)

$\dfrac{A_{eff}}{K}\left[\beta^2 + \tan^2 \Lambda_{c/2_V}\right]^{1/2} = 3.193$

$\dfrac{C_{L_\alpha}}{A_{eff}} = 1.08$ (figure 4.1.3.2-49)

$(C_{L_\alpha})_{V(BH)} = \left(\dfrac{C_{L_\alpha}}{A_{eff}}\right)A_{eff} = 2.57$ per rad

$\left(1 + \dfrac{\partial\sigma}{\partial\beta}\right)\dfrac{q_V}{q_\infty} = 0.724 + 3.06\ \dfrac{S_V/S_W}{1 + \cos \Lambda_{c/4_W}} + 0.4\ \dfrac{z_W}{d} + 0.009\ A_W = 1.230$ (equation 5.4.1-a)

$k = 0.87$ (figure 5.3.1.1-22d)

Solution:

$$(\Delta C_{Y_\beta})_{V(WBH)} = -k(C_{L_\alpha})_{V(BH)} \left(1 + \frac{\partial \sigma}{\partial \beta}\right) \frac{q_V}{q_\infty} \frac{S_V}{S_W} \quad \text{(equation 5.3.1.1-b)}$$

$$= -0.734 \text{ per rad}$$

This compares with an experimental value of -0.76 per radian obtained from reference 6.

2. Method 2

Given: A configuration consisting of wing, body, and twin vertical panels mounted on the tips of a horizontal tail. Find the effect of adding the twin vertical panels to the configuration.

Twin Vertical Tail Characteristics

$A_V = 1.39$ $b_V = 5.0$ ft $b'_V = 4.0$ ft $S_V = 18.0$ ft $\phi_{TE_V} = 10°$

Additional Characteristics

$S_W = 144.0$ sq ft $\ell_B = 55.0$ ft $b_H = 12.0$ ft $r_f = 1.50$ ft

Compute:

$b'_V/b_V = 0.80$

$\frac{A_{eff}}{A} = 1.20$ (figure 5.3.1.1-24a)

$A_{eff} = 1.67$

$(C_{Y_\beta})_{V_{eff}} = 2.40$ (figure 5.3.1.1-24b)

$2r_f/b_V = 0.6$

$b_H/\ell_B = 0.22$

$\frac{(C_{Y_\beta})_{V(WBH)}}{(C_{Y_\beta})_{V_{eff}}} = 0.61$ (figure 5.3.1.1-24c)

Solution:

$$(\Delta C_{Y_\beta})_{V(WBH)} = -\frac{(C_{Y_\beta})_{V(WBH)}}{(C_{Y_\beta})_{V_{eff}}} \frac{2S_V}{S_W} \quad \text{(equation 5.3.1.1-c)}$$

$$= -0.366 \text{ per rad}$$

3. Method 3

Given: A configuration of reference 10 consisting of wing, body, horizontal tail, and vertical tail. Find the effect of adding the vertical tail to the wing-body-horizontal tail configuration.

Vertical Tail Characteristics

$A_V = 1.40$ $A_{V_e} = 1.37$ $S_V = 48.6$ sq in. $S_{V_e} = 36.2$ sq in. $\Lambda_{c/2_V} = 39.4°$

$\lambda_V = 0.645$ $\lambda_{V_e} = 0.60$ $b_V = 8.25$ in. NACA 65008 airfoil

Additional Characteristics

$M = 0.13$ $r_1 = 1.20$ $r_2 = 2.65$ $\frac{b_H}{2} = 6.70$ in. $S_W = 324$ sq in.

Compute:

$(c\ell_\alpha)_V = 6.67$ per rad (Section 4.1.1.2)

$K = \frac{(c\ell_\alpha)_V}{2\pi} = 1.06$ (ratio of section lift-curve slope to 2π)

$2A_{V_e} = 2.74$

$\frac{2A_{V_e}}{K}[\beta^2 + \tan^2 \Lambda_{c/2_V}]^{1/2} = 3.26$

$\frac{(C_{L_\alpha})_V}{2A_{V_e}} = 1.08$ per rad (figure 4.1.3.2-49)

$(C_{L_\alpha})_V = (1.08)(2A_{V_e}) = 2.96$ per rad (based on S_{V_e})

Determine the apparent-mass factor due to adding the upper vertical stabilizer to the wing-body-horizontal tail configuration. In this case the empennage consists of the body, horizontal tail, and upper vertical stabilizer. The apparent-mass factor to be found is that due to adding the upper vertical stabilizer to the combination of body and horizontal tail, $K_{V(HB)}$

$\left(\frac{r_1}{r_2}\right) = 0.451$, $\left(r_2/\frac{b}{2}\right)_H = 0.396$, $\left(\frac{r_1}{b}\right)_{\substack{U \\ \text{existing} \\ \text{panel}}} = 1.000$, $\left(\frac{r_1}{b}\right)_{\substack{V \\ \text{added} \\ \text{panel}}} = 0.1455$

Using the above parameters and table 5.3.1.1-A it is seen that $K_{V(HB)}$ is obtained by interpolation from figures 5.3.1.1-25s, -25t, -25u for $r_1/r_2 = 0.333$, 5.3.1.1-25y, -25z, -25aa for $r_1/r_2 = 0.667$; 5.3.1.1-25c, -25d, -25e for $r_1/r_2 = 1.000$. An interpolation between those values of $K_{V(BH)}$ gives, for $r_1/r_2 = 0.451$

$K_{V(BH)} = 1.135$.

Solution

5.3.1.1-7

$(\Delta C_{Y_\beta})_p = -K(C_{L_\alpha})_p \frac{S_{p_e}}{S_W}$ (equation 5.3.1.1-d)

$(\Delta C_{Y_\beta})_{V(WBH)} = -K_{V(HB)} (C_{L_\alpha})_V \frac{S_{V_e}}{S_W}$

$= (-1.135)(2.96)\left(\frac{36.2}{324}\right)$

$= -0.375$ per rad (based on S_W)

This corresponds to an experimental value of -0.367 per radian obtained from reference 10.

B. TRANSONIC

The side force on a vertical panel depends on three general factors. These are the lift characteristics of the panel itself, the effect of the wing-body wake and sidewash, and the interference effects of the body and horizontal surface.

The lift characteristics of the isolated panel at transonic speeds can be estimated by methods such as that described in paragraph B of Section 4.1.3.2. The wake and sidewash, on the other hand, are affected by the detailed geometry of the flow field, which can be radically changed by relatively minor variations in the vehicle geometry. This is true because of the sensitivity of transonic flow to local contour and area distribution changes and because of shock-induced boundary-layer separation. In addition, the vertical panel is usually contained in a small segment of the flow field so that local variations in the field can have pronounced effects upon the resultant forces on the tail. The interference effects of the body and horizontal tail at transonic speeds are likewise sensitive to local configuration geometry and cannot be eliminated.

Because of the above reasons, the vertical tail contribution to the sideslip derivative C_{Y_β} is difficult to estimate reliably, and its value is usually obtained by wind-tunnel testing or estimated from comparison with similar configurations.

DATCOM METHOD

No method is available in the literature for estimating this derivative and none is presented in the Datcom. However, some data in this speed regime can be found in references 11, 12, and 13.

C. SUPERSONIC

The problem of estimating the effectiveness of panels in the empennage in generating side forces due to sideslip at supersonic speeds is complicated by the presence of shock waves. These shock waves cause marked regions of differentiation on the surfaces of an added panel (see sketch b). Each region is characterized by different Mach numbers, pressures, and velocity directions. In addition, vortices from the body and the wake from the forward lifting surfaces can have important effects on the forces generated. The method presented herein, taken from reference 3, does not account for the effects of vortices and wakes. However, these effects are small at low angles of attack.

DATCOM METHOD

The method of this Section is for estimating the increment in C_{Y_β} due to the addition of a panel (either a vertical stabilizer or a horizontal tail) in the empennage. The vertical panel contribution includes the effects of all existing panels on the added panel. An extension of the method to determine the total empennage side force due to sideslip at supersonic speeds which results from the addition of all panels present in the empennage is presented in paragraph C of Section 5.6.1.1.

The method is based on the same apparent mass concept as used in Method 3 of paragraph A. A weighted apparent mass factor is obtained for each region defined by a system of Mach lines characteristic of the configuration. The total effective apparent mass K' is then determined and used to obtain the desired force contribution of the added panel.

This method is limited to configurations in which the horizontal tail is mounted on the body or configurations with no horizontal tail.

Contribution of Vertical Panel

When adding a vertical panel to a configuration, the following general procedure is used. However, a more thorough understanding will be gained by studying the sample problems.

Step 1. Construct the Mach lines $\left(\mu = \sin^{-1}\frac{1}{M}\right)$ emenating from the exposed root chord leading and trailing edges of all panels other than that to be added, as shown in sketch (b). (This is an approximation to the horizontal panel flow field boundaries strictly applicable to a flat plate airfoil at zero angle of attack and does not account for the effects of vortices and wakes.)

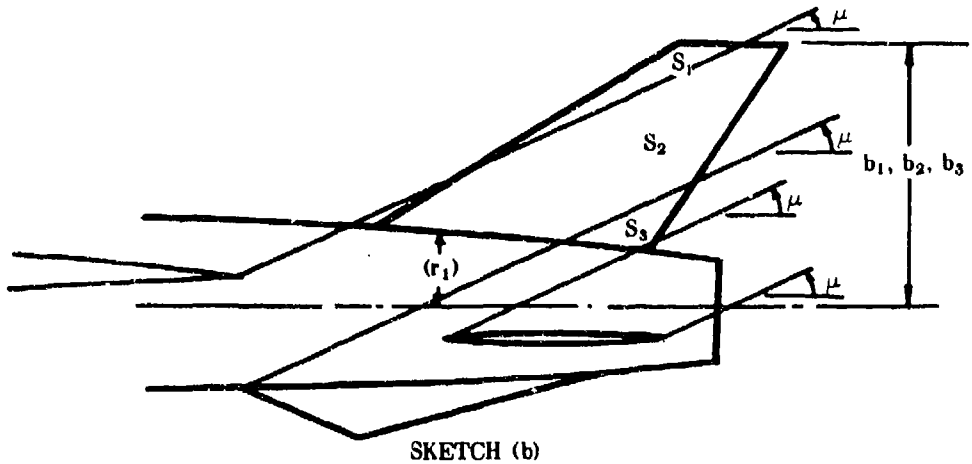

SKETCH (b)

Step 2. Determine the areas or regions on the added panel affected by each vehicle component, S_1, S_2, S_3, etc.

Step 3. Determine the body-radius-to-semi-span ratios for each region for both the horizontal and vertical surfaces. The vertical span of a given region is taken as the total span of the added panel measured to the body center line, as shown in sketch (b). The semi-span of horizontal surfaces (wings and horizontal tails) is the maximum semi-span of these surfaces. The radius of the body for a given region is taken to be the average radius for that region.

Step 4. The apparent mass factors K for each region are determined from figures 5.3.1.1-25a through 5.3.1.1-25nn using the geometry of each region as determined in Step 3. In determining the K factors for each region any point lying forward of the Mach line from the leading-edge body juncture of a panel does not feel the presence of the panel, and any point lying behind the shock wave drawn from the trailing-edge body juncture of a panel does not feel the presence of the panel. For example, referring to sketch (b), the upper vertical panel is divided into three regions of influence. Region S_1 senses the presence of the body and the wing; region S_2 only the body; and region S_3 the body and the lower vertical stabilizer. Interpolation for the appropriate geometry must frequently be made when using these charts. It is recommended that at least three points be used in these interpolations because of the nonlinearities of the characteristics involved. (See Method 3 of paragraph A for a general discussion on the use of the K charts.)

Step 5. Each apparent mass factor is reduced by the ratio of the area of its region on the added panel (Step2) to the total exposed panel area.

Step 6. The total effective apparent-mass factor for the added panel K′ is then the sum of those calculated for each region (Step 5). For example in the case illustrated in sketch (b), K′ of the upper vertical panel in the presence of wing, body, horizontal tail, and ventral is given as

$$K' = K_{V(WB)} \frac{S_1}{S_{V_e}} + K_{V(B)} \frac{S_2}{S_{V_e}} + K_{V(BU)} \frac{S_3}{S_{V_e}}$$

Step 7. The side-force curve slope (based on total wing area) of a vertical panel added to an empennage is given by

$$(\Delta C_{Y_\beta})_p = -K'(C_{N_\alpha})_p \frac{S_{p_e}}{S_w} \qquad 5.3.1.1\text{-f}$$

where the subscript $_p$ and S_{p_e} are as defined in Method 3 of paragraph A, and $(C_{N_\alpha})_p$ is the normal-force-curve slope of the isolated vertical panel mounted on a reflection plane, from paragraph C of Section 4.1.3.2, based on twice the aspect ratio defined by the average exposed span and exposed area.

Contribution of Horizontal Tail

In determining the total empennage side force due to sideslip which results from the addition of all panels present in the empennage the horizontal tail must be added first (see paragraph C, Section 5.6.1.1). Although the horizontal tail contribution to C_{Y_β} is usually small and for most calculations can be neglected; it can provide a significant contribution to the sideslip derivative C_{n_β}.

The contribution to the sideslip derivative C_{Y_β} (based on total wing area) of a horizontal tail added to a body is given by

$$(\Delta C_{Y_\beta})_{H(B)} = K_{H(B)} (C_{Y_\beta})_B \frac{S_{act}}{S_{ext}} \frac{S_{B_{Ref}}}{S_W} \qquad 5.3.1.1\text{-g}$$

where $K_{H(B)}$, $(C_{Y_\beta})_B$, and $S_{B_{Ref}}$ are as defined in Method 3 of paragraph A

$\frac{S_{act}}{S_{ext}}$ is the ratio of the actual projected side area of the fuselage to that of the extended fuselage as determined by Mach lines $\left(\mu = \sin^{-1} \frac{1}{M}\right)$ originating from the leading and trailing edge of the exposed root chord (see sketch (c))

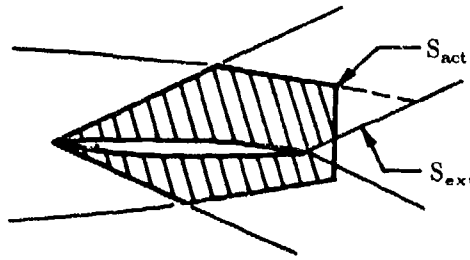

SKETCH (c)

This method is substantiated in table 5.3.1.1-C (from reference 3).

Sample Problems

1. Given: The configuration of reference 16 consisting of wing, body, horizontal tail, and upper vertical stabilize
Find the effect of adding the vertical tail to the wing-body-horizontal tail combination.

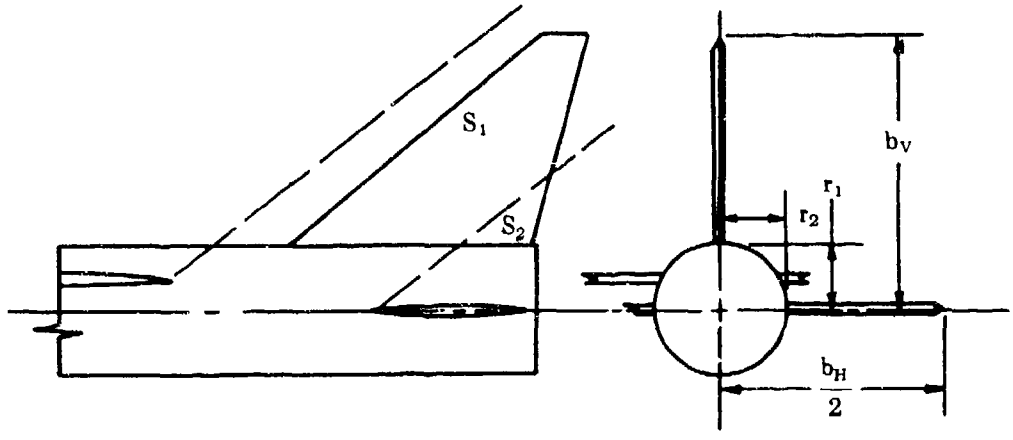

Vertical Tail Characteristics

$A_V = 1.59$	$A_{V_e} = 1.48$	$S_V = 35.3$ sq in.	$S_{V_e} = 21.9$ sq in.	$\Lambda_{LE_V} = 50.4^\circ$
$\lambda_V = 0.153$	$\lambda_{V_e} = 0.192$	$b_V = 7.48$ in.	NACA 65A005 airfoil	

Additional Characteristics

$M = 1.61$ $\mu = \sin^{-1}\frac{1}{M} = 38.5°$ $r_1 = 1.78$ in. $r_2 = 1.78$ in.

$\frac{b_H}{2} = 6.06$ in. $S_W = 160.4$ sq in. $S_1 = 19.9$ sq in. $S_2 = 2.0$ sq in.

$z_H = 0$ (horizontal tail on body centerline)

Compute:

$2A_{V_e} \tan \Lambda_{LE_V} = 3.575$

$\beta = \sqrt{M^2 - 1} = 1.265$

$\frac{\tan \Lambda_{LE_V}}{\beta} = 0.955$

$\beta(C_{N_\alpha})_V = 3.90$ per rad (figures 4.1.3.2-56a, -56b, -56c interpolated for $\lambda_{V_e} = 0.192$)

$(C_{N_\alpha})_V = 3.08$ per rad (based on S_{V_e})

Determine the effective apparent mass ratio due to adding the vertical stabilizer to the wing-body-horizontal stabilizer combination. The empennage in this case consists of body, horizontal stabilizer and vertical stabilizer. The effective apparent mass ratio to be found is that due to adding the vertical stabilizer to the body and horizontal tail, $K'_{V(HB)}$.

Referring to the configuration sketch, the region S_1 senses only the body, while S_2 senses both the body and the horizontal stabilizer. Therefore, the effective apparent mass ratio is given by

$$K'_{V(HB)} = K_{V(B)} \frac{S_1}{S_{V_e}} + K_{V(HB)} \frac{S_2}{S_{V_e}}$$

Determine $K_{V(B)}$

$$\left(\frac{r_1}{r_2}\right) = 1.000; \left(\frac{r_1}{b}\right)_{\substack{V \\ \text{added} \\ \text{panel}}} = 0.238; \left(\frac{r_1}{b}\right)_{\substack{U \\ \text{existing} \\ \text{panel}}} = 1.000$$

using the above parameters and table 5.3.1.1-A it is seen that $K_{V(B)}$ is obtained from figure 5.3.1.1-25a

$K_{V(B)} = 1.25$

Determine $K_{V(HB)}$

$$\left(\frac{r_1}{r_2}\right) = 1.000; \left(\frac{r_2}{b_H/2}\right) = 0.293; \left(\frac{r_1}{b}\right)_{\substack{V \\ \text{added} \\ \text{panel}}} = 0.238; \left(\frac{r_1}{b}\right)_{\substack{U \\ \text{existing} \\ \text{panel}}} = 1.000$$

Using the above parameters and table 5.3.1.1-A it is seen that $K_{V(HB)}$ is obtained from figures 5.3.1.1-25b, -25c, and -25d interpolated for $\left(r_2/\frac{b_H}{2}\right) = 0.293$

$K_{V(HB)} = 1.375$

$$K'_{V(HB)} = (1.25)\left(\frac{19.9}{21.9}\right) + (1.375)\left(\frac{2.0}{21.9}\right) = 1.26$$

Solution:

$$(\Delta C_{Y_\beta}) = -K' (C_{N_\alpha})_p \frac{S_{o_o}}{S_W} \quad \text{(equation 5.3.1.1-f)}$$

$$(\Delta C_{Y_\beta})_{V(WBH)} = -K'_{V(HB)} (C_{N_\alpha})_V \frac{S_{V_e}}{S_W}$$

$$= (-1.26)\ (3.08)\left(\frac{21.90}{160.4}\right)$$

$$= -0.529 \text{ per rad (based on } S_W)$$

This compares with an experimental value of -0.486 per radian from reference 16.

2. Given: The configuration of reference 18 consisting of wing, body, upper vertical stabilizer and lower vertical stabilizer. Find the effect of adding the upper vertical stabilizing surface to the wing-body-lower vertical stabilizer combination.

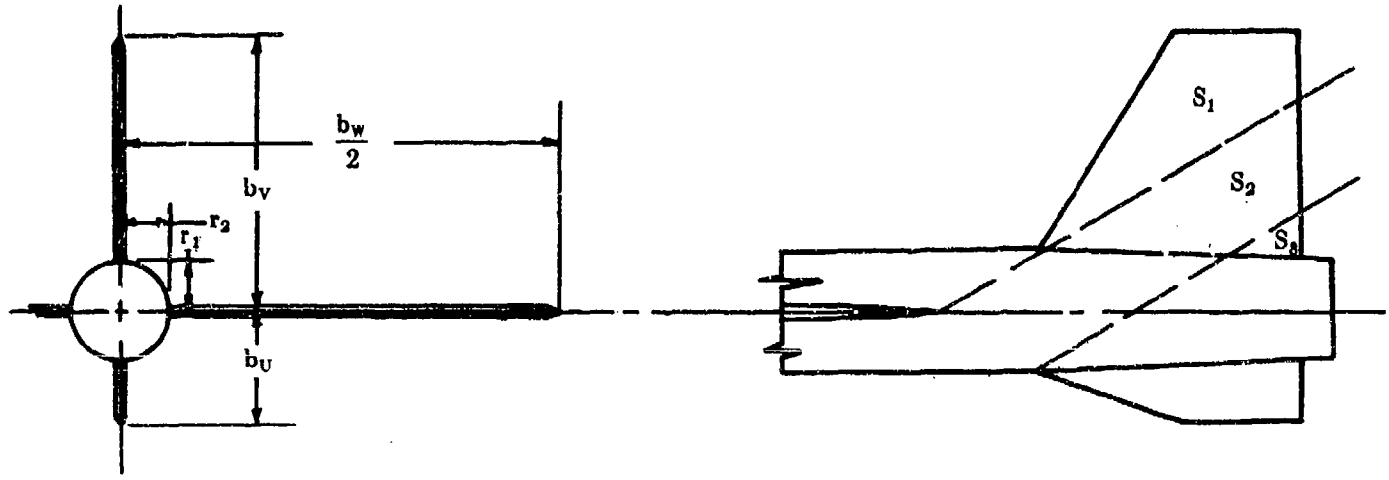

Upper Vertical Tail Characteristics

$A_V = 1.29$	$A_{V_e} = 1.12$	$S_V = 43.5$ sq in.	$S_{V_e} = 31.6$ sq in.	$\Lambda_{LE_V} = 32.5°$
$\lambda_V = 0.42$	$\lambda_{V_e} = 0.482$	$b_V = 7.48$ in.	airfoil: wedge nose, slab sides (constant thickness)	

Additional Characteristics

$M = 2.01$	$\mu = \sin^{-1}\frac{1}{M} = 29.8°$		$r_1 = 1.50$ in.	$r_2 = 1.50$ in.
$S_W = 144$ sq in.	$\frac{b_W}{2} = 12.0$ in.	$S_1 = 16.35$ sq in.	$S_2 = 14.10$ sq in.	$S_3 = 1.15$ sq in.
$z_W = 0$ (wing on body centerline)		$b_U = 3.05$ in.		

Compute:

$2A_{V_e} \tan \Lambda_{LE_V} = 1.425$

$\beta = \sqrt{M^2 - 1} = 1.744$

$\frac{\tan \Lambda_{LE_V}}{\beta} = 0.365$

$\beta(C_{N_\alpha})_V = 3.68$ per rad (figures 4.1.3.2-56c, -56d, -56e interpolated for $\lambda_{V_e} = 0.482$)

$(C_{N_\alpha})_V = 2.12$ per rad (based on S_{V_e})

Determine the effective apparent mass ratio due to adding the upper vertical stabilizer to the wing-body-lower vertical stabilizer combination. The empennage in this case consists of body, upper vertical stabilizer and lower vertical stabilizer (ventral). The effective apparent mass ratio to be found is that due to adding the upper vertical stabilizer to the body and ventral, $K'_{V(BU)}$.

Referring to the configuration sketch, the region S_1 senses the wing and the body, S_2 senses only the body and S_3 senses both the body and the ventral. Therefore, the effective apparent mass ratio is given by

$$K'_{V(BU)} = K_{V(WB)} \frac{S_1}{S_{V_e}} + K_{V(B)} \frac{S_2}{S_{V_e}} + K_{V(BU)} \frac{S_3}{S_{V_e}}$$

Determine $K_{V(WB)}$

$$\left(\frac{r_1}{r_2}\right) = 1.000; \left(\frac{r_2}{b_w/2}\right) = 0.125; \left(\frac{r_1}{b}\right)_{\substack{V \\ \text{added} \\ \text{panel}}} = 0.200$$

The ventral surface is not felt in region S_1, therefore

$$\left(\frac{r_1}{b}\right)_{\substack{U \\ \text{existing} \\ \text{panel}}} = 1.000$$

Using the above parameters and table 5.3.1.1-A it is seen that $K_{V(WB)}$ is obtained from figures 5.3.1.1-25b, -25c, -25d interpolated for $(r_2/\frac{b_w}{2}) = 0.125$

$K_{V(WB)} = 1.36$

Determine $K_{V(B)}$

$$\left(\frac{r_1}{r_2}\right) = 1.000; \left(\frac{r_1}{b}\right)_{\substack{V \\ \text{added} \\ \text{panel}}} = 0.200; \left(\frac{r_1}{b}\right)_{\substack{U \\ \text{existing} \\ \text{panel}}} = 1.000 \text{ (region } S_2 \text{ does not sense the ventral)}$$

Using the above parameters table 5.3.1.1-A it is seen that $K_{V(B)}$ is obtained from figure 5.3.1.1-25a

$K_{V(B)} = 1.13$

Determine $K_{V(BU)}$

$$\left(\frac{r_1}{r_2}\right) = 1.000; \left(\frac{r_1}{b}\right)_{\substack{V \\ \text{added} \\ \text{panel}}} = 0.200; \left(\frac{r_1}{b}\right)_{\substack{U \\ \text{existing} \\ \text{panel}}} = 0.492$$

Using the above parameters and table 5.3.1.1-A it is seen that $K_{V(BU)}$ is obtained from figure 5.3.1.1-25a interpolated for $(r_1/b)_U = 0.492$

$$K_{V(BU)} = 1.24$$

$$K'_{V(BU)} = (1.36)\left(\frac{16.35}{31.60}\right) + (1.13)\left(\frac{14.10}{31.60}\right) + (1.24)\left(\frac{1.15}{31.60}\right)$$

$$= 1.253$$

Solution:

$$(\Delta C_{Y_\beta})_p = -K' (C_{N_\alpha})_p \frac{S_{p_e}}{S_w} \quad \text{(equation 5.3.1.1-f)}$$

$$(\Delta C_{Y_\beta})_{V(WBU)} = -K'_{V(BU)} (C_{N_\alpha})_V \frac{S_{V_e}}{S_w}$$

$$= (-1.253)\ (2.12)\left(\frac{31.60}{144.0}\right)$$

$$= -0.583 \text{ per rad (based on } S_w)$$

This compares with an experimental value of -0.601 per radian from reference 18.

D. HYPERSONIC

A general discussion of hypersonic flow is given in paragraph D of Section 4.1.3.3 and in the references cited therein. The application of theories to tail components is complicated by the flow disturbances of forward components (body and wings) in the form of vortices, shock waves, and wakes. In general, these effects have not been generalized and specific configurations must either be compared to similar configurations for which data exist or be submitted to a test program. The recommendations of the Datcom for this speed regime are necessarily tentative and will be updated as information becomes available.

DATCOM METHOD

For configurations in which the tail panels are mounted on the body, it is recommended that the supersonic method described in paragraph C be applied at the higher Mach numbers. However, this method has not been substantiated beyond a Mach number of 6.86 (see table 5.3.1.1-C).

Alternatively, the vertical-panel contribution to C_{Y_β} may be estimated by the hypersonic small-disturbance theory, which gives a local pressure coefficient of

$$C_p = (\beta \pm \delta)^2 \left(\frac{\gamma + 1}{2} \pm \sqrt{\frac{(\gamma + 1)^2}{4} + \frac{4}{(M^2 - 1)(\beta \pm \delta)^2}} \right) \qquad 5.3.1.1\text{-h}$$

where δ is the local slope of the surface of the vertical panel with respect to the vertical plane of symmetry in radians

γ is the ratio of specific heats

β is the sideslip angle in radians

The sign of $(\beta \pm \delta)$ should be chosen to give the correct local angle of sideslip.

The plus sign before the radical in equation 5.3.1.1-h applies to the compression side of the surface and the minus sign to the expansion side. The equation is strictly valid only for sharp-edged sections and for $\delta << 1$. For a slab-sided section the pressure coefficient becomes the side-force coefficient directly (based on exposed panel area).

For very high Mach numbers, Newtonian flow can be assumed. The pressure coefficient for this case is

$$C_p = 2\sin^2(\beta \pm \delta) \qquad 5.3.1.1\text{-i}$$

Care must be taken to assure that portions of the panels that are "blanketed" by forward components, i.e., are not "seen" from the free-stream direction, are not included in the calculation. In these regions the pressure coefficient is assumed to be zero. The pressure coefficient is also assumed to be zero on the leeward side of the panel when the sideslip angle β is greater than the local panel slope δ.

These methods have not been substantiated, since not enough test data are available.

Sample Problem

Given:

$\frac{S_1}{S_V} = .5$ $\quad \frac{S_3}{S_V} = .2$ $\quad \frac{S_2}{S_V} = .3$ $\quad M = 5.0$ $\quad \gamma = 1.4$

Compute (for $\beta = 1^\circ$):

$$\frac{\gamma + 1}{2} = 1.20$$

$$\frac{(\gamma + 1)^2}{4} = 1.44$$

$$M^2 - 1 = 24$$

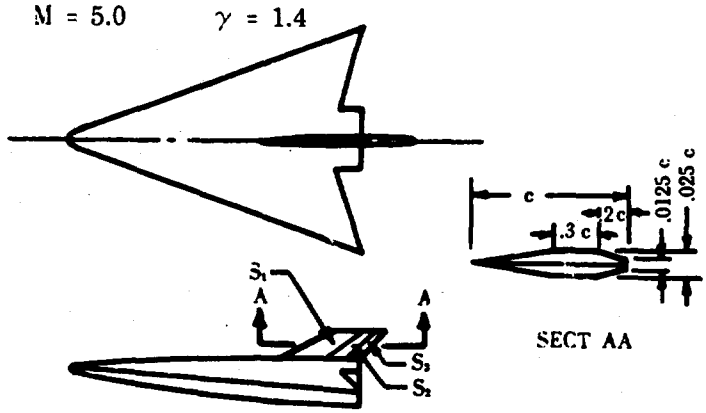

Region	$\beta \pm \delta$ (rad)	
	Compression Side*	Expansion Side*
1	.04240	+.00750
2	.01745	−.01745
3	−.01396	−.04886

Values of pressure coefficient, C_p, calculated for each region by means of equation 5.3.1.1-h are listed in the following table (plus signs are used for flow compressions and minus signs for flow expansions in both tables).

Region	C_p	
	Compression Side	Expansion Side
1	.01960	+.00300
2	.00748	−.00674
3	−.00546	−.01728

*For a similar slab-sided surface. In actuality, both sides of region 1 are in compression and both sides of region 3 are in an expansion field.

Solution:

The sum of the pressure coefficients acting on the two sides of a given region is given by the difference of the two pressure coefficients

$$(C_p)_{\substack{\text{compression}\\ \text{side}}} - (C_p)_{\substack{\text{extension}\\ \text{side}}} = \Delta C_p$$

Thus, combining the pressure coefficients for each region and converting to side force coefficient gives

$$\Delta C_Y = \Delta C_{p1} \frac{S_1}{S_V} + \Delta C_{p2} \frac{S_2}{S_V} + \Delta C_{p3} \frac{S_3}{S_V}$$

$$= .0166 \times .5 + .01422 \times .3 + .01182 \times .2$$

$$= .015$$

Therefore

$$(\Delta C_{Y_\beta})_V = -.015 \text{ per degree or } -.86 \text{ per radian}$$

This is essentially the configuration of reference 19.

TABLE 5.3.1.1-A

APPARENT MASS FACTOR INDEX

Figure 5.3.1.1-25( )	$\frac{r_1}{r_2}$	Horizontal Surface Position	$\left(\frac{r_2}{b/2}\right)_H$ or $\left(\frac{r_2}{b/2}\right)_W$	$\left(\frac{r_1}{b}\right)$ added vertical panel	$\left(\frac{r_1}{b}\right)$ existing vertical panel
a	1.000	——	——	0 to 1.0	0.1 to 1.0
b	1.000	Mid	0	0 to 1.0	0 to 1.0
c			0.2		0.1 to 1.0
d			0.4		0.1 to 1.0
e			0.6		0.1 to 1.0
f			0.8		0.1 to 1.0
g	1.000	Tangent to body on same side as added panel	0	0 to 1.0	0 to 1.0
h			0.2		0.1 to 1.0
i			0.4		0.1 to 1.0
j			0.6		0.1 to 1.0
k			0.8		0.1 to 1.0
l	1.000	Tangent to body on side opposite added panel	0	0 to 1.0	0 to 1.0
m			0.2		0.1 to 1.0
n			0.4		0.1 to 1.0
o			0.6		0.1 to 1.0
p			0.8		0.1 to 1.0
q	0.333	——	——	0 to 1.0	0.1 to 1.0
r	0.333	Mid	0	0 to 1.0	0 to 1.0
s			0.2		0.1 to 1.0
t			0.4		0.1 to 1.0
u			0.6		0.1 to 1.0
v			0.8		0.1 to 1.0
w	0.667	——	——	0 to 1.0	0.1 to 1.0
x	0.667	Mid	0	0 to 1.0	0 to 1.0
y			0.2		0.1 to 1.0
z			0.4		0.1 to 1.0
aa			0.6		0.1 to 1.0
bb			0.8		0.1 to 1.0
cc	1.500	——	——	0 to 1.0	0.1 to 1.0
dd	1.500	Mid	0	0 to 1.0	0 to 1.0
ee			0.2		0.1 to 1.0
ff			0.4		0.1 to 1.0
gg			0.6		0.1 to 1.0
hh			0.8		0.1 to 1.0
ii	3.000	——	——	0 to 1.0	0.1 to 1.0
jj	3.000	Mid	0	0 to 1.0	0 to 1.0
kk			0.2		0.1 to 1.0
ll			0.4		0.1 to 1.0
mm			0.6		0.1 to 1.0
nn			0.8		0.1 to 1.0
oo	1.000	Mid or tangent position	0 to ∞	1.0	1.0

SUBSONIC
D

Ref.	Configuration Sketch	Surface	A	b (in)	λ_V	λ_{V_e}	Λ_{LE} (deg)	Airfoil
6	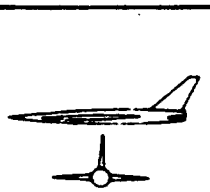	W	3.0	41.56	— —	— —	53.1	— —
		H	4.0	22.42	— —	— —	— —	— —
		V_S	1.50	13.28	.160	.195	54.0	NACA 0003.5-64
		V_L	1.50	15.23	.160	.189	54.0	NACA 0003.5-64
8		W	2.31	36.50	— —	— —	— —	— —
		V	2.18	10.37	0	0	42.5	NACA 65-006
		W	2.31	36.50	— —	— —	— —	— —
		V	2.18	11.74	0	0	42.5	NACA 65-006
	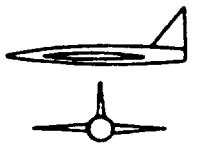	W_1	2.31	36.50	— —	— —	60.0	— —
		W_2	2.31	36.50	— —	— —	60.0	— —
		W_3	2.31	36.50	— —	— —	60.0	— —
		V	2.18	14.23	0	0	42.5	NACA 65-006
9	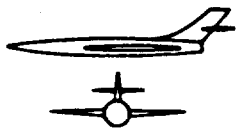	W	4.0	36.00	— —	— —	46.7	— —
		H	4.0	16.08	— —	— —	— —	— —
		V	1.18	10.19	.500	.61	57.5	NACA 63(10)A009
10	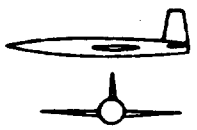	W	4.0	36.00	— —	— —	3.6	— —
		H	4.0	16.10	— —	— —	— —	— —
		V	2.02	9.90	.600	.647	3.5	NACA 65A008
	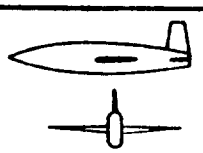	W	4.0	36.00	— —	— —	— —	— —
		H	4.0	16.10	— —	— —	— —	— —
		V	2.02	9.90	.600	.678	3.5	NACA 65A008
	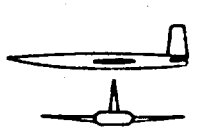	W	4.0	36.00	— —	— —	— —	— —
		H	4.0	16.10	— —	— —	— —	— —
		V	2.02	9.90	.600	.630	3.5	NACA 65A008

*This table is a condensed form of that appearing in reference 3. Additional substantiation can be obtained from this r

TABLE 5.3.1.1-B*

SUBSONIC CONTRIBUTION OF VERTICAL PANELS TO C_{Y_β}
DATA SUMMARY AND SUBSTANTIATION

A	b (in)	λ_V	λ_{V_e}	Λ_{LE} (deg)	Airfoil	r_1/r_2	x/c_v	Panel Added	M	Method 1		
										$k(C_{L_\alpha})_{V(BH)}$ (per rad)	$\left(1+\frac{\partial\sigma}{\partial\beta}\right)\frac{q_v}{q_\infty}$	(ΔC_{Y_β}) Calc. (per rad)
							.50	$BWHV_S$-BW	.25	.431	1.115	−.481
3.0	41.56	—	—	53.1	—	1.000	.55	$BWHV_L$-BW	.25	.597	1.230	−.734
4.0	22.42	—	—	—	—		—	BV_S-B	.25	.428	1.0	−.428
1.50	13.28	.160	.195	54.0	NACA 0003.5-64		—	BV_L-B	.25	.578	1.0	−.578
1.50	15.23	.160	.189	54.0	NACA 0003.5-64		.55	BHV_L-B	.25	.597	1.0	−.597
							.50	BHV_S-B	.25	.431	1.0	−.431
2.31	36.50	—	—	—	—	1.000	—	BV-B	.17	.254	1.0	−.254
2.18	10.37	0	0	42.5	NACA 65-006							
2.31	36.50	—	—	—	—	1.000	—	BV-B	.17	.317	1.0	−.317
2.18	11.74	0	0	42.5	NACA 65-006							
2.31	36.50	—	—	60.0	—	1.000	—	BW_1V-BW_1	.17	.446	1.050	−.468
2.31	36.50	—	—	60.0	—		—	BW_2V-BW_2	.17	.446	.918	−.409
2.31	36.50	—	—	60.0	—		—	BW_3V-BW_3	.17	.446	1.184	−.528
2.18	14.23	0	0	42.5	NACA 65-006		—	BV-B	.17	.446	1.0	−.446
4.0	36.00	—	—	46.7	—	1.000	1.00	BWHV-BW	.6	.461	1.247	−.575
4.0	16.08	—	—	—	—		—	BV-B	.6	—	—	—
1.18	10.19	.500	.61	57.5	NACA 63(10)A009							
4.0	36.00	—	—	3.6	—	1.000	.25	BWHV-BW	.13	.430	.990	−.426
4.0	16.10	—	—	—	—		.25	BHV-BH	.13	—	—	—
2.02	9.90	.600	.647	3.5	NACA 65A008							
4.0	36.00	—	—	—	—	2.210	.25	BHV-BH	.13	—	—	—
4.0	16.10	—	—	—	—							
2.02	9.90	.600	.678	3.5	NACA 65A008							
4.0	36.00	—	—	—	—	.451	.25	BHV-BH	.13	—	—	—
4.0	16.10	—	—	—	—							
2.02	9.90	.600	.630	3.5	NACA 65A008							

aring in reference 3. Additional substantiation can be obtained from this reference.

2

TABLE 5.3.1.1-B*

BUTION OF VERTICAL PANELS TO C_{Y_β}
IMARY AND SUBSTANTIATION

x/c_r	Panel Added	M	Method 1			Method 3			(ΔC_{Y_β}) Test (per rad)	Percent Error e	
			$k(C_{L_\alpha})_{V(BH)}$ (per rad)	$\left(1+\frac{\partial\sigma}{\partial\beta}\right)\frac{q_v}{q_\infty}$	(ΔC_{Y_β}) Calc. (per rad)	$(C_{L_\alpha})_V$ (per rad)	K	(ΔC_{Y_β}) Calc. (per rad)		Method 1	Method 3
.50	$BWHV_S$-BW	.25	.431	1.115	−.481	—	—	—	−.54	10.9	—
.55	$BWHV_L$-BW	.25	.597	1.230	−.734	—	—	—	−.76	3.4	—
—	BV_S-B	.25	.428	1.0	−.428	.370	1.16	−.429	−.44	2.7	2.5
—	BV_L-B	.25	.578	1.0	−.578	.514	1.07	−.550	−.56	3.2	1.8
.55	BHV_L-B	.25	.597	1.0	−.597	.514	1.25	−.642	−.63	5.2	1.9
.50	BHV_S-B	.25	.431	1.0	−.431	.370	1.34	−.496	−.47	8.3	5.5
—	BV-B	.17	.254	1.0	−.254	.239	.94	−.225	−.25	1.6	10.0
—	BV-B	.17	.317	1.0	−.317	.293	1.01	−.296	−.30	5.7	1.3
—	BW_1V-BW_1	.17	.446	1.050	−.468	—	—	—	−.43	8.8	—
—	BW_2V-BW_2	.17	.446	.918	−.409	—	—	—	−.34	20.3	—
—	BW_3V-BW_3	.17	.446	1.184	−.528	—	—	—	−.49	7.8	—
—	BV-B	.17	.446	1.0	−.446	.401	1.15	−.461	−.42	6.2	9.8
1.00	BWHV-BW	.6	.461	1.247	−.575	—	—	—	−.46	25.0	—
—	BV-B	.6	—	—	—	.460	1.07	−.492	−.49	—	0.4
.25	BWHV-BW	.13	.430	.990	−.426	—	—	—	−.51	16.5	—
.25	BHV-BH	.13	—	—	—	.400	1.26	−.504	−.53	—	4.9
.25	BHV-BH	.13	—	—	—	.331	1.53	−.506	−.53	—	4.5
.25	BHV-BH	.13	—	—	—	.448	1.11	−.497	−.49	—	1.4

3

TABLE 5.3.1.1-C*
SUPERSONIC CONTRIBUTION OF VERTICAL PANELS TO C_{Y_β}
DATA SUMMARY AND SUBSTANTIATION

Ref.	Configuration Sketch	r_1/r_2	Surface	A	b (in)	$\lambda_{L.E.}$	$\Lambda_{L.E.}$ (deg)	Panel Added	M	$(C_{Y_\alpha})_V$ (per rad)
15	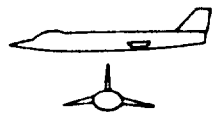	1.000	W	2.45	10.48	.427	27.1	BWV-BW	1.82	−.418
			V	1.32	3.80	.378	44.0			
16	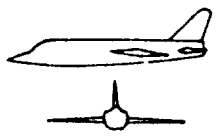	1.000	W	4.0	25.32	.538	38.1	BV-B	1.61	−.420
			H	3.5	12.12	.541	38.5	BWHV -BWH	1.61	−.420
			V	3.0	7.48	.192	50.4			
1	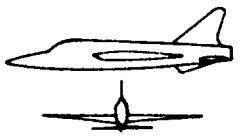	1.170	W	3.18	19.08	.483	48.0			
			H	3.06	9.12	.517	48.0	BWHU-BWH	2.01	−.021
			V	1.73	7.08	.392	49.2	BWHUV-BWHU	2.01	−.398
			U	—	2.56	.00	70.2			
17		.940	W	3.86	22.41	.313	49.7	BWV_0-BW	1.61	−.247
								BWV_0-BW	2.01	−.195
			H	3.54	15.74	.402	49.6	$BWHV_0$-BWH	1.61	−.247
			V_0	1.10	7.20	.416	23.5	$BWHV_0$-BWH	2.01	−.195
			V_{ext}	1.61	8.66	.260	23.5	$BWHV_{ext}$-BWH	1.61	−.321
			$V_{127\%}$	1.45	8.74	.290	23.5	$BWHV_{127\%}$-BWH	1.61	−.349
18		1.000	W	4.	24.00	.225	49.4	BWV-BW	1.41	−.788
			V	1.29	8.59	.235	20.6	BWV-BW	2.01	−.470
18		1.000	W	4.	24.00	.225	49.4	BWV-BW	1.41	−.810
			V	1.29	8.59	.235	41.6	BWV-BW	2.01	−.482
18		1.000	W	4.	24.00	.225	49.4	BWV-BW	1.41	−.761
			V	1.29	8.59	.235	52.1	BWV-BW	2.01	−.512
18	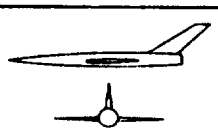	1.000	W	4.	24.00	.225	49.4	BWV-BW	1.41	−.679
			V	1.29	8.59	.235	62.5	BWV-BW	2.01	−.554
20	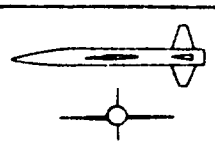	1.0	W	3.00	4.33	.140	38.83	BWHUV-BWUV	6.86	.0670
			H	3.52	2.69	.261	22.63	BWHUV-BWH	6.86	.1110
			V = U	1.50	1.35	.333	22.63	BWHUV-BW	6.86	—

*This table is a condensed form of that appearing in reference 3. Additional substantiation can be obtained from this reference.

C*

RTICAL PANELS TO C_{Y_β}

STANTIATION

Panel Added	M	$(C_{l_\alpha})_V$ (per rad)	K'	(ΔC_{Y_β}) Calc. (per rad)	(ΔC_{Y_β}) Test (per rad)	Percent Error e
BWV-BW	1.82	−.418	1.41	−.589	−.56	5.2
BV-B	1.61	−.420	1.25	−.525	−.52	0.96
BWHV -BWH	1.61	−.420	1.26	−.529	−.487	8.6
BWHU-BWH	2.01	−.021	2.76	−.056	−.057	1.8
BWHUV-BWHU	2.01	−.398	1.32	−.525	−.52	1.0
BWV_ϕ-BW	1.61	−.247	1.45	−.358	−.33	8.5
BWV_ϕ-BW	2.01	−.195	1.72	−.335	−.30	11.7
$BWHV_\phi$-BWH	1.61	−.247	1.49	−.368	−.37	.5
$BWHV_\phi$-BWH	2.01	−.195	1.72	−.335	−.30	11.7
$BWHV_{\text{ext}}$-BWH	1.61	−.321	1.32	−.424	−.41	3.4
$BWHV_{127\phi}$-BWH	1.61	−.349	1.35	−.471	−.44	7.0
BWV-BW	1.41	−.788	1.06	−.836	−.92	9.1
BWV-BW	2.01	−.470	1.16	−.545	−.65	16.2
BWV-BW	1.41	−.810	1.04	−.842	−.88	4.3
BWV-BW	2.01	−.482	1.12	−.540	−.60	10.0
BWV-BW	1.41	−.761	1.04	−.792	−.85	6.8
BWV-BW	2.01	−.512	1.06	−.542	−.53	2.3
BWV-BW	1.41	−.679	1.04	−.706	−.67	5.4
BWV-BW	2.01	−.554	1.04	−.586	−.50	17.2
BWHUV-BWUV	6.86	.0670	1.79	−.120	—	—
BWHUV-BWH	6.86	.1110	1.758	−.195	—	—
BWHUV-BW	6.86	—	—	−.315**	−.321	1.9

l from this reference.

**Sum of the two terms above.

REFERENCES

1. Decker, J., et al: USAF Stability and Control Handbook. M-03671, 1956. (C) Title Unclassified
2. Anon.: Royal Aeronautical Society Data Sheets—Aerodynamics, 1955. (U)
3. Goodwin, F. K., and Kaattari, G. E.: Estimation of Directional Stability Derivatives at Small Angles and Supersonic Speeds. NASA Memo 12-2-58A, 1958. (U)
4. Bryson, A. E., Jr.: Evaluation of the Inertia Coefficients of the Cross Section of a Slender Body. Jour. Aero. Sci., Vol. 21, No. 6, June 1954. (U)
5. Spencer, B., Jr.: A Simplified Method for Estimating Subsonic Lift-Curve Slope at Low Angles of Attack for Irregular Planform Wings. NASA TM X-525, 1961. (C) Title Unclassified
6. Savage, H. F., and Tinling, B. E.: The Subsonic Static Aerodynamic Characteristics of an Airplane Model Having a Triangular Wing of Aspect Ratio 3. II—Lateral and Directional Characteristics. NACA TN 4042, 1957. (U)
7. Paulson, J. W., and Boisseau, P. C.: Low-Speed Investigation of the Effect of Small Canard Surfaces on the Directional Stability of a Sweptback-Wing Fighter-Airplane Model. NACA RM L56F19a, 1956. (C) Title Unclassified
8. Goodman, A., and Thomas, D. F., Jr.: Effects of Wing Position and Fuselage Size on the Low-Speed Static and Rolling Stability Characteristics of a Delta-Wing Model. NACA TN 3063, 1954. (U)
9. Wiggins, J. W., Kuhn, R. E., and Fournier, P. G.: Wind-Tunnel Investigation to Determine the Horizontal- and Vertical-Tail Contributions to the Static Lateral Stability Characteristics of a Complete-Model Swept-Wing Configuration at High Subsonic Speeds. NACA TN 3818, 1956. (U)
10. Letko, W., and Williams, J. L.: Experimental Investigation at Low Speed of Effects of Fuselage Cross Section on Static Longitudinal and Lateral Stability Characteristics of Models Having 0° and 45° Sweptback Surfaces. NACA TN 3551, 1955. (U)
11. Hallissy, J. M., Jr.: Transonic Wind-Tunnel Measurements of Static Lateral and Directional Stability and Vertical-Tail Loads for a Model with a 45° Sweptback Wing. NACA RM L55L19, 1956. (U)
12. Arabian, D. D., and Schmeer, J. W.: Lateral Stability and Control Measurements of a Fighter-Type Airplane With Low-Aspect-Ratio Unswept Wing and a Tee-Tail. NACA RM L55F08, 1956. (U)
13. Osborne, R. S.: Aerodynamic Characteristics of a 0.0667-Scale Model of the North American X-15 Research Airplane at Transonic Speeds. NASA TM X-24, 1959. (U)
14. Spearman, M. L., Robinson, R. B., and Driver, C.: The Effects of the Addition of Small Fuselage-Mounted Fins on the Static Directional Stability Characteristics of a Model of a 45° Swept-Wing Airplane at Angles of Attack Up to 15.3° at a Mach Number of 2.01. NACA RM L56D16A, 1956. (C) Title Unclassified
15. Spearman, M. L., and Driver, C.: Longitudinal and Lateral Stability Characteristics of a Low-Aspect-Ratio Unswept-Wing Airplane Model at Mach Numbers of 1.82 and 2.01. NACA RM L56H06, 1957. (U)
16. Spearman, M. L.: Static Lateral and Directional Stability and Effective Sidewash Characteristics of a Model of a 35° Swept-Wing Airplane at a Mach Number of 1.61. NACA RM L56E23, 1956. (U)
17. Spearman, M. L., and Robinson, R. B.: Static Lateral Stability and Control Characteristics of a Model of a 45° Swept-Wing Fighter Airplane With Various Vertical Tails at Mach Numbers of 1.41, 1.61, and 2.01. NACA RM L56D05, 1956. (U)
18. Spearman, M. L., and Robinson, R. B.: Investigation of the Aerodynamic Characteristics in Pitch and Sideslip of a 45° Swept-Wing Airplane Configuration With Various Vertical Locations of the Wing and Horizontal Tail. Static Lateral and Directional Stability; Mach Numbers of 1.41 and 2.01. NACA RM L57J25a, 1957. (U)
19. Dennis, D. H., and Petersen, R. H.: Aerodynamic Performance and Static Stability at Mach Numbers Up to 5 of Two Airplane Configurations With Favorable Lift Interference. NASA Memo 1-8-59A, 1959. (U)
20. Ridyard, H. W., Fetterman, D. E., Jr., and Penland, J. A.: Static Lateral Stability Data From an Exploratory Investigation at a Mach Number of 6.86 of an Airplane Configuration Having a Wing of Trapezoidal Planform. NACA RM L55A21a, 1955. (U)

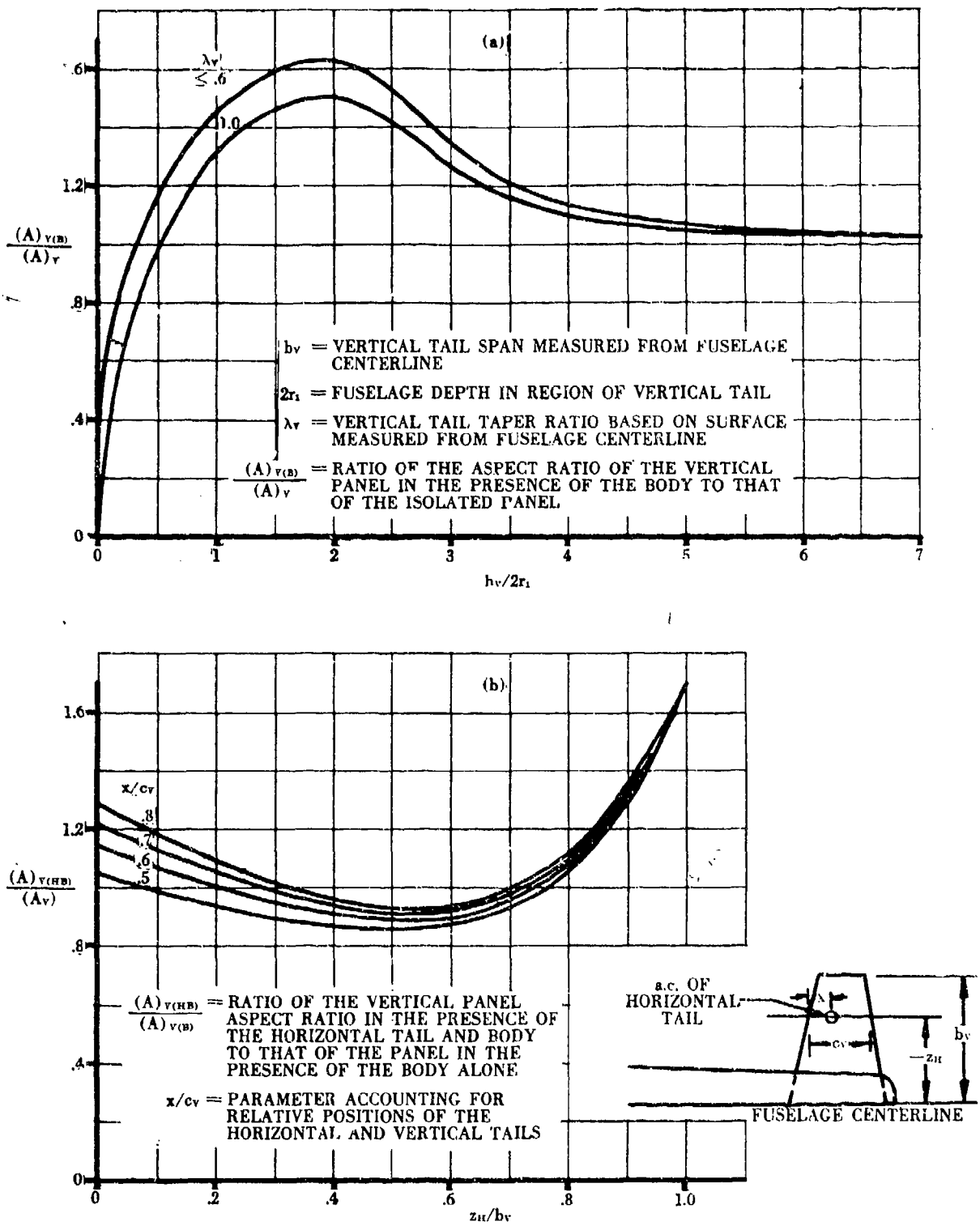

FIGURE 5.3.1.1-22 CHARTS FOR ESTIMATING THE SIDESLIP DERIVATIVE $(C_{Y_\beta})_{V(WBH)}$ FOR SINGLE VERTICAL TAILS

SUBSONIC

METHOD 1--SINGLE VERTICAL TAILS

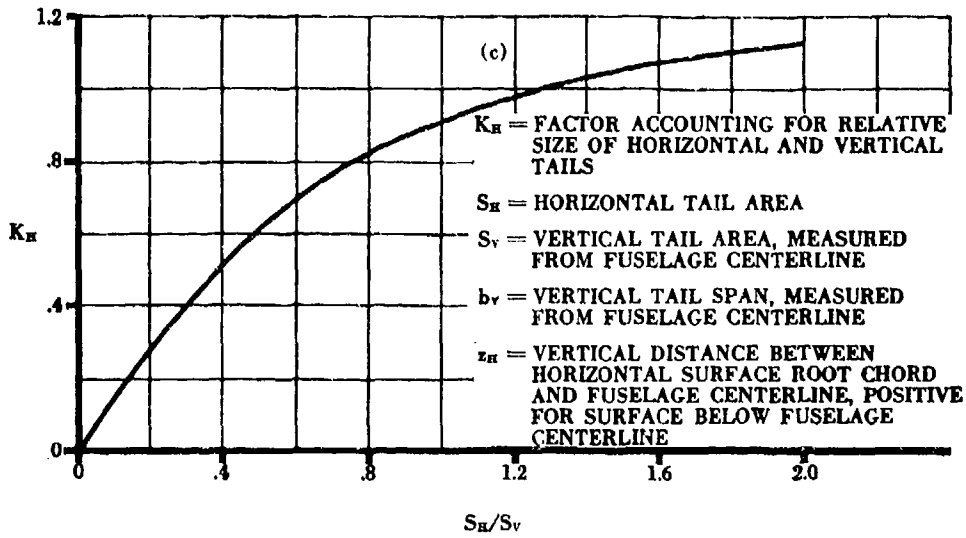

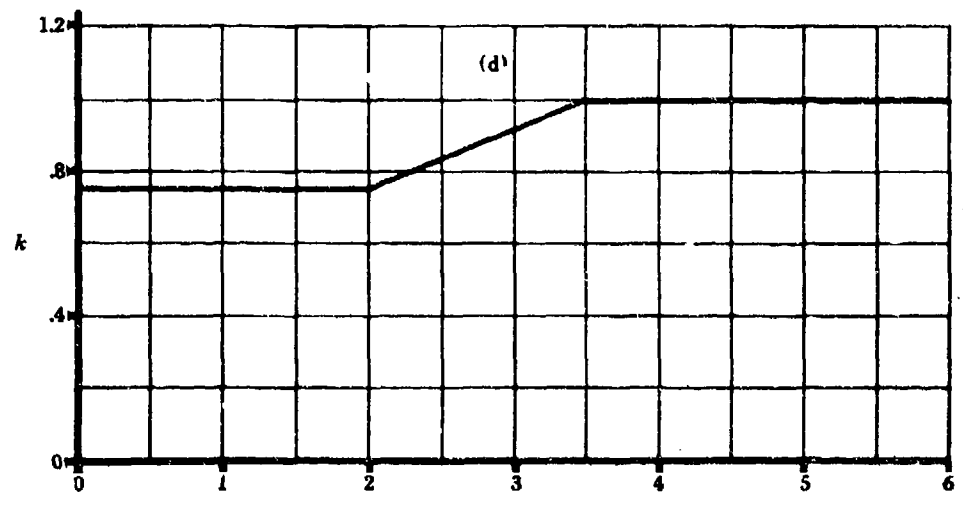

FIGURE 5.3.1.1-22(CONTD) CHARTS FOR ESTIMATING THE SIDESLIP DERIVATIVE $(C_{Y_\beta})_{V(WBH)}$ FOR SINGLE VERTICAL TAILS

SUBSONIC

METHOD 2—TWIN VERTICAL TAILS

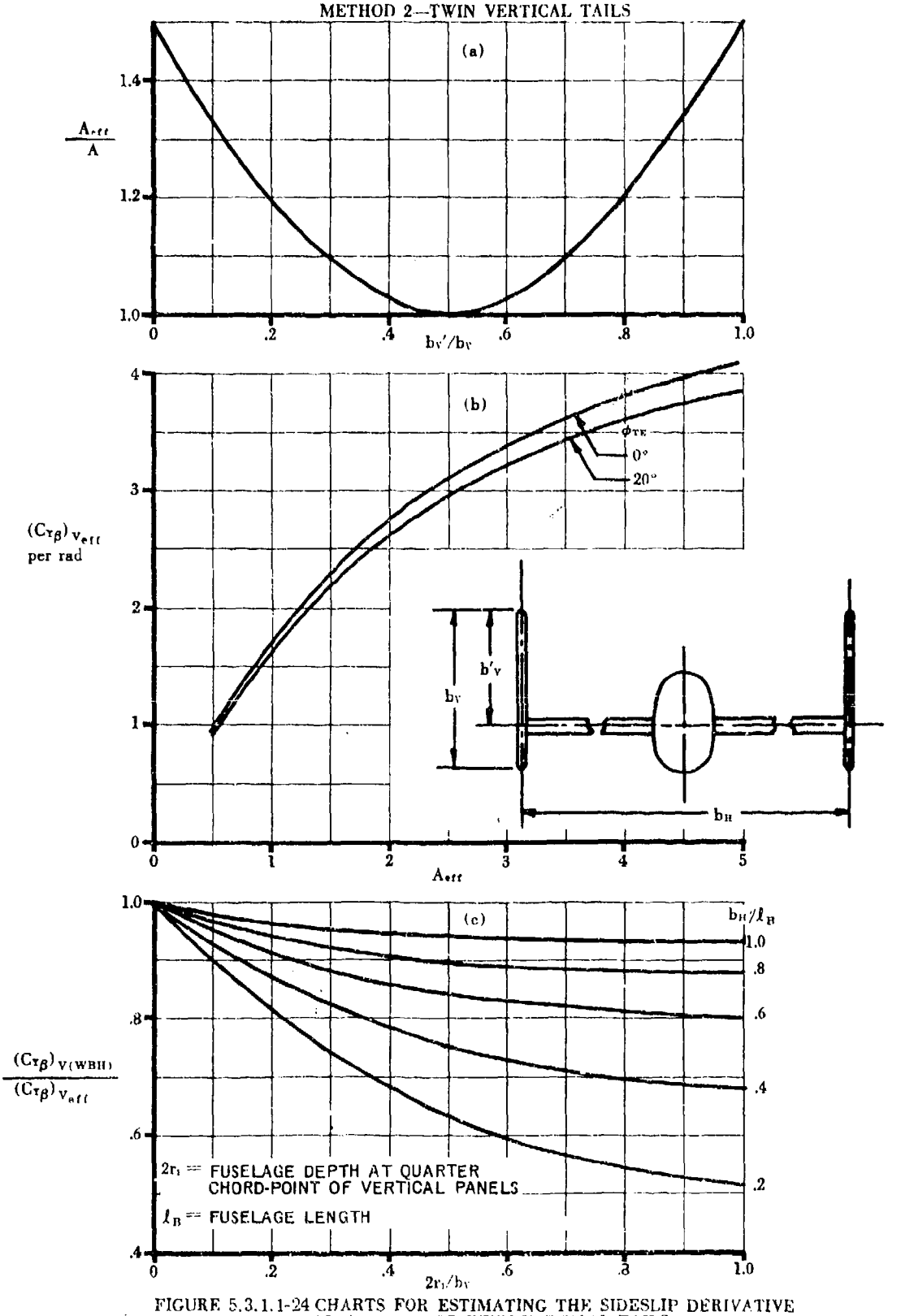

FIGURE 5.3.1.1-24 CHARTS FOR ESTIMATING THE SIDESLIP DERIVATIVE $(C_{Y\beta})_{V(WBH)}$ FOR TWIN VERTICAL TAILS.

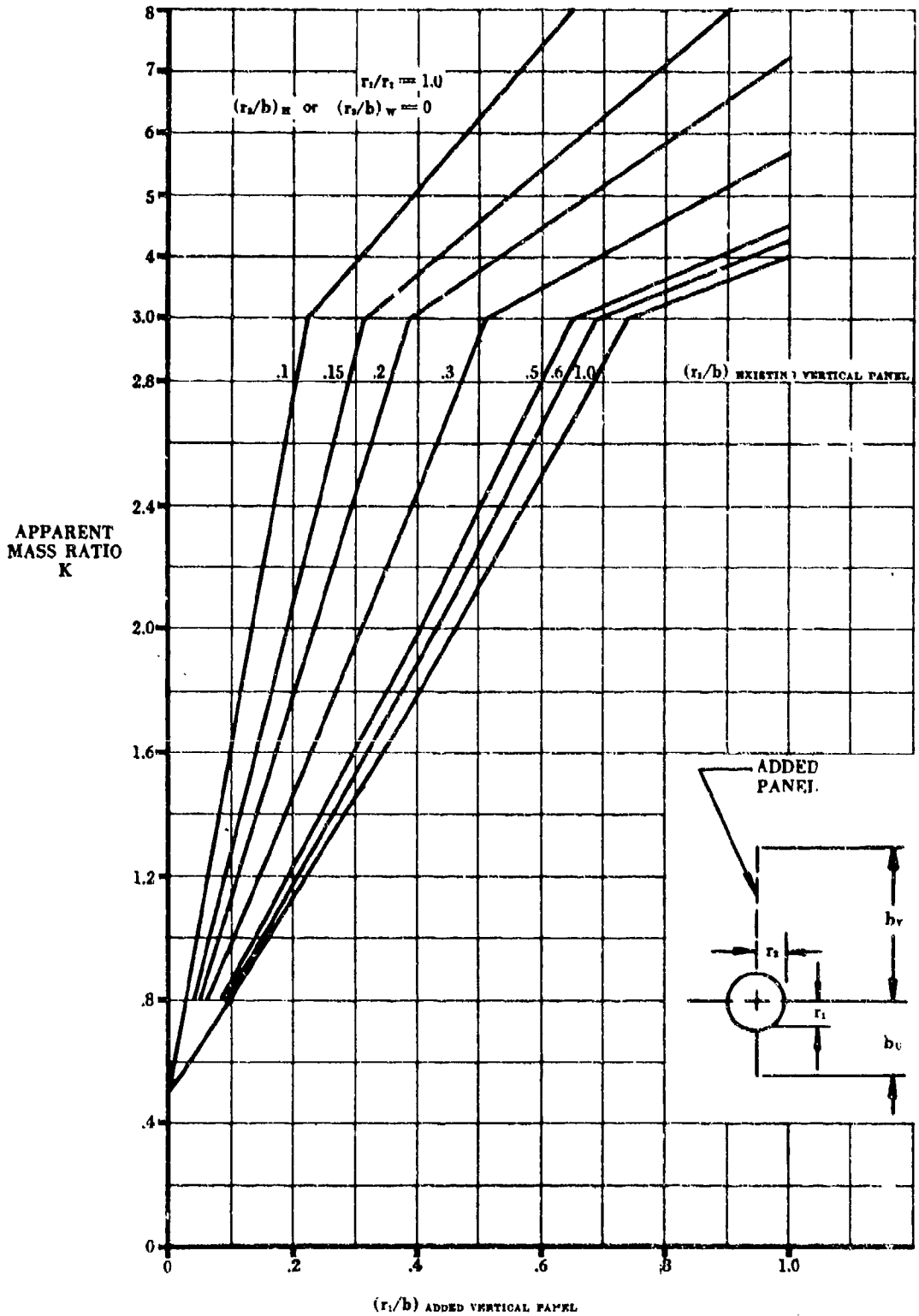

FIGURE 5.3.1.1-25a APPARENT MASS FACTORS

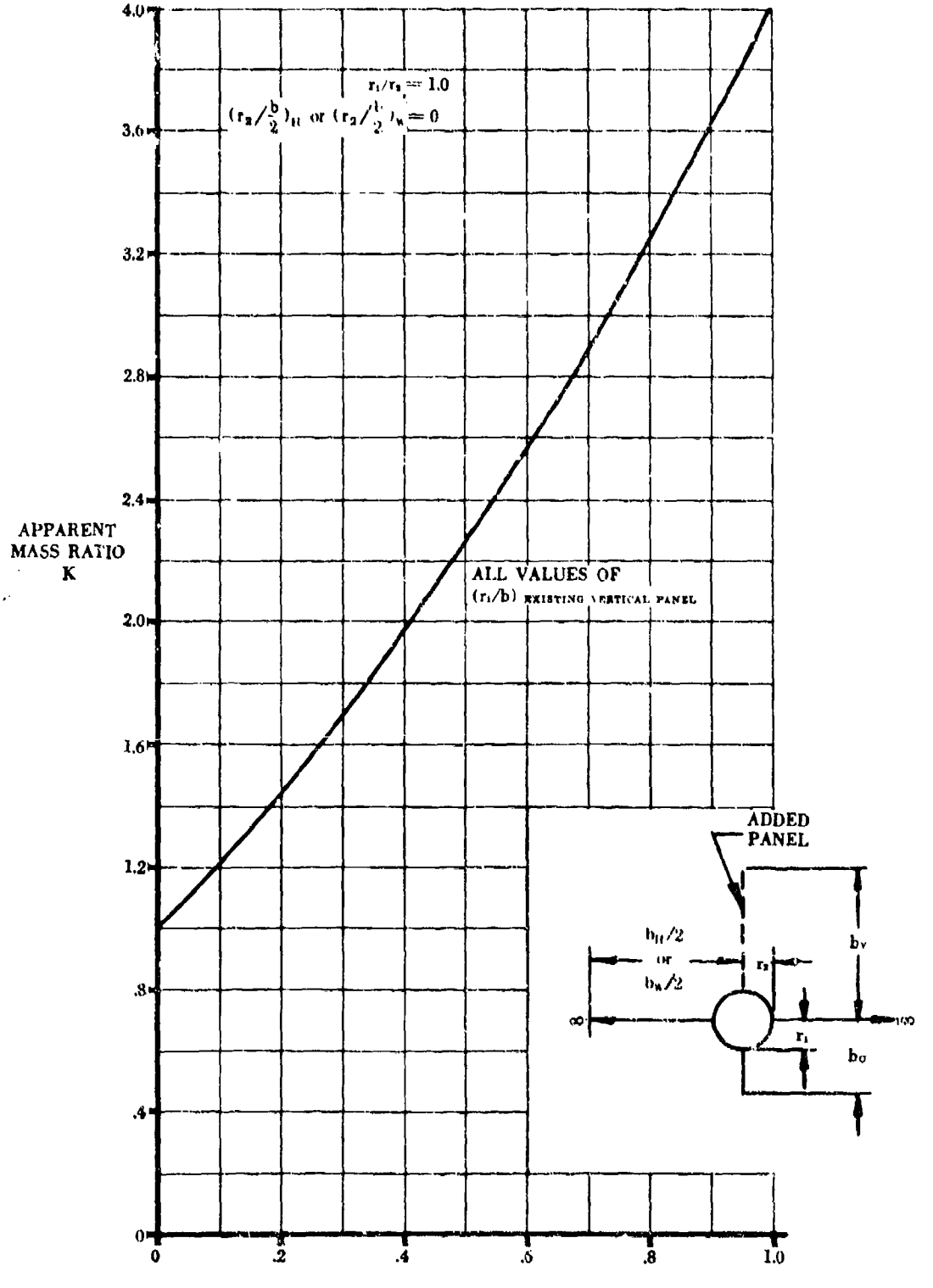

FIGURE 5.3.1.1-25b APPARENT MASS FACTORS (CONTD)

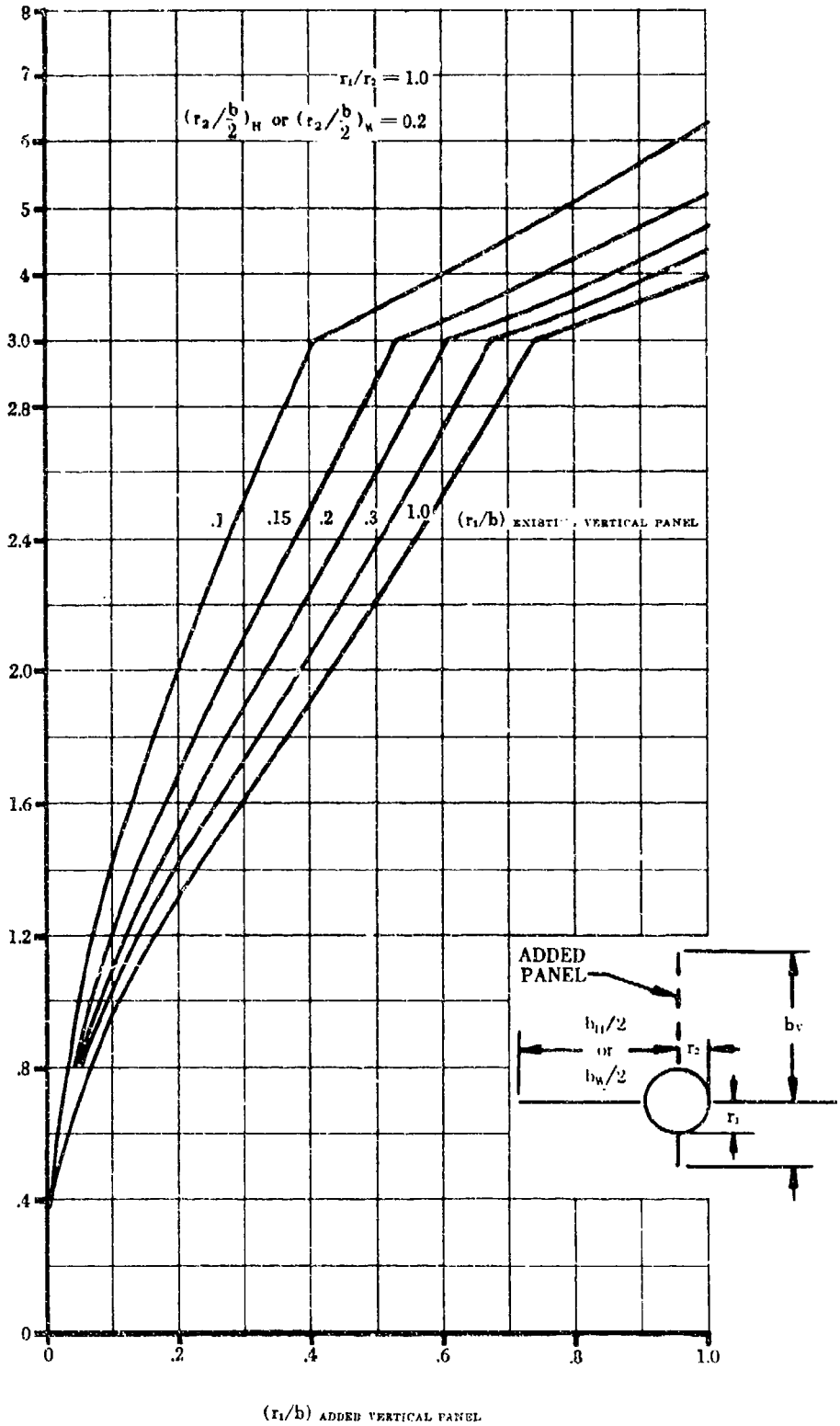

FIGURE 5.3.1.1-25c APPARENT MASS FACTORS (CONTD)

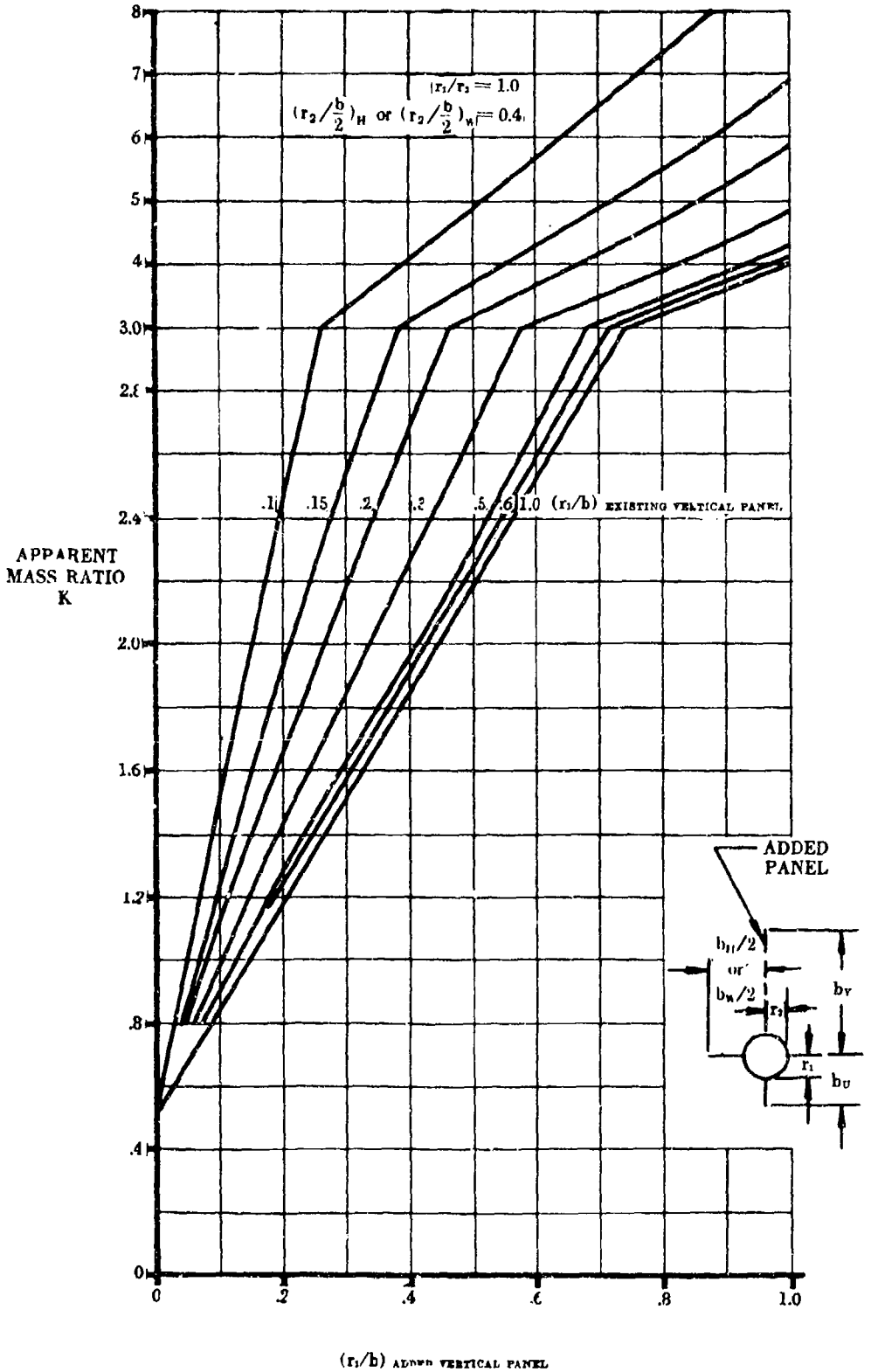

FIGURE 5.3.1.1-25d APPARENT MASS FACTORS (CONTD)

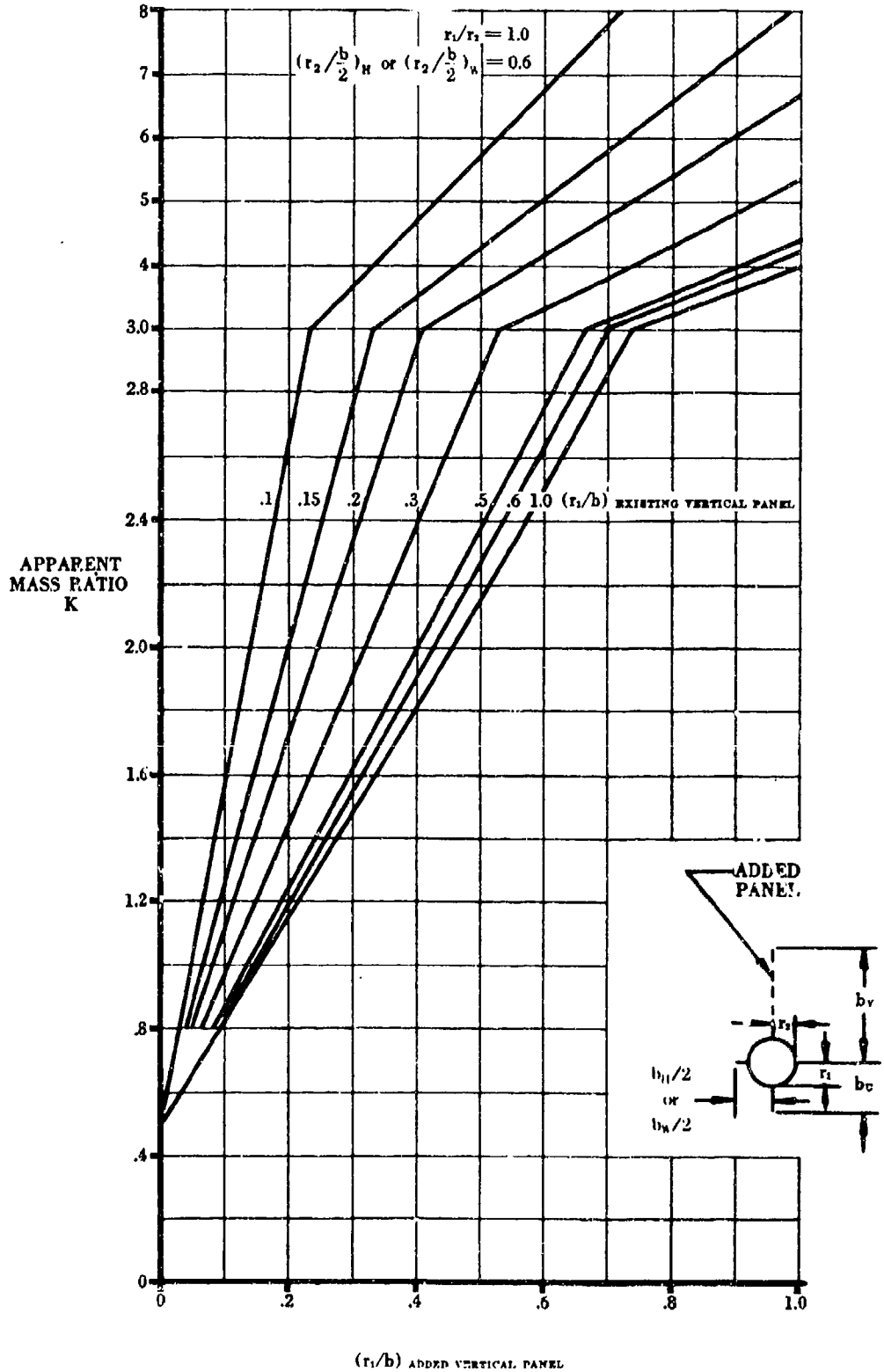

FIGURE 5.3.1.1-25e APPARENT MASS FACTORS (CONTD)

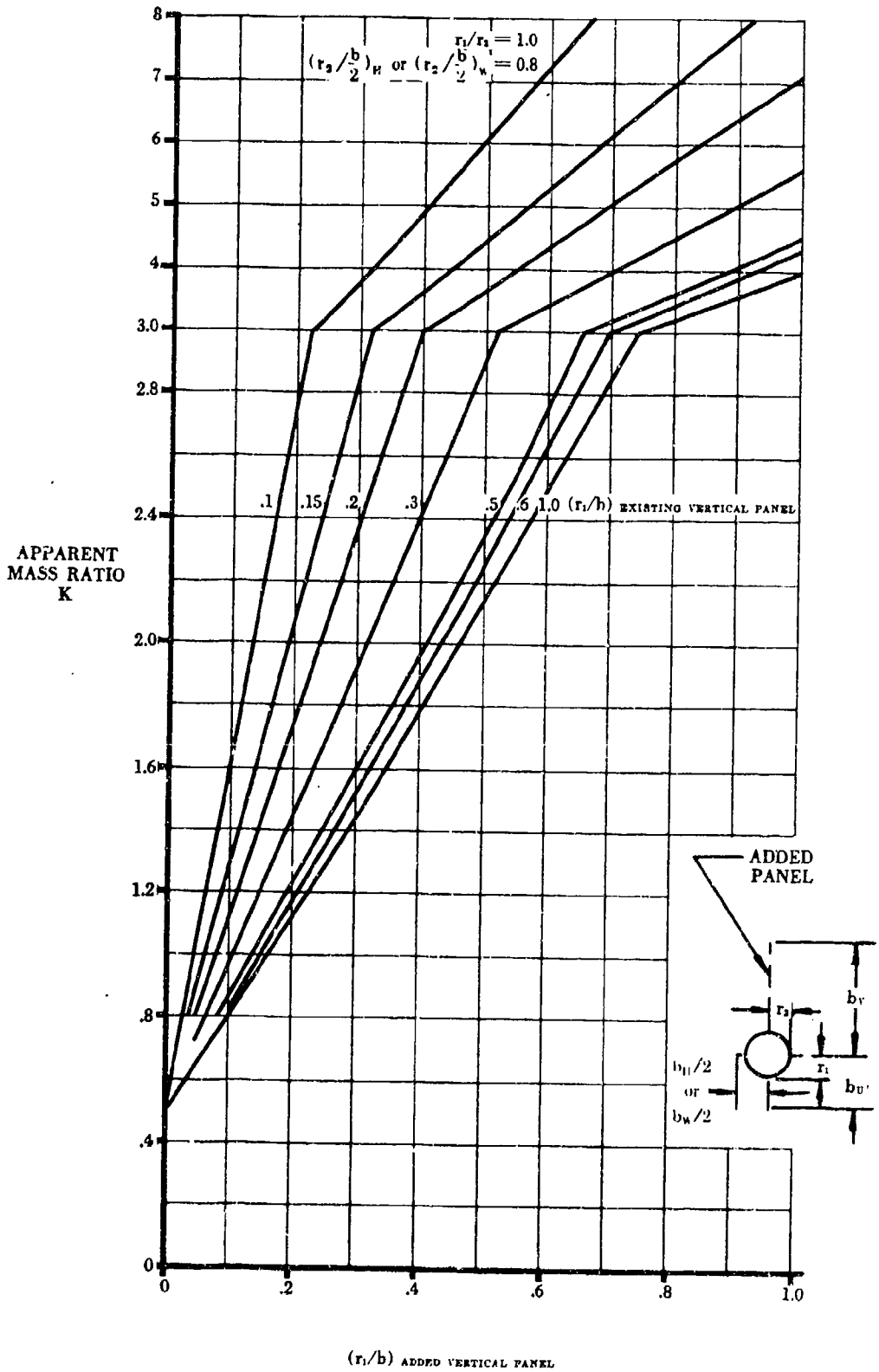

FIGURE 5.3.1.1-25f APPARENT MASS FACTORS (CONTD)

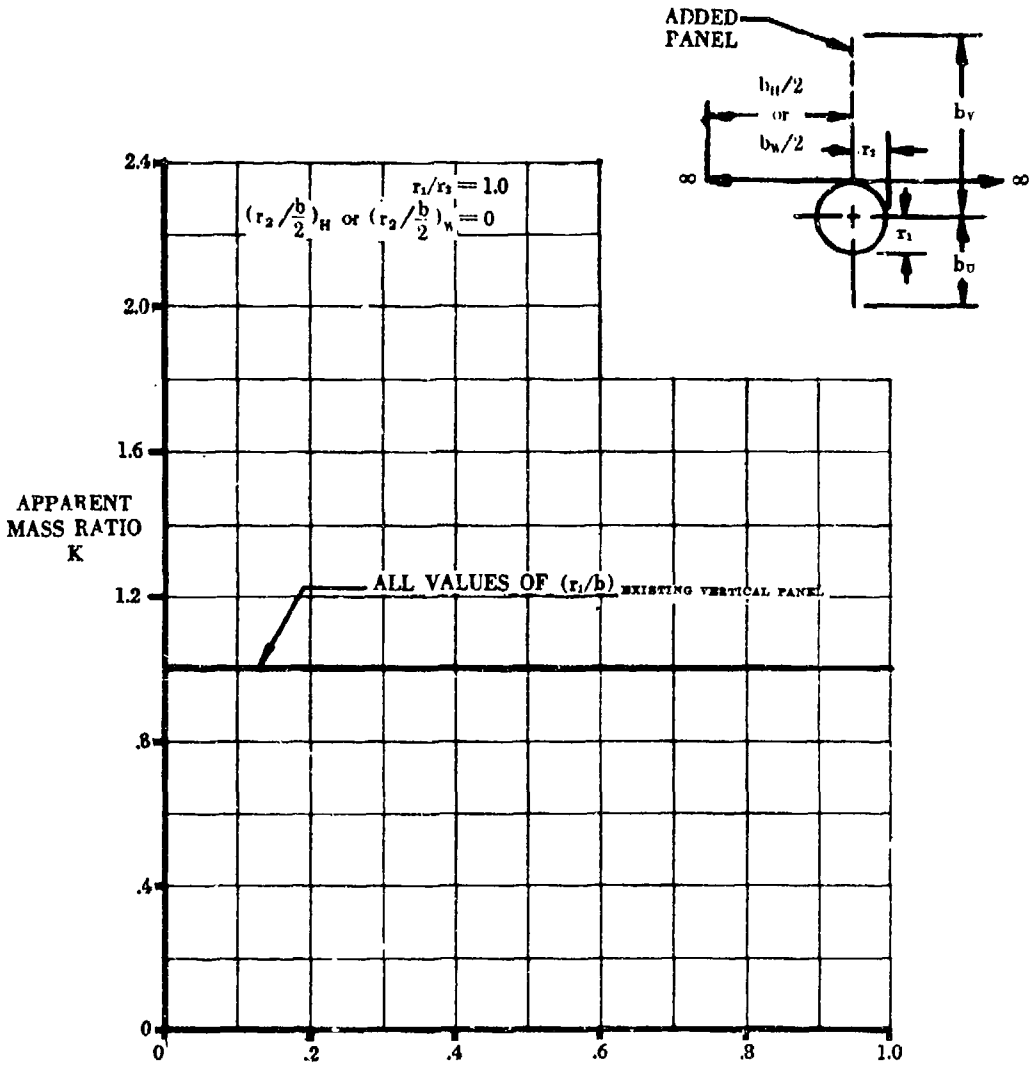

FIGURE 5.3.1.1-25g APPARENT MASS FACTORS (CONTD)

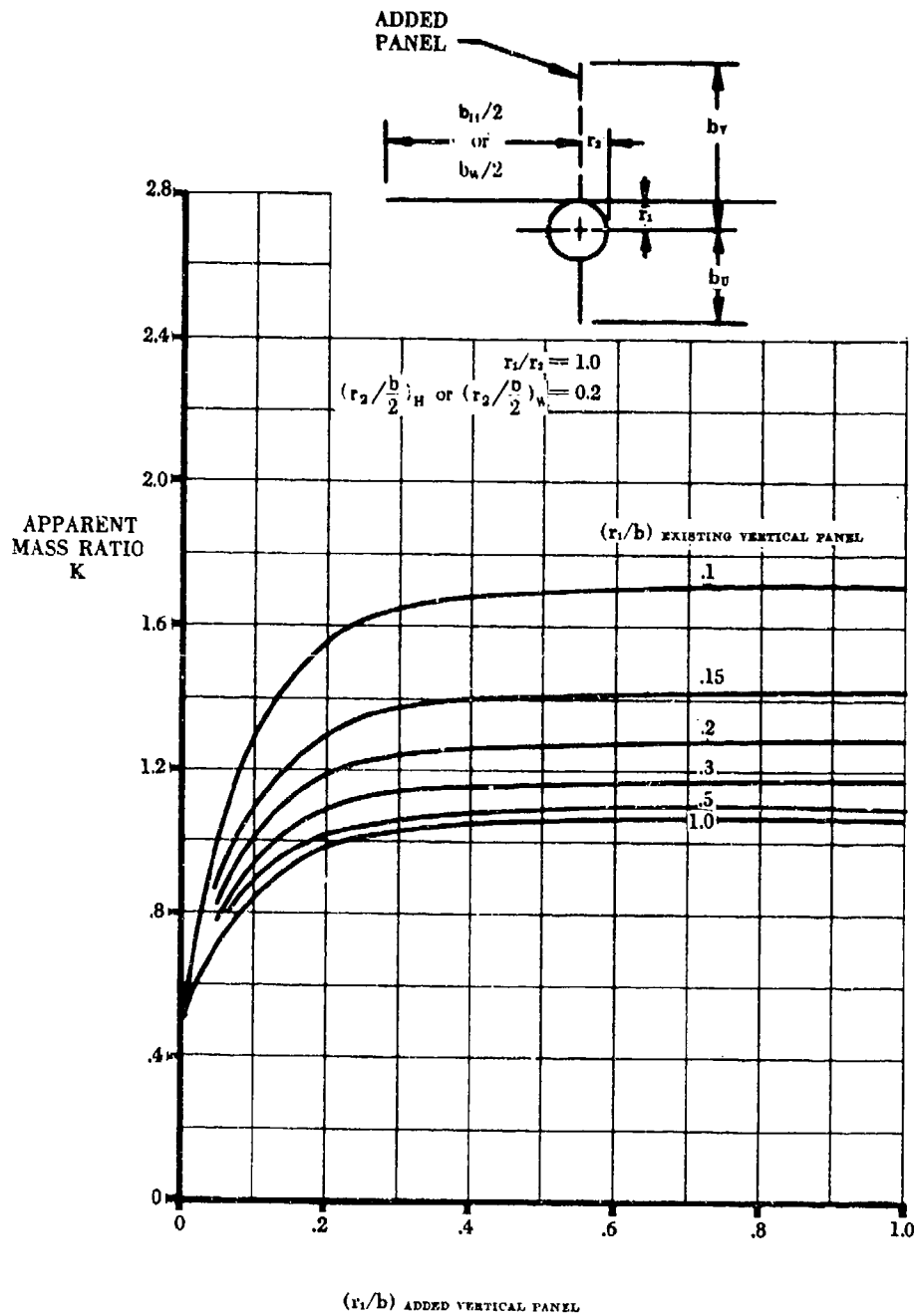

FIGURE 5.3.1.1-25h APPARENT MASS FACTORS (CONTD)

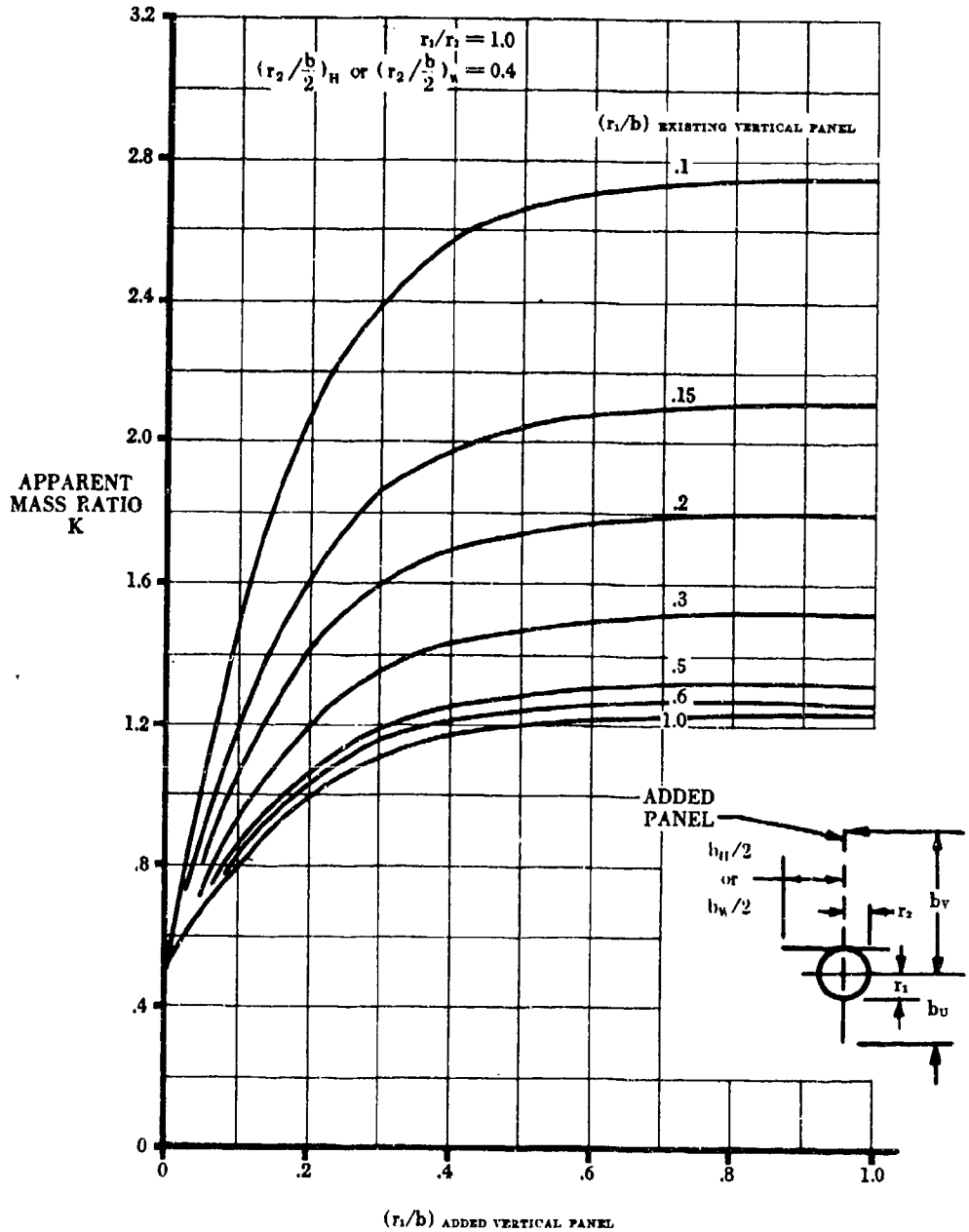

FIGURE 5.3.1.1-25i APPARENT MASS FACTORS (CONTD)

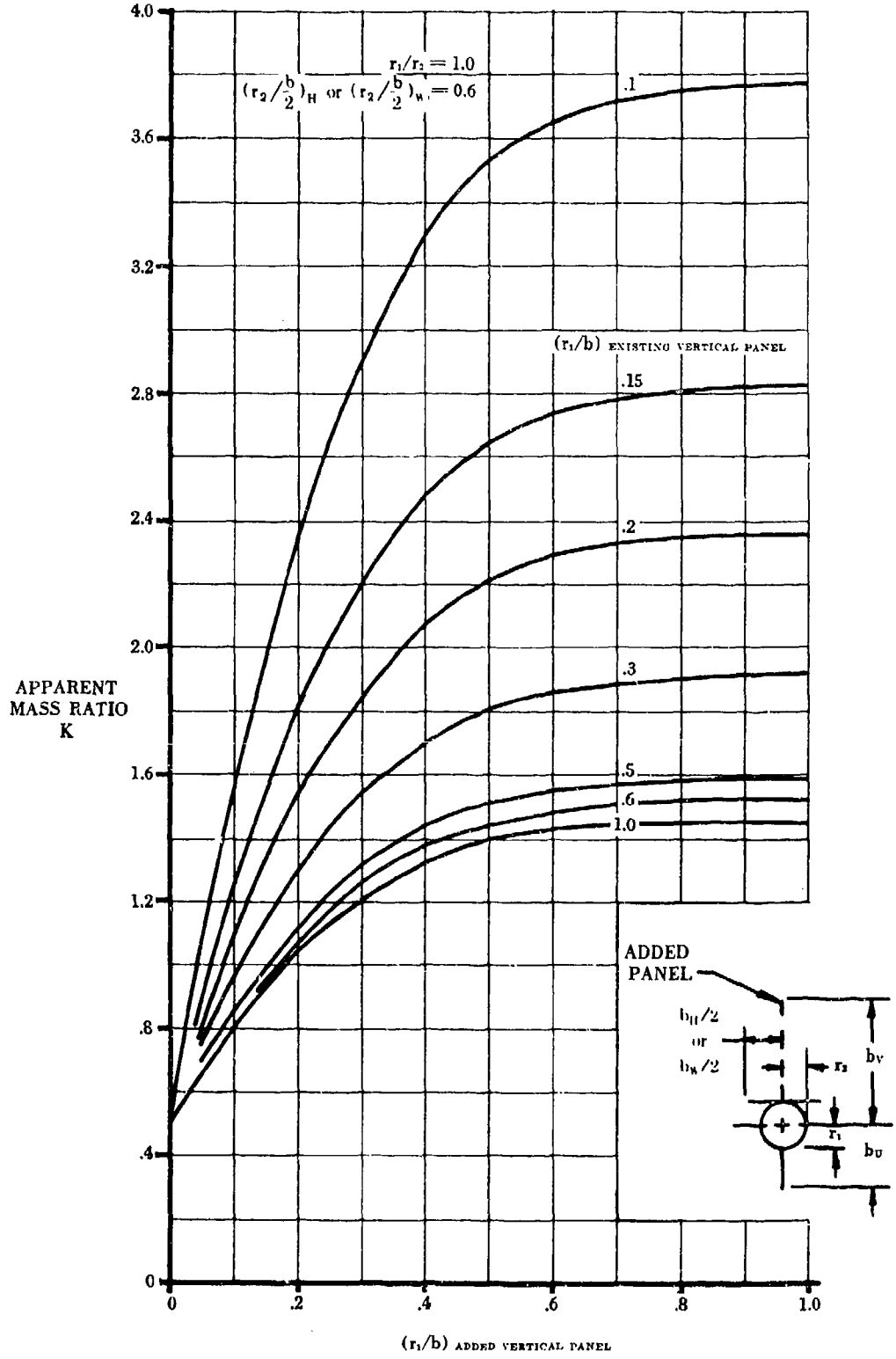

FIGURE 5.3.1.1-25j APPARENT MASS FACTORS (CONTD)

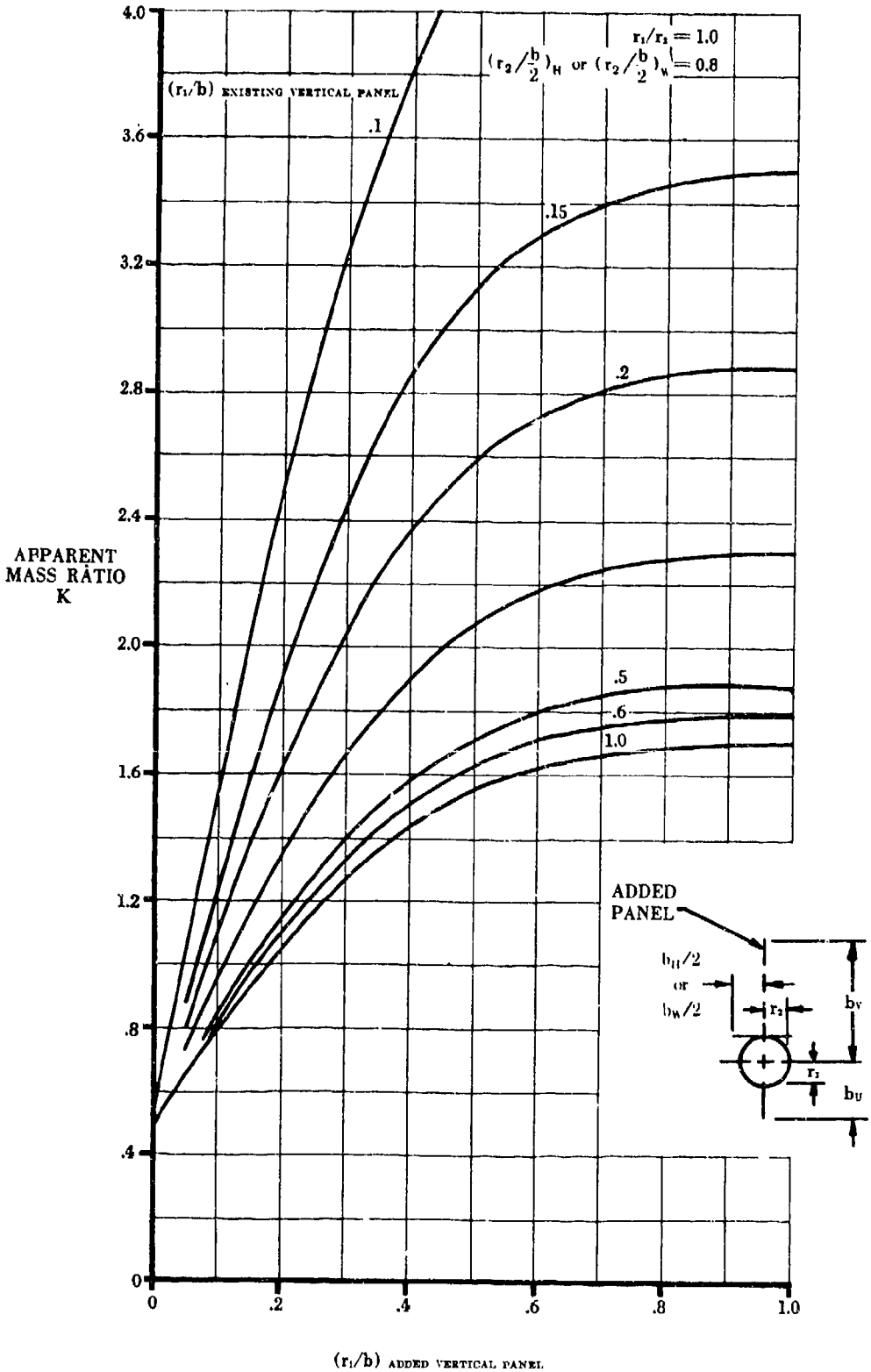

FIGURE 5.3.1.1-25k APPARENT MASS FACTORS (CONTD)

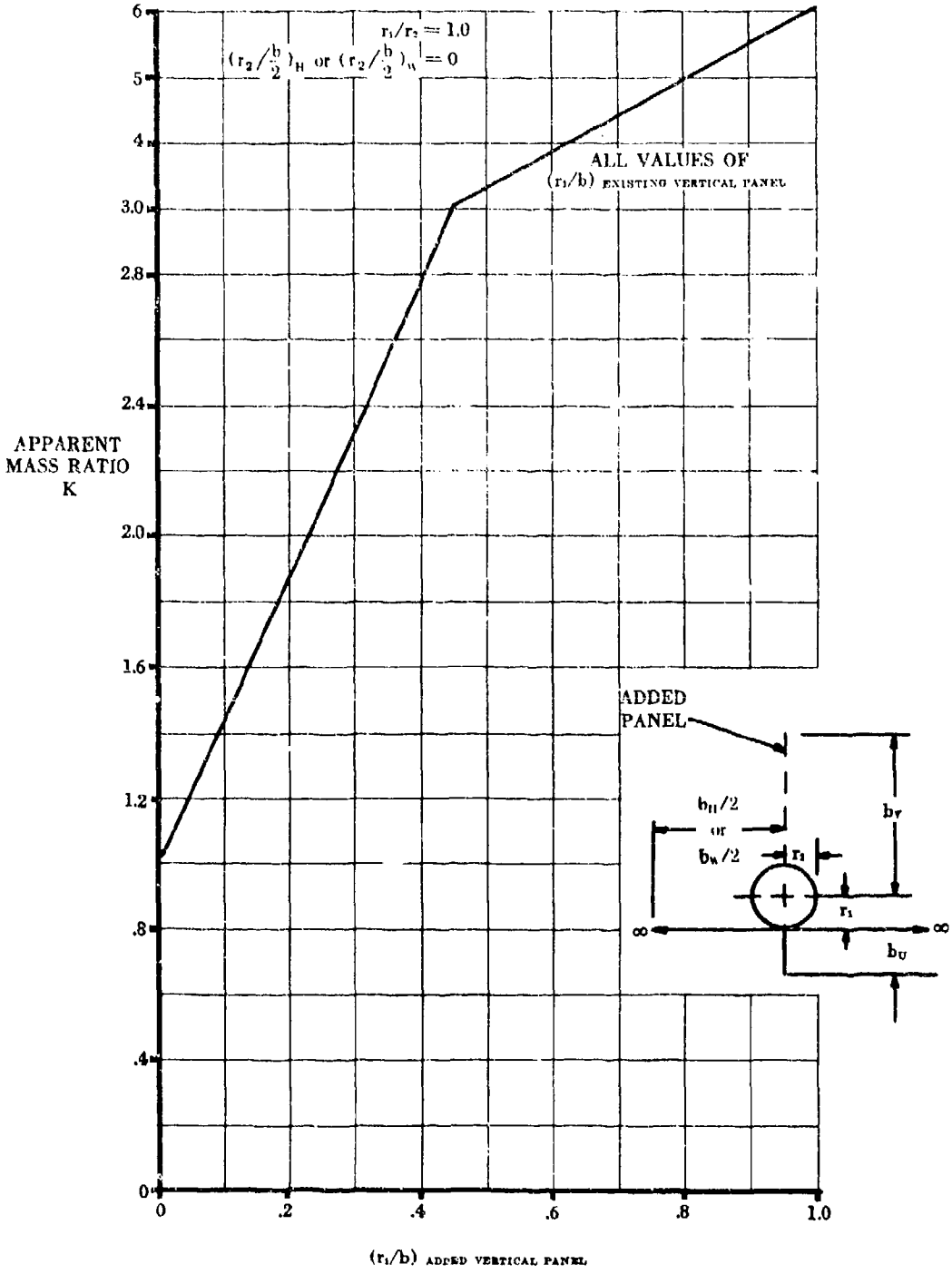

FIGURE 5.3.1.1-251 APPARENT MASS FACTORS (CONTD)

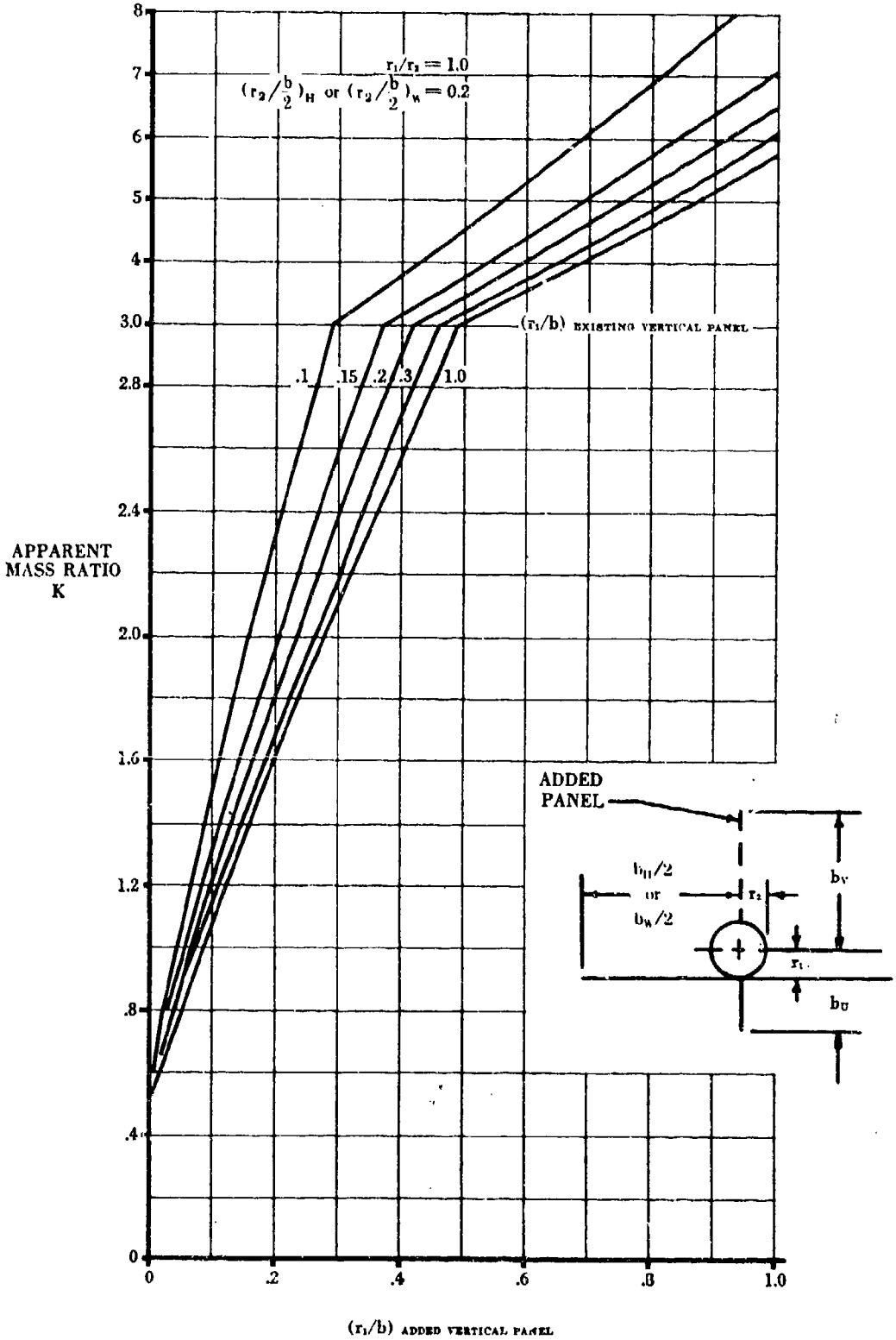

FIGURE 5.3.1.1-25m APPARENT MASS FACTORS (CONTD)

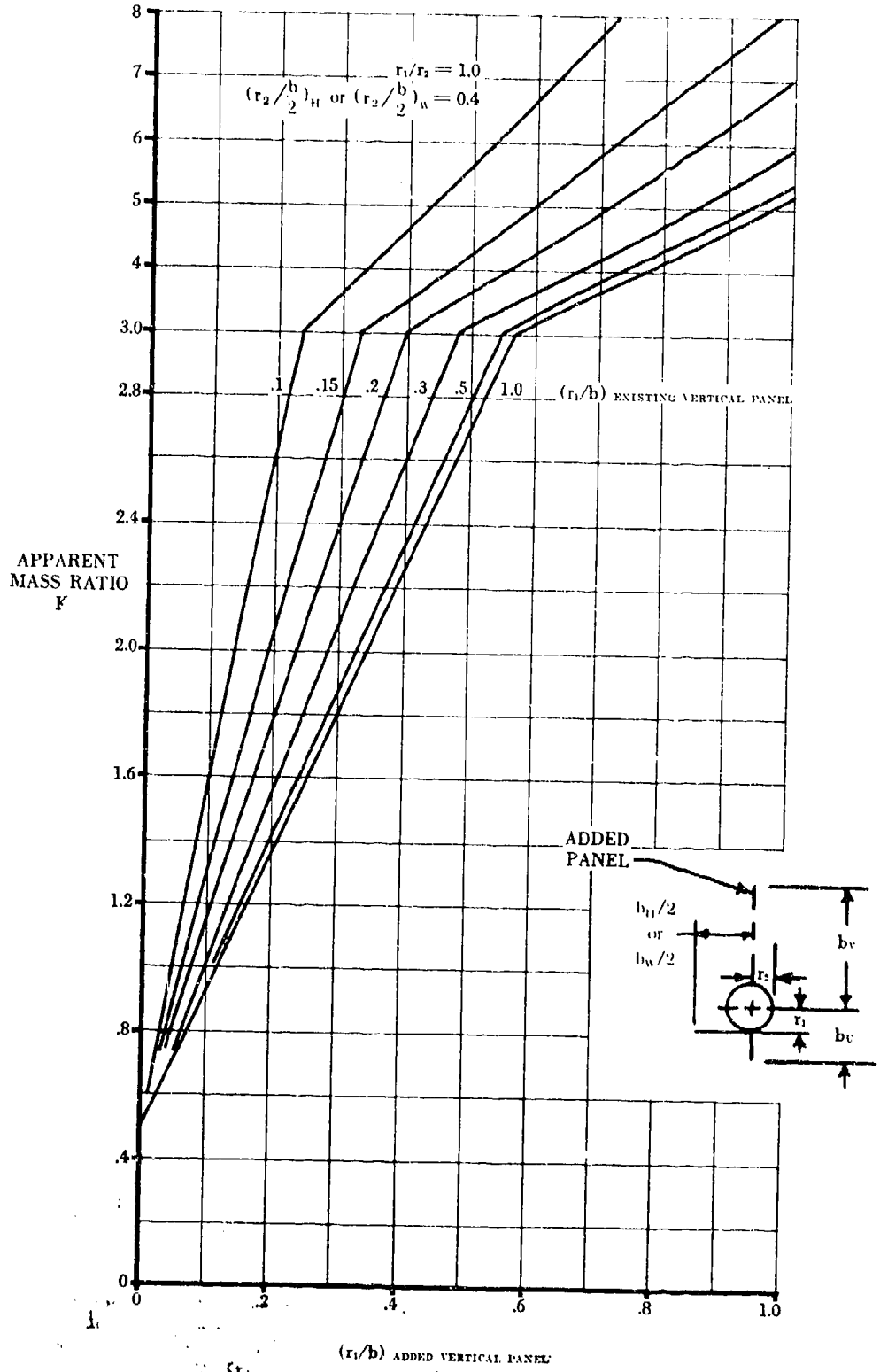

FIGURE 5.3.1.1-25n APPARENT MASS FACTORS (CONTD)

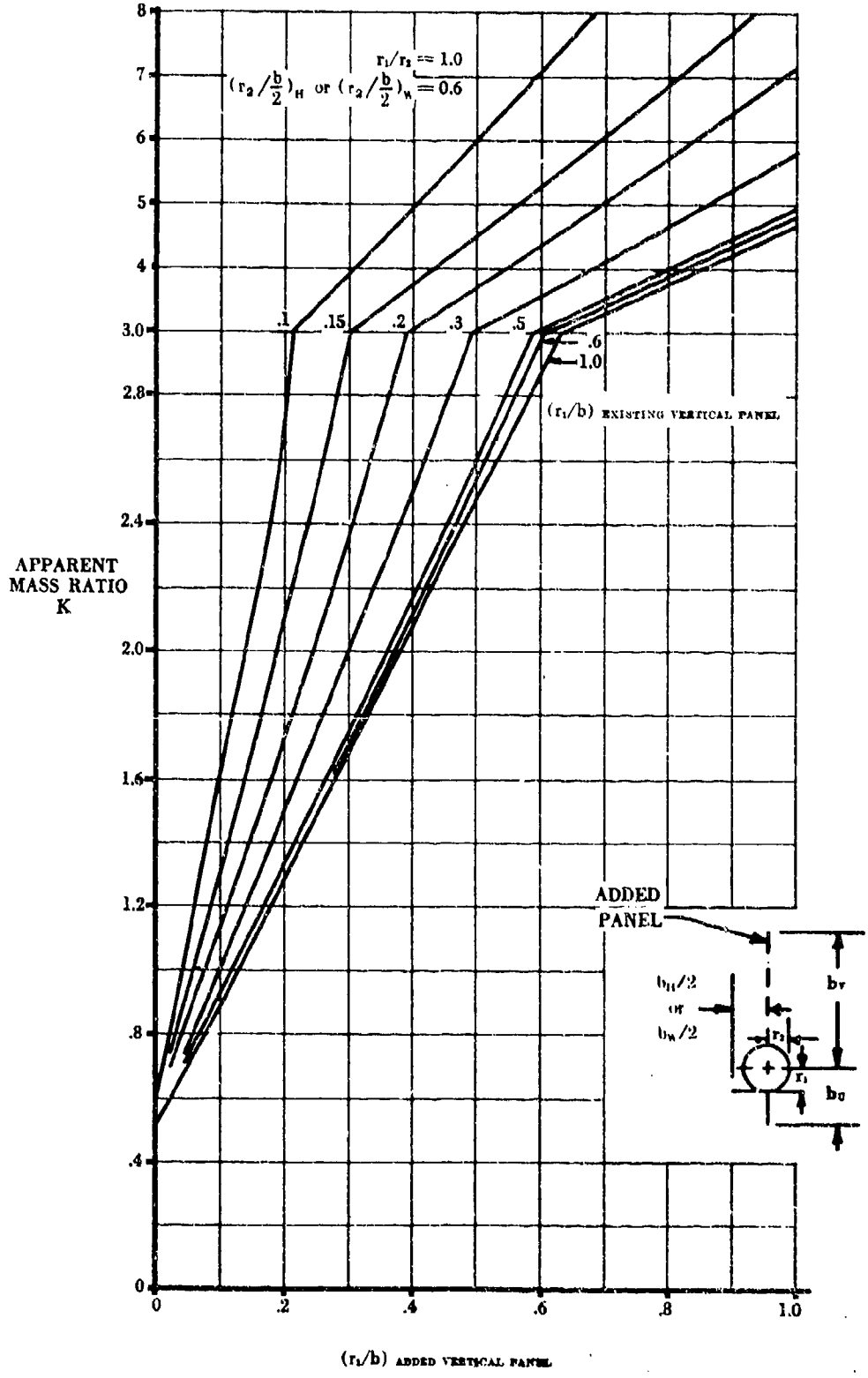

FIGURE 5.3.1.1-25 APPARENT MASS FACTORS (CONTD)

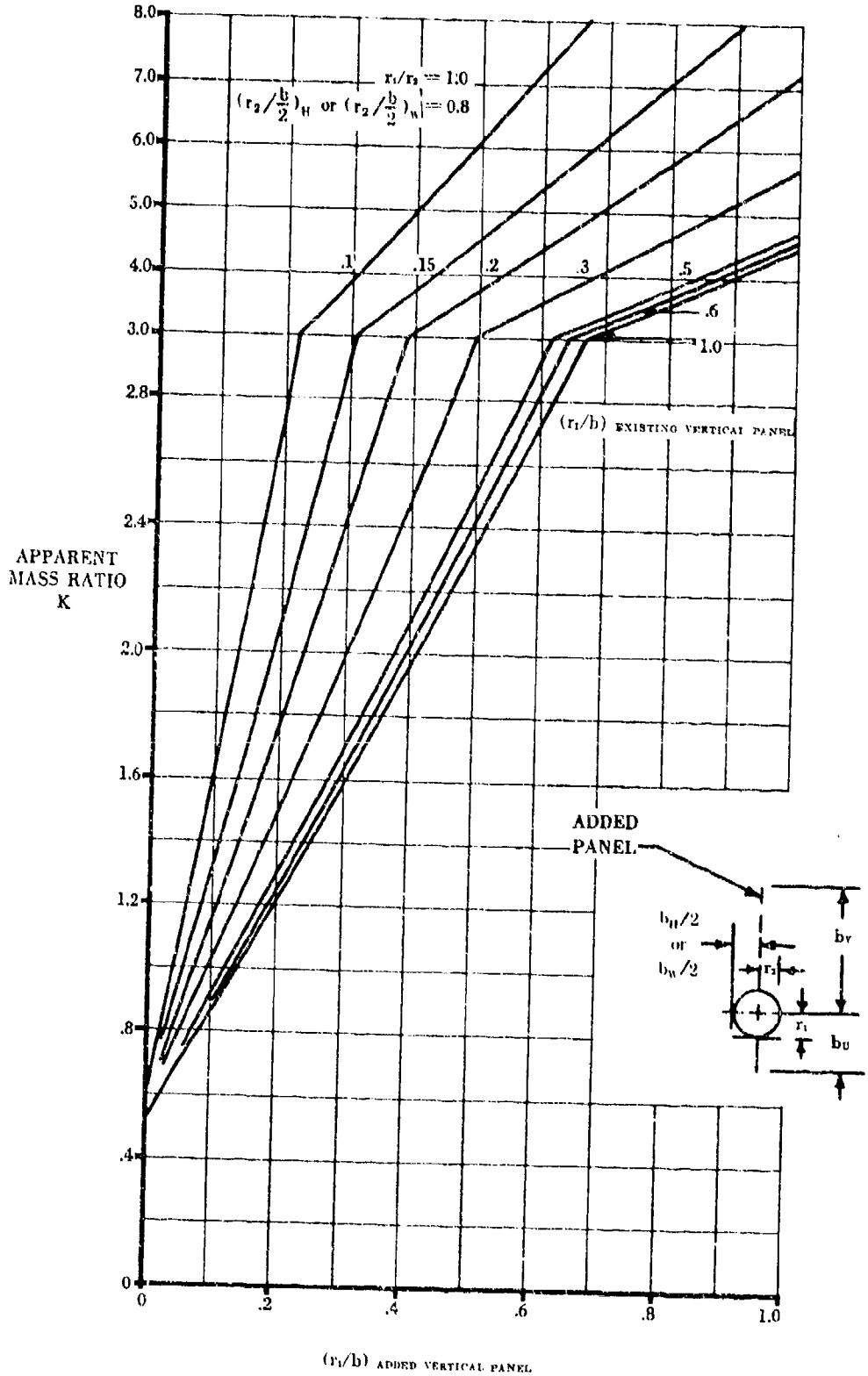

FIGURE 5.3.1.1-25p APPARENT MASS FACTORS (CONTD)

SUBSONIC AND SUPERSONIC

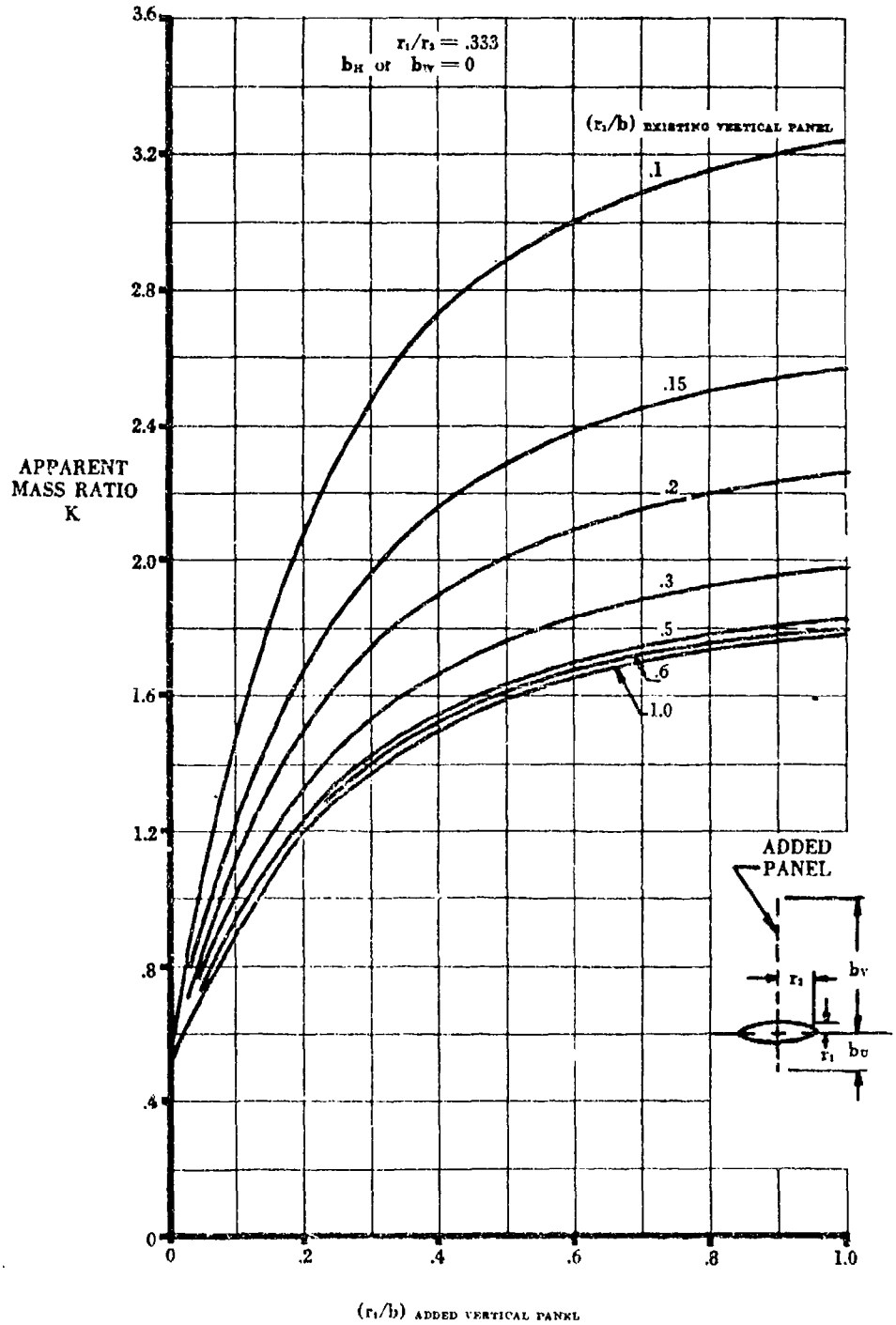

FIGURE 5.3.1.1-25q APPARENT MASS FACTORS (CONTD)

SUBSONIC AND SUPERSONIC

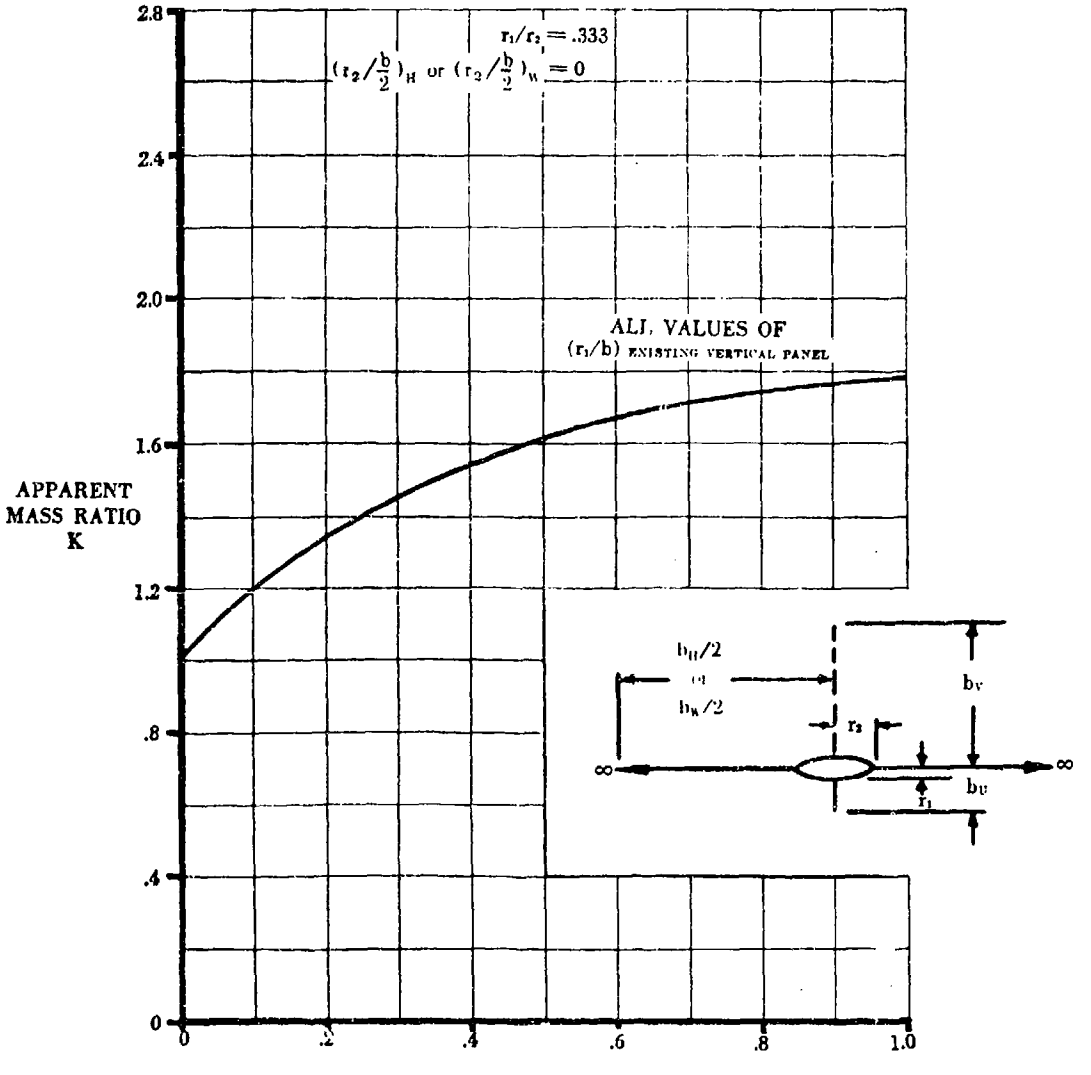

FIGURE 5.3.1.1-25r APPARENT MASS FACTORS (CONTD)

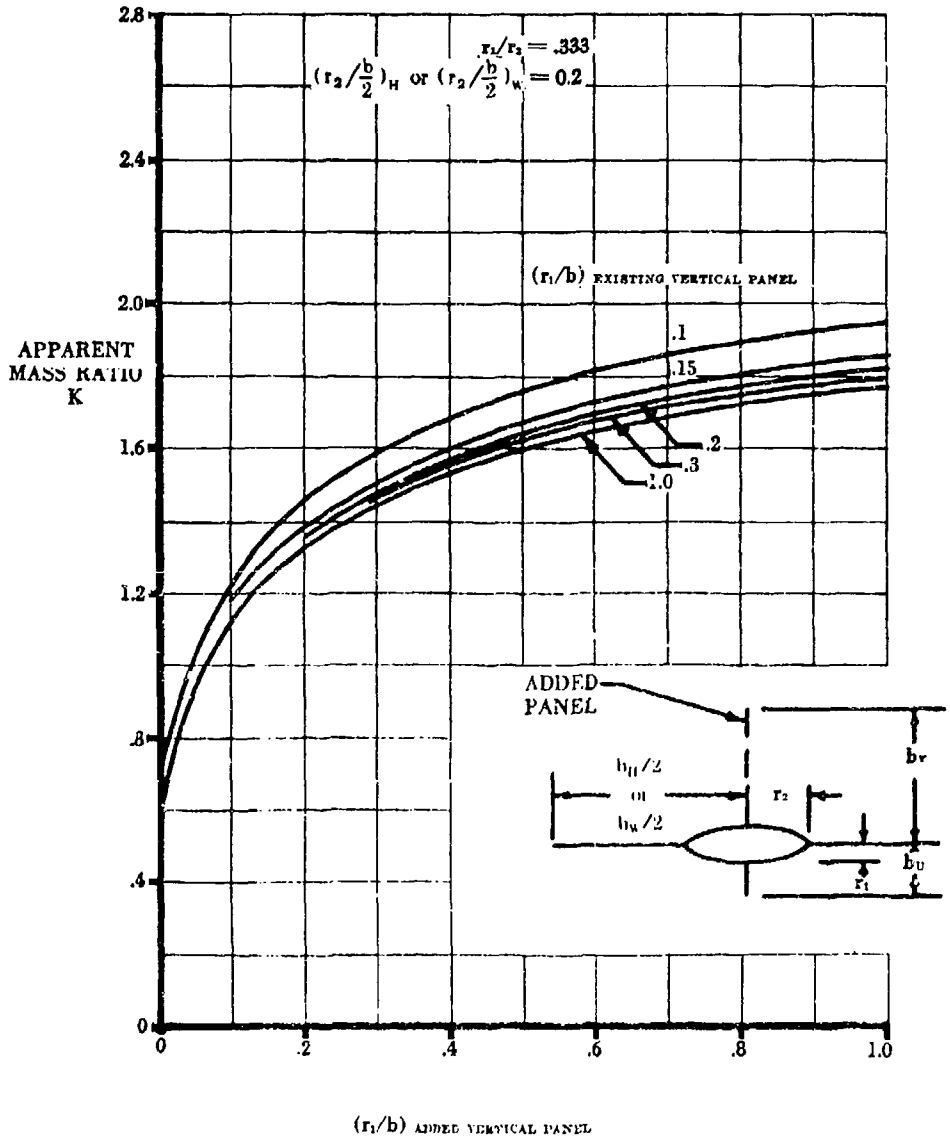

FIGURE 5.1.1-25: APPARENT MASS FACTORS (CONTD)

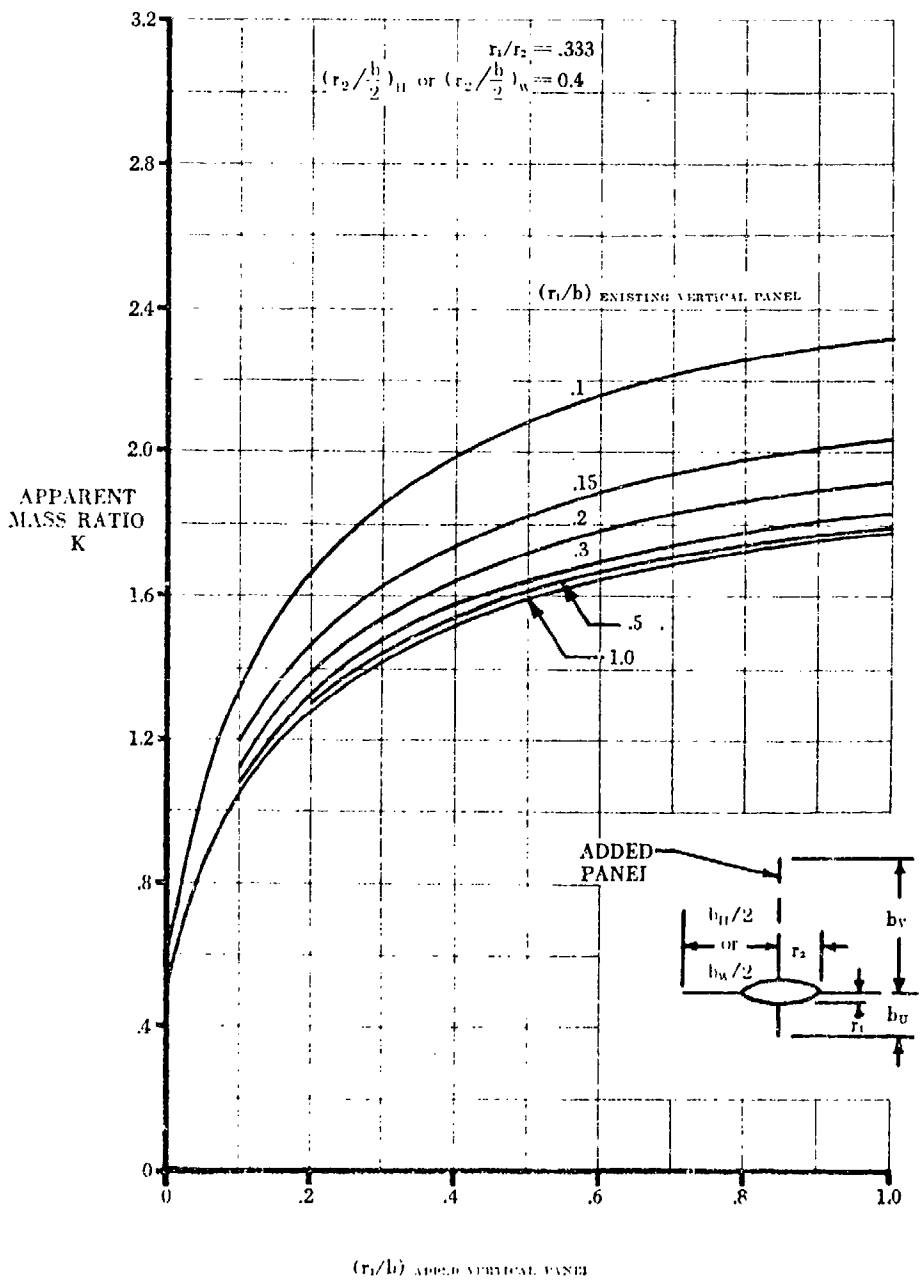

FIGURE 5.3.1.1-25t APPARENT MASS FACTORS (CONTD)

SUBSONIC AND SUPERSONIC

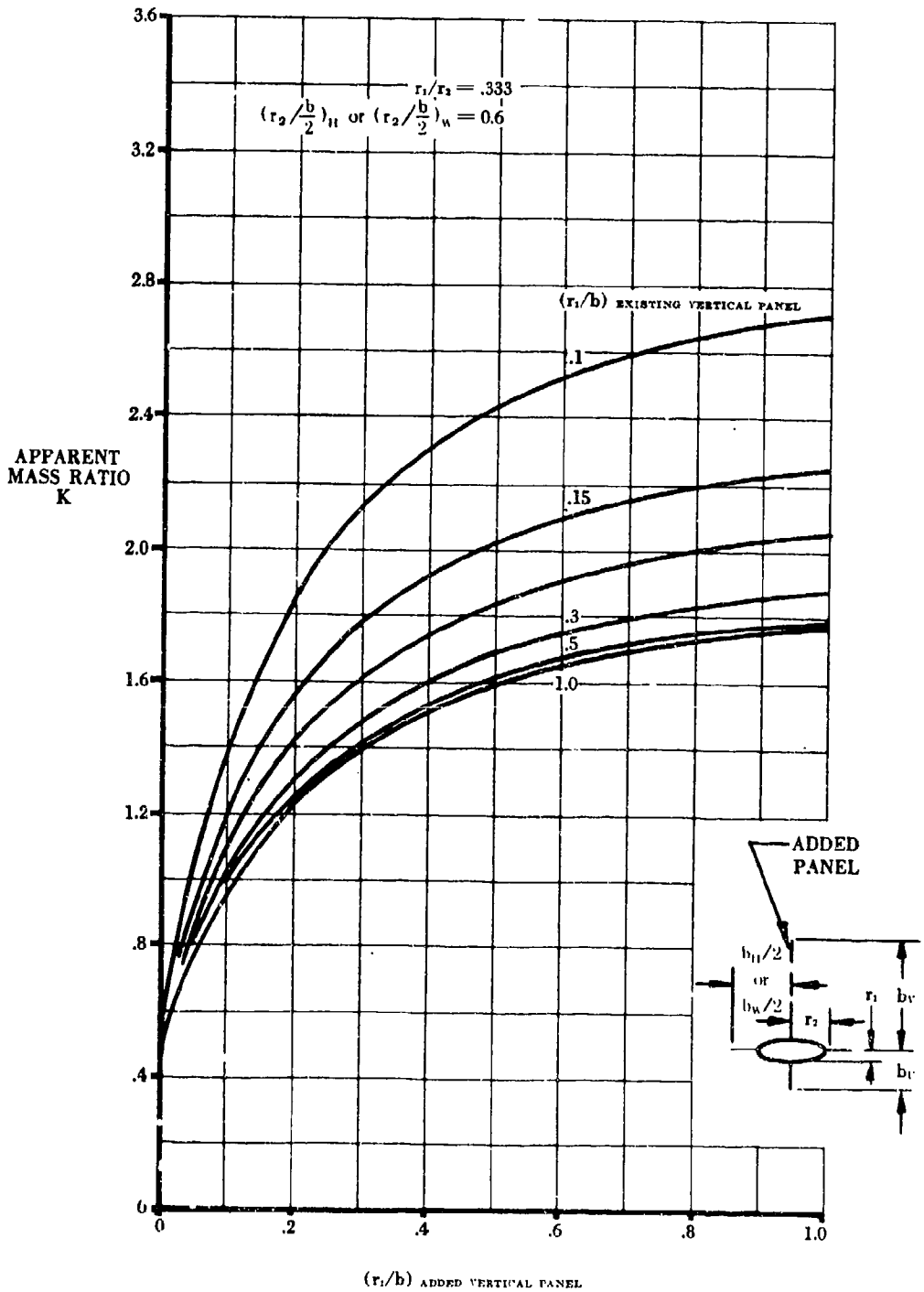

FIGURE 5.3.1.1-25u APPARENT MASS FACTORS (CONTD)

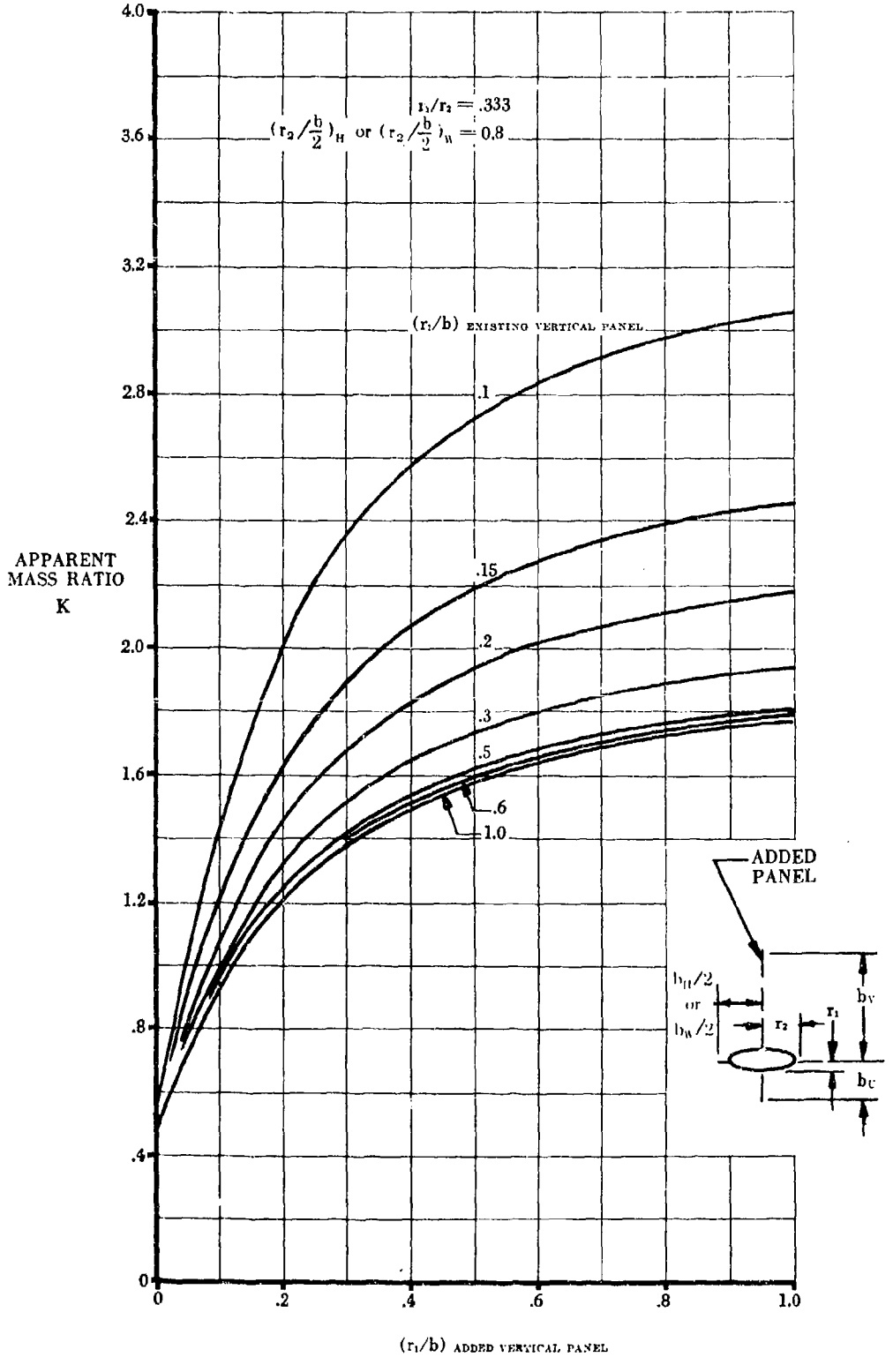

FIGURE 5.3.1.1-25v APPARENT MASS FACTORS (CONTD)

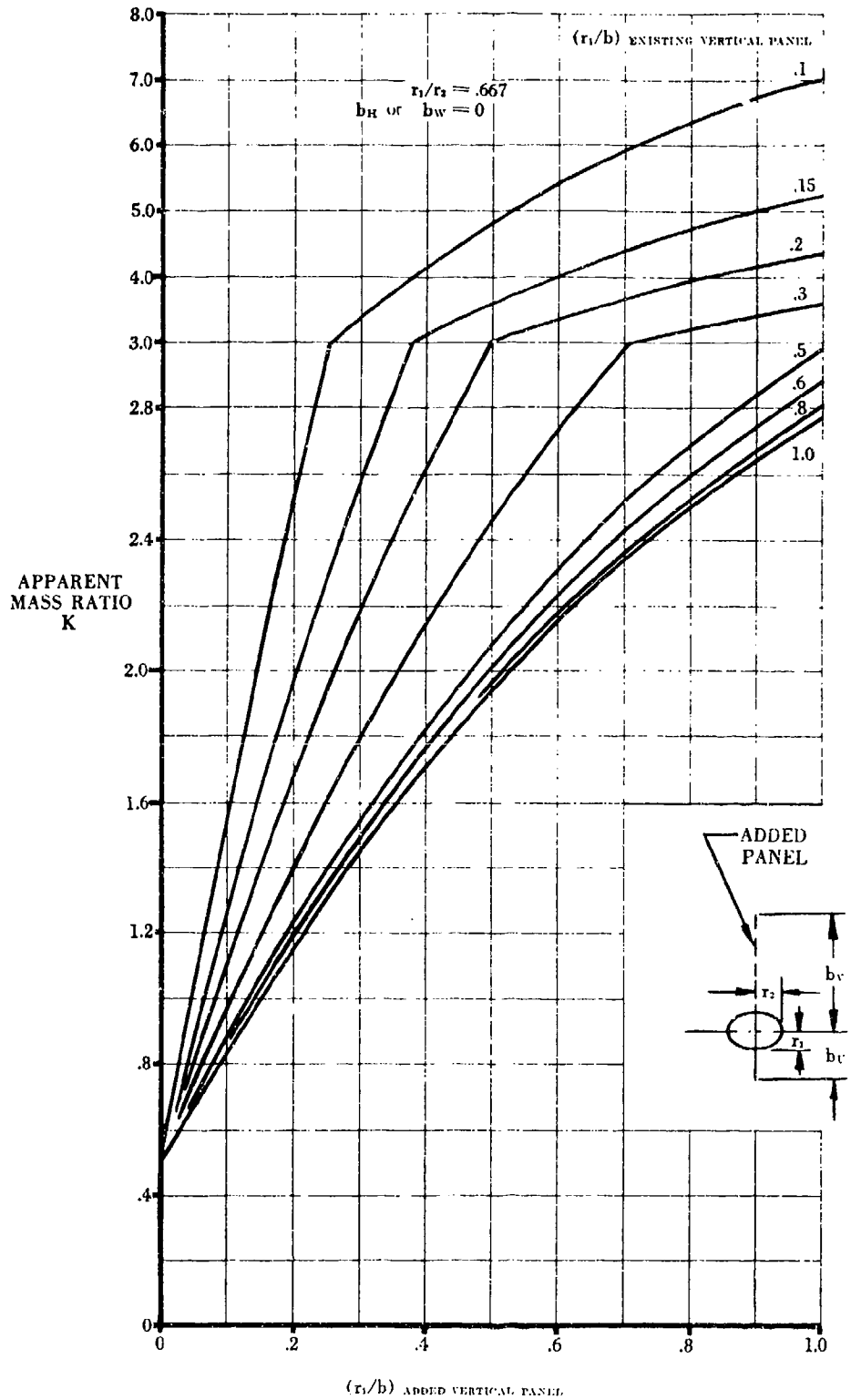

FIGURE 5.3.1.1-25w APPARENT MASS FACTORS (CONTD)

SUBSONIC AND SUPERSONIC

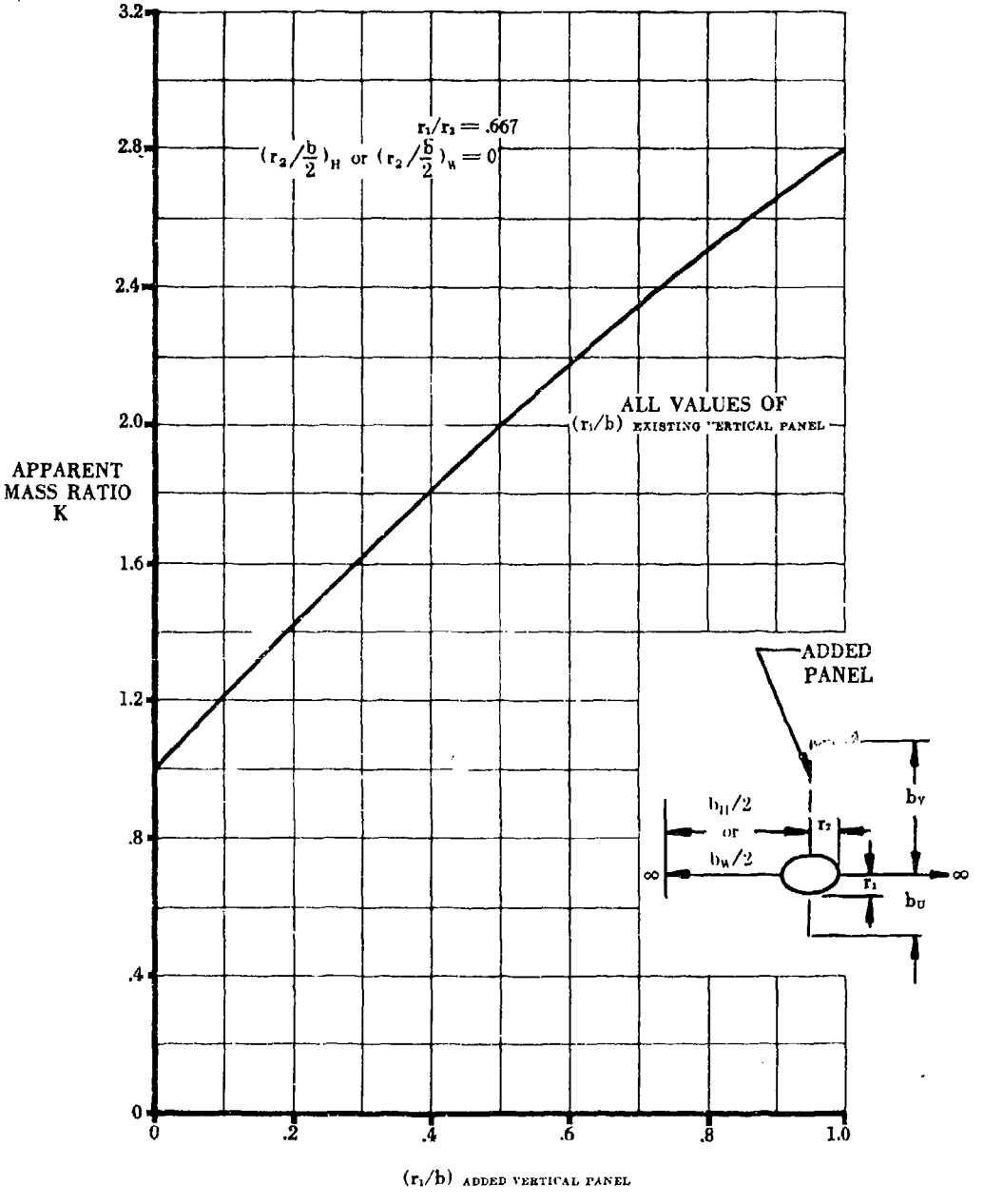

FIGURE 5.3.1.1-25x APPARENT MASS FACTORS (CONTD)

SUBSONIC AND SUPERSONIC

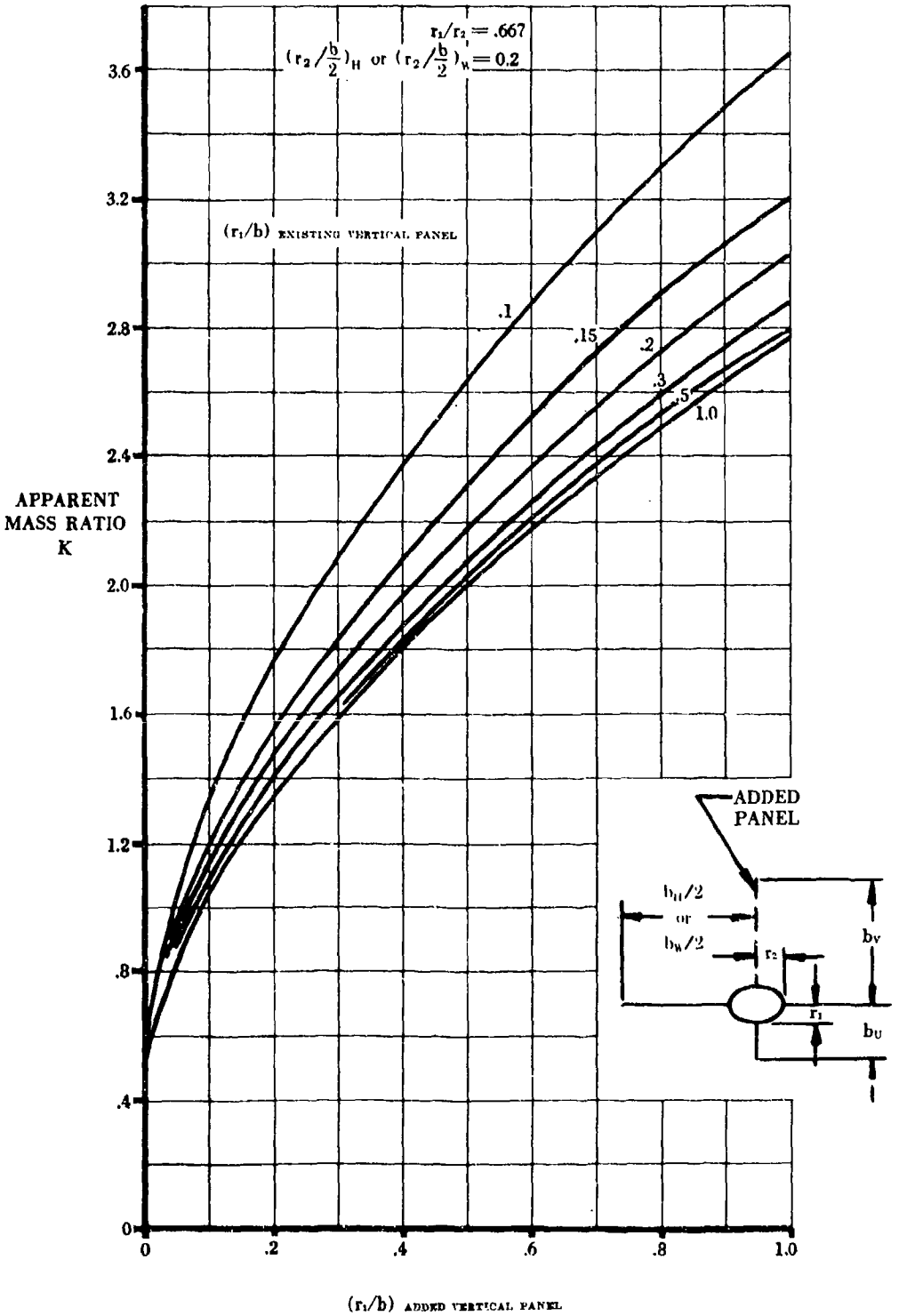

FIGURE 5.3.1.1-25y APPARENT MASS FACTORS (CONTD)

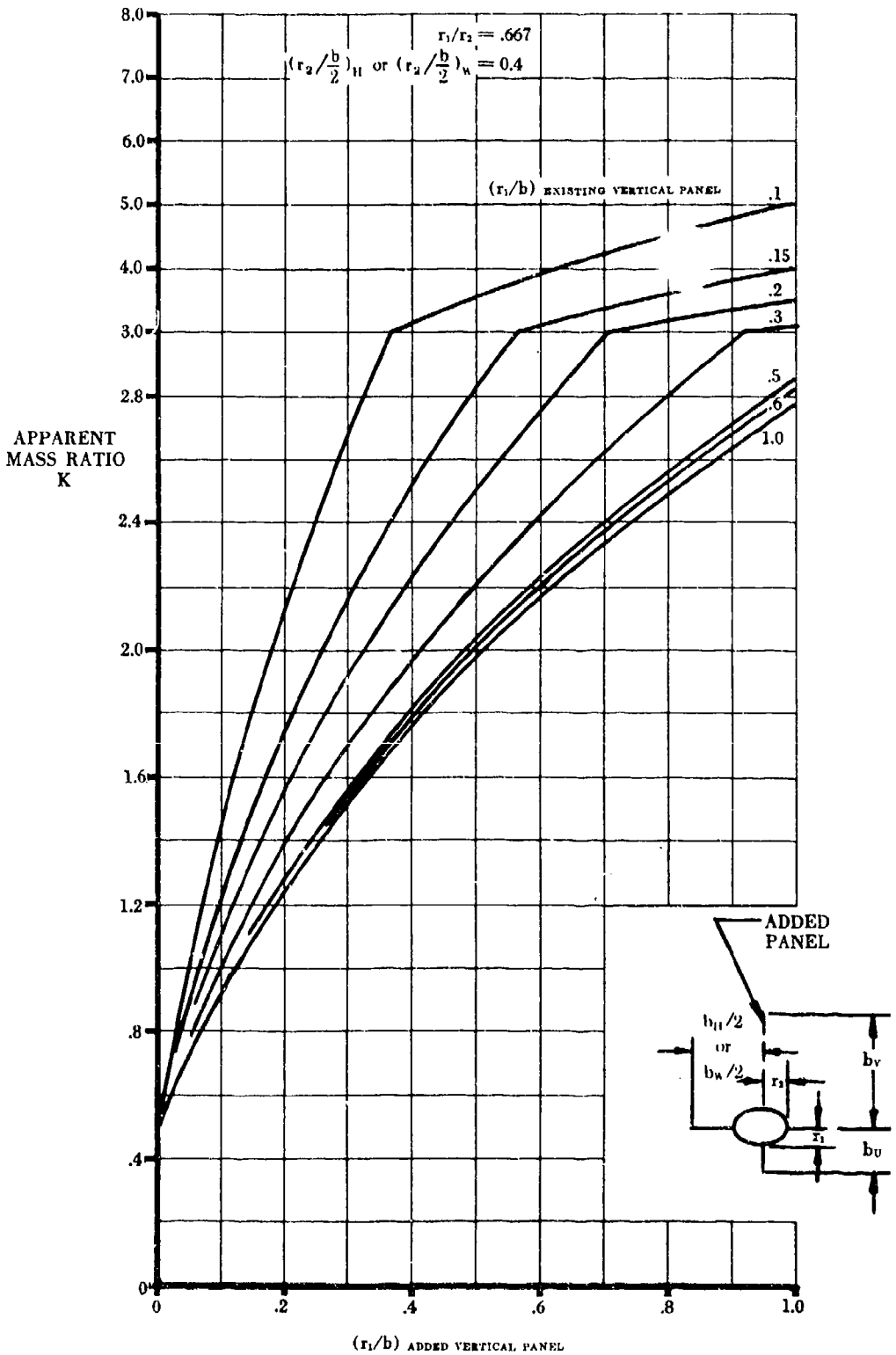

FIGURE 5.3.1.1-25z APPARENT MASS FACTORS (CONTD)

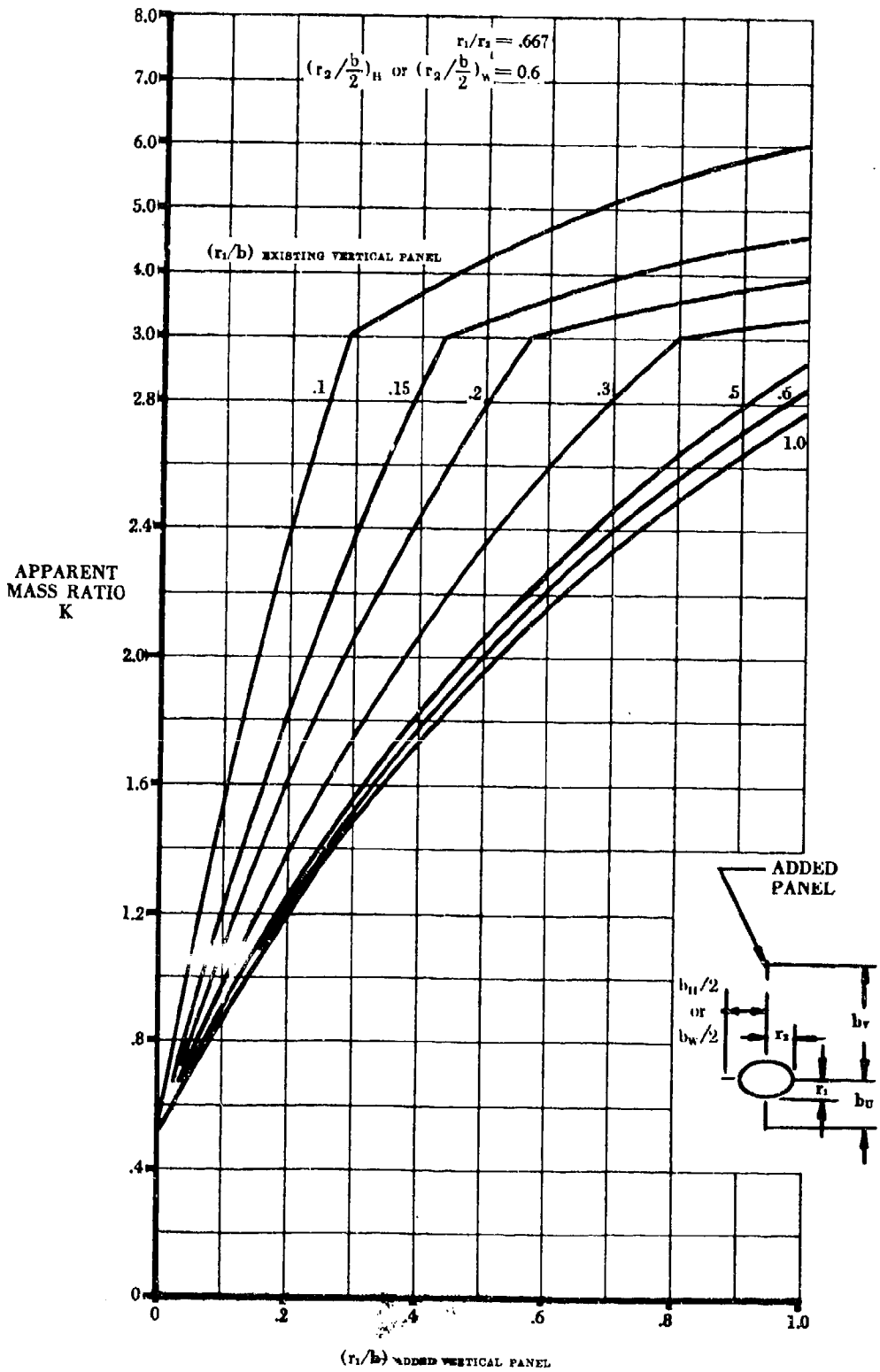

FIGURE 5.3.1.1-2 APPARENT MASS FACTORS (CONTD)

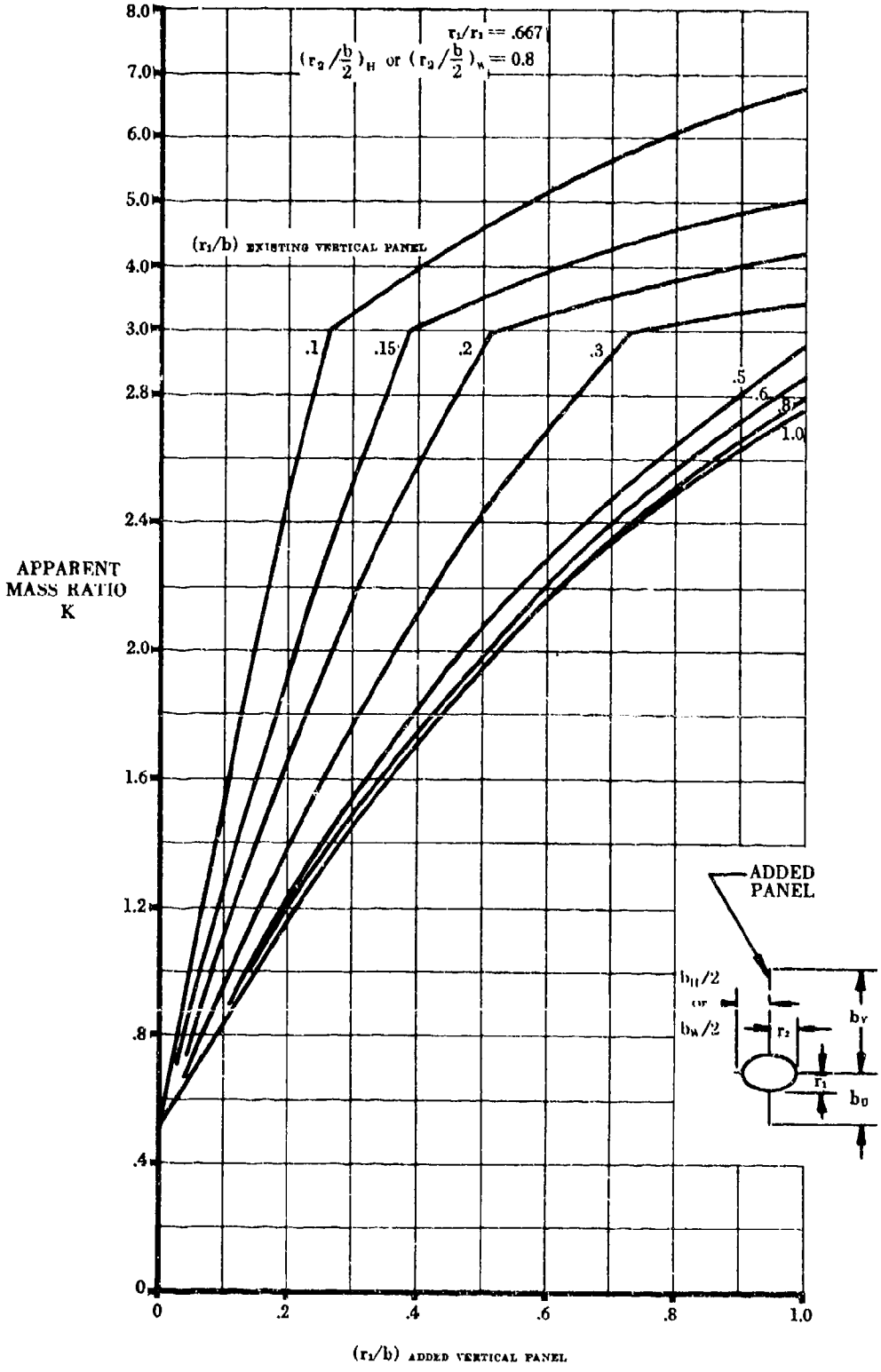

FIGURE 5.3.1.1-25bb APPARENT MASS FACTORS (CONTD)

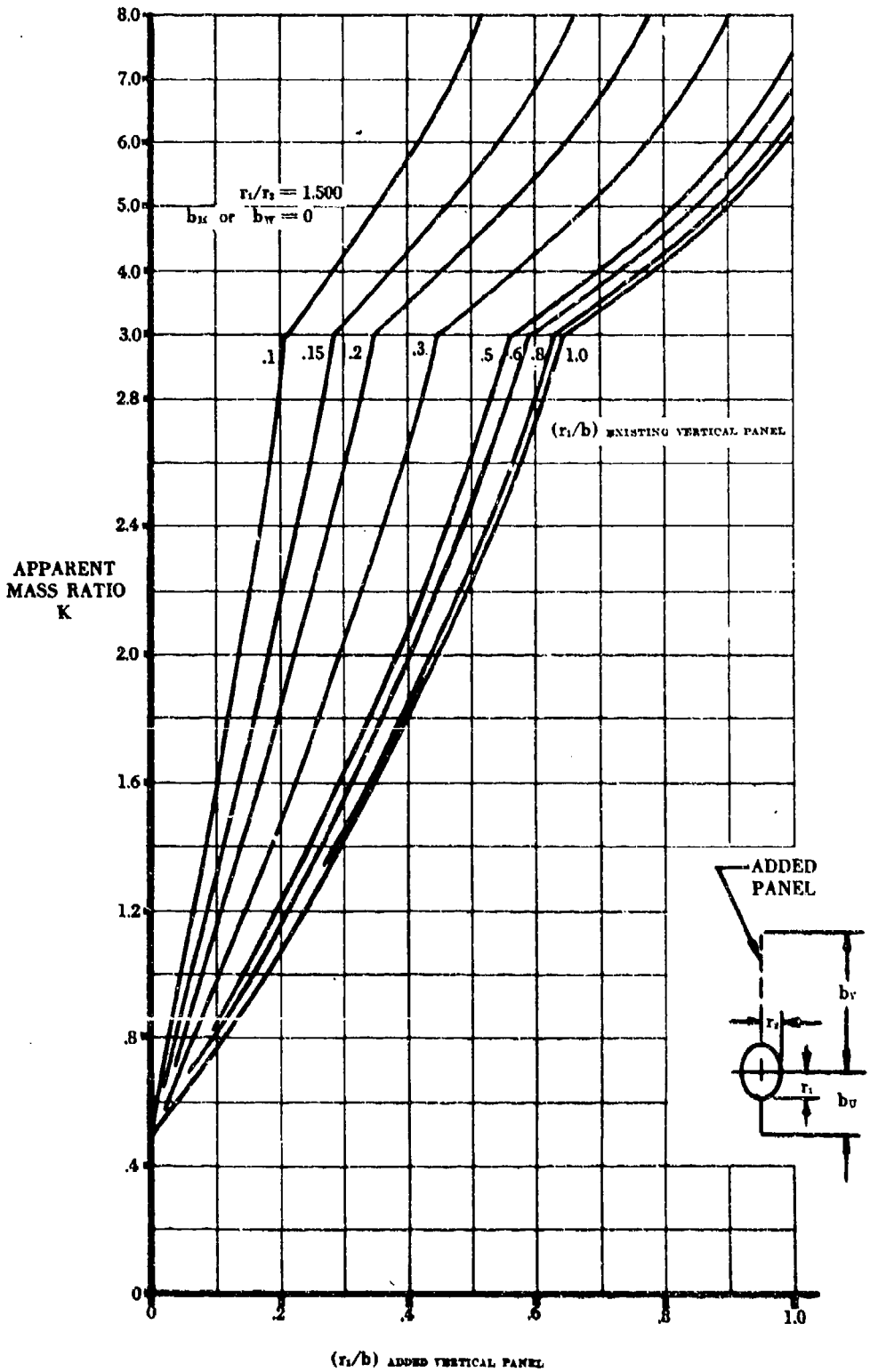

FIGURE 5.3.1.1-25cc APPARENT MASS FACTORS (CONTD)

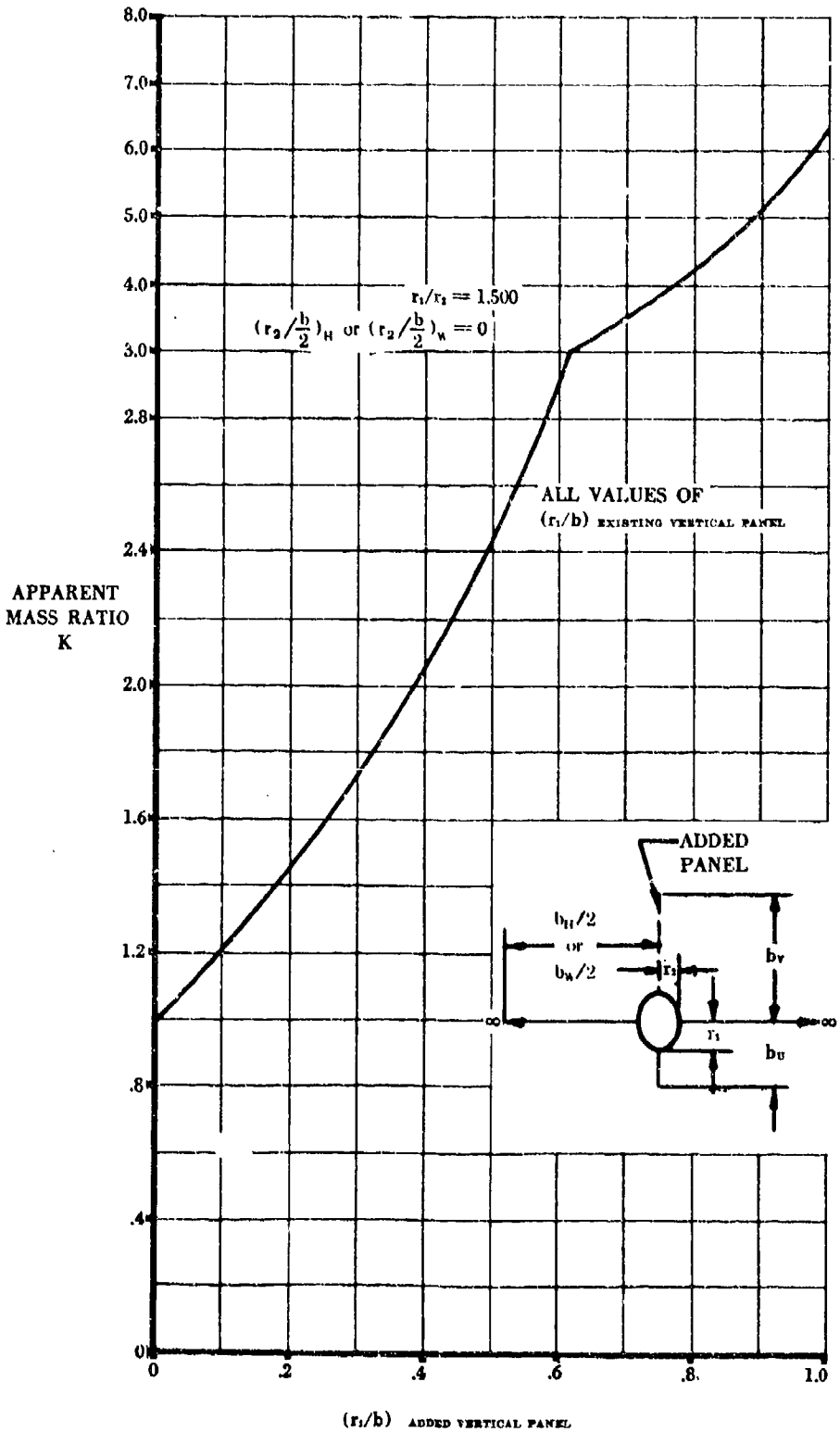

FIGURE 5.3.1.1-25dd APPARENT MASS FACTORS (CONTD)

SUBSONIC AND SUPERSONIC

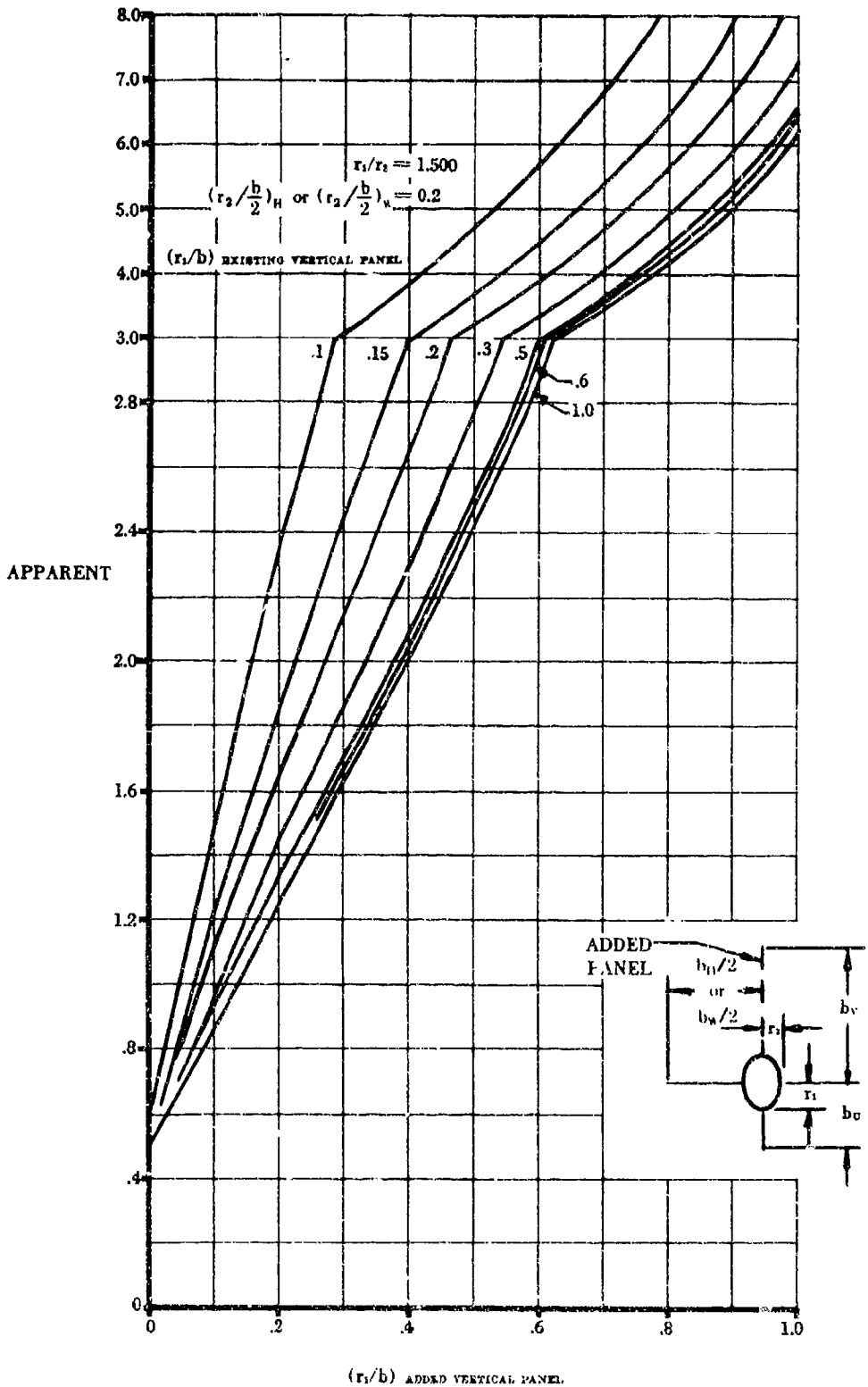

FIGURE 5.3.1.1-25ee APPARENT MASS FACTORS (CONTD)

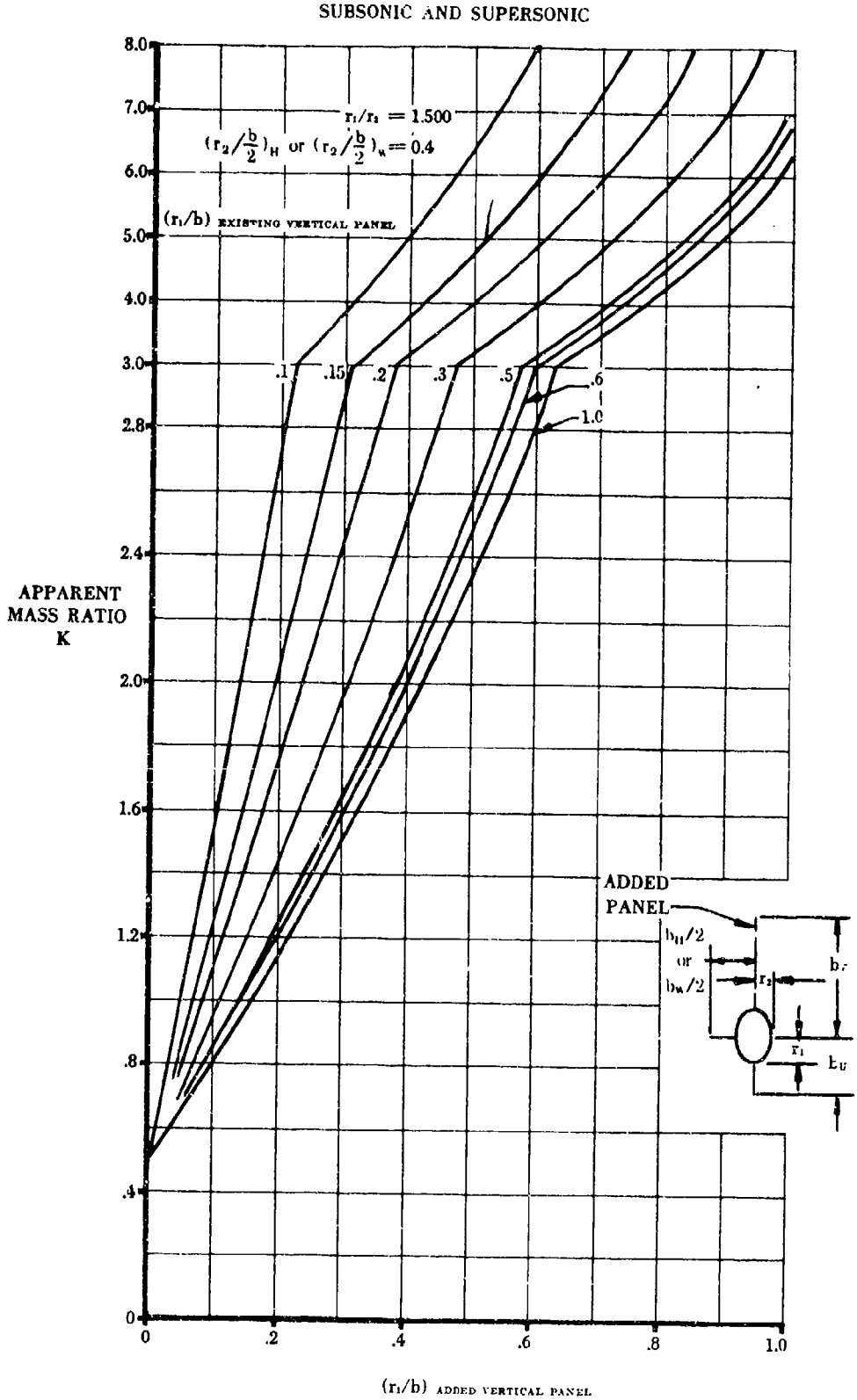

FIGURE 5.3.1.1-25ff APPARENT MASS FACTORS (CONTD)

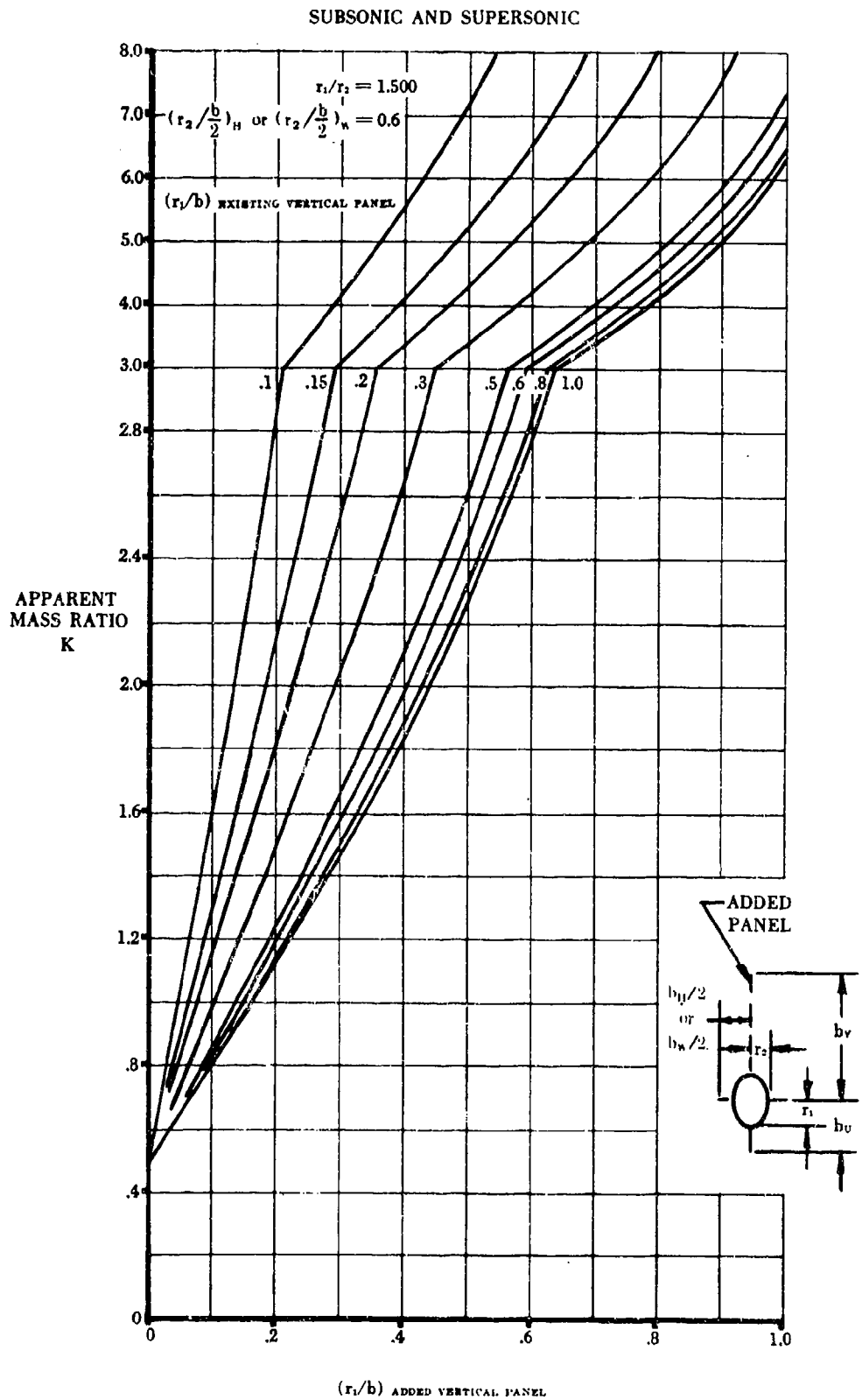

FIGURE 5.3.1.1-25gg APPARENT MASS FACTORS (CONTD)

SUBSONIC AND SUPERSONIC

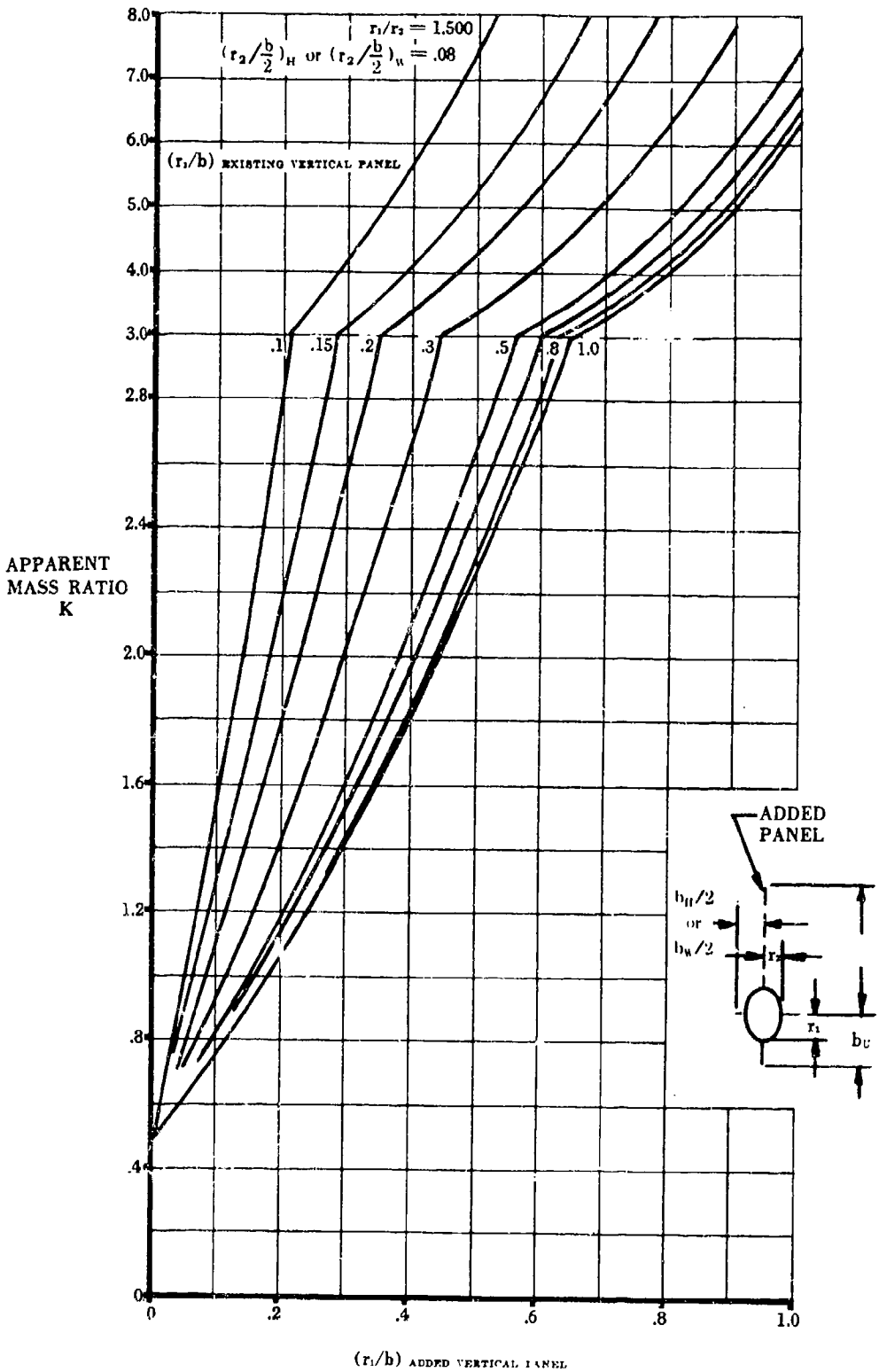

FIGURE 5.3.1.1-25hh APPARENT MASS FACTORS (CONTD)

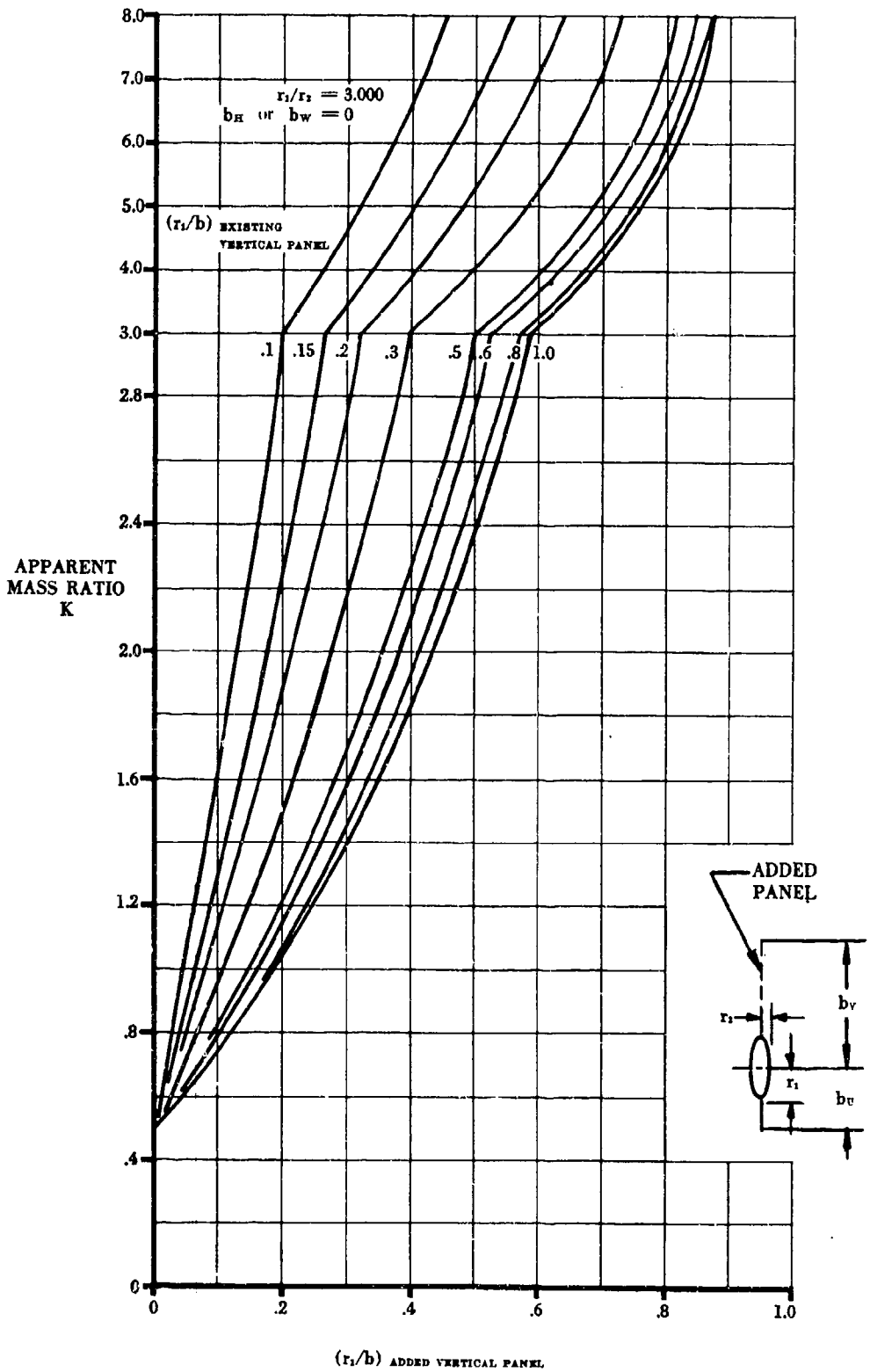

FIGURE 5.3.1.1-25ii APPARENT MASS FACTORS (CONTD)

SUBSONIC AND SUPERSONIC

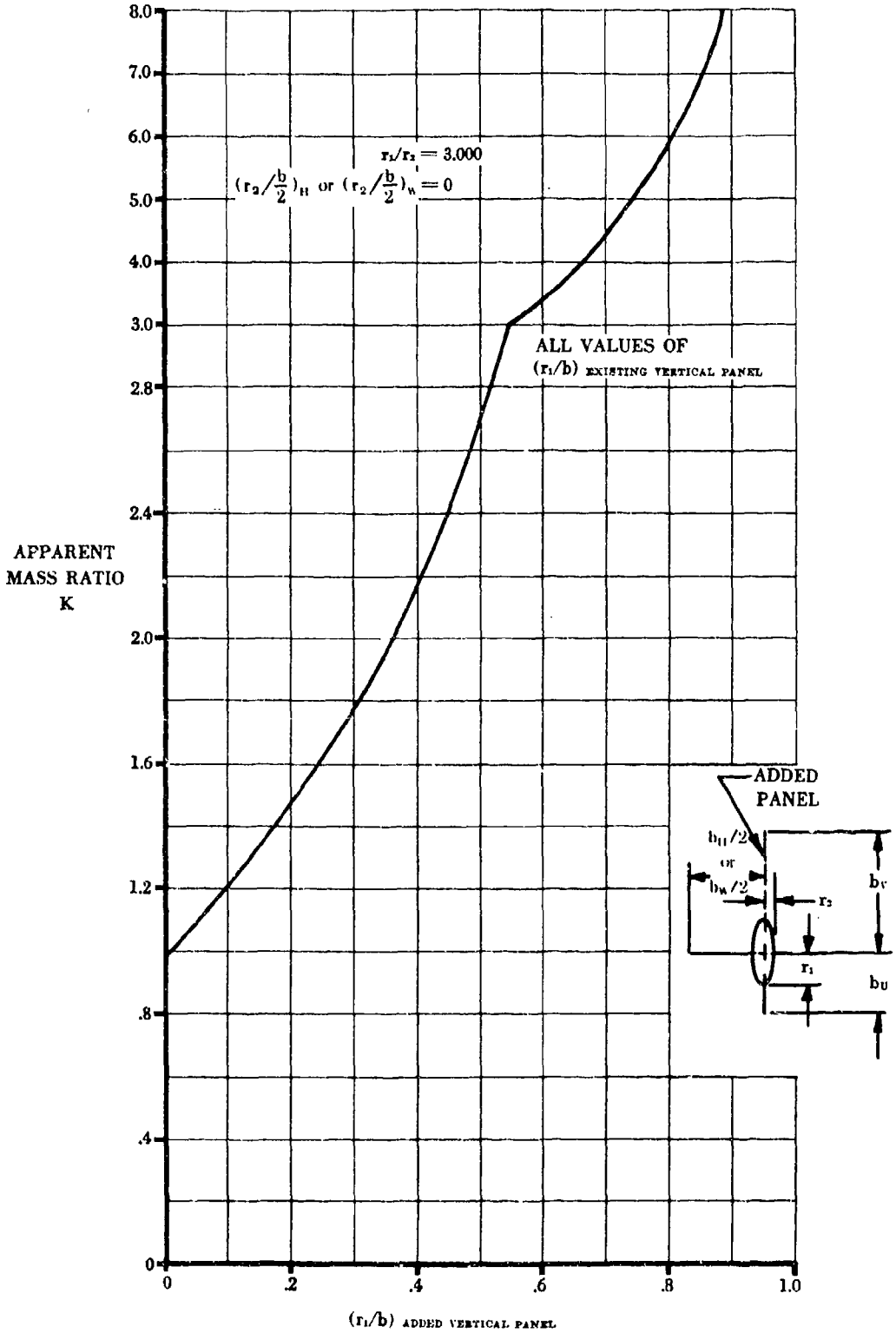

FIGURE 5.3.1.1-25jj APPARENT MASS FACTORS (CONTD)

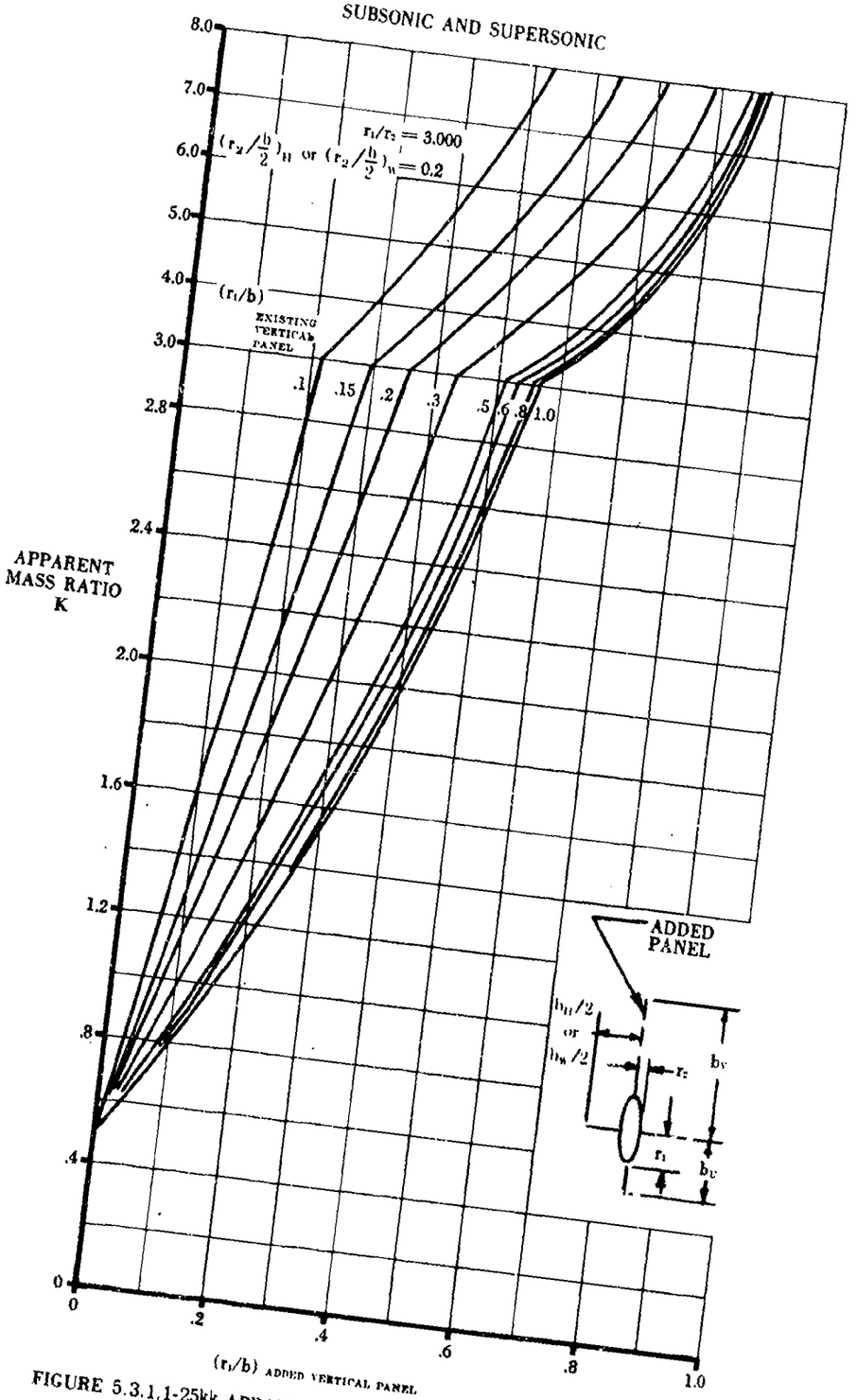

FIGURE 5.3.1.1-25kk APPARENT MASS FACTORS (CONTD)

SUBSONIC AND SUPERSONIC

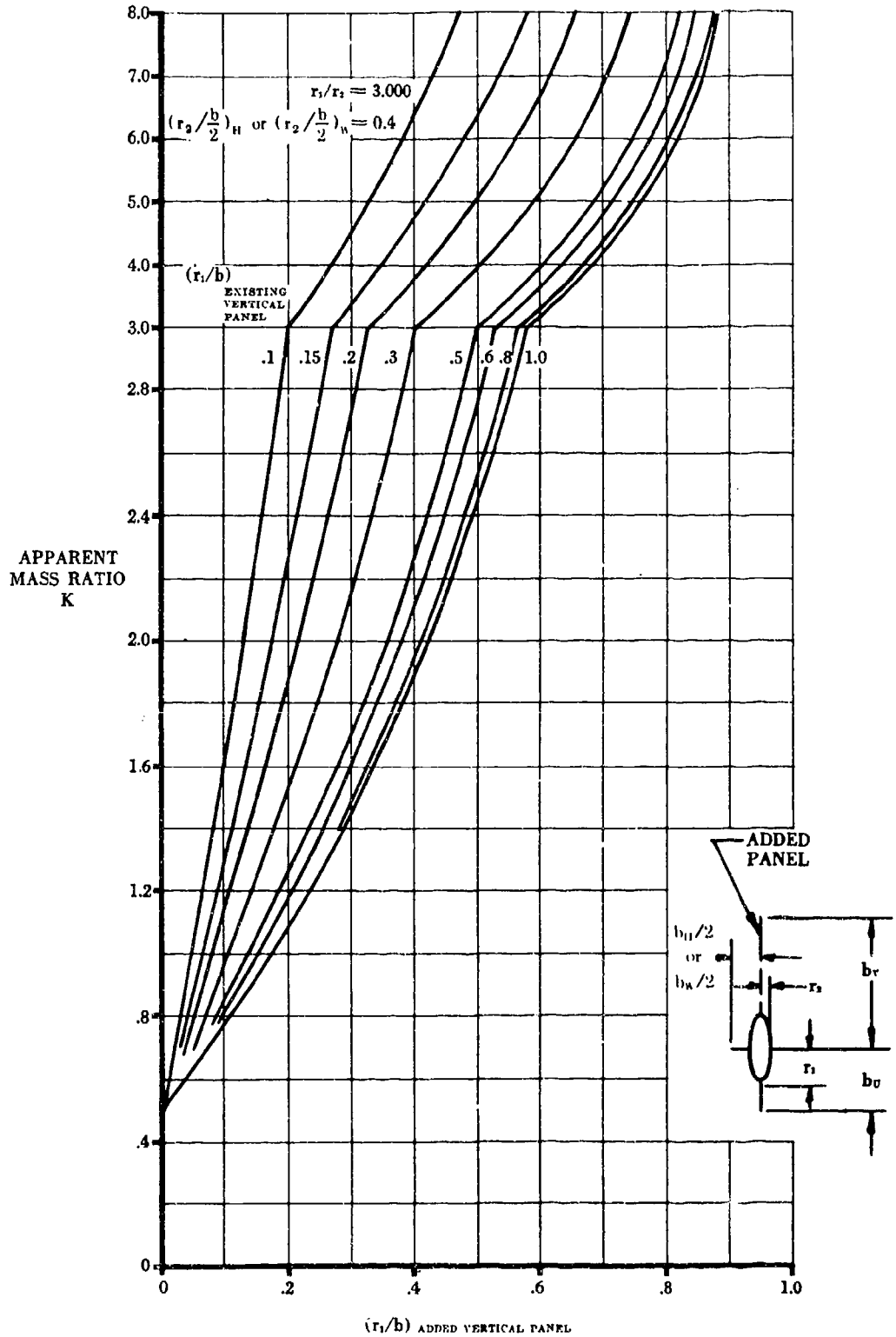

FIGURE 5.3.1.1-2511 APPARENT MASS FACTORS (CONTD)

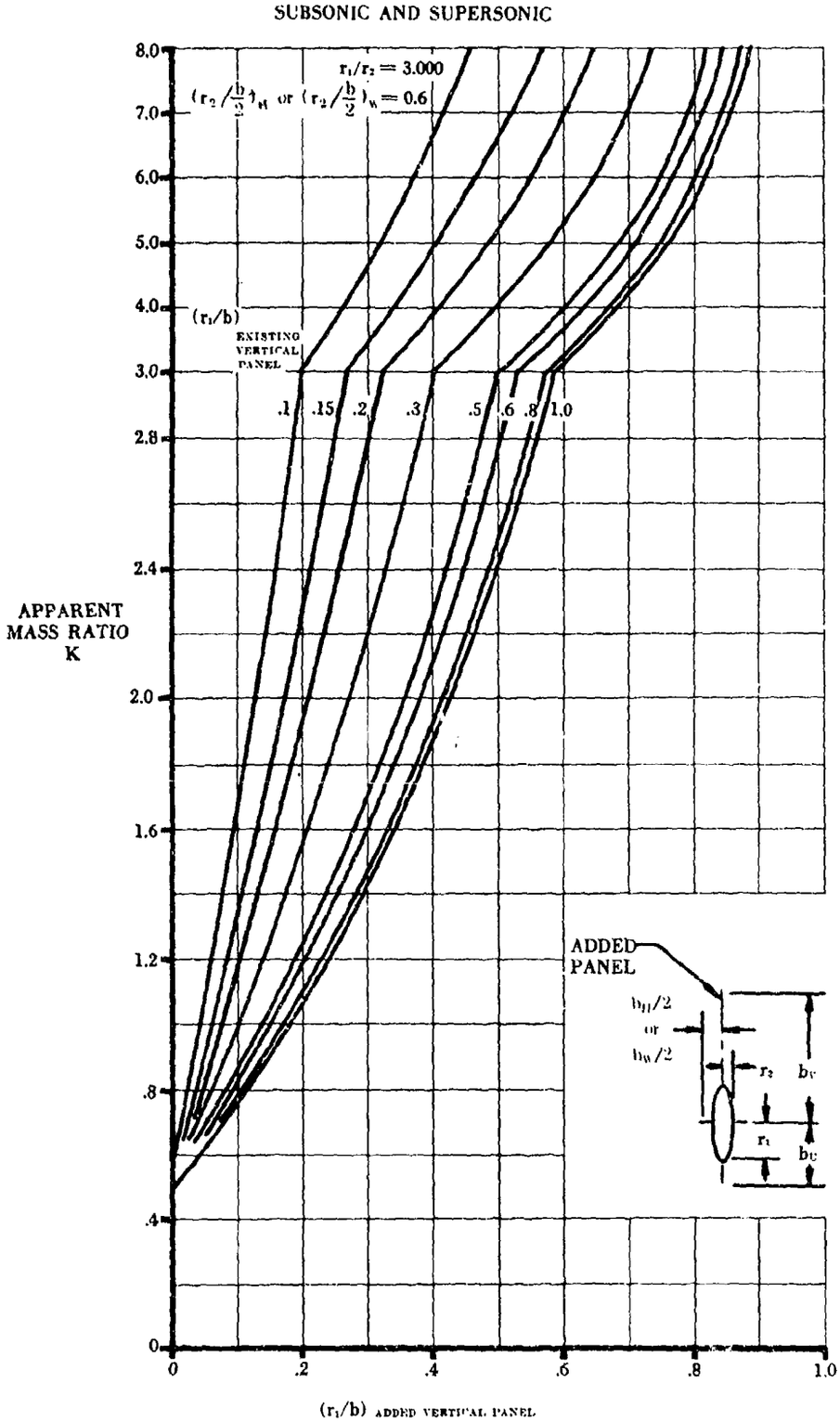

FIGURE 5.3.1.1-25mm APPARENT MASS FACTORS (CONTD)

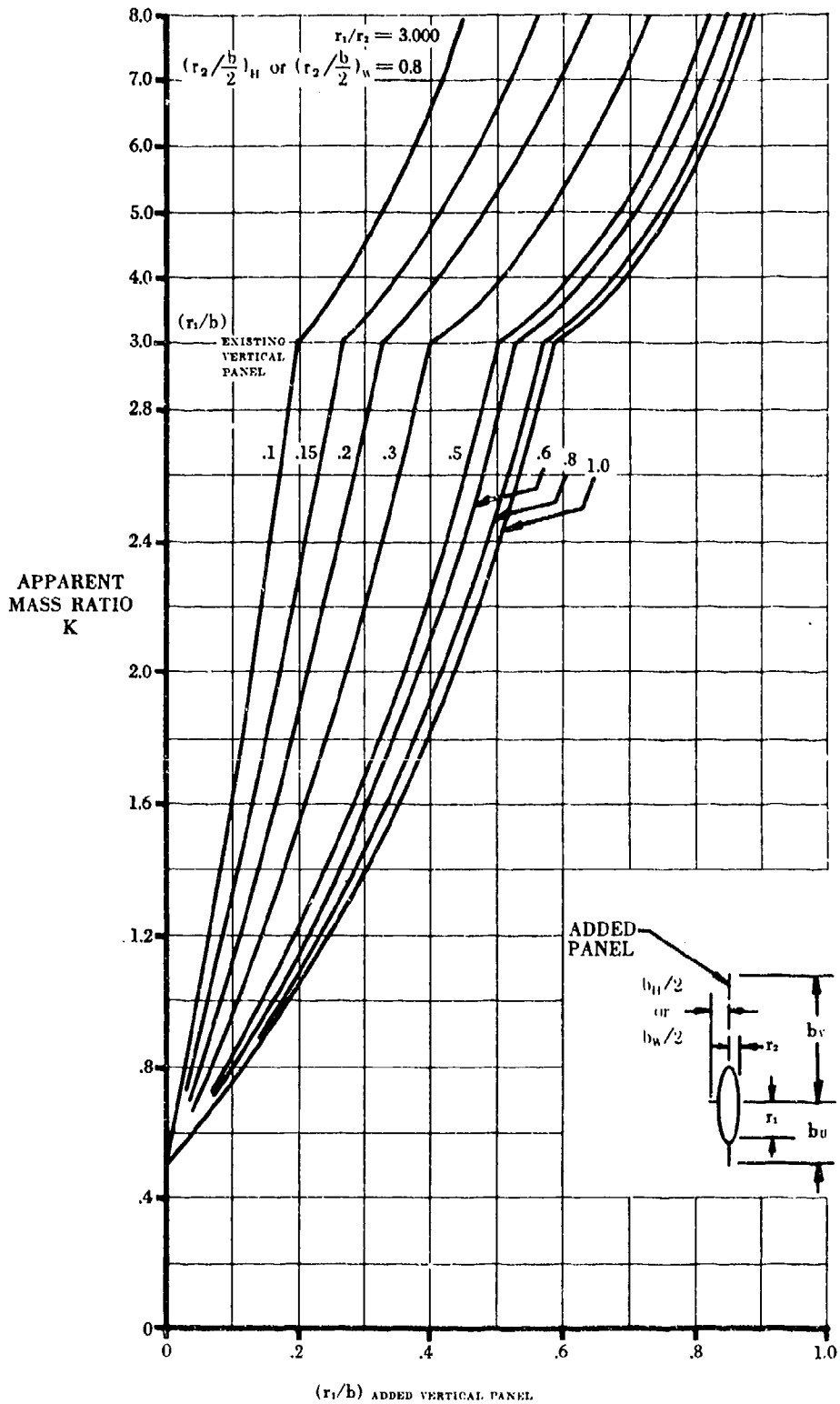

FIGURE 5.3.1.1-25nn APPARENT MASS FACTORS (CONTD)

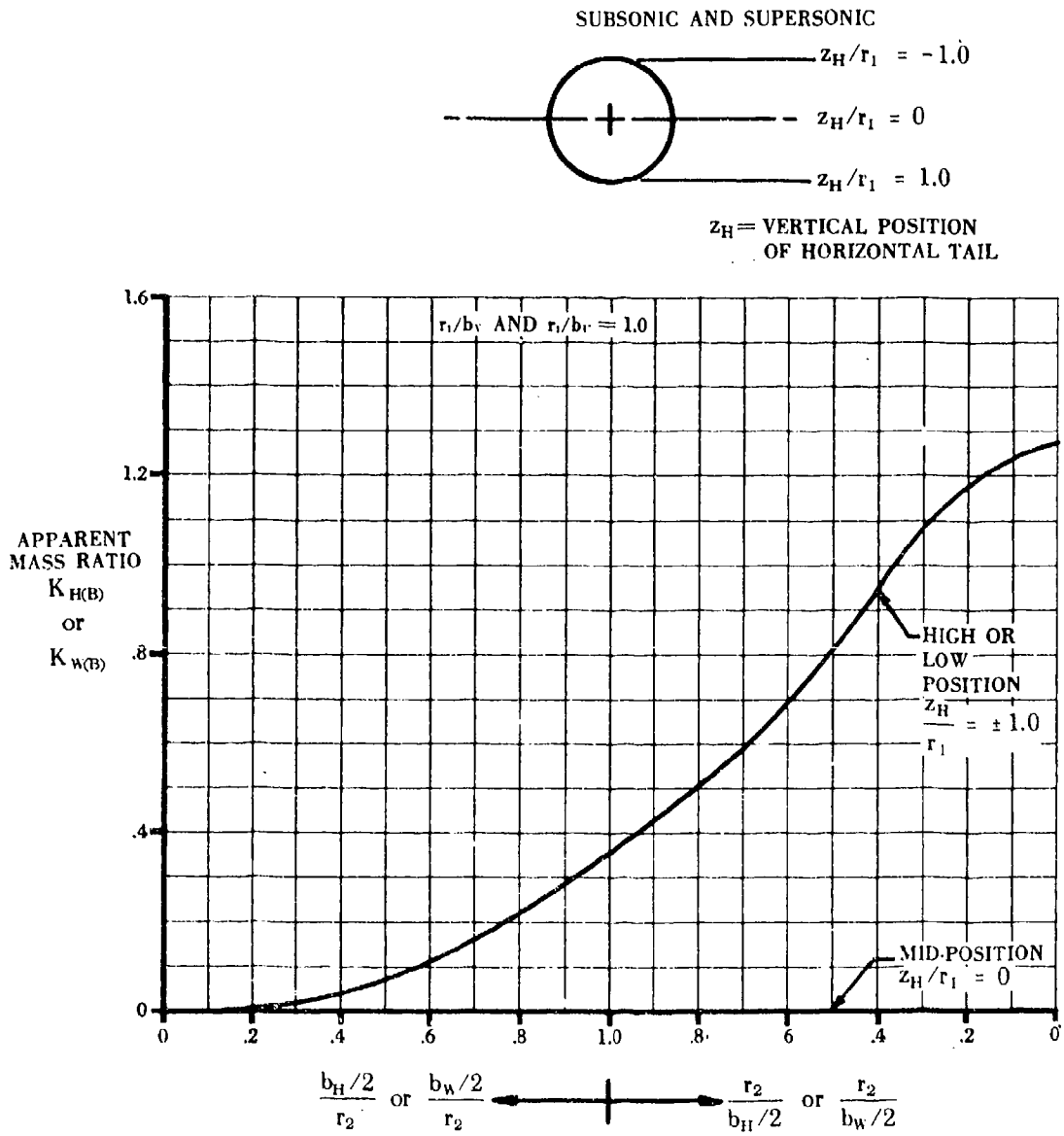

FIGURE 5.3.1.1-2500 APPARENT MASS FACTORS (CONTD)

5.3.1.2 TAIL-BODY SIDE-FORCE COEFFICIENT C_Y AT ANGLE OF ATTACK

The tail-body side force developed at combined angles is nonlinear with respect to both sideslip and angle of attack because of the body-vortex induced sidewash on the upper vertical tail and the cross-coupling of upwash and sidewash velocities. To obtain the sideslip derivative C_{Y_β}, it is recommended that C_Y be calculated at several angles of attack for a small sideslip angle ($\beta \leq 4^\circ$). Then at each angle of attack the side force is assumed linear with sideslip for small values of β so that

$$C_{Y_\beta} \approx \frac{C_Y}{\beta}.$$

A. SUBSONIC

The analysis of tail-body combinations at subsonic speeds and zero angle of attack is described in paragraph A of Section 5.3.1.1. At combined sideslip and angle of attack, however, two other phenomena must be considered: the body-vortex interference, and the cross-coupling effect of sideslip and angle-of-attack induced cross-flow velocities. Unfortunately neither of these phenomena can be estimated at other than supersonic speeds.

The method presented herein is restricted to first-order approximations at relatively low angles of attack.

DATCOM METHOD

It is recommended that the methods of paragraph A of Section 5.3.1.1 be used in the linear-lift angle-of-attack region.

B. TRANSONIC

As stated for the subsonic case the body-vortex interference and cross-coupling of upwash and sidewash velocities due to combined angles cannot be estimated at other than supersonic speeds.

Furthermore, as stated in paragraph B of Section 5.3.1.1, no method is available for estimating the side force on a vertical panel at zero angle of attack.

DATCOM METHOD

No method is available for estimating this coefficient and none is presented in the Datcom.

C. SUPERSONIC

The method of this Section is an extension of that presented as Method 3 of paragraph A and in paragraph C of Section 5.3.1.1. The discussion appearing there also applies here and will not be repeated. At combined sideslip and angle of attack, however, two additional effects must be considered. The cross-coupling effect of sideslip and angle of attack induces cross-flow velocities at the tail panels, and at angle of attack the body sheds vortices which proceed downstream to cause interference at the tail.

The method presented herein does not account for interferences existing between a wing and tail surfaces. If a wing is present in the configuration three additional types of interference exist between the wing and tail panels at supersonic speeds. These interferences produce additional nonlinear effects which are accounted for in paragraph C of Section 5.6.1.2.

DATCOM METHOD

The method presented in this Section for estimating the tail contribution to the sideslip coefficient C_Y is from reference 1, and uses the apparent-mass concept described in Method 3 of paragraph A in Section 5.3.1.1. The method prescribes the order in which the tail panels should be added to the configuration for analysis purposes.

This order is:

The horizontal tail is always added first, but the method is valid only for configurations with a horizontal tail mounted on the body or for configurations with no horizontal tail.

The remaining tail panels are then added, starting with the most aft and working forward (the position is measured in a streamwise direction to the leading edge of the exposed root chord).

The proper weighting of the apparent-mass ratios, which accounts for partial-panel areas affected by existing panels, is outlined in paragraph C of Section 5.3.1.1. The result is an effective apparent-mass factor K'.

For tail-body configurations at angle of attack, the horizontal-tail pressure field is not delineated by Mach lines alone. The pressure field produced is bounded by shock waves at the upper trailing edge and the lower leading edge (at positive angles of attack). If the airfoil is assumed to be thin, it is an easy matter to define the expansion and compression fields by direct application of shock-expansion theory. We assume that the flow in the region of the tail is the two-dimensional shock-expansion field corresponding to the exposed root chord of the horizontal surface. Any effects of horizontal surface-body interference or horizontal surface section in distorting the shock-expansion field are neglected. This method is also used in Section 5.6.1.2 to define the pressure field produced by a wing. The method is described below:

Upper surface of panel:

1. Find the leading-edge Mach line $\mu = \sin^{-1} \frac{1}{M_\infty}$ (measured relative to the free stream).
2. Find Mach number M_1 aft of expansion from figure 4.4.1-82. Read ν at M_∞. Then read M_1 at $\nu + \alpha = \nu_1$.
3. Find trailing-edge shock angle. Enter figure 4.4.1-81 at $-\delta' = \alpha$ and read θ_1 at M_1 (measured relative to the chord plane of the horizontal surface).

Lower surface of panel:

1. Find leading-edge shock angle. Enter figure 4.4.1-81 at $-\delta' = \alpha$ and read θ at M_∞ (measured relative to the free stream).
2. Find Mach number M_2 beneath wing from figure 4.4.1-82. Read ν at M_∞. Then read M_2 at $\nu - \alpha = \nu_2$.
3. Find trailing-edge Mach line (end of expansion), $\mu = \sin^{-1} \frac{1}{M_\infty}$ (measured relative to the free stream).

For a specified initial Mach number there is a maximum value of the angle of attack for which there exists an oblique shock solution. Or, conversely, for a specified angle of attack there is a minimum initial Mach number for which there is an oblique shock solution. The relation between Mach number and angle of attack below which no oblique shock solutions may be obtained is indicated in sketch (a).

SKETCH (a)

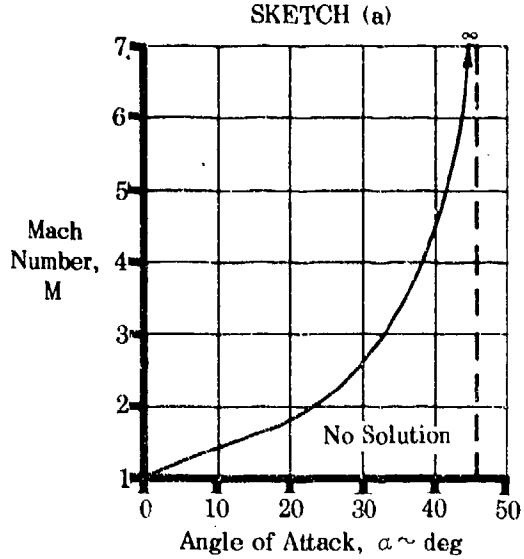

The pressure-field boundaries produced by a horizontal tail are defined in sketch (b) which shows the body area influenced by the horizontal tail. Compare this with sketch (c) of Section 5.3.1.1.

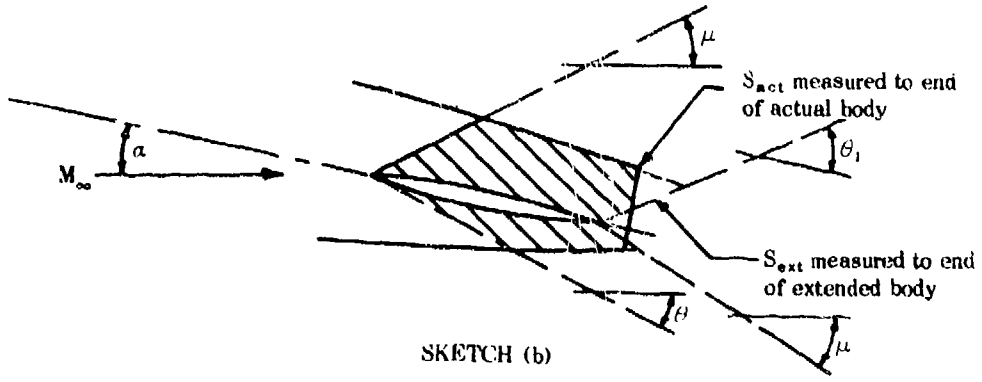

SKETCH (b)

The pressure-field boundaries of a typical tail-body configuration are illustrated in sketch (c). For this example the vertical tail exposed root-chord leading edge is aft of the ventral fin exposed root-chord leading edge; therefore, the ventral fin has no effect on the vertical tail since it is added later. At the angle of attack and Mach number represented the horizontal tail influences both the vertical tail and the ventral fin; however, the vertical tail does not influence the ventral fin.

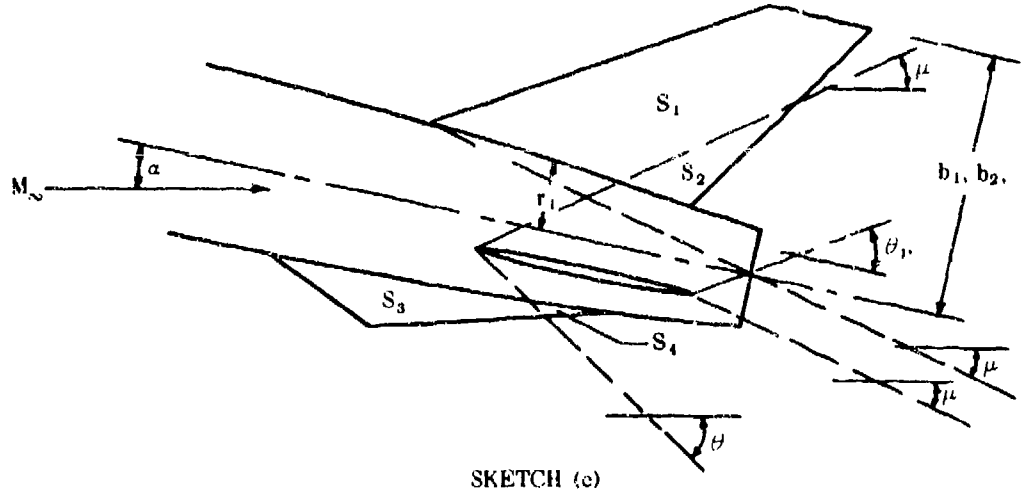

SKETCH (c)

The modifying effect of angle of attack on the tail contribution to the side-force coefficient is accounted for by the cross-coupling interference factor K_ϕ, developed from slender-body theory in reference 2.

The effect of body-vortex induced sidewash on the upper vertical tail side-force coefficient is calculated using interference factors from references 3 and 4, and vortex strengths and positions from Section 4.3.1.3. A simplified model of body-vortex separation is shown in sketch (d). At some distance x_s behind the body nose a pair of vortices separates from the body. As the vortices progress downstream, they increase in strength as a result of small vortex filaments originating on the body and feeding into the vortex cores. The positions and vortex strengths of a body of revolution are dependent upon angle of attack and the axial distance x behind the body nose. These vortex strengths and positions are presented in Section 4.3.1.3 as functions only of a single nondimensional parameter and the results are presented in the y - z coordinate system. In the method that follows these vortex strengths and positions are resolved into vertical tail reference coordinates for the configuration at combined angle of attack and sideslip. The estimation procedure for finding vortex positions and strengths is restricted to circular bodies; therefore, the Datcom method is not valid for other body shapes.

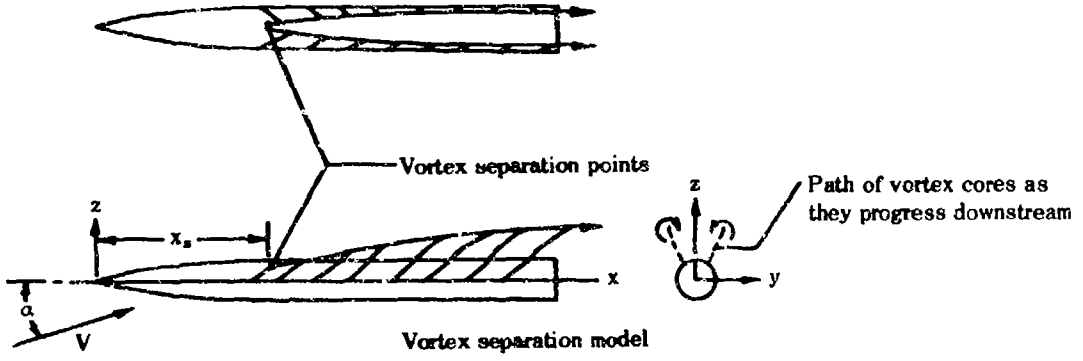

Vortex separation model

SKETCH (d)

The contribution of the tail panels to the side-force coefficient is determined from the following equation

$$C_{Y_{H(B)V(B)U(B)}} = C_{Y_{H(B)}} + C_{Y_V} + C_{Y_U} \qquad 5.3.1.2\text{-a}$$

where

$C_{Y_{H(B)}}$ is the contribution of the horizontal tail in the presence of the body, calculated by equation 5.3.1.2-b

C_{Y_V} is the contribution of the vertical tail, including body and horizontal tail interference effects, effects of cross-coupling of α and β, and effects of body vortices, and may include ventral fin interference. Calculate by equation 5.3.1.2-c.

C_{Y_U} is the contribution of the ventral fin, including body and horizontal tail interference effects, and effects of cross-coupling of α and β, and may include vertical tail interference. Calculate by equation 5.3.1.2-g. (Ventral fins are not affected by body vortices.)

The following procedure is used in determining the contributions of the tail panels:

Step 1

Determine the contribution of the horizontal tail in the presence of the body. The procedure is completely analogous to that for determining the contribution of the wing in the presence of the body in Section 5.2.1.2. This is always calculated first but cannot be analyzed if the panel is not body-mounted. The equation is

$$C_{Y_{H(B)}} = 2\eta_B K_{H(B)} k(\alpha) \frac{S_B}{S_W} \frac{S_{act}}{S_{ext}} \beta - \frac{c_{d_c}\left(c_{Y_c}\right)_H d}{S_W} \beta(\beta - \alpha') \qquad 5.3.1.2\text{-b}$$

where the first term on the right-hand side is the forebody cross-flow effect and is taken as zero for the midtail case, and the second term on the right-hand side is an approximate effect of the horizontal inhibiting the viscous cross-flow occuring along the body at large angles of attack.

η_B is the Mach number correction to the horizontal tail-body interference coefficient from figure 5.2.1.2-7 using the exposed root chord of the horizontal tail and the average body diameter at the horizontal tail

$K_{H(B)}$ is the horizontal tail-body interference coefficient, or apparent-mass ratio, from figure 5.3.1.1-2500. For tail positions other than midtail ($K_{H(B)} = 0$) or tangent, a nonlinear interpolation is described in Method 3, paragraph A, Section 5.3.1.1.

$k(\alpha)$ is the angle-of-attack correction to the horizontal tail-body interference coefficient obtained from figure 5.2.1.2-8 using the exposed root chord of the horizontal tail and the average body diameter at the horizontal tail. For tail positions other than midtail ($k(\alpha) = 0$) or tangent, a nonlinear interpolation is described in Method 3, paragraph A, Section 5.3.1.1.

$\frac{S_{act}}{S_{ext}}$ is the ratio of the actual projected side area of the fuselage to that of the extended fuselage as illustrated in sketch (b). These areas are bounded by the shock waves and expansion fans of the horizontal tail.

c_{d_c} is the cross-flow drag coefficient, obtained from figure 4.2.1.2-35b, with $M_c = M_\infty \sin \alpha'$

$\left(c_{r_e}\right)_H$ is the exposed root chord of the horizontal tail

β is the sideslip angle in radians

α' is the angle of inclination, $\alpha' = \sqrt{\alpha^2 + \beta^2}$, in radians

Step 2

Determine the vertical tail contribution by

$$C_{Y_V} = C_{Y_{V(K,\phi)}} + C_{Y_{V(\Gamma_B)}} \qquad 5.3.1.2\text{-c}$$

where

$C_{Y_{V(K,\phi)}}$ accounts for horizontal tail-body interference and cross-coupling of α and β acting on the vertical stabilizer, given by equation 5.3.1.2-d

$C_{Y_{V(\Gamma_B)}}$ accounts for the effect of body vortices on the vertical stabilizer, given by equation 5.3.1.2-e

Compute:

$$C_{Y_{V(K,\phi)}} = \left[K'_V - K_{\phi_V}\, \alpha \tan \Lambda_{LE_V}\right] (-C_{N_\alpha})_V\, \beta\, \frac{S_{V_e}}{S_W} \qquad 5.3.1.2\text{-d}$$

where

K'_V is the effective apparent-mass ratio of the vertical tail, as described in paragraph C of Section 5.3.1.1, but refers to sketch (c) of this Section. This factor includes the presence of the horizontal tail; but does not include the presence of the ventral fin if the ventral fin is farther forward than the vertical tail as measured from the leading edges of the exposed root chords.

K_{ϕ_V} is the cross-coupling interference factor of the vertical tail, from figure 5.3.1.2-12

α is the angle of attack in radians

Λ_{LE_V} is the sweepback angle of the vertical tail leading edge

$(C_{N_\alpha})_V$ is the normal-force-curve slope of the vertical tail as defined in paragraph C of Section 5.3.1.1

Compute:

$$C_{Y_{V(\Gamma_B)}} = \Delta i_v \left[\frac{\Gamma_B}{2\pi\, \alpha'\, Vr}\right] \frac{(-C_{N_\alpha})_V\, \alpha'\, S_{V_e}}{\left(\frac{b_V}{r} - 1\right) S_W} \qquad 5.3.1.2\text{-e}$$

where

$\frac{\Gamma_B}{2\pi\, \alpha'\, Vr}$ is the nondimensional vortex strength obtained from figure 4.3.1.3-15 of Section 4.3.1.3 with α replaced by α' in all cases and x taken as the distance from the body nose to the midpoint of the MAC of the exposed panel.

α' is the angle of inclination in radians: $\alpha' = \sqrt{\alpha^2 + \beta^2}$

r is the average radius of the body along the vertical tail exposed root chord

Δi_v is the vortex interference factor:

$\Delta i_v = i_{v_1} - i_{v_2}$. The values of i_{v_1} and i_{v_2} are given in figure 5.3.1.2-13, where they are presented as functions of the positions of the body vortices at the vertical tail

$\frac{z_{v_1}}{b_v}$, $\frac{y_{v_1}}{b_v}$, $\frac{z_{v_2}}{b_v}$, and $\frac{y_{v_2}}{b_v}$ (see sketch (e)). These are given by

$$\left.\begin{aligned}
\frac{z_{v_1}}{b_v} &= \frac{r}{b_v}\left[\frac{z_0}{r}\cos\phi + \frac{y_0}{r}\sin\phi\right] \\
\frac{y_{v_1}}{b_v} &= \frac{r}{b_v}\left[\frac{z_0}{r}\sin\phi - \frac{y_0}{r}\cos\phi\right] \\
\frac{z_{v_2}}{b_v} &= \frac{r}{b_v}\left[\frac{z_0}{r}\cos\phi - \frac{y_0}{r}\sin\phi\right] \\
\frac{y_{v_2}}{b_v} &= \frac{r}{b_v}\left[\frac{z_0}{r}\sin\phi + \frac{y_0}{r}\cos\phi\right]
\end{aligned}\right\} \quad 5.3.1.2\text{-f}$$

where $\phi = \tan^{-1}\frac{\beta}{\alpha}$

$\frac{z_0}{r}$ is the vertical position of the body vortex in the y - z coordinate system from figure 4.3.1.3-13b

$\frac{y_0}{r}$ is the lateral position of the body vortex in the y - z coordinate system from figure 4.3.1.3-14

In reading these last two figures α must be replaced by α' in all cases and x is taken as the distance from the body nose to the midpoint of the MAC of the exposed panel.

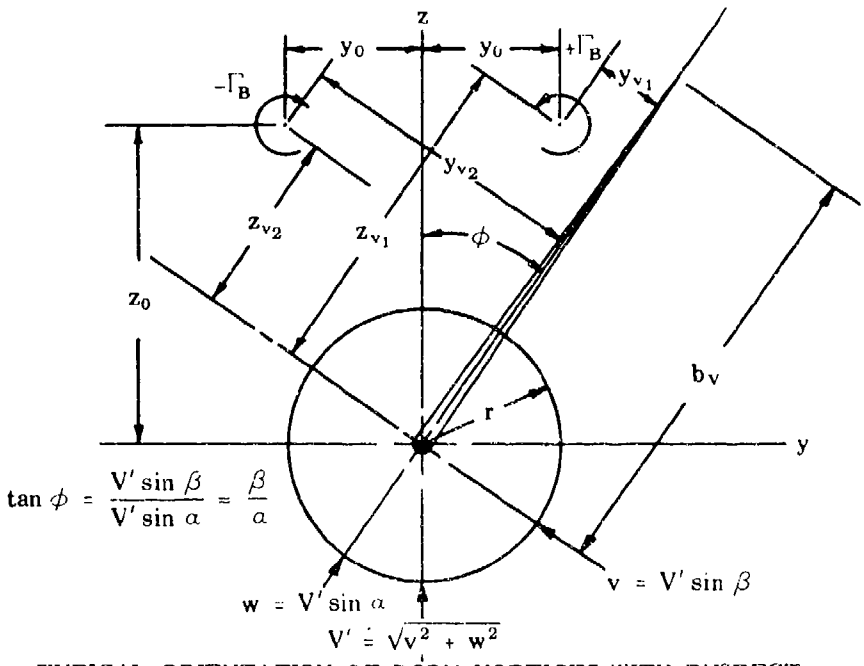

TYPICAL ORIENTATION OF BODY VORTICES WITH RESPECT TO TAIL PLANE FOR CONFIGURATION AT COMBINED ANGLES

SKETCH (e)

Step 3

Determine the ventral fin contribution by

$$C_{Y_U} = C_{Y_{U(K,\Phi)}} = \left[K'_U + K_{\Phi_U} \alpha \tan \Lambda_{LE_U}\right] (-C_{N_\alpha})_U \beta \frac{S_{U_e}}{S_w} \qquad 5.3.1.2\text{-g}$$

where

K'_U is the effective apparent-mass ratio of the ventral fin, as described in paragraph C of Section 5.3.1.1, but refers to sketch (c) of this Section. This factor includes the presence of a horizontal tail; but does not include the presence of the vertical tail if the vertical tail is farther forward than the ventral fin, as measured from the leading edge of the exposed root chords.

K_{Φ_U} is the cross-coupling interference factor of the ventral fin from figure 5.3.1.2-12

Λ_{LE_U} is the sweepback angle of the ventral fin leading edge

$(C_{N_\alpha})_U$ is the normal-force-curve slope of the ventral fin as defined in paragraph C of Section 5.3.1.1

Step 4

All terms are now available for substitution into equation 5.3.1.2-a for finding $C_{Y_{H V(U)}}$.

Values for the incremental coefficient resulting from the addition of upper vertical tails to circular bodies, calculated using equation 5.3.1.2-c, are compared with experimental results in figure 5.3.1.2-11. It is evident from the experimental data that a strong destabilizing effect occurs with increasing angle of attack and that this effect is accurately predicted by the Datcom method over the angle-of-attack range of the tests.

Sample Problem

Given: The configuration of reference 5 consisting of body, vertical tail, and ventral tail. This is the same configuration as that of sample problem 2, paragraph C, Section 5.3.1.1. Find the side-force coefficient developed by the vertical and ventral tails in the presence of a body at $\alpha = 12^\circ$ and $\beta = 4^\circ$.

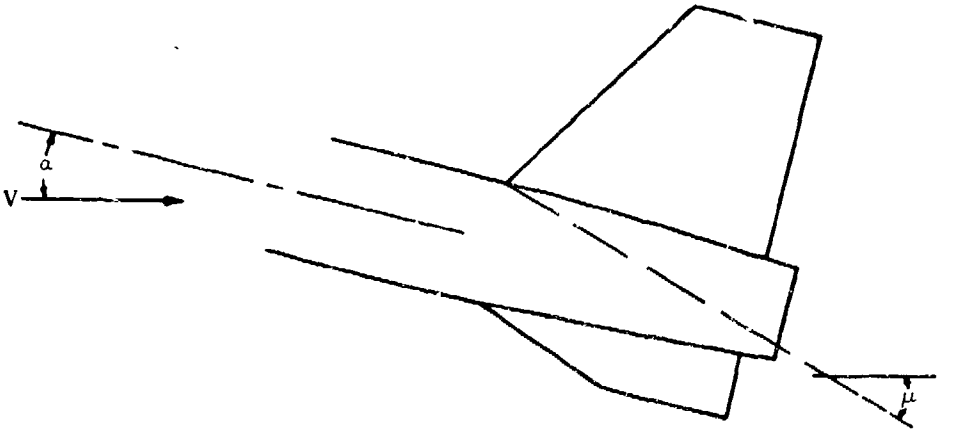

Body Characteristics

Ogive cylinder, with slight boattail d = 3.33 in. $r_1 = r_2 = 1.5$ in. (average values in region of tail panels)

Vertical Tail Characteristics

$S_{V_e} = 31.6$ sq in. $b_V = 7.48$ in. $\Lambda_{LE_V} = 32.5^\circ$ $A_{V_e} = 1.12$

$\lambda_{V_e} = 0.482$

Ventral Tail Characteristics

S_{U_e} = 8.54 sq in. b_U = 3.05 in. Λ_{LE_U} = 70° A_{U_e} = 0.35

λ_{U_e} = 0.428

Additional Characteristics

M = 2.01 α = 12° = 0.209 rad β = 4° = 0.070 rad

$\alpha' = \sqrt{\alpha^2 + \beta^2}$ = 12.65° = 0.221 rad S_W = 144.0 sq in.

x/r = 21.87 (x measured from nose to 50-percent-chord point of MAC of exposed vertical panel)

At positive angle of attack, vertical-tail exposed root-chord leading edge is aft of ventral-fin exposed root-chord leading edge.

Ventral fin is not influenced by presence of vertical tail at this angle of attack and Mach number.

Compute:

Step 1. Determine the horizontal-tail contribution $C_{Y_{H(B)}}$

$C_{Y_{H(B)}}$ = 0 (horizontal tail off)

Step 2. Determine the vertical tail contribution C_{Y_V}

Vertical tail interference and cross-coupling term $C_{Y_{V(\alpha,\phi)}}$

Determine K'_V = 1.13 (figure 5.3.1.1-25a) at (r_1/r_2) = 1.000; $(r_1/b)_{V_{\text{added panel}}}$ = 0.200; $(r_1/b)_{U_{\text{existing panel}}}$ = 1.000;

Determine K_{ϕ_V} = 0.687 (figure 5.3.1.2-12 at $(r_1/b)_V$ = 0.200)

Determine $(C_{N_\alpha})_V$ using $2A_{V_e}$

$(C_{N_\alpha})_V$ = 2.12 per rad (based on S_{V_e}) (sample problem 2, paragraph C, Section 5.3.1.1)

$$C_{Y_{V(\alpha,\phi)}} = \left[K'_V - K_{\phi_V}\, \alpha \tan \Lambda_{LE_V}\right] (-C_{N_\alpha})_V\, \beta\, \frac{S_{V_e}}{S_W} \qquad \text{(equation 5.3.1.2-d)}$$

$$= [1.13 - (0.687)(0.209)\tan 32.5^\circ]\,(-2.12)\,(0.070)\left(\frac{31.6}{144.0}\right)$$

$$= -0.0339 \text{ (based on } S_W)$$

Effect of body vortices on vertical tail contribution $C_{Y_{V(\Gamma_B)}}$

$\frac{x_a}{r}$ = 10.6 (figure 4.3.1.3-13a at α' = 12.65°)

$\frac{\alpha'(x - x_a)}{r}$ = 0.221 (21.87 - 10.6) = 2.49

$\frac{\Gamma_B}{2\pi\,\alpha' Vr}$ = 0.86 (figure 4.3.1.3-15 at α' = 12.65°)

$\frac{y_0}{r}$ = 0.71 (figure 4.3.1.3-14 at α' = 12.65°)

$\frac{z_0}{r}$ = 1.53 (figure 4.3.1.3-13b at α' = 12.65°)

$$\phi = \tan^{-1}\frac{\beta}{a} = \tan^{-1}\frac{4}{12} = 18.4^\circ$$

Calculate position of vortices at vertical tail

$$\frac{z_{v_1}}{b_v} = \frac{r}{b_v}\left[\frac{z_0}{r}\cos\phi + \frac{y_0}{r}\sin\phi\right] \qquad \text{(equation 5.3.1.2-f)}$$

$$= \frac{1.50}{7.48}\,(1.53\cos 18.4^\circ + 0.71\sin 18.4^\circ)$$

$$= 0.336$$

$$\frac{y_{v_1}}{b_v} = \frac{r}{b_v}\left[\frac{z_0}{r}\sin\phi - \frac{y_0}{r}\cos\phi\right] \qquad \text{(equation 5.3.1.2-f)}$$

$$= \frac{1.50}{7.48}\,(1.53\sin 18.4^\circ - 0.71\cos 18.4^\circ)$$

$$= -0.038$$

$$\frac{z_{v_2}}{b_v} = \frac{r}{b_v}\left[\frac{z_0}{r}\cos\phi - \frac{y_0}{r}\sin\phi\right] \qquad \text{(equation 5.3.1.2-f)}$$

$$= \frac{1.50}{7.48}\,(1.53\cos 18.4^\circ - 0.71\sin 18.4^\circ)$$

$$= 0.246$$

$$\frac{y_{v_2}}{b_v} = \frac{r}{b_v}\left[\frac{z_0}{r}\sin\phi + \frac{y_0}{r}\cos\phi\right] \qquad \text{(equation 5.3.1.2-f)}$$

$$= \frac{1.50}{7.48}\,(1.53\sin 18.4^\circ + 0.71\cos 18.4^\circ)$$

$$= 0.232$$

Find vortex interference factor

$$\left.\begin{aligned} i_{v_1} &= -1.4 \\ i_{v_2} &= -0.9 \end{aligned}\right\} \qquad \text{(figure 5.3.1.2-13a)}$$

$$\Delta i_v = i_{v_1} - i_{v_2} = (-1.4) - (-0.9) = -0.5$$

$$C_{Y_{V(\Gamma_B)}} = \Delta i_v\left[\frac{\Gamma_B}{2\pi\alpha' V_r}\right]\frac{(-C_{N_\alpha})_V\,\alpha' S_{V_e}}{\left(\frac{b_V}{r} - 1\right)S_W} \qquad \text{(equation 5.3.1.2-e)}$$

$$= (-0.5)\,(0.86)\,\frac{(-2.12)\,(0.221)\,(31.6)}{\left(\frac{7.48}{1.5} - 1\right)(144.0)}$$

$$= 0.01104 \text{ (based on } S_W\text{)}$$

Total vertical tail contribution:

$$C_{Y_V} = C_{Y_{V(K,\phi)}} + C_{Y_{V(\Gamma_B)}} \qquad \text{(equation 5.3.1.2-c)}$$

$$= (-0.0339) + (0.01104)$$

$$= -0.0229 \text{ (based on } S_w)$$

Step 3. Determine the ventral tail contribution C_{Y_U}

Ventral fin interference and cross-coupling term $C_{Y_{U(K,\phi)}}$

Determine $K'_U = 2.11$ (figure 5.3.1.1-25a) at $(r_1/r_2) = 1.000$; $(r_1/b)_{U_{\text{added panel}}} = 0.492$; $(r_1/b)_{V_{\text{existing panel}}} = 1.000$

(no horizontal tail, and ventral fin is out of vertical tail influence).

Determine $K_{\phi_U} = 0.535$ (figure 5.3.1.2-12 at $(r_1/b)_U = 0.492$)

Determine $(C_{N_\alpha})_U$ using $2A_{U_e}$

$(C_{N_\alpha})_U = 1.09$ per rad (Section 4.*.3.2; based on S_{U_e})

Total ventral fin contribution:

$$C_{Y_U} = C_{Y_{U(K,\phi)}} = [K'_U + K_{\phi_U} \alpha \tan \Lambda_{LE_U}] (-C_{N_\alpha})_U \beta \frac{S_{U_e}}{S_w} \qquad \text{(equation 5.3.1.2-g)}$$

$$= [2.11 + (0.535)(0.209) \tan 70^\circ] (-1.09)(0.070)\left(\frac{8.54}{144.0}\right)$$

$$= -0.0109 \text{ (based on } S_w)$$

Solution:

$$C_{Y_{HVU(B)}} = C_{Y_{H(B)}} + C_{Y_V} + C_{Y_U} \qquad \text{(equation 5.3.1.2-a)}$$

$$= 0 + (-0.0229) + (-0.0109)$$

$$= -0.0338 \text{ (based on } S_w)$$

REFERENCES

1. Kaattari, G. E.: Estimation of Directional Stability Derivatives at Moderate Angles and Supersonic Speeds. NASA Memo 12-1-58A, 1959. (U)

2. Spahr, J. R.: Contribution of the Wing Panels to the Forces and Moments of Supersonic Wing-Body Combinations at Combined Angles. NACA TN 4146, 1958. (U)

3. Pitts, W. C., Nielsen, J. N., and Kaattari, G. E.: Lift and Center of Pressure of Wing-Body-Tail Combinations at Subsonic, Transonic, and Supersonic Speeds. NACA TR 1307, 1959. (U)

4. Spahr, J. R.: Theoretical Prediction of the Effects of Vortex Flows on the Loading, Forces, and Moments of Slender Aircraft. NASA TR R-10 1961, (U)

5. Spearman, M. L., Driver, C., and Hughes, W. C.: Investigation of Aerodynamic Characteristics in Pitch and Sideslip of a 45° Sweptback-Wing Airplane Model with Various Vertical Locations of Wing and Horizontal Tail – Basic-Data Presentation, M = 2.01. NACA RM L54L06, 1955. (U)

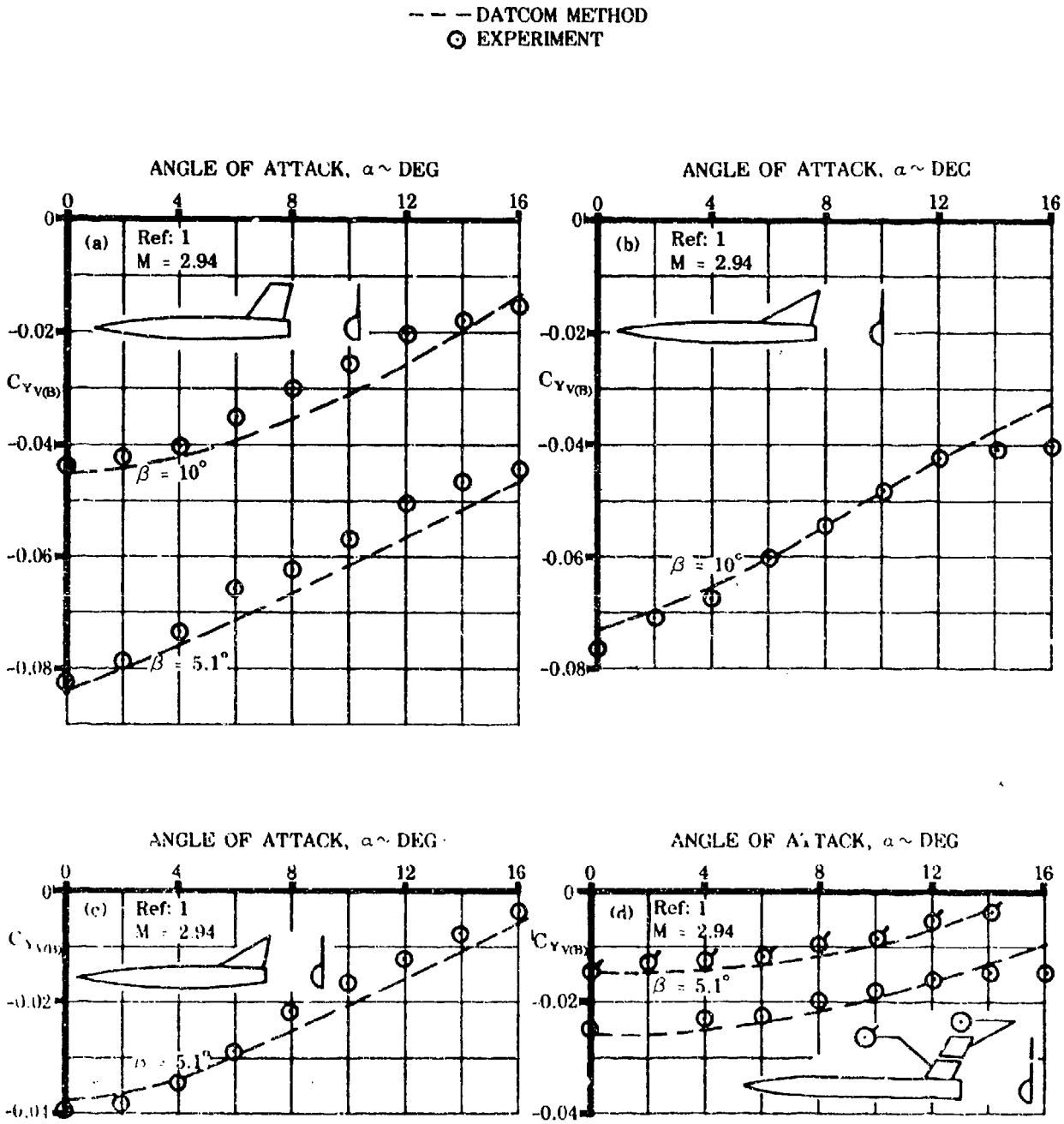

FIGURE 5.3.1.2-11 COMPARISON OF EXPERIMENTAL AND CALCULATED SIDE-FORCE COEFFICIENT INCREMENTS DUE TO ADDING A VERTICAL TAIL TO A BODY

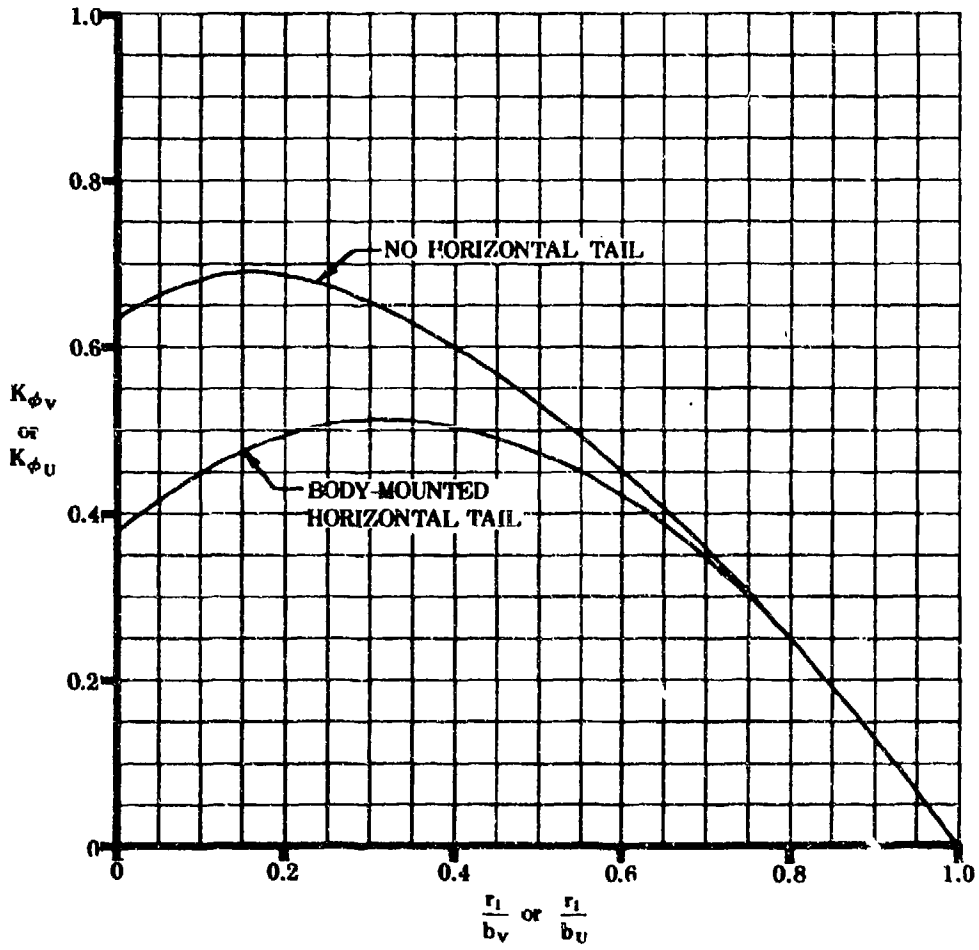

FIGURE 5.3.1.2-12 CROSS-COUPLING INTERFERENCE FACTOR

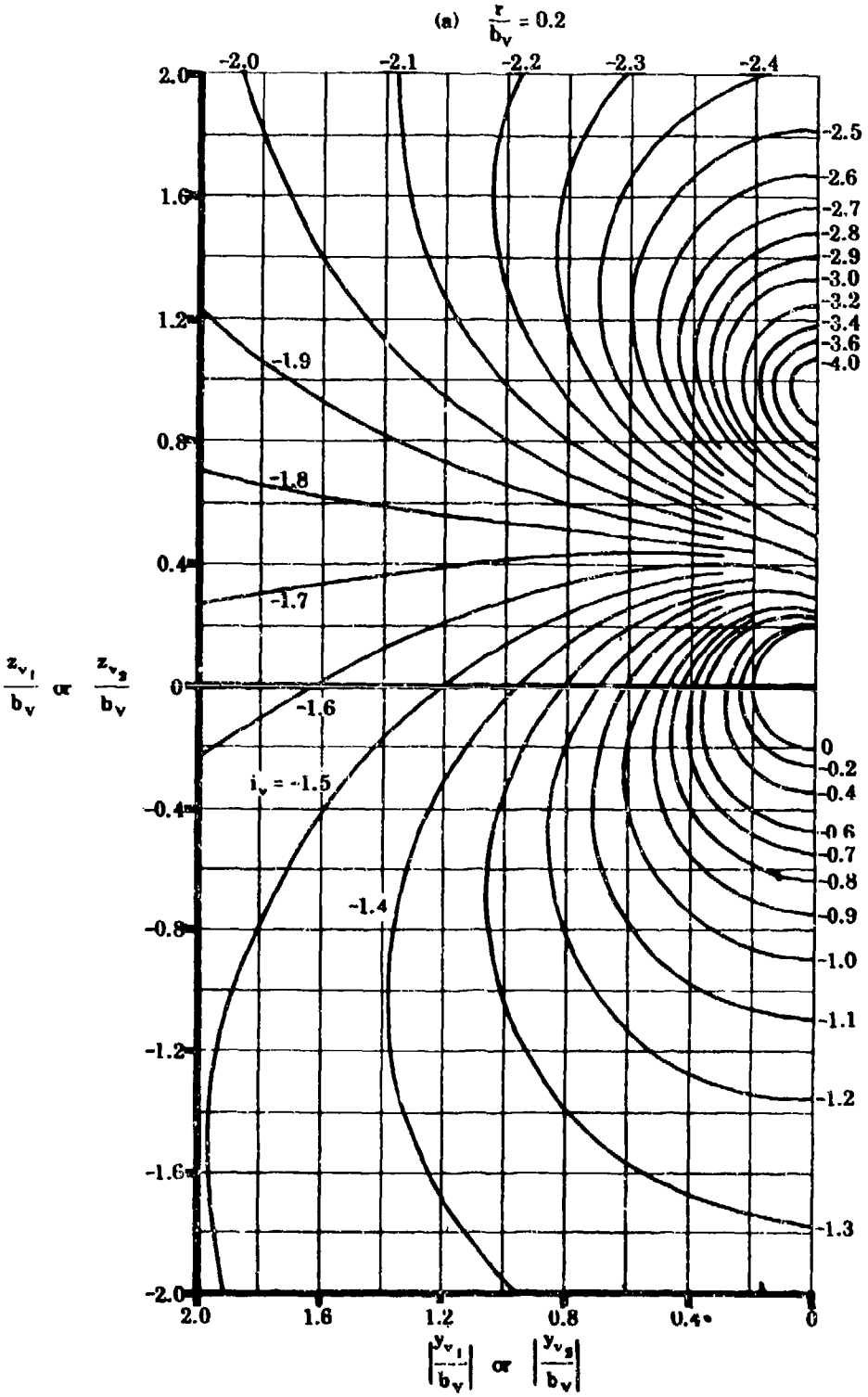

FIGURE 5.3.1.2-13 VORTEX INTERFERENCE FACTOR

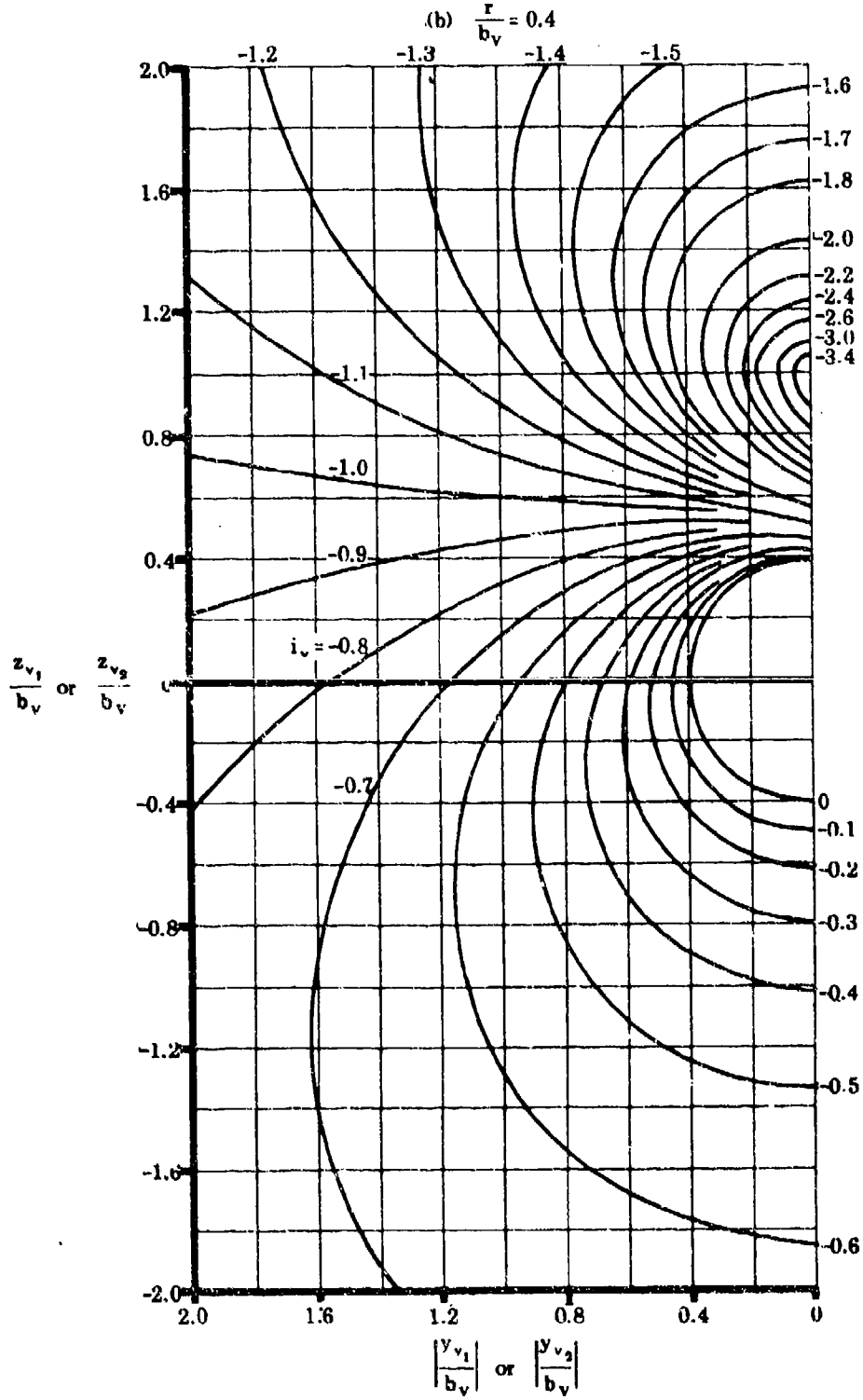

FIGURE 5.3.1.2-13 VORTEX INTERFERENCE FACTOR (contd)

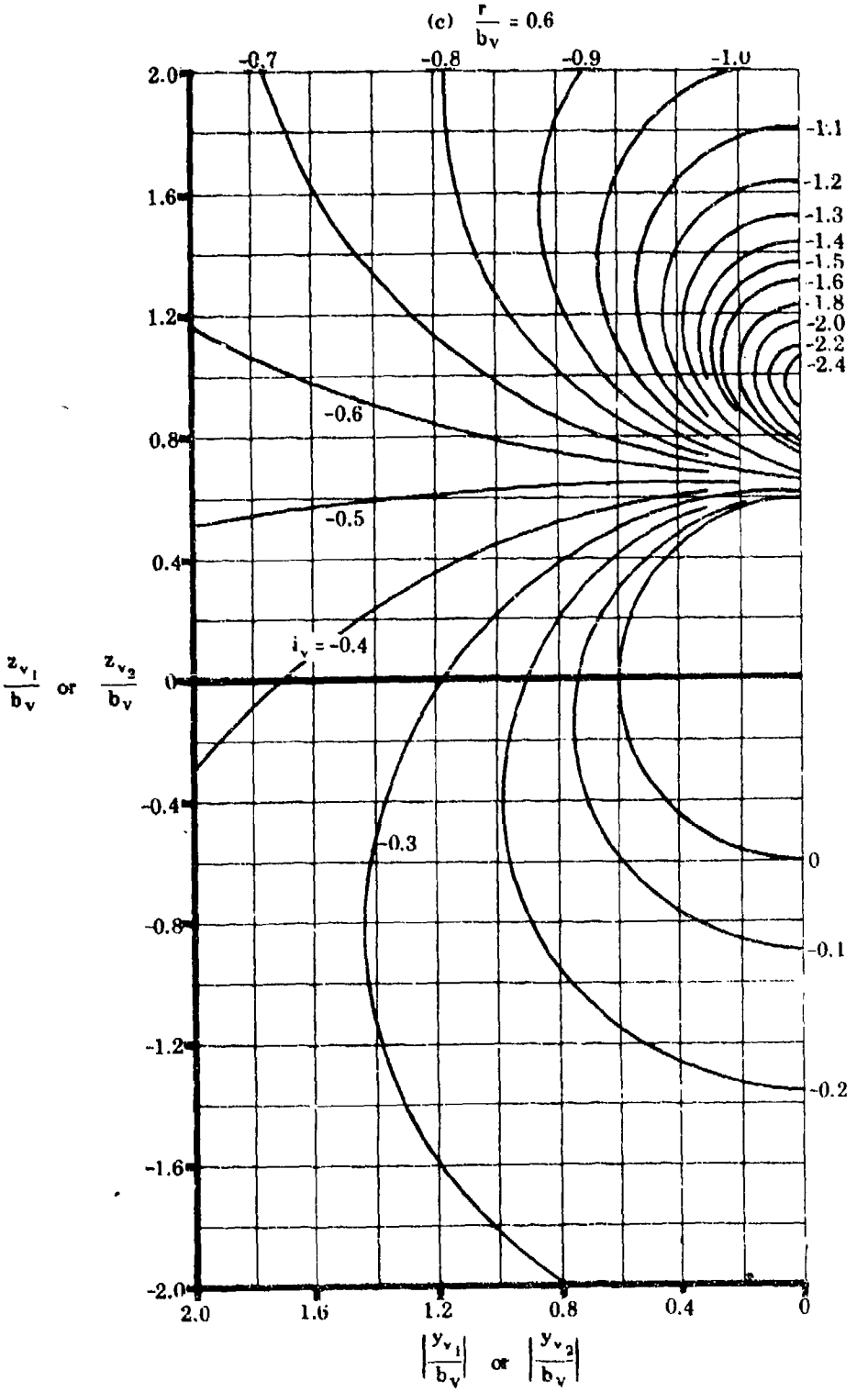

FIGURE 5.3.1.2-13 VORTEX INTERFERENCE FACTOR (contd)

5.3.2 TAIL-BODY SIDESLIP DERIVATIVE C_{l_β}

5.3.2.1 TAIL-BODY SIDESLIP DERIVATIVE C_{l_β} IN THE LINEAR ANGLE-OF-ATTACK RANGE

The method of estimating the contribution of panels in the empennage to the sideslip derivative C_{l_β} is similar to that for estimating the contribution of panels in the empennage to C_{n_β}. That is, the side force generated by an added panel is multiplied by an appropriate moment arm in order to obtain the rolling-moment contribution.

A refinement is required in the case of the contribution of a vertical panel (either an upper or lower vertical panel), since the pressure field that is generated by the vertical panel is reflected on the surface of the horizontal tail. These induced loads on the horizontal tail are perpendicular to this surface and therefore do not significantly affect the vehicle yawing moments or side forces. They do, however, contribute to the rolling moments and hence must not be neglected. The rolling-moment contribution of the horizontal tail is positive (opposes that due to the vertical panel) when the horizontal surface is in the low position with respect to the vertical panel. The rolling-moment contribution has no effect when the horizontal tail is mounted near the midspan of the vertical panel and is negative for the horizontal surface in the high position.

At subsonic speeds these contributions are usually small, and reasonable results are obtained when they are neglected. (Actually they would be quite difficult to estimate.) At transonic speeds they can be quite pronounced, because the pressure field of the entire horizontal surface is strongly influenced by the presence of the vertical panel. At supersonic speeds the interferences are restricted to regions on the horizontal surfaces within the boundaries defined by the shock-wave pattern of the vertical panel. As the Mach number increases, the region of influence decreases because the shock pattern becomes more swept. It is to be expected, therefore, that this horizontal-tail effect will become less significant as the supersonic Mach number increases.

Because of the complexity of the problem, no method for predicting the effects of panels in the empennage at transonic speeds is presented, and the method presented for supersonic speeds does not account for the horizontal-tail contribution. However, the effect of the presence of a horizontal tail is accounted for at supersonic speeds in computing the contribution of a vertical panel.

A. SUBSONIC

The contribution of panels in the empennage to the vehicle sideslip derivative C_{l_β} is based on the values of the panel contribution to C_{Y_β} estimated by the methods of Paragraph A. of Section 5.3.1.1.

In addition to the pressure forces induced on the horizontal tail by the vertical tail, there can be other forces for a configuration having either significant twist and/or dihedral on the horizontal tail. If the horizontal tail is large relative to the wing, the effects of twist and/or dihedral may be worthy of consideration. To consider these effects on the horizontal tail, the method of Section 5.1.2.1 is used; i.e., treating the horizontal tail as an isolated wing. (Caution should be exercised to make certain that the horizontal-tail contribution to C_{l_β} is converted to the same reference area and

length $S_W b_W$ as the wing-body contribution, before adding them together.) However, since the horizontal-tail contribution is very small for most configurations in the subsonic speed regime, the method presented here neglects this contribution.

As mentioned above, reasonable results are obtained at subsonic speeds when the horizontal-tail contribution is neglected. However, in using Method 3 of Paragraph A, Section 5.3.1.1, if a horizontal tail is present in the empennage, its effect on the vertical-tail contribution must be accounted for by proper use of the apparent-mass factor (K) charts. If Method 1 or Method 2 of Paragraph A, Section 5.3.1.1 is used, the effect of a horizontal tail on the vertical-tail contribution is implicitly accounted for by the method.

DATCOM METHOD

The contribution of a vertical panel to the sideslip derivative C_{l_β} is estimated by

$$\left(\Delta C_{l_\beta}\right)_p = \left(\Delta C_{Y_\beta}\right)_p \frac{z_p \cos\alpha - \ell_p \sin\alpha}{b_W} \qquad 5.3.2.1\text{-a}$$

where

p is the subscript referring to the added vertical panel (either an upper vertical stabilizing surface V or a lower vertical stabilizing surface U).

$\left(\Delta C_{Y_\beta}\right)_p$ is the side force due to sideslip of the added vertical panel determined as follows:

For configurations with horizontal panels mounted on the body or with no horizontal panels, use Method 1 or Method 3 of Paragraph A, Section 5.3.1.1.

For configurations with horizontal panels mounted on the vertical panel, use Method 1 of Paragraph A, Section 5.3.1.1.

For twin-vertical-panel configurations, use Method 2 of Paragraph A, Section 5.3.1.1.

z_p is the distance in the z-direction (normal to the longitudinal body axis) between the moment reference center (usually the vehicle center of gravity) and the MAC of the added panel, positive for the panel above the body.

ℓ_p is the distance parallel to the longitudinal body axis between the moment reference center (usually the vehicle center of gravity) and the quarter-chord point of the MAC of the added panel, positive for the added panel behind the moment reference center. The aerodynamic center of the vertical panel could be used, but the inaccuracies of the basic method do not warrant this degree of refinement.

b_W is the span of the wing.

All geometry used in determining the moment arms for the above method is based on the vertical panel extended to the body center line.

For a wingless configuration, b_W is replaced by the vehicle reference length and $(\Delta C_{Y_\beta})_p$ is based on the vehicle reference area.

Results calculated at zero angle of attack by this method are compared to experimental data in Table 5.3.2.1-A. The detailed geometry of the configurations used in this table is given in Table 5.3.1.1-B. It should be noted that the values of ΔC_{Y_β} used in Table 5.3.2.1-A are not test data, but are calculated by the method of Section 5.3.1.1. The errors inherent in estimating ΔC_{Y_β} are therefore implicitly included in Table 5.3.2.1-A. However, the errors due to ΔC_{Y_β} and those due to the moment arm can be separated by comparing the errors for a given configuration from Table 5.3.1.1-B (for ΔC_{Y_β}) with those of Table 5.3.2.1-A (for ΔC_{l_β}).

Sample Problems

1. Given: The configuration of Reference 1 consisting of a wing, body, horizontal tail, and upper vertical tail. This is the same configuration as that of Sample Problem 1, Paragraph A, Section 5.3.1.1. Some of the characteristics are repeated.

Wing Characteristics:

$S_W = 576.0$ sq in. $\quad b_W = 41.56$ in. $\quad z_W = 0$

Additional Characteristics:

$M = 0.25 \quad \ell_V = 24.89$ in. (c.g. to $(\bar{c}/4)_V$) $\quad z_V = 5.78$ in. (c.g. to $(MAC)_V$)

$\alpha = 0, 2°, 4°, 6°$

Compute:

$\left(\Delta C_{Y_\beta}\right)_{V(WBH)}$ = −0.734 per rad (based on S_W) (Sample Problem 1, Paragraph A, Section 5.3.1.1)

Solution:

$$\left(\Delta C_{l_\beta}\right)_p = \left(\Delta C_{Y_\beta}\right)_p \frac{z_p \cos\alpha - \ell_p \sin\alpha}{b_W} \quad \text{(Equation 5.3.2.1-a)}$$

$$\left(\Delta C_{l_\beta}\right)_{V(WBH)} = \left(\Delta C_{Y_\beta}\right)_{V(WBH)} \frac{z_V \cos\alpha - \ell_V \sin\alpha}{b_W}$$

$$= -0.734 \left(\frac{5.78 \cos\alpha - 24.89 \sin\alpha}{41.56}\right) \text{ per rad (based on } S_W b_W)$$

Test results from Reference 1 are listed in Column 6 of the calculation table.

(1) α (deg)	(2) $z_V \cos\alpha$ (in.)	(3) $\ell_V \sin\alpha$ (in.)	(4) $\frac{z_V \cos\alpha - \ell_V \sin\alpha}{b_W}$ [(2) − (3)]/41.56	(5) $(\Delta C_{l_\beta})_{V(WBH)}$ −0.734 (4) (per rad)	(6) $(\Delta C_{l_\beta})_{V(WBH)}$ (test) (per rad)
0	5.780	0	0.1390	−0.1020	−0.0877
2	5.777	0.870	0.1180	−0.0865	−0.0802
4	5.766	1.740	0.0967	−0.0710	−0.0653
6	5.750	2.600	0.0758	−0.0556	−0.0464

2. Given: The configuration of Reference 2 consisting of a wing, body, horizontal tail, and vertical tail. This is the same configuration as that of Sample Problem 3, Paragraph A, Section 5.3.1.1. Some of the characteristics are repeated.

Wing Characteristics:

S_W = 324 sq in. $\quad b_W$ = 36.0 in. $\quad z_W$ = 0

Additional Characteristics:

M = 0.13 $\quad \ell_V$ = 16.70 in. (c.g. to $(\bar{c}/4)_V$) $\quad z_V$ = 3.78 in. (c.g. to $(MAC)_V$)

α = 0, 2°, 4°, 6°

Compute:

$\left(\Delta C_{Y_\beta}\right)_{V(WBH)}$ = −0.375 per rad (based on S_W) (Sample Problem 3, Paragraph A, Section 5.3.1.1)

Solution:

$$\left(\Delta C_{l_\beta}\right)_p = \left(\Delta C_{Y_\beta}\right)_p \frac{z_p \cos\alpha - \ell_p \sin\alpha}{b_W} \quad \text{(Equation 5.3.2.1-a)}$$

$$\left(\Delta C_{l_\beta}\right)_{V(WBH)} = \left(\Delta C_{Y_\beta}\right)_{V(WBH)} \frac{z_V \cos\alpha - \ell_V \sin\alpha}{b_W}$$

$$= -0.375\left(\frac{3.78\cos\alpha - 16.70\sin\alpha}{36.0}\right) \text{ per rad (based on } S_W b_W)$$

Test results from Reference 2 are listed in Column 6 of the calculation table.

(1) α (deg)	(2) $z_V \cos\alpha$ (in.)	(3) $\ell_V \sin\alpha$ (in.)	(4) $\frac{z_V \cos\alpha - \ell_V \sin\alpha}{b_W}$ [(2) − (3)]/36.0	(5) $(\Delta C_{l_\beta})_{V(WBH)}$ −0.375 (4) (per rad)	(6) $(\Delta C_{l_\beta})_{V(WBH)}$ (test) (per rad)
0	3.780	0	0.105	−0.0394	−0.0401
2	3.778	0.582	0.0887	−0.0333	−0.0287
4	3.771	1.166	0.0723	−0.0271	−0.0115
6	3.759	1.745	0.0560	−0.0210	−0.0067

B. TRANSONIC

A brief discussion of the flow phenomena associated with a vertical panel at transonic speeds is given in Paragraph B of Section 5.3.1.1. The rolling moments due to the vertical panel are partly determined by the transonic lift-curve-slope characteristics of the isolated tail and partly by the wake and wash characteristics of the wing-body combination. In addition, the impingement on the horizontal-tail surface of the pressure field generated by the vertical panel can cause rolling moments. This latter effect can be large, since the pressure field at transonic speeds is frequently strong and is propagated to large distances from the source. The entire horizontal surface is therefore usually immersed in the field of the vertical panel.

DATCOM METHOD

Because of the complexity of the problem, no explicit method is available in the literature for estimating the contribution of a vertical panel to C_{l_β} at transonic speeds and none is presented in the Datcom. Some examples of the limited data available in the literature are shown in Figure 5.3.2.1-13.

C. SUPERSONIC

The procedure for estimating the rolling-moment contribution due to vertical panels at supersonic speeds is essentially the same as that at subsonic speeds. That is, the rolling-moment contribution of a vertical panel is based on the sideslip derivative ΔC_{Y_β} as obtained from Section 5.3.1.1. The problem of estimating the forces generated on vertical panels is complicated by the presence of shock waves. This effect is discussed in Paragraph C of Section 5.3.1.1.

As stated in the introduction to this section, no method is available for determining the horizontal-tail contribution to the derivative C_{l_β}. However, the effect of the horizontal tail on the vertical-tail contribution is accounted for by proper use of the apparent-mass factor (K) charts in determining the vertical-panel side force.

This method is limited to configurations in which the horizontal tail is mounted on the body or configurations with no horizontal tail.

DATCOM METHOD

The contribution of a vertical panel to the sideslip derivative C_{l_β} at supersonic speeds is given by Equation 5.3.2.1-a.

$$\left(\Delta C_{l_\beta}\right)_p = \left(\Delta C_{Y_\beta}\right)_p \frac{z_p \cos\alpha - \ell_p \sin\alpha}{b_W}$$

where the subscript p, z_p, and b_W are defined in Paragraph A, and

$\left(\Delta C_{Y_\beta}\right)_p$ is the side force due to sideslip of an added vertical panel obtained from Paragraph C of Section 5.3.1.1. (If a horizontal panel is present, its effect on the vertical panel must be included.)

ℓ_p is the distance parallel to the longitudinal body axis between the moment reference center and the 50-percent-chord point of the MAC of the added vertical panel, positive for the panel aft of the moment reference center. The aerodynamic center of the vertical panel could be used, but the inaccuracies of the basic method do not warrant this degree of refinement.

All geometry used in determining the moment arms of the vertical panels is based on the exposed panel.

For a wingless configuration the remarks following the Datcom method of Paragraph A above are also applicable here.

Results calculated at zero angle of attack by this method are compared to experimental data in Table 5.3.2.1-B. The detailed geometry of the configurations used in this table is given in Table 5.3.1.1-C. It should be noted that the values of ΔC_{Y_β} used in Table 5.3.2.1-B are calculated by the method of Paragraph C of Section 5.3.1.1.

Sample Problems

1. Given: The configuration of Reference 3 consisting of a wing, body, horizontal tail, and upper vertical stabilizer. This is the same configuration as that of Sample Problem 1, Paragraph C, Section 5.3.1.1. Some of the characteristics are repeated.

   Wing Characteristics:

   $S_W = 160.4$ sq in. $\quad b_W = 25.31$ in. $\quad z_W = 0$

   Additional Characteristics:

   $M = 1.61 \quad \ell_V = 11.40$ in. (c.g. to $(\bar{c}/2)_{V_e}$) $\quad z_V = 4.0$ in. (c.g. to $(MAC)_{V_e}$)

   $\alpha = 0, 2^\circ, 4^\circ, 6^\circ$

Compute:

$\left(\Delta C_{Y_\beta}\right)_{V(WBH)}$ = −0.529 per rad (based on S_W) (Sample Problem 1, Paragraph C, Section 5.3.1.1)

Solution:

$$\left(\Delta C_{l_\beta}\right)_p = \left(\Delta C_{Y_\beta}\right)_p \frac{z_p \cos\alpha - \ell_p \sin\alpha}{b_W} \quad \text{(Equation 5.3.2.1-a)}$$

$$\left(\Delta C_{l_\beta}\right)_{V(WBH)} = \left(\Delta C_{Y_\beta}\right)_{V(WBH)} \frac{z_V \cos\alpha - \ell_V \sin\alpha}{b_W}$$

$$= 0.529 \left(\frac{4.0 \cos\alpha - 11.40 \sin\alpha}{25.31}\right) \quad \text{per rad (based on } S_W b_W\text{)}$$

Test values from Reference 3 are listed in Column 6 of the calculation table.

① α (deg)	② $z_V \cos\alpha$ (in.)	③ $\ell_V \sin\alpha$ (in.)	④ $\frac{z_V \cos\alpha - \ell_V \sin\alpha}{b_W}$ [② − ③]/25.31	⑤ $\left(\Delta C_{l_\beta}\right)_{V(WBH)}$ −0.529 ④ (per rad)	⑥ $\left(\Delta C_{l_\beta}\right)_{V(WBH)}$ (test) (per rad)
0	4.000	0	0.158	−0.0836	−0.1010
2	3.998	0.398	0.143	−0.0756	−0.0930
4	3.990	0.796	0.126	−0.0667	−0.0803
6	3.978	1.191	0.110	−0.0582	−0.0647

2. Given: The configuration of Reference 4 consisting of a wing, body, upper vertical stabilizer, and lower vertical stabilizer. This is the same configuration as that of Sample Problem 2, Paragraph C, Section 5.3.1.1. Some of the characteristics are repeated.

Wing Characteristics:

S_W = 144.0 sq in. b_W = 24.0 in. z_W = 0

Additional Characteristics:

M = 2.01 ℓ_V = 12.0 in. (c.g. to $(\bar{c}/2)_{V_e}$) z_V = 4.15 in. (c.g. to $(MAC)_{V_e}$)

α = 0, 2°, 4°, 6°

Compute:

$$\left(\Delta C_{Y_\beta}\right)_{V(WBU)} = -0.583 \text{ per rad (based on } S_W\text{) (Sample Problem 2, Paragraph C, Section 5.3.1.1)}$$

Solution:

$$\left(\Delta C_{l_\beta}\right)_p = \left(\Delta C_{Y_\beta}\right)_p \frac{z_p \cos\alpha - \ell_p \sin\alpha}{b_W} \quad \text{(Equation 5.3.2.1-a)}$$

$$\left(\Delta C_{l_\beta}\right)_{V(WBU)} = \left(\Delta C_{Y_\beta}\right)_{V(WBU)} \frac{z_V \cos\alpha - \ell_V \sin\alpha}{b_W}$$

$$= -0.583 \left(\frac{4.15 \cos\alpha - 12.0 \sin\alpha}{24.0}\right) \text{ per rad (based on } S_W b_W\text{)}$$

Test values from Reference 4 are listed in Column 6 of the calculation table.

①	②	③	④	⑤	⑥
α (deg)	$z_V \cos\alpha$ (in.)	$\ell_V \sin\alpha$ (in.)	$\frac{z_V \cos\alpha - \ell_V \sin\alpha}{b_W}$ [(②) − (③)] /24.0	$\left(\Delta C_{l_\beta}\right)_{V(WBU)}$ −0.583 (④) (per rad)	$\left(\Delta C_{l_\beta}\right)_{V(WBU)}$ (test) (per rad)
0	4.150	0	0.173	−0.1010	−0.0745
2	4.147	0.419	0.155	−0.0905	−0.0774
4	4.140	0.838	0.138	−0.0805	−0.0803
6	4.127	1.264	0.120	−0.0700	−0.0830

D. HYPERSONIC

A general discussion of hypersonic flows is given in the introduction to Paragraph D of Section 4.1.3.5 and in several standard texts. No explicit method exists for estimating the contribution of an added tail panel to the sideslip derivative C_{l_β} at hypersonic speeds.

The supersonic method for estimating the derivative $\left(\Delta C_{Y_\beta}\right)_p$ (Paragraph C, Section 5.3.1.1) has been substantiated to reasonably high Mach numbers (6.86) and can be used for estimating the contribution of an added vertical panel, as in Paragraph C above. However, the method should be applied with caution, since the basic assumptions are increasingly violated as the Mach number increases. The hypersonic small-disturbance theory and Newtonian theory can also be used to estimate the forces and therefore the moments on the vertical panel. Newtonian flow, however, is limited to the upper range of hypersonic Mach numbers.

DATCOM METHODS

Method 1

Extended Supersonic Method

The method described in Paragraph C of this section can be used up to Mach numbers of approximately 7.

Method 2

Hypersonic Small-Disturbance Theory

Equation 5.3.2.1-a can be used to estimate hypersonic values of the vertical-panel contribution $(\Delta C_{l_\beta})_V$, where $(\Delta C_{Y_\beta})_V$ in this equation is obtained from Equation 5.3.1.1-h, and ℓ_p is determined as in Paragraph C above.

Method 3

Newtonian Theory

Equation 5.3.2.1-a is again used, but the vertical-panel contribution $(\Delta C_{Y_\beta})_V$ in this equation is based upon the use of Equation 5.3.1.1-i for this case, and ℓ_p is determined as in Paragraph C above. This method is most successful in the upper range of hypersonic Mach numbers.

Because of the general lack of test data in this speed regime, no substantiation tables are presented.

Sample Problem

Method 2

Given: The configuration of Reference 5. This is the same configuration as that of the sample problem, Paragraph D, Section 5.3.1.1. Some of the characteristics are repeated.

Wing Characteristics:

$S_W = 19.15$ sq in. $\quad b_W = 5.60$ in. $\quad z_W = 0$

Additional Characteristics:

$M = 5.0 \quad z_V = 0.795$ in. (c.g. to $(MAC)_{V_e}$) $\quad \alpha = 0$

Compute:

$$\frac{z_V}{b_W} = \frac{0.795}{5.60} = 0.142$$

$\left(\Delta C_{Y_\beta}\right)_V$ = −0.86 per rad (based on S_W) (Sample Problem, Paragraph D, Section 5.3.1.1)

Solution:

$$\left(\Delta C_{l_\beta}\right)_V = \left(\Delta C_{Y_\beta}\right)_p \frac{z_p \cos\alpha - \ell_p \sin\alpha}{b_W} \quad \text{(Equation 5.3.2.1-a)}$$

$$\left(\Delta C_{l_\beta}\right)_V = \left(\Delta C_{Y_\beta}\right)_V \frac{z_V}{b_W} \quad (\alpha = 0)$$

$$= -0.86\,(0.142)$$

$$= -0.122 \text{ per rad (based on } S_W b_W)$$

This corresponds to an experimental value (based on $S_W b_W$) of −0.1146 per radian obtained from Reference 5.

REFERENCES

1. Savage, H. F., and Tinling, B. E.: The Subsonic Static Aerodynamic Characteristics of an Airplane Model Having a Triangular Wing of Aspect Ratio 3. II – Lateral and Directional Characteristics. NACA TN 4042, 1957. (U)

2. Letko, W., and Williams, J. L.: Experimental Investigation at Low Speed of Effects of Fuselage Cross Section on Static Longitudinal and Lateral Stability Characteristics of Models Having 0° and 45° Sweptback Surfaces. NACA TN 3561, 1955. (U)

3. Spearman, M. L.: Static Lateral and Directional Stability and Effective Sidewash Characteristics of a Model of a 35° Swept-Wing Airplane at a Mach Number of 1.61. NACA RM L56E23, 1956. (U)

4. Spearman, M. L., and Robinson, R. B.: Investigation of the Aerodynamic Characteristics in Pitch and Sideslip of a 45° Swept-Wing Configuration with Various Vertical Locations of the Wing and Horizontal Tail. Static Lateral and Directional Stability; Mach Numbers of 1.41 and 2.01. NACA RM L57J25a, 1957. (U)

5. Dennis, D. H., and Petersen, R. H.: Aerodynamic Performance and Static Stability at Mach Numbers Up to 5 of Two Airplane Configurations with Favorable Lift Interference. NASA Memo 1-8-59A. 1959. (U)

TABLE 5.3.2.1-A[1]

SUBSONIC CONTRIBUTION OF VERTICAL PANELS TO C_{l_β}

DATA SUMMARY AND SUBSTANTIATION

Ref.[2]	Configuration Sketch	M	Panel Added	$(\Delta C_{Y_\beta})_V$ Calc. (per rad)	$\frac{z_V}{b_W}$	$(\Delta C_{l_\beta})_V$ Calc. (per rad)	$(\Delta C_{l_\beta})_V$ Test (per rad)	Percent Error e
6	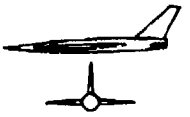	.25	$BWHV_S$-BW	−.481	.121	−.058	−.060	3.3
		.25	$BWHV_L$-BW	−.734	.139	−.102	−.091	12.1
		.25	BV_S-B	−.428	.121	−.052	−.065	20.0
		.25	BV_L-B	−.578	.139	−.080	−.102	21.6
		.25	BHV_L-BH	−.597	.139	−.083	−.095	12.6
		.25	BHV_S-BH	−.431	.121	−.052	−.058	10.3
8		.17	BV-B	−.254	.095	−.024	−.023	4.3
		.17	BV-B	−.317	.107	−.034	−.034	0
	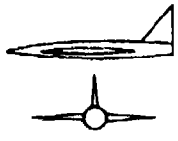	.17	BV-B	−.446	.130	−.058	−.071	18.3
		.17	BW_1V-BW_1	−.468	.130	−.061	−.069	11.6
		.17	BW_2V-BW_2	−.409	.130	−.053	−.052	1.9
		.17	BW_3V-BW_3	−.528	.130	−.069	−.080	13.7
9	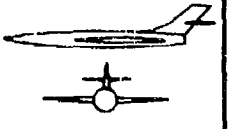	.6	BWHV-BW	−.575	.125	−.072	−.069	4.3
10	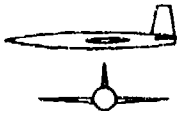	.13	BWHV-BW	−.426	.126	−.054	−.057	5.3

1. Refer to Table 5.3.1.1-B for configuration data
2. These references are found in Section 5.3.1.1

TABLE 5.3.2.1-B[1]

SUPERSONIC CONTRIBUTION OF VERTICAL PANELS TO C_{l_β}

DATA SUMMARY AND SUBSTANTIATION

Ref.[2]	Configuration Sketch	M	Panel Added	$(\Delta C_{Y_\beta})_V$ Calc. (per rad)	$\frac{z_v}{b_w}$	$(\Delta C_{l_\beta})_V$ Calc. (per rad)	$(\Delta C_{l_\beta})_V$ Test (per rad)	Percent Error e
16	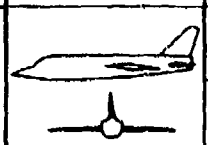	1.61	BV-B	-.525	.158	-.083	−.083	0
		1.61	BWHV -BWH	-.529	.158	-.084	−.101	16.8
17		1.61	BWV_o-BW	−.358	.145	−.052	−.049	6.1
		2.01	BWV_o-BW	−.335	.145	−.048	−.034	41.2
		1.61	$BWHV_o$-BWH	−.368	.136	−.050	−.043	16.3
		2.01	$BWHV_o$-BWH	−.335	.145	−.048	−.034	41.2
		1.61	$BWHV_{ext}$-BWH	−.424	.151	−.064	−.054	18.5
		1.61	$BWHV_{187\%}$-BWH	−.471	.146	−.069	−.060	15.0
18		1.41	BWV-BW	−.836	.182	−.152	−.126	20.6
		2.01	BWV-BW	−.545	.182	−.099	−.103	3.9
18		1.41	BWV-BW	−.842	.182	−.153	−.126	21.4
		2.01	BWV-BW	−.540	.182	−.098	−.100	2.0
18		1.41	BWV-BW	−.792	.182	−.144	−.126	14.3
		2.01	BWV-BW	−.542	.182	−.099	−.092	7.6
18		1.41	BWV-BW	−.706	.182	−.128	−.097	32.0
		2.01	BWV-BW	−.586	.182	−.107	−.086	24.4
19		5.0	BWV-BW	−.860[3]	.142	−.122	−.123	.8

1. Refer toTable 5.3.1.1-C for configuration data
2. These references are found in Section 5.3.1.1
3. Refer to Sample Problem, Paragraph D, Section 5.3.1.1

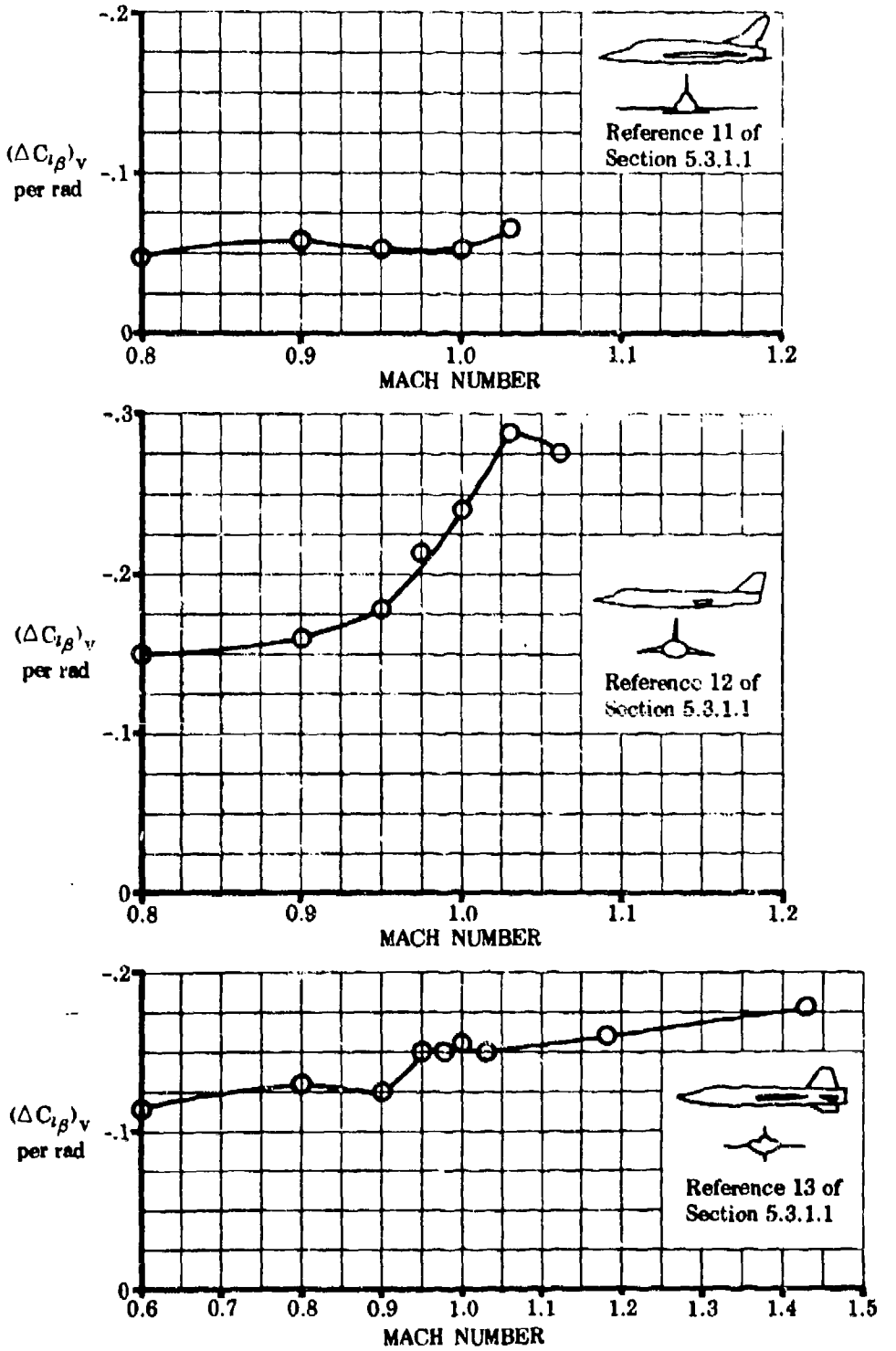

FIGURE 5.3.2.1-13 TYPICAL TRANSONIC DATA

3.3 TAIL-BODY SIDESLIP DERIVATIVE C_{n_β}

5.3.3.1 TAIL-BODY SIDESLIP DERIVATIVE C_{n_β} IN THE LINEAR ANGLE-OF-ATTACK RANGE

The contribution of panels present in the empennage to the vehicle sideslip derivative C_{n_β} is estimated by the methods of this Section. The methods generally include the interference effects of other vehicle components.

Detailed discussion of the various aerodynamic aspects of adding tail panels to flight vehicles is given in Section 5.3.1.1 and is not repeated here.

A. SUBSONIC

The methods of estimating the contribution of panels present in the empennage to the sideslip derivative C_{n_β} are based on the methods for estimating the contribution of panels present in the empennage to the sideslip derivative C_{Y_β} in Section 5.3.1.1. The moment arm through which the panel side force acts can be taken as (a) the distance parallel to the longitudinal axis between the vehicle center of gravity and the quarter-chord point of the mean aerodynamic chord of the panel or (b) the distance parallel to the longitudinal axis between the vehicle center of gravity and the actual aerodynamic center of the panel. In most cases the former approximation is used, since the inaccuracies of estimating the side force of the panel do not warrant the refinements of (b). For short-coupled configurations, however, where the tail-length distance is relatively short and the size of the panel may be large, significant differences between results estimated by (a) and (b) may result; in such cases (b) is recommended.

DATCOM METHOD

Method 1

Simplified Method

The contribution of a panel to the sideslip derivative C_{n_β} at subsonic speeds is given by

$$(\Delta C_{n_\beta})_p = -(\Delta C_{Y_\beta})_p \frac{\ell_p}{b_w} \qquad 5.3.3.1\text{-a}$$

where the subscript $_p$ refers to panels present in the empennage

$(\Delta C_{Y_\beta})_p$ is the side force due to sideslip of the added panel determined as follows:

For configurations with the horizontal panel mounted on the body, or with no horizontal panel, use Method 1 or Method 3 of paragraph A, Section 5.3.1.1.

For configurations with the horizontal panel mounted on the vertical, use Method 1 of paragraph A, Section 5.3.1.1.

For twin-vertical panel configurations, use Method 2 of paragraph A, Section 5.3.1.1.

ℓ_p is the distance parallel to the longitudinal axis between the moment reference center (usually the vehicle center of gravity) and the quarter-chord point of the MAC of the added panel, positive for the added panel behind the moment reference center.

b_w is the span of the wing

Method 2

Refined Method

In this case the contribution of a panel to the sideslip derivative C_{n_β} is given by

$$(\Delta C_{n_\beta})_p = -(\Delta C_{Y_\beta})_p \frac{[\ell_p + (x_{a.c.})_p]}{b_w} \qquad 5.3.3.1\text{-b}$$

where $(\Delta C_{Y_\beta})_p$, ℓ_p, and b_W are defined in Method 1 above, and

$(x_{c.c.})_p$ is the distance between the quarter-chord point of the MAC of the added panel as determined from paragraph A of Section 4.1.4.2, positive for the a.c. behind the quarter-chord point. (In determining the vertical panel a.c. use the aspect ratio of the panel mounted on an infinite reflection plane.)

All geometry for the added panel of these methods is based on the panel extended to the body centerline.

Methods 1 and 2 of paragraph A, Section 5.3.1.1 lump the total empennage increment in C_{Y_β} into a single parameter. On the other hand, Method 3 gives the increment due to the addition of one panel (either a horizontal or vertical panel) including the mutual aerodynamic interference effects of all other panels present. An extension of Method 3 to determine the total empennage side force due to sideslip at subsonic speeds which results from the addition of all panels present in the empennage is presented in paragraph A of Section 5.5.1.1.

For a wingless configuration, b_W is replaced by the reference length for the vehicle, and $(\Delta C_{Y_\beta})_p$ is based on the vehicle reference area.

Table 5.3.3.1-A compares results calculated by Method 1 with test data. The test cases for this table are the same as those used for table 5.3.1.1-B. Pertinent detailed information for table 5.3.3.1-A is therefore found in table 5.3.1.1-B and is not repeated.

Sample Problems

1. Method 1

Given: The configuration of reference 1, consisting of wing, body, horizontal tail, and upper vertical tail. This is the same configuration as that of sample problem 1, paragraph A, Section 5.3.1.1. Some of the characteristics are repeated. Find the effect of adding the vertical tail to the wing-body-horizontal tail configuration.

Wing Characteristics

S_W = 576.0 sq in. b_W = 41.56 in. z_W = 0

Additional Characteristics

M = 0.25 ℓ_V = 24.89 in. (c.g. to $(\bar{c}/4)_V$)

Compute:

$$\frac{\ell_V}{b_W} = \frac{24.89}{41.56} = 0.599$$

$(\Delta C_{Y_\beta})_{V(WBH)}$ = -0.734 per rad (based on S_W) (sample problem 1, paragraph A, Section 5.3.1.1)

Solution:

$$(\Delta C_{n_\beta})_p = -(\Delta C_{Y_\beta})_p \frac{\ell_p}{b_W} \qquad \text{(equation 5.3.3.1-a)}$$

$$(\Delta C_{n_\beta})_{V(WBH)} = -(\Delta C_{Y_\beta})_{V(WBH)} \frac{\ell_V}{b_W}$$

$$= -(-0.734)(0.599)$$

$$= 0.440 \text{ per rad (based on } S_W b_W)$$

This compares with an experimental value of 0.415 per radian obtained from reference 1.

2. Method 1

Given: The configuration of reference 2, consisting of wing, body, horizontal tail, and vertical tail. This is the same configuration as that of sample problem 3, paragraph A, Section 5.3.1.1. Some of the characteristics are repeated. Find the effect of adding the vertical tail to the wing-body-horizontal tail combination.

Wing Characteristics

S_w = 324 sq in. b_w = 36.0 in. z_w = 0

Additional Characteristics

M = 0.13 ℓ_v = 16.70 in. (c.g. to $(\bar{c}/4)_v$)

Compute:

$$\frac{\ell_v}{b_w} = \frac{16.7}{36.0} = 0.464$$

$(\Delta C_{Y_\beta})_{V(WBH)}$ = -0.375 per rad (based on S_w) (sample problem 3, paragraph A, Section 5.3.1.1)

Solution:

$$(\Delta C_{n_\beta})_v = -(\Delta C_{Y_\beta})_v \frac{\ell_v}{b_w} \qquad \text{(equation 5.3.3.1-a)}$$

$$(\Delta C_{n_\beta})_{V(WBH)} = -(\Delta C_{Y_\beta})_{V(WBH)} \frac{\ell_v}{b_w}$$

$$= -(-0.375)\,(0.464)$$

$$= 0.174 \text{ per rad (based on } S_w b_w)$$

This compares with an experimental value of 0.178 per radian obtained from reference 2.

B. TRANSONIC

A brief discussion of the flow phenomena associated with forces generated on a vertical panel at transonic speeds is given in paragraph B of Section 5.3.1.1. As in the case for the vertical tail contribution to C_{Y_β}, the transonic characteristics of the sideslip derivative C_{n_β} are closely associated with the transonic lift-curve-slope characteristics of the isolated panel (see introduction to paragraph B of Section 4.1.3.2).

DATCOM METHOD

No method is available for estimating the contribution of a tail panel to the sideslip derivative C_{n_β} and none is presented in the Datcom. Figure 5.3.3.1-11 presents some available information for this derivative.

C. SUPERSONIC

As in the subsonic case, the method of estimating supersonic values of $(\Delta C_{n_\beta})_v$ is based on the values of $(\Delta C_{Y_\beta})_v$ estimated by the method of Section 5.3.1.1. The problem of estimating the forces generated on vertical panels is complicated by the presence of shock waves. See paragraph C of Section 5.3.1.1 for a detailed description of this method. The moment arm through which the added vertical panel side force acts can be taken as (a) the distance parallel to the longitudinal axis between the vehicle center of gravity and the 50-percent-chord point of the mean aerodynamic center of the vertical panel, or (b) the distance parallel to the longitudinal axis between the vehicle center of gravity and the actual aerodynamic center of the vertical panel. For short-coupled configurations the latter approximation is, of course, more accurate. At supersonic speeds the centroid of area of the region of interference approximates the moment arm in the case of the increment gained by adding a horizontal surface.

This method is limited to configurations in which the horizontal tail is mounted on the body or configurations with no horizontal tail.

DATCOM METHODS

Method 1

Simplified Method

The contribution of an added panel (either a horizontal or vertical panel) to the sideslip derivative C_{n_β} at supersonic speeds is given by equation 5.3.3.1-a

$$(\Delta C_{n_\beta})_p = -(\Delta C_{Y_\beta})_p \frac{\ell_p}{b_W}$$

where the subscript p and b_W are defined in paragraph A, and

$(\Delta C_{Y_\beta})_p$ is the side force due to sideslip of an added panel obtained from paragraph C of Section 5.3.1.1

ℓ_p is the distance parallel to the longitudinal axis between the vehicle moment center and the 50-percent-chord point of the MAC of an added vertical panel, positive for the vertical panel aft of the vehicle moment center. In the case of the increment gained by adding a horizontal panel, ℓ_p is the distance parallel to the longitudinal axis between the vehicle moment center and the centroid of area of the region of interference, positive for the horizontal panel aft of the vehicle moment center. (See sketch (c) of Section 5.3.1.1 for definition of area of region of interference.)

Method 2

Refined Method

For a more refined estimate of the contribution of an added panel to the sideslip derivative C_{n_β}, equation 5.3.3.1- is used

$$(\Delta C_{n_\beta})_p = -(\Delta C_{Y_\beta})_p \frac{[\ell_p + (x_{a.c.})_p]}{b_W}$$

where $(\Delta C_{Y_\beta})_p$, ℓ_p, and b_W are defined in Method 1 above, and

$(x_{a.c.})_p$ is the distance parallel to the longitudinal axis between the 50-percent-chord point of the MAC of an added vertical panel and the aerodynamic center of the added panel obtained from paragraph C of Section 4.1.4.2, positive for the a.c. behind the 50-percent-chord point. (In determining the vertical panel a.c. use the aspect ratio of the isolated panel mounted on an infinite reflection plane.)

In the case of the increment gained by adding a horizontal panel, the moment arm is treated as in Method 1 above.

All geometry used in determining the moment arms of the vertical panels in the above methods is based on the exposed panel.

For a wingless configuration the remarks following the Datcom methods of paragraph A above are also applicable here.

Table 5.3.3.1-B compares results obtained by Method 1 with experimental data. The test configurations used in this table are the same as those used in Table 5.3.1.1-C. Detailed geometric variables are given in this latter table.

Sample Problems

1. Method 1

Given: The configuration of reference 3 consisting of wing, body, horizontal tail, and upper vertical stabilizer. This is the same configuration as that of sample problem 1, paragraph C, Section 5.3.1.1. Some of the characteristics are repeated. Find the effect of adding the vertical tail to the wing-body-horizontal tail combination.

Wing Characteristics

S_w = 160.4 sq in. b_w = 25.31 in. z_w = 0

Additional Characteristics

M = 1.61 ℓ_v = 11.40 in. (c.g. to $(\bar{c}/2)_{v_e}$)

Compute:

$$\frac{\ell_v}{b_w} = \frac{11.40}{25.31} = 0.450$$

$(\Delta C_{Y_\beta})_{V(WBH)}$ = -0.529 per rad (based on S_w) (sample problem 1, paragraph C, Section 5.3.1.1)

Solution:

$$(\Delta C_{n_\beta})_p = -(\Delta C_{Y_\beta})_p \frac{\ell_p}{b_w} \qquad \text{(equation 5.3.3.1-a)}$$

$$(\Delta C_{n_\beta})_{V(WBH)} = -(\Delta C_{Y_\beta})_{V(WBH)} \frac{\ell_v}{b_w}$$

$$= -(-0.529)\,(0.450)$$

$$= 0.238 \text{ per rad (based on } S_w b_w)$$

This compares with an experimental value of 0.218 per radian obtained from reference 3.

2. Method 1

Given: The configuration of reference 4 consisting of wing, body, upper vertical stabilizer, and lower vertical stabilizer. This is the same configuration as that of sample problem 2, paragraph C, Section 5.3.1.1. Some of the characteristics are repeated. Find the effect of adding the upper vertical stabilizer to the wing-body-lower vertical stabilizer combination.

Wing Characteristics

S_w = 144.0 sq in. b_w = 24.0 in. z_w = 0

Additional Characteristics

M = 2.01 ℓ_v = 12.00 in. (c.g. to $(\bar{c}/2)_{v_e}$)

Compute:

$$\frac{\ell_v}{b_w} = \frac{12.00}{24.0} = 0.500$$

$(\Delta C_{Y_\beta})_{V(WBU)}$ = -0.583 per rad (based on S_w) (sample problem 2, paragraph C, Section 5.3.1.1)

Solution:

$$(\Delta C_{n_\beta})_p = -(\Delta C_{Y_\beta})_p \frac{\ell_p}{b_w} \qquad \text{(equation 5.3.3.1-a)}$$

$$(\Delta C_{n_\beta})_{V(WBU)} = -(\Delta C_{Y_\beta})_{V(WBU)} \frac{\ell_v}{b_w}$$

$$= -(-0.583)\,(0.500)$$

$$= 0.2915 \text{ per rad (based on } S_w b_w)$$

This compares with an experimental value of 0.277 per radian obtained from reference 4.

D. HYPERSONIC

A general discussion of hypersonic flows is given in the introduction to paragraph D of Section 4.1.3.3 and in several standard texts. No explicit method exists for estimating the contribution of an added tail panel to the sideslip derivative C_{n_β} at hypersonic speeds.

The supersonic method for estimating the derivative $(\Delta C_{Y_\beta})_p$ (paragraph C, Section 5.3.1.1) has been substantiated to reasonably high Mach numbers (6.86) and can be used for estimating $(\Delta C_{n_\beta})_p$ as in paragraph C above. However, the method should be applied with caution, since the basic assumptions are increasingly violated as the Mach number increases. The hypersonic small-disturbance theory and Newtonian Theory can also be used to estimate the forces and therefore the moments on the vertical panel. Newtonian flow, however, is limited to the upper range of hypersonic Mach numbers.

DATCOM METHODS

Method 1

Extended Supersonic Method

The method described in paragraph C can be used up to Mach numbers of approximately 7.

Method 2

Hypersonic Small-Disturbance Theory

Equation 5.3.3.1-a or 5.3.3.1-b can be used to estimate hypersonic values of $(\Delta C_{n_\beta})_V$, where $(\Delta C_{Y_\beta})_V$ is obtained from equation 5.3.1.1-h and ℓ_p is as defined in paragraph C above. This method is generally limited to small angles of flow deflection.

Method 3

Newtonian Theory

Equation 5.3.3.1-a or 5.3.3.1-b can be used, but $(\Delta C_{Y_\beta})_V$ is obtained by using equation 5.3.1.1-i to determine C_p in this case. ℓ_p is as defined in paragraph C above. This method is most successful at the high hypersonic Mach numbers.

Because of the general lack of test data in this speed regime, no substantiation table is presented.

Method 2

Sample Problem

Given: The configuration of reference 5. This is the same configuration as that of the sample problem, paragraph D, Section 5.3.1.1. Some of the characteristics are repeated. Find the effect of adding the vertical stabilizer to the wing-body configuration.

Wing Characteristics

S_W = 19.15 sq in. $\quad b_W$ = 5.60 in.

Additional Characteristics

M = 5.0 $\quad \ell_V$ = 2.79 in. (c.g. to $(\bar{c}/2)_{V_e}$)

Compute:

$$\frac{\ell_V}{b_W} = \frac{2.79}{5.60} = 0.499$$

$(\Delta C_{Y_\beta})_V$ = -0.86 per rad (based on S_W) (sample problem, paragraph D, Section 5.3.1.1)

Solution:

$$(\Delta C_{n_\beta})_p = -(\Delta C_{Y_\beta})_p \frac{\ell_p}{b_W} \qquad \text{(equation 5.3.3.1-a)}$$

$$(\Delta C_{n_\beta})_V = -(\Delta C_{Y_\beta})_V \frac{\ell_V}{b_W}$$

$= -(-0.36)\,(0.499)$

$= 0.430$ per rad (based on $S_w b_w$)

This corresponds to an experimental value of 0.59 per radian obtained from reference 5.

REFERENCES

1. Savage, H. F., and Tinling, B. E.: The Subsonic Static Aerodynamic Characteristics of an Airplane Model Having a Triangular Wing of Aspect Ratio 3. II - Lateral and Directional Characteristics. NACA TN 4042, 1957. (U)

2. Letko, W., and Williams, J. L.: Experimental Investigation at Low Speed of Effects of Fuselage Cross Section on Static Longitudinal and Lateral Stability Characteristics of Models Having 0° and 45° Sweptback Surfaces. NACA TN 3551, 1955. (U)

3. Sperman, M. L.: Static Lateral and Directional Stability and Effective Sidewash Characteristics of a Model of a 35° Swept-Wing Airplane at a Mach Number of 1.61. NACA RM L56E23, 1956. (U)

4. Spearman, M. L., and Robinson, R. B.: Investigation of the Aerodynamic Characteristics in Pitch and Sideslip of a 45° Swept-Wing Airplane Configuration with Various Vertical Locations of the Wing and Horizontal Tail. Static Lateral and Directional Stability; Mach Numbers of 1.41 and 2.01. NACA RM L57J25a, 1957. (U)

5. Dennis, D. H., and Petersen, R. H.: Aerodynamic Performance and Static Stability at Mach Numbers Up to 5 of Two Airplane Configuration with Favorable Lift Interference. NASA Memo 1-6-59A, 1959. (U)

TABLE 5.3.3.1-A[1,2,3]

SUBSONIC CONTRIBUTION OF VERTICAL PANELS TO C_{n_β}

DATA SUMMARY AND SUBSTANTIATION

Ref.[3]	Configuration Sketch	M	Panel Added	$(\Delta C_{Y_\beta})_V$ Calc. (per rad)	$\frac{\ell_V}{b_W}$ Method 1	$(\Delta C_{n_\beta})_V$ Calc. (per rad)	$(\Delta C_{n_\beta})_V$ Test (per rad)	Percent Error e
6		.25	$BWHV_R$-BWH	−.481	.463	.223	.24	7.1
		.25	$BWHV_L$-BWH	−.734	.443	.325	.31	4.8
		.25	BV_R-B	−.428	.620	.265	.31	14.5
		.25	BV_L-B	−.578	.599	.346	.39	11.3
		.25	BHV_L-BH	−.597	.599	.358	.41	12.7
		.25	BHV_R-BH	−.431	.620	.267	.32	16.6
8		.17	BV-B	−.254	.58	.147	.14	5.0
		.17	BV-B	−.317	.57	.181	.18	.6
	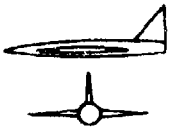	.17	BV-B	−.446	.56	.250	.26	3.8
		.17	BW_1V-BW_1	−.468	.56	.262	.25	4.8
		.17	BW_2V-BW_2	−.409	.56	.229	.18	27.2
		.17	BW_3V-BW_3	−.528	.56	.296	.30	1.3
9	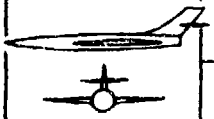	.6	BWHV-BW	−.575	.425	.244	.23	6.1
		.6	BV-B	−.492	.425	.209	.24	12.9
10	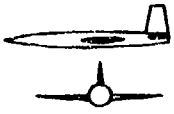	.13	BWHV-BW	−.426	.464	.198	.21	5.7
		.13	BHV-BH	−.504	.464	.234	.22	6.4
	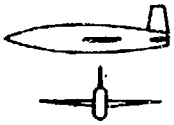	.13	BHV-BH	−.506	.464	.235	.21	11.9

TABLE 5.3.3.1-A[1,2,3] (CONTD)

Ref.[3]	Configuration Sketch	M	Panel Added	$(\Delta C_{Y_\beta})_V$ Calc. (per rad)	$\frac{\ell_v}{b_w}$ Method 1	$(\Delta C_{n_\beta})_V$ Calc. (per rad)	$(\Delta C_{n_\beta})_V$ Test (per rad)	Percent Error e
10	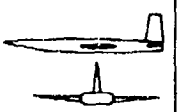	.13	BHV-BH	−.497	.464	.230	.20	15.0

NOTES:

1. This table is a condensed form of that appearing in reference 2. Additional substantiation can be obtained from this reference.
2. Refer to table 5.3.1.1-B for configuration data.
3. These references are found in Section 5.3.1.1.

TABLE 5.3.3.1-B[1,2,3]

SUPERSONIC CONTRIBUTION OF VERTICAL PANELS TO C_{n_β}

DATA SUMMARY AND SUBSTANTIATION

Ref.[3]	Configuration Sketch	M	Panel Added	$(\Delta C_{Y_\beta})_V$ Calc. (per rad)	$\frac{\ell_v}{b_w}$	$(\Delta C_{n_\beta})_V$ Calc. (per rad)	$(\Delta C_{n_\beta})_V$ Test (per rad)	Percent Error e
15	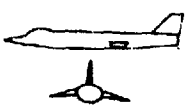	1.82	BWV-BW	−.589	.768	.453	.43	5.3
16	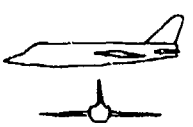	1.61	BV-B	−.525	.450	.236	.22	7.3
		1.61	BWHV -BWH	−.529	.450	.238	.218	9.2
14	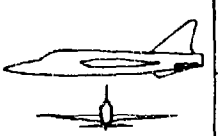	2.01	BWHU-BWH	−.056	.439	.025	.034	26.5
		2.01	BWHUV-BWHU	−.525	.575	.302	.30	.7
17		1.61	BWV_{0}-BW	−.358	.403	.144	.14	2.9
		2.01	BWV_{0}-BW	−.335	.403	.135	.12	12.5
		1.61	$BWHV_{0}$-BWH	−.368	.403	.148	.15	1.3
		2.01	$BWHV_{0}$-BWH	−.335	.403	.135	.12	12.5
		1.61	$BWHV_{+31}$-BWH	−.424	.414	.176	.17	3.5
		1.61	$BWHV_{+27^{0}}$-BWH	−.471	.410	.193	.17	13.5

TABLE 5.3.3.1-B[1,2,3] (CONTD)

Ref.[3]	Configuration Sketch	M	Panel Added	$(\Delta C_{Y_\beta})_V$ Calc. (per rad)	$\frac{\ell_V}{b_W}$	$(\Delta C_{n_\beta})_V$ Calc. (per rad)	$(\Delta C_{n_\beta})_V$ Test (per rad)	Percent Error e
18		1.41	BWV-BW	−.836	.465	.389	.37	5.1
		2.01	BWV-BW	−.545	.469	.256	.31	17.4
18		1.41	BWV-BW	−.842	.564	.475	.42	13.1
		2.01	BWV-BW	−.540	.564	.305	.30	1.7
18		1.41	BWV-BW	−.792	.630	.499	.45	10.9
		2.01	BWV-BW	−.542	.630	.342	.30	14.0
18		1.41	BWV-BW	−.706	.748	.528	.36	46.7
		2.01	BWV-BW	−.586	.748	.438	.32	36.9
20	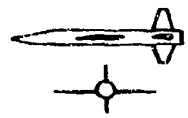	6.86	BWHUV-BW	−.315	.645	.203	.18	12.8

NOTES:

1. This table is a condensed form of that appearing in reference 2. Additional substantiation can be obtained from this reference.
2. Refer to table 5.3.1.1-C for configuration data.
3. These references are found in Section 5.3.1.1.

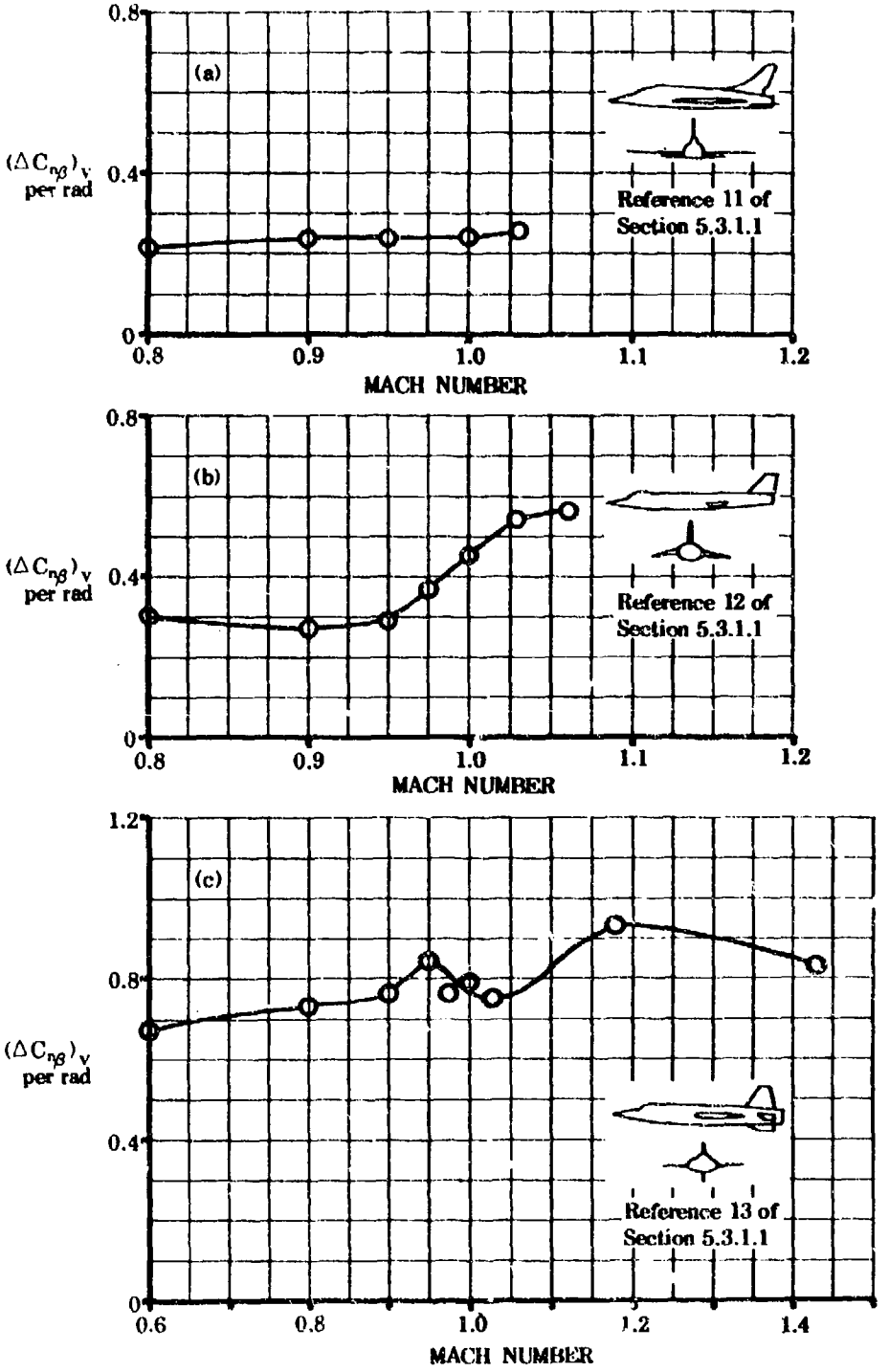

FIGURE 5.3.3.1-11. TYPICAL TRANSONIC DATA

5.3.3.2 TAIL-BODY YAWING-MOMENT COEFFICIENT C_n AT ANGLE OF ATTACK

The tail-body yawing moment developed at combined angles is nonlinear with respect to both sideslip and angle of attack because of the body-vortex induced sidewash on the upper vertical tail and the cross-coupling of upwash and sidewash velocities. To obtain the derivative C_{n_β}, it is recommended that C_n be calculated at several angles of attack for a small sideslip angle ($\beta \leq 4^o$). Then, at each angle of attack, the yawing moment is assumed linear with sideslip for small values of β so that

$$C_{n_\beta} \approx \frac{C_n}{\beta}$$

A. SUBSONIC

The comments appearing in Paragraph A of Section 5.3.1.2 apply here also. The method presented herein is restricted to first-order approximations at relatively low angles of attack.

DATCOM METHOD

It is recommended that the method of Paragraph A of Section 5.3.3.1 be used in the linear-lift angle-of-attack range.

B. TRANSONIC

The comments appearing in Paragraph B of Section 5.3.1.2 apply here also and will not be repeated.

DATCOM METHOD

No method is available for estimating this coefficient at angle of attack and none is presented in the Datcom.

C. SUPERSONIC

The comments in Paragraph C of Section 5.3.1.2 apply here also. As noted therein, the method for determining the side-force coefficient at angle of attack does not account for wing-tail interference effects. The yawing-moment coefficient at angle of attack for a configuration including a wing at supersonic speeds must be obtained from Paragraph C of Section 5.6.3.2.

DATCOM METHOD

The method for estimating the empennage contribution to the yawing moment at combined angles is essentially that of Section 5.3.1.2. The yawing-moment coefficient is obtained simply by applying the proper moment arms to the various side-force coefficients that comprise the total tail contribution. As noted in Section 5.3.1.2, the method is limited to circular bodies, and to the analysis of horizontal-tail effects only when the surface is body-mounted.

The contribution of the tail panels to the yawing-moment coefficient is given as

$$(C_n)_{HVU(B)} = -\frac{\ell_H \cos\alpha + z_H \sin\alpha}{b_W}(C_Y)_{H(B)} - \frac{\ell_V \cos\alpha + z_V \sin\alpha}{b_W}(C_Y)_V$$

$$-\frac{\ell_U \cos\alpha + z_U \sin\alpha}{b_W}(C_Y)_U \qquad 5.3.3.2\text{-a}$$

where

$(C_Y)_{H(B)}$ is defined under Equation 5.3.1.2-a.

$(C_Y)_V$ is defined under Equation 5.3.1.2-a.

$(C_Y)_U$ is defined under Equation 5.3.1.2-a.

ℓ_H is the distance from the moment reference center to the center of pressure of the horizontal-tail interference side force, measured parallel to the longitudinal axis. The c.p. is taken at the centroid of the interference area, indicated by shading in Sketch (a) of Section 5.3.1.2.

z_H is the distance to the center of pressure of the horizontal-tail interference side force, measured from, and normal to, the longitudinal axis. z_H is positive when the c.p. is above the longitudinal axis. (The c.p. location is as assumed above.)

ℓ_V is the distance from the moment reference center to the center of pressure of the upper vertical tail, measured parallel to the longitudinal axis.

z_V is the distance to the center of pressure of the upper vertical tail, measured from, and normal to, the longitudinal axis. z_V is positive when the c.p. is above the longitudinal axis.

ℓ_U is the distance from the moment reference center to the center of pressure of the ventral fin, measured parallel to the longitudinal axis.

z_U is the distance to the center of pressure of the ventral fin, measured from, and normal to, the longitudinal axis. z_U is negative when the c.p. is below the longitudinal axis.

For the vertical panels the center of pressure is taken as the 50-percent-chord point of the mean aerodynamic chord of the exposed panel.

Values for the incremental coefficient resulting from the addition of upper vertical tails to circular bodies, calculated using the Datcom method, are compared with experimental results in Figure 5.3.3.2-4. It is evident from the experimental data that a strong destabilizing effect occurs with increasing angle of attack, and that this effect is fairly accurately predicted by the Datcom method over the angle-of-attack range of the tests.

Sample Problem

Given: Configuration of Sample Problem, Paragraph C, Section 5.3.1.2. No horizontal tail. Some characteristics are repeated. Find the yawing-moment coefficient developed by a vertical tail and a ventral fin.

Wing Characteristics:

$\alpha = 12°$ $\quad S_W = 144.0$ sq in.

Additional Characteristics:

$\ell_V = 12.0$ in. $\quad \ell_U = 12.0$ in. $\quad b_W = 24.0$ in. $\quad z_V = 4.15$ in. $\quad z_U = -2.15$ in.

$\left.\begin{aligned}(C_Y)_V &= -0.0229 \\ (C_Y)_U &= -0.0109\end{aligned}\right\}$ (based on S_W) (Sample Problem, Paragraph C, Section 5.3.1.2)

$M = 2.01$

Solution:

$$(C_n)_{VU(B)} = -\frac{\ell_V \cos\alpha + z_V \sin\alpha}{b_W}(C_Y)_V - \frac{\ell_U \cos\alpha + z_U \sin\alpha}{b_W}(C_Y)_U$$ (Equation 5.3.3.2-a, horizontal tail off)

$$= -\frac{12.0 \cos 12° + 4.15 \sin 12°}{24.0}(-0.0229) - \frac{12.0 \cos 12° - 2.15 \sin 12°}{24.0}(-0.0109)$$

$= 0.0171$ (based on $S_W b_W$)

REFERENCE

1. Kaettari, G. E.: Estimation of Directional Stability Derivatives at Moderate Angles and Supersonic Speeds. NASA Memo 12-1-58A, 1959. (U)

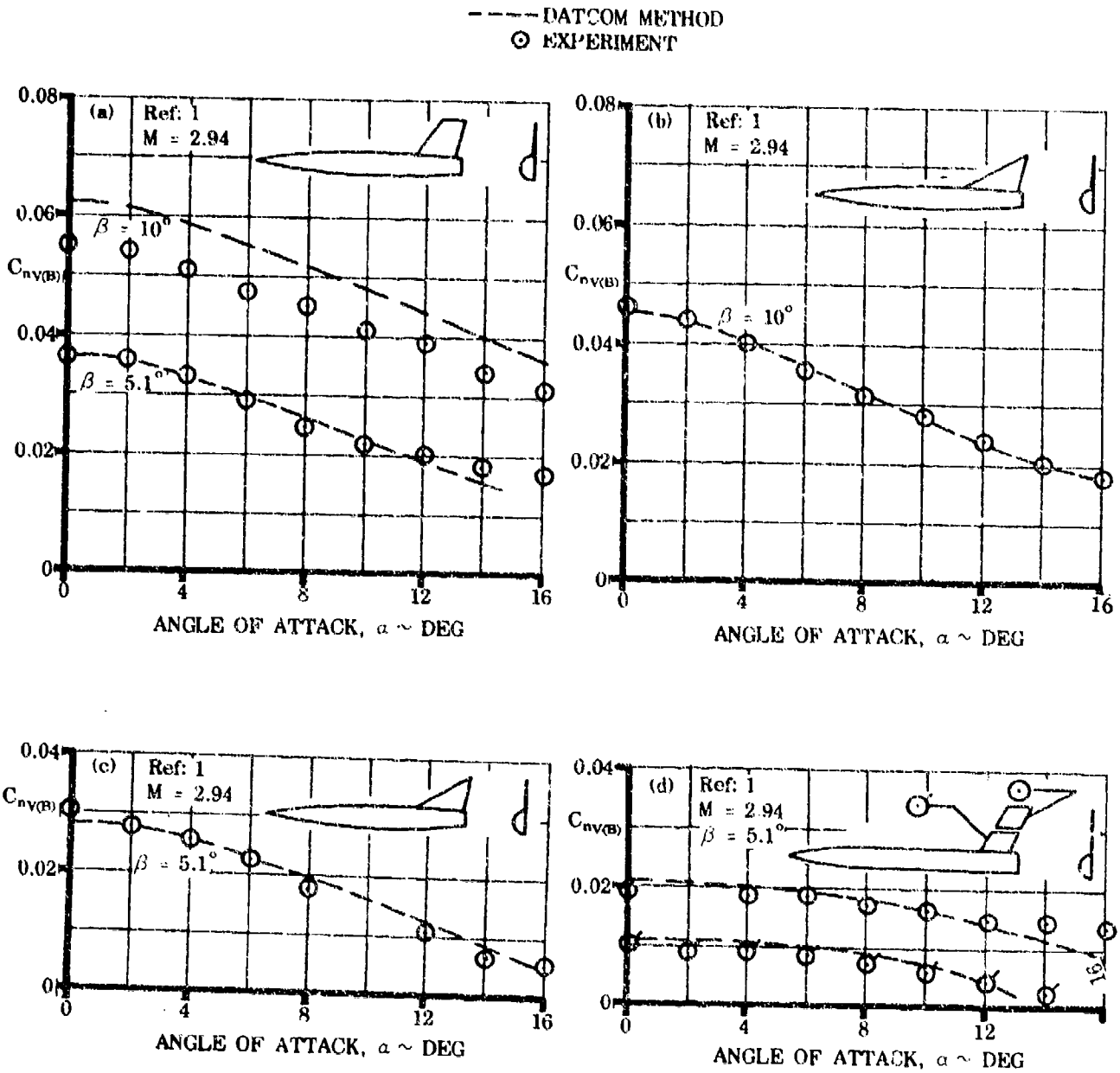

FIGURE 5.3.3.2-4 COMPARISON OF EXPERIMENTAL AND CALCULATED YAWING-MOMENT COEFFICIENT INCREMENTS DUE TO ADDING A VERTICAL TAIL TO A BODY

5.4 FLOW FIELDS IN SIDESLIP

5.4.1 WING-BODY WAKE AND SIDEWASH IN SIDESLIP

For a wing-body combination there are two contributions to the sidewash present at a vertical tail – that due to the body and that due to the wing.

The sidewash due to a body arises from the side force developed by a body in yaw. As a result of this side force a vortex system is produced, which in turn induces lateral-velocity components at the vertical tail. This sidewash from the body causes a destabilizing flow in the airstream beside the body. Above and below the fuselage, however, the flow is stabilizing.

The sidewash arising from a wing in yaw is small compared to that of a body. The flow above the wake center line moves inboard and the flow below the wake center line moves outboard.

For conventional aircraft the combination of the wing-body flow fields is such as to cause almost no sidewash effect below the wake center line.

At subsonic speeds an empirical equation is presented that gives the total sidewash effect directly, i.e., the combined sidewash angle and dynamic-pressure loss.

At supersonic speeds no generalized method is available.

DATCOM METHOD

A. SUBSONIC

A simple algebraic equation is presented that predicts the combined sidewash and dynamic-pressure parameter:

$$\left(1 + \frac{\partial\sigma}{\partial\beta}\right) \frac{q_V}{q_\infty}$$

This empirically derived expression is

$$\left(1 + \frac{\partial\sigma}{\partial\beta}\right) \frac{q_V}{q_\infty} = 0.724 + 3.06 \frac{\frac{S_V}{S_W}}{1 + \cos\Lambda_{c/4\,W}} + .4 \frac{z_W}{d} + 0.009A_W \qquad 5.4.1\text{-a}$$

where

σ is the sidewash at the vertical tail, positive out the left wing

S_V is the vertical tail area, including the submerged area to the fuselage center line, square feet

z_W is the distance, parallel to the Z-axis, from wing root quarter-chord point to fuselage center line, feet. This value is positive for the quarter-chord point below the fuselage center line.

d is the maximum fuselage depth, feet

A comparison of test data with results calculated from Equation 5.4.1-a is shown in Table 5.4.1-A.

TABLE 5.4.1-A

Ref.	$\Lambda_{c/4_W}$ (deg)	A	z_W/d	$\frac{S_V}{S_W}$	$\left(1+\frac{\partial\sigma}{\partial\beta}\right)\frac{q_t}{q_\infty}$ Test	$\left(1+\frac{\partial\sigma}{\partial\beta}\right)\frac{q_{fy}}{q_\infty}$ Calc.	$\lvert e\rvert$ Percent Error
1	45	4	0	.272	1.233	1.246	1.1
2	0	4	−.333	.150	.925	.889	3.9
	0	4	0	.150	1.004	.989	1.5
	0	4	.333	.150	1.090	1.089	0.1
	45	4	−.333	.150	.994	.929	6.5
	45	4	0	.150	1.067	1.029	3.5
	45	4	.333	.150	1.210	1.129	6.7
3	45	3	.390	.150	1.210	1.176	2.8
	45	3	.390	.244	1.140	1.345	18.0
4	60	2	0	.150	1.068	1.048	1.9
	60	6	0	.150	1.10	1.084	1.3
5	45	2	0	.150	.998	1.021	2.3
	45	6	0	.150	1.023	1.057	3.3
6	0	2	0	.150	1.007	.971	3.6
	0	6	0	.150	.968	.989	2.2
7	0	4	0	.150	1.010	.989	2.1
	0	4	0	.150	.902	.989	9.6
	0	4	0	.150	.966	.989	2.4
	45	4	0	.150	1.040	1.029	1.1
	45	4	0	.150	.950	1.029	8.3
	45	4	0	.150	1.037	1.029	0.8
8	45	3	0	.203	1.170	1.124	3.9
	45	3	0	.203	1.13	1.124	.5
	45	3	0	.267	1.20	1.237	3.1
	45	3	0	.267	1.252	1.237	1.2
	45	3	−.354	.203	1.030	.973	5.5
	45	3	−.354	.205	1.060	.973	8.2
	45	3	−.354	.267	1.152	1.086	5.7
	45	3	−.354	.267	1.082	1.086	0.4
9	52.5	2.31	−.333	.084	.743	.772	3.9
	52.5	2.31	−.333	.127	.792	.854	7.8
	52.5	2.31	−.333	.110	.740	.811	9.6
	52.5	2.31	−.333	.145	.792	.874	10.3
	52.5	2.31	−.333	.156	.728	.895	23.0
	52.5	2.31	.333	.004	1.155	1.038	10.1
	52.5	2.31	.333	.127	1.073	1.110	3.4
	52.5	2.31	.333	.110	1.060	1.077	1.6
	52.5	2.31	.333	.145	1.097	1.140	3.9
	52.5	2.31	.333	.156	1.147	1.161	1.2

Ref.	$\Lambda_{c/4}$ (deg)	A	z_v/d	$\frac{S_v}{S_w}$	$\left(1+\frac{\partial\sigma}{\partial\beta}\right)\frac{q_v}{q_\infty}$ Test	$\left(1+\frac{\partial\sigma}{\partial\beta}\right)\frac{q_v}{q_\infty}$ Calc.	$\lvert e\rvert$ Percent Error
10	45	4	0	.150	1.09	1.029	5.6
	45	4	0	.150	.963	1.029	6.9
	45	4	0	.150	1.034	1.029	0.5
	45	4	0	.150	1.030	1.029	0.1
11	63	3.5	0	.168	1.130	1.207	6.8
12	56.5	2	0	.266	1.136	1.274	12.1
13	45	6	0	.151	1.053	1.049	3.4
	45	6	0	.151	1.082	1.049	6.8
14	0	5.9	.063	.160	1.030	1.047	1.7
15	40	2.5	.125	.165	1.070	1.083	1.2
16	35.92	6.95	—.387	.307	1.140	1.152	1.0
17	33.21	2.91	.417	.266	1.263	1.364	8.0
					Average Error $= \frac{\Sigma\lvert e\rvert}{n} = 4.7\%$		

REFERENCES

1. Wiggins, J. W.; Kuhn, R. E.; and Fournier, P. G.: Wind-Tunnel Investigation to Determine the Horizontal- and Vertical-Tail Contributions to the Static Lateral Stability Characteristics of a Complete-Model Swept-Wing Configuration at High Subsonic Speeds. NACA TN 3818, November, 1956. (U)

2. Letko, W.: Experimental Investigation at Low Speed of the Effects of Wing Position on the Static Stability of Models Having Fuselages of Various Cross Section and Unswept and 45° Sweptback Surfaces. NACA TN 3857, November, 1956. (U)

3. Jaquet, B. M., and Fletcher, H. S.: Effect of Fuselage Nose Length and a Canopy on the Static Longitudinal and Lateral Stability Characteristics of 45° Sweptback Airplane Models Having Fuselages with Square Cross Sections. NACA TN 3962, April, 1957. (U)

4. Wolhart, W. D., and Thomas, D. F., Jr.: Static Longitudinal and Lateral Stability Characteristics at Low Speed of 60° Sweptback Midwing Models Having Wings With an Aspect Ratio of 2, 4, and 6. NACA TN 4397, September, 1958. (U)

5. Thomas, D. F., Jr. and Wolhart, W. D.: Static Longitudinal and Lateral Stability Characteristics at Low Speed of 45° Sweptback Midwing Models Having Wings With an Aspect Ratio of 2, 4, and 6. NACA TN 4077, September, 1957. (U)

6. Wolhart, W. D., and Thomas, D. F., Jr.: Static Longitudinal and Lateral Stability Characteristics at Low Speeds of Unswept-Midwing Models Having Wings With an Aspect Ratio of 2, 4, and 6. NACA TN 3649, May, 1956. (U)

7. Letko, W., and Williams, J. L.: Experimental Investigation at Low Speed of Effects of Fuselage Cross Section on Static Longitudinal and Lateral Stability Characteristics of Models Having 0° and 45° Sweptback Surface. NACA TN 3551, December, 1955. (U)

8. Savage, H. F. and Tinling, B. E.: The Subsonic Static Aerodynamic Characteristics of an Airplane Model Having a Triangular Wing of Aspect Ratio 3. II-Lateral and Directional Characteristics. NACA TN 4042, August, 1957. (U)

9. Goodman, A., and Thomas, D. F., Jr.: Effects of Wing Position and Fuselage Size on Low-Speed Static and Rolling Stability Characteristics of a Delta Wing Model. NACA TN 3063, February, 1954. (U)

10. Brewer, J. D., and Lichtenstein, J. H.: Effect of Horizontal Tail on Low-Speed Static Lateral Stability Characteristics of a Model Having 45° Sweptback Wing and Tail Surfaces. NACA TN 2010, January, 1950. (U)

11. McCormack, G. M.: Aerodynamic Study of a Wing-Fuselage Combination Employing a Wing Swept Back 63° — Aerodynamic Characteristics in Sideslip of a Large-Scale Model Having a 63° Swept-Back Vertical Tail. NACA RM A9F14, October 7, 1949. (U)

12. Graham, D., and Soenig, D. G.: Tests in the Ames 40- by 80-Foot Wind Tunnel of an Airplane Configuration With an Aspect Ratio 2 Triangular Wing and an All-Movable Horizontal Tail — Lateral Characteristics. NACA RM A51L03, February 11, 1952. (U)

13. Griner, R. F.: Static Lateral Stability Characteristics of an Airplane Model Having a 47.7° Sweptback Wing of Aspect Ratio 6 and the Contribution of Various Model Components at a Reynolds Number of 4.45×10^6. NACA RM L53G09, September 1, 1953. (U)

14. Williams, J. L.: Measured and Estimated Lateral Static and Rotary Derivatives of a 1/12-Scale Model of a High Speed Fighter Airplane with Unswept Wings. NACA RM L53K09, January 11, 1954. (U)

15. Schuldenfrei, M., Comisarow, P., and Goodson, K. W.: Stability and Control Characteristics of an Airplane Model Having a 45.1° Swept-Back Wing With Aspect Ratio 3.87 and Taper Ratio 0.49. NACA RM L7B25, May 8, 1947. (U)

16. Hinds, W. E., and Graves, J. D.: Low-Speed Stability and Control Characteristics of the Model XA3D-1 Airplane. Douglas Aircraft Co. Report ES 15582, 1951. (U)

17. Cagle, B., and Kerhofer, W.: Report on Subsonic Wind Tunnel Tests of a 0.10-Scale Model of the Douglas (El Segundo) A4D-1 Airplane. CWT Rept. 732, 1955. (U)

5.5 LOW-ASPECT-RATIO WINGS AND WING-BODY COMBINATIONS IN SIDESLIP

During recent years much work has been done on problems associated with the design and operation of advanced flight vehicles. These vehicles include re-entry configurations and those designed for hypersonic cruise. The requirement that these vehicles operate within the atmosphere at hypersonic speeds necessitates the use of configurations that are not well suited for subsonic flight at low altitudes. For the most part, the configurations proposed for this type of mission feature extremely low aspect ratios of the order of two or less, and thick, generously rounded lifting surfaces. These configurations also often have large blunt bases.

The use of conventional subsonic theories and related test data does not result in adequate estimates of the aerodynamic characteristics for this type of vehicle. The methods presented in this section for estimating the aerodynamic characteristics of advanced flight vehicles at subsonic speeds are necessarily semiempirical in nature. The methods are based on test data, which have been correlated with the aid of the extension of available theory. A large portion of the material is related to delta or modified-delta configurations, since a major portion of the pertinent theory and test results relates to these planforms.

In the following group of sections (5.5.1, 5.5.2, and 5.5.3) methods are presented for estimating the side force, rolling moment, and yawing moment on specific types of advanced flight vehicles over the linear sideslip-angle range and at angles of attack up to 20°.

The pertinent aerodynamic forces and moments acting on the vehicle are illustrated on figure 5.5-6. These forces and moments are presented in a normal-force axis system that is introduced in Section 4.8. The reference axes are oriented with respect to the particular configuration under consideration such that the normal force is zero at zero angle of attack and also so that the rolling moment due to sideslip is zero for zero normal force.

The axis designated $X' - X'$ in figure 5.5-6 is the zero-normal-force reference axis defined in Section 4.8 as the axis passing through the centroid of the base area and the most forward point on the vehicle nose. If this axis is parallel to the free stream, the normal force acting on the body is zero by definition, and the zero-normal-force angle of attack α_{N_0} is specified (see Section 4.8.1.1).

Although the position of the axes such that the normal force is zero at zero angle of attack is readily determined, there is no accurate way of establishing the position of the axes for an arbitrary configuration such that the rolling moment due to sideslip is zero at zero normal force.

In the sections that follow, the position of the axis which results in zero rolling moment due to sideslip at zero normal force has been defined by using available test data. The required axis position, represented by axis $0 - 0$ of figure 5.5-6, is parallel to the $X' - X'$ axis and located at a distance Δ from $X' - X'$, where Δ is given by

$$\Delta = \left[\frac{K'_{l_{\beta_{X'X'}}}}{K_{Y_\beta}} \right]_{N_0} b$$

The data in the following sections are presented with respect to this "zero normal force – zero rolling moment" axis system. In this axis system the normal-force coefficient, angle of attack, side-force derivative with respect to sideslip, rolling-moment derivative with respect to sideslip, and yawing-moment derivative with respect to sideslip are designated by C_N', α', K_{Y_β}, K'_{l_β}, and K'_{n_β}, respectively.

The lateral-directional characteristics for the defined body-axis system are related to the more familiar stability-axis system by

$$K_{Y_\beta} = C_{Y_\beta}$$

$$K'_{l_\beta} = C_{l_\beta} \cos \alpha' - C_{n_\beta} \sin \alpha' - K_{Y_\beta} \frac{\Delta}{b}$$

$$K'_{n_\beta} = C_{n_\beta} \cos \alpha' + C_{l_\beta} \sin \alpha'$$

For symmetrical configurations (symmetry about the Z = 0 plane)

$$\alpha' = \alpha$$

$$K'_{l_\beta} = K_{l_\beta}$$

$$K'_{n_\beta} = K_{n_\beta}$$

A general notation list is included in this section for all sections included under Section 5.5.

Sketches showing planform geometry for nearly all configurations analyzed in Sections 5.5.1.1 through 5.5.3.2 are presented in table 4.8-A

NOTATION

SYMBOL	DEFINITION	SECTION
A	aspect ratio of surface	Several
b	surface span	Several
c_r	surface root chord	5.5.3.1 5.5.3.2
h_b	maximum height of base	Several
ℓ_B	total length of body	Several
N'_1	uniform distribution of normal force acting on a pure delta wing	5.5.2.1
N'_2	concentrated component of normal force acting on leading edge of a pure delta wing	5.5.2.1
N'_{2_L}	left leading-edge component of concentrated normal force	5.5.2.1

SYMBOL	DEFINITION	SECTION
N'_{2_R}	right leading-edge component of concentrated normal force	5.5.2.1
$R_{\frac{1}{3}\ LE}$	effective radius of round leading-edge wing, perpendicular to leading edge at $c_r/3$ from the nose (see figure 4.8.1.2-11b)	5.5.1.2 5.5.2.2 5.5.3.1 5.5.3.2
S	planform area	Several
S_{B_S}	projected side area of configuration	Several
$\left(S_{B_S}\right)_{.2c_r}$	projected side area of configuration forward of $.2c_r$	5.5.3.1 5.5.3.2
V_∞	free-stream velocity	5.5.2.1
$(x_{c.p.})_p$	chordwise distance from the configuration nose to the center of pressure of the pressure component of the side force, positive for c.p. aft of nose	5.5.3.1 5.5.3.2
$x_{centroid_{S_{B_S}}}$	chordwise distance from the nose of the configuration to the centroid location of the projected side area, positive aft of the nose	5.5.3.1 5.5.3.2
$x_{centroid_W}$	chordwise distance from the nose of the configuration to the centroid location of the wing planform, positive aft of the nose	5.5.3.1 5.5.3.2
α_{N_0}	angle of attack at zero normal force	5.5
α'	angle of attack $(\alpha - \alpha_{N_0})$, (see figure 4.8-12)	5.5 5.5.2.2
β	angle of sideslip, positive nose left	Several
Δ	1. perpendicular distance between zero-normal-force reference axis X'–X' and "zero normal force – zero rolling moment" reference axis 0 – 0, positive for 0 – 0 below X'–X' (see figure 5.5-6)	5.5
	2. distance of c.p. of leading-edge component of normal force on a pure delta wing, measured from and normal to the root chord (see sketch (b), Section 5.5.2.1)	5.5.2.1
$\delta_\perp$	total wedge angle of sharp-leading-edged wing, perpendicular to leading edge at $c_r/3$ from nose (see figure 4.8.1.2-11a)	5.5.1.2 5.5.2.2
$\delta_{e_\perp}$	effective wedge angle of sharp-leading-edged wing, perpendicular to leading edge at $c_r/3$ from nose (see figure 4.8.1.2-11a)	5.5.1.2 5.5.2.2

SYMBOL	DEFINITION	SECTION
$\delta_{L_\perp}$	average lower-surface angle of sharp-leading-edged wing, perpendicular to wing leading edge at $c_r/3$ from nose (see figure 4.8.1.2-11a)	5.5.1.2 5.5.2.2
θ	wing semiapex angle	5.5.2.1 5.5.2.2
Λ_{LE}	sweepback angle of wing leading edge	Several
λ	taper ratio, $\frac{\text{tip chord}}{\text{root chord}}$	Several
C_f	skin-friction coefficient for incompressible flow	5.5.1.1 5.5.3.1
C_{l_β}	rate of change of rolling-moment coefficient with sideslip angle, $\frac{\partial C_l}{\partial \beta}$ (stability axes)	5.5
$C_{N'}$	normal-force coefficient $\frac{N'}{qS}$ measured with respect to zero-normal-force reference plane	5.5.1.2 5.5.2.1 5.5.2.2 5.5.3.2
$(C_{N'})_{20}$	value of coefficient at $\alpha' = 20^\circ$	5.5.1.2 5.5.2.2
C_{n_β}	rate of change of yawing-moment coefficient with sideslip angle, $\frac{\partial C_n}{\partial \beta}$ (stability axis)	5.5
C_{Y_β}	rate of change of side-force coefficient with sideslip angle, $\frac{\partial C_Y}{\partial \beta}$ (stability axes)	5.5
K'_{l_β}	rate of change of rolling-moment coefficient with sideslip angle, $\frac{\partial K_l}{\partial \beta}$, referred to the defined body axes	5.5 5.5.2.1 5.5.2.2
$\left(\frac{K'_{l_\beta}}{C_{N'}}\right)_\Delta$	valve of parameter for a pointed-nose delta wing	5.5.2.2
$\left[\left(\frac{K'_{l_\beta}}{C_{N'}}\right)_{calc}\right]_{20}$	calculated valve of parameter at $\alpha' = 20^\circ$	5.5.2.2
$K'_{l_{\beta_{XX'}}}$	value of derivative referred to zero-normal-force axis	5.5

SYMBOL	DEFINITION	SECTION
$K'_{l_{\beta_{N_0}}}$	value of derivative near zero-normal-force	5.5.2.1 5.5.2.2
$\left[\frac{K'_{l_{\beta_{N_0}}}}{C_{N'}}\right]_{\Delta}$	value of parameter for pointed-nose delta wing	5.5.2.1 5.5.2.2
$\Delta\left[\frac{K'_{l_\beta}}{C_{N'}}\right]_B$	increment in value of $\frac{K'_{l_\beta}}{C_{N'}}$ of thin delta wing due to nose blunting	5.5.2.1 5.5.2.2
$\frac{\left(K'_{l_\beta} / C_{N'}\right)_{20}}{\left[\left(K'_{l_\beta} / C_{N'}\right)_{calc}\right]_{20}}$	sideslip-derivative correlation factor for K'_{l_β} at $\alpha' = 20^o$	5.5.2.2
$\Delta\frac{\left(K'_{l_\beta}/C_{N'}\right)_{20}}{\left[\left(K'_{l_\beta}/C_{N'}\right)_{calc}\right]_{20}}$	increment in correlation factor at $\alpha' = 20^o$ due to thickness effects	5.5.2.2
K'_{n_β}	rate of change of yawing-moment coefficient with sideslip angle, $\frac{\partial K_n}{\partial \beta}$, referred to the defined body axes	5.5 5.5.3.1 5.5.3.2
$K'_{n_{\beta_{N_0}}}$	value of derivative at zero normal force	5.5.3.1
K_{Y_β}	rate of change of side-force coefficient with sideslip angle, $\frac{\partial K_Y}{\partial \beta}$, referred to the defined body axis	5.5 5.5.1.1 5.5.1.2 5.5.3.2
$K_{Y_{\beta_{N_0}}}$	value of derivative at zero normal force	5.5.1.1 5.5.1.2 5.5.3.1
$\left(K_{Y_\beta}\right)_{20}$	value of derivative at $\alpha' = 20^o$	5.5.1.2
$\Delta\left(K_{Y_\beta}\right)_{20}$	increment in derivative accounting for change in α' from 0 to 20^o	5.5.1.2
$\left[\frac{K_{Y_\beta}}{(C_{N'})^2}\right]_{20}$	sideslip-derivative correlation factor for K_{Y_β} at $\alpha' = 20^o$	5.5.1.2

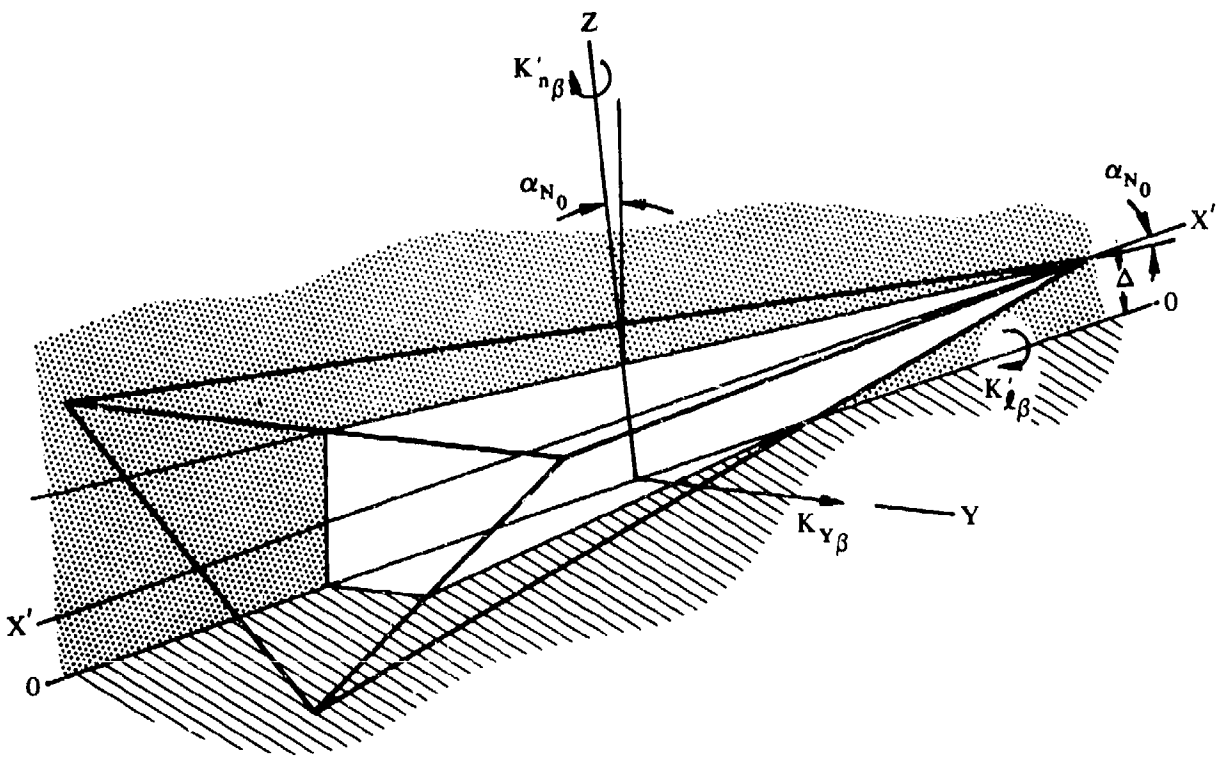

FIGURE 5.5-6 CONFIGURATION GEOMETRY – REFERENCE BODY AXES

5.5.1 WING, WING-BODY SIDESLIP DERIVATIVE K_{Y_β}

5.5.1.1 WING, WING-BODY SIDESLIP DERIVATIVE K_{Y_β} AT ZERO NORMAL FORCE

A. SUBSONIC

This section presents a method, taken from reference 1, for estimating the sideslip derivative K_{Y_β} at zero normal force for delta and modified-delta configurations at subsonic speeds.

The side force at zero normal force is assumed to be composed of two parts, side force due to skin friction and side force due to the pressures acting on the configuration. For thin configurations (essentially zero side area) the side force can be taken as equal to the skin-friction drag of the wing. As the thickness is increased, the influence of pressure distribution is introduced and the side force increases. However, this increase would be expected to be relatively small until the thickness becomes large enough so that the flow separates, causing the pressure drag to become appreciable. It is reported in reference 1 that many attempts were made to relate this phenomenon to existing theories, but without success. The available theories are usually appropriate only when the flow is attached or when the point of separation is known, as in the case of a thin, sharp-leading-edged delta wing. For the case of a moderately thick delta wing, the cross-flow components associated with sideslip tend to induce separation in an unpredictable manner. Therefore, the method presented is based on an empirical correlation of available test data.

The design chart presented was obtained by relating the sideslip derivative at zero normal force to the side area of the configuration. For zero side area, $K_{Y_{\beta N_0}}$ is taken to be equal to the incompressible skin-friction coefficient of the wing. For the purpose of the Datcom, the skin-friction coefficient of the wing is taken as $C_f = 0.006$. Therefore, for a wing with zero side area, $K_{Y_{\beta N_0}} = -0.006$ per radian.

Factors which might be expected to influence side force, but which are not isolated in the analysis, include planform geometry, aspect ratio, section thickness, and camber.

DATCOM METHOD

The zero-normal-force sideslip derivative $K_{Y_{\beta N_0}}$ of a delta or modified-delta configuration, based on planform area, is obtained from the procedure outlined in the following steps:

Step 1. From the configuration geometry determine the projected side area of the configuration S_{B_S} and the planform area S.

Step 2. Obtain $K_{Y_{\beta N_0}}$ as a function of S_{B_S}/S from figure 5.5.1.1-6 .

Values of the zero-normal-force sideslip derivative calculated by using this method are compared with test results in table 5.5.1.1-A. It should be noted that a considerable amount of scatter was involved in the data correlation used to define the design chart. A more accurate correlation was not obtainable because of the limited availability of test data and the uncertainties in the test results.

Sample Problem

Given: The delta-series configuration of reference 6 designated D-2. This is a sharp-edged delta model with a symmetrical diamond-shape cross section and a blunt trailing edge.

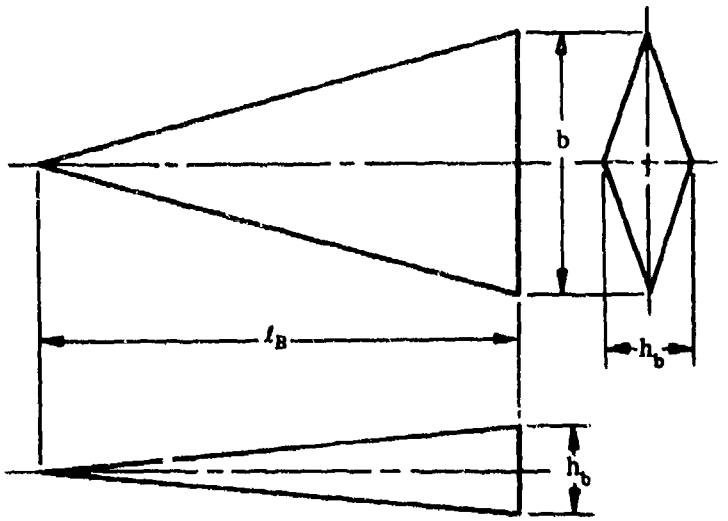

ℓ_B = 23.0 in.

b = 12.374 in.

h_b = 4.32 in.

Compute:

$$S = \frac{1}{2}\ell_B b$$

$$= \frac{1}{2}(23.0)(12.374) = 142.3 \text{ sq in.}$$

$$S_{B_S} = \frac{1}{2}\ell_B h_b = \frac{1}{2}(23.0)(4.32) = 49.68 \text{ sq. in.}$$

$$\frac{S_{B_S}}{S} = \frac{49.68}{142.3} = 0.349$$

Solution:

$K_{Y_{\beta_{N_0}}}$ = −0.110 per rad (based on S) (figure 5.5.1.1-6)

This compareds with a test value of −0.122 per radian from reference 6.

REFERENCES

1. Seeger, D. B., and Ross, R.: Investigation of the Low-Speed Stability and Control Characteristics of Advanced Flight Vehicles. ASD-TDR-63-671, 1963. (C) Title Unclassified

2. Seeger, D. B., and Meyer, J. E.: An Investigation of the Subsonic Aerodynamic Characteristics and the Landing Flare Maneuver for Hypersonic Re-entry Configurations. ASD-TDR-62-271, 1962. (C) Title Unclassified

3. Mantz, K., and Seeger, D. B.: Tests to Determine the Subsonic Pressures, Forces and Moments Acting on a Hypersonic Re-entry Configuration. ASD-TDR-62-270, 1962. (C) Title Unclassified

4. Mantz, K., Seeger, D. B., and Ross, R.: Tests to Determine Subsonic Pressures, Forces and Moments Acting on a Hypersonic Re-entry Configuration. ASD-TDR-62-270, Supplement 1, 1963. (U)

5. Sipe, O. E., and Seeger, D. B.: Tests to Determine Subsonic Aerodynamic Characteristics of Hypersonic Re-entry Configurations. ASD-TR-61-485, 1961. (C) Title Unclassified

6. Mantz, D., Seeger, D. B., and Ross, R.: Tests to Determine Subsonic Aerodynamic Characteristics of Hypersonic Re-entry Configurations. ASD-TR-61-485, Supplement 1, 1963. (U)

7. Graham, D., and Koenig, D. G.: Tests in the Ames 40- by 80-Foot Wind Tunnel of an Airplane Configuration With an Aspect Ratio 2 Triangular Wing and an All-Movable Horizontal Tail – Lateral Characteristics. NACA RM A51L03, 1952. (U)

8. Jaquet, B. M., and Brewer, J. D.: Low-Speed Static-Stability and Rolling Characteristics of Low-Aspect-Ratio Wings of Triangular and Modified Plan Forms. NACA RM L8L29, 1949. (U)

9. McKinney, M. O., Jr., and Drake, H. M.: Flight Characteristics at Low Speed of Delta-Wing Models. NACA RM L7K07, 1948. (U)

10. Keating, R. F. A.: Low-Speed Wind-Tunnel Tests on Sharp-Edged Gothic Wings of Aspect-Ratio 3/4. ARC CP 576, 1961. (U)

11. Goodman, A., and Thomas, D.: Effects of Wing Position and Fuselage Size on the Low-Speed Static and Rolling Stability Characteristics of a Delta-Wing Model. NACA TR 1224, 1955. (U)

12. Whittle, E. F., Jr., and Lovell, J. C.: Full-Scale Investigation of an Equilateral Triangular Wing Having 10-Percent Thick Biconvex Airfoil Sections. NACA RM L8G05, 1948. (U)

13. Olstad, W. B., Mugler, J. P., Jr., and Cahn, M. S.: Static Longitudinal and Lateral Stability Characteristics of a Right Triangular Pyramidal Lifting Re-entry Configuration at Transonic Speeds. NASA TN D-655, 1961. (U)

14. Ware, G. M.: Low-Subsonic-Speed Static Stability of Right-Triangular-Pyramid and Half-Cone Lifting Re-entry Configurations. NASA TN D-646, 1961. (U)

15. Paulson, J. W.: Low-Speed Static Stability and Control Characteristics of a Right Triangular Pyramid Re-entry Configuration. NASA Memo 4-11-59L, 1959. (U)

16. Ribner, H.: The Stability Derivatives of Low-Aspect-Ratio Triangular Wings at Subsonic and Supersonic Speeds. NACA TN 1423, 1947. (U)

17. Queijo, M.: Theoretical Span Load Distributions and Rolling Moments for Sideslipping Wings of Arbitrary Planform in Incompressible Flow. NACA TR 1269, 1956. (U)

18. Jones, R. T.: Properties of Low-Aspect-Ratio Pointed Wings at Speeds Below and Above the Speed of Sound. NACA TR 835, 1946. (U)

19. Edwards, G. G., and Savage, H. F.: The Subsonic Aerodynamic Characteristics of Some Blunt Delta Configurations with 75° Sweepback. NASA TM X-581, 1961. (C) Title Unclassified

20. McDevitt, J. B., and Rakich, J. V.: The Aerodynamic Characteristics of Several Thick Delta Wings at Mach Numbers to 5 and Angles of Attack to 50°. NASA TM X-162, 1960. (C) Title Unclassified

21. Hoerner, S. F.: Fluid Dynamic Drag. Published by author, 1958. (U)

22. Goodwin, F. K., and Kaattari, G. E.: Estimation of Directional Stability Derivatives at Small Angles and Subsonic and Supersonic Speeds. NASA Memo 12-2-58A, 1958. (U)

23. Harvey, J. K.: Some Measurements on a Yawed Slender Delta Wing with Leading Edge Separation. ARC 20451, R&M 3160, 1958. (U)

24. Nonweiler, T.: Theoretical Stability Derivatives of a Highly Swept Delta Wing and Slender Body Combination. College of Aeronautics, Cranfield, Report 50, 1958. (U)

25. Örnberg, T.: A Note on the Flow Around Delta Wings. Swedish Technical Note, K.T.H. Aero TN 38, 1954. (U)

26. Paulson, J. W.: Low-Speed Static Stability Characteristics of Two Configurations Suitable for Lifting Re-entry From Satellite Orbit. NASA Memo 10-22-58L, 1958. (C) Title Unclassified

27. Paulson, J. W., Shanks, R. E., and Johnson, J. L.: Low-Speed Flight Characteristics of Re-entry Vehicles of the Glide-Landing Type. NASA TM X-331, 1960. (C) Title Unclassified

28. Paulson, J. W., and Shanks, R. E.: Investigation of Low-Subsonic Flight Characteristics of a Model of a Hypersonic Boost-Glide Configuration Having a 78° Delta Wing. NASA TN D-894, 1961. (U)

29. Ware, G. M., and Shanks, R. E.: Investigation of the Low-Subsonic Flight Characteristics of a Model of a Re-entry Configuration Having a 75° Delta Wing. NASA TM X-084, 1962. (C) Title Unclassified

30. Weber, J.: Some Effects of Flow Separation on Slender Delta Wings. RAE Aero 2425, ARC 18073, 1955. (C) Title Unclassified

31. Campbell, J. P., and McKinney, M. O.: Summary of Methods for Calculating Dynamic Lateral Stability and Response and for Estimating Lateral Stability Derivatives. NACA TR 1098, 1952. (U)

32. Fink, P. T.: Some Low Speed Aerodynamic Properties of Cones. Experiments done in the Imperial College Aeronautical Laboratory. ARC 17,632, 1955. (C) Title Unclassified

33. Lee, G. H.: Note on the Flow Around Delta Wings with Sharp Leading Edges. ARC R&M 3070, 1958. (U)

34. Levacic, I.: Rolling Moment Due to Sideslip. Part II. The Effect of Sweepback and Planform. ARC 9278, 1945. (U)

TABLE 5.5.1.1-A

SUBSONIC ZERO-NORMAL-FORCE SIDE-FORCE DERIVATIVE WITH RESPECT TO SIDESLIP

DELTA PLANFORM CONFIGURATIONS

DATA SUMMARY

Ref.	Configuration	A	Λ_{LE} (deg)	$\frac{S_{B_S}}{S}$	$K_{Y_{\beta_{N_0}}}$ Calc. (per rad)	$K_{Y_{\beta_{N_0}}}$ Test (per rad)	$\Delta K_{Y_{\beta_{N_0}}}$ Calc.-Test (per rad)
4	D-50	1.076	75	0.386	−0.150	−0.227	0.077
6	D-1	1.075	75	0.386	−0.150	−0.107	−0.043
↓	D-2	1.076	75	0.349	−0.110	−0.122	0.012
↓	D-5	1.076	75	0.386	−0.150	−0.219	0.069
↓	D-6	1.868	65	0.236	−0.030	−0.021	−0.009
↓	D-10	1.702	75	0.296	−0.060	−0.060	0
↓	WB-3	1.074	75	0.282	−0.051	−0.137	0.086
7	Wing Alone	2.00	63.4	0.050	−0.004	−0.010	0.006
8	2	2.31	60	0.116	−0.008	−0.015	0.007
9	1	3.00	53	0.045	−0.003	0	−0.003
↓	4	2.00	63	0.050	−0.004	0	−0.004
↓	6	1.00	76	0.050	−0.004	0	−0.004
↓	8	0.50	83	0.070	−0.005	0	−0.005
10	Wing Alone	0.75	Gothic	0.125	−0.009	0	−0.009
11	Wing Alone	2.31	60	0.045	−0.003	0	−0.003
12	Wing Alone	2.31	60	0.145	−0.011	−0.017	0.006
13	1	0.742	79.5	0.491	−0.325	−0.335	0.010
14	a	0.783	79.5	0.535	−0.412	−0.413	0.001
↓	b(basic)	0.783	79.5	0.491	−0.325	−0.344	0.019
↓	b(R = 1.5 in.)	0.809	79.5	0.500	−0.337	−0.321	−0.016
↓	d	0.783	79.5	0.518	−0.375	−0.372	−0.003
15	1	0.780	79.4	0.528	−0.395	−0.401	0.006

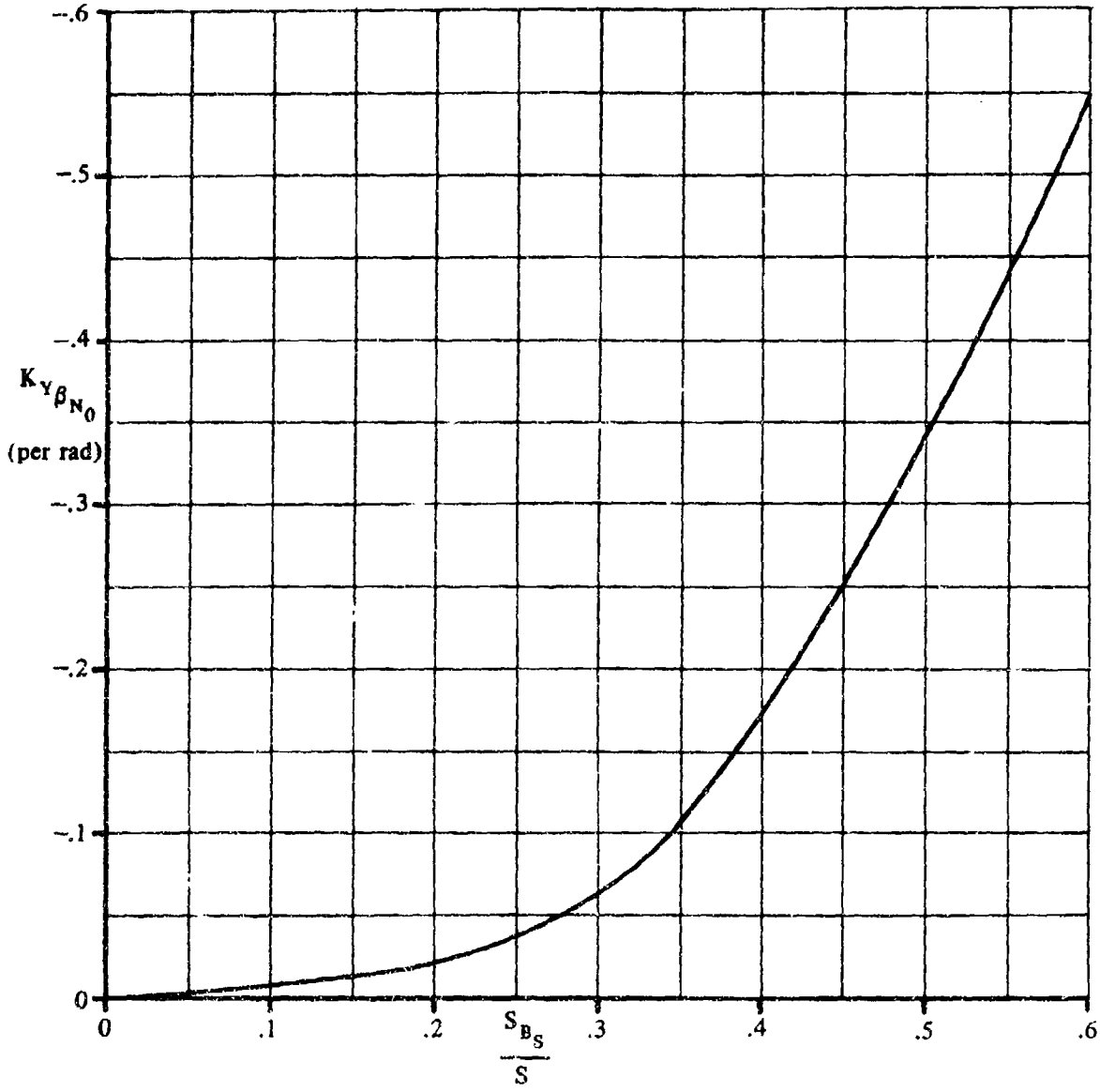

FIGURE 5.5.1.1-6 SIDE-FORCE DERIVATIVE WITH RESPECT TO SIDESLIP AT ZERO NORMAL FORCE – DELTA AND MODIFIED DELTA CONFIGURATIONS

5.5.1.2 WING, WING-BODY SIDESLIP-DERIVATIVE K_{Y_β} VARIATION WITH ANGLE OF ATTACK

A. SUBSONIC

This section presents a method for estimating the effects of angle of attack on the sideslip derivative K_{Y_β} of a delta or modified-delta planform re-entry configuration.

The Datcom method is taken from reference 1. An empirical correlation is presented for estimating K_{Y_β} at $\alpha' = 20^o$, and this correlation has been related to the normal-force coefficient to estimate K_{Y_β} at intermediate angles of attack.

Leading-edge shape was shown to have an important influence on the side force as well as on its variation with angle of attack. A lifting delta wing is characterized by two vortices that extend aft of the nose, at or somewhat inboard of the wing tips. These vortices move with respect to the wing as it is sideslipped, tending to remain fixed with respect to the free stream. Minimum pressures and, as a result, maximum local lifts, are observed in the area immediately below the cores of these vortices. It would, therefore, be expected that the side force produced by sideslipping a delta wing would depend to a significant degree upon the shape of the wing below the vortices. For example, if the minimum pressure acts on a region where the surface of the wing is sloped so that the contribution to side force is large, the value of K_{Y_β} would be expected to differ from that observed on a configuration with flat upper surfaces. During the study reported in reference 1 available test results were analyzed in an attempt to isolate this phenomenon; however, the results were not conclusive. Therefore, the influence of cross-sectional shape other than that related to leading-edge rounding or leading-edge angle is not included in the correlation curve presented in the Datcom method.

Test data show that K_{Y_β} tends to become more negative as angle of attack is increased for wings with small leading-edge radii, while the opposite is true for configurations with generously rounded leading edges. This phenomenon can be explained as follows: On a lifting delta wing the upper-surface pressures on the up-stream leading edge decrease as the sideslip angle is increased and the upper-surface pressures acting on the down-stream edge increase. If the leading-edge radius is large so that the flow does not separate readily, and so that these pressures are effective over a relatively large area, the change in K_{Y_β} due to increases in $C_N{}'$ is positive. For sharper leading edges, the combination of the flow separating readily at the leading edges and the small side area in the vicinity of the minimum pressures at the up-stream leading edge results in a reduction in K_{Y_β} as $C_N{}'$ is increased. This observation led to the development of the estimation procedure. Since the change in K_{Y_β} with C_N depends upon the pressure distribution produced by the lifting process, it was assumed that a correlation procedure could be developed that relates K_{Y_β} to the normal-force coefficient. The expression used in the correlation procedure is

$$K_{Y_\beta} = K_{Y_{\beta_{N_0}}} + \left(K_{Y_{\beta_{20}}} - K_{Y_{\beta_{N_0}}}\right)\left[\frac{C_{N'}}{C_{N'_{20}}}\right]^2$$

Semiempirical correlation curves based on the above expression and test values at $\alpha' = 20^o$ are presented in the Datcom method for delta and modified-delta wings with either round or sharp leading edges. These design charts are considered valid for sideslip angles between $\pm 5^o$ and angles of attack up to 20^o.

DATCOM METHOD

The variation of the sideslip derivative K_{Y_β} with angle of attack for a delta or modified-delta configuration at low speeds, based on planform area, is obtained from the procedure outlined in the following steps:

Step 1. Determine the effective leading-edge angle $\delta_{e_\perp}$ for sharp leading edges or the effective leading-edge radius $R_{\frac{1}{3}LE}$ for round leading edges. These parameters are functions of the configuration geometry in a plane normal to the leading edge at $\frac{1}{3}c_r$ from the nose. The applicable configuration geometry is illustrated on figures 4.8.1.2-11a and 4.8.1.2-11b.

Step 2. Determine the variation of sideslip derivative with angle of attack by

$$K_{Y_\beta} = K_{Y_{\beta_{N_0}}} + \left[\frac{\Delta K_{Y_\beta}}{(C_N')^2}\right]_{20} (C_N')^2 \qquad 5.5.1.2\text{-a}$$

where

$K_{Y_{\beta_{N_0}}}$ is the side force due to sideslip at zero normal force obtained by using the method of Section 5.5.1.1.

C_N' is the normal-force coefficient at angle of attack obtained by using the method of Section 4.8.1.2.

$\left[\frac{K_{Y_\beta}}{(C_N')^2}\right]_{20}$ is the semiempirical correlation factor for the sideslip derivative K_{Y_β} for delta and modified-delta configurations. It is presented as a function of effective leading-edge radius $R_{\frac{1}{3}LE}$ and S_{B_S}/S for configurations with round leading edges in figure 5.5.1.2-8, and as a function of effective leading-edge angle $\delta_{e_\perp}$ and S_{B_S}/S for configurations with sharp leading edges in figure 5.5.1.2-9.

S_{B_S}/S is the ratio of the projected side area of the configuration to the planform area.

It should be noted that a considerable amount of scatter was involved in the data correlation used to define the design charts. In the case of sharp-leading-edged configurations it was necessary to estimate the nature of the effect of leading-edge angle on the basis of very few test data. Therefore, the accuracy of the design chart for sharp leading edges (figure 5.5.1.2-9) is questionable.

Nonlinearities in the variation of side force with sideslip may appear if the upper-surface slope is such that spanwise components of normal force, due to the negative pressures under the vortex, appear only for a limited range of sideslip angles. As indicated in the introduction, the available data are not sufficient to allow isolation of this effect. However, it should be realized that a constant value of K_{Y_β} valid for $\beta = \pm 5^o$ may not be a useful representation of the physical phenomena involved.

The variation of the sideslip derivative K_{Y_β} with normal force calculated by this method is compared with test data in table 5.5.1.2-A.

Sample Problem

Given: A delta model with a symmetrical diamond cross section, a blunt trailing edge, and round leading edges. This is model D-6 of reference 6. This is the configuration of sample problem 1 of Section 4.8.1.2.

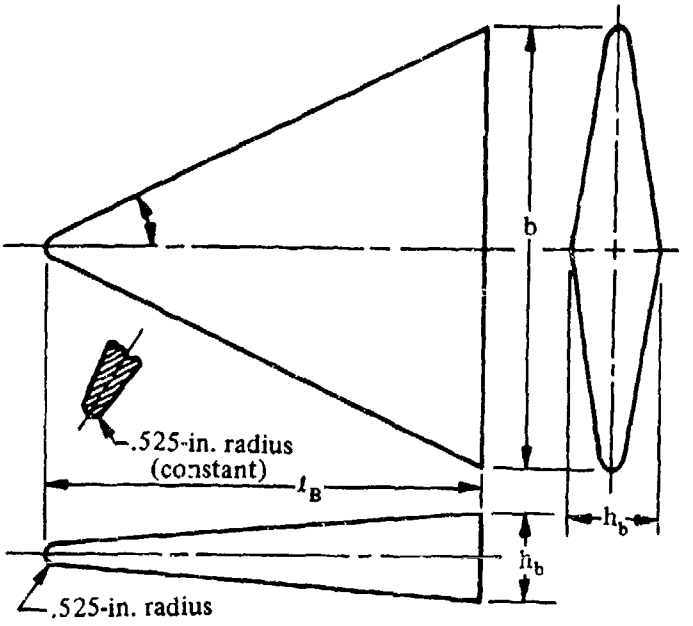

$A = 1.868$ $b = 22.116$ in.

$S = 261.95$ sq in.

$R_{\frac{1}{3}LE} = 0.525$ in.

$S_{B_S} = 61.82$ sq in.

The following variation of C_N' with α' from sample problem 1 of Section 4.8.1.2:

α	0	5°	10°	15°	20°
C_N'	0	0.2017	0.4122	0.6323	0.8618

Compute:

$S_{B_S}/S = 61.82/261.95 = 0.236$

$K_{Y\beta_{N_0}} = -0.030$ per rad (figure 5.5.1.1-6)

$R_{\frac{1}{3}LE}/b = 0.525/22.116 = 0.0237$

$\left[\frac{\Delta K_{Y_\beta}}{(C_N')^2}\right]_{20} = -0.095$ per rad (figure 5.5.1.2-8)

Solution:

$$K_{Y_\beta} = K_{Y_{\beta_{N_0}}} + \left[\frac{\Delta K_{Y_\beta}}{(C_{N'})^2}\right]_{20} (C_{N'})^2 \quad \text{(equation 5.5.1.2-a)}$$

$$= -0.030 + (-0.095)\ (C_{N'})^2$$

①	②	③	④	⑤
α (deg)	$C_{N'}$ (given)	$(C_{N'})^2$ ②^2	$-0.095\,(C_{N'})^2$ -0.095 ③	K_{Y_β} (based on S) (per rad) $-0.030 +$ ④
0	0	0	0	−0.030
5	0.2017	0.041	−0.004	−0.034
10	0.4122	0.170	−0.016	−0.046
15	0.6323	0.400	−0.038	−0.068
20	0.8618	0.743	−0.071	−0.101

The calculated results are compared with test values in sketch (a) and in table 5.5.1.2-A.

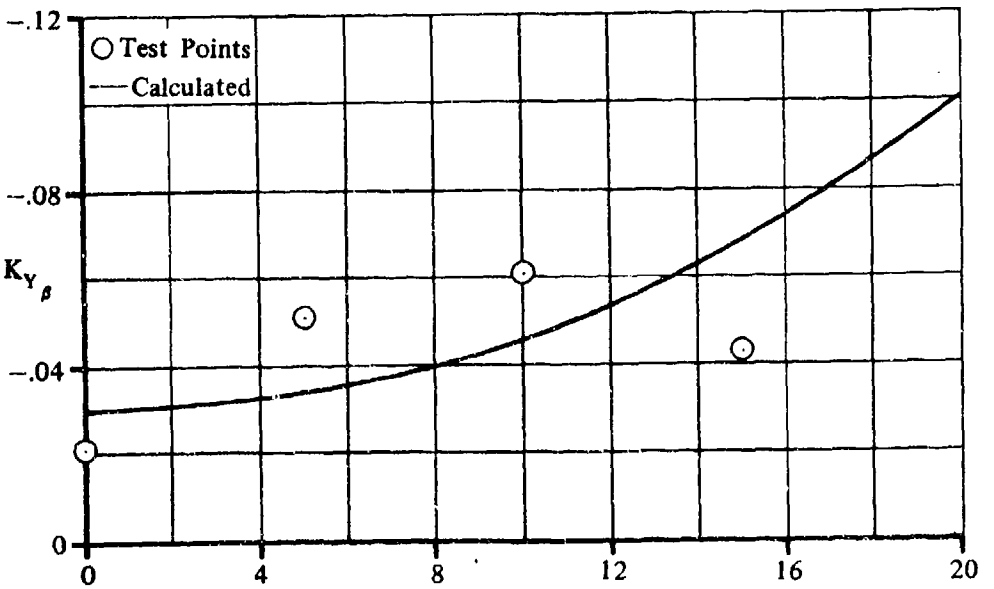

SKETCH (a)

REFERENCES

1. Seeger, D. B., and Ross, R.: Investigation of the Low-Speed Stability and Control Characteristics of Advanced Flight Vehicles. ASD-TDR-63-671, 1963. (C) Title Unclassified

2. Seeger, D. B., and Meyer, J. E.: An Investigation of the Subsonic Aerodynamic Characteristics and the Landing Flare Maneuver for Hypersonic Re-entry Configurations. ASD-TDR-62-271, 1962. (C) Title Unclassified

3. Mantz, K., and Seeger, D. B.: Tests to Determine the Subsonic Pressures, Forces and Moments Acting on a Hypersonic Re-entry Configuration. ASD-TDR-62-270, 1962. (C) Title Unclassified

4. Mantz, K , Seeger, D. B., and Ross, R.: Tests to Determine Subsonic Pressures, Forces and Moments Acting on a Hypersonic Re-entry Configuration. ASD-TDR-62-270, Supplement 1, 1963. (U)

5. Sipe, O. E., and Seeger, D. B.: Tests to Determine Subsonic Aerodynamic Characteristics of Hypersonic Re-entry Configurations. ASD-TR-61-485, 1961. (C) Title Unclassified

6. Mantz, D., Seeger, D. B., and Ross, R.: Tests to Determine Subsonic Aerodynamic Characteristics of Hypersonic Re-entry Configurations. ASD-TR-61-485, Supplement 1, 1963. (U)

7. Graham, D., and Koenig, D. G.: Tests in the Ames 40- by 80-Foot Wind Tunnel of an Airplane Configuration With an Aspect Ratio 2 Triangular Wing and an All-Movable Horizontal Tail — Lateral Characteristics. NACA RM A51L03, 1952. (U)

8. Jaquet, B. M., and Brewer, J. D.: Low-Speed Static-Stability and Rolling Characteristics of Low-Aspect-Ratio Wings of Triangular and Modified Plan Forms. NACA RM L8L29, 1949. (U)

9. McKinney, M. O., Jr., and Drake, H. M.: Flight Characteristics at Low Speed of Delta-Wing Models. NACA RM L7K07, 1948. (U)

10. Keating, R. F. A.: Low-Speed Wind-Tunnel Tests on Sharp-Edged Gothic Wings of Aspect-Ratio 3/4. ARC CP 576, 1961. (U)

11. Goodman, A., and Thomas, D.: Effects of Wing Position and Fuselage Size on the Low-Speed Static and Rolling Stability Characteristics of a Delta-Wing Model. NACA TR 1224, 1955. (U)

12. Whittle, E. F., Jr., and Lovell, J. C.: Full-Scale Investigation of an Equilateral Triangular Wing Having 10-Percent Thick Biconvex Airfoil Sections. NACA RM L8G05, 1948. (U)

13. Olstad, W. B., Mugler, J. P., Jr., and Cahn, M. S.: Static Longitudinal and Lateral Stability Characteristics of a Right Triangular Pyramidal Lifting Re-entry Configuration at Transonic Speeds. NASA TN D-655, 1961. (U)

14. Ware, G. M.: Low-Subsonic-Speed Static Stability of Right-Triangular-Pyramid and Half-Cone Lifting Re-entry Configurations. NASA TN D-646, 1961. (U)

15. Paulson, J. W.: Low-Speed Static Stability and Control Characteristics of a Right Triangular Pyramid Re-entry Configuration. NASA Memo 4-11-59L, 1959. (U)

16. Ribner, H.: The Stability Derivatives of Low-Aspect-Ratio Triangular Wings at Subsonic and Supersonic Speeds. NACA TN 1423, 1947. (U)

17. Queijo, M.: Theoretical Span Load Distributions and Rolling Moments for Sideslipping Wings of Arbitrary Planform in Incompressible Flow. NACA TR 1269, 1956. (U)

18. Jones, R. T.: Properties of Low-Aspect-Ratio Pointed Wings at Speeds Below and Above the Speed of Sound. NACA TR 835, 1946. (U)

19. Edwards, G. G., and Savage, H. F.: The Subsonic Aerodynamic Characteristics of Some Blunt Delta Configurations with 75° Sweepback. NASA TM X-581, 1961. (C) Title Unclassified

20. McDevitt, J. B., and Rakich, J. V.: The Aerodynamic Characteristics of Several Thick Delta Wings at Mach Numbers to 6 and Angles of Attack to 50°. NASA TM X-162, 1960. (C) Title Unclassified

21. Hoerner, S. F.: Fluid Dynamic Drag. Published by author, 1958. (U)

22. Goodwin, F. K., and Kaattari, G. E.: Estimation of Directional Stability Derivatives at Small Angles and Subsonic and Supersonic Speeds. NASA Memo 12-2-58A, 1958. (U)

23. Harvey, J. K.: Some Measurements on a Yawed Slender Delta Wing with Leading Edge Separation. ARC 20461, R&M 3160, 1958. (U)

24. Nonweiler, T.: Theoretical Stability Derivatives of a Highly Swept Delta Wing and Slender Body Combination. College of Aeronautics, Cranfield, Report 50, 1958. (U)

25. Örnberg, T.: A Note on the Flow Around Delta Wings. Swedish Technical Note, K.T.H. Aero TN 38, 1954. (U)

26. Paulson, J. W.: Low-Speed Static Stability Characteristics of Two Configurations Suitable for Lifting Re-entry From Satellite Orbit. NASA Memo 10-22-58L, 1958. (C) Title Unclassified

27. Paulson, J. W., Shanks, R. E., and Johnson, J. L.: Low-Speed Flight Characteristics of Re-entry Vehicles of the Glide-Landing Type. NASA TM X-331, 1960. (C) Title Unclassified

28. Paulson, J. W., and Shanks, R. E.: Investigation of Low-Subsonic Flight Characteristics of a Model of a Hypersonic Boost-Glide Configuration Having a 78° Delta Wing. NASA TN D-894, 1961. (U)

29. Ware, G. M., and Shanks, R. E.: Investigation of the Low-Subsonic Flight Characteristics of a Model of a Re-entry Configuration Having a 75° Delta Wing. NASA TM X-684, 1962. (C) Title Unclassified

30. Weber, J.: Some Effects of Flow Separation on Slender Delta Wings. RAE Aero 2425, ARC 18073, 1955. (C) Title Unclassified

31. Campbell, J. P., and McKinney, M. O.: Summary of Methods for Calculating Dynamic Lateral Stability and Response and for Estimating Lateral Stability Derivatives. NACA TR 1098, 1952. (U)

32. Fink, P. T.: Some Low Speed Aerodynamic Properties of Cones. Experiments done in the Imperial College Aeronautical Laboratory. ARC 17,632, 1955. (C) Title Unclassified

33. Lee, G. H.: Note on the Flow Around Delta Wings with Sharp Leading Edges. ARC R&M 3070, 1958. (U)

34. Levacic, I.: Rolling Moment Due to Sideslip. Part II. The Effect of Sweepback and Planform. ARC 9278, 1945. (U)

TABLE 5.5.1.2-A

SUBSONIC SIDE-FORCE DERIVATIVE WITH RESPECT TO SIDESLIP -- VARIATION WITH NORMAL FORCE

DELTA PLANFORM CONFIGURATIONS

DATA SUMMARY

Ref	Configuration	A	Λ_{LE} (deg)	$\frac{S_{B_S}}{S}$	Leading Edge	C_N'	K_{Y_β} Calc. (per rad)	K_{Y_β} Test (per rad)	ΔK_{Y_β} Calc.-Test (per rad)
5	D-50	1.076	75	0.386	Round $R_1 = 1.05$ in. $\frac{-LE}{3}$	0	−0.150	−0.224	0.074
						.2	−0.124	−0.215	0.091
						.4	−0.044	−0.205	−0.161
						.6	0.088	—	—
6	D-1	1.075	75	0.386	Round $R_1 = .525$ in. $\frac{-LE}{3}$	0	−0.150	−0.107	−0.043
						.2	−0.150	−0.100	−0.050
						.4	−0.150	−0.117	−0.033
						.6	−0.150	−0.157	0.007

TABLE 5.5.1.2-A (CONTD)

Ref.	Configuration	A	Λ_{LE} (deg)	$\frac{S_{B_S}}{S}$	Leading Edge	C_N'	K_{Y_β} Calc. (per rad)	K_{Y_β} Test (per rad)	ΔK_{Y_β} Calc.-Test (per rad)
6	D-2	1.076	75	0.349	Sharp $\delta_{e_\perp} = 68°$	0	−0.110	−0.122	0.012
						.2	−0.097	−0.070	−0.027
						.4	−0.056	−0.003	−0.053
						.6	0.012	0.057	−0.045
	D-5	1.076	75	0.386	Round $R_1 = 1.05$ in. $\frac{}{3}$LE	0	−0.150	−0.219	0.069
						.2	−0.124	−0.208	0.084
						.4	−0.044	−0.196	0.152
						.6	0.088	—	—
	D-6	1.868	65	0.236	Round $R_1 = .525$ in. $\frac{}{3}$LE	0	−0.030	−0.021	−0.009
						.2	−0.034	−0.051	0.017
						.41	−0.046	−0.061	0.015
						.63	−0.068	−0.043	−0.025
						.86	−0.101	—	—
	W8-3	1.074	75	0.282	Round $R_1 = .250$ in. $\frac{}{3}$LE	0	−0.051	−0.137	0.086
						.2	−0.055	−0.184	0.129
						.4	−0.069	−0.231	0.162
						.6	−0.091	−0.277	0.186
14	b(basic)	0.783	79.5	0.491	Round $R_1 = .250$ in. $\frac{}{3}$LE	0	−0.325	−0.344	0.019
						.2	−0.353	−0.482	0.129
						.4	−0.435	−0.521	0.086
						.6	−0.573	−0.539	−0.034
	b(R=1.5 in.)	0.808	79.5	0.500	Round $R_1 = .250$ in. $\frac{}{3}$LE	0	−0.337	−0.321	−0.016
						.2	−0.365	−0.475	0.110
						.4	−0.451	−0.548	0.097
						.6	−0.593	−0.557	−0.036
15	1	0.780	79.4	0.528	Round $R_1 = .50$ in. $\frac{}{3}$LE	0	−0.395	−0.401	0.006
						2	−0.416	−0.476	0.060
						.4	−0.480	−0.548	0.068
						.6	−0.586	−0.586	0

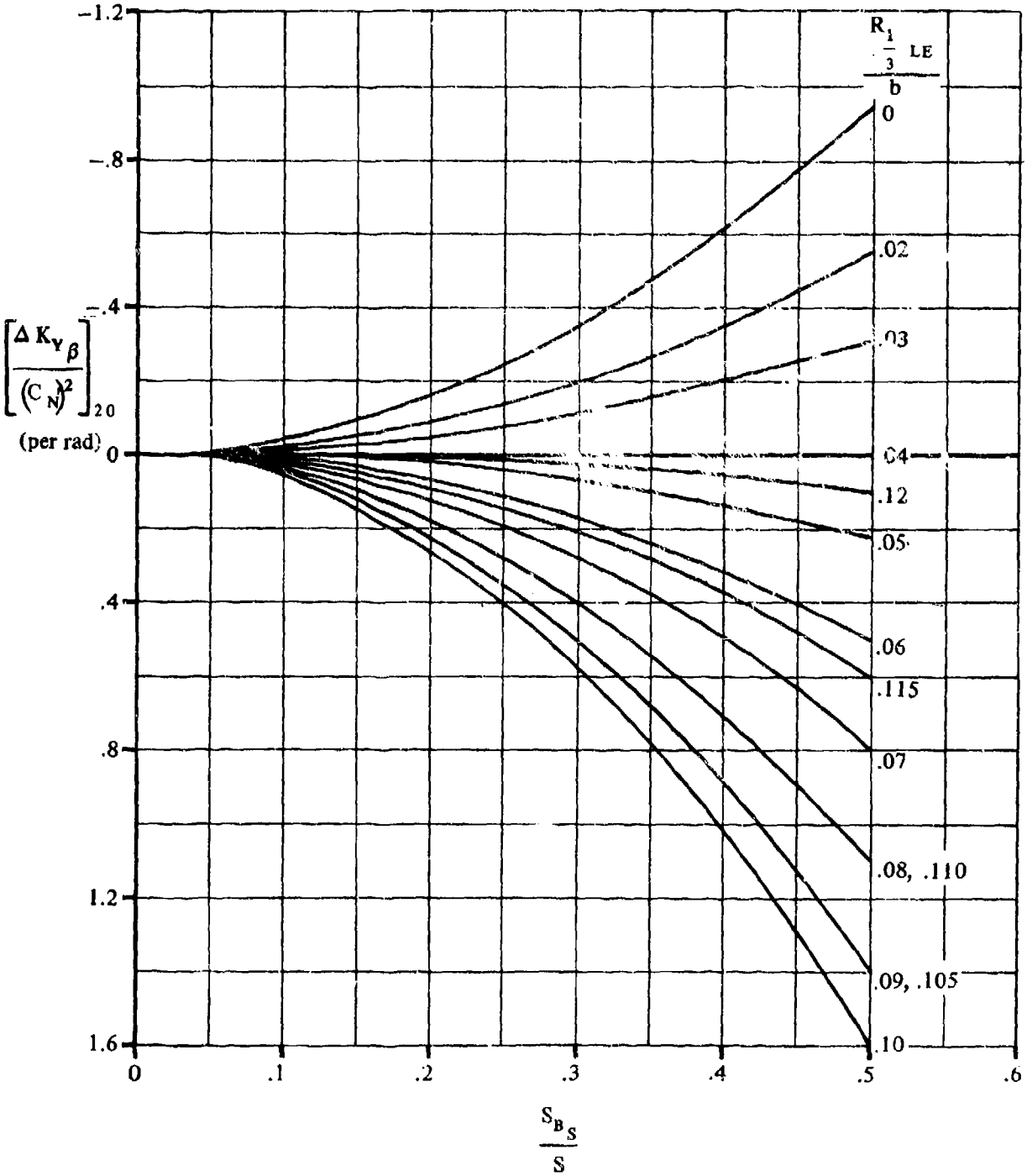

FIGURE 5.5.1.2-8 SIDE-FORCE-DERIVATIVE CORRELATION FACTOR FOR K_{Y_β} AT $\alpha' = 20^o$ – DELTA AND MODIFIED-DELTA CONFIGURATIONS WITH ROUND LEADING EDGES

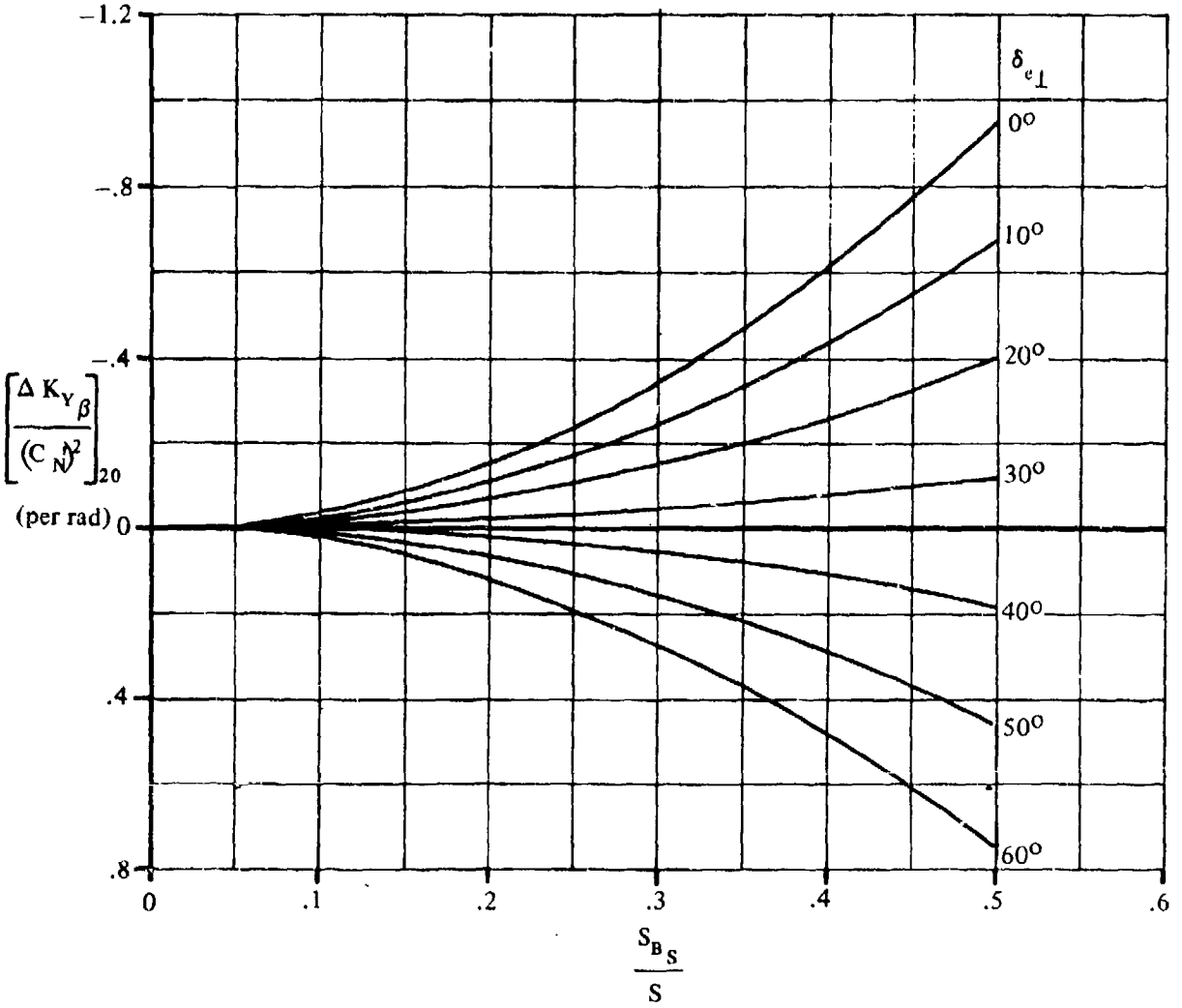

FIGURE 5.5.1.2-9 SIDE-FORCE-DERIVATIVE CORRELATION FACTOR FOR K_{Y_β} AT $\alpha' = 20^o$ – DELTA AND MODIFIED-DELTA CONFIGURATIONS WITH SHARP LEADING EDGES

5.5.2 WING, WING-BODY SIDESLIP DERIVATIVE K'_{l_β}

5.5.2.1 WING, WING-BODY SIDESLIP DERIVATIVE K'_{l_β} NEAR ZERO NORMAL FORCE

A. SUBSONIC

This section presents a method for estimating the sideslip derivative K'_{l_β} near zero normal force for delta and modified-delta configurations at subsonic speeds.

The subsonic rolling moment due to sideslip of a thin delta wing of vanishing aspect ratio ($A < 1$) with sharp leading edges and a pointed nose can be satisfactorily predicted at low lift coefficients by using the method presented in Section 5.1.2.1. However, this procedure is inadequate for proposed re-entry configurations. These configurations range in aspect ratio from low values of the order of 1/2 up to 2, and, for the most part, have thick, generously rounded lifting surfaces and blunt nose shapes.

The Datcom method is taken from reference 1. The method is semiempirical and was developed by first describing the pertinent aerodynamic phenomena in terms of a conceptual model and then using available experimental data to adjust the final theoretical results.

In determining the rolling moment due to sideslip of thin delta wings near zero normal force, it was necessary to define the spanwise variation of the normal-force loading due to sideslip, the longitudinal and lateral shifts in the configuration center of pressure due to sideslip, and the effect of sideslip on the total normal force. Briefly, the analysis proceeded as follows: From symmetry considerations and experimental results it was concluded that the total normal force is independent of sideslip angle near zero sideslip. Experimental data also show that the longitudinal position of the center of pressure does not change as the wing is sideslipped through small sideslip angles. Therefore, it was concluded that the change in K'_{l_β} results because of the spanwise shifts in normal force. It was then assumed that the normal force acting on a pure delta wing at zero sideslip can be divided into two components, one distributed uniformly over the planform and the other concentrated at the leading edge. The magnitude of the concentrated component at any spanwise station is proportional to the local chord. In accordance with this concept, the resultant of the uniform load acts at a point 2/3 of the root chord aft of the wing apex, and the resultant of the leading-edge component acts at a point 1/3 of the root chord aft of the wing apex (see sketch (a)). It was further assumed that when the wing is sideslipped, the center of

SKETCH (a)

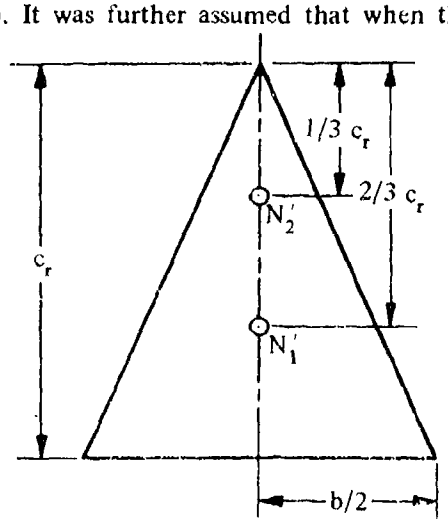

pressure of the uniform load moves normal to the root chord so as to maintain a line from the trailing edge of the root chord to the center of pressure in a plane parallel to the free stream. It was also assumed that the center of pressure of the leading-edge component moves normal to the root chord some distance Δ that is a function of the angle of sideslip (see sketch (b)). Any rolling-moment

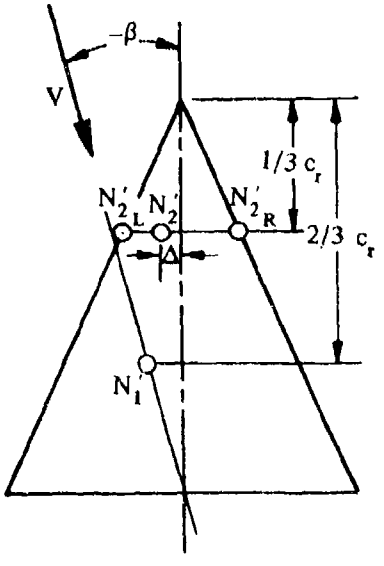

GEOMETRY FOR DEFINING THE EFFECT OF SIDESLIP ON CENTER-OF-PRESSURE POSITION – PURE DELTA WING

SKETCH (b)

contribution from the leading-edge component results from a normal-force differential between the right and left leading-edge components. The lateral position of their center of pressure is determined by balancing their rolling moments about the roll axis. By using the results given in reference 2 for the variation of the leading-edge component of normal force and the configuration geometry described by sketches (a) and (b), an expression was derived for the rolling moment due to sideslip of a thin delta wing near zero normal force. Finally, test data were used to refine the derived expression.

The final correlation is presented as figure 5.5.2.1-8a in the Datcom.

The effect of nose blunting was determined by analyzing a simplified model wherein a portion of the nose of a pure delta wing is removed by a straight cut normal to the root chord. The lateral center-of-pressure movement predicted by this technique is different from that observed, since actual nose blunting usually consists of rounding the forward part of the wing rather than cutting it off sharply. Therefore, an empirical factor was applied, based on the results of reference 3, to compensate for this difference.

It would be expected that thickness would influence rolling moment due to sideslip. The difference in the pressure distribution on the upper and lower surfaces of a lifting delta wing and the variation of the center-of-pressure locations due to thickness should result in an increment of rolling moment due to sideslip. However, during the study reported in reference 1, it was not possible to isolate the expected thickness effects with any degree of confidence. Therefore, the Datcom method does not include an increment showing the effect of thickness on rolling moment.

The Datcom method is considered valid for normal-force coefficients up to 0.3.

DATCOM METHOD

The rolling moment due to sideslip near zero normal force for delta and modified-delta configurations, based on the product of the planform area and span Sb, at low speeds is given by

$$K'_{l\beta_{N_0}} = C_{N'} \left\{ \left[\frac{K'_{l\beta_{N_0}}}{C_{N'}} \right]_{\Delta} + \Delta \left[\frac{K'_{l\beta}}{C_{N'}} \right]_{B} \right\} \quad \text{(per radian)} \qquad 5.5.2.1\text{-a}$$

where

$C_{N'}$ is the normal-force coefficient.

$\left[\frac{K'_{l\beta_{N_0}}}{C_{N'}} \right]_{\Delta}$ is the ratio of the sideslip derivative $K'_{l\beta}$ at zero normal force to the normal-force coefficient for a pointed-nose delta configuration. This parameter is obtained from figure 5.5.2.1-8a as a function of the wing semiapex angle θ.

$\Delta \left[\frac{K'_{l\beta}}{C_{N'}} \right]_{B}$ is the increment of the ratio of sideslip derivative $K'_{l\beta}$ to the normal-force coefficient, due to nose blunting. This parameter is obtained from figure 5.5.2.1-8b as a function of the configuration semiapex angle θ and the aspect ratio. The semiapex angle is measured as illustrated on figure 5.5.2.1-8b and the aspect ratio is that of the blunt-nose configuration.

A comparison of the rolling moment due to sideslip near zero normal force calculated by this method with test data is presented as table 5.5.2.1-A.

Sample Problem

Given: A blunt-nose delta-wing model with a symmetrical cross section and a blunt trailing edge. This is model D-5 of reference 7.

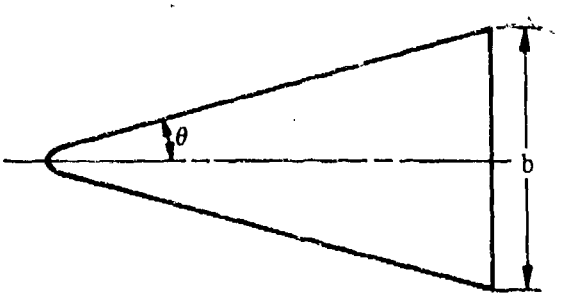

A = 1.076 θ = 15° S = 160.19 sq in. b = 13.13 in.

Compute:

$$\left[\frac{K'_{l\beta_{N_0}}}{C_{N'}}\right]_\Delta = -0.65 \text{ per rad} \quad \text{(figure 5.5.2.1-8a)}$$

$$1 - \frac{4 \tan \theta}{A} = 1 - \frac{4 \tan 15^\circ}{1.076} = 0.0041$$

$$\Delta\left[\frac{K'_{l\beta}}{C_{N'}}\right]_B = 0.033 \text{ per rad} \quad \text{(figure 5.5.2.1-8b)}$$

Solution:

$$\frac{K'_{l\beta}}{C_{N'}} = \left\{\left[\frac{K'_{l\beta_{N_0}}}{C_{N'}}\right]_\Delta + \Delta\left[\frac{K'_{l\beta}}{C_{N'}}\right]_B\right\} \quad \text{(equation 5.5.2.1-a)}$$

$$= -0.65 + 0.033$$

$$= -0.617 \text{ per rad (based on Sb)}$$

This compares with a test value of −0.556 per radian from reference 7.

REFERENCES

1. Seeger, D. B., and Ross, R.: Investigation of the Low-Speed Stability and Control Characteristics of Advanced Flight Vehicles. ASD-TDR-63-671, 1963. (C) Title Unclassified

2. Seeger, D. B., and Meyer, J. E.: An Investigation of the Subsonic Aerodynamic Characteristics and the Landing Flare Maneuver for Hypersonic Re-entry Configurations. ASD-TDR-62-271, 1962. (C) Title Unclassified

3. Edwards, G. G., and Savage, H. F.: The Subsonic Aerodynamic Characteristics of Some Blunt Delta Configurations with 75° Sweepback. NASA TM X-681, 1961. (C) Title Unclassified

4. Mantz, K., and Seeger, D. B.: Tests to Determine the Subsonic Pressures, Forces and Moments Acting on a Hypersonic Re-entry Configuration. ASD-TDR-62-270, 1962. (C) Title Unclassified

5. Mantz, K., Seeger, D. B., and Ross, R.: Tests to Determine Subsonic Pressures, Forces and Moments Acting on a Hypersonic Re-entry Configuration. ASD-TDR-62-270, Supplement 1, 1963. (U)

6. Sipe, O. E., and Seeger, D. B.: Tests to Determine Subsonic Aerodynamic Characteristics of Hypersonic Re-entry Configurations. ASD-TR-61-485, 1961. (C) Title Unclassified

7. Mantz, K., Seeger, D. B., and Ross, R.: Tests to Determine Subsonic Aerodynamic Characteristics of Hypersonic Re-entry Configurations. ASD-TR-61-485, Supplement 1, 1963. (U)

8. Graham, D., and Koenig, D. G.: Tests in the Ames 40- by 80-Foot Wind Tunnel of an Airplane Configuration with an Aspect Ratio 2 Triangular Wing and an All-Movable Horizontal Tail – Lateral Characteristics. NACA RM A51L03, 1952. (U)

9. Jaquet, B. M., and Brewer, J. D.: Low-Speed Static-Stability and Rolling Characteristics of Low-Aspect-Ratio Wings of Triangular and Modified Triangular Plan Forms. NACA RM L8L29, 1949. (U)

10. McKinney, M. O., Jr., and Drake, H. M.: Flight Characteristics at Low Speed of Delta-Wing Models. NACA RM L7K07, 1948. (U)

11. Jaquet, B. M., and Brewer, J. D.: Effects of Various Outboard and Central Fins on Low-Speed Static-Stability and Rolling Characteristics of a Triangular-Wing Model. NACA RM L9E18, 1949. (U)

12. Keating, R. F. A.: Low-Speed Wind-Tunnel Tests on Sharp-Edged Gothic Wings of Aspect-Ratio 3/4. ARC CP 576, 1961. (U)

13. Goodman, A., and Thomas, D.: Effects of Wing Position and Fuselage Size on the Low-Speed Static and Rolling Stability Characteristics of a Delta-Wing Model. NACA TR 1224, 1955. (U)

14. Tosti, L. P.: Low Speed Static Stability and Damping-in-Roll Characteristics of Some Swept and Unswept Low-Aspect-Ratio Wings. NACA TN 1468, 1947. (U)

15. Lange/Wacke: Test Report on Three- and Six-Component Measurements on a Series of Tapered Wings of Small Aspect Ratio. (Partial Report: Triangular Wing.) NACA TM 1176, 1948. (U)

16. Whittle, E. F., Jr., and Lovell, J. C.: Full-Scale Investigation of an Equilateral Triangular Wing Having 10-Percent Thick Biconvex Airfoil Sections. NACA RM L8G05, 1948. (U)

17. Olstad, W. B., Mugler, J. P., Jr., and Cahn, M. S.: Static Longitudinal and Lateral Stability Characteristics of a Right Triangular Pyramidal Lifting Re-entry Configuration at Transonic Speeds. NASA TN D-655, 1961. (U)

18. Ware, G. M.: Low-Subsonic-Speed Static Stability of Right-Triangular-Pyramid and Half-Cone Lifting Re-entry Configurations. NASA TN D-646, 1961. (U)

19. Paulson, J. W., and Shanks, R. E.: Investigation of Low-Subsonic Flight Characteristics of a Model of a Hypersonic Boost-Glide Configuration Having a 78° Delta Wing. NASA TN D-894, 1961. (U)

20. Paulson, J. W.: Low-Speed Static Stability and Control Characteristics of a Right Triangular Pyramid Re-entry Configuration. NASA Memo 4-11-59L, 1959. (U)

21. Anderson, A. E.: An Investigation of a Large-Scale Triangular Wing of Aspect Ratio Two. – I. Characteristics of a Wing Having a Double-Wedge Airfoil Section with Maximum Thickness at 20-Percent Chord. NACA RM A7F06, 1947. (U)

22. McDevitt, J. B., and Rakich, J. V.: The Aerodynamic Characteristics of Several Thick Delta Wings at Mach Numbers to 6 and Angles of Attack to 50°. NASA TM X-162, 1960. (C) Title Unclassified

23. Shanks, R. E.: Investigation of the Low-Subsonic Flight Characteristics of a Model of an All-Wing Hypersonic Boost-Glide Configuration Having Very High Sweep. NASA TN D-369, 1960. (U)

24. Boisseau, P. C.: Investigation of the Low-Subsonic Flight Characteristics of a Model of a Re-entry Vehicle with a Thick Flat 75° Delta Wing and a Half-Cone Fuselage. NASA TN D-1007, 1962. (U)

TABLE 5.5.2.1-A

SUBSONIC ROLLING MOMENT DUE TO SIDESLIP NEAR ZERO NORMAL FORCE

DELTA PLANFORM CONFIGURATIONS

DATA SUMMARY

Ref.	Configuration	A	θ (deg)	Nose Configuration	$\left[\frac{K_{\zeta\beta_{N_0}}}{C'_N}\right]$ Calc. (per rad)	$\left[\frac{K_{\zeta\beta_{N_0}}}{C'_N}\right]$ Test (per rad)	$\Delta\left[\frac{K_{\zeta\beta_{N_0}}}{C'_N}\right]$ (Calc.-Test) (per rad)
6	D-50	1.076	15.0	blunt	−0.617	−0.586	−.031
7	D-1	1.076	15.0	blunt	−0.617	−0.544	−.073
	D-2	1.076		sharp	−0.617	−0.500	−.117
	D-5	1.076		sharp	−0.617	−0.556	−.061
	D-6	1.868	25.0	blunt	−0.345	−0.368	.023
	WB-1	1.094	15.0	blunt	−0.557	−0.585	.028
	WB-3	1.074		blunt	−0.600	−0.560	−.040
	WB-4	1.147		blunt	−0.504	−0.456	−.048
8	Wing alone	2.00	26.17	sharp	−0.330	−0.320	−.010
9	1	2.31	30.0	sharp	−0.286	−0.636	.350
	2			sharp	−0.286	−0.585	.299
	3			sharp	−0.286	−0.585	.299
	4	1.07	15.0	sharp	−0.630	−0.970	.340
	7	4.00	45.0	sharp	−0.172	−0.320	.148
10	1	3.00	37.0	sharp	−0.218	−0.186	−.032
	4	2.00	27.0	sharp	−0.323	−0.246	−.077
	6	1.00	14.0	sharp	−0.675	−0.825	.150
	8	0.50	7.0	sharp	−1.370	−2.060	.690
11	Wing alone	2.31	30.0	sharp	−0.286	−0.370	.084
13	Wing alone	2.31	30.0	sharp	−0.286	−0.380	.094
14	11	3.00	37.0	sharp	−0.218	−0.225	.007
	12	2.00	26.2	sharp	−0.330	−0.262	−.068
	13	1.00	14.0	sharp	−0.675	−0.520	−.155
	14	0.50	7.1	sharp	−1.35	−0.936	−.414

TABLE 5.5.2.1-A (CONTD)

Ref.	Configuration	A	ϵ (deg)	Nose Configuration	$\left[\frac{K_\zeta \beta_{N_0}}{C_{N'}}\right]$ Calc. (per rad)	$\left[\frac{K'_\zeta \beta_{N_0}}{C_{N'}}\right]$ Test (per rad)	$\Delta\left[\frac{K'_\zeta \beta_{N_0}}{C_{N'}}\right]$ (Calc.-Test) (per rad)
15	1	3.00	37.0	sharp	−0.172	−0.122	−.050
	2	2.00	26.2	sharp	−0.330	−0.190	−.140
	3	1.33	18.03	sharp	−0.503	−0.404	−.099
	4	1.00	14.0	sharp	−0.675	−0.528	−.147
16	Wing alone	2.31	60.0	sharp	−0.286	−0.320	.034
17	1	0.742	10.5	blunt	−0.886	−1.00	.134
18	a	0.783	10.5	blunt	−0.721	−0.670	−.051
	b(basic)	0.783		blunt	−0.721	−0.710	−.011
	b(R=1.5 in.)	0.808		blunt	−0.678	−0.690	.012
	d	0.783		blunt	−0.721	−0.800	.079
19	Delta wing boost-glide	0.740	12.0	sharp	−0.800	−0.940	.140
20	Rt. triangular pyramid	0.780	10.6	blunt	−0.722	−0.580	−.142
21	Wing alone	2.0	26.6	sharp	−0.330	−0.186	−.144

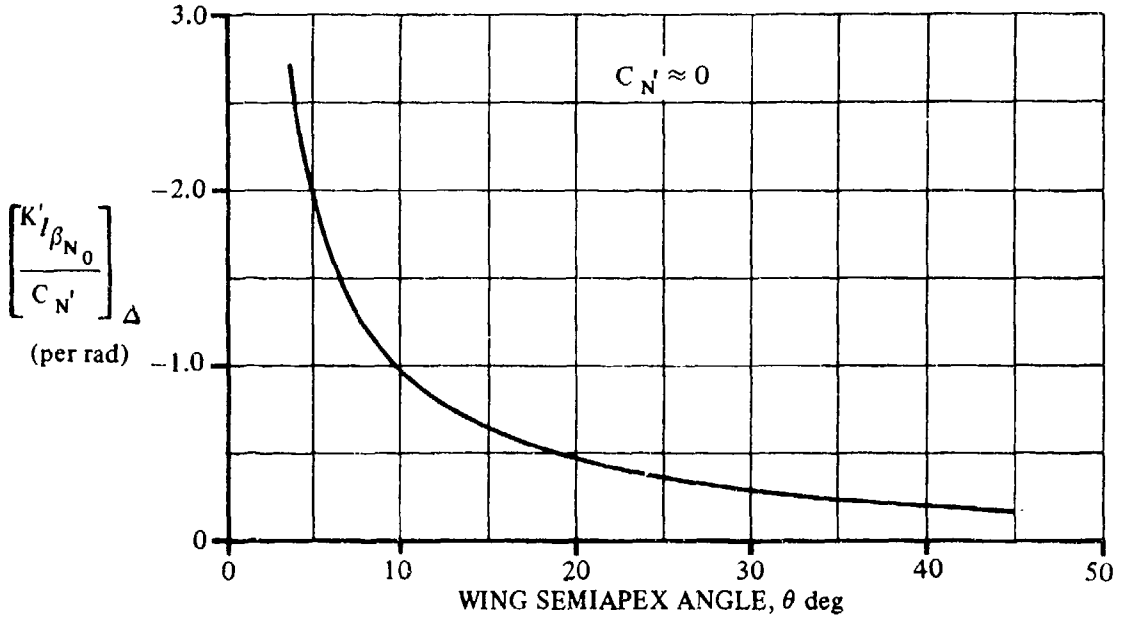

FIGURE 5.5. 2.1-8a ROLLING MOMENT DUE TO SIDESLIP
POINTED-NOSED DELTA CONFIGURATIONS

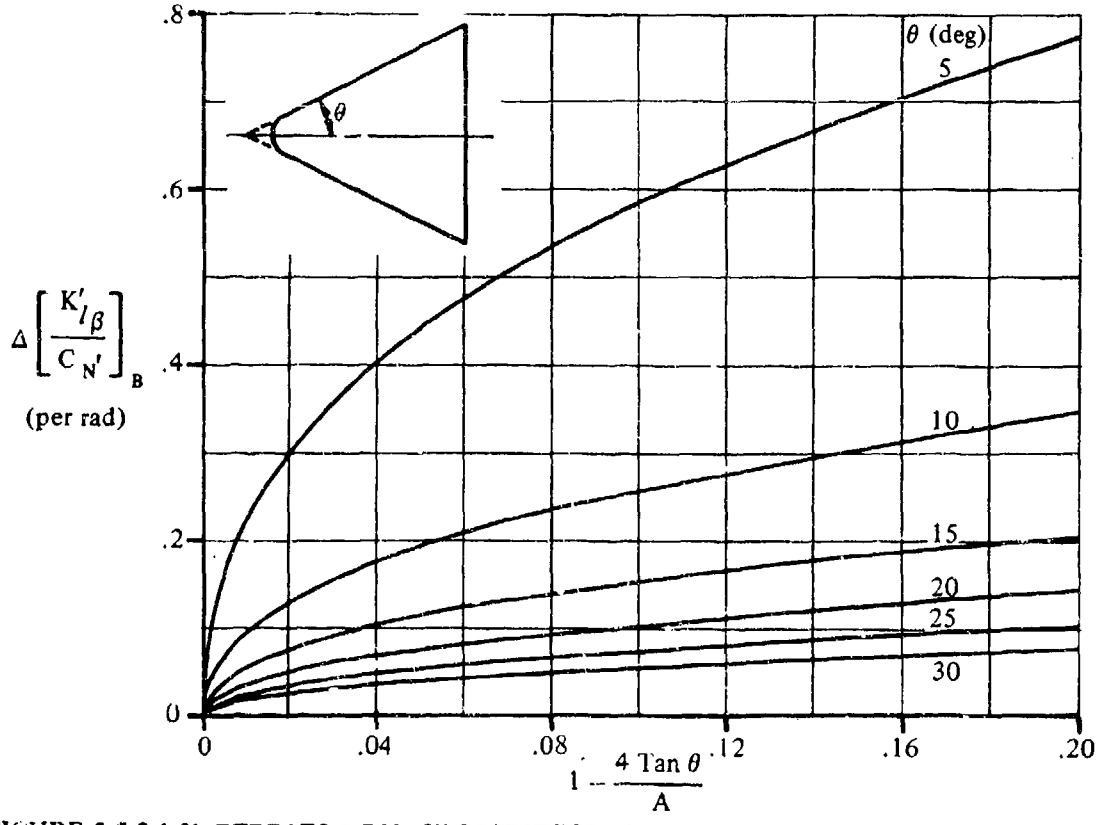

FIGURE 5.5.2.1-8b EFFECTS OF NOSE BLUNTING ON ROLLING MOMENT DUE TO SIDESLIP
DELTA AND BLUNTED DELTA CONFIGURATIONS

5.5.2.2 WING, WING-BODY SIDESLIP-DERIVATIVE K'_{l_β} VARIATION WITH ANGLE OF ATTACK

A. SUBSONIC

This section presents a method, taken from reference 1, for estimating the sideslip-derivative K'_{l_β} variation with angle of attack for delta and modified-delta configurations at subsonic speeds.

The variation of K'_{l_β} with angle of attack for a thin delta wing is based on the conceptual model described briefly in Section 5.5.2.1, and the semiempirical technique used to obtain the variation of normal force with angle of attack is that described in reference 2. It is shown in reference 2 that the longitudinal position of the center of pressure and the distribution of the load over the surface of an unyawed, thin delta wing are both independent of angle of attack. As noted in Section 5.5.2.1, experimental data also show that the longitudinal position of the center of pressure does not change as the wing is sideslipped through small sideslip angles. Therefore, it was concluded that the ratio of the normal-force component that is considered to act at the leading edge to that uniformly distributed over the wing (see discussion in Section 5.5.2.1) does not change, and that the change in K'_{l_β} with angle of attack results because of the spanwise shift in one or both of these normal-force components as the angle of attack is increased. In accordance with these considerations, the variation of the sideslip derivative K'_{l_β} with angle of attack is related to the normal-force coefficient by

$$\frac{\left(K'_{l_\beta}/C_{N'}\right)_{\text{linear}}}{\left(K'_{l_\beta}/C_{N'}\right)_{\text{nonlinear}}} = \frac{\left(C_{N'}\right)_{\text{linear}}}{\left(C_{N'}\right)_{\text{nonlinear}}}$$

The technique used to obtain a correlation of normal force in reference 2 (see Section 4.8.1.2) was then applied to determine a reference value for K'_{l_β} at $\alpha' = 20^\circ$. The correlation parameters used were leading-edge radius and leading-edge angle for thin delta wings with round and sharp leading edges, respectively. It was then assumed that the variation of $K'_{l_\beta}/C_{N'}$ within the angle-of-attack range from 0 to 20° is parabolic. It should be noted that as the leading-edge radius approaches zero, the rolling-moment coefficient with respect to sideslip approaches the same value as for a sharp leading edge. Therefore, a configuration with a small leading-edge radius can be analyzed as one having a sharp leading edge.

As wing thickness is increased, the pressure distribution on the upper and lower surfaces of a sideslipping delta wing at angle of attack become significantly different. A couple will be introduced due to this pressure distribution and a corresponding rolling-moment increment will result. An empirical correlation, taken from reference 1, is presented to account for this thickness effect. This correlation is based on data at $\alpha' = 20^\circ$ only; however, it is applied over the angle-of-attack range from 0 to 20° in the Datcom.

The increment in rolling-moment coefficient with respect to sideslip due to nose blunting is assumed invariant with angle of attack. Therefore, the effect of nose blunting is taken as that presented in Section 5.5.2.1.

The Datcom method is considered valid for sideslip angles between ±10° and angles of attack up to 20°.

DATCOM METHOD

The sideslip-derivative K'_{l_β} variation with angle of attack for a delta or modified-delta configuration at subsonic speeds, based on the product of planform area and span Sb, is obtained from the procedure outlined in the following steps:

Step 1. Determine the effective leading-edge angle $\delta_{e_\perp}$ for sharp leading edges or the effective leading-edge radius $R_{\frac{1}{3}\,LE}$ for round leading edges. These parameters are functions of the configuration geometry in a plane normal to the leading edge at $\frac{1}{3} c_r$ from the nose. The applicable configuration geometry is illustrated on figure 4.8.1.2-11a and 4.8.1.2-11b.

Step 2. Determine the ratio $\left[\frac{K'_{l_{\beta_{N_0}}}}{C_{N'}}\right]_\Delta$ of the sideslip derivative K'_{l_β} near zero normal force to the normal-force coefficient for a thin, pointed-nose delta wing. This parameter is obtained from figure 5.5.2.1-8a as a function of the wing semiapex angle θ.

Step 3. Determine the calculated value of $K'_{l_\beta}/C_{N'}$ at $\alpha' = 20^o$ by

$$\left[\left(\frac{K'_{l_\beta}}{C_{N'}}\right)_{calc}\right]_{20} = \frac{1}{1 + \frac{0.152}{\tan\theta}} \left[\frac{K'_{l_{\beta_{N_0}}}}{C_{N'}}\right]_\Delta \quad \text{(per radian)} \qquad 5.5.2.2\text{-a}$$

where θ is the semiapex angle in degrees and $\left[\frac{K'_{l_{\beta_{N_0}}}}{C_{N'}}\right]_\Delta$ is obtained from step 2.

Step 4. Obtain the empirical correlation factor for the ratio of K'_{l_β} to normal-force coefficient at $\alpha' = 20^o$. This parameter is expressed as $\frac{\left(K'_{l_\beta}/C_{N'}\right)_{20}}{\left[\left(K'_{l_\beta}/C_{N'}\right)_{calc}\right]_{20}}$ and is presented as a function of the effective leading-edge radius for configurations with round leading edges in figure 5.5.2.2-12a, and as a function of leading-edge angle for configurations with sharp leading edges in figure 5.5.2.2-12b.

Step 5. Obtain the empirical correlation factor for the increment in the ratio of K'_{l_β} to normal-force coefficient due to thickness effects at $\alpha' = 20^o$. This parameter is expressed as $\Delta \frac{\left(K'_{l_\beta}/C_{N'}\right)_{20}}{\left[\left(K'_{l_\beta}/C_{N'}\right)_{calc}\right]_{20}}$ and is presented in figure 5.5.2.2-13 as a function of the ratio of the projected side area of the configuration to the planform area S_{B_S}/S.

Step 6. Determine the ratio of the increment in sideslip derivative K'_{l_β} to the normal-force coefficient due to nose blunting $\Delta\left[\frac{K'_{l_\beta}}{C_{N'}}\right]_B$ from figure 5.5.2.1-8b as a function of the configuration semiapex angle θ and the aspect ratio. The semiapex angle is measured as illustrated on figure 5.5.2.1-8b and the aspect ratio is that of the blunt-nose configuration.

Step 7. Using the terms obtained in steps 2 through 6 determine the variation of the ratio of $K'_{l_\beta}/C_{N'}$ with α' by

$$\frac{K'_{l_\beta}}{C_{N'}} = \left[\frac{K'_{l_{\beta_{N_0}}}}{C_{N'}}\right]_\Delta \left[1 - \left(\frac{\alpha'}{20}\right)^2\right] + \left(\left\{ \frac{\left(K'_{l_\beta}/C_{N'}\right)_{20}}{\left[\left(K'_{l_\beta}/C_{N'}\right)_{calc}\right]_{20}} + \Delta \frac{\left(K'_{l_\beta}/C_{N'}\right)_{20}}{\left[\left(K'_{l_\beta}/C_{N'}\right)_{calc}\right]_{20}} \right\} \left[\left(\frac{K'_{l_\beta}}{C_{N'}}\right)_{calc}\right]_{20} + \Delta\left[\frac{K'_{l_\beta}}{C_{N'}}\right]_B \right)\left(\frac{\alpha'}{20}\right)^2 \quad \text{(per radian)}$$

5.5.2.2-b

where α' is in degrees.

Step 8. Determine the variation of K'_{l_β} with angle of attack by

$$K'_{l_\beta} = \left(\frac{K'_{l_\beta}}{C_{N'}}\right) C_{N'} \qquad \text{5.5.2.2-c}$$

where $\left(K'_{l_\beta}/C_{N'}\right)$ is from step 7 and $C_{N'}$ is the normal-force coefficient at angle of attack obtained from Section 4.8.1.2.

The variation of the sideslip derivative K'_{l_β} with angle of attack calculated by this method is compared with test data in table 5.5.2.2-A. The variations of $C_{N'}$ with angle of attack, used to obtain the calculated values of K'_{l_β} in table 5.5.2.2-A, were calculated by using the method of Section 4.8.1.2.

It should be noted that a considerable amount of scatter was involved in the data correlation used to define the design charts. In the case of sharp-leading-edged configurations it was necessary to estimate the nature of the effect of leading-edge angle on the basis of very few test data. Therefore, the accuracy of the design chart used for sharp leading edges (figure 5.5.2.2-12b) is questionable.

The lift distribution over a lifting delta wing is such that maximum local lifts occur in the area immediately below the cores of the shed vortices (see discussion in Section 5.5.1.2). Since these vortices do not move with the wing as it is sideslipped, the region of high local lift may act on the surface at one sideslip angle while the wing-vortex which produces it may be outboard of the leading edge at

another. Therefore, nonlinearities in the variation of rolling moment with sideslip may exist with low-aspect-ratio delta planforms. The available data are not sufficient to allow isolation of this effect. However, it should be realized that a constant value of K'_{l_β} valid for $\beta = \pm 10^o$ may not be a useful representation of the physical phenomena involved.

Sample Problems

1. Round Leading Edge

Given: A delta wing model of reference 6 designated D-6. This is the configuration of sample problem 1 of Section 4.8.1.2.

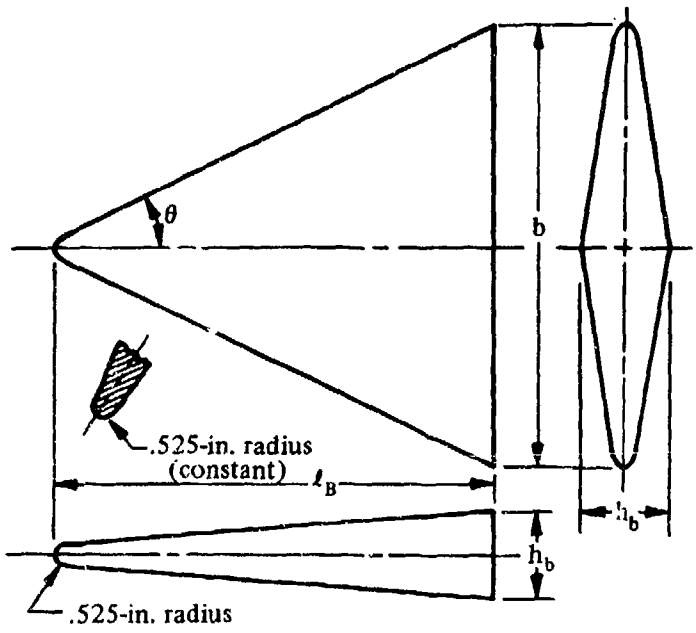

$A = 1.868$ $b = 22.116$ in. $S = 261.95$ sq in. $S_{B_S} = 61.82$ sq in.

$R_{\frac{1}{3}\,LE} = 0.525$ in. $\theta = 25^o$ $h_b = 4.32$ in.

The following variation of $C_{N'}$ with α' from sample problem 1 of Section 4.8.1.2:

α'	0	5^o	10^o	15^o	20^o
$C_{N'}$	0	0.2017	0.4122	0.6323	0.8618

Compute:

$$\left[\frac{K'_{l_{\beta_{N_0}}}}{C_{N'}}\right]_\Delta = -0.36 \text{ per rad} \quad \text{(figure 5.5.2.1-8a)}$$

$$\left[\left(\frac{K'_{l_\beta}}{C_{N'}}\right)_{calc}\right]_{20} = \frac{1}{1+\frac{0.152}{\tan\theta}}\left[\frac{K'_{l_{\beta_{N_0}}}}{C_{N'}}\right]_\Delta \quad \text{(equation 5.5.2.2-a)}$$

$$= \frac{1}{1+\frac{0.152}{\tan 25^\circ}} \quad (-0.36)$$

$$= -0.271 \text{ per rad}$$

$$R_{\frac{1}{3}LE}/b = 0.525/22.116 = 0.0237$$

$$\frac{\left(K'_{l_\beta}/C_{N'}\right)_{20}}{\left[\left(K'_{l_\beta}/C_{N'}\right)_{calc}\right]_{20}} = 0.655 \quad \text{(figure 5.5.2.2-12a)}$$

$$S_{B_S}/S = 61.82/261.95 = 0.236$$

$$\Delta\frac{\left(K'_{l_\beta}/C_{N'}\right)_{20}}{\left[\left(K'_{l_\beta}/C_{N'}\right)_{calc}\right]_{20}} = 0.10 \quad \text{(figure 5.5.2.2-13)}$$

$$1-\frac{4\tan\theta}{A} = 1-\frac{4\tan 25^\circ}{1.868} = 0.0015$$

$$\Delta\left[\frac{K'_{l_\beta}}{C_{N'}}\right]_B = 0.005 \text{ per rad} \quad \text{(figure 5.5.2.1-8b)}$$

$$\frac{K'_{l_\beta}}{C_{N'}} = \left[\frac{K'_{l_{\beta_{N_0}}}}{C_{N'}}\right]_\Delta\left[1-\left(\frac{\alpha'}{20}\right)^2\right] + \left(\left\{\frac{\left(K'_{l_\beta}/C_{N'}\right)_{20}}{\left[\left(K'_{l_\beta}/C_{N'}\right)_{calc}\right]_{20}} + \Delta\frac{\left(K'_{l_\beta}/C_{N'}\right)_{20}}{\left[\left(K'_{l_\beta}/C_{N'}\right)_{calc}\right]_{20}}\right\}\left[\left(\frac{K'_{l_\beta}}{C_{N'}}\right)_{calc}\right]_{20} + \Delta\left[\frac{K'_{l_\beta}}{C_{N'}}\right]_B\right)\left(\frac{\alpha'}{20}\right)^2 \quad \text{(equation 5.5.2.2-b)}$$

$$= (-0.36)\left[1 - \left(\frac{\alpha'}{20}\right)^2\right] + \left(\{0.655 + 0.10\}[-0.271] + 0.005\right)\left(\frac{\alpha'}{20}\right)^2$$

$$= -0.36 + 0.36\left(\frac{\alpha'}{20}\right)^2 - 0.200\left(\frac{\alpha'}{20}\right)^2$$

$$= -0.36 + 0.160\left(\frac{\alpha'}{20}\right)^2 \text{ per rad}$$

Solution:

$$K'_{l_\beta} = \left(\frac{K'_{l_\beta}}{C_{N'}}\right) C_{N'} \quad \text{(equation 5.5.2.2-c)}$$

$$= \left[-0.36 + 0.160\left(\frac{\alpha'}{20}\right)^2\right] C_N \text{ per rad}$$

①	②	③	④	⑤	⑥
α' (deg)	$C_{N'}$ (given)	$\alpha'/20$ ① /20	$0.160\left(\frac{\alpha'}{20}\right)^2$ 0.160 ③ ^{2}	$\frac{K'_{l_\beta}}{C_{N'}}$ (per rad) −0.36 + ④	K'_{l_β} (based on Sb) eq. 5.5.2.2-c (per rad) ⑤ ②
0	0	0	0	−0.360	0
5	0.202	0.25	0.010	−0.350	−0.071
10	0.412	0.50	0.040	−0.320	−0.132
15	0.632	0.75	0.090	−0.270	−0.171
20	0.862	1.00	0.160	−0.200	−0.172

The calculated results are compared with test values from reference 6 in sketch (a) and in table 5.5.2.2-A.

2. Sharp Leading Edge

Given: The hypersonic boost-glide configuration of reference 8 without tip cones and ventrals.

$A = 0.74$ $\quad b = 35.40$ in. $\quad S = 11.70$ sq ft $\quad S_{B_S} = 3.39$ sq ft

$\delta_{e_\perp} = 10.1^\circ$ $\quad \theta = 12^\circ$

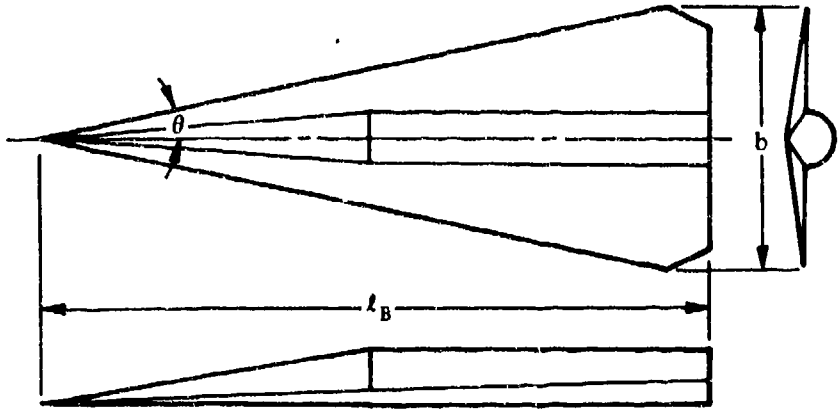

The following variation of $C_{N'}$ with α', calculated by using the method of Section 4.8.1.2:

α'	0	5°	10°	15°	20°
$C_{N'}$	0	0.119	0.276	0.471	0.704

Compute:

$$\left[\frac{K'_{l_{\beta_{N_0}}}}{C_{N'}}\right]_{\Delta} = -0.800 \text{ per rad} \quad \text{(figure 5.5.2.1-8a)}$$

$$\left[\left(\frac{K'_{l_\beta}}{C_{N'}}\right)_{calc}\right]_{20} = \frac{1}{1 + \frac{0.152}{\tan\theta}} \left[\frac{K'_{l_{\beta_{N_0}}}}{C_{N'}}\right]_{\Delta} \quad \text{(equation 5.5.2.2-a)}$$

$$= \frac{1}{1 + \frac{0.152}{\tan 12^o}} (-0.800)$$

$$= -0.466 \text{ per rad}$$

$$\frac{\left(K'_{l_\beta}/C_{N'}\right)_{20}}{\left[\left(K'_{l_\beta}/C_{N'}\right)_{calc}\right]_{20}} = 0.950 \quad \text{(figure 5.5.2.2-12b)}$$

$$S_{B_S}/S = 3.39/11.70 = 0.290$$

$$\Delta \frac{\left(K'_{l_\beta}/C_{N'}\right)_{20}}{\left[\left(K'_{l_\beta}/C_{N'}\right)_{calc}\right]_{20}} = 0.12 \quad \text{(figure 5.5.2.2-13)}$$

$$\Delta\left[\frac{K'_{l_\beta}}{C_{N'}}\right]_B = 0 \text{ (no nose bluntness)}$$

$$\frac{K'_{l_\beta}}{C_{N'}} = \left[\frac{K'_{l_{\beta_{N_0}}}}{C_{N'}}\right]_\Delta \left[1 - \left(\frac{\alpha'}{20}\right)^2\right] + \left(\left\{\frac{\left(K'_{l_\beta}/C_{N'}\right)_{20}}{\left[\left(K'_{l_\beta}/C_{N'}\right)_{calc}\right]_{20}}\right.\right.$$

$$\left. + \Delta\frac{\left(K'_{l_\beta}/C_{N'}\right)_{20}}{\left[\left(K'_{l_\beta}/C_{N'}\right)_{calc}\right]_{20}}\right\}\left[\left(\frac{K'_{l_\beta}}{C_{N'}}\right)_{calc}\right]_{20}$$

$$\left. + \Delta\left[\frac{K'_{l_\beta}}{C_{N'}}\right]_B\right)\left(\frac{\alpha'}{20}\right)^2 \quad \text{(equation 5.5.2.2-b)}$$

$$= (-0.800)\left[1 - \left(\frac{\alpha'}{20}\right)^2\right] + \left(\{0.950 + 0.12\}[-0.466] + 0\right)\left(\frac{\alpha'}{20}\right)^2$$

$$= -0.800 + 0.800\left(\frac{\alpha'}{20}\right)^2 - 0.499\left(\frac{\alpha'}{20}\right)^2$$

$$= -0.800 + 0.301\left(\frac{\alpha'}{20}\right)^2 \text{ per rad}$$

Solution:

$$K'_{l_\beta} = \left(\frac{K'_{l_\beta}}{C_{N'}}\right) C_{N'} \quad \text{(equation 5.5.2.2-c)}$$

$$= \left[-0.800 + 0.301\left(\frac{\alpha'}{20}\right)^2\right] C_{N'} \text{ per rad}$$

①	②	③	④	⑤	⑥
α' (deg)	C_N' (given)	$\alpha'/20$ ① /20	$0.301\left(\frac{\alpha'}{20}\right)^2$ 0.301 ③ ^{2}	$\frac{K'_{l_\beta}}{C_N'}$ (per rad) −0.800 + ④	K'_{l_β} (based on Sb) eq. 5.5.2.2-c (per rad) ⑤ ②
0	0	0	0	−0.800	0
5	0.119	0.25	0.019	−0.781	−0.093
10	0.276	0.50	0.075	−0.725	−0.200
15	0.471	0.75	0.169	−0.631	−0.297
20	0.704	1.00	0.301	−0.499	−0.351

The calculated results are compared with test values from reference 8 in sketch (a) and in table 5.5.2.2-A.

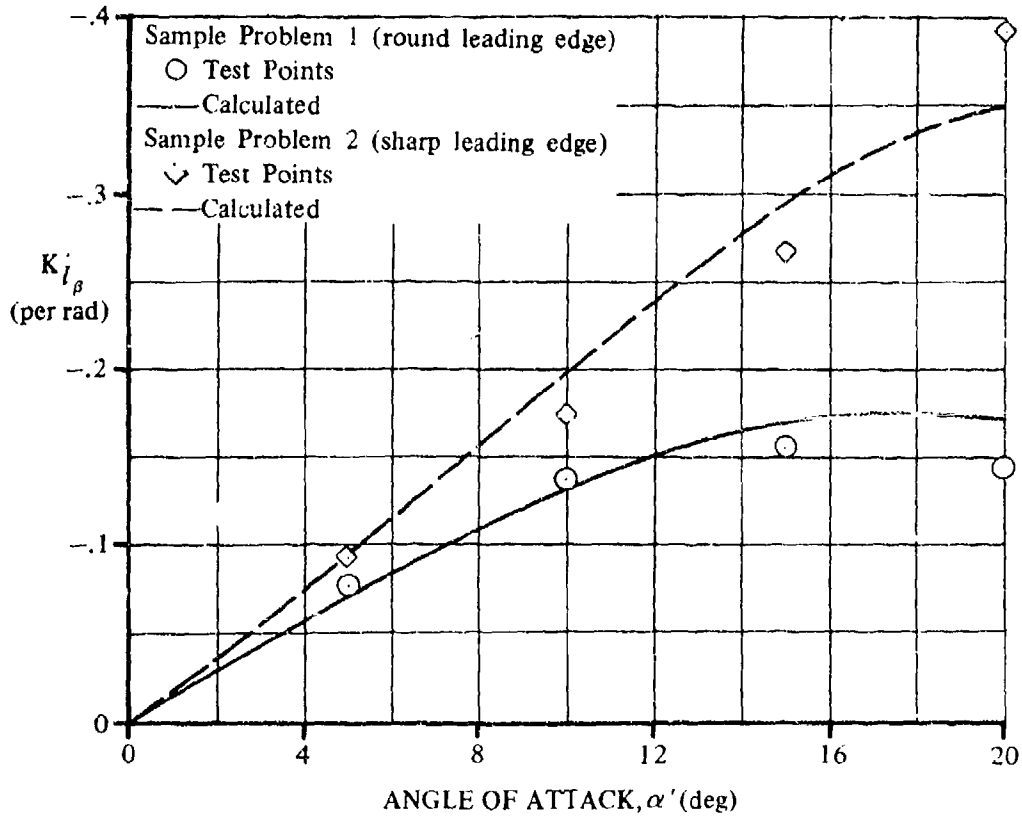

SKETCH (a)

REFERENCES

1. Seeger, D. B., and Ross, R.: Investigation of the Low-Speed Stability and Control Characteristics of Advanced Flight Vehicles. ASD-TDR-63-671, 1963. (C) Title Unclassified

2. Seeger, D. B., and Meyer, J. E.: An Investigation of the Subsonic Aerodynamic Characteristics and the Landing Flare Maneuver for Hypersonic Re-entry Configurations. ASD-TDR-62-271, 1962. (C) Title Unclassified

3. Mantz, K., and Seeger, D. B.: Tests to Determine the Subsonic Pressures, Forces and Moments Acting on a Hypersonic Re-entry Configuration. ASD-TDR-62-270, 1962. (C) Title Unclassified

4. Mantz, K., Seeger, D. B., and Ross, R.: Tests to Determine Subsonic Pressures, Forces and Moments Acting on a Hypersonic Re-entry Configuration. ASD-TDR-62-270, Supplement 1, 1963. (U)

5. Sipe, O. E., and Seeger, D. B.: Tests to Determine Subsonic Aerodynamic Characteristics of Hypersonic Re-entry Configurations. ASD-TR-61-485, 1961. (C) Title Unclassified

6. Mantz, K., Seeger, D. B., and Ross, R.: Tests to Determine Subsonic Aerodynamic Characteristics of Hypersonic Re-entry Configurations. ASD-TR-61-485, Supplement 1, 1963. (U)

7. Ware, G. M.: Low-Subsonic-Speed Static Stability of Right-Triangular-Pyramid and Half-Cone Lifting Re-entry Configurations. NASA TN D-646, 1961. (U)

8. Paulson, J. W., and Shanks, R. E.: Investigation of Low-Subsonic Flight Characteristics of a Model of a Hypersonic Boost-Glide Configuration Having a 78° Delta Wing. NASA TN D-894, 1961. (U)

9. Edwards, G. G., and Savage, H. F.: The Subsonic Aerodynamic Characteristics of Some Blunt Delta Configurations with 75° Sweepback. NASA TM X-581, 1961. (C) Title Unclassified

10. McDevitt, J. B., and Rakich, J. V.: The Aerodynamic Characteristics of Several Thick Delta Wings at Mach Numbers to 6 and Angles of Attack to 50°. NASA TM X-162, 1960. (C) Title Unclassified

TABLE 5.5.2.2-A

SUBSONIC ROLLING MOMENT WITH RESPECT TO SIDESLIP — VARIATION WITH ANGLE OF ATTACK

DELTA PLANFORM CONFIGURATIONS

DATA SUMMARY

Ref.	Configuration	A	θ (deg)	$\frac{S_{B_S}}{S}$	Leading Edge	α (deg)	K'_{l_β} Calc. (per rad)	K'_{l_β} Test (per rad)	$\Delta K'_{l_\beta}$ Calc.-Test (per rad)
4	D50	1.076	15	0.386	Round $R_1 = \frac{1}{3} LE = 2.10$ in.	0	0	0	0
						5	−0.076	−0.077	0.001
						10	−0.148	−0.138	−0.010
						15	−0.210	−0.183	−0.027
						20	−0.257	−0.212	−0.045

TABLE 5.5.2.2-A (CONTD)

Ref.	Configuration	A	θ (deg)	$\frac{S_{B_S}}{S}$	Leading Edge	α (deg)	K'_{l_β} Calc. (per rad)	K'_{l_β} Test (per rad)	$\Delta K'_{l_\beta}$ Calc.-Test (per rad)
6	D-2	1.076	15	0.349	Sharp $\delta_{e_\perp} = 58^\circ$	0	0	0	0
						5	-0.079	-0.070	-0.009
						10	-0.162	-0.148	-0.014
						15	-0.186	-0.210	0.025
						20	-0.118	-0.274	0.156
	D-5	1.076	15	0.386	Round $R_{\frac{1}{3}LE} = 1.05$ in.	0	0	0	0
						5	-0.076	-0.067	-0.009
						10	-0.147	-0.138	-0.009
						15	-0.210	-0.195	-0.015
						20	-0.257	-0.250	-0.007
	D-6	1.86R	25	0.236	Round $R_{\frac{1}{3}LE} = .525$ in.	0	0	0	0
						5	-0.071	-0.078	0.007
						10	-0.132	-0.137	0.005
						15	-0.171	-0.155	-0.016
						20	-0.172	-0.143	-0.029
7	d	0.783	10.5	0.518	Round $R_{\frac{1}{3}LE} = .50$ in.	0	0	0	0
						5	-0.086	-0.090	0.004
						10	-0.160	-0.172	0.012
						15	-0.208	-0.246	0.038
						20	-0.173	-0.215	0.042
8	Hypersonic-boost-glide without tip cones and ventrals	0.74	12	0.29	Sharp $\delta_{e_\perp} = 10.1^\circ$	0	0	0	0
						5	-0.093	-0.091	-0.002
						10	-0.200	-0.174	-0.026
						15	-0.297	-0.267	-0.030
						20	-0.361	-0.392	0.041

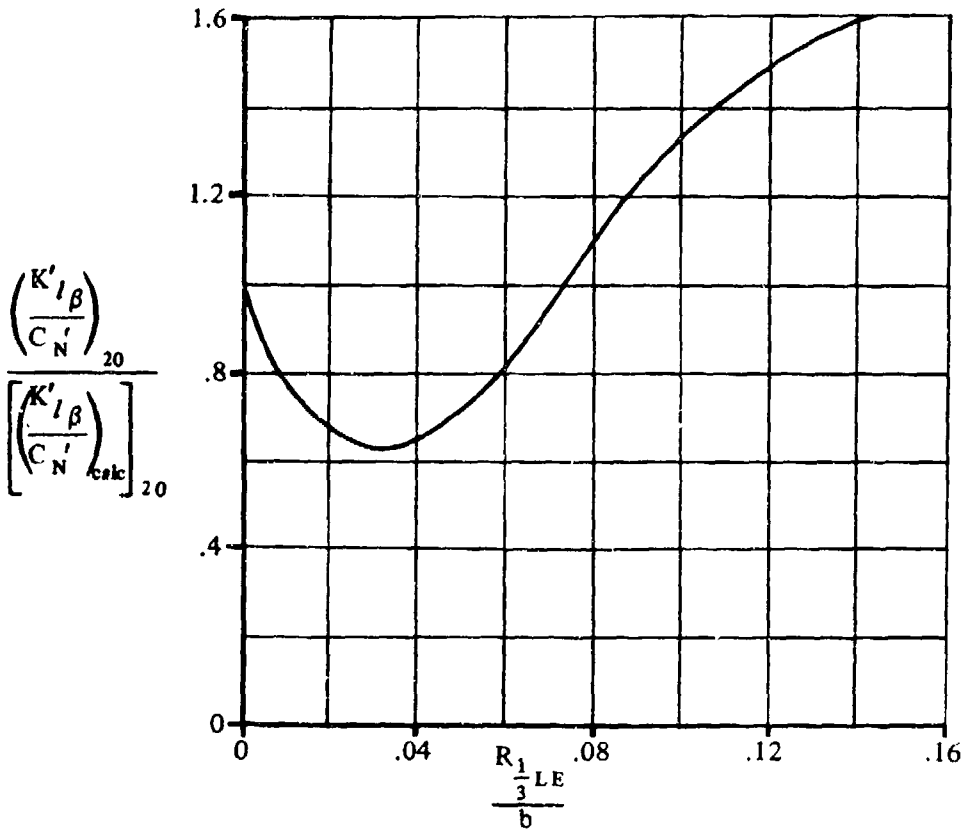

FIGURE 5.5.2.2-12a ROLLING-MOMENT-DERIVATIVE CORRELATION FACTOR AT $\alpha' = 20^o$ – DELTA CONFIGURATIONS WITH ROUND LEADING EDGES

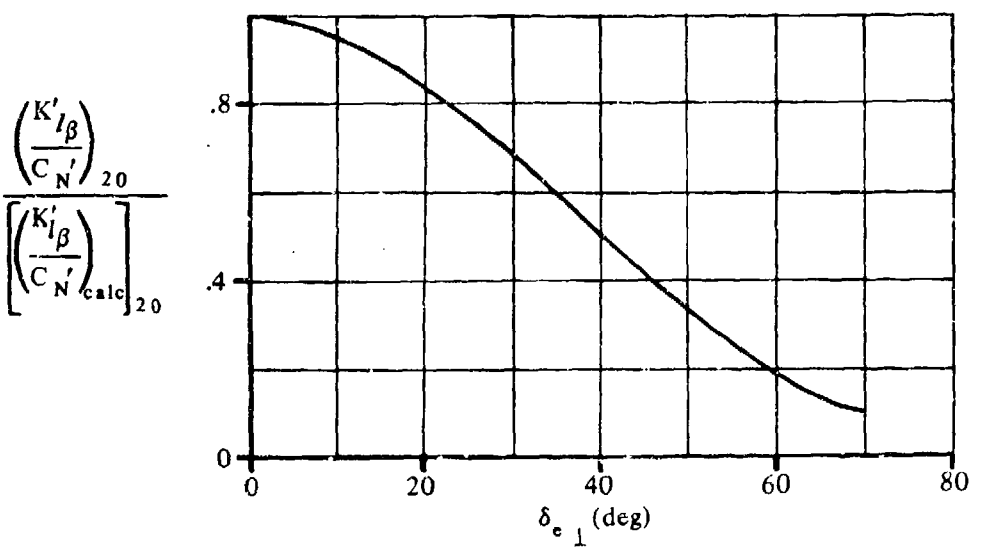

FIGURE 5.5.2.2-12b ROLLING-MOMENT-DERIVATIVE CORRELATION FACTOR AT $\alpha' = 20^o$ – DELTA CONFIGURATIONS WITH SHARP LEADING EDGES

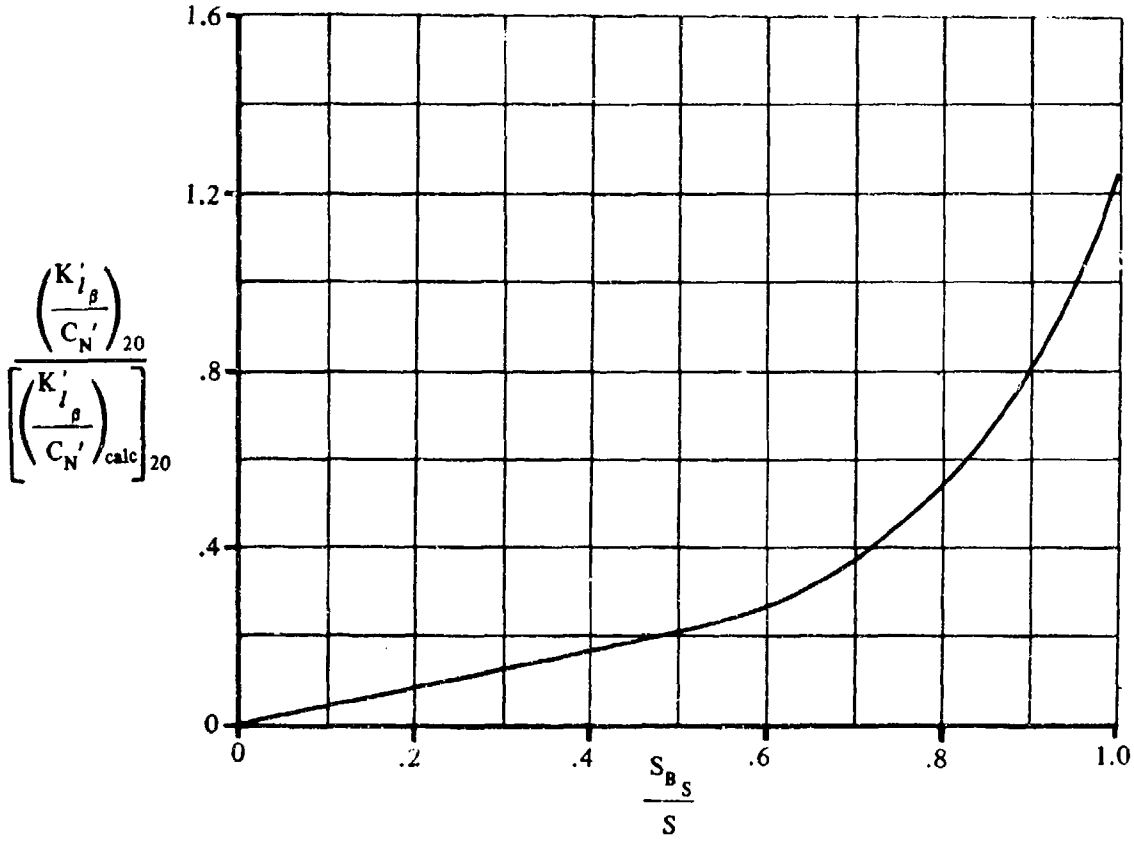

FIGURE 5.5.2.2-13 EFFECTS OF CONFIGURATION THICKNESS ON ROLLING MOMENT DUE TO SLIDESLIP AT $\alpha' = 20^\circ$ – DELTA CONFIGURATIONS

5.5.3 WING, WING-BODY SIDESLIP DERIVATIVE K'_{n_β}

5.5.3.1 WING, WING-BODY SIDESLIP DERIVATIVE K'_{n_β} AT ZERO NORMAL FORCE

A. SUBSONIC

This section presents a method, taken from reference 1, for estimating $K'_{n_{\beta_{N_0}}}$, the yawing-moment coefficient with respect to sideslip at zero normal force, for delta and modified-delta configurations at subsonic speeds.

The yawing moment due to sideslip is estimated by determining the side force due to sideslip and determining its effective point of application. The side force due to sideslip at zero normal force is estimated by using the method of Section 5.5.1.1.

The nature of the side force, and consequently the location of the center of pressure, is basically different for thin and for thick wings. As noted in Section 5.5.1.1, the side force at zero normal force is assumed to be composed of two parts, side force due to skin friction and side force due to the pressure acting on the configuration. For thin wings the side force is produced primarily by skin friction, and the side-force center of pressure can be related to the wing planform. As the wing thickness is increased, the side force is produced primarily by the difference in pressure distribution between the right and left sides. While the wing planform area would be expected to influence this pressure distribution, the side-area distribution has a major effect. In accordance with these considerations, the skin-friction drag component is assumed to act at the centroid of the planform area and the pressure-drag component at the center of pressure of the side area of the configuration.

An empirical correlation was used to determine the position of the resultant of the side-force components. It was assumed that the center-of-pressure position of the pressure component depends primarily on the shape of the side area and that the influence of other geometric parameters can be neglected. Test data indicated that nose shape has an important influence on this center-of-pressure location, and the final correlation is presented as a function of the ratio of the side area forward of the 20-percent root-chord point (see figure 5.5.3.1-6) to the total side area.

The zero-normal-force sideslip derivative $K_{Y_{\beta_{N_0}}}$ for very thin wings is taken to be equal to the incompressible skin-friction coefficient of the wing, which is taken as $C_f = 0.006$, so that $K_{Y_{\beta_{N_{0_{\substack{\text{thin}\\\text{wing}}}}}}} = -0.006$ per radian, based on planform area. This value is maintained constant for thicker wings, since the side force due to pressure is much greater than that produced by friction and a more accurate value of it is not required.

DATCOM METHOD

The zero-normal-force sideslip derivative $K'_{n_{\beta_{N_0}}}$ of a delta or modified-delta configuration, based on the product of planform area and span Sb, and taken about an axis at the nose of the configuration, is determined from the procedure outlined in the following steps:

Step 1. From the configuration geometry determine the following:

S_{B_S} the projected side area of the configuration

$(S_{B_S})_{.2c_r}$ the projected side area of the configuration forward of 0.2 c_r

$x_{centroid_W}$ the distance from the nose of the configuration to the centroid location of the wing planform, positive aft of the nose

$x_{centroid_{S_{B_S}}}$ the distance from the nose of the configuration to the centroid location of the projected side area, positive aft of the nose

Step 2. Determine $K'_{n_{\beta_{N_0}}}$ by

$$K'_{n_{\beta_{N_0}}} = \left(K_{Y_{\beta_{N_0}}} + 0.006\right) \frac{(x_{c.p.})_p}{x_{centroid_{S_{B_S}}}} \frac{x_{centroid_{S_{B_S}}}}{b} - 0.006 \frac{x_{centroid_W}}{b} \text{ (per radian)} \qquad 5.5.3.1\text{-a}$$

where

$K_{Y_{\beta_{N_0}}}$ is the side-force coefficient due to sideslip at zero normal force, obtained from Section 5.5.1.1.

$\frac{(x_{c.p.})_p}{x_{centroid_{S_{B_S}}}}$ is the ratio of the center-of-pressure location of the pressure component of side force to the centroid location of the projected side area.

This parameter is obtained from figure 5.5.3.1-6 as a function of $(S_{B_S})_{.2c_r}/S_{B_S}$.

b is the wing span.

A comparison of $K'_{N_{\beta N_0}}$ calculated by using this method with test results is presented as table 5.5.3.1-A. The sideslip derivatives $K_{Y_{\beta N_0}}$, used to obtain the calculated values of $K'_{n_{\beta N_0}}$ in table 5.5.3.1-A, were calculated by using the method of Section 5.5.1.1.

It should be noted that a considerable amount of scatter was involved in the data correlation used to define the center-of-pressure location of the pressure component of side force. For configurations with values of $(S_{B_S})_{.2c_r}/S_{B_S}$ greater than approximately 0.15, the location of $(x_{c.p.})_p$ is not well established.

Sample Problem

Given: A delta-series configuration of reference 6 designated D-2.

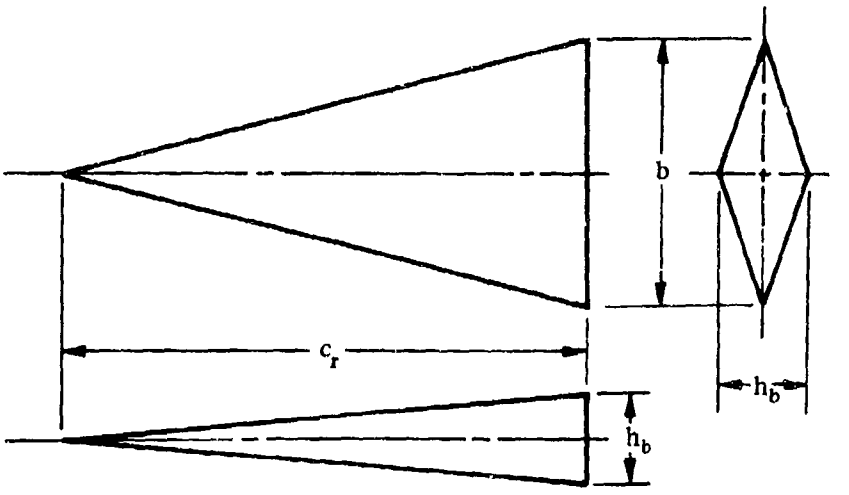

$S = 142.3$ sq in. $\quad S_{B_S} = 49.68$ sq in. $\quad \left(S_{B_S}\right)_{.2c_r} = 1.99$ sq in.

$c_r = 23.0$ in. $\quad b = 12.374$ in. $\quad h_b = 4.32$ in.

Compute:

$S_{B_S}/S = 49.68/142.3 = 0.349$

$K_{Y_{\beta_{N_0}}} = -0.110$ per rad (figure 5.5.1.1-6)

$x_{centroid_W} = 2c_r/3 = 2(23.0)/3 = 15.33$ in.

$x_{centroid_{S_{B_S}}} = 2c_r/3 = 15.33$ in.

$\left(S_{B_S}\right)_{.2c_r}/S_{B_S} = 1.99/49.68 = 0.040$

$\dfrac{(x_{c.p.})_p}{x_{centroid_{S_{B_S}}}} = 1.04$ (figure 5.5.3.1-6)

Solution:

$$K'_{n_{\beta_{N_0}}} = \left(K_{Y_{\beta_{N_0}}} + 0.006\right) \frac{(x_{c.p.})_p}{x_{centroid_{S_{B_S}}}} \frac{x_{centroid_{S_{B_S}}}}{b} - 0.006 \frac{x_{centroid_W}}{b} \quad \text{(equation 5.5.3.1-a)}$$

$$= (-0.110 + 0.006)\,(1.04)\,\frac{15.33}{12.374} - 0.006\,\frac{15.33}{12.374}$$

$$= -0.1414 \text{ per rad (based on Sb)}$$

This compares with a test value of −0.1485 per radian from reference 6.

REFERENCES

1. Seeger, D. B., and Ross, R.: Investigation of the Low-Speed Stability and Control Characteristics of Advanced Flight Vehicles. ASD-TDR-63-671, 1963. (C) Title Unclassified

2. Seeger, D. B., and Meyer, J. E.: An Investigation of the Subsonic Aerodynamic Characteristics and the Landing Flare Maneuver for Hypersonic Re-entry Configurations. ASD-TDR-62-271, 1962. (C) Title Unclassified

3. Mantz, K., and Seeger, D. B.: Tests to Determine the Subsonic Pressures, Forces and Moments Acting on a Hypersonic Re-entry Configuration. ASD-TDR-62-270, 1962. (C) Title Unclassified

4. Mantz, K., Seeger, D. B., and Ross, R.: Tests to Determine Subsonic Pressures, Forces and Moments Acting on a Hypersonic Re-entry Configuration. ASD-TDR-62-270, Supplement 1, 1963. (U)

5. Sipe, O. E., and Seeger, D. B.: Tests to Determine Subsonic Aerodynamic Characteristics of Hypersonic Re-entry Configurations. ASD-TR-61-485, 1961. (C) Title Unclassified

6. Mantz, K., Seeger, D. B., and Ross, R.: Tests to Determine Subsonic Aerodynamic Characteristics of Hypersonic Re-entry Configurations. ASD-TR-61-485, Supplement 1, 1963. (U)

7. Graham, D., and Koenig, D.G.: Tests in the Ames 40- by 80-Foot Wind Tunnel of an Airplane Configuration with an Aspect Ratio 2 Triangular Wing and an All-Movable Horizontal Tail – Lateral Characteristics. NACA RM A51L03, 1952. (U)

8. Jaquet, B. M., and Brewer, J. D.: Low-Speed Static-Stability and Rolling Characteristics of Low-Aspect-Ratio Wings of Triangular and Modified Triangular Plan Forms. NACA RM L8L29, 1949. (U)

9. McKinney, M. O., Jr., and Drake, H. M.: Flight Characteristics at Low Speed of Delta-Wing Models. NACA RM L7K07, 1948. (U)

10. Goodman, A., and Thomas, D.: Effects of Wing Position and Fuselage Size on the Low-Speed Static and Rolling Stability Characteristics of a Delta-Wing Model. NACA TR 1224, 1955. (U)

11. Lange/Wacke: Test Report on Three- and Six-Component Measurements on a Series of Tapered Wings of Small Aspect Ratio. (Partial Report: Triangular Wing.) NACA TM 1176, 1948. (U)

12. Whittle, E. F., Jr., and Lovell, J. C.: Full-Scale Investigation of an Equilateral Triangular Wing Having 10-Percent Thick Biconvex Airfoil Sections. NACA RM L8G05, 1948. (U)

13. Edwards, G. G., and Savage, H. F.: The Subsonic Aerodynamic Characteristics of Some Blunt Delta Configurations with 75° Sweepback. NASA TM X-581, 1961. (U)

14. McDevitt, J. B., and Rakich, J. V.: The Aerodynamic Characteristics of Several Thick Delta Wings at Mach Numbers to 6 and Angles of Attack to 50°. NASA TM X-162, 1960. (C) Title Unclassified

15. Keating, R. F. A.: Low-Speed Wind-Tunnel Tests on Sharp-Edged Gothic Wings of Aspect-Ratio 3/4. ARC CP 576, 1961. (U)

16. Olsted, W. B., Mugler, J. P., Jr., and Cahn, M. S.: Static Longitudinal and Lateral Stability Characteristics of a Right Triangular Pyramidal Lifting Re-entry Configuration at Transonic Speeds. NASA TN D-655, 1961. (U)

17. Ware, G. M.: Low-Subsonic-Speed Static Stability of Right-Triangular-Pyramid and Half-Cone Lifting Re-entry Configurations. NASA TN D-646, 1961. (U)

18. Paulson, J. W.: Low-Speed Static Stability and Control Characteristics of a Right Triangular Pyramid Re-entry Configuration. NASA Memo 4-11-59L, 1959. (U)

19. Anderson, A. E.: An Investigation at Low-Speed of a Large-Scale Triangular Wing of Aspect Ratio Two. – I. Characteristics of a Wing Having a Double-Wedge Airfoil Section with Maximum Thickness at 20-Percent Chord. NACA RM A7F06, 1947. (U)

TABLE 5.5.3.1-A

SUBSONIC YAWING MOMENT DUE TO SIDESLIP AT ZERO NORMAL FORCE

DELTA PLANFORM CONFIGURATIONS

DATA SUMMARY

Ref.	Configuration	A	b (in.)	$\frac{S_{B_S}}{S}$	$\frac{(S_{B_S})_{.2c_r}}{S_{B_S}}$	$x_{centroid_{S_{B_S}}}$ (in.)	$x_{centroid_W}$ (in.)	$K'_{n_{\beta_{N_0}}}$ Calc. (per rad)	$K'_{n_{\beta_{N_0}}}$ Test (per rad)	$\Delta K'_{n_{\beta_{N_0}}}$ Calc.-Test (per rad)
4	D-50	1.076	26.26	0.386	0.102	27.66	29.78	–0.164	–0.2407	0.0767
6	D-1	1.075	13.13	0.386	0.102	13.83	14.89	–0.164	–0.109	–0.055
	D-2	1.076	12.37	0.349	0.040	15.33	15.33	–0.141	–0.1485	0.0075
	D-5	1.076	13.13	0.386	0.102	13.83	14.89	–0.164	–0.223	0.059
	D-6	1.868	22.12	0.236	0.102	13.83	15.11	–0.020	0.0138	–0.0338
	WB-1	1.094	12.44	0.282	0.129	11.50	12.55	–0.041	–0.0705	0.0295
	WB-3	1.074	11.10	0.282	0.089	12.31	12.57	–0.059	–0.152	0.093
	WB-4	1.147	14.17	0.293	0.189	10.00	12.11	–0.005	–0.073	0.068
9	1	3.00	34.00	0.045	0.215	10.46	15.09	–0.003	0	–0.003
	4	2.00	27.20	0.050	0.215	10.46	14.72	–0.003	0	–0.003
	6	1.00	17.00	0.050	0.215	10.46	13.81	–0.005	0	–0.006
	8	0.50	27.70	0.070	0.212	13.00	18.47	–0.004	0	–0.004
10	Wing Alone	2.31	36.50	0.045	0.167	14.40	21.07	–0.0033	–0.0114	0.0081
11	1	3.00	59.06	0.108	0.207	16.54	26.24	–0.003	–0.012	0.009
	2	2.00	48.23	0.162	0.207	20.28	32.15	–0.004	–0.0287	0.0247
	3	1.33	39.37	0.244	0.207	24.82	39.37	–0.006	–0.0372	0.0312
	4	1.00	34.09	0.325	0.207	28.65	45.48	–0.008	–0.0344	0.0264
17	a	0.783	21.10	0.536	0.051	35.38	35.38	–0.718	–0.743	0.025
	b(basic)	0.783	21.10	0.491	0.051	35.38	35.38	–0.588	–0.585	0.019
	b(R=1.5 in.)	0.808	21.10	0.500	0.072	31.55	31.55	–0.524	–0.572	0.048
	d	0.783	21.10	0.581	0.051	35.38	35.38	–0.653	–0.709	0.056
18	1	0.780	21.10	0.528	0.051	35.38	35.38	–0.688	–0.615	–0.073
19	Wing Alone	2.00	26(ft)	0.050	0.128	10(ft)	16.67(ft)	–0.003	0	–0.003

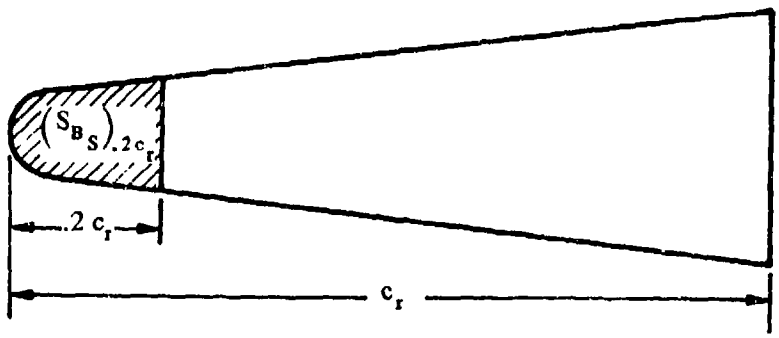

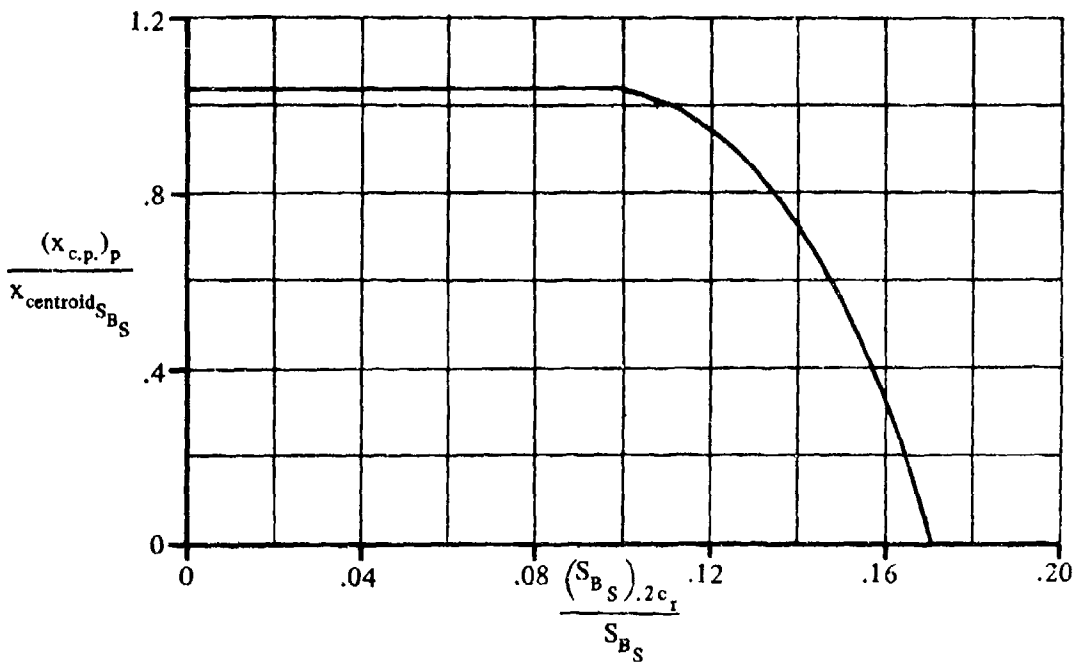

FIGURE 5.5.3.1-6 SIDE-FORCE CENTER OF PRESSURE DELTA AND MODIFIED DELTA CONFIGURATIONS

5.5.3.2 WING, WING-BODY SIDESLIP-DERIVATIVE K'_{n_β} VARIATION WITH ANGLE OF ATTACK

A. SUBSONIC

This section presents a method, taken from reference 1, for estimating the sideslip-derivative K'_{n_β} variation with angle of attack for delta and modified-delta configurations at subsonic speeds.

Although the pressure distribution over a configuration is altered as a result of the lifting process, test data show that side-force center-of-pressure location is not affected appreciably by normal force. Therefore, the change in directional stability is attributed to the change in side force due to sideslip as angle of attack is increased.

Because the location of the side-force center of pressure is considered to be independent of angle of attack, the relationships established in Section 5.5.3.1 for determining the location of the side-force center of pressure at zero normal force are also applicable to this section. Furthermore, the nature of the breakdown of the side force at zero normal force may also be applied at any angle of attack, and the expression for determining the directional stability at angle of attack is the same as that presented in Section 5.5.3.1 for determining K'_{n_β} at zero normal force.

The Datcom method is considered valid for sideslip angles between $\pm 5^o$ and angles of attack from 0 to 20^o.

DATCOM METHOD

The variation of the sideslip derivative K'_{n_β} with angle of attack, based on the product of planform area and span Sb and referred to a moment center at the nose of the configuration, for a delta or modified-delta configuration at subsonic speeds is given by

$$K'_{n_\beta} = \left(K_{Y_\beta} + 0.006\right)\frac{\left(x_{c.p.}\right)_p}{x_{centroid_{S_{B_S}}}}\frac{x_{centroid_{S_{B_S}}}}{b} - 0.006\frac{x_{centroid_W}}{b} \text{ (per radian)} \qquad 5.5\,3.2\text{-a}$$

where K_{Y_β} is the side force due to sideslip at angle of attack, obtained from Section 5.5.1.2, and all the remaining terms are described in Section 5.5.3.1.

A comparison of the variation of K'_{n_β} with normal-force variation calculated by using this method with test data is presented as table 5.5.3.2-A.

The comments pertaining to nonlinearities in the variation of side force with sideslip in Section 5.5.1.2 also apply to the side-force center-of-pressure location.

Sample Problem

Given: A delta-series model of reference 6 designated D-2. This is the configuration of the sample problem of Section 5.5.3.1.

$S = 142.3$ sq in. $\quad S_{B_S} = 49.68$ sq in. $\quad (S_{B_S})_{.2c_r} = 1.99$ sq in.

$c_r = 23.0$ in. $\quad b = 12.374$ in. $\quad \delta_{e_\perp} = 58^\circ$

The following results from the sample problem of Section 5.5.3.1:

$$K_{Y_{\beta_{N_0}}} = -0.110 \text{ per rad} \qquad \frac{(x_{c.p.})_p}{x_{centroid_{S_{B_S}}}} = 1.04$$

$$x_{centroid_{S_{B_S}}} = x_{centroid_W} = 15.33 \text{ in.} \qquad S_{B_S}/S = 0.349$$

Compute:

$$\left[\frac{\Delta K_{Y_\beta}}{(C_{N'})^2}\right]_{20} = 0.335 \text{ per rad} \quad \text{(figure 5.5.1.2-9)}$$

$$K_{Y_\beta} = K_{Y_{\beta_{N_0}}} + \left[\frac{\Delta K_{Y_\beta}}{(C_{N'})^2}\right]_{20} (C_{N'})^2 \quad \text{(equation 5.5.1.2-a)}$$

$$= -0.110 + (0.335)(C_{N'})^2$$

① $C_{N'}$	② $(C_{N'})^2$ ① ^{2}	③ $(0.335)(C_{N'})^2$ 0.335 ②	④ K_{Y_β} (based on S) −0.110 + ③
0	0	0	−0.110
0.2	0.04	0.0134	−0.097
0.4	0.16	0.0536	−0.056
0.6	0.36	0.1206	0.011

Solution:

$$K'_{n_\beta} = (K_{Y_\beta} + 0.006)\frac{(x_{c.p.})_p}{x_{centroid_{S_{B_S}}}}\frac{x_{centroid_{S_{B_S}}}}{b} - 0.006\frac{x_{centroid_W}}{b} \quad \text{(equation 5.5.3.2-a)}$$

$$= (K_{Y_\beta} + 0.00\,)(1.04)\,\frac{15.33}{12.374} - 0.006\,\frac{15.33}{12.374}$$

$$= 1.288\,K_{Y_\beta} + 0.0003$$

① $C_{N'}$	② K_{Y_β} (based on S) (per rad)	③ $1.288\,K_{Y_\beta}$ 1.288 ②	④ K'_{n_β} (based on Sb) (per rad) ③ +0.0003
0	–0.110	–0.1417	–0.1414
0.2	–0.097	–0.1249	–0.1246
0.4	–0.056	–0.0721	–0.0718
0.6	0.011	0.0142	0.0145

The calculated results are compared with test values in sketch (a) and in table 5.5.3.2-A.

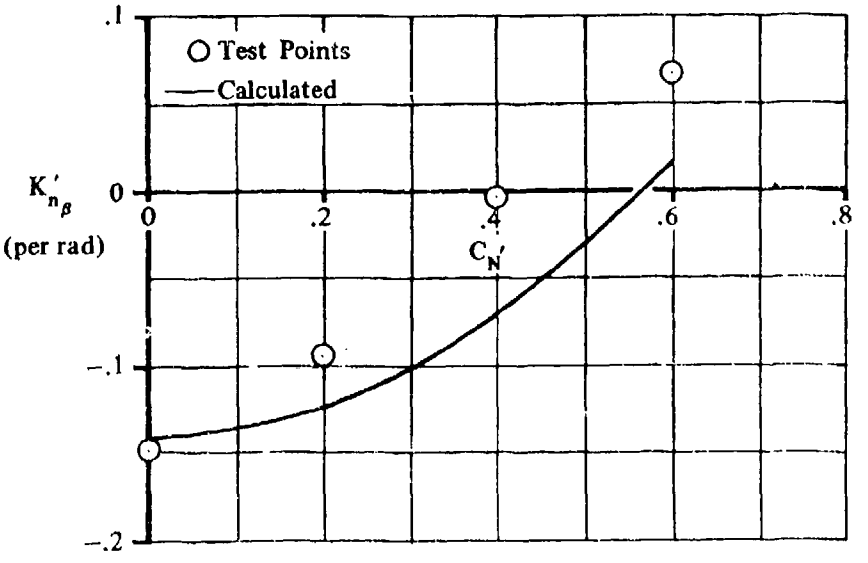

SKETCH (a)

REFERENCES

1. Seeger, D. B., and Ross, R.: Investigation of the Low-Speed Stability and Control Characteristics of Advanced Flight Vehicles. ASD-TDR-63-671, 1963. (C) Title Unclassified

2. Seeger, D. B., and Meyer, J. E.: An Investigation of the Subsonic Aerodynamic Characteristics and the Landing Flare Maneuver for Hypersonic Re-entry Configurations. ASD-TDR-62-271, 1962. (C) Title Unclassified

3. Mantz, K., and Seeger, D. B.: Tests to Determine the Subsonic Pressures, Forces and Moments Acting on a Hypersonic Re-entry Configuration. ASD-TDR-62-270, 1962. (C) Title Unclassified

4. Mantz, K., Seeger, D. B., and Ross, R.: Tests to Determine Subsonic Pressures, Forces and Moments Acting on a Hypersonic Re-entry Configuration. ASD-TDR-62-270, Supplement 1, 1963. (U)

5. Sipe, O. E., and Seeger, D. B.: Tests to Determine Subsonic Aerodynamic Characteristics of Hypersonic Re-entry Configurations. ASD-TR-61-485, 1961. (C) Title Unclassified

6. Mantz, K., Seeger, D. B., and Ross, R.: Tests to Determine Subsonic Aerodynamic Characteristics of Hypersonic Re-entry Configurations. ASD-TR-61-485, Supplement 1, 1963. (U)

7. Graham, D., and Koenig, D. G.: Tests in the Ames 40- by 80-Foot Wind Tunnel of an Airplane Configuration with an Aspect Ratio 2 Triangular Wing and an All-Movable Horizontal Tail — Lateral Characteristics. NACA RM A51L03, 1952. (U)

8. Jaquet, B. M., and Brewer, J. D.: Low-Speed Static-Stability and Rolling Characteristics of Low-Aspect-Ratio Wings of Triangular and Modified Triangular Plan Forms. NACA RM L8L29, 1949. (U)

9. McKinney, M. O., Jr., and Drake, H. M.: Flight Characteristics at Low Speed of Delta-Wing Models. NACA RM L7K07, 1948. (U)

10. Keating, R. F. A.: Low-Speed Wind-Tunnel Tests on Sharp-Edged Gothic Wings of Aspect-Ratio 3/4. ARC CP 576, 1961. (U)

11. Goodman, A., and Thomas, D.: Effects of Wing Position and Fuselage Size on the Low-Speed Static and Rolling Stability Characteristics of a Delta-Wing Model. NACA TR 1224, 1955. (U)

12. Whittle, E. F., Jr., and Lovell, J. C.: Full-Scale Investigation of an Equilateral Triangular Wing Having 10-Percent Thick Biconvex Airfoil Sections. NACA RM L8G05, 1948. (U)

13. Olstad, W. B., Mugler, J. P., Jr., and Cahn, M. S.: Static Longitudinal and Lateral Stability Characteristics of a Right Triangular Pyramidal Lifting Re-entry Configuration at Transonic Speeds. NASA TN D-665, 1961. (U)

14. Ware, G. M.: Low-Subsonic-Speed Static Stability of Right-Triangular-Pyramid and Half-Cone Lifting Re-entry Configurations. NASA TN D-546, 1961. (U)

15. Edwards, G. G., and Savege, H. F.: The Subsonic Aerodynamic Characteristics of Some Blunt Delta Configurations with 75° Sweepback. NASA TM X-581, 1961. (U)

16. McDevitt, J. B., and Rakich, J. V.: The Aerodynamic Characteristics of Several Thick Delta Wings at Mach Numbers to 6 and Angles of Attack to 50°. NASA TM X-162, 1960. (C) Title Unclassified

TABLE 5.5.3.2-A

SUBSONIC YAWING MOMENT WITH RESPECT TO SIDESLIP
VARIATION WITH ANGLE OF ATTACK

DELTA PLANFORM CONFIGURATIONS

DATA SUMMARY*

Ref.	Configuration	A	$C_{N'}$	K'_{n_β} Calc. (per rad)	K'_{n_β} Test (per rad)	$\Delta K'_{n_\beta}$ Calc.-Test (per rad)
4	D-60	1.076	0	−0.164	−0.2407	0.0767
			0.2	−0.164	−0.2196	0.0556
			0.4	−0.164	−0.2036	0.0395
			0.6	−0.164	—	—
6	D-1	1.075	0	−0.164	−0.109	−0.055
			0.2	−0.164	−0.1024	−0.0616
			0.4	−0.164	−0.1257	−0.0384
			0.6	−0.164	−0.1786	0.0146
	D-2	1.076	0	−0.1414	−0.1485	0.0071
			0.2	−0.1246	−0.0947	−0.0299
			0.4	−0.0718	−0.0040	−0.0678
			0.6	0.0145	0.0662	−0.0517
	D-5	1.076	0	−0.164	−0.233	0.069
			0.2	−0.135	−0.214	0.079
			0.4	−0.0489	−0.1963	0.1474
			0.6	0.084	—	—
	D-6	1.868	0	−0.0200	0.0138	−0.0338
			0.2	−0.0224	0.031	−0.0534
			0.4	−0.0309	0.0368	−0.0677
			0.6	−0.0452	0.0279	−0.0731
14	a	0.783	0	−0.718	−0.743	0.025
			0.2	−0.744	−0.937	0.193
			0.4	−0.941	−1.006	0.065
			0.6	−1.220	−1.018	−0.202

TABLE 5.5.3.2-A (CONTD)

Ref.	Configuration	A	$C_{N'}$	K'_{n_β} Calc. (per rad)	K'_{n_β} Test (per rad)	$\Delta K'_{n_\beta}$ Calc.-Test (per rad)
14	b(basic)	0.783	0	−0.586	−0.585	0.019
			0.2	−0.615	−0.760	0.145
			0.4	−0.762	−0.875	0.113
			0.6	−1.006	−0.950	−0.056
	b(R=1.5 in.)	0.808	0	−0.524	−0.572	0.048
			0.2	−0.568	−0.765	0.197
			0.4	−0.700	−0.912	0.212
			0.6	−0.921	−0.962	0.041

5.6 WING-BODY-TAIL COMBINATIONS IN SIDESLIP

5.6.1 WING-BODY-TAIL SIDESLIP DERIVATIVE C_{Y_β}

5.6.1.1 WING-BODY-TAIL SIDESLIP DERIVATIVE C_{Y_β} IN THE LINEAR ANGLE-OF-ATTACK RANGE

The information contained in this Section is for estimating the side-force-curve slope C_{Y_β} of wing-body-tail combinations at low angles of attack. In general, it consists of a synthesis of material presented in other Sections. The method of Section 5.3.1.1 based on the apparent-mass concept for the determination of increments in C_{Y_β} due to the addition of one panel to an empennage is extended herein to determine the total empennage sideslip derivative C_{Y_β} at low angles of attack resulting from the addition of all the panels present in the empennage. The methods presented include the mutual interference effects of other vehicle components.

The main contributions to the derivative C_{Y_β} will come from the fuselage and the vertical stabilizers. The wing contribution is a function of α^2 and can usually be neglected at low angle of attack. A discussion of the various aerodynamic aspects associated with the build-up of vehicle components in relation to side force are discussed in Sections 5.2.1.1 and 5.3.1.1 and are not repeated here.

The methods presented herein are based on the procedure of totaling the coefficient of the wing-body configuration and the incremental coefficient of the total empennage resulting from the addition of all panels present in the empennage.

A. SUBSONIC

Three methods of estimating the subsonic derivative C_{Y_β} of a complete configuration are presented, differing in their treatment of the incremental coefficient of the total empennage. Methods 1 and 2 treat the mutual interference effects of the wing-body wake and sidewash independently of the body and horizontal tail end-plate effects and lump the total empennage increment into a single parameter. On the other hand, Method 3 utilizes a build-up procedure to determine the total empennage increment wherein the mutual interference effects are lumped into a single effectiveness parameter for each panel in the empennage.

DATCOM METHODS

Method 1

For configurations with a single vertical stabilizer and with horizontal-stabilizer height ranging from positions on the body to the top of the vertical stabilizer or configurations with a single vertical stabilizer and with no horizontal stabilizer the side force due to sideslip is given by

$$C_{Y_\beta} = (C_{Y_\beta})_{WB} + (\Delta C_{Y_\beta})_{VOLBD} \qquad 5.6.1.1\text{-a}$$

where

$(C_{Y_\beta})_{WB}$ is obtained from Section 5.2.1.1

$(\Delta C_{Y_\beta})_{VOLBD}$ is the total empennage increment in C_{Y_β} obtained from Method 1, paragraph A, Section 5.3.1.1

Method 2

For configurations with twin vertical panels mounted on the tips of a horizontal tail or wing the side force due to sideslip is given by equation 5.6.1.1-a

$$C_{Y_\beta} = (C_{Y_\beta})_{WB} + (\Delta C_{Y_\beta})_{VOLBD}$$

where

$(\Delta C_{Y_\beta})_{VOLBD}$ is the total empennage increment in C_{Y_β} obtained from Method 2, paragraph A, Section 5.3.1.1

Method 3

The estimation of the total empennage side-force derivative by this method is based on the apparent-mass concept for the determination of increments in C_{Y_β} due to the addition of one panel to an empennage, presented as Method 3 of paragraph A of Section 5.3.1.1. That method is extended herein to determine the total sideslip derivative C_{Y_β} resulting from the addition of all panels present in the empennage. The method is limited to configurations in which the horizontal tail is mounted on the body or configurations with no horizontal tail.

The total empennage contribution to C_{Y_β} is obtained by adding the increments gained by successive additions of the panels in the empennage to the wing-body configuration. The order of build-up should proceed as follows:

1. Determine the increment in C_{Y_β} due to adding the horizontal stabilizer to the wing-body configuration, $(\Delta C_{Y_\beta})_{H(WB)}$
2. Determine the increment in C_{Y_β} due to adding the upper vertical stabilizing surface to the combination of wing, body, and horizontal stabilizer, $(\Delta C_{Y_\beta})_{V(WBH)}$
3. Determine the increment in C_{Y_β} due to adding the lower vertical stabilizing surface to the combination of wing, body, horizontal stabilizer, and upper vertical stabilizer, $(\Delta C_{Y_\beta})_{(V)(WBHV)}$

The side force due to sideslip for the complete configuration is given by

$$C_{Y_\beta} = (C_{Y_\beta})_{WB} + \Sigma_p (\Delta C_{Y_\beta})_p \qquad 5.6.1.1\text{-b}$$

where the subscript p refers to the panels present in the empennage

$(C_{Y_\beta})_{WB}$ is obtained from Section 5.2.1.1

$(\Delta C_{Y_\beta})_p$ is the increment in C_{Y_β} gained by successive additions of the panels in the empennage obtained from Method 3, paragraph A, Section 5.3.1.1

For a wingless configuration, $(\Delta C_{Y_\beta})_p$ is based on the vehicle reference area and the contribution of the body to the total derivative can be obtained from Section 4.2.1.1 as $(C_{Y_\beta})_B = -(C_{L_\alpha})_B$, based on the vehicle reference area.

Sample Problems

1. Method 1

Given: A configuration of reference 1 consisting of wing, body, horizontal tail, and vertical tail.

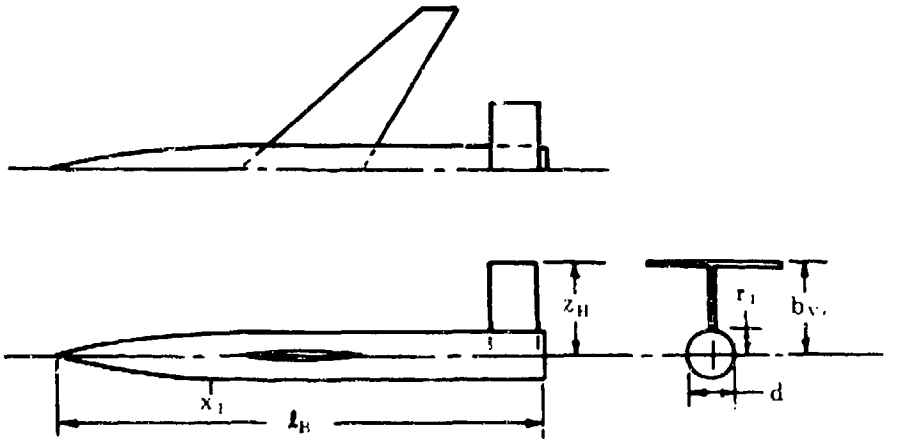

Wing Characteristics

$A_W = 4.00$ $S_W = 36.0$ sq in. $\Lambda_{c/4_W} = 45°$ $\Gamma = 0$ $z_W = 0$

Horizontal Tail Characteristics

$A_H = 2.78$ $S_H = 9.0$ sq in. $z_H = -3.30$ in.

Vertical Tail Characteristics

$A_V = 1.835$ $S_V = 5.94$ sq in. $\Lambda_{c/2_V} = 0$ $b_V = 3.30$ in. $\lambda_V = 1.00$

NACA 65A006 airfoil

Body Characteristics

$\ell_B = 18.25$ in. $x_1 = 5.83$ in. $V_B^{2/3} = 10.4$ sq in. $d = 1.667$ in.

Additional Characteristics

$M = 0.60$ $r_1 = 0.8335$ in. $x/c_v = 0.25$

Compute:

Step 1. Determine the wing-body contribution to C_{Y_β} using the method of Section 5.2.1.1.

$K_i = 1.0$ (midwing)

$f = \frac{\ell_B}{d} = 10.95$

$(k_2 - k_1) = 0.95$ (figure 4.2.1.1-20a)

$x_1/\ell_B = 0.319$

$x_0/\ell_B = 0.545$ (figure 4.2.1.1-20b)

$x_0 = (0.545)(18.25) = 9.95$ in.

$S_0 = \pi\left(\frac{d}{2}\right)^2 = 2.18$ sq in.

$$(C_{Y_\beta})_{WB} = K_i(C_{Y_\beta})_B\left(\frac{\text{Body Reference Area}}{S_w}\right) + (\Delta C_{Y_\beta})_\Gamma \qquad \text{(equation 5.2.1.1-a)}$$

$$= K_i\left(\frac{-2\,(k_2 - k_1)\,S_0}{V_B^{2/3}}\right)\left(\frac{V_B^{2/3}}{S_w}\right) + (\Delta C_{Y_\beta})_\Gamma$$

$$= 1.00\left(\frac{(-2)(0.95)(2.18)}{10.4}\right)\left(\frac{10.4}{36.0}\right) + 0$$

$= -0.115$ per rad (based on S_w)

Step 2. Determine the total empennage contribution to C_{Y_β} using Method 1, Paragraph A, Section 5.3.1.1.

$(c\ell_\alpha)_V = 6.57$ per rad (Section 4.1.1.2)

$\kappa = \frac{(c\ell_\alpha)_V}{2\pi} = 1.05$ (ratio of incompressible section lift-curve slope to 2π)

$b_V/2r_1 = 1.98$

$k = 0.76$ (figure 5.3.1.1-22d)

$\frac{(A)_{V(B)}}{A_V} = 1.50$ (figure 5.3.1.1-22a)

$(A)_{V(B)} = 1.50\,(A_V) = 2.75$

$S_H/S_V = 1.518$

$K_H = 1.06$ (figure 5.3.1.1-22c)

$z_H/b_V = -1.00$

$\frac{(A)_{V(HB)}}{(A)_{V(B)}} = 1.70$ (figure 5.3.1.1-22b)

$S_V/S_W = 0.165$

$z_W/d = 0$

$$A_{eff} = (A)_{V(B)} \left\{ 1 + K_H \frac{(A)_{V(HB)}}{(A)_{V(B)}} - 1 \right\} \qquad \text{(equation 5.3.1.1-a)}$$

$$= 2.75 \{1 + 1.06 [1.70 - 1]\} = 4.79$$

$$\frac{A_{eff}}{K} [\beta^2 + \tan^2 \Lambda_{c/2_V}]^{1/2} = 3.65$$

$\frac{(C_{L_\alpha})_V}{A_{eff}} = 1.02$ per rad (figure 4.1.3.2-49)

$(C_{L_\alpha})_V = 4.88$ per rad

$$\left(1 + \frac{\partial \sigma}{\partial \beta}\right) \frac{q_V}{q_\infty} = 0.724 + 3.06 \frac{S_V/S_W}{1 + \cos \Lambda_{c/4_W}} + 0.4 \frac{z_W}{d} + 0.009 A_W \qquad \text{(equation 5.4.1-a)}$$

$$= 0.724 + 3.06 \frac{(0.165)}{(1.707)} + 0 + 0.036$$

$$= 1.056$$

$$(\Delta C_{Y_\beta})_{V(WBH)} = -k (C_{L_\alpha})_V \left(1 + \frac{\partial \sigma}{\partial \beta}\right) \frac{q_V}{q_\infty} \frac{S_V}{S_W} \qquad \text{(equation 5.3.1.1-b)}$$

$$= -(0.76)(4.88)(1.056)(0.165)$$

$$= -0.645 \text{ per rad (based on } S_W)$$

Solution:

$$C_{Y_\beta} = (C_{Y_\beta})_{WB} + (\Delta C_{Y_\beta})_{V(WBH)} \qquad \text{(equation 5.6.1.1-a)}$$

$$= -0.115 - 0.645$$

$$= -0.760 \text{ per rad (based on } S_W)$$

The experimental results (based on S_W) from reference 1, are $(C_{Y_\beta})_{WB} = -0.143$ per radian, $(\Delta C_{Y_\beta})_{V(WBH)} = -0.716$ per radian, and $C_{Y_\beta} = -0.859$ per radian.

2. Method 2

Given: A configuration of reference 1, consisting of wing, body, horizontal tail, and twin vertical tails mounted o the tips of the horizontal tail. The wing and body are identical to those of sample problem 1 and their characteristics are not repeated.

Vertical Tail Characteristics

$b_V = 2.00$ in.	$b_V' = 1.00$ in.	$S_V = 3.60$ sq in.	$A_V = 1.11$
NACA 65A006 airfoil		$\phi_{TE_V} = 7^\circ$	

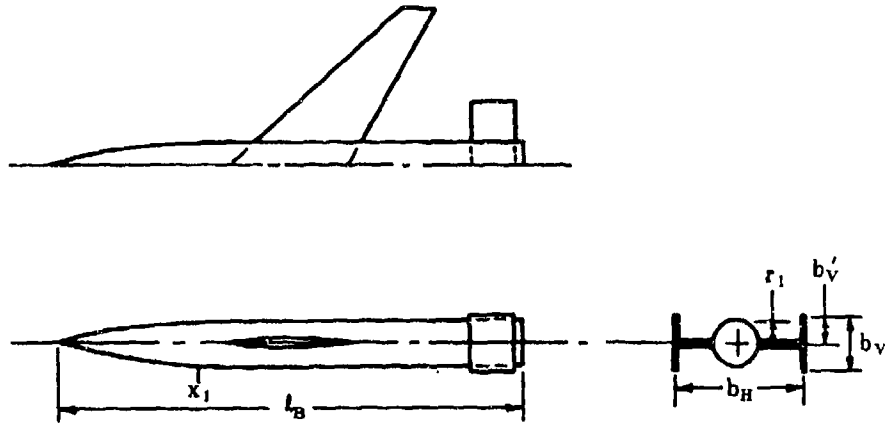

Additional Characteristics

r_1 = 0.8335 in. b_H = 4.80 in. M = 0.60

Compute:

Step 1. Determine the wing-body contribution to C_{Y_β} using the Method of Section 5.3.1.1.

$(C_{Y_\beta})_{WB}$ = -0.115 per rad (sample problem 1)

Step 2. Determine the total empennage contribution to C_{Y_β} using Method 2, paragraph A, Section 5.3.1.1.

b_V'/b_V = 0.50

$\frac{A_{eff}}{A}$ = 1.0 (figure 5.3.1.1-24a)

A_{eff} = 1.11

$(C_{Y_\beta})_{V_{eff}}$ = 1.78 per rad (figure 5.3.1.1-24b)

$2r_1/b_V$ = 0.8335

$\frac{b_H}{\ell_B} = \frac{4.80}{18.25}$ = 0.263

$\frac{(C_{Y_\beta})_{V(WBH)}}{(C_{Y_\beta})_{V_{eff}}}$ = 0.595 (figure 5.3.1.1-24c)

$$(\Delta C_{Y_\beta})_{V(WBH)} = -\frac{(C_{Y_\beta})_{V(WBH)}}{(C_{Y_\beta})_{V_{eff}}} (C_{Y_\beta})_{V_{eff}} \frac{2S_V}{S_W} \qquad \text{(equation 5.3.1.1-c)}$$

$$= -(0.595)\,(1.78)\,\frac{2(3.60)}{36.0}$$

= -0.212 per rad (based on S_W)

Solution:

$$C_{Y_\beta} = (C_{Y_\beta})_{WB} + (\Delta C_{Y_\beta})_{V(WBH)} \qquad \text{(equation 5.3.1.1-a)}$$

= -0.115 - 0.212

= -0.327 per rad (based on S_W).

The experimental results (based on S_W) from reference 1 are $(C_{Y_\beta})_{WB} = -0.143$ per radian, $(\Delta C_{Y_\beta})_{V(WBH)} = -0.258$ per radian, and $C_{Y_\beta} = -0.401$ per radian.

3. Method 3

Given: The configuration of reference 2, consisting of wing, body, horizontal tail, and upper vertical tail.

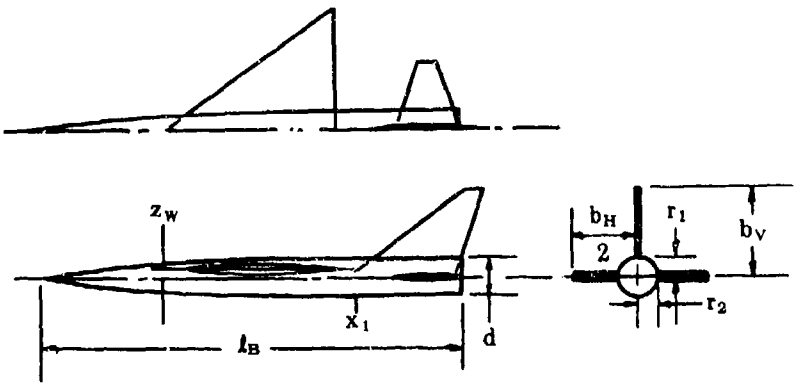

Wing Characteristics

$A_W = 3.0$ $S_W = 576$ sq in. $z_W = -2.08$ in. $\Gamma = 0$

Horizontal Tail Characteristics

$A_H = 4.0$ $b_H/2 = 11.21$ in. $z_H = 0$

Vertical Tail Characteristics

$A_V = 1.50$ $A_{V_e} = 1.43$ $S_V = 153.7$ sq in. $S_{V_e} = 109.7$ sq in.

$\Lambda_{\alpha/2_V} = 41.9^\circ$ $\lambda_V = 0.16$ $\lambda_{V_e} = 0.189$ $b_V = 15.23$ in.

NACA 0003.5-64 airfoil

Body Characteristics

$l_B = 72.0$ in. $x_1 = 54.0$ in. $V_B^{2/3} = 133.0$ sq in. $d = 6.0$ in.

Additional Characteristics

$M = 0.25$ $r_1 = 2.76$ in. $r_2 = 2.76$ in

Compute:

Step 1. Determine the wing-body contribution to C_{Y_β} using the method of Section 5.2.1.1.

$$\frac{z_W}{d/2} = \frac{-2.08}{3.0} = -0.694$$

$K_1 = 1.58$ (figure 5.2.1.1-7)

$$f = \frac{l_B}{d} = 12.0$$

$k_2 - k_1 = 0.955$ (figure 4.2.1.1-20a)

$x_1/l_B = 0.75$

$x_0/\ell_B = 0.765$ (figure 4.2.1.1-20b)

$x_0 = (0.765)(72.0) = 55.08$ in.

$S_0 = \pi\left(\frac{d}{2}\right)^2 = 28.28$ sq in.

$$(C_{Y_\beta})_{WB} = K_I (C_{Y_\beta})_B \left(\frac{\text{Body Reference Area}}{S_W}\right) + (\Delta C_{Y_\beta})_\Gamma \qquad \text{(equation 5.2.1.1-a)}$$

$$= K_I \left(\frac{-2(k_2 - k_1) S_0}{V_B^{2/3}}\right)\left(\frac{V_B^{2/3}}{S_W}\right) + (\Delta C_{Y_\beta})_\Gamma$$

$$= 1.58\left(\frac{(-2)(0.955)(28.28)}{133.0}\right)\left(\frac{133.0}{576.0}\right) + 0$$

$$= -0.1480 \text{ per rad (based on } S_W)$$

Step 2. Determine the total empennage contribution to C_{Y_β} using Method 3, paragraph A, Section 5.3.1.1 to determine the contributions of individual panels.

$(c\ell_\alpha)_V = 6.18$ per rad (Section 4.1.1.2)

$$\kappa = \frac{(c\ell_\alpha)_V}{2\pi} = 0.984 \text{ (ratio of incompressible section lift-curve slope to } 2\pi)$$

$2A_{V_e} = 2.86$

$$\frac{2A_{V_e}}{\kappa}\left[\beta^2 + \tan^2 \Lambda_{c/2_V}\right]^{1/2} = 3.84$$

$$\frac{(C_{L_\alpha})_V}{2A_{V_e}} = 0.995 \text{ per rad (figure 4.1.3.2-49)}$$

$(C_{L_\alpha})_V = (0.995)(2A_{V_e}) = 2.85$ per rad (based on S_{V_e})

Determine the increment in C_{Y_β} due to adding the horizontal tail to the wing-body configuration. In this case the empennage consists of the body and the horizontal tail. The apparent-mass ratio to be found is that due to adding the horizontal tail to the body, $K_{H(B)}$.

$z_H/r_1 = 0$

$K_{H(B)} = 0$ (figure 5.3.1.1-25oo)

$$(\Delta C_{Y_\beta})_{H(WB)} = K_{H(B)} (C_{Y_\beta})_B \frac{S_{B_{Ref}}}{S_W} \qquad \text{(equation 5.3.1.1-e)}$$

$$= 0$$

Determine the increment in C_{Y_β} due to adding the upper vertical stabilizer to the wing-body-horizontal tail configuration. In this case the empennage consists of body, horizontal tail, and upper vertical stabilizer. The apparent-mass ratio to be found is that due to adding the upper vertical stabilizer to the combination of body and horizontal tail, $K_{V(BH)}$.

$$r_1/r_2 = 1.000;\ \frac{r_2}{b_H/2} = 0.246;\ (r_1/b)_{V_{\substack{\text{existing}\\\text{panel}}}} = 1.000;\ (r_1/b)_{V_{\substack{\text{added}\\\text{panel}}}} = 0.181$$

By using the above parameters and Table 5.3.1.1-A, $K_{V(BH)}$ can be obtained from figures 5.3.1.1-25b, -25c, and -25d interpolated for a value of $\frac{r_2}{b_H/2} = 0.246$.

$K_{V(BH)} = 1.225$

$$(\Delta C_{Y_\beta})_{V(WBH)} = -K_{V(BH)} (C_{L_\alpha})_V \frac{S_{V_e}}{S_W} \qquad \text{(equation 5.3.1.1-d)}$$

$$= -(1.225)(2.85) \frac{109.7}{576}$$

$$= -0.665 \text{ per rad (based on } S_W)$$

Solution:

$$C_{Y_\beta} = (C_{Y_\beta})_{WB} + \Sigma_p (\Delta C_{Y_\beta})_p \qquad \text{(equation 5.6.1.1-b)}$$

$$= (C_{Y_\beta})_{WB} + (\Delta C_{Y_\beta})_{H(WB)} + (\Delta C_{Y_\beta})_{V(WBH)}$$

$$= -0.1480 + 0 - 0.665$$

$$= -0.813 \text{ per rad (based on } S_W)$$

The experimental results (based on S_W) from reference 2 are $(C_{Y_\beta})_{WB} = -0.149$ per radian, $(\Delta C_{Y_\beta})_{V(WBH)} = -0.556$ per radian, and $C_{Y_\beta} = -0.705$ per radian.

B. TRANSONIC

A brief discussion of the flow phenomena associated with forces generated on a vertical panel at transonic speeds is given in paragraph B of Section 5.3.1.1. The effect of wing-body wake and sidewash, and the mutual interference effects between component combinations at transonic sp[illegible] are extremely sensitive to changes in local contour.

At the present time these effects cannot be predicted with accuracy and the vehicle sideslip derivative C_{Y_β} is usually obtained by wind-tunnel testing or estimated from comparison with similar configurations.

DATCOM METHOD

No method is available in the literature for estimating the vehicle sideslip derivative C_{Y_β} at transonic speeds and none is presented in the Datcom. Some typical transonic data for this derivative are presented as figure 5.6.1.1-14.

C. SUPERSONIC

The procedure for estimating the supersonic sideslip derivative C_{Y_β} of a wing-body-tail configuration is essentially the same as that at subsonic speeds. The problem of estimating the contribution of the empennage is complicated by the presence of shock waves. This effect is discussed in paragraph C of Section 5.3.1.1.

DATCOM METHOD

The side force due to sideslip for the complete configuration at supersonic speeds is given by equation 5.6.1.1-b

$$C_{Y_\beta} = (C_{Y_\beta})_{WB} + \Sigma_p (\Delta C_{Y_\beta})_p$$

where the subscript p refers to panels present in the empennage

$(C_{Y_\beta})_{WB}$ is obtained from Section 5.2.1.1

$(\Delta C_{Y_\beta})_p$ are the increments in C_{Y_β} gained by successive additions of the panels in the empennage obtained from paragraph C, Section 5.3.1.1

The order of configuration build-up will generally proceed as outlined for subsonic speeds (Method 3, paragraph A). The one exception to that build-up procedure is the case at supersonic speeds where the vertical panels are stag-

gered along the body so that their leading edges intersect the body at different locations. In this case, the panel whose leading edge intersects the body farthest aft is added first.

This method is limited to configurations in which the horizontal tail is mounted on the body or configurations with no horizontal tail.

For a wingless configuration the remarks following the Datcom methods of paragraph A above are also applicable at supersonic speeds.

Sample Problem

Given: The configuration of reference 3 consisting of wing, body, horizontal tail upper vertical tail, and lower vertical tail.

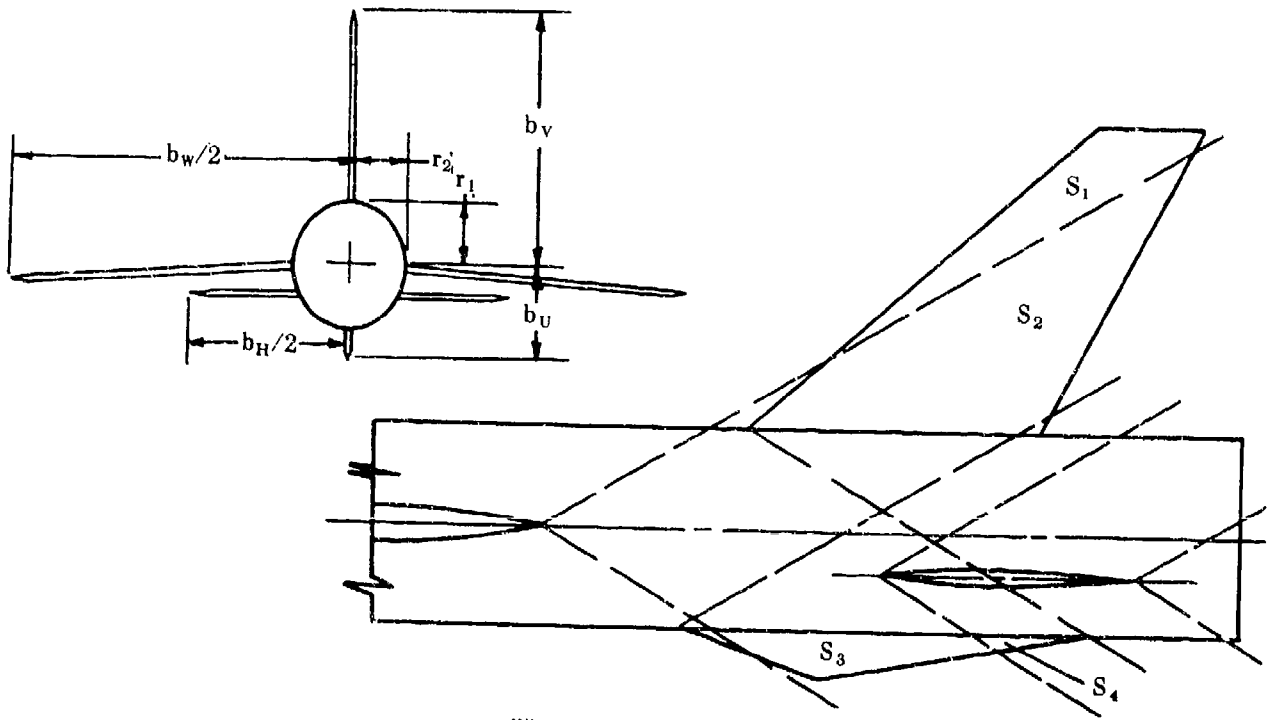

Wing Characteristics

$A_W = 3.18$	$S_W = 114.5$ sq in.	$b_W = 19.08$ in.	$z_W = 0$	$\Gamma = -3.5°$

Horizontal Tail Characteristics

$A_H = 3.06$	$b_H = 9.12$ in.	$z_H = 0.84$ in.

Vertical Tail Characteristics

$A_{V_e} = 1.48$	$S_{V_e} = 19.20$ sq in.	$\Lambda_{LE_V} = 49.2°$	$b_V = 7.08$ in.	$\lambda_{V_e} = 0.392$

Ventral Tail Characteristics

$A_{U_e} = 0.2025$	$S_{U_e} = 3.24$ sq in.	$\Lambda_{LE_U} = 70.2°$	$b_U = 2.56$ in.	$\lambda_U = 0$

Additional Characteristics

$M = 2.01$	$\mu = \sin^{-1} 1/M = 29.8°$	$r_1 = 1.75$ in.	$r_2 = 1.496$ in.
$r_1/r_2 = 1.170$	$S_1 = 4.63$ sq in.	$S_2 = 14.56$ sq in.	$S_3 = 2.74$ sq in.
$S_4 = 0.50$ sq in.	$\frac{S_{act}}{S_{ext}} = 0.875$		

Compute:

Step 1. Determine the wing-body contribution to C_{Y_β}.

The Datcom does not present methods at supersonic speeds that will predict the side-force characteristics of the wing-body configuration of this sample problem. In such cases it is suggested that test results of a similar configuration be used, if available, and corrected for the difference in relative size of the fuselage and wing for the two configurations. If the vertical location of the wing on the fuselage is not similar, a correction for wing-fuselage interference must also be made.*

An experimental result for $(C_{Y_\beta})_{WB}$ is not available for this configuration. Use is made of the experimental result for $(C_{Y_\beta})_{WBH}$. However, the increment due to adding the horizontal tail to the wing-body configuration will be computed for the sake of completeness.

$(C_{Y_\beta})_{\substack{WBH \\ test}} = -0.315$ per rad (based on S_W)

Step 2. Determine the total empennage contribution to C_{Y_β} using the method of paragraph C, Section 5.3.1.1 to determine the contributions of individual panels.

Upper Vertical Panel

$2A_{V_e} \tan \Lambda_{LE_V} = 3.42$

$\dfrac{\tan \Lambda_{LE_V}}{\beta} = \dfrac{1.1585}{1.744} = 0.664$

$\beta(C_{N_\alpha})_V = 4.10$ per rad

(figures 4.1.3.2-56c,-56d, -56e interpolated for $\lambda_{V_e} = 0.392$)

$(C_{N_\alpha})_V = 2.35$ per rad (based on S_{V_e})

Lower Vertical Panel

$2A_{U_e} \tan \Lambda_{LE_U} = 1.125$

$\dfrac{\beta}{\tan \Lambda_{LE_U}} = 0.628$

$\tan \Lambda_{LE_U} (C_{N_\alpha})_U = 1.73$ per rad (figure 4.1.3.2-56d)

$(C_{N_\alpha})_U = 0.622$ per rad (based on S_{U_e})

Determine the increment in C_{Y_β} due to adding the horizontal tail to the wing-body configuration. In this case the empennage consists of the body and the horizontal tail. The apparent-mass ratio to be found is that due to adding the horizontal tail to the body, $K_{H(B)}$.

$\left(\dfrac{z_H}{r_1}\right) = \dfrac{0.84}{1.75} = 0.480; \left(\dfrac{r_2}{b_H/2}\right) = \dfrac{1.496}{4.56} = 0.328$

From figure 5.3.1.1-25oo, values of $K_{H(B)}$ are obtained for $\left(\dfrac{z_H}{r_1}\right) = 1.0, 0, -1.0$ at $\left(\dfrac{r_2}{b_H/2}\right) = 0.328$

Since K charts are not presented for the case of a horizontal surface added to an elliptical body the body is considered circular and an interpolation is performed to obtain

$K_{H(B)}$ at $\left(\dfrac{z_H}{r_1}\right) = 0.480$**

$K_{H(B)} = 0.130$

The side-force-curve slope of the body is given by slender-body theory. $(C_{Y_\beta})_B = -2$ per rad (based on S_B)

$(\Delta C_{Y_\beta})_{H(WB)} = K_{H(B)} (C_{Y_\beta})_B \dfrac{S_{B_{Ref}}}{S_W} \dfrac{S_{act}}{S_{ext}}$ (equation 5.3.1.1-g)

$= (0.130)(-2)\left(\dfrac{\pi r_1 r_2}{114.5}\right)(0.875)$

*See reference 5 for discussion of design corrections.

**See Method 3, paragraph A, Section 5.3.1.1 for interpolation procedure.

$$= (0.130)(-2)\left[\frac{(\pi)(1.75)(1.496)}{114.5}\right](0.875)$$

$$= -0.0163 \text{ per rad (based on } S_W)$$

Determine the increment in C_{Y_β} due to adding the upper vertical stabilizer to the wing-body-horizontal stabilizer combination. The empennage in this case consists of the body, horizontal tail, and upper vertical stabilizer. The apparent-mass ratio to be found is that due to adding the upper vertical stabilizer to the body and horizontal tail, $K_{V(HB)}$.

In the configuration sketch part of the upper vertical panel S_1 senses only the wing-body combination, while S_2 senses only the body. Therefore, the effective apparent-mass ratio is given by

$$K'_{V(HB)} = K_{V(WB)} \frac{S_1}{S_{V_e}} + K_{V(B)} \frac{S_2}{S_{V_e}}$$

Determine $K_{V(WB)}$:

$$\left(\frac{r_1}{r_2}\right) = 1.170; \left(\frac{r_2}{b_W/2}\right) = 0.157; \left(\frac{r_1}{b}\right)_{\substack{V \\ \text{added} \\ \text{panel}}} = 0.247; \left(\frac{r_1}{b}\right)_{\substack{U \\ \text{existing} \\ \text{panel}}} = 1.000$$

By using the above parameters and table 5.3.1.1-A it is seen that $K_{V(WB)}$ can be obtained from figures 5.3.1.1-25b, -25c, -25e, and 5.3.1.1-25x, -25y, -25z, and 5.3.1.1-25dd, -25ee, -25ff, interpolated for

$\frac{r_2}{b_W/2} = 0.157$ and $r_1/r_2 = 1.170$.

$$K_{V(WB)} = 1.49$$

Determine $K_{V(B)}$:

$$\left(\frac{r_1}{r_2}\right) = 1.170; \left(\frac{r_1}{b}\right)_{\substack{V \\ \text{added} \\ \text{panel}}} = 0.247; \left(\frac{r_1}{b}\right)_{\substack{U \\ \text{existing} \\ \text{panel}}} = 1.000$$

By using the above parameters and table 5.3.1.1-A it is seen that $K_{V(B)}$ can be obtained from figures 5.3.1.1-25a, -25w, and -25cc, interpolated for $r_1/r_2 = 1.170$

$$K_{V(B)} = 1.27$$

$$K'_{V(HB)} = (1.49)\left(\frac{4.63}{19.20}\right) + (1.27)\left(\frac{14.57}{19.20}\right) = 1.32$$

$$(\Delta C_{Y_\beta})_{V(WBH)} = -K'_{V(HB)} (C_{N_\alpha})_V \frac{S_{V_e}}{S_W} \qquad \text{(equation 5.3.1.1-f)}$$

$$= -(1.32)(2.35)\frac{19.20}{114.5}$$

$$= -0.520 \text{ per rad (based on } S_W)$$

Determine the increment in C_{Y_β} due to adding the lower vertical stabilizer to the wing-body-horizontal stabilizer-upper vertical stabilizer combination. The empennage in this case consists of body, horizontal tail, upper vertical stabilizer, and lower vertical stabilizer. The apparent-mass ratio to be found is that due to adding the lower vertical stabilizer to the combination of body, horizontal tail, and upper vertical stabilizer, $K_{U(BHV)}$.

In the configuration sketch part of the lower vertical stabilizer S_3 senses only the body, while S_4 senses both the body and horizontal tail. Therefore, the effective apparent-mass ratio is given by

$$K'_{U(BHV)} = K_{U(B)} \frac{S_3}{S_{U_e}} + K_{U(BH)} \frac{S_4}{S_{U_e}}$$

Determine $K_{U(B)}$:

$$\left(\frac{r_1}{r_2}\right) = 1.170; \left(\frac{r_1}{b}\right)_{\substack{U \\ \text{added} \\ \text{panel}}} = 0.685; \left(\frac{r_1}{b}\right)_{\substack{V \\ \text{existing} \\ \text{panel}}} = 1.000$$

By using the above parameters and table 5.3.1.1-A it is seen that $K_{U(B)}$ can be obtained from figures 5.3.1.1-25a, -25w, and -25cc, interpolated for $r_1/r_2 = 1.170$.

$$K_{U(B)} = 3.0$$

Determine $K_{U(BH)}$:

$$\left(\frac{r_1}{r_2}\right) = 1.170; \left(\frac{r_1}{b}\right)_{\substack{U \\ \text{added} \\ \text{panel}}} = 0.685; \left(\frac{r_1}{b}\right)_{\substack{V \\ \text{existing} \\ \text{panel}}} = 1.000; \left(\frac{r_2}{b_H/2}\right) = 0.328; \left(\frac{z_H}{r_1}\right) = 0.480$$

Since the horizontal tail is located below the body centerline and the body is elliptical, we have a horizontal tail-body combination not covered by the K charts of Section 5.3.1.1. To handle this case, either the body has to be considered circular and an interpolation made for horizontal tail height, or the horizontal tail has to be assumed to be located at the mid-position and an interpolation made between r_1/r_2 ratios. A comparison between figures 5.3.1.1-25d, -25z, and 25ff shows that a small variation in cross section has a significant effect on the apparent-mass ratio in the region of $(r_1/b)_U = 0.685$. Therefore, an interpolation for body shape will be made rather than for horizontal tail height.

From figures 5.3.1.1-25c, -25d, -25e and 5.3.1.1-25y, -25z, -25aa and 5.3.1.1-25ee, -25ff, -25gg obtain $K_{U(BH)}$ interpolated for $\frac{r_2}{b_H/2} = 0.328$. An interpolation between those values of $K_{U(BH)}$ gives, for $(r_1/r_2) = 1.170$

$$K_{U(BH)} = 3.04$$

$$K'_{U(BHV)} = (3.0)\left(\frac{2.74}{3.24}\right) + (3.04)\left(\frac{0.50}{3.24}\right)$$

$$= 3.01$$

$$(\Delta C_{Y_\beta})_{U(WBHV)} = -K'_{U(BHV)} (C_{N_\alpha})_U \frac{S_{U_e}}{S_W} \qquad \text{(equation 5.3.1.1-f)}$$

$$= -(3.01)(0.622) \frac{3.24}{114.5}$$

$$= -0.053 \text{ per rad (based on } S_W)$$

Solution:

$$C_{Y_\beta} = (C_{Y_\beta})_{WB} + \Sigma_p (\Delta C_{Y_\beta})_p \qquad \text{(equation 5.6.1.1-b)}$$

$$= (C_{Y_\beta})_{WB} + (\Delta C_{Y_\beta})_{H(WB)} + (\Delta C_{Y_\beta})_{V(WBH)} + (\Delta C_{Y_\beta})_{U(WBHV)}$$

For this sample problem use is made of the test result for $(C_{Y_\beta})_{WBH}$, so

$$C_{Y_\beta} = (C_{Y_\beta})_{WBH} + (\Delta C_{Y_\beta})_{V(WBH)} + (\Delta C_{Y_\beta})_{U(WBHV)}$$

$$= (-0.315) + (-0.520) + (-0.053)$$

$$= -0.888 \text{ per rad (based on } S_W)$$

The experimental result from reference 3 is $C_{Y_\beta} = -0.888$ per radian (based on S_W).

REFERENCES

1. Sleeman, W. C., Jr.: An Experimental Study at High Subsonic Speeds of Several Tail Configurations on a Model Having a 45° Sweptback Wing. NACA RM L57C08, 1957. (U)

2. Savage, H. F., and Tinling, B. E.: The Subsonic Static Aerodynamic Characteristics of an Airplane Model Having a Triangular Wing of Aspect Ratio 3. II - Lateral and Directional Characteristics. NACA TN 4042, 1957. (U)

3. Spearman, M. L., Robinson, R. B., and Driver, C.: The Effects of the Addition of Small Fuselage-Mounted Fins on the Static Directional Stability Characteristics of a Model of a 45° Sweptwing Airplane at Angles of Attack up to 15.3° at a Mach Number of 2.01. NACA RM L56D16a, 1956. (U)

4. Goodwin, F. K., and Kaattari, G. E.: Estimation of Directional Stability Derivatives at Small Angles and Subsonic and Supersonic Speeds. NASA Memo 12-2-58A, 1958. (U)

5. Campbell, J. P., and McKinney, M. O.: Summary of Methods for Calculating Dynamic Lateral Stability and Respone and for Estimating Lateral Stability Derivatives. NACA TR 1098, 1952. (U)

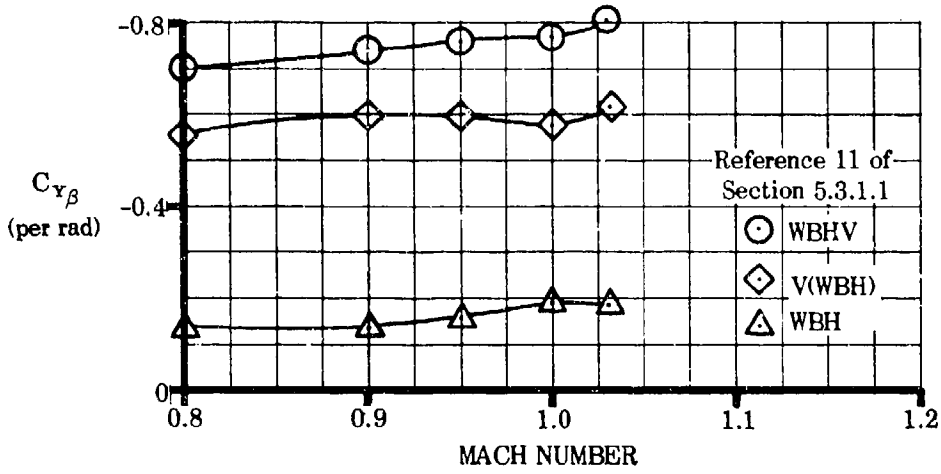

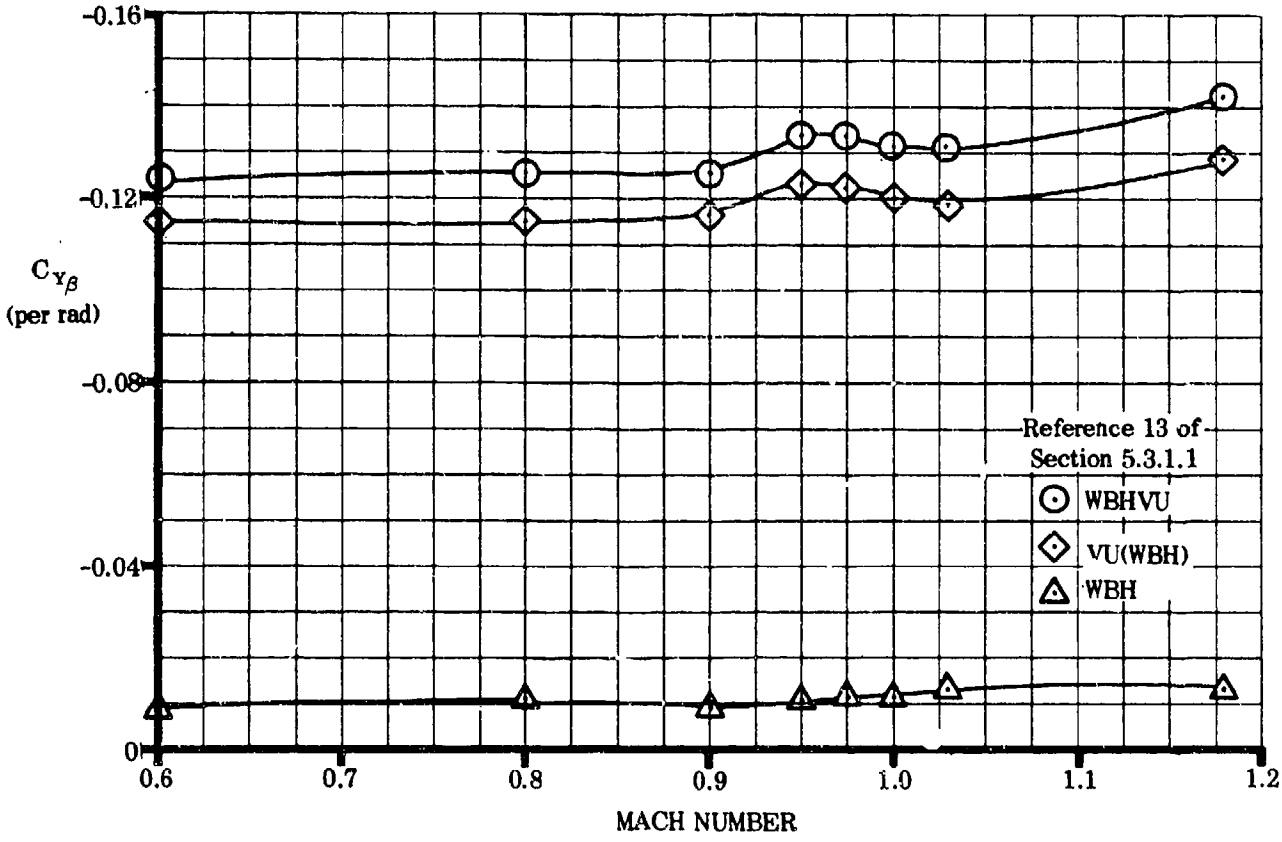

FIGURE 5.6.1.1-14 TYPICAL TRANSONIC DATA

5.6.1.2 WING-BODY-TAIL SIDE-FORCE COEFFICIENT C_Y AT ANGLE OF ATTACK

The wing-body-tail side force developed at combined angles is nonlinear with respect to both sideslip and angle of attack for the reasons cited in the introductory remarks of Sections 5.2.1.2 and 5.3.1.2, and as in those Sections, to obtain C_{Y_β}, it is recommended that C_Y be calculated at several angles of attack for a small sideslip angle ($\beta \leq 4^\circ$). Then at each angle of attack the side force is assumed linear with sideslip for small values of β so that

$$C_{Y_\beta} \approx \frac{C_Y}{\beta}.$$

A. SUBSONIC

No method is presently available for determining the wing-body-tail side force at large angles of attack and subsonic speeds. The method presented herein is restricted to first-order approximations at relatively low angles of attack.

DATCOM METHOD

It is recommended that the method of paragraph A of Section 5.6.1.1 be used, with consideration given to the angle-of attack restriction presented in figure 5.1.1.1-4.

B. TRANSONIC

The comments appearing in paragraph B of Section 5.6.1.1 are equally appropriate here.

DATCOM METHOD

No method is available for estimating this coefficient and none is presented in the Datcom.

C. SUPERSONIC

The analysis of wing-body-tail configurations at combined angles is taken from reference 1 and is accomplished through a combination of the methods of Sections 5.2.1.2 and 5.3.1.2. Therefore, the discussions in paragraph C of those Sections apply to this Section as well. Note in Section 5.3.1.2 that the method is limited to configurations with circular bodies, and to the analysis of horizontal tail effects only when that surface is body-mounted.

In addition to the phenomena previously discussed, three types of interference exist between the wing and tail surfaces. If the vertical tail panels are in the wing-flow field, mutual interaction occurs in the same way as that between horizontal and vertical tail panels. This effect is taken into account through the apparent-mass factor concept. Secondly, there is interference due to the wing-flow field which alters the local dynamic pressure and Mach number acting on the vertical tail surfaces. This is a nonlinear effect of angle of attack and is taken into account by a tail effectiveness parameter η_W based on two-dimensional shock-expansion theory. Wing-vertical tail interference also results from the effect of the wing-flow field on the body vortices. The positions and strengths of the body vortices are both influenced by the wing. The wing-flow field cuts off the body feeding vortex sheet along the length of the exposed wing root chord and the body vortex path is curved as it passes through the wing-flow field. The effect of the wing is taken into account herein by an approximation to the method of reference 2. It is assumed that both vortex strengths and positions are those about a body alone, foreshortened by the length of the exposed wing root chord. This assumption satisfactorily accounts for the effect of the wing-flow field on vortex strength but neglects the effect of the wing-flow field in altering the path of the vortices; however, the error introduced at small angles of sideslip is negligible.

Two methods are discussed in reference 2 for approximating the effect of the wing-flow field on the body vortex positions. One method is based on two-dimensional shock-expansion theory which precludes accurate prediction of lateral vortex positions and also restricts the results to configurations with slender wing panels. A second method applicable to slender configurations is suggested in which the calculation of the vortex paths with the wing panels

present can be made by using slender-body theory and proceeding step by step. However, the practical calculation of the paths with any degree of accuracy requires the use of automatic computing methods.

Sections 5.2.1.2 and 5.3.1.2 have considered separately wing-body and tail-body configurations. Wing-body-tail configurations may be classified as either uncoupled, coupled, or partially coupled, depending on the physical relationship between the wing-flow field and the tail. The three classes of configurations are illustrated in sketch (a). For the uncoupled configurations a body section separates the wing from the empennage so that the wing-flow field does not directly impinge on the tail surfaces. For the coupled configuration the tail surfaces are totally enveloped in the wing-flow field. Partially coupled configurations have partial coupling between the wing-flow field and the tail. The primary difference between the three classes of configurations in so far as the present theory is concerned is that the shock-expansion effects of the wing on the tail are neglected when dealing with uncoupled configurations.

The wing-flow field at angle of attack and supersonic speeds is defined by the method outlined in Section 5.3.1.2 for determining the horizontal tail-flow field at angle of attack and supersonic speeds.

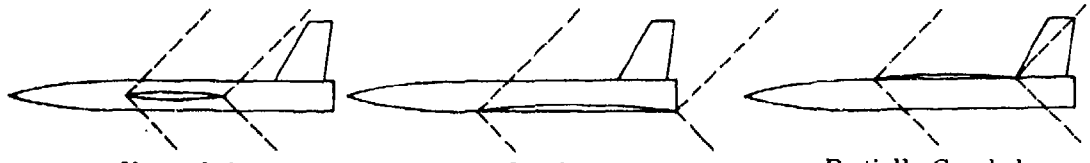

SKETCH (a)

DATCOM METHOD

The method for determining the wing-body-tail side-force coefficient at combined angles is given by

$$C_{Y_{WBHVU}} = C_{Y_{WB}} + C_{Y_{HVU(WB)}} \qquad 5.6.1.2\text{-a}$$

where

$C_{Y_{WB}}$ is the wing-body contribution obtained from equation 5.2.1.2-a

$C_{Y_{HVU(WB)}}$ is the empennage contribution obtained from equation 5.6.1.2-b

The contribution of the empennage is given by

$$C_{Y_{HVU(WB)}} = C_{Y_{H(B)}} + C_{Y_{V(\eta)}} + C_{Y_{U(\eta)}} \qquad 5.6.1.2\text{-b}$$

where

$C_{Y_{H(B)}}$ is the horizontal tail contribution obtained from equation 5.3.1.2-b

$C_{Y_{V(\eta)}}$ is the vertical tail contribution obtained from equation 5.6.1.2-c

$C_{Y_{U(\eta)}}$ is the ventral fin contribution obtained from equation 5.6.1.2-d

The order in which the tail panels should be added to the wing-body configuration for analysis purposes parallels that prescribed in Section 5.3.1.2 for a tail-body configuration.

The contribution of the vertical tail is given by

$$C_{Y_{V(\eta)}} = C_{Y_{V(K,\phi)}} + C_{Y_{V(\Gamma_B)}} \qquad 5.6.1.2\text{-c}$$

for uncoupled configurations, and by

$$C_{Y_{V(\eta)}} = [C_{Y_{V(K,\phi)}} + C_{Y_{V(\Gamma_B)}}]\ \eta_{W_V} \qquad 5.6.1.2\text{-c}$$

for coupled or partially coupled configurations;

where

$C_{Y_{V(K,\phi)}}$ accounts for α and β cross-coupling and any mutual interaction between the vertical tail and other surfaces in the empennage and is given by equation 5.3.1.2-d. In addition, any impingement of the wing-flow field on the vertical tail must be considered in determining the effective apparent-mass factor K'_V. The method for defining the wing flow field is the same as for the horizontal tail, and is given step-by-step in paragraph C, Section 5.3.1.2. Note that the upper trailing edge is marked by a shock wave rather than a Mach line.

$C_{Y_{V(\Gamma_B)}}$ accounts for the effect of body vortices on the vertical stabilizer, and includes influence of the wing on the vortex strength. The wing effect is approximated by foreshortening the body length by the exposed wing root chord c_{r_e} when finding vortex strength and position from figures 4.3.1.3-13b, 4.3.1.3-14, and 4.3.1.3-15. That is, the figures are entered with $\frac{\alpha'(x - x_s - c_{r_e})}{r}$, rather than $\frac{\alpha(x - x_s)}{r}$.* The results are then applied to equations 5.3.1.2-f and 5.3.1.2-e to obtain $C_{Y_{V(\Gamma_B)}}$.**

η_{W_V} is the tail effectiveness parameter of the upper vertical stabilizer obtained from figure 5.6.1.2-9 as a function of angle of attack and Mach number. These charts take into account the changes in dynamic pressure and Mach number at the tail by direct application of two-dimensional shock-expansion theory. Any effects of wing-body interference or wing section in distorting the shock-expansion field are neglected.

For a specified initial Mach number there is a maximum value of the angle of attack for which there exists an oblique shock solution. Or, conversely, for a specified angle of attack there is a minimum initial Mach number for which there is an oblique shock solution. The relation between Mach number and angle of attack below which no solutions for η_W may be obtained is indicated in sketch (a) of Section 5.3.1.2.

The procedure for using these charts is

Step 1: Draw on transparent paper the relative positions of the wing exposed root chord and the vertical surfaces. Choose the scale so that the exposed chord length coincides with that shown in figure 5.6.1.2-9 .

Step 2: Overlay the drawing on the figure to locate the tail in the proper influence zone.

Step 3: The vertical tail is divided into several areas. The average value of η_{W_V} in each area is multiplied by the ratio of its area to S_{V_e}.

Step 4: Sum the weighted values of η_{W_V} to obtain the total tail effectiveness parameter η_{W_V}.

Step 5: Interpolation for angle of attack and/or Mach number may be necessary. If so, a three-point interpolation for α should be made using weighted values of η_{W_V}. Two points are sufficient for Mach number interpolation.

The contribution of the ventral fin is given by

$$C_{Y_{U(\eta)}} = C_{Y_U} \qquad 5.6.1.2\text{-d}$$

for uncoupled configurations, and by

$$C_{Y_{U(\eta)}} = C_{Y_U}\,\eta_{W_U} \qquad 5.6.1.2\text{-d}'$$

for coupled or partially coupled configurations;

* If x_s indicates vortex separation aft of the exposed wing root-chord leading edge, then only that portion of c_{r_e} aft of the indicated separation point is subtracted.

** The vortex positions given by equation 5.3.1.2-f are the positions at a given longitudinal station about the body alone foreshortened by c_{r_e} and do not include the effects of the wing-flow field in altering the paths of the vortices.

where

C_{Y_U} accounts for α and β cross-coupling and any mutual interaction between the vertical tail and other surfaces in the empennage, and is given by equation 5.3.1.2-g. In addition, any impingement of the wing flow field on the ventral tail must be considered in determing the effective apparent-mass factor K'_U.

η_{W_U} is the tail effectiveness parameter of the ventral fin and is obtained from figure 5.6.1.2-9 by following the steps describing the determination of η_{W_V}.

As noted in paragraph C of Section 5.3.1.2, the body vortices do not affect the ventral fin.

Values for the incremental coefficient resulting from the addition of vertical tails to wing-body configurations, calculated using the Datcom method, are compared with experimental results in figure 5.6.1.2-8. The correlation between experiment and estimate is relatively good at $\beta = 5.1°$ and poor at $\beta = 10°$. The poor correlation at $\beta = 10°$ can be attributed to the assumption that the body vortex positions are those about a body foreshortened by the length of the exposed wing root chord. This assumption neglects the effects of the wing-flow field on the body vortex positions and poor correlation can be expected at higher sideslip angles where viscous lateral cross-flow effects become important.

Sample Problem

Given: Configuration of sample problem, paragraph C, Sections 5.2.1.2 (with slight boattail) and 5.3.1.2. There is no horizontal tail on this configuration. Some of the characteristics are repeated. Find the side-force coefficient developed by the wing-body-tail combination at $\alpha = 12°$, $\beta = 4°$, and $M = 2.01$.

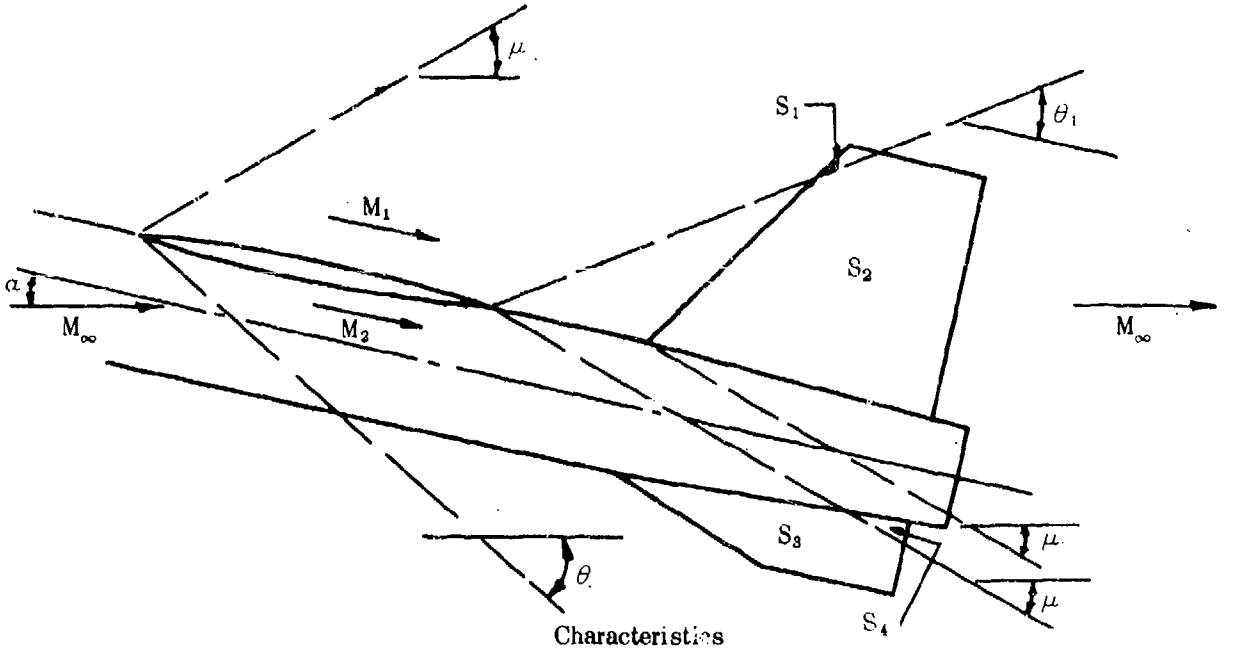

Characteristics

$\frac{r_1}{b_V} = 0.200$ $\frac{r_1}{b_U} = 0.492$. $\Lambda_{LE_V} = 32.5°$ $\Lambda_{LE_U} = 70°$ $S_W = 144.0$ sq in.

$b_W = 24.0$ in. $c_{r_e} = 8.90$ in.

$S_{V_e} = 31.6$ sq in. $S_{U_e} = 8.54$ sq in. $S_1 = 0.40$ sq in. $S_2 = 31.2$ sq in. $S_3 = S_{U_e} = 8.54$ sq in.

x = 32.8 in. (x measured from nose to 50-percent-chord point of MAC of exposed vertical panel)

$C_{Y_{WB}} = -0.400$ (sample problem, paragraph C, Section 5.2.1.2)

$C_{Y_{H(B)}} = 0$ (no horizontal tail on this configuration)

At positive angle of attack, vertical-tail exposed root-chord leading edge is aft of ventral-fin exposed root-chord leading edge.

Ventral fin is not influenced by presence of upper vertical tail at this angle of attack and Mach number.

Configuration is partially coupled at this angle of attack and Mach number.

Compute:

Determine the vertical tail contribution $C_{Y_{V(\eta)}}$

K'_V = 1.13 (method of paragraph C, Section 5.3.1.1 with S_1 = 0.40 sq in. and S_2 = 31.2 sq in.)

K_{ϕ_V} = 0.687 figure 5.3.1.2-12 at $(r_1/b)_V$ = 0.200)

$(C_{N_\alpha})_V$ = 2.12 per rad (based on S_{V_e}) (sample problem, paragraph C, Section 5.3.1.2)

$$C_{Y_{V(\kappa,\phi)}} = [K'_V - K_{\phi_V} \alpha \tan \Lambda_{LE_V}] (-C_{N_\alpha})_V \beta \frac{S_{V_e}}{S_W} \qquad \text{(equation 5.3.1.2-d)}$$

$$= [1.13 - (0.687)(0.209) \tan 32.5^\circ] (-2.12) (0.070) \left(\frac{31.6}{144.0}\right)$$

$$= -0.0339 \text{ (based on } S_W)$$

For the purpose of finding vortex characteristics:

$\frac{x_s}{r}$ = 10.6 (figure 4.3.1.3-13a at α' = 12.65°)

Vortex separation is forward of exposed wing root-chord leading edge.

$$\frac{\alpha'(x - x_s - c_{r_e})}{r} = 0.221\left(\frac{32.8}{1.50} - 10.6 - \frac{8.90}{1.50}\right) = 1.180$$

$\frac{y_0}{r}$ = 0.63 (figure 4.3.1.3-14)

$\frac{z_0}{r}$ = 1.25 (figure 4.3.1.3-13b)

$\frac{\Gamma_B}{2\pi\alpha' V r}$ = 0.62 (figure 4.3.1.3-15)

} at $\frac{\alpha'(x - x_s - c_{r_e})}{r}$

ϕ = 18.4° (sample problem, paragraph C, Section 5.3.1.2)

then the positions of the body vortices at the vertical tail (neglecting the effect of the wing-flow field in altering the paths of the vortices) are:

$$\frac{z_{v_1}}{b_V} = \frac{r}{b_V}\left[\frac{z_0}{r}\cos\phi + \frac{y_0}{r}\sin\phi\right] \qquad \text{(equation 5.3.1.2-f)}$$

$$= \frac{1.50}{7.48}\left[1.25\cos 18.4^\circ + 0.63 \sin 18.4^\circ\right] = 0.278$$

$$\frac{y_{v_1}}{b_V} = \frac{r}{b_V}\left[\frac{z_0}{r}\sin\phi - \frac{y_0}{r}\cos\phi\right] \qquad \text{(equation 5.3.1.2-f)}$$

$$= \frac{1.50}{7.48}\left[1.25 \sin 18.4^\circ - 0.63 \cos 18.4^\circ\right] = -0.0408$$

$$\frac{z_{v_2}}{b_V} = \frac{r}{b_V}\left[\frac{z_0}{r}\cos\phi - \frac{y_0}{r}\sin\phi\right] \qquad \text{(equation 5.3.1.2-f)}$$

$$= \frac{1.50}{7.48}\left[1.25\cos 18.4^\circ - 0.63\sin 18.4^\circ\right] = 0.198$$

$$\frac{y_{v_2}}{b_V} = \frac{r}{b_V}\left[\frac{z_0}{r}\sin\phi + \frac{y_0}{r}\cos\phi\right] \qquad \text{(equation 5.3.1.2-f)}$$

$$= \frac{1.50}{7.48}\left[1.25\sin 18.4^\circ + 0.63\cos 18.4^\circ\right] = 0.199$$

$$\left.\begin{aligned} i_{v_1} &= -0.9 \\ i_{v_2} &= -0.6 \end{aligned}\right\} \qquad \text{(figure 5.3.1.2-13a)}$$

$$\Delta i_v = i_{v_1} - i_{v_2} = (-0.9) - (-0.6) = -0.3$$

$$C_{Y_{V(\Gamma_B)}} = \Delta i_v\left[\frac{\Gamma_B}{2\pi\alpha' Vr}\right]\left[\frac{(-C_{N_\alpha})_V\,\alpha' S_{V_e}}{\left(\frac{b_V}{r} - 1\right) S_W}\right] \qquad \text{(equation 5.3.1.2-e)}$$

$$= (-0.3)(0.62)\left[\frac{(-2.12)(0.221)(31.6)}{\left(\frac{7.48}{1.5} - 1\right)(144.0)}\right]$$

$$= 0.00478 \text{ (based on } S_W)$$

Determine tail effectiveness parameter η_{W_V}

By interpolation using figures 5.6.1.2-9g, -9h, and -9i, obtain $\eta_{W_V} = 0.98$ (see steps 1 through 5, page 5.6.1.2-3)

$$C_{Y_{V(\eta)}} = \left[C_{Y_{V(K,\phi)}} + C_{Y_{V(\Gamma_B)}}\right]\eta_{W_V} \qquad \text{(equation 5.6.1.2-c')}$$

$$= [(-0.0339) + (0.00478)](0.98)$$

$$= -0.0285 \text{ (based on } S_W)$$

Determine the ventral fin contribution $C_{Y_{U(\eta)}}$

$K'_U = 3.15$ (method of paragraph C, Section 5.3.1.1 with $S_s \approx S_{U_e} = 8.54$ sq in.)

$K_{\phi_U} = 0.535$ (figure 5.3.1.2-12 at $(r_1/b)_U = 0.492$)

$C_{N_{\alpha_U}} = 1.09$ per rad (based on S_{U_e}) (sample problem, paragraph C, Section 5.3.1.2)

$$C_{Y_U} = C_{Y_{U(K,\phi)}} = \left[K'_U + K_{\phi_U}\,\alpha\tan\Lambda_{LE_U}\right](-C_{N_\alpha})_U\,\beta\,\frac{S_{U_e}}{S_W} \qquad \text{(equation 5.3.1.2-g)}$$

$$= \left[3.15 + (0.535)(0.209)\tan 70^\circ\right](-1.09)(0.070)\left(\frac{8.54}{144.0}\right)$$

$$= -0.0156 \text{ (based on } S_W)$$

Determine the tail effectiveness parameter η_{W_U}

By interpolation using figures 5.6.1.2-9g, -9h, and -9i, obtain $\eta_{W_U} = 1.20$ (see steps 1 through 5, page 5.6.1.2-3)

$C_{Y_{U(\eta)}} = C_{Y_U}\ \eta_{W_U}$ (equation 5.6.1.2-d')

$= (-0.0156)\ (1.20)$

$= -0.0187$ (based on S_W)

Determine total empennage contribution

$C_{Y_{HVU(WB)}} = C_{Y_{H(B)}} + C_{Y_{V(\eta)}} + C_{Y_{U(\eta)}}$ (equation 5.6.1.2-b)

$= 0 + (-0.0285) + (-0.0187)$

$= -0.0472$ (based on S_W)

Solution:

$C_{Y_{WBHVU}} = C_{Y_{WB}} + C_{Y_{HVU(WB)}}$ (equation 5.6.1.2-a)

$= (-0.0400) + (-0.0472)$

$= -0.0872$ (based on S_W)

This compares with an experimental value (based on S_W) of $C_{Y_{WBHVU}} = -0.096$ from reference 3.

REFERENCES

1. Kaattari, G. E.: Estimation of Directional Stability Derivatives at Moderate Angles and Supersonic Speeds. NACA Memo 12-1-58A, 1959. (U)

2. Nielsen, J. N.: The Effect of Body Vortices and the Wing Shock-Expansion Field on the Pitch-Up Characteristics of Supersonic Airplanes. NACA RM A57L23, 1958. (C) Title Unclassified.

3. Spearman, L. M., Driver, C., and Hughes, W. C.: Investigation of Aerodynamic Characteristics in Pitch and Sideslip of a 45° Sweptback-Wing Airplane Model with Various Vertical Locations of Wing and Horizontal Tail. NACA RM L54L05, 1955. (U)

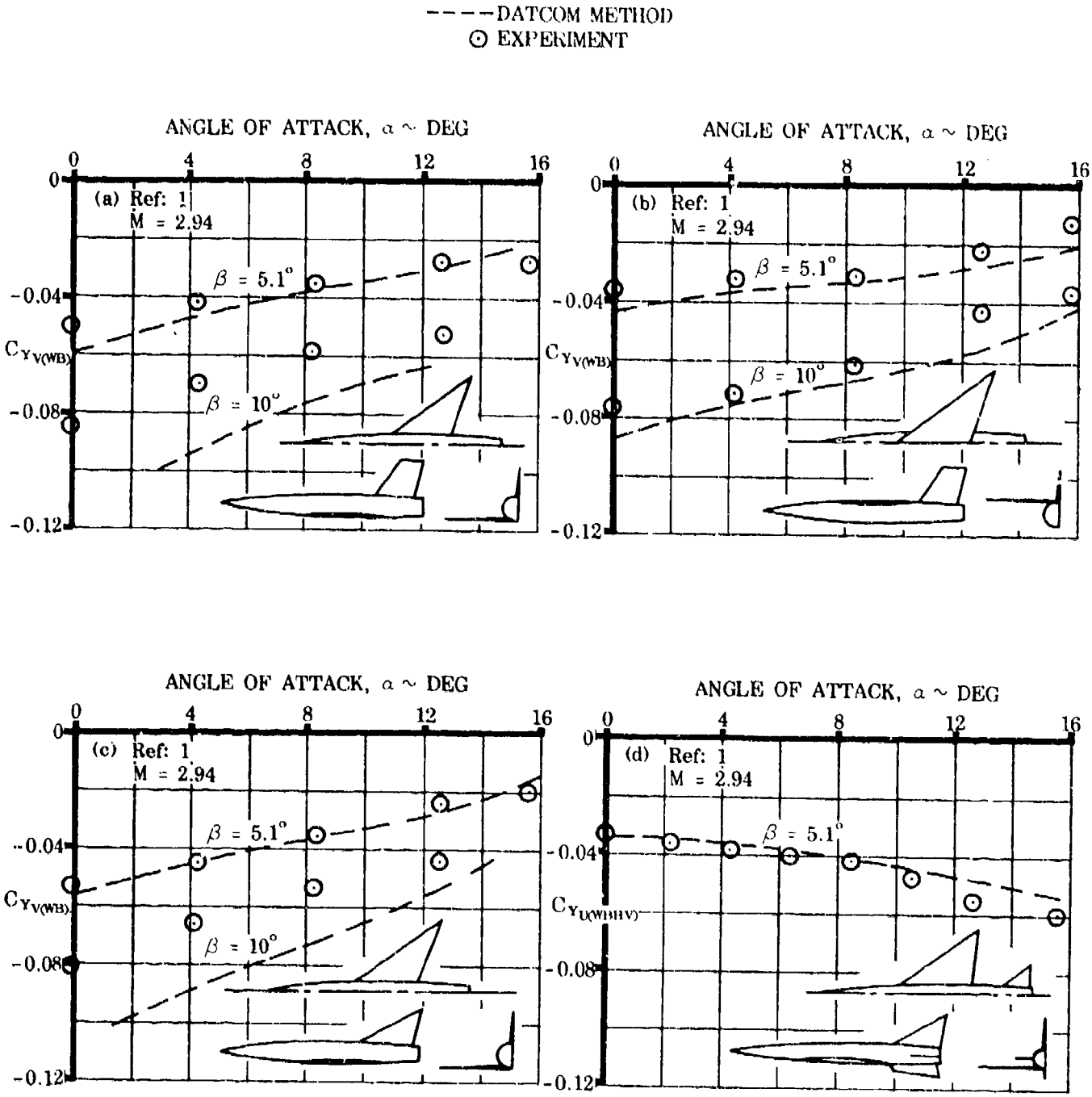

FIGURE 5.6.1.2-8 COMPARISON OF EXPERIMENTAL AND CALCULATED SIDE-FORCE COEFFICIENT INCREMENTS DUE TO ADDING A VERTICAL TAIL TO A WING-BODY

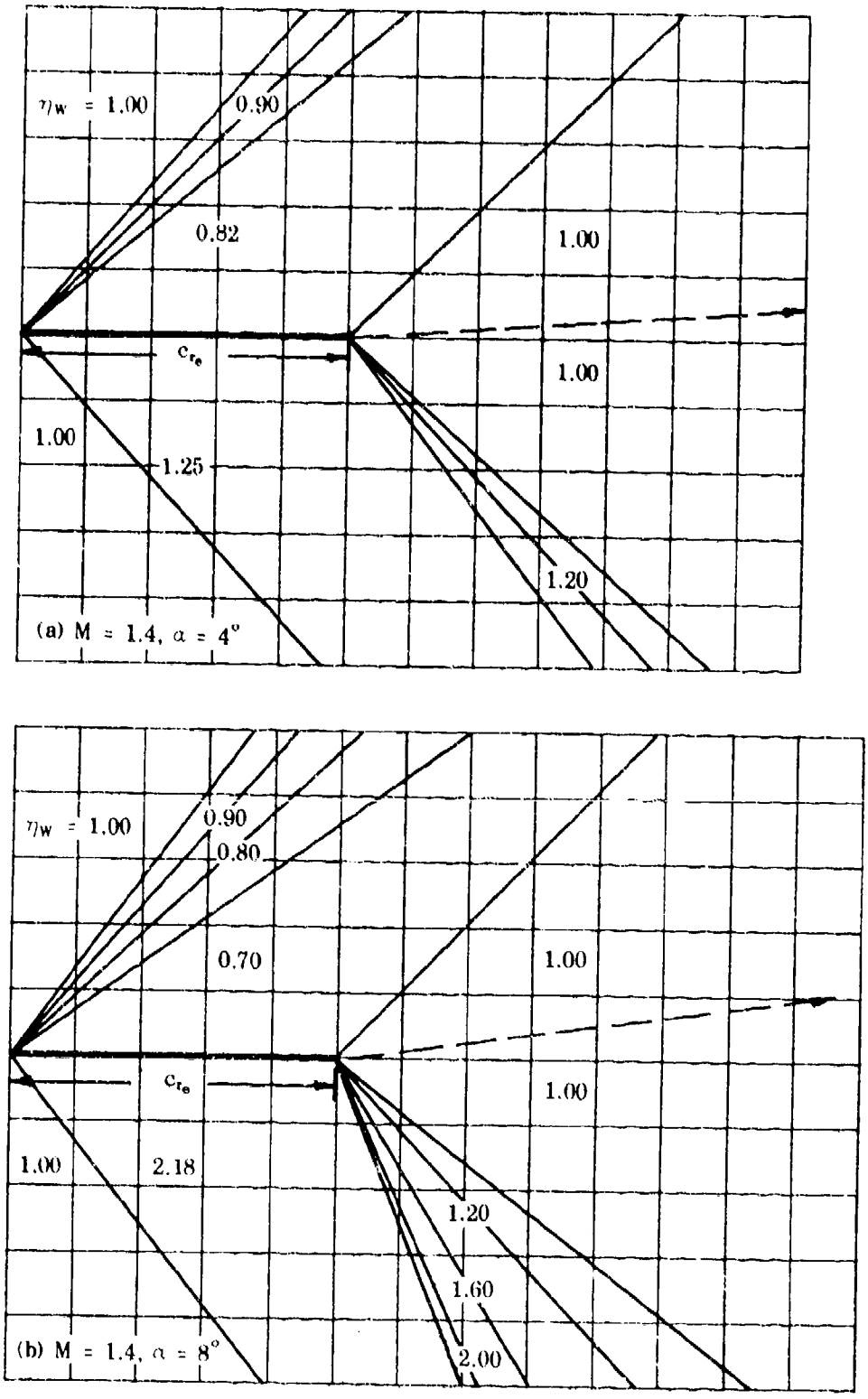

FIGURE 5.6.1.2-9 TAIL EFFECTIVENESS PARAMETER

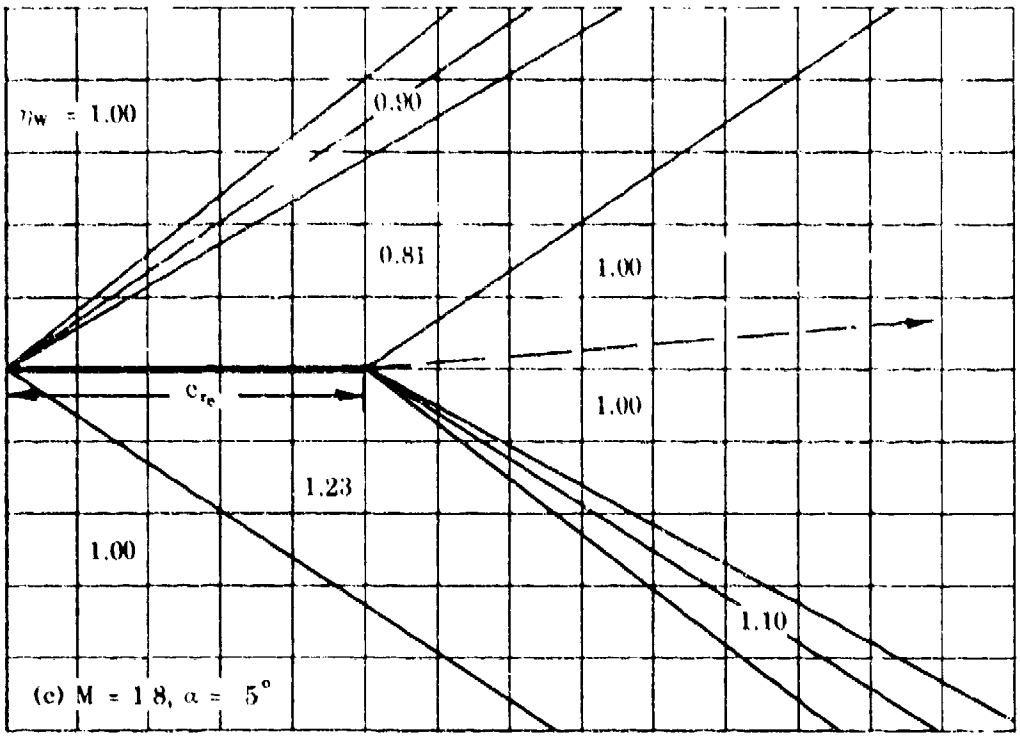

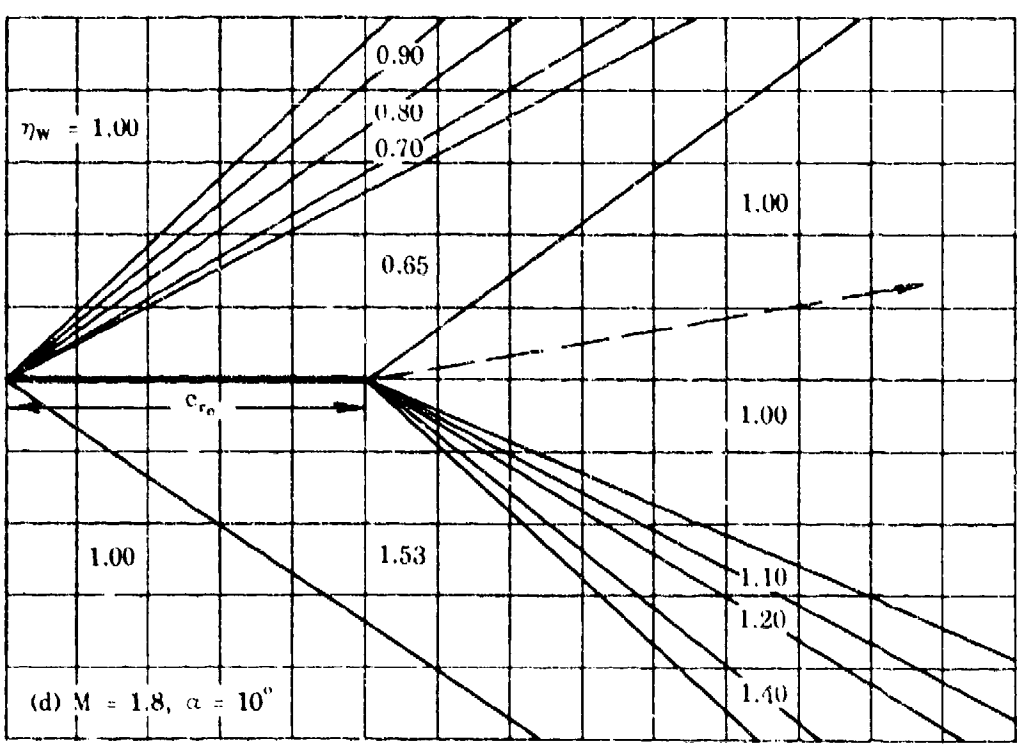

FIGURE 5.6.1.2-9 TAIL EFFECTIVENESS PARAMETER (contd)

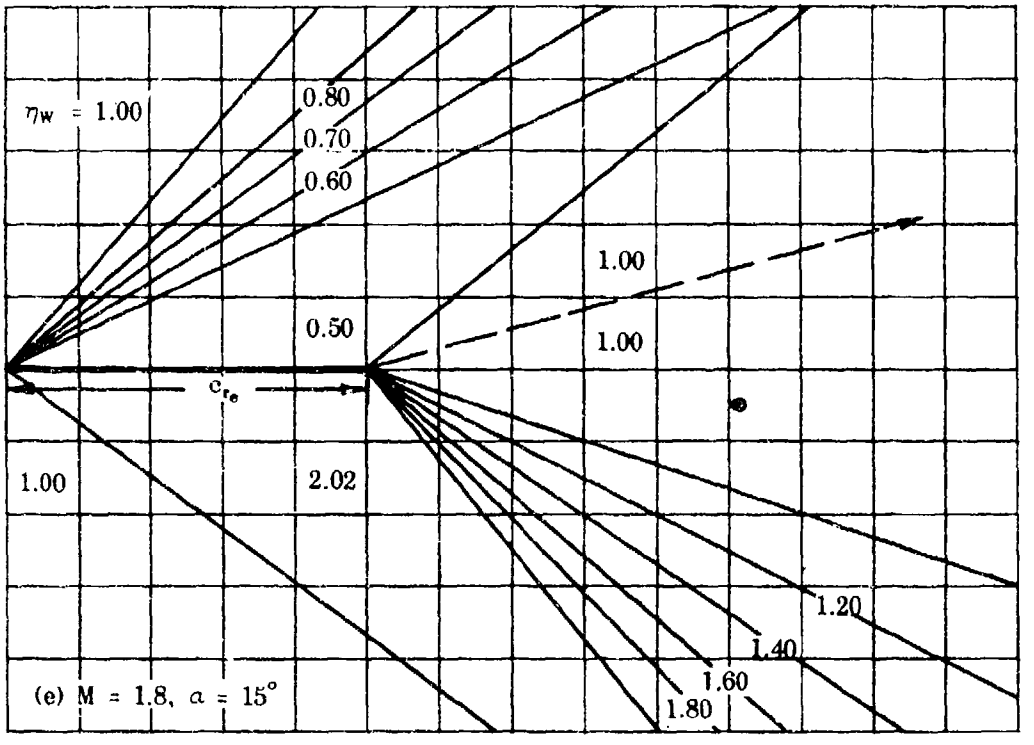

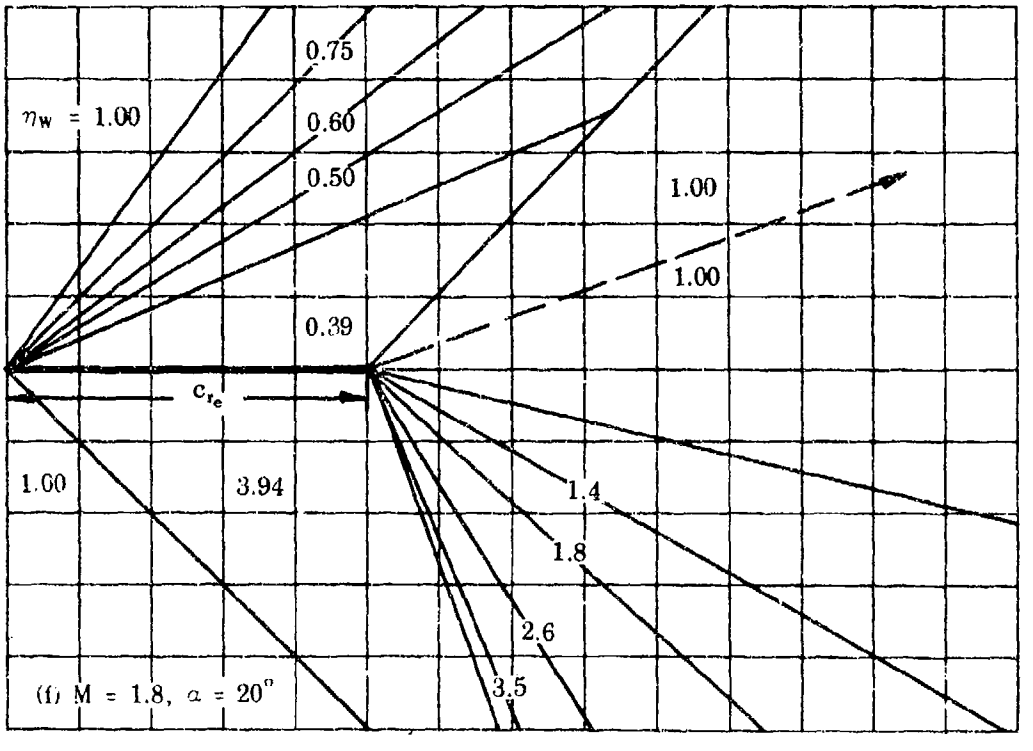

FIGURE 5.6.1.2-9 TAIL EFFECTIVENESS PARAMETER (contd)

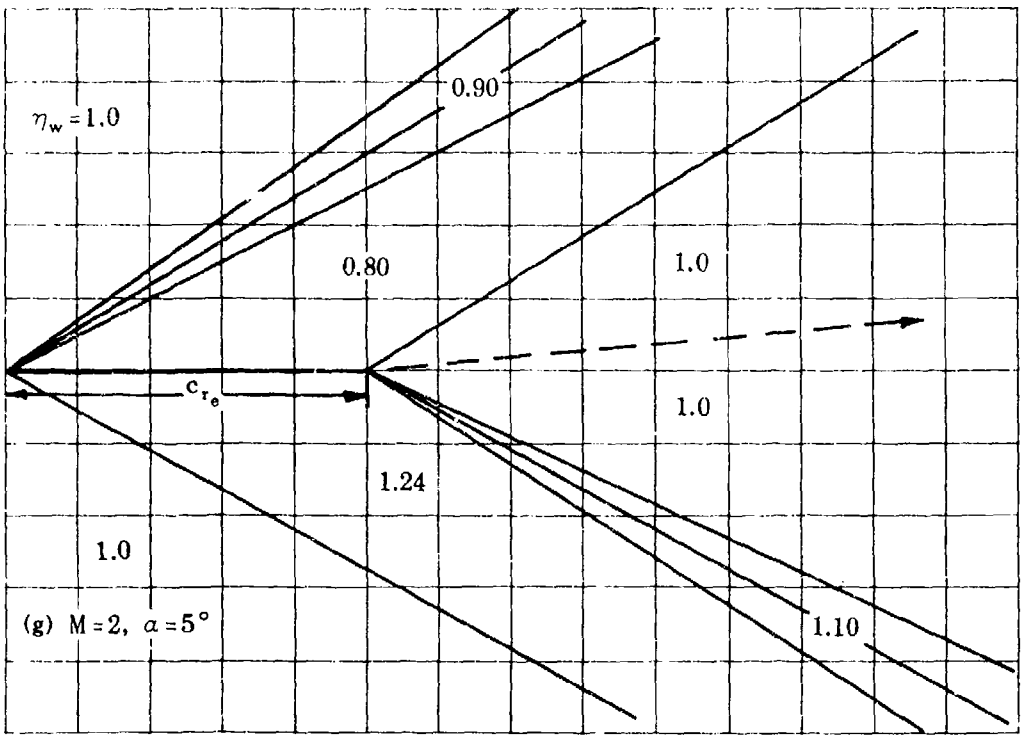

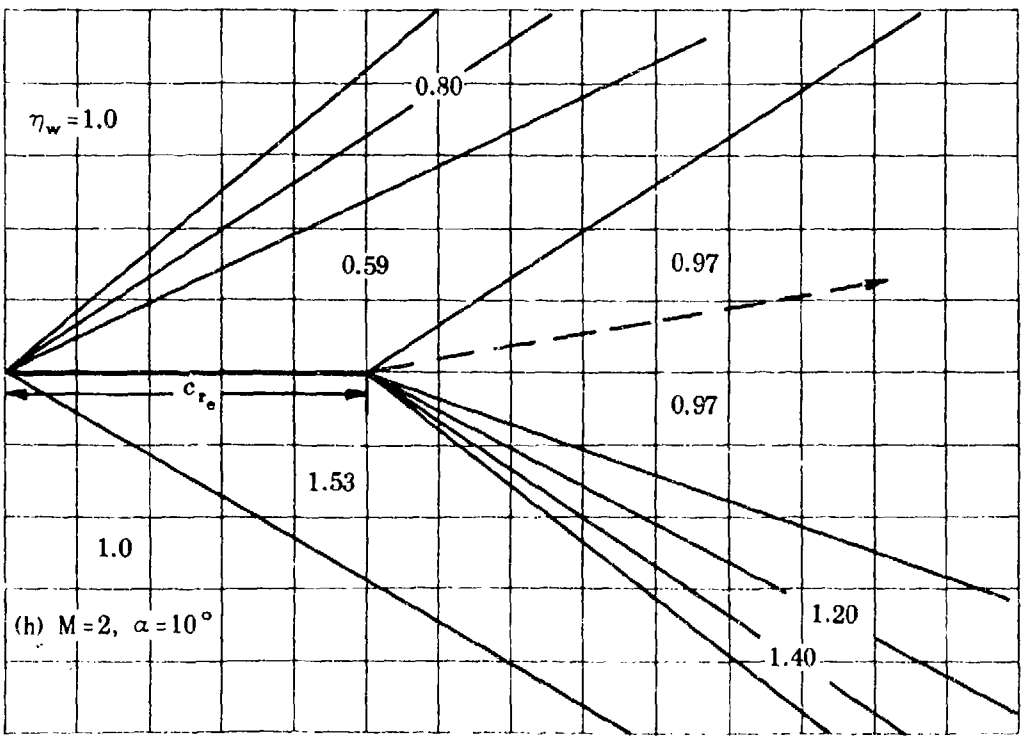

FIGURE 5.6.1.2-9 TAIL EFFECTIVENESS PARAMETER (contd)

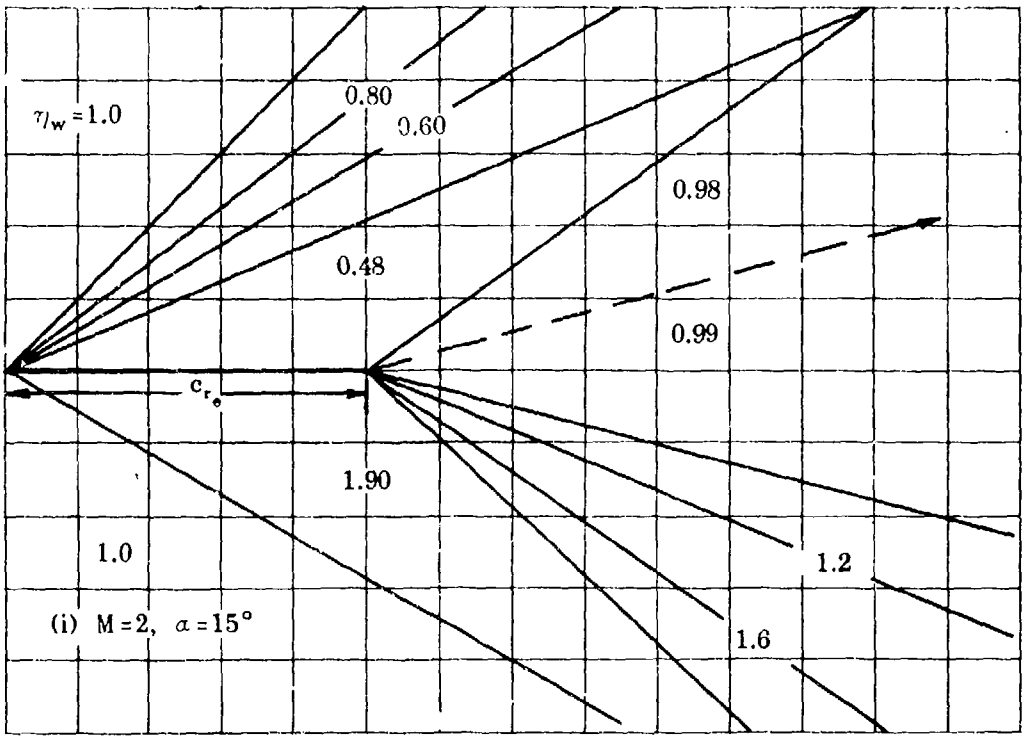

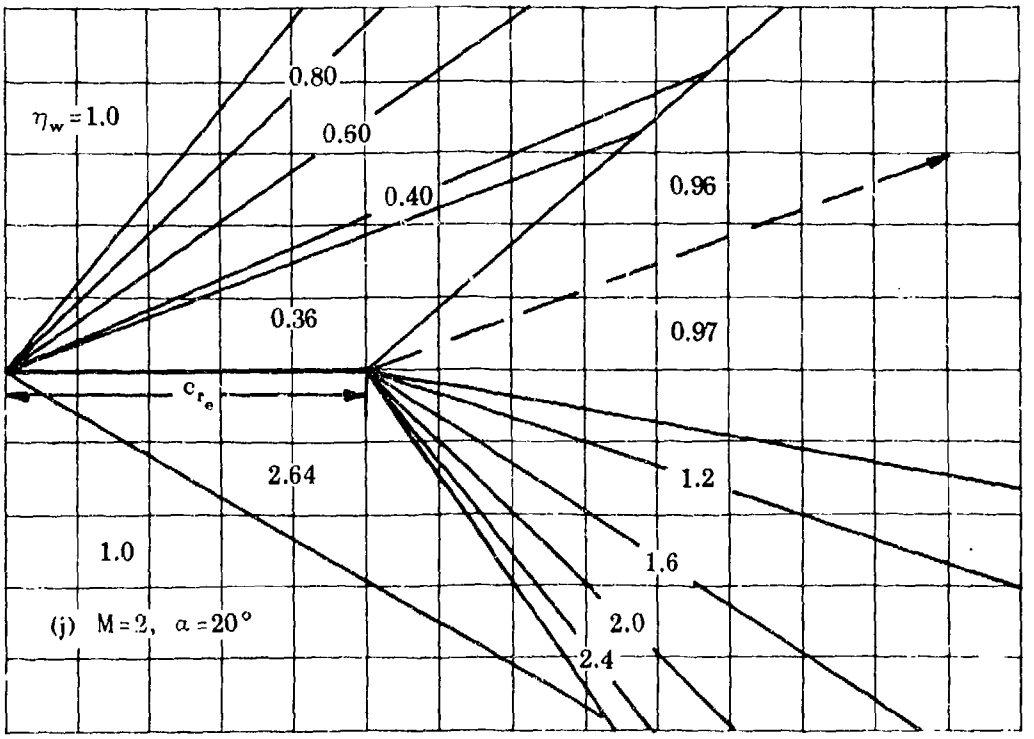

FIGURE 5.6.1.2-9 TAIL EFFECTIVENESS PARAMETER (contd)

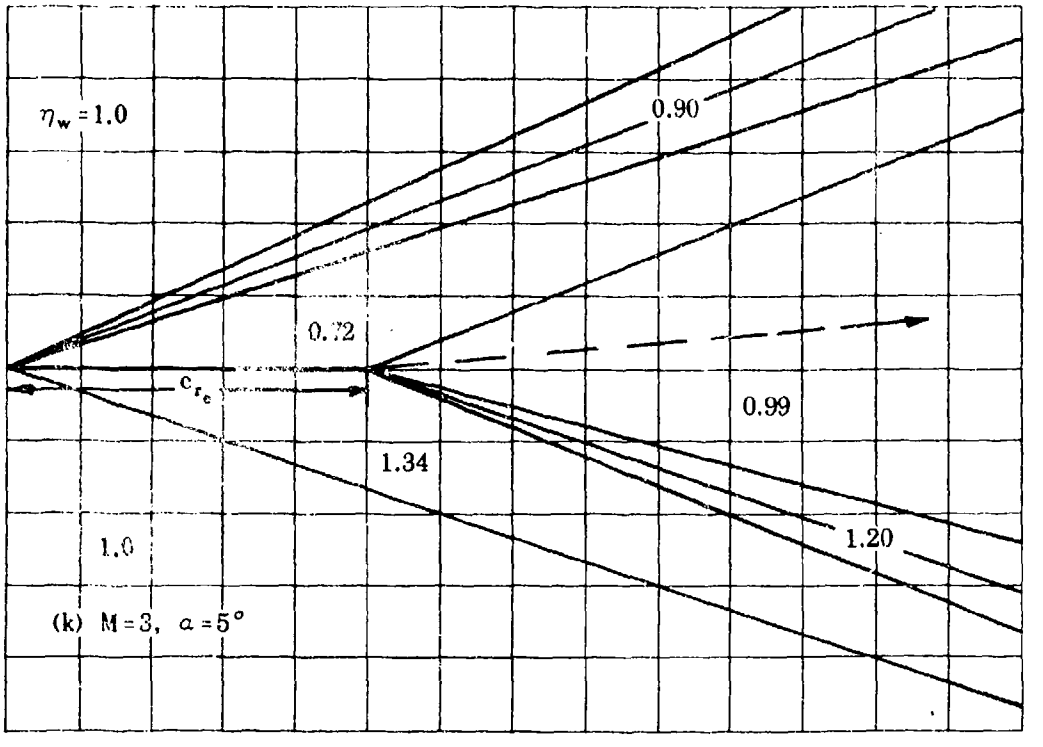

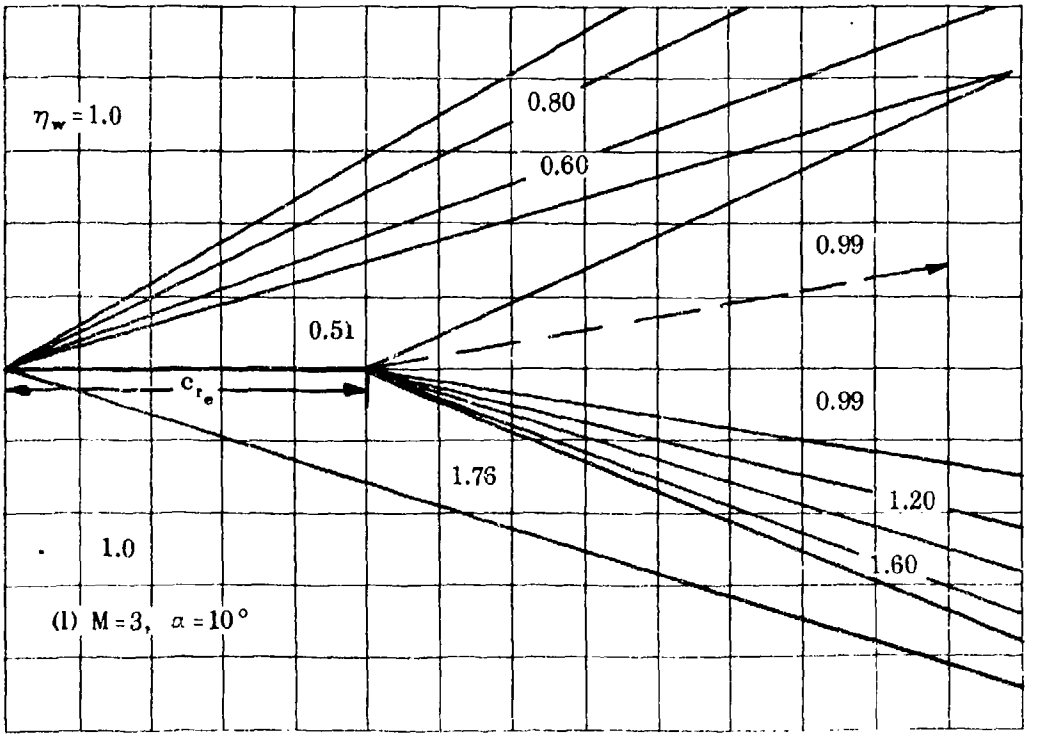

FIGURE 5.6.1.2-9 TAIL EFFECTIVENESS PARAMETER (contd)

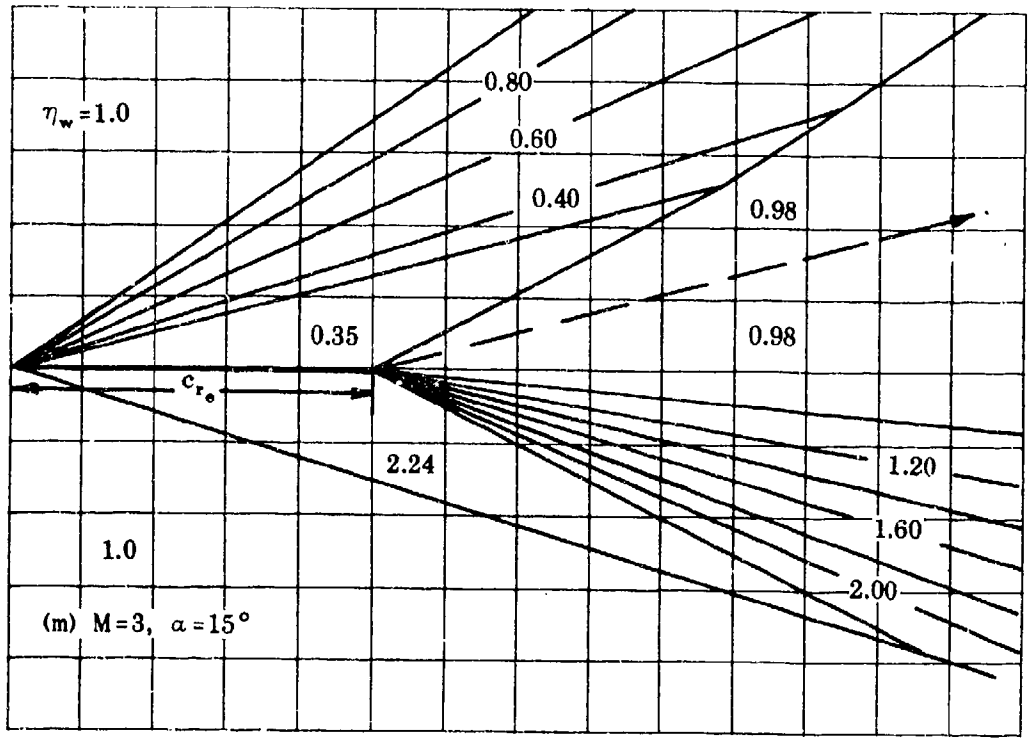

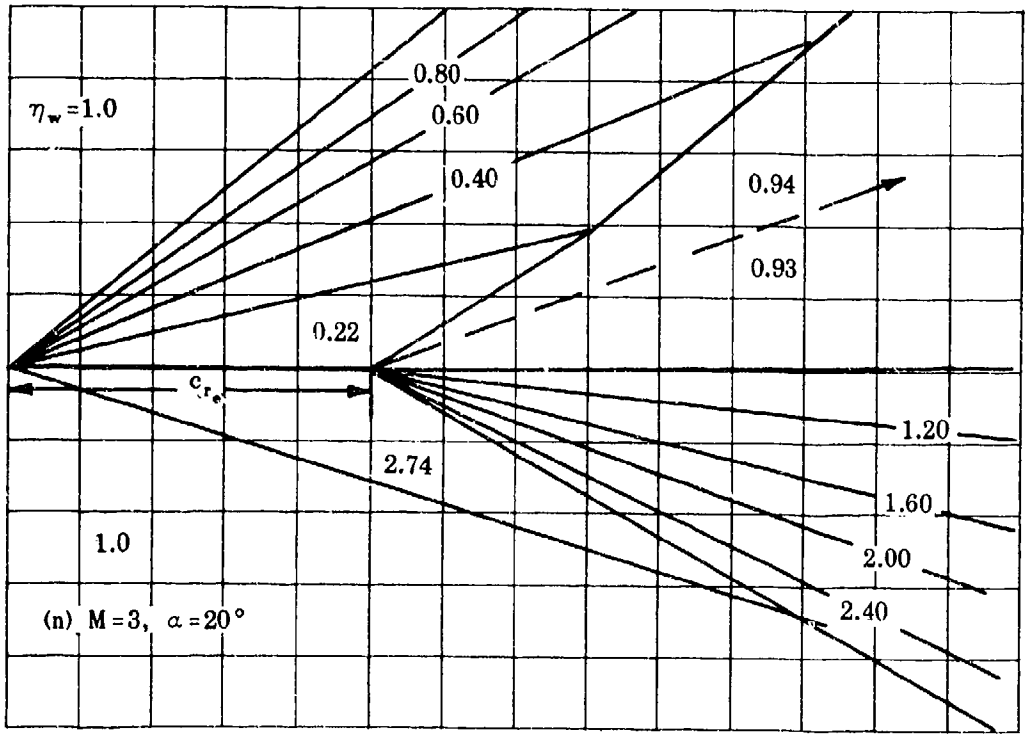

FIGURE 5.6.1.2-9 TAIL EFFECTIVENESS PARAMETER (contd)

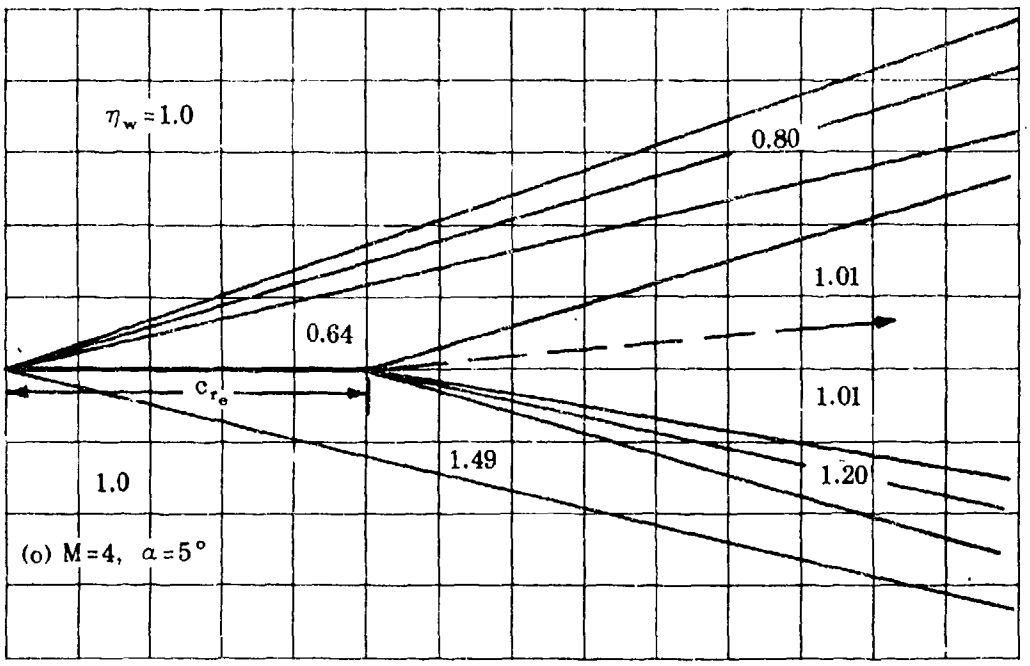

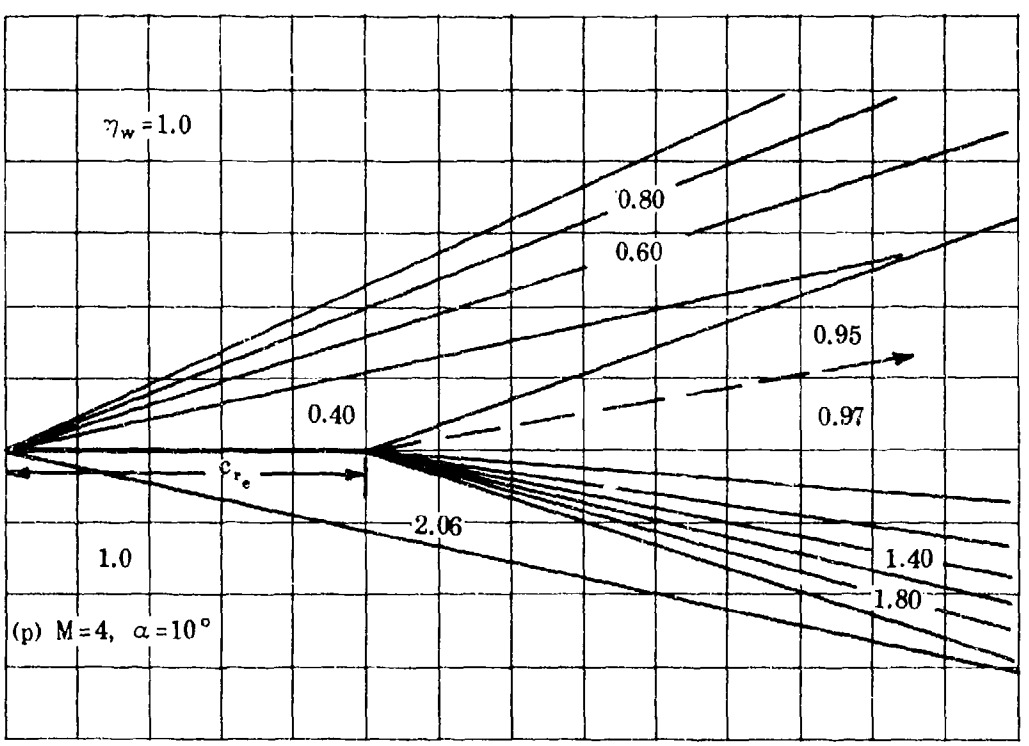

FIGURE 5.6.1.2-9 TAIL EFFECTIVENESS PARAMETER (contd)

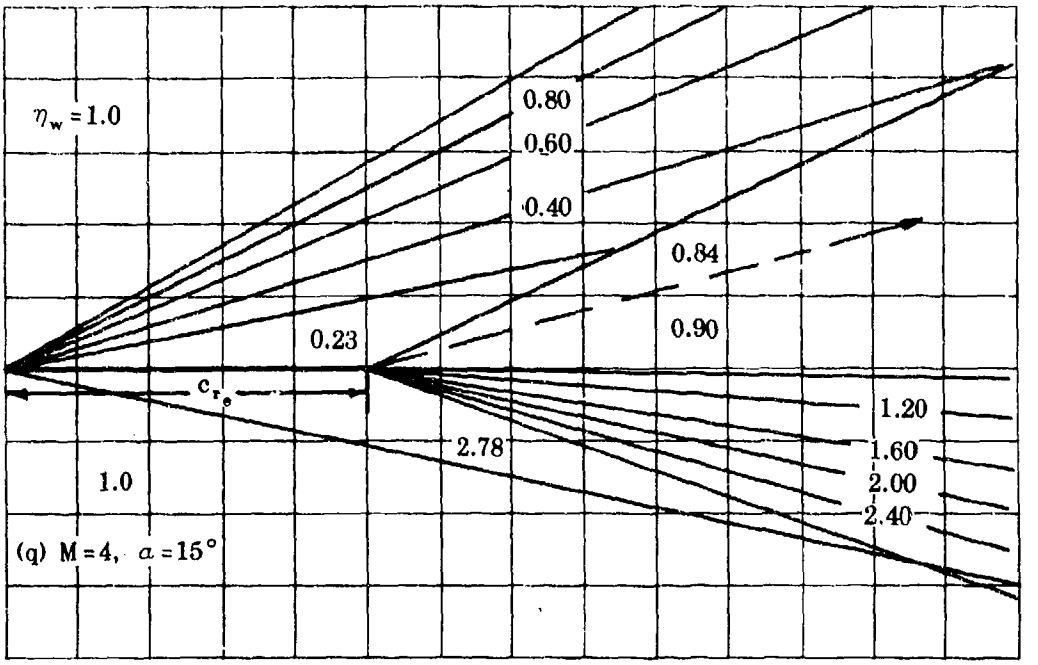

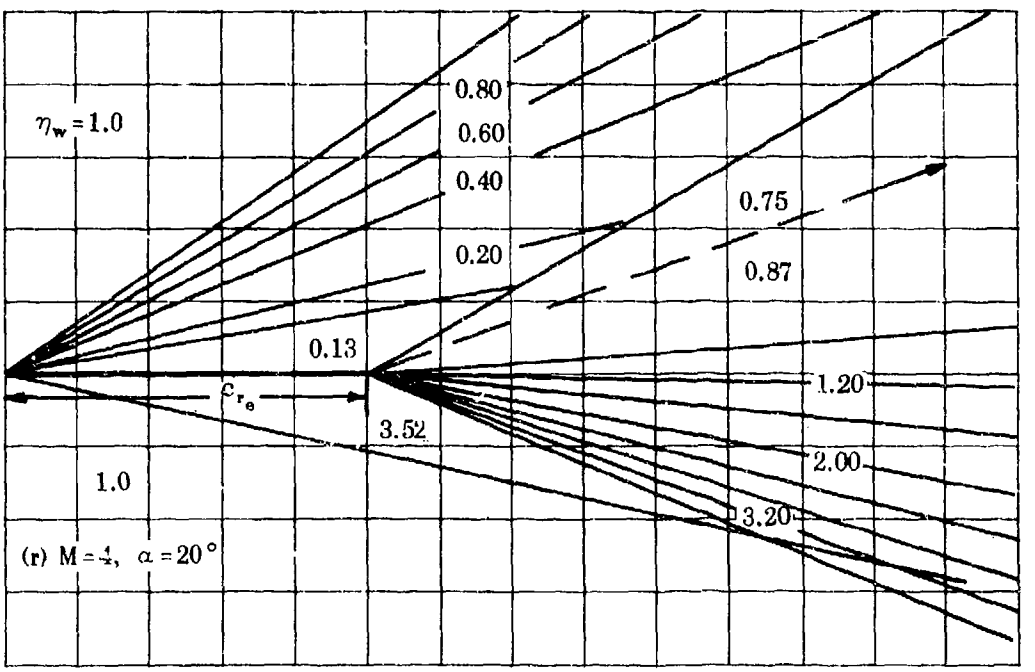

FIGURE 5.6.1.2-9 TAIL EFFECTIVENESS PARAMETER (contd)

5.6.2 WING-BODY-TAIL SIDESLIP DERIVATIVE C_{l_β}

5.6.2.1 WING-BODY-TAIL SIDESLIP DERIVATIVE C_{l_β} IN THE LINEAR ANGLE-OF-ATTACK RANGE

The information contained in this section is for estimating the rolling moment due to sideslip C_{l_β} of wing-body-tail configurations at low angles of attack. In general, it consists of a synthesis of material presented in other sections. Discussions of the various aerodynamic aspects of vehicle components and component combinations in sideslip are presented in other sections and are not repeated here.

The effect of a horizontal tail is more important in estimating C_{l_β} than C_{Y_β} and C_{n_β}, since the tail itself contributes to C_{l_β} in addition to affecting the vertical-panel contribution. The effect of the horizontal tail on the vertical-panel contribution and a discussion regarding the effects of the induced pressure field on the horizontal tail that is generated by the vertical panel are discussed in the introduction to Section 5.3.2.1 and are not repeated here.

For most configurations at subsonic speeds the horizontal-tail contribution is usually very small, and reasonable results can be obtained when it is neglected. However, for configurations employing a large horizontal tail with either significant twist and/or dihedral, the contribution may be worthy of consideration. For such a configuration the contribution of the horizontal tail may be estimated by using the method of Section 5.1.2.1; i.e., by treating the horizontal tail as an isolated wing. (Caution should be exercised to make certain the horizontal-tail contribution to C_{l_β} is converted to the same reference area and length $S_W b_W$ as the wing-body contribution, before adding them together.) However, since the horizontal-tail contribution is very small for most configurations in the subsonic speed regime, the method presented here neglects its contribution.

At transonic and supersonic speeds the horizontal-tail contribution should not be neglected. At transonic speeds the pressure field of the entire horizontal surface is affected by the presence of the vertical panel; while at supersonic speeds the effects are restricted to regions on the horizontal surface within boundaries defined by the shock-wave pattern of the vertical tail. Because of the complexity of the problem, no method is presented at transonic speeds. The method presented at supersonic speeds does not include the contribution of a horizontal tail; however, the effect of the horizontal tail on the vertical-tail contribution is accounted for as in Section 5.3.2.1.

The methods presented are similar to those of Section 5.6.1.1, in that the derivative of the configuration is given as the sum of the contributions of the wing-body combination and the empennage combination. The method of estimating the empennage contribution to C_{l_β} is similar to that for estimating the empennage contribution to C_{n_β} in Section 5.6.3.1. That is, the side-force contributions of the panels of the empennage are multiplied by an appropriate moment arm to obtain their individual contributions to the derivative C_{l_β}.

A. SUBSONIC

The method of estimating the subsonic values of the empennage contribution to the derivative C_{l_β} is based on the values of C_{Y_β} estimated by the methods of Paragraph A of Section 5.3.1.1. If the apparent-mass-concept method (Method 3, Paragraph A, Section 5.3.1.1) is used, the build-up

procedure outlined in Method 3 of Paragraph A of Section 5.6.1.1 must be applied in determining the individual side-force derivatives, with one exception. That is, the horizontal-tail increment is not to be expressed explicitly as a contributing term in the total empennage contribution; however, the effect of the presence of the horizontal tail must be considered in computing the contributions of the vertical panels.

For most configurations, the presence of flaps at a given lift coefficient causes C_{l_β} to become a larger negative value (see References 1 through 7). The exceptions to this are a few cases at low lift coefficients where C_{l_β} becomes a lower negative value (References 8, 9, and 10). However, the incremental changes in C_{l_β} vary dramatically with variations in lift coefficient for different configurations. This variation in the incremental change in C_{l_β} with flaps extended prevents the formulation of a hand procedure to estimate the flap effects on C_{l_β}.

Comparison of the subsonic method presented here with available flight-test data (References 11 through 15) supplements the substantiation of the method based on wind-tunnel data that is presented in Sections 5.2.2.1 and 5.3.2.1. A typical comparison of flight-test data (Reference 11) with the predicted variation of C_{l_β} as a function of $C_{L_{trim}}$ is shown in Sketch (a).

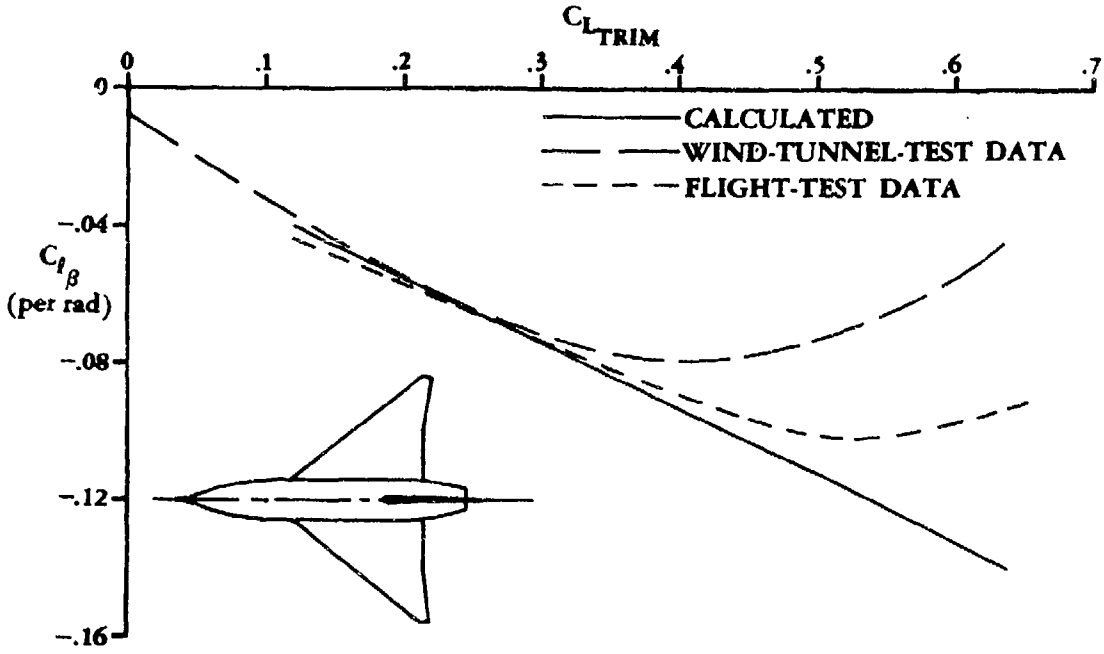

SKETCH (a)

As implied in the introduction to this section, the Datcom method at subsonic speeds is applicable to a configuration with a horizontal tail in the empennage.

DATCOM METHOD

The rolling moment (about the longitudinal stability axis) due to sideslip of a wing-body-tail configuration, referred to an arbitrary moment center and based on wing area and wing span, is given by

$$C_{l_\beta} = \left(C_{l_\beta}\right)_{WB} + \sum_p \left\{ \left(\Delta C_{Y_\beta}\right)_p \left[\frac{z_p \cos\alpha - \ell_p \sin\alpha}{b_W} \right] \right\} \qquad 5.6.2.1\text{-a}$$

where

p is the subscript referring to the vertical panels present in the empennage (either an upper vertical stabilizer V or a lower vertical stabilizer U).

$\left(C_{l_\beta}\right)_{WB}$ is the contribution of the wing-body configuration to the total rolling moment due to sideslip, obtained from Paragraph A, Section 5.2.2.1.

$\left(\Delta C_{Y_\beta}\right)_p$ is the side force due to sideslip of the added vertical panel determined as follows:

For configurations with the horizontal panel mounted on the body or for configurations with no horizontal panel, use Method 1 or Method 3, Paragraph A, Section 5.3.1.1. If Method 1 of Paragraph A of Section 5.3.1.1 is used, the total empennage increment is given by a single term. If Method 3 of Paragraph A of Section 5.3.1.1 is used, the build-up procedure outlined in Method 3 of Paragraph A of Section 5.6.1.1 must be applied to determine the individual increment of each added vertical panel*.

For configurations with a horizontal panel mounted on the vertical panel, use Method 1, Paragraph A, Section 5.3.1.1. The total empennage increment is given by a single term.

For configurations with twin vertical panels mounted on the tips of a horizontal panel, use Method 2, Paragraph A, Section 5.3.1.1. The total empennage increment is given by a single term.

z_p is the distance measured normal to the longitudinal body axis between the moment reference center and the MAC of the vertical panel, positive for the panel above the body.

ℓ_p is the distance parallel to the longitudinal body axis between the vehicle moment center and the quarter-chord point of the MAC of the vertical panel, positive for the panel aft of the vehicle moment center.**

b_W is the span of the wing.

All geometry used in determining the moment arms for the above method is based on the vertical panel extended to the body center line.

*See remarks of Paragraph A above, regarding horizontal-panel effects when using Method 3 of Paragraph A of Section 5.3.1.1.

**The aerodynamic center of the vertical panel could be used, but the inaccuracies of the basic method do not warrant this degree of refinement.

For a wingless configuration, b_W is replaced by the vehicle reference length, $\left(\Delta C_{Y_\beta}\right)_p$ is based on the vehicle reference area, and the contribution of the body alone to the total derivative may be ignored.

Sample Problems

1. Given: A configuration of Reference 16 consisting of a wing, body, horizontal tail, and vertical tail. This is the same configuration as that of Sample Problem 1, Paragraph A, Section 5.6.1.1. Some of the characteristics are repeated.

Wing Characteristics:

$A_W = 4.0$ $S_W = 36.0$ sq in. $b_W = 12.0$ in. $\lambda_W = 0.30$

$\Lambda_{c/2_W} = 40.9°$ $\Gamma = 0$ $z_W = 0$ (midwing)

Additional Characteristics:

$M = 0.60$ $\ell_V = 6.035$ in. $z_V = 1.65$ in. $\ell_f = 14.3$ in.

C_L	α (deg) (test)
0	0
0.1	1.55
0.2	3.20
0.3	4.65

Compute:

$$\frac{\ell_f}{b_W} = 1.192$$

$$\left(\frac{C_{l_\beta}}{C_L}\right)_{\Lambda_{c/2_W}} = -0.0035 \text{ per deg} \quad \text{(Figure 5.1.2.1-27)}$$

$$\cos \Lambda_{c/2_W} = 0.755$$

$$M \cos \Lambda_{c/2_W} = 0.453$$

$$\frac{A_W}{\cos \Lambda_{c/2_W}} = 5.30$$

$K_{M_\Lambda} = 1.035$ (Figure 5.1.2.1-28a)

$K_f = 0.91$ (Figure 5.2.2.1-26)

$\left(\frac{C_{l_\beta}}{C_L}\right)_\Lambda = -0.001$ (Figure 5.1.2.1-28b)

$$\left(C_{l_\beta}\right)_{WB} = C_L \left[\left(\frac{C_{l_\beta}}{C_L}\right)_{\Lambda_{c/2_W}} K_{M_\Lambda} K_f + \left(\frac{C_{l_\beta}}{C_L}\right)_\Lambda\right] \text{ per deg} \quad \text{(Equation 5.2.2.1-c)}$$

$$= C_L \left[(-0.0035)(1.035)(0.91) + (-0.001)\right]$$

$$= -0.0043\, C_L \text{ per deg}$$

$\left(\Delta C_{Y_\beta}\right)_{V(WBH)} = -0.645$ per rad (Sample Problem 1, Paragraph A, Section 5.6.1.1)

$= -0.01125$ per deg (based on S_W)

Solution:

$$C_{l_\beta} = \left(C_{l_\beta}\right)_{WB} + \sum_p \left\{\left(\Delta C_{Y_\beta}\right)_p \left[\frac{z_p \cos\alpha - \ell_p \sin\alpha}{b_W}\right]\right\} \quad \text{(Equation 5.6.2.1-a)}$$

$$= \left(C_{l_\beta}\right)_{WB} + \left(\Delta C_{Y_\beta}\right)_{V(WBH)} \left[\frac{z_V \cos\alpha - \ell_V \sin\alpha}{b_W}\right]$$

$$= -0.0043\, C_L + (-0.01125) \left(\frac{1.65\cos\alpha - 6.035\sin\alpha}{12.0}\right) \text{ per deg (based on } S_W b_W)$$

① C_L	② α (deg)	③ $(C_{l_\beta})_{WB}$ (per deg) -0.0043 ①	④ $z_V \cos\alpha$ (in.)	⑤ $\ell_V \sin\alpha$ (in.)	⑥ $\frac{z_V\cos\alpha - \ell_V\sin\alpha}{b_W}$ [④ − ⑤]/12.0	⑦ $(C_{l_\beta})_{V(WBH)}$ (per deg) -0.01125 ⑥	⑧ C_{l_β} (per deg) ③ + ⑦
0	0	0	1.660	0	0.1375	−0.00155	−0.00155
0.1	1.55	−0.00043	1.649	0.163	0.1236	−0.00139	−0.00182
0.2	3.20	−0.00086	1.647	0.337	0.1090	−0.00123	−0.00209
0.3	4.65	−0.00129	1.644	0.490	0.0962	−0.00108	−0.00237

These results are compared with experimental results from Reference 16 in Sketch (b).

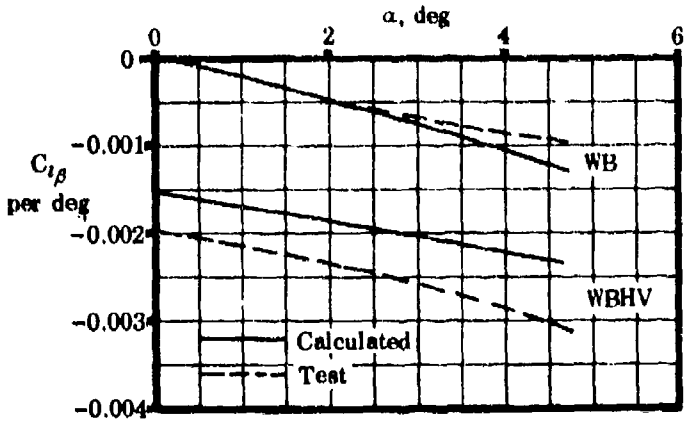

SKETCH (b)

2. Given: The configuration of Reference 17 consisting of a wing, body, horizontal tail, and vertical tail. This is the same configuration as that of Sample Problem 3, Paragraph A, Section 5.6.1.1. Some of the characteristics are repeated.

Wing Characteristics:

$A_W = 3.0$ $S_W = 576$ sq in. $b_W = 41.56$ in. $\lambda_W = 0$

$\Lambda_{c/2_W} = 33.6°$ $\Gamma = 0$ $z_W = -2.08$ in.

Additional Characteristics:

$M = 0.25$ $\ell_V = 24.89$ in. $z_V = 5.78$ in. $\ell_f = 51.13$ in.

$d = 6.0$ in. $h = 6.0$ in.

C_L	α (deg) (test)
0	0
0.1	2.0
0.2	4.0
0.3	6.?

Compute:

$$\frac{\ell_f}{b_W} = 1.23$$

$$\left(\frac{C_{l_\beta}}{C_L}\right)_{\Lambda_{c/2_W}} = -0.0027 \text{ per deg} \quad \text{(Figure 5.1.2.1-27c)}$$

$$\cos \Lambda_{c/2_W} = 0.8329$$

$$M \cos \Lambda_{c/2_W} = 0.2082$$

$$\frac{A}{\cos \Lambda_{c/2_W}} = 3.60$$

$$K_{M_\Lambda} = 1.000 \quad \text{(Figure 5.1.2.1-28a)}$$

$$K_f = 1.000 \quad \text{(Figure 5.2.2.1-26)}$$

$$\left(\frac{C_{l_\beta}}{C_L}\right)_A = -0.001 \quad \text{(Figure 5.1.2.1-28b)}$$

$$\left(\Delta C_{l_\beta}\right)_{z_W} = \frac{1.2\sqrt{A}}{57.3} \frac{z_w}{b} \left(\frac{2d}{b}\right) \text{ per deg} \quad \text{(Equation 5.2.2.1-c)}$$

$$= \frac{(1.2)(1.732)}{57.3} \left(\frac{-2.08}{41.56}\right) (0.2885)$$

$$= -0.000524 \text{ per deg}$$

$$\left(C_{l_\beta}\right)_{WB} = C_L \left[\left(\frac{C_{l_\beta}}{C_L}\right)_{\Lambda_{c/2_W}} K_{M_\Lambda} K_f + \left(\frac{C_{l_\beta}}{C_L}\right)_A\right] + \left(\Delta C_{l_\beta}\right)_{z_W} \text{ per deg} \quad \text{(Equation 5.2.2.1-c)}$$

$$= C_L \left[(-0.0027)(1.00)(1.00) + (-0.001)\right] + (-0.00052)$$

$$= -0.0037\, C_L - 0.00052$$

$$\left(\Delta C_{Y_\beta}\right)_{V(WBH)} = 0.665 \text{ per rad} \quad \text{(Sample Problem 3, Paragraph A, Section 5.6.1.1)}$$

$$= -0.0116 \text{ per deg (based on } S_w\text{)}$$

Solution:

$$C_{l_\beta} = \left(C_{l_\beta}\right)_{WB} + \sum_p \left\{ \left(\Delta C_{Y_\beta}\right)_p \left[\frac{z_p \cos\alpha - \ell_p \sin\alpha}{b_W} \right] \right\} \qquad \text{(Equation 5.6.2.1-a)}$$

$$= \left(C_{l_\beta}\right)_{WB} + \left(\Delta C_{Y_\beta}\right)_{V(WBH)} \left[\frac{z_V \cos\alpha - \ell_V \sin\alpha}{b_W} \right]$$

$$= -0.0037\, C_L - 0.00052 + (-0.0116) \left(\frac{5.78 \cos\alpha - 24.89 \sin\alpha}{41.56} \right)$$

per deg (based on $S_W b_W$)

① C_L	② α (deg)	③ $(C_{l_\beta})_{WB}$ (per deg) -0.0037 ① -0.00052	④ $z_V \cos\alpha$ (in.)	⑤ $\ell_V \sin\alpha$ (in.)	⑥ $\frac{z_V \cos\alpha - \ell_V \sin\alpha}{b_W}$ [④ − ⑤]/41.56	⑦ $(C_{l_\beta})_{V(WBH)}$ (per deg) -0.01185 ⑥	⑧ C_{l_β} (per deg) ③ + ⑦
0	0	−0.00052	5.780	0	0.1390	−0.00161	−0.00213
0.1	2.0	−0.00089	5.777	0.870	0.1180	−0.00137	−0.00226
0.2	4.0	−0.00126	5.766	1.740	0.0969	−0.00112	−0.00238
0.3	5.7	−0.00163	5.752	2.475	0.0790	−0.00092	−0.00255

These results are compared with experimental results from Reference 17 in Sketch (c).

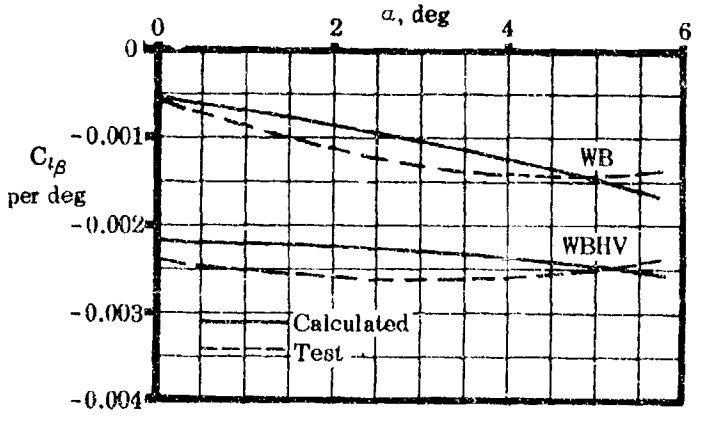

SKETCH (c)

B. TRANSONIC

A brief discussion of the flow phenomena associated with the forces generated on vertical panels at transonic speeds is given in Paragraph B of Section 5.3.1.1. At the present time there are no methods available to predict the effect of wing-body wake and sidewash or the mutual interference effects between vehicle components on the sideslip characteristics at transonic speeds. In addition, the effects of the impingement of the pressure field generated by the vertical panel on the horizontal-tail surface are difficult to evaluate.

DATCOM METHOD

No explicit method is available in the literature for estimating the vehicle sideslip derivative C_{l_β} at transonic speeds and none is presented in the Datcom. Some typical transonic data for this derivative are presented as Figure 5.6.2.1-15.

C. SUPERSONIC

The procedure for estimating the supersonic sideslip derivative C_{l_β} is essentially the same as that at subsonic speeds. That is, the rolling-moment contributions of vertical panels are based on the sideslip derivative C_{Y_β}. The problem of estimating the forces generated on vertical panels is complicated by the presence of shock waves. This effect is discussed in Paragraph C of Section 5.3.1.1.

As stated in the introduction to this section, no method is available for determining the horizontal-tail contribution to the derivative C_{l_β}. However, the effect of the horizontal tail on the vertical-tail contribution is accounted for by proper use of the apparent-mass factor (K) charts in determining the vertical-panel side force.

DATCOM METHOD

The rolling moment (about the longitudinal stability axis) due to sideslip of a wing-body-vertical-tail configuration, referred to an arbitrary moment center and based on wing area and wing span, is given by Equation 5.6.2.1-a:

$$C_{l_\beta} = \left(C_{l_\beta}\right)_{WB} + \sum_p \left\{ \left(\Delta C_{Y_\beta}\right)_p \left[\frac{z_p \cos\alpha - \ell_p \sin\alpha}{b_W} \right] \right\}$$

where C_{l_β}, $\left(C_{l_\beta}\right)_{WB}$, z_p, and b_W are defined in Paragraph A above, and

$\left(\Delta C_{Y_\beta}\right)_p$ is the side force due to sideslip of an added vertical panel from Paragraph C of Section 5.3.1.1. The build-up procedure outlined in Paragraph C of Section 5.6.1.1 (neglecting the contribution of a horizontal tail) must be applied in determining the individual increment of each added panel. The effect of the presence of a horizontal tail must be considered in computing the contributions of the vertical panels.

ℓ_p is the distance parallel to the longitudinal body axis between the moment reference center and the 50-percent chord of the MAC of the added vertical panel, positive for panel aft of the vehicle moment center.*

All geometry used in determining the moment arms of the vertical panels is based on the exposed panel.

For a wingless configuration the remarks following the Datcom methods of Paragraph A above are also applicable at supersonic speeds.

Sample Problem

Given: The configuration of Reference 18 consisting of a wing, body, upper vertical tail, and lower vertical tail. This is the same configuration as that of the sample problem of Paragraph C, Section 5.6.1.1 with the horizontal tail removed. Some characteristics are repeated.

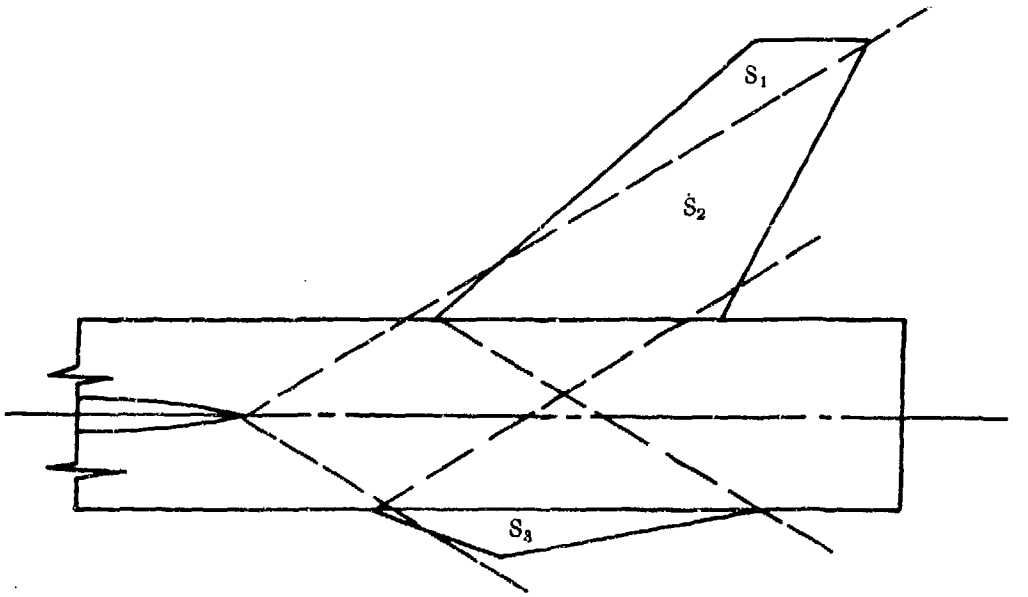

Wing Characteristics:

A_W = 3.1[illegible] S_W = 114.5 sq in. z_W = 0 Γ = −3.5°

λ_W = 0.468 Λ_{LE_W} 48.08° No twist b_W = 19.08 in.

Vertical-Tail Characteristics:

A_{V_e} = 1.48 S_{V_e} = 19.20 sq in. Λ_{LE_V} = 49:2° b_V = 7.08 in.

*See footnote at bottom of Page 5.6.2.1-3.

$\lambda_{V_e} = 0.392$

Ventral-Tail Characteristics:

$A_{U_e} = 0.2025$ $S_{U_e} = 3.24$ sq in. $\Lambda_{LE_U} = 70.2°$ $b_U = 2.56$ in.

$\lambda_{U_e} = 0$

Additional Characteristics:

$M = 2.01$ $\mu = \sin^{-1}(1/M) = 29.8°$ $r_1 = 1.75$ in.

$r_2 = 1.496$ in. $r_1/r_2 = 1.170$ $S_1 = 4.63$ sq in.

$S_2 = 14.56$ sq in. $S_3 = S_{U_e} = 3.24$ sq in. $d/b_W = 0.157$

$\ell_V = 10.65$ in. $z_V = 4.05$ in. $\ell_U = 8.40$ in. $z_U = -2.05$ in.

$C_N = 0.10, \alpha = 2.20°$ (test)

Compute:

Step 1. Determine the wing-body contribution $\left(C_{l_\beta}\right)_{WB}$

$\sqrt{M^2 - 1} = 1.744$

$\Lambda_{LE_W} = 0.84$ rad; $1 + \Lambda_{LE_W} = 1.84$; $1 + \dfrac{\Lambda_{LE_W}}{2} = 1.42$

$1 + \lambda_W \left(1 + \Lambda_{LE_W}\right) = 1.860$

$\dfrac{\tan \Lambda_{LE_W}}{\sqrt{M^2 - 1}} = 0.639$

$\dfrac{M^2 \cos^2 \Lambda_{LE_W}}{A} = \dfrac{(4.04)(0.445)}{3.18} = 0.565$

$\left(\dfrac{\tan \Lambda_{LE_W}}{4}\right)^{4/3} = (0.2785)^{4/3} = 0.182$

Dihedral effect

$A_W \sqrt{M^2 - 1} = 5.55; \sqrt{M^2 - 1} \cot \Lambda_{LE_W} = 1.57$

$C_{l_p} = -0.28$ per rad (Figure 7.3.2.2-6)

$$\left(\frac{1 + 2\lambda}{1 + 3\lambda}\right)_W = 0.805$$

$$\frac{C_{l_\beta}}{\Gamma} = \frac{2}{(57.3)^2} \left(\frac{1 + 2\lambda}{1 + 3\lambda}\right)_W C_{l_p} = -0.000137 \text{ (per deg)}^2 \quad \text{(Equation 5.1.2.1-d)}$$

$$\frac{\Delta C_{l_\beta}}{\Gamma} = -0.0005 \sqrt{A_W} \left(\frac{d}{b_W}\right)^2 = -0.000022 \text{ (per deg)}^2 \quad \text{(Equation 5.2.2.1-b)}$$

$$\Gamma \left(\frac{C_{l_\beta}}{\Gamma} + \frac{\Delta C_{l_\beta}}{\Gamma}\right) = -0.000159\,\Gamma$$

$\left(C_{N_\alpha}\right)_W = 0.041$ per deg (based on S_W) (Section 4.1.3.2)

$$\left(C_{l_\beta}\right)_{WB} = -0.061\, C_N \left(C_{N_\alpha}\right)_W [1 + \lambda (1 + \Lambda_{LE})]_W \left(1 + \frac{\Lambda_{LE}}{2}\right)_W \left(\frac{\tan \Lambda_{LE_W}}{\sqrt{M^2 - 1}}\right)$$

$$\left[\frac{M^2 \cos^2 \Lambda_{LE_W}}{A_W} + \left(\frac{\tan \Lambda_{LE_W}}{4}\right)^{4/3}\right] + \Gamma \left(\frac{C_{l_\beta}}{\Gamma} + \frac{\Delta C_{l_\beta}}{\Gamma}\right)$$

(Equation 5.2.2.1-d)

$$= (-0.061)\, C_N\, (0.041)\, (1.860)\, (1.420)\, (0.639)\, [0.565 + 0.182]$$

$$+ (-3.5)\, (-0.000159)$$

$$= -0.00315\, C_N + 0.000556 \text{ per deg (based on } S_W b_W)$$

Step 2. Determine the empennage contribution

$\left(\Delta C_{Y_\beta}\right)_{V(WB)} = -0.520$ per rad (based on S_W) (Sample problem of Paragraph C, Section 5.6.1.1)

$= 0.0091$ per deg

The vertical tail in the sample problem of Paragraph C, Section 5.6.1.1 does not "see" the horizontal tail; therefore the increment in C_{Y_β} of the vertical tail in the presence of a wing and body is identical to $\left(\Delta C_{Y_\beta}\right)_{V(WBH)}$ calculated in Section 5.6.1.1.

Calculate the increment in C_{Y_β} due to adding the lower vertical panel to the wing-body-upper-vertical-panel combination. In the configuration sketch the ventral panel senses only the body. The effective apparent mass ratio is

$$K'_{U(BV)} = K_{U(B)} = 3.0 \quad \text{(Section 5.3.1.1 with } (r_1/r_2) = 1.170, (r_1/b)_{U_{\text{added panel}}} = 0.685, \text{ and } (r_1/b)_{V_{\text{existing panel}}} = 1.000\text{)}$$

$\left(C_{N_\alpha}\right)_U = 0.622$ per rad (based on S_{U_e}) (Sample problem, Paragraph C, Section 5.6.1.1)

$$\left(\Delta C_{Y_\beta}\right)_{U(WBV)} = -K'_{U(BV)} \left(C_{N_\alpha}\right)_U \frac{S_{U_e}}{S_W} \quad \text{(Equation 5.3.1.1-f)}$$

$$= (-3.0)\,(0.622)\left(\frac{3.24}{114.5}\right)$$

$$= -0.0527 \text{ per rad (based on } S_W\text{)}$$

$$= -0.00092 \text{ per deg}$$

Solution:

$$C_{l_\beta} = \left(C_{l_\beta}\right)_{WB} + \sum_p \left\{ \left(\Delta C_{Y_\beta}\right)_p \left[\frac{z_p \cos\alpha - \ell_p \sin\alpha}{b_W} \right] \right\} \quad \text{(Equation 5.6.2.1-a)}$$

$$= \left(C_{l_\beta}\right)_{WB} + \left(\Delta C_{Y_\beta}\right)_{V(WB)} \left[\frac{z_V \cos\alpha - \ell_V \sin\alpha}{b_W} \right]$$

$$+ \left(\Delta C_{Y_\beta}\right)_{U(WBV)} \left[\frac{z_U \cos\alpha - \ell_U \sin\alpha}{b_W} \right]$$

$$= (-0.00315\ C_N + 0.000556) + (-0.0091)\left[\frac{4.05\cos\alpha - 10.65\sin\alpha}{19.08}\right]$$

$$+ (-0.00092)\left[\frac{(-2.05)\cos\alpha - 8.40\sin\alpha}{19.08}\right]$$

$$= [-0.00315\ (0.1) + 0.000556] + [(-0.00193)\cos 2.2^\circ + 0.00508\sin 2.2^\circ]$$

$$+ [0.00010\cos 2.2^\circ + 0.000405\sin 2.2^\circ]$$

$$= 0.00024 + (-0.00173) + (0.000116)$$

$$= -0.001374 \text{ per deg (based on } S_W b_W)$$

REFERENCES

1. Purser, P. E., and Spearman, M. L.: Wind-Tunnel Tests at Low Speed of Swept and Yawed Wings Having Various Plan Forms. NACA TN 2445, 1951. (U)

2. Graham, D., and Koenig, D.: Tests in the Ames 40- by 80-Foot Wind Tunnel of an Airplane Configuration with an Aspect Ratio 2 Triangular Wing and an All-Movable Horizontal Tail – Lateral Characteristics. NACA RM A5IL03, 1952. (U)

3. Koenig, D.. Tests in the Ames 40- by 80-Foot Wind Tunnel of an Airplane Configuration with an Aspect Ratio 3 Triangular Wing and an All-Movable Horizontal Tail – Longitudinal and Lateral Characteristics. NACA RM A52L15, 1953. (U)

4. Griner, R. F.: Static Lateral Stability Characteristics of an Airplane Model Having a 47.7° Sweptback Wing of Aspect Ratio 6 and the Contribution of Various Model Components at a Reynolds Number of 4.45×10^6. NACA RM L53G09, 1953. (U)

5. Letko, W., and Goodman, A.: Preliminary Wind-Tunnel Investigation at Low Speed of Stability and Control Characteristics of Sweptback Wings. NACA TN 1046, 1946. (U)

6. Fink, M. P., and Freeman, D. C., Jr.: Full-Scale Wind-Tunnel Investigation of Static Longitudinal and Lateral Characteristics of a Light Twin-Engine Airplane. NACA TN D-4983, 1969. (U)

7. Fink, M. P., and Freeman, D. C., Jr.: Full-Scale Wind-Tunnel Investigation of the Static Longitudinal and Lateral Characteristics of a Light Single-Engine Airplane. NACA TN D-5700, 1970. (U)

8. Franks, R. W.: Tests in the Ames 40- by 80-Foot Wind Tunnel of an Airplane Model with an Aspect Ratio 4 Triangular Wing and an All-Movable Horizontal Tail – High-Lift Devices and Lateral Controls. NACA RM A52K13, 1953. (U)

9. Lockwood, V. E., and Watson, J. M.: Stability and Control Characteristics at Low Speed of an Airplane Model Having a 38.7° Sweptback Wing with Aspect Ratio 4.51, Taper Ratio 0.54, and Conventional Tail Surfaces. NACA TN 1742, 1948. (U)

10. Neeley, R. H., and Conner, D. W.: Aerodynamic Characteristics of a 42° Swept-Back Wing with Aspect Ratio 4 and 64_1-112 Airfoil Sections at Reynolds Numbers from 1,700,000 to 9,500,000. NACA RM L7D14, 1947. (U)

11. Perry, D. H., Morrall, J. C., and Port, W. G. A.: Low Speed Flight Tests on a Tailless Delta Wing Aircraft (Avro 707B). Part 3 – Lateral Stability and Control. ARC CP 1106, 1970. (U)

12. Brown, S. C., and Holleman, E. C.: Experimental and Predicted Lateral-Directional Dynamic-Response Characteristics of a Large Flexible 35° Swept-Wing Airplane at an Altitude of 35,000 Feet. NACA TN 3874, 1956. (U)

13. Wolowicz, C. H., and Redless, H. A.: Effects of Jet Exhausts on Flight-Determined Longitudinal and Lateral Dynamic Stability Characteristics of the Douglas D-558-II Research Airplane. NACA RM H57G09, 1957. (U)

14. DC-8 Unpublished Data. (U)

15. DC-9 Unpublished Data. (U)

16. Sleeman, W. C., Jr.: An Experimental Study at High Subsonic Speeds of Several Tail Configurations on a Model Having a 45° Sweptback Wing. NACA RM L57C08, 1957. (U)

17. Savage, H. F., and Tinling, B. E.: The Subsonic Static Aerodynamic Characteristics of an Airplane Model Having a Triangular Wing of Aspect Ratio 3. II – Lateral and Directional Characteristics. NACA TN 4042, 1957. (U)

18. Spearman, M. L., Robinson, R. B., and Driver, C.: The Effects of the Addition of Small Fuselage-Mounted Fins on the Static Directional Stability Characteristics of a Model of a 45° Sweptback Wing Airplane at Angles of Attack up to 15.3° at a Mach Number of 2.01. NACA RM L56D16a. 1956. (U)

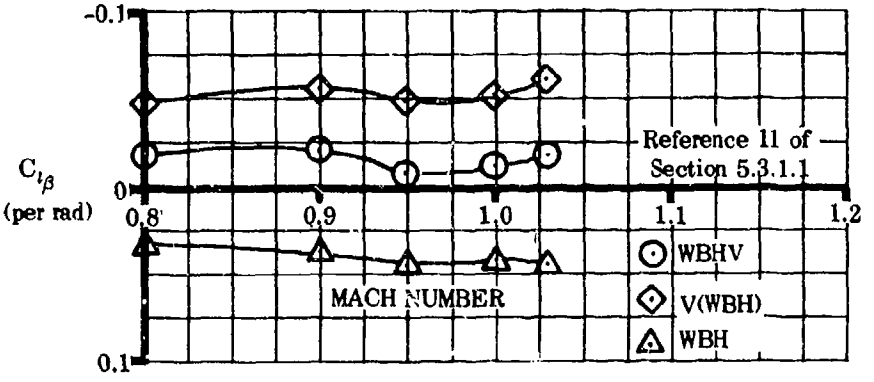

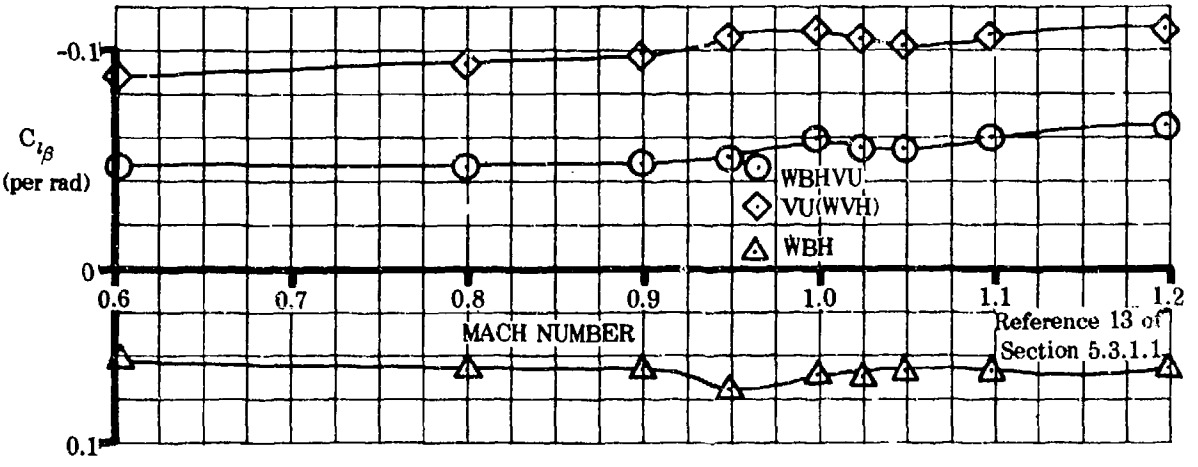

FIGURE 5.6.2.1-15 TYPICAL TRANSONIC DATA

5.6.3 WING-BODY-TAIL SIDESLIP DERIVATIVE C_{n_β}

5.6.3.1 WING-BODY-TAIL SIDESLIP DERIVATIVE C_{n_β} IN THE LINEAR ANGLE-OF-ATTACK RANGE

The information contained in this Section is for estimating the yawing moment due to sideslip C_{n_β} of wing-body-tail combinations at low angles of attack. In general, it consists of a synthesis of material presented in other Sections. Discussion of the various aerodynamic aspects of vehicle components in sideslip is given in other Sections of the Datcom and is not repeated here.

The methods presented are based on the procedure of totaling the wing-body contribution and the total empennage increment as was done in Section 5.6.1.1 for the determination of side force due to sideslip for a complete configuration. The yawing moment of the complete empennage is determined by applying the appropriate moment arm to each of the incremental values of side force which make up the total, as determined in Section 5.6.1.1.

A. SUBSONIC

The methods of estimating the subsonic values of the empennage contribution to the derivative C_{n_β} are based on the values of C_{Y_β} estimated by the methods of paragraph A of Section 5.3.1.1. If the apparent-mass-concept method (Method 3, paragraph A, Section 5.3.1.1) is used, the build-up procedure outlined in Method 3 of paragraph A of Section 5.6.1.1 must be applied in determining the individual panel side-force derivatives.

Two methods of determining the moment arm through which the empennage panel side force acts at subsonic speeds are presented in Section 5.3.3.1. The moment arm can be taken as (a) the distance parallel to the longitudinal axis between the vehicle moment center and the quarter-chord point of the mean aerodynamic chord of the added panel or (b) the distance parallel to the longitudinal axis between the vehicle moment center and the aerodynamic center of the added panel. For most cases the simplified approximation (a) is used. However, for short coupled configurations where the tail length distance is relatively short and the size of the added panel large the refined approximation (b) is recommended.

DATCOM METHODS

Method 1

Simplified Method

The yawing moment due to sideslip of a wing-body-tail configuration, referred to an arbitrary moment center and based on the wing area and wing span, is given by

$$C_{n_\beta} = (C_{n_\beta})_{WB} + \Sigma_p \left[-(\Delta C_{Y_\beta})_p \frac{\ell_p}{b_w} \right] \qquad 5.6.3.1\text{-a}$$

where the subscript $_p$ refers to panels present in the empennage

$(C_{n_\beta})_{WB}$ is the contribution of the wing-body combination to the total yawing moment due to sideslip, obtained from Section 5.2.3.1

$(\Delta C_{Y_\beta})_p$ is the side force due to sideslip of the added panel determined as follows

For configurations with the horizontal panel mounted on the body, or for configurations with no horizontal panel use Method 1 or Method 3, paragraph A, Section 5.3.1.1. If Method 1 of paragraph A of Section 5.3.1.1 is used, the total empennage increment is given by a single term. If Method 3 of paragraph A of Section 5.3.1.1 is used, the build-up procedure outlined in Method 3 of paragraph A of Section 5.6.1.1 must be applied to determine the individual increment of each added panel.

For configurations with a horizontal panel mounted on the vertical panel, use Method 1, paragraph A, Section 5.3.1.1. The total empennage increment is given by a single term.

For configurations with twin vertical panels mounted on the tips of a horizontal panel use Method 2, paragraph A, Section 5.3.1.1. The total empennage increment is given by a single term.

ℓ_p is the distance parallel to the longitudinal axis between the vehicle moment center and the quarter-chord point of the MAC of the added panel, positive for the panel aft of the vehicle moment center

b_W is the span of the wing

Method 2

Refined Method

In this case the sideslip derivative C_{n_β}, referred to an arbitrary moment center and based on wing area and wing span, is given by

$$C_{n_\beta} = (C_{n_\beta})_{WB} + \Sigma_p \left[-(\Delta C_{Y_\beta})_p \left(\frac{\ell_p + (x_{a.c.})_p}{b_W} \right) \right] \qquad 5.6.3.1\text{-b}$$

where $(C_{n_\beta})_{WB}$, $(\Delta C_{Y_\beta})_p$, ℓ_p, and b_W are defined in Method 1 above, and

$(x_{a.c.})_p$ is the distance parallel to the longitudinal axis between the quarter-chord point of the MAC of the added panel and the aerodynamic center of the added panel obtained from paragraph A of Section 4.1.4.2, positive for the a.c. behind the quarter-chord point of the MAC. (In determining the vertical panel a.c. use the aspect ratio of the panel mounted on an infinite reflection plane).

All geometry used in determining the moment arms for the above methods is based on the panel extended to the body centerline.

For a wingless configuration, b_W is replaced by the vehicle reference length, $(\Delta C_{Y_\beta})_p$ is based on the vehicle reference area, and the contribution of the body to the total derivative can be obtained from Section 4.2.2.1 as $(C_{n_\beta})_B \approx -(C_{m_\alpha})_B$, based on the vehicle reference area.

Sample Problems

1. Method 1

Given: A wing-body-horizontal tail-vertical tail configuration of reference 1. This is the same configuration as that of sample problem 1, paragraph A, Section 5.6.1.1. Some of the characteristics are repeated.

Wing Characteristics

S_W = 36.0 sq in. b_W = 12.0 in.

Body Characteristics

ℓ_B = 18.25 in. x_m = 10.42 in. S_{B_S} = 25.6 sq in. h_1/h_2 = 0.950

h/w = 1.000

Additional Characteristics

M = 0.60 R_ℓ = 7.43×10^6 (based on ℓ_B) ℓ_V = 6.035 in.

α = 0

Compute:

$\frac{x_m}{\ell_B} = 0.572$

$\left(\frac{h_1}{h_2}\right)^{1/2} = 0.975$

$\frac{\ell_B^2}{S_{B_S}} = 13.00$

Using the above computed parameters and the Reynolds number obtain K_N from figure 5.2.3.1-5

$K_N = 0.0014$

$$(C_{n_\beta})_{WB} = -K_N \frac{S_{B_S}}{S_W} \frac{\ell_B}{b_W} \text{ per deg} \qquad \text{(equation 5.2.3.1-a)}$$

$$= -(0.0014)\left(\frac{25.6}{36.3}\right)\left(\frac{18.25}{12.0}\right)$$

$$= -0.00151 \text{ per deg (based on } S_W b_W)$$

$$= -0.0865 \text{ per rad (based on } S_W b_W)$$

$(\Delta C_{Y_\beta})_{V(WBH)} = -0.645$ per rad (based on S_W) (sample problem 1, paragraph A, Section 5.6.1.1)

Solution:

$$C_{n_\beta} = (C_{n_\beta})_{WB} + \Sigma_p \left[-(\Delta C_{Y_\beta})_p \frac{\ell_p}{b_W} \right] \qquad \text{(equation 5.6.3.1-a)}$$

$$= (C_{n_\beta})_{WB} + \left[-(\Delta C_{Y_\beta})_{V(WBH)} \frac{\ell_V}{b_W} \right]$$

$$= -0.0865 + \left[-(-0.645)\left(\frac{6.035}{12.0}\right) \right]$$

$$= -0.0865 + 0.324$$

$$= 0.2375 \text{ per rad (based on } S_W b_W)$$

The experimental results (based on $S_W b_W$) from reference 1 are $(C_{n_\beta})_{WB} = -0.063$ per radian, $(\Delta C_{n_\beta})_{V(WBH)} = 0.350$ per radian, and $C_{n_\beta} = 0.286$ per radian.

2. Method 1

Given: The wing-body-horizontal tail-vertical tail configuration of reference 2. This is the same configuration as that of sample problem 3, paragraph A, Section 5.6.1.1. Some characteristics are repeated.

Wing Characteristics

$S_W = 576$ sq in. $\quad b_W = 41.56$ in.

Body Characteristics

$\ell_B = 72.0$ in. $\quad x_m = 39.60$ in. $\quad S_{B_S} = 349.9$ sq in. $\quad h_1/h_2 = 0.730$

$h/w = 1.000$

Additional Characteristics

$M = 0.25$ $\quad R_\ell = 9.73 \times 10^6$ (based on ℓ_B) $\quad \ell_V = 24.89$ in.

$\ell_H = 26.2$ in. $\quad \alpha = 0$

Compute:

$$\frac{x_m}{\ell_B} = 0.550$$

$$\left(\frac{h_1}{h_2}\right)^{1/2} = 0.854$$

$$\frac{\ell_B^2}{S_{B_S}} = 14.80$$

Using the parameters computed above and the Reynolds number obtain K_N from figure 5.2.3.1-5

$K_N = 0.0013$

$(C_{n_\beta})_{WB} = -K_N \frac{S_{B_S}}{S_W} \frac{\ell_B}{b_W}$ per deg (equation 5.2.3.1-a)

$= -(0.0013)\left(\frac{349.9}{576.0}\right)\left(\frac{72.0}{41.56}\right)$

$= -0.001365$ per deg (based on $S_W b_W$)

$= -0.0782$ per rad (based on $S_W b_W$)

From sample problem 3, paragraph A, Section 5.6.1.1

$(\Delta C_{Y_\beta})_{H(WB)} = 0$

$(\Delta C_{Y_\beta})_{V(WBH)} = -0.665$ per rad (based on S_W)

Solution:

$C_{n_\beta} = (C_{n_\beta})_{WB} + \Sigma_p \left[-(\Delta C_{Y_\beta})_p \frac{\ell_p}{b_W}\right]$ (equation 5.6.3.1-a)

$= (C_{n_\beta})_{WB} + \left[-(\Delta C_{Y_\beta})_{H(WB)} \frac{\ell_H}{b_W}\right] + \left[-(\Delta C_{Y_\beta})_{V(WBH)} \frac{\ell_V}{b_W}\right]$

$= -0.0782 + 0 + \left[-(-0.665)\left(\frac{24.89}{41.56}\right)\right]$

$= -0.0782 + 0.398$

$= 0.3198$ per rad (based on $S_W b_W$)

The experimental results (based on $S_W b_W$) from reference 2 are $(C_{n_\beta})_{WB} = -0.057$ per radian, $(\Delta C_{n_\beta})_{V(WBH)} = 0.409$ per radian, and $C_{n_\beta} = 0.352$ per radian.

B. TRANSONIC

A brief discussion of the flow phenomena associated with forces generated on vertical panels at transonic speeds is given in paragraph B of Section 5.3.1.1. At the present time there are no methods available to predict the effect of wing-body wake and sidewash or the mutual interference effects between vehicle components on the sideslip characteristics at transonic speeds.

DATCOM METHOD

No explicit method is available for estimating the vehicle sideslip derivative C_{n_β} at transonic speeds and none is presented in the Datcom. Some typical transonic data for this derivative are presented as figure 5.6.3.1-8.

C. SUPERSONIC

The procedure for estimating the supersonic sideslip derivative C_{n_β} of a wing-body-tail configuration is essentially the same as that at subsonic speeds. The problem of estimating the forces generated on vertical panels is complicated by the presence of shock waves. This effect is discussed in paragraph C of Section 5.3.1.1.

The moment arm through which an added vertical panel acts can be taken as (a) the distance parallel to the longitudinal axis between the vehicle moment center and the 50-percent-chord point of the mean aerodynamic chord of the added vertical panel or (b) the distance parallel to the longitudinal axis between the vehicle moment center and

the aerodynamic center of the added vertical panel. For short-coupled configurations with a large vertical panel the latter approach is recommended. At supersonic speeds the centroid of area of the region of interference approximates the center of pressure in the case of the increment gained by adding a horizontal surface.

This method is limited to configurations in which the horizontal tail is mounted on the body or configurations with no horizontal tail.

DATCOM METHODS

Method 1

Simplified Method

The yawing moment due to sideslip of a wing-body-tail configuration, referred to an arbitrary moment center and based on wing area and wing span, is given by equation 5.6.3.1-a

$$C_{n_\beta} = (C_{n_\beta})_{WB} + \Sigma_p \left[-(\Delta C_{Y_\beta})_p \frac{\ell_p}{b_W} \right]$$

where $(C_{n_\beta})_{WB}$ is defined in paragraph A above, and

$(\Delta C_{Y_\beta})_p$ is the side force due to sideslip of an added panel obtained from paragraph C, Section 5.3.1.1. The build-up procedure outlined in paragraph C of Section 5.6.1.1 must be applied in determining the individual increment of each added panel.

ℓ_p is the distance parallel to the longitudinal axis between the vehicle moment center and the 50-percent-chord point of the MAC of an added vertical panel, positive for the vertical panel aft of of the vehicle moment center. In the case of the increment gained by adding a horizontal panel, ℓ_p is the distance parallel to the longitudinal axis between the vehicle moment center and the centroid of the area of the region of interference, positive for the horizontal panel aft of the vehicle moment center.

Method 2

Refined Method

In this case the sideslip derivative C_{n_β}, referred to an arbitrary moment center and based on wing area and wing span, is given by equation 5.6.3.1-b

$$C_{n_\beta} = (C_{n_\beta})_{WB} + \Sigma_p \left[-(\Delta C_{Y_\beta})_p \left(\frac{\ell_p + (x_{a.c.})_p}{b_W} \right) \right]$$

where $(C_{n_\beta})_{WB}$, $(\Delta C_{Y_\beta})_p$, and ℓ_p are defined in Method 1 above, and

$(x_{a.c.})_p$ is the distance parallel to the longitudinal axis between the 50-percent-chord point of the MAC of an added vertical panel and the aerodynamic center of the added panel obtained from paragraph C of Section 4.1.4.2, positive for the a.c. behind the 50-percent-chord point. (In determining the vertical panel a.c. use the aspect ratio of the isolated panel mounted on an infinite reflection plane.)

In the case of the increment gained by adding a horizontal panel, the moment arm is treated as in Method 1 above.

All geometry used in determining the moment arms of the vertical panels in the above methods is based on the exposed panel.

For a wingless configuration the remarks following the Datcom methods of paragraph A above are also applicable at supersonic speeds.

Sample Problem

Method 1

Given: The wing-body-horizontal tail-upper vertical tail-lower vertical tail configuration of reference 3. This is the same configuration as that of the sample problem of paragraph C, Section 5.6.1.1. Some characteristics are repeated..

Wing Characteristics

S_W = 114.5 sq in. b_W = 19.08 in.

Body Characteristics

ℓ_B = 32.88 in. x_m = 18.00 in. S_{B_S} = 92.24 sq in. h_1/h_2 = 1.1175

h/w = 1.340

Additional Characteristics

M = 2.01 R_ℓ = 3.38 · 10^6 (based on ℓ_B) α = 0

ℓ_V = 10.65 in. ℓ_U = 8.40 in. ℓ_H = 11.45 in. (c.g. to centroid of region of interference)

Compute:

$$\frac{x_m}{\ell_B} = 0.548$$

$$\left(\frac{h_1}{h_2}\right)^{1/4} = 1.058$$

$$\frac{\ell_B^2}{S_{B_S}} = 11.72$$

Using the parameters computed above and the Reynolds number obtain K_N from figure 5.2.3.1-5

K_N = 0.0017

$$(C_{n_\beta})_{WB} = -K_N \frac{S_{B_S}}{S_W} \frac{\ell_B}{b_W} \text{ per deg} \qquad \text{(equation 5.2.3.1-a)}$$

$$= -(0.0017)\left(\frac{92.24}{114.5}\right)\left(\frac{32.88}{19.08}\right)$$

$$= -0.00236 \text{ per deg (based on } S_W b_W)$$

$$= -0.135 \text{ per rad (based on } S_W b_W)$$

$(\Delta C_{Y_\beta})_{H(WB)}$ = −0.0163 per rad (based on S_W)
$(\Delta C_{Y_\beta})_{V(WBH)}$ = −0.520 per rad (based on S_W)
$(\Delta C_{Y_\beta})_{U(WBHV)}$ = −0.053 per rad (based on S_W)

(sample problem, paragraph C, Section 5.6.1.1.)

Solution:

$$C_{n_\beta} = (C_{n_\beta})_{WB} + \Sigma_p \left[-(\Delta C_{Y_\beta})_p \frac{\ell_p}{b_W} \right] \qquad \text{(equation 5.6.3.1-a)}$$

$$= (C_{n_\beta})_{WB} + \left[-(\Delta C_{Y_\beta})_{H(WB)} \frac{\ell_H}{b_W} \right] + \left[-(\Delta C_{Y_\beta})_{V(WBH)} \frac{\ell_V}{b_W} \right] + \left[-(\Delta C_{Y_\beta})_{U(WBHV)} \frac{\ell_U}{b_W} \right]$$

$$= -0.135 + \left[-(0.0163)\left(\frac{11.45}{19.08}\right)\right] + \left[-(-0.520)\left(\frac{10.65}{19.08}\right) + \left[-(0.053)\left(\frac{8.40}{19.08}\right)\right]\right.$$

$$= -0.135 + 0.0098 + 0.290 + 0.0233$$

$$= 0.1881 \text{ per rad (based on } S_w b_w)$$

The experimental results from reference 3 (based on $S_w b_w$) are $(C_{n_\beta})_{WBH} = -0.169$ per radian, $(\Delta C_{n_\beta})_{V(WBH)} = 0.338$ per radian, $(\Delta C_{n_\beta})_{U(WBHV)} = 0.0286$ per radian, and $C_{n_\beta} = 0.1975$ per radian.

REFERENCES

1. Sleeman, W. C., Jr.: An Experimental Study at High Subsonic Speeds of Several Tail Configurations on a Model Having a 45° Sweptback Wing. NACA RM L57C08, 1957. (U)

2. Savage, H. F., and Tinling, B. E.: The Subsonic Static Aerodynamic Characteristics of an Airplane Model Having a Triangular Wing of Aspect Ratio 3. II - Lateral and Directional Characteristics. NACA TN 4042, 1957. (U)

3. Spearman, M. L., Robinson, R. B., and Driver, C.: The Effects of the Addition of Small Fuselage-Mounted Fins on the Static Directional Stability Characteristics of a Model of a 45° Sweptback Wing Airplane at Angles of Attack up to 15.5° at a Mach Number of 2.01. NACA RM L56D16a, 1956. (U)

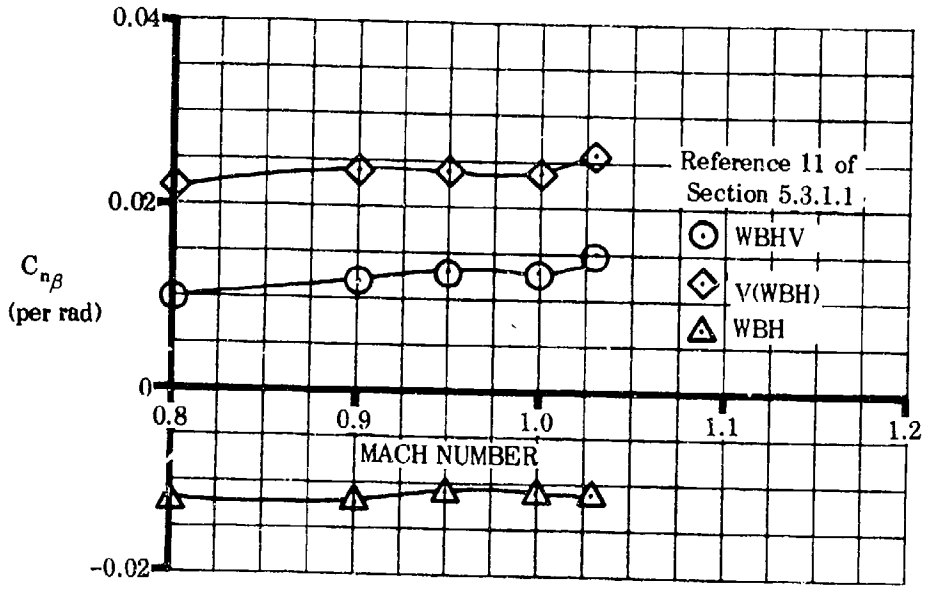

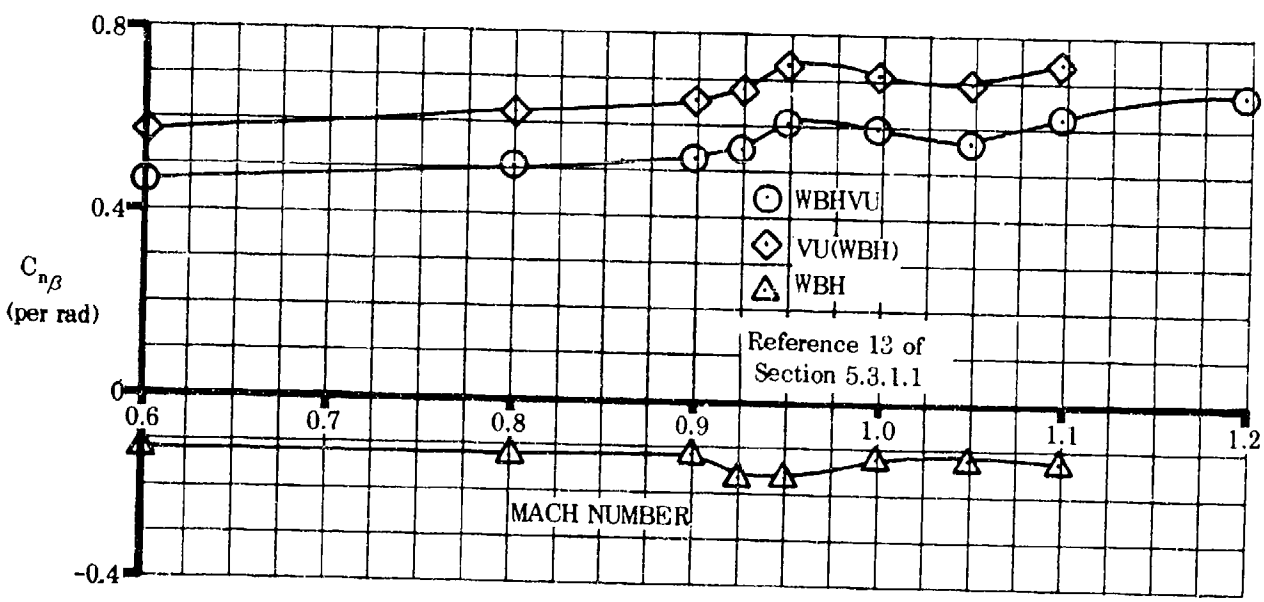

FIGURE 5.6.3.1-8 TYPICAL TRANSONIC DATA

5.6.3.2 WING-BODY-TAIL YAWING-MOMENT COEFFICIENT C_n AT ANGLE OF ATTACK

The wing-body-tail yawing moment developed at combined angles is nonlinear with respect to both sideslip and angle of attack for the reasons cited in the introductory remarks of Sections 5.2.1.2 and 5.3.1.2. To obtain the derivative C_{n_β} it is recommended that C_n be calculated at several angles of attack for a small sideslip angle ($\beta \leq 4°$). Then at each angle of attack the yawing moment is assumed linear with sideslip for small values of β so that

$$C_{n_\beta} \approx \frac{C_n}{\beta}$$

A. SUBSONIC

No method is presently available for determining the wing-body-tail yawing moment at large angles of attack and subsonic speeds. The method presented herein is restricted to first-order approximations at relatively low angles of attack.

DATCOM METHOD

It is recommended that the method of Section 5.6.3.1 be used in the linear-lift angle-of-attack range.

B. TRANSONIC

The comments appearing in Paragraph B of Section 5.6.1.1 are equally appropriate here.

DATCOM METHOD

No method is available for estimating this coefficient and none is presented in the Datcom.

C. SUPERSONIC

The discussion of Paragraph C in Section 5.6.1.2 applies here also and will not be repeated.

DATCOM METHOD

The method for estimating the wing-body-tail yawing moment at combined angles is basically that of Section 5.6.1.2. The yawing-moment coefficient is obtained simply by applying the proper moment arms to the various side-force coefficients calculated in that section. The restrictions noted in Section 5.6.1.2 also apply here.

The wing-body yawing-moment coefficient is given by

$$(C_n)_{WBHVU} = (C_n)_{WB} + (C_n)_{HVU(WB)} \qquad 5.6.3.2\text{-a}$$

where

$(C_n)_{WB}$ is the wing-body contribution obtained from Equation 5.2.3.2-a

$(C_n)_{HVU(WB)}$ is the empennage contribution obtained from Equation 5.6.3.2-b.

The contribution of the empennage is given by

$$(C_n)_{HVU(WB)} = -\frac{\ell_H \cos\alpha + z_H \sin\alpha}{b_W}(C_Y)_{H(B)} - \frac{\ell_V \cos\alpha + z_V \sin\alpha}{b_W}(C_Y)_{V(\eta)} - \frac{\ell_U \cos\alpha + z_U \sin\alpha}{b_W}(C_Y)_{U(\eta)} \qquad 5.6.3.2\text{-b}$$

where

$(C_Y)_{H(B)}$ is from Equation 5.3.1.2-b.

$(C_Y)_{V(\eta)}$ is from Equation 5.6.1.2-c.

$(C_Y)_{U(\eta)}$ is from Equation 5.6.1.2-d.

ℓ_H, z_H, ℓ_V, z_V, ℓ_U, z_U are defined under Equation 5.3.3.2-a.

Values for the incremental coefficient resulting from the addition of vertical tails to wing-body configurations, calculated using the Datcom method, are compared with experimental results in Figure 5.6.3.2-4. The assessment of the correlation parallels that of the incremental side-force coefficient, and the comments appearing in Section 5.6.1.2 are equally applicable here.

Sample Problem

Given: Configuration of Sample Problem, Paragraph C, Sections 5.2.3.2 (with slight boattail) and 5.6.1.2. There is no horizontail tail on this configuration. Some of the characteristics are repeated. Find the yawing-moment coefficient developed by the wing-body-tail configuration at $\alpha = 12°$, $\beta = 4°$, and $M = 2.01$.

Characteristics:

$\ell_V = 12.0$ in. $z_V = 4.15$ in. $\ell_U = 12.0$ in. $z_U = -2.15$ in. $b_W = 24.0$ in.

$(C_n)_{WB}$ = −0.00695 (Sample Problem, Paragraph C, Section 5.2.3.2)

$(C_Y)_{H(B)}$ = 0 (no horizontal tail on this configuration)

$(C_Y)_{V(\eta)}$ = −0.0285
$(C_Y)_{U(\eta)}$ = −0.0187
} (Sample Problem, Paragraph C, Section 5.6.1.2)

Compute:

$$(C_n)_{HVU(WB)} = -\frac{\ell_H \cos\alpha + z_H \sin\alpha}{b_W}(C_Y)_{H(B)} - \frac{\ell_V \cos\alpha + z_V \sin\alpha}{b_W}(C_Y)_{V(\eta)}$$

$$- \frac{\ell_U \cos\alpha + z_U \sin\alpha}{b_W}(C_Y)_{U(\eta)} \qquad \text{(Equation 5.6.3.2-b)}$$

$$= 0 - \frac{(12.0)\cos 12^\circ + (4.15)\sin 12^\circ}{24.0}(-0.0285)$$

$$- \frac{(12.0)\cos 12^\circ + (-2.15)\sin 12^\circ}{24.0}(-0.0187)$$

$$= 0.0238 \text{ (based on } S_W b_W)$$

Solution:

$$(C_n)_{WBHVU} = (C_n)_{WB} + (C_n)_{HVU(WB)} \qquad \text{(Equation 5.6.3.2-a)}$$

$$= -0.00695 + 0.0238$$

$$= 0.01685 \text{ (based on } S_W b_W)$$

This compares with an experimental value (based on $S_W b_W$) of $(C_n)_{WBHVU}$ = 0.0175 from Reference 2.

REFERENCES

1. Kasttari, G. E.: Estimation of Directional Stability Derivatives at Moderate Angles and Supersonic Speeds. NASA Memo 12-1-58A, 1959. (U)

2. Spearman, L. M., Driver, C., and Hughes, W. C.: Investigation of Aerodynamic Characteristics in Pitch and Sideslip of a 45° Sweptback-Wing Airplane Model with Various Vertical Locations of Wing and Horizontal Tail – Basic-Data Presentation, M = 2.01. NACA RM L54L06, 1955. (U)

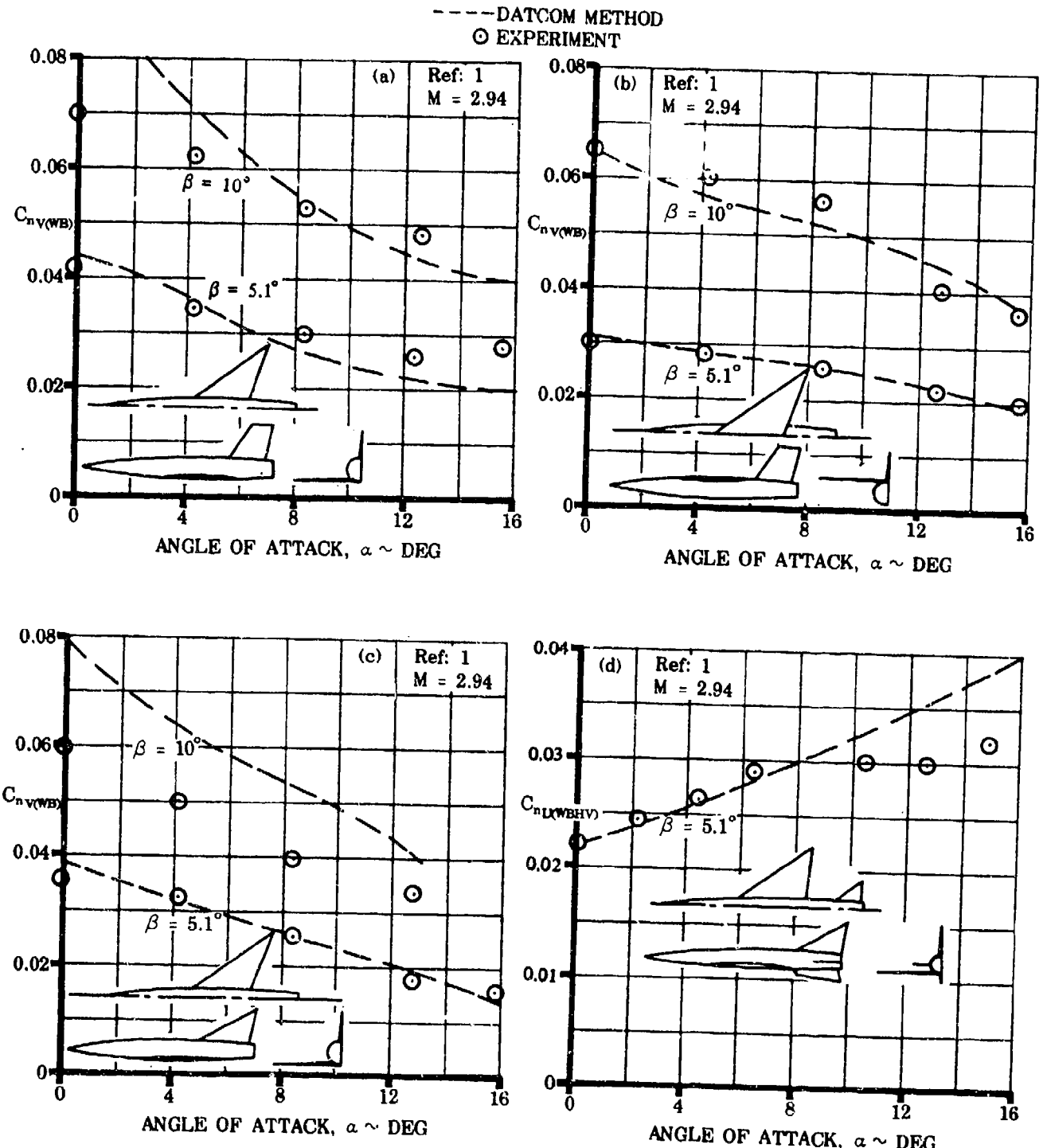

FIGURE 5.6.3.2-4 COMPARISON OF EXPERIMENTAL AND CALCULATED YAWING-MOMENT COEFFICIENT INCREMENTS DUE TO ADDING A VERTICAL TAIL TO A WING-BODY

6.1 SYMMETRICALLY DEFLECTED FLAPS AND CONTROL DEVICES ON WING-BODY AND TAIL-BODY COMBINATIONS

6.1.1 SECTION LIFT WITH HIGH-LIFT AND CONTROL DEVICES

Conventional aerodynamic high-lift and control devices, and jet flaps are similar in that each functions by changing the lift generated by the portion of wing ahead of and/or behind it. Although their stability-and-control and performance applications are quite different, no distinction is made in this section between the aerodynamic characteristics of these devices. The fundamental aerodynamic characteristics of each are discussed in the appropriate sections.

The methods of this section provide the section lift characteristics of the following:

High-Lift Devices

Split flaps	Fowler flaps
Plain flaps	Jet flaps
Single-slotted flaps	Leading-edge flaps
Double-slotted flaps	Slats

Control Devices

Trailing-edge flap types

Spoilers (plug and flap types)

In general, sufficient information is presented in the Datcom to permit the complete lift characteristics of a given device to be calculated. The complete lift characteristics can then be constructed as in the following sketch.

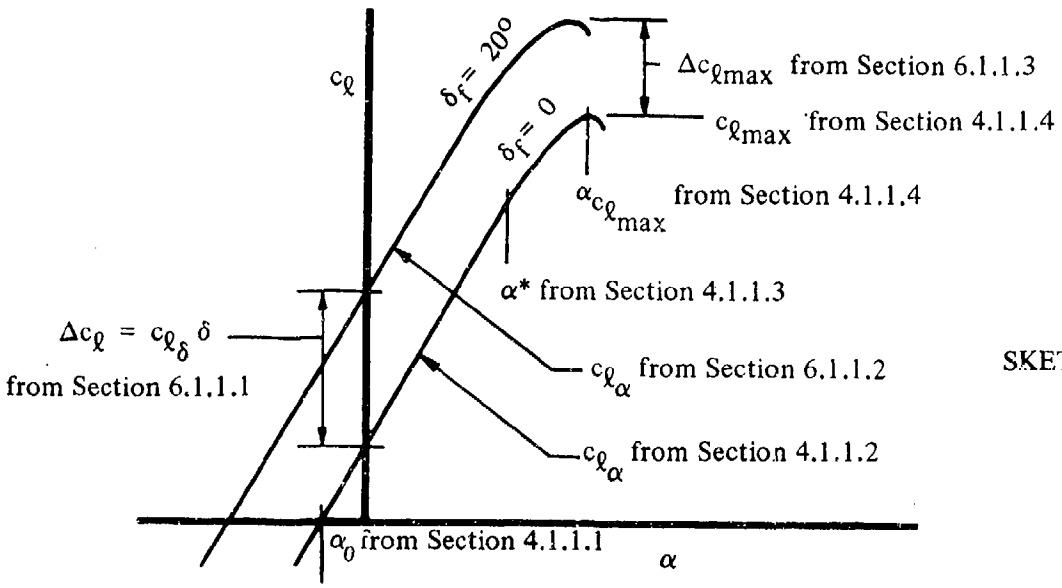

SKETCH (a)

6.1.1.1 SECTION LIFT EFFECTIVENESS OF HIGH-LIFT AND CONTROL DEVICES

Lift effectiveness is defined and used in the literature in several ways. For linear systems, the rate of change of lift with control or flap deflection at constant angle of attack is frequently used. This parameter is defined as

$$c_{\ell_\delta} = \left(\frac{\partial c_\ell}{\partial \delta}\right)_\alpha \qquad 6.1.1.1\text{-a}$$

In cases where nonlinear effects must be accounted for, it is customary to use lift increments for flap deflections at constant angle of attack. Another convention frequently used is the rate of change of zero-lift angle of attack with flap deflection.

$$\left(\frac{\partial \alpha}{\partial \delta}\right)_{c_\ell=0} = \alpha_\delta = -\frac{\left(c_{\ell_\delta}\right)_\alpha}{\left(c_{\ell_\alpha}\right)_\delta} \qquad 6.1.1.1\text{-b}$$

Again, for nonlinear characteristics, increments in angle of attack at zero lift are used. Several of these definitions of lift effectiveness are used in this section, depending upon the particular device being discussed.

In the linear-lift range, α_δ can be obtained from c_{ℓ_δ}, and vice versa, by means of Equations 6.1.1.1-a and 6.1.1.1-b.

The methods presented in this section are limited to subsonic flow.

A. TRAILING-EDGE FLAPS

Trailing-edge flaps operating in the linear-lift range change the lift of the basic airfoil by changing the effective airfoil angle of attack. The means by which each type of flap accomplishes this end is discussed in the following paragraphs. Various types of flaps in common usage are illustrated in Section 6.1.1.3.

Plain Trailing-Edge Flaps

For plain, sealed trailing-edge flaps the theoretical derivative c_{ℓ_δ} is a function of flap-chord-to-wing-chord ratio and airfoil thickness ratio. Increasing airfoil thickness increases the theoretical lift increment for a given flap deflection.

The boundary layer for plain flapped airfoils is shed at the trailing edge of the flap. Lift increments are therefore sensitive to the conditions of the boundary layer – the thicker the boundary layer the lower the value of c_{ℓ_δ} derived from the flap. Since boundary layers are thicker on thick airfoils than on thin airfoils, actual c_{ℓ_δ} values tend to be lower for the thick airfoils.

In general, for a given increase in airfoil thickness ratio the reduction in c_{ℓ_δ} due to viscous effects is greater than the increase in c_{ℓ_δ} as predicted from inviscid-flow theory In the charts of this section, viscous effects are accounted for by using the experimental lift-curve slope as a parameter, since c_{ℓ_α} is influenced by viscous effects in the same manner as c_{ℓ_δ}.

Because of the sensitivity of plain flaps to the boundary layer, the flow separates over the flap surface at relatively small deflection angles. The linear range of c_{ℓ_δ} for plain flaps is therefore limited to the range from 0 to 10° or 15° of flap deflection. An empirical correction factor is applied in this section to account for the nonlinear effects at high flap deflection.

Slotted Trailing-Edge Flaps

For efficiently designed slotted trailing-edge flaps the airfoil boundary layer is shed at the slot lip and a new boundary layer forms over the flap surface. The lift derived from efficiently designed slotted flaps is therefore not affected by the boundary layer of the basic airfoil. Experimental data for slotted flaps support this observation.

Fowler Flaps

Many flap designs have been developed in which the instantaneous center of rotation moves rearward as the flap deflects. An example of such a flap is the Fowler flap.

Aerodynamically, Fowler flaps function in the same way as single-slotted flaps. Additional lift benefits are derived from such flaps because of the increase in planform area due to flap translation.

The effect of translation can be approximated by calculating the increase in airfoil chord as a function of flap deflection.

Split Flaps

The deflection of split trailing-edge flaps causes a wide wake to appear behind the airfoil. This wake prevents the realization of the full increase in circulation due to flap deflection. The rate of increase of lift with flap deflection is therefore lower than that for the corresponding plain flap. The rate also decreases continuously with increasing flap deflection, because the wake widens as the flap deflection is increased.

B. JET FLAPS

The term jet flap has been used to describe a propulsive jet emitted from the wing trailing edge as a plane jet at an angle of inclination to the mainstream. In three dimensions, the jet is distributed in the spanwise direction on a wing. Such an integrated jet-flap system is depicted schematically in Sketch (a), along with a definition of the section jet momentum coefficient C_μ.

In order that the Datcom user may better understand the jet-flap concept, a brief discussion covering the salient aspects of the jet-flap principle is presented. This general discussion is taken essentially from References 1 and 2.

The primary objective of a jet-flap system is to increase significantly the lift component beyond that which a conventional mechanical flap system can possibly attain. The lift of a jet flap can be attributed to three different sources as follows:

1. Direct-lift component of the jet reaction. This is directly proportional to the jet momentum emitted at the trailing edge.

2. Circulation generated around the airfoil. Since the amount of circulation greatly exceeds that of a corresponding pure airfoil, it is sometimes termed supercirculation. Physically, this additional increase in lift may be explained as follows: The air on the upper surface of the airfoil is drawn down by the deflected jet, creating a suction, while the air flow below is blocked by the jet, producing pressure. Both effects tend to increase lift on the airfoil. Scientists investigating jet lift prefer to call this circulation effect the magnification of the direct jet lift.

3. Automatic boundary-layer control. The jet tends to prevent the flow above the airfoil from separating by reducing the adverse pressure gradient which the boundary layer must negotiate. Some reduction of the adverse pressure gradient can be attributed to the jet entrainment.

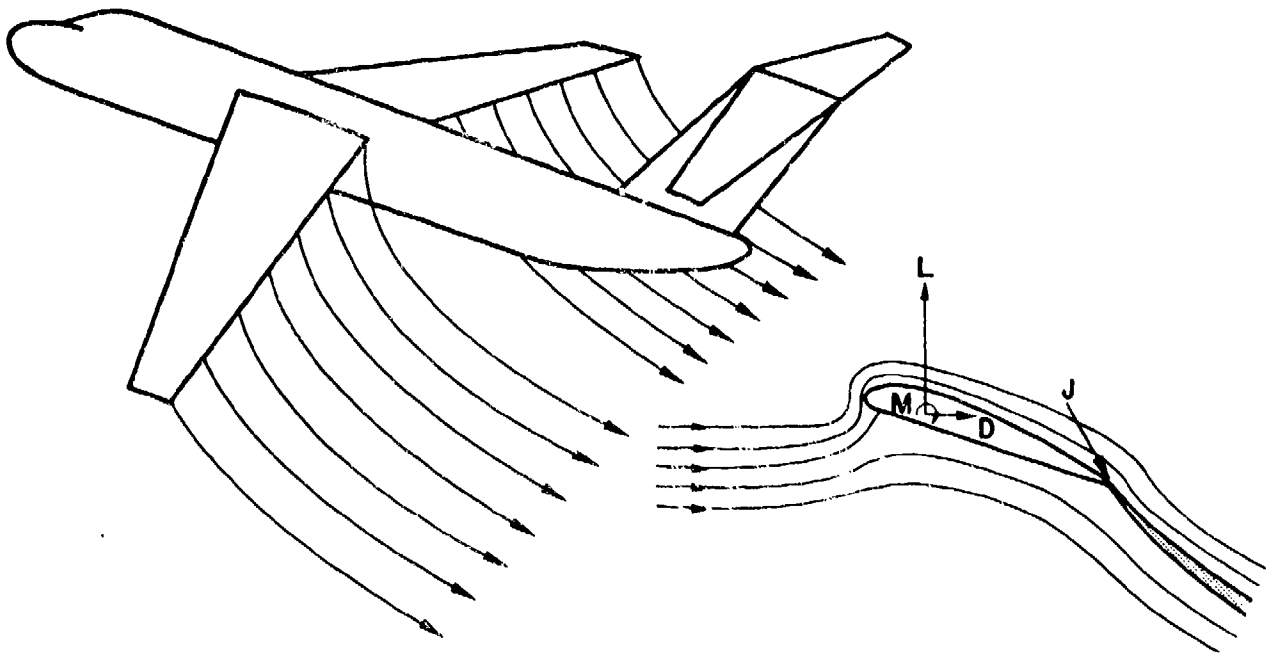

$$C_\mu = \frac{m_j V_j}{1/2\,\rho\, V^2\, c} = \frac{J}{qc} \quad \text{and} \quad C'_\mu = \frac{m_j V_j}{1/2\,\rho\, V^2\, c'} = \frac{J}{qc'}$$

where

C_μ is the section nondimensional trailing-edge jet momentum coefficient.

m_j is the mass-flow rate of the gas efflux (per section).

V_j is the velocity of the gas efflux leaving the trailing edge of the airfoil.

J is the jet momentum; i.e., the product of m_j and V_j.

ρ is the density of the free stream.

V is the velocity of the free stream.

c is the airfoil chord.

c is the extended airfoil chord (see Figures 6.1.1.1-44 through -46 and Figure 6.1.1.1-48).

q is the free-stream dynamic pressure.

SKETCH (a)

The above effect that dominates the lift contribution depends on the magnitude of the jet momentum. The boundary-layer control effect is most significant when the jet momentum is small ($C_\mu < 1$), while the supercirculation effect predominates when the momentum is moderate or large.

With respect to the supercirculation, the downward extending jet acts generally in a manner similar to that of a mechanical flap. Although the jet sheet extends downstream to infinity, only its initial portion, before it has been curved around so as to become almost straight, could significantly affect

the flow. Therefore, its effect is analogous to some specific mechanical flap of finite extension. As the jet momentum is increased, the jet would penetrate farther into the mainstream, corresponding to a larger mechanical flap. The name "jet flap" was derived from such analogy.

The basic jet-flap scheme, often referred to as an internal-flow system, essentially requires the gas to be ducted through the wing either to the trailing edge or to a slot at the knee of a flap which is used for varying the jet angle. Several alternatives to the basic jet-flap scheme have been devised for directing the gas efflux to the trailing edge. Some of these concepts are shown in Sketch (b). For the external-flow system shown in Sketch (b), the gas from the engine is ducted or directed outside the wing. With an underslung podded engine, the round jet may be guided to impinge on a mechanical flap system and form a flattened jet sheet. Alternatively, with the engine mounted on the top, the exit nozzle may be elongated spanwise to generate a plane jet sheet. Another approach shown in Sketch (b) is the augmentor-wing concept. With this scheme the jet efflux can also be used to drive an ejector system that will, in turn, augment the thrust by the entrainment of the free-stream flow.

The fact that all these concepts exhibit a flat jet sheet at the trailing edge, which characteristically has the same effect of inducing supercirculation, provides the basis for a common theoretical analysis.

The analysis of jet-flap problems inherently requires that the wing and jet be treated as an integrated system. Thus far, theoretical treatments of jet-flap aerodynamic problems have been based on linearized small-disturbance concepts. In the context of linearized theory, the basic difference between the jet wing and a conventional wing is that, in addition to the wing planform, the jet sheet itself should be regarded as a discontinuity sheet in longitudinal velocity. Roughly speaking, the jet-flapped wing may be treated as if the wing planform were extended to infinity. Unfortunately, the shape of the jet sheet, unlike that of the wing, is not known. Thus a dynamic boundary condition must be introduced for the jet, in contrast to the kinematic boundary condition for the wing. Therefore, the development of an analytical solution for aerodynamic characteristics of a jet-flapped wing encounters two difficulties. One is due to the mixed boundary conditions; the other is due to the fact that the boundary conditions are prescribed over a region of semi-infinite extent. An elegant solution for the two-dimensional jet-flap problem has been obtained by Spence in References 3 and 4. His approach is based on the assumptions that the flows inside and outside the jet are irrotational and at constant, although not necessarily equal, densities. Since entrainment into the jet is neglected, it can be regarded as if bounded by streamlines. These simplifications enable a relation between the pressure differences across the jet and its curvature to be found. The limiting case of a thin, high-speed jet is considered by assuming that the jet has zero thickness but finite momentum. Airfoil thickness is neglected, the airfoil and jet are assumed near zero angle of attack, and the airfoil and jet boundary conditions are transferred to the semi-infinite line through the trailing edge and parallel to the undisturbed flow. The result of these approximations is the representation of the flow by a mixed-boundary-value problem on this semi-infinite line. Spence has obtained three basic solutions: angle of attack, flap deflection, and jet deflection. Close agreement has been obtained between Spence's theory and the experimental results of Dimmock (Reference 5) over the range of jet momentum and jet deflection angles of practical interest.

Several experimental and theoretical studies have been conducted to investigate the effects of ground proximity on jet-flapped wings. Insofar as theoretical methods are concerned, however, only a simple mathematical representation of the two-dimensional jet-flap airfoil has been formulated (Reference 6).

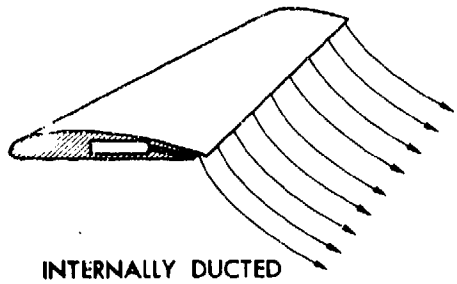

INTERNALLY DUCTED
JET FLAP

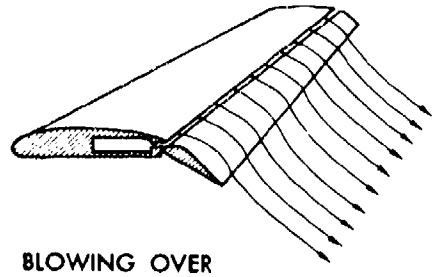

BLOWING OVER
MECHANICAL FLAP

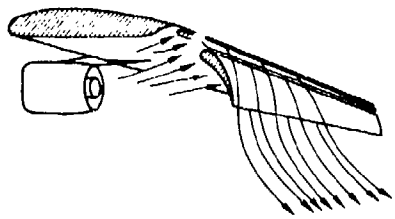

EXTERNALLY BLOWN
JET FLAP

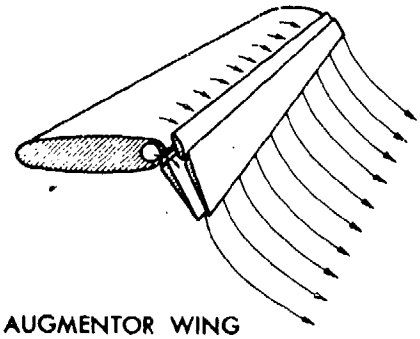

AUGMENTOR WING

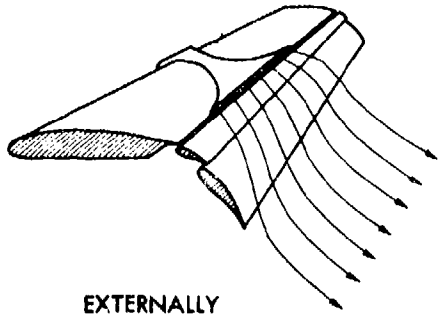

EXTERNALLY
DUCTED JET FLAP

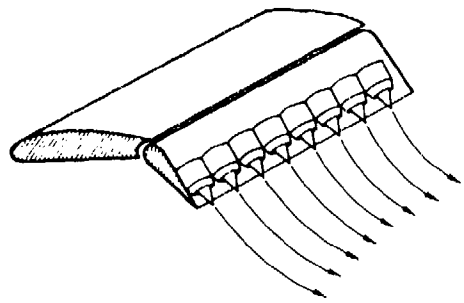

MULTI-FAN ON FLAP

SKETCH (b)

C. LEADING-EDGE FLAPS AND SLATS

Leading-Edge Flaps

Leading-edge flaps change the lift of an airfoil by changing the effective angle of attack in the same way that trailing-edge flaps do. Unlike trailing-edge flaps, however, a positive leading-edge-flap deflection (nose down) causes a loss in lift instead of an increase in lift. In general, the change in lift per degree of flap deflection is smaller for leading-edge flaps than for trailing-edge flaps.

Leading-edge-flap effectiveness is not affected by the airfoil boundary layer.

Leading-Edge Slats

The lift parameter c_{ℓ_δ} for leading-edge slats is affected by two factors. First, the deflection or rotation of the slat causes a loss in lift similar to that of leading-edge flaps. Secondly, slat extension or translation increases the planform area.

D. SPOILERS

Spoilers are generally used for two reasons -- for roll control when deflected asymmetrically and for high drag generation when deflected symmetrically. Only the section-lift aspects of spoilers are discussed herein.

Many types of spoilers have been developed, depending upon control-power limitations, structural limitations, and aerodynamic requirements. Some of the more commonly used types are illustrated in Sketch (c).

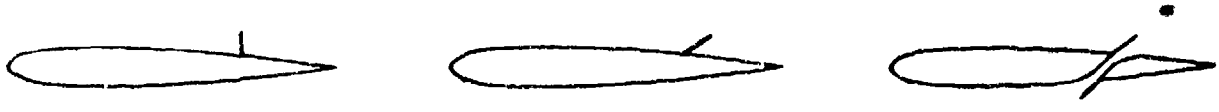

PLUG SPOILER | FLAP SPOILER | SLOTTED SPOILER

SKETCH (c) TYPICAL SPOILER ARRANGEMENTS

Unlike flaps, spoilers operate by causing a loss in airfoil lift – rather than an increase – by separating the flow downstream. The effective angle of attack is decreased and the lift correspondingly reduced. There are two viewpoints that can be used in explaining the operation of spoilers. One is to consider the pressure field over the airfoil and the other is to consider the effect of the spoiler on the wake pattern. These viewpoints are discussed in the following paragraphs.

For flap- and plug-type spoilers the pressure loading forward of the spoiler (difference in upper- and lower-surface pressures) is reduced, and the local lift is reduced accordingly. Aft of the spoiler the pressure loading is increased because of high suction pressures behind the spoiler on the upper surface. The increase in lift aft of the spoiler, however, does not offset the decrease in lift forward of the spoiler, and a total loss in lift results. These phenomena are illustrated in Sketch (d).

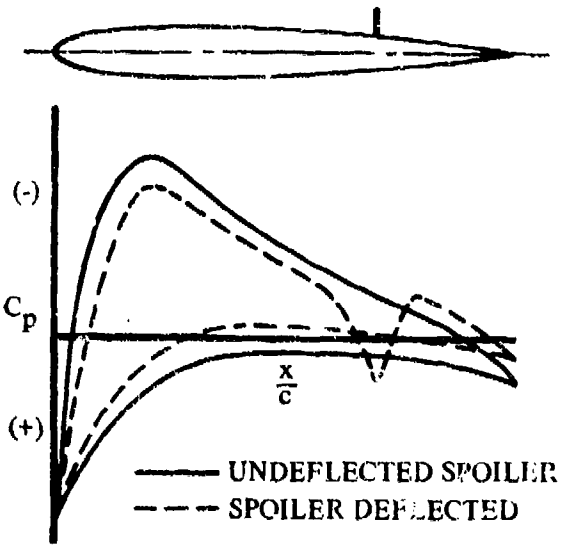

SKETCH (d) TYPICAL AIRFOIL PRESSURE DISTRIBUTION FOR PLUG-TYPE SPOILER

For large spoiler deflections a wide wake exists behind the spoiler, the width of which depends upon spoiler height, location, and airfoil angle of attack. The lift generated from the airfoil is related to the width and direction of the wake with respect to the free stream.

At subsonic and transonic speeds the wake characteristics vary nonlinearly with angle of attack and spoiler deflection. Therefore, the corresponding lift characteristics are also nonlinear, as shown in Sketch (e). The loss in effectiveness at high angles of attack should be noted. This loss, which is particularly pronounced for thin wings, can be greatly alleviated by the use of leading-edge flaps (Reference 7) or by incorporating a slot behind the spoiler, as discussed below (Reference 8).

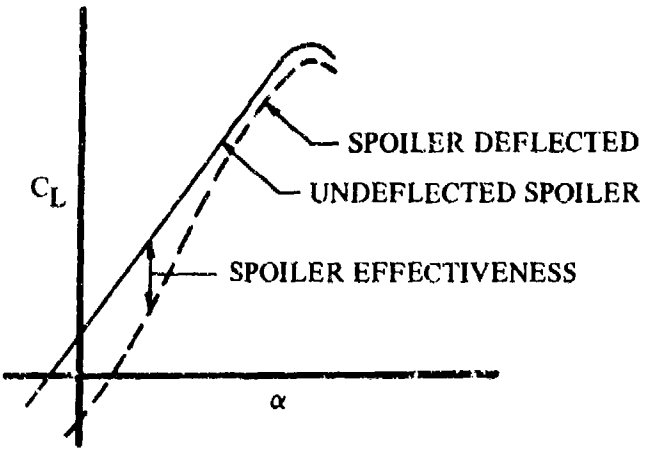

SKETCH (e) TYPICAL LIFT CURVES FOR PLUG-TYPE SPOILER

For small deflections of plug- and flap-type spoilers, the flow reattaches behind the spoiler and the spoiler becomes ineffective. This generally occurs for spoiler deflections less than one percent of the airfoil chord. This problem is discussed in detail in Reference 9.

One commonly used variation of the flap-type spoiler is the slotted spoiler with a deflector on the lower surface (see Sketch (c)). This system has several advantages. First, the air that is ducted from the underside of the airfoil relieves the upper-surface suction pressures behind the spoiler and increases the spoiler effectiveness. Secondly, the problem of flow reattachment does not occur for small spoiler deflections. Thirdly, the opposing aerodynamic loads on the spoiler and deflector can be used to achieve low actuation power requirements.

The information presented in this section is limited to the region near zero lift, where the spoiler lift characteristics are essentially linear with angle of attack.

DATCOM METHODS

A. TRAILING-EDGE FLAPS

Plain Flaps

The section lift increment due to the deflection of plain trailing-edge flaps with sealed gaps, based on the method of Reference 10, is given by

$$\Delta c_{\ell} = \delta_f \left[\frac{c_{\ell_\delta}}{\left(c_{\ell_\delta}\right)_{theory}} \right] \left(c_{\ell_\delta}\right)_{theory} K' \qquad 6.1.1.1\text{-c}$$

where

$\left(c_{\ell_\delta}\right)_{theory}$ is the theoretical flap-lift effectiveness from Figure 6.1.1.1-39a for a given airfoil thickness ratio and flap-chord-to-airfoil-chord ratio.

$\dfrac{c_{\ell_\delta}}{\left(c_{\ell_\delta}\right)_{theory}}$ is an empirical correction factor obtained from Figure 6.1.1.1-39b

The parameter $c_{\ell_\alpha}/\left(c_{\ell_\alpha}\right)_{theory}$ used in reading this chart is obtained from Section 4.1.1.2 (Figure 4.1.1.2-8a).

δ_f is the flap deflection.

K' is an empirical correction factor from Figure 6.1.1.1-40. This factor has been derived from a large body of test data (References 11 through 28). It corrects Δc_{ℓ} for nonlinear effects at high flap deflections.

This method does not include the effects of unsealed gaps, beveled trailing edges, or compressibility.

In general, the effectiveness of the control is reduced when the gap is unsealed. This effect is more pronounced for airfoils with beveled trailing edges than for airfoils with true-contour trailing edges.

The method may be applied to true-contour airfoils or airfoils with slightly modified trailing-edge contours. The method should not be applied to airfoils with beveled trailing edges. Not enough experimental data are available to allow a quantitative prediction of the effect of bevel. However, the data do show a decrease in control effectiveness with increasing bevel.

Compressibility will have serious effects on the lift effectiveness of plain trailing-edge controls. Experimental data (References 17, 18, and 57 through 59) show decreases in lift effectiveness up to one half the low-speed values at high subsonic speeds. Although there are not enough data to allow a quantitative prediction of compressibility effects, they do demonstrate significant effects of airfoil thickness, control size, and trailing-edge angle on the control effectiveness as the Mach number is increased. The onset of an abrupt loss in control effectiveness is delayed to higher Mach numbers by a reduction in airfoil thickness (References 58 and 59), an increase in control size (Reference 17), or a reduction in trailing-edge angle (References 56 and 57).

A comparison of low-speed test data with Δc_ℓ of plain-flapped airfoils calculated by this method is presented as Table 6.1.1.1-A.

Single-Slotted Flaps

Two methods are presented for estimating the section lift increment due to the deflection of single-slotted flaps. Both methods are applicable in the high-flap-deflection range and limited to the low-speed regime. Method 1 is preferable when test data are available for the section lift-curve slope of the unflapped airfoil. When no section lift-curve-slope test data are available, Method 2 should be used.

Method 1

The section life increment due to the deflection of single-slotted flaps is given by

$$\Delta c_\ell = -c_{\ell_\alpha} \alpha_\delta \delta_f \qquad \text{6.1.1.1-d}$$

where

c_{ℓ_α} is the section lift-curve slope of the unflapped airfoil, including the effects of compressibility, obtained from test data or Section 4.1.1.2.

α_δ is the section lift-effectiveness parameter of single-slotted flaps obtained from the empirical correlation of Figure 6.1.1.1-41. This parameter, based on the data of References 29 through 50, is presented as a function of flap deflection for several values of the ratio of flap chord to airfoil chord c_f/c.

δ_f is the flap deflection.

A comparison of test data with Δc_ℓ due to single-slotted flaps calculated by this method is presented as Table 6.1.1.1-B.

Method 2

This method (Reference 70) uses the theoretical lift effectiveness of a simple trailing-edge flap as obtained from thin-airfoil theory, modified by an empirical lift-effectiveness parameter. The section-lift increment due to the deflection of single-slotted flaps is given by

$$\Delta c_\ell = c_{\ell_\delta} \delta_f \eta_1 \frac{c'}{c} \qquad \text{6.1.1.1-e}$$

where

c_{ℓ_δ} is the theoretical lift effectiveness from thin-airfoil theory of a simple trailing-edge flap, obtained from Figure 6.1.1.1-42 as a function of flap-chord ratio c_1/c (see Figure 6.1.1.1-44 for a geometric representation of c_1/c).

δ_f is the flap deflection in degrees.

η_1 is the empirical lift-efficiency factor for single-slotted flaps, obtained from Figure 6.1.1.1-43a as a function of the effective turning angle Φ,

where

$$\Phi = \delta_f + \phi_{TE_{upper}} \qquad 6.1.1.1\text{-f}$$

where

$$\phi_{TE_{upper}} = \tan^{-1}\left(\frac{Y_{90} - Y_{100}}{0.10}\right) \qquad 6.1.1.1\text{-g}$$

Y_{90} is the upper-surface ordinate of the flap at 90% chord in the retracted position, in fractions of the chord.

Y_{100} is the upper-surface ordinate of the flap at 100% chord in the retracted position, in fractions of the chord.

$\frac{c'}{c}$ is the ratio of the extended-wing chord to the basic wing chord. (See Figure 6.1.1.1-44 for a schematic definition.)

A comparison of test data with Δc_2 due to single-slotted flaps calculated by this method is presented as Table 6.1.1.1-C. These data are the same data that appear in Table 6.1.1.1-B.

It is virtually impossible to present quantitative information on the effects of the various geometric and aerodynamic variables involved because of the lack of systematic experimental data. Although a large body of test data is available, the data consist of a large number of unrelated combinations of airfoils and slotted flaps. The configurations listed in Table 6.1.1.1-B include wide variations in chordwise position of slot lip, slot-entry shape, slot-lip shape, flap-nose shape, and position of the flap with respect to the slot lip.

Because of the number of variables involved and the design parameters not considered in the Datcom methods, the comparison between theory and experiment cannot be analyzed by examining the isolated effect of any one variable.

Fowler Flaps

Section lift increments for Fowler flaps are obtained by using the methods presented for single-slotted flaps. Fowler flaps are included in the empirical correlation of slotted-flap lift effectiveness in Figure 6.1.1.1-41 of Method 1. It should be noted, however, that this design chart

applies only when the Fowler flap is near its fully extended position and the slot is properly developed. Method 2 predicts an increase in lift increment that is directly proportional to the ratio of the extended chord to the retracted chord.

Not enough test data for airfoils are available to fully substantiate these methods. However, the accuracy of the methods when applied to Fowler flaps near their fully extended position and with a properly developed slot should be comparable to that shown for the single-slotted flap methods in Tables 6.1.1.1-B and 6.1.1.1-C.

Double-Slotted Flaps

Two methods, taken from Reference 70, are presented for estimating the section lift increment due to the deflection of a double-slotted flap. Both methods are applicable in the high-flap-deflection range and limited to the low-speed regime. Method 1 is applicable to the conventional vane-plus-aft-flap configuration as shown in Figure 6.1.1.1-45 where $c_1/c_2 \leq 0.60$. Method 2 is applicable to a double-slotted configuration where the two flap-chord segments are approximately equal (see Figure 6.1.1.1-46). This configuration is referred to as a double-deflected flap in several references.

Method 1

The section lift increment due to the deflection of double-slotted flaps of the conventional vane-plus-aft-flap combination is given by

$$\Delta c_\ell = \eta_1 \, c_{\ell_{\delta_{f_1}}} \, \delta_{f_1} \left(\frac{c + c_1}{c} \right) + \eta_2 \, c_{\ell_{\delta_{f_2}}} \left(\delta_{f_1} + \delta_{f_2} \right) \left(\frac{c'}{c} \right) \qquad 6.1.1.1\text{-h}$$

where

η_1, η_2 are the empirical lift-efficiency factors for the vane and aft-flap segments obtained from Figure 6.1.1.1-43a, based on c_1/c and c_2/c, respectively, and the effective turning angle Φ,

where

$$\Phi = \delta_{f_1} + \phi_{TE_{upper}} \qquad \text{(vane segment)}$$

$$\Phi = \delta_{f_1} + \delta_{f_2} + \phi_{TE_{upper}} \qquad \text{(flap segment)}$$

and $\phi_{TE_{upper}}$ is defined in Equation 6.1.1.1-g.

$c_{\ell_{\delta_{f_1}}}, c_{\ell_{\delta_{f_2}}}$ are the theoretical lifting-efficiency factors for the vane and aft-flap segments obtained from Figure 6.1.1.1-42 and based on c_1/c and c_2/c, respectively.

All remaining parameters are illustrated and defined in Figure 6.1.1.1-45.

A comparison of test data with Δc_ℓ due to double-slotted flaps calculated by this method is presented in Table 6.1.1.1-D.

Method 2

The section lift increment due to the deflection of double-slotted flaps with approximately equal flap-chord segments is given by

$$\Delta c_{\ell} = \eta_1 \, c_{\ell_{\delta_{f_1}}} \, \delta_{f_1} \left(\frac{c_a'}{c} \right) + \eta_2 \eta_t \, c_{\ell_{\delta_{f_2}}} \, \delta_{f_2} \left(1 + \frac{c' - c_a'}{c} \right) \qquad 6.1.1.1\text{-i}$$

where

η_1, η_2 are the empirical lift-efficiency factors for the forward- and aft-flap segments obtained from Figure 6.1.1.1-43a, based on c_1'/c and c_2/c, respectively, and the effective turning angle Φ,

where

$$\Phi = \delta_{f_1} + \phi_{TE_{upper}} \qquad \text{(forward segment)}$$

$$\Phi = \delta_{f_2} + \phi_{TE_{upper}} \qquad \text{(aft segment)}$$

and $\phi_{TE_{upper}}$ is defined in Equation 6.1.1.1-g.

$c_{\ell_{\delta_{f_1}}}, c_{\ell_{\delta_{f_2}}}$ are the theoretical lifting-efficiency factors for the forward- and aft-flap segments obtained from Figure 6.1.1.1-42, based on c_1'/c and c_2/c, respectively.

η_t is the turning-efficiency factor of the aft flap obtained from Figure 6.1.1.1-43b, based on the forward- and aft-flap-deflection angles.

All remaining parameters are illustrated and defined in Figure 6.1.1.1-46.

No substantiation table is presented for this method because of the lack of test data for this type of configuration. However, for those cases that have been evaluated, the accuracy of the method is analogous to that of Method 1 above.

The double-slotted flap may be defined as a single-slotted flap with a turning vane in the slot. Consequently, the important design parameters for double-slotted flaps are more complicated than those for single-slotted flaps, particularly in relation to determining the efficiency of flow through the slot. As in the case for single-slotted flaps, a lack of systematic test data precludes quantitative examination of the effects of the various geometric and aerodynamic variables involved.

Because of the design parameters not considered in the Datcom method, the comparison between theory and experiment cannot be analyzed by examining the isolated effect of any one variable.

Split Flaps

The section lift increment due to the deflection of split flaps is given by

$$\Delta c_{\ell} = -c_{\ell_\alpha} \alpha_\delta \delta_f \qquad 6.1.1.1\text{-j}$$

where

c_{ℓ_α} is the section lift-curve slope of the unflapped airfoil, including the effects of compressibility, obtained from Section 4.1.1.2.

α_δ is the section lift-effectiveness parameter of split flaps obtained from the empirical curves of Figure 6.1.1.1-47. This parameter, based on the curves presented in Reference 53, is presented as a function of flap deflection for several values of the ratio of flap chord to airfoil chord c_f/c.

δ_f is the flap deflection, measured tangent to airfoil lower-surface contour at trailing edge.

A comparison of test data with Δc_{ℓ} due to split flaps calculated by this method is presented as Table 6.1.1.1-E.

B. JET FLAPS

Methods that are adaptable to a handbook application are not available for all jet-flap schemes. The method presented below is applicable to the pure jet-flap concept and the internally-blown-flap (IBF) and externally-blown-flap (EBF) concepts with a plain trailing-edge flap. For an IBF or EBF concept with a single-slotted or multislotted flap configuration, this method should be used only as a first approximation. No handbook method is currently available to analyze the section lift increment due to an augmentor-wing concept.

The method presented herein is a combination of methods presented in References 2 and 70 (based on Spence's theoretical results). The pertinent geometrical parameters are defined and illustrated in Figure 6.1.1.1-48. No substantiation of the method is presented herein; however, the method has been acknowledged as being substantiated in the literature (References 1 and 4).

This method is capable of estimating the lift increments in the linear-lift range (preferably at zero angle of attack) for three types of configurations:

1. Pure jet flap
2. IBF or EBF
3. Combination jet-flap and plain-flap deflection (see Figure 6.1.1.1-48)

It is of particular interest to note that the factor $[1 + k_t(t/c')]$ in Equation 6.1.1.1-k below corrects the pressure lift contribution for thickness effects, under the constraint of no trailing-edge separation. No values for the lifting-efficiency factor are available as a function of flap setting and jet momentum coefficient. For this reason, the user must exercise caution not to apply the method to conditions where trailing-edge separation exists and/or low values of jet momentum coefficient prevail.

It should be noted that the flap-chord value c_f/c' used in Figure 6.1.1.1-49 is not the true mechanical flap length for flaps with Fowler-type motion. For Fowler-type flaps, the flap chord is the length from the flap trailing edge to the intersection of the flap-chord and wing-chord lines.

The section lift increment due to flap deflection and jet efflux of a jet-flap combination, based on the retracted airfoil chord c, is given by

$$\Delta c_\ell = \left\{ \left[1 + k_t \left(\frac{t}{c'} \right) \right] \delta_f \left(c_{\ell_{\delta_f}} - C'_\mu \right) + C'_\mu \, \delta_f \right.$$

$$\left. + \left[1 + k_t \left(\frac{t}{c'} \right) \right] \delta_j \left(c_{\ell_{\delta_j}} - C'_\mu \right) + C'_\mu \, \delta_j \right\} \frac{c'}{c} \qquad \text{6.1.1.1-k}$$

where

k_t is the airfoil-theory thickness factor; i.e.,

$k_t = 1.0$ for elliptic airfoils

$= 0.637$ for parabolic airfoils

For airfoil sections other than elliptic or parabolic, a value of 0.80 for k_t is suggested (Reference 70).

$\frac{t}{c'}$ is the airfoil thickness ratio, based on the extended chord; see Figure 6.1.1.1-48.

$c_{\ell_{\delta_f}}$ is the rate of change of section lift coefficient with respect to flap deflection obtained from Figure 6.1.1.1-49 as a function of the trailing-edge jet momentum C_μ' and the ratio of the flap chord to the extended wing chord c_f/c'. (The term c'_{ℓ_α} appearing in Figure 6.1.1.1-49 is the jet-flap lift-curve slope uncorrected for thickness effects.)

As noted above, the flap-chord value c_f is the length from the flap trailing edge to the intersection of the flap-chord and wing-chord lines.

C_μ' is the section nondimensional trailing-edge jet-momentum coefficient based on the extended airfoil chord (defined in Sketch (a) of this section).

δ_f is the flap deflection in radians, see Figure 6.1.1.1-48.

$c_{\ell_{\delta_j}}$ is the rate of change of section lift coefficient with respect to the jet deflection obtained from Figure 6.1.1.1-49 as a function of the trailing-edge jet momentum C_μ'.

δ_j is the trailing-edge jet momentum angle in radians, with respect to the trailing-edge camber line, see Figure 6.1.1.1-48.

$\frac{c'}{c}$ is the ratio of the extended wing chord to the retracted wing chord.

C. LEADING-EDGE FLAPS AND SLATS

The available experimental section characteristics for leading-edge devices (References 15, 69, and 76) are insufficient to allow substantiation of the methods presented. However, the methods should provide results that are suitable for first approximations for flapped airfoils with geometric parameters within the boundaries of thin-airfoil theory. Consequently, the methods are considered applicable for airfoil-flap configurations with $t/c \leq 0.10$ and with small flap deflections, in the linear-lift range (preferably at zero angle of attack).

It should be noted that the c_{ℓ_δ} values for all leading-edge devices are of opposite sign from the values for trailing-edge flaps.

Leading-Edge Flaps

The method presented below is taken from Reference 70 and is based on thin-airfoil theory. The section lift increment due to leading-edge flap deflection is given by

$$\Delta c_\ell = c_{\ell_\delta} \delta_f \qquad 6.1.1.1\text{-}l$$

where

c_{ℓ_δ} is the leading-edge flap-effectiveness parameter obtained from Figure 6.1.1.1-50 as a function of the nose-flap-chord to wing-chord ratio c_f/c.

δ_f is the nose-flap deflection in degrees, as shown in Figure 6.1.1.1-51.

Krueger Flaps

The method presented below is a modification of the method presented immediately above (Reference 70), to account for the chord extension associated with Krueger leading-edge devices.

No substantiation of this method is presented because of the lack of test data. The section lift increment due to a Krueger leading-edge flap deflection is given by

$$\Delta c_\ell = c_{\ell_\delta} \delta_f \frac{c'}{c} \qquad 6.1.1.1\text{-}m$$

where

c_{ℓ_δ} is the leading-edge flap-effectiveness parameter obtained from Figure 6.1.1.1-50 as a function of the Krueger flap-chord to wing-chord ratio c_f/c'

δ_f is the Krueger flap deflection, in degrees, as shown in Figure 6.1.1.1-51.

$\frac{c'}{c}$ is the ratio of the extended wing chord to airfoil chord as shown in Figure 6.1.1.1-51.

Leading-Edge Slats

The method presented here is a modification of the method presented for leading-edge flaps (Reference 70); i.e., it is modified to account for the chord extension associated with leading-edge slats. The section lift increment due to a leading-edge slat deflection is given by

$$\Delta c_\ell = c_{\ell_\delta} \delta_f \frac{c'}{c} \qquad \text{6.1.1.1-m}$$

where

c_{ℓ_δ} is the leading-edge flap-effectiveness parameter obtained from Figure 6.1.1.1-50 as a function of the leading-edge-slat-chord to wing-chord ratio c_f/c'.

δ_f is the slat deflection, in degrees, as shown in Figure 6.1.1.1-51.

$\frac{c'}{c}$ is the ratio of the extended wing chord to airfoil chord as shown in Figure 6.1.1.1-51.

D. SPOILERS

The section lift increment due to either plug or flap spoilers is given by

$$\Delta c_\ell = -c_{\ell_\alpha} \Delta\alpha'_s \qquad \text{6.1.1.1-n}$$

where

c_{ℓ_α} is the lift-curve slope of the basic airfoil, including compressibility effects, from Section 4.1.1.2.

$\Delta\alpha'_s$ is the spoiler lift-effectiveness parameter expressed in terms of change in zero-lift angle of attack, from Figure 6.1.1.1-52. This design chart, taken from Reference 55, was developed from data obtained by testing a series of airfoils with various plug-spoiler configurations.

In Figure 6.1.1.1-52, the parameter x_s is the distance from the nose of the airfoil to the spoiler lip, and h_s is the height of the spoiler measured from and normal to the airfoil mean line at x_s.

Experimental section characteristics (Reference 77) for airfoils with plain or plug spoilers are too meager to allow substantiation of this method. However, if a reliable value of c_{ℓ_α} is used, the method should provide results that can be used with confidence within the limitations of the design chart for determining $\Delta\alpha'_s$.

The lift effectiveness of a slotted spoiler with a deflector on the lower surface is greater (causes larger lift loss) than that of plug and flap spoilers. No known method is available for predicting the section lift effectiveness of slotted spoilers.

Sample Problems

1. Plain Trailing-Edge Flap

Given: The flapped airfoil of Reference 13.

NACA 0009 airfoil $\quad c_f/c = 0.20 \quad \delta_f = 50^o \quad R_\ell = 2.76 \times 10^6$

$\tan\frac{1}{2}\phi_{TE} = 0.099$ (streamwise airfoil geometry)

Compute:

$(c_{\ell_\delta})_{theory} = 3.61$ per rad $= 0.063$ per deg (Figure 6.1.1.1-39a)

$\frac{c_{\ell_\alpha}}{(c_{\ell_\alpha})_{theory}} = 0.837$ (Figure 4.1.1.2-8a)

$\frac{c_{\ell_\delta}}{(c_{\ell_\delta})_{theory}} = 0.725$ (Figure 6.1.1.1-39b)

$K' = 0.543$ (Figure 6.1.1.1-40)

Solution:

$$\Delta c_\ell = \delta_f \left[\frac{c_{\ell_\delta}}{(c_{\ell_\delta})_{theory}}\right] (c_{\ell_\delta})_{theory} \; K' \qquad \text{(Equation 6.1.1.1-c)}$$

$= (50)(0.725)(0.063)(0.543)$

$= 1.24$

This compares with a test value of 1.15 from Reference 13.

2. Single-Slotted Trailing-Edge Flap (Method 1)

Given: The flapped airfoil of Reference 41 with the slot lip at 0.84 c.

NACA 65-210 airfoil $\quad c_f/c = 0.25 \quad \delta_f = 50^o$

Low Speed; $\beta = 1.0 \quad R_\ell = 6.0 \times 10^6$

$\tan\frac{1}{2}\phi'_{TE} = 0.084$ (streamwise airfoil geometry)

Compute:

c_{ℓ_α} (Section 4.1.1.2)

$$\frac{c_{\ell_\alpha}}{(c_{\ell_\alpha})_{theory}} = 0.879 \qquad \text{(Figure 4.1.1.2-8a)}$$

$$(c_{\ell_\alpha})_{theory} = 6.78 \text{ per rad} \qquad \text{(Figure 4.1.1.2-8b)}$$

$$c_{\ell_\alpha} = \frac{1.05}{\beta}\left[\frac{c_{\ell_\alpha}}{(c_{\ell_\alpha})_{theory}}\right](c_{\ell_\alpha})_{theory} \qquad \text{(Equation 4.1.1.2-a)}$$

$$= \frac{1.05}{1.0}(0.879)\,(6.78)/57.3 = 0.109 \text{ per deg}$$

α_δ = −0.300 (Figure 6.1.1.1-41)

Solution:

$$\Delta c_\ell = -c_{\ell_\alpha}\,\alpha_\delta\,\delta_f \qquad \text{(Equation 6.1.1.1-d)}$$

$$= -(0.109)\,(-0.300)\,(50)$$

$$= 1.64$$

This compares with a test value of 1.73 from Reference 41.

3. Single-Slotted Trailing-Edge Flap (Method 2)

Given: The flapped airfoil of Reference 41 with the slot lip at 0.84 c
(same sample problem as presented for Method 1)

NACA 65-210 airfoil $\quad \frac{c_f}{c} = 0.25 \quad \frac{c'}{c} = 1.078 \quad \alpha = 0$

$Y_{90} = 0.01327\,c \quad Y_{100} = 0 \quad \delta_f = 50°$

Low Speed; $\beta = 1.0$

Compute:

c_{ℓ_δ} = 0.0668 per deg (Figure 6.1.1.1-42)

$$\phi_{TE_{upper}} = \tan^{-1}\left(\frac{Y_{90} - Y_{100}}{0.10}\right) \qquad \text{(Equation 6.1.1.1-g)}$$

$$= \tan^{-1}\left(\frac{0.01327 - 0}{0.10}\right)$$

$$= 7.56^{o}$$

$$\Phi = \delta_f + \phi_{TE_{upper}} \qquad \text{(Equation 6.1.1.1-f)}$$

$$= 50 + 7.56 = 57.56^{o}$$

$$\eta_1 = 0.455 \qquad \text{(Figure 6.1.1.1-43a)}$$

$$\Delta c_\ell = c_{\ell_\delta}\, \delta_f\, \eta_1 \frac{c'}{c} \qquad \text{(Equation 6.1.1.1-e)}$$

$$= (0.0668)\,(50)\,(0.455)\,(1.078)$$

$$= 1.64$$

This compares with a test value of 1.73 from Reference 41.

4. Double-Slotted Trailing-Edge Flap (Method 1)

Given: The flapped airfoil of Reference 64.

NACA 64-208 airfoil	$c_1/c = 0.056$	$c_2/c = 0.25$	$c'/c = 1.127$
$M = 0.18$	$\delta_{f_1} = 25^{o}$	$\delta_{f_2} = 25^{o}$	$\alpha = 0$
$Y_{90} = 0.01067c$	$Y_{100} = 0$		

Compute:

$c_{\ell_{\delta_{f_1}}}$ = 0.0327 per deg (Figure 6.1.1.1-42)

$c_{\ell_{\delta_{f_2}}}$ = 0.0668 per deg (Figure 6.1.1.1-42)

$$\phi_{TE_{upper}} = \tan^{-1}\left(\frac{Y_{90} - Y_{100}}{0.10}\right) \qquad \text{(Equation 6.1.1.1-g)}$$

$$= \tan^{-1}\left(\frac{0.01067 - 0}{0.10}\right)$$

$$= 6.1^{o}$$

$$\Phi = \delta_{f_1} + \phi_{TE_{upper}} \quad \text{(vane segment)}$$

$$= 25 + 6.1 = 31.1^{o}$$

$$\Phi = \delta_{f_1} + \delta_{f_2} + \phi_{TE_{upper}} \quad \text{(flap segment)}$$

$$= 25 + 25 + 6.1 = 56.1^{o}$$

$$\left.\begin{aligned} \eta_1 &= 0.640 \\ \eta_2 &= 0.470 \end{aligned}\right\} \quad \text{(Figure 6.1.1.1-43a)}$$

$$\Delta c_{\ell} = \eta_1 \, c_{\ell_{\delta_{f_1}}} \, \delta_{f_1} \left(\frac{c + c_1}{c}\right) + \eta_2 \, c_{\ell_{\delta_{f_2}}} \left(\delta_{f_1} + \delta_{f_2}\right)\left(\frac{c'}{c}\right) \quad \text{(Equation 6.1.1.1-h)}$$

$$= (0.640)(0.0327)(25)(1.056) + (0.470)(0.0668)(50)(1.127)$$

$$= 0.552 + 1.770$$

$$= 2.32$$

This compares with a test value of 2.07 from Reference 64.

5. Double-Slotted Trailing-Edge Flap (Method 2)

Given: The flapped airfoil of Reference 78.

NACA 23012 airfoil $\quad c_1'/c = 0.40 \quad c_2/c = 0.2566$

$c_{\ell}'/c = 1.10 \quad c'/c = 1.14 \quad \delta_{f_1} = 30^{o} \quad \delta_{f_2} = 20^{o}$

Low Speed; $\beta = 1.0 \quad Y_{90} = 0.0168c \quad Y_{100} = 0.0013c$

Compute:

$c_{\ell_{\delta_{f_1}}} = 0.082$ per deg (Figure 6.1.1.1-42)

$c_{\ell_{\delta_{f_2}}} = 0.0672$ per deg (Figure 6.1.1.1-42)

$$\phi_{TE_{upper}} = \tan^{-1}\left(\frac{Y_{90} - Y_{100}}{0.10}\right) \qquad \text{(Equation 6.1.1.1-g)}$$

$$= \tan^{-1}\left(\frac{0.0168 - 0.0013}{0.10}\right)$$

$$= 8.8^{o}$$

$$\Phi = \delta_{f_1} + \phi_{TE_{upper}} \qquad \text{(forward segment)}$$

$$= 30 + 8.8 = 38.8^{o}$$

$$\Phi = \delta_{f_2} + \phi_{TE_{upper}} \qquad \text{(aft segment)}$$

$$= 20 + 8.8 = 28.8^{o}$$

$$\left.\begin{aligned} \eta_1 &= 0.69 \\ \eta_2 &= 0.71 \end{aligned}\right\} \qquad \text{(Figure 6.1.1.1-43a)}$$

$\eta_t = 0.84$ (extrapolated from Figure 6.1.1.1-43b)

$$\Delta c_{\ell} = \eta_1 \, c_{\ell_{\delta_{f_1}}} \, \delta_{f_1} \left(\frac{c_a'}{c}\right) + \eta_2 \, \eta_t \, c_{\ell_{\delta_{f_2}}} \, \eta_{f_2} \left(1 + \frac{c' - c_a'}{c}\right) \qquad \text{(Equation 6.1.1.1-i)}$$

$$= (0.69)\,(0.082)\,(30)\,(1.10) + (0.71)\,(0.84)\,(0.0672)\,(20)\,[1 + (1.14 - 1.10)]$$

$$= 1.867 + 0.834$$

$$= 2.70$$

This compares with a test value of 2.69 from Reference 78.

6. Split Trailing-Edge Flap

Given: The flapped airfoil of Reference 75

$\delta_f = 60^{o}$ NACA 23012 airfoil $c_f/c = 0.40$

$c_{\ell_\alpha} = 0.107$ per deg (test data)

Compute:

$\alpha_\delta = -0.30$ (Figure 6.1.1.1-47)

Solution:

$$\Delta c_{\ell} = -c_{\ell_{\alpha}} \alpha_{\delta} \delta_f \qquad \text{(Equation 6.1.1.1-j)}$$

$$= -(0.107)(-0.30)(60)$$

$$= 1.92$$

This compares with a test value of 1.71 from Reference 75.

7. Jet Flaps

Given: The pure jet-flap configuration of Reference 5.

Elliptic airfoil $\quad \frac{t}{c} = 0.125 \quad C_{\mu} = 4.0 \quad \frac{c'}{c} = 1.0$

$\frac{c_f}{c} = 0 \quad \delta_f = 0 \quad \alpha = 0 \quad \delta_j = 31.4^{\circ}$

Compute:

$k_t = 1.0$ (elliptic value)

$c_{\ell_{\delta_j}} = 9.60$ per rad (Figure 6.1.1.1-49)

$$\Delta c_{\ell} = \left\{ \left[1 + k_t \left(\frac{t}{c'} \right) \right] \delta_f \left(c_{\ell_{\delta_f}} - C'_{\mu} \right) + C'_{\mu} \delta_f \right.$$

$$\left. + \left[1 + k_t \left(\frac{t}{c'} \right) \right] \delta_j \left(c_{\ell_{\delta_j}} - C'_{\mu} \right) + C'_{\mu} \delta_j \right\} \frac{c'}{c} \qquad \text{(Equation 6.1.1.1-k)}$$

Since $\delta_f = 0$, the first two terms drop out.

$$\Delta c_{\ell} = [1 + (1.0)(0.125)] \frac{31.4}{57.3} (9.60 - 4.0) + 4.0 \left(\frac{31.4}{57.3} \right)$$

$$= 3.452 + 2.192$$

$$= 5.64 \text{ (based on } c)$$

This compares with a test value of 5.59 from Reference 5.

8. Leading-Edge Flaps

Given: The flapped airfoil of Reference 15.

NACA 0006 airfoil $\quad c_f/c = 0.15 \quad \delta_f = 20^o$

$M = 0.15$

Compute:

$c_{\ell_\delta} = -0.00286$ per deg (Figure 6.1.1.1-50)

$\Delta c_\ell = c_{\ell_\delta} \delta_f$ (Equation 6.1.1.1-ℓ)

$= (-0.00286)(20)$

$= -0.057$

This compares with a test value of −0.07 from Reference 15.

9. Leading-Edge Slats

Given: The flapped airfoil of Reference 69.

NACA 65A010 airfoil $\quad c_f/c = 0.17 \quad \delta_f = 25.6^o$

Low Speed $\quad R_\ell = 7.0 \times 10^6 \quad c'/c = 1.12$

Compute:

$c_{\ell_\delta} = -0.00350$ per deg (Figure 6.1.1.1-50)

$\Delta c_\ell = c_{\ell_\delta} \delta_f \frac{c'}{c}$ (Equation 6.1.1.1-m)

$= (-0.00350)(25.6)(1.12)$

$= -0.100$

This compares with a test value of −0.19 from Reference 69.

REFERENCES

1. Lopez, M.L., and Shen, C.C.: Recent Developments in Jet Flap Theory and Its Application to STOL Aerodynamic Analysis. AIAA Paper 71-578, 1971. (U)

2. Lopez, M.L., Shen, C.C., and Wasson, N.F.: A Theoretical Method for Calculating the Aerodynamic Characteristics of Arbitrary Jet-Flapped Wings. Douglas Aircraft Company, MDC J5519-01, 1972. (U)

3. Spence, D.A.: Lift Coefficient of a Thin Jet-Flapped Wing. Proc. Roy. Soc., Vol. A238, 1956. (U)

4. Spence, D.A.: The Lift on a Thin Aerofoil With a Jet Augmented Flap. Aero. Quart. Vol. 9, 1958. (U)

5. Dimmock, N.A.: Some Early Jet Flap Experiments. Aero. Quart. Vol. 8, 1957. (U)

6. Lissaman, P.B.S.: A Linear Theory for the Jet Flap in Ground Effect. AIAA Jour. Vol. 6, 1968. (U)

7. Fitzpatrick, J.E., and Woods, R.L.: Low-Speed Lateral-Control Characteristics of an Unswept Wing With Hexagonal Airfoil Sections and Aspect Ratio 2.5 Equipped With Spoilers and With Sharp- and Thickened-Trailing-Edge Flap-Type Ailerons at a Reynolds Number of 7.6×10^6. NACA RM L52B15, 1952. (U)

8. Lowry, J.G.: Data on Spoiler-Type Ailerons. NACA RM L53I24a, 1953. (U)

9. Newman, B.G.: The Reattachment of a Turbulent Boundary Layer Behind a Spoiler. Rept. A.64, Aero. Res. Lab. (Melbourne), October 1949. (U)

10. Anon.: Royal Aeronautical Society Data Sheets - Aerodynamics, Vol. IV. (Controls 01.01.03), 1956. (U)

11. Spearman, M.L.: Wind-Tunnel Investigation of an NACA 0009 Airfoil With 0.25- and 0.50-Airfoil-Chord Plain Flaps Tested Independently and in Combination. NACA TN 1517, 1948. (U)

12. Rogallo, F.M.: Collection of Balanced Aileron Test Data. NACA WR L-419, 1944. (U)

13. Sears, R.I.: Wind-Tunnel Data on the Aerodynamic Characteristics of Airplane Control Surfaces. NACA WR L-663, 1943. (U)

14. Rose, L.M., and Altman, J.M.: Low-Speed Experimental Investigation of a Thin Faired, Double-Wedge Airfoil Section With Nose and Trailing-Edge Flaps. NACA TN 1934, 1949. (U)

15. Gambucci, B.J.: Section Characteristics of the NACA 0006 Airfoil With Leading-Edge and Trailing-Edge Flaps. NACA TN 3797, 1956. (U)

16. Abbott, I.H., von Doenhoff, A.E., and Stivers, L.S., Jr.: Summary of Airfoil Data. NACA TR 824, 1945. (U)

17. Ilk, R.J.: Characteristics of a 15-Percent-Chord and a 35-Percent-Chord Plain Flap on the NACA 0006 Airfoil Section at High Subsonic Speeds. NACA RM A7H19, 1947. (U)

18. Luoma, A.A.: An Investigation of the Section Characteristics of Plain Unsealed Ailerons on an NACA 66, 1-115 Airfoil Section in the Langley 8-Foot High-Speed Tunnel. NACA TN 1596, 1949. (U)

19. Spearman, L.M.: Wind-Tunnel Investigation of Control-Surface Characteristics. XXIII - A 0.25-Airfoil-Chord Flap With Tab Having a Chord Twice the Flap Chord on an NACA 0009 Airfoil. NACA WR L-47, 1945. (U)

20. Street, W.G., and Ames, M.B., Jr.: Pressure-Distribution Investigation of an N.A.C.A. 0009 Airfoil With a 50-Percent-Chord Plain Flap and Three Tabs. NACA TN 734, 1939. (U)

21. Ames, M.B., Jr. and Sears, R.I.: Pressure-Distribution Investigation of an N.A.C.A. 0009 Airfoil With a 30-Percent-Chord Plain Flap and Three Tabs. NACA TN 759, 1940. (U)

22. Ames, M.B.,Jr., and Sears, R.I.: Determination of Control-Surface Characteristics From NACA Plain-Flap and Tab Data. NACA TR 721, 1941. (U)

23. Braslow, A.L.: Two-Dimensional Wind-Tunnel Investigation of Sealed 0.22-Airfoil-Chord Internally Balanced Ailerons of Different Contour on an NACA $65_{(112)}$-213 Airfoil. NACA TN 1099, 1946. (U)

24. Lockwood, V.E.: Wind-Tunnel Investigation of Control-Surface Characteristics. XVII Beveled-Trailing-Edge Flaps of 0.20, 0.30, and 0.40 Airfoil Chord on an NACA 0009 Airfoil. NACA WR L-686, 1944. (U)

25. Klein, M.M.: Pressure Distributions and Force Tests of an NACA 65-210 Airfoil Section With a 50-Percent-Chord Flap. NACA TN 1167, 1947. (U)

26. Abbott, I.H., and Greenburg, H.: Tests in the Variable-Density Wind Tunnel of the NACA 23012 Airfoil With Plain and Split Flaps. NACA TR 661, 1949. (U)

27. Ames, M.B.,Jr.: Wind-Tunnel Investigation of Two Airfoils With 25-Percent-Chord Gwinn and Plain Flaps. NACA TN 763, 1940. (U)

28. Cahill, J.F., et al: Aerodynamic Forces and Loadings on Symmetrical Circular-Arc Airfoils with Plain Leading-Edge and Plain Trailing-Edge Flaps. NACA TR 1146, 1953. (U)

29. Harris, T.A., and Purser, P.E.: Wind-Tunnel Investigation of an NACA 23012 Airfoil With Two Sizes of Balanced Split Flap. NACA WR L-441, 1940. (U)

30. Underwood, W.J., and Abbott, F.T., Jr.: Test of NACA 66,2-116, a = 0.6 Airfoil Section Fitted With Pressure Balance and Slotted Flaps for the Wing of the XP-63 Airplane. NACA WR L-701, 1942. (U)

31. Holtzclaw, R.W.: Wind-Tunnel Investigation of the Effects of Spoilers on the Characteristics of a Low-Drag Airfoil Equipped With a 0.25-Chord Slotted Flap. NACA WR A-92, 1945. (U)

32. Holtzclaw, R.W., and Welsman, Y.: Wind-Tunnel Investigation of the Effects of Slot Shape and Flap Location on the Characteristics of a Low-Drag Airfoil Equipped With a 0.25-Chord Slotted Flap. NACA WR A-8., 1944. (U)

33. Swanson, R.S., and Schuldenfrei, M.J.: Wind-Tunnel Investigation of an NACA 23021 Airfoil With Two Sizes of Balanced Split Flaps. NACA WR L-449, 1941. (U)

34. Bogdonoff, S.M.: Tests of Two Models Representing Intermediate Inboard and Outboard Wing Sections of the XB-36 Airplane. NACA WR L-662, 1943. (U)

35. Abbott, I.H.: Tests of Four Models Representing Intermediate Sections of the XB-33 Airplane Including Sections With Slotted Flaps and Ailerons. NACA WR L-704, 1942. (U)

36. Duschik, F.: Wind-Tunnel Investigation of an N.A.C.A. 23021 Airfoil With Two Arrangements of a 40-Percent-Chord Slotted Flap. NACA TN 728, 1939. (U)

37. Recant, I.G.: Wind-Tunnel Investigation of an N.A.C.A. 23030 Airfoil With Various Arrangements of Slotted Flaps. NACA TN 755, 1940. (U)

38. Harris, T.A.: Wind-Tunnel Investigation of an N.A.C.A. 23012 Airfoil With Two Arrangements of a Wide-Chord Slotted Flap. NACA TN 715, 1939. (U)

39. Lowry, J.G.: Wind-Tunnel Invertigation of an NACA 23012 Airfoil With Several Arrangements of Slotted Flaps With Extended Lips. NACA TN 808, 1941. (U)

40. Racisz, S.F.: Investigation of NACA $65_{(112)}$A111 (Approx.) Airfoil With 0.35-Chord Slotted Flap at Reynolds Numbers Up to 25 Million. NACA TN 1463, 1947. (U)

41. Cahill, J.F.: Two-Dimensional Wind-Tunnel Investigation of Four Types of High-Lift Flap on an NACA 65-210 Airfoil Section. NACA TN 1191, 1947. (U)

42. Goodwin, M.D.: Single-Slotted Trailing-Edge Flap Combined With Plain or Slotted Leading-Edge Flap. WADC TR 6356, Part 3, 1953. (U)

43. Wenzinger, C.J., and Harris, T.A.: Wind-Tunnel Investigation of an N.A.C.A. 23021 Airfoil With Various Arrangements of Slotted Flaps. NACA TR 677, 1939. (U)

44. Jones, R., and Bell, A.H.: Further Experiments on an NACA 23021 Aerofoil With a 15-Percent Handley Page Slotted Flap in the Compressed Air Tunnel. ARC R&M 2519, 1954. (U)

45. Harris, T.A., and Lowry, J.G.: Pressure Distribution Over an NACA 23021 Airfoil With a Slotted and a Split Flap. NACA TR 718, 1941. (U)

46. Wenzinger, C.J., and Harris, T.A.: Wind-Tunnel Investigation of an N.A.C.A. 23012 Airfoil With Various Arrangements of Slotted Flaps. NACA TR 664, 1939. (U)

47. Wenzinger, C.J., and Gauvain, W.E.: Wind-Tunnel Investigation of an N.A.C.A. 23012 Airfoil With A Slotted Flap and Three Types of Auxiliary Flap. NACA TR 679, 1939. (U)

48. Wenzinger, C.J., and Delano, J.B.: Pressure Distribution Over an N.A.C.A. 23012 Airfoil With a Slotted and Plain Flap. NACA TR 633, 1938. (U)

49. Abbott, I.H., and Fullmer, F.F., Jr.: Wind-Tunnel Investigation of an NACA 63, 4-420 Section With 25-Percent-Chord Slotted Flap. NACA ACR 3I21, 1943. (U)

50. Wenzinger, C.J., and Anderson, W.B.: Pressure Distribution Over Airfoils With Fowler Flaps. NACA TR 620, 1938. (U)

51. Anon: Royal Aeronautical Society Data Sheets - Aerodynamics. Vol. IV (Flaps 01.01.08), 1949. (U)

52. Anon: Royal Aeronautical Society Data Sheets - Aerodynamics. Vol.IV (Flaps 01.01.09), 1959. (U)

53. James, H. A., and Hunton, L. W.: Estimation of Incremental Pitching Moments Due to Trailing-Edge Flaps on Swept and Triangular Wings. NACA TN 4040, 1957. (U)

54. Roshko, A.: Computation of the Increment of Maximum Lift Due to Flaps, Douglas Aircraft Company Rept., SM 23626, 1959. (U)

55. Franks, R.W.: The Application of a Simplified Lifting-Surface Theory to the Prediction of the Rolling Effectiveness of Plain Spoiler Ailerons at Subsonic Speeds. NACA RM A54H26a, 1954. (U)

56. Stevenson, D.B., and Adler, A.A.: High-Speed Wind-Tunnel Tests of an NACA 0009-64 Airfoil Having a 33.4-Percent-Chord Flap With an Overhang 20.1 Percent of the Flap Chord. NACA TN 1417, 1947. (U)

57. Stevenson, D.B., and Byrne, R.W.: High-Speed Wind-Tunnel Tests of an NACA 16-009 Airfoil Having a 32.9-Percent-Chord Flap With an Overhang 20.7 Percent of the Flap Chord. NACA TN 1406, 1947. (U)

58. Lindsey, W.F.: Effect of Compressibility on the Pressures and Forces Acting on a Modified NACA 65,3-019 Airfoil Having a 0.20-Chord Flap. NACA WR L-76, 1946. (U)

59. Stivers, L.S., Jr.: The Effectiveness at High Speeds of a 20-Percent-Chord Plain Trailing-Edge Flap on the NACA 65-210 Airfoil Section. NACA RM A7A17, 1947. (U)

60. Underwood, W.J., Braslow, A.L., and Cahill, J.F.: Two-Dimensional Wind-Tunnel Investigation of 0.20-Airfoil-Chord Plane Ailerons of Different Contour on an NACA 65_1-210 Airfoil Section. NACA WR L-151, 1945. (U)

61. Wenzinger, C.J.: Wind-Tunnel Investigation of Ordinary and Split Flaps on Airfoils of Different Profile. NACA TR 554, 1936. (U)

62. Purser, P.E., Fischel, J., and Riebe, J.M.: Wind-Tunnel Investigation of an NACA 23012 Airfoil With a 0.30-Airfoil-Chord Double Slotted Flap. NACA WR L-469, 1943. (U)

63. Fischel, J., and Riebe, J.M.: Wind-Tunnel Investigation of an NACA 23021 Airfoil With a 0.32-Airfoil-Chord Double Slotted Flap. NACA WR L-7, 1944. (U)

64. Cahill, J.F., and Racisz, S.F.: Wind-Tunnel Investigation of Seven Thin NACA Airfoil Sections to Determine Optimum Double Slotted Flap Configurations. NACA TN 1545, 1948. (U)

65. Quinn, J.H., Jr.: Tests of the NACA 64_1A212 Airfoil Section With a Slat, a Double Slotted Flap, and Boundary-Layer Control By Suction. NACA TN 1293, 1947. (U)

66. Bogdonoff, S.M.: Wind-Tunnel Investigation of a Low-Drag Airfoil Section With a Double Slotted Flap. NACA WR L-697, 1943. (U)

67. Quinn, J.H. Jr.: Wind-Tunnel Investigation of Boundary-Layer Control By Suction on the NACA 65_3-418, a = 1.0 Airfoil Section With a 0.29-Airfoil-Chord Double Slotted Flap. NACA TN 1071, 1946. (U)

68. Quinn, J.H., Jr.: Wind-Tunnel Investigation of the NACA 65_4-421 Airfoil Section With a Double Slotted Flap and Boundary-Layer Control by Suction. NACA TN 1395, 1947. (U)

69. Kelly, J.A., and Hayter, N-L.F.: Lift and Pitching Moment at Low Speeds of the NACA 64A010 Airfoil Section Equipped With Various Combinations of a Leading-Edge Slat, Leading-Edge Flap, Split Flap, and Double Slotted Flap. NACA TN 3007, 1953. (U)

70. Ramsay, J.C., and Laudeman, E.C.: STOL Tactical Aircraft Investigation State-of-the-Art Design Compendium. Prepared under USAF Contract F33615-71-C-1754, 1971. (U)

71. Visconti, F.: Wind-Tunnel Investigation of Air Loads Over a Double Slotted Flap on the NACA 65(216)-215, a = 0.8 Airfoil Section, NACA RM L7A30, 1947. (U)

72. Cahill, J.F.: Aerodynamic Data for a Wing Section of the Republic XF-12 Airplane Equipped With a Double Slotted Flap. NACA WR L-544, 1946. (U)

73. McKee, P.B., Jr.: Double Slotted Trailing-Edge Flap Combined With a Plain or Slotted Leading-Edge Flap. WADC TR 6356, Part 2, 1952. (U)

74. Fullmer, F.F.: Wind-Tunnel Investigation of NACA 66(215)-216, 66,1-212, and 65_1-212 Airfoils With 0.20-Airfoil-Chord Split Flaps. NACA WR L-140, 1944. (U)

75. Wenzinger, C.J., and Harris, T.A.: Wind-Tunnel Investigation of N.A.C.A. 23012, 23021, and 23030 Airfoils With Various Sizes of Split Flap. NACA TR 668, 1939. (U)

76. McKee, P.B., Jr.: Plain and Slotted Leading-Edge Flaps With a Conventional Split Trailing-Edge Flap. WADC TR 6356, Part 1, 1951. (U)

77. Velasco, C.E.: High-Speed Wind-Tunnel Investigation of Spoilers for Lateral Control on the NACA 65,-210 Airfoil Section. NACA MR A5K02, 1945. (U)

78. Harris, T.A., and Recant, I.G.: Wind-Tunnel Investigation of NACA 23012, 23021 and 23030 Airfoils Equipped With 40-Percent-Chord Double-Slotted Flaps. NACA TR 723, 1941. (U)

TABLE 6.1.1.1-A
PLAIN TRAILING-EDGE FLAP EFFECTIVENESS
DATA SUMMARY AND SUBSTANTIATION

Ref.	Airfoil Section	M	$R_\ell \times 10^{-6}$	c_f/c	δ_f (deg)	K′	Δc_ℓ Calc	Δc_ℓ Test	Percent Error
47	23012	.105	3.5	0.10	10	1.000	0.267	0.265	0.8
					20	.900	0.478	0.430	11.2
					30	.710	0.566	0.545	3.9
					40	.640	0.680	0.685	- 0.7
					50	.595	0.790	0.795	- 0.6
					60	.560	0.893	0.895	- 0.2
61	Clark Y	.105	0.61	0.10	10	1.000	0.18	0.22	-18.2
					30	.710	0.39	0.40	- 2.5
					45	.615	0.501	0.545	- 8.1
					60	.560	0.61	0.60	1.7
13	0009	.10	2.76	0.15	10	1.000	0.37	0.39	- 5.1
					20	.890	0.65	0.57	14.0
					30	.695	0.76	0.73	4.1
					40	.616	0.90	0.84	7.1
					50	.567	1.03	0.97	6.2
					60	.531	1.16	1.09	6.4
20	0009	.09	3.4	0.15	10	1.000	0.37	0.40	- 7.5
					20	.890	0.66	0.60	10.0
					30	.695	0.77	0.73	5.5
17	0006	.3	1.0	0.15	5.5	1.000	0.21	0.24	-12.5
					10.5	1.000	0.39	0.45	-13.3
30	66, 2 – 116 a = 0.6	–	6.0	0.167	10	.887	0.66	0.62	6.5
					30	.685	0.762	0.845	- 9.8
					40	.610	0.905	1.045	-13.4
					50	.560	1.038	1.180	-12.0
13	0009	.10	2.76	0.20	10	1.000	0.43	0.42	2.4
					20	.880	0.76	0.74	2.7
					30	.670	0.87	0.85	2.4
					40	.592	1.02	0.99	3.0
					50	.540	1.19	1.15	3.5
					60	.501	1.30	1.24	4.8

TABLE 6.1.1.1-A (CONTD)

Ref.	Airfoil Section	M	$R_\ell \times 10^{-6}$	c_f/c	δ_f (deg)	K'	Δc_ℓ Calc	Δc_ℓ Test	e Percent Error
48	23012	.105	3.5	0.20	15	.978	0.595	0.660	- 9.8
↓	↓	↓	↓	↓	30	.670	0.815	0.860	- 5.2
46	23012	.105	3.5	0.20	10	1.000	0.407	0.355	14.6
↓	↓	↓	↓	↓	20	.880	0.714	0.655	9.0
↓	↓	↓	↓	↓	30	.670	0.815	0.797	2.3
↓	↓	↓	↓	↓	45	.565	1.031	1.025	0.6
↓	↓	↓	↓	↓	60	.501	1.219	1.245	- 2.1
61	23012	.105	0.61	0.20	15	.978	0.43	0.50	-14.0
↓	↓	↓	↓	↓	30	.670	0.58	0.67	-13.4
↓	↓	↓	↓	↓	45	.565	0.74	0.89	-16.9
↓	↓	↓	↓	↓	60	.501	0.87	1.02	-14.7
28	Circular Arc 0.06c	.15	6.0	0.20	20	.880	0.82	0.87	- 5.7
↓	↓	↓	↓	↓	40	.592	1.10	1.07	2.8
↓	↓	↓	↓	↓	60	.501	1.40	1.39	0.7
↓	Circular Arc 0.10c	.15	6.0	0.20	20	.880	0.67	0.69	- 2.9
↓	↓	↓	↓	↓	40	.592	0.90	1.07	-15.9
↓	↓	↓	↓	↓	60	.501	1.15	1.37	-16.1
60	65_1 - 210	.07	1.0	0.20	5	1.000	0.24	0.28	-14.3
↓	↓	↓	↓	↓	10	1.000	0.49	0.60	-18.3
↓	↓	.17	9.0	0.20	5	1.000	0.28	0.25	12.0
↓	↓	↓	↓	↓	10	1.000	0.55	0.48	14.6
↓	↓	↓	↓	↓	15	.978	0.81	0.67	20.9
↓	↓	↓	↓	↓	20	.880	0.97	0.81	19.8
16	63, 3 - 618	.2	6.0	0.20	10	1.000	0.45	0.45	0
↓	↓	↓	↓	↓	20	.880	0.79	0.654	20.8
↓	↓	↓	↓	↓	30	.670	0.90	0.80	12.5
↓	↓	↓	↓	↓	40	.592	1.06	0.97	9.3
↓	↓	↓	↓	↓	50	.540	1.21	1.09	11.0
↓	↓	↓	↓	↓	60	.501	1.36	1.20	13.5

TABLE 6.1.1.1-A (CONTD)

Ref.	Airfoil Section	M	$R_\ell \times 10^{-6}$	c_f/c	δ_f (deg)	K′	Δc_ℓ Calc	Δc_ℓ Test	e Percent Error
12	66 (215) - 216 a = 1.0	.2	6.0	0.20	10	1.000	0.40	0.43	- 7.0
↓	↓	↓	↓	↓	20	.880	0.71	0.70	1.4
16	66 (215) - 216	.2	6.0	0.20	10	1.000	0.40	0.44	- 9.1
↓	↓	↓	↓	↓	40	.592	0.95	1.10	-13.6
↓	↓	↓	↓	↓	50	.540	1.08	1.34	-19.4
↓	↓	↓	↓	↓	60	.501	1.21	1.50	-19.3
23	$65_{(112)}$ - 213	.15	8.0	0.22	10	1.000	0.53	0.58	- 8.6
↓	↓	↓	↓	↓	15	.978	0.78	0.68	14.7
↓	↓	↓	↓	↓	20	.870	0.93	0.86	8.1
11	0009	.09	2.58	0.25	5	1.000	0.246	0.235	4.0
↓	↓	↓	↓	↓	10	1.000	0.493	0.473	4.2
↓	↓	↓	↓	↓	15	.978	0.720	0.680	5.9
↓	↓	↓	↓	↓	20	.840	0.825	0.800	3.1
↓	↓	↓	↓	↓	25	.701	0.860	0.835	3.0
↓	↓	↓	↓	↓	30	.640	0.943	0.850	10.9
27	23015	.105	0.61	0.25	10	1.000	0.29	0.287	1.0
↓	↓	↓	↓	↓	30	.640	0.56	0.530	5.7
↓	↓	↓	↓	↓	45	.540	0.703	0.725	- 3.0
↓	↓	↓	↓	↓	60	.480	0.833	0.933	-10.7
14	Double Wedge	.17	5.8	0.25	10	1.000	0.57	0.60	- 5.0
↓	↓	↓	↓	↓	20	.840	0.96	1.08	-11.1
↓	↓	↓	↓	↓	40	.569	1.30	1.30	0
↓	↓	↓	↓	↓	50	.518	1.48	1.50	- 1.3
↓	↓	↓	↓	↓	60	.480	1.65	1.65	0
13	0009	.10	2.76	0.30	10	1.000	0.55	0.59	- 6.8
↓	↓	↓	↓	↓	20	.800	0.88	0.87	1.1
↓	↓	↓	↓	↓	30	.607	1.00	0.96	4.2
15	0006	.15	4.5	0.30	20	.800	0.95	1.10	-13.6
↓	↓	↓	↓	↓	35	.607	1.26	1.32	- 4.5
↓	↓	↓	↓	↓	50	.495	1.47	1.62	- 9.3

TABLE 6.1.1.1-A (CONTD)

Ref.	Airfoil Section	M	$R\ell \times 10^{-6}$	c_f/c	δ_f (deg)	K′	Δc_ℓ Calc	Δc_ℓ Test	e Percent Error
21	0009	.09	3.4	0.30	10	1.000	0.56	0.55	1.8
					20	.800	0.89	0.80	11.3
					30	.607	1.02	0.90	13.3
					40	.540	1.21	1.07	13.1
					45	.515	1.15	1.28	-10.2
13	0015	.10	2.76	0.30	20	.800	0.75	0.78	- 3.8
					30	.607	0.85	0.99	-14.1
61	Clark Y	.105	0.61	0.30	10	1.000	0.391	0.475	-17.7
					30	.607	0.712	0.755	- 5.7
					45	.540	0.951	0.935	1.7
					60	.460	1.080	1.040	3.8
13	66-009	.105	1.43	0.30	10	1.000	0.56	0.57	- 1.8
					20	.800	0.90	0.80	12.5
					30	.607	1.03	0.90	14.4
57	16-009	.4	1.1	0.329	10.3	1.000	0.43	0.47	- 8.5
56	0009-64	.4	1.1	0.334	5.9	1.000	0.288	0.332	-13.3
					7.9	1.000	0.386	0.415	- 7.0
					9.9	1.000	0.483	0.495	- 2.4
17	0006	.3	1.0	0.35	4.9	1.000	0.30	0.34	-11.8
					10.2	1.000	0.62	0.68	- 8.8
11	0009	.09	2.58	0.50	5	1.000	0.37	0.36	2.8
					10	.998	0.74	0.71	4.2
					15	.910	1.01	0.99	2.0
					20	.685	1.01	1.02	- 1.0
					25	.590	1.09	1.05	3.8
					30	.542	1.20	1.14	5.3
20	0009	.09	3.4	0.50	10	.998	0.75	0.80	- 6.3
					20	.685	1.03	1.02	1.0
					30	.542	1.22	1.25	- 2.4
					40	.485	1.46	1.52	- 3.9
					45	.466	1.58	1.65	- 4.2
25	65-210	< .15	6.0	0.50	4	1.000	0.33	0.31	6.5
					7	1.000	0.57	0.65	-12.3
					10	1.000	0.82	0.85	- 3.5

Average Error = $\frac{\Sigma|e|}{n}$ = 7.75%

TABLE 6.1.1.1-8.
SINGLE-SLOTTED TRAILING-EDGE FLAP EFFECTIVENESS
DATA SUMMARY AND SUBSTANTIATION

Ref.	Airfoil Section	Config.(1)	M	β	$R_\ell \times 10^{-6}$	c_f/c	δ_f (deg)	c_{ℓ_α} (per deg)	$-\alpha_\delta$	Δc_ℓ Calc	Δc_ℓ Test	e Percent Error
29	23012	2a*	0.105	0.995	3.5	0.15	30	0.104	.322	1.00	1.00	0
33	23021	2a*	0.105	0.995	3.5	0.15	60	0.097	.150	0.87	1.20	-27.5
44	23021	2b	LS	1.0	7.1	0.15	60	0.097	.150	0.87	0.83	4.8
34	63 (420) - 222 a = 0.1	1b	LS	1.0	9.0	0.243	30	0.118	.445	1.58	1.41	12.1
							40		.385	1.82	1.58	15.2
							45		.345	1.83	1.46	25.3
							20		.480	1.13	1.12	1.0
							30		.445	1.58	1.40	12.9
41	65-210	2c	LS	1.0	6.0	0.25	30	0.109	.453	1.48	1.46	1.4
							40		.397	1.73	1.78	- 2.8
							45		.356	1.75	1.87	- 6.4
							50		.300	1.62	1.73	- 6.4
							30		.453	1.48	1.54	- 3.9
							36.3		.421	1.67	1.72	- 2.9
							41.3		.388	1.75	1.82	- 3.8
							46.5		.340	1.72	1.73	- 0.6
							30		.453	1.48	1.41	5.0
							35		.428	1.63	1.54	5.8
							40		.397	1.73	1.81	- 4.4
29	23012	2a*	0.105	0.995	3.5	0.25	40	0.104	.397	1.65	1.76	- 6.3
31	66, 2 - 216 a = 0.6	1c	0.19	0.982	5.1	0.25	10	0.105	.509	0.53	0.47	12.8
							20		.490	1.03	0.995	3.5
							30		.453	1.43	1.33	7.5
							40		.397	1.67	1.56	7.1
							45		.356	1.68	1.63	3.1
32	66, 2 - 216 a = 0.6	2c	0.19	0.982	5.1	0.25	10	0.105	.509	0.53	0.48	10.4
							20		.490	1.03	1.00	3.0
							30		.453	1.43	1.335	7.1
							40		.397	1.67	1.565	6.7
							45		.356	1.68	1.63	3.1
		2b					10		.509	0.534	0.495	7.9
							20		.490	1.03	1.01	2.0
							30		.453	1.43	1.53	- 6.5
							40		.397	1.67	1.70	- 1.8
							45		.356	1.68	1.61	4.3

TABLE 6.1.1.1-B. (CONTD)

Ref.	Airfoil Section	Config.(1)	M	β	$R_\ell \times 10^{-6}$	c_f/c	δ_f (deg)	c_{ℓ_α} (per deg)	$-\alpha_\delta$	Δc_ℓ Calc	Δc_ℓ Test	e Percent Error
30	66, 2 - 116 a = 0.6	1b	LS	1.0	6.0	0.25	15	0.110	.500	0.83	0.70	18.6
↓	↓	↓	↓	↓	↓	↓	45	↓	.356	1.76	1.80	- 2.3
33	23021	2a*	0.105	0.995	3.5	0.25	40	0.097	.397	1.54	1.76	-12.5
42	Mod. Double Wedge	1b	0.25	0.97	6.9	0.253	40	0.101	.398	1.61	1.60	0.6
35	65, 2-222 a = 0.1	1a	LS	1.0	6.0	0.256	20	0.120	.495	1.19	1.06	12.3
↓	↓	↓	↓	↓	↓	↓	30	↓	.460	1.66	1.50	10.7
↓	↓	↓	↓	↓	↓	↓	40	↓	.400	1.92	1.52	26.3
47	23012	1b	0.105	0.995	3.5	0.257	10	0.104	.515	0.54	0.48	12.5
↓	↓	↓	↓	↓	↓	↓	20	↓	.495	1.03	1.00	3.0
↓	↓	↓	↓	↓	↓	↓	30	↓	.460	1.44	1.48	- 2.7
↓	↓	↓	↓	↓	↓	↓	40	↓	.400	1.66	1.64	1.2
↓	↓	↓	↓	↓	↓	↓	50	↓	.305	1.59	1.59	0
43	23021	2b	0.105	0.995	3.5	0.257	10	0.097	.515	0.50	0.49	2.0
↓	↓	↓	↓	↓	↓	↓	20	↓	.495	0.96	1.05	- 8.6
↓	↓	↓	↓	↓	↓	↓	30	↓	.460	1.34	1.30	3.1
↓	↓	↓	↓	↓	↓	↓	40	↓	.400	1.55	1.52	2.0
↓	↓	↓	↓	↓	↓	↓	50	↓	.305	1.48	1.60	- 7.5
↓	↓	↓	↓	↓	↓	↓	60	↓	.220	1.28	1.71	-25.1
↓	↓	1b	↓	↓	↓	↓	20	↓	.495	0.96	0.98	- 2.0
↓	↓	↓	↓	↓	↓	↓	30	↓	.460	1.34	1.23	8.9
↓	↓	↓	↓	↓	↓	↓	40	↓	.400	1.55	1.17	32.5
↓	↓	↓	↓	↓	↓	↓	50	↓	.305	1.48	1.37	8.0
↓	↓	↓	↓	↓	↓	↓	60	↓	.220	1.28	1.46	-12.3
37	23030	1b	0.105	0.995	3.5	0.257	10	0.080	.515	0.41	0.41	0
↓	↓	↓	↓	↓	↓	↓	20	↓	.495	0.79	0.90	-12.2
↓	↓	↓	↓	↓	↓	↓	30	↓	.460	1.10	1.15	- 4.3
↓	↓	↓	↓	↓	↓	↓	40	↓	.400	1.28	1.18	8.5
↓	↓	↓	↓	↓	↓	↓	50	↓	.305	1.22	1.20	1.7
↓	↓	↓	↓	↓	↓	↓	60	↓	.220	1.06	1.40	-24.3
46	23012	2a*	0.105	0.995	3.5	0.267	30	0.104	.469	1.46	1.71	-14.6
↓	↓	2b	↓	↓	↓	↓	50	↓	.313	1.63	1.53	6.5
39	23012	1b*	0.105	0.995	3.5	0.30	40	0.104	.440	1.83	1.84	- 0.5
↓	↓	1a	↓	↓	↓	↓	10	↓	.550	0.57	0.57	0
↓	↓	↓	↓	↓	↓	↓	20	↓	.531	1.10	1.02	7.8
↓	↓	↓	↓	↓	↓	↓	30	↓	.496	1.55	1.48	4.7
↓	↓	↓	↓	↓	↓	↓	40	↓	.440	1.83	1.82	0.5
↓	↓	↓	↓	↓	↓	↓	50	↓	.338	1.76	1.96	-10.2

TABLE 6.1.1.1-8. (CONTD)

Ref.	Airfoil Section	Conf 2[1]	M	β	$R_\ell \times 10^{-6}$	c_f/c	δ_f (deg)	$c\ell_\alpha$ (per deg)	$-\alpha_\delta$	Δc_ℓ Calc	Δc_ℓ Test	e Percent Error
39	23012	1b	0.105	0.995	3.5	0.30	10	0.104	.550	0.57	0.54	5.6
							20		.531	1.10	1.16	- 5.2
							30		.496	1.55	1.58	- 1.9
							40		.440	1.83	1.58	15.8
40	65(112)A111	2c	0.20	0.98	9.0	0.35	35	0.105	.499	1.83	1.95	- 6.2
							40		.466	1.96	1.85	5.9
							45		.425	2.01	2.13	- 5.6
38	23012	1b	0.105	0.995	3.5	0.40	10	0.104	.597	0.62	0.63	- 1.6
							20		.583	1.21	1.32	- 8.3
							30		.550	1.72	1.91	- 9.9
							40		.492	2.05	1.76	16.5
							50		.398	2.07	2.09	- 1.0
		1a					10		.597	0.62	0.48	29.2
							20		.583	1.21	1.24	- 2.4
							30		.550	1.72	1.78	- 3.4
							40		.492	2.05	1.73	18.5
							50		.398	2.07	2.06	0.5
36	23021	1b	0.105	0.995	3.5	0.40	10	0.100	.597	0.60	0.65	- 7.7
							20		.583	1.17	1.17	0
							30		.550	1.65	1.53	7.8
							40		.492	1.97	1.53	28.8
							50		.398	1.99	1.73	15.0
37	23030	1b	0.105	0.995	3.5	0.40	10	0.080	.597	0.48	0.52	- 7.7
							20		.583	0.93	1.07	-13.1
							30		.550	1.32	1.35	- 2.2
							40		.492	1.57	1.40	12.1
							50		.398	1.59	1.66	- 4.2

*Fowler flap

(1)Slot-flap configuration (see sketch below)

Average Error = $\frac{\Sigma|e|}{n}$ = 7.9%

Flap Nose Shape

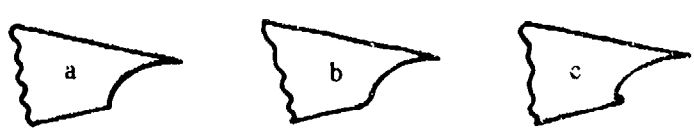

Sharp Rounded Closed

Slot-Entry Shape

TABLE 6.1.1.1-C
SINGLE-SLOTTED TRAILING-EDGE FLAP EFFECTIVENESS
DATA SUMMARY AND SUBSTANTIATION
(See TABLE 6.1.1.1-B for slot-flap configuration)

Ref.	Airfoil Section	M	$R_\ell \times 10^{-6}$	c_f/c	δ_f (deg)	$\frac{c_1}{c}$	Φ (deg)	$c\ell_\delta$ (per deg)	η_1	$\Delta c\ell_{calc}$	$\Delta c\ell_{test}$	e Percent Error
29	23012	0.105	3.5	0.15	30	1.149	38.80	0.0528	0.615	1.12	1.00	12.0
33	23021	0.105	3.5	0.15	60	1.157	74.25	0.0528	0.350	1.28	1.20	6.7
44	23021	LS	7.1	0.15	60	1.03	73.9	0.0528	0.35	1.14	0.83	37.3
34	63(420)-422 a = 0.1	LS	9.0	0.243	30	1.07	42.1	0.066	0.62	1.32	1.41	−6.4
↓	↓	↓	↓	↓	40	↓	52.1	↓	0.52	1.48	1.58	−6.3
↓	↓	↓	↓	↓	45	↓	57.1	↓	0.46	1.47	1.46	0.7
↓	↓	↓	↓	↓	20	↓	32.1	↓	0.697	0.99	1.12	−11.6
↓	↓	↓	↓	↓	30	↓	42.1	↓	0.62	1.32	1.40	−5.7
41	65-210	LS	6.0	0.25	29.1	1.075	37.6	0.0668	0.66	1.38	1.45	−4.8
↓	↓	↓	↓	↓	39.1	1.078	47.6	↓	0.57	1.61	1.78	−9.4
↓	↓	↓	↓	↓	44.1	1.076	52.56	↓	0.51	1.63	1.86	−12.4
↓	↓	↓	↓	↓	49.1	1.076	57.56	↓	0.455	1.61	1.72	−6.4
↓	↓	↓	↓	↓	28.2	1.144	37.0	↓	0.66	1.42	1.52	−6.6
↓	↓	↓	↓	↓	34.5	1.141	43.3	↓	0.61	1.60	1.71	−6.4
↓	↓	↓	↓	↓	39.5	1.135	48.3	↓	0.56	1.68	1.80	−6.7
↓	↓	↓	↓	↓	44.7	1.146	53.5	↓	0.50	1.70	1.73	−1.7
↓	↓	↓	2.4	↓	27.5	1.27	33.7	↓	0.69	1.57	1.40	12.1
↓	↓	↓	↓	↓	32.5	1.25	38.7	↓	0.65	1.76	1.53	15.0
↓	↓	↓	↓	↓	37.5	1.21	43.7	↓	0.61	1.89	1.80	5.0
29	23012	0.105	3.5	0.25	40	1.25	48.8	0.0668	0.56	1.87	1.98	−5.5
31	66,2-216 a = 0.6	0.19	5.1	0.25	10	1.029	21	0.0668	0.73	0.50	0.47	6.4
↓	↓	↓	↓	↓	20	1.043	31	↓	0.70	0.976	0.995	−1.9
↓	↓	↓	↓	↓	30	1.058	41	↓	0.633	1.34	1.33	0.8
↓	↓	↓	↓	↓	40	1.068	51	↓	0.53	1.51	1.56	−3.2
↓	↓	↓	↓	↓	45	1.073	56	↓	0.47	1.52	1.63	−6.7
32	66,2-216 a = 0.6	0.19	5.1	0.25	10	1.029	21	0.0668	0.73	0.50	0.48	4.2
↓	↓	↓	↓	↓	20	1.043	31	↓	0.73	0.976	1.00	−2.4
↓	↓	↓	↓	↓	30	1.058	41	↓	0.633	1.34	1.335	0.4
↓	↓	↓	↓	↓	40	1.068	51	↓	0.53	1.51	1.565	−3.5
↓	↓	↓	↓	↓	45	1.073	56	↓	0.47	1.52	1.63	−6.7
↓	↓	↓	↓	↓	10	1.014	21	↓	0.73	0.495	0.495	0
↓	↓	↓	↓	↓	20	1.029	31	↓	0.70	0.96	1.01	−5.0
↓	↓	↓	↓	↓	30	1.043	41	↓	0.633	1.32	1.53	−13.7
↓	↓	↓	↓	↓	40	1.058	51	↓	0.53	1.50	1.70	−11.8
↓	↓	↓	↓	↓	45	1.066	56	↓	0.47	1.51	1.61	−6.2
30	66,2-116 a = 0.6	LS	6.0	0.25	15	1.023	26.3	0.0668	0.718	0.74	0.70	5.7
↓	↓	↓	↓	↓	45	1.066	56.3	↓	0.467	1.50	1.80	−16.7
33	23021	0.105	3.5	0.25	40	1.255	54.25	0.0668	0.49	1.64	1.76	−6.8
42	Mod. Double Wedge	0.25	6.9	0.253	40	1.006	46.42	0.0672	0.58	1.57	1.60	−1.9
35	65,2-222 a = 0.1	LS	6.0	0.256	20	1.058	31.3	0.0675	0.70	1.00	1.06	−5.7
↓	↓	↓	↓	↓	30	↓	41.3	↓	0.63	1.35	1.50	−10.0
↓	↓	↓	↓	↓	40	↓	51.3	↓	0.53	1.51	1.52	−0.7
47	23012	0.105	3.5	0.257	10	1.03	18.8	0.0676	0.73	0.51	0.48	6.3
↓	↓	↓	↓	↓	20	1.05	28.8	↓	0.71	1.01	1.00	1.0
↓	↓	↓	↓	↓	30	1.06	38.8	↓	0.65	1.40	1.48	−5.4
↓	↓	↓	↓	↓	40	1.0705	48.8	↓	0.56	1.62	1.64	−1.2
↓	↓	↓	↓	↓	50	1.08	58.8	↓	0.445	1.62	1.59	1.9

TABLE 6.1.1.1-C (CONTD)

Ref.	Airfoil Section	M	$R_\ell \times 10^{-6}$	c_f/c	δ_f (deg)	$\frac{c_1}{c}$	Φ (deg)	$c\ell_\delta$ (per deg)	η_1	$\Delta c\ell_{calc}$	$\Delta c\ell_{test}$	e Percent Error
43	23021	0.105	3.5	0.257	10	1.035	24.25	0.0676	0.72	0.50	0.49	2.0
					20	1.035	34.25		0.685	0.96	1.05	−8.6
					30	1.07	44.25		0.603	1.31	1.30	−0.8
					40	1.07	54.25		0.49	1.42	1.52	−6.6
					50	1.07	64.25		0.405	1.46	1.60	−8.8
					60	1.06	74.25		0.36	1.55	1.77	−12.4
					20	1.037	34.25		0.685	0.96	0.98	−2.0
					30	1.05	44.25		0.603	1.28	1.23	4.1
					40	1.063	54.25		0.49	1.41	1.17	20.5
					50	1.054	64.25		0.405	1.44	1.37	5.1
					60	1.065	74.25		0.36	1.55	1.46	6.2
37	23030	0.105	3.5	0.257	10	1.02	29.57	0.0676	0.706	0.49	0.41	19.5
					20	1.072	39.57		0.644	0.93	0.90	3.3
					30	1.08	49.57		0.550	1.20	1.15	4.3
					40	1.103	59.57		0.438	1.31	1.18	11.0
					50	1.122	69.57		0.403	1.53	1.20	27.5
					60	1.118	79.57		0.35	1.59	1.40	13.6
46	23012	0.105	3.5	0.267	30	1.26	38.8	0.069	0.65	1.69	1.86	−9.1
39	23012	0.105	3.5	0.30	40	1.31	48.8	0.0725	0.57	1.95	2.17	−10.1
					10	1.20	18.8		0.743	0.65	0.78	−16.7
					20		28.8		0.72	1.25	1.22	2.5
					30		38.8		0.664	1.73	1.67	3.6
					40		48.8		0.57	1.98	2.01	−1.5
					50		58.8		0.458	1.99	2.16	−7.9
					10	1.20	18.8	0.0725	0.743	0.65	0.73	−11.0
					20		28.8		0.72	1.25	1.38	−9.4
					30		38.8		0.664	1.73	1.79	−3.3
					40		48.8		0.57	1.98	1.79	10.6
40	$65_{(112)}A111$	0.20	2.4	0.35	35	1.186	43.13	0.0775	0.64	2.06	1.95	5.6
					40	1.2	48.15		0.49	1.83	1.85	−1.1
					45	1.2	53.15		0.525	2.20	2.13	3.3
38	23012	0.105	3.5	0.40	10	1.065	18.8	0.082	0.77	0.67	0.63	6.3
					20	1.088	28.8		0.75	1.34	1.32	1.5
					30	1.103	38.8		0.69	1.87	1.91	2.1
					40	1.093	48.8		0.59	2.12	1.76	20.5
					50	1.09	58.8		0.48	2.15	2.09	2.9
					10	1.082	18.8		0.77	0.68	0.57	19.3
					20	1.10	28.8		0.75	1.35	1.24	8.9
					30	1.102	38.8		0.69	1.87	1.78	5.1
					40	1.11	48.8		0.59	2.15	1.73	24.3
					50	1.09	58.8		0.48	2.15	2.06	4.4
36	23021	0.105	3.5	0.40	10	1.032	24.25	0.082	0.761	0.64	0.65	−1.5
					20	1.075	34.25		0.724	1.28	1.17	9.4
					30	1.085	44.25		0.639	1.71	1.53	11.8
					40	1.095	54.25		0.53	1.90	1.53	24.2
					50	1.095	64.25		0.435	1.95	1.73	12.7
37	23030	0.105	3.5	0.40	10	1.04	29.57	0.082	0.745	0.64	0.52	23.0
					20	1.08	39.57		0.684	1.21	1.07	13.1
					30	1.10	49.57		0.583	1.58	1.35	17.0
					40	1.15	59.57		0.475	1.79	1.40	27.9
					50	1.16	69.57		0.402	1.91	1.56	15.1

Average Error = $\frac{\Sigma|e|}{n}$ = 8.3%.

TABLE 6.1.1.1-D
DOUBLE-SLOTTED TRAILING-EDGE FLAP EFFECTIVENESS
DATA SUMMARY AND SUBSTANTIATION

Ref.	Airfoil Section	M	ϕTE_{UPPER} (deg)	$\frac{c'}{c}$	$\frac{c_1}{c}$	$\frac{c_2}{c}$	δf_1 (deg)	δf_2 (deg)	$\Delta c_{\ell_{calc}}$	$\Delta c_{\ell_{test}}$	e Percent Error
73	Wedge	0.25	7.2	1.085	0.04	0.25	20	30	2.04	1.96	4.1
64	64-208	0.18	6.1	1.127	0.056	0.25	25	25	2.33	2.17	7.4
41	65-210	–	7.6	1.139	0.075	0.25	15	25	2.14	1.99	7.5
↓	↓	↓	↓	1.146	↓	↓	20	↓	2.29	2.14	7.0
				1.143			25		2.40	2.26	6.2
				1.148			30		2.51	2.30	9.1
				1.133			35		2.57	2.23	15.2
64	1410	0.18	8.0	1.141	0.075	0.25	25	25	2.36	2.49	–5.2
↓	63-210	↓	6.4	1.133	0.075	0.25	↓	↓	2.44	2.51	–2.8
	65-210		7.6	1.143	0.075	0.25			2.36	2.23	5.8
	66-210		8.9	1.144	0.075	0.25		30	2.36	2.36	0
	64-208		6.1	1.148	0.075	0.25	30	15	2.62	2.364	10.8
	64_1-212		7.4	1.152	0.075	0.25	↓	20	2.51	2.52	–0.4
↓	64-210	↓	6.8	1.139	0.075	0.25		25	2.53	2.61	–3.1
69	64A010	0.06	5.9	1.133	0.075	0.25	30	22.7	2.54	2.34	8.6
↓	↓	0.20	5.9	↓	↓	↓	↓	↓	2.54	2.26	12.4
65	64_1A212	–	9.8	1.106	0.083	0.229	26	29	2.24	2.55	–12.0
71	65(216)-215 a = 0.8	0.12	8.0	1.114	0.096	0.248	10	15	1.59	1.61	–1.2
↓	↓	↓	↓	1.118	↓	↓	↓	20	1.76	1.85	–4.9
				1.121				25	1.92	1.98	–3.0
				1.125				30	2.00	2.165	–7.6
				1.133				40	2.01	2.37	–15.2
				1.137				45	2.04	2.50	–18.4
↓	↓	↓	↓	1.151	↓	↓	↓	60	2.29	2.55	–10.2
72	R-4,40-318-1	–	16.5	1.137	0.092	0.238	5	35	1.52	1.74	–12.6
↓	↓	↓	↓	1.155	↓	↓	20	20	1.96	1.68	16.7
	R-4,40-413-6			1.216			25	35	2.33	2.50	–6.8
↓	↓	↓	↓	1.180	↓	↓	↓	40	2.32	2.63	–11.8
64	66-210	0.18	8.9	1.172	0.10	0.25	25	35	2.54	2.28	11.4
66	$65_3$118	0.105	9.0	1.175	0.10	0.245	23	42	2.51	2.83	–11.3
67	65_3-418	–	13.2	1.163	0.106	0.236	21	44	2.37	2.62	–9.6
62	23012	0.105	8.8	1.221	0.1165	0.2566	25	35	2.69	2.53	6.5
68	65_4-421	–	14.1	1.166	0.109	0.235	20	31	2.17	2.23	–2.7
63	23021	0.105	14.3	1.229	0.147	0.2566	30	40	3.07	2.78	10.5

Average Error = $\frac{\Sigma|e|}{n}$ = 8.2%.

TABLE 6.1.1.1-E
SPLIT TRAILING-EDGE FLAP EFFECTIVENESS
DATA SUMMARY AND SUBSTANTIATION

Ref	Airfoil Section	M	$R_\ell \times 10^{-6}$	c_f/c	δ_f	Δc_ℓ Calc	Δc_ℓ Test	e Percent Error
75	23012	0.105	3.5	0.10	15	0.38	0.37	2.7
					30	0.62	0.64	−3.1
					45	0.835	0.82	1.8
					60	0.985	0.94	4.8
					75	1.05	1.02	2.9
	23021				15	0.35	0.32	9.4
					30	0.57	0.63	−9.5
					45	0.765	0.88	−13.1
					60	0.90	1.05	−14.3
					75	0.96	1.15	−16.5
69	64A010	0.06	2	0.20	66	1.31	1.35	−3.0
		0.12	4			1.43	1.36	5.1
		0.17	6			1.43	1.36	5.1
		0.20	7			1.43	1.36	5.1
26	23012	—	8		5	0.23	0.17	37.5
					10	0.39	0.32	21.9
					15	0.51	0.45	13.3
					20	0.615	0.58	6.0
					30	0.83	0.84	−1.2
					45	1.12	1.09	2.8
46		0.105	3.5		60	1.34	1.34	0
					75	1.51	1.41	7.1
74	66,1-212	~0.15	6		40	0.99	1.09	−9.2
					50	1.16	1.25	−7.2
					60	1.29	1.37	−5.8
					70	1.41	1.42	−0.7
	65_1-212				40	1.05	1.06	−0.9
					50	1.23	1.205	2.1
					60	1.37	1.36	0.7
					70	1.50	1.36	10.3
	66(215)-216				40	1.11	1.17	−5.1
					50	1.29	1.37	−5.8
					60	1.44	1.44	0
					70	1.58	1.54	2.6
45	23021	0.085	3.56		15	0.47	0.51	−7.8
					30	0.76	0.95	−20.0
					45	1.03	1.27	−18.9
					60	1.23	1.52	−19.1
					75	1.38	1.65	−16.4
75	23012	0.105	3.5	0.30	15	0.665	0.63	5.6
					30	1.05	1.06	−0.9
					45	1.41	1.37	2.9
					60	1.72	1.55	11.0
					75	1.99	1.64	21.3
	23021				15	0.61	0.67	−9.0
					30	0.96	1.20	−20.0
					45	1.29	1.59	−18.9
					60	1.57	1.84	−14.7
					75	1.82	1.96	−7.1
	23012			0.40	15	0.77	0.70	10.0
					30	1.21	1.22	−0.8
					45	1.59	1.55	2.6
					60	1.93	1.71	12.9
	23021				15	0.70	0.80	−12.5
					30	1.11	1.42	−21.8
					45	1.46	1.86	−21.5
					60	1.76	2.12	−17.0

$$\text{Average Error} = \frac{\Sigma |e|}{\eta} = 9.3\%$$

PLAIN TRAILING-EDGE FLAPS

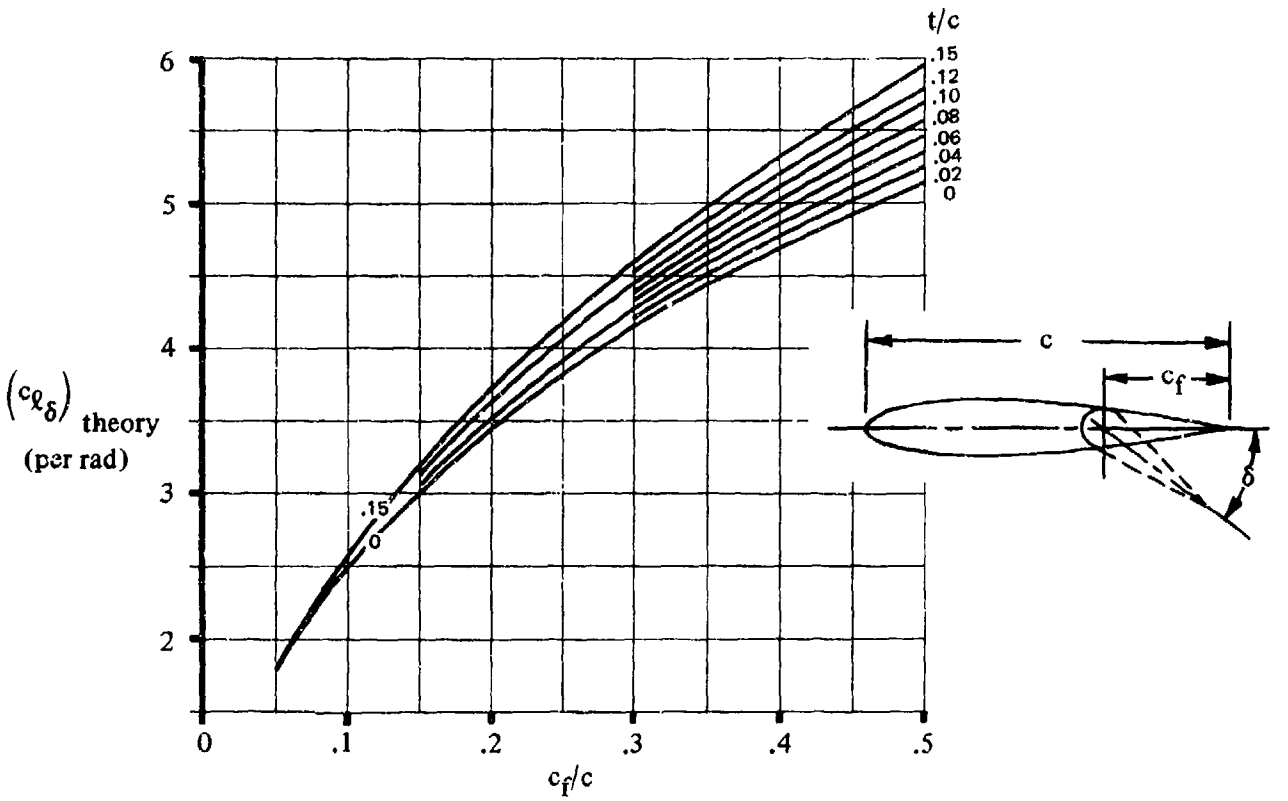

FIGURE 6.1.1.1-39a THEORETICAL LIFT EFFECTIVENESS OF PLAIN TRAILING-EDGE FLAPS

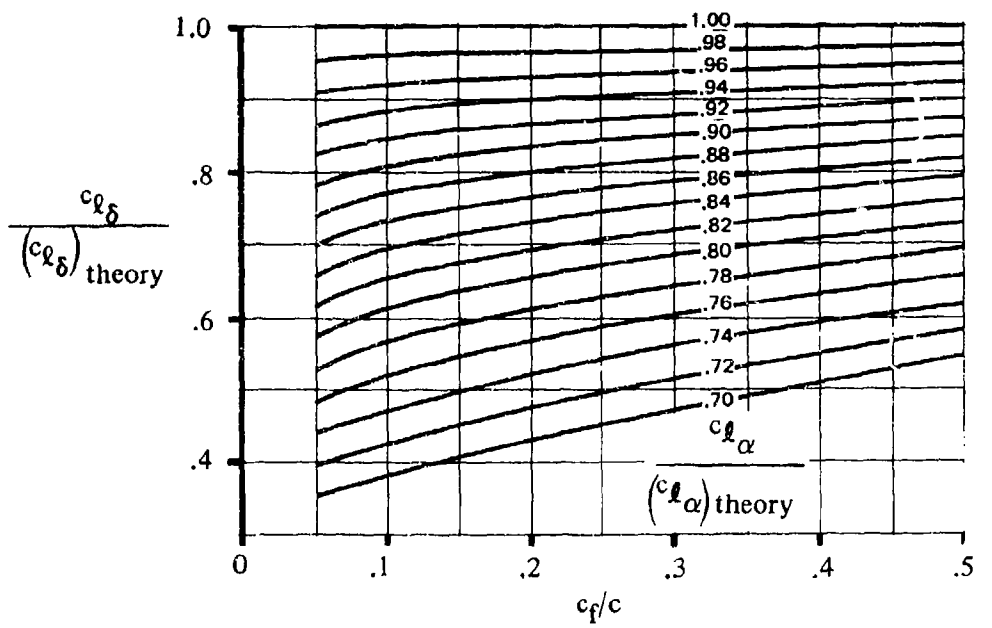

FIGURE 6.1.1.1-39b EMPIRICAL CORRECTION FOR LIFT EFFECTIVENESS OF PLAIN TRAILING-EDGE FLAPS

PLAIN TRAILING-EDGE FLAPS

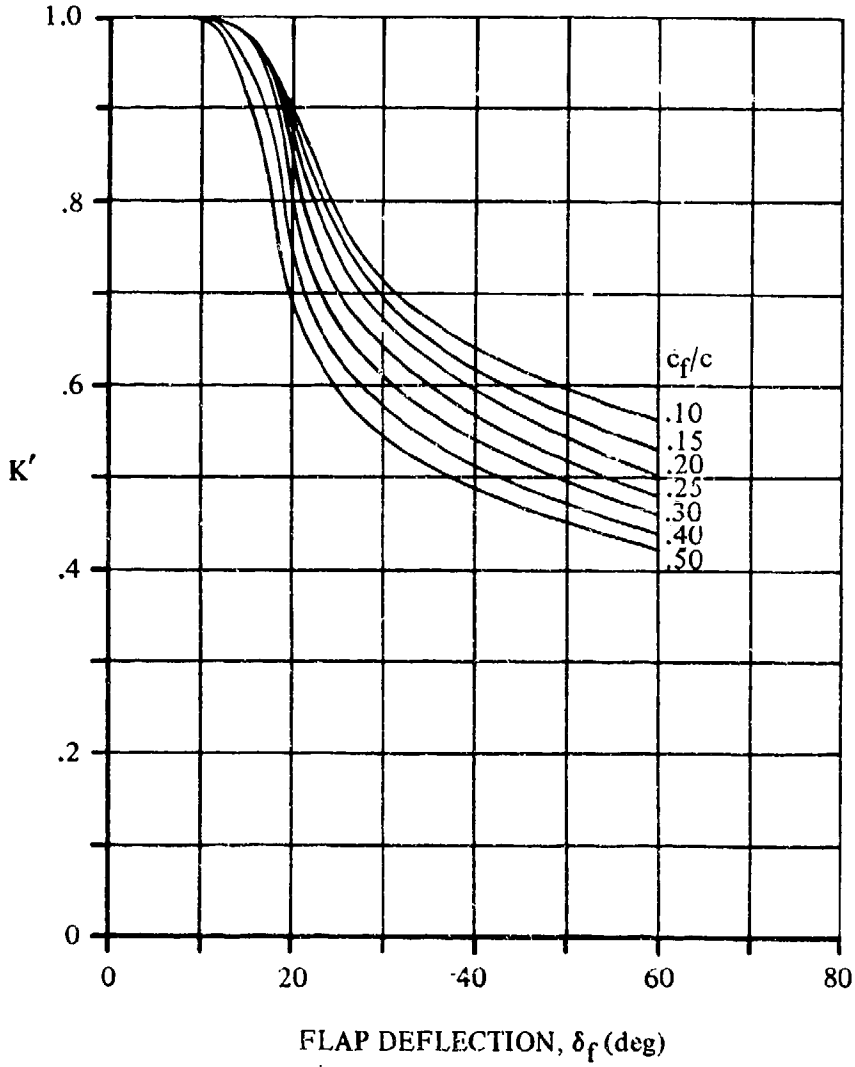

FIGURE 6.1.1.1-40 EMPIRICAL CORRECTION FOR LIFT EFFECTIVENESS OF PLAIN TRAILING-EDGE FLAPS AT HIGH FLAP DEFLECTIONS

SINGLE-SLOTTED FLAPS

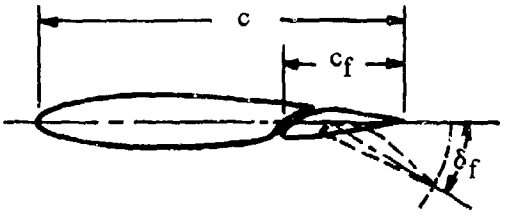

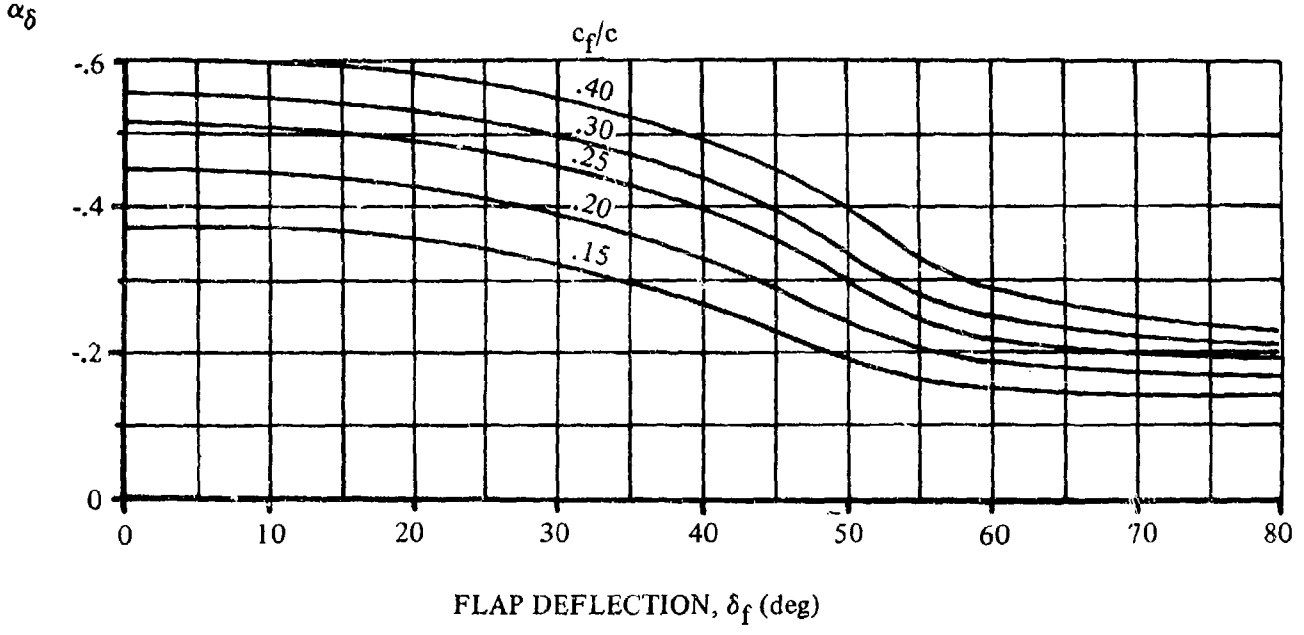

FIGURE 6.1.1.1-41 SECTION LIFT-EFFECTIVENESS PARAMETER OF SINGLE-SLOTTED FLAPS

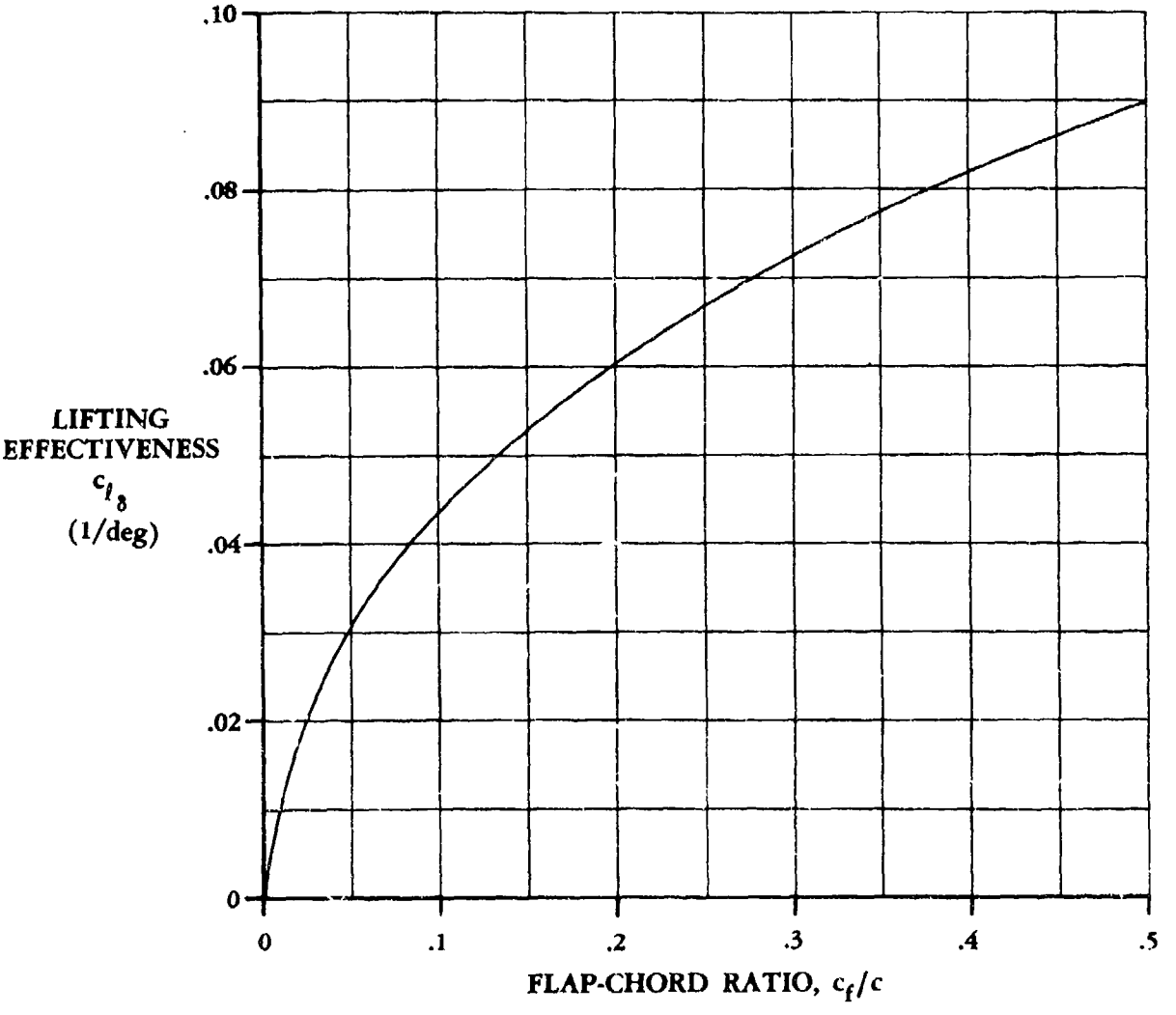

Note: The c_f/c values needed for using this figure are defined under "Datcom Methods," based on the geometric parameters shown in Figures 6.1.1.1-44 through -46.

FIGURE 6.1.1.1-42 THEORETICAL LIFTING EFFECTIVENESS OF TRAILING-EDGE FLAPS

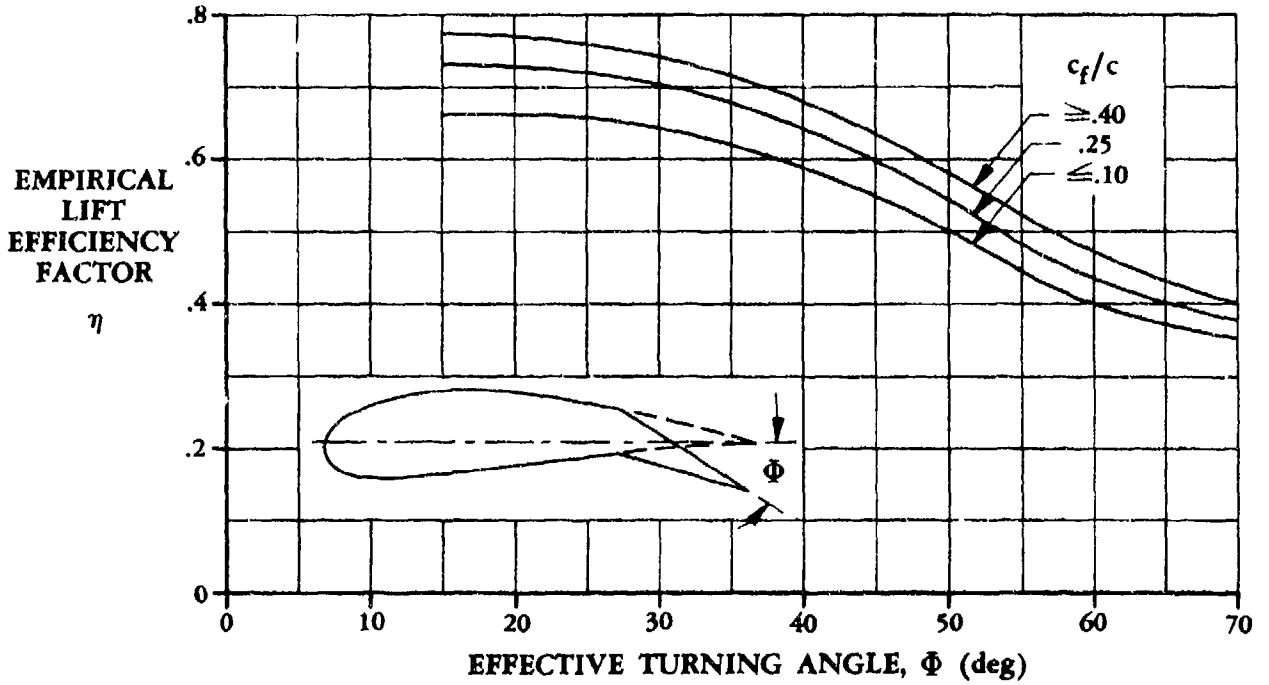

FIGURE 6.1.1.1-43a EMPIRICAL LIFTING-EFFICIENCY FACTORS FOR SLOTTED FLAPS

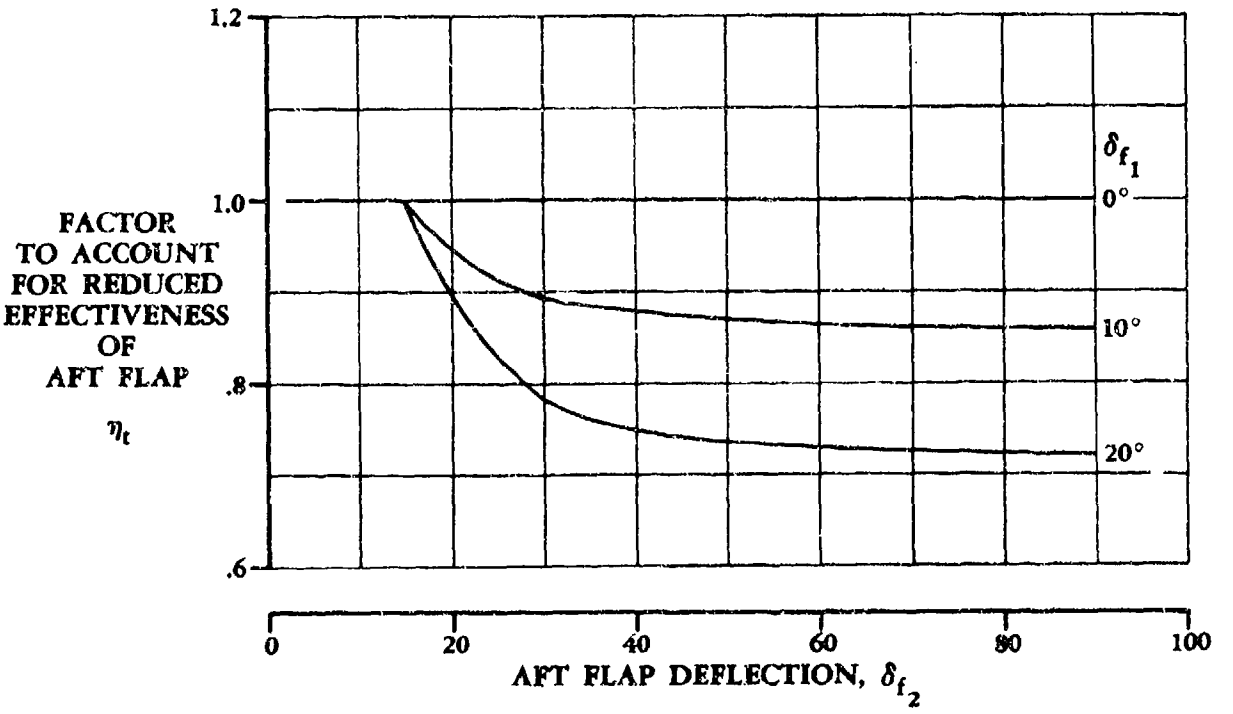

FIGURE 6.1.1.1-43b TURNING EFFICIENCY OF AFT FLAPS

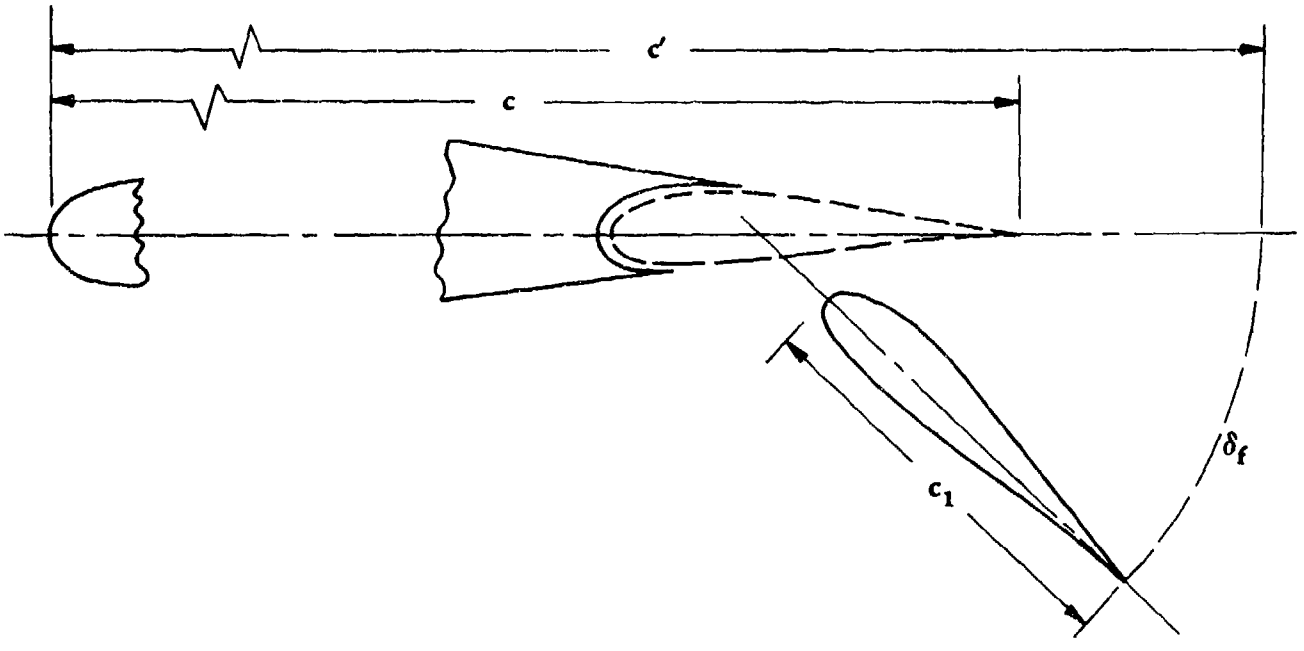

c wing chord (flap in neutral position).

c_1 flap chord.

c' extended wing chord due to flap extension. In measuring c', the flap trailing edge is rotated from its deflected position about the intersection of the flap chord and the chord of the airfoil section, until the two chords coincide.

δ_f flap deflection.

FIGURE 6.1.1.1-44 SINGLE-SLOTTED FLAP GEOMETRIC PARAMETERS

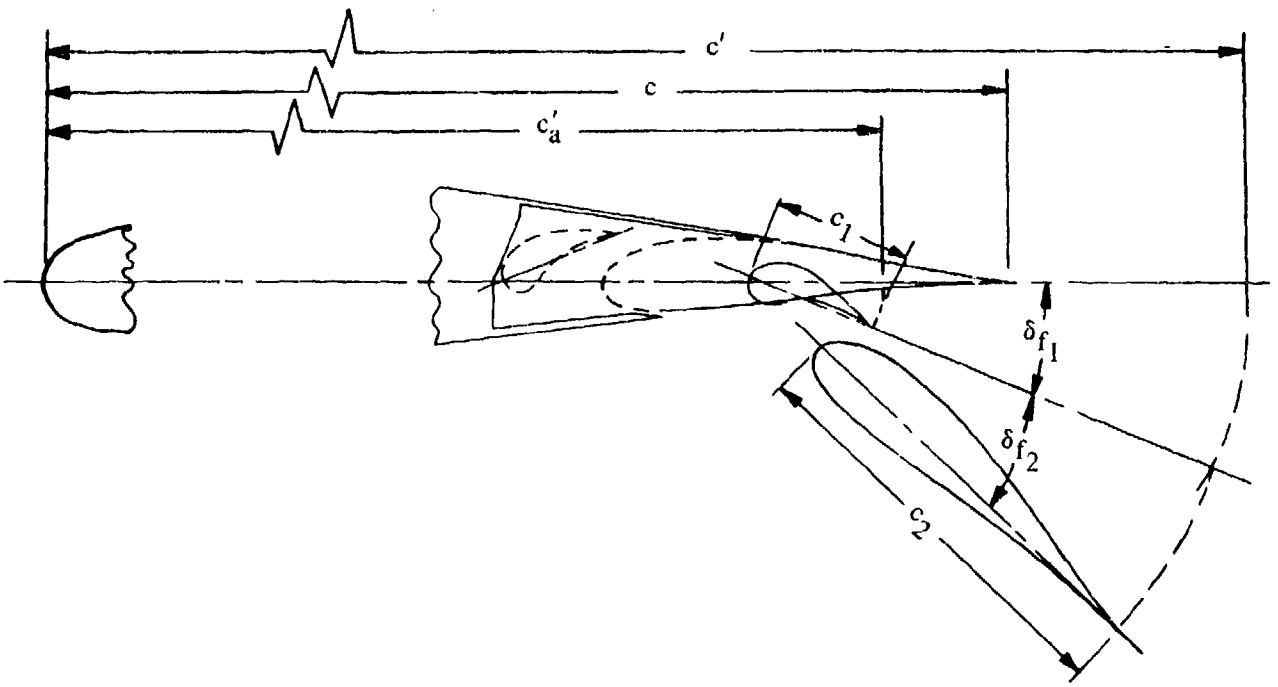

c wing chord (flap in neutral position).

c'_a extended wing chord due to forward-flap extension. In measuring c_a, first rotate the forward flap from its deflected position about the point of intersection of the forward-flap chord and the chord of the airfoil section, until the two chords coincide.

c' extended wing chord due to the double-slotted flaps. In measuring c', the aft flap is first rotated from its deflected position about the point of intersection of the aft-flap chord and the chord of the forward flap, until the two chords coincide. Then both flaps are rotated from the deflection of the forward flap about the point of intersection of the forward-flap chord with the wing chord, until these two coincide.

δ_{f_1} flap deflection of the forward flap.

δ_{f_2} flap deflection of the aft flap.

c_1 forward-flap chord.

c_2 aft-flap chord.

FIGURE 6.1.1.1-45 DOUBLE-SLOTTED FLAP GEOMETRIC PARAMETERS

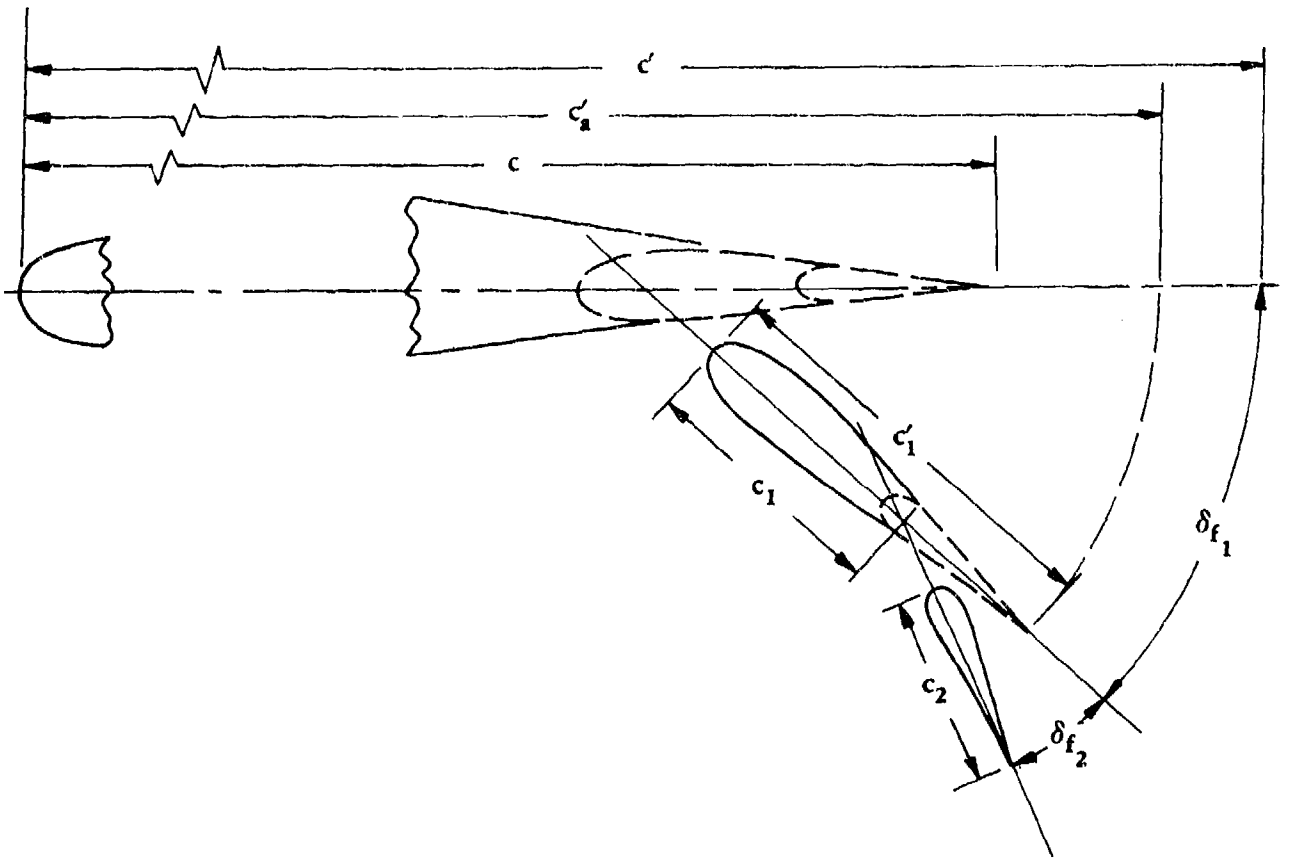

c wing chord (flap in neutral position).

c'_a extended wing chord due to complete forward-flap extension. In measuring c'_a, first rotate the complete forward flap (usually includes aft flap) about the point of intersection of the forward-flap chord and the chord of the airfoil section, until the two chords coincide.

c' extended wing chord due to the deflection of the double-slotted flaps. In measuring c', the aft flap is first rotated from its deflected position about the point of intersection of the aft-flap chord and the chord of the forward flap, until the two chords coincide. Then both flaps are rotated from the deflection position of the forward flap about the point of intersection of the forward-flap chord with the wing chord, until these two coincide.

c_1 forward-flap chord (actual).

c_1' forward-flap chord (complete airfoil).

c_2 aft-flap chord.

δ_{f_1} flap deflection of the forward flap.

δ_{f_2} flap deflection of the aft flap.

FIGURE 6.1.1.1-46 DOUBLE-SLOTTED FLAP GEOMETRIC PARAMETERS

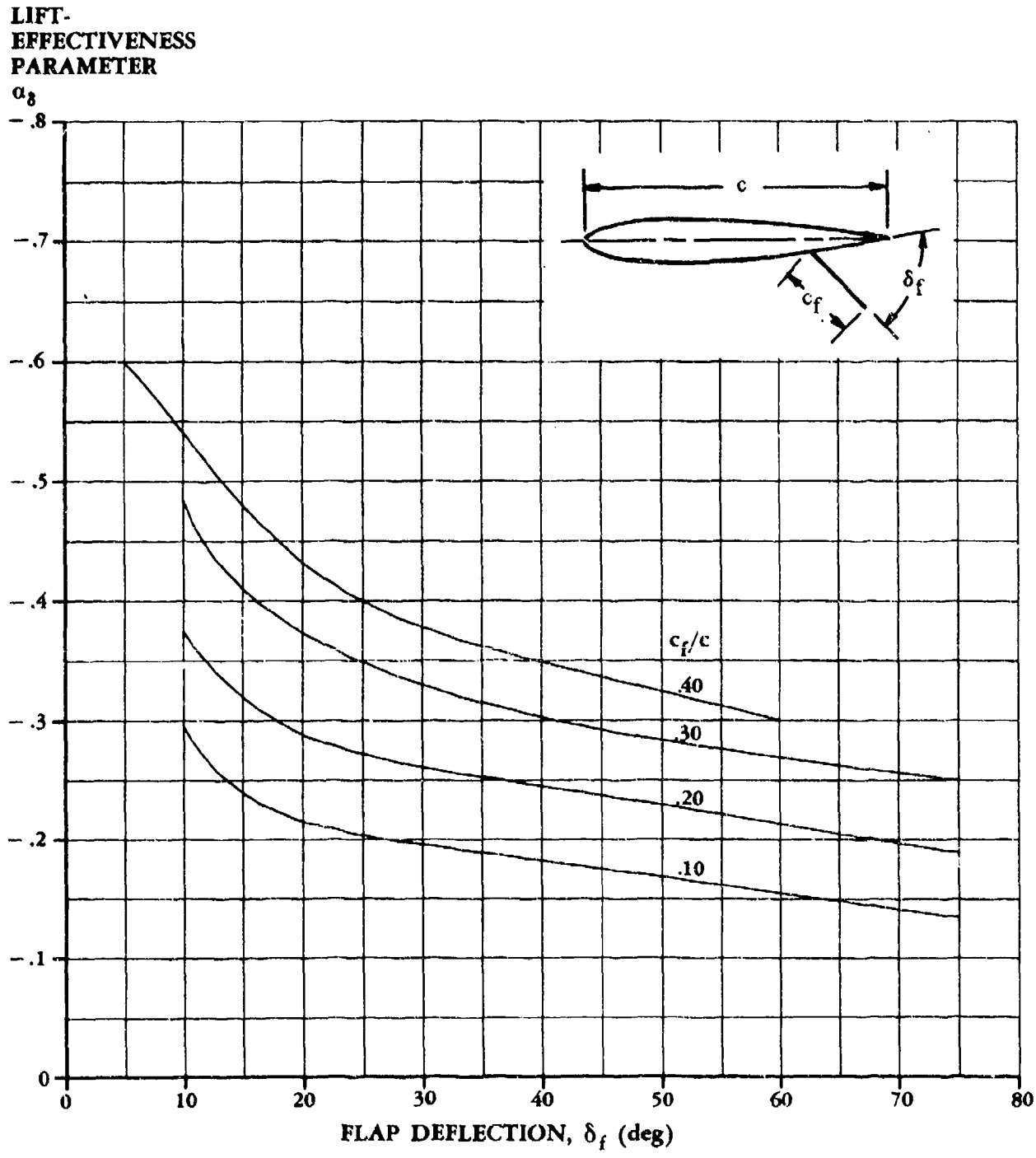

FIGURE 6.1.1.1-47 SECTION LIFT-EFFECTIVENESS PARAMETER OF SPLIT FLAPS

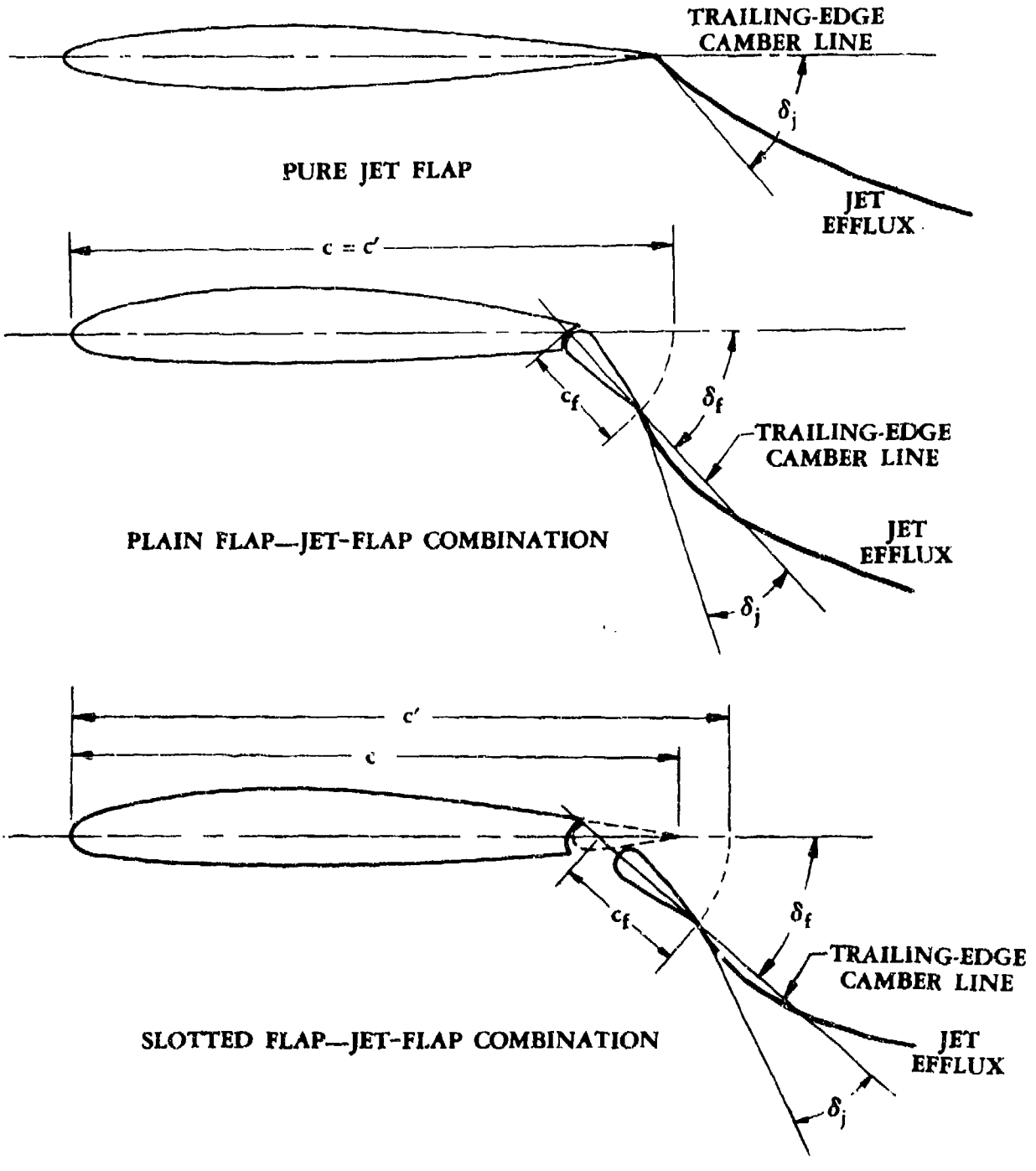

δ_j is the initial trailing-edge jet momentum angle in radians, measured with respect to the trailing-edge camber line of the airfoil.

δ_f is the flap deflection in radians, measured with respect to the airfoil chord.

FIGURE 6.1.1.1-48 JET-FLAP GEOMETRIC PARAMETERS

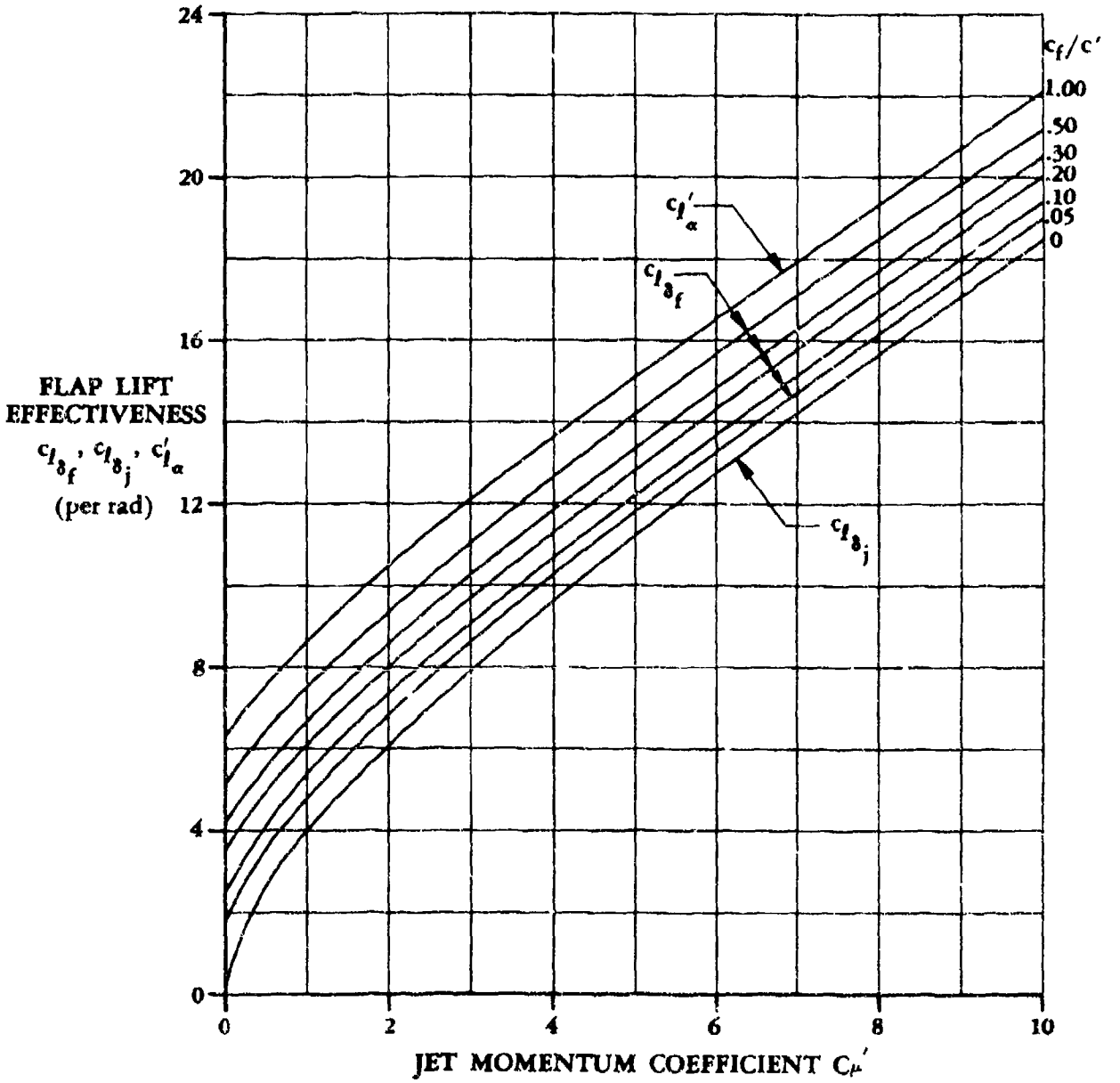

FIGURE 6.1.1.1-49 TWO DIMENSIONAL JET-FLAP THEORETICAL RESULTS

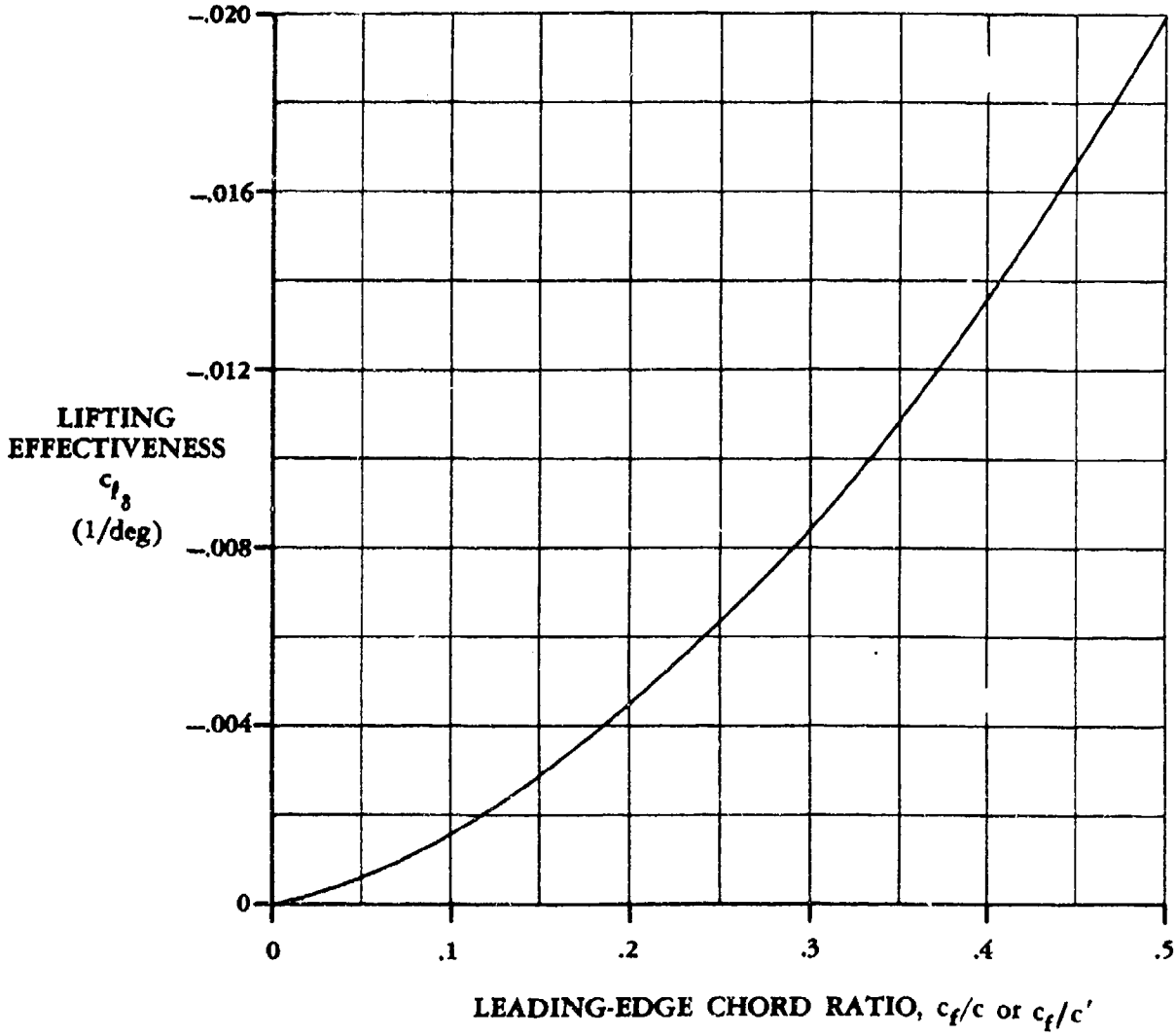

Note: The c_f/c or c_f/c' values needed for using this figure are schematically illustrated in the next figure.

FIGURE 6.1.1.1-50 THEORETICAL LIFTING EFFECTIVENESS OF LEADING-EDGE DEVICES

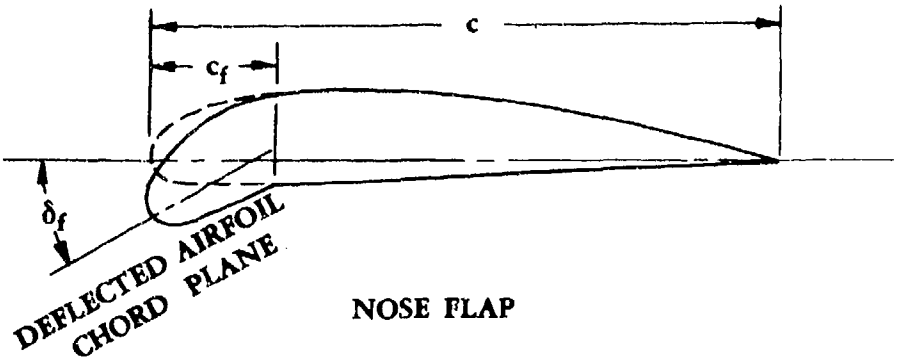

NOSE FLAP

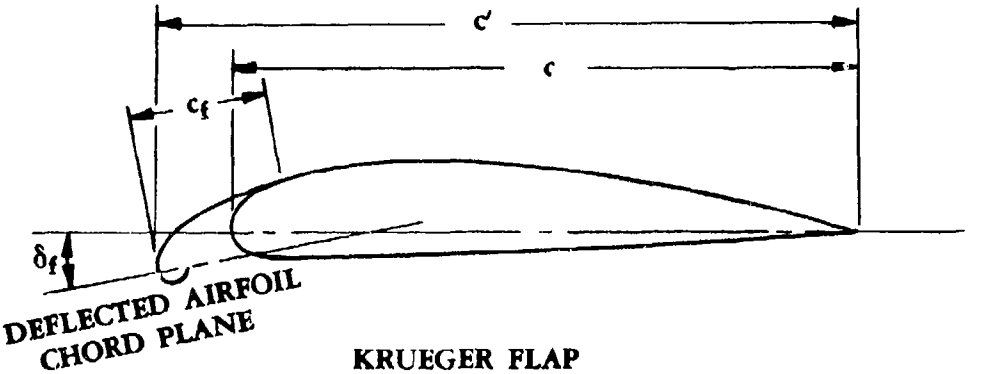

KRUEGER FLAP

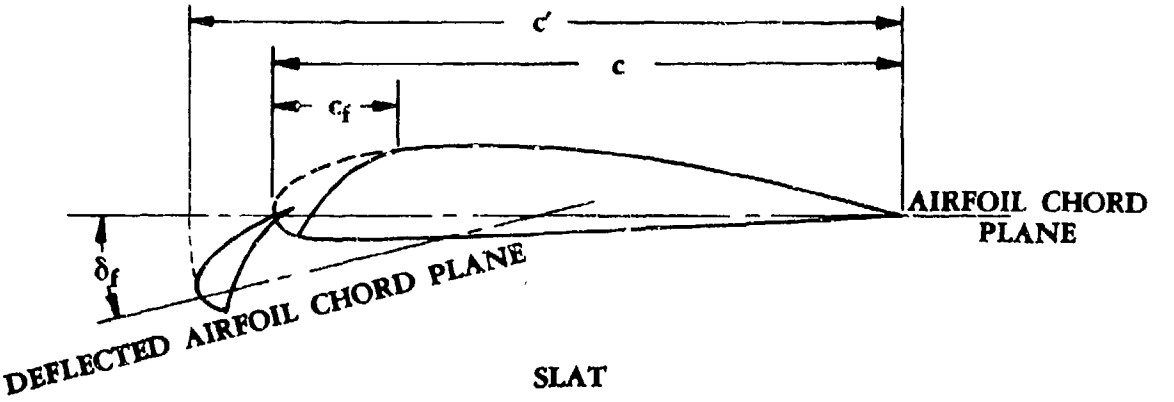

SLAT

c' is the extended wing chord due to the deflection of the leading-edge device. In measuring c' the leading-edge device is rotated to the wing-chord line from its deflected position, about the point of intersection of the leading-edge-flap chord and the wing chord.

FIGURE 6.1.1.1-51 GEOMETRY OF LEADING-EDGE DEVICES

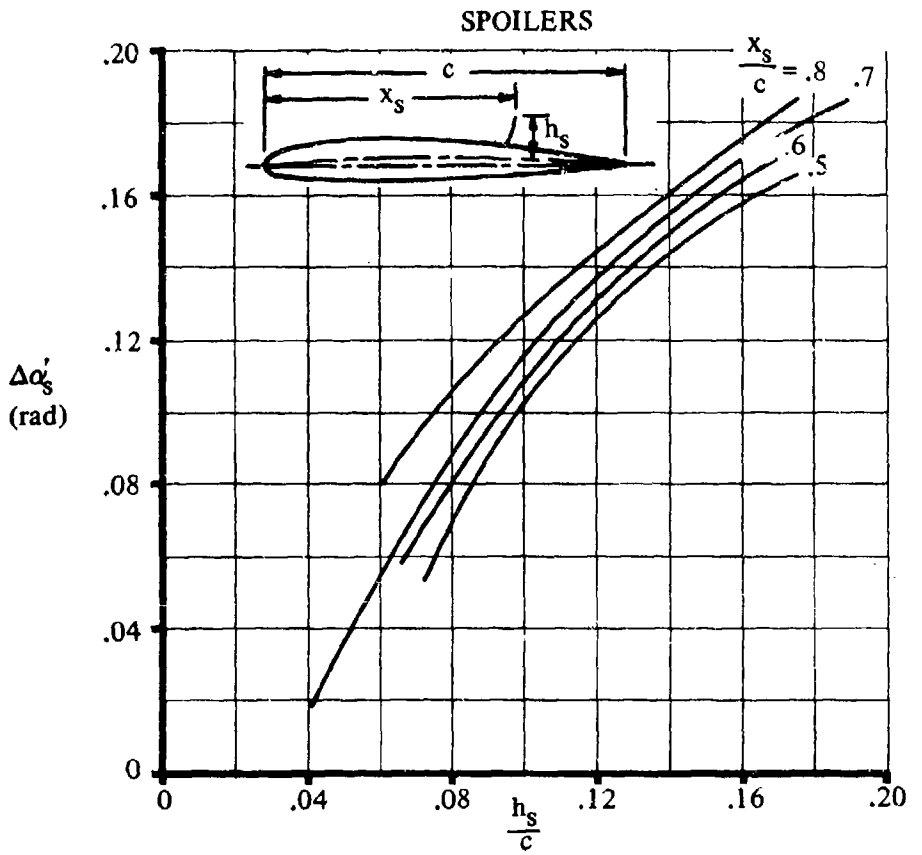

FIGURE 6.1.1.1-52 SPOILER LIFT EFFECTIVENESS – LOW SPEEDS

6.1.1.2 SECTION LIFT-CURVE SLOPE WITH HIGH-LIFT AND CONTROL DEVICES

Trailing-Edge Flaps

Thin-airfoil theory shows that the lift-curve slope of a cambered section is the same as that of the corresponding uncambered airfoil. Experimental data verify this theoretical prediction for the angle-of-attack and flap-deflection ranges for which the flow is attached over both the wing and flap surfaces.

Flow separation on the wing or flap causes the lift-curve slope to be lower than the theoretical value. Sketch (a) shows a typical set of lift curves for trailing-edge flaps at various deflections. The approximate points at which the curves become appreciably nonlinear for a given flap deflection are shown by the arrows.

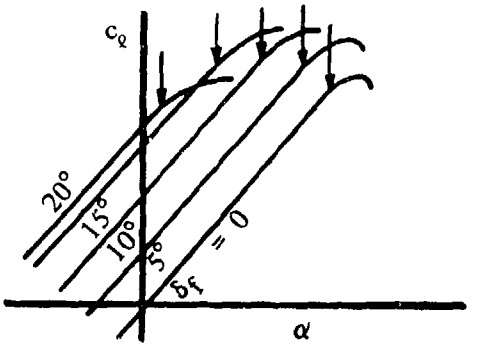

SKETCH (a) TYPICAL LIFT CURVES FOR TRAILING-EDGE FLAPS

The sketch is typical of all types of trailing-edge flaps except split flaps, which have somewhat different lift characteristics. When a split flap is deflected, a reduced pressure exists in the wedge-shaped region between the flap and the wing. This reduced pressure creates a favorable pressure gradient near the wing trailing edge, which causes the boundary layer at the upper-surface trailing edge to be thinner for the flap-deflected condition than for the undeflected condition. Consequently, lift-curve slope for small split-flap deflections is greater than that of the unflapped airfoil. This effect is particularly pronounced on thick airfoils.

For flaps that translate as they deflect, the lift-curve slope is increased because of the increased effective area of the flapped section. Fowler flaps are the most commonly used flaps of this type.

Reference 1 contains a comprehensive summary of two-dimensional trailing-edge control-surface data, including data for the nonlinear angle-of-attack and flap-deflection ranges.

Jet Flaps

The lift-curve slope for a jet-flap airfoil is dependent upon the jet momentum trailing-edge coefficient C_μ. The method presented herein is Spence's adaptation of thin-airfoil theory as presented in References 2 and 3. In summary, Spence applies thin-airfoil theory to inviscid, incompressible flow past a thin, two-dimensional wing at a small incidence, with a jet of zero thickness and finite momentum emerging at a small angle of incidence from the trailing edge. The flow inside the jet is assumed to be irrotational and is bounded by vortex sheets that prevent mixing

with the mainstream. For flaps that extend as well as rotate, a correction is applied to account for the increased planform area. For more details regarding the fundamental concepts of jet flaps, the reader is referred to the discussion presented in Section 6.1.1.1.

Leading-Edge Flaps

The lift-curve slope of an airfoil with a leading-edge flap is very nearly the same as that of the unflapped airfoil. For slats that extend forward as well as rotate, a correction must be made for the increased planform area. Typical lift curves are shown in Sketch (b).

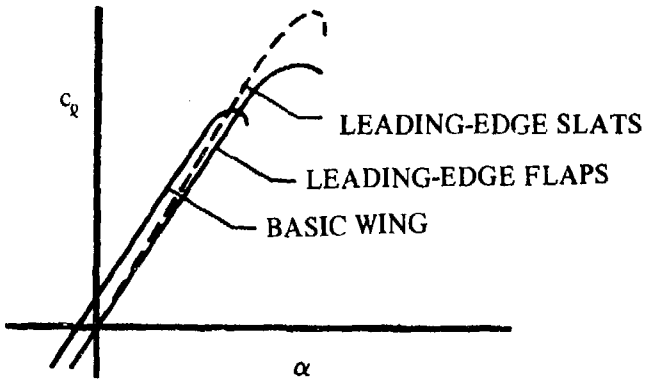

SKETCH (b) TYPICAL LIFT CURVES FOR LEADING-EDGE FLAPS AND SLATS

Spoilers

The lift curves of airfoils with spoilers extended are extremely nonlinear, particularly at subsonic speeds. Sketch (c) shows a typical set of lift curves for an airfoil with and without plug and slotted spoilers. Leading-edge flaps in conjunction with plug spoilers tend to linearize the lift curve at high angles of attack. This effect is similar to that achieved by adding a slot and deflector behind a plug spoiler.

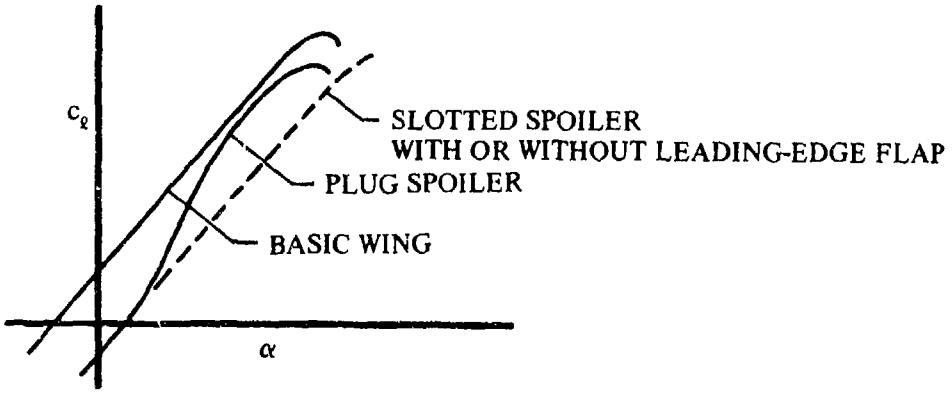

SKETCH (c) EFFECT OF SLOT AND LEADING-EDGE FLAP ON SPOILER LIFT CURVES

The Datcom methods presented below for trailing-edge flaps, jet flaps, leading-edge flaps and slats, and spoilers are limited to subsonic flow.

DATCOM METHODS

The approximate flap deflections at which flow separation and appreciable lift-curve-slope losses occur with increasing flap deflection are shown in Table 6.1.1.2-A for various types of flaps. Values for both good and poor designs are shown. Flap design is very critical to airfoil section and flap geometry. The effects of these variables on maximum lift are discussed in detail in Section 6.1.1.3.

1. Fixed-Hinge Trailing- and Leading-Edge Flaps

For these flaps the lift-curve slope is assumed to be the same as that of the unflapped section for unseparated flow conditions.

2. Translating Trailing-Edge Flaps and Leading-Edge Devices (Slats and Krueger Flaps)

For devices whose hinge line translates with deflection, the lift-curve slope is given by

$$\left(c_{\ell_\alpha}\right)_\delta = \frac{c'}{c}\left(c_{\ell_\alpha}\right)_{\delta=0} \qquad 6.1.1.2\text{-a}$$

where

$\left(c_{\ell_\alpha}\right)_{\delta=0}$ is the lift-curve slope of the unflapped airfoil, including compressibility effects, from Section 4.1.1.2

$\left(c_{\ell_\alpha}\right)_\delta$ is the lift-curve slope at leading- or trailing-edge deflection δ.

c is the chord of the unflapped airfoil.

c' is the effective chord of the flapped airfoil at any flap deflection. In measuring c' of a single-slotted trailing-edge flap or a leading-edge device, the flap or leading-edge device is rotated from its deflected position about the point of intersection of the flap or leading-edge-device chord with the wing chord, until the two coincide. In measuring c' of a double-slotted flap, the reader is referred to Figures 6.1.1.1-45 and 6.1.1.1-46.

3. Jet Flaps

The method presented here applies to the same configurations as indicated for the jet-flap method of Section 6.1.1.1; i.e., the pure jet flap and the internally-blown-flap (IBF) and externally-blown-flap (EBF) concepts with plain trailing-edge flaps. For an IBF or EBF concept with a single-slotted or multislotted flap configuration, this method should be used only as a first approximation.

No substantiation of the method is presented; however, the method has been acknowledged as being substantiated in the literature (References 4 and 5).

It should be noted that the term $[1 + k_t(t/c')]$ is used as a correction for airfoil thickness effects and applies to the pressure lift contribution calculated by thin-airfoil theory. This correction can be justified only if there is no trailing-edge separation.

For jet-flap configurations the total section lift-curve slope, based on the retracted airfoil chord, is given by

$$c_{\ell_\alpha} = \left\{\left[1 + k_t\left(\frac{t}{c'}\right)\right]\left(c'_{\ell_\alpha} - C'_\mu\right) + C'_\mu\right\}\frac{c'}{c} \qquad 6.1.1.2\text{-b}$$

where

k_t is the airfoil-theory thickness factor; i.e.,

k_t = 1.0 for elliptic airfoils

= 0.637 for parabolic airfoils

For airfoil sections other than elliptic or parabolic, a value of 0.80 for k_t is suggested (Reference 2).

$\frac{t}{c'}$ is the airfoil thickness ratio, based on the extended wing chord

c'_{ℓ_α} is the jet-flap lift-curve slope uncorrected for thickness effects obtained from Figure 6.1.1.1-49, based on the extended wing chord, as a function of C'_μ.

C'_μ is the section nondimensional trailing-edge jet momentum coefficient, based on the extended wing chord (defined in Sketch (a) of Section 6.1.1.1).

$\frac{c'}{c}$ is the ratio of the extended wing chord to airfoil chord, where c' is obtained as described in Section 6.1.1.1 for the appropriate flap geometry.

4. Spoilers

For the purposes of the Datcom the lift-curve slope of an airfoil with a spoiler, for the conditions $\alpha > 0$ and $c_\ell < 0$, is assumed to be the same as that of the basic airfoil.

Sample Problems

1. Translating Trailing-Edge Flap

Given: The flapped airfoil of Reference 7.

NACA 23012 airfoil Single-slotted flap $\delta_f = 30°$ $c'/c = 1.154$

$M = 0.105$; $\beta = 0.995$ $R_\ell = 3.5 \times 10^6$

$\tan 1/2\,\phi'_{TE} = 0.132$ (streamwise airfoil geometry)

Compute:

$$\left(c_{\ell_\alpha}\right)_{\delta=0} = 0.102 \text{ per deg} \quad \text{(Section 4.1.1.2)}$$

Solution:

$$\left(c_{\ell_\alpha}\right)_{\delta} = \frac{c'}{c}\left(c_{\ell_\alpha}\right)_{\delta=0} \quad \text{(Equation 6.1.1.2-a)}$$

$$= (1.154)\,(0.102)$$

$$= 0.118 \text{ per deg}$$

This compares with a test value of 0.120 per degree from Reference 7.

2. Jet Flap

Given: The pure jet-flap configuration of Reference 6.

Elliptic airfoil $\quad \frac{t}{c} = 0.125 \quad C_\mu = 4.0$

$$\frac{c_f}{c} = 0 \qquad \delta_f = 0 \qquad \delta_j = 31.4^\circ \qquad \frac{c'}{c} = 1.0$$

Compute:

$$k_t = 1.0 \text{ (elliptic airfoil)}$$

$$c'_{\ell_\alpha} = 13.63 \text{ per rad} \quad \text{(Figure 6.1.1.1-49)}$$

$$c_{\ell_\alpha} = \left\{\left[1 + k_t\left(\frac{t}{c'}\right)\right]\left(c'_{\ell_\alpha} - C'_\mu\right) + C'_\mu\right\}\frac{c'}{c} \quad \text{(Equation 6.1.1.2-b)}$$

$$= \left\{[1 + (1.0)(0.125)]\,(13.63 - 4.0) + 4.0\right\}\,1.0$$

$$= 14.83 \text{ per rad (based on c)}$$

This compares with a test value of 16.1 from Reference 6.

REFERENCES

1. Sears, R.I.: Wind-Tunnel Data on the Aerodynamic Characteristics of Airplane Control Surfaces. NACA WR L-663, 1943. (U)

2. Ramsey, J.C., and Laudeman, E.C.: STOL Tactical Aircraft Investigation State-of-the-Art Design Compendium. Prepared under USAF Contract F33615-71-C-1764, 1971. (U)

3. Hayashi, T.T.: The Two Dimensional Jet Flap Theory. Douglas Aircraft Company, MDC J1089, to be published. (U)

4. Lopez, M.L., and Shen, C.C.: Recent Developments in Jet Flap Theory and Its Application to STOL Aerodynamic Analysis. AIAA Paper 71-678, 1971. (U)

5. Spence, D.A.: Lift Coefficient of a Thin Jet-Flapped Wing. Proc. Roy. Soc., Vol. A238, 1956. (U)

6. Dimmock, N.A.: Some Early Jet Flap Experiments. Aero. Quart. Vol. 8, 1957. (U)

7. Harris, T.A., and Purser, P.E.: Wind-Tunnel Investigations of an NACA 23012 Airfoil with Two Sizes of Balanced Split Flap. NACA WR L-441, 1940. (U)

TABLE 6.1.1.2-A

APPROXIMATE RANGE OF FLAP DEFLECTION FOR LINEAR-LIFT CHARACTERISTICS AT ZERO ANGLE OF ATTACK

Flap Type	δ_f (deg)	
	Poor Design	Good Design
Plain	0 to 10	0 to 20
Single Slotted and Fowler	0 to 20	0 to 30
Double Slotted	0 to 30	0 to 60
Split	0 to 30 or 45	

6.1.1.3 SECTION MAXIMUM LIFT WITH HIGH-LIFT AND CONTROL DEVICES

The maximum-lift increments obtainable by the use of leading- and trailing-edge flaps are strongly influenced by the flow characteristics of unflapped sections near the stall. The lift of unflapped sections near and at the stall is discussed in detail in Sections 4.1.1.3 and 4.1.1.4.

A discussion of the aerodynamic aspects of airfoil flaps is given in Reference 1, some of the more salient points of which are summarized in the following paragraphs.

Trailing-edge flaps increase the maximum lift of a section by means of the camber effect. Theoretically, the incremental load distribution due to flap deflection reaches a peak in the region of the flap hinge line, has a smaller peak at the leading edge, and falls to zero at the trailing edge. Thus the pressure gradient of the upper surface forward of the flap is relieved, although the gradient over the flap itself is greatly increased. The flow over the flap therefore separates at moderate angles, i.e., 10° to 15° for plain flaps. However, the separation is contained behind the flap hinge line and does not progress forward over the wing until the flap deflections become large. Lift continues to increase with flap deflection after separation takes place over the flap, but the rate of increase is considerably less than that for the small flap-deflection range where the flow is completely attached. Maximum lift is obtained just before the separation progresses forward of the flap or the flow separates from the leading edge.

Leading-edge flaps increase the maximum lift of airfoils by lowering the high peak suction pressures near the nose and thereby delaying leading-edge separation. Nose-flap deflection has only a second-order effect on the flow near the trailing edge. Maximum lift for a given flap deflection is achieved when the angle of attack is increased to the point where the pressure distribution around the nose approximates the pressure distribution of the unflapped section just before the stall. Leading-edge stall ensues as in the case of the unflapped section. This problem is treated theoretically in Reference 2.

Thin airfoils stall as a result of leading-edge separation, and thick airfoils as a result of trailing-edge separation (see Section 4.1.1.3). Since trailing-edge flaps primarily affect trailing-edge separation without significantly altering the nose pressures, they are most effective on thick wings. Leading-edge flaps, on the other hand, delay leading-edge separation without significantly altering the trailing-edge flow and are therefore most effective on thin wings.

The stall angle of attack of an airfoil having a leading-edge flap is quite different from that of an airfoil having a trailing-edge flap. Leading-edge flaps produce increases in lift by enabling the airfoil to reach higher angles of attack. Therefore, the angle of attack at stall is considerably higher for an airfoil having a leading-edge flap than that for the unflapped airfoil. Trailing-edge flaps, on the other hand, produce increases in maximum lift by means of the camber effect and actually stall at an angle of attack below that of the unflapped airfoil. These trends are illustrated in the accompanying sketch. A consideration of these stalling angles is often a critical item in practice.

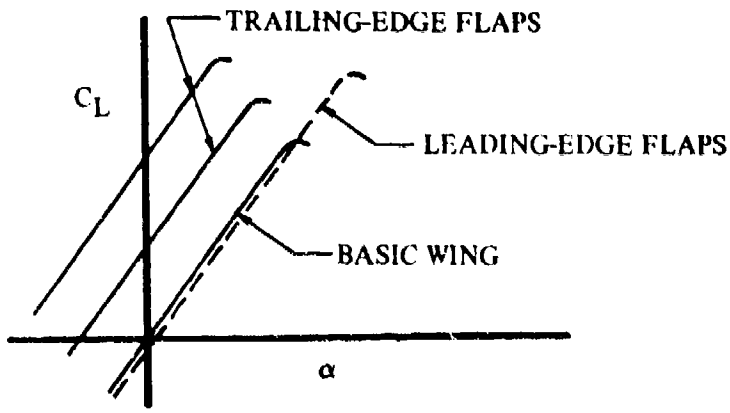

SKETCH (a) TYPICAL LIFT CURVES FOR LEADING-EDGE AND TRAILING-EDGE FLAPS

Specific comments concerning high-lift trailing-edge devices in common use are given in the following paragraphs. The accompanying sketch illustrates the various types of flaps. Not all of those shown are explicitly discussed.

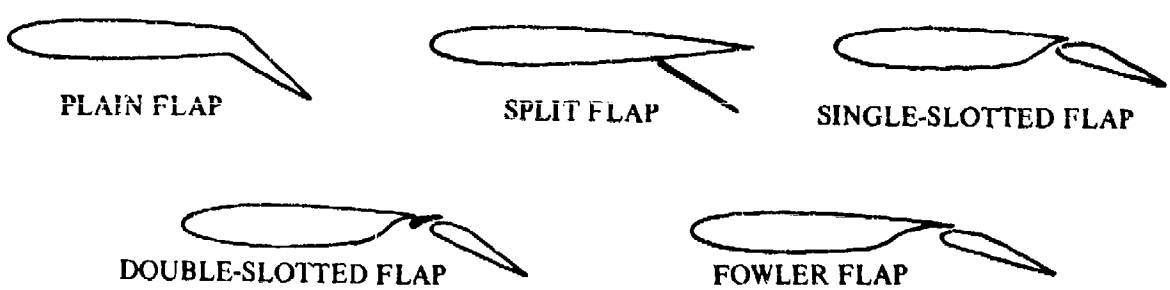

SKETCH (b) TYPICAL TRAILING-EDGE FLAPS

Plain Flaps

The preceding discussion of trailing-edge flaps is applicable to plain flaps and no further comments are required.

Split Flaps

When a split flap is deflected, a region of reduced pressure exists between the upper surface of the flap and the lower surface of the airfoil. This reduced pressure creates a favorable pressure gradient over the top rear surface of the airfoil. Trailing-edge separation is thus suppressed, and final stall often occurs at the airfoil nose.

Slotted Flaps

The crucial factor in the design of a slotted flap is the slot. The slot sheds the boundary layer at the slot lip and allows a new boundary layer to develop over the flap. The slot also directs air in a direction tangential to the surface of the flap. Flow attachment can therefore be maintained to relatively large flap deflections. For instance, efficiently designed double-slotted flaps can prevent flow separation at deflections as high as 60°.

The design of slots for slotted flaps is very critical. Several rules of thumb have been developed for efficiently designing these flaps. First, the flap (and vane) and airfoil must overlap for all deflections when viewed in planform. Secondly, the jet issuing from the slot should also be directed in a direction tangential to the flap surface. Long shroud lengths often show advantages, since they have better control over the direction of the jet.

The flaps (and vanes) of a slotted flap carry considerably more lift than the corresponding plain flap with the same chord and deflection angle. These surfaces are, in reality, in tandem with the wing and derive beneficial induced-camber effects associated with tandem configurations.

Fowler Flaps

Aerodynamically, Fowler flaps function in the same way as single-slotted flaps. Additional lift benefits are obtained, however, from the increased chord due to translation of these flaps.

Jet Flaps

The recent developments in high-lift technology have led to the widespread consideration of the jet-flap scheme (see Section 6.1.1.1 for a sketch of the various types and a discussion of the salient aspects). Comments regarding the maximum lift increment due to power effects of a jet-flap scheme are given in the following paragraphs.

The increment in lift due to power effects of a jet-flap configuration is strongly dependent upon the trailing-edge jet momentum coefficient C_{μ}. Since the jet-flap theory as developed by Spence assumes inviscid flow, it cannot be utilized to predict the achievable maximum lift coefficient. An expression has been developed in Reference 3 for the increment in maximum lift of a two-dimensional jet-flapped airfoil with supercirculation. The analysis is limited to airfoils that exhibit a leading-edge stall. Under these circumstances it is suggested that the pressure distribution around the leading edge would be similar for the flapped- and plain-wing sections at stall.

Reference 4 summarizes an attempt to correlate test data with the method presented in Reference 3. The predicted values of $\Delta c_{\ell_{max}}$ due to power underestimated the experimental data by a considerable margin. These results tend to indicate that an airfoil with blowing does not stall at the same leading-edge pressure coefficient as the airfoil without blowing, but at considerably lower pressure coefficients. The test data used for the attempted correlation indicated a wide scatter band as a function of C_{μ}. This scatter prevents the application of an empirical modification to the method. Consequently, no method is presented herein. Further investigations are required and more test data needed to yield a more accurate and reliable method.

DATCOM METHODS

The following Datcom methods for trailing-edge and leading-edge flaps are limited to subsonic flow.

1. Trailing-Edge Flaps

An empirical method from Reference 2 for predicting maximum lift increments for plain, split, and slotted flaps is presented in Figures 6.1.1.3-12a through 6.1.1.3-13b. The maximum lift increment is given by

$$\Delta c_{\ell_{max}} = k_1 k_2 k_3 \left(\Delta c_{\ell_{max}}\right)_{base} \qquad 6.1.1.3\text{-a}$$

where

$\left(\Delta c_{\ell_{max}}\right)_{base}$ is the section maximum lift increment for 25-percent chord flaps at the reference flap-deflection angle from Figure 6.1.1.3-12a. (Reference flap-deflection angles are denoted in Figure 6.1.1.3-13a.)

k_1 is a factor accounting for flap-chord-to-airfoil-chord ratios other than 0.25 from Figure 6.1.1.3-12b.

k_2 is a factor accounting for flap deflections other than the reference values from Figure 6.1.1.3-13a.

k_3 is a factor accounting for flap motion as a function of flap deflection from Figure 6.1.1.3-13b.

A comparison of experimental data with results based on these charts is shown in Table 6.1.1.3-A.

2. Leading-Edge Flaps

A method is developed in Reference 5 for predicting the maximum lift increment for leading-edge flaps, slats, and Krueger flaps. The method is based on an extension of thin-airfoil theory, using empirical factors that were developed using available test data.

The available Krueger-flap test data were found to be dependent largely upon the trailing-edge flap deflection. Consequently, the method for Krueger flaps from Reference 5 is not presented, since it does not account for the trailing-edge flap deflections.

The method presented herein gives reasonable results when applied to leading-edge flap deflections less than 30°, as indicated by the comparison of test data with predicted results, shown in Table 6.1.1.3-B.

For leading-edge slats it is not advisable to use the method herein for deflections greater than 20°. The method tends to overpredict the maximum lift increment for larger deflections, as shown in Table 6.1.1.3-B.

The maximum lift increment for leading-edge flaps and slats is given by

$$\Delta c_{\ell_{max}} = c_{\ell_{\delta_{max}}} \eta_{max} \eta_{\delta} \delta_f \frac{c'}{c} \qquad 6.1.1.3\text{-b}$$

where

$c_{\ell_{\delta_{max}}}$ is the theoretical maximum lifting effectiveness obtained from Figure 6.1.1.3-14 as a function of the leading-edge flap-chord ratio c_f/c.

η_{max} is the empirical factor accounting for the maximum lifting efficiency obtained from Figure 6.1.1.3-15 as a function of the ratio of the leading-edge radius to the thickness ratio of the airfoil.

The reason for the discontinuity in the slat curve presented in Figure 6.1.1.3-15 is that older NACA test data are used to establish the left-hand portion of the curve, while more recent test data (as indicated in Reference 5) are used for the right-hand portion. An attempt was made to resolve this discontinuity; however, no modifications were made because of the lack of test data in the region of the discontinuity.

η_{δ} is the empirical factor accounting for changes in flap deflection from the optimum deflection obtained from Figure 6.1.1.3-16 as a function of deflection angle.

δ_f is the leading-edge deflection angle in radians (see Figure 6.1.1.1-51).

$\frac{c'}{c}$ is the ratio of the extended wing chord due to leading-edge flap extension to the retracted wing chord (see Figure 6.1.1.1-51).

Sample Problems

1. Trailing-Edge Flap

Given: The flapped airfoil of Reference 6.

NACA 65-210 airfoil Double-slotted flap $\delta_{f_1} = 15^o$ $\delta_{f_2} = 25^o$

$\delta_f = 40^o$ $c_f/c = 0.312$ $R_{\ell} = 6.0 \times 10^6$

Compute:

$\left(\Delta c_{\ell_{max/base}}\right) = 1.165$ (Figure 6.1.1.3-12a)

$k_1 = 1.250$ (Figure 6.1.1.3-12b, extrapolated)

$k_2 = 0.950$ (Figure 6.1.1.3-13a)

$$\frac{\text{Actual Flap Angle}}{\text{Reference Flap Angle}} = \frac{40}{50} = 0.80$$

$k_3 = 0.870$ (Figure 6.1.1.3-13b)

Solution:

$$\Delta c_{\ell_{max}} = k_1 k_2 k_3 \left(\Delta c_{\ell_{max}}\right)_{base} \quad \text{(Equation 6.1.1.3-a)}$$

$$= (1.250)(0.950)(0.870)(1.165)$$

$$= 1.20$$

This compares with a test value of 1.33 from Reference 6.

2. Leading-Edge Flap

Given: The flapped airfoil of Reference 7.

NACA 64A010 airfoil • Leading-edge radius = 0.687% c

$\frac{t}{c} = 0.10$ Nose flap $\delta_f = 30^o$ $\frac{c_f}{c} = 0.15$ $\frac{c'}{c} = 1.0$

Compute:

$c_{\ell_{\delta_{max}}} = 1.44$ per rad (Figure 6.1.1.3-14)

$\eta_{max} = 0.99$ (Figure 6.1.1.3-15)

$\eta_\delta = 0.82$ (Figure 6.1.1.3-16)

Solution:

$$\Delta c_{\ell_{max}} = c_{\ell_{\delta_{max}}} \eta_{max} \eta_\delta \delta_f \frac{c'}{c} \quad \text{(Equation 6.1.1.3-b)}$$

$$= (1.44)(0.99)(0.82)\ \frac{30}{57.3}\ (1.0)$$

$$= 0.612$$

This compares with a test value of 0.56 from Reference 7.

REFERENCES

1. Nonweiler, T.: Flaps, Slots, and Other High-Lift Aids. Aircraft Engineering, September 1955. (U)

2. Anon.: Approximate Relationships for Determining Airplane Maximum Lift Coefficients. Douglas Aircraft Company Report SM 13874, 1950. (U)

3. Perry, D. H.: A Review of Some Published Data on the External-Flow Jet-Augmented Flap. ARC CP 1194, 1972. (U)

4. Levinsky, E. S., and Ramsey, J. C.: Methodology for Estimating STOL Aircraft High Lift System Characteristics. AIAA Paper 72-779, Aug.1972. (U)

5. Ramsey, J. C., and Laudeman, E. C.: STOL Tactical Aircraft Investigation State-of-the-Art Design Compendium. Prepared Under USAF Contract F33615-71-C-1754, 1971. (U)

6. Cahill, J. F.: Two-Dimensional Wind-Tunnel Investigation of Four Types of High-Lift Flap on an NACA 65-210 Airfoil Section. NACA TN 1191, 1947. (U)

7. Kelly, J. A., and Hayter, N. L. F.: Lift and Pitching Moment at Low Speeds of the NACA 64A010 Airfoil Section Equipped with Various Combinations of a Leading-Edge Slat, Leading-Edge Flap, Split Flap, and Double Slotted Flap. NACA TN 3007, 1953. (U)

8. Roshko, A.: Computation of the Increment of Maximum Lift Due to Flaps. Douglas Aircraft Company Report SM 23626, 1959. (U)

9. Spearman, M. L.: Wind-Tunnel Investigation of an NACA 0009 Airfoil with 0.25- and 0.50-Airfoil-Chord Plain Flaps Tested Independently and in Combination. NACA TN 1517, 1948. (U)

10. Rose, L. M., and Altman, J. M.: Low-Speed Experimental Investigation of a Thin, Faired, Double-Wedge Airfoil Section with Nose and Trailing-Edge Flaps. NACA TN 1934, 1949. (U)

11. Gambucci, B. J.: Section Characteristics of the NACA 0006 Airfoil with Leading-Edge and Trailing-Edge Flaps. NACA TN 3797, 1956. (U)

12. Cahill, J. F., Underwood, W. J., Nuber, R. J., and Cheesman, G. A.: Aerodynamic Forces and Loadings on Symmetrical Circular-Arc Airfoils with Plain Leading-Edge and Plain Trailing-Edge Flaps. NACA TR 1146, 1953. (U)

13. Lockwood, V. E.: Wind-Tunnel Investigation of Control-Surface Characteristics. XVII – Beveled-Trailing-Edge Flaps of 0.20, 0.30, and 0.40 Airfoil Chord of an NACA 0009 Airfoil. NACA WR L-666, 1944. (U)

14. Jacobs, E. N., Pinkerton, R. M., and Greenberg, H.: Tests of Related Forward-Camber Airfoils in the Variable-Density Wind Tunnel. NACA TR 610, 1937. (U)

15. Cahill, J. F., and Racisz, S. F.: Wind-Tunnel Investigation of Seven Thin NACA Airfoil Sections to Determine Optimum Double-Slotted-Flap Combinations. NACA TN 1545, 1948. (U)

16. Wenzinger, C. J., and Harris, T. A.: Wind-Tunnel Investigation of an NACA 23012 Airfoil with Various Arrangements of Slotted Flaps. NACA TR 664, 1939. (U)

17. Wenzinger, C. J., and Harris, T. A.: Wind-Tunnel Investigation of NACA 23012, 23021, and 23030 Airfoils with Various Sizes of Split Flap. NACA TR 668, 1939. (U)

18. Underwood, W. J., and Abbott, F. T., Jr.: Test of NACA 66,2-116, a = 0.6 Airfoil Section Fitted with Pressure Balance and Slotted Flaps for the Wing of the XP-63 Airplane. NACA WR L-701, 1942. (U)

19. Lowry, J. G.: Wind-Tunnel Investigation of an NACA 23012 Airfoil with Several Arrangements of Slotted Flaps with Extended Lips. NACA TN 808, 1941. (U)

20. Holtzclaw, R. W.: Wind-Tunnel Investigation of the Effects of Spoilers on the Characteristics of a Low-Drag Airfoil Equipped with a 0.25-Chord Slotted Flap. NACA WR A-92, 1945. (U)

21. Rogallo, F. M.: Aerodynamic Characteristics of a Slot-Lip Aileron and Slotted Flap for Dive Brakes. NACA WR L-337, 1941. (U)

22. Harris, T. A.: Wind-Tunnel Investigation of an NACA 23012 Airfoil with Two Arrangements of a Wide-Chord Slotted Flap. NACA TN 715, 1939. (U)

23. Cahill, J. F.: Aerodynamic Data for a Wing Section of the Republic XF-12 Airplane Equipped with a Double Slotted Flap. NACA WR L-544, 1946. (U)

24. Bogdonoff, S. M.: Wind-Tunnel Investigation of a Low-Drag Airfoil Section with a Double Slotted Flap. NACA WR L-697, 1943. (U)

25. Fischel, J., and Riebe, J. M.: Wind-Tunnel Investigation of an NACA 23021 Airfoil with a 0.32-Airfoil-Chord Double Slotted Flap. NACA WR L-7, 1944. (U)

26. Purser, P. E., Fischel, J., and Riebe, J. M.: Wind-Tunnel Investigation of an NACA 23012 Airfoil with a 0.30-Airfoil-Chord Double Slotted Flap. NACA WR L-469, 1943. (U)

27. Harris, T. A., and Recant, I. G.: Wind-Tunnel Investigation of NACA 23012, 23021, and 23030 Airfoils Equipped with 40-Percent-Chord Double Slotted Flaps. NACA TR 723, 1941. (U).

28. Wenzinger, C. J., and Anderson, W. B.: Pressure Distribution Over Airfoils with Fowler Flaps. NACA TR 620, 1938. (U)

29. Rose, L. M., and Altman, J. M.: Low-Speed Investigation of a Thin, Faired, Double-Wedge Airfoil Section with Nose Flaps of Various Chords. NACA TN 2018, 1950. (U)

30. Gottlieb, S. M.: Two-Dimensional Wind-Tunnel Investigation of Two NACA 6-Series Airfoils with Leading-Edge Slats. NACA L8K22, 1949. (U)

31. Hunton, L. W., and James, H. A.: Use of Two-Dimensional Data in Estimating Loads on a 45° Sweptback Wing with Slats and Partial-Span Flaps. NACA TN 3040, 1953. (U)

32. Weick, F. E., and Platt, R. C.: Wind-Tunnel Tests on Model Wing with Fowler Flap and Specially Developed Leading-Edge Slot. NACA TN 459, 1933. (U)

33. Moss, G. F.: Systematic Wind-Tunnel Tests with Slats on a 10 Percent Thick Symmetrical Wing Section (EQ 1040 Profile). ARC R&M 2705, 1952. (U)

34. Wenzinger, C. J., and Shortal, J. A.: The Aerodynamic Characteristics of a Slotted Clark Y Wing as Affected by the Auxiliary Airfoil Position. NACA TR 400, 1931. (U)

35. Koven, W., and Graham, R. R.: Wind-Tunnel Investigation of High-Lift and Stall-Control Devices on a 37° Sweptback Wing of Aspect Ratio 6 at High Reynolds Numbers. NACA RM L8D29, 1948. (U)

TABLE 6.1.1.3-A

LOW-SPEED SECTION MAXIMUM-LIFT INCREMENTS FOR TRAILING-EDGE FLAP DEFLECTION
DATA SUMMARY AND SUBSTANTIATION

Ref.	Airfoil	Flap Type	$R_\ell \times 10^{-6}$	c_f/c	δ_f (deg)	$c_{\ell_{max}}$ ($\delta_f = 0$)	$\Delta c_{\ell_{max}}$ Calc	$\Delta c_{\ell_{max}}$ Test	e *Percent Error
9	NACA 0009	Plain	2.58	.25	10	.885	.27	.23	17.4
10	Double Wedge t/c = 4.23%	↓	5.8	.25	60	.84	.97	.89	9.0
11	NACA 0006	↓	4.5	.30	50	.94	.91	.76	19.7
12	6-percent-thick circular arc	↓	6.0	.20	60	.73	.84	.91	−7.7
12	10-percent-thick circular arc	↓	6.0	.20	60	.67	.75	.98	−23.5
13	NACA 0009	↓	2.76	.20	30	1.15	.56	.43	−30.2
13	NACA 0009	↓	2.39	.30	30	.975	.64	.57	12.3
13	NACA 0009	↓	2.39	.40	30	1.0	.66	.53	24.5
6	NACA 65-210	Split	6.0	.20	60	1.29	.75	.78	−3.8
14	NACA 0012	↓	8.0	.20	60	1.66	.84	.69	21.7
15	NACA 1410	↓	6.0	.20	60	1.51	.74	.82	−9.8
16	NACA 23012	↓	3.5	.20	60	1.55	.84	.98	−14.3
17	NACA 23012	↓	3.5	.10	60	1.55	.59	.75	−21.3
17	NACA 23021	↓	3.5	.40	60	1.36	1.73	1.54	12.3
18	NACA 66,2-116 a = .6	Single Slotted	6.0	.2505	45	1.45	1.67	1.29	29.5
6	NACA 65-210	↓	2.4	.25	30	1.22	.79	.90	−12.2
6	NACA 65-210	↓	2.4	.25	30	1.22	.79	.84	−6.0
19	NACA 23012	↓	3.5	.30	40	1.55	1.24	1.36	−8.8
20	NACA 66,2-216 a = .6	↓	5.1	.25	45	1.46	1.67	1.42	17.6
21	NACA 23012	↓	3.5	.2566	30	1.52	.88	1.03	−14.6
22	NACA 23012	↓	3.5	.40	40	1.53	1.27	1.30	−2.3
6	NACA 65-210	Double Slotted	2.4	.312	40	1.22	1.20	1.30	−7.7
6	NACA 65-210	↓	6	.312	40	1.29	1.20	1.33	−9.8
6	NACA 65-210	↓	9	.312	50	1.4	1.47	1.20	22.5
23	Between R-4,40-318-1 and R-4,40-313-6	↓	3.5	.238	40	1.39	1.37	1.35	1.5
23	Between R-4,40-318-1 and R-4,40-313-6	↓	14	.238	40	1.55	1.37	1.31	4.6
24	NACA 65,3-118 a = 1.0	↓	6	.309	45	1.61	1.98	1.59	24.5
25	NACA 23021	↓	3.5	.32	50	1.35	2.30	1.86	23.7
26	NACA 23012	↓	3.5	.30	50	1.55	1.65	1.63	1.2
27	NACA 23012	↓	3.5	.40	40	1.55	1.82	1.91	−4.7
15	NACA 63-210	↓	6	.25	50	1.52	1.17	1.38	−15.2
6	NACA 65-210	Fowler	2.4	.25	35	1.22	1.03	.99	4.0
6	NACA 65-210	↓	9	.25	35	1.4	1.03	1.04	−1.0
16	NACA 23012	↓	3.5	.2667	40	1.55	1.47	1.09	34.9
19	NACA 23012	↓	3.5	.30	40	1.55	1.65	1.75	−5.7
28	NACA 23012	↓	2.9	.40	30	1.16	1.71	1.70	0.6
28	Clark Y	↓	~2	.20	30	1.35	.84	1.16	−27.6

*based on flapped airfoil

$$\text{Average Error} = \frac{\Sigma|e|}{n} = 13.7\%$$

TABLE 6.1.1.3-B

LOW-SPEED SECTION MAXIMUM-LIFT INCREMENTS FOR LEADING-EDGE FLAP AND SLAT DEFLECTION DATA SUMMARY AND SUBSTANTIATION

Ref.	Airfoil	Type	t/c	c_f/c	δ_f (deg)	$\Delta c\ell_{max}$ Calc	$\Delta c\ell_{max}$ Test	$\Delta(\Delta c\ell_{max_{calc}} - \Delta c\ell_{max_{test}})$
7	64A010	Flap	0.10	0.15	15	0.373	0.39	−0.017
↓	↓	↓	↓	↓	30	0.612	0.56	0.052
↓	↓	↓	↓	↓	45	0.280	0.46	−0.180
29	Double Wedge	↓	0.0423	0.12	5	0.068	0.145	−0.077
↓	↓	↓	↓	0.16	↓	0.076	0.145	−0.069
↓	↓	↓	↓	0.20	↓	0.085	0.155	−0.070
↓	↓	↓	↓	0.12	10	0.136	0.14	−0.004
↓	↓	↓	↓	0.16	↓	0.155	0.17	−0.015
↓	↓	↓	↓	0.20	↓	0.170	0.20	−0.030
↓	↓	↓	↓	0.25	↓	0.182	0.225	−0.043
↓	↓	↓	↓	0.12	15	0.204	0.185	0.019
↓	↓	↓	↓	0.16	↓	0.232	0.26	−0.028
↓	↓	↓	↓	0.20	↓	0.254	0.28	−0.026
↓	↓	↓	↓	0.12	20	0.272	0.255	0.017
↓	↓	↓	↓	0.16	↓	0.310	0.335	−0.025
↓	↓	↓	↓	0.20	↓	0.339	0.345	−0.006
↓	↓	↓	↓	0.25	↓	0.364	0.445	−0.081
↓	↓	↓	↓	0.12	25	0.320	0.37	−0.050
↓	↓	↓	↓	0.16	↓	0.364	0.445	−0.081
↓	↓	↓	↓	0.20	↓	0.399	0.41	−0.011
↓	↓	↓	↓	0.25	↓	0.428	0.515	−0.087
↓	↓	↓	↓	0.12	30	0.335	0.41	−0.075
↓	↓	↓	↓	0.16	↓	0.381	0.485	−0.104
↓	↓	↓	↓	0.20	↓	0.417	0.465	−0.048
↓	↓	↓	↓	0.25	↓	0.448	0.515	−0.067
↓	↓	↓	↓	0.12	35	0.314	0.43	−0.116
↓	↓	↓	↓	0.16	↓	0.358	0.195	0.163
↓	↓	↓	↓	0.20	↓	0.392	0.18	0.212
↓	↓	↓	↓	0.25	↓	0.421	0.515	−0.094
7	64A010	Slat	0.10	0.17	25.6	0.736	0.90	−0.164
30	64_1-212	↓	0.12	0.14	14.3	0.70	0.60	0.100
↓	65A109	↓	0.09	↓	24.3	0.61	0.69	−0.080
31	64A010	↓	0.10	0.17	15	0.577	0.66	−0.083
32	Clark Y	↓	0.117	0.13	11.5	0.456	0.76	−0.304
↓	↓	↓	↓	↓	14	0.556	0.79	−0.234

TABLE 6.1.1.3-B (CONTD)

Ref.	Airfoil	Type	t/c	c_f/c	δ_f (deg)	$\Delta c\ell_{max}$ Calc	$\Delta c\ell_{max}$ Test	$\Delta\left(\Delta c\ell_{max_{calc}} - \Delta c\ell_{max_{test}}\right)$
32	Clark Y	Slat	0.117	0.13	16.5	0.646	0.76	−0.114
					14	0.542	0.705	−0.163
					19	0.685	0.77	−0.085
					21.5	0.720	0.55	0.170
					19	0.691	0.683	0.008
					24	0.734	0.722	0.012
					26.5	0.729	0.715	0.014
33	EQ 1040		0.10	0.20	5.1	0.204	0.340	−0.136
					11.1	0.443	0.585	−0.142
					16.4	0.641	0.600	0.041
					20.7	0.946	0.190	0.756
				0.30	16.2	0.780	0.785	−0.005
					18.2	0.843	0.852	−0.009
					20.3	0.880	0.910	−0.030
					22.3	0.907	0.642	0.265
					8.0	0.403	0.630	−0.227
					11.1	0.559	0.730	−0.171
					15.1	0.760	0.755	0.005
					13.9	0.656	0.682	−0.026
					15.9	0.742	0.685	0.057
					19.0	0.850	0.698	0.152
34	Clark Y		0.117	0.13	32.5	0.602	0.223	0.379
					25	0.723	0.344	0.379
					16.5	0.641	0.507	0.134
					7.5	0.302	0.436	−0.134
					20.5	0.680	0.213	0.467
					15	0.573	0.472	0.101
					8.5	0.332	0.521	−0.189
					9.5	0.351	0.289	0.062
					5.5	0.209	0.483	−0.274
35	64_1-212		0.12	0.14	14	0.286	0.15	0.136
Average $\Delta\left\lvert\Delta c\ell_{max_{calc}} - \Delta c\ell_{max_{test}}\right\rvert$ = 0.116								

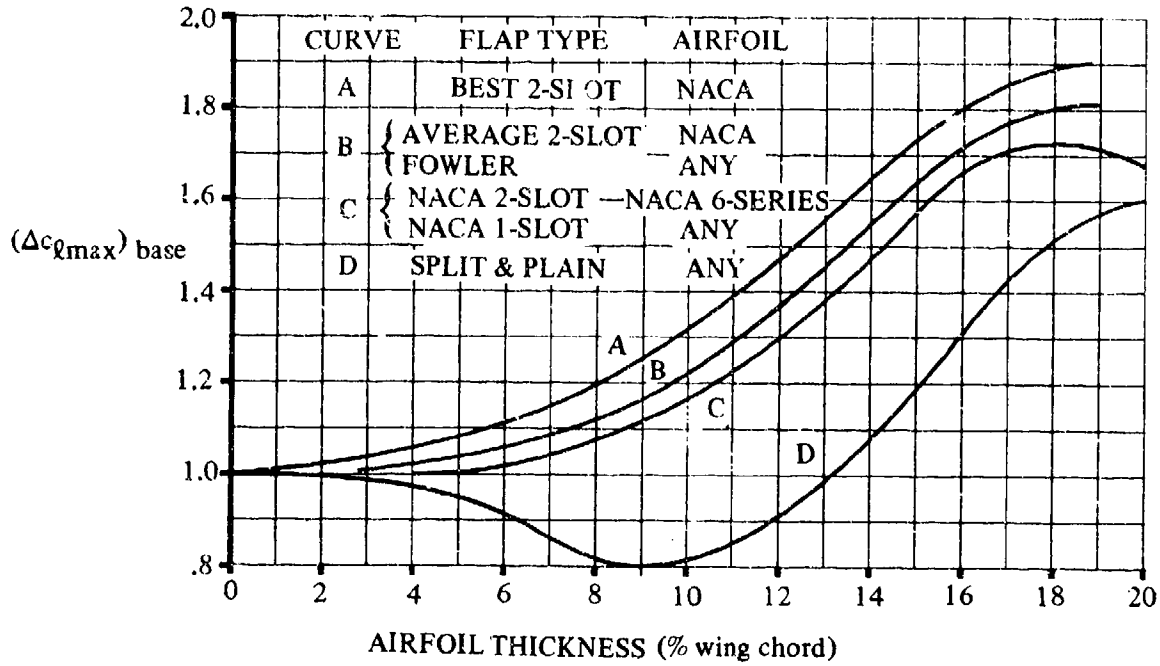

FIGURE 6.1.1.3-12a MAXIMUM-LIFT INCREMENTS FOR 25%-CHORD FLAPS AT REFERENCE FLAP ANGLE

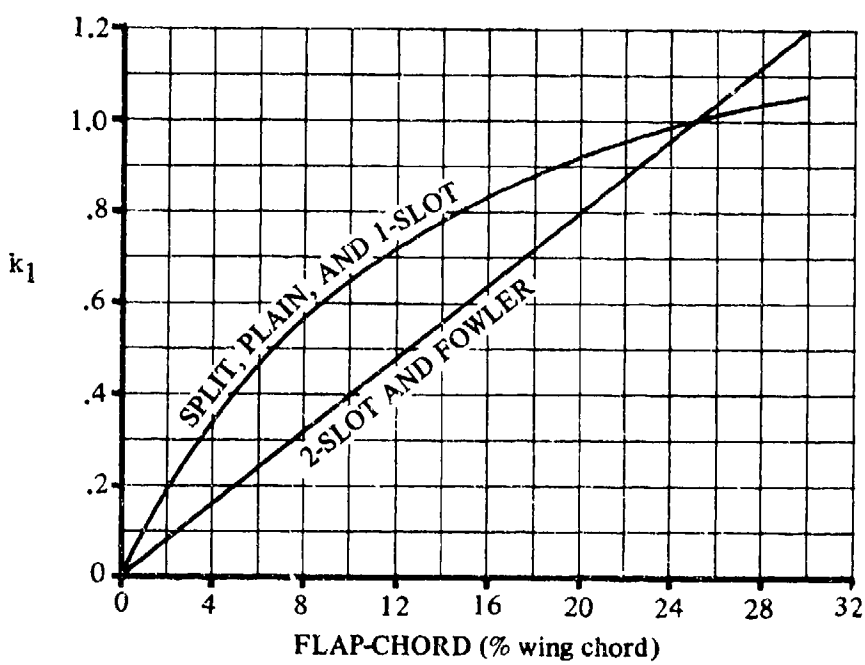

FIGURE 6.1.1.3-12b FLAP-CHORD CORRECTION FACTOR

TRAILING-EDGE FLAPS

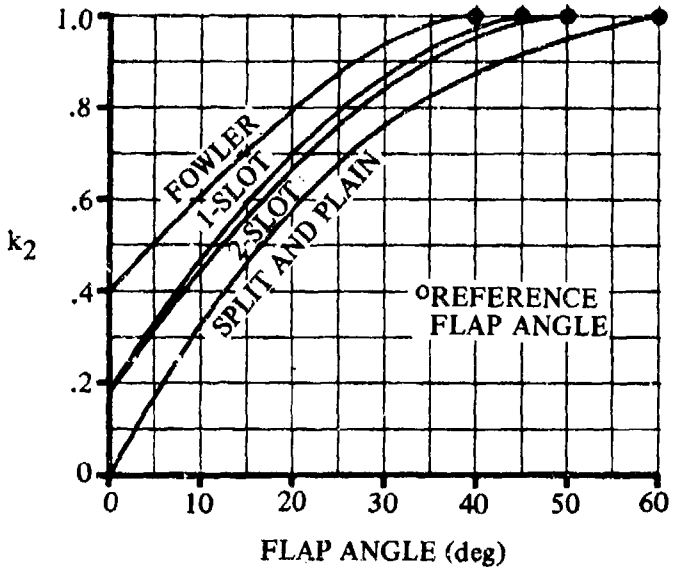

FIGURE 6.1.1.3-13a FLAP-ANGLE CORRECTION FACTOR

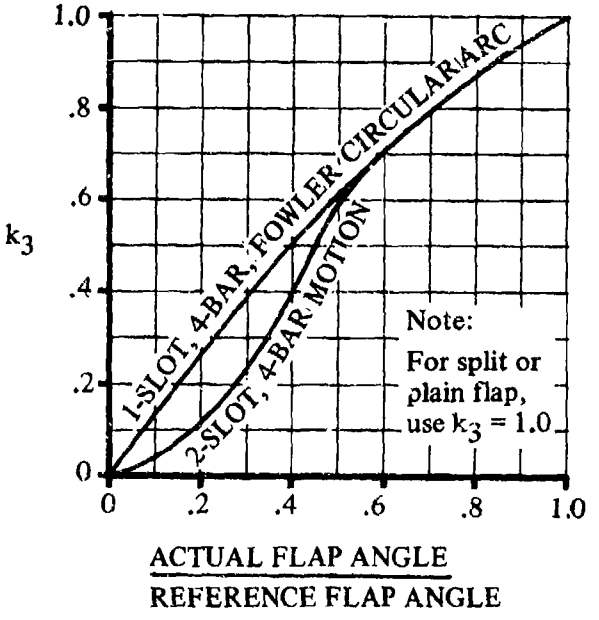

FIGURE 6.1.1.3-13b FLAP-MOTION CORRECTION FACTOR

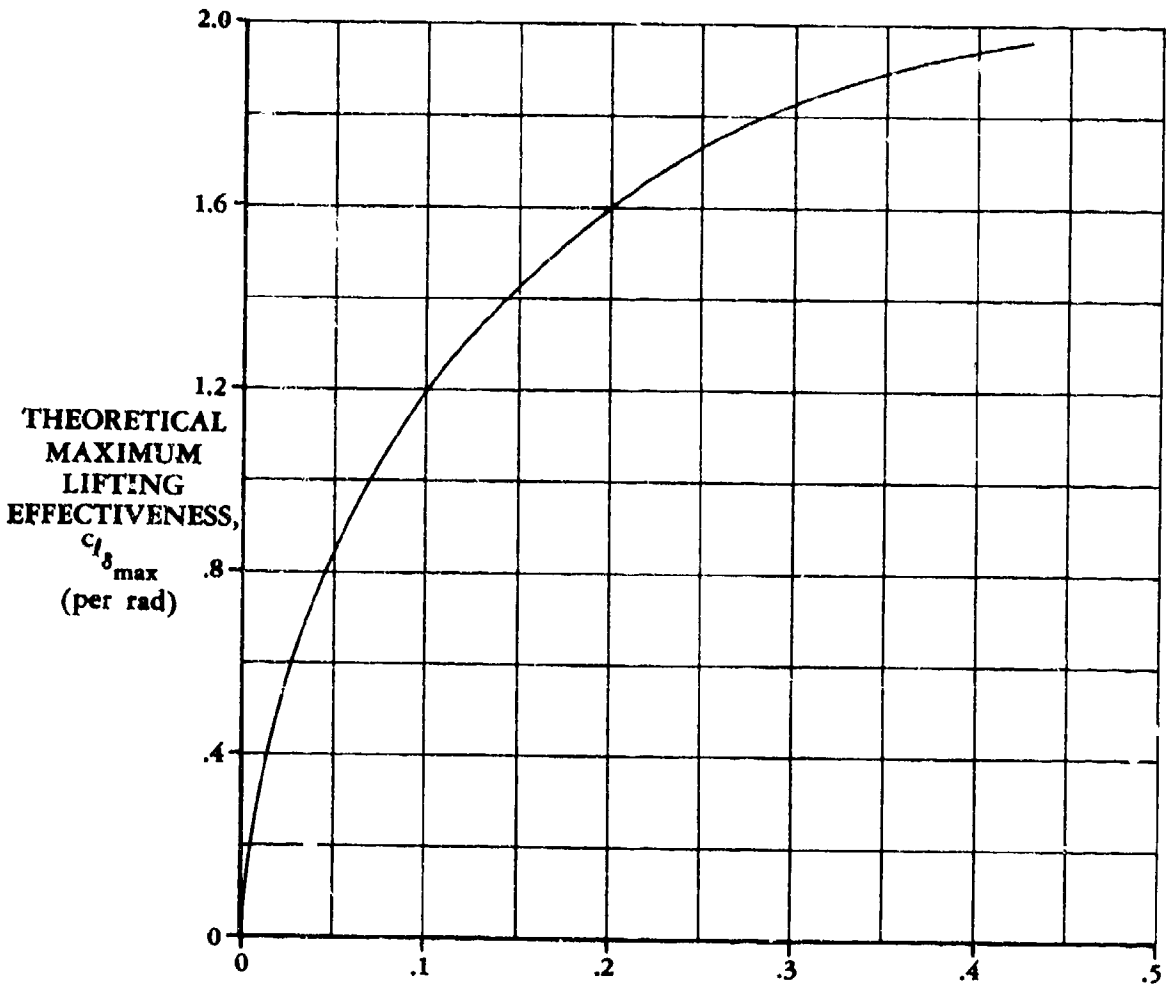

FIGURE 6.1.1.3-14 THEORETICAL MAXIMUM-LIFT EFFECTIVENESS

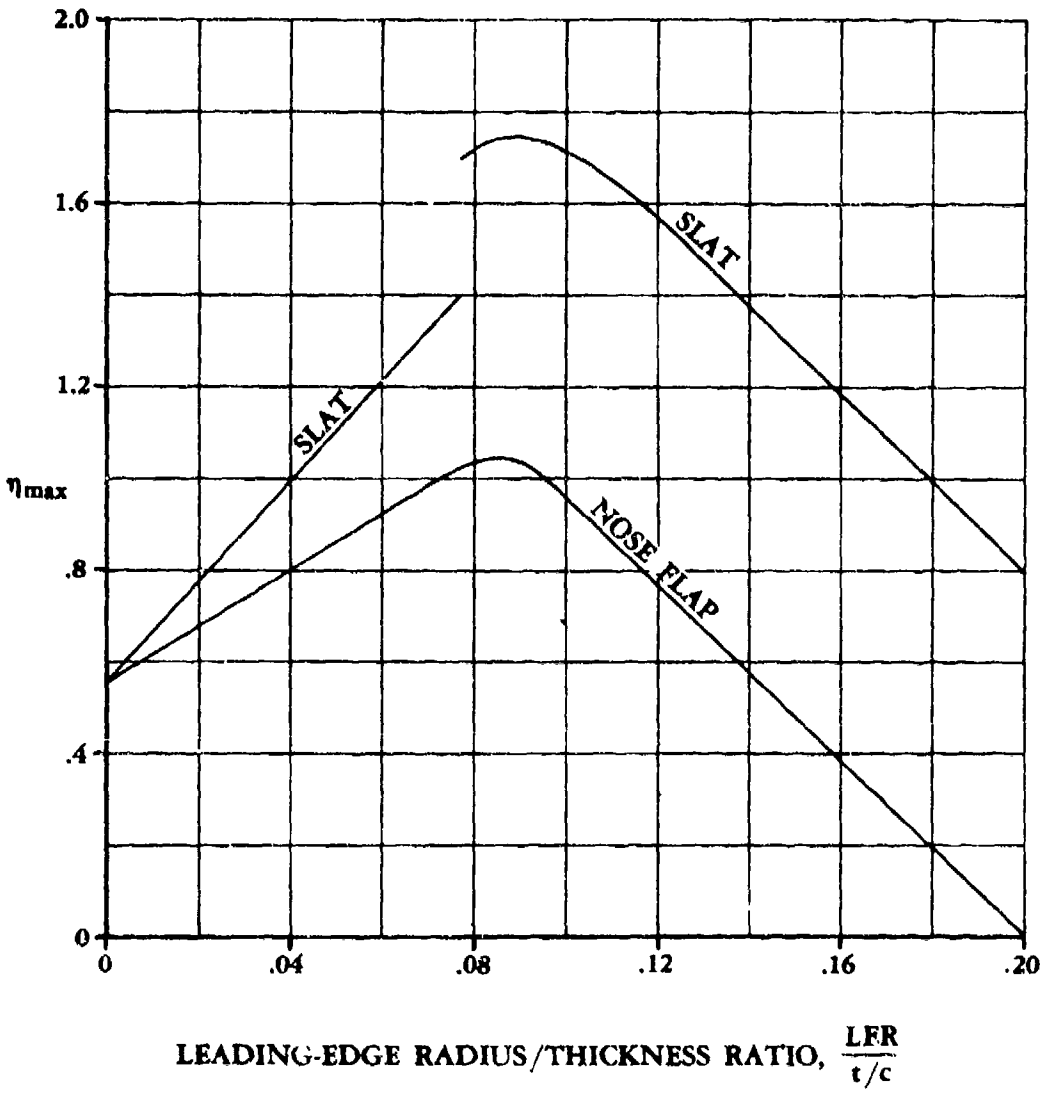

FIGURE 6.1.1.3-15 MAXIMUM-LIFT EFFICIENCY FOR LEADING-EDGE DEVICES

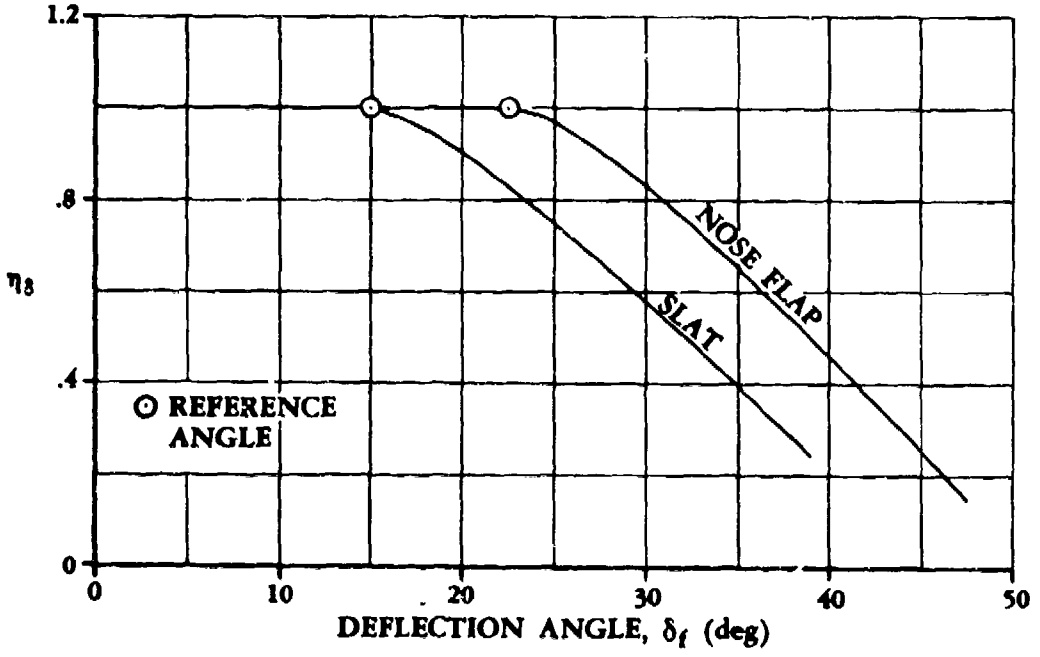

FIGURE 6.1.1.3-16 DEFLECTION-ANGLE CORRECTION FACTOR

6.1.2 SECTION PITCHING MOMENT WITH HIGH-LIFT AND CONTROL DEVICES

6.1.2.1 SECTION PITCHING-MOMENT INCREMENT Δc_m DUE TO HIGH-LIFT AND CONTROL DEVICES

The use of high-lift and control devices alters the basic airfoil load distribution, thus affecting the section pitching moment, as well as the lift.

Methods are presented in this section for estimating the pitching-moment characteristics for most common high-lift devices in use today and for some of the blown flaps being considered for STOL aircraft. These methods are valid only in the subsonic regime in the linear-lift region (preferably near zero angle of attack). The effect of these devices on the variation of pitching moment with angle of attack is presented in Section 6.1.2.2, except for the jet flap, which is presented in this section. Considerations of clarity and simplicity of presentation dictated this deviation from standard Datcom practice.

The assumption is made that the characteristics of a trailing-edge flap are independent of any leading-edge device, and/or the characteristics of a leading-edge device are independent of any mechanical trailing-edge flap. In reality this is not quite true, but the methods of this section are not sufficiently refined to account for these interference effects. This assumption cannot be justified in the case of the more powerful jet flap.

Trailing-Edge Mechanical Flaps

Sketch (a) shows a typical loading on an airfoil with a plain flap deflected and undeflected. The incremental load due to the flap exhibits a peak over the airfoil leading edge and a peak over the hinge line. The higher loading at the hinge predominates, giving a nose-down moment.

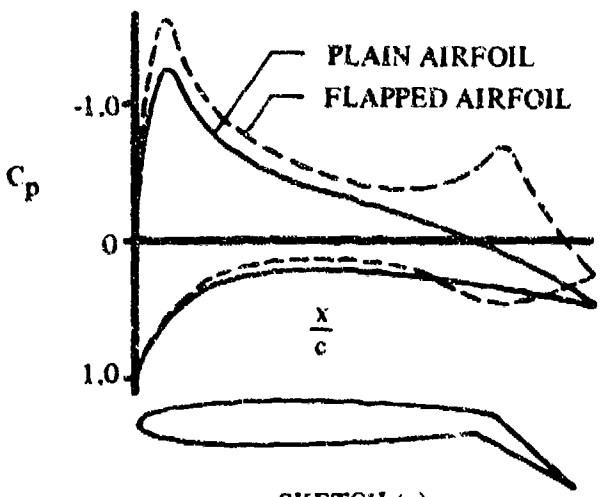

SKETCH (a)

For conditions where the flow is attached, the center-of-pressure location of the additional load due to flaps does not shift position with flap deflection. Therefore, the pitching moment is directly proportional to the lift increment. As the flow breaks down, the center of pressure usually moves forward by a small amount, causing a mild pitch-up. The Datcom method is fairly accurate, even for high values of flap deflection.

Sketch (b) illustrates typical flap pitching-moment curves plotted as a function of flap deflection for a given ratio of flap chord to wing chord. The lift and pitching-moment variation with flap angle are usually linear as long as the flow is attached. Plain flaps maintain attached flow and exhibit linear characteristics at small angles of attack and flap deflections. Single-, double-, and triple-slotted flaps assure attached flow for increasingly higher angles of incidence and flap deflections and give linear characteristics over a much larger range. Split flaps have no significant range of linear characteristics as a result of the wide wake caused by the split trailing edge.

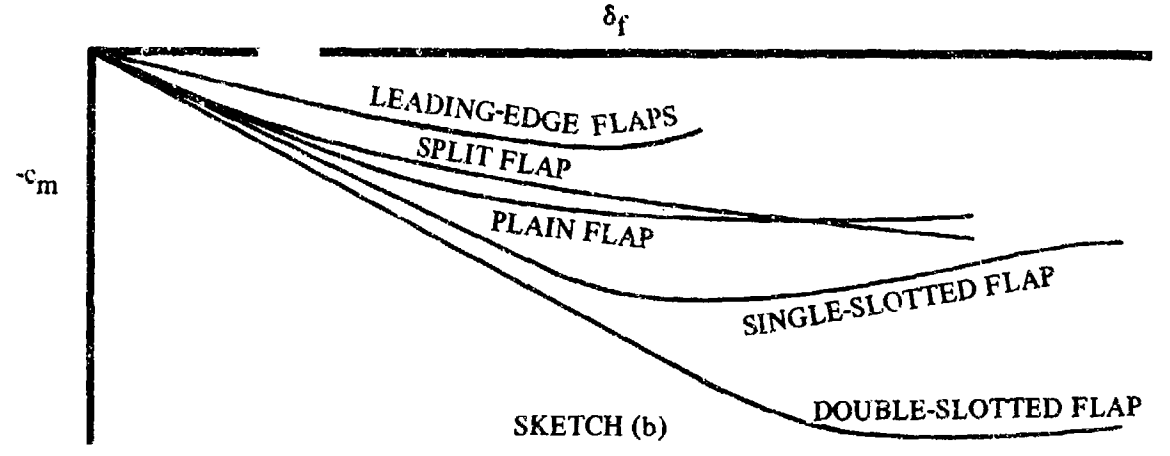

SKETCH (b)

Theoretically, the center-of-pressure location is a function of the ratio of the flap chord to airfoil chord, showing a forward shift with increasing flap-chord ratios. Although test data for plain and split flaps do not match the theoretical center-of-pressure location, they do show the same trend as theory. Slotted flaps do not follow this trend. Data for slotted flaps were analyzed for extended airfoil chords of 10 to 40 percent. Virtually all of the data indicated a center-of-pressure location between 41 and 47 percent of the extended airfoil chord, showing no dependence upon the ratio of flap chord to airfoil chord. Therefore, an average center-of-pressure location of 44 percent has been assumed (see Figure 6.1.2.1-35a) for all slotted flaps, independent of the ratio of flap chord to airfoil chord.

Leading-Edge Mechanical Devices

Leading-edge devices produce a nose-down pitching moment, similar to trailing-edge flaps, because they delay the stall by lowering the high peak loading at the leading edge. The method presented is for conventional leading-edge devices, based on thin-wing theory from Reference 1. Efforts to substantiate this method by using available test data have proved unsatisfactory. The test data exhibit nonlinear characteristics which linear theory is intrinsically unable to handle. Therefore, this method should be applied only to thin airfoils with small leading-edge devices.

Jet Flaps

The pitching-moment increment for a jet-flap airfoil is dependent upon the jet momentum trailing-edge coefficient C'_μ and the ratio of flap chord to the extended wing chord. The method presented herein is Spence's adaptation of thin-airfoil theory as presented in Reference 2. In summary, Spence applies thin-airfoil theory to inviscid, incompressible flow past a thin, two-dimensional wing at small incidence, with a jet emerging at a small angle of incidence from the trailing edge. The flow inside the jet is assumed to be irrotational. In addition, the jet is bounded by vortex sheets that prevent mixing with the mainstream and maintains finite momentum as its thickness decreases to zero. For flaps that extend as well as rotate, a correction is applied to account for the increased chord length.

The definitions of aerodynamic center $x_{a.c.}$ and center of pressure $x_{c.p.}$ are well established for conventional aircraft. However, for jet-flap configurations the jet reaction is a new component that must be accounted for when considering the location of the aerodynamic center and center of pressure. In order to maintain consistency, the Datcom defines the aerodynamic center for jet-flap configurations as that point about which the *total* pitching moment is invariant with the *total* lift; i.e., $dC_m/dC_L = 0$ at a given Mach number and trailing-edge jet momentum coefficient. In essence, the aerodynamic center is a function of the trailing-edge jet momentum coefficient C_μ. For conventional wing sections the aerodynamic center is located on the wing chord line. However, for jet-flap configurations it becomes necessary to define the measurement of $x_{a.c.}$ off the wing-chord line, as shown in Sketch (c), to simplify the calculation of the pitching moment about any reference location.

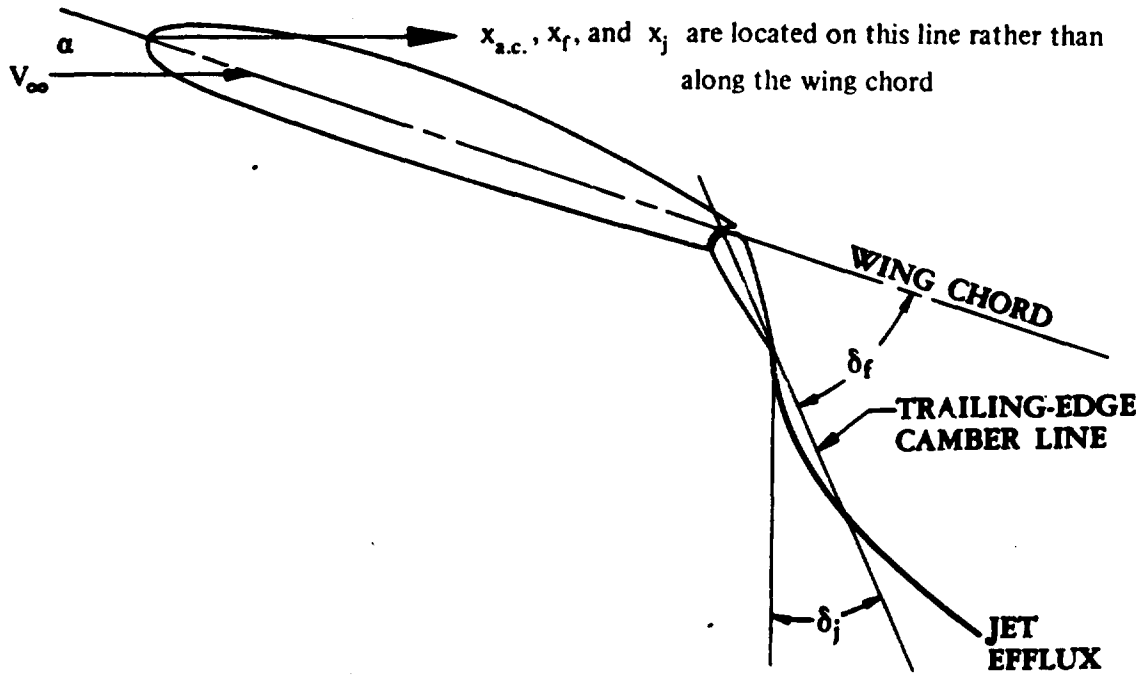

$$\frac{x_f}{c} = -\frac{c_{m_{\delta_f}}}{c_{\ell_{\delta_f}}} \qquad \frac{x_j}{c} = -\frac{c_{m_{\delta_j}}}{c_{\ell_{\delta_j}}}$$

where

$c_{m_{\delta_f}}$ is the flap pitching-moment effectiveness measured about the leading edge.

$c_{\ell_{\delta_f}}$ is the rate of change of section lift effectiveness due to flap deflection.

$c_{m_{\delta_j}}$ is the rate of change of pitching-moment coefficient measured about the leading edge with respect to the jet deflection. (The parameters $c_{m_{\delta_j}}$ and $c_{\ell_{\delta_j}}$ are due to the jet efflux not being emitted at the same angle as the trailing-edge camber line, i.e., the flap deflection.)

$c_{\ell_{\delta_j}}$ is the rate of change of section lift coefficient with respect to the jet deflection.

SKETCH (c) JET-FLAP AERODYNAMIC CENTER AND CENTER OF LIFT

There are two additional parameters shown and defined in Sketch (c), x_f and x_j. The center-of-lift term x_f is analogous to the conventional flap center-of-pressure location, except that it also includes the reaction component of the jet. For this reason it is not the true "center-of-pressure location"; i.e., it is the location where the total lift increment due to flap deflection is assumed to act.

The term x_j is analogous to a center-of-pressure location of the incremental load due to the jet efflux acting at an angle to the trailing-edge camber line. However, it is not a true center-of-pressure location for this incremental load, because of the inclusion of the reaction component; therefore, it is also referred to as the center of lift.

For more details regarding the fundamental concepts of jet flaps, the reader is referred to the discussion presented in Section 6.1.1.1. (Sketch (b) of Section 6.1.1.1 illustrates some of the blown-flap concepts now being investigated for STOL aircraft.)

Spoilers

Pitching-moment changes due to spoilers are generally smaller than those for flap-type control surfaces. For this reason they are useful on thin, swept wings where wing twist due to control deflection is a problem. Many wind-tunnel programs have therefore been conducted on swept wings, but few have been conducted on airfoil sections. Reference 3, published in 1953, contains a comprehensive bibliography of spoiler studies made up to that time.

Because of the scarcity of two-dimensional spoiler data, no generalized methods are presented in this section for section pitching moment due to spoiler deflection.

DATCOM METHODS

1. Trailing-Edge Mechanical Flaps

Two methods are presented for estimating the section pitching-moment increment due to the deflection of mechanical trailing-edge flaps. Method 1 is applicable to plain, split, and multislotted flaps with or without extensible flaps. Method 2 is applicable only to plain flaps.

In view of the ease of application of Method 2 and the fact that it predicts plain-flap section pitching moments as accurately as Method 1 does, Method 2 is the preferred Datcom plain-flap method.

Method 1 (Plain, Split, and Multislotted Flaps)

This method is empirical in nature and limited to the low-speed regime. The section pitching-moment increment due to trailing-edge flaps, based on the square of the wing chord c^2, is given by

$$\Delta c_m = \Delta c_\ell \left[\frac{x_{ref}}{c} - \left(\frac{x_{c.p.}}{c'} \right) \left(\frac{c'}{c} \right) \right] \qquad 6.1.2.1\text{-a}$$

where

Δc_ℓ is the lift increment for a given flap type and deflection, from test data or as determined by the appropriate method of Section 6.1.1.1.

$\frac{x_{ref}}{c}$ is the desired pitching-moment reference point expressed as a fraction of the basic airfoil chord, measured positive aft from the airfoil leading edge, parallel to the wing chord.

$\frac{x_{c.p.}}{c'}$ is the center-of-pressure location of the incremental load due to flaps, expressed as a fraction of the extended airfoil chord, measured positive aft from the airfoil leading edge, parallel to the wing chord. This parameter is obtained from Figure 6.1.2.1-35a as a function of the ratio of flap chord to airfoil chord c_f/c.

$\frac{c'}{c}$ is the ratio of the extended wing chord to the airfoil chord as shown in Figures 6.1.1.1-44 through -46.

A comparison of low-speed test data with calculated values of Δc_m using this method is presented in Tables 6.1.2.1-A and -C through -E.

Method 2 (Plain Flaps)

Pitching-moment increments for plain trailing-edge flaps are presented in Figure 6.1.2.1-35b. These increments are given about the quarter-chord, based on the square of the airfoil chord c^2, as a function of flap deflection and the ratio of flap chord to airfoil chord c_f/c. This figure is limited to the linear-lift range and subcritical Mach numbers.

A comparison of low-speed test data with Δc_m calculated by this method is presented in Table 6.1.2.1-B.

2. Conventional Leading-Edge Devices

The section pitching-moment increment due to mechanical leading-edge devices, based on the square of the wing chord c^2, is given by thin-airfoil theory as

$$\Delta c_{m_{LE}} = c'_{m_{\delta_{LE}}} \left(\frac{c'}{c}\right)^2 \delta_{f_{LE}} + \left(\frac{x_{ref}}{c} + \frac{c' - c}{c}\right) \Delta c_\ell + c_m \left[\left(\frac{c'}{c}\right)^2 - 1\right] + 0.75\, c_\ell \left(\frac{c'}{c}\right)\left(\frac{c'}{c} - 1\right) \qquad 6.1.2.1\text{-b}$$

where

c'_{m_δ} is the theoretical flap pitching-moment effectiveness (about the leading edge), obtained from Figure 6.1.2.1-36 as a function of the ratio of the leading-edge flap chord to the extended airfoil chord $c_{f_{LE}}/c'$.

$\frac{c'}{c}$ is the ratio of the extended wing chord to the basic airfoil chord as shown in Figure 6.1.1.1-51.

$\delta_{f_{LE}}$ is the deflection of the leading-edge device in degrees (see Figure 6.1.1.1-51).

$\frac{x_{ref}}{c}$ is the desired pitching-moment reference point expressed as a fraction of the basic airfoil chord, measured positive aft from the airfoil leading edge with the leading-edge device retracted, parallel to the wing chord.

Δc_ℓ is the lift increment due to a given leading-edge-device deflection, from test data or as determined by the appropriate method in Section 6.1.1.1, based on c.

c_m is the section pitching-moment coefficient with the flaps retracted, based on c^2. This parameter should be obtained from the test data, if available, or from Section 4.1.2.1.

c_ℓ is the section lift coefficient with the flaps retracted, based on c. This parameter should be obtained from test data, if available, or from Sections 4.1.1.1 and 4.1.1.2.

The use of this method is demonstrated in Sample Problem 3.

3. Jet Flaps

Methods that are adaptable to a handbook application are not available for all jet-flap schemes. The method presented below is applicable to the pure jet-flap concept, and the internally-blown-flap (IBF) and externally-blown-flap (EBF) concepts with a plain trailing-edge flap. For an IBF or EBF concept with a single-slotted or multislotted flap configuration, this method should be used only as a first approximation. No handbook method is currently available to analyze the section pitching-moment increment due to an augmentor-wing concept.

For EBF flaps the user is cautioned that if the flap does not "capture" or "intercept" all of the jet exhaust, the result of this method may be erroneous. Reference 57 considers a design where part of the jet passes below the flap. Furthermore, a technique to be used in analyzing such a design is proposed. Unfortunately, this technique is cumbersome, and no satisfactory cases to check its accuracy have been found in the available literature. Therefore, it is not included in the Datcom. It should be noted, however, that the lack of such a technique is not a serious restriction, since most configurations avoid the problem by use of jet deflectors and/or canted thrust axes to ensure that the entire engine exhaust is flattened and directed at the flap knee.

It should be noted that the airfoil thickness correction used in the method of Section 6.1.1.1 in determining the section lift increment of a jet-flap combination (see Equation 6.1.1.1-p) does not apply to the section pitching moment. Therefore, the lift coefficients calculated in this section for use in determining section pitching moment are not the same as those calculated in Sections 6.1.1.1 and 6.1.1.2 and should be considered only as intermediate values generated during the calculation of the pitching moment. The actual lift of the airfoil must be calculated by using the more exact procedures of Sections 6.1.1.1 and 6.1.1.2.

The user is reminded that the theory on which this method is based is linear and as such cannot predict any nonlinearities; e.g., those that may arise from separated flow.

The flap deflection angles and the flap-chord values to be used in this method are not defined in the conventional manner. Instead, the user must use his best judgment to approximate the particular flap system by constructing a simple-hinged multideflected flap system. The primary goal of the simple-hinged multideflected flap system is to duplicate the mean-camber-line distribution of the actual flap system. A schematic illustration is presented in the following discussion (Sketches (d) through (f)) that depicts the determination of the flap chords and flap angles for a triple-slotted-flap system. The treatment of less complex flap systems follows from this example.

Determine the mean-camber-line distributions of the flap components as in Sketch (d).

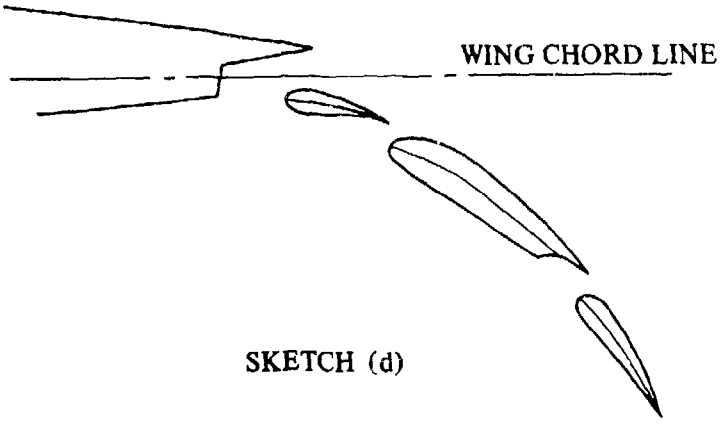

SKETCH (d)

Approximate the actual mean-camber-line distribution with straight-line segments (keeping in mind the total mean-camber-line distribution) as in Sketch (e). Extend the straight-line segments until they intersect each other, so as to define the flap-chord lengths as shown.

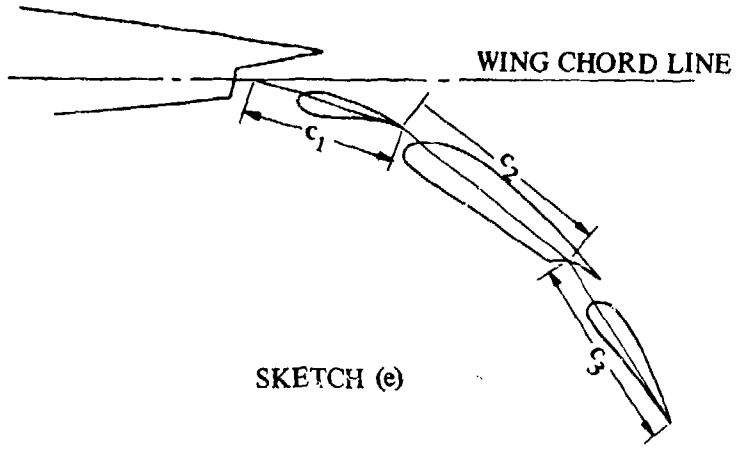

SKETCH (e)

Determine the flap deflection angles from the straight-line segments relative to the wing chord line as shown in Sketch (f).

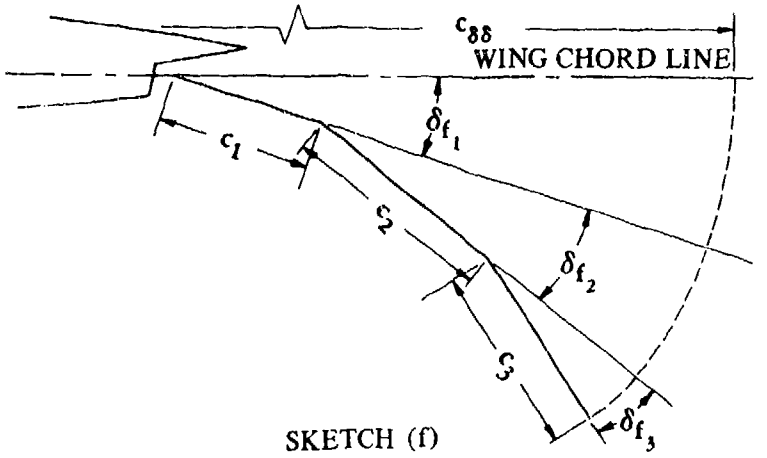

SKETCH (f)

The determination of the extended wing-chord $c_{\delta\delta}$ in Sketch (f) is found by the following procedure. The aft flap segment c_3 is first rotated from its deflected position about the point of intersection of c_2 and c_3, until the two chords coincide. Then the total chord of c_2 and c_3 is rotated about the intersection of c_1 and c_2 until these two chords coincide. Then the total chord of c_1, c_2, and c_3 is rotated about the intersection of the wing chord and c_1 until it intersects the wing chord.

In the method outlined below, the computation of the pitching moment is broken down into components due to the leading-edge device, the angle of attack, the mechanical flap, and the jet flap. This division can be somewhat misleading because in each term there appears the parameter $c_{\delta\delta}/c$, which is the ratio of the airfoil chord with all flaps extended to the basic airfoil chord. Thus each term is actually dependent upon the total extended airfoil chord $c_{\delta\delta}$. For example, a change in $c_{\delta\delta}$ due to a deflection of the leading-edge device will affect the contribution of each component, not just the component due to the leading-edge device.

No substantiation is given for the method presented below; however, the method has been acknowledged in the literature as being accurate to within 10 percent (References 12 and 16). Although an insufficient number of configurations have been analyzed to provide a meaningful substantiation table, the ones that have been analyzed indicate that this method is more accurate in estimating the pitching-moment change with flap angle than in estimating the variation of pitching moment with angle of attack. This may be accounted for by the tendency of wings developing very high lift coefficients to have significant flow separation even at low angles of attack. The variation in the amount of separated flow with angle of attack may be affecting c_{m_α} significantly.

The section pitching-moment increment of an airfoil due to a trailing-edge jet flap at an angle of attack, based on the square of the wing chord c^2, is given by

$$\Delta c_m = (\Delta c_m)_{\delta f_{LE}} + (\Delta c_m)_\alpha + (\Delta c_m)_{\delta f} + (\Delta c_m)_{\delta_j} \qquad 6.1.2.1\text{-c}$$

where

$(\Delta c_m)_{\delta f_{LE}}$ is the pitching-moment increment due to the deflection of a leading-edge device. (If there is no leading-edge device, $(\Delta c_m)_{\delta f_{LE}} = 0$.)

$(\Delta c_m)_\alpha$ is the pitching-moment increment due to the angle of attack of the airfoil. (If $\alpha = 0$, $(\Delta c_m)_\alpha = 0$.)

$(\Delta c_m)_{\delta f}$ is the pitching-moment increment due to trailing-edge flaps. The flap system is treated as a series of plain flaps using the principle of superposition. The pitching moments of all of these flaps are then summed to give the total. This is illustrated schematically in Sketch (g) by using a triple-slotted flap. The treatment of less complex flap systems follows from this example. (For airfoils with no trailing-edge mechanical flaps, $(\Delta c_m)_{\delta f} = 0$.)

$(\Delta c_m)_{\delta_j}$ is the pitching-moment increment due to the jet sheet acting at an angle δ_j to the trailing-edge camber line. This term may be present with a pure jet flap, or in the case of EBF and IBF systems where the total turning angle of the jet exceeds the total deflection angle of the mechanical flap segments. (If $\delta_j = 0$, $(\Delta c_m)_{\delta_j} = 0$.)

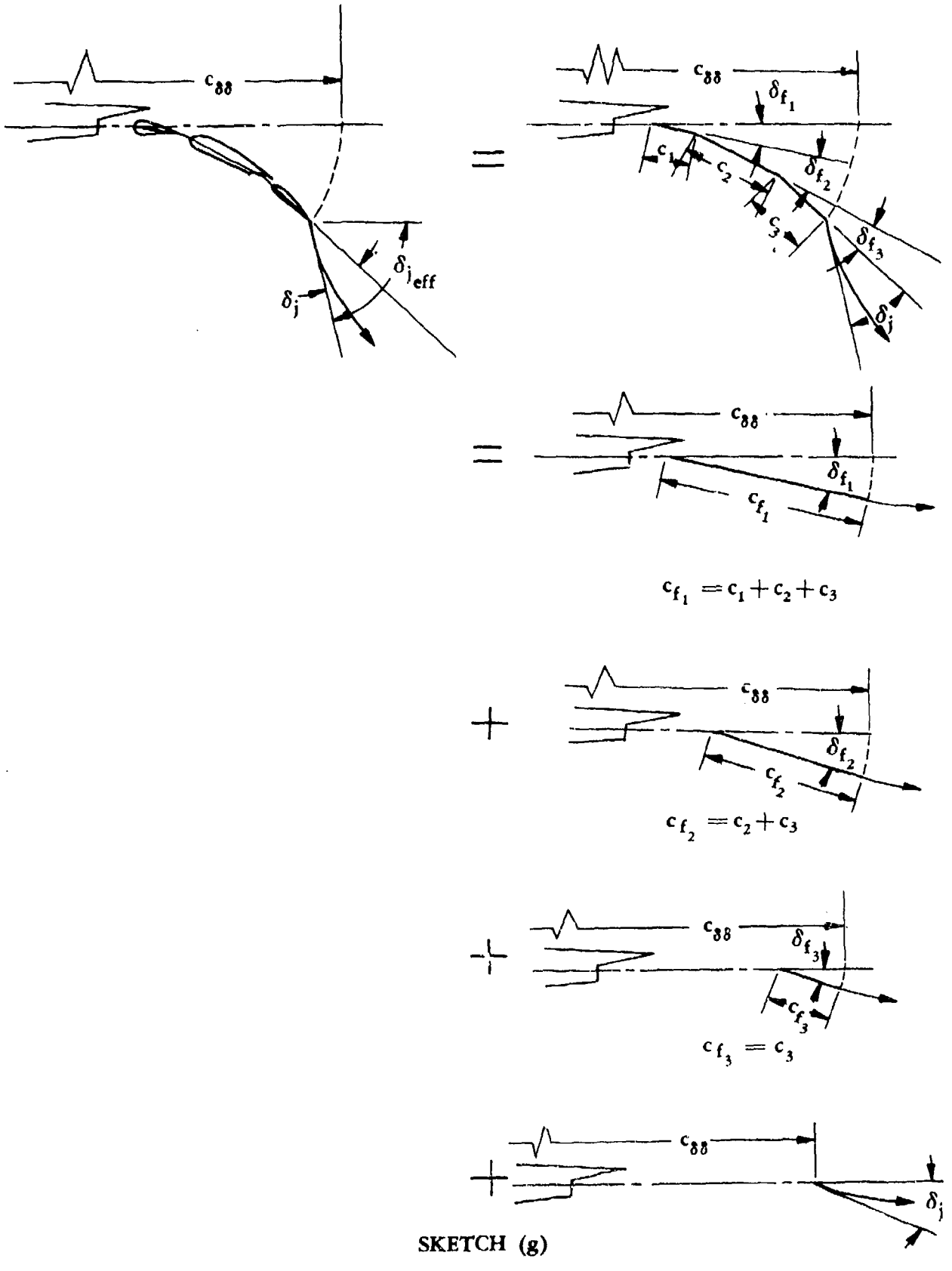
$c_{\delta\delta}$
$\delta_{j_{eff}}$
δ_j
=
$c_{\delta\delta}$
δ_{f_1}
c_1
c_2
δ_{f_2}
c_3
δ_{f_3}
δ_j
=
$c_{\delta\delta}$
δ_{f_1}
c_{f_1}
$c_{f_1} = c_1 + c_2 + c_3$
+
$c_{\delta\delta}$
δ_{f_2}
c_{f_2}
$c_{f_2} = c_2 + c_3$
+
$c_{\delta\delta}$
δ_{f_3}
c_{f_3}
$c_{f_3} = c_3$
+
$c_{\delta\delta}$
δ_j

SKETCH (g)

The above terms of Equation 6.1.2.1-c are evaluated by using Steps 1 through 4, respectively, below.

Step 1. Determine $(\Delta c_m)_{\delta_{f_{LE}}}$ by

$$(\Delta c_m)_{\delta_{f_{LE}}} = \Delta c_1 \, x_1 - \Delta c_2 \, x_2 + \Delta c_{m_3} \qquad 6.1.2.1\text{-d}$$

a. Evaluate the following expressions:

$$\Delta c_1 = \frac{\delta_{f_{LE}}}{57.3} K \, c_{\ell_{\delta_a}} \qquad 6.1.2.1\text{-e}$$

$$\Delta c_2 = \frac{\delta_{f_{LE}}}{57.3} K \, c_{\ell_\alpha} \qquad 6.1.2.1\text{-f}$$

where

$\Delta c_1, \Delta c_2$ are terms analagous to section lift coefficients. However, the thickness correction is not applied.

$\delta_{f_{LE}}$ is the deflection of the leading-edge device in degrees, as shown in Figure 6.1.1.1-51.

K is equal to $c_{\delta\delta}/c$, the ratio of the extended wing chord to the retracted wing chord. (Note that the extended wing chord includes the extensions of both leading- and trailing-edge flaps. The definition of the extended chord lengths is shown in Figures 6.1.1.1-44 through -46 for trailing-edge flaps and Figure 6.1.1.1-51 for leading-edge flaps.)

$c_{\ell_{\delta_a}}$ is the section lift effectiveness due to the deflection of a hypothetical flap of chord c_a.

$$c_a = c_{\delta\delta} - c_{f_{LE}} \qquad 6.1.2.1\text{-g}$$

where $c_{f_{LE}}$ is the chord of the leading-edge flap defined in Figure 6.1.1.1-51. This parameter is obtained from Figure 6.1.1.1-49 as a function of $c_a/c_{\delta\delta}$* and the trailing-edge jet momentum C'_μ. C'_μ is the section nondimensional trailing-edge jet momentum coefficient based on the extended airfoil chord $c_{\delta\delta}$, $C'_\mu = C_\mu \frac{c}{c_{\delta\delta}}$ (see Sketch (a) Section 6.1.1.1).

*When using Figure 6.1.1.1-49 in this section, it is necessary to substitute $c_a/c_{\delta\delta}$ or $c_f/c_{\delta\delta}$ for c_f/c' on the figure.

c_{ℓ_α} is the jet-flap lift-curve slope obtained from Figure 6.1.1.1-49 at $c_f/c_{\delta\delta} = 1$,* as a function of the trailing-edge jet momentum coefficient C'_μ.

b. Determine the corresponding moment arms:

$$x_1 = \frac{x_m}{c} + \left(\frac{c'_{LE}}{c} - 1\right) - \frac{x_a}{c_{\delta\delta}} \frac{c_{\delta\delta}}{c} \qquad 6.1.2.1\text{-h}$$

$$x_2 = \frac{x_m}{c} + \left(\frac{c'_{LE}}{c} - 1\right) - \frac{x_{a.c.}}{c_{\delta\delta}} \frac{c_{\delta\delta}}{c} \qquad 6.1.2.1\text{-i}$$

where

$\frac{x_m}{c}$ is the desired pitching-moment reference point expressed as a fraction of the basic airfoil chord, measured positive aft from the basic airfoil leading edge, parallel to the wing chord.

$\frac{c'_{LE}}{c}$ is the ratio of the airfoil chord with only the leading-edge device extended to the basic airfoil chord.

$\frac{x_a}{c_{\delta\delta}}$ is the center-of-lift location of the incremental load due to flap deflection. This parameter is obtained from Figure 6.1.2.1-37 as a function of $c_a/c_{\delta\delta}$ and the trailing-edge jet momentum C'_μ. It is measured positive aft from the extended-airfoil leading edge, parallel to the free stream.

$\frac{x_{a.c.}}{c_{\delta\delta}}$ is the aerodynamic-center location obtained from Figure 6.1.2.1-37 at $c_f/c_{\delta\delta} = 1.0$, as a function of C'_μ. It is measured positive aft from the extended-airfoil leading edge, parallel to the free stream.

$\frac{c_{\delta\delta}}{c}$ is defined in Step 1a. (See definition of K.)

c. Determine Δc_{m_3} from

$$\Delta c_{m_3} = C_\mu \frac{c_{f_{LE}}}{c} \sin \delta_{f_{LE}} \qquad 6.1.2.1\text{-j}$$

*When using Figure 6.1.1.1-49 in this section, it is necessary to substitute $c_a/c_{\delta\delta}$ or $c_f/c_{\delta\delta}$ for c_f/c' on the figure.

where

C_μ is the section nondimensional trailing-edge jet momentum coefficient based on the basic airfoil chord (see Sketch (a) Section 6.1.1.1).

$\frac{c_{f_{LE}}}{c}$ is the ratio of the chord of the leading-edge flap, as defined in Figure 6.1.1.1-51, to the basic airfoil chord.

$\delta_{f_{LE}}$ is defined in Step 1a.

Step 2. Determine $(\Delta c_m)_\alpha$ by

$$(\Delta c_m)_\alpha = \Delta c_4 \, x_2 + \Delta c_{m4} \qquad 6.1.2.1\text{-k}$$

a. Evaluate Δc_4 from

$$\Delta c_4 = \frac{\alpha}{57.3} K \, c_{\ell_\alpha} \qquad 6.1.2.1\text{-}\ell$$

where

Δc_4 is a term analagous to the section lift coefficient. However, the thickness correction is not applied.

α is the angle of attack of the airfoil in degrees.

K and c_{ℓ_α} are defined in Step 1a above.

b. Evaluate Δc_{m4} from

$$\Delta c_{m4} = -C_\mu \left[\frac{x_m}{c} + \left(\frac{c'_{LE}}{c} - 1 \right) \right] \frac{\alpha}{57.3} \qquad 6.1.2.1\text{-m}$$

All terms have been previously defined in the preceding steps.

Step 3. Determine $(\Delta c_m)_{\delta_f}$ from

$$(\Delta c_m)_{\delta_f} = \sum_{i=1}^{n} (\Delta c_5)_i \, (x_5)_i \qquad 6.1.2.1\text{-n}$$

The subscript n refers to the total flap segments; i.e., in triple-slotted flaps, n = 3, double-slotted flaps, n = 2, and single-slotted or plain flaps, n = 1. The subscript i refers to a particular flap segment, where the forward segment is 1 and the aft segment is n.

a. Evaluate $(\Delta c_5)_i$ from

$$(\Delta c_5)_i = \frac{\delta_{f_i}}{57.3} K c_{\ell_{\delta f_i}} \qquad 6.1.2.1\text{-o}$$

where

$(\Delta c_5)_i$ is a term analagous to the section lift coefficient. However, the thickness correction is not applied.

δ_{f_i} is the deflection of the i^{th} flap segment in degrees. The value of the last flap segment used in this instance depends upon the effective jet angle $\delta_{j_{eff}}$, determined by using Equation 6.1.4.1-d of Section 6.1.4.1 or obtained from test data. If $\delta_{j_{eff}} > \sum_{i=1}^{n} \delta_{f_i}$, then the last flap deflection is that determined from constructing the straight line elements relative to the wing-chord line as depicted in Sketches (f) and (g). If $\delta_{j_{eff}} \leq \sum_{i=1}^{n} \delta_{f_i}$, then the last flap deflection is given by

$$\delta_{f_n} = \delta_{j_{eff}} - \sum_{i=1}^{n-1} \delta_{f_i} \qquad 6.1.2.1\text{-p}$$

$c_{\ell_{\delta f_i}}$ is the rate of change of section lift coefficient with respect to flap deflection. The value is obtained from Figure 6.1.1.1-49 as a function of the trailing-edge jet momentum coefficient C'_μ and the ratio of the flap chord (of the i^{th} flap segment) to the extended airfoil chord $c_{f_i}/c_{\delta\delta}$. For flaps with Fowler-type motion, the flap chord is defined as shown in Sketch (g).

K is defined in Step 1a.

b. Determine the corresponding moment arm

$$(x_5)_i = \frac{x_m}{c} + \left(\frac{c'_{LE}}{c} - 1\right) - \frac{x_{f_i}}{c_{\delta\delta}} \frac{c_{\delta\delta}}{c} \qquad 6.1.2.1\text{-q}$$

where

$\frac{x_{f_i}}{c_{\delta\delta}}$ is the center-of-lift location of the incremental load due to the deflection of the i^{th} flap segment. This parameter is obtained from Figure 6.1.2.1-37 as a function of the trailing-edge jet momentum C'_μ and the ratio of the flap chord to the extended wing-chord $c_{f_i}/c_{\delta\delta}$.

All other terms have been defined in Step 1b above.

Step 4. Determine $(\Delta c_m)_{\delta_j}$ from

$$(\Delta c_m)_{\delta_j} = \Delta c_6 \, x_6 \qquad 6.1.2.1\text{-r}$$

a. Evaluate Δc_6 from

$$\Delta c_6 = \frac{\delta_j}{57.3} K \, c_{\ell_{\delta_j}} \qquad 6.1.2.1\text{-s}$$

where

Δc_6 is a term analagous to the section lift coefficient. However, the thickness correction is not applied.

δ_j is the deflection of a pure jet flap, in degrees, relative to the trailing-edge camber line (see Sketch (g)). For IBF and EBF systems if

$$\delta_{j_{eff}} > \sum_{i=1}^{n} \delta_{f_i}, \text{ then}$$

$$\delta_j = \delta_{j_{eff}} - \sum_{i=1}^{n} \delta_{f_i} \qquad 6.1.2.1\text{-t}$$

If not, then $\delta_j = 0$. Terms are defined in Step 3a.

$c_{\ell_{\delta_j}}$ is the rate of change of section lift coefficient with respect to jet deflection, obtained from Figure 6.1.1.1-49 at $c_f/c_{\delta\delta} = 0$, as a function of the trailing-edge jet momentum coefficient C'_μ.

K is defined in Step 1a.

b. Determine the corresponding moment arm

$$x_6 = \frac{x_m}{c} + \left(\frac{c'_{LE}}{c} - 1\right) - \frac{x_j}{c_{\delta\delta}} \frac{c_{\delta\delta}}{c} \qquad 6.1.2.1\text{-u}$$

where

$\frac{x_j}{c_{\delta\delta}}$ is the center-of-lift location of the incremental load due to the jet deflection. This parameter is obtained from Figure 6.1.2.1-37 at $c_f/c_{\delta\delta} = 0$, as a function of the trailing-edge jet momentum coefficient C'_μ.

All other terms have been defined in Step 1b above.

Theoretically, this equation, within the context of linearized theory, is exact only for an airfoil of zero thickness. Unlike the lift equation, no comparable wing-chord thickness correction exists for the pitching-moment increment.

Sample Problems

1. Plain Trailing-Edge Flap (Method 1)

Given: A flapped airfoil from Reference 11.

Clark Y airfoil $c_f/c = 0.30$ $\delta_f = 45^o$ $t/c = 0.117$

$R_\ell = 0.61 \times 10^6$ $\tan\frac{1}{2}\phi'_{TE} = 0.142$ $x_{ref}/c = 0.25$ $c'/c = 1.0$

Compute:

$(c_{\ell_\delta})_{theory} = 4.51$ per rad (Figure 6.1.1.1-39a)

$\frac{c_{\ell_\alpha}}{(c_{\ell_\alpha})_{theory}} = 0.721$ (Figure 4.1.1.2-8a)

$\frac{c_{\ell_\delta}}{(c_{\ell_\delta})_{theory}} = 0.516$ (Figure 6.1.1.1-39b)

$K' = 0.518$ (Figure 6.1.1.1-40)

$$\Delta c_{\ell} = \delta_f \left[\frac{c_{\ell_\delta}}{(c_{\ell_\delta})_{theory}} \right] (c_{\ell_\delta})_{theory} K' \qquad \text{(Equation 6.1.1.1-c)}$$

$$= \frac{45}{57.3} (0.516)(4.51)(0.518)$$

$$= 0.947$$

$x_{c.p.}/c' = 0.425$ (Figure 6.1.2.1-35a)

Solution:

$$\Delta c_m = \Delta c_{\ell} \left[\frac{x_{ref}}{c} - \left(\frac{x_{c.p.}}{c'} \right) \left(\frac{c'}{c} \right) \right] \qquad \text{(Equation 6.1.2.1-a)}$$

$$= (0.947)\ [0.25 - (0.425)(1)]$$

-0.166 (based on c^2 and measured about c/4)

This compares with a test value of -0.195 from Reference 11.

2. Plain Trailing-Edge Flap (Method 2)

Given: A flapped airfoil from Reference 40.

NACA 65_1-210 airfoil $\quad c_f/c = 0.20 \quad \delta_f = 15^o \quad x_{ref}/c = 0.25$

Solution:

$\Delta c_m = -0.130$ (based on c^2 and measured about c/4) (Figure 6.1.2.1-35b)

This compares with a test value of -0.142 from Reference 40.

3. Plain Leading-Edge Flap

Given: The flapped airfoil of Reference 9.

NACA 0006 airfoil $\quad c_{f_{LE}}/c = 0.15 \quad \delta_{f_{LE}} = 20^o \quad M = 0.15$

$x_{ref}/c = 0.25 \quad \Delta c_{\ell} = -0.057$ (Example 8, Section 6.1.1.1)

$c'/c = 1.0 \quad \alpha = 0 \quad c_{\ell} = 0 \quad c_m = 0$

Compute:

$c_{m_{\delta_{LE}}} = -0.00116$ per deg (Figure 6.1.2.1-36)

$$\Delta c_{m_{LE}} = c'_{m_{\delta_{LE}}} \left(\frac{c'}{c}\right)^2 \delta_{f_{LE}} + \left[\frac{x_{ref}}{c} + \frac{c' - c}{c}\right] \Delta c_{\ell} + c_m \left[\left(\frac{c'}{c}\right)^2 - 1\right] + 0.75\, c_{\ell}\left(\frac{c'}{c}\right)\left(\frac{c'}{c} - 1\right)$$

(Equation 6.1.2.1-b)

$= -0.00116\,(1.0)^2\,(20) + (0.25 + 0)(-0.057) + 0[(1.0)^2 - 1.0] + 0.75\,(0)(1)(1 - 1)$

$= -0.0232 - 0.0143$

$= -0.0375$ (based on c^2 and measured about c/4)

This compares with a test value of −0.026 from Reference 9.

4. Jet Flaps

Given: The IBF airfoil with a double-slotted trailing-edge Fowler flap and leading-edge Krueger flap.

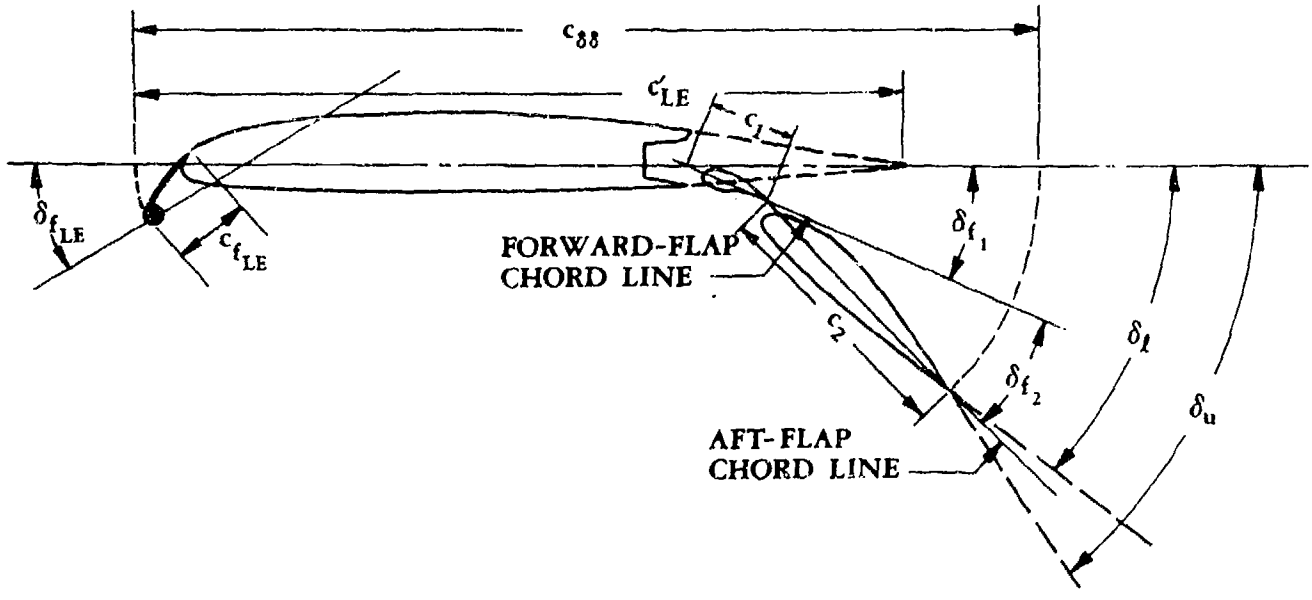

$C_\mu = 5.0$	$\frac{c_{\delta\delta}}{c} = 1.174$	$\frac{c_{f_{LE}}}{c} = 0.105$	$\frac{c'_{LE}}{c} = 1.068$	
$\frac{c_2}{c} = 0.306$	$\frac{c_1}{c} = 0.074$	$\frac{x_m}{c} = 0.25$	$\alpha = 3.0^o$	
$\delta_{f_{LE}} = 30^o$	$\delta_{f_1} = 30^o$	$\delta_{f_2} = 15^o$	$\delta_u = 56^o$	$\delta_\ell = 38^o$

Compute:

Step 1. $(\Delta c_m)_{\delta f_{LE}}$

$$K = \frac{c_{\delta\delta}}{c} = 1.174$$

$$c_a = c_{\delta\delta} - c_{f_{LE}} \quad \text{(Equation 6.1.2.1-g)}$$

$$\frac{c_a}{c_{\delta\delta}} = 1 - \frac{c_{f_{LE}}}{c} \Big/ \frac{c_{\delta\delta}}{c}$$

$$= 1 - \frac{0.105}{1.174}$$

$$= 0.9106$$

$$C'_\mu = \frac{C_\mu}{c_{\delta\delta}/c}$$

$$= \frac{5.0}{1.174}$$

$$= 4.259$$

$$\left.\begin{aligned} c_{\ell_{\delta_a}} &= 13.83 \quad \text{per rad} \\ c_{\ell_\alpha} &= 14.00 \quad \text{per rad} \end{aligned}\right\} \text{(Figure 6.1.1.1-49)}$$

$$\Delta c_1 = \frac{\delta_{f_{LE}}}{57.3} K\, c_{\ell_{\delta_a}} \quad \text{(Equation 6.1.2.1-e)}$$

$$= \frac{30}{57.3}(1.174)(13.83)$$

$$= 8.501$$

$$\Delta c_2 = \frac{\delta_{f_{LE}}}{57.3} K\, c_{\ell_\alpha} \quad \text{(Equation 6.1.2.1-f)}$$

$$= \frac{30}{57.3}(1.174)(14.00)$$

$$= 8.605$$

$$\left.\begin{aligned} \frac{x_a}{c_{\delta\delta}} &= 0.235 \\ \frac{x_{a.c.}}{c_{\delta\delta}} &= 0.202 \end{aligned}\right\} \quad \text{(Figure 6.1.2.1-37)}$$

$$x_1 = \frac{x_m}{c} + \left(\frac{c'_{LE}}{c} - 1\right) - \frac{x_a}{c_{\delta\delta}} \frac{c_{\delta\delta}}{c} \quad \text{(Equation 6.1.2.1-h)}$$

$$= 0.25 + (1.068 - 1) - (0.235)(1.174)$$

$$= 0.0421$$

$$x_2 = \frac{x_m}{c} + \left(\frac{c'_{LE}}{c} - 1\right) - \frac{x_{a.c.}}{c_{\delta\delta}} \frac{c_{\delta\delta}}{c} \quad \text{(Equation 6.1.2.1-i)}$$

$$= 0.25 + (1.068 - 1) - (0.202)(1.174)$$

$$= 0.0809$$

$$\Delta c_{m_3} = C_\mu \frac{c_{f_{LE}}}{c} \sin \delta_{f_{LE}} \quad \text{(Equation 6.1.2.1-j)}$$

$$= (5.0)(0.105)(\sin 30^o)$$

$$= 0.2625$$

$$(\Delta c_m)_{\delta f_{LE}} = \Delta c_1 \, x_1 - \Delta c_2 \, x_2 + \Delta c_{m_3} \quad \text{(Equation 6.1.2.1-d)}$$

$$= (8.501)(0.0421) - (8.605)(0.0809) + (0.2625)$$

$$= -0.0757$$

Step 2. $(\Delta c_m)_\alpha$

$$\Delta c_4 = \frac{\alpha}{57.3} K \, c_{\ell_\alpha} \quad \text{(Equation 6.1.2.1-ℓ)}$$

$$= \frac{3.0}{57.3} (1.174)(14.00)$$

$$= 0.861$$

$$\Delta c_{m_4} = -C_\mu \left[\frac{x_m}{c} + \left(\frac{c'_{LE}}{c} - 1\right)\right] \frac{\alpha}{57.3} \quad \text{(Equation 6.1.2.1-m)}$$

$$= -(5.0)[0.25 + (1.068 - 1)] \frac{(3.0)}{57.3}$$

$$= -0.0832$$

$$(\Delta c_m)_\alpha = \Delta c_4 \, x_2 + \Delta c_{m_4} \quad \text{(Equation 6.1.2.1-k)}$$

$$= (0.861)(0.0809) - 0.0832$$

$$= -0.0135$$

Step 3. $(\Delta c_m)_{\delta_f}$

n = 2, since there are two flap segments

$$\delta_{j_{eff}} = \frac{1}{2}(\delta_u + \delta_\ell) \quad \text{(Equation 6.1.4.1-d)}$$

$$= \frac{1}{2}(56 + 38)$$

$$= 47^o$$

Therefore, since $\delta_{j_{eff}} > \sum_{i=1}^{n} \delta_{f_i} = (\delta_{f_1} + \delta_{f_2}) = 45^o$, $\delta_{f_2} = 15^o$ (see Step 3a)

$$\frac{c_{f_1}}{c} = \frac{c_1}{c} + \frac{c_2}{c} \quad \text{(See Sketch (g))}$$

$$= 0.074 + 0.306$$

$$= 0.380$$

$$\frac{c_{f_1}}{c_{\delta\delta}} = \frac{c_{f_1}}{c} \Big/ \frac{c_{\delta\delta}}{c}$$

$$= 0.380/1.174$$

$$= 0.3237$$

For i = 1 (forward flap segment)

$$c_{\ell_{\delta_{f_1}}} = 12.33 \text{ per rad} \quad \text{(Figure 6.1.1.1-49)}$$

$$(\Delta c_5)_1 = \frac{\delta_{f_1}}{57.3} K \, c_{\ell_{\delta_{f_1}}} \quad \text{(Equation 6.1.2.1-o)}$$

$$= \frac{30}{57.3}(1.174)(12.33)$$

$$= 7.579$$

$$\frac{x_{f_1}}{c_{\delta\delta}} = 0.490 \quad \text{(Figure 6.1.2.1-37)}$$

$$(x_5)_1 = \frac{x_m}{c} + \left(\frac{c'_{LE}}{c} - 1\right) - \frac{x_{f_1}}{c_{\delta\delta}} \frac{c_{\delta\delta}}{c} \quad \text{(Equation 6.1.2.1-q)}$$

$$= 0.25 + (1.068 - 1) - (0.490)(1.174)$$

$$= -0.2573$$

For i = 2 (aft flap segment)

$$\frac{c_{f_2}}{c_{\delta\delta}} = \frac{c_{f_2}}{c} \Big/ \frac{c_{\delta\delta}}{c}$$

$$= 0.306/1.174 = 0.2606$$

$$c_{\ell_{\delta_{f_2}}} = 12.05 \quad \text{per rad} \quad \text{(Figure 6.1.1.1-49)}$$

$$(\Delta c_5)_2 = \frac{\delta_{f_2}}{57.3} K \, c_{\ell_{\delta_{f_2}}} \quad \text{(Equation 6.1.2.1-o)}$$

$$= \frac{15}{57.3}(1.174)(12.05)$$

$$= 3.703$$

$$\frac{x_{f_2}}{c_{\delta\delta}} = 0.521 \quad \text{(Figure 6.1.2.1-37)}$$

$$(x_5)_2 = \frac{x_m}{c} + \left(\frac{c_{LE}}{c} - 1\right) - \frac{x_{f_2}}{c_{\delta\delta}} \frac{c_{\delta\delta}}{c} \quad \text{(Equation 6.1.2.1-q)}$$

$$= 0.25 + (1.068 - 1) - (0.521)(1.174)$$

$$= -0.2937$$

$$(\Delta c_m)_{\delta_f} = \sum_{i=1}^{n} (\Delta c_5)_i (x_5)_i \quad \text{(Equation 6.1.2.1-n)}$$

$$= (\Delta c_5)_1 (x_5)_1 + (\Delta c_5)_2 (x_5)_2$$

$$= (7.579)(-0.2573) + (3.703)(-0.2937)$$

$$= -3.0376$$

Step 4. $(\Delta c_m)_{\delta_j}$

$c_{\ell_{\delta_j}} = 10.07$ per rad (Figure 6.1.1.1-49)

Since $\delta_{j_{eff}} > \sum_{i=1}^{n} \delta_{f_1}$ (Step 3), then

$$\delta_j = \delta_{j_{eff}} - \sum_{i=1}^{n} \delta_{f_i}$$

$$= \delta_{j_{eff}} - (\delta_{f_1} + \delta_{f_2})$$

$$= 47 - (30 + 15)$$

$$= 2^o$$

$$\Delta c_6 = \frac{\delta_j}{57.3} K\, c_{\ell_{\delta_j}} \quad \text{(Equation 6.1.2.1-s)}$$

$$= \frac{2}{57.3} (1.174)(10.07)$$

$$= 0.4126$$

$$\frac{x_j}{c_{\delta\delta}} = 0.658 \quad \text{(Figure 6.1.2.1-37)}$$

$$x_6 = \frac{x_m}{c} + \left(\frac{c'_{LE}}{c} - 1\right) - \frac{x_j}{c_{\delta\delta}} \frac{c_{\delta\delta}}{c} \quad \text{(Equation 6.1.2.1-u)}$$

$$= 0.25 + (1.068 - 1) - (0.658)(1.174)$$

$$= -0.4545$$

$$(\Delta c_m)_{\delta_j} = \Delta c_6 \, x_6 \quad \text{(Equation 6.1.2.1-r)}$$

$$= (0.4164)(-0.4545)$$

$$= -0.1875$$

Solution:

$$\Delta c_m = (\Delta c_m)_{\delta_{f_{LE}}} + (\Delta c_m)_\alpha + (\Delta c_m)_{\delta_f} + (\Delta c_m)_{\delta_j} \quad \text{(Equation 6.1.2.1-c)}$$

$$= -0.0757 - 0.0135 - 3.0376 - 0.1875$$

$$= -3.314 \quad \text{(based on } c^2\text{)}$$

REFERENCES

1. Hebert, J.: Procedure for Estimating the Aerodynamic Characteristics of Two-Dimensional Passive High Lift Devices. General Dynamics Convair Division TN-70-AVLABS-07, 1970. (U)

2. Hayashi, T. T.: The Two Dimensional Jet Flap Theory. Douglas Aircraft Company, MDC J1089, to be published. (U)

3. Lowry, J. G.: Data on Spoiler-Type Ailerons. NACA RM L53124a, 1953. (U)

4. Dimmock, N. A.: An Experimental Introduction to the Jet Flap. ARC CP 344, 1957. (U)

5. Spence, D. A.: The Lift on a Thin Airfoil with a Blown Flap. RAE TN Aero 2450, 1956. (U)

6. Cahill, J. F.: Two-Dimensional Wind-Tunnel Investigation of Four Types of High-Lift Flap on an NACA 65-210 Airfoil Section. NACA TN 1191, 1947. (U)

7. Harris, T. A., and Recant, I. G.: Wind-Tunnel Investigation of NACA 23012, 23021, and 23030 Airfoils Equipped with 40-Percent-Chord Double Slotted Flaps. NACA TR 723, 1941. (U)

8. Wenzinger, C. J., and Harris, T. A.: Wind-Tunnel Investigation of NACA 23012, 23021, and 23030 Airfoils with Various Sizes of Split Flap. NACA TR 668, 1939. (U)

9. Gambucci, B. J.: Section Characteristics of the NACA 0006 Airfoil with Leading-Edge and Trailing-Edge Flaps. NACA TN 3797, 1956. (U)

10. Kelly, J. A., and Hayter, N. L. F.: Lift and Pitching Moment at Low Speeds of the NACA 64A010 Airfoil Section Equipped with Various Combinations of a Leading-Edge Slat, Leading-Edge Flap, Split Flap and Double Slotted Flap. NACA TN 3007, 1953. (U)

11. Wenzinger, C. J.: Wind-Tunnel Investigation of Ordinary and Split Flaps on Airfoils of Different Profile. NACA TR 554, 1936. (U)

12. Ramsey, J. C., and Lauderman, E. C.: STOL Tactical Aircraft Investigation State-of-the-Art Design Compendium. Prepared under USAF Contract F33615-71-C-1754, 1971. (U)

13. May, F. W.: State-of-the-Art Design Compendium – STOL Aerodynamic Technology (Internally Blown Flaps). Boeing D180-14299-1, 1972. (U)

14. Kriechbaum, G., et al.: State-of-the-Art Design Compendium – STOL Aerodynamic Technology (Vectored Thrust and Mechanical Flaps). Boeing D180-14239-1, 1972. (U)

15. Jacobs, W. F., and Paterson, J. H.: The Jet-Flapped Wing in Two- and Three-Dimensional Flow. IAS Preprint 791, 1958. (U)

16. Korbacher, G. K., and Sridhar, K.: A Review of the Jet Flap. UTIA Review No. 14, 1960. (U)

17. Rogallo, F. M.: Collection of Balanced Aileron Test Data. NACA WR L-419, 1944. (U)

18. Rose, L. M., and Altman, J. M.: Low-Speed Experimental Investigation of a Thin Faired, Double-Wedge Airfoil Section with Nose and Trailing-Edge Flaps. NACA TN 1934, 1949. (U)

19. Street, W. G., and Ames, M. B., Jr.: Pressure Distribution Investigation of an NACA 0009 Airfoil with a 50-Percent Chord Plain Flap and Three Tabs. NACA TN 734, 1939. (U)

20. Ames, M. B., Jr. and Sears, R. I.: Pressure-Distribution Investigation of an NACA 0009 Airfoil with a 30-Percent Chord Plain Flap and Three Tabs. NACA TN 759, 1940. (U)

21. Abbott, I. H., and Greenburg, H.: Tests in the Variable-Density Wind Tunnel of the NACA 23012 Airfoil with Plain and Split Flaps. NACA TR 661, 1949. (U)

22. Cahill, J. F., et al.: Aerodynamic Forces and Loadings on Symmetrical Circular-Arc Airfoils with Plain Leading-Edge and Plain Trailing-Edge Flaps. NACA TR 1146, 1953. (U)

23. Harris, T. A., and Purser, P. E.: Wind-Tunnel Investigation of an NACA 23012 Airfoil with Two Sizes of Balanced Split Flap. NACA WR L-441, 1940. (U)

24. Holtzclaw, R. W.: Wind-Tunnel Investigation of the Effects of Spoilers on the Characteristics of a Low-Drag Airfoil Equipped with a 0.25-Chord Slotted Flap. NACA WR A-92, 1945. (U)

25. Holtzclaw, R. W., and Weisman, Y.: Wind-Tunnel Investigation of the Effects of Slot Shape and Flap Location on the Characteristics of a Low-Drag Airfoil Equipped with a 0.25-Chord Slotted Flap. NACA WR A-80, 1944. (U)

26. Swanson, R. S., and Schuldenfrei, M. J.: Wind-Tunnel Investigation of an NACA 23021 Airfoil with Two Sizes of Balanced Split Flaps. NACA WR L-449, 1941. (U)

27. Bogdonoff, S. M.: Tests of Two Models Representing Intermediate Inboard and Outboard Wing Sections of the XB-36 Airplane. NACA WR L-662, 1943. (U)

28. Duschik, F.: Wind-Tunnel Investigation of an NACA 23021 Airfoil with Two Arrangements of a 40-Percent-Chord Slotted Flap. NACA TN 728, 1939. (U)

29. Recant, I. G.: Wind-Tunnel Investigation of an NACA 23030 Airfoil with Various Arrangements of Slotted Flaps. NACA TN 755, 1940. (U)

30. Harris, T. A.: Wind-Tunnel Investigation of an NACA 23012 Airfoil with Two Arrangements of a Wide-Chord Slotted Flap. NACA TN 715, 1939. (U)

31. Lowry, J. G.: Wind-Tunnel Investigation of an NACA 23012 Airfoil with Several Arrangements of Slotted Flaps with Extended Lips. NACA TN 808, 1941. (U)

32. Wenzinger, C. J., and Harris, T. A.: Wind-Tunnel Investigation of an NACA 23021 Airfoil with Various Arrangements of Slotted Flaps. NACA TR 677, 1939. (U)

33. Jones, R., and Bell, A. H.: Further Experiments on an NACA 23021 Aerofoil with a 15-Percent Handley Page Slotted Flap in the Compressed Air Tunnel. ARC R&M 2519, 1954. (U)

34. Harris, T. A., and Lowry, J. G.: Pressure Distribution Over an NACA 23021 Airfoil with a Slotted and a Split Flap. NACA TR 718, 1941. (U)

35. Wenzinger, C. J., and Harris, T. A.: Wind-Tunnel Investigation of an NACA 23012 Airfoil with Various Arrangements of Slotted Flaps. NACA TR 664, 1939. (U)

36. Wenzinger, C. J., and Gauvain, W. E.: Wind-Tunnel Investigation of an NACA 23012 Airfoil with a Slotted Flap and Three Types of Auxiliary Flap. NACA TR 679, 1939. (U)

37. Wenzinger, C. J., and Delano, J. B.: Pressure Distribution Over an NACA 23012 Airfoil with a Slotted and Plain Flap. NACA TR 633, 1938. (U)

38. Stevenson, D. B., and Adler, A. A.: High-Speed Wind-Tunnel Tests of an NACA 0009-64 Airfoil Having a 33.4-Percent Chord Flap with an Overhang 20.1 Percent of the Flap Chord. NACA TN 1417, 1947. (U)

39. Stevenson, D. B., and Byrne, R. W.: High-Speed Wind-Tunnel Tests of an NACA 16-009 Airfoil Having a 32.9-Percent Chord Flap with an Overhang 20.7 Percent of the Flap Chord. NACA TN 1406, 1947. (U)

40. Underwood, W. J., Braslow, A. L., and Cahill, J. F.: Two-Dimensional Wind-Tunnel Investigation of 0.20-Airfoil Chord Plain Ailerons of Different Contour on an NACA 65_1-210 Airfoil Section. NACA WR L-151, 1945. (U)

41. Purser, P. E., Fischel, J., and Riebe, J. M.: Wind-Tunnel Investigation of an NACA 23012 Airfoil with a 0.30-Airfoil-Chord Double Slotted Flap. NACA WR L-469, 1943. (U)

42. Fischel, J., and Riebe, J. M.: Wind-Tunnel Investigation of an NACA 23021 Airfoil with a 0.32-Airfoil-Chord Double Slotted Flap. NACA WR L-7, 1944. (U)

43. Cahill, J. F., and Racisz, S. F.: Wind-Tunnel Investigation of Seven Thin NACA Airfoil Sections to Determine Optimum Double-Slotted-Flap Configurations. NACA TN 1545, 1948. (U)

44. Bogdonoff, S. M.: Wind-Tunnel Investigation of a Low-Drag Airfoil Section with a Double Slotted Flap. NACA WR L-697, 1943. (U)

45. Quinn, J. H., Jr.: Wind-Tunnel Investigation of Boundary-Layer Control by Suction on the NACA 65_3-418, a = 1.0 Airfoil Section with a 0.29-Airfoil-Chord Double Slotted Flap. NACA TN 1071, 1945. (U)

46. Fullmer, F. F.: Wind-Tunnel Investigation of NACA 66(215)-216, 66,1-212 and 65_1-212 Airfoils with 0.20-Airfoil-Chord Split Flaps. NACA WR L-140, 1944. (U)

47. Gauvain,W.E.: Wind-Tunnel Tests of a Clark Y Wing with "Maxwell" Leading Edge Slots. NACA TN 598, 1937. (U)

48. McKee, P. B., Jr.: Plain and Slotted Leading-Edge Flaps with a Conventional Split Trailing-Edge Flap. WADC TR 6356, Part 1, 1951. (U)

49. Spence, D. A.: Lift Coefficient of a Thin Jet-Flapped Wing. Proc. Roy. Soc., Vol. A238, 1956. (U)

50. Cahill, J. F.: Summary of Section Data on Trailing-Edge High-Lift Devices. NACA TR 938, 1949. (U)

51. James, H. A., and Hunton, L. W.: Estimation of Incremental Pitching Moments Due to Trailing-Edge Flaps on Swept and Triangular Wings. NACA TN 4040, 1957. (U)

52. Sears, R. I.: Wind-Tunnel Data on the Aerodynamic Characteristics of Airplane Control Surfaces. NACA WR L-663, 1943. (U)

53. Cahill, J. F.: Aerodynamic Data for a Wing Section of the Republic XF-12 Airplane Equipped with a Double-Slotted Flap. NACA WR L-544, 1946. (U)

54. Rose, L. M., and Altman, J. M.: Low-Speed Investigation of a Thin, Faired, Double-Wedge Airfoil Section with Nose Flaps of Various Chord. NACA TN 2018, 1950. (U)

55. Kelly, J. A.: Effects of Modifications to the Leading-Edge Region on the Stalling Characteristics of the NACA 63_1-012 Airfoil Section. NACA TN 2228, 1950. (U)

56. Nuber, R. J., and Gottlieb, S. M.: Two-Dimensional Wind-Tunnel Investigation at High Reynolds Numbers of an NACA 65A006 Airfoil with High-Lift Devices. NACA RM L7K06, 1948. (U)

57. Rensselaer, D. J. and Kelly, R.: Aerodynamic Design Compendium for Externally Blown Flaps. North American Rockwell NA-71-1105, 1971. (U)

TABLE 6.1.2.1-A
PLAIN TRAILING-EDGE FLAP PITCHING MOMENT EFFECTIVENESS
(METHOD 1)
DATA SUMMARY AND SUBSTANTIATION

Ref.	Airfoil Section	c_f/c	x_{ref}/c	δ_f (deg)	Δc_m Calc.	Δc_m Test	e Percent Error
36	23012	0.10	0.238	10	−0.063	−0.070	−10.0
				20	−0.113	−0.105	7.6
				30	−0.134	−0.130	3.1
				40	−0.161	−0.160	0.6
				50	−0.187	−0.180	3.9
				60	−0.212	−0.195	8.7
11	Clark Y	0.10	0.250	10	−0.041	−0.070	−41.4
				30	−0.088	−0.125	−29.6
				45	−0.113	−0.159	−28.9
				60	−0.137	−0.165	−17.0
35	23012	0.20	0.238	10	−0.086	−0.090	−4.4
				20	−0.151	−0.150	0.7
				30	−0.173	−0.180	−3.9
				45	−0.219	−0.215	1.9
				60	−0.258	−0.240	7.5
37	23012	0.20	0.250	15	−0.119	−0.122	−2.5
				30	−0.163	−0.170	−4.1
11	23012	0.20	0.250	15	−0.086	−0.130	−33.8
				30	−0.116	−0.178	−34.8
				45	−0.148	−0.220	−32.7
				60	−0.174	−0.235	−26.0
22	Circular Arc 0.06c	0.20	0.250	20	−0.164	−0.133	23.3
				40	−0.220	−0.174	26.4
				60	−0.280	−0.220	27.3
	Circular Arc 0.10c	0.20	0.250	20	−0.134	−0.130	3.1
				40	−0.180	−0.188	−4.3
				60	−0.230	−0.220	4.5
40	65_1-210	0.20	0.250	5	−0.048	−0.062	−22.6
				10	−0.098	−0.110	−10.9
				5	−0.056	−0.051	9.8
				10	−0.110	−0.101	8.9
				15	−0.162	−0.142	14.1
				20	−0.194	−0.166	16.9

TABLE 6.1.2.1-A (CONTD)

Ref.	Airfoil Section	c_f/c	x_{ref}/c	δ_f (deg)	Δc_m Calc.	Δc_m Test	e Percent Error
18	Double Wedge	0.25	0.250	10	−0.107	−0.100	7.0
				20	−0.180	−0.163	10.4
				40	−0.244	−0.194	26.8
				50	−0.278	−0.220	26.4
				60	−0.309	−0.225	37.3
9	0006	0.30	0.250	20	−0.166	−0.180	−7.8
				35	−0.221	−0.205	7.8
				50	−0.257	−0.250	2.8
20	0009	0.30	0.250	10	−0.098	−0.100	−2.0
				20	−0.156	−0.160	−2.5
				30	−0.179	−0.170	5.3
				40	−0.212	−0.200	6.0
				45	−0.201	−0.220	−8.6
11	Clark Y	0.30	0.250	10	−0.068	−0.100	−32.0
				30	−0.125	−0.170	−26.5
				45	−0.166	−0.195	−14.9
				60	−0.189	−0.185	2.2
39	16-009	0.329	0.250	10.3	−0.072	−0.075	−4.0
38	0009-64	0.334	0.250	5.9	−0.048	−0.059	−18.7
				7.9	−0.064	−0.072	−11.7
				9.9	−0.080	−0.089	−10.1
19	0009	0.50	0.250	10	−0.094	−0.086	9.3
				20	−0.129	−0.150	−14.0
				30	−0.153	−0.196	−21.9
				40	−0.183	−0.239	−23.4
				45	−0.198	−0.258	−23.3

Average Error = $\frac{\Sigma|e|}{n}$ = 14.2%

TABLE 6.1.2.1-B
PLAIN TRAILING-EDGE FLAP PITCHING-MOMENT EFFECTIVENESS
(METHOD 2)
DATA SUMMARY AND SUBSTANTIATION

Ref.	Airfoil Section	c_f/c	δ_f (deg)	$\Delta c_{m_{c/4}}$ Calc.	$\Delta c_{m_{c/4}}$ Test	e Percent Error
36	23012	0.10	10	−0.053	−0.073	−27.4
↓	↓	↓	20	−0.103	−0.110	−6.4
↓	↓	↓	30	−0.140	−0.137	2.2
↓	↓	↓	40	−0.162	−0.168	−3.6
↓	↓	↓	50	−0.173	−0.190	−8.9
↓	↓	↓	60	−0.178	−0.206	−13.6
11	Clark Y	0.10	10	−0.053	−0.070	−24.3
↓	↓	↓	30	−0.140	−0.125	12.0
↓	↓	↓	45	−0.168	−0.159	5.7
↓	↓	↓	60	−0.178	−0.165	7.9
35	23012	0.20	10	−0.090	−0.094	−4.3
↓	↓	↓	20	−0.162	−0.158	2.5
↓	↓	↓	30	−0.200	−0.190	5.3
↓	↓	↓	45	−0.223	−0.227	−1.8
↓	↓	↓	60	−0.236	−0.255	−7.5
37	23012	0.20	15	−0.130	−0.122	6.6
↓	↓	↓	30	−0.200	−0.170	17.6
11	23012	0.20	15	−0.130	−0.130	0
↓	↓	↓	30	−0.200	−0.178	12.4
↓	↓	↓	45	−0.223	−0.220	1.4
↓	↓	↓	60	−0.236	−0.235	0.4
22	Circular Arc 0.06c	0.20	20	−0.162	−0.133	21.8
↓	↓	↓	40	−0.217	−0.174	24.7
↓	↓	↓	60	−0.236	−0.220	7.3
↓	Circular Arc 0.10c	0.20	20	−0.162	−0.130	24.6
↓	↓	↓	40	−0.217	−0.188	15.4
↓	↓	↓	60	−0.236	−0.220	7.3

TABLE 6.1.2.1-8 (CONTD)

Ref.	Airfoil Section	c_f/c	δ_f (deg)	$\Delta c_{m_{c/4}}$ Calc.	$\Delta c_{m_{c/4}}$ Test	e Percent Error
40	65_1-210	0.20	5	−0.048	−0.062	−22.6
			10	−0.390	−0.110	−18.2
			5	−0.048	−0.051	−5.9
			10	−0.090	−0.101	−10.9
			15	−0.130	−0.142	−8.5
			20	−0.162	−0.166	−2.4
18	Double Wedge	0.25	10	−0.110	−0.100	10.0
			20	−0.195	−0.163	19.6
			40	−0.268	−0.194	38.1
			50	−0.283	−0.220	28.6
			60	−0.292	−0.225	29.8
9	0006	0.30	20	−0.167	−0.180	−7.2
			35	−0.237	−0.205	15.6
			50	−0.258	−0.250	3.2
20	0009	0.30	10	−0.090	−0.100	−10.0
			20	−0.167	−0.160	4.4
			30	−0.218	−0.170	28.2
			40	−0.243	−0.200	21.5
			45	−0.252	−0.220	14.5
11	Clark Y	0.30	10	−0.090	−0.100	−10.0
			30	−0.218	−0.170	28.2
			45	−0.252	−0.195	29.2
			60	−0.265	−0.185	43.2
39	16-009	0.329	10.3	−0.093	−0.075	24.0
38	0009-64	0.334	5.9	−0.051	−0.059	−13.6
			7.9	−0.070	−0.072	−3.4
			9.9	−0.090	−0.089	1.1
19	0009	0.50	10	−0.077	−0.086	−10.5
			20	−0.144	−0.150	−4.0
			30	−0.195	−0.196	−0.5
			40	−0.235	−0.239	−1.7
			45	−0.250	−0.258	−3.1

Average Error = $\frac{\Sigma |e|}{n}$ = 12.6%

TABLE 6.1.2.1-C
SINGLE-SLOTTED TRAILING-EDGE FLAP PITCHING-MOMENT EFFECTIVENESS
(METHOD 1)
DATA SUMMARY AND SUBSTANTIATION

Ref.	Airfoil Section	c_f/c	c'/c	x_{ref}/c	δ_f (deg)	Δc_m Calc.	Δc_m Test	e Percent Error
23	23012	0.15	1.150	0.238	30	−0.300	−0.300	0
26	23021	0.15	1.150	0.223	60	−0.366	−0.380	−3.7
27	63(420)-222, a = 0.1	0.243	1.070	0.260	40	−0.327	−0.300	9.0
23	23012	0.25	1.250	0.238	40	−0.583	−0.620	−6.0
26	23021	0.25	1.250	0.223	40	−0.540	−0.520	3.8
24	66,2-216,	0.25	1.029	0.250	10	−0.101	−0.105	−3.8
↓	a = 0.6	↓	1.043	↓	20	−0.204	−0.240	−15.0
↓	↓	↓	1.058	↓	30	−0.289	−0.327	−11.6
↓	↓	↓	1.068	↓	40	−0.332	−0.384	−13.5
↓	↓	↓	1.073	↓	50	−0.338	−0.405	−16.5
25	66,2-216,	0.25	1.014	0.250	10	−0.097	−0.112	−13.4
↓	a = 0.6	↓	1.029	↓	20	−0.194	−0.234	−17.1
↓	↓	↓	1.043	↓	30	−0.276	−0.360	−23.3
↓	↓	↓	1.058	↓	40	−0.323	−0.410	−21.2
↓	↓	↓	1.066	↓	50	−0.331	−0.400	−17.3
6	65-210	0.25	1.144	0.250	28.2	−0.359	−0.425	−15.5
↓	↓	↓	1.141	↓	34.5	−0.404	−0.445	−9.2
↓	↓	↓	1.135	↓	39.5	−0.420	−0.500	−16.0
↓	↓	↓	1.145	↓	44.7	−0.428	−0.462	−7.4
↓	↓	↓	1.075	↓	29.1	−0.308	−0.360	−14.4
↓	↓	↓	1.078	↓	39.1	−0.361	−0.420	−14.1
↓	↓	↓	1.076	↓	44.1	−0.363	−0.445	−18.4
↓	↓	↓	1.076	↓	49.1	−0.359	−0.395	−9.1
36	23012	0.257	1.030	0.238	10	−0.110	−0.110	0
↓	↓	↓	1.050	↓	20	−0.226	−0.240	−5.8
↓	↓	↓	1.060	↓	30	−0.320	−0.355	−9.9
↓	↓	↓	1.070	↓	40	−0.377	−0.395	−4.6
↓	↓	↓	1.080	↓	50	−0.384	−0.355	8.2
21	23021	0.257	1.035	0.223	10	−0.116	−0.130	−10.8
↓	↓	↓	1.035	↓	20	−0.223	−0.270	−17.4
↓	↓	↓	1.070	↓	30	−0.324	−0.350	−7.4
↓	↓	↓	1.070	↓	40	−0.352	−0.400	−12.0
↓	↓	↓	1.070	↓	50	−0.362	−0.405	−10.6
↓	↓	↓	1.060	↓	60	−0.377	−0.405	−6.9

TABLE 6.1.2.1-C (CONTD)

Ref.	Airfoil Section	c_f/c	c'/c	x_{ref}/c	δ_f (deg)	Δc_m Calc.	Δc_m Test	e Percent Error
21	23021	0.257	1.037	0.223	20	−0.224	−0.255	−12.2
			1.050		30	−0.306	−0.330	−7.3
			1.063		40	−0.345	−0.320	7.8
			1.054		50	−0.347	−0.340	2.1
			1.065		60	−0.381	−0.360	5.8
35	23012	0.267	1.260	0.238	30	−0.533	−0.600	−11.2
31	23012	0.30	1.200	0.238	10	−0.189	−0.205	−7.8
					20	−0.363	−0.325	11.7
					30	−0.502	−0.435	15.4
					40	−0.574	−0.540	6.3
					50	−0.577	−0.560	3.0
					10	−0.189	−0.220	−14.1
					20	−0.363	−0.395	−8.1
					30	−0.502	−0.500	0.4
					40	−0.574	−0.515	11.5
			1.310		10	−0.236	−0.320	−26.3
					20	−0.449	−0.525	−14.5
					30	−0.602	−0.685	−12.1
					40	−0.661	−0.700	−5.6
28	23021	0.40	1.032	0.223	10	−0.148	−0.155	−4.5
			1.075		20	−0.320	−0.310	3.2
			1.085		30	−0.435	−0.400	8.8
			1.055		40	−0.458	−0.390	17.5
			1.095		50	−0.505	−0.425	18.8
29	23030	0.40	1.040	0.140	10	−0.203	−0.195	4.1
			1.080		20	−0.406	−0.410	−1.0
			1.100		30	−0.544	−0.545	−0.2
			1.150		40	−0.655	−0.570	14.9
			1.160		50	−0.707	−0.650	8.8
30	23012	0.40	1.065	0.238	10	−0.155	−0.145	6.9
			1.088		20	−0.323	−0.300	7.7
			1.103		30	−0.462	−0.440	5.0
			1.093		40	−0.515	−0.355	45.1
			1.090		50	−0.519	−0.420	23.6
			1.082		10	−0.162	−0.150	8.0
			1.100		20	−0.332	−0.300	10.7
			1.102		30	−0.462	−0.405	14.1
			1.110		40	−0.538	−0.400	34.5
			1.090		50	−0.519	−0.420	23.6

Average Error = $\frac{\Sigma|e|}{n}$ = 11.2%

TABLE 6.1.2.1-D
DOUBLE-SLOTTED TRAILING-EDGE FLAP PITCHING-MOMENT EFFECTIVENESS
(METHOD 1)
DATA SUMMARY AND SUBSTANTIATION

Ref.	Airfoil Section	c_1/c	c_2/c	c'/c	x_{ref}/c	δ_{f_1} (deg)	δ_{f_2} (deg)	Δc_m Calc.	Δc_m Test	e Percent Error
41	23012	0.170	0.257	1.221	0.238	25	35	−0.804	−0.713	12.8
42	23021	0.147	0.257	1.229	0.223	30	40	−0.976	−0.773	26.3
43	64-208	0.056	0.250	1.127	0.250	25	25	−0.573	−0.541	5.9
↓	1410	0.075	0.250	1.141	↓	25	25	−0.595	−0.606	−1.8
↓	63-210	↓	↓	1.138	↓	25	25	−0.612	−0.578	5.9
↓	65-210	↓	↓	1.143	↓	25	25	−0.597	−0.584	2.2
↓	66-210	↓	↓	1.144	↓	25	30	−0.598	−0.583	2.6
↓	64-208	↓	↓	1.148	↓	30	15	−0.668	−0.568	17.6
↓	64-212	↓	↓	1.152	↓	30	20	−0.645	−0.606	6.4
↓	64-210	↓	↓	1.139	↓	30	25	−0.635	−0.633	0.3
↓	66-210	0.100	0.250	1.172	↓	25	35	−0.675	−0.563	19.9
6	65-210	0.075	0.250	1.139	0.250	15	25	−0.537	−0.550	−2.3
↓	↓	↓	↓	1.146	↓	20	25	−0.582	−0.583	−0.2
↓	↓	↓	↓	1.143	↓	25	25	−0.607	−0.590	2.9
↓	↓	↓	↓	1.148	↓	30	25	−0.640	−0.590	8.5
↓	↓	↓	↓	1.133	↓	35	25	−0.639	−0.557	14.7
10	64A010	0.075	0.250	1.133	0.250	30	22.7	−0.631	−0.550	14.7
↓	↓	↓	↓	↓	↓	30	22.7	−0.631	−0.520	21.4
44	65_3-118	0.100	0.245	1.175	0.250	23	42	−0.670	−0.714	−6.2
7	23012	0.143	0.257	1.145	0.238	30	20	−0.737	−0.654	12.7
↓	↓	↓	↓	1.160	↓	30	30	−0.806	−0.703	14.9
↓	↓	↓	↓	1.110	↓	10	40	−0.509	−0.527	−3.4
↓	↓	↓	↓	1.110	↓	20	10	−0.459	−0.472	−2.8
↓	↓	↓	↓	1.115	↓	40	0	−0.545	−0.410	32.9
↓	↓	↓	↓	1.101	↓	0	30	−0.358	−0.342	4.7

Average Error = $\frac{\Sigma|e|}{n}$ = 9.8%

TABLE 6.1.2.1-E
SPLIT TRAILING-EDGE FLAP PITCHING-MOMENT EFFECTIVENESS
(METHOD 1)
DATA SUMMARY AND SUBSTANTIATION

Ref.	Airfoil Section	c_f/c	x_{ref}/c	δ_f (deg)	Δc_m Calc.	Δc_m Test	e Percent Error
8	23012	0.10	0.236	15	−0.085	−0.085	0
↓	↓	↓	↓	30	−0.147	−0.145	1.4
↓	↓	↓	↓	45	−0.185	−0.185	0
↓	↓	↓	↓	60	−0.211	−0.196	8.2
↓	↓	↓	↓	75	−0.225	−0.185	21.6
8	23021	0.10	0.223	15	−0.123	−0.080	53.8
↓	↓	↓	↓	30	−0.207	−0.150	38.0
↓	↓	↓	↓	45	−0.267	−0.210	27.2
↓	↓	↓	↓	60	−0.305	−0.250	22.0
↓	↓	↓	↓	75	−0.328	−0.250	31.2
46	66,1-212	0.20	0.250	40	−0.204	−0.205	−0.5
↓	↓	↓	↓	50	−0.228	−0.219	4.1
↓	↓	↓	↓	60	−0.246	−0.235	4.7
↓	↓	↓	↓	70	−0.258	−0.234	10.3
46	65_1-212	0.20	0.250	40	−0.204	−0.191	6.8
↓	↓	↓	↓	50	−0.228	−0.212	7.5
↓	↓	↓	↓	60	−0.246	−0.221	11.3
↓	↓	↓	↓	70	−0.258	−0.211	22.3
46	66(215)-216	0.20	0.250	40	−0.236	−0.232	1.7
↓	↓	↓	↓	50	−0.264	−0.257	2.7
↓	↓	↓	↓	60	−0.286	−0.262	9.2
↓	↓	↓	↓	70	−0.304	−0.264	15.2
21	23012	0.20	0.238	5	−0.036	−0.026	38.5
↓	↓	↓	↓	10	−0.070	−0.060	16.7
↓	↓	↓	↓	15	−0.106	−0.090	17.8
↓	↓	↓	↓	20	−0.134	−0.116	15.5
↓	↓	↓	↓	30	−0.179	−0.170	5.3
↓	↓	↓	↓	45	−0.228	−0.214	6.5

TABLE 6.1.2.1-E (CONTD)

Ref.	Airfoil Section	c_f/c	x_{ref}/c	δ_f (deg)	Δc_m Calc	Δc_m Test	e Percent Error
34	23021	0.20	0.250	15	−0.134	−0.103	30.1
↓	↓	↓	↓	30	−0.224	−0.200	12.0
↓	↓	↓	↓	45	−0.292	−0.252	15.9
↓	↓	↓	↓	60	−0.332	−0.280	18.6
↓	↓	↓	↓	75	−0.358	−0.271	32.1
8	23012	0.30	0.238	15	−0.110	−0.115	−4.3
↓	↓	↓	↓	30	−0.185	−0.185	0
↓	↓	↓	↓	45	−0.236	−0.230	2.6
↓	↓	↓	↓	60	−0.267	−0.242	10.3
8	23021	0.30	0.223	15	−0.160	−0.140	14.3
↓	↓	↓	↓	30	−0.267	−0.245	9.0
↓	↓	↓	↓	45	−0.345	−0.325	6.2
↓	↓	↓	↓	60	−0.394	−0.360	9.4
↓	↓	↓	↓	75	−0.422	−0.365	15 6
8	23012	0.40	0.238	15	−0.110	−0.102	7.8
↓	↓	↓	↓	30	−0.188	−0.185	1.6
↓	↓	↓	↓	45	−0.238	−0.230	3.5
↓	↓	↓	↓	60	−0.269	−0.245	9.8
8	23021	0.40	0.223	15	−0.163	−0.153	6.5
↓	↓	↓	↓	30	−0.271	−0.272	−0.4
↓	↓	↓	↓	45	−0.350	−0.360	−2.8
↓	↓	↓	↓	60	−0.402	−0.407	−1.2

$$\text{Average Error} = \frac{\Sigma|e|}{n} = 12.5\%$$

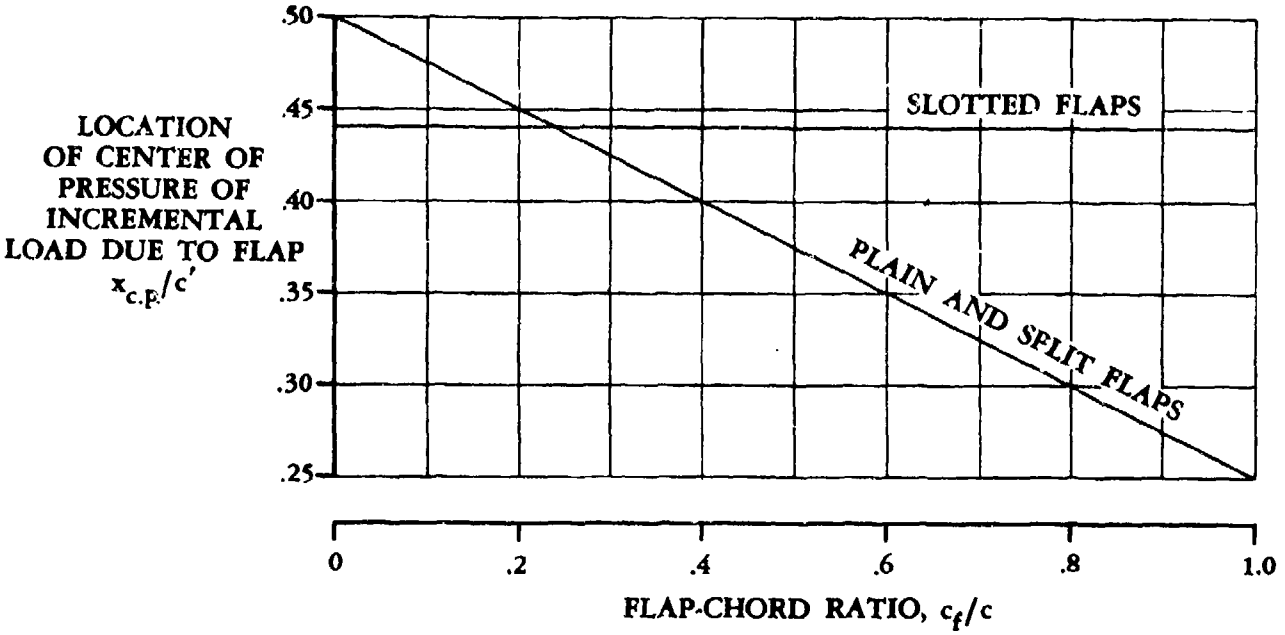

FIGURE 6.1.2.1-35a EMPIRICAL LOCATION OF CENTER OF PRESSURE OF INCREMENTAL LOAD DUE TO TRAILING-EDGE, MECHANICAL FLAPS

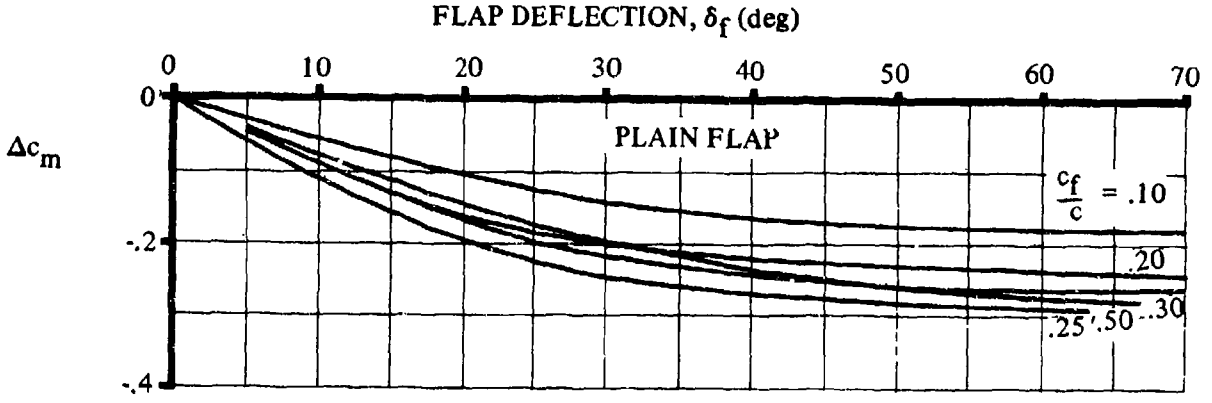

FIGURE 6.1.2.1-35b EFFECT OF TRAILING-EDGE FLAP DEFLECTION AND FLAP-CHORD-TO-WING-CHORD RATIO ON SECTION INCREMENTAL PITCHING MOMENT DUE TO PLAIN FLAPS

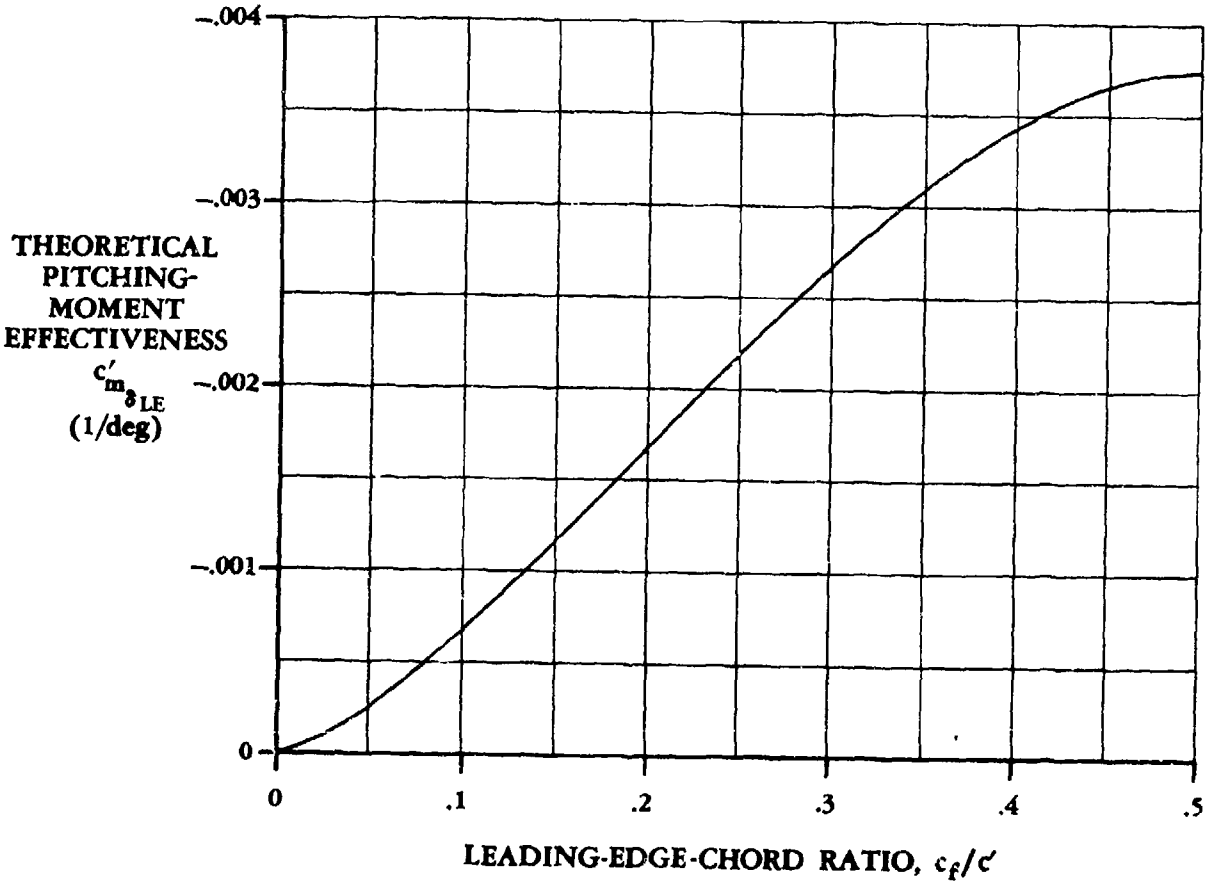

FIGURE 6.1.2.1-36 THEORETICAL PITCHING-MOMENT EFFECTIVENESS OF LEADING-EDGE DEVICES

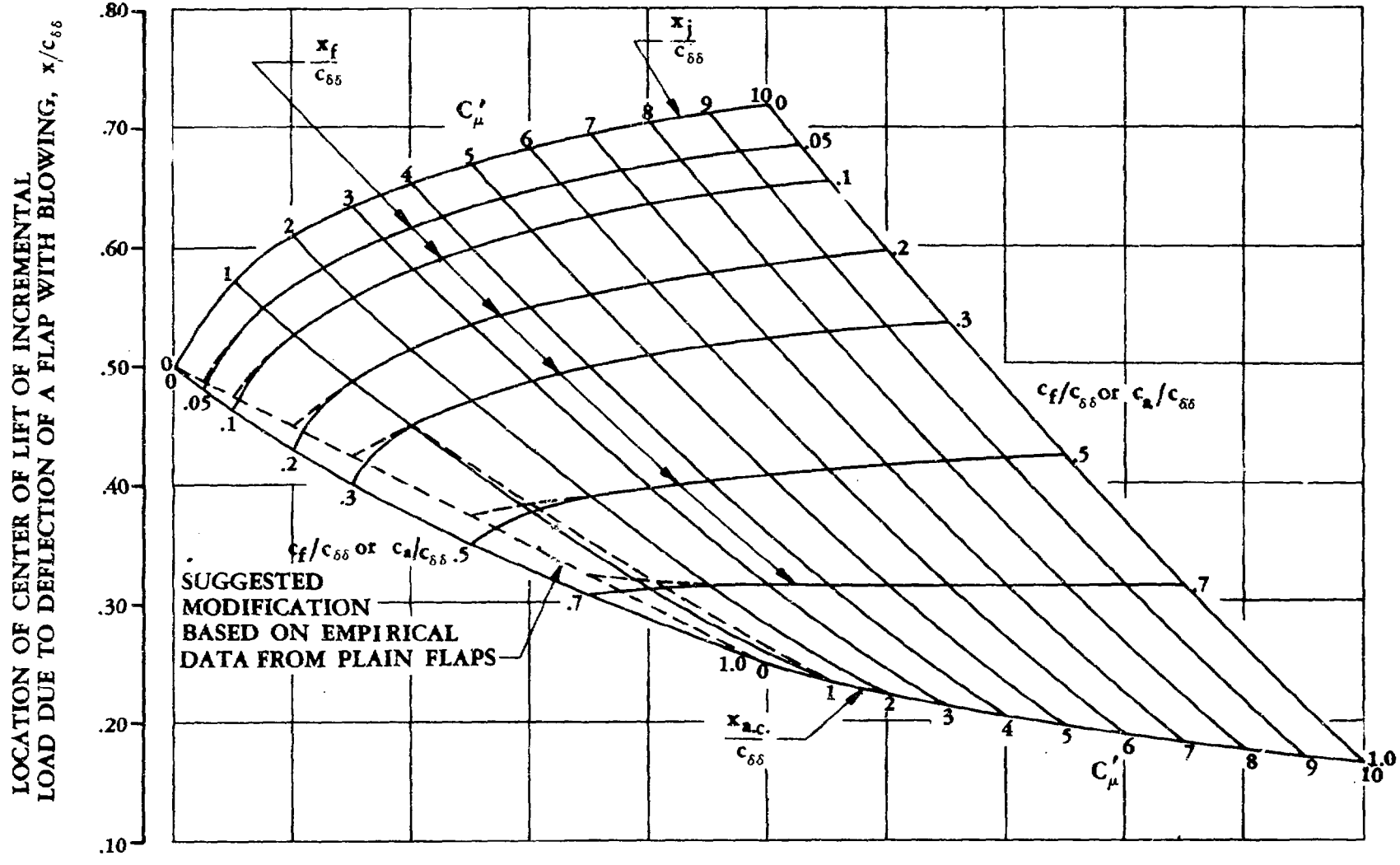

FIGURE 6.1.2.1-37 THEORETICAL LOCATION OF CENTER OF PRESSURE OF INCREMENTAL LOAD DUE TO DEFLECTION OF A FLAP WITH A JET EMERGING FROM THE TRAILING EDGE

6.1.2.2 SECTION DERIVATIVE c_{m_α} WITH HIGH-LIFT AND CONTROL DEVICES

Mechanical Flaps

According to thin-airfoil theory, camber, such as that due to flaps, does not affect the moment-curve slope of an airfoil section. Experimental data verify this for the angle-of-attack and flap-deflection ranges for which the flow is attached over the airfoil and flap surfaces. This aspect of the subject is discussed with respect to lift for various types of flaps in Section 6.1.1.2.

A typical set of data is shown in Sketch (a) for plain trailing-edge flaps.

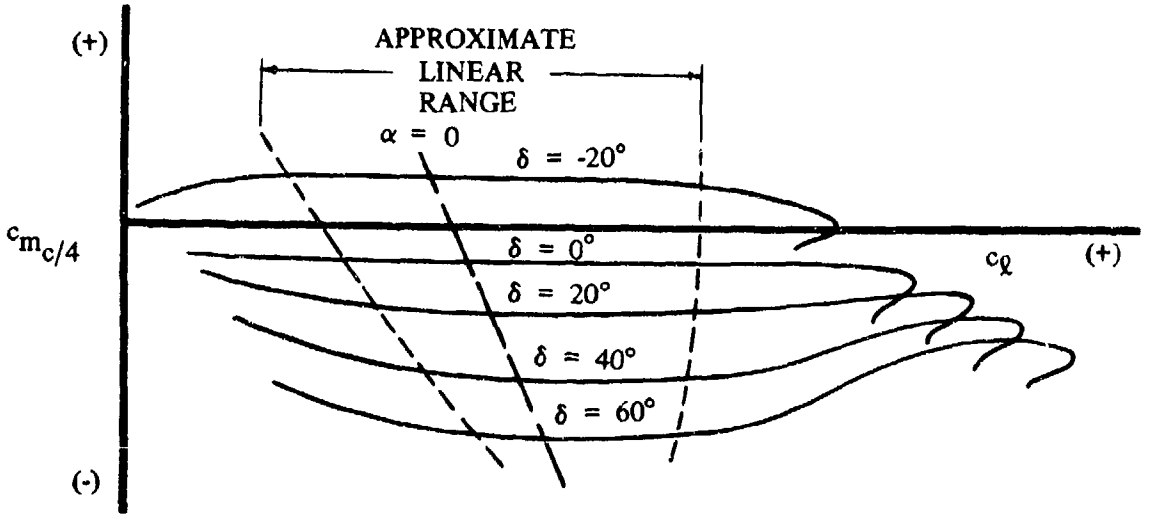

SKETCH (a)

The approximate linear range is noted in the sketch. At angles of attack above the linear range the flow separates over the flap surface, and the additional loading due to the flap is lost. A pitch-up tendency results. At angles of attack below the linear range the flow separates on the underside of the airfoil, causing a forward shift in center of pressure and a nose-up moment change.

Theoretically, the pitching-moment-curve slope is affected both by leading- and trailing-edge devices that extend beyond the chord of the basic airfoil. These changes, predicted by thin-airfoil theory, along with a recommended empirical factor for trailing-edge devices, are presented in Reference 1. Attempts to substantiate these equations by using available test data of References 2 through 8 have proved unsatisfactory. The test data from these references do not indicate a consistent dependence of pitching-moment-curve slope upon airfoil-chord extension as predicted by thin-airfoil theory.

Jet Flaps

The aerodynamic-center location for a jet-flap airfoil is dependent upon the trailing-edge jet momentum coefficient C_μ and upon the extent to which leading- and trailing-edge flaps extend beyond the basic airfoil.

Considerations of clarity and simplicity of presentation dictated a deviation from normal Datcom practice in that the effect of jet flaps on c_{m_α} was included in Section 6.1.2.1, which deals with the pitching-moment increment Δc_m.

DATCOM METHODS

1. Leading- and Trailing-Edge Mechanical Flaps

The parameter dc_m/dc_ℓ for various flap deflections is the same as that for zero flap deflection for angles of attack near zero. However, the linear range for this parameter becomes very small at the higher flap deflections.

2. Jet Flaps

The variation of pitching moment with angle of attack for airfoil sections equipped with jet flaps is covered in the jet-flap method of Section 6.1.2.1. The range of applicability and the limitations of the method are discussed there and in Section 6.1.1.1.

REFERENCES

1. Hebert, J., Jr., et al.: STOL Tactical Aircraft Investigation, Volume II Design Compendium. AFFDL-TR-73-21-Volume II, 1973. (U)
2. Recant, I. G.: Wind-Tunnel Investigation of an N.A.C.A. 23030 Airfoil with Various Arrangements of Slotted Flaps. NACA TN 755, 1940. (U)
3. Wenzinger, C. J., and Harris, T. A.: Wind-Tunnel Investigation of an N.A.C.A. 23021 Airfoil with Various Arrangements of Slotted Flaps. NACA TR 677, 1939. (U)
4. Harris, T. A., and Purser, P. E.: Wind-Tunnel Investigation of an N.A.C.A. 23012 Airfoil with Two Sizes of Balanced Split Flap. NACA WR L-441, 1940. (U)
5. Swanson, R. S., and Schuldenfrei, M. J.: Wind-Tunnel Investigation of an N.A.C.A. 23021 Airfoil with Two Sizes of Balanced Split Flaps. NACA WR L-449, 1941. (U)
6. Holtzclaw, R. W., and Weisman, Y.: Wind-Tunnel Investigation of the Effects of Slot Shape and Flap Location on the Characteristics of a Low-Drag Airfoil Equipped with a 0.25-Chord Slotted Flap. NACA WR A-80, 1944. (U)
7. Holtzclaw, R. W.: Wind-Tunnel Investigation of the Effects of Spoilers on the Characteristics of a Low-Drag Airfoil Equipped with a 0.25-Chord Slotted Flap. NACA WR A-92, 1945. (U)
8. Harris, T. A., and Recant, I. G.: Wind-Tunnel Investigation of N.A.C.A. 23012, 23021, and 23030 Airfoils Equipped with 40-Percent-Chord Double Slotted Flaps. NACA TR 723, 1941. (U)
9. Sears, R. I.: Wind-Tunnel Data on the Aerodynamic Characteristics of Airplane Control Surfaces. NACA WR L-663, 1943. (U)
10. Lowry, T. G.: Wind-Tunnel Investigation of an N.A.C.A. 23012 Airfoil with Several Arrangements of Slotted Flaps with Extended Lips. NACA TN 808, 1941. (U)
11. Wenzinger, C. J., and Harris, T. A.: Wind-Tunnel Investigation of an N.A.C.A. 23012 Airfoil with Various Arrangements of Slotted Flaps. NACA TR 664, 1939. (U)

6.1.2.3 SECTION PITCHING MOMENT NEAR MAXIMUM LIFT WITH HIGH-LIFT AND CONTROL DEVICES

It is shown in reference 1 that near maximum-lift conditions the pitching-moment increment due to flap deflection is a function of the corresponding lift increment and is nearly independent of flap and airfoil geometry. The summary chart from this reference is presented in this section for estimating pitching-moment increments due to flap deflection at high angles of attack. The flap types covered include plain, slotted, and Fowler trailing-edge flaps and leading-edge flaps and slats. The chart is applicable only to that part of the c_m versus c_ℓ curve just below the moment break.

DATCOM METHOD

Section pitching-moment increments due to high-lift and control devices are obtained from figure 6.1.2.3-3. The section-lift increment Δc_ℓ used in reading this chart is obtained from the appropriate method of Section 6.1.1.1. The section-lift increment for airfoils with both leading-edge and trailing-edge devices is obtained by adding the individual increments calculated by the methods of Section 6.1.1.1.

The design chart is based on the test data of references 2 through 28. The accuracy of the method, within the boundaries of the test points on the chart, is dependent upon the accuracy of the value of Δc_ℓ used in reading the design chart. The limitations of the method are the same as those of the methods of Section 6.1.1.1 for determining the section-lift increments.

REFERENCES

1. Bidwell, J.M., and Cahill, J.F.: Survey of Two-Dimensional Data on Pitching-Moment Changes Near Maximum Lift Caused by Deflection of High-Lift Devices. NACA RM L9J03, 1949. (U)

2. Cahill, J.F.: Summary of Section Data on Trailing-Edge High-Lift Devices. NACA RM L8D09, 1948. (U)

3. Wenzinger, C.J., and Harris, T.A.: Wind-Tunnel Investigation of an NACA 23012 Airfoil With Various Arrangements of Slotted Flaps. NACA TR 664, 1939. (U)

4. Abbott, I.H., and Greenberg, H.: Tests in the Variable-Density Wind Tunnel of the NACA 23012 Airfoil with Plain and Split Flaps. NACA TR 661, 1939. (U)

5. Klein, M.M.: Pressure Distributions and Force Tests of an NACA 65-210 Airfoil Section with a 50-Percent-Chord Flap. NACA TN 1167, 1947. (U)

6. Wenzinger, C.J., and Harris, T.A.: Wind-Tunnel Investigation of NACA 23012, 23021, and 23030 Airfoils with Various Sizes of Split Flap. NACA TR 668, 1939. (U)

7. Schuldenfrei, M.J.: Wind-Tunnel Investigation of an NACA 23012 Airfoil with a Handley Page Slat and Two Flap Arrangements. NACA WR L-261, 1942. (U)

8. Harris, T.A., and Purser, P.E.: Wind-Tunnel Investigation of an NACA 23012 Airfoil with Two Sizes of Balanced Split Flap. NACA WR L-441, 1940. (U)

9. Lowry, J.G.: Wind-Tunnel Investigation of an NACA 23012 Airfoil with Several Arrangements of Slotted Flaps with Extended Lips. NACA TN 808, 1941. (U)

10. Harris, T.A.: Wind-Tunnel Investigation of an NACA 23012 Airfoil with Two Arrangements of a Wide-Chord Slotted Flap. NACA TN 715, 1939. (U)

11. Purser, P.E., Fischel, J., and Riebe, J.M.: Wind-Tunnel Investigation of an NACA 23012 Airfoil with a 0.30-Airfoil-Chord Double Slotted Flap. NACA WR L-469, 1943. (U)

12. Wenzinger, C.J., and Harris, T.A.: Wind-Tunnel Investigation of an NACA 23021 Airfoil with Various Arrangements of Slotted Flaps. NACA TR 677, 1939. (U)

13. Duschik, F.: Wind-Tunnel Investigation of an NACA 23021 Airfoil with Two Arrangements of a 40-Percent-Chord Slotted Flap. NACA TN 728, 1939. (U)

14. Fischel, J., and Riebe, J.M.: Wind-Tunnel Investigation of an NACA 23021 Airfoil with a 0.32-Airfoil-Chord Double Slotted Flap. NACA WR L-7, 1944. (U)

15. Holtzclaw, R.W., and Weisman, Y.: Wind-Tunnel Investigation of the Effects of Slot Shape and Flap Location on the Characteristics o. Low-Drag Airfoil Equipped with a 0.25-Chord Slotted Flap. NACA WR A-92, 1944. (U)

16. Abbott, I.H., and Fullmer, F.F., Jr.: Wind-Tunnel Investigation of NACA 63, 4-420 Airfoil with 25-Percent-Chord Slotted Flap. NACA ACR 3I21, 1943. (U)

17. Gillis, C.L., and McKee, J.W.: Wind-Tunnel Investigation of an NACA 23012 Airfoil with an 18.05-Percent-Chord Maxwell Slat and with Trailing-Edge Flaps. NACA WR L-574, 1941. (U)

18. Lowry, J.G., and McKee, J.W.: Wind-Tunnel Investigation of an NACA 23012 Airfoil with a 30-Percent-Chord Maxwell Slat and With Trailing-Edge Flaps. NACA WR L-693, 1941. (U)

19. Weick, F.E., and Platt, R.C.: Wind-Tunnel Tests on Model Wing With Fowler Flap and Specially Developed Leading-Edge Slot. NACA TN 459, 1933. (U)

20. Lemme, H.G.: Force and Pressure-Distribution Measurements on a Rectangular Wing with a Slotted Droop Nose and with Either Plain and Split Flaps in Combination or a Slotted Flap. NACA TM 1108, 1947. (U)

21. Lemme, H.A.: Force and Pressure-Distribution Measurements on a Rectangular Wing with Double-Hinged Nose. NACA TM 1117, 1947.(U)

22. Gauvain, W.E.: Wind-Tunnel Tests of a Clark Y Wing with "Maxwell" Leading-Edge Slots. NACA TN 598, 1937. (U)

23. Fullmer, F.F., Jr.: Two-Dimensional Wind-Tunnel Investigation of the NACA 64_1-012 Airfoil Equipped with Two Types of Leading-Edge Flap. NACA TN 1277, 1947. (U)

24. Fullmer, F.F., Jr.: Two-Dimensional Wind-Tunnel Investigation of an NACA 64-009 Airfoil Equipped with Two Types of Leading-Edge Flap. NACA TN 1624, 1948. (U)

25. Underwood, W.J., and Nuber, R.J.: Two-Dimensional Wind-Tunnel Investigation at High Reynolds Numbers of Two Symmetrical Circular-Arc Airfoil Sections with High-Lift Devices. NACA RM L6K22, 1947. (U)

26. Nuber, R.J., and Cheesman, G.A.: Two-Dimensional Wind-Tunnel Investigation of a 6-Percent-Thick Symmetrical Circular-Arc Airfoil Section with Leading-Edge and Trailing-Edge High-Lift Devices Deflected in Combination. NACA RM L9G20, 1949. (U)

27. Nuber, R.J., and Gottlieb, S.M.: Two-Dimensional Wind-Tunnel Investigation at High Reynolds Numbers of an NACA 65A006 Airfoil with High-Lift Devices. NACA RM L7K06, 1948. (U)

28. Thompson, M.J.: A Simple Method for Determining the Aerodynamic Center of an Airfoil. Jour. Aero. Sci., February 1938. (U)

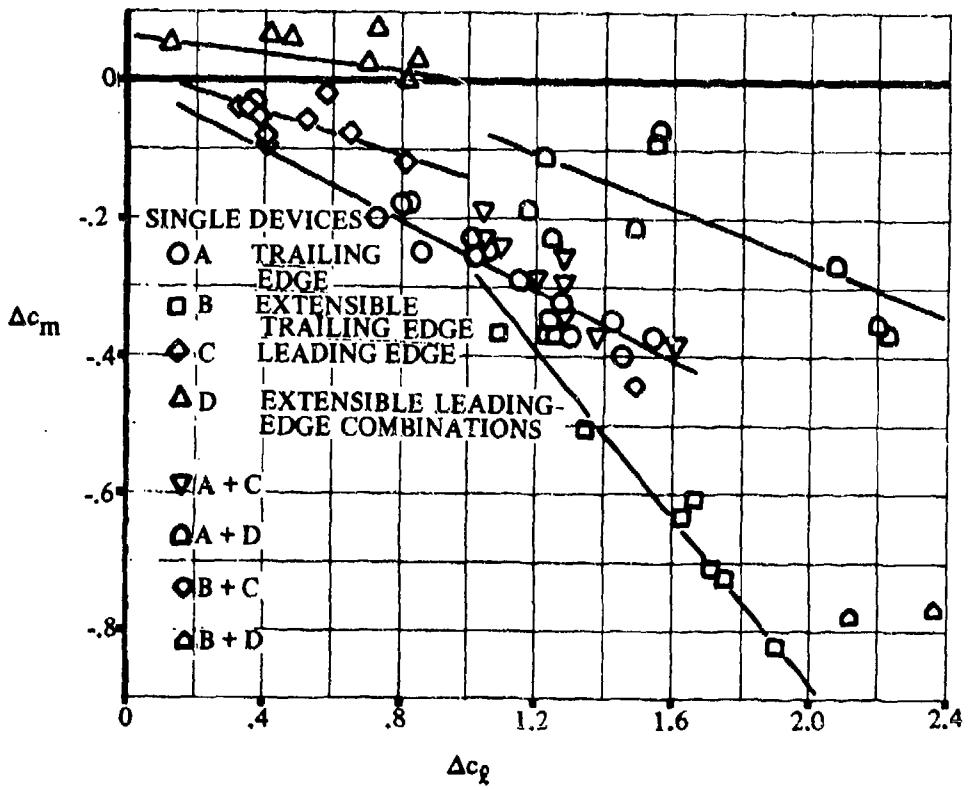

FIGURE 6.1.2.3-3 SECTION PITCHING-MOMENT INCREMENTS OF VARIOUS TYPES OF HIGH-LIFT DEVICES

6.1.3 SECTION HINGE MOMENT OF HIGH-LIFT AND CONTROL DEVICES

Hinge moments are affected by many factors, such as balance ratio, balance shape, basic airfoil characteristics, trailing-edge angle, trailing-edge bluntness, gap size and geometry, tab controls and trimmers, etc. Hinge moments are also nonlinear with angle of attack and flap deflection, particularly at moderate to large angles. The hinge moments of trailing-edge controls are sensitive to boundary-layer conditions and hence to Reynolds-number effects. All of the above items cause the prediction of hinge moments to be very difficult. Test data on the particular configuration under consideration or one closely resembling it should always be preferred to characteristics obtained from generalized methods. (Summaries of early hinge-moment test data used in determining the effects of various factors on hinge moments can be found in References 1 and 2.)

The methods presented in subsequent sections are limited to the range of flap deflections and angles of attack for which the hinge moments are linear, i.e., those conditions for which the flow is attached over the control surface. The angles of attack and flap deflections at which the flow separates over a plain, sealed control are interrelated and depend upon the flap-chord-to-wing-chord ratio. Approximate boundaries for linear control effectiveness are presented in Figure 6.1.3-2. This chart, taken from Reference 3, is based on test data on an NACA 0009 airfoil.

The sign convention for hinge moments is that a positive hinge moment tends to rotate the control-surface trailing edge down, i.e., a positive control deflection.

REFERENCES

1. Sears, R. I.: Wind-Tunnel Data on the Aerodynamic Characteristics of Airplane Control Surfaces. NACA WR L-663, 1943. (U)

2. Axelson, J. A.: A Summary and Analysis of Wind Tunnel Data on the Lift and Hinge-Moment Characteristics of Control Surfaces up to a Mach Number of 0.90. NACA RM A7L02, 1948. (U)

3. Ames, M. B., Jr., and Sears, R. I.: Determination of Control-Surface Characteristics from NACA Plain-Flap and Tab Data. NACA TR 721, 1941. (U)

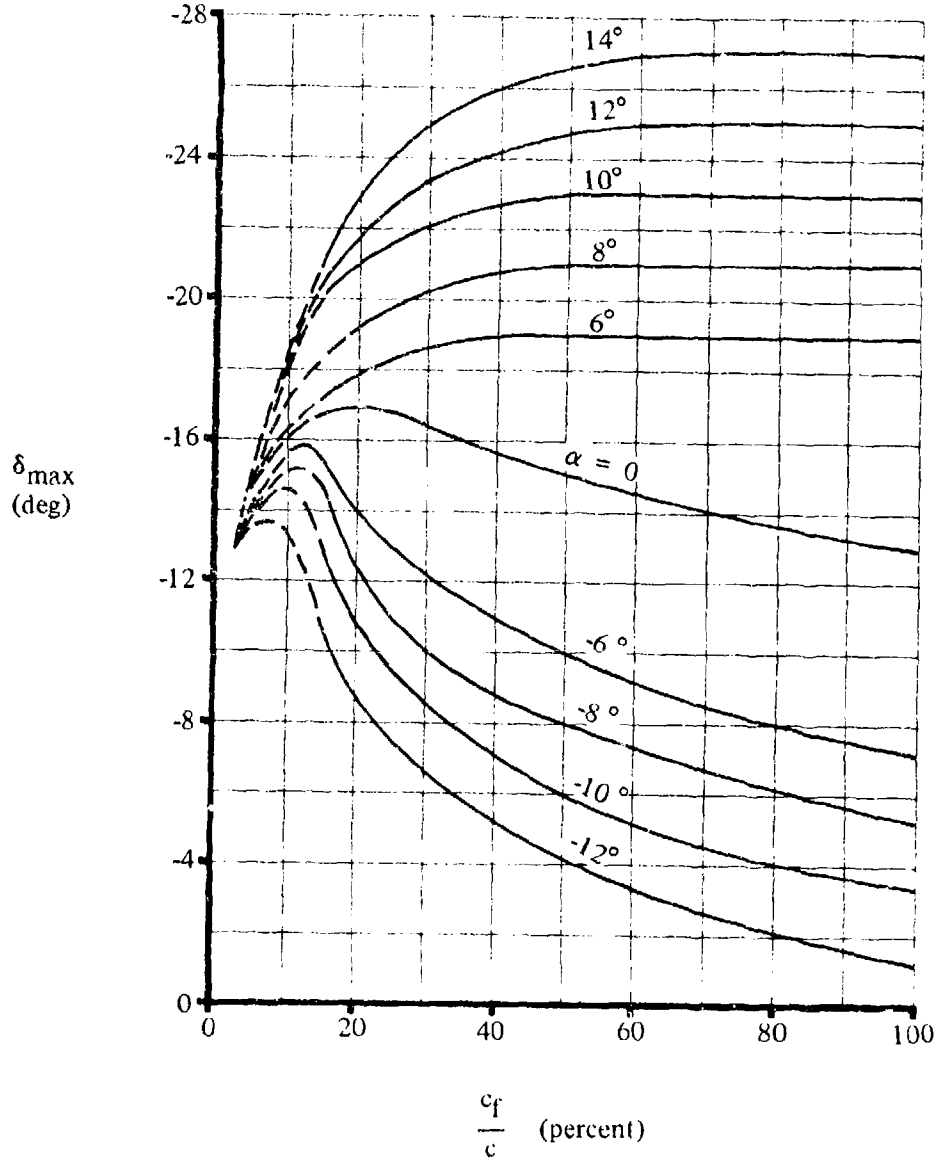

FIGURE 6.1.3-2 APPROXIMATE MAXIMUM CONTROL-SURFACE DEFLECTIONS FOR LINEAR CONTROL CHARACTERISTICS OF A PLAIN, SEALED FLAP (NACA 0009 AIRFOIL)

6.1.3.1 SECTION HINGE-MOMENT DERIVATIVE c_{h_α} OF HIGH-LIFT AND CONTROL DEVICES

For the angle-of-attack range where the flow is attached over the control surface, the variation of hinge moment with angle of attack is linear. At some angle of attack, depending upon the control deflection and airfoil and control geometry, the flow separates from the flap surface. The rate of change of hinge moment with flap deflection increases beyond this point at an increased rate. This increase can be attributed to the increased loading at the trailing edge on the leeward side that accompanies separation, i.e., the aft movement of the center-of-pressure location. The approximate angle of attack at which the flow separates from the surface of a plain, sealed flap on an NACA 0009 airfoil is shown as a function of flap deflection angle and flap-chord-to-control-chord ratio in Figure 6.1.3-2.

Those additional parameters that restrict the linear range are large trailing-edge angles, large nose-balance ratios, blunt (control) nose shapes, and relatively large airfoil thickness ratios. The linear hinge-moment range is generally smaller than the corresponding linear lift-increment range due to control deflection.

Seal and Gap Effects

Unsealing the gap between the nose of the control surface and the basic airfoil affects the hinge-moment derivative of both plain and balanced controls. For most cases, the hinge-moment derivative c_{h_α} becomes more positive when the gap is unsealed. Experimental data indicate that this effect tends to be larger for balanced controls. The method presented herein does not quantitatively account for the effect of unsealing the gap. In effect, seals or gaps produce a change in the pressure distribution along the control surface. Therefore, many factors must be considered when analyzing the effects of gaps or seals, i.e., type and/or location of seal, nose shape, balancing, and the particular pressure distribution of the airfoil. Sketch (a) illustrates the pressure distributions for a

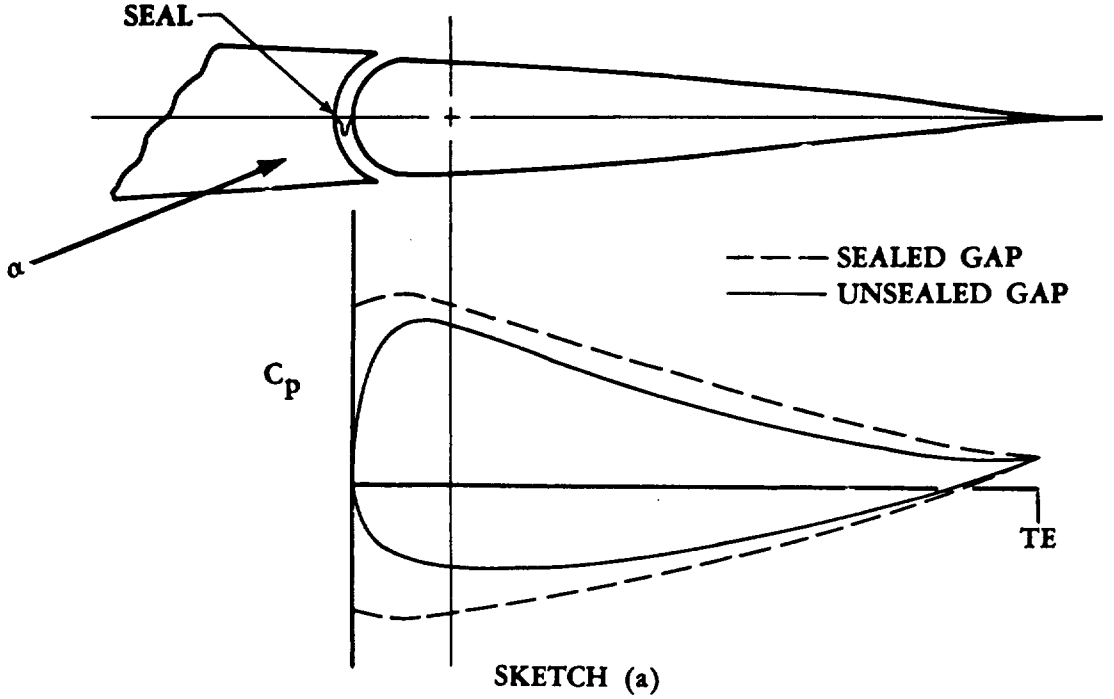

SKETCH (a)

sealed and unsealed gap on a particular control. (This pressure distribution should not be construed as being true for all configurations.) In viewing the change in the pressure distribution, the effect of the hinge-line location (balanced control) becomes evident when determining the effect of the seal or gap on the hinge-moment derivative.

In view of the difficulty of predicting the effects of seals and gaps, experimental data should be used whenever possible. Figures 6.1.3.1-9 and -10 (from Reference 1) show the effects of fixing transition and sealing the tab gap on a modified NACA 65_1-012 airfoil. For these data, the flap-chord-to-wing-chord ratio is 0.25, the tab-chord-to-flap-chord ratio is 0.25, and the flap gap is sealed.

DATCOM METHOD

A. SUBSONIC

The method presented for estimating the hinge moment of trailing-edge controls due to angle of attack at low speeds is taken from Reference 2. It is based on the theories and data of References 3, 4, and 5, and applies to sealed controls (at the nose) in the linear hinge-moment range only. It is not valid for horn-balanced controls. The hinge-moment derivative c_{h_α} is based on the control chord squared c_f^2 (where the control chord c_f is measured from the hinge line aft to the trailing edge).

The method is broken down into a logical sequence of calculations that account for various factors in the following order:

1. Radius-nose, sealed, plain trailing-edge control for which the thickness condition

$$\tan\frac{\phi'_{TE}}{2} = \tan\frac{\phi''_{TE}}{2} = \tan\frac{\phi_{TE}}{2} = \frac{t}{c}$$

   is satisfied.

2. Thickness distribution when

$$\tan\frac{\phi'_{TE}}{2} = \tan\frac{\phi''_{TE}}{2} = \tan\frac{\phi_{TE}}{2} = \frac{t}{c}$$

   is not satisfied.

3. Various control nose shapes and the effect of nose balance.

4. Effects of Mach number.

The semiempirical method for determining the section hinge-moment derivative c_{h_α} is as follows:

Step 1. Calculate the hinge-moment derivative c'_{h_α} for a radius-nose, sealed, trailing-edge flap for the following thickness condition:

$$\tan\frac{\phi'_{TE}}{2} = \tan\frac{\phi''_{TE}}{2} = \tan\frac{\phi_{TE}}{2} = \frac{t}{c}$$

by

$$c'_{h_\alpha} = \left[\frac{c'_{h_\alpha}}{(c_{h_\alpha})_{theory}}\right](c_{h_\alpha})_{theory} \quad \text{(per radian)} \qquad 6.1.3.1\text{-a}$$

where

ϕ'_{TE} is the trailing-edge angle defined as the angle between straight lines passing through points at 90 and 99 percent of the chord on the upper and lower airfoil surfaces.

ϕ''_{TE} is the trailing-edge angle defined as the angle between straight lines passing through points at 95 and 99 percent of the chord on the upper and lower airfoil surfaces.

ϕ_{TE} is the trailing-edge angle defined as the angle between tangents to the upper and lower airfoil surfaces at the trailing edge.

$\dfrac{c'_{h_\alpha}}{(c_{h_\alpha})_{theory}}$ is the ratio of the actual to the theoretical hinge-moment derivative for a radius-nose, sealed-gap, plain trailing-edge flap, obtained from Figure 6.1.3.1-11a.

$(c_{h_\alpha})_{theory}$ is the theoretical hinge-moment derivative for airfoils having $\tan\frac{\phi'_{TE}}{2} = \tan\frac{\phi''_{TE}}{2} = \tan\frac{\phi_{TE}}{2} = \frac{t}{c}$.
This parameter is obtained from Figure 6.1.3.1-11b.

The parameter $c_{\ell_\alpha}/(c_{\ell_\alpha})_{theory}$ used in reading this chart is obtained from Figure 4.1.1.2-8a.

Step 2. If the thickness condition in Step 1 is satisfied, Step 2 may be omitted. However, if the thickness condition in Step 1 is not satisfied, correct the hinge-moment derivative c'_{h_α} of Step 1 to account for the particular thickness distribution by

$$c''_{h_\alpha} = c'_{h_\alpha} + 2(c_{\ell_\alpha})_{theory}\left[1 - \frac{c_{\ell_\alpha}}{(c_{\ell_\alpha})_{theory}}\right]\left(\tan\frac{\phi''_{TE}}{2} - \frac{t}{c}\right) \quad \text{(per radian)}$$

6.1.3.1-b

where

c'_{h_α} is obtained from Equation 6.1.3.1-a in Step 1.

$(c_{\ell_\alpha})_{theory}$ is the theoretical section lift-curve slope obtained from Figure 4.1.1.2-8b as a function of airfoil thickness ratio.

The parameters $c_{\ell_\alpha}/(c_{\ell_\alpha})_{theory}$ and $\frac{\phi''_{TE}}{2}$ are obtained as noted above in Step 1.

For a beveled trailing edge, ϕ''_{TE} should be taken as equal to the angle of the bevel.

It is stated in Reference 2 that under the restriction that there is no separated flow, c_{h_α} for a radius-nose control can be determined by using the above equations with an accuracy of ±0.05 per radian.

Step 3. Correct the hinge-moment derivative to account for nose-shape and nose-balance effects by using the following equation (taken from Reference 5):

$$(c_{h_\alpha})_{balance} = c''_{h_\alpha}\left[\frac{(c_{h_\alpha})_{balance}}{c''_{h_\alpha}}\right] \quad \text{(per radian)} \qquad 6.1.3.1\text{-c}$$

where

c''_{h_α} is obtained from Step 2, or is equal to c'_{h_α} from Step 1 if the thickness correction is not required.

$\frac{(c_{h_\alpha})_{balance}}{c''_{h_\alpha}}$ is obtained from Figure 6.1.3.1-12a for noses of various shapes. The nose shapes corresponding to the curves in Figure 6.1.3.1-12a are shown in Figure 6.1.3.1-12b. The balance ratio used in Figure 6.1.3.1-12a is defined by

$$\text{Balance ratio} = \sqrt{\left(\frac{c_b}{c_f}\right)^2 - \left(\frac{t_c}{2c_f}\right)^2} \qquad 6.1.3.1\text{-d}$$

where

c_b is the chord of the balance.

c_f is the chord of the control aft of the hinge line.

t_c is the thickness of the control at the hinge line.

Figure 6.1.3.1-12a is taken from Reference 6 and is based on a limited amount of experimental data on sealed controls. Small changes in nose shape, trailing-edge contour, and air flow may have significant effects on the hinge-moment derivative of balanced control surfaces.

Step 4. Mach-number effects should be approximated by the use of test data whenever possible. However, when no test data are available, the Mach-number effects may be roughly approximated by using the Prandtl-Glauert correction; i.e.,

$$(c_{h_\alpha})_M = \frac{(c_{h_\alpha})_{\text{low speed}}}{\sqrt{1 - M^2}}$$

Sample Problem

Given: The flapped airfoil of Reference 7.

NACA 0015 airfoil Plain trailing-edge flap $c_f/c = 0.30$

Round-nose control $c_b/c_f = 0.35$ $t_c/(2c_f) = 0.1527$

Sealed gap $\tan\frac{\phi'_{TE}}{2} = 0.164$ $\tan\frac{\phi''_{TE}}{2} = 0.169$ $\tan\frac{\phi_{TE}}{2} = 0.169$

Low speed $R_\ell = 2.76 \times 10^6$

Compute:

Determine the hinge-moment derivative for a radius-nose, sealed, trailing-edge flap

$(c_{h_\alpha})_{\text{theory}} = -0.507$ per rad (Figure 6.1.3.1-11b)

$\frac{c_{\ell_\alpha}}{(c_{\ell_\alpha})_{\text{theory}}} = 0.760$ (Figure 4.1.1.2-8a)

$\frac{c'_{h_\alpha}}{(c_{h_\alpha})_{\text{theory}}} = 0.320$ (Figure 6.1.3.1-11a)

$$c'_{h_\alpha} = \left[\frac{c'_{h_\alpha}}{(c_{h_\alpha})_{\text{theory}}}\right](c_{h_\alpha})_{\text{theory}} \quad \text{(Equation 6.1.3.1-a)}$$

$= (0.320)(-0.507)$

$= -0.162$ per rad

Determine if the thickness condition is satisfied; i.e.,

$$\tan\frac{\phi'_{TE}}{2} = \tan\frac{\phi''_{TE}}{2} = \tan\frac{\phi_{TE}}{2} = \frac{t}{c}$$

$$0.164 \neq 0.169 = 0.169 \neq 0.15$$

Determine the hinge-moment derivative accounting for the thickness distribution

$$(c_{\ell_\alpha})_{theory} = 7.04 \text{ per rad} \quad \text{(Figure 4.1.1.2-8b)}$$

$$c''_{h_\alpha} = c'_{h_\alpha} + 2(c_{\ell_\alpha})_{theory}\left[1 - \frac{c_{\ell_\alpha}}{(c_{\ell_\alpha})_{theory}}\right]\left(\tan\frac{\phi''_{TE}}{2} - \frac{t}{c}\right) \quad \text{(Equation 6.1.3.1-b)}$$

$$= -0.162 + 2(7.04)[1 - 0.760](0.169 - 0.150)$$

$$= -0.0978 \text{ per rad}$$

Determine the effect of nose shape and nose balance

$$\text{Balance ratio} = \sqrt{\left(\frac{c_b}{c_f}\right)^2 - \left(\frac{t_c}{2c_f}\right)^2} \quad \text{(Equation 6.1.3.1-d)}$$

$$= \sqrt{(0.35)^2 - (0.1527)^2}$$

$$= 0.315$$

$$\frac{(c_{h_\alpha})_{balance}}{c''_{h_\alpha}} = 0.50 \quad \text{(Figure 6.1.3.1-12a)}$$

$$(c_{h_\alpha})_{balance} = c''_{h_\alpha}\left[\frac{(c_{h_\alpha})_{balance}}{c''_{h_\alpha}}\right] \quad \text{(Equation 6.1.3.1-c)}$$

$$= (-0.0978)(0.50)$$

$$= -0.0489 \text{ per rad}$$

$$= -0.000853 \text{ per deg}$$

This compares with a test value of −0.00145 per degree from Reference 7.

B. TRANSONIC

No method is available for predicting the section hinge-moment derivative c_{h_α} at transonic speeds.

C. SUPERSONIC

The method for determining c_{h_α} at supersonic speeds is based on the theory of Reference 8. The theory applies to airfoils with sharp leading and trailing edges, where the angles of attack and flap-deflection angles are small. In addition, the flow field is assumed to be everywhere supersonic and inviscid.

DATCOM METHOD

The hinge-moment derivative c_{h_α} at supersonic speeds for a symmetric, straight-sided flap with $c_f/c < 1/2$, regardless of the airfoil section ahead of the flap, is given by

$$c_{h_\alpha} = -C_1 + C_2 \phi_{TE} \qquad 6.1.3.1\text{-e}$$

where C_1 and C_2 are thickness correction factors to the supersonic flat-plate derivative.

$$C_1 = \frac{2}{\sqrt{M^2 - 1}} \text{ per radian}$$

$$C_2 = \frac{(\gamma + 1)M^4 - 4(M^2 - 1)}{2(M^2 - 1)^2} \text{ per radian}$$

ϕ_{TE} is the trailing-edge angle in radians.

γ is the ratio of specific heats, $\gamma = 1.4$.

For a symmetric, circular-arc airfoil with $c_f/c < 1/2$, c_{h_α} is given by

$$c_{h_\alpha} = -C_1 + \left(\frac{\Delta c_{h_\alpha}}{t/c}\right)\frac{t}{c} \qquad 6.1.3.1\text{-f}$$

where C_1 is defined above, and

$\frac{\Delta c_{h_\alpha}}{t/c}$ is a thickness correction factor for symmetric, circular-arc airfoils obtained from Figure 6.1.3.1-13.

The method becomes somewhat complicated for more general airfoil shapes. Other airfoil shapes are treated in Reference 8.

Sample Problem

Given: Symmetric, circular-arc airfoil.

$t/c = 0.06$ $\qquad c_f/c = 0.30$ $\qquad M = 2.0$

Compute:

$$C_1 = \frac{2}{\sqrt{M^2 - 1}} \frac{1}{57.3} = 0.020 \text{ per deg}$$

$$\frac{\Delta c_{h_\alpha}}{t/c} = 0.0008 \text{ per deg} \quad \text{(Figure 6.1.3.1-13)}$$

Solution:

$$c_{h_\alpha} = -C_1 + \left(\frac{\Delta c_{h_\alpha}}{t/c}\right)\frac{t}{c} \quad \text{(Equation 6.1.3.1-f)}$$

$$= -0.020 + (0.0008)(0.06)$$

$$= -0.01995 \text{ per deg}$$

REFERENCES

1. Brewer, J. D., and Queijo, M. J.: Wind-Tunnel Investigation of the Effect of Tab Balance on Tab and Control-Surface Characteristics. NACA TN 1403, 1947. (U)
2. Anon.: Royal Aeronautical Society Data Sheets – Aerodynamics, Vol. IV, (Controls 04.01.01), 1956. (U)
3. Anon.: Royal Aeronautical Society Data Sheets – Aerodynamics, Vol. IV, (Controls 04.01.00), 1950. (U)
4. Garner, H. C.: Charts for Low-Speed Characteristics of Two-Dimensional Trailing Edge Flaps. ARC 18,528, 1956. (U)
5. Woods, L. C.: The Theory of Aerofoils with Hinged Flaps in Two-Dimensional Compressible Flow. ARC CP 138, 1952. (U)
6. Anon.: Royal Aeronautical Society Data Sheets – Aerodynamics, Vol. IV, (Controls 04.01.03), 1949. (U)
7. Sears, R. I., and Hoggard, H. P., Jr.: Wind-Tunnel Investigation of Control-Surface Characteristics. VII – A Medium Aerodynamic Balance of Two Nose Shapes Used with a 30-Percent-Chord Flap on an NACA 0015 Airfoil. NACA WR L-448, 1942. (U)
8. Lock, C. N. H.: Examples of the Application of Busemann's Formula to Evaluate the Aerodynamic Force Coefficients on Supersonic Aerofoils. ARC R&M 2101, 1944. (U)

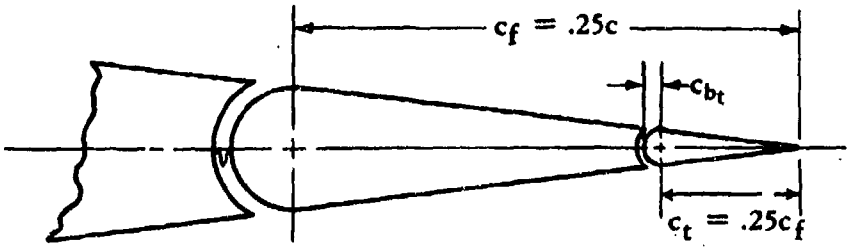

	TAB GAP	TRANSITION STRIPS
———	.004c	AT .01c
— — —	SEALED	AT .01c
——— –	.004c	OFF
——— – –	SEALED	OFF

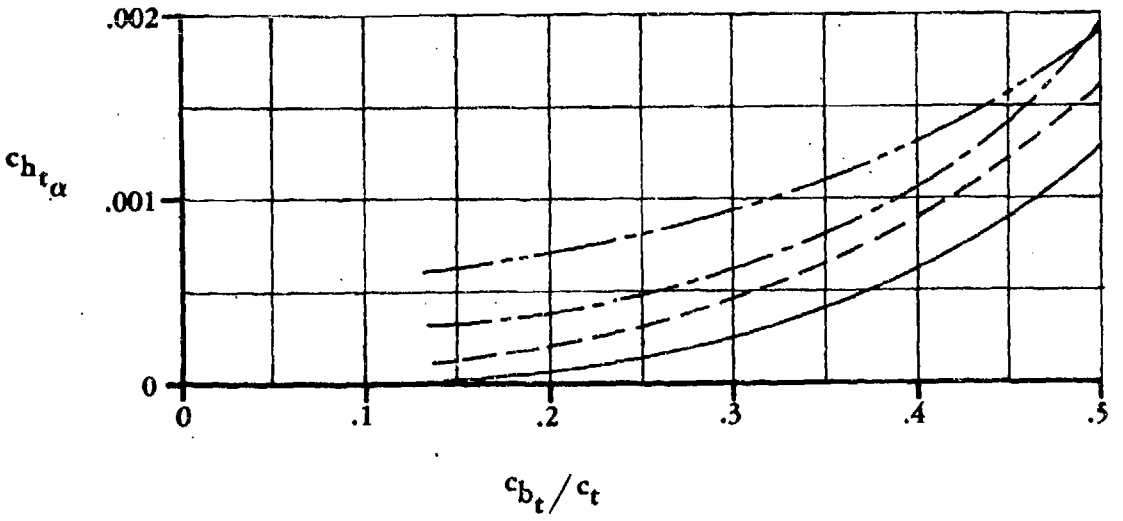

FIGURE 6.1.3.1-9 EFFECT OF SEALED AND UNSEALED TAB GAPS AND TRANSITION STRIPS ON TAB SECTION HINGE MOMENTS

SUBSONIC SPEEDS

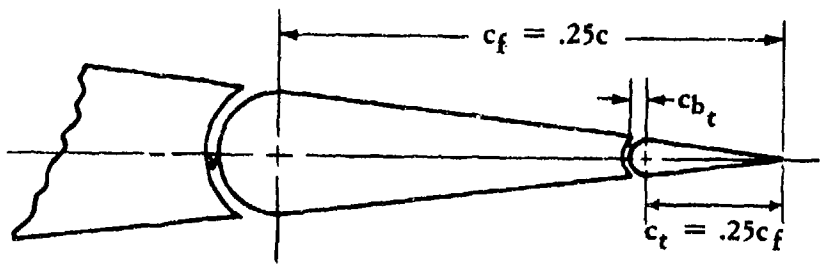

	TAB GAP	TRANSITION STRIPS
———	.004c	AT .01c
— — —	SEALED	AT .01c
——— —	.004c	OFF
——— — -	SEALED	OFF

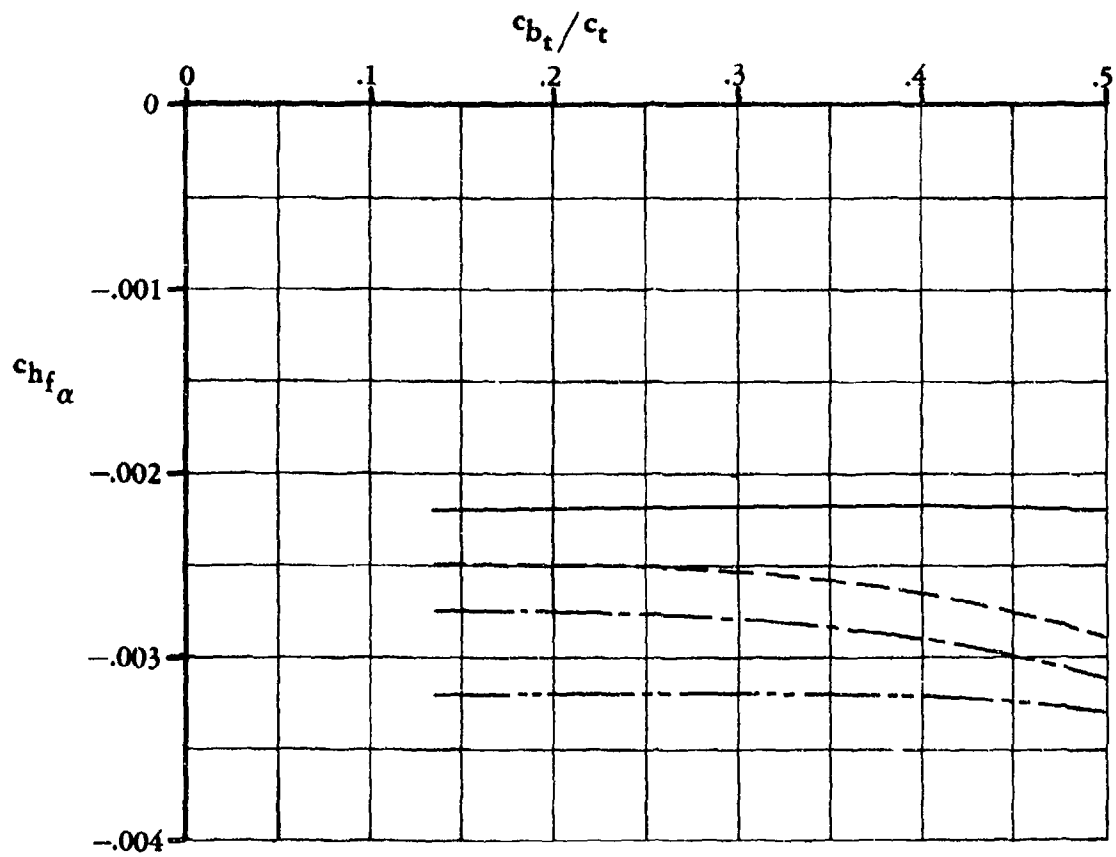

FIGURE 6.1.3.1-10 EFFECT OF SEALED AND UNSEALED TAB GAPS AND TRANSITION STRIPS ON FLAP SECTION HINGE MOMENTS

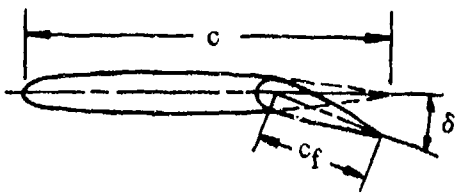

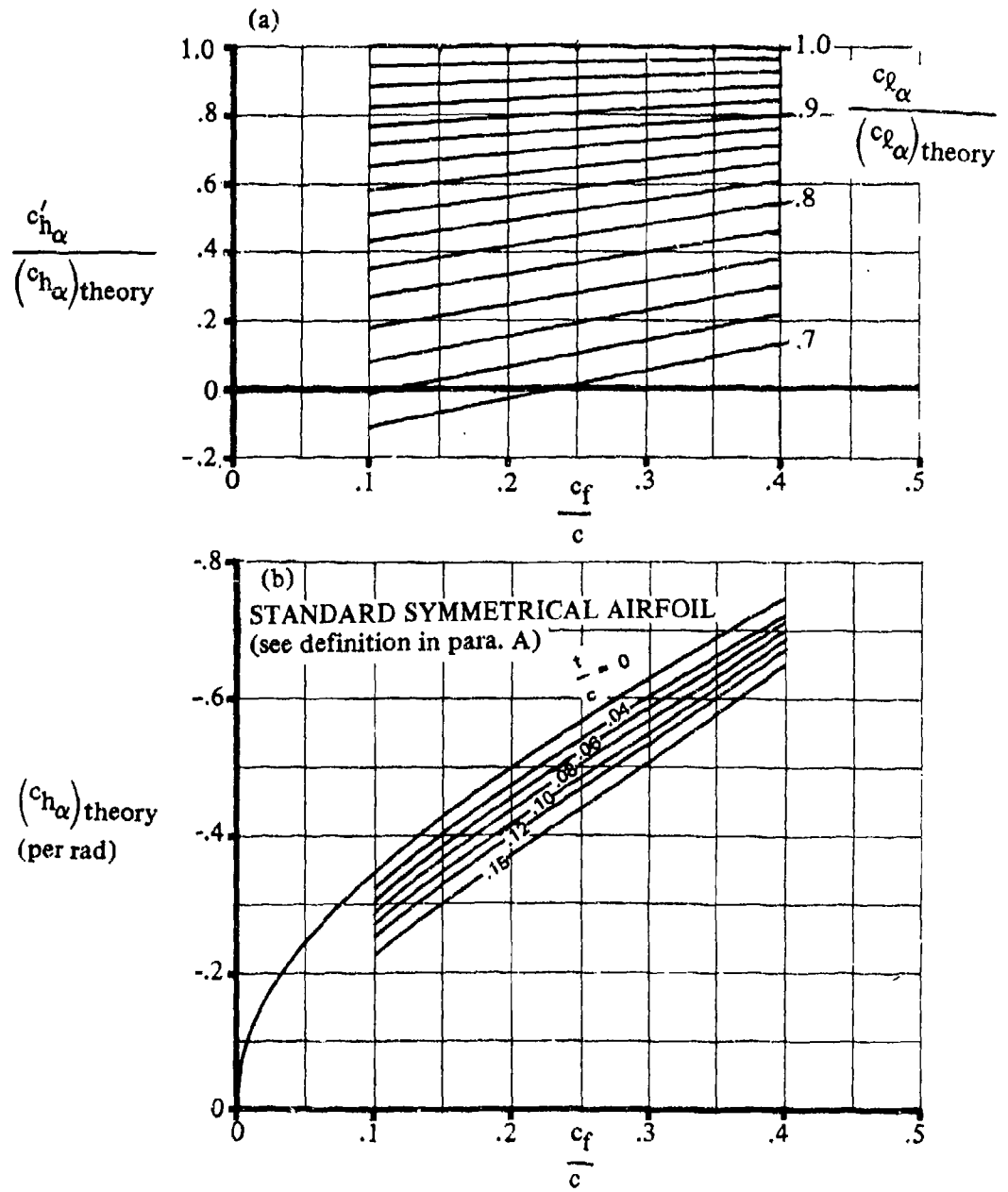

FIGURE 6.1.3.1-11 RATE OF CHANGE OF SECTION HINGE-MOMENT COEFFICIENT WITH ANGLE OF ATTACK FOR A PLAIN FLAP

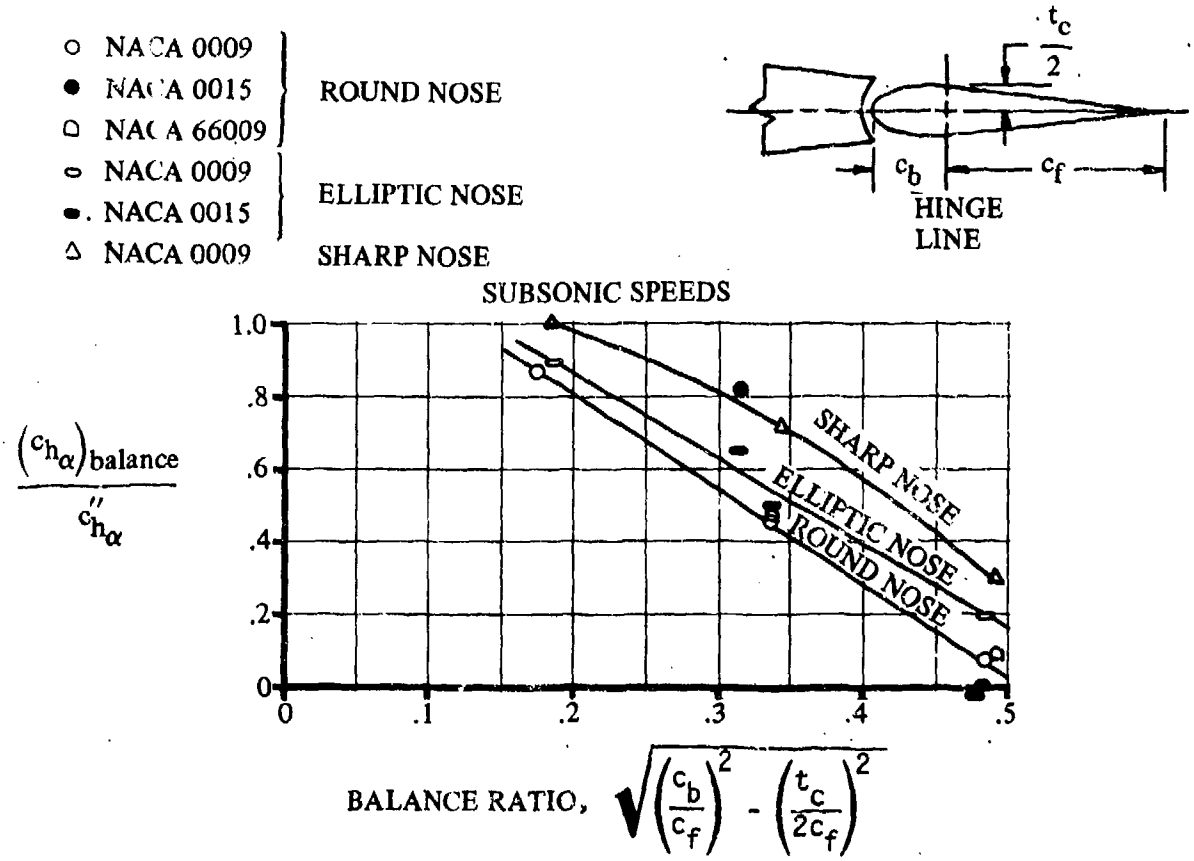

FIGURE 6.1.3.1-12a EFFECT OF NOSE BALANCE ON SECTION CONTROL HINGE-MOMENT COEFFICIENT

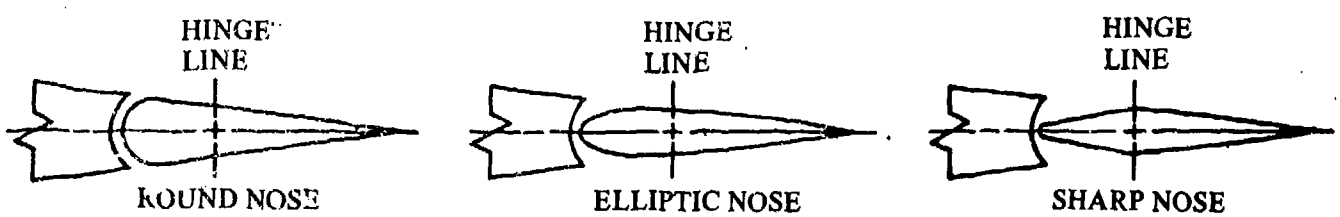

FIGURE 6.1.3.1-12b CONTROL-SURFACE SECTION NOSE SHAPES SHOWN FOR A 35% BALANCE

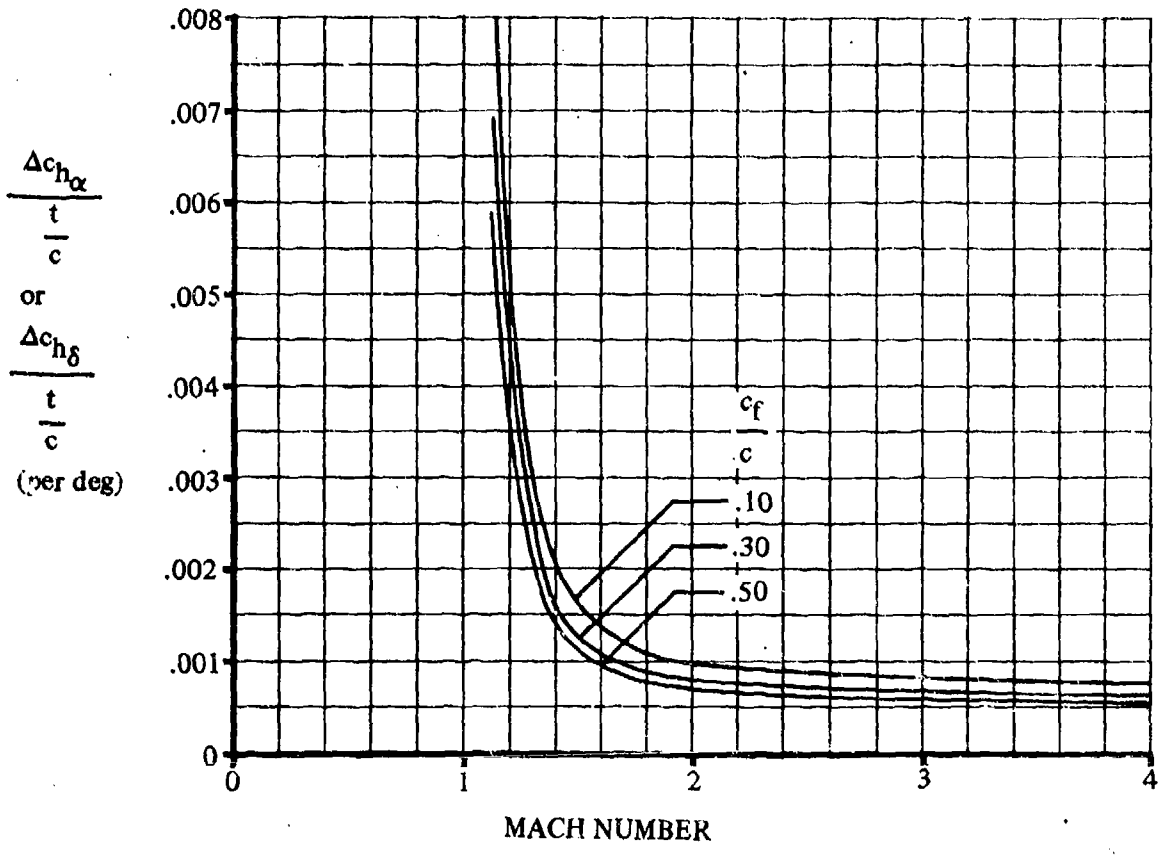

FIGURE 6.1.3.1-13 THICKNESS CORRECTION FACTOR FOR HINGE-MOMENT DERIVATIVES FOR SYMMETRIC, CIRCULAR-ARC AIRFOILS

6.1.3.2 SECTION HINGE-MOMENT DERIVATIVE c_{h_δ} OF HIGH-LIFT AND CONTROL DEVICES

For small control deflections, where the flow is attached over the control surface, the variation of hinge moment with control deflection is linear. At some deflection angle, depending upon the angle of attack and airfoil and control geometry, the flow separates from the flap surface. The rate of change of hinge moment with flap deflection increases beyond this point at an increased rate, as shown in Sketch (a). This increase can be attributed to the increased loading at the trailing edge on the leeward side that accompanies separation; i.e., the aft movement of the center-of-pressure location. The approximate deflection angle at which the flow separates from the surface of a plain, sealed flap on an NACA 0009 airfoil is shown as a function of angle of attack and flap-chord-to-control-chord ratio in Figure 6.1.3-2.

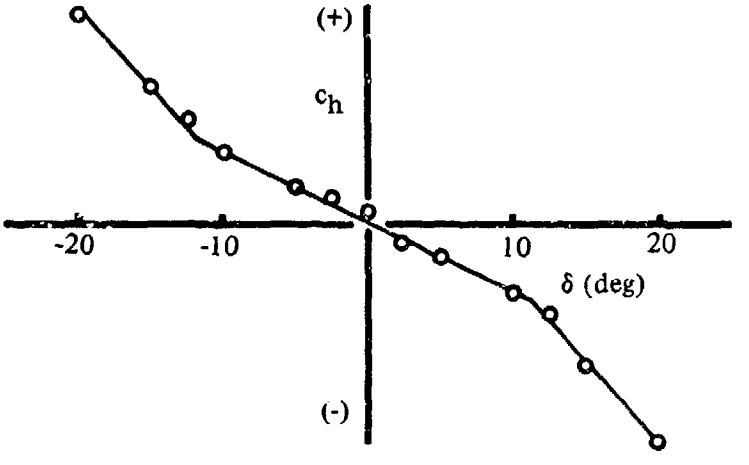

TYPICAL CURVE OF HINGE MOMENT
SKETCH (a)

The additional parameters that restrict the linear range are large trailing-edge angles, large nose-balance ratios, blunt (control) nose shapes, and relatively large airfoil thickness ratios. The effect of large nose-balance ratios is shown in Sketch (b) (from Reference 1).

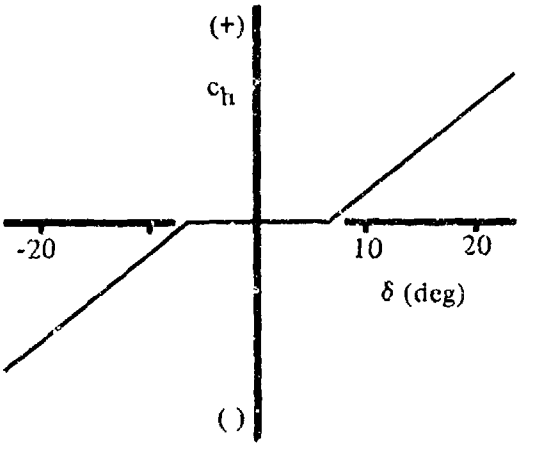

HINGE MOMENT WITH VERY
LARGE NOSE BALANCE
SKETCH (b)

The effect of beveled trailing edges is shown in Sketch (c) (from Reference 1). The linear hinge-moment range is generally smaller than the corresponding linear lift-increment range due to control deflection.

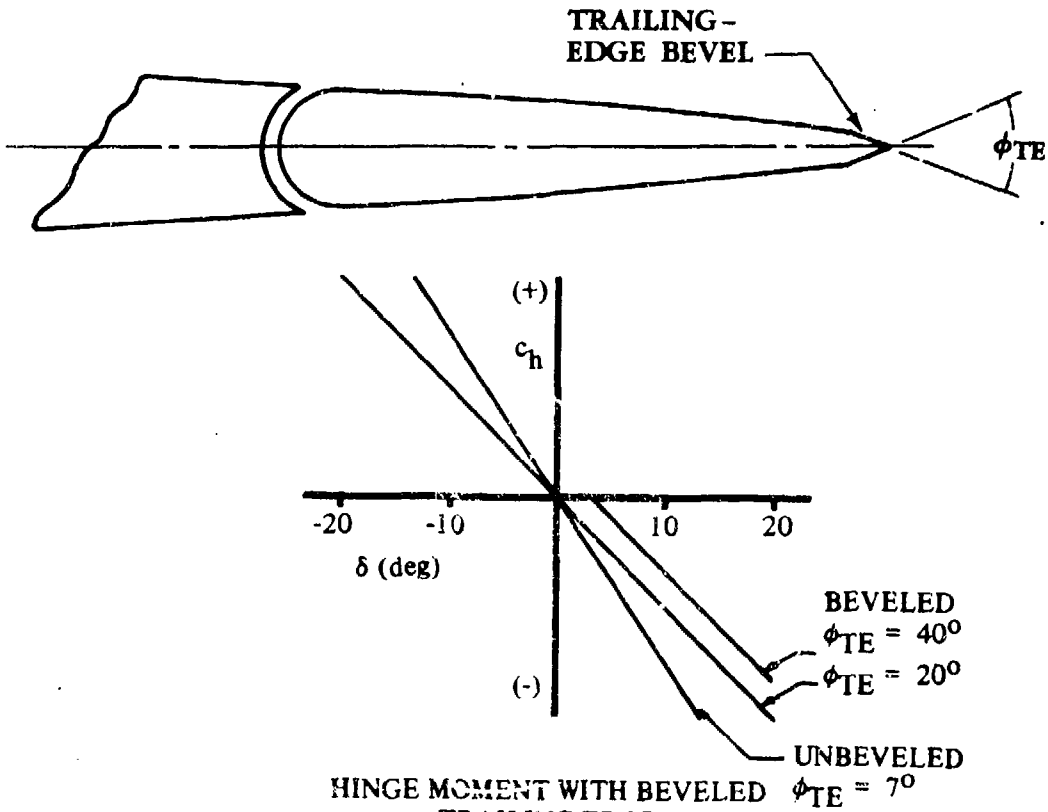

SKETCH (c)

Unsealing the gap between the nose of the control surface and the basic airfoil affects the hinge-moment derivative of both plain and balanced controls. The method presented herein does not quantitatively account for the effect of unsealing the gap (see Section 6.1.3.1 for a discussion of the salient aspects). Figures 6.1.3.2-10 and -11 (from Reference 2) illustrate the effect of fixing transition and sealing the tab gap on a modified NACA 65_1-012 airfoil. For these data, the flap-chord-to-wing-chord ratio is 0.25, the tab-chord-to-flap-chord ratio is 0.25, and the flap gap is sealed.

DATCOM METHOD

A. SUBSONIC

The method presented for estimating the hinge moment due to trailing-edge control deflection at low speeds is taken from Reference 3 and closely parallels the method presented in Section 6.1.3.1 for predicting the hinge-moment derivative c_{h_α}. This method is based on the theories and data of References 4, 5, and 6. The method applies to sealed controls (at the nose) in the linear hinge-moment range only. It is not valid for horn-balanced controls. The hinge-moment derivative c_{h_δ} is based on the control chord squared c_f^2 (where the control chord c_f is measured from the hinge line aft to the trailing edge).

The method is broken down into a logical sequence of calculations that account for various factors in the following order:

1. Radius-nose, sealed, plain trailing-edge control for which the condition

$$\tan\frac{\phi'_{TE}}{2} = \tan\frac{\phi''_{TE}}{2} = \tan\frac{\phi_{TE}}{2} = \frac{t}{c}$$

is satisfied.

2. Thickness distribution when

$$\tan\frac{\phi'_{TE}}{2} = \tan\frac{\phi''_{TE}}{2} = \tan\frac{\phi_{TE}}{2} = \frac{t}{c}$$

is not satisfied.

3. Various control nose shapes and the effect of nose balance.

4. Effects of Mach number.

The semiempirical method for determining the section hinge-moment derivative c_{h_δ} is as follows:

Step 1. Calculate the hinge-moment derivative c'_{h_δ} for a radius-nose, sealed, trailing-edge flap for the following thickness condition

$$\tan\frac{\phi'_{TE}}{2} = \tan\frac{\phi''_{TE}}{2} = \tan\frac{\phi_{TE}}{2} = \frac{t}{c}$$

by

$$c'_{h_\delta} = \left[\frac{c'_{h_\delta}}{(c_{h_\delta})_{theory}}\right](c_{h_\delta})_{theory} \quad \text{(per radian)} \qquad 6.1.3.2\text{-a}$$

where

ϕ'_{TE} is the trailing-edge angle defined as the angle between straight lines passing through points at 90 and 99 percent of the chord on the upper and lower airfoil surfaces.

ϕ''_{TE} is the trailing-edge angle defined as the angle between straight lines passing through points at 95 and 99 percent of the chord on the upper and lower airfoil surfaces.

ϕ_{TE} is the trailing-edge angle defined as the angle between tangents to the upper and lower airfoil surfaces at the trailing edge.

$\frac{c'_{h_\delta}}{(c_{h_\delta})_{theory}}$ is the ratio of the actual to the theoretical hinge-moment derivative for a radius-nose, sealed-gap, plain trailing-edge flap, obtained from Figure 6.1.3.2-12a.

The parameter $c_{\ell_\alpha}/(c_{\ell_\alpha})_{theory}$ used in reading this chart is obtained from Figure 4.1.1.2-8a.

$(c_{h_\delta})_{theory}$ is the theoretical hinge-moment derivative for airfoils having

$$\tan\frac{\phi'_{TE}}{2} = \tan\frac{\phi''_{TE}}{2} = \tan\frac{\phi_{TE}}{2} = \frac{t}{c}$$

This parameter is obtained from Figure 6.1.3.2-12b.

Step 2. If the thickness condition in Step 1 is satisfied, Step 2 may be omitted. However, if the thickness condition in Step 1 is not satisfied, correct the hinge-moment derivative c'_{h_δ} of Step 1 to account for the particular thickness distribution by

$$c''_{h_\delta} = c'_{h_\delta} + 2(c_{\ell_\delta})_{theory}\left[1 - \frac{c_{\ell_\delta}}{(c_{\ell_\delta})_{theory}}\right]\left(\tan\frac{\phi''_{TE}}{2} - \frac{t}{c}\right) \quad \text{(per radian)}$$

6.1.3.2-b

where

c'_{h_δ} is obtained from Equation 6.1.3.2-a in Step 1.

$(c_{\ell_\delta})_{theory}$ is the theoretical lift due to flap deflection, obtained from Figure 6.1.1.1-39a.

$\frac{c_{\ell_\delta}}{(c_{\ell_\delta})_{theory}}$ is the ratio of the actual to the theoretical lift due to flap deflection, obtained from Figure 6.1.1.1-39b as a function of $c_{\ell_\alpha}/(c_{\ell_\alpha})_{theory}$ and c_f/c.

The parameters $c_{\ell_\alpha}/(c_{\ell_\alpha})_{theory}$ and $\tan\frac{\phi''_{TE}}{2}$ are obtained as noted in Step 1.

For a beveled trailing edge, ϕ''_{TE} should be taken as equal to the angle of bevel.

It is stated in Reference 3 that under the restriction that there is no separated flow, c_{h_δ} for a radius-nose control can be determined from the above equations with an accuracy of ±0.05 per radian.

Step 3. Correct the hinge-moment derivative to account for nose-shape and nose-balance effects (taken from Reference 5) by

$$(c_{h_\delta})_{balance} = c''_{h_\delta} \left[\frac{(c_{h_\delta})_{balance}}{c''_{h_\delta}} \right] \text{ (per radian)} \qquad 6.1.3.2\text{-c}$$

where

c''_{h_δ} is obtained from Equation 6.1.3.2-b, or is equal to c'_{h_δ} in Step 1, if the thickness correction is not required.

$\frac{(c_{h_\delta})_{balance}}{c''_{h_\delta}}$ is obtained from Figure 6.1.3.2-13 for noses of various shapes. The nose shapes corresponding to the curves in Figure 6.1.3.2-13 are shown in Figure 6.1.3.1-12b of Section 6,1.3.1. The balance ratio as used in Figure 6.1.3.2-13 is defined by Equation 6.1.3.1-d of Section 6.1.3.1.

Figure 6.1.3.2-13 is taken from Reference 6 and is based on a limited amount of experimental data on sealed controls. Small changes in nose shape, trailing-edge contour, and air flow may have significant effects on the hinge-moment derivative of balanced control surfaces.

Step 4. Mach-number effects should be approximated by the use of test data whenever possible. However, when no test data are available, the Mach-number effects may be roughly approximated by using the Prandtl-Glauert correction; i.e.,

$$(c_{h_\delta})_M = \frac{(c_{h_\delta})_{low\ speed}}{\sqrt{1 - M^2}} \qquad 6.1.3.2\text{-e}$$

Sample Problem

Given: The flapped airfoil of Reference 8. This is the same configuration as that of the sample problem of Paragraph A, Section 6.1.3.1.

NACA 0015 airfoil Plain trailing-edge flap $c_f/c = 0.30$

Round-nose control $c_b/c_f = 0.35$ $t_c/(2c_f) = 0.1527$

Sealed gap $\tan\frac{\phi'_{TE}}{2} = 0.164$ $\tan\frac{\phi''_{TE}}{2} = 0.169$ $\tan\frac{\phi_{TE}}{2} = 0.169$

Low speed $R_\ell = 2.76 \times 10^6$

Compute:

Determine the hinge-moment derivative for a radius-nose, sealed, trailing-edge flap

$$(c_{h_\delta})_{theory} = -0.825 \text{ per rad} \quad \text{(Figure 6.1.3.2-12b)}$$

$$\frac{c_{\ell_\alpha}}{(c_{\ell_\alpha})_{theory}} = 0.760 \quad \text{(Figure 4.1.1.2-8a)}$$

$$\frac{c'_{h_\delta}}{(c_{h_\delta})_{theory}} = 0.780 \quad \text{(Figure 6.1.3.2-12a)}$$

$$c'_{h_\delta} = \left[\frac{c'_{h_\delta}}{(c_{h_\delta})_{theory}}\right](c_{h_\delta})_{theory} \quad \text{(Equation 6.1.3.2-a)}$$

$$= (0.780)(-0.825)$$

$$= -0.644 \text{ per rad}$$

Determine if the thickness condition is satisfied; i.e.,

$$\tan\frac{\phi'_{TE}}{2} = \tan\frac{\phi''_{TE}}{2} = \tan\frac{\phi_{TE}}{2} = \frac{t}{c}$$

$$0.164 \neq 0.169 = 0.169 \neq 0.15$$

Determine the hinge-moment derivative accounting for the thickness distribution

$$(c_{\ell_\delta})_{theory} = 4.60 \text{ per rad} \quad \text{(Figure 6.1.1.1-39a)}$$

$$\frac{c_{\ell_\delta}}{(c_{\ell_\delta})_{theory}} = 0.605 \quad \text{(Figure 6.1.1.1-39b)}$$

$$c''_{h_\delta} = c'_{h_\delta} + 2(c_{\ell_\delta})_{theory}\left[1 - \frac{c_{\ell_\delta}}{(c_{\ell_\delta})_{theory}}\right]\left(\tan\frac{\phi''_{TE}}{2} - \frac{t}{c}\right) \quad \text{(Equation 6.1.3.2-b)}$$

$$= -0.644 + 2(4.60)[1 - 0.605](0.169 - 0.150)$$

$$= -0.575 \text{ per rad}$$

Determine the effect of nose shape and nose balance

$$\text{Balance ratio} = \sqrt{\left(\frac{c_b}{c_f}\right)^2 - \left(\frac{t_c}{2c_f}\right)^2} \quad \text{(Equation 6.1.3.1-d)}$$

$$= \sqrt{(0.35)^2 - (0.1527)^2}$$

$$= 0.315$$

$$\frac{(c_{h_\delta})_{\text{balance}}}{c''_{h_\delta}} = 0.42 \quad \text{(Figure 6.1.3.2-13)}$$

$$(c_{h_\delta})_{\text{balance}} = c''_{h_\delta}\left[\frac{(c_{h_\delta})_{\text{balance}}}{c''_{h_\delta}}\right] \quad \text{(Equation 6.1.3.2-c)}$$

$$= (-0.575)(0.42)$$

$$= -0.2415 \text{ per rad}$$

$$= -0.00421 \text{ per deg}$$

This compares with a test value of −0.0030 per degrec from Reference 8.

B. TRANSONIC

No method is available for predicting the section hinge-moment derivative c_{h_δ} at transonic speeds.

C. SUPERSONIC

The method for determining c_{h_δ} at supersonic speeds is based on the theory of Reference 7. The theory applies to airfoils with sharp leading and trailing edges, where the angles of attack and flap deflection angles are small. In addition, the flow field is assumed to be everywhere supersonic and inviscid.

DATCOM METHOD

The hinge-moment derivative c_{h_δ} at supersonic speeds for a symmetric, straight-sided flap with $c_f/c < 1/2$, regardless of the airfoil section ahead of the flap, is given by

$$c_{h_\delta} = -C_1 + C_2 \phi_{TE} \qquad 6.1.3.2\text{-d}$$

where C_1 and C_2 are thickness correction factors to the supersonic flat-plate derivative.

$$C_1 = \frac{2}{\sqrt{M^2 - 1}} \text{ per radian}$$

$$C_2 = \frac{(\gamma + 1)M^4 - 4(M^2 - 1)}{2(M^2 - 1)^2} \text{ per radian}$$

ϕ_{TE} is the trailing-edge angle in radians.

γ is the ratio of specific heats, $\gamma = 1.4$.

For a symmetric, circular-arc airfoil with $c_f/c < 1/2$, c_{h_δ} is given by

$$c_{h_\delta} = -C_1 + \left(\frac{\Delta c_{h_\delta}}{t/c}\right)\frac{t}{c} \qquad 6.1.3.2\text{-e}$$

where C_1 is defined above, and

$\frac{\Delta c_{h_\delta}}{t/c}$ is a thickness correction factor for symmetric, circular-arc airfoils, obtained from Figure 6.1.3.1-13.

The method becomes somewhat complicated for more general airfoil shapes. Other airfoil shapes are treated in Reference 7.

Sample Problem

Given: Symmetric, circular-arc airfoil.

$t/c = 0.06$ $\qquad$ $c_f/c = 0.30$ $\qquad$ $M = 2.0$

Compute:

$$C_1 = \frac{2}{\sqrt{M^2 - 1}}\frac{1}{57.3} = 0.020 \text{ per deg}$$

$$\frac{\Delta c_{h_\delta}}{t/c} = 0.0008 \text{ per deg} \quad \text{(Figure 6.1.3.1-13)}$$

Solution:

$$c_{h_\delta} = -C_1 + \left(\frac{\Delta c_{h_\delta}}{t/c}\right)\frac{t}{c} \quad \text{(Equation 6.1.3.2-e)}$$

$$= -0.020 + (0.0008)(0.06)$$

$$= -0.01995 \text{ per deg}$$

REFERENCES

1. Anon.: Royal Aeronautical Society Data Sheets – Aerodynamics, Vol. IV, (Controls 04.01.00), 1950. (U)

2. Brewer, J. D., and Queijo, M. J.: Wind-Tunnel Investigation of the Effect of Tab Balance on Tab and Control-Surface Characteristics. NACA TN 1403, 1947. (U)

3. Anon.: Royal Aeronautical Society Data Sheets – Aerodynamics, Vol. IV, (Controls 04.01.02), 1956. (U)

4. Garner, H. C.: Charts for Low-Speed Characteristics of Two-Dimensional Trailing Edge Flaps. ARC 18,528, 1956. (U)

5. Woods, L. C.: The Theory of Aerofoils with Hinged Flaps in Two-Dimensional Compressible Flow. ARC CP 138, 1952. (U)

6. Anon.: Royal Aeronautical Society Data Sheets – Aerodynamics, Vol. IV, (Controls 04.01.03), 1949. (U)

7. Lock, C. N. H.: Examples of the Application of Busemann's Formula to Evaluate the Aerodynamic Force Coefficients on Supersonic Aerofoils. ARC R&M 2101, 1944. (U)

8. Sears, R. I., and Hoggard, H. P., Jr.: Wind-Tunnel Investigation of Control-Surface Characteristics. VII – A Medium Aerodynamic Balance of Two Nose Shapes Used with a 30-Percent-Chord Flap on an NACA 0015 Airfoil. NACA WR L-448, 1942. (U)

SUBSONIC SPEEDS

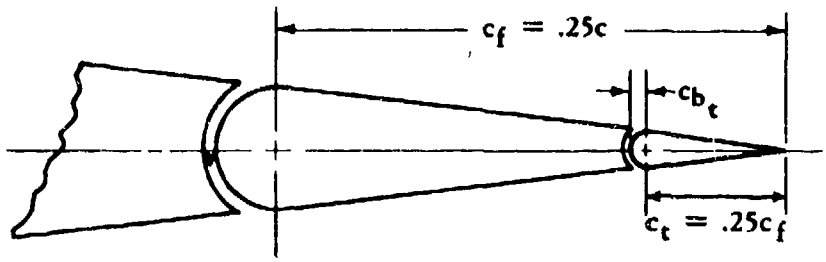

	TAB GAP	TRANSITION STRIPS
———	.004c	AT .01c
— — —	SEALED	AT .01c
——— –	.004c	OFF
——— – –	SEALED	OFF

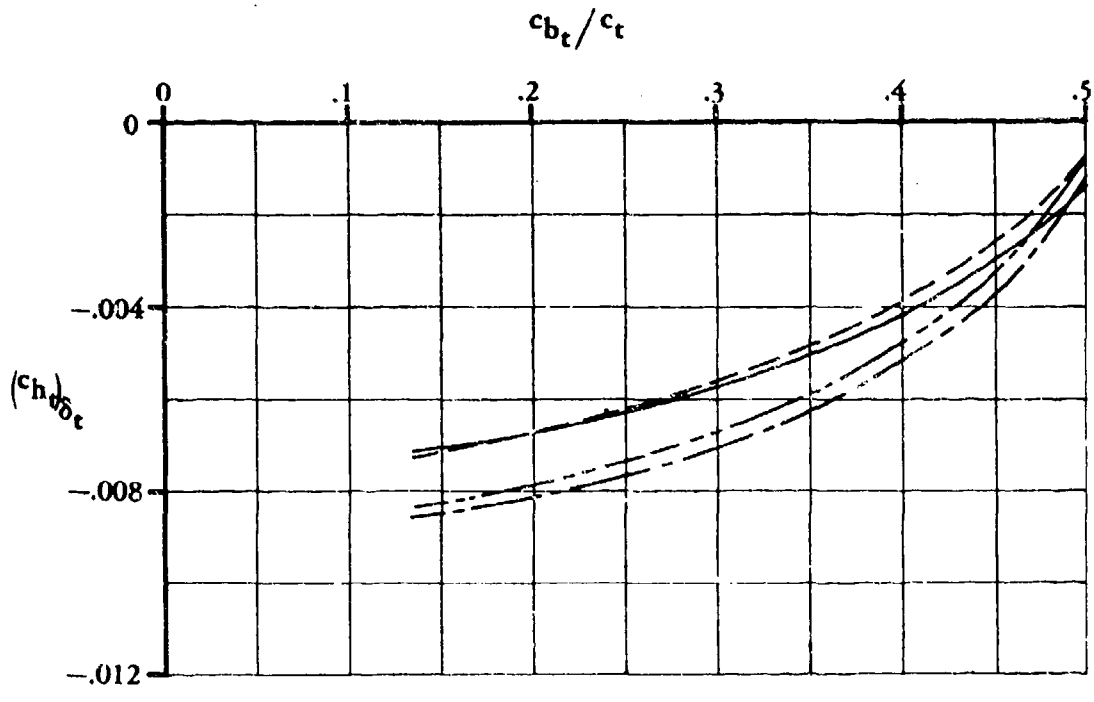

FIGURE 6.1.3.2-10 EFFECT OF SEALED AND UNSEALED TAB GAPS AND TRANSITION STRIPS ON TAB SECTION HINGE MOMENTS

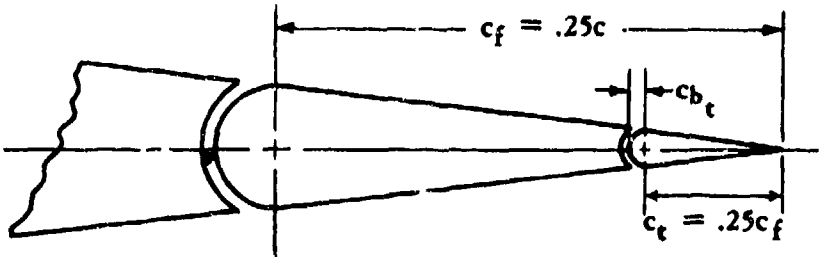

TAB GAP	TRANSITION STRIPS
——— .004c	AT .01c
— — — SEALED	AT .01c
——— - .004c	OFF
——— - - SEALED	OFF

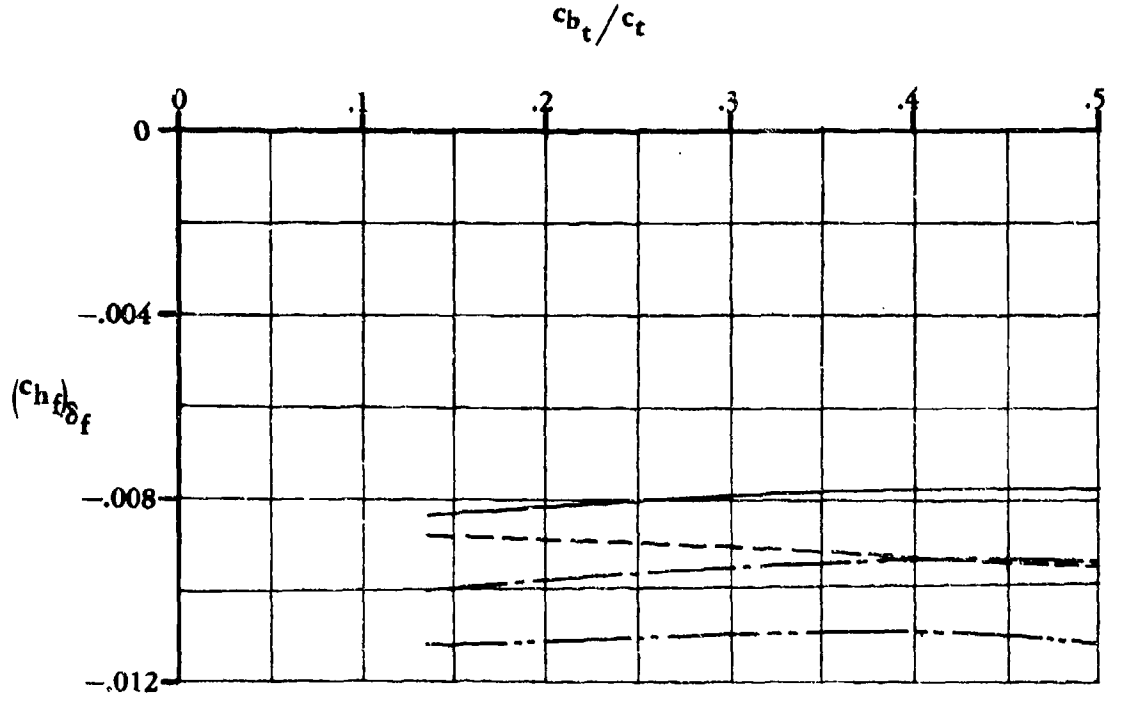

FIGURE 6.1.3.2-11 EFFECT OF SEALED AND UNSEALED TAB GAPS AND TRANSITION STRIPS ON FLAP SECTION HINGE MOMENTS

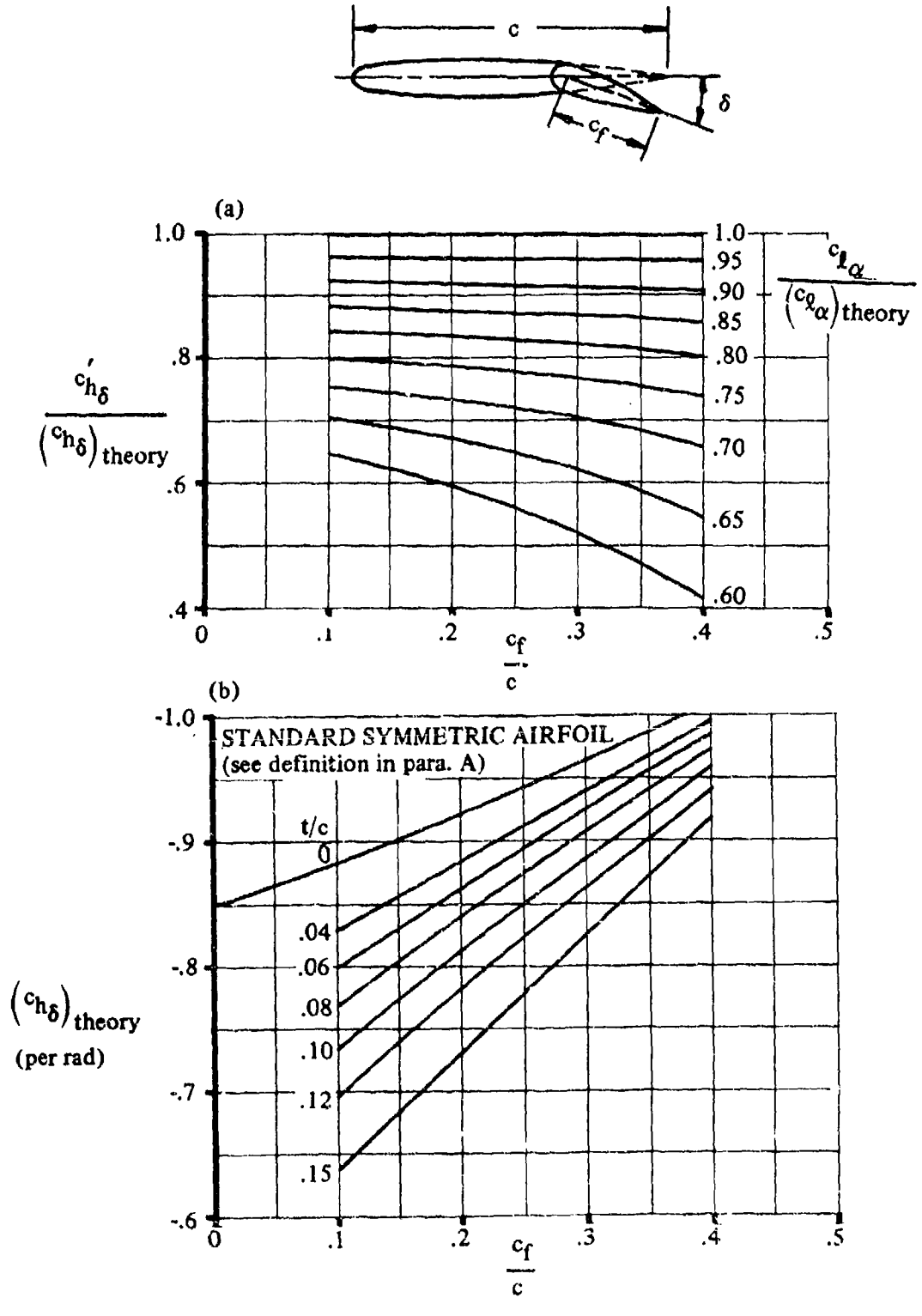

FIGURE 6.1.3.2-12 RATE OF CHANGE OF HINGE-MOMENT COEFFICIENT WITH CONTROL DEFLECTION FOR A PLAIN FLAP

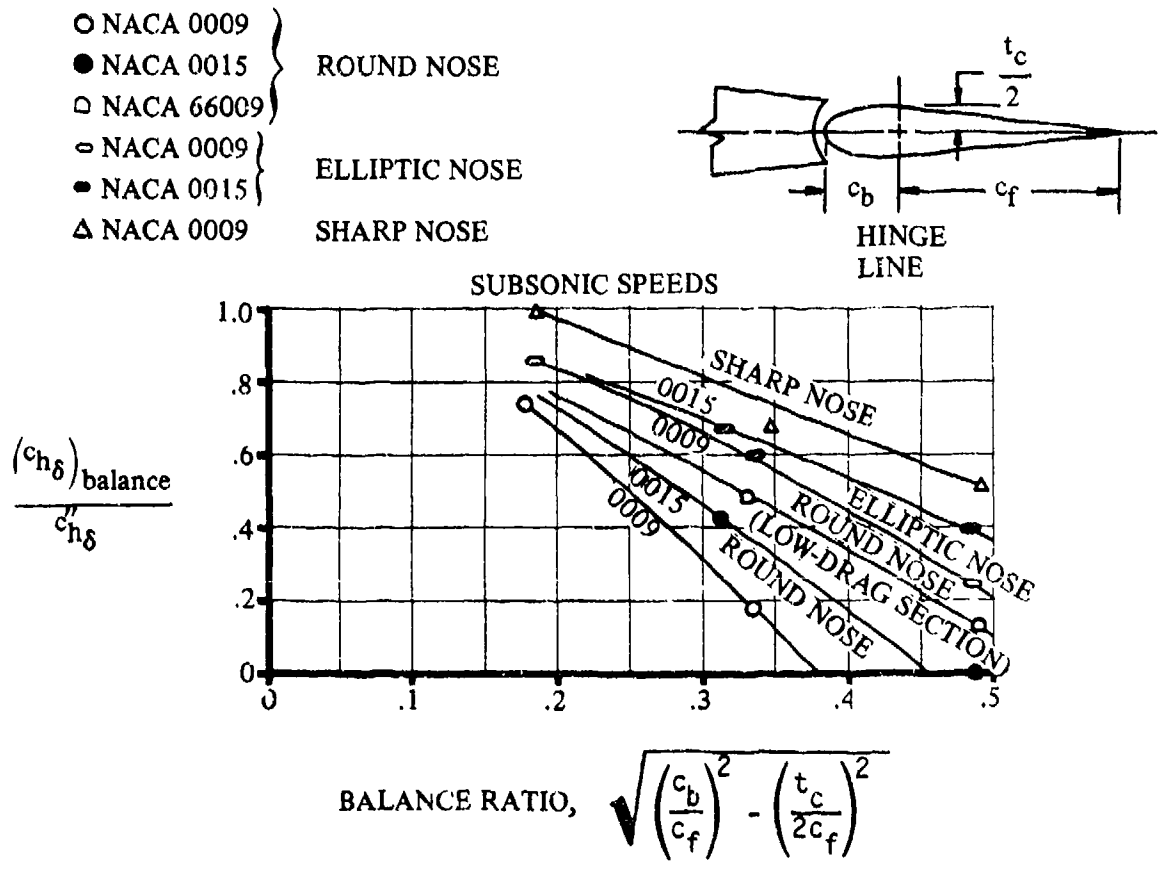

FIGURE 6.1.3.2-13 EFFECT OF NOSE BALANCE ON SECTION CONTROL HINGE-MOMENT COEFFICIENT

6.1.3.3 SECTION HINGE-MOMENT DERIVATIVE $(c_{h_f})_{\delta_t}$ OF CONTROL SURFACE DUE TO CONTROL TABS

A deflected tab on a control surface causes pressure changes on the surfaces of the tab and control. Because of the large moment arms associated with these incremental pressures, large changes in control-surface hinge moments result. In addition, these incremental changes in the pressure distribution can be influenced by a sealed or unsealed surface where the tab meets the control.

DATCOM METHOD

The following method is taken from Reference 1 and is based on the two-dimensional NACA 0009 airfoil test data for round-nose, unbalanced controls with sealed flap and tab gaps. This method is limited to the low-speed linear hinge-moment range and should be restricted to tab deflections of approximately $\pm 18^{\circ}$ and the combinations of control deflection and angle of attack as indicated in Figure 6.1.3-2.

The change in the low-speed section hinge-moment coefficient of a control due to tab deflection, measured at constant values of angle of attack and flap deflection, can be expressed as

$$\left(\frac{\partial c_{h_f}}{\partial \delta_t}\right)_{\alpha, \delta_f} = \left(\frac{\partial c_{h_f}}{\partial \delta_t}\right)_{c_\ell, \delta_f} - \left(\frac{\partial c_{h_f}}{\partial c_\ell}\right)_{\delta_t, \delta_f} \left(\frac{\partial c_\ell}{\partial \alpha}\right)_{\delta_t, \delta_f} \left(\frac{\partial \alpha}{\partial \delta_t}\right)_{c_\ell, \delta_f} \qquad 6.1.3.3\text{-a}$$

where

$\left(\frac{\partial c_{h_f}}{\partial \delta_t}\right)_{c_\ell, \delta_f}$ is the change in control section hinge-moment coefficient due to tab deflection, measured at constant values of lift and flap deflection. This value is obtained from Figure 6.1.3.3-4a.

$\left(\frac{\partial c_{h_f}}{\partial c_\ell}\right)_{\delta_t, \delta_f}$ is the change in control section hinge-moment coefficient due to lift variation, measured at constant values of tab and flap deflection. This value is obtained from Figure 6.1.3.3-4b (modified from Reference 1 to reflect the characteristics of a flat-sided flap contour -- like a conventional elevator).

$\left(\frac{\partial c_\ell}{\partial \alpha}\right)_{\delta_t, \delta_f}$ is the section lift-curve slope of the primary panel (wing, horizontal tail, etc.) at constant values of tab and flap deflection. This value can be obtained from Section 4.1.1.2.

$\left(\frac{\partial \alpha}{\partial \delta_t}\right)_{c_\ell, \delta_f}$ is the rate of change of angle of attack due to a change in tab deflection in the linear range at constant values of lift and flap deflection. This value can be obtained from Figure 6.1.3.3-5.

The above method does not quantitatively account for the effect of unsealing the tab gap. In view of the difficulty of predicting the effects of seals and gaps, experimental data should be used whenever possible. Figure 6.1.3.3-6a (from Reference 2) shows the effects of fixing transition and sealing the tab gap on a modified NACA 65_1-012 airfoil. For these data, the flap-chord-to-wing-chord ratio is 0.25, the tab-chord-to-flap-chord ratio is 0.25, and the flap gap is sealed.

The effects of tab nose shape are also not accounted for in the above method, and experimental data should be used whenever possible. However, the effect of tab nose shape as a function of nose balance is presented in Figure 6.1.3.3-6b (from Reference 2) for a NACA 65_1-012 airfoil with a tab gap of 0.004c and transition strips at 0.01c.

Other parameters not accounted for in this method include the effects of airfoil thickness and trailing-edge angle. Unfortunately, not enough data are available to evaluate the effects of either of these variables on the section hinge-moment derivative. Additional test data, including the effects of these variables on a limited number of flapped configurations, are presented in References 3 through 9.

Sample Problem

Given: The flap and tab configuration of Reference 2.

NACA 65_1-012 airfoil — Plain trailing-edge flap (sealed)

$c_f/c = 0.25$ — Round-nose flap

Plain trailing-edge tab (sealed) — $c_t/c_f = 0.25$ — Round-nose tab

Low speed — $R_\ell = 4.59 \times 10^6$

Compute:

$$\left(\frac{\partial c_{h_f}}{\partial \delta_t}\right)_{c_\ell, \delta_f} = -0.0124 \text{ per deg} \quad \text{(Figure 6.1.3.3-4a)}$$

$$\left(\frac{\partial c_{h_f}}{\partial c_\ell}\right)_{\delta_t, \delta_f} = -0.046 \quad \text{(Figure 6.1.3.3-4b)}$$

$$\left(\frac{\partial \alpha}{\partial \delta_t}\right)_{c_\ell, \delta_f} = -0.255 \quad \text{(Figure 6.1.3.3-5)}$$

$c_{\ell_\alpha} = 0.11$ per deg (Table 4.1.1-B)

Solution:

$$\left(\frac{\partial c_{h_f}}{\partial \delta_t}\right)_{\alpha,\,\delta_f} = \left(\frac{\partial c_{h_f}}{\partial \delta_t}\right)_{c_\ell,\,\delta_f} - \left(\frac{\partial c_{h_f}}{\partial c_\ell}\right)_{\delta_t,\,\delta_f} \left(\frac{\partial c_\ell}{\partial \alpha}\right)_{\delta_t,\,\delta_f} \left(\frac{\partial \alpha}{\partial \delta_t}\right)_{c_\ell,\,\delta_f}$$

(Equation 6.1.3.3-a)

$$= -0.0124 - (-0.046)(0.11)(-0.255)$$

$$= -0.0124 - 0.0013$$

$$= -0.0137 \text{ per deg}$$

This compares with test values of –0.0115 per degree with transition strips and –0.0138 per degree without transition strips, from Reference 2.

REFERENCES

1. Ames, M. B., Jr., and Sears, R. I.: Determination of Control-Surface Characteristics from NACA Plain Flap and Tab Data. NACA TR 721, 1941. (U)

2. Brewer, J. D., and Queijo, M. J.: Wind-Tunnel Investigation of the Effect of Tab Balance on Tab and Control-Surface Characteristics. NACA TN 1403, 1947. (U)

3. Batson, A. S., and Skelton, W. C.: Lift and Hinge Moment on Two-Dimensional Tabbed Controls at Low Speeds. ARC 17285, 1955. (U)

4. Sears, R. I., and Liddell, R. B.: Wind-Tunnel Investigation of Control-Surface Characteristics. VI – A 30-Percent-Chord Plain Flap on the 0015 Airfoil. NACA L-454, 1942. (U)

5. Sears, R. I., and Hoggard, H. P., Jr.: Wind-Tunnel Investigation of Control-Surface Characteristics. VII – A Medium Aerodynamic Balance of Two Nose Shapes Used with a 30-Percent-Chord Flap on an NACA 0015 Airfoil. NACA L-448, 1942. (U)

6. Sears, R. I., and Clarence, G. L.: Wind-Tunnel Investigation of Control-Surface Characteristics. VIII – A Large Aerodynamic Balance of Two Nose Shapes Used with a 30-Percent-Chord Flap on an NACA 0015 Airfoil. NACA L-378, 1942. (U)

7. Clarence, G. L., and Lockwood, V. E.: Wind-Tunnel Investigation of Control-Surface Characteristics. XIII – Various Flap Overhangs Used with a 30-Percent-Chord Flap on an NACA 66-009 Airfoil. NACA L-314, 1943. (U)

8. Wright, K. C.: Measurements of Two-Dimensional Derivatives on a Wing-Aileron-Tab System with a 1541 Section Aerofoil. Part II – Direct Tab and Cross Aileron-Tab Derivatives. ARC R&M 3029, 1958. (U)

9. Ames, M. B., Jr.: Wind-Tunnel Investigation of Control-Surface Characteristics. III – A Small Aerodynamic Balance of Various Nose Shapes Used with a 30-Percent-Chord Flap on an NACA 0009 Airfoil. NACA L-301, 1941. (U)

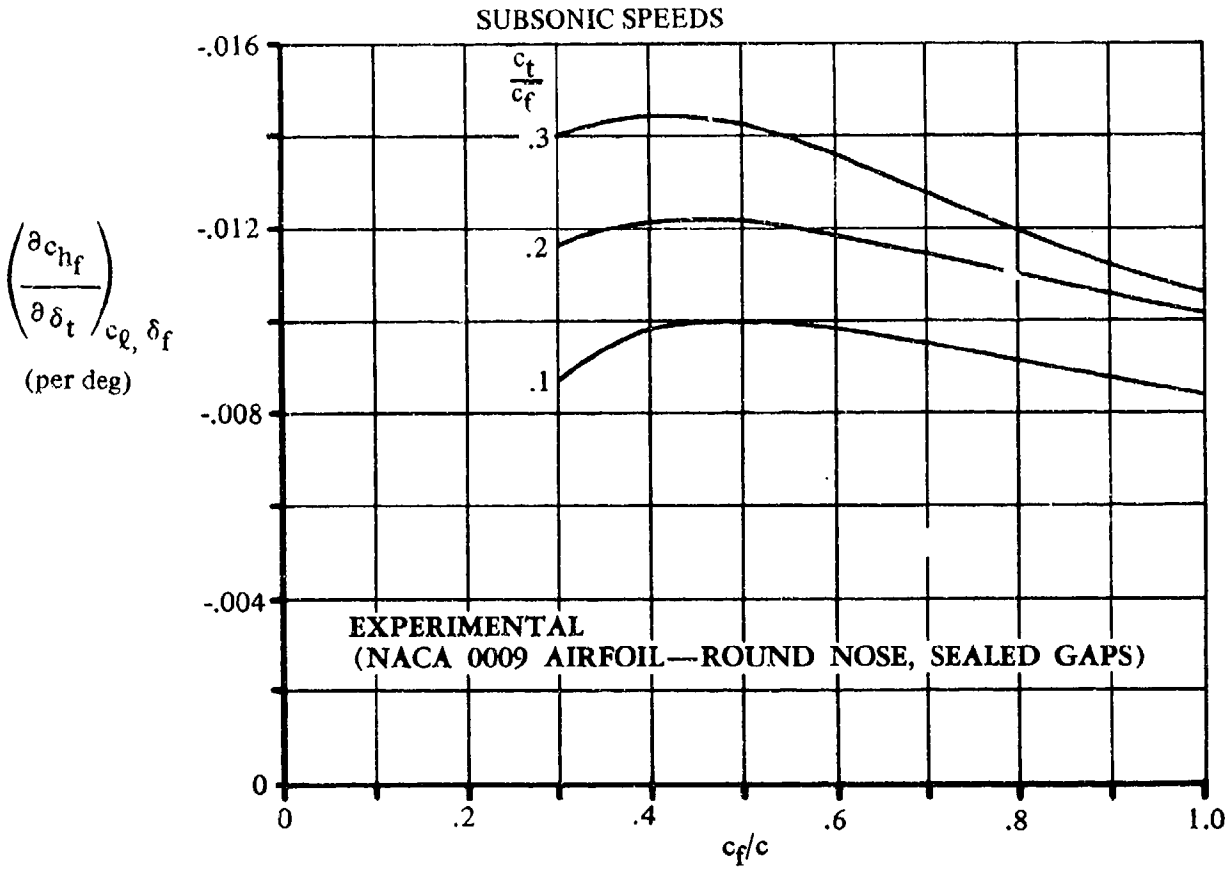

FIGURE 6.1.3.3-4a EFFECT OF TAB DEFLECTION ON CONTROL-SURFACE SECTION HINGE MOMENTS

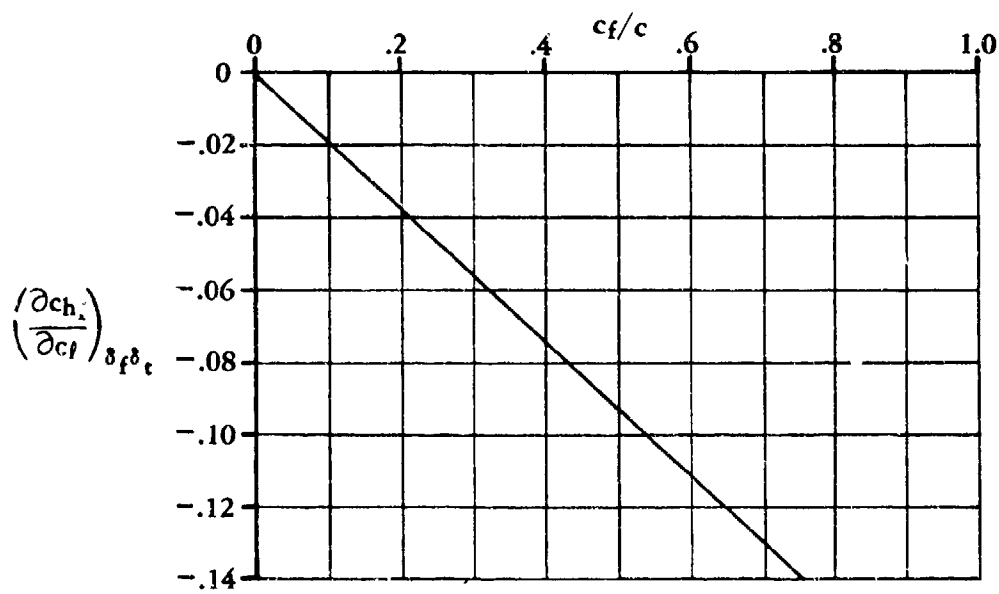

FIGURE 6.1.3.3-4b EFFECT OF SECTION LIFT COEFFICIENT ON FLAP SECTION HINGE MOMENTS

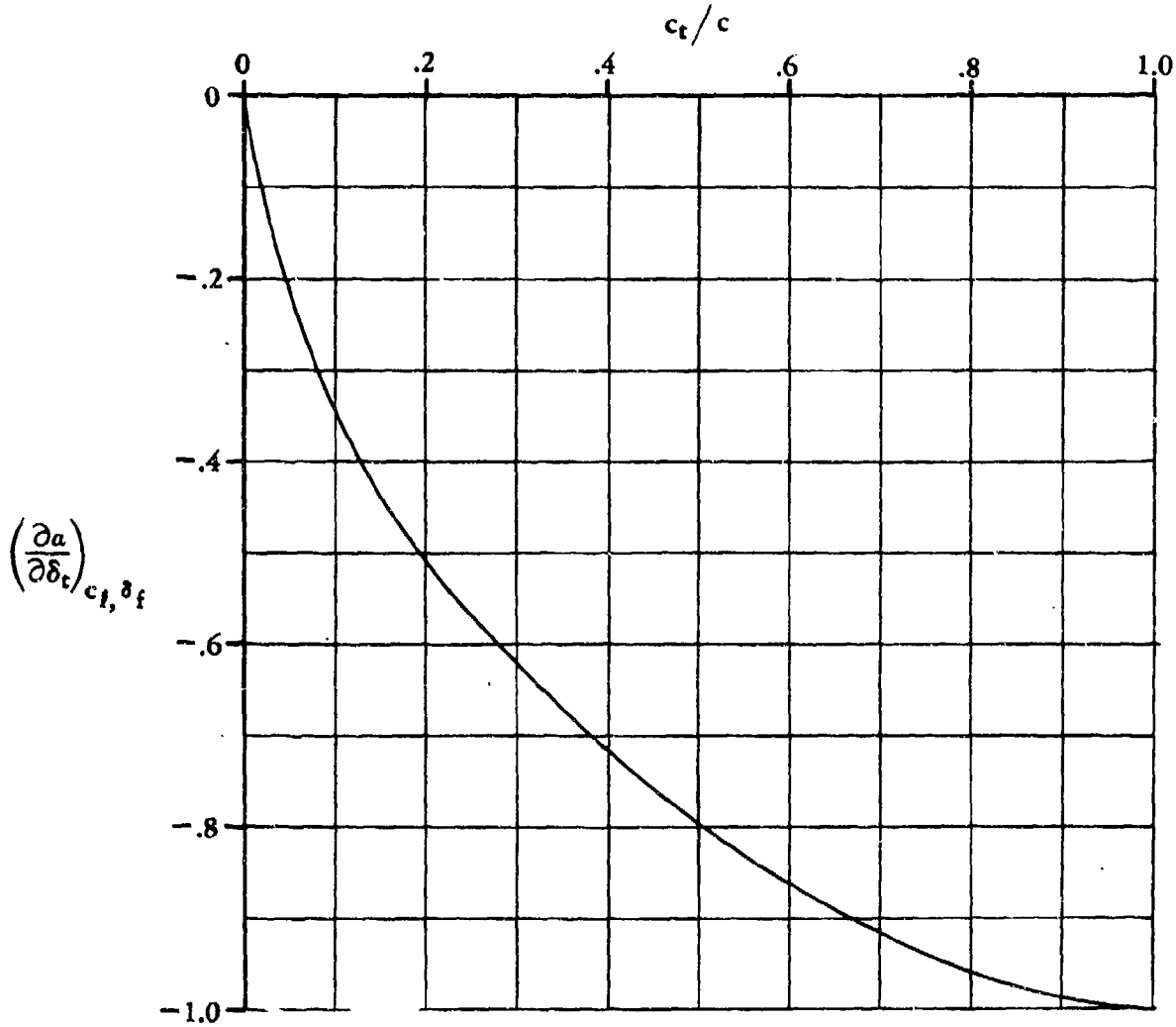

FIGURE 6.1.3.3-5 RATE OF CHANGE OF ANGLE OF ATTACK DUE TO A CHANGE IN TAB DEFLECTION

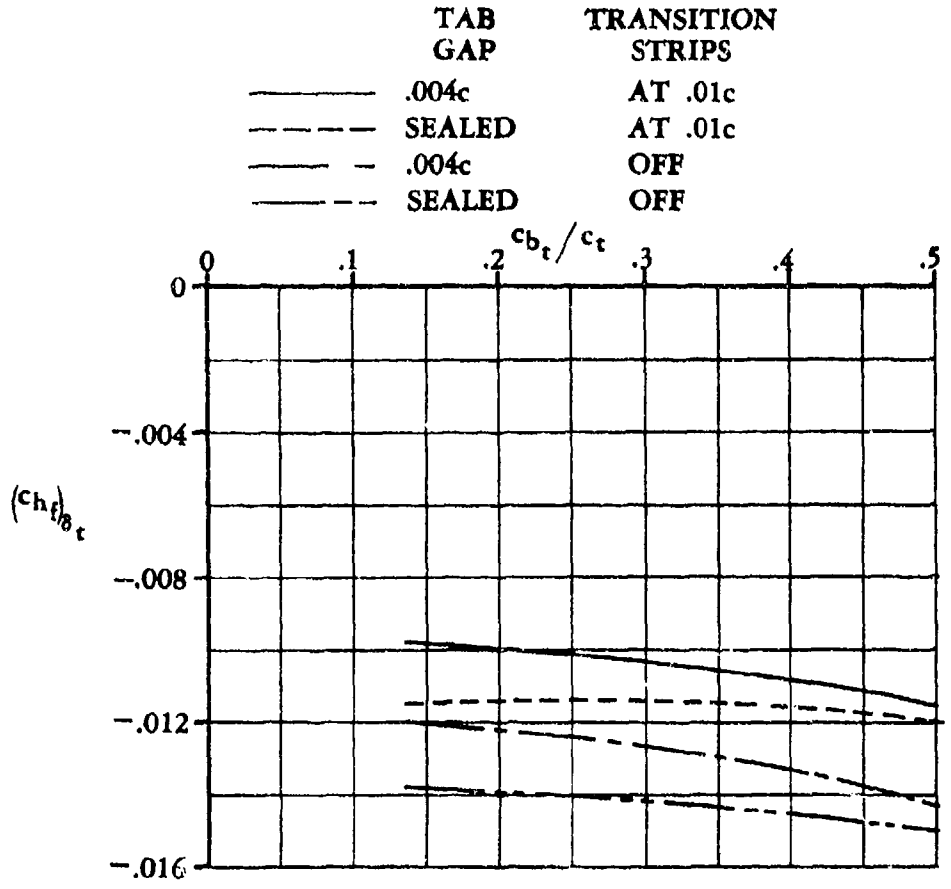

FIGURE 6.1.3.3-6a EFFECT OF SEALED AND UNSEALED TAB GAPS AND TRANSITION STRIPS ON FLAP SECTION HINGE MOMENTS

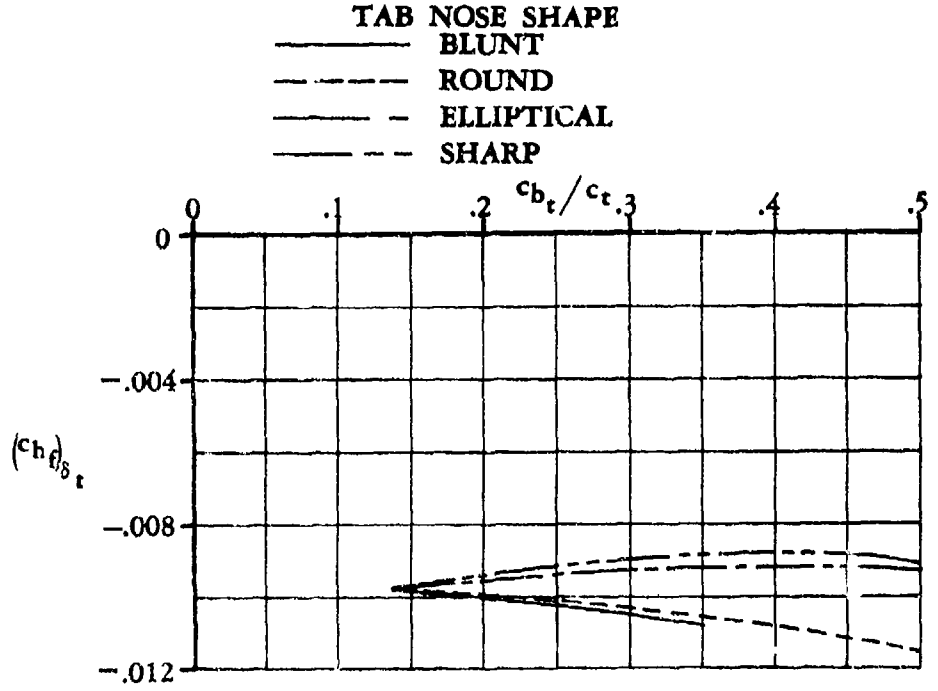

FIGURE 6.1.3.3-6b EFFECT OF TAB NOSE SHAPE AND AERODYNAMIC BALANCE ON FLAP SECTION HINGE MOMENTS

6.1.3.4 SECTION HINGE-MOMENT DERIVATIVE $(c_{h_t})_{\delta_f}$ OF CONTROL TAB DUE TO CONTROL SURFACE

A deflected flap or control surface causes pressure changes on the surfaces of the tab and control. These pressure changes on the tab generally result in a change in the tab hinge moment.

DATCOM METHOD

The following method is taken from Reference 1 and is based on the two-dimensional NACA 0009 airfoil test data for round-nose, unbalanced controls, with sealed flap and tab gaps. This method is limited to the low-speed linear hinge-moment range and should be restricted to flap deflections of approximately $\pm 18^{o}$ and the combinations of control deflection and angle of attack as indicated in Figure 6.1.3-2.

The change in the low-speed tab section hinge-moment coefficient due to flap deflection, measured at constant values of angle of attack and tab deflection, can be expressed as

$$\left(\frac{\partial c_{h_t}}{\partial \delta_f}\right)_{\alpha, \delta_t} = \left(\frac{\partial c_{h_t}}{\partial \delta_f}\right)_{c_\ell, \delta_t} - \left(\frac{\partial c_{h_t}}{\partial c_\ell}\right)_{\delta_f, \delta_t} \left(\frac{\partial c_\ell}{\partial \alpha}\right)_{\delta_f, \delta_t} \left(\frac{\partial \alpha}{\partial \delta_f}\right)_{c_\ell, \delta_t} \qquad 6.1.3.4\text{-a}$$

where

$\left(\frac{\partial c_{h_t}}{\partial \delta_f}\right)_{c_\ell, \delta_t}$ is the change in tab section hinge-moment coefficient due to control deflection, measured at constant values of lift and tab deflection. This value is obtained from Figure 6.1.3.4-4a.

$\left(\frac{\partial c_{h_t}}{\partial c_\ell}\right)_{\delta_f, \delta_t}$ is the change in tab section hinge-moment coefficient with respect to lift coefficient, measured at constant values of flap and tab deflections. This value is obtained from Figure 6.1.3.4-4b.

$\left(\frac{\partial c_\ell}{\partial \alpha}\right)_{\delta_f, \delta_t}$ is the section lift-curve slope of the primary panel (wing, horizontal tail, etc.) at constant values of tab and flap deflection. This value can be obtained from Section 4.1.1.2.

$\left(\frac{\partial \alpha}{\partial \delta_f}\right)_{c_\ell, \delta_t}$ is the rate of change of angle of attack due to a change in flap deflection in the linear range at constant values of lift and tab deflection. This value can be obtained from Figure 6.1.3.4-5.

The above method does not quantitatively account for the effect of unsealing the tab gap. In view of the difficulty of predicting the effects of seals and gaps, experimental data should be used whenever possible. Figure 6.1.3.4-6a (from Reference 2) shows the effects of fixing transition and sealing the tab gap on a modified NACA 65_1-012 airfoil. For these data, the flap-chord-to-wing-chord ratio is 0.25, the tab-chord-to-flap-chord ratio is 0.25, and flap gap is sealed.

The effects of tab nose shape are not accounted for in the above method and experimental data should be used whenever possible. However, the effect of tab nose shape as a function of nose balance is presented in Figure 6.1.3.4-6b (from Reference 2) for a NACA 65_1-012 airfoil with a tab gap of 0.004c and transition strips at 0.01c.

Other parameters not accounted for in the above method include the effects of airfoil thickness and trailing-edge angle. Unfortunately, not enough test data are available to evaluate the effects of either of these variables on the section hinge-moment derivative. Additional test data, including the effects of these variables on a limited number of flapped configurations, are presented in References 3 through 9 of Section 6.1.3.3.

Sample Problem

Given: The flap and tab configuration of Reference 2.

NACA 65_1-012 airfoil		Plain trailing-edge flap (sealed)	
$c_f/c = 0.25$	Round-nose flap	Plain trailing-edge tab (sealed)	
$c_t/c_f = 0.25$	Round-nose tab	Low speed	$R_\ell = 4.59 \times 10^6$

Compute:

$$\left(\frac{\partial c_{h_t}}{\partial \delta_f}\right)_{c_\ell, \delta_t} = -0.00188 \text{ per deg} \quad \text{(Figure 6.1.3.4-4a)}$$

$$\left(\frac{\partial c_{h_t}}{\partial c_\ell}\right)_{\delta_f, \delta_t} = -0.011 \quad \text{(Figure 6.1.3.4-4b)}$$

$$\left(\frac{\partial \alpha}{\partial \delta_f}\right)_{c_\ell, \delta_t} = -0.569 \quad \text{(Figure 6.1.3.4-5)}$$

c_{ℓ_α} = 0.11 per deg (Table 4.1.1-B)

Solution:

$$\left(\frac{\partial c_{h_t}}{\partial \delta_f}\right)_{\alpha, \delta_t} = \left(\frac{\partial c_{h_t}}{\partial \delta_f}\right)_{c_\ell, \delta_t} - \left(\frac{\partial c_{h_t}}{\partial c_\ell}\right)_{\delta_f, \delta_t} \left(\frac{\partial c_\ell}{\partial \alpha}\right)_{\delta_f, \delta_t} \left(\frac{\partial \alpha}{\partial \delta_f}\right)_{c_\ell, \delta_t}$$

(Equation 6.1.3.4-a)

$$= -0.00188 - (-0.011)(0.11)(-0.569)$$

$$= -0.00188 - 0.00069$$

$$= -0.00257 \text{ per deg}$$

This compares with test values of −0.0012 per degree with transition strips and −0.0026 per degree without transition strips, from Reference 2.

REFERENCES

1. Ames, M. B., Jr., and Sears, R. I.: Determination of Control-Surface Characteristics from NACA Plain Flap and Tab Data. NACA TR 721, 1941. (U)

2. Brewer, J. D., and Queijo, M. J.: Wind-Tunnel Investigation of the Effect of Tab Balance on Tab and Control-Surface Characteristics. NACA TN 1403, 1947. (U)

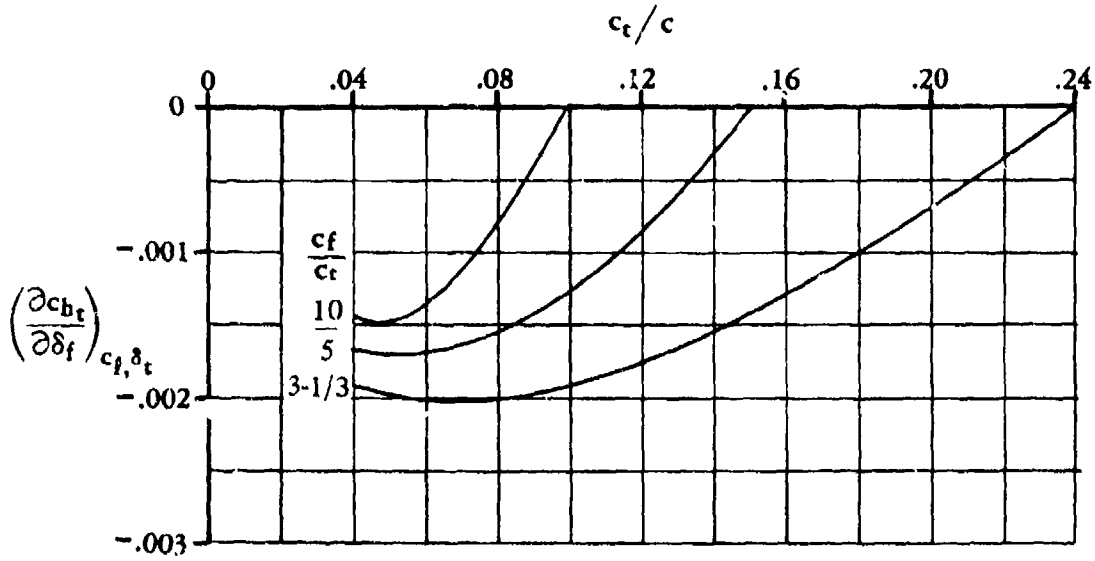

FIGURE 6.1.3.4-4a EFFECT OF FLAP DEFLECTION ON TAB SECTION HINGE MOMENTS

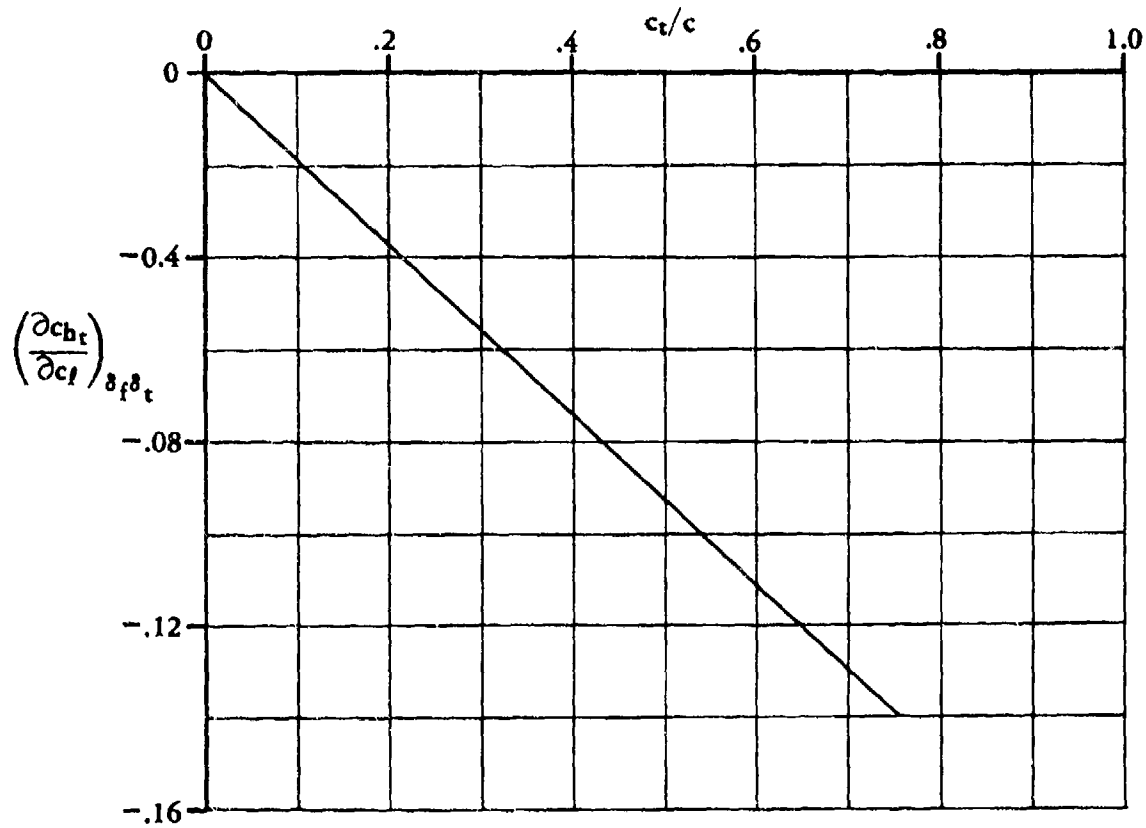

FIGURE 6.1.3.4-4b EFFECT OF SECTION LIFT COEFFICIENT ON TAB SECTION HINGE MOMENTS

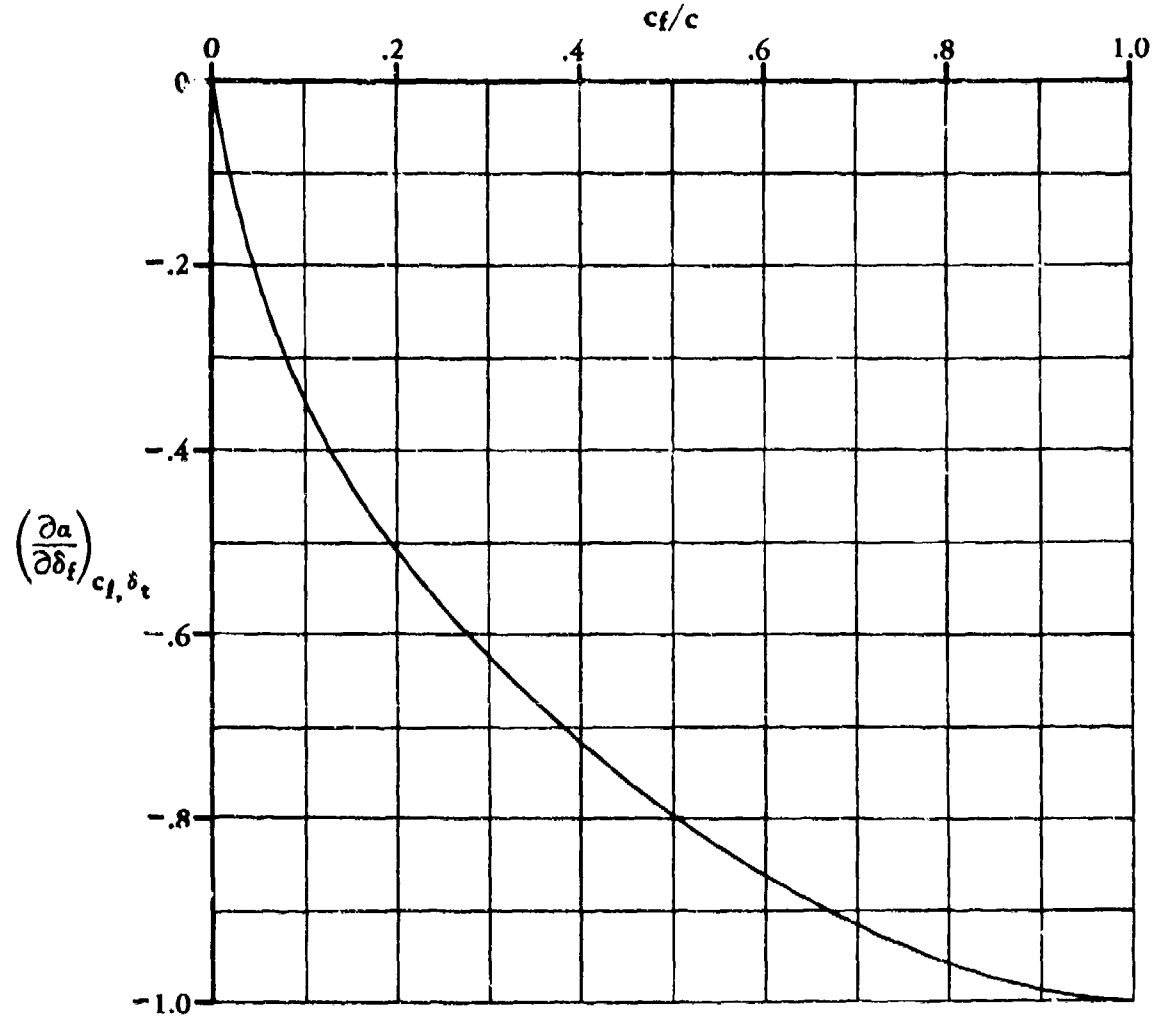

FIGURE 6.1.3.4-5 RATE OF CHANGE OF ANGLE OF ATTACK DUE TO A CHANGE IN FLAP DEFLECTION

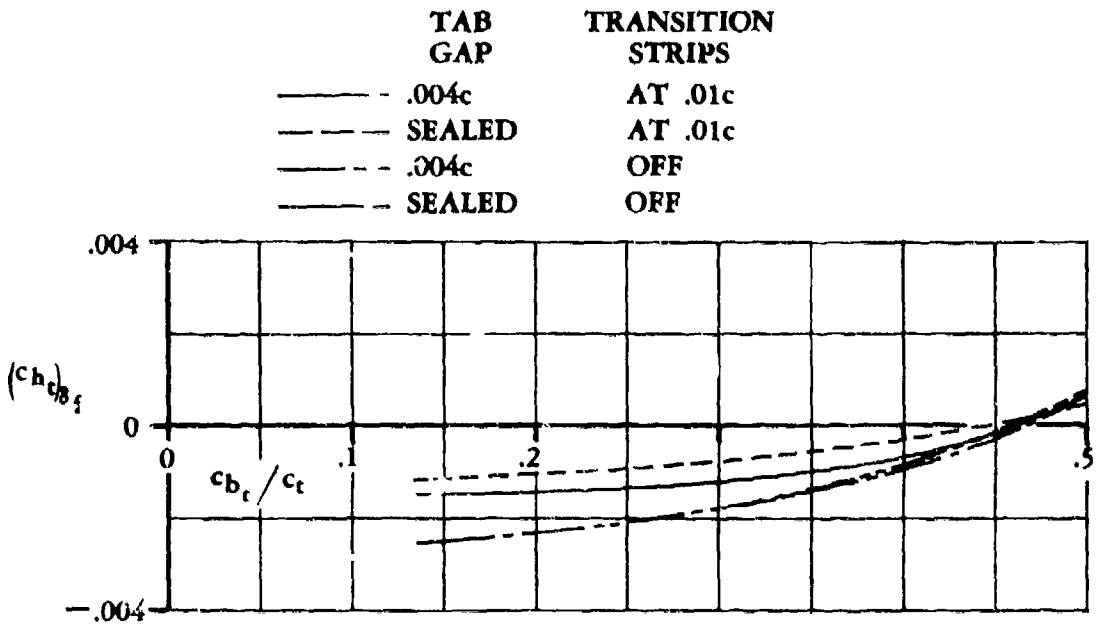

FIGURE 6.1.3.4-6 a EFFECT OF SEALED AND UNSEALED TAB GAPS AND TRANSITION STRIPS ON TAB SECTION HINGE MOMENTS

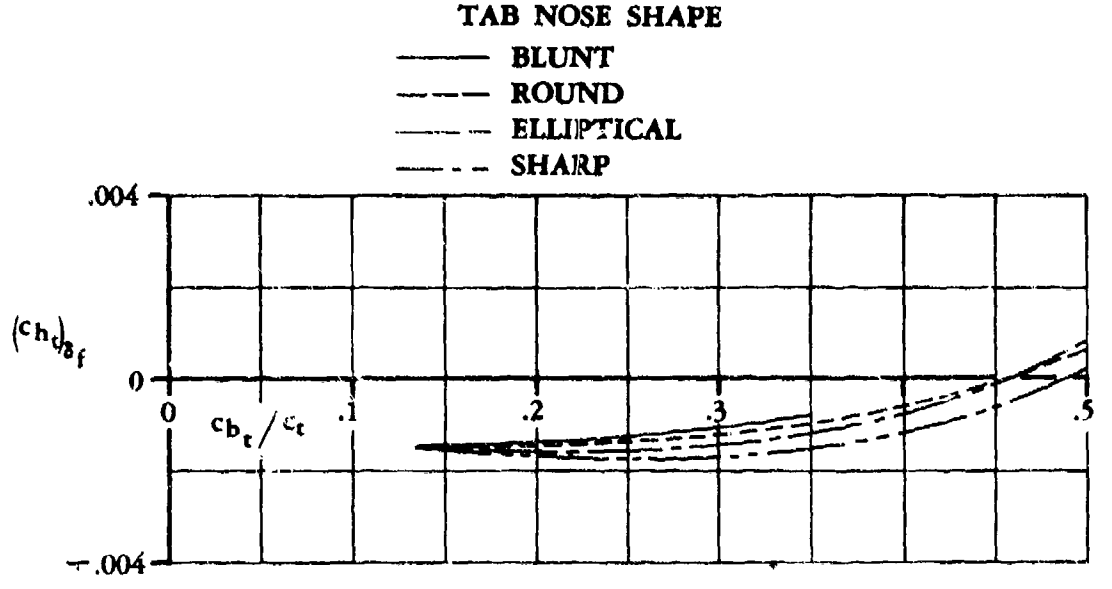

FIGURE 6.1.3.4-6 b EFFECT OF TAB NOSE SHAPE AND AERODYNAMIC BALANCE ON TAB SECTION HINGE MOMENTS

6.1.4 WING LIFT WITH HIGH-LIFT AND CONTROL DEVICES

6.1.4.1 CONTROL DERIVATIVE C_{L_δ} OF HIGH-LIFT AND CONTROL DEVICES

A. SUBSONIC

Mechanical Flaps

The method used to estimate lift due to flap deflection at subsonic speeds is designed to make maximum use of experimental airfoil section data when such data are available. This approach is taken from Reference 1, wherein various existing methods have been combined to obtain a simple procedure with general application.

Jet Flaps

Two methods are presented for estimating the jet-flap lift increment at small angles of attack (see Section 6.1.1.1 for a sketch of the various jet-flap types and a discussion of the salient aspects). More accurate and sophisticated lift methods than those presented here have been developed for analyzing jet-flap configurations (such as the method presented in Reference 2). However, the more sophisticated methods are not amenable to a handbook solution; i.e., they require the use of a computer. Other modifications and approaches to the jet-flap problem are presented and discussed in detail in Reference 3.

The first method (taken from Reference 4) evaluates the lift increment due to both flap deflection and power effects for an internally-blown-flap (IBF) configuration. This method is based on the theoretical two-dimensional jet-flap lift increment modified by Maskell's theoretical correction factor for finite-aspect-ratio effects and a crude part-span factor to account for partial-span flaps. This method has not been substantiated because of the lack of published three-dimensional IBF data. However, the method has yielded results within ten percent of test data for those cases that have been evaluated (References 4 and 5).

The second method (taken from Reference 6) is used to evaluate the lift increment due only to power effects for an externally-blown-flap (EBF) configuration. This method is based on Spence's two-dimensional jet-flap lift increment, modified by Hartunian's theoretical correction factor for finite-aspect-ratio effects and the ratio of flapped wing area to reference wing area to account for partial-span effects. Substantiation of this method has not been presented here; however, a substantiation of the method does appear in Reference 6 with an indicated average error of about 10 percent.

The nondimensional trailing-edge jet momentum coefficient for three-dimensional jet-flap configurations is denoted by C_J. The relationship to the two-dimensional jet momentum coefficient C_μ (see Section 6.1.1.1 for definition) can be expressed as

$$C_J = \frac{1}{qS} \int_{-b/2}^{b/2} J \, dy$$

$$= \frac{1}{S} \int_{-b/2}^{b/2} c\, C_\mu \, dy \qquad \text{6.1.4.1-1}$$

where

J is the jet momentum at the trailing edge.

dy is the spanwise wing increment.

q is the free-stream dynamic pressure.

S is the reference wing area.

b is the wing span.

c is the wing chord.

DATCOM METHODS

1. Mechanical Leading- and Trailing-Edge Devices

The lift increment developed by deflection of a control surface is given by

$$\Delta C_L = \Delta c_\ell \left(\frac{C_{L_\alpha}}{c_{\ell_\alpha}} \right) \left[\frac{(\alpha_\delta)_{C_L}}{(\alpha_\delta)_{c_\ell}} \right] K_b \qquad 6.1.4.1\text{-a}$$

where

Δc_ℓ is the section lift increment due to control deflection. Test data on the particular flapped airfoil are preferred, but the increment can be estimated by the applicable method of Section 6.1.1.1.

C_{L_α} is the lift-curve slope of the wing with the flap retracted, based on the wing reference area, obtained from the appropriate wing method of Paragraph A of Section 4.1.3.2.

c_{ℓ_α} is the section lift-curve slope of the basic airfoil, including the effects of compressibility, obtained from Section 4.1.1.2.

$\frac{(\alpha_\delta)_{C_L}}{(\alpha_\delta)_{c_\ell}}$ is the ratio of the three-dimensional flap-effectiveness parameter to the two-dimensional flap-effectiveness parameter, obtained from Figure 6.1.4.1-14 as a function of wing aspect ratio and the theoretical value of $(\alpha_\delta)_{c_\ell}$. The theoretical value of $(\alpha_\delta)_{c_\ell}$ is obtained from the inset chart of Figure 6.1.4.1-14.

When experimental values of the section lift increment Δc_ℓ are used in Equation 6.1.4.1-a, the value of $(\alpha_\delta)_{c_\ell}$ used to obtain $(\alpha_\delta)_{C_L}/(\alpha_\delta)_{c_\ell}$ from Figure 6.1.4.1-14 should be calculated using

$$(\alpha_\delta)_{c_\ell} = -\frac{(\Delta c_\ell)_{\text{experiment}}}{(c_{\ell_\alpha})\ \delta_f}$$

with one exception; i.e., for area-suction- and blowing-type flaps, use the inset chart of Figure 6.1.4.1-14.

K_b is the flap-span factor obtained from Figure 6.1.4.1-15 as illustrated in Sketch (a). (Note: η is the span station, $\eta = \frac{\text{control span ordinate}}{b/2}$.)

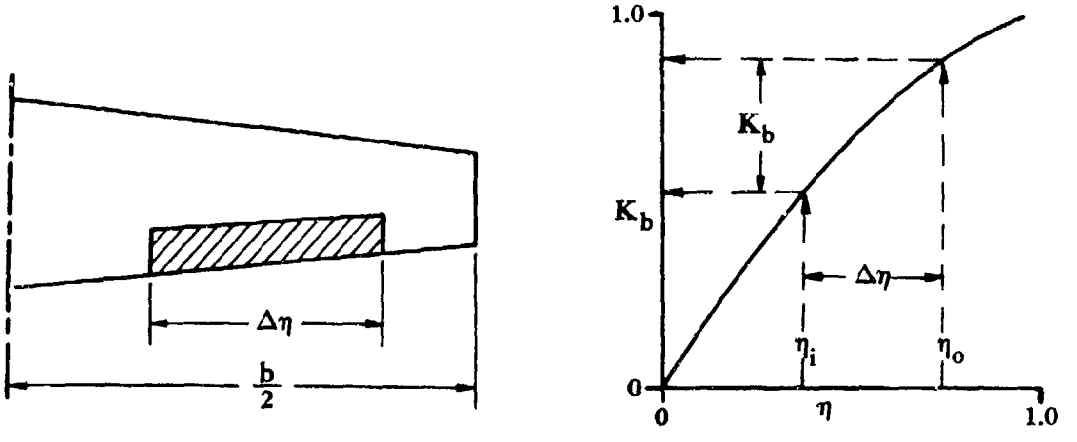

SKETCH (a)

It should be noted that the control deflection angles and all dimensions are measured in planes parallel or perpendicular to the plane of symmetry.

This method is restricted to the limitations of the methods used to evaluate the section lift increments from Section 6.1.1.1.

Equation 6.1.4.1-a is applicable to leading-edge flaps and slats, and plain, split, and slotted trailing-edge flaps. The lift increment due to combinations of leading-edge and trailing-edge devices may be estimated by applying Equation 6.1.4.1-a to each device separately and adding the individual increments.

For the case of arbitrary spanwise distribution of control chord (constant-chord controls on tapered wings or tapered controls on untapered wings), the control can be divided into spanwise steps and the lift increment found by the summation of ΔC_L values due to each spanwise step based on the average values of Δc_ℓ and $(\alpha_\delta)_{c_\ell}$ over that spanwise step.

Low-speed values of ΔC_L at $\alpha = 0$, calculated using the Datcom method, are compared with test values in Figures 6.1.4.1-16a, -16b, and -16c for wing-control combinations employing plain, split, and slotted trailing-edge controls, respectively. All parameters used in the calculations were estimated by using methods from the appropriate sections of the Datcom. The values of $(\alpha_\delta)_{c_\ell}$ used in the calculations were obtained from the inset of Figure 6.1.4.1-14. The ranges of Reynolds numbers and geometric parameters of the test configurations are noted on the correlation charts.

2. Jet-Flap IBF Configuration

The lift increment due to flap deflection and power effects for an IBF configuration is given by

$$\Delta C_L = \Delta c_\ell \left[\frac{A_t + \frac{2C'_J}{\pi}}{A_t + 2 + 0.604(C'_J)^{1/2} + 0.876\, C'_J} \right] \frac{S_{W_f}}{S_W} \qquad 6.1.4.1\text{-b}$$

where

Δc_ℓ is the section lift increment due to flap deflection and power effects. Test data on the particular flapped airfoil are preferred, but the increment can be estimated by the jet-flap method of Section 6.1.1.1. (When using Section 6.1.1.1 the value of C'_J is substituted for the value of C'_μ.)

A_t is the aspect ratio of the wing based on the total wing area S_t, including any increase in wing area due to flap extension.

C'_J is the three-dimensional trailing-edge jet momentum coefficient, based on the blown-flap affected wing area S_{W_f}, i.e.,

$$C'_J = C_J \frac{S_W}{S_{W_f}}$$

$\frac{S_{W_f}}{S_W}$ is the ratio of the blown-flap affected wing area (schematically illustrated in Section 2.2.2) to the wing reference area. The blown-flap affected area includes any increase in wing area due to flap extension.

As indicated above, this method has not been thoroughly substantiated and therefore should be applied with caution.

It should be noted that the total lift coefficient for an IBF configuration can be found by adding the lift increment from Equation 6.1.4.1-b to the flaps-retracted power-off lift coefficient, obtained from test data or the appropriate methods of Section 4.

3. Jet-Flap EBF Configuration

The effective jet deflection angle $\delta_{j_{eff}}$ and the trailing-edge momentum coefficient C_J are not specifically defined for EBF configurations. This is due to the jet sheet being somewhat diffuse rather than infinitesimally thin as assumed in jet-flap theory. For this reason it becomes necessary to obtain the effective jet angle from static force tests, or to relate the jet angle to the trailing-edge flap geometry. From correlation of test data (indicated in Reference 6), the best results are obtained when the engine exhaust jet momentum is used directly to define the trailing-edge momentum coefficient. Any losses in thrust must therefore be considered in the determination of drag.

The lift increment due to power effects for an EBF configuration is given by

$$\Delta C_L = 4\pi d_o \left[\frac{\pi A_t + 2C_J'}{\pi A_t + c_{\ell_\alpha}' + 2.01\, C_J'}\right] \frac{\delta_{j_{eff}}}{57.3} \frac{S_{W_f}}{S_W} \qquad 6.1.4.1\text{-c}$$

where

$4\pi d_o$ is the theoretical effect of blowing on the lift derivative. This parameter is obtained from Figure 6.1.4.1-18 as a function of the flap chord ratio c_f/c' and trailing-edge jet momentum coefficient C_J'. (See Figure 6.1.4.1-19a for a schematic definition of c_f/c'.)

A_t is the aspect ratio of the wing based on the total wing area S_t, including any increase in wing area due to flap extension.

C_J' is the three-dimensional trailing-edge jet momentum coefficient, based on the blown-flap-affected wing area S_{W_f}, i.e., $C_J' = C_J\, S_W/S_{W_f}$.

c_{ℓ_α} is the two-dimensional jet-flap lift-curve slope uncorrected for thickness effects. This term is obtained from Figure 6.1.1.1-49, using the trailing-edge jet momentum coefficient C_J' in place of C_μ'.

$\delta_{j_{eff}}$ is the effective jet deflection angle with respect to the airfoil chord, in degrees. If possible, this value should be obtained from static force tests. When test data are not available, the effective flap deflection angle may be approximated by using

$$\delta_{j_{eff}} = \frac{1}{2}(\delta_u + \delta_\ell) \qquad 6.1.4.1\text{-d}$$

where the values for δ_u and δ_ℓ are shown schematically in Figure 6.1.4.1-19b.

$\frac{S_{W_f}}{S_W}$ is the ratio of the flap-affected wing area (schematically illustrated in Section 2.2.2) to the wing reference area. The flap-affected area includes any increase in wing area due to flap extension.

It should be noted that the total lift coefficient for an EBF configuration can be found by adding the lift increment from Equation 6.1.4.1-c, the power-off mechanical-flap lift increment from Equation 6.1.4.1-a, and the flap-retracted power-off lift coefficient, obtained from test data or the appropriate methods of Section 4.

Sample Problems

1. Mechanical Flaps

Given: The sweptback wing of Reference 7.

$A = 3.78$ $\lambda = 0.586$ $\Lambda_{c/2} = 45.46^o$

NACA 65A006 airfoil Plain trailing-edge flap $c_f/c = 0.224$

$b_f/b = 0.469$ $\eta_i = 0.141$ $\eta_o = 0.610$ $\delta_f = 22.1^o$ (streamwise)

Low speed; $\beta = 1.0$ $R_\ell = 6.1 \times 10^6$

$\tan(\phi'_{TE}/2) = 0.0717$ (streamwise airfoil section geometry)

Compute:

c_{ℓ_α} and Δc_ℓ (Sections 4.1.1.2 and 6.1.1.1)

$$\frac{c_{\ell_\alpha}}{(c_{\ell_\alpha})_{theory}} = 0.887 \quad \text{(Figure 4.1.1.2-8a)}$$

$$(c_{\ell_\alpha})_{theory} = 6.58 \text{ per rad} \quad \text{(Figure 4.1.1.2-8b)}$$

$$c_{\ell_\alpha} = \frac{1.05}{\beta}\left[\frac{c_{\ell_\alpha}}{(c_{\ell_\alpha})_{theory}}\right](c_{\ell_\alpha})_{theory} \quad \text{(Equation 4.1.1.2-a)}$$

$$= (1.05)(0.887)(6.58) = 6.13 \text{ per rad}$$

$$(c_{\ell_\delta})_{theory} = 3.77 \text{ per rad} \quad \text{(Figure 6.1.1.1-39a)}$$

$$\frac{c_{\ell_\delta}}{(c_{\ell_\delta})_{theory}} = 0.817 \quad \text{(Figure 6.1.1.1-39b)}$$

$K' = 0.780$ (Figure 6.1.1.1-40)

$$\Delta c_\ell = \delta_f\left[\frac{c_{\ell_\delta}}{(c_{\ell_\delta})_{theory}}\right](c_{\ell_\delta})_{theory} K' \quad \text{(Equation 6.1.1.1-c)}$$

$$= \left(\frac{22.1}{57.3}\right)(0.817)(3.77)(0.780)$$

$$= 0.927$$

Wing lift-curve slope (Section 4.1.3.2)

$$\kappa = \frac{c_{\ell_\alpha}}{2\pi} = \frac{6.13}{2\pi} = 0.976$$

$$\frac{A}{\kappa}\left(\beta^2 + \tan^2 \Lambda_{c/2}\right)^{1/2} = \frac{3.78}{0.976}\left[1.0 + (1.0162)^2\right]^{1/2} = 5.52$$

$$\frac{C_{L_\alpha}}{A} = 0.798 \text{ per rad} \quad \text{(Figure 4.1.3.2-49)}$$

$$C_{L_\alpha} = 3.016 \text{ per rad}$$

$(\alpha_\delta)_{c_\ell} = -0.576$ (Inset, Figure 6.1.4.1-14)

$$\frac{(\alpha_\delta)_{C_L}}{(\alpha_\delta)_{c_\ell}} = 1.083 \quad \text{(Figure 6.1.4.1-14)}$$

$$\left.\begin{aligned}(K_b)_{\eta_i} &= 0.190 \\ (K_b)_{\eta_o} &= 0.740\end{aligned}\right\} \text{(Figure 6.1.4.1-15)}$$

$$K_b = (K_b)_{\eta_o} - (K_b)_{\eta_i} = 0.550$$

Solution:

$$\Delta C_L = \Delta c_\ell \left(\frac{C_{L_\alpha}}{c_{\ell_\alpha}}\right)\left[\frac{(\alpha_\delta)_{C_L}}{(\alpha_\delta)_{c_\ell}}\right] K_b \quad \text{(Equation 6.1.4.1-a)}$$

$$= (0.927)\,\frac{3.016}{6.13}\,(1.083)(0.550)$$

$$= 0.272$$

This compares with a test value of 0.255 from Reference 7.

2. Jet-Flap IBF Configuration

Given: The IBF configuration of Reference 5.

NACA 4424 airfoil $\quad \delta_f = 30^o \quad \delta_j = 22^o$

$\frac{c_f}{c} = 0.11 \quad \frac{c'}{c} = 1.0 \quad A = 6.0 \quad A_t = 6.0$

$C_j = 2.80 \quad \frac{t}{c} = 0.24 \quad \frac{S_{W_f}}{S_W} = 0.783 \quad \frac{S_t}{S_W} = 1.0$

Compute:

$$C_J' = C_J \frac{S_W}{S_{W_f}}$$

$$= (2.80) \frac{1}{0.783}$$

$$= 3.576$$

k_t = 0.80 (average airfoil)

$c_{\ell_{\delta_f}}$ = 10.0 per rad

$c_{\ell_{\delta_j}}$ = 8.9 per rad

Figure 6.1.1.1-49

$$\Delta c_\ell = \left\{ \left[1 + k_t \left(\frac{t}{c'} \right) \right] \delta_f \left(c_{\ell_{\delta_f}} - C_\mu' \right) + C_\mu' \delta_f \right.$$

$$\left. + \left[1 + k_t \left(\frac{t}{c'} \right) \right] \delta_j \left(c_{\ell_{\delta_j}} - C_\mu' \right) + C_\mu' \delta_j \right\} \frac{c'}{c} \qquad \text{(Equation 6.1.1.1-k)}$$

$$= [1 + (0.80)(0.24)] \frac{30}{57.3} (10.0 - 3.576) + 3.576 \frac{30}{57.3}$$

$$+ [1 + (0.80)(0.24)] \frac{22}{57.3} (8.9 - 3.576) + 3.576 \frac{22}{57.3}$$

$$= 4.01 + 1.87 + 2.44 + 1.37$$

$$= 9.69$$

Solution:

$$\Delta C_L = \Delta c_\ell \left[\frac{A_t + \frac{2C_J'}{\pi}}{A_t + 2 + 0.604 (C_J')^{1/2} + 0.876 C_J'} \right] \frac{S_{W_f}}{S_W} \qquad \text{(Equation 6.1.4.1-b)}$$

$$= 9.69 \left[\frac{6.0 + \frac{2(3.576)}{\pi}}{6.0 + 2.0 + 0.604 (3.576)^{1/2} + 0.876 (3.576)} \right] 0.783$$

$$= 5.12 \text{ (lift increment due to flap deflection and power effects)}$$

This compares with a test value of 5.03 from Reference 5.

3. Jet-Flap EBF Configuration

Given: The EBF configuration of Reference 8.

$\frac{c_f}{c} = 0.556$ $\quad \frac{c'}{c} = 1.336$ (without leading-edge extension) $\quad \frac{t}{c} \simeq 0.12$

$S_W = 8.43\ ft^2$ $\quad S_{W_f} = 9.58\ ft^2$ $\quad S_t = 10.84\ ft^2$

$A = 7.23$ $\quad A_t = 5.62$ $\quad C_J = 1.74$

$\delta_u = 61^o$ $\quad \delta_\ell = 50^o$

Compute:

$$C_J' = C_J\left(\frac{S_W}{S_{W_f}}\right)$$

$$= 1.74\left(\frac{8.43}{9.58}\right) = 1.53$$

$$\delta_{j_{eff}} = \frac{1}{2}(\delta_u + \delta_\ell) \quad \text{(Equation 6.1.4.1-d)}$$

$$= \frac{1}{2}(61 + 50)$$

$$= 55.5^o$$

$$\frac{c_f}{c'} = \left(\frac{c_f}{c}\right)\left(\frac{c}{c'}\right)$$

$$= \frac{0.556}{1.336} = 0.416$$

$c_{\ell_\alpha}' = 9.66$ per rad (Figure 6.1.1.1-49)

$4\pi d_o = 3.48$ (Figure 6.1.4.1-18)

Solution:

$$\Delta C_L = 4\pi d_o\left[\frac{\pi A_t + 2C_J'}{\pi A_t + c_{\ell_\alpha}' + 2.01\,C_J'}\right]\left(\frac{\delta_{j_{eff}}}{57.3}\right)\left(\frac{S_{W_f}}{S_W}\right) \quad \text{(Equation 6.1.4.1-c)}$$

$$= 3.48\left[\frac{\pi(5.62) + (2)(1.53)}{\pi(5.62) + 9.66 + (2.01)(1.53)}\right]\left(\frac{55.5}{57.3}\right)\left(\frac{9.58}{8.43}\right)$$

$$= 2.61 \text{ (lift increment due to power effects only)}$$

This compares with a test value of 2.45 from Reference 8.

B. TRANSONIC

No accurate method is available for predicting the control derivative C_{L_δ} at transonic speeds. Mixed flow conditions and interrelated shockwave and boundary-layer-separation effects cause extreme nonlinearities in this parameter in the transonic regime. The method presented herein is based on the observation that experimental data indicate that C_{L_δ} follows the same trend as the lift-curve slope through the transonic regime.

DATCOM METHOD

A first-order approximation to the control derivative C_{L_δ} at transonic speeds for mechanical trailing-edge flaps is given by

$$C_{L_\delta} = C_{L_{\delta M=0.6}} \left(\frac{C_{l_\delta}}{C_{l_{\delta M=0.6}}} \right) \qquad 6.1.4.1\text{-e}$$

where

$C_{L_{\delta M=0.6}}$ is the lift effectiveness, calculated by the method of Paragraph A of this section, at M = 0.6, i.e.,

$$C_{L_\delta} = \frac{\Delta C_L}{\delta_f}$$

$\frac{C_{l_\delta}}{C_{l_{\delta M=0.6}}}$ is the ratio of the rolling-effectiveness parameter at the Mach number in question to that at M = 0.6, obtained by the method of Paragraph B of Section 6.2.1.1.

C. SUPERSONIC

At supersonic speeds, the lift effectiveness of plain trailing-edge controls is predicted by the theoretical method presented in Reference 9. The restrictions used in the derivation of the method are as follows:

1. Leading and trailing edges of the control surface are swept ahead of the Mach lines from the deflected controls.

2. Control root and tip chords are parallel to the plane of symmetry.

3. Controls are located either at the wing tip or far enough inboard so that the outermost Mach lines from the deflected controls do not cross the wing tip.

4. Innermost Mach lines from the deflected controls do not cross the wing root chord.

5. Wing planform has leading edges swept ahead of the Mach lines and has streamwise tips.

6. Controls are not influenced by the tip conical flow from the opposite wing panel or by the interaction of the wing-root Mach cone with the wing tip.

DATCOM METHOD

The trailing-edge flap effectiveness C_{L_δ} at supersonic speeds for a symmetric, straight-sided flap is given by

$$C_{L_\delta} = \left(1 - \frac{C_2}{C_1}\phi_{TE}\right) C'_{L_\delta} \frac{S_f}{S_W} \qquad 6.1.4.1\text{-f}$$

where $\left(1 - \frac{C_2}{C_1}\phi_{TE}\right)$ is a thickness correction factor to the supersonic flat-plate derivative.

$$C_1 = \frac{2}{\sqrt{M^2 - 1}} \text{ (per radian)}$$

$$C_2 = \frac{(\gamma + 1)M^4 - 4(M^2 - 1)}{2(M^2 - 1)^2} \text{ (per radian)}$$

ϕ_{TE} is the trailing-edge angle in radians, measured normal to the control hinge line.

γ is the ratio of specific heats, $\gamma = 1.4$.

C'_{L_δ} is the lift effectiveness of one symmetric, straight-sided flap, based on the area of the flap. This parameter is obtained from Figures 6.1.4.1-20a through 6.1.4.1-20j for flaps located at the wing tip and from Figure 6.1.4.1-25 for flaps located inboard from the wing tip.

$\frac{S_f}{S_W}$ is the ratio of the total flap area (both sides of wing) to the total wing area.

It should be noted that control deflection angles are measured streamwise.

Not enough supersonic test data are available to allow substantiation of this method.

Sample Problem

Given: A wing-flap configuration with the following characteristics:

$S_W = 46.5$ sq ft $\qquad \bar{c}_W = 4.0$ ft $\qquad b_W = 12.0$ ft

$\lambda_W = 0.55$ $\qquad \Lambda_{LE} = 42^o$ $\qquad \Lambda_{TE} = 27.7^o$

Symmetric, straight-sided inboard flap

$\Lambda_{HL} = 30.8^{o}$ $S_f = 4.71$ sq ft $b_f = 6.5$ ft $\lambda_f = 0.715$ $\phi_{TE} = 3^{o}$

Additional Characteristics:

$M = 1.90$; $\beta = 1.62$

Compute:

$$C_1 = \frac{2}{\sqrt{M^2 - 1}} = 1.235 \text{ per rad}$$

$$C_2 = \frac{(\gamma + 1)M^4 - 4(M^2 - 1)}{2(M^2 - 1)^2} \text{ per rad}$$

$$= \frac{(2.4)(1.90)^4 - 4\,[(1.90)^2 - 1]}{2[(1.90)^2 - 1]^2} = \frac{20.84}{13.62} = 1.53 \text{ per rad}$$

$$\frac{\tan \Lambda_{TE}}{\beta} = \frac{0.5250}{1.62} = 0.324$$

$\beta C'_{L_\delta} = 0.074$ per deg (Figure 6.1.4.1-25)

$C'_{L_\delta} = 0.0457$ per deg

Solution:

$$C_{L_\delta} = \left(1 - \frac{C_2}{C_1}\phi_{TE}\right) C'_{L_\delta} \frac{S_f}{S_W} \quad \text{(Equation 6.1.4.1-f)}$$

$$= \left[1 - \left(\frac{1.53}{1.235}\right)\left(\frac{3.0}{57.3}\right)\right] (0.0457)\ \frac{4.71}{46.5}$$

$$= 0.00433 \text{ per deg}$$

REFERENCES

1. Lowry, J. G., and Polhamus, E. C.: A Method for Predicting Lift Increment Due to Flap Deflection at Low Angles of Attack in Incompressible Flow. NACA TN 3911, 1957. (U)

2. Lopez, M. L., and Shen, C. C.: Recent Developments in Jet Flap Theory and Its Application to STOL Aerodynamic Analysis. AIAA Paper 71-578, 1971. (U)

3. Korbacher, G. K., and Sridhar, K.: A Review of the Jet Flap. Univ. of Toronto, UTIA Review 14, 1960. (U)

4. Alexander, A. J., and Williams, J.: Wind-Tunnel Experiments on a Rectangular-Wing Jet-Flap Model of Aspect Ratio 6. ARC R&M 3329, 1964. (U)

5. Butler, S. F. J., Guyett, M. B., and Moy, B. A.: Six-Component Low-Speed Tunnel Tests of Jet-Flap Complete Models with Variation of Aspect Ratio, Dihedral and Sweepback, Including the Influence of Ground Proximity. ARC R&M 3441, 1961. (U)

6. May, F., and Widdison, C. A.: STOL High-Lift Design Study. Vol. I – State-of-the-Art Review of STOL Aerodynamic Technology. AFFDL-TR-71-26 Vol. I, 1971. (U)

7. Barnett, U. R., Jr., and Lipson, S.: Effects of Several High-Lift and Stall-Control Devices on the Aerodynamic Characteristics of a Semispan 49° Sweptback Wing. NACA RM L52D17a, 1952. (U)

8. Grafton, S. B., Parlett, L. P., and Smith, C. C.: Dynamic Stability Derivatives of a Jet Transport Configuration with High Thrust-Weight Ratio and An Externally Blown Jet Flap. NASA TN D-6440, 1971. (U)

9. Goin, K. L.: Equations and Charts for the Rapid Estimation of Hinge-Moment and Effectiveness Parameters for Trailing-Edge Controls Having Leading and Trailing Edges Swept Ahead of the Mach Lines. NACA TR 1041, 1951. (U)

10. Abbott, I. H., and Greenberg, H.: Tests in the Variable-Density Wind Tunnel of the NACA 23012 Airfoil with Plain and Split Flaps. NACA TR 661, 1939. (U)

11. Smith, D. W., and Reed, V. D.: Subsonic Static Longitudinal Stability and Control Characteristics of a Wing-Body Combination Having a Pointed Wing of Aspect Ratio 2 With Constant-Percent-Chord Trailing Edge Elevons. NACA RM A53C20, 1953. (U)

12. Wenzinger, C. J.: Wind-Tunnel Investigation of Ordinary and Split Flaps on Airfoils of Different Profile. NACA TR 554, 1936. (U)

13. Lipson, S., and Barnett, U. R., Jr.: Comparison of Semispan and Full-Span Tests of a 47.5° Sweptback Wing with Symmetrical Circular-Arc Sections and Having Drooped-Nose Flaps, Trailing-Edge Flaps, and Ailerons. NACA RM L51H15, 1951. (U)

14. Schwier, W.: Lift Increase by Blowing Out Air, Tests on Airfoil of 12 Percent Thickness, Using Various Types of Flap. NACA TM 1148, 1947. (U)

15. Guryansky, E. R., and Lipson, S.: Effect of High-Lift Devices on the Longitudinal and Lateral Characteristics of a 45° Sweptback Wing With Symmetrical Circular-Arc Sections. NACA RM L8D06, 1948. (U)

16. Pearson, H. A., and Anderson, R. F.: Calculation of the Aerodynamic Characteristics of Tapered Wings With Partial-Span Flaps. NACA TR 665, 1939. (U)

17. Pratt, G. L., and Shields, E. R.: Low-Speed Longitudinal Characteristics of a 45°Sweptback Wing of Aspect Ratio 8 With High-Lift and Stall-Control Devices at Reynolds Numbers from 1,500,000 to 4,800,000. NACA RM L51J04, 1952. (U)

18. Sivells, J. C., and Spooner, S. H.: Investigation in the Langley 19-Foot Pressure Tunnel of Two Wings of NACA 65-210 Airfoil Sections with Various Type Flaps. NACA TR 942, 1949. (U)

19. Graham, R. R., and Conner, D. W.: Investigation of High-Lift and Stall-Control Devices on an NACA 64-Series 42° Sweptback Wing With and Without Fuselage. NACA RM L7G09, 1947. (U)

20. Woods, R. L., and Spooner, S. H.: Effects of High-Lift and Stall-Control Devices, Fuselage, and Horizontal Tail on a Wing Sweptback 42° at the Leading Edge and Having Symmetrical Circular-Arc Airfoil Sections at Reynolds Number of 6.9×10^6. NACA RM L9B11, 1949. (U)

21. Foster, G. V., and Fitzpatrick, J. E.: Longitudinal-Stability Investigation of High-Lift and Stall-Control Devices on a 52° Sweptback Wing With and Without Fuselage and Horizontal Tail at a Reynolds Number of 6.8×10^6. NACA RM L8J08, 1948. (U)

22. Graham, D., and Koenig, D. G.: Tests in the Ames 40- by 80-Foot Wind Tunnel of an Airplane Configuration With an Aspect Ratio 2 Triangular Wing and an All-Moveable Horizontal Tail – Longitudinal Characteristics. NACA RM A51B21, 1951. (U)

23. Spooner, S. H., and Mollenberg, E. F.: Positioning Investigation of Single Slotted Flaps on a 47.7° Sweptback Wing at Reynolds Numbers of 4.0×10^6 and 6.0×10^6. NACA RM L50H29, 1950. (U)

24. Mollenberg, E. F., and Spooner, S. H.: Low-Speed Investigation of the Effects of Single Slotted and Doubled Slotted Flaps on a 47.7° Sweptback Wing – Fuselage Combination at a Reynolds Number of 6.0×10^6. NACA RM L51E24, 1951. (U)

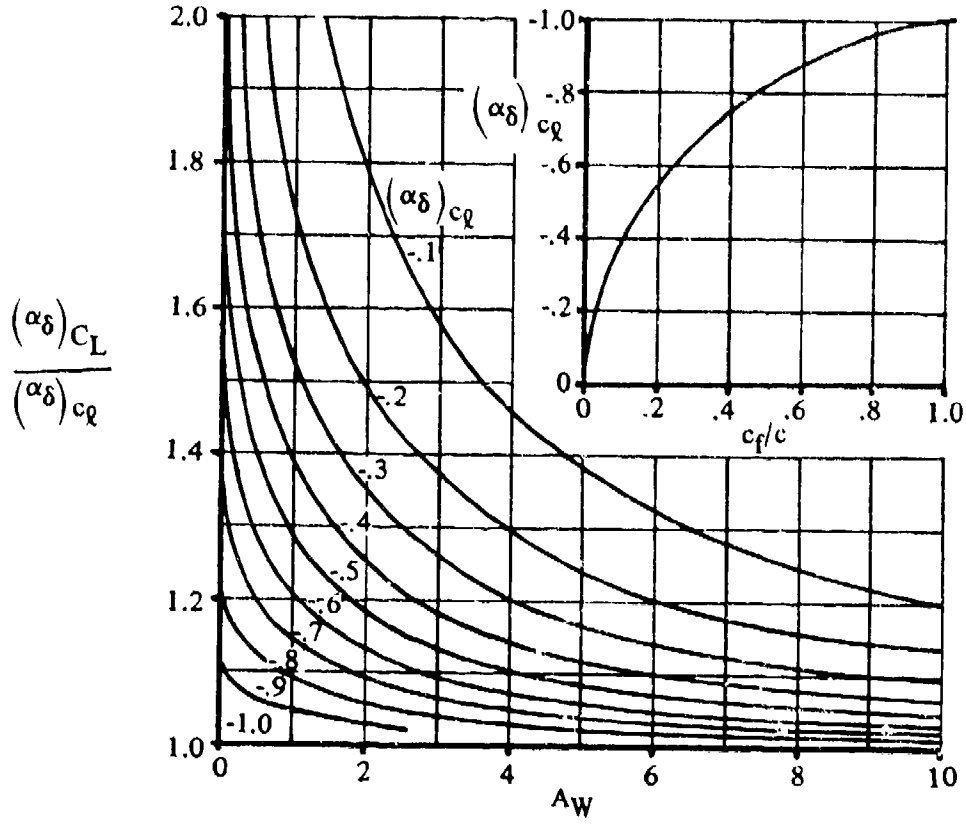

FIGURE 6.1.4.1-14 FLAP-CHORD FACTOR

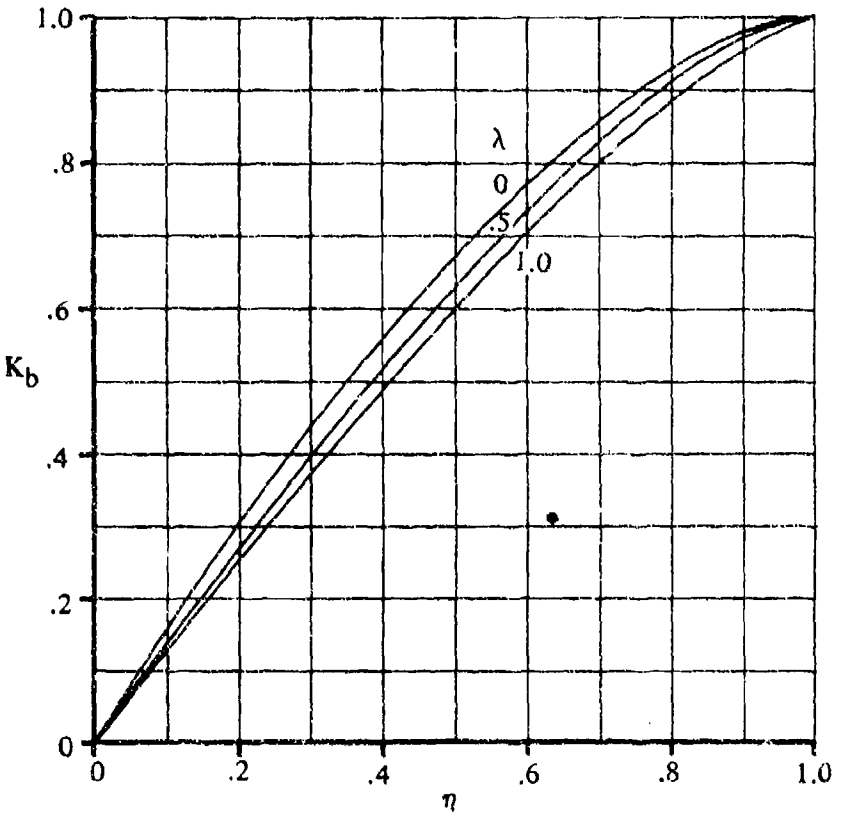

FIGURE 6.1.4.1-15 SPAN FACTOR FOR INBOARD FLAPS

(a) PLAIN FLAPS

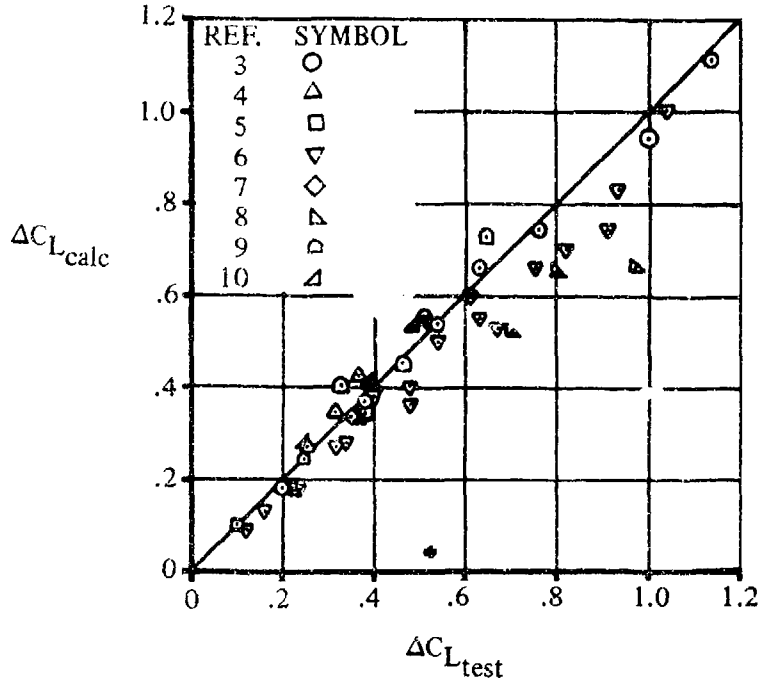

$0.6 \leq R_\ell \times 10^6 \leq 15.0$
$2.0 \leq A \leq 6.0$
$0 \leq \lambda \leq 1.0$
$0 \leq \Lambda_{c/2} \leq 45.5^o$
$0.30 \leq b_f/b \leq 1.0$
$0.10 \leq c_f/c \leq 0.25$
$5^o \leq \delta \leq 60^o$

(b) SPLIT FLAPS

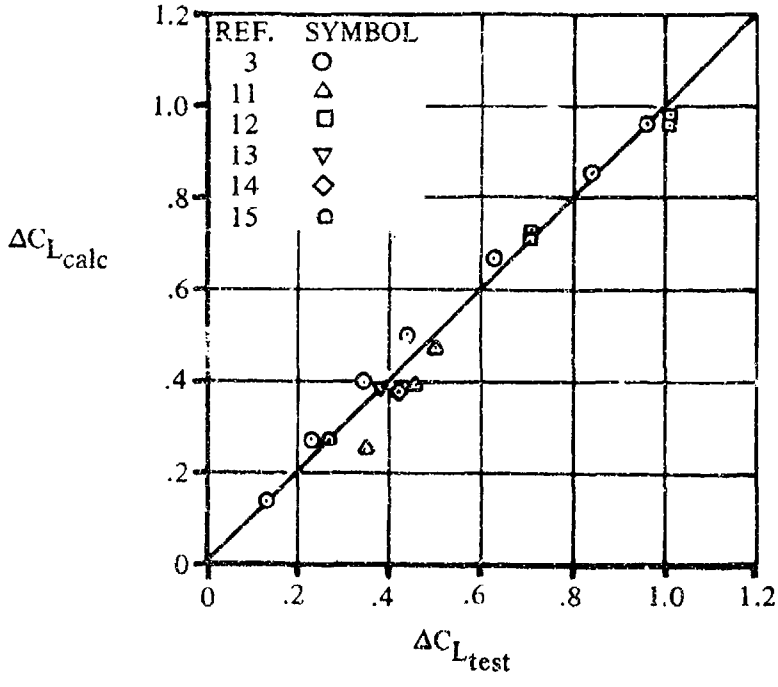

$4.0 \leq R_\ell \times 10^6 \leq 8.4$
$3.94 \leq A \leq 8.02$
$0.40 \leq \lambda \leq 1.0$
$-2.72^o \leq \Lambda_{c/2} \leq 48.3^o$
$0.35 \leq b_f/b \leq 1.0$
$0.177 \leq c_f/c \leq 0.20$
$5^o \leq \delta \leq 60^o$

FIGURE 6.1.4.1-16 CORRELATION OF CALCULATED AND EXPERIMENTAL DATA FOR THE INCREMENTAL LIFT DEVELOPED BY DEFLECTION OF CONTROLS AT SUBSONIC SPEEDS

(c) SLOTTED FLAPS

SINGLE SLOTTED

4.0	≤	$R_\ell \times 10^6$	≤	14.6
2.0	≤	A	≤	9.02
0	≤	λ	≤	0.40
-2.72°	≤	$\Lambda_{c/2}$	≤	56.3°
0.306	≤	b_f/b	≤	0.975
0.20	≤	c_f/c	≤	0.22
9.4°	≤	δ	≤	45°

DOUBLE SLOTTED

$R_\ell = 4.4 \times 10^6$
A = 9.02
λ = 0.40
$\Lambda_{c/2}$ = -2.72°
b_f/b = 0.60
c'/c = 1.144
δ = 50°

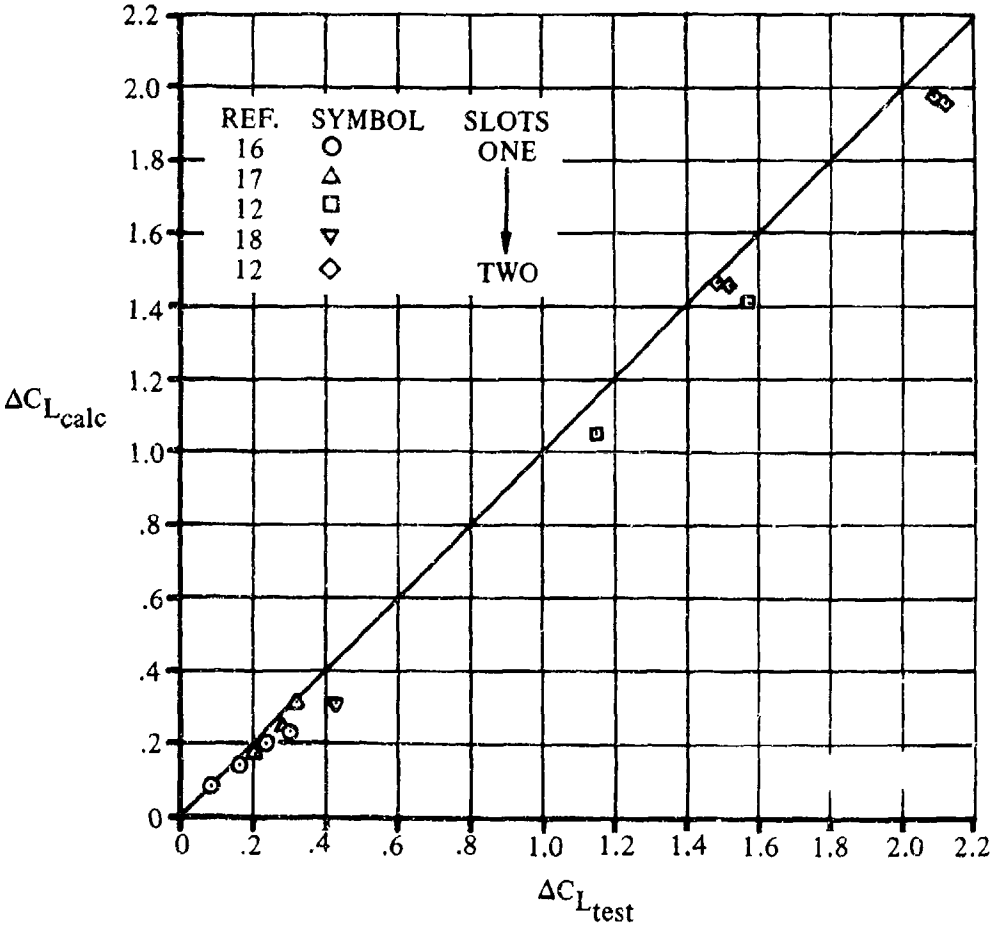

FIGURE 6.1.4.1-16 (CONTD)

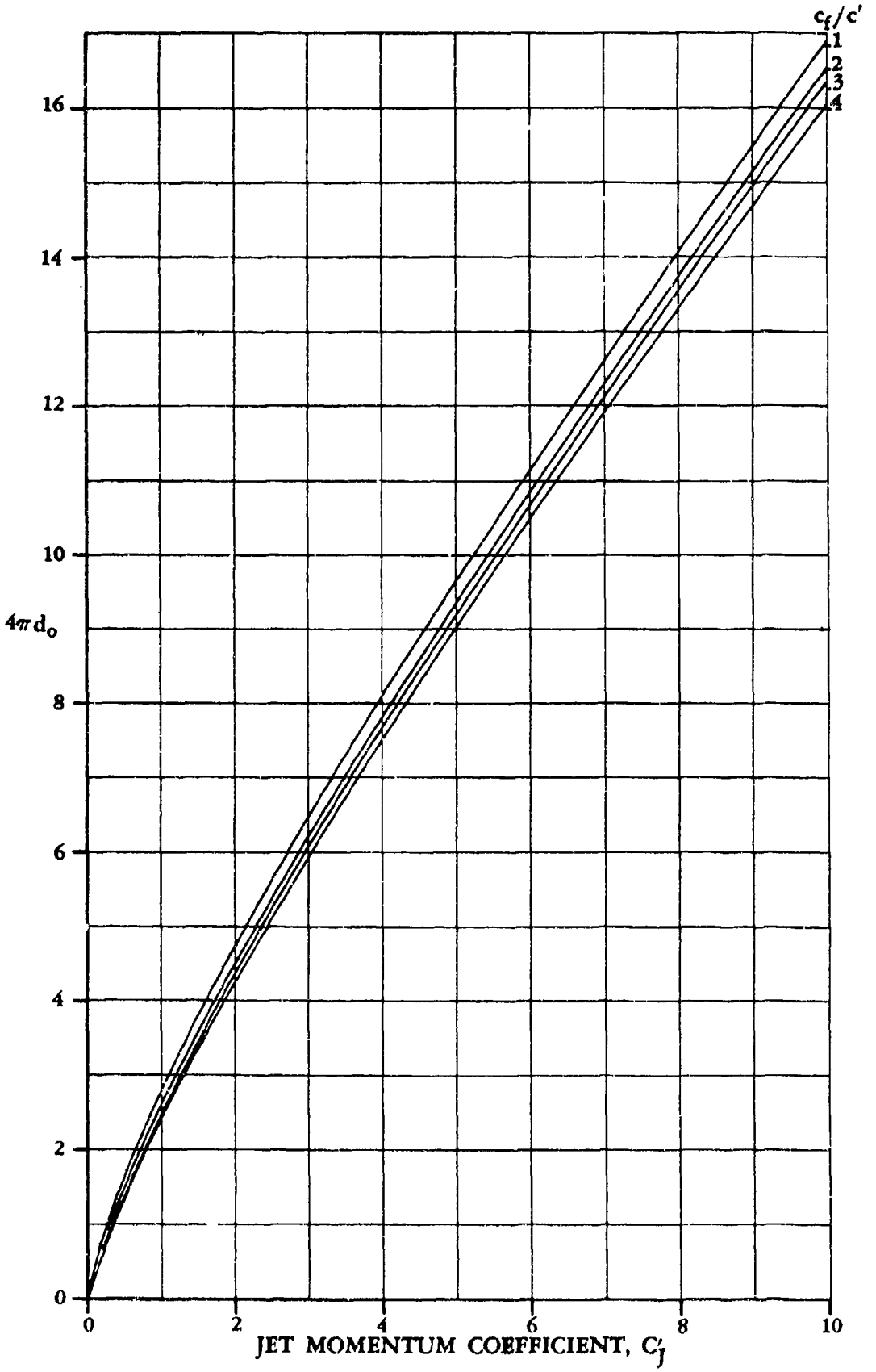

FIGURE 6.1.4.1-18 THEORETICAL CHANGE IN LIFT DERIVATIVE DUE TO BLOWING

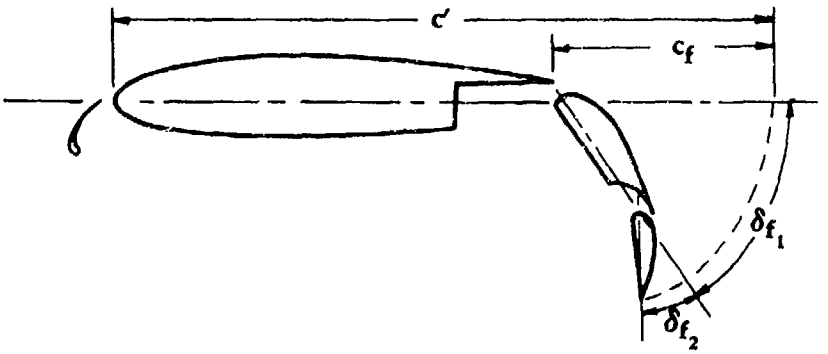

FIGURE 6.1.4.1-19a. FLAP CHORD FOR AN EBF CONFIGURATION

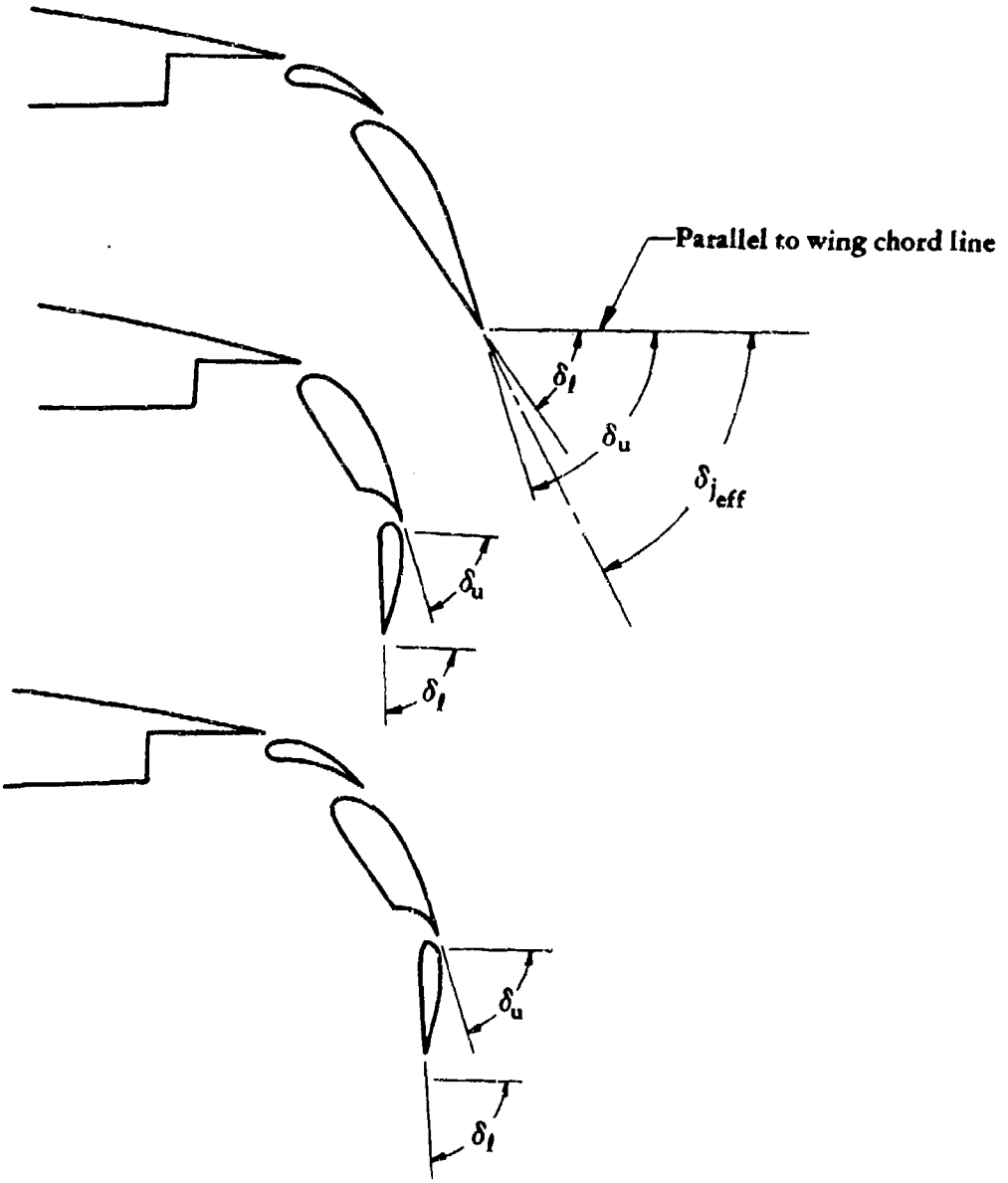

FIGURE 6.1.4.1-19b. EFFECTIVE JET DEFLECTION ANGLE FOR AN EBF CONFIGURATION

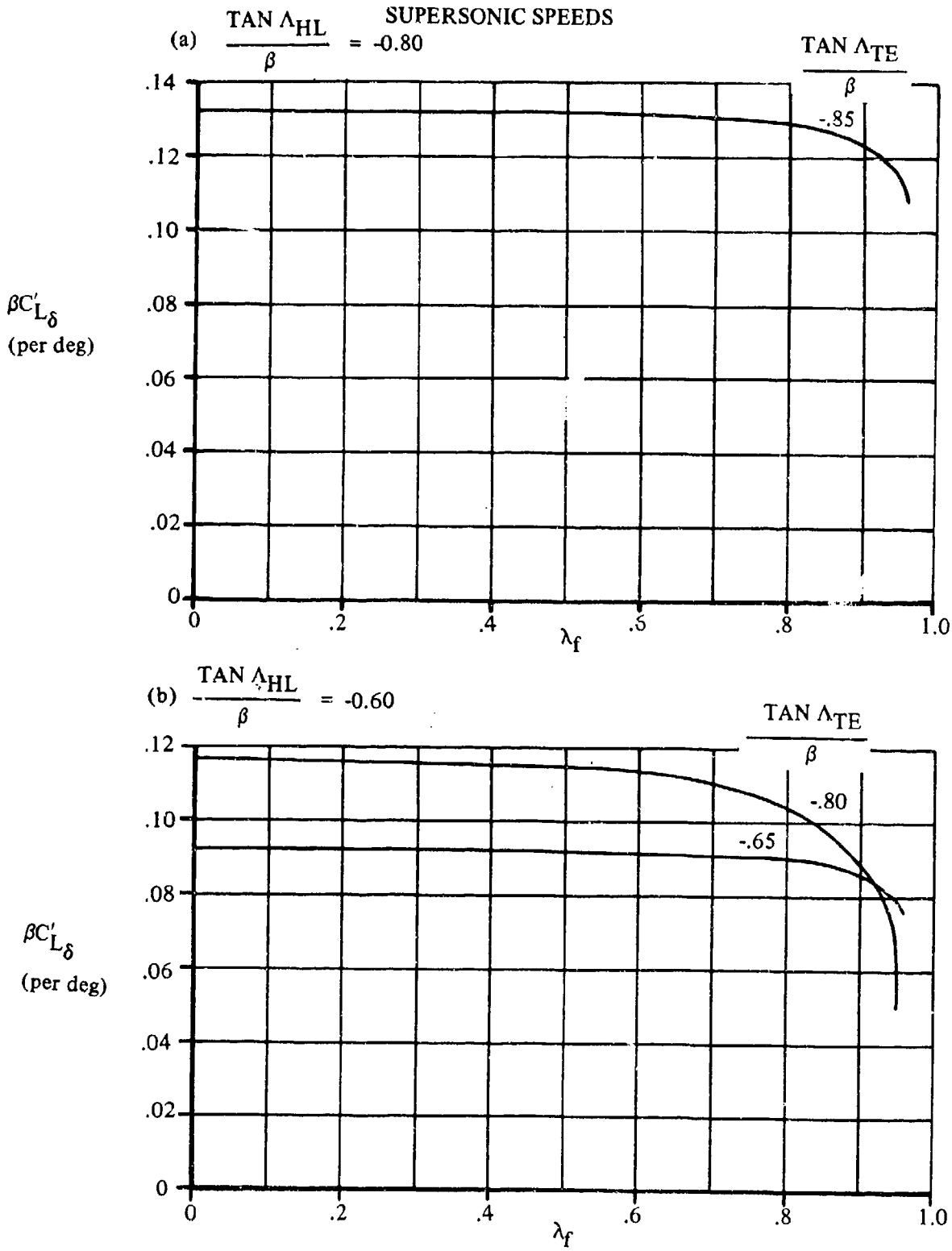

FIGURE 6.1.4.1-20 LIFT PARAMETER FOR DEFLECTED TRAILING-EDGE FLAPS LOCATED AT THE WING TIP

(c) $\frac{\text{TAN } \Lambda_{HL}}{\beta} = -0.40$

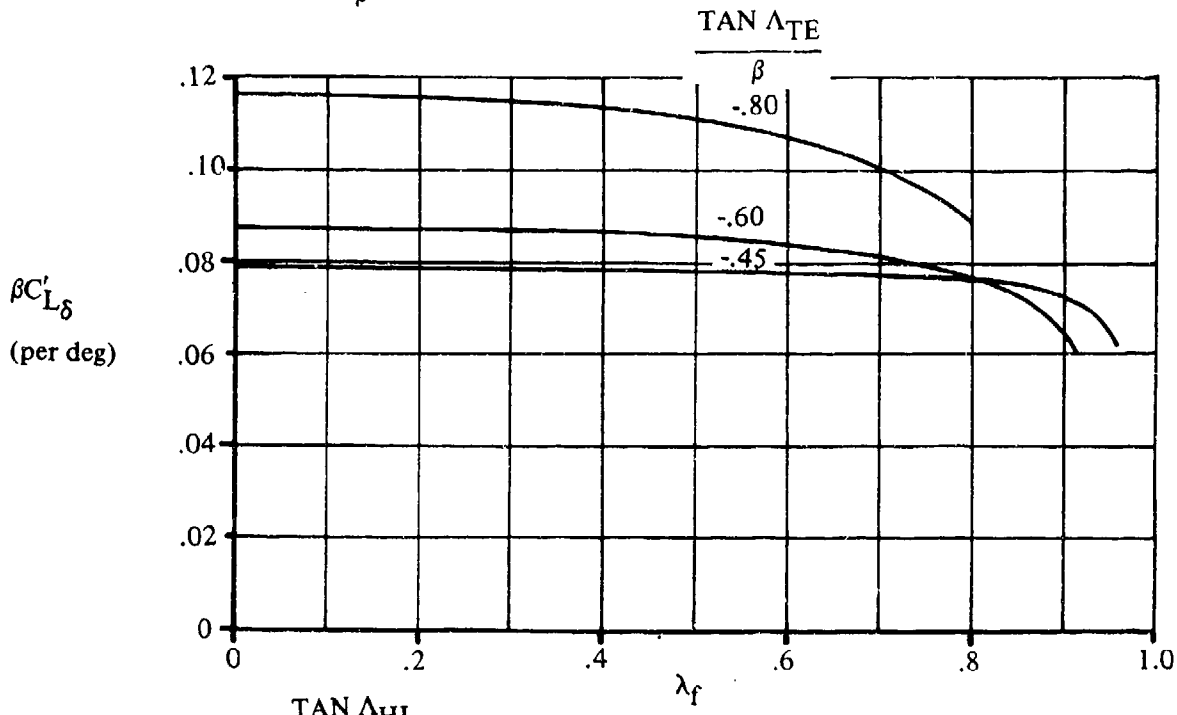

(d) $\frac{\text{TAN } \Lambda_{HL}}{\beta} = -0.20$

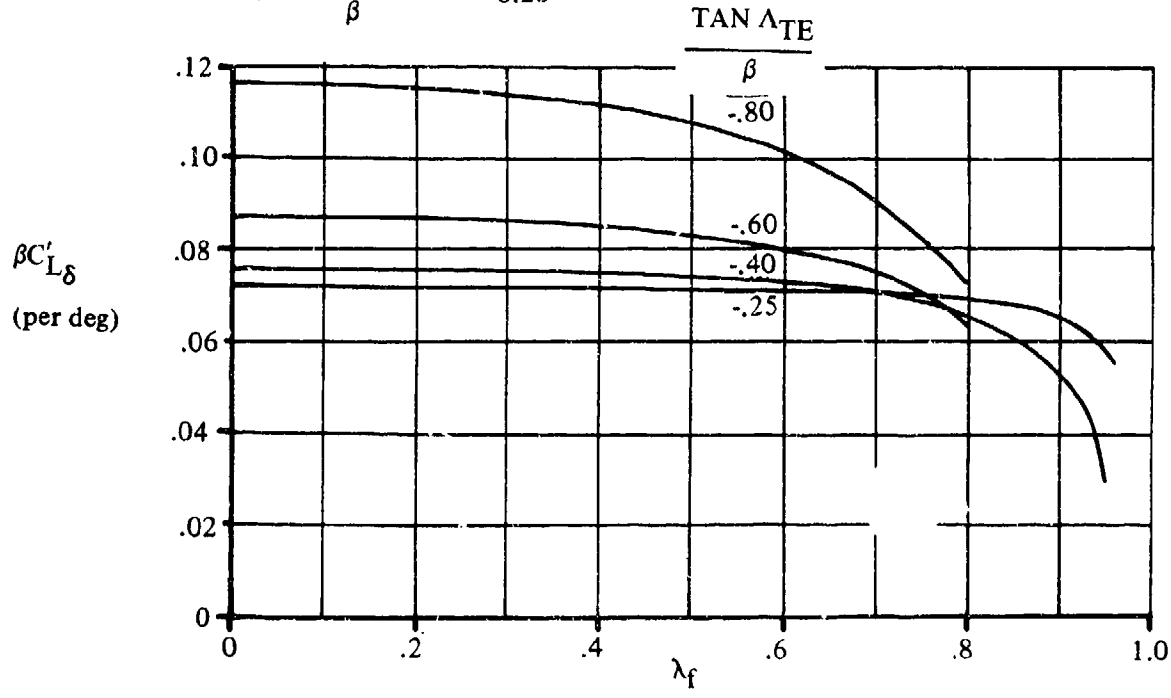

FIGURE 6.1.4.1-20(CONTD)

(e) $\frac{\text{TAN } \Lambda_{HL}}{\beta} = 0$

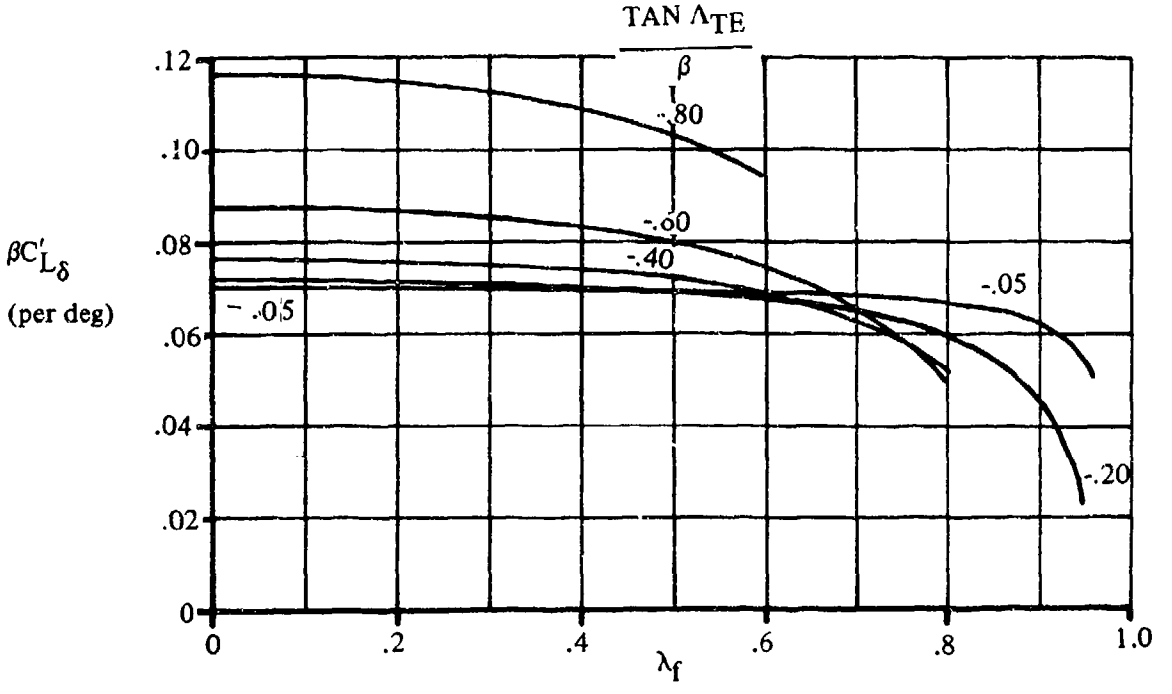

(f) $\frac{\text{TAN } \Lambda_{HL}}{\beta} = 0.20$

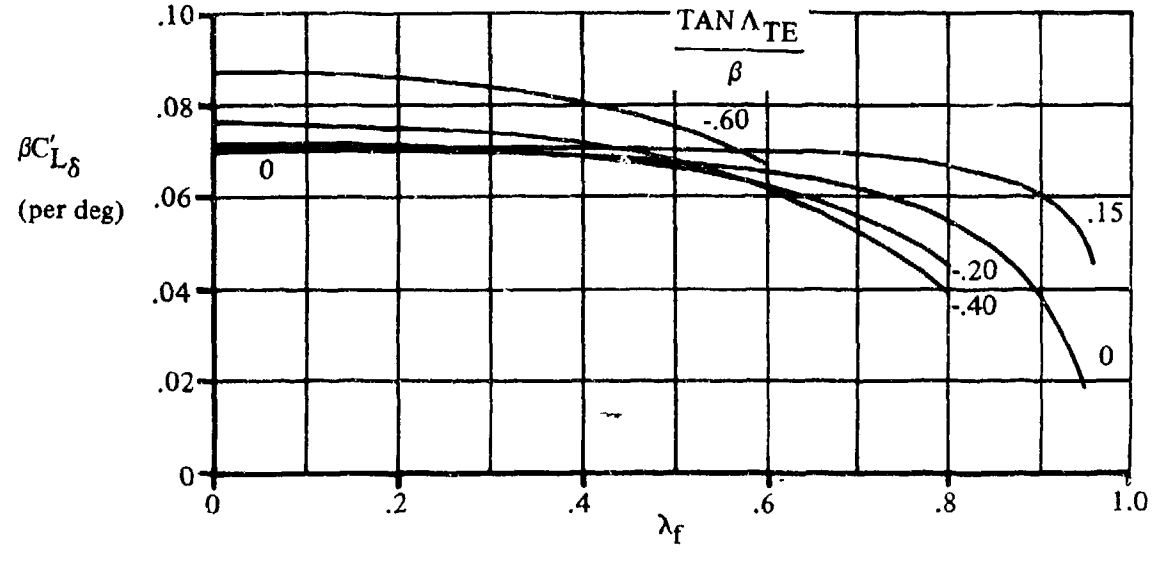

FIGURE 6.1.4.1-20(CONTD)

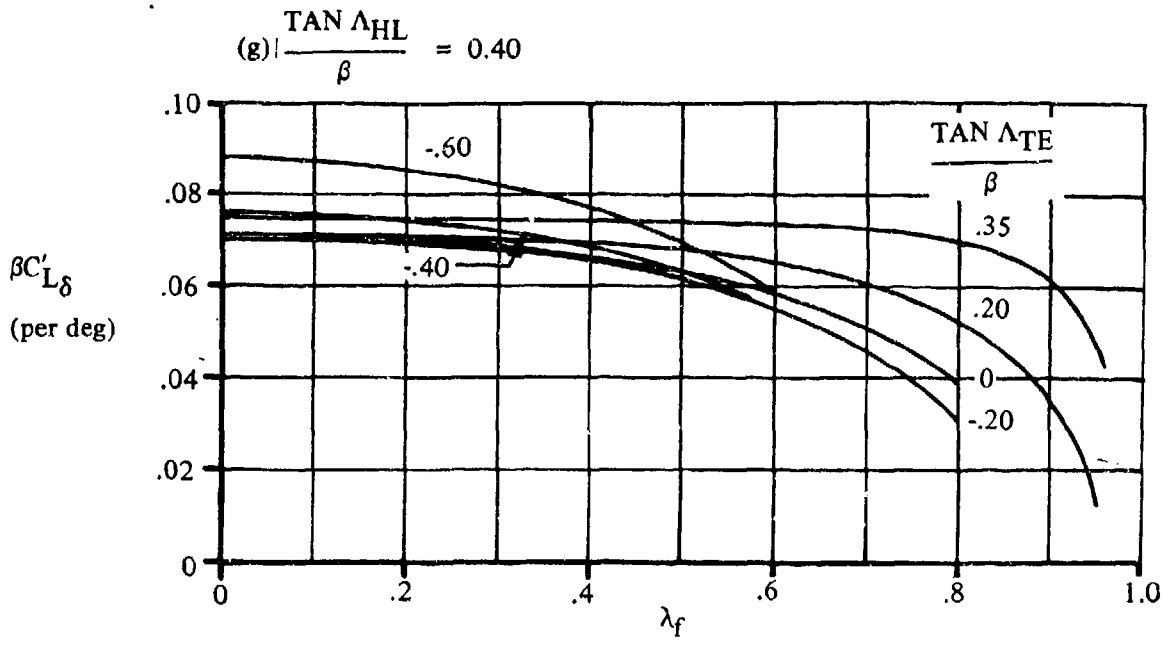

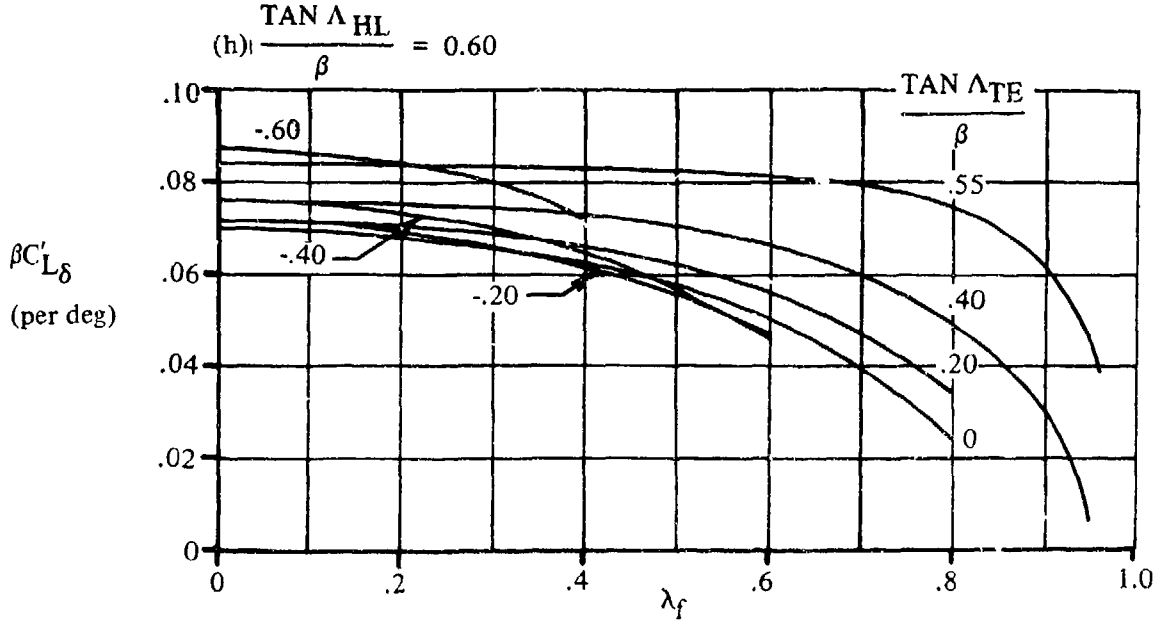

FIGURE 6.1.4.1-20 (CONTD)

SUPERSONIC SPEEDS

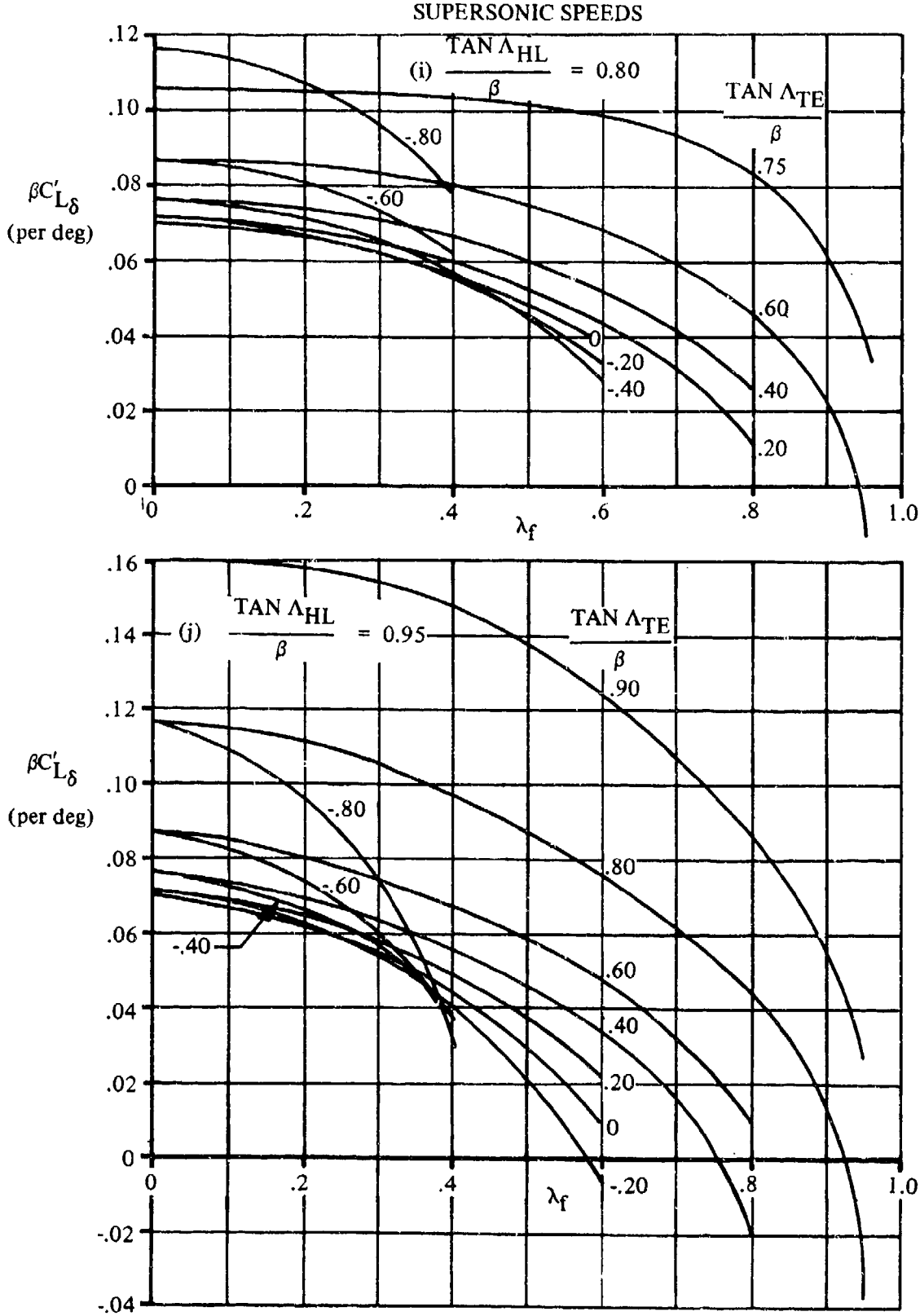

FIGURE 6.1.4.1-20 (CONTD)

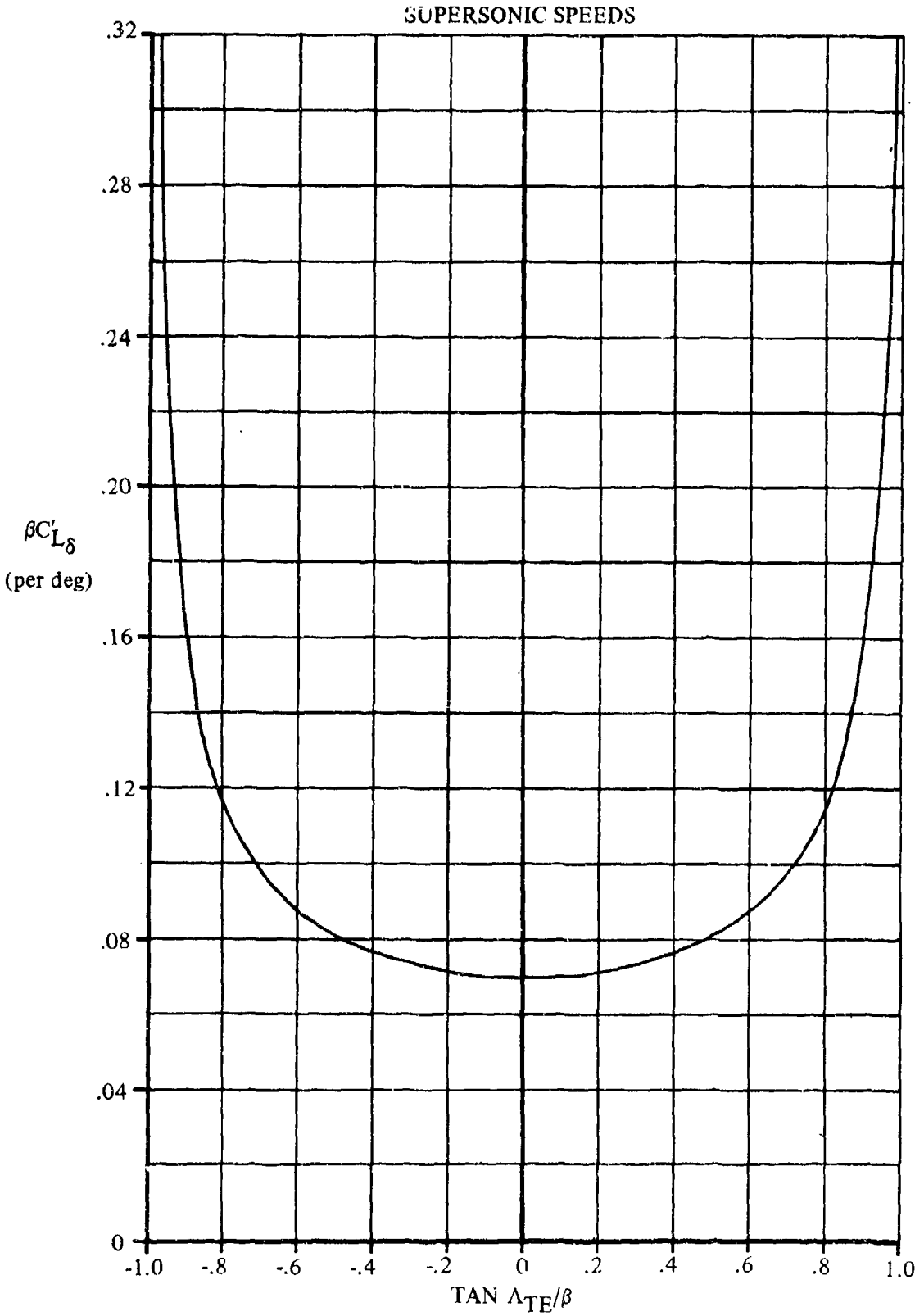

FIGURE 6.1.4.1-25 LIFT PARAMETERS FOR DEFLECTED TRAILING-EDGE FLAPS LOCATED INBOARD FROM WING TIP

6.1.4.2 WING LIFT-CURVE SLOPE WITH HIGH-LIFT AND CONTROL DEVICES

According to linear wing theory, camber, such as that due to flaps, does not affect the lift-curve slope. Linear theory also predicts that, for translating types of leading- or trailing-edge flaps, the lift-curve slope will increase as a result of the additional wing area. Recently, linear theory has also been applied to wings with blown flaps and shows an increase in lift-curve slope with increasing trailing-edge jet momentum. Within the limitation that the flow does not separate from the surface of the wing or flap, experimental data verify these predictions.

The effects of these devices on the two-dimensional airfoil section lift-curve slope are discussed in Section 6.1.1.2. The discussion and methods of that section are directly applicable to the three-dimensional wing.

DATCOM METHODS

1. Leading- and Trailing-Edge Mechanical Flaps

For wings with nontranslating leading- and trailing-edge flaps, the lift-curve slope of the flap-deflected wing is assumed to be the same as that of the flap-retracted wing, as given in Section 4.1.3.2. This assumption is valid for the linear-lift range of angles of attack and flap deflection.

For wings with translating leading- and trailing-edge flaps, a correction is made to the flaps-up lift-curve slope by means of the equation

$$\left(C_{L_\alpha}\right)_\delta = \left[\left(\frac{c'}{c} - 1\right)\frac{S_{W_f}}{S_W}\right]\left(C_{L_\alpha}\right)_{\delta=0} + \left(C_{L_\alpha}\right)_{\delta=0} \qquad \text{6.1.4.2-a}$$

where

$\left(C_{L_\alpha}\right)_\delta$ is the lift-curve slope of the flap-deflected wing, based on the area of the flap-retracted wing.

$\left(C_{L_\alpha}\right)_{\delta=0}$ is the lift-curve slope of the flap-retracted wing from test data or Section 4.1.3.2.

$\frac{S_{W_f}}{S_W}$ is the ratio of the flap-affected wing area to the wing reference area. The area S_{W_f} is schematically illustrated in Section 2.2.2, and does not include any increase in wing due to flap extensions.

$\frac{c'}{c}$ is the ratio of the extended wing chord to the chord of the flap-retracted wing. In measuring c' of a single-slotted trailing-edge flap or a leading-edge slat, the flap or slat is rotated from its deflected position about the point of intersection of the flap or slat chord with the wing chord until the two coincide. In measuring c' of a double-slotted flap, the aft flap is first rotated from its deflected position about the point of intersection of the aft-flap chord and the chord of the forward flap until the two chords coincide; then both flaps are rotated from the deflection of the

forward flap about the point of intersection of the forward-flap chord with the wing chord until these two coincide. (See Figures 6.1.1.1-44 through -46, and -51.)

For the case of arbitrary spanwise distribution of flap chord (constant-chord flaps on tapered wings or tapered flaps on untapered wings), the flap can be divided into spanwise steps and the correction factor to be applied to the flaps-up lift-curve slope found by the summation of the correction factors due to each spanwise step based on the average value of c'/c and S_{W_f}/S_W over that spanwise step.

2. Jet Flaps

The method presented herein for estimating the lift-curve slope of a wing with a blown flap is a modification of the method presented in Reference 1. Similar methods appear in References 2 and 3. The assumptions made in the development of the method are as follows: inviscid flow, elliptical loading, high-aspect-ratio configuration, full-span trailing-edge flaps, and constant spanwise sectional momentum coefficient. Despite these limitations, the theory has been successfully adapted to handle configurations outside the range of these assumptions. Specifically, this method is strictly valid only for the pure jet-flap and the internally-blown-flap (IBF) systems; however, it has been applied with good success to wings with externally-blown flaps (EBF).

This method uses an aspect-ratio correction factor based on Hartunian's work (Reference 4). Mathematically, the aspect-ratio correction factor allows the method to be applied to wings of any aspect ratio. However, the validity of the method for aspect ratios less than five is unknown. The fact that the data presented in Figure 6.1.4.2-9 allow the method to be applied to low-aspect-ratio configurations must not be construed to mean that the Datcom recommends such use.

The corrections of the method for part-span blowing and large trailing-edge flap deflections are not inherent in Hartunian's aspect-ratio correction factor.

An implicit assumption of this method is that the flow on the unblown wing is attached. Unfortunately, the blown-flap systems now being tested do not always exhibit attached flow for an unblown condition. However, such designs are acceptable, since blowing provides a type of automatic boundary-layer control that causes the flow to reattach. But it does prohibit the use of experimental data to determine the lift-curve slope of the unblown flap-deflected wing where separation is a possibility.

The lift-curve slope (near zero angle of attack) of a wing with a trailing-edge jet flap, based on the flap-retracted wing area, is given by

$$C_{L_\alpha} = \left(C_{L_\alpha}\right)_\delta \left\{\left[K(A_t, C_J') - 1\right] K_b + 1\right\} + \frac{C_J \left(\cos \delta_{j_{eff}} - 1\right)}{57.3} \qquad 6.1.4.2\text{-b}$$

where

$\left(C_{L_\alpha}\right)_\delta$ is the lift-curve slope of the unblown flap-deflected wing, with attached flow. This parameter can be obtained from experimental data if no separation exists, or from the mechanical-flap method of this section.

$K(A_t C_J')$ is the jet momentum aspect-ratio correction factor obtained from Figure 6.1.4.2-9 as a function of A_t and C_J', where

A_t is the aspect ratio of the wing based on the total wing area S_t, including any increase in wing area due to flap extension.

C_J' is the three-dimensional trailing-edge jet momentum coefficient based on the blown-flap affected area S_{W_f}; i.e.,

$$C_J' = C_J \frac{S_W}{S_{W_f}}$$

where

S_{W_f}/S_W is the ratio of the blown-flap affected area (schematically illustrated in Sketch (a)) to the wing reference area. The blown-flap affected area includes any increase in wing area due to flap extensions.

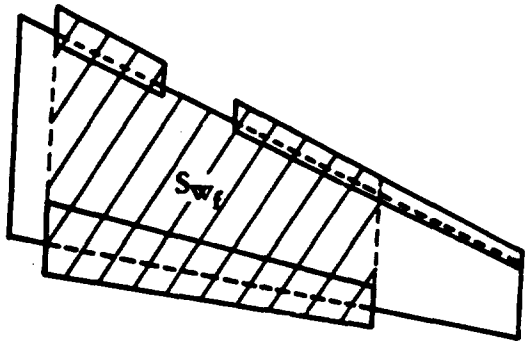

SKETCH (a)

K_b is the flap-span factor from Figure 6.1.4.1-15, using the $\lambda = 1$ curve, as illustrated in Sketch (a) of Section 6.1.4.1.

C_J is the trailing-edge jet momentum coefficient based on the flap-retracted wing area.

$\delta_{j_{eff}}$ is the effective jet deflection angle with respect to the airfoil chord, in degrees. If possible, this value should be obtained from static force tests. When test data are not available for an externally-blown-flap (EBF) configuration, the effective flap deflection angle may be approximated by using Equation 6.1.4.1-d, i.e.,

$$\delta_{j_{eff}} = \frac{1}{2}(\delta_u + \delta_\ell)$$

where the values for δ_u and δ_ℓ are shown schematically in Figure 6.1.4.1-19b.

A data summary and substantiation of this method are presented in Table 6.1.4.2-A.

Sample Problems

1. Leading-edge slat

Given: The wing of Reference 5 with a 50-percent-span leading-edge slat.

$A = 6.0 \qquad \Lambda_{c/2} = 32.8^{\circ} \qquad \lambda = 0.50 \qquad c'/c = 1.10 \qquad S_{W_f}/S_W = 0.429$

Low speed; $\beta = 1.0 \qquad \kappa = 1.0$ (assumed)

Compute:

$$\frac{A}{\kappa}\left[\beta^2 + \tan^2 \Lambda_{c/2}\right]^{1/2} = (6.0)\left[1.0 + (0.6445)^2\right]^{1/2} = 7.14$$

$$\frac{(C_{L_\alpha})_{\delta=0}}{A} = 0.67 \text{ per rad} \quad \text{(Figure 4.1.3.2-49)}$$

$$(C_{L_\alpha})_{\delta=0} = 4.02 \text{ per rad} = 0.0702 \text{ per deg}$$

Solution:

$$(C_{L_\alpha})_\delta = \left[\left(\frac{c'}{c} - 1\right)\frac{S_{W_f}}{S_W}\right](C_{L_\alpha})_{\delta=0} + (C_{L_\alpha})_{\delta=0} \quad \text{(Equation 6.1.4.2-a)}$$

$$= [(1.10 - 1.0)(0.420)]\ 0.0702 + 0.0702$$

$$= 0.0732 \text{ per deg (based on } S_W)$$

This compares with a test value of 0.0720 per degree from Reference 5.

2. Jet Flap

Given: The sweptback wing-body configuration of Reference 6 with a trailing-edge double-slotted EBF system.

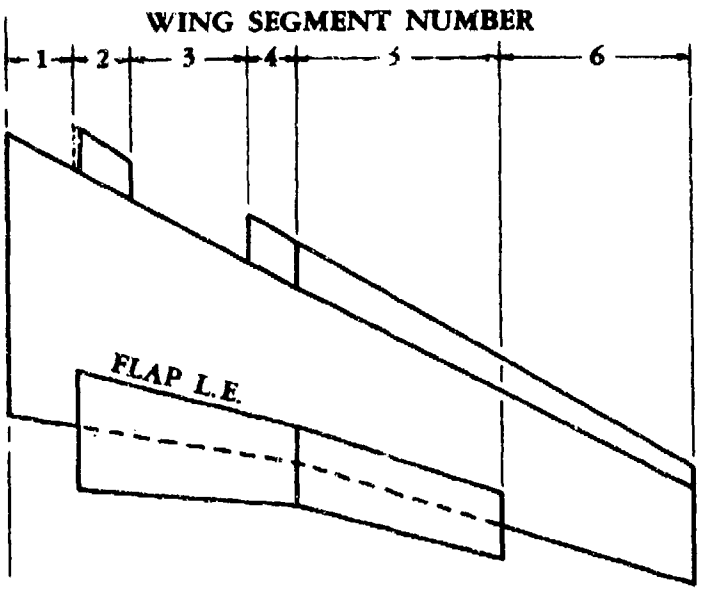

Note: All leading-edge and trailing-edge devices are shown rotated into the wing plane.

Wing Characteristics:

$A = 7.75$ $S_W = 7.87\ ft^2$ $b = 95.08$ in.

$\lambda = 0.336$ $c_r = 19.49$ in. $c_t = 6.54$ in.

$\bar{c} = 13.22$ in. $y_{\bar{c}} = 19.33$ in.

To facilitate calculations, the wing has been divided into segments as shown in the preceding sketch. The divisions are made at the sweep discontinuity and at the discontinuities in leading- and trailing-edge flaps.

Sections	$S(ft^2)$ (flaps retracted)	c'/c	$S_t(ft^2)$ (flaps extended)
1	1.253	1.000	1.253
2	0.909	1.421	1.311
3	1.650	1.253	2.069
4	0.617	1.521	0.933
5	2.076	1.521	3.178
6	1.365	1.268	1.847
Value for the entire wing	7.870		$10.59\ ft^2$

Flap Characteristics:

Double-slotted trailing-edge flap:

Forward segment: $c_f/c = 0.22$ $\delta_{f_1} = 30^o$

Aft segment: $c_f/c = 0.24$ $\delta_{f_2} = 30^o$

$\eta_i = 0.102$ $\eta_o = 0.720$ $\delta_{j_{eff}} = 60^o$

Krueger leading-edge flap:

Inboard segment: $c_f/c = 0.168$

Outboard segment: $c_f/c = 0.268$

Additional Characteristics:

$R_\ell = 0.35 \times 10^6$ $\quad V = 50$ ft/sec $\quad C_J = 3.18$

Low speed; $\beta = 1.0$ $\quad \kappa = 1.0$ (assumed) $\quad \Lambda_{c/2} = 21.1^\circ$ (average value)

Compute:

Determine the unblown lift-curve slope for both leading- and trailing-edge flap extension.

$$\frac{A}{\kappa}\left[\beta^2 + \tan^2 \Lambda_{c/2}\right]^{1/2} = \frac{7.75}{1.0}\left[1.0 + (0.3859)^2\right]^{1/2} = 8.307$$

$$\frac{(C_{L_\alpha})_{\delta=0}}{A} = 0.602 \text{ per rad} \quad \text{(Figure 4.1.3.2-49)}$$

$$(C_{L_\alpha})_{\delta=0} = 4.666 \text{ per rad} = 0.0814 \text{ per deg}$$

Since the wing has been divided into 6 segments, Equation 6.1.4.2-a should be written as

$$(C_{L_\alpha})_\delta = \sum_{n=1}^{6}\left[\left(\frac{c'}{c} - 1\right)\frac{S_{W_f}}{S_W}\right](C_{L_\alpha})_{\delta=0} + (C_{L_\alpha})_{\delta=0} \quad \text{(Equation 6.1.4.2-a)}$$

$$= \left[(1.0 - 1.0)\frac{0}{7.87} + (1.421-1.0)\frac{0.909}{7.87} + (1.253-1.0)\frac{1.650}{7.87} + (1.521-1.0)\frac{0.617}{7.87}\right.$$

$$\left. + (1.521-1.0)\frac{2.076}{7.87} + (1.278-1.0)\frac{1.365}{7.87}\right]0.0814 + 0.0814$$

$$= (0.3264)(0.0814) + 0.0814$$

$$= 0.108$$

Determine the blown lift-curve slope for both leading- and trailing-edge flap extension.

$$A_t = \frac{(95.08)^2}{(144)(10.59)} = 5.928$$

The value of S_{W_f} is found by adding the flap-extended wing area for segments 2 through 5; i.e., $S_{W_f} = 7.491$ ft^2.

$$C_J' = C_J\frac{S_W}{S_{W_f}}$$

$$= 3.18\frac{7.87}{7.491}$$

$$= 3.34$$

$$K(A_t, C_J') = 1.795 \quad \text{(Figure 6.1.4.2-9)}$$

$$\left.\begin{aligned}(K_b)_{\eta_i} &= 0.13 \\ (K_b)_{\eta_o} &= 0.82\end{aligned}\right\} \quad \text{(Figure 6.1.4.1-15)}$$

$$K_b = 0.82 - 0.13 = 0.69$$

Solution:

$$C_{L_\alpha} = (C_{L_\alpha})_\delta \left\{[K(A_t, C_J') - 1]\, K_b + 1\right\} + \frac{C_J(\cos \delta_{j_{eff}} - 1)}{57.3} \quad \text{(Equation 6.1.4.2-b)}$$

$$= (0.108)\left\{[1.795 - 1](0.69) + 1\right\} + \frac{3.18(0.50 - 1)}{57.3}$$

$$= 0.167 - 0.0277$$

$$= 0.139 \text{ per deg}$$

This compares with a test value of 0.130 per degree from Reference 6.

REFERENCES

1. May, F.W.: State-of-the-Art Design Compendium – STOL Aerodynamic Technology (Internally Blown Jet Flaps). Boeing D180-14299-1, 1971. (U)

2. Ramsey, J.C., and Lausdeman, E.C.: STOL Tactical Aircraft Investigation State-of-the-Art Design Compendium. Prepared under USAF Contract F33615-71-C-1754, 1971. (U)

3. May, F.W., and Widdison, C.A.: STOL High-Lift Design Study. Vol. 1. State-of-the-Art Review of STOL Aerodynamic Technology. AFFDL-TR-71-26, Vol. 1, 1971. (U)

4. Hartunian, R.A.: The Finite Aspect Ratio Jet Flap. CAL A1-1190-A-3, 1959. (U)

5. Koven, W., and Graham, R.R.: Wind-Tunnel Investigation of High-Lift and Stall Control Devices on a 37° Sweptback Wing of Aspect Ratio 6 at High Reynolds Numbers. NACA RM L8D29, 1948. (U)

6. Freeman, D.C., Jr., Parlett, L.P., and Henderson, R.L.: Wind-Tunnel Investigation of a Jet Transport Airplane Configuration with an External-Flow Jet Flap and Inboard Pod-Mounted Engines. NASA TN D-7004, 1970. (U)

7. Smith, C.C., Jr.: Effect of Engine Position and High-Lift Devices on Aerodynamic Characteristics of an External-Flow Jet-Flap STOL Model. NASA TN D-6222, 1971. (U)

8. Alexander, A.J., and Williams, J.: Wind-Tunnel Experiments on a Rectangular-Wing Jet-Flap Model of Aspect Ratio 6. ARC R&M 3329, 1964. (U)

9. Aoyagi, K., and Hall, L.P.: Wind-Tunnel Investigation of a Large 35° Swept-Wing Jet Transport Model with an External-Flow Jet-Augmented Double-Slotted Flap. NASA TN D-6482, 1971. (U)

10. Vogler, R.D.: Wind-Tunnel Investigation of a Four-Engine Externally Blown Jet-Flap STOL Airplane Model. NASA TN D-7034, 1970. (U)

11. Turner, T.R.: Low-Speed Investigation of a Full-Span Internal-Flow Jet-Augmented Flap on a High-Wing Model with a 35° Swept Wing of Aspect Ratio 7.0. NASA TN D-434, 1960. (U)

12. Campbell, J.P., and Johnson, J.L., Jr.: Wind-Tunnel Investigation of an External-Flow Jet-Augmented Slotted Flap Suitable for Application to Airplanes with Pod-Mounted Jet Engines. NACA TN 3898, 1956. (U)

13. Aerodynamic Subdivision, Douglas Aircraft Company: Summary of Low Speed Wind Tunnel Data on Several Externally Blown Flap STOL Transport Configurations. MDC J5431, 1972. (U)

TABLE 6.1.4.2-A

EFFECT OF JET MOMENTUM ON LIFT-CURVE SLOPE
DATA SUMMARY AND SUBSTANTIATION
SUBSONIC

Ref	A	$\Lambda_{c/2}$ (deg)	$\delta_{j_{eff}}$ (deg)	Flap Type	C_J	C_{L_α} Calc	C_{L_α} Test	e Percent Error
6	7.75	21.1	60	Double-slotted EBF with L. E. Krueger	1.06	0.122	0.110	10.9
↓	↓	↓	↓	↓	2.12	0.133	0.130	2.3
↓	↓	↓	↓	↓	3.18	0.141	0.130	8.5
↓	↓	↓	↓	↓	4.24	0.146	0.139	5.0
7*	7.0	0	35	Double-slotted EBF with L. E. slat	2.75	0.153	0.178	−14.0
↓	↓	↓	↓	↓	4.13	0.168	0.200	−16.0
↓	↓	↓	↓	↓	5.50	0.181	0.220	−17.7
↓	↓	↓	55	↓	4.13	0.167	0.160	4.4
↓	↓	↓	↓	↓	5.50	0.179	0.192	−6.8
8	6.0	0	30	Plain IBF	0.95	0.097	0.100	−3.0
↓	↓	↓	↓	↓	2.07	0.115	0.116	−0.9
9	7.82	32.4	20	Double-slotted EBF with	2.0	0.128	0.145	−11.7
↓	↓	↓	50	L. E. slat	2.0	0.118	0.114	3.5
10	7.0	21.3	60	Double-slotted EBF with	2.0	0.120	0.120	0
↓	↓	↓	↓	L. E. slat	3.0	0.127	0.127	0
13	7.0	21.8	23	Double-slotted EBF with	2.0	0.125	0.147	−15.0
↓	↓	↓	60	L. E. slat & flap	3.0	0.124	0.144	−13.9
↓	7.0	3.1	60	L. E. slat	2.9	0.158	0.133	18.8
11	7.0	31.9	18.8	Plain IBF	3.09	0.125	0.149	−16.1
12	6.52	26.9	60	Single-slotted EBF	2.95	0.103	0.112	−8.0

$$\text{Average Error} = \frac{\Sigma|e|}{n} = 8.8\%$$

*The data indicate that the flow is probably unattached, which may account for the large errors in this case.

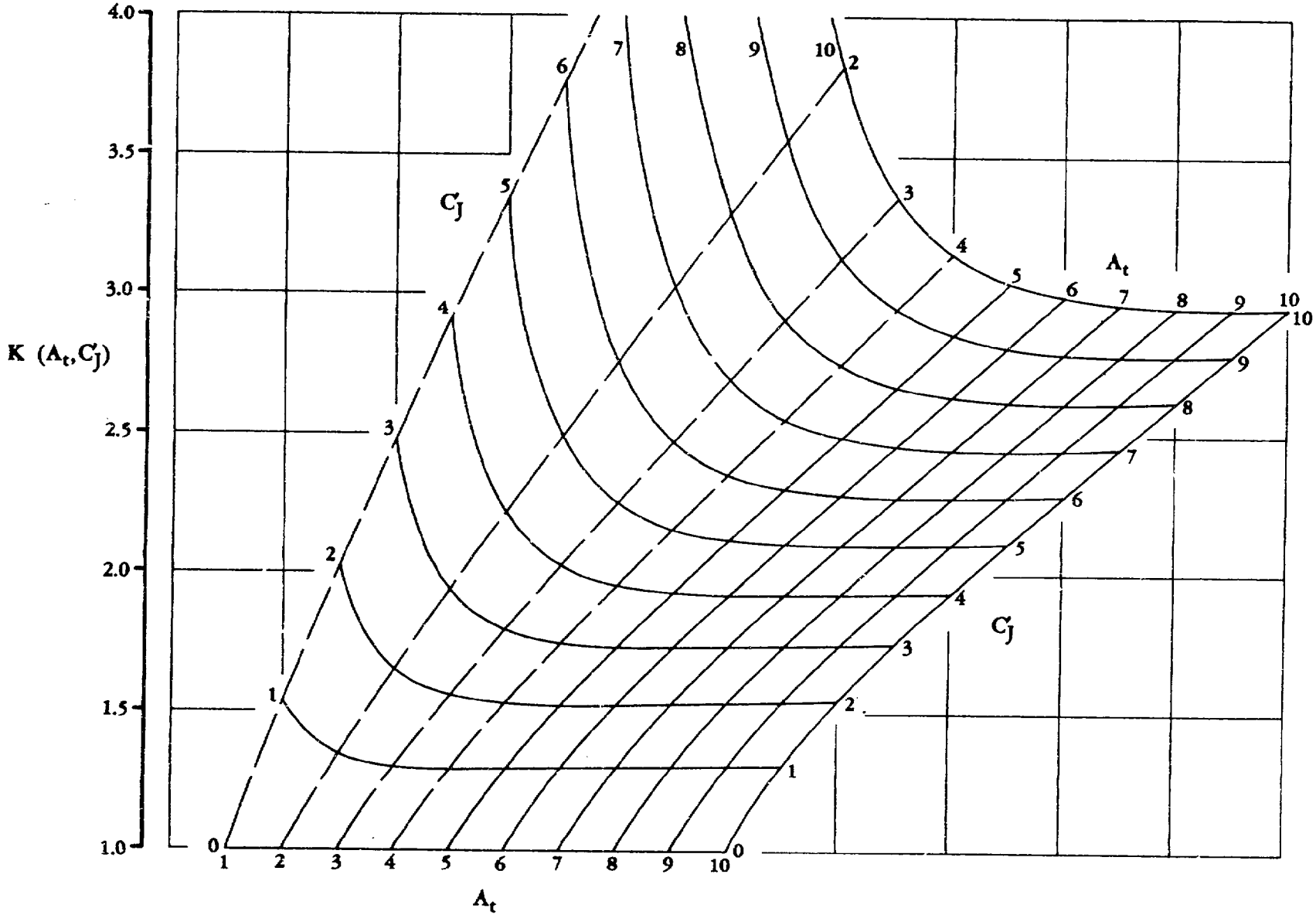

FIGURE 6.1.4.2-9 JET MOMENTUM FACTOR FOR BLOWN FLAPS

6.1.4.3 WING MAXIMUM LIFT WITH HIGH-LIFT AND CONTROL DEVICES

The estimation of wing maximum-lift coefficient is at best approximate. The stalling characteristics of various kinds of wings often take on an entirely different character from the stalling characteristics of airfoil sections. Stall may begin at the wing tips or may occur initially at the inboard flapped sections, depending upon the amount of sweep, taper ratio, and the difference in stall angle between the flapped and unflapped sections. Leading-edge devices can markedly alter the character of the stall. Large crossflow components on the wing at the stall make estimates based on section data inaccurate.

Tabulated data from 142 reports are presented in Reference 1. Results are shown for many planforms with and without various configurations of leading- and trailing-edge flaps, fences, and slats. Values of $C_{L_{max}}$ and $\alpha_{C_{L_{max}}}$ are given in tabular form. Summary data from Reference 1 are shown in Figures 6.1.4.3-7 through 6.1.4.3-9.

Figure 6.1.4.3-7 illustrates the effect of sweep on the maximum lift effectiveness of trailing-edge flaps. It can be seen that at high angles of sweep, flap deflection can actually decrease maximum lift. This results partially from the additional induced effects when flaps are deflected, causing the tips to stall. Figure 6.1.4.3-8 shows representative effects on $C_{L_{max}}$ of two sweptback wings with varying flap-span ratios.

Because of their boundary-layer-control properties, double-slotted flaps are capable of producing larger $C_{L_{max}}$ increments.

Maximum lift increments of leading-edge and trailing-edge flaps cannot, in general, be added when these devices are used in combination. A brief summary of maximum lift coefficients for swept wings is presented in Figure 6.1.4.3-9.

Separate methods are presented herein for estimating the wing maximum lift due to each of the following: mechanical trailing-edge flaps, slats, and jet flaps (externally-blown flaps only).

Mechanical Trailing-Edge Flaps

The Datcom method for trailing-edge flaps is semiempirical and converts two-dimensional data into three-dimensional characteristics as affected by wing planform, airfoil section characteristics across the span, flap type and geometry, and flap span. The method is intended to be used as a first-order approximation of wing maximum-lift coefficients when experimental data are not available.

Slats

The Datcom method for slats is an empirical method that assumes a section maximum-lift value of 1.28. This method estimates the maximum obtainable lift increment for a particular slat span, slat-chord-to-wing-chord ratio, and wing quarter-chord sweep. If a test value for the slat section maximum lift is available, it can be substituted for the assumed value of 1.28. Attempts to use the predicted section maximum-lift value from Section 6.1.1.3 have been unsatisfactory, as the resulting estimates underpredicted the test values. The method has not been substantiated beyond the test data that were used to formulate the method (which indicated a variation in agreement). Therefore, the method is intended to be used only as a first approximation of the slat maximum-lift increment when experimental data are not available.

Jet Flaps

The jet-flap method presented is for predicting the maximum-lift coefficient for an externally-blown-flap (EBF) configuration; no method is currently presented for an internally-blown-flap (IBF) configuration. The Datcom method for EBF configurations is an empirical approximation

taken from Reference 2. The maximum-lift coefficient therein is reasoned to be a function of the total camber of the wing, and blowing is considered to act as an effective camber increase. The measurement of the increase in camber is taken to be the component of thrust normal to the airfoil. This method is intended to be a first-order approximation of the maximum-lift increment due to power effects. Substantiation of this method is not presented here; however, a substantiation of the method does appear in References 2 and 3.

A semiempirical method for an EBF configuration, based on the assumption of a leading-edge stall and the use of basic jet-flap theory, is given in Reference 3. The method provides good correlation with measured values when an empirical factor is added. However, the use of this method depends upon the availability of test data for the effective jet deflection angle, the measured turning efficiency, and the power-off stall angle of attack. If these test data are available, this method is preferable to the Datcom method presented herein.

DATCOM METHODS

1. Mechanical Trailing-Edge Flaps

The increment in maximum-lift coefficient due to trailing-edge flap deflection is given by the equation

$$\Delta C_{L_{max}} = \Delta c_{\ell_{max}} \frac{S_{W_f}}{S_W} K_\Lambda \qquad 6.1.4.3\text{-a}$$

where

$\Delta c_{\ell_{max}}$ is the increment in airfoil section maximum-lift coefficient due to trailing-edge flaps, obtained from Section 6.1.1.3.

$\frac{S_{W_f}}{S_W}$ is the ratio of the flap-affected wing area to the total wing area. The flap-affected wing area does not include any increase in wing area due to flap extension.

K_Λ is an empirically derived correction factor that accounts for the effects of wing planform. This parameter is obtained from Figure 6.1.4.3-10 as a function of the sweepback of the wing quarter-chord line.

It should be noted that the flap deflection angles and all dimensions are measured in planes parallel or perpendicular to the plane of symmetry.

2. Slats

The increment in maximum-lift coefficient due to leading-edge slat deflection, based on the wing reference area, is given by

$$\Delta C_{L_{max}} = 1.28 \left(\frac{c_f/c}{0.18}\right) \left(\frac{b_{slat}}{b_e}\right)^2 \cos^2 \Lambda_{c/4} \qquad 6.1.4.3\text{-b}$$

where

$\frac{c_f}{c}$ is the ratio of the leading-edge-slat chord to the wing chord (see Figure 6.1.1.1-51).

$\frac{b_{slat}}{b_e}$ is the ratio of the total slat span to the exposed wing span. For a segmented leading-edge slat, b_{slat} is the total span of the segments. (See Section 4.3.1.2 for the definition of the exposed wing span.)

$\Lambda_{c/4}$ is the sweep of the quarter chord.

3. Jet Flaps

The increment in maximum-lift coefficient due to power effects for an EBF configuration is approximated from Figure 6.1.4.3-12, as a function of the thrust normal to the airfoil, defined as

$$\eta_t C_J \sin \delta_{j_{eff}}$$

where

η_t is the static turning efficiency defined as the resultant force divided by the gross thrust. This value should be obtained from test data if available, or it may be approximated for double- or triple-slotted flaps from Figure 6.1.4.3-11, as a function of the effective jet deflection angle. (See Sketch (a).)

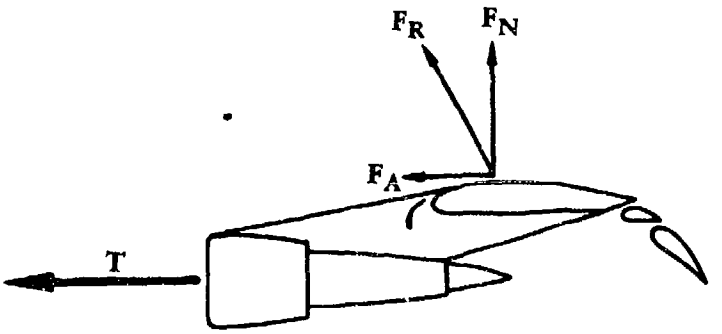

$$\delta_{j_{eff}} = \tan^{-1} (F_N/F_A)$$

$$\eta_t = F_R/T$$

SKETCH (a)

C_J is the nondimensional trailing-edge jet momentum coefficient based on the gross engine thrust and the wing reference area. (See Section 6.1.4.1 for a definition.)

$\delta_{j_{eff}}$ is the effective jet deflection angle with respect to the airfoil chord. If possible, this value should be obtained from static force tests. When test data are not available, the effective flap deflection angle may be approximated by using Equation 6.1.4.1-d; i.e.,

$$\delta_{j_{eff}} = \frac{1}{2} (\delta_u + \delta_\ell)$$

where δ_u and δ_ℓ are defined in Section 6.1.4.1.

Sample Problems

1. Mechanical Trailing-Edge Flaps

Given: The wing-flap configuration of Reference 2.

$A = 5.1$ $\quad \lambda = 0.383$ $\quad \Lambda_{c/4} = 46^{o}$

NACA 64-210 airfoil (Ł286c) $\quad (t/c)_{streamwise} = 0.072$

Single-slotted flap $\quad c_f/c = 0.258$ $\quad \delta_f = 15.6^{o}$

$\frac{S_{W_f}}{S_W} = 0.378$ $\quad R_{\ell} = 6.0 \times 10^{6}$

Compute:

$\Delta c_{\ell_{max}}$ (Section 6.1.1.3)

$\left(\Delta c_{\ell_{max}}\right)_{base} = 1.045$ (Figure 6.1.1.3-12a)

$k_1 = 1.010$ (Figure 6.1.1.3-12b)

$k_2 = 0.605$ (Figure 6.1.1.3-13a)

$\frac{\text{Actual flap angle}}{\text{Reference flap angle}} = \frac{15.6}{45} = 0.347$

$k_3 = 0.445$ (Figure 6.1.1.3-13b)

$\Delta c_{\ell_{max}} = k_1 k_2 k_3 \left(\Delta c_{\ell_{max}}\right)_{base}$ (Equation 6.1.1.3-a)

$= (1.010)\ (0.605)\ (0.445)\ (1.045)$

$= 0.284$

$K_{\Lambda} = 0.730$ (Figure 6.1.4.3-10)

Solution:

$\Delta C_{L_{max}} = \Delta c_{\ell_{max}} \frac{S_{W_f}}{S_W} K_{\Lambda}$ (Equation 6.1.4.3-a)

$= (0.284)\ (0.378)\ (0.730)$

$= 0.0784$ (based on S_W)

This compares with a test value of 0.075 from Reference 2.

2. Slats

Given: The wing-body configuration of an A4D-1 Flight Trainer

$$\frac{c_f}{c} = 0.177 \qquad \Lambda_{c/4} = 33.2^{o} \qquad \frac{b_{slat}}{b_e} = 0.535$$

Compute:

$$\Delta C_{L_{max}} = 1.28 \left(\frac{c_f/c}{0.18}\right)\left(\frac{b_{slat}}{b_e}\right)^2 \cos^2 \Lambda_{c/4} \qquad \text{(Equation 6.1.4.3-b)}$$

$$= (1.28) \left(\frac{0.177}{0.18}\right) (0.535)^2 (0.700)$$

$$= 0.252 \text{ (based on } S_W)$$

This compares with a test value of 0.295.

3. Jet-Flap EBF Configuration

Given: The wing-body configuration of Reference 5.

$C_J = 3.18$ $\qquad \delta_f = 60^{o}$ $\qquad \delta_u \simeq 73^{o}$ $\qquad \delta_\ell \simeq 52^{o}$

Double-Slotted Flaps

Compute:

$$\delta_{j_{eff}} = \frac{1}{2} (\delta_u + \delta_\ell) \qquad \text{(Equation 6.1.4.1-d)}$$

$$= \frac{1}{2} (73 + 52)$$

$$= 62.5^{o}$$

$\eta_t = 0.583$ (Figure 6.1.4.3-11)

$\eta_t C_j \sin \delta_{j_{eff}} = (0.583)\ (3.18)\ (0.887) = 1.644$

$\Delta C_{L_{max}} = 4.65$ (Figure 6.1.4.3-12, lift increment due only to power effects, based on S_W)

This compares with a test value of 5.35 from Reference 5.

REFERENCES

1. Furlong, G. C., and McHugh, J. G.: A Summary and Analysis of the Low-Speed Longitudinal Characteristics of Swept Wings at High Reynolds Number. NACA TR 1339, 1957. (U)

2. May, F., and Widdison, C. A.: STOL High-Lift Design Study. Vol. I — State-of-the-Art Review of STOL Aerodynamic Technology. AFFDL-TR-71-26, Vol. I, 1971. (U)

3. Moorhouse, D. J.: A Practical Look at the Stall and High-Lift Operation of Externally Blown Flap STOL Transport Configurations. AGARD Preprint No. 102, 1972. (U)

4. Spooner, S. H., and Mollenberg, E. F.: Positioning Investigation of Single-Slotted Flaps on a 47.7° Sweptback Wing at Reynolds Numbers of 4.0×10^6 and 6.0×10^6. NACA RM L50H29, 1950. (U)

5. Freeman, D. C., Jr., Parlett, L. P., and Henderson, R. L.: Wind-Tunnel Investigation of a Jet Transport Airplane Configuration with an External-Flow Jet Flap and Inboard Pod-Mounted Engines. NASA TN D-7004, 1970. (U)

(a)

NACA 23012 (perpendicular to leading edge)

λ = 1.0 **half-span split flap**

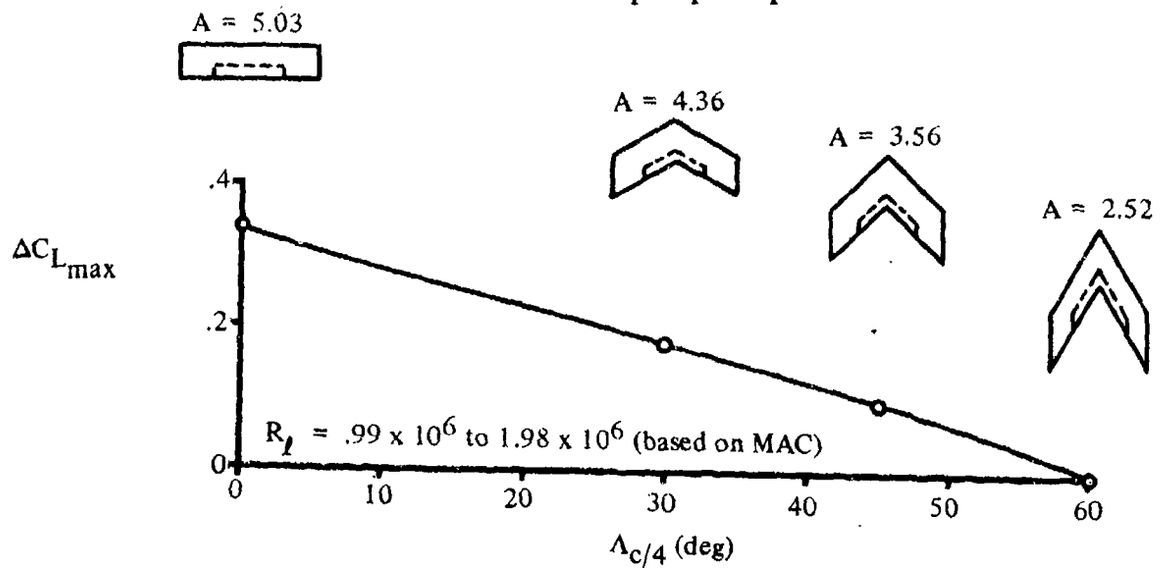

(b)

NACA 65A006 (parallel to plane of symmetry)

A = 4 λ = .6 **half-span split flap**

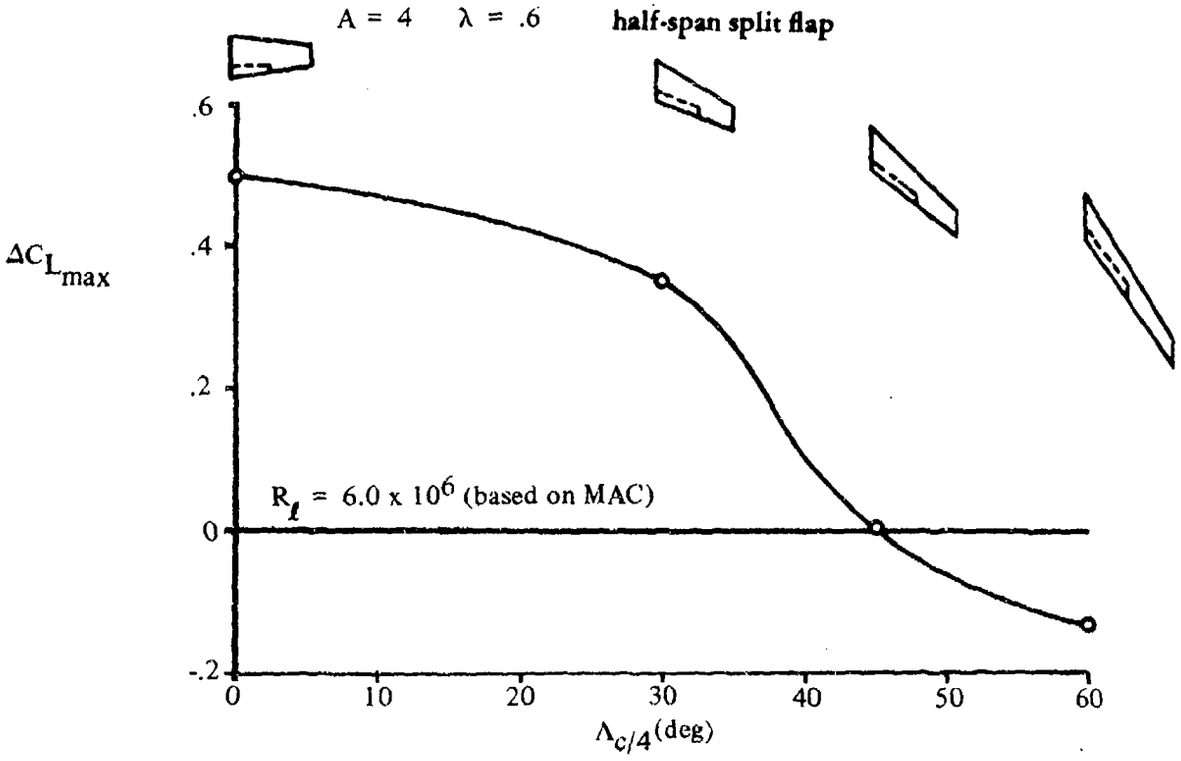

FIGURE 6.1.4.3-7 TYPICAL EFFECTS OF WING SWEEP ON MAXIMUM-LIFT INCREMENTS DUE TO SPLIT TRAILING-EDGE FLAPS

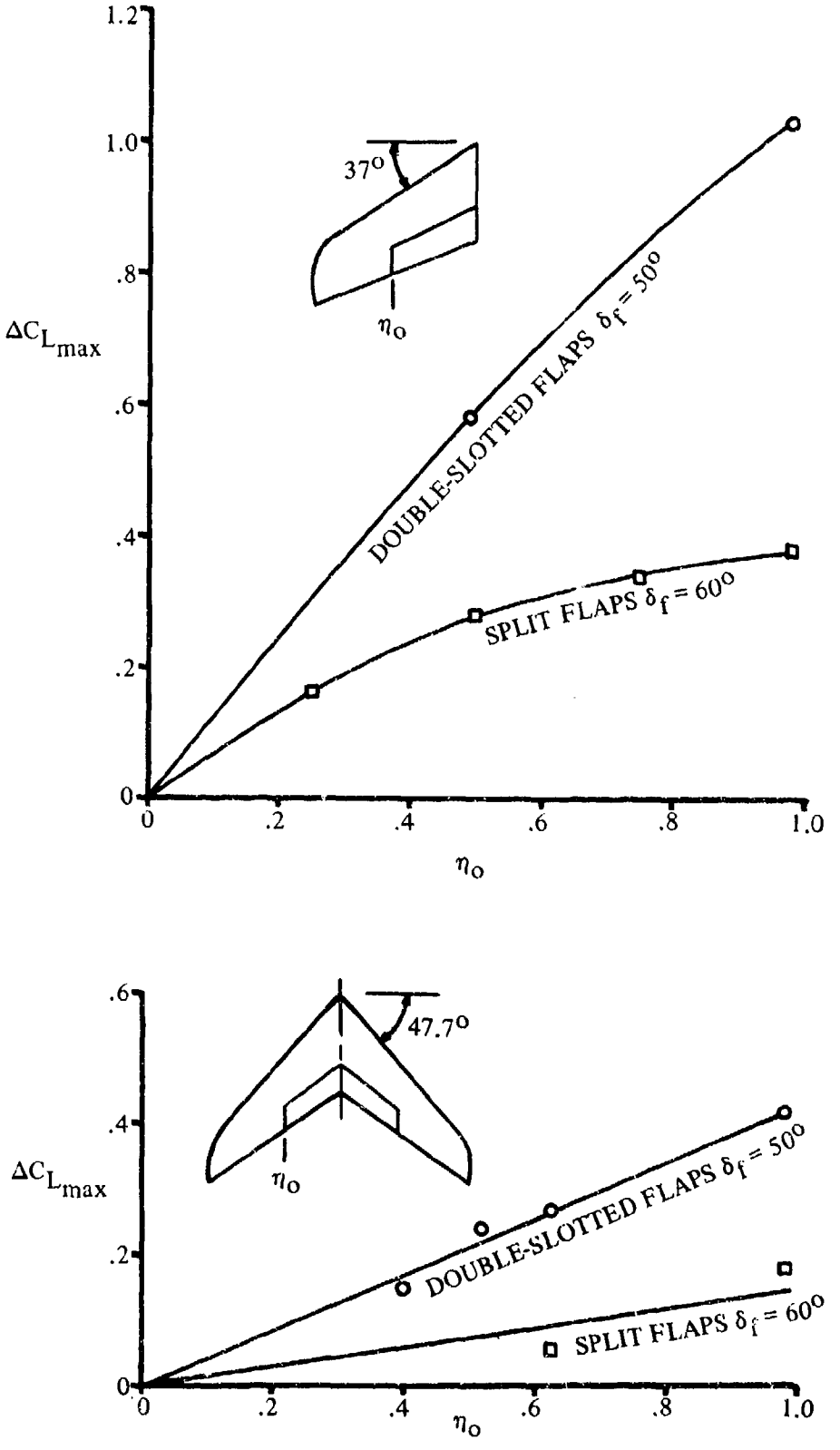

FIGURE 6.1.4.3-8 EFFECT OF SPANWISE FLAP EXTENT ON WING MAXIMUM LIFT INCREMENT

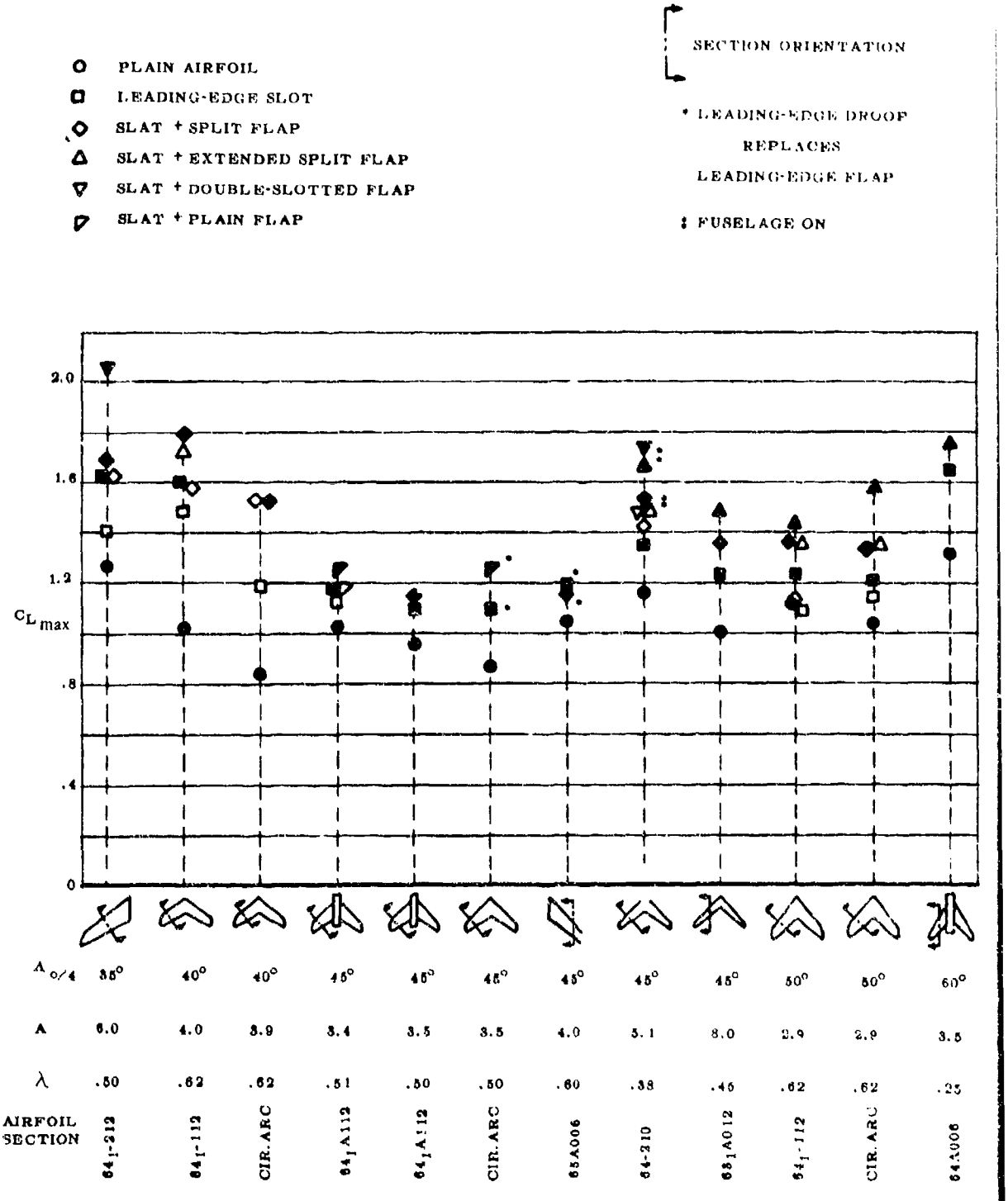

FIGURE 6.1.4.3-9 SUMMARY CHART OF MAXIMUM LIFT COEFFICIENTS OBTAINED WITH VARIOUS TYPES OF TRAILING-EDGE FLAPS

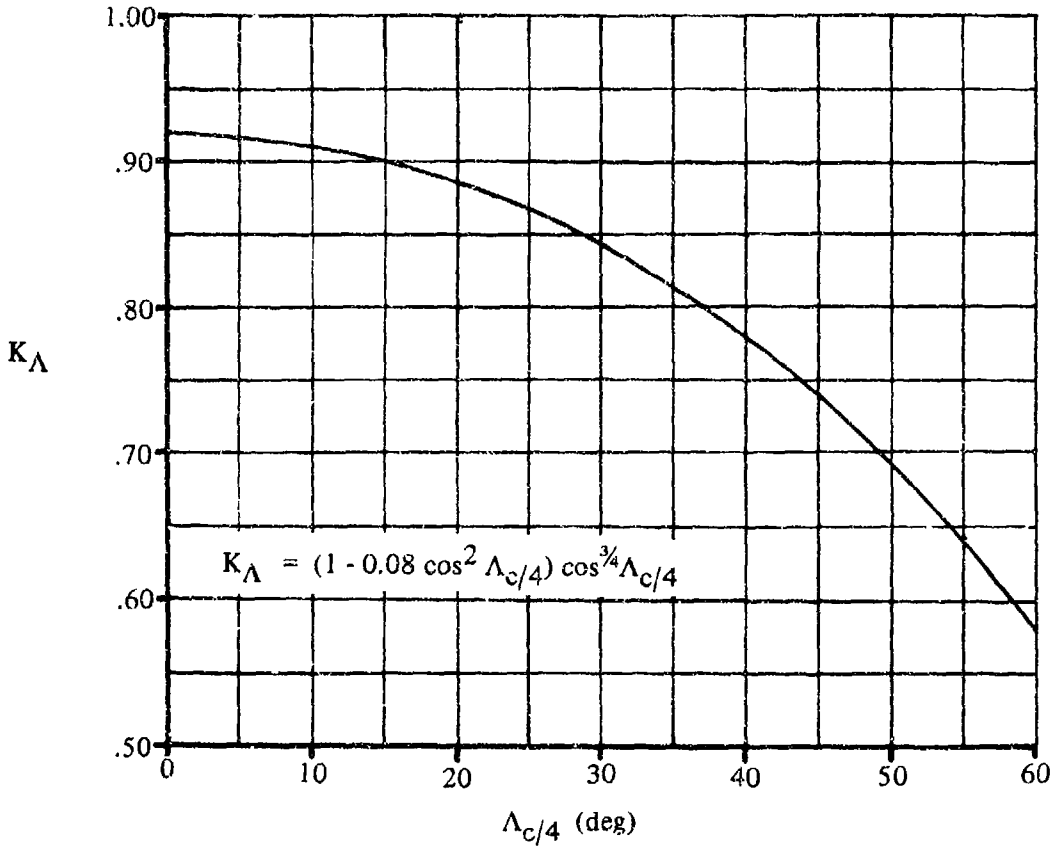

FIGURE 6.1.4.3-10 PLANFORM CORRECTION FACTOR — TRAILING-EDGE FLAPS

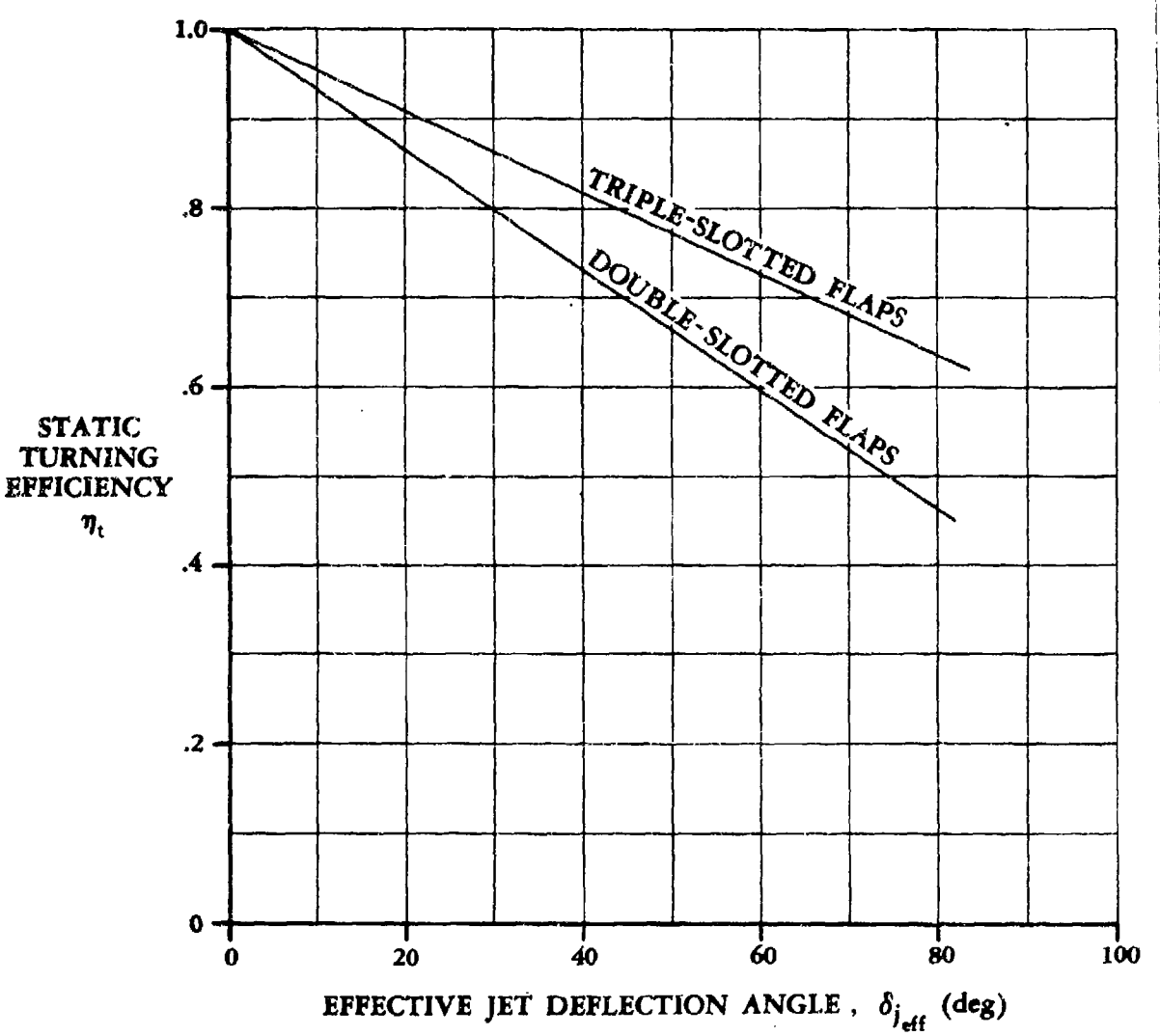

FIGURE 6.1.4.3-11 FLAP TURNING EFFICIENCY

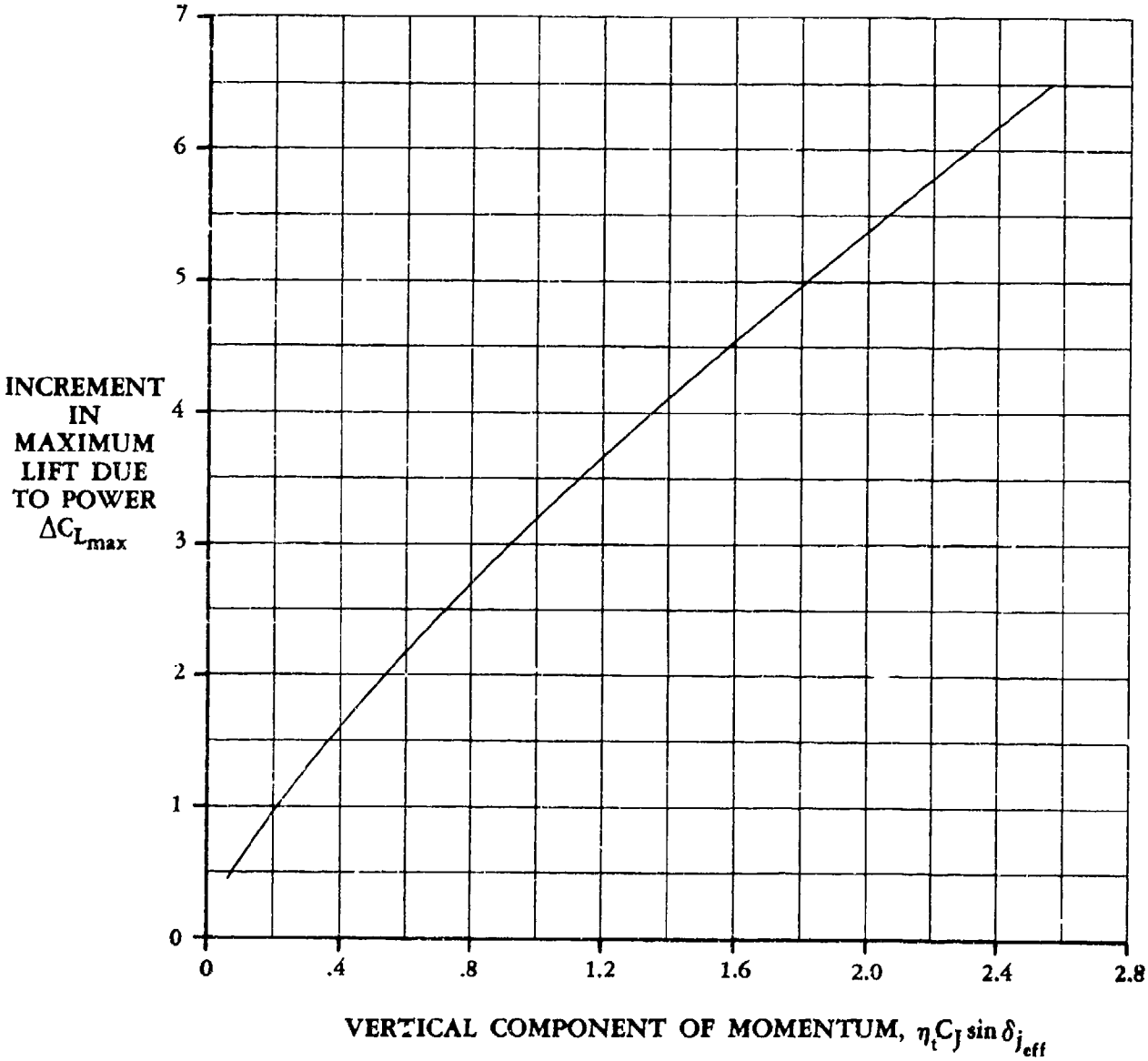

FICURE 6.1.4.3-12 CORRELATION OF MAXIMUM LIFT DUE TO POWER

6.1.5 WING PITCHING MOMENT WITH HIGH-LIFT AND CONTROL DEVICES

The following sections give the effect of flap deflection on wing pitching-moment coefficient at subsonic, transonic, and supersonic speeds. Section data from other portions of the Datcom are used. Although the methods are developed for trailing-edge flaps, they can be applied to leading-edge flaps, slats, and spoilers, provided the proper section data are available or can be estimated. However, the methods presented are applicable to the angle-of-attack and flap-deflection ranges for which linear aerodynamic control characteristics exist. A chart showing the linear-lift range for a particular airfoil is shown in Section 6.1.3. In general, the linear-lift range for wings is considerably shorter than that shown in this chart, particularly for swept and low-aspect-ratio wings. For swept wings, the effects of spanwise boundary-layer flow, induced camber, and leading-edge vortices are pronounced and tend to nonlinearize the control or flap characteristics. For low-aspect-ratio wings, section characteristics are not important and, generally, the linear range is shorter than those of their section counterparts.

Leading- and trailing-edge flaps frequently have a pronounced effect upon the longitudinal stability characteristics of wings. Reference 1 gives a summary of these effects. Figures 6.1.5-2a and 6.1.5-2b are reproduced from this reference. Figure 6.1.5-2a shows the increase in stability that can be obtained from leading-edge flaps, slats, and fences. The basic curve is also shown in Section 4.1.4.3. Figure 6.1.5-2b shows the effect of spanwise extent of leading- and trailing-edge flaps on longitudinal stability for a particular wing.

REFERENCE

1. Furlong, G.C., and McHugh, J.G.: A Summary and Analysis of the Low-Speed Longitudinal Characteristics of Swept Wings at High Reynolds Number. NACA TR 1339, 1957. (U)

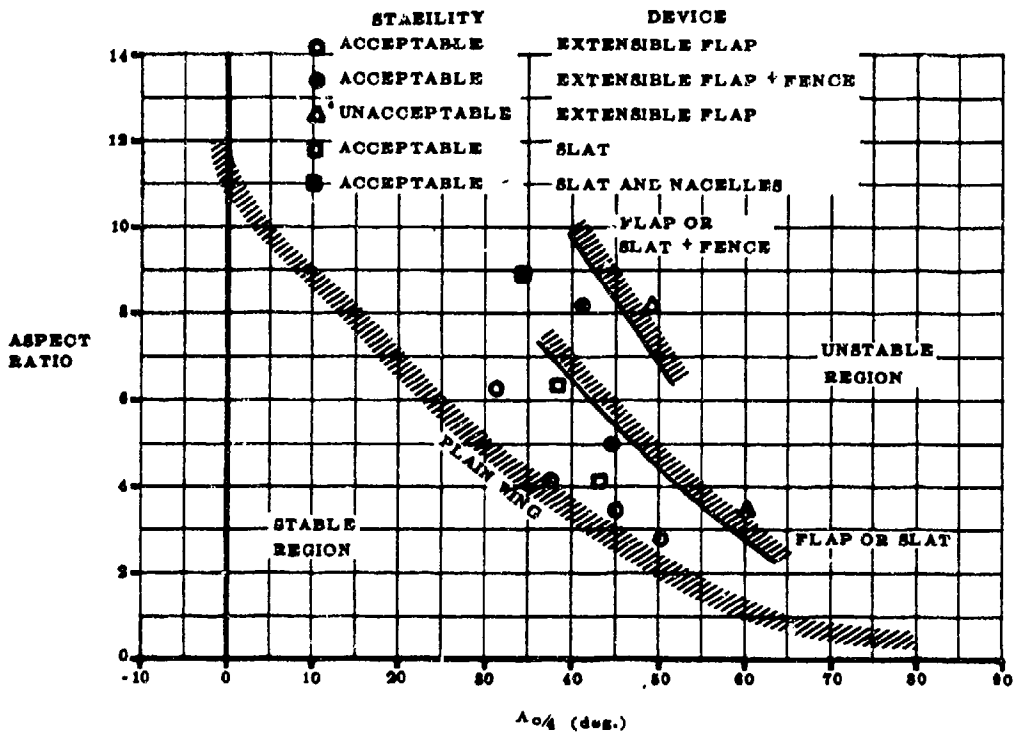

FIGURE 6.1.5-2a INFLUENCE OF SEVERAL TYPES OF STALL-CONTROL DEVICES ON LONGITUDINAL STABILITY BOUNDARY FOR WINGS WITH $\lambda > .4$

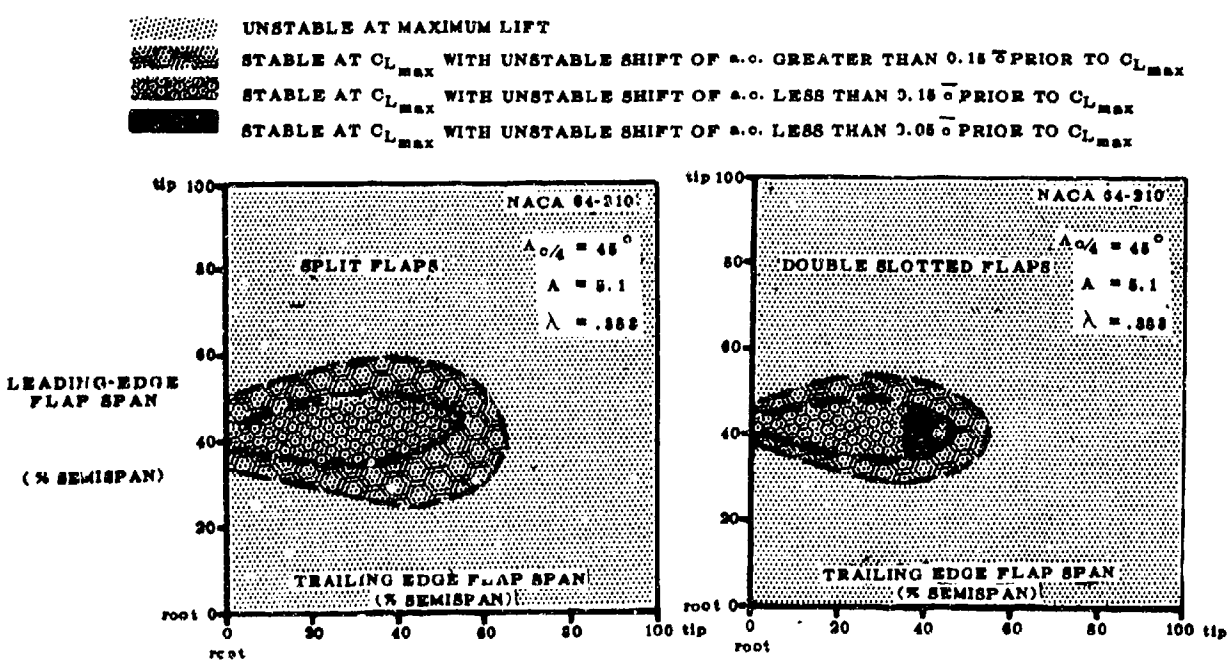

FIGURE 6.1.5-2b EFFECTS OF LEADING-EDGE AND TRAILING-EDGE FLAPS ON LONGITUDINAL STABILITY CHARACTERISTICS OF A SWEPTBACK WING

6.1.5.1 PITCHING-MOMENT INCREMENT ΔC_m DUE TO HIGH-LIFT AND CONTROL DEVICES

A. SUBSONIC

Methods are presented in this section for estimating the pitching-moment characteristics for most common high-lift devices in use today and for some of the blown flaps being considered for STOL aircraft. These methods are valid only in the linear-lift region (preferably near zero angle of attack). The effect of these devices on the variation of pitching moment with angle of attack is presented in Section 6.1.5.2, except for the jet flap, which is presented in this section. Considerations of clarity and simplicity of presentation dictated this deviation from standard Datcom practice. The reader is referred to Sections 6.1.1.1 and 6.1.2.1 for a discussion of the salient aspects regarding the various types of high-lift devices.

The assumption is made that the characteristics of a trailing-edge flap are independent of any leading-edge device, and/or the characteristics of a leading-edge device are independent of any mechanical trailing-edge flap. In reality this is not quite true, but the methods of this section are not sufficiently refined to account for these interference effects. This assumption cannot be justified in the case of the more powerful jet flap.

Trailing-Edge Mechanical Flaps

Two methods are presented for estimating the pitching-moment increment due to trailing-edge mechanical flaps at small angles of attack and low speeds. Both methods are applicable to all types of flaps and to high-flap-deflection ranges, provided proper section data are used.

Method 1 (Reference 1) is substantially easier to apply than Method 2 (Reference 2). A data summary and substantiation of Method 1 are presented in Table 6.1.5.1-A. The resulting mean error of the pitching-moment increment due to flap deflection is ±0.053. For configurations with quarter-chord sweep angles greater than 45°, caution should be exercised, since the accuracy of the method is questionable in this range.

Method 2 uses linear theory for subsonic compressible flow, together with two-dimensional airfoil data adjusted for the effects of sweep. The additional feature of this method is that it requires the determination of the spanwise loading of the wing due to flap deflection. It is this feature that makes this method cumbersome to use. This method is not substantiated here; however, a substantiation of the method does appear in Reference 2 with a reported mean error of pitching-moment increment due to flap deflection of ±0.02.

Leading-Edge Mechanical Devices

Although the second method described above should be equally applicable to leading-edge devices, no substantiation of such use has been found. The use of a method as complex as this one cannot be justified when the small pitching moments and nonlinear characteristics of leading-edge devices are considered. Therefore, a simpler method is presented for estimating the effect of conventional leading-edge devices on the pitching moment. This method is based on the thin-airfoil, two-dimensional method, uncorrected for three-dimensional effects. Although the accuracy of the method is not as good as desired, no trends in three-dimensional parameters, such as aspect ratio, taper ratio, or sweep, have been observed that would improve the accuracy.

The lack of accuracy is to be expected, since the linear theory is intrinsically unable to handle the large deflections typical of leading-edge devices or to predict the nonlinear characteristics evident in the test data.

Jet Flaps

The method presented herein (taken in part from Reference 3) adapts the jet-flap method for airfoils, presented in Section 6.1.2.1, for use on finite-aspect-ratio wings. As such, it applies to the same concepts and is subject to the same limitations that are listed in that section. The user is referred to the discussions in Sections 6.1.1.1 and 6.1.2.1 for a complete understanding of this method.

The jet-flap method assumes that the entire flap is immersed in a uniform-jet-flow field. For externally-blown-flap (EBF) systems on swept wings, where this assumption is obviously not valid, the method contains a procedure for making an approximate estimate of the spanwise distribution of the jet. However, this cannot be expected to yield better than a rough estimate of the true pitching moment. This is due to the fact that the pitching moment cannot be accurately estimated without a detailed knowledge of the spanwise extent of the wing influenced by the jet.

Unfortunately, the jet spreading problem is very difficult to treat, and to date little in the way of analytical or empirical methods has been developed. Solution of the problem, which is simply to determine the spanwise distribution of trailing-edge jet momentum, requires that the flow details of the impingement, spreading, and turning process be known. Such a flow solution, which involves the viscid/inviscid interaction of the jet impinging on the wing-flap system, is clearly beyond the scope of the Datcom.

The wing pitching moment is calculated by applying correction factors for finite aspect ratio to Spence's adaptation of thin-airfoil theory to the two-dimensional jet-flap problem. The correction factors adjust the center-of-lift location and the magnitude of the lift increment. The first is from Reference 4 and is based on conventional flap data; the second is from Reference 38 and is based on Maskell's theoretical correction for three-dimensional effects. This method does not account for sweep or taper effects, except insofar as they affect the geometric relationship between the center of gravity and the wing. This should not be a serious restriction, since the jet-flap system is usually applied to high-aspect-ratio wings with low to moderate sweepback. The maximum sweep angle and taper ratio for which this method is valid have not been determined.

DATCOM METHODS

1. Trailing-Edge Mechanical Flaps

Method 1

This method assumes a constant flap-chord-to-wing-chord ratio. In the case of arbitrary spanwise distribution of flap chord (constant-chord flaps on tapered wings or tapered flaps on untapered wings), the flaps should be divided into spanwise steps. The pitching-moment contributions from each spanwise step are then calculated and added together to obtain the total increment for the flap.

At low angles of attack, the change in pitching-moment increment due to flap deflection based on $S_W \bar{c}_W$ taken about $\bar{c}_W/4$ is given by

$$\Delta C_{m_f} = \Delta C_m + K_\Lambda \left(\frac{A}{1.5}\right) \Delta C_L \tan \Lambda_{c/4} \qquad 6.1.5.1\text{-a}$$

where

$$\Delta C_m = K_p \left\{ \left(\frac{\Delta C'_m}{\Delta C_L}\right) \Delta C_L \left(\frac{c'}{c}\right)^2 - 0.25\, C_L \left(\frac{c'}{c}\right)\left(\frac{c'}{c} - 1\right) + C_m \left[\left(\frac{c'}{c}\right)^2 - 1\right] \right\} \qquad 6.1.5.1\text{-b}$$

where

K_p is the flap-span factor as a function of taper ratio and flap location, obtained from Figure 6.1.5.1-61 as illustrated in Sketch (a). Note: η is the span station, $\eta = \dfrac{\text{control span ordinate}}{b/2}$

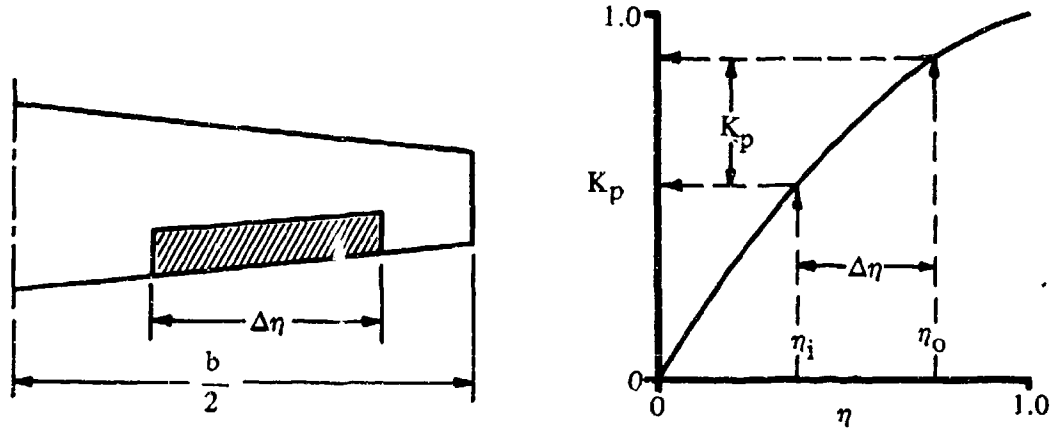

SKETCH (a)

$\dfrac{\Delta C'_m}{\Delta C_L}$ is the ratio of the pitching-moment increment to lift increment for a full-span flap on a rectangular wing, obtained from Figure 6.1.5.1-60 as a function of wing thickness and flap-chord-to-extended-wing-chord ratio.

ΔC_L is the lift increment due to flap deflection, obtained from the appropriate equation (determined by the particular flap type) of Section 6.1.4.1 using the following assumptions:

1. full-span flap
2. wing aspect ratio of 6
3. no sweep, $\Lambda_{c/2} = 0$

(Note: the above assumptions are to be used for all calculations involved in calculating ΔC_L.)

$\frac{c'}{c}$ is the ratio of the extended wing chord to the retracted wing chord (see Figures 6.1.1.1-44 through -46 for a graphical illustration).

C_L is the wing-body lift coefficient with the flap retracted. This value should be obtained from test data if available, or from Sections 4.1.3.1* and 4.3.1.2.

C_m is the wing-body pitching-moment coefficient with the flap retracted. This value should be obtained from test data if available, or from Section 4.3.2.2 supplemented with a test-data value for $\left(C_{m_0}\right)_{WB}$

K_Λ is the conversion factor for a partial-span flap on a sweptback wing obtained from Figure 6.1.5.1-57 in a similar manner as K_p; i.e., see the illustration in Sketch (a).

A is the wing aspect ratio.

$\Lambda_{c/4}$ is the sweep of the wing quarter-chord.

Method 2

This method requires the determination of the span loading due to flap deflection (Reference 5) and the chordwise center-of-pressure location for stations across the span. Once these quantities are determined, the incremental pitching moment can be calculated by an integration process. The pitching-moment increment ΔC_{m_f} is obtained by using the procedure outlined in the following steps:

Step 1. Determine the spanwise loading coefficient G/δ of full wing-chord flaps. The spanwise loading coefficient G/δ of full wing-chord flaps is obtained as a function of span station, $\eta = \frac{\text{span ordinate}}{b/2}$, from Figures 6.1.5.1-62a through 6.1.5.1-62d for appropriate values of $\beta A/\kappa$, Λ_β, and λ, where $\kappa = c_{\ell_{\alpha_M}}/(2\pi/\beta)$ and $\Lambda_\beta = \tan^{-1}\ (\tan \Lambda_{c/4}/\beta)$.

It should be noted that Figures 6.1.5.1-62a through 6.1.5.1-62d present the spanwise loading coefficients for full wing-chord flaps that extend from the plane of symmetry out to span stations of $\eta_o = 0.195$, $\eta_o = 0.556$, and $\eta_o = 1.0$ (Figure 6.1.5.1-62a also includes $\eta_o = 0.831$). The results for other flap spans are obtained by interpolating the results of the particular flap spans presented in Figures 6.1.5.1-62a through 6.1.5.1-62d. The final step in the interpolation procedure is to cross-plot the results of the variation of the loading parameter at given stations as a function of flap span η_f for desired values of the parameters $\beta A/\kappa$, Λ_β, and λ (see Sketch (b)).

*The wing-body zero-lift angle of attack is obtained from the wing-alone data of Section 4.1.3.1. Test data from a similar configuration should be used if available. Wing surface velocity is increased by the presence of the fuselage; therefore, when the fuselage is below the wing, the lift is reduced, and with the fuselage above the wing, the lift will be increased. This effect is generally small, unless wing-mounted bodies, such as stores or nacelles, are close to the fuselage or to each other.

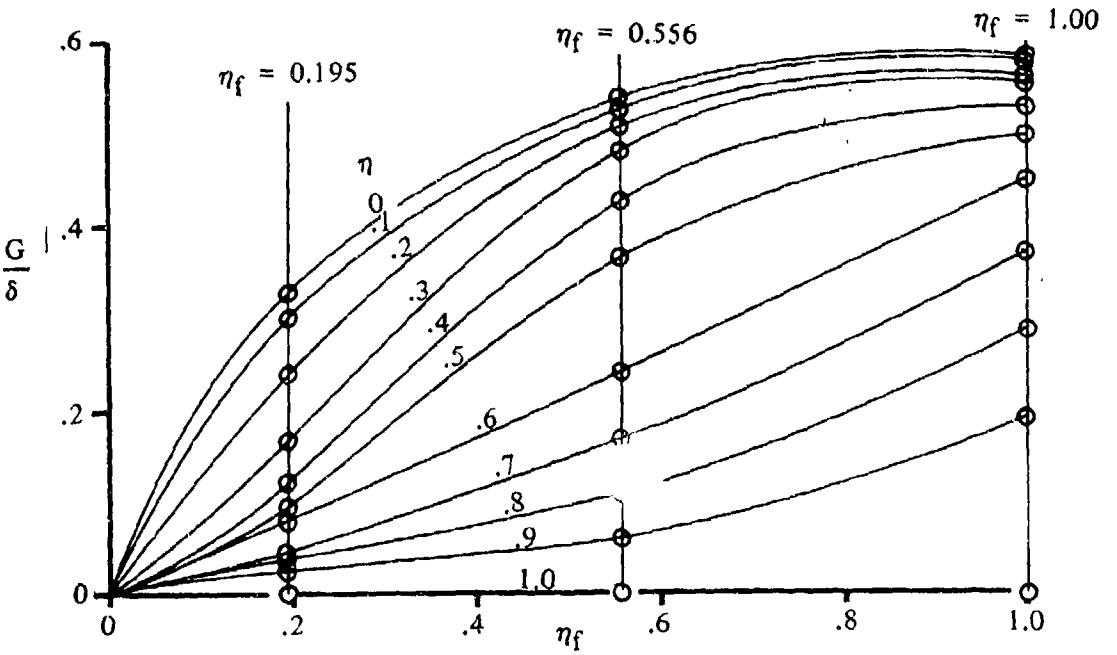

SKETCH (b)

The spanwise loading is then read from this cross plot at the desired values of η_f (η_i and η_o). Note that for cases where Figure 6.1.5.1-62a applies, i.e., where $\beta A/\kappa = 0$, the cross plot represented by Sketch (b) is obtained directly, since no intermediate steps are required to interpolate for λ or Λ_β.

The following procedure is used to determine the spanwise loading of the actual flap:

a. For flaps that extend from the plane of symmetry outboard, tabulate the loading for an inboard flap extending from the plane of symmetry to the outboard station of the actual flap, as shown in Sketch (c).

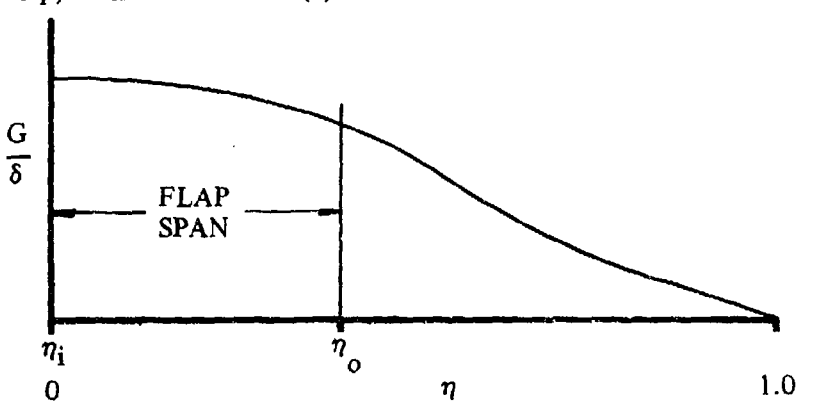

SKETCH (c)

b. For partial-span flaps that extend from the wing tip inboard, the charts are used as follows: Tabulate the loading G/δ for a full-span flap. Tabulate the loading G/δ for an inboard flap extending from the plane of symmetry to the inboard station of the actual flap. Subtract the loadings of the above tabulations at each span station to obtain the loading of the actual flap (see Sketch (d)).

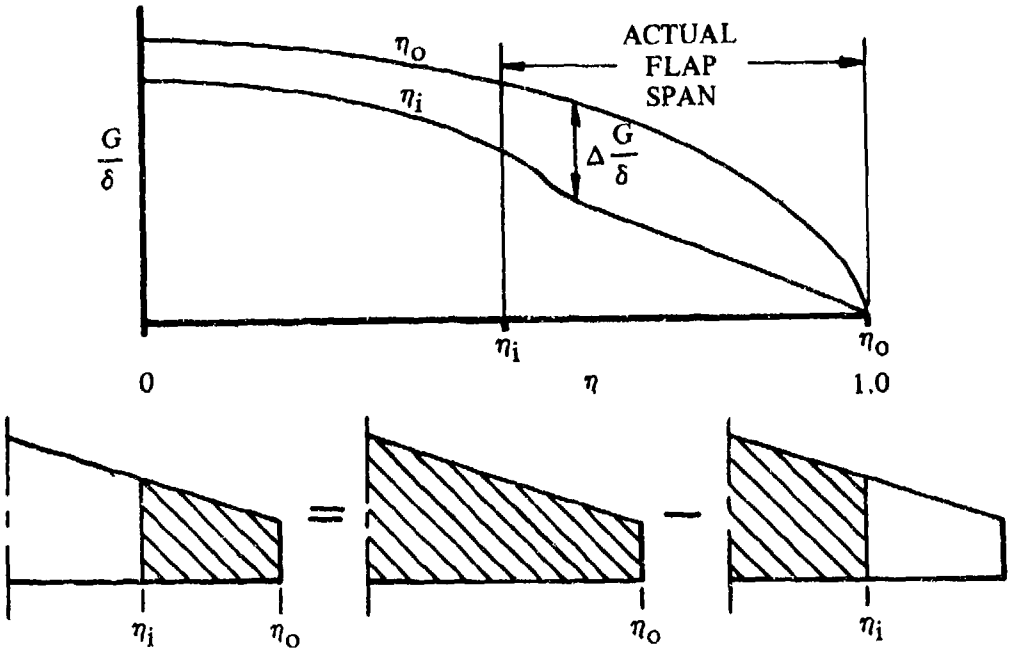

SKETCH (d)

c. For partial-span flaps that have outboard ends inboard of the wing tip and inboard ends outboard of the plane of symmetry, the charts are used as follows: Tabulate the loading function G/δ for flaps extending from the plane of symmetry to the outboard station of the actual flap. Tabulate the loading function G/δ for a flap extending from the plane of symmetry to the inboard end of the actual flap. Subtract the loadings of the above tabulations at each span station to obtain the loading of the actual flap (see Sketch (e)).

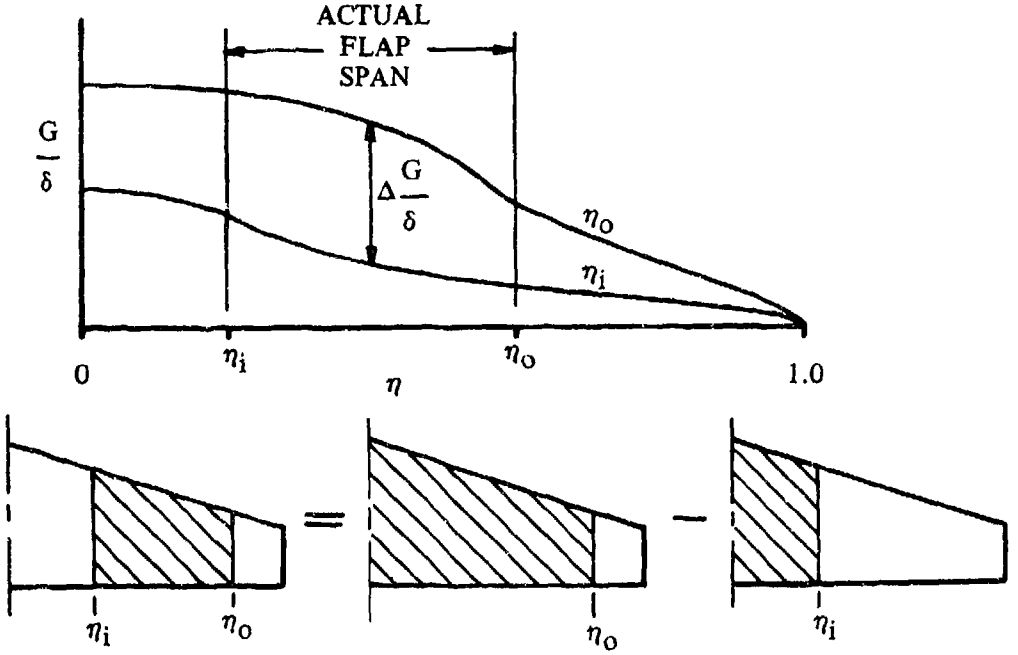

SKETCH (e)

Step 2. Determine the incremental section lift coefficient as a function of span station η by*

$$c_{\ell_\Lambda} = -\frac{2b}{c}\frac{G}{\delta}\alpha_\delta \delta \qquad 6.1.5.1\text{-c}$$

where

c_{ℓ_Λ} is the incremental section lift coefficient due to flap deflection.

b is the total wing span.

c is the local chord at the span station in question.

$\frac{G}{\delta}$ is the loading coefficient of a full wing-chord flap at the span station in question, obtained from Step 1.

α_δ is the two-dimensional lift-effectiveness parameter expressed as

$$\alpha_\delta = -\frac{\left(c_{\ell_\delta}\right)_\alpha}{\left(c_{\ell_\alpha}\right)_\delta} \quad \text{(Equation 6.1.1.1-b)}$$

where

c_{ℓ_δ} is the lift effectiveness of the flapped airfoil from the appropriate method of Section 6.1.1.1.

c_{ℓ_α} is the airfoil section lift-curve slope (including the effects of compressibility) from Section 4.1.1.2.

For area-suction and blowing-type flaps the theoretical value of α_δ is presented as a function of c_f/c in the inset of Figure 6.1.4.1-14.

When experimental values of the section lift increment Δc_ℓ are available for plain, split, or slotted flaps, the lift-effectiveness parameter should be calculated using

$$\alpha_\delta = -\frac{(\Delta c_\ell)_{\text{experiment}}}{(c_{\ell_\alpha})_\delta}$$

δ is the streamwise flap deflection in radians. This value may be obtained from

$$\delta = \tan^{-1}(\cos \Lambda_{HL} \tan \delta_{\perp HL}) \qquad 6.1.5.1\text{-d}$$

*In the theory, sections of a yawed infinite wing are dealt with. See Reference 2 for details of the theoretical treatment of sweep and taper.

where

Λ_{HL} is the sweep angle of the flap hinge line.

$\delta_{\perp HL}$ is the flap deflection measured normal to the flap hinge line.

The product $(G/\delta)\alpha_\delta$ in Equation 6.1.5.1-c converts the spanwise loading distribution of full wing-chord flaps, $c_f/c = 1.0$, to the spanwise loading distribution of partial wing-chord flaps. For the case of arbitrary spanwise distribution of flap chord (constant-chord flaps on tapered wings or tapered flaps on untapered wings), the flap can be divided into spanwise steps and a new value for α_δ for each segment determined. The load distribution due to each spanwise step is then determined by the product of G/δ and the average value of α_δ over that spanwise step.

Step 3. Determine the chordwise center-of-pressure location $x_{c.p.}$ for stations across the span.

For this calculation the wing span is divided into not more than three types of regions. These regions are illustrated schematically in Sketch (f), and consist of:

a. Span stations included in the flapped section.

b. Span stations adjacent to the flap ends where the distance from the ends of the flap $\Delta\eta$ is less than $|0.20|$.

c. Span stations not influenced by the flap span, $\Delta\eta \geq |0.20|$.

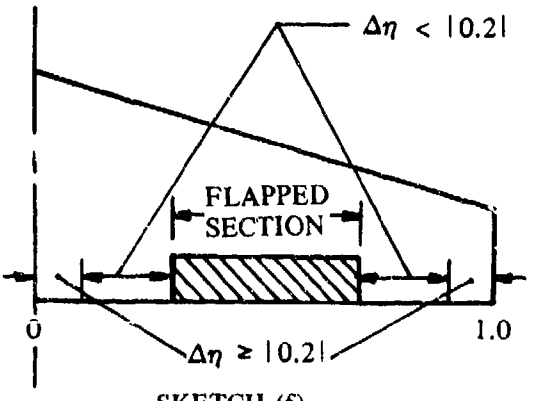

SKETCH (f)

The chordwise center-of-pressure location in each region is obtained as follows:

a. For the span stations included in the flapped section

$$x_{c.p.} = 0.25 - \frac{\Delta c_m}{c_{\ell_{\Lambda=0}}} \qquad 6.1.5.1\text{-e}$$

where

Δc_m is the section incremental pitching moment obtained from Section 6.1.2.1 by the appropriate trailing-edge mechanical-flap method using c_f/c and δ', where δ' is the flap deflection in the plane normal to the constant-percent chord line through $x_{c.p._b}$, given by

$$\delta' = \tan^{-1} \frac{\tan \delta}{\cos \Lambda_b} \qquad 6.1.5.1\text{-f}$$

where Λ_b is the sweepback of the constant-percent chord line through the center of pressure of the basic loading, given by

$$\tan \Lambda_b = \tan \Lambda_{c/4} - \frac{4}{A}(x_{c.p._b} - 0.25) \frac{1-\lambda}{1+\lambda} \qquad 6.1.5.1\text{-g}$$

where $x_{c.p._b}$ is the chordwise center-of-pressure position (basic loading) for a plain flap from Figure 6.1.5.1-67b.

$c_{\ell_{\Lambda=0}}$ is the incremental section lift coefficient as a function of span station, referred to the basic load line, by

$$c_{\ell_{\Lambda=0}} = \frac{c_{\ell_\Lambda}}{\cos^2 \Lambda_b} \qquad 6.1.5.1\text{-h}$$

where c_{ℓ_Λ} is obtained from Step 2.

b. For the span stations adjacent to the flap ends where the distance from the ends of the flap $\Delta\eta$ is less than |0.20|,

$$x_{c.p.} = 0.25 - K\left(\frac{\Delta c_m}{c_{\ell_{\Lambda=0}}}\right)_{\substack{\text{edge of} \\ \text{flap}}} \qquad 6.1.5.1\text{-i}$$

where

K is obtained from Figure 6.1.5.1-67a as a function of distance from the end of the flap.

$\left(\frac{\Delta c_m}{c_{\ell_{\Lambda=0}}}\right)_{\substack{\text{edge}\\ \text{of}\\ \text{flap}}}$ is the value determined in Step 3a at the span station corresponding to the edge of the flap.

c. For span stations not influenced by the flap span, i.e., $\Delta\eta \geq |0.20|$, the theoretical chordwise center-of-pressure position is assumed to be the quarter-chord point.

A typical variation of chordwise center-of-pressure location for stations across the span is illustrated in Sketch (g).

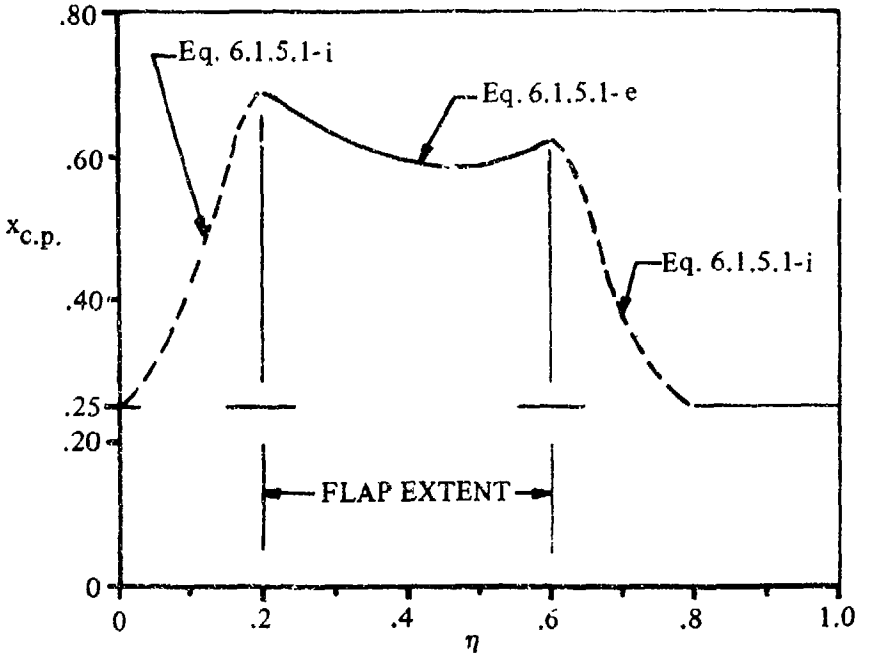

SKETCH (g)

Step 4. For wings with swept quarter-chord, the chordwise center-of-pressure position at each span station must be referred to the quarter-chord of the MAC by

$$\frac{x}{\bar{c}} = (\eta - \bar{\eta})\frac{b/2}{\bar{c}}\tan\Lambda_{c/4} + \frac{c\,(x_{c.p.} - 0.25)}{\bar{c}} \qquad 6.1.5.1\text{-j}$$

where

$\bar{\eta}$ is the lateral distance of the wing MAC from the body center line in semispans.

x is the distance of the local center of pressure aft of the quarter-chord of the MAC.

Step 5. With the local centers of pressure and the span loading known, determine the change in pitching moment due to flap deflection, based on $S_W \bar{c}_W$ taken about the quarter-chord of the wing MAC, by integrating across the span as follows:

$$\Delta C_{m_f} = \int_0^{1.0} - \left[c_{\ell_\Lambda} \frac{c}{c_{av}} \left(\frac{x}{\bar{c}} \right) \right] d\eta \qquad 6.1.5.1\text{-k}$$

where c_{ℓ_Λ} is from Step 2, $(x/\bar{c})$ is from Steps 3 and 4, and c/c_{av} is the ratio of the local chord at a given span station to the average chord ($c_{av} = S_W/b_W$).

2. Leading-Edge Devices

This method assumes a constant flap-chord-to-wing-chord ratio. In the case of an arbitrary spanwise distribution of leading-edge flap chord, the flaps should be divided into spanwise steps. The pitching-moment contributions from each spanwise step are then calculated and added to obtain the total increment for the leading-edge device.

The pitching-moment increment due to mechanical leading-edge devices, based on $S_W \bar{c}_W$, is given by

$$\Delta C_m = \left[c'_{m_{\delta_{LE}}} \left(\frac{\bar{c}'}{\bar{c}} \right) + \left(\frac{x_m}{\bar{c}} - \frac{x_{LE}}{\bar{c}} \right) c'_{\ell_\delta} \right] \frac{S_{W_f}}{S_W} \delta_f$$

$$+ \left\{ C_m \left[\left(\frac{\bar{c}'}{c} \right)^2 - 1 \right] + 0.75\, C_L \left(\frac{\bar{c}'}{c} \right) \left(\frac{\bar{c}' - c}{c} \right) \right\} \Delta\eta \qquad 6.1.5.1\text{-}\ell$$

where

$c'_{m_{\delta_{LE}}}$ is the theoretical two-dimensional, flap pitching-moment effectiveness about the leading edge, obtained from Figure 6.1.2.1-36 as a function of the ratio of flap chord to the extended airfoil chord c_f/c'. (See Figures 6.1.1.1-51 for the definition of flap chord c_f.)

$\bar{c}'$ is the mean aerodynamic chord of the wing segment affected by the leading-edge device (see Sketch (h)). The wing chord is the extended-wing chord due to an extension of the leading-edge device. The trailing-edge flaps, if any, are considered retracted.

$\bar{c}$ is the wing mean aerodynamic chord (MAC).

c is the retracted or basic-airfoil chord at the spanwise station of the MAC of the wing segment affected by the leading-edge device (see Sketch (h)).

$\frac{x_m}{\bar{c}}$ is the moment-reference-center location in fractions of the wing MAC, measured positive aft from the aircraft reference-axis origin (usually the aircraft nose or wing apex) parallel to the longitudinal axis.

$\frac{x_{LE}}{\bar{c}}$ is the location of the leading edge of the mean aerodynamic chord of the wing segment affected by the leading edge device, in fractions of the wing MAC. This parameter is measured positive aft from the aircraft reference-axis origin (see Sketch (h)).

c'_{ℓ_δ} is the two-dimensional leading-edge flap effectiveness parameter obtained from Figure 6.1.1.1-50 as a function of the flap-chord ratio $c_f/\bar{c}'$, instead of c_f/c.

Sw_f is the area of the wing segment affected by the leading-edge device (see Sketch (h)).

S_W is the wing reference area.

δ_f is the leading-edge-device deflection, measured parallel to the free stream in degrees (see Figure 6.1.1.1-51).

C_m is the wing-body pitching-moment coefficient at a given angle of attack, with the leading- and trailing-edge flaps retracted. This parameter should be obtained from test data, if available, or by using Section 4.3.2.2 supplemented with a test-data value for $(C_{m_0})_{WB}$.

C_L is the wing-body lift coefficient at a given angle of attack, with the leading-edge and trailing-edge flaps retracted. This parameter should be obtained from test data, if available, or from Sections 4.1.3.1*, 4.1.3.2, and 4.3.1.2.

$\Delta\eta$ is the flap span in fractions of the wing semispan (see Sketch (h)).

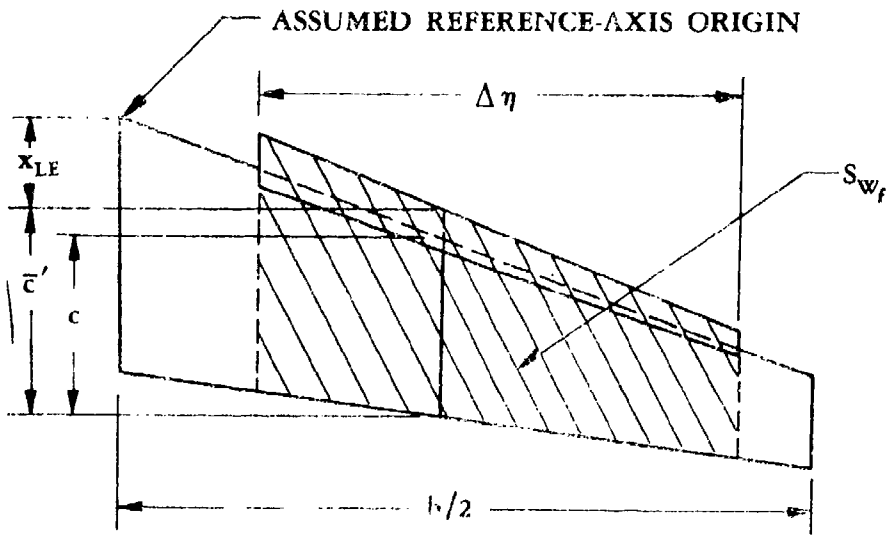

SKETCH (h)

*The wing-body zero-lift angle of attack is obtained from the ... tion should be used if available.

3. Jet Flaps

The method presented herein pertains to the same concepts as noted in Section 6.1.1.1; i.e., the pure jet-flap concept and the IBF and EBF concepts with a plain trailing-edge flap. For an IBF or EBF concept with a single-slotted or multislotted flap configuration, this method should be used only as a first approximation.

Because of the complexity of calculating the pitching moment due to a trailing-edge jet flap, the method is presented in a stepwise procedure. This procedure assumes that the wing employs a leading-edge device; however, it will also handle configurations without leading-edge devices. In using the method, all flap-chord lengths and flap deflections are measured in a streamwise direction.

The computation of the pitching moment is broken down into components due to the leading-edge device, the angle of attack, the mechanical flap, and the jet flap. This division can be somewhat misleading because in each term there appears the parameter $c_{\delta\delta}/c$, which is the ratio of the airfoil chord with all flaps extended to the basic airfoil chord. Thus each term is actually dependent upon the total extended airfoil chord $c_{\delta\delta}$. For example, a change in $c_{\delta\delta}$ due to a deflection of the leading-edge device will affect the contribution of each component, not just the component due to the leading-edge device.

No substantiation of the method is presented herein because of the scarcity of data for which enough information is available to make a meaningful comparison. The available data indicate an average error of approximately ±20 percent. For those configurations that have been analyzed by using this method, the results indicate that this method is more accurate in estimating the pitching-moment increment due to flap deflection than in estimating the variation of pitching moment with angle of attack. This may be accounted for by the tendency of wings developing very high lift coefficients to have significant flow separation even at low angles of attack. The variation in the amount of separated flow with angle of attack may be affecting C_{m_α} significantly.

The wing pitching-moment increment (omitting the zero-lift pitching moment at $C_\mu = 0$) due to a trailing-edge jet flap with or without a leading-edge device is obtained from the following procedure. All of the area terms are assumed to be total values, not semispan values, i.e., to include both the left- and right-wing contributions.

Step 1. Divide the wing into spanwise sections that exhibit the same geometric and flow characteristics, i.e., no geometric discontinuities.

a. The blown wing area will determine one or more spanwise sections. The blown wing area is defined as the basic wing area that is affected by the jet flap, excluding any increase in wing area due to Fowler motion of the leading- and/or trailing-edge devices. For a pure jet-flap configuration with the efflux at the trailing edge, S_J is defined as the streamwise basic wing area ahead of the jet flap. For EBF configurations, the jet spreading angle γ must be considered before S_J can be determined. Therefore, it is suggested that the user determine the spreading angle for his particular configuration from test data on a similar configuration. However, if no such test data are available, the Datcom recommends that a value of 12^o be used for the spreading angle γ. An example for determining S_J for an EBF configuration is presented in Sketch (i). In this example the value of S_J has been increased slightly so as to include that portion of the wing ahead of the inboard tip of the flap. The reason for this adjustment is explained in part (b).

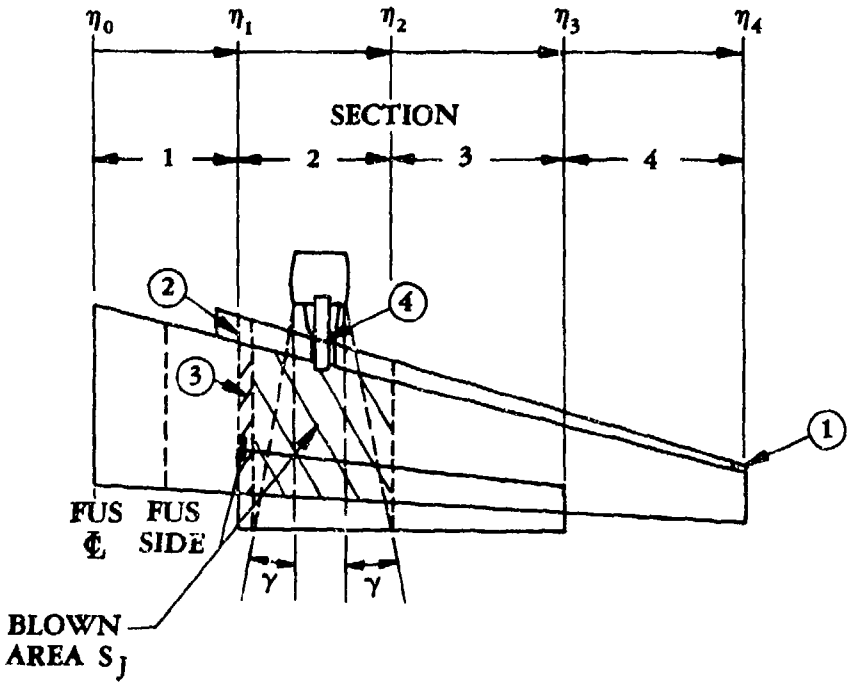

SKETCH (i)

b. The basic criterion for dividing the wing is the avoidance of discontinuities. The sections are determined such that the ratio of the extended wing chord (including both leading- and trailing-edge devices) to the basic wing chord is constant or approximately constant, and the ratio of the flap chord to the basic wing chord is constant or approximately constant; i.e., $c_{\delta\delta}/c$ is constant and c_f/c is constant. A schematic illustration for determining these spanwise sections for an EBF configuration is presented in Sketch (i). In order to minimize the number of spanwise sections, it is suggested that small changes are assumed to be made to the actual configuration. In Sketch (i) some of the assumptions made were: 1) the outboard wing slat station was assumed to be at the wing tip, 2) the inboard tip of the slat was neglected, 3) the jet spreading was assumed to extend to the inboard station of the flap, and 4) no discontinuity was assumed in the slat due to the engine pylon.

Step 2. The pitching-moment increment of each spanwise section is now calculated by treating each wing section as a two-dimensional airfoil. The calculation of the pitching-moment increments is performed by strictly applying the jet-flap method of Section 6.1.2.1 (not the mechanical leading- or trailing-edge methods) to evaluate each section individually. To prevent a duplication of effort, the material of Section 6.1.2.1 is not repeated here. It is therefore advised that the reader become familiar with the jet-flap method of Section 6.1.2.1 before proceeding further. However, before the jet-flap method of Section 6.1.2.1 can be applied to the three-dimensional wing sections, the following terms x_m/c, C_μ, K, $x_{f_i}/c_{\delta\delta}$, $x_j/c_{\delta\delta}$, and α_L (for α) must be redefined as follows:

$\frac{x_m}{c}$ redefined as the ratio of the distance from the wing leading edge to the unique unswept reference line (which may lie on or aft of a conventional wing configuration) to the local chord, such that x_m/c has a constant value for straight-tapered wings. (This reference location eliminates the need for calculating the spanwise center-of-pressure location for each wing section.) For non-straight-tapered wings there can be more than one value. Sketch (j) presents an example of a non-straight-tapered wing where two values of x_m/c are required. The determination of x_m/c is defined by

$$\frac{x_m}{c} = \frac{1+\lambda}{1-\lambda}\left(\frac{A_s}{4}\right)\tan \Lambda_{LE} \qquad 6.1.5.1\text{-m}$$

where

λ is the taper ratio of the particular spanwise wing section.

A_s is the aspect ratio of the particular spanwise wing section.

Λ_{LE} is the sweep of the leading-edge angle of the particular spanwise wing section.

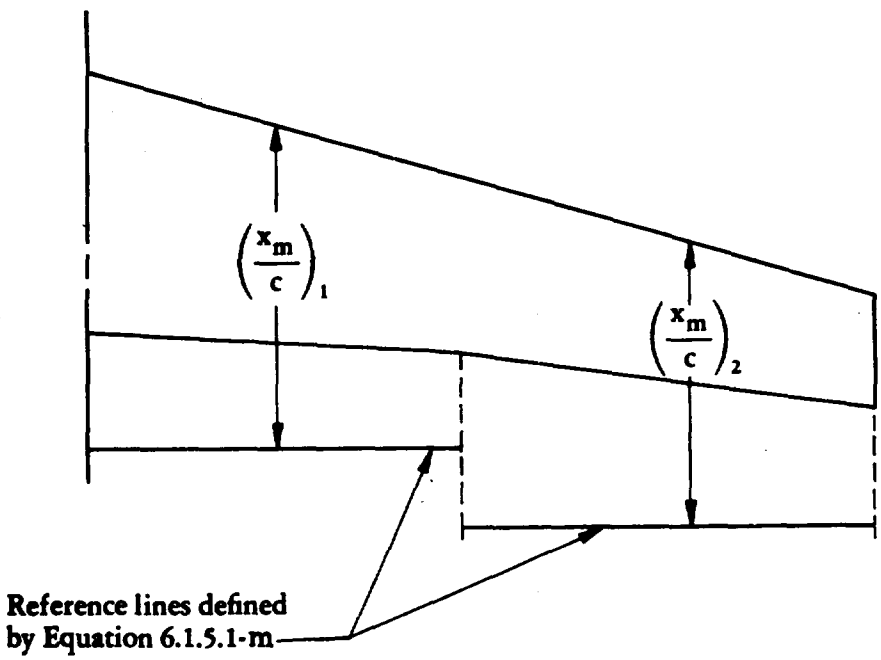

SKETCH (j)

However, a problem arises in the case of untapered wings ($\lambda = 1$), since x_m/c in Equation 6.1.5.1-m becomes indeterminate. Therefore, for an untapered wing or wing section, Equation 6.1.5.1-m is modified to the following:

$$\frac{x_m}{c} = \frac{\Delta x_r}{c} \qquad 6.1.5.1\text{-n}$$

where

Δx_f is the distance between the wing apex and the desired moment reference center, measured positive aft.

c is the basic wing chord.

C_μ is the section nondimensional trailing-edge jet momentum coefficient. For those sections that are outside of the blown area, $C_\mu = 0$. For those sections within the blown area, the following approximation is used to determine the relationship between C_μ and C_J:

$$C_\mu = C_J \eta_t \frac{S_W}{S_J} \qquad 6.1.5.1\text{-o}$$

where

C_J is the nondimensional trailing-edge jet momentum coefficient based on the gross engine thrust and the wing reference area. (See Section 6.1.4.1 for an exact definition.)

η_t is the static turning efficiency defined as the resultant force divided by the gross thrust (see Section 6.1.4.3, Sketch (a)). This value should be obtained from test data if possible, or from Figure 6.1.4.3-11 for slotted flaps. Although Figure 6.1.4.3-11 represents a reasonable average of the available data, the data scatter is large. Since this method cannot be expected to yield good results if the error in η_t is large, it is imperative that test data be used if available.

$\frac{S_W}{S_J}$ is the ratio of the wing reference area to the blown wing area.

K redefined here to apply to each wing section individually, based on the following expression

$$K = \left[\frac{A_t + 2\,C'_\mu/\pi}{A_t + 2 + 0.604\,(C'_\mu)^{1/2} + 0.876\,C'_\mu} \right] \frac{c_{\delta\delta}}{c} \qquad 6.1.5.1\text{-p}$$

where

$\frac{c_{\delta\delta}}{c}$ is the ratio of the extended wing chord, including the extensions of both the leading- and trailing-edge devices, to the basic wing chord of the particular spanwise wing section.

A_t is the aspect ratio of the total wing based on the extended wing chord, i.e., $A_t = A(c/c_{\delta\delta})$, using the particular section value for $c/c_{\delta\delta}$.

C'_μ is the section nondimensional trailing-edge jet momentum coefficient based on the extended wing chord $c_{\delta\delta}$, i.e., $C'_\mu = C_\mu (c/c_{\delta\delta})$.

$\frac{x_{f_i}}{c_{\delta\delta}}, \frac{x_j}{c_{\delta\delta}}$ are the center-of-lift location of the incremental load due to the deflection of the i^{th} flap segment and the center-of-lift location of the incremental load due to the jet deflection, respectively. In this section these terms are applied to each spanwise wing section and are corrected for three-dimensional effects by

$$\frac{x_{f_i}}{c_{\delta\delta}} = \left(\frac{x_{f_i}}{c_{\delta\delta}}\right)_{2D} \left[\frac{(x_{c.p.})_{3D}}{(x_{c.p.})_{2D}}\right]_i \qquad 6.1.5.1\text{-q}$$

$$\frac{x_j}{c_{\delta\delta}} = \left(\frac{x_j}{c_{\delta\delta}}\right)_{2D} \left[\frac{(x_{c.p.})_{3D}}{(x_{c.p.})_{2D}}\right]_j \qquad 6.1.5.1\text{-r}$$

where

$\left(\frac{x_{f_i}}{c_{\delta\delta}}\right)_{2D}$ is the two-dimensional center-of-lift location of the incremental load due to deflection of the i^{th} trailing-edge flap segment. This parameter is obtained, as defined in Section 6.1.2.1, from Figure 6.1.2.1-37 as a function of the ratio of the flap chord to the extended airfoil chord $c_{f_i}/c_{\delta\delta}$ and C'_μ.

$\left[\frac{(x_{c.p.})_{3D}}{(x_{c.p.})_{2D}}\right]_i$ is the ratio of the center-of-lift location for a finite-aspect-ratio wing to the center-of-lift location for an infinite-aspect-ratio wing for the incremental load due to deflection of the i^{th} trailing-edge flap segment. This parameter is obtained from Figure 6.1.5.1-68 as a function of $c_{f_i}/c_{\delta\delta}$ and $1/A_t$.

$\left(\frac{x_j}{c_{\delta\delta}}\right)_{2D}$ is the two-dimensional center-of-lift location of the incremental load due to the jet momentum acting at some angle to the trailing-edge camber line. This parameter is obtained from Figure 6.1.2.1-37 at $c_f/c_{\delta\delta} = 0$, as a function of the trailing-edge jet momentum C'_μ.

$\left[\frac{(x_{c.p.})_{3D}}{(x_{c.p.})_{2D}}\right]_j$ is the ratio of the center-of-lift location for a finite-aspect-ratio wing to the center-of-lift location for an infinite-aspect-ratio wing for the incremental load due to the jet momentum acting at some angle to the trailing-edge camber line. This parameter is obtained from Figure 6.1.5.1-68 at $c_f/c_{\delta\delta} = 0$, as a function of $1/A_t$.

α_L is the local angle of attack for the particular spanwise wing section under consideration. For wings with twist, this value will change from section to section. It is suggested that the change be approximated by using the average twist incidence for each section.

Step 3. Compute the sum of the wing section pitching-moment increments from Step 2 according to the following:

$$C_{m_m} = \sum_{k=1}^{p} \Delta c_m \, (K_{b_k} - K_{b_{k-1}}) \qquad 6.1.5.1\text{-s}$$

where

k is the number of the wing section (numbered from the fuselage center line outboard).

p is the total number of wing sections.

Δc_m is the section pitching-moment increment for the particular spanwise section, obtained from the jet-flap procedure of Section 6.1.2.1.

$K_{b_k}, K_{b_{k-1}}$ are the values of the span factor for the outboard and inboard ends, respectively, of the k^{th} wing section. This parameter is obtained from Figure 6.1.4.1-15 as a function of basic-wing taper ratio λ and the span stations η_k and η_{k-1} of the streamwise cuts defining the k^{th} wing section nondimensionalized by the wing semispan (see Sketch (i)).

Step 4. Calculate the lift contribution to the pitching-moment increment for each wing section according to

$$C_{\lambda_k} = \left[\Delta c_1 - \Delta c_2 + \Delta c_4 + \sum_{i=1}^{n} (\Delta c_5)_i + \Delta c_6\right](K_{b_k} - K_{b_{k-1}}) \qquad 6.1.5.1\text{-t}$$

where

$\Delta c_1, \Delta c_2, \Delta c_4, (\Delta c_5)_i$, and Δc_6 are the terms analogous to lift generated during the execution of the jet-flap procedure of Section 6.1.2.1.

$K_{b_k}, K_{b_{k-1}}$ are defined in Step 3 above.

Step 5. The total wing pitching-moment increment due to a jet flap at some angle of attack is calculated by using one of two equations presented below. For a tapered wing, Equation 6.1.5.1-u is used; while for an untapered wing, Equation 6.1.5.1-v should be used. Both equations convert the pitching moments for each wing panel about $x_m/c_{\delta\delta}$ to the desired moment-reference-center location, based on $S_W \bar{c}_W$.

$$\Delta C_m = C_{m_m} + \eta_t C_J \frac{\Delta z}{\bar{c}} + \sum_{k=1}^{p} \left\{ \left[C_\mu \frac{\alpha_L}{57.3} \frac{S_k}{S_W} - C_{\lambda_k} \right] \frac{\Delta x_k}{\bar{c}} \right\} \qquad 6.1.5.1\text{-u}$$

where

$\frac{\Delta z}{\bar{c}}$ is the vertical distance between the desired moment-reference-center location and the quarter-chord of the MAC, positive for the wing below the desired location. (This is an approximation because an exact solution would require accounting for the vertical distance for each blown wing section.)

$\frac{\Delta x_k}{\bar{c}}$ is the longitudinal distance between the moment-reference-center location and the location of the chord station for zero sweep. This parameter is measured positive aft from the moment reference center as illustrated in Sketch (k).

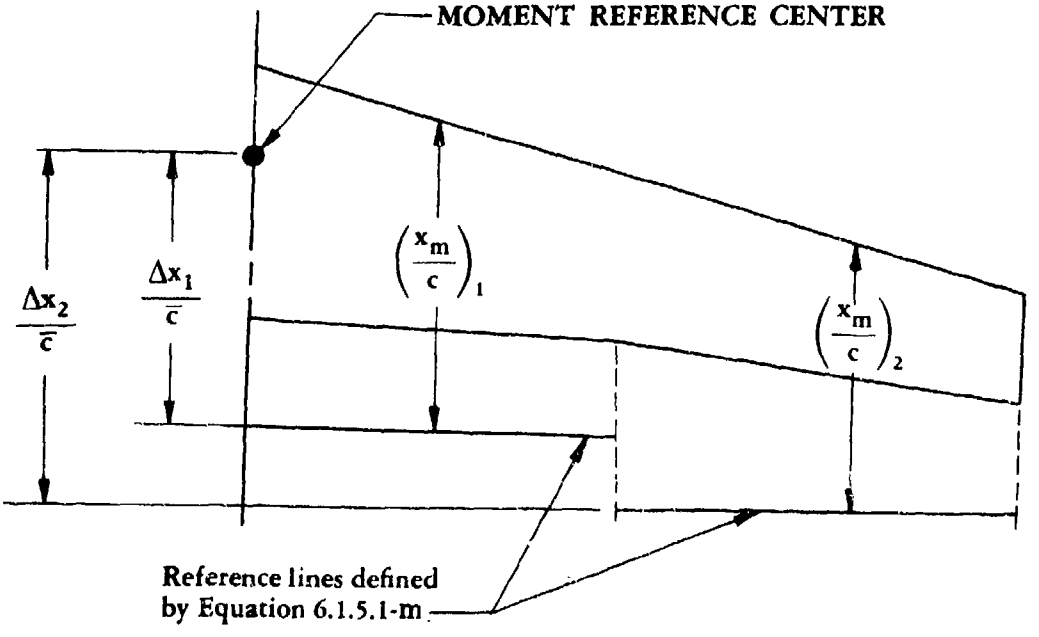

SKETCH (k)

For an untapered wing this distance can be found by using

$$\frac{\Delta x_k}{\bar{c}} = \frac{\eta_k - \eta_{k-1}}{2} \frac{b}{2} \frac{\tan \Lambda}{c} \qquad 6.1.5.1\text{-v}$$

S_k is the area of the k^{th} wing section with all flaps retracted.

All remaining terms have been defined in the previous steps.

Sample Problems

1. Single-Slotted Trailing-Edge Flap (Method 1)

Given: The sweptback wing-body configuration of Reference 32 with a single-slotted flap.

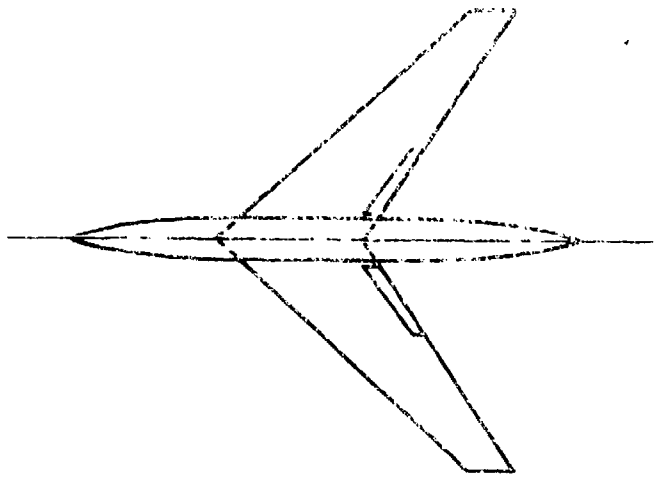

Wing Characteristics:

$A = 5.1$ $\quad b/2 = 74.75$ in. $\quad \lambda = 0.383$ $\quad \Lambda_{c/4} = 44.6°$

$c_r = 42.36$ in. $\quad c_t = 16.24$ in. $\quad S_W = 30.35$ ft^2 $\quad \bar{c} = 31.22$ in.

NACA 64-210 $\downarrow$ 0.286 c $\quad \frac{t}{c} = 0.075$ (streamwise) $\quad \frac{Y_{90}}{2} = 0.671\%$ c

$\frac{Y_{99}}{2} = 0.04\%$ c $\quad a = 0$ $\quad C_m = -0.034$ (test data)

$C_L = 0.025$ (test data)

Flap Characteristics:

Single-slotted flap $\quad \frac{c_f}{c} = 0.286$ (streamwise) $\quad \frac{c'}{c} = 1.05$

$\eta_i = 0.144 \quad \eta_o = 0.45 \quad \delta_f = 30.68°$ (streamwise)

Additional Characteristics:

$M = 0.14; \beta = 0.99 \quad R_\ell = 6 \times 10^6$

Compute:

$$\tan \frac{1}{2} \phi'_{TE} = \frac{\frac{Y_{90}}{2} - \frac{Y_{99}}{2}}{9}$$

$$= \frac{0.671 - 0.04}{9} = 0.07$$

$$\frac{c_{\ell_\alpha}}{\left(c_{\ell_\alpha}\right)_{theory}} = 0.873 \quad \text{(Figure 4.1.1.2-8a)}$$

$\left(c_{\ell_\alpha}\right)_{theory} = 6.66$ per rad (Figure 4.1.1.2-8a)

$$c_{\ell_\alpha} = \frac{1.05}{\beta}\left[\frac{c_{\ell_\alpha}}{\left(c_{\ell_\alpha}\right)_{theory}}\right]\left(c_{\ell_\alpha}\right)_{theory} \quad \text{(equation 4.1.1.2-a)}$$

$$= \frac{1.05}{0.99}(0.873)(6.66)$$

$= 6.167$ per rad

$\alpha_\delta = -0.483$ (Figure 6.1.1.1-4l)

$\Delta c_\ell = -c_{\ell_\alpha} \alpha_\delta \delta_f$ (equation 6.1.1.1-c)

$= -(6.167)(-0.483)\frac{30.68}{57.3}$

$= 1.595$

$$\left.\begin{aligned} A &= 6.0 \\ \Lambda_{c/2} &= 0 \end{aligned}\right\}$$ Method 1 assumptions for calculating ΔC_L

$$\kappa = \frac{c_{\ell_\alpha}}{\beta} \Big/ \frac{2\pi}{\beta} = \frac{6.167}{2\pi} = 0.9815$$

$$\frac{A}{\kappa}\left[\beta^2 + \tan^2 \Lambda_{c/2}\right]^{1/2} = \frac{6}{0.9815}\,(0.99) = 6.05$$

$$\frac{C_{L_\alpha}}{A} = 0.747 \text{ per rad} \quad \text{(Figure 4.1.3.2-49)}$$

$$C_{L_\alpha} = 6(0.747) = 4.48 \text{ per rad}$$

$$\left(\alpha_\delta\right)_{c_\ell} = -0.655 \quad \text{(Figure 6.1.4.1-14 insert)}$$

$$\frac{\left(\alpha_\delta\right)_{C_L}}{\left(\alpha_\delta\right)_{c_\ell}} = 1.04 \quad \text{(Figure 6.1.4.1-14)}$$

$K_b = 1.0$ (assume full-span flaps for calculating ΔC_L)

$$\Delta C_L = \Delta c_\ell \left(\frac{C_{L_\alpha}}{c_{\ell_\alpha}}\right)\left[\frac{\left(\alpha_\delta\right)_{C_L}}{\left(\alpha_\delta\right)_{c_\ell}}\right] K_b \quad \text{(Equation 6.1.4.1-a)}$$

$$= (1.595)\left(\frac{4.48}{6.167}\right)(1.04)(1.0)$$

$$= 1.205$$

$$\frac{c_f}{c'} = \frac{c_f}{c}\,\frac{c}{c'}$$

$$= \frac{0.286}{1.05} = 0.272$$

$$\frac{\Delta C'_m}{\Delta C_L} = -0.271 \quad \text{(Figure 6.1.5.1-60)}$$

$$\left(K_p\right)_{\eta=0.144} = 0.27 \quad \text{(Figure 6.1.5.1-61)}$$

$$\left(K_p\right)_{\eta=0.45} = 0.72 \quad \text{(Figure 6.1.5.1-61)}$$

$$K_p = \left(K_p\right)_{\eta_o} - \left(K_p\right)_{\eta_i}$$

$$= 0.72 - 0.27 = 0.45$$

$$\Delta C_m = K_p\left\{\left(\frac{\Delta C'_m}{\Delta C_L}\right)\Delta C_L\left(\frac{c'}{c}\right)^2 - 0.25\, C_L\left(\frac{c'}{c}\right)\left(\frac{c'}{c} - 1\right) + C_m\left[\left(\frac{c'}{c}\right)^2 - 1\right]\right\}$$

(Equation 6.1.5.1-b)

$$= 0.45\left\{(-0.271)\,(1.205)\,(1.05)^2 - 0.25(0.025)\,(1.05)\,(0.05) - 0.034\left[(1.05)^2 - 1\right]\right\}$$

$$= 0.45\left\{-0.36 - 0.0003 - 0.0035\right\}$$

$$= -0.164$$

$$\left(K_\Lambda\right)_{\eta=0.144} = 0.0365 \quad \text{(Figure 6.1.5.1-57a through -57d, interpolated)}$$

$$\left(K_\Lambda\right)_{\eta=0.45} = 0.0615 \quad \text{(Figure 6.1.5.1-57a through -57d, interpolated)}$$

$$K_\Lambda = \left(K_\Lambda\right)_{\eta_o} - \left(K_\Lambda\right)_{\eta_i}$$

$$= 0.0615 - 0.0365 = 0.025$$

Solution:

$$\Delta C_{m_f} = \Delta C_m + K_\Lambda\left(\frac{A}{1.5}\right)\Delta C_L \tan \Lambda_{c/4} \quad \text{(Equation 6.1.5.1-a)}$$

$$= -0.164 + (0.025)\left(\frac{5.1}{1.5}\right)(1.205)\,(0.9874)$$

$$= -0.164 + 0.101$$

$$= -0.063 \text{ (based on the product of wing area and wing mean aerodynamic chord and referred to a moment center at } \bar{c}/4)$$

This compares with a test value of $\Delta C_{m_f} = -0.074$ from Reference 32.

2. Plain Trailing-Edge Flap (Method 2)

Given: The sweptback wing of Reference 13 with a partial-span plain trailing-edge flap. This is the same configuration as Sample Problem 1 of Paragraph A of Section 6.1.4.1.

Wing Characteristics:

$A = 3.78$ $\quad b/2 = 16.97$ ft $\quad \lambda = 0.586$ $\quad \Lambda_{c/4} = 47.35^{o}$

$c_r = 11.315$ ft $\quad \bar{\eta} = 0.456$ $\quad \bar{c} = 9.09$ ft $\quad c_{av} = 8.98$ ft

NACA 65A006 airfoil (streamwise)

Flap Characteristics:

Plain trailing-edge flap $\quad \Lambda_{HL} = 43^{o}$ $\quad c_f/c = 0.224$ (streamwise)

$\eta_i = 0.10$ $\quad \eta_o = 0.58$ $\quad \delta_{\perp HL} = 30^{o}$ $\quad \delta = 22.1^{o}$ (streamwise)

Additional Characteristics:

Low speed; $\beta = 1.0$ $\quad R_\ell = 6.1 \times 10^{6}$

Compute:

Step 1. Determine the spanwise loading coefficient G/δ (see Step 1c of Datcom Method 2)

$c_{\ell_\alpha} = 6.13$ per rad (Sample Problem 1, Paragraph A, Section 6.1.4.1)

$$\kappa = \frac{c_{\ell_\alpha}}{2\pi} = \frac{6.13}{2\pi} = 0.976$$

$$\frac{\beta A}{\kappa} = \frac{(1.0)(3.78)}{0.976} = 3.87$$

$$\Lambda_\beta = \tan^{-1}\left(\frac{\tan \Lambda_{c/4}}{\beta}\right) = \tan^{-1}\left(\frac{\tan 47.35^{o}}{1.0}\right) = 47.35^{o}$$

Obtain the spanwise loading coefficient G/δ for a full wing-chord flap extending from the plane of symmetry to the inboard station of the actual flap ($\eta_i = 0.10$), and for a full wing-chord flap extending from the plane of symmetry to the outboard end of the actual flap ($\eta_o = 0.58$). Since the span loadings for these particular flap spans are not presented in Figures 6.1.5.1-62a through 6.1.5.1-62d, the interpolation procedure described in Step 1 of Datcom Method 2 must be applied. The cross-plotted results of the variation of the loading parameter at given span stations as a function of flap span for the desired values of $\beta A/\kappa$, Λ_β, and λ are presented in Sketch (h).

The spanwise loading coefficients for a full wing-chord flap that extends from the plane of symmetry to the inboard station $\eta_i = 0.100$ and for a full wing-chord flap that extends from the plane of symmetry to the outboard station $\eta_o = 0.58$ are read from Sketch (h) at η_i and η_o. These spanwise loading coefficients are presented in Sketch (i).

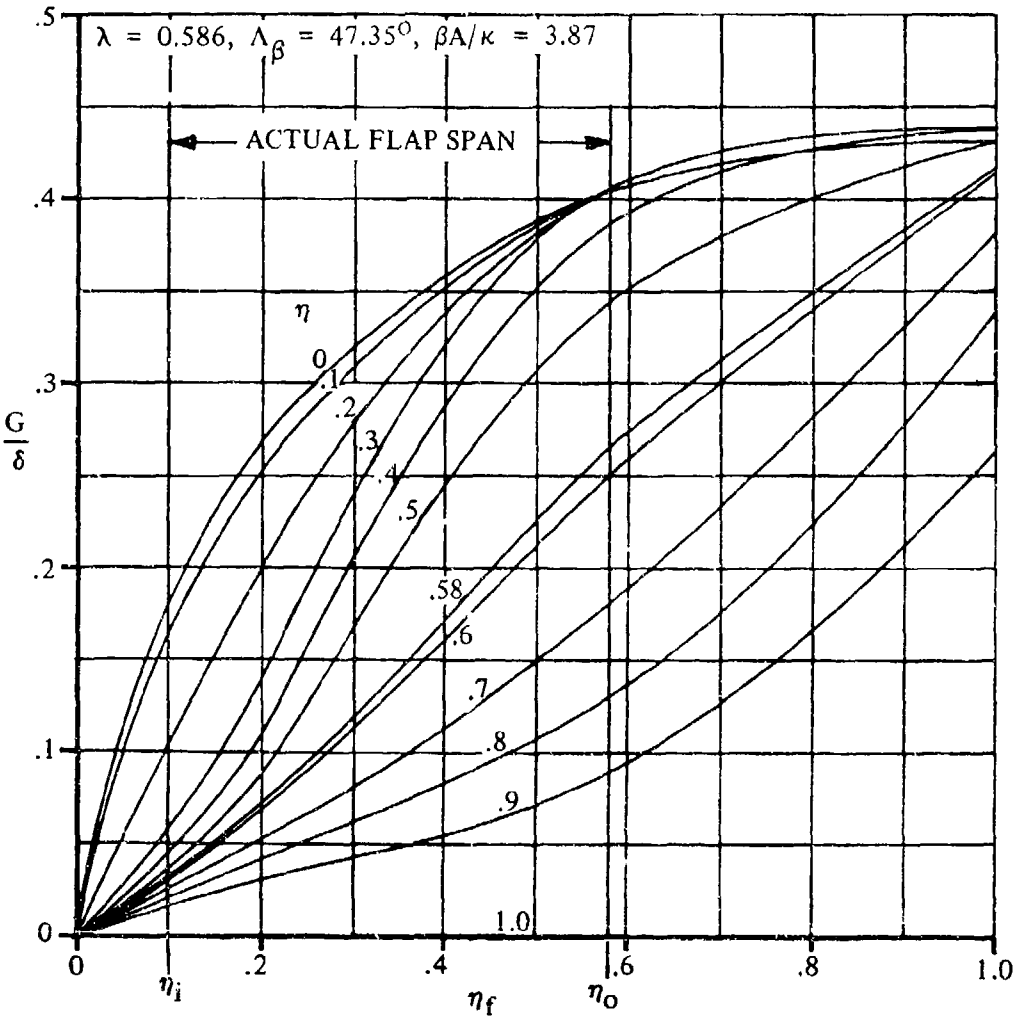

VARIATION OF LOADING COEFFICIENT WITH FLAP SPAN

SKETCH (h)

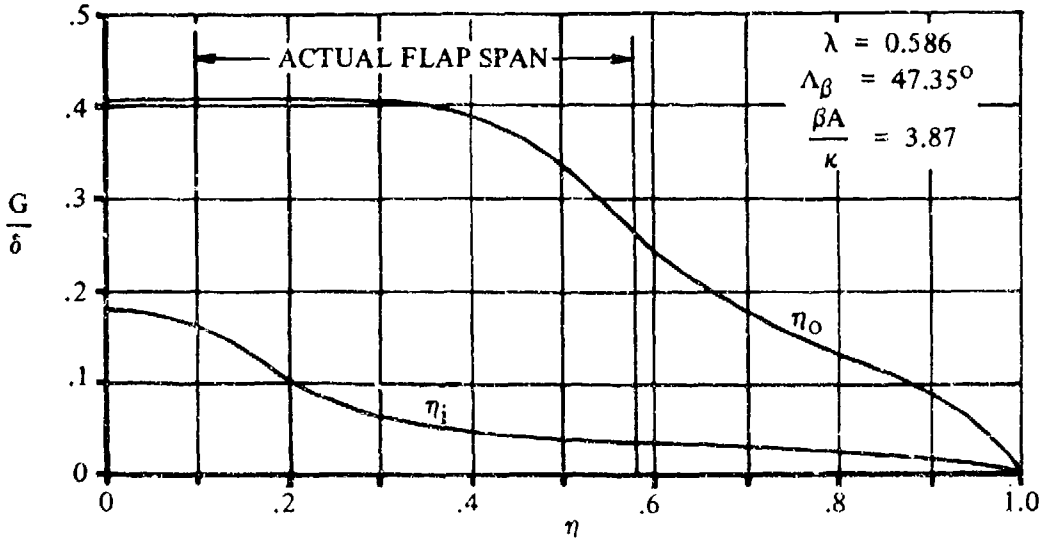

VARIATION OF SPANWISE LOADING COEFFICIENT

SKETCH (i)

Step 2. Determine the incremental section lift coefficient as a function of span station η.

$$c_{\ell_\Lambda} = -\frac{2b}{c}\frac{G}{\delta}\alpha_\delta\delta \quad \text{(Equation 6.1.5.1-c)}$$

$$\Delta c_\ell = 0.927 \quad \text{(Sample Problem 1, Paragraph A, Section 6.1.4.1)}$$

$$\alpha_\delta = -\frac{\left(c_{\ell_\delta}\right)_\alpha}{\left(c_{\ell_\alpha}\right)_\delta} \quad \text{(Equation 6.1.1.1-b)}$$

$$= -\frac{\Delta c_\ell}{\left(c_{\ell_\alpha}\right)_\delta \delta} = -\frac{0.927}{(6.13)\,\frac{22.1}{57.3}} = -0.392$$

INCREMENTAL SECTION LIFT COEFFICIENT

① η	② $\left(\frac{G}{\delta}\right)_{\eta_o}$ = 0.58	③ $\left(\frac{G}{\delta}\right)_{\eta_i}$ = 0.10	④ $\frac{G}{\delta}$ ② − ③	⑤ $\alpha_\delta\delta$ (rad)	⑥ c Local Chord (ft)	⑦ c_{ℓ_Λ} -2b ④ ⑤ / ⑥ Eq. 6.1.5.1-c
0	0.404	0.180	0.224	-0.151	11.315	0.203
η_i	0.404	0.163	0.241		10.847	0.228
.2	0.404	0.103	0.301		10.379	0.297
.3	0.405	0.057	0.348		9.911	0.360
.4	0.386	0.045	0.341		9.443	0.370
.5	0.344	0.036	0.308		8.975	0.352
η_o	0.265	0.031	0.234		8.600	0.279
.6	0.250	0.030	0.220		8.507	0.265
.7	0.180	0.025	0.155		8.039	0.198
.8	0.129	0.021	0.108		7.571	0.146
.9	0.088	0.016	0.072		7.103	0.104
1.0	0	0	0		6.635	0

Step 3. Determine the chordwise center-of-pressure location $x_{c.p.}$ for stations across the span.

$$x_{c.p._b} = 0.665 \quad \text{(Figure 6.1.5.1-67b)}$$

$$\tan\Lambda_b = \tan\Lambda_{c/4} - \frac{4}{A}\left(x_{c.p._b} - 0.25\right)\left(\frac{1-\lambda}{1+\lambda}\right) \quad \text{(Equation 6.1.5.1-g)}$$

$$= 1.0856 - \frac{4}{3.78}(0.665 - 0.25)\left(\frac{0.414}{1.586}\right) = 0.9710$$

$\Lambda_b = \tan^{-1}(0.9710) = 44.15^o$

$\cos \Lambda_b = 0.7175$

$\cos^2 \Lambda_b = 0.5148$

$\delta' = \tan^{-1}\left(\frac{\tan \delta}{\cos \Lambda_b}\right)$ (Equation 6.1.5.1-f)

$= \tan^{-1}\left(\frac{\tan 22.1^o}{\cos 44.15^o}\right) = \tan^{-1}(0.5660) = 29.5^o$

$\Delta c_{m_f} = -0.205$ (Figure 6.1.2.1-35b at δ' and c_f/c)

CHORDWISE CENTER-OF-PRESSURE LOCATION

	FLAPPED SECTION			ADJACENT TO FLAP ENDS, $\Delta\eta < \lvert\eta_{0.20}\rvert$			
	(8)	(9)	(10)	(11)	(12)	(13)	(14)
η	$c\ell_{\Lambda=0}$ (7)/$\cos^2 \Lambda_b$ Eq. 6.1.5.1-h	$\frac{\Delta c_{m_f}}{c\ell_{\Lambda=0}}$ $\frac{-0.205}{(8)}$	$x_{c.p.}$ Flapped Section 0.25-(9)	K Fig. 6.1.5.1-67a	$\left(\frac{\Delta c_{m_f}}{c\ell_{\Lambda=0}}\right)_{\text{edge of flap}}$	$x_{c.p.}$ @ $\Delta\eta < \lvert\eta_{0.20}\rvert$ 0.25-(11)(12) Eq. 6.1.5.1-i	$x_{c.p.}$ Summary
0	–	–	–	0.33	−0.463	0.403	0.403
η_i	0.443	−0.463	0.713	– –	– – –	– –	0.713
.2	0.577	−0.355	0.605	– –	– – –	– –	0.605
.3	0.699	−0.293	0.543	– –	– – –	– –	0.543
.4	0.719	−0.285	0.535	– –	– – –	– –	0.535
.5	0.684	−0.300	0.550	– –	– – –	– –	0.550
η_o	0.542	−0.378	0.626	– –	– – –	– –	0.628
.6	– –	– – –	– –	0.955	−0.378	0.611	0.611
.7	– –	– – –	– –	0.210	−0.378	0.329	0.329
.8	– –	– – –	– –	– –	– – –	– –	0.250
.9	– –	– – –	– –	– –	– – –	– –	0.250
1.0	– –	– – –	– –	– –	– – –	– –	0.250

The calculated variation of chordwise center-of-pressure location for stations across the span is plotted in Sketch (j)

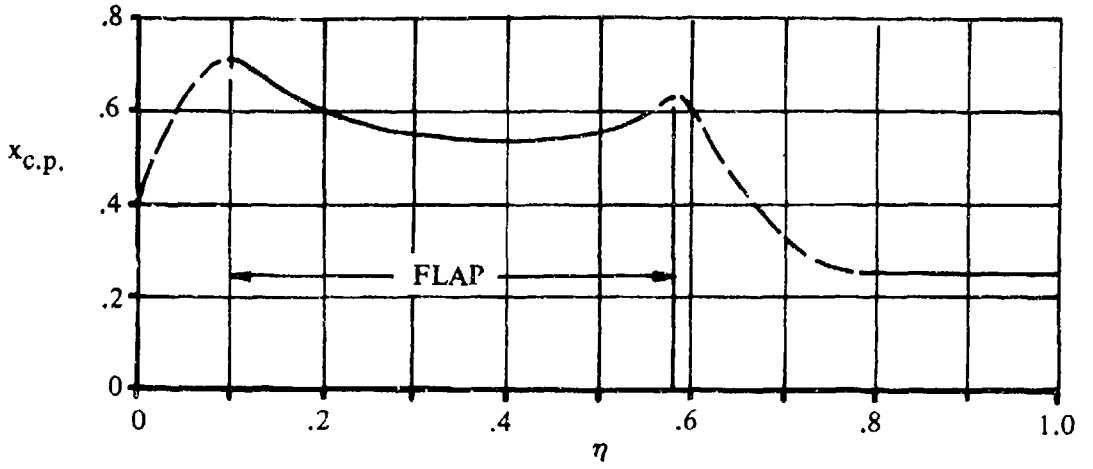

VARIATION OF CHORDWISE CENTER-OF-PRESSURE LOCATION
SKETCH (j)

Solution:

$$\Delta C_{m_f} = \int_0^{1.0} - \left[c_{\ell_\Lambda} \left(\frac{c}{c_{av}} \right) \left(\frac{x}{\bar{c}} \right) \right] d\eta \quad \text{(Equation 6.1.5.1-k)}$$

$$\frac{x}{\bar{c}} = (\eta - \bar{\eta}) \frac{b/2}{\bar{c}} \tan \Lambda_{c/4} + \frac{c(x_{c.p.} - 0.25)}{\bar{c}} \quad \text{(Equation 6.1.5.1-j)}$$

	(15)	(16)	(17)	(18)	(19)	(20)
η	$\frac{c}{c_{av}}$ (6) / 8.98	$\frac{c}{\bar{c}}$ (6) / 9.09	$(\eta - \bar{\eta}) \frac{b/2}{\bar{c}} \tan \Lambda_{c/4}$	$(x_{c.p.} - .25) \frac{c}{\bar{c}}$ [(14) − .25] (16)	$\frac{x}{\bar{c}}$ (17) + (18)	Δc_{m_f} − [(7) (15) (19)] $\Delta\eta$ Eq. 6.1.5.1-k
0	1.260	1.245	−0.924	0.190	−0.734	0.00930
η_i	1.208	1.193	−0.721	0.552	−0.169	0.00465
.2	1.156	1.142	−0.519	0.405	−0.114	0.00391
.3	1.104	1.090	−0.316	0.319	0.003	−0.00012
.4	1.051	1.039	−0.113	0.296	0.183	−0.00712
.5	0.999	0.987	0.089	0.296	0.385	−0.01354
η_o	0.958	0.946	0.251	0.358	0.609	–
.6	0.947	0.936	0.292	0.338	0.630	−0.01581
.7	0.895	0.884	0.494	0.070	0.564	−0.00999
.8	0.843	0.833	0.697	0	0.697	−0.00858
.9	0.791	0.781	0.899	0	0.899	−0.00740
1.0	0.739	0.730	1.102	0	1.102	0
					$\Delta c_{m_f} = \Sigma =$	−0.0473

This compares with a test value of $\Delta C_{m_f} = -0.040$ from Reference 13.

3. Krueger Leading-Edge Flap

Given: The sweptback wing-body configuration of Reference 35 with a leading-edge Krueger flap.

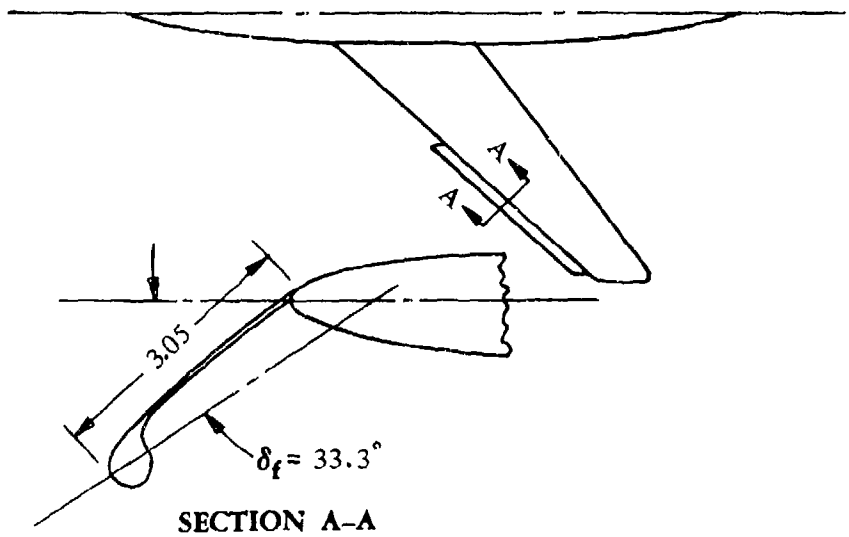

SECTION A–A

Wing Characteristics:

$A = 5.1$ $b/2 = 74.75$ in. $\lambda = 0.383$ $\Lambda_{c/4} = 45.35^{o}$ $\Lambda_{LE} = 47.72^{o}$

$c_r = 42.36$ in. $c_t = 16.24$ in. $S_W = 30.35$ ft^2 $\bar{c} = 31.22$ in.

$y_{\bar{c}} = 31.81$ in. $\alpha = 2^{o}$

Flap Characteristics:

Krueger leading-edge flap $c_{f_{1_{LE}}} = 3.05$ in. $\delta^{*}_{f_{1_{LF}}} = 33.3^{o}$

Constant flap chord $\eta_i = 0.50$ $\eta_o = 0.975$

Additional Characteristics:

$M = 0.14$; $\beta = 0.99$ $R_\ell = 6 \times 10^6$ $C_L = 0.17$

$x_m = 42.79$ in. (aft of wing apex) $C_m = -0.040$ (flaps retracted)

*δ_f is defined according to Figure 6.1.1.1-51, not as defined in Reference 35.

Compute:

Determine $\bar{c}'$

$$c_{f_{LE}} = \frac{c_{f_{LE}}}{\cos \Lambda_{LE}} = \frac{3.05}{0.6727} = 4.53 \text{ in.}$$

$c = c_r - \eta (c_r - c_t)$ (see Section 2.2.2)

At η_i, $c = 42.36 - (0.50)(42.36 - 16.24) = 29.30$ in.

$c' = c + c_f = 29.30 + 4.53 = 33.83$ in.

At η_o, $c = 42.36 - (0.975)(42.36 - 16.24) = 16.89$ in.

$c' = 16.89 + 4.53 = 21.42$ in.

$$\lambda_f = \frac{(c')_{\eta_o}}{(c')_{\eta_i}} = \frac{21.42}{33.83} = 0.633$$

$$\bar{c}' = \frac{2}{3}(c')_{\eta_i}\left(\frac{1 + \lambda_f + \lambda_f^2}{1 + \lambda_f}\right) \quad \text{(Section 2.2.2)}$$

$$= \frac{2}{3}(33.83)\left(\frac{1 + 0.633 + 0.633^2}{1 + 0.633}\right)$$

$= 28.09$ in.

Determine $c_{m'_{\delta_{LE}}}$ and $c_{\ell'_\delta}$ (assuming constant flap-to-chord ratio)

$$\frac{c_{f_{LE}}}{\bar{c}'} = \frac{4.53}{28.09} = 0.161$$

$c_{m'_{\delta_{LE}}} = -0.00127$ per deg (Figure 6.1.2.1-36)

$c_{\ell'_\delta} = -0.00320$ per deg (Figure 6.1.1.1-50)

Determine x_{LE}

$$y_{\bar{c}'} = \frac{1}{3}(\Delta\eta)(b/2)\left(\frac{1 + 2\lambda_f}{1 + \lambda_f}\right) + (\eta_i)(b/2) \quad \text{(Section 2.2.2)}$$

$$= \frac{1}{3}(0.975 - 0.50)(74.75)\left(\frac{1 + 2(0.633)}{1 + 0.633}\right) + 0.5(74.75)$$

$= 16.42 + 37.375 = 53.80$ in.

$$x_{LE} = y_{\bar{c}'} \tan \Lambda_{LE} - c_f$$

$$= 53.80\,(1.0998) - 4.53$$

$$= 54.64 \text{ in.}$$

Determine S_{W_f}

$$S_{W_f} = [(c')_{\eta_i} + (c')_{\eta_o}]\,(\Delta\eta)(b/2)$$

$$= (33.83 + 21.42)(0.975 - 0.50)(74.75)$$

$$= 1961.72 \text{ in.}^2 = 13.62 \text{ ft}^2$$

Determine δ_f (streamwise)

$$\delta_f = \tan^{-1}(\tan \delta_{f_{\perp LE}} \cos \Lambda_{LE}) \quad \text{(Equation 6.1.5.1-d)}$$

$$= \tan^{-1}[(0.6569)(0.6727)]$$

$$= 23.84^{\circ} \text{ (streamwise)}$$

Determine c

$$\text{At } \eta_{\bar{c}'},\ c = c_r - \frac{y_{\bar{c}'}}{b/2}(c_r - c_t) \quad \text{(Section 2.2.2)}$$

$$= 42.36 - \frac{53.80}{74.75}(42.36 - 16.24) = 23.56 \text{ in.}$$

Solution:

$$\Delta C_m = \left[c_{m'_{\delta_{LE}}} \left(\frac{\bar{c}'}{\bar{c}}\right) + \left(\frac{x_m}{\bar{c}} - \frac{x_{LE}}{\bar{c}}\right) c_{\ell'_\delta} \right] \frac{S_{W_f}}{S_W} \delta_f$$

$$+ \left\{ C_m \left[\left(\frac{\bar{c}'}{c}\right)^2 - 1 \right] + 0.75\, C_L \left(\frac{\bar{c}'}{c}\right) \left(\frac{\bar{c}'}{c} - 1\right) \right\} \Delta\eta \quad \text{(Equation 6.1.5.1-}\ell\text{)}$$

$$= \left[(-0.00127)\left(\frac{28.09}{31.22}\right) + \left(\frac{42.79}{31.22} - \frac{54.64}{31.22}\right)(-0.00320) \right] \frac{13.62}{30.35}(23.84)$$

$$+ \left\{ (-0.040)\left[\left(\frac{28.09}{23.56}\right)^2 - 1 \right] + 0.75\,(0.17) \left(\frac{28.09}{23.56}\right) \left(\frac{28.09}{23.56} - 1\right) \right\} (0.975 - 0.50)$$

$$= (-0.00114 + 0.00121)(10.70) + (-0.0169 + 0.0293)(0.475)$$

$$= 0.00075 + 0.00589$$

$$= 0.00664$$

This compares with a test value of $\Delta C_m = 0.003$ from Reference 35.

4. Trailing-Edge Jet Flap

Given: The wing with the EBF system shown below.

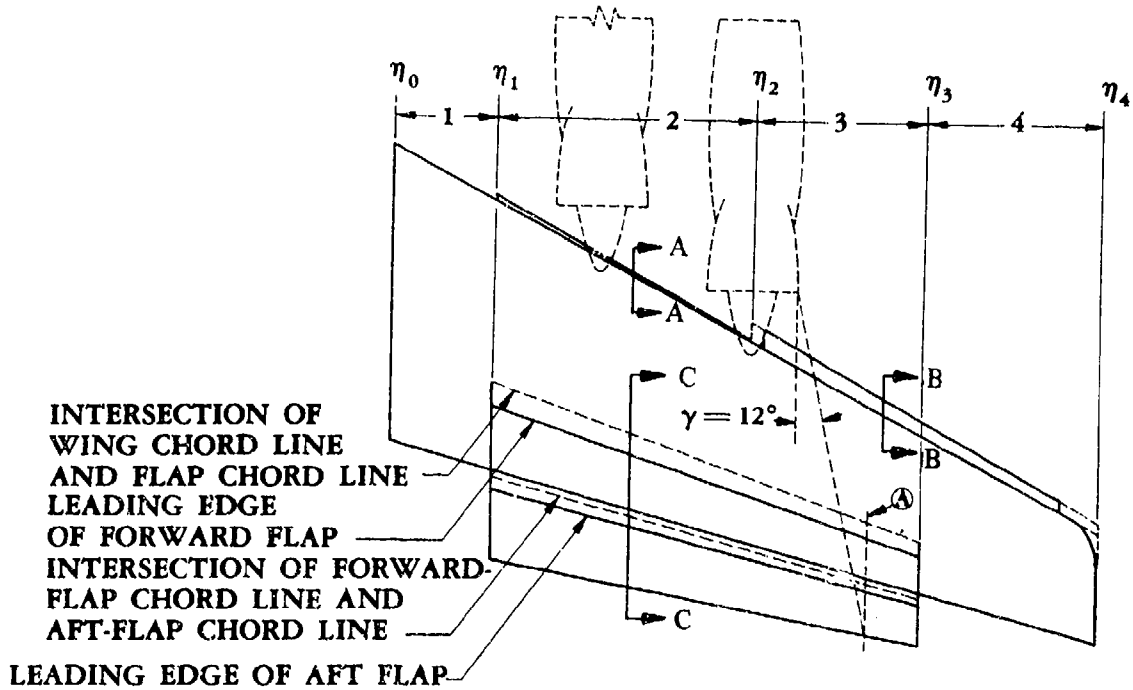

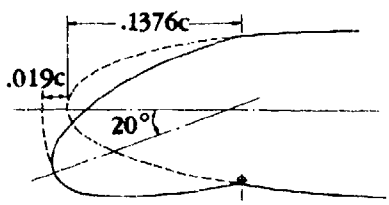

SECTION A–A

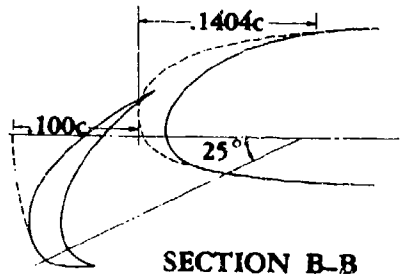

SECTION B–B

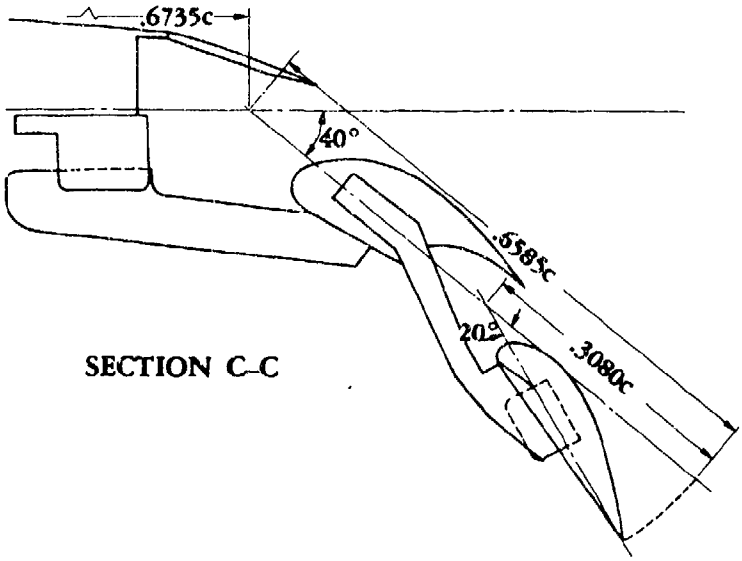

SECTION C–C

$A = 7.0$ $\lambda = 0.3714$ $b = 5.9360$ ft $\Lambda_{c/4} = 25^{O}$

$c_r = 14.84$ in. $\bar{c} = 10.8886$ in. $S_W = 5.0337$ ft^2

$x_{c.g.} = 10.72$ in. aft of wing apex $\Delta z_{c.g.} = -1.922$ in. (below MAC quarter-chord)

$\alpha_W = 0$ $C_J = 3.0$ $\eta_t = 0.81$

$\delta_{j_{eff}} = 57.5^{O}$ } (from static force-test data)

$\delta_{f_1} = 40^{O}$ $\delta_{f_2} = 20^{O}$

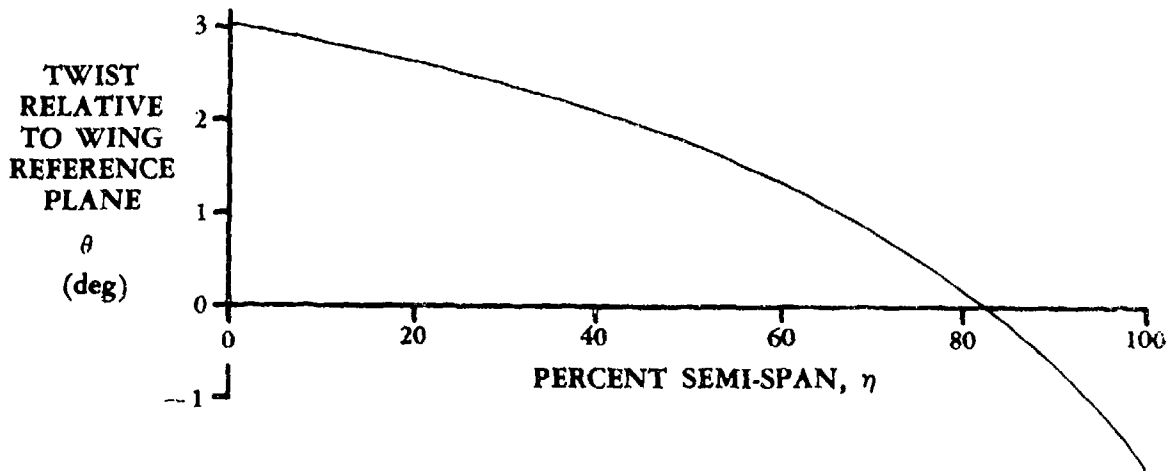

Wing section, k	1	2	3	4
Span station of outboard streamwise cut, η_k	0.1443	0.5076	0.7515	1.0
Span station of inboard streamwise cut, η_{k-1}	0	0.1443	0.5076	0.7515
Leading-edge device	None	Drooped leading edge	Slat	Slat
$\delta_{f_{LE}}$	0	20^{O}	25^{O}	25^{O}
Trailing-edge device	None	Double-slot Fowler flap	Double-slot Fowler flap	None
$c_{f_{LE}}/c$	0	0.1376	0.1404	0.1404
c'_{LE}/c	1.0	1.019	1.100	1.100
c_1/c	0	0.3505	0.3505	0
c_2/c	0	0.3080	0.3080	0
$c_{\delta\delta}/c$	1.0	1.351	1.432	1.100

Compute:

Step 1. Divide the wing into four sections as indicated in the drawing. The wing-tip is squared off and the slats extended to avoid definition of additional small wing sections. It was assumed that blowing affects the entire trailing-edge flap.*

Find $S_J = S_2 + S_3$ (the area ahead of the flap)

$$c_t = \lambda c_r = (0.3714)(14.84) = 5.512 \text{ in.}$$

$$c = c_r - \eta_k(c_r - c_t)$$

At η_1, $c = 14.84 - 0.1443(14.84 - 5.51) = 13.49$ in.

At η_2, $c = 14.84 - 0.5076(14.84 - 5.51) = 10.10$ in.

At η_3, $c = 14.84 - 0.7515(14.84 - 5.51) = 7.83$ in.

$$S_2 = \frac{1}{2}\frac{(13.49 + 10.10)}{12}(0.5076 - 0.1443)(5.9360) = 2.120 \text{ ft}^2$$

$$S_3 = \frac{1}{2}\frac{(10.10 + 7.83)}{12}(0.7515 - 0.5076)(5.9360) = 1.082 \text{ ft}^2$$

$$S_J = 2.120 + 1.082 = 3.202 \text{ ft}^2$$

Because of the lengthiness of the calculations for various parameters in Steps 2 through 5, the calculations for only wing section 2 will be presented in detail. However, the calculated components for each wing section are listed in summary tables with the detailed calculations for wing section 2.

*For purposes of illustration only, an additional division, Ⓐ in the sketch, is shown. It is made at the intersection of the jet and the extended flap trailing edge, by assuming that the jet spreading is 12 degrees. If the wing had been equipped with a full-span trailing-edge flap, division A would have been used as η_3 instead of $\eta_3 = 0.7515$.

Step 2. Δc_m (Section 6.1.2.1. Note, however, that several terms have been redefined in Section 6.1.5.1; e.g., C_μ, K, $\frac{x_m}{c}$, α_L, $\frac{x_{f_i}}{c_{\delta\delta}}$, and $\frac{x_j}{c_{\delta\delta}}$)

Find $(\Delta c_m)_{\delta f_{LE}}$ (Wing Section 2)

$$\left.\begin{aligned} \delta_{f_{LE}} &= 20^o \\ \frac{c_{f_{LE}}}{c} &= 0.1376 \end{aligned}\right\} \text{ (given)}$$

$$c_a = c_{\delta\delta} - c_{f_{LE}} \quad \text{(Equation 6.1.2.1-g)}$$

$$\frac{c_a}{c_{\delta\delta}} = 1 - \frac{c_{f_{LE}}}{c} \Big/ \frac{c_{\delta\delta}}{c}$$

$$= 1 - \frac{0.1376}{1.351}$$

$$= 0.8981$$

$$C_\mu = C_J \eta_t \frac{S_W}{S_J} \quad \text{(Equation 6.1.5.1-o)}$$

$$= (3.0)(0.81)\frac{5.0337}{3.202}$$

$$= 3.820$$

$$C_\mu' = C_\mu \frac{c}{c_{\delta\delta}} \quad \text{(defined in Section 6.1.2.1 Step 1a)}$$

$$= 3.820/1.351$$

$$= 2.828$$

$$c_{\ell_{\delta_a}} = 11.6 \text{ per rad} \quad \text{(Figure 6.1.1.1-49)}$$

$$c_{\ell_\alpha} = 11.8 \text{ per rad} \quad \text{(Figure 6.1.1.1-49)}$$

$$A_t = A\frac{c}{c_{\delta\delta}} = \frac{7.0}{1.351} = 5.181$$

$$K = \left[\frac{A_t + 2 C'_\mu/\pi}{A_t + 2 + 0.604(C'_\mu)^{1/2} + 0.876\, C'_\mu} \right] \frac{c_{\delta\delta}}{c} \quad \text{(Equation 6.1.5.1-p)}$$

$$= \left[\frac{5.181 + 2(2.828)/\pi}{5.181 + 2 + 0.604(2.828)^{1/2} + 0.876(2.828)} \right] (1.351)$$

$$= \frac{6.981(1.351)}{10.674}$$

$$= 0.8836$$

$$\Delta c_1 = \frac{\delta_{f_{LE}}}{57.3} K\, c_{\ell_{\delta_a}} \quad \text{(Equation 6.1.2.1-e)}$$

$$= \frac{20}{57.3}(0.8836)(11.6)$$

$$= 3.5776$$

$$\Delta c_2 = \frac{\delta_{f_{LE}}}{57.3} K\, c_{\ell_\alpha} \quad \text{(Equation 6.1.2.1-f)}$$

$$= \frac{20}{57.3}(0.8836)(11.8)$$

$$= 3.6393$$

$$\tan \Lambda_{LE} = \tan \Lambda_{c/4} - \frac{4}{A}\left(-\frac{1}{4}\right)\frac{1-\lambda}{1+\lambda} \quad \text{(Section 2.2.2)}$$

$$= 0.4663 - \frac{4}{7}\left(-\frac{1}{4}\right)\frac{1-0.3714}{1.3714}$$

$$= 0.5318$$

$$\frac{x_m}{c} = \left(\frac{1+\lambda}{1-\lambda}\right)\frac{A_s}{4}\tan\Lambda_{LE} \quad \text{(Equation 6.1.5.1-m)}$$

$$= \left(\frac{1.3714}{1-0.3714}\right)\frac{7}{4}(0.5318)$$

$$= 2.0304$$

$$\frac{x_a}{c_{\delta\delta}} = 0.245 \quad \text{(Figure 6.1.2.1-37)}$$

$$\frac{x_{a.c.}}{c_{\delta\delta}} = 0.215 \quad \text{(Figure 6.1.2.1-37)}$$

$$x_1 = \frac{x_m}{c} + \left(\frac{c'_{LE}}{c} - 1\right) - \frac{x_a}{c_{\delta\delta}}\frac{c_{\delta\delta}}{c} \quad \text{(Equation 6.1.2.1-h)}$$

$$= 2.0304 + (1.019 - 1) - 0.245\,(1.351)$$

$$= 1.718$$

$$x_2 = \frac{x_m}{c} + \left(\frac{c'_{LE}}{c} - 1\right) - \frac{x_{a.c.}}{c_{\delta\delta}}\frac{c_{\delta\delta}}{c} \quad \text{(Equation 6.1.2.1-i)}$$

$$= 2.0304 + (1.019 - 1) - 0.215(1.351)$$

$$= 1.759$$

$$\Delta c_{m_3} = C_\mu \frac{c_{f_{LE}}}{c}\sin\delta_{f_{LE}} \quad \text{(Equation 6.1.2.1-j)}$$

$$= 3.820\,(0.1376)(0.3420)$$

$$= 0.1798$$

$$(\Delta c_m)_{\delta f_{LE}} = \Delta c_1\, x_1 - \Delta c_2\, x_2 + \Delta c_{m_3} \quad \text{(Equation 6.1.2.1-d)}$$

$$= (3.5776)(1.718) - (3.6393)(1.759) + 0.1798$$

$$= -0.0754 \quad \text{(for Wing Section 2)}$$

$(\Delta c_m)_{\delta f_{LE}}$ Summary

Wing Section	1	2	3	4
δf_{LE} (given)	0	20°	25°	25°
$\frac{c_{f_{LE}}}{c}$ (given)	0	0.1376	0.1404	0.1404
$\frac{c_a}{c_{\delta\delta}}$ (From Eq. 6.1.2.1-g)		0.8981	0.9020	0.8724
C_μ (Eq. 6.1.5.1-o)	0	3.820	3.820	0
C'_μ	0	2.828	2.668	0
$c\ell_{\delta_a}$ (per rad) (Fig. 6.1.1.1-49)		11.6	11.4	6.1
$c\ell_\alpha$ (per rad) (Fig. 6.1.1.1-49)		11.8	11.6	6.3
A_t	7.0	5.181	4.888	6.364
K (Eq. 6.1.5.1-p)	0.7778	0.8836	0.9237	0.8370
Δc_1 (Eq. 6.1.2.1-e)		3.5776	4.594	2.228
Δc_2 (Eq. 6.1.2.1-f)		3.6393	4.675	2.301
$\frac{x_m}{c}$ (Eq. 6.1.5.1-m)		2.0304	2.0304	2.0304
$\frac{x_a}{c_{\delta\delta}}$ (Fig. 6.1.2.1-37)		0.245	0.246	0.274
$\frac{x_{a.c.}}{c_{\delta\delta}}$ (Fig. 6.1.2.1-37)		0.215	0.216	0.249
x_1 (Eq. 6.1.2.1-h)		1.718	1.778	1.829
x_2 (Eq. 6.1.2.1-i)		1.759	1.821	1.8565
Δc_{m_3} (Eq. 6.1.2.1-j)		0.1798	0.2267	0
$(\Delta c_m)_{\delta f_{LE}}$ (Eq. 6.1.2.1-d)	0 (no LE device)	−0.0754	-0.1183	−0.1968

Find $(\Delta c_m)_\alpha$

$$\alpha_L = \alpha_W + \theta$$

$$= 0 + \theta$$

Wing Section	1	2	3	4
$\alpha_L = \theta$ (from given plot)	2.91	2.30	1.19	−0.42
*K	0.7778	0.8836	0.9237	0.8370
*$c\ell_\alpha$ (per rad)	6.3	11.8	11.6	6.3
$\Delta c_4 = \frac{\alpha_L}{57.3} K\, c\ell_\alpha$ (Eq. 6.1.2.1-ℓ)	0.2489	0.4185	0.2225	−0.03865
*C_μ	0	3.820	3.820	0
*$\frac{x_m}{c}$		2.0304	2.0304	2.0304
$\frac{c'_{LE}}{c}$ (given)	1.0	1.019	1.100	1.100
$\Delta c_{m_4} = -C_\mu \left[\frac{x_m}{c} + \left(\frac{c'_{LE}}{c} - 1\right)\right] \frac{\alpha_L}{57.3}$ (Eq. 6.1.2.1-m)	0	−0.3142	−0.1690	0
*x_2	1.781	1.759	1.821	1.8565
$(\Delta c_m)_\alpha = \Delta c_4\, x_2 + \Delta c_{m_4}$ (Eq. 6.1.2.1-k)	0.4433	0.4219	0.2362	−0.0717

*From preceding $(\Delta c_m)_{\delta_{f_{LE}}}$ calculations.

Find $(\Delta c_m)_{\delta_f}$ (Wing Section 2)

n = 2

Forward flap

$\delta_{f_1} = 40^o$

$c_{f_1} = c_1 + c_2$ (Sketch (g) Section 6.1.2.1)

$$\frac{c_{f_1}}{c_{\delta\delta}} = \frac{c_1 + c_2}{c} \Big/ \frac{c_{\delta\delta}}{c}$$

$= (0.3505 + 0.3080)/1.351$

$= 0.4874$

$C'_\mu = 2.828$ (previous $(\Delta c_m)_{\delta f_{LE}}$ calculations)

$c_{\ell_{\delta f_1}} = 10.6$ per rad (Figure 6.1.1.1-49)

$K = 0.8836$ (see previous table for $(\Delta c_m)_\alpha$)

$$(\Delta c_5)_1 = \frac{\delta_{f_1}}{57.3} K c_{\ell_{\delta f_1}}$$ (Equation 6.1.2.1-o)

$$= \frac{40}{57.3} (0.8836)(10.6)$$

$= 6.538$

$$\left(\frac{x_{f_1}}{c_{\delta\delta}}\right)_{2D} = 0.402$$ (Figure 6.1.2.1-37)

$A_t = 5.181$ (previous $(\Delta c_m)_{\delta f_{LE}}$ calculations)

$$\frac{1}{A_t} = \frac{1}{5.181} = 0.1930$$

$$\left[\frac{(x_{c.p.})_{3D}}{(x_{c.p.})_{2D}}\right]_1 = 1.085 \quad \text{(Figure 6.1.5.1-68)}$$

$$\frac{x_{f_1}}{c_{\delta\delta}} = \left(\frac{x_{f_1}}{c_{\delta\delta}}\right)_{2D} \left[\frac{(x_{c.p.})_{3D}}{(x_{c.p.})_{2D}}\right]_1 \quad \text{(Equation 6.1.5.1-q)}$$

$$= (0.402)(1.085)$$

$$= 0.436$$

$$(x_5)_1 = \frac{x_m}{c} + \left(\frac{c'_{LE}}{c} - 1\right) - \frac{x_{f_1}}{c_{\delta\delta}} \frac{c_{\delta\delta}}{c} \quad \text{(Equation 6.1.2.1-q)}$$

$$= 2.0304 + (1.019 - 1) - 0.436(1.351)$$

$$= 1.460$$

Aft flap

$$\delta_{f_2} = \delta_{jeff} - \sum_{i=1}^{n-1} \delta_{f_i} \quad \text{(Equation 6.1.2.1-p)}$$

$$= 57.5 - 40$$

$$= 17.5^{o}$$

$c_{f_2} = c_2$ (Sketch (g) Section 6.1.2.1)

$$\frac{c_{f_2}}{c_{\delta\delta}} = \frac{c_2}{c} \Big/ \frac{c_{\delta\delta}}{c}$$

$$= 0.3080/1.351$$

$$= 0.2280$$

$C'_\mu = 2.828$ (previous $(\Delta c_m)_{\delta f_{LE}}$ calculations)

$c_{\ell_{\delta f_2}} = 9.5$ per rad (Figure 6.1.1.1-49)

$K = 0.8836$ (see previous table for $(\Delta c_m)_\alpha$)

$$(\Delta c_5)_2 = \frac{\delta_{f_2}}{57.3} K c_{\ell_{\delta f_2}} \quad \text{(Equation 6.1.2.1-o)}$$

$$= \frac{17.5}{57.3}(0.8836)(9.5)$$

$$= 2.564$$

$$\left(\frac{x_{f_2}}{c_{\delta\delta}}\right)_{2D} = 0.518 \quad \text{(Figure 6.1.2.1-37)}$$

$A_t = 5.181$ (previous $(\Delta c_m)_{\delta f_{LE}}$ calculation)

$$\frac{1}{A_t} = \frac{1}{5.181} = 0.1930$$

$$\left[\frac{(x_{c.p.})_{3D}}{(x_{c.p.})_{2D}}\right]_2 = 1.140 \quad \text{(Figure 6.1.5.1-68)}$$

$$\frac{x_{f_2}}{c_{\delta\delta}} = \left(\frac{x_{f_2}}{c_{\delta\delta}}\right)_{2D} \left[\frac{(x_{c.p.})_{3D}}{(x_{c.p.})_{2D}}\right]_2 \quad \text{(Equation 6.1.5.1-q)}$$

$$= (0.518)(1.140)$$

$$= 0.5905$$

$$(x_5)_2 = \frac{x_m}{c} + \left(\frac{c'_{LE}}{c} - 1\right) - \frac{x_{f_2}}{c_{\delta\delta}} \frac{c_{\delta\delta}}{c} \quad \text{(Equation 6.1.2.1-q)}$$

$$= 2.0304 + (1.019 - 1) - 0.5905(1.351)$$

$$= 1.252$$

$$(\Delta c_m)_{\delta_f} = \sum_{i=1}^{n} (\Delta c_5)_i (x_5)_i \quad \text{(Equation 6.1.2.1-n)}$$

$$= (6.538)(1.460) + (2.564)(1.252)$$

$$= 12.7556 \quad \text{(for Wing Section 2)}$$

$(\Delta c_m)_{\delta_f}$ Summary

Wing Section	1	2	3	4
$*C'_\mu$		2.828	2.668	
*K		0.8836	0.9237*	
$*1/A_t$		0.1930	0.2046	
Forward Flap				
$c\ell_{\delta_{f_1}}$ (per rad) (Fig. 6.1.1.1-49)		10.6	10.4	
$(\Delta c_5)_1$ (Eq. 6.1.2.1-o)		6.538	6.706	
$\left(\frac{x_{f_1}}{c_{\delta\delta}}\right)_{2D}$ (Fig. 6.1.2.1-37)		0.402	0.400	
$\left[\frac{(x_{c.p.})_{3D}}{(x_{c.p.})_{2D}}\right]_1$ (Fig. 6.1.5.1-68)		1.085	1.090	
$\frac{x_{f_1}}{c_{\delta\delta}}$ (Eq. 6.1.5.1-q)		0.436	0.436	
$(x_5)_1$ (Eq. 6.1.2.1-q)		1.460	1.5060	
Aft Flap				
$c\ell_{\delta_{f_2}}$ (per rad) (Fig. 6.1.1.1-49)		9.5	9.25	
$(\Delta c_5)_2$ (Eq. 6.1.2.1-o)		2.564	2.609	
$\left(\frac{x_{f_2}}{c_{\delta\delta}}\right)_{2D}$ (Fig. 6.1.2.1-37)		0.518	0.515	
$\left[\frac{(x_{c.p.})_{3D}}{(x_{c.p.})_{2D}}\right]_2$ (Fig. 6.1.5.1-68)		1.140	1.147	

*From preceding $(\Delta c_m)_{\delta_{f_{LE}}}$ calculations

Wing Section	1	2	3	4
$\frac{x_{f_2}}{c_{\delta\delta}}$ (Eq. 6.1.5.1-q)		0.5905	0.5907	
$(x_5)_2$ (Eq. 6.1.2.1-q)		1.252	1.2845	
$(\Delta c_m)_{\delta_f} = \sum_{i=1}^{n} (\Delta c_5)_i (x_5)_i$ (Equation 6.1.2.1-n)	0 (no TE flaps)	12.7556	13.4505	0 (no TE flaps)

Find $(\Delta c_m)_{\delta_j}$

$$\delta_{j_{eff}} < \sum_{i=1}^{n} \delta_{f_i}$$

For $57.5 < 40 + 20$, then $\delta_j = 0$

$$\Delta c_6 = \frac{\delta_j}{57.3} K c_{\ell_{\delta_j}} \quad \text{(Equation 6.1.2.1-s)}$$

$= 0$ (all wing sections)

$$(\Delta c_m)_{\delta_j} = \Delta c_6 \, x_6 \quad \text{(Equation 6.1.2.1-r)}$$

$= 0$

$$\Delta c_m = (\Delta c_m)_{\delta_{f_{LE}}} + (\Delta c_m)_\alpha + (\Delta c_m)_{\delta_f} + (\Delta c_m)_{\delta_j} \quad \text{(Equation 6.1.2.1-c)}$$

Wing Section	1	2	3	4
$(\Delta c_m)_{\delta_{f_{LE}}}$ (Eq. 6.1.2.1-d)	0	−0.0754	−0.1183	−0.1968
$(\Delta c_m)_\alpha$ (Eq. 6.1.2.1-k)	0.4433	0.4219	0.2363	−0.0717
$(\Delta c_m)_{\delta_f}$ (Eq. 6.1.2.1-n)	0	12.7556	13.4505	0
$(\Delta c_m)_{\delta_j}$ (Eq. 6.1.2.1-r)	0	0	0	0
Δc_m (Eq. 6.1.2.1-c)	0.4433	13.10	13.57	−0.2685

Step 3. C_{m_m}

Wing Section, k	1	2	3	4
η_k	0.1443	0.5076	0.7515	1.0
η_{k-1}	0	0.1443	0.5076	0.7515
K_{b_k} (Fig. 6.1.4.1-15)	0.205	0.650	0.880	1.0
$K_{b_{k-1}}$ (Fig. 6.1.4.1-15)	0	0.205	0.650	0.880
$K_{b_k} - K_{b_{k-1}}$	0.205	0.445	0.230	0.120
Δc_m (from preceding Step 2)	0.4433	13.10	13.57	−0.2673

$$C_{m_m} = \sum_{k=1}^{p} \Delta c_m (K_{b_k} - K_{b_{k-1}}) \quad \text{(Equation 6.1.5.1-s)}$$

$$= (0.4433)(0.205)+(13.10)(0.445)+(13.57)(0.230)+(-0.2673)(0.120)$$

$$= 9.009$$

Step 4. $C_{\lambda_k} = [\Delta c_1 - \Delta c_2 + \Delta c_4 + \sum_{i=1}^{n} (\Delta c_5)_i + \Delta c_6](K_{b_k} - K_{b_{k-1}})$ (Equation 6.1.5.1-t)

Wing Section, k	1	2	3	4
*Δc_1	0	3.5776	4.594	2.228
*Δc_2	0	3.6393	4.675	2.301
*Δc_4	0.2489	0.4185	0.2225	−0.03865
*$\sum_{i=1}^{n} (\Delta c_5)_i$	0	6.538+ 2.564	6.706+ 2.609	0
*Δc_6	0	0	0	0
**$(K_{b_k} - K_{b_{k-1}})$	0.205	0.445	0.230	0.120
C_{λ_k} (Eq. 6.1.5.1-t)	0.0510	4.212	2.175	−0.01340

*From preceding Step 2

**From preceding Step 3

Step 5. ΔC_m

$$\frac{\Delta z}{\bar{c}} = \frac{-1.922}{10.8886} = -0.1765$$

$$\frac{\Delta x_k}{\bar{c}} = \frac{x_m}{c}\left(\frac{c}{\bar{c}}\right) - \frac{x_{c.g.}}{\bar{c}}$$

$$= 2.0304\left(\frac{14.84}{10.8886}\right) - \frac{10.72}{10.8886}$$

$$= 1.783$$

Wing Section, k	1	2	3	4
C_{λ_k} (preceding Step 4)	0.0510	4.212	2.175	−0.0134
C_μ (preceding Step 2)	0	3.820	3.820	0
$\frac{\alpha_L}{57.3}$ (preceding Step 2)		0.04014	0.02077	
$\frac{S_k}{S_W}$ (preceding Step 1)		0.4212	0.2150	
$C_\mu \frac{\alpha_L}{57.3}\frac{S_k}{S_W}$	0	0.0646	0.0171	0

$$\Delta C_m = C_{m_m} + \eta_t C_J \frac{\Delta z}{\bar{c}} + \sum_{k=1}^{p} \left\{\left[C_\mu \frac{\alpha_L}{57.3}\frac{S_k}{S_W} - C_{\lambda_k}\right]\frac{\Delta x_k}{\bar{c}}\right\} \quad \text{(Equation 6.1.5.1-u)}$$

$$= 9.009+(0.81)(3.0)(-0.1765)$$

$$+\{(0-0.0510)+(0.0646-4.212)+(0.0171-2.175)+[0-(-0.01340)]\}\ (1.783)$$

$$= 9.009-0.4289-11.310$$

$$= -2.729 \quad \text{(based on } S_W \bar{c}_W\text{)}$$

B. TRANSONIC

The following method for the estimation of C_{m_δ} at transonic speeds is based on a procedure similar to that of Reference 6 and is developed empirically from test data of References 7 through 10. The only readily available test data for pitching-moment effectiveness at transonic speeds are those of References 7 through 10. Therefore, the method has not been substantiated independently of these test data.

DATCOM METHOD

A first-order approximation to the pitching-moment effectiveness at transonic speeds is given by

$$C_{m_\delta} = -C_{L_\delta} \frac{x}{\bar{c}} \qquad 6.1.5.1\text{-w}$$

where

C_{L_δ} is the lift effectiveness of the control surfaces from the method of Paragraph B of Section 6.1.4.1.

$\frac{x}{\bar{c}}$ is the distance, in percent of MAC, of the chordwise center-of-pressure location aft of the wing moment reference point.

$$\frac{x}{\bar{c}} = -\frac{b}{\bar{c}} \tan \Lambda_{LE} \left[\frac{1 + 2\lambda}{6(1 + \lambda)} - 2 \frac{\left(C_{l_\delta}\right)_{M = 0.6}}{\left(C_{L_\delta}\right)_{M = 0.6}} \right] + \left(\frac{x_{c.p.}}{c_{c.p.}}\right) \frac{c_{c.p.}}{\bar{c}} - \frac{x_{MRP}}{\bar{c}} \qquad 6.1.5.1\text{-x}$$

where

$\left(C_{l_\delta}\right)_{M = 0.6}$ is the roll effectiveness of the control surface at M = 0.6, based on the total wing span with one control deflected. This parameter is one-half the value of C_{l_δ} obtained by the method of Paragraph A of Section 6.2.1.1.

$\left(C_{L_\delta}\right)_{M = 0.6}$ is the lift effectiveness of the control surfaces at M = 0.6 from Paragraph A of Section 6.1.4.1.

$\frac{x_{MRP}}{\bar{c}}$ is the distance, in percent of MAC, from the leading edge of the MAC to the moment reference point, positive for the moment reference point aft of the leading edge of the MAC.

$\frac{x_{c.p.}}{c_{c.p.}}$ is the empirically derived chordwise center-of-pressure location of the incremental load due to surface deflection, determined by

$$\frac{x_{c.p.}}{c_{c.p.}} = \left(\frac{x_{c.p.}}{c_{c.p.}}\right)_1 + K\left(\frac{c_f}{c} - 0.2\right) \qquad 6.1.5.1\text{-y}$$

where $\left(x_{c.p.}/c_{c.p.}\right)_1$ and K are empirically derived factors presented as functions of Mach number and $\Lambda_{c/4}$ in Figures 6.1.5.1-69a and 6.1.5.1-69b, respectively. The flap-chord ratio c_f/c is measured in the streamwise direction.

$\frac{c_{c.p.}}{\bar{c}}$ is the wing chord at the spanwise center-of-pressure location, in percent of MAC given by

$$\frac{c_{c.p.}}{\bar{c}} = \frac{c_r}{\bar{c}}\left[1 - 4(1-\lambda)\frac{\left(C_{l_\delta}\right)_{M=0.6}}{\left(C_{L_\delta}\right)_{M=0.6}}\right] \qquad 6.1.5.1\text{-}z$$

where $\left(C_{l_\delta}\right)_{M=0.6}$ and $\left(C_{L_\delta}\right)_{M=0.6}$ are defined above.

The planform parameters of the empirical data used to derive Figures 6.1.5.1-69a and 6.1.5.1-69b are: A = 4.0, λ = 0.6, t/c = 0.06, $0 \leq \Lambda_{c/4} \leq 60^o$, and a 0.30c plain sealed flap.

Sample Problem

Given: The configuration of Reference 8 with a partial-span plain trailing-edge flap.

Wing Characteristics:

A = 4.0 b/2 = 4.243 in. λ = 0.60 $\Lambda_{c/4} = 35^o$ $\Lambda_{LE} = 37.33^o$

NACA 65A006 airfoil (streamwise) $x_{MRP} = \frac{\bar{c}}{4}$ $c_r/\bar{c}$ = 1.183 $\frac{b}{\bar{c}}$ = 3.918

Flap Characteristics:

Plain trailing-edge flap c_f/c = 0.30 $\Lambda_{HL} = 30.44^o$

η_i = 0.57 η_o = 1.0 $\delta = 16^o$ (streamwise)

Additional Characteristics:

M = 0.90 $\left(C_{l_\delta}\right)_{M=0.6}$ = 0.0014 per deg (test value for semispan model, based on S_W and b_W)

$\left(C_{l_\delta}\right)_{M=0.9}$ = 0.00135 per deg (test value for semispan model, based on S_W and b_W)

$\left(C_{L_\delta}\right)_{M=0.6}$ = 0.0105 per deg (test value for full-span model, based on S_W)

Compute:

Chordwise center-of-pressure location

$$\frac{c_{c.p.}}{\bar{c}} = \frac{c_r}{\bar{c}}\left[1 - 4(1-\lambda)\frac{\left(C_{l_\delta}\right)_{M=0.6}}{\left(C_{L_\delta}\right)_{M=0.6}}\right] \qquad \text{(Equation 6.1.5.1-z)}$$

$$= 1.183\left[1 - 4(0.4)\ \frac{0.0014}{0.0105}\right]$$

$$= 0.931$$

$$\left(\frac{x_{c.p.}}{c_{c.p.}}\right)_1 = 0.880 \quad \text{(Figure 6.1.5.1-69 a)}$$

$K = -0.690$ (Figure 6.1.5.1-69b)

$$\frac{x_{c.p.}}{c_{c.p.}} = \left(\frac{x_{c.p.}}{c_{c.p.}}\right)_1 + K\left(\frac{c_f}{c} - 0.2\right) \qquad \text{(Equation 6.1.5.1-y)}$$

$$= (0.880) + (-0.690)(0.30 - 0.20)$$

$$= 0.811$$

$$\frac{x}{\bar{c}} = -\frac{b}{\bar{c}}\tan\Lambda_{LE}\left[\frac{1+2\lambda}{6(1+\lambda)} - 2\,\frac{\left(C_{l_\delta}\right)_{M=0.6}}{\left(C_{L_\delta}\right)_{M=0.6}}\right] + \left(\frac{x_{c.p.}}{c_{c.p.}}\right)\frac{c_{c.p.}}{\bar{c}} - \frac{x_{MRP}}{\bar{c}} \qquad \text{(Equation 6.1.5.1-x)}$$

$$= (-3.918)(0.7626)\left[\frac{2.20}{9.60} - 2\left(\frac{0.0014}{0.0105}\right)\right] + (0.811)(0.931) - 0.25$$

$$= 0.112 + 0.755 - 0.25$$

$$= 0.617$$

Lift effectiveness at M = 0.9 (Section 6.1.4.1)

$$C_{L_\delta} = \left(C_{L_\delta}\right)_{M=0.6}\left(\frac{C_{l_\delta}}{C_{l_{\delta_{M=0.6}}}}\right) \qquad \text{(Equation 6.1.4.1-e)}$$

$$= 0.0105\left(\frac{0.00135}{0.0014}\right)$$

$$= 0.0101 \text{ per deg}$$

Solution:

$$C_{m_\delta} = - C_{L_\delta} \frac{x}{\bar{c}} \quad \text{(Equation 6.1.5.1-w)}$$

$$= - (0.0101)(0.617)$$

$$= - 0.00623 \text{ per deg}$$

The test value at M = 0.90 from Reference 8 is – 0.0065 per degree.

C. SUPERSONIC

The procedure for estimating trailing-edge control effectiveness at supersonic speeds is based on the method presented in Reference 11. The restrictions used in the derivation of the method are listed below.

1. Leading and trailing edges of the control surface are swept ahead of the Mach lines from the deflected controls.
2. Control root and tip chords are parallel to the plane of symmetry.
3. Controls are located either at the wing tip or far enough inboard so that the outermost Mach lines from the deflected controls do not cross the wing tip.
4. Innermost Mach lines from the deflected controls do not cross the wing root chord.
5. Wing planform has leading edges swept ahead of the Mach lines and has streamwise tips.
6. Controls are not influenced by the tip conical flow from the opposite wing panel or by the interaction of the wing-root Mach cone with the wing tip.

DATCOM METHOD

The pitching-moment effectiveness C_{m_δ} at supersonic speeds for symmetric, straight-sided controls, based on total wing area and $\bar{c}$, is given by

$$C_{m_\delta} = K_1 \frac{1}{3} \frac{b_f}{\bar{c}} \frac{c_{r_f}}{S_W} C'_{m_\delta} - K_2 \frac{1}{2} \frac{b_f}{\bar{c}} \frac{S_f}{S_W} C'_{l_\delta} - K_3 \frac{x_f}{\bar{c}} \frac{S_f}{S_W} C'_{L_\delta} \quad \text{6.1.5.1-aa}$$

where

$$K_1 = \left(1 - \frac{C_2}{C_1} \phi_{TE}\right) (1 + \lambda_f + \lambda_f^2)$$

$$K_2 = \left(1 - \frac{C_2}{C_1} \phi_{TE}\right) \tan \Lambda_{HL}$$

$$K_3 = \left(1 - \frac{C_2}{C_1} \phi_{TE}\right)$$

where $\left(1 - \frac{C_2}{C_1}\phi_{TE}\right)$ is a thickness correction factor to the supersonic flat-plate derivative.

$$C_1 = \frac{2}{\sqrt{M^2 - 1}} \text{ per radian}$$

$$C_2 = \frac{(\gamma + 1)M^4 - 4(M^2 - 1)}{2(M^2 - 1)^2} \text{ per radian}$$

ϕ_{TE} is the trailing-edge angle in radians, measured normal to the control hinge line.

γ is the ratio of specific heats, $\gamma = 1.4$.

b_f is the control span (both sides of wing).

S_f is the control area (both sides of wing).

λ_f is the taper ratio of the control.

Λ_{HL} is the sweep of the control hinge line.

c_{r_f} is the root chord of the control.

x_f is the distance of the leading edge of the control root chord behind the wing axis of pitch.

C'_{m_δ} is the pitching-moment effectiveness of one symmetric, straight-sided control, based on twice its moment area about the hinge line, from Figures 6.1.5.1-70 through 6.1.5.1-73b, according to the control planform as follows:

(a) Tapered controls with outboard edge coincident with wing tip, use Figure 6.1.5.1-70.

(b) Tapered controls with outboard edge not coincident with wing tip, use Figure 6.1.5.1-73a.

(c) Untapered controls with outboard edge coincident with wing tip, use Figure 6.1.5.1-73b.

(d) Untapered controls with outboard edge not coincident with wing tip, use Figure 6.1.5.1-73a.

C'_{L_δ} is the lift effectiveness of one symmetric, straight-sided control, based on the area of the control, obtained from Paragraph C of Section 6.1.4.1.

C'_{l_δ} is the rolling-moment effectiveness of one symmetric, straight-sided control about its root chord line, based on the area and span of one control, obtained from Paragraph C of Section 6.2.1.1.

It should be noted that control deflection angles are measured streamwise.

For swept-forward wings and controls with inverse taper, see Reference 11 for the proper values of C'_{m_δ}, C'_{L_δ} and C'_{l_δ}.

Thickness correction factors for other than symmetrical, straight-sided controls can be determined from Reference 11.

The computation of pitching-moment effectiveness for leading-edge controls and trailing-edge controls with subsonic leading edges can be accomplished with the aid of Reference 12.

Not enough test data are available to allow substantiation of the method.

Sample Problem

Given: A wing-control configuration with the following characteristics:

Wing Characteristics:

S_W = 46.5 sq ft $\quad \bar{c}$ = 4.0 ft $\quad b$ = 12.0 ft $\quad \Lambda_{LE} = 42^\circ$

$\Lambda_{TE} = 27.7^\circ$

Control Characteristics:

Symmetric, straight-sided inboard flap

S_f = 4.71 sq ft (both sides of wing) $\quad b_f$ = 6.5 ft (both sides of wing)

λ_f = 0.715 $\quad c_{r_f}$ = 0.85 ft $\quad x_f$ = 1.768 ft $\quad \phi_{TE} = 3^\circ$

$\Lambda_{HL} = 30.8^\circ$

Additional Characteristics:

$M = 1.90$; $\beta = 1.62$

Compute:

$$C_1 = \frac{2}{\sqrt{M^2 - 1}} = 1.235$$

$$C_2 = \frac{(\gamma + 1) M^4 - 4 (M^2 - 1)}{2 (M^2 - 1)^2} = \frac{(2.4) (1.90)^4 - 4 \left[(1.90)^2 - 1\right]}{2 \left[(1.90)^2 - 1\right]^2} = \frac{20.84}{13.62} = 1.53$$

$$K_1 = \left(1 - \frac{C_2}{C_1} \phi_{TE}\right) \left(1 + \lambda_f + \lambda_f^2\right)$$

$$= \left[1 - \left(\frac{1.53}{1.235}\right)\left(\frac{3.0}{57.3}\right)\right]\left[1 + 0.715 + (0.715)^2\right] = (0.935)(2.226) = 2.08$$

$$K_2 = \left(1 - \frac{C_2}{C_1}\phi_{TE}\right)(\tan \Lambda_{HL}) = (0.935)(0.5961) = 0.557$$

$$K_3 = \left(1 - \frac{C_2}{C_1}\phi_{TE}\right) = 0.935$$

$$\frac{\tan \Lambda_{TE}}{\beta} = \frac{0.5250}{1.62} = 0.324$$

$$\frac{\tan \Lambda_{HL}}{\beta} = \frac{0.5961}{1.62} = 0.368$$

$\beta C'_{m_\delta}$ = -0.0360 per deg (Figure 6.1.5.1-73a)

C'_{m_δ} = -0.0222 per deg

$\beta C'_{L_\delta}$ = 0.0750 per deg (Figure 6.1.4.1-25)

C'_{L_δ} = 0.0463 per deg

$\beta C'_{l_\delta}$ = 0.0340 per deg (Figure 6.2.1.1-28, interpolated)

C'_{l_δ} = 0.0210 per deg

Solution:

$$C_{m_\delta} = K_1 \frac{1}{3}\frac{b_f}{\bar{c}}\frac{c_{r_f}}{S_W} C'_{m_\delta} - K_2 \frac{1}{2}\frac{b_f}{\bar{c}}\frac{S_f}{S_W} C'_{l_\delta} - K_3 \frac{x_f}{\bar{c}}\frac{S_f}{S_W} C'_{L_\delta}$$ (Equation 6.1.5.1-aa)

$$= (2.08)\frac{1}{3}\left(\frac{6.5}{4.0}\right)\left(\frac{0.85}{46.5}\right)(-0.0222) - (0.557)\frac{1}{2}\left(\frac{6.5}{4.0}\right)\left(\frac{4.71}{46.5}\right)(0.0210)$$

$$-(0.935)\left(\frac{1.768}{4.0}\right)\left(\frac{4.71}{46.5}\right)(0.0463)$$

$$= (-0.000457) - (0.000963) - (0.00194)$$

$$= -0.00336 \text{ per deg}$$

REFERENCES

1. Anon: Royal Aeronautical Society Data Sheets – Aerodynamics, Vol. IV. (Flaps 08.01.01 and 08.01.02), 1956. (U)

2. James, H. A., and Hunton, L. W.: Estimation of Incremental Pitching Moments Due to Trailing-Edge Flaps on Swept and Triangular Wings. NACA TN 4040, 1957. (U)

3. May, F., and Widdison, C. A.: STOL High-Lift Design Study. Vol. 1. State-of-the-Art Review of STOL Aerodynamic Technology. AFFDL-TR-71-26 Vol. 1, 1971. (U)

4. Campbell, L. J., Blanks, C. F., and Leaver, D. A.: Aerodynamic Characteristics of Rectangular Wings of Small Aspect Ratio. ARC R&M 3142, 1960. (U)

5. DeYoung, J.: Theoretical Symmetric Span Loading Due to Flap Deflection for Wings of Arbitrary Plan Form at Subsonic Speeds. NACA TR 1071, 1952. (U)

6. Decker, J., et al.: USAF Stability and Control Handbook. M-03671, 1956. (C) Title Unclassified

7. Smith, W. G.: Wind-Tunnel Investigation at Subsonic and Supersonic Speeds of a Model of a Tailless Fighter Airplane Employing a Low-Aspect-Ratio Sweptback Wing – Stability and Control. NACA RM A52J30, 1953. (U)

8. Thompson, R. F.: Lateral-Control Investigation of Flap-Type Controls on a Wing with Quarter-Chord Line Swept Back 35°, Aspect Ratio 4, Taper Ratio 0.6, and NACA 65A006 Airfoil Section. NACA RM L9L12a, 1950. (U)

9. Vogler, R. D.: Lateral-Control Investigation of Flap-Type Controls on a Wing with Quarter-Chord Line Swept Back 45°, Aspect Ratio 4, Taper Ratio 0.6, and NACA 65A006 Airfoil Section. Transonic-Bump Method. NACA RM L9F29a, 1949. (U)

10. Hammond, A. D.: Lateral-Control Investigation of Flap-Type Controls on a Wing with Unswept Quarter-Chord Line, Aspect Ratio 4, Taper Ratio 0.6, and NACA 65A006 Airfoil Section. NACA RM L50A03, 1950. (U)

11. Goin, K. L.: Equations and Charts for the Rapid Estimation of Hinge-Moment and Effectiveness Parameters for Trailing-Edge Controls Having Leading and Trailing Edges Swept Ahead of the Mach Lines. NACA TR 1041, 1951. (U)

12. Heaslet, M. A., and Spreiter, J. R.: Reciprocity Relations in Aerodynamics. NACA TN 2700, 1952. (U)

13. Barnett, U. R., Jr., and Lipson, S.: Effects of Several High-Lift and Stall-Control Devices on the Aerodynamic Characteristics of a Semispan 49° Sweptback Wing. NACA RM L52D17a, 1952. (U)

14. Maki, R. L., and Embry, U. R.: Effects of High-Lift Devices and Horizontal-Tail Location on the Low-Speed Characteristics of a Large-Scale 45° Swept-Wing Airplane Configuration. NACA RM A54E10, 1954. (U)

15. Kelly, M. W., and Tolhurst, W. H., Jr.: The Use of Area Suction to Increase the Effectiveness of a Trailing-Edge Flap on a Triangular Wing of Aspect Ratio 2. NACA RM A54A25, 1954. (U)

16. Fink, M. P., and Cocke, B. W.: A Low-Speed Investigation of the Aerodynamic Control, and Hinge-Moment Characteristics of Two Types of Controls and Balancing Tabs on a Large-Scale Thin Delta-Wing – Fuselage Model. NACA RM L54B03, 1954. (U)

17. Lock, R. C., Ross, J. G., and Meiklem, P.: Wind-Tunnel Tests on a 90°-Apex Delta Wing of Variable Aspect Ratio (Sweepback 36.8°). Part II – Measurements of Downwash and Effect of High Lift Devices. ARC CP 83, 1948. (U)

18. Trouncer, J., and Moss, G. F.: Low-Speed Wind-Tunnel Tests on Two 45 Degree Sweptback Wings of Aspect Ratios 4.5 and 3.0 (Models A and B) ARC R&M 2710, 1953. (U)

19. Franks, R. W.: Tests in the Ames 40- by 80-foot Wind Tunnel of Two Airplane Models Having Aspect Ratio 2 Trapezoidal Wings of Taper Ratios 0.33 and 0.20. NACA RM A52L16, 1953. (U)

20. Riebe, J. M., and MacLeod, R. G.: Low-Speed Wind-Tunnel Investigation of a Thin 60° Delta Wing with Double Slotted, Single Slotted, Plain, and Split Flaps. NACA RM L52J29, 1953. (U)

21. Riebe, J. M., and Graven, J. C., Jr.: Low-Speed Investigation of the Effects of Location of a Delta and a Straight Tail on the Longitudinal Stability and Control of a Thin Delta Wing with Extended Double Slotted Flaps. NACA RM L53J26, 1954. (U)

22. Guryansky, E. R., and Lipson, S.: Effect of High-Lift Devices on the Longitudinal and Lateral Characteristics of a 45° Sweptback Wing with Symmetrical Circular-Arc Sections. NACA RM L8D06, 1948. (U)

23. Foster, G. V., Mollenberg, E. F., and Woods, R. L.: Low-Speed Longitudinal Characteristics of an Unswept Hexagonal Wing with and without a Fuselage and a Horizontal Tail Located at Various Positions at Reynolds Numbers from 2.8×10^6 to 7.6×10^6. NACA RM L52L11b, 1953. (U)

24. Pratt, G. L., and Shields, E. R.: Low-Speed Longitudinal Characteristics of a 45° Sweptback Wing of Aspect Ratio 8 with High-Lift and Stall-Control Devices at Reynolds Numbers from 1,500,000 to 4,800,000. NACA L51J04, 1952. (U)

25. Franks, R. W.: Tests in the Ames 40- by 80-Foot Wind Tunnel of an Airplane Model with an Aspect Ratio 4 Triangular Wing and an All-Movable Horizontal Tail – High Lift Devices and Lateral Controls. NACA A52K13, 1953. (U)

26. Weiberg, J. A., and Page, V. R.: Large-Scale Wind-Tunnel Tests of an Airplane Model with an Unswept, Aspect Ratio-10 Wing, Four Propellers, and Blowing Flaps. NASA TN D-25, 1959. (U)

27. Goodson, K. W., and Few, A. G., Jr.: Low-Speed Static Longitudinal and Lateral Stability Characteristics of a Model with Leading-Edge Chord-Extensions Incorporated on a 40° Sweptback Circular-Arc Wing of Aspect Ratio 4 and Taper Ratio 0.50. NACA RM L52I18, 1952. (U)

28. Griner, R. F., and Foster, G. V.: Low-Speed Longitudinal and Wake Air-Flow Characteristics at a Reynolds Number of 6.0×10^6 of a 52° Sweptback Wing Equipped with Various Spans of Leading-Edge and Trailing-Edge Flaps, a Fuselage, and a Horizontal Tail at Various Vertical Positions. NACA RM L50K29, 1951. (U)

29. Salmi, R. J.: Horizontal-Tail Effectiveness and Downwash Surveys for Two 47.7° Sweptback Wing-Fuselage Combinations with Aspect Ratios of 5.1 and 6.0 at a Reynolds Number of 6.0×10^6. NACA RM L50K06, 1951. (U)

30. Foster, G. V., and Griner, R. F.: Low-Speed Longitudinal and Wake Air-Flow Characteristics at a Reynolds Number of 5.5×10^6 of a Circular-Arc 52° Sweptback Wing with a Fuselage and a Horizontal Tail at Various Vertical Positions. NACA RM L51C30, 1951. (U)

31. Tinling, B. E., and Lopez, A. E.: The Effects of Nacelles and of Extended Split Flaps on the Longitudinal Characteristics of a Wing-Fuselage-Tail Combination Having a Wing with 40° of Sweepback and an Aspect Ratio of 10. NACA RM A53D06, 1953. (U)

32. Spooner, S. H., and Mollenberg, E. F.: Positioning Investigation of Single Slotted Flaps on a 47.4° Sweptback Wing at Reynolds Numbers of 4.0×10^6 and 6.0×10^6. NACA RM L50H29, 1950. (U)

33. Riebe, J. M., and Graven, J. C., Jr.: Low-Speed Investigation of the Effects of Location of a Delta Horizontal Tail on the Longitudinal Stability and Control of a Fuselage and Thin Delta Wing with Double Slotted Flaps Including the Effects of a Ground Board. NACA RM L53H19a, 1953. (U)

34. Anderson, A. E.: An Investigation at Low Speed of a Large-Scale Triangular Wing of Aspect Ratio Two – II. The Effect of Airfoil Section Modifications and the Determination of the Wake Downwash. NACA RM A7H28, 1947. (U)

35. Mollenberg, E. F. and Spooner, S. H.: Low-Speed Investigation of the Effects of Single Slotted and Double Slotted Flaps on a 47.7° Sweptback-Wing-Fuselage Combination at a Reynolds Number of 6.0×10^6. NACA RM L51E24, 1951. (U)

36. Freeman, D. C., Jr., Parlett, L. P., and Henderson, R. L.: Wind-Tunnel Investigation of a Jet Transport Airplane Configuration with an External-Flow Jet Flap and Inboard Pod-Mounted Engines. NASA TN D-7004, 1970. (U)

37. Smith, C. C., Jr.: Effect of Engine Position and High-Lift Devices on Aerodynamic Characteristics of an External-Flow Jet-Flap STOL Model. NASA TN D-6222, 1971. (U)

38. Alexander, A. J. and Williams, J.: Wind-Tunnel Experiments on a Rectangular-Wing Jet-Flap Model of Aspect-Ratio 6. ARC R&M 3329, 1964. (U)

39. Koenig, D. G., and Corsiglia, V. R.: Aerodynamic Characteristics of a Large-Scale Model with an Unswept Wing and Augmented Jet Flap. NASA TN D-4610, 1968. (U)

40. Campbell, J. P., and Johnson, J. L.: Wind-Tunnel Investigation of an External-Flow Jet-Augmented Slotted Flap Suitable for Application to Airplanes with Pod-Mounted Jet Engines. NACA TN 3898, 1956. (U)

41. Renselaer, D. J., and Kelly, R.: Aerodynamic Design Compendium for Externally Blown Flaps. NA-71-1105, 1971. (U)

42. Kriechbaum, G., Letsinger, G., May, F. W., Morell, E. J., and Vincent, J. H.: State of the Art Design Compendium – STOL Aerodynamic Technology (Vectored Thrust and Mechanical Flaps), Boeing D180-14239-1, 1971. (U)

43. May, F. W.: State of the Art Design Compendium – STOL Aerodynamic Technology (Internally Blown Jet Flaps). Boeing, D180-14299-1, 1971. (U)

44. Hebert, J., Jr., et al.: STOL Tactical Aircraft Investigation. Vol II Design Compendium. AFFDL-TR-73-21-Vol II, 1973. (U)

TABLE 6.1.5.1-A
EFFECT OF FLAP DEFLECTION ON PITCHING MOMENT
DATA SUMMARY AND SUBSTANTIATION
METHOD 1 SUBSONIC

Ref.	A	λ	$\Lambda_{c/4}$ (deg)	t/c	Flap Type	δ_f (deg)	$\left(\Delta C_m\right)_{\delta_f}$ calc.	$\left(\Delta C_m\right)_{\delta_f}$ test	$\Delta\left(\Delta C_m\right)_{\delta_f}$ calc.-test
13	3.78	0.586	47.35	0.06	Plain	30	−0.065	−0.04	−0.025
↓	↓	↓	↓	↓	↓	45	−0.087	−0.05	−0.037
14	3.5	0.3	45	0.10	Double Slotted	50	−0.370	−0.280	−0.090
Unpub. data	6.8	0.3	35	0.115	Double Slotted	45	−0.351	−0.418	0.067
15	2.0	0	56.3	0.05	Plain	59	−0.258	−0.185	−0.073
16	2.31	0	52.4	0.03	Plain	30	−0.146	−0.196	0.050
17	3.0	0.143	36.9	0.10	Split	60	−0.228	−0.184	−0.044
18	4.5	0.25	45	0.14	Split	60	−0.091	−0.103	0.012
↓	3.0	↓	↓	↓	↓	↓	−0.150	−0.123	−0.027
19	2.0	0.33	36.87	0.05	Single Slotted	40	−0.329	−0.263	−0.066
↓	↓	0.20	45	↓	↓	↓	−0.330	−0.260	−0.070
20	2.31	0	52.4	0.03	Plain	54	−0.254	−0.165	−0.089
↓	↓	↓	↓	↓	Split	60	−0.154	−0.164	0.010
↓	↓	↓	↓	↓	Single Slotted	59.75	−0.252	−0.172	−0.080
↓	↓	↓	↓	↓	Double Slotted	64	−0.547	−0.413	−0.134
21	2.31	0	52.4	0.03	Single Slotted	40.3	−0.249	−0.336	0.087
21	2.31	0	52.4	0.03	Double Slotted	61.3	−0.440	−0.622	0.182
22	3.5	0.5	44.9	0.074	Plain	52.2	−0.092	−0.072	−0.020
↓	↓	↓	↓	↓	↓	↓	−0.329	−0.183	−0.146
23	2.5	0.625	5.27	0.06	Plain	50	−0.031	−0.089	0.058
↓	↓	↓	↓	↓	↓	↓	−0.221	−0.151	−0.070
24	8.0	0.45	45	0.12	Split	50	−0.068	−0.008	−0.060
25	4.0	0	36.9	0.05	Single Slotted	40	−0.244	−0.153	−0.091
26	9.86	0.5	0	0.17	Plain	40	−0.080	−0.170	0.090
27	4.0	0.5	40	0.08	Plain	41.7	−0.063	−0.060	−0.003
28	2.88	0.625	50.24	0.08	Split	48.1	−0.033	−0.021	−0.012
↓	↓	↓	↓	↓	↓	↓	−0.072	−0.082	0.010
↓	↓	↓	↓	↓	↓	↓	−0.048	−0.021	−0.027
↓	↓	↓	↓	↓	↓	↓	−0.121	−0.080	−0.041
29	5.1	0.383	45.35	0.075	Split	50.8	−0.028	−0.020	−0.008
↓	6.0	0.313	↓	↓	↓	↓	−0.039	−0.027	−0.012
↓	5.1	0.383	↓	↓	Double Slotted	36.5	−0.114	−0.050	−0.064
↓	6.0	0.313	↓	↓	↓	↓	−0.078	−0.087	0.009
30	2.84	0.616	49.9	0.053	Split	49.3	−0.103	−0.135	0.032
↓	↓	↓	↓	↓	↓	↓	−0.029	−0.033	0.004
31	10.0	0.4	40	0.10	Split	23.86	−0.023	+0.010	−0.033
↓	↓	↓	↓	↓	↓	53	+0.027	+0.039	−0.012
32	5.1	0.383	44.6	0.075	Single Slotted	30.7	−0.063	−0.074	0.011
33	2.31	0	52.4	0.03	Double Slotted	40.3	−0.303	−0.328	0.025
34	2.0	0	56.3	0.05	Split	44.5	−0.229	−0.174	−0.055

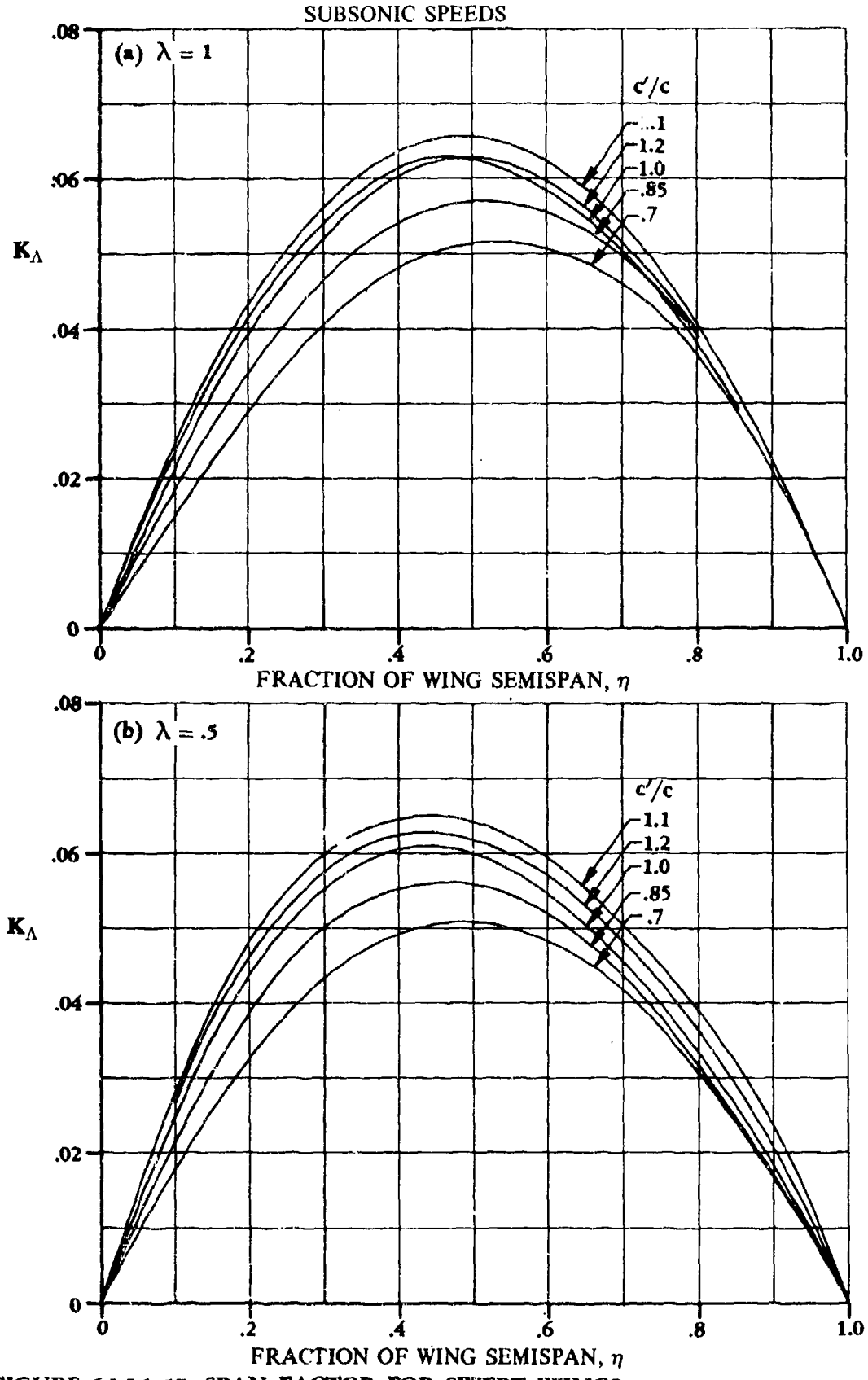

FIGURE 6.1.5.1-57 SPAN FACTOR FOR SWEPT WINGS

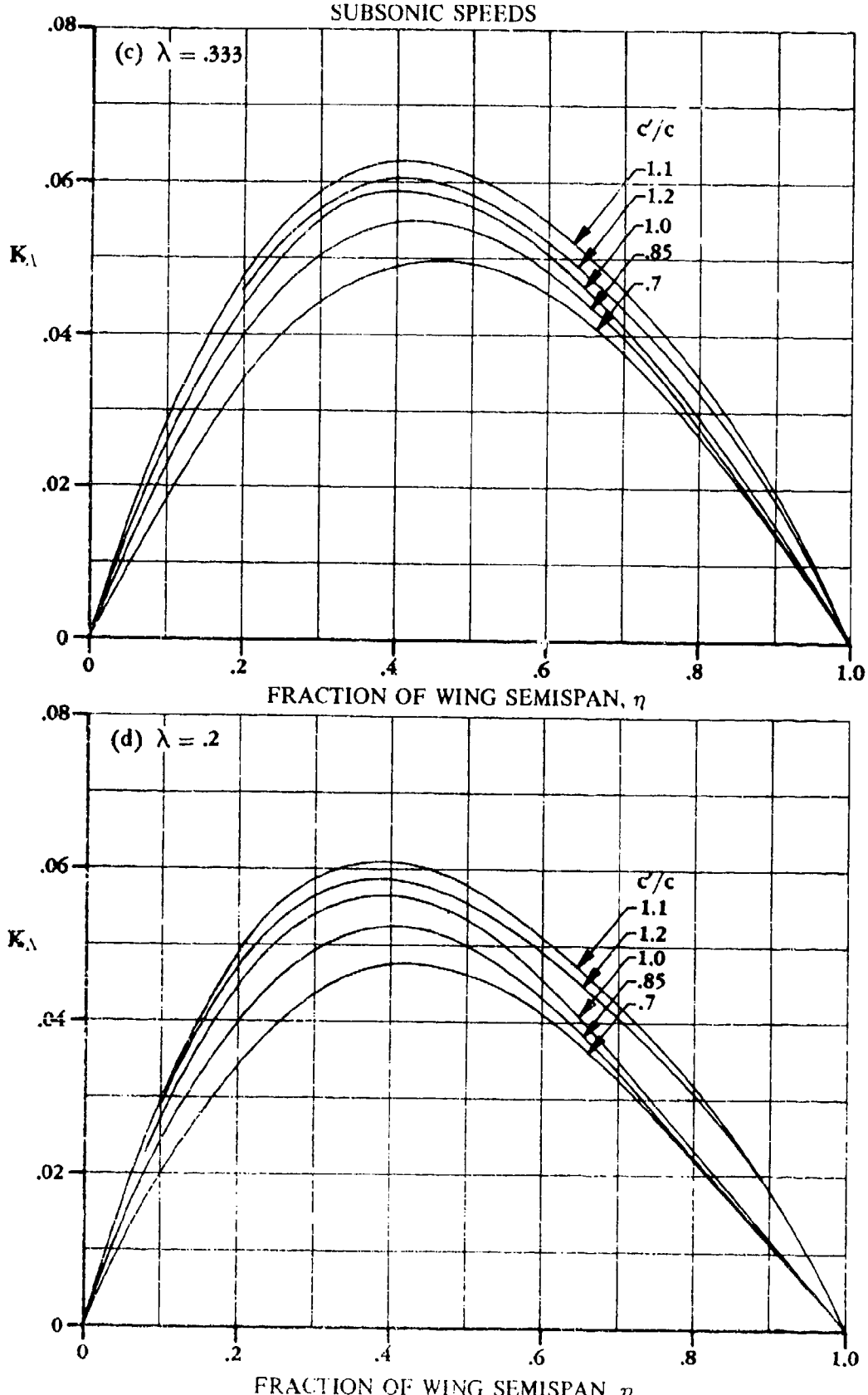

FIGURE 6.1.5.1-57 **(CONTD)**

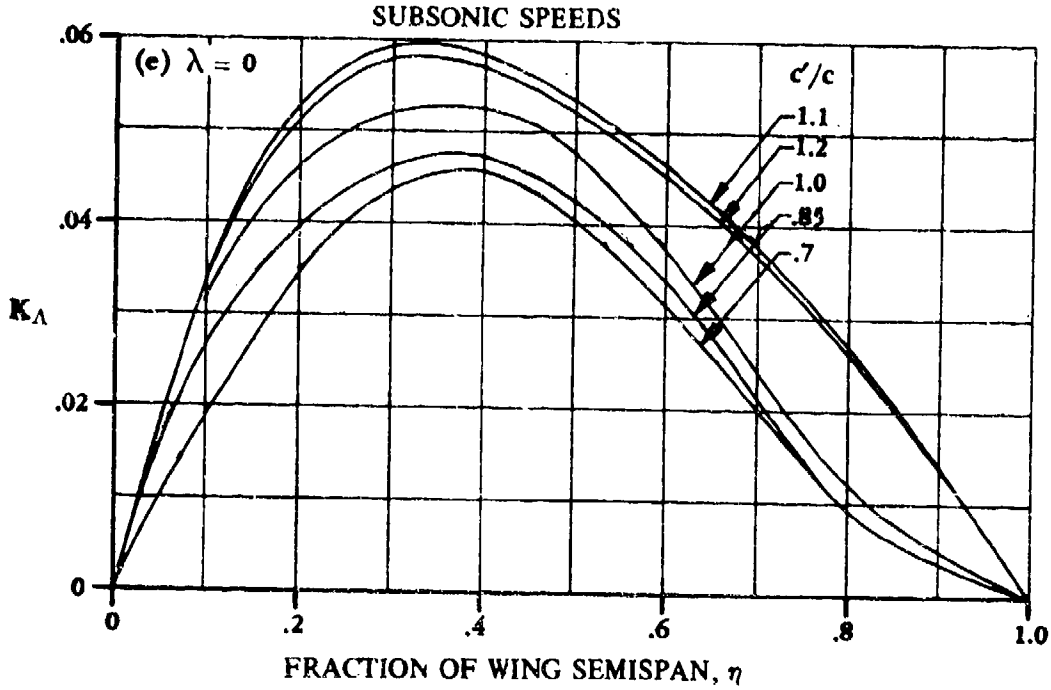

FIGURE 6.1.5.1-57 (CONTD)

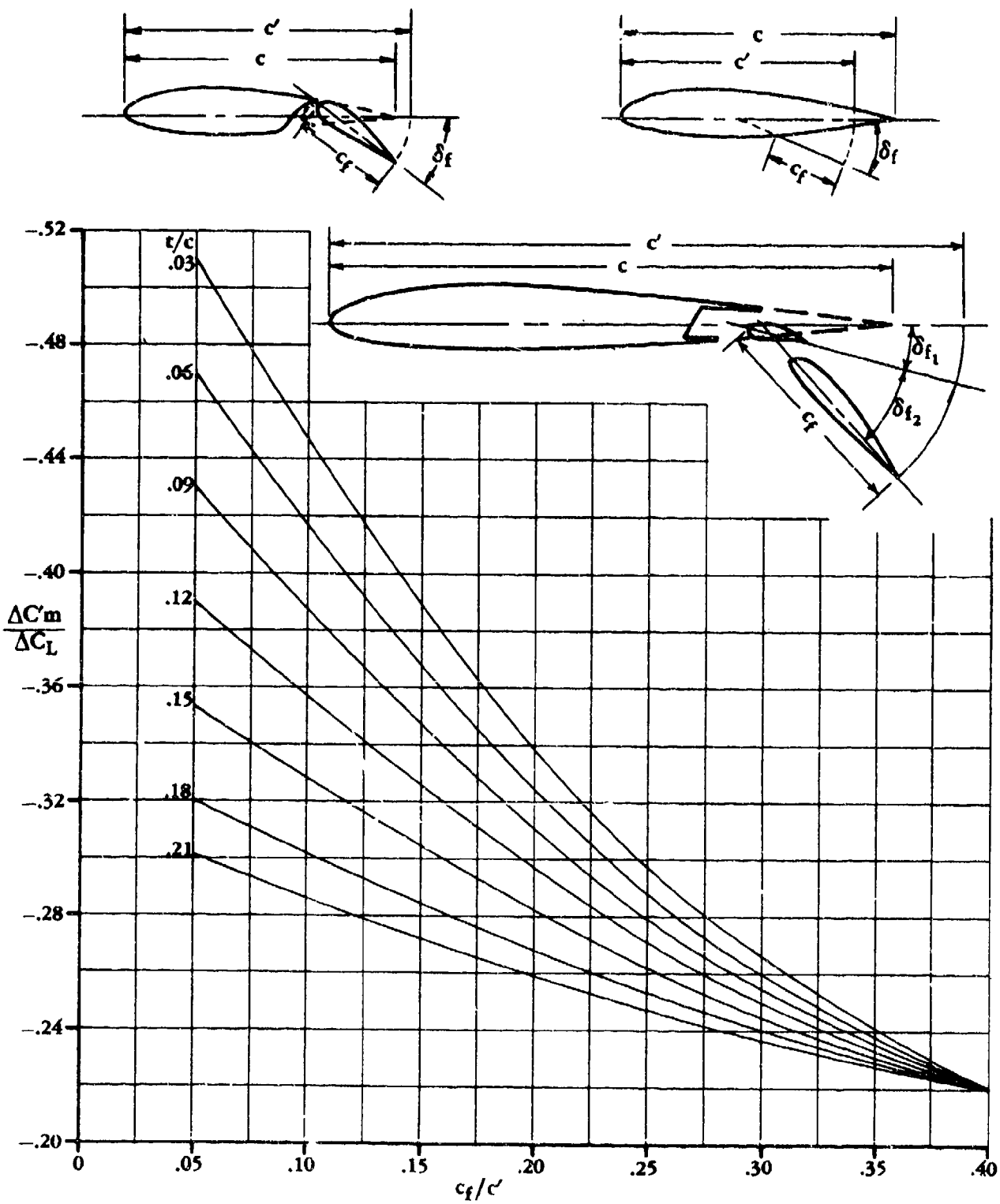

FIGURE 6.1.5.1-60 RATIO OF PITCHING-MOMENT-COEFFICIENT INCREMENT TO LIFT-COEFFICIENT INCREMENT DUE TO FLAPS FOR UNSWEPT WINGS

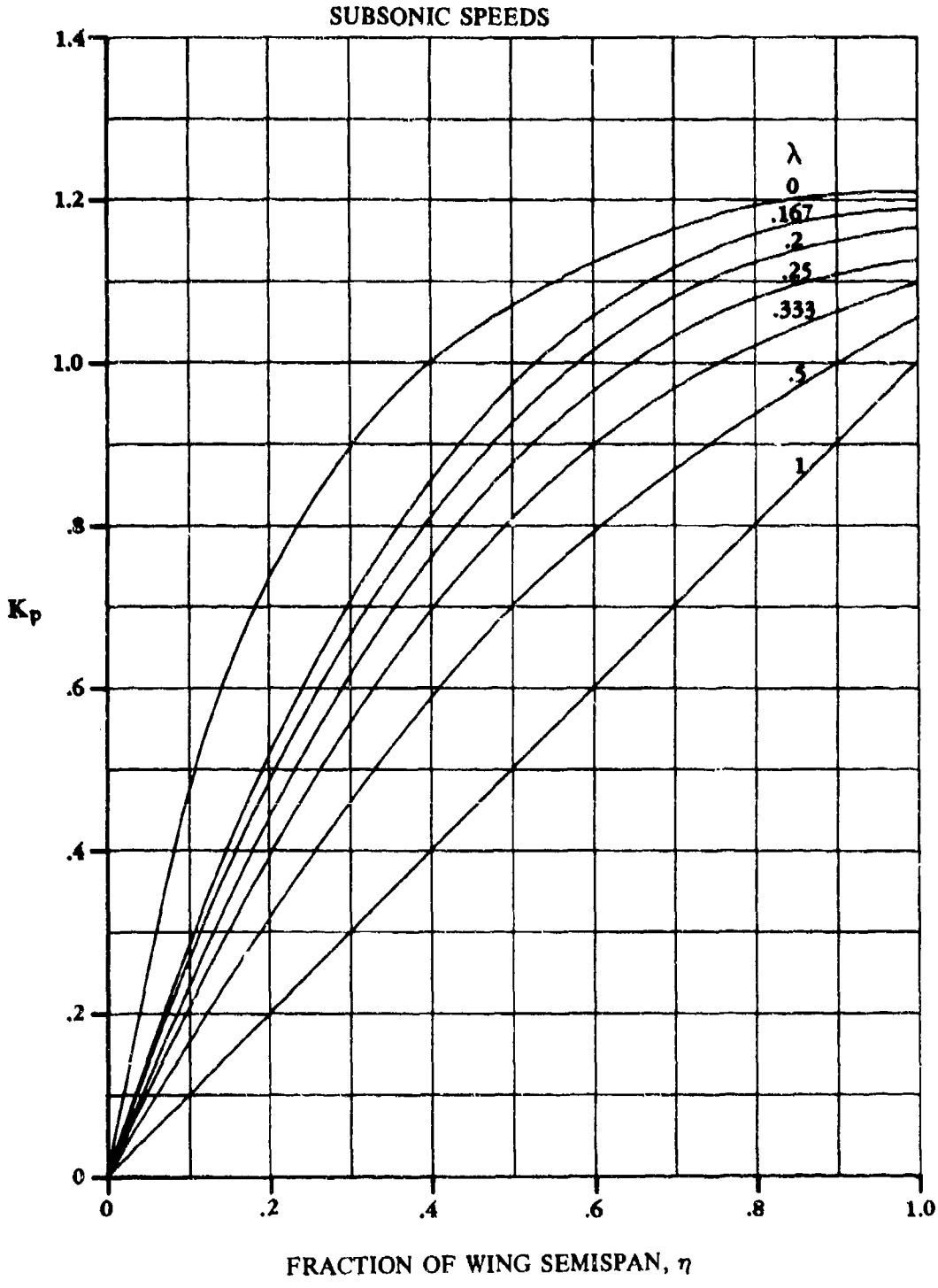

FIGURE 6.1.5.1-61 CONVERSION FACTOR FOR PARTIAL-SPAN FLAPS

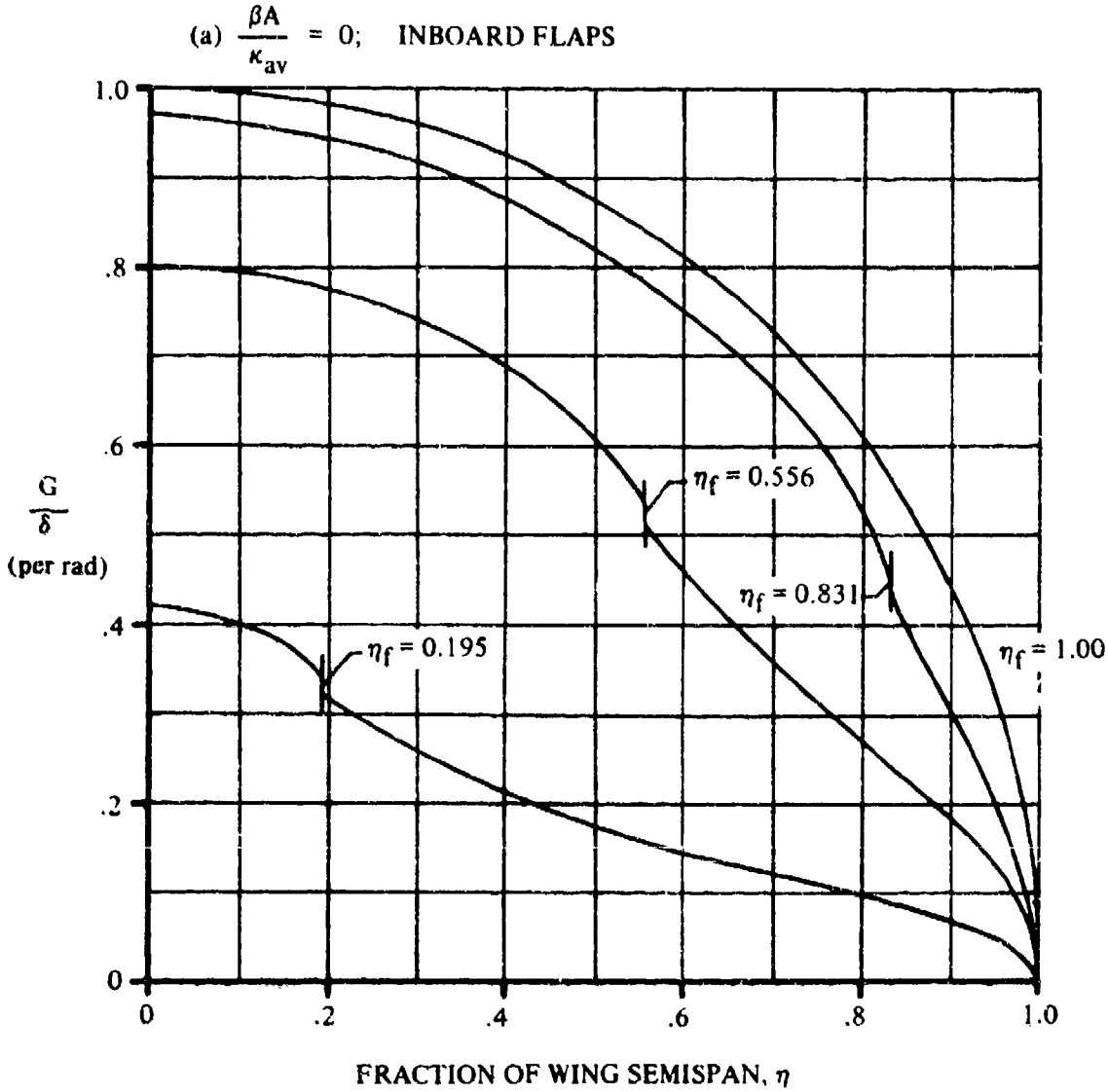

FIGURE 6.1.5.1-62 SPANWISE LOAD DISTRIBUTION DUE TO SYMMETRIC FLAP DEFLECTION FOR STRAIGHT-TAPERED WING. $c_f/c = 1$.

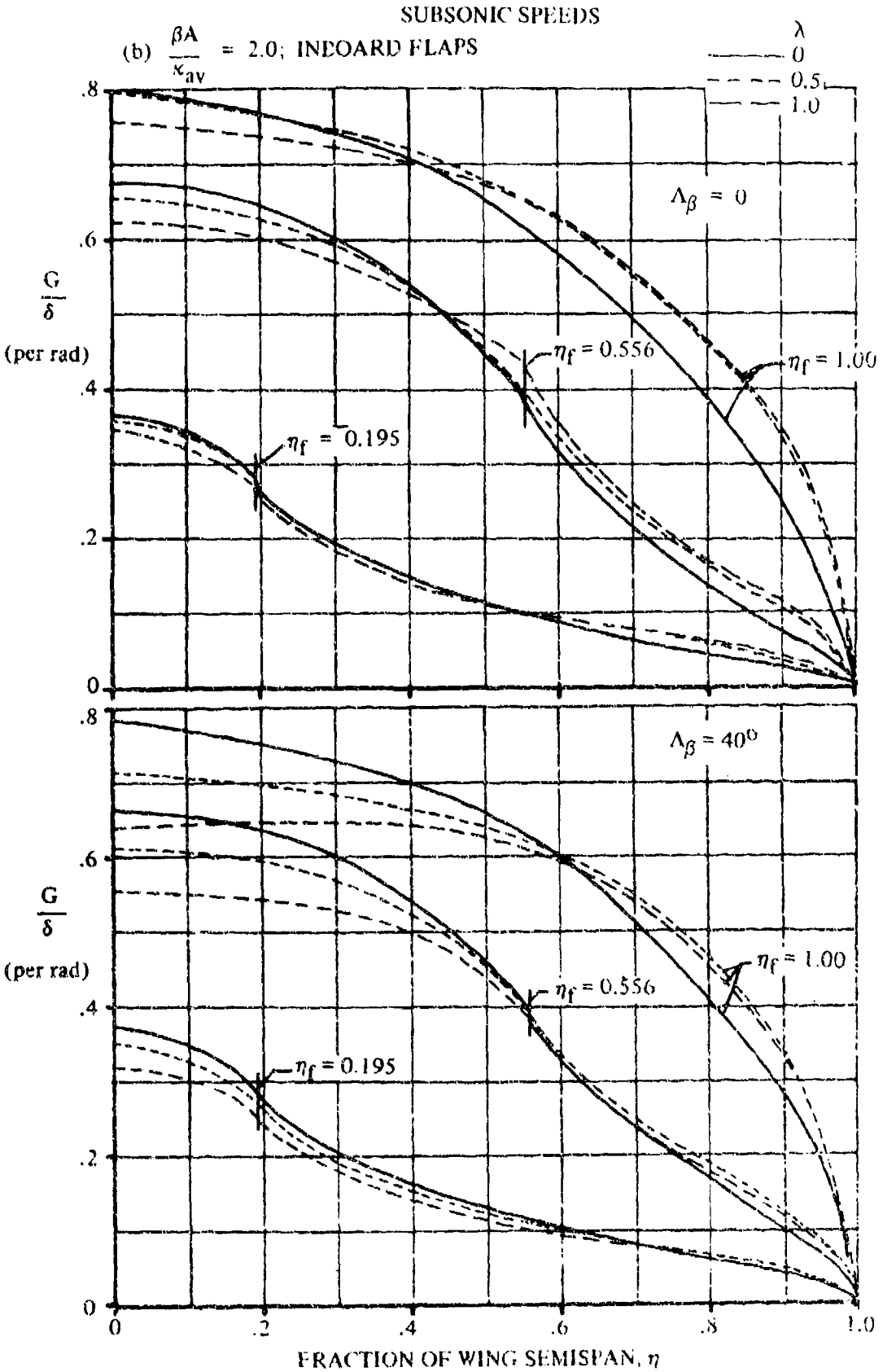

FIGURE 6.1.5.1-62 (CONTD)

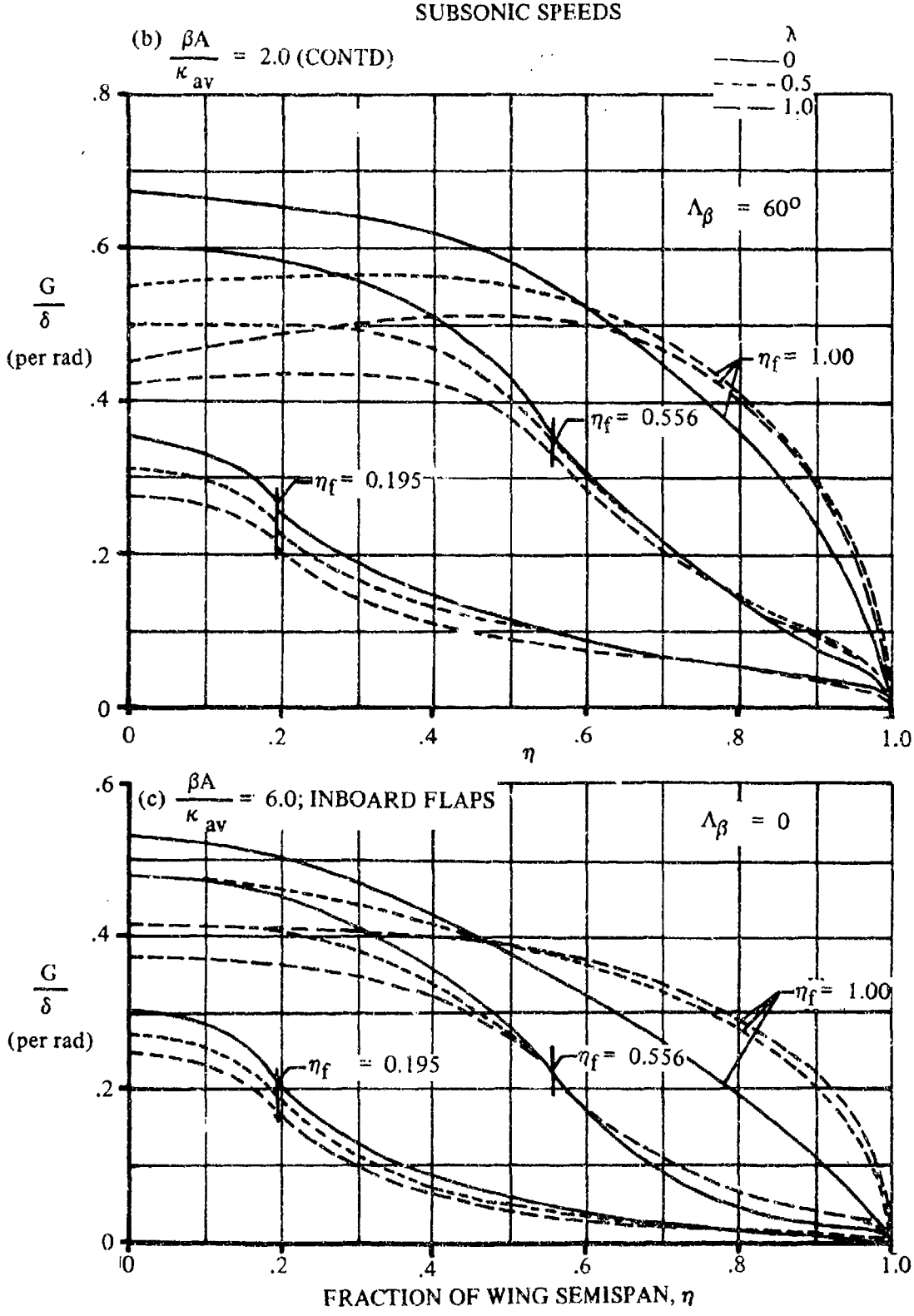

FIGURE 6.1.5.1-62 (CONTD)

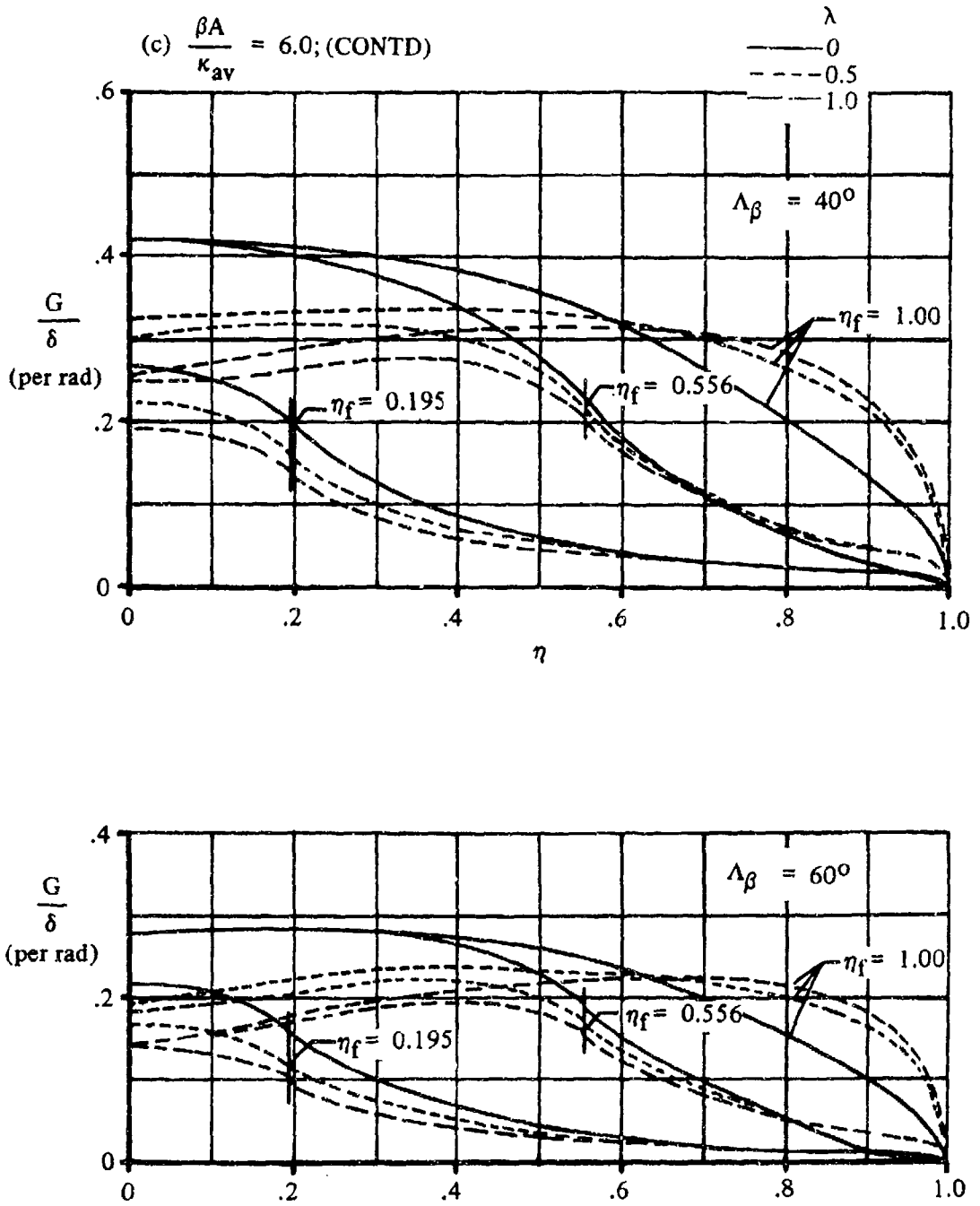

FIGURE 6.1.5.1-62 (CONTD)

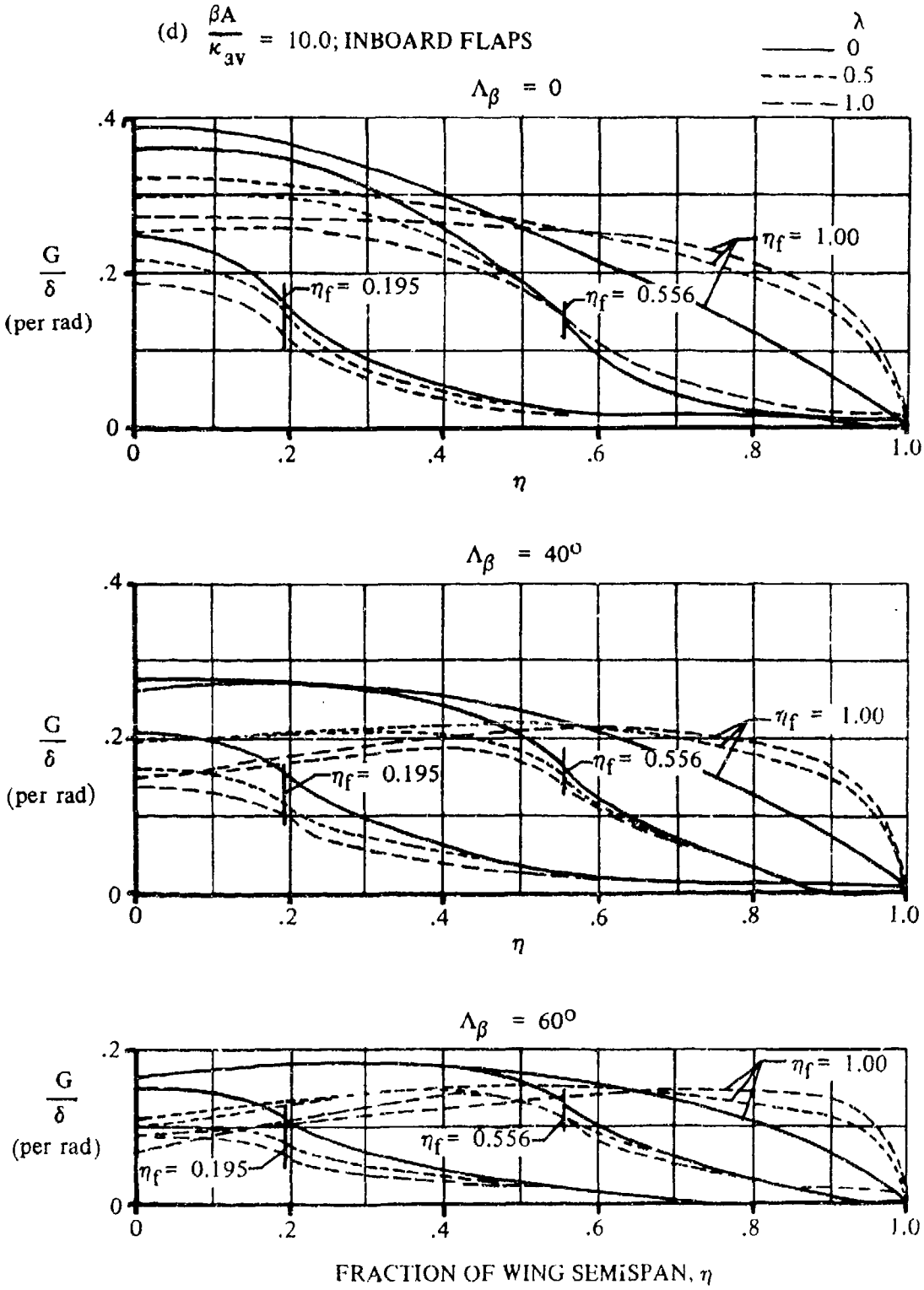

FIGURE 6.1.5.1-62 (CONTD)

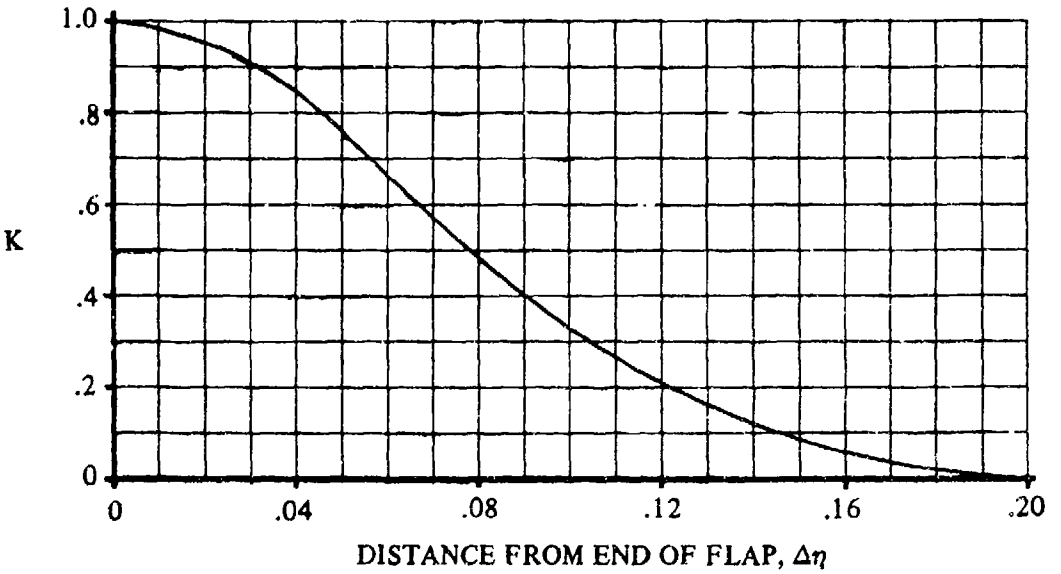

FIGURE 6.1.5.1-67a ESTIMATION OF SECTION CENTER-OF-PRESSURE LOCATION FOR UNFLAPPED SECTIONS NEAR END OF FLAPS

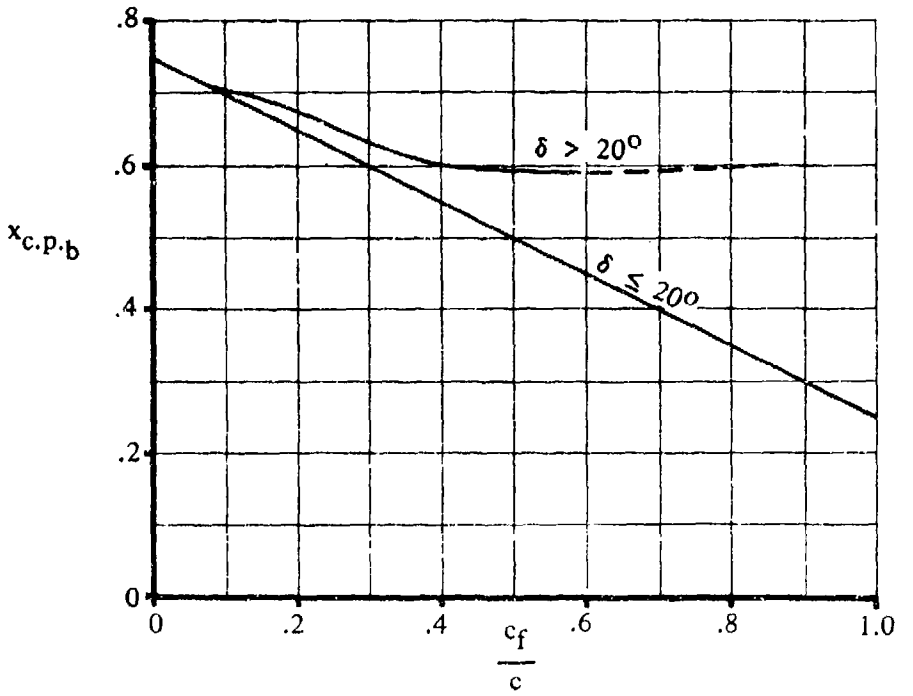

FIGURE 6.1.5.1-67b VARIATION OF SECTION-BASIC-LOADING CENTER OF PRESSURE WITH FLAP-CHORD RATIO

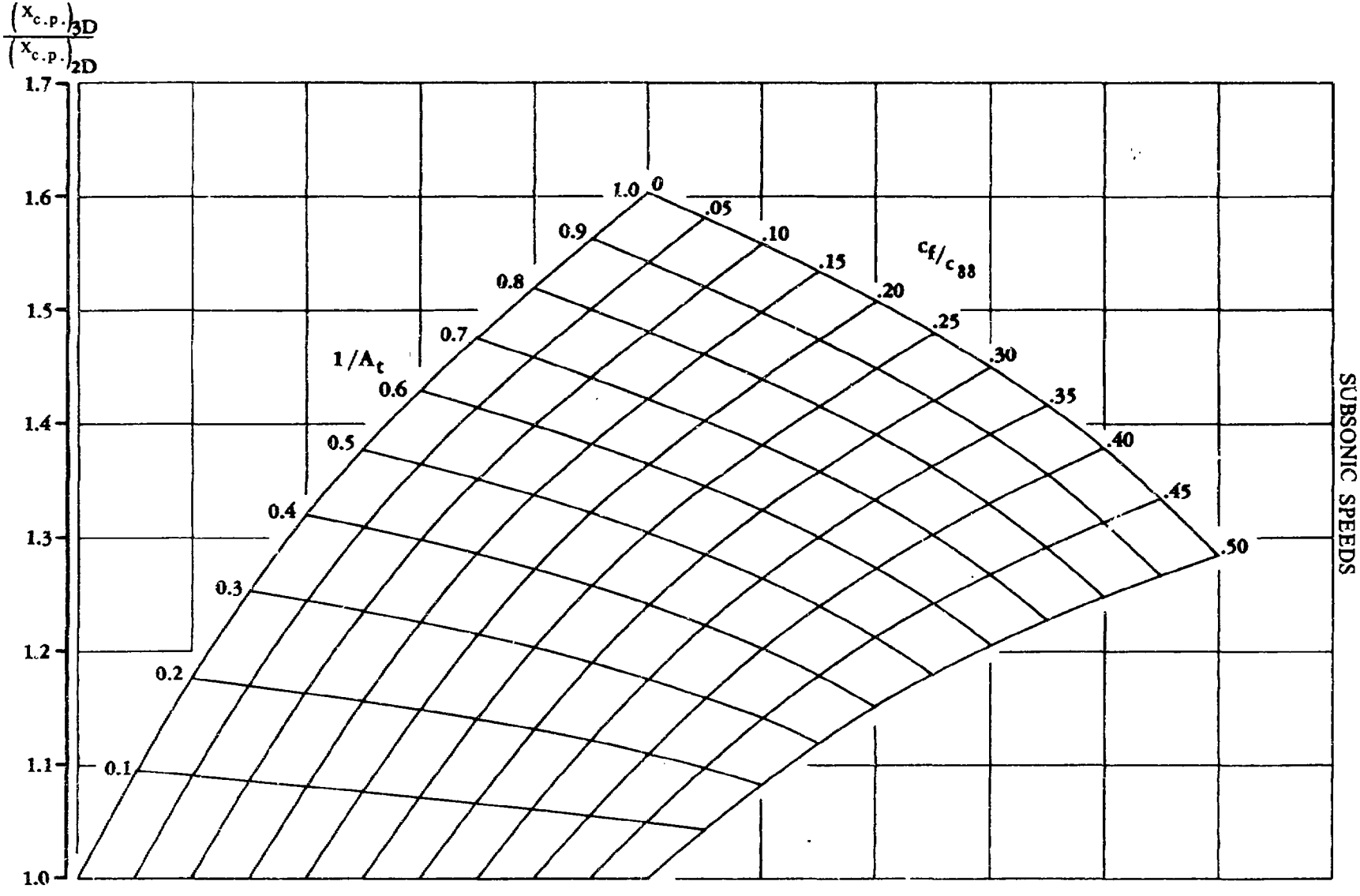

FIGURE 6.1.5.1-68 RATIO OF CENTER OF PRESSURE LOCATION FOR A WING TO CENTER OF PRESSURE LOCATION FOR AN AIRFOIL

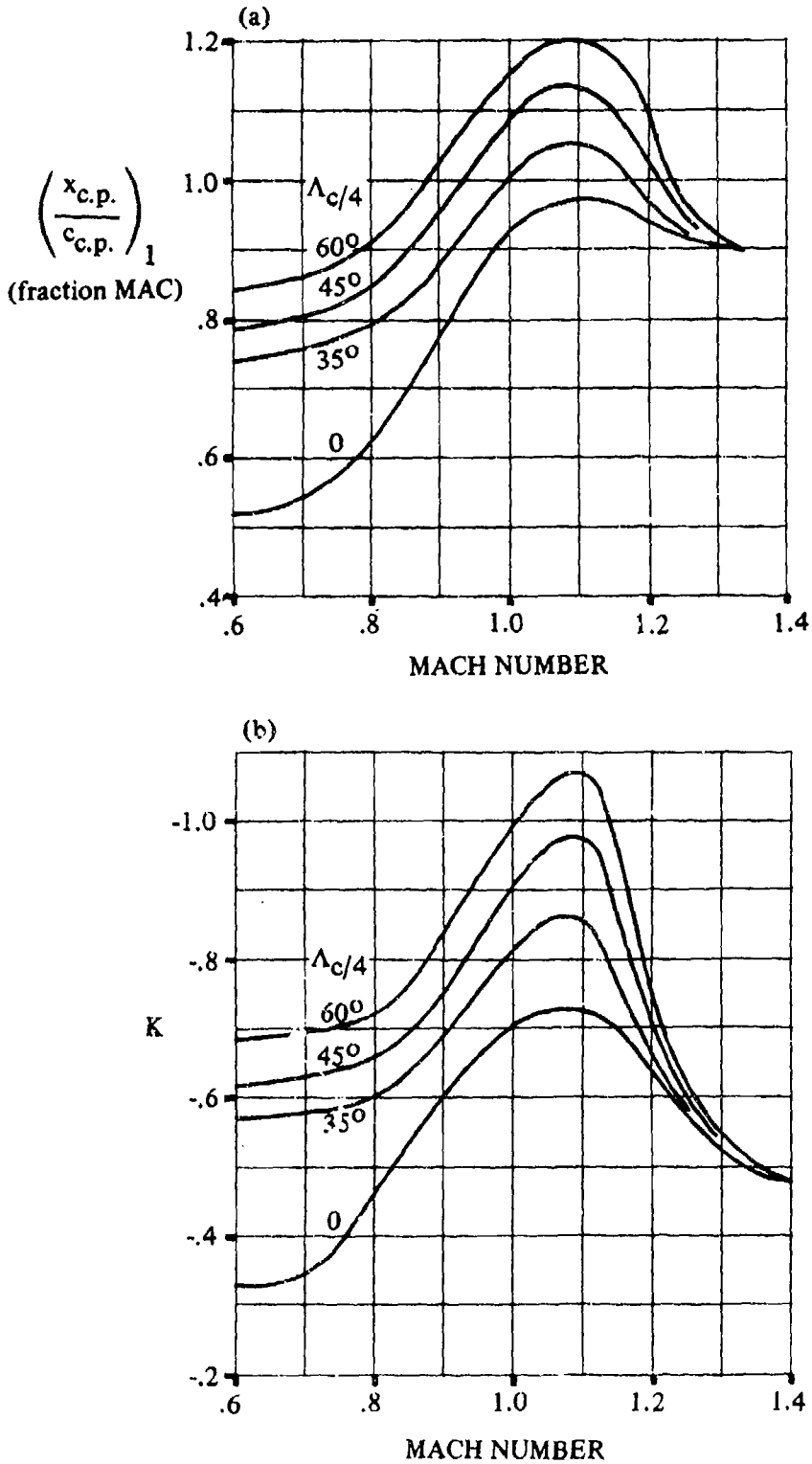

FIGURE 6.1.5.1-69 TRANSONIC CONTROL-SURFACE PITCH-EFFECTIVENESS PARAMETERS

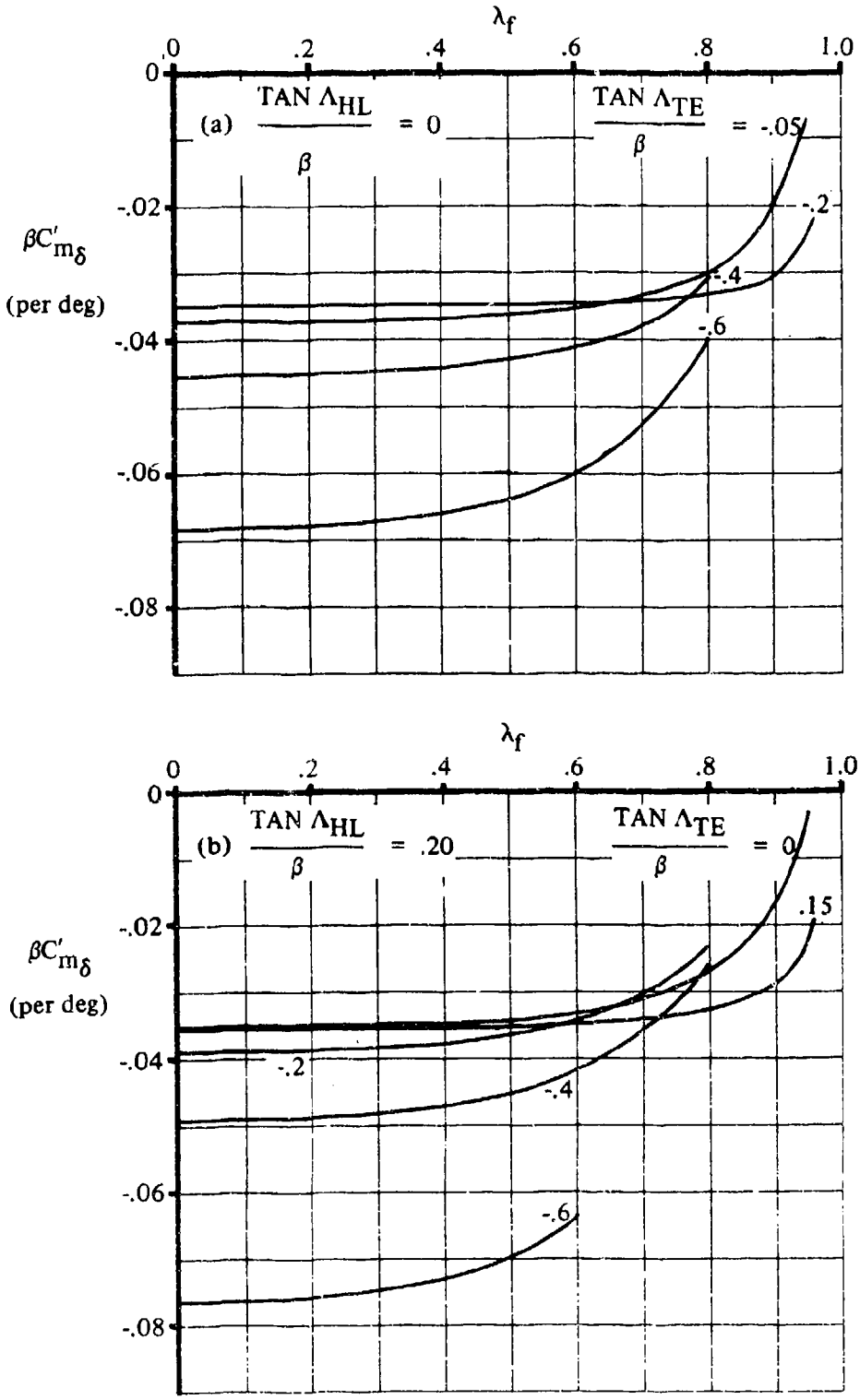

FIGURE 6.1.5.1-70 PITCHING-MOMENT DERIVATIVE FOR TAPERED CONTROL SURFACES HAVING OUTBOARD EDGE COINCIDENT WITH WING TIP

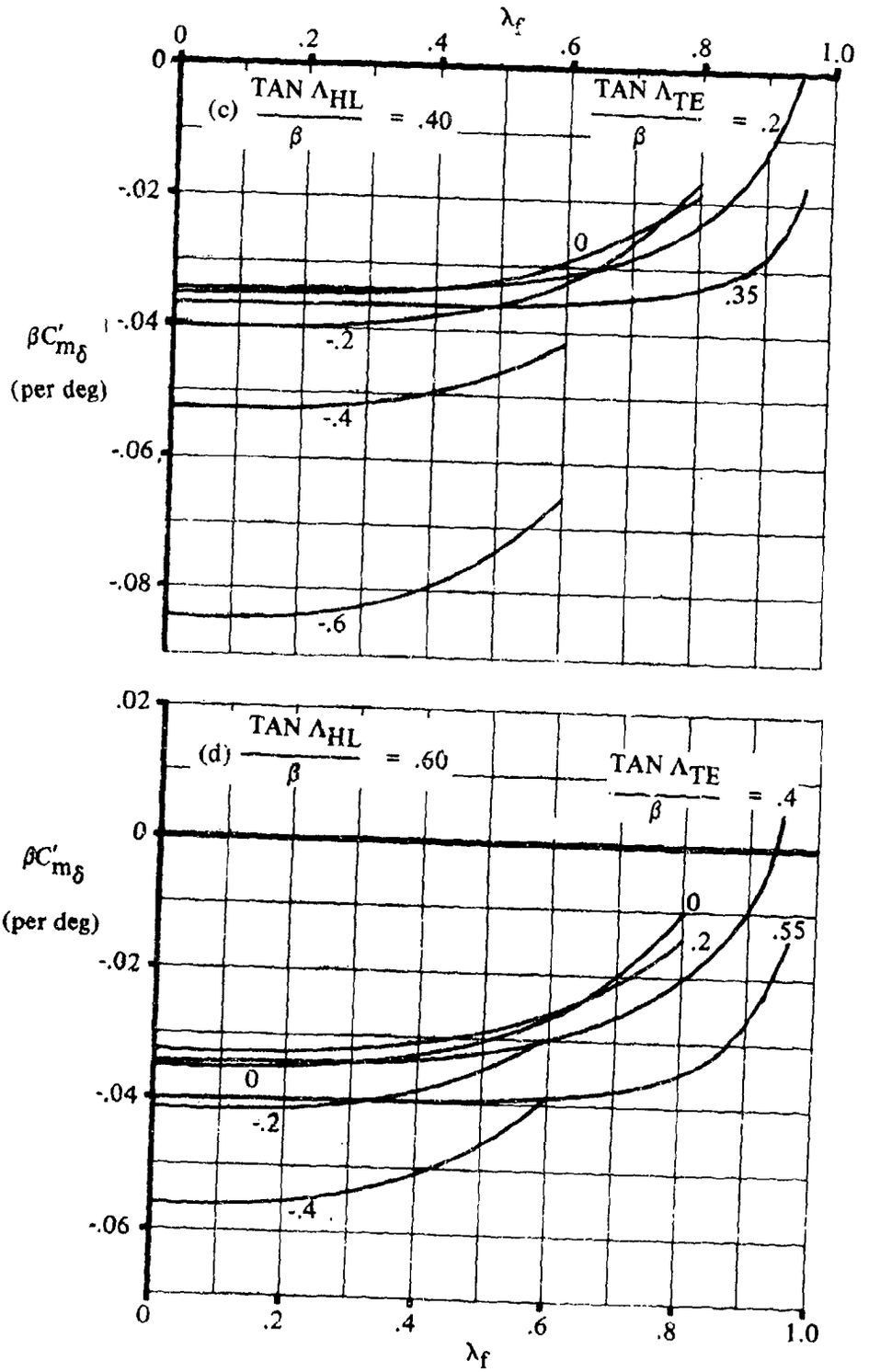

FIGURE 6.1.5.1-70 (CONTD)

SUPERSONIC SPEEDS

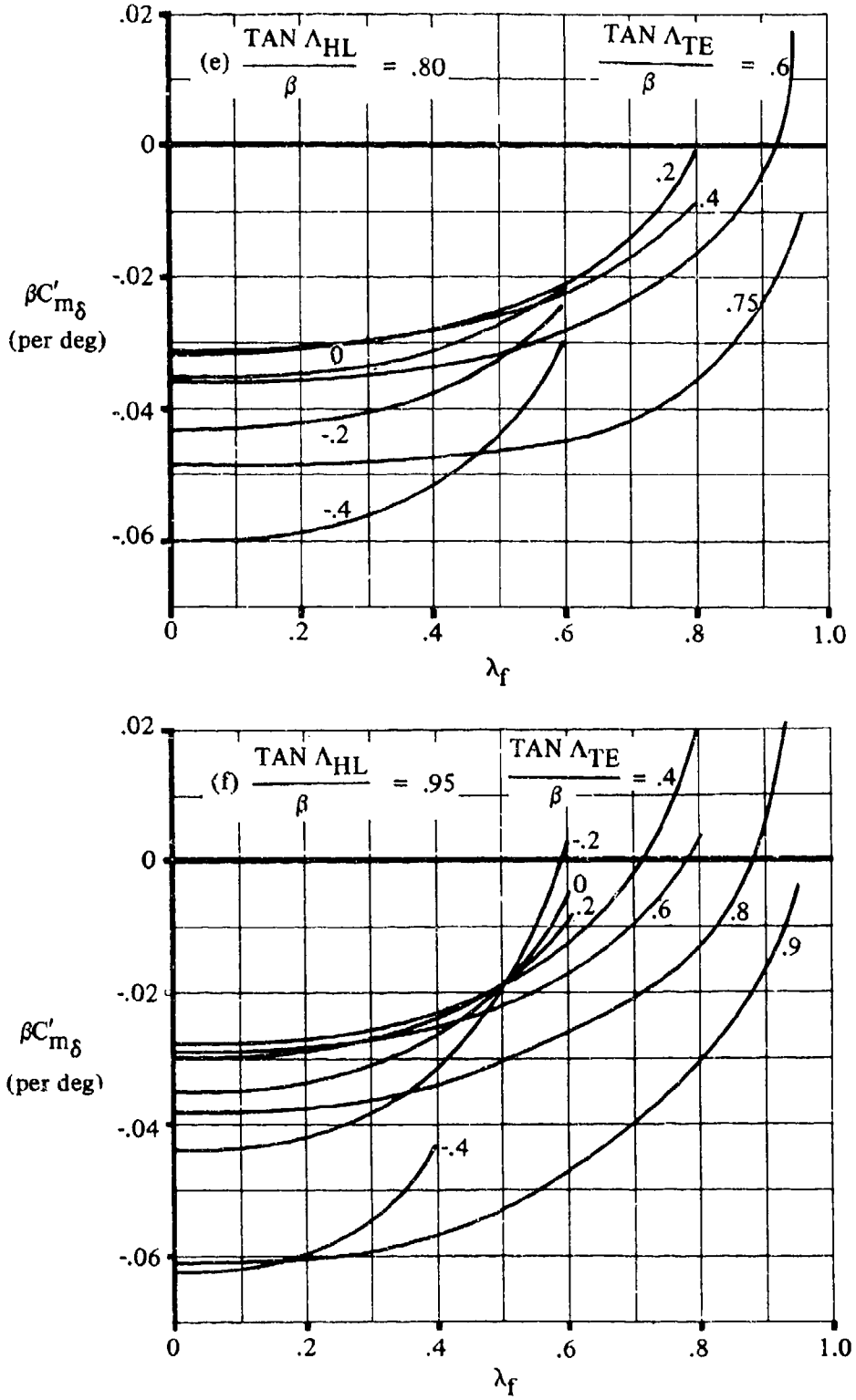

FIGURE 6.1.5.1-70 (CONTD)

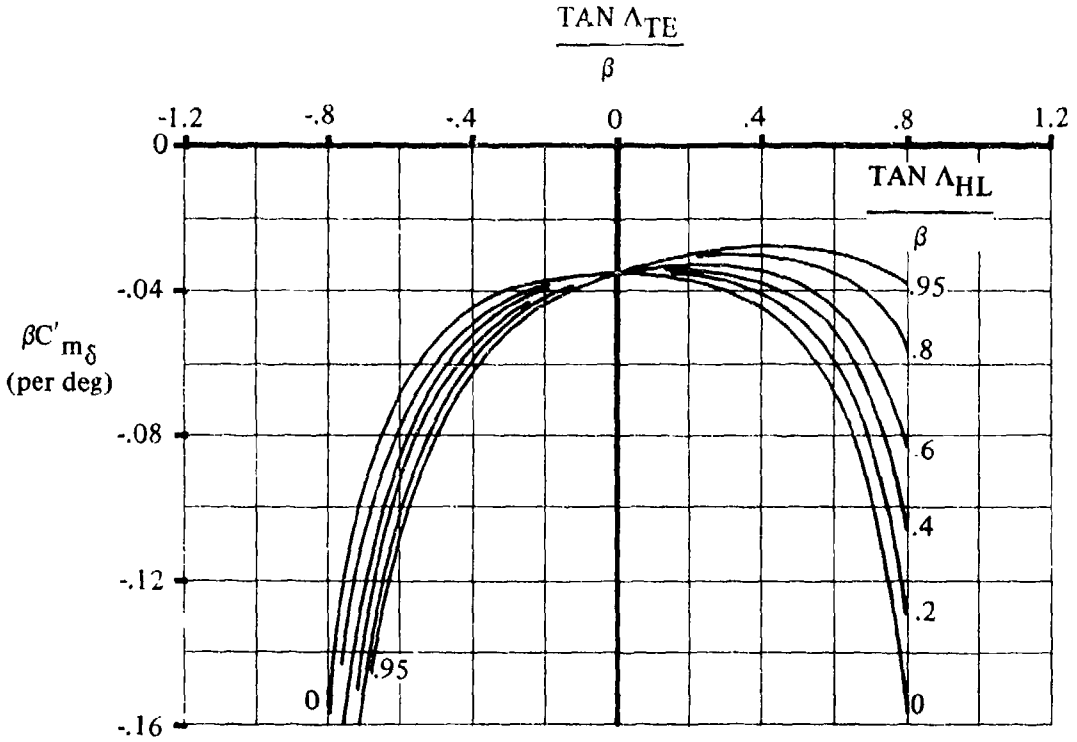

FIGURE 6.1.5.1-73a PITCHING-MOMENT DERIVATIVE FOR TAPERED AND UNTAPERED TRAILING-EDGE FLAPS HAVING OUTBOARD EDGE NOT COINCIDENT WITH WING TIP

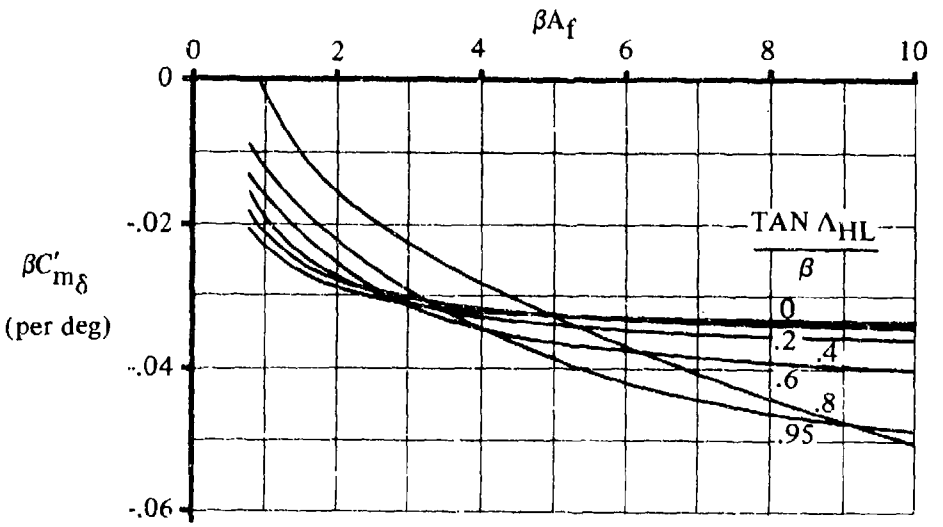

FIGURE 6.1.5.1-73b PITCHING-MOMENT DERIVATIVE FOR UNTAPERED TRAILING-EDGE CONTROL SURFACES LOCATED AT THE WING TIP

6.1.5.2 WING DERIVATIVE C_{m_α} WITH HIGH-LIFT AND CONTROL DEVICES

Mechanical Flaps

According to lifting-line or lifting-surface theory, camber, such as that due to flaps, does not affect the variation of pitching moment with angle of attack over the region where there is no flow separation. The theory is substantiated by experiment over the linear angle-of-attack and flap-deflection ranges (References 1 and 2).

Theoretically, the pitching-moment-curve slope of both wings and airfoils is affected by leading- and/or trailing-edge flaps that extend beyond the basic airfoil chord. However, the changes in C_{m_α} for airfoils (as predicted by linear theory) cannot be substantiated with test data (see Section 6.1.2.2). In addition, the effect of extended flaps on C_{m_α} for a wing of finite aspect ratio is not treated in detail in any of the literature surveyed for Datcom. Therefore, no method is presented to account for the effects of extended flaps on C_{m_α}.

Jet Flaps

The aerodynamic-center location for a wing with a jet flap is dependent upon the trailing-edge jet momentum coefficient C_μ and upon the extent to which leading- and trailing-edge flaps extend beyond the basic wing.

Considerations of clarity and simplicity of presentation dictated a deviation from normal Datcom practice in that the effect of jet flaps on C_{m_α} was included in Section 6.1.5.1, which deals with the pitching-moment increment ΔC_m.

DATCOM METHOD

1. Mechanical Flaps

The variation of wing pitching moment with angle of attack for various flap deflections is assumed to be the same as that for zero flap deflection over the linear-lift range (see Section 6.1.3, particularly Figure 6.1.3-2).

2. Jet Flaps

The variation of pitching moment with angle of attack for wings equipped with jet flaps is covered in the jet-flap method of Section 6.1.5.1. The range of applicability and the limitations of the method are discussed there and in Sections 6.1.1.1 and 6.1.2.1.

REFERENCES

1. Boyd, J. W., and Pfyl, F. A.: Experimental Investigation of Aerodynamically Balanced Trailing-Edge Control Surfaces on an Aspect Ratio 2 Triangular Wing at Subsonic and Supersonic Speeds. NACA RM A52L04, 1953. (U)

2. Furlong, G. C., and McHugh, J. G.: A Summary and Analysis of the Low-Speed Longitudinal Characteristics of Swept Wings at High Reynolds Number. NACA TR 1339, 1957. (U)

6.1.6 HINGE MOMENTS OF HIGH-LIFT AND CONTROL DEVICES

This section presents approximate methods for determining hinge-moment derivatives at subsonic and supersonic speeds. At subsonic speeds the method, based on lifting-line theory, is believed to be of sufficient accuracy to be used for preliminary-design work. This method is best suited for higher-aspect-ratio wings.

The methods presented for supersonic speeds have one stringent restriction: the leading edges of the wing planform must be swept ahead of the Mach lines. The methods are based on conical-flow solutions. Since hinge-moment variation with Mach number at transonic speeds becomes somewhat erratic, no method is presented for calculating transonic hinge moments. However, some trends in the transonic range can be noted from References 1 through 4. As the critical Mach number is passed, a shock forms on the upper surface of the airfoil and moves rearward with increasing Mach number. The airfoil pressure distribution changes from one that is approximately triangular, with a peak negative pressure forward, to one more nearly rectangular, with lower pressures at the trailing edge. In general, this causes hinge moments to become more negative. Sketch (a) presents some typical hinge-moment-derivative variations with Mach number.

It should be noted that in the more normal or stable case, where C_{h_α} and C_{h_δ} are negative at subsonic speeds, hinge-moment derivatives decrease in a somewhat regular fashion through the transonic range and then increase slightly to their supersonic value. Most of the very erratic variations of C_{h_α} and C_{h_δ} occur when these values are near zero or positive at subsonic speeds. It can also be seen that in the transonic region some hinge-moment derivatives can change sign.

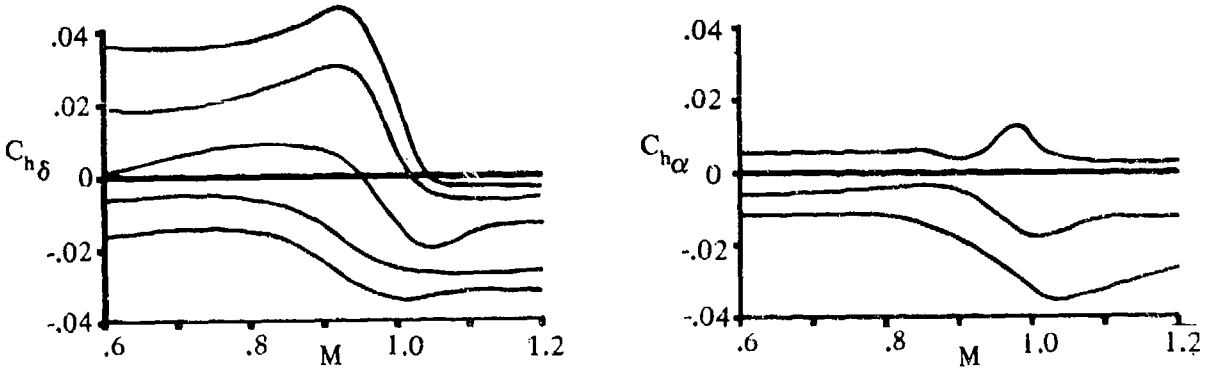

SKETCH (a)

REFERENCES

1. Thompson, R. F.: Investigation of a 42.7° Sweptback Wing Model to Determine the Effects of Trailing - Edge Thickness on the Aileron Hinge-Moment and Flutter Characteristics at Transonic Speeds. NACA RM L50J06, 1950. (U)

2. Lord, D. R., and Czarnecki, K. R.: Recent Information on Flap and Tip Controls. NACA RM L53I17a, 1953. (U)

3. Thompson, R.F.: Hinge-Moment, Lift, and Pitching-Moment Characteristics of a Flap-Type Control Surface Having Various Hinge-Line Locations on a 4-Percent-Thick 60° Delta Wing – Transonic Bump Method. NACA RM L54B08, 1954. (U)

4. Hieser, G.: Transonic Investigation of the Effectiveness and Loading Characteristics of a Flap-Type Aileron With and Without Paddle Balances on an Unswept-Wing–Fuselage Model. NACA RM L56B02, 1956. (U)

5. Runckel, J. F., and Hieser, G.: Normal-Force and Hinge-Moment Characteristics at Transonic Speeds of Flap-Type Ailerons at Three Spanwise Locations on a 4-Percent-thick Sweptback-Wing – Body Model and Pressure-Distribution Measurements on an Inboard Aileron. NACA RM L57I23, 1957. (U)

6.1.6.1 HINGE-MOMENT DERIVATIVE C_{h_α} OF HIGH-LIFT AND CONTROL DEVICES

A. SUBSONIC

The hinge-moment derivative due to angle of attack can be approximated from the method of Reference 1. The method is based on lifting-line theory, with additional lifting-surface corrections to account for sweep.

The method is based on equations in terms of section parameters; therefore, the accuracy of the method is dependent upon the accuracy with which the section characteristics can be estimated. Test data on the particular airfoil-flap combination under consideration or one closely resembling it should always be preferred to characteristics obtained from generalized methods. Calculated values and test data for several different configurations are presented in Table 6.1.6.1-A to illustrate the accuracy of the method and summarize available test data.

The method is directly applicable to control surfaces having constant chord ratios and constant airfoil contours across the span. For configurations with variable chord ratios or variable airfoil contours across the span, it is suggested that average values of the section characteristics be used. Furthermore, the accuracy of the method in predicting the effects of finite-wing parameters decreases as the wing aspect ratio decreases. Application of the method to wings with aspect ratios of three or less should be avoided.

Experimental data have shown that for sweptback wings the shape of the ends of the control surface can have a critical effect on the hinge-moment parameters. The Datcom method is applicable to controls with the control-surface ends cut parallel to the plane of symmetry. For configurations with wing cutouts, or with control surfaces that do not have ends parallel to the plane of symmetry, it is suggested that empirical procedures be used to estimate C_{h_α}.

The effect of subcritical Mach-number corrections on hinge moments appears to be small for control surfaces having trailing-edge angles less than approximately 12°. Therefore the Datcom method, which neglects subcritical Mach-number effects, may be applied over a large portion of the subcritical Mach-number range.

DATCOM METHOD

The hinge-moment derivative due to angle of attack of a sealed, plain trailing-edge control at subsonic speeds, based on the product of the control-surface area and the control-surface chord $S_c c_c$ (area and chord aft of the hinge line), is approximated by

$$C_{h_\alpha} = \frac{A \cos \Lambda_{c/4}}{A + 2 \cos \Lambda_{c/4}} \left(c_{h_\alpha}\right)_{\text{balance}} + \Delta C_{h_\alpha} \qquad \text{6.1.6.1-a}$$

where

$\left(c_{h_\alpha}\right)_{\text{balance}}$ is the section hinge-moment derivative due to angle of attack. Test data on the particular flapped airfoil are preferred, but the derivative can be approximated by the method of Paragraph A of Section 6.1.3.1. (This term could be c'_{h_α} or c''_{h_α} from Section 6.1.3.1.)

ΔC_{h_α} is an approximate lifting-surface correction which accounts for induced-camber effects. It is obtained by multiplying the quantity $\frac{\Delta C_{h_\alpha}}{c_{\ell_\alpha} B_2 K_\alpha \cos\Lambda_{c/4}}$, from Figure 6.1.6.1-19a, by its denominator

where

c_{ℓ_α} is the airfoil section lift-curve slope obtained by using the method of Section 4.1.1.2.

B_2 accounts for the effect of control-surface and balance chord ratios. This parameter is obtained from Figure 6.1.6.1-19c. The primed values of the control-surface and balance chord ratios used in reading Figure 6.1.6.1-19c, refer to measurements normal to the wing quarter-chord line.

K_α accounts for the effect of control-surface span. This parameter is defined by

$$K_\alpha = \frac{(K_\alpha)_{\eta_i}(1-\eta_i) - (K_\alpha)_{\eta_o}(1-\eta_o)}{\eta_o - \eta_i} \qquad 6.1.6.1\text{-b}$$

where

η_i is the inboard span station of the control,
$\eta_i = \frac{\text{inboard span ordinate}}{b/2}$

$(K_\alpha)_{\eta_i}$ is obtained from Figure 6.1.6.1-19b as a function of the inboard spanwise location (η_i) of the control panel.

η_o is the outboard span station of the control,
$\eta_o = \frac{\text{outboard span ordinate}}{b/2}$

$(K_\alpha)_{\eta_o}$ is obtained from Figure 6.1.6.1-19b as a function of the outboard spanwise location (η_o) of the control panel.

Sample Problem

Given: The flapped wing configuration of Reference 8

Wing Characteristics:

$A = 3.43$ $\lambda = 0.44$ $\Lambda_{c/4} = 48.7^o$

$t/c = 0.086$ (streamwise) $\tan\frac{\phi'_{TE}}{2} = 0.0697$ (streamwise)

$\tan \frac{\phi''_{TE}}{2}$ = 0.0523 (streamwise)

NACA 65-012 airfoil (normal to .50c of unswept wing)

Flap Characteristics:

Plain trailing-edge flap | Sealed gap | Λ_{HL} = 41°

c_f/c = 0.167 (streamwise) | c'_f/c' = 0.20 (normal to .25c)

c_b/c_f = 0.090 (streamwise) | c'_b/c'_f = 0.115 (normal to .25c)

$t_c/(2c_f)$ = 0.090 (streamwise) | Round-nosed control

η_i = 0.586 | η_o = 0.99

Additional Characteristics:

Low speed | R_{ℓ} = 2.2 x 10^6

Compute:

Section hinge-moment derivative c_{h_α} (Section 6.1.3.1)

$\left(c_{h_\alpha}\right)_{theory}$ = -0.384 per rad (Figure 6.1.3.1-11b)

$\frac{c_{\ell_\alpha}}{\left(c_{\ell_\alpha}\right)_{theory}}$ = 0.855 (Figure 4.1.1.2-8a)

$\frac{c'_{h_\alpha}}{\left(c_{h_\alpha}\right)_{theory}}$ = 0.600 (Figure 6.1.3.1-11a)

$c'_{h_\alpha} = \left[\frac{c'_{h_\alpha}}{\left(c_{h_\alpha}\right)_{theory}}\right] \left(c_{h_\alpha}\right)_{theory}$ (Equation 6.1.3.1-a)

= (0.600) (-0.384) = -0.230 per rad

$\left(c_{\ell_\alpha}\right)_{theory}$ = 6.715 per rad (Figure 4.1.1.2-8b)

Balance ratio = $\sqrt{\left(\frac{c_b}{c_f}\right)^2 - \left(\frac{t_c}{2c_f}\right)^2}$ = 0 (Equation 6.1.3.1-d)

$\left(c_{h_\alpha}\right)_{balance} / c''_{h_\alpha}$ = 1.0 (Figure 6.1.3.1-12a)

$$c''_{h_\alpha} = c'_{h_\alpha} + 2\left(c_{\ell_\alpha}\right)_{\text{theory}} \left[1 - \frac{c_{\ell_\alpha}}{\left(c_{\ell_\alpha}\right)_{\text{theory}}}\right] \left(\tan\frac{\phi''_{TE}}{2} - \frac{t}{c}\right) \quad \text{(Equation 6.1.3.1-b)}$$

$$= -0.230 + 2\,(6.715)\,[1 - 0.855]\quad (0.0523 - 0.086)$$

$$= -0.296 \text{ per rad} = -0.00516 \text{ per deg}$$

$$\left(c_{h_\alpha}\right)_{\text{balance}} = c''_{h_\alpha}\left[\left(c_{h_\alpha}\right)_{\text{balance}} / c''_{h_\alpha}\right] \quad \text{(Equation 6.1.3.1-c)}$$

$$= -0.00516 \text{ per deg}$$

Induced camber effect ΔC_{h_α}

$$c_{\ell_\alpha} = \frac{1.05}{\beta}\left[\frac{c_{\ell_\alpha}}{\left(c_{\ell_\alpha}\right)_{\text{theory}}}\right]\left(c_{\ell_\alpha}\right)_{\text{theory}} \quad \text{(Equation 4.1.1.2-a)}$$

$$= \left(\frac{1.05}{1.0}\right)(0.855)(6.715)$$

$$= 6.03 \text{ per rad}$$

$$= 0.105 \text{ per deg}$$

$B_2 = 0.885$ (Figure 6.1.6.1-19c)

$\left.\begin{aligned}(K_\alpha)_{\eta_i} &= 2.18\\ (K_\alpha)_{\eta_o} &= 4.20\end{aligned}\right\}$ (Figure 6.1.6.1-19b)

$$K_\alpha = \frac{(K_\alpha)_{\eta_i}(1-\eta_i) - (K_\alpha)_{\eta_o}(1-\eta_o)}{\eta_o - \eta_i} \quad \text{(Equation 6.1.6.1-b)}$$

$$= \frac{(2.18)(1-0.586) - (4.20)(1-0.99)}{0.99 - 0.586}$$

$$= 2.13$$

$$c_{\ell_\alpha} B_2 K_\alpha \cos\Lambda_{c/4} = (0.105)(0.885)(2.13)(0.66) = 0.1306 \text{ per deg}$$

$$\frac{\Delta C_{h_\alpha}}{c_{\ell_\alpha} B_2 K_\alpha \cos\Lambda_{c/4}} = 0.0125 \quad \text{(Figure 6.1.6.1-19a)}$$

$$\Delta C_{h_\alpha} = (0.0125)(0.1306) = 0.00163 \text{ per deg}$$

Solution:

$$C_{h_\alpha} = \frac{A \cos \Lambda_{c/4}}{A + 2 \cos \Lambda_{c/4}} \left(c_{h_\alpha}\right)_{\text{balance}} + \Delta C_{h_\alpha} \qquad \text{(Equation 6.1.6.1-a)}$$

$$= \frac{(3.43)(0.6600)}{(3.43) + (2)(0.6600)} (-0.00516) + 0.00163$$

$$= -0.00083 \text{ per deg}$$

This compares with a test value of −0.0014 per degree from Reference 8.

B. TRANSONIC

No method is available for the prediction of the hinge-moment derivative C_{h_α} at transonic speeds. Because of the mixed-flow conditions and interrelated shock-wave and boundary-layer-separation effects encountered at transonic speeds, the prediction of C_{h_α} by theoretical means is extremely difficult. Experimental results for C_{h_α} at transonic speeds are presented in References 2 through 5.

C. SUPERSONIC

The supersonic three-dimensional hinge moment due to angle of attack can be computed for trailing-edge control surfaces by the method presented in Reference 6. The method is based on linearized theory and applies to tapered and untapered trailing-edge control surfaces, with the following restrictions:

1. Control root and tip chords are parallel to the plane of symmetry.
2. Wing planform has leading edges swept ahead of the Mach lines and has streamwise tips.
3. Controls are not influenced by the tip conical flow from the opposite wing panel or by the interaction of the wing-root Mach cone with the wing tip.

Calculated values and test data for several different configurations are presented in Table 6.1.6.1-B to illustrate the accuracy of the method and summarize available test data.

For leading-edge control surfaces or for trailing-edge control surfaces with subsonic leading edges, reverse-flow techniques (see Reference 7) can be used.

DATCOM METHOD

The method consists of determining the pressure-area-moment for an infinitely thin flat-plate control by assuming two-dimensional loading and then subtracting the losses in loading resulting from the interference of the wing-root and wing-tip conical flows.

Combinations of wing-root and wing-tip conical-flow cases for a typical wing-planform-control configuration are illustrated by the relative positions of the Mach lines in Sketch (a).

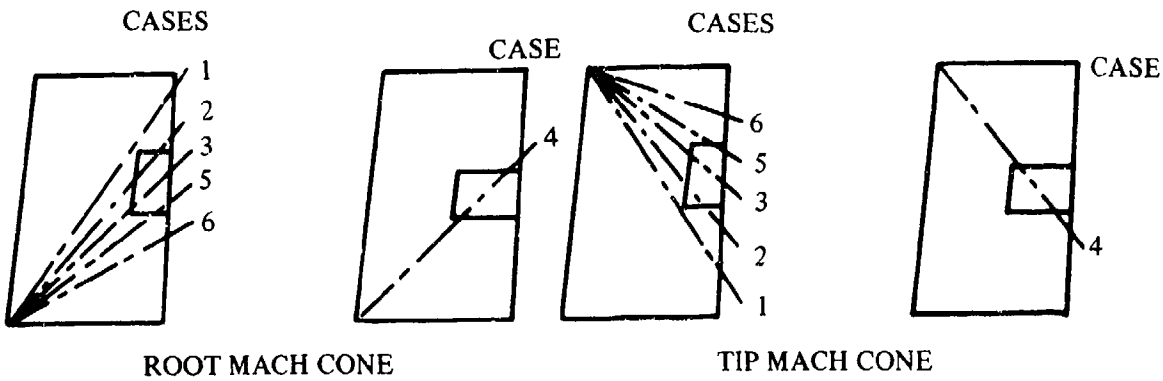

SKETCH (a)

For a given Mach number and wing-control combination (which determines the wing-root and wing-tip conical-flow case), the conical-flow losses are obtained by dividing the conical regions into a series of triangular segments, each having its origin at the apex of the Mach cone, and summing the loss in pressure-area-moment $P'S_L x$ for those segments. The procedure to be followed in summing $P'S_L x$ for the triangular segments is illustrated for the most general wing-root and wing-tip conical-flow case (Case 1) in Figure 6.1.6.1-21. Table 6.1.6.1-C is a general computing form for summing a pressure-area-moment parameter representing a loss in loading from the two-dimensional loading of the triangular segments of the conical-flow region defined by Case 1.

Figure 6.1.6.1-21 and Table 6.1.6.1-C can be adapted to compute the pressure-area-moment parameter for wing-root and wing-tip conical-flow Cases 2 through 5 by determining the proper regions that will be affected by the Mach cones. For wing-root and wing-tip conical-flow Case 6, there is no loss in loading from the two-dimensional loading value.

The hinge-moment derivative C_{h_α} at supersonic speeds for a symmetric, straight-sided control, based on the product of the control-surface area and the control-surface chord $S_c c_c$ (area and chord aft of hinge line), is given by

$$\left(C_{h_\alpha}\right)_{t/c} = \left(1 - \frac{C_2}{C_1}\phi_{TE}\right)\left(C_{h_\alpha}\right)_{t/c\,=\,0} \qquad 6.1.6.1\text{-c}$$

where

$\left(1 - \frac{C_2}{C_1}\phi_{TE}\right)$ is a thickness correction factor to the supersonic flat-plate derivative.

$C_1 = \frac{2}{\sqrt{M^2 - 1}}$ per radian

$$C_2 = \frac{(\gamma + 1)\, M^4 - 4\,(M^2 - 1)}{2\,(M^2 - 1)^2} \quad \text{per radian}$$

ϕ_{TE} is the trailing-edge angle in radians, measured normal to the control hinge line.

γ is the ratio of specific heats, $\gamma = 1.4$.

For a symmetrical biconvex airfoil the thickness correction factor in Equation 6.1.6.1-c is

$$1 - \frac{2\,C_2 \left(\frac{t}{c}\right)'}{3\,C_1\,(1 + k)\cos\left(\Lambda_{LE} - \Lambda_{HL}\right)} \left\{ 2 \left[1 + 2 \left(\frac{x_h}{c}\right)' \right] - k \left[1 - \left(\frac{x_h}{c}\right)' \right]^2 \right\}$$

where

$\left(\frac{t}{c}\right)'$ is the maximum airfoil-thickness ratio, measured in a plane normal to the control hinge axis.

$\left(\frac{x_h}{c}\right)'$ is the chordwise location of the control hinge axis, measured in a plane normal to the control hinge axis.

$$k = \tan\left(\Lambda_{LE} - \Lambda_{HL}\right) \tan\left(\Lambda_{LE} - \Lambda_{TE}\right)$$

Thickness correction factors for other airfoil sections can be determined from Reference 6.

$\left(C_{h_\alpha}\right)_{t/c\,=\,0}$ is the supersonic flat-plate hinge-moment derivative.

The procedure for calculating $\left(C_{h_\alpha}\right)_{t/c\,=\,0}$ is outlined in the following steps:

Step 1. Construct the wing-root and wing-tip Mach lines on a layout of the wing-control configuration, and determine the wing-root and wing-tip conical-flow case by referring to Sketch (a).

If the wing-root and wing-tip conical-flow case is Case 6, there is no loss of loading from the two-dimensional value. For this case calculate β and g as presented in Step 2, then

$$\left(C_{h_\alpha}\right)_{t/c\,=\,0} = \frac{-2}{57.3\,\beta\sqrt{1 - g^2}} \quad \text{(per degree)} \qquad 6.1.6.1\text{-d}$$

Step 2. Compute the following geometric and Mach-number parameters (see Sketch (b)):

$$\beta = \sqrt{M^2 - 1}$$

$$g = \frac{\tan \Lambda_{LE}}{\beta}$$

$$a = \frac{\tan \Lambda_{HL}}{\beta}$$

$$d = \frac{\tan \Lambda_{TE}}{\beta}$$

$$K_1 = \beta y_o$$

$$K_2 = \beta y_i$$

$$K_3 = \beta\left(\frac{b}{2} - y_i\right)$$

$$K_4 = \beta\left(\frac{b}{2} - y_o\right)$$

$$K_5 = \beta (y_o)^2$$

$$K_6 = \frac{1}{\beta (1 - d)}$$

$$K_7 = \frac{1}{\beta (1 - a)}$$

$$K_8 = \beta (y_i)^2$$

$$K_9 = \beta\left(\frac{b}{2} - y_i\right)^2$$

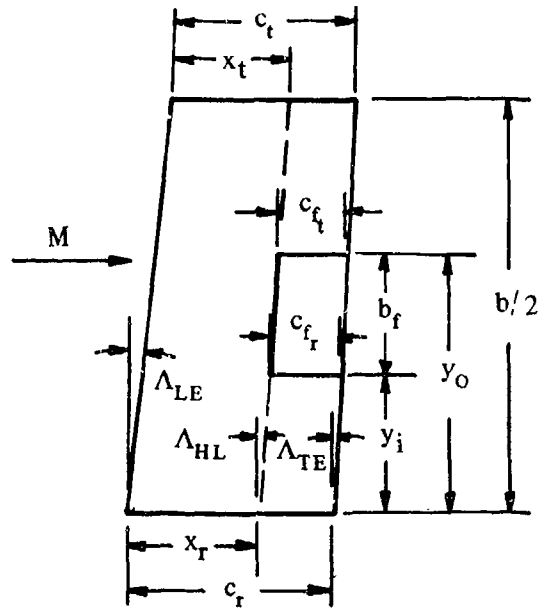

SKETCH (b)

$$K_{10} = \frac{1}{\beta (1 + d)}$$

$$K_{11} = \frac{1}{\beta (1 + a)}$$

$$K_{12} = \beta\left(\frac{b}{2} - y_o\right)^2$$

Step 3. Determine the regions (triangular segments numbered (1) through (8) on Figure 6.1.6.1-21) that are affected by the wing-root and wing-tip conical-flow case determined in Step 1.

The regions affected for each case are:

Conical-Flow Case (Sketch (a))	Wing-Root and Wing-Tip Conical Flow Regions Affected
1	1, 2, 3, 4, 5, 6, 7, 8
2	1, 3, 4, 5, 7, 8
3	3, 5, 7, 8
4	1, 3, 4, 7
5	3, 7
6	None

Step 4. Calculate the pressure-area-moment parameter representing a loss in loading from the two-dimensional loading value for each of the wing-root and wing-tip conical-flow regions affected by using the computing procedure presented in Table 6.1.6.1-C.

Step 5. Sum the values of the pressure-area-moment parameter calculated in Step 4 for the affected regions and obtain $\left(C_{h_\alpha}\right)_{t/c = 0}$ by

$$\left(C_{h_\alpha}\right)_{t/c = 0} = \frac{-2}{57.3\,\beta\sqrt{1 - g^2}} \left\{1 - \frac{\Sigma P' \left(3x\sqrt{1 + \beta^2 a^2}\right) 2S_L}{2M_a \left[3\sqrt{1 + \beta^2 a^2}\right]}\right\} \text{(per deg)} \quad 6.1.6.1\text{-e}$$

where

$$2M_a \left[3\sqrt{1 + \beta^2 a^2}\right] = b_f \frac{\left(c_{f_r}\right)^3 - \left(c_{f_t}\right)^3}{c_{f_r} - c_{f_t}} \quad 6.1.6.1\text{-f}$$

for tapered controls, and

$$2M_a \left[3\sqrt{1 + \beta^2 a^2}\right] = 3\, b_f \left(c_{f_r}\right)^2 \quad 6.1.6.1\text{-g}$$

for untapered controls.

SYMBOLS AND DEFINITIONS USED IN COMPUTATION OF $\left(C_{h_\alpha}\right)_{t/c = 0}$

n, r' nondimensional coordinates used in integration of wing-root and wing-tip conical pressures. Equations are given in column (1) of Table 6.1.6.1-C for calculating n and r'. Values of n are required to enter the design charts for P' and $t_{c.p.}$ for conical-flow Regions 3, 4, 5, and 6. Values of r' are required to enter the design charts for P' and $t_{c.p.}$ for conical-flow Regions 1, 2, 7, and 8.

P' the loss of loading of the average value of the local pressure ratio (C_p/C_{p_o}) over the conical-flow region. This parameter is obtained from Figure 6.1.6.1-22 for conical-flow regions intersecting the wing-root Mach cone and from Figure 6.1.6.1-34 for conical-flow regions intersecting the wing-tip Mach cone.

C_p is the pressure coefficient $(\Delta p/q)$ for a three-dimensional wing.

C_{p_o} is the two-dimensional pressure coefficient.

$t_{c.p.}$ nondimensional parameter used in calculating the moment-arm parameter $3x\sqrt{1 + \beta^2 a^2}$. $t_{c.p.}$ is obtained from Figure 6.1.6.1-22 for conical-flow regions intersecting the wing-root Mach cone and from Figure 6.1.6.1-34 for conical-flow regions intersecting the wing-tip Mach cone.

x distance of the center of loading of a conical-flow region from the control hinge axis measured normal to the hinge axis (see Sketch (c)). Equations are given in Column (4) of Table 6.1.6.1-C for calculating the moment-arm parameter $3x\sqrt{1+\beta^2 a^2}$ for the appropriate conical-flow region; hence, explicit values of x are not required.

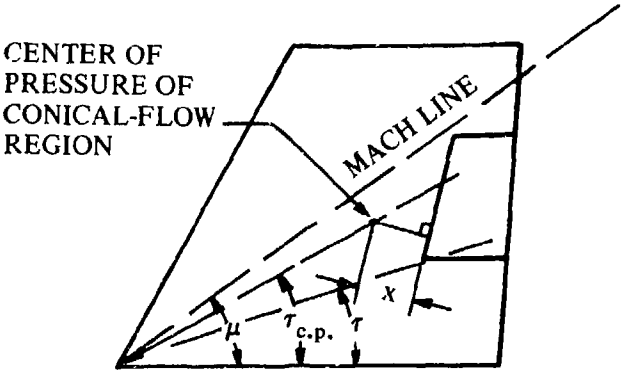

SKETCH (c)

$\tau_{c.p.}$ angle of a ray in the conical-flow field which passes through the center of pressure.

τ angle denoting an arbitrary position of the ray in the conical-flow field.

S_L area of a loaded region. Equations are given in Column (5) of Table 6.1.6.1-C for determining $2S_L$.

M_a area moment of a control surface about its hinge axis.

$$M_a = \frac{\left(c_{f_r}\right)^2 b_f}{6} \cos \Lambda_{HL} \left(\lambda^2{}_f + \lambda_f + 1\right)$$

where λ_f is the control-surface taper ratio.

η angle of sweep of the line intersecting conical-flow regions of the wing at angle of attack. In reading values of P' and $t_{c.p.}$ from Figures 6.1.6.1-22a through 6.1.6.1-22j, and from Figures 6.1.6.1-34a through 6.1.6.1-34d, $\eta = \Lambda_{HL}$ for conical-flow Regions 5 and 6, and

$\eta = \Lambda_{TE}$ for conical-flow Regions 3 and 4.

The sample problem below illustrates use of the method for obtaining $\left(C_{h_\alpha}\right)_{t/c\,=\,0}$

Sample Problem

Given: A wing-control configuration with the following characteristics:

$A = 6.19$ $\lambda = 0.55$ $b/2 = 6.0$ ft $\Lambda_{LE} = 41.9^{o}$

$\Lambda_{TE} = 27.57^{o}$ $\Lambda_{HL} = 30.85^{o}$ $c_t = 2.75$ ft $c_r = 5.0$ ft

$x_t = 2.20$ ft $x_r = 4.0$ ft $c_{f_t} = 0.606$ ft $c_{f_r} = 0.850$ ft

$b_f = 3.25$ ft $y_i = 2.0$ ft $y_o = 5.25$ ft

Additional Characteristics:

$M = 1.80$; $\beta = 1.4967$

Compute:

Step 1. Determine the wing-root and wing-tip conical-flow case.

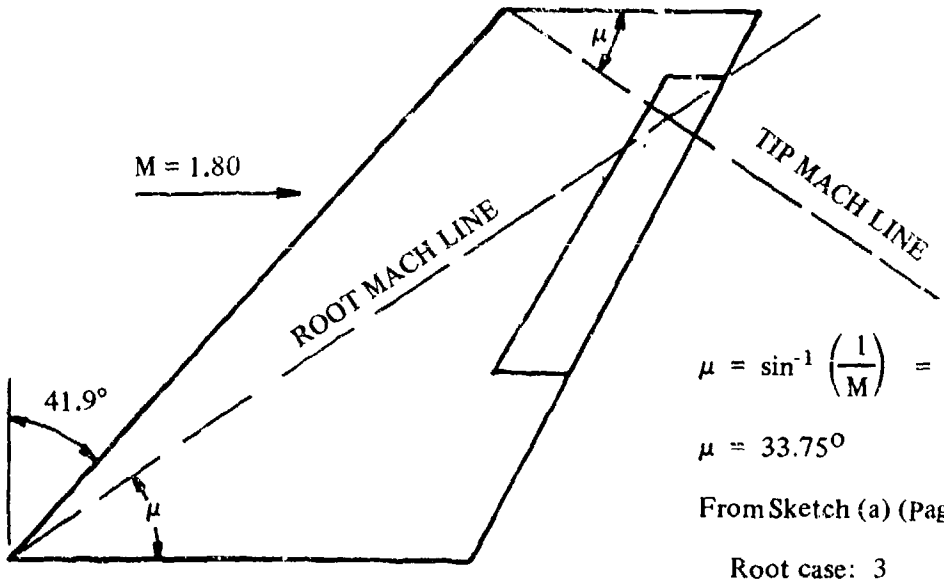

$$\mu = \sin^{-1}\left(\frac{1}{M}\right) = \sin^{-1}\left(\frac{1}{1.80}\right)$$

$\mu = 33.75^{o}$

From Sketch (a) (Page 6.1.6.1-6):

Root case: 3

Tip case: 3

Step 2. Compute the required geometric and Mach-number parameters.

$$g = \frac{\tan \Lambda_{LE}}{\beta} = \frac{0.8972}{1.4967} = 0.5995$$

$$a = \frac{\tan \Lambda_{HL}}{\beta} = \frac{0.5973}{1.4967} = 0.3991$$

$$d = \frac{\tan \Lambda_{TE}}{\beta} = \frac{0.5221}{1.4967} = 0.3488$$

$$K_1 = \beta y_o = (1.4967)(5.25) = 7.8577 \text{ ft}$$

$$K_2 = \beta y_i = (1.4967)(2.0) = 2.9934 \text{ ft}$$

$$K_3 = \beta\left(\frac{b}{2} - y_i\right) = (1.4967)(6.0 - 2.0) = 5.9868 \text{ ft}$$

$$K_4 = \beta\left(\frac{b}{2} - y_o\right) = (1.4967)(6.0 - 5.25) = 1.1225 \text{ ft}$$

$$K_5 = \beta\left(y_o\right)^2 = (1.4967)(5.25)^2 = 41.2528 \text{ sq ft}$$

$$K_6 = \frac{1}{\beta(1 - d)} = \frac{1}{(1.4967)(1 - 0.3488)} = 1.0260$$

$$K_7 = \frac{1}{\beta(1 - a)} = \frac{1}{(1.4967)(1 - 0.3991)} = 1.1119$$

$$K_8 = \beta\left(y_i\right)^2 = (1.4967)(2.0)^2 = 5.9868 \text{ sq ft}$$

$$K_9 = \beta\left(\frac{b}{2} - y_i\right)^2 = (1.4967)(6.0 - 2.0)^2 = 23.9472 \text{ sq ft}$$

$$K_{10} = \frac{1}{\beta(1 + d)} = \frac{1}{(1.4967)(1 + 0.3488)} = 0.4954$$

$$K_{11} = \frac{1}{\beta(1 + a)} = \frac{1}{(1.4967)(1 + 0.3991)} = 0.4775$$

$$K_{12} = \beta\left(\frac{b}{2} - y_o\right)^2 = (1.4967)(6.0 - 5.25)^2 = 0.8419 \text{ sq ft}$$

Step 3. Determine the wing-root and wing-tip conical-flow regions affected.

From the chart of Step 3 of the Datcom method the affected wing-root and wing-tip conical-flow regions are: 3, 5, 7, and 8.

Step 4. Using the computing form, presented as Table 6.1.6.1-C, calculate the pressure-area-moment parameter representing a loss in loading from the two-dimensional loading value of the affected conical-flow Regions.

	Conical-Flow Region	① n or r' See Column ① Table 6.1.6.1-C	② P' See Table 6.1.6.1-C	③ $t_{c.p.}$ See Table 6.1.6.1-C	④ $3x\sqrt{1+\beta^2a^2}$ See Column ④ Table 6.1.6.1-C	⑤ $2S_L$ See Column ⑤ Table 6.1.6.1-C	⑥ $P'\left(3x\sqrt{1+\beta^2a^2}\right)2S_L$ ② ④ ⑤ (cu ft)
ROOT MACH CONE	3	0.6101	0.258	0.736	-2.4978	15.649	-10.085
	5	0.5503	0.245	–	4.00	9.7901	9.5943
	7	1.0191	0.300	0.645	5.1073	6.1011	9.3480
	8	0.7354	0.277	0.695	-5.7755	4.4027	- 7.0435
TIP MACH CONE	3	0.4495	0.280	0.662	-0.9512	1.6840	0.4485
	5	0.2862	0.224	–	2.20	0.6614	0.3259
	7	1.1011	0.314	0.609	2.0177	0.9270	0.5873
	8	0.5608	0.236	0.751	-2.7147	0.4721	- 0.3025
						$\Sigma P'\left(3x\sqrt{1+\beta^2a^2}\right)2S_L = \Sigma$ ⑥ =	1.9760

Solution:

$$2M_a\left[3\sqrt{1+\beta^2a^2}\right] = b_f\,\frac{\left(c_{f_r}\right)^3 - \left(c_{f_t}\right)^3}{c_{f_r} - c_{f_t}} \qquad \text{(Equation 6.1.6.1-f)}$$

$$= 3.25\,\frac{(0.850)^3 - (0.606)^3}{(0.850) - (0.606)} = 5.22 \text{ cu ft}$$

$$\left(C_{h_\alpha}\right)_{t/c\,=\,0} = \frac{-2}{57.3\,\beta\sqrt{1-g^2}}\left\{1 - \frac{\Sigma P'\left(3x\sqrt{1+\beta^2a^2}\right)2S_L}{2M_a\left[3\sqrt{1+\beta^2a^2}\right]}\right\} \qquad \text{(Equation 6.1.6.1-e)}$$

$$= \frac{-2}{(57.3)(1.4967)\left(\sqrt{1-(0.5995)^2}\right)}\left\{1 - \frac{1.9760}{5.22}\right\}$$

$$= -0.0181 \text{ per deg}$$

REFERENCES

1. Toll, T. A., and Schneiter, L. E.: Approximate Relations for Hinge-Moment Parameters of Control Surfaces on Swept wings at Low Mach Numbers. NACA TN 1711, 1948. (U)

2. Thompson, R. F.: Hinge-Moment, Lift, and Pitching-Moment Characteristics of a Flap-Type Control Surface Having Various Hinge-Line Locations on a 4-Percent-Thick 60° Delta Wing – Transonic-Bump Method. NACA RM L54B08, 1954. (U)

3. Thompson, R. F.: Investigation of a 42.7° Sweptback Wing Model to Determine the Effects of Trailing-Edge Thickness on the Aileron Hinge-Moment and Flutter Characteristics at Transonic Speeds. NACA RM L50J06, 1950. (U)

4. Hieser, G.: Transonic Investigation of the Effectiveness and Loading Characteristics of a Flap-Type Aileron With and Without Paddle Balances on an Unswept-Wing-Fuselage Model. NACA RM L56B02, 1956. (U)

5. Runckel, J. F., and Hieser, G.: Normal-Force and Hinge-Moment Characteristics at Transonic Speeds of Flap-Type Ailerons at Three Spanwise Locations on a 4-Percent-Thick Sweptback-Wing-Body Model and Pressure Distribution Measurements on an Inboard Aileron. NASA TN D-842, 1961. (U)

6. Goin, K. L.: Equations and Charts for the Rapid Estimation of Hinge-Moment and Effectiveness Parameters for Trailing-Edge Controls Having Leading and Trailing Edges Swept Ahead of the Mach Lines. NACA TR 1041, 1951. (U)

7. Heaslet, M. A., and Spreiter, J. R.: Reciprocity Relations in Aerodynamics, NACA TN 2700, 1952. (U)

8. Fischel, J., and Schneiter, L. E.: An Investigation at Low Speed of a 51.3° Sweptback Semispan Wing Equipped With 16.7-Percent-Chord Plain Flaps and Ailerons Having Various Spans and Three Trailing-Edge Angles. NACA RM L&H20, 1943. (U)

9. Dods, J. B., Jr.: Wind-Tunnel Investigation of Horizontal Tails. III – Unswept and 35° Swept-back Plan Forms of Aspect Ratio 6. NACA RM A8H30, 1948. (U)

10. Tinling, B. E., and Dickson, J. K.: Tests of a Model Horizontal Tail of Aspect Ratio 4.5 in the Ames 12-Foot Pressure Wind Tunnel. I – Quarter-Chord Line Swept Back 35°. NACA RM A9G13, 1949 (U)

11. Kolbe, C. D., and Bandettini, A.: Investigation in the Ames 12-Foot Pressure Wind Tunnel of a Model Horizontal Tail of Aspect Ratio 3 and Taper Ratio 0.5 Having the Quarter-Chord Line Swept Back 45°. NACA RM A51D02, 1951. (U)

12. Johnson, H. I.: Measurements of Aerodynamic Characteristics of a 35° Sweptback NACA 65-009 Airfoil Model with 1/4-Chord Plain Flap by the NACA Wing-Flow Method. NACA RM L7F13, 1947. (U)

13. Morrill, C. P., Jr., and Boddy, L. E.: High-Speed Stability and Control Characteristics of a Fighter Airplane Model with a Swept-Back Wing and Tail. NACA RM A7K28, 1948. (U)

14. Cleary, J. W., and Boddy, L. E.: Wind-Tunnel Investigation of a 45° Swept-Back Wing Having a Symmetrical Root and a Highly Cambered Tip, Including the Effects of Fences and Lateral Controls. NACA RM A53I21, 1953. (U)

15. Pfyl, F. A.: Aerodynamic Study of a Wing-Fuselage Combination Employing a Wing Swept Back 63° – Effectiveness of an Inboard Elevon as a Longitudinal and Lateral-Control Device at Subsonic and Supersonic Speeds. NACA RM A51I18, 1951. (U)

16. Hammond, A. D.: The Effect of Various Aerodynamic Balances on the Low-Speed Lateral-Control and Hinge-Moment Characteristics of a 0.20-Chord Partial-Span Outboard Aileron on a Wing with Leading Edge Swept Back 51.3° NACA RM L52G03, 1952. (U)

17. Schneiter, L. E., and Hagerman, J. R.: Wind-Tunnel Investigation at High Subsonic Speeds of the Lateral-Control Characteristics of an Aileron and a Stepped Spoiler on a Wing with Leading Edge Swept Back 51.3°. NACA RM L9D06, 1949. (U)

18. Fischel, J., and Schneiter, L. E.: An Investigation at Low Speeds of a 51.3° Sweptback Semispan Wing with a Raked Tip and with 16.7-Percent-Chord Ailerons Having Three Spans and Three Trailing-Edge Angles. NACA RM L8F29, 1948. (U)

19. Dods, J. B., Jr.: Wind-Tunnel Investigation of Horizontal Tails. II – Unswept and 35° Swept-Back Plan Forms of Aspect Ratio 4.5. NACA RM A8B11, 1948. (U)

20. Harper, J. J.: Wind-Tunnel Investigation of Effects of Various Aerodynamic Balance Shapes and Sweepback on Control Surface Characteristics of Semispan Tail Surfaces with NACA 0009, 0015, 66-009, 66(215)-014, and Circular-Arc Airfoil Sections. NACA TN 2495, 1951. (U)

21. Lord, D. R., and Driver, C.: Investigation of the Effect of Balancing Tabs on the Hinge-Moment Characteristics of a Trailing-Edge Flap-Type Control on a Trapezoidal Wing at a Mach Number of 161. NACA RM L54F22, 1954. (U)

22. Sivells, J. C., and Goin, K. L.: Experimental and Calculated Hinge Moments of Two Ailerons on a 42.7° Sweptback Wing at a Mach Number of 1.9. NACA RM L8K24a, 1949. (U)

23. Conner, D. W., and Mitchell, M. H., Jr.: Control Effectiveness and Hinge-Moment Measurements at a Mach Number of 1.9 of a Nose Flap and Trailing-Edge Flap on a Highly Tapered Low-Aspect-Ratio Wing. NACA RM L8K17a, 1949. (U)

24. Lord, D. R., and Czarnecki, K. R.: Aerodynamic Characteristics of Several Flap-Type Trailing-Edge Controls on a Trapezoidal Wing at Mach Numbers of 1.61 and 2.01. NACA RM L54D19, 1954. (U)

25. Spearman, M. L., and Webster, R. A.: An Investigation at Mach Numbers of 1.40 and 1.59 of the Effects of Aileron Profile on the Aerodynamic Characteristics of a Complete Model of a Supersonic Aircraft Configuration. NACA RM L50J31, 1951. (U)

26. Boatright, W. B., and Rainey, R. W.: Hinge-Moment Measurement of a Wing with Leading-Edge and Trailing-Edge Flaps at a Mach Number of 1.93. NACA RM L8K12a, 1949. (U)

27. Dunning, R. W., and Ulman, E. F.: Aerodynamic Characteristics at Mach Number 4.04 of a Rectangular Wing of Aspect Ratio 1.33 having a 6-Percent-Thick Circular-Arc Profile and a 30-Percent-Chord Full-Span Trailing-Edge Flap. NACA RM L53D03, 1953. (U)

28. Robinson, R. L.: An Investigation of a Supersonic Aircraft Configuration having a Tapered Wing with Circular Arc Sections and 40^{0} Sweepback – Static Lateral Control Characteristics at Mach Numbers of 1.40 and 1.59. NACA RM L50I11, 1950. (U)

TABLE 6.1.6.1-A

SUBSONIC HINGE-MOMENT DERIVATIVE DUE TO ANGLE OF ATTACK
DATA SUMMARY AND SUBSTANTIATION

Ref.	M	A	$\Lambda_{c/4}$ (deg)	λ	Type of Control Surface	C_{h_α} Calc	C_{h_α} Test	ΔC_{h_α} Calc-Test
9	0.23	6.0	5.7	0.5	Elevator	−0.00268	−0.0030	0.0003
10	0.21	4.5	35.3	0.5	Elevator	−0.00273	−0.0034	0.0007
	0.6					−0.00209	−0.0028	0.0007
	0.8					−0.00310	−0.0022	−0.0009
	0.85					−0.00365	−0.0016	−0.0021
	0.9					−0.00460	−0.0015	−0.0031
11	0.25	3.0	45.6	0.5	Elevator	−0.00167	−0.0030	0.0013
	0.6					−0.00145	−0.0030	0.0015
	0.8					−0.00231	−0.0027	0.0004
	0.9					−0.00360	−0.0025	−0.0011
12	0.55	3.04	35.0	1.0	Flap	−0.00211	−0.0057	0.0036
	0.8					−0.00368	−0.0045	0.0008
	0.9					−0.00558	−0.0044	−0.0012
13	0.3	4.785	35.22	0.513	Aileron	0.00296	−0.0024	0.0054
	0.6					0.00234	−0.0022	0.0045
	0.8					0.00233	0	0.00233
	0.85					0.00236	−0.002	0.00438
	0.875					0.00241	0	0.00241
	0.9					0.00249	−0.004	0.00649
	0.3	4.65	35.59	0.450	Elevator	0.00154	0	0.00154
	0.6					0.00101	−0.0015	0.0025
	0.8					0.000889	−0.0028	0.0037
	0.85					0.000866	−0.0026	0.0035
	0.875					0.000851	−0.0042	0.0051
	0.9					0.000847	−0.0047	0.0055
4	0.7	4.0	4.8	0.5	Aileron	−0.00418	−0.0013	−0.0029
	0.8					−0.00546	−0.0030	−0.0025
	0.9					−0.00842	0.0013	−0.0097
14	0.25	5.515	45.0	0.532	Aileron	−0.000982	−0.00244	0.00146
	0.8					−0.00280	−0.00195	−0.00085
	0.9					−0.00392	−0.00280	−0.00112
	0.25					−0.000986	−0.00244	0.00145
	0.8					−0.00280	−0.00195	−0.00085
	0.9					−0.00393	−0.0028	−0.0011
15	0.6	3.50	60.8	0.25	Elevon	−0.000858	−0.0039	0.0030
	0.9					−0.00166	−0.0059	0.0042
16	0.328	3.06	38.7	0.49	Aileron	−0.000753	−0.0002	−0.0006
	0.328				Aileron	0.000920	0.0011	−0.0002

TABLE 6.1.6.1-A (CONTD)

Ref.	M	A	$\Lambda_{c/4}$ (deg)	λ	Type of Control Surface	C_{h_α} Calc	C_{h_α} Test	ΔC_{h_α} Calc-Test
17	0.302	3.06	38.7	0.49	Aileron	−0.000713	−0.001	0.0003
	0.499					−0.00113	−0.001	−0.0001
	0.7					−0.00184	−0.001	−0.0008
	0.8					−0.00255	−0.001	−0.0016
8	0.12	3.43	48.6	0.44	Aileron	0.000427	−0.0024	0.0028
						0.000661	−0.0015	0.0022
						0.00124	−0.0011	0.0023
						−0.000303	−0.0025	0.0022
						0.000143	−0.0011	0.0012
						0.00472	0.0015	0.0032
						−0.000214	−0.0015	0.0013
18	0.12	3.58	48.7	0.44	Aileron	−0.00141	−0.0035	0.0021
						0.0000304	−0.0016	0.0016
						0.00351	0.0022	0.0013
						−0.00123	−0.0026	0.0014
						0.000207	−0.0011	0.0013
						0.00369	0.0026	0.0011
						−0.000754	−0.0019	0.0011
						0.000683	−0.0008	0.0015
						0.00417	0.0027	0.0015
19	0.17	4.5	7.6	0.5	Elevator	−0.00240	−0.0020	−0.0004
			35.3			−0.00158	−0.0021	0.0005
20	0.12	3.36	13.5	0.4	Flap	−0.00186	−0.0016	−0.0003
						−0.000532	0	−0.0005
						−0.00118	−0.0003	−0.0009
		3.30	40.0	0.4	Flap	−0.00581	−0.0028	−0.0030
						−0.000417	−0.0012	0.0008
						0.00109	0.0040	−0.0029
						0.000920	0.0039	−0.0030
		3.36	13.5	0.4	Flap	−0.00262	−0.0036	0.0010
						−0.000860	−0.0037	0.0028
						−0.00169	−0.0038	0.0021
						−0.00104	0	−0.00104
						0.0000177	−0.0002	0.00022
						−0.000520	−0.0003	−0.0002
						0.000369	0	0.00037
						0.000800	0.0006	0.0002
						0.000511	0.0004	0.0001
		3.36	13.5	0.4	Flap	0.000181	−0.0022	0.0024
						0.000626	−0.0034	0.0040
						0.000325	−0.0044	0.0047
						0.00374	0.001	0.0027
						0.00283	0.0013	0.0015
						0.00317	0.0008	0.0024

Average $\Delta \left| C_{h_{\alpha_{calc}}} - C_{h_{\alpha_{test}}} \right| = 0.0020$

TABLE 6.1.6.1-B

SUPERSONIC HINGE-MOMENT DERIVATIVE DUE TO ANGLE OF ATTACK
DATA SUMMARY AND SUBSTANTIATION

Ref.	M	A	Λ_{LE} (deg)	λ	C_{h_α} Calc	C_{h_α} Test	$\Delta (C_{h_\alpha})$ Calc-Test
21	1.61	3.1	23	0.4	–0.0193	–0.0183	–0.001
22	1.9	4.0	42.7	0.5	–0.0177	–0.010	–0.0077
″	″	″	″	″	–0.0177	–0.014	–0.0037
23	1.9	1.06	45	0.31	–0.0056	–0.003	–0.0026
24	1.61	3.1	23	0.4	–0.0278	–0.0133	–0.0145
″	″	″	″	″	–0.0203	–0.020	–0.0003
″	″	″	″	″	–0.0222	–0.019	–0.0032
″	″	″	″	″	–0.0193	–0.0175	–0.0018
″	″	″	″	″	–0.0215	–0.023	0.0015
″	″	″	″	″	–0.0236	–0.0217	–0.0019
″	2.01	″	″	″	–0.0168	–0.0163	–0.0005
″	″	″	″	″	–0.0172	–0.015	–0.0022
″	″	″	″	″	–0.0154	–0.0146	–0.0008
25	1.59	4.0	42.7	0.5	–0.0108	–0.012	0.0012
″	″	″	″	″	–0.0108	–0.012	0.0012
″	″	″	″	″	–0.0108	–0.013	0.0022
″	″	″	″	″	–0.0108	–0.017	0.0062
26	1.93	3.14	9.33	0.59	–0.0127	–0.009	–0.0037
27	4.04	1.33	0	1.0	–0.00479	–0.006	0.00121
28	1.59	1.0	42.7	0.5	–0.0107	–0.0163	0.0056
	1.59	1.17	40.6	0.337	–0.0041	–0.0043	0.0002

Average $\Delta \left| C_{h_{\alpha_{calc}}} - C_{h_{\alpha_{test}}} \right| = 0.00301$

TABLE 6.1.6.1–C
COMPUTING FORM FOR SUMMING PRESSURE-AREA-MOMENT PARAMETER OF TRIANGULAR SEGMENTS OF WING-ROOT AND WING-TIP CONICAL-FLOW REGIONS

	Figures for Determining Columns ② & ③	Conical-Flow Region	① Enter Figure at Following Value of n or r′	② P′	③ $t_{c.p.}$	④ Value of $3x\sqrt{1+\beta^2 a^2}$	⑤ Value of $2S_L$	⑥ $P'\left(3x\sqrt{1+\beta^2 a^2}\right)2S_L$ (cu ft)
ROOT MACH CONE	6.1.6.1–22k through 6.1.6.1–22ℓ	1	$r' = \frac{c_r}{K_1} \cdot (1-d)$			$\frac{2K_1(1-at_{c.p.})}{t_{c.p.}} \cdot 3x_r$	①K_5	
		2	$r' = \frac{x_r}{K_1} \cdot (1-a)$			$3x_r \cdot \frac{2K_1(1-at_{c.p.})}{t_{c.p.}}$	①K_5	
	6.1.6.1–22a through 6.1.6.1–22j	3	$n = 1-\frac{K_2}{c_r}(1-d)$			$\frac{2c_r(1-at_{c.p.})}{(1-dt_{c.p.})} \cdot 3x_r$	①$(c_r)^2K_6$	
		4	$n = 1-\frac{K_1}{c_r}(1-d)$			$3x_r \cdot \frac{2c_r(1-at_{c.p.})}{(1-dt_{c.p.})}$	①$(c_r)^2K_6$	
	6.1.6.1–22a through 6.1.6.1–22j	5	$n = 1-\frac{K_2}{x_r}(1-a)$		–	x_r	①$(x_r)^2K_7$	
		6	$n = 1-\frac{K_1}{x_r}(1-a)$		–	$-x_r$	①$(x_r)^2K_7$	
	6.1.6.1–22k through 6.1.6.1–22ℓ	7	$r' = \frac{c_r}{K_2} \cdot (1-d)$			$3x_r \cdot \frac{2K_2(1-at_{c.p.})}{t_{c.p.}}$	①K_8	
		8	$r' = \frac{x_r}{K_2} \cdot (1-a)$			$\frac{2K_2(1-at_{c.p.})}{t_{c.p.}} \cdot 3x_r$	①K_8	
TIP MACH CONE	6.1.6.1–34e through 6.1.6.1–34f	1	$r' = \frac{c_t}{K_3} \cdot (1+d)$			$\frac{2K_3(1+at_{c.p.})}{t_{c.p.}} \cdot 3x_t$	①K_9	
		2	$r' = \frac{x_t}{K_3} \cdot (1+a)$			$3x_t \cdot \frac{2K_3(1+at_{c.p.})}{t_{c.p.}}$	①K_9	
	6.1.6.1–34a through 6.1.6.1–34d	3	$n = 1-\frac{K_4(1+d)}{c_t}$			$\frac{2c_t(1+at_{c.p.})}{(1+dt_{c.p.})} \cdot 3x_t$	①$(c_t)^2K_{10}$	
		4	$n = 1-\frac{K_3(1+d)}{c_t}$			$3x_t \cdot \frac{2c_t(1+at_{c.p.})}{(1+dt_{c.p.})}$	①$(c_t)^2K_{10}$	
	6.1.6.1–34a through 6.1.6.1–34d	5	$n = 1-\frac{K_4(1+a)}{x_t}$		–	x_t	①$(x_t)^2K_{11}$	
		6	$n = 1-\frac{K_3(1+a)}{x_t}$		–	$-x_t$	①$(x_t)^2K_{11}$	
	6.1.6.1–34e through 6.1.6.1–34f	7	$r' = \frac{c_t}{K_4} \cdot (1+d)$			$3x_t \cdot \frac{2K_4(1+at_{c.p.})}{t_{c.p.}}$	①K_{12}	
		8	$r' = \frac{x_t}{K_4} \cdot (1+a)$			$\frac{2K_4(1+at_{c.p.})}{t_{c.p.}} \cdot 3x_t$	①K_{12}	
						$\Sigma P'\left(3x\sqrt{1+\beta^2 a^2}\right)2S_L =$		

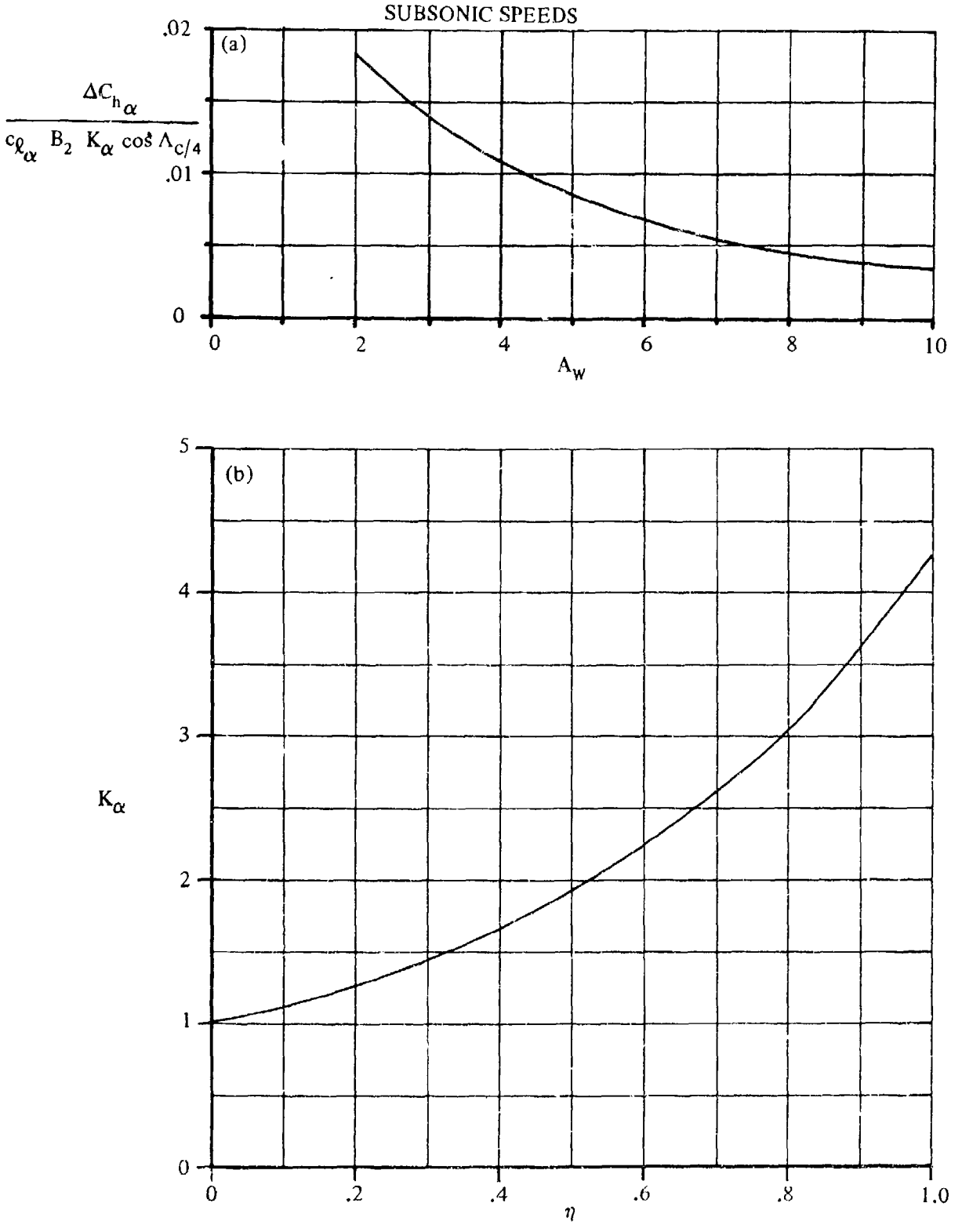

FIGURE 6.1.6.1-19 CHARTS FOR INDUCED-CAMBER CORRECTIONS TO HINGE-MOMENT PARAMETERS OF FINITE-SPAN WINGS

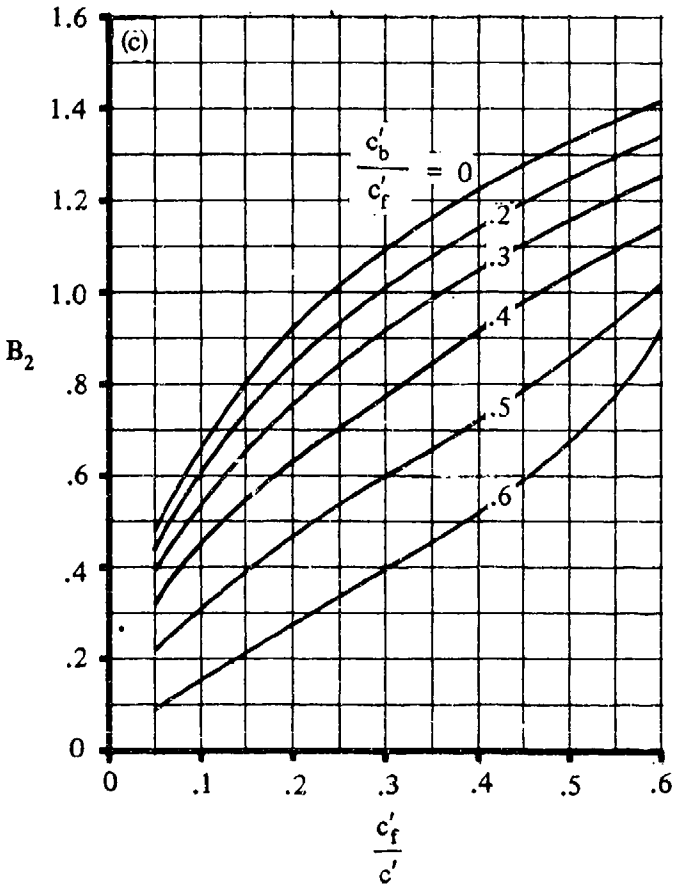

FIGURE 6.1.6.1-19 (CONTD)

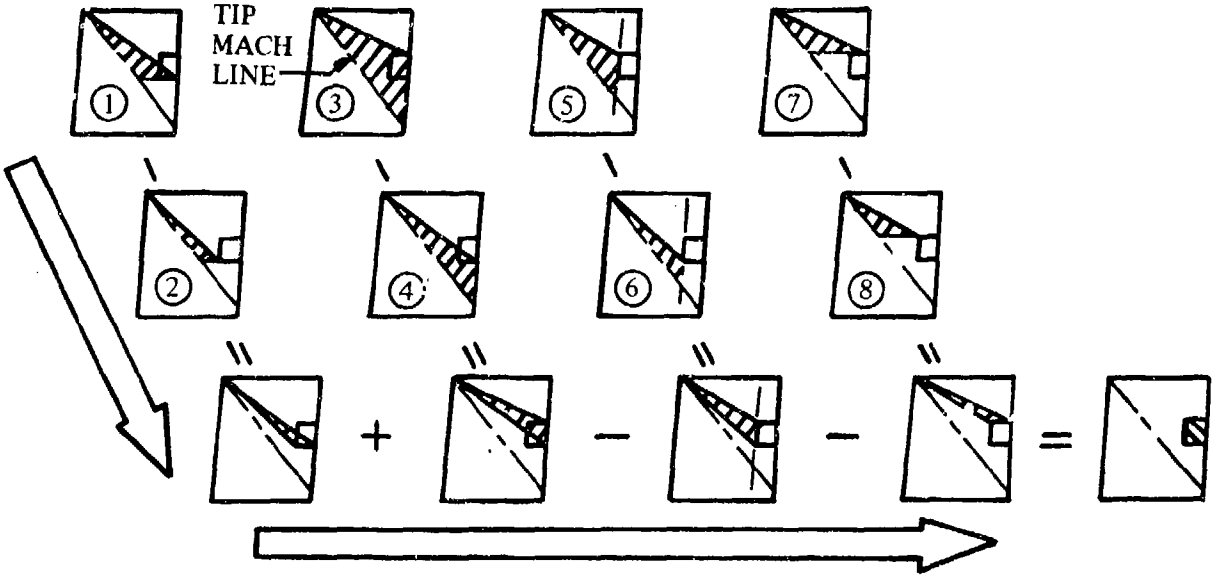

TIP CONICAL-FLOW REGIONS

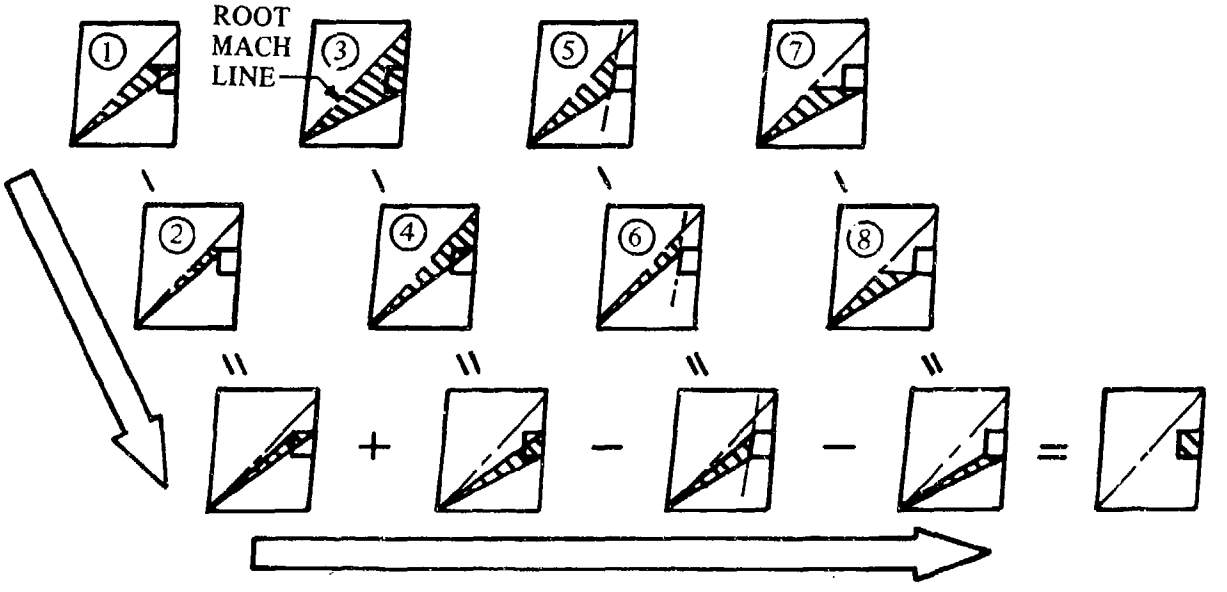

ROOT CONICAL-FLOW REGIONS

Arrows show procedure for summing pressure-area-moment parameter. (Encircled numbers correspond to regions as designated in computing form for pressure-area-moment parameter.) Table 6.1.6.1-A

FIGURE 6.1.6.1-21 DEFINITION OF CONICAL-FLOW REGIONS

(a) $\frac{\text{TAN } \Lambda_{LE}}{\beta} = 0.10$

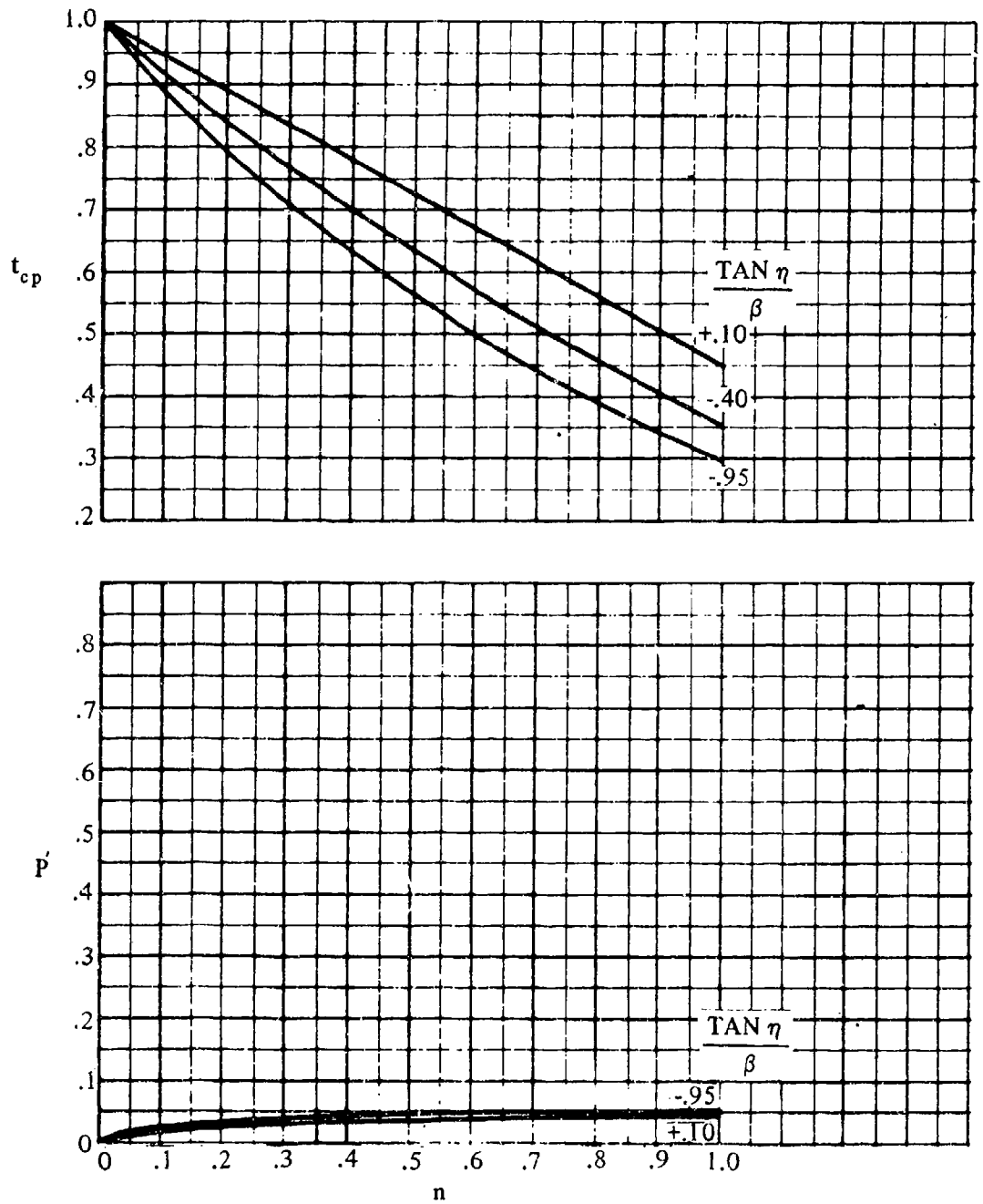

FIGURE 6.1.6.1-22 LOADING DISTRIBUTIONS IN THE CONICAL-FLOW REGIONS INTERSECTING THE WING-ROOT MACH CONE

(b) $\frac{\text{TAN } \Lambda_{LE}}{\beta} = 0.20$

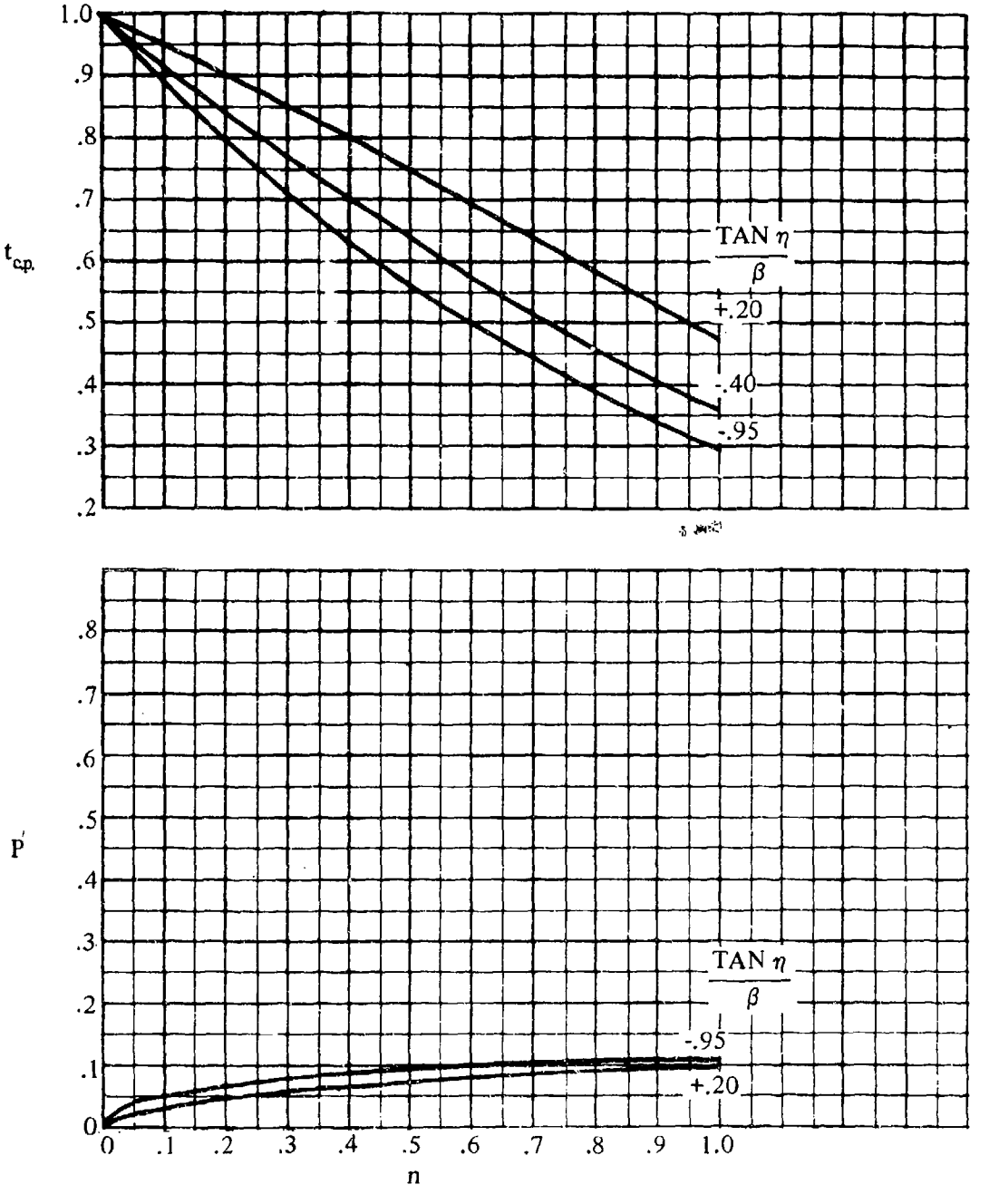

FIGURE 6.1.6.1-22 (CONTD)

(c) $\frac{\text{TAN } \Lambda_{LE}}{\beta} = 0.30$

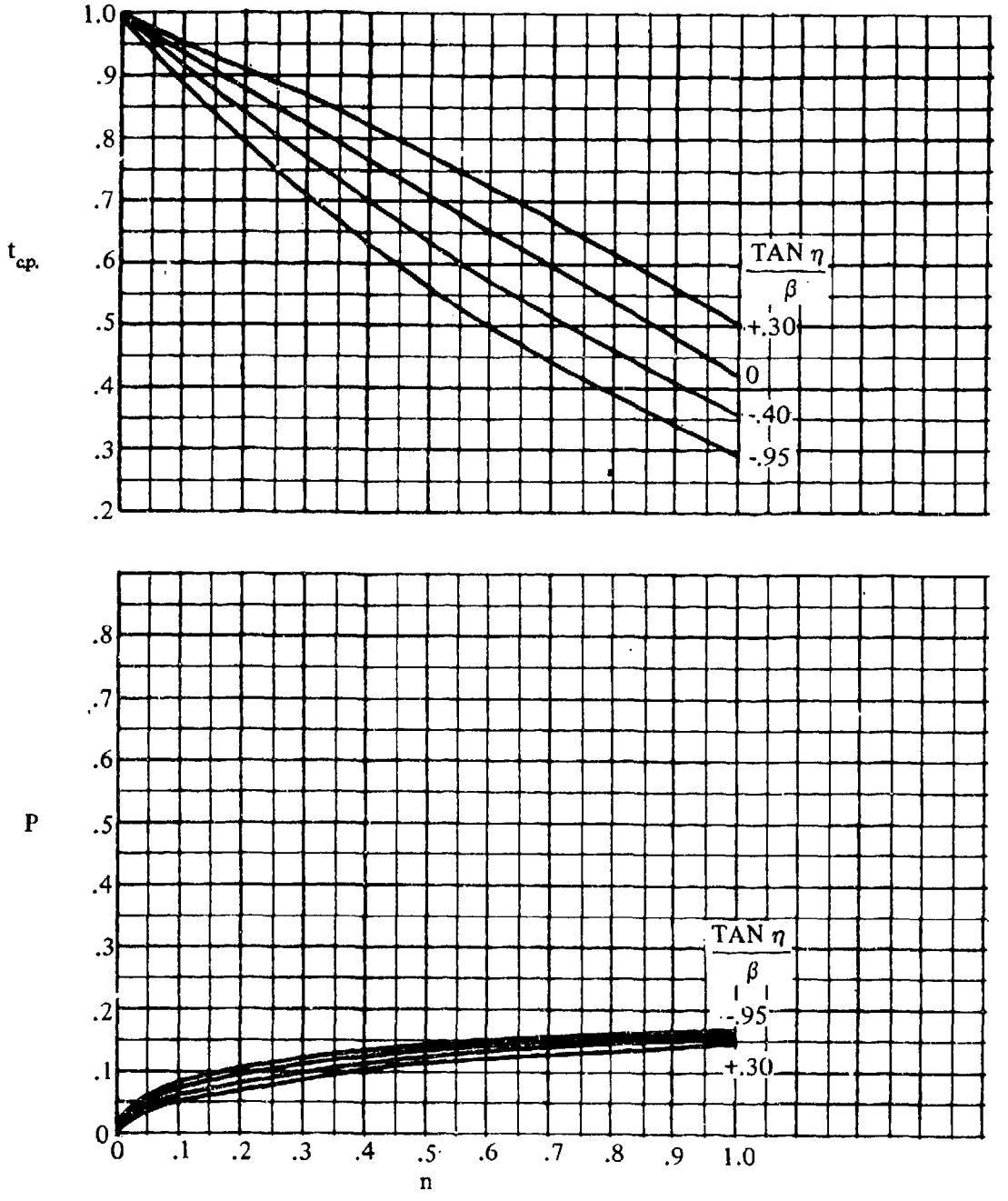

FIGURE 6.1.6.1-22 (CONTD)

SUPERSONIC SPEEDS

(d) $\frac{\text{TAN } \Lambda_{LE}}{\beta} = 0.40$

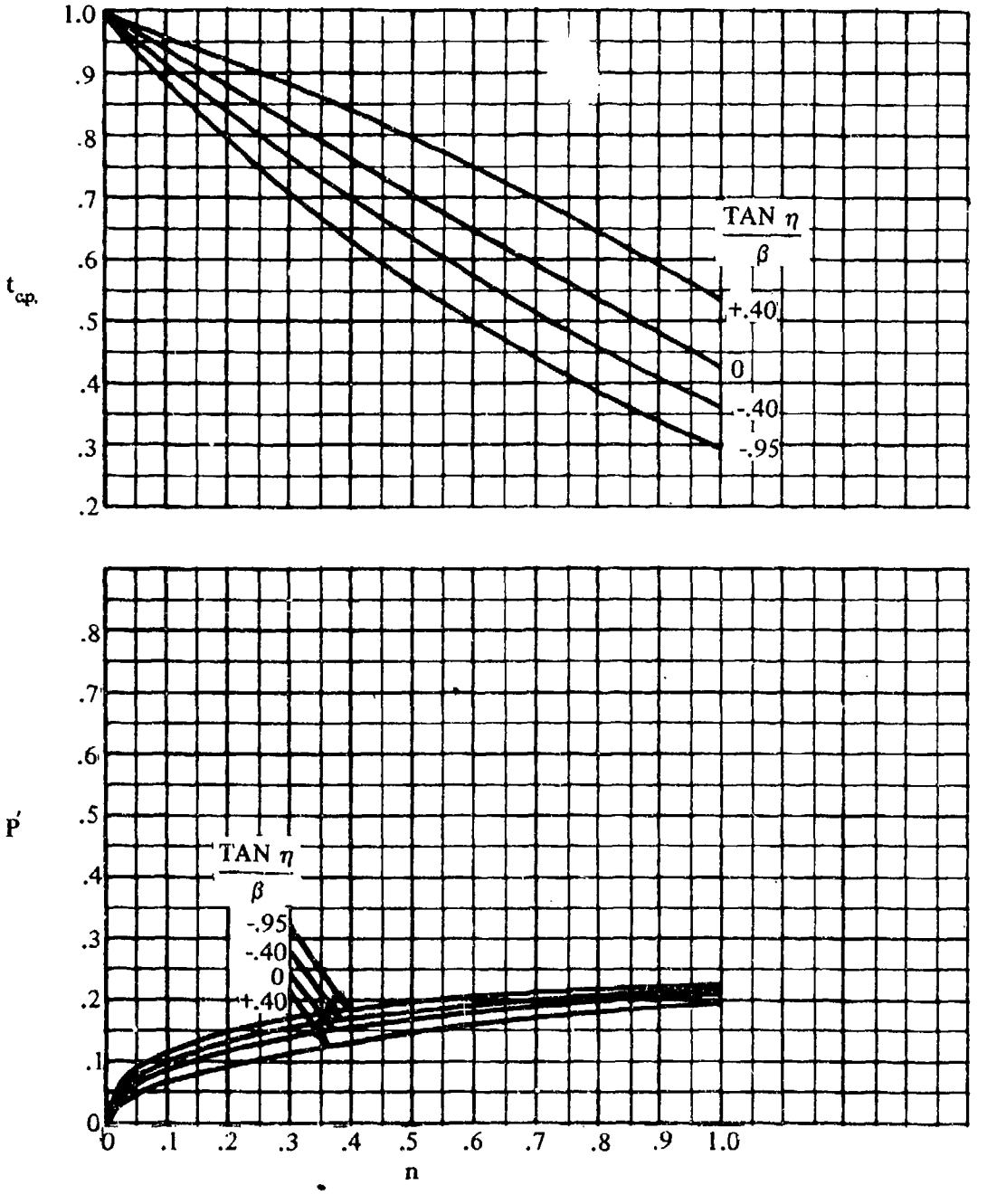

FIGURE 6.1.6.1-22 (CONTD)

SUPERSONIC SPEEDS

(e) $\frac{\text{TAN } \Lambda_{LE}}{\beta} = 0.50$

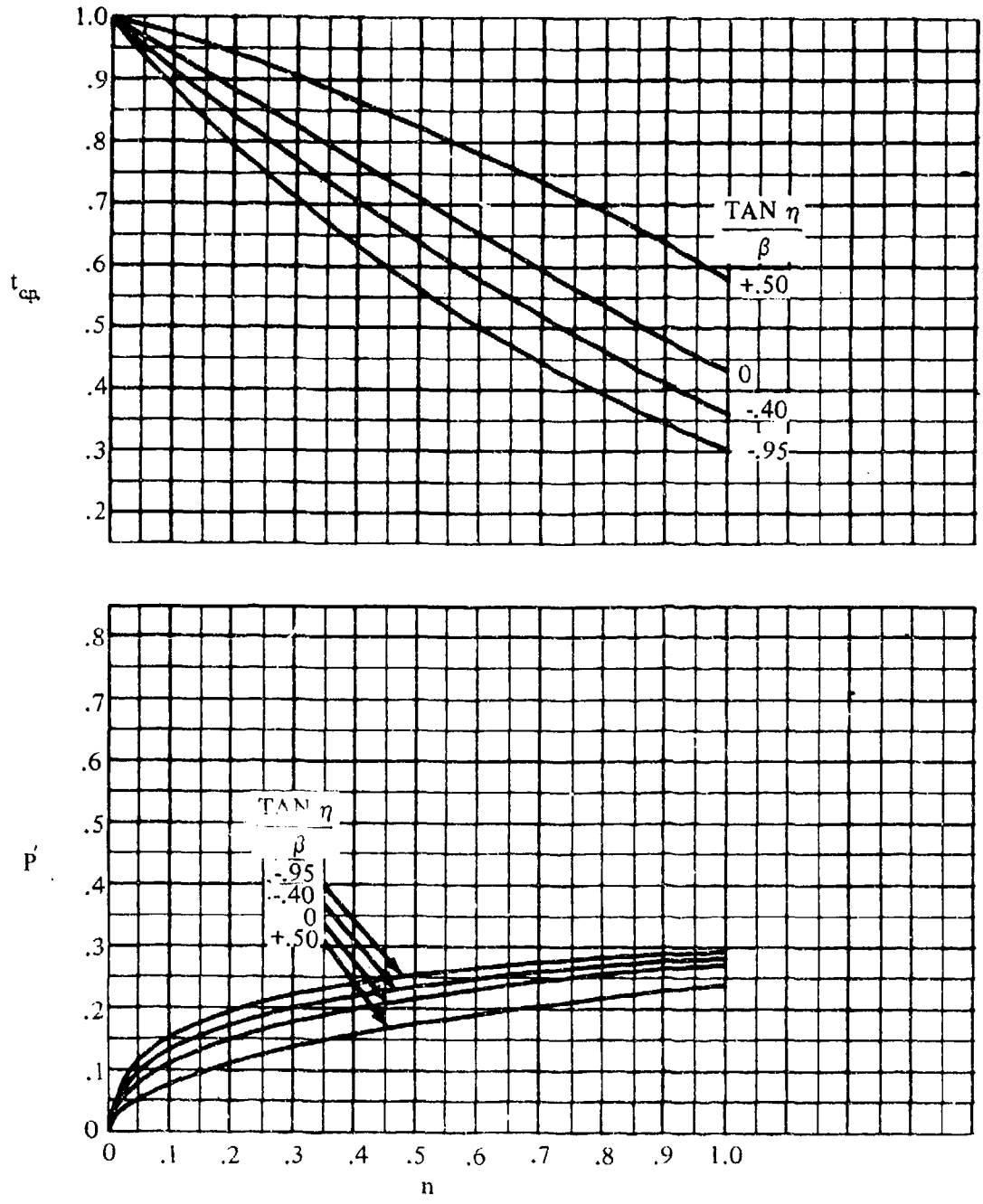

FIGURE 6.1.6.1-22 (CONTD)

SUPERSONIC SPEEDS

(f) $\frac{\text{TAN } \Lambda_{LE}}{\beta} = 0.60$

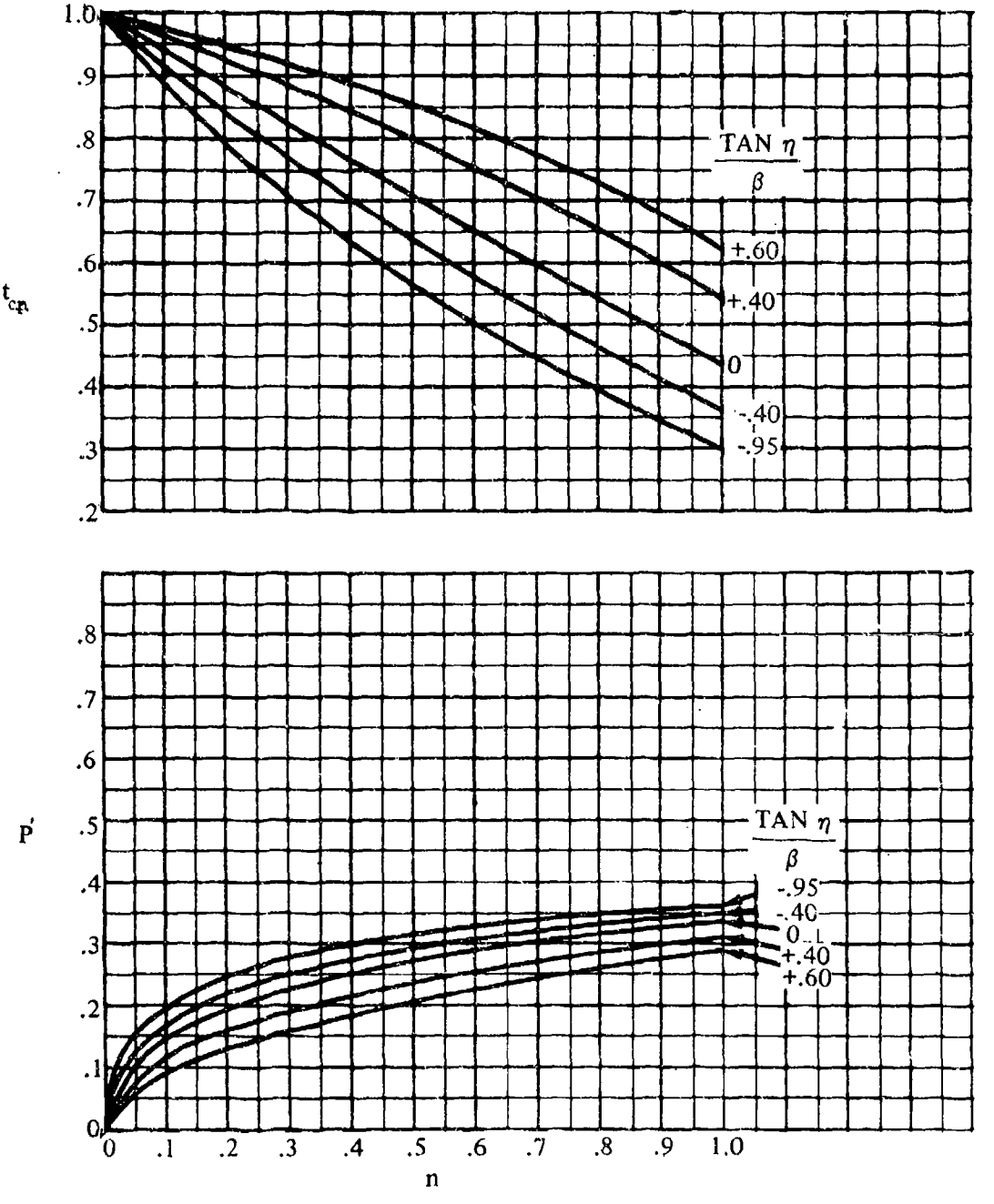

FIGURE 6.1.6.1-22 (CONTD)

SUPERSONIC SPEEDS

(g) $\frac{\text{TAN } \Lambda_{LE}}{\beta} = 0.70$

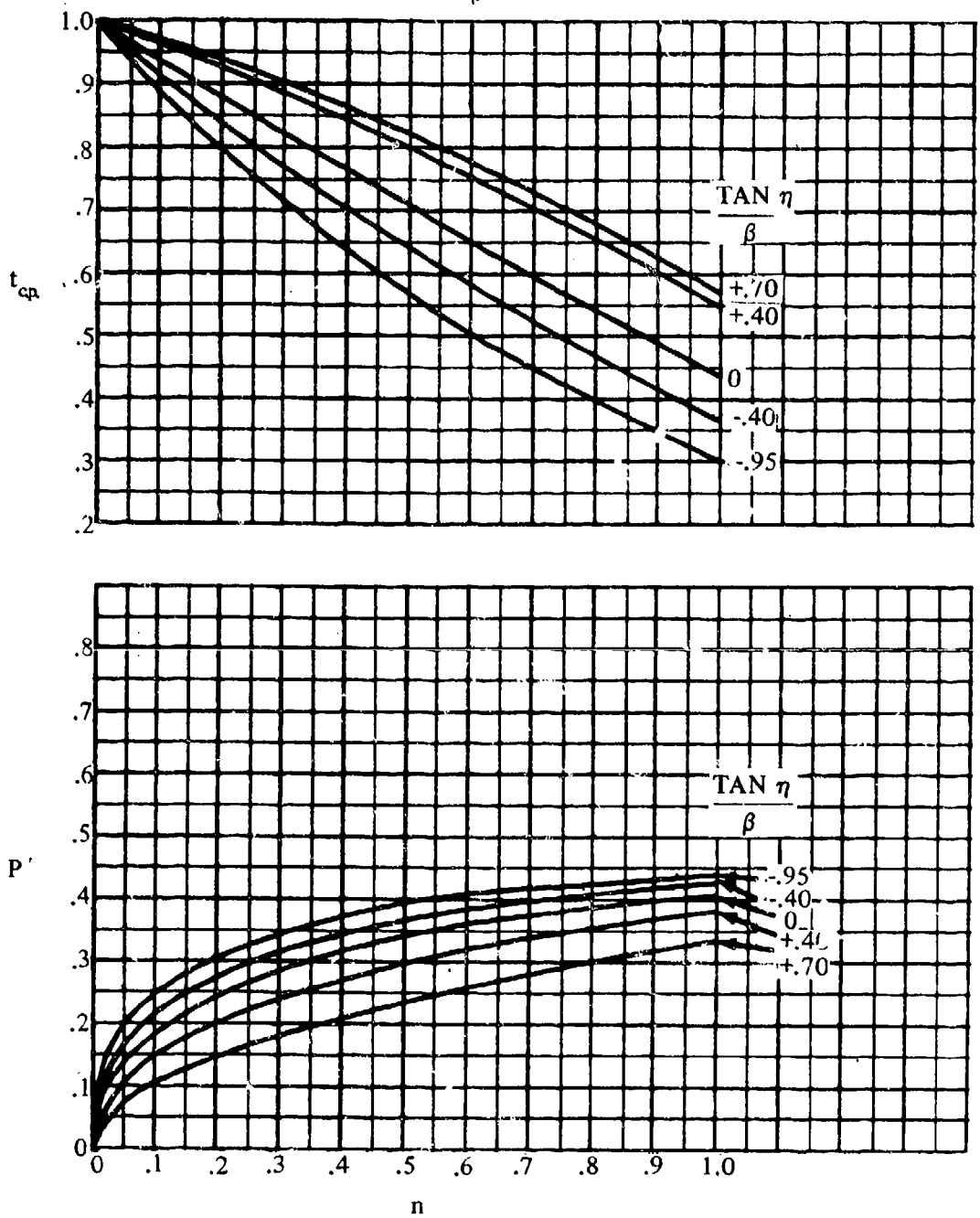

FIGURE 6.1.6.1-22 (CONTD)

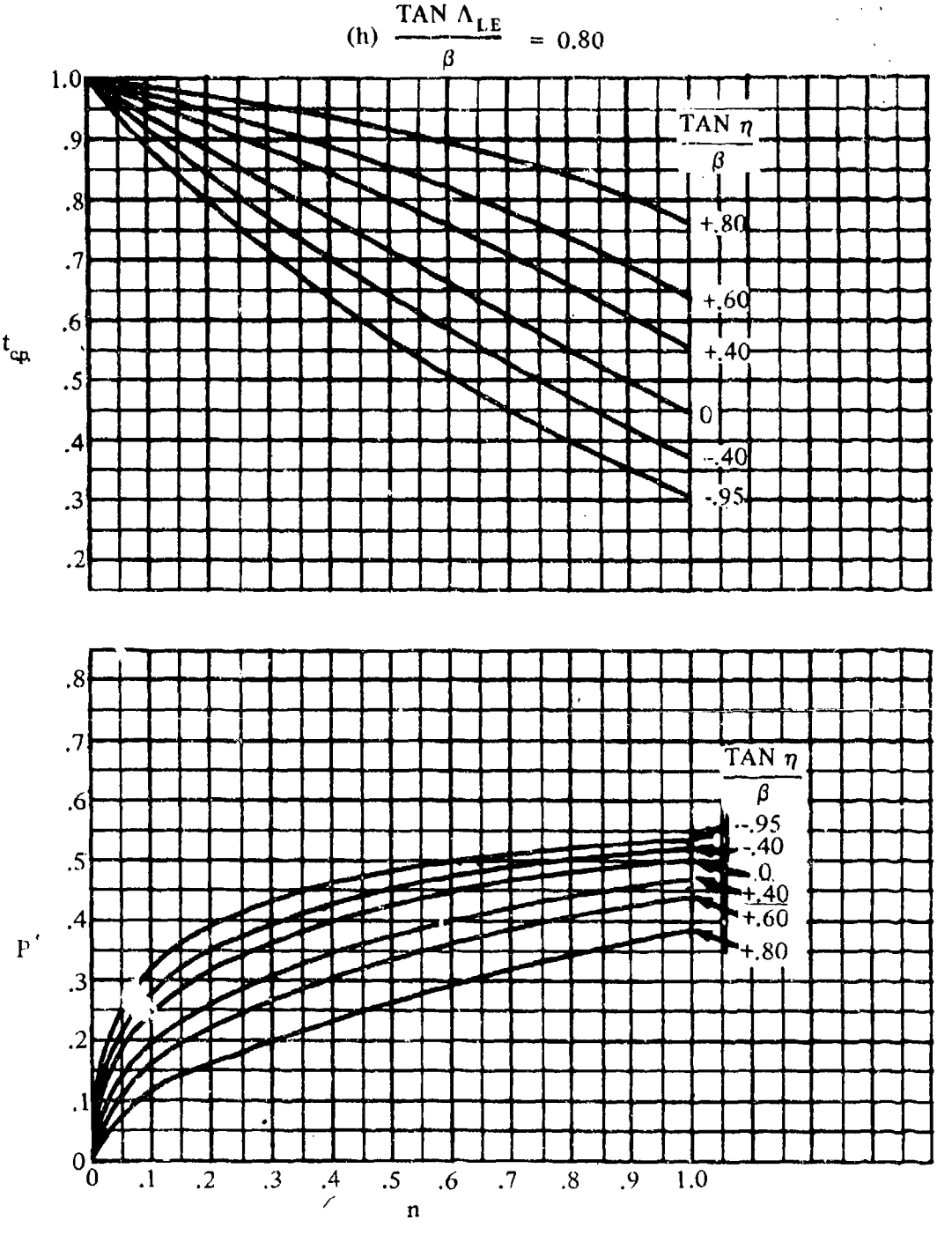

FIGURE 6.1.6.1-22 (CONTD)

SUPERSONIC SPEEDS

(i) $\frac{\text{TAN } \Lambda_{LE}}{\beta} = 0.90$

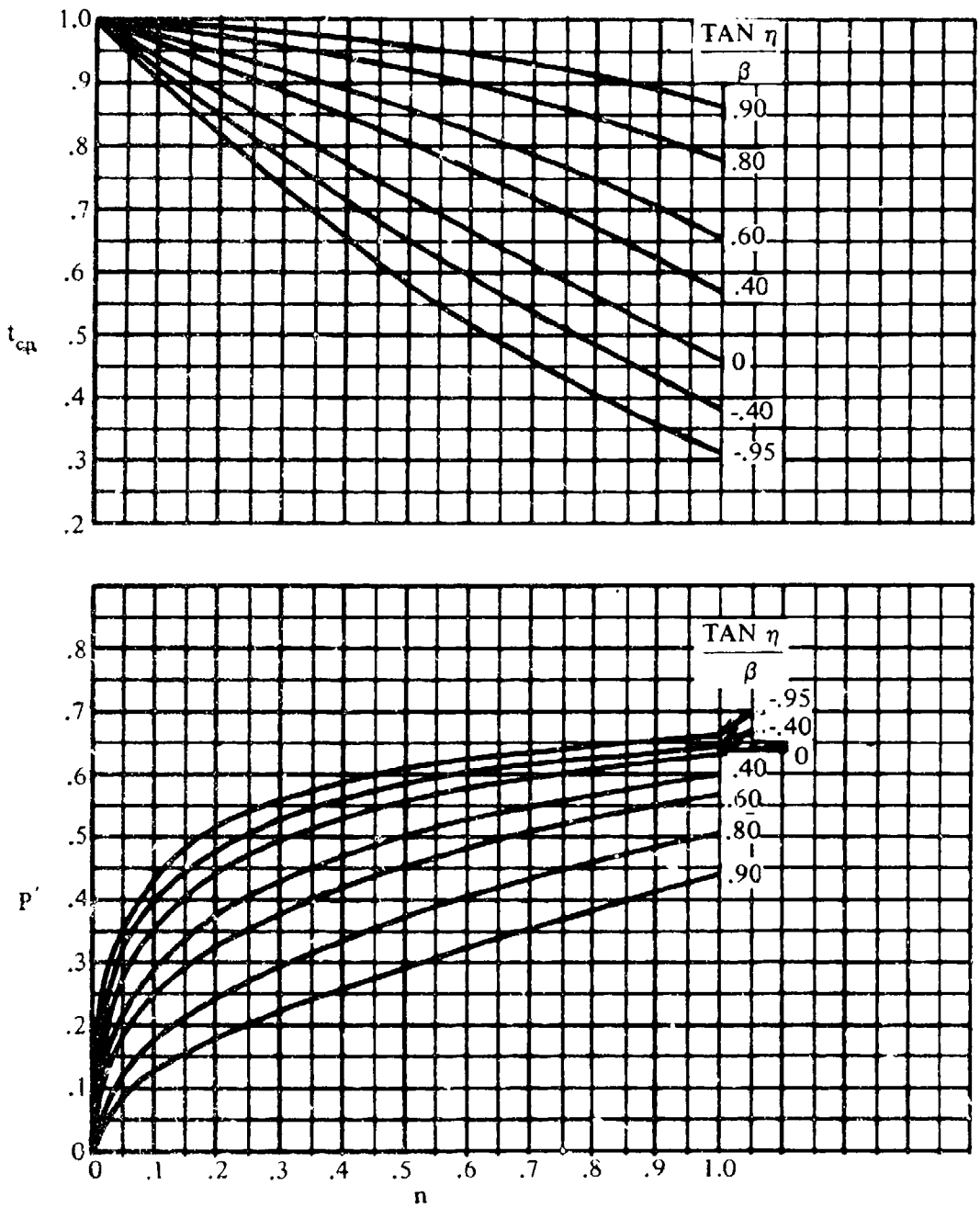

FIGURE 6.1.6.1-22 (CONTD)

SUPERSONIC SPEEDS

(j) $\frac{\text{TAN } \Lambda_{LE}}{\beta} = 0.95$

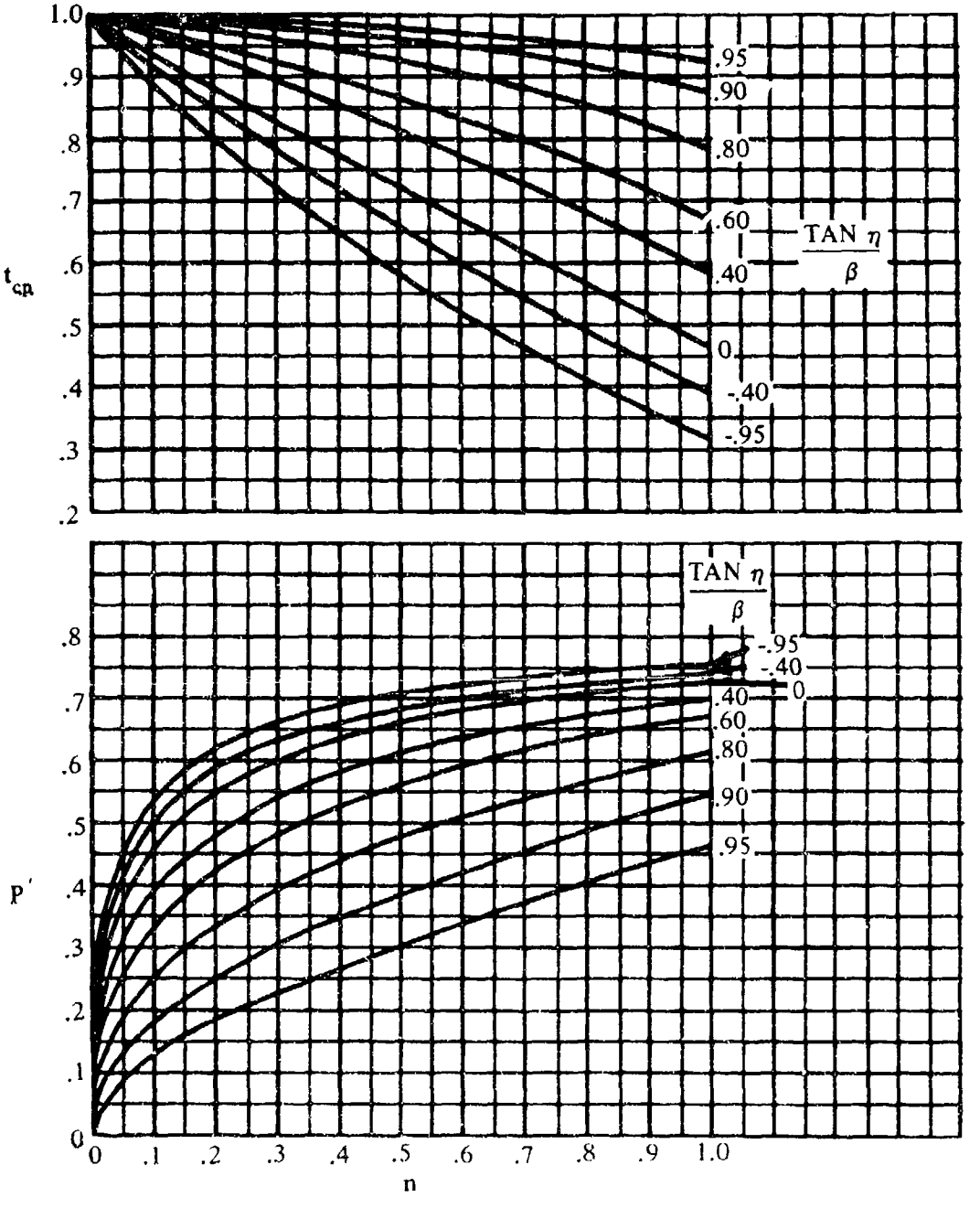

FIGURE 6.1.6.1-22 (CONTD)

SUPERSONIC SPEEDS

(k) r′ = 0 TO 1.0

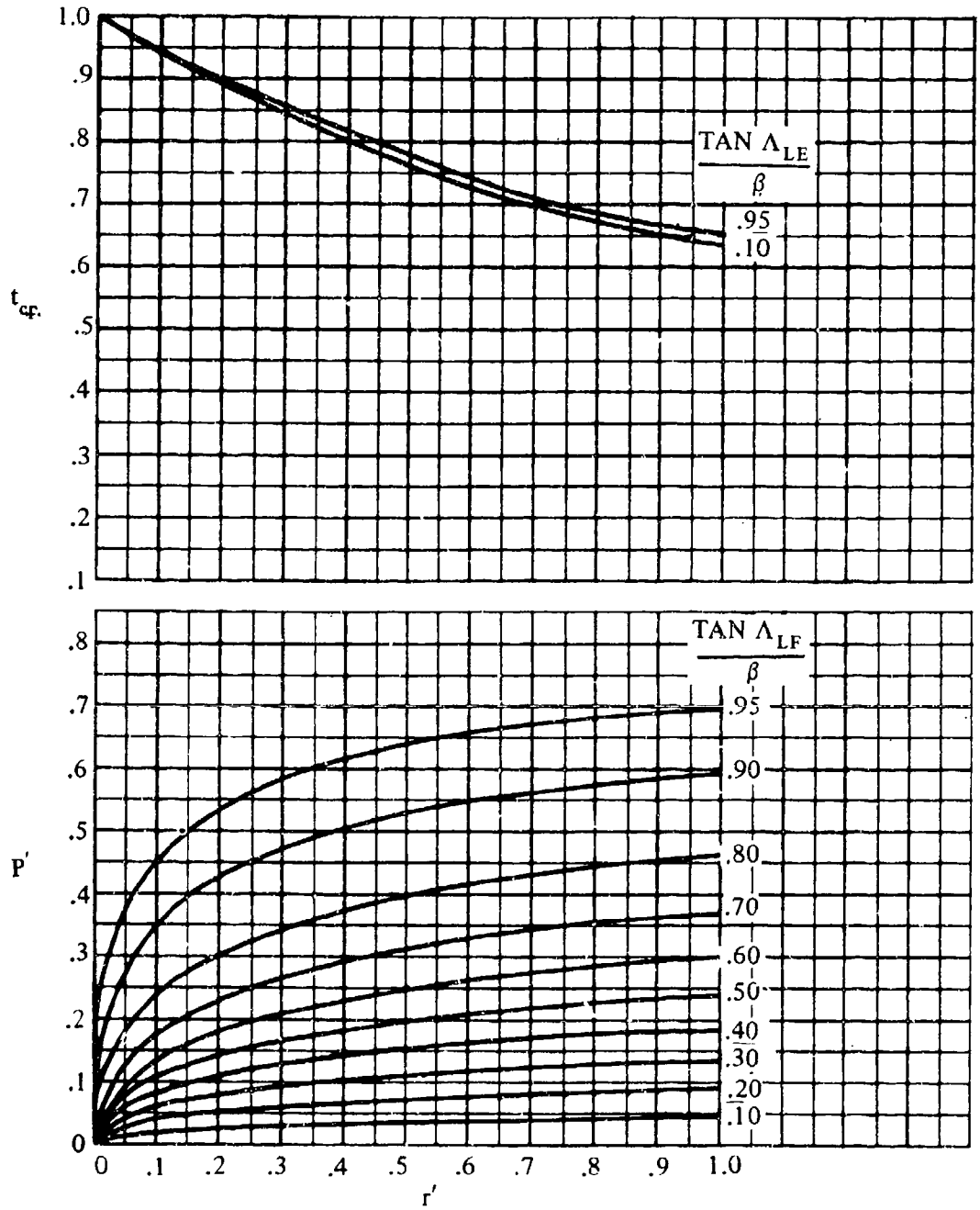

FIGURE 6.1.6.1-22 (CONTD)

SUPERSONIC SPEEDS

(ℓ) r′ = 1.0 TO 10.0

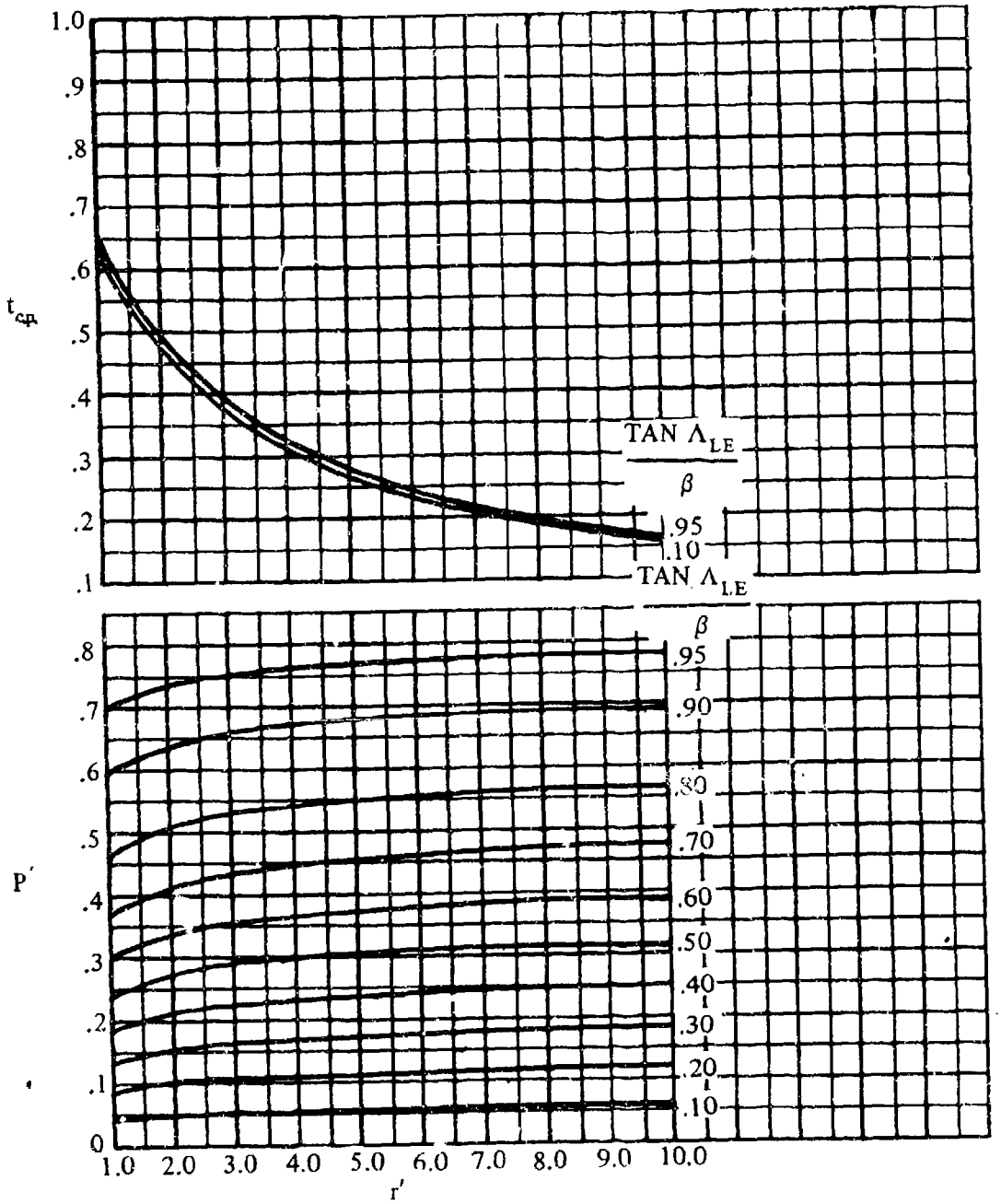

FIGURE 6.1.6.1-22 (CONTD)

SUPERSONIC SPEEDS

(a) $\frac{\text{TAN } \Lambda_{LE}}{\beta} = 0$

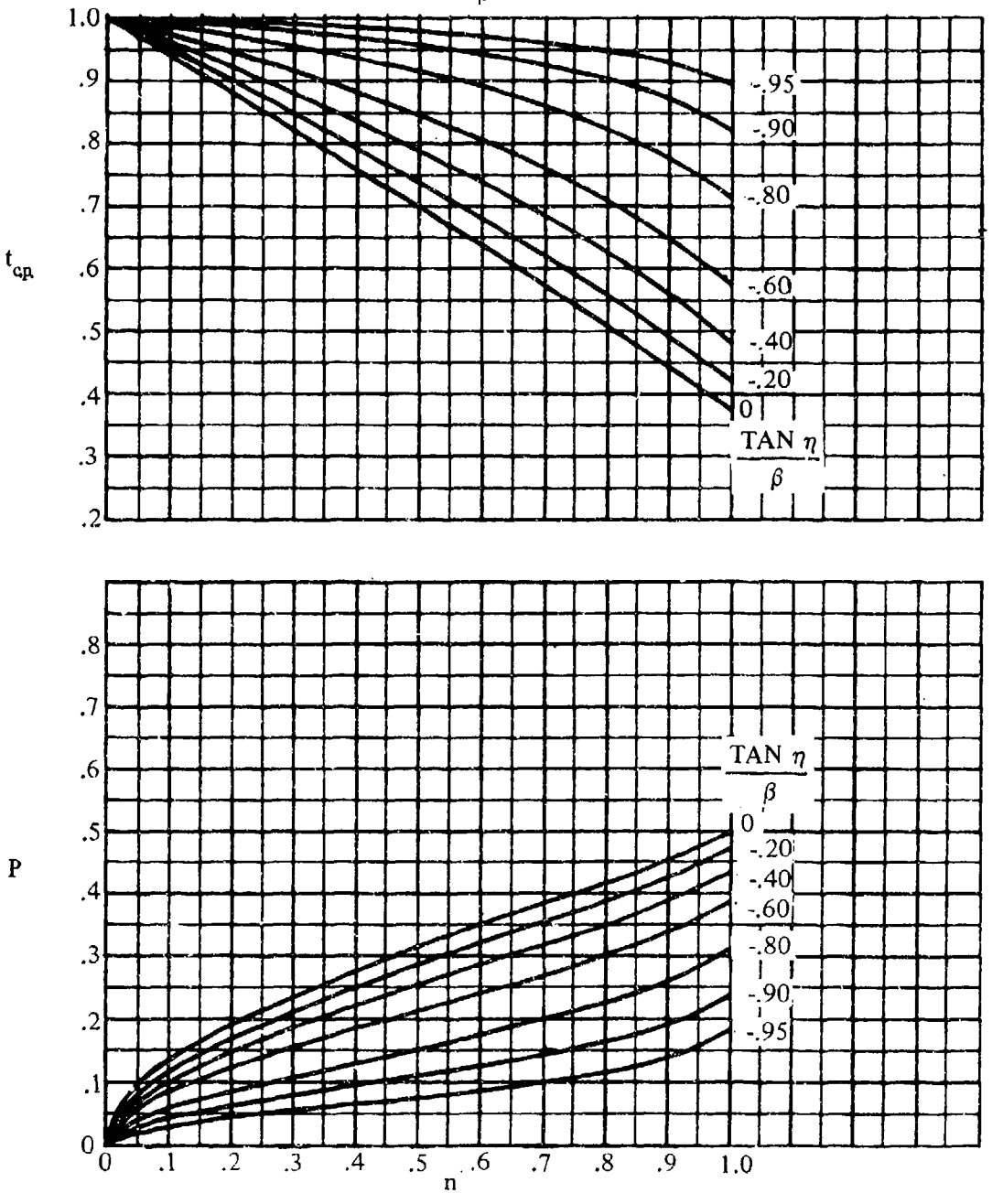

FIGURE 6.1.6.1-34 LOADING DISTRIBUTION IN THE CONICAL-FLOW REGIONS INTERSECTING THE WING-TIP MACH CONE

SUPERSONIC SPEEDS

(b) $\frac{\text{TAN } \Lambda_{LE}}{\beta} = 0.20$

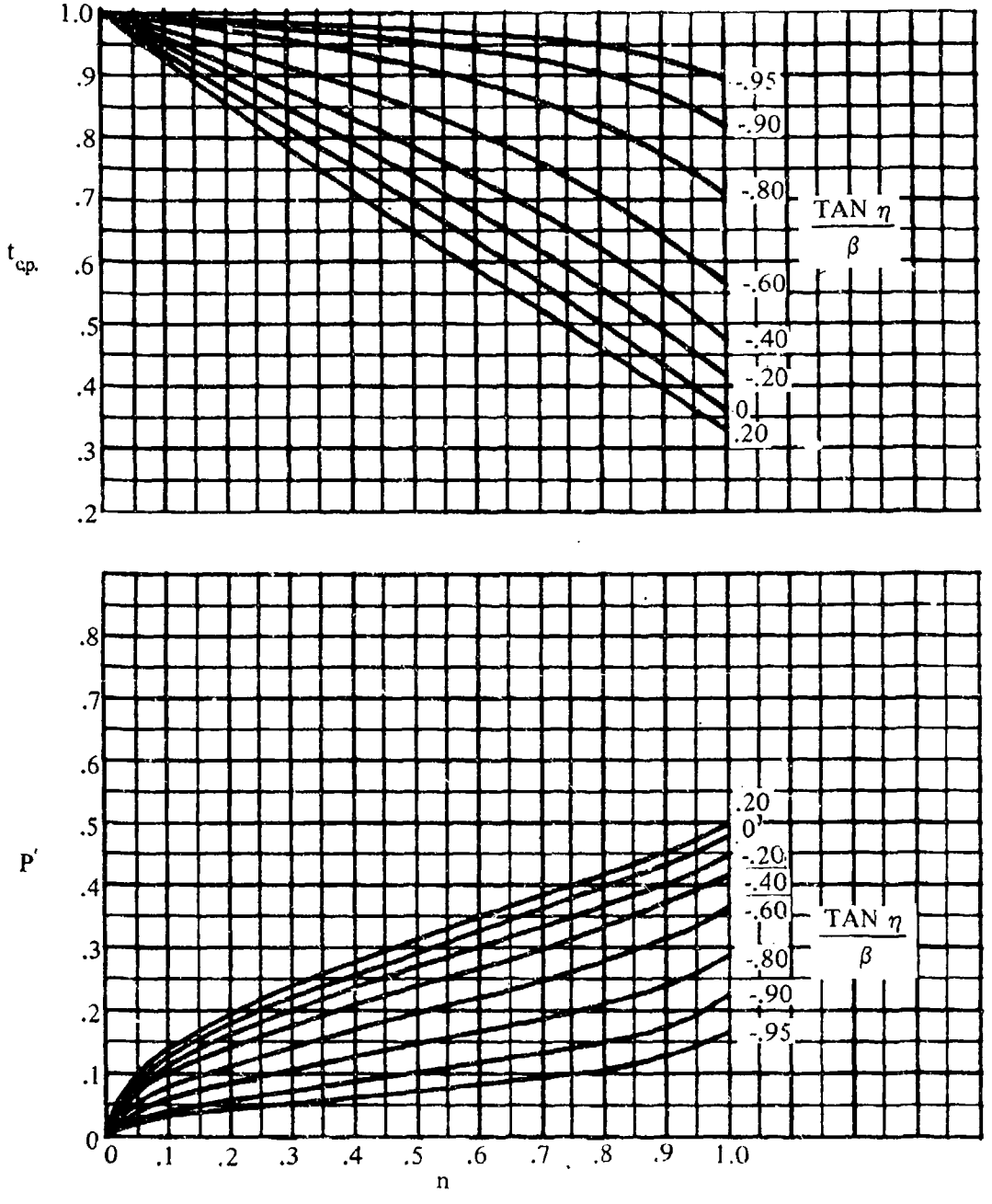

FIGURE 6.1.6.1-34 (CONTD)

SUPERSONIC SPEEDS

(c) $\frac{\text{TAN } \Lambda_{LE}}{\beta} = 0.50$

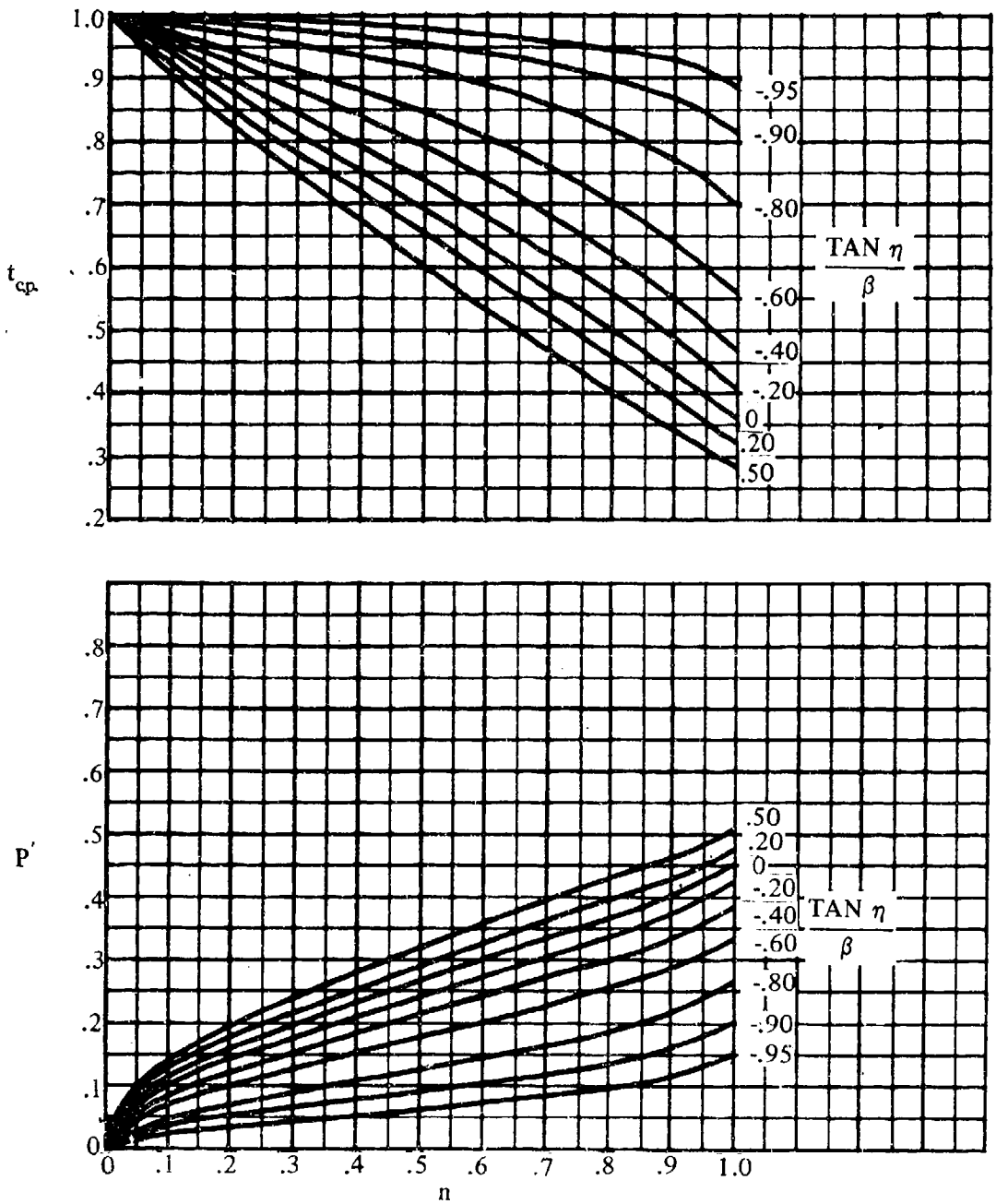

FIGURE 6.1.6.1-34 (CONTD)

SUPERSONIC SPEEDS

(d) $\frac{\text{TAN } \Lambda_{LE}}{\beta} = 0.95$

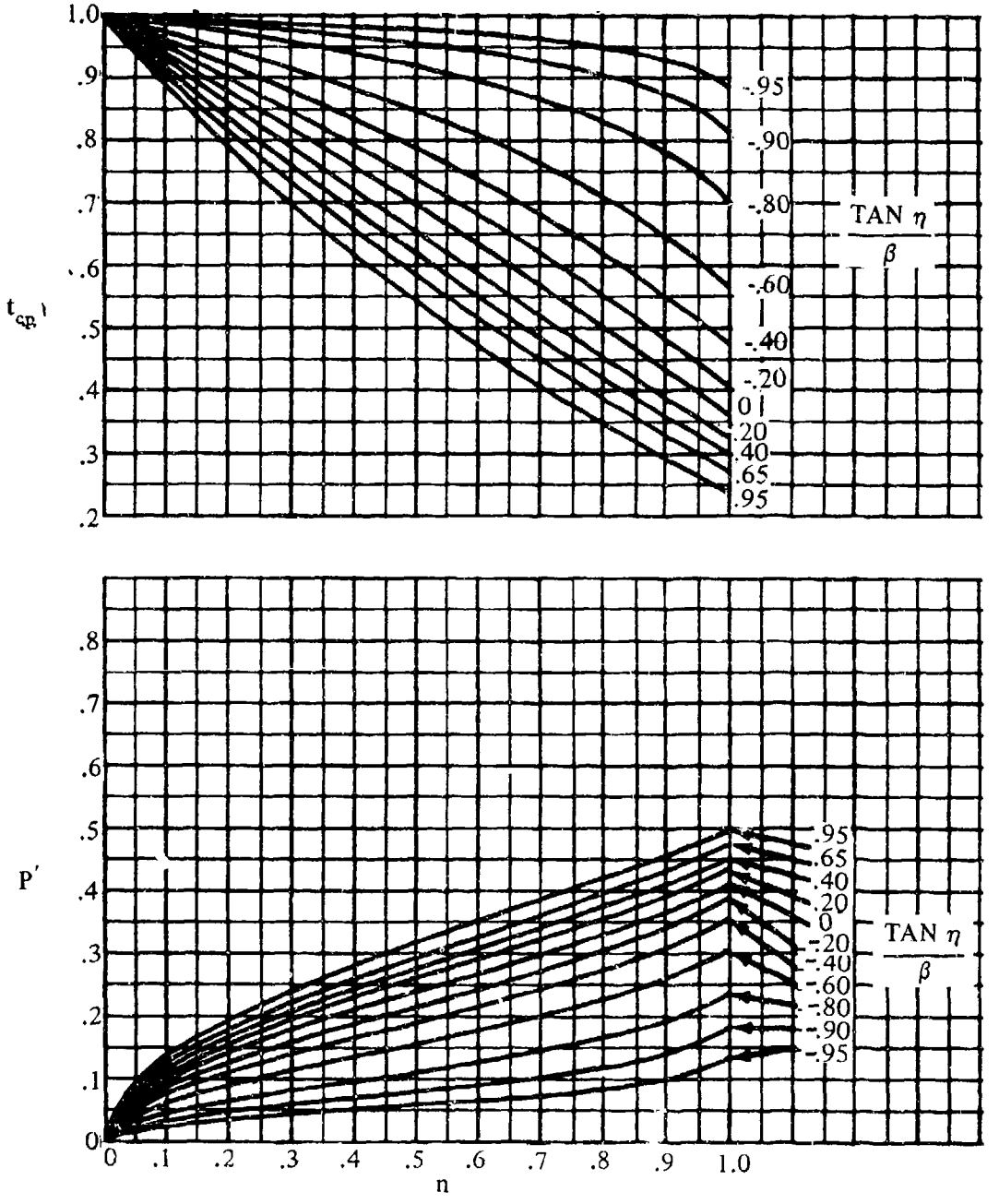

FIGURE 6.1.6.1-34 (CONTD)

SUPERSONIC SPEEDS

(e) $r' = 0$ TO 1.0

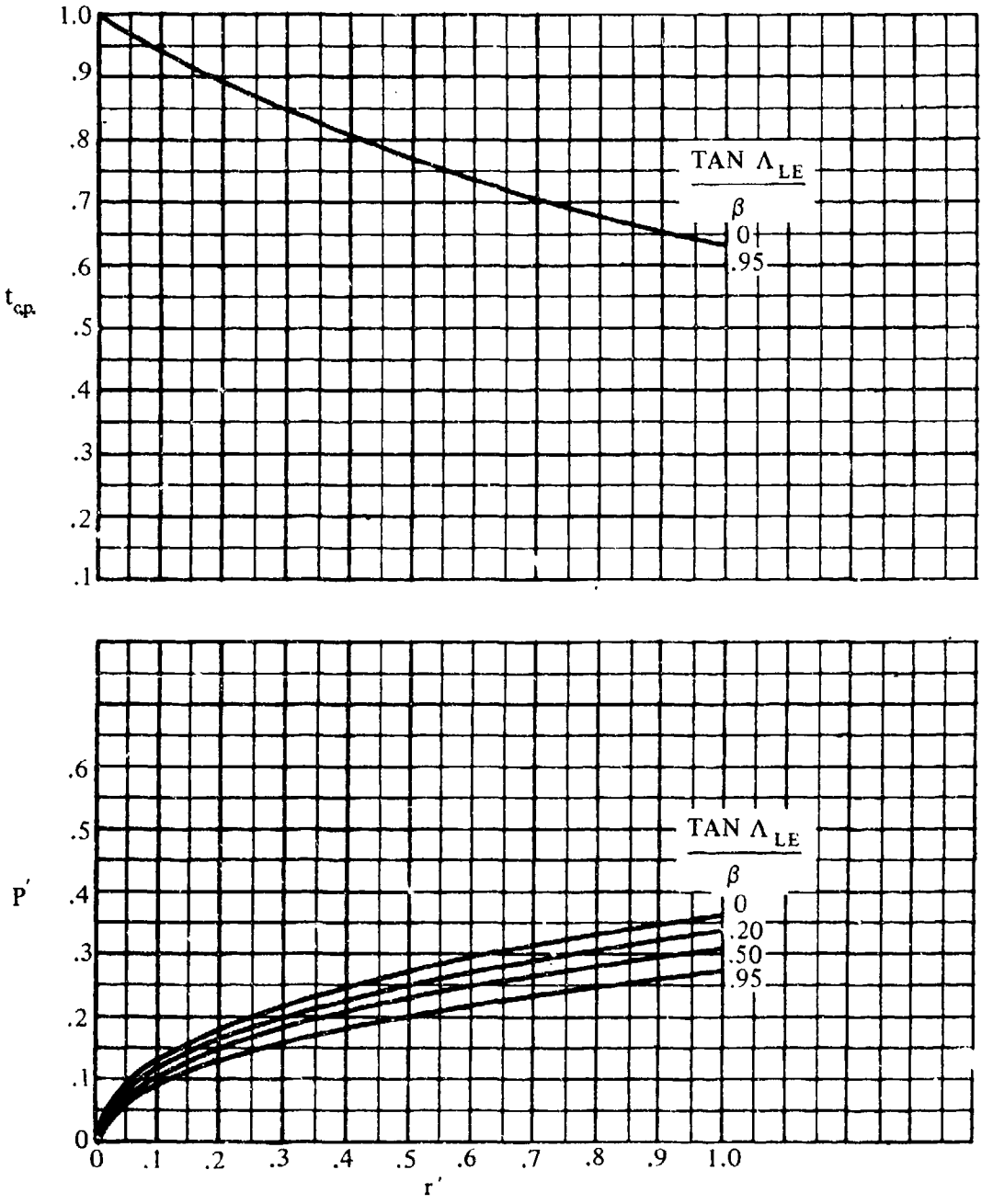

FIGURE 6.1.6.1-34 (CONTD)

SUPERSONIC SPEEDS

(f) r′ = 1.0 TO 10.0

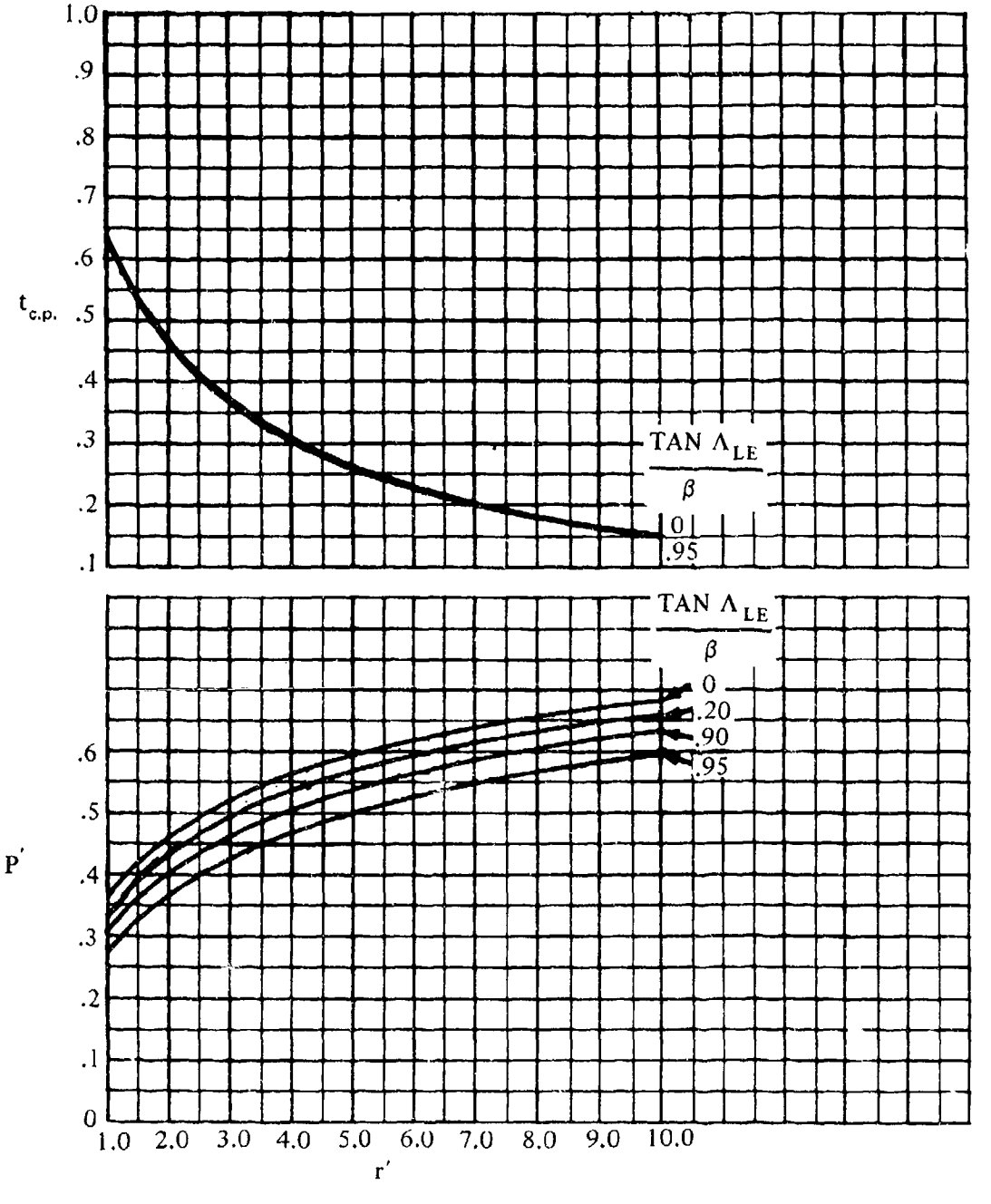

FIGURE 6.1.6.1-34 (CONTD)

6.1.6.2 HINGE-MOMENT DERIVATIVE C_{h_δ} OF HIGH-LIFT AND CONTROL DEVICES

A. SUBSONIC

The hinge-moment derivative due to control deflection can be approximated from the method of Reference 1. The method is based on lifting-line theory, with additional lifting-surface corrections to account for sweep.

The method is based on equations in terms of section parameters; therefore, the accuracy of the method is dependent upon the accuracy with which the section characteristics can be estimated. Test data on the particular airfoil-flap combination under consideration or one closely resembling it should always be preferred to characteristics obtained from generalized methods. Calculated values and test data for several different configurations are presented in Table 6.1.6.2-A to illustrate the accuracy of the method and summarize available test data.

The method is directly applicable to control surfaces having constant chord ratios and constant airfoil contours across the span. For configurations with variable chord ratios or variable airfoil contours across the span, it is suggested that average values of the section characteristics be used. Furthermore, the accuracy of the method in predicting the effects of finite-wing parameters decreases as the wing aspect ratio decreases. Application of the method to wings with aspect ratios of three or less should be avoided.

Experimental data have shown that for sweptback wings the shape of the ends of the control surface can have a critical effect on the hinge-moment parameters. The Datcom method is applicable to controls with the control-surface ends cut parallel to the plane of symmetry. For configurations with wing cutouts, or with control surfaces that do not have ends parallel to the plane of symmetry, it is suggested that empirical procedures be used to estimate C_{h_δ}.

The effect of subcritical Mach-number corrections on hinge moments appears to be small for control surfaces having trailing-edge angles less than approximately 12°. Therefore, the Datcom method, which neglects subcritical Mach-number effects, may be applied over a large portion of the subcritical Mach-number range.

DATCOM METHOD

The hinge-moment derivative due to the deflection of a sealed, plain trailing-edge control at subsonic speeds, based on the product of the control-surface area and the control-surface chord $S_c c_c$ (area and chord aft of the hinge line), is approximated by

$$C_{h_\delta} = \cos\Lambda_{c/4}\,\cos\Lambda_{HL}\left[\left(c_{h_\delta}\right)_{\text{balance}} + \alpha_\delta\left(c_{h_\alpha}\right)_{\text{balance}}\frac{2\cos\Lambda_{c/4}}{A + 2\cos\Lambda_{c/4}}\right] + \Delta C_{h_\delta} \quad 6.1.6.2\text{-a}$$

where

$\left(c_{h_\alpha}\right)_{\text{balance}}$ is the section hinge-moment derivative due to angle of attack. Test data on the particular flapped airfoil are preferred, but the derivative can be approximated by the method of Paragraph A of Section 6.1.3.1. (This term could be c'_{h_α} or c''_{h_α} from Section 6.1.3.1.)

$\left(c_{h_\delta}\right)_{\text{balance}}$ is the section hinge-moment derivative due to control deflection. Test data on the particular flapped airfoil are preferred, but the derivative can be approximated by the method of Paragraph A of Section 6.1.3.2. (This term could be c'_{h_δ} or c''_{h_δ} from Section 6.1.3.2.)

α_δ is the two-dimensional lift-effectiveness parameter expressed as

$$\alpha_\delta = -\frac{\left(c_{\ell_\delta}\right)_\alpha}{\left(c_{\ell_\alpha}\right)_\delta} \qquad \text{(Equation 6.1.1.1-b)}$$

where

c_{ℓ_δ} is the lift effectiveness of the sealed, plain trailing-edge control obtained by using the method of Section 6.1.1.1.

c_{ℓ_α} is the airfoil section lift-curve slope (including the effects of compressibility) from Section 4.1.1.2.

When experimental values of the section lift increment Δc_ℓ are available, the lift effectiveness parameter should be calculated using

$$(\alpha_\delta)_{c_\ell} = -\frac{\left(\Delta c_\ell\right)_{\text{experiment}}}{\left(c_{\ell_\alpha}\right)_\delta \delta}$$

ΔC_{h_δ} is an approximate lifting-surface correction which accounts for induced-camber effects. It is obtained by multiplying the quantity $\dfrac{\Delta C_{h_\delta}}{c_{\ell_\delta} B_2 K_\delta \cos\Lambda_{c/4} \cos\Lambda_{HL}}$, from Figure 6.1.6.2-15a, by its denominator. The primed values of the control-surface and wing chord ratios, used in reading Figure 6.1.6.2-15a, refer to measurements normal to the wing quarter-chord line.

The terms in the denominator are defined below, except for c_{ℓ_δ}, which is defined above.

B_2 accounts for the effect of the control surface and balance chord ratios. This parameter is obtained from Figure 6.1.6.1-19c,where the primed values of the control-surface and balance-chord ratios refer to measurements normal to the quarter-chord line.

K_δ accounts for the effect of control-surface span. This parameter is defined by

$$K_\delta = \frac{(K_\delta)_{\eta_i}(1-\eta_i) - (K_\delta)_{\eta_o}(1-\eta_o)}{\eta_o - \eta_i} \qquad 6.1.6.2\text{-b}$$

where

η_i is the inboard span station of the control,

$$\eta_i = \frac{\text{inboard span ordinate}}{b/2}$$

$(K_\delta)_{\eta_i}$ is obtained from Figure 6.1.6.2-15b as a function of the inboard spanwise location (η_i) of the control panel.

η_o is the outboard span station of the control,

$$\eta_o = \frac{\text{outboard span ordinate}}{b/2}$$

$(K_\delta)_{\eta_o}$ is obtained from Figure 6.1.6.2-15b as a function of the outboard spanwise location (η_o) of the control panel.

Sample Problem

Given: The flapped wing configuration of Reference 8. This is the configuration of the sample problem of Paragraph A, Section 6.1.6.1. The characteristics are repeated.

Wing Characteristics:

$A = 3.43$ $\lambda = 0.44$ $\Lambda_{c/4} = 48.7^o$ NACA 65-012 airfoil (normal to .50c of unswept wing)

$t/c = 0.086$ (streamwise) $\tan\frac{\phi'_{TE}}{2} = 0.0697$ (streamwise)

$$\tan\frac{\phi''_{TE}}{2} = 0.0523 \text{ (streamwise)}$$

Flap Characteristics:

Plain trailing-edge flap Sealed gap $\Lambda_{HL} = 41^{o}$

$c_f/c = 0.167$ (streamwise) $c'_f/c' = 0.20$ (normal to .25c)

$c_b/c_f = 0.090$ (streamwise) $c'_b/c'_f = 0.115$ (normal to .25c)

$t_c/(2c_f) = 0.090$ (streamwise) Round-nosed control

$\eta_i = 0.586$ $\eta_o = 0.99$ $\delta = 0$

Additional Characteristics:

Low speed $R_\ell = 2.2 \times 10^6$

$\left(c_{h_\alpha}\right)_{balance} = -0.00516$ per deg

$c_{\ell_\alpha} = 0.105$ per deg

$\dfrac{c_{\ell_\alpha}}{\left(c_{\ell_\alpha}\right)_{theory}} = 0.855$

} (Sample Problem, Paragraph A, Section 6.1.6.1)

Compute:

Lift effectiveness (Section 6.1.1.1)

$\left(c_{\ell_\delta}\right)_{theory} = 3.29$ per rad (Figure 6.1.1.1-39a)

$\dfrac{c_{\ell_\delta}}{\left(c_{\ell_\delta}\right)_{theory}} = 0.745$ (Figure 6.1.1.1-39b)

$K' = 1.0$ (Figure 6.1.1.1-40)

$$c_{\ell_\delta} = \frac{\Delta c_\ell}{\delta_f} = \left[\frac{c_{\ell_\delta}}{\left(c_{\ell_\delta}\right)_{theory}}\right]\left(c_{\ell_\delta}\right)_{theory} K' \quad \text{(Equation 6.1.1.1-c)}$$

$= (0.745)(3.29)(1.0) = 2.45$ per rad

$$\alpha_\delta = - \frac{\left(c_{\ell_\delta}\right)_\alpha}{\left(c_{\ell_\alpha}\right)_\delta} \qquad \text{(Equation 6.1.1.1-b)}$$

$$= - \frac{2.45}{(0.105)} \frac{1}{57.3} = -0.407$$

Section hinge-moment derivative c_{h_δ} (Section 6.1.3.2)

$$\left(c_{h_\delta}\right)_{\text{theory}} = -0.810 \text{ per rad} \qquad \text{(Figure 6.1.3.2-12b)}$$

$$\frac{c'_{h_\delta}}{\left(c_{h_\delta}\right)_{\text{theory}}} = 0.883 \qquad \text{(Figure 6.1.3.2-12a)}$$

$$c'_{h_\delta} = \left[\frac{c'_{h_\delta}}{\left(c_{h_\delta}\right)_{\text{theory}}} \right] \left(c_{h_\delta}\right)_{\text{theory}} \qquad \text{(Equation 6.1.3.2-a)}$$

$$= (0.883)(-0.810) = -0.715 \text{ per rad}$$

$$\text{Balance ratio} = \sqrt{\left(\frac{c_b}{c_f}\right)^2 - \left(\frac{t_c}{2c_f}\right)^2} = 0 \qquad \text{(Equation 6.1.3.1-d)}$$

$$\frac{\left(c_{h_\delta}\right)_{\text{balance}}}{c''_{h_\delta}} = 1.0 \qquad \text{(Figure 6.1.3.2-13)}$$

$$c''_{h_\delta} = c'_{h_\delta} + 2\left(c_{\ell_\delta}\right)_{\text{theory}} \left[1 - \frac{\left(c_{\ell_\delta}\right)}{\left(c_{\ell_\delta}\right)_{\text{theory}}} \right] \left(\tan \frac{\phi''_{TE}}{2} - \frac{t}{c} \right) \qquad \text{(Equation 6.1.3.2-b)}$$

$$= (-0.715) + 2(3.29)\ [1 - 0.745]\ (0.0523 - 0.086)$$

$$= -0.7715 \text{ per rad} = -0.0135 \text{ per deg}$$

$$\left(c_{h_\delta}\right)_{\text{balance}} = c''_{h_\delta} \left[\frac{\left(c_{h_\delta}\right)_{\text{balance}}}{c''_{h_\delta}} \right] \qquad \text{(Equation 6.1.3.2-c)}$$

$$= -0.0135 \text{ per deg}$$

Induced camber effect ΔC_{h_δ}

$B_2 = 0.885$ (Figure 6.1.6.1-19 c)

$$\left.\begin{aligned}(K_\delta)_{\eta_i} &= 2.0\\ (K_\delta)_{\eta_o} &= 4.25\end{aligned}\right\} \quad \text{Figure 6.1.6.2-15b}$$

$$K_\delta = \frac{(K_\delta)_{\eta_i}(1 - \eta_i) - (K_\delta)_{\eta_o}(1 - \eta_o)}{\eta_o - \eta_i} \qquad \text{(Equation 6.1.6.2-b)}$$

$$= \frac{(2.0)(1 - 0.586) - (4.25)(1 - 0.99)}{0.99 - 0.586}$$

$$= 1.944$$

$$c_{\ell_\delta} B_2 K_\delta \cos \Lambda_{c/4} \cos \Lambda_{HL} = \frac{2.45}{57.3}(0.885)(1.944)(0.660)(0.7547)$$

$$= 0.03665 \text{ per deg}$$

$$\frac{\Delta C_{h_\delta}}{c_{\ell_\delta} B_2 K_\delta \cos \Lambda_{c/4} \cos \Lambda_{HL}} = 0.0218 \qquad \text{(Figure 6.1.6.2-15a)}$$

$$\Delta C_{h_\delta} = (0.0218)(0.03665) = 0.000799 \text{ per deg}$$

Solution:

$$C_{h_\delta} = \cos \Lambda_{c/4} \cos \Lambda_{HL} \left[\left(c_{h_\alpha}\right)_{\text{balance}} + \alpha_\delta \left(c_{h_\alpha}\right)_{\text{balance}} \frac{2 \cos \Lambda_{c/4}}{A + 2 \cos \Lambda_{c/4}} \right] + \Delta C_{h_\delta}$$

(Equation 6.1.6.2-a)

$$= (0.6600)(0.7547)\left[(-0.0135) + (-0.407)(-0.00516) \frac{2(0.6600)}{3.43 + 2(0.6600)} \right] + 0.000799$$

$$= -0.00563 \text{ per deg}$$

The test value from Reference 8 is -0.0031 per degree.

B. TRANSONIC

No method is available for the prediction of the hinge-moment derivative C_{h_δ} at transonic speeds. Because of the mixed-flow conditions and interrelated shock-wave and boundary-layer-separation effects encountered at transonic speeds, the prediction of C_{h_δ} by theoretical means is extremely difficult. Experimental results for C_{h_δ} at transonic speeds are presented in References 2 through 5.

C. SUPERSONIC

The supersonic three-dimensional hinge moment due to control deflection can be computed for trailing-edge surfaces by the method of Reference 6. The method is based on linearized theory and applies to tapered and untapered control surfaces with the following restrictions:

1. Leading and trailing edges of the control surface are swept ahead of the Mach lines from the deflected controls.
2. Control root and tip chords are parallel to the plane of symmetry.
3. Controls are located either at the wing tip or far enough inboard so that the outermost Mach lines from the deflected controls do not cross the wing tip.
4. Innermost Mach lines from the deflected controls do not cross the wing root chord.
5. The wing planform has leading edges swept ahead of the Mach lines and has streamwise tips.
6. Controls are not influenced by the tip conical flow from the opposite wing panel or by the interaction of the wing-root Mach cone with the wing tip.

Calculated values and test data for several different configurations are presented in Table 6.1.6.2-B to illustrate the accuracy of the method and summarize available test data.

For leading-edge control surfaces and for trailing-edge control surfaces with subsonic leading edges, reverse-flow techniques (see Reference 7) can be used.

DATCOM METHOD

The hinge-moment derivative C_{h_δ} at supersonic speeds for a symmetric, straight-sided control, based on the product of the control-surface area and the control-surface chord $S_c c_c$ (area and chord aft of the hinge line), is approximated by

$$C_{h_\delta} = \frac{1}{\beta}\left(1 - \frac{C_2}{C_1}\,\phi_{TE}\right)\beta C'_{h_\delta} \qquad 6.1.6.2\text{-c}$$

where

$\left(1 - \frac{C_2}{C_1}\phi_{TE}\right)$ is a thickness correction factor to the supersonic flat-plate derivative.

$$C_1 = \frac{2}{\sqrt{M^2 - 1}} \text{ per radian}$$

$$C_2 = \frac{(\gamma+1)M^4 - 4(M^2 - 1)}{2(M^2 - 1)^2} \text{ per radian}$$

ϕ_{TE} is the trailing-edge angle in radians, measured normal to the control hinge line.

γ is the ratio of specific heats, $\gamma = 1.4$.

For a symmetrical biconvex airfoil the airfoil thickness correction factor in Equation 6.1.6.2-c is

$$1 - \frac{4}{3}\frac{C_2}{C_1}\left(\frac{t}{c}\right)'\left[1 + 2\left(\frac{x_h}{c}\right)'\right]$$

where

$\left(\frac{t}{c}\right)'$ is the maximum airfoil-thickness ratio, measured in a plane normal to the control hinge axis.

$\left(\frac{x_h}{c}\right)'$ is the chordwise location of the control hinge axis, measured in a plane normal to the control hinge axis.

Thickness correction factors for other airfoil sections can be determined from Reference 6.

$\beta C'_{h_\delta}$ is the supersonic flat-plate hinge-moment parameter obtained from Figure 6.1.6.2-17. For tapered controls this parameter is a function of tan Λ_{HL}/β, tan Λ_{TE}/β, and the control taper ratio λ_f. For untapered controls it is a function of tan Λ_{HL}/β, tan Λ_{TE}/β, and the control aspect-ratio parameter βA_f.

Sample Problem

Given: Wing with a tapered, trailing-edge control.

$\Lambda_{HL} = 31^\circ$ $\Lambda_{TE} = 27.6^\circ$ $\lambda_f = 0.713$ $\phi_{TE} = 3^\circ$

Symmetric, flat-sided section $M = 1.80$; $\beta = 1.50$

Compute:

$$C_1 = \frac{2}{\sqrt{M^2 - 1}} = \frac{2}{1.5} = 1.33 \text{ per rad}$$

$$C_2 = \frac{(\gamma+1) M^4 - 4 (M^2 - 1)}{2(M^2 - 1)^2} = \frac{(2.4) (1.8)^4 - 4(2.24)}{2(2.24)^2} = 1.62 \text{ per rad}$$

$$\left(1 - \frac{C_2}{C_1} \phi_{TE}\right) = \left[1 - \left(\frac{1.62}{1.33}\right)\frac{3.0}{57.3}\right] = 0.936$$

$$\frac{\tan \Lambda_{HL}}{\beta} = \frac{0.6009}{1.5} = 0.401$$

$$\frac{\tan \Lambda_{TE}}{\beta} = \frac{0.5228}{1.5} = 0.349$$

$\beta C'_{h_\delta}$ =−0.0335 per deg (Figure 6.1.6.2-17c)

Solution:

$$C_{h_\delta} = \frac{1}{\beta}\left(1 - \frac{C_2}{C_1} \phi_{TE}\right) \beta C'_{h_\delta} \qquad \text{(Equation 6.1.3.2-c)}$$

$$= \frac{0.936}{1.5} (-0.0335) = -0.0209 \text{ per deg}$$

REFERENCES

1. Toll, T. A., and Schneiter, L. E.: Approximate Relations for Hinge-Moment Parameters of Control Surfaces on Swept wings at Low Mach Numbers. NACA TN 1711, 1948. (U)

2. Thompson, R. F.: Hinge-Moment, Lift, and Pitching-Momeeent Characteristics of a Flap-Type Control Surface Having Various Hinge-Line Locations on a 4-Percent-Thick 60° Delta Wing – Transonic-Bump Method. NACA RM L54B08, 1954. (U)

3. Thompson, R. F.: Investigation of a 42.7° Sweptback Wing Model to Determine the Effects of Trailing-Edge Thickness on the Aileron Hinge-Moment and Flutter Characteristics at Transonic Speeds. NACA RM L50J06, 1950. (U)

4. Hieser, G.: Transonic Investigation of the Effectiveness and Loading Characteristics of a Flap-Type Aileron With and Without Paddle Balances on an Unswept-Wing-Fuselage Model. NACA RM L56B02, 1956. (U)

5. Runckel, J. F., and Hieser, G.: Normal-Force and Hinge-Moment Characteristics at Transonic Speeds of Flap-Type Ailerons at Three Spanwise Locations on a 4-Percent-Thick Sweptback-Wing-Body Model and Pressure Distribution Measurements on an Inboard Aileron. NASA TN D-842, 1961. (U)

6. Goin, K. L.: Equations and Charts for the Rapid Estimation of Hinge-Moment and Effectiveness Parameters for Trailing-Edge Controls Having Leading and Trailing Edges Swept Ahead of the Mach Lines. NACA TR 1041, 1951. (U)

7. Heaslet, M. A., and Spreiter, J. R.: Reciprocity Relations in Aerodynamics, NACA TN 2700, 1952. (U)

8. Fischel, J., and Schneiter, L. E.: An Investigation at Low Speed of a 51.3° Sweptback Semispan Wing Equipped With 16.7-Percent-Chord Plain Flaps and Ailerons Having Various Spans and Three Trailing-Edge Angles. NACA RM L&H20, 1948. (U)

9. Dods, J. B., Jr.: Wind-Tunnel Investigation of Horizontal Tails. III – Unswept and 35° Swept-back Plan Forms of Aspect Ratio 6. NACA RM A8H30, 1948. (U)

10. Tinling, B. E., and Dickson, J. K.: Tests of a Model Horizontal Tail of Aspect Ratio 4.5 in the Ames 12-Foot Pressure Wind Tunnel. I – Quarter-Chord Line Swept Back 35°. NACA RM A9G13, 1949. (U)

11. Kolbe, C. D., and Bandettini, A.: Investigation in the Ames 12-Foot Pressure Wind Tunnel of a Model Horizontal Tail of Aspect Ratio 3 and Taper Ratio 0.5 Having the Quarter-Chord Line Swept Back 45°. NACA RM A51D02, 1951. (U)

12. Johnson, H. I.: Measurements of Aerodynamic Characteristics of a 35° Sweptback NACA 65-009 Airfoil Model with 1/4-Chord Plain Flap by the NACA Wing-Flow Method. NACA RM L7F13, 1947. (U)

13. Morrill, C. P., Jr., and Boddy, L. E.: High-Speed Stability and Control Characteristics of a Fighter Airplane Model with a Swept-Back Wing and Tail. NACA RM A7K28, 1948. (U)

14. Cleary, J. W., and Boddy, L. E.: Wind-Tunnel Investigation of a 45° Swept-Back Wing Having a Symmetrical Root and a Highly Cambered Tip, Including the Effects of Fences and Lateral Controls. NACA RM A53I21, 1953. (U)

15. Pfyl, F. A.: Aerodynamic Study of a Wing-Fuselage Combination Employing a Wing Swept Back 63° – Effectiveness of an Inboard Elevon as a Longitudinal and Lateral-Control Device at Subsonic and Supersonic Speeds. NACA RM A51I18, 1951. (U)

16. Hammond, A. D.: The Effect of Various Aerodynamic Balances on the Low-Speed Lateral-Control and Hinge-Moment Characteristics of a 0.20-Chord Partial-Span Outboard Aileron on a Wing with Leading Edge Swept Back 51.3°. NACA RM L52G03, 1952. (U)

17. Schneiter, L. E., and Hagerman, J. R.: Wind-Tunnel Investigation at High Subsonic Speeds of the Lateral-Control Characteristics of an Aileron and a Stepped Spoiler on a Wing with Leading Edge Swept Back 51.3°. NACA RM L9D06, 1949. (U)

18. Moseley, W. C., Jr., and Gainer, T. G.: Some Effects of Control Profile and Control Trailing-Edge Angle on the Oscillating Hinge-Moment and Flutter Characteristics of Flap-Type Controls at Transonic Speeds. NASA TM X-170, 1960. (U)

19. Fischel, J., and Schneiter, L. E.: An Investigation at Low Speeds of a 51.3° Sweptback Semispan Wing with a Raked Tip and with 16.7-Percent-Chord Ailerons Having Three Spans and Three Trailing-Edge Angles. NACA RM L8F29, 1948. (U)

20. Dods, J. B., Jr.: Wind-Tunnel Investigation of Horizontal Tails. II – Unswept and 35° Swept-Back Plan Forms of Aspect Ratio 4.5. NACA RM A8B11, 1948. (U)

21. Harper, J. J.: Wind-Tunnel Investigation of Effects of Various Aerodynamic Balance Shapes and Sweepback on Control-Surface Characteristics of Semispan Tail Surfaces with NACA 0009, 0015, 66-009, 66(215)-014, and Circular-Arc Airfoil Sections. NACA TN 2495, 1951. (U)

22. Lord, D. R., and Driver, C.: Investigation of the Effect of Balancing Tabs on the Hinge-Moment Characteristics of a Trailing-Edge Flap-Type Control on a Trapezoidal Wing at a Mach Number of 1.61. NACA RM L54F22, 1954. (U)

23. Sivells, J. C., and Goin, K. L.: Experimental and Calculated Hinge Moments of Two Ailerons on a 42.7° Swentback Wing at a Mach Number of 1.9. NACA RM L8K24a, 1949. (U)

24. Conner, D. W., and Mitchell, M. H., Jr.: Control Effectiveness and Hinge-Moment Measurements at a Mach Number of 1.9 of a Nose Flap and Trailing-Edge Flap on a Highly Tapered Low-Aspect-Ratio Wing. NACA RM L8K17a, 1949. (U)

25. Lord, D. R., and Czarnecki, K. R.: Aerodynamic Characteristics of Several Flap-Type Trailing-Edge Controls on a Trapezoidal Wing at Mach Numbers of 1.61 and 2.01. NACA RM L54D19, 1954. (U)

26. Spearman, M. L., and Webster, R. A.: An Investigation at Mach Numbers of 1.40 and 1.59 of the Effects of Aileron Profile on the Aerodynamic Characteristics of a Complete Model of Supersonic Aircraft Configuration. NACA RM L50J31, 1951. (U)

27. Boatright, W. B., and Rainey, R. W.: Hinge-Moment Measurement of a Wing with Leading-Edge and Trailing-Edge Flaps at a Mach Number of 1.93. NACA RM L8K12a, 1949. (U)

28. Dunning, R. W., and Ulman, E. F.: Aerodynamic Characteristics at Mach Number 4.04 of a Rectangular Wing of Aspect Ratio 1.33 having a 6-Percent-Thick Circular-Arc Profile and a 30-Percent-Chord Full-Span Trailing-Edge Flap. NACA RM L53D03, 1953. (U)

29. Robinson, R. L.: An Investigation of a Supersonic Aircraft Configuration having a Tapered Wing with Circular-Arc Sections and 40° Sweepback – Static Lateral Control Characteristics at Mach Numbers of 1.40 and 1.59. NACA RM L50I11, 1950. (U)

TABLE 6.1.6.2-A

SUBSONIC HINGE-MOMENT DERIVATIVE DUE TO CONTROL DEFLECTION
DATA SUMMARY AND SUBSTANTIATION

Ref.	M	A	$\Lambda_{c/4}$ (deg)	λ	Type of Control Surface	C_{h_δ} Calc	C_{h_δ} Test	ΔC_{h_δ} Calc-Test
9	0.23	6	5.7	0.5	Elevator	−0.0118	−0.0104	−0.0014
10	0.21	4.5	35.3	0.5	Elevator	−0.00830	−0.0081	−0.0002
↓	0.6	↓	↓	↓	↓	−0.00976	−0.0094	−0.0004
↓	0.8	↓	↓	↓	↓	−0.0132	−0.0118	−0.0014
↓	0.85	↓	↓	↓	↓	−0.0151	−0.0128	−0.0023
↓	0.9	↓	↓	↓	↓	−0.0184	−0.0147	−0.0037
11	0.25	3	45.6	0.5	Elevator	−0.00608	−0.0067	0.0006
↓	0.6	↓	↓	↓	↓	−0.00725	−0.0079	0.0006
↓	0.8	↓	↓	↓	↓	−0.00991	−0.0083	−0.0016
↓	0.9	↓	↓	↓	↓	−0.0139	−0.0087	−0.0052
12	0.55	3.04	35.0	1.0	Flap	−0.00956	−0.0085	−0.0011
↓	0.8	↓	↓	↓	↓	−0.0136	−0.010	−0.0036
↓	0.9	↓	↓	↓	↓	−0.0190	−0.010	−0.0090
13	0.3	4.785	35.22	0.513	Aileron	−0.00431	−0.0057	0.0014
↓	0.6	↓	↓	↓	↓	−0.00586	−0.0046	−0.0013
↓	0.8	↓	↓	↓	↓	−0.00829	−0.0043	−0.0040
↓	0.85	↓	↓	↓	↓	−0.00962	−0.0040	−0.0056
↓	0.875	↓	↓	↓	↓	−0.0106	−0.0040	−0.0066
↓	0.9	↓	↓	↓	↓	−0.0119	−0.0055	−0.0064
↓	0.3	4.65	35.59	0.450	Elevator	−0.00593	−0.0063	0.0004
↓	0.6	↓	↓	↓	↓	−0.00755	−0.0040	−0.0036
↓	0.8	↓	↓	↓	↓	−0.0103	−0.0024	−0.0079
↓	0.85	↓	↓	↓	↓	−0.0119	−0.0020	−0.0099
↓	0.875	↓	↓	↓	↓	−0.0130	−0.0006	−0.0124
↓	0.9	↓	↓	↓	↓	−0.0144	0	−0.0144
4	0.7	4.0	4.8	0.5	Aileron	−0.0164	−0.0110	−0.0054
↓	0.8	↓	↓	↓	↓	−0.0199	−0.0130	−0.0069
↓	0.9	↓	↓	↓	↓	−0.0281	−0.0185	−0.0096
14	0.25	5.515	45.0	0.532	Aileron	−0.00554	−0.005	−0.0005
↓	0.8	↓	↓	↓	↓	−0.00945	−0.006	−0.0035
↓	0.9	↓	↓	↓	↓	−0.0131	−0.006	−0.0071
↓	0.25	↓	↓	↓	↓	−0.00552	−0.005	−0.0005
↓	0.8	↓	↓	↓	↓	−0.00941	−0.006	−0.0034
↓	0.9	↓	↓	↓	↓	−0.0130	−0.006	−0.0070
15	0.6	3.50	60.8	0.25	Elevon	−0.00337	−0.0029	−0.0005
	0.9					−0.00626	−0.0035	−0.0028
16	0.328	3.06	38.7	0.49	Aileron	−0.00571	−0.0031	−0.0026
↓	0.328	↓	↓	↓	↓	0.00363	−0.0013	0.0049
↓		↓	↓	↓	↓			

TABLE 6.1.6.2-A (CONTD)

Ref.	M	A	$\Lambda_{c/4}$ (deg)	λ	Type of Control Surface	C_{h_δ} Calc	C_{h_δ} Test	ΔC_{h_δ} Calc-Test
17	0.302	3.06	38.7	0.49	Aileron	−0.00566	−0.0043	−0.0014
	0.499					−0.00633	−0.0043	−0.0020
	0.7					−0.00787	−0.0047	−0.0032
	0.8					−0.00955	−0.0048	−0.0048
18	0.6	3.0	0	1.0	Flap	−0.00225	−0.005	0.0027
	0.7					−0.00262	−0.004	0.0014
	0.8					−0.00327	−0.0026	−0.0007
	0.85					−0.00383	−0.0095	0.0057
	0.9					−0.00478	−0.005	0.0002
	0.6					−0.00301	−0.005	0.0020
	0.7					−0.00347	−0.004	0.0005
	0.8					−0.00429	−0.005	0.0007
	0.85					−0.00499	−0.0055	0.0005
	0.9					−0.00619	−0.002	−0.0042
	0.6					−0.00390	−0.0053	0.0014
	0.7					−0.00447	−0.0043	−0.0002
	0.8					−0.00547	−0.001	−0.0045
	0.85					−0.00634	−0.004	−0.0023
	0.9					−0.00782	−0.0043	−0.0035
	0.6					−0.00564	−0.012	0.0064
	0.7					−0.00641	−0.011	0.0046
	0.8					−0.00779	−0.011	0.0032
	0.85					−0.00901	−0.012	0.0030
	0.9					−0.0111	−0.0145	0.0034
8	0.12	3.43	48.6	0.44	Aileron	−0.00477	−0.0064	0.0016
						−0.00469	−0.0060	0.0013
						−0.00447	−0.0057	0.0012
						−0.00504	−0.0067	0.0017
						−0.00489	−0.0064	0.0015
						−0.00178	−0.0035	0.0017
						−0.00543	−0.0069	0.0015
19	0.12	3.58	48.7	0.44	Aileron	−0.00592	−0.0071	0.0012
						−0.00494	−0.0056	0.0007
						−0.00219	−0.0025	0.0003
						−0.00586	−0.0073	0.0014
						−0.00488	−0.0058	0.0009
						−0.00214	−0.0028	0.0007
						−0.00568	−0.0070	0.0013

TABLE 6.1.6.2-A (CONTD)

Ref.	M	A	$\Lambda_{c/4}$ (deg)	λ	Type of Control Surface	C_{h_δ} Calc	C_{h_δ} Test	ΔC_{h_δ} Calc-Test
19	0.12	3.58	48.7	0.44	Aileron	−0.00471	−0.0057	0.0010
↓	↓	↓	↓	↓	↓	−0.00199	−0.0023	0.0003
20	0.17	4.5	7.6	0.5	Elevator	−0.0109	−0.0095	−0.0014
↓	↓	↓	35.3	↓	↓	−0.00775	−0.0069	−0.0009
21	0.12	3.36	13.5	0.4	Flap	−0.0102	−0.0068	−0.0034
↓	↓	↓	↓	↓	↓	−0.00558	−0.0032	−0.0024
↓	↓	↓	↓	↓	↓	−0.00768	−0.0041	−0.0036
↓	↓	3.30	40.0	0.4	Flap	−0.00698	−0.0078	0.0008
↓	↓	↓	↓	↓	↓	−0.00376	−0.0049	0.0011
↓	↓	↓	↓	↓	↓	−0.00455	−0.0012	−0.0034
↓	↓	↓	↓	↓	↓	−0.00251	0.0005	−0.0030
↓	↓	3.36	13.5	0.4	Flap	−0.00735	−0.0100	0.0026
↓	↓	↓	↓	↓	↓	−0.00392	−0.0082	0.0043
↓	↓	↓	↓	↓	↓	−0.00550	−0.0086	0.0031
↓	↓	↓	↓	↓	↓	−0.00608	−0.0059	−0.0002
↓	↓	↓	↓	↓	↓	−0.00318	−0.0054	0.0022
↓	↓	↓	↓	↓	↓	−0.00452	−0.0054	0.0009
↓	↓	↓	↓	↓	↓	−0.00536	−0.0048	−0.0006
↓	↓	↓	↓	↓	↓	−0.00335	−0.0036	0.0002
↓	↓	↓	↓	↓	↓	−0.00412	−0.0040	−0.0001
↓	↓	↓	↓	↓	↓	−0.00539	−0.0110	0.0056
↓	↓	↓	↓	↓	↓	−0.00279	−0.0094	0.0066
↓	↓	↓	↓	↓	↓	−0.00426	−0.0112	0.0069
↓	↓	↓	↓	↓	↓	−0.00197	−0.0019	−0.0001
↓	↓	↓	↓	↓	↓	−0.000815	−0.0022	0.0014
↓	↓	↓	↓	↓	↓	−0.00149	−0.0027	0.0012
Average $\Delta \left\lvert C_{h_{\delta_{calc}}} - C_{h_{\delta_{test}}} \right\rvert$ = 0.0029								

TABLE 6.1.6.2-B

SUPERSONIC HINGE-MOMENT DERIVATIVE DUE TO CONTROL DEFLECTION
DATA SUMMARY AND SUBSTANTIATION

Ref.	M	A	Λ_{LE} (deg)	λ	C_{h_δ} Calc	C_{h_δ} Test	$\Delta(C_{h_\delta})$ Calc-Test
22	1.61	3.1	23	0.4	−0.0209	−0.0210	0.0001
23	1.9	4.0	42.7	0.5	−0.0122	−0.010	−0.0022
↓	↓	↓	↓	↓	−0.0122	−0.014	0.0018
24	1.9	1.06	45	0.31	−0.0151	−0.010	−0.0051
25	1.61	3.1	23	0.4	−0.0192	−0.021	0.0018
↓	↓	↓	↓	↓	−0.0196	−0.019	−0.0006
↓	↓	↓	↓	↓	−0.0207	−0.020	−0.0007
↓	↓	↓	↓	↓	−0.0209	−0.021	0.0001
↓	↓	↓	↓	↓	−0.0232	−0.0245	0.0013
↓	↓	↓	↓	↓	−0.0255	−0.026	0.0005
↓	2.01	↓	↓	↓	−0.0146	−0.015	0.0004
↓	↓	↓	↓	↓	−0.0152	−0.016	0.0008
↓	↓	↓	↓	↓	−0.0153	−0.016	0.0007
26	1.59	4.0	42.7	0.5	−0.0169	−0.012	−0.0049
↓	↓	↓	↓	↓	−0.0169	−0.012	−0.0049
↓	↓	↓	↓	↓	−0.0169	−0.016	−0.0009
↓	↓	↓	↓	↓	−0.0169	−0.017	0.0001
27	1.93	3.14	9.33	0.59	−0.0124	−0.011	−0.0014
28	4.04	1.33	0	1.0	−0.00464	−0.0056	0.001
29	1.59	4.0	42.7	0.5	−0.0166	−0.0157	−0.0009
|	1.59	1.17	40.6	0.337	−0.0149	−0.0031	−0.0118

Average $\Delta \left| C_{h_{\delta\,calc}} - C_{h_{\delta\,test}} \right| = 0.0020$

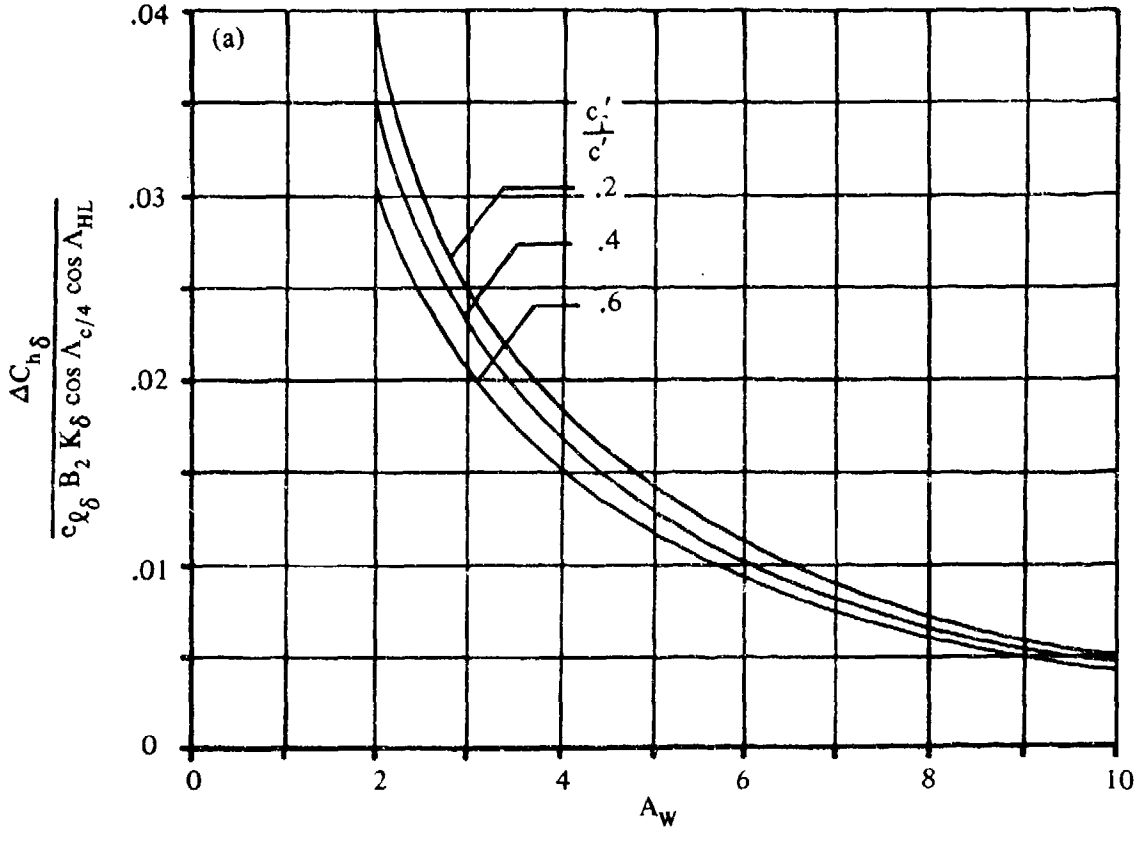

FIGURE 6.1.6.2-15 CHARTS FOR INDUCED-CAMBER CORRECTIONS TO HINGE-MOMENT PARAMETERS OF FINITE-SPAN WINGS

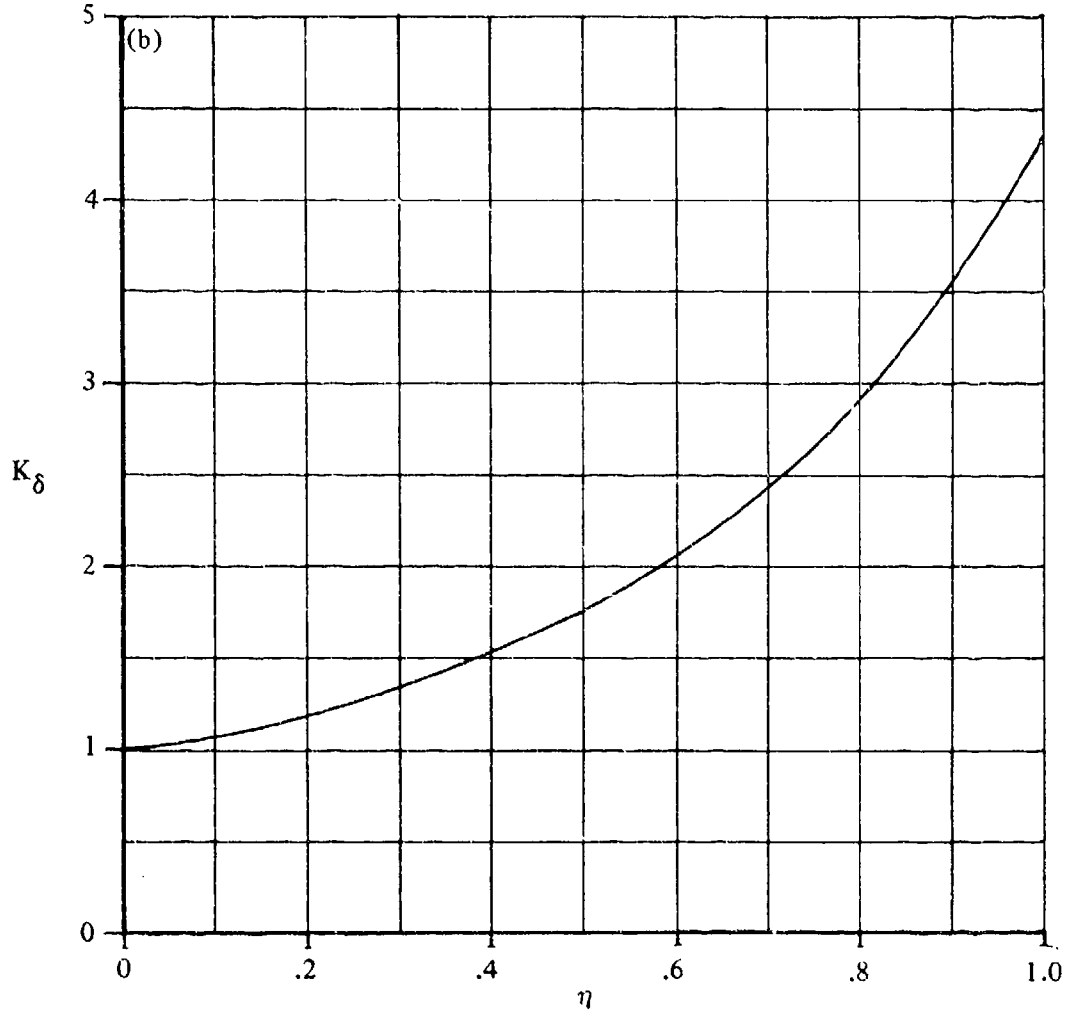

FIGURE 6.1.6.2 -15 (CONTD)

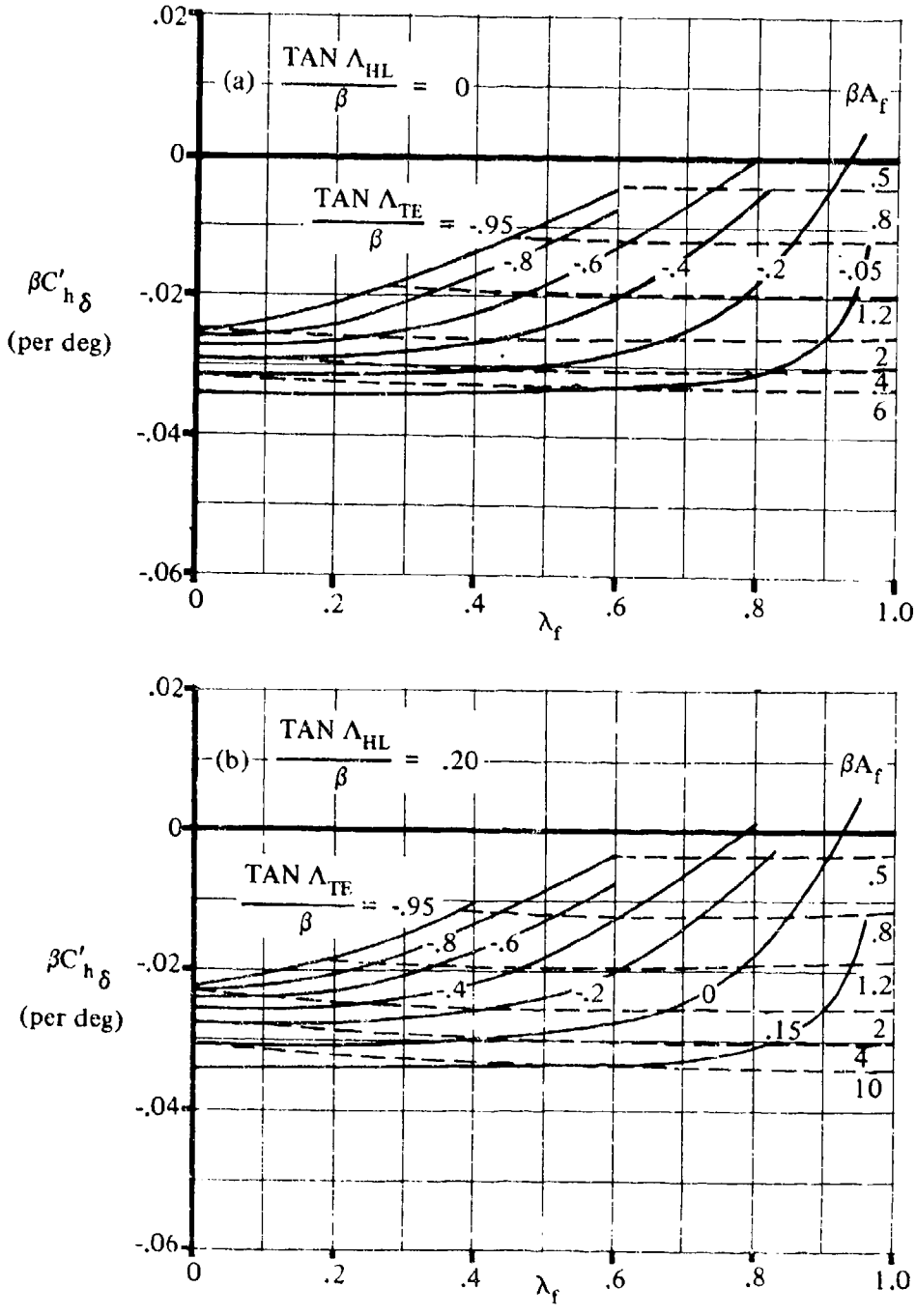

FIGURE 6.1.6.2-17 SUPERSONIC THEORETICAL HINGE-MOMENT DERIVATIVE C_{h_δ}

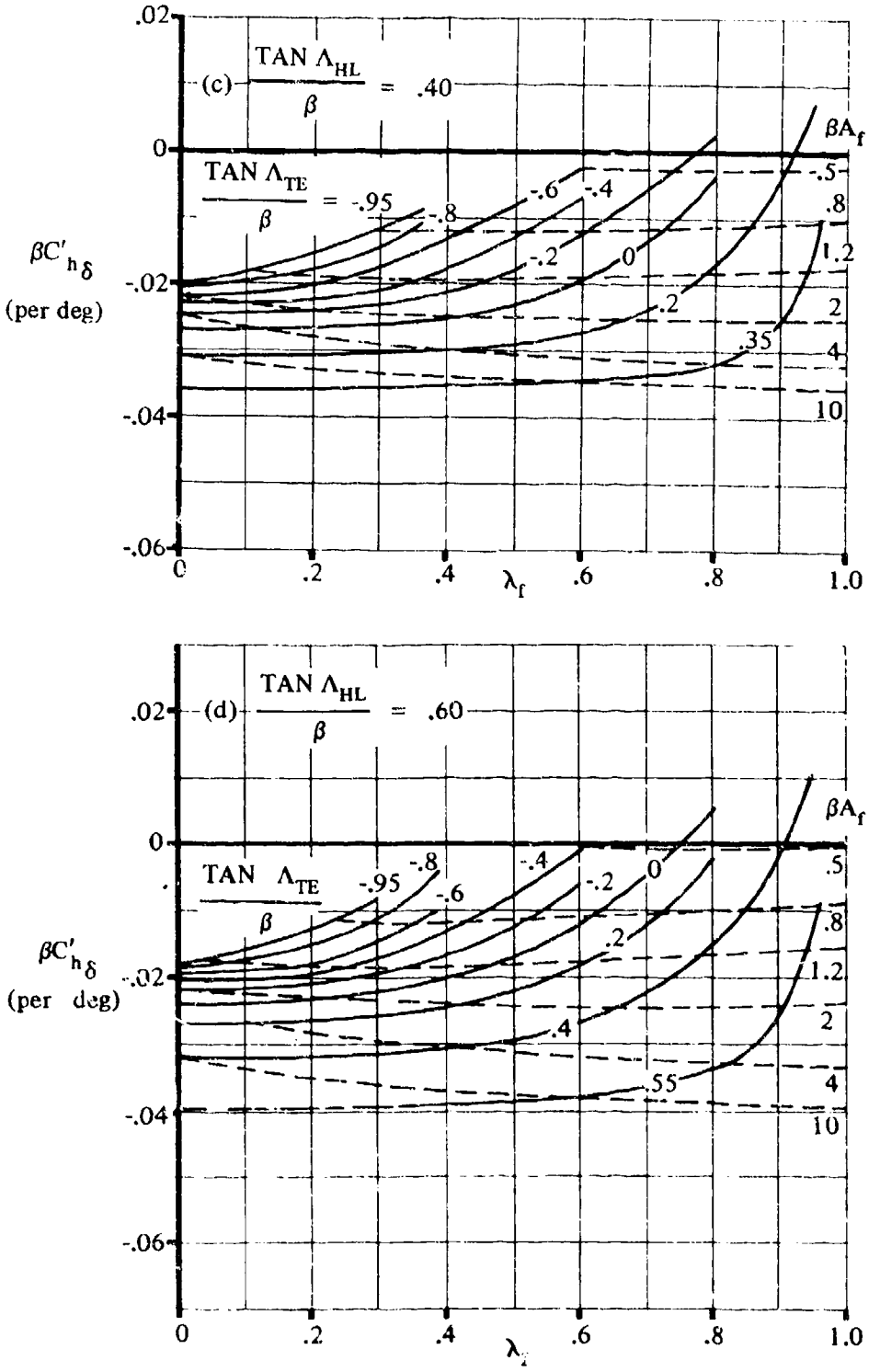

FIGURE 6.1.6.2-17 (CONTD)

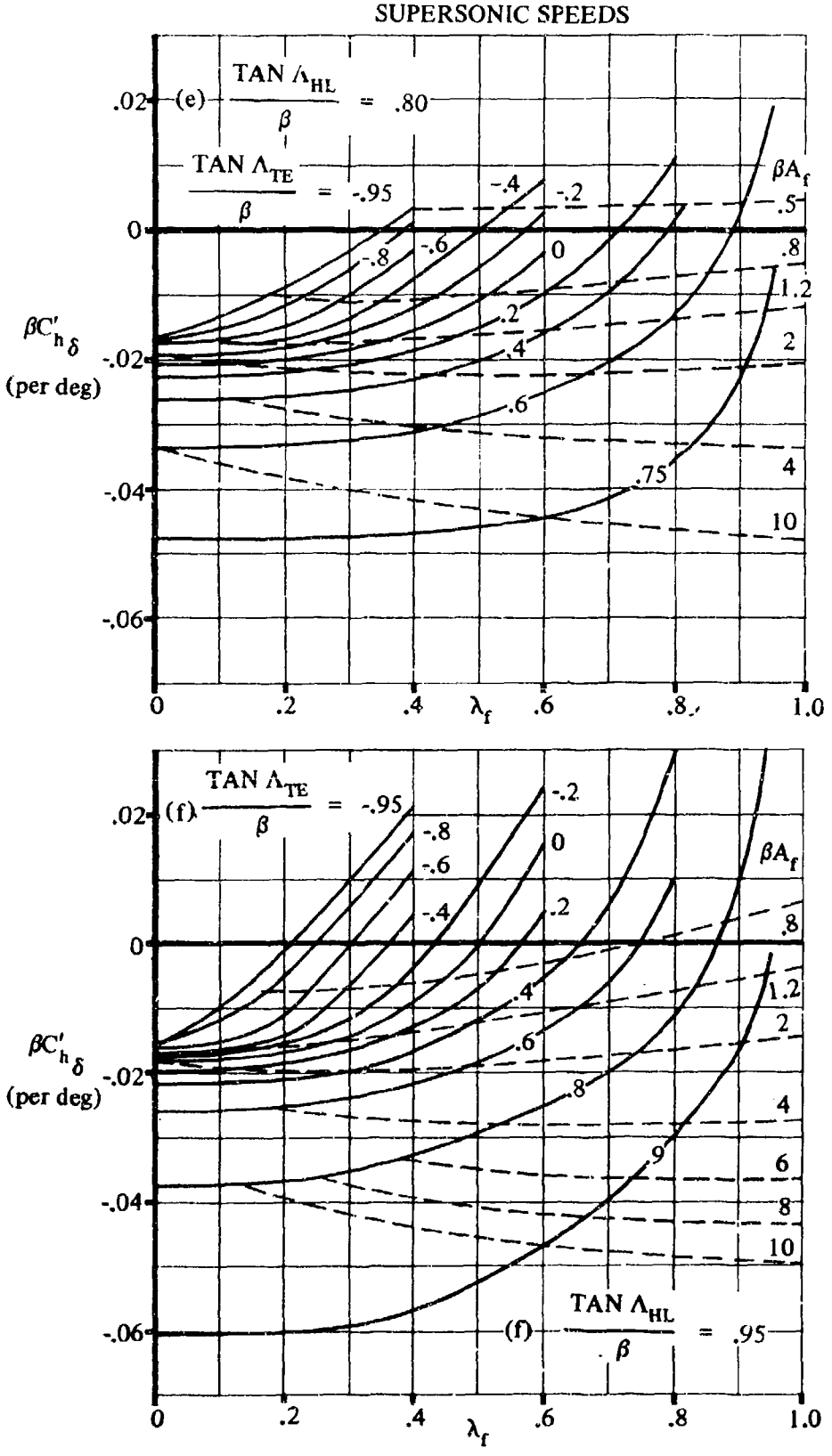

FIGURE 6.1.6.2-17 (CONTD)

6.1.7 DRAG OF HIGH-LIFT AND CONTROL DEVICES

There are two types of movable control surfaces. Control surfaces or flaps may exist as movable portions of primary lifting surfaces, such as ailerons on a wing or elevators attached to stabilizers. A control surface may also exist as an independent lifting surface, such as an "all-flying" horizontal tail. The drag due to deflection of the latter type of control is treated simply as the drag of the surface at a different angle of attack. This section of the Datcom is therefore concerned only with the drag due to deflection of flaps or control surfaces that are movable parts of primary lifting surfaces.

The deflection of flaps or control surfaces causes two increments of drag. First, the profile drag of the primary-surface – movable-surface combination is changed. Second, if the two surfaces are producing a force normal to the local flow direction, the deflection of the control surface will produce a different span-loading distribution and may therefore change the induced drag of the surfaces. Both profile-drag and induced-drag effects are considered in the Datcom.

A. SUBSONIC

The changes of both induced drag and profile drag due to control or flap deflection are considered. The change of induced drag is caused by a change in span-loading distribution. The induced drag is calculated first without flap or control surfaces deflected and then with these surfaces deflected. The increment of drag thus obtained is the change of induced drag due to flap or control-surface deflection.

The method of calculating induced drag used in this Section is limited to the flap deflections and angles of attack for which the flow is attached over the control surface. The approximate maximum control deflections for linear control characteristics are given in figure 6.1.3-2. This chart, based on test data for an NACA 0009 airfoil, is intended only to serve as a guide.

DATCOM METHOD

To calculate the induced drag for a spanwise symmetrically loaded wing, the span-loading distribution is determined by the method of Section 6.1.5.1. A finite number m of spanwise stations on the full-span wing is chosen. Each station is indicated by the integers v and n, which are related to span location by the equation

$$\eta = \cos\frac{v\pi}{m+1} = \cos\frac{n\pi}{m+1} \qquad 6.1.7\text{-a}$$

The number of span stations m must be an odd integer. If the span loading is a smooth curve, m may be relatively small, for example, 7, 9, or 11. If the span loading is not smooth, m should be larger, for example, 13, 15, or 17.

For a given flap deflection δ, the span loading is given by

$$G_v = \left(\frac{G}{\delta}\right)_v (\alpha_\delta)\,\delta \qquad 6.1.7\text{-b}$$

where α_δ is obtained from Section 6.1.1.1, δ is the streamwise control deflection, and $(G/\delta)_v$ is determined as outlined in step 1 of Method 2 in paragraph A of Section 6.1.5.1.

The induced drag can be expressed, by the method of reference 1, as

$$C_{D_i} = \frac{\pi A}{m+1}\left[G_k\left\{ b_{kk}\,G_k - \sum_{n=1}^{k}(1-\delta_{kn})\,B_{kn}\,G_n \right\} + 2\sum_{v=1}^{k-1} G_v\left\{ b_{vv}\,G_v - \sum_{n=1}^{k}(1-\delta_{vn})\,B_{vn}\,G_n \right\}\sin\phi_v \right] \qquad 6.1.7\text{-c}$$

where

$$k = \frac{m+1}{2} \qquad 6.1.7\text{-d}$$

$$b_{vv} = \frac{m+1}{4 \sin \phi_v} \quad \text{for } n = v \qquad \text{6.1.7-e}$$

$$= b_{kk} \quad \text{for } v = n = k$$

$$b_{vn} = \frac{\sin \phi_n}{(\cos \phi_n - \cos \phi_v)^2} \left(\frac{1 - (-1)^{n-v}}{2\,(m+1)} \right) \quad \text{for } n \neq v \qquad \text{6.1.7-f}$$

$$\delta_{vn} = 1 \quad \text{for } v = n \qquad \text{6.1.7-g}$$

$$\delta_{vn} = 0 \quad \text{for } v \neq n \qquad \text{6.1.7-h}$$

$$B_{vn} = b_{vn} \quad \text{for } n = \frac{m+1}{2} = k \qquad \text{6.1.7-i}$$

$$B_{vn} = b_{vn} + b_{v,\,m+1-n} \quad \text{for } n \neq \frac{m+1}{2} = k \qquad \text{6.1.7-j}$$

$$\phi = \cos^{-1} \eta \qquad \text{6.1.7-k}$$

$$\phi_v = \frac{v\pi}{m+1} \qquad \text{6.1.7-}\ell$$

$$\phi_n = \frac{n\pi}{m+1} \qquad \text{6.1.7-m}$$

$$G_v = \left(\frac{G}{\delta} \right)_v (\alpha_\delta)\, \delta \quad \text{(equation 6.1.7-b)}$$

$$= G_n \quad \text{for } n = v$$

$$= G_k \quad \text{for } n = k$$

The sample problem at the end of this section demonstrates the use of equation 6.1.7-c. Step 1 of the sample problem is an evaluation of the terms of equation 6.1.7-c that are functions only of m, and hence of n and v. Once calculated for a given number of span locations m, Step 1 need not be repeated. Therefore, when using m = 11 or m = 21, one may utilize the results of Step 1 in the sample problem, and begin the calculations at Step 2.

Equation 6.1.7-c gives the induced drag coefficient at a given angle of attack and a given flap deflection. The corresponding lift coefficient is

$$C_L = \frac{\pi A}{m+1} \left[G_k + 2 \sum_{n=1}^{k-1} G_n \sin \phi_n \right] \qquad \text{6.1.7-n}$$

where the terms of equation 6.1.7-n are defined as in equa' 6.1.7-c.

SKETCH (a)

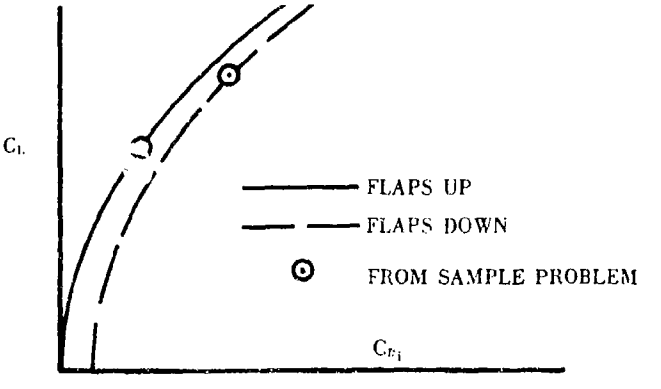

Equations 6.1.7-c and 6.1.7-n are evaluated at several angles of attack, both with flaps up and with flaps down. The induced drag coefficient C_{D_i} is then plotted versus C_L for flaps up and flaps down, as shown in sketch (a). The increment of C_{D_i} between these curves, at constant C_L, is the induced drag due to flap deflection at a given lift coefficient.

The increment of profile drag due to control or flap deflection can be expressed as a change of the minimum drag coefficient for the polar of the primary surface with undeflected control or flap. The minimum drag coefficient is then

$$(C_D)_{min} = (C_{D_{min}})_{flaps\ up} + \Delta C_{D_{min}} \qquad 6.1.7\text{-o}$$

where

$$\Delta C_{D_{min}} = \Delta c_{d_f} K_b + K' \frac{(\Delta C_{L_f})^2}{\pi A} \qquad 6.1.7\text{-p}$$

Δc_{d_f} is the airfoil section drag coefficient with deflected flap given in figures 6.1.7-22 and 6.1.7-23 as a function of deflection and of $\frac{c_f}{c}$ for plain and for single-slotted flaps.

K_b is given in figure 6.1.4.1-15 as a function of taper ratio and flap span ratio.

K' is the flap span factor given in figures 6.1.7-24(a), (b), and (c), taken from reference 2.

ΔC_{L_f} is determined by the mechanical flap method of Section 6.1.4.1

The shift of the polar without flap or control deflection can now be drawn (figure 6.1.7-27). The increment of induced drag due to flap or control deflection is added to the basic polar. The resulting curve is then translated parallel to the C_D-axis until the minimum C_D agrees with the value given by equation 6.1.7-o.

Sample Problem

Given: The flapped-wing configuration with the following characteristics.

Wing Characteristics:

$A = 6.35 \quad \lambda = 0.50 \quad \Lambda_{c/4} = 40^o \quad S_W = 567$ sq ft

$c_r = 12.6$ ft $\quad \bar{c} = 9.8$ ft $\quad b_W/2 = 30.0$ ft

NACA 63_1012 airfoil (streamwise) $\quad \tan \frac{\phi'_{TE}}{2} = 0.073$

Flap Characteristics:

Plain trailing-edge flap Sealed gap

$\eta_i = 0.195 \quad \eta_o = 0.556 \quad \delta = 11.3^o$ (streamwise)

$c_f/c = 0.20$ (streamwise)

Additional characteristics:

Low speed; $\beta = 1.0$ $\left(C_{D_{min}}\right)_{\delta = 0} = 0.0203$ $\alpha = 10^{o}$

$R_{\ell} = 9.0 \times 10^{6}$

Compute:

Step 1. Parameters that are functions of m are evaluated. These parameters remain constant for any particular value of m. Tables are presented in this section for m = 11 and 21, (tables 6.1.7-A through 6.1.7-F). In case it is desired to use some other value of m, the procedure for calculating these parameters is outlined below. Equations 6.1.7-a through 6.1.7-m are used.

Let $m = 11$

$m + 1 = 12$

$k = \frac{m+1}{2} = 6$

$v = 1$ to k (1 to 6)

$n = 1$ to k (1 to 6)

(1)

v	ϕ_v	$\sin \phi_v$	$\cos \phi_v = \eta$
1			
2			
3		Equation 6.1.7-*l*	
4			
5			
6			

(2)

$(\cos \phi_n - \cos \phi_v)^2$						
n	v					
	1	2	3	4	5	6
1						
2						
3						
4						
5						
6						

(3)

$\frac{1-(-1)^{n-v}}{2(m+1)}$						
n	v					
	1	2	3	4	5	6
1						
2						
3						
4						
5						
6						

(4)

b_{vn}						
n	v					
	1	2	3	4	5	6
1						
2						
3	Equations 6.1.7-e and 6.1.7-f					
4						
5						
6						

(5)

$(\cos \phi_{m+1-n} - \cos \phi_v)^2$						
n	v					
	1	2	3	4	5	6
1						
2						
3						
4						
5						
6						

(6)

$\frac{1-(-1)^{(m+1-n)-v}}{2(m+1)}$						
n	v					
	1	2	3	4	5	6
1						
2						
3						
4						
5						
6						

(7)

$b_{v,\,m+1-n}$						
n	v					
	1	2	3	4	5	6
1						
2						
3	Equations 6.1.7-e and 6.1.7-f, with (m + 1 − n) substituted for n					
4						
5						
6						

(8)

$1 - \delta_{vn}$						
n	v					
	1	2	3	4	5	6
1						
2						
3	Equations 6.1.7-g and 6.1.7-h					
4						
5						
6						

(9)

B_{vn}						
n	v					
	1	2	3	4	5	6
1						
2						
3	Equations 6.1.7-i and 6.1.7-j					
4						
5						
6						

(10)

$(1 - \delta_{vn})\, B_{vn}$						
n	v					
	1	2	3	4	5	6
1						
2						
3						
4						
5						
6						

Step 2. Spanwise loading coefficient G_v.

The following spanwise loading coefficients must be obtained:

1. Basic loading without flaps
2. Incremental loading due to flap deflection
3. Basic loading with flaps

1. Basic loading without flaps:

The variation of G/δ with η_v is determined as outlined in step 1 of Method 2 in paragraph A of Section 6.1.5.1.

$$c_{\ell_\alpha} = 0.116 \text{ per deg} = 6.65 \text{ per rad (table 4.1.1-B)}$$

$$\kappa = \frac{c_{\ell_\alpha}}{2\pi} = \frac{6.65}{2\pi} = 1.06$$

$$\frac{\beta A}{\kappa} = \frac{(1.0)(6.35)}{1.06} = 6.0$$

$$\Lambda_\beta = \tan^{-1}\left(\frac{\tan \Lambda_{c/4}}{\beta}\right) = \tan^{-1}\left(\frac{\tan 40^o}{1.0}\right) = 40^o$$

The variation of G/δ with η_v is then the spanwise loading from figure 6.1.5.1-62c with $\eta_o = 1.0$ (wing treated as a full-span flap). The desired loading coefficient G_v is calculated as follows:

$$G_v = -\left(\frac{G}{\delta}\right)\alpha_\delta \ \delta \quad \text{(equation 6.1.7-b)}$$

$\alpha_\delta = -1.0$ (wing treated as a full wing-chord flap)

$\delta = \sigma$ (radians) = 0.175 rad

Then

$$G_v = \left(\frac{G}{\delta}\right)_v \alpha$$

The calculation is shown below.

η	$\left(\frac{G}{\delta}\right)_v$ per rad	α rad	G_v
0	.32	.175	.0560
.1	.33	.175	.0578
.2	.34	.175	.0595
.3	.34	.175	.0595
.4	.34	.175	.0595
.5	.33	.175	.0578
.6	.32	.175	.0560
.7	.30	.175	.0525
.8	.26	.175	.0455
.9	.21	.175	.0368
1.0	0	.175	0

2. Incremental loading due to flap deflection:

The variation of G/δ with η_v may be read directly from figure 6.1.5.1-62c at $\eta_i = 0.195$ and $\eta_o = 0.556$. Then, the difference in the spanwise loading of those tabluations at each span station is the spanwise loading of the actual full-chord flap. (See sketch (b), Section 6.1.5.1.)

Flap effectiveness α_δ

$$\frac{c_{\ell_\alpha}}{\left(c_{\ell_\alpha}\right)_{theory}} = 0.899 \quad \text{(figure 4.1.1.2-8a)}$$

$$\frac{c_{\ell_\delta}}{\left(c_{\ell_\delta}\right)_{theory}} = 0.836 \quad \text{(figure 6.1.1.1-39b)}$$

$$\left(c_{\ell_\delta}\right)_{theory} = 3.68 \text{ per rad} \quad \text{(figure 6.1.1.1-39a)}$$

$K' = 0.999$ (figure 6.1.1.1-40)

$$\Delta c_\ell = \delta \left[\frac{c_{\ell_\delta}}{\left(c_{\ell_\delta}\right)_{theory}}\right] \left(c_{\ell_\delta}\right)_{theory} K' \quad \text{(equation 6.1.1.1-c)}$$

$$= \frac{11.3}{57.3} (0.836)(3.68)(0.999) = 0.606$$

$$\alpha_\delta = -\frac{\Delta c_\ell}{\left(c_{\ell_\alpha}\right)_\delta \delta} \quad \text{(equation 6.1.1.1-b)}$$

$$= -\frac{0.606}{(0.116)(11.3)} = -0462$$

$$G_v = -\left(\frac{G}{\delta}\right)_v \alpha_\delta \delta \quad \text{(equation 6.1.7-b)}$$

$$= -\left(\frac{G}{\delta}\right)_v (-0.462)(11.3/57.3) = 0.0911 \left(\frac{G}{\delta}\right)_v$$

η	$\left(\frac{G}{\delta}\right)_{\eta_o} = 0.556$ (fig. 6.1.5.1-62c)	$\left(\frac{G}{\delta}\right)_{\eta_i} = 0.195$ (fig. 6.1.5.1-62c)	$\left(\frac{G}{\delta}\right)_v$ $(\ )_{\eta_o} - (\ )_{\eta_i}$	G_v
0	0.30	0.22	0.08	0.0073
.1	0.31	0.21	0.10	0.0091
.2	0.32	0.15	0.17	0.0155
.3	0.32	0.10	0.22	0.0200
.4	0.30	0.07	0.23	0.0210
.5	0.23	0.05	0.18	0.0164
.6	0.17	0.04	0.13	0.0118
.7	0.11	0.03	0.08	0.0073
.8	0.07	0.02	0.05	0.0046
.9	0.05	0.02	0.03	0.0027
1.0	0	0	0	0

3. Basic loading with flaps:

The incremental loading due to flap deflection is added to the basic loading without flaps to obtain the basic loading with flaps.

η	G_v basic loading without flaps	G_v incremental loading due to flaps	G_v basic loading with flaps
0	0.0560	0.0073	0.0633
.1	0.0578	0.0091	0.0669
.2	0.0595	0.0155	0.0750
.3	0.0595	0.0200	0.0795
.4	0.0595	0.0210	0.0805
.5	0.0578	0.0164	0.0742
.6	0.0560	0.0118	0.0678
.7	0.0525	0.0073	0.0598
.8	0.0455	0.0046	0.0501
.9	0.0368	0.0027	0.0395
1.0	0	0	0

The above loadings are plotted in sketch (b), in order that values of G_v may be read for any desired η_v.

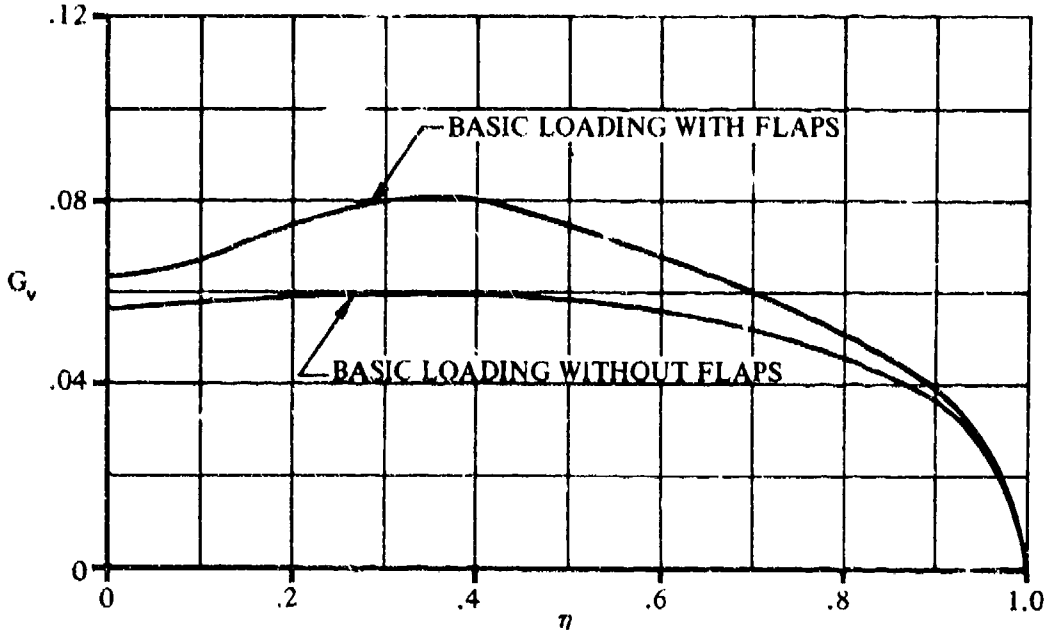

SKETCH (b)

Step 3 C_{D_i} due to flaps

Let $C_{D_i} = \frac{\pi A}{m+1} \{N_1 + N_2\}$ (equation 6.1.7-c)

where

$$N_1 = G_k \left\{ b_{kk} G_k - \sum_{n=1}^{k} \left[\left(1 - \delta_{vn}\right) B_{kn} G_n \right] \right\}$$

$$N_2 = 2 \sum_{v=1}^{k-1} \left(G_v \left\{ b_{vv} G_v - \sum_{n=1}^{k} \left[\left(1 - \delta_{vn}\right) B_{vn} G_n \right] \right\} \sin \phi_v \right)$$

$m + 1 = 12 \qquad k = 6 \qquad \frac{\pi A}{m+1} = \frac{\pi (6.35)}{12} = 1.662$

C_{D_i} must be calculated for the following loadings:

Case 1. Basic loading without flaps

Case 2. Basic loading with flaps

Case 1. (Calculations for basic loading without flaps)

Tabulate G_v for v = 1 to k

v	η (table 6.1.7-A)	G_v [from sketch (b)]
1	.9659	.0205
2	.8660	.0400
3	.7071	.0520
4	.5000	.0578
5	.2588	.0595
6	0	.0560

Calculate N_1

for v = k = 6, n = k = 6

①	②	③
G_k	b_{kk} table 6.1.7-B	$b_{kk} G_k$ = ① ②
.0560	3.000	.1680

for v = k = 6

①	②	③	④
n	$(1 - \delta_{vn}) B_{kn}$ table 6.1.7-C	G_n	② ③
1	.04622	.0205	.0009
2	0	.0400	0
3	.2356	.0520	.0123
4	0	.0578	0
5	2.404	.0595	.1430
6	0	.0560	0

$$\sum_{n=1}^{k} ④ = 0.1562$$

$$N_1 = 0.560 \{0.1680 - 0.1562\} = 0.000661$$

Calculate N_2

for v = 1

①	②	③	④	⑤
v	n	$(1 - \delta_{vn})\ B_{vn}$ table 6.1.7-C	G_n	③ ④
1	1	0	.0205	0
	2	4.187	.0400	.1675
	3	0	.0520	0
	4	.3660	.0578	.0212
	5	0	.0595	0
	6	.08931	.0560	.0050

$$\sum_{n=1}^{k} ⑤ = 0.1937$$

Repeat the above calculation for v = 2 through 5. The summations are listed below.

$$[a] = \sum_{n=1}^{k} \left(1 - \delta_{vn}\right) B_{vn}\, G_n \quad \text{for } v = 1 \text{ to } k-1$$

v	1	2	3	4	5
[a]	.1937	.1838	.1762	.1664	.1544

①	⑨	⑧	⑥	⑧	⑥	⑦	⑧
v	$\sin \phi_v$ table 6.1.7-A	b_{vv} table 6.1.7-B	G_v	$b_{vv} G_v$ = ⑧ ⑥	[a]	⑥ − [a]	⑦ ⑥ ⑧
1	.2588	11.59	.0205	.2376	.1937	.0439	.000233
2	.5000	6.000	.0400	.2400	.1838	.0562	.001124
3	.7071	4.243	.0520	.2206	.1762	.0444	.001633
4	.8660	3.464	.0578	.2002	.1664	.0338	.001692
5	.9659	3.106	.0595	.1848	.1544	.0304	.001747

$$2 \sum_{v=1}^{k-1} ⑧ = 0.01286$$

Solution for Case 1

$$C_{D_i} = \frac{\pi A}{m+1}\,[N_1 + N_2] = 1.662\ [0.000661 + 0.01286]$$

$$= 0.0225 \text{ (basic loading without flaps)}$$

Case 2. (Calculations for basic loading with flaps at $\alpha = 10^o$)

Tabulate G_v for v = 1 to k

v	n	G_v sketch (b)
1	.9659	.0220
2	.8660	.0432
3	.7071	.0590
4	.5000	.0747
5	.2588	.0784
6	0	.0635

Calculate N_1

for v = k = 6, n = k = 6

①	②	③
G_k	b_{kk} table 6.1.7-B	$b_{kk}\,G_k$ ① ②
.0635	3.00	.1905

for v = k = 6

①	②	③	④
n	$(1-\delta_{vn})\,B_{i\,n}$ table 6.1.7-C	G_n	$(1-\delta_{kn})\,B_{kn}\,G_n$ ② ③
1	.04622	.0220	.00102
2	0	.0432	0
3	.2356	.0590	.01390
4	0	.0747	0
5	2.404	.0784	.1885
6	0	.0635	0

$$\sum_{n=1}^{k} ④ = 0.2034$$

$$N_1 = 0.0635\,\{0.1905 - 0.2034\} = -0.000819$$

Calculate N_2

for $v = 1$

① v	② n	③ $(1-\delta_{vn})B_{vn}$ (table 6.1.7-C)	④ G_n	⑤ $(1-\delta_{vn})B_{vn}G_n$ ③ ④
1	1	0	.0220	0
	2	4.187	.0432	.1809
	3	0	.0590	0
	4	.3660	.0747	.0273
	5	0	.0784	0
	6	.08931	.0635	.0057

$$\sum_{n=1}^{k} ⑤ = 0.2139$$

Repeat the above calculation for $v = 2$ through 5. The summations are listed below.

$$[a] = \sum_{n=1}^{k} \left(1-\delta_{vn}\right) B_{vn} G_n \quad \text{for } v = 1 \text{ to } k-1$$

v	1	2	3	4	5
[a]	.2139	.2089	.2121	.2052	.1873

① v	② $\sin\phi_v$ table 6.1.7-A	③ b_{vv} table 6.1.7-B	④ G_v	⑤ $b_{vv}G_v$ ③ ④	⑥ [a]	⑦ ⑤ − [a]	⑧ ⑦ ④ ②
1	.2588	11.59	.0220	.2550	.2139	.0411	.000234
2	.5000	6.00	.0432	.2592	.2089	.0503	.001086
3	.7071	4.243	.0590	.2503	.2121	.0382	.001595
4	.8660	3.464	.0747	.2588	.2052	.0536	.003465
5	.9659	3.106	.0784	.2435	.1873	.0562	.002456

$$N_2 = 2\sum_{v=1}^{k=1} ⑧ = 0.02127$$

$$C_{D_i} = \frac{\pi A}{m+1}\left[N_1 + N_2\right] = 1.662\ [-0.000819 + 0.02127]$$

$$= 0.0340 \text{ (basic loading with flaps deflected } 11.3^{o} \text{ at } \alpha = 10^{o})$$

Step 4. Determine the lift coefficient C_L for Cases 1 and 2.

Case 1. (Basic Loading without flaps)

Case 2. (Basic Loading with flaps)

$G_k = 0.0635$ for $v = k = 6$

①	②	③	④
n	G_n	$\sin \phi_n$ table 6.1.7-A	$G_n \sin \phi_n$ ② ③
1	.0220	.2588	.00569
2	.0432	.5000	.02160
3	.0590	.7071	.04172
4	.0747	.8660	.06469
5	.0784	.9659	.07573

$$2 \sum_{n=1}^{k-1} \text{④} = 0.4189$$

$$C_L = \frac{\pi A}{m+1} \left[G_k + 2 \sum_{n=1}^{k-1} G_n \sin \phi_n \right] \quad \text{(equation 6.1.7-n)}$$

$= 1.662\,[0.0635 + 0.4189]$

$= 0.8017$ (basic loading with flaps deflected 11.3° at $\alpha = 10^\circ$)

Step 5. Determine the profile drag increment due to flaps $\Delta C_{D_{min}}$

$\Delta c_{d_f} = 0.0050$ (figure 6.1.7-22)

$$\left.\begin{aligned} K_{b_{(\eta_o = 0.556)}} &= 0.688 \\ K_{b_{(\eta_i = 0.195)}} &= 0.265 \end{aligned}\right\} \quad \text{(figure 6.1.4.1-15)}$$

$K_b = K_{b_{(\eta_o)}} - K_{b_{(\eta_i)}} = 0.424$

$K' \doteq 1.01$ (figures 6.1.7-24a through -24c, interpolated)

ΔC_{L_f} (Section 6.1.4.1)

$$\left.\begin{aligned} \Delta c_{\ell} &= 0.606 \\ \alpha_{\delta} &= -0.462 \\ c_{\ell_{\alpha}} &= 6.65 \text{ per rad} \end{aligned}\right\} \quad \text{(Step 2, above)}$$

$$\frac{(\alpha_{\delta})_{C_L}}{(\alpha_{\delta})_{c_{\ell}}} = 1.056 \text{ (figure 6.1.4.1-14) (at } (\alpha_{\delta})_{c_{\ell}} = 0.55 \text{ from inset of figure 6.1.4.1-14)}$$

$$\frac{A}{\kappa}\left[\beta^2 + \tan^2 \Lambda_{c/2}\right]^{1/2} = \frac{6.35}{1.06}\left[1 + (0.7866)^2\right]^{1/2} = 7.62$$

$$C_{L_{\alpha}}/A = 0.640 \text{ per rad (figure 4.1.3.2-49)}$$

$$C_{L_{\alpha}} = (0.640)(6.35) = 4.06 \text{ per rad}$$

$$\Delta C_{L_f} = \Delta c_{\ell}\left(\frac{C_{L_{\alpha}}}{c_{\ell_{\alpha}}}\right)\left[\frac{(\alpha_{\delta})_{C_L}}{(\alpha_{\delta})_{c_{\ell}}}\right] K_b \text{ (equation 6.1.4.1-a)}$$

$$= (0.606)\left(\frac{4.06}{6.65}\right)[1.056]\ (0.424)$$

$$= 0.166$$

$$\Delta C_{D_{min}} = \Delta c_{d_f} K_b + K'\frac{\left(\Delta C_{L_f}\right)^2}{\pi A} \text{ (equation 6.1.7-p)}$$

$$= (0.0050)(0.424) + (1.31)\frac{(0.166)^2}{\pi(6.35)}$$

$$= 0.00212 + 0.00181$$

$$= 0.00393$$

Step 6. Determine the minimum drag coefficient with flaps deflected

$$C_{D_{min}} = \left(C_{D_{min}}\right)_{\delta=0} + \Delta C_{D_{min}} \text{ (equation 6.1.7-o)}$$

$$= 0.0203 + 0.0039$$

$$= 0.0242$$

At this point, the lift coefficients and induced-drag coefficients are known at $\alpha = 10^{o}$ for flaps deflected 11.3^{o}. The minimum drag coefficient with flaps deflected is also known. Steps 2 through 4 must now be repeated at several angles of attack to determine the variation of C_{D_f} with C_L, as shown in sketch (a)

on page 6.1.7-2 for flaps undeflected and flaps deflected 11.3°. These values are plotted in the form of figure 6.1.7-27 to give a flap-deflected drag polar.

B. TRANSONIC

At transonic Mach numbers, the drag increment due to control deflection is extremely difficult to estimate. The transonic flow about an airfoil, which has locally subsonic and supersonic regions, is very sensitive to changes in airfoil section. The supersonic flow regions frequently terminate with a nearly normal shock wave, causing an abrupt increase in pressure at that point. The location of this shock wave can be greatly influenced by control deflection, which results in changes to the pressure distribution, and hence causes an unpredictable drag increment. The complexity of the mixed flows prevents the use of either simple theory or empirical analysis for general treatment of the problem.

DATCOM METHOD

Because of the extreme sensitivity of the mixed flows at transonic Mach numbers, no Datcom Method is given to estimate the drag increment due to control deflection.

C. SUPERSONIC

At supersonic speeds, the drag due to control-surface deflection can be considered in two parts – a change of wave or pressure drag, and a change of skin-friction drag.

DATCOM METHOD

The increment of wave drag of the primary surface with control surface deflected is

$$\Delta(C_{D_{wave}}) = \left[\frac{(C_{D_{wave}})}{(C_{D_{wave}})_{\delta=0}} - 1\right](C_{D_{wave}})_{\delta=0} \qquad 6.1.7\text{-q}$$

where $(C_{D_{wave}})_{\delta=0}$ is determined by the method of Section 4.1.5.1.

The ratio $\dfrac{(C_{D_{wave}})}{(C_{D_{wave}})_{\delta=0}}$ can be estimated by linear theory and is approximated by

$$\frac{(C_{D_{wave}})}{(C_{D_{wave}})_{\delta=0}} = \left[1 - \frac{\bar{c}_f}{c}\right] + \left[\frac{\bar{c}_f}{c}\right]\left[\frac{\alpha+\delta}{\alpha}\right]^2\left[\frac{S_{n1} + \frac{1}{2}S_1}{S} + 1 - \frac{S_{n1} + S_1}{S}\right] \qquad 6.1.7\text{-r}$$

where

$\dfrac{\bar{c}_f}{c}$ is the ratio of mean flap chord to primary-surface chord

α is the angle of attack of the primary surface with $\delta=0$

δ is the deflection of the control surface relative to the primary surface, positive for trailing edge down

S_{n1} is the part of the primary-surface planform area forward of and including the flap area that is not influenced by the primary-surface tip [see figure 6.1.7-28 (b)]

S_1 is the part of the primary-surface planform area forward of and including the flap area that is influenced by the primary-surface tip [see figure 6.1.7-28 (b)]

The effect of control surface or flap deflection on drag is

$$(C_D)_\delta = (C_D)_{\delta=0} + \Delta(C_{D_{wave}}) + \Delta(C_{D_f}) \qquad 6.1.7\text{-s}$$

Although procedures can be devised for estimating the change of skin-friction drag due to control surface or flap deflection, the estimated changes are so small as to be of the order of the reading accuracy of the charts of reference 3 that are used in the calculations. Therefore the change of skin-friction drag due to control deflection will be assumed to be zero.

Sample Problem

Given:

Configuration of sample problem 1, Method 1, paragraph C, Section 4.1.5.1.

$\Lambda_{c/4} = 35°$ $A = 4.0$ $t/c = 0.06$

Smooth surface Stabilized flight

$R_\ell = 10^7$ Round-nose airfoil

$M = 2.0$ $(C_{D_f})_{\delta=0} = 0.00521$ $(C_{D_{wave}})_{\delta=0} = (\Delta C_{D_o})_{\delta=0} = 0.0171$

Additional characteristics:

$\frac{S_w}{2} = 200$ sq ft $\frac{b_w}{2} = 20$ ft

$\lambda = 0.3$ $c_r = 15.40$ ft

full-span flap $\frac{\delta_f}{c} = 0.20$

$\alpha = 5°$ $\delta = -8°$ $(C_D)_{\delta=0} = 0.0395$ (at $\alpha = 5°$)

The pertinent Mach line is shown below.

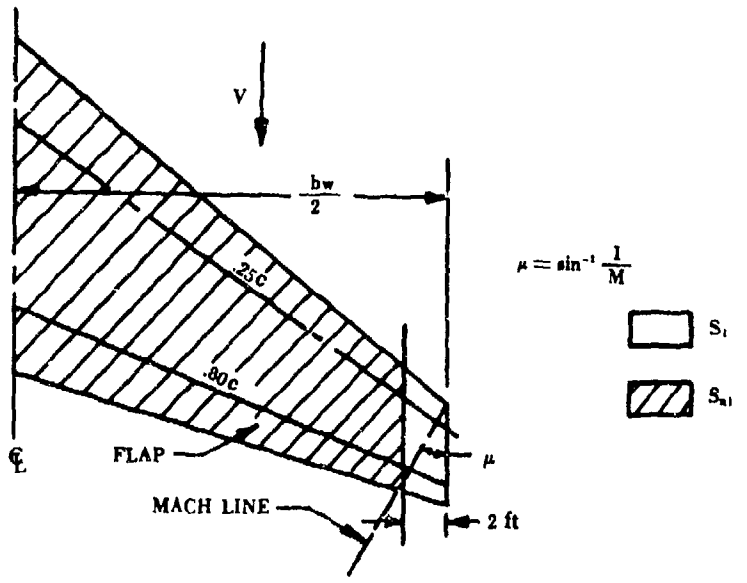

$S_l = 10$ sq ft

$S_{al} = 190$ sq ft

Compute:

$\Delta C_{D_{wave}}$ calculation:

$$\left[1 - \frac{\delta_f}{c}\right] = 0.8$$

$$\left[\frac{\alpha+\delta}{\alpha}\right]^2 = 0.36$$

$$\left[\frac{S_{n1}+\frac{1}{2}S_l}{S}\right] = \frac{195}{200} = 0.975$$

$$\left[\frac{S_{n1}+S_l}{S}\right] = 1.0$$

$$\frac{C_{D_{wave}}}{(C_{D_{wave}})_{\delta=0}} = \left[1-\frac{\bar{c}_f}{c}\right]+\left[\frac{\bar{c}_f}{c}\right]\left[\frac{\alpha+\delta}{\alpha}\right]^2\left[\frac{S_{n1}+\frac{1}{2}S_l}{S}+1-\frac{S_{n1}+S_l}{S}\right] \quad \text{(equation 6.1.7-r)}$$

$$= 0.8 + 0.2\,(0.36)\,(0.975)$$

$$= 0.8702$$

$$\Delta C_{D_{wave}} = \left[\frac{C_{D_{wave}}}{(C_{D_{wave}})_{\delta=0}} - 1\right](C_{D_{wave}})_{\delta=0} \quad \text{(equation 6.1.7-q)}$$

$$= [0.8702 - 1]\,(0.0171)$$

$$= -0.00222$$

Solution for drag with flap deflection:

For $\alpha = 5°$

$$(C_D)_{\delta=-8°} = (C_D)_{\delta=0} + \Delta C_{D_{wave}} + \Delta C_{D_f} \quad \text{(equation 6.1.7-s)}$$

$$= 0.0395 + (-0.00222) + 0$$

$$= 0.03728$$

TABLE 6.1.7-A

v	ϕ_v deg	sin ϕ_v	cos ϕ_v = η
1	15.0	.2588	.9659
2	30.0	.5000	.8660
3	45.0	.7071	.7071
4	60.0	.8660	.5000
5	75.0	.9659	.2588
6	90.0	1.0	0

TABLE 6.1.7-B

	b_{vn}					
n	v					
	1	2	3	4	5	6
1	11.59	2.161	0	.09934	0	.02311
2	4.175	6.000	1.650	0	.1130	0
3	0	2.334	4.243	1.374	0	.1178
4	.3324	0	1.683	3.464	1.240	0
5	0	.2183	0	1.383	3.106	1.202
6	.08931	0	.1667	0	1.244	3.000

TABLE 6.1.7-C

$(1 - \delta_{vn})B_{vn}$						
n	v					
	1	2	3	4	5	6
1	0	2.167	0	.1094	0	.04622
2	4.187	0	1.667	0	.1459	0
3	0	2.358	0	1.414	0	.2356
4	.3660	0	1.733	0	1.365	0
5	0	.2819	0	1.523	0	2.404
6	.08931	0	.1667	0	1.244	0

Note: m = 11 for tables 6.1.7-A, -B, and -C

m = 21 for tables 6.1.7-D, -E, and -F

TABLE 6.1.7-D

v	ϕ_v deg	$\sin \phi_v$	$\cos \phi_v = \eta$
1	8.18	.1423	.9898
2	16.36	.2817	.9595
3	24.54	.4153	.9097
4	32.73	.5407	.8412
5	40.91	.6549	.7557
6	49.09	.7557	.6549
7	57.27	.8412	.5407
8	65.46	.9097	.4153
9	73.64	.9595	.2817
10	81.82	.9898	.1423
11	90.00	1.0	0

TABLE 6.1.7-E

b_{vn}											
n	v										
	1	2	3	4	5	6	7	8	9	10	11
1	38.65	7.044	0	.2929	0	.05764	0	.01959	0	.009004	0
2	13.95	19.52	5.163	0	.3083	0	.07300	0	.02787	0	.01391
3	0	7.611	13.24	4.023	0	.2907	0	.07723	0	.03205	0
4	1.113	0	5.238	10.17	3.362	0	.2721	0	.07851	0	.03473
5	0	.7167	0	4.072	8.398	2.930	0	.2568	0	.07910	0
6	.3061	0	.5291	0	3.381	7.278	2.634	0	.2466	0	.08008
7	0	.2180	0	.4234	0	2.932	6.538	2.431	0	.2409	0
8	.1253	0	.1692	0	.3567	0	2.628	6.046	2.316	0	.2397
9	0	.09493	0	.1393	0	.3131	0	2.443	5.732	2.244	0
10	.06263	0	.07639	0	.1195	0	.2835	0	2.315	5.557	2.222
11	0	.04937	0	.06423	0	.1060	0	.2635	0	2.244	5.500

TABLE 6.1.7-F

$(1 - \delta_{vn}) B_{vn}$											
n	v										
	1	2	3	4	5	6	7	8	9	10	11
1	0	7.046	0	.2948	0	.06003	0	.02287	0	.01405	0
2	13.95	0	5.167	0	.3127	0	.07869	0	.03618	0	.02782
3	0	7.616	0	4.029	0	.2984	0	.08798	0	.04910	0
4	1.120	0	5.246	0	3.372	0	.2850	0	.09800	0	.06946
5	0	.7268	0	4.084	0	2.945	0	.2785	0	.1160	0
6	.3188	0	.5431	0	3.398	0	2.658	0	.2858	0	.1602
7	0	.2310	0	.4384	0	2.951	0	2.459	0	.2883	0
8	.1463	0	.1928	0	.3869	0	2.673	0	2.401	0	.4794
9	0	.1232	0	.1739	0	.3628	0	2.533	0	2.487	0
10	.09772	0	.1170	0	.1753	0	.3799	0	2.565	0	4.444
11	0	.04937	0	.06423	0	.1060	0	.2635	0	2.244	0

REFERENCES

1. DeYoung, J.: Theoretical Symmetric Span Loading Due to Flap Deflection for Wings of Arbitrary Plan Form at Subsonic Speeds. NACA Report 1071, 1952. (U)
2. Young, A. D.: The Aerodynamic Characteristics of Flaps. British Report No. Aero 2185, February 1947. (U)
3. Ames Research Staff: Equations, Tables, and Charts for Compressible Flow. NASA Report 1135, 1953. (U)

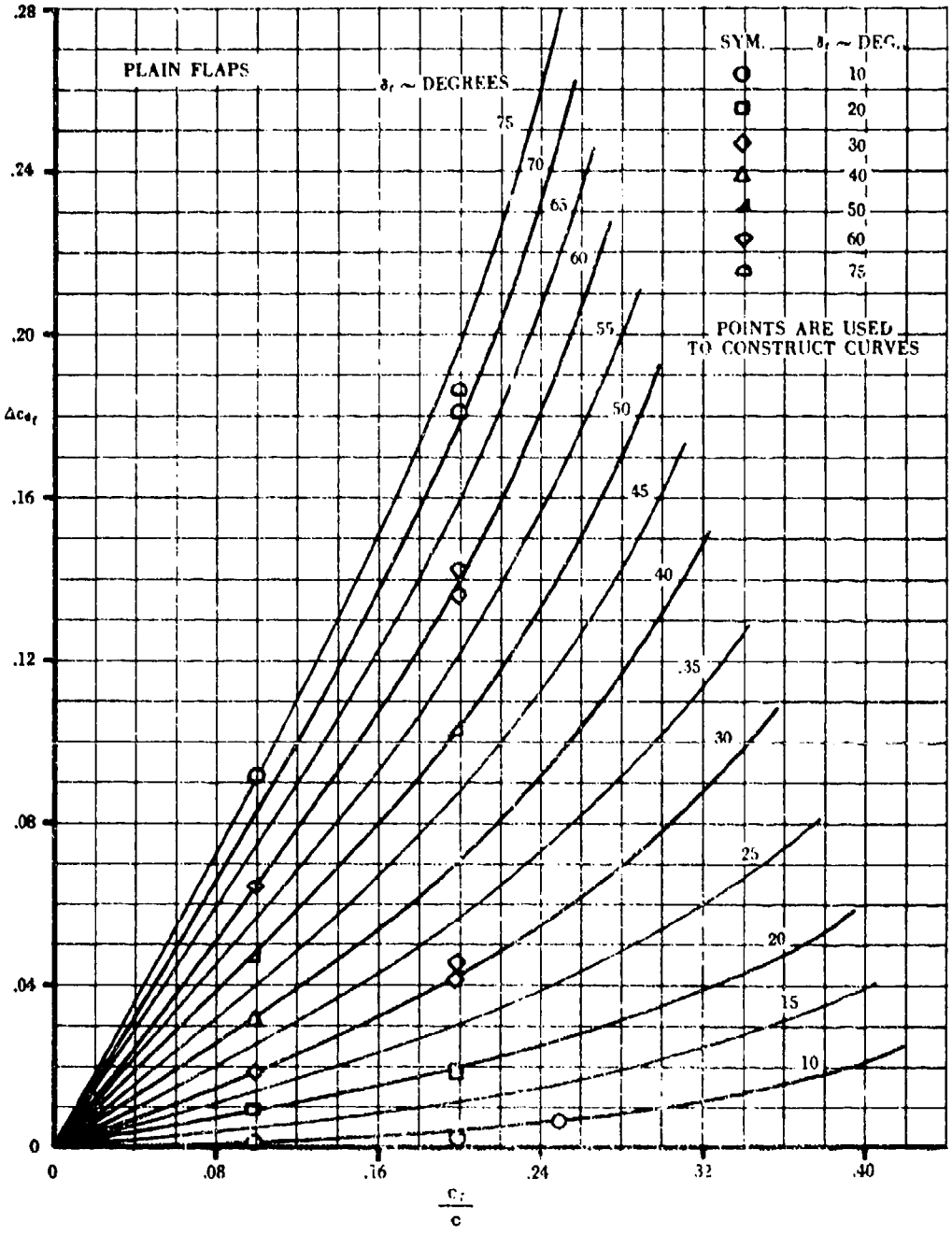

FIGURE 6.1.7-22 TWO-DIMENSIONAL DRAG INCREMENT DUE TO FLAPS

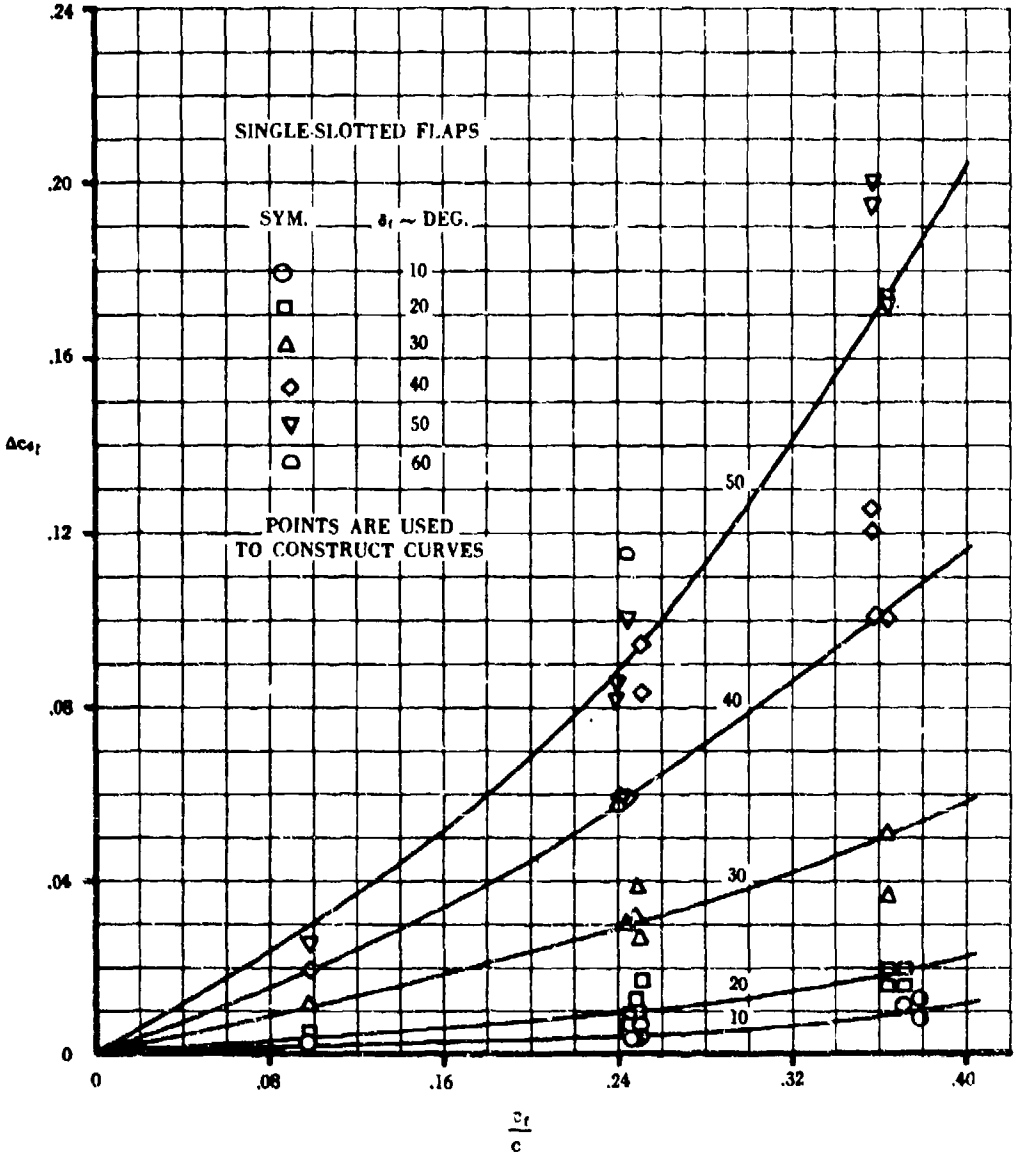

FIGURE 6.1.7-23 TWO-DIMENSIONAL DRAG INCREMENT DUE TO FLAPS

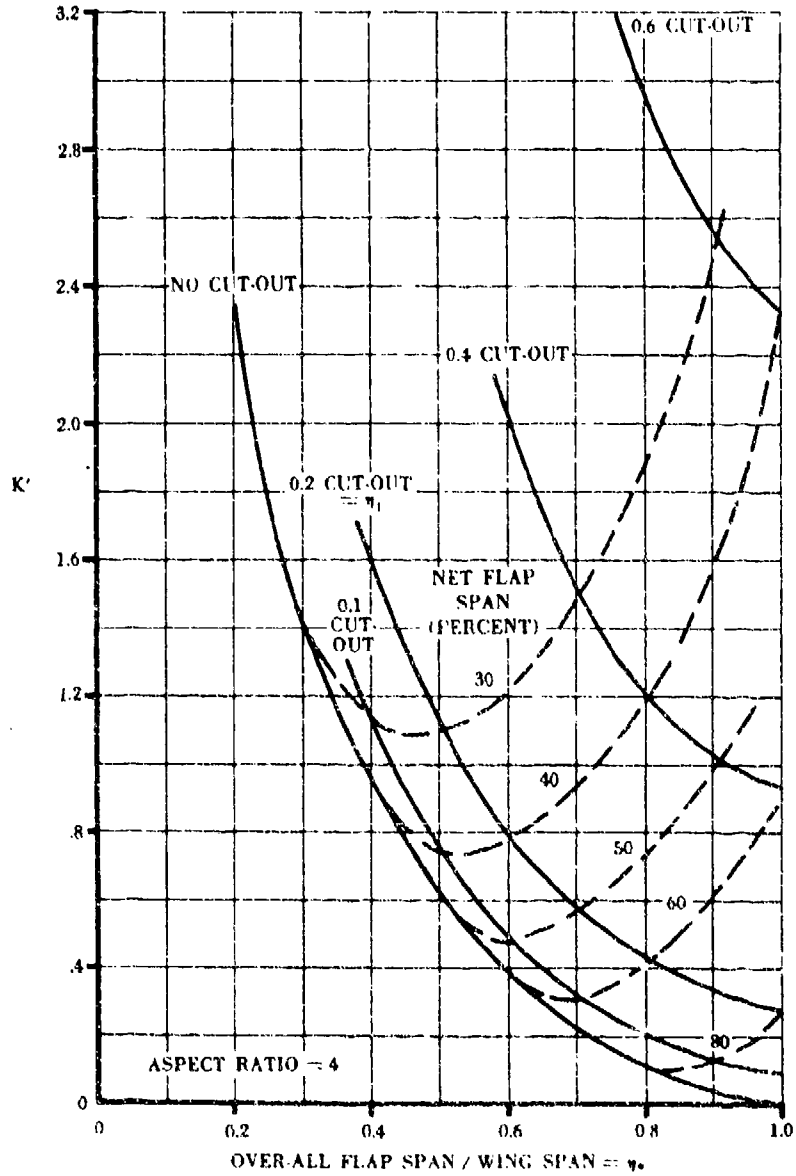

FIGURE 6.1.7-24 (a) FACTOR K' FOR CALCULATING INDUCED DRAG OF AN ELLIPTIC WING WITH PART-SPAN FLAPS AND CUT-OUT

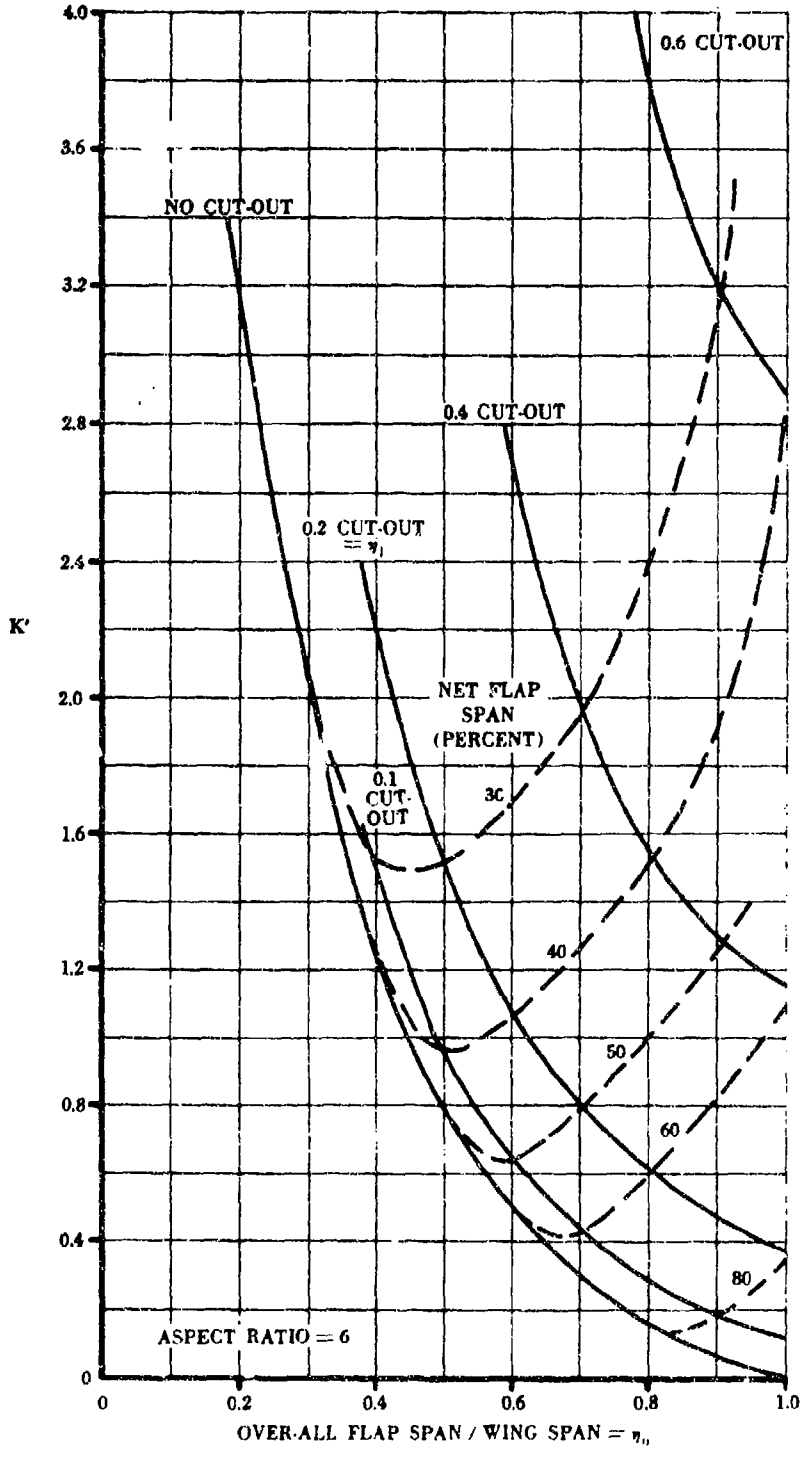

FIGURE 6.1.7-24 (b) FACTOR K' FOR CALCULATING INDUCED DRAG OF AN ELLIPTIC WING WITH PART-SPAN FLAPS AND CUT-OUT

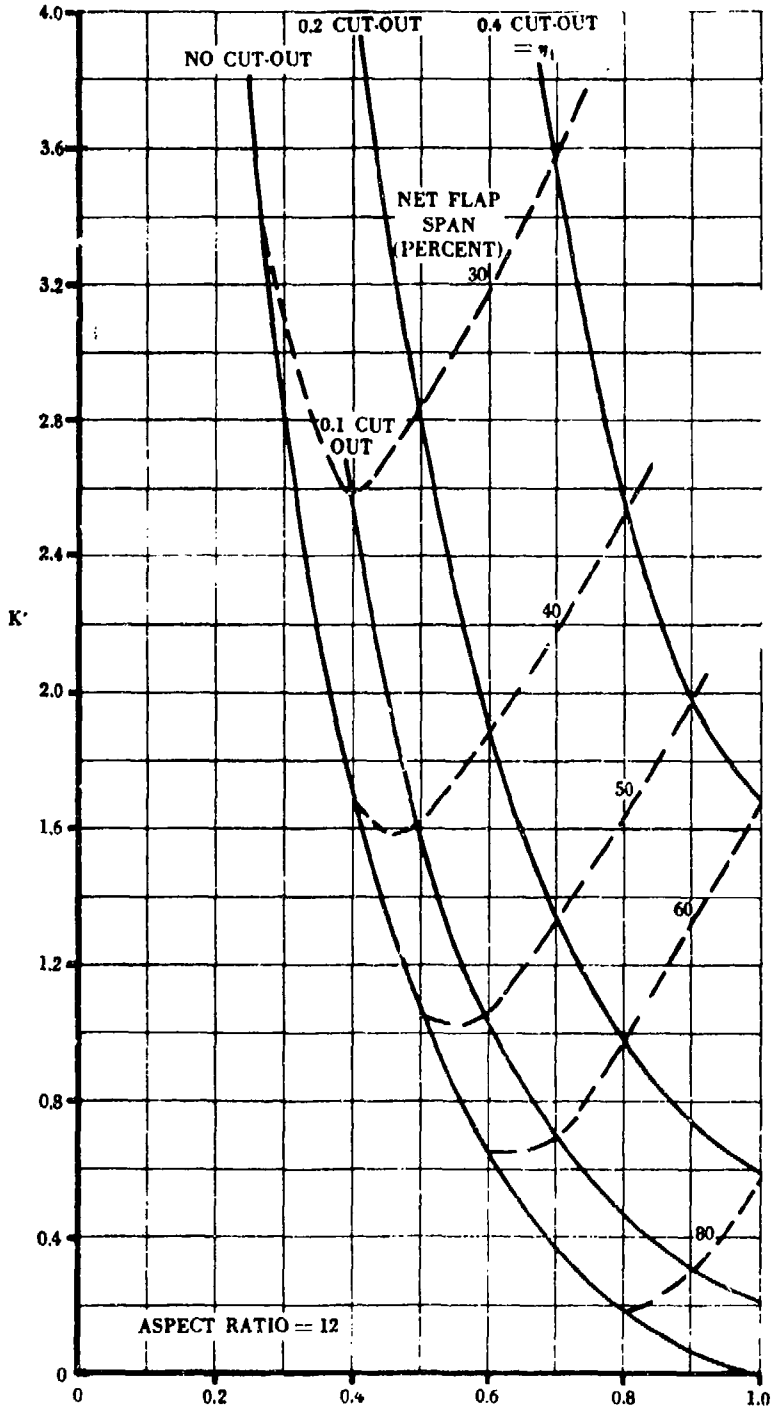

FIGURE 6.1.7-24 (c) FACTOR K' FOR CALCULATING INDUCED DRAG OF AN ELLIPTIC WING WITH PART-SPAN FLAPS AND CUT-OUT

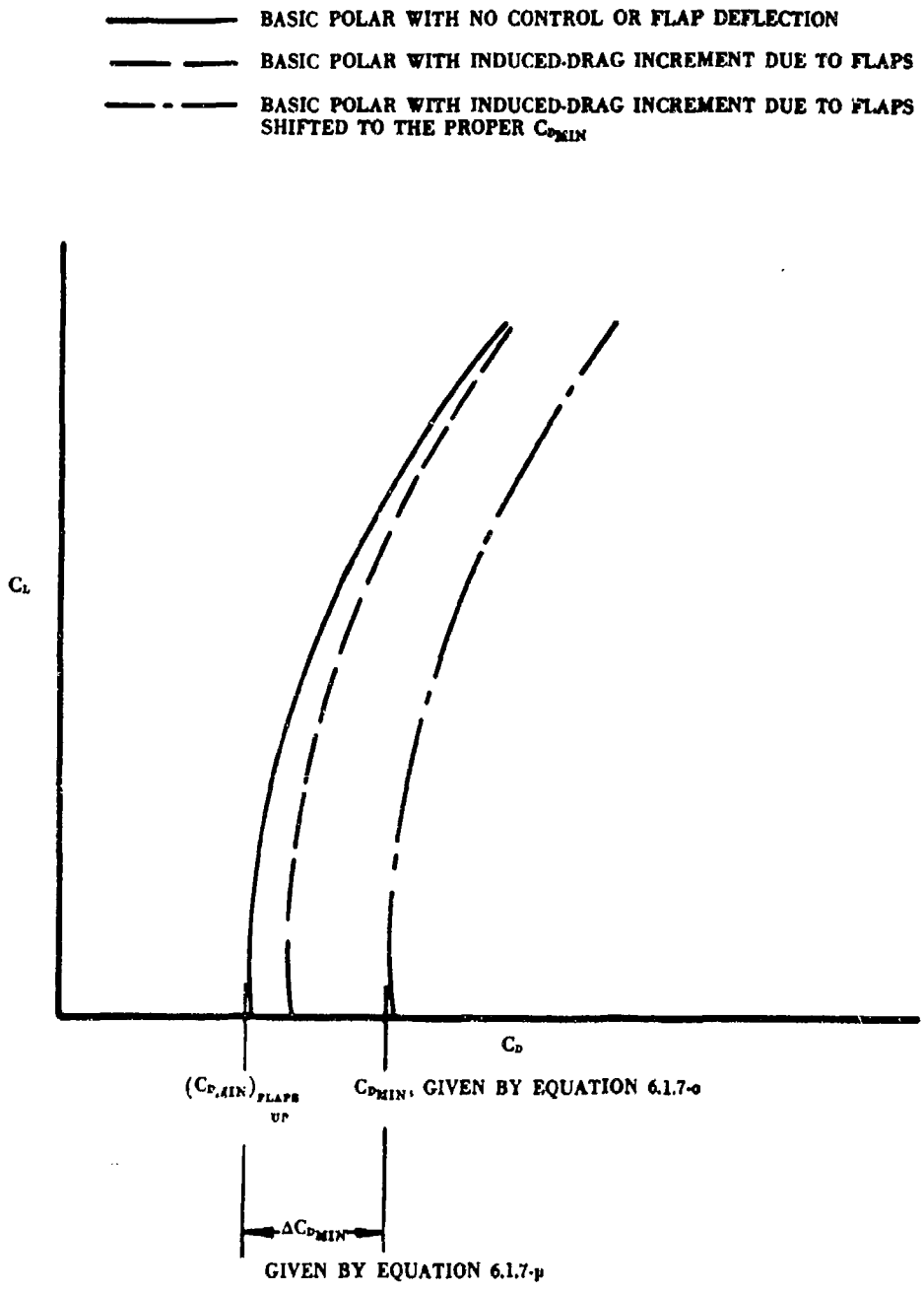

FIGURE 6.1.7-27 CONSTRUCTION OF FLAPS-DEFLECTED DRAG POLAR

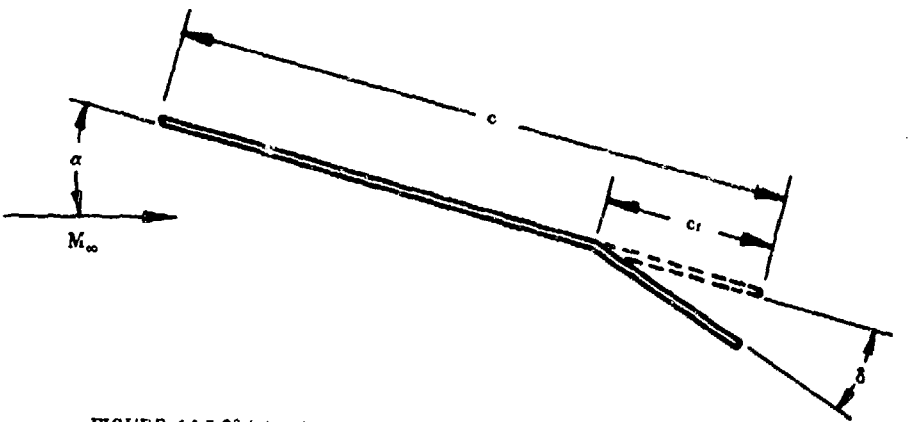

FIGURE 6.1.7-28 (a) CROSS SECTION OF AERODYNAMIC SURFACE

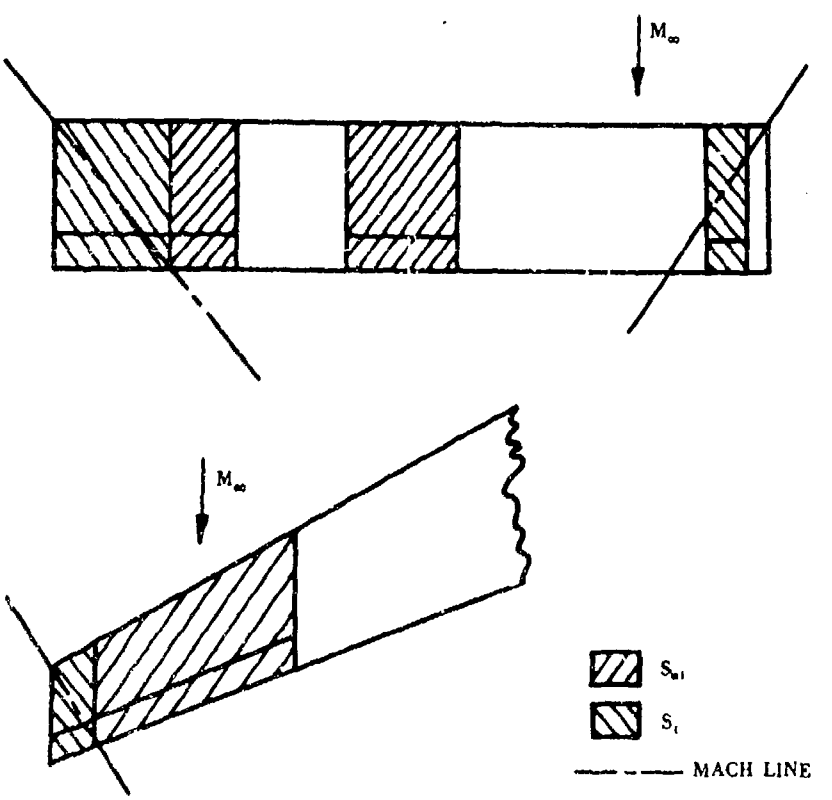

FIGURE 6.1.7-28 (b) EXAMPLES OF S_{el} AND S_t

6.2 ASYMMETRICALLY DEFLECTED CONTROLS ON WING-BODY AND TAIL-BODY CONTROL COMBINATIONS

6.2.1 ROLLING MOMENT DUE TO ASYMMETRIC DEFLECTION OF CONTROL DEVICES

6.2.1.1 ROLLING MOMENT DUE TO CONTROL DEFLECTION

Methods are presented in this section for estimating the rolling moment due to control deflection at subsonic, transonic, and supersonic speeds. Plain trailing-edge flap-type controls and spoilers are included. The fundamental means by which each of these devices changes the lift of a wing, and hence the rolling moment, is discussed in Section 6.1.1.1.

A discussion of the aerodynamic aspects of spoilers on three-dimensional wings is given in reference 1. This reference also contains an extensive bibliography of spoiler tests. The following discussion summarizes the conclusions of this reference.

At subsonic and transonic speeds, spoilers do not, in general, provide linear variation of effectiveness with spoiler projection, particularly at small deflections (see sketch (a)). This deficiency can be corrected by the use of a slot or slot-deflector behind the spoiler.

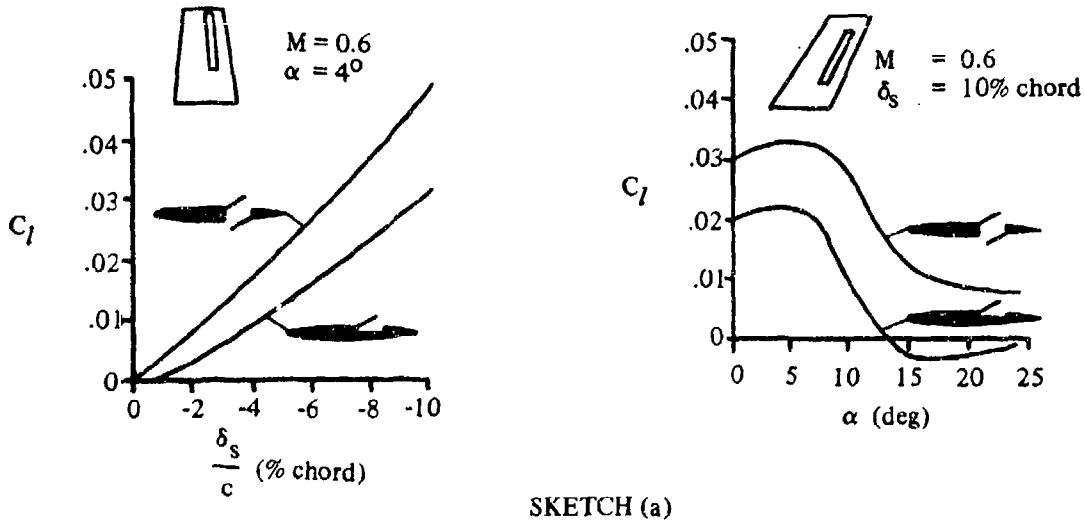

SKETCH (a)

For thin wings at high angles of attack plain spoilers are ineffective. This ineffectiveness can be partially overcome by the use of a slot behind the spoiler and by the use of leading-edge devices. Sketch (b) shows the effect of a drooped leading-edge extension on the rolling effectiveness of a plain and of a slotted spoiler.

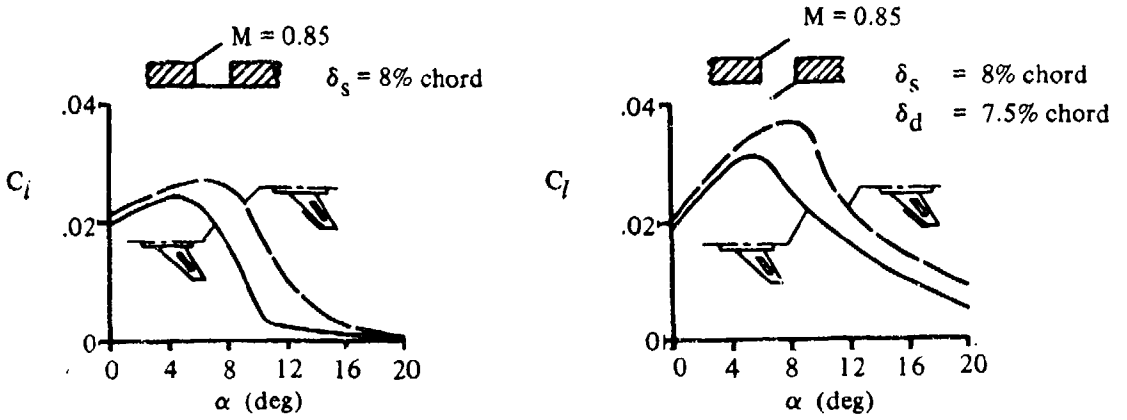

EFFECT OF DROOPED WING LEADING-EDGE EXTENSION ON SPOILER EFFECTIVENESS

SKETCH (b)

In order to achieve maximum effectiveness, spoilers should be located toward the rear portion of the wing for the following reasons:

1. The ineffectiveness of spoilers at small deflections increases with distance from the trailing edge.

2. The lag time at low speeds becomes excessively long for forward-mounted spoilers.

The optimum spanwise extent and position of spoilers are determined primarily by wing sweep. The higher the sweep angle, the farther inboard the spoilers should be placed. Sketch (c) shows the spoiler rolling moment for a spoiler extending from the wing tip to any inboard station y_i. The ineffectiveness of tip-located spoilers on swept wings is apparent.

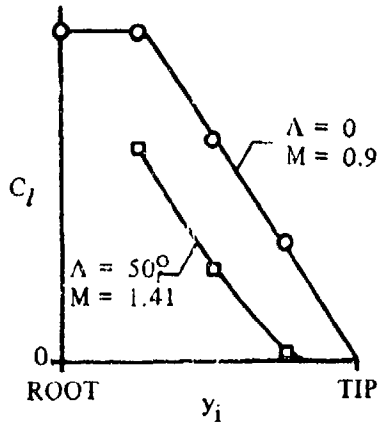

SKETCH (c)

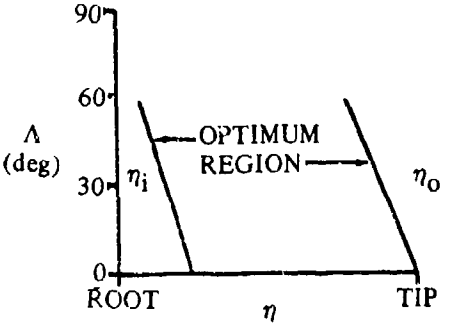

SKETCH (d)

The optimum spanwise location of spoilers as a function of wing sweep is shown in sketch (d).

A. SUBSONIC

Plain Trailing-Edge Flaps

A simplified lifting-surface theory is used in reference 2 to obtain the rolling-moment effectiveness C_{l_δ} for plain trailing-edge controls at subcritical Mach numbers. The theory is applicable to wings for which $\beta A \geq 2$ and $\Lambda_\beta < 60^o$, where $\Lambda_\beta = \tan^{-1}(\tan \Lambda_{c/4}/\beta)$. The Prandtl-Glauert compressibility correction is used to account for subcritical compressibility effects. In this section the theory of reference 2 is used up to M = 0.6. Since the theory is based on potential flow, the results are valid for attached-flow conditions only, i.e., wing angle of attack and surface deflection where no flow separation exists.

Two-dimensional lift-curve slopes for specific wing sections are used to adjust the wing lift distribution. It should be noted that the design charts from reference 2 give results for two full-chord controls antisymmetrically deflected. Then, absolute values of the section-lift effectiveness $|\alpha_\delta|$ for a specific configuration are used to adjust the theory to realistic values. This results in positive values of C_{l_δ} for antisymmetric control deflections. The proper sign of the rolling-moment coefficient will result from the expression $C_l = C_{l_\delta} \dfrac{(\delta_L - \delta_R)}{2}$ *

Spoilers

The method for predicting the effectiveness of plug and flap type spoilers is taken from reference 3. The method is based on the simplified lifting-surface theory developed for flap-type controls in reference 2, used with section spoiler data and an empirical correction for the effective spanwise location on swept wings. The results are valid for attached flow conditions only.

A design chart based on the empirical results of reference 4 is presented for the prediction of the subsonic rolling effectiveness of spoiler-slot-deflector controls.

DATCOM METHODS

Plain Trailing-Edge Flaps

The wing trailing-edge control derivative C_{l_δ} at subcritical Mach numbers, based on the total wing area and wing span, is obtained from the procedure outlined in the following steps:

Step 1. Obtain the rolling-moment effectiveness parameter $\beta C'_{l_\delta}/\kappa$ of two full-chord controls ($c_f/c = 1.0$) antisymmetrically deflected, as a function of $\beta A/\kappa$ and Λ_β, from figure 6.2.1.1-23.

The parameter κ is the ratio of the two-dimensional lift-curve slope at the appropriate Mach number to $2\pi/\beta$, i.e., $(c_{\ell_\alpha})_M / 2\pi/\beta$. The two-dimensional lift-curve slope is obtained from Section 4.1.1.2. For wings with airfoil sections varying in a reasonably linear manner with span, the lift-curve slope of the section at the MAC of the flapped portion of the wing is adequate.

The parameter Λ_β is the compressible sweep parameter, given as $\Lambda_\beta = \tan^{-1}(\tan \Lambda_{c/4}/\beta)$.

*The usual convention is implied. Positive rolling moment is right wing down. Positive control deflection is trailing edge down.

Figure 6.2.1.1-23 gives directly the effectiveness parameter for control spans measured from the plane of symmetry outboard. For partial-span controls having the inboard edge of the control at spanwise station η_i and the outboard edge at η_o, the effectiveness parameter is obtained as illustrated in sketch (e).

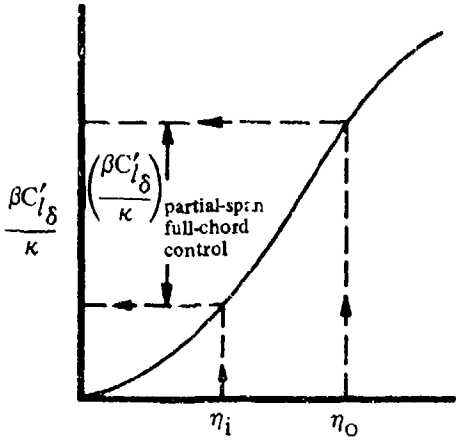

SKETCH (e)

Step 2. Determine the rolling effectiveness of two full-chord controls antisymmetrically deflected by

$$C'_{l_\delta} = \frac{\kappa}{\beta}\left(\frac{\beta C'_{l_\delta}}{\kappa}\right) \qquad 6.2.1.1\text{-a}$$

Step 3. Determine the rolling effectiveness of the partial-chord controls (c_f/c < 1.0) of constant-percent-chord (c_f/c = constant) antisymmetrically deflected by

$$C_{l_\delta} = |\alpha_\delta| C'_{l_\delta} \qquad 6.2.1.1\text{-b}$$

where C'_{l_δ} is obtained from equation 6.2.1.1-a and $|\alpha_\delta|$ is the absolute value of the section lift effectiveness. α_δ is obtained from Section 6.1.1.1 for the particular control under consideration. For antisymmetric control deflections the value of α_δ is based on the deflection of one surface.

The effect of a differential control deflection is taken into account by considering C_{l_δ} of each control as one-half the antisymmetric value (equation 6.2.1.1-b) where $|\alpha_\delta|$ is considered separately for each control and based on its respective deflection. Then, the total rolling-moment coefficient for differential-control deflection is obtained by

$$C_l = \left(\frac{C_{l_\delta}}{2}\right)_L \delta_L - \left(\frac{C_{l_\delta}}{2}\right)_R \delta_R$$

For arbitrary spanwise distribution of control chord (constant-chord controls on tapered wings or tapered controls on untapered wings), the control is divided into spanwise steps, and the total C_{l_δ} value is found by summing the C_{l_δ} values due to each spanwise step, based on the average $|\alpha_\delta|$ values over that spanwise step.

It should be noted that in applying this method the control deflection angles and all dimensions are measured in planes parallel and perpendicular to the plane of symmetry.

The relationship between streamwise control deflection δ, control deflection measured normal to the control hinge line $\delta_{\perp_{HL}}$, and sweep of the flap hinge line Λ_{HL} is

$$\tan \delta = \cos \Lambda_{HL} \tan \delta_{\perp_{HL}}$$

The relationship between a C_{l_δ} value defined for a streamwise deflection and the corresponding value defined normal to the hinge line is

$$C_{l_\delta} = C_{l_{\delta_{\perp_{HL}}}} \cos \Lambda_{HL}$$

Sample problem 1 on page 6.2.1.1-7 illustrates the use of this method.

There are not enough experimental data available to substantiate this method. However, for configurations within the limitations of the method it is expected that the accuracy of the calculated results will be within ±10 percent.

Spoilers

Plug or Flap-Type Spoilers

The rolling-moment coefficient of a plug or a flap-type spoiler deflected on one wing panel only, based on the total wing area and wing span, is given by

$$C_l = \frac{C'_{l_\delta}}{2} \Delta\alpha'_s \qquad \text{6.2.1.1-c}$$

where

C'_{l_δ} is the rolling-moment effectiveness of two full-chord controls antisymmetrically deflected, obtained as outlined in the above method for plain-trailing-edge controls, but with effective locations of the inboard and outboard ends of the control used in place of their geometric locations in reading figure 6.2.1.1-23.

$\Delta\alpha'_s$ is the spoiler lift effectiveness expressed in terms of the change in zero-lift angle of attack. This parameter is presented as a function of effective spoiler height for four spoiler chordwise locations in figure 6.1.1.1-52. In using this figure, x_s is the distance from the nose of the airfoil to the spoiler lip, and h_s is the height of the spoiler measured from and normal to the airfoil mean line at x_s (see sketch (f)).

SKETCH (f)

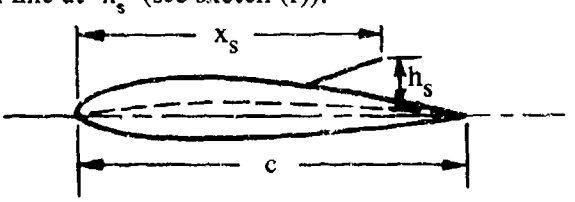

The effective locations of the inboard and outboard ends of the spoiler, used in reading figure 6.2.1.1-23, are given by

$$\left.\begin{aligned} \eta_{i_{eff}} &= \eta_i + \Delta\eta_i \\ \eta_{o_{eff}} &= \eta_o + \Delta\eta_o \end{aligned}\right\} \qquad 6.2.1.1.\text{-d}$$

where η_i and η_o are the spanwise locations of the inboard and outboard ends of the spoiler, respectively, and $\Delta\eta_i$ and $\Delta\eta_o$ are effective increments in the spoiler spanwise locations due to the spanwise flow of the spoiler wake for partial-span spoilers. These increments in spoiler spanwise locations are given by

$$\left.\begin{aligned} \Delta\eta_i &= \frac{4\left(1 - \frac{x'_s}{c}\right)}{A(1+\lambda)}\left[1 - (1-\lambda)\,\eta_i\right]\frac{\cos\Lambda_{TE}\,\sin\theta}{\cos(\Lambda_{TE}+\theta)} \\ \Delta\eta_o &= \frac{4\left(1 - \frac{x'_s}{c}\right)}{A(1+\lambda)}\left[1 - (1-\lambda)\,\eta_o\right]\frac{\cos\Lambda_{TE}\,\sin\theta}{\cos(\Lambda_{TE}+\theta)} \end{aligned}\right\} \qquad 6.2.1.1.\text{-e}$$

where θ is an empirically determined angle obtained from figure 6.2.1.1-26a as a function of the spoiler sweepback. The spoiler sweepback is determined from the expression

$$\tan\Lambda_s = \tan\Lambda_{c/4} - \frac{4\left[0.75 - \left(1 - \frac{x'_s}{c}\right)\right]}{A}\left(\frac{1-\lambda}{1+\lambda}\right)$$

In using this method, if $\eta_{o_{eff}}$ exceeds 1.0, which would be the case for the spoiler extending almost to the wing tip on a highly swept wing, the value of C'_{l_δ} at $\eta_o = 1.0$ is used.

The effective spanwise extent of an arbitrarily located spoiler as used in this method is illustrated in sketch (g).

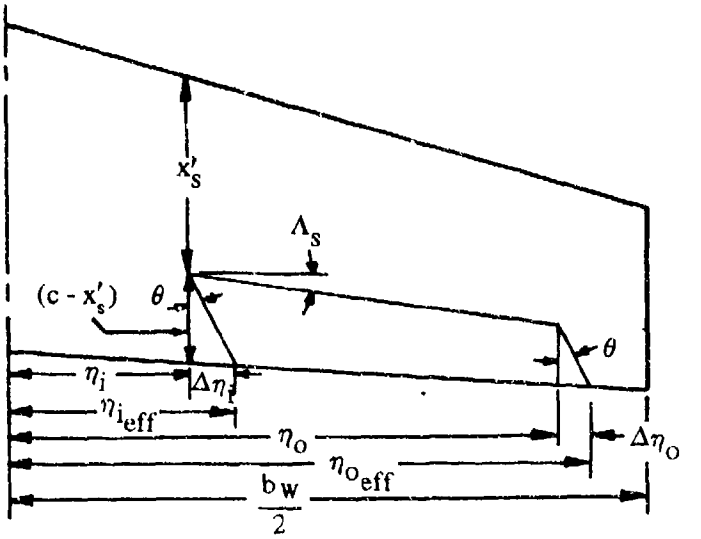

SKETCH (g)

Sample problem 2 on page 6.2.1.1-9 illustrates the use of this method.

Comparisons of test data with results calculated by using this method are presented as table 6.2.1.1-A. Additional comparisons between test and calculated values are given in reference 3.

Only spoilers of constant-percent-chord height (h_s/c = constant) were included in the analysis of reference 3; however, it is implied therein that the method should give acceptable results for arbitrary spanwise distribution of spoiler control chord.

Spoiler-Slot-Deflector

The rolling-moment coefficient of a spoiler-slot-deflector on one wing panel, based on the total wing area and wing span, is given by

$$(C_l)_{\text{spoiler-slot-deflector}} = K(C_l)_{\text{plain spoiler}} \qquad 6.2.1.1\text{-f}$$

where

$(C_l)_{\text{plain spoiler}}$ is the rolling-moment coefficient of a plain flap-type spoiler deflected on one wing panel, based on the total wing area and wing span, determined by using equation 6.2.1.1-c.

K is the ratio of the rolling-moment coefficient of a spoiler-slot-deflector to that of a plain spoiler, obtained from figure 6.2.1.1-26b, as a function of the ratio of spoiler deflection to deflector deflection δ_s/δ_d. The spoiler and deflector deflections are illustrated in figure 6.2.1.1-26b. Note the difference between the spoiler-height measurement h_s used in determining C_l of the plain spoiler and the δ_s and δ_d measurements for the spoiler-slot-deflector control.

Figure 6.2.1.1-26b is based on the empirical results of reference 4. The wing planform of the test configuration is a straight-tapered wing with $A = 4.0$, $\lambda = 0.6$, $\Lambda_{c/4} = 32.6^\circ$, and with an NACA 65006 airfoil section in the streamwise direction. The method has not been verified by comparison with other test results. Nevertheless, the method is expected to give acceptable results over the linear-lift range for configurations with $\beta A \geq 2$ and $\Lambda_\beta < 60^\circ$, and at Mach numbers up to 0.6.

The use of this method is illustrated in sample problem 3 on page 6.2.1.1-12.

Sample Problems

1. Plain Trailing-Edge-Flap Ailerons

Given: The following wing-aileron configuration:

Wing Characteristics:

$A_W = 3.78$ $\lambda_W = 0.586$ $\Lambda_{c/4} = 47.35^\circ$

NACA 65009 airfoil (streamwise) $\tan \phi'_{TE}/2 = 0.0776$ (streamwise airfoil section geometry)

Aileron Characteristics:

Plain trailing-edge flap $c_f/c = 0.30$ $\eta_i = 0.75$ $\eta_o = 0.95$

$\delta_L = 15^o$ $\delta_R = -15^o$

Additional Characteristics:

$M = 0.40$; $\beta = 0.917$ $R_\ell = 9 \times 10^6$

Compute:

C'_{l_δ}

$$\frac{c_{\ell_\alpha}}{\left(c_{\ell_\alpha}\right)_{theory}} = 0.893 \quad \text{(figure 4.1.1.2-8a)}$$

$$\left(c_{\ell_\alpha}\right)_{theory} = 6.58 \text{ per rad} \quad \text{(figure 4.1.1.2-8b)}$$

$$\left(c_{\ell_\alpha}\right)_M = \frac{1.05}{\beta}\left[\frac{c_{\ell_\alpha}}{\left(c_{\ell_\alpha}\right)_{theory}}\right]\left(c_{\ell_\alpha}\right)_{theory} \quad \text{(equation 4.1.1.2-a)}$$

$$= \frac{1.05}{0.917}\,(0.893)\,(6.58) = 6.73 \text{ per rad}$$

$$\kappa = \frac{\left(c_{\ell_\alpha}\right)_M}{2\pi/\beta} = \frac{6.73}{2\pi/\beta} = 0.981$$

$$\frac{\beta A}{\kappa} = \frac{(0.917)\,(3.78)}{0.981} = 3.53$$

$$\Lambda_\beta = \tan^{-1}\frac{\tan \Lambda_{c/4}}{\beta} = \tan^{-1}\left(\frac{1.0856}{0.917}\right) = 49.8^o$$

$$\left.\begin{aligned}\left(\frac{\beta C'_{l_\delta}}{\kappa}\right)_{\eta_i = 0.75} &= 0.320 \text{ per rad}\\ \left(\frac{\beta C'_{l_\delta}}{\kappa}\right)_{\eta_o = 0.95} &= 0.420 \text{ per rad}\end{aligned}\right\} \quad \text{(figures 6.2.1.1-23a through -23c, interpolated)}$$

$$C'_{l_\delta} = \frac{\kappa}{\beta}\left[\left(\frac{\beta C'_{l_\delta}}{\kappa}\right)_{\eta_o} - \left(\frac{\beta C'_{l_\delta}}{\kappa}\right)_{\eta_i}\right] \quad \text{(equation 6.2.1.1-a)}$$

$$= \frac{0.981}{0.917}\,[0.420 - 0.320] = 0.107 \text{ per rad}$$

Section lift effectiveness α_δ (Section 6.1.1.1)

$$\left(c_{\ell_\delta}\right)_{\text{theory}} = 4.35 \text{ per rad (figure 6.1.1.1-39a)}$$

$$\frac{c_{\ell_\delta}}{\left(c_{\ell_\delta}\right)_{\text{theory}}} = 0.840 \text{ (figure 6.1.1.1-39b)}$$

$$K' = 0.98 \text{ (figure 6.1.1.1-40)}$$

$$\Delta c_\ell = \delta\left[\frac{c_{\ell_\delta}}{\left(c_{\ell_\delta}\right)_{\text{theory}}}\right]\left(c_{\ell_\delta}\right)_{\text{theory}} K' \text{ (equation 6.1.1.1-c)}$$

$$= \frac{15.0}{57.3}(0.840)(4.35)(0.98) = 0.937$$

$$\alpha_\delta = -\frac{\left(c_{\ell_\delta}\right)_\alpha}{\left(c_{\ell_\alpha}\right)_\delta} \text{ (equation 6.1.1.1-b)}$$

$$= -\frac{\Delta c_\ell}{\left(c_{\ell_\alpha}\right)_\delta^\delta} = -\frac{(0.937)}{(6.73)\frac{15.0}{57.3}} = -0.532$$

Solution:

$$C_{l_\delta} = C'_{l_\delta}\,|\alpha_\delta| \text{ (equation 6.2.1.1-b)}$$

$$= (0.107)(0.532) = 0.0569 \text{ per rad}$$

The rolling-moment coefficient is given by

$$C_l = \left(\frac{C_{l_\delta}}{2}\right)_L \delta_L - \left(\frac{C_{l_\delta}}{2}\right)_R \delta_R$$

$$= \frac{0.0569}{2(57.3)}\,[15 - (-15)] = 0.0149 \text{ (based on } S_w b_w)$$

2. Spoiler

Given: The wing-body configuration of reference 4 with a partial-span constant-chord spoiler hinged at the 55-percent-chord line.

Wing Characteristics:

$A_w = 4.0$ $\quad \lambda_w = 0.60$ $\quad S_w = 324.0$ sq in. $\quad b_w = 36.0$ in.

$\Lambda_{c/4} = 32.6^o$ $\quad \Lambda_{TE} = 24.3^o$ $\quad$ NACA 65006 airfoil (streamwise)

Spoiler Characteristics:

$$\eta_i = \frac{y_i}{b/2} = 0.139 \qquad \eta_o = \frac{y_o}{b/2} = 0.639 \qquad \frac{c_s}{c} = 0.150$$

Spoiler projection δ_s measured from the airfoil surface at 0.70c, and corresponding spoiler chordwise location

$$\frac{\delta_s}{c} = 0.100$$

$$\frac{x_s}{c} = 0.662$$

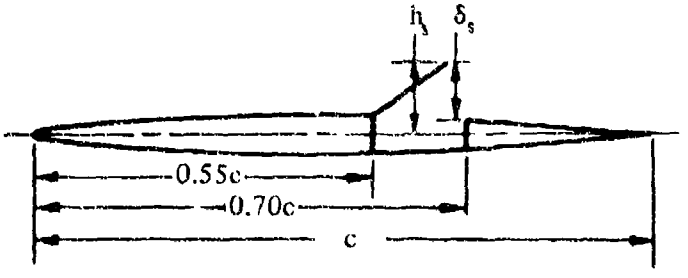

Additional Characteristics:

$M = 0.40$; $\beta = 0.917$

Compute:

Determine C'_{l_δ}

$c_{\ell_\alpha} = 0.105$ per deg $= 6.02$ per rad (table 4.1.1-B)

$$\left(c_{\ell_\alpha}\right)_M = \frac{c_{\ell_\alpha}}{\beta} = \frac{6.02}{0.917} = 6.56 \text{ per rad}$$

$$\kappa = \frac{\left(c_{\ell_\alpha}\right)_M}{2\pi/\beta} = \frac{6.56}{2\pi/\beta} = 0.958$$

$$\Lambda_\beta = \tan^{-1}\frac{\tan\Lambda_{c/4}}{\beta} = \tan^{-1}\frac{0.6395}{0.917} = 34.9^o$$

$$\frac{\beta A}{\kappa} = \frac{0.917\,(4.0)}{0.958} = 3.85$$

Determine $\eta_{i_{eff}}$ and $\eta_{o_{eff}}$

$$\tan\Lambda_s = \tan\Lambda_{c/4} - \frac{4\left[0.75 - \left(1 - \frac{x_s}{c}\right)\right]}{A}\left(\frac{1-\lambda}{1+\lambda}\right)$$

$$= 0.6395 - \frac{4}{4.0}\,[0.75 - (1 - 0.662)]\,\frac{0.40}{1.60}$$

$$= 0.6395 - (0.412)(0.25) = 0.5365$$

$$\Lambda_s = \tan^{-1} 0.5365 = 28.2^{\circ}$$

$$\theta = 28.3^{\circ} \text{ (figure 6.2.1.1-26a)}$$

$$\frac{\cos \Lambda_{TE} \sin \theta}{\cos (\Lambda_{TE} + \theta)} = \frac{0.9114\,(0.4741)}{0.6074} = 0.7114$$

$$\frac{4\left(1 - \frac{x'_s}{c}\right)}{A(1+\lambda)} = \frac{4\,(1 - 0.662)}{4.0\,(1.60)} = 0.211$$

$$[1 - (1 - \lambda)\,\eta_i] = [1 - (1 - 0.6)\,(0.139)] = 0.944$$

$$[1 - (1 - \lambda)\,\eta_o] = [1 - (1 - 0.6)\,(0.639)] = 0.744$$

$$\left.\begin{aligned} \Delta\eta_i &= \frac{4\left(1 - \frac{x'_s}{c}\right)}{A(1+\lambda)}\,[1 - (1 - \lambda)\,\eta_i]\,\frac{\cos \Lambda_{TE} \sin \theta}{\cos (\Lambda_{TE} + \theta)} \\ &= (0.211)\,(0.944)\,(0.7114) = 0.142 \end{aligned}\right\} \text{(equation 6.2.1.1-e)}$$

$$\left.\begin{aligned} \Delta\eta_o &= \frac{4\left(1 - \frac{x'_s}{c}\right)}{A(1+\lambda)}\,[1 - (1 - \lambda)\,\eta_o]\,\frac{\cos \Lambda_{TE} \sin \theta}{\cos (\Lambda_{TE} + \theta)} \\ &= (0.211)\,(0.744)\,(0.7114) = 0.112 \end{aligned}\right\}$$

$$\left.\begin{aligned} \eta_{i_{eff}} &= \eta_i + \Delta\eta_i = 0.139 + 0.142 = 0.281 \\ \eta_{o_{eff}} &= \eta_o + \Delta\eta_o = 0.639 + 0.112 = 0.751 \end{aligned}\right\} \text{(equation 6.2.1.1-d)}$$

$$\left.\begin{aligned} \left(\frac{\beta C'_{l\,\delta}}{\kappa}\right)_{\eta_{i_{eff}}} &= 0.061 \text{ per rad} \\ \left(\frac{\beta C'_{l\,\delta}}{\kappa}\right)_{\eta_{o_{eff}}} &= 0.350 \text{ per rad} \end{aligned}\right\} \text{(figures 6.2.1.1-23a through -23c, interpolated)}$$

$$C'_{l_\delta} = \frac{\kappa}{\beta}\left[\left(\frac{\beta C'_{l_\delta}}{\kappa}\right)_{\eta_{o_{eff}}} - \left(\frac{\beta C'_{l_\delta}}{\kappa}\right)_{\eta_{i_{eff}}}\right] \quad \text{(equation 6.2.1.1-a)}$$

$$= \frac{0.958}{0.917}\left[0.350 - 0.061\right] = 0.302 \quad \text{per rad}$$

Determine $\Delta\alpha'_s$

The upper-surface ordinate of the NACA 65006 airfoil section at 0.70c is 0.0194c. (see reference 5)

$$\frac{h_s}{c} = \frac{\delta_s}{c} + 0.0194 = 0.100 + 0.0194 = 0.1194$$

$\Delta\alpha'_s = 0.134$ (figure 6.1.1.1-52 at $x_s/c, h_s/c$)

Solution:

$$C_l = \frac{C'_{l_\delta}}{2}\Delta\alpha'_s \quad \text{(equation 6.2.1.1-c)}$$

$$= \left(\frac{0.302}{2}\right)(0.134)$$

$= 0.0202$ (based on $S_W b_W$) (Spoiler deflected on one wing panel)

This result compares with a test value of 0.0215 from reference 4.

3. Spoiler-Slot-Deflector

Given: The wing-body configuration of reference 4 with a partial-span constant-chord spoiler-slot-deflector on one wing panel. This is the configuration of sample problem 2 with the addition of a slot opening between the 55- and 70-percent-chord lines extending from $\eta_i = 0.139$ to $\eta_o = 0.639$, and a 0.15c deflector hinged at the 0.70 chord line.

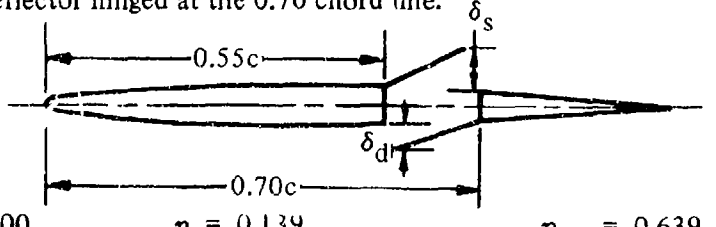

$S_W = 324.0$ sq in.

$b_W = 36.0$ in.

$\frac{\delta_s}{c} = 0.100$ $\eta_i = 0.139$ $\eta_o = 0.639$

$(C_l)_{\text{plain spoiler}} = 0.0202$ (sample problem 2)

$\frac{\delta_d}{c} = 0.025,\ 0.050,\ 0.075,\ 0.100$

Solution:

$$(C_l)_{\text{spoiler-slot-deflector}} = K(C_l)_{\text{plain spoiler}} \qquad \text{(equation 6.2.1.1-f)}$$

$$= (0.0202)\,K \qquad \text{(based on } S_w\, b_w\text{)}$$

① $\frac{\delta_s}{c}$	② $\frac{\delta_d}{c}$	③ δ_s/δ_d ① / ②	④ K figure 6.2.1.1-26b	⑤ $(C_l)_{\text{spoiler-slot-deflector}}$ (.0202) ④	⑥ $(C_l)_{\text{spoiler-slot-deflector}}$ (Test)
0.100	0.025	4.00	1.35	0.0273	0.0290
0.100	0.050	2.00	1.70	0.0343	0.0350
0.100	0.075	1.33	1.57	0.0317	0.0350
0.100	0.100	1.00	1.34	0.0271	0.0300

B. TRANSONIC

No accurate method is available for predicting C_{l_δ} at transonic speeds. Mixed flow conditions and interrelated shock-wave and boundary-layer-separation effects cause extreme nonlinearities in this parameter. The discussion of paragraph B of Section 4.1.3.2 gives some insight into these effects for plain wings.

The method presented here is intended to give a first-order approximation only and to provide a guide to aid in fairing between subcritical and supersonic speeds.

Published experimental data in the transonic speed range are available for only a specific flap-type control tested on a wing-planform series in which only the wing sweep was varied (references 6 through 9).

DATCOM METHOD

No specific charts are presented for determining the transonic rolling effectiveness of lateral-control devices. The best source of information of this type is experimental data on similar configurations. If such information is not available, the following approach may be used as a guide in fairing between subcritical and supersonic speeds.

A first-order approximation of the transonic rolling effectiveness of lateral-control devices is given by

$$C_l = (C_l)_{M=0.6} \frac{(C_{L_\alpha})}{(C_{L_\alpha})_{M=0.6}} \qquad \text{6.2.1.1-g}$$

where

$(C_l)_{M=0.6}$ is the rolling effectiveness of the control at M = 0.6, obtained by using the appropriate method of paragraph A of this section.

$\left(C_{L_\alpha}\right)$ is the transonic wing-lift-curve slope, obtained from paragraph B of Section 4.1.3.2.

$\left(C_{L_\alpha}\right)_{M=0.6}$ is the wing-lift-curve slope at M = 0.6, obtained by using the straight-tapered wing method of paragraph A of Section 4.1.3.2 (figure 4.1.3.2-41).

C. SUPERSONIC

Plain Trailing-Edge Flaps

Supersonic linear theory is used in reference 10 to derive conical-flow solutions for the rolling effectiveness of wing trailing-edge flap-type control surfaces. The theory is based on the following assumptions (see sketch (h)):

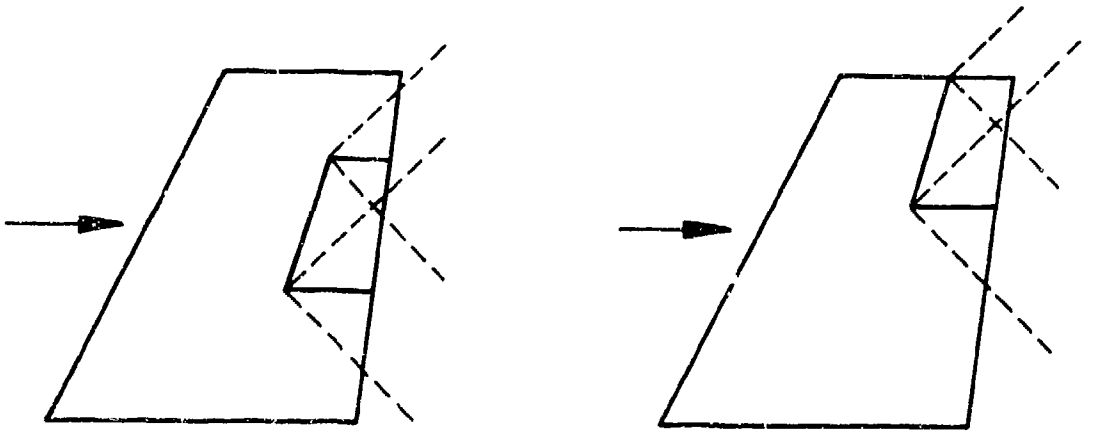

SKETCH (h)

1. The leading (hinge line) and trailing edges of the control surface are supersonic (swept ahead of the Mach lines).

2. The control surfaces are located at the wing tip or are far enough inboard to prevent the outermost Mach lines from the control surface from crossing the wing tip.

3. The innermost Mach lines from the deflected control surface do not cross the root chord.

4. The root and tip chords of the control surfaces are streamwise.

5. Controls are not influenced by the tip conical flow from the opposite wing panel or by the interaction of the wing-root Mach cone with the wing tip.

An approximate correction is given in reference 10 to account for the effect of airfoil thickness in the case of slab-sided controls.

Spoilers

The method presented for determining the supersonic rolling moment due to spoilers is taken from reference 11. The derivation is based on an analysis, presented in reference 12, of the pressure distributions adjacent to the spoiler. Although data on spoiler rolling characteristics at supersonic speeds are limited, the method appears satisfactory for both plug and flap-type spoilers within the Mach number range of the available data (M = 1.6 to 3.0).

No method is presented for determining the supersonic rolling moment due to spoiler-slot-deflectors. Published test data on spoiler-slot-deflector characteristics at supersonic speeds are extremely limited. References 13 and 14 present test data on spoiler-slot-deflector controls at supersonic speeds.

DATCOM METHODS

Plain Trailing-Edge Flaps

The supersonic rolling effectiveness of plain trailing-edge flap-type controls is given by

$$C_{l_\delta} = \left(1 - \frac{C_2}{C_1}\phi_{TE}\right) C'_{L_\delta} \frac{S_f}{S_W} \frac{1}{2}\left[\frac{y_i}{b_W} + \left(\frac{b_f}{2\,b_W}\right)\frac{C'_{l_\delta}}{C'_{L_\delta}}\right] \qquad 6.2.1.1\text{-h}$$

where

C_{l_δ} is the control-surface rolling effectiveness of one control surface deflected on one wing panel, based on the total wing area and span.

C'_{l_δ} is the theoretical rolling-moment derivative based on total control area S_f for thin wings for the following cases:

(a) Tapered control surfaces with outboard edge coincident with wing tip (use figure 6.2.1.1-27).

(b) Tapered control surfaces with outboard edge not coincident with wing tip (use figure 6.2.1.1 -28).

(c) Untapered control surfaces with outboard edge coincident with wing tip (use figure 6.2.1.1 -29a).

(d) Untapered control surface with outboard edge not coincident with wing tip (use figure 6.2.1.1 -29b).

$\frac{S_f}{S_W}$ is the ratio of the total control area (both sides of wing) to the total wing area.

$\frac{b_f}{b_W}$ is the ratio of the total control span (both sides of wing) to the total wing span.

$\frac{y_i}{b_W}$ is the distance from the wing root chord to the control root chord in wing spans.

$\left(1 - \frac{C_2}{C_1}\phi_{TE}\right)$ is a thickness correction factor to the supersonic flat-plate derivative.

$$C_1 = \frac{2}{\sqrt{M^2 - 1}} \text{ (per radian)}$$

$$C_2 = \frac{(\gamma + 1)\,M^4 - 4\,(M^2 - 1)}{2\,(M^2 - 1)^2} \quad \text{(per radian)}$$

θ_{TE} is the trailing-edge angle in radians, measured normal to the control hinge line.

γ is the ratio of specific heats, $\gamma = 1.4$.

C'_{L_δ} is the lift-effectiveness of one symmetric, straight-sided control, based on the area of the control. This parameter is obtained from figures 6.1.4.1-20a through 6.1.4.1-20j for controls located at the wing tip, and from figure 6.1.4.1-25 for controls located inboard from the wing tip.

It should be noted that in applying this method the control deflection angle and all dimensions (with the exception of ϕ_{TE}) are measured in planes parallel and perpendicular to the plane of symmetry.

The limitations of this method are noted in the introduction to paragraph C. A comparison of test values with results calculated by this method is presented as table 6.2.1.1-B.

Sample problem 1 at the conclusion of this paragraph illustrates the use of the method.

Spoilers

Plug and Flap-Type Spoilers

The supersonic rolling-moment coefficient of a plug or a flap-type spoiler deflected on one panel, based on the total wing area and span, is obtained from figure 6.2.1.1-30 as a function of Mach number and configuration geometry.

A comparison of test values with results calculated by using this method is presented as table 6.2.1.1-C.

Sample problem 2 at the conclusion of this paragraph illustrates the use of the method.

Sample Problems

1. Plain Trailing-Edge-Flap Ailerons

Given: The wing-body-tail configuration of reference 18, with plain trailing-edge ailerons.

Wing Characteristics:

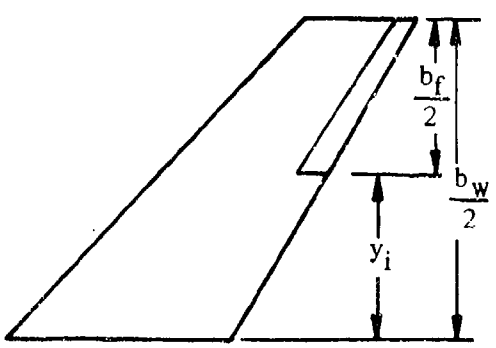

$S_W = 166.8$ sq in. $\quad b_W = 25.86$ in.

$\lambda_W = 0.50 \quad A_W = 4.0$

$\Lambda_{c/4} = 40^\circ \quad \Lambda_{TE} = 30.5^\circ$

$\Lambda_{LE} = 42.7^\circ$

Control Characteristics:

Symmetric, straight-sided outboard control $\Lambda_{HL} = 33.26^{o}$ $\lambda_f = 0.666$

$b_f = 12.93$ in. (both sides of wing) $S_f = 13.89$ sq in. (both sides of wing)

$\frac{y_i}{b_w} = 0.25$ $\phi_{TE} = 6^{o}$ $c_f/c = 0.20$

Additional Characteristics:

$M = 1.61$; $\beta = 1.262$; $M^2 - 1 = 1.592$

Compute:

$$C_1 = \frac{1}{\sqrt{M^2 - 1}} = \frac{1}{1.262} = 0.792 \text{ per rad}$$

$$C_2 = \frac{(\gamma + 1) M^4 - 4 (M^2 - 1)}{2 (M^2 - 1)^2} = \frac{(2.40) (1.61)^4 - 4 (1.592)}{2 (1.592)^2} = 1.925 \text{ per rad}$$

$$\frac{\tan \Lambda_{HL}}{\beta} = \frac{0.6558}{1.262} = 0.520; \quad \frac{\tan \Lambda_{TE}}{\beta} = \frac{0.5891}{1.262} = 0.467$$

$\beta C'_{L_\delta} = 0.0745$ per deg (figures 6.1.4.1-20g through -20i, interpolated)

$C'_{L_\delta} = 0.0590$ per deg

$\beta C'_{l_\delta} = 0.0370$ per deg (figure 6.2.1.1-27)

$C'_{l_\delta} = 0.0293$ per deg

Solution:

$$C_{l_\delta} = \left(1 - \frac{C_2}{C_1} \phi_{TE}\right) C'_{L_\delta} \frac{S_f}{S_w} \frac{1}{2}\left[\frac{y_i}{b_w} + \left(\frac{b_f}{2b_w}\right)\frac{C'_{l_\delta}}{C'_{L_\delta}}\right] \text{ (equation 6.2.1.1-h)}$$

$$= \left[1 - \frac{1.925}{0.792}\left(\frac{6}{57.3}\right)\right](0.0590) \frac{13.89}{166.8} \left(\frac{1}{2}\right)\left[0.25 + \frac{6.465}{25.86}\left(\frac{0.0293}{0.0590}\right)\right]$$

$= 0.000686$ per deg (based on $S_w b_w$) (one control surface deflected on one wing panel)

This compares with a test value of 0.00056 per degree from reference 18.

2. Plug and Flap-Type Spoilers

Given: The wing-body-tail configuration of reference 18, equipped with plug and flap-type spoilers.

Wing Characteristics:

$A_W = 4.0 \qquad \lambda_W = 0.500 \qquad \Lambda_{c/4} = 40^o$

Spoiler Characteristics:

Case	Type	$\frac{y_i}{b_W/2}$	$\frac{y_o}{b_W/2}$	Chordwise Location %c	$\frac{\delta_s}{c}$
1	Plug	0.15	0.95	0.55	0.05
2	Flap	0.15	0.95	0.55	0.05
3	Plug	0.15	0.95	0.65	0.02
4	Plug	0.15	0.55	0.65	0.05
5	Plug	0.15	0.55	0.65	0.02

Additional Characteristics:

$M = 1.61$

Compute:

Case	$\frac{y_i + y_o}{b_W/2}$	$\frac{b_s}{b_W/2}$	$(C_l)_{calc}$ figure 6.2.1.1-30	$(C_l)_{test}$ @$\alpha = 0^o$
1	1.10	0.80	0.0070	0.0085
2	1.10	0.80	0.0070	0.0080
3	1.10	0.80	0.0030	0.0017
4	0.70	0.40	0.0030	0.0045
5	0.70	0.40	0.0016	0.0006

REFERENCES

1. Lowry, J.G.: Data on Spoiler-Type Ailerons. NACA RM L53I24a, 1953. (U)

2. DeYoung, J.: Theoretical Antisymmetric Span Loading for Wings of Arbitrary Planform at Subsonic Speeds. NACA TR 1056, 1951. (U)

3. Banks, R.: The Application of a Simplified Lifting-Surface Theory to the Prediction of the Rolling Effectiveness of Plain Spoiler Ailerons at Subsonic Speeds. NACA RM A54H26a, 1954. (U)

4. Vogler, R.D.: Wind-Tunnel Investigation at High Subsonic Speeds of a Spoiler-Slot-Deflector Combination an an NASA 65A006 Wing with Quarter-Chord Line Swept Back 32.6°. NACA RM L53D17, 1953. (U)

5. Abbott, I.H., von Doenhoff, A.E., and Stivers, L.S., Jr.: Summary of Airfoil Data. NACA TR 824, 1945. (U)

6. Hammond, A.D.: Lateral-Control Investigation of Flap-Type Controls on a Wing with Unswept Quarter-Chord Line, Aspect Ratio 4, Taper Ratio 0.6 and NACA 65A006 Airfoil Section--Transonic Bump Method. NACA RM L50A03, 1950. (U)

7. Thompson, R.F.: Lateral-Control Investigation of Flap-Type Controls on a Wing With Quarter-Chord Line Swept Back 35°, Aspect Ratio 4, Taper Ratio 0.6, and NACA 65A006 Airfoil Section. NACA RM L9L12a, 1950. (U)

8. Vogler, R.D.: Lateral-Control Investigation of Flap-Type Controls on a Wing With Quarter-Chord Line Swept Back 45°, Aspect Ratio 4, Taper Ratio 0.6, and NACA 65A006 Airfoil Section--Transonic-Bump Method. NACA RM L9F29a, 1949. (U)

9. Vogler, R.D.: Lateral-Control Investigation of Flap-Type Controls on a Wing With Quarter-Chord Line Swept Back 60°, Aspect Ratio 4, Taper Ratio 0.6, and NACA 65A006 Airfoil Section--Transonic-Bump Method. NACA RM L50A17, 1950. (U)

10. Goin, K.L.: Equations and Charts for the Rapid Estimation of Hinge-Moment and Effectiveness Parameters for Trailing-Edge Controls Having Leading and Trailing Edges Swept Ahead of the Mach Lines. NACA TR 1041, 1951. (U)

11. Decker, J.L., et al: USAF Stability and Control Handbook. M-03671, 1956. (C) Title Unclassified

12. Lord, D.R., and Czarnecki, K.R.: Loads Associated with Spoilers at Supersonic Speeds. NACA RM L55E12a, 1955. (U)

13. Foster, G.V.: Effects of Spoiler-Slot Deflector Control on the Aerodynamic Characteristics at a Mach Number of 2.01 of a Variable-Wing-Sweep Configuration With the Outer Wing Panels Swept Back 75°. NASA TM X-273, 1960. (U)

14. Lord, D.R., and Moring, R.: Aerodynamic Characteristics of a Spoiler-Slot-Deflector Control on a 45° Sweptback Wing at Mach Numbers of 1.61 and 2.01. NACA RM L57E16a, 1957. (U)

15. Franks, R.W.: Tests in the Ames 40- by 80-Foot Wind Tunnel of the Aerodynamic Characteristics of Four Airplane Models with Plain Spoiler Ailerons. NACA RM A54H26, 1954. (U)

16. Vogler, R.D.: Wind-Tunnel Investigation at High Subsonic Speeds of Spoilers of Large Projection on an NACA 65A006 Wing With Quarter-Chord Line Swept Back 32.6°. NACA RM L51L10, 1952. (U)

17. Fischel, J., and Hagerman, J.R.: Effect of Aspect Ratio and Sweepback on the Low-Speed Lateral Control Characteristics of Untapered Low-Aspect-Ratio Wings Equipped With Retractable Ailerons. NACA TN 2347, 1951. (U)

18. Hamilton, C.V., and Driver, C.: An Investigation of a Supersonic Aircraft Configuration Having a Tapered Wing with Circular-Arc Sections and 40° Sweepback. – Stability and Control Characteristics at a Mach Number of 1.61 of the Complete Configuration Equipped With Spoilers. NACA RM L54F15, 1954. (U)

19. Conner, D.W., and Mitchell, M.H., Jr.: Effect of Spoiler on Airfoil Pressure Distribution and Effects of Size and Location of Spoilers on the Aerodynamic Characteristics of a Tapered Unswept Wing of Aspect Ratio 2.5 at a Mach Number of 1.90. NACA RM L50L20, 1951. (U)

20. Wong, N.D.: An Investigation of the Control Effectiveness of Tip Ailerons and Spoilers on a Low-Aspect-Ratio Trapezoidal-Wing Airplane Model at Mach Numbers From 1.55 to 2.35. NACA RM A57I26a, 1957. (U)

21. Kindell, W.H.: Effects of Span and Spanwise and Chordwise Location on the Control Effectiveness of Spoilers on a 60° Sweptback Wing at Mach Numbers of 1.41 and 1.96. NACA RM L53B09, 1953. (U)

22. Guy, L.D.: Effects of Overhang Balance on the Hinge-Moment and Effectiveness Characteristics of an Unswept Trailing-Edge Control on a 60° Delta Wing at Transonic and Supersonic Speeds. NACA RM L54G12a, 1954. (U)

23. Spearman, M.L., and Driver, C.: Longitudinal and Lateral Stability and Control Characteristics at Mach Number 2.01 of a 60° Delta-Wing Airplane Configuration Equipped with a Canard Control and With Wing Trailing-Edge Flap Controls. NACA RM L58A20, 1958. (U)

24. Guy, L.D.: Hinge-Moment and Effectiveness Characteristics of an Aspect-Ratio-8.2 Flap-Type Control on a 60° Delta Wing at Mach Numbers From 0.72 to 1.96. NACA RM L56J17, 1957. (U)

25. Guy, L.D., and Brown, H.V.: Effects of an Inset Tab on the Hinge-Moment and Effectiveness Characteristics of an Unswept Trailing-Edge Control on a 60° Delta Wing at Mach Numbers From 0.75 to 1.96. NACA RM L54K16a, 1955. (U)

TABLE 6.2.1.1-A
SUBSONIC ROLLING-MOMENT EFFECTIVENESS OF PLUG
AND FLAP-TYPE SPOILERS

DATA SUMMARY

Ref.	Airfoil Section	A	λ	$\Lambda_{c/4}$ (deg)	$\frac{\delta_s}{c}$	$\frac{h_s}{c}$	$\frac{x_s}{c}$	$\frac{\eta_i}{b/2}$	$\frac{\eta_o}{b/2}$	$\frac{b_s}{b/2}$	M	C_{l_δ} Calc	C_{l_δ} Test	ΔC_{l_δ} Calc-Test
15	NACA65A006	3.00	0.40	40.6	0.10	0.1174	0.70	0.15	0.60	0.45	0.13	0.0148	0.0155	-0.0007
									0.80	0.65		0.0208	0.0215	-0.0007
									1.00	0.85		0.0225	0.0261	-0.0036
					0.15	0.1674		0.15	0.60	0.45		0.0192	0.0219	-0.0027
									0.80	0.65		0.0269	0.0300	-0.0031
									1.00	0.85		0.0291	0.0344	-0.0053
					0.10	0.1174	0.60	0.15	0.60	0.45		0.0139	0.0112	0.0027
					0.10	0.1174	0.80	0.15	0.60	0.45		0.0152	0.0190	-0.0038
	NACA0012-64	4.78	0.51	35.0	0.10	0.1366	0.70	0.10	0.60	0.50	0.13	0.0287	0.0300	-0.0013
								0.40	0.80	0.40		0.0231	0.0257	-0.0026
16	NACA65A006	4.0	0.60	32.6	0.15	0.1694	0.70	0.139	0.639	0.50	0.40	0.0281	0.0322	-0.0041
											0.60	0.0290	0.0350	-0.0060
											0.80	0.0298	0.0341	-0.0043
4	NACA65A006	4.0	0.60	32.6	0.05	0.0694	0.692	0.139	0.639	0.50	0.40	0.0112	0.0100	0.0012
					0.075	0.0944	0.681					0.0189	0.0180	0.0009
					0.10	0.1194	0.662					0.0220	0.0215	0.0005
17	NACA64A010	4.13	1.00	0	0.02	0.0483	0.07	0.376	0.976	0.60	0.26	0.0077	0.0085	-0.0008
					0.06	0.0883						0.0233	0.0270	-0.0037

$$\text{Average Error} = \frac{\Sigma|\Delta C_{l_\delta}|}{n} = 0.0027$$

TABLE 6.2.1.1-B
SUPERSONIC ROLLING EFFECTIVENESS OF PLAIN TRAILING-EDGE-FLAP AILERONS

DATA SUMMARY

Ref.	λ_f	Λ_{HL} (deg)	Λ_{TE} (deg)	ϕ_{TE} (deg)	$\frac{b_f}{b_W}$	$\frac{S_f}{S_W}$	$\frac{Y_i}{b_W}$	M	c_{l_δ} (per deg) Calc	c_{l_δ} (per deg) Test	Δc_{l_δ} (per deg) Calc-Test
18	0.666	33.26	30.5	9.0	0.50	0.0834	0.25	1.61	0.000686	0.000560	0.000126
22	1.00	0	0	7.62	0.536	0.0746	0.086	1.96	0.000242	0.000223	0.000019
↓	↓	↓	↓	↓	↓	↓	↓	1.41	0.000401	0.000313	0.000088
23	1.00	0	0	9.2	0.338	0.0615	0.0776	2.01	0.000151	0.000180	-0.000029
24	1.00	0	0	7.62	0.536	0.0401	0.086	1.96	0.000130	0.000098	0.000032
↓	↓	↓	↓	↓	↓	↓	↓	1.41	0.000218	0.000180	0.000036
25	1.00	0	0	7.64	0.402	0.075	0.150	1.96	0.000312	0.000270	0.000042
↓	↓	↓	↓	↓	↓	↓	↓	1.41	0.000515	0.000415	0.000100
										Average Error = $\frac{\Sigma\lvert\Delta c_{l_\delta}\rvert}{n}$ =	0.000069

TABLE 6.2.1.1-C
SUPERSONIC ROLLING MOMENT DUE TO SPOILER DEFLECTION

DATA SUMMARY

Ref.	Spoiler	A	λ	$\Lambda_{c/4}$ (deg)	$\frac{Y_i}{b_W/2}$	$\frac{Y_o}{b_W/2}$	Spoiler Chordwise Location (%c)	$\frac{\delta_s}{c}$	M	c_l Calc	c_l Test	Δc_l Calc.-Test
18	Plug	4.0	0.50	40.0	0.15	0.95	0.55	0.05	1.61	0.0070	0.0085	-0.0015
↓	Flap	↓	↓	↓	↓	↓	↓	↓	↓	0.0070	0.0080	-0.0010
↓	Plug	↓	↓	↓	↓	↓	0.65	0.02	↓	0.0030	0.0017	0.0013
↓	↓	↓	↓	↓	↓	0.55	↓	0.05	↓	0.0030	0.0045	-0.0015
↓	↓	↓	↓	↓	↓	↓	↓	0.02	↓	0.0016	0.0005	0.0011
14	Flap	3.50	0.30	45.0	0.13	0.78	0.75	0.04	1.61	0.0049	0.0055	-0.0006
↓	↓	↓	↓	↓	↓	↓	↓	0.05	↓	0.0066	0.0100	-0.0034
↓	↓	↓	↓	↓	↓	↓	↓	0.075	↓	0.0087	0.0115	-0.0028
↓	↓	↓	↓	↓	↓	↓	↓	0.04	2.01	0.0040	0.0030	0.0010
↓	↓	↓	↓	↓	↓	↓	↓	0.05	↓	0.0055	0.0052	0.0003
↓	↓	↓	↓	↓	↓	↓	↓	0.075	↓	0.0080	0.0085	-0.0005

TABLE 6.2.1.1-C (CONTD)

Ref.	Spoiler	A	λ	$\Lambda_{c/4}$ (deg)	$\frac{y_i}{b_w/2}$	$\frac{y_o}{b_w/2}$	Spoiler Chordwise Location (%c)	$\frac{\delta_s}{c}$	M	c_l Calc	c_l Test	Δc_l Calc-Test
19	Plug	2.50	0.625	5.3	0.20	0.95	0.75	0.05	1.90	0.0067	0.0075	-0.0008
								0.02		0.0019	0.0030	-0.0011
					0.45			0.05		0.0052	0.0060	-0.0008
								0.02		0.0019	0.0017	0.0002
					0.70			0.05		0.0024	0.0033	-0.0009
								0.02		0.0020	0.0018	0.0002
					0.45	0.70		0.05		0.0024	0.0032	-0.0008
								0.02		0.0012	0.0013	-0.0001
20	Flap	3.20	0.40	19.2	0.28	0.75	0.77	0.037	1.55	0.0031	0.0035	-0.0004
								0.095		0.0084	0.0078	0.0006
								0.037	1.90	0.0028	0.0025	0.0003
								0.095		0.0069	0.0053	0.0016
								0.037	2.35	0.0027	0.0011	0.0016
								0.095		0.0065	0.0037	0.0028
21	Plug	2.50	0.625	47.16	0.20	0.95	0.65	0.04	1.41	0.0075	0.0084	-0.0009
								0.06		0.0130	0.0110	0.0020
								0.04	1.96	0.0046	0.0045	0.0001
								0.06		0.0082	0.0075	0.0007
						0.70		0.04	1.41	0.0052	0.0075	-0.0023
								0.06		0.0062	0.0092	-0.0030
								0.04	1.96	0.0029	0.0035	-0.0006
								0.06		0.0043	0.0050	-0.0007
						0.45		0.04	1.41	0.0020	0.0034	-0.0014
								0.06		0.0030	0.0060	-0.0030
								0.04	1.96	0.0011	0.0020	-0.0009
								0.06		0.0020	0.0040	-0.0020

$$\text{Average Error} = \frac{\Sigma|\Delta c_l|}{n} = 0.0012$$

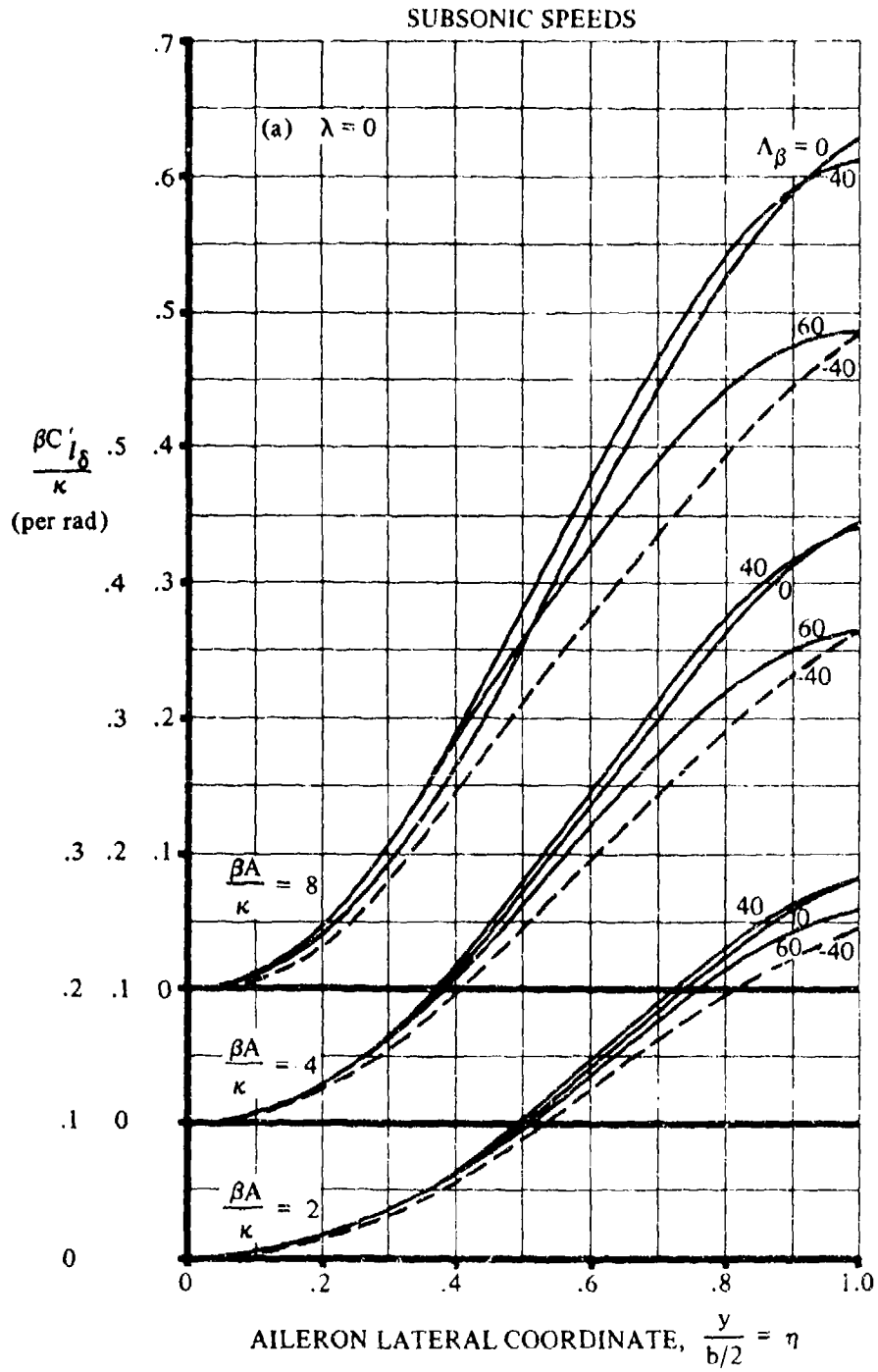

FIGURE 6.2.1.1-23 SUBSONIC AILERON ROLLING-MOMENT PARAMETER

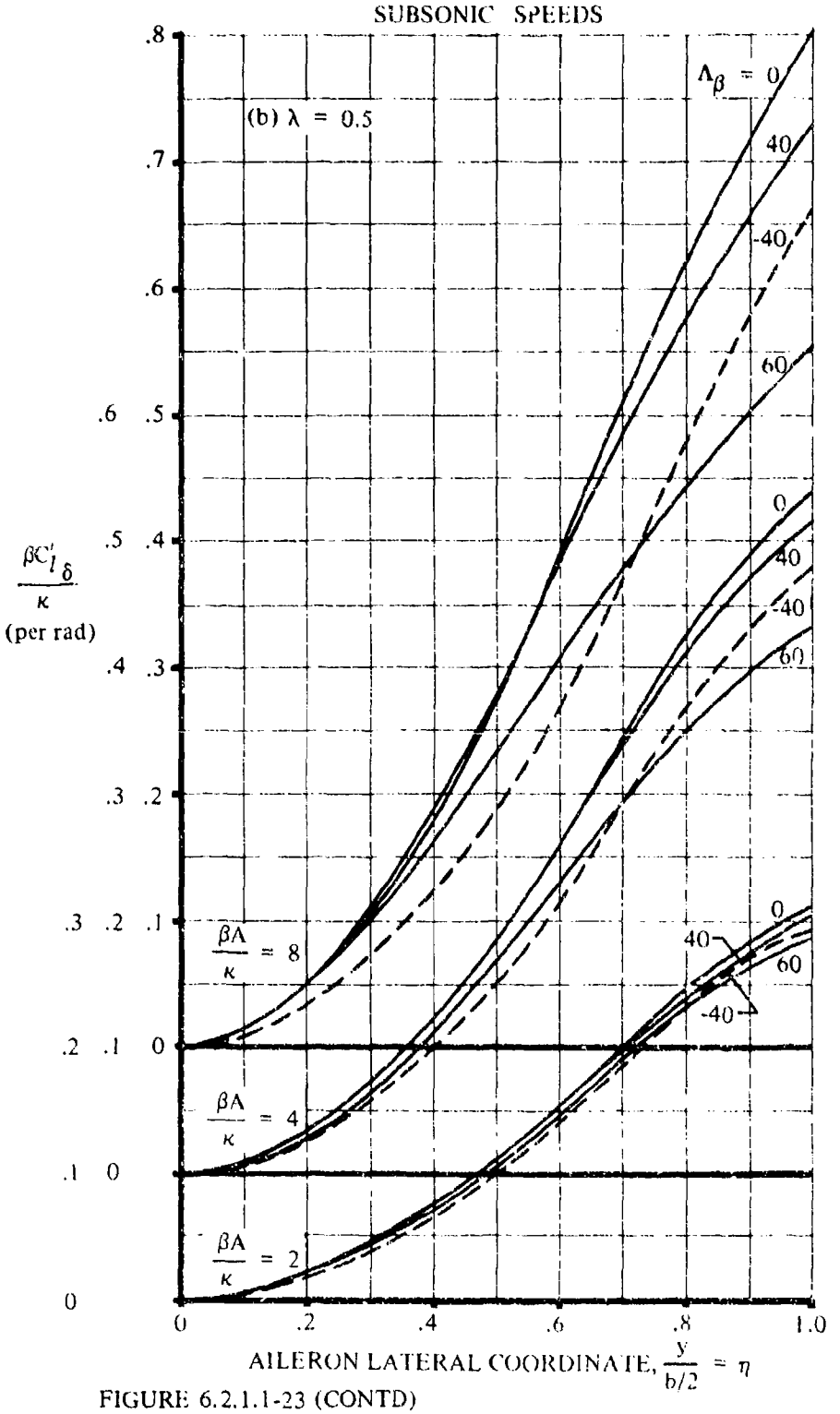

FIGURE 6.2.1.1-23 (CONTD)

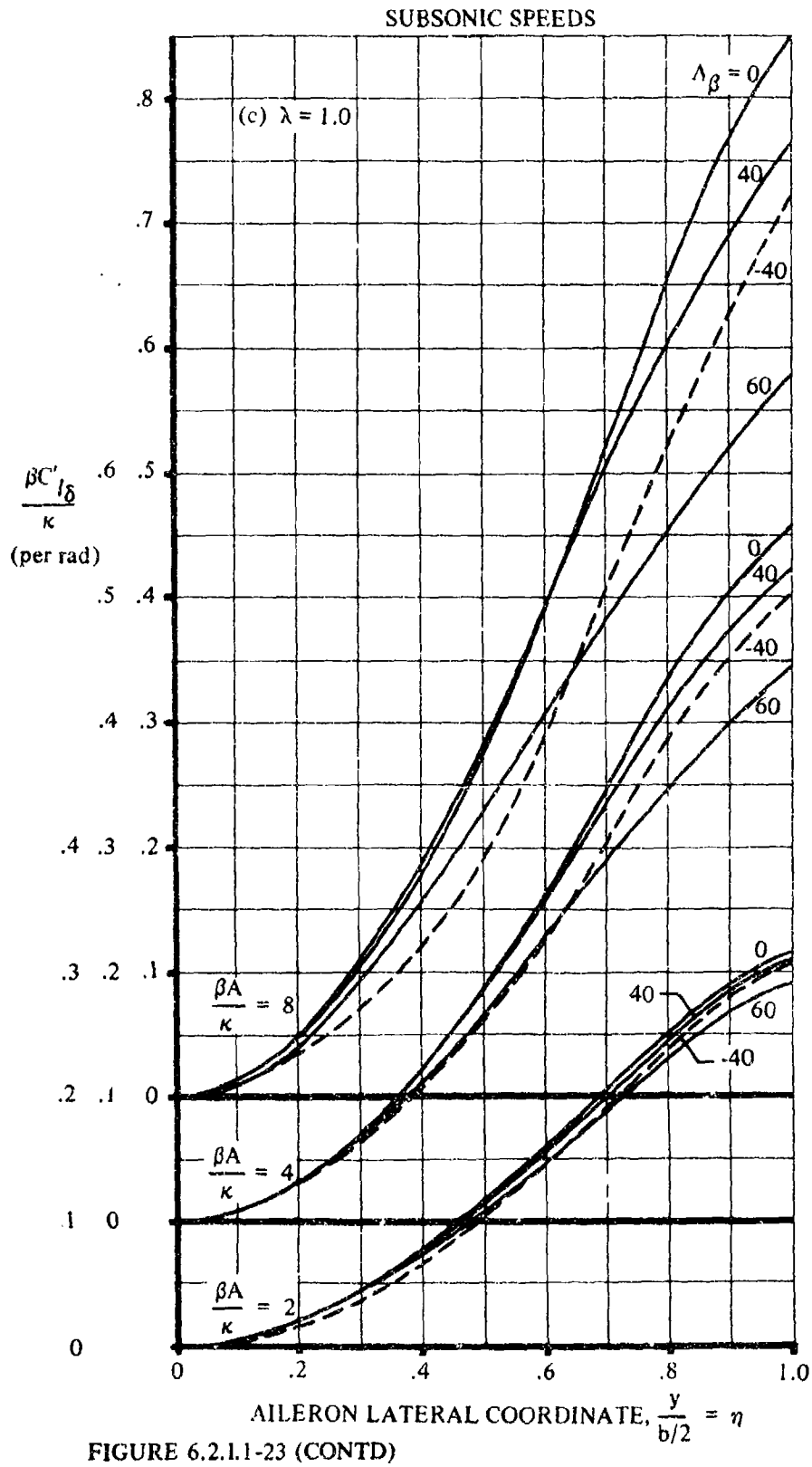

FIGURE 6.2.1.1-23 (CONTD)

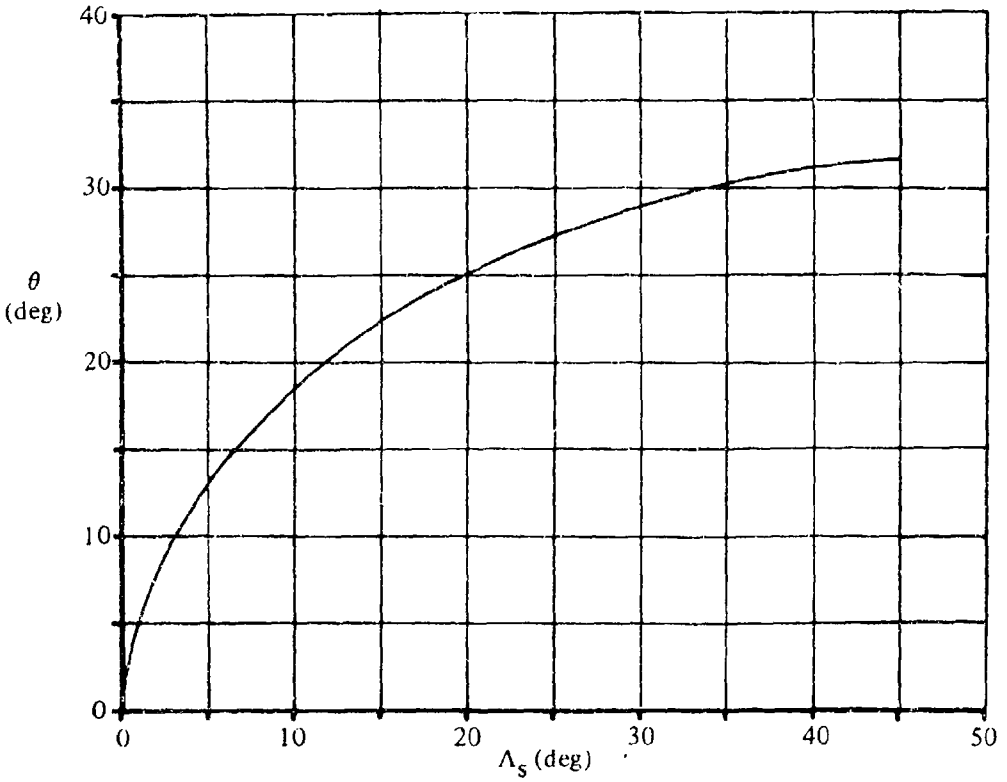

FIGURE 6.2.1.1-26a VARIATION OF θ WITH ANGLE OF SWEEPBACK OF SPOILER

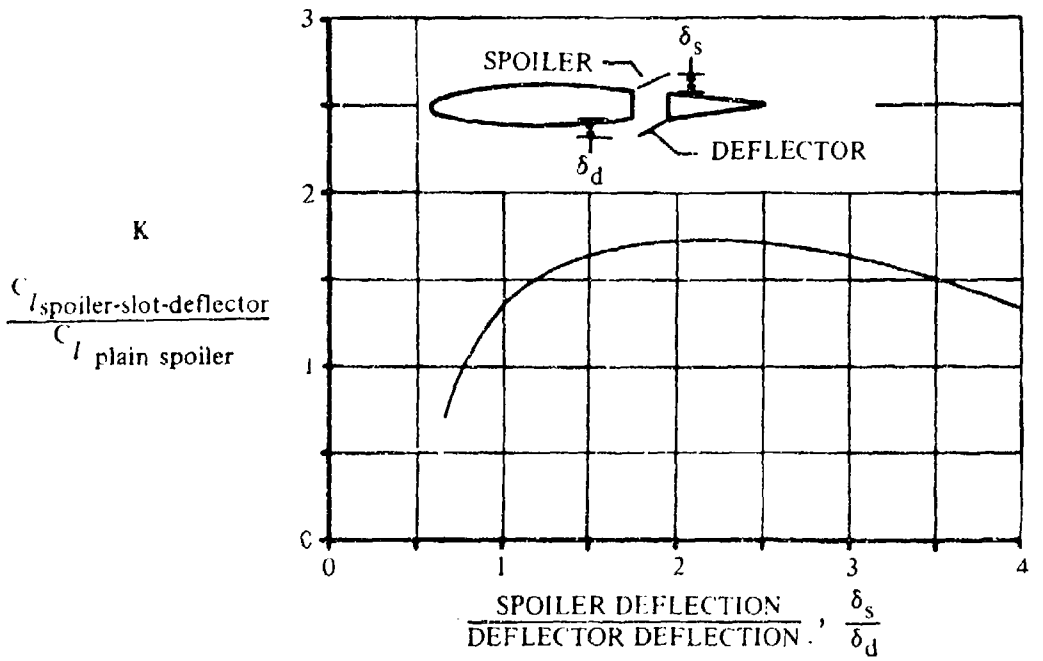

FIGURE 6.2.1.1-26b EFFECT OF SPOILER SLOT AND DEFLECTOR ON SPOILER ROLLING EFFECTIVENESS

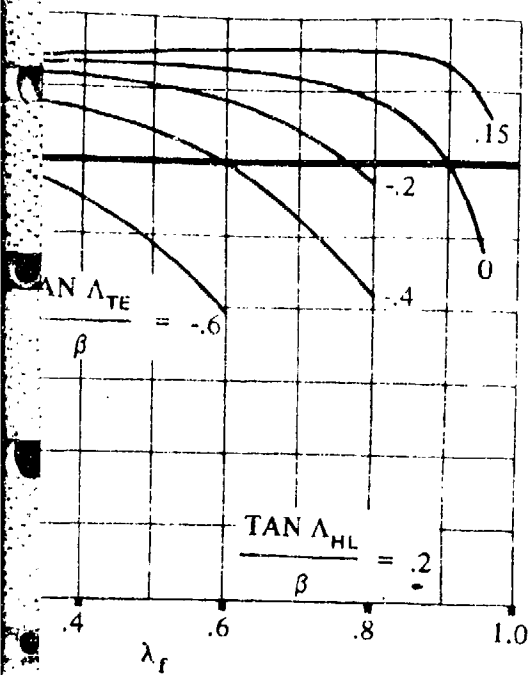
.15
-.2
0
-.4
AN Λ_{TE} / β = -.6
TAN Λ_{HL} / β = .2
.4
.6
.8
1.0
λ_f

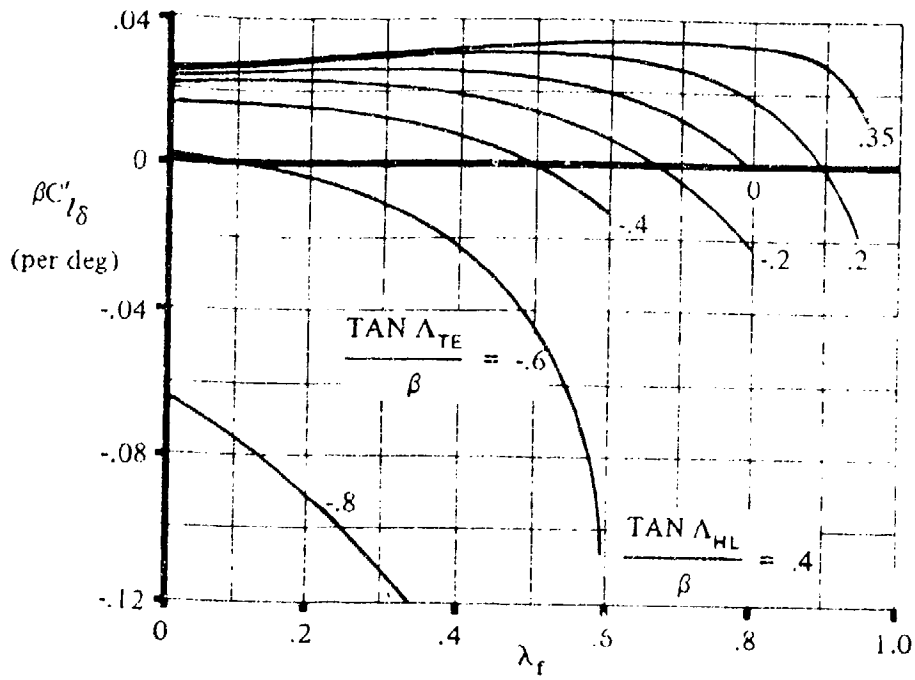
.04
0
-.04
-.08
-.12
$\beta C'_{l_\delta}$
(per deg)
.35
0
-.4
-.2
.2
TAN Λ_{TE} / β = -.6
-.8
TAN Λ_{HL} / β = .4
0
.2
.4
.6
.8
1.0
λ_f

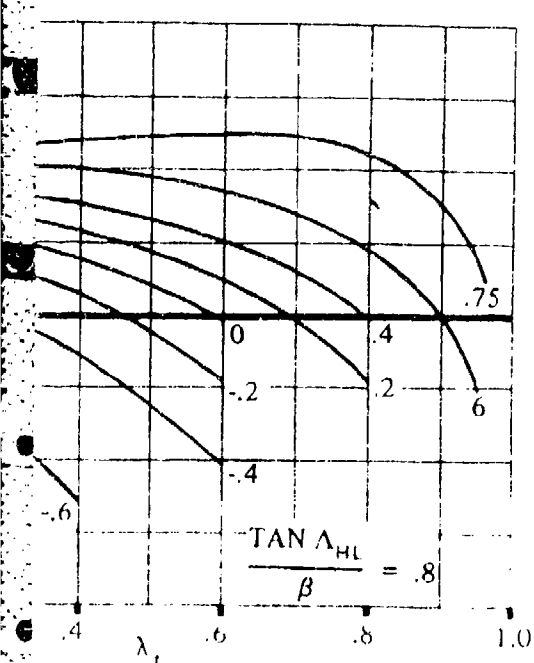
.75
0
.4
-.2
.2
6
-.4
-.6
TAN Λ_{HL} / β = .8
.4
.6
.8
1.0
λ_f

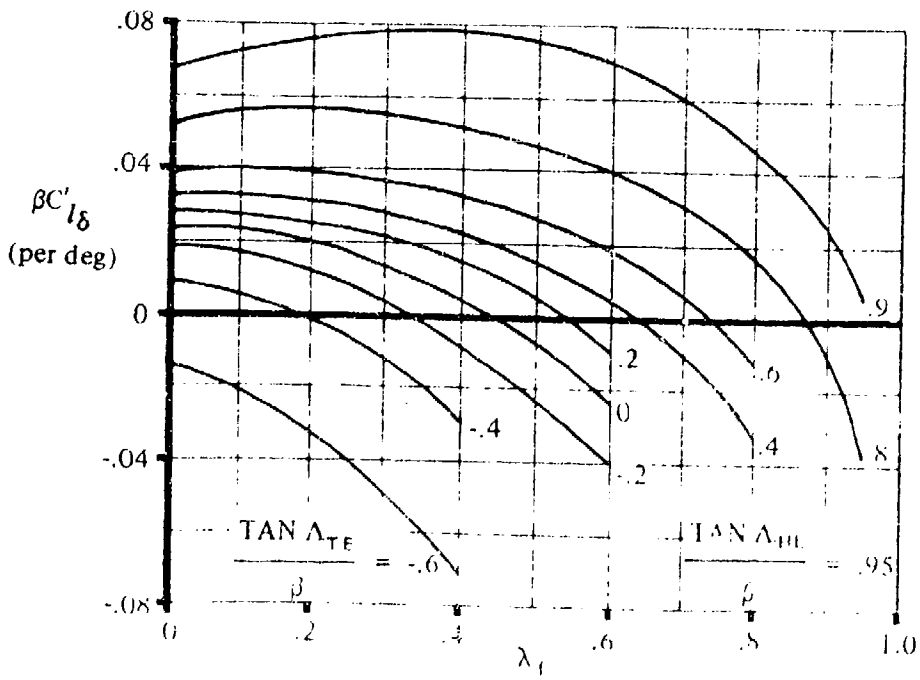
.08
.04
0
-.04
-.08
$\beta C'_{l_\delta}$
(per deg)
.9
.6
.2
0
-.4
.4
-.2
.8
TAN Λ_{TE} / β = -.6
TAN Λ_{HL} / β = .95
0
.2
.4
.6
.8
1.0
λ_f

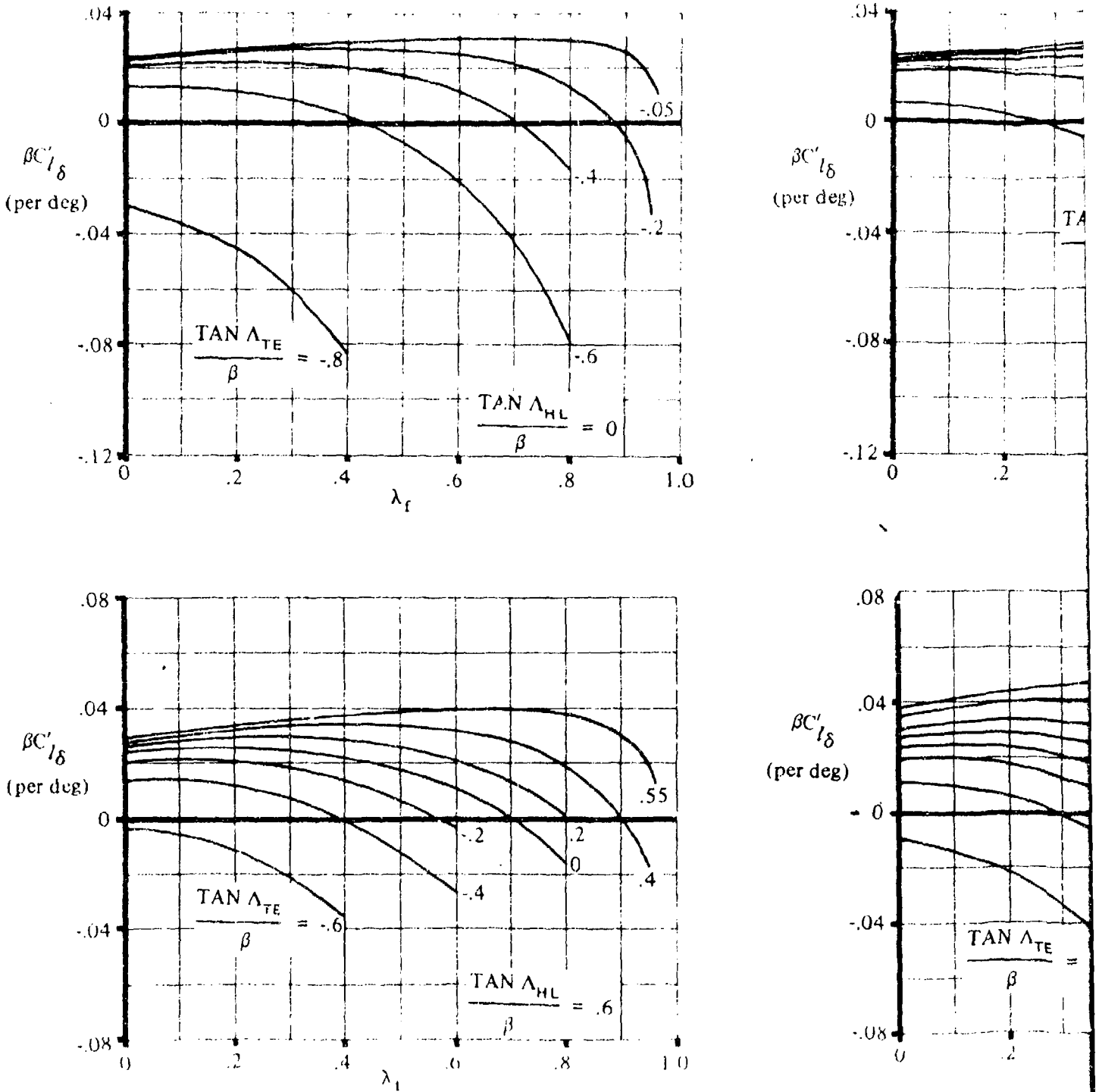

FIGURE 6.2.1.1-27 ROLLING-MOMENT DERIVATIVE FOR TAPERED CONTROL SURFACES HAVING OUTBOARD EDGE COINCIDENT WITH WING TIP

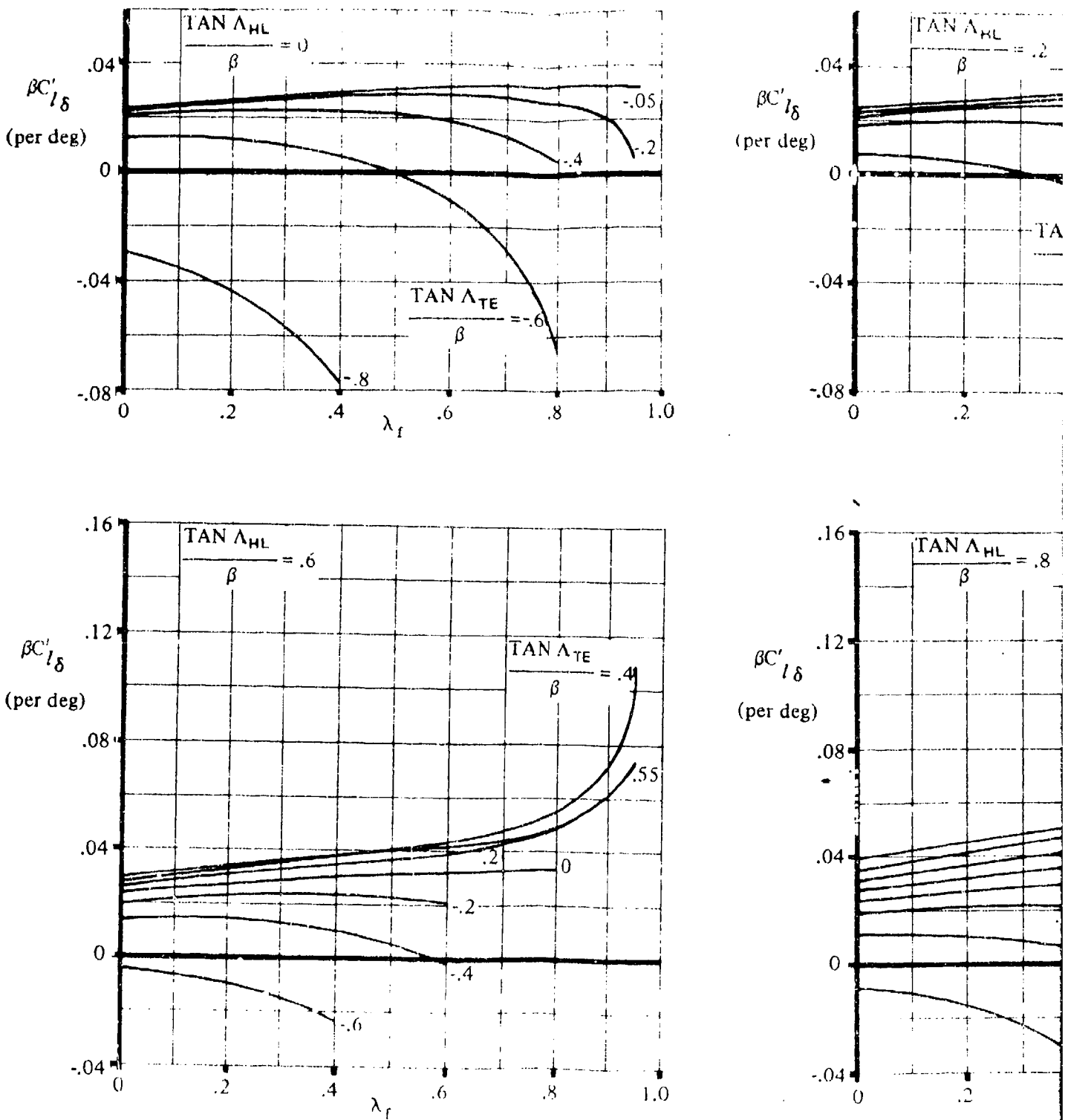

FIGURE 6.2.1.1-28 ROLLING-MOMENT DERIVATIVE FOR TAPERED CONTROL SURFACES HAVING OUTBOARD EDGE NOT COINCIDENT WITH WING TIP

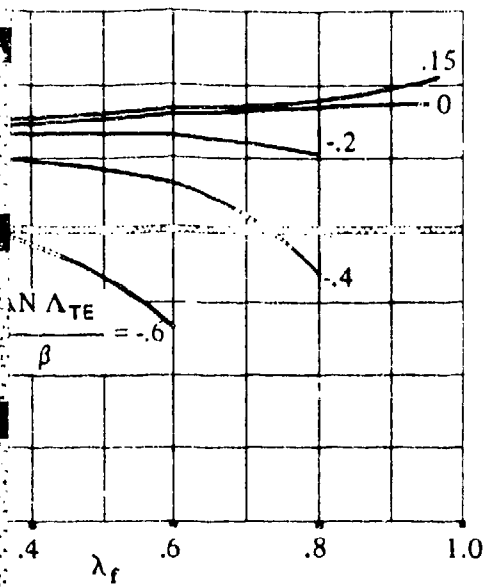
.15
0
-.2
-.4
$\frac{\tan \Lambda_{TE}}{\beta}$ = -.6
.4
.6
.8
1.0
λ_f

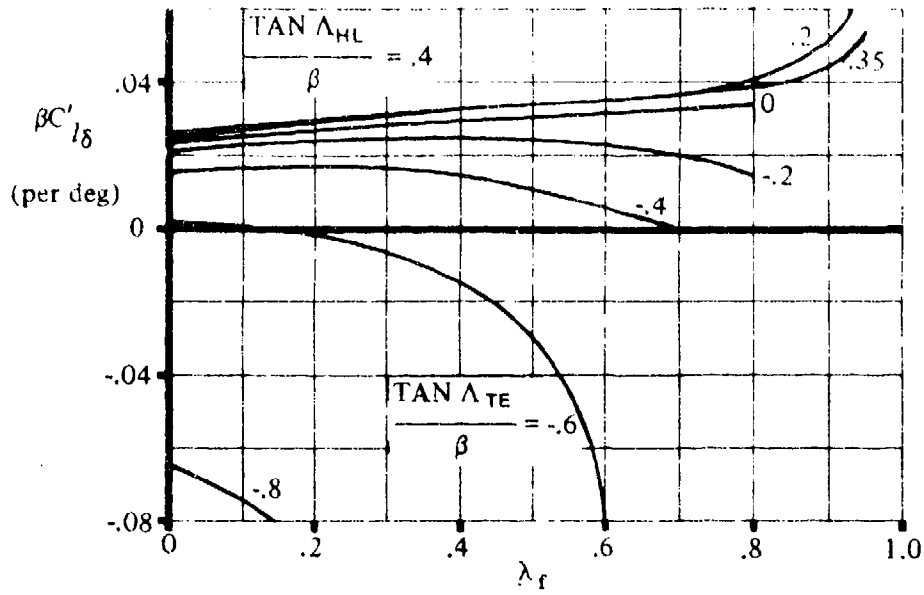
$\frac{\tan \Lambda_{HL}}{\beta}$ = .4
.2
.35
0
-.2
-.4
$\beta C'_{l_\delta}$
(per deg)
.04
0
-.04
-.08
$\frac{\tan \Lambda_{TE}}{\beta}$ = -.6
-.8
0
.2
.4
.6
.8
1.0
λ_f

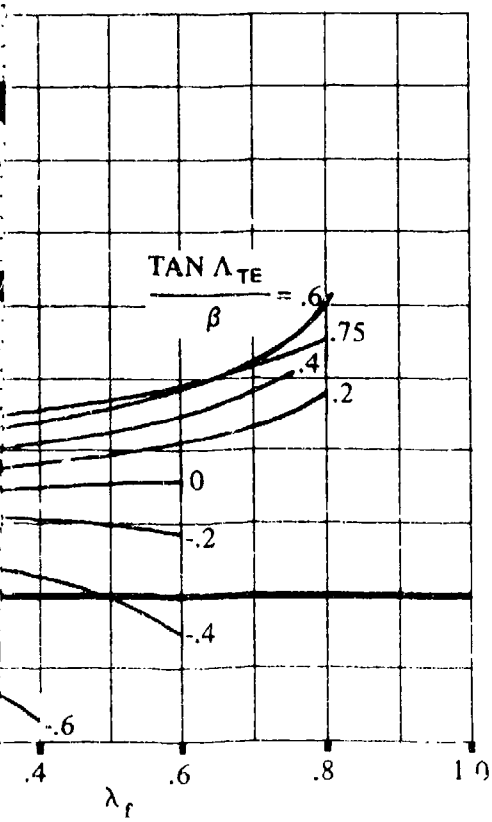
$\frac{\tan \Lambda_{TE}}{\beta}$ = .6
.75
.4
.2
0
-.2
-.4
-.6
.4
.6
.8
1.0
λ_f

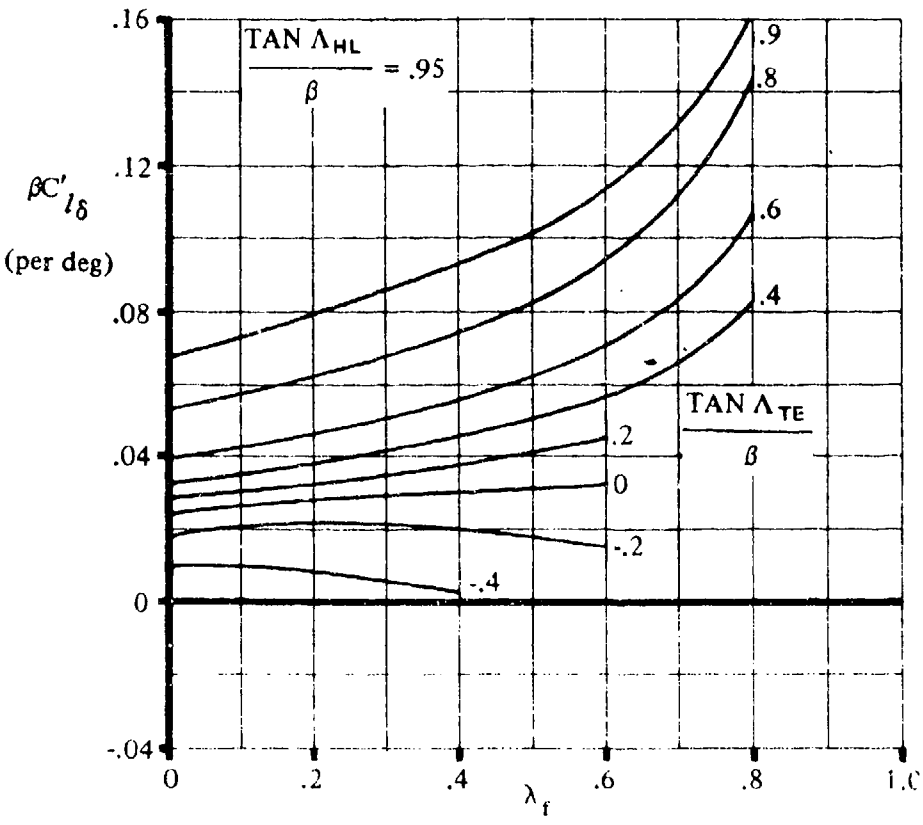
$\frac{\tan \Lambda_{HL}}{\beta}$ = .95
.9
.8
.6
.4
.2
0
-.2
-.4
$\frac{\tan \Lambda_{TE}}{\beta}$
$\beta C'_{l_\delta}$
(per deg)
.16
.12
.08
.04
0
-.04
0
.2
.4
.6
.8
1.0
λ_f

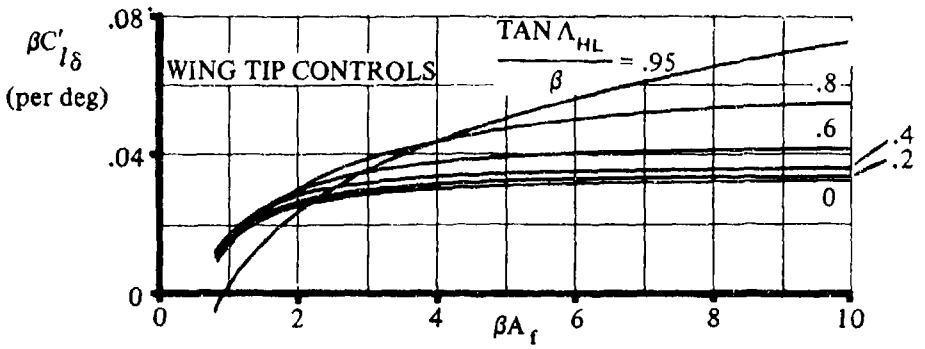

FIGURE 6.2.1.1-29a ROLLING-MOMENT DERIVATIVE FOR UNTAPERED CONTROL SURFACES HAVING OUTBOARD EDGE COINCIDENT WITH WING TIP

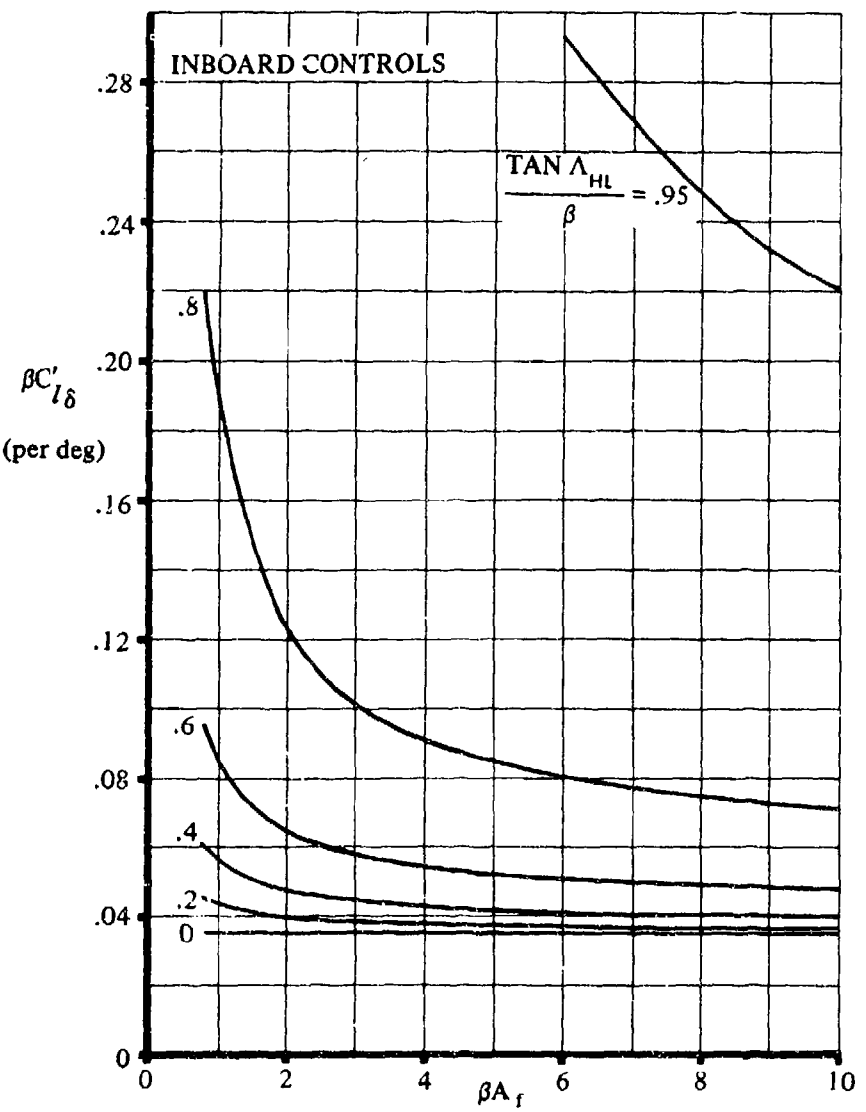

FIGURE 6.2.1.1-29b ROLLING-MOMENT DERIVATIVE FOR UNTAPERED CONTROL SURFACES HAVING OUTBOARD EDGE NOT COINCIDENT WITH WING TIP

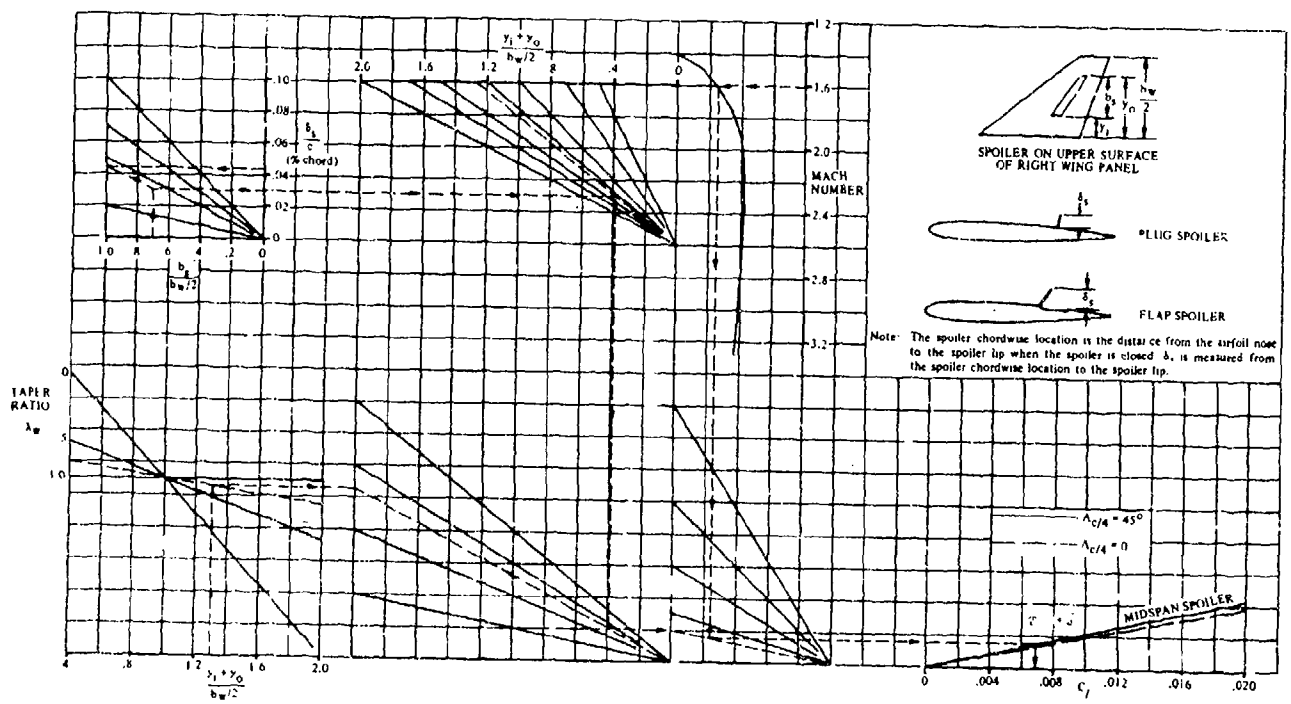

FIGURE 6.2.1.1-30 SPOILER ROLLING MOMENTS AT SUPERSONIC SPEEDS BASED ON TOTAL WING AREA

6.2.1.2 ROLLING MOMENT DUE TO A DIFFERENTIALLY DEFLECTED HORIZONTAL STABILIZER

A large amount of theoretical and experimental work has been directed toward the development of efficient roll-control devices. The initial studies and tests concentrated on ailerons, optimizing their size and location to maximize the available roll-control power. However, the more recent studies have investigated auxiliary surfaces or techniques that supplement aileron control to improve aircraft maneuverability. Among these auxiliary devices considered is the differentially deflected horizontal stabilizer.

Methods are presented in this section for estimating the rolling moments generated by a differentially deflected horizontal tail, at subsonic, transonic, and supersonic speeds. These methods are valid only for body-mounted horizontal tails (due to the empirical tail-effectiveness parameter) and are applicable throughout the angle-of-attack range until separation is encountered on the horizontal tail. No provisions are made to estimate the effects of flap deflections, horizontal-tail dihedral, or the rolling-moment contribution of the vertical tail; i.e., they are assumed to be negligible. Comparisons of the estimated and experimental values indicate relatively good correlation to moderate angles of attack (see Tables 6.2.1.2-A and -B).

Body vortices can have a strong influence on the horizontal-tail loading at high angles of attack. For body vortices, the flow separates just above or behind the area of minimum pressure along the side of the body near the nose and wraps up into a pair of symmetrical vortices that proceed downstream. The point at which separation first takes place depends upon the angle of attack (the higher the angle of attack, the nearer the nose separation occurs), the nose-profile shape (the blunter the nose, the nearer the nose separation occurs), and body cross-sectional shape (sharply curving lateral contours promote early separation). The vortices increase in size and strength with increasing downstream distance. These body vortices are accounted for in the methods herein by using the vortex interference charts found in Section 4.3.1.3. However, the effect of the wing shock-expansion field on the body vortices is neglected in the supersonic method.

Wing vortices are of equal interest in determining the horizontal-tail loading at high angles of attack. For closely-coupled configurations having wings and tails of nearly equal span, the wing-vortex effects can be of particular significance. The wing-vortex effects are accounted for in the downwash gradient parameter $\partial\bar{\epsilon}/\partial\alpha$ calculated in Section 4.4.1. (Care should be used to select the method best suited for the configuration.)

To familiarize the reader with the more salient aspects associated with horizontal-tail roll control, a basic discussion is presented. The discussion is supplemented by graphical comparisons of tail-roll-control and aileron-roll-control characteristics to illustrate similarities and differences. (Both the discussion and the illustrations are taken from Reference 1, except where noted.)

The interest in evaluating roll control for a differentially deflected horizontal tail is, in general, due to the inadequate roll-control power provided by conventional roll-control systems; i.e., ailerons and/or spoilers in the transonic and supersonic speed regimes. This inadequacy is due primarily to wing twist and shock-induced separation of the boundary layer ahead of the control surface. For a thin flexible wing of a high-speed airplane, the deflection of conventional outboard ailerons can produce a substantial amount of wing twist that can result in a significant reduction in roll-control

effectiveness. The boundary-layer separation results in a loss of roll-control effectiveness, as well as an increase in buffet and drag and a decrease in lift.

The most recent results of tail-roll-control investigations (Reference 2) indicate that tail roll control is best suited as an auxiliary roll-control device, where only moderate differential deflections are required.

In general, three basic considerations should be kept in mind when designing a tail-roll-control system:

(1) The tail must provide adequate effectiveness without excessive deflections (large tail and good effectiveness).

(2) The longitudinal trim requirements of the tail should be minimized to avoid interaction of roll and pitch controls.

(3) The horizontal tail should be positioned vertically to avoid excessive favorable or adverse yawing moments.

The first item requires no discussion, as the advantages are apparent. The second item can be a critical factor and is worthy of careful consideration. For a specific configuration, a wind-tunnel test is required to determine the interaction effects, since no methods presently exist for estimating this effect. Both the effects of roll control on pitching moments and the variation of roll control with angle of attack for different stabilizer settings must be considered. It is necessary to avoid stabilizer trim settings where the roll control might be limited or significantly reduced because of separation on the horizontal tail as a result of high angles of attack. For example, the landing configuration for some aircraft may produce control interaction problems. The effects of Item 3 above are discussed in detail in Section 6.2.2.2.

Mach Number Effects

From the limited available test data (References 1 through 8), it can be concluded that the variation of tail-roll-control effectiveness C_{l_δ} with Mach number is small. Within the subsonic regime, the effectiveness is relatively constant. In the supersonic regime, a slight increase in C_{l_δ} is noted at a Mach number of approximately 1.2, and then a progressive decrease in effectiveness is noted with increasing Mach number because of the decreasing lift-curve slope of the horizontal tail.

In the subsonic regime, values for C_{l_δ} due to tail roll control are approximately one-half to one-third of those produced by conventional ailerons at comparable speeds. In the supersonic speed regime, values for C_{l_δ} due to tail roll control are comparable to those obtained by using ailerons. However, since there will usually be more control deflection available for the ailerons, they will provide more roll control, assuming no aileron reversal is encountered due to wing twist.

Angle-of-Attack Effects

For subsonic Mach numbers, the variation of C_{l_δ} with angle of attack is not large for most configurations. However, for some configurations C_{l_δ} can decrease to one-half its original value at

α = 16° to 20° (Reference 8). For aileron control at subsonic speeds, the effectiveness generally drops off rapidly with increasing angle of attack, so that at high angles of attack the values of C_{l_δ} can begin to approximate those for tail roll control (Reference 3). Sketch (a) presents representative trends for both aileron and horizontal-tail deflections at four different Mach numbers as a function of angle of attack. (These results were obtained on wind-tunnel models with essentially rigid wings.) In contrast to the subsonic speed regime, at M = 1.61 the aileron effectiveness increases with angle of attack while the tail roll control decreases with angle of attack.

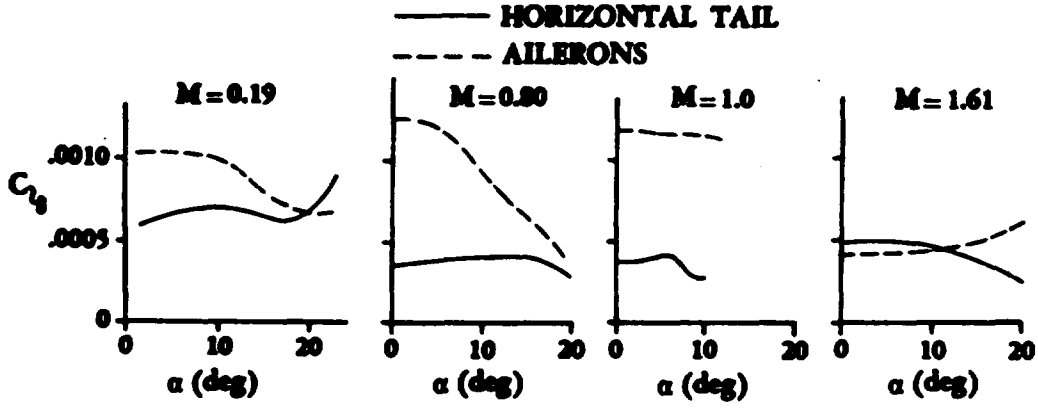

SKETCH (a)

Flap Effects

The effects of flaps on the tail roll control are shown in Sketch (b) for two different configurations. Both configurations show a detrimental effect of flaps at low lift coefficients. However, as the lift coefficient is increased, the tail roll control increases to equal or exceed the flap-retracted value of C_{l_δ}. Insufficient data exist to determine if this trend is consistent for all configurations.

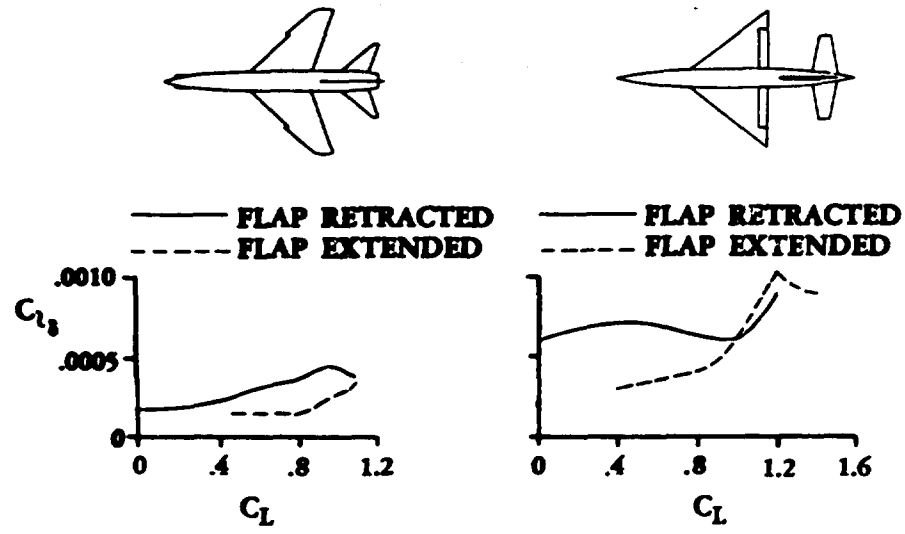

SKETCH (b)

Dihedral Effects

Reference 6 presents the results of a systematic variation of dihedral angle from 0 to -30° on the lateral-control effectiveness and the stabilizer characteristics for tail roll control at subsonic speeds. The results of the investigation show a small variation in the roll effectiveness C_{l_δ} with negative tail-dihedral angle. These small variations did not form a set pattern, but rather were dependent upon the initial stabilizer angle prior to differential deflection.

Aeroelastic Effects

The effects of wing flexibility are analyzed in the literature (References 1 and 4) through an overall rolling effectiveness parameter $(pb/2V)/\delta$, which can be expressed as C_{l_δ}/C_{l_p}. Thus, for a flexible-wing airplane in comparison to a rigid-wing airplane, greater rolling effectiveness will be realized for the flexible-wing aircraft because of the reduction in the wing contribution to roll damping C_{l_p}. Sketch (c) presents a comparison of data for a stiff and a flexible wing for both tail roll control and aileron roll control as a function of Mach number. These data illustrate the wing-twist problem encountered for thin flexible wings employing ailerons at supersonic speeds. In contrast, the horizontal-tail roll control shows no adverse effects, but rather an increase for the flexible wing. Thus one can conclude that for certain cases, i.e., a thin flexible-wing configuration at supersonic speeds, the tail-roll-control contribution may be superior to that of conventional ailerons.

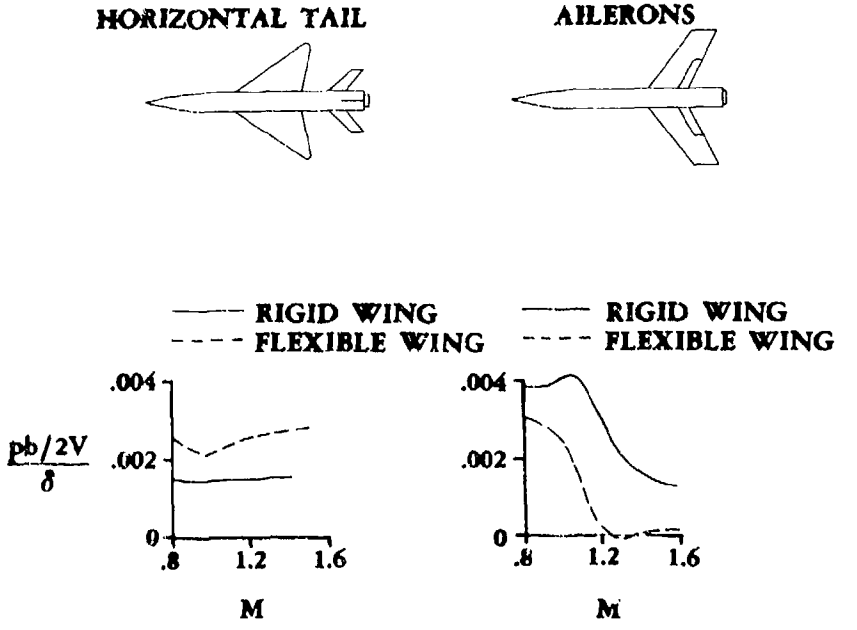

SKETCH (c)

A SUBSONIC

DATCOM METHOD

The following method is a modification of the method found in Reference 1, with the additional terms accounting for the effects of downwash, body vortices, and tail effectiveness. At angles of attack less than six degrees the body vortex interference factor $i_{v_{B(H)}}$ can be neglected. The roll-control effectiveness of a body-mounted differentially deflected horizontal stabilizer, based on $S_W b_W$, is given by

$$C_{l_\delta} = \frac{1}{2}\left[\left(1 - \frac{\pi A_W}{57.3}\frac{\partial\bar{\epsilon}}{\partial\alpha}\right) + i_{v_{B(H)}}\left(\frac{\Gamma}{2\pi\alpha Vr}\right)\left(\frac{r}{b_{H_e}/2}\right)\right]\eta\left(\frac{q_H}{q}\right)\frac{\bar{y}_H S_{H_e}}{b_W S_W}\left(C_{L_{\alpha_H}}\right)_e \qquad 6.2.1.2\text{-a}$$

The proper sign of the rolling-moment coefficient will result from the expression $C_l = C^*_{l_\delta}(\delta_L - \delta_R)$. The subscript e refers to the exposed surface (see Section 4.3.1.2 for a definition of exposed surfaces), and

A_W is the aspect ratio of the total wing.

$\frac{\partial\bar{\epsilon}}{\partial\alpha}$ is the average rate of change of downwash with respect to angle of attack at the horizontal tail, obtained from Section 4.4.1. Care should be exercised to select the method of Section 4.4.1 best suited for the aircraft configuration.

$i_{v_{B(H)}}$ is the vortex interference factor for a lifting surface mounted on the body center line. This parameter is given in Figures 4.3.1.3-7a through -7ℓ for various exposed-tail taper ratios, relative exposed-tail sizes, and vortex center-line positions.

The vertical and lateral vortex positions required to obtain $i_{v_{B(H)}}$ are $\frac{z_o}{r}$ and $\frac{y_o}{r}$, respectively. At any given station x, they may be obtained from Figures 4.3.1.3-13b and 4.3.1.3-14, respectively, as functions of the parameter $\frac{\alpha(x - x_s)}{r}$ where

α is the angle of attack in radians.

x is the distance from the body nose to the quarter-chord point of the MAC of the exposed horizontal tail for subsonic flow. (However, for supersonic flow x is measured to the midchord point of the MAC of the exposed horizontal tail.)

r is the average body radius in the region of the horizontal tail. For noncircular bodies use the average body depth in the region of the horizontal tail.

*It should be noted that the definition of C_{l_δ} based on the total differential deflection (consistent with the literature) does not agree with C_{l_δ} in other sections.

$\frac{x_s}{r}$ is the nondimensional position of vortex separation, from Figure 4.3.1.3-13a.

It should be noted that Figures 4.3.1.3-7a through -7ℓ give the vortex interference factors for a lifting surface mounted on the body center line. If the lifting surface is not mounted on the body center line, the vertical distance of the body vortices from the body center line, obtained from Figure 4.3.1.3-13b, must be corrected to their distance from the tail before obtaining $i_{v_{B(H)}}$. This is illustrated in the sample problem following the subsonic method.

In using Figures 4.3.1.3-7a through -7ℓ a possible problem can develop when interpolation must be made with respect to λ and $\frac{r}{b_W/2}$. For positions of the vortex near the body, the interpolation in $\frac{r}{b_W/2}$ can carry the vortex inside the body. Under these circumstances, it is recommended that the interpolation be made using $\frac{y_o - r}{b_W/2 - r}$ for the vortex lateral position in place of $\frac{y_o}{b_W/2}$, to avoid vortex positions inside the body.

For noncylindrical bodies, caution must be exercised in using the curves in Section 4.3.1.3 as they are based entirely on cylindrical body shapes.

$\frac{\Gamma}{2\pi\alpha V r}$ is the nondimensional vortex strength from Figure 4.3.1.3-15.

$\frac{r}{b_{H_e}/2}$ is the ratio of the average radius of the body (or average fuselage depth for noncircular bodies) in the region of the tail to the semispan of the exposed tail.

$\eta\left(\frac{q_H}{q}\right)$ is the tail-effectiveness factor for configurations with body-mounted horizontal tails, obtained from Figure 6.2.1.2-22 (from Reference 9).

b_W is the total wing span.

$\frac{S_{H_e}}{S_W}$ is the ratio of the area of the exposed horizontal tail to the total wing area.

$\bar{y}_H$ is the lateral c.p. coordinate of the horizontal tail, measured from and normal to the longitudinal axis. This parameter is given by

$$\bar{y}_H = \eta_{c.p.}\left(\frac{b_{H_e}}{2}\right) + r \qquad 6.2.1.2\text{-b}$$

where

$\eta_{c.p.}$ is the spanwise location of the c.p. of the exposed horizontal tail (based on the exposed aspect ratio, sweep, and exposed taper ratio), obtained from Figure 6.2.1.2-23 (from Reference 10).

$\frac{b_{H_e}}{2}$ is the semispan of the exposed horizontal tail.

r is the body radius in the region of the horizontal tail. For noncircular bodies use the average body depth in the region of the horizontal tail.

$\left(C_{L_{\alpha_H}}\right)_e$ is the lift-curve slope of the exposed horizontal stabilizer, obtained from Section 4.1.3.2. Care should be exercised to use the appropriate method in determining this parameter because of its significant influence.

The total angular deflection of the control surfaces δ is measured in a plane parallel to the plane of symmetry, and is positive for the left control surface deflected trailing edge down and the right control surface deflected trailing edge up.

Sample Problem

Given: The configuration of Reference 3

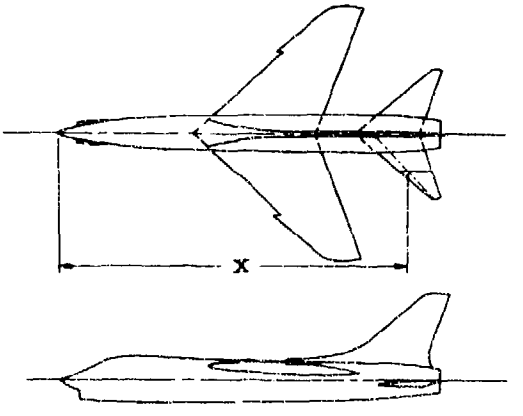

Wing Characteristics:

S_W = 666.7 sq in. b_W = 47.56 in. A_W = 3.39

λ_W = 0.247 $\Lambda_{c/4}$ = 42° Root Section NACA 65-006

Tip Section NACA 65-005

Horizontal-Tail Characteristics:

S_{H_e} = 102.4 sq in. b_{H_e} = 18.24 in. b_H = 24.11 in.

A_{H_e} = 3.25 A_H = 3.50 λ_{H_e} = 0.187

λ_H = 0.148 $\Lambda_{c/4}$ = 45° $\Lambda_{c/2}$ = 38.2°

h_H = −3.0 in. ℓ_H = 18.25 in.

Additional Characteristics:

Low speed; $\beta \cong 1.0$ d_H = 5.87 in. x = 66.0 in.

r = 2.935 in. z' = 0.49 in.

Compute:

Calculate $\left(C_{L_{\alpha_H}}\right)_e$ from Section 4.1.3.2

c_{ℓ_α} = 0.105 per deg (Table 4.1.1-B, for 65-006)

$$\kappa = \frac{\left(c_{\ell_\alpha}\right)_M}{2\pi/\beta} = \frac{c_{\ell_\alpha}/\beta}{2\pi/\beta} = \frac{57.3\,(0.105)}{2\pi} = 0.9576$$

$$\frac{A_{H_e}}{\kappa}\left[\beta^2 + \tan^2\Lambda_{c/2}\right]^{1/2} = \frac{3.25}{0.9576}\left[1.0 + (0.788)^2\right]^{1/2} = 4.32$$

$$\frac{\left(C_{L_{\alpha_H}}\right)_e}{A_{H_e}} = 0.935 \text{ per rad} \quad \text{(Figure 4.1.3.2-49)}$$

$$\left(C_{L_{\alpha_H}}\right)_e = 3.039 \text{ per rad}$$

$$= 0.0530 \text{ per deg}$$

Calculate $\eta\left(\frac{q_H}{q}\right)$

$$\frac{d_H}{b_H} = \frac{5.87}{24.11} = 0.243$$

$\eta\left(\frac{q_H}{q}\right)$ = 0.789 (Figure 6.2.1.2-22)

Calculate $\bar{y}_H$

$$(\Lambda_\beta)_H = \tan^{-1}\left(\frac{\tan \Lambda_{c/4}}{\beta}\right) = \tan^{-1}\left(\frac{1}{1}\right) = 45°$$

$$\frac{\beta A_{H_e}}{\kappa} = \frac{(1)(3.25)}{0.9576} = 3.394$$

$\eta_{c.p.} = 0.429$ (Figure 6.2.1.2-23)

$$\bar{y}_H = \eta_{c.p.}\left(\frac{b_{H_e}}{2}\right) + r \quad \text{(Equation 6.2.1.2-b)}$$

$$= (0.429)\left(\frac{18.24}{2}\right) + 2.935 = 6.85$$

$$\frac{\bar{y}_H S_{H_e}}{b_W S_W} = \frac{6.85}{47.56}\,\frac{102.4}{666.7} = 0.0221$$

Calculate $\frac{\partial \bar{\epsilon}}{\partial \alpha}$ from Section 4.4.1. (Method 2 is used because this configuration is similar to other configurations used in the substantiation of the method presented in Table 4.4.1-B.)

$$\frac{\partial \bar{\epsilon}}{\partial \alpha} = 4.44\left[K_A\, K_\lambda\, K_H\, (\cos \Lambda_{c/4})^{1/2}\right]^{1.19} \quad \text{(Equation 4.4.1-h)}$$

$K_A = 0.183$ (Figure 4.4.1-69a)

$K_\lambda = 1.324$ (Figure 4.4.1-69b)

$$\frac{2\ell_H}{b} = \frac{2(18.25)}{47.56} = 0.767$$

$$\frac{2h_H}{b} = \frac{2(-3.0)}{47.56} = -0.126$$

$K_H = 1.16$ (Figure 4.4.1-70, extrapolated)

$$\frac{\partial \bar{\epsilon}}{\partial \alpha} = 4.44\,[(0.183)(1.324)(1.16)(0.862)]^{1.19}$$

$$= 4.44\,[0.2423]^{1.19} = 4.44\,[0.1851]$$

$$= 0.822$$

Calculate the body vortex interference factors from Section 4.3.1.3

$$\frac{r}{\left(b_{H_e}/2\right)} = \frac{2.935}{9.12} = 0.322$$

$$\alpha\left(\frac{x - x_s}{r}\right) = \frac{\alpha}{57.3}\left(\frac{66.0}{2.935} - \frac{x_s}{r}\right) = \frac{\alpha}{57.3}\left(22.5 - \frac{x_s}{r}\right)$$

①	②	③	④	⑤	⑥	⑦	⑧
α (deg)	x_s/r (Fig. 4.3.1.3-13a)	$\frac{\alpha}{57.3}\left(\frac{x - x_s}{r}\right)$	y_o/r (Fig. 4.3.1.3-14)	z_o/r (Fig. 4.3.1.3-13b)	z_o/r (corrected)*	$\frac{\Gamma}{2\pi\alpha Vr}$ (Fig. 4.3.1.3-15)	$\frac{y_o}{b_{H_e}/2}$ ④ (0.322)
0	–	–	–	–	–	–	–
4	–	–	–	–	–	–	–
8	16.9	0.782	0.600	1.13	1.297	0.55	0.193
12	11.25	2.356	0.705	1.62	1.787	0.895	0.227
16	8.55	3.895	0.747	1.90	2.067	1.215	0.241
20	7.0	5.410	0.762	2.075	2.242	1.58	0.245

①	⑨	⑩	⑪
α (deg)	$\frac{z_o}{b_{H_e}/2}$ ⑥ (0.322)	$i_{v_{B(H)}}$ (Fig. 4.3.1.3-7a-ℓ)	$i_{v_{B(H)}}\left(\frac{\Gamma}{2\pi\alpha Vr}\right)\left(\frac{r}{b_{H_e}/2}\right)$ ⑩ ⑦ (0.322)
0	–	–	–
4	–	–	–
8	0.418	–0.190	–0.03365
12	0.575	–0.300	–0.08646
16	0.666	–0.296	–0.1158
20	0.722	–0.297	–0.1511

*The vertical location of the body vortex must be adjusted to account for the true location of the horizontal tail (Figures 4.3.1.3-7a through -7ℓ assume the horizontal tail is mounted on the body center line). Since the horizontal tail is located below the body center line, the vertical distance of the vortex is increased; i.e., $\left(\frac{z_o}{r}\right)_{\text{corrected}} = \frac{z_o}{r} + \frac{z'}{r}$ where z' is the distance of the horizontal tail below the center line.

Solution:

$$C_{l_\delta} = \frac{i}{2}\left[\left(1 - \frac{\pi A_W}{57.3}\frac{\partial\bar{\epsilon}}{\partial a}\right) + i_{v_{B(H)}}\left(\frac{\Gamma}{2\pi\alpha Vr}\right)\left(\frac{r}{b_{H_e}/2}\right)\right]\eta\left(\frac{q_H}{q}\right)\frac{\bar{y}_H S_{H_e}}{b_W S_W}\left(C_{L_{\alpha_H}}\right)_e$$

(Equation 6.2.1.2-a)

$$= \frac{1}{2}\left[\left\{1 - \frac{\pi(3.39)}{57.3}(0.822)\right\} + i_{v_{B(H)}}\left(\frac{\Gamma}{2\pi\alpha Vr}\right)\left(\frac{r}{b_{H_e}/2}\right)\right](0.789)(0.0221)(0.0530)$$

$$= 0.000391 + 0.000462\left[i_{v_{B(H)}}\left(\frac{\Gamma}{2\pi\alpha Vr}\right)\left(\frac{r}{b_{H_e}/2}\right)\right]$$

α (deg)	$i_{v_{B(H)}}\left(\frac{\Gamma}{2\pi\alpha Vr}\right)\left(\frac{r}{b_{H_e}/2}\right)$	C_{l_δ} (per deg)
0	–	0.000391
4	–	0.000391
8	–0.03365	0.000375
12	–0.08646	0.000351
16	–0.1158	0.000338
20	–0.1511	0.000321

The calculated results are compared with test values from Reference 3 in Sketch (d).

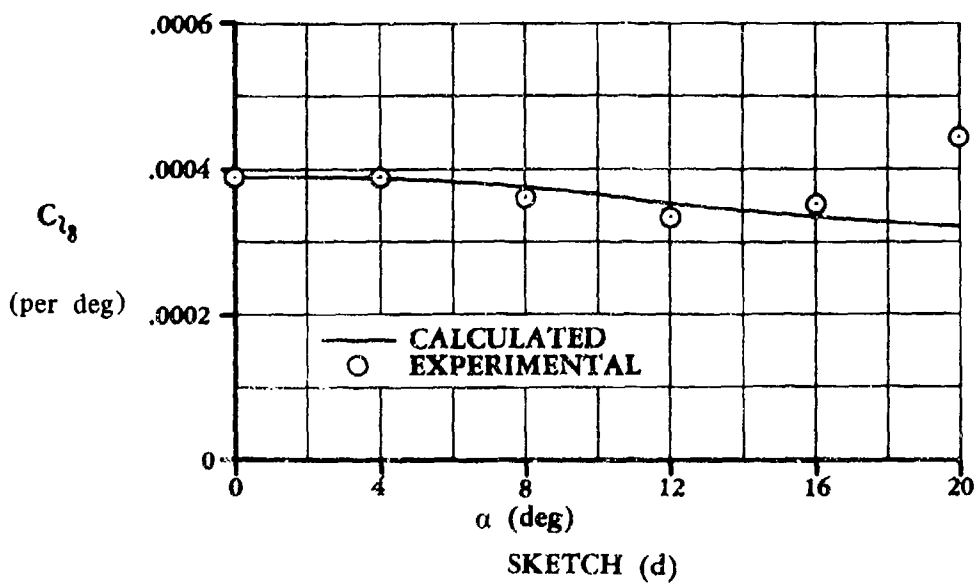

SKETCH (d)

B. TRANSONIC

DATCOM METHOD

Because Mach number effects on roll-control effectiveness are very small, no separate solution is presented in the transonic regime. The existing methods are considered to be applicable in the transonic regime; i.e., the subsonic method for $M < 1.0$, and the supersonic method for $M > 1.0$. However, it should be emphasized that the transonic methods must be used to calculate the various components of the roll-control-effectiveness equations; i.e., the values of $\partial\bar{\epsilon}/\partial\alpha$, $\left(C_{L_{\alpha_H}}\right)_e$, and $\left(C_{N_{\alpha_H}}\right)_e$, in the transonic speed regime.

C. SUPERSONIC

DATCOM METHOD

The following method is a modification of the method found in Reference 1, with the additional terms accounting for the effects of body vortices and tail effectiveness. In contrast to the subsonic method, this method accounts for the tail effectiveness and the downwash due to wing vortices in the empirical factor of 0.35. At angles of attack less than six degrees the body vortex interference factor $i_{v_{B(H)}}$ can be neglected. The roll-control effectiveness of a body-mounted differentially deflected horizontal stabilizer, based on $S_W b_W$, is given by

$$C_{l_\delta} = 0.35\left[i_{v_{B(H)}}\left(\frac{\Gamma}{2\pi\alpha V r}\right)\left(\frac{r}{b_{H_e}/2}\right) + \left(k_{H(B)} + k_{B(H)}\right)\right]\left(C_{N_{\alpha_H}}\right)_e \frac{\bar{y}_H S_{H_e}}{b_W S_W} \qquad 6.2.1.2\text{-c}$$

The proper sign of the rolling-moment coefficient will result from the expression $C_l = C_{l_\delta}(\delta_L - \delta_R)$. The subscript e refers to the exposed surface (see Section 4.3.1.2 for a definition of exposed surfaces), and

$k_{H(B)}$ and $k_{B(H)}$ are tail-body interference factors obtained from Figures 4.3.1.2-12b and -12a, respectively, of Section 4.3.1.2. Care should be taken to use the appropriate empennage geometry with these figures; i.e., the average body diameter in the region of the horizontal tail and the horizontal-tail span.

$\left(C_{N_{\alpha_H}}\right)_e$ is the normal-force variation with angle of attack of the exposed horizontal tail obtained from Paragraph C of Section 4.1.3.2. Care should be exercised to use the correct method for the specific geometry and to apply the appropriate correction factors where applicable, e.g., those on Figure 4.1.3.2-60.

$\bar{y}_H$ is the lateral center-of-pressure coordinate of the horizontal tail measured from and normal to the longitudinal axis. For the supersonic case, it is assumed that the lateral center-of-pressure coordinate is located at the 40-percent position of the semispan of the exposed tail; i.e.,

$$\bar{y}_H = 0.4\left(\frac{b_{H_e}}{2}\right) + r \qquad 6.2.1.2\text{-d}$$

All remaining terms have been previously defined in the subsonic method of this section. (It should be noted that the c.p. of the horizontal tail at supersonic speeds is assumed to be located at the midchord point of the exposed tail MAC in defining the parameter x.)

The total angular deflection of the control surfaces δ is measured in a plane parallel to the plane of symmetry, and is positive for the left control surface deflected trailing edge down and the right control surface deflected trailing edge up.

Sample Problem

Given: Model 2 of Reference 8

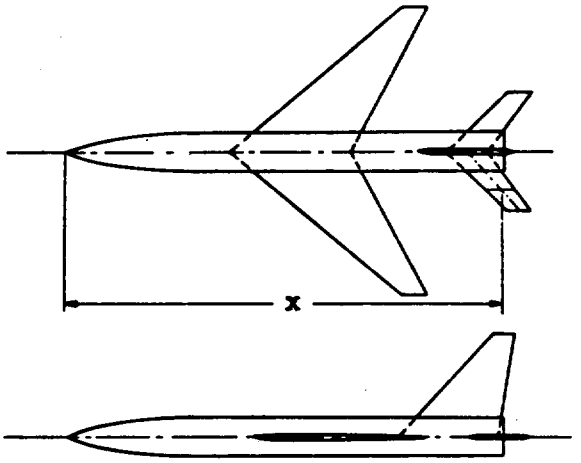

Wing Characteristics:

S_W = 144.0 sq in. b_W = 24.0 in. $\Lambda_{c/4}$ = 45°

Horizontal-Tail Characteristics:

S_{H_e} = 18.24 sq in. b_H = 10.73 in. b_{H_e} = 7.4 in.

A_H = 4.0 A_{H_e} = 3.0 λ_H = 0.6 λ_{H_e} = 0.685

$\Lambda_{c/4}$ = 45° Λ_{LE} = 46.7° Airfoil: Double Wedge; t/c = 0.04

Additional Characteristics:

M = 2.01; β = 1.744 r = 1.665 in. x = 36.59 in.

Compute:

Calculate $\left(C_{N_{\alpha_H}}\right)_e$ from Section 4.1.3.2

$$\frac{\tan \Lambda_{LE}}{\beta} = \frac{1.0625}{1.744} = 0.609$$

$$A_{H_e} \tan \Lambda_{LE} = (3.0)(1.0625) = 3.1875$$

$\beta\left(C_{N_\alpha}\right) = 4.02$ per rad (Figure 4.1.3.2-56 (d), (e), (f), interpolated)

$C_{N_\alpha} = 2.305$ per rad

$\beta \cot \Lambda_{LE} = (1.744)(0.9424) = 1.64$ (supersonic leading edge)

The supersonic wing lift-curve-slope correction factor will be applied because of the supersonic leading edge.

t/c = 0.04 and double-wedge airfoil

$\Delta y = 0.25$ (Figure 2.2.1-8)

$$\Delta y_\perp = \frac{\Delta y}{\cos \Lambda_{LE}} = \frac{0.25}{0.6858} = 0.365$$

$$\frac{C_{N_\alpha}}{\left(C_{N_\alpha}\right)_{theory}} = 0.995 \quad \text{(Figure 4.1.3.2-60)}$$

$$\left(C_{N_{\alpha_H}}\right)_e = (0.995)(2.305) = 2.293 \text{ per rad} = 0.040 \text{ per degree}$$

Calculate the tail-body interference factors from Section 4.3.1.2

$$\frac{d_H}{b_H} = \frac{2(1.665)}{10.73} = 0.3103$$

$k_{B(H)} = 0.324$ (Figure 4.3.1.2-12a)

$\beta A_{H_e} = (1.744)(3.0) = 5.232$

$k_{H(B)} = 0.983$ (Figure 4.3.1.2-12b)

$k_{B(H)} + k_{H(B)} = 0.324 + 0.983 = 1.307$

Calculate the lateral center-of-pressure coordinate

$$\bar{y}_H = 0.4\left(\frac{b_{H_e}}{2}\right) + r \quad \text{(Equation 6.2.1.2-d)}$$

$$= (0.4)(3.7) + 1.665 = 3.145 \text{ in.}$$

$$\frac{\bar{y}_H S_{H_e}}{b_W S_W} = \frac{(3.145)(18.24)}{(24.0)(144.0)} = 0.0166$$

Calculate the body vortex interference factors from Section 4.3.1.3

$$\frac{r}{b_{H_e}/2} = \frac{1.665}{3.7} = 0.45$$

$$\alpha\left(\frac{x - x_s}{r}\right) = \frac{\alpha}{57.3}\left(\frac{36.59}{1.665} - \frac{x_s}{r}\right) = \frac{\alpha}{57.3}\left(21.98 - \frac{x_s}{r}\right)$$

①	②	③	④	⑤	⑥	⑦	⑧
α (deg)	x_s/r (Fig. 4.3.1.3-13a)	$\frac{\alpha}{57.3}\left(\frac{x - x_s}{r}\right)$	y_o/r (Fig. 4.3.1.3-14)	z_o/r (Fig. 4.3.1.3-13b)	z_o/r (corrected)*	$\frac{\Gamma}{2\pi\alpha Vr}$ (Fig. 4.3.1.3-15)	$\frac{y_o}{b_{H_e}/2}$ ④ (0.45)
0	–	–	–	–	–	–	–
4	–	–	–	–	–	–	–
8	17.0	0.695	0.590	1.110	1.110	0.54	0.265
12	11.15	2.268	0.700	1.600	1.600	0.87	0.315
16	8.52	3.758	0.742	1.880	1.880	1.18	0.334

①	⑨	⑩	⑪
α (deg)	$\frac{z_o}{b_{H_e}/2}$ ⑥ (0.45)	$i_{v_{B(H)}}$ (Fig. 4.3.1.3-7a-ℓ)	$i_{v_{B(H)}}\left(\frac{\Gamma}{2\pi\alpha Vr}\right)\left(\frac{r}{b_{H_e}/2}\right)$ ⑩ ⑦ (0.45)
0	–	–	–
4	–	–	–
8	0.499	–0.125	–0.0304
12	0.720	–0.226	–0.0885
16	0.846	–0.242	–0.1286

*$\left(\frac{z_o}{r}\right)_{\text{corrected}} = \frac{z_o}{r} - 0 = \frac{z_o}{r}$ (tail located on body center line).

Solution:

$$C_{l_\delta} = 0.35\left[i_{v_{B(H)}} \left(\frac{\Gamma}{2\pi\alpha V r}\right)\left(\frac{r}{b_{H_e}/2}\right) + \left(k_{H(B)} + k_{B(H)}\right)\right] \left(C_{N_{\alpha_H}}\right)_e \frac{\bar{y}_H S_{H_e}}{b_W S_W}$$

(Equation 6.2.1.2-c)

$$= 0.35\left[i_{v_{B(H)}} \left(\frac{\Gamma}{2\pi\alpha V r}\right)\left(\frac{r}{b_{H_e}/2}\right) + 1.307\right] (0.040)(0.0166)$$

$$= 0.000232\left[i_{v_{B(H)}} \left(\frac{\Gamma}{2\pi\alpha V r}\right)\left(\frac{r}{b_{H_e}/2}\right)\right] + 0.000303$$

α (deg)	$i_{v_{B(H)}}\left(\frac{\Gamma}{2\pi\alpha V r}\right)\left(\frac{r}{b_{H_e}/2}\right)$	C_{l_δ} (per deg)
0	–	0.000303
4	–	0.000303
8	−0.0304	0.000296
12	−0.0885	0.000282
16	−0.1285	0.000273

The calculated results are compared with test values from Reference 8 in Sketch (e).

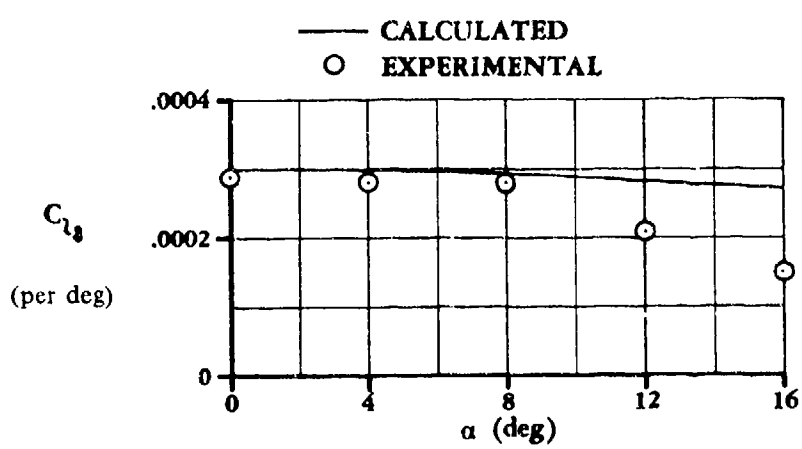

SKETCH (e)

REFERENCES

1. Campbell, J. P.: The Use of the Horizontal Tail for Roll Control. NACA RM L55L16a, 1956. (U)

2. McAllister, J. D., et al.: Wing Roll Control Devices for Transonic High Lift Conditions. Part I – Fixed Wing Configuration. AFFDL-TR-69-124, 1970. (U)

3. Boisseau, P. C.: Low-Speed Roll Effectiveness of a Differentially Deflected Horizontal-Tail Surface on a 42° Swept-Wing Model. NACA RM L56E03, 1956. (U)

4. English, R. D.: Free-Flight Investigation, Including Some Effects of Wing Aeroelasticity, of the Rolling Effectiveness of an All-Movable Horizontal Tail With Differential Incidence at Mach Numbers from 0.6 to 1.5. NACA RM L54K30, 1955. (U)

5. Mitchell, J. L., and Vitale, A. J.: Free-Flight Investigation of the Control Effectiveness of a Differentially Deflected Horizontal Tail at Mach Numbers from 0.8 to 1.6. NACA RM L56B20, 1956. (U)

6. Fournier, P. G.: Effect of Tail Dihedral on Lateral Control Effectiveness at High Subsonic Speeds of Differentially Deflected Horizontal-Tail Surfaces on a Configuration Having a Thin Highly Tapered Wing. NASA Memo 12-1-58L, 1959. (U)

7. Critzos, C. C.: Lateral-Control Investigation at Transonic Speeds of Differentially Deflected Horizontal-Tail Surfaces for a Configuration Having a 6-Percent-Thick 45° Sweptback Wing. NACA RM L55I26, 1955. (U)

8. Spearman, M. L.: Limited Investigation of Effects of Differential Horizontal-Tail Deflection on Lateral Control Characteristics of Two Swept-Wing Airplane Models at Mach Numbers from 1.4 to 2.0. NACA RM L56I20, 1956. (U)

9. Neely, R. H., and Griner, R. F.: Summary and Analysis of Horizontal-Tail Contribution to Longitudinal Stability of Swept Wing Airplanes at Low Speeds. NASA TR R-49, 1959. (U)

10. DeYoung, J., and Harper, C. W.: Theoretical Symmetric Span Loading at Subsonic Speeds for Wings Having Arbitrary Plan Form. NACA TR 921, 1948. (U)

11. Koenig, D. G.: Tests in the Ames 40- by 80-Foot Wind Tunnel of an Airplane Configuration with an Aspect Ratio 3 Triangular Wing and an All-Movable Horizontal Tail – Longitudinal and Lateral Characteristics. NACA RM A52L15, 1953. (U)

12. Spearman, M. L. and Foster, G. V.: Stability and Control Characteristics at a Mach Number of 2.01 of a Variable-Sweep-Wing Configuration with Outboard Wing Panels Swept Back 75°. NASA TM X-32, 1959. (U)

13. Shaw, D. S.: Supersonic Investigation of the Static Stability, Performance, and Control of a Variable-Sweep Tactical Fighter Model. Phase 1, NASA TM X-1045, 1965. (C) Title Unclassified

14. Graham, D., and Koenig, D. G.: Tests in the Ames 40- by 80-Foot Wind Tunnel of an Airplane Configuration with an Aspect Ratio 2 Triangular Wing and an All-Movable Horizontal Tail – Lateral Characteristics. NACA RM A51L03, 1952. (U)

TABLE 6.2.1.2-A
SUBSONIC TAIL-ROLL-CONTROL EFFECTIVENESS DATA SUMMARY AND SUBSTANTIATION

Ref.	M	A_W	λ_W	b_W (in.)	Λ_{LE_W}	A_{H_e}	λ_{H_e}	b_H (in.)	Λ_{LE_H}	α	C_{l_δ} Calc.	C_{l_δ} Test	ΔC_{l_δ}
2	0.7	4.07	0.3	22.52	31.5°	2.146	0	13.06	57.5°	0	0.000872	0.00114	−0.000268
										4	0.000872	0.00116	−0.000288
										8	0.000836	0.00132	−0.000484
										12	0.000784	0.00112	−0.000336
										16	0.000741	0.00112	−0.000379
3	0.05	3.39	0.247	47.56	47.2°	3.25	0.187	24.11	50.5°	0	0.000391	0.00039	0
										4	0.000391	0.00039	0
										8	0.000375	0.000361	0.000014
										12	0.000351	0.000336	0.000015
										16	0.000338	0.000352	−0.000014
										20	0.000321	0.000445	−0.000124
6	0.6	3.0	0.14	27.39	38.7°	3.084	0.588	16.12	18.8°	0	0.000575	0.00069	−0.000115
										5	0.000575	0.00069	−0.000115
										10	0.000544	0.00074	−0.000196
										15	0.000506	0.00077	−0.000264
11	0.13	2.99	0	367.7	53.2°	3.977	0.50	221.4	10°	0	0.000787	0.00055	0.000237
										4	0.000787	0.00065	0.000137
										8	0.000740	0.00081	−0.00007
										12	0.000720	0.00084	−0.00012
										16	0.000696	0.00078	−0.000084
										20	0.000674	0.00072	−0.000046

TABLE 6.2.1.2-A (CONTD)

Ref.	M	A_W	λ_W	b_W (in.)	Λ_{LE_W}	A_{H_e}	λ_{H_e}	b_H (in.)	Λ_{LE_H}	α	C_{l_δ} Calc.	C_{l_δ} Test	ΔC_{l_δ}
7	0.96	4.0	0.6	72.0	46.7°	3.275	0.668	30.7	46.6°	0	0.000358	0.000315	0.000043
										4	0.000358	0.00040	−0.000042
	0.90									0	0.000367	0.000325	0.000042
										4	0.000367	0.000373	−0.000006
										8	0.000345	0.00045	−0.000105
										12	0.000327	0.000385	−0.000058
										16	0.000311	0.000325	−0.000014
	0.80									0	0.000352	0.00035	0.000002
										4	0.000352	0.00040	−0.000048
										8	0.000332	0.00035	−0.000018
										12	0.000315	0.000415	−0.0001
										16	0.000299	0.000368	−0.000069
										20	0.000284	0.000265	0.000019
2	0.9	4.07	0.3	22.52	31.5°	2.146	0	13.06	57.5°	0	0.000954	0.00119	−0.000236
										4	0.000954	0.00119	−0.000236
										8	0.000914	0.00130	−0.000386
										12	0.000856	0.00112	−0.000264
										16	0.000813	0.00088	−0.000067
	0.8									0	0.000913	0.00124	−0.000327
										4	0.000913	0.00122	−0.000307
										8	0.000875	0.00126	−0.000385
										12	0.000820	0.00122	−0.0004
										16	0.000774	0.00096	−0.000186

TABLE 6.2.1.2-B
SUPERSONIC TAIL-ROLL-CONTROL EFFECTIVENESS DATA SUMMARY AND SUBSTANTIATION

Ref.	M	A_W	λ_W	b_W (in.)	Λ_{LE_W}	A_{H_e}	λ_{H_e}	b_H (in.)	Λ_{LE_H}	α	C_{l_δ} Calc.	C_{l_δ} Test	ΔC_{l_δ}
8 Model 1	1.61	4	0.5	25.31	38.1°	3.0	0.468	12.12	39.5°	0	0.000455	0.00049	−0.000035
										4	0.000455	0.00049	−0.000035
										8	0.000454	0.00046	−0.000006
										12	0.000435	0.000425	0.000010
										16	0.000423	0.00036	0.000063
	2.01									0	0.000371	0.00040	−0.000029
										4	0.000371	0.00040	−0.000029
										8	0.000370	0.00039	−0.000020
										12	0.000354	0.00034	0.000014
										16	0.000345	0.00025	0.000095
8 Model 2	1.41	4	0.2	24.0	49.4°	3.0	0.685	10.73	46.7°	0	0.000402	0.00042	−0.000018
										4	0.000402	0.00039	0.000012
										8	0.000393	0.00035	0.000043
										12	0.000374	0.00034	0.000034
										16	0.000362	0.00028	0.000082
	2.01									0	0.000303	0.00029	0.000013
										4	0.000303	0.00028	0.000023
										8	0.000296	0.00028	0.000016
										12	0.000282	0.00021	0.000072
										16	0.000273	0.00015	0.000123
12	2.01	1.86	0.13	22.68	60°	2.23	0.197	15.4	60°	0	0.000644	0.00050	0.000144
										4	0.000644	0.00055	0.000094
										8	0.000605	0.00050	0.000105
										12	0.000580	0.00043	0.00015
										16	0.000551	0.00038	0.000171

TABLE 6.2.1.2-B (CONTD)

Ref.	M	A_W	λ_W	b_W (in.)	Λ_{LE_W}	A_{H_e}	λ_{H_e}	b_H (in.)	Λ_{LE_H}	α	C_{l_δ} Calc.	C_{l_δ} Test	ΔC_{l_δ}
7	1.00	4.0	0.6	72.0	46.7°	3.275	0.668	30.7	46.7°	0	0.000387	0.000350	0.000037
										4	0.000387	0.000365	0.000022
										8	0.000370	0.000300	0.000070
	1.05									0	0.00036	0.00035	0.00001
										4	0.00036	0.00040	−0.00004
2	1.20	4.07	0.3	22.52	31.5°	2.146	0	13.06	57.5°	0	0.00148	0.00135	0.00013
										4	0.00148	0.00137	0.00011
										8	0.00143	0.00140	0.00003
										12	0.00138	0.00131	0.00007
										16	0.00121	0.00112	0.00009
13	1.60	7.564	–	31.50	72.5°	2.111	0.186	14.834	57.5°	0	0.000872	(a)	
										5	0.000872		
										10	0.000840		
										15	0.000810		
										20	0.000769		
	2.16									0	0.000703		
										5	0.000703		
										10	0.000678		
										15	0.000655		
	2.50									0	0.000610		
										5	0.000610		
										10	0.000588		
										15	0.000568		

(a) This information is classified CONFIDENTIAL.

SUBSONIC SPEEDS

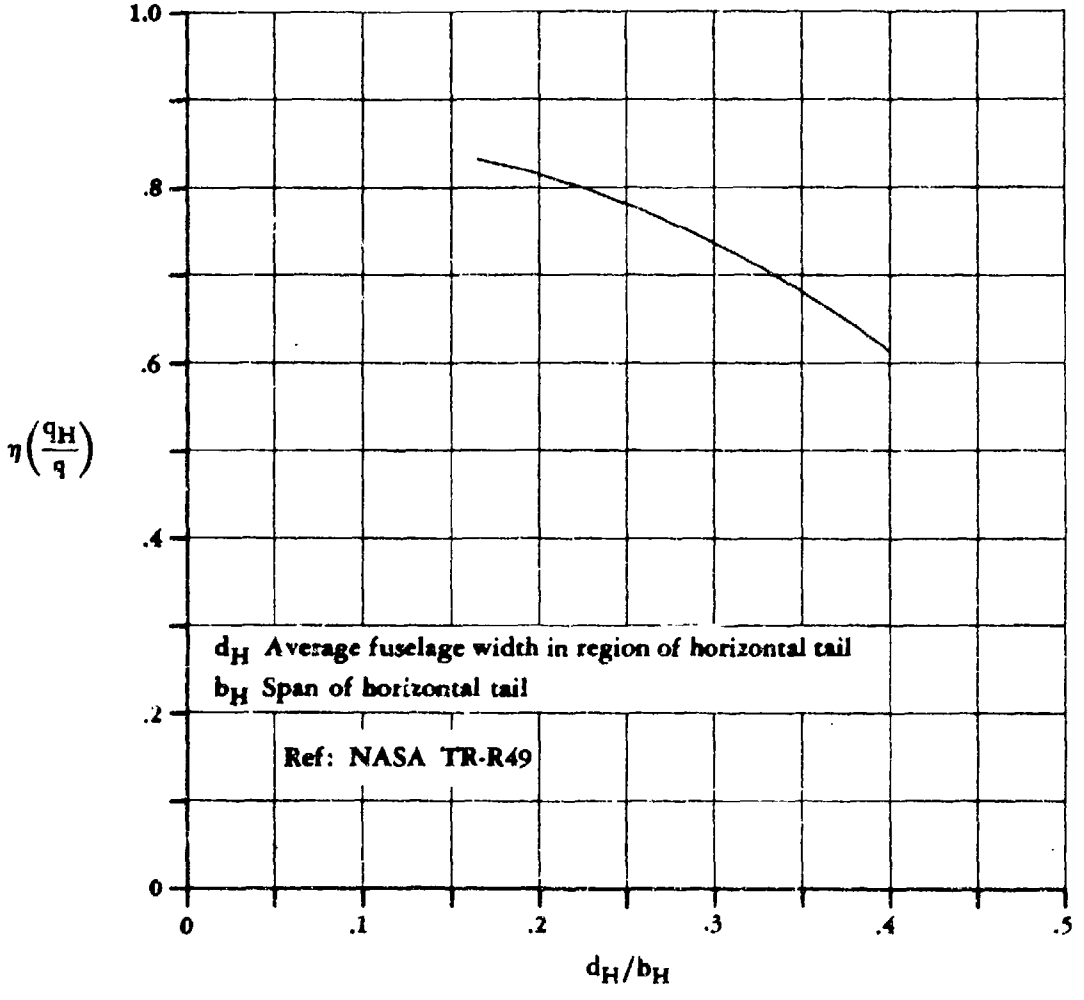

FIGURE 6.2.1.2-22 TAIL EFFECTIVENESS FOR BODY-MOUNTED HORIZONTAL TAILS

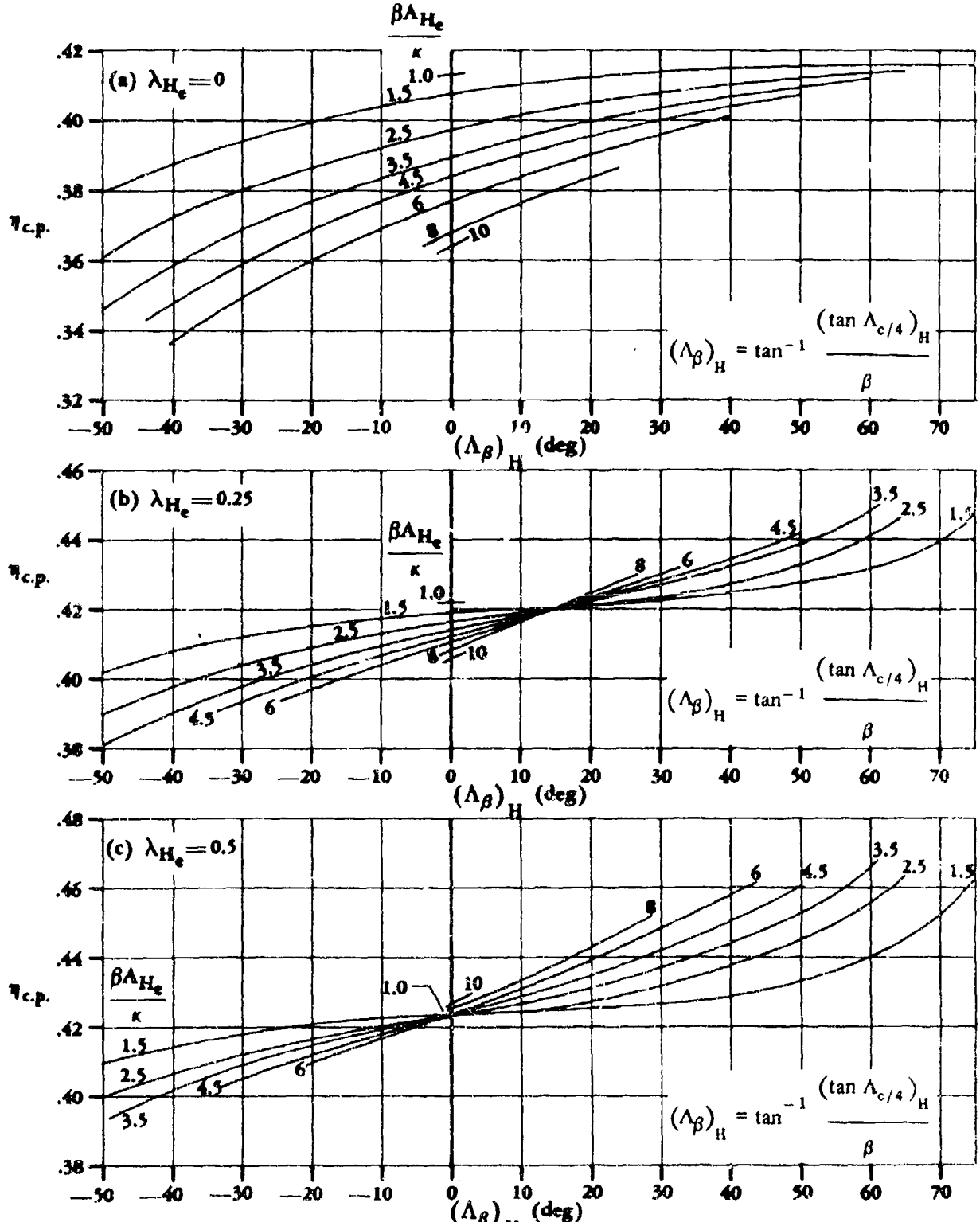

FIGURE 6.2.1.2-23 VARIATION OF SPANWISE LOCATION OF CENTER OF PRESSURE WITH COMPRESSIBLE SWEEP, ASPECT RATIO, AND TAPER RATIO

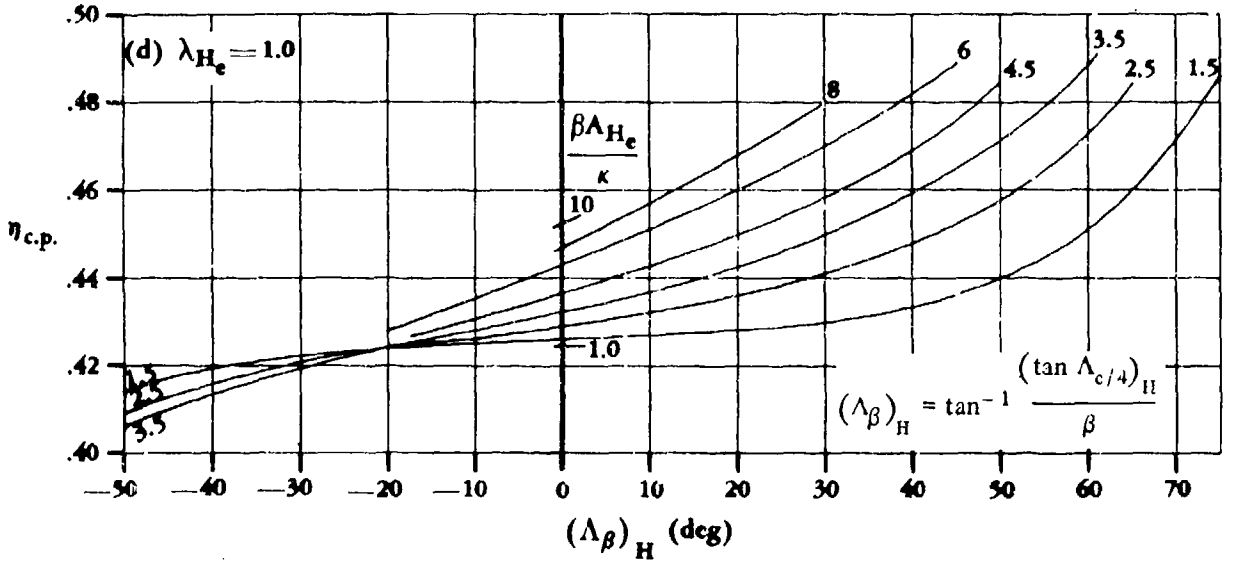

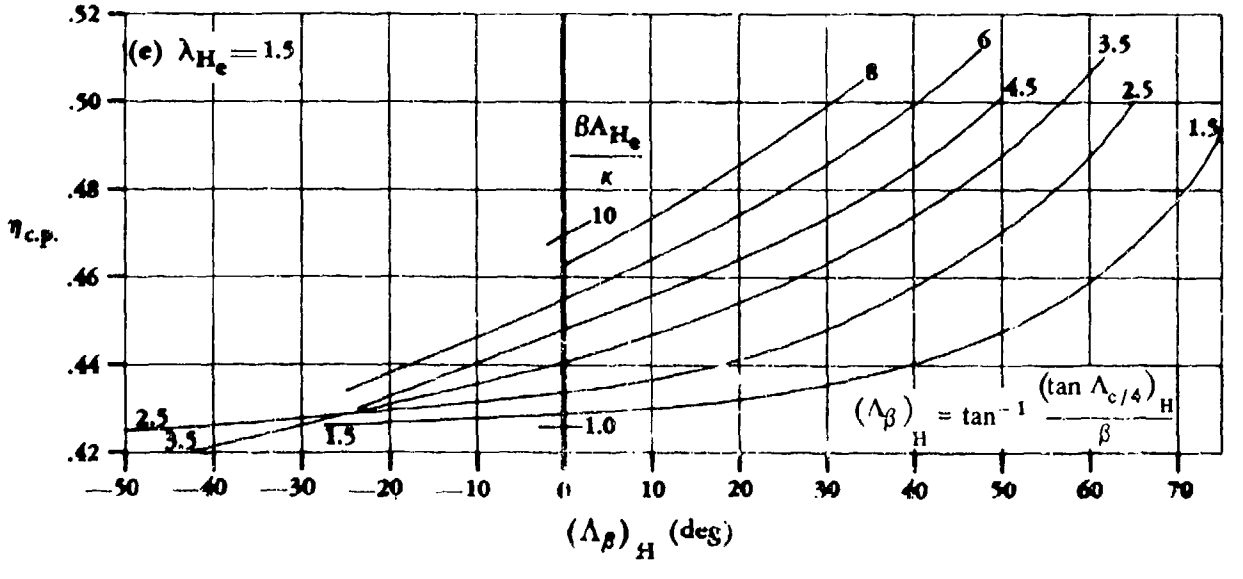

FIGURE 6.2.1.2-23 (CONTD)

6.2.2 YAWING MOMENT DUE TO ASYMMETRIC DEFLECTION OF CONTROL DEVICES

6.2.2.1 YAWING MOMENT DUE TO CONTROL DEFLECTION

Yawing moments due to aileron deflection arise from two sources. The first is the asymmetric change in the induced drag of the wings; the induced drag of the wing with the down-going aileron increases and that of the wing with the up-going aileron decreases. The second is the increase in profile drag due to flap deflection. The profile drag increases almost equally for positive and for negative flap deflections. The yawing moments due to the profile-drag increments of antisymmetrically deflected ailerons therefore tend to cancel. The methods of this section for estimating the yawing moment due to aileron deflection are derived from induced-drag changes and neglects contributions due to profile drag.

For spoilers that deflect on one wing panel at a time, the profile drag cannot be neglected. The methods presented for estimating the yawing moment due to spoiler deflection therefore include the contributions due to induced-drag and profile-drag changes.

Additional discussion on the aerodynamic aspects of aileron and spoiler controls is found in Sections 6.1.1.1, 6.1.1.2, 6.1.1.3, and 6.2.1.1.

A. SUBSONIC

DATCOM METHODS

Aileron-Type Controls

The method for determining the yawing moment of plain trailing-edge-flap controls is taken from Reference 1 The method is empirical in nature and is based on a limited amount of test data.

For aileron-type controls that extend to the wing tip, the yawing moment due to aileron deflection resulting from the unsymmetrical change in induced drag may be approximated by

$$C_n = KC_L C_{l_\delta} \frac{(\delta_L - \delta_R)}{2} \qquad 6.2.2.1\text{-a}$$

where

- K is an empirical factor, depending upon planform geometry, obtained from Figure 6.2.2.1-9. This design chart is taken from Reference 1 and is based on the data of References 2 through 7.
- C_{l_δ} is the rolling effectiveness of the aileron (per radian), obtained by using the method of Paragraph A of Section 6.2.1.1 for the appropriate subcritical Mach number.
- C_L is the lift coefficient for zero aileron deflection.
- δ_R is the right-hand control deflection in radians (positive trailing edge down).
- δ_L is the left-hand control deflection in radians (positive trailing edge down).

For aileron-type controls not extending to the wing tip, Equation 6.2.2.1-a is used to compute the difference in the yawing moments of two hypothetical ailerons—one extending from the inboard location of the actual aileron to the wing tip and the other extending from the outboard location of the actual aileron to the wing tip. The difference in the yawing moments of these two hypothetical ailerons gives the yawing moment of the actual aileron.

The method is valid for attached-flow conditions only; i.e., wing angle of attack and control deflection where no flow separation exists.

A sample problem illustrating the use of this method is presented on Page 6.2.2.1-3.

Not enough test data are available to permit either an independent verification or an extension of this method. Therefore, caution should be used in applying the method to configurations whose geometric parameters fall outside the ranges of those of the configurations of References 2 through 7 (see Figure 6.2.2.1-9).

Spoilers

Plug and Flap-Type Spoilers

The subsonic yawing moment due to spoiler deflection is obtained from Figures 6.2.2.1-10 and 6.2.2.1-11 for straight wings and swept wings, respectively. The charts are from Reference 1 and are based on the data of References 6 through 11. They are applicable to plug and to flap-type spoilers at zero angle of attack and for spoiler heights above the wing surface between 2 and 10 percent of the local wing chord. However, the applicability of the charts to inboard spoilers on swept wings is questionable.

Not enough experimental data are available to permit either an independent verification or an extension of this method. Therefore, the method is limited to the ranges of parameters presented on the design charts. It should be noted that the swept-wing design chart is based on test data from configurations with a constant spoiler chordwise location of 0.70c.

The design chart values of C_n are for a spoiler deflected on one panel based on the total wing area and wing span.

Sample Problem 2 on Page 6.2.2.1-4 illustrates the use of this method.

Spoiler-Slot-Deflector

The use of spoiler-slot-deflector combinations increases the effectiveness and hence the yawing moment due to spoiler deflection. The yawing moment due to a spoiler-slot-deflector combination at zero angle of attack, where the spoiler deflection is equal to the deflector deflection ($\delta_s/\delta_d = 1.0$) is given by

$$(C_n)_{\text{spoiler-slot-deflector}} = K\,(C_n)_{\text{plain spoiler}} \qquad 6.2.2.1\text{-b}$$

where

K — is the ratio of the yawing-moment coefficient of a spoiler-slot-deflector to that of a plain spoiler, obtained from Figure 6.2.2.1-12 as a function of the compressible sweep parameter $M \cos \Lambda_{c/4}$. This chart is based on data from References 12 through 14.

$(C_n)_{\text{plain spoiler}}$ — is the yawing-moment coefficient of a plain flap-type spoiler deflected on one wing panel, based on the total wing area and span, obtained from either Figure 6.2.2.1-10 or 6.2.2.1-11.

For higher angles of attack, a decrease in C_n due to plug and to flap spoilers is experienced. As the stall is approached, the yawing moment for these spoilers becomes zero. The use of a slot and deflector in combination with a plug or a flap spoiler improves its effectiveness at high angles of attack (see Section 6.2.1.1) and hence gives a significant yawing-moment increment for these angles.

Not enough test data are available to extend this method to configurations employing differential spoiler-deflector deflections.

Application of this method is illustrated by Sample Problem 3 on Page 6.2.2.1-4.

Sample Problems

1. Aileron-Type Control

Given: The wing-control configuration of Reference 4.

Wing-Control Characteristics:

$A_W = 3.94$ $\quad \lambda_W = 0.625$ $\quad \Lambda_{LE} = 42^o$ $\quad b_W = 11.38$ ft

$S_W = 32.8$ sq ft $\quad \frac{y_i}{b_W/2} = 0.50$ $\quad \delta_L = 15^o$ $\quad \delta_R = -15^o$

Additional Characteristics:

Low speed

α (deg)	C_L	C_{l_δ} (per rad)	
2	0.110	0.1180	Test results
4	0.230	0.1158	
6	0.350	0.1126	

Compute:

$K = -0.261$ (Figure 6.2.2.1-9)

$\frac{\delta_L - \delta_R}{2} = 15^o = 0.262$ rad

Solution.

$$C_n = KC_L C_{l_\delta} \frac{(\delta_L - \delta_R)}{2} \text{ (Equation 6.2.2.1-a)}$$

$$= (-0.261)(0.262) C_L C_{l_\delta}$$

$$= -0.0684 C_L C_{l_\delta}$$

①	②	③	④	⑤	⑥
α (deg)	C_L	C_{l_δ} (per rad)	②③	$(C_n)_{calc}$ -0.0684 ④	$(C_n)_{test}$
2	0.110	0.1180	0.01298	-0.00089	-0.0010
4	0.230	0.1158	0.02663	-0.00182	-0.0018
6	0.350	0.1126	0.03941	-0.00270	-0.0026

These test data have been used in the derivation of Figure 6.2.2.1-9; therefore, the sample problem is not an independent verification of the method.

2. Spoiler

Given: The wing-control configuration of Reference 15.

Wing-Control Characteristics:

S_W = 324 sq in. $\quad \lambda_W = 0.60 \quad A_W = 4.0 \quad b_W$ = 36.0 in. $\quad \Lambda_{LE} = 35.1^o$

Flap-type spoiler $\quad x_s/c = 0.70 \quad \frac{b_s}{b_W/2} = 0.50$

$\frac{y_o}{b_W/2} = 0.639 \quad \frac{\delta_s}{c} = 0.025, 0.05, 0.075, 0.100$

Solution:

$\frac{\delta_s}{c}$	$\frac{C_n}{\delta_s/c}$ Fig. 6.2.2.1-11	C_n Calc	C_n Test
.025	0.04	0.0010	0.00085
.050	0.04	0.0020	0.0020
.075	0.04	0.0030	0.0031
.100	0.04	0.0040	0.0034

3. Spoiler-Slot-Deflector

Given: The wing-control configuration of Reference 15. This is the configuration of Sample Problem 2 with the addition of a slot opening and a hinged deflector.

Wing-Control Characteristics:

S_W = 324.0 sq in. $\quad b_W$ = 36.0 in. $\quad \Lambda_{c/4} = 32.6^o \quad \frac{\delta_s}{c} = \frac{\delta_d}{c}$

The following test values of $(C_n)_{\text{plain spoiler}}$:

$\frac{\delta_s}{c}$	$(C_n)_{\text{plain spoiler}}$ (test results from Ref. 15)
.025	0.00085
.050	0.0020
.075	0.0031
.100	0.0034

Additional Characteristics:

$M = 0.40$

Compute:

$M \cos \Lambda_{c/4} = 0.40\ (0.8425) = 0.3370$

$K = 2.33$ (Figure 6.2.2.1-12)

Solution:

$(C_n)_{\substack{\text{spoiler-}\\\text{slot-}\\\text{deflector}}} = K\,(C_n)_{\substack{\text{plain}\\\text{spoiler}}}$ (Equation 6.2.2.1-b)

$\frac{\delta_s}{c}$	$(C_n)_{\text{plain spoiler}}$	$(C_n)_{\text{spoiler-slot-deflector}}$ Calc	$(C_n)_{\text{spoiler-slot-deflector}}$ Test
.025	0.00085	0.0020	0.0025
.050	0.0020	0.0047	0.0042
.075	0.0031	0.0072	0.0080
.100	0.0034	0.0079	0.0090

B. TRANSONIC

Force and moment characteristics at transonic speeds are difficult to generalize because of the nonlinear nature of the flow equations and interacting shock-wave–boundary-layer separation effects (see Section 4.1.3.2). The method presented here is intended to give a first-order approximation only and to provide a guide to aid in fairing between subcritical and supersonic speeds.

DATCOM METHOD

No specific charts are presented for determining the transonic yawing moment of lateral-control devices. The best source of information of this type is experimental data on similar configurations. If such information is not available, the following approach may be used as a guide in fairing between subcritical and supersonic speeds.

A first-order approximation of the transonic yawing moment of lateral-control devices is given by

$$C_n = (C_n)_{M=0.6} \frac{C_{L_\alpha}}{(C_{L_\alpha})_{M=0.6}} \qquad 6.2.2.1\text{-c}$$

where

$(C_n)_{M=0.6}$ is the yawing moment of the control at $M = 0.6$, obtained by using the appropriate method of Paragraph A of this section.

(C_{L_α}) is the transonic wing-lift-curve slope, obtained from Paragraph B of Section 4.1.3.2.

$(C_{L_\alpha})_{M = 0.6}$ is the wing-lift-curve slope at M = 0.6; obtained by using the straight-tapered-wing method of Paragraph A of Section 4.1.3.2 (Figure 4.1.3.2-49).

It should be noted that this approximation applied to spoilers neglects the effect of transonic wave drag, which can be very significant. Therefore, when applied to spoilers, the method should be considered only for the purpose of establishing the trend through the transonic region, and not as an approximation of the magnitude of the yawing moment.

C. SUPERSONIC

Methods are presented at supersonic speeds for approximating the yawing moment due to aileron-type controls and to plug or to flap-type spoilers. No method is presented for estimating the supersonic yawing moment due to spoiler-slot-deflectors. Published test data on spoiler-slot-deflector characteristics at supersonic speeds are extremely limited. References 16 and 17 present test data on spoiler-slot-deflector controls at supersonic speeds.

DATCOM METHOD

Aileron-Type Controls

Supersonic values of yawing moment due to flap deflection are obtained from Figure 6.2.2.1-13. This chart is taken from Reference 1 and is based on the method of computing drag due to lift in Reference 18 and on a limited amount of test data from References 19 and 20.

Not enough test data are available to permit either an independent verification or an extension of this method. Therefore, caution should be used in applying the method to configurations whose geometric parameters fall outside those of the configurations of References 19 and 20 (see Figure 6.2.2.1-13).

Spoilers

Plug and Flap-Type Spoilers

The supersonic yawing-moment coefficient due to spoiler deflection of a plug or a flap-type spoiler, deflected on one panel, based on the total wing area and span, is obtained from Figure 6.2.2.1-14 as a function of Mach number and configuration geometry. The design chart is based on the data from References 10 and 21 through 23.

A comparison of test values with results calculated by using this method is presented as Table 6.2.2.1-A.

REFERENCES

1. Decker, J., et al: USAF Stability and Control Handbook. M-03671, 1956. (C) Title Unclassified

2. Fitzpatrick, J.E., and Woods, R.L.: Low-Speed Lateral-Control Characteristics of an Unswept Wing With Hexagonal Airfoil Sections and Aspect Ratio 2.5 Equipped with Spoilers and With Sharp- and Thickened-Trailing-Edge Flap-Type Ailerons at a Reynolds Number of 7.6×10^6. NACA RM L52B15, 1952. (U)

3. Graham, R.R., and Koven, W.: Lateral-Control Investigation on a 37° Sweptback Wing of Aspect Ratio 6 at a Reynolds Number of 6,800,000. NACA RM L8K12, 1949. (U)

4. Spooner, S.H., and Woods, R.L.: Low-Speed Investigation of Aileron and Spoiler Characteristics of a Wing Having 42° Sweepback of the Leading Edge and Circular-Arc Airfoil Sections at Reynolds Numbers of Approximately 6.0×10^6. NACA RM L9A07, 1949. (U)

5. Bollech, T.V., and Pratt, G.L.: Investigation of Low-Speed Aileron Control Characteristics at a Reynolds Number of 6,800,000 of a Wing With Leading Edge Swept Back 42° With and Without High-Lift Devices. NACA RM L9E24, 1949. (U)

6. Pasamanick, J., and Sellers, T.B.: Low-Speed Investigation of the Effect of Several Flap and Spoiler Ailerons on the Lateral Characteristics of a 47.5° Sweptback-Wing-Fuselage Combination at a Reynolds Number of 4.4 x 10^6. NACA RM L50J20, 1950. (U)

7. Fischel, J., Naeseth, R.L., Hagerman, J.R., and O'Hare, W.M.: Effect of Aspect Ratio on the Low-Speed Lateral Control Characteristics of Untapered Low-Aspect-Ratio Wings Equipped With Flap and With Retractable Ailerons. NACA TR 1091, 1952. (U)

8. Franks, R.W.: Tests in the Ames 40- by 80-Foot Wind Tunnel of the Aerodynamic Characteristics of Airplane Models with Plain Spoiler Ailerons. NACA RM A54H26, 1954. (U)

9. Fischel, J., and Hammond, A.D.: Investigation of Effect of Span and Spanwise Location of Plain and Stepped Spoiler Ailerons on Lateral Control Characteristics of a Wing With Leading Edge Swept Back 51.3°. NACA RM L9K02, 1950. (U)

10. Johnson, H.S.: Wind-Tunnel Investigation at High Subsonic Speeds of the Effect of Spoiler Profile on the Lateral Control Characteristics of a Wing-Fuselage Combination With Quarter-Chord Line Swept Back 32.6° and NACA 65A006 Airfoil Section. NACA RM L53J05a, 1953. (U)

11. Fischel, J., and Tamburello, V.: Investigation of the Effect of Span, Spanwise Location, and Chordwise Location of Spoilers on Lateral Control Characteristics on a Tapered Wing. NACA TN 1294, 1947. (U)

12. Vogler, R.D.: Wind-Tunnel Investigation at Transonic Speeds of a Spoiler-Slot-Deflector Combination on an Unswept NACA 65A006 Wing. NACA RM L53J21, 1953. (U)

13. Hammond, A.D., and Brown, A.E.: Results of an Investigation at High Subsonic Speeds to Determine Lateral-Control and Hinge-Moment Characteristics of a Spoiler-Slot-Deflector Configuration on a 35° Sweptback Wing. NACA RM L57C20, 1957. (U)

14. Hammond, A.D.: Wind-Tunnel Investigation of the Effect of Aspect Ratio and Chordwise Location on Effectiveness of Plain Spoilers on Thin Untapered Wings at Transonic Speeds. NACA RM L56F20, 1956. (U)

15. Vogler, R.D.: Wind-Tunnel Investigation at High Subsonic Speeds of a Spoiler-Slot-Deflector Combination on an NACA 65A006 Wing With Quarter-Chord Line Swept Back 32.6°. NACA RM L53D17, 1953. (U)

16. Foster, G.V.: Effects of Spoiler-Slot-Deflector Control on the Aerodynamic Characteristics at a Mach Number of 2.01 of a Variable-Wing-Sweep Configuration with the Outer Wing Panels Swept Back 75°. NASA TM X-273, 1960. (U)

17. Lord, D.R., and Moring, R.: Aerodynamic Characteristics of a Spoiler-Slot-Deflector Control on a 45° Sweepback Wing at Mach Numbers of 1.61 and 2.01. NACA RM L57E16a, 1957. (U)

18. Polhamus, E.C.: Drag Due to Lift at Mach Numbers up to Two. NACA RM L53I22b, 1953. (U)

19. Mitchell, M.H., Jr.: Effects of Varying the Size and Location of Trailing-Edge Flap-Type Controls on the Aerodynamic Characteristics of an Unswept Wing at a Mach Number of 1.9. NACA RM L50F08, 1950. (U)

20. Jacobsen, C.R.: Effects on Control Effectiveness of Systematically Varying the Size and Location of Trailing-Edge Flaps on a 45° Sweptback Wing at a Mach Number of 1.9. NACA RM L51I26, 1951. (U)

21. Kindell, W.H.: Effects of Span and Spanwise and Chrodwise Location on the Control Effectiveness of Spoilers on a 50° Sweptback Wing at Mach Numbers of 1.41 and 1.96. NACA RM L53B09, 1953. (U)

22. Conner, D.W., and Mitchell, M.H., Jr.: Effects of Spoiler on Airfoil Pressure Distribution and Effects of Size and Location of Spoilers on the Aerodynamic Characteristics of a Tapered Unswept Wing of Aspect Ratio 2.5 at a Mach Number of 1.90. NACA RM L50L20, 1951. (U)

23. Wong, N.D.: An Investigation of the Control Effectiveness of Tip Ailerons and Spoilers on a Low-Aspect-Ratio Trapezoidal-Wing Airplane Model at Mach Numbers from 1.55 to 2.35. NACA RM A57I26a, 1957. (U)

24. Hamilton, C.V., and Driver, C.: An Investigation of a Supersonic Aircraft Configuration Having a Tapered Wing with Circular-Arc Sections and 40° Sweepback—Stability and Control Characteristics at a Mach Number of 1.61 of the Complete Configuration Equipped With Spoilers. NACA RM L54F15, 1954. (U)

TABLE 6.2.2.1-A
SUPERSONIC YAWING MOMENT DUE TO SPOILER DEFLECTION

DATA SUMMARY

Ref.	Spoiler	A	λ	$\Lambda_{c/4}$ (deg)	$\frac{y_i}{b_w/2}$	$\frac{y_o}{b_w/2}$	Spoiler Chordwise Location (%c)	$\frac{\delta_s}{c}$	M	C_n Calc	C_n Test	ΔC_n Calc - Test
24	Plug	4.0	0.50	40.0	0.15	0.95	0.55	0.05	1.61	0.0052	0.0053	-0.0001
	Flap									0.0052	0.0062	-0.0010
	Plug						0.65			0.0052	0.0070	-0.0018
						0.55				0.0021	0.0020	0.0001
								0.02		0.0010	0.0010	0
22	Plug	2.50	0.625	5.3	0.20	0.95	0.75	0.05	1.90	0.0040	0.0056	-0.0016
								0.02		0.0018	0.0021	-0.0003
					0.45			0.05		0.0030	0.0049	-0.0019
								0.02		0.0015	0.0012	0.0003
					0.70			0.05		0.0015	0.0026	-0.0011
								0.02		0.0008	0.0008	0
					0.45			0.05		0.0030	0.0020	0.0010
								0.02		0.0015	0.0004	0.0011
23	Flap	3.20	0.40	19.2	0.28	0.75	0.77	0.037	1.55	0.0025	-0.0008	0.0033
								0.095		0.0060	-0.0008	0.0068
								0.037	1.90	0.0016	0	0.0016
								0.095		0.0040	0	0.0040
								0.037	2.35	0.0011	0.0025	-0.0014
								0.095		0.0030	0.0025	0.0005
21	Plug	2.50	0.625	47.16	0.20	0.95	0.65	0.04	1.96	0.0033	0.0026	0.0007
								0.06		0.0045	0.0043	0.0002
						0.70		0.04		0.0018	0.0014	0.0004
								0.06		0.0025	0.0019	0.0006
						0.45		0.04		0.0010	0.0005	0.0005
								0.06		0.0012	0.0011	0.0001

Average Error = $\frac{|\Delta C_n|}{n}$ = 0.0012

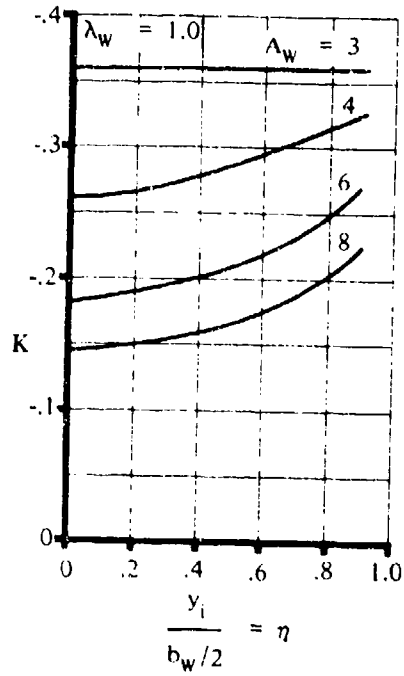

$1.13 \leq A_w \leq 6.13$

$0.5 \leq \lambda_w \leq 1.0$

$0 \leq \frac{y_i}{b_w/2} \leq 0.775$

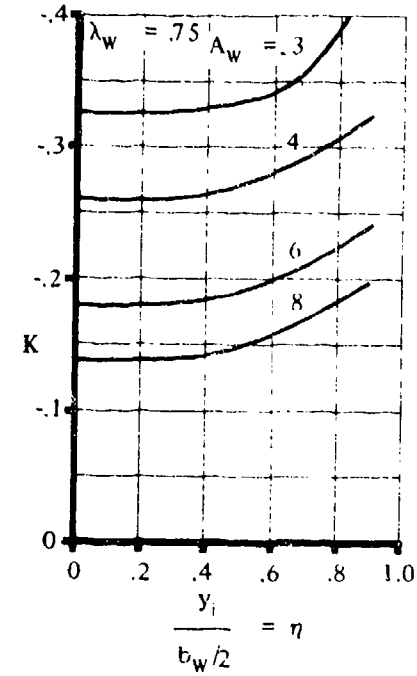

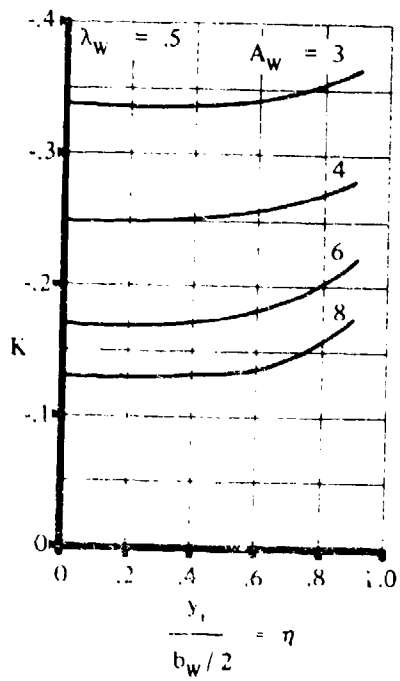

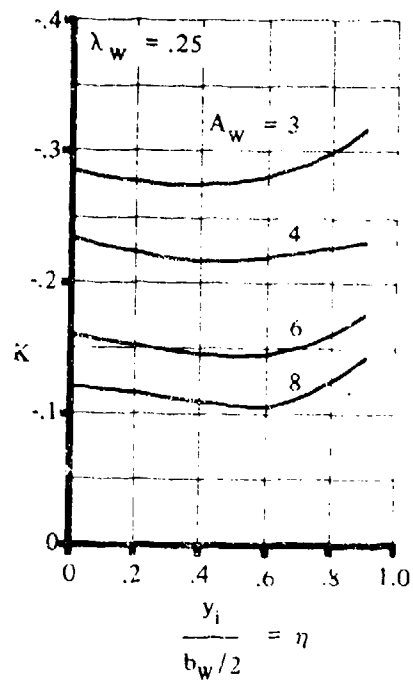

FIGURE 6.2.2.1-9 CORRELATION CONSTANT FOR DETERMINING YAWING MOMENT DUE TO AILERON DEFLECTION

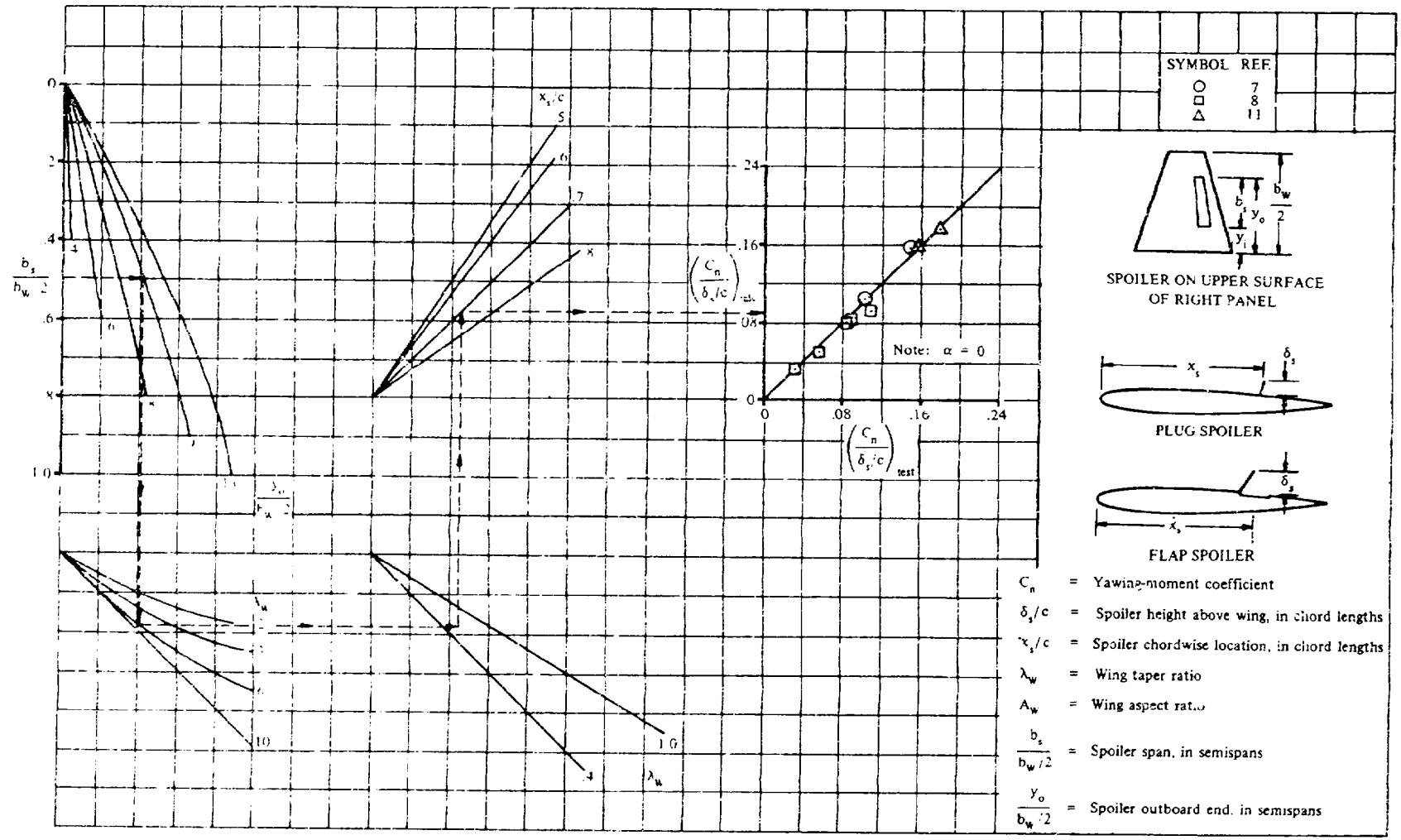

FIGURE 6.2.2.1-10 YAWING MOMENT DUE TO SPOILER CONTROL SURFACES FOR STRAIGHT WINGS AT SUBSONIC SPEEDS AT LOW ANGLES OF ATTACK

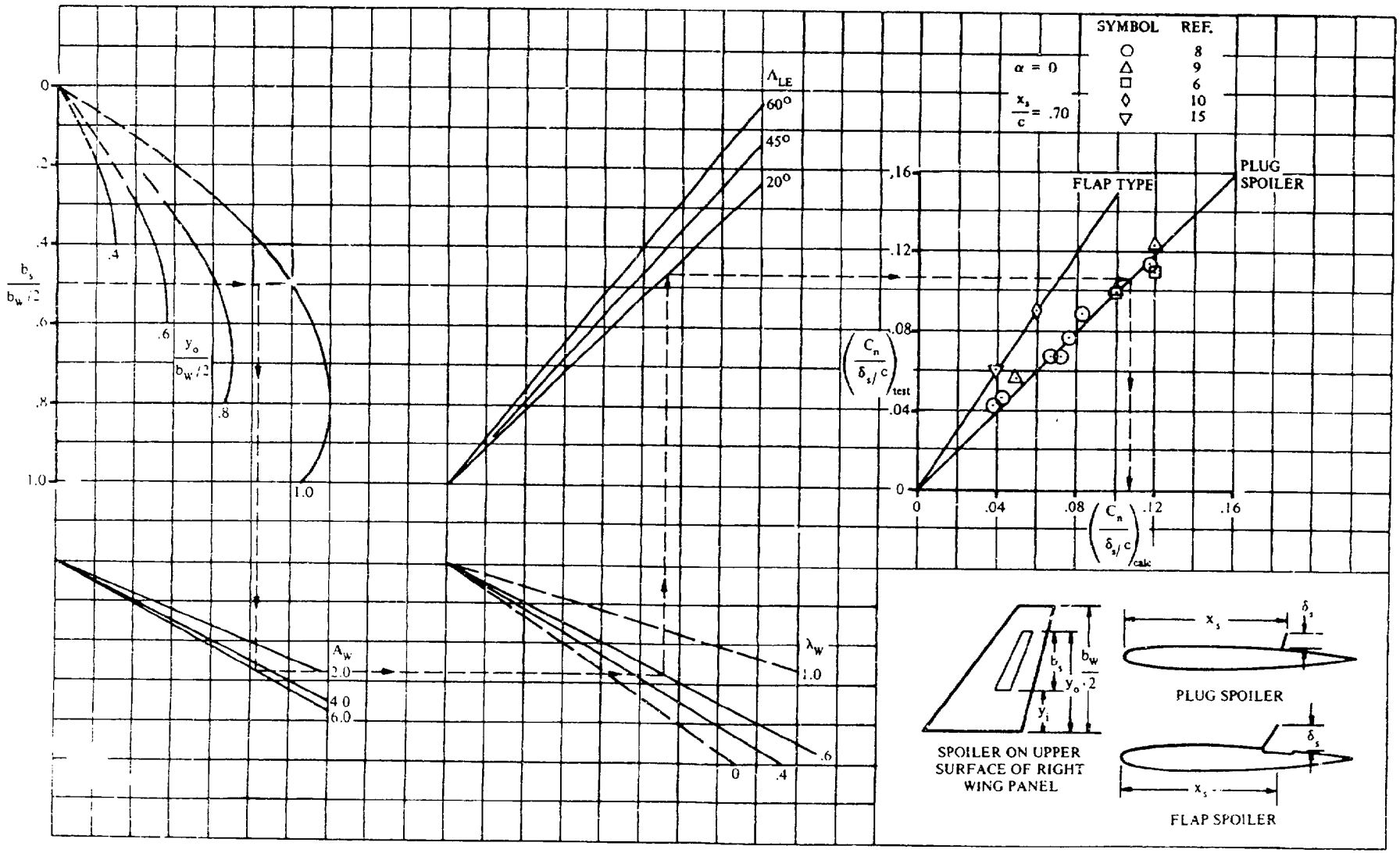

FIGURE 6.2.2.1-11 YAWING MOMENT DUE TO SPOILER CONTROL SURFACES FOR SWEPTBACK WINGS AT SUBSONIC SPEEDS AND LOW ANGLES OF ATTACK

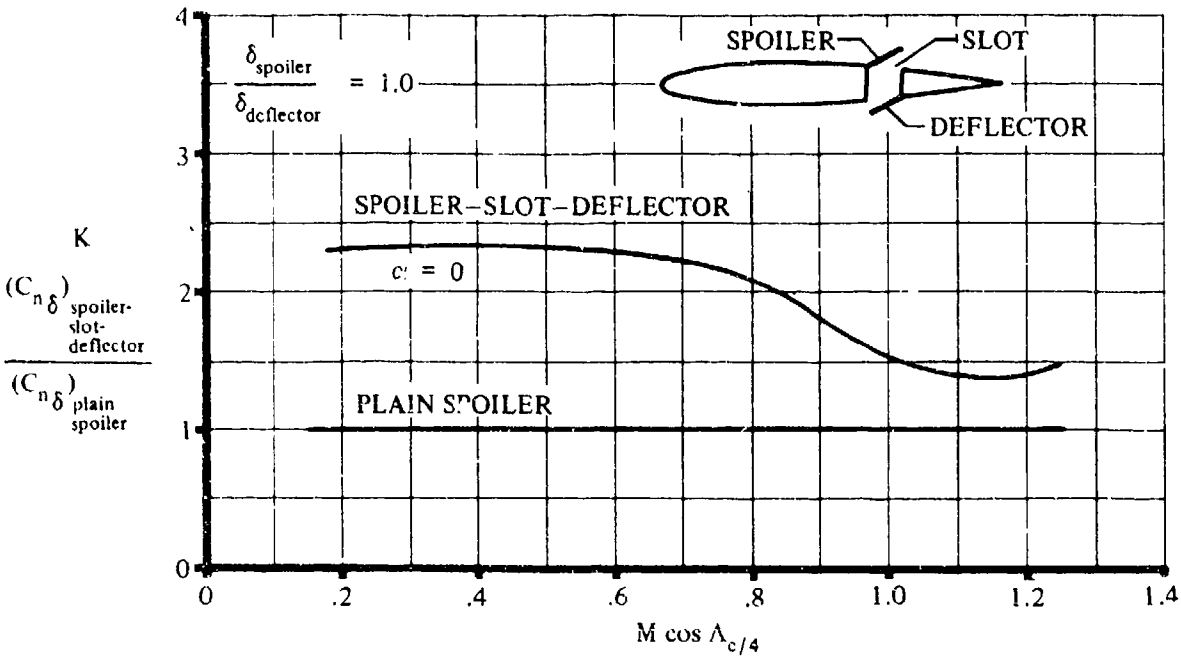

FIGURE 6.2.2.1-12 EFFECT OF SLOT AND DEFLECTOR ON SPOILER YAWING MOMENT

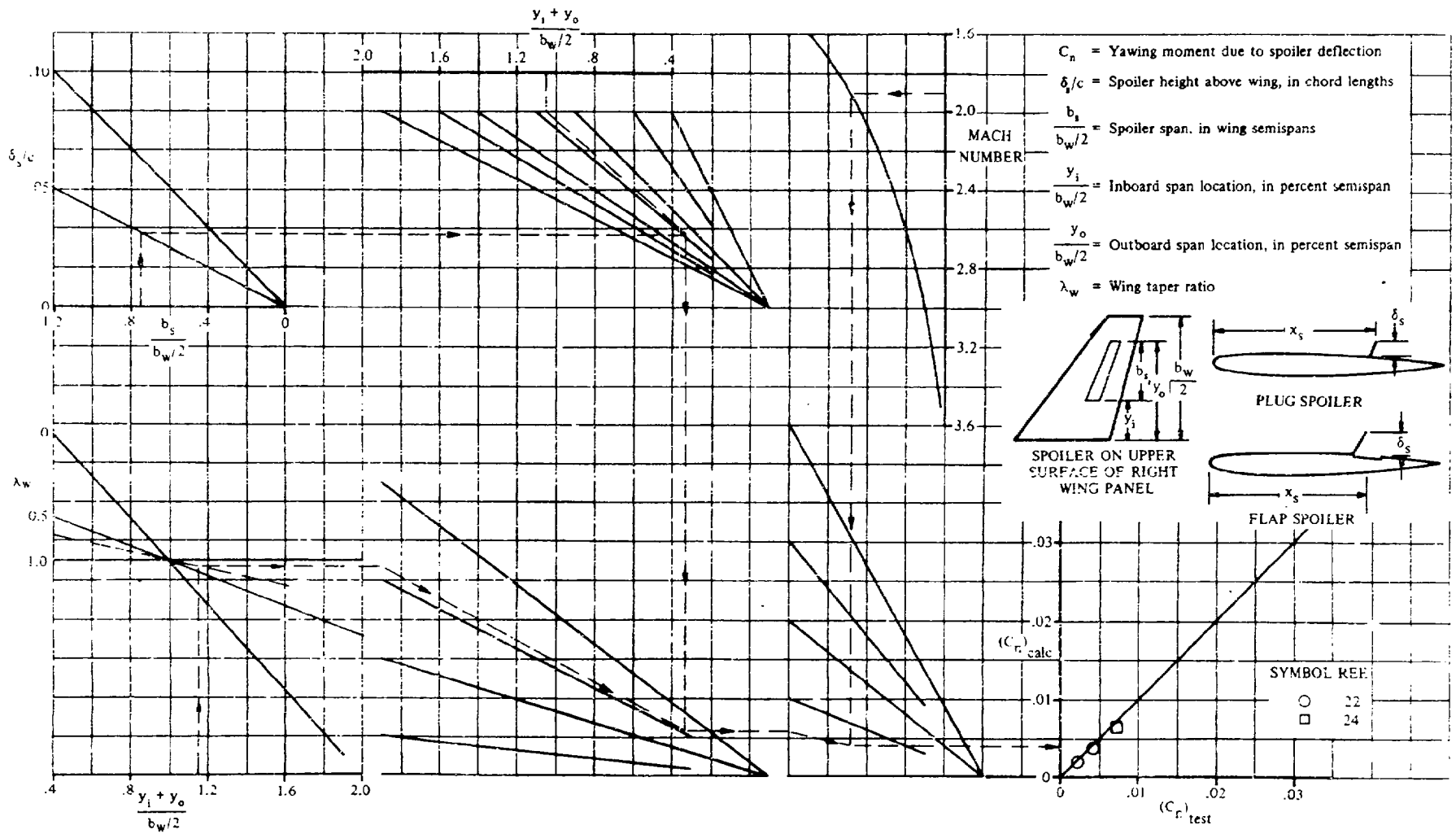

FIGURE 6.2.2.1-14 SPOILER YAWING MOMENT AT SUPERSONIC SPEEDS

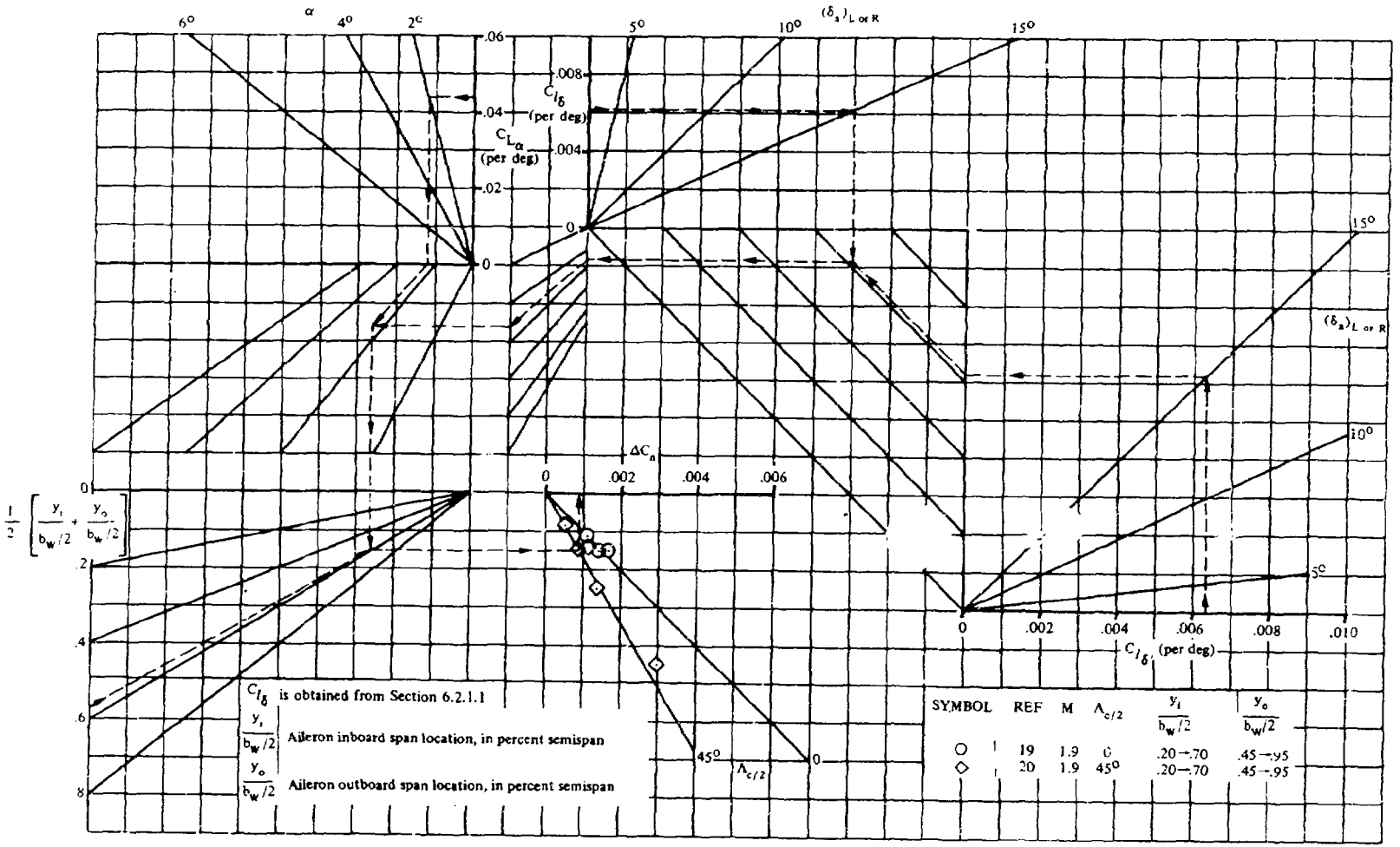

FIGURE 6.2.2.1-13 YAWING MOMENT DUE TO AILERON DEFLECTION AT SUPERSONIC SPEEDS

6.2.2.2 YAWING MOMENT DUE TO A DIFFERENTIALLY DEFLECTED HORIZONTAL STABILIZER

No methods are available for estimating the yawing moments due to a differentially deflected horizontal stabilizer, and the data available for correlation are limited. However, a brief discussion, taken essentially from Reference 1, is given pertaining to the qualitative and quantitative aspects of yawing moments associated with tail roll control.

Associated with tail roll control are yawing moments, varying in magnitude and direction as a function of Mach number, angle of attack, and vehicle geometry. These yawing moments can be attributed to (1) the pressure differential induced on the vertical tail as a result of the differentially deflected horizontal tail, (2) the drag component associated with each horizontal-tail panel, and (3) the dihedral of the horizontal tail. For most configurations and test conditions, the differential pressure on the vertical tail is the dominating factor.

Yawing-moment data are generally presented in the form of the parameter $C_{n_\delta}/C_{l_\delta}$ (ratio of yawing moment to rolling moment produced by roll control). For low-horizontal-tail configurations, tail roll control up to $M \approx 1.0$ produces very large favorable yawing moments, which decrease with increasing angle of attack but tend to remain positive over the angle-of-attack range ($\alpha \approx 0$ to $22°$) for which test data are available. These large yawing moments are due primarily to the induced pressure differential on the vertical panel. This pressure differential on the vertical tail also tends to reduce the rolling moment for a low-tail configuration.

At supersonic speeds, the load carry-over from the horizontal tail to the vertical tail decreases with increasing Mach number. The attendant result is that at supersonic speeds the tail roll control will produce smaller favorable yawing moments at low angles of attack and possibly adverse yawing moments at high angles of attack. For a specific configuration, if the Mach number is high enough, adverse yaw due to tail roll control is a possibility throughout the angle-of-attack range. Sketch (a) presents representative yawing-moment data produced by roll control for a low-tail configuration as a function of Mach number and angle of attack.

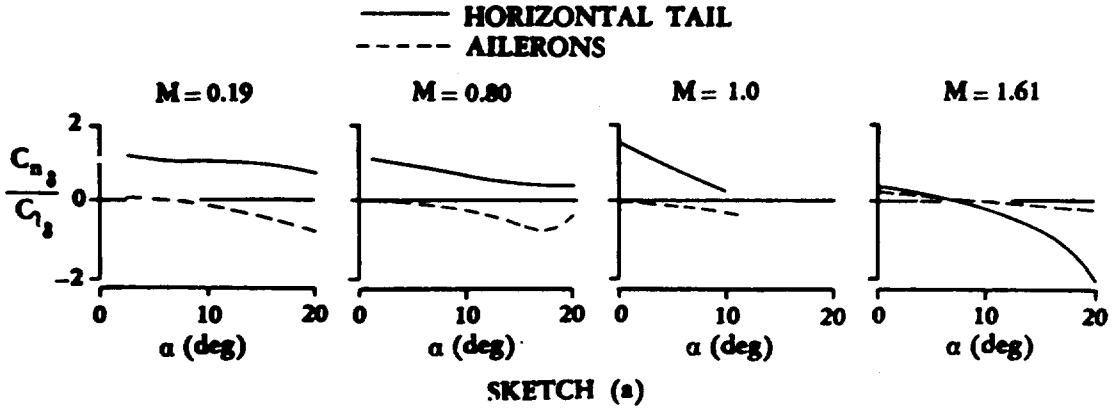

SKETCH (a)

The vertical position of the horizontal tail is the most important parameter in determining the relative magnitude and direction of the yawing moment due to roll control (References 1 and 2). The variations in yawing moment due to roll control shown in Sketch (b) are representative of the

effect of the horizontal-tail location. These variations would enable the designer to position the horizontal tail to avoid large undesirable yawing moments, longitudinal stability permitting. In this connection, it may also be pointed out that if a ventral fin is used on the airplane for high-speed stability, the yawing moments for a low tail position would be smaller. If the yawing moments cannot be adjusted to a satisfactory value by positioning the tail, it might be necessary to adjust them by linking the rudder in with the tail roll control.

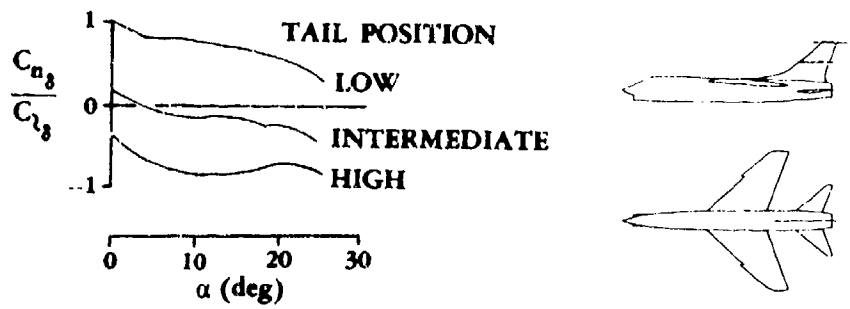

SKETCH (b)

Dihedral Effects

The results of dihedral variation on yawing moment due to roll $C_{n_\delta}/C_{l_\delta}$ are of significant importance. The lateral component of the horizontal-tail loads increases with negative dihedral, and the load induced on the vertical tail by differential horizontal-tail deflection is reduced by increases in negative dihedral. The combined effect of these two phenomena is a substantial increase in the yawing-moment parameter $C_{n_\delta}/C_{l_\delta}$ with increasing negative dihedral angle over a large angle-of-attack range. The variation of the yawing moment due to tail roll control is shown in Sketch (c) (Reference 3). Consequently, if negative tail dihedral is employed on a low-tail configuration to improve the linearity of the pitching-moment curves, for example, and differential tail deflection is utilized to augment low-speed roll control; then the favorable yawing moment associated with tail roll control will be aggravated further. Of course, if a ventral fin is employed on the configuration, the loads induced on the ventral would be increased, tending to offset the additional yawing moment due to negative dihedral; however, this effect would not be strong enough to cancel the effect created by negative dihedral. On the other hand, for low-tail configurations at supersonic speeds where the yawing moment due to tail roll control is adverse, negative tail dihedral would be favorable.

SUBSONIC SPEEDS

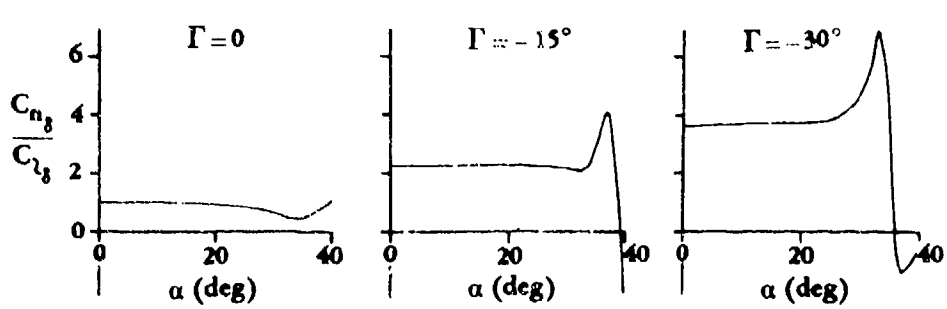

SKETCH (c)

Flap Effects

The effects of flaps on yawing moment due to roll control are shown for two different configurations in Sketch (d). Both configurations show a substantial increase of $C_{n_\delta}/C_{l_\delta}$ with flap deflection at low lift coefficients. This increase is primarily the result of a decrease in roll effectiveness C_{l_δ}.

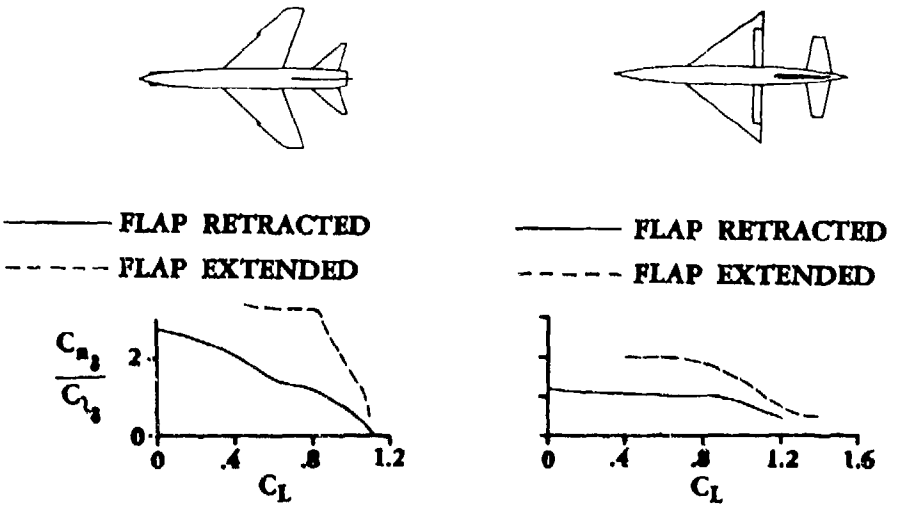

SKETCH (d)

REFERENCES

1. Campbell, J. P.: The Use of the Horizontal Tail for Roll Control. NACA RM L55L16a, 1956. (U)

2. Boisseau, P. C.: Low-Speed Roll Effectiveness of a Differentially Deflected Horizontal-Tail Surface on a 42° Swept-Wing Model. NACA RM L56E03, 1956. (U)

3. Fournier, P. G.: Effect of Tail Dihedral on Lateral Control Effectiveness at High Subsonic Speeds of Differentially Deflected Horizontal-Tail Surfaces on a Configuration Having a Thin Highly Tapered Wing. NASA Memo 12-1-58L, 1959. (U)

6.2.3 SIDE FORCE DUE TO ASYMMETRIC DEFLECTION OF CONTROL DEVICES

The side-force increment due to the asymmetric deflection of control devices on a plain wing is usually small enough to be neglected. At supersonic speeds, however, strong shock waves can be generated from deflected controls. These shock waves frequently impinge on vehicle components and cause considerable forces and moments by means of their direct pressure effect and by boundary-layer-separation effects.

For the purpose of the Datcom, it is assumed that the side force due to asymmetric control deflection is sufficiently small to be neglected. Some data on the side force due to asymmetric control deflection on wing-body combinations at supersonic speeds may be found in reference 1.

REFERENCE

1. Smith, W. G., and Intrieri, P. F.: Some Aspects of Aileron Deflection on the Static Lateral and Directional Aerodynamic Characteristics of Four Contemporary Airplane Models. NACA RM A57E22, 1957. (U)

6.3 SPECIAL CONTROL METHODS

6.3.1 AERODYNAMIC CONTROL EFFECTIVENESS AT HYPERSONIC SPEEDS

The interest in aircraft and re-entry vehicles operating at hypersonic speeds has created the need for establishing preliminary-design methods for predicting the effectiveness of aerodynamic controls of such vehicles at hypersonic speeds.

This section presents a procedure, taken from reference 1, for applying the correlation results presented in reference 1 to the prediction of hypersonic control effectiveness.

The development of efficient hypersonic vehicles involves solutions of complex problems associated with the severe environment of hypersonic flight. Control characteristics, particularly at hypersonic speeds, are greatly affected by flow separation phenomena. Flow separation can occur ahead of deflected flaps, on the leeward side of a surface inclined at large angles of attack, near the impingement of a shock wave upon the boundary layer of a body, and on a curved surface. Control effectiveness may be increased, limited, or completely nullified because of boundary-layer separation. Pressure distributions over the control and the basic configuration can be greatly altered because of separation effects. Heat-transfer rates are changed on the control surfaces and the basic configuration both upstream and downstream of the control. The interaction region is characterized by a reduction of local heating rates in the separated region and a substantial heating rate increase at the reattachment point. It is therefore essential to understand the flow-separation phenomena and to describe the flow conditions in the separated region.

In reference 1, semiempirical correlations are developed for the characteristic parameters of a separated flow at hypersonic speeds. These correlations describe the pressure and heat-transfer distributions in terms of local flow properties by defining characteristic magnitudes and distance parameters. Knowing these quantities, relations for incremental aerodynamic force and moment coefficients are developed.

In order that the Datcom user may better understand the control effectiveness methods presented in this section, general discussions of hypersonic flow separation and the effects of the influence of separation on controls are presented. These general discussions are essentially quoted from reference 2 and present only the salient aspects of hypersonic-flow separation and its influence on aerodynamic controls. The reader can obtain a more thorough review of hypersonic-flow separation phenomena from references 1 and 3.

HYPERSONIC-FLOW SEPARATION

Separated flows are characterized by the prevailing type of boundary layer: laminar, turbulent, or transitional. The pressure rise and the extent of the separated region depend upon the characteristics of the boundary layer.

In general, boundary-layer separation occurs whenever the streamwise pressure increase along a surface is sufficient to overcome the forces acting to accelerate a fluid particle, or when the streamline curvature necessary to follow the surface contour cannot be sustained by the pressure gradient normal to the surface. In steady-flow aerodynamic problems the only forces acting to accelerate the low-momentum fluid near the wall against a pressure gradient are the shear forces between layers of fluid. Because the momentum of the fluid near the wall is quite low, a relatively small amount of deceleration by the pressure gradient is sufficient to bring about separation. Turbulent flow helps to delay the occurrence of separation, because the turbulent fluctuations increase the effective shear forces and thereby increase the adverse pressure force necessary to reverse the flow of the fluid near the wall.

The greatly increased effective viscosity due to turbulent fluctuations enables the equilibrium between pressure and shear forces near the wall to occur at much greater adverse pressure rises in turbulent boundary layers. Because of the connection between pressure rise and flow turning angle, this higher pressure corresponds to a much shorter, thicker separated zone for the same initial boundary-layer thickness. Cases presented by Schlichting (reference 4) and Howarth (reference 5) show turbulent pressure rises twice the lami-

nar ones, while the laminar separation zone extends 10 times farther than the turbulent one. A similar thickening (and simultaneous pressure rise) occurs in a transitional separation when the mixing zone becomes turbulent, and the downstream flow soon approaches a condition very similar to the equivalent turbulent separation. Upstream of the transition point, the flow has the character of the corresponding laminar separation zone. The location of the transition point therefore plays a distinct role in determining the pressure distribution (see references 6 and 7).

Present indications are that shock-induced laminar separation pressure distributions, and to a limited extent turbulent ones, are independent of the type of geometry producing separation (see reference 6). However, the turbulent peak pressure rise often depends significantly on geometry (references 6 and 8 through 11). This difference in dependence can probably be attributed to the greatly increased effective viscosity in turbulent flow enabling the wall contour within the separated zone to transmit its effect more strongly to the outer flow.

Typical surface pressure distributions for laminar and turbulent boundary layers are presented in sketches (a) and (b), respectively.

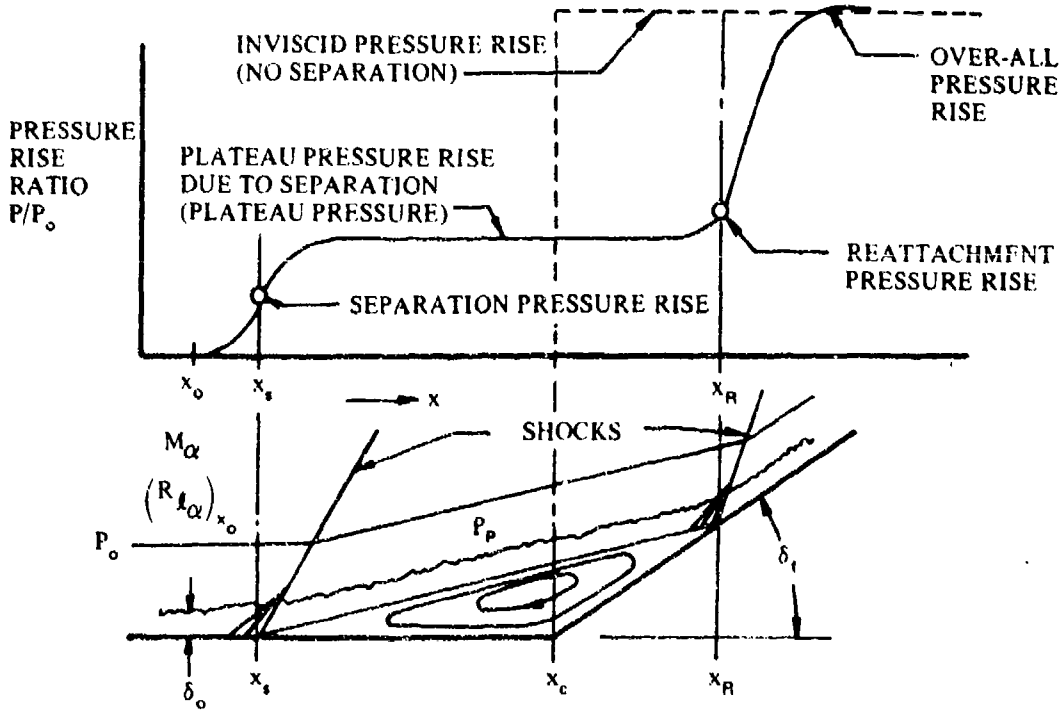

WALL PRESSURE DISTRIBUTION IN THE VICINITY OF LAMINAR SEPARATION

SKETCH (a)

The laminar boundary layer has a characteristic plateau where the pressure remains almost constant over most of the separated flow region. The separation pressure coefficient is based on the pressure rise from the undisturbed stream to the separation point. As explicitly mentioned by Love (reference 12), this is not to be confused with the pressure rise needed to cause separation.

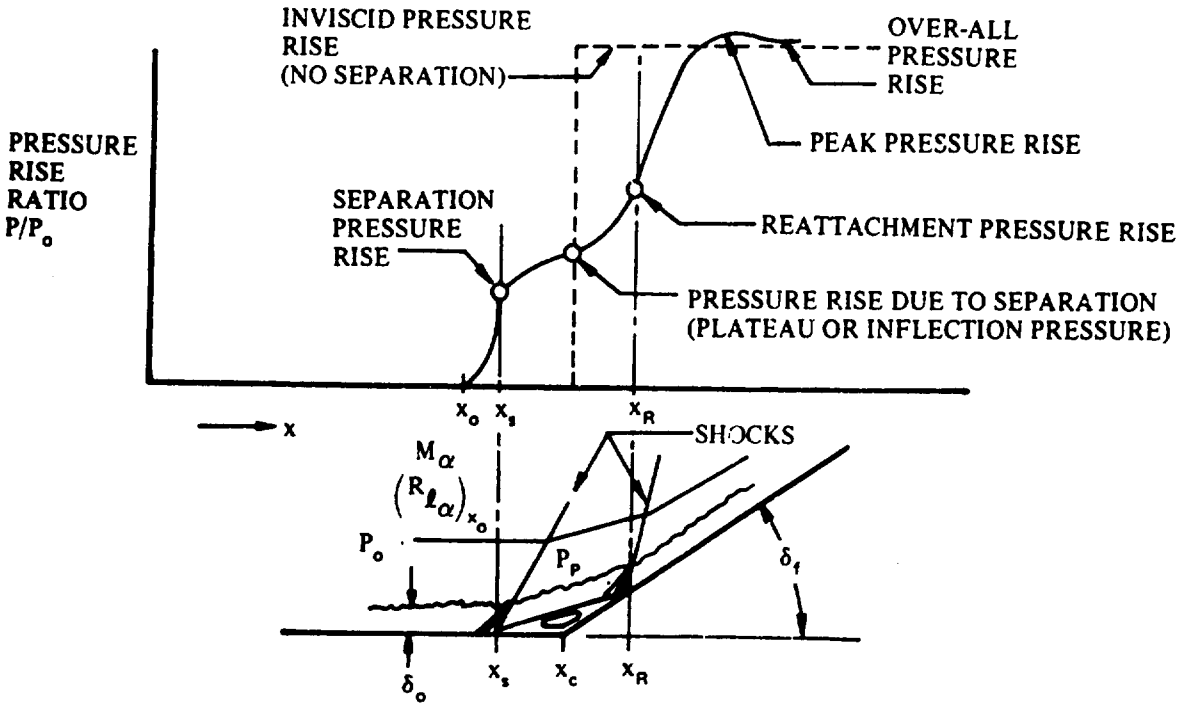

WALL PRESSURE DISTRIBUTION IN THE VICINITY OF TURBULENT SEPARATION

SKETCH (b)

The separated turbulent boundary-layer pressure distribution has no plateau region but rises to an inflection value. The final pressure after reattachment is usually that given by inviscid theory. Occasionally, a situation arises wherein there is a pressure rise above the inviscid value followed by an expansion to the inviscid value. This is caused by a lower local entropy level due to the multiple-shock compression of the inviscid flow near the separation and reattachment points. The multiple-shock compression is a more efficient process than the single-shock compression, resulting in a higher local total pressure. It has been observed occasionally in three-dimensional hypersonic separation, and there is good reason to expect it in other situations at high Mach numbers where multiple oblique-shock compression can exist.

The critical pressure-rise coefficient, referred to herein as the incipient pressure-rise coefficient $C_{p_{inc}}$, corresponds to the minimum over-all pressure for which separation will occur (see references 4, 7, 9, 10, 12, and 13). The current indications are that it is independent of the particular geometry causing the pressure rise (see references 11 and 14), although this may not prove to be a general rule. $C_{p_{inc}}$ is much greater and is a much weaker function of Reynolds number for turbulent boundary layers ($C_{p_{inc}} \sim (R_\ell)^{1/10}$) than for laminar boundary layers ($C_{p_{inc}} \sim (R_\ell)^{1/4}$). Recent correlations presented in reference 1 substantiate this 1/4-power Reynolds-number dependence for laminar boundary layers; however, the range of Reynolds numbers of the available test data is too small to validate the 1/10-power relation for turbulent boundary layers. Nevertheless, this dependence does correlate the available turbulent data over the ranges of the test conditions.

The pressure rise due to separation (plateau pressure) is of the same order of magnitude as the critical pressure rise, and exhibits the same type of dependence on Mach and Reynolds numbers. Detailed correlation formulas for predicting the pressure-distribution parameters in various situations are developed in reference 1, and are presented in the Datcom method in the form of design charts.

Two further points should be made concerning the general characteristics of laminar and turbulent separations. First, the high altitudes and large stream-to-wall temperature ratios characteristic of hypersonic flight greatly increase the probability of finding laminar flow. And second, the large viscous interaction associated with high Mach number and low Reynolds number will often make it very difficult to determine experimentally or theoretically whether separation has even occurred, let alone the separation location. For those conditions where separation is difficult to detect, the effect of separation on loads is quite small, but the understanding of the flow and the prediction of heat transfer and flow stability become uncertain.

The stability and steadiness of separated flows cannot be predicted with certainty using present information. In general, cavities appear to be the most unstable type of separated geometry. Unsteadiness can result from a hysteresis between laminar and turbulent separated-zone conditions if the flow conditions and geometry are of certain types, e.g., a sharply deflected ramp near the transition point of a flat plate. Whether all separated-zone instabilities are associated with transition or whether other mechanisms participate must be determined by future investigations. The resonant frequency of a cavity would be one important parameter in such an investigation. Violent macroscopic flow fluctuations affect heat-transfer rates and wall shear forces near the separation and reattachment points because of the Reynolds stress effect.

The relationships between heat transfer and separation in laminar and turbulent flow are poorly understood. Chapman (reference 15) theoretically estimates a ratio of heat transfer in a laminar separated zone to that in the attached layer, of 0.56. The experiments of Larson (reference 16) substantiate this estimate. Chapman mentions that turbulent separation regions can have heat-transfer rates as high as six times the equivalent rates for the attached layer at low Mach numbers, but this ratio decreases greatly with increasing Mach number. The turbulent-flow measurements of Larson do not show this high ratio at low Mach numbers, but the theory appears to approach the measurements at high Mach numbers. Larson states that the discrepancy is probably due to the failure of the theory to include the proper temperature – heat-transfer relationships for the experiments. It appears doubtful whether very large increases in heat transfer will ever be found in steady, separated regions. In short, turbulent and transitional separations may lead to heat-transfer rates higher than the equivalent attached boundary layer, but at high Mach numbers the ratio appears to be about 0.50 to 0.70, which is not indicated satisfactorily by present theory. Local increases in heat-transfer rate near reattachment are mentioned in reference 16, but these were not always found by the other investigators mentioned in reference 16.

The converse effect, i.e., the effect of heat-transfer on separation characteristics, is also not understood (see references 16 through 25). Sogin states in his survey report (reference 24) that there is much disagreement between theory and experiment regarding the effects of heat transfer on either laminar or turbulent separated flows. Thus, theoretical results for laminar boundary layers (references 17 through 23 and 32 and 33) indicate separation should be delayed by cooling; experimental results in references 32 and 33 tend to substantiate this theory, while those in references 16 and 26 through 28 do not. Gadd further states that if the turbulent boundary layer could be treated analytically it should also show separation delayed by cooling (references 26 and 27), but poor experimental agreement is obtained. The resolution of this uncertainty is very important, as it bears directly on the application of wind-tunnel data (equilibrium wall) to flight problems (usually cold wall).

INFLUENCE OF SEPARATION ON CONTROLS

Control characteristics, particularly at hypersonic speeds, are often greatly affected by separation. As previously noted, control effectiveness may be increased, limited, or completely nullified because of boundary-layer separation. Pressure distributions over controls and on the basic configuration may be greatly altered due to separation effects, changing drastically the moment coefficients predicted by inviscid theory. Heat-transfer rates are changed on the control surfaces and on the basic configuration both upstream and downstream of the control. Separation effects must therefore be considered in both the design and loca-

tion of controls. In general, separation tends to smooth out the sharp changes in pressure distributions predicted by inviscid theory, and can cause local "hot spots" which have heat-transfer rates many times higher than those that would exist for attached boundary layers. Separated flow phenomena are frequently unsteady and three-dimensional in nature, and undergo large changes with transition from laminar to turbulent flow, further complicating the analytical treatment of a design. Thus, for example, hysteresis effects are noticeable in the C_m versus α curves for some control configurations.

Aerodynamic forces and moments on a vehicle may be changed as much by changing the pressure distribution on the basic configuration as they would be by changes in the normal forces acting on controls. Leading-edge controls, for example, usually are not directly influenced by separation but, by causing separation, they can affect the pressures and heat-transfer rates over the entire configuration. Some effects of separation associated with controls on windward and leeward surfaces and some important three-dimensional and unsteady flow effects of separation on control characteristics are presented below.

Leading-Edge Controls

Leading-edge controls contemplated for hypersonic vehicles include flaps, spoilers, fins, spikes, and all-movable noses. The importance of separation for such controls is in the influence on the entire flow field downstream of the control. Separation behind a deflected leading-edge flap makes any control or stabilizing surface downstream of the flap ineffectual. Heat-transfer rates on the surface are reduced in the separated-flow region, but if the boundary layer reattaches on the surface the heat-transfer rate at reattachment can be several times larger than that for an attached boundary layer. The control forces and hinge moments of leading-edge fins and flaps would not be directly influenced by separation. Fins, which may be canards, create strong vortices which can cause boundary-layer transition and contribute to the possibility of unsteady flow over the downstream surfaces of the configuration. Comparable effects would be expected for large amounts of all-movable nose deflection which, nevertheless, is anticipated to be a very effective trimming device at high angles of attack. The importance of leading-edge controls in influencing the entire afterbody is epitomized by the use of spikes. Flow-separation spikes in front of blunt bodies may reduce the total drag of the body by effectively streamlining it. Average heat-transfer rates in the separated-flow region created by the spike are significantly reduced in laminar flow, although the local heat-transfer rate at reattachment may be quite high. Deflectable spikes might be used as control devices because they alter the pressure distribution in the forward region of a body. The separated-flow region caused by spikes, however, is frequently unsteady, which is a most unsatisfactory control characteristic. If these problems can be worked out, spike controls could become a very effective system for blunt vehicles.

Downstream Controls

Frequently control surfaces located downstream of the leading edge are also used as stabilizing devices. Their effectiveness, however, may be greatly affected by upstream separation of the boundary layer. The inviscid estimate of the pressure rise due to deflecting a control into the local stream is a discontinuous jump in the pressure distribution on the surface at the leading edge of the control. A similar sudden increase in the inviscid pressure distribution occurs at the trailing-edge shock required to recompress the flow over an expansion surface. In the actual flow, the sudden pressure rise may be transmitted upstream through the subsonic portion of the boundary layer, and separation may occur far upstream as a result. This is particularly likely for hypersonic flow, where shocks are highly swept, and for laminar boundary layers, which have thicker subsonic portions than turbulent boundary layers. Depending upon flow conditions, the boundary layer may be separated over the major portion of the surface, thereby greatly influencing the effectiveness of controls located downstream on either compression or expansion surfaces.

Laminar boundary-layer separation ahead of a deflected flap on the windward surface of a vehicle spreads the flow-deflection pressure rise over a much larger region than does turbulent separation. The effectiveness of the flap in creating a moment is lessened both by the decrease in the pressure distribution on the flap and by any pressure increase occurring on the surface upstream of the moment reference center. These effects tend to restrict the desired rearward movement of the center of pressure and reduce the effectiveness of the control. In extreme cases the center-of-pressure location with laminar separation may be well forward of that for a turbulent boundary layer.

The extent of the separated-flow region and the pressures imposed on the surface depend on the flap deflection, flow conditions, and nature of the boundary layer ahead of the flap. Reattachment of the separated flow on the flap is usually accompanied by a local heat-transfer rate several times larger than that corresponding to an attached boundary layer; the average heat transfer to the separated-flow region, however, is reduced. Similarly, separation affects the pressure distribution on vehicles having flared-skirt-type stabilizing surfaces. Laminar boundary-layer flow ahead of small protuberances yields pressure distributions closer to the inviscid predictions than does turbulent flow. A small step on a surface is effectively streamlined by laminar separation far ahead of it, whereas for turbulent separation, a strong shock exists ahead of the step and there is a large increase in the local pressure.

Separation on the leeward side of a vehicle may make shielded controls (i.e., controls which do not "see" the free stream) useless. Several factors combine in making leading-edge separation from the leeward surface of hypersonic vehicles particularly probable. Large angles of attack may be desirable for many hypersonic flight paths. Because high Mach number flows have small limiting expansion angles, much of the upper surface feels only the leakage flow from the boundary layer where the Mach number is lower. The pressure rise due to the strong trailing-edge shock may be propagated far forward through the thick hypersonic boundary layer, thus increasing the possibility of leading-edge separation.Another factor enhancing the probability of separation is the likelihood of the boundary layer being laminar with consequently thicker subsonic regions and at the same time less able to overcome an adverse pressure gradient than the corresponding turbulent boundary layer. The effectiveness of controls located entirely within the separated-flow region, such as trailing-edge flaps or fins, would be nullified. On the other hand, flow separation over notches (cavities) may advantageously be used to control the drag of a hypersonic vehicle; for essentially the same average rate of heat transfer to a hypersonic vehicle, the drag may be increased by an order of magnitude by the employment of notches in the surface of the vehicle. Separation influences both the type and the location of control devices. Spoilers, for example, would be ineffectual on leeward surfaces of hypersonic vehicles even if they were near the leading edge. Positive controls that always "see" the free stream are required.

Three-Dimensional and Unsteady Flow Effects

Separated-flow regions rarely are purely two-dimensional and usually are unsteady. Although much insight into separation phenomena may be gained by using two-dimensional flow analyses, there are important effects that must be considered three-dimensionally. One such effect is the large venting of the separated region in front of a ramp of finite span. The fluid in the separated region, having low velocity and relatively high pressure, expands readily into the low-pressure stream at the tip, and the mass balance of the two-dimensional separation is upset. Another case is that associated with the streamwise flow in the corner at the juncture of a fin and the surface of the configuration. A strong vortex may be set up in such a corner with extreme rates of heat transfer associated with the vortical motion. Another important three-dimensional effect is the coupling effect of a control on another surface. The shock wave ahead of a blunt control or ahead of a separated-flow region may impinge on a transverse surface. Thus, the deflection of a vertical fin or rudder may cause nonsymmetrical separation on the horizontal surface and create an undesired rolling or pitching moment. Particularly for separation occurring near the point of transition of a laminar to turbulent boundary layer, the point of separation and the associated shock wave may

oscillate about some mean position. Large buffeting loads may be experienced on the surface and on adjoining surfaces of the configuration. Unsteady flow in cavities in the surface of a missile may also cause structural failure. Laminar boundary-layer separation with large center-of-pressure shift may be experienced at a small control deflection, while if the deflection is increased and then decreased to its initial value, the separation may be turbulent with a far different value of pitching moment because of the different center-of-pressure location. This hysteresis is extremely difficult to predict, and can be quite dangerous.

In high Mach number flows, the pressure loads produced by compression surfaces are much greater than those produced by expansion surfaces. Consequently, the most effective aerodynamic controls usually employ deflections which involve compression of the local flow. Therefore, shock-induced separation, either ahead of a compression surface or due to an incident shock, is the type most prevalent with hypersonic controls and has been treated most extensively in the literature.

When separation occurs in high-speed flight, the changes in the pressure distribution and heat-transfer rate can have catastrophic effects. Trim and stability are radically affected by sudden center-of-pressure shifts and changes in pressure magnitude. Local hot spots at separation and reattachment points can cause failure of thermal protection. Heat-transfer rates can also be greatly increased by streamwise vortices originating from three-dimensional separations.

HYPERSONIC CONTROL EFFECTIVENESS

The method presented in this section to determine the aerodynamic control effectiveness at hypersonic speeds is taken from reference 1. The method is intended for use over a broad range of flight conditions encountered by a typical hypersonic cruise/glide vehicle. However, it should be noted that the semiempirical correlation charts used in the method are based on presently available data covering a limited range of test conditions and that the validity of extrapolations for conditions outside the experimental range has not been established. The range of variables covered by experimental data is indicated on the correlation charts.

The flight conditions encountered by a typical hypersonic vehicle are illustrated by the altitude-velocity envelop presented as sketch (c).

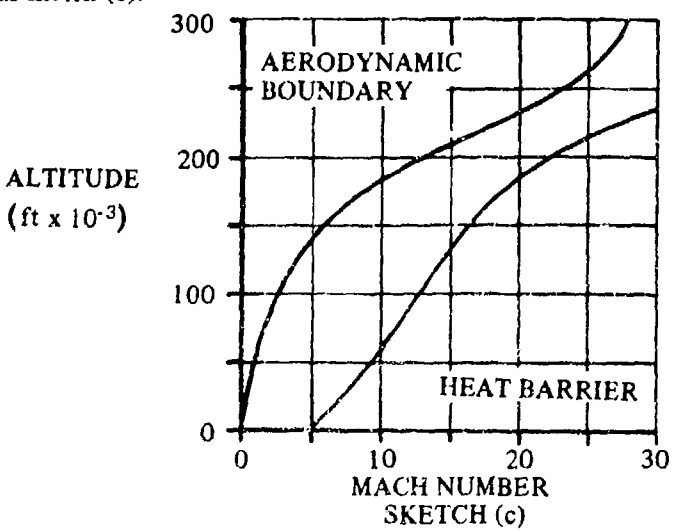

SKETCH (c)

For a given velocity the maximum attainable altitude is determined by the minimum dynamic pressure which will sustain flight, and the minimum altitude is a function of the vehicle's capability to withstand aerodynamic heating. The Datcom method is restricted to free-stream flight conditions in the flight envelop for Mach numbers greater than 5.0.

The angle of attack of the vehicle is limited by vehicle performance and structural heating conditions. The angle of attack below which the L/D ratio is favorable and structural heating is not excessive is approximately 20°. Therefore, the angle-of-attack range of the Datcom method is $0 \leq \alpha \leq 20^{\circ}$. Since the study conducted in connection with reference 1 was concerned primarily with flat-plate surfaces, the angle of attack also represents the flow-deflection angle in the method that follows.

The prediction method has been derived on the basis of compression-corner flow separation. It is limited to the analysis of controls on windward surfaces, and is applicable only to regions where the assumption of two-dimensional flow is valid.

In applying the method to complex three-dimensional configurations, the degree of deviation from two-dimensional flow should be established so that the proper method of determining the local-flow properties can be selected. Then the correlations presented herein can be applied to the separated-flow region. For such approximations exact streamline direction is not as important as static pressure and Mach number. However, there can be substantial reductions in control effectiveness due to finite span. Section V of reference 1 presents some insight into methods that can be employed to determine the degree of deviation from two-dimensional flow when the actual flow is three-dimensional. The use of flow-visualization studies, and lengthwise and spanwise pressure distributions on similar models are suggested. Reference 1 presents brief summaries of separated three-dimensional flow on fin-plate configurations, flat surfaces with compression flaps and end plates, and delta wings with variations (blunt leading edges, pyramidal configurations with and without flat-bottom surfaces, etc.)

Since leeward surfaces in hypersonic flow are generally ineffective, the restriction of the method to the analysis of controls on the windward surface is not a serious limitation.

For many practical cases the control surfaces are located near the trailing edge of essentially planar surfaces and are sufficiently far from the leading edge for bluntness effects to be negligible. For such cases, the local-flow properties upstream of the control surface are approximately the same as flow conditions behind an oblique shock, and oblique-shock properties can be used to define the local-flow properties. The Datcom method is restricted to cases of this sort.

The Datcom method consists of first determining the local-flow properties upstream of the control surface. Then by using the local-flow properties, a complete pressure distribution is defined for compression-corner flow separation in terms of interaction parameters and pressure levels for either laminar or turbulent separated-flow conditions. Finally, the pressure distribution is integrated to obtain the two-dimensional force and moment increments produced by separated compression-corner flow. Force and moment equations have been developed in terms of the distances and pressure levels which define the pressure distribution. These equations are presented in the Datcom method.

The local-flow conditions have been determined by using oblique-shock properties for a number of conditions in the flight envelop. The design charts presented in this section include local-flow properties based on both perfect-gas and equilibrium-real-gas assumptions. For the flight regimes where flow properties deviate from those given by oblique-shock theory for a perfect gas, equilibrium-real-gas effects have been determined by means of similarity parameters from approximate theory and the effective ratio of specific heats presented in reference 29 (see Sections III and VI of reference 1). In using the local-flow charts (figure 6.3.1-31 through -49) the equilibrium-real-gas curves are used for velocity-altitude conditions and flow-deflection angles where the equilibrium-real-gas value differs from the perfect-gas value.

The equations used for the prediction of the separated-flow pressure distributions are developed in reference 1. Where applicable, the final equations are presented on the design charts of this section; however, the developments of the semiempirical correlations for laminar and turbulent separated flows are not discussed herein.

In reference 1 the transition phenomenon is investigated and a criterion for establishing the location of transition based on the results of Deem and Murphy (reference 30) is established. The minimum pressure rise required to cause flow separation, and incipient-separation criteria for both laminar and turbulent flow, are based on test data.

The characteristics of the separated-flow region of a typical pressure profile are illustrated in sketch (d). The distance parameters are based on a common reference line which is defined for various model configurations as a geometrical shock impingement point, hinge line (for corner flow), or the forward face of a step.

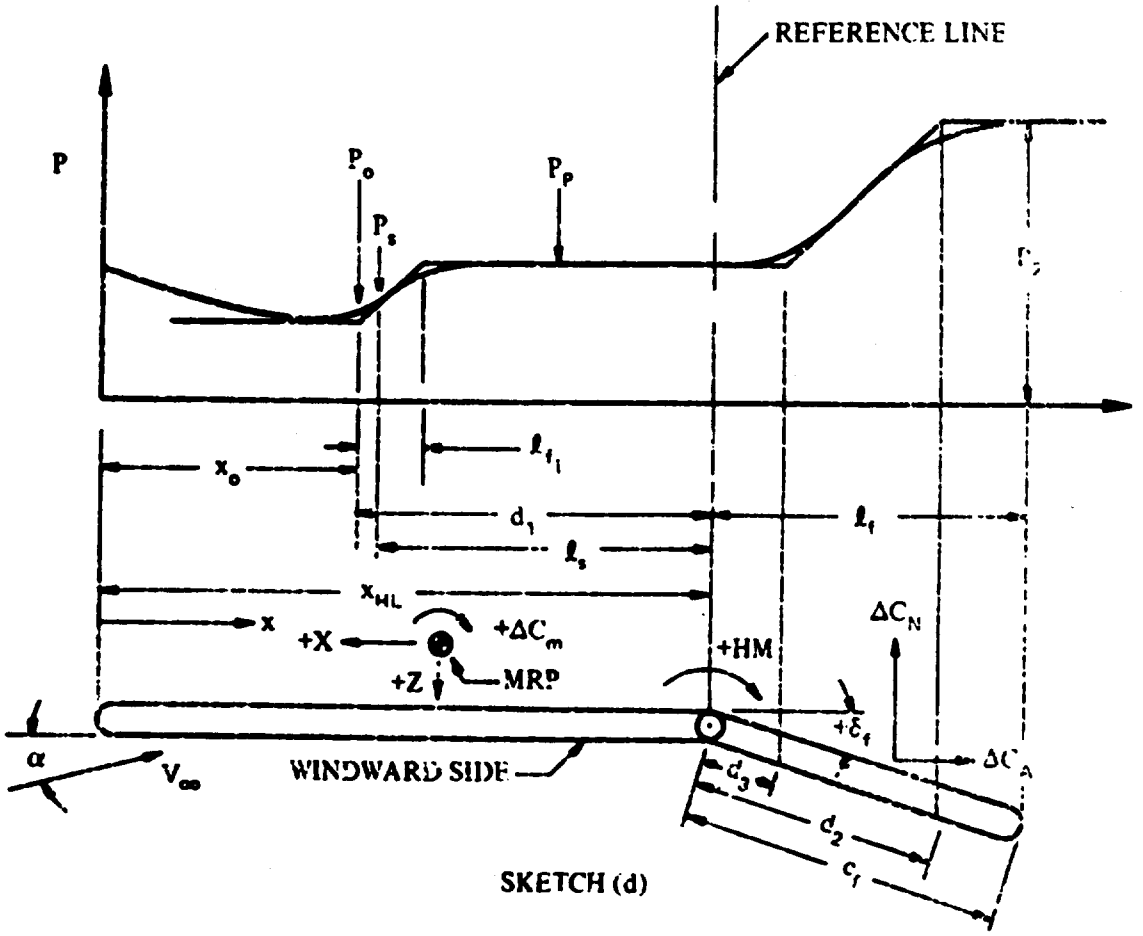

SKETCH (d)

NOTATION

Symbol	Definition
x_o	beginning of pressure interaction (point where pressure just begins to rise)
d_1	upstream pressure interaction length (distance from the beginning of interaction to the reference line)
ℓ_{f_i}	free interaction length (distance from the beginning of interaction to the point where the pressure distribution reaches the straight section of the pressure plateau)
d_2	downstream interaction length (distance from the reference line to the point of intersection of two lines tangent to the pressure curve in the downstream region, measured along the chord (see sketch (d))
d_3	distance from the reference line to the point of intersection of two lines tangent to the pressure curve as illustrated in sketch (d)
ℓ_s	separation length (distance from the separation point to the reference line)

Symbol	Definition
ℓ_f	length of the control (undeflected)
c_f	control chord
d_{LE}	diameter of leading edge
x_{HL}	distance of the control hinge line measured from the nose of the configuration
δ_f	control deflection, positive trailing edge down
b	span of surface
C_A	axial-force coefficient
C_p	pressure coefficient
C_m	pitching-moment coefficient
C_N	normal-force coefficient
HM	hinge moment
L	reference length
P	pressure
q	dynamic pressure
R_ℓ	Reynolds number
S	reference area
T	temperature
V	velocity
x	longitudinal coordinate, measured from leading edge to point of interest
α	angle of attack or flow-deflection angle
γ	ratio of specific heats
δ	boundary-layer thickness
θ	shock-wave angle measured from upstream flow direction
ϕ	angle associated with geometry of separation
Λ_{LE}	leading-edge-sweep angle

Symbol	Definition
	SUBSCRIPTS
HL	hinge line
inc	incipient
MRP	moment reference point
P	plateau
α	local condition upstream of interaction
o	point where interaction begins
∞	free stream
2	peak value, downstream portion of pressure distribution
t	transition point
c.p.	center of pressure
w	wall
s	separation
	SUPERSCRIPT
*	reference condition

DATCOM METHOD

The control effectiveness at hypersonic speeds of a deflected control located on the windward surface is obtained from the procedure outlined in the following steps:**

Step 1. Determine the local-flow conditions:

The ratios of pressure, temperature, Mach number, and Reynolds number behind an oblique shock to their respective values in the free stream are obtained from figures 6.3.1-31, -37, -43, and -49, respectively.

**The subscript α used throughout the Datcom method has two different meanings as follows: (1) The value of the parameter being considered is its local value upstream of interaction, examples being $(C_{p\infty})_\alpha$, P_α, M_α, $R\ell_\alpha$; (2) The value of the parameter being considered is its value at some specific location downstream of interaction, referred to local conditions upstream of interaction, examples being $(C_{p_\alpha})_2$, $(R\ell_\alpha)_{HL}$, $(C_{p_\alpha})_P$.

The pressure coefficient upstream of the control surface, referred to free-stream conditions, is given by

$$(C_{p_\infty})_\alpha = \frac{(P_\alpha/P_\infty) - 1}{\frac{\gamma}{2} M_\infty^2} \qquad 6.3.1\text{-a}$$

Step 2. Determine if the flow is laminar or turbulent:

It is assumed that the state of the boundary layer is laminar if $x_t > x_{HL}$, and turbulent if $x_t < x_{HL}$. Based on the results of Deem and Murphy (reference 29) and recent experimental data, the following expression for transition distance is given in reference 1:

$$x_t(\text{feet}) = \frac{5.38 \times 10^2 + 1.94 \times 10^2 \, (M_\alpha - 3)^{3/2} (\cos \Lambda)^{1/2}}{(R\ell_\alpha/\text{in.})^{0.6}} \qquad 6.3.1\text{-b}$$

For configurations with no sweepback ($\Lambda = 0$), the state of the boundary layer at the hinge line is obtained from figure 6.3.1-55 as a function of $\left(R\ell_{\alpha/HL}\right.$ and M_α, where

$$\left(R\ell_{\alpha}\right)_{HL} = x_{HL} \left(R\ell_\alpha\right)$$

Of course, if the transition Reynolds number is known, then the transition distance is given by $x_t = \left(R\ell_{\alpha}\right)_{x_t} / R\ell_\alpha$, where $R\ell_\alpha$ is the Reynolds number per foot.

Step 3. Determine if flow separation exists:

Obtain the pressure coefficient for incipient separation $\left(C_{p_\alpha}\right)_{inc}$ from figure 6.3.1-56 for laminar flow or figure 6.3.1-57 for turbulent flow.

Obtain the final pressure-rise coefficient by

$$\left(C_{p_\alpha}\right)_2 = \frac{(P_2/P_\alpha) - 1}{\frac{\gamma}{2} M_\alpha^2} \qquad 6.3.1\text{-c}$$

where P_2/P_α is obtained from figure 6.3.1-58 as a function of M_α. For laminar flow the average of the isentropic and single-shock values should be used for $M_\alpha < 6$, and the single-shock value should be used for $M_\alpha > 6$. For turbulent flow use the single-shock value. If $\left(C_{p_\alpha}\right)_2 \geq \left(C_{p_\alpha}\right)_{inc}$, the flow is separated.

Step 4. Determine the separation location if separated flow exists:

If flow separation exists an iterative procedure is required to determine the separation location. For a given local Mach number M_α, the upstream interaction distance d_1 is a function of the plateau-pressure level P_p, which is a function of the Reynolds number at the interaction point $\left(R\ell_{\alpha/x_0}\right.$.

Therefore, for any interaction point x_o a corresponding plateau-pressure level and upstream interaction distance must be defined. In solving for the interaction location, the upstream interaction distances corresponding to a number of assumed interaction locations are calculated until the point is found for which the sum of the downstream distance to the interaction point and the upstream interaction distance is equal to the distance to the hinge line; i.e., $x_o + d_1 = x_{HL}$. The procedure is as follows:

a. Assume an interaction location x_o (For vehicles of practical dimensions the difference between x_o and x_{HL} will be small).

b. Calculate the Reynolds number for the assumed x_o by $\left(R_{\ell_\alpha}\right)_{x_o} = x_o\left(R_{\ell_\alpha}\right)$, and obtain the plateau-pressure level $\left(C_{p_\alpha}\right)_P$ as a function of $\left(R_{\ell_\alpha}\right)_{x_o}$ and M_α from figure 6.3.1-59 or figure 6.3.1-60 for laminar or turbulent flow, respectively.

c. Obtain the upstream interaction distance, nondimensionalized by boundary-layer thickness d_1/δ_o, as a function of $\left(C_{p_\alpha}\right)_P$ and M_α from figure 6.3.1-61 or figure 6.3.1-62 for laminar or turbulent flow, respectively.

d. For a given wall temperature, obtain the reference temperature Reynolds-number ratio $\left(R_{\ell_\alpha}^*/R_{\ell_\alpha}\right)$ as a function of T_w/T_α and M_α from figure 6.3.1-63 or figure 6.3.1-64 for laminar or turbulent flow, respectively.

e. Calculate the reference temperature Reynolds number by $R_{\ell_\alpha}^* = \left(R_{\ell_\alpha}^*/R_{\ell_\alpha}\right)R_{\ell_\alpha}$, and obtain the corresponding boundary-layer thickness δ_o from figure 6.3.1-65 or figure 6.3.1-66 for laminar or turbulent flow, respectively, by $\delta_o = (\delta_o/\sqrt{x_o})\sqrt{x_o}$.

f. Calculate the upstream interaction distance by $d_1 = (d_1/\delta_o)\delta_o$.

g. Sum d_1 and x_o. If $d_1 + x_o \neq x_{HL}$, repeat the procedure until $d_1 + x_o = x_{HL}$.

Step 5. Having determined the separation point x_o, define the windward pressure distribution (see sketch (d)) as follows:

a. Calculate the Reynolds number for x_o by $\left(R_{\ell_\alpha}\right)_{x_o} = x_o\left(R_{\ell_\alpha}\right)$.

b. Obtain the plateau-pressure level $(C_{p_\alpha})_P$ as a function of $\left(R_{\ell_\alpha}\right)_{x_o}$ and M_α from figure 6.3.1-59 or figure 6.3.1-60 for laminar or turbulent flow, respectively.

c. Calculate the plateau pressure, referred to free-stream conditions, by

$$\left(C_{p_\infty}\right)_P = \left(C_{p_\alpha}\right)_P \left(\frac{M_\alpha}{M_\infty}\right)^2 \frac{P_\alpha}{P_\infty} + \left(C_{p_\infty}\right)_\alpha \qquad 6.3.1\text{-d}$$

where M_α/M_∞, P_α/P_∞, and $\left(C_{p_\infty}\right)_\alpha$ are obtained from step 1.

d. Obtain the free interaction length nondimensionalized by boundary-layer thickness ℓ_{f_i}/δ_o as a function of $(C_{p_\alpha})_P$ and M_α from figure 6.3.1-67 or figure 6.3.1-68 for laminar or turbulent flow, respectively.

e. Calculate the free interaction length by $\ell_{f_i} = \left(\ell_{f_i}/\delta_o\right)\delta_o$ where δ_o is the boundary-layer thickness determined as outlined in step 4e.

f. Obtain the upstream interaction distance nondimensionalized by boundary-layer thickness d_1/δ_o as a function of $(C_{p_\alpha})_P$ and M_α from figure 6.3.1-61 or figure 6.3.1-62 for laminar or turbulent flow, respectively.

g. Calculate the upstream interaction distance by $d_1 = (d_1/\delta_o)\delta_o$.

h. Obtain the downstream interaction length d_2 from figure 6.3.1-69 or figure 6.3.1-70 for laminar or turbulent flow, respectively.

i. Determine the downstream interaction length to the pressure rise d_3. For turbulent flow $d_3 = 0$. For laminar flow the ratio d_3/d_1 is obtained from figure 6.3.1-71 as a function of flap deflection δ_f and the equivalent flow-deflection angle ϕ for $(C_{p_\alpha})_P$.

The equivalent flow-deflection angle for $(C_{p_\alpha})_P$ may be obtained as a function of the shock-wave angle θ and M_α. The shock-wave angle is given by

$$\theta = \sin^{-1}\sqrt{\frac{6(P_P/P_\alpha)+1}{7(M_\alpha)^2}} \qquad 6.3.1\text{-e}$$

where

$$\frac{P_P}{P_\alpha} = (C_{p_\alpha})_P \frac{\gamma}{2}(M_\alpha)^2 + 1 \qquad 6.3.1\text{-f}$$

Enter figure 4.4.1-81 with θ and M_α and read $\phi = |\delta'|$.

j. Calculate the peak flap pressure, referred to free-stream conditions, by

$$(C_{p_\infty})_2 = (C_{p_\alpha})_2 \left(\frac{M_\alpha}{M_\infty}\right)^2 \frac{P_\alpha}{P_\infty} + (C_{p_\infty})_\alpha \qquad 6.3.1\text{-g}$$

where M_α/M_∞, P_α/P_∞, and $(C_{p_\infty})_\alpha$ are obtained from step 1, and $(C_{p_\alpha})_2$ is obtained from step 2 (equation 6.3.1-c).

Step 6. The windward pressure distribution may now be constructed as illustrated in sketch (e).

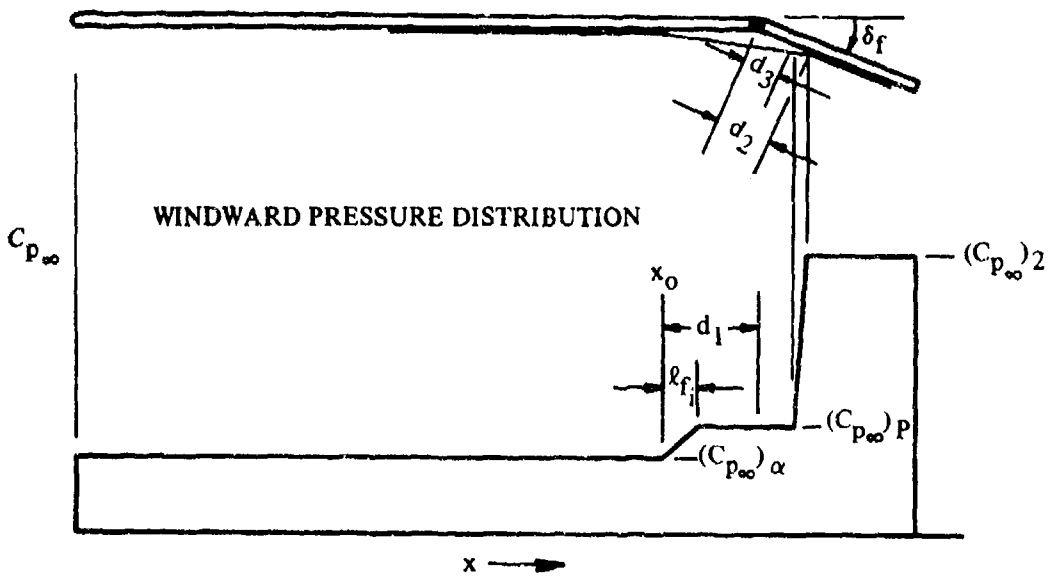

SKETCH (e)

Step 7. The two-dimensional force and moment increments produced on the windward surface of a deflected control are given by

Normal-force increment:

$$\frac{\Delta C_N S}{b} = \left[(C_{p_\infty})_P - (C_{p_\infty})_\alpha\right]\left[d_1 - \frac{\ell_{f_i}}{2} + \cos\delta_f c_f\right] + \left[(C_{p_\infty})_2 - (C_{p_\infty})_P\right](\cos\delta_f)\left[c_f - \frac{d_2}{2} - \frac{d_3}{2}\right] \text{ (ft)} \qquad 6.3.1\text{-h}$$

Increment of pitching moment about HL due to normal force increment:

$$\left[\frac{(\Delta C_m)_{HL} SL}{b}\right]_{\Delta C_N} = \left[(C_{p_\infty})_P - (C_{p_\infty})_\alpha\right]\left[\frac{(\ell_{f_i})^2}{6} - \frac{(\ell_{f_i})(d_1)}{2} + \frac{(d_1)^2}{2} - \frac{\cos^2\delta_f (c_f)^2}{2}\right]$$

$$- \left[(C_{p_\infty})_2 - (C_{p_\infty})_P\right](\cos^2\delta_f)\left[\frac{(c_f)^2}{2} - \frac{(d_2)^2}{6} - \frac{d_2 d_3}{6} - \frac{(d_3)^2}{6}\right] \text{ (ft)}^2 \qquad 6.3.1\text{-i}$$

Center of pressure of normal-force increment, measured from the MRP, negative aft:

$$(x_{c.p.})_{\Delta C_N} = -(x_{HL} - x_{MRP}) + \frac{\left[(\Delta C_m)_{HL} L\right]_{\Delta C_N}}{\Delta C_N} \text{ (ft)} \qquad 6.3.1\text{-j}$$

Axial-force increment:

$$\frac{\Delta C_A S}{b} = (\sin\delta_f)\left\{\left[(C_{p_\infty})_P - (C_{p_\infty})_\alpha\right] c_f + \left[(C_{p_\infty})_2 - (C_{p_\infty})_P\right]\left[c_f - \frac{d_2}{2} - \frac{d_3}{2}\right]\right\} \text{ (ft)} \qquad 6.3.1\text{-k}$$

Increment of pitching moment about HL due to axial-force increment:

$$\left[\frac{(\Delta C_m)_{HL}\,SL}{b}\right]_{\Delta C_A} = -(\sin^2\delta_f)\left\{\left[(C_{p_\infty})_P - (C_{p_\infty})_\alpha\right]\frac{(c_f)^2}{2} + \left[(C_{p_\infty})_2 - (C_{p_\infty})_P\right]\left[\frac{(c_f)^2}{2} - \frac{(d_2)^2}{6} - \frac{d_2 d_3}{6} - \frac{(d_3)^2}{6}\right]\right\} \quad (ft)^2 \qquad 6.3.1\text{-}\ell$$

Center of pressure of axial-force increment, measured from the MRP, positive down:

$$(z_{c.p.})_{\Delta C_A} = z_{HL} - \frac{\left[(\Delta C_m)_{HL}L\right]_{\Delta C_A}}{\Delta C_A} \quad (ft) \qquad 6.3.1\text{-m}$$

Increment of pitching moment about vehicle MRP:

$$\left[\frac{(\Delta C_m)_{MRP}S}{b}L\right] = \left[\frac{(\Delta C_N)\,S}{b}(x_{c.p.})\right]_{\Delta C_N} - \left[\frac{(\Delta C_A)\,S}{b}(z_{c.p.})\right]_{\Delta C_A} \quad (ft)^2 \qquad 6.3.1\text{-n}$$

Windward component of control hinge moment (based on absolute pressure):

$$\frac{HM}{bq} = -\left\{(C_{p_\infty})_2\frac{(c_f)^2}{2} - \frac{1}{6}\left[(C_{p_\infty})_2 - (C_{p_\infty})_F\right]\left[(d_2)^2 + d_2 d_3 + (d_3)^2\right]\right\} \quad (ft)^2 \qquad 6.3.1\text{-o}$$

An approximate correction for the effect of finite control span on the two-dimensional pressure distribution in the separated region over the control is presented as figure 6.3.1-72. This empirical correlation, taken from reference 1, is based on a limited amount of test data. Unfortunately, not enough test data are available for partial-span control effect to identify the effects of Mach number, Reynolds number, or control position.

Two sample problems are presented at the conclusion of this section. The first sample problem is straightforward in that the Datcom method is directly applicable. The second sample problem illustrates an application of the method to a flight condition where the separated region extends forward to the leading edge of the configuration.

It should be recalled that the use of oblique-shock relations implies small leading-edge-bluntness effects and negligible viscous effects. On bodies with a blunted leading edge, pressure near the leading edge will be higher than that predicted by the oblique-shock theory. When leading-edge bluntness is not zero, the actual value for M_α will be between that given by oblique-shock and shock-loss theories. Values of M_α on surfaces with leading edges of various bluntness dimensions were obtained from test data during the analysis conducted in connection with reference 1. It is suggested therein that oblique-shock properties result in acceptable values of local Mach number M_α for

$$\frac{0.1375\,\frac{x_{HL}}{d_{LE}} + 2.0}{M_\infty} > 1.0$$

If the leading-edge bluntness is comparatively large, the local-flow properties should be calculated by other available methods, such as tangent-wedge, blast-wave, or the Moeckel shock-loss theory (reference 31). Blunt leading edges or large viscous-induced pressure gradients also reduce the boundary-layer thickness. The effects of leading-edge bluntness and viscous interaction on the flow properties along a body surface are discussed in Section III of reference 1.

Sample Problems

1.

Given: A two-dimensional flat plate with negligible thickness.

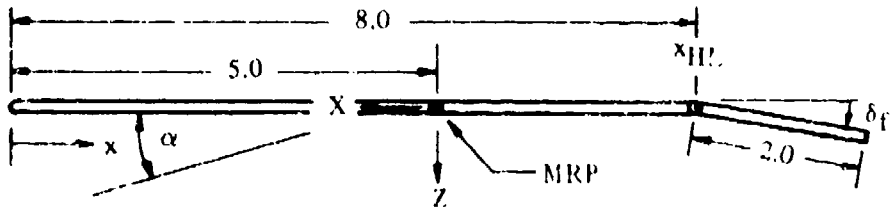

$L = 10.0$ ft $\quad x_{MRP} = 5.0$ ft $\quad x_{HL} = 8.0$ ft $\quad z_{HL} = 0 \quad c_f = 2.0$ ft

$\delta_f = 10^o \quad R_{\ell_\infty} = 1.06 \times 10^5$ per ft

Altitude: 150,000 ft $\quad P_\infty = 2.84$ lb/(ft)$^2 \quad T_\infty = 480^o$ R

$T_w = 1500^o$R $\quad \alpha = 15^o$ Negligible viscous interaction (assumed)

$M_\infty = 10.0$

Compute:

Determine the local flow conditions:

$$\frac{P_\alpha}{P_\infty} = 13.5 \text{ (figure 6.3.1-31c)}$$

$$\frac{T_\alpha}{T_\infty} = 3.0 \text{ (figure 6.3.1-37c) (equilibrium real gas)}$$

$$M_\alpha = 5.5 \text{ (figure 6.3.1-43c) (equilibrium real gas)}$$

$$\frac{R_{\ell_\alpha}}{R_{\ell_\infty}} = 1.94 \text{ (figure 6.3.1-49c) (equilibrium real gas)}$$

$$T_\alpha = T_\infty \frac{T_\alpha}{T_\infty} = 1440^o \text{ R}$$

$$R_{\ell_\alpha} = R_{\ell_\infty} \frac{R_{\ell_\alpha}}{R_{\ell_\infty}} = 2.06 \times 10^5 \text{ per ft}$$

$$\frac{\delta_o}{\sqrt{x_o}} = 0.0215 \text{ (figure 6.3.1-65)}$$

$$\delta_o = \sqrt{x_o}\,\frac{\delta_o}{\sqrt{x_o}} = (\sqrt{7.0})\,(0.0215) = 0.057 \text{ ft}$$

$$d_1 = \delta_o \left(\frac{d_1}{\delta_o}\right) = (0.057)\,(20.0) = 1.14 \text{ ft}$$

$d_1 + x_o = 1.14 + 7.0 = 8.14 \text{ ft} > x_{HL}$. Try a second iteration.

Second iteration (assume $x_o = 6.5$ ft)

$$\left(R\ell_\alpha\right)_{x_o} = x_o \left(R\ell_\alpha\right) = (6.5)\,(2.06 \times 10^5) = 1.339 \times 10^6$$

$$\left(C_{p_\alpha}\right)_f = 0.019 \text{ (figure 6.3.1-59)}$$

$$\frac{d_1}{\delta_o} = 21.5 \text{ (figure 6.3.1-61)}$$

$$\frac{\delta_o}{\sqrt{x_o}} = 0.0215 \text{ (calculation to determine } \delta_o/\sqrt{x_o} \text{ is same as first iteration)}$$

$$\delta_o = \sqrt{x_o}\,\frac{\delta_o}{\sqrt{x_o}} = \sqrt{6.5}\,(0.0215) = 0.055 \text{ ft}$$

$$d_1 = \delta_o \left(\frac{d_1}{\delta_o}\right) = (0.055)\,(21.5) = 1.183 \text{ ft}$$

$d_1 + x_o = 1.183 + 6.50 = 7.683 \text{ ft} < x_{HL}$

The flow separation point is now determined graphically. $x_o = 6.85$ ft

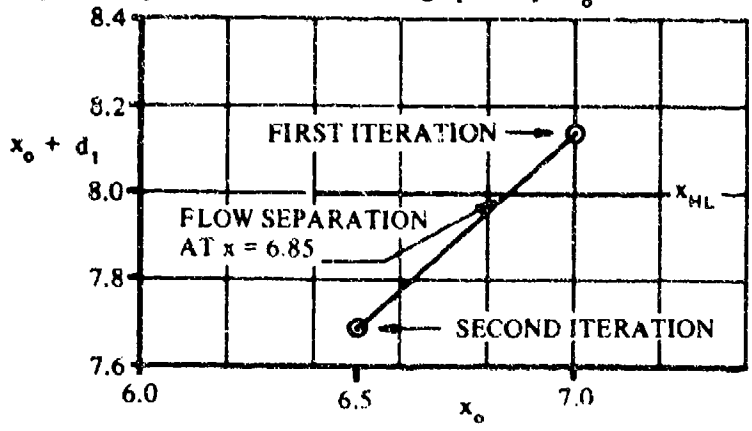

Define the windward pressure distribution:

$$\left(R_{\ell_\alpha}\right)_{x_o} = x_o \left(R_{\ell_\alpha}\right) = (6.85)(2.06 \times 10^5) = 1.41 \times 10^6$$

$$\left(C_{p_{\alpha_P}}\right) = 0.019 \text{ (figure 6.3.1-59)}$$

$$\left(C_{p_\infty}\right)_P = \left(C_{p_\alpha}\right)_P \left(\frac{M_\alpha}{M_\infty}\right)^2 \frac{P_\alpha}{P_\infty} + \left(C_{p_\infty}\right)_\alpha \text{ (equation 6.3.1-d)}$$

$$= (0.019)\left(\frac{5.5}{10.0}\right)^2 (13.5) + 0.179 = 0.257$$

$$\frac{\ell_{f_i}}{\delta_o} = 8.0 \text{ (figure 6.3.1-67)}$$

$$\delta_o = \sqrt{x_o}\ \frac{\delta_o}{\sqrt{x_o}} = \sqrt{6.85}\,(0.0215) = 0.056 \text{ ft}$$

$$\ell_{f_i} = \delta_o \left(\frac{\ell_{f_i}}{\delta_o}\right) = (0.056)(8.0) = 0.448 \text{ ft}$$

$$\frac{d_1}{\delta_o} = 21.4 \text{ (figure 6.3.1-61)}$$

$$d_1 = \delta_o \left(\frac{d_1}{\delta_o}\right) = (0.056)(21.4) = 1.20 \text{ ft}$$

$$\frac{c_f}{d_1} = \frac{2.0}{1.20} > 1; \text{ therefore, } \frac{d_2}{\sqrt{(c_f)(d_1)}} = \frac{d_2}{d_1} = 0.506 \text{ (figure 6.3.1-69)}$$

$$d_2 = d_1 \left(\frac{d_2}{d_1}\right) = (1.20)(0.506) = 0.607 \text{ ft}$$

Equivalent flow deflection angle for $\left(C_{p_\alpha}\right)_P$

$$\frac{P_P}{P_\alpha} = \left(C_{p_\alpha}\right)_P \frac{\gamma}{2} (M_\alpha)^2 + 1 \text{ (equation 6.3.1-f)}$$

$$= (0.019)\left(\frac{1.4}{2}\right)(5.5)^2 + 1 = 1.402$$

$$\theta = \sin^{-1}\sqrt{\frac{6(P_p/P_\alpha)+1}{7(M_\alpha)^2}} \quad \text{(equation 6.3.1-e)}$$

$$= \sin^{-1}\sqrt{\frac{6(1.402)+1}{7(5.5)^2}} = 12.2^{o}$$

$\phi = 2.6^{o}$ ($\phi = |\delta'|$ at M_α and θ from figure 4.4.1-81)

$$\frac{d_3}{d_1} = 0.35 \quad \text{(figure 6.3.1-71)}$$

$$d_3 = d_1\left(\frac{d_3}{d_1}\right) = (1.20)(0.35) = 0.42 \text{ ft}$$

$$\left(C_{p_\infty}\right)_2 = \left(C_{p\alpha}\right)_2\left(\frac{M_\alpha}{M_\infty}\right)^2\frac{P_\alpha}{P_\infty} + \left(C_{p_\infty}\right)_\alpha \quad \text{(equation 6.3.1-g)}$$

$$= (0.100)\left(\frac{5.5}{10.0}\right)^2(13.5) + (0.179) = 0.587$$

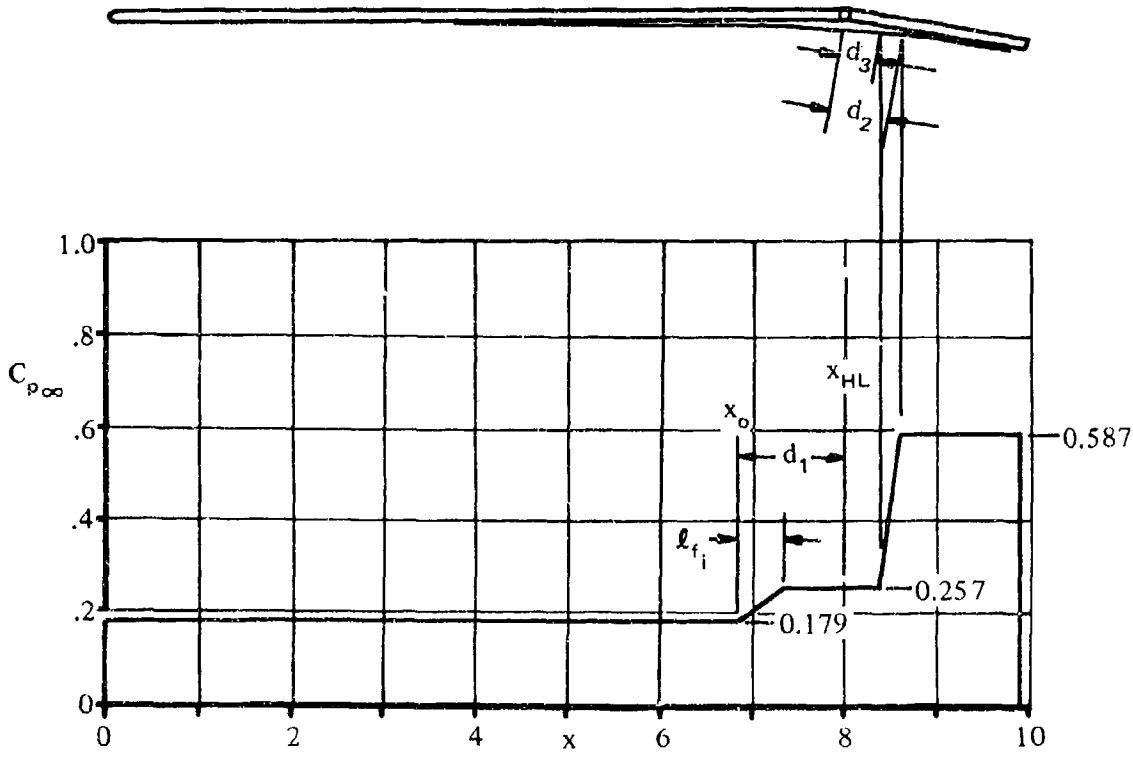

Solution:

Normal-force increment:

$$\frac{\Delta C_N S}{b} = \left[\left(C_{p_\infty}\right)_P - \left(C_{p_\infty}\right)_\alpha\right]\left[d_1 - \frac{\ell_{f_i}}{2} + \cos\delta_f c_f\right] + \left[\left(C_{p_\infty}\right)_2 - \left(C_{p_\infty}\right)_P\right](\cos\delta_f)\left[c_f - \frac{d_2}{2} - \frac{d_3}{2}\right]$$

(equation 6.3.1-h)

$$= [(0.257) - (0.179)]\left[1.20 - \frac{0.448}{2} + (0.985)(2.0)\right]$$

$$+ [(0.587) - (0.257)](0.985)\left[2.0 - \frac{0.607}{2} - \frac{0.42}{2}\right]$$

$$= 0.713 \text{ ft}$$

Increment of pitching moment about HL due to normal force increment:

$$\left[\frac{(\Delta C_m)_{HL} SL}{b}\right]_{\Delta C_N} = \left[\left(C_{p_\infty}\right)_P - \left(C_{p_\infty}\right)_\alpha\right]\left[\frac{(\ell_{f_i})^2}{6} - \frac{(\ell_{f_i})(d_1)^2}{2} + \frac{(d_1)^2}{2} - \frac{\cos^2\delta_f (c_f)^2}{2}\right]$$

$$- \left[\left(C_{p_\infty}\right)_2 - \left(C_{p_\infty}\right)_P\right](\cos^2\delta_f)\left[\frac{(c_f)^2}{2} - \frac{(d_2)^2}{6} - \frac{(d_2 d_3)}{6} - \frac{(d_3)^2}{6}\right]$$

(equation 6.3.1-i)

$$= [(0.257) - (0.179)]\left[\frac{(0.448)^2}{6} - \frac{(0.448)(1.20)}{2} + \frac{(1.20)^2}{2}\right.$$

$$\left. - \frac{(0.985)^2 (2.0)^2}{2}\right] - [(0.587) - (0.257)](0.985)^2\left[\frac{(2.0)^2}{2} - \frac{(0.607)^2}{6}\right.$$

$$\left. - \frac{(0.607)(0.42)}{6} - \frac{(0.42)^2}{6}\right]$$

$$= -0.713 \text{ (ft)}^2$$

Center of pressure for normal-force increment referred to MRP:

$$(x_{c.p.})_{\Delta C_N} = -(x_{HL} - x_{MRP}) + \frac{[(\Delta C_m)_{HL} L]_{\Delta C_N}}{\Delta C_N} \quad \text{(equation 6.3.1-j)}$$

$$= -(8.0 - 5.0) + \frac{-0.713}{0.713}$$

$$= -4.00 \text{ ft} \quad (4.00 \text{ feet aft of MRP})$$

Axial-force increment:

$$\frac{\Delta C_A S}{b} = (\sin \delta_f) \left\{ \left[\left(C_{p_\infty}\right)_P - \left(C_{p_\infty}\right)_\alpha \right] c_f + \left[\left(C_{p_\infty}\right)_2 - \left(C_{p_\infty}\right)_P \right] \left[c_f - \frac{d_2}{2} - \frac{d_3}{2} \right] \right\} \quad \text{(equation 6.3.1-k)}$$

$$= (0.174) \left\{ [(0.257) - (0.179)] (2.0) + [(0.587) - (0.257)] \left[2.0 - \frac{0.607}{2} - \frac{0.42}{2} \right] \right\}$$

$$= 0.1125 \text{ ft}$$

Increment of pitching moment about HL due to axial force:

$$\left[\frac{(\Delta C_m)_{HL} SL}{b} \right]_{\Delta C_A} = -(\sin^2 \delta_f) \left\{ \left[\left(C_{p_\infty}\right)_P - \left(C_{p_\infty}\right)_\alpha \right] \frac{(c_f)^2}{2} + \left[\left(C_{p_\infty}\right)_2 - \left(C_{p_\infty}\right)_P \right] \left[\frac{(c_f)^2}{2} - \frac{(d_2)^2}{6} - \frac{d_2 d_3}{6} - \frac{(d_3)^2}{6} \right] \right\} \quad \text{(equation 6.3.1-ℓ)}$$

$$= -(0.174)^2 \left\{ [(0.257) - (0.179)] \frac{(2.0)^2}{2} + [(0.587) - (0.257)] \left[\frac{(2.0)^2}{2} - \frac{(0.607)^2}{6} - \frac{(0.607)(0.42)}{6} - \frac{(0.42)^2}{6} \right] \right\}$$

$$= -0.0234 \text{ (ft)}^2$$

Center of pressure of axial-force increment:

$$(z_{c.p.})_{\Delta C_A} = Z_{HL} - \frac{[(\Delta C_m)_{HL} L]_{\Delta C_A}}{\Delta C_A} \quad \text{(equation 6.3.1-m)}$$

$$= 0 - \left(\frac{-0.0234}{0.1125} \right)$$

$$= 0.208 \text{ (ft)}$$

Increment of pitching moment about vehicle MRP:

$$\left[\frac{(\Delta C_m)_{MRP} S}{b} L \right] = \left[\frac{(\Delta C_N) S}{b} (x_{c.p.}) \right]_{\Delta C_N} - \left[\frac{(\Delta C_A) S}{b} (z_{c.p.}) \right]_{\Delta C_A} \quad \text{(equation 6.3.1-n)}$$

$$= (0.713) (-4.00) - (0.1125) (0.208) = -2.875 \text{ (ft)}^2$$

Windward component of control hinge moment (based on absolute pressure):

$$\frac{HM}{bq} = -\left\{ \left(C_{p_\infty}\right)_2 \frac{(c_f)^2}{2} - \frac{1}{6} \left[\left(C_{p_\infty}\right)_2 - \left(C_{p_\infty}\right)_P \right] [(d_2)^2 + d_2 d_3 + (d_3)^2] \right\} \quad \text{(equation 6.3.1-o)}$$

$$= -\left\{(0.587)\frac{(2.0)^2}{2} - \frac{1}{6}[(0.587) - (0.257)][(0.607)^2 + (0.607)(0.42) + (0.42)^2]\right\}$$

$$= -1.130\ (\text{ft})^2$$

2.

Given: A two-dimensional flat plate with negligible thickness.

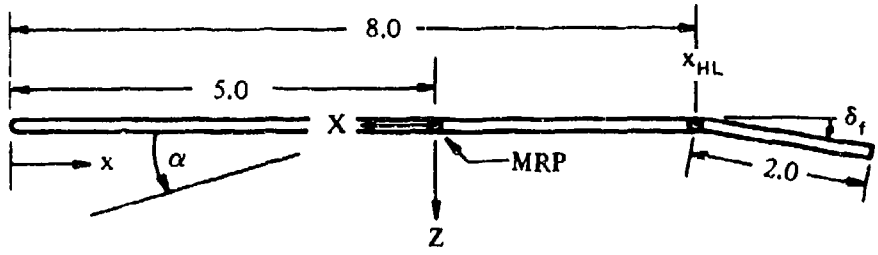

$L = 10.0$ ft $\quad x_{MRP} = 5.0$ ft $\quad x_{HL} = 8.0$ ft $\quad z_{HL} = 0$

$c_f = 2.0$ ft $\quad \delta_f = 10^o \quad R_{\ell_\infty} = 3.27 \times 10^4$ per ft

Altitude: 200,000 ft $\quad P_\infty = 0.413$ lb/(ft)^2 $\quad T_\infty = 458^o$ R

$T_w = 2000^o$ R $\quad \alpha = 10^o$ Negligible viscous interaction (assumed)

$M_\infty = 20$

Compute:

Determine the local-flow conditions:

$\frac{P_\alpha}{P_\infty} = 21$ (figure 6.3.1-31d) (equilibrium real gas)

$\frac{T_\alpha}{T_\infty} = 4.30$ (figure 6.3.1-37d) (equilibrium real gas)

$M_\alpha = 9.80$ (figure 6.3.1-43d) (equilibrium real gas)

$\frac{R_{\ell_\alpha}}{R_{\ell_\infty}} = 1.87$ (figure 6.3.1-49d) (equilibrium real gas)

$T_\alpha = T_\infty \frac{T_\alpha}{T_\infty} = 1970^o$R

$$R_{\ell_\alpha} = R_{\ell_\infty} \frac{R_{\ell_\alpha}}{R_{\ell_\infty}} = 6.11 \times 10^4 \text{ per ft}$$

$$\left(C_{p_\infty}\right)_\alpha = \frac{(P_\alpha/P_\infty) - 1}{\frac{\gamma}{2} M_\infty^2} = \frac{21.0 - 1}{\frac{1.4}{2}(20)^2} = 0.071 \text{ (equation 6.3.1-a)}$$

Determine if the flow is laminar or turbulent:

$$\left(R_{\ell_\alpha}\right)_{HL} = x_{HL} \left(R_{\ell_\alpha}\right) = (8.0)(6.11 \times 10^4) = 4.9 \times 10^5$$

At $\left(R_{\ell_\alpha}\right)_{HL}$ and M_α, figure 6.3.1-55 indicates a laminar boundary layer.

Determine if separation exists:

$$\left(C_{p_\alpha}\right)_{inc} = 0.019 \text{ (figure 6.3.1-56)}$$

$$\frac{P_2}{P_\alpha} = 6.80 \text{ (figure 6.3.1-58) (single-shock value)}$$

$$\left(C_{p_{\alpha/2}}\right)_2 = \frac{(P_2/P_\alpha) - 1}{\frac{\gamma}{2} M_\alpha^2} = \frac{6.80 - 1}{\frac{1.4}{2}(9.8)^2} = 0.0863 \text{ (equation 6.3.1-c)}$$

Since $\left(C_{p_\alpha}\right)_2 > \left(C_{p_\alpha}\right)_{inc}$, the flow is separated.

Determine the separation location (see step 4 of Datcom method for iteration procedure):

First iteration (assume x_o = 7.0 ft)

$$\left(R_{\ell_{\alpha/x_o}}\right) = x_o \left(R_{\ell_\alpha}\right) = (7.0)(6.11 \times 10^4) = 4.277 \times 10^5$$

$$\left(C_{p_{\alpha/P}}\right) = 0.0185 \text{ (figure 6.3.1-59)}$$

$$\frac{d_1}{\delta_o} = 110 \text{ (figure 6.3.1-61)}$$

$$\frac{T_w}{T_\alpha} = \frac{2000}{1970} = 1.015$$

$$\frac{R_{\ell_\alpha}^*}{R_{\ell_\alpha}} = 0.079 \text{ (figure 6.3.1-63)}$$

$$R_{\ell_\alpha}^* = R_{\ell_\alpha}\left(\frac{R_{\ell_\alpha}^*}{R_{\ell_\alpha}}\right) = (6.11 \times 10^4)(0.079) = 4.83 \times 10^3$$

$$\frac{\delta_o}{\sqrt{x_o}} = 0.075 \text{ (figure 6.3.1-65)}$$

$$\delta_o = \sqrt{x_o}\,\frac{\delta_o}{\sqrt{x_o}} = \sqrt{7.0}\,(0.075) = 0.199 \text{ ft}$$

$$d_1 = \delta_o\left(\frac{d_1}{\delta_o}\right) = (0.199)(110) = 21.89 \text{ ft}$$

$d_1 + x_o = 21.89 + 7.0 = 28.89 \text{ ft} > x_{HL}$. Try a second iteration.

Second iteration (assume $x_o = 4.0$ ft)

$$\left(R_{\ell_\alpha}\right)_{x_o} = x_o\left(R_{\ell_\alpha}\right) = (4.0)(6.11 \times 10^4) = 2.444 \times 10^5$$

$$\left(C_{p_\alpha}\right)_p = 0.023 \text{ (figure 6.3.1-59)}$$

$$\frac{d_1}{\delta_o} = 230 \text{ (figure 6.3.1-61)}$$

$$\frac{\delta_o}{\sqrt{x_o}} = 0.075 \text{ (calculation to determine } \delta_o/\sqrt{x_o} \text{ is same as first iteration)}$$

$$\delta_o = \sqrt{x_o}\,\frac{\delta_o}{\sqrt{x_o}} = \sqrt{4.0}\,(0.075) = 0.150 \text{ ft}$$

$$d_1 = \delta_o\left(\frac{d_1}{\delta_o}\right) = (0.150)(230) = 34.50 \text{ ft}$$

$d_1 + x_o = 34.50 + 4.0 = 38.50 \text{ ft} > x_{HL}$. Try a third iteration.

Third iteration (assume $x_o = 2.0$ ft)

$$\left(R_{\ell_\alpha}\right)_{x_o} = x_o\left(R_{\ell_\alpha}\right) = (2.0)(6.11 \times 10^4) = 1.222 \times 10^5$$

$$\left(C_{p_\alpha}\right)_p = 0.0255 \text{ (figure 6.3.1-59)}$$

$$\frac{d_1}{\delta_o} = 350 \text{ (figure 6.3.1-61)}$$

$$\frac{\delta_o}{\sqrt{x_o}} = 0.075 \text{ (calculation to determine } \delta_o/\sqrt{x_o} \text{ is same as first and second iteration)}$$

$$\delta_o = \sqrt{x_o}\frac{\delta_o}{\sqrt{x_o}} = \sqrt{2.0}\ (0.075) = 0.106 \text{ ft}$$

$$d_1 = \delta_o\left(\frac{d_1}{\delta_o}\right) = (0.106)\,(350) = 37.10 \text{ ft}$$

$$d_1 + x_o = 37.10 + 2.0 = 39.10 \text{ ft} > x_{HL}$$

The magnitudes of d_1 from the iterations indicate that the region of separation extends forward to the leading edge of the plate. For this case it is assumed that the plateau-pressure region extends forward to the leading edge. Then, $d_1 = x_{HL}$ and $\ell_{f_i} = 0$ (see sketch (d)).

Define the windward pressure distribution:

Assume the plateau pressure corresponds to the wedge pressure for a local flow deflection angle of ϕ degrees as illustrated below.

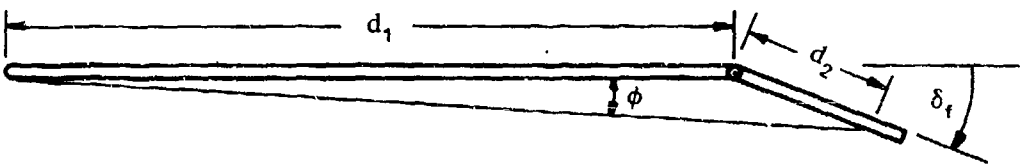

Then, by using d_1, d_2, and δ_f the angle ϕ can be defined. Knowing ϕ the plateau-pressure level is obtained by using oblique-shock relations.

Assume $d_1 = x_{HL} = 8.0$ ft

$$\frac{c_f}{d_1} = \frac{2.0}{8.0} = 0.25 \le 0.25; \text{ therefore, } \frac{d_2}{\sqrt{(c_f)\,(d_1)}} = 2\frac{d_2}{d_1} = 0.475 \text{ (figure 6.3.1-69)}$$

$$d_2 = \frac{0.475\, d_1}{2} = 1.90 \text{ ft}$$

$$\phi = \tan^{-1}\frac{d_2 \sin\delta_f}{d_1 + d_2\cos\delta_f} = \tan^{-1}\frac{(1.90)\,(0.174)}{8.0 + (1.90)\,(0.985)}$$

$$= \tan^{-1} 0.0335 = 1.9^o$$

$$\theta = 7.25^o \text{ (θ is obtained from figure 4.4.1-81 at } M_\alpha = 9.8 \text{ and } \phi = |\delta'|)$$

$$\frac{P_P}{P_\alpha} = \frac{7M_\alpha^2 \sin^2 \theta - 1}{6} \quad \text{(equation 6.3.1-e)}$$

$$= \frac{7(9.8)^2 (\sin 7.25^o)^2 - 1}{6} = 1.62$$

$$\left(C_{p_\alpha}\right)_P = \frac{(P_P/P_\alpha) - 1}{\frac{\gamma}{2} M_\alpha^2} \quad \text{(equation 6.3.1-f)}$$

$$= \frac{(1.62) - 1}{\frac{1.4}{2}(9.8)^2}$$

$$= 0.00922$$

$$\left(C_{p_\infty}\right)_P = \left(C_{p_\alpha}\right)_P \left(\frac{M_\alpha}{M_\infty}\right)^2 \frac{P_\alpha}{P_\infty} + \left(C_{p_\infty}\right)_\alpha \quad \text{(equation 6.3.1-d)}$$

$$= (0.00922)\left(\frac{9.8}{20.0}\right)^2 (21) + 0.071 = 0.117$$

$$\left(\frac{d_3}{d_1}\right) = 0.250 \quad \text{(figure 6.3.1-71)}$$

$d_3 = d_1\left(\frac{d_3}{d_1}\right) = (8.0)(0.25) = 2.0$ ft. However, d_3 must be less than or equal to d_2 (see sketch (d)). Therefore, let $d_3 = d_2 = 1.90$ ft

$$\left(C_{p_\infty}\right)_2 = \left(C_{p_\alpha}\right)_2 \left(\frac{M_\alpha}{M_\infty}\right)^2 \frac{P_\alpha}{P_\infty} + \left(C_{p_\infty}\right)_\alpha \quad \text{(equation 6.3.1-g)}$$

$$= (0.0863)\left(\frac{9.8}{20.0}\right)^2 (21) + 0.071 = 0.506$$

The windward pressure distribution is illustrated in the following sketch. The solutions for the force and moment increments are not shown, since the use of equations 6.3.1-h through 6.3.1-o is illustrated in sample problem 1.

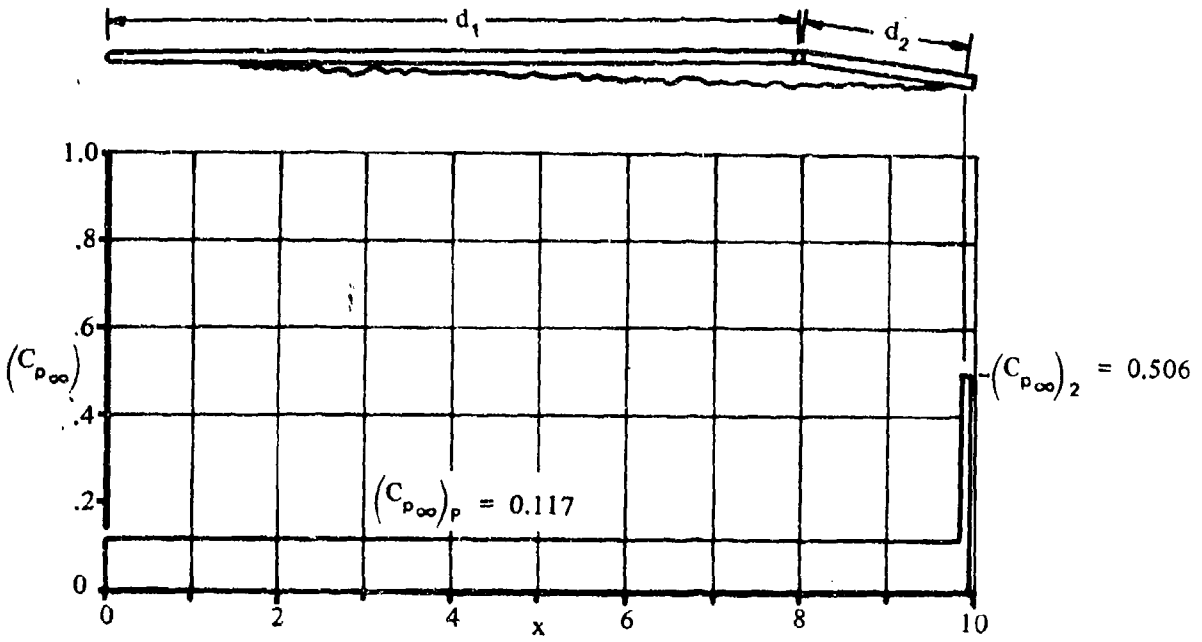

REFERENCES

1. Popinski, Z., and Ehrlich, C.F.: Development of Design Methods for Predicting Hypersonic Aerodynamic Control Characteristics. AFFDL-TR-66-35, 1966. (U)

2. Kaufman, L.G., II, Oman, R.A., Hartofilis, S.A., et al: A Review of Hypersonic Flow Separation and Control Characteristics. ASD-TDR-62-168, 1962. (U)

3. Wuerer, J.E., et al: Flow Separation in High-Speed Flight, A Review of the State-of-the-Art. Douglas Aircraft Co., Report SM-46429, 1965. (U)

4. Schlichting, H.: Boundary-Layer Theory. McGraw-Hill Book Co., New York, 1955. (U)

5. Modern Developments in Fluid Dynamics -- High-Speed Flow. Edited by L. Howarth, Vol. I, Oxford University Press, 1953. (U)

6. Chapman, D.R., Kuehn, D., and Larson, H.K.: Investigation of Separated Flows in Supersonic and Transonic Streams with Emphasis on the Effects of Transition. NACA TR 1356, 1958. (U)

7. Sterrett, J.R., and Emery, J. C.: Extension of Boundary-Layer-Separation Criteria to a Mach Number of 6.5 by Utilizing Flat Plates With Forward-Facing Steps. NASA TN D-618, 1960. (U)

8. Hammitt, A.G.: The Interaction of Shock Waves and Turbulent Boundary Layers. JAS, Vol. 25, No. 6, 1958. (U)

9. Lange, R.H.: Present Status of Information Relative to the Prediction of Shock-Induced Boundary-Layer Separation. NACA TN 3065, 1954. (U)

10. Reshotko, E., and Tucker, M.: Effect of a Discontinuity on Turbulent Boundary-Layer-Thickness Parameters with Application to Shock-Induced Separation. NACA TN 3454, 1955. (U)

11. Drougge, G.: An Experimental Investigation of the Influence of Strong Adverse Pressure Gradients on Turbulent Boundary Layers at Supersonic Speeds. Aero. Res. Inst. of Sweden, Report No. 46, 1953. (U)

12. Love, E.S.: Pressure Rise Associated with Shock-Induced Boundary Layer Separation. NACA TN 3601, 1955. (U)

13. Shapiro, A.H.: The Dynamics and Thermodynamics of Compressible Fluid Flow. Vol. II, The Ronald Press Co., New York, 1954. (U)

14. Schuh, H.: On Determining Turbulent Boundary-Layer Separation in Incompressible and Compressible Flow. JAS, Vol. 22, No. 5, 1955. (U)

15. Chapman, D.R.: A Theoretical Analysis of Heat Transfer in Regions of Separated Flows. NACA TN 3792, 1956. (U)

16. Larson, H.K.: Heat Transfer in Separated Flows. JAS, Vol. 26, No. 11, 1959. (U)

17. Cohen, C.B., and Reshotko, E.: Similar Solutions for the Compressible Laminar Boundary Layer With Heat Transfer and Pressure Gradient. NACA TR 1293, 1956. (U)

18. Cohen, C.B., and Reshotko, E.: The Compressible Laminar Boundary Layer With Heat Transfer and Arbitrary Pressure Gradient. NACA TR 1294, 1956. (U)

19. Gadd, G.E.: The Numerical Integration of the Laminar Compressible Boundary-Layer Equations, With Special Reference to the Position of Separation When the Wall is Cooled. ARC 15101, FM1771, 1952. (U)

20. Gadd, G.E.: A Theoretical Investigation of the Effects of Mach Number, Reynolds Number, Wall Temperature and Surface Curvature on Laminar Separation in Supersonic Flow. ARC 18449, 1956. (U)

21. Gadd, G.E.: A Review of Theoretical Work Relevant to the Problem of Heat-Transfer Effects on Laminar Separation. ARC 18495, 1956. (U)

22. Illingworth, C.R.: The Effect of Heat Transfer on the Separation of a Compressible Laminar Boundary Layer. Quart. Fluid Mech. & Appl. Math. 7, 8, 1954. (U)

23. Morduchow, M., and Grape, R.G.: Separation Stability and Other Properties of Compressible Laminar Boundary Layer With Pressure Gradient and Heat Transfer. NACA TN 3296, 1955. (U)

24. Sogin, H.H., Burkhard, K., and Richardson, P.D.: Heat Transfer in Separated Flows – Part I: Preliminary Experiments on Heat Transfer From an Infinite Bluff Plate to an Air Stream. Part II: Survey on Separated Flows With Special Reference to Heat Transfer. Aeronautical Research Lab., Melbourne, ARL-4, 1961. (U)

25. Kuo, Y.H.: Dissociation Effects in Hypersonic Viscous Flows. JAS, Vol. 24, No. 5, 1957. (U)

26. Gadd, G.E.: An Experimental Investigation of Heat Transfer Effects on Boundary Layer Separation in Supersonic Flow. Jour. Fluid Mech., Vol. 2, Part 2, 1957. (U)

27. Gadd, G.E., and Holder, D.W.: The Behavior of Supersonic Boundary Layers in the Presence of Shock Waves. IAS Paper 59-138, 1959. (U)

28. Gadd, G.E.: Boundary Layer Separation in the Presence of Heat Transfer. AGARD Rpt. 280, 1960. (U)

29. Bertram, M.H., and Cook, B.S.: The Correlation of Oblique Shock Parameters for Ratios of Specific Heats From 1 to 5/3 With Application to Real Gas Flows. NASA TR R-171, 1963. (U)

30. Deem, R.E., and Murphy, J.S.: Flat-Plate Boundary-Layer Transition at Hypersonic Speeds. AIAA Paper No. 65-128, 1965. (U)

31. Moeckel, W.E.: Some Effects of Bluntness on Boundary-Layer Transition and Heat Transfer at Supersonic Speeds. NACA TR 1312, 1957. (U)

32. Abbott, D. E., Holt, M., and Nielsen, J. N.: Investigation of Hypersonic Flow Separation and Its Effects on Aerodynamic Control Characteristics. ASD-TDR-62-963, 1962. (U)

33. Nielsen, J. N., Lynes, L. L., and Goodwin, F. K.: Calculation of Laminar Separation with Free Interaction by the Method of Integral Relations, Part II – Two-Dimensional Supersonic Nonadiabatic Flow and Axisymmetric Supersonic Adiabatic and Nonadiabatic Flows. AFFDL-TR-65-107, 1966. (U)

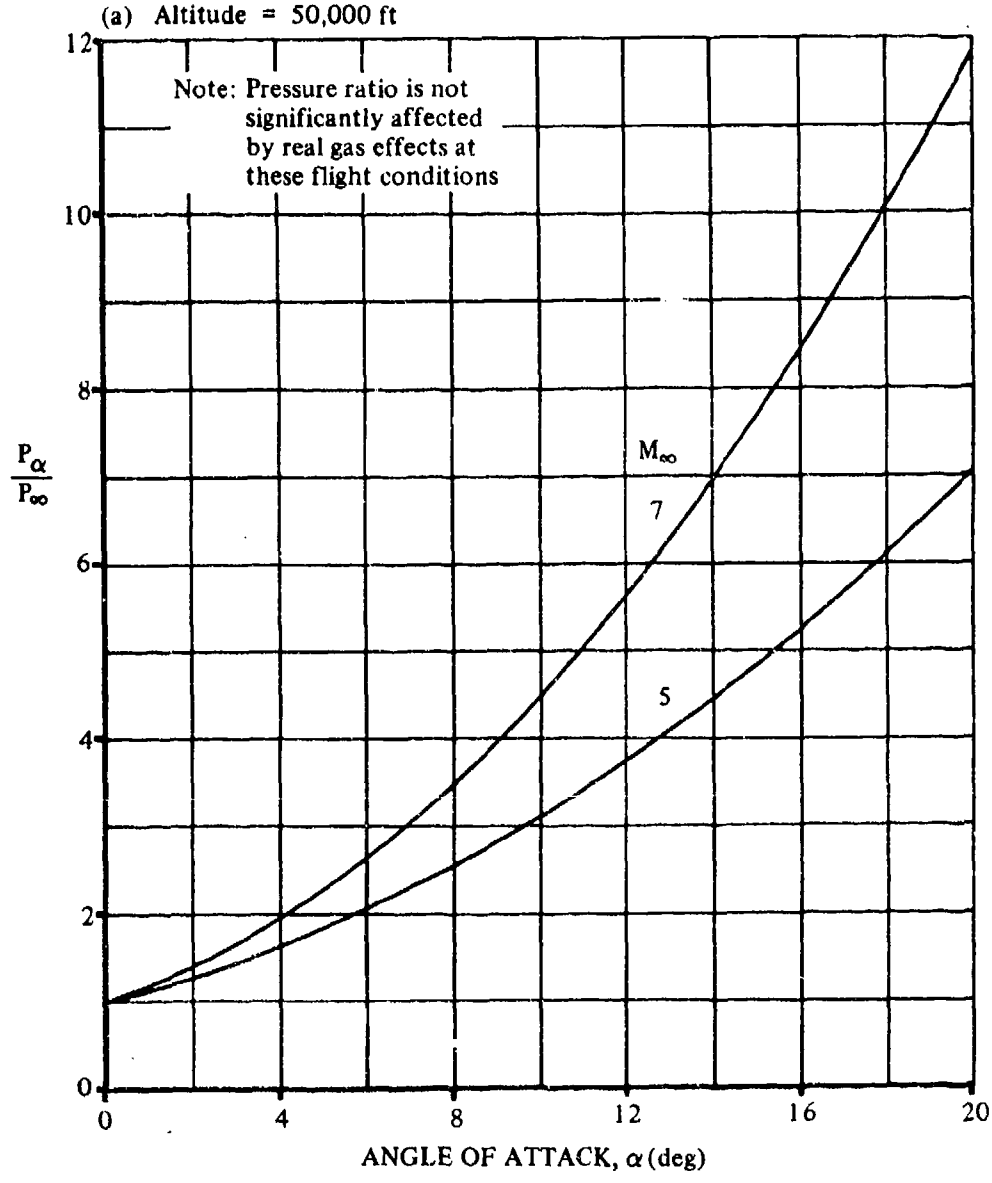

FIGURE 6.3.1-31 OBLIQUE SHOCK PRESSURE RATIO INCLUDING REAL GAS EFFECTS

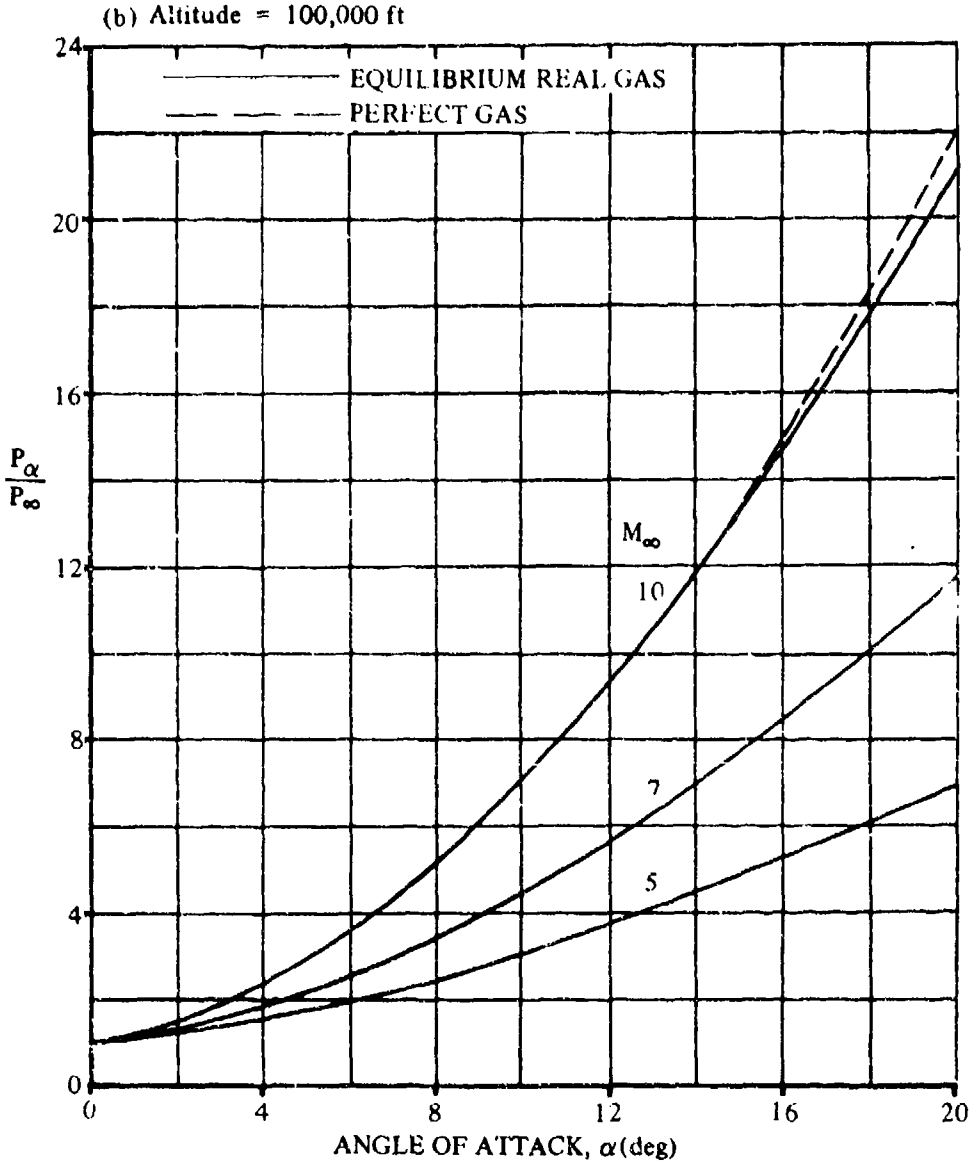

FIGURE 6.3.1-31 (CONTD)

(c) Altitude = 150,000 ft

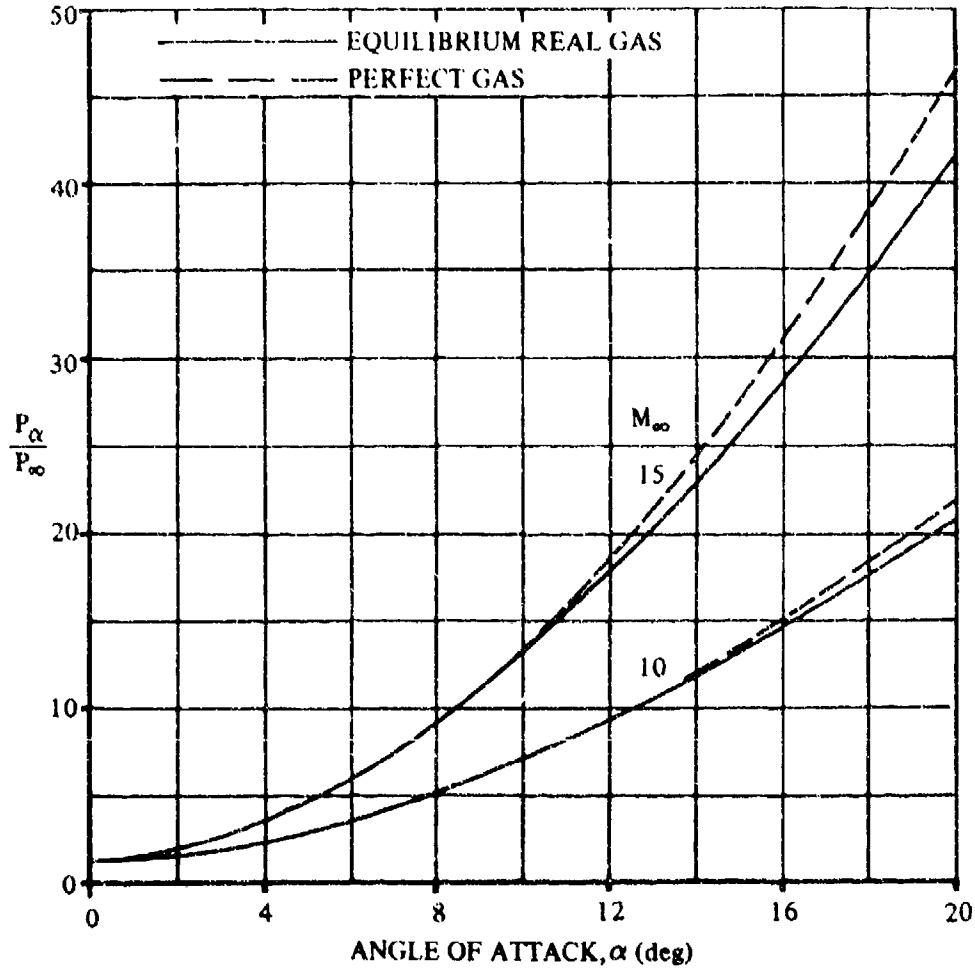

FIGURE 6.3.1-31 (CONTD)

(d) Altitude = 200,000 ft

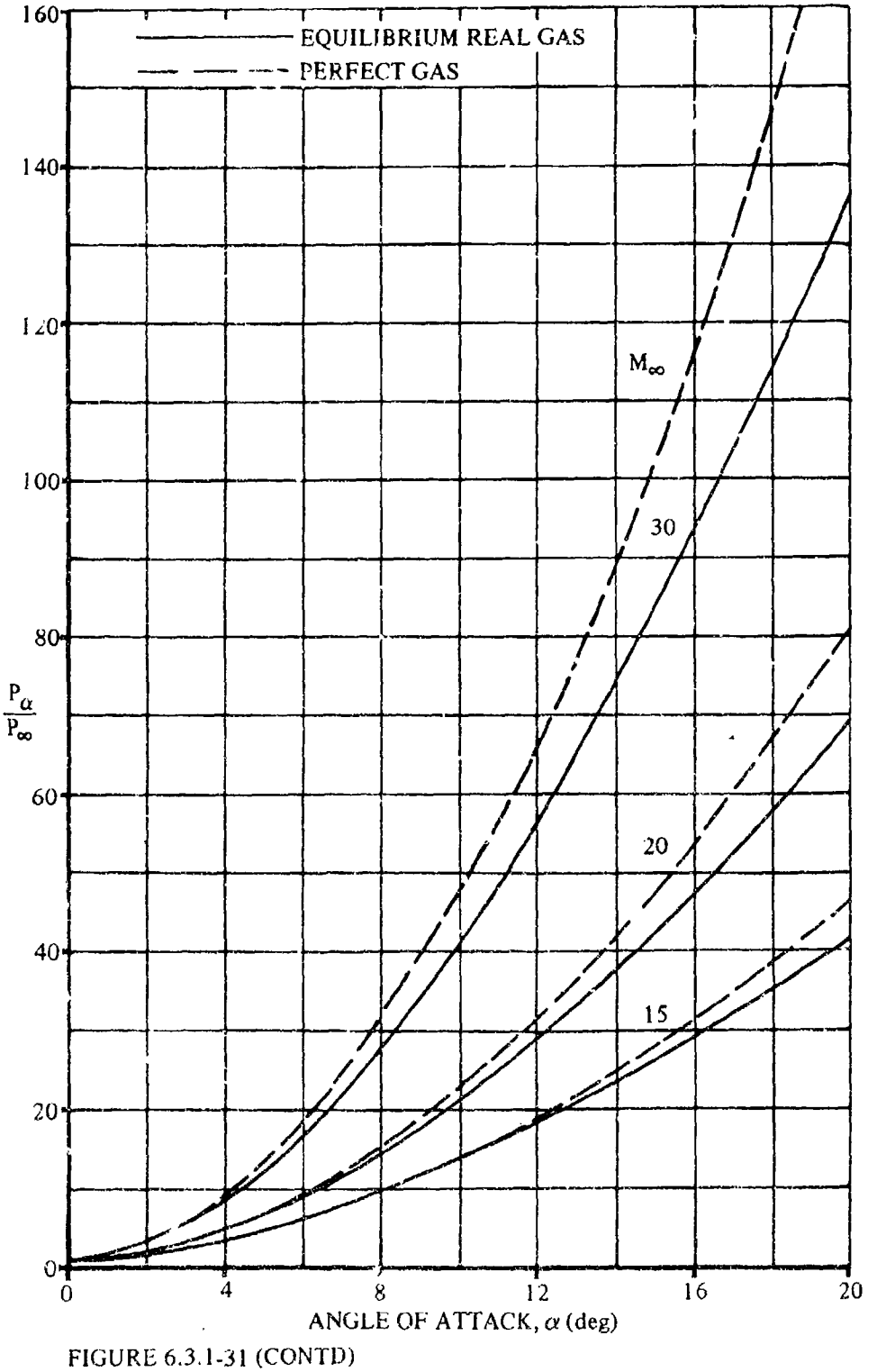

FIGURE 6.3.1-31 (CONTD)

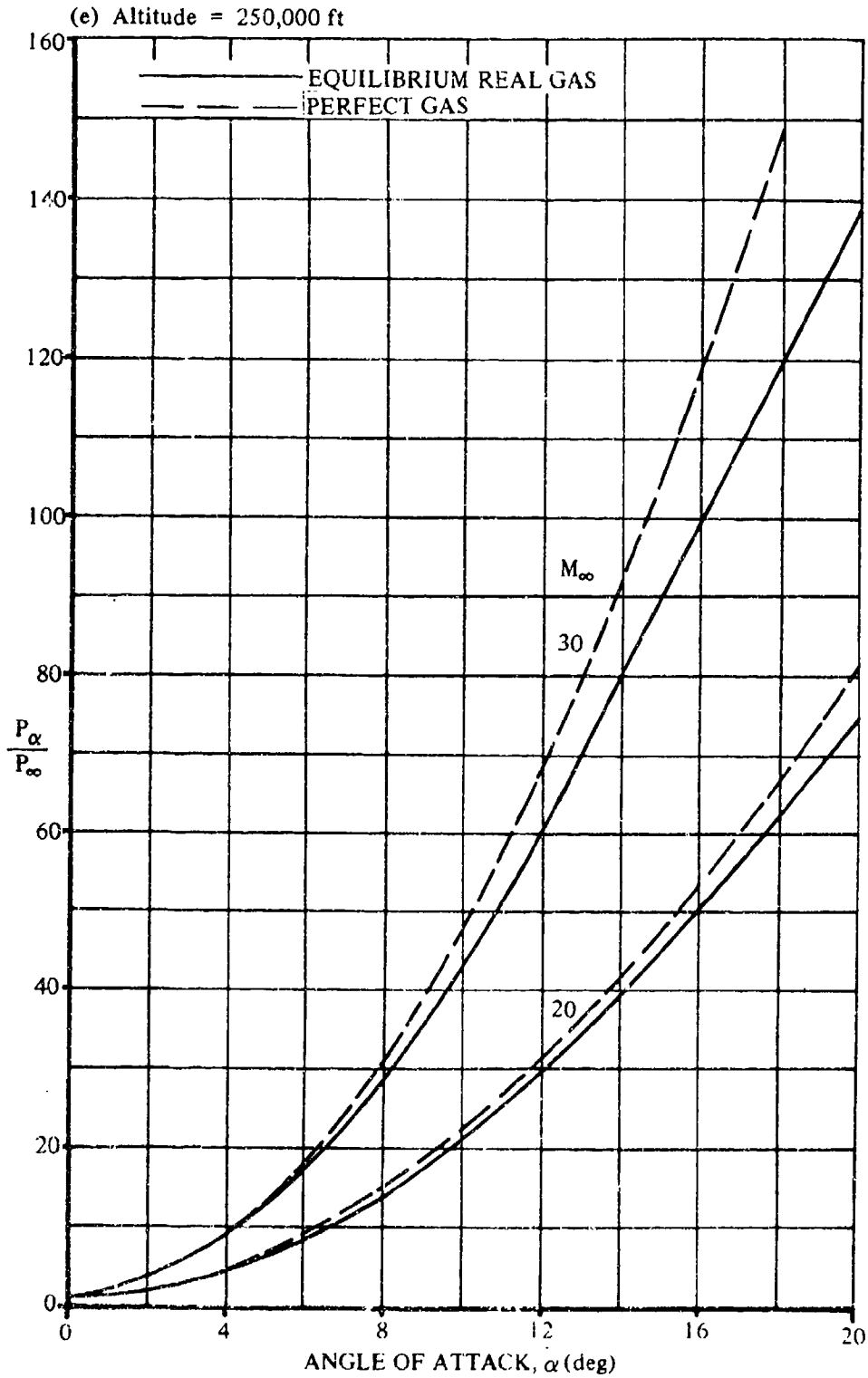

FIGURE 6.3.1-31 (CONTD)

(f) Altitude = 300,000 ft

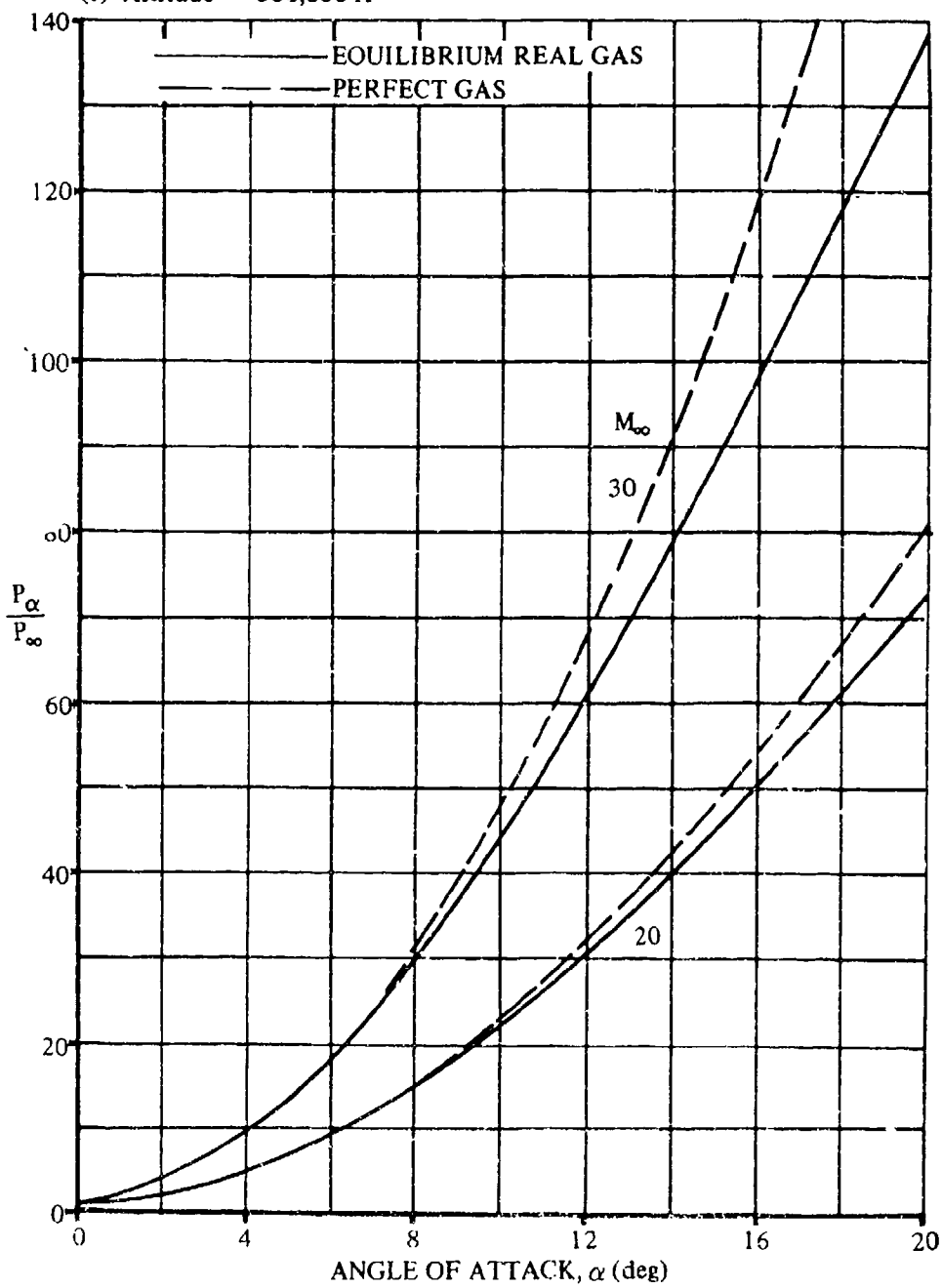

FIGURE 6.3.1-31 (CONTD)

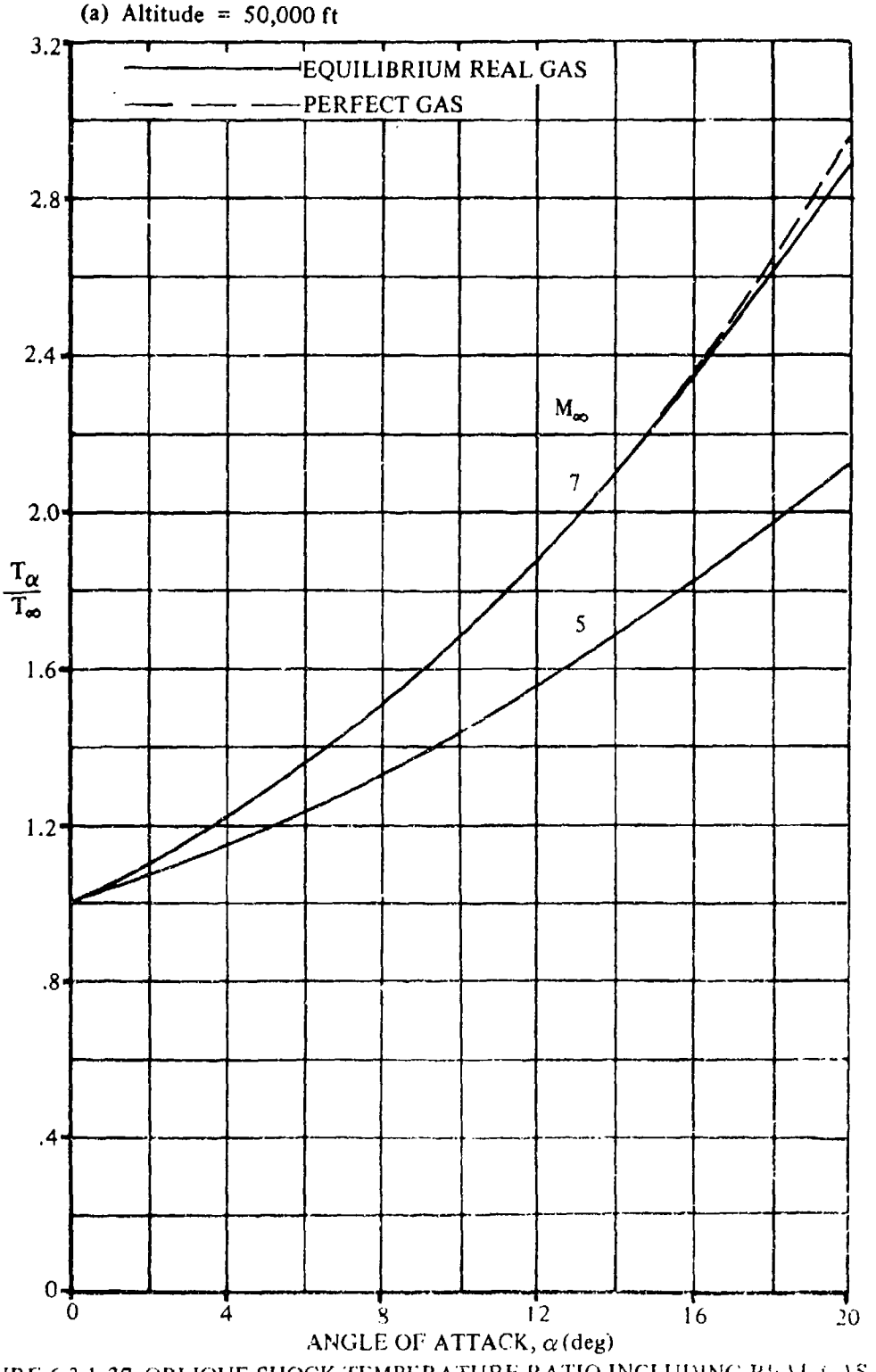

FIGURE 6.3.1-37 OBLIQUE SHOCK TEMPERATURE RATIO INCLUDING REAL GAS EFFECTS

(b) Altitude = 100,000 ft

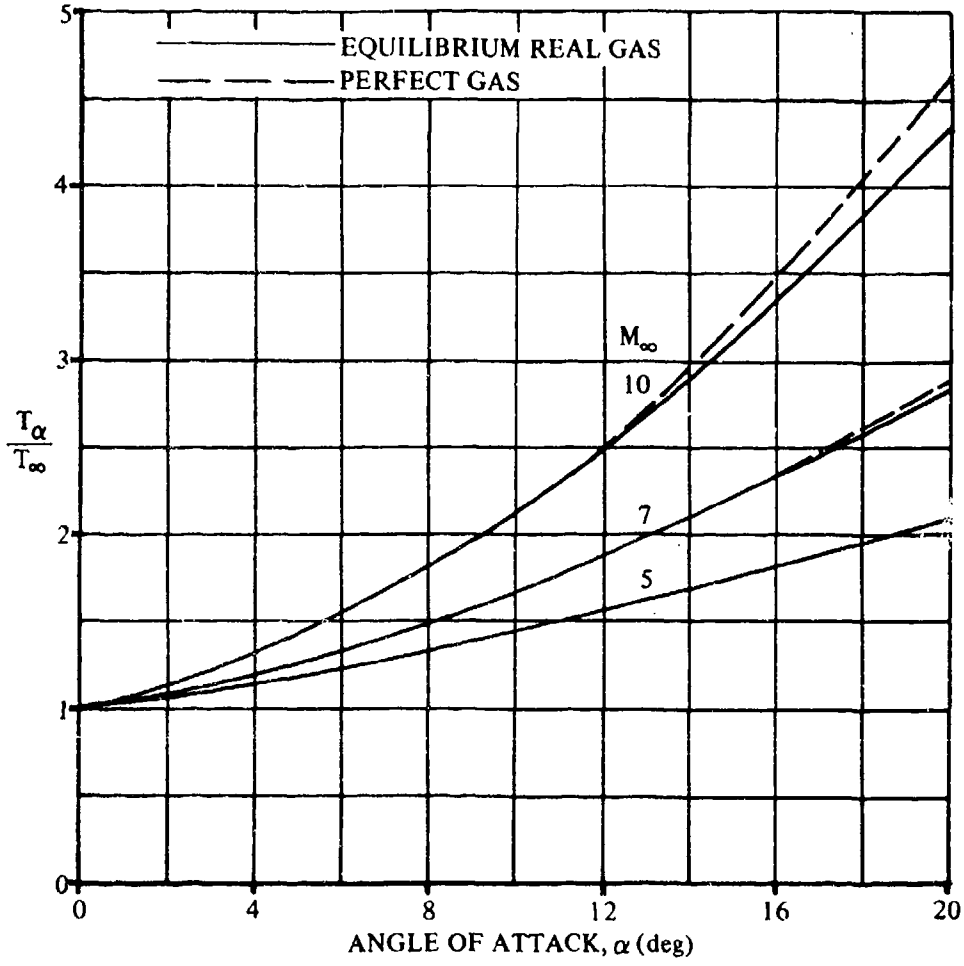

FIGURE 6.3.1-37 (CONTD)

(c) Altitude = 150,000 ft

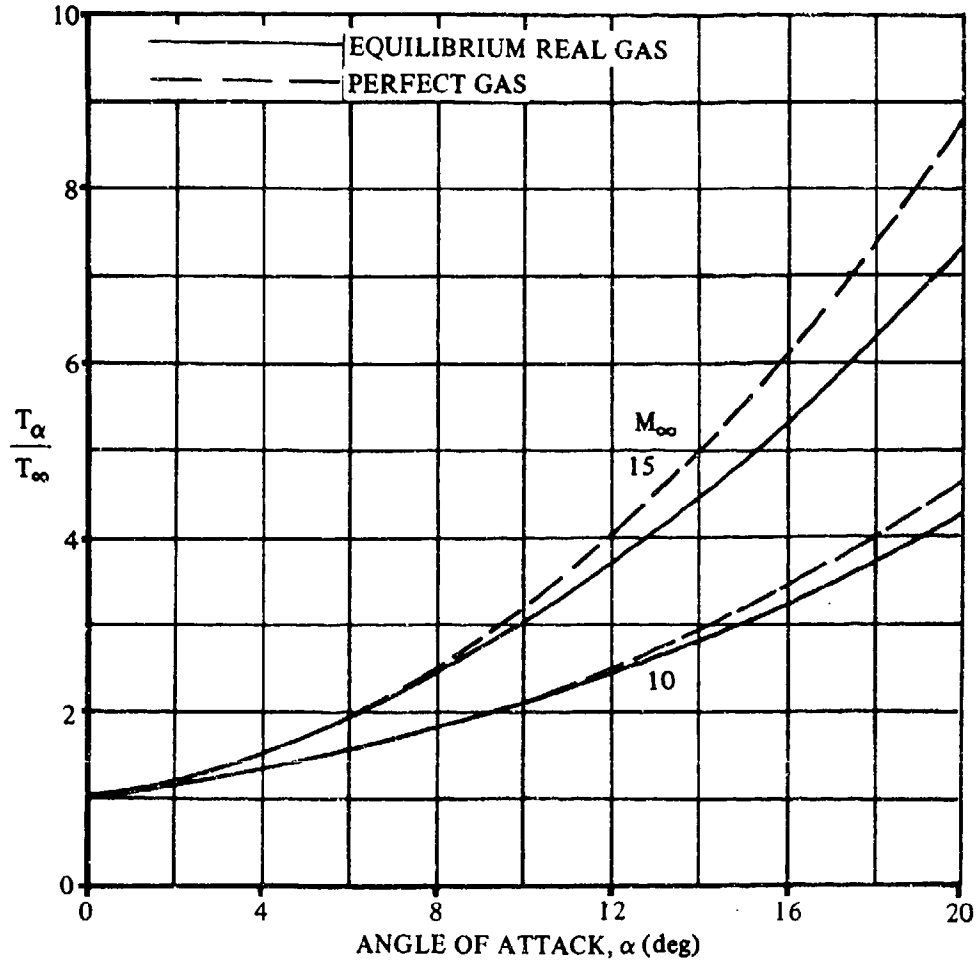

FIGURE 6.3.1-37 (CONTD)

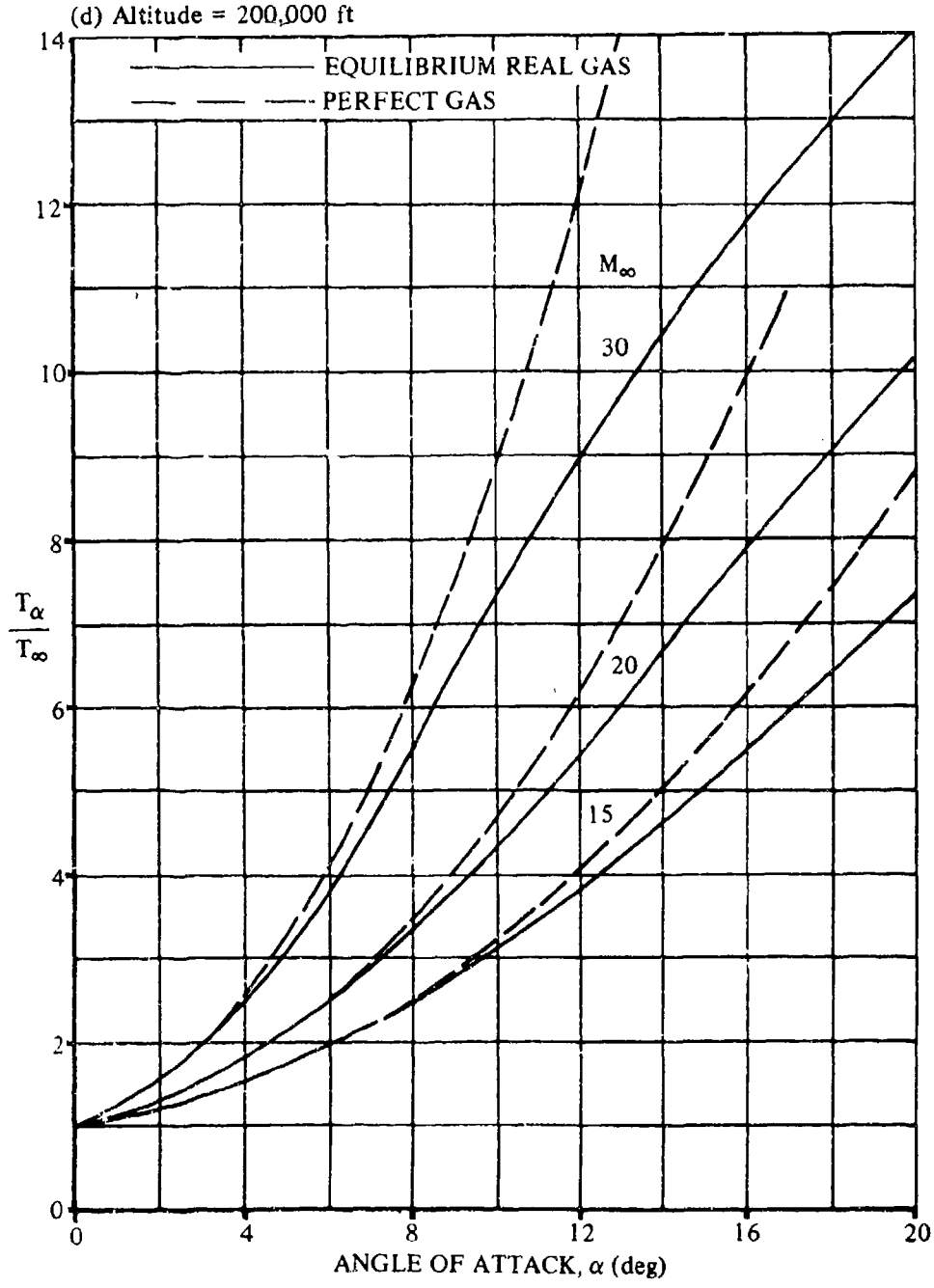

FIGURE 6.3.1-37 (CONTD)

(e) Altitude = 250,000 ft

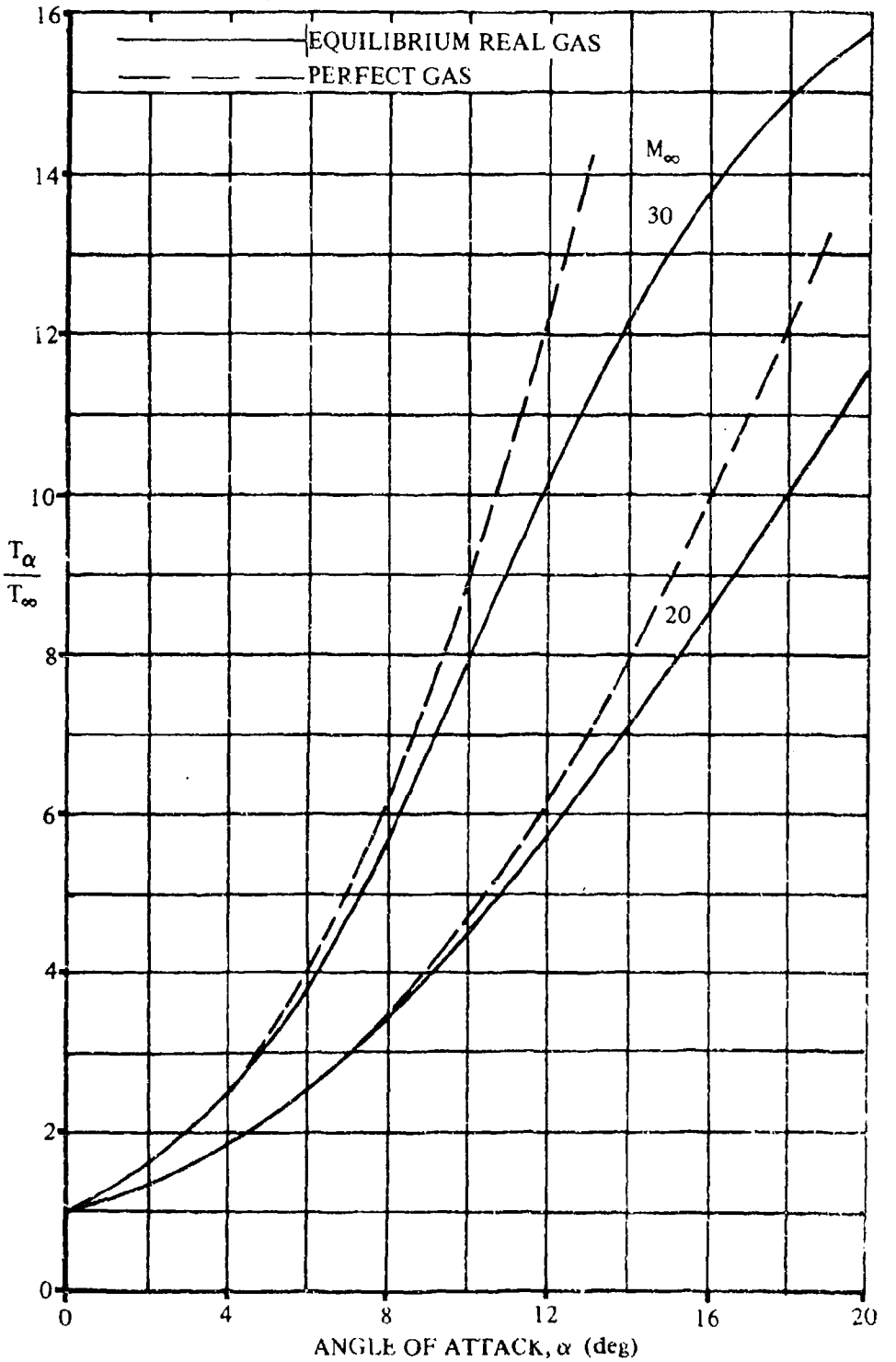

FIGURE 6.3.1-37 (CONTD)

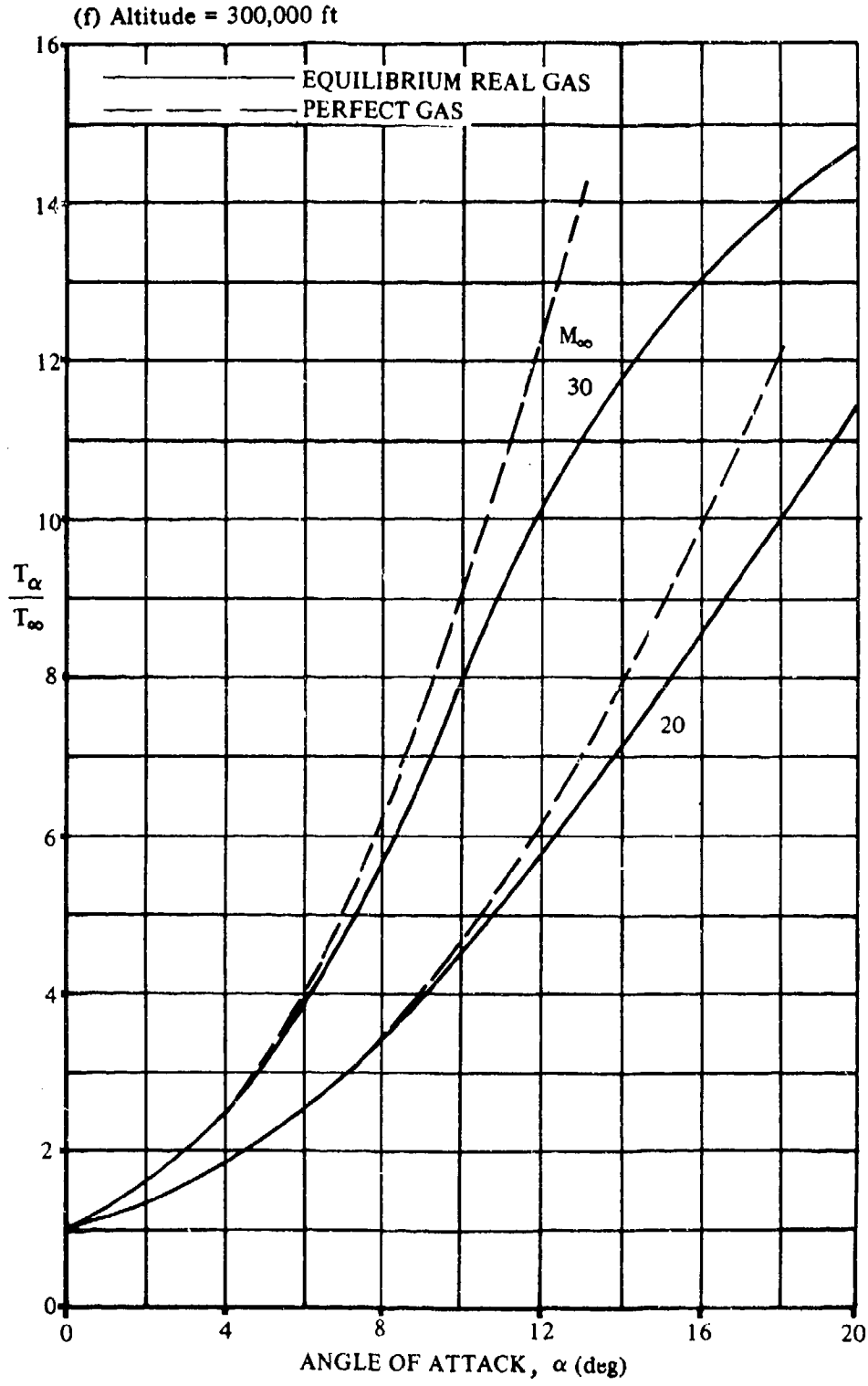

FIGURE 6.3.1-37 (CONTD)

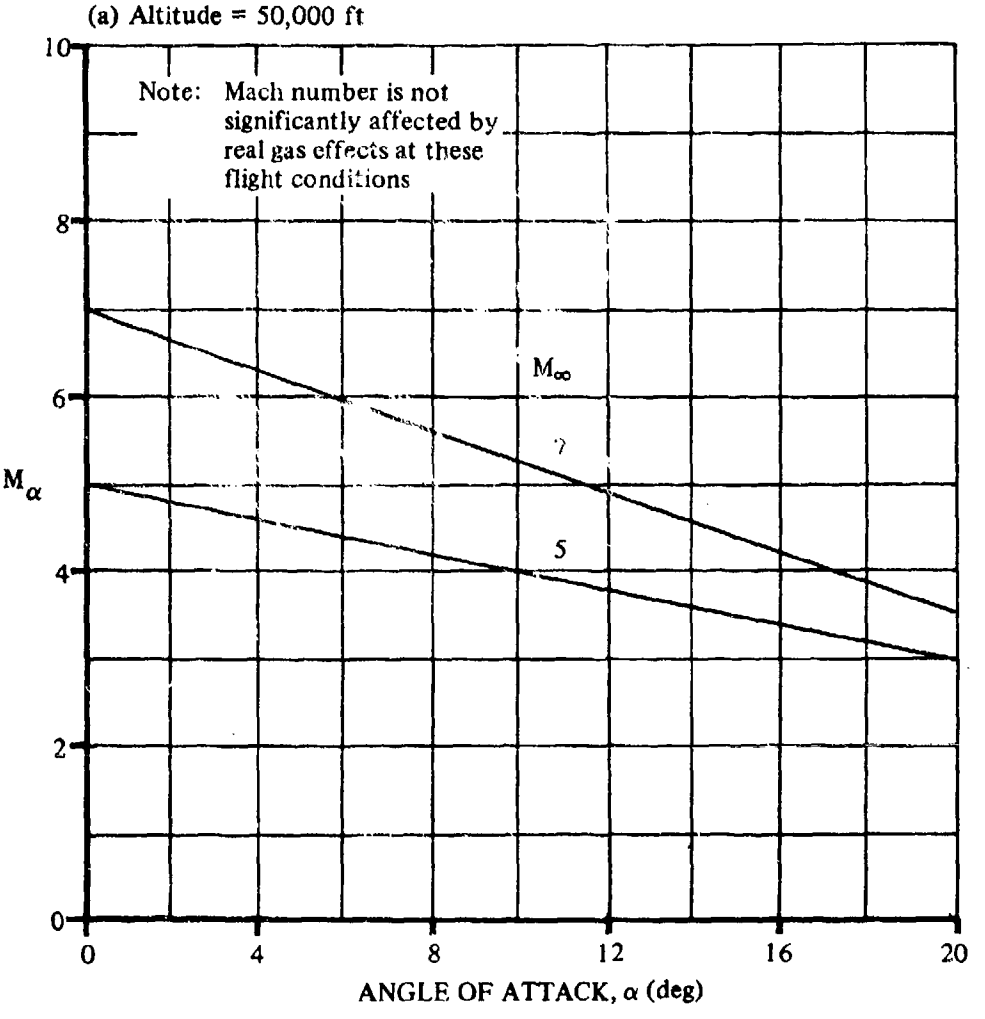

FIGURE 6.3.1-43 MACH NUMBER BEHIND AN OBLIQUE SHOCK INCLUDING REAL GAS EFFECTS

(b) Altitude = 100,000 ft

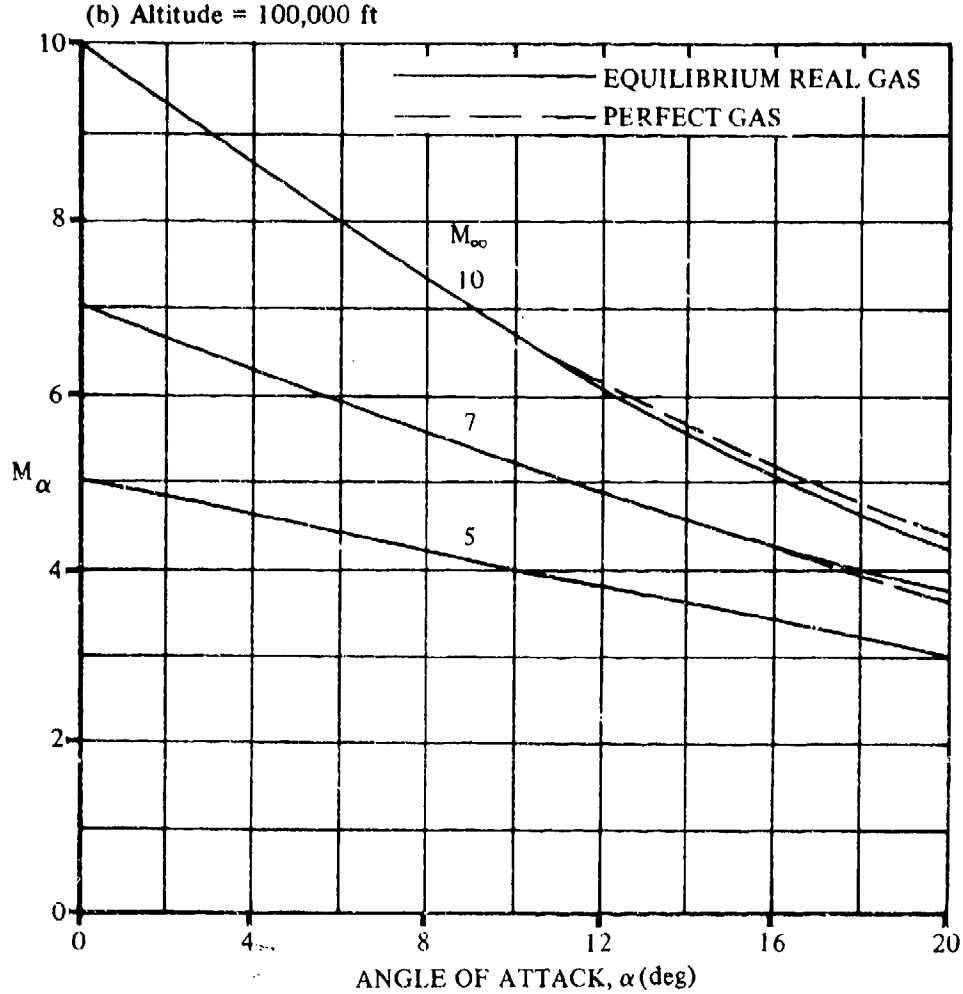

FIGURE 6.3.1-43 (CONTD)

(c) Altitude = 150,000 ft

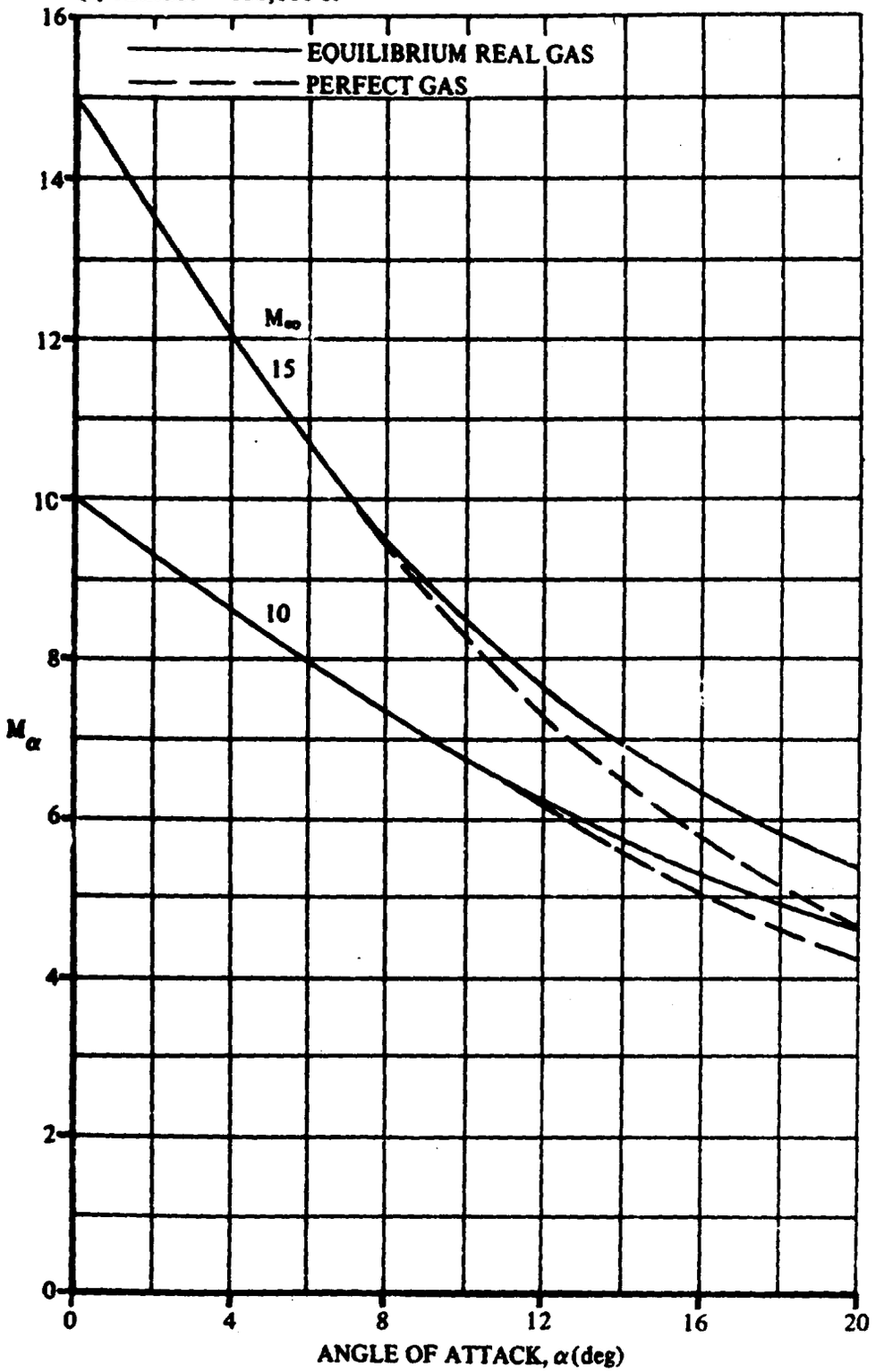

FIGURE 6.3.1-43 (CONTD)

(d) Altitude = 200,000 ft

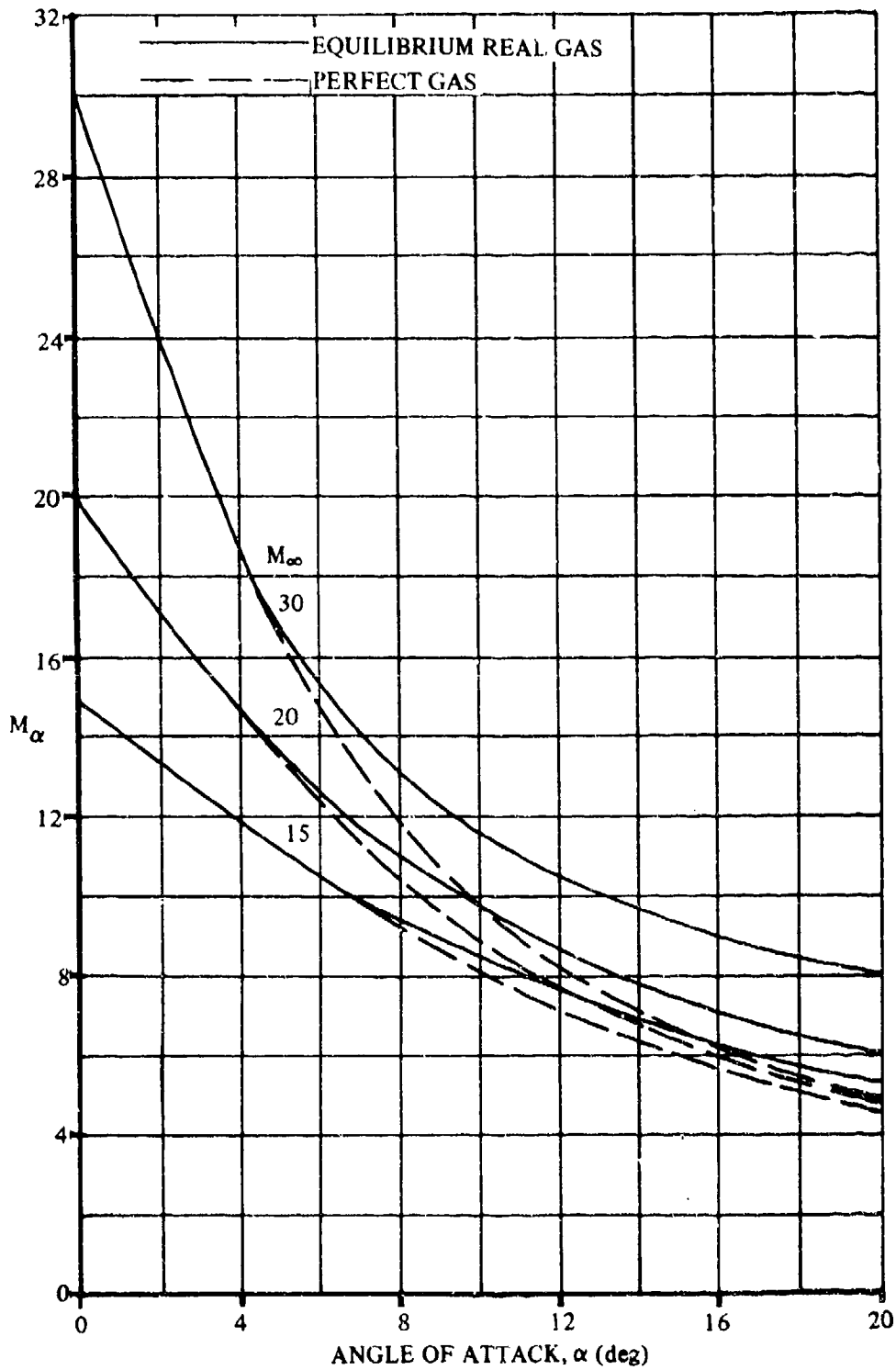

FIGURE 6.3.1-43 (CONTD)

(e) Altitude = 250,000 ft

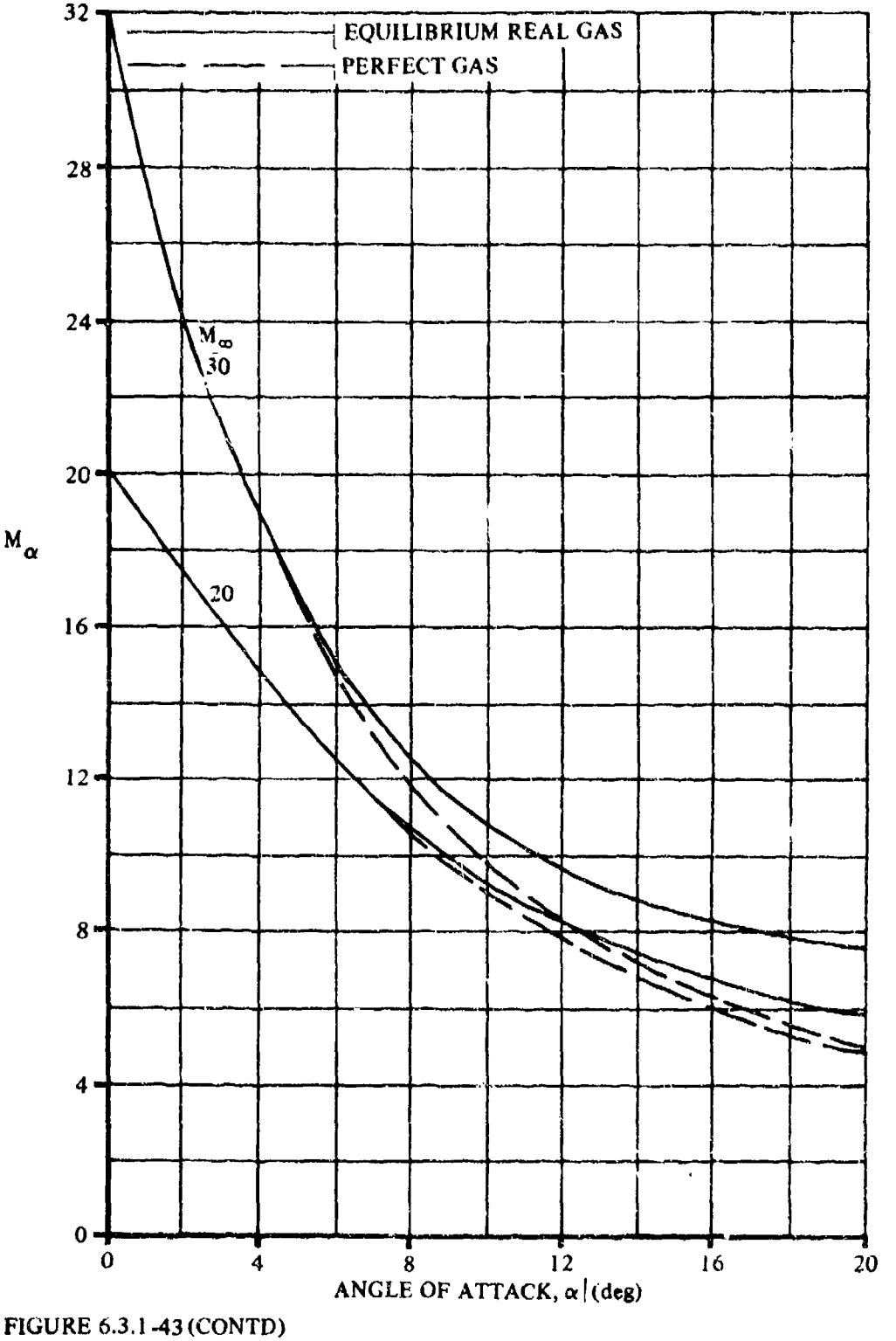

FIGURE 6.3.1-43 (CONTD)

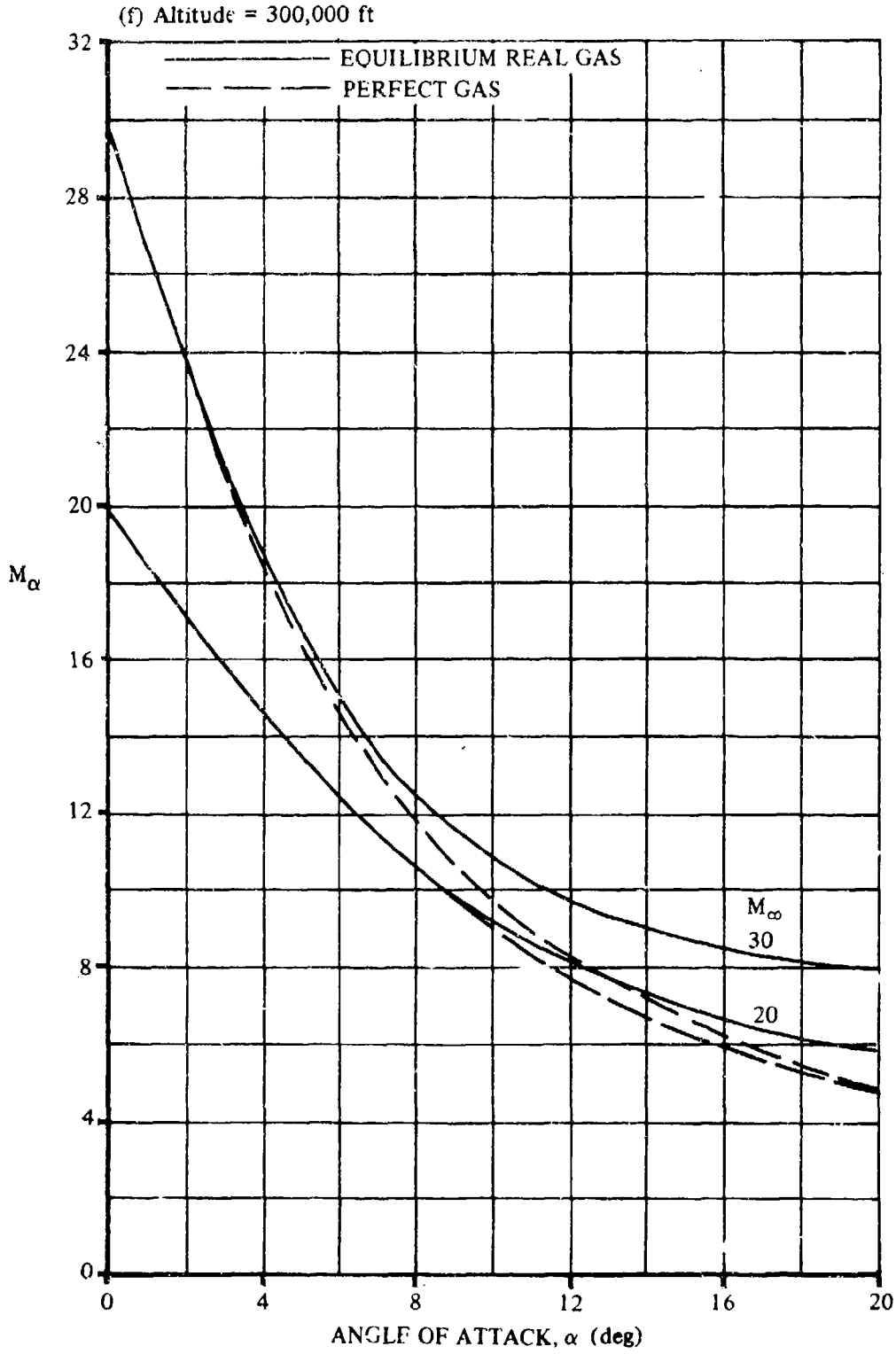

FIGURE 6.3.1-43 (CONTD)

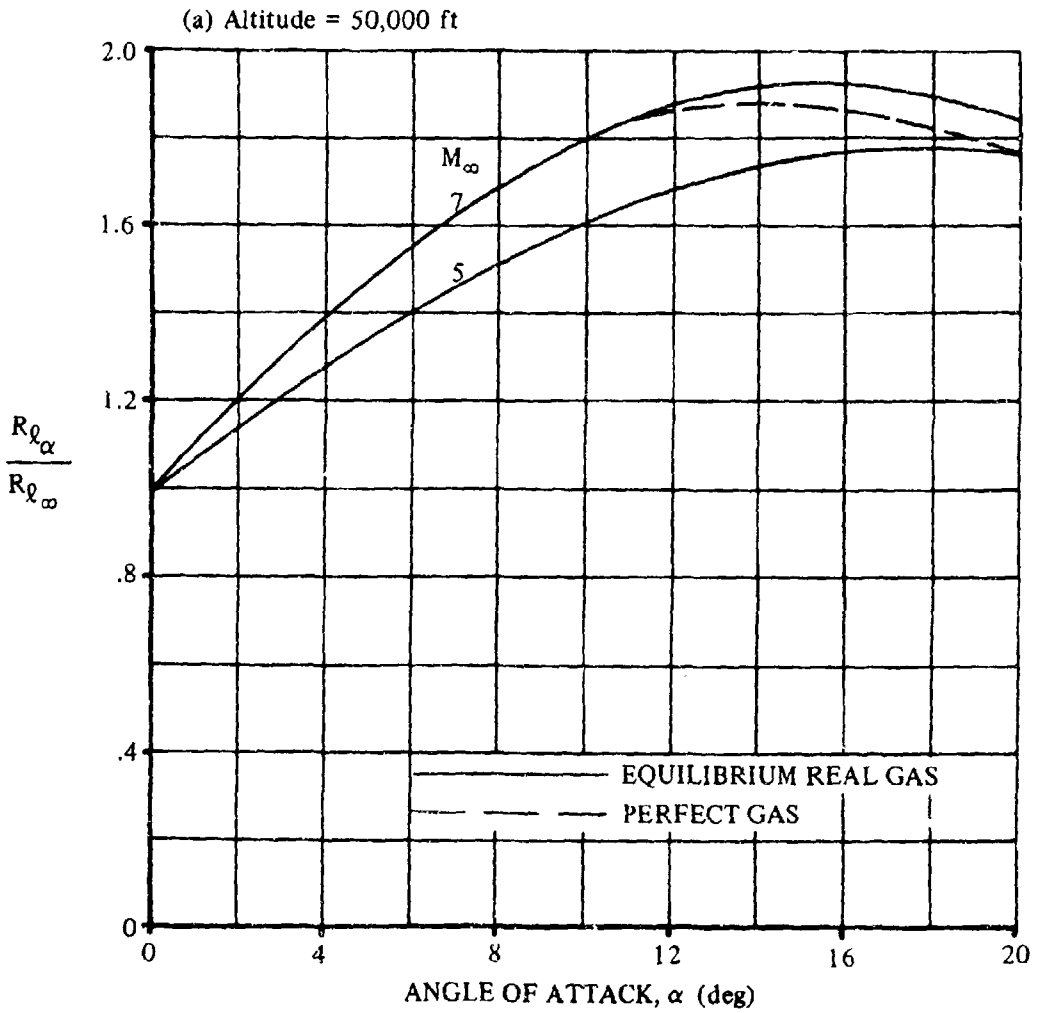

FIGURE 6.3.1-49 OBLIQUE SHOCK REYNOLDS-NUMBER RATIO INCLUDING REAL GAS EFFECTS

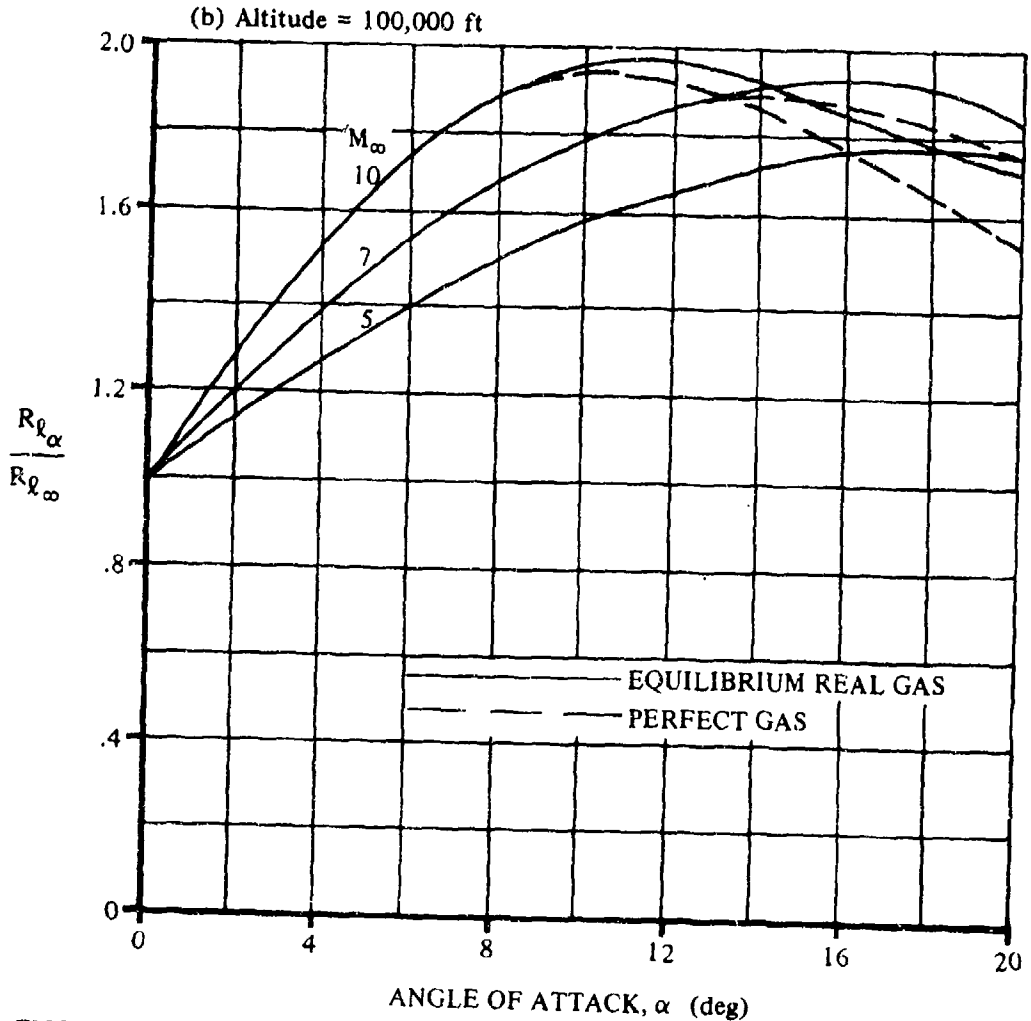

FIGURE 6.3.1-49 (CONTD)

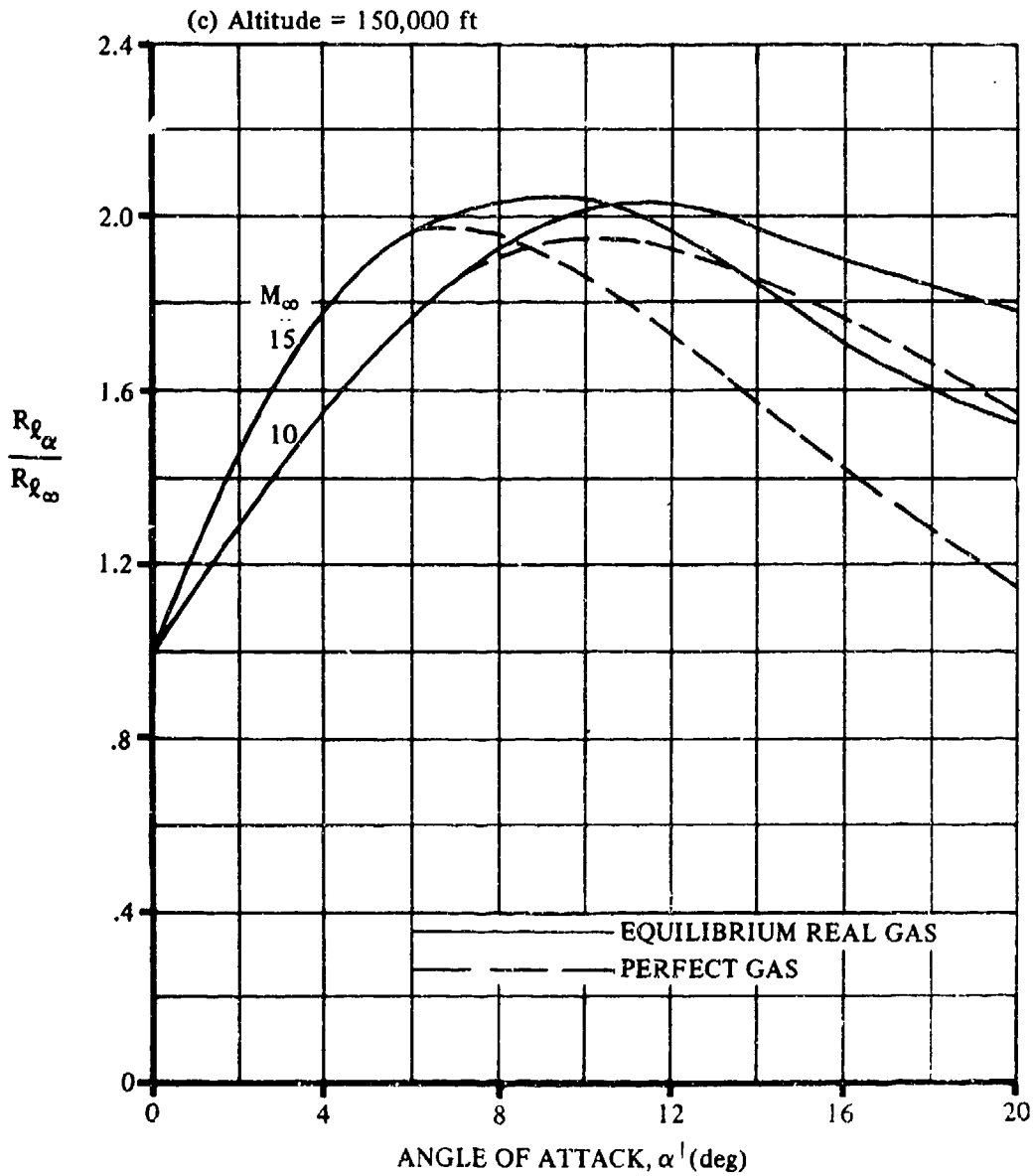

FIGURE 6.3.1-49 (CONTD)

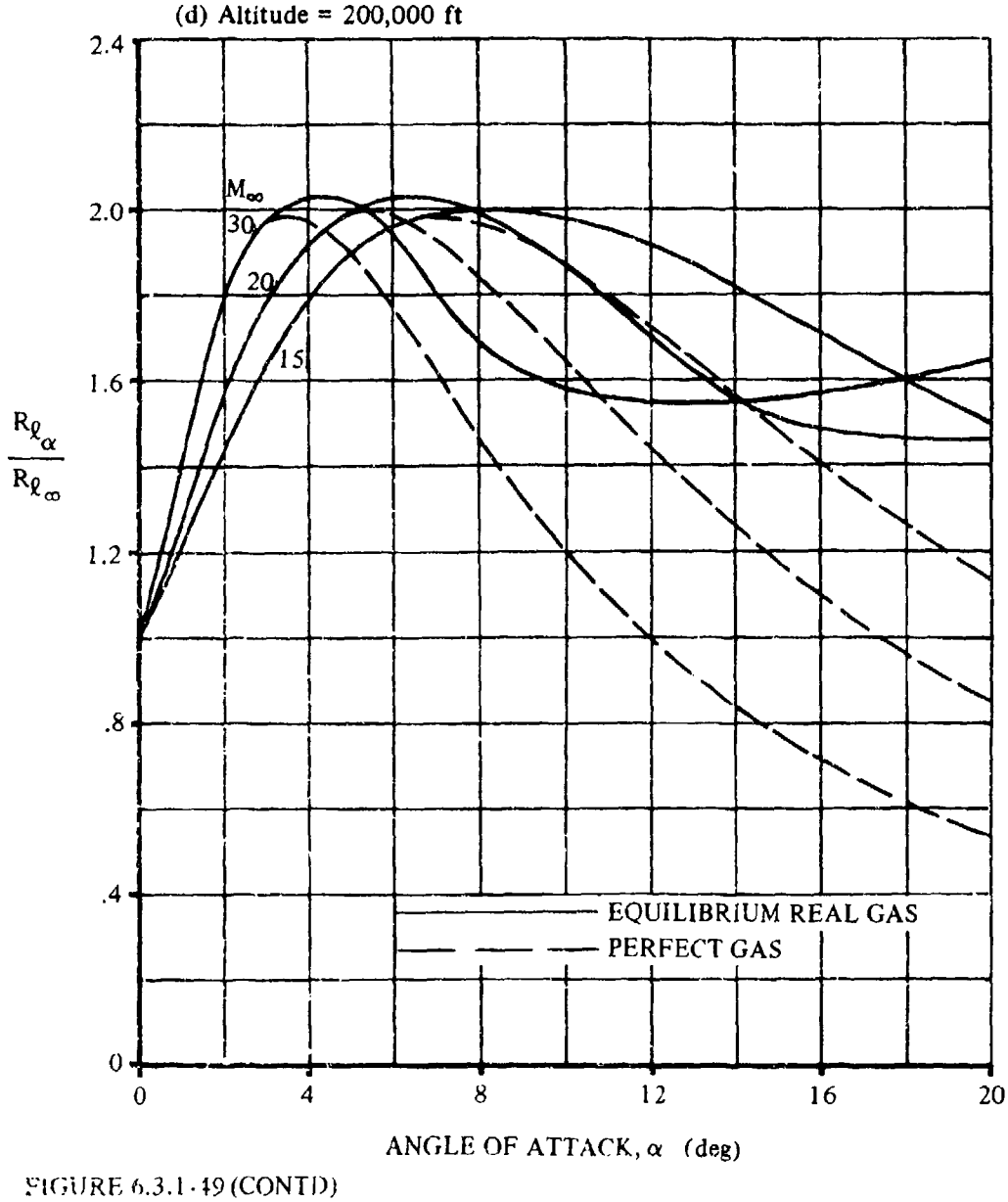

FIGURE 6.3.1-49 (CONTD)

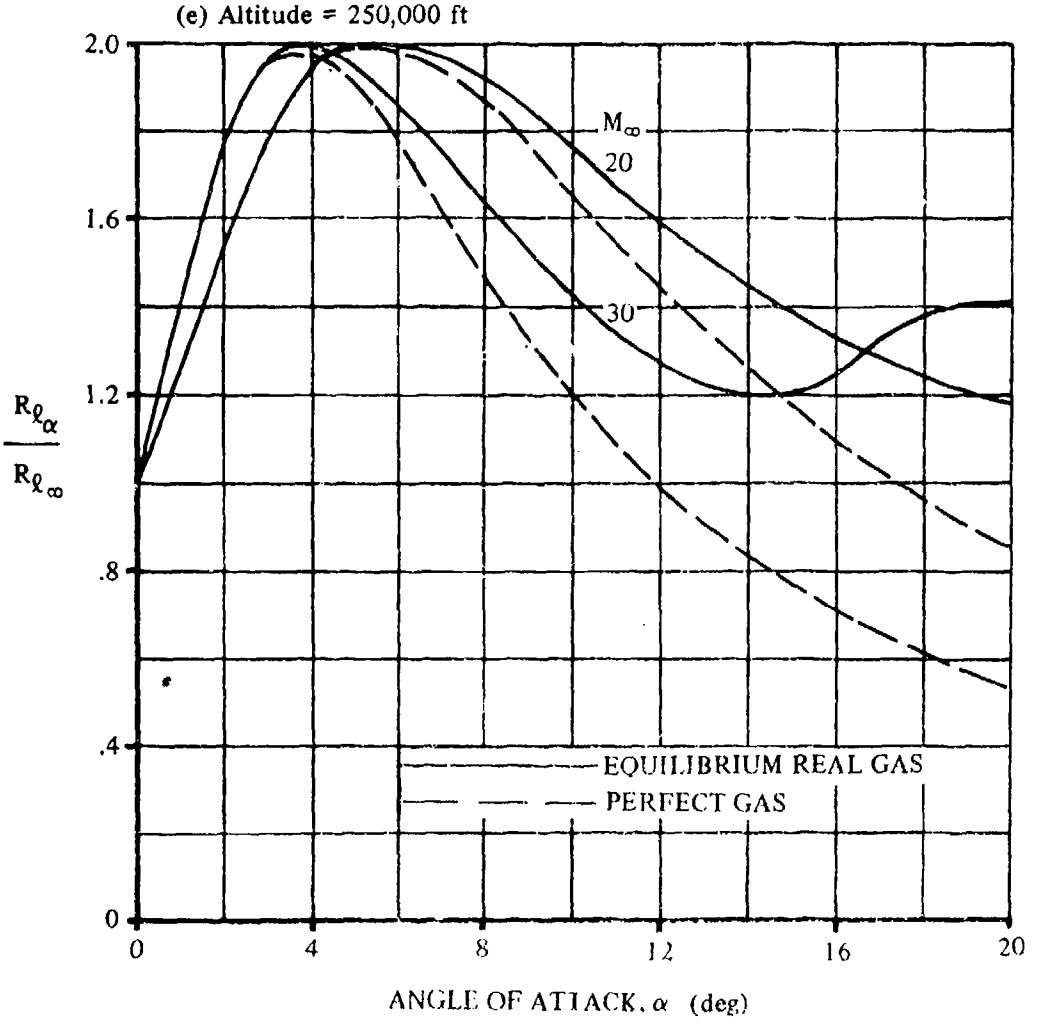

FIGURE 6.3.1-49 (CONTD)

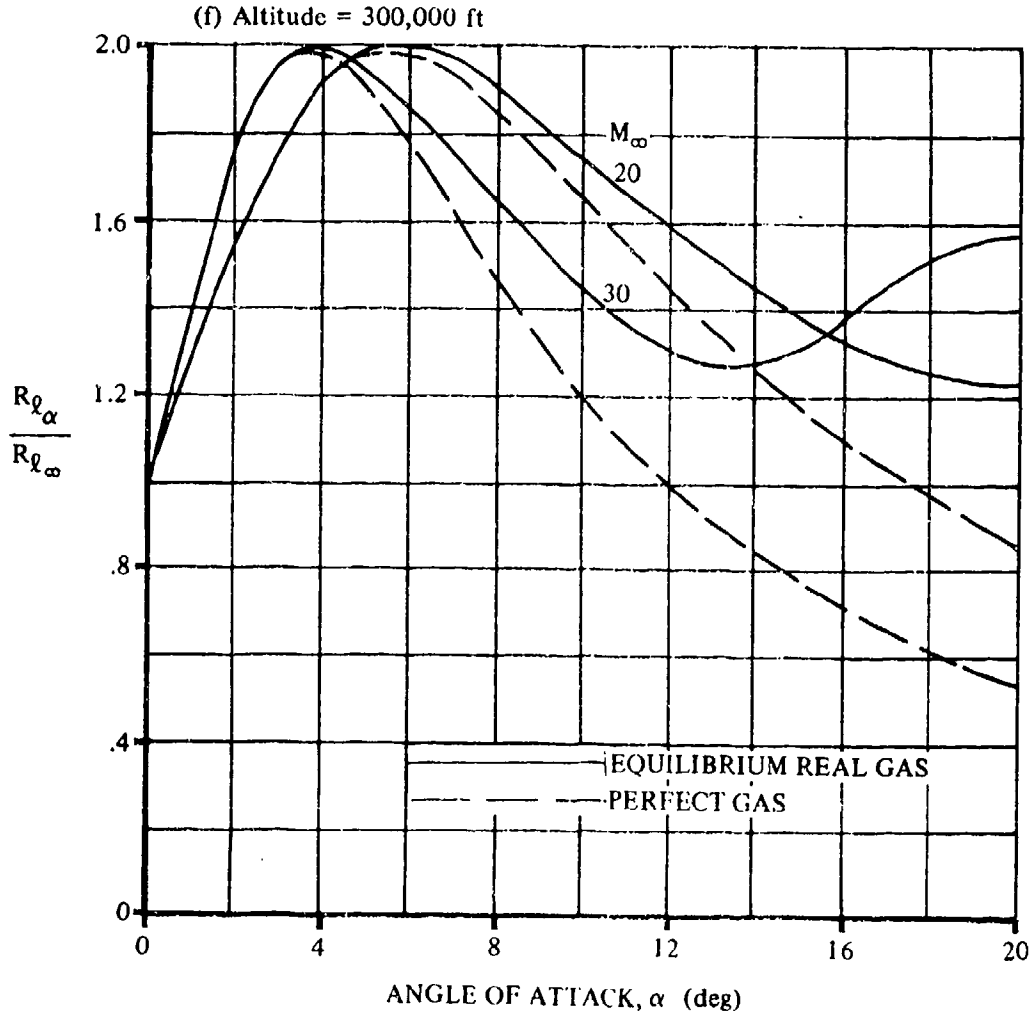

FIGURE 6.3.1-49 (CONTD)

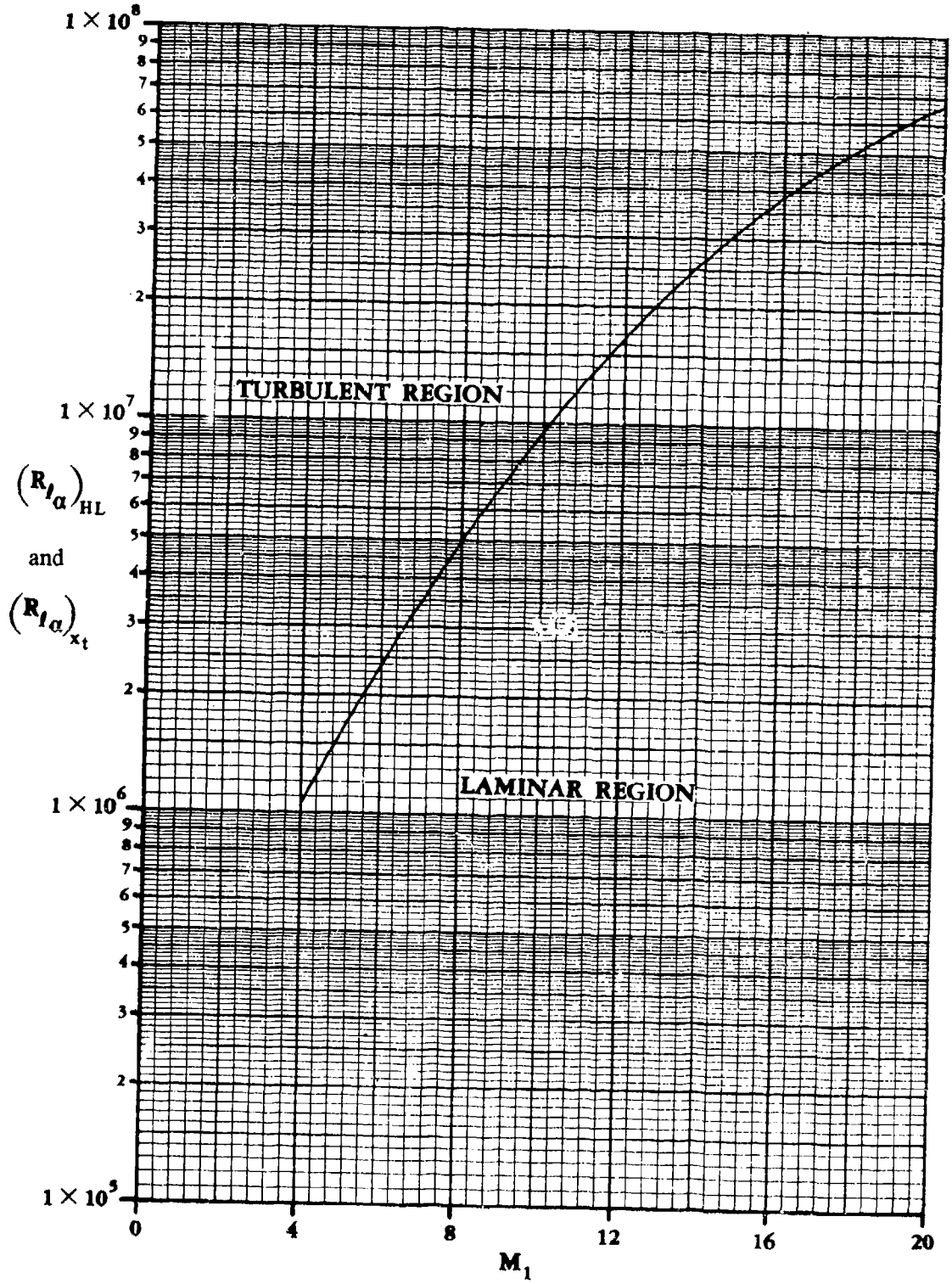

FIGURE 6.3.1-55 REGIONS FOR FXISTENCE OF THE LAMINAR AND TURBULENT BOUNDARY LAYERS

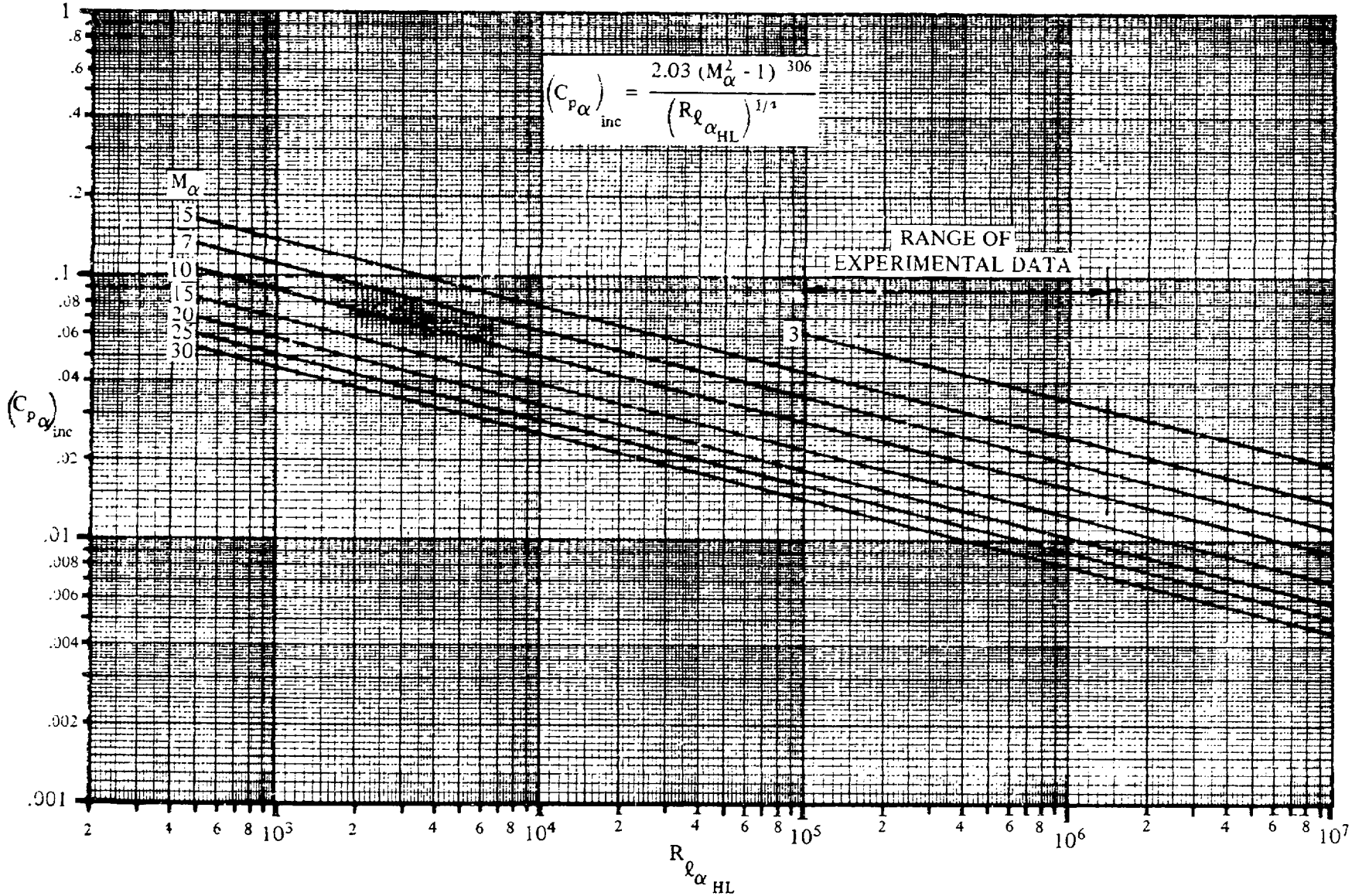

FIGURE 6.3.1-56 PRESSURE COEFFICIENT FOR INCIPIENT BOUNDARY-LAYER SEPARATION IN LAMINAR FLOW

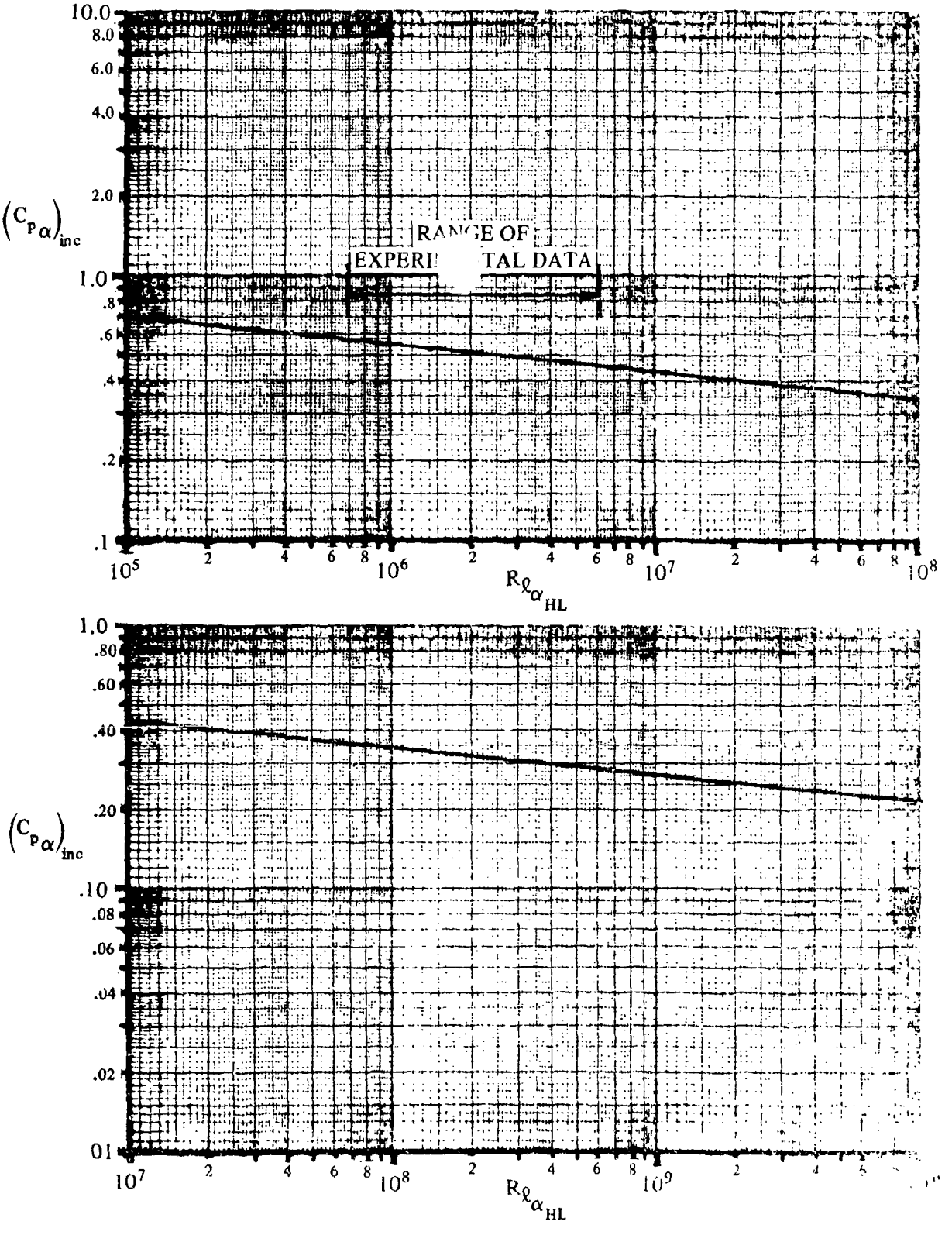

FIGURE 6.3.1-57 PRESSURE COEFFICIENT FOR INCIPIENT BOUNDARY-LAYER SEPARATION IN TURBULENT FLOW

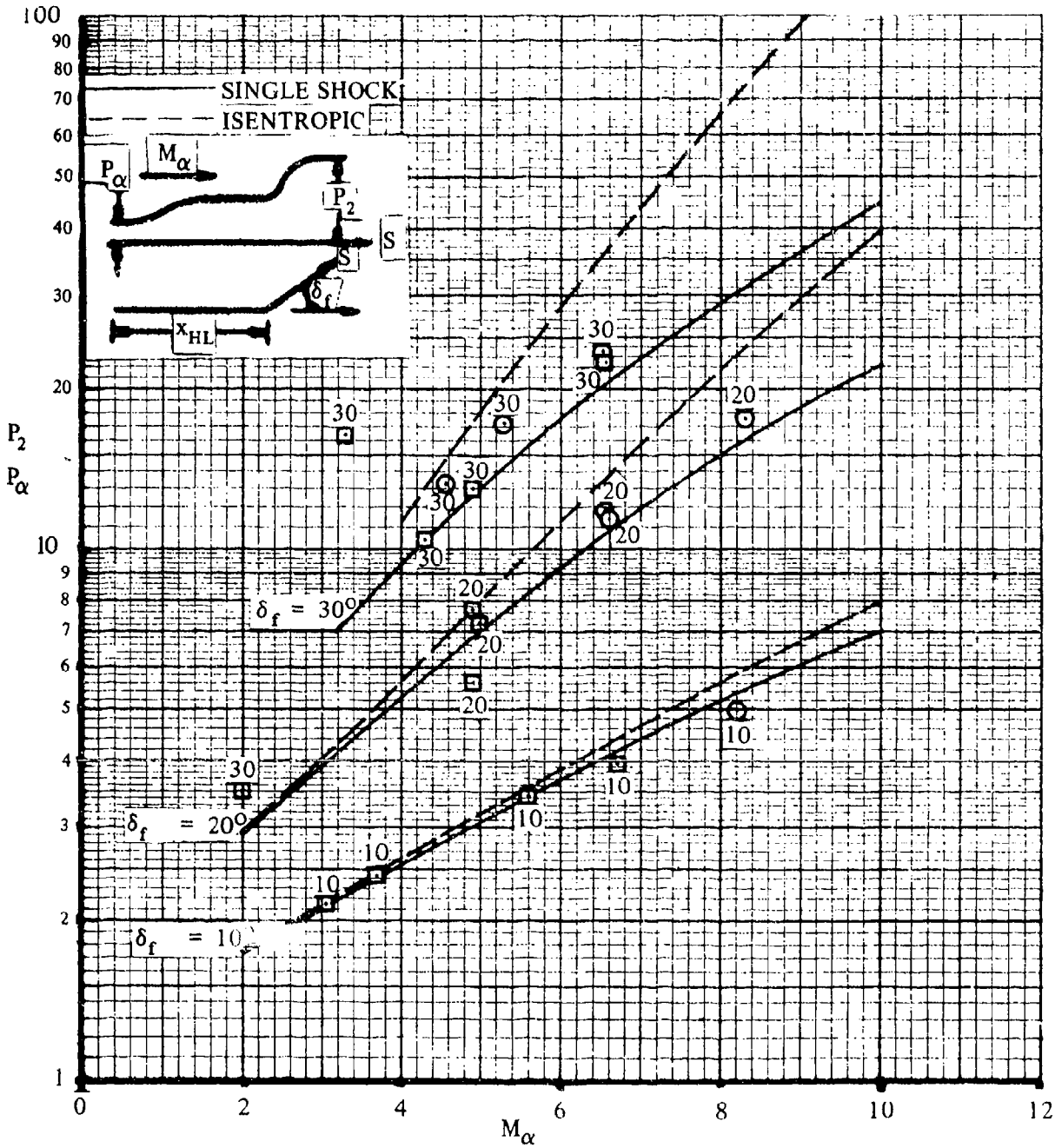

FIGURE 6.3.1-58 PEAK FLAP PRESSURE FOR ISENTROPIC AND SINGLE-SHOCK COMPRESSION

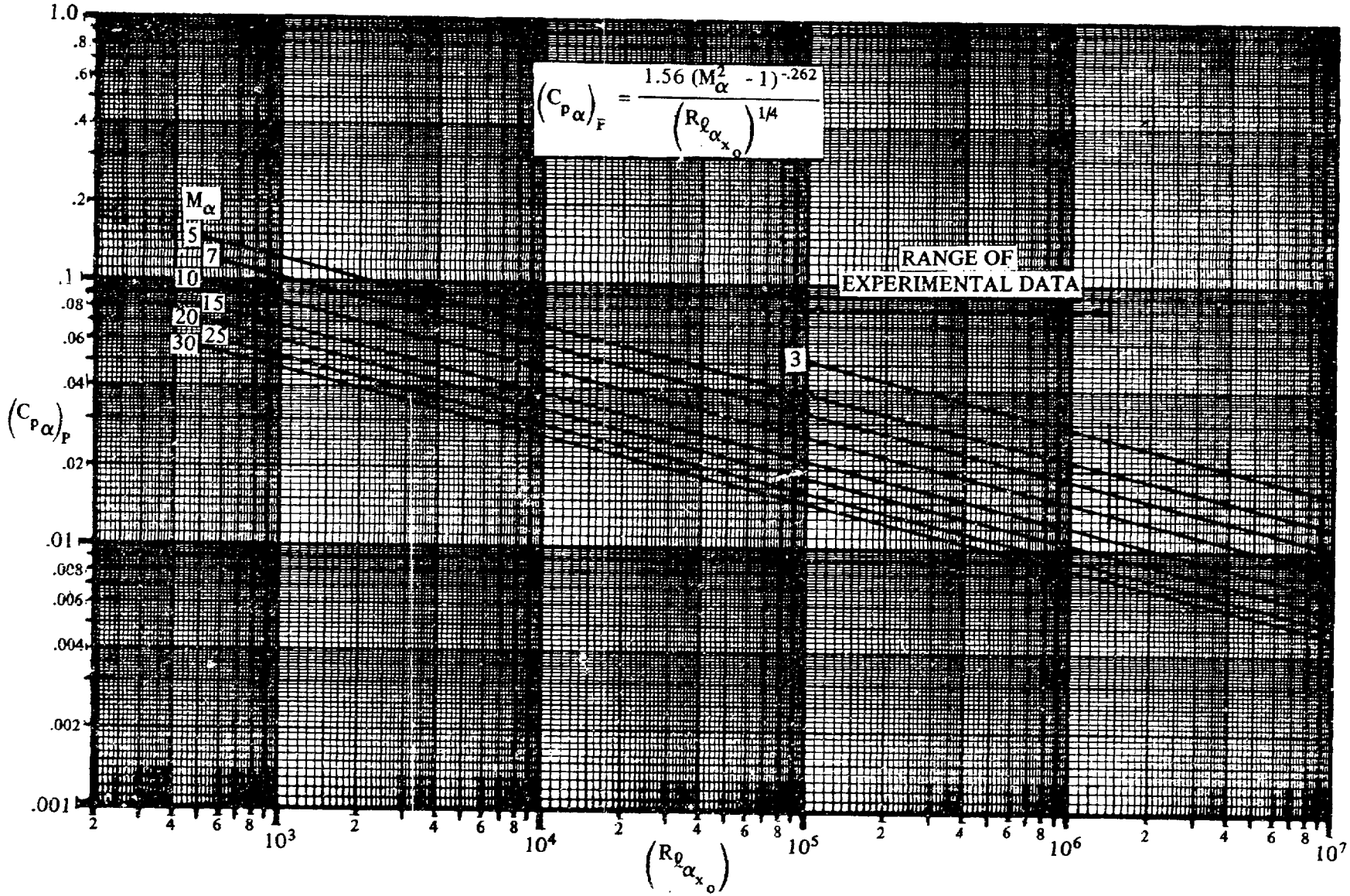

FIGURE 6.3.1-59 LAMINAR PLATEAU-PRESSURE COEFFICIENT

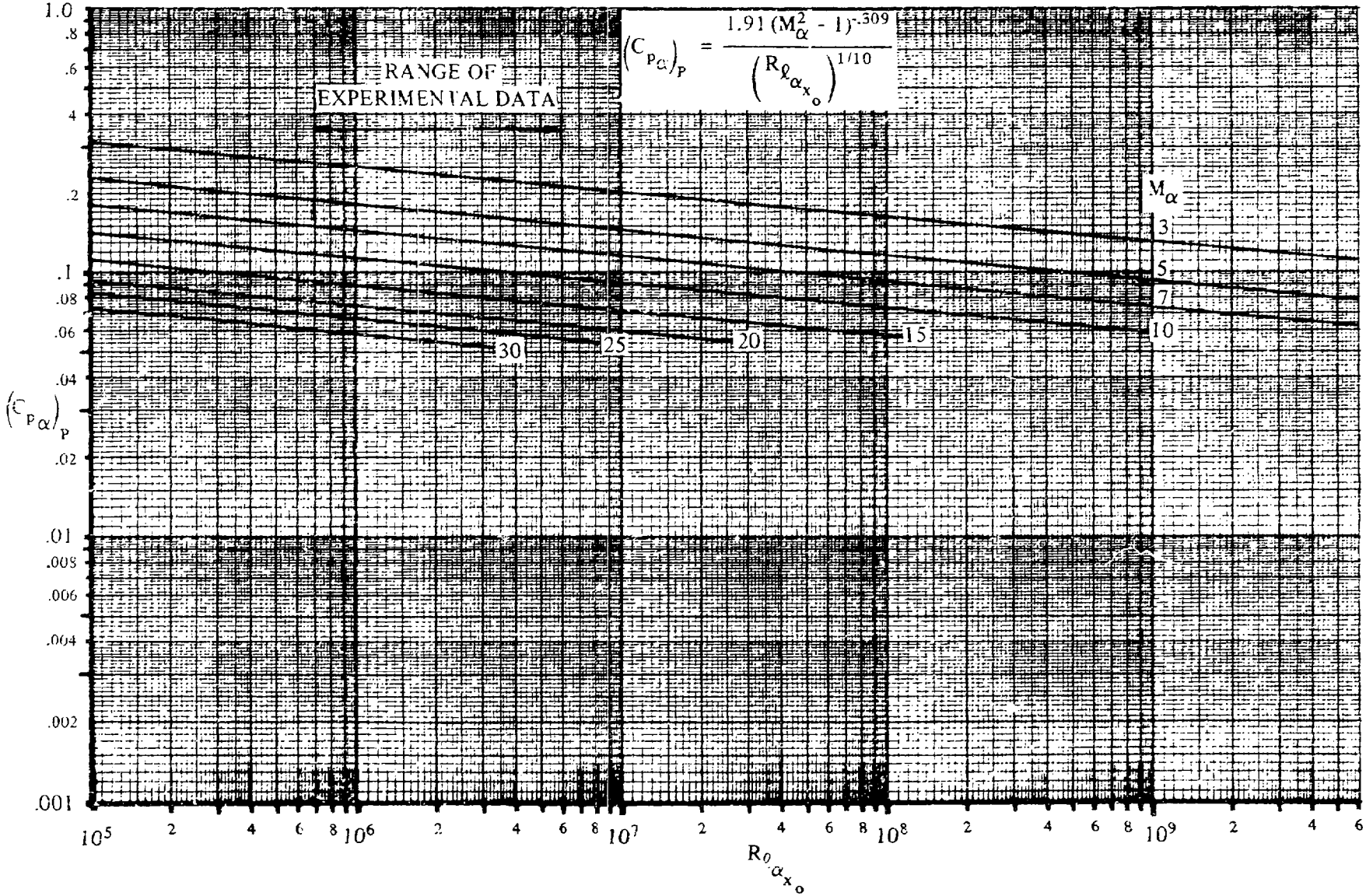

FIGURE 6.3.1 -60 TURBULENT PLATEAU-PRESSURE COEFFICIENT

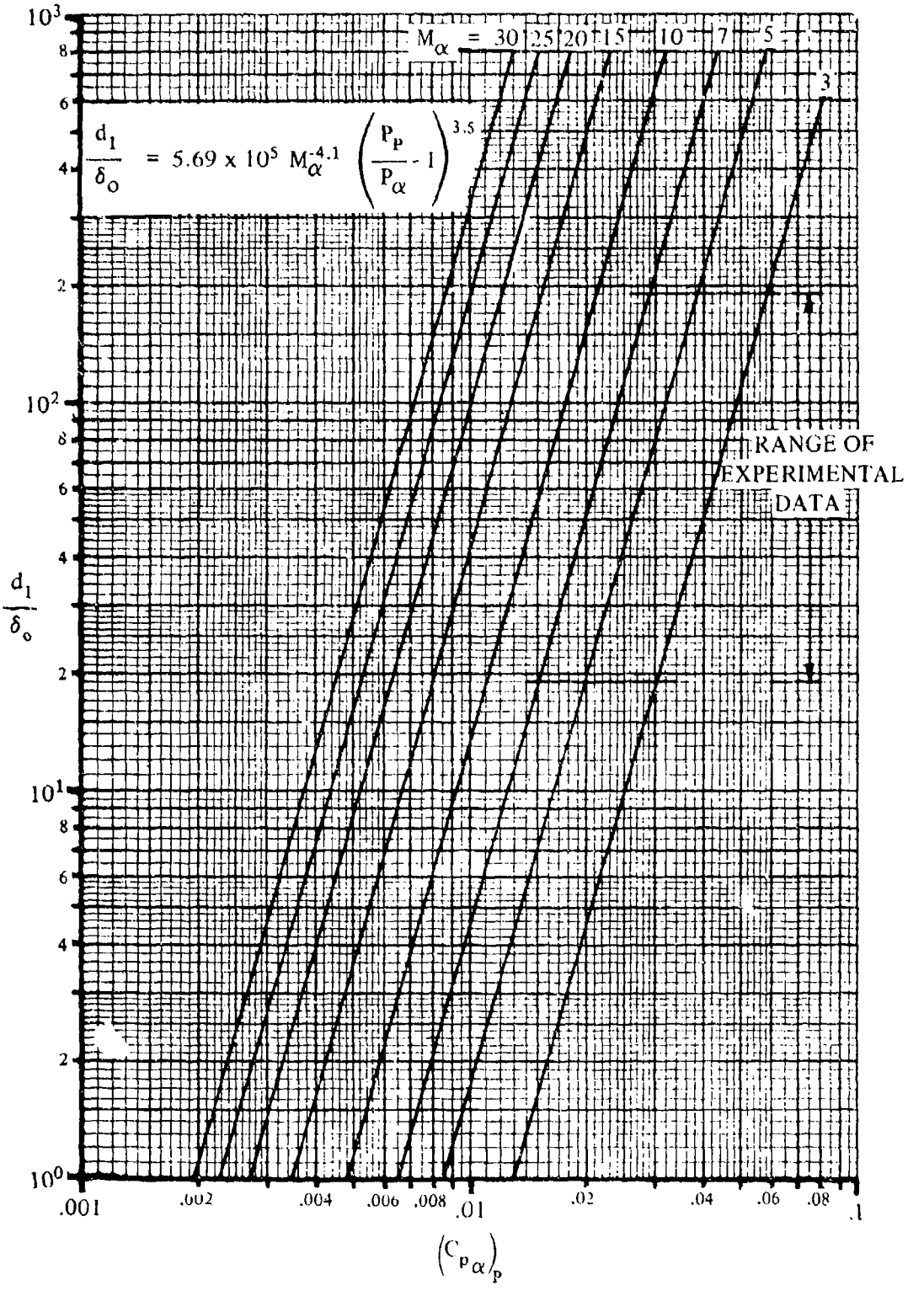

FIGURE 6.3.1-61 UPSTREAM INTERACTION DISTANCE FOR LAMINAR FLOW

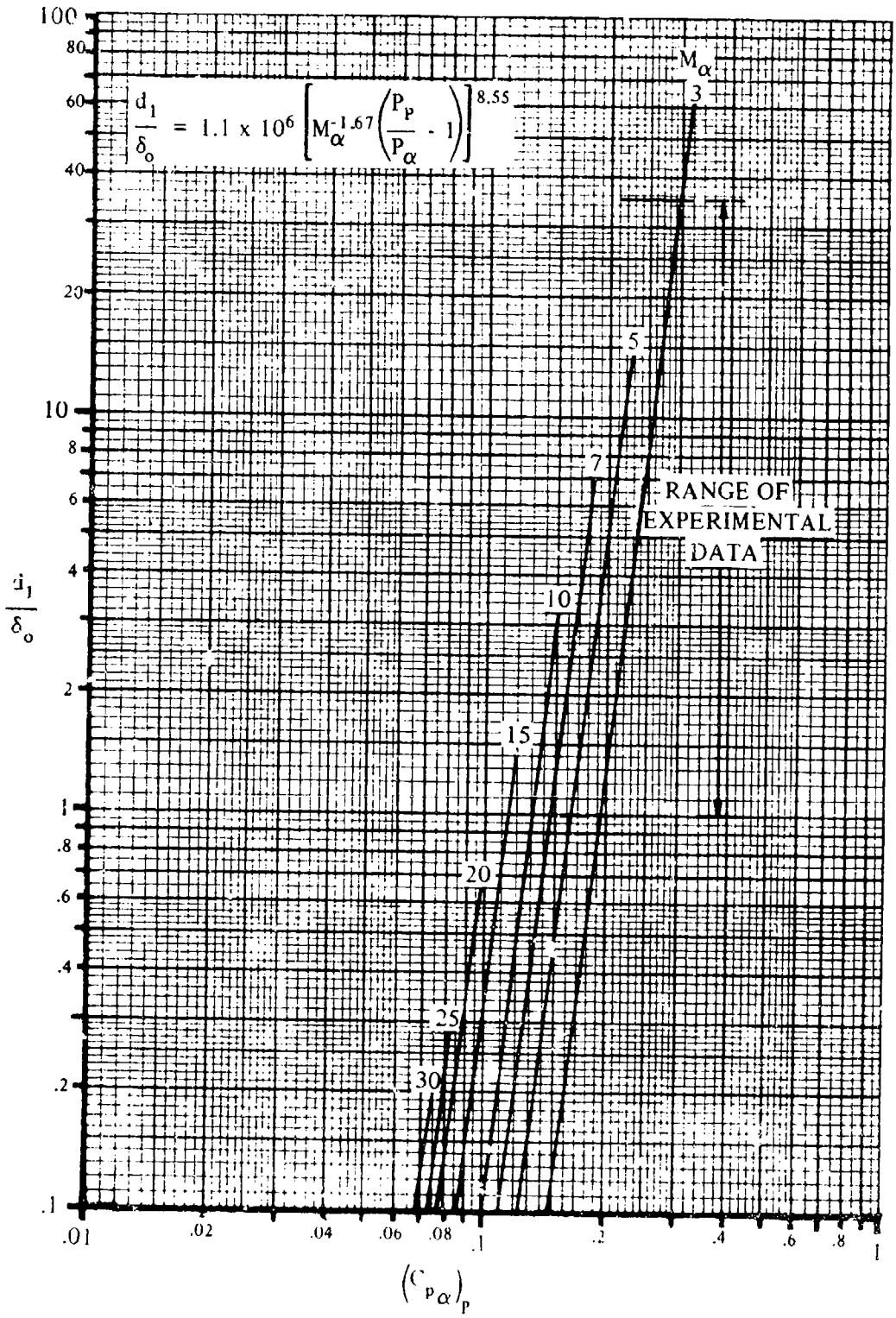

FIGURE 6.3.1 -62 UPSTREAM INTERACTION DISTANCE FOR TURBULENT FLOW

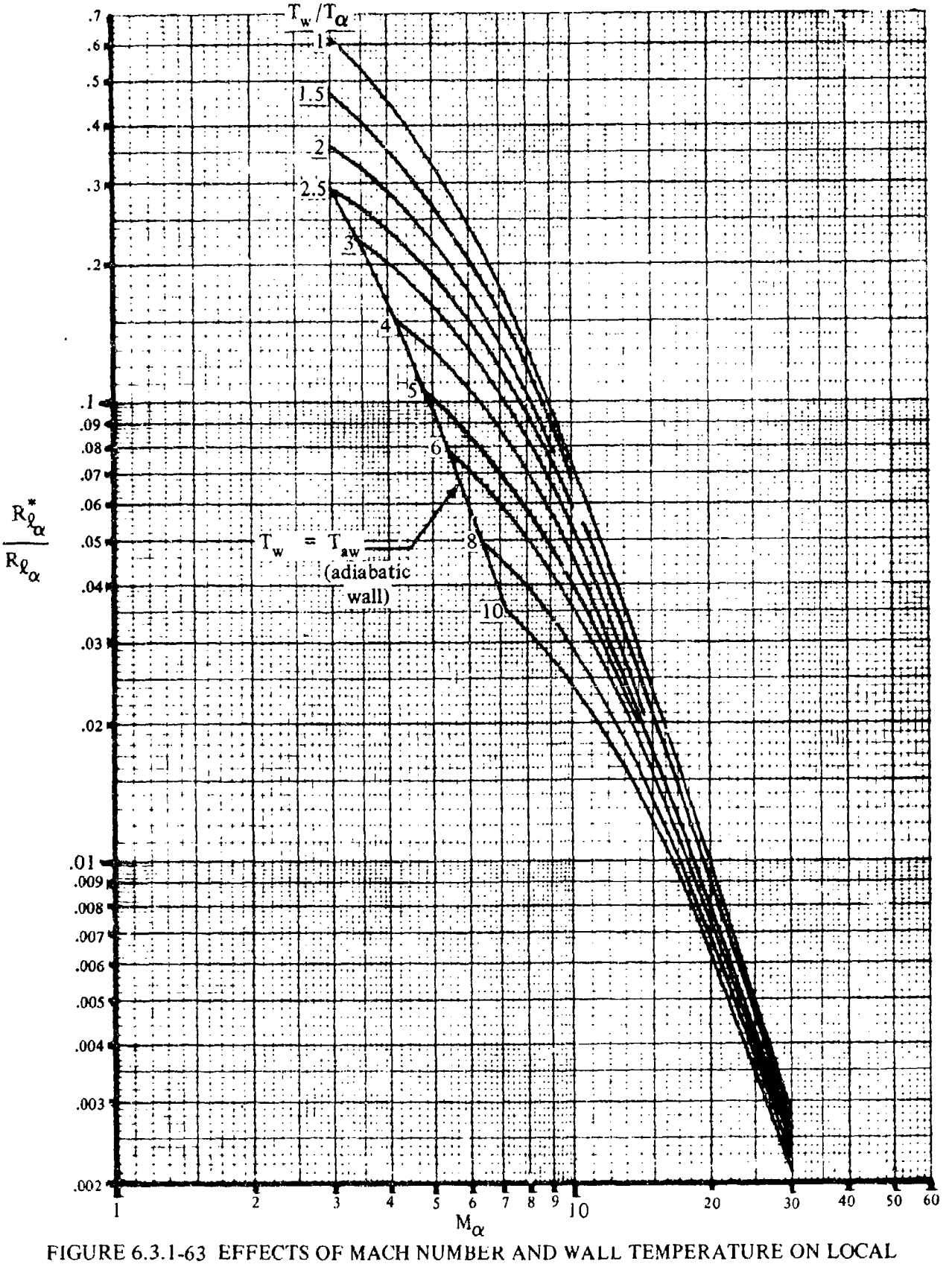

FIGURE 6.3.1-63 EFFECTS OF MACH NUMBER AND WALL TEMPERATURE ON LOCAL REFERENCE TEMPERATURE REYNOLDS-NUMBER RATIO (LAMINAR)

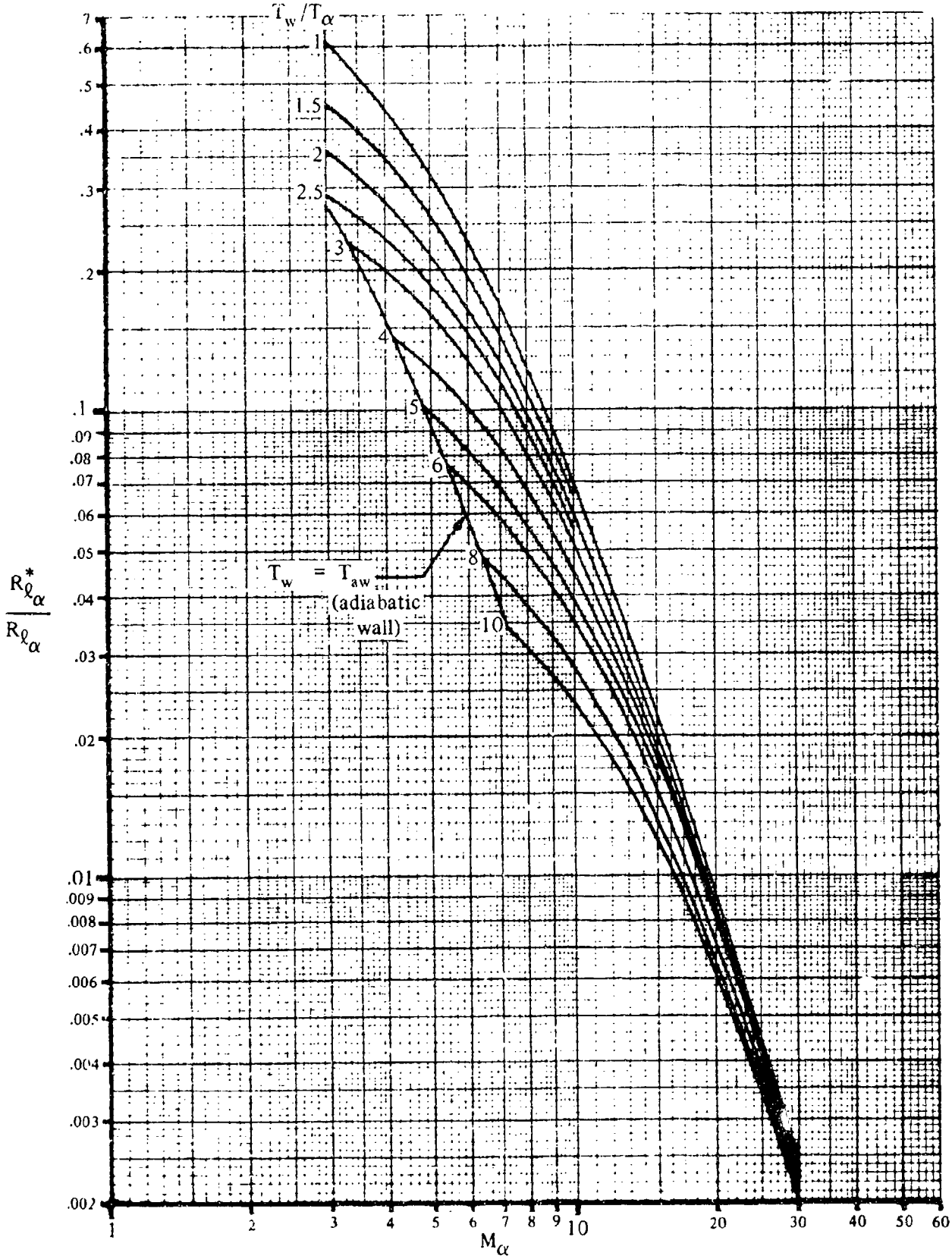

FIGURE 6.3.1-64. EFFECTS OF MACH NUMBER AND WALL TEMPERATURE ON LOCAL REFERENCE TEMPERATURE REYNOLDS-NUMBER RATIO (TURBULENT)

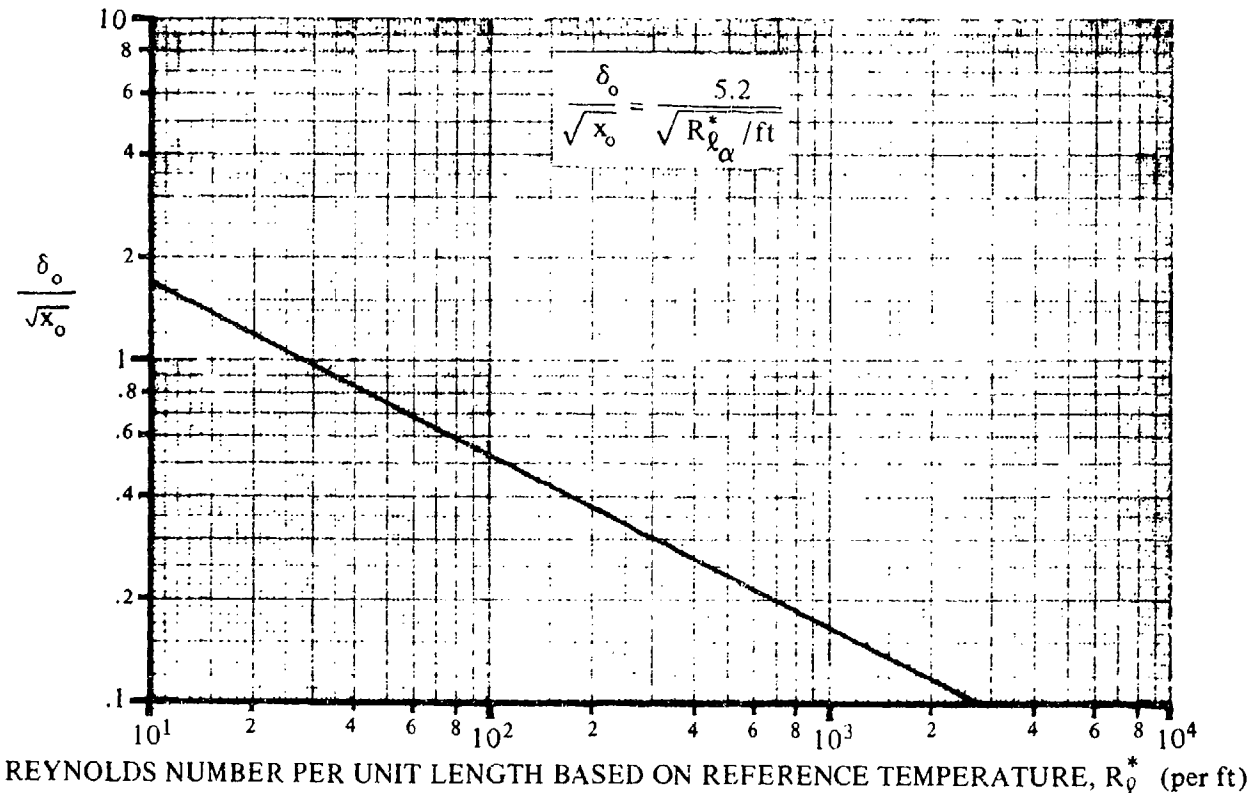

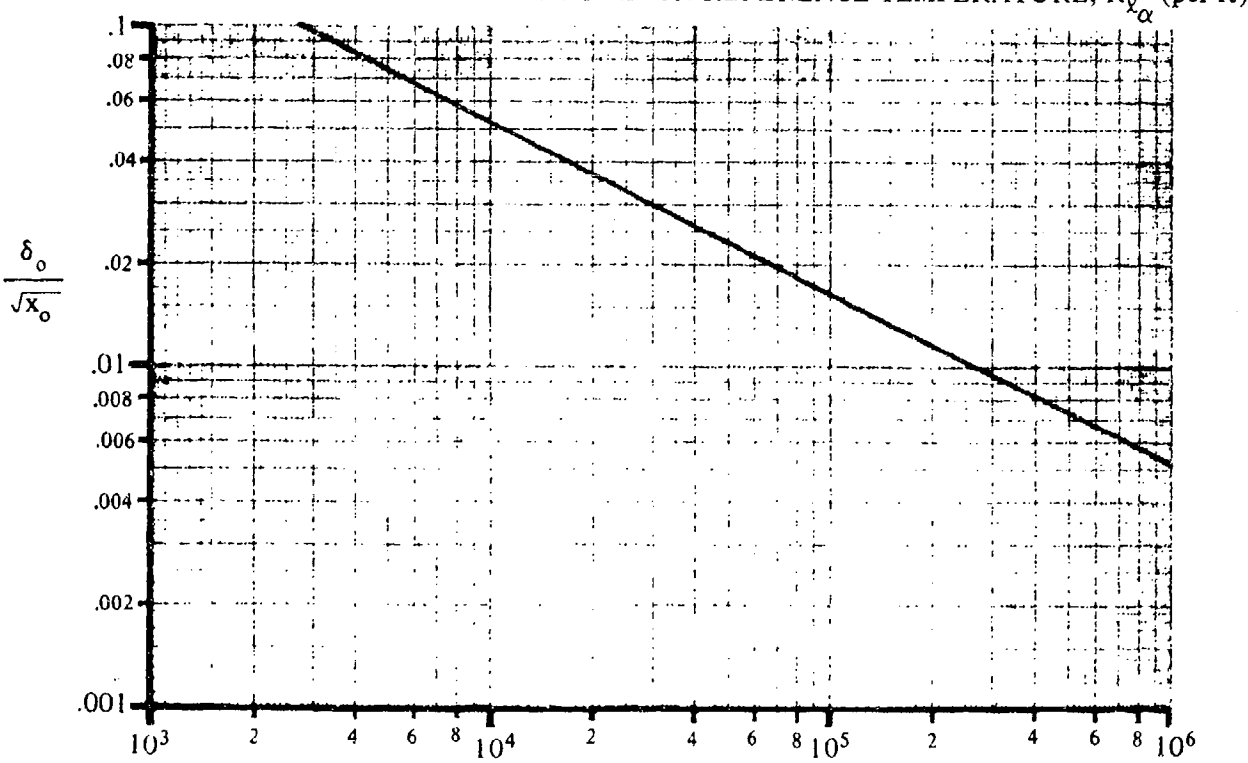

FIGURE 6.3.1-65 LAMINAR BOUNDARY-LAYER THICKNESS

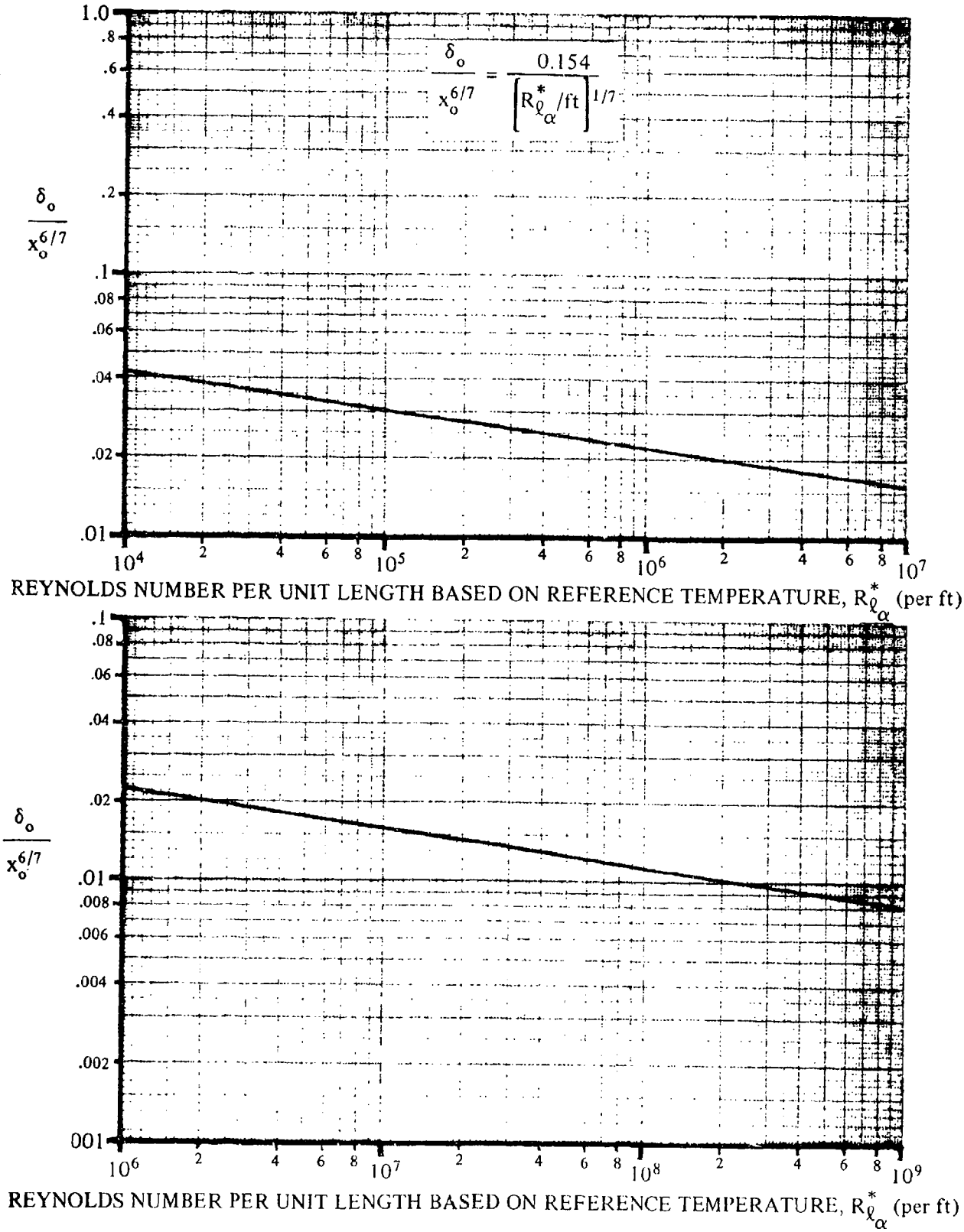

FIGURE 6.3.1-66. TURBULENT BOUNDARY LAYER THICKNESS

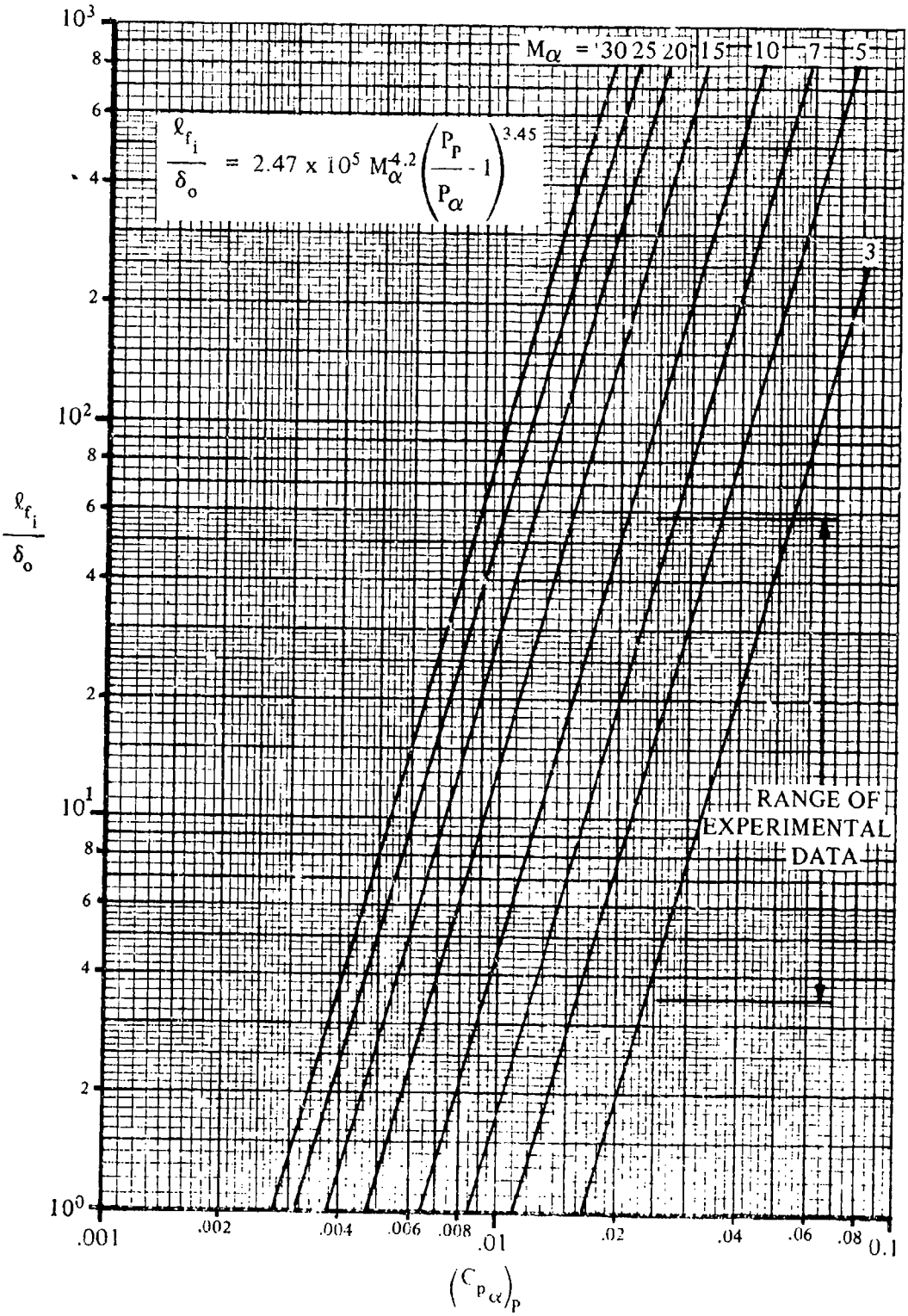

FIGURE 6.3.1-67 FREE INTERACTION LENGTH FOR LAMINAR FLOW

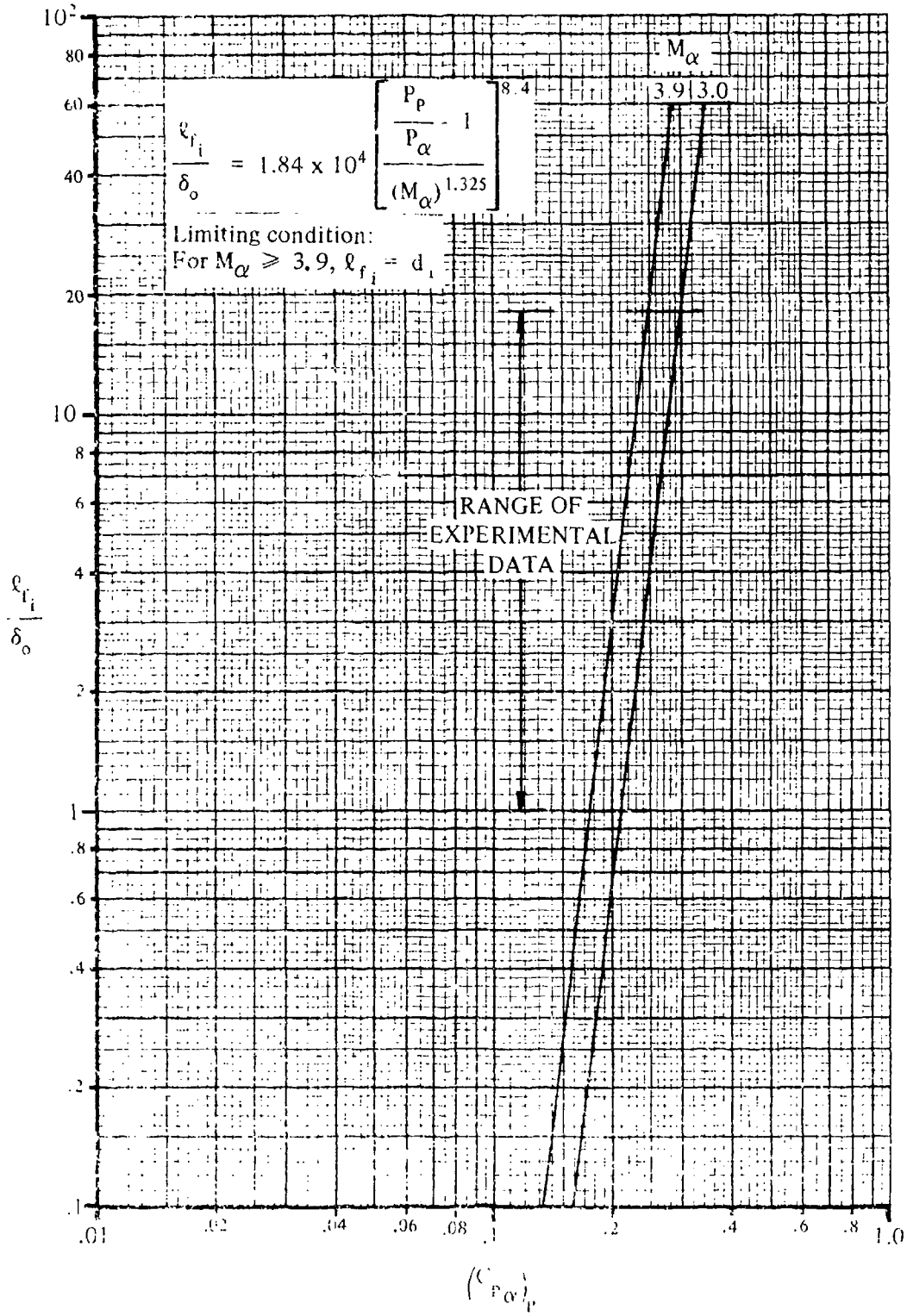

FIGURE 6.3.1-68 FREE INTERACTION LENGTH FOR TURBULENT FLOW

Limiting conditions:

1. If $\frac{c_f}{d_1} \geq 1$, then $\frac{d_2}{\sqrt{c_f d_1}} = \frac{d_2}{d_1}$

2. If $\frac{c_f}{d_1} \leq 0.25$, then $\frac{d_2}{\sqrt{c_f d_1}} = 2\frac{d_2}{d_1}$

(c_f = flap chord)

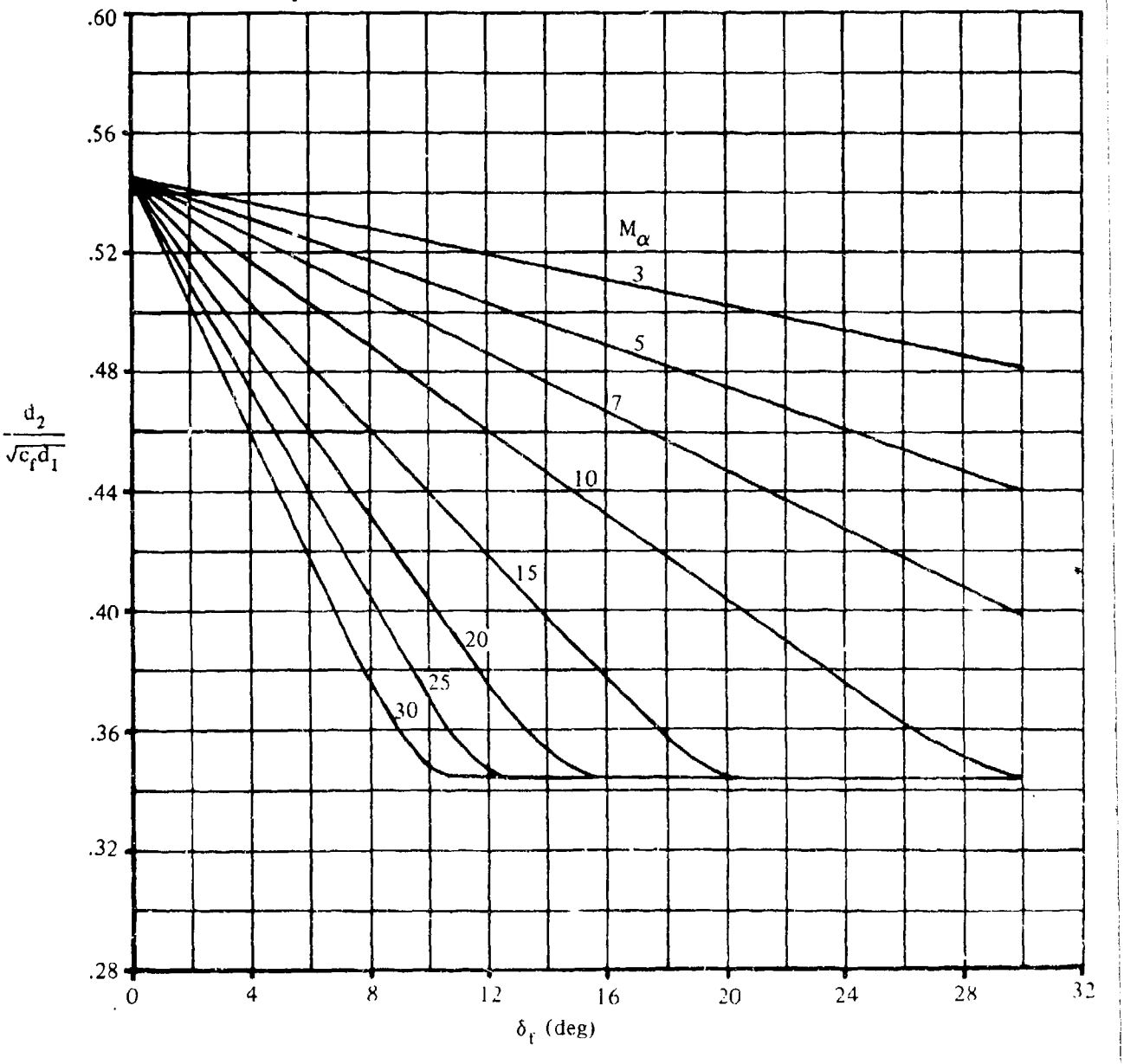

FIGURE 6.3.1-69 DOWNSTREAM INTERACTION DISTANCE TO PEAK PRESSURE ON FLAP FOR LAMINAR FLOW

Limiting conditions

1. If $\frac{c_f}{d_1} \geq 1$, then $\frac{d_2}{\sqrt{c_f d_1}} = \frac{d_2}{d_1}$

2. If $\frac{c_f}{d_1} \leq 0.25$, then $\frac{d_2}{\sqrt{c_f d_1}} = 2\frac{d_2}{d_1}$

(c_f = flap chord)

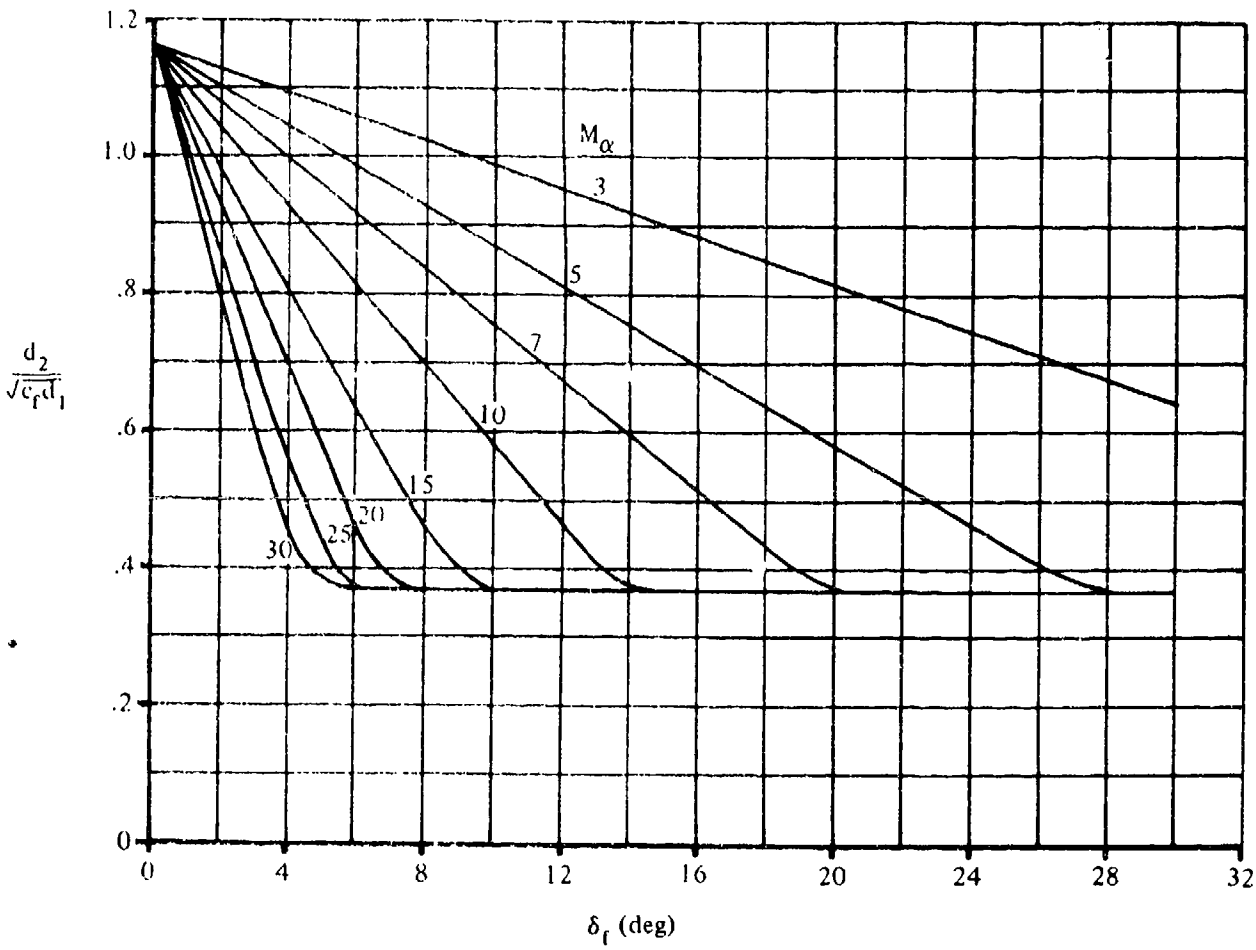

FIGURE 6.3.1-70 DOWNSTREAM INTERACTION DISTANCE TO PEAK PRESSURE ON FLAP FOR TURBULENT FLOW

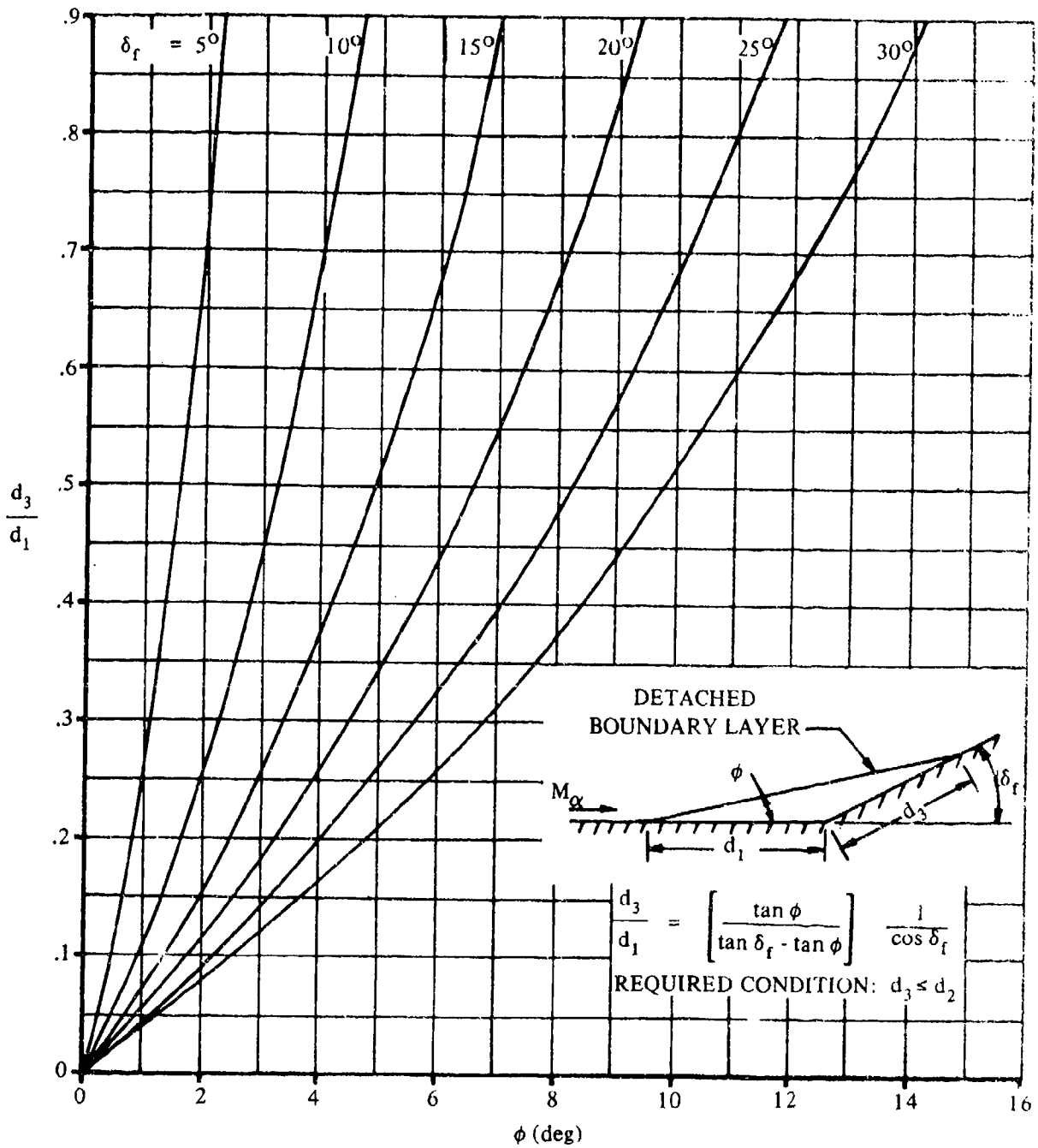

FIGURE 6.3.1-71 DOWNSTREAM INTERACTION DISTANCE TO PRESSURE RISE ON FLAP FOR LAMINAR FLOW

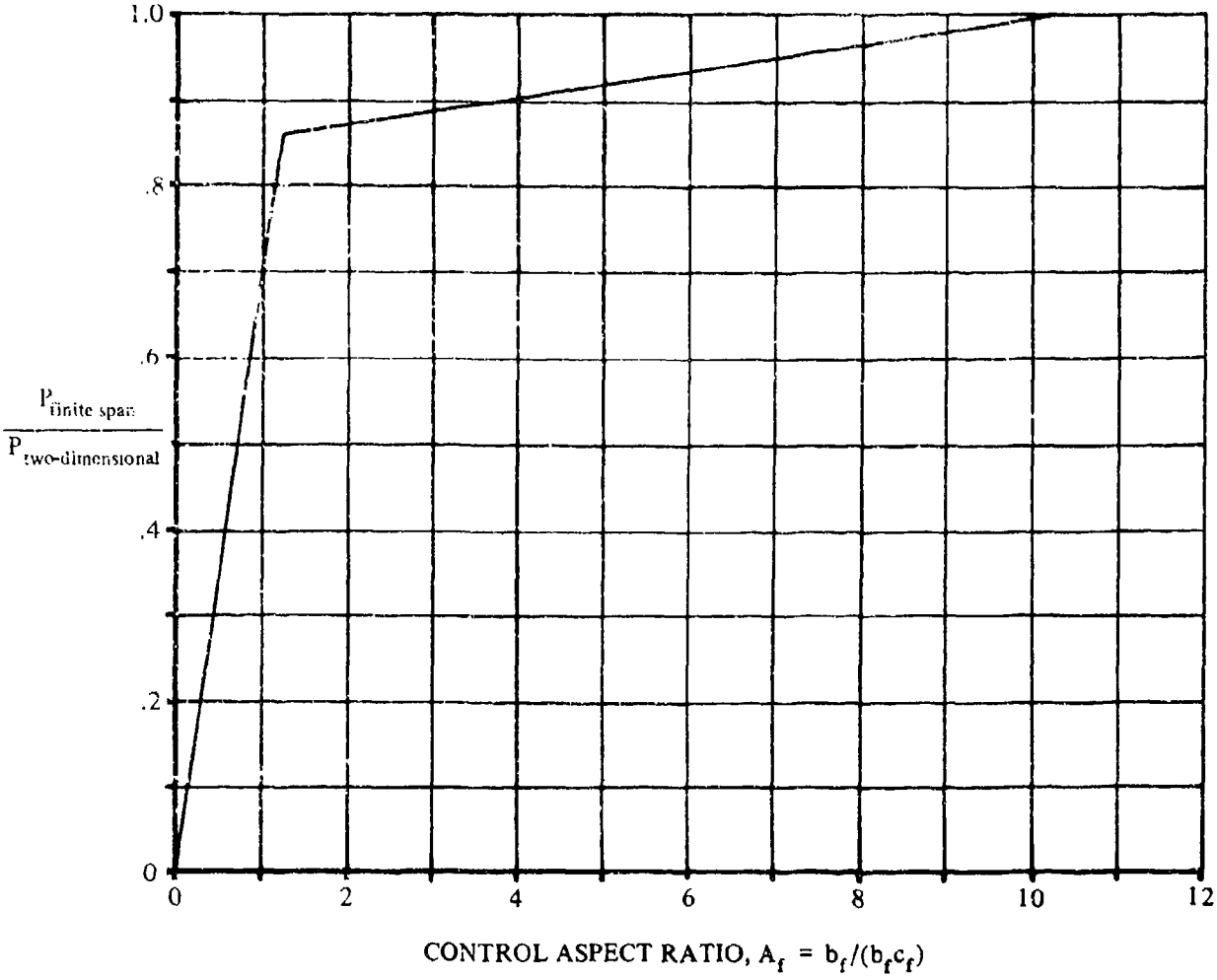

FIGURE 6.3.1-72 EFFECT OF FINITE CONTROL SPAN ON THE TWO-DIMENSIONAL PRESSURE DISTRIBUTION IN THE SEPARATED-FLOW REGION

6.3.2 TRANSVERSE-JET CONTROL EFFECTIVENESS

The interest in evaluating the feasibility of using transverse-jet control systems on high-speed flight vehicles within the atmosphere has created the need for establishing preliminary-design methods for predicting transverse-jet control effectiveness.

This section presents a procedure, taken from reference 1, for sizing a two-dimensional transverse-jet control system in hypersonic flow.

A transverse-jet control system is a control system that uses one or more jets as spoilers. Flow separation generally limits the use of conventional flap-type systems; however, it serves as the basic phenomenon in achieving an effective transverse-jet control system. The jet spoiler creates flow separation in the region surrounding the jet by forcing the primary flow to turn around the obstruction created by the jet exhaust. Transverse-jet control systems are often referred to as jet-interaction control systems to emphasize the important contribution provided by the jet-interaction phenomenon.

Transverse-jet control systems consist of a variety of different types and sizes of thrust units mounted on aerodynamic surfaces. The thrust can be provided by solid or liquid propellant rocket engines or bleed-thrust control units. These thrust units may be large single units or a group of small units strategically located.

In analyzing the performance of transverse jets, several theories have been developed that provide estimates of the principal parameters upstream and downstream of the nozzle. However, the complexity of the interaction has prevented obtaining a detailed physical description of the flow field. This has restricted investigators to limiting the scope of their analyses until fundamentals of the flow have been firmly established. Thus, the Datcom method presented herein is subject to limitations. The primary restriction limits analyses to two-dimensional nozzles. Considerable effort (references 2, 3, 4, and 5) has been directed towards analyzing the three-dimensional problem; however, no acceptable design methods are currently available. The other limiting condition pertains to the pressure forces downstream of the nozzle exit. Because of the conflicting theories regarding the merits of the downstream forces, all nozzles are assumed to be located at the aft end of their respective surfaces. Thus, no consideration is given to possible aft-end forces in the Datcom method; however, they are considered in the discussion of interaction forces.

The advantages (reference 6) of transverse jets in high-speed flow in comparison with conventional aerodynamic control systems have provided the impetus for investigating the possible implementation of transverse-jet control systems. The primary advantage is the possibility of achieving control forces greater than the impulse provided by the jet reaction. This increased force or amplification is due to the favorable interaction of the transverse jet with the local stream flow. The jet interaction substantially alters the surface pressure distribution and results in large additional surface loads, which augment the simple reaction force of the jet. Experimental tests have indicated that properly designed systems can achieve interaction forces that exceed the reaction jet force by factors of four or five.

A second advan age is the possible reduced control response time for transverse jets in comparison to conventional systems. This reduced response time enables the vehicle to be designed with less static stability. A potential increase in reliability provides a third advantage, since redundance is more readily achieved with a less severe weight penalty than for conventional systems and because rocket technology is felt to be more advanced than the technology involved in building high-speed actuators and the integral components required to operate in an extreme temperature environment. Another benefit is the wide range of flight conditions in which transverse jets can provide control forces, as compared with the limited envelope for conventional systems. Improvements are also derived from the elimination of structural problems associated with control surfaces and related heat-transfer problems prevalent in hypersonic flow.

Inherent with transverse jets are many problems and disadvantages which must be solved or accounted for before successful implementation can be achieved. The most crucial problem is the lack of a thorough knowledge involving the jet-interaction process. This prevents formulating a completely reliable prediction technique. Distinct disadvantages are the weight penalties imposed by the propulsion system and the limited quantity of propellant available for a given mission. Associated problems are also encountered in the growth potential when mission requirements change.

An evaluation and design comparison of transverse-jet controls and conventional aerodynamic control systems are presented in reference 6. The conclusions of the report are: (1) high L/D re-entry vehicles with the vehicle trimmed to maximum L/D are favorable to transverse-jet control systems, if trajectory control by roll control is used; (2) if a winged re-entry vehicle is to be maneuvered in pitch to angles appreciably different from the angle of attack required for maximum L/D, conventional flap-type aerodynamic controls are preferable. Additional comparisons regarding transverse jets, solid spoilers, and flap deflections can be found in references 6 and 7.

In order that the Datcom user may better understand the control-effectiveness methods presented in this section, a general discussion of hypersonic-flow separation and the effect of the jet-interaction phenomena upon augmenting the control force is presented. This general discussion is essentailly quoted from Section 6.3.1 of the Datcom and from reference 1. A more detailed description of hypersonic-flow separation and jet-interaction phenomena can be found in references 1, 2, 3, 4, and 8. A summary of the literature pertaining to transverse jets can be found in reference 9. A summation of the contents of each document is given, along with a qualitative discussion of the data and/or theory presented.

Hypersonic-Flow Separation

Separated flows are characterized by the prevailing type of boundary layer: laminar, turbulent, or transitional. The pressure rise and the extent of the separated region depend upon the characteristics of the boundary layer.

In general, boundary-layer separation occurs whenever the streamwise pressure increase along a surface is sufficient to overcome the forces acting to accelerate a fluid particle, or when the streamline curvature necessary to follow the surface contour cannot be sustained by the pressure gradient normal to the surface. In steady-flow aerodynamics the only forces acting to accelerate the low-momentum fluid near the wall against a pressure gradient are the shear forces between

layers of fluid. Because the momentum of the fluid near the wall is quite low, a relatively small amount of deceleration by the pressure gradient is sufficient to bring about separation. Turbulent flow helps to delay the occurrence of separation, because the turbulent fluctuations increase the effective shear forces and thereby increase the adverse pressure force necessary to reverse the flow of the fluid near the wall.

The greatly increased effective viscosity due to turbulent fluctuations enables the equilibrium between pressure and shear forces near the wall to occur at much greater adverse pressure rises in a turbulent boundary layer. Because of the connection between pressure rise and flow turning angle, this higher pressure corresponds to a much shorter, thicker separated zone for the same initial boundary-layer thickness. Cases presented by Schlichting (reference 10) and Howarth (reference 11) show turbulent pressure rises twice the laminar ones; whereas the laminar separation zone extends much farther than the turbulent one.

A similar thickening (and simultaneous pressure rise) occurs in a transitional separation when the mixing zone becomes turbulent and the downstream flow soon approaches a condition very similar to the equivalent turbulent separation. Upstream of the transition point, the flow has the character of the corresponding laminar separation zone. The location of the transition point therefore plays a significant role in determining the pressure distribution (see references 12 and 13).

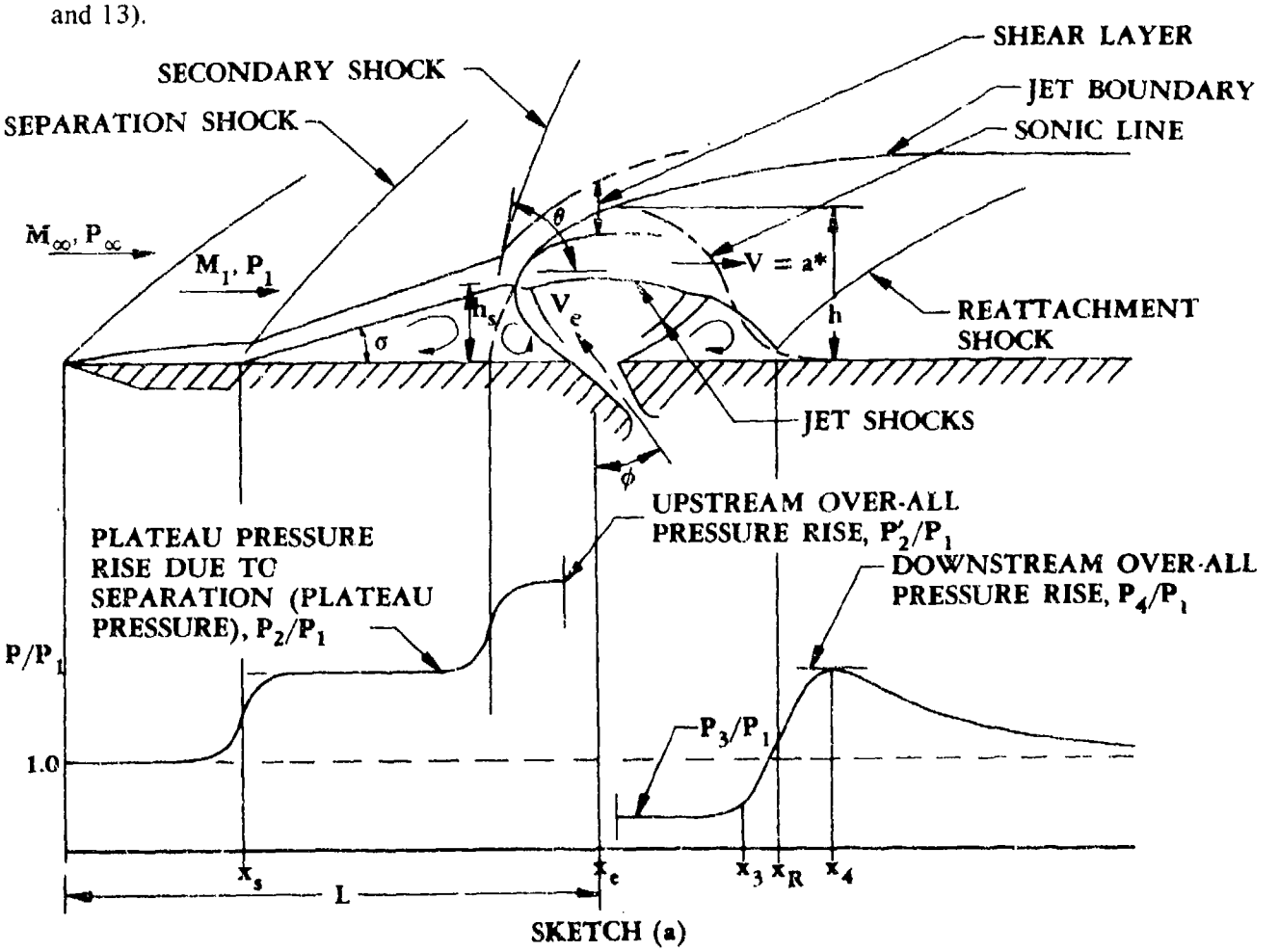

SKETCH (a)

JET INTERACTION FLOW MODEL FOR LAMINAR SEPARATION

Present indications are that shock-induced laminar-separation pressure distributions, and to a limited extent turbulent ones, are independent of the type of disturbing force that produces separation (see reference 12). However, the turbulent peak pressure rise often depends significantly on the disturbing force (references 12 and 14 through 17). This difference in dependence can probably be attributed to the greatly increased effective viscosity in turbulent flow, enabling the wall contour within the separated zone to transmit its effect more strongly to the outer flow.

Typical jet-interaction flow fields for laminar and turbulent boundary layers are presented in sketches (a) and (b), respectively (reference 1).

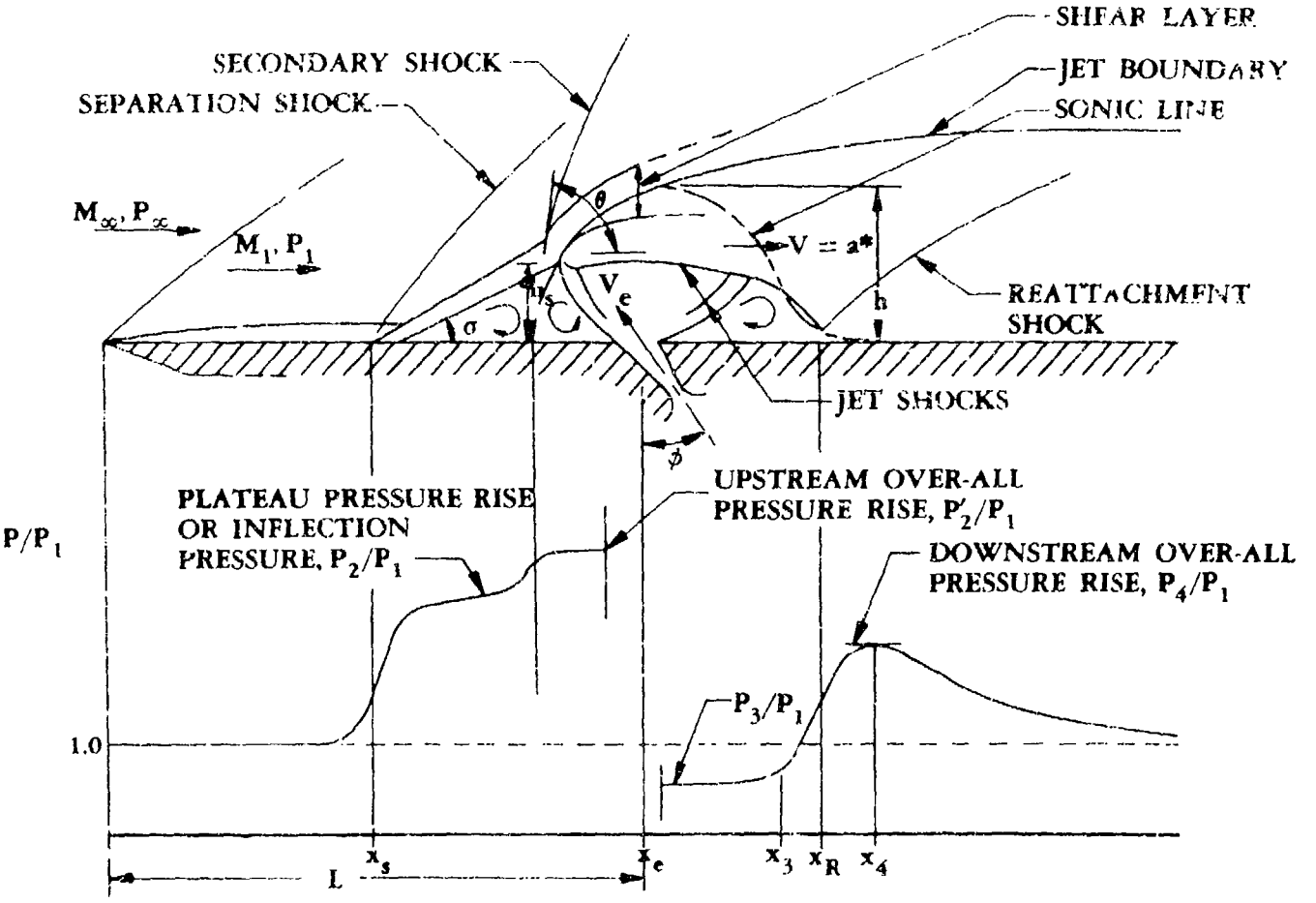

SKETCH (b)

JET INTERACTION FLOW MODEL FOR TURBULENT SEPARATION

For the upstream region, laminar boundary-layer separation has a characteristic plateau where the pressure remains almost constant over most of the separated flow region. The plateau pressure level depends only on local flow conditions at the location of the separation point (see reference 12). The upstream turbulent boundary-layer-separation pressure distribution is not characterized by a long pressure plateau region as in the case of laminar separation. Instead, the turbulent separation produces an increasing pressure gradient that exhibits an inflection point or a very

short plateau pressure, which appears to be dependent only upon the Mach number. Although some discrepancies exist in the literature (references 1, 4, and 18) regarding upstream pressure trends with boundary-layer condition, the majority of the later references indicate that larger upstream forces are exhibited for laminar separated boundary layers. These larger forces can be attributed to the integrated loads for the longer, lower pressure regions of laminar flow, being larger than those for the shorter, higher pressure regions of turbulent flow.

The problem of locating the boundary-layer transition point is one that has received wide-spread attention from theoreticians and experimentalists. However, no universally applicable prediction technique has been obtained. The best approach for predicting the transition point is to examine wind-tunnel data that most nearly approximate the actual flow conditions. Techniques for correlating the transition data from various sources are available. Reference 19 presents one such technique for correlating data for cone-shaped configurations. In the absence of similar wind-tunnel data, the method presented in the Datcom can serve as an approximate estimation for determining the state of the boundary layer or transition point.

Jet-Interaction Phenomena

The most prominent feature of jet-interaction phenomena is the formation of a strong jet shock that is nearly normal to the jet flow direction, resulting in a recompression and subsonic flow on the downstream side of the nozzle. Reference 8 indicates that because the injected stream must be turned by the primary flow, it acts as an obstruction, and as such, produces a strong shock in the primary flow. This shock interacts with the boundary layer on the wall and causes it to separate. Both the initial shock and the resulting boundary-layer separation produce a region of high pressure near the point of injection. This is the source of the interaction force that augments the simple reaction force of the jet.

Kaufman, in reference 20, describes the interaction pressure downstream of the nozzle as characteristically having a low-pressure region followed by a pressure rise to the reattachment value. At reattachment, the pressure can be either larger or smaller than the undisturbed free-stream pressure. Downstream of reattachment, the pressure approaches its undisturbed value asymptotically.

The low-pressure region downstream of the nozzle can have an adverse effect on the interaction force if the nozzle is not located at the aft end. However, the increasing pressure at reattachment can in some cases predominate, yielding a favorable force if the aft end of the surface is of sufficient length to capture the major portion of the positive pressure region.

The reattachment of the boundary layer downstream of the jet is not well understood. Experiments have indicated a pressure rise similar to that at separation, with the gradient at reattachment usually being in excess of that at separation.

The downstream pressure distributions have frequently been compared to pressure distributions behind rearward-facing steps. These pressure distributions have been estimated by using various base-flow analyses. As indicated by Kaufman (reference 20), determining the proper start conditions for the base-flow models has been difficult. This is due to the existence of large gradients in the flow and no detailed flow-field measurements in this region to guide the

selection of the proper jet-flow conditions to be utilized as the initial conditions in the base-flow analyses.

As stated earlier, the Datcom method does not account for aft-end forces, because all nozzles are assumed to be located at the aft end of their respective surfaces.

Three-Dimensional Effects

Three-dimensional flow fields result from low-aspect-ratio jets located on both flat plates and more complicated bodies. Reference 2 presents a description of the flow field and the relative differences between two- and three-dimensional flow. The more salient aspects are presented here for the reader's benefit.

Three-dimensional effects in the jet-interaction flow field are not well understood quantitatively. This is partly due to the fact that less effort has been devoted to the three-dimensional problem, but more significantly because of the general complexity of three-dimensional flow. The boundary-layer-separation problem alone is not very well understood for three-dimensional flow. Unfortunately, the more significant differences between two- and three-dimensional flow fields are observed to be the extent of the boundary-layer separation and the geometry of the shocks. In contrast to two-dimensional flow, the three-dimensional boundary-layer separation is greatly reduced as a result of the lateral flow component, allowing the boundary layer to bleed off around the sides of the plume. This minimizes the viscous effects and creates a largely inviscid phenomenon.

The most obvious concern with three-dimensional flow is the possible loss in effectiveness due to end effects. However, reference 5 points out that integration of the pressure distribution over a 7-degree cone shows that the normal-force coefficient obtained is the same as the normal-force coefficient per unit span of a two-dimensional jet with the same jet mass flux. This behavior is attributed to a favorable interaction between the cross flow and the main stream, which increases the effective span of the jet. However, this conclusion was based on limited test data and has not been corroborated for various flow conditions.

Unlike a jet on a flat plate, an adverse interaction has been observed to occur frequently on three-dimensional bodies. This is attributed to the effect of "wraparound," i.e., the propagation of the disturbance to the sides or the underside of the body. Much of the interaction force created by three-dimensional nozzles results from the high-pressure region immediately behind the bow shock, which forms a hyperbolic high-pressure ridge on the surface of the body extending out from the region of the nozzle. In addition, the low-pressure region directly downstream of the nozzle, which has an adverse effect on the interaction force, is virtually as effective on a cylindrical body as on a flat plate; therefore, negative interaction forces commonly occur on such vehicles.

Although the existing method of analysis in reference 2 provides fair agreement with experimental data, additional sophistication in the shock-body interaction analysis is contemplated, and improved correlation is expected. References 4, 5, 18, and 21 offer additional information regarding the pressure distributions and jet-interaction phenomena for three-dimensional flow.

Jet-Interaction Control Effectiveness

For obvious reasons it is desirable to obtain the highest possible jet-interaction forces. This leads to the consideration of various nozzle inclination angles. Figure 6.3.2-41 (reference 1) presents the amplification factor versus injection angle for various values of nozzle exit velocities and normal sonic amplification factors. From this figure it can be seen that substantial gains in performance may be achieved by inclining the nozzle upstream, provided that large amplification factors (control force normal to wall normalized with respect to vacuum thrust of sonic nozzle) are realized from a normal sonic nozzle. The reason for this is apparent when it is realized that inclining the nozzle upstream tends to increase the interaction force and to decrease the normal component of thrust. Hence, if only a moderate interaction force is realized for a normal sonic nozzle, then little may be gained by upstream injection because of the loss in the normal component of thrust. However, if injection normal to the wall produces a large interaction force relative to the thrust, then substantial improvement may be realized by inclining the nozzle. Maurer in reference 22 states that the optimum injection angles against the main stream were in the range of $15° < \phi < 45°$

Inherent with obtaining the maximum control-force effectiveness is locating the nozzle to achieve the most desirable pressure distribution. Unfortunately, many discrepancies and questions are found in the literature regarding the contribution of aft-end forces. Pressure distributions downstream of the nozzle can be found in references 1, 8, 20, 23, and 24; to list a few. Barnes (reference 1) found that the aft interaction forces due to a laminar boundary layer are considerably smaller than the forward forces (see sketch (c)). In contrast, he found that for

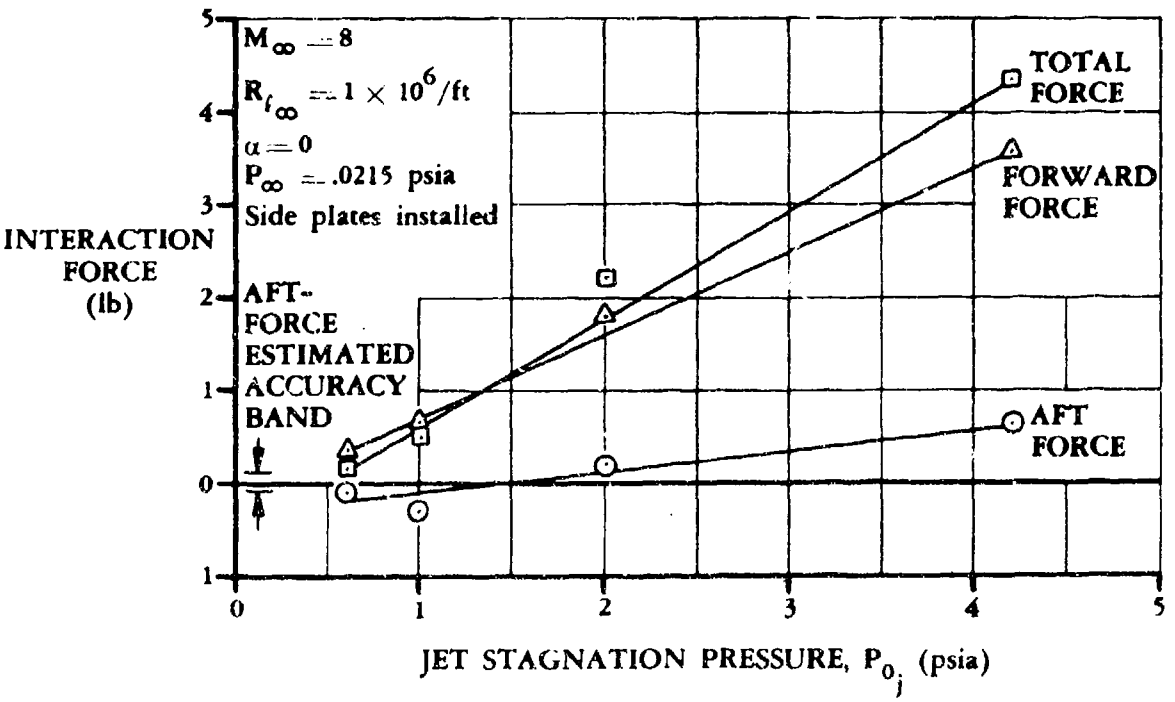

SKETCH (c)

JET INTERACTION FORCES FOR A LAMINAR BOUNDARY LAYER

turbulent flows the aft-end forces added significantly to the total force, as is evident in sketch (d). However, the contribution of downstream forces in turbulent flow was found to decrease rapidly as the mass-flow rate increased. Although these sketches do not hold true for all nozzle configurations and flow conditions, they do indicate the relative contribution available from aft-end forces. Kaufman (reference 20), in addition to corroborating the findings of Barnes, found that the reattachment pressure increased strongly with increasing Mach number. Spaid and Zukoski, in reference 8, indicate a dependence of downstream pressure on Mach number, mass-flow rate, and injectant fluid properties. With helium as an injectant, higher downstream static pressure levels were obtained in comparison with those for nitrogen.

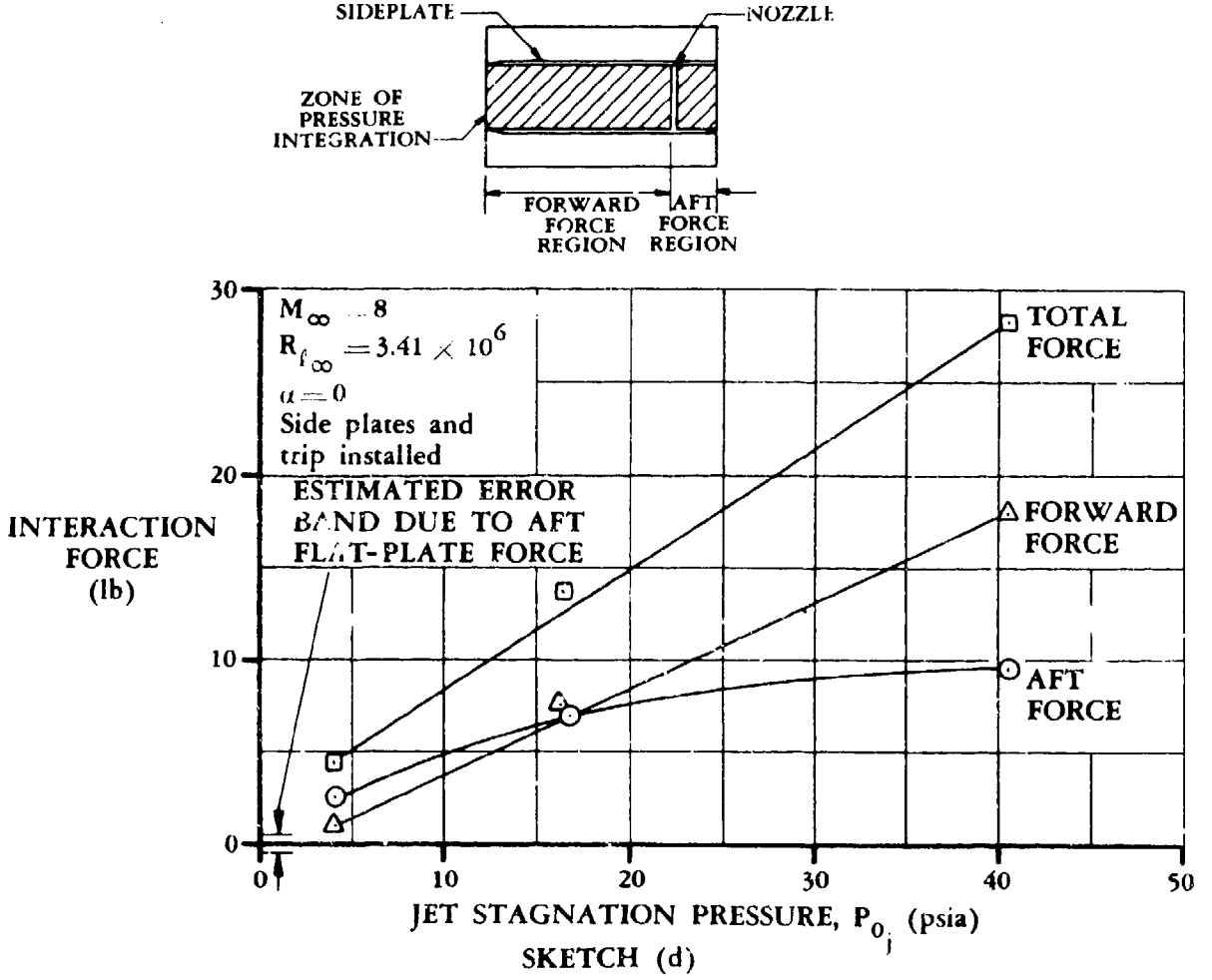

SKETCH (d)

JET INTERACTION FORCES FOR A TURBULENT BOUNDARY LAYER

An iterative method, utilizing experimental data classified according to nozzle aspect ratios (span/width), is presented in reference 20, which predicts upstream and downstream pressure distributions. The results of the method agree qualitatively with experimental data, although more theoretical analyses must be developed before it becomes a reliable predicting technique.

In general, because of the complexity involved in the interaction phenomena, no consistent nozzle angle or location yields the optimum design for the large range of possible applications and environments; each case must be considered separately.

Although the supersonic jet experiences an increase in reaction force over the sonic jet, it also experiences a decrease in the interaction force; it is not obvious which occurrence dominates. The decreased interaction force is a result of a lower pressure at the exit for a supersonic jet. This prevents the jet from expanding into a full plume upon leaving the nozzle, consequently the interaction force decreases. An example of the relative effect of nozzle exit velocity on surface pressure is shown in sketch (e), from reference 1. The Datcom method predicts improved performance by obtaining supersonic velocities at the nozzle exit. Although experimental data indicate that supersonic nozzles exhausting normal to a wall produce virtually no change in control force, the Datcom method predicts a moderate gain. Experiments show that a beneficial effect occurs principally at positive upstream injection angles.

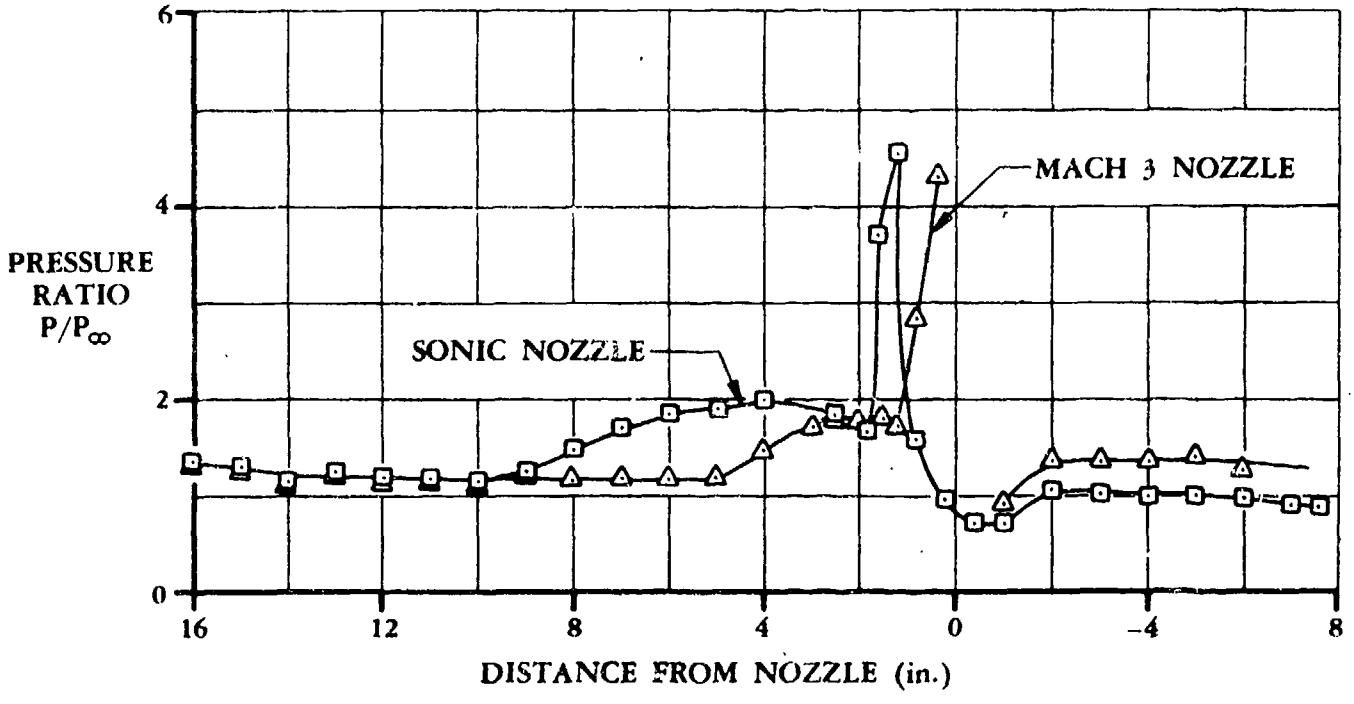

SKETCH (e)

COMPARISON OF NORMAL SONIC AND NORMAL MACH 3 CIRCULAR NOZZLE CENTER-LINE PRESSURE DISTRIBUTIONS

Experimental data show that jet-flow parameters are dominating factors in the jet-interaction phenomena. The more prominent features of the flow are determined by the strength of the jet. For very weak jets (jets with very low pressure ratios (P_{0_j}/P_1)), the jet behavior has been described by Kaufman in reference 20 as similar to film cooling of the surface. There are no separated flow regions, and boundary-layer analysis can describe the resulting flow. In reference 25, Kaufman considers weak jets and focuses his work on the downstream pressure distributions.

Because the Datcom method applies only to strong jets (jets sufficient to induce separation of the boundary layer), it is pertinent to ascertain if separation exists. Available data are not conclusive, but it appears that the minimum nozzle exit pressure P_e to achieve separation must be of the order of twice the plateau pressure P_2 in the separated boundary layer. Turbulent

flow yields a higher plateau pressure, hence it is the determining condition for establishing a minimum jet-strength requirement. The minimum jet-pressure ratio (P_{0_j}/P_1) required to induce separation is presented in figure 6.3.2-43 (reference 1). At pressure ratios substantially below those in figure 6.3.2-43, the Datcom method is probably not valid.

When pressure ratios are above the minimum required, some discrepancy exists in the literature regarding the effect on the amplification factor. Werle in reference 26 concludes that a slight loss in effectiveness is displayed as P_{0_j}/P_1 approaches infinity, while Barnes in reference 1 indicates virtually no change in amplification factor. Reference 20 contains a summary of available jet-interaction data wherein pertinent flow parameters along with the various slot geometries are tabulated.

The Datcom method does not explicitly account for variations in angle of attack. These changes in angle of attack must be accounted for in evaluating local flow conditions and the state of the boundary layer. At high angles of attack, with the jet on the leeward side, caution must be used. The flow will begin to separate, and the jet will essentially be exhausting into a dead-air region that results in the interaction force decreasing to zero. Pressure distributions for small variations in angle of attack can be found in references 1 and 20 for flat plates, and in reference 3 for an ogive-cylinder.

Several methods for modulating the control force have been suggested. The more pragmatic methods are: pulsing the jet with a constant jet pressure with a pulse duration proportional to the impulse required, using multiple nozzles which are individually actuated, varying the jet plenum pressure, and combinations of these.

The Datcom equations describing the upstream jet interaction have been obtained from a momentum balance method. Several other techniques have been used by investigators in their attempts to establish the most complete and reliable prediction scheme. Blast-wave analogy has been used in references 2 and 27. Other investigators (references 5 and 28) employ finite difference techniques in conjunction with various methods in an attempt to describe the flow field.

NOTATION

SYMBOL	DEFINITION
a	speed of sound
b	span of slot nozzle (normal to flow direction)
c	nozzle discharge coefficient
C_{f_0}	vacuum-thrust coefficient
C_{F_c}	control-force coefficient
C_p	pressure coefficient, $C_p = (P - P_1)/q_1$

SYMBOL	DEFINITION
C_x	drag coefficient
d_e	width of nozzle exit in the flow direction
d_{LE}	diameter of surface leading edge
d_t	width of nozzle throat
F_c	control force
F_{j_0}	vacuum thrust
h	maximum height of sonic line above surface (effective jet height)
h_s	maximum height of separated boundary layer above the surface
I_{sp}	jet vacuum specific impulse
K	upstream amplification factor (control force normal to the surface normalized with respect to vacuum thrust of sonic nozzle)
K_o	upstream amplification factor of normal sonic nozzle
L	distance of nozzle from plate leading edge
M	Mach number
$\dot{m}$	nozzle mass-flow rate
P	pressure
P_{0_j}	jet plenum pressure
q	dynamic pressure, $q = \rho V^2/2$
R_{ℓ_L}	Reynold number based on length L (dimensionless)
R_{ℓ_s}	Reynolds number based on the distance to the separation point (dimensionless)
R_{ℓ_∞}	unit Reynolds number based on free-stream conditions
SF	safety factor

SYMBOL	DEFINITION
V	velocity
x_{cp}	center-of-pressure location measured relative to leading edge
α	angle of attack (positive with jet on lee side of model)
γ	specific-heat ratio of jet gases
θ	angle of secondary shock
λ	mean free path (average distance traveled between molecular collisions)
ξ	pressure ratio across secondary shock
ρ	density
σ	boundary-layer separation angle
ϕ	inclination of nozzle center line relative to an axis normal to surface

SUBSCRIPTS

cr	corrected
e	nozzle-exit conditions
max	maximum value
min	minimum value
R	reattachment conditions
s	separation conditions
t	throat conditions
trim	trim condition
1	ambient conditions on plate in the absence of a jet
2	conditions in the region of the separated boundary layer
2′	conditions at the second peak pressure in the separated boundary layer
3	conditions in the separated region just before the reattachment shock
4	conditions in the region corresponding to the peak downstream pressure after the reattachment shock

SYMBOL	DEFINITION
∞	undisturbed free-stream conditions
	SUPERSCRIPT
*	sonic conditions

DATCOM METHOD

A method for sizing a two-dimensional transverse-jet control system, modulated by varying the jet plenum pressure, is presented in the following procedure. This method is based on a continuum concept and is valid in the Mach number range of 2 to 20. When the mean free path of the surrounding flow λ approaches 0.1 of the jet width d_t, the method begins to break down. The method is completely invalid when the mean free path equals the jet width. The method is invalid because of angle-of-attack effects when (1) the angle of attack is such that the leading-edge shock interacts with the jet-interaction region, or (2) the boundary layer is separated at the jet location prior to jet discharge.

For a transverse-jet control system that is modulated by pulsing the jet with a constant jet plenum pressure, the sizing procedure is similar to the Datcom method. The primary objective is to determine the maximum jet plenum pressure required to satisfy the trim and separation requirements. This enables the nozzle throat width to be calculated.

The Datcom method consists of first obtaining a time history of the local-flow parameters at the nozzle exit prior to jet discharge. These parameters are then used in conjunction with the time history of the control force required to trim the vehicle, to obtain a control-force coefficient. This control-force coefficient is then corrected, and the sonic amplification factor is obtained as a function of the state of the boundary layer and the Reynolds number. The true value for the amplification factor is then obtained from design charts that account for the nozzle inclination angle and nozzle exit Mach number. From the local Mach number and the nozzle exit conditions, values for the minimum jet plenum pressure required to induce flow separation are obtained. This minimum jet plenum pressure and the vacuum thrust, calculated using the true amplification factor, allow calculation of the nozzle throat diameter. This in turn permits the calculation of the jet plenum pressure and propellant weight requirements to trim the vehicle.

Step 1. Determine if the boundary layer is separated at the jet location prior to jet discharge.

Because of the complex nature of boundary-layer separation at hypersonic speeds, no single criterion is available to accurately determine the location of separation. Exact locations can only be determined through wind-tunnel testing. However, for preliminary-design conditions, the simple Newtonian-shadowing criterion may be used. For a nozzle located on the leeward side, this criterion assumes the location of the separation point to be just downstream of the leading edge when the leeward surface is not directly visible to the free stream. Thus, using the Newtonian-shadowing criterion restricts the Datcom method to transverse-jet control systems located on the windward surface.

If the boundary layer is separated prior to jet discharge, the jet-interaction force is probably nil. For this case, the only force is that due to the reaction of the jet, nullifying the Datcom method.

Step 2. Determine the time-history values required for the control force F_c to trim or maneuver the vehicle, the associated free-stream Mach Number M_∞, and the associated angle of attack α_∞.

These parameters must be obtained from an outside source because of the numerous possibilities for vehicle design and mission trajectories. The jet-interaction center of pressure can be assumed to be located at the nozzle for determining the time history of the control force.

Step 3. Determine the time-history values of the local-flow parameters: P_1, q_1, M_1, and $R\ell_L$ in the absence of jet exhaust. The ratios of pressure, dynamic pressure, Mach number, and Reynolds number behind an oblique shock to their respective values in the free stream can be obtained from figures 6.3.2-30, -31, -32, and -33, respectively. These oblique shock ratios are valid so long as the following relationship holds:

$$\frac{0.1375 \dfrac{L}{d_{LE}} + 2.0}{M_\infty} > 1.0$$

For a thick leading edge and for high Mach numbers, the above relationship becomes invalid, disallowing the calculation of the local-flow parameters by oblique-shock theory. This requires calculating the local-flow properties by other available methods, such as tangent-wedge, blast-wave, Newtonian-impact (reference 29), or the Moeckel shock-loss theory (reference 30).

Step 4. Determine the time history of the state of the boundary layer from wind-tunnel data that approximate the actual flow conditions, or as a function of M_1 and $R\ell_L$ from figure 6.3.2-34.

Step 5. Make the following initial choices regarding nozzle geometry, if not already established.

a. Assume a nozzle span b that is as large as the vehicle geometry permits.

b. Choose a nozzle injection angle ϕ, where $0 < \phi < 45°$

Step 6. Determine the nozzle exit Mach number M_e and the jet vacuum specific impulse I_{sp}.

The calculation of these parameters requires knowledge of the propellant as well as of the plenum temperature and nozzle shape. It is therefore advisable that these parameters be determined by the propulsion engineer and designer.

Step 7. Determine the time-history values of the control-force coefficient C_{F_c} by

$$C_{F_c} = \frac{F_c}{q_1 bL} \qquad 6.3.2\text{-a}$$

Step 8. Calculate the value of the vacuum-thrust coefficient using the value of specific-heat ratio associated with the propellant by

$$C_{f_0} = \left(\frac{2}{\gamma + 1}\right)^{\frac{\gamma}{\gamma-1}} (\gamma + 1) \qquad 6.3.2\text{-b}$$

Step 9. Calculate the time-history values of the corrected control-force coefficient by

$$\left(C_{F_c}\right)_{cr} = \left(\frac{F_c}{q_1 bL}\right)\left(\frac{1.268}{C_{F_0}}\right) \qquad 6.3.2\text{-c}$$

Step 10. From the Reynolds number and the state of the boundary layer at each time interval, select the appropriate figure from the sizing charts (figures 6.3.2 -35a through -35e and -40) and determine the time-history values of the amplification factor K_o for a normal sonic nozzle. For a laminar boundary layer interpolate between figures 6.3.2 -35a through -35e. For a turbulent boundary layer, which is independent of Reynolds number, use figure 6.3.2-40.

Step 11. Determine the time-history values of the true amplification factor K from figure 6.3.2-41 or 6.3.2-42, or by

$$K = (K_o - 1)\left[1 + \frac{\gamma}{\gamma + 1}\,\frac{V_e}{a_t}\sin\phi\right] + \left[\frac{V_e}{a_t} + \frac{a_t}{V_e}\right]\frac{\cos\phi}{2} \qquad 6.3.2\text{-d}$$

where

$$\frac{V_e}{a_t} = \left[\frac{(\gamma + 1)M_e^2}{2 + (\gamma - 1)M_e^2}\right]^{1/2} \qquad 6.3.2\text{-e}$$

Step 12. Calculate the time-history values of the vacuum thrust by

$$F_{j_0} = \frac{F_c}{K} \qquad 6.3.2\text{-f}$$

Step 13. Determine a time-history value of the minimum jet plenum pressure required to induce separation $\left(P_{0_j}\right)_{min}$ as follows:

a. Obtain the time history of the minimum jet plenum pressure ratio $\left(P_{0j}/P_1\right)_{min}$ as a function of V_e/a_t and M_1 from figure 6.3.2-43.

b. Multiply these pressure ratios by the corresponding value of local pressure P_1 to obtain $\left(P_{0_j}\right)_{min}$; i.e.,

$$\left(P_{0_j}\right)_{min} = \left(P_{0_j}/P_1\right)_{min} P_1 \qquad 6.3.2\text{-g}$$

Step 14. From the time-history values in steps 12 and 13, determine the maximum value of the vacuum thrust $\left(F_{j_{0/}}\right)_{max}$ and the maximum value of plenum pressure $\left(P_{0_j}\right)_{max}$

Step 15. Calculate, using experimental data if available, a value for the nozzle discharge coefficient c (defined as the ratio of the actual nozzle flow to the flow calculated by isentropic laws). In reference 31, relations are given relating the nozzle discharge coefficient to the velocity coefficient, polytropic efficiency, and other nozzle parameters. However, all these relationships require some experimental k. owledge of the nozzle.

If no experimental data are available for the nozzle, a value of 0.90 can be assumed with concurrence of the nozzle designer. This value was the lower bound for nozzle discharge coefficients experienced by the investigators in reference 1. However, caution must be used because values as low as 0.71 for nozzle discharge coefficients have also been reported (reference 3).

Step 16. Calculate the nozzle throat width required to provide a vacuum thrust at least as large as the peak value predicted to trim the vehicle. The use of a safety factor to allow for dynamics and contingencies may be desirable (see sample problem). Compute the nozzle throat width as follows:

$$d_t = \frac{\left(F_{j_0}\right)_{max} SF}{c\, C_{f_0}\, b \left(P_{0_j}\right)_{max}} \qquad 6.3.2\text{-h}$$

Step 17. Calculate the time-history values of the jet plenum pressure required to trim the vehicle by

$$\left(P_{0_j}\right)_{trim} = \frac{F_{j_0}}{c C_{f_0}\, b\, d_t} \qquad 6.3.2\text{-i}$$

The jet plenum pressure required to trim the vehicle should always exceed the minimum jet plenum pressure required to induce separation $(P_{0_j})_{min}$ in step 13. When the jet plenum pressure required to trim the vehicle is less than the minimum jet plenum pressure required to induce separation, two choices are available: (a) the throat width can be reduced with a corresponding increase in jet plenum pressure; (b) no

change can be made, with a loss in effectiveness (amplification factor) for a short period of time. The second choice is preferable because economically and structurally it is advantageous to keep the jet plenum pressure as low as possible.

Step 18. Calculate the time-history values of the mass-flow rate by

$$\dot{m} = \frac{F_{j_0}}{I_{sp}} \qquad 6.3.2\text{-j}$$

Step 19. Calculate the required propellant weight by integrating the time history of the mass-flow rate.

Step 20. Revise the preliminary estimates made in step 5 and reiterate to obtain an optimum configuration based on trade-offs between system weight, jet-plenum-pressure requirements, and the available control force.

The approach described above is based on the assumption that the jet-interaction center of pressure is located at the nozzle (step 2). In many practical applications this assumption introduces only a small error, particularly for turbulent boundary layers and for relatively low-aspect-ratio nozzles. Present knowledge of jet interaction does not allow an accurate determination of the center of pressure, particularly for laminar boundary layers. However, an approximate method from reference 1 is presented.

The most extreme forward location of the center of pressure results from a two-dimensional nozzle located at the end of a plate. This location can be evaluated and used as a guide in estimating the true center-of-pressure location.

For three-dimensional nozzles the longitudinal extent of the separated boundary layer is much closer to the nozzle than for the two-dimensional case. Experimental data indicate that for most three-dimensional configurations one-half of the calculated value will be conservative and should suffice for preliminary-design purposes.

Step 21. Determine the time-history values of the center-of-pressure location for each time increment as follows:

a. For laminar flow

(1) Assume a value for the separation Reynolds number $R\ell_s$ of approximately one-fifth the Reynolds number based on the nozzle location $R\ell_L$. (It should be noted that although $R\ell_s$ is based on the separation location, it does not give an accurate value for the separation location.)

(2) Calculate the plateau-pressure coefficient C_{p_2} by

$$C_{p_2} = \frac{1.60}{\left[R\ell_s (M_1^2 - 1)\right]^{1/4}} \qquad 6.3.2\text{-k}$$

where

$$C_{p_2} = \frac{P_2 - P_1}{q_1}$$

(3) Calculate the total drag coefficient of the interaction phenomena by

$$C_x = 4.75\ C_{p_2} \qquad 6.3.2\text{-}\ell$$

(4) Calculate the normalized effective jet height by

$$\frac{h}{L} = \left(\frac{P_{0_j}\ d_t}{P_1 L}\right)\left(\frac{2\ C_{f_0}}{\gamma C_x M_1^{\ 2} + 2}\right) \qquad 6.3.2\text{-m}$$

(5) Calculate the plateau pressure by

$$P_2 = C_{p_2}\ q_1 + P_1 \qquad 6.3.2\text{-n}$$

(6) Calculate the tangent of the boundary-layer separation angle by

$$\tan \sigma = \left[\frac{5(\xi - 1)}{7\ M_1^{\ 2} - 5(\xi - 1)}\right]\left[\frac{7\ M_1^{\ 2} - (6\xi + 1)}{6\xi + 1}\right]^{1/2} \qquad 6.3.2\text{-o}$$

where

$$\xi = \frac{P_2}{P_1} \qquad 6.3.2\text{-p}$$

(7) Calculate a new value for the normalized effective jet height by

$$\left(\frac{h}{L}\right)_{new} = \left(1 - \frac{R_{\ell_s}}{R_{\ell_L}}\right) \tan \sigma \qquad 6.3.2\text{-q}$$

(8) If $\left(\frac{h}{L}\right)_{new}$ given by equation 6.3.2-q is not equal to $\left(\frac{h}{L}\right)$ given by equation 6.3.2-m, i.e., $\left(\frac{h}{L}\right)_{new} \neq \left(\frac{h}{L}\right)$, choose a new value for R_{ℓ_s} in step 21.a.(1) and iterate until $\left(\frac{h}{L}\right)_{new} = \left(\frac{h}{L}\right)$.

(9) Calculate the normalized center-of-pressure location with respect to the nozzle location by

$$\frac{x_{cp}}{L} = (1 - G) + G \left[1 - \frac{G}{2} \left(\frac{C_{F_c}}{C_{p_2}} \right) \right] \qquad 6.3.2\text{-r}$$

where

$$G \cong 1 - \frac{1}{K} \qquad 6.3.2\text{-s}$$

and C_{p_2} is based on the correct value of $R\ell_s$. (step 21.a.(2))

b. For turbulent flow

(1) Calculate the plateau-pressure coefficient C_{p_2}

For $M_1 \leq 5$

$$C_{p_2} = 0.41 + 0.481\, M_1 - 0.0509\, M_1^2 + 0.0061\, M_1^3 \qquad 6.3.2\text{-t}$$

For $M_1 > 5$

$$C_{p_2} = 0.2257 - 0.0232\, M_1 + 0.0014\, M_1^2 - 0.00003\, M_1^3 \qquad 6.3.2\text{-u}$$

(2) Calculate the normalized center-of-pressure location with respect to the nozzle location by

$$\frac{x_{cp}}{L} = (1 - G) + G \left[1 - \frac{G}{2} \left(\frac{C_{F_c}}{C_{p_2}} \right) \right] \qquad \text{(equation 6.3.2-r)}$$

where

$$G \cong 1 - \frac{1}{K} \qquad \text{(equation 6.3.2-s)}$$

If the calculated value for the center of pressure appears to introduce a significant error into the determination of the required control force in step 2, a new control force should be calculated and the procedure repeated for sizing the nozzle.

Sample Problem

Given: A transverse jet located at the trailing edge of a flat plate

$L = 10.0$ ft $\quad b = 2.0$ ft $\quad \phi = 30^{o} \quad V_e/a_t = 2.0$

$M_e = 2.39 \quad \gamma = 1.2 \quad I_{sp} = 225.0$ sec $\quad c = 0.90$

The sample problem presents a hypothetical case which serves to illustrate the Datcom method. The time-history values of the control force F_c must be calculated or established prior to the application of the Datcom method. For a real problem, the time-history values of the free-stream Mach number M_∞ and the angle of attack α_∞ must also be determined prior to the application of the Datcom method, in order to obtain the time-history values of the local-flow parameters.

TABLE 6.3.2-A

SAMPLE TRANSVERSE-JET SIZING CALCULATIONS

1. Time (sec)	1	2	3	4	5
2. Control Force, F_c (lb)	1000	2000	1000	500	200
3. Local Mach No., M_1	10.0	9.0	8.0	7.0	6.0
4. Reynolds No., $R\ell_L$	1×10^8	5×10^7	1×10^7	5×10^6	1×10^6
5. Local Pressure, P_1 (lb/in.^{2})	1.70	0.65	0.25	0.10	0.04
6. Dynamic Pressure, q_1 (lb/in.^{2})	119	36.8	11.2	3.43	1.01
7. Boundary Layer	turb	turb	turb	turb	lam
8. Control-Force Coeff., $C_{F_c} = F_c/(q_1\, b\, L)$	0.00292	0.0189	0.0310	0.0506	0.0688
9. Corrected Force Coeff., $\left(C_{F_c}\right)_{cr}$	0.00296	0.0192	0.0314	0.0513	0.0698
10. Sonic Amplification Factor, K_o	2.53	2.15	2.10	2.05	2.80
11. Amplification Factor, K	3.44	2.86	2.78	2.70	3.86
12. Vacuum Thrust, F_{j_0} (lb)	291	700	360	185	51.8
13. Min. Pressure Ratio, $(P_{0_j}/P_1)_{min}$	560	510	465	420	375
14. Min. Jet Pressure, $(P_{0_j})_{min}$ (lb/in.^{2})	950	332	116	42	15
15. Jet Pressure, $(P_{0_j})_{trim}$ (lb/in.^{2})	316	760	391	201	56.3
16. Mass-Flow Rate, $\dot{m}$ (lb/sec)	1.29	3.12	1.60	0.82	0.23

With the time-history values of the local-flow parameters completed in items 3 through 7 of table 6.3.2-A, the calculation for the sample problem continues for $t = 1$ second with step 4.

Determine the state of the boundary layer from wind-tunnel test data or as a function of M_1 and $R\ell_L$ from figure 6.3.2-34.

Determine the control-force coefficient

$$C_{F_c} = \frac{F_c}{q_1 bL} \qquad \text{(equation 6.3.2-a)}$$

$$= \frac{1000}{(119)(2)(10)(144)}$$

$$= 0.00292$$

Determine the vacuum-thrust coefficient

$$C_{f_0} = \left(\frac{2}{\gamma + 1}\right)^{\frac{\gamma}{\gamma-1}} (\gamma + 1) \qquad \text{(equation 6.3.2-b)}$$

$$= \left(\frac{2}{1.2 + 1}\right)^{\frac{1.2}{1.2-1}} (1.2 + 1)$$

$$= 1.25$$

Determine the corrected control-force coefficient

$$\left(C_{F_c}\right)_{cr} = \left(\frac{F_c}{q_1 bL}\right)\left(\frac{1.268}{C_{f_0}}\right) \qquad \text{(equation 6.3.2-c)}$$

$$= (0.00292)\left(\frac{1.268}{1.250}\right)$$

$$= 0.00296$$

Determine the sonic amplification factor

$K_o = 2.53$ (figure 6.3.2-40)

Determine the true amplification factor

$K = 3.44$ (figure 6.3.2-41)

Determine the vacuum thrust

$$F_{j_0} = \frac{F_c}{K} \qquad \text{(equation 6.3.2-f)}$$

$$= \frac{1.000}{3.44}$$

$$= 291 \text{ lb}$$

Determine the minimum jet plenum pressure required to induce separation

$$\left(\frac{P_{0_j}}{P_1}\right)_{min} = 560 \qquad \text{(figure 6.3.2-43)}$$

$$\left(P_{0_j}\right)_{min} = \left(\frac{P_{0_j}}{P_1}\right)_{min} P_1 \qquad \text{(equation 6.3.2-g)}$$

$$= (560)\ (1.70)$$

$$= 950 \text{ lb/in.}^2$$

The remaining steps cannot be based on one time segment; i.e., the total time history of the various parameters must be considered.

Determine the throat width

$$d_t = \frac{\left(F_{j_0}\right)_{max} SF}{c\, C_{f_0}\, b \left(P_{0_j}\right)_{max}} \qquad \text{(equation 6.3.2-h)}$$

$$= \frac{(700)\ (1.25)}{(0.9)\ (1.25)\ (24)\ (950)}$$

$$= 0.0341 \text{ in.}$$

The safety factor is determined from the maximum thrust and the maximum jet plenum pressure. The maximum thrust required is 700 lb; however, a value of 900 lb should allow for contingencies. If the design value for the maximum jet pressure required to induce separation is chosen to be 1000 lb/in.^{2} rather than the value of 950 lb/in.^{2} in table 6.3.2-A, the safety factor can be expressed as

$$SF = \frac{\left(F_{j_0}\right)_{max}}{\left(P_{0_j}\right)_{max}}\Bigg|_{design} \frac{\left(P_{0_j}\right)_{max}}{\left(F_{j_0}\right)_{max}}$$

$$= \left(\frac{900}{1000}\right)\left(\frac{950}{700}\right)$$

$$= 1.21, \text{ use } 1.25$$

The jet plenum pressures required to trim the vehicle are calculated based on the throat width by using equation 6.3.2-i. These calculated plenum pressures must always exceed the plenum pressure required to induce separation (950 lb/in.^{2} at the initial time period of one second). The jet plenum pressures required for trim (item 15 in the table) were computed as follows:

$$\left(P_{0_j}\right)_{trim} = \frac{F_{j_0}}{c\, C_{f_0}\, b\, d_t} \qquad \text{(equation 6.3.2-i)}$$

$$= \frac{F_{j_0}}{(0.9)\,(1.25)\,(24)\,(0.0341)}$$

$$= 1.086\, F_{j_0}$$

It is seen that the jet plenum pressures required for trim (item 15) are less than the specified minimum value at the initial time of one second. Two choices are available: either the throat width can be reduced with a corresponding increase in jet pressure or, if this proves to be detrimental to the system weight, then some loss in effectiveness can probably be accepted for a short time period in order to avoid increasing the jet pressure. The proper choice depends upon the sensitivity of the control-system weight to an increase in jet plenum pressure.

The propellant weight required to trim the vehicle is obtained from the integral of the mass-flow rate $\dot{m}$ in item 16. For the sample problem, the required propellant weight to trim the vehicle is 7.06 lb.

In order to arrive at an optimum nozzle design in any particular application, several iterations of the above procedure should be made with systematic variations in the initial assumptions. If extensive sizing studies are required and if suitable computing facilities are available, a computer program, described in reference 1, should be used.

Determine the center-of-pressure location.

Two cases are presented to illustrate the procedure: one where the boundary layer is turbulent and one where the boundary layer is laminar.

Case I t = 4 seconds (turbulent flow)

$M_1 = 7.0$

$C_{F_c} = 0.0506$ } (table 6.3.2-A)

$K = 2.70$

$$C_{p_2} = 0.2257 - 0.0232\, M_1 + 0.0014\, M_1^{\,2} - 0.00003\, M_1^{\,3} \qquad \text{(equation 6.3.2-u)}$$

$$= 0.2257 - 0.0232\,(7) + 0.0014\,(49) - 0.00003\,(343)$$

$$= 0.1216$$

$$G \cong 1 - \frac{1}{K} \qquad \text{(equation 6.3.2-s)}$$

$$= 1 - \frac{1}{2.70} = 0.63$$

$$\frac{x_{cp}}{L} = (1 - G) + G \left[1 - \frac{G}{2}\left(\frac{C_{F_c}}{C_{p_2}}\right)\right] \qquad \text{(equation 6.3.2-r)}$$

$$= (1 - 0.63) + 0.63 \left[1 - \frac{0.63}{2}\left(\frac{0.0506}{0.1216}\right)\right]$$

$$= 0.917$$

$$x_{cp} = (0.917)\, L$$

$$= (0.917)\,(10)$$

$$= 9.17 \text{ ft from leading edge}$$

Case II t = 5 seconds (laminar flow)

$M_1 = 6.0$

$C_{F_c} = 0.0688$ } (table 6.3.2-A)

$K = 3.86$

$P_{0_j} = 56.3$ lb/in.^{2}

$P_1 = 0.04$ lb/in.^{2} } (table 6.3.2-A)

$q_1 = 1.01$ lb/in.^{2}

First iteration (assume $R_{\ell_s} = 1 \times 10^5$)

$$C_{p_2} = \frac{1.60}{\left[R_{\ell_s} (M_1^2 - 1)\right]^{1/4}} \qquad \text{(equation 6.3.2-k)}$$

$$= \frac{1.60}{[10^5 (36 - 1)]^{1/4}}$$

$$= 0.037$$

$$C_x = 4.75\ C_{p_2} \qquad \text{(equation 6.3.2-ℓ)}$$

$$= (4.75)\ (0.037)$$

$$= 0.1758$$

$$\frac{h}{L} = \left[\frac{P_{0_j}\ d_t}{P_1\ L}\right] \left[\frac{2\ C_{f_0}}{\gamma\ C_x\ M_1^2 + 2}\right] \qquad \text{(equation 6.3.2-m)}$$

$$= \left[\frac{(56.3)\ (0.0341)}{(0.04)\ (10)\ (12)}\right] \left[\frac{(2)\ (1.25)}{(1.2)\ (0.1758)\ (36) + 2}\right]$$

$$= (0.400)\ (0.2605)$$

$$= 0.104$$

$$P_2 = C_{p_2}\ q_1 + P_1 \qquad \text{(equation 6.3.2-n)}$$

$$= (0.037)\ (1.01) + 0.04$$

$$= 0.0774 \text{ lb/in.}^2$$

$$\xi = \frac{P_2}{P_1} = \frac{0.0774}{0.04} = 1.93 \qquad \text{(equation 6.3.2-p)}$$

$$\tan \sigma = \left[\frac{5(\xi - 1)}{7 M_1^2 - 5(\xi - 1)}\right]\left[\frac{7 M_1^2 - (6\xi + 1)}{6\xi + 1}\right]^{1/2} \qquad \text{(equation 6.3.2-o)}$$

$$= \left[\frac{5(0.93)}{7(36) - 5(0.93)}\right]\left[\frac{7(36) - [6(1.93) + 1]}{6(1.93) + 1}\right]^{1/2}$$

$$= (0.0188)(4.36)$$

$$= 0.082$$

$$\left(\frac{h}{L}\right)_{new} = \left(1 - \frac{R_{\ell_s}}{R_{\ell_L}}\right)\tan \sigma \qquad \text{(equation 6.3.2-q)}$$

$$= \left(1 - \frac{10^5}{10^6}\right)(0.0819)$$

$$= 0.0738$$

Since $0.0738 \neq 0.104$, try a second iteration.

Second iteration (assume $R_{\ell_s} = 5 \times 10^4$)

$$C_{p_2} = \frac{1.60}{[(5 \times 10^4)(36 - 1)]^{1/4}} = 0.044 \qquad \text{(equation 6.3.2-k)}$$

$$C_x = (4.75)(0.044) = 0.209 \qquad \text{(equation 6.3.2-ℓ)}$$

$$\frac{h}{L} = \left[\frac{(56.3)(0.0341)}{(0.04)(10)(12)}\right]\left[\frac{2(1.25)}{(1.2)(0.209)(36) + 2}\right] \qquad \text{(equation 6.3.2-m)}$$

$$= (0.400)(0.227)$$

$$= 0.0908$$

$$P_2 = (0.044)(1.01) + 0.04 = 0.0844 \text{ lb/in.}^2 \qquad \text{(equation 6.3.2-n)}$$

$$\xi = \frac{P_2}{P_1} = \frac{0.0844}{0.04} = 2.11 \qquad \text{(equation 6.3.2-p)}$$

$$\tan \sigma = \left[\frac{5\,(1.11)}{252 - 5\,(1.11)}\right] \left[\frac{252 - [6\,(2.11) + 1]}{6\,(2.11) + 1}\right]^{1/2} \qquad \text{(equation 6.3.2-o)}$$

$$= (0.0225)\,(4.18)$$

$$= 0.094$$

$$\left(\frac{h}{L}\right)_{new} = \left(1 - \frac{5 \times 10^4}{10^6}\right)(0.094) = 0.0893 \qquad \text{(equation 6.3.2-q)}$$

Since $0.0893 \neq 0.0908$, try a third iteration.

Third iteration (assume $R_{\ell_s} = 4.85 \times 10^4$)

$$C_{p_2} = \frac{1.60}{[(4.85 \times 10^4)\,(36 - 1)]^{1/4}} = 0.0443 \qquad \text{(equation 6.3.2-k)}$$

$$C_x = (4.75)\,(0.0443) = 0.210 \qquad \text{(equation 6.3.2-}\ell\text{)}$$

$$\frac{h}{L} = \left[\frac{(56.3)\,(0.0341)}{(0.04)\,(10)\,(12)}\right] \left[\frac{(2)\,(1.25)}{(1.2)\,(0.210)\,(36) + 2}\right] \qquad \text{(equation 6.3.2-m)}$$

$$= (0.400)\,(0.226)$$

$$= 0.0904$$

$$P_2 = (0.0443)\,(1.01) + 0.04 = 0.0847 \text{ lb/in.}^2 \qquad \text{(equation 6.3.2-n)}$$

$$\xi = \frac{P_2}{P_1} = \frac{0.0847}{0.04} = 2.118 \qquad \text{(equation 6.3.2-p)}$$

$$\tan \sigma = \left[\frac{5\,(1.118)}{252 - 5\,(1.118)}\right] \left[\frac{252 - [6\,(2.118) + 1]}{6\,(2.118) + 1}\right]^{1/2} \qquad \text{(equation 6.3.2-o)}$$

$$= (0.0227)\,(4.17)$$

$$= 0.0947$$

$$\left(\frac{h}{L}\right)_{new} = \left(1 - \frac{4.95 \times 10^4}{10^6}\right)(0.0947) = 0.0901 \qquad \text{(equation 6.3.2-q)}$$

$0.0901 \cong 0.0904$; therefore $R_{\ell_s} = 4.85 \times 10^4$

$C_{p_2} = 0.0443$

$$G \cong 1 - \frac{1}{K} = 1 - \frac{1}{3.86} = 0.741 \qquad \text{(equation 6.3.2-s)}$$

$$\frac{x_{cp}}{L} = (1 - G) + G \left[1 - \frac{G}{2}\left(\frac{C_{F_c}}{C_{p_2}}\right)\right] \qquad \text{(equation 6.3.2-r)}$$

$$= (1 - 0.741) + 0.741 \left[1 - \frac{0.741}{2}\left(\frac{0.0688}{0.0443}\right)\right]$$

$$= 0.574$$

Since the value of $x_{cp}/L = 0.574$ is a conservative estimate of the most extreme forward position for a two-dimensional nozzle, the actual value is probably close to 0.75 or 0.80 (see discussion prior to step 21). Since the center of pressure for t = 5 seconds is not close to the nozzle location, it would be advisable to calculate a new control force based on the approximate value of x_{cp} = 7.5 ft and repeat the sizing calculation for t = 5 seconds.

REFERENCES

1. Barnes, J. W., Davis, J. G., and Tang, H. H.: Control Effectiveness of Transverse Jets Interacting With a High-Speed Free Stream. Vol. I. Design Charts, Theoretical and Experimental Results. AFFDL TR-67-90, Vol. I, 1967. (U)

2. Cassel, L. A., Davis, J. G., and Engh, D. P.: Lateral Jet Control Effectiveness Prediction for Axisymmetric Missile Configurations. Army Missile Command, RD-TR-68-5, 1968. (U)

3. Phinney, R. E., Werle, M. J., and Knott, J.: Slot Jet Interaction Studies of an Ogive Cylinder at M_∞ = 4 and 5. Naval Ordnance Lab., NOL TR-68-143, 1968. (U)

4. Strike, W. T., Schueler, C. J., and Deitering, J. S.: Interactions Produced by Sonic Lateral Jets Located on Surfaces in a Supersonic Stream. AEDC-TDR-63-22, 1963. (U)

5. Zakkay, V., Erdos, J., and Calarese, W.: An Investigation of the Interaction Between a Transverse Sonic Jet and a Hypersonic Stream. N.Y. Univ., NYU-AA-68-27, 1968. (U)

6. Swanson, R. S.: Parametric and Preliminary Design Comparison of Transverse Jet Controls and Flap-Type Aerodynamic Controls for Re-entry Vehicles and High-Speed Cruise Aircraft. AFFDL TR-68-98, 1968. (U)

7. Heyser, A., and Maurer, F.: Experimental Investigations on Solid Spoilers and Jet Spoilers at Mach Numbers of 0.6 to 2.8. Cal. Inst. of Tech., JPL, Trans. No. 32, 1964. (U)

8. Spaid, F. W., and Zukoski, E. E.: A Study of the Interaction of Gaseous Jets From Transverse Slots With Supersonic External Flows. Douglas Aircraft Company DP 4480, 1967. (U)

9. Spring, D. J., Street, T. A., and Amick, J. L.: Transverse Jet Experiments and Theories – A Survey of the Literature. US Army Missile Command RD-TR-67-4, 1967. (U)

10. Schlichting, H.: Boundary-Layer Theory. McGraw-Hill Co., New York, 1955. (U)

11. Howarth, L. (edit): Modern Developments in Fluid Dynamics -- High-Speed Flow. Vol. I. Oxford Univ. Press, 1953. (U)

12. Chapman, D. R., Kuehn, D., and Larson, H. K.: Investigation of Separated Flows in Supersonic and Transonic Streams With Emphasis on the Effects of Transition. NACA TR 1356, 1958. (U)

13. Sterrett, J. R., and Emery, J. C.: Extension of Boundary-Layer-Separation Criteria to a Mach Number of 6.5 by Utilizing Flat Plates With Forward-Facing Steps. NASA TN D-618, 1960. (U)

14. Hammitt, A. G.: The Interaction of Shock Waves and Turbulent Boundary Layers. JAS, Vol. 25, No. 6, 1958. (U)

15. Lange, R. H.: Present Status of Information Relative to the Prediction of Shock-Induced Boundary-Layer Separation. NACA TN 3065, 1954. (U)

16. Reshotko, E., and Tucker, M.: Effect of a Discontinuity on Turbulent Boundary-Layer-Thickness Parameters With Application to Shock-Induced Separation. NACA TN 3454, 1955. (U)

17. Drougge, G.: An Experimental Investigation of the Influence of Strong Adverse Pressure Gradients of Turbulent Boundary Layers at Supersonic Speeds. Aero. Res. Inst. of Sweden, Rept. No. 46, 1953. (U)

18. Amick, J. L., and Hays, P. B.: Interaction Effects of Side Jets Issuing From Flat Plates and Cylinders Alined With a Supersonic Stream. WADD TR-60-329, 1960. (U)

19. Shaw, W. J.: Static Stability Characteristics of Cones, Including Effects of Nose Bluntness, Ablation Interactions, and Selected Protuberance Configurations. McDonnell Douglas Corp. DAC-63190, 1969. (U)

20. Kaufman, L. G., II, and Koch, F.: High Speed Flows Past Transverse Jets. Grumman Aircraft Eng. Corp. RE-348, 1968. (U)

21. Maurer, F.: Three-Dimensional Effects in Shock-Separated Flow Regions Ahead of Lateral Control Jets Issuing From Slot Nozzles of Finite Length. Published in the proceedings of a Specialists' Meeting, sponsored by the AGARD Fluid Dynamics Panel held in Rhode-Saint Genese, Belgium, 1966. (U)

22. Maurer, F.: Interference Effects Produced by Gaseous Side-Jets Issuing Into a Supersonic Stream. Deutsche Luft-und Raumfahrt Forschungsbericht 65-04, 1965. (U)

23. Volz, W. C., and Werle, M. J.: Jet Interaction Studies. Naval Ordnance Lab., White Oak, 1966. (U)

24. Orth, R. C., and Funk, J. A.: An Experimental and Comparative Study in Jet Penetration in Supersonic Flow. AIAA Paper 67-225, 1967. (U)

25. Kaufman, L. G., II: Classification of Interactions Due to High-Speed Flows Past Transverse Jets. Grumman Aircraft Eng. Corp., Research Rept. RE-154, 1962. (U)

26. Werle, M. J.: A Critical Review of Analytical Methods for Estimating Control Forces Produced by Secondary Injection. Naval Ordnance Lab., NOL TR-68-5, 1968 (U)

27. Evers, J. L.: A Study of the Bow Shock Induced by Secondary Injection Into Supersonic and Hypersonic Flows. Von Karman Inst. for Fluid Dynamics, TN 29, 1965. (U)

28. Coxe, E. F.: Interaction of a Two Dimensional Jet With a Deflecting Stream. So. Carolina Univ. Ph.D. Thesis, 1967. (U)

29. Truitt, R. W.: Hypersonic Aerodynamics. The Ronald Press Company, New York, 1959. (U)

30. Moeckel, W. E.: Some Effects of Bluntness on Boundary-Layer Transition and Heat Transfer at Supersonic Speeds. NACA TR 1312, 1957. (U)

31. Emmons, H. W. (edit): Fundamentals of Gas Dynamics. Princeton University Press, Princeton, N.J., 1958. (U)

32. Nunn, R. H., and Ulrich, R. D.: Jet Reaction Control for Atmospheric Flight: A Review and Summary of the Literature. Naval Weapons Center NWC-TP-4559, 1969. (C) Title Unclassified

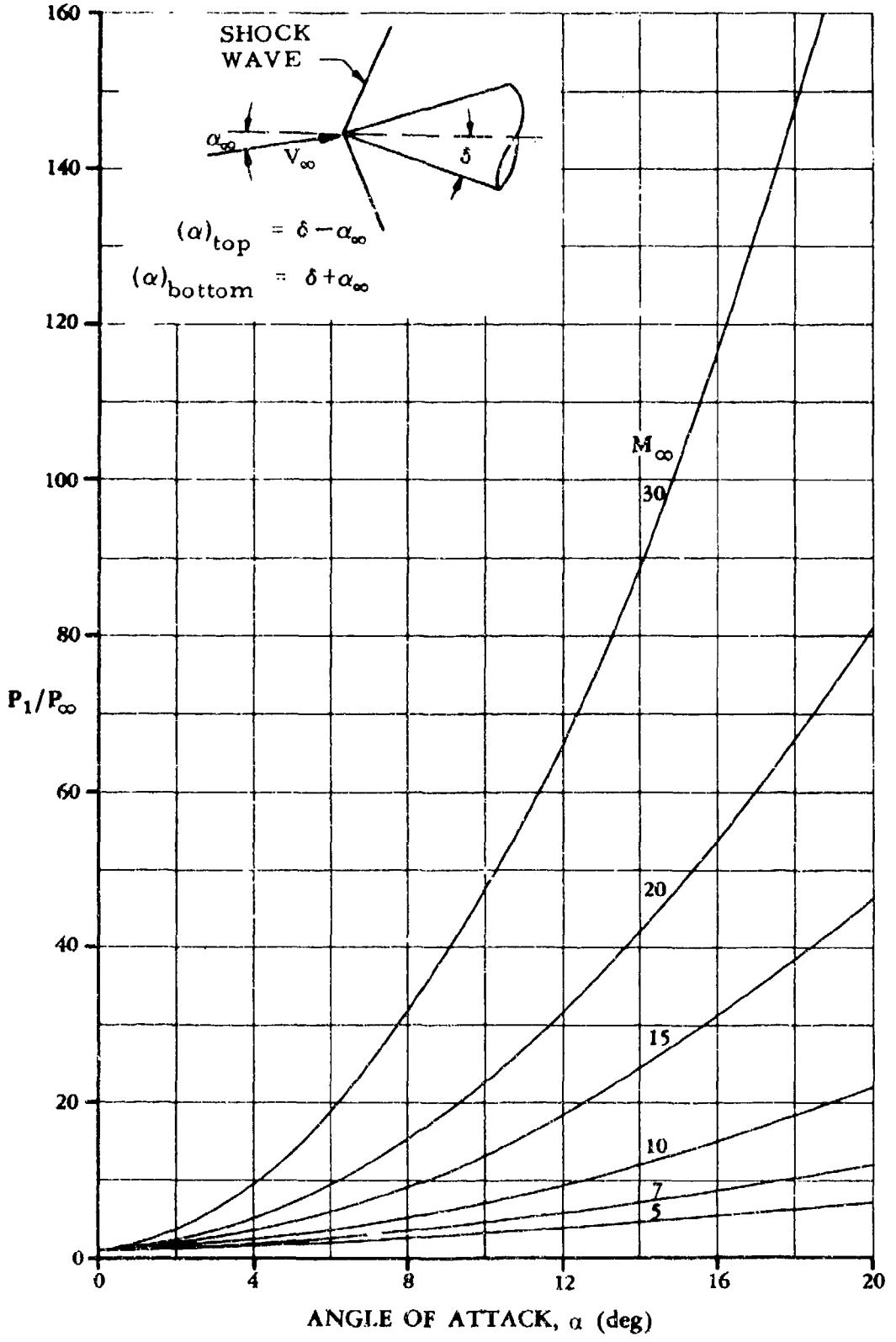

FIGURE 6.3.2-30 OBLIQUE SHOCK PRESSURE RATIO FOR PERFECT GAS

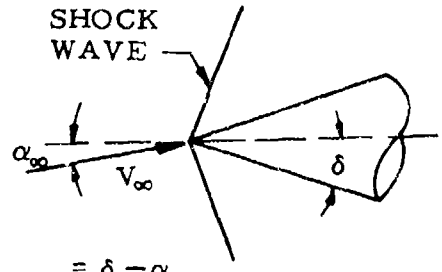

$$(\alpha)_{top} = \delta - \alpha_\infty$$

$$(\alpha)_{bottom} = \delta + \alpha_\infty$$

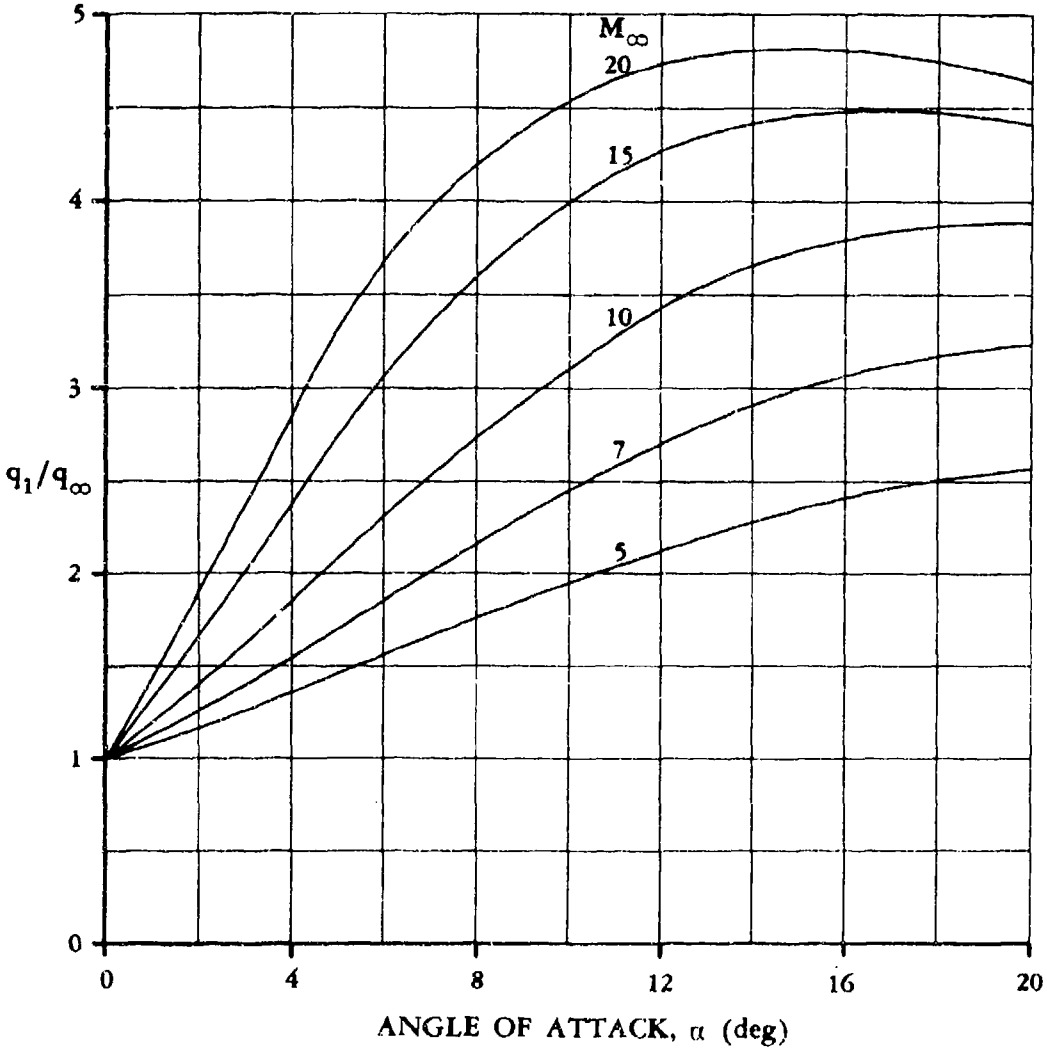

FIGURE 6.3.2-31 OBLIQUE SHOCK DYNAMIC-PRESSURE RATIO FOR PERFECT GAS

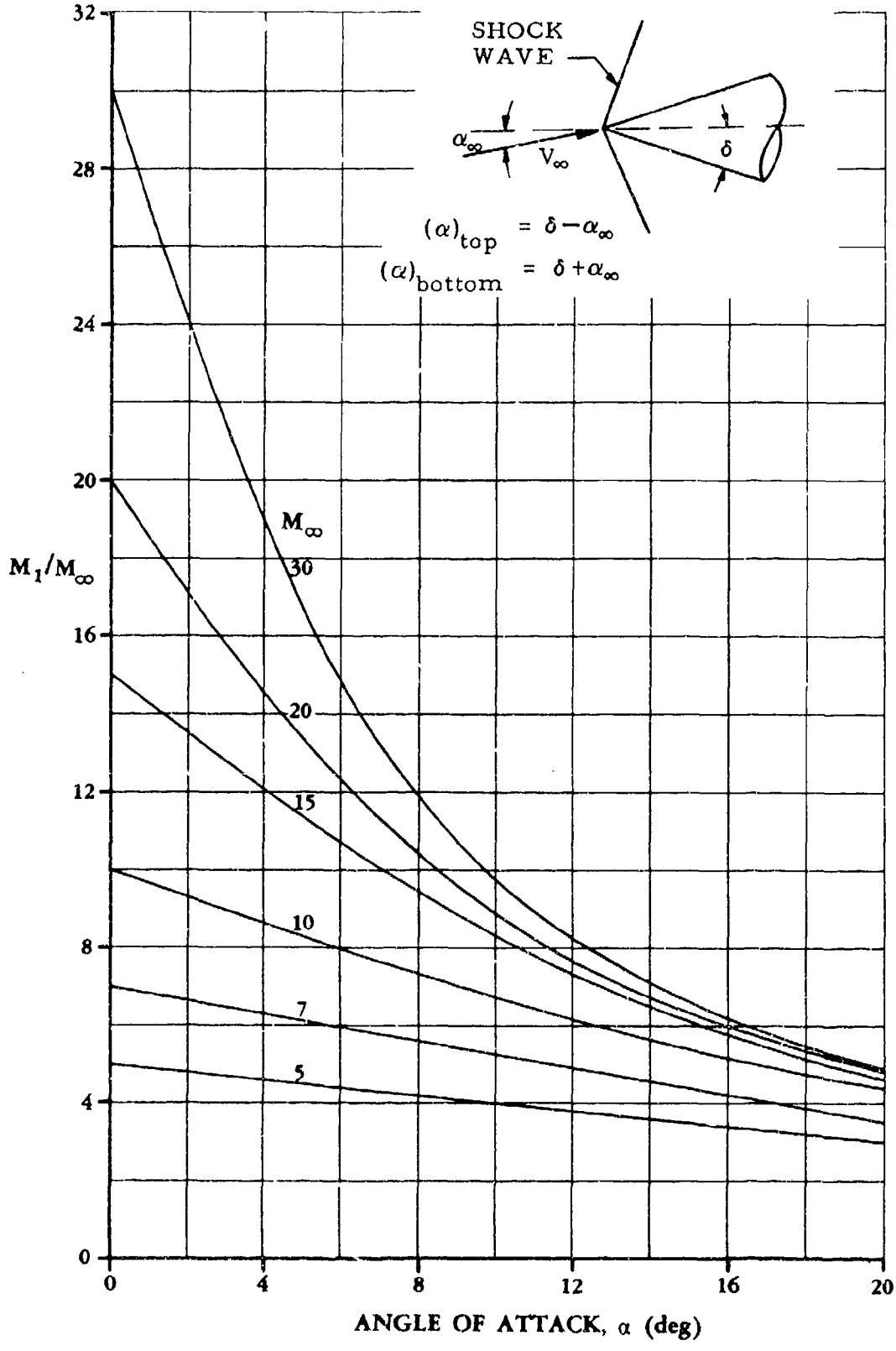

FIGURE 6.3.2-32 **OBLIQUE SHOCK MACH NUMBERRATIO FOR PERFECT GAS**

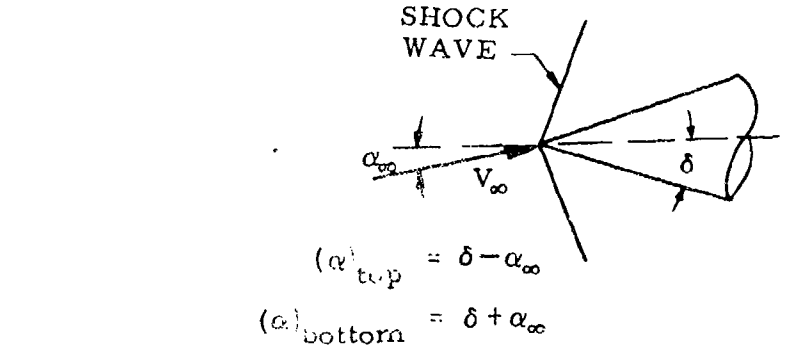

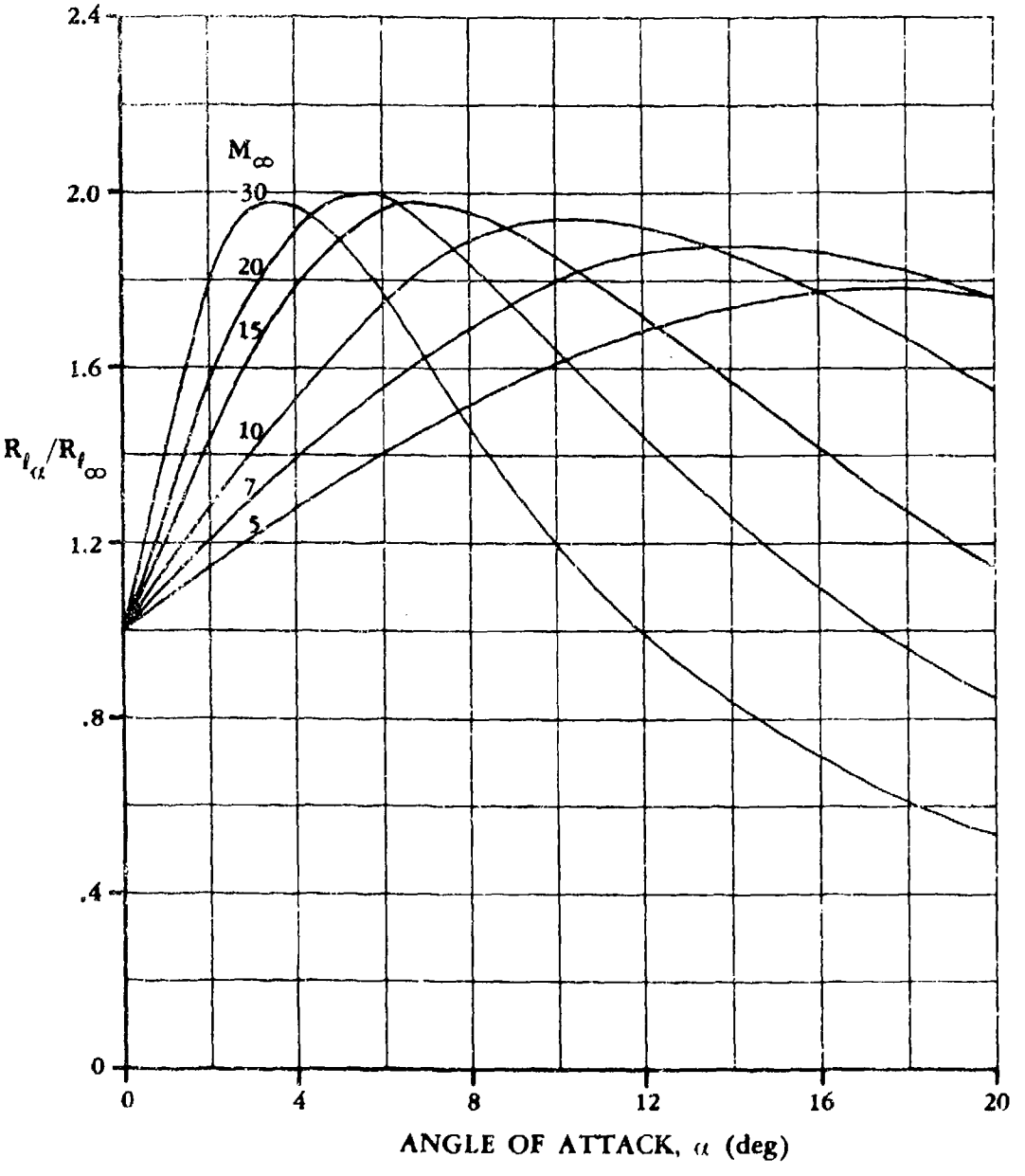

FIGURE 6.3.2-33 OBLIQUE SHOCK REYNOLDS-NUMBER RATIO FOR PERFECT GAS

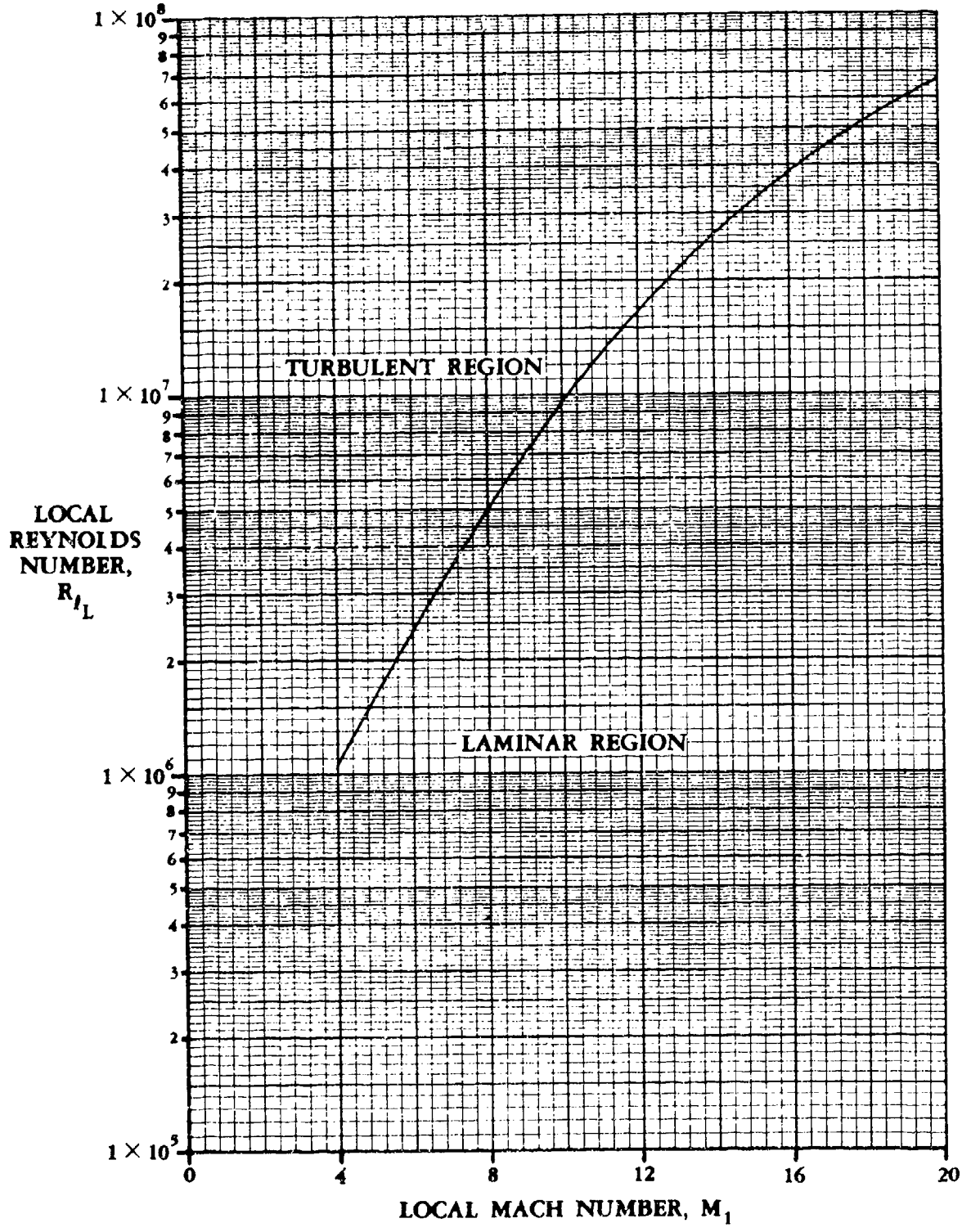

FIGURE 6.3.2-34 REGIONS FOR EXISTENCE OF THE LAMINAR AND TURBULENT BOUNDARY LAYERS

(a) $R_{\ell_L} = 1 \times 10^5$

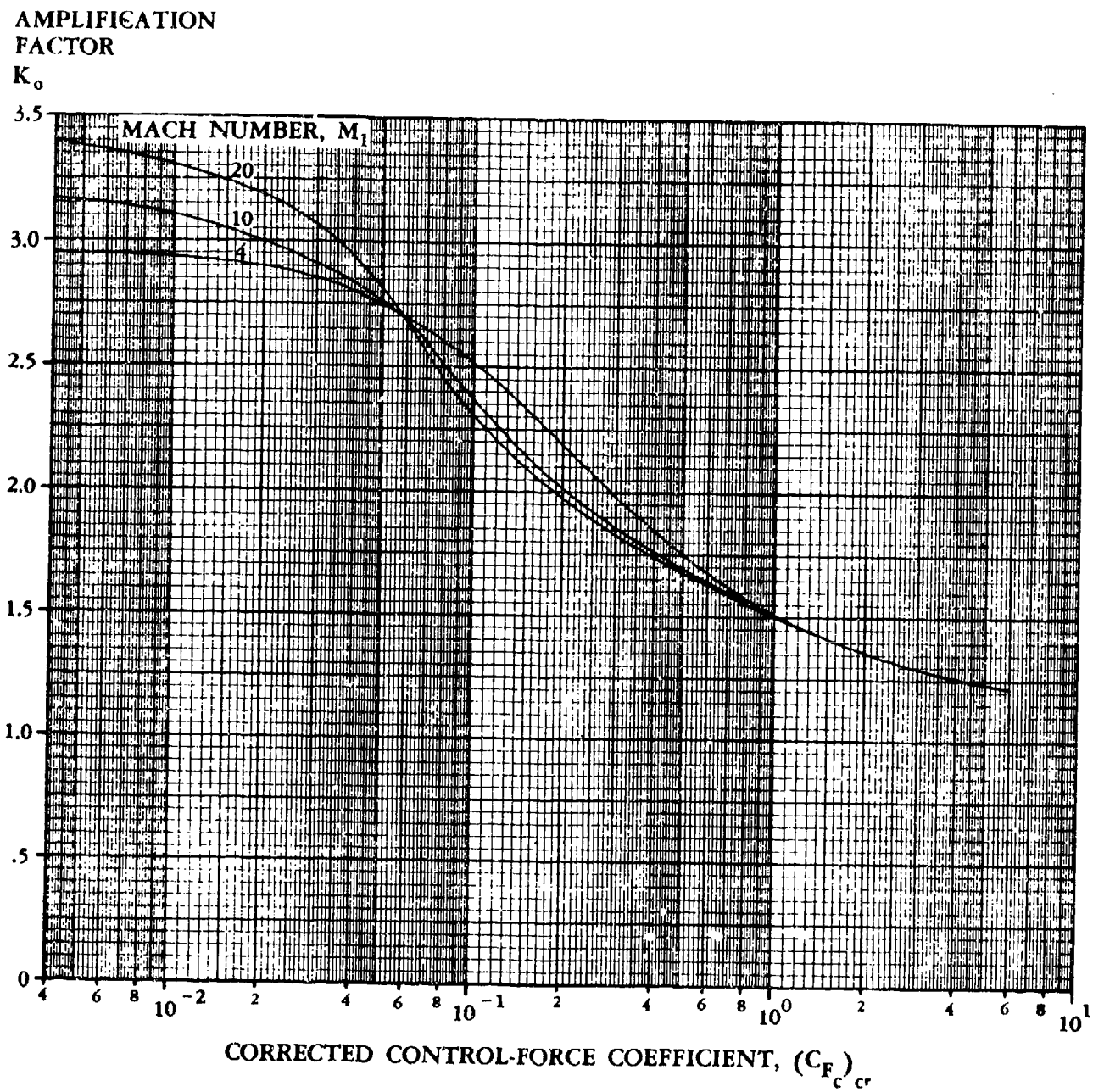

FIGURE 6.3.2-35 AMPLIFICATION FACTOR VERSUS CONTROL-FORCE COEFFICIENT FOR LAMINAR BOUNDARY LAYER

(b) $R_{\ell_L} = 1 \times 10^6$

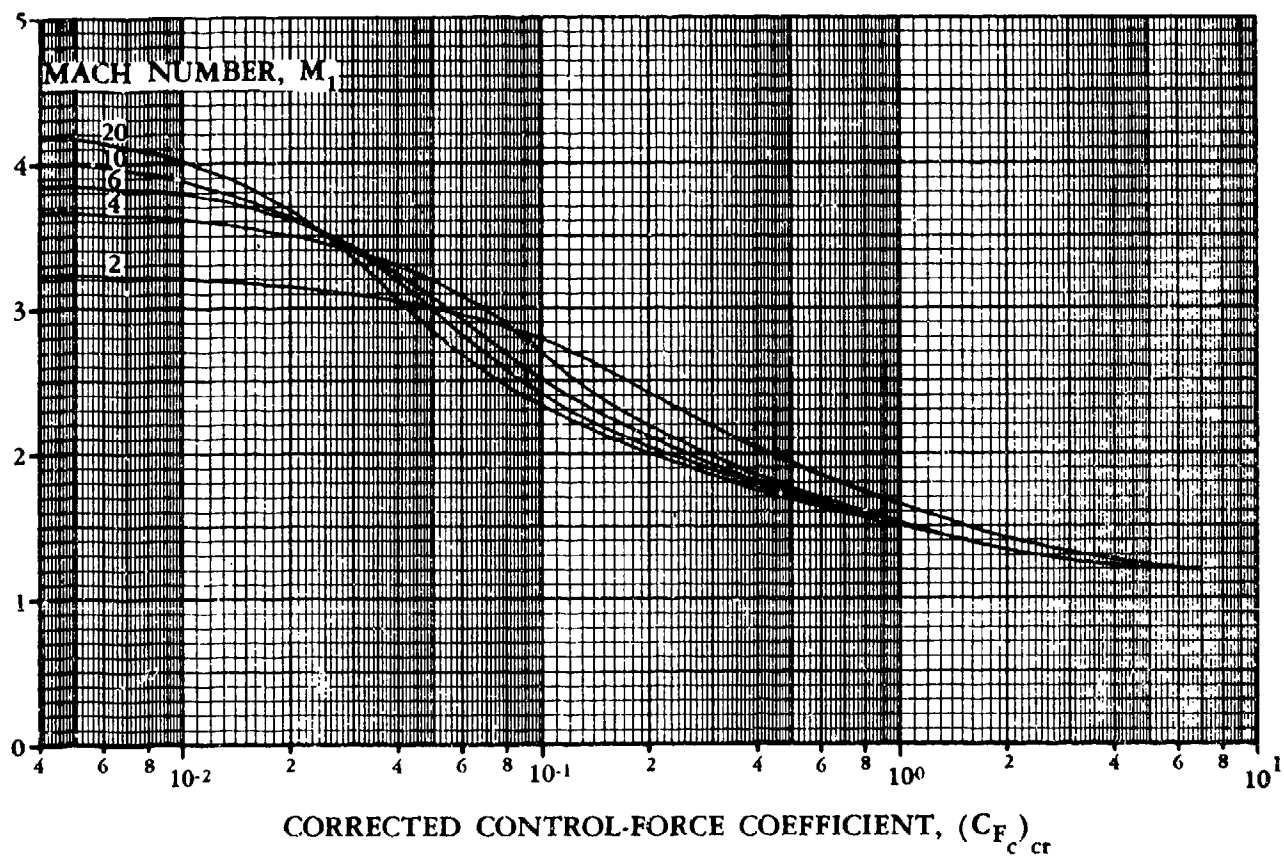

FIGURE 6.3.2-35 (CONTD)

(c) $R_{\ell_L} = 1 \times 10^7$

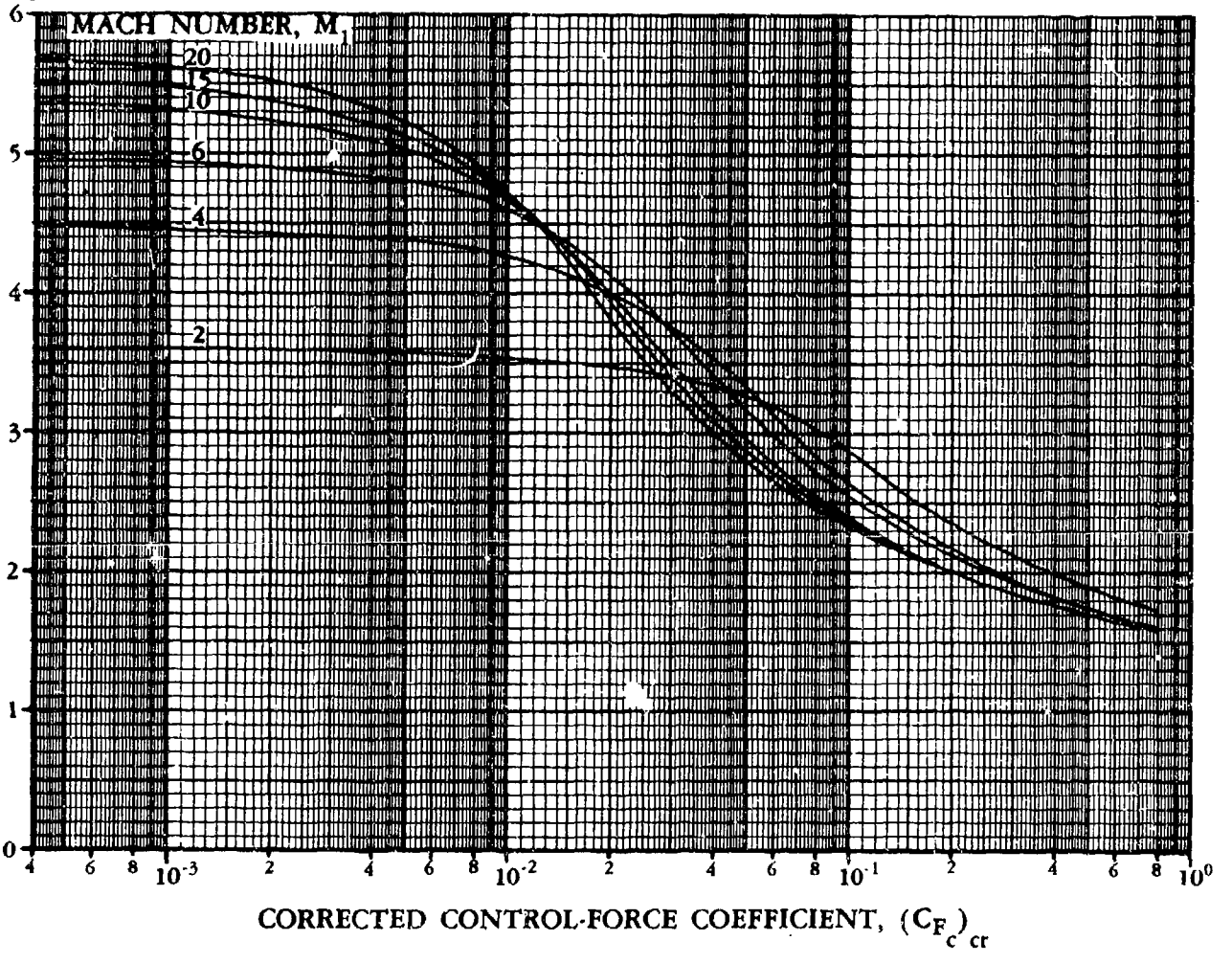

FIGURE 6.3.2-35 (CONTD)

(d) $R_{\ell_L} = 1 \times 10^8$

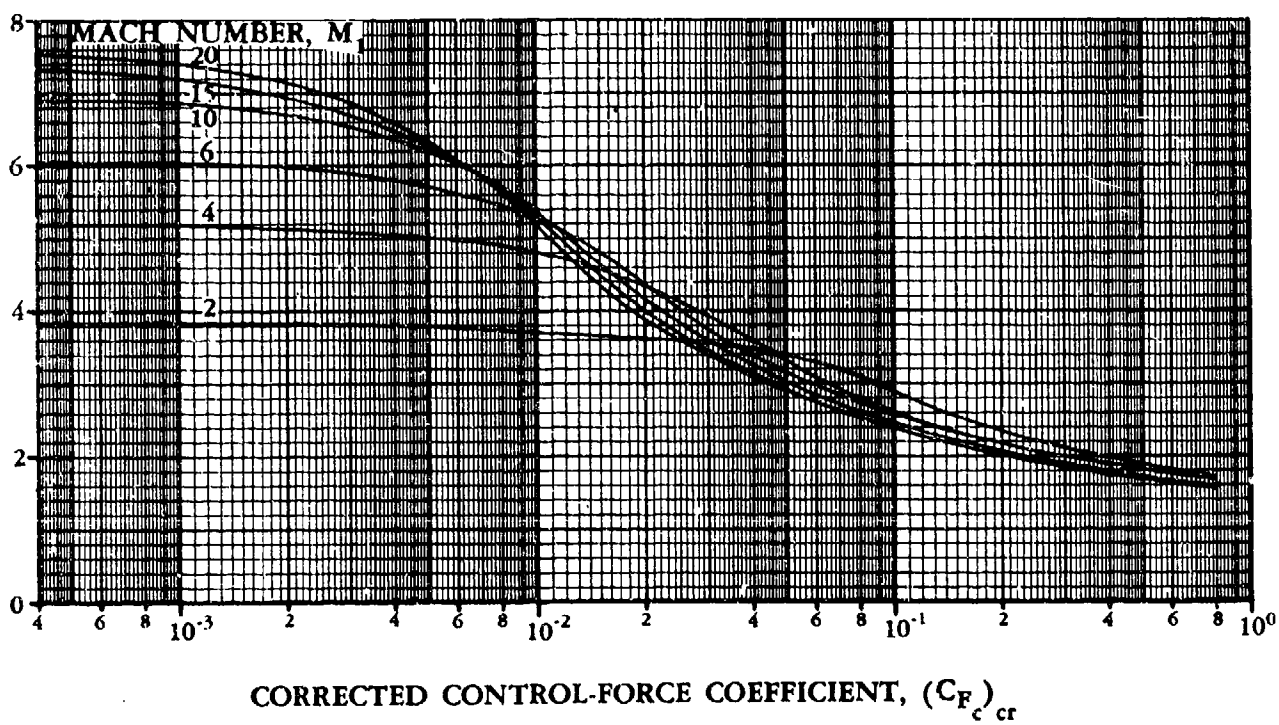

FIGURE 6.3.2-35 (CONTD)

(e) $R_{\ell_L} = 1 \times 10^9$

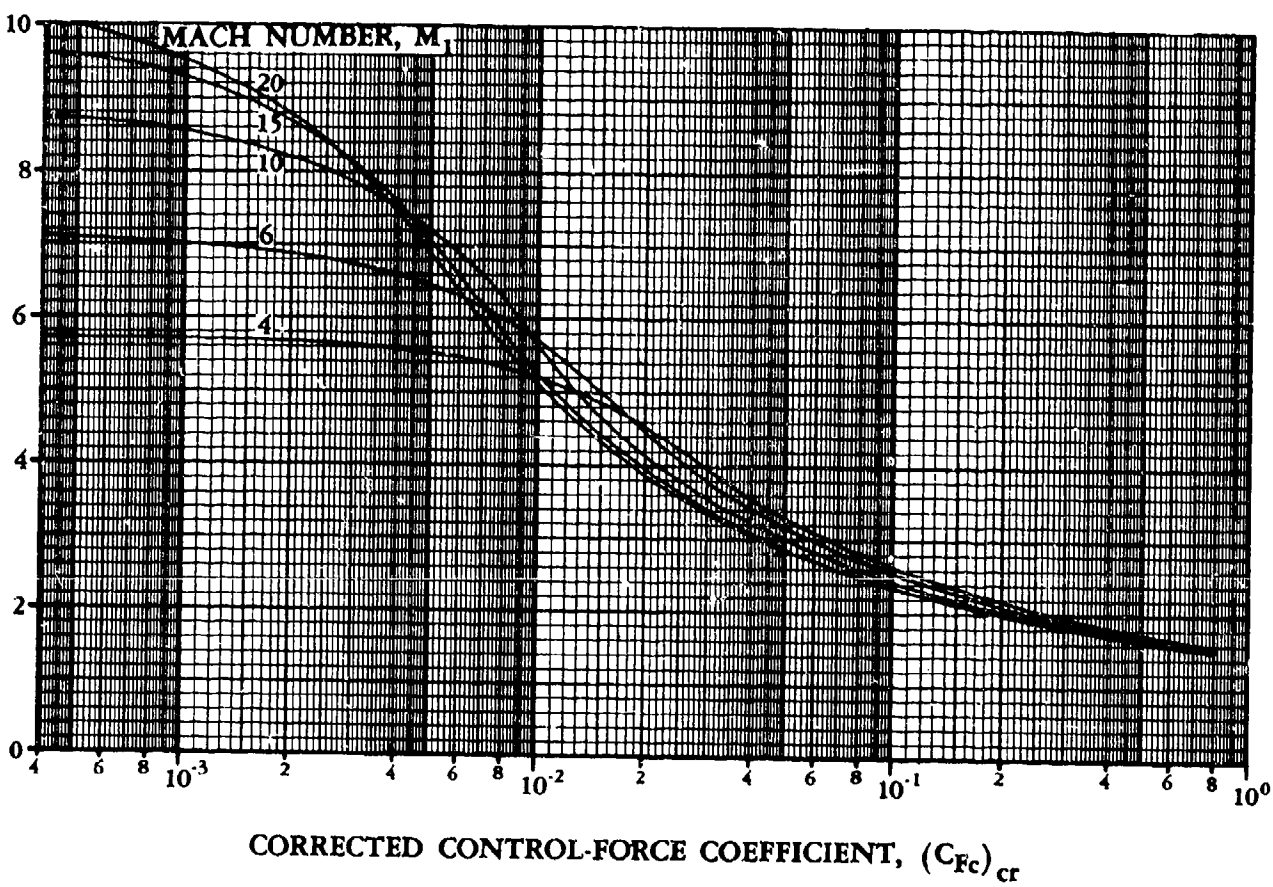

FIGURE 6.3.2-35 (CONTD)

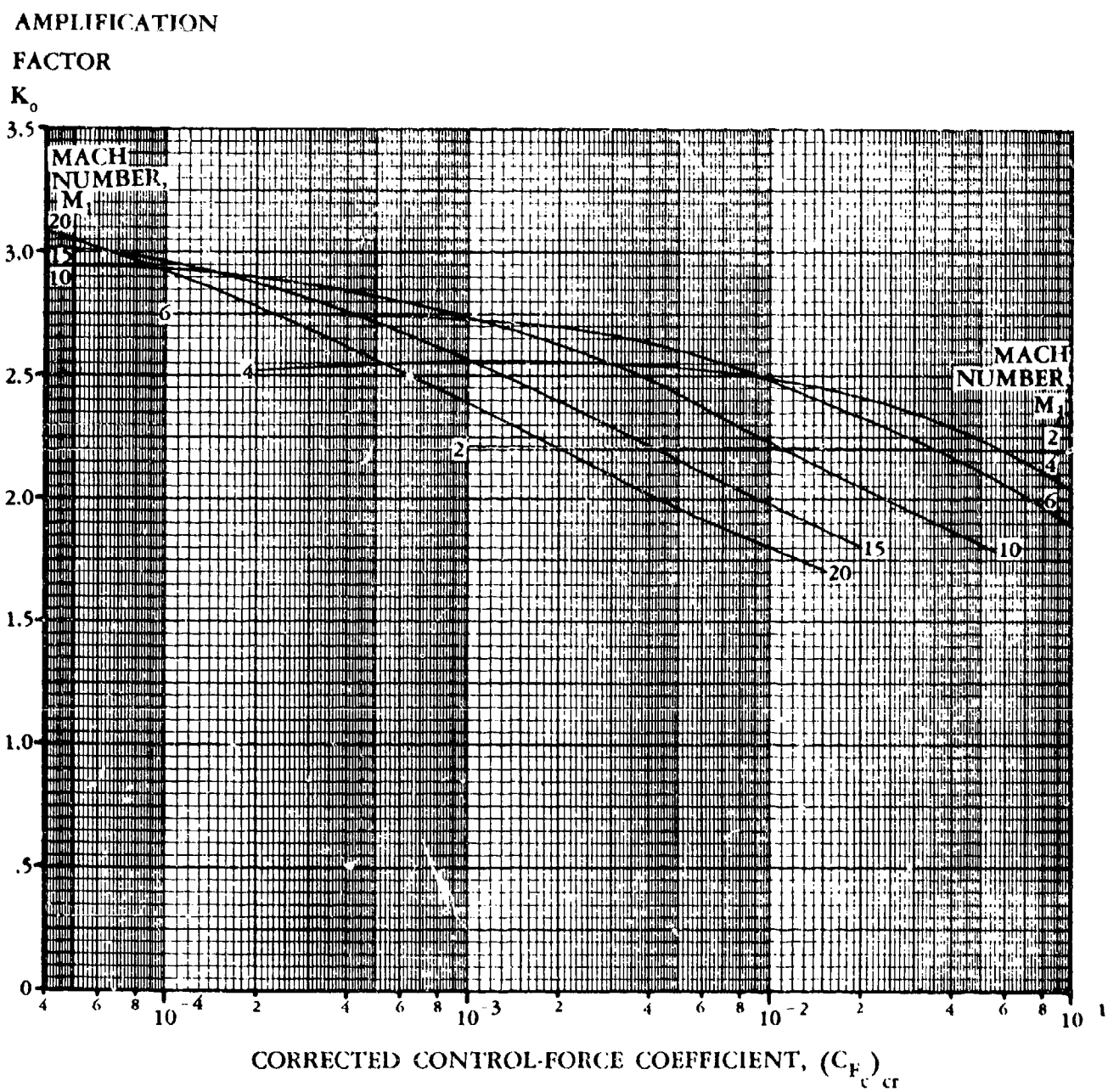

FIGURE 6.3.2-40 AMPLIFICATION FACTOR VERSUS CONTROL-FORCE COEFFICIENT FOR TURBULENT BOUNDARY LAYER

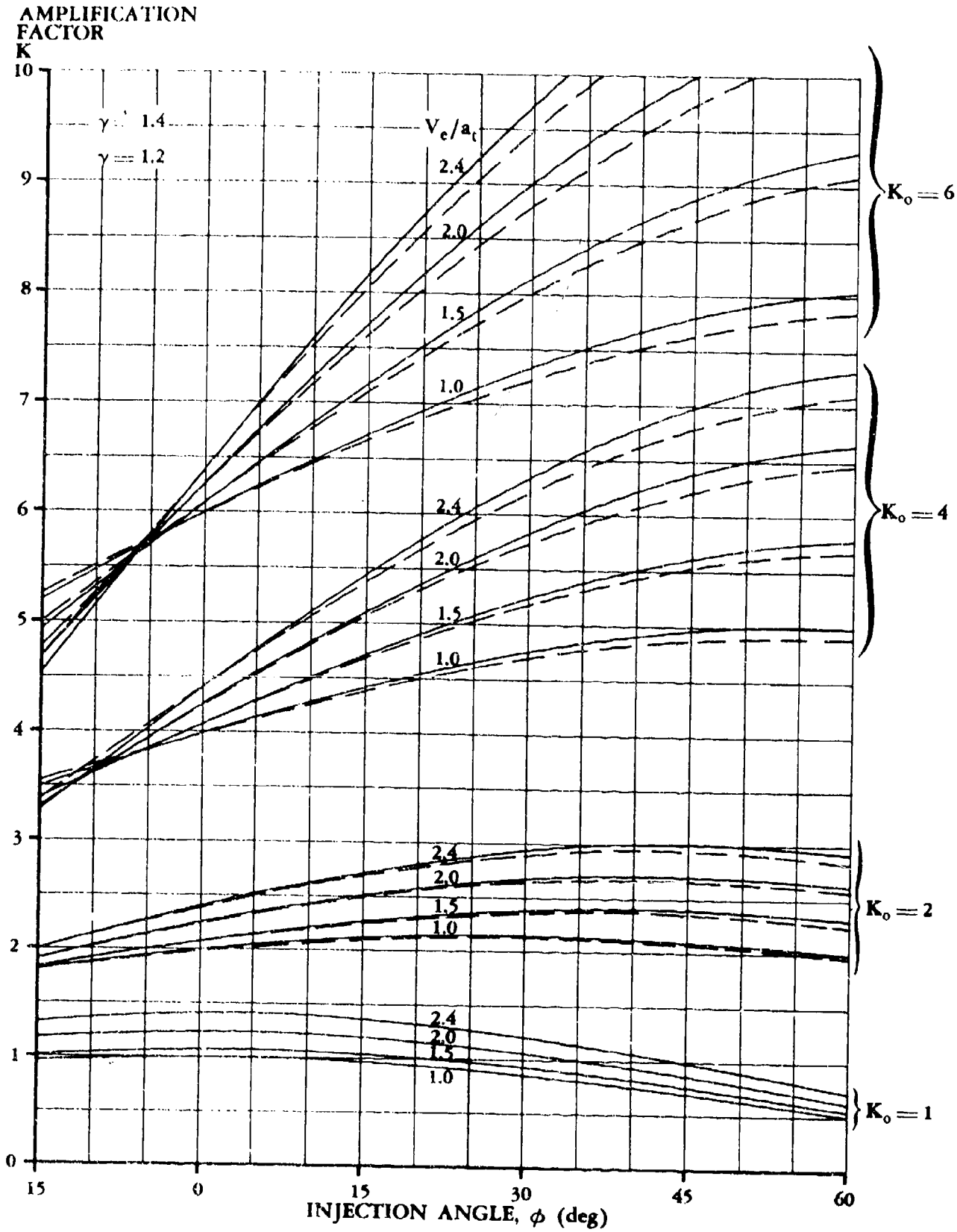

FIGURE 6.3.2-41 AMPLIFICATION FACTOR FOR INCLINED SUPERSONIC JETS

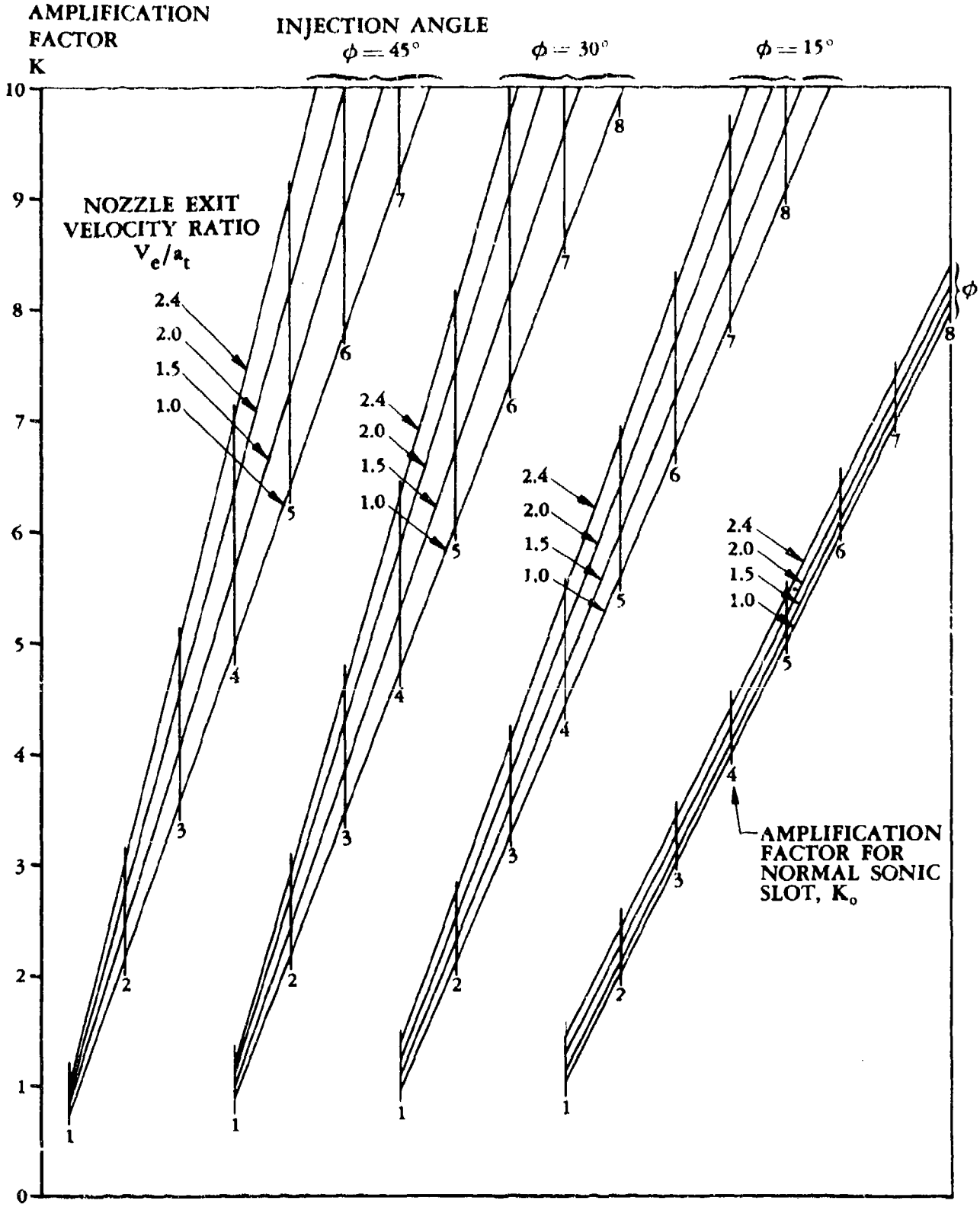

FIGURE 6.3.2-42 AMPLIFICATION FACTOR FOR INCLINED SUPERSONIC JETS

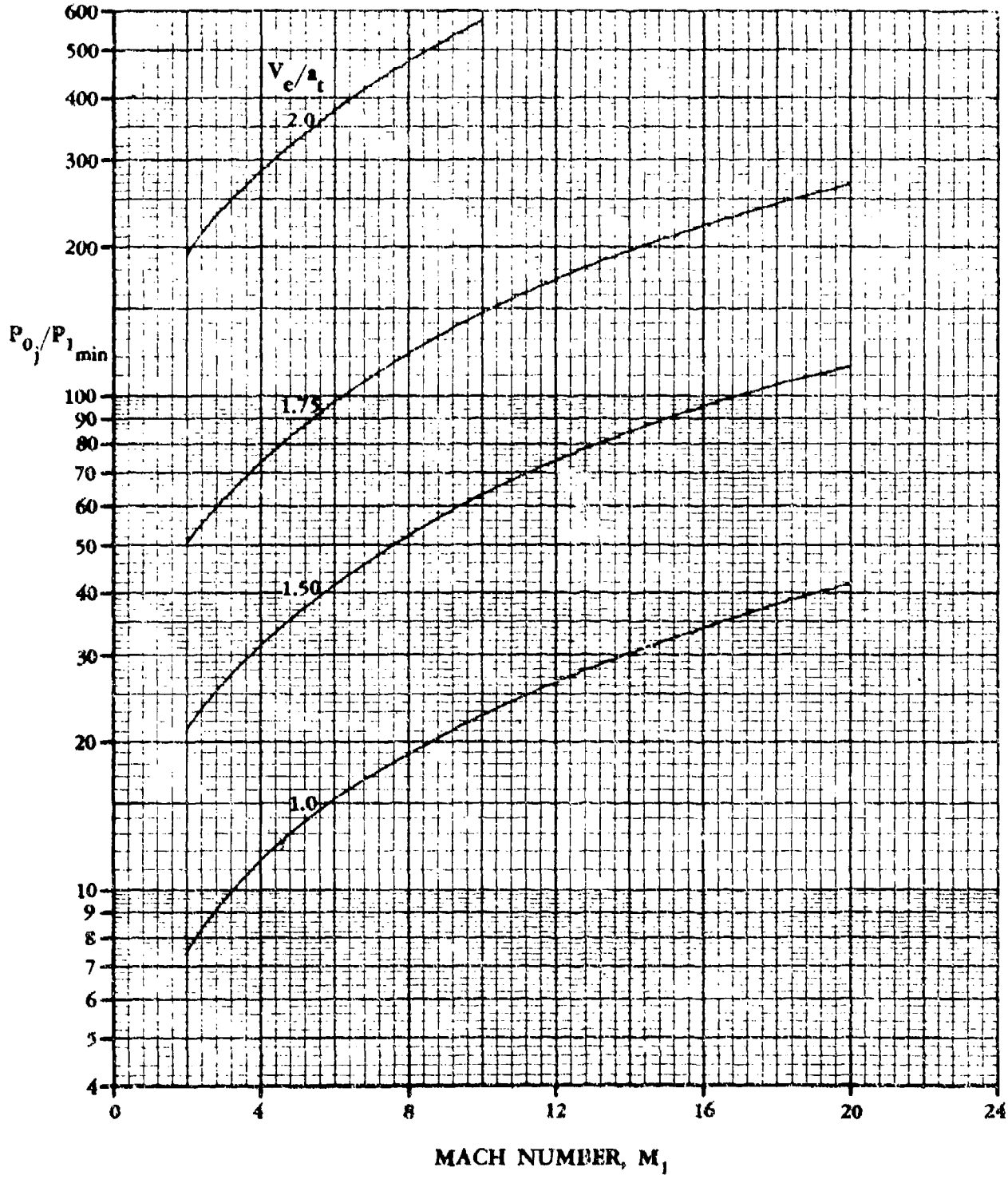

FIGURE 6.3.2-43 MINIMUM JET PRESSURE RATIO FOR CHOKED NOZZLE FLOW

6.3.4 AERODYNAMICALLY BOOSTED CONTROL-SURFACE TABS

Aerodynamically boosted control-surface tabs have been successfully used to reduce the forces on reversible-control systems many years. Linear methods from Reference 1 are presented herein for estimating the stick forces for a variety of the most commonly used control-surface-tab systems. Because of the compressibility effects on tabs at high speeds, the application of these methods should be restricted to subsonic flow; i.e., speeds below the surface critical Mach number or not above a Mach number of 0.90, whichever is least.

In order that the Datcom user may better understand the complex design considerations for a tab system, a general discussion (essentially taken from Reference 1) of pertinent design parameters for control-surface-tab systems is presented. For more details regarding tab systems the reader is referred to References 1 through 6. For a discussion and method of springy tabs or downsprings, the reader is specifically referred to Reference 6.

System Description

Aerodynamically boosted control systems can be divided into two distinct classifications: direct-control systems and indirect-control systems. Aerodynamic boost in direct-control systems includes nose aerodynamic balance, internal pressure balance on the main control surface, and may also include a tab "geared" to the main control surface. Sketch (a) illustrates the simple form of direct control without a tab, called "pure direct control."

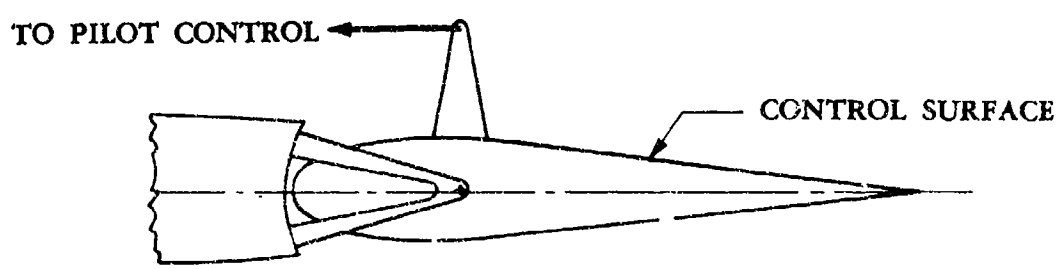

SKETCH (a) PURE DIRECT CONTROL

Sketch (b) illustrates the simple form of direct control with a tab, called a "geared tab."

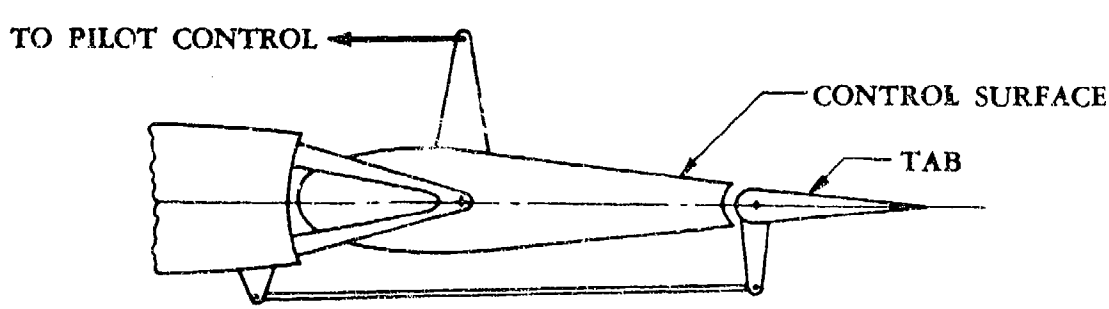

SKETCH (b) GEARED TAB

The most commonly used aerodynamically boosted control systems* fall into the indirect-control classification. Indirect-control systems may be subdivided into two types, one in which the pilot has direct control over both the tab and the main control surface and one in which he controls only the tab. Those systems in which the pilot has direct control over both the tab and the main control surface are referred to as link-tab systems. The three types of link-tab systems are plain linked tab, spring tab, and geared spring tab, shown schematically in Sketch (c).

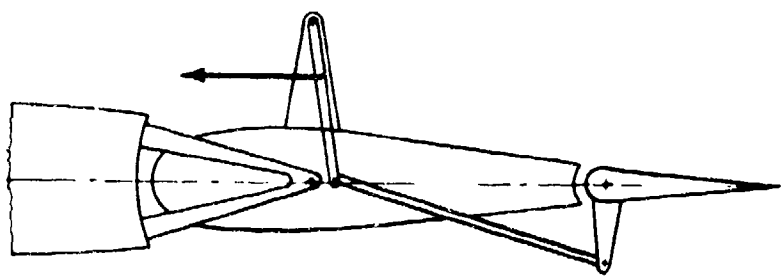

PLAIN LINKED TAB

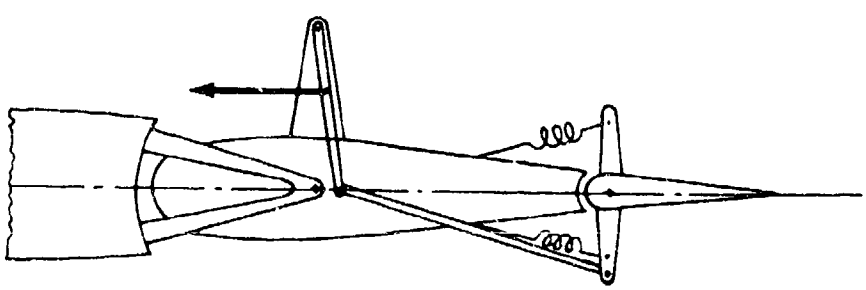

SPRING TAB

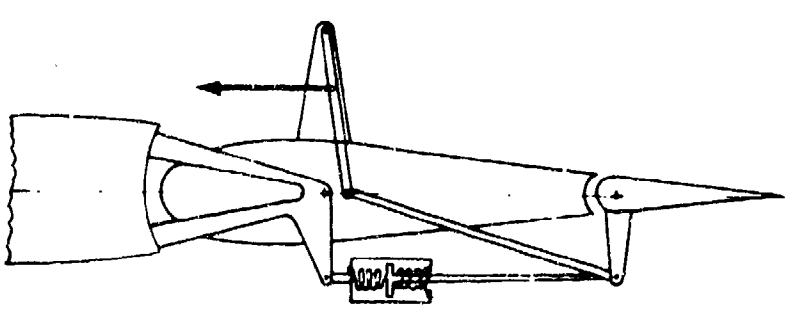

GEARED SPRING TAB

SKETCH (c)

*The control surface may be either an elevator, aileron, or rudder, throughout the discussion.

The fundamental relationship of the three tab systems is depicted in Sketch (c). It is evident that a spring-tab system is a plain linked tab with a spring added. The geared spring tab includes all the components of a spring tab, but with the spring arranged in series with a geared tab link.

The second type of indirect-control system is distinguished from the link-tab systems in that the pilot controls only the tab and is therefore called the pure-flying-tab system. The three types of flying-tab systems are the pure flying tab, spring flying tab, and the geared flying tab as shown schematically in Sketch (d).

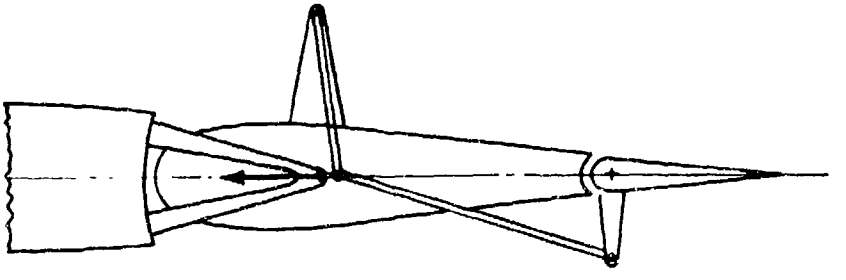

PURE FLYING TAB

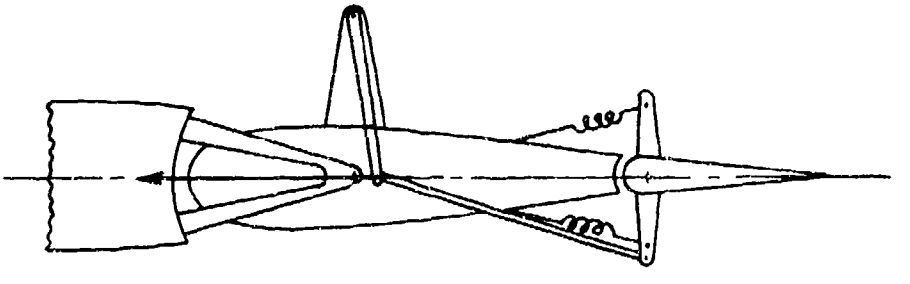

SPRING FLYING TAB

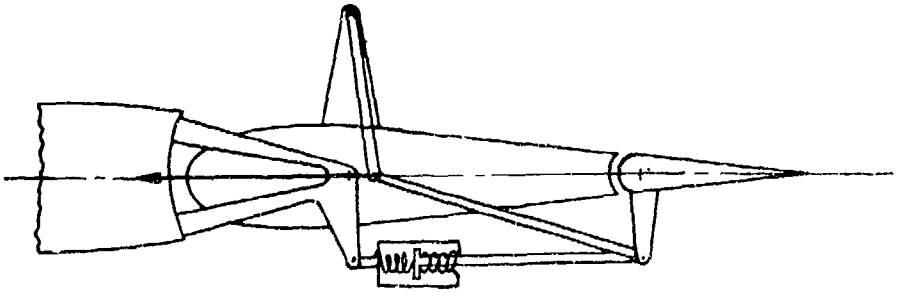

GEARED FLYING TAB

SKETCH (d)

Again, the fundamental relationship of the three tab systems is evident in Sketch (d).

It should be noted that both the plain linked tab and the pure flying tab have been called "servo-tabs" in much of the literature. However, since they are not identical systems, because of the different location of the cockpit control connecting point, it is important to maintain some distinction between the two.

In making any comprehensive analysis of aerodynamically boosted control-surface-tab systems, it is desirable first to reduce the special cases to be considered to the minimum number. Such a study reveals that all of the previously mentioned systems are but special cases of one general system. A schematic illustration of this general tab system is shown in Sketch (e). Table 6.3.4-A which accompanies the generalized control system, describes the specific tab system as a function of the cockpit control connecting point, along with the presence of a spring and its location.

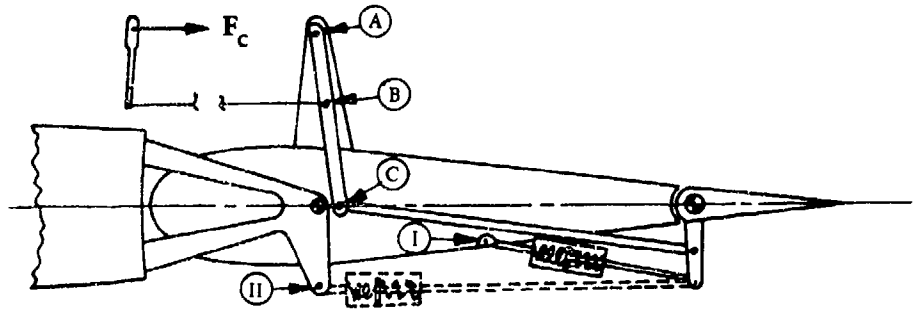

GENERALIZED CONTROL SYSTEM SCHEMATIC DIAGRAM
SKETCH (e)

TABLE 6.3.4-A

Cockpit Control Connecting Point	Tab Spring Configuration	Type of Control System
A	No Spring	Pure Direct Control
A	II	Geared Tab
B	No Spring	Plain Linked Tab
B	I	Spring Tab
B	II	Geared Spring Tab
C	II	Geared Flying Tab
C	I	Spring Flying Tab
C	No Spring	Pure Flying Tab

For a complete understanding of this general control-tab system, it is essential that the system kinematics are clearly understood. The key feature of the tab linkage is the fact that point C in Sketch (e) is not fixed to the control surface; i.e., it is free to translate; whereas, point A in Sketch (e) is fixed to the control surface and can translate only with movement of the control. It should also be noted that the spring configuration I in Sketch (e) corresponds to the case where the tab gearing link is connected to the hinge bracket at the main control-surface hinge line.

Key Linkage Parameters

The tab-system designer determines the type of tab system and the system force characteristics by his selection of three key linkage parameters. These key linkage parameters are:

- o The aerodynamic boost link ratio R_L, which is an index to the relative location of the pilot connecting point (A, B, or C in Sketch (e))
- o The tab spring effectiveness k
- o The tab gearing β, which is determined by the connecting linkage between the tab and the hinge bracket

Boost Link Ratio R_L

The boost link ratio R_L is specifically defined as the rate of change of the tab deflection with respect to control-surface deflection with the control column fixed; i.e.,

$$R_L = \left(\frac{\partial \delta_{tc}}{\partial \delta_c} \right)_{\substack{\text{stick} \\ \text{fixed}}} \qquad 6.3.4\text{-a}$$

For a general tab system as shown in Sketch (f), the value of R_L can be approximated by the system geometry by

$$R_L = \frac{\ell_2}{\ell_1} \frac{\ell}{\ell_t} \qquad 6.3.4\text{-b}$$

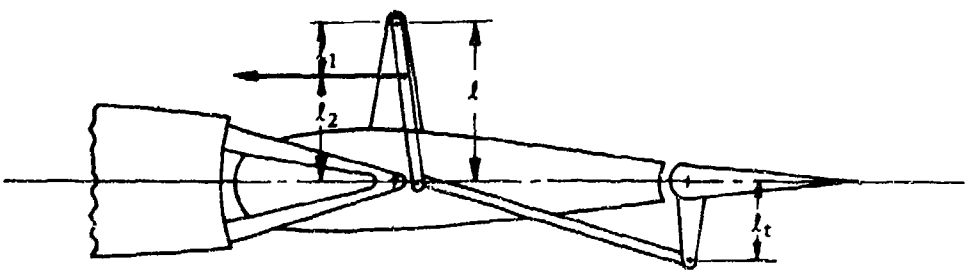

SKETCH (f)

From this relationship, the value of R_L can be seen as a direct indication of the cockpit control connecting point. Thus, when the value of R_L is zero, the tab system corresponds to a pure flying tab as shown in Sketch (d). Likewise, when the value of R_L is infinite, the tab system becomes a direct-control system (with a free-floating tab).

Tab Spring Effectiveness k

The tab spring effectiveness k is defined as the rate of change of moment on the tab due to the spring with respect to tab deflection, based on the product of tab area and chord; i.e.,

$$k = -\left(\frac{\partial M_{tc}}{\partial \delta_{tc}}\right)_{spring} \frac{1}{S_{tc}\bar{c}_{tc}} \qquad 6.3.4\text{-c}$$

Thus, typical units of k could be lb/ft^2-deg or $lb/in.^2$-deg.

Control Tab Gearing Ratio β

The control-tab-gearing ratio β is specifically defined as the rate of change of the tab deflection with respect to control-surface deflection with $k = \infty$ and the stick free; i.e.,

$$\beta = \left(\frac{\partial \delta_{tc}}{\partial \delta_c}\right)_{\substack{stick \\ free}} \text{ with } k = \infty \qquad 6.3.4\text{-d}$$

So, for a tab system without any connecting linkage between the tab and the hinge bracket, the value of β is zero, i.e., no gearing. For a geared system, the specific value of β is determined by the location of the connecting linkage relative to the control-surface hinge line.

Linkage-Parameter Effects on Forces

For discussion purposes, consider a plain-linked-tab system on a control surface that requires a pilot force of two hundred pounds to control the main surface, tab free, and a two-pound pilot force for a pure-flying-tab control. By applying one pound of pilot force to the tab, one-half the total work required to move the main surface is performed by the tab itself. Then by applying one hundred pounds of force to the main surface, the remaining one-half of the work is made up by the pilot directly, and the total pilot effort is 100 + 1 or 101 pounds. Thus, the link ratio R_L defines the proportions of the force division. At infinite link ratio, the pilot force will be two hundred pounds; at zero link ratio, two pounds. Therefore, a reduction in link ratio R_L results in a reduction of pilot force.

The use of a spring on the tab increases the tab hinge moments, and therefore increases the forces of a plain-linked-tab system. In the preceding example the force required to move the tab may be increased to, say, twenty pounds. For the same linkage, then, the total pilot force would be 100 + 10 or 110 pounds. Essentially, the spring effect adds an element of locked-tab hinge moment and reduces slightly the free-tab contribution. (This concept may be more clearly understood by referring to Equations 6.3.4-k and -o, which divide the control column force into contributions due to the free-tab, locked-tab, and gearing components.) Since the increase due to the locked-tab element is always greater than the corresponding decrease in the free-tab contribution, the pilot force will increase with increasing tab spring effectiveness.

Tab gearing β in the boost direction always reduces the pilot forces (by an increment rather than by a percentage), although the magnitude of the effect depends upon the values of the tab spring effectiveness k and the link ratio R_L. The effects of the spring and link ratio, however, are not so simply stated. Here both the magnitude and direction of the effect of one depend upon the value of the other and also on the tab gear ratio. In order to understand the interrelations between these parameters, it is necessary first to examine the "aerodynamic" characteristics of a spring. By this is meant the relationship of aircraft speed to the spring effect.

Normal aerodynamic coefficients are of course independent of speed if compressibility and aeroelastic effects are neglected. However, the spring characteristics are represented aerodynamically as (k/q) where q is the local dynamic pressure of the airstream. At zero airspeed the aerodynamic spring characteristic is infinite for all finite values of k. However, at infinite airspeed the aerodynamic spring characteristic is zero for all values of k. Hence, the characteristics of any system incorporating a tab spring correspond to those with the tab locked as in pure direct control (or geared as a geared tab) at zero airspeed, and to a system with no spring at infinite airspeed.

The individual effects of the linkage parameters are interrelated, but are nevertheless independent of the type of system used. It may be surmised that "special tab arrangements" are in themselves not that significant. What is more important is the matter of choosing proper values of the linkage parameters for a design application, rather than choosing a particular type of system. To illustrate this point, Sketch (g) shows three different tab systems for a particular control surface on an aircraft. Each tab system has been adjusted to yield nearly equivalent force characteristics over the speed range considered.

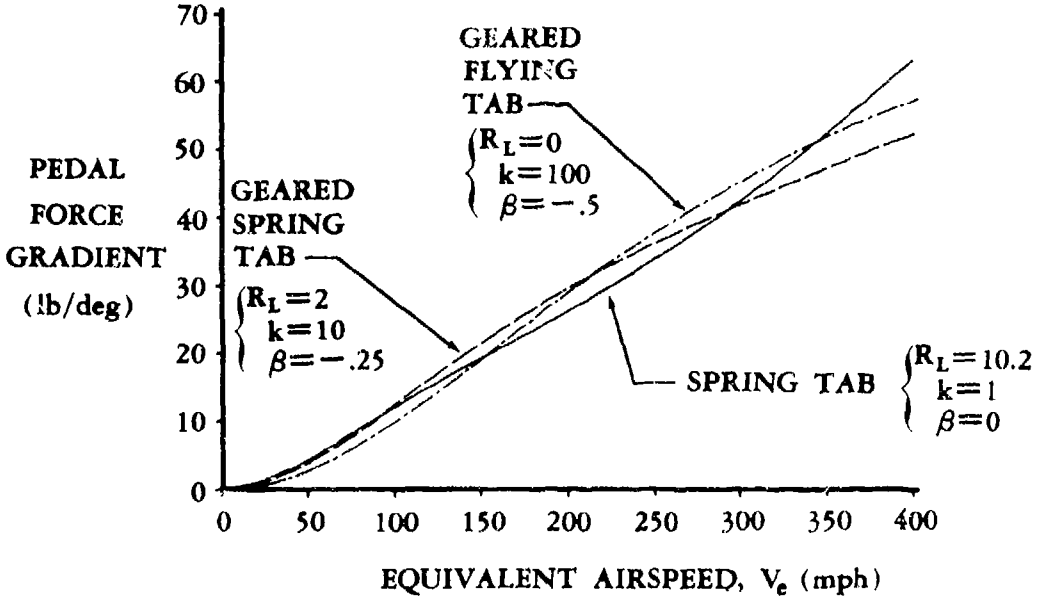

SKETCH (g)

DATCOM METHOD

The Datcom Method presents the fundamental relationship between the pilot forces and the tab and control-surface moments from which the control-column forces are evaluated.

The control-column force equations are presented in such a manner that the individual contributions of the various factors, i.e., tab-free, tab-fixed, and gearing contributions can be readily identified. It should be noted that two control-column force equations are presented, both of which define a general tab control system for an elevator, rudder, aileron, or other control system having linear characteristics. The two equations presented are based on different independent variables for the convenience of the user (they provide identical values of control-column force).

Because of the lengthy control-column force equations, a summary table and shorthand notation has been used to simplify the presentation of equations. In order to facilitate this presentation, the following general notation list is provided.

NOTATION*

SYMBOL		DEFINITION
A_c	=	$\dfrac{S_{tc}\bar{c}_{tc}}{S_c\bar{c}_c}$.
B_1	=	$\left(\partial C_{h_c}/\partial\delta_c\right)_{\delta_{tc},\alpha_s,\delta_{tt}}$
B_2	=	$\left(\partial C_{h_c}/\partial\delta_{tc}\right)_{\delta_c,\alpha_s,\delta_{tt}}$
B_3	=	$\left(\partial C_{h_c}/\partial\alpha_s\right)_{\delta_c,\delta_{tc},\delta_{tt}}$
B_4	=	$\left(\partial C_{h_c}/\partial\delta_{tt}\right)_{\delta_c,\delta_{tc}\alpha_s}$
$\bar{c}_{(\ )}$		surface mean aerodynamic chord (movable surfaces are defined by their area aft of the hinge line, and the MAC is of that area)
C_{h_c}		is the hinge-moment coefficient of the particular control surface, i.e., $H_c/qS_c\bar{c}_c$)(either an elevator, rudder, or aileron)
$C_{h_{tc}}$		is the hinge-moment coefficient of the control tab, i.e., $H_{tc}/qS_{tc}\bar{c}_{tc}$)
C_L		lift coefficient, positive up or to the right

*Units are not specified for derivatives, lengths, or areas. It is up to the user to choose his units and be consistent throughout.

SYMBOL	DEFINITION
C_{L_s}	lift coefficient of surface to which the main control surface is attached, i.e., C_{L_H}, C_{L_V}, or C_{L_W} (total lift, including lift due to control deflection, tab deflection, and angle of attack)
C_{L_H}	is the horizontal-tail lift coefficient (total lift, including lift due to control deflection, tab deflection, and angle of attack)
C_{L_V}	is the vertical-tail lift coefficient (total lift, including lift due to control deflection, tab deflection, and angle of attack)
C_{L_W}	is the wing lift coefficient (total lift, including lift due to control deflection, tab deflection, and angle of attack)
C_{L_α}	airplane lift-curve slope
$C_{L_{\alpha_H}}$	airplane lift-curve slope with respect to the tail angle of attack
$C_1 = \left(\partial C_{L_s}/\partial \delta_c\right)_{\delta_{tc}, \delta_{tt}, \alpha_s}$	
$C_2 = \left(\partial C_{L_s}/\partial \delta_{tc}\right)_{\delta_c, \alpha_s, \delta_{tt}}$	
$C_3 = \left(\partial C_{L_s}/\partial \alpha_s\right)_{\delta_c, \delta_{tc}, \delta_{tt}}$	
$C_4 = \left(\partial C_{L_s}/\partial \delta_{tt}\right)_{\delta_c, \alpha_s, \delta_{tc}}$	
$D_1 = \left(\partial C_{h_{tc}}/\partial \delta_c\right)_{\delta_{tc}, \alpha_s}$	
$D_2 = \left(\partial C_{h_{tc}}/\partial \delta_{tc}\right)_{\delta_c, \alpha_s}$	
$D_3 = \left(\partial C_{h_{tc}}/\partial \alpha_s\right)_{\delta_c, \delta_{tc}}$	
$E_1 = B_1/C_1$	
$E_2 = B_2 - C_2E_1$	
$E_3 = B_3 - C_3E_1$	
$E_4 = B_4 - C_4E_1$	
F_c	control-column force in lb (pull force is positive)

SYMBOL		DEFINITION
F_s		elevator stick force in lb (pull force is positive)
F_p		rudder-pedal force in lb (push on left pedal is positive)
F_1	=	D_1/C_1
F_2	=	$D_2 - C_2F_1$
F_3	=	$D_3 - C_3F_1$
F_4	=	$-C_4F_1$
$G_{(\ )}$		pilot gearing factor (see Equations 6.3.4-f and -f')
$G_{c_{max}}$		maximum stick gearing (see Equation 6.3.4-i)
$H_{(\ )}$		control hinge moment
k		tab spring effectiveness, in lb/ft^2-deg (see Equation 6.3.4-c)
n'		airplane normal acceleration or load factor in g's
q		local dynamic pressure (lb/ft^2)
q_∞		free-stream dynamic pressure (lb/ft^2)
R_1, R_2		shorthand notation for tab and main surface hinge moments and key linkage parameters, obtained from Table 6.3.4-B
R_L		aerodynamic boost link ratio (see Equations 6.3.4-a and -b)
$S_{(\ )}$		surface area (movable surfaces are defined by their area aft of the hinge line)
T_1, T_2		shorthand notation for tab and main surface hinge moments and key linkage parameters, obtained from Table 6.3.4-C
V		airspeed
W		aircraft weight
x_c		fore and aft displacement of control column, positive forward
$x_{c_{max}}$		maximum displacement of control column, positive forward

SYMBOL		DEFINITION
x_p		fore and aft displacement of right rudder pedal, positive forward
α		angle of attack, positive for lift increase
α_s		angle of attack of the surface to which the main control surface is attached, i.e., α_H, α_V, or α_W
α_H		angle of attack of the horizontal tail
α_V		angle of attack of the vertical tail
α_W		angle of attack of the wing
β		control-tab gear ratio (see Equation 6.3.4-d)
ϵ		downwash at the horizontal tail
Δ_r	=	$-\delta_{tc_{max}}/\delta_{c_{max}}$ for a maximum control deflection (the value of Δ_r is positive because $\delta_{tc_{max}}$ and $\delta_{c_{max}}$ will have opposite signs)
$\delta_{c_{max}}$		the maximum deflection of the main control surface, in degrees
$\delta_{(\ )}$		surface deflection, positive for trailing edge down or to the left, in degrees
σ		air density ratio, ρ/ρ_o
ϕ_β		lift efficiency factor for a geared tab system, $1 + \beta C_2/C_1$

SUBSCRIPTS

c	main control surface (elevator, rudder, aileron, etc.)
e	elevator
H	horizontal tail
p	control pedal
r	rudder
s	surface to which the main control surface is attached, i.e., horizontal tail, vertical tail, or wing
tc	control tab
tt	trim tab

The following relationship from Reference 1 is derived from basic considerations of system equilibrium and fundamental laws, giving a relationship between pilot forces and the tab and control surface moments, as

$$F_c = G_c H_c = G_{tc} H_{tc} = -G_c R_L H_{tc} \qquad 6.3.4\text{-e}$$

where the control-surface stick gearing G_c and the tab stick gearing G_{tc} are defined as

$$G_c = \frac{1}{57.3\left(\frac{\partial x_c}{\partial \delta_c}\right)_{tc}} \qquad 6.3.4\text{-f}$$

$$G_{tc} = \frac{1}{57.3\left(\frac{\partial x_c}{\partial \delta_{tc}}\right)_{c}} \qquad 6.3.4\text{-f}'$$

Using Equation 6.3.4-e, the aerodynamic boost link ratio R_L can be expressed as a function of the stick and tab gearing, i.e.,

$$R_L = \frac{-G_{tc}}{G_c}$$

Since the aerodynamic boost link ratio must be positive, it becomes evident that the control surface stick gearing G_c and the tab stick gearing G_{tc} must have opposite signs.

The particular form of Equation 6.3.4-e that is used is dependent upon the value of the boost link ratio; i.e.,

$$F_c = G_c H_c \qquad \text{for} \qquad R_L = \infty$$

$$F_c = G_{tc} H_{tc} \qquad \text{for} \qquad R_L = 0$$

$$F_c = -G_c R_L H_{tc} \qquad \text{for} \qquad 0 < R_L < \infty$$

The control surface moments M_c for a general tab system (see Sketch (e)) can be expressed as*

$$H_c = S_c \bar{c}_c q[B_1 \delta_c + B_2 \delta_{tc} + B_3 \alpha_s + B_4 \delta_{tt} + \frac{k}{q} A_c \beta(\delta_{tc} - \beta\delta_c)] \qquad 6.3.4\text{-g}$$

*These moment equations are applicable for symmetrical, untwisted control surfaces that yield a value of zero for H_c and H_{tc} when δ_c, δ_{tc}, δ_{tt}, and α_s are all zero.

and the tab surface moments M_{t_c} for a general tab system can be expressed as*

$$H_{t_c} = S_{t_c}\bar{c}_{t_c}q[D_1\delta_c + D_2\delta_{t_c} + D_3\alpha_s - \frac{k}{q}(\delta_{t_c} - \beta\delta_c)] \qquad 6.3.4\text{-h}$$

Equation 6.3.4-e is the primary aerodynamic relationship from which the stick forces are evaluated. It defines not only the force-moment relationships, but also the system equilibrium Therefore, analysis of any control system can be made if the control-surface and control-tab hinge-moment characteristics and the system motion characteristics are known.

Another significant parameter is the maximum stick gearing $G_{c_{max}}$ defined by

$$G_{c_{max}} = \frac{1}{57.3\left(\frac{\partial x_c}{\partial \delta_c}\right)_{max}} \qquad 6.3.4\text{-i}$$

The stick gearing G_c is related to the maximum stick gearing by the following:

$$\frac{G_c}{G_{c_{max}}} = \frac{R_L + \Delta_r}{R_L} \qquad 6.3.4\text{-j}$$

From this equation it is evident that the value of the ratio $G_c/G_{c_{max}}$ is greater than one. This simply means that the cockpit control travel must be greater than that required to bottom the control with the tab fixed. Sufficient control travel must exist to bottom the control surface and the control surface tab simultaneously, while allowing for cable stretch.

Control Column Forces

The analysis of a typical tab system requires detailed knowledge of the tab and control hinge-moment characteristics as a function of the main-control-surface angle of attack. For a particular angle of attack, Sketch (h) illustrates the typical hinge-moment and gearing data required to analyze any tab control system.

These data should preferably be obtained from wind-tunnel-test data or may be estimated by using the hinge-moment methods of Section 6.1.6. Because of the lengthy control-column force equations, a summary table and shorthand notation will be used to simplify the presentation of the equations. The format in which the control-column force equations are presented, i.e., tab-free, tab-fixed, and gearing contributions, is used so that the contribution of the various factors can be more readily identified.

*These moment equations are applicable for symmetrical, untwisted control surfaces that yield a value of zero for H_c and H_{t_c} when δ_c, δ_{t_c}, δ_{t_t}, and α_s are all zero.

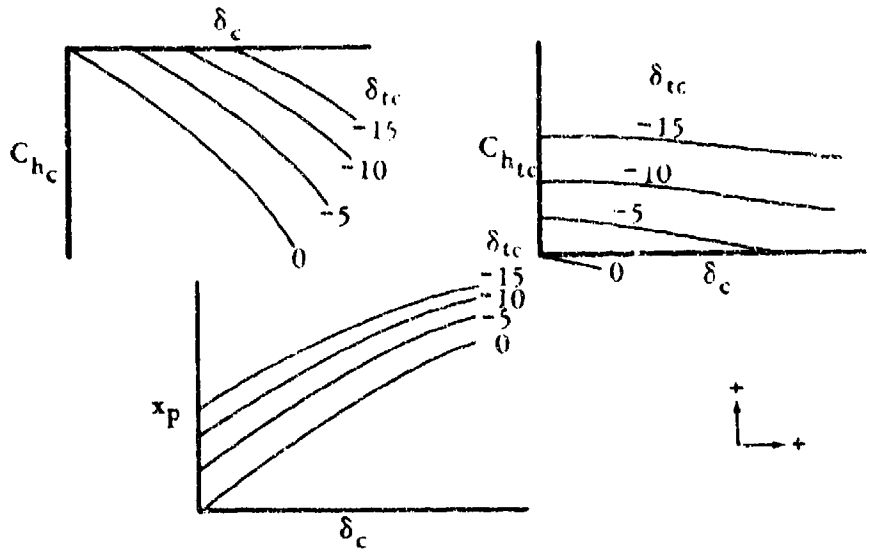

SKETCH (h)

The two control-column force equations presented herein are modifications of Equation 6.3.4-e, with the variable δ_{tc} being eliminated. These equations are for a general tab control system on an elevator, rudder, aileron, or other control system having linear aerodynamic characteristics. (For example, when evaluating an elevator tab system, the terms $\bar{c}_c$, δ_c, C_{h_c}, α_s, etc., become $\bar{c}_e$, δ_e, C_{h_e}, α_H, etc., respectively.) The first equation is based on the independent variables δ_c, α_s, and δ_{tt}; while the second equation is based on the independent variables C_L, α_s, and δ_{tt}. Either equation may be used depending upon the preference of the user.

The first equation for estimating the control-column force characteristics, based on the independent variables δ_c, α_s, and δ_{tt}, is

$$F_c = G_{c_{max}} S_c \bar{c}_c q \left[C_{h_{c_{\substack{tab \\ free}}}} R_1 + C_{h_{c_{\substack{tab \\ locked}}}} R_2 + \Delta C_{h_{c_{\substack{tab \\ gearing}}}} R_2 \right] \qquad 6.3.4\text{-k}$$

where

$G_{c_{max}}$ is the maximum stick gearing available as defined by Equation 6.3.4-i. The value of $G_{c_{max}}$ is finite for all tab systems with a finite boost link ratio. However, for flying-tab systems where $R_L = 0$, the value of $G_{c_{max}}$ is zero. To avoid a problem when using Equation 6.3.4-k, the user should realize that the R_1 and R_2 terms for flying-tab systems in Table 6.3.4-B contain the parameter Δ_r. The product of $G_{c_{max}}$ and Δ_r yields $G_{tc_{max}}$ or the maximum gearing of the tab, which has a finite value. Thus, for flying-tab systems a finite value of $G_{c_{max}}$ is not possible; however, Equation 6.3.4-k is still applicable when $G_{tc_{max}}$ is used to replace the product of $G_{c_{max}}$ and Δ_r.

q is the dynamic-pressure ratio. This value must be consistent with whatever value is used to nondimensionalize the hinge-moment coefficients in Equations 6.3.4-ℓ, -m, and -n. If the hinge-moment coefficients are based on wind-tunnel-test data, they are probably nondimensionalized with respect to the free-stream dynamic-pressure ratio. If the Datcom is used to estimate the hinge-moment coefficients, the local dynamic-pressure ratio should be used. (Local dynamic-pressure ratio may be obtained from Section 4.4.1 for an empennage panel.)

$$C_{h_{c_{\substack{tab \\ free}}}} = \left(B_1 - D_1 \frac{B_2}{D_2}\right)\delta_c + \left(B_3 - D_3 \frac{B_2}{D_2}\right)\alpha_s + B_4 \delta_{tt} \qquad 6.3.4\text{-}\ell$$

$$C_{h_{c_{\substack{tab \\ locked}}}} = B_1 \delta_c + B_3 \alpha_s + B_4 \delta_{tt} \qquad 6.3.4\text{-m}$$

$$\Delta C_{h_{c_{gearing}}} = (\beta B_2 + \beta A_c D_1 + \beta^2 A_c D_2)\delta_c + (\beta A_r D_3)\alpha_s \qquad 6.3.4\text{-n}$$

The values for R_1 and R_2 are found from Table 6.3.4-B as a function of the specific type of tab system. This table also summarizes values for the three key linkage parameters R_L, k, and β for each specific type of tab system, using an "F" to denote finite values for the parameters.

The second equation for estimating the control-column force characteristics, based on the independent variables C_{L_s}, α_s, and δ_{tt}, is

$$F_c = G_{c_{max}} S_c \bar{c}_c q \left[C_{h_{c_{\substack{tab \\ free}}}} T_1 + C_{h_{c_{\substack{tab \\ locked}}}} T_2 + \Delta C_{h_{c_{gearing}}} T_2\right] \qquad 6.3.4\text{-o}$$

where

$G_{c_{max}}$ is the maximum stick gearing available as defined by Equation 6.3.4-i. The same comments made about $G_{c_{max}}$ for spring tab systems, when using Equation 6.3.4-k, also apply to the application of Equation 6.3.4-o (see discussion following Equation 6.3.4-k).

q is the dynamic-pressure ratio as defined above for Equation 6.3.4-k. (Consistent with whatever value was used to nondimensionalize the hinge-moment coefficients in Equations 6.3.4-p, -q, and -r.)

TABLE 6.3.4-B

Specific Type of System	Linkage R_L	Linkage k	Linkage β	R_1	R_2
Geared Tab	∞	∞	F*	0	1
Pure Direct Control	∞	∞	0	0	1
Geared Spring Tab	F	F	F	$\dfrac{(R_L + \Delta_r)}{R_L + \dfrac{B_2}{A_c D_2} - \dfrac{k}{qD_2}(R_L - \beta)}$	$\dfrac{-(k/qD_2)(R_L + \Delta_r)}{R_L + \dfrac{B_2}{A_c D_2} - \dfrac{k}{qD_2}(R_L - \beta)}$
Spring Tab	F	F	0	$\dfrac{(R_L + \Delta_r)}{R_L + \dfrac{B_2}{A_c D_2} - \dfrac{k}{qD_2}(R_L)}$	$\dfrac{-(k/qD_2)(R_L + \Delta_r)}{R_L + \dfrac{B_2}{A_c D_2} - \dfrac{k}{qD_2}(R_L)}$
Plain Linked Tab	F	0	0	$\dfrac{(R_L + \Delta_r)}{R_L + \dfrac{B_2}{A_c D_2}}$	0
Geared Flying Tab	0	F	F	$\dfrac{\Delta_r}{\dfrac{B_2}{A_c D_2} + \dfrac{k}{qD_2}\beta}$	$\dfrac{-(k/qD_2)\,\Delta_r}{\dfrac{B_2}{A_c D_2} + \dfrac{k}{qD_2}\beta}$
Spring Flying Tab	0	F	0	$\dfrac{\Delta_r}{\dfrac{B_2}{A_c D_2}}$	$\dfrac{-(k/qD_2)\,\Delta_r}{\dfrac{B_2}{A_c D_2}}$
Pura Flying Tab	0	0	0	$\dfrac{\Delta_r}{\dfrac{B_2}{A_c D_2}}$	0

*Denotes a finite value.

$$C_{h_{c_{\substack{tab\\free}}}} = \left(E_1 - F_1\frac{E_2}{F_2}\right)C_{L_s} + \left(E_3 - F_3\frac{E_2}{F_2}\right)\alpha_s + \left(E_4 - F_4\frac{E_2}{F_2}\right)\delta_{tt} \qquad 6.3.4\text{-p}$$

$$C_{h_{c_{\substack{tab\\locked}}}} = E_1 C_{L_s} + E_3\alpha_s + E_4\delta_{tt} \qquad 6.3.4\text{-q}$$

$$\Delta C_{h_{c_{gearing}}} = \beta\left(E_1\frac{C_2}{C_1} + A_c\frac{F_2}{C_1} + \frac{E_2}{C_1} + A_c\phi_\beta F_1\right)C_{L_s} + \beta\left(E_3\frac{C_2}{C_1} - \beta A_c C_3\frac{F_2}{C_1} - C_3\frac{E_2}{C_1} + \phi_\beta A_c F_3\right)\alpha_s + \beta\left(E_4\frac{C_2}{C_1} - \beta A_c C_4\frac{F_2}{C_1} - C_4\frac{E_2}{C_1} + \phi_\beta A_c F_4\right)\delta_{tt}$$

6.3.4-r

The values for T_1 and T_2, along with values for the key linkage parameters, are found from Table 6.3.4-C as a function of the specific type of tab system.

TABLE 6.3.4-C

Specific Type of System	Linkage R_L	Linkage k	Linkage β	T_1	T_2
Geared Tab	∞	∞	F*	0	$1/\phi_\beta$
Pure Direct Control	∞	∞	0	0	1
Geared Spring Tab	F	F	F	$\dfrac{(R_L+\Delta_r)}{R_L+\frac{E_2}{A_cF_2}-\frac{k}{qF_2}\phi_\beta(R_L-\beta)}$	$\dfrac{-(k/qF_2)(R_L+\Delta_r)}{R_L+\frac{E_2}{A_cF_2}-\frac{k}{qF_2}\phi_\beta(R_L-\beta)}$
Spring Tab	F	F	0	$\dfrac{(R_L+\Delta_r)}{R_L+\frac{E_2}{A_cF_2}-\frac{k}{qF_2}(R_L)}$	$\dfrac{-(k/qF_2)(R_L+\Delta_r)}{R_L+\frac{E_2}{A_cF_2}-\frac{k}{qF_2}(R_L)}$
Plain Linked Tab	F	0	0	$\dfrac{(R_L+\Delta_r)}{R_L+\frac{E_2}{A_cF_2}}$	0
Geared Flying Tab	0	F	F	$\dfrac{\Delta_r}{\frac{E_2}{A_cF_2}+\frac{k}{qF_2}\phi_\beta(\beta)}$	$\dfrac{-(k/qF_2)\,\Delta_r}{\frac{E_2}{A_cF_2}+\frac{k}{qF_2}\phi_\beta(\beta)}$
Spring Flying Tab	0	F	0	$\dfrac{\Delta_r}{\frac{E_2}{A_cF_2}}$	$\dfrac{-(k/qF_2)\,\Delta_r}{\frac{E_2}{A_cF_2}}$
Pure Flying Tab	0	0	0	$\dfrac{\Delta_r}{\frac{E_2}{A_cF_2}}$	0

*Denotes a finite value.

Tab Lift Loss

In achieving large control-column force reductions, tabs generate loads opposite to those on the main control surface. Thus, the net lift or efficiency of the main control surface is reduced by some amount. A typical value for loss in lift efficiency for a transport-type aircraft is 15%. The majority of the lift losses range from 5 to 20%. The maximum loss will occur for the pure flying-tab system. The efficiency of a control surface employing a tab may be expressed as

$$\eta = 1 - \frac{\Delta C_{L_{tc}} \text{ (lift loss due to tab)}}{\Delta C_{L_c} \text{ (iift increment due to control surface)}} \qquad 6.3.4\text{-s}$$

This can also be expressed as

$$\eta = 1 + \left(\frac{\partial C_{L_c}}{\partial \delta_{tc}}\right)\left(\frac{\partial \delta_c}{\partial C_{L_c}}\right)\frac{\delta_{tc}}{\delta_c} \qquad 6.3.4\text{-t}$$

For most cases, the critical case occurs when the trim tab angle and the angle of attack are zero, allowing δ_{tc}/δ_c to be expressed as

$$\frac{\delta_{tc}}{\delta_c} = \frac{B_1 + R_L A_c D_1 + \frac{k}{q}\beta A_c R_L - \frac{k}{q}A_c \beta^2}{B_2 + R_L A_c D_2 - \frac{k}{q}A_c R_L + \frac{k}{q}A_c \beta} \qquad 6.3.4\text{-u}$$

Thus, the efficiency of a tab system can be evaluated by using Equation 6.3.4-t where Equation 6.3.4-u is used for the relationship of δ_{tc}/δ_c.

Design Criteria

The design of tab boost systems can be a complex iterative process involving many variables. The mechanical limitations vary for various aircraft designs. However, Table 6.3.4-D (from Reference 1) presents a summary of the practical design criteria that will apply to most systems.

TABLE 6.3.4-D
SUGGESTED DESIGN CRITERIA
FOR AERODYNAMIC BOOST SYSTEMS

Parameter	Maximum Range of Values	Design Limitations
Link Ratio R_L	0, .1 to 10, ∞	Mechanical-Linkage Design
Spring Rate k	Any	Minimum Value Depends on Preload
Gear Ratio β	0 to $-\left(.002+\frac{\partial C_{h_c}}{\partial \delta_c}\right)\left(\frac{\partial C_{h_c}}{\partial \delta_{tc}}\right)$	Nonlinearity and Overbalance
Spring Preload	Min. Value: As required to overcome tab system friction Max. Value: No more than required to obtain desired force level	Good Tab Centering Minimize Variation of Elevator Control Forces with Speed
Tab Size	Minimum: To control main surface to maximum deflection Maximum: To give $\frac{\partial C_{h_c}}{\partial \delta_c} \Big/ \frac{\partial C_{h_c}}{\partial \delta_{tc}} = 0.5$	Adequate Tab Power Overbalance with Free Tab
$\frac{\partial C_{h_c}}{\partial \delta_c} = B_1$	$-B_1 > 0.002$	Overbalance and Nonlinearity

The following sample problem illustrates the use of the control-column force equations as applied to a given elevator spring-tab control system. No attempt is made herein to present a numerical example of the design of a tab boost system.

Sample Problem

Given: An elevator spring-tab control system on a transport-type aircraft.

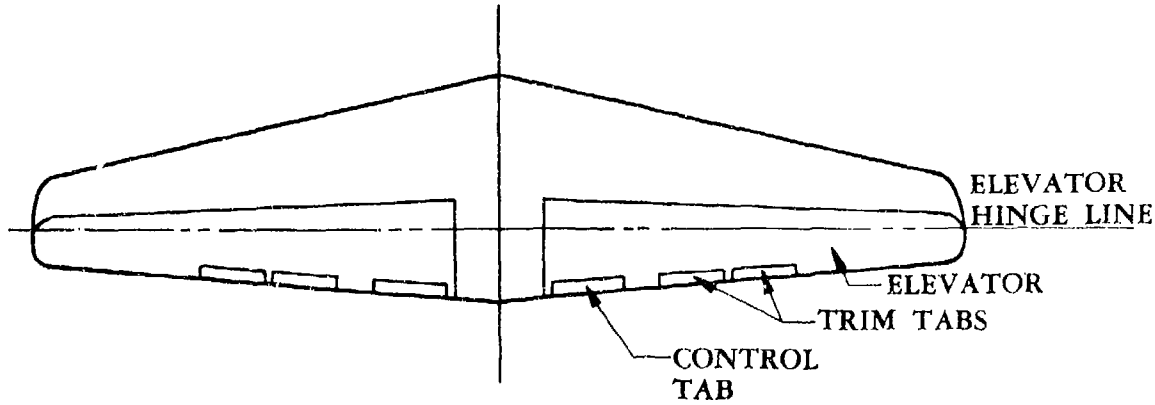

HORIZONTAL TAIL

Horizontal Tail Characteristics:

$S_e \bar{c}_e G_{e_{max}} = 162.0 \text{ ft}^2$

$\alpha_H = 2.5^o \qquad \delta_{tt} = -3.0^o \qquad \delta_e = 10^o$

$B_1 = \dfrac{\partial C_{h_e}}{\partial \delta_e} = -0.0040 \text{ per deg} \qquad B_2 = \dfrac{\partial C_{h_e}}{\partial \delta_{tc}} = -0.0046 \text{ per deg}$

$B_3 = \dfrac{\partial C_{h_e}}{\partial \alpha_H} = -0.0017 \text{ per deg} \qquad B_4 = \dfrac{\partial C_{h_e}}{\partial \delta_{tt}} = -0.0044 \text{ per deg}$

$\delta_{e_{max}} = 15^o, -30^o \qquad q = 150 \text{ lb/ft}^2 \text{ (sea level)}$

Tab Characteristics:

$R_L = 4.1 \qquad k = 0.244 \text{ lb/ft}^2\text{-deg} \qquad \beta = 0 \qquad \delta_{tc_{max}} = \pm 20^o$

$A_e = \dfrac{S_{tc} \bar{c}_{tc}}{S_e \bar{c}_e} = 0.0169 \qquad D_1 = \dfrac{\partial C_{h_{tc}}}{\partial \delta_e} = -0.0025 \text{ per deg}$

$D_2 = \dfrac{\partial C_{h_{tc}}}{\partial \delta_{tc}} = -0.0085 \text{ per deg} \qquad D_3 = \dfrac{\partial C_{h_{tc}}}{\partial \alpha_H} = -0.0014 \text{ per deg}$

Compute the control-column force required to deflect the elevator 10^o TED at a free-stream dynamic pressure of 150 lb/ft^2.

Determine the values of R_1 and R_2 for a spring-tab system

$$R_1 = \frac{R_L + \Delta_r}{R_L + \dfrac{B_2}{A_e D_2} - \dfrac{k}{qD_2} R_L} \qquad \text{(Table 6.3.4-B)}$$

$$R_1 = \frac{4.1 + \dfrac{20.0}{15.0}}{4.1 + \dfrac{-0.0046}{(0.0169)(-0.0085)} - \dfrac{(0.244)(4.1)}{150.0(-0.0085)}}$$

$$= \frac{5.433}{36.907} = 0.1472$$

$$R_2 = \frac{-\frac{k}{qD_2}(R_L + \Delta_r)}{R_L + \frac{B_2}{A_e D_2} - \frac{k}{qD_2} R_L} = -\frac{k}{qD_2} R_1 \qquad \text{(Table 6.3.4-B)}$$

$$= \frac{-(0.244)}{(150.0)(-0.0085)}(0.1472)$$

$$= 0.02817$$

Determine the tab-free hinge-moment coefficient

$$C_{h_{e_{\substack{tab \\ free}}}} = \left(B_1 - D_1 \frac{B_2}{D_2}\right)\delta_e + \left(B_3 - D_3 \frac{B_2}{D_2}\right)\alpha_H + B_4 \delta_{tt} \qquad \text{(Equation 6.3.4-l)}$$

$$= \left[-0.0040 + 0.0025\left(\frac{-0.0046}{-0.0085}\right)\right]10 + \left[-0.0017 + 0.0014\left(\frac{-0.0046}{-0.0085}\right)\right]2.5$$

$$+ (-0.0044)(-3.0)$$

$$= -0.01563$$

Determine the locked-tab hinge-moment coefficient

$$C_{h_{e_{\substack{tab \\ locked}}}} = B_1 \delta_e + B_3 \alpha_H + B_4 \delta_{tt} \qquad \text{(Equation 6.3.4-m)}$$

$$= (-0.0040)\ 10 + (-0.0017)\ 2.5 + (-0.0044)(-3.0)$$

$$= -0.03105$$

Solution:

$$F_s = G_{e_{max}} S_e \bar{c}_e q \left[C_{h_{e_{\substack{tab \\ free}}}} R_1 + C_{h_{e_{\substack{tab \\ locked}}}} R_2 + \Delta C_{h_{e_{\substack{tab \\ gearing}}}} R_2\right] \qquad \text{(Equation 6.3.4-k)}$$

$$F_s = (162.0)(150)[(-0.01563)(0.1472) + (-0.03105)(0.02817) + 0]$$

$$= (162.0)(150)(-0.003175)$$

$$= -77.16 \text{ lb}$$

Therefore, for the given tab system, a push force of 77.16 lb is required to achieve an elevator deflection of 10^{o} at a free-stream dynamic pressure of 150 lb/ft^2.

REFERENCES

1. Dunn, O. R.. Aerodynamically Boosted Surface Controls and Their Application to the DC-6 Transport. IAS Paper presented May 24, 1949. (U)

2. Kolk, W. R.: Modern Flight Dynamics. Prentice-Hall, Inc., Englewood Cliffs, N.J., 1961. (U)

3. Perkins, C. D., and Hage, R. E.: Airplane Performance Stability and Control. John Wiley and Sons, Inc., N.Y. 1949. (U)

4. Toll, T. A.: Summary of Lateral-Control Research. NACA TR 868, 1947. (U)

5. Mendelsohn, R. A.: A Semigraphical Method of Computing Stick Forces for Spring-Tab Controls Having Nonlinear Hinge-Moment Characteristics. Jour. of Aero. Sci., February 1948. (U)

6. Woodcock, R. J., and Drake, D. E.: Estimation of Flying Qualities of Piloted Airplanes. AFFDL-TR-65-218, 1966. (U)

7 DYNAMIC DERIVATIVES

Dynamic derivatives are associated with those aerodynamic forces and moments caused by the angular velocities and linear accelerations of the vehicle motion. A detailed discussion of wing, body, and wing-body dynamic derivatives is given in the introduction to each of the subject sections. In most cases the methods presented are based on theories that necessarily assume attached-flow conditions. They are thus limited to low angles of attack except for high-aspect-ratio wings below stall at subsonic speeds.

In general, dynamic derivatives for attached-flow conditions are smaller and of less importance than those for separated-flow conditions. For separated-flow conditions the derivatives become functions of the amplitude and frequency of oscillation. Such conditions exist on low-aspect-ratio wings and bodies at all speeds and at all angles of attack except for a narrow range around zero.

Because of the limited amount of data at high angles of attack and the complexity of deriving adequate generalized methods, particularly for the frequency and amplitude variations, no methods are presented that cover separated-flow conditions. Rather, a literature summary is presented in table 7-A and a bibliography on pages 7-1 through -10.

REFERENCES

1. Anon.: A General Investigation of Hypersonic Stability and Control Under Trimmed Flight Conditions. Flight Sci. Lab. R-63-011-104, 1964. (U)

2. Bauer, R. C.: An Investigation of the Influence of Several Shape Parameters on the Dynamic Stability of Ballistic Re-entry Configurations. Phase I. Effect of Afterbody Configuration at Mach Numbers 0.5 Through 1.5. AEDC-TN-59-78, 1959. (U)

3. Beam, B. H.: The Effects of Oscillation Amplitude and Frequency on the Experimental Damping in Pitch of a Triangular Wing Having an Aspect Ratio of 4. NACA RM A52G07, 1952. (U)

4. Beam, B. H., Reed, V. D., and Lopez, A. E.: Wind-Tunnel Measurements at Subsonic Speeds of the Static and Dynamic-Rotary Stability Derivatives of a Triangular-Wing Airplane Model Having a Triangular Vertical Tail. NACA RM A55A28, 1955. (U)

5. Bennett, C. V., and Johnson, J. L.: Experimental Determination of the Damping in Roll and Aileron Rolling Effectiveness of Three Wings Having 2°, 42°, and 62° Sweepback. NACA TN 1278, 1947. (U)

6. Bielat, R. P., and Wiley, H. G.: Dynamic Longitudinal and Directional Stability Derivatives for a 45° Sweptback-Wing Airplane Model at Transonic Speeds. NASA TM X-39, 1959. (U)

7. Bird, J. D., Jaquet, B. M., and Cowan, J. W.: Effect of Fuselage and Tail Surfaces on Low-Speed Yawing Characteristics of a Swept-Wing Model as Determined in Curved-Flow Test Section of Langley Stability Tunnel. NACA RM L8G13, 1948. (U)

8. Bird, J. D., Jaquet, B. M., and Cowan, J. W.: Effect of Fuselage and Tail Surfaces on Low-Speed Yawing Characteristics of a Swept-Wing Model as Determined in Curved-Flow Test Section of Langley Stability Tunnel. NACA TN 2483, 1951. (U)

9. Bird, J. D., Lichtenstein, J. H., and Jaquet, B. M.: Investigation of the Influence of Fuselage and Tail Surfaces on Low-Speed Static Stability and Rolling Characteristics of a Swept-Wing Model. NACA TN 2741, 1952. (U)

10. Bird, J. D.: Some Theoretical Low-Speed Span Loading Characteristics of Swept Wings in Roll and Sideslip. NACA TN 1839, 1949. (U)

11. Bird, J. D.: Some Theoretical Low-Speed Span Loading Characteristics of Swept Wings in Roll and Sideslip. NACA TR 969, 1950. (U)

12. Bird, J. D., and Jaquet, B. M.: A Study of the Use of Experimental Stability Derivatives in the Calculation of the Lateral Disturbed Motions of a Swept-Wing Airplane and Comparison with Flight Results. NACA TN 2013, 1950. (U)

13. Bird, J. D., Lichtenstein, J. H., and Jaquet, B. M.: Investigation of the Influence of Fuselage and Tail Surfaces on Low-Speed Static Stability and Rolling Characteristics of a Swept-Wing Model. NACA RM L7H15, 1947. (U)

14. Bland, W. M., Jr.: Effect of Fuselage Interference on the Damping in Roll of Delta Wings of Aspect Ratio 4 in the Mach Number Range Between 0.6 and 1.6 as Determined with Rocket-Propelled Vehicles. NACA RM L52E13, 1952. (U)

15. Bland, W. M., Jr., and Dietz, A. E.: Some Effects of Fuselage Interference, Wing Interference, and Sweepback on the Damping in Roll of Untapered Wings as Determined by Techniques Employing Rocket-Propelled Vehicles. NACA RM L51D25, 1951. (U)

16. Bland, W. M., Jr., and Sandahl, C. A.: A Technique Utilizing Rocket-Propelled Test Vehicles for the Measurement of the Damping in Roll of Sting-Mounted Models and Some Initial Results for Delta and Uptwept Tapered Wings. NACA RM L50D24, 1950. (U)

17. Bond R., and Packard, B. B.: Unsteady Aerodynamic Forces on a Slender Body of Revolution in Supersonic Flow. NASA TN D-859, 1961. (U)

18. Bradley, W. G.: Measurement of the Lateral Stability Derivatives of a Morane-Saulnier M.S 760 'Paris' Aircraft G-APRU. CoA Report Aero. 185, 1965. (U)

19. Brewer, J. D., and Fisher, L. R.: Effect of Taper Ratio on the Low-Speed Rolling Stability Derivatives of Swept and Unswept Wings of Aspect Ratio 2.61. NACA TN 2555, 1951. (U)

20. Brown, C. E. and Heinke, H. S., Jr.: Preliminary Wind-Tunnel Tests of Triangular and Rectangular Wings in Steady Roll at Mach Numbers of 1.62 and 1.92. NACA RM L8L30, 1949. (U)

21. Brown, C. E., and Adams, M. C.: Damping in Pitch and Roll of Triangular Wings at Supersonic Speeds. NACA TR 892, 1948. (U)

22. Buell, D. A., Reed, V. D., and Lopez, A. E.: The Static and Dynamic-Rotary Stability Derivatives at Subsonic Speeds of an Airplane Model with an Unswept Wing and a High Horizontal Tail. NACA RM A56I04, 1956. (U)

23. Campbell, J. P., and Woodling, C. H.: Calculated Effects of the Lateral Acceleration Derivatives on the Dynamic Lateral Stability of a Delta-Wing Airplane. NACA RM L54K26, 1955. (U)

24. Campbell, J. P., and Mathews, W. O.: Experimental Determination of the Yawing Moment Due to Yawing Contributed by the Wing, Fuselage, and Vertical Tail of a Midwing Airplane Model. NACA L-387, 1943. (U)

25. Campbell, J. P., Johnson, J. L., Jr., and Hewes, D. E.: Low-Speed Study of the Effect of Frequency on the Stability Derivatives of Wings Oscillating in Yaw with Particular Reference to High Angle-of-Attack Conditions. NACA RM L55H05, 1955. (U)

26. Campbell, J. P., and Goodman, A.: A Semiempirical Method for Estimating the Rolling Moment Due to Yawing of Airplanes. NACA TN 1984, 1949. (U)

27. Chapman, R., Jr., and Morrow, J. D.: Longitudinal Stability and Drag Characteristics at Mach Numbers from 0.70 to 1.37 of Rocket-Propelled Models Having a Modified Triangular Wing. NACA RM L52A31, 1952. (U)

28. Clay, J. T.: Nose Bluntness, Cone Angle, and Mach Number Effects on the Stability Derivatives of Slender Cones. ARL 67-0185, 1967. (U)

29. Cole, I. J., and Margolis, K.: Lift and Pitching Moment at Supersonic Speeds Due to Constant Vertical Acceleration for Thin Sweptback Tapered Wings with Streamwise Tips. Supersonic Leading and Trailing Edges. NACA TN 3196, 1954. (U)

30. Conlin, L. T., and Orlik-Rückemann, K. J.: Comparison of Some Experimental and Theoretical Data on Damping-in-Roll of a Delta-Wing Body Configuration at Supersonic Speeds. NRC LR-266, 1959. (U)

31. Cox, A. P., and Butler, S. F. J.: Low-Speed Wind-Tunnel Measurements of Damping in Yaw ($n_{\dot{\psi}}$) on an A.R.9 Jet-Flap Model. ARC CP 869, 1967. (U)

32. Curtiss, H. C., Jr.: Some Basic Considerations Regarding the Longitudinal Dynamics of Aircraft and Helicopters. Princeton Univ. Report 562, 1961. (U)

33. D'Aiutolo, C. T.: Low-Amplitude Damping-in-Pitch Characteristics of Tailless Delta-Wing Body Combinations at Mach Numbers from 0.80 to 1.35 as Obtained with Rocket-Powered Models. NACA RM L54D29, 1954. (U)

34. D'Aiutolo, C. T., and Parker, R. N.: Preliminary Investigation of the Low-Amplitude Damping in Pitch of Tailless Delta- and Swept-Wing Configurations at Mach Numbers from 0.7 to 1.35. NACA RM L52G09, 1952. (U)

35. D'Aiutolo, C. T., and Mason, H. P.: Preliminary Results of the Flight Investigation Between Mach Numbers of 0.80 and 1.36 of a Rocket-Powered Model of a Supersonic Airplane Configuration Having a Tapered Wing with Circular-Arc Section and 40° Sweepback. NACA RM L50H29a, 1950. (U)

36. Delaney, B. R., and Thompson, W. E.: Dynamic Stability Characteristics in Pitch and in Yaw for a Model of a Variable-Sweep Supersonic Transport Configuration at Mach Numbers of 2.40, 2.98, and 3.60. NASA TM X-761, 1963. (U)

37. Dietz, A. E., and Edmondson, J. L.: The Damping in Roll of Rocket-Powered Test Vehicles Having Rectangular Wings with a NACA 65-006 and Symmetrical Double-Wedge Airfoil Sections of Aspect Ratio 4.5. NACA RM L50B10, 1950. (U)

38. Dorrance, W. H.: Nonsteady Supersonic Flow About Pointed Bodies of Revolution. Jour. of Aero. Sci., Vol. 18, No. 8, 1951. (U)

39. Dubose, H. C.: Static and Dynamic Stability of Blunt Bodies. AGARD Rept. 347, 1961. (U)

40. Edmondson, J. L., and Sanders, E. C., Jr.: A Free-Flight Technique for Measuring Damping in Roll by Use of Rocket-Powered Models and Some Initial Results for Rectangular Wings. NACA RM L9I01, 1949. (U)

41. Emerson, H. F., and Robison, R. C.: Experimental Wind-Tunnel Investigation of the Transonic Damping-in-Pitch Characteristics of Two Wing-Body Combinations. NASA Memo 11-30-58A, 1958. (U)

42. Ericsson, L. E., and Reding, J. P.: Aerodynamic Effects of Bulbous Bases. NASA CR-1339, 1969. (U)

43. Ericsson, L. E.: Effect of Boundary Layer Transition on Vehicle Dynamics. AIAA Paper 69-106, 1969. (U)

44. Feigenbaum, D., and Goodman, A.: Preliminary Investigation at Low Speeds of Swept Wings in Rolling Flow. NACA RM L7E09, 1947. (U)

45. Fink, M. R., and Carroll, J. B.: Hypersonic Static and Dynamic Stability of Wing-Fuselage Configurations. UAL C910188-17, 1965. (U)

46. Fisher, L. R.: Approximate Corrections for the Effects of Compressibility on the Subsonic Stability Derivatives of Swept Wings. NACA TN 1854, 1949. (U)

47. Fisher, L. R., and Fletcher, H. S.: Effect of Lag of Sidewash on the Vertical-Tail Contribution to Oscillatory Damping in Yaw of Airplane Models. NACA TN 3356, 1955. (U)

48. Fisher, L. R.: Equations and Charts for Determining the Hypersonic Stability Derivatives of Combinations of Cone Frustums Computed by Newtonian Impact Theory. NASA TN D-149, 1959. (U)

49. Fisher, L. R.: Experimental Determination of the Effects of Frequency and Amplitude on the Lateral Stability Derivatives for a Delta, a Swept, and an Unswept Wing Oscillating in Yaw. NACA RM A56L19, 1956. (U)

50. Fisher, L. R.: Experimental Determination of the Effects of Frequency and Amplitude on the Lateral Stability Derivatives for a Delta, a Swept, and an Unswept Wing Oscillating in Yaw. NACA TR 1357, 1958. (U)

51. Fisher, L. R.: Experimental Determination of the Effects of Frequency and Amplitude of Oscillation on the Roll-Stability Derivatives for a 60° Delta-Wing Airplane Model. NASA TN D-232, 1960. (U)

52. Fisher, L. R., and Michael, W. H., Jr.: An Investigation of the Effect of Vertical-Fin Location and Area on Low-Speed Lateral Stability Derivatives of a Semitailless Airplane Model. NACA RM L51A10, 1951. (U)

53. Fisher, L. R., Lichtenstein, J. H., and Williams, K. D.: A Preliminary Investigation of the Effects of Frequency and Amplitude on an Unswept-Wing Model Oscillating in Roll. NACA TN 3554, 1956. (U)

54. Fletcher, H. S.: Low-Speed Experimental Determination of the Effects of Leading-Edge Radius and Profile Thickness on Static and Oscillatory Lateral Stability Derivatives for a Delta Wing with 60° of Leading-Edge Sweep. NACA TN 4341, 1958. (U)

55. Gillis, C. L., Peck, R. F., and Vitale, A. J.: Preliminary Results from a Free-Flight Investigation at Transonic and Supersonic Speeds of the Longitudinal Stability and Control Characteristics of an Airplane Configuration with a Thin Straight Wing of Aspect Ratio 3. NACA RM L9K25a, 1950. (U)

56. Gillis, C. L., and Chapman, R., Jr.: Summary of Pitch-Damping Derivatives of Complete Airplane and Missile Configurations as Measured in Flight at Transonic and Supersonic Speeds. NACA RM L52K20, 1953. (U)

57. Gillis, C. L., and Vitale, A. J.: Wing-on and Wing-off Longitudinal Characteristics of an Airplane Configuration Having a Thin Unswept Tapered Wing of Aspect Ratio 3, as Obtained from Rocket-Propelled Models at Mach Numbers from 0.8 to 1.4. NACA RM L50K16, 1951. (U)

58. Gilmore, A. W., et al.: Investigation of Dynamic Stability Derivatives of Vehicles Flying at Hypersonic Velocity. ASD-TDR-62-460, 1963. (U)

59. Goodman, A., and Thomas, D. F., Jr.: Effects of Wing Position and Fuselage Size on the Low-Speed Static and Rolling Stability Characteristics of a Delta-Wing Model. NACA TN 3063, 1954. (U)

60. Goodman, A., and Adair, G. H.: Estimation of the Damping in Roll of Wings Through the Normal Flight Range of Lift Coefficient. NACA TN 1924, 1949. (U)

61. Goodman, A., and Fisher, L. R.: Investigation at Low Speeds of the Effect of Aspect Ratio and Sweep on Rolling Stability Derivatives of Untapered Wings. NACA TN 1835, 1949. (U)

62. Goodman, A., and Fisher, L. R.: Investigation at Low Speeds of the Effect of Aspect Ratio and Sweep on Rolling Stability Derivatives of Untapered Wings. NACA TR 968, 1950. (U)

63. Goodman, A., and Brewer, J. D.: Investigation at Low Speeds of the Effect of Aspect Ratio and Sweep on Static and Yawing Stability Derivatives of Untapered Wings. NACA TN 1669, 1948. (U)

64. Goodman, A., and Feigenbaum, D.: Preliminary Investigation at Low Speeds of Swept Wings in Yawing Flow. NACA RM L7I09, 1948. (U)

65. Greenwood, G. H.: Free-Flight Measurements of the Dynamic Longitudinal-Stability Characteristics of a Wind Tunnel Interference Model (M = 0.92 to 1.35). ARC CP 648, 1963. (U)

66. Guyett, P. R., and Curran, J. D.: Aerodynamic Derivative Measurements on a Rectangular Wing of Aspect Ratio 3.3. ARC R&M 3171, 1961. (U)

67. Harmon, S. M.: Stability Derivatives at Supersonic Speeds of Thin Rectangular Wings with Diagonals Ahead of Tip Mach Lines. NACA TR 925, 1949. (U)

68. Harmon, S. M.: Stability Derivatives of Thin Rectangular Wings at Supersonic Speeds. NACA TN 1706, 1948. (U)

69. Harmon, S. M., and Jeffreys, I.: Theoretical Lift and Damping in Roll of Thin Wings with Arbitrary Sweep and Taper at Supersonic Speeds – Supersonic Leading and Trailing Edges. NACA TN 2114, 1950. (U)

70. Henderson, A., Jr.: Pitching-Moment Derivatives C_{m_q} and $C_{m_{\dot{\alpha}}}$ at Supersonic Speeds for a Slender-Delta-Wing and Slender-Body Combination and Approximate Solutions for Broad-Delta-Wing and Slender-Body Combinations. NACA TN 2553, 1951. (U)

71. Hewes, D. E.: Low-Speed Measurement of Static Stability and Damping Derivatives of a 60° Delta-Wing Model for Angles of Attack of 0° to 90°. NACA RM L54G22a, 1954. (U)

72. Hoerner, S.: Forces and Moments on a Yawed Airfoil. NACA TM 906, 1939. (U)

73. Holleman, E. C.: Longitudinal Frequency-Response and Stability Characteristics of the Douglas D-558-II Airplane as Determined from Transient Response to a Mach Number of 0.96. NACA RM L52E02, 1952. (U)

74. Holt, C. F., and Kron, G. J.: Delta Wing Stability in the Pitch Plane. AIAA Student Jour., Feb. 1965. (U)

75. Hopko, R. N.: A Flight Investigation of the Damping in Roll and Rolling Effectiveness Including Aeroelastic Effects of Rocket-Propelled Missile Models Having Cruciform, Triangular, Interdigitated Wings and Tails. NACA RM L51D16, 1951. (U)

76. Howe, R. M.: An Investigation of the Relative Effect of Stability Derivatives on the Dynamic Characteristics of the F-100A. WADC TN 57-297, 1957. (U)

77. Hui, W. H.: Stability Derivatives of Sharp Wedges in Viscous Hypersonic Flow Including the Effects of Thickness and Wave Reflection. Univ. of Southampton, AASU Rept. 278, 1967. (U)

78. Hunt, G. K.: Free-Flight Model Measurements of the Dynamic Stability of a Supersonic Strike Aircraft (TSR2). ARC CP 918, 1967. (U)

79. Hunton, L. W., and Dew, J. K.: Measurements of the Damping in Roll of Large-Scale Swept-Forward and Swept-Back Wings in Rolling Flow. NACA RM A7D11, 1947. (U)

80. Ishii, T., and Yanagizawa, M.: Measurements of the Aerodynamic Derivatives of an Oscillating Biconvex-Flat Airfoil in Supersonic Flow at Mach Number 2 to 3. National Aerospace Lab. of Japan, TR-57T, 1963. (U)

81. Jaffe, P., and Prislin, R. H.: Effect of Boundary Layer Transition on Dynamic Stability Over Large Amplitudes of Oscillation. AIAA Paper 64-427, 1964. (U)

82. Jaquet, B. M., and Brewer, J. D.: Effects of Various Outboard and Central Fins on Low-Speed Static-Stability and Rolling Characteristics of a Triangular-Wing Model. NACA RM L9E18, 1949. (U)

83. Jaquet, B. M., and Fletcher, H. S.: Experimental Steady-State Yawing Derivatives of a 60° Delta-Wing Model as Affected by Changes in Vertical Position of the Wing and in Ratio of Fuselage Diameter to Wing Span. NACA TN 3843, 1956. (U)

84. Jaquet, B. M., and Brewer, J. D.: Low-Speed Static-Stability and Rolling Characteristics of Low-Aspect-Ratio Wings of Triangular and Modified Triangular Plan Forms. NACA RM L8L29, 1949. (U)

85. Johnson, J. L., Jr.: Low-Speed Measurements of Rolling and Yawing Stability Derivatives of a 60° Delta-Wing Model. NACA RM L54G27, 1954. (U)

86. Johnson, J. L., Jr.: Low-Speed Measurements of Static Stability, Damping in Yaw, and Damping in Roll of a Delta, a Swept, and an Unswept Wing for Angles of Attack from 0° to 90°. NACA RM L56B01, 1956. (U)

87. Jones, A. L., and Alksne, A.: The Damping Due to Roll of Triangular, Trapezoidal, and Related Plan Forms in Supersonic Flow. NACA TN 1548, 1948. (U)

88. Kemp, W. B., Jr., and Becht, R. E.: Damping-in-Pitch Characteristics at High Subsonic and Transonic Speeds of Four 35° Sweptback Wings. NACA L53G29a, 1953. (U)

89. Kennet, H., Ashley, H., and Stapleford, R. L.: Forces and Moments on Oscillating Slender Wing-Body Combinations at Supersonic Speed. Part II — Applications and Comparison with Experiment. OSR TN 58-114, MIT Fluid Dynamics Research Group Rept. 57-5, 1957. (U)

90. Kennet, H., and Ashley, H.: Review of Unsteady Aerodynamic Studies in the Fluid Dynamics Research Group, 1955-1958. OSR TN 59-6, MIT Fluid Dynamics Research Group Rept. 58-5, 1958. (U)

91. Kilgore, R. A., and Hillje, E. R.: Some Transonic Dynamic Longitudinal and Directional Stability Parameters of a Canard Airplane Model Designed for Supersonic Flight. NASA TM X-633, 1961. (U)

92. Kind, R. J., and Orlik-Rückemann, K.: Stability Derivatives of Sharp Cones in Viscous Hypersonic Flow. NRC LR-427, 1965. (U)

93. Kuhn, R. E., and Myers, B. C., II: Effects of Mach Number and Sweep on the Damping-in-Roll Characteristics of Wings of Aspect Ratio 4. NACA RM L9E10, 1949. (U)

94. Kuhn, R. E.: Notes on Damping in Roll and Load Distributions in Roll at High Angles of Attack and High Subsonic Speed. NACA RM L53G13a, 1953. (U)

95. Kuhn, R. E., and Wiggins, J. W.: Wind-Tunnel Investigation to Determine the Aerodynamic Characteristics in Steady Roll of a Model at High Subsonic Speeds. NACA RM L52K24, 1953. (U)

96. Lamplkin, B. A., and Tunnell, P. J.: Static and Dynamic Rotary Stability Derivatives of an Airplane Model with an Unswept Wing and a High Horizontal Tail at Mach Numbers of 2.5, 3.0, and 3.5. NACA RM A58F17, 1958. (U)

97. Landahl, M. T.: The Flow Around Oscillating Low Aspect Ratio Wings at Transonic Speeds. Royal Institute of Technology, KTH Aero TN 40, 1954. (U)

98. Landahl, M. T.: Forces and Moments on Oscillating Slender Wing-Body Combinations of Sonic Speed. OSR TN 56-109, MIT Fluid Dynamics Research Group Rept. 56-1, 1956. (U)

99. Lehrian, D. E.: Calculation of Stability Derivatives for Oscillating Wings. ARC R&M 2922, 1956. (U)

100. Letko, W., and Brewer, J. D.: Effect of Airfoil Profile of Symmetrical Sections on the Low-Speed Rolling Derivatives of 45° Sweptback-Wing Models of Aspect Ratio 2.61 NACA L8L31a, 1949. (U)

101. Letko, W., and Jaquet, B. M.: Effect of Airfoil Profile of Symmetrical Sections on the Low-Speed Static-Stability and Yawing Derivatives of 45° Sweptback Wing Models of Aspect Ratio 2.61. NACA RM L8H10, 1948. (U)

102. Letko, W., and Fletcher, H. S.: Effects of Frequency and Amplitude on the Yawing Derivatives of Triangular, Swept, and Unswept Wings and of a Triangular-Wing-Fuselage Combination With and Without a Trianguiar Tail Performing Sinusoidal Yawing Oscillations. NACA TN 4390, 1958. (U)

103. Letko, W., and Wolhart, W. D.: Effect of Sweepback on the Low-Speed Static and Rolling Stability Derivatives of Thin Tapered Wings of Aspect Ratio 4. NACA RM L9F14, 1949. (U)

104. Letko, W., and Cowan, J. W.: Effect of Taper Ratio on Low-Speed Static and Yawing Stability Derivatives of 45° Sweptback Wings with Aspect Ratio of 2.61. NACA TN 1671, 1948. (U)

105. Letko, W., and Riley, D. R.: Effect of an Unswept Wing on the Contributions of Unswept-Tail Configurations to the Low-Speed Static- and Rolling-Stability Derivatives of a Midwing Airplane Model. NACA TN 2175, 1950. (U)

106. Letko, W.: Effect of Vertical-Tail Area and Length on the Yawing Stability Characteristics of a Model Having a 45° Sweptback Wing. NACA TN 2358, 1951. (U)

107. Letko, W.: Experimental Determination at Subsonic Speeds of the Oscillatory and Static Lateral Stability Derivatives of a Series of Delta Wings with Leading-Edge Sweep from 30° to 86.5°. NACA RM L57A30, 1957. (U)

108. Lichtenstein, J. H., and Williams, J. L.: Effect of Frequency of Sideslipping Motion on the Lateral Stability Derivatives of a Typical Delta-Wing Airplane. NACA RM L57F07, 1957. (U)

109. Lichtenstein, J. H.: Effect of High-Lift Devices on the Low-Speed Static Lateral and Yawing Stability Characteristics of an Untapered 45° Sweptback Wing. NACA TN 2689, 1952. (U)

110. Lockwood, V. E.: Damping-in-Roll Characteristics of a 42.7° Sweptback Wing as Determined from a Wind-Tunnel Investigation of a Twisted Semispan Wing. NACA L9F15, 1949. (U)

111. Lockwood, V. E.: Effects of Sweep on the Damping-in-Roll Characteristics of Three Sweptback Wings Having an Aspect Ratio of 4 at Transonic Speeds. NACA RM L50J19, 1950. (U)

112. Lomax, H., and Heaslet, M. A.: Damping-in-Roll Calculations for Slender Swept-Back Wings and Slender Wing-Body Combinations. NACA TN 1950, 1949. (U)

113. Lopez, A. E., Buell, D. A., and Tinling, B. E.: The Static and Dynamic Rotary Stability Derivatives at Subsonic Speeds of an Airplane Model Having Wing and Tail Surfaces Swept Back 45°. NASA Memo 5-16-59A, 1959. (U)

114. MacLachlan, R., and Letko, W.: Correlation of Two Experimental Methods of Determining the Rolling Characteristics of Unswept Wings. NACA TN 1309, 1947. (U)

115. MacLachlan, R., and Fisher, L. R.: Wind-Tunnel Investigation at Low Speeds of the Pitching Derivatives of Untapered Swept Wings. NACA RM L8G19, 1948. (U)

116. Maggin, B., and Bennett, C. V.: Low-Speed Stability and Damping-in-Roll Characteristics of Some Highly Swept Wings. NACA TN 1286, 1947. (U)

117. Malvestuto, F. S., Jr., and Hoover, D. M.: Lift and Pitching Derivatives of Thin Sweptback Tapered Wings with Streamwise Tips and Subsonic Leading Edges at Supersonic Speeds. NACA TN 2250, 1951. (U)

118. Malvestuto, F. S., Jr., and Hoover, D. M.: Supersonic Lift and Pitching Moment of Thin Sweptback Tapered Wings Produced by Constant Vertical Acceleration — Subsonic Leading Edges and Supersonic Trailing Edges. NACA TN 2315, 1951. (U)

119. Malvestuto, F. S., Jr., Margolis, K., and Ribner, H. S.: Theoretical Lift and Damping in Roll at Supersonic Speeds of Thin Sweptback Tapered Wings with Streamwise Tips, Subsonic Leading Edges, and Supersonic Trailing Edges. NACA TR 970, 1950. (U)

120. Malvestuto, F. S., Jr., Margolis, K., and Ribner, H. S.: Theoretical Lift and Damping in Roll of Thin Sweptback Wings of Arbitrary Taper and Sweep at Supersonic Speeds – Subsonic Leading Edges and Supersonic Trailing Edges. NACA TN 1860, 1950. (U)

121. Malvestuto, F. S., Jr., and Margolis, K.: Theoretical Stability Derivatives of Thin Sweptback Wings Tapered to a Point with Sweptforward Trailing Edges for a Limited Range of Supersonic Speeds. NACA TR 971, 1950. (U)

122. Mangler, K. W.: A Method of Calculating the Short-Period Longitudinal Stability Derivatives of a Wing in Linearized Unsteady Compressible Flow. ARC R&M 2924, 1957. (U)

123. Mantle, P. J.: On the Rolling Motion of Low-Aspect-Ratio Delta Wings. Jour. of Aero. Sci., May 1961. (U)

124. Mantle, P. J.: Some Free Flight Results of the Lift Curve Slope and Rolling Derivatives of Low Aspect Ratio Delta Wings. Canadian Arm. Res. and Devel. Est. TM AB-67, 1960. (U)

125. Margolis, K., and Babbitt, P. J.: Theoretical Calculations of the Stability Derivatives at Supersonic Speeds for a High-Speed Airplane Configuration. NACA RM L53G17, 1953. (U)

126. Martin, J. C., Margolis, K., and Jeffreys, I.: Calculation of Lift and Pitching Moments Due to Angle of Attack and Steady Pitching Velocity at Supersonic Speeds for Thin Sweptback Tapered Wings with Streamwise Tips and Supersonic Leading and Trailing Edges. NACA TN 2699, 1952. (U)

127. Martina, A. P.: Method for Calculating the Rolling and Yawing Moments Due to Rolling for Unswept Wings With or Without Flaps or Ailerons by Use of Nonlinear Section Lift Data. NACA TN 2937, 1953. (U)

128. McDearmon, R. W., and Heinke, H. S., Jr.: Investigations of the Damping in Roll of Swept and Tapered Wings at Supersonic Speeds. NACA RM L53A13, 1953. (U)

129. Miles, J. W.: Quasi-Stationary Airfoil Theory in Compressible Flow. Jour. of Aero. Sci., Vol. 16, No. 8, August 1949. (U)

130. Mitcham, G. L., Crabill, N. L., and Stevens, J. E.: Flight Determination of the Drag and Longitudinal Stability and Control Characteristics of a Rocket-Powered Model of a 60° Delta-Wing Airplane from Mach Numbers of 0.75 to 1.70. NACA L51104, 1951. (U)

131. Mitcham, G. L., and Blanchard, W. S., Jr.: Summary of the Aerodynamic Characteristics and Flying Qualities Obtained from Flights of Rocket-Propelled Models of an Airplane Configuration Incorporating a Sweptback Inversely Tapered Wing at Transonic and Low Supersonic Speeds. NACA RM L50G18a, 1950. (U)

132. Myers, B. C., II, and Kuhn, R. E.: High-Subsonic Damping-in-Roll Characteristics of a Wing with the Quarter-Chord Line Swept Back 35° and with Aspect Ratio 3 and Taper Ratio 0.6. NACA RM L9C23, 1949. (U)

133. Nethaway, J. E., and Clark, J.: Flight Tests to Investigate the Dynamic Lateral-Stability Characteristics of a 45-deg. Delta, Cropped to Give Three Aspect Ratios. ARC R&M 3243, 1962. (U)

134. Ohman, L. H.: A Surface Flow Solution and Stability Derivatives for Bodies of Revolution in Complex Supersonic Flow. Part I – Theory and Some Representative Results. NRL LR-418, 1964. (U)

135. Ohman, L. H.: A Surface Flow Solution and Stability Derivatives for Bodies of Revolution in Complex Supersonic Flow. Part II – Results for Two Families of Bodies of Revolution for $1.1 \leqslant M \leqslant 5$. NRL LR-419, 1964. (U)

136. Orlik-Rückemann, K. J.: Stability Derivatives of Sharp Wedges in Viscous Hypersonic Flow. NRC LR-431, 1965. (U)

137. Orlik-Rückemann, K. J., and Laberge, J. G.: Static and Dynamic Longitudinal Stability Characteristics of a Series of Delta and Sweptback Wings at Supersonic Speeds. NRC LR-396, 1966. (U)

138. Parks, J. H.: Longitudinal Aerodynamic Characteristics of a Model Airplane Configuration Equipped with a Scaled X-1 Airplane Wing. NACA RM L51L10a, 1952. (U)

139. Parks, J. H., and Kohlet, A. B.: Longitudinal Stability, Trim, and Drag Characteristics of a Rocket-Propelled Model of an Airplane Configuration Having a 45° Sweptback Wing and an Unswept Horizontal Tail. NACA RM L52F05, 1952. (U)

140. Pearson, H. A., and Jones, R. T.: Theoretical Stability and Control Characteristics of Wings with Various Amounts of Taper and Twist. NACA TR 635, 1938. (U)

141. Peck, R. F., and Mitchell, J. L.: Rocket-Model Investigation of Longitudinal Stability and Drag Characteristics of an Airplane Configuration Having a 60° Delta Wing and High Unswept Horizontal Tail. NACA RM L52K04a, 1953. (U)

142. Piland, R. O.: Summary of the Theoretical Lift, Damping-in-Roll, and Center-of-Pressure Characteristics of Various Wing Plan Forms at Supersonic Speeds. NACA TN 1977, 1949. (U)

143. Pinsker, W. J. G.: A Semiempirical Method for Estimating the Rotary Rolling Moment Derivatives of Swept and Slender Wings. ARC CP 524, 1960. (U)

144. Platzer, M. F., and Sheror, A. D.: Dynamic Stability Analysis of Bodies of Revolution in Supersonic Flow. AIAA Paper 67-607, 1967. (U)

145. Platzer, M. F., and Hoffman, G. H.: Quasi-Slender Body Theory for Slowly Oscillating Bodies of Revolution in Supersonic Flow. NASA TN D-3440, 1966. (U)

146. Polhamus, E. C.: A Simple Method of Estimating the Subsonic Lift and Damping in Roll of Sweptback Wings. NACA TN 1862, 1949. (U)

147. Queijo, M. J and Jaquet, B. M.: Calculated Effects of Geometric Dihedral on the Low-Speed Rolling Derivatives of Swept Wings. NACA TN 1732, 1948. (U)

148. Queijo, M. J., and Jaquet, B. M.: Investigation of Effects of Geometric Dihedral on Low-Speed Static Stability and Yawing Characteristics of an Untapered 45° Sweptback-Wing Model of Aspect Ratio 2.61. NACA TN 1668, 1948. (U)

149. Queijo, M. J., et al.: Preliminary Measurements of the Aerodynamic Yawing Derivatives of a Triangular, a Swept, and an Unswept Wing Performing Pure Yawing Oscillations, with a Description of the Instrument Employed. NACA RM L55L14, 1956. (U)

150. Queijo, M. J., and Wells, E. G.: Wind-Tunnel Investigation of the Low-Speed Static and Rotary Stability Derivatives of a 0.13-Scale Model of the Douglas D-558-II Airplane in the Landing Configuration. NACA RM L52G07, 1952. (U)

151. Quinn, B.: The Hypersonic Roll Damping Derivative of a Blunt Cone. ARL 68-0137, 1968. (U)

152. Ribner, H.: The Stability Derivatives of Low-Aspect-Ratio Triangular Wings at Subsonic and Supersonic Speeds. NACA TN 1423, 1947. (U)

153. Ribner, H. S., and Malvestuto, F. S., Jr.: Stability Derivatives of Triangular Wings at Supersonic Speeds. NACA TR 908, 1948. (U)

154. Rightley, E. C.: Dynamic Stability Derivatives for a 10° Blunt Cone at Mach Numbers from 0.5 to 21. Sandia Corp. Report SC-R-65-907, 1965. (U)

155. Ross, A. J.: The Lateral Oscillation of Slender Aircraft. ARC CP 845, 1966. (U)

156. Sadoff, M., Ankenbruck, H. O., and O'Hare, W.: Stability and Control Measurements Obtained During USAF-NACA Cooperative Flight-Test Program on the X-4 Airplane (USAF NO. 46-677). NACA RM A51H09, 1951. (U)

157. Sanders, E. C., Jr., and Edmondson, J. L.: Damping in Roll of Rocket-Powered Test Vehicles Having Swept, Tapered Wings of Low Aspect Ratio. NACA RM L51G06, 1951. (U)

158. Sanders, E. C., Jr.: Damping in Roll of Straight and 45° Swept Wings of Various Taper Ratios Determined at High Subsonic, Transonic, and Supersonic Speeds with Rocket-Powered Models. NACA RM L51H14, 1951. (U)

159 Scruton, C., Woodgate, L., and Alexander, A. J.: Measurement of the Aerodynamic Derivatives for Swept Wings of Low Aspect Ratio Describing Pitching and Plunging Oscillations in Incompressible Flow. ARC R&M 2925, 1957. (U)

160. Scruton, C., et al.: Measurement of Pitching-Moment Derivatives for Aerofoils Oscillating in Two-Dimensional Supersonic Flow. ARC R&M 3234, 1962. (U)

161. Smith, C. B., and Beane, B. J.: Damping in Pitch of Bodies of Revolution at Supersonic Speeds. IAS Preprint 311, 1951. (U)

162. Statler, I.C., Tufts, O.B., and Hirtreiter, W. J.: The Development and Evaluation of the CAL/Air Force Dynamic Wind-Tunnel Testing System. Part I – Description and Dynamic Tests of an F-80 Model. AFFDL-TR-66-153 Part I, 1967. (U)

163. Statler, I. C.: The Development and Evaluation of the CAL/Air Force Dynamic Wind-Tunnel Testing System. Part II – Dynamic Tests of an F-104 Model. AFFDL-TR-66-153 Part II, 1967. (U)

164. Statler, I.C.: Dynamic Stability at High Speeds from Unsteady Flow Theory. Jour of Aero Sci, Vol. 17, No. 4, 1950. (U)

165. Stone, D. G., and Sandahl, C. A.: A Comparison of Two Techniques Utilizing Rocket-Propelled Vehicles for the Determination of the Damping-in-Roll Derivative. NACA L51A16, 1951. (U)

166. Swanson, R. S., and Priddy, E. L.: Lifting-Surface-Theory Values of the Damping in Roll and of the Parameter Used in Estimating Aileron Stick Forces. NACA L-53, 1945. (U)

167. Thomas, H. H. B. M., and Ross, A. J.: The Calculation of the Rotary Lateral Stability Derivatives of a Jet-Flapped Wing. ARC R&M 3277, 1962. (U)

168. Thompson, J. S., Fail, R. A., and Inglesby, J. V.: Low Speed Wind Tunnel Measurements of the Oscillatory Lateral Stability Derivatives for a Model of a Slender Aircraft (HP 115) Including the Effects of Frequency Parameter. RAE TR 69018, 1969. (U)

169. Tobak, M.: Damping in Pitch of Low-Aspect-Ratio Wings at Subsonic and Supersonic Speeds. NACA RM A52L04a, 1953. (U)

170. Tobak, M., and Lessing, H. C.: Estimation of Rotary Stability Derivatives at Subsonic and Transonic Speeds. AGARD Report 343, 1961. (U)

171. Tobak, M., Reese, D. E. Jr., and Beam, B. H.: Experimental Damping in Pitch of 45° Triangular Wings. NACA RM A50J26, 1950. (U)

172. Tobak, M., and Wehrend, W. R.: Stability Derivatives of Cones at Supersonic Speeds. NACA TN 3788, 1956. (U)

173. Toll, T. A., and Queijo, M. J.: Approximate Relations and Charts for Low-Speed Stability Derivatives of Swept Wings. NACA TN 1581, 1948. (U)

174. Tosti, L. P.: Low-Speed Static Stability and Damping-in-Roll Characteristics of Some Swept and Unswept Low-Aspect-Ratio Wings. NACA TN 1468, 1947. (U)

175. Triplett, W. C., and Van Dyke, R. D., Jr.: Preliminary Flight Investigation of the Dynamic Longitudinal-Stability Characteristics of a 35° Swept-Wing Airplane. NACA RM A50J09a, 1950. (U)

176. Tucker, W. A., and Piland, R. O.: Estimating of the Damping in Roll of Supersonic-Leading-Edge Wing-Body Combinations. NACA TN 2151, 1950. (U)

177. Turner, K. J., Ross, A. J., and Earley, G.: The Dynamic Stability Derivatives of a Slender Wing, a Comparison of Theory with Free-Flight Model Tests at Near-Zero Lift, M = 8.0 to 2.4. ARC CP 995, 1968. (U)

178. Turner, K. J., and Hunt, G. K.: Free-Flight Measurements for the Transonic Roll-Damping Characteristics of Three Related Wings of Aspect Ratio 2.83. ARC R&M 3274, 1962. (U)

179. Turner, K. J.: Measurements of Dynamic Stability from Three Simplified Free-Flight Models of a Supersonic Research Aircraft (Bristol T.188) Over the Mach Number Range 1.2-2.6. ARC CP 816, 1965. (U)

180. Vitale, A. J., McFall, J. C., Jr., and Morrow, J. D.: Longitudinal Stability and Drag Characteristics at Mach Numbers from 0.75 to 1.5 of an Airplane Configuration Having a 30° Swept Wing of Aspect Ratio 2.24 as Obtained from Rocket-Propelled Models. NACA L51K06, 1952. (U)

181. Walchner, O., and Clay, J. T.: Hypersonic Stability Derivatives of Blunted Slender Cones. AIAA Journal, Vol 8, No. 4, April 1965. (U)

182. Walker, H. J., and Ballantyne, M. B.: Pressure Distribution and Damping in Steady Roll at Supersonic Mach Numbers of Flat Swept-Back Wings with Subsonic Edges. NACA TN 2047, 1950. (U)

183. Wehrend, W. R., Jr.: A Wind-Tunnel Investigation of the Effect of Changes in Base Contour on the Damping in Pitch of a Blunted Cone NASA TN D-2062, 1963. (U)

184. Wehrend, W. R., Jr.: Wind-Tunnel Investigation of the Static and Dynamic Stability Characteristics of a 10° Semivertex Angle Blunted Cone. NASA TN D-1202, 1962. (U)

185. Wiggins, J. W.: Wind-Tunnel Investigation of Effect of Sweep on Rolling Derivatives at Angles of Attack up to 13° and at High Subsonic Mach Numbers, Including a Semiempirical Method of Estimating the Rolling Derivatives. NACA TN 4185, 1958. (U)

186. Wiggins, J. W.: Wind-Tunnel Investigation at High Subsonic Speeds to Determine the Rolling Derivatives of Two Wing-Fuselage Combinations Having Triangular Wings, Including a Semiempirical Method of Estimating the Rolling Derivatives. NACA RM L53L18a, 1953. (U)

187. Williams, J. L.: Measured and Estimated Lateral Static and Rotary Derivatives of a 1/12-Scale Model of a High-Speed Fighter Airplane with Unswept Wings. NACA RM L53K09, 1954. (U)

188. Wolhart, W. D.: Influence of Wing and Fuselage on the Vertical-Tail Contribution to the Low-Speed Rolling Derivatives of Midwing Airplane Models with 45° Swept Back Surfaces. NACA TN 2587, 1951. (U)

189 Wood, R. M., and Murphy, C. H.: Acrodynamic Derivatives for Both Steady and Nonsteady Motion of Slender Bodies. Jour. of Aero. Sci., Vol. 22, No. 12, 1955. (U)

190. Woodgate, L., and Pugh, P. G.: Measurements of the Pitching-Moment Derivatives on a Sharp-Edged Delta Wing in Incompressible Flow. ARC R&M 3379, 1963. (U)

191. Wright, B. R., and Brower, M. L.: Aerodynamic Damping and Oscillatory Stability in Pitch for a Model of a Typical Subsonic Jet-Transport Airplane. NASA TN D-3159, 1966. (U)

192. Zartarian, G., and Ashley, H.: Forces and Moments on Oscillating Slender Wing-Body Combinations at Supersonic Speed, Part I – Basic Theory. OSR TN 57-386, MIT Fluid Dynamics Research Group Rpt. 57-2, 1957. (U)

TABLE 7-A

DYNAMIC DERIVATIVES

Ref.	Derivative	A	$\Lambda_{(\ )}$ (deg)	λ	M	Freq.	Ampl.	Config.
2	$C_{m_q} + C_{m_{\dot{\alpha}}}$	–	–	–	.5 → 1.5	X	X	B
3	$C_{m_q} + C_{m_{\dot{\alpha}}}$	4	45 LE	0	.10 → .95	X	X	WB
4	$C_{m_q} + C_{m_{\dot{\alpha}}}, C_{\ell_p}, C_{n_p}$, $C_{\ell_r} - C_{\ell_{\dot{\beta}}}, C_{n_r} - C_{n_{\dot{\beta}}}$	2.2	60 LE	.03	.25 → .95	X	X	WB
5	C_{ℓ_p}	10 5.9 2.5	2 c/4 42 62	.5	Low speed	–	–	W
6	$C_{m_q} + C_{m_{\dot{\alpha}}}$, $C_{n_r} - C_{n_{\dot{\beta}}} \cos\alpha$	4	45 c/4	.2	.70 → 1.15	X	X	WBHV, BHV, WBH, WBV
7	$C_{Y_r}, C_{n_r}, C_{\ell_r}$	2.63	45 c/4	1.0	.13	–	–	W, WB
8	$C_{Y_r}, C_{n_r}, C_{\ell_r}$	2.61	45 c/4	1.0	.13	–	–	W, WB
9	$C_{\ell_p}, C_{n_p}, C_{Y_p}$	2.61	45 c/4	1.0	.17	–	–	W, WB
10	C_{n_r} (theor.)	1.5, 3.5, 6	0, 30, 45, 60 c/4	0, .5, 1.5	Low speed	–	–	W
11	C_{ℓ_p} (theor.)	1.5, 3.5, 6, 10	0, 30, 45, 60 c/4	0, .5, 1.0	Low speed	–	–	W
12	$C_{n_p}, C_{\ell_p}, C_{Y_p}$, $C_{n_r}, C_{\ell_r}, C_{Y_r}$	4.51	35 c/4	1.84	.17 .13	–	–	WB

TABLE 7-A (CONTD)

Ref.	Derivative	A	$\Lambda_{(\ )}$ (deg)	λ	M	Freq.	Ampl.	Config.
13	$C_{\ell_p}, C_{Y_p}, C_{n_p}$	2.63	45 LE	1.0	.17	–	–	W, WB
14	C_{ℓ_p}	4	45 LE	0	.6 → 1.6	–	–	W, WB
15	C_{ℓ_p}	3.7	0, 45 LE	1.0	.6 → 1.7	–	–	W, WB
16	C_{ℓ_p}	4.0	45 LE 0 c/2	0 .5	.6 → 1.7	–	–	W, WB
17	$C_{m_q} + C_{m_{\dot{\alpha}}}$	–	–	–	1.1 → 2.4	X	–	B
19	$C_{Y_p}, C_{n_p}, C_{\ell_p}$	2.61	0 c/4 45 c/4	.5, 1.0 .5, .25, 1.0	.17	–	–	W
20	βC_{ℓ_p}	1.47 → 4.0	0 → 45 LE (12 configurations)	1.0, 0	1.62, 1.92	–	–	WB
21	C_{L_q}, C_{m_q} C_{ℓ_p} (theor.)	4 cot Λ_{LE}	$\tan^{-1}\frac{4}{A}$ LE	0	Supersonic	–	–	W
22	$C_{m_q} + C_{m_{\dot{\alpha}}}, C_{\ell_p}, C_{n_p}$, $C_{\ell_r} - C_{\ell_{\dot{\beta}}}, C_{n_r} - C_{n_{\dot{\beta}}}$	2.44	27 LE	.38	.25 → .94	X	X	WBHV, WBV, B, WB, BV, BHV
23	$C_{n_p}, C_{\ell_p}, C_{n_r}, C_{\ell_r}$, $C_{n_{\dot{\beta}}}, C_{\ell_{\dot{\beta}}}$ (theor.)	2.2	60 LE	0	–	X	–	WBV
24	$C_{n_{\dot{r}}}$	6 6.7	0 LE –	1.0 .40	Low speed	–	–	W WB
25	$C_{n_r} - C_{n_{\dot{\beta}}}$ $C_{\ell_r} - C_{\ell_{\dot{\beta}}}$	2.31 2.61 3.0	60 LE 45 c/4 0 c/2	0 .25 .50	Low speed	X	X	W
26	C_{ℓ_r}	1.34 2.61 5.16 2.61 4 2.31	0 LE 45 60 45 45 52.2 c/4	1.0 .50, .25 .6 0	Low speed	–	–	W, WB
27	$C_{m_q} + C_{m_{\dot{\alpha}}}$	2.53	50.66 c/4	0	.70 → 1.37	–	–	WB
28	$C_{m_q} + C_{m_{\dot{\alpha}}}$	–	–	–	14.2	–	–	B
29	$C_{L_{\dot{\alpha}}}, C_{m_{\dot{\alpha}}}$ (theor.)	$\beta A = 3 \rightarrow 20$ $\beta A = 2 \rightarrow 20$	$\beta \cot \Lambda_{LE} = 1 \rightarrow \infty$ $\beta \cot \Lambda_{LE} = 1 \rightarrow \infty$	0, .25, .5, .75 1.0	Supersonic	–	–	W
30	C_{ℓ_p}	2	63.4 LE	0	1.35 → 2.03	X	X	WBV
31	$C_{n_{\dot{\beta}}}$	9.20	6 c/4	.48	Low speed	X	X	W, WB, WBV, WBHV

TABLE 7-A (CONTD)

Ref.	Derivative	A	$\Lambda_{(\ )}$ (deg)	λ	M	Freq.	Ampl.	Config.
33	$C_{m_q} + C_{m_{\dot\alpha}}$	2 3	63.43 LE 53.07 LE	0	.80 → 1.35	–	–	WB
34	$C_{m_q} + C_{m_{\dot\alpha}}$	.4 3 3.6	45 LE 37.5 ↓ 39. ↓	0 .6 .4	.7 → 1.35	–	–	WB
35	$C_{m_q} + C_{m_{\dot\alpha}}$	4	40 c/4	.5	.80 → 1.36	–	–	WB
36	$C_{m_q} + C_{m_{\dot\alpha}}, C_{m_\alpha} - k^2 C_{m_{\dot q}}$, $C_{\ell_\beta} \cos\alpha + k^2 C_{\ell_{\dot r}}$, $C_{n_r} - C_{n_{\dot\beta}} \cos\alpha$, $C_{n_\beta} \cos\alpha + k^2 C_{n_{\dot r}}$	1.56	70/75 LE	–	2.4, 2.98, 3.6	X	X	WBHV, WBV, WBH
37	C_{ℓ_p}	4.5	0 LE	1.0	.85 → 1.45	–	–	WB
38	$C_{L_{\dot\alpha}}, C_{m_{\dot\alpha}}, C_{L_q}, C_{m_q}$ (theor.)	–	–	–	Supersonic	X	X	B
39	$C_{m_q} + C_{m_{\dot\alpha}}$	–	–	–	.7 → 5.0	X	X	B
40	C_{ℓ_p}	3.71	0 LE	1.0	.85 → 1.40	–	–	WB
41	$C_{m_q} + C_{m_{\dot\alpha}}$	2 3	63.4 LE –	0 .4065	.6 → 1.18	X	X	WB
42	$C_{m_q}, C_{m_q} + C_{m_{\dot\alpha}}$, $C_{m_\alpha} - \bar\omega^2 C_{m_{\dot q}}$	–	–	–	.25 → 5	X	X	B
43	$C_{m_q} + C_{m_{\dot\alpha}}$	–	–	–	5, 6, 7, 8	–	–	B
44	$C_{Y_p}, C_{n_p}, C_{\ell_p}$	2.61 5.16 2.61 1.34	–45 LE 0 ↓ 45 ↓ 60 ↓	1.0	.17	–	–	W
45	$C_{m_q} + C_{m_{\dot\alpha}}, C_{m_q}$	.4 (exposed) .8 ↓ 1.6 ↓	0 LE 79 ↓ 70 ↓	1 0 0	4.8, 8.08, 10, 17	X	–	B, WB
46	$C_{L_q}, C_{m_q}, C_{\ell_{\dot r}}$, $C_{\ell_p}, C_{n_p}, C_{Y_p}$, C_{ℓ_p} (theor.)	4 4 2, 6 ↓ 4 ↓	30 c/4 50 ↓ 0 30 45 0 30 45 ↓	– – 1.0 ↓ 1.0, .5 ↓	0 → 1.0 0 → 1.0 0 → .9 ↓	–	–	W
47	C_{n_r}	4	45, 0 c/4	.6	Low speed	–	–	WB

TABLE 7-A (CONTD)

Ref.	Derivative	A	$\Lambda_{(\ )}$ (deg)	λ	M	Freq.	Ampl.	Config.
48	C_{L_q}, C_{m_q} (theor.)	–	–	–	Hypersonic	–	–	B
49	C_{ℓ_r}, C_{n_r}, $C_{n_r} - C_{n_{\dot\beta}}, C_{\ell_r} - C_{\ell_{\dot\beta}}$	2.31 4	60 LE 0, 45 c/4	0 .6	.13	X	X	W
50	C_{n_r}, C_{ℓ_r}	2.31 4	60 LE 0, 45 c/4	0 .6	.13	X	X	W
51	C_{n_p}, C_{ℓ_p}	2.31	60 LE	0	.13	X	X	W, WB
52	$C_{Y_p}, C_{n_p}, C_{\ell_p}$	3.60	41.57 LE	.455	.13, .16	–	–	W, WB
53	$C_{Y_p}, C_{n_p}, C_{\ell_p}$	6	2 c/4	.5	.13	X	X	WB
54	$C_{n_r} - C_{n_{\dot\beta}}, C_{\ell_r} - C_{\ell_{\dot\beta}}$	2.31	60 LE	0	.13	X	X	W
55	$C_{m_q} + C_{m_{\dot\alpha}}$	3	16 c/4	.4	.9 → 1.35	–	–	WB
56	$C_{m_q} + C_{m_{\dot\alpha}}$	1.87 → 6.02	1.9 → 60 c/4 (18 configurations)	0 → 1.63	.6 → 1.7	–	–	WB
57	$C_{m_q} + C_{m_{\dot\alpha}}$	3	16 c/4	.4	.8 → 1.4	–	–	WB
58	C_{N_q} (theor.), C_{m_q}, $C_{m_q} + C_{m_{\dot\alpha}}$	1.456	70 LE	0	8.08	–	X	B, W
59	$C_{Y_p}, C_{n_p}, C_{\ell_p}$	2.31	60 LE	0	.17	–	–	W, WB
60	C_{ℓ_p}	1.34 → 5.9	0 → 60 c/4 (22 configurations)	0 → 1.0	0 → 1.3	–	–	W
61	$C_{\ell_p}, C_{n_p}, C_{Y_p}$	1.34 2.61 5.16	0 LE 45 60 0 45 60 0 45 60	1.0	.13, .17	–	–	W
62	$C_{\ell_p}, C_{n_p}, C_{Y_p}$	1.34 2.61 5.16	0 LE 45 60 0 45 60 0 45 60	1.0	.17	–	–	W

TABLE 7-A (CONTD)

Ref.	Derivative	A	$\Lambda_{(\ )}$ (deg)	λ	M	Freq.	Ampl.	Config.
63	$C_{\ell_r}, C_{Y_r}, C_{n_r}$	1.34 2.61 5.16	0 LE 45 60 0 45 60 0 45 60	1.0	.13	–	–	W
64	$C_{n_r}, C_{Y_r}, C_{\ell_r}$	2.61 5.16 2.61 1.34	–45 LE 0 45 60	1.0	.13	–	–	W
65	$C_{m_q} + C_{m_{\dot{\alpha}}}$ (theor.)	2.83	45 c/2	.333	.92 → 1.35	X	–	WB
66	$C_{L_q}, C_{m_q}, C_{\ell_q}, C_{L_{\dot{\alpha}}}, C_{m_{\dot{\alpha}}}$, $C_{\ell_{\dot{\alpha}}}, C_{m_p}, C_{\ell_p}$, $C_{L_p} + .263\, C_{L_{\dot{\alpha}}}$, and other combinations	3.35	0	1.0	0 → .125	X	X	W
67	$C_{L_q}, C_{m_q}, C_{\ell_p}, C_{Y_p}$, $C_{n_p}, C_{\ell_r}, C_{Y_r}, C_{n_r}$, (theor.)	βA = 1 → 20	0 LE	1.0	Supersonic	–	–	W
68	C_{ℓ_p} or C_{ℓ_r}, C_{Y_p} or C_{Y_r}, C_{n_p} or C_{n_r} (theor.)	βA = 0 → 20	–	–	Supersonic	–	–	W
69	C_{ℓ_p} (theor.)	2, 4 2, 4 0 → 10 2, 4 βA = 3, 4, 5, 6, 8, 10, 12, 16, 20	53 LE 0 → 60 53 53 β cos Λ = 1 → ∞	.5 .5 .5 0 → 1.0 0, .25, .5, .75, 1.0	1.2 → 2.6 2 2 2	–	–	W
70	$C_{m_q} + C_{m_{\dot{\alpha}}}$ (theor.)	1.07 2.31 4 6.93	75 LE 60 45 30	0	1 → 5 1 → 3 1 → 1.8 1 → 1.5	–	–	WB
71	$C_{\ell_p} + C_{\ell_\beta} \sin\theta$, $C_{n_r} - C_{n_{\dot{\beta}}} \cos\theta$	2.2	60 LE	0	Low speed	–	–	WB
72	C_{ℓ_r}, C_{n_r} (theor.)	6, 1.25	0 LE	1.0	–	–	–	W
73	$C_{m_q} + C_{m_{\dot{\alpha}}}$	3.57	35 .3c	.565	.6 → .96	–	–	WB
74	C_{L_q}, C_{m_q} (theor.)	2	60 LE	0	.13	–	–	W
75	C_{ℓ_p}	2.3	45, 60 LE	0	.8 → 1.8	–	–	WB

TABLE 7-A (CONTD)

Ref.	Derivative	A	$\Lambda_{(\ )}$ (deg)	λ	M	Freq.	Ampl.	Config.
76	$C_{L_q}, C_{m_q}, C_{L_{\dot{\alpha}}}, C_{m_{\dot{\alpha}}}$, $C_{Y_p}, C_{\ell_p}, C_{n_p}$, $C_{Y_r}, C_{\ell_r}, C_{n_r}$ (theor.)	–	–	–	.6, 1.2	–	–	WBHV
77	C_{m_q} (theor.)	–	78 → 88 LE	0	10, 17	–	–	W
78	$C_{m_q} + C_{m_{\dot{\alpha}}}, C_{\ell_p}, C_{n_r}$	1.96	–	0	.74 → 1.4	X	X	WBHV
79	C_{ℓ_p}	3.12 4.69 4.62 4.84 3.64	–45 c/4 –30 0 30 45	.38 .40 .55 .44 .42	Low speed, high speed	–	–	W
81	$C_{m_q} + C_{m_{\dot{\alpha}}}$	–	–	– *	2.01, 3.02, 4.56	X	–	B
82	$C_{Y_p}, C_{n_p}, C_{\ell_p}$	2.31	60 LE	0	.13	–	–	W, WB
83	$C_{Y_r}, C_{n_r}, C_{\ell_r}$	2.31	60 LE	0	.13	–	–	WB
84	$C_{Y_p}, C_{n_p}, C_{\ell_p}$	2.31 1.07 4 3 2 1	60 LE 75 45	0 0 0 .15 .36 .58	.13	–	–	W
85	$C_{\ell_p}, C_{n_p}, C_{n_r}$	2.2	60 LE	0	Low speed	–	–	WB
86	C_{ℓ_p}, C_{n_r}	2.31 2.61 3.0	60 LE 45 c/4 0 c/2	0 .25 .50	Low speed	X	–	W
87	βC_{ℓ_p} (theor.)	–	0 LE	1.0, 0	Supersonic	–	–	W
88	$C_{m_q} + C_{m_{\dot{\alpha}}}$	3	35 c/4	.6	High subsonic, transonic	–	–	W
89	$C_{m_q} + C_{m_{\dot{\alpha}}}$, $C_{m_q} + C_{m_{\dot{\alpha}}}$ (theor.)	2.309	60 LE	0	Supersonic	–	–	WB
90	$C_{m_q} + C_{m_{\dot{\alpha}}}$, $C_{m_q} + C_{m_{\dot{\alpha}}}$ (theor.)	2.0	63.4 LE	0	Transonic	X	X	WB
91	$C_{m_q} + C_{m_{\dot{\alpha}}}$, $C_{n_r} - C_{n_{\dot{\beta}}} \cos \alpha$	.904	62 LE	.418	.8, .9, 1.0, 1.2	X	X	WB + Canard
92	C_{L_q}, C_{m_q} (theor.)	–	–	–	8.8, 17	–	–	B

TABLE 7-A (CONTD)

Ref.	Derivative	A	$\Lambda_{(\ )}$ (deg)	λ	M	Freq.	Ampl.	Config.
93	C_{ℓ_p}	4	3.6, 32.6, 46 c/4	.6	.4 → .91	–	–	W
94	C_{ℓ_p}	4 2.31	3.6, 32.6, 45 c/4 60 LE	.6 0	.2 → .91	–	–	WB
95	$C_{n_p}, C_{Y_p}, C_{\ell_p}$	4	45 c/4	.6	.4 → .95	–	–	WB
96	$C_{m_q} + C_{m_{\dot{\alpha}}}$, $C_{n_r} - C_{n_{\dot{\beta}}} \cos\alpha$, $C_{\ell_r} - C_{\ell_{\dot{\beta}}} \cos\alpha$, $C_{\ell_p} + C_{\ell_{\dot{\beta}}} \sin\alpha$, $C_{n_p} + C_{n_{\dot{\beta}}} \sin\alpha$	2.44	27 LE	.38	2.5, 3.0, 3.5	X	X	WB, WBHV
97	$C_{L_{\dot{\alpha}}}, C_{m_{\dot{\alpha}}}, C_{L_q}, C_{m_q}$, $C_{m_q} + C_{m_{\dot{\alpha}}}$ (theor.)	1.0 1.5 2.0 2.5 3.0 3.5 4.0	75.9 LE 69.5 63.4 58. 53.1 48.8 45	0	Transonic	X	X	W
98	$C_{L_{\dot{\alpha}}}, C_{m_{\dot{\alpha}}}, C_{L_q}, C_{m_q}$, $C_{m_q} + C_{m_{\dot{\alpha}}}$ (theor.)	1.5 2.0 2.5	69.5 LE 63.4 58.	0	Transonic	X	X	B, W, WB
99	$C_{L_q}, C_{m_q}, C_{L_{\dot{\alpha}}}, C_{m_{\dot{\alpha}}}$ (theor.)	1.2 2.0 3.0 1.32	68.2 LE	.143 .389	Subsonic Subsonic .4 → .9 Subsonic	X X X X	X X X X	W
100	$C_{Y_p}, C_{n_p}, C_{\ell_p}$	2.61	45 LE	1.0	.17	–	–	W
101	$C_{Y_r}, C_{n_r}, C_{\ell_r}$	2.61	45 LE	1.0	.13	–	–	W
102	C_{ℓ_r}, C_{n_r}	2.31 4	60 LE 45, 0 c/4	0 .6	Low speed	X	X	W, WB
103	$C_{Y_p}, C_{n_p}, C_{\ell_p}$	4	46.7 c/4	.6	.13	–	–	W
104	$C_{Y_r}, C_{n_r}, C_{\ell_r}$	2.61	45 c/4	1.0, .50, .25	.13	–	–	W
105	$C_{Y_p}, C_{n_p}, C_{\ell_p}$	4	0 c/4	.6	.17	–	–	W, WB
106	$C_{Y_r}, C_{n_r}, C_{\ell_r}$	4	45 c/4	.6	.13	–	–	W, WB
107	$C_{\ell_r} - C_{\ell_{\dot{\beta}}}$ $C_{n_r} - C_{n_{\dot{\beta}}}$	.53 1.07 2.31	82.5 LE 75 60	0	.13	X	X	W

TABLE 7-A (CONTD)

Ref.	Derivative	A	$\Lambda_{(\ )}$ (deg)	λ	M	Freq.	Ampl.	Config.
108	$C_{Y_r}, C_{n_r}, C_{\ell_r}, C_{Y_p}, C_{n_p}, C_{\ell_p}, C_{n_r} - C_{n_{\dot\beta}}, C_{\ell_r} - C_{\ell_{\dot\beta}}$	2.31	60 LE	0	.13	X	X	WB
109	$C_{\ell_r}, C_{n_r}, C_{Y_r}$	2.61	45 LE	1.0	.13	–	–	W
110	C_{ℓ_p}	4	42.7 LE	.5	.6 → 1.15, 1.9	–	–	W
111	C_{ℓ_p}	4	0 c/4 35 ↓ 45 ↓	.6	.6, .7, .8, .85, .9, .95, 1.0, 1.05, 1.10, 1.15	–	–	WB
112	C_{ℓ_p} (theor.)	Low	45 LE	0, ~1.0	Low	–	–	W, WB
113	$C_{\ell_p}, C_{n_p}, C_{\ell_r}, C_{n_r}, C_{m_q} + C_{m_{\dot\alpha}}, C_{n_r} - C_{n_{\dot\beta}}, C_{\ell_r} - C_{\ell_{\dot\beta}}$	3.56	45 c/4	.3	.23 → .94	X	X	B, WB, WBH, BH, WBHV, BHV, BV
114	C_{ℓ_p}	6.38 6.	0 LE 18.4 ↓	1.0 .333	Subsonic	–	–	W
115	C_{m_q}, C_{L_q}	1.34 2.61 5.16 2.61	0 LE 45 ↓ 60 ↓ –45 ↓	1.0	.13	–	–	W
116	C_{ℓ_p}	2 3 5.9	42 LE –38, 42 LE –38, 42 LE	.793 .707 .50	Low speed	–	–	W
117	C_{L_q}, C_{m_q} C_{L_q} (theor.)	βA = 2 → 10 2.4 2 → 9 2.4 2.4	– 53 LE 53 ↓ 45 → 66 ↓ 53 ↓	.25, .50, .75 .5 .5 .5 0 → .75	Supersonic Supersonic 1.5 1.414 1.414	–	–	W
118	$C_{L_{\dot\alpha}}, C_{m_{\dot\alpha}}$ (theor.)	βA = 2 → 10	$\beta \cot \Lambda_{LE}$ = 0 → 1	.25, .50, .75	Supersonic	–	–	W
119	C_{ℓ_p} (theor.)	2, 4 1.65 → 5.4 2, 4	53 LE 53 ↓ 45 → 56 ↓	.5	1.2 → 1.6 1.5 1.414	–	–	W
120	C_{ℓ_p} (theor.)	2, 4 2, 4 1.8, 5.4 2, 4 βA = 2, 3, 4, 5, 6, 8, 10	53 LE 45 → 60 ↓ 53 ↓ 53 ↓ $\beta \cos \Lambda$ = 0 → 1.0	.5 .5 .5 0, .7 0, .25, .50	1.2 → 1.6 1.414 1.5 1.414	–	–	W

TABLE 7-A (CONTD)

Ref.	Derivative	A	$\Lambda_{(\ )}$ (deg)	λ	M	Freq.	Ampl.	Config.
121	$C_{L_{\dot\alpha}}, C_{m_{\dot\alpha}}, C_{L_q}, C_{m_q}$ $C_{\ell_p}, C_{n_p}, C_{Y_p}, C_{\ell_r}$, C_{n_r}, C_{Y_r} (theor.)	$\frac{\beta A}{4} < 1$	$\beta \cot \Lambda_{LE} \leq 1$ $\beta \cot \Lambda_{LE} > \left\lvert 1 - \frac{4 \cot \Lambda_{LE}}{A} \right\rvert$	0	Supersonic	--	--	W
122	$C_{L_{\dot\alpha}}, C_{m_{\dot\alpha}}, C_{L_q}, C_{m_q}$, $C_{m_q} + C_{m_{\dot\alpha}}$ (theor.)	$4 \cot \Lambda_{LE}$	$\tan^{-1}\frac{4}{A}$ LE	0	Subsonic, transonic, supersonic	X	X	W
123	$C_{\ell_p}/(AR)^3$	.5, 1, 2	--	0	1.2 → 2.5	--	--	W
124	$C_{\ell_p}/(AR)^3$	.5, 1, 2	--	0	--	--	--	W
125	$C_{m_q} + C_{m_{\dot\alpha}}$ (theor.)	3.20	55 LE	0	1.414 → 3.0	--	--	WBH
126	C_{L_q}, C_{m_q} (theor.)	$\beta A = 3 \rightarrow 20$ $\beta A = 2 \rightarrow 20$	$\beta \cot \Lambda_{LE} = 1 \rightarrow \infty$	0, .25, .5, .75 1.0	Supersonic	--	--	W
127	C_{ℓ_p}, C_{n_p} (theor.)	4 9.021	-- --	.6 .4	--	--	--	W
128	C_{ℓ_p}	1.82 → 3.4	21.2 → 70 LE (28 configurations)	0, .25	1.62, 1.93, 2.41	--	--	W
129	C_{m_q} (theor.)	--	--	--	Supersonic	X	X	W
130	$C_{m_q} + C_{m_{D\alpha}}$	2.31	60 LE	0	.75 → 1.70	--	--	WB
131	$C_{m_q} + C_{m_{D\alpha}}$	3.07	40 c/2	1.626	.55 → 1.2	--	--	WB
132	C_{ℓ_p}	3	35 c/4	.6	.4 → .91	--	--	WB
133	$C_{\ell_r}, C_{n_p}, C_{\ell_p}$ (theor.) C_{n_r}	3.8 3.0 2.3	45 LE	.026 .147 .274	.2 → .9	X	--	WBHV
134	$C_{N_q}, C_{N_{\dot\alpha}}, C_{m_q}, C_{m_{\dot\alpha}}$, $C_{m_q} + C_{m_{\dot\alpha}}$ (theor.)	--	--	--	1.1 → 5	--	--	B
135	$C_{N_q}, C_{N_{\dot\alpha}}, C_{m_q}, C_{m_{\dot\alpha}}$ (theor.)	--	--	--	1.1 → 5	--	--	B
136	$C_{m_q} + C_{m_{\dot\alpha}}$ (theor.)	--	87, 84, 81 LE	0	9, 17	--	--	W
137	$C_{m_{\dot\theta}}, C_{L_{\dot\theta}}$	3. 2. 1.25 3 2. 1.25	49.1 LE 60 70.1 49.1 60 70.1	.072 ↓ .238 ↓	1.22 → 2, .5 → 1.14	X	X	W

TABLE 7-A (CONTD)

Ref.	Derivative	A	$\Lambda_{(\ )}$ (deg)	λ	M	Freq.	Ampl.	Config.
138	$C_{m_q} + C_{m_{\dot{\alpha}}}$	6.02	0 .4c	.5	.6 → 1.17	X	–	WB
139	$C_{m_q} + C_{m_{\dot{\alpha}}}$	4	45 c/4	.6	.63 → 1.16	–	–	WB
140	$C_{n_r}, C_{\ell_r}, C_{n_p}, C_{\ell_p}$ (theor.)	6, 10, 16	0 c/4	1, .50, .25	–	–	–	W
141	$C_{m_q} + C_{m_{\dot{\alpha}}}$	2.31	60 LE	0	.9 → 1.37	–	–	WB
142	C_{ℓ_p} (theor.)	2 → 8	0 → 69.4 LE (44 configurations)	0 → 1.0	Supersonic	–	–	W
143	C_{ℓ_p}	.75, 1.0	–	0	Low speed	–	–	W
144	$C_{N_{\dot{\alpha}}} + C_{N_q}$ (theor.), $C_{m_q} + C_{m_{\dot{\alpha}}}$	–	–	–	.7 → 8.2, 1.1 → 2.4	–	–	B
145	$C_{m_q} + C_{m_{\dot{\alpha}}}$, $C_{N_{\dot{\alpha}}} + C_{N_q}$ (theor.)	–	–	–	1.2 → 3.0	–	–	B
146	C_{ℓ_p} (theor.)	1.0 → 5	0 – 60 c/4	0 → 1.0	–	–	–	W
147	$C_{Y_p}, C_{n_p}, C_{\ell_p}$	2.61	45 LE	1.0	Low speed	–	–	W
148	$C_{\ell_r}, C_{n_r}, C_{Y_r}$	2.61	45 LE	1.0	.13	–	–	W
149	$C_{n_r}, C_{\ell_r}, C_{Y_r}$	2.31 4.0	60 LE 0, 45 c/4	0 .6	Low speed	–	–	W
150	$C_{Y_p}, C_{n_p}, C_{\ell_p}, C_{Y_r}, C_{n_r}, C_{\ell_r}$	3.57	35 c/3	.565	.13, .17	–	–	WB
151	C_{ℓ_p} (theor.)	–	–	–	14	–	–	B
152	$C_{L_q}, C_{m_q}, C_{\ell_p}, C_{\ell_r}, C_{n_p}, C_{n_r}, C_{Y_p}, C_{Y_r}$ (theor.)	< .5	–	0	Subsonic Supersonic	–	–	W
153	$C_{L_{\dot{\alpha}}}, C_{m_{\dot{\alpha}}}, C_{\ell_r}, C_{Y_r}$ C_{n_p}, C_{Y_p} (theor.)	$\frac{\beta A}{4} < 1$	$\beta \cot \Lambda_{LE} \leq 1$	0	Supersonic	–	–	W
154	$C_{m_q} + C_{m_{\dot{\alpha}}}$	Varies	Varies	Varies	.5 → 21	X	X	B
155	C_{ℓ_r}, C_{n_r} (theor.) C_{n_p}, C_{ℓ_p}	1	–	0	Low speed	–	–	W + fin

TABLE 7-A (CONTD)

Ref.	Derivative	A	$\Lambda_{(\ )}$ (deg)	λ	M	Freq.	Ampl.	Config.
156	$C_{m_q} + C_{m_{\dot{\alpha}}}$	3.6	41.57 LE	.456	.4 → .88	–	–	WB
157	C_{ℓ_p}	4	42.7 LE	.5	.7 → 1.4	–	–	WB
		3.5	36.5	.56				
		2.9	23.1	.41				
		4	37.4, 46.7, 60.9	.6				
		3.5	63	.25				
		6	46.2	.6				
158	C_{ℓ_p}	3.71	0, 45 c/4	1, .5, .3, 0	.8 → 1.45	–	–	WB
159	C_{L_q}, C_{m_q}	1.2	68.2 LE	.143	Subsonic	X	–	W
		1.6		0				
		1.32		.389				
160	$C_{m_{\dot{\theta}}}$	4.4	0	1	1.37 → 2.43	X	–	W
161	C_{m_q} (theor.)	–	–	–	Supersonic	–	–	B
162	$C_{L_{\dot{\alpha}}}, C_{m_{\dot{\alpha}}}, C_{L_q}, C_{m_q}$	–	–	–	.5 → .8	X	–	WBHV
163	$C_{L_{\dot{q}}}, C_{m_{\dot{q}}}, C_{L_q}, C_{m_q}$	2.46	–	–	.70 → 1.10	X	–	WBHV
164	$C_{L_{\dot{\alpha}}}, C_{m_{\dot{\alpha}}}, C_{L_q}, C_{m_q}$ (theor.)	–	–	–	.30, .50, .70, .75	X	X	WBH
165	C_{ℓ_p}	3.7	–	1.0	.6 → 1.4	–	–	WB
166	C_{ℓ_p} (theor.)	6	–	1, .5, .25	–	–	–	W
167	$C_{\ell_p}, C_{\ell_r}, C_{n_p}, C_{n_r}$ (theor.)	4, 6, 8	–	–	–	–	–	W
168	$C_{n_r} - C_{n_{\dot{\beta}}} \cos\alpha$, $C_{Y_r} - C_{Y_{\dot{\beta}}} \cos\alpha$, $C_{\ell_r} - C_{\ell_{\dot{\beta}}} \cos\alpha$, $C_{n_p} + C_{n_{\dot{\beta}}} \sin\alpha$, $C_{Y_p} + C_{Y_{\dot{\beta}}} \sin\alpha$, $C_{\ell_p} + C_{\ell_{\dot{\beta}}} \sin\alpha$	.92	74 LE	0	.094 → .267	X	–	WBV
169	$C_{m_q} + C_{m_{\dot{\alpha}}}$	2	63.4 LE	0	1.2 → 1.9	–	–	WB
		3	53	↓				
		4	45					
		3	45	.403				
		3	19.1	.407				

TABLE 7-A (CONTD)

Ref.	Derivative	A	$\Lambda_{(\ )}$ (deg)	λ	M	Freq.	Ampl.	Config.
170	$C_{L_{\dot\alpha}}, C_{m_{\dot\alpha}}, C_{L_q}, C_{m_q}$, $C_{m_q} + C_{m_{\dot\alpha}}$ (theor.)	$0 < \beta A < 4$	$\tan^{-1}\frac{4}{A}$ LE	0	0 → 1.0	–	–	W
171	$C_{m_q} + C_{m_{\dot\alpha}}$	4	45 LE	0	1.15 → 1.70	–	–	W, WB
172	$C_{L_{\dot\alpha}}, C_{m_{\dot\alpha}}, C_{L_q}, C_{m_q}$ (theor.)	–	–	–	Supersonic, hypersonic	–	–	B
173	$C_{\ell_p}, C_{n_p}, C_{Y_p}$, $C_{\ell_r}, C_{n_r}, C_{Y_r}$, C_{L_q}, C_{m_q}	2.61 5.16 2.61 1.34	–45 LE 0 45 60	1.0	Low speed	–	–	W
174	C_{ℓ_p}	.5 → 10	0 → 80.4 c/4 (17 configurations)	0 → 1.0	Low speed	–	–	W
175	$C_{m_q} + C_{m_{\dot\alpha}}$	4.79	35.23 c/4	.51	.6 → 1.04	–	–	WB
176	C_{ℓ_p} (theor.)	–	0 –	1.0 0	–	–	–	WB
177	$C_{m_q} + C_{m_{\dot\alpha}}, C_{\ell_p}$, $C_{n_r} - C_{n_{\dot\beta}}$	.866	73.3 LE	0	1.06 → 1.8	X	–	W + fin
178	C_{ℓ_p}	2.83	27.95, 53.55 LE 49.97	.33 .066	.7 → 1.4	–	–	WBV
179	C_{ℓ_p}, C_{n_r}	3.1	0/38/65 LE	(.13)	1.2 → 2.6	X	–	WBHV
180	$C_{m_q} + C_{m_{\dot\alpha}}$	2.24	60 c/4	.333	.75 → 1.50	–	–	WB
181	C_{m_q} (theor.)	–	–	–	–	–	–	B
182	C_{ℓ_p}	3.5	63 LE	.25	1.2 → 1.7	–	–	W
183	$C_{m_q} + C_{m_{\dot\alpha}}$	–	–	–	.25 → 2.20	–	X	B
184	$C_{m_q} + C_{m_{\dot\alpha}}$	–	–	–	.65 → 2.20	X	X	B
185	$C_{Y_p}, C_{n_p}, C_{\ell_p}$	4	3.6, 32.6, 45, 60 c/4	.6	.5 → .95	–	–	WB
186	$C_{\ell_p}, C_{n_p}, C_{Y_p}$	4 2.31	45 LE 60	0	.5 → .95	–	–	WB
187	$C_{Y_p}, C_{n_p}, C_{\ell_p}$, $C_{Y_r}, C_{n_r}, C_{\ell_r}$	5.90	0 LE	.473	.13, .17	–	–	WB

TABLE 7-A (CONTD)

Ref.	Derivative	A	$\Lambda_{(\ )}$ (deg)	λ	M	Freq.	Ampl.	Config.
188	$C_{Y_p}, C_{n_p}, C_{\ell_p}$	4	45 c/4	.6	.17	–	–	W
189	$C_{L_{\dot\alpha}}, C_{m_{\dot\alpha}}, C_{L_q}, C_{m_q}$ (theor.)	–	–	–	Supersonic	–	–	B
190	C_{m_q}	1.484	–	0	.09, .18	X	X	W
191	$C_{m_q} + C_{m_{\dot\alpha}}$ $C_{m_\alpha} - k^2 C_{m_{\dot q}}$	7.035	41.5/37.5 LE	(.33)	.20 → .94	X	X	WB
192	$C_{L_{\dot\alpha}}, C_{m_{\dot\alpha}}, C_{L_q}, C_{m_q}$, $C_{m_q} + C_{m_{\dot\alpha}}$ (theor.)	1.5 2.0 2.5	69.5 LE 63.4 ↓ 58 ↓	0	Supersonic	–	–	B, W, WB

7.1 WING DYNAMIC DERIVATIVES

The methods presented in this section are to be used for the estimation of pitching, acceleration, rolling, and yawing dynamic derivatives of isolated lifting surfaces. The methods and charts applicable to this section are based on lifting-surface theory for subsonic speeds and on linearized theory for supersonic speeds. The charts are thus limited to conditions for which the flow is essentially attached over the surface of the wing, i.e., the linear lift-curve range. This means that at subsonic speeds the methods are valid for high-aspect-ratio wings up to stall angles of attack but are limited for low-aspect-ratio wings to low angles of attack.

For wings operating under conditions of partially separated flow, such as low-aspect-ratio wings at moderate to high angles of attack, experimental data, e.g., references 1 and 2, show that substantial nonlinearities exist in the dynamic derivatives. In addition, tests made by wind-tunnel oscillating-mode techniques show that the dynamic derivatives are functions of both the amplitude and frequency of oscillation. In general, dynamic derivatives for separated-flow conditions are larger and therefore more significant than for attached-flow conditions. Because of the complexity of the separated-flow case, no quantitative information on these effects is presented in the Datcom. Instead, a qualitative discussion of the characteristics of dynamic derivatives under partially separated-flow conditions is given.

Flow separation on wings at angles of attack below stall is discussed in Sections 4.1.3.3 and 4.1.3.4. The dominant feature of flow over low-aspect-ratio or swept wings, i.e., wings for which flow separation below stall is important, is the leading-edge vortex. The strength of the leading-edge vortex is determined by wing planform and airfoil leading-edge geometry.

In general, large leading-edge sweep angles and sharp airfoil sections are conducive to high vortex strengths. The strength of the leading-edge vortex, in turn, determines the nature and magnitude of the nonlinear static force, moment, and dynamic-derivative characteristics. The effects of geometry on the dynamic derivatives of a triangular wing at low speed are presented in reference 3.

Partially separated flow over a wing causes the dynamic derivatives to be frequency-dependent. The reason is that a change in wing attitude changes the boundary-layer conditions, which, in turn, alter the flow-separation pattern. The time required for the flow to adjust to a change in attitude is appreciable, and the dynamic derivatives become functions of the rate change of attitude (or frequency). The flow about wings with essentially attached flow is less dependent upon the boundary layer and therefore adjusts more rapidly to attitude changes. Hence the dynamic derivatives for these conditions are not frequency-dependent over the practical frequency range.

For wings that exhibit nonlinearities in their static forces and moments (partially separated flow exists), the dynamic derivatives also depend upon the amplitude of the attitude changes. For instance, sketch (a) (reference 2) shows the rolling moment in sideslip for a triangular wing at high angles of attack. It is clear that the rotary derivative C_{l_r} depends upon the amplitude of oscillation about the Z-axis.

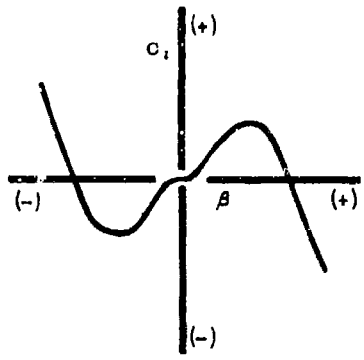

SKETCH (a)

REFERENCES

1. Campbell, J. P., Johnson, J. L., Jr., and Hewes, D. E.: Low-Speed Study of the Effect of Frequency on the Stability Derivatives of Wings Oscillating in Yaw with Particular Reference to High Angle-of-Attack Conditions. NACA RM L55H05, 1955. (U)

2. Johnson, J. L., Jr.: Low-Speed Measurements of Static Stability, Damping in Yaw, and Damping in Roll of a Delta, a Swept, and an Unswept Wing for Angles of Attack from 0° to 90°. NACA RM L56B01, 1956. (U)

3. Fletcher, H. S.: Low-Speed Experimental Determination of the Effects of Leading-Edge Radius and Profile Thickness on Static and Oscillatory Lateral Stability Derivatives for a Delta Wing with 60° of Leading-Edge Sweep. NACA TN 4341, 1958. (U)

7.1.1 WING PITCHING DERIVATIVES

7.1.1.1 WING PITCHING DERIVATIVE C_{L_q}

The wing pitching derivative C_{L_q} is generally small compared to other terms in the equations of motion and is frequently neglected. However, methods are presented for determining C_{L_q} of the wing in subsonic and supersonic speed ranges. The supersonic value of C_{L_q} is used in estimating supersonic values of C_{m_q} in Section 7.1.1.2.

If the wing pitching derivative C_{L_q} is to be used in method 1 of Section 7.3.1.1 to obtain $(C_{L_q})_{WB}$, the exposed wing planform area should be used for all calculations in the Datcom methods. Using the exposed planform area will yield C_{L_q} based on the product of exposed wing area and exposed wing MAC, rather than the product of total wing area and wing MAC as indicated.

DATCOM METHODS

A. SUBSONIC

The equation for estimating the subsonic pitching derivative $C_{L_q}^{*}$ (derived in reference 1), based on the product of wing area and wing MAC $S_W \bar{c}_W$, is given by

$$C_{L_q} = \left(\frac{1}{2} + 2\,\frac{\bar{x}}{\bar{c}}\right) C_{L_\alpha} \qquad 7.1.1.1\text{-a}$$

where $\frac{\bar{x}}{\bar{c}}$ can be expressed as

$$\frac{\bar{x}}{\bar{c}} = \frac{x_{a.c.}}{\bar{c}} - \frac{x_{c.g.}}{\bar{c}} \qquad 7.1.1.1\text{-b}$$

and

$\bar{x}$ is the distance between the center of gravity and the aerodynamic center, positive for aerodynamic center behind center of gravity.

$\frac{x_{a.c.}}{\bar{c}} = \left(\frac{x_{a.c.}}{c_r}\right)_{4.1.4.2} \left(\frac{c_r}{\bar{c}}\right)$, the longitudinal distance from the wing leading-edge vertex to the aerodynamic center measured in mean aerodynamic chords, positive aft.

$\frac{x_{c.g.}}{\bar{c}}$ is the longitudinal distance from the wing leading-edge vertex to the center of gravity measured in mean aerodynamic chords, positive aft.

C_{L_α} is the wing lift-curve slope (Section 4.1.3.2) at the Mach number under consideration, based on the total wing area.

Sample Problem

Given:

$A = 4.0$ $\quad \lambda = 0.68$ $\quad \Lambda_{LE} = 46.3°$ $\quad \frac{c_r}{\bar{c}} = 1.18$

$\frac{x_{c.g.}}{c_r}$ = 1.04 (from planform geometry with c.g. at $\bar{c}/4$) $\quad M = 0.20$

C_{L_α} = 3.20 per rad (Section 4.1.3.2)

Compute:

Calculate $\frac{x_{a.c.}}{c_r}$ using the method of Section 4.1.4.2

$\tan \Lambda_{LE} = 1.046$

$A \tan \Lambda_{LE} = 4.18$

$\beta = 0.98$

$\beta/\tan \Lambda_{LE} = 0.937$

$\frac{x_{a.c.}}{c_r}$ = 1.05 (figures 4.1.4.2-26d, -26e, -26f)

Calculate the distance between the center of gravity and the aerodynamic center

$$\frac{\bar{x}}{\bar{c}} = \frac{x_{a.c.}}{\bar{c}} - \frac{x_{c.g.}}{\bar{c}} \quad \text{(equation 7.1.1.1-b)}$$

$$= \left(\frac{x_{a.c.}}{c_r} - \frac{x_{c.g.}}{c_r} \right) \frac{c_r}{\bar{c}}$$

$= (1.05 - 1.04)\ 1.18$

$= 0.0118$

Solution:

Calculate the wing pitching derivative

$$C_{L_q} = \left(\frac{1}{2} + 2\,\frac{\bar{x}}{\bar{c}}\right) C_{L_\alpha} \quad \text{(equation 7.1.1.1-a)}$$

$$= \left[\frac{1}{2} + 2(0.0118)\right] 3.20$$

$= (0.52)\ (3.20)$

$= 1.66$ per rad (based on $S_W \bar{c}_W$)

B. TRANSONIC

There are few data and no theory available on the derivative C_{L_q} in the transonic region. For the purpose of the Datcom, it is suggested that equation 7.1.1.1-a be applied in the transonic region.

C. SUPERSONIC

The supersonic value of C_{L_q}, based on the product of wing area and wing MAC $S_W \bar{c}_W$, is given by

$$C_{L_q} = C_{L_q}{}' + 2\left(\frac{\bar{x}}{\bar{c}}\right) C_{N_\alpha} \quad \text{(per radian)} \qquad 7.1.1.1\text{-c}$$

where

$$\frac{\bar{x}}{\bar{c}} = \frac{x_{a.c.}}{\bar{c}} - \frac{x_{c.g.}}{\bar{c}} \qquad 7.1.1.1\text{-b}$$

and

C_{L_q} is referred to body axis with the origin at the wing aerodynamic center and is obtained as indicated below, based on the product of total wing area and wing MAC $S_W \bar{c}_W$.

C_{N_α} is the wing normal-force-curve slope (Section 4.1.3.2) at the Mach number under consideration, based on the total wing area (per radian).

Methods of estimating C_{L_q}'

1. Wings with subsonic leading edges ($\beta \cot \Lambda_{LE} < 1.0$)

For wings with subsonic leading edges, C_{L_q}' is obtained by the method of reference 3 for $\lambda = 0$ and by the method of reference 4 for $\lambda = 0.25$ to 1.0. The following methods are not valid if the Mach line from the trailing-edge vertex intersects the leading edge or if the wing-tip Mach lines intersect on the wings or intersect the opposite wing tips.

a. Zero-taper-ratio wings ($\lambda = 0$)

C_{L_q}' is derived in reference 3 as

$$C_{L_q}' = \frac{\pi}{2} A[3G(\beta C) F_3(N) - 2E''(\beta C) F_4(N)] + 2 \frac{(d - x_{a.c.})}{\bar{c}} C_{N_\alpha} \text{ (per radian)}$$

7.1.1.1-d

where

$E''(\beta C)$ and $G(\beta C)$ are obtained from figure 7.1.1.1-8.

$F_3(N)$ and $F_4(N)$ are obtained from figure 7.1.1.1-9.

d is two-thirds the basic triangular wing root chord $\left(d = \frac{2}{3} c_{r_B}\right)$. (See sketch (a).)

A is the aspect ratio of the wing.

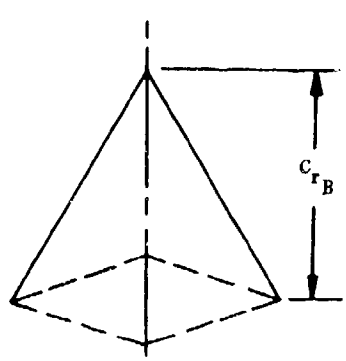

SKETCH (a)

b. Wings with $\lambda = 0.25$ to 1.0

$C_{L_q}{}'$ is derived in reference 4 as

$$C_{L_q}{}' = C_{L_q}{}'' - 2\left(\frac{x_{a.c.}}{\bar{c}}\right) C_{N_\alpha} \quad \text{(per radian)} \qquad 7.1.1.1\text{-e}$$

where

$C_{L_q}{}''$ is referred to body axis with the origin at the wing leading-edge vertex and is obtained from figures 7.1.1.1-10a, 7.1.1.1-10b, and 7.1.1.1-10c, for $\lambda = 0.25, 0.50$, and 0.75, respectively, and from the equations of reference 4 for $\lambda > 0.75$.

2. Wings with supersonic leading edges ($\beta \cot \Lambda_{LE} > 1.0$)

For wings with supersonic leading edges, $C_{L_q}{}'$ is obtained from figures 7.1.1.1-11a through 7.1.1.1-11k. This method, derived in reference 5, is valid for the range of Mach numbers for which the Mach lines from the leading-edge vertex intersect the trailing edge. An additional limitation is that the foremost Mach line from either wing tip may not intersect the remote half of the wing.

Sample Problem

Given:

$A = 3.46$ $\quad \Lambda_{LE} = 60^\circ$ $\quad \frac{c_r}{\bar{c}} = 1.50$ $\quad M = 1.50$ $\quad \lambda = 0$

$b = 16$ ft $\quad$ c.g. at $\frac{\bar{c}}{4}$ $\quad c_r = 9.25$ ft $\quad \bar{c} = 6.17$ ft

Compute:

$$\beta = \sqrt{M^2 - 1} = 1.12$$

$$\beta \cot \Lambda_{LE} = 0.647 \text{ (subsonic leading edge)}$$

$$N = 1 - \frac{4 \cot \Lambda_{LE}}{A} = 0.333$$

$$\left.\begin{aligned} E''(\beta C) &= 0.770 \\ G(\beta C) &= 0.570 \end{aligned}\right\} \text{ (figure 7.1.1.1-8)}$$

$$\left.\begin{aligned} F_3(N) &= 0.913 \\ F_4(N) &= 1.12 \end{aligned}\right\} \text{ (figure 7.1.1 1-9)}$$

Obtain C_{N_α} from Section 4.1.3.2

$\beta/\tan \Lambda_{LE} = 0.647$

$A \tan \Lambda_{LE} = 6.0$

$\tan \Lambda_{LE}\, C_{N_\alpha} = 5.40$ per rad (figure 4.1.3.2-56a)

$C_{N_\alpha} = 3.12$ per rad

Obtain $\frac{x_{a.c.}}{\bar{c}}$ from Section 4.1.4.2

$\frac{x_{a.c.}}{c_r} = 0.90$ (figure 4.1.4.2-26a)

$$\frac{x_{a.c.}}{\bar{c}} = \left(\frac{x_{a.c.}}{c_r}\right)\left(\frac{c_r}{\bar{c}}\right) = 1.35$$

$x_{a.c.} = 1.35\ \bar{c} = (1.35)(6.17) = 8.33$

Calculate $\frac{\bar{x}}{\bar{c}}$

$\frac{x_{c.g.}}{c_r} = 0.67$ (from planform geometry with c.g. at $\bar{c}/4$)

$$\frac{\bar{x}}{\bar{c}} = \left(\frac{x_{a.c.}}{\bar{c}} - \frac{x_{c.g.}}{\bar{c}}\right) \quad \text{(equation 7.1.1.1-b)}$$

$$= \left(\frac{x_{a.c.}}{c_r} - \frac{x_{c.g.}}{c_r}\right)\frac{c_r}{\bar{c}}$$

$= (0.90 - 0.67)\ 1.50 = 0.345$

Calculate d from the characteristics of the basic triangular wing (see sketch (a))

$$A_B = \frac{b^2}{\frac{1}{2}\, b\, c_{r_b}} = \frac{4}{\tan \Lambda_{LE}} = \frac{4}{1.732} = 2.31$$

$$c_{r_b} = \frac{2b}{A_B} = \frac{2(16)}{2.31} = 13.85 \text{ ft}$$

$$d = \frac{2}{3} c_{r_b} = \frac{2}{3} (13.85) = 9.233 \text{ ft}$$

Solution for C_{L_q}'

$$C_{L_q}' = \frac{\pi A}{2} [3G(\beta C) F_3(N) - 2E''(\beta C) F_4(N)] + 2 \frac{(d - x_{a.c.})}{\bar{c}} C_{N_\alpha}$$

(equation 7.1.1.1-d)

$$= \frac{\pi}{2} (3.46) [3(0.57) (0.913) - 2(0.77) (1.12)] + 2 \frac{(9.233 - 8.33)}{6.17} (3.12)$$

$$= -0.891 + 0.913$$

$$= 0.022 \text{ per rad} \quad (\text{based on } S_W \bar{c}_W)$$

Solution for C_{L_q}

$$C_{L_q} = C_{L_q}' + 2\left(\frac{\bar{x}}{\bar{c}}\right) C_{N_\alpha} \quad \text{(equation 7.1.1.1-c)}$$

$$= 0.022 + 2(0.345)\, 3.12$$

$$= 2.175 \text{ per rad} \quad (\text{based on } S_W \bar{c}_W)$$

REFERENCES

1. Toll, T., and Queijo, M.: Approximate Relations and Charts for Low-Speed Stability Derivatives of Swept Wings. NACA TN 1581, 1948. (U)

2. MacLachlan, R., and Fisher, L. R.: Wind-Tunnel Investigation at Low Speeds of the Pitching Derivatives of Untapered Swept Wings. NACA RM L8G19, 1948. (U)

3. Malvestuto, F. S., Jr., and Margolis, K.: Theoretical Stability Derivatives of Thin Sweptback Wings Tapered to a Point with Sweptback or Sweptforward Trailing Edges for a Limited Range of Supersonic Speeds. NACA TR 971, 1950. (U)

4. Malvestuto, F. S., Jr., and Hoover, D. M.: Lift and Pitching Derivatives of Thin Sweptback Tapered Wings with Streamwise Tips and Subsonic Leading Edges at Supersonic Speeds. NACA TN 2294, 1951. (U)

5. Martin, J. C., Margolis, K., and Jeffreys, I.: Calculation of Lift and Pitching Moments Due to Angle of Attack and Steady Pitching Velocity at Supersonic Speeds for Thin Sweptback Tapered Wings with Streamwise Tips and Supersonic Leading and Trailing Edges. NACA TN 2699, 1952. (U)

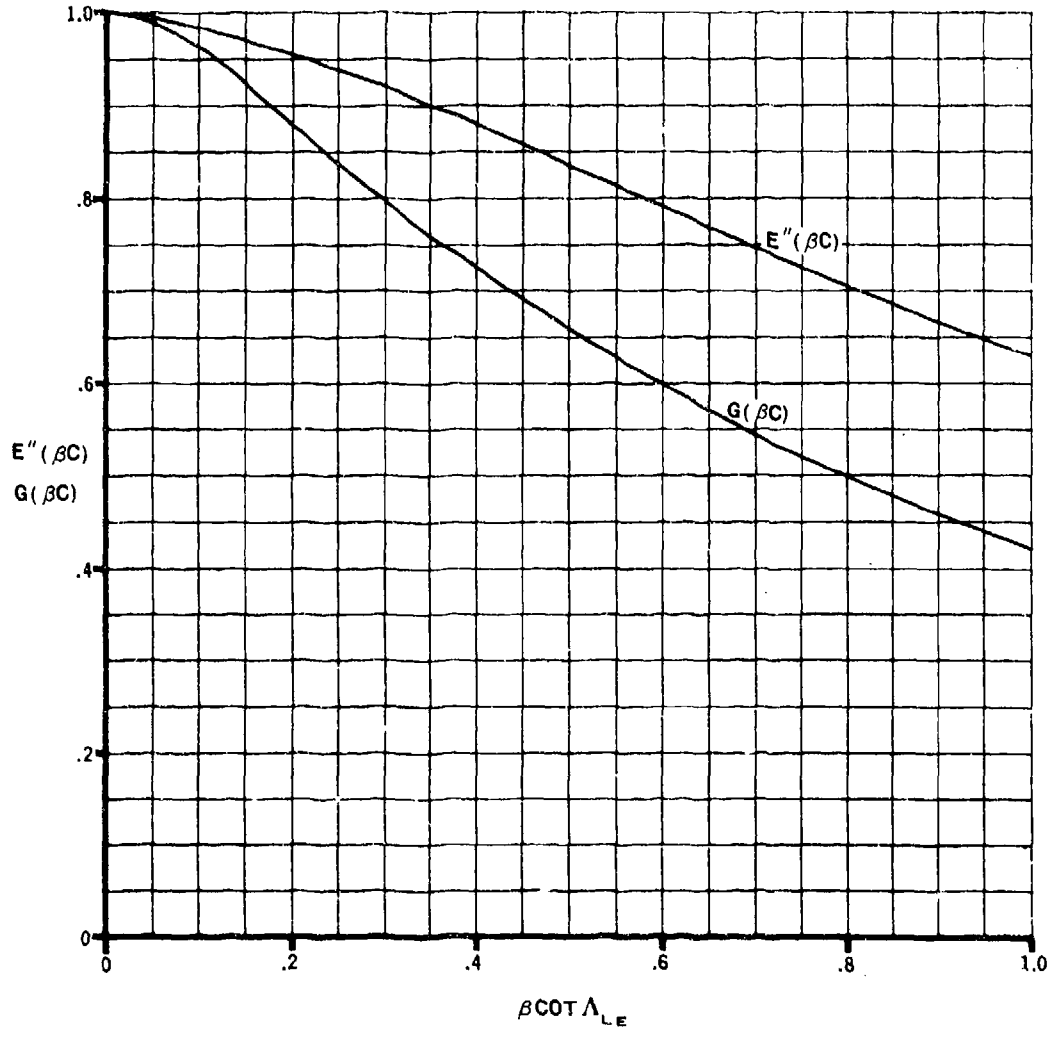

FIGURE 7.1.1.1-8 ELLIPTIC INTEGRAL FACTORS OF THE STABILITY DERIVATIVE

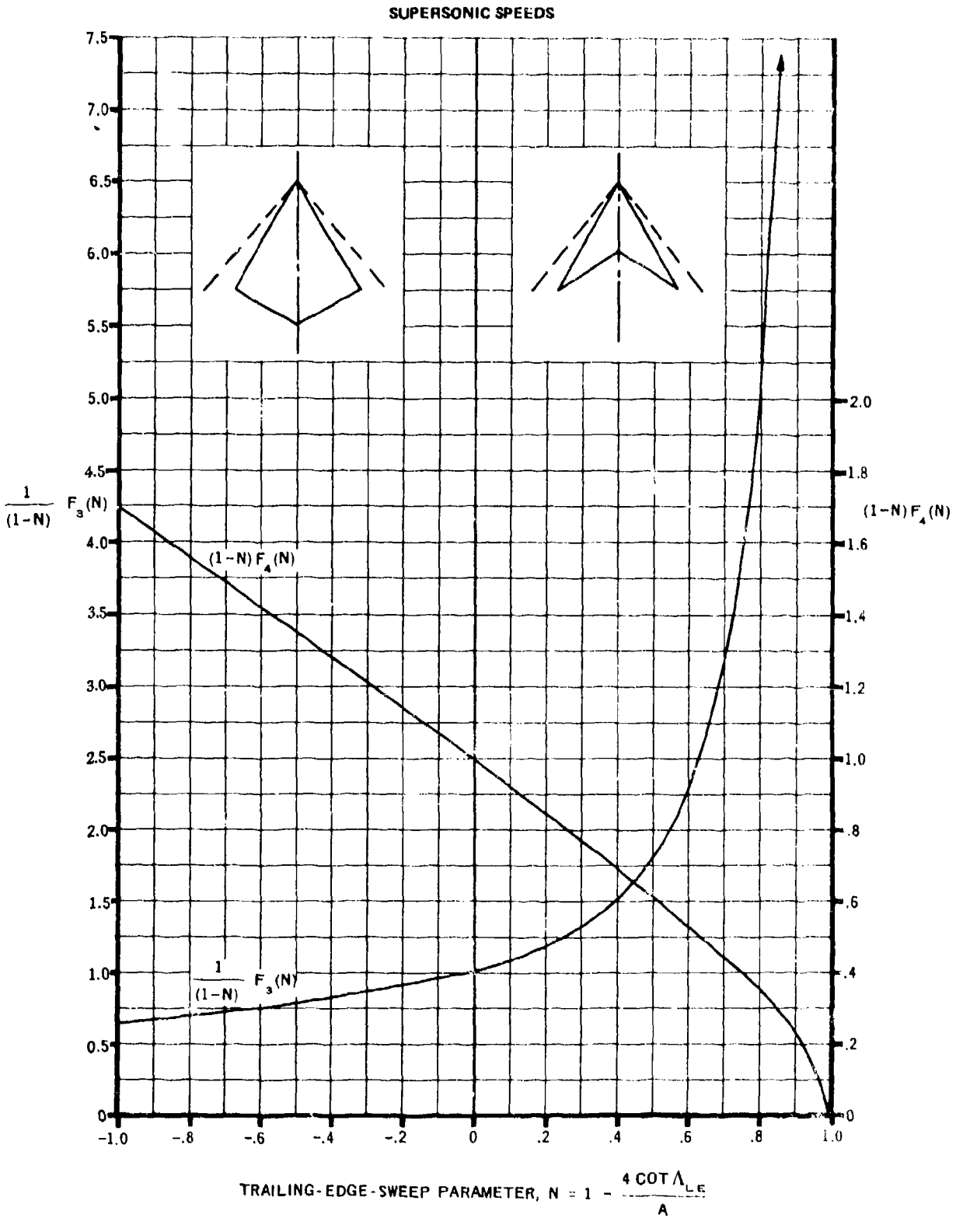

FIGURE 7.1.1.1-9 F(N) FACTORS OF THE STABILITY DERIVATIVE

SUBSONIC LEADING EDGE

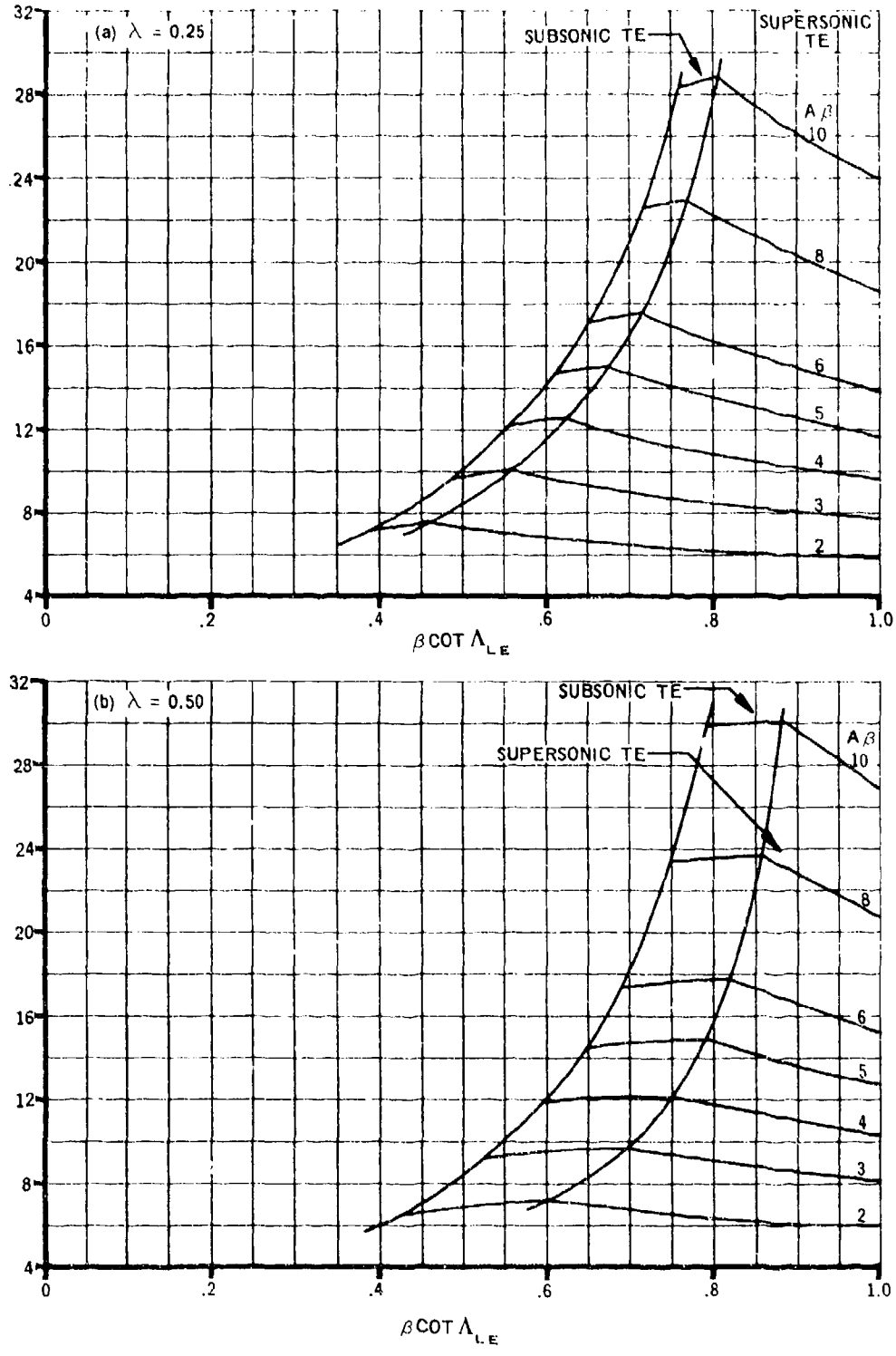

FIGURE 7.1.1.1-10 VARIATION OF $\beta C_{L_q}''$ WITH $\beta \cot \Lambda_{LE}$

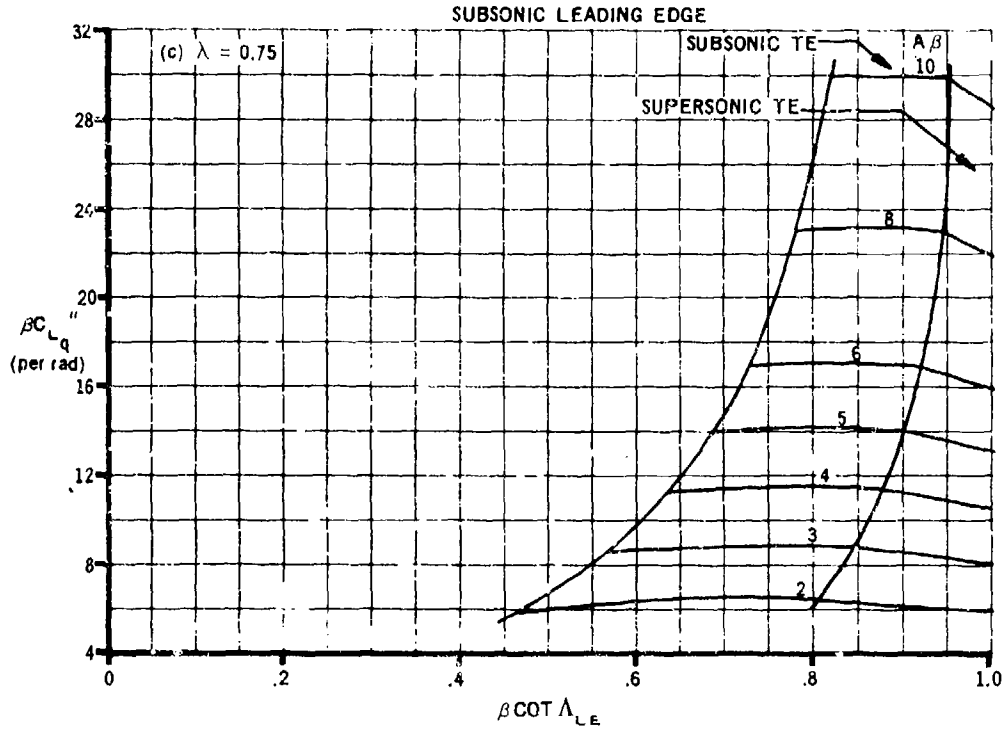

FIGURE 7.1.1.1-10(CONTD)

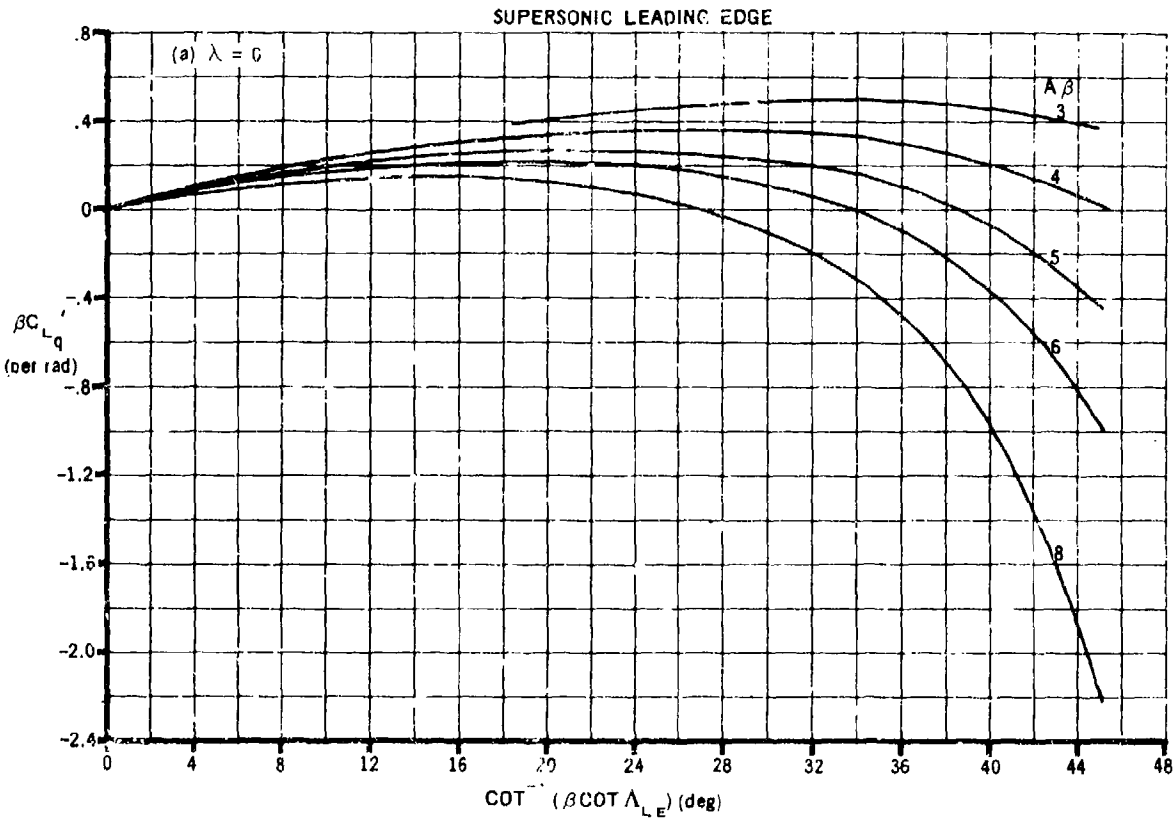

FIGURE 7.1.1.1-11 VARIATION OF $\beta C_{L_q}'$ WITH $\cot^{-1}(\beta \cot \Lambda_{LE})$

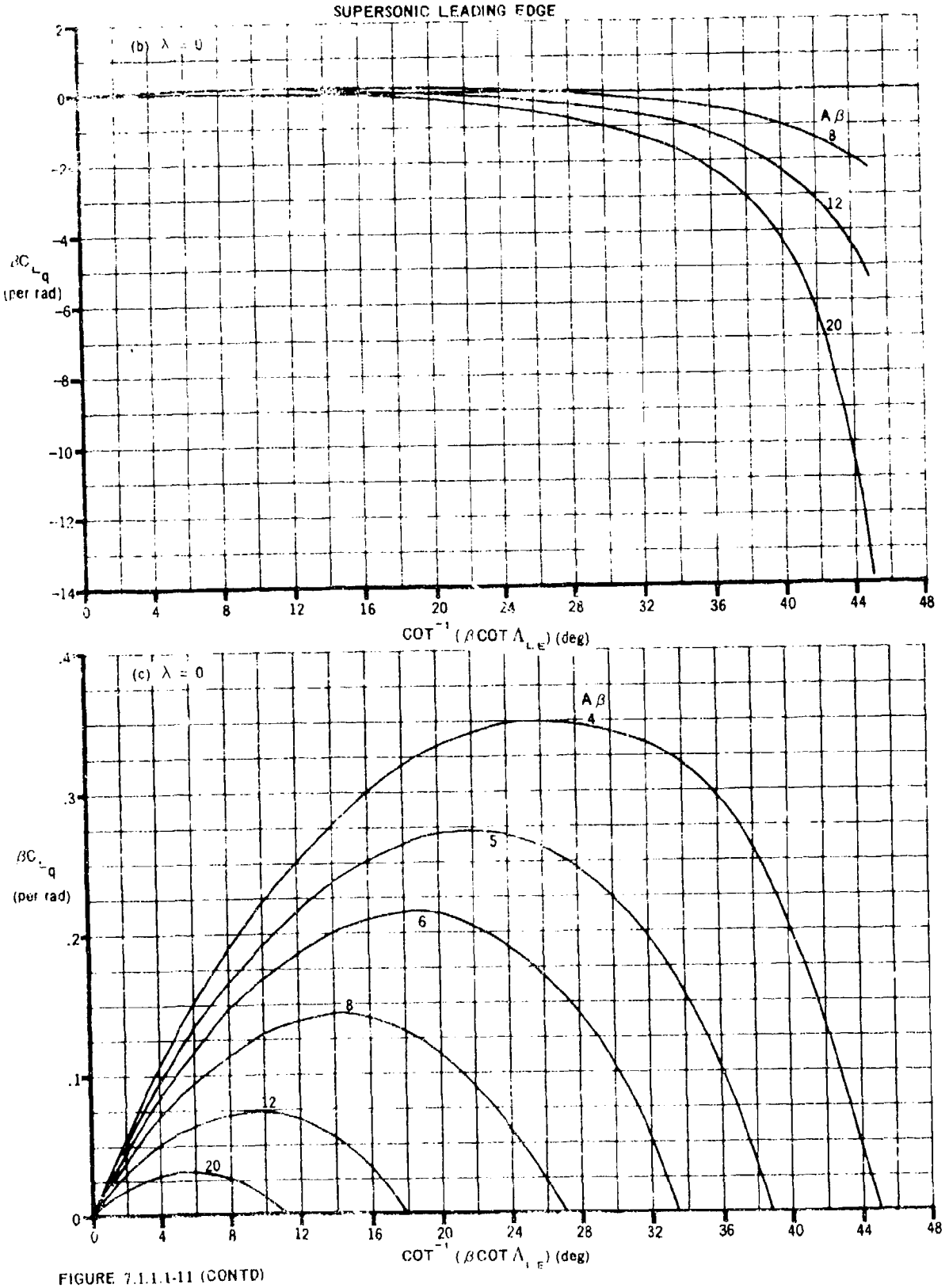

FIGURE 7.1.1.1-11 (CONTD)

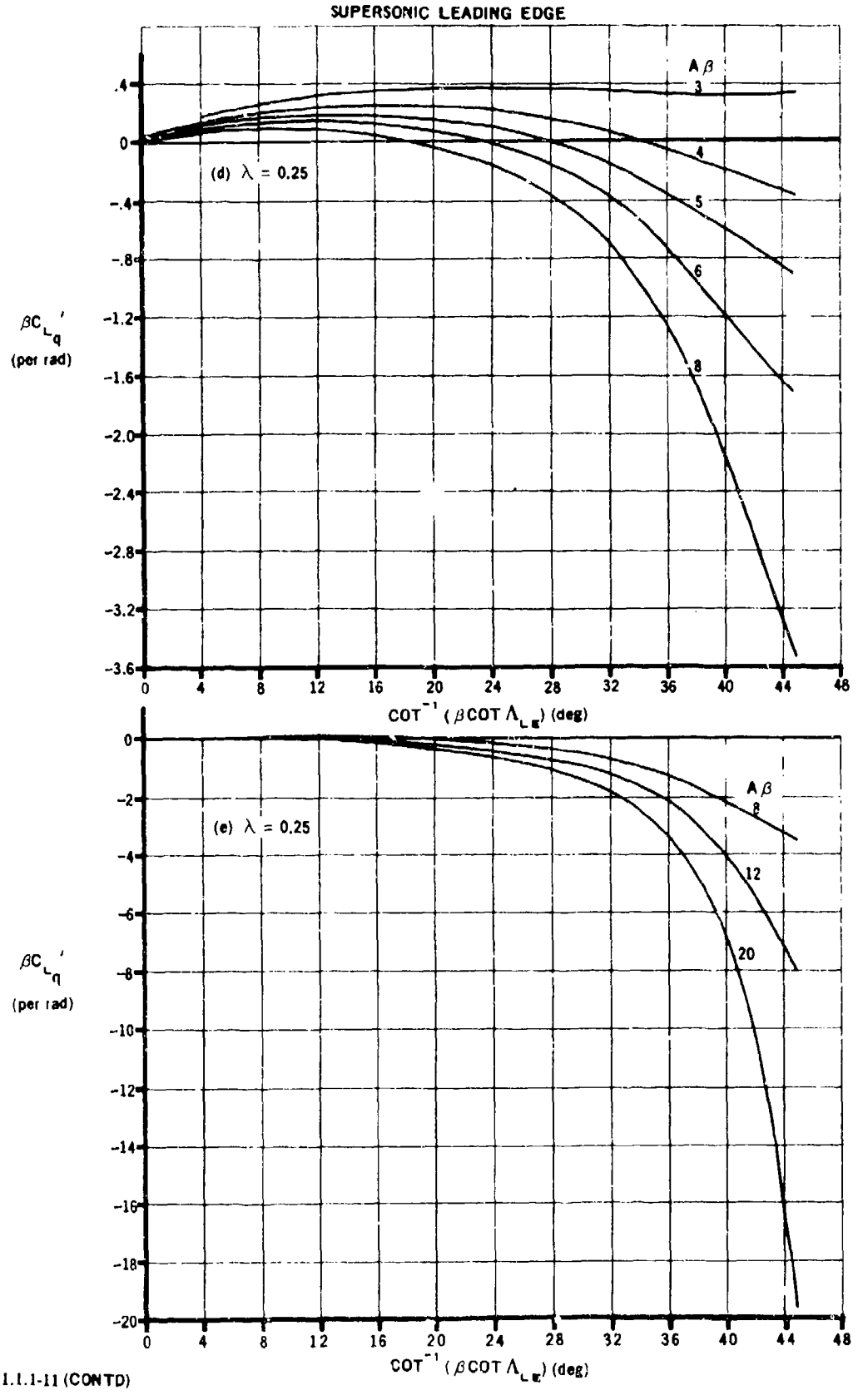

FIGURE 7.1.1.1-11 (CONTD)

SUPERSONIC LEADING EDGE

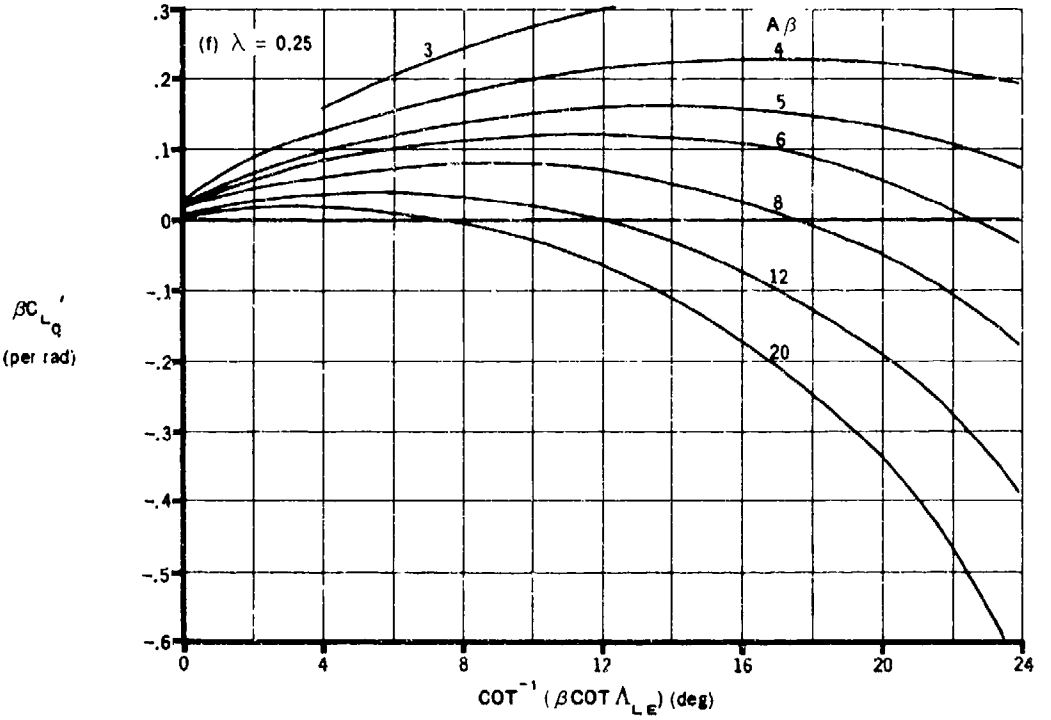

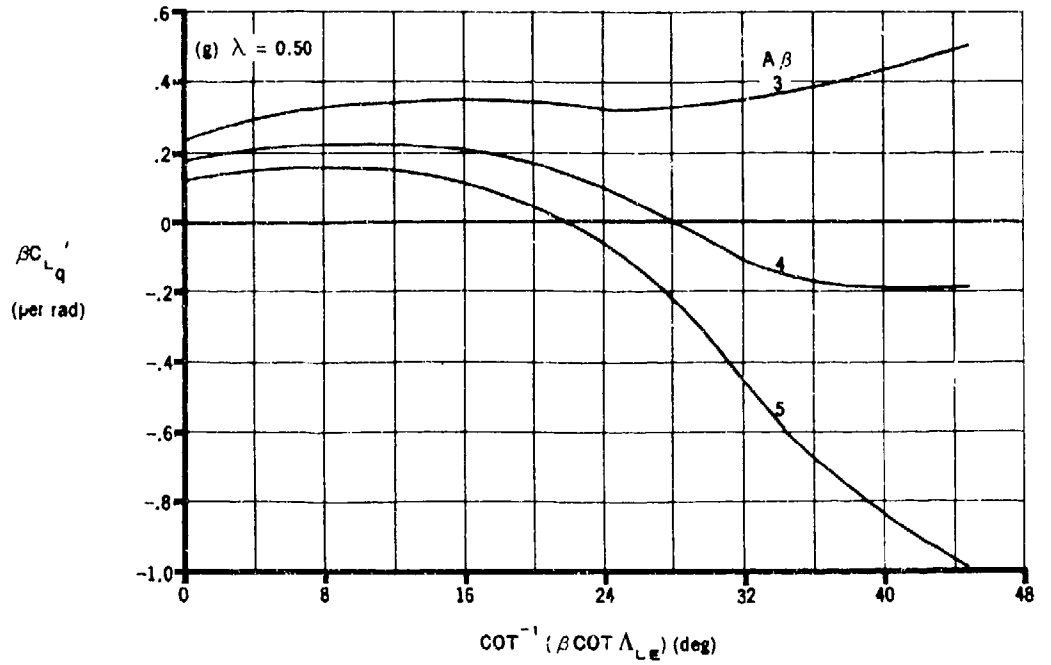

FIGURE 7.1.1.1-11 (CONTD)

SUPERSONIC LEADING EDGE

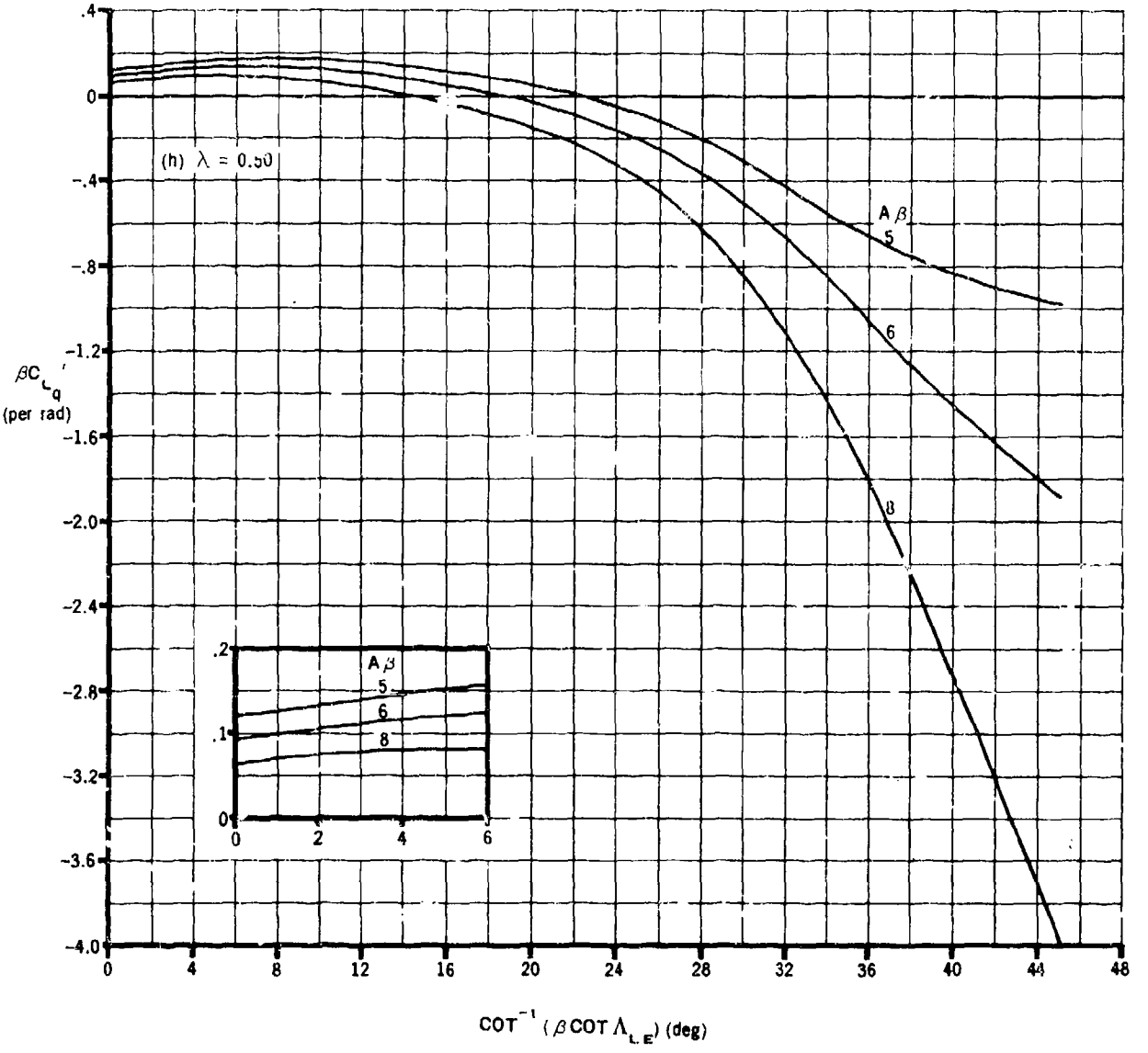

FIGURE 7.1.1.1-11 (CONTD)

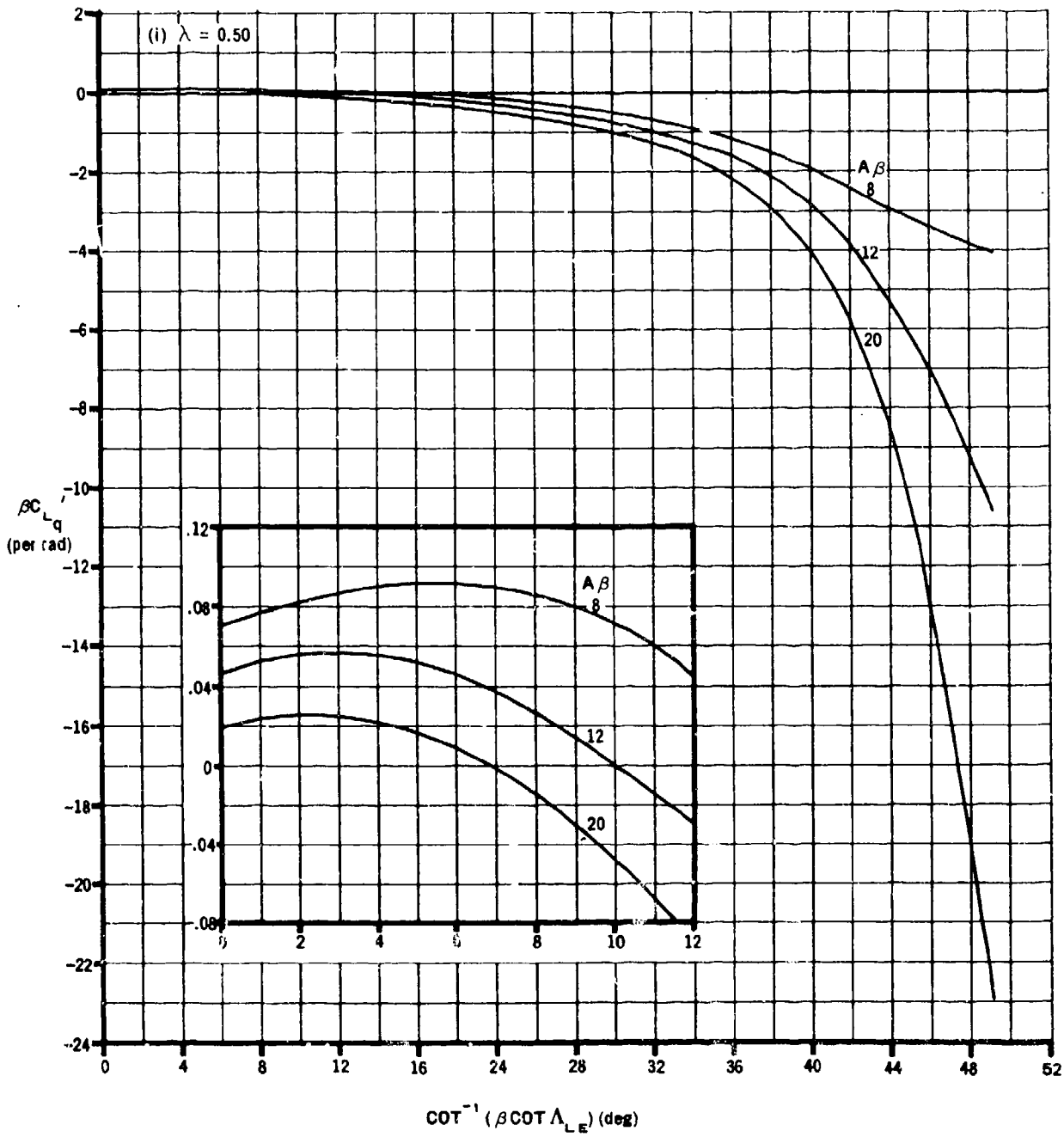

FIGURE 7.1.1.1-11 (CONTD)

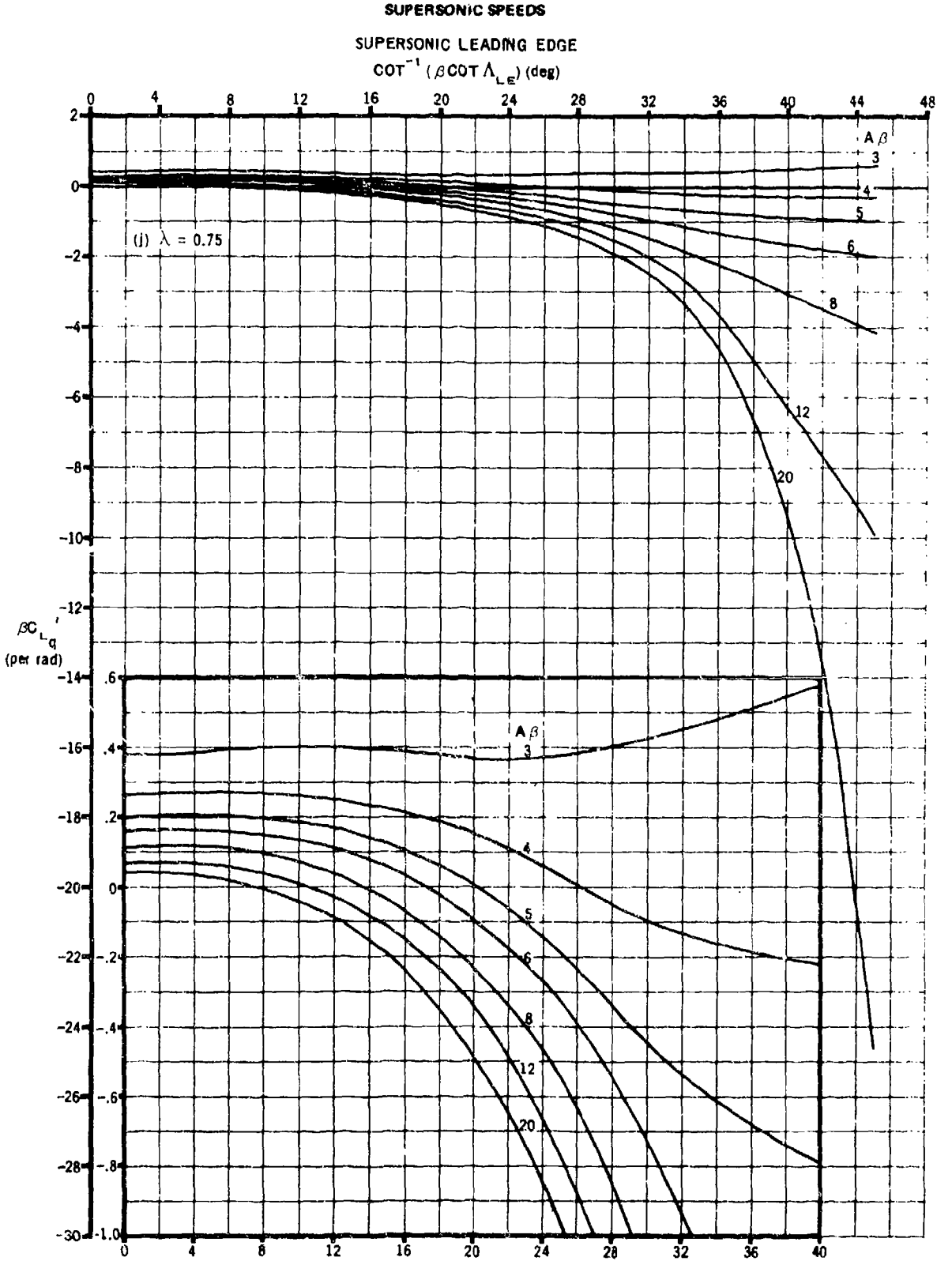

FIGURE 7.1.1.1-11 (CONTD)

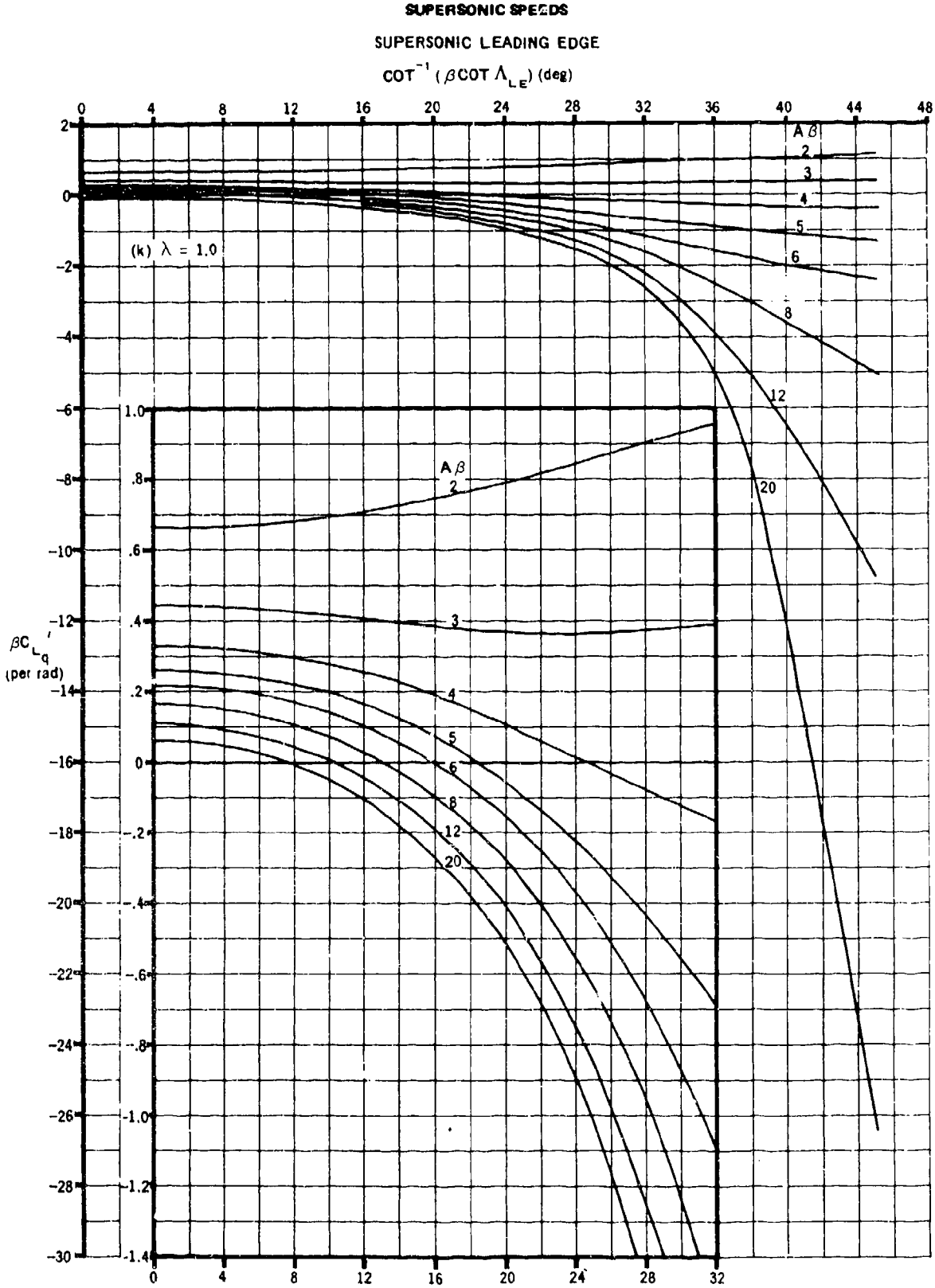

FIGURE 7.1.1.1-11 (CONTD)

7.1.1.2 WING PITCHING DERIVATIVE C_{m_q}

When a wing rotates in pitch about a given center of gravity at an angular velocity θ in a free-stream velocity V_∞, changes in local angle of attack are produced that are proportional to w/V (w is the local vertical disturbance velocity). For wings having sweepback, an additional increment in angle of attack is produced that is a function of spanwise wing station. These local changes in angle of attack produce an effective angle-of-attack increment for the complete wing that results in a pitching-moment increment. This pitching-moment increment is expressed as the wing contribution to the derivative C_{m_q}.

If the wing pitching derivative C_{m_q} is to be used in method 1 of Section 7.3.1.2 to obtain $(C_{m_q})_{WB}$, the exposed wing planform area should be used for all calculations in the Datcom methods. Using the exposed planform area will yield C_{m_q} based on the product of exposed wing area and the square of exposed wing MAC, rather than the product of total wing area and the square of wing MAC as indicated.

DATCOM METHOD

A. SUBSONIC

The low-speed value ($M \approx 0.2$) of C_{m_q}, based on the product of total wing area and the square of wing MAC $S_W \bar{c}_W{}^2$, is given by

$$\left(C_{m_q}\right)_{M \approx 0.2} = -0.7\, c_{\ell_\alpha} \cos \Lambda_{c/4} \left\{ \frac{A\left[\frac{1}{2}\,\frac{\bar{x}}{\bar{c}} + 2\left(\frac{\bar{x}}{\bar{c}}\right)^2\right]}{A + 2\cos\Lambda_{c/4}} + \frac{1}{24}\left(\frac{A^3 \tan^2 \Lambda_{c/4}}{A + 6\cos\Lambda_{c/4}}\right) + \frac{1}{8} \right\} \quad \text{(per radian)} \quad 7.1.1.2\text{-a}$$

where

$\frac{\bar{x}}{\bar{c}}$ is defined in Section 7.1 .1.

c_{ℓ_α} is the wing section lift curve slope from Section 4.1.1 (per radian).

This equation is a modified form of that derived in reference 1. The equation was modified in reference 2 by the empirical factor 0.7. It is strictly applicable to aspect ratios between 1 and 6. For aspect ratios of about 10 or 12 the empirical factor should be approximately 0.9, but there are no experimental data available to show how this empirical factor should vary for intermediate aspect ratios. It is suggested that a smooth fairing be used.

For higher subsonic speeds the derivative C_{m_q}, based on the product of wing area and the square of wing MAC $S_W \bar{c}_W{}^2$, is obtained by applying an approximate compressibility correction derived in reference 3:

$$\left(C_{m_q}\right)_{M>0.2} = \left[\frac{\frac{A^3 \tan^2 \Lambda_{c/4}}{AB + 6\cos\Lambda_{c/4}} + \frac{3}{B}}{\frac{A^3 \tan^2 \Lambda_{c/4}}{A + 6\cos\Lambda_{c/4}} + 3}\right] \left(C_{m_q}\right)_{M\approx 0.2} \quad \text{(per radian)} \qquad 7.1.1.2\text{-b}$$

where

$\left(C_{m_q}\right)_{M\approx 0.2}$ is obtained from equation 7.1.1.2-a.

$B = \sqrt{1 - M^2 \cos^2 \Lambda_{c/4}}$

Sample Problem

Given: Same wing as in sample problem of paragraph A, Section 7.1.1.1.

$A = 4.0 \qquad \lambda = 0.68 \qquad \Lambda_{c/4} = 45^\circ \qquad \frac{c_r}{\bar{c}} = 1.18$

Additional Characteristics:

Airfoil: 64-006 Smooth airfoil surface $M = 0.2, 0.6$

$\frac{\bar{x}}{\bar{c}} = 0.0118$ (sample problem, paragraph A, Section 7.1.1.1)

Compute:

$c_{\ell_\alpha} = 0.109$ per deg (table 4.1.1-B)

$\cos \Lambda_{c/4} = 0.707$; $\tan \Lambda_{c/4} = 1.0$

At $M = 0.6$, $B = \sqrt{1 - M^2 \cos^2 \Lambda_{c/4}} = \sqrt{1 - (0.36)(0.50)} = 0.905$

Solution ($M = 0.2$):

$$\left(C_{m_q}\right)_{M\approx 0.2} = -0.7\, c_{\ell_\alpha} \cos\Lambda_{c/4} \left\{\frac{A\left[\frac{1}{2}\frac{\bar{x}}{\bar{c}} + 2\left(\frac{\bar{x}}{\bar{c}}\right)^2\right]}{A + 2\cos\Lambda_{c/4}} + \frac{1}{24}\left(\frac{A^3 \tan^2 \Lambda_{c/4}}{A + 6\cos\Lambda_{c/4}}\right) + \frac{1}{8}\right\}$$

(equation 7.1.1.2-a)

$$= (-0.7)\,(0.109)\,(57.3)\,(0.707)\left\{\frac{4\left[\frac{1}{2}\,(0.0118) + 2(0.0118)^2\right]}{4 + 2(0.707)}\right.$$

$$\left. + \frac{1}{24}\left[\frac{(4)^3\,(1)}{4 + 6(0.707)}\right] + \frac{1}{8}\right\}$$

$$= -3.090\left[\frac{0.0247}{5.414} + \frac{1}{24}\left(\frac{64}{8.242}\right) + \frac{1}{8}\right]$$

$$= -3.090(0.00456 + 0.3235 + 0.125)$$

$$= -1.400 \text{ per rad } \left(\text{based on } S_W \bar{c}_W{}^2\right)$$

Solution (M = 0.6):

$$\left(C_{m_q}\right)_{M>0.2} = \left[\frac{\frac{A^3 \tan^2 \Lambda_{c/4}}{AB + 6\cos\Lambda_{c/4}} + \frac{3}{B}}{\frac{A^3 \tan^2 \Lambda_{c/4}}{A + 6\cos\Lambda_{c/4}} + 3}\right]\left(C_{m_q}\right)_{M\approx 0.2} \quad \text{(equation 7.1.1.2-b)}$$

$$= \left[\frac{\frac{(4)^3\,(1)}{4(0.905) + 6(0.707)} + \frac{3}{0.905}}{\frac{(4)^3\,(1)}{4 + 6(0.707)} + 3}\right](-1.40)$$

$$= \left[\frac{\frac{64}{7.862} + 3.31}{\frac{64}{8.242} + 3}\right](-1.40)$$

$$= \left(\frac{8.14 + 3.31}{7.77 + 3}\right)(-1.40)$$

$$= -1.49 \text{ per rad } \left(\text{based on } S_W \bar{c}_W{}^2\right)$$

B. TRANSONIC

At transonic speeds the derivative C_{m_q}, based on the product of wing area and the square of wing MAC $S_W \bar{c}_W{}^2$, is estimated by

$$C_{m_q} = \frac{\left(C_{L_\alpha}\right)_M - \left(C_{L_\alpha}\right)_{M_{cr}}}{\left(C_{L_\alpha}\right)_{M=1.2} - \left(C_{L_\alpha}\right)_{M_{cr}}} \left[\left(C_{m_q}\right)_{M=1.2} - \left(C_{m_q}\right)_{M_{cr}}\right] + \left(C_{m_q}\right)_{M_{cr}} \quad \text{(per radian)} \qquad 7.1.1.2\text{-c}$$

where

C_{L_α} is the wing lift-curve slope (Section 4.1.3.2) at the Mach number under consideration, based on the total wing area (per radian).

$\left(C_{m_q}\right)_{M=1.2}$ is obtained from the supersonic method of paragraph C of this section, based on the product of wing area and the square of wing MAC $S_W \bar{c}_W{}^2$ (per radian).

$\left(C_{m_q}\right)_{M_{cr}}$ is obtained from equation 7.1.1.2-b at the critical Mach number, based on the product of wing area and the square of wing MAC $S_W \bar{c}_W{}^2$ (per radian).

For this purpose the critical Mach number M_{cr} is taken equal to the force-break Mach number M_{fb} defined in paragraph B of Section 4.1.3.2.

C. SUPERSONIC

The supersonic value of C_{m_q}, referred to body axis and for any center-of-gravity location and based on the product of wing area and the square of wing MAC $S_W \bar{c}_W{}^2$, is given by

$$C_{m_q} = C_{m_q}{}' - \left(\frac{\bar{x}}{\bar{c}}\right) C_{L_q} \quad \text{(per radian)} \qquad 7.1.1.2\text{-d}$$

where

C_{L_q} is obtained from Section 7.1.1.1, based on the product of wing area and wing MAC (per radian).

$\frac{\bar{x}}{\bar{c}}$ is defined in Section 7.1.1.1.

$C_{m_q}{}'$ is referred to body axis with the origin at the wing aerodynamic center, based on the product of wing area and the square of wing MAC $S_W \bar{c}_W{}^2$, and obtained as indicated below.

Methods for estimating C_{m_q}'

1. Wings with subsonic leading edges ($\beta \cot \Lambda_{LE} < 1.0$)

For wings with subsonic leading edges, C_{m_q}' is obtained by the method of reference 4 for $\lambda = 0$ and by the method of reference 5 for $\lambda = 0.25$ to 1.0. The following methods are not valid if the Mach line from the trailing-edge vertex intersects the leading edge or if the wing-tip Mach lines intersect on the wings or intersect the opposite wing tips.

a. Zero-taper-ratio wings ($\lambda = 0$)

C_{m_q}' is derived in reference 4 as

$$C_{m_q}' = -\frac{3}{16}\pi A \left\{ G(\beta C)\, F_7(N) + \frac{16}{3} E''(\beta C) \left[\frac{F_5(N)}{F_{11}(N)}\right] \right\} - \left(\frac{d - x_{a.c.}}{\bar{c}}\right) C_{L_q}' + 2\left(\frac{d - x_{a.c.}}{\bar{c}}\right)^2 C_{N_\alpha} \quad \text{(per radian)} \qquad 7.1.1.2\text{-e}$$

where

$G(\beta C)$ and $E''(\beta C)$ are obtained from figure 7.1.1.1-8.

$F_5(N)$, $F_7(N)$, and $F_{11}(N)$ are obtained from figure 7.1.1.2-8.

$\frac{x_{a.c.}}{\bar{c}}$ is defined in paragraph A of Section 7.1.1.1.

C_{N_α} is the wing normal-force-curve slope (Section 4.1.3.2) at the Mach number under consideration, based on the total wing area (per radian).

d is defined in paragraph C of Section 7.1.1.1.

C_{L_q}' is obtained from paragraph C of Section 7.1.1.1, based on the product of wing area and wing MAC (per radian).

b. Wings with $\lambda = 0.25$ to 1.0

C_{m_q}' is derived in reference 5 as

$$C_{m_q}' = C_{m_q}'' + \left(\frac{x_{a.c.}}{\bar{c}}\right) C_{L_q}'' \quad \text{(per radian)} \qquad 7.1.1.2\text{-f}$$

where

C_{m_q}'' is referred to body axis with the origin at the wing leading-edge vertex and is obtained from figures 7.1.1.2-9a, 7.1.1.2-9b, and 7.1 1.2-9c, for $\lambda = 0.25$, 0.50, and 0.75, respectively, and from the equations of reference 5 for $\lambda > 0.75$ (per radian).

C_{L_q}'' is obtained from paragraph C of Section 7.1.1.1, based on the product of wing area and wing MAC (per radian).

$\frac{x_{a.c.}}{\bar{c}}$ is defined in paragraph A of Section 7.1.1.1.

2. Wings with supersonic leading edges ($\beta \cot \Lambda_{LE} > 1.0$)

For wings with supersonic leading edges, C_{m_q}' is obtained from figures 7.1.1.2-10a through 7.1.1.2-10k. This method is derived in reference 6 and is valid for the range of Mach numbers for which the Mach lines from the leading-edge vertex intersect the trailing edge. An additional limitation is that the foremost Mach line from either wing tip may not intersect the remote half of the wing.

Sample Problem

Given: Same wing as in sample problem of paragraph C, Section 7.1.1.1.

$A = 3.46$ $\quad \lambda = 0$ $\quad \Lambda_{LE} = 60°$ $\quad \frac{c_r}{\bar{c}} = 1.50$ $\quad b = 16$ ft

c.g. at $\frac{\bar{c}}{4}$ $\quad M = 1.50$ $\quad \bar{c} = 6.17$ ft $\quad c_r = 9.25$ ft

From sample problem of paragraph C, Section 7.1.1.1:

$\beta \cot \Lambda_{LE} = 0.647$ (subsonic leading edge)

$N = 0.333$ $\quad E''(\beta C) = 0.770$ $\quad G(\beta C) = 5.70$ $\quad C_{N_\alpha} = 3.12$ per rad

$C_{L_q}' = 0.022$ per rad $\quad C_{L_q} = 2.175$ per rad $\quad \frac{d - x_{a.c.}}{\bar{c}} = 0.146$ $\quad \frac{\bar{x}}{\bar{c}} = 0.345$

Compute:

$$\left.\begin{aligned} F_5(N) &= 0.133 \\ F_7(N) &= -0.200 \\ F_{11}(N) &= 0.660 \end{aligned}\right\} \text{ (figure 7.1.1.2-8)}$$

Solution:

$$C_{m_q}' = -\frac{3}{16}\pi A\left\{G(\beta C)\,F_7(N) + \frac{16}{3}\,E''(\beta C)\left[\frac{F_5(N)}{F_{11}(N)}\right]\right\}$$

$$-\left(\frac{d - x_{a.c.}}{\bar{c}}\right) C_{L_q}' + 2\left(\frac{d - x_{a.c.}}{\bar{c}}\right)^2 C_{N_\alpha} \quad \text{(equation 7.1.1.2-e)}$$

$$= -\frac{3}{16}\,\pi(3.46)\left[(0.570)\,(-0.200) + \frac{16}{3}\,(0.770)\,\frac{0.133}{0.660}\right]$$

$$-\,(0.146)\,(0.022) + 2(0.146)^2\,(3.12)$$

$$= -2.038(-0.1140 + 0.8276) - 0.0032 + 0.1330$$

$$= -1.325 \text{ per rad}$$

$$C_{m_q} = C_{m_q}' - \left(\frac{\bar{x}}{\bar{c}}\right) C_{L_q} \quad \text{(equation 7.1.1.2-d)}$$

$$= -1.325 - (0.345)\,(2.175)$$

$$= -2.075 \text{ per rad (based on } S_W \bar{c}_W{}^2)$$

REFERENCES

1. Toll, T., and Queijo, M.: Approximate Relations and Charts for Low-Speed Stability Derivatives of Swept Wings. NACA TN 1581, 1948. (U)

2. MacLachlan, R., and Fisher, L. R.: Wind-Tunnel Investigation at Low Speeds of the Pitching Derivatives of Untapered Swept Wings. NACA RM L8G19, 1948. (U)

3. Fisher, L. R.: Approximate Corrections for the Effects of Compressibility on the Subsonic Stability Derivatives of Swept Wings. NACA TN 1854, 1949. (U)

4. Malvestuto, F. S., Jr., and Margolis, K.: Theoretical Stability Derivatives of Thin Sweptback Wings Tapered to a Point with Sweptback or Sweptforward Trailing Edges for a Limited Range of Supersonic Speeds. NACA TR 971, 1950. (U)

5. Malvestuto, F. S., Jr., and Hoover, D. M.: Lift and Pitching Derivatives of Thin Sweptback Tapered Wings with Streamwise Tips and Subsonic Leading Edges at Supersonic Speeds. NACA TN 2294, 1951. (U)

6. Martin, J., Margolis, K., and Jeffreys, I.: Calculation of Lift and Pitching Moments Due to Angle of Attack and Steady Pitching Velocity at Supersonic Speeds for Thin Sweptback Tapered Wings with Streamwise Tips and Supersonic Leading and Trailing Edges. NACA TN 2699, 1952. (U)

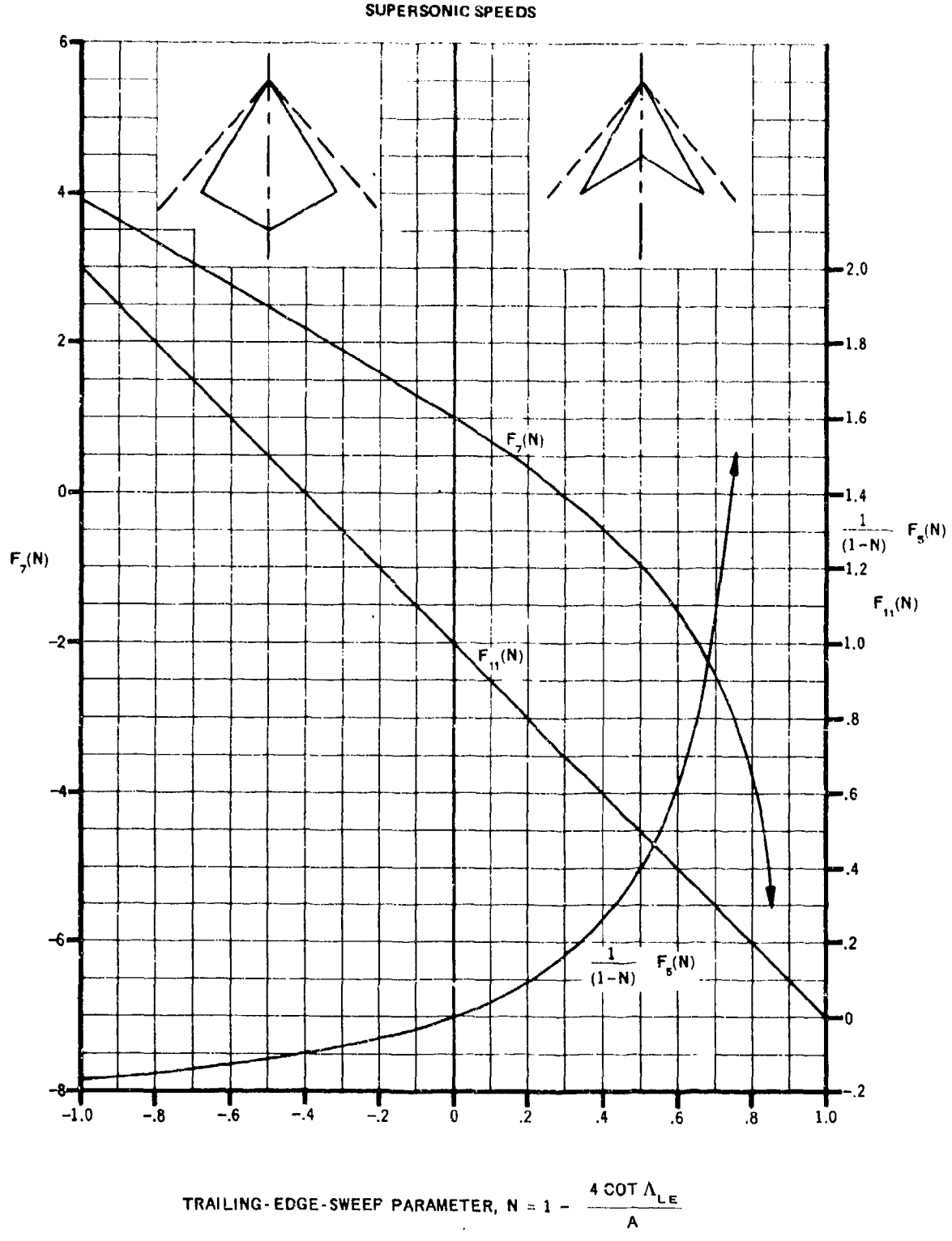

FIGURE 7.1.1.2-8 F(N) FACTORS OF THE STABILITY DERIVATIVE

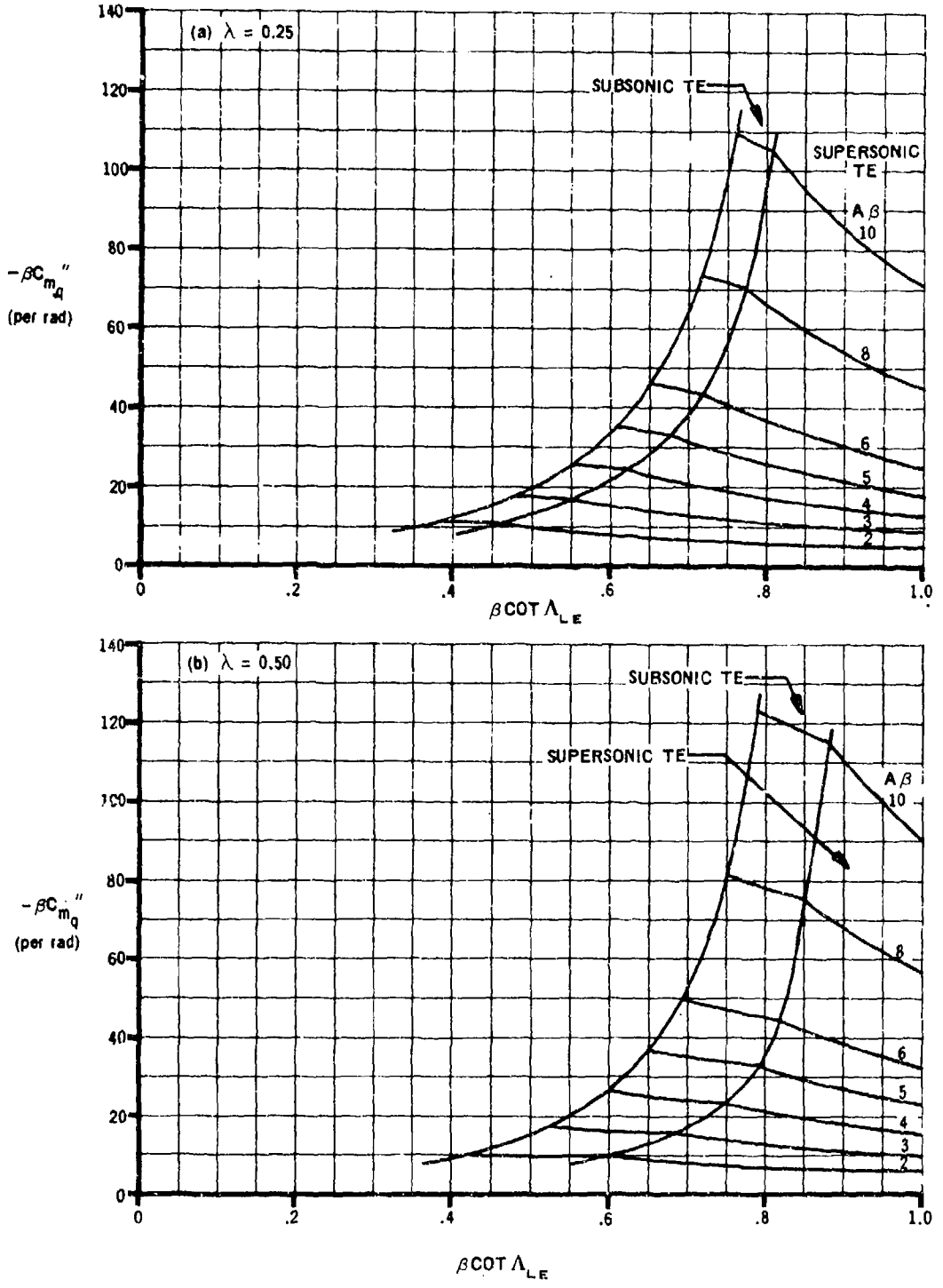

FIGURE 7.1.1.2-9 VARIATION OF $\beta C_{m_q}''$ WITH $\beta \cot \Lambda_{LE}$

SUBSONIC LEADING EDGE

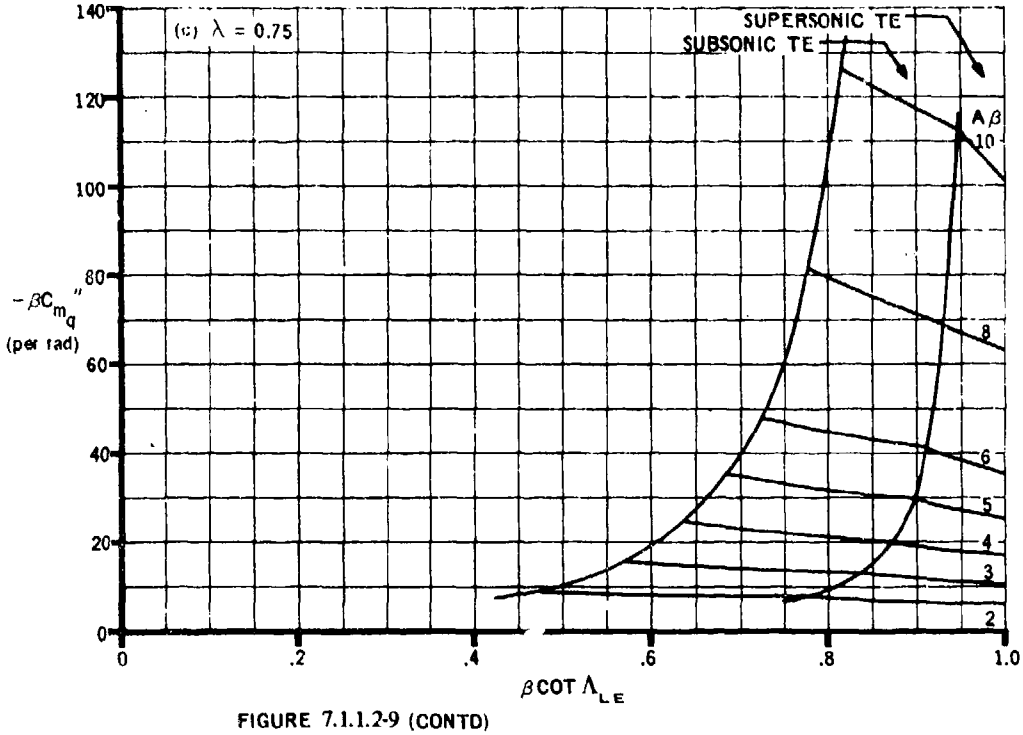

FIGURE 7.1.1.2-9 (CONTD)

SUPERSONIC LEADING EDGE

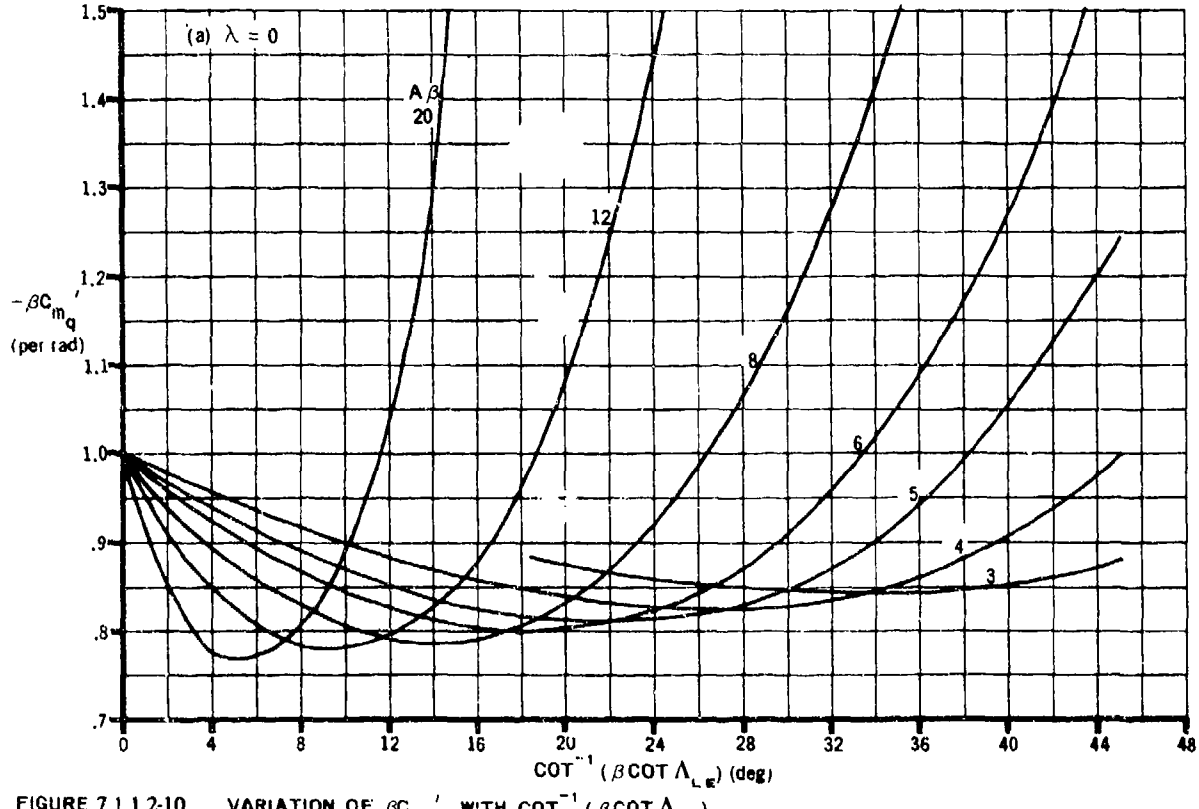

FIGURE 7.1.1.2-10 VARIATION OF $\beta C_{m_q}'$ WITH $\cot^{-1}(\beta \cot \Lambda_{LE})$

SUPERSONIC LEADING EDGE

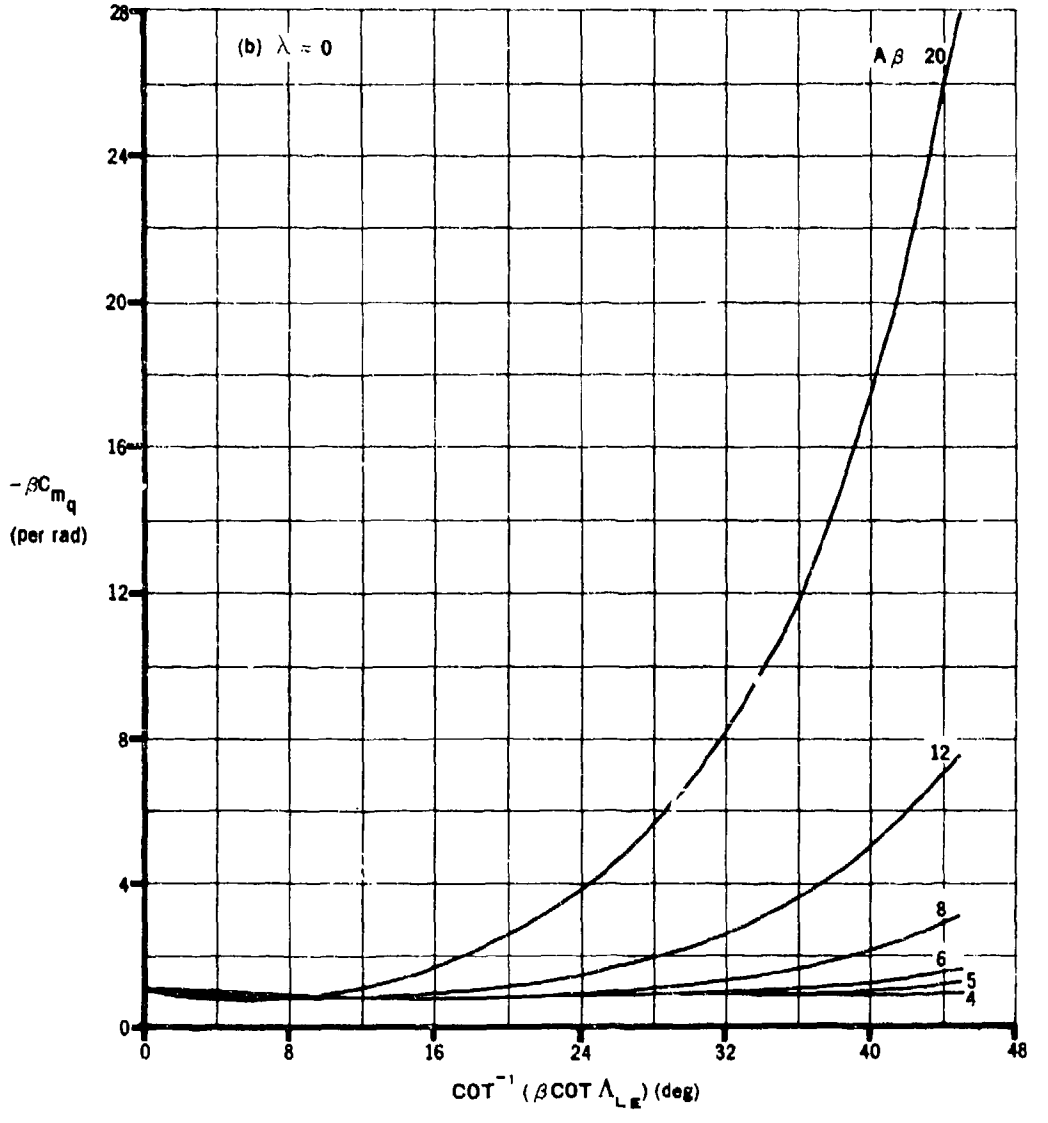

FIGURE 7.1.1.2-10 (CONTD)

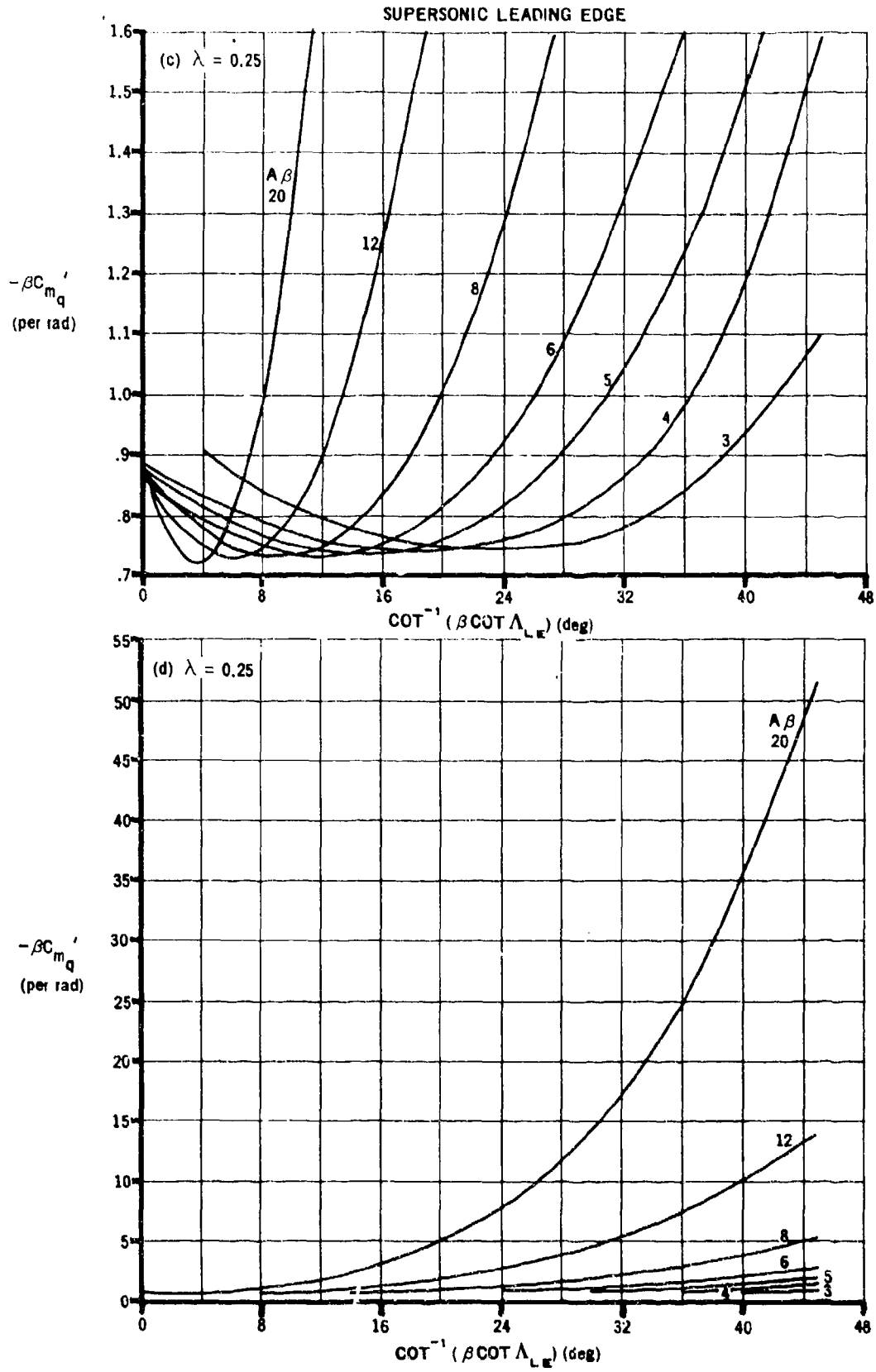

FIGURE 7.1.1.2-10 (CONTD)

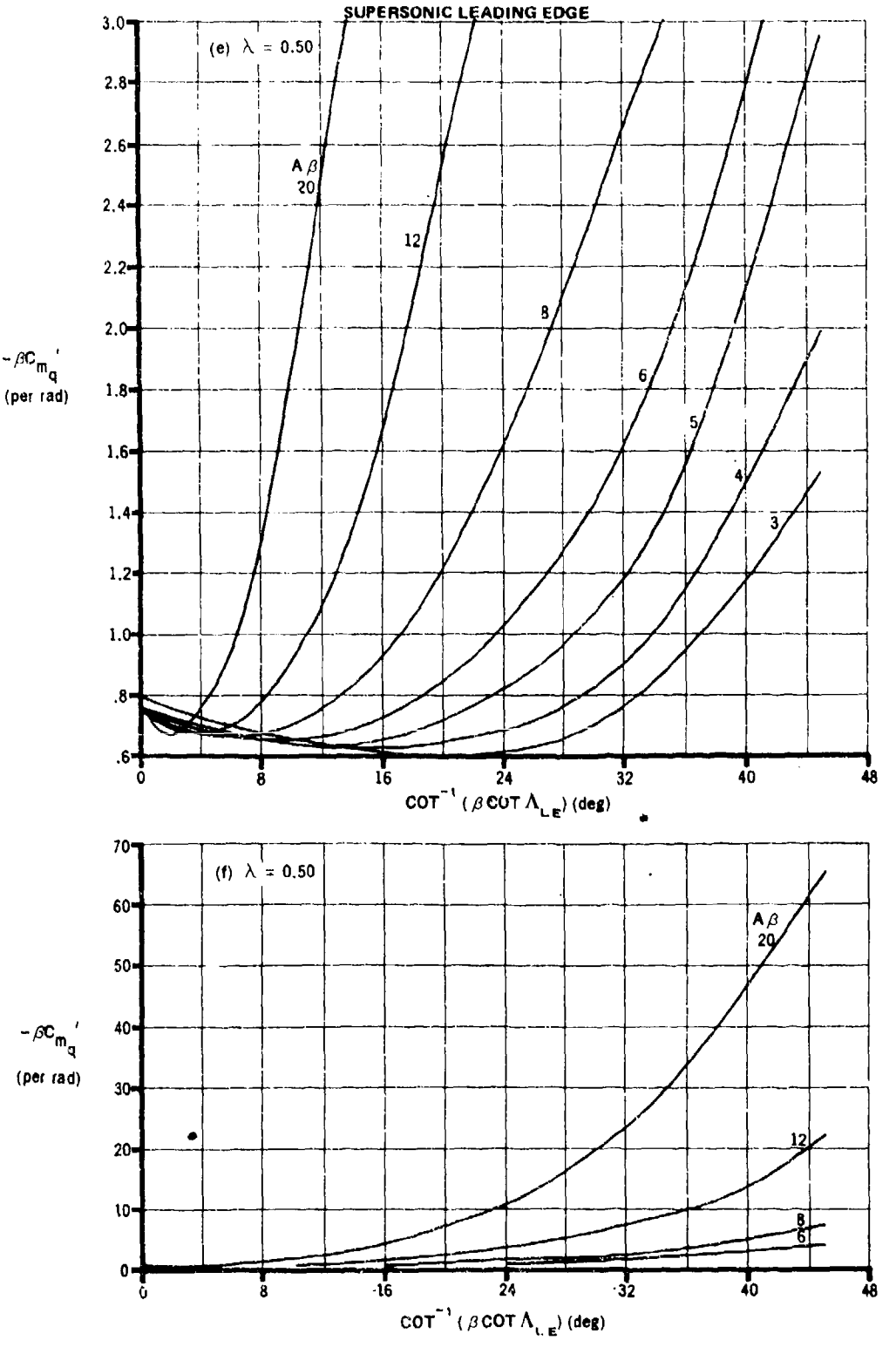

FIGURE 7.1.1.2-10 (CONTD)

SUPERSONIC LEADING EDGE

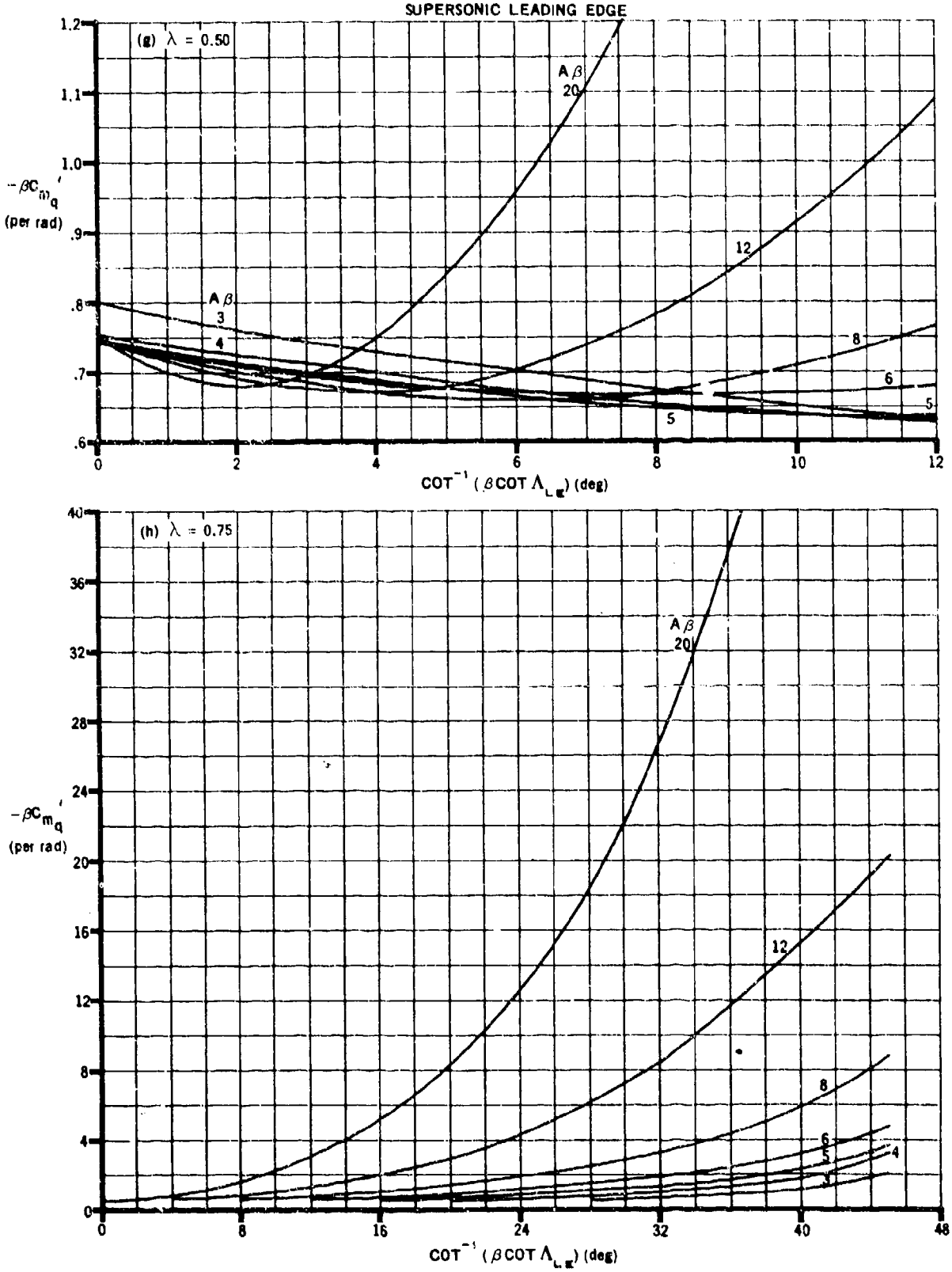

FIGURE 7.1.1.2-10 (CONTD)

SUPERSONIC LEADING EDGE

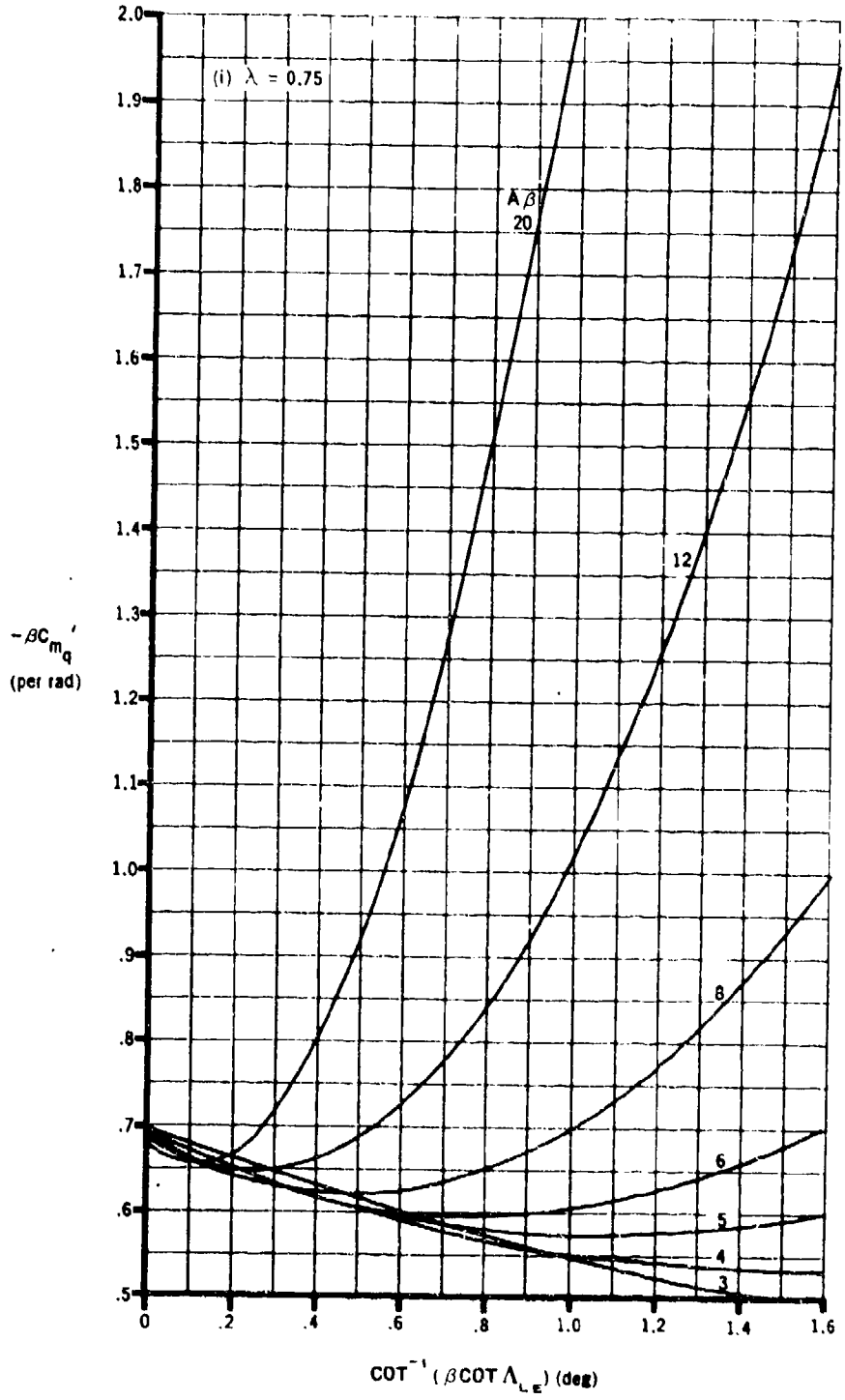

FIGURE 7.1.1.2-10 (CONTD)

SUPERSONIC LEADING EDGE

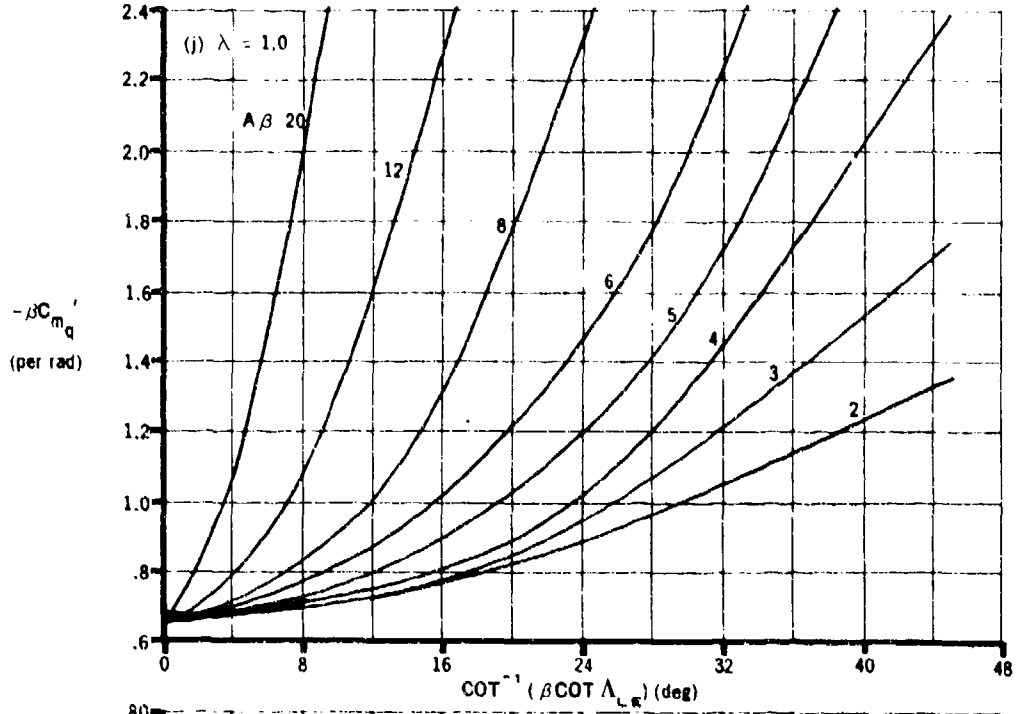

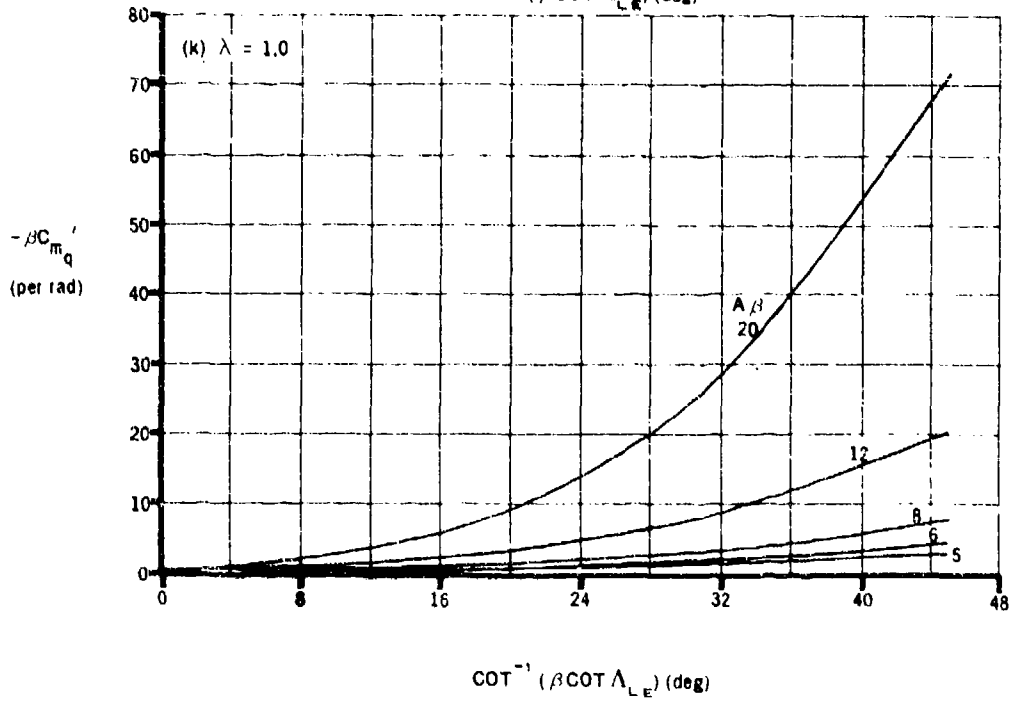

FIGURE 7.1.1.2-10 (CONTD)

7.1.1.3 WING PITCHING DERIVATIVE C_{D_q}

This section presents a method for estimating the wing contribution to the pitching derivative C_{D_q} at subsonic speeds. This derivative is the change in drag coefficient due to a change in pitching velocity at a constant angle of attack and is defined as

$$C_{D_q} = \frac{\partial C_D}{\partial\left(\frac{q\bar{c}}{2V}\right)}, \text{ where } C_D \text{ is based on } S_W.$$

In general, this derivative is small and has a negligible effect on longitudinal stability; hence, it is usually neglected.

A. SUBSONIC

The method presented herein uses the Weissinger method of Reference 1 to calculate the section lift due to angle of attack, twist, and pitch rate. The lift is then rotated through the local downwash angle due to each of these effects to produce a chordwise component of force.

DATCOM METHOD

Design charts for predicting the wing contribution to C_{D_q} are available only at Mach numbers of 0.2 and 0.8. The wing pitching derivative C_{D_q} is given by

$$C_{D_q} = C_{D_{q_0}}(-\theta) + \frac{\partial C_{D_q}}{\partial \alpha_F}\,\alpha_F + \frac{\partial C_{D_q}}{\partial\left(\frac{q\bar{c}}{2V}\right)}\left(\frac{q\bar{c}}{2V}\right) \qquad 7.1.1.3\text{-a}$$

where

$C_{D_{q_0}}$ is the contribution due to zero-angle-of-attack loading obtained from Figures 7.1.1.3-3a through -3f as a function of wing aspect ratio, taper ratio, and sweep.

θ is the wing twist in degrees between the root and tip sections, negative for washout (see Figure 5.1.2.1-30b).

$\frac{\partial C_{D_q}}{\partial \alpha_F}$ is the contribution due to angle of attack obtained from Figures 7.1.1.3- 7a through - 7f as a function of wing aspect ratio, taper ratio, and sweep.

α_F is the fuselage angle of attack in degrees.

$\frac{\partial C_{D_q}}{\partial\left(\frac{q\bar{c}}{2V}\right)}$ is the contribution due to the rate of change of pitch obtained from Figures 7.1.1.3-12a through -12f as a function of wing aspect ratio, taper ratio, and sweep.

q is the pitch rate in degrees per second.

$\bar{c}$ is the wing mean aerodynamic chord.

V is the free-stream velocity.

Sample Problem

Given: The following wing-body configuration

Wing Characteristics:

$A = 7$ $\quad \lambda = 0.25$ $\quad \Lambda_{LE} = 35^{\circ}$

$\bar{c} = 25.0$ ft $\quad S_W = 3500$ ft^2 $\quad \theta = -5.0^{\circ}$

Additional Characteristics:

$M = 0.8$ $\quad \alpha_F = 1^{\circ}$ $\quad q = 5$ deg/sec

$V = 796$ ft/sec $\quad (h = 30{,}000$ ft)

Compute:

$C_{D_{q_0}} = 0.00036$ per deg^2 (interpolated using Figures 7.1.1.3-3d, -3e, and -3f)

$\dfrac{\partial C_{D_q}}{\partial \alpha_F} = 0.000876$ per deg^2 (interpolated using Figures 7.1.1.3- 7d, - 7e, and - 7f)

$\dfrac{\partial C_{D_q}}{\partial \left(\frac{q\bar{c}}{2V}\right)} = 0.00061$ per deg^2 (interpolated using Figures 7.1.1.3-12d, -12e, and -12f)

$\dfrac{q\bar{c}}{2V} = \dfrac{(5)(25)}{2(796)} = 0.0785$ deg

Solution:

$$C_{D_q} = C_{D_{q_0}}(-\theta) + \frac{\partial C_{D_q}}{\partial \alpha_F}\alpha_F + \frac{\partial C_{D_q}}{\partial \left(\frac{q\bar{c}}{2V}\right)}\left(\frac{q\bar{c}}{2V}\right) \qquad \text{(Equation 7.1.1.3-a)}$$

$$= (0.00036)(+5.0) + (0.000876)(1.0) + (0.00061)(0.0785)$$

$$= 0.00272 \text{ per deg}$$

B. TRANSONIC

No method is presented.

C. SUPERSONIC

No method is presented.

REFERENCE

1. De Young, J., and Harper, C. W.: Theoretical Symmetric Span Loading at Subsonic Speeds for Wings Having Arbitrary Planform. NACA TR 921, 1948. (U)

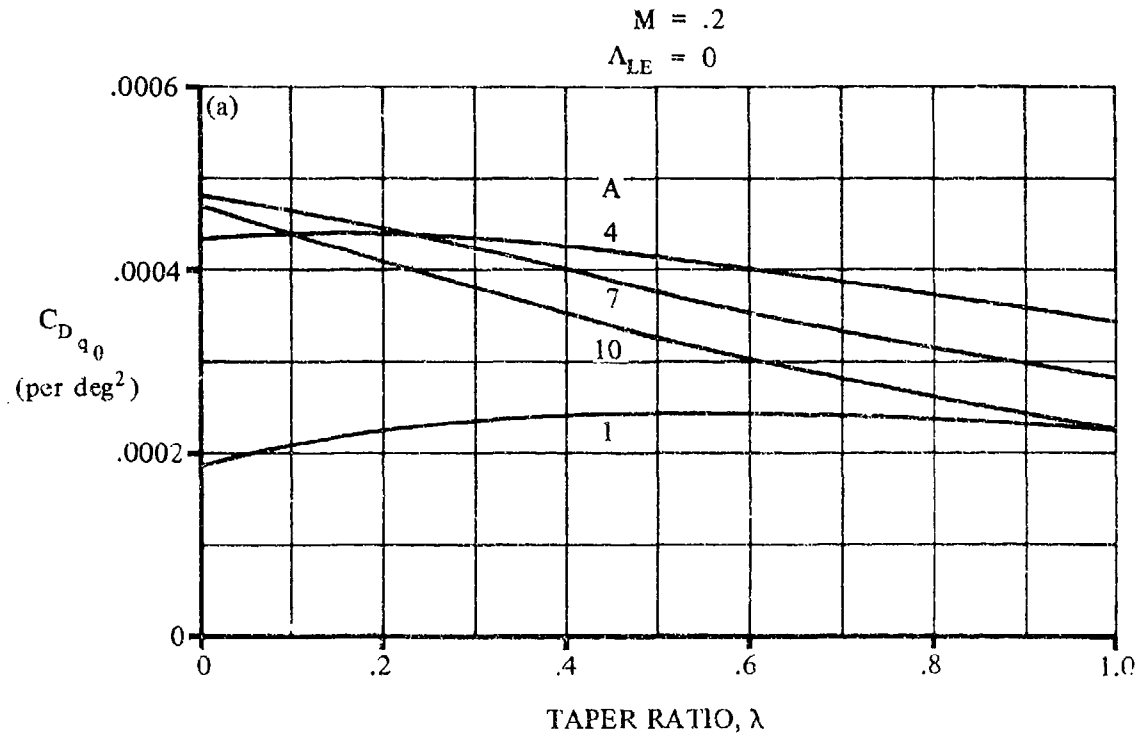

FIGURE 7.1.1.3-3 THE ZERO-ANGLE-OF-ATTACK LOADING CONTRIBUTION TO THE WING PITCHING DERIVATIVE C_{D_q}

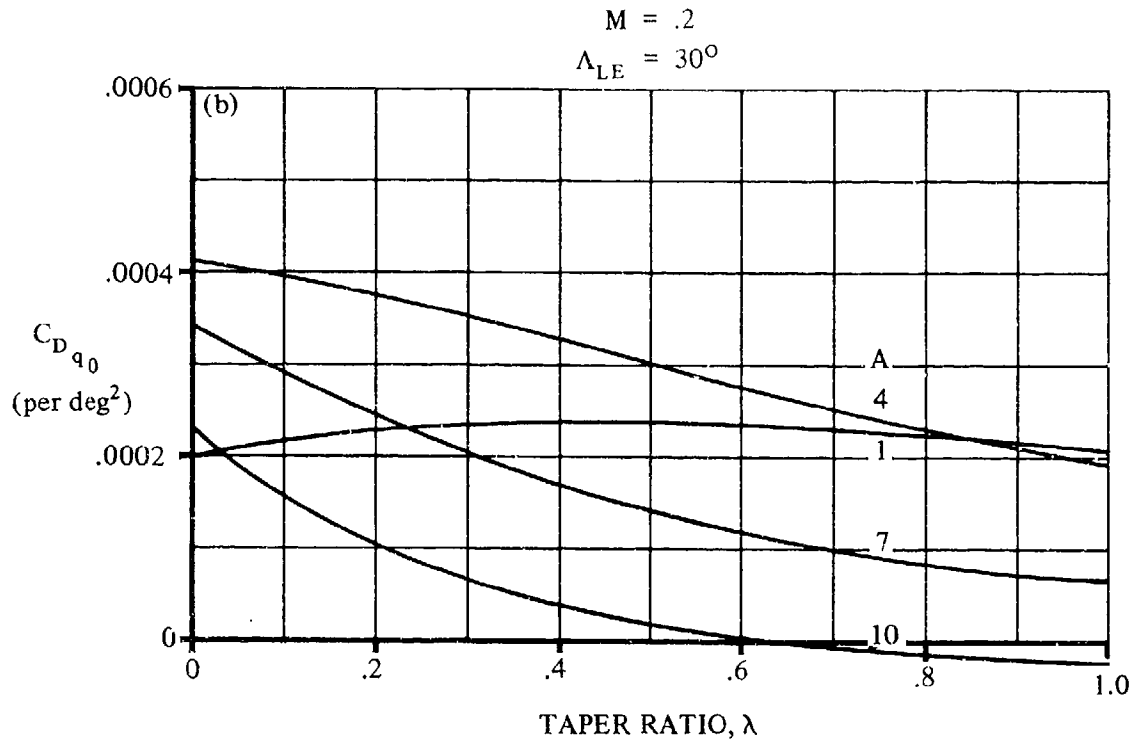

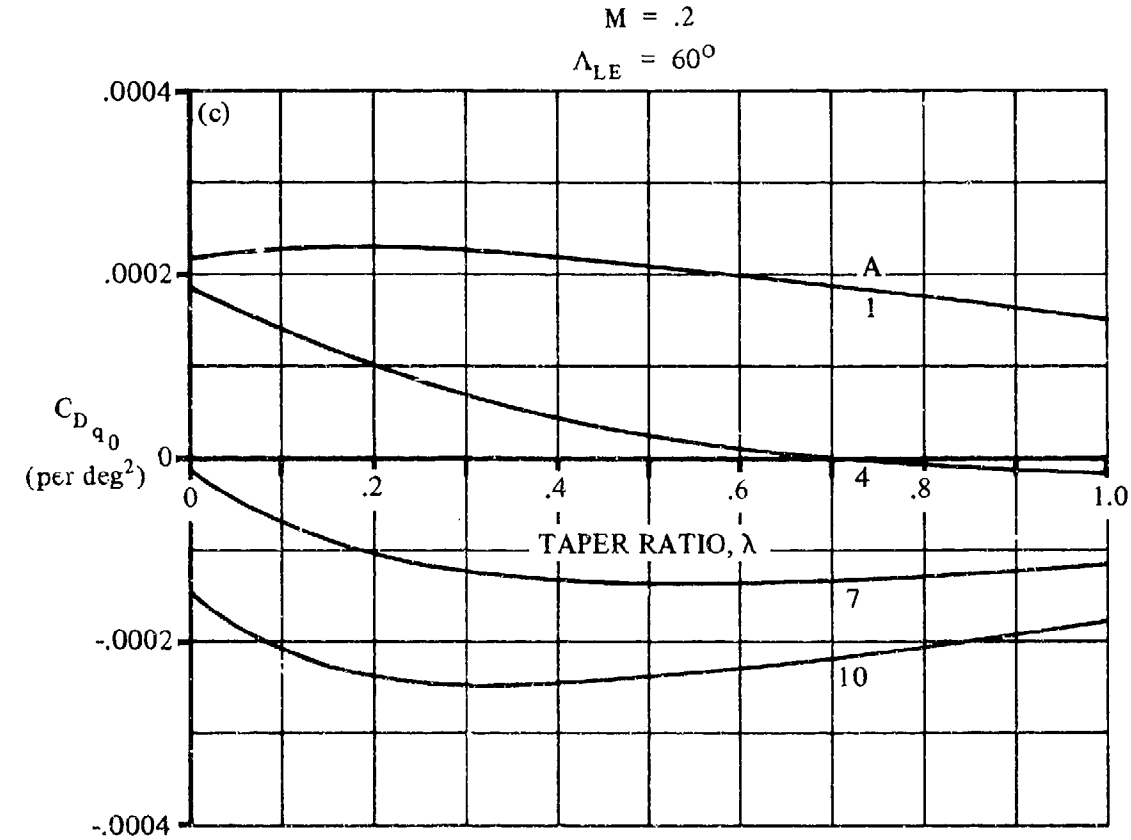

FIGURE 7.1.1.3-3(CONTD)

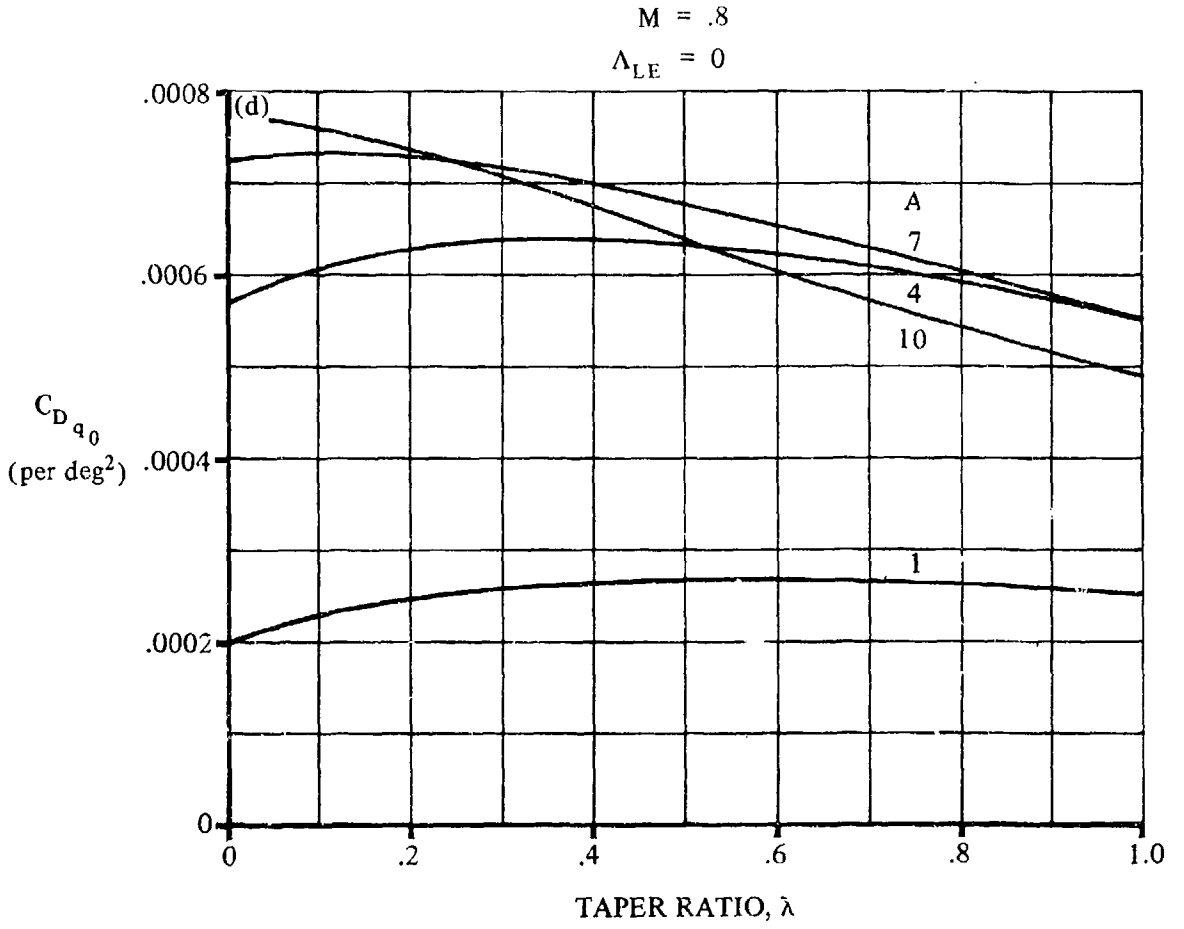

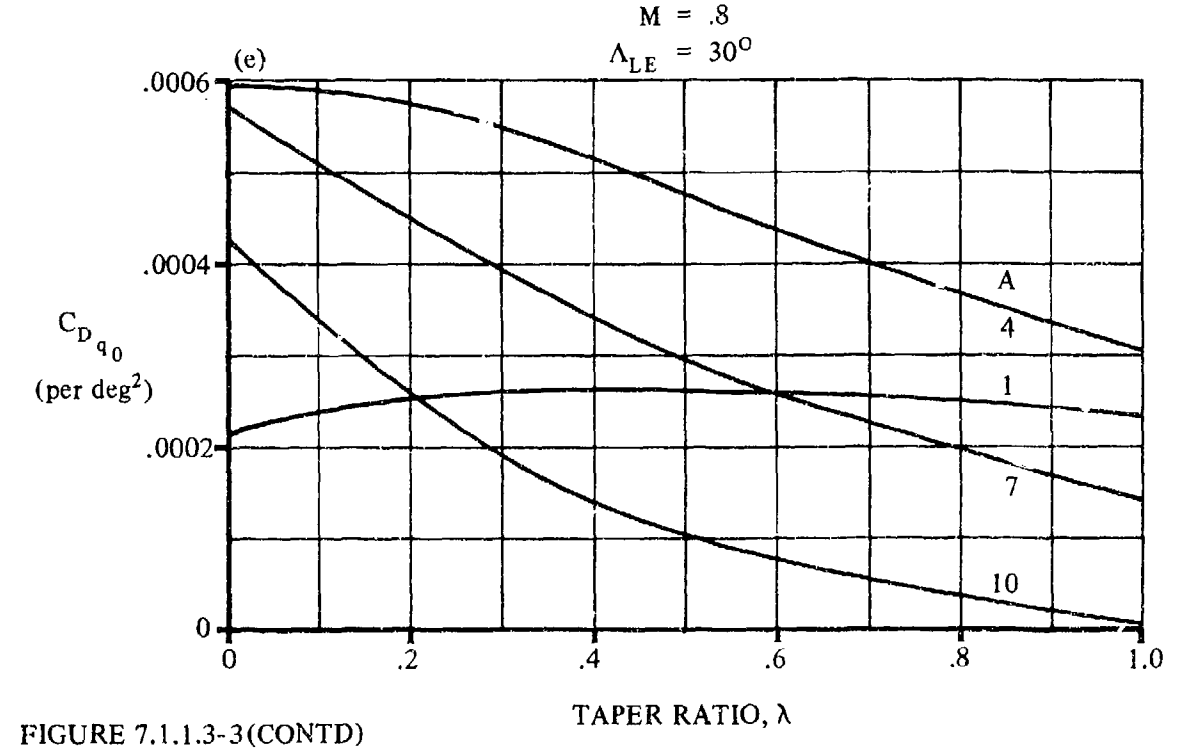

FIGURE 7.1.1.3-3(CONTD)

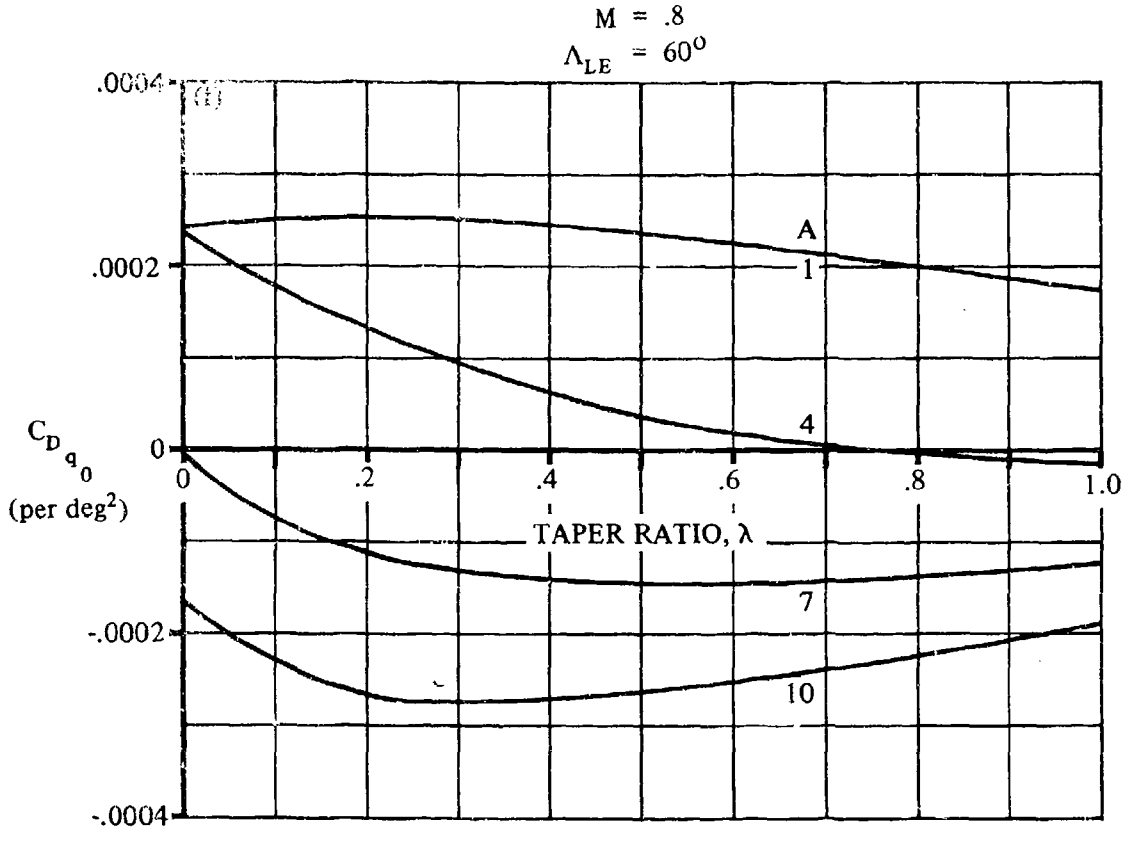

FIGURE 7.1.1.3-3 (CONTD)

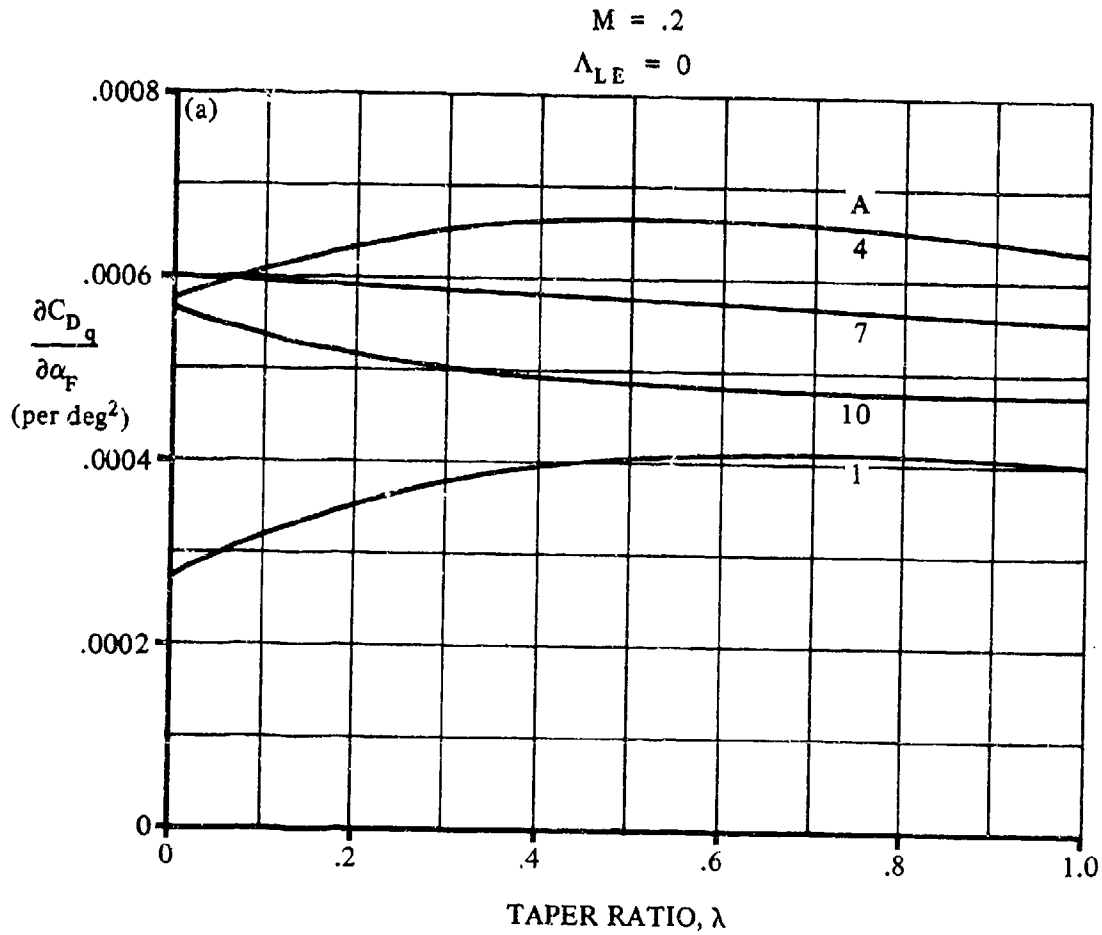

FIGURE 7.1.1.3- 7 THE ANGLE-OF-ATTACK CONTRIBUTION TO THE WING PITCHING DERIVATIVE C_{D_q}

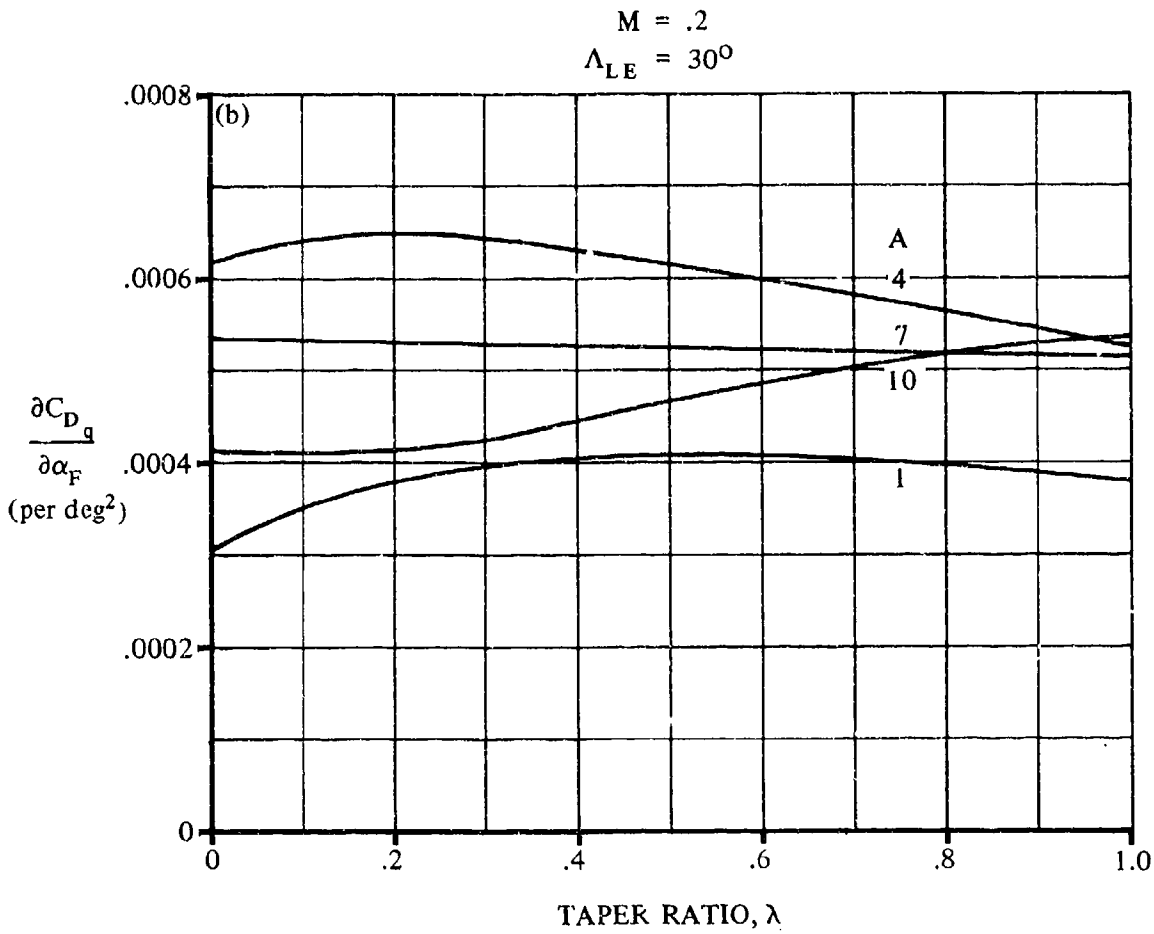

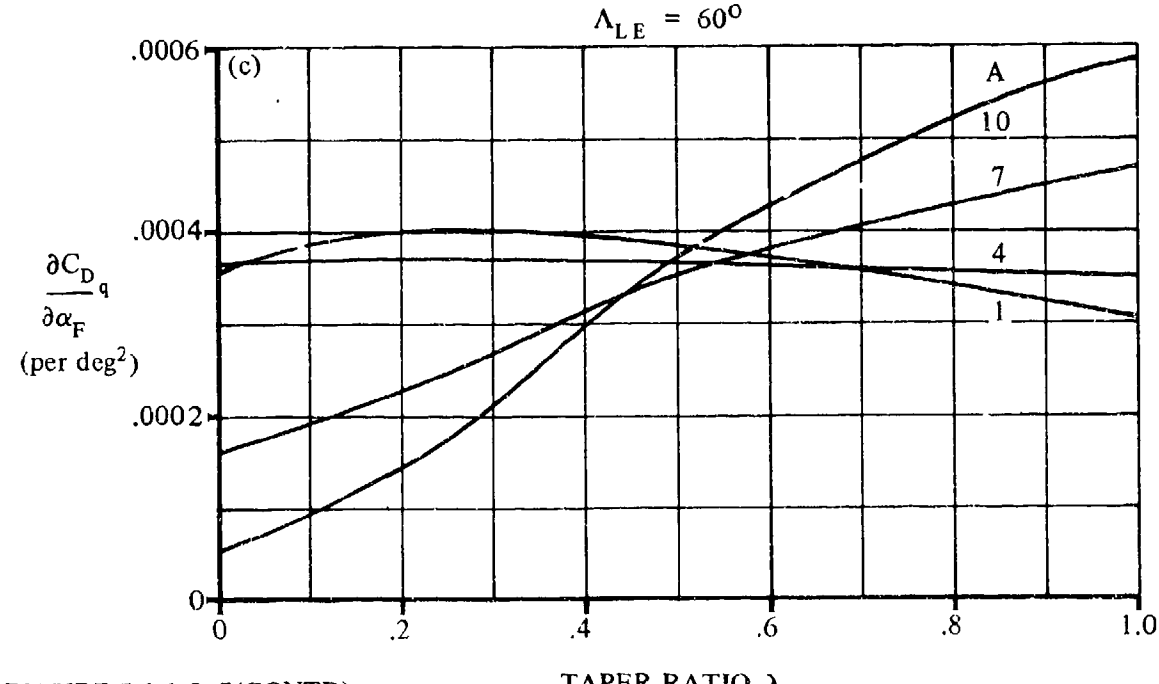

FIGURE 7.1.1.3- 7(CONTD)

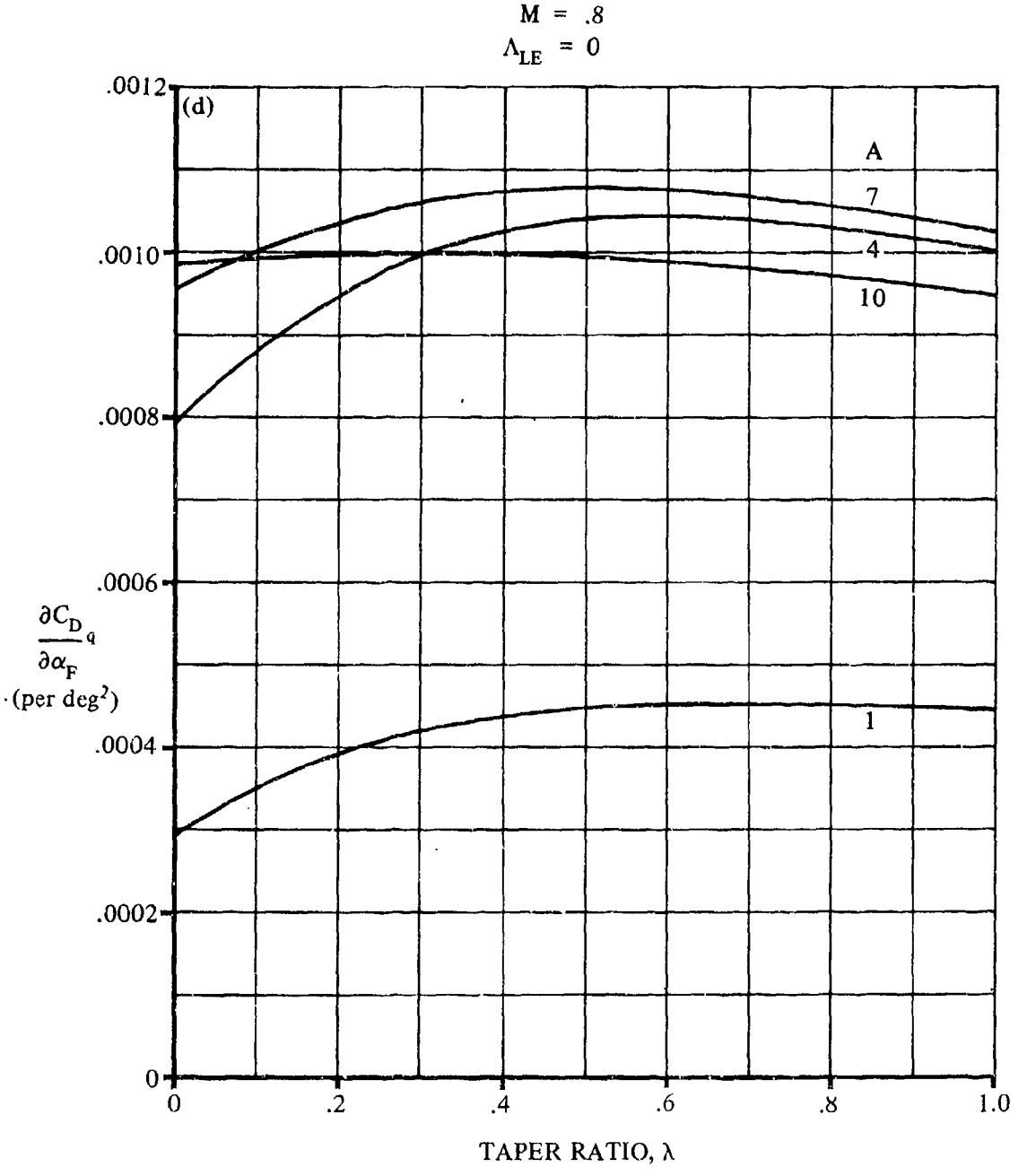

FIGURE 7.1.1.3- 7(CONTD)

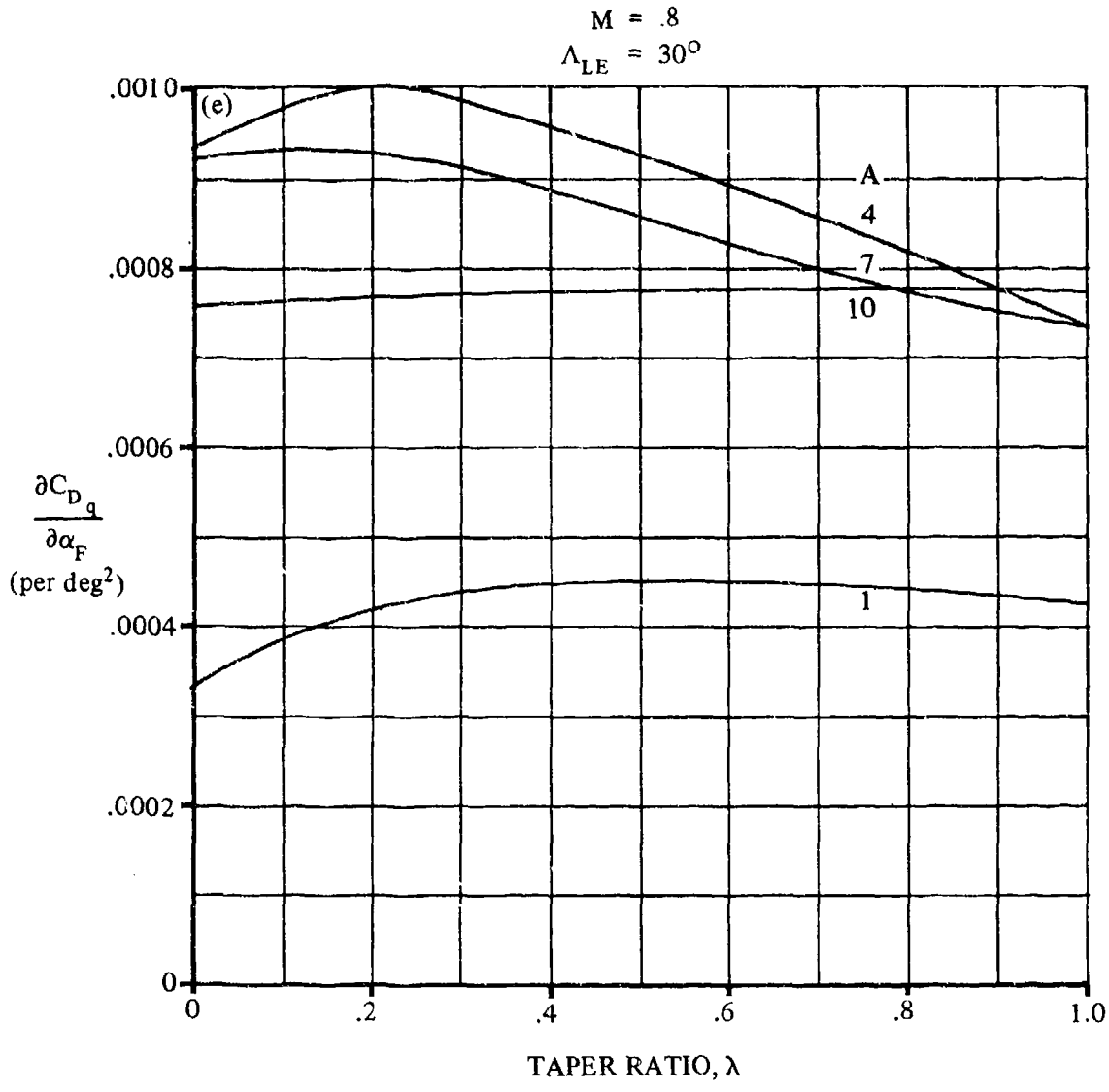

FIGURE 7.1.1.3- 7(CONTD)

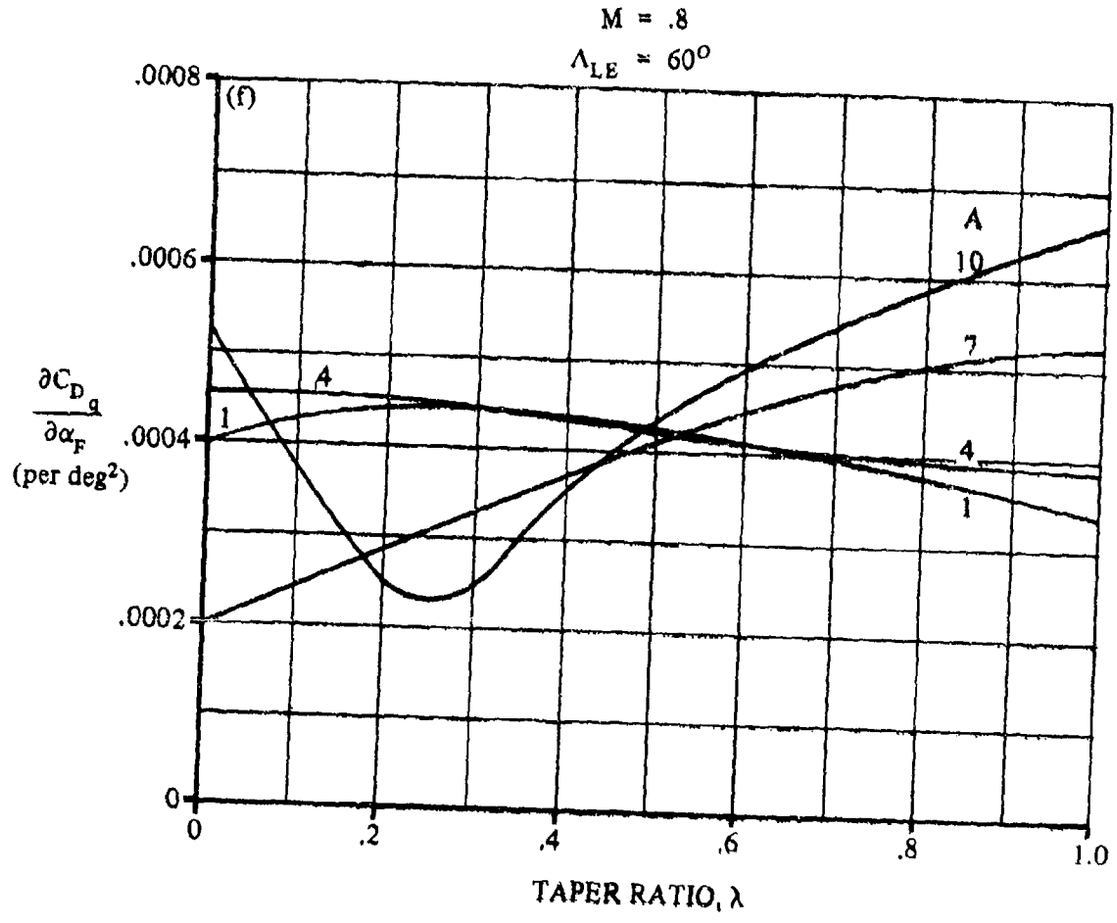

FIGURE 7.1.1.3-7(CONTD)

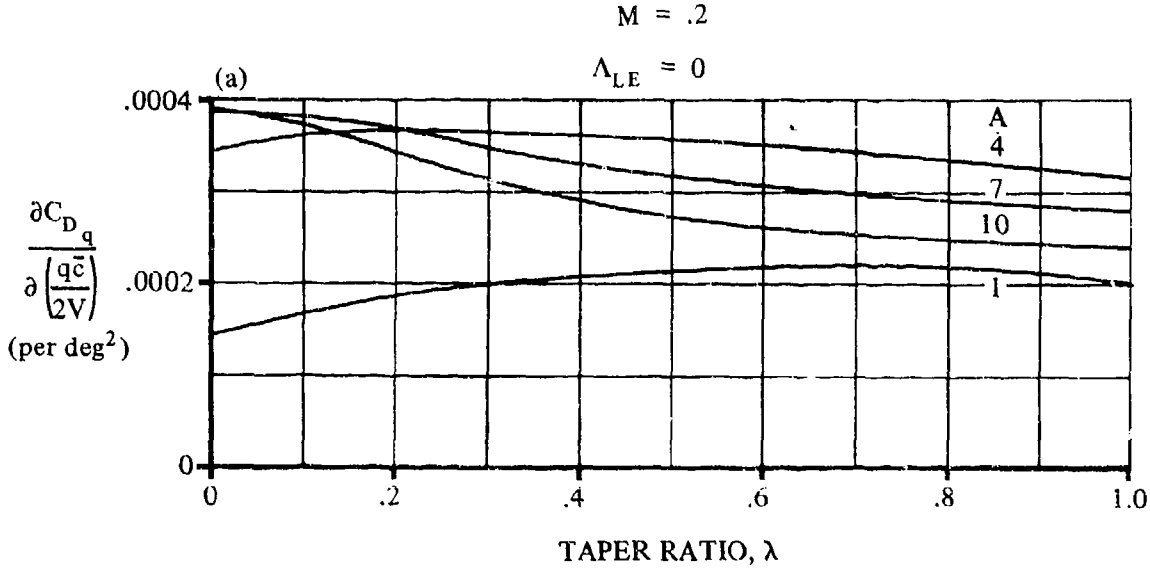

FIGURE 7.1.1.3-12 THE PITCH-RATE CONTRIBUTION TO THE WING PITCHING DERIVATIVE C_{D_q}

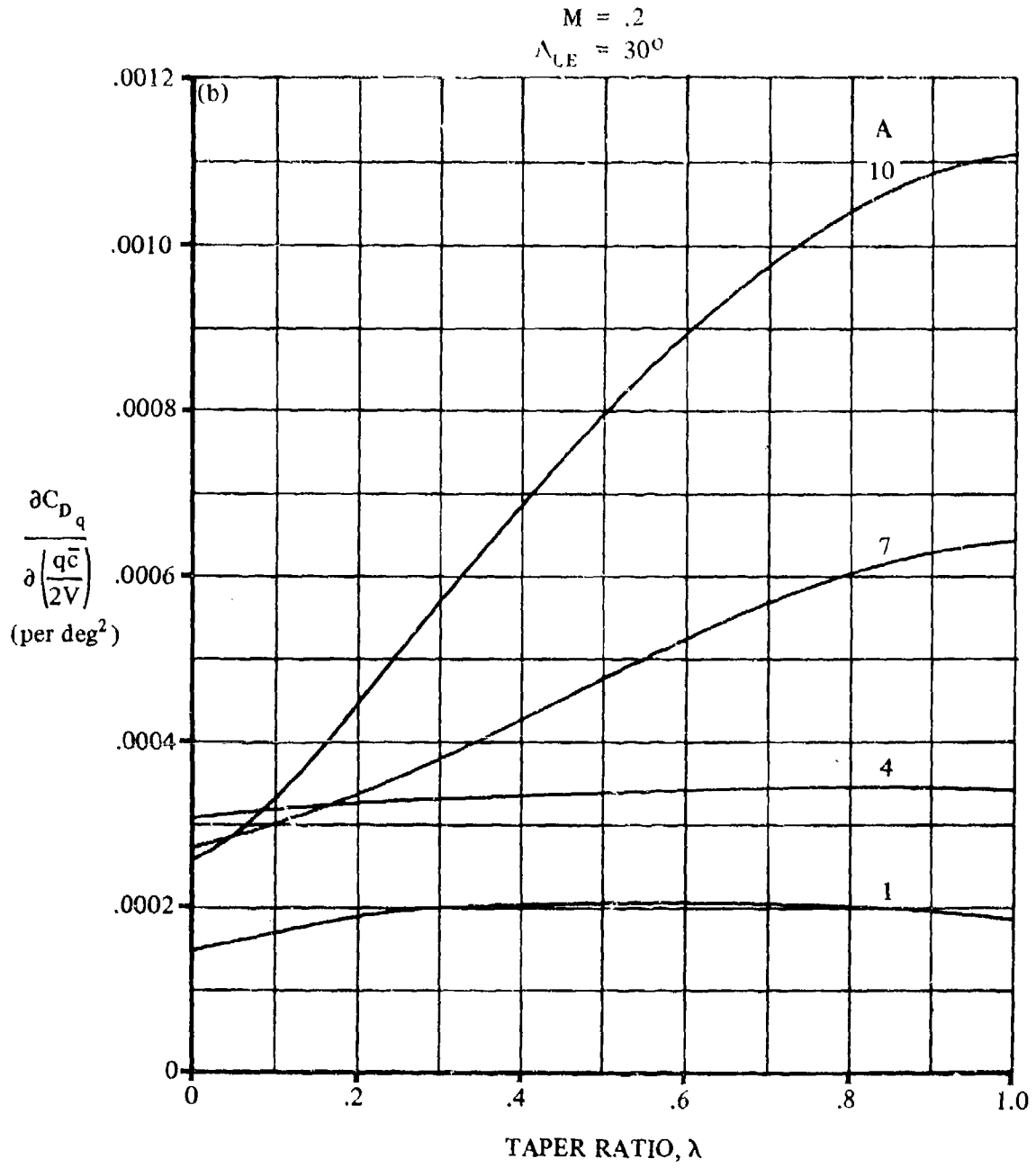

FIGURE 7.1.1.3-12 (CONTD)

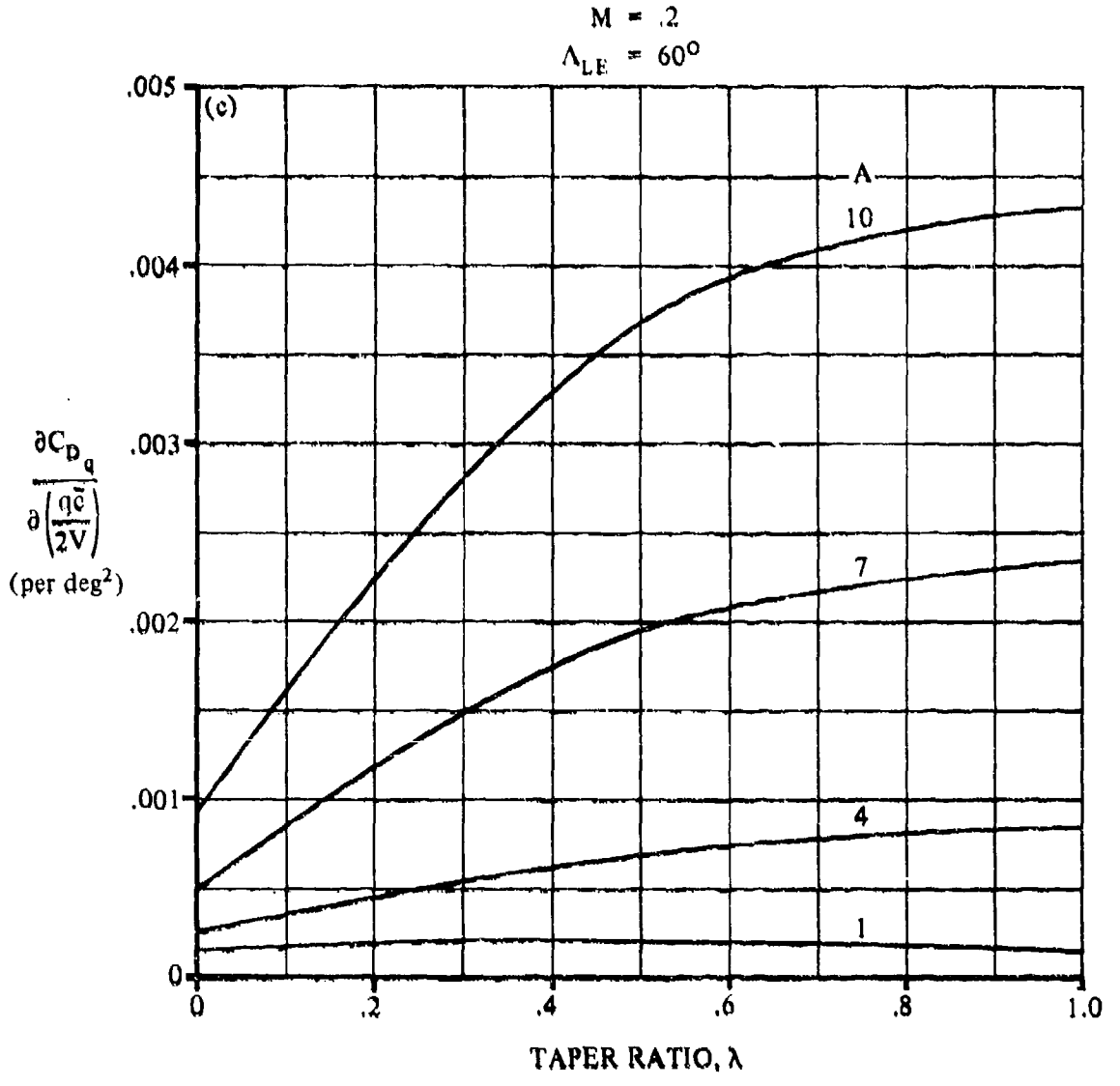

FIGURE 7.1.1.3-12 (CONTD)

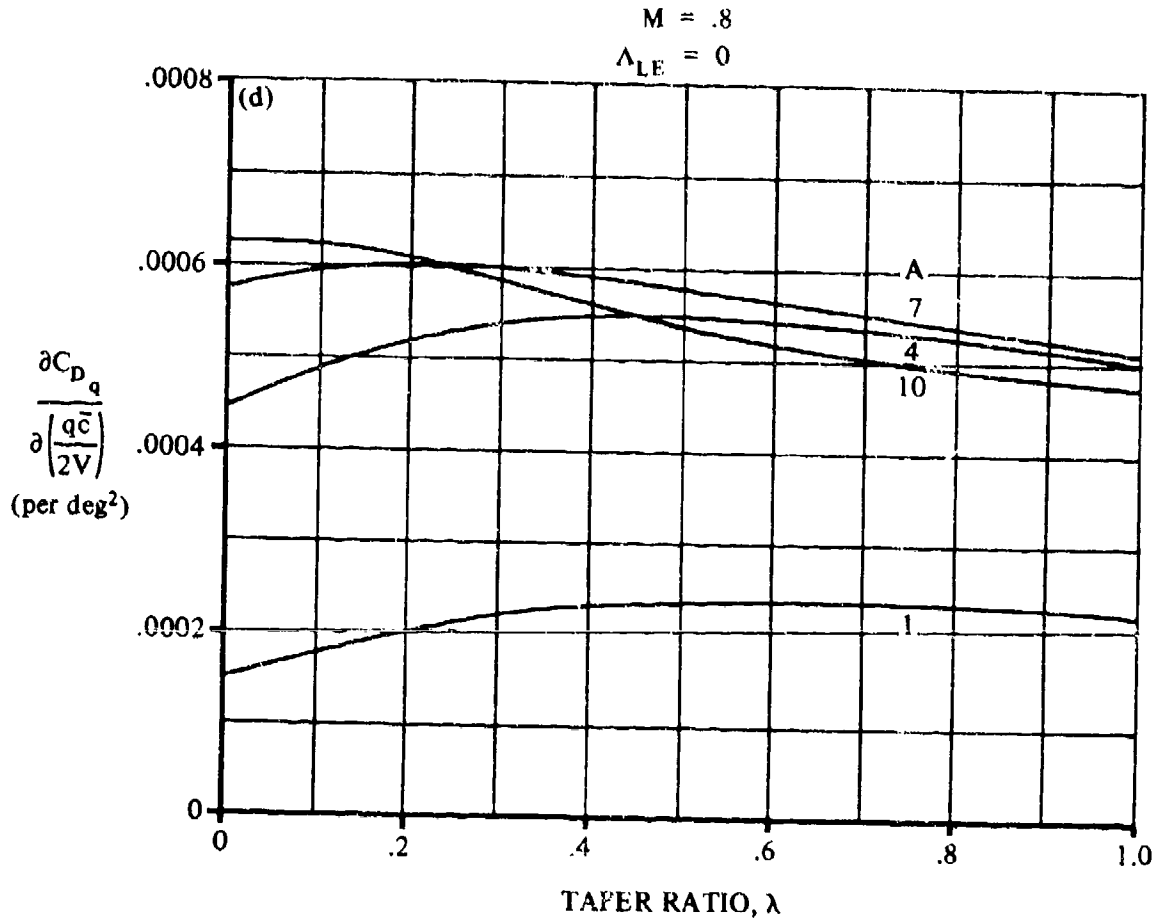

FIGURE 7.1.1.3-12 (CONTD)

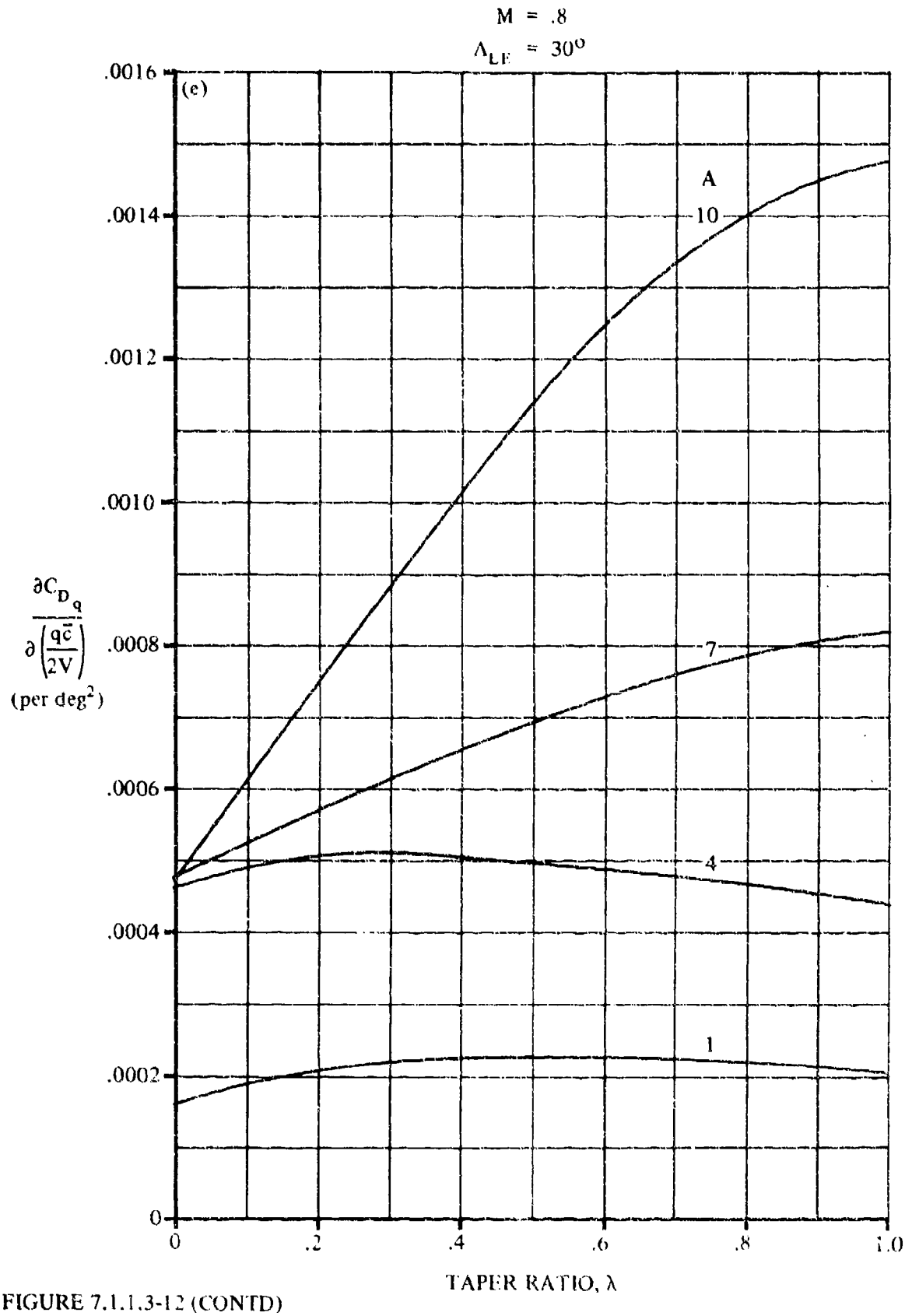

FIGURE 7.1.1.3-12 (CONTD)

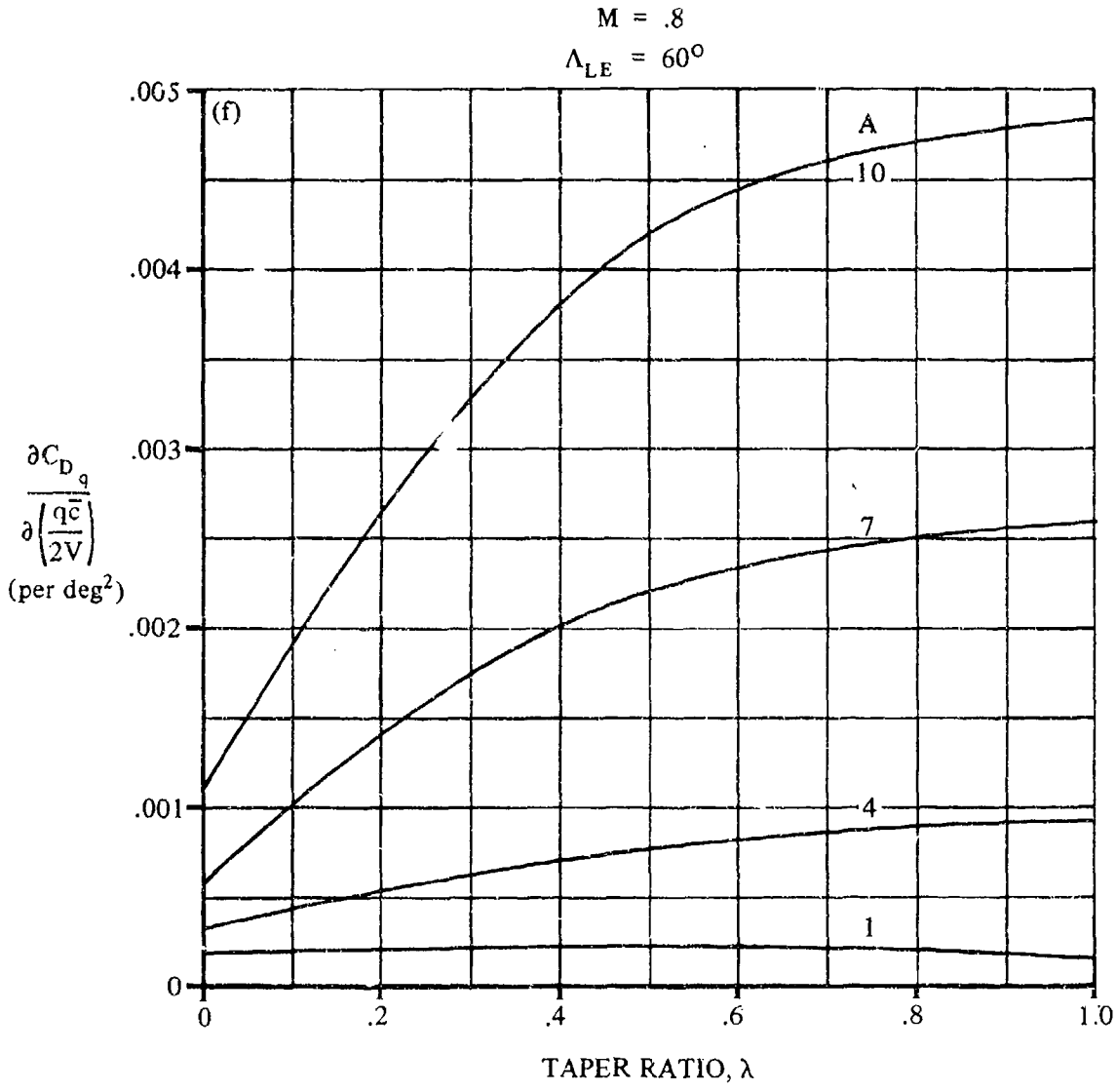

FIGURE 7.1.1.3-12 (CONTD)

7.1.2 WING ROLLING DERIVATIVES

7.1.2.1 WING ROLLING DERIVATIVE C_{Y_p}

This section presents methods for estimating the wing contribution to the rolling derivative C_{Y_p} at subsonic and supersonic speeds. This derivative is the change in side-force coefficient with change in wing-tip helix angle and is expressed as

$$C_{Y_p} = \frac{\partial C_Y}{\partial\left(\frac{pb}{2V_\infty}\right)}$$

A. SUBSONIC

The wing rolling derivative C_{Y_p} results from the angle-of-attack distribution and the tip-suction effects of rolling wings.

The angle-of-attack distribution caused by rolling produces incremental changes in aerodynamic forces. For wings having sweep and/or dihedral, these incremental changes have components in the lateral direction, causing a side force. The contribution to C_{Y_p} due to the angle-of-attack distribution caused by rolling is derived in reference 1, based on simple sweep theory. This result is limited to swept, untapered wings at low lift coefficients. The effect of taper ratio has been derived based on the experimental results presented in reference 2. The effect of dihedral is taken from reference 3. Although the expression for the dihedral effect has been derived specifically for untapered wings, it should be reasonably reliable for wings of any taper ratio over the range of wing dihedral angles of practical interest.

The side force due to rolling of unswept wings is not accounted for by the theory of reference 1. This value is presumed to be caused by tip suction and is given by the empirical expression developed in reference 4. Experimental results show that the tip-suction effect is independent of sweep and varies inversely as the aspect ratio.

The method of reference 5 is applied to extrapolate the potential-flow values to high lift coefficients by using experimental values of the lift and drag at high lift coefficients. If experimental lift and drag data for the particular planform of interest are not available at the chosen Mach number, no attempt should be made to estimate the variation of C_{Y_p} with lift coefficient. The negligible importance of this derivative does not warrant the effort involved in estimating the wing lift and drag variation. Furthermore, no known general method for estimating the variation of drag coefficient will give results reliable enough to use in determining the correction factor for extrapolating the potential-flow values to higher lift coefficients.

DATCOM METHOD

The variation of the wing rolling derivative C_{Y_p} with lift coefficient, based on the product of the wing area and wing span, is given by

$$C_{Y_p} = K\left[\left(\frac{C_{Y_p}}{C_L}\right)_{\substack{C_L=0 \\ M}} C_L\right] + \left(\Delta C_{Y_p}\right)_\Gamma \qquad \text{(per radian)} \qquad 7.1.2.1\text{-a}$$

where

$\left(\frac{C_{Y_p}}{C_L}\right)_{\substack{C_L=0 \\ M}}$ is the slope of the side force due to rolling at zero lift given by

$$\left(\frac{C_{Y_p}}{C_L}\right)_{\substack{C_L=0 \\ M}} = \frac{A + 4\cos\Lambda_{c/4}}{AB + 4\cos\Lambda_{c/4}} \; \frac{AB + \cos\Lambda_{c/4}}{A + \cos\Lambda_{c/4}} \left(\frac{C_{Y_p}}{C_L}\right)_{\substack{C_L=0 \\ M=0}} \qquad 7.1.2.1\text{-b}$$

where $B = \sqrt{1 - M^2\cos^2\Lambda_{c/4}}$ and

$\left(\frac{C_{Y_p}}{C_L}\right)_{\substack{C_L=0 \\ M=0}}$ is the slope of the low-speed side force due to rolling at zero lift, obtained from figure 7.1.2.1-9 as a function of aspect ratio, sweep of the quarter-chord, and taper ratio. This chart has been derived by using the results of references 1, 2, and 4. Equation 7.1.2.1-b modifies the low-speed value by means of the Prandtl-Glauert rule to yield approximate corrections for the first-order three-dimensional effects of compressible flow up to the critical Mach number.

C_L is the wing lift coefficient.

$\left(\Delta C_{Y_p}\right)_\Gamma$ is the increment in C_{Y_p} due to dihedral given by

$$\left(\Delta C_{Y_p}\right)_\Gamma = \left[3\sin\Gamma\left(1 - 2\frac{z}{b/2}\sin\Gamma\right)\right]\left(C_{l_p}\right)_{\substack{\Gamma=0 \\ C_L=0}} \qquad \text{(per radian)} \qquad 7.1.2.1\text{-c}$$

where

Γ is the geometric dihedral angle in degrees, positive for the wing tip above the plane of the root chord.

z is the vertical distance between the c.g and the wing root quarter-chord point, positive for the c.g. above the wing root chord. (This parameter is independent of angle of attack.)

b is the wing span.

$\left(C_{l_p}\right)_{\substack{\Gamma=0 \\ C_L=0}}$ is the roll-damping derivative of the wing without dihedral and at zero lift. This value is obtained from paragraph A of Section 7.1.2.2 and is given by (see equation 7.1.2.2-a)*

$$\left(C_{l_p}\right)_{\substack{\Gamma=0 \\ C_L=0}} = \left(\frac{\beta C_{l_p}}{\kappa}\right)_{C_L=0} \frac{\kappa}{\beta} \quad \text{(per radian)}$$

K is a dimensionless correction factor used to extrapolate the potential-flow values to high lift coefficients. At zero lift this factor is taken as 1.0. At lift coefficients other than zero this factor accounts for the variation of profile drag with lift coefficient and is given by

$$K = \frac{\frac{\partial}{\partial \alpha}\left(C_L \tan\alpha\right) - \frac{\partial}{\partial \alpha}\left(C_D - C_{D_0}\right)}{\frac{\partial}{\partial \alpha}\left(C_L \tan\alpha\right) - \frac{\partial}{\partial \alpha}\left(\frac{C_L{}^2}{\pi A}\right)} \qquad 7.1.2.1\text{-d}$$

Test values of lift and drag at the chosen Mach number for the particular planform of interest must be used in evaluating equation 7.1.2.1-d. The terms of equation 7.1.2.1-d are evaluated by taking the slopes of $C_L \tan\alpha$, $C_D - C_{D_0}$, and $C_L{}^2/(\pi A)$, plotted versus angle of attack.

If reliable values of the static-force coefficients are available, the method should provide results within ±20 percent accuracy throughout the lift-coefficient range to the stall.

Sample Problem

Given: The wing designated 32.6-4-0.6-006 of references 5 and 8.

Wing Characteristics:

$A = 4.0 \qquad \lambda = 0.60 \qquad \Lambda_{c/4} = 32.6^\circ \qquad \Gamma = 0$

$S = 2.25$ sq ft

Additional Characteristics:

$M = 0.7$

The following test values from reference 8 at $M = 0.7$

$C_{D_0} = 0.01$

*The effect of profile drag on the roll damping at zero lift is neglected.

C_L	.05	.1	.2	.3	.4	.5	.6	.7
α	.75	1.50	2.95	4.30	5.60	7.20	8.80	11.20
C_D	.011	.0115	.015	.021	.033	.0535	.078	.145

Compute:

Determine C_{Y_p}/C_L at zero lift

$$\left(C_{Y_p}\right)_{\substack{C_L=0 \\ M=0}} = 0.42 \text{ per rad} \qquad \text{(figure 7.1.2.1- 9)}$$

$$B = \sqrt{1 - M^2 \cos^2 \Lambda_{c/4}} = \sqrt{1 - (0.7)^2 (\cos 32.6^o)^2} = 0.808$$

$$\frac{A + 4 \cos \Lambda_{c/4}}{AB + 4 \cos \Lambda_{c/4}} = \frac{4.0 + 4 \cos 32.6^o}{(4.0)(0.808) + 4 \cos 32.6^o} = 1.116$$

$$\frac{AB + \cos \Lambda_{c/4}}{A + \cos \Lambda_{c/4}} = \frac{(4.0)(0.808) + \cos 32.6^o}{4.0 + \cos 32.6^o} = 0.8414$$

$$\frac{A + 4 \cos \Lambda_{c/4}}{AB + 4 \cos \Lambda_{c/4}} \frac{AB + \cos \Lambda_{c/4}}{A + \cos \Lambda_{c/4}} = (1.116)(0.8414) = 0.939$$

$$\left(\frac{C_{Y_p}}{C_L}\right)_{\substack{C_L=0 \\ M}} = \frac{A + 4 \cos \Lambda_{c/4}}{AB + 4 \cos \Lambda_{c/4}} \frac{AB + \cos \Lambda_{c/4}}{A + \cos \Lambda_{c/4}} \left(\frac{C_{Y_p}}{C_L}\right)_{\substack{C_L=0 \\ M=0}} \qquad \text{(equation 7.1.2.1-b)}$$

$$= (0.939)(0.42) = 0.394$$

Determine the K factor

$$K = \frac{\frac{\partial}{\partial \alpha}(C_L \tan\alpha) - \frac{\partial}{\partial \alpha}(C_D - C_{D_0})}{\frac{\partial}{\partial \alpha}(C_L \tan\alpha) - \frac{\partial}{\partial \alpha}\left(\frac{C_L^2}{\pi A}\right)} \qquad \text{(equation 7.1.2.1-d)}$$

①	②	③	④	⑤	⑥	⑦
C_L	α Test (deg)	tan α tan ②	C_L tanα ① ③	C_D Test	$C_D - C_{D_0}$ ⑤ -- 0.01	$C_L^2/(\pi A)$ ①^2/(4π)
.05	.75	.01309	.0007	.011	.001	.0002
.10	1.5	.02619	.0026	.0115	.0015	.0008
.20	2.95	.05153	.0103	.015	.005	.0032
.30	4.30	.07519	.0226	.021	.011	.0072
.40	5.60	.09805	.0392	.033	.023	.0127
.50	7.20	.1263	.0632	.0535	.0435	.0199
.60	8.80	.1548	.0929	.078	.068	.0287
.70	11.20	.1980	.1396	.145	.135	.0390

Plot $C_L \tan \alpha$, $C_D - C_{D_0}$, and $C_L^2/(\pi A)$ versus angle of attack (see sketch (a)).

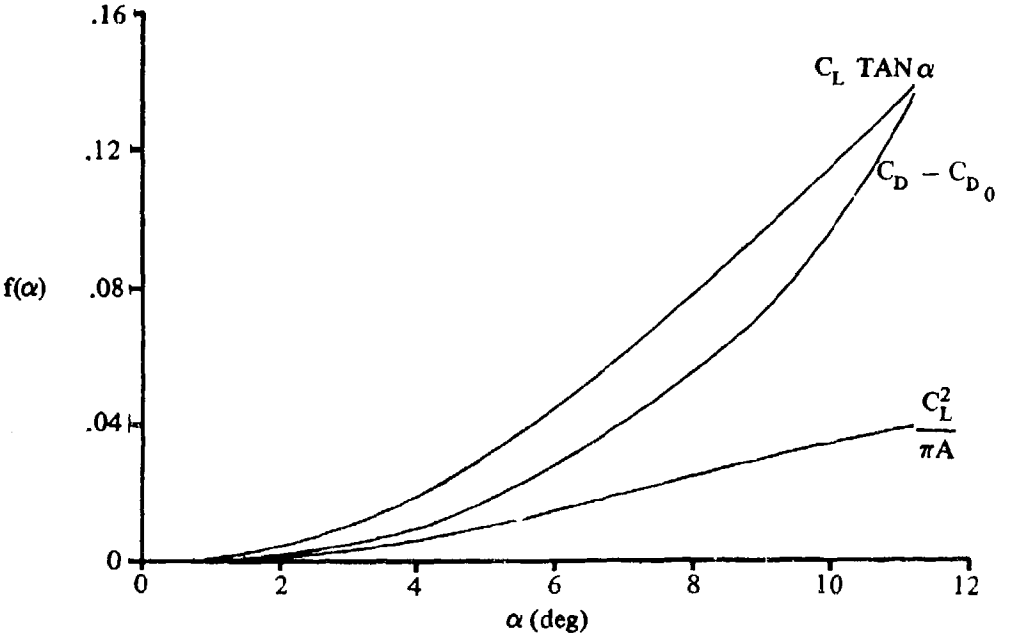

SKETCH (a)

① C_L	② $\frac{\partial}{\partial\alpha}(C_L \tan\alpha)$	③ $\frac{\partial}{\partial\alpha}(C_D - C_{D_0})$	④ $\frac{\partial}{\partial\alpha}\left(\frac{C_L^2}{\pi A}\right)$	⑤ K (② − ③)/(② − ④) (eq. 7.1.2.1-d)
0	–	–	–	1.000
.05	.0018	.00095	.0002	.531
.10	.0040	.0012	.00115	.982
.20	.0066	.0030	.0022	.818
.30	.0105	.0066	.00325	.538
.40	.0136	.0116	.0044	.228
.50	.0168	.0152	.0049	.135
.60	.0184	.0195	.0052	– .083
.70	.01865	.0279	.0031	– .595

Solution:

$$C_{Y_p} = K\left[\left(\frac{C_{Y_p}}{C_L}\right)_{\substack{C_L=0 \\ M}} C_L\right] + \left(\Delta C_{Y_p}\right)_\Gamma \qquad \text{(equation 7.1.2.1-a)}$$

$$= K\left[(0.394)\, C_L\right] + 0 = 0.394\, K\, C_L$$

C_L	K	C_{Y_p} (based on $S_W b_W$) (per rad) (eq. 7.1.2.1-a)
0	1.000	0
.05	.531	.0105
.10	.982	.0387
.20	.818	.0645
.30	.538	.0636
.40	.228	.0359
.50	.135	.0266
.60	– .083	–.0196
.70	– .595	–.1641

The calculated results are compared with test values from reference 5 in sketch (b).

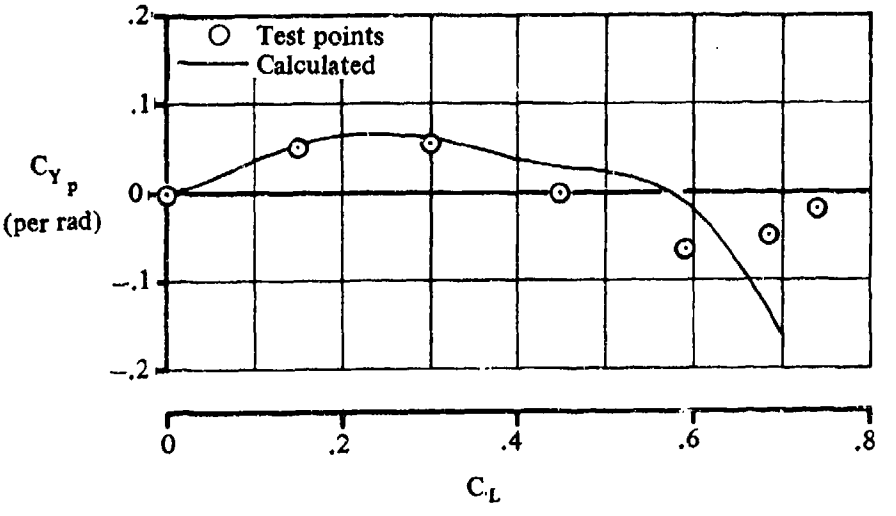

SKETCH (b)

B. TRANSONIC

No generalized method is available in the literature for estimating transonic values of the rolling derivative C_{Y_p}. Furthermore, no known experimental results are available for this derivative at transonic speeds.

C. SUPERSONIC

At supersonic speeds a design chart based on theoretical calculations is presented for estimating the rolling derivative C_{Y_p} at low values of the lift coefficient. The design chart is based on the results of reference 6 for wings with subsonic leading edges and supersonic trailing edges, and the results of reference 7 for wings with supersonic leading edges and either subsonic or supersonic trailing edges. The results of both references 6 and 7 are based on linearized-supersonic-flow theory and are therefore restricted to thin, swept-back, tapered wings with streamwise tips. The lateral force due to rolling is taken as that arising entirely from suction forces on the wing edges. For wings with supersonic leading edges no suction forces are induced along the leading edges, and the determination of C_{Y_p} involves only the unbalanced suction forces along the wing tips. Therefore, for zero-taper wings with supersonic leading edges the theory gives $C_{Y_p} = 0$.

No experimental data are available for this derivative at supersonic speeds. Therefore, the validity of linearized-supersonic-flow theory for estimating C_{Y_p} cannot be determined.

DATCOM METHOD

The wing contribution to the rolling derivative C_{Y_p} at supersonic speeds and at low values of the lift coefficient is obtained from figure 7.1.2.1-10 as a function of the wing aspect ratio, taper ratio, leading-edge sweep, and Mach number.

Sample Problem

Given: Tapered, swept-back wing.

$A = 3.22 \qquad \lambda = 0.25 \qquad \Lambda_{LE} = 55.2^{o}$

$M = 2.41; \ \beta = 2.19$

Compute:

$\beta A = (2.19)(3.22) = 7.07$

Solution:

$$\frac{C_{Y_p}}{\alpha} = 0.50 \text{ per rad}^2 \text{ (based on } S_W b_W \text{) (figure 7.1.2.1-10)}$$

REFERENCES

1. Toll, T. A., and Queijo, M. J.: Approximate Relations and Charts for Low-Speed Stability and Control Derivatives of Swept Wings. NACA TN 1581, 1948. (U)

2. Brewer, J. D., and Fisher, L. R.: Effect of Taper Ratio on the Low-Speed Rolling Stability Derivatives of Swept and Unswept Wings of Aspect Ratio 2.61. NACA TN 2555, 1951. (U)

3. Queijo, M. J., and Jaquet, B. M.: Calculated Effects of Geometric Dihedral on the Low-Speed Rolling Derivatives of Swept Wings. NACA TN 1732, 1948. (U)

4. Goodman, A., and Fisher, L. R.: Investigation at Low Speeds of the Effect of Aspect Ratio and Sweep on Rolling Stability Derivatives of Untapered Wings. NACA TR 968, 1950. (U)

5. Wiggins, J. W.: Wind-Tunnel Investigation of Effect of Sweep on Rolling Derivatives at Angles of Attack Up to 13° and at High Subsonic Mach Numbers, Including a Semiempirical Method of Estimating the Rolling Derivatives. NACA TN 4185, 1958. (U)

6. Margolis, K.: Theoretical Calculations of the Lateral Force and Yawing Moment Due to Rolling at Supersonic Speeds for Sweptback Tapered Wings With Streamwise Tips. Subsonic Leading Edges. NACA TN 2122, 1950. (U)

7. Harmon, S. M., and Martin, J. C.: Theoretical Calculations of the Lateral Force and Yawing Moment Due to Rolling at Supersonic Speeds for Sweptback Tapered Wings With Streamwise Tips. Supersonic Leading Edges. NACA TN 2156, 1950. (U)

8. Wiggins, J. W., and Kuhn, R. E.: Wind-Tunnel Investigation of the Aerodynamic Characteristics in Pitch of Wing-Fuselage Combinations at High Subsonic Speeds. Sweep Series. NACA RM L52D18, 1952. (U)

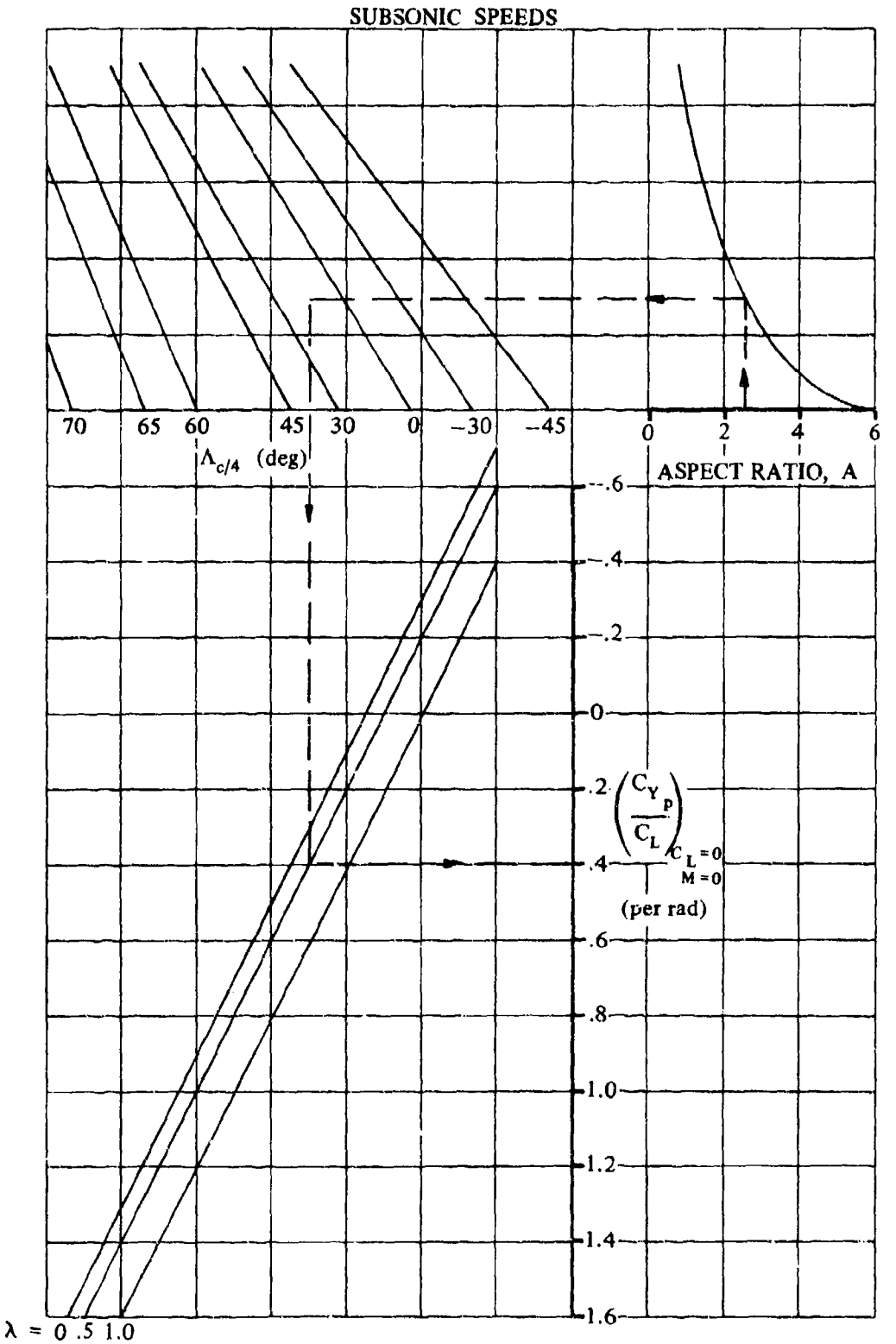

FIGURE 7.1.2.1-9 WING ROLLING DERIVATIVE, C_{Y_p}

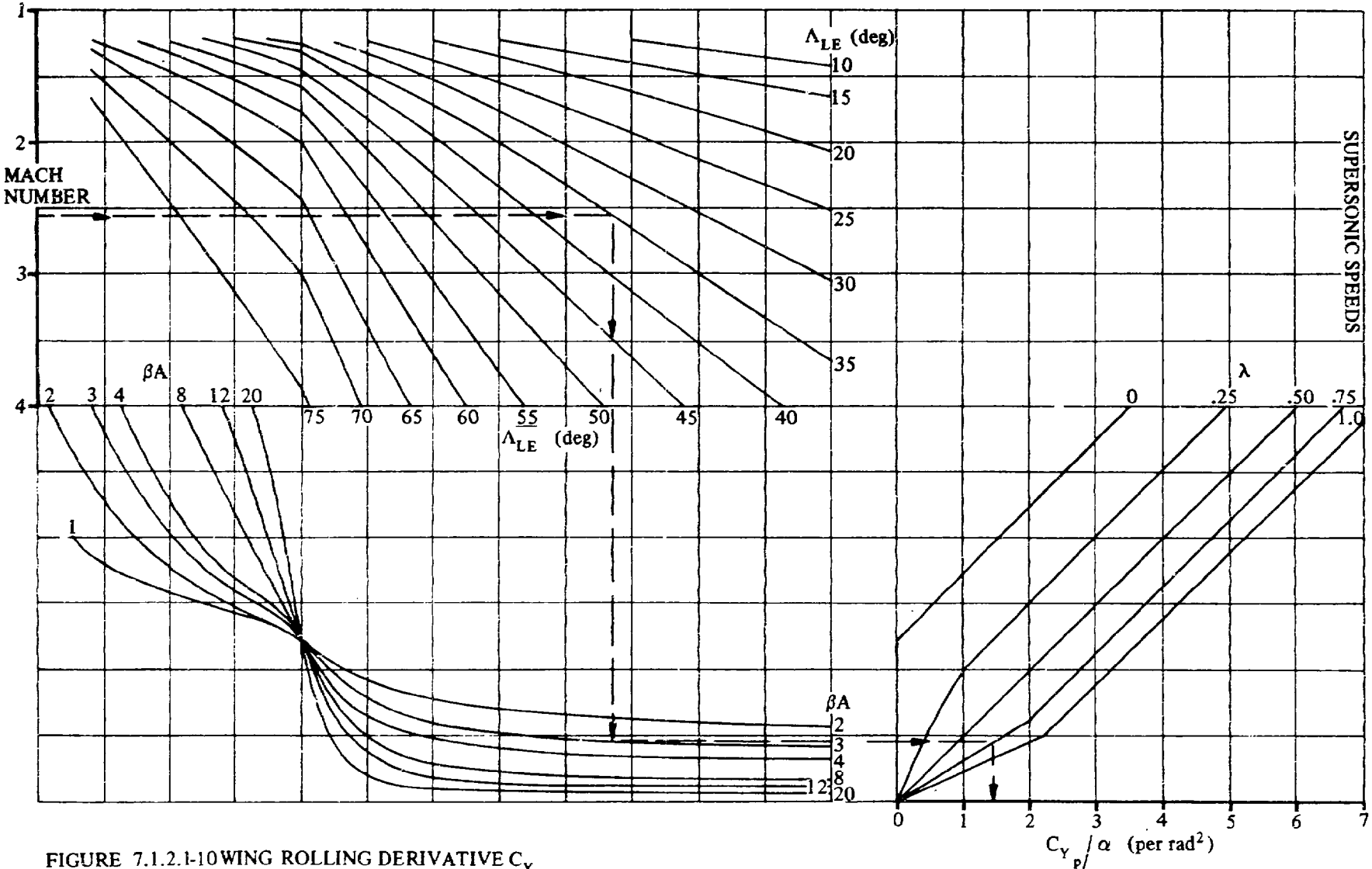

FIGURE 7.1.2.1-10 WING ROLLING DERIVATIVE C_{Y_p}

7.1.2.2 WING ROLLING DERIVATIVE C_{l_p}

This section presents methods for estimating the wing contribution to the rolling derivative C_{l_p} at subsonic and supersonic speeds. This derivative is the change in rolling-moment coefficient with change in wing-tip helix angle and is expressed as

$$C_{l_p} = \frac{\partial C_l}{\partial\left(\frac{pb}{2V_\infty}\right)}$$

A. SUBSONIC

The wing rolling derivative C_{l_p} at subsonic speeds is a function of the wing lift-curve slope, the wing drag, and geometric dihedral. The effects of dihedral become significant when the displacement of the rolling axis from the wing root chord is moderate or large.

For unswept wings of moderately high aspect ratio the lift-curve slope undergoes only small changes throughout the lift-coefficient range, and the drag contribution is relatively unimportant. Therefore, potential flow values of C_{l_p} at zero lift are generally satisfactory at all lift coefficients below the stall for these planforms.

Several methods are available for estimating the potential flow value of C_{l_p}. Reference 1 presents design charts for C_{l_p} at zero lift of unswept wings based on lifting-line theory. An effective edge-velocity correction is applied to the lifting-line theory results of reference 1 in reference 2. Finally the results of reference 2 are modified for the effects of sweep in reference 3. A similar method that accounts for the effects of sweep on the edge-velocity correction is presented in reference 4. Reference 5 presents a more rigorous method of estimating C_{l_p} for wings of arbitrary planform at zero lift, based on the simplified lifting-surface theory of Weissinger for determining the additional span loading due to rolling. The Datcom method for estimating C_{l_p} at zero lift is taken from reference 6. It is essentially that of reference 5 corrected for compressibility effects and extended to a wider range of planform parameters.

For wings of moderate to high aspect ratios and with moderate sweep, the value of C_{l_p} in the nonlinear-lift range is estimated to a first approximation by assuming that variations in the lift-curve slope will affect C_{l_p} in the same proportion as C_{L_α}.

On low-aspect-ratio and/or highly swept wings, the flow separates and forms a stable leading-edge vortex that is responsible for the generation of considerable additional lift on the outer portions of the wing. The drag associated with these high lift coefficients causes significant changes in C_{l_p}. The increment in C_{l_p} due to drag is derived in reference 7, based on the strip-theory procedure of reference 3. Since the effects of drag due to lift and of profile drag on the roll-damping derivative are not of equal importance, they are considered separately in determining the increment due to drag.

The correction for geometric dihedral is considered in detail in reference 8. Although the expression for the dihedral effect has been derived specifically for untapered wings, it should be reasonably reliable for wings of any taper ratio over the range of wing dihedral angles of practical interest.

The Datcom method accounts for the variations in wing lift-curve slope, drag due to lift, and profile

drag, as well as the effect of dihedral. The method requires knowledge of the variation of lift and drag over the angle-of-attack range to the stall for the particular configuration at the appropriate Mach number. Therefore, this method is quite readily applied if experimental lift and drag data are available.

DATCOM METHOD

The value of the wing rolling derivative C_{l_p} at a given lift coefficient at subsonic speeds, based on the product of the wing area and the square of the wing span $S_W b_W^2$, is given by

$$C_{l_p} = \left(\frac{\beta C_{l_p}}{\kappa}\right)_{C_L=0} \left(\frac{\kappa}{\beta}\right) \frac{(C_{L_\alpha})_{C_L}}{(C_{L_\alpha})_{C_L=0}} \frac{(C_{l_p})_\Gamma}{(C_{l_p})_{\Gamma=0}} + (\Delta C_{l_p})_{drag} \quad \text{(per radian)} \qquad 7.1.2.2\text{-a}$$

where

$\left(\frac{\beta C_{l_p}}{\kappa}\right)_{C_L=0}$ is the roll-damping parameter at zero lift, obtained from figure 7.1.2.2-20 as a function of Λ_β and $\beta A/\kappa$.

The parameter κ is the ratio of the two-dimensional lift-curve slope at the appropriate Mach number to $2\pi/\beta$; i.e., $(c_{\ell_\alpha})_M/(2\pi/\beta)$. The two-dimensional lift-curve slope is obtained from Section 4.1.1.2. For wings with airfoil sections varying in a reasonably linear manner with span, the average value of the lift-curve slopes of the root and tip sections is adequate.

The parameter Λ_β is the compressible sweep parameter given as

$$\Lambda_\beta = \tan^{-1}\left(\frac{\tan \Lambda_{c/4}}{\beta}\right), \text{ where } \beta = \sqrt{1 - M^2}\,.$$

$(C_{L_\alpha})_{C_L=0}$ is the wing lift-curve slope at zero lift, obtained from test data or estimated by using the straight-tapered wing method of paragraph A of Section 4.1.3.2 at the appropriate Mach number.

$(C_{L_\alpha})_{C_L}$ is the wing lift-curve slope at any lift coefficient below the stall, obtained from test data or estimated by using the straight-tapered wing method of paragraph A of Section 4.1.3.3 at the appropriate Mach number.

$\frac{(C_{l_p})_\Gamma}{(C_{l_p})_{\Gamma=0}}$ is the dihedral-effect parameter given by

$$\frac{(C_{l_p})_\Gamma}{(C_{l_p})_{\Gamma=0}} = \left[1 - 2\frac{z}{b/2}\sin\Gamma + 3\left(\frac{z}{b/2}\right)^2 \sin^2\Gamma\right] \qquad 7.1.2.2\text{-b}$$

where

Γ is the geometric dihedral angle, positive for the wing tip above the plane of the root chord.

z is the vertical distance between the c.g. and the wing root chord, positive for the c.g. above the root chord.

b is the wing span.

$\left(\Delta C_{l_p}\right)_{drag}$ is the increment in the roll-damping derivative due to drag, given by

$$\left(\Delta C_{l_p}\right)_{drag} = \frac{\left(C_{l_p}\right)_{C_{D_L}}}{C_L^{\,2}} C_L^{\,2} - \frac{1}{8} C_{D_0} \quad \text{(per radian)} \qquad 7.1.2.2\text{-c}$$

where

$\frac{\left(C_{l_p}\right)_{C_{D_L}}}{C_L^{\,2}}$ is the drag-due-to-lift roll-damping parameter obtained from figure 7.1.2.2-24 as a function of A and $\Lambda_{c/4}$.

C_L is the wing lift coefficient below the stall.

C_{D_0} is the profile or total zero-lift drag coefficient. If experimental data are not available, C_{D_0} may be estimated by the method of paragraph A of Section 4.1.5.1 at the appropriate Mach number.

This method includes the effects of compressibility and may be applied up to the critical Mach number. (The drag-due-to-lift term does not include a Mach number correction; however, it is small except at high C_L where the Mach number is generally low.)

The most important factor considered in this method is the variation of the wing lift-curve slope. If reliable values of this parameter are available over the lift-coefficient range, the method will in most cases give satisfactory results over that C_L range for configurations with aspect ratios of approximately 2 or greater.

For wings of low aspect ratio and/or high sweep the accuracy of the method rapidly deteriorates with increasing C_L, even when experimental values of lift and drag are used. The error results from the fact that the high values of $\left(C_{l_p}\right)_{C_{D_L}}$ obtained from figure 7.1.2.2-24 for these configurations are not realized in practice. Therefore, as C_L increases the calculated values of the roll-damping derivative become progressively smaller than those given by experiment.

A comparison of the roll-damping derivative calculated by using this method with test results is presented as table 7.1.2.2-A. Experimental values of lift and drag have been used in evaluating the roll-damping derivative of all the configurations listed in the table. Several additional references containing test results of the damping-in-roll characteristics of straight-tapered wings are listed in table 7-A.

Sample Problem

Given: Model 8 of reference 17.

Wing Characteristics:

$A = 3.0 \qquad \lambda = 0.15 \qquad \Lambda_{c/4} = 36.9^{o} \qquad \Gamma = 0$

Airfoil Characteristics:

NACA 0012 airfoil $\qquad \frac{Y_{90}}{2} = 1.448 \qquad \frac{Y_{99}}{2} = 0.260$

Additional Characteristics:

$M = 0.13; \quad \beta = 0.992 \qquad R_{\ell} = 1.254 \times 10^{6} \qquad C_{D_0} = 0.036$ (test value)

The following test values from reference 17:

C_L	0	.1	.2	.3	.4	.5	.6	.7	.8
C_{L_α}	.0525	.0525	.0525	.053	.053	.054	.054	.050	.030

Compute:

Determine the roll-damping parameter at zero lift $\left(\frac{\beta C_{l_p}}{\kappa}\right)_{C_L = 0}$

$$\tan \frac{1}{2}\phi'_{TE} = \frac{\frac{Y_{90}}{2} - \frac{Y_{99}}{2}}{9} = \frac{1.448 - 0.26}{9} = 0.132$$

$\frac{c_{\ell_\alpha}}{(c_{\ell_\alpha})_{theory}} = 0.768$ (figure 4.1.1.2-8a, extrapolated by plotting vs $\log_{10} R_{\ell}$)

$(c_{\ell_\alpha})_{theory} = 6.88$ (figure 4.1.1.2-8b)

$$(c_{\ell_\alpha})_M = \frac{1.05}{\beta} \frac{c_{\ell_\alpha}}{(c_{\ell_\alpha})_{theory}} (c_{\ell_\alpha})_{theory} \qquad \text{(equation 4.1.1.2-a)}$$

$$= \frac{1.05}{0.992} (0.768)(6.88) = 5.59 \text{ per rad}$$

$$\kappa = \frac{(c_{\ell_\alpha})_M}{2\pi/\beta} = \frac{5.59}{2\pi/0.992} = 0.883$$

$$\frac{\beta A}{\kappa} = \frac{(0.992)\,(3.0)}{0.883} = 3.37$$

$$\Lambda_\beta = \tan^{-1}\left(\frac{\tan \Lambda_{c/4}}{\beta}\right) = \tan^{-1}\left(\frac{0.7508}{0.992}\right) = \tan^{-1} 0.7569 = 37.12^\circ$$

$$\left(\frac{\beta C_{l_p}}{\kappa}\right)_{C_L=0} = -0.251 \text{ per rad} \quad \text{(figure 7.1.2.2-20, interpolated)}$$

Determine the dihedral-effect parameter

$$\frac{(C_{l_p})_\Gamma}{(C_{l_p})_{\Gamma=0}} = 1.0 \quad \text{(equation 7.1.2.2-b at } \Gamma = 0)$$

Determine the increment in roll damping due to drag $(\Delta C_{l_p})_{drag}$

$$\frac{(C_{l_p})_{C_{D_L}}}{C_L^{\,2}} = -0.034 \text{ (figure 7.1.2.2-24)}$$

$$(\Delta C_{l_p})_{drag} = \frac{(C_{l_p})_{C_{D_L}}}{C_L^{\,2}} C_L^{\,2} - \frac{1}{8} C_{D_0} \quad \text{(equation 7.1.2.2-c)}$$

$$= (-0.034) C_L^{\,2} - \frac{1}{8}\, 0.036 \text{ per rad}$$

① C_L	② $C_L^{\,2}$	③ $\frac{1}{8} C_{D_0}$	④ ΔC_{l_p} $-.034$ ② $-$ ③
0	0	0.0045	−0.0045
0.1	0.01		−0.0048
0.2	0.04		−0.0059
0.3	0.09		−0.0076
0.4	0.16		−0.0099
0.5	0.25		−0.0130
0.6	0.36		−0.0167
0.7	0.49		−0.0212
0.8	0.64		−0.0263

Solution:

$$C_{l_p} = \left(\frac{\beta C_{l_p}}{\kappa}\right)_{C_L=0} \left(\frac{\kappa}{\beta}\right) \frac{\left(C_{L_\alpha}\right)_{C_L}}{\left(C_{L_\alpha}\right)_{C_L=0}} \frac{\left(C_{l_p}\right)_\Gamma}{\left(C_{l_p}\right)_{\Gamma=0}} + \left(\Delta C_{l_p}\right)_{drag} \quad \text{(equation 7.1.2.2-a)}$$

$$= (-0.251)\ \frac{0.883}{0.992}\ \frac{\left(C_{L_\alpha}\right)_{C_L}}{\left(C_{L_\alpha}\right)_{C_L=0}}\ (1.0) + \left(\Delta C_{l_p}\right)_{drag}$$

$$= -0.223\ \frac{\left(C_{L_\alpha}\right)_{C_L}}{\left(C_{L_\alpha}\right)_{C_L=0}} + \left(\Delta C_{l_p}\right)_{drag}$$

①	②	③	④	⑤
C_L	$\left(C_{L_\alpha}\right)_{C_L}$ (test results)	$\frac{\left(C_{L_\alpha}\right)_{C_L}}{\left(C_{L_\alpha}\right)_{C_L=0}}$ ② /0.0525	$\left(\Delta C_{l_p}\right)_{drag}$ (per rad) (eq. 7.1.2.2-c)	C_{l_p} (based on $S_W b_W^2$) (per rad) −0.223 ③ + ④
0	0.0625	1.00	−0.0045	−0.2275
0.1	↓	↓	−0.0048	−0.2278
0.2	↓	↓	−0.0059	−0.2289
0.3	0.063	1.01	−0.0076	−0.2328
0.4	↓	↓	−0.0099	−0.2361
0.5	0.064	1.03	−0.0130	−0.2427
0.6	↓	↓	−0.0167	−0.2464
0.7	0.060	0.952	−0.0212	−0.2335
0.8	0.030	0.571	−0.0263	−0.1536

The calculated results are compared with test values in sketch (a) and in table 7.1.2.2-A.

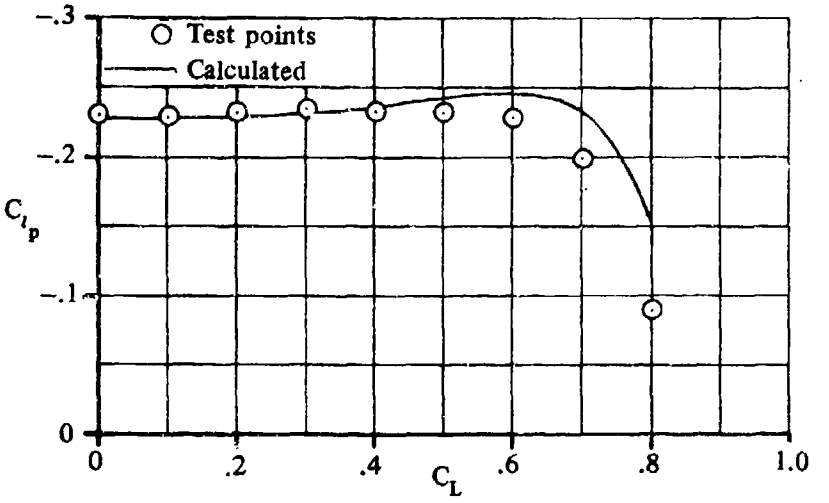

SKETCH (a)

B. TRANSONIC

There are no reliable methods for estimating the derivative C_{l_p} in the transonic region. Although this derivative might be expected to vary with Mach number in the same manner as the lift-curve slope, this trend is not exhibited by experimental data. A considerable quantity of test data is available, however, and reference should be made to table 7-A.

C. SUPERSONIC

At supersonic speeds design charts based on theoretical calculations are presented for estimating the rolling derivative C_{l_p} of wings of vanishing thickness.

The design charts are those of reference 9 and are based on the results presented in the following references:

Reference 10 – in the region of supersonic leading and trailing edges

Reference 11 – in the region of subsonic leading edges and supersonic trailing edges

Reference 12 – for values of $\beta A < 2$

The results presented in references 10 and 11 are based on linearized supersonic-flow theory while those of reference 12 are based on slender-wing theory. The slender-wing-theory value of C_{l_p} for $\beta A = 0$ was used to establish a straight-line relationship between slender-wing theory and the low limit of the linearized supersonic-flow theory. Thin airfoils have been assumed in these theories. Thickness effects are not important except for conditions where the Mach lines lie on or near the wing leading edge. Under these conditions the wing-leading-edge shock position is displaced forward from its theoretical position by the finite thickness effects of the leading edge. This displacement results in substantial losses in normal-force-curve slope and consequently, in roll damping.

The empirical chart presented in Section 4.1.3.2 for determining the leading-edge-thickness effect on the normal-force-curve slope of straight-tapered wings has been adopted in this section to determine the leading-edge-thickness effect on the roll damping. This chart is presented as figure 7.1.2.2-27 in the form

of a ratio of the actual roll-damping derivative to the theoretical roll-damping derivative. For straight-tapered wings with sharp leading edges, the airfoil nose semiwedge angle (measured normal to the wing leading edge) determines the shock position relative to the wing. Experimental data indicate that the parameter corresponding to the nose semiwedge angle is $\Delta y_\perp = \Delta y/\cos \Lambda_{LE}$, where Δy is the difference between the upper-surface ordinates at the 6-percent- and 0.15-percent-chord stations. The parameter Δy is presented for several airfoil shapes in figure 2.2.1-8. For double-wedge and biconvex airfoils there is a linear relationship between $\Delta y_\perp$ and the leading-edge semiwedge angle, given by

$$\Delta y_\perp = 5.85 \tan \delta_\perp$$

Either $\Delta y_\perp$ or $\delta_\perp$ may be used to calculate the thickness effects.

The Datcom method is applicable to straight-tapered wings of arbitrary taper ratio with wing tips parallel to the free stream and with subsonic or supersonic leading edges and supersonic trailing edges. A further restriction is that the foremost Mach line from the tip may not intersect the remote half-wing.

Wings with inverse taper ($\lambda > 1$) have not been considered. Wings with swept-forward leading edges are included through the use of the reversibility theorem (references 13 and 14). The reversibility theorem states that the roll-damping derivative C_{l_p} of the wing in forward flight equals the roll-damping derivative of the same wing in reverse flight.

DATCOM METHOD

The wing contribution to the roll-damping derivative C_{l_p} at supersonic speeds, based on the product of wing area and the square of the wing span $S_W b_W^2$, is given by

$$C_{l_p} = \left[\frac{\left(C_{l_p}\right)_{\text{theory}}}{A}\right] A \; \frac{C_{l_p}}{\left(C_{l_p}\right)_{\text{theory}}} \quad \text{(per radian)} \qquad \text{7.1.2.2-d}$$

where

A is the wing aspect ratio.

$\dfrac{\left(C_{l_p}\right)_{\text{theory}}}{A}$ is the theoretical roll-damping parameter obtained from figures 7.1.2.2-25a through 7.1.2.2-25e.

$\dfrac{C_{l_p}}{\left(C_{l_p}\right)_{\text{theory}}}$ is the empirical thickness correction factor obtained from figure 7.1.2.2-27.

The sonic trailing-edge boundaries on figures 7.1.2.2-25a through 7.1.2.2-25e represent an upper limit for the true theoretical values of the derivatives. Values below the sonic trailing-edge boundary are for wings with subsonic trailing edges and are in violation of one of the basic assumptions of the theory. For configurations with subsonic trailing edges ($\beta \cot \Lambda_{TE} < 1$) the design charts will overestimate the roll-damping derivative.

It should be noted that the "kinks" in the curves of figures 7.1.2.2-25a through 7.1.2.2-25e correspond to the conditions of sonic leading or trailing edges. Experimental evidence shows that these "kinks" do not occur in practice.

Comparisons of the supersonic roll-damping derivative in the linear-lift range calculated by this method with test results are presented in tables 7.1.2.2-B and 7.1.2.2-C. The configurations listed in table 7.1.2.2-B have supersonic leading edges, while those of table 7.1.2.2-C have either sonic or subsonic leading edges. The roll damping is predicted quite accurately by the Datcom method when the wing leading edges are supersonic. However, when the wing leading edges are sonic or subsonic, the calculated roll damping is in almost all cases considerably greater than that given by experiment. Application of the thickness correction factor presented as figure 7.1.2.2-27 improves the agreement between the calculated and experimental values of roll damping in almost all cases presented in table 7.1.2.2-C, since this factor represents a reduction in roll damping. For wings with subsonic leading edges the theoretical results presented in figures 7.1.2.2-25a through 7.1.2.2-25e show the poorest agreement with experiment at the lower values of $\beta \cot \Lambda_{LE}$ for a given value of βA.

Sample Problem

Given: Wing 14 of reference 23.

$\Lambda_{LE} = 60^{\circ}$ $\Lambda_{c/4} = 53.4^{\circ}$ $A = 3.12$ $\lambda = 0.25$

Airfoil: Constant 3/16-in. thickness with symmetrical 5° bevel on all edges in a direction parallel to the root chord.

$\delta_{\perp} = 10^{\circ}$

$M = 2.41$; $\beta = 2.19$

Compute:

$\beta A = (2.19)(3.12) = 6.83$

$A \tan \Lambda_{c/2} = (3.12)(\tan 53.4^{\circ}) = 4.20$

$\dfrac{(C_{l_p})_{theory}}{A} = -0.0716$ per rad (figure 7.1.2.2-25b)

$\beta \cot \Lambda_{LE} = 2.19 (\cot 60^{\circ}) = 1.265$ (supersonic leading edge)

$\dfrac{\tan \Lambda_{LE}}{\beta} = \dfrac{\tan 60^{\circ}}{2.19} = 0.791$

$\dfrac{C_{l_p}}{(C_{l_p})_{theory}} = 0.865$ (figure 7.1.2.2-27)

Solution:

$$C_{l_p} = \left[\frac{\left(C_{l_p}\right)_{\text{theory}}}{A}\right] A \quad \frac{C_{l_p}}{\left(C_{l_p}\right)_{\text{theory}}} \quad \text{(equation 7.1.2.2-d)}$$

$$= (-0.0716)\ (3.12)\ (0.865)$$

$$= -0.193 \text{ per rad} \quad \text{(based on } S_w b_w^2\text{)}$$

This compares with a test result of −0.188 per radian from reference 23.

REFERENCES

1. Pearson, H. A., and Jones, R. T.: Theoretical Stability and Control Characteristics of Wings With Various Amounts of Taper and Twist. NACA TR 635, 1938. (U)

2. Swanson, R. S., and Priddy, E. L.: Lifting-Surface-Theory Values of the Damping in Roll and of the Parameter Used in Estimating Aileron Stick Forces. NACA WR L-53, 1945. (U)

3. Toll, T. A., and Queijo, M. J.: Approximate Relations and Charts for Low-Speed Stability Derivatives of Swept Wings. NACA TN 1581, 1948. (U)

4. Polhamus, E. C.: A Simple Method of Estimating the Subsonic Lift and Damping in Roll of Sweptback Wings. NACA TN 1862, 1949. (U)

5. Bird, J. D.: Some Theoretical Low-Speed Span-Loading Characteristics of Swept Wings in Roll and Sideslip. NACA TR 969, 1950. (U)

6. De Young, J.: Theoretical Antisymmetric Span Loading for Wings of Arbitrary Plan Form at Subsonic Speeds. NACA TR 1056, 1951. (U)

7. Goodman, A., and Adair, G. H.: Estimation of the Damping in Roll of Wings Through the Normal Flight Range of Lift Coefficient. NACA TN 1924, 1949. (U)

8. Queijo, M. J., and Jaquet, B. M.: Calculated Effects of Geometric Dihedral on the Low-Speed Rolling Derivatives of Swept Wings. NACA TN 1732, 1948. (U)

9. Anon: Royal Aeronautical Society Data Sheets – Aerodynamics, Vol. III (Aircraft S.06.03.01), 1957. (U)

10. Harmon, S. M., and Jeffreys, I.: Theoretical Lift and Damping in Roll of Thin Wings With Arbitrary Sweep and Taper at Supersonic Speeds. Supersonic Leading and Trailing Edges. NACA TN 2114, 1950. (U)

11. Malvestuto, F. S., Jr., Margolis, K., and Ribner, H. S.: Theoretical Lift and Damping in Roll at Supersonic Speeds of Thin Sweptback Wings of Arbitrary Taper and Sweep at Supersonic Speeds. Subsonic Leading Edges and Supersonic Trailing Edges. NACA TR 970, 1950. (U)

12. Mangler, K. W.: Calculations of the Pressure Distribution Over a Wing at Sonic Speeds. ARC R&M 2888, 1955. (U)

13. Harmon, S. M.: Theoretical Relations Between the Stability Derivatives of a Wing in Direct and in Reverse Supersonic Flow. NACA TN 1943, 1949. (U)

14. Brown, C. E.: The Reversibility Theorem for Thin Airfoils in Subsonic and Supersonic Flow. NACA TN 1944, 1949. (U)

15. Letko, W., and Wolhart, W. D.: Effect of Sweepback on the Low-Speed Static and Rolling Stability Derivatives of Thin Tapered Wings of Aspect Ratio 4. NACA RM L9F14, 1949. (U)

16. Jaquet, B. M., and Brewer, J. D.: Effects of Various Outboard and Central Fins on Low-Speed Static-Stability and Rolling Characteristics of a Triangular-Wing Model. NACA RM L9E18, 1949. (U)

17. Jaquet, B. M., and Brewer, J. D.: Low-Speed Static-Stability and Rolling Characteristics of Low-Aspect-Ratio Wings of Triangular and Modified Triangular Plan Forms. NACA RM L8L29, 1949. (U)

18. Bird, J. D., Lichtenstein, J. H., and Jaquet, B. M.: Investigation of the Influence of Fuselage and Tail Surfaces on Low-Speed Static Stability and Rolling Characteristics of a Swept-Wing Model. NACA TN 2741, 1952. (U)

19. Fisher, L. R., and Michael, W. H., Jr.: An Investigation of the Effect of Vertical-Fin Location and Area on Low-Speed Lateral Stability Derivatives of a Semitailless Airplane Model. NACA RM L51A10, 1951. (U)

20. Goodman, A., and Thomas, D. F., Jr.: Effect of Wing Position and Fuselage Size on the Low-Speed Static and Rolling Stability Characteristics of a Delta-Wing Model. NACA TR 1224, 1955. (U)

21. Letko, W. and Riley, D. R.: Effect of an Unswept Wing on the Contribution of Unswept-Tail Configurations to the Low-Speed Static and Rolling-Stability Derivatives of a Midwing Airplane Model. NACA TN 2175, 1950. (U)

22. Wiggins, J. W., and Kuhn, R. E.: Wind-Tunnel Investigation of the Aerodynamic Characteristics in Pitch of Wing-Fuselage Combinations at High Subsonic Speeds — Sweep Series. NACA RM L52D18, 1952. (U)

23. McDearmon, R. W., and Heinke, H. S., Jr.: Investigations of the Damping in Roll of Swept and Tapered Wings at Supersonic Speeds. NACA RM L53A13, 1953. (U)

24. Bland, W. M., Jr., and Sandahl, C. A.: A Technique Utilizing Rocket-Propelled Test Vehicles for the Measurement of the Damping in Roll of Sting-Mounted Models and Some Initial Results for Delta and Unswept Tapered Wings. NACA RM L50D24, 1950. (U)

25. Bland, W. M., Jr., and Dietz, A. E.: Some Effects of Fuselage Interference, Wing Interference, and Sweepback on the Damping in Roll of Untapered Wings as Determined by Techniques Employing Rocket-Propelled Vehicles. NACA RM L51D25, 1951. (U)

TABLE 7.1.2.2-A

SUBSONIC WING ROLLING DERIVATIVE C_{l_p}

DATA SUMMARY

Ref.	A	λ	$\Lambda_{c/4}$ (deg)	Airfoil Section	Γ (deg)	M	R_ℓ x 10^{-6}	C_L	C_{L_α} (per deg) (test)	C_{D_0} (test)	C_{l_p} Calc. (per rad)	C_{l_p} Test (per rad)	e Percent Error
15	4.0	0.60	3.6	65A006	0	0.13	0.72	0	0.065	0.033	−0.322	−0.345	6.7
								0.1	0.072		−0.356	−0.346	− 2.9
								0.2	0.072		−0.357	−0.347	−2 9
								0.3	0.072		−0.357	−0.348	−2.6
								0.4	0.067		−0.334	−0.355	5.9
								0.5	0.067		−0.334	−0.370	9.7
								0.6	0.063		−0.316	−0.370	14.6
								0.7	0.047		−0.240	−0.275	12.7
			32.6					0	0.062	0.033	−0.308	−0.330	6.7
								0.1	0.062		−0.308	−0.330	6.7
								0.2	0.062		−0.309	−0.336	8.0
								0.3	0.066		−0.329	−0.360	8.6
								0.4	0.066		−0.330	−0.387	14.7
								0.5	0.066		−0.332	−0.370	10.3
								0.6	0.061		−0.309	−0.295	−4.7
								0.7	0.046		−0.234	−0.195	−20.0
								0.8	0.027		−0.145	−0.085	−70.6

TABLE 7.1.2.2-A (CONTD)

Ref.	A	λ	$\Lambda_{c/4}$ (deg)	Airfoil Section	Γ (deg)	M	R_ℓ x 10−6	C_L	C_{L_α} (per deg) (test)	C_{D_0} (test)	C_{l_p} Calc. (per rad)	C_{l_p} Test (per rad)	e Percent Error
15	4.0	0.60	46.7	65A006	0	0.13	0.72	0	0.062	0.033	−0.287	−0.300	4.3
								0.1	0.062		−0.288	−0.305	5.6
								0.2	0.062		−0.288	−0.335	14.0
								0.3	0.066		−0.309	−0.378	18.3
								0.4	0.066		−0.312	−0.392	20.4
								0.5	0.066		−0.315	−0.382	17.5
								0.6	0.059		−0.285	−0.350	18.6
								0.7	0.046		−0.230	−0.297	22.6
								0.8	0.036		−0.193	−0.256	24.6
16	2.31	0	52.2	$65_{(06)}-006.5$	0	0.13	1.624	0	0.045	0.020	−0.172	−0.165	− 4.2
								0.1			−0.173	−0.175	1.1
								0.2			−0.176	−0.180	2.2
								0.3			−0.180	−0.180	0
								0.4			−0.186	−0.182	−2.2
								0.5			−0.195	−0.182	−7.1
								0.6			−0.205	−0.180	−13.9
								0.7			−0.218	−0.179	−21.8
								0.8			−0.233	−0.172	−35.5
17	3.0	0.15	36.9	0012	0	0.13	1.254	0	0.0525	0.036	−0.228	−0.230	0.9
								0.1	0.0525		−0.228	−0.230	0.9
								0.2	0.0525		−0.229	−0.232	1.3
								0.3	0.053		−0.233	−0.235	0.9
								0.4	0.053		−0.235	−0.232	−1.3
								0.5	0.054		−0.243	−0.232	−4.7
								0.6	0.054		−0.246	−0.228	−7.9
								0.7	0.050		−0.234	−0.198	−18.1
								0.8	0.030		−0.154	−0.090	−71.1
	2.31	0	52.2				1.624	0	0.041	0.033	−0.168	−0.150	−12.0
								0.1			−0.169	−0.150	−12.7
								0.2			−0.172	−0.150	−14.7
								0.3			−0.176	−0.149	−18.1
								0.4			−0.183	−0.143	−28.0
								0.5			−0.191	−0.138	−38.4
								0.6	0.0435		−0.212	−0.128	−65.6
								0.7	0.0435		−0.225	−0.120	−87.5
								0.8	0.045		−0.245	−0.127	−92.9

TABLE 7.1.2.2-A (CONTD)

Ref.	A	λ	$\Lambda_{c/4}$ (deg)	Airfoil Section	Γ (deg)	M	R_ℓ x 10^{-6}	C_L	C_{L_α} (per deg) (test)	C_{D_0} (test)	C_{l_p} Calc. (per rad)	C_{l_p} Test (per rad)	e Percent Error
	4.0	0	38.9				1.232	0	0.056	0.037	−0.239	−0.227	− 5.3
								0.1			−0.239	−0.230	−3.9
								0.2			−0.240	−0.230	−4.3
								0.3			−0.241	−0.235	−2.6
								0.4			−0.243	−0.228	−6.6
								0.5			−0.245	−0.200	−22.5
								0.6	0.0545		−0.242	−0.160	−51.2
								0.7	0.047		−0.214	−0.117	−82.9
								0.8	0.037		−0.178	–	–
	2.0	0.36	38.9				1.335	0	0.036	0.041	−0.183	−0.228	19.7
								0.1	0.041		−0.208	−0.221	5.9
								0.2	0.044		−0.224	−0.231	3.0
								0.3			−0.226	−0.232	2.6
								0.4			−0.229	−0.222	−3.2
								0.5			−0.233	−0.228	−2.2
								0.6			−0.238	−0.242	1.7
								0.7	0.043		−0.239	−0.250	4.4
								0.8	0.053		−0.295	−0.240	−22.9
18	2.61	1.00	45.0	0012(I_{LE})	0	0.17	1.40	0	0.0452	0.023	−0.218	−0.230	5.2
								0.1			−0.218	−0.232	6.0
								0.2			−0.219	−0.235	6.8
								0.3			−0.223	−0.240	7.1
								0.4			−0.227	−0.242	6.2
								0.5	0.048		−0.245	−0.256	4.3
								0.6	0.050		−0.260	−0.275	5.5
								0.7	0.065		−0.339	−0.318	−6.6
								0.8	0.0745		−0.393	−0.385	−2.1
19	3.60	0.455	38.16	0010-64	0	0.16	1.138	0	0.0515	0.018	−0.271	−0.266	− 1.9
								0.1	0.055		−0.290	−0.261	−11.1
								0.2			−0.290	−0.279	−3.9
								0.3			−0.292	−0.290	−0.7
								0.4	0.056		−0.300	−0.299	−0.3
								0.5	0.054		−0.292	−0.292	0
								0.6	0.046		−0.254	−0.248	−2.4
								0.7	0.035		−0.200	−0.150	−33.3
								0.8	0.017		−0.110	−0.125	12.0

TABLE 7.1.2.2-A (CONTD)

Ref.	A	λ	$\Lambda_{c/4}$ (deg)	Airfoil Section	Γ (deg)	M	R_ℓ x 10^{-6}	C_L	C_{L_α} (per deg) (test)	C_{D_0} (test)	C_{l_p} Calc. (per rad)	C_{l_p} Test (per rad)	e Percent Error
20	2.31	0	52.4	65A003	0	0.17	2.06	0	0.042	0.015	−0.170	−0.160	− 6.3
								0.1			−0.171	−0.155	−10.3
								0.2			−0.175	−0.158	−10.8
								0.3	0.0455		−0.193	−0.165	−17.0
								0.4	0.047		−0.205	−0.165	−24.2
								0.5	0.048		−0.218	−0.162	−34.6
								0.6	0.048		−0.228	−0.155	−47.1
								0.7	0.047		−0.236	−0.150	−57.3
								0.8	0.047		−0.250	−0.157	−59.2
21	4.0	0.6	0	65A008	0	0.166	0.88	0	0.061	0.027	−0.317	−0.330	3.9
								0.1			−0.317	−0.340	6.8
								0.2			−0.318	−0.370	14.1
								0.3			−0.318	−0.392	18.9
								0.4			−0.320	−0.384	16.7
								0.5			−0.321	−0.355	9.6
								0.6			−0.321	−0.336	4.5

Average Error = $\frac{\Sigma|e|}{n}$ = 11.5%

TABLE 7.1.2.2-8

SUPERSONIC WING ROLLING DERIVATIVE C_{l_p}

SUPERSONIC LEADING EDGES

DATA SUMMARY

Ref.	A	λ	Λ_{LE} (deg)	M	$\beta \cot \Lambda_{LE}$	Airfoil Section	$\delta_\perp$ (deg)	$\frac{(C_{l_p})_{theory}}{A}$ (per rad)	$\frac{C_{l_p}}{(C_{l_p})_{theory}}$	C_{l_p} Calc. (per rad)	C_{l_p} Test (per rad)	e Percent Error
23	3.07	0	60.0	2.41	1.27	Beveled Flat Plate	10.0	−0.0536	0.865	−0.142	−0.139	2.2
	1.90	0.25	60.0	2.41	1.27		10.0	−0.0982	0.865	−0.161	−0.163	− 1.2
	1.91	0.25	55.0	1.93	1.16		8.75	−0.1126	0.860	−0.185	−0.195	− 5.1
	↓	↓	↓	2.41	1.54		↓	−0.0980	0.913	−0.171	−0.188	− 9.0
	2.37	0.25	55.0	1.93	1.16		8.75	−0.1016	0.860	−0.207	−0.210	− 1.4
	↓	↓	↓	2.41	1.54		↓	−0.0834	0.913	−0.181	−0.200	− 9.5
	3.12	0.25	60.0	2.41	1.27		10.0	−0.0716	0.865	−0.193	−0.188	2.7
	3.22	0.25	55.2	1.93	1.15		8.75	−0.0853	0.850	−0.234	−0.225	4.0
	↓	↓	↓	2.41	1.53		↓	−0.0669	0.915	−0.197	−0.211	− 6.6
	3.12	0.25	45.0	1.62	1.27		7.08	−0.1010	0.895	−0.282	−0.272	3.3
	↓	↓	↓	1.93	1.65		↓	−0.0839	0.945	−0.248	−0.253	− 2.0
				2.41	2.20			−0.0642	1.000	−0.200	−0.190	5.3
	1.83	0	55.0	1.93	1.16		8.75	−0.0972	0.860	−0.163	−0.160	− 4.4
	↓	↓	↓	2.41	1.54		↓	−0.0758	0.913	−0.127	−0.138	− 8.0
	1.82	0	50.0	1.62	1.07		7.8	−0.1070	0.863	−0.166	−0.185	−10.3
	↓	↓	↓	1.93	1.39		↓	−0.0960	0.902	−0.158	−0.176	−10.2
				2.41	1.84			−0.0755	0.965	−0.132	−0.138	− 4.3
	2.34	0	54.9	1.93	1.16		8.7	−0.0815	0.860	−0.164	−0.170	− 3.5
	↓	↓	↓	2.41	1.55		↓	−0.0625	0.913	−0.133	−0.155	−14.2
	2.31	0	45.0	1.62	1.27		7.08	−0.0982	0.895	−0.203	−0.210	− 3.3
	↓	↓	↓	1.93	1.65		↓	−0.0790	0.945	−0.172	−0.187	− 8.0
				2.41	2.20			−0.0610	1.000	−0.141	−0.140	0.7
	2.34	0	40.4	1.62	1.50		6.57	−0.0962	0.933	−0.210	−0.229	− 8.3
	↓	↓	↓	1.93	1.94		↓	−0.0775	0.995	−0.180	−0.170	5.9
				2.41	2.59			−0.0599	1.000	−0.140	−0.155	− 9.7

TABLE 7.1.2.2-B (CONTD)

Ref.	A	λ	Λ_{LE} (deg)	M	$\beta \cot \Lambda_{LE}$	Airfoil Section	$\Delta y_{\perp}$	$\frac{(C_{l_p})_{theory}}{A}$ (per rad)	$\frac{C_{l_p}}{(C_{l_p})_{theory}}$	C_{l_p} Calc. (per rad)	C_{l_p} Test (per rad)	e Percent Error
23	3.07	0	45.0	1.62	1.27	Beveled Flat Plate	7.08	−0.0795	0.895	−0.218	−0.214	1.9
				1.93	1.65			−0.0627	0.945	−0.181	−0.200	− 9.5
				2.41	2.20			−0.0483	1.000	−0.148	−0.144	2.8
	3.02	0	33.4	1.62	1.93		6.08	−0.0778	1.000	−0.235	−0.225	4.4
				1.93	2.50			−0.0613	1.000	−0.185	−0.178	3.9
				2.41	3.34			−0.0480	1.000	−0.145	−0.134	8.2
	1.88	0.25	33.5	1.62	1.93		6.0	−0.1292	1.000	−0.243	−0.257	− 5.4
				1.93	2.50			−0.1163	1.000	−0.219	−0.210	4.3
				2.41	3.31			−0.0960	1.000	−0.180	−0.167	7.8
	2.33	0.25	45.0	1.62	1.27		7.08	−0.1163	0.895	−0.243	−0.240	1.3
				1.93	1.65			−0.1032	0.945	−0.227	−0.235	− 3.4
				2.41	2.00			−0.0823	1.000	−0.192	−0.186	3.2
	2.41	0.25	27.3	1.62	2.46		5.64	−0.1172	1.000	−0.282	−0.275	2.5
				1.93	3.20			−0.0990	1.000	−0.239	−0.225	6.2
				2.41	4.25			−0.0780	1.000	−0.188	−0.178	5.6
	2.37	0.25	27.4	1.62	2.46		5.65	−0.1185	1.000	−0.281	−0.267	5.2
				1.93	3.19			−0.0998	1.000	−0.237	−0.218	8.7
				2.41	4.25			−0.0790	1.000	−0.187	−0.173	8.1
	3.22	0.25	21.2	1.62	3.28		5.36	−0.0965	1.000	−0.311	−0.317	− 1.9
				1.93	4.25			−0.0775	1.000	−0.250	−0.220	13.6
				2.41	5.65			−0.0606	1.000	−0.195	−0.175	11.4
	2.32	0	60.0	2.41	1.27		10.0	−0.0651	0.865	−0.131	−0.138	− 5.1
	2.81	0	55.0	1.93	1.16		8.75	−0.0858	0.860	−0.207	−0.167	24.0
				2.41	1.54			−0.0651	0.913	−0.167	−0.160	4.4
	3.40	0	50.0	1.62	1.07		7.8	−0.0778	0.855	−0.226	−0.205	10.2
				1.93	1.39			−0.0595	0.905	−0.183	−0.205	−10.7
				2.41	1.84			−0.0453	0.965	−0.149	−0.156	− 4.5

TABLE 7.1.2.2-B (CONTD)

Ref.	A	λ	Λ_{LE} (deg)	M	$\beta \cot \Lambda_{LE}$	Airfoil Section	$\Delta y_{\perp}$	$\frac{(C_{l_p})_{theory}}{A}$ (per rad)	$\frac{C_{l_p}}{(C_{l_p})_{theory}}$	C_{l_p} Calc. (per rad)	C_{l_p} Test (per rad)	e Percent Error
24	4.00	0	45.0	1.485	1.097	Symmetrical dbl. wedge t/c = 0.04	3.24	−0.075	0.934	−0.280	−0.280	0
	4.00	0	45.0	1.485	1.097	Symmetrical dbl. wedge t/c = 0.09	7.3	−0.075	0.867	−0.260	−0.230	13.0
	4.00	0.50	9.5	1.70	8.21	Symmetrical dbl. wedge t/c = 0.046	2.67	−0.084	1.000	−0.336	−0.350	− 4.0
				1.485	6.56			−0.100	1.000	−0.400	−0.406	− 1.2
				1.414	5.98			−0.106	1.000	−0.424	−0.440	− 3.6
25	3.70	1.00	0	1.60	∞	65A009	16.6	−0.101	1.000	−0.374	−0.342	9.4
				1.50				−0.1075	1.000	−0.398	−0.360	10.6
				1.414				−0.1140	1.000	−0.423	−0.376	12.5
				1.30				−0.1235	1.000	−0.467	−0.390	17.2
	3.70	1.00	45.0	1.60	1.25	65A009	16.6	−0.101	0.812	−0.303	−0.310	− 2.3
				1.50	1.12			−0.105	0.792	−0.308	−0.307	0.3

Average Error = $\frac{\Sigma |e|}{n}$ = 6.2%

TABLE 7.1.2.2-C

SUPERSONIC WING ROLLING DERIVATIVE C_{l_p}

SUBSONIC OR SONIC LEADING EDGE

DATA SUMMARY

Ref.	A	λ	Λ_{LE} (deg)	M	$\beta \cot \Lambda_{LE}$	Airfoil Section	$\Delta y_{\perp}$	$\frac{(C_{l_p})_{theory}}{A}$ (per rad)	$\frac{C_{l_p}}{(C_{l_p})_{theory}}$	C_{l_p} Calc. (per rad)	C_{l_p} Test (per rad)	e Percent Error
23	1.82	0	70.0	1.62	0.465	Beveled Flat Plate	1.52	−0.0810	1.000	−0.147	−0.120	22.5
				1.93	0.600			−0.0795	0.922	−0.134	−0.114	17.5
				2.41	0.800			−0.0769	0.820	−0.115	−0.090	27.8
	2.34	0	69.9	1.62	0.465		1.52	−0.0707	1.000	−0.165	−0.092	79.3
				1.93	0.605			−0.0698	0.920	−0.150	−0.098	53.1
				2.41	0.805			−0.0669	0.818	−0.128	−0.080	60.0
	2.33	0	65.0	1.62	0.595		1.22	−0.0797	0.914	−0.175	−0.140	25.0
				1.93	0.770			−0.0770	0.850	−0.152	−0.116	31.0
				2.41	1.000			−0.0683	0.800	−0.127	−0.118	7.6
	3.06	0	65.0	1.62	0.595		1.22	−0.0686	0.940	−0.197	−0.143	37.8
				1.93	0.770			−0.0662	0.850	−0.173	−0.116	49.1
				2.41	1.000			−0.0587	0.800	−0.144	−0.109	32.1
	3.07	0	60.0	1.62	0.735		1.03	−0.0752	0.880	−0.203	−0.174	16.7
				1.93	0.955			−0.0705	0.820	−0.177	−0.158	12.0
	1.87	0.25	70.0	1.62	0.465		1.52	−0.0937	1.000	−0.175	−0.098	78.6
				1.93	0.600			−0.0943	0.922	−0.162	−0.116	39.7
				2.41	0.800			−0.0916	0.820	−0.140	−0.086	[illegible].8
	1.84	0.25	64.7	1.62	0.604		1.21	−0.1058	0.938	−0.183	−0.187	− 2.1
				1.93	0.782			−0.1046	0.845	−0.162	−0.135	20.0
				2.41	1.000			−0.0988	0.807	−0.147	−0.113	30.1
	1.90	0.25	60.0	1.62	0.735		1.03	−0.1115	0.880	−0.187	−0.219	−14.6
				1.93	0.955			−0.1097	0.820	−0.171	−0.176	− 2.8
	1.91	0.25	55.0	1.62	0.890		0.90	−0.1175	0.840	−0.188	−0.222	−15.3
	2.37	0.25	70.0	1.62	0.465		1.52	−0.0805	1.000	−0.191	−0.142	34.5
				1.93	0.600			−0.0833	0.922	−0.182	−0.118	54.2
				2.41	0.800			−0.0822	0.820	−0.160	−0.098	66.7

TABLE 7.1.2.2-C (CONTD)

Ref.	A	λ	Λ_{LE} (deg)	M	$\beta \cot \Lambda_{LE}$	Airfoil Section	$\Delta y_{\perp}$	$\frac{(c_{l_p})_{theory}}{A}$ (per rad)	$\frac{c_{l_p}}{(c_{l_p})_{theory}}$	c_{l_p} Calc. (per rad)	c_{l_p} Test (per rad)	ε Percent Error
23	2.34	0.25	65.0	1.62	0.595	Beveled Flat Plate	1.22	−0.0955	0.940	−0.210	−0.183	14.8
				1.93	0.770			−0.0934	0.850	−0.186	−0.127	46.5
				2.41	1.000			−0.0870	0.800	−0.163	−0.127	28.3
	2.37	0.25	55.0	1.62	0.802		0.90	−0.1092	0.840	−0.218	−0.221	− 1.4
	3.06	0.25	65.1	1.62	0.592		1.22	−0.0825	0.950	−0.239	−0.155	54.2
				1.93	0.765			−0.0818	0.850	−0.213	−0.132	61.4
				2.41	1.000			−0.0757	0.800	−0.185	−0.120	54.2
	3.12	0.25	60.0	1.62	0.735		1.03	−0.0905	0.900	−0.248	−0.230	7.8
				1.93	0.955			−0.0870	0.820	−0.222	−0.205	8.3
	3.22	0.25	55.2	1.62	0.885		0.90	−0.0948	0.840	−0.256	−0.228	12.3
	1.83	0	65.0	1.62	0.890		0.90	−0.1040	0.840	−0.160	−0.156	2.6
	2.34	0	54.9	1.62	0.885		0.895	−0.0957	0.835	−0.187	−0.187	0
	2.32	0	60.0	1.62	0.735		1.03	−0.0890	0.880	−0.181	−0.158	14.6
				1.93	0.955			−0.0858	0.820	−0.163	−0.155	5.2
	2.81	0	55.0	1.62	0.880		0.90	−0.0890	0.840	−0.210	−0.172	22.1
24	4.00	0	45.0	1.414	1.000	Symmetrical dbl. wedge t/c = 0.04	0.332	−0.095	0.910	−0.309	−0.280	10.4
	4.00	0	45.0	1.414	1.000	Symmetrical dbl. wedge t/c = 0.09	0.75	−0.095	0.848	−0.288	−0.230	25.2
25	3.70	1.00	45.0	1.414	1.000	65A009	1.74	−0.106	0.770	−0.302	−0.265	14.0
				1.30	0.830			−0.1055	0.800	−0.312	−0.311	0.3

Average Error = $\frac{\Sigma|\varepsilon|}{n}$ = 28.4%

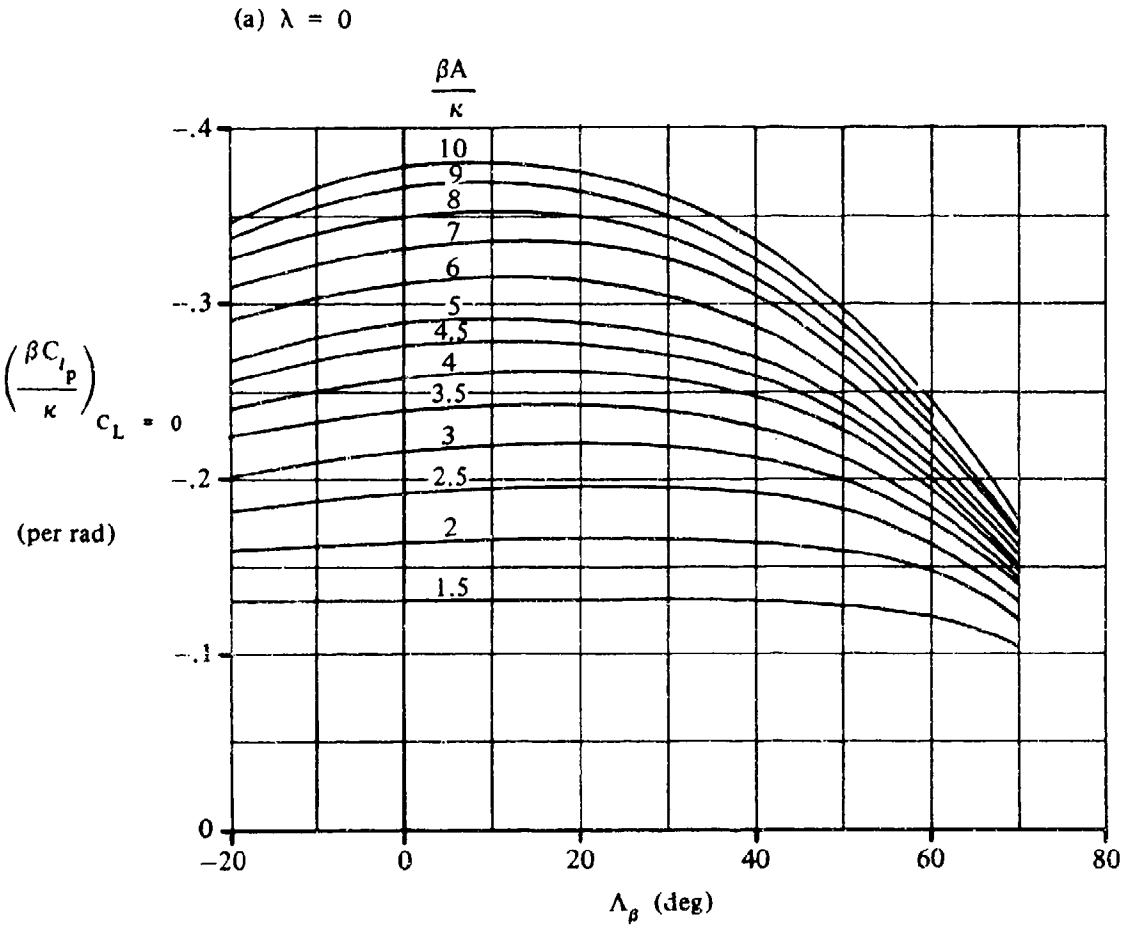

FIGURE 7.1.2.2-20 ROLL-DAMPING PARAMETER AT ZERO LIFT

(b) $\lambda = 0.25$

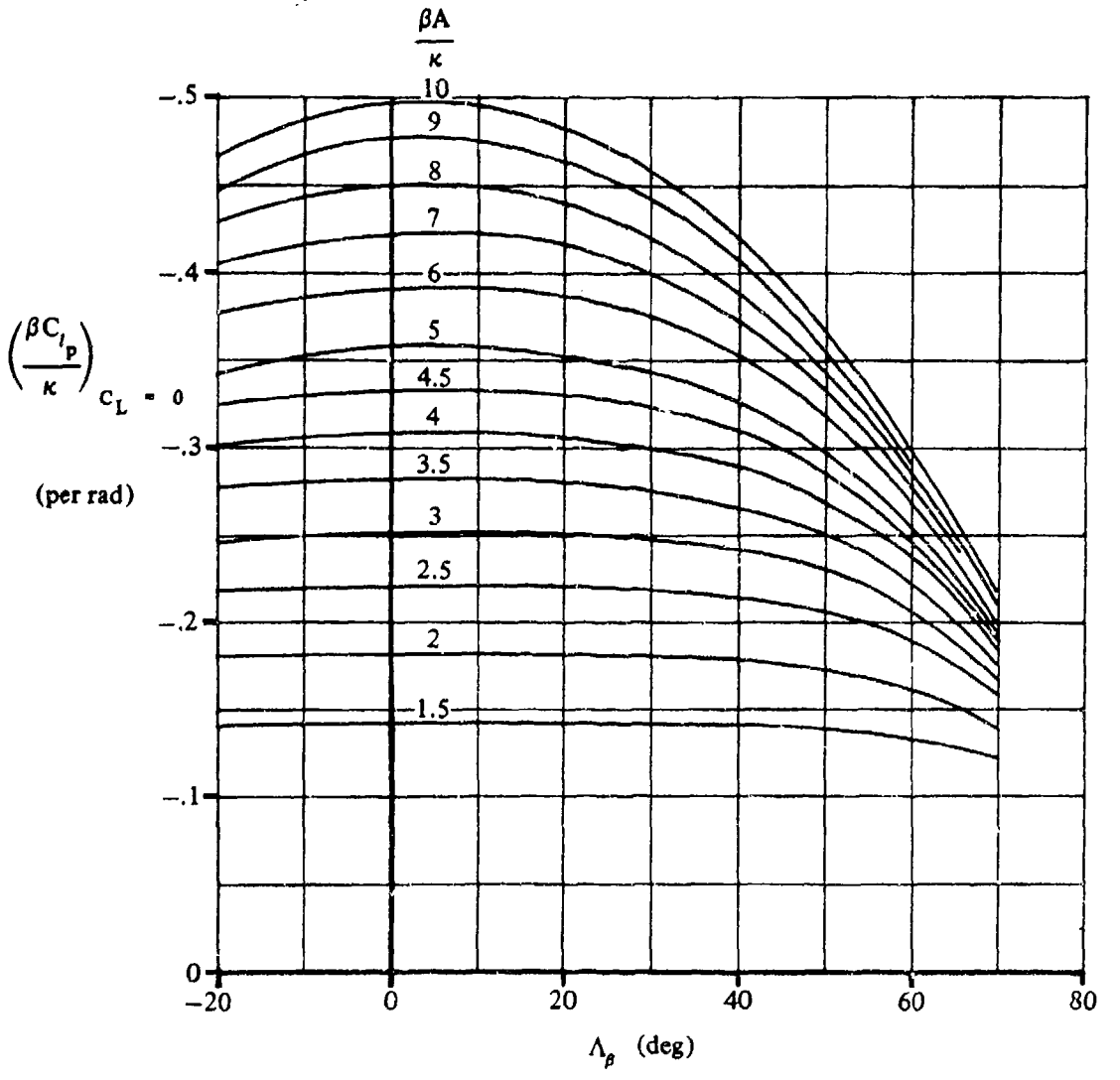

FIGURE 7.1.2.2-20 (CONTD)

(c) $\lambda = 0.50$

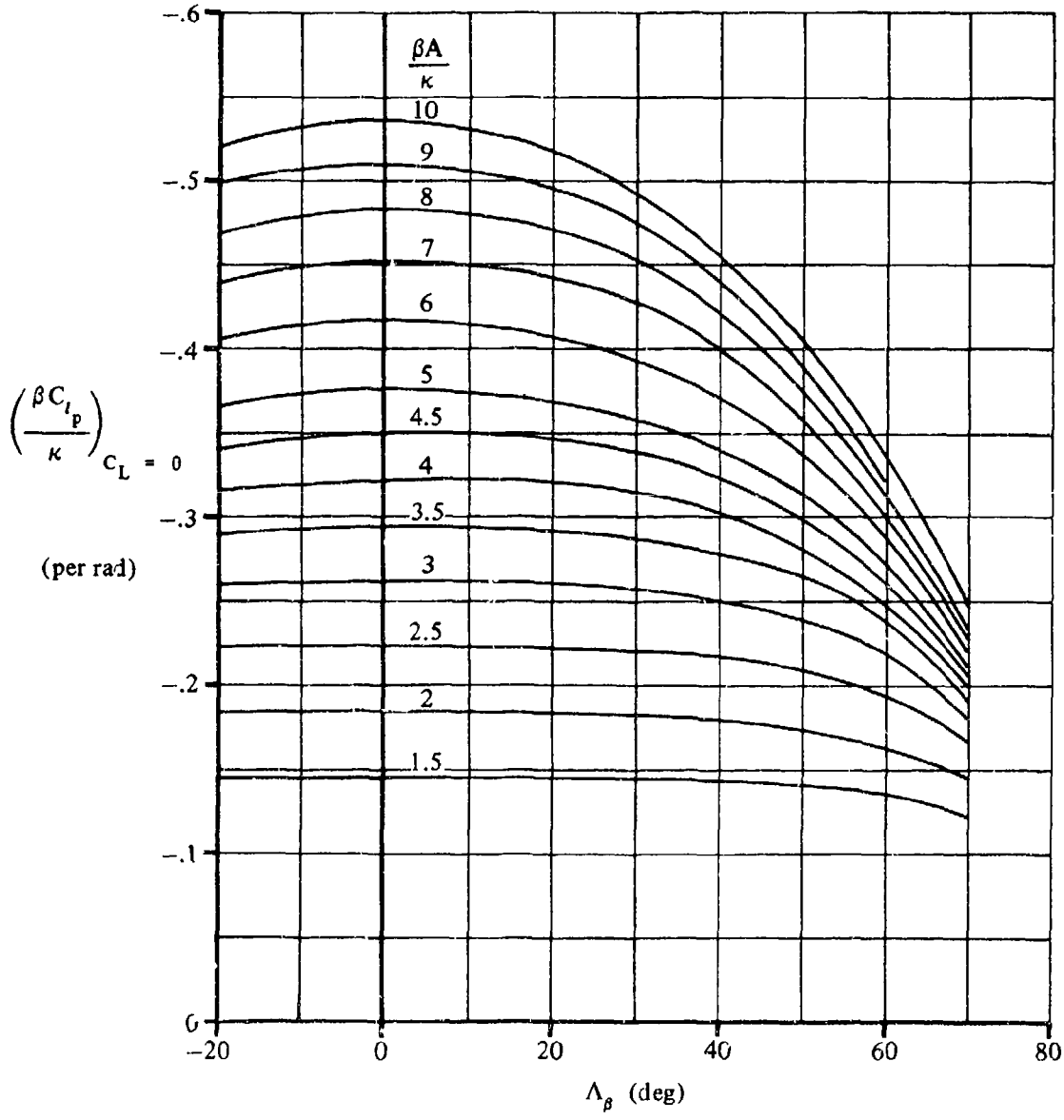

FIGURE 7.1.2.2-20 (CONTD)

(d) $\lambda = 1.0$

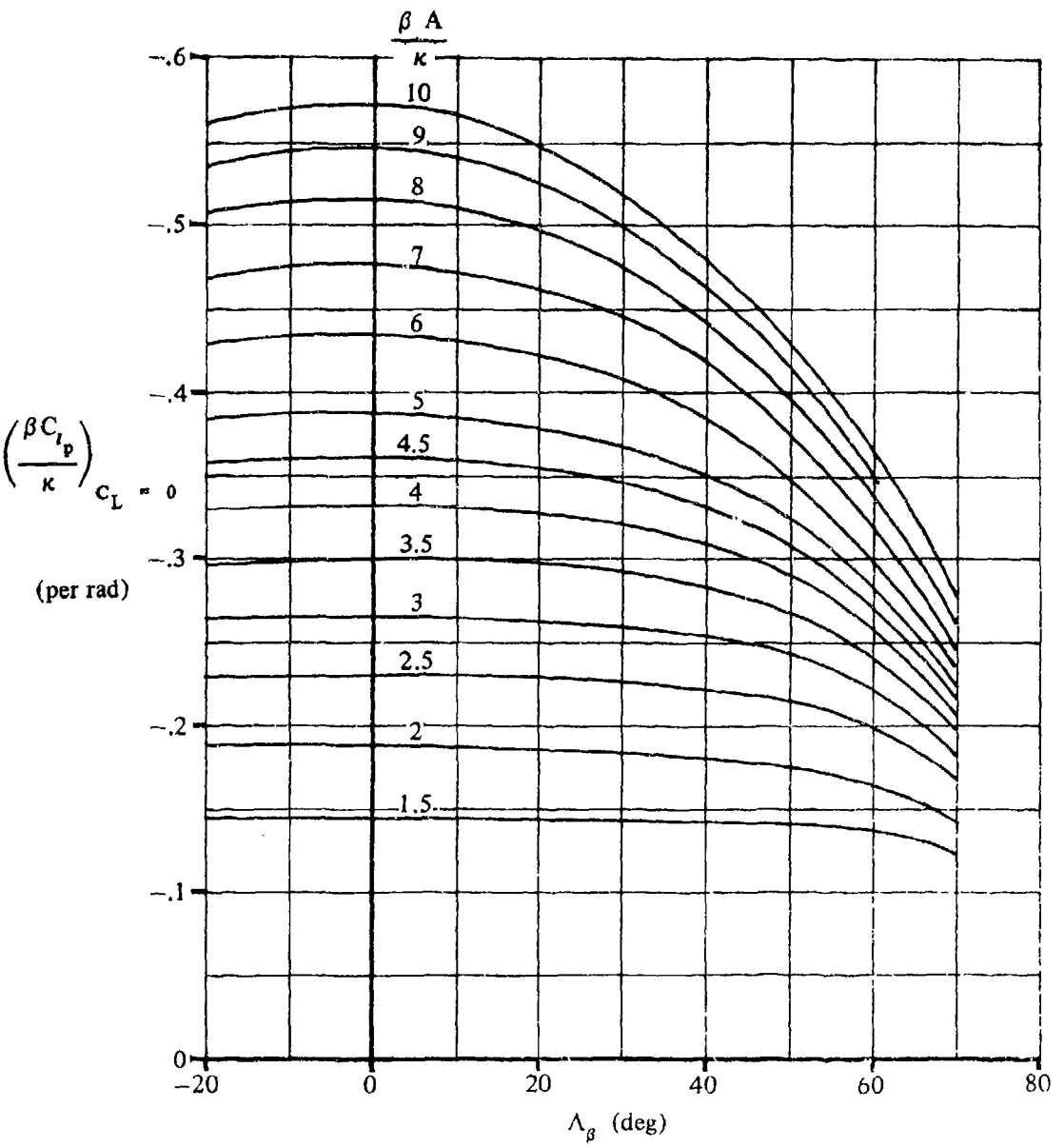

FIGURE 7.1.2.2-20 (CONTD)

SUBSONIC SPEEDS

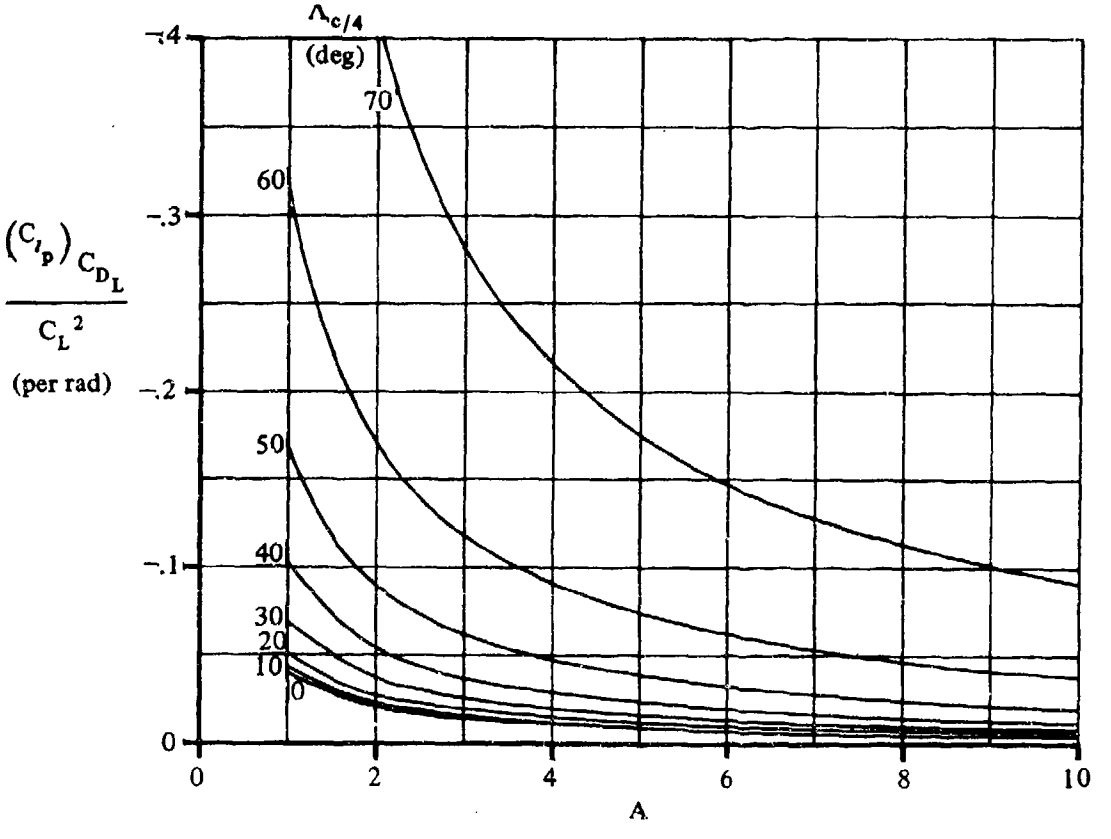

FIGURE 7.1.2.2-24 DRAG-DUE-TO-LIFT ROLL-DAMPING PARAMETER

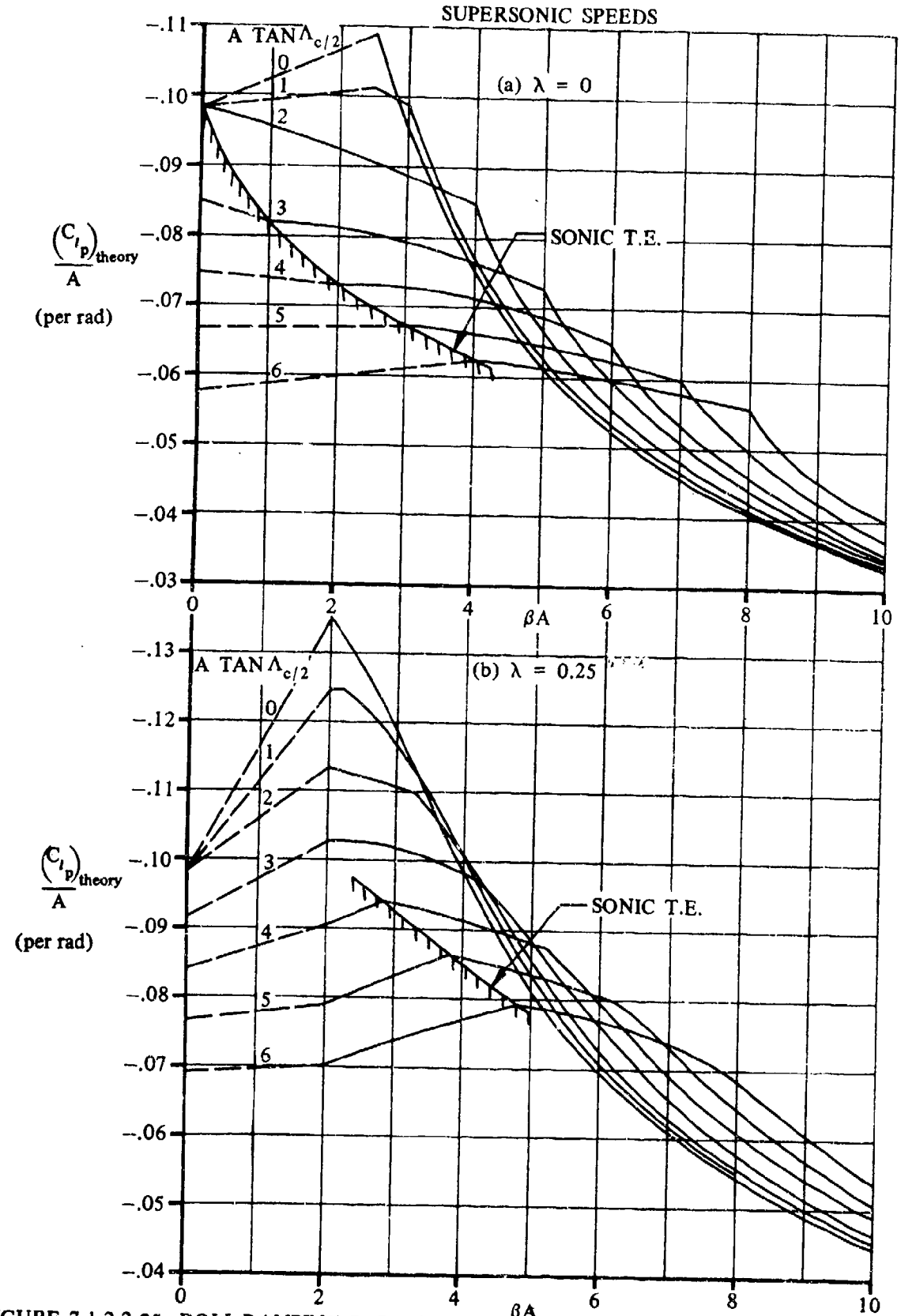

FIGURE 7.1.2.2-25 ROLL-DAMPING PARAMETER

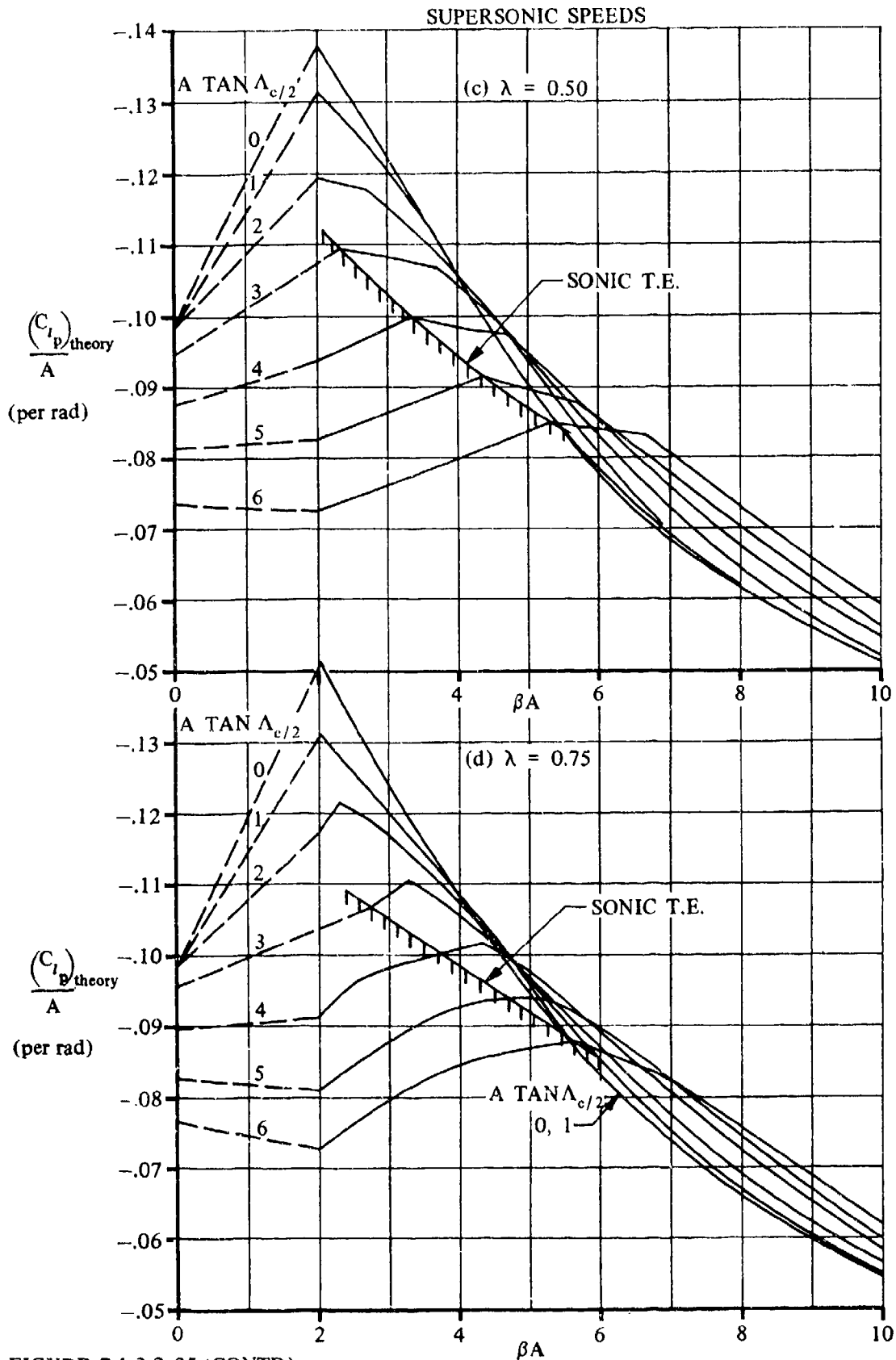

FIGURE 7.1.2.2-25 (CONTD)

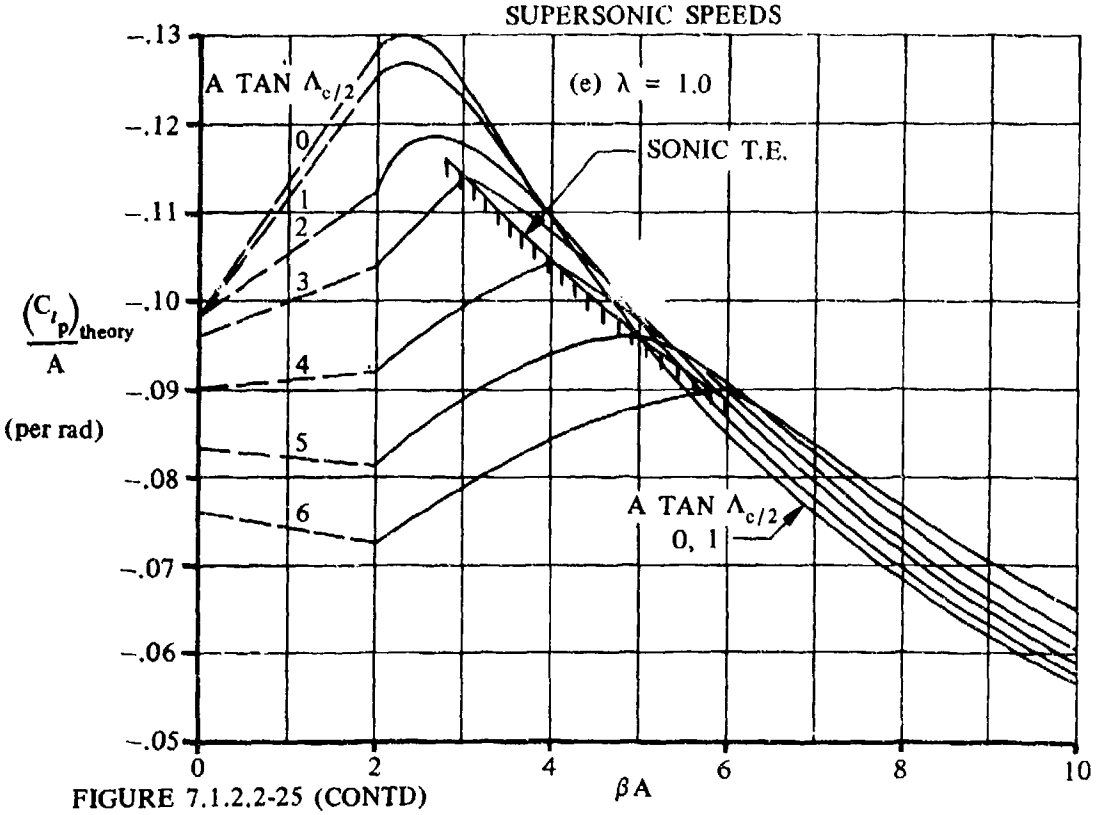

FIGURE 7.1.2.2-25 (CONTD)

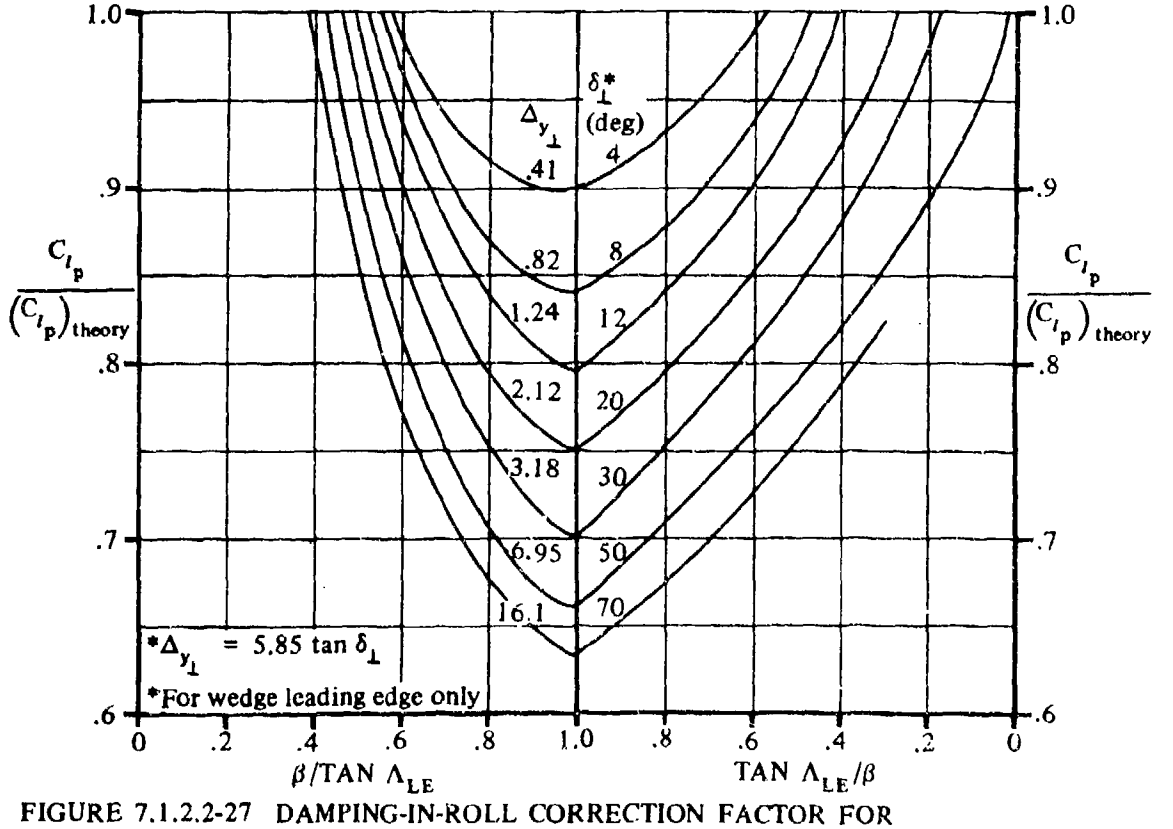

FIGURE 7.1.2.2-27 DAMPING-IN-ROLL CORRECTION FACTOR FOR SONIC-LEADING-EDGE REGION

7.1.2.3 WING ROLLING DERIVATIVE C_{n_p}

This section presents methods for estimating the wing contribution to the rolling derivative C_{n_p} at subsonic and supersonic speeds. This derivative is the change in yawing-moment coefficient with change in wing-tip helix angle and is expressed as

$$C_{n_p} = \frac{\partial C_n}{\partial\left(\frac{pb}{2V_\infty}\right)}$$

A SUBSONIC

The wing rolling derivative C_{n_p} results because the unsymmetrical lift distribution causes a difference in drag between the wing panels when the wing is rolling.

The method for estimating the wing rolling derivative C_{n_p} is derived from an analysis of references 1 through 5. The method is applicable over the lift-coefficient range up to the stall, providing reliable values of lift and drag are available over this range.

The value of C_{n_p} near zero-lift coefficient is the potential-flow value based on simple-sweep theory from reference 1. The effects of linear wing twist and symmetric flap deflection are taken from references 1 and 3. Geometric dihedral also causes an increment in yawing moment that is associated with the increment in lateral force. The empirical results of reference 4 show that this increment is independent of lift coefficient over the low to moderate lift-coefficient range and increases at the higher values of lift coefficient. However, over the range of wing dihedral angles of practical interest the increment in C_{n_p} due to dihedral is very small and may be neglected.

At moderate or high lift coefficients, a comparatively large change in C_{n_p}/C_L occurs, especially for swept wings, due to the rise in drag associated with the increase in lift. In references 2 and 5, methods are presented for evaluating C_{n_p} over the lift-coefficient range up to the stall by using a correction factor to account for the variation of profile drag with lift coefficient. Results obtained by using the methods of both references 2 and 5 for estimating C_{n_p} over the lift-coefficient range have been analyzed and the method of reference 5 selected for the Datcom.

Theoretically, the tip-suction contribution to the lateral force also contributes to the yawing moment. Since this contribution is inversely proportional to aspect ratio, the increment in C_{n_p} due to tip suction becomes quite significant for highly swept and/or low-aspect-ratio planforms. A comparison has been made of C_{n_p} calculated with and without the tip-suction effect of reference 5 with test results. In all cases better agreement was obtained when the tip-suction effects were neglected. The analysis indicates a loss in tip suction particularly at the higher lift coefficients. Therefore, the effect of tip suction has been omitted from the Datcom.

If experimental lift and drag data for the particular planform of interest are not available at the chosen Mach number, no attempt should be made to estimate the variation of C_{n_p} with lift coefficient. No known general method for estimating the variation of drag coefficient will give results reliable enough to use in determining the correction factor for extrapolating the potential-flow values to higher lift coefficients.

DATCOM METHOD

The variation of the wing rolling derivative C_{n_p} with lift coefficient at subsonic speeds, based on the product of the wing area and the square of the wing span $S_W b_W^2$, is given by

$$C_{n_p} = -C_{l_p} \tan\alpha - K\left[-C_{l_p} \tan\alpha - \left(\frac{C_{n_p}}{C_L}\right)_{\substack{C_L=0 \\ M}} C_L\right] + \left(\frac{\Delta C_{n_p}}{\theta}\right)\theta$$

$$+ \left[\frac{\Delta C_{n_p}}{\left(\frac{\partial\alpha}{\partial\delta}\right)_f \delta_f}\right]\left(\frac{\partial\alpha}{\partial\delta}\right)_f \delta_f \qquad \text{(per radian)} \qquad 7.1.2.3\text{-a}$$

where

C_{l_p} is the roll-damping derivative at the appropriate Mach number estimated by using the method of paragraph A of Section 7.1.2.2.

α is the angle of attack in degrees.

C_L is the lift coefficient.

$\left(\frac{C_{n_p}}{C_L}\right)_{\substack{C_L=0 \\ M}}$ is the slope of the yawing moment due to rolling at zero lift given by

$$\left(\frac{C_{n_p}}{C_L}\right)_{\substack{C_L=0 \\ M}} = \left(\frac{A + 4\cos\Lambda_{c/4}}{AB + 4\cos\Lambda_{c/4}}\right)\left[\frac{AB + \frac{1}{2}(AB + \cos\Lambda_{c/4})\tan^2\Lambda_{c/4}}{A + \frac{1}{2}(A + \cos\Lambda_{c/4})\tan^2\Lambda_{c/4}}\right]\left(\frac{C_{n_p}}{C_L}\right)_{\substack{C_L=0 \\ M=0}}$$

7.1.2.3-b

where $B = \sqrt{1-M^2\cos^2\Lambda_{c/4}}$ and

$\left(\frac{C_{n_p}}{C_L}\right)_{\substack{C_L=0 \\ M=0}}$ is the slope of the low-speed yawing moment due to rolling at zero lift given by

$$\left(\frac{C_{n_p}}{C_L}\right)_{\substack{C_L=0 \\ M=0}} = -\frac{1}{6}\,\frac{A + 6(A + \cos\Lambda_{c/4})\left(\frac{\bar{x}}{\bar{c}}\,\frac{\tan\Lambda_{c/4}}{A} + \frac{\tan^2\Lambda_{c/4}}{12}\right)}{A + 4\cos\Lambda_{c/4}}$$

(per radian)
7.1.2.3-c

where $\bar{x}$ is the distance from the center of gravity to the aerodynamic center, positive when the a.c. is aft of the c.g. and c is the wing mean aerodynamic chord. Equation 7.1.2.3-b modifies the low-speed value of equation 7.1.2.3-c by means of the Prandtl-Glauert rule to yield approximate corrections for the first-order three-dimensional effects of compressible flow up to the critical Mach number.

$\frac{\Delta C_{n_p}}{\theta}$ is the effect of linear wing twist obtained from figure 7.1.2.3-12.

θ is the wing twist between the root and tip stations in degrees, negative for washout (see figure 7.1.2.3-12).

$\frac{\Delta C_{n_p}}{\left(\frac{\partial \alpha}{\partial \delta}\right)_f \delta_f}$ is the effect of symmetric flap deflection obtained from figure 7.1.2.3-13.

δ_f is the streamwise flap deflection in degrees.

$\left(\frac{\partial \alpha}{\partial \delta}\right)_f$ is the two-dimensional lift-effectiveness parameter α_δ obtained from Section 6.1.1.1.

K is a dimensionless correction factor used to extrapolate the potential-flow values to high lift coefficients. This is the same correction factor used in Section 7.1.2.1 to account for the variation of profile drag with lift coefficient. At zero lift this factor is taken as 1.0. At lift coefficients other than zero this factor accounts for the variation of profile drag with lift coefficient and is given by

$$K = \frac{\frac{\partial}{\partial \alpha}(C_L \tan \alpha) - \frac{\partial}{\partial \alpha}\left(C_D - C_{D_0}\right)}{\frac{\partial}{\partial \alpha}(C_L \tan \alpha) - \frac{\partial}{\partial \alpha}\left(\frac{C_L^2}{\pi A}\right)} \qquad 7.1.2.3\text{-d}$$

Test values of lift and drag at the chosen Mach number for the particular planform of interest must be used in evaluating equation 7.1.2.3-d. The terms of this equation are evaluated by taking the slopes of $C_L \tan \alpha$, $(C_D - C_{D_0})$, and $C_L^2/(\pi A)$, plotted versus angle of attack.

If reliable values of the static-force coefficients are available, the method should provide results within ±20 percent accuracy throughout the lift-coefficient range to the stall.

Sample Problem

Given: The wing designated 45-4.0-0.6-006 of references 5 and 8.

Wing Characteristics:

$A = 4.0 \quad \lambda = 0.6 \quad \Lambda_{c/4} = 45^o \quad \theta = 0$

$S = 2.25$ sq ft $\quad b = 3.0$ ft

NACA 65A006 Airfoil $\quad \bar{x} = 0$ [origin of moments (c.g.) located at $x_{a.c.}$]

Additional Characteristics:

$M = 0.70; \ \beta = 0.714 \quad R_\ell = 3.1 \times 10^6$

The following values of α and C_D are test results from reference 8. The variation of C_{l_p} with C_L has been calculated using the method of paragraph A of Section 7.1.2.2.

C_L	0	.1	.2	.3	.4	.5	.6	.7	.75
α	0	1.70	3.30	4.90	6.55	8.00	9.60	11.80	13.20
C_D	.011	.012	.016	.024	.040	.063	.094	.138	.170
C_{l_p}	−.314	− .314	− .313	− .312	− .326	− .325	− .280	− .181	− .156

Compute:

Determine the slope of the yawing moment due to rolling at zero lift $\left(\frac{C_{n_p}}{C_L}\right)_{\substack{C_L=0 \\ M}}$

$$\left(\frac{C_{n_p}}{C_L}\right)_{\substack{C_L=0 \\ M=0}} = -\frac{1}{6}\,\frac{A + 6(A + \cos\Lambda_{c/4})\left(\frac{\bar{x}}{\bar{c}}\,\frac{\tan\Lambda_{c/4}}{A} + \frac{\tan^2\Lambda_{c/4}}{12}\right)}{A + 4\cos\Lambda_{c/4}} \quad \text{(equation 7.1.2.3-c)}$$

$$= -\frac{1}{6}\,\frac{4.0 + 6\,(4.0 + \cos 45^o)\left(0 + \frac{\tan^2 45^o}{12}\right)}{4.0 + 4\cos 45^o}$$

$$= -\frac{1}{6}\,\frac{4.0 + 6\,(4.7071)\left(0 + \frac{1}{12}\right)}{4.0 + 2.828} = -0.155 \text{ per rad}$$

$$B = \sqrt{1 - M^2 \cos^2 \Lambda_{c/4}} = \sqrt{1 - (0.7)^2 (0.7071)^2} = 0.87$$

$$\frac{A + 4 \cos \Lambda_{c/4}}{AB + 4 \cos \Lambda_{c/4}} = \frac{4.0 + (4.0)(0.7071)}{(4.0)(0.87) + (4.0)(0.7071)} = \frac{6.828}{6.308} = 1.082$$

$$\frac{AB + \frac{1}{2}(AB + \cos \Lambda_{c/4}) \tan^2 \Lambda_{c/4}}{A + \frac{1}{2}(A + \cos \Lambda_{c/4}) \tan^2 \Lambda_{c/4}} = \frac{(4.0)(0.87) + \frac{1}{2}[(4.0)(0.87) + 0.7071](1)}{4.0 + \frac{1}{2}[4.0 + 0.7071](1)}$$

$$= \frac{5.574}{6.354} = 0.877$$

$$\left(\frac{C_{n_p}}{C_L}\right)_{\substack{C_L = 0 \\ M}} = \left(\frac{A + 4 \cos \Lambda_{c/4}}{AB + 4 \cos \Lambda_{c/4}}\right) \left[\frac{AB + \frac{1}{2}(AB + \cos \Lambda_{c/4}) \tan^2 \Lambda_{c/4}}{A + \frac{1}{2}(A + \cos \Lambda_{c/4} \tan^2 \Lambda_{c/4}}\right] \left(\frac{C_{n_p}}{C_L}\right)_{\substack{C_L = 0 \\ M = 0}}$$

(equation 7.1.2.3-b)

$$= (1.082)(0.877)(-0.155) = -0.147 \text{ per rad}$$

Determine the K factor

$$K = \frac{\frac{\partial}{\partial \alpha}(C_L \tan\alpha) - \frac{\partial}{\partial \alpha}(C_D - C_{D_0})}{\frac{\partial}{\partial \alpha}(C_L \tan\alpha) - \frac{\partial}{\partial \alpha}\left(\frac{C_L^2}{\pi A}\right)}$$ (equation 7.1.2.3-d)

①	②	③	④	⑤	⑥	⑦
C_L	α Test (deg)	$\tan\alpha$ $\tan$ ②	$C_L \tan\alpha$ ① ③	C_D Test	$C_D - C_{D_0}$ ⑤ − 0.011	$C_L^2/(\pi A)$ $①^2/(4\pi)$
0	0	0	0	.011	0	0
.1	1.70	.02968	.00297	.012	.001	.00080
.2	3.30	.05766	.01153	.016	.005	.00318
.3	4.90	.08573	.02572	.024	.013	.00716
.4	6.55	.1148	.04592	.040	.029	.01273
.5	8.00	.1406	.07027	.063	.052	.01990
.6	9.60	.1691	.1015	.094	.083	.02860
.7	11.80	.2089	.1462	.138	.127	.03900
.75	13.20	.2345	.1759	.170	.159	.04478

Plot $C_L \tan\alpha$, $C_D - C_{D_0}$, and $C_L^2/(\pi A)$ versus angle of attack (see sketch (a)).

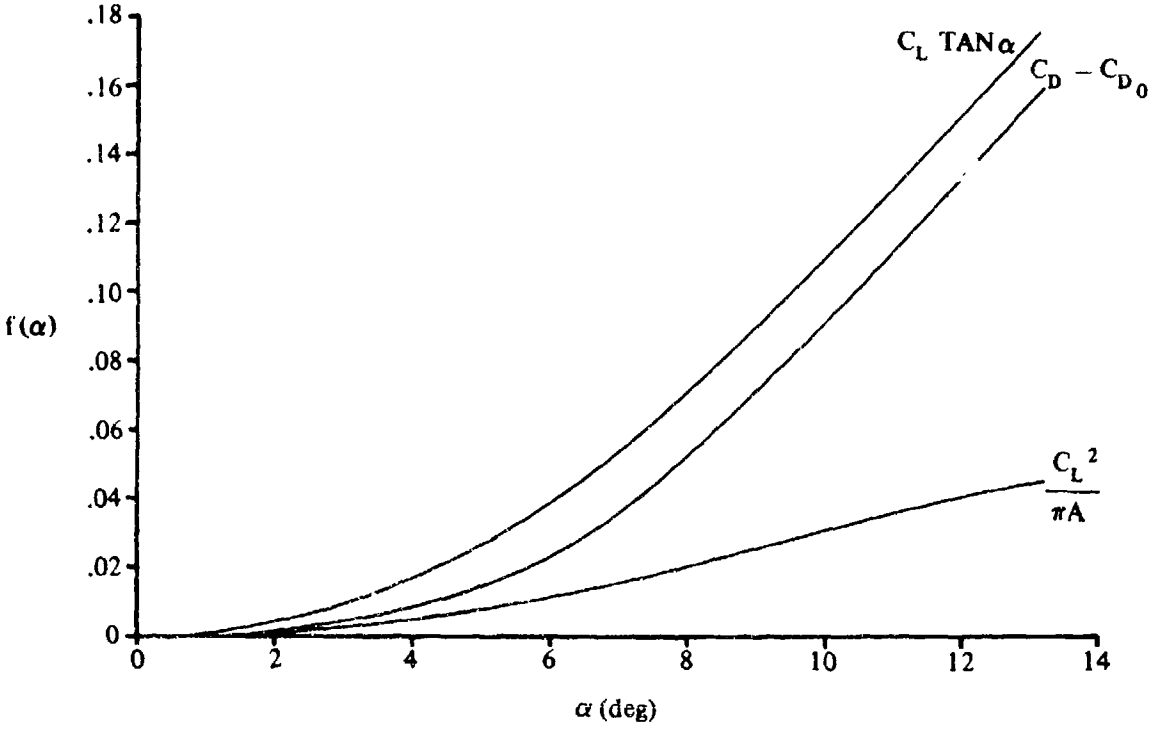

SKETCH (a)

①	②	③	④	⑤
C_L	$\frac{\partial}{\partial\alpha}(C_L \tan\alpha)$	$\frac{\partial}{\partial\alpha}(C_D - C_{D_0})$	$\frac{\partial}{\partial\alpha}\left(\frac{C_L^2}{\pi A}\right)$	$(② - ③)/(② - ④)^K$ (eq. 7.1.2.3-d)
0	–	–	–	1.00
.1	.0033	.0014	.0010	.826
.2	.00755	.0036	.0019	.699
.3	.01055	.0069	.0030	.483
.4	.01440	.0128	.0040	.154
.5	.01720	.0173	.00515	– .008
.6	.0195	.0195	.0051	0
.7	.0212	.0215	.0041	– .018
.75	.0216	.0220	.0039	– .023

Solution:

$$C_{n_p} = -C_{l_p} \tan\alpha - K\left[-C_{l_p}\tan\alpha - \left(\frac{C_{n_p}}{C_L}\right)_{\substack{C_L=0 \\ M}} C_L\right] \qquad \text{(equation 7.1.2.3-a)}$$

$$= -C_{l_p}\tan\alpha - K\left[-C_{l_p}\tan\alpha - (-0.147)\,C_L\right] = -C_{l_p}\tan\alpha\,(1-K) - 0.147\,C_L\,K$$

① C_L	② C_{l_p} Sec. 7.1.2.2 (per rad)	③ $C_{l_p \tan\alpha}$ ② $\tan\alpha$	④ K	⑤ $1-K$ $1-$④	⑥ $-C_{l_p}\tan\alpha(1-K)$ $-$③⑤	⑦ $0.147\,K\,C_L$ 0.147④①	⑧ C_{n_p} based on $S_W b_W^2$ eq. 7.1.2.3-a (per rad) ⑥ − ⑦
0	−.314	0	1.00	0	0	0	0
.1	−.314	−.0093	.826	.174	.00162	.0121	−.0105
.2	−.313	−.0180	.699	.301	.00542	.0206	−.0152
.3	−.312	−.0267	.483	.517	.0138	.0213	−.0075
.4	−.326	−.0374	.154	.846	.0317	.0091	.0226
.5	−.325	−.0457	−.008	1.008	.0460	0	.0460
.6	−.280	−.0474	0	1.00	.0474	0	.0474
.7	−.181	−.0378	−.018	1.018	.0385	−.0019	.0404
.75	−.156	−.0366	−.023	1.023	.0374	−.0025	.0399

The calculated results are compared with test values from reference 5 in sketch (b).

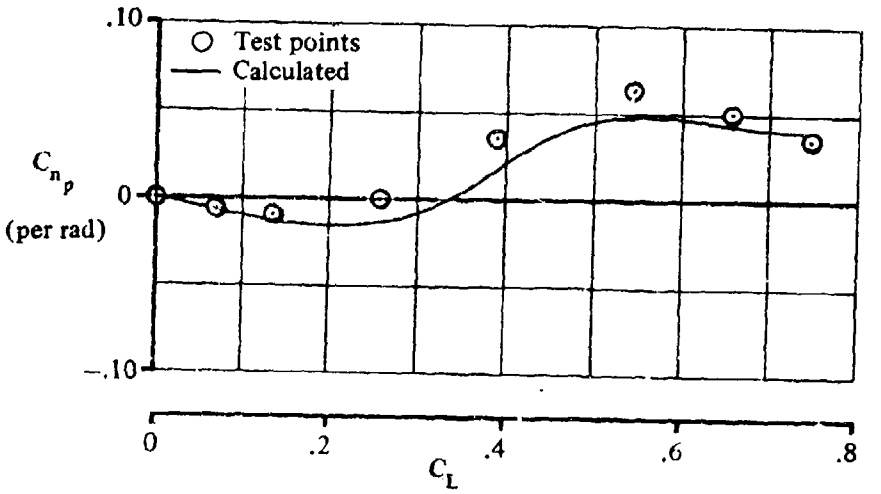

SKETCH (b)

B. TRANSONIC

No generalized method is available in the literature for estimating transonic values of the rolling derivative C_{n_p}. Furthermore, no known experimental results are available for this derivative at transonic speeds.

C. SUPERSONIC

At supersonic speeds design charts based on theoretical calculations are presented for estimating the rolling derivative C_{n_p} at low values of the lift coefficient.

The design charts are based on the results of reference 6 for wings with subsonic leading edges and supersonic trailing edges, and on the results of reference 7 for wings with supersonic leading edges and either subsonic or supersonic trailing edges. The results of both references 6 and 7 are based on linearized-supersonic-flow theory and are therefore restricted to thin, swept-back, tapered wings with streamwise tips. The yawing moment due to rolling is taken as that arising entirely from suction forces on the wing edges. For wings with supersonic leading edges no suction forces are induced along the leading edges; consequently, the determination of C_{n_p} involves only the unbalanced suction forces along the wing tips. Therefore, no design chart is presented for zero-taper wings with supersonic leading edges, since the theory gives $C_{n_p} = 0$.

The design charts for wings with subsonic leading edges give values of C_{n_p} that are referred to body axes with the origin located at the wing apex. The design charts for wings with supersonic leading edges give values of C_{n_p} that are referred to body axes with the origin located at the projection of the leading edge of the tip on the wing root chord. The Datcom method presents transformation formulas for conversion from body axes to stability axes with the origin located at an arbitrary distance from the leading edge.

No experimental data are available for this derivative at supersonic speeds. Therefore, the validity of linearized-supersonic-flow theory for estimating C_{n_p} cannot be determined.

DATCOM METHOD

Subsonic Leading Edges ($\beta \cot \Lambda_{LE} < 1$)

For wings with subsonic leading edges the contribution to the rolling derivative C_{n_p} at supersonic speeds, and at low values of the lift coefficient is given by

$$\frac{C_{n_p}}{\alpha} = \left(\frac{C_{n_p}}{\alpha}\right)_{\substack{\text{body}\\ \text{axis}}} + \frac{2\, x_{c.g.}}{A(1+\lambda)} \left(\frac{C_{Y_p}}{\alpha}\right) - \left(C_{l_p} - C_{n_r}\right) \quad \text{(per radian}^2\text{)} \qquad 7.1.2.3\text{-e}$$

where

$\frac{C_{n_p}}{\alpha}$ is the supersonic yawing moment due to rolling referred to stability axes with the origin at the center of gravity.

$\left(\frac{C_{n_p}}{\alpha}\right)_{\substack{body \\ axis}}$ is the supersonic yawing moment due to rolling referred to body axes with the origin at the wing apex, given by

$$\left(\frac{C_{n_p}}{\alpha}\right)_{\substack{body \\ axis}} = \left(\frac{C_{n_p}}{\alpha}\right)_1 + \left(\frac{C_{n_p}}{\alpha}\right)_2 + \left(\frac{C_{n_p}}{\alpha}\right)_3 \quad \text{(per radian}^2\text{)} \qquad 7.1.2.3\text{-f}$$

where

$\left(\frac{C_{n_p}}{\alpha}\right)_1$ is obtained from figure 7.1.2.3-14a through 7.1.2.3-14d as a function of βA, $\beta \cot \Lambda_{LE}$, and taper ratio. For $\lambda = 0$, $(C_{n_p}/\alpha)_1 = 0$.

$\left(\frac{C_{n_p}}{\alpha}\right)_2$ and $\left(\frac{C_{n_p}}{\alpha}\right)_3$ are obtained from figure 7.1.2.3-16 as a function of $\beta \cot \Lambda_{LE}$.

$x_{c.g.}$ is the distance from the wing apex to the center of gravity in root chords, positive when the c.g. is aft of the wing apex.

$\frac{C_{Y_p}}{\alpha}$ is the supersonic side force due to rolling obtained by using the method of paragraph C of Section 7.1.2.1.

C_{l_p} is the supersonic roll-damping derivative obtained by using the method of paragraph C of Section 7.1.2.2.

C_{n_r} is the supersonic yaw-damping derivative. It is negligible except for very low-aspect-ratio wings. References are noted in paragraph C of Section 7.1.3.3 that outline approximate methods that may be used to determine this derivative.

α is the angle of attack in radians.

Supersonic Leading Edges ($\beta \cot \Lambda_{LE} > 1$)

For wings with supersonic leading edges the contribution to the rolling derivative C_{n_p} at supersonic speeds and at low values of the lift coefficient is given by

$$\frac{C_{n_p}}{\alpha} = \left(\frac{C_{n_p}}{\alpha}\right)_{\substack{body \\ axis}} + \left[\frac{2\,x_{c.g.}}{A(1+\lambda)} - \frac{1}{2}\tan \Lambda_{LE}\right] \frac{C_{Y_p}}{\alpha} - C_{l_p} \quad \text{(per radian}^2\text{)}$$

7.1.2.3-g

where

$\frac{C_{n_p}}{\alpha}$ is the supersonic yawing moment due to rolling referred to stability axes with the origin at the center of gravity.

$\left(\frac{C_{n_p}}{\alpha}\right)_{\substack{body \\ axis}}$ is the supersonic yawing moment due to rolling referred to body axes with the origin at the projection of the leading edge of the tip on the wing root chord. It is obtained from figures 7.1.2.3-17a through 7.1.2.3-17d as a function of βA, β cot Λ_{LE}, and taper ratio. No design chart is presented for zero-taper wings since $(C_{n_p}/\alpha)_{\substack{body \\ axis}} = 0$ for these planforms. For wings with taper ratios less than 0.25 ($\lambda < 0.25$) values of $(C_{n_p}/\alpha)_{\substack{body \\ axis}}$ should be obtained by extrapolating values from figures 7.1.2.3-17a through 7.1.2.3-17d.

The remaining terms in equation 7.1.2.3-g are defined under the subsonic-leading-edge case.

Sample Problem

Given: Tapered, swept-back wing

$A = 3.22$ $\lambda = 0.25$ $\Lambda_{LE} = 55.2^o$ $\Lambda_{c/2} = 46.8^o$

$M = 2.41$; $\beta = 2.19$ $x_{c.g.} = 0.742$

Compute:

β cot $\Lambda_{LE} = (2.19)$ (cot 55.2^o) $= 1.522$ (supersonic leading edge)

$\beta A = (2.19)(3.22) = 7.07$

$\frac{C_{Y_p}}{\alpha} = 0.50$ per rad^2 (figure 7.1.2.1-10)

$\left(\frac{C_{n_p}}{\alpha}\right)_{\substack{body \\ axis}} = -0.0114$ per rad^2 (figure 7.1.2.3-17a)

A tan $\Lambda_{c/2} = (3.22)$ (tan 46.8^o) $= 3.433$

$\frac{C_{l_p}}{A} = -0.066$ per rad (figure 7.1.2.2-25b)

$$C_{l_p} = (-0.066)\,(3.22) = -0.213 \text{ per rad}$$

Solution:

$$\frac{C_{n_p}}{\alpha} = \left(\frac{C_{n_p}}{\alpha}\right)_{\substack{\text{body}\\ \text{axis}}} + \left[\frac{2\,x_{c.g.}}{A(1+\lambda)} - \frac{1}{2}\tan\Lambda_{LE}\right]\frac{C_{Y_p}}{\alpha} - C_{l_p} \qquad \text{(equation 7.1.2.3-g)}$$

$$= -0.0114 + \left[\frac{2\,(0.742)}{3.22\,(1+0.25)} - \frac{1}{2}\tan 55.2^{o}\right]0.50 - (-0.213)$$

$$= -0.0114 + [0.3687 - 0.7194]\,0.50 + 0.213$$

$$= 0.026 \text{ per rad}^2 \qquad \text{(referred to stability axes with origin at } x_{c.g.} \text{ and based on } S_W b_W^2\text{)}$$

REFERENCES

1. Toll, T. A., and Queijo, M. J.: Approximate Relations and Charts for Low-Speed Stability and Control Derivatives of Swept Wings. NACA TN 1581, 1948. (U)

2. Goodman, A., and Fisher, L. R.: Investigation at Low Speeds of the Effect of Aspect Ratio and Sweep on Rolling Stability Derivatives of Untapered Wings. NACA TR 968, 1950. (U)

3. Pinsker, W.: The Aerodynamic Coefficients of Free Lateral Motion. DVL UM 1144/1 and 1144/2, 1943. (U)

4. Queijo, M. J., and Jaquet, B. M.: Calculated Effects of Geometric Dihedral on the Low-Speed Rolling Derivatives of Swept Wings. NACA TN 1732, 1948. (U)

5. Wiggins, J. W.: Wind-Tunnel Investigation of Effect of Sweep on Rolling Derivatives at High Angles of Attack up to 13° and at High Subsonic Mach Numbers, Including a Semiempirical Method of Estimating the Rolling Derivatives. NACA TN 4185, 1958. (U)

6. Margolis, K.: Theoretical Calculations of the Lateral Force and Yawing Moment Due to Rolling at Supersonic Speeds for Sweptback Tapered Wings With Streamwise Tips. Subsonic Leading Edges. NACA TN 2122, 1950. (U)

7. Harmon, S. M., and Martin, J. C.: Theoretical Calculations of the Lateral Force and Yawing Moment Due to Rolling at Supersonic Speeds for Sweptback Tapered Wings With Streamwise Tips. Supersonic Leading Edges. NACA TN 2156, 1950. (U)

8. Kuhn, R. E., and Wiggins, J. W.: Wind-Tunnel Investigation of the Aerodynamic Characteristics in Pitch of Wing-Fuselage Combinations at High Subsonic Speeds. Aspect Ratio Series. NACA RM L52A29, 1952. (U)

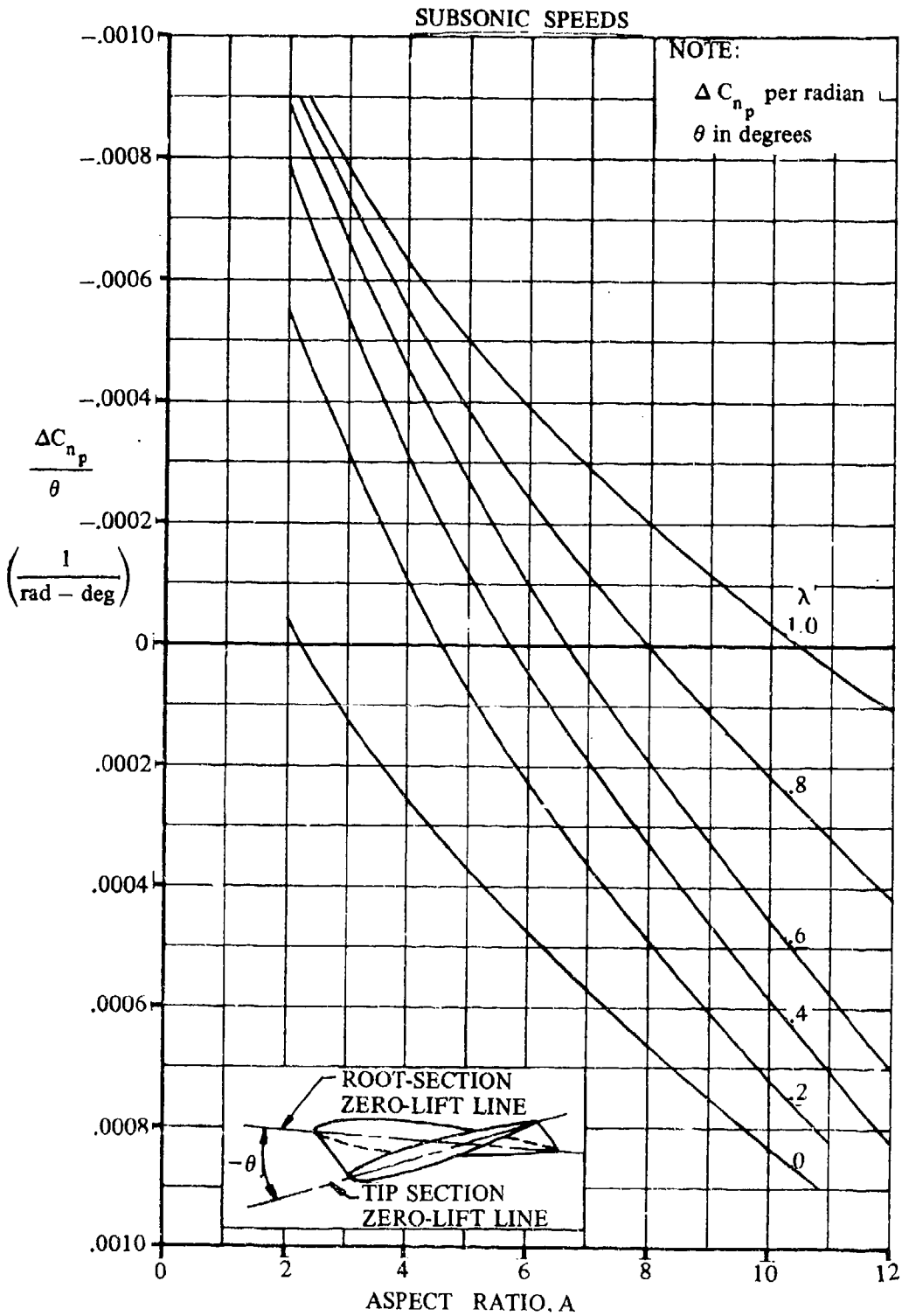

FIGURE 7.1.2.3–12 EFFECT OF WING TWIST ON WING ROLLING DERIVATIVE C_{n_p}

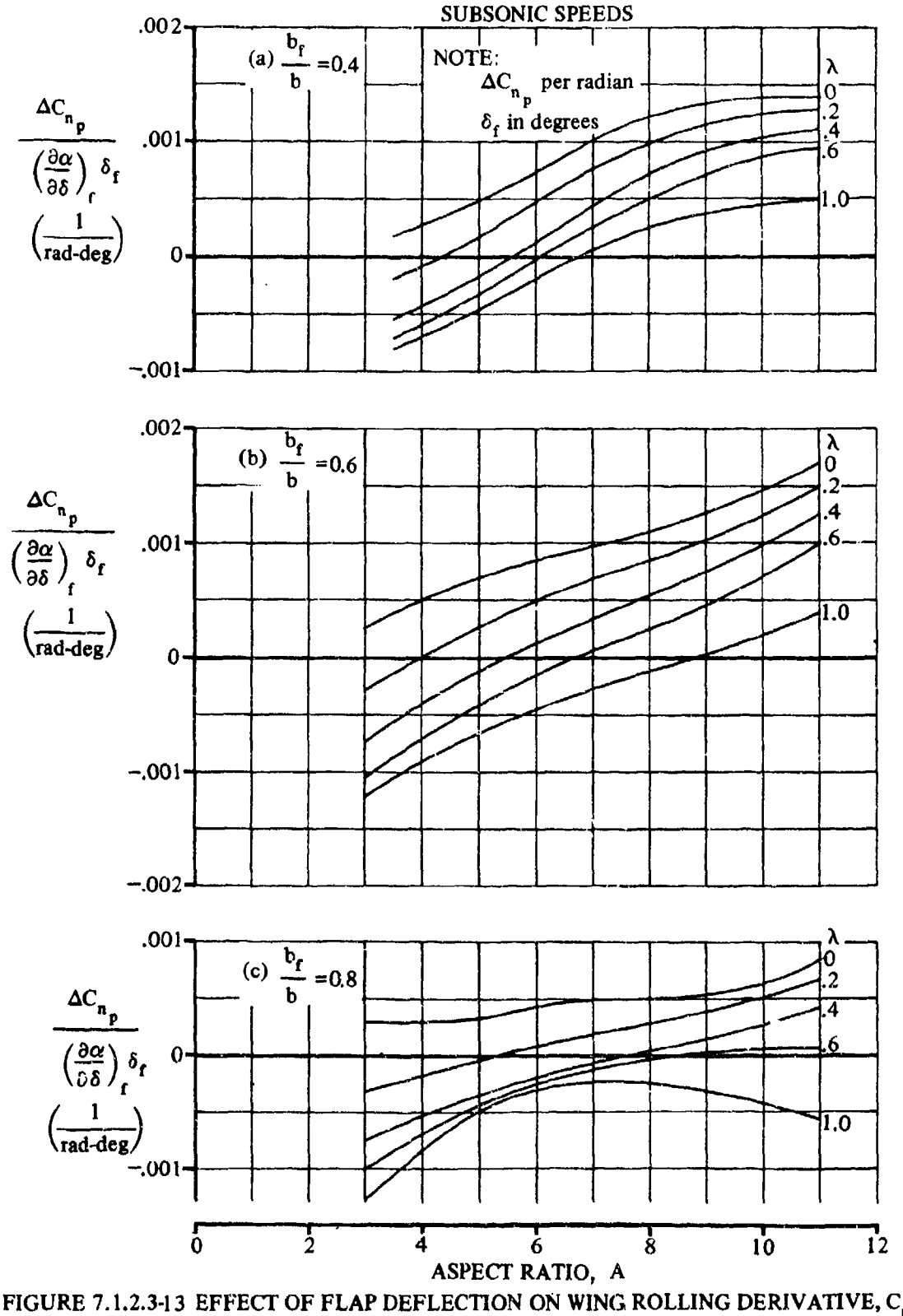

FIGURE 7.1.2.3-13 EFFECT OF FLAP DEFLECTION ON WING ROLLING DERIVATIVE, C_{n_p}

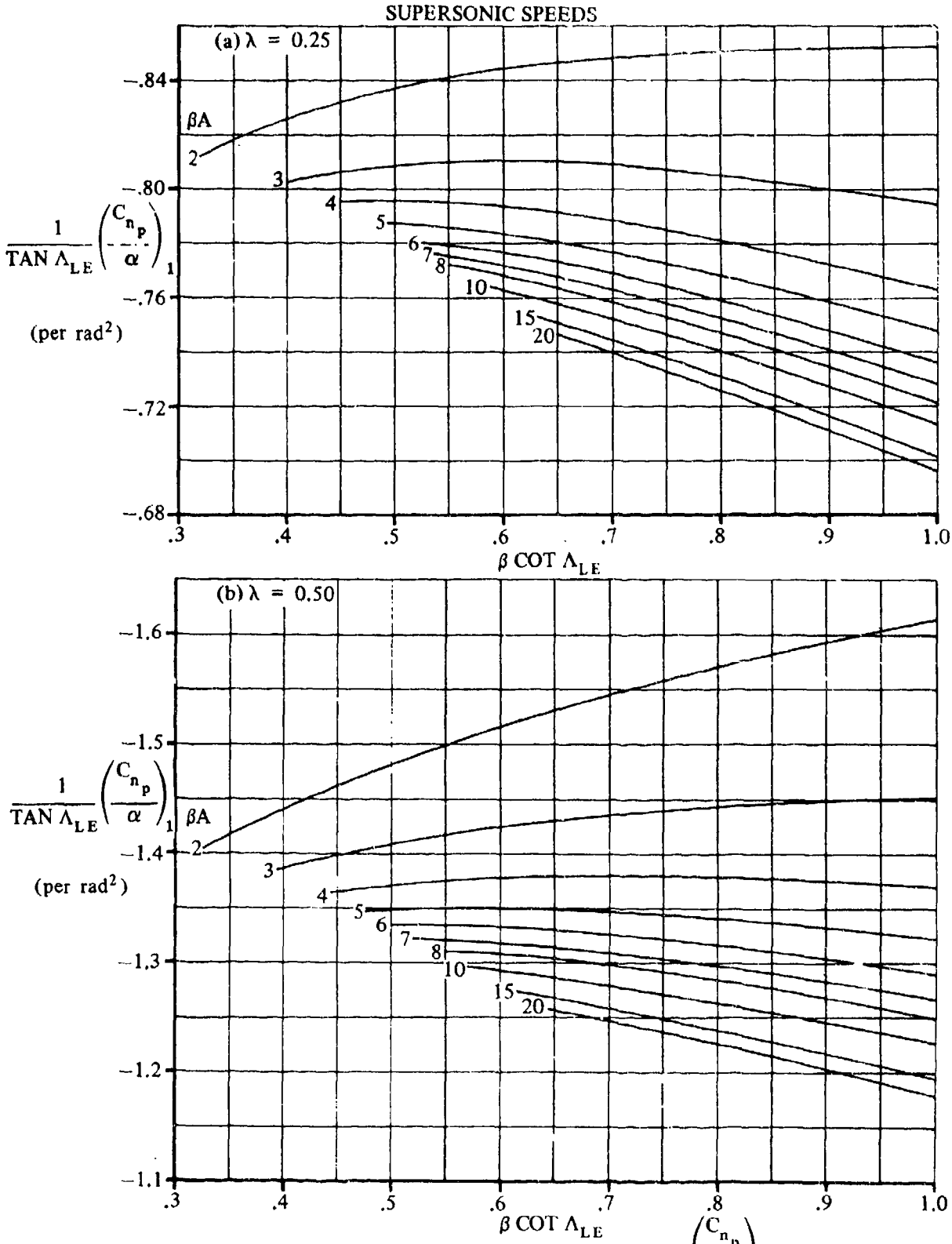

FIGURE 7.1.2.3-14 YAWING-MOMENT-DUE-TO-ROLLING COMPONENT $\left(\frac{C_{n_p}}{\alpha}\right)_1$ - SUBSONIC LEADING EDGE

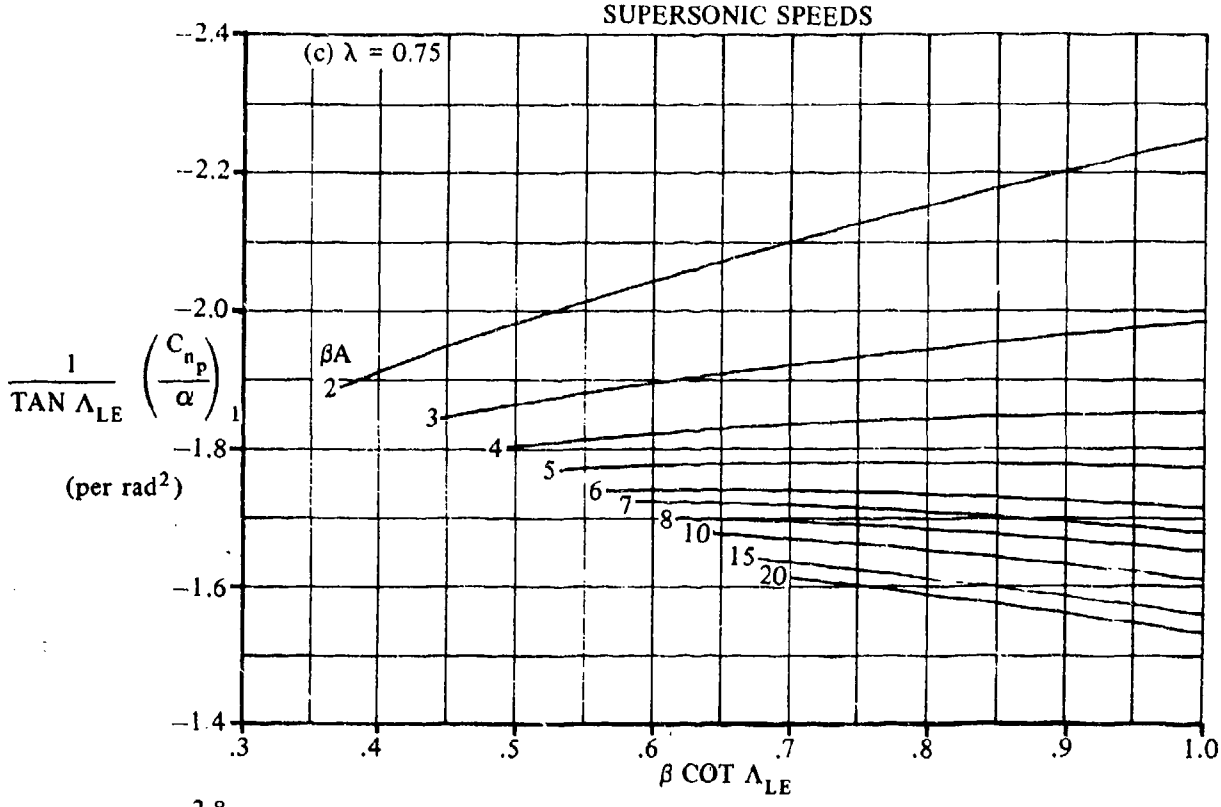

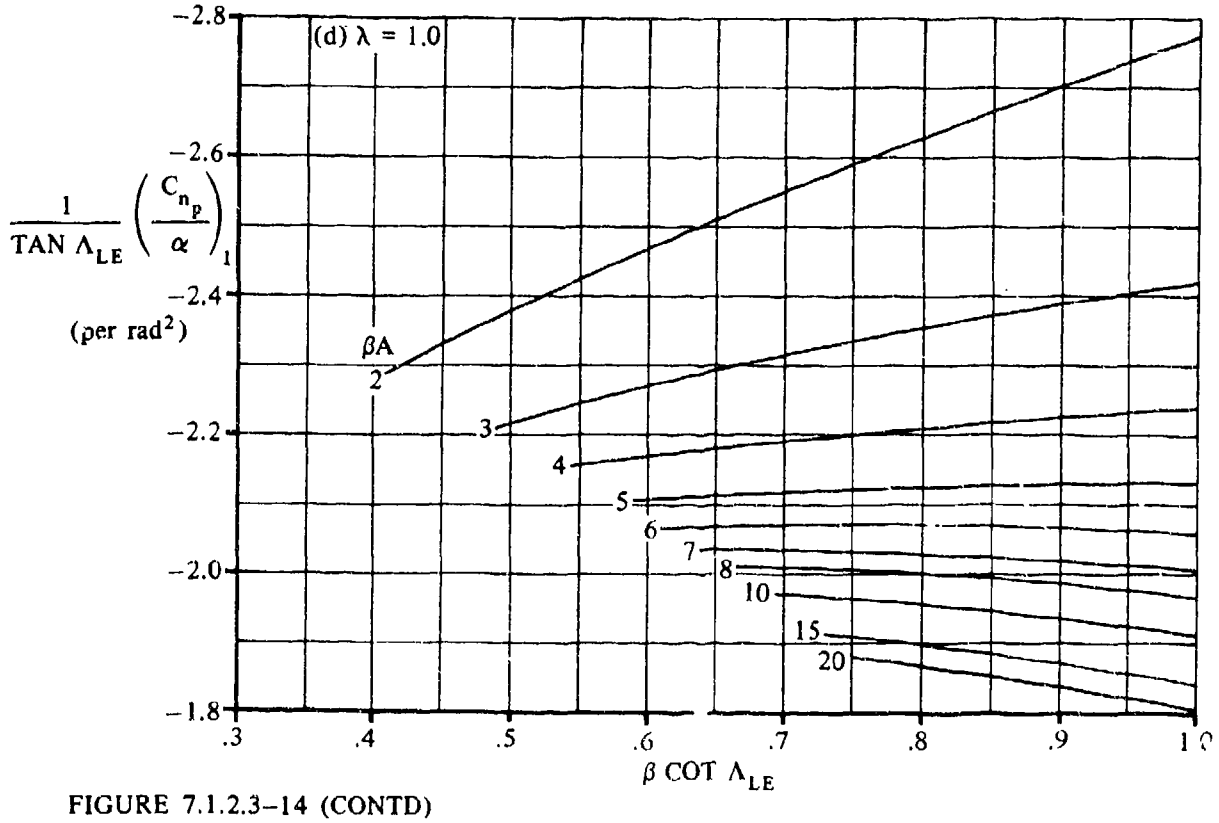

FIGURE 7.1.2.3–14 (CONTD)

SUPERSONIC SPEEDS

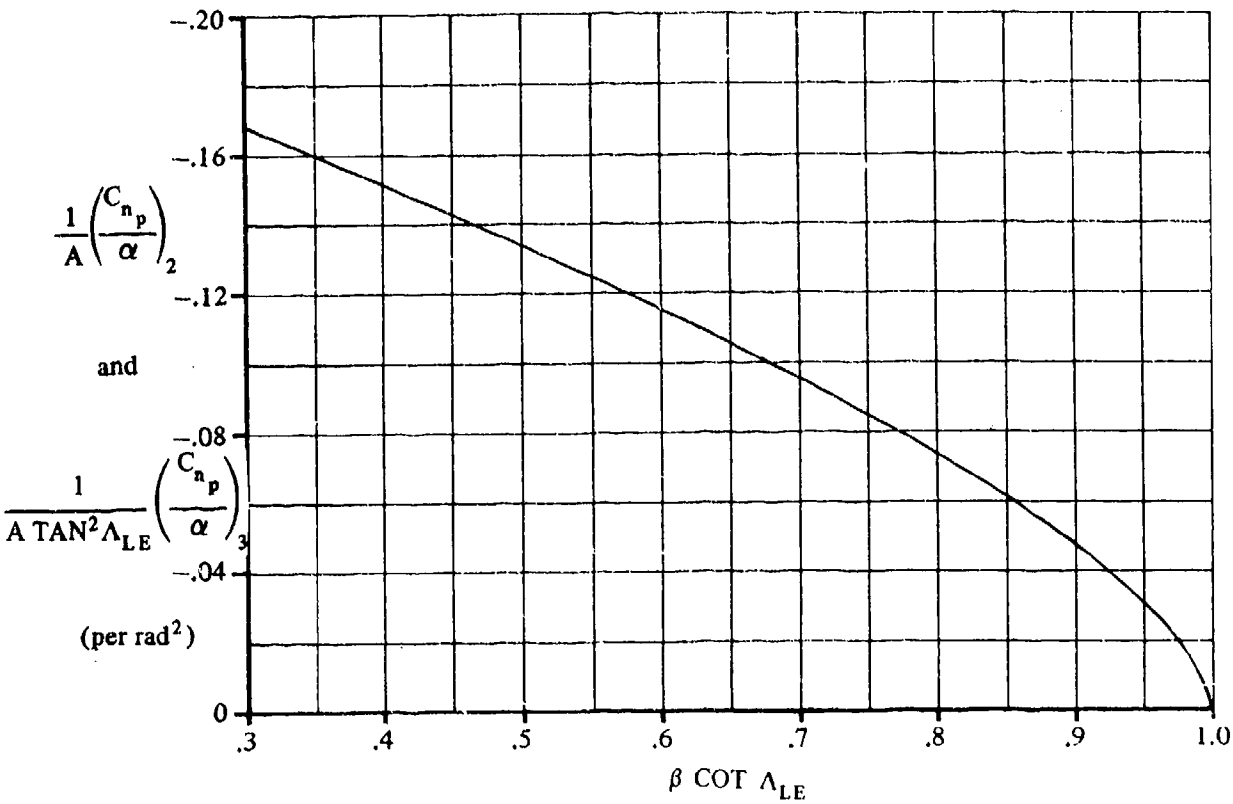

FIGURE 7.1.2.3-16 YAWING-MOMENT-DUE-TO-ROLLING COMPONENTS $\left(\frac{C_{n_p}}{\alpha}\right)_2$ AND $\left(\frac{C_{n_p}}{\alpha}\right)_3$

SUBSONIC LEADING EDGES

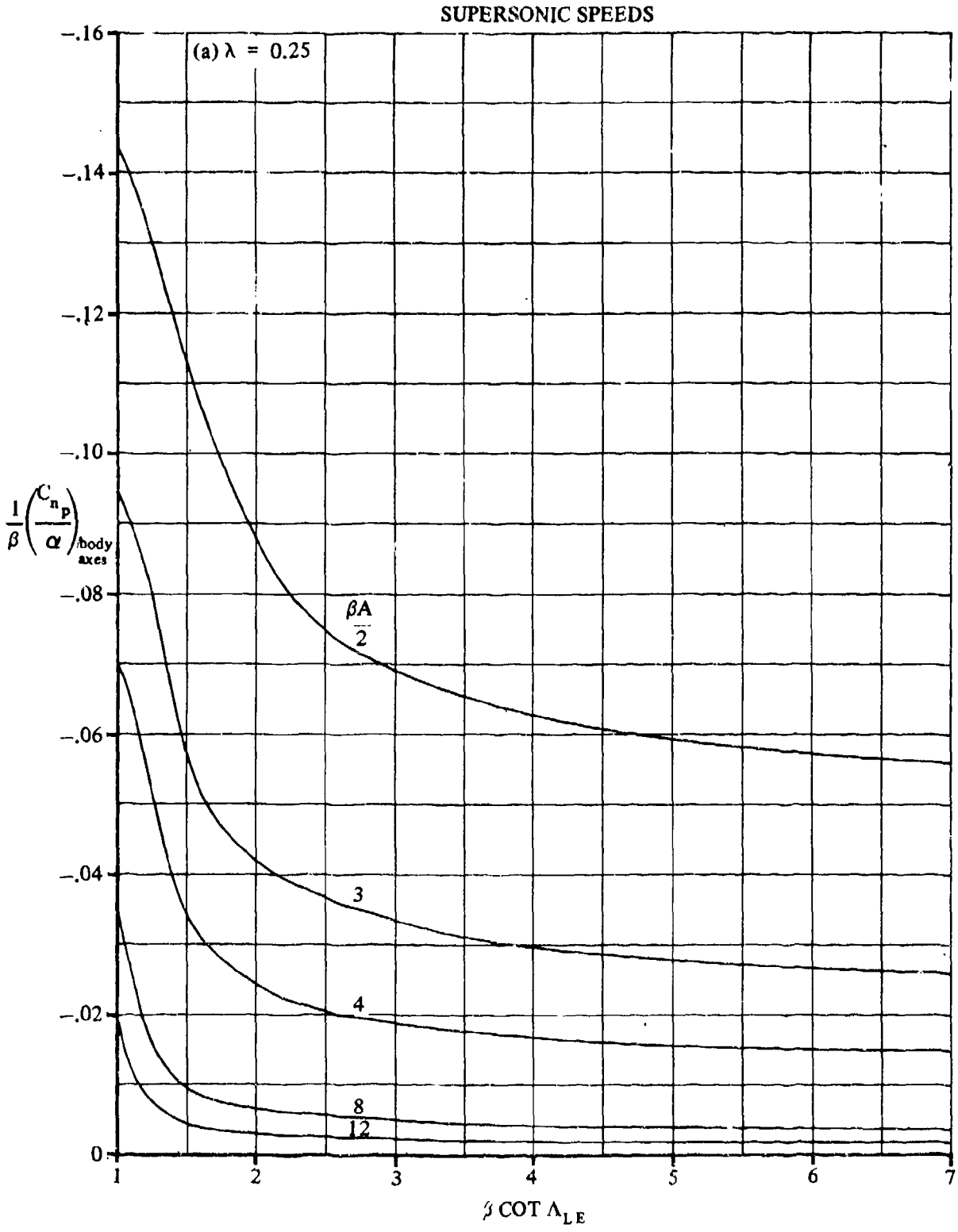

FIGURE 7.1.2.3-17 YAWING MOMENT DUE TO ROLLING – SUPERSONIC LEADING EDGES – BODY AXES

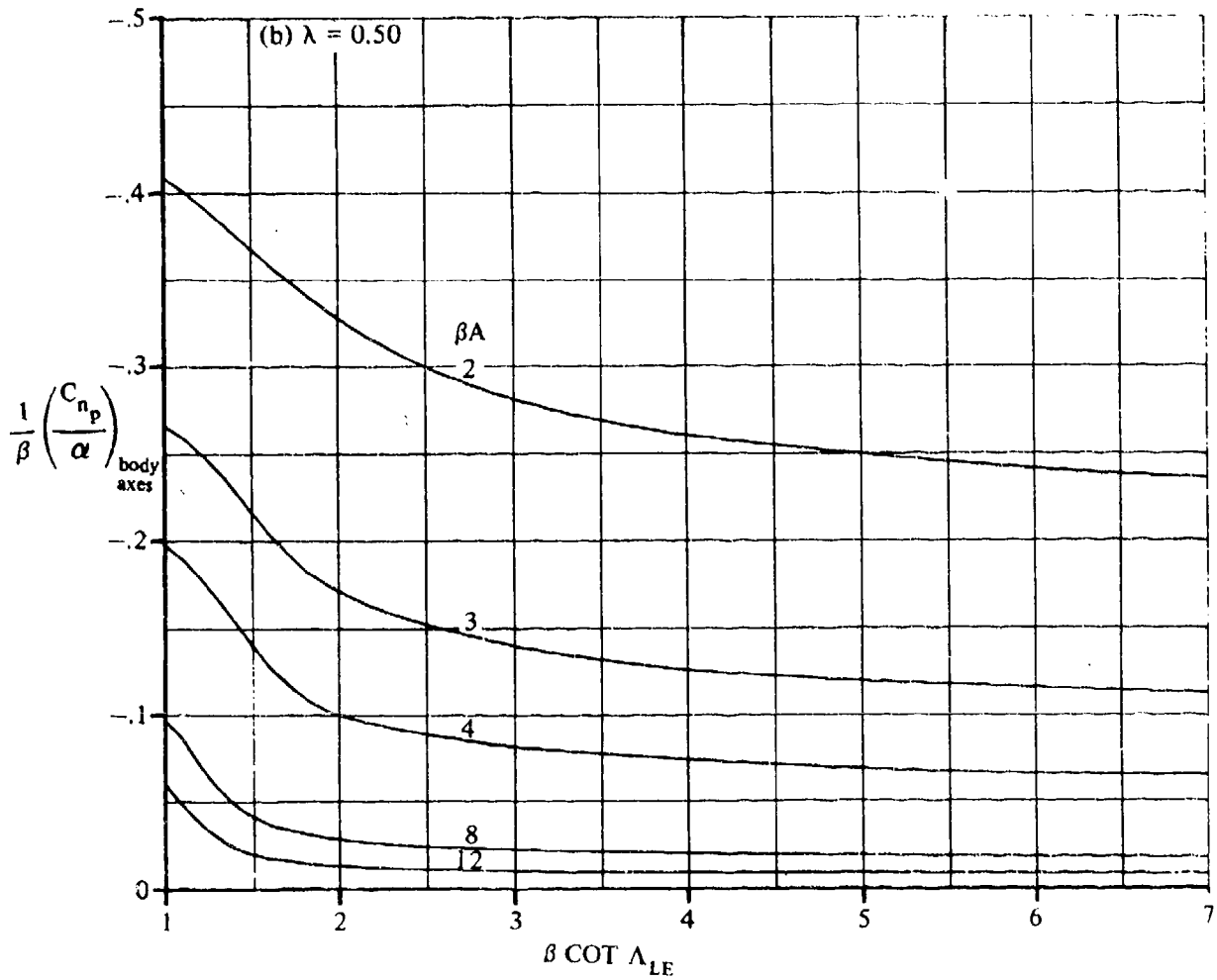

FIGURE 7.1.2.3–17 (CONTD)

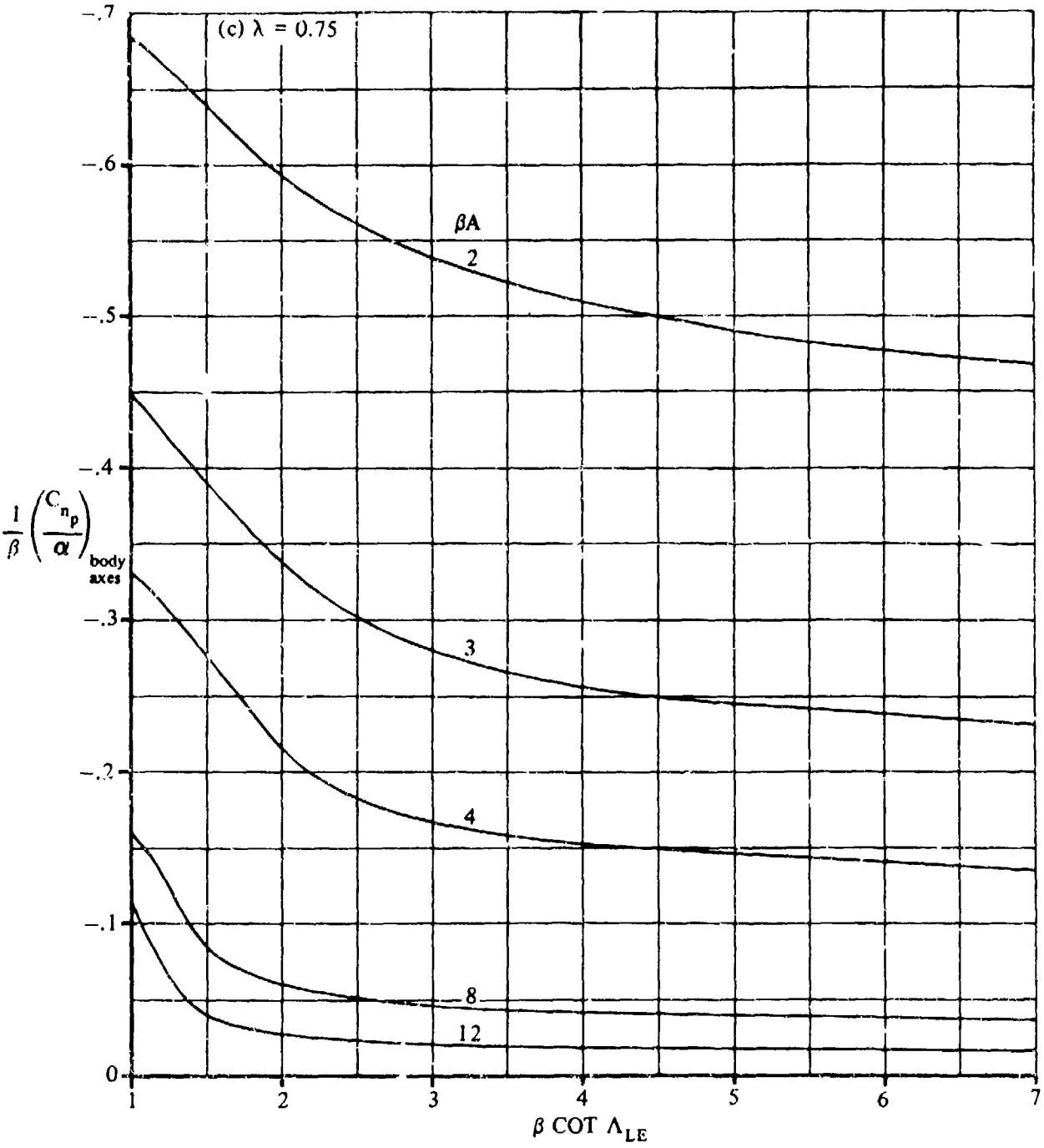

FIGURE 7.1.2.3-17 (CONTD)

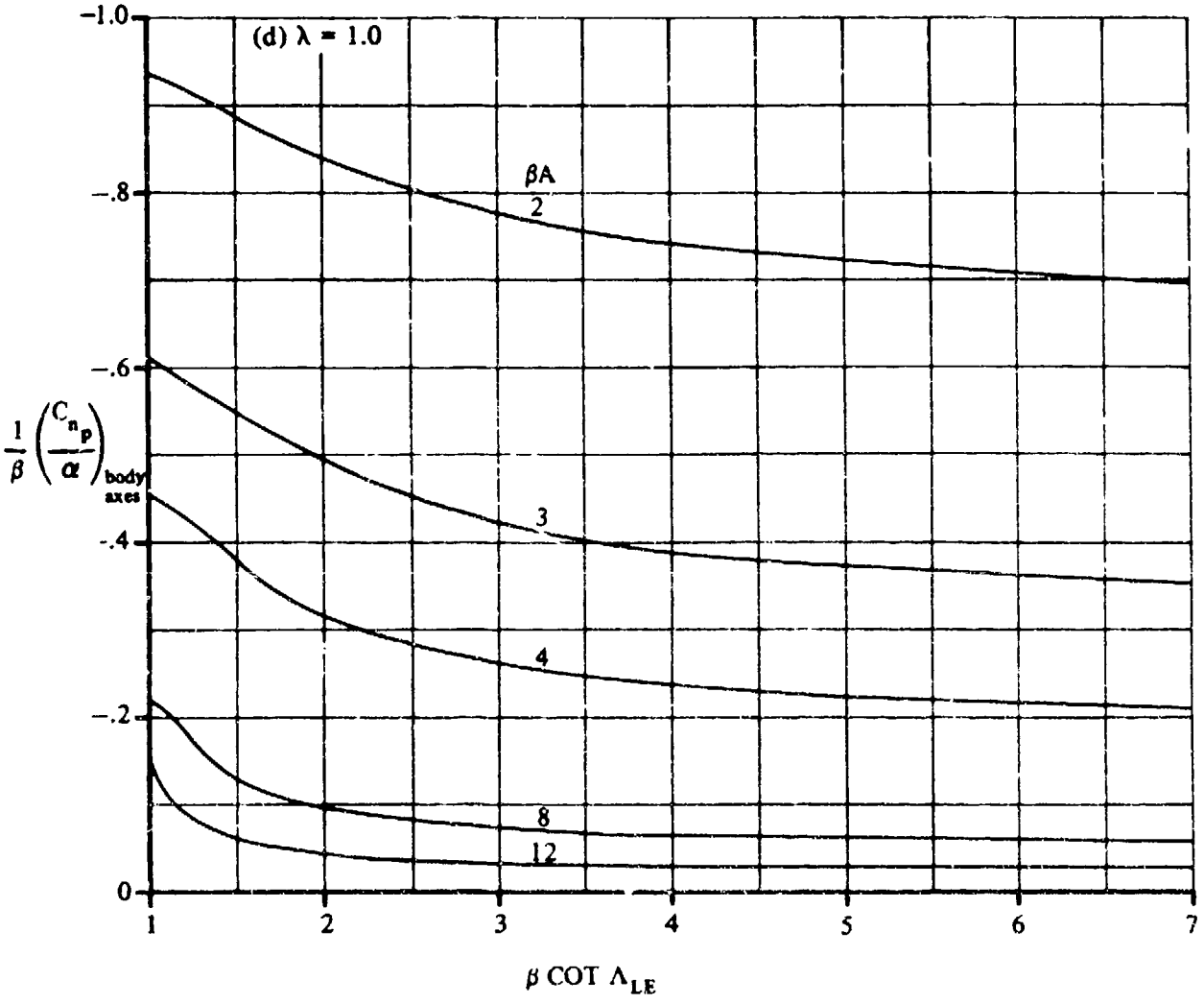

FIGURE 7.1.2.8–17 (CONTD)

7.1.3 WING YAWING DERIVATIVES

7.1.3.1 WING YAWING DERIVATIVE C_{Y_r}

This section recommends methods for estimating the wing contribution to the yawing derivative C_{Y_r} at subsonic and supersonic speeds. However, at subsonic, transonic, and supersonic speeds no generalized methods are available for estimating the wing contribution to C_{Y_r}. This derivative is the change in side-force coefficient with variation in yawing velocity and is expressed as

$$C_{Y_r} = \frac{\partial C_Y}{\partial\left(\frac{rb}{2V_\infty}\right)}$$

A. SUBSONIC

The wing contribution to C_{Y_r} is best evaluated from available experimental data (see table 7-A and references 1, 2, 3, and 4), since no generalized method is available in the literature. However, a method is available in reference 1 for wings with a taper ratio of one and moderate sweep at low subsonic speeds. The range and accuracy of this method are limited and generally inadequate for making reliable estimates of the wing contribution.

Since the wing contribution to C_{Y_r} is usually quite small in comparison to the vertical-tail contribution, it is sometimes neglected.

B. TRANSONIC

No generalized method is available in the literature for estimating transonic values of the wing contribution to the yawing derivative C_{Y_r}. Furthermore, there is a scarcity of experimental data for this derivative at transonic speeds.

C. SUPERSONIC

No generalized method is available in the literature for estimating supersonic values of the wing contribution to the yawing derivative C_{Y_r}. A few theoretical methods are available for specific configurations (see table 7-A). Although the use of experimental data for a similar configuration is preferable to theoretical methods, experimental data are so scarce that the use of the limited theoretical methods becomes the only alternative for most configurations.

REFERENCES

1. Toll, T. A., and Queijo, M. J.: Approximate Relations and Charts for Low-Speed Stability Derivatives of Swept Wings. NACA TN 1581, 1948. (U)

2. Queijo, M. J., and Jaquet, B. M.: Investigation of Effects of Geometric Dihedral on Low-Speed Static Stability and Yawing Characteristics of an Untapered 45° Sweptback-Wing Model of Aspect Ratio 2.61. NACA TN 1668, 1948. (U)

3. Goodman, A., and Brewer, J. D.: Investigation at Low Speeds of the Effect of Aspect Ratio and Sweep on Static and Yawing Stability Derivatives of Untapered Wings. NACA TN 1669, 1948. (U)

4. Letko, W., and Cowan, J. W.: Effect of Taper Ratio on Low-Speed Static and Yawing Stability Derivatives of 45° Sweptback Wings with Aspect Ratio of 2.61. NACA TN 1671, 1948. (U)

7.1.3.2 WING YAWING DERIVATIVE C_{l_r}

This section presents a method for estimating the wing contribution to the yawing derivative C_{l_r} at subsonic speeds. No generalized methods are available for estimating C_{l_r} at transonic and supersonic speeds; however, theoretical methods for determining this derivative at supersonic speeds for special classes of wing planforms are discussed. This derivative is the change in rolling-moment coefficient with change in the yawing-velocity parameter and is expressed as

$$C_{l_r} = \frac{\partial C_l}{\partial\left(\frac{rb}{2V_\infty}\right)}$$

A. SUBSONIC

The wing yawing derivative C_{l_r} results from the lift differential between the wing panels when the vehicle is yawed about its vertical axis.

Over the range of lift coefficients for which C_{l_r} is linear with C_L, the derivative C_{l_r} for wings without geometric dihedral, twist, or flaps is based on the lifting-line theory of reference 1 for aspect ratios greater than three and on the experimental data of references 2 and 3 for aspect ratios less than three. The increment in C_{l_r} due to geometric dihedral is taken from reference 4. The effects of symmetric flap deflection and wing twist are taken from reference 1.

In addition to the increments in C_{l_r} due to dihedral, twist, and flaps, an additional increment in C_{l_r} arises due to C_{Y_r} if the center of gravity does not lie at the same height as the quarter-chord point of the wing MAC. This contribution is obtained from the expression

$$(\Delta C_{l_r})_{\text{side force}} = -C_{Y_r}\frac{z}{b}$$

where z is the vertical distance between the center of gravity and the quarter-chord point of the wing MAC, positive for the c.g. above $\bar{c}/4$. The side force due to yawing C_{Y_r} is small except at high angles of attack. Therefore, this increment in C_{l_r} is omitted from the Datcom method.

The fore and aft movement of the center of gravity also affects C_{l_r}, but this effect is neglected because of the questionable accuracy of the basic effect of wing sweep.

The method of reference 5 is applied to extrapolate the potential-flow value of C_{l_r} to higher lift coefficients. The method is semiempirical in that it requires test values to determine the correction factors to be applied to the theory. Analysis of experimental data shows that the discrepancies between theoretical and experimental values of C_{l_r} for wings are similar to the discrepancies between theoretical and experimental values of the static derivative C_{l_β}. Based on this analysis, a correction factor is applied in reference 5, which is the incremental value of C_{l_β} obtained by subtracting the experimental value from the theoretical value.

Experimental data indicate that for unswept wings C_{l_r} is nearly proportional to the lift coefficient until maximum lift occurs. For sweptback wings, a linear variation is obtained over only a limited lift range, which is reduced as sweep increases. At high lift coefficients C_{l_r} decreases, and for sweptback wings may become negative near maximum lift.

If reliable values of the rolling moment due to sideslip C_{l_β} are available, the method should provide results within ±20-percent accuracy over the lift-coefficient range for which C_{l_r} is approximately linear with C_L.

DATCOM METHOD

The variation of the wing yawing derivative C_{l_r} with lift coefficient, based on the product of the wing area and the square of the wing span $S_W b_W^2$, is given by

$$C_{l_r} = C_L\left(\frac{C_{l_r}}{C_L}\right)_{\substack{C_L=0\\M}} + (\Delta C_{l_r})_{C_L} + \left(\frac{\Delta C_{l_r}}{\Gamma}\right)\Gamma + \left(\frac{\Delta C_{l_r}}{\theta}\right)\theta + \left[\frac{\Delta C_{l_r}}{\left(\frac{\partial\alpha}{\partial\delta}\right)_f \delta_f}\right]\left(\frac{\partial\alpha}{\partial\delta}\right)_f \delta_f \quad \text{(per radian)} \qquad 7.1.3.2\text{-a}$$

where

$\left(\frac{C_{l_r}}{C_L}\right)_{\substack{C_L=0\\M}}$ is the slope of the rolling moment due to yawing at zero lift given by

$$\left(\frac{C_{l_r}}{C_L}\right)_{\substack{C_L=0\\M}} = \frac{1 + \frac{A(1-B^2)}{2B(AB+2\cos\Lambda_{c/4})} + \frac{AB+2\cos\Lambda_{c/4}}{AB+4\cos\Lambda_{c/4}}\,\frac{\tan^2\Lambda_{c/4}}{8}}{1 + \frac{A+2\cos\Lambda_{c/4}}{A+4\cos\Lambda_{c/4}}\,\frac{\tan^2\Lambda_{c/4}}{8}}\left(\frac{C_{l_r}}{C_L}\right)_{\substack{C_L=0\\M=0}} \qquad 7.1.3.2\text{-b}$$

where $B = \sqrt{1-M^2\cos^2\Lambda_{c/4}}$ and

$\left(\frac{C_{l_r}}{C_L}\right)_{\substack{C_L=0\\M=0}}$ is the slope of the low-speed rolling moment due to yawing at zero lift, obtained from figure 7.1.3.2-10 as a function of aspect ratio, sweep of the quarter-chord, and taper ratio. This chart has been derived by using the results of references 1, 2, and 3. Equation 7.1.3.2-b modifies the low-speed value by means of the Prandtl-Glauert rule to yield approximate corrections for the first-order three-dimensional effects of compressible flow up to the critical Mach number.

C_L is the wing lift coefficient.

$(\Delta C_{l_r})_{C_L}$ is a semiempirical correction factor used to extrapolate the potential-flow values of C_{l_r} to higher lift coefficients. This parameter is given by

$$(\Delta C_{l_r})_{C_L} = C_L \left(\frac{C_{l_\beta}}{C_L}\right) - \left(C_{l_\beta}\right)_{test} \qquad \text{(per radian)} \qquad 7.1.3.2\text{-c}$$

where

$\frac{C_{l_\beta}}{C_L}$ is the theoretical value of the slope of the rolling moment due to sideslip at zero lift obtained by using the method of paragraph A of Section 5.1.2.1, neglecting the effects of twist and dihedral. In applying this method the compressibility correction to the sweep contribution should be considered.

$\left(C_{l_\beta}\right)_{test}$ is the experimental value of the rolling moment due to sideslip at the appropriate Mach number.

$\frac{\Delta C_{l_r}}{\Gamma}$ is the increment in C_{l_r} due to dihedral, given by

$$\frac{\Delta C_{l_r}}{\Gamma} = \frac{1}{12} \frac{\pi A \sin \Lambda_{c/4}}{A + 4 \cos \Lambda_{c/4}} \qquad \text{(per radian}^2\text{)} \qquad 7.1.3.2\text{-d}$$

Γ is the geometric dihedral angle in radians, positive for the wing tip above the plane of the root chord.

$\frac{\Delta C_{l_r}}{\theta}$ is the increment in C_{l_r} due to wing twist obtained from figure 7.1.3.2-11.

θ is the wing twist between the root and tip sections in degrees, negative for washout (see figure 7.1.3.2-11).

$\frac{\Delta C_{l_r}}{\left(\frac{\partial \alpha}{\partial \delta}\right)_f \delta_f}$ is the effect of symmetric flap deflection obtained from figure 7.1.3.2-12.

δ_f is the streamwise flap deflection in degrees.

$\left(\frac{\partial \alpha}{\partial \delta}\right)_f$ is the two-dimensional lift-effectiveness parameter α_δ obtained from Section 6.1.1.1.

The expression given for the effect of dihedral (equation 7.1.3.2-d) is based on an extension of the simple-sweep theory of reference 6. It has been shown by comparison with test data that the increment in C_{l_Γ} due to dihedral is underestimated by equation 7.1.3.2-d. However, it has not been possible to improve upon the simple-sweep-theory result because of a lack of experimental data.

Furthermore, not enough data are available to examine the validity of the lifting-line-theory results presented for the increments in C_{l_Γ} due to either twist or flap deflection.

A comparison of the slope of the rolling moment due to yawing at zero lift, obtained by using figure 7.1.3.2-10, with test results is presented as table 7.1.3.2-A.

The sample problem illustrates the application of the method over the lift-coefficient range to the stall.

Sample Problem

Given: The sweptback, untapered wing of reference 4.

Wing Characteristics:

$A = 2.61 \qquad \lambda = 1.0 \qquad \Lambda_{c/4} = 45^o \qquad \Lambda_{c/2} = 45^o \qquad \Gamma = 10^o \qquad \theta = 0$

Additional Characteristics:

Low speed; $M \approx 0$

The following test values from reference 4:

C_L	0	.1	.2	.3	.4	.5	.6	.7	.8	.9	1.0	1.1
C_{l_β} (per rad)	−.0458	−.1031	−.140	−.176	−.206	−.235	−.260	−.274	−.260	−.211	−.102	.0287

Compute:

$\left(\frac{C_{l_\Gamma}}{C_L}\right)_{\substack{C_L=0 \\ M=0}}$ = 0.419 per rad (figure 7.1.3.2-10)

Determine the theoretical value of C_{l_β}/C_L (Section 5.1.2.1)

$$\left(\frac{C_{l_\beta}}{C_L}\right)_{\Lambda_{c/2}} = -0.0038 \text{ per deg} \qquad \text{(figure 5.1.2.1-27)}$$

$$\left(\frac{C_{l_\beta}}{C_L}\right)_{A} = -0.0044 \text{ per deg} \qquad \text{(figure 5.1.2.1-28b)}$$

$$K_{M_\Lambda} = 1.0 \quad \text{(figure 5.1.2.1-28a for } M \approx 0)$$

$$C_{l_\beta} = C_L\left[\left(\frac{C_{l_\beta}}{C_L}\right)_{\Lambda_{c/2}} K_{M_\Lambda} + \left(\frac{C_{l_\beta}}{C_L}\right)_{A}\right] + \Gamma\left(\frac{C_{l_\beta}}{\Gamma} K_{M_\Gamma}\right) + \theta \tan \Lambda_{c/4} \frac{\Delta C_{l_\beta}}{\theta \tan \Lambda_{c/4}}$$

(equation 5.1.2.1-a)

Neglecting the effects of twist and dihedral

$$\frac{C_{l_\beta}}{C_L} = \left[\left(\frac{C_{l_\beta}}{C_L}\right)_{\Lambda_{c/2}} K_{M_\Lambda} + \left(\frac{C_{l_\beta}}{C_L}_{/A}\right)\right]$$

$$= (-0.0038)(1.0) + (-0.0044)$$

$$= -0.0082 \text{ per deg}$$

$$= -0.470 \text{ per rad}$$

$$(\Delta C_{l_r})_{C_L} = C_L\left(\frac{C_{l_\beta}}{C_L}\right) - (C_{l_\beta})_{test} \qquad \text{(equation 7.1.3.2-c)}$$

$$= C_L\,(-0.470) - (C_{l_\beta})_{test} \qquad \text{(see calculation table)}$$

$$\frac{\Delta C_{l_r}}{\Gamma} = \frac{1}{12}\,\frac{\pi A \sin \Lambda_{c/4}}{A + 4\cos \Lambda_{c/4}} \qquad \text{(equation 7.1.3.2-d)}$$

$$= \frac{1}{12}\,\frac{\pi(2.61)(\sin 45^o)}{2.61 + 4\cos 45^o} = \frac{1}{12}\,\frac{\pi(2.61)(0.7071)}{2.61 + 4(0.7071)}$$

$$= 0.0884 \text{ per rad}^2$$

Solution:

$$C_{l_r} = C_L \left(\frac{C_{l_r}}{C_L}\right)_{\substack{C_L = 0 \\ M = 0}} + (\Delta C_{l_r})_{C_L} + \left(\frac{\Delta C_{l_r}}{\Gamma}\right)\Gamma \qquad \text{(equation 7.1.3.2-a)}$$

$$= C_L\,(0.419) + [C_L\,(-0.470) - C_{l_{\beta\ \text{test}}}] + (0.0884)\,\frac{10}{57.3}$$

$$= 0.419\,C_L + [-0.470\,C_L - C_{l_{\beta\ \text{test}}}] + 0.0154$$

①	②	③	④	⑤	⑥
C_L	C_{l_β} (test) (per rad)	$\left(\frac{C_{l_r}}{C_L}\right)_{C_L}$ $C_L = 0$, $M = 0$ 0.419 ①	$\left(\frac{C_{l_\beta}}{C_L}\right) C_L$ −0.470 ①	$(\Delta C_{l_r})_{C_L}$ (eq. 7.1.3.2-c) ④ − ② (per rad)	C_{l_r} (based on $S_W b_W^2$) (eq. 7.1.3.2-a) ③ + ⑤ + 0.0154 (per rad)
0	−.0458	0	0	.0458	.0612
.1	−.1031	.0419	−0.0470	0.0561	0.1134
.2	−.1400	.0838	−0.0940	0.0460	0.1452
.3	−.1760	.1257	−0.1410	0.0350	0.1761
.4	−.2060	.1676	−0.1880	0.0180	0.2010
.5	−.2350	.2095	−0.2350	0	0.2249
.6	−.2600	.2514	−0.2820	−0.0220	0.2448
.7	−.2740	.2933	−0.3290	−0.0550	0.2537
.8	−.2600	.3352	−0.3760	−0.1160	0.2346
.9	−.2110	.3771	−0.4230	−0.2120	0.1805
1.0	−.1020	.4190	−0.4700	−0.3680	0.0664
1.1	0287	.4609	−0.5170	−0.5457	−0.0694

The calculated results are compared with test values from reference 4 in sketch (a).

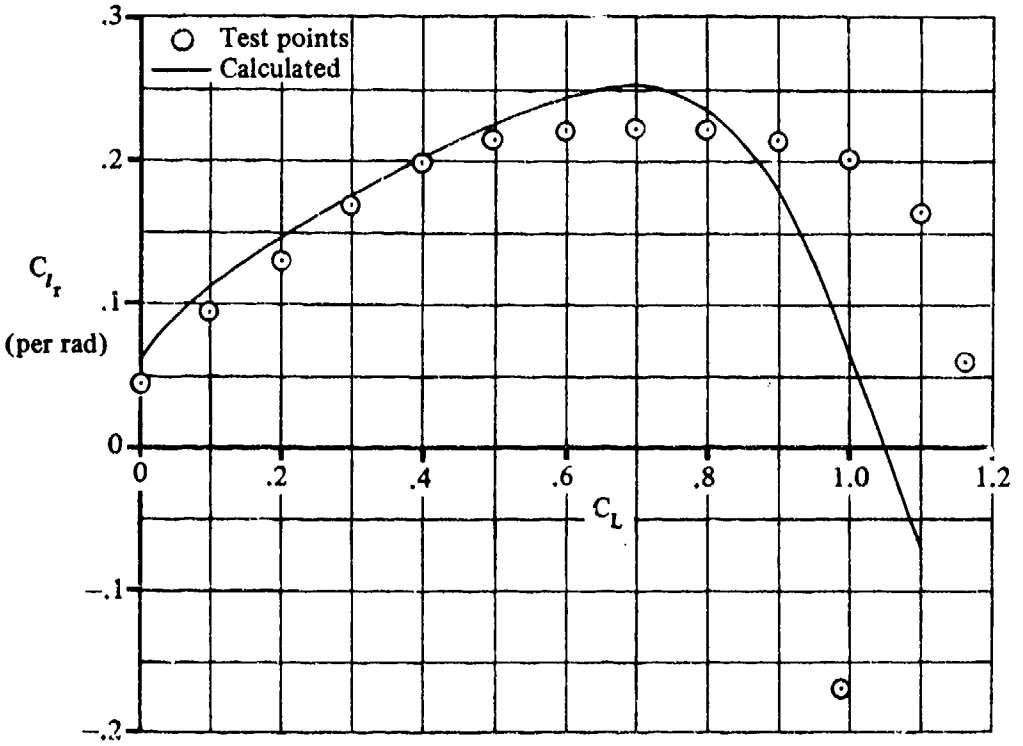

SKETCH (a)

B. TRANSONIC

In the transonic speed regime no theoretical methods are available for estimating the wing yawing derivative C_{l_r}. Furthermore, no known experimental results are available for this derivative at transonic speeds.

C. SUPERSONIC

No general method is available for evaluating the wing contribution to the yawing derivative C_{l_r} at supersonic speeds. However, methods are presented in references 7, 8, and 9 for evaluating C_{l_r} for special classes of wing planforms. The results presented in these references are based on supersonic linear theory. The methods are restricted to estimating C_{l_r} over a limited range of Mach numbers for zero-thickness wings with no dihedral. Furthermore, the methods are considered tentative, since the spanwise variation of Mach number in the case of yawing has been neglected.

REFERENCES

1. Pinsker, W.: The Aerodynamic Coefficients of Free Lateral Motion. DVL UM 1144/1 and UM 1144/2, 1943. (U)

2. Goodman, A., and Brewer, J. D.: Investigation at Low Speeds of the Effect of Aspect Ratio and Sweep on Static and Yawing Stability Derivatives of Untapered Wings. NACA TN 1669, 1948. (U)

3. Letko, W., and Cowan, J. W.: Effect of Taper Ratio on Low-Speed Static and Yawing Stability Derivatives of 45° Sweptback Wings With Aspect Ratio of 2.61. NACA TN 1671, 1948. (U)

4. Queijo, M. J., and Jaquet, B. M.: Investigation of Effects of Geometric Dihedral on Low-Speed Static Stability and Yawing Characteristics of an Untapered 45° Sweptback-Wing Model of Aspect Ratio 2.61. NACA TN 1668, 1948. (U)

5. Campbell, J. P., and Goodman, A.: A Semiempirical Method for Estimating the Rolling Moment Due to Yawing of Airplanes. NACA TN 1984, 1949. (U)

6. Toll, T. A., and Queijo, M. J.: Approximate Relations and Charts for Low-Speed Stability Derivatives of Swept Wings. NACA TN 1581, 1948. (U)

7. Ribner, H. S., and Malvestuto, F. S., Jr.: Stability Derivatives of Triangular Wings at Supersonic Speeds. NACA TR 908, 1948. (U)

8. Harmon, S. M.: Stability Derivatives at Supersonic Speeds of Thin Rectangular Wings With Diagonals Ahead of Tip Mach Lines. NACA TR 925, 1949. (U)

9. Malvestuto, F. S., Jr., and Margolis, K.: Theoretical Stability Derivatives of Thin Sweptback Wings Tapered to a Point With Sweptback or Sweptforward Trailing Edges for a Limited Range of Supersonic Speeds. NACA TR 971, 1950. (U)

10. Lichtenstein, J. H.: Effect of High-Lift Devices on the Low-Speed Static Lateral and Yawing Stability Characteristics of an Untapered 45° Sweptback Wing. NACA TN 2689, 1952. (U)

11. Letko, W.: Effect of Vertical-Tail Area and Length on the Yawing Stability Characteristics of a Model Having a 45° Sweptback Wing. NACA TN 2358, 1951. (U)

12. Williams, J. L.: Measured and Estimated Lateral Static and Rotary Derivatives of a 1/12-Scale Model of a High-Speed Fighter Airplane with Unswept Wings. NACA RM L53K09, 1954. (U)

13. Goodman, A., and Feigenbaum, D.: Preliminary Investigation at Low Speeds of Swept Wings in Yawing Flow. NACA RM L7I09, 1948. (U)

14. Letko, W., and Jaquet, B. M.: Effect of Airfoil Profile of Symmetrical Sections on the Low-Speed Static-Stability and Yawing Derivatives of 45° Sweptback Wing Models of Aspect Ratio 2.61. NACA RM L8H10, 1948. (U)

15. Bird, J. D., Jaquet, B. M., and Cowan, J. W.: Effect of Fuselage and Tail Surfaces on Low-Speed Yawing Characteristics of a Swept-Wing Model as Determined in Curved-Flow Test Section of Langley Stability Tunnel. NACA TN 2483, 1951. (U)

16. Jaquet, B. M., and Fletcher, H. S.: Experimental Steady-State Yawing Derivatives of a 60° Delta-Wing Model as Affected by Changes in Vertical Position of the Wing and in Ratio of Fuselage Diameter to Wing Span. NACA TN 3843, 1956. (U)

TABLE 7.1.3.2-A

SUBSONIC WING ROLLING MOMENT DUE TO YAWING

DATA SUMMARY

Ref.	A	λ	$\Lambda_{c/4}$ (deg)	C_{l_r}/C_L Calc. (per rad)	C_{l_r}/C_L Test (per rad)	e Percent Error
10	2.61	1.0	45.0	0.419	0.415	1.0
11	4.00	0.60	45.0	0.413	0.396	4.3
12	5.90	0.473	−3.5	0.240	0.225	6.7
13	1.34	1.0	60.0	0.445	0.470	− 5.3
↓	5.16	1.0	0	0.260	0.220	18.2
2	1.34	1.0	0	0.195	0.161	21.1
↓	↓	↓	45.0	0.353	0.350	0.9
↓	2.61	↓	0	0.230	0.260	−11.5
↓	↓	↓	60.0	0.525	0.558	− 5.9
↓	5.16	↓	45.0	0.475	0.480	− 1.0
↓	↓	↓	60.0	0.596	0.550	8.4
5	2.61	0.50	45.0	0.365	0.300	21.7
↓	↓	0.25	45.0	0.302	0.315	− 4.1
↓	2.31	0	52.2	0.295	0.285	3.5

$$\text{Average Error} = \frac{\Sigma|e|}{n} = 8.1\%$$

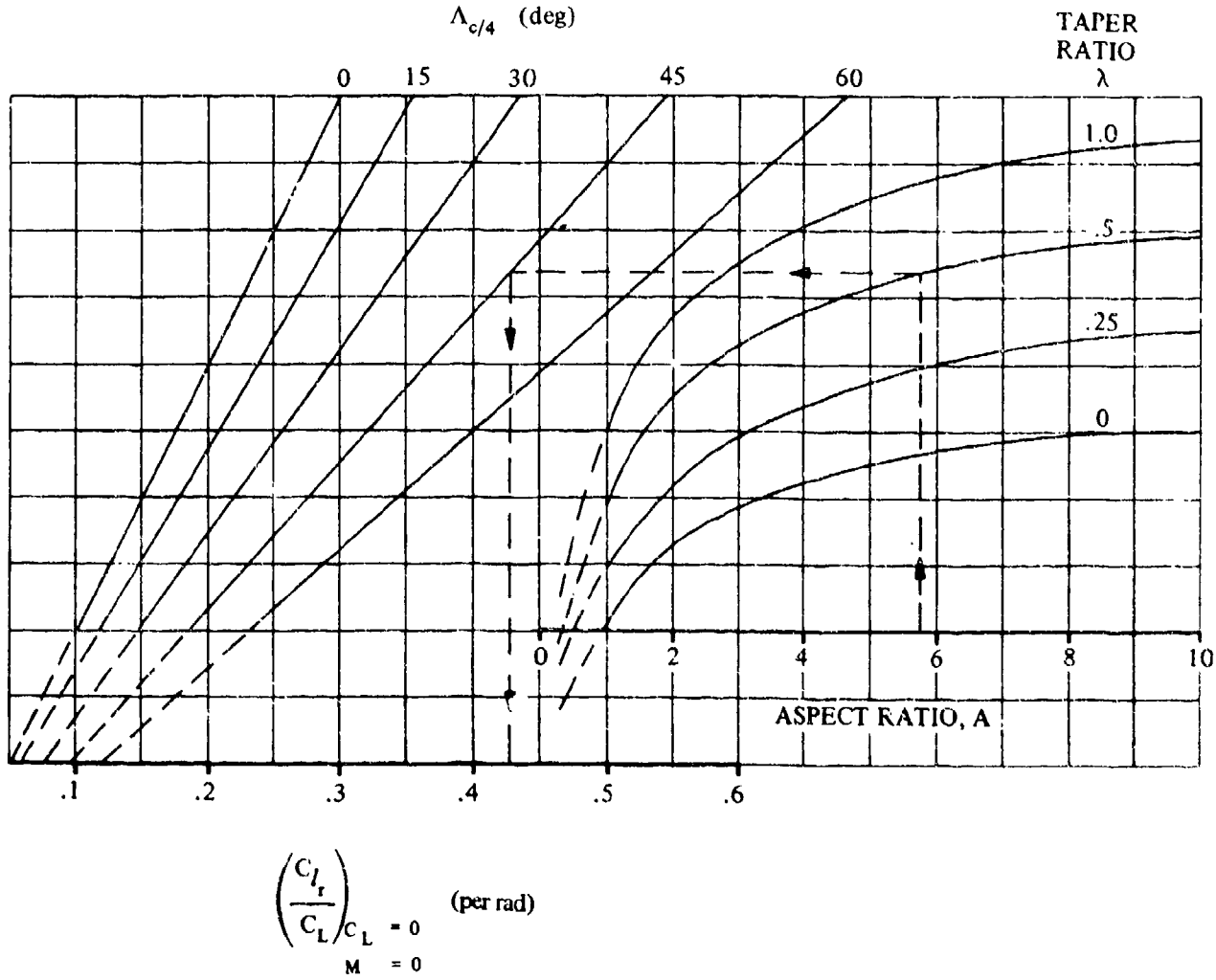

FIGURE 7.1.3.2-10 WING YAWING DERIVATIVE C_{l_r}

SUBSONIC SPEEDS

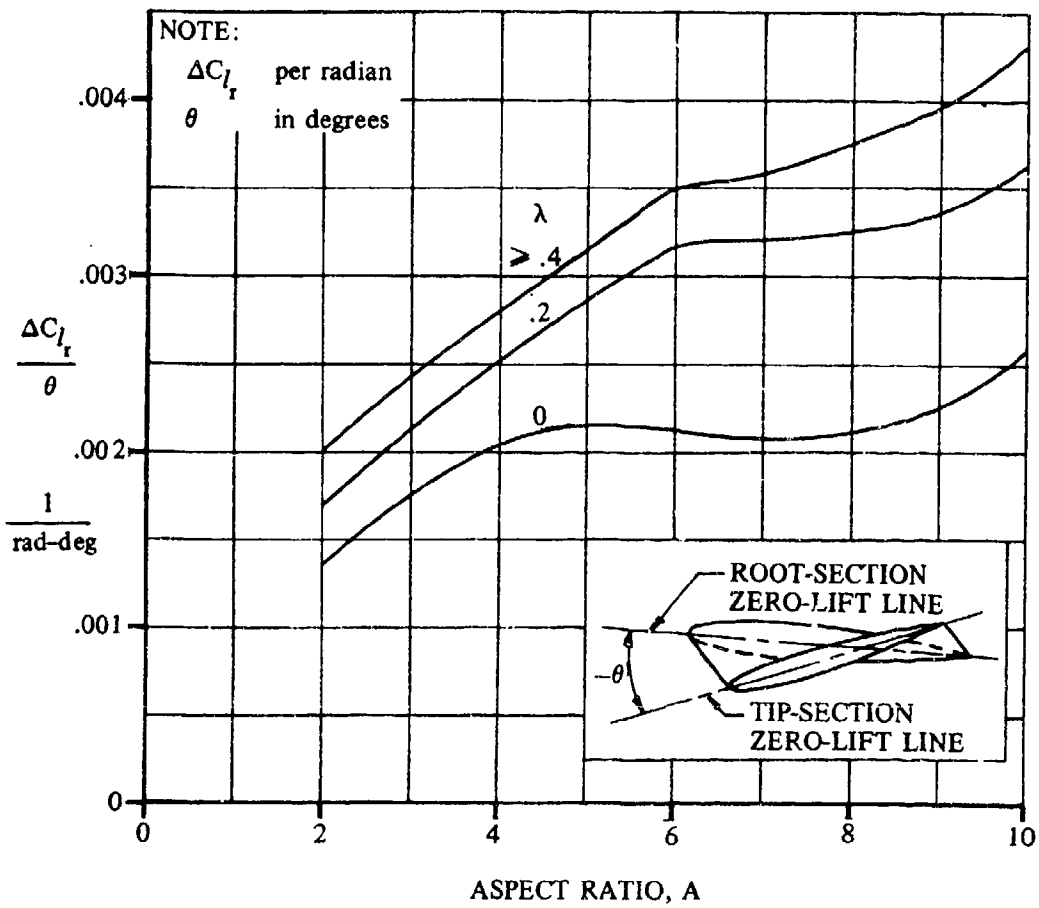

FIGURE 7.1.3.2–11 EFFECT OF WING TWIST ON WING YAWING DERIVATIVE C_{l_r}

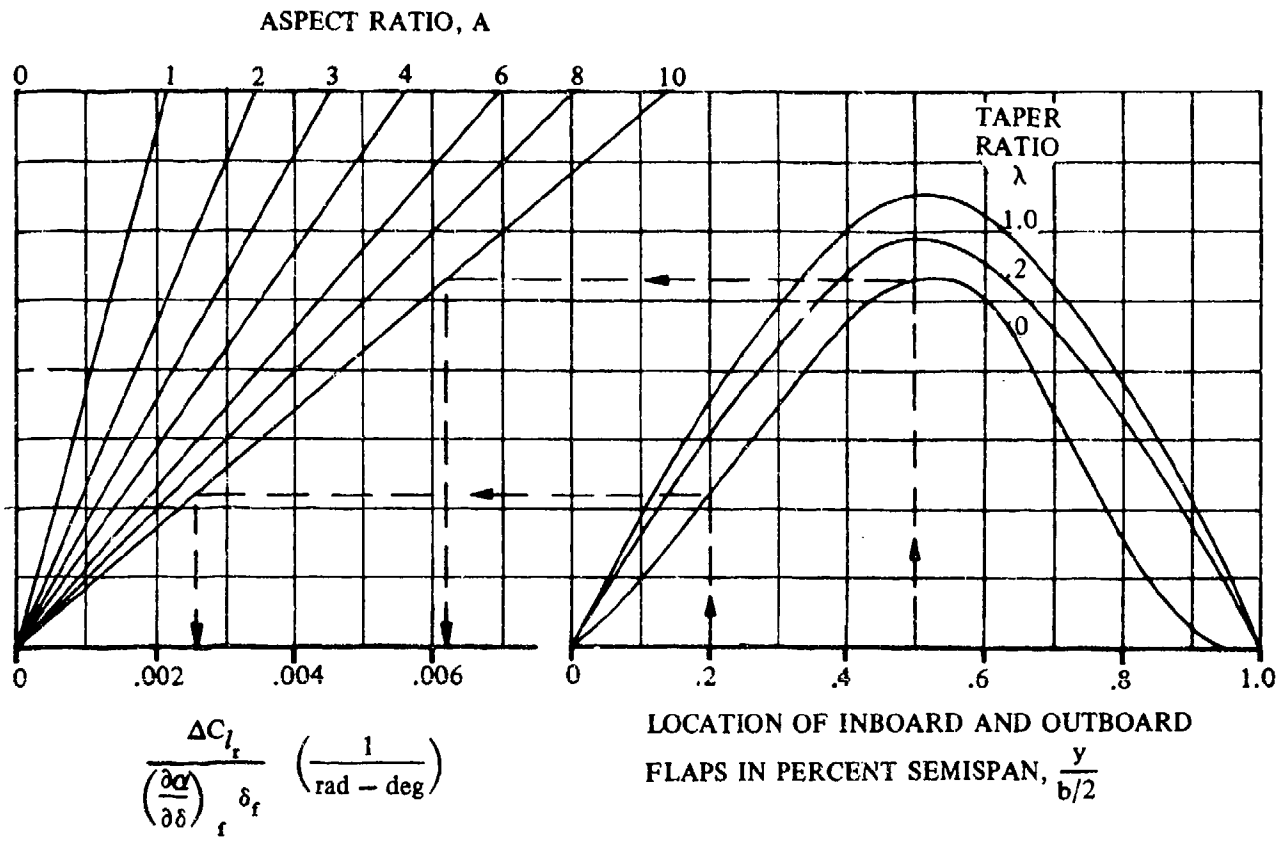

NOTE:

ΔC_{l_r} per radian

δ_f in degrees

NOTE: $$\frac{\Delta C_{l_r}}{\left(\frac{\partial \alpha'}{\partial \delta}\right)_f \delta_f} = \left[\frac{\Delta C_{l_r}}{\left(\frac{\partial \alpha'}{\partial \delta}\right)_f \delta_f}\right]_{\text{outboard}} - \left[\frac{\Delta C_{l_r}}{\left(\frac{\partial \alpha'}{\partial \delta}\right)_f \delta_f}\right]_{\text{inboard}}$$

FIGURE 7.1.3.2-12 EFFECT OF FLAPS ON C_{l_r}

7.1.3.3 WING YAWING DERIVATIVE C_{n_r}

This section presents a method for estimating the wing contribution to the yawing derivative C_{n_r} at subsonic speeds. No generalized methods are available for estimating C_{n_r} at transonic and supersonic speeds; however, theoretical methods for determining this derivative at supersonic speeds for special classes of wing planforms are discussed. This derivative is the change in yawing-moment coefficient with change in the yawing-velocity parameter. It is commonly referred to as the yaw damping and is expressed as

$$C_{n_r} = \frac{\partial C_n}{\partial\left(\frac{rb}{2V_\infty}\right)}$$

A. SUBSONIC

The wing yawing derivative C_{n_r} is due to the antisymmetrical lift and drag distributions over the wing resulting from the yawing velocity.

The wing contribution to the yaw damping in the range of lift coefficients for which C_{n_r} varies linearly with C_L is composed of two major contributions; namely, that resulting from the drag due to lift and that resulting from the profile drag. The contribution resulting from the drag due to lift is given to a first approximation by the simple-sweep-theory result of reference 1. It is a negative quantity except for highly swept wings in which case it can become positive.

The increment in C_{n_r} due to profile drag is also taken from reference 1. Although the spanwise distribution of profile drag is required for an accurate determination of the effect of profile drag on C_{n_r}, the profile drag has been assumed constant over the wing surface in the analysis reported in reference 1. This approximation greatly simplifies the analysis, since it allows the profile-drag effect to be expressed as a function of only the wing geometry.

Flaps and wing twist will also induce increments in C_{n_r}, primarily as a result of their influencing the lift distribution across the span. However, the technique of the superposition of lift distribution proportional to angle of attack, which was used to determine the effects of either flaps and/or twist on the rotary derivatives C_{n_p} and C_{l_r}, cannot be applied in this case. The contribution of the drag-due-to-lift component to C_{n_r} increases as the square of the angle of attack. Therefore, a breakdown of the lift distribution proportional to angle of attack is not possible. No methods are available in the literature for estimating the effects of flaps or wing twist on the wing contribution to C_{n_r}. Furthermore, not enough test data are available to allow derivation of an empirical method.

The wing side force due to yawing C_{Y_r} will also produce a yawing moment when the center of gravity does not lie at the same longitudinal station as the quarter-chord of the wing MAC. However, the side force due to yawing is small except at high angles of attack; consequently, this increment in C_{n_r} is omitted from the Datcom.

Experimental data indicate that for unswept wings the yaw damping is nearly proportional to the lift coefficient until maximum lift occurs. On the other hand, for sweptback wings linear variations of C_{n_r} are obtained over only a limited lift coefficient range, which is reduced as sweep and/or aspect ratio increase. Experimental data also show that, in general, the yaw damping of a sweptback wing

changes sign and becomes positive at some moderate lift coefficient. The lift coefficient at which this change in sign occurs is reduced as wing sweep and/or aspect ratio increase.

Results obtained by using the Datcom method agree reasonably well with test data over the range of lift coefficients for which C_{n_r} varies linearly with C_L.

Since the wing contribution to the total C_{n_r} of the airplane is small, no method has been developed to account for the effects of compressibility. For the purpose of the Datcom the effects of compressibility are accounted for by evaluating the wing profile-drag coefficient at the desired Mach number.

Experimental data show that the effect of wing dihedral on the yaw damping is negligible.

Because of the insignificance of the wing contribution to the total yaw damping and the approximate nature of the Datcom method, the method is applicable to wings with twist and/or symmetric flap deflection as well as to plain wings.

DATCOM METHOD

The variation of the wing yawing derivative C_{n_r} with lift coefficient at subsonic speeds, based on the product of the wing area and the square of the wing span $S_W b_W^2$, is given by

$$C_{n_r} = \left(\frac{C_{n_r}}{C_L^2}\right) C_L^2 \div \left(\frac{C_{n_r}}{C_{D_0}}\right) C_{D_0} \qquad \text{(per radian)} \qquad 7.1.3.3\text{-a}$$

where

C_L is the wing lift coefficient.

$\frac{C_{n_r}}{C_L^2}$ is the low-speed drag-due-to-lift yaw-damping parameter obtained from figure 7.1.3.3-6 as a function of wing aspect ratio, taper ratio, sweepback, and c.g. position.

$\frac{C_{n_r}}{C_{D_0}}$ is the low-speed profile-drag yaw-damping parameter obtained from figure 7.1.3.3-7 as a function of the wing aspect ratio, sweep-back, and c.g. position.

C_{D_0} is the wing profile drag coefficient evaluated at the appropriate Mach number. For this application C_{D_0} is assumed to be the profile drag associated with the theoretical ideal drag due to lift and is given by

$$C_{D_0} = C_D - \frac{C_L^2}{\pi A}$$

where C_D is the total drag coefficient at a given lift coefficient, obtained from experimental data.

Sample Problem

Given: The delta-wing model of references 5 and 6.

Wing Characteristics:

$A = 2.31 \qquad \lambda = 0 \qquad \Lambda_{c/4} = 52.4^{o} \qquad \theta = 0$

$\bar{x}/\bar{c} = 0$ (c.g. at $\bar{c}/4$)

Additional Characteristics:

$M = 0.13$

The following test values from reference 6.

C_L	0	.1	.2	.3	.4	.5	.6	.7	.8
C_D	.017	.020	.029	.047	.074	.105	.141	.184	.235

Compute:

$$\frac{C_{n_r}}{C_L^{\,2}} = 0.0080 \text{ per rad} \qquad \text{(figure 7.1.3.3-6)}$$

$$\frac{C_{n_r}}{C_{D_0}} = -0.68 \text{ per rad} \qquad \text{(figure 7.1.3.3-7)}$$

Solution:

$$C_{n_r} = \left(\frac{C_{n_r}}{C_L^{\,2}}\right) C_L^{\,2} + \left(\frac{C_{n_r}}{C_{D_0}}\right) C_{D_0} \qquad \text{(equation 7.1.3.3-a)}$$

$$= +0.008\, C_L^{\,2} + (-0.68)\, C_{D_0}$$

①	②	③	④	⑤	⑥	⑦	⑧
C_L	C_L^2 ①^2	$\left(\frac{C_{n_r}}{C_L^2}\right)C_L^2$ (0.008) ②	C_D (test)	$\frac{C_L^2}{\pi A}$ ②/(π 2.31)	C_{D_0} $C_D - C_L^2/(\pi A)$ ④ − ⑤	$\left(\frac{C_{n_r}}{C_{D_0}}\right)C_{D_0}$ (−0.68) ⑥	C_{n_r} (based on $S_W b_W^2$) (eq. 7.1.3.3-a) ③ + ⑦ (per rad)
0	0	0	.017	0	.0170	−.0116	−.0116
.1	.01	.00008	.020	.00138	.0186	−.0127	−.0126
.2	.04	.0003	.029	.00551	.0235	−.0160	−.0157
.3	.09	.0007	.047	.01240	.0346	−.0236	−.0228
.4	.16	.0013	.074	.0220	.0520	−.0354	−.0331
.5	.25	.0020	.105	.0344	.0706	−.0480	−.0460
.6	.36	.0029	.141	.0496	.0914	−.0621	−.0592
.7	.49	.0039	.184	.0675	.1165	−.0792	−.0753
.8	.64	.0051	.235	.0882	.1468	−.0998	−.0947

The calculated results are compared with test values from reference 5 in sketch (d).

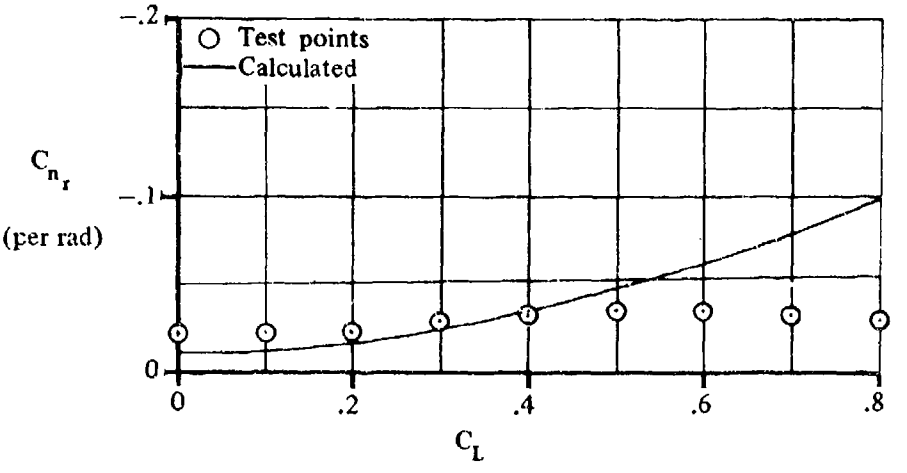

SKETCH (a)

B. TRANSONIC

In the transonic speed regime no theoretical methods are available for estimating the wing yawing derivative C_{n_r}. Furthermore, no known experimental results are available for this derivative at transonic speeds.

C. SUPERSONIC

No general method is available for evaluating the wing contribution to the yawing derivative C_{n_r} at supersonic speeds. However, methods are presented in references 2, 3, and 4 for evaluating C_{n_r} for special classes of wing planforms. The results presented in these references are based on supersonic linear theory. The methods are restricted to estimating C_{n_r} over a limited range of Mach numbers for zero-thickness wings with no dihedral. Furthermore, the methods are considered tentative, since the spanwise variation of Mach number in the case of yawing has been neglected.

REFERENCES

1. Toll, T. A., and Queijo, M. J.: Approximate Relations and Charts for Low-Speed Stability Derivatives of Swept Wings. NACA TN 1581, 1948. (U)

2. Ribner, H. S., and Malvestuto, F. S., Jr.: Stability Derivatives of Triangular Wings at Supersonic Speeds. NACA TR 908, 1948. (U)

3. Harmon, S. M.: Stability Derivatives at Supersonic Speeds of Thin Rectangular Wings With Diagonals Ahead of Tip Mach Lines. NACA TR 925, 1949. (U)

4. Malvestuto, F. S., Jr., and Margolis, K.: Theoretical Stability Derivatives of Thin Sweptback Wings Tapered to a Point With Sweptback and Sweptforward Trailing Edges for a Limited Range of Supersonic Speeds. NACA TR 971, 1950. (U)

5. Jaquet, B. M., and Fletcher, H. S.: Experimental Steady-State Yawing Derivatives of a 60° Delta-Wing Model as Affected by Changes in Vertical Position of the Wing and in Ratio of Fuselage Diameter to Wing Span. NACA TN 3843, 1956. (U)

6. Goodman, A., and Thomas, D. F., Jr.: Effects of Wing Position and Fuselage Size on the Low-Speed Static and Rolling Stability Characteristics of a Delta-Wing Model. NACA TR 1224, 1955. (U)

7. Williams, J. L.: Measured and Estimated Lateral Static and Rotary Derivatives of a 1/12-Scale Model of a High-Speed Fighter Airplane With Unswept Wings. NACA RM L53K09, 1954. (U)

8. Goodman, A., and Brewer, J. D.: Investigation at Low Speed of the Effect of Aspect Ratio and Sweep on Static and Yawing Stability Derivatives of Untapered Wings. NACA TN 1659, 1948. (U)

9. Bird, J. D., Jaquet, B. M., and Cowan, J. W.: Effect of Fuselage and Tail Surfaces on Low-Speed Yawing Characteristics of a Swept-Wing Model as Determined in Curved-Flow Test Section of Langley Stability Tunnel. NACA TN 2483, 1951. (U)

10. Letko, W., and Jaquet, B. M.: Effect of Airfoil Profile of Symmetrical Sections on the Low-Speed Static-Stability and Yawing Derivatives of 45° Sweptback Wing Models of Aspect Ratio 2.61. NACA RM L8H10, 1948. (U)

11. Letko, W.: Effect of Vertical-Tail Area and Length on the Yawing Stability Characteristics of a Model Having a 45° Sweptback Wing. NACA TN 2358, 1951. (U)

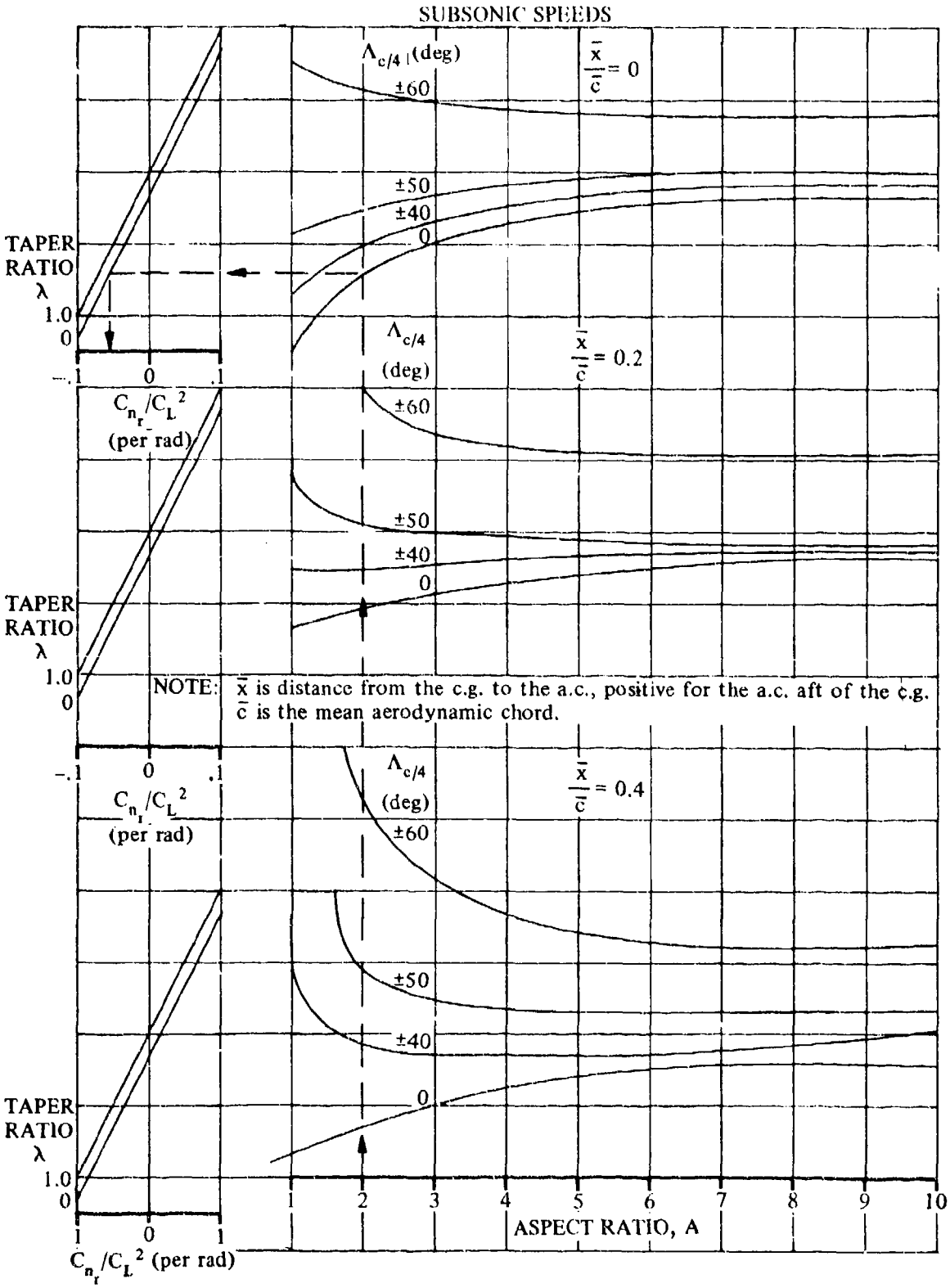

FIGURE 7.1.3.3-6 LOW-SPEED DRAG-DUE-TO-LIFT YAW-DAMPING PARAMETER

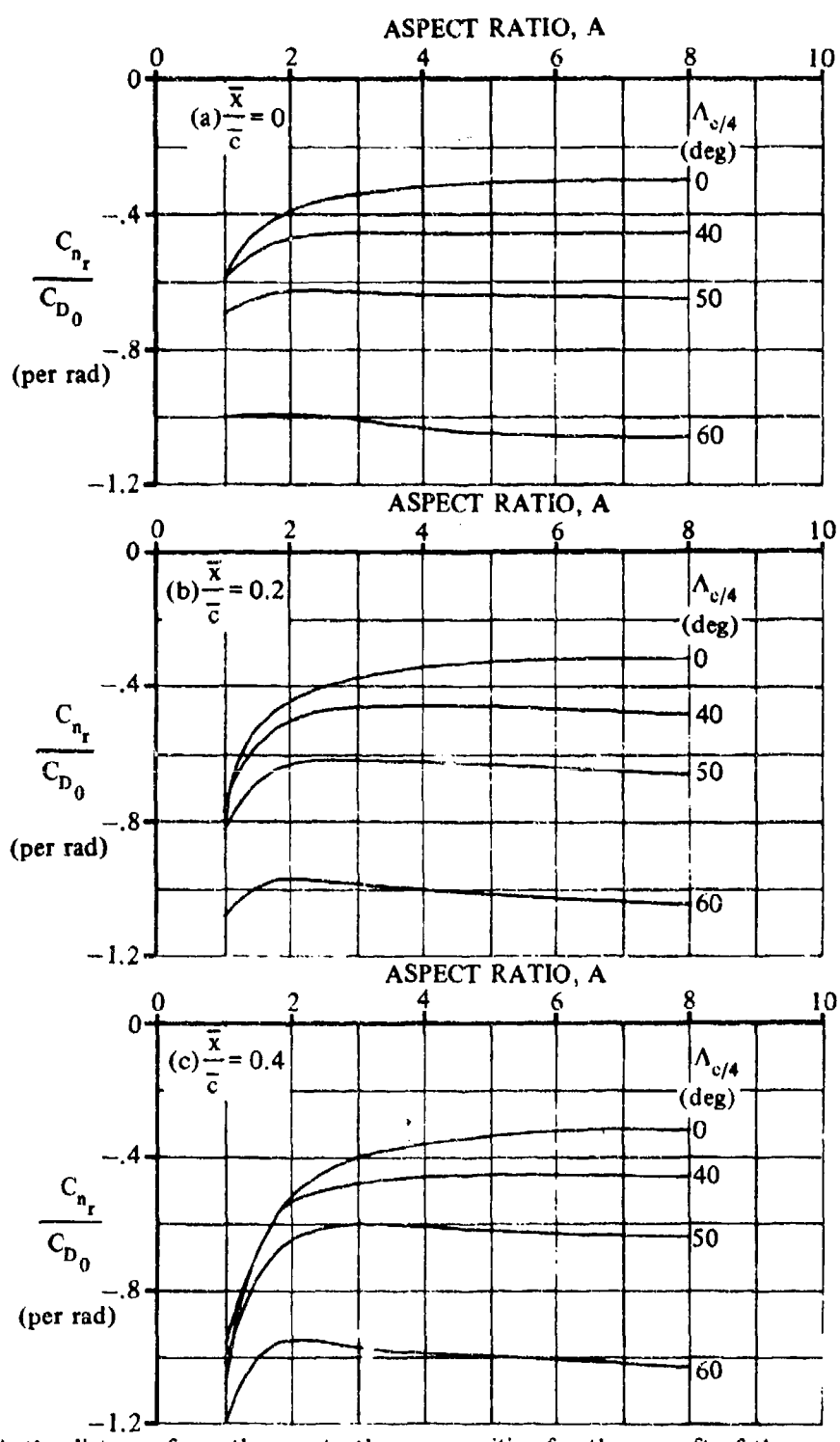

NOTE: $\bar{x}$ is the distance from the c.g. to the a.c., positive for the a.c. aft of the c.g.
$\bar{c}$ is the wing mean aerodynamic chord.

FIGURE 7.1.3.3-7 LOW-SPEED PROFILE-DRAG YAW-DAMPING PARAMETER

7.1.4 WING ACCELERATION DERIVATIVES

7.1.4.1 WING ACCELERATION DERIVATIVE $C_{L_{\dot{\alpha}}}$

Methods are presented for estimating the wing contribution to the derivative $C_{L_{\dot{\alpha}}}$ at low angles of attack for a triangular planform the subsonic and low transonic speed ranges and for planforms with the leading edge swept back and the trailing edge swept back or swept forward in the supersonic speed range. In addition, the supersonic results are directly applicable to wings with sweptforward leading edges, in view of the reversibility theorem (see reference 5). This derivative is used in estimating $C_{m_{\dot{\alpha}}}$ in Section 7.1.4.2.

If the wing acceleration derivative $C_{L_{\dot{\alpha}}}$ is to be used in method 1 of Section 7.3.4.1 to obtain $(C_{L_{\dot{\alpha}}})_{WB}$, the exposed wing planform area should be used for all calculations in the Datcom methods. Using the exposed planform area will yield $C_{L_{\dot{\alpha}}}$ based on the product of the exposed wing area and the exposed wing MAC, rather than the product of wing area and wing MAC as indicated.

DATCOM METHODS

A. SUBSONIC

An equation for estimating the subsonic acceleration derivative $C_{L_{\dot{\alpha}}}$ of a triangular wing (derived in reference 1), based on the product of wing area and wing MAC $S_W \bar{c}_W$, is given by

$$C_{L_{\dot{\alpha}}} = 1.5 \left(\frac{x_{a.c.}}{c_r} \right) C_{L_\alpha} + 3\, C_L(g) \quad \text{(per radian)} \qquad 7.1.4.1\text{-a}$$

where

C_{L_α} is the wing lift-curve slope (Section 4.1.3.2) at the Mach number under consideration, based on the total wing area (per radian).

$\frac{x_{a.c.}}{c_r}$ is obtained from Section 4.1.4.2.

$C_L(g)$ is the lift-coefficient correction term obtained from figure 7.1.4.1-6 (per radian).

Because of the restrictions placed on the lift-coefficient correction term, this method is valid only for $0 < \beta A < 4$.

Explicit expressions for estimating $C_{L_{\dot{\alpha}}}$ of other wing planforms in the subsonic region are not available at this time.

Sample Problem

Given:

$A = 4.0 \qquad \lambda = 0 \qquad \Lambda_{LE} = 45^\circ \qquad C_{L_\alpha} = 4.0$ per rad (Section 4.1.3.2)

$M = 0.6$

Compute:

$\beta = \sqrt{1 - M^2} = 0.80$

$\tan \Lambda_{LE} = 1.0$

$\beta / \tan \Lambda_{LE} = 0.80$

$\beta A = 3.20$

$A \tan \Lambda_{LE} = 4.0$

$\frac{x_{a.c.}}{c_r} = 0.570$ (figure 4.1.4.2-26a)

$\frac{-\beta^2 C_L(g)}{\pi A/2} = 0.1245$ per rad (figure 7.1.4.1-6)

$C_L(g) = -1.22$ per rad

Solution:

$$C_{L_{\dot{\alpha}}} = 1.5 \left(\frac{x_{a.c.}}{c_r} \right) C_{L_\alpha} + 3\, C_L(g) \quad \text{(equation 7.1.4.1-a)}$$

$$= (1.5)\,(0.570)\,(4.0) + (3)\,(-1.22)$$

$$= -0.240 \text{ per rad (based on } S_W \bar{c}_W)$$

B. TRANSONIC

The value of $C_{L_{\dot{\alpha}}}$ of a triangular wing from the critical Mach number to M = 1.0 is given by the method of paragraph A, provided $0 < \beta A < 4$.

There is no general theory available in the literature that gives the transonic values of $C_{L_{\dot{\alpha}}}$, either for additional wing-geometry parameters or for Mach numbers greater than 1.0. Furthermore, there is a scarcity of test data in the transonic region for any wing planform.

C. SUPERSONIC

The supersonic value of $C_{L_{\dot{\alpha}}}$, based on the product of wing area and wing MAC $S_W \bar{c}_W$, is derived in references 2 and 3 for wings with subsonic leading edges and in reference 4 for wings with supersonic leading edges.

1. Wings with subsonic leading edges ($\beta \cot \Lambda_{LE} < 1.0$)

For wings with subsonic leading edges, $C_{L_{\dot{\alpha}}}$ is obtained by the method of reference 2 for $\lambda = 0$ and by the method of reference 3 for $\lambda = 0.25$ to 1.0. The following methods are not valid if the Mach line from the vertex of the trailing edge intersects the leading edge or if the wing-tip Mach lines intersect on the wings or intersect the opposite wing tips.

a. Zero-taper-ratio wings ($\lambda = 0$)

$C_{L_{\dot{\alpha}}}$ is derived in reference 2 as

$$C_{L_{\dot{\alpha}}} = -\frac{\pi A M^2}{2\beta^2}\left[-3G(\beta C)\,F_3(N) + 2E''(\beta C)\,F_2(N) + \frac{1}{M^2}\,E''(\beta C)\,F_1(N)\right] \quad \text{(per radian)} \qquad 7.1.4.1\text{-b}$$

where

$E''(\beta C)$ and $G(\beta C)$ are obtained from figure 7.1.1.1-8.

$F_1(N)$, $F_2(N)$, and $F_3(N)$ are obtained from figure 7.1.4.1-7.

b. Wings with $\lambda = 0.25$ to 1.0

$C_{L_{\dot{\alpha}}}$ is derived in reference 3 as

$$C_{L_{\dot{\alpha}}} = \frac{M^2}{\beta^2}\left(C_{L_{\dot{\alpha}}}\right)_1 - \frac{1}{\beta^2}\left(C_{L_{\dot{\alpha}}}\right)_2 \quad \text{(per radian)} \qquad 7.1.4.1\text{-c}$$

where

$\left(C_{L_{\dot{\alpha}}}\right)_1$ and $\left(C_{L_{\dot{\alpha}}}\right)_2$ are obtained from figures 7.1.4.1-8a through 7.1.4.1-8f for $\lambda = 0.25$, 0.50, and 0.75 and from the equations of reference 3 for $\lambda > 0.75$.

2. Wings with supersonic leading edges ($\beta \cot \Lambda_{LE} > 1.0$)

For wings with supersonic leading edges, $C_{L_{\dot{\alpha}}}$ (derived in reference 4) is given by equation 7.1.4.1-c with $(C_{L_{\dot{\alpha}}})_1$ and $(C_{L_{\dot{\alpha}}})_2$ obtained from figures 7.1.4.1-11a through 7.1.4.1-11o.

Figures 7.1.4.1-11a through 7.1.4.1-11o are valid for the range of Mach numbers for which the Mach lines from the leading-edge vertex intersect the trailing edge. An additional limitation is that the foremost Mach line from either wing tip may not intersect the remote half-wing.

Sample Problem

1. Wing with subsonic leading edge

Given:

$A = 5.80 \qquad \lambda = 0 \qquad \Lambda_{LE} = 60^\circ \qquad M = 1.50$

Compute:

$$\beta = \sqrt{M^2 - 1} = 1.12$$

$$\cot \Lambda_{LE} = 0.5774$$

$$\beta \cot \Lambda_{LE} = 0.647$$

$$N = 1 - \frac{4 \cot \Lambda_{LE}}{A} = 0.602$$

$E''(\beta C) = 0.770$
$G(\beta C) = 0.570$
} (figure 7.1.1.1-8)

$F_1(N) = 0.520$
$F_2(N) = 1.090$
$F_3(N) = 0.907$
} (figure 7.1.4.1-7)

Solution:

$$C_{L_{\dot{\alpha}}} = -\frac{\pi A M^2}{2\beta^2}\left[-3G(\beta C)\,F_3(N) + 2E''(\beta C)\,F_2(N) + \frac{1}{M^2}\,E''(\beta C)\,F_1(N)\right]$$

(equation 7.1.4.1-b)

$$= -\frac{\pi(5.80)(2.25)}{2(1.25)}\left[-3(0.570)(0.907) + 2(0.770)(1.090) + \frac{1}{2.25}(0.770)(0.520)\right]$$

$= -5.22\,\pi(-1.551 + 1.679 + 0.178)$

$= -5.02$ per rad (based on $S_W \bar{c}_W$)

2. Wing with supersonic leading edge

Given:

$A = 4.0$ $\quad \lambda = 0.25$ $\quad \Lambda_{LE} = 45°$ $\quad M = 2.0$

Compute:

$\beta = \sqrt{M^2 - 1} = 1.732$

$\beta A = 6.928$

$\cot \Lambda_{LE} = 1.00$

$\beta \cot \Lambda_{LE} = 1.732$

$\cot^{-1} (\beta \cot \Lambda_{LE}) = 30°$

$\beta \left(C_{L_{\dot{\alpha}}}\right)_1 = -0.390$ per rad (figure 7.1.4.1-11d)

$\left(C_{L_{\dot{\alpha}}}\right)_1 = -0.225$ per rad

$\beta \left(C_{L_{\dot{\alpha}}}\right)_2 = 4.200$ per rad (figure 7.1.4.1-11f)

$\left(C_{L_{\dot{\alpha}}}\right)_2 = 2.425$ per rad

Solution:

$$C_{L_{\dot{\alpha}}} = \frac{M^2}{\beta^2} \left(C_{L_{\dot{\alpha}}}\right)_1 - \frac{1}{\beta^2} \left(C_{L_{\dot{\alpha}}}\right)_2 \text{ (equation 7.1.4.1-c)}$$

$$= \frac{4}{3} (-0.225) - \frac{1}{3} (2.425)$$

$= -1.108$ per rad (based on $S_W \bar{c}_W$)

REFERENCES

1. Tobak, M., and Lessing, H. C.: Estimation of Rotary Stability Derivatives at Subsonic and Transonic Speeds. Agard Report No. 343, Apr 1961. (U)

2 Malvestuto, F. S., Jr., and Margolis, K.: Theoretical Stability Derivatives of Thin Sweptback Wings Tapered to a Point with Sweptback or Sweptforward Trailing Edges for a Limited Range of Supersonic Speeds. NACA TR 971, 1950. (U)

3. Malvestuto, F. S., Jr., and Hoover, D. M.: Supersonic Lift and Pitching Moment of Thin Sweptback Tapered Wings Produced by Constant Vertical Acceleration. Subsonic Leading Edges and Supersonic Trailing Edges. NACA TN 2315, Mar 1951. (U)

4. Cole, I. J., and Margolis, K.: Lift and Pitching Moment at Supersonic Speeds due to Constant Vertical Acceleration for Thin Sweptback Tapered Wings with Streamwise Tips. Supersonic Leading and Trailing Edges. NACA TN 3196, Jul 1954. (U)

5. Harmon, S. M.: Theoretical Relations Between the Stability Derivatives of a Wing in Direct and Reverse Supersonic Flow. NACA TN 1943, 1949. (U)

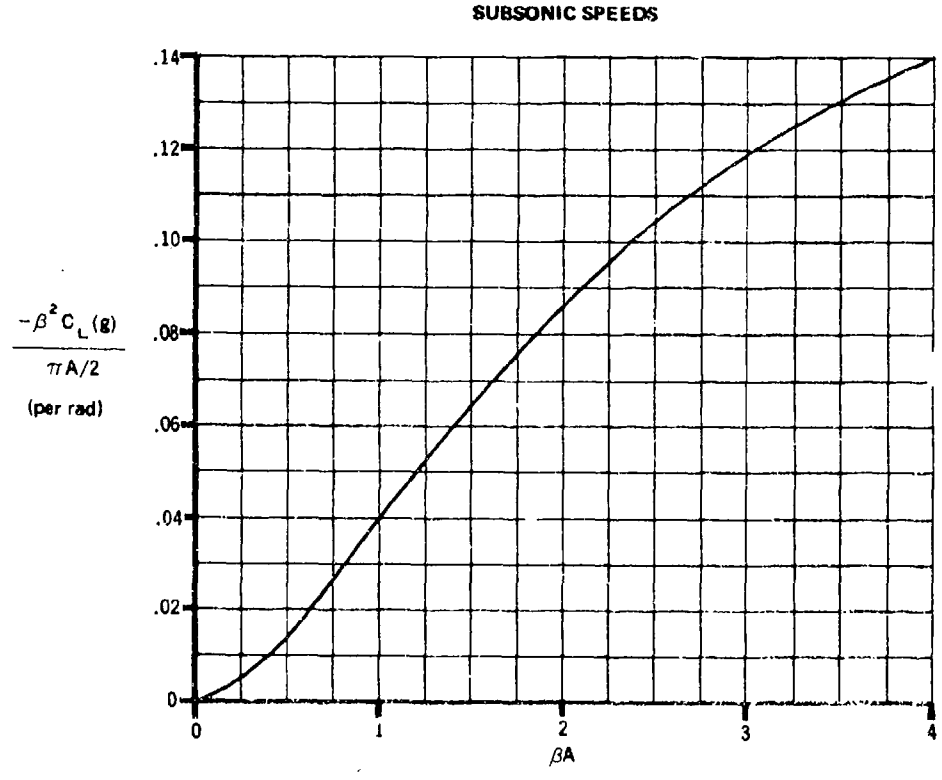

FIGURE 7.1.4.1-6 VARIATION OF LIFT-COEFFICIENT CORRECTION TERM WITH βA. TRIANGULAR WING. $0 < \beta A \leq 4$.

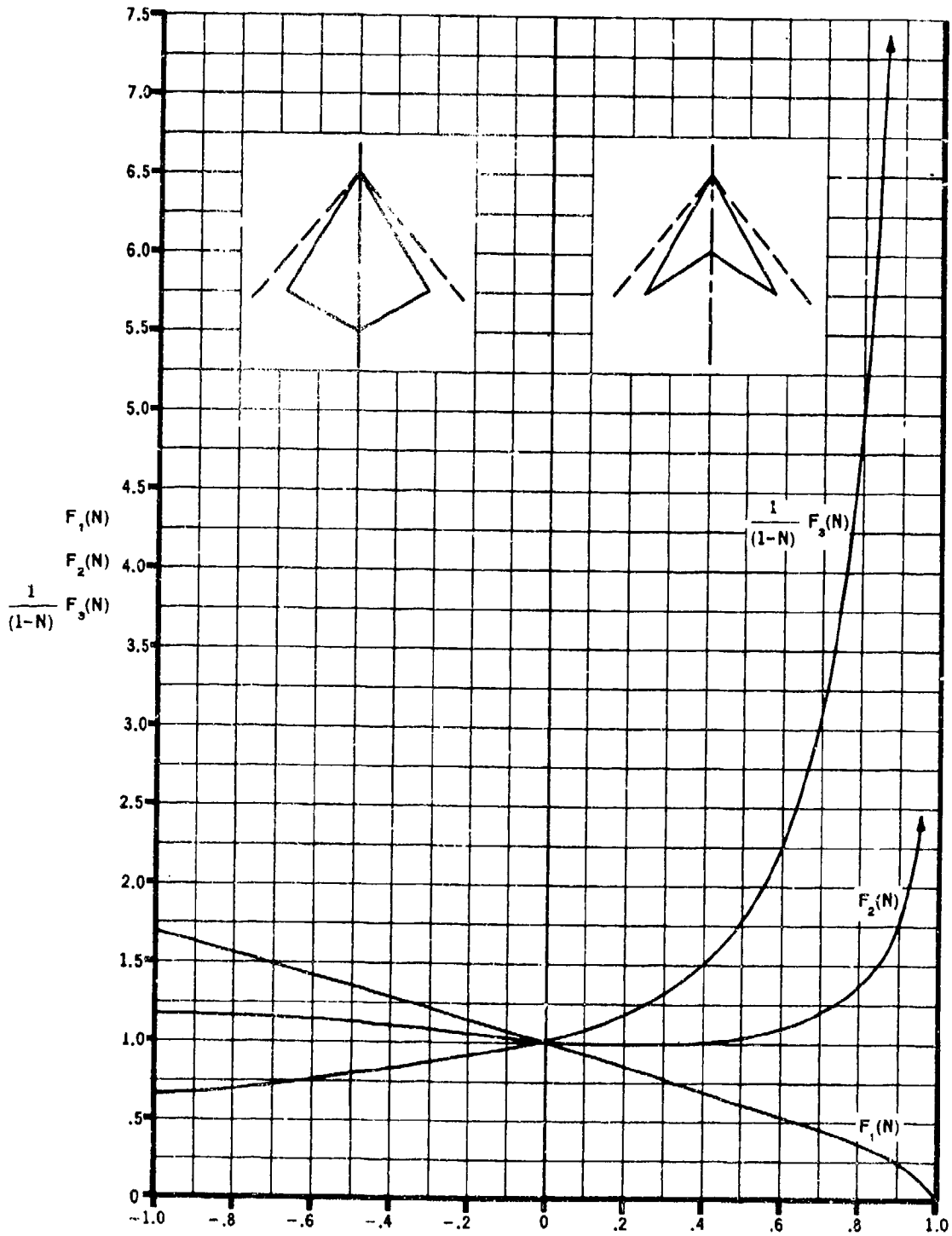

FIGURE 7.1.4.1-7 F(N) FACTORS OF THE STABILITY DERIVATIVE

SUBSONIC LEADING EDGE

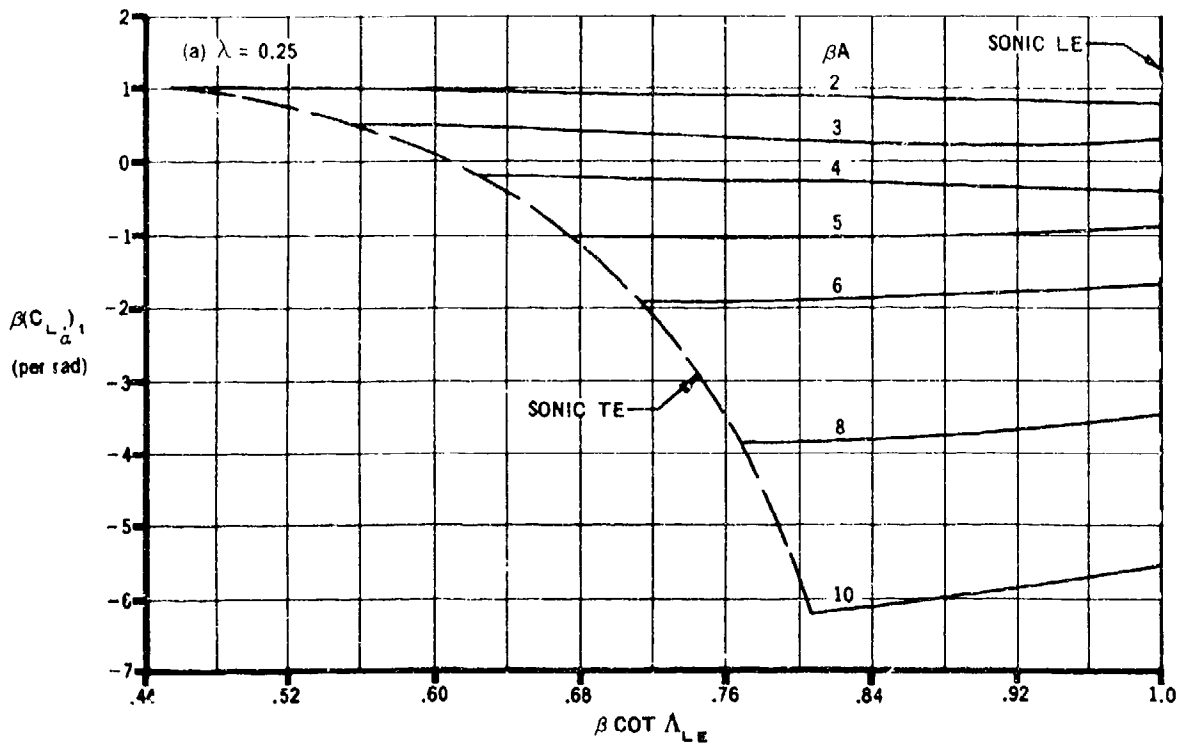

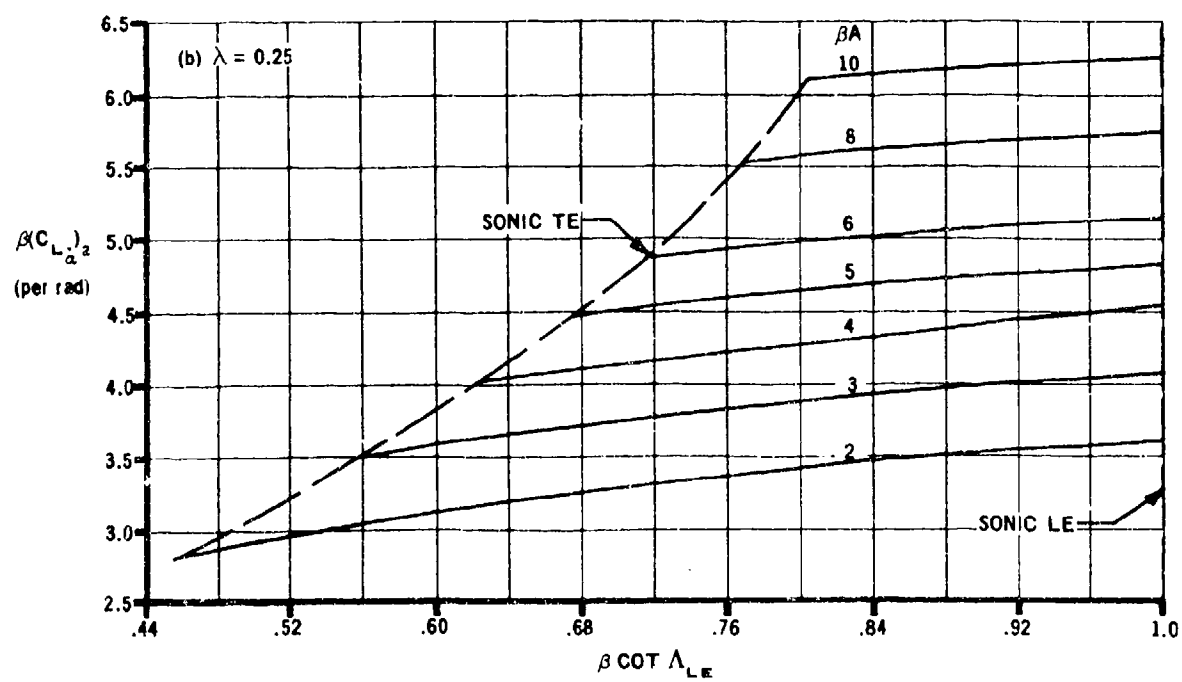

FIGURE 7.1.4.1-8 VARIATION OF $\beta(C_{L_\alpha})_1$ AND $\beta(C_{L_\alpha})_2$ WITH β COT Λ_{LE}

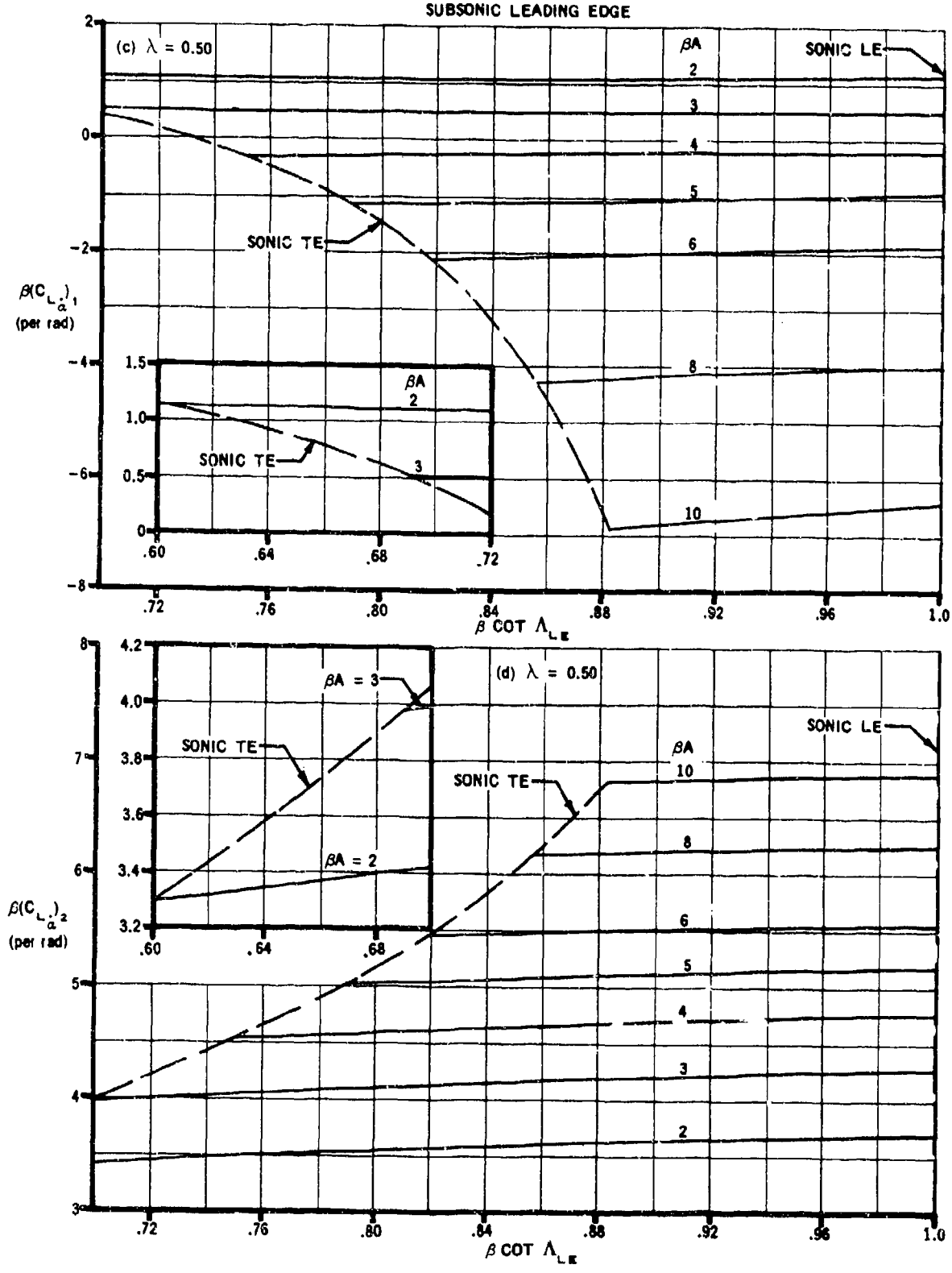

FIGURE 7.1.4.1-8 (CONTD)

SUBSONIC LEADING EDGE

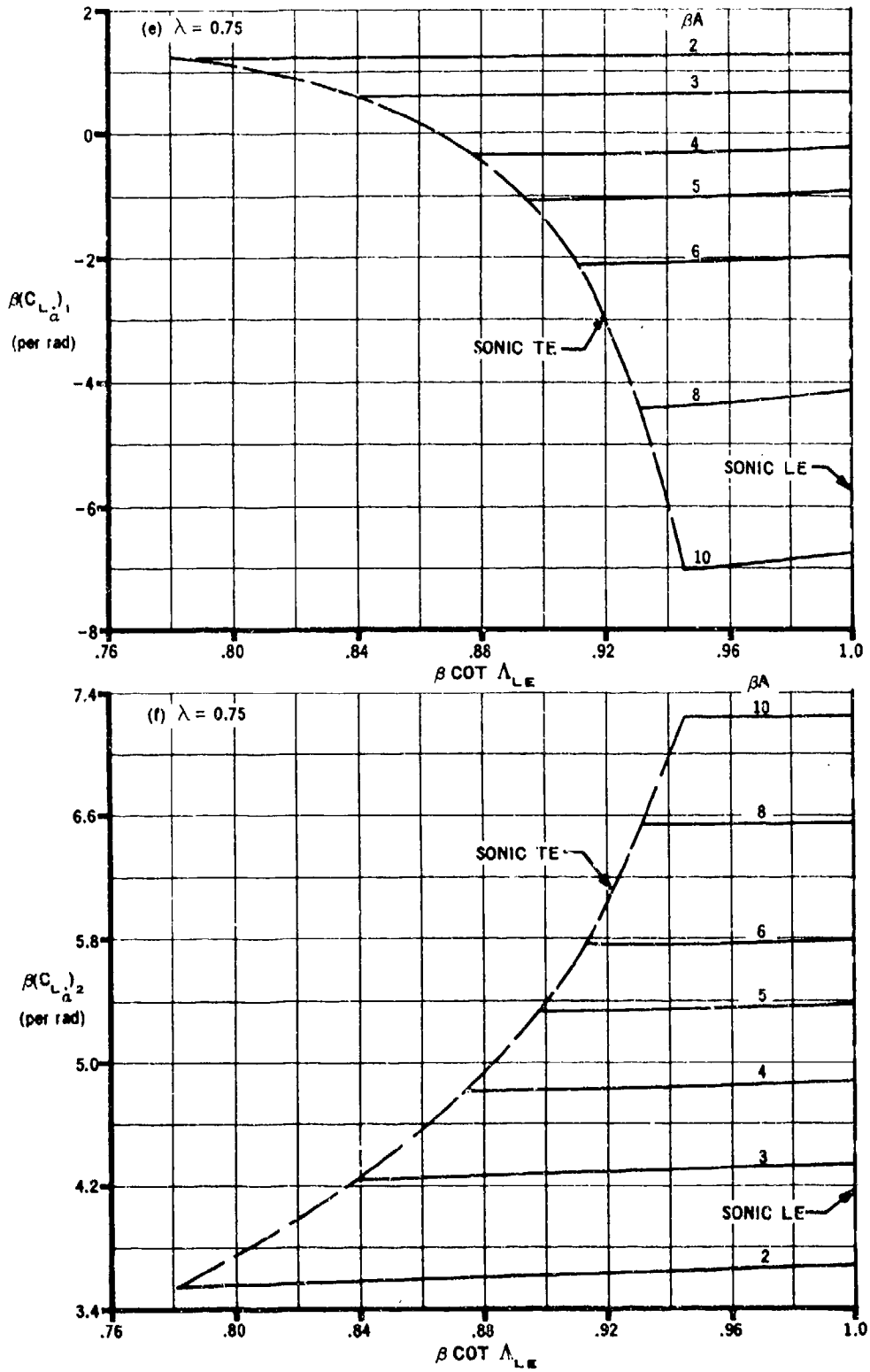

FIGURE 7.1.4.1-8 (CONTD)

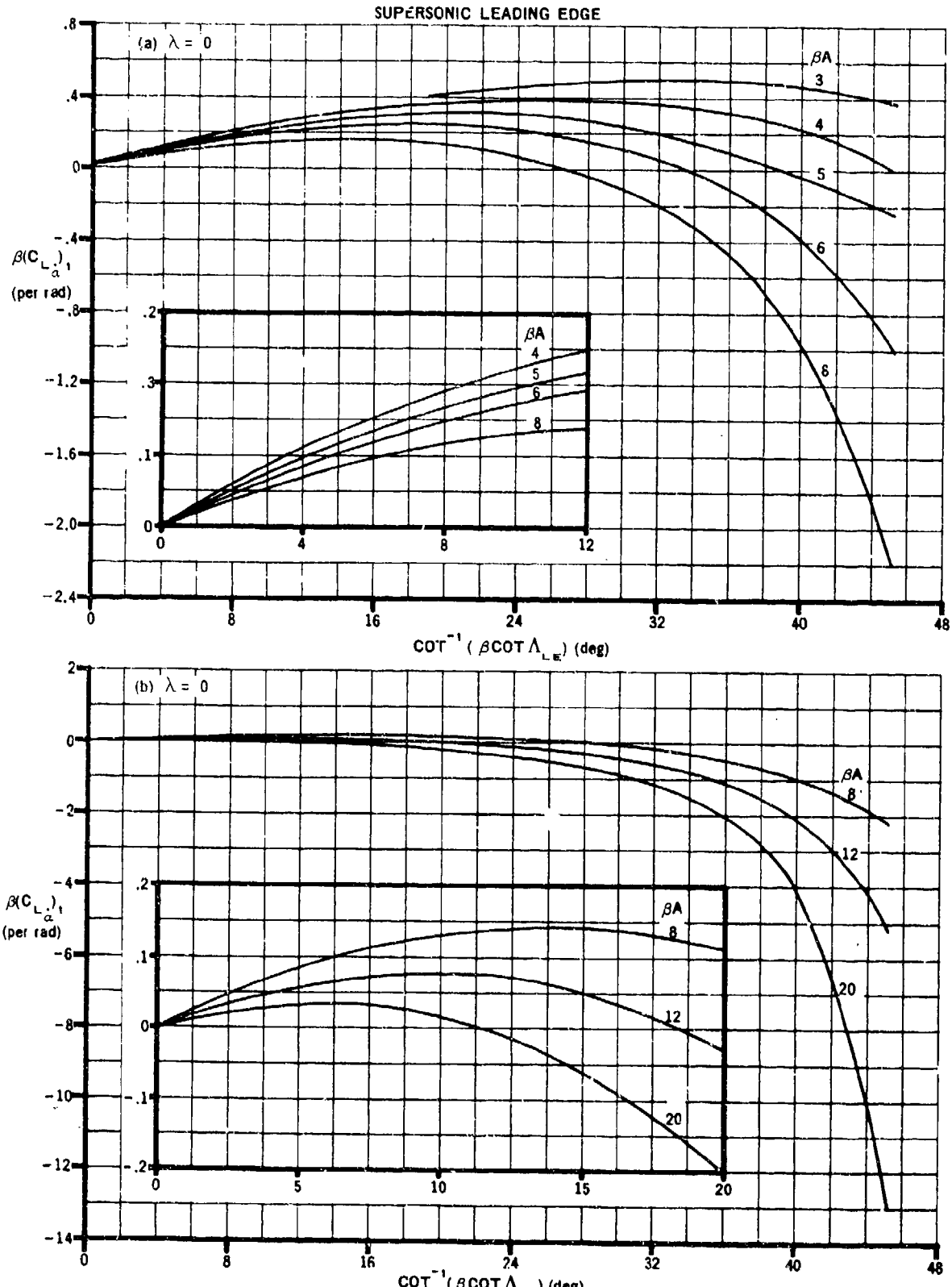

FIGURE 7.1.4.1-11 VARIATION OF $\beta(C_{L_\alpha})_1$ AND $\beta(C_{L_\alpha})_2$ WITH $\cot^{-1}(\beta \cot \Lambda_{L.E.})$

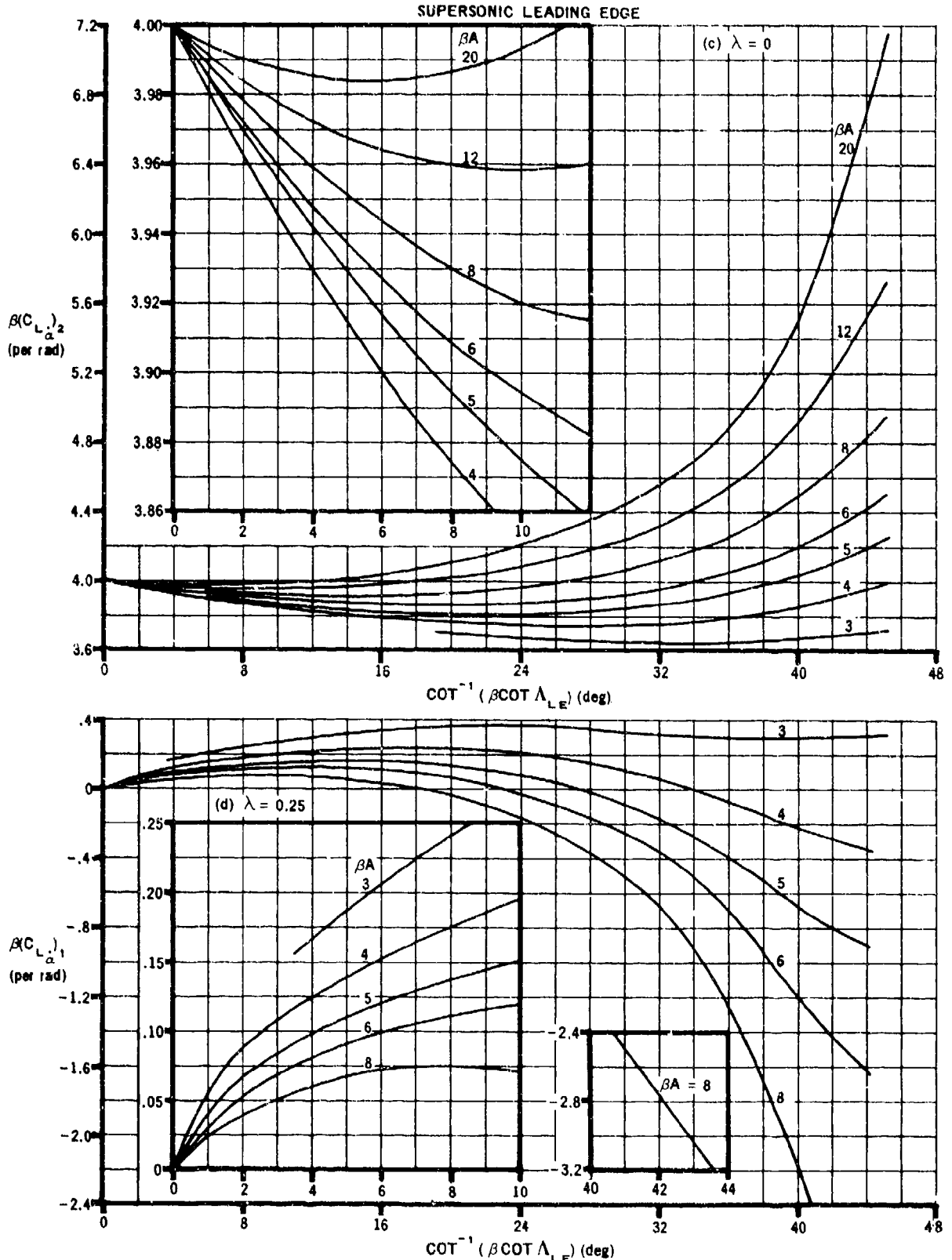

FIGURE 7.1.4.1-11 (CONTD)

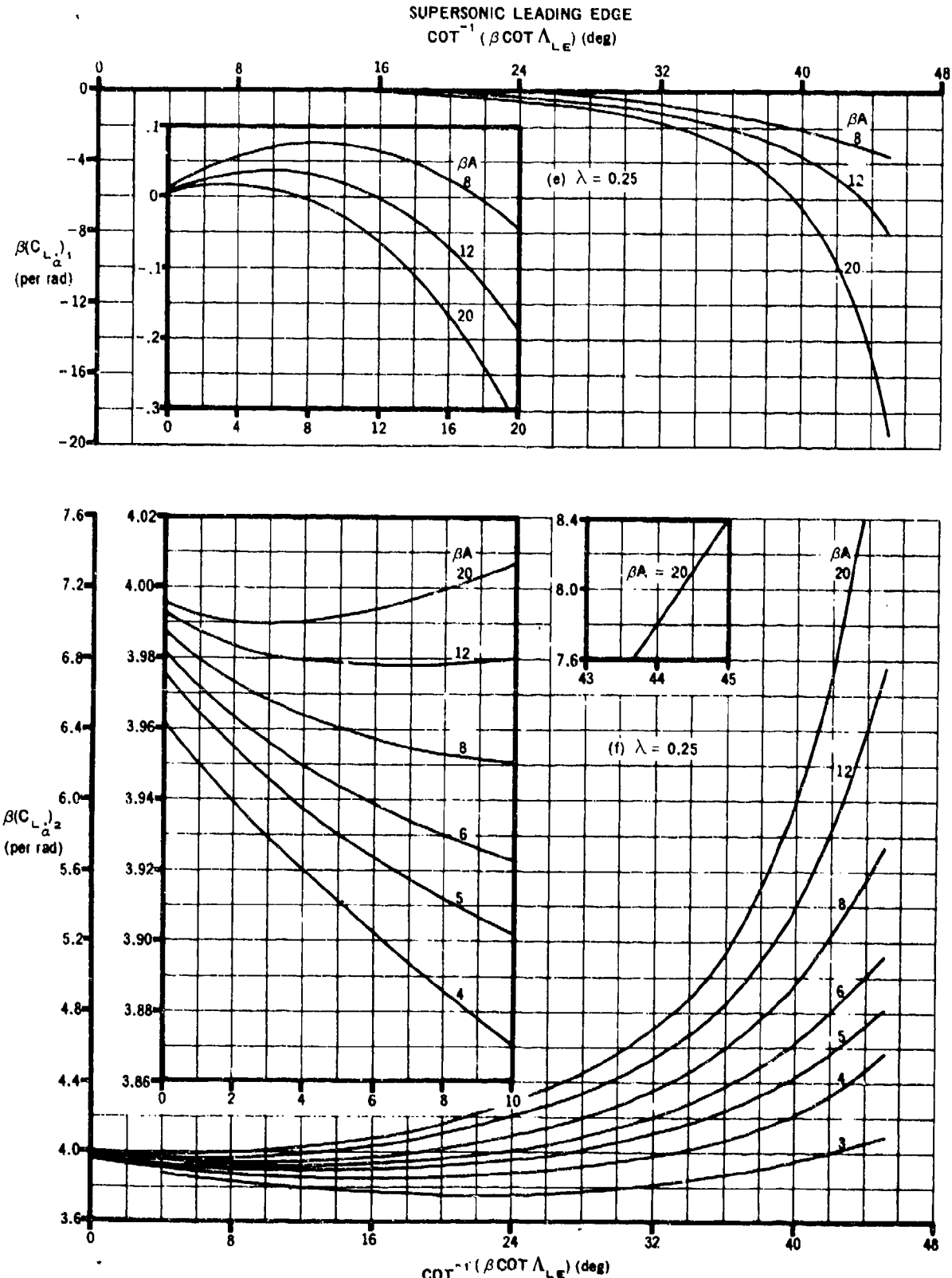

FIGURE 7.1.4.1-11 (CONTD)

SUPERSONIC LEADING EDGE

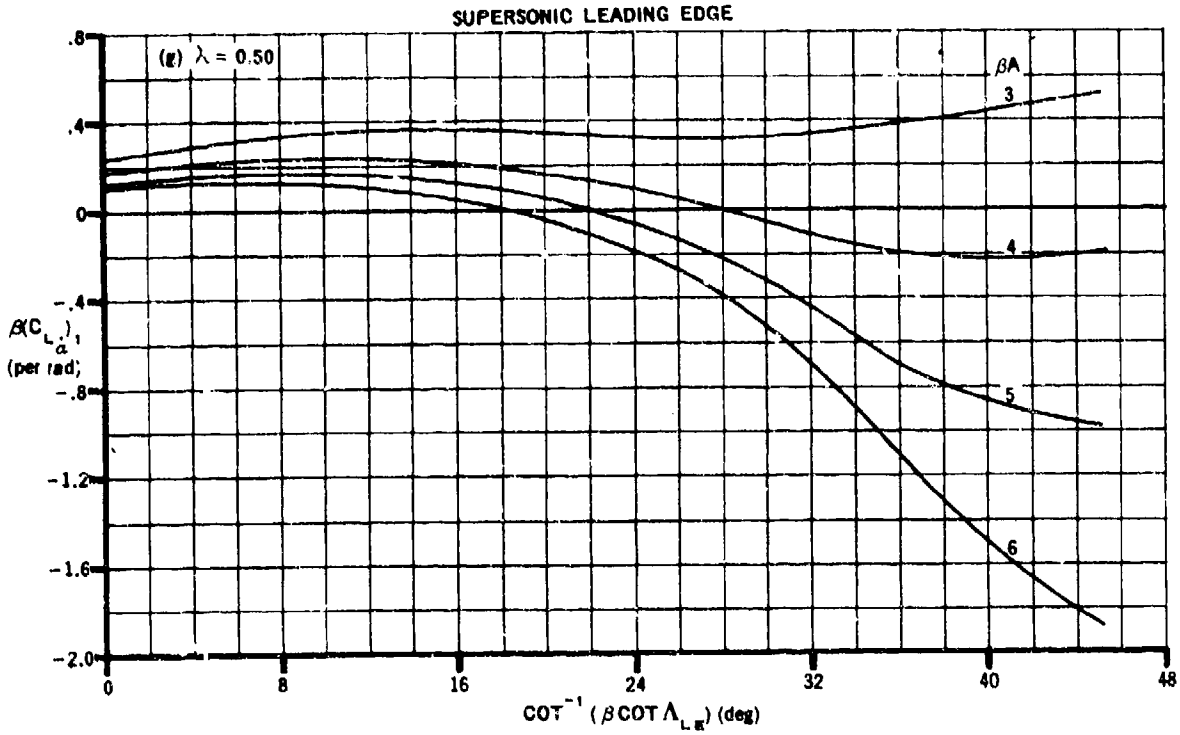

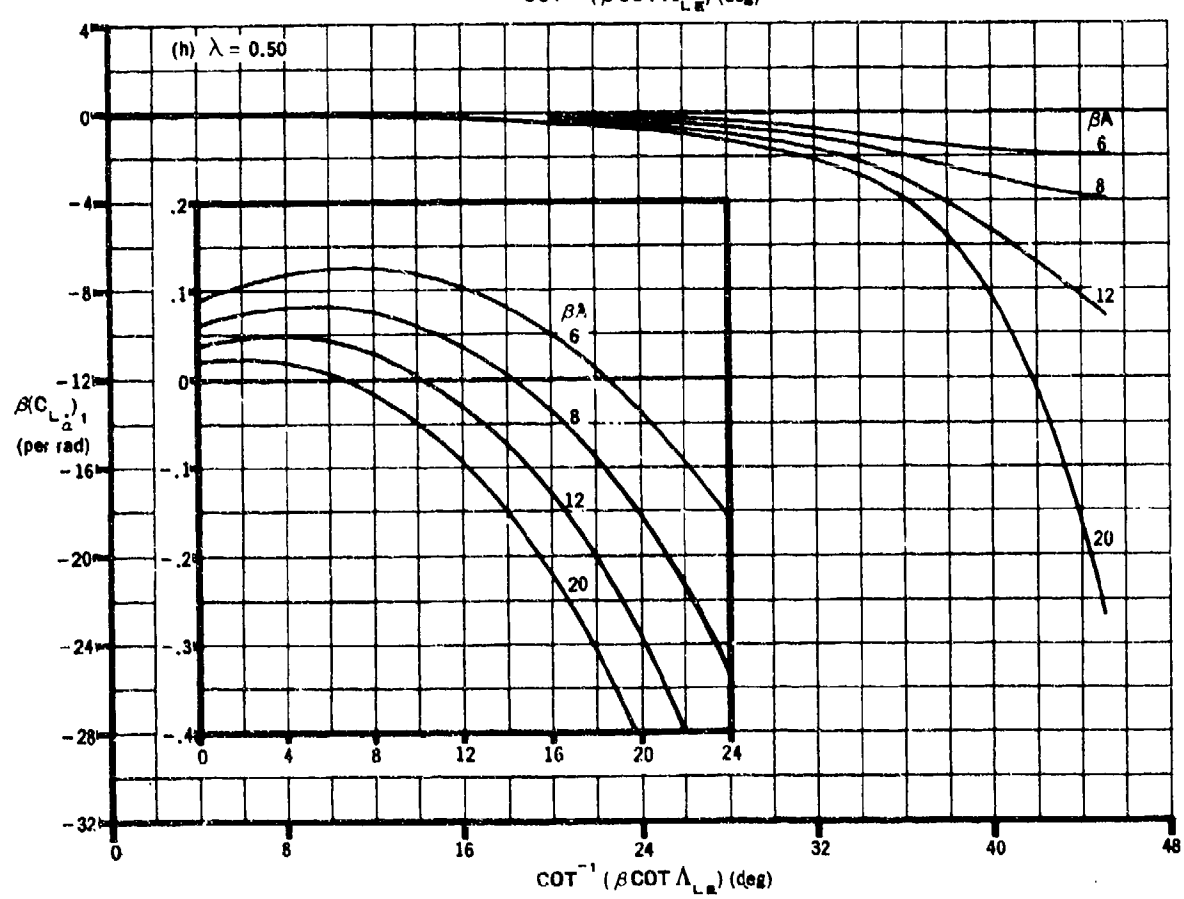

FIGURE 7.1.4.1-11 (CONTD)

SUPERSONIC LEADING EDGE

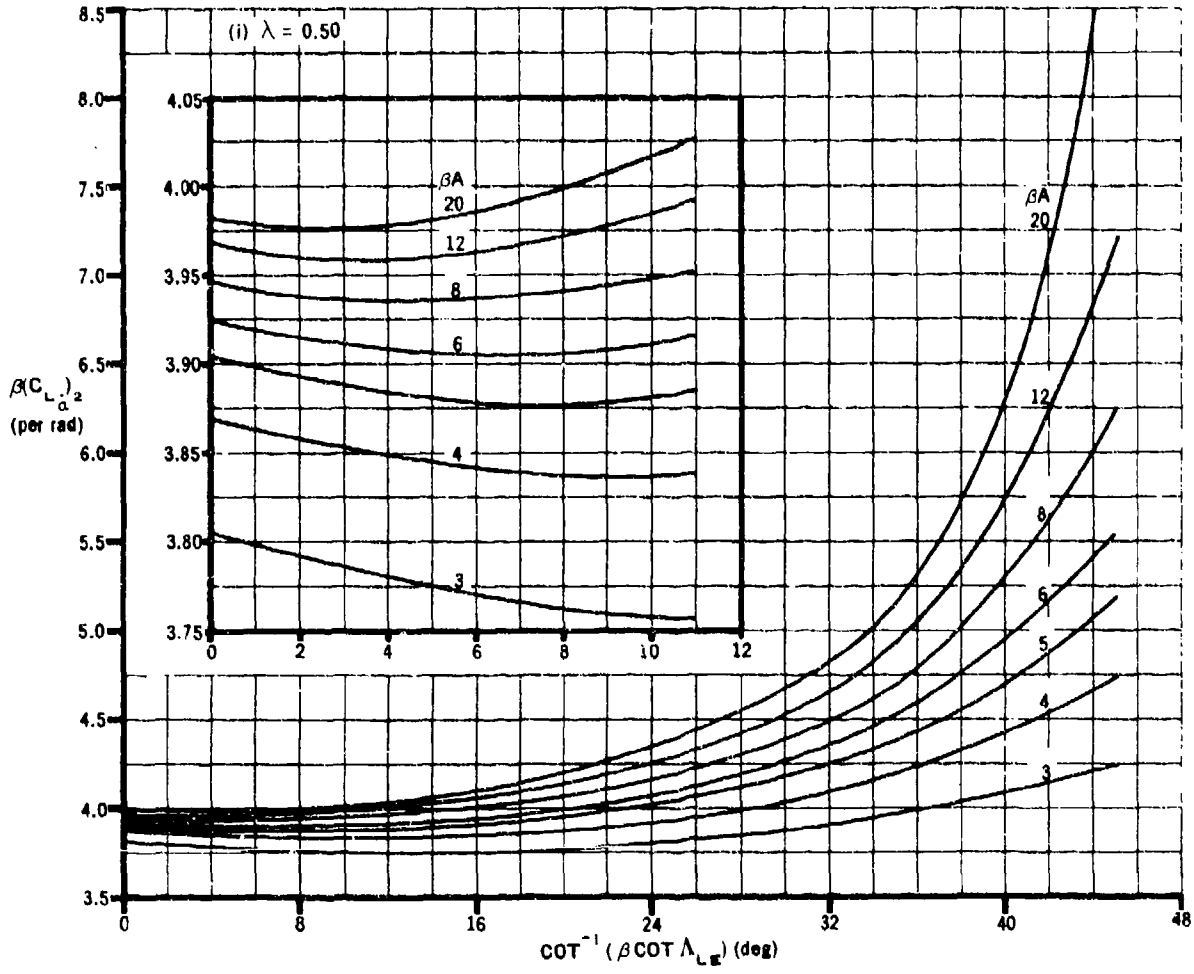

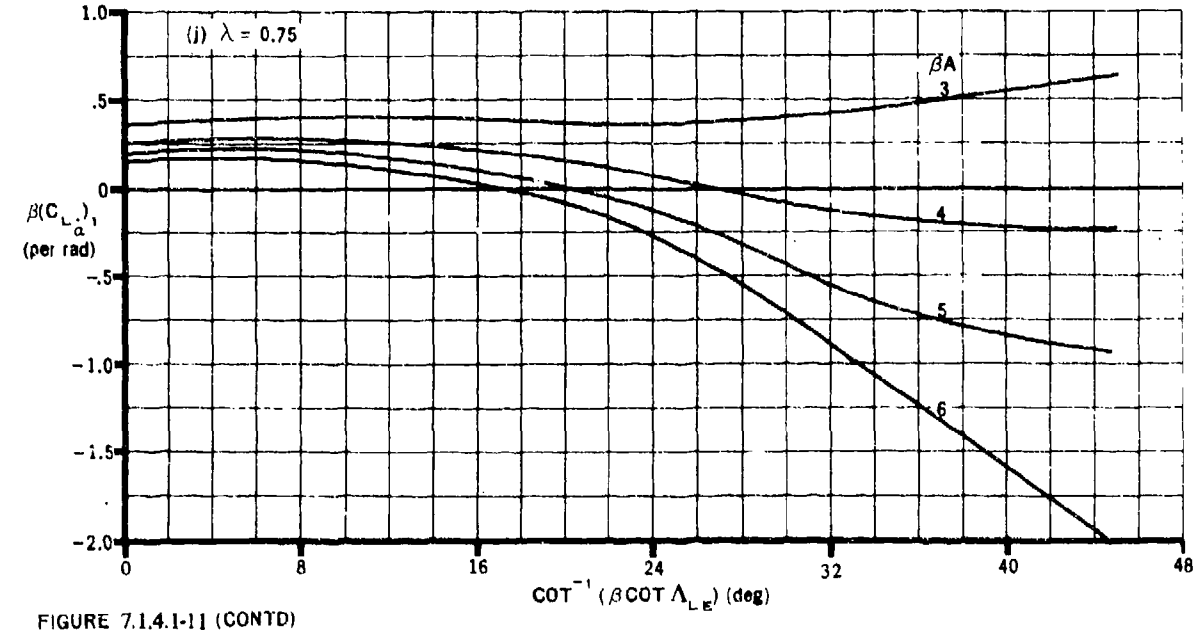

FIGURE 7.1.4.1-11 (CONTD)

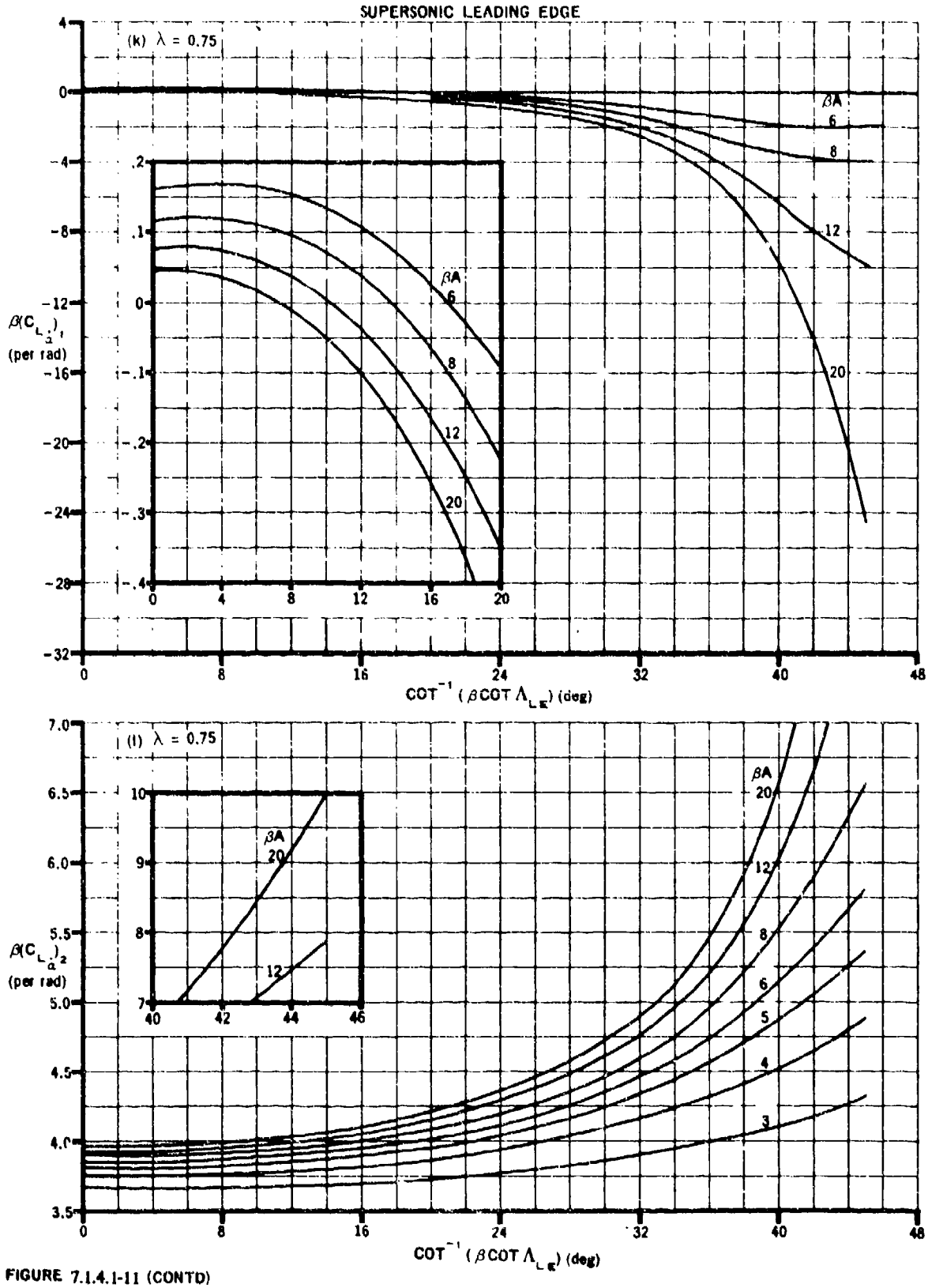

FIGURE 7.1.4.1-11 (CONTD)

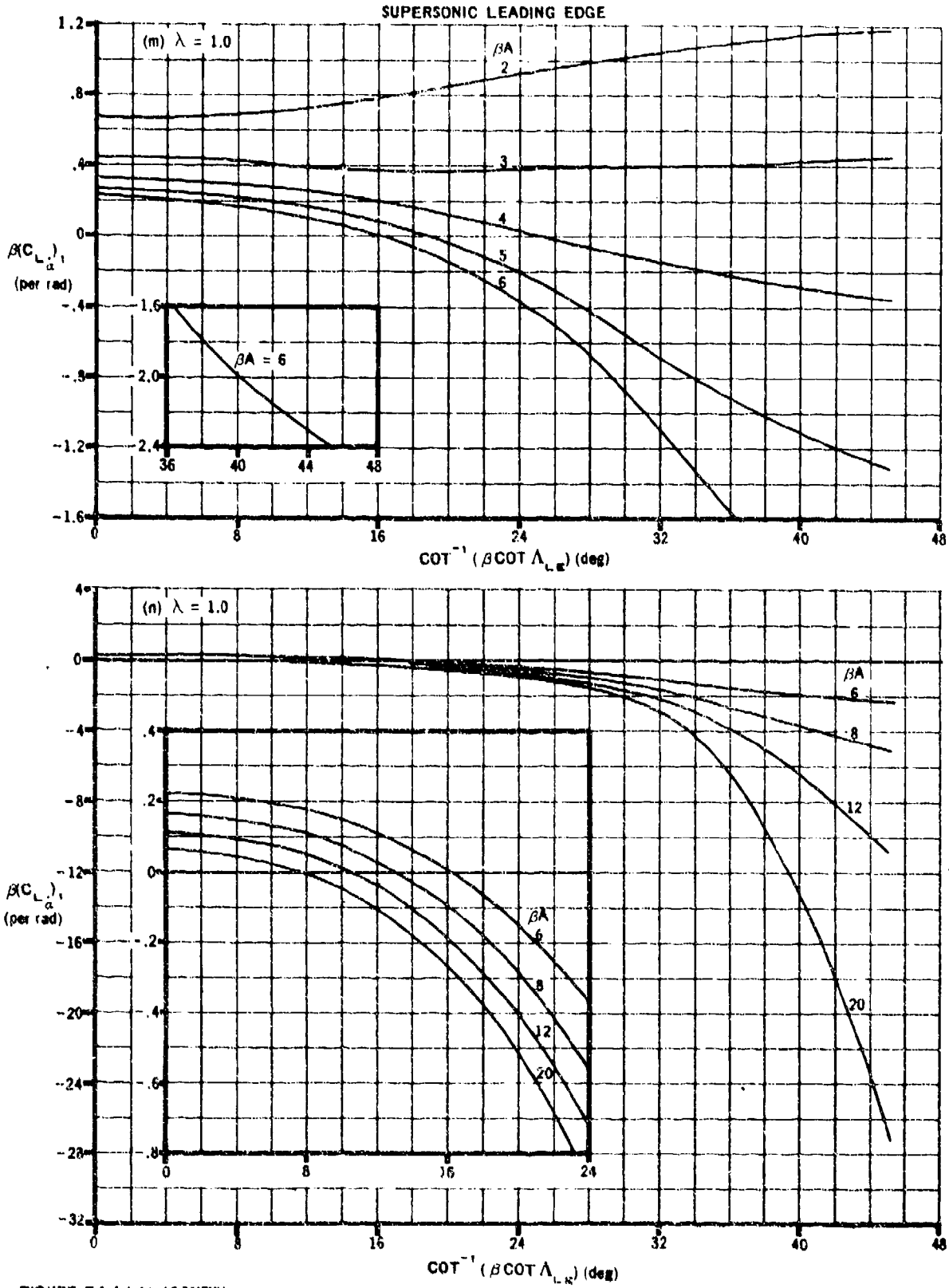

FIGURE 7.1.4.1-11 (CONTD)

SUPERSONIC LEADING EDGE

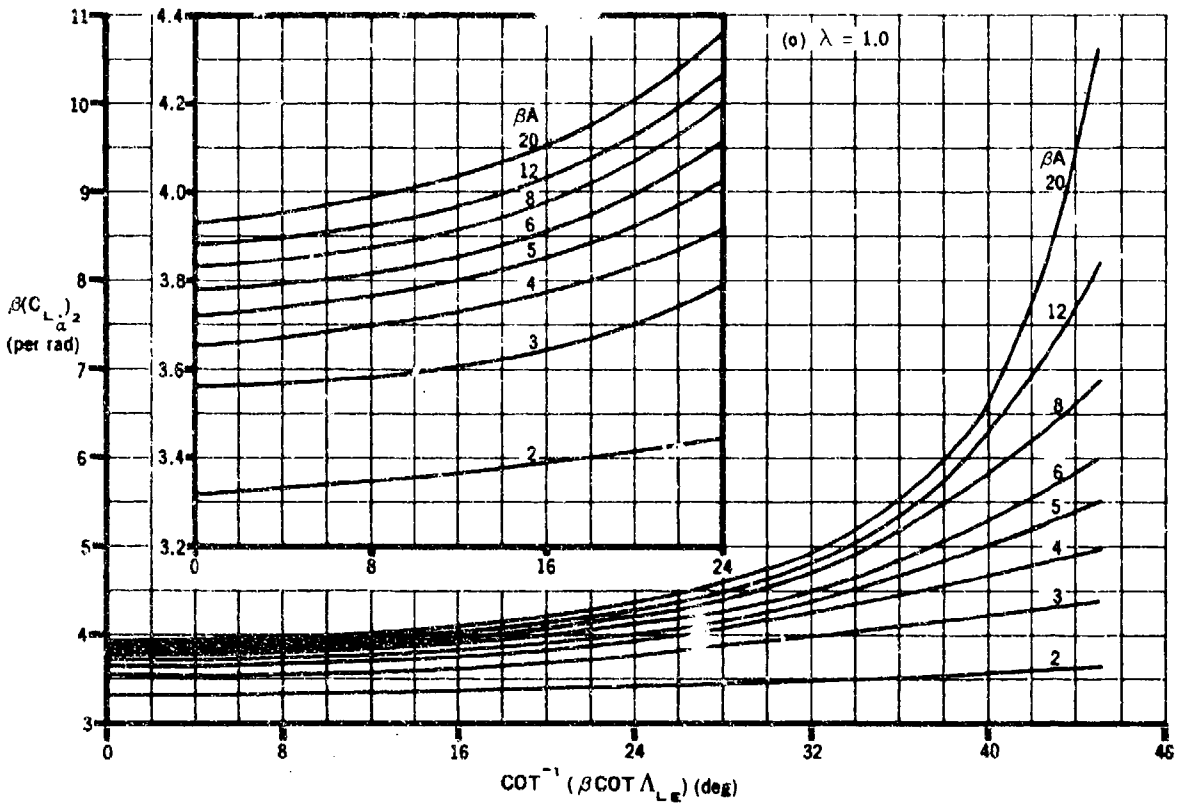

FIGURE 7.1.4.1-11 (CONTD)

7.1.4.2 WING ACCELERATION DERIVATIVE $C_{m_{\dot{\alpha}}}$

Methods are presented for estimating the wing contribution to the derivative $C_{m_{\dot{\alpha}}}$ for a triangular planform in the subsonic and low transonic speed ranges and for planforms with the leading edge swept back and the trailing edge swept back or swept forward in the supersonic speed range.

If the wing acceleration derivative $C_{m_{\dot{\alpha}}}$ is to be used in method 1 of Section 7.3.4.2 to obtain $(C_{m_{\dot{\alpha}}})_{WB}$, the exposed wing planform area should be used for all calculations in the Datcom methods. Using the exposed planform area will yield $C_{m_{\dot{\alpha}}}$ based on the product of the exposed wing area and the square of the exposed wing MAC, rather than the product of the wing area and the square of the wing MAC as indicated.

DATCOM METHODS

A. SUBSONIC

The subsonic value of $C_{m_{\dot{\alpha}}}$, based on the product of wing area and the square of wing MAC $S_W \bar{c}_W^{\,2}$, referred to body axis and for any center-of-gravity location is given by

$$C_{m_{\dot{\alpha}}} = C_{m_{\dot{\alpha}}}'' + \left(\frac{x_{c.g.}}{\bar{c}}\right) C_{L_{\dot{\alpha}}} \quad \text{(per radian)} \qquad 7.1.4.2\text{-a}$$

where

$C_{m_{\dot{\alpha}}}''$ is referred to body axis with the origin at the wing leading-edge vertex and is obtained as indicated below (per radian).

$\frac{x_{c.g.}}{\bar{c}}$ is the longitudinal distance from the wing leading-edge vertex to the center of gravity, measure l in mean aerodynamic chords, positive aft.

$C_{L_{\dot{\alpha}}}$ is obtained from Section 7.1.4.1, based on the product of wing area and wing MAC (per radian).

A method of estimating the subsonic acceleration derivative $C_{m_{\dot{\alpha}}}''$ of a triangular wing is derived in reference 1 as

$$C_{m_{\dot{\alpha}}}'' = -\frac{81}{32}\left(\frac{x_{a.c.}}{c_r}\right)^2 C_{L_\alpha} + \frac{9}{2} C_{m_0}(g) \quad \text{(per radian)} \qquad 7.1.4.2\text{-b}$$

where

C_{L_α} is the wing lift-curve slope (Section 4.1.3.2) at the Mach number under consideration, based on the total wing area (per radian).

$\frac{x_{a.c.}}{c_r}$ is obtained from Section 4.1.4.2.

$C_{m_0}(g)$ is the pitching-moment-coefficient correction term obtained from figure 7.1.4.2-8 (per radian).

Because of restrictions placed on the pitching-moment-coefficient correction term, equation 7.1.4.2-b is valid only for $0 < \beta A < 4$.

Explicit expressions for estimating $C_{m_{\dot\alpha}}$ of other wing planforms in the subsonic region are not available. An approximation may be made by subtracting the value of C_{m_q} (Section 7.1.1.2) from the appropriate test value of total pitch damping $\left(C_{m_q} + C_{m_{\dot\alpha}}\right)$ taken from table 7-A. Tests indicate that the relative importance of body damping of a conventional configuration in subsonic flow is small; therefore the use of wing-body test data of total pitch damping in this region is acceptable for an approximation, provided the test data are for a conventional design.

Sample Problem

Given: Same wing as in sample problem of paragraph A, Section 7.1.4.1

$A = 4.0$ $\lambda = 0$ $\Lambda_{LE} = 45°$ $C_{L_\alpha} = 4.0$ per rad (Section 4.1.3.2)

$\frac{x_{c.g.}}{\bar{c}} = 0.75$ (from planform geometry with c.g. at $\bar{c}/4$) $M = 0.6$

From sample problem of paragraph A, Section 7.1.4.1

$\frac{x_{a.c.}}{c_r} = 0.570$ $\beta = 0.8$ $\beta A = 3.20$ $C_{L_{\dot\alpha}} = -0.240$ per rad

Compute:

$\frac{\beta^2 C_{m_0}(g)}{\pi A/2} = 0.071$ per rad (figure 7.1.4.2-8)

$C_{m_0}(g) = 0.697$ per rad

Solution:

$$C_{m_{\dot{\alpha}}}'' = -\frac{81}{32}\left(\frac{x_{a.c.}}{c_r}\right)^2 C_{L_\alpha} + \frac{9}{2} C_{m_0}(g) \quad \text{(equation 7.1.4.2-b)}$$

$$= -\frac{81}{32}(0.570)^2(4.0) + \frac{9}{2}(0.697)$$

$$= -0.153 \text{ per rad}$$

$$C_{m_{\dot{\alpha}}} = C_{m_{\dot{\alpha}}}'' + \left(\frac{x_{c.g.}}{\bar{c}}\right) C_{L_{\dot{\alpha}}} \quad \text{(equation 7.1.4.2-a)}$$

$$= -0.153 + (0.75)(-0.240)$$

$$= -0.333 \text{ per rad (based on } S_W \bar{c}_W^2)$$

B. TRANSONIC

The variation of $C_{m_{\dot{\alpha}}}$ of a triangular wing from the critical Mach number to M = 1.0 is given by the method of paragraph A, provided $0 < \beta A < 4$.

There is no generalized theory available in the literature that gives the transonic values of $C_{m_{\dot{\alpha}}}$, either for additional wing-geometry parameters or for Mach numbers greater than 1.0. An approximation may be made by subtracting the value of C_{m_q} (Section 7.1.1.2) from the appropriate test value of total pitch damping $\left(C_{m_q} + C_{m_{\dot{\alpha}}}\right)$ taken from table 7-A. Although the importance of body damping in this region is unknown because of a lack of experimental data, wing-body test data of total pitch damping will probably have to be utilized if an approximation of $C_{m_{\dot{\alpha}}}$ is to be made, simply because of the lack of sufficient wing-alone test data. This method of analysis gives only a rough approximation and is limited to conventional designs where test data are available.

C. SUPERSONIC

The supersonic value of $C_{m_{\dot{\alpha}}}$, based on the product of wing area and the square of wing MAC $S_W \bar{c}_W^2$, referred to body axis and for any center-of-gravity location, is given by equation 7.1.4.2-a, i.e.,

$$C_{m_{\dot{\alpha}}} = C_{m_{\dot{\alpha}}}'' + \left(\frac{x_{c.g.}}{\bar{c}}\right) C_{L_{\dot{\alpha}}} \qquad \text{(per radian)}$$

where the parameters are defined in paragraph A and the supersonic value of $C_{m_{\dot{\alpha}}}''$ is obtained as indicated below.

Methods for estimating $C_{m_{\dot{\alpha}}}''$

1. Wings with subsonic leading edges ($\beta \cot \Lambda_{LE} < 1.0$)

For wings with subsonic leading edges, $C_{m_{\dot{\alpha}}}''$ is obtained by the method of reference 2 for $\lambda = 0$ and by the method of reference 3 for $\lambda = 0.25$ to 1.0. The following methods are not valid if the Mach line from the vertex of the trailing edge intersects the leading edge or if the wing-tip Mach lines intersect on the wings or intersect the opposite wing tips.

a. Zero-taper-ratio wings ($\lambda = 0$)

$C_{m_{\dot{\alpha}}}''$ is derived in reference 2 as

$$C_{m_{\dot{\alpha}}}'' = -\frac{3\pi AM^2}{16\beta^2}\left[G(\beta C)\, F_7(N) + \frac{16}{3}\, E''(\beta C)\, \frac{F_5(N)}{F_{11}(N)}\right]$$

$$+ \frac{16AM^2}{9\beta^2}\left[E''(\beta C)\, F_8(N)\right] + \frac{\pi A}{16\beta^2}\left[E''(\beta C)\, F_6(N)\right] - \left(\frac{d}{\bar{c}}\right) C_{L_{\dot{\alpha}}}$$

(per radian) 7.1.4.2-c

where

$E''(\beta C)$ and $G(\beta C)$ are obtained from figure 7.1.1.1-8.

$F_5(N)$, $F_7(N)$, and $F_{11}(N)$ are obtained from figure 7.1.1.2-8.

$F_6(N)$ and $F_8(N)$ are obtained from figure 7.1.4.2-9.

d is two-thirds the basic triangular wing root chord, $d = \frac{2}{3} c_{r_B}$ (see sketch (a), Section 7.1.1.1).

$C_{L_{\dot{\alpha}}}$ is obtained from paragraph C of Section 7.1.4.1, based on the product of wing area and wing MAC.

b. Wings with $\lambda = 0.25$ to 1.0

$C_{m_{\dot{\alpha}}}''$ is derived in reference 3 as

$$C_{m_{\dot{\alpha}}}'' = \frac{M^2}{\beta^2}\left(C_{m_{\dot{\alpha}}}\right)_1 - \frac{1}{\beta^2}\left(C_{m_{\dot{\alpha}}}\right)_2 \text{ (per radian)} \qquad 7.1.4.2\text{-d}$$

where

$\left(C_{m_{\dot{\alpha}}}\right)_1$ and $\left(C_{m_{\dot{\alpha}}}\right)_2$ are obtained from figures 7.1.4.2-10a through 7.1.4.2-10f for λ = 0.25, 0.50, and 0.75 and from the equations of reference 3 for $\lambda > 0.75$.

2. Wings with supersonic leading edges ($\beta \cot \Lambda_{LE} > 1.0$)

For wings with supersonic leading edges $C_{m_{\dot{\alpha}}}''$ is derived in reference 4 as

$$C_{m_{\dot{\alpha}}}'' = \frac{M^2}{\beta^2}\left(C_{m_{\dot{\alpha}}}\right)_1 + \left(\frac{M^2}{\beta^2} + 1\right)\left(C_{m_{\dot{\alpha}}}\right)_2 \quad \text{(per radian)} \qquad 7.1.4.2\text{-e}$$

where

$\left(C_{m_{\dot{\alpha}}}\right)_1$ and $\left(C_{m_{\dot{\alpha}}}\right)_2$ are obtained from figures 7.1.4.2-13a through 7.1.4.2-13p.

Figures 7.1.4.2-13a through 7.1.4.2-13p are valid for the range of Mach numbers for which the Mach lines from the leading-edge vertex intersect the trailing edge. An additional limitation is that the foremost Mach line from either wing tip may not intersect the remote half-wing.

Sample Problems

1. Wing with subsonic leading edge

Given: Same wing as in sample problem 1 of paragraph C, Section 7.1.4.1.

$A = 5.80 \quad \lambda = 0 \quad \Lambda_{LE} = 60° \quad$ c.g. at $\frac{\bar{c}}{4} \quad b = 16$ ft $\quad M = 1.50$

$\frac{x_{c.g.}}{\bar{c}} = 1.50$ (from planform geometry with c.g. at $\bar{c}/4$)

From sample problem 1 of paragraph C, Section 7.1.4.1:

$\beta = 1.12 \qquad \beta \cot \Lambda_{LE} = 0.647 \qquad N = 0.602$

$E''(\beta C) = 0.770 \qquad G(\beta C) = 0.570 \qquad C_{L_{\dot{\alpha}}} = -5.02$ per rad

Compute:

$$\left.\begin{aligned} F_5(N) &= 0.251 \\ F_7(N) &= -1.620 \\ F_{11}(N) &= 0.395 \end{aligned}\right\} \text{(figure 7.1.1.2-8)}$$

$$\left.\begin{aligned} F_6(N) &= -2.600 \\ F_8(N) &= 0.880 \end{aligned}\right\} \text{(figure 7.1.4.2-9)}$$

Obtain d from the characteristics of the basic triangular wing (see sketch (a), Section 7.1.1.1).

$$A_B = \frac{4}{\tan \Lambda_{LE}} = 2.31$$

$$c_{r_B} = \frac{2b}{A_B} = 13.85 \text{ ft}$$

$$d = \frac{2}{3} c_{r_B} = 9.233 \text{ ft}$$

$$c_r = \frac{2b}{A} = 5.517 \text{ ft}$$

$$\bar{c} = 3.678 \text{ ft}$$

Solution:

$$C_{m_{\dot{\alpha}}}'' = -\frac{3\pi AM^2}{16\beta^2}\left[G(\beta C)\, F_7(N) + \frac{16}{3} E''(\beta C) \frac{F_5(N)}{F_{11}(N)}\right]$$

$$+ \frac{16AM^2}{9\beta^2}\left[E''(\beta C)\, F_8(N)\right] + \frac{\pi A}{16\beta^2}\left[E''(\beta C)\, F_6(N)\right] - \left(\frac{d}{\bar{c}}\right) C_{L_{\dot{\alpha}}}$$

(equation 7.1.4.2-c)

$$= -\frac{3\pi(5.80)\,(2.25)}{16(1.25)}\left[(0.570)\,(-1.620) + \frac{16}{3}\,(0.770)\,\frac{(0.251)}{(0.395)}\right]$$

$$+ \frac{16(5.80)\,(2.25)}{9(1.25)}\left[(0.770)\,(0.880)\right] + \frac{\pi(5.80)}{16(1.25)}\left[(0.770)\,(-2.600)\right]$$

$$- \frac{(9.233)}{(3.678)}\,(-5.02)$$

$$= -6.15(-0.9234 + 2.610) + 12.576 - 1.824 + 12.602$$

$$= 12.98 \text{ per rad}$$

$$C_{m_{\dot{\alpha}}} = C_{m_{\dot{\alpha}}}'' + \frac{x_{c.g.}}{\bar{c}} C_{L_{\dot{\alpha}}} \quad \text{(equation 7.1.4.2-a)}$$

$$= 12.98 + (1.5)(-5.02)$$

$$= 5.45 \text{ per rad (based on } S_W \bar{c}_W{}^2)$$

2. Wing with supersonic leading edge

Given: Same wing as in sample problem 2 of paragraph C, Section 7.1.4.1.

$$A = 4.0 \qquad \lambda = 0.25 \qquad \Lambda_{LE} = 45° \qquad \text{c.g. at } \frac{\bar{c}}{4} \qquad M = 2.0$$

$$\frac{x_{c.g.}}{\bar{c}} = 0.964 \text{ (from planform geometry with c.g. at } \bar{c}/4)$$

From sample problem 2 of paragraph C, Section 7.1.4.1:

$$\beta = 1.732 \qquad \beta A = 6.928 \qquad \beta \cot \Lambda_{LE} = 1.732$$

$$\cot^{-1}(\beta \cot \Lambda_{LE}) = 30° \qquad C_{L_{\dot{\alpha}}} = -1.108 \text{ per rad}$$

Compute:

$$\beta \left(C_{m_{\dot{\alpha}}}\right)_1 = 11.80 \text{ per rad} \quad \text{(figure 7.1.4.2-13d)}$$

$$\left(C_{m_{\dot{\alpha}}}\right)_1 = 6.813 \text{ per rad}$$

$$\beta \left(C_{m_{\dot{\alpha}}}\right)_2 = -5.530 \text{ per rad} \quad \text{(figure 7.1.4.2-13f)}$$

$$\left(C_{m_{\dot{\alpha}}}\right)_2 = -3.193 \text{ per rad}$$

Solution:

$$C_{m_{\dot{\alpha}}}'' = \frac{M^2}{\beta^2} \left(C_{m_{\dot{\alpha}}}\right)_1 + \left(\frac{M^2}{\beta^2} + 1\right) \left(C_{m_{\dot{\alpha}}}\right)_2 \quad \text{(equation 7.1.4.2-e)}$$

$$= \frac{4}{3}(6.813) + \left(\frac{4}{3} + 1\right)(-3.193)$$

$$= 9.08 - 7.45$$

$$= 1.63 \text{ per rad}$$

$$C_{m_{\dot{\alpha}}} = C_{m_{\dot{\alpha}}}'' + \frac{x_{c.g.}}{\bar{c}} C_{L_{\dot{\alpha}}} \quad \text{(equation 7.1.4.2-a)}$$

$$= 1.63 + (0.964)(-1.108)$$

$$= 0.562 \text{ per rad (based on } S_W \bar{c}_W{}^2)$$

REFERENCES

1. Tobak, M., and Lessing, H. C.: Estimation of Rotary Stability Derivatives at Subsonic and Transonic Speeds. AGARD Report 343, 1961. (U)

2. Malvestuto, F. S., Jr., and Margolis, K.: Theoretical Stability Derivatives of Thin Sweptback Wings Tapered to a Point with Sweptback or Sweptforward Trailing Edges for a Limited Range of Supersonic Speeds. NACA TR 971, 1950. (U)

3. Malvestuto, F. S., Jr., and Hoover, D. M.: Supersonic Lift and Pitching Moment of Thin Sweptback Tapered Wings Produced by Constant Vertical Acceleration. Subsonic Leading Edges and Supersonic Trailing Edges. NACA TN 2315, 1951. (U)

4. Cole, I. J., and Margolis, K.: Lift and Pitching Moment at Supersonic Speeds due to Constant Vertical Acceleration for Thin Sweptback Tapered Wings with Streamwise Tips. Supersonic Leading and Trailing Edges. NACA TN 3196, 1954. (U)

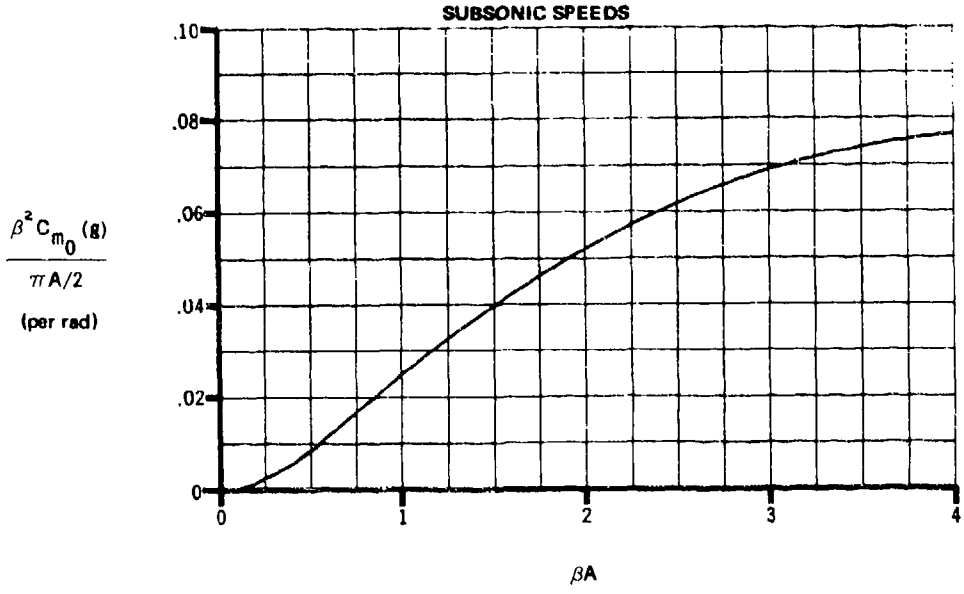

FIGURE 7.1.4.2-8 VARIATION OF PITCHING-MOMENT COEFFICIENT CORRECTION TERM WITH βA, TRIANGULAR WING $0 < \beta A \leq 4$.

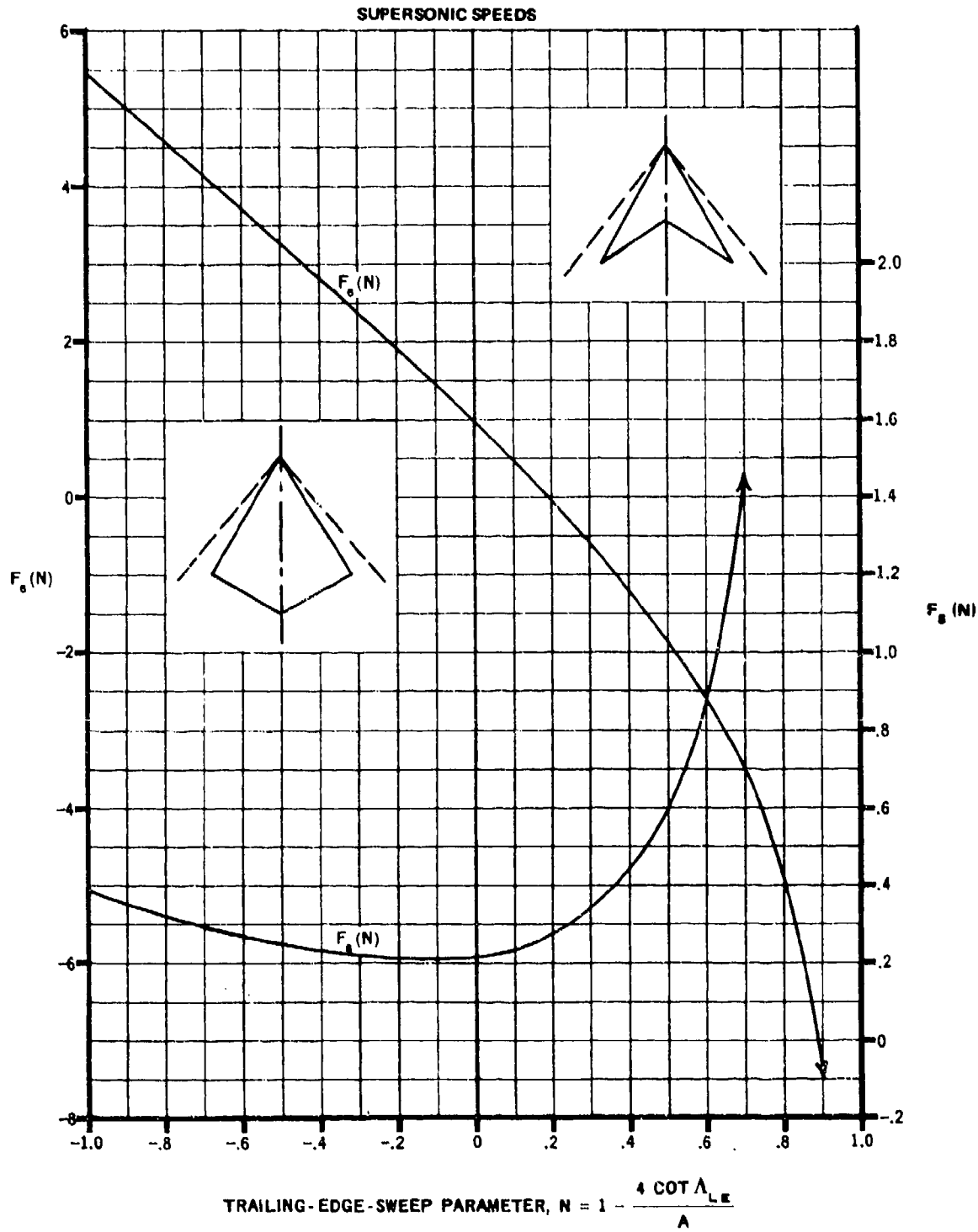

FIGURE 7.1.4.2-9 F(N) FACTORS OF THE STABILITY DERIVATIVE

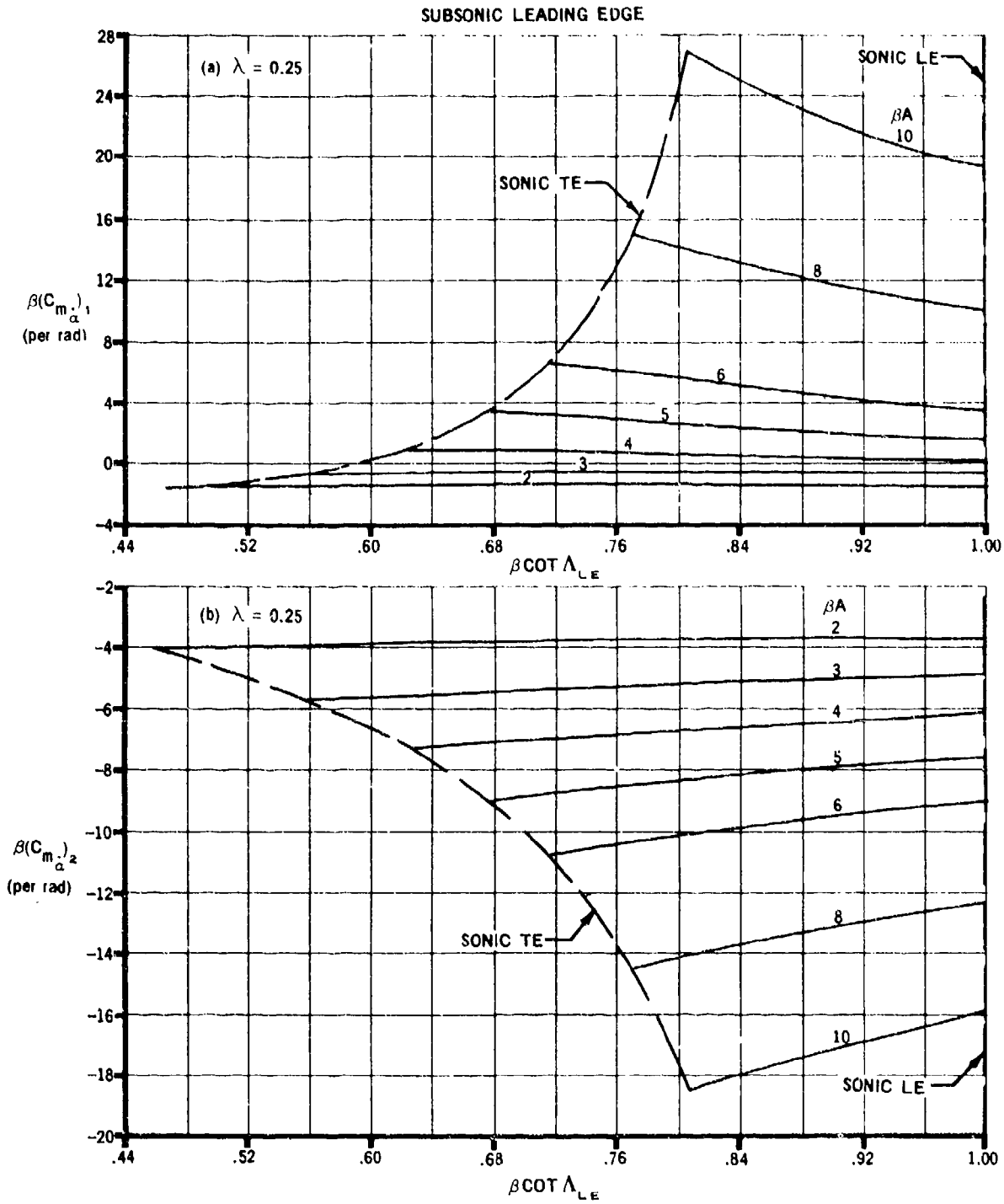

FIGURE 7.1.4.2-10 VARIATION OF $\beta(C_{m_\alpha})_1$ AND $\beta(C_{m_\alpha})_2$ WITH βCOT Λ_{LE}

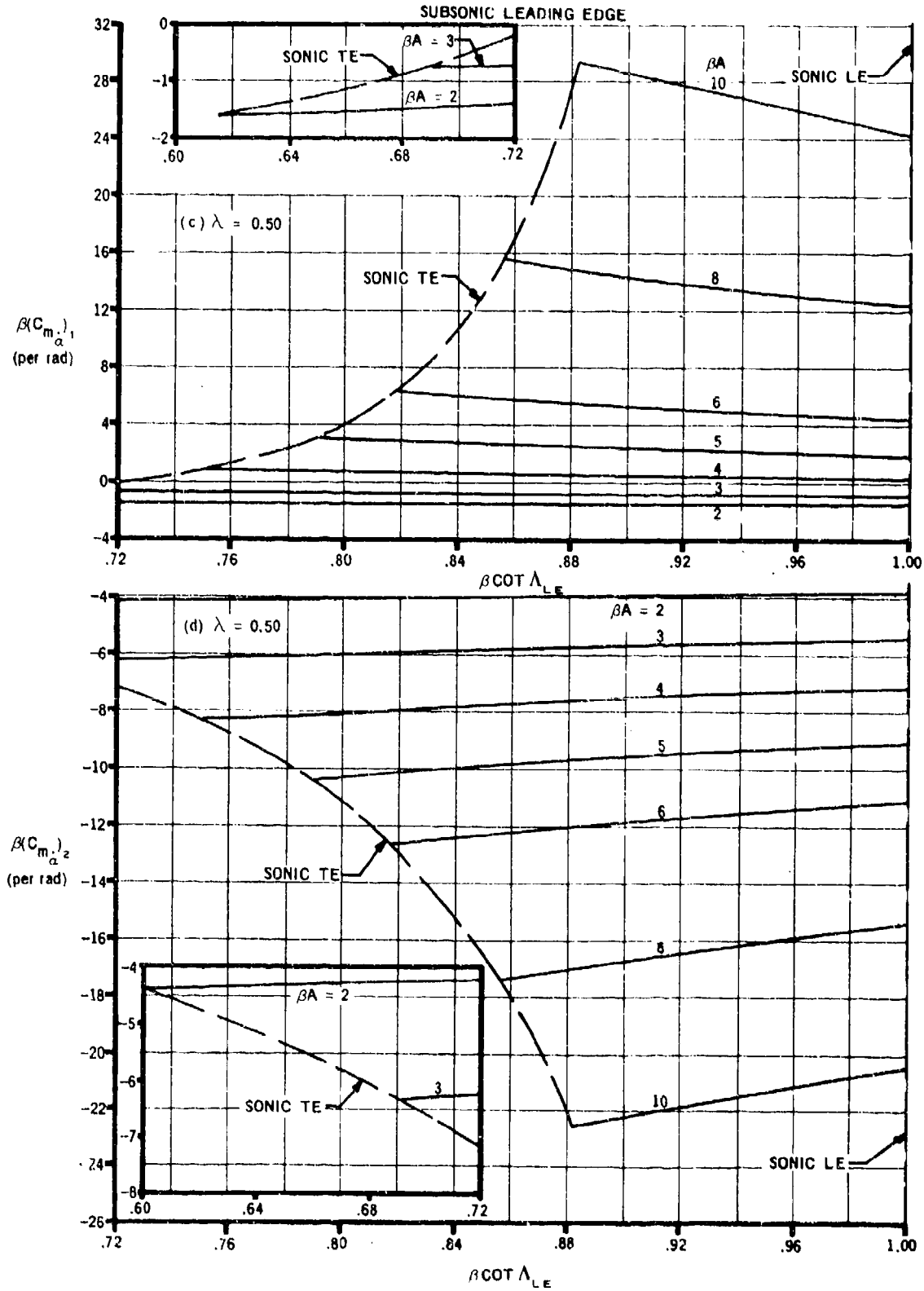

FIGURE 7.1.4.2-10 (CONTD)

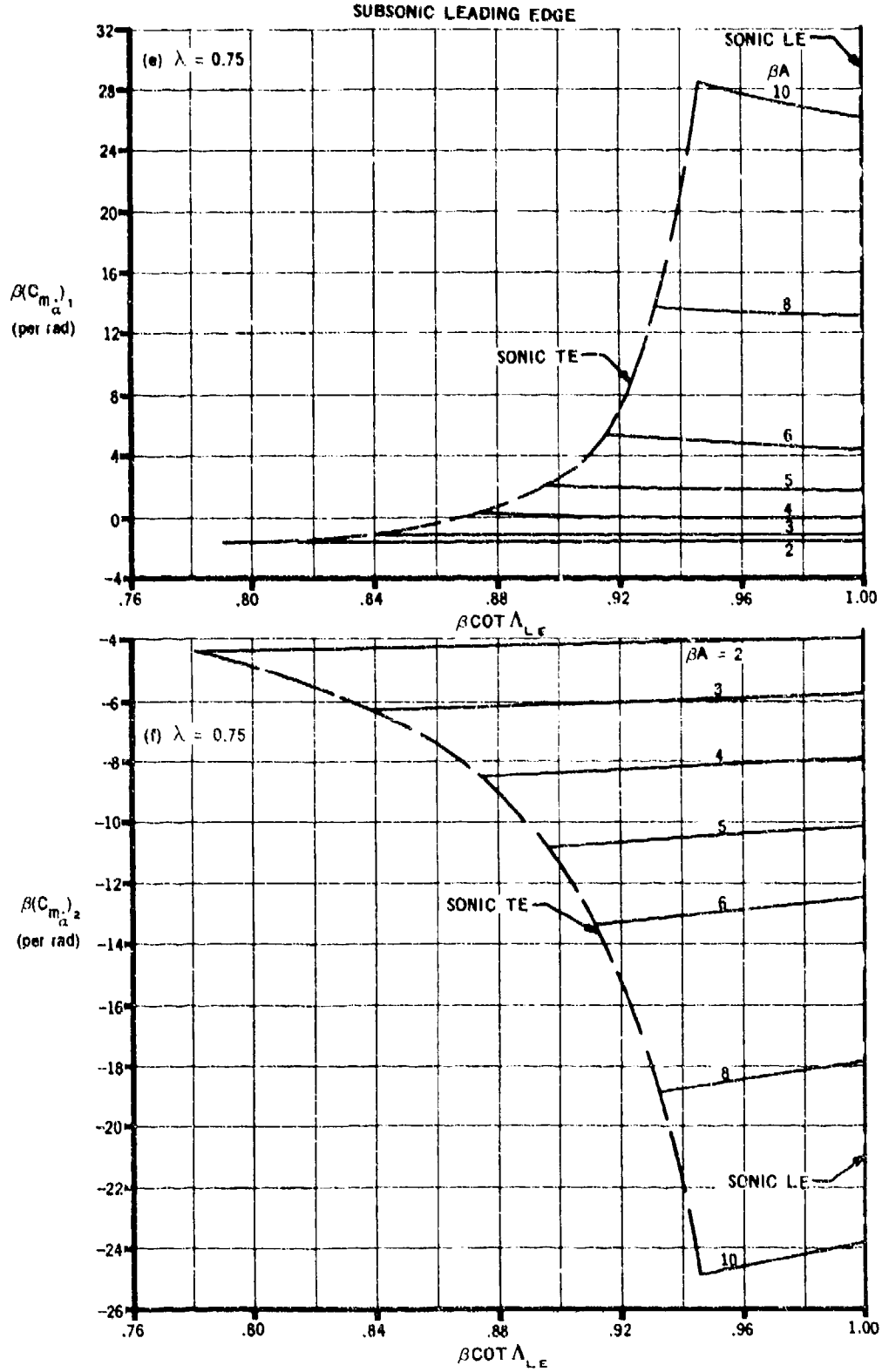

FIGURE 7.1.4.2-10 (CONTD)

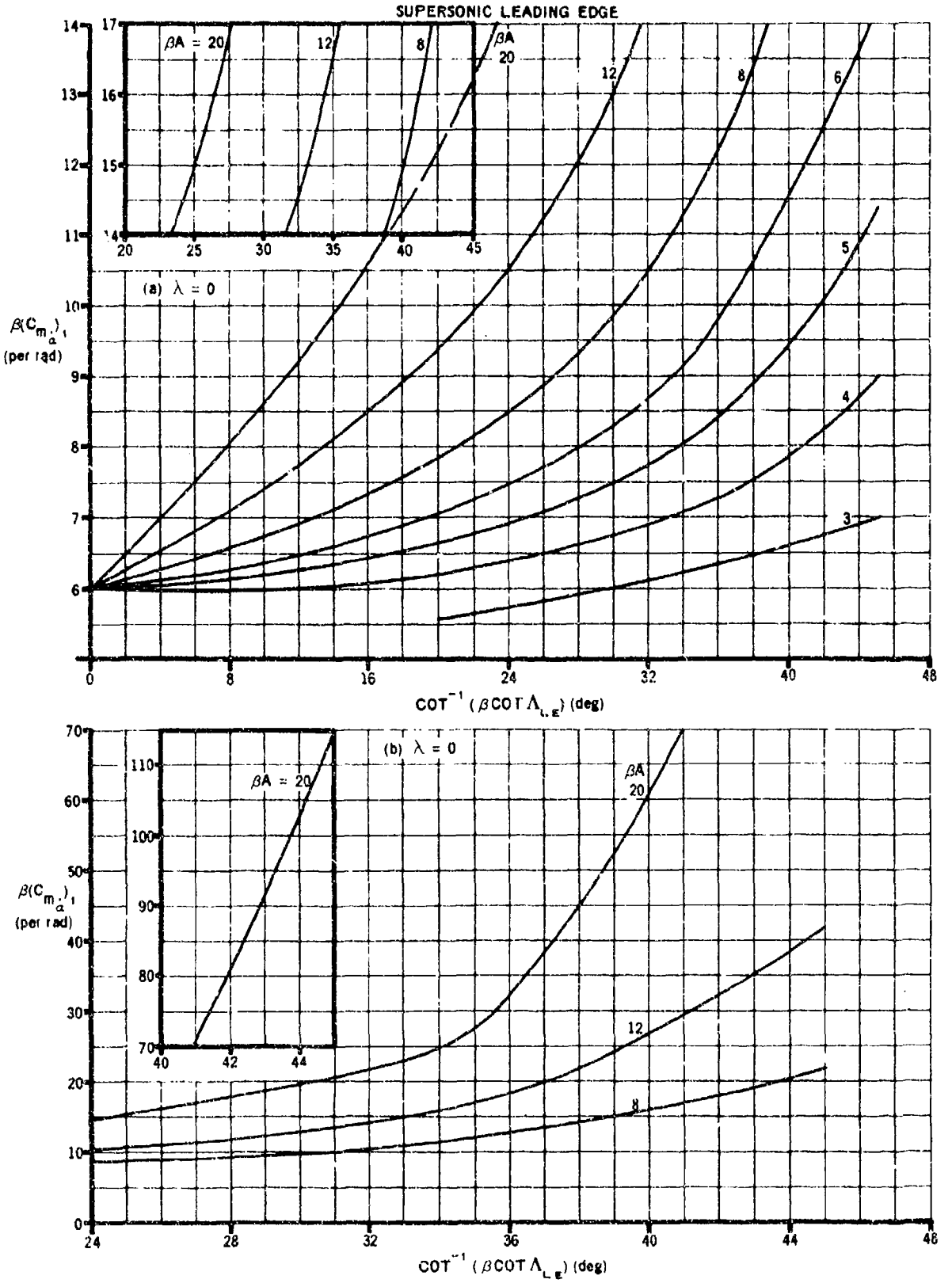

FIGURE 7.1.4.2-13 VARIATION OF $\beta(C_{m_\alpha})_1$ AND $\beta(C_{m_\alpha})_2$ WITH $\cot^{-1}(\beta \cot \Lambda_{L.E})$

SUPERSONIC LEADING EDGE

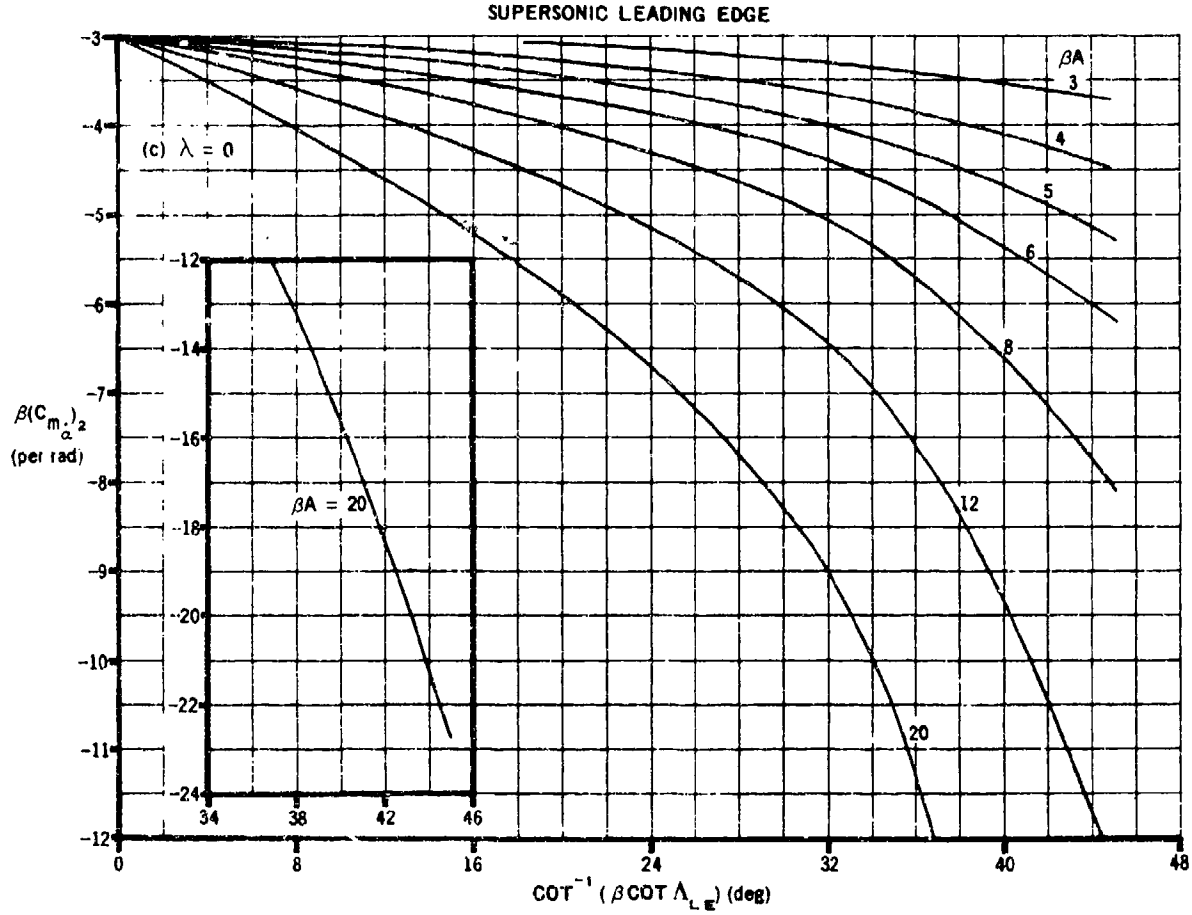

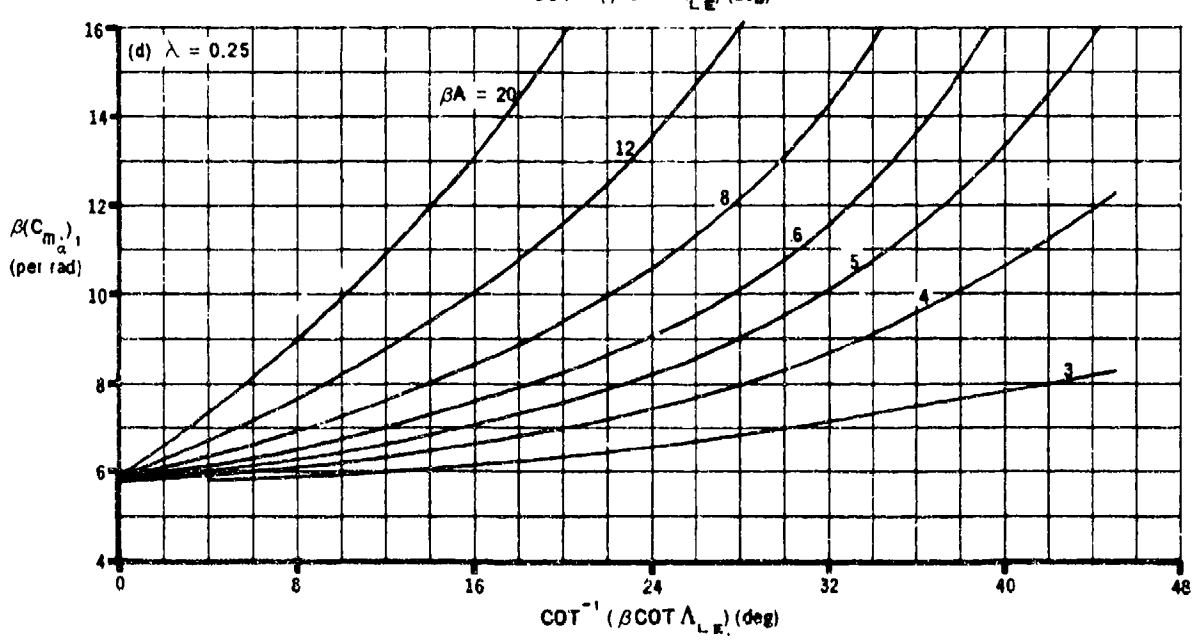

FIGURE 7.1.4.2-13 (CONTD)

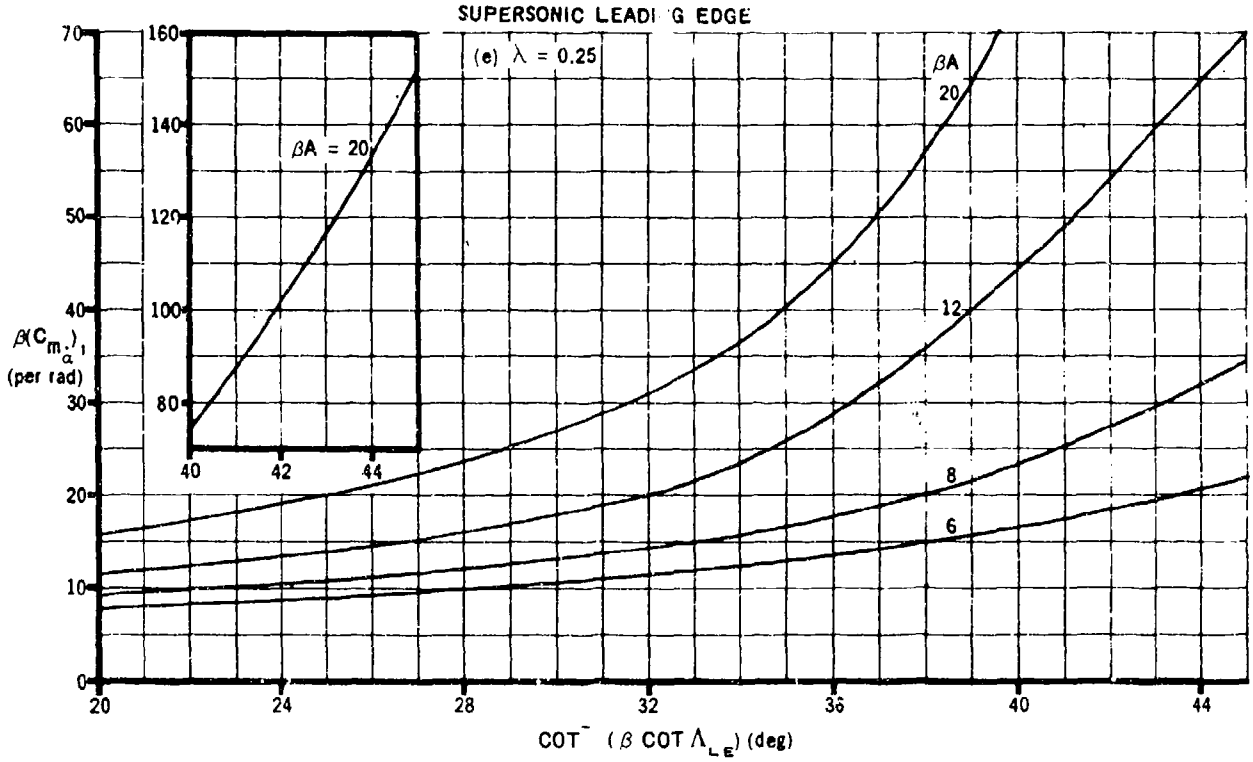

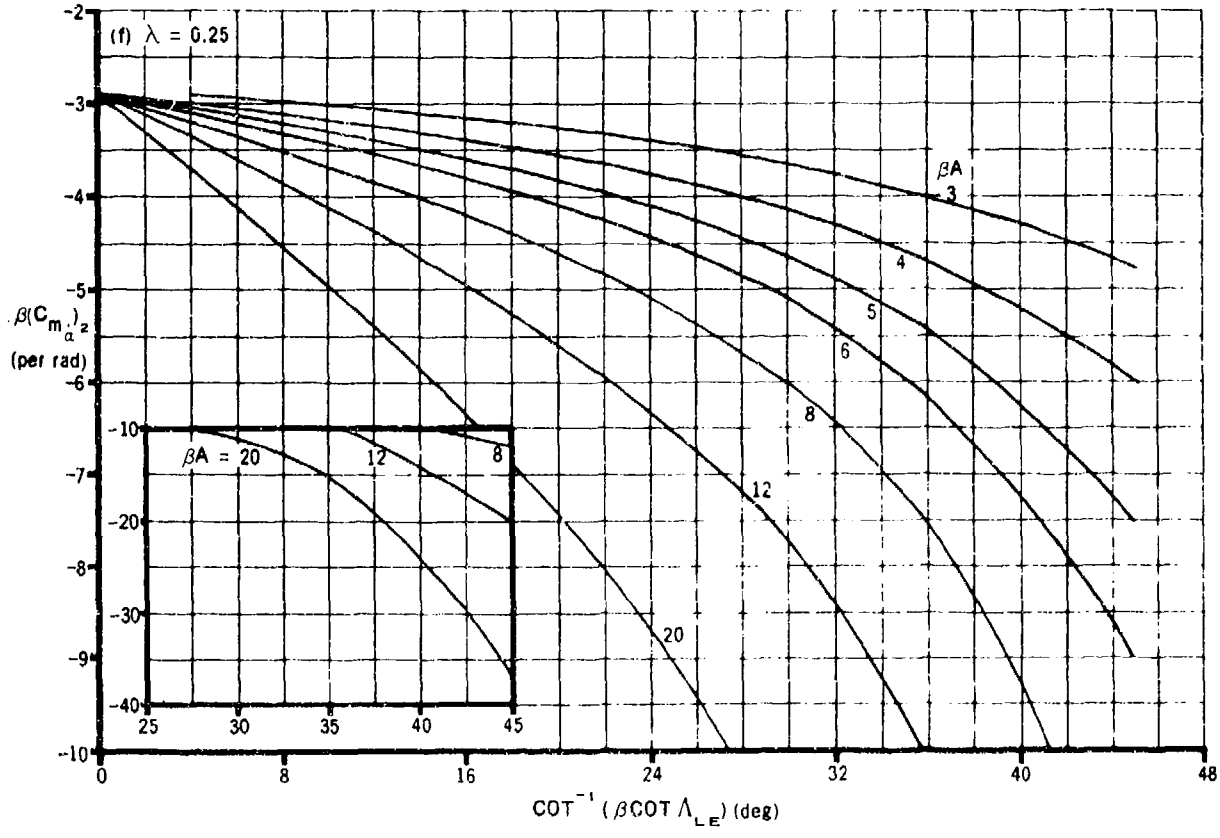

FIGURE 7.1.4.2-13 (CONTD)

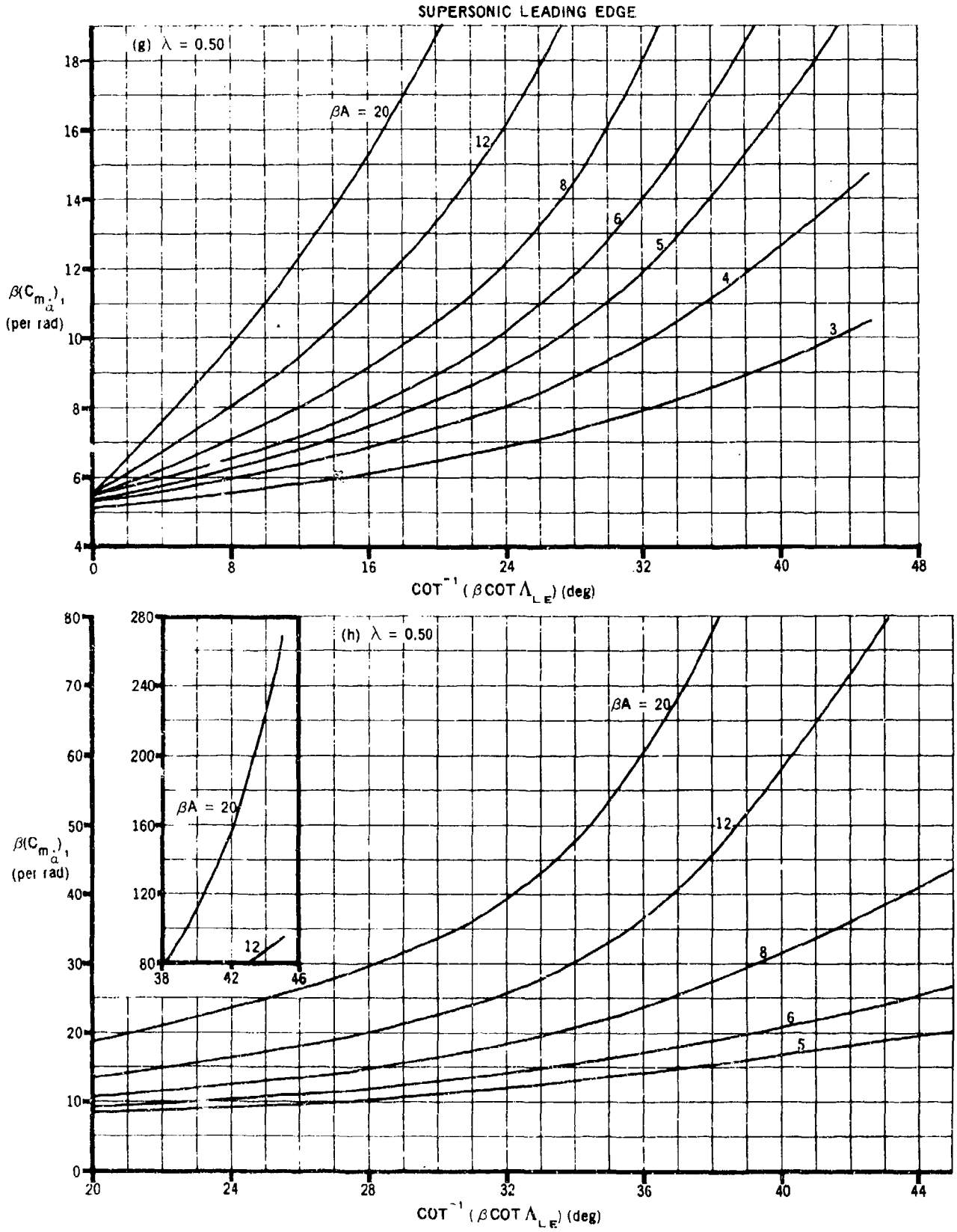

FIGURE 7.1.4.2-13 (CONTD)

SUPERSONIC LEADING EDGE

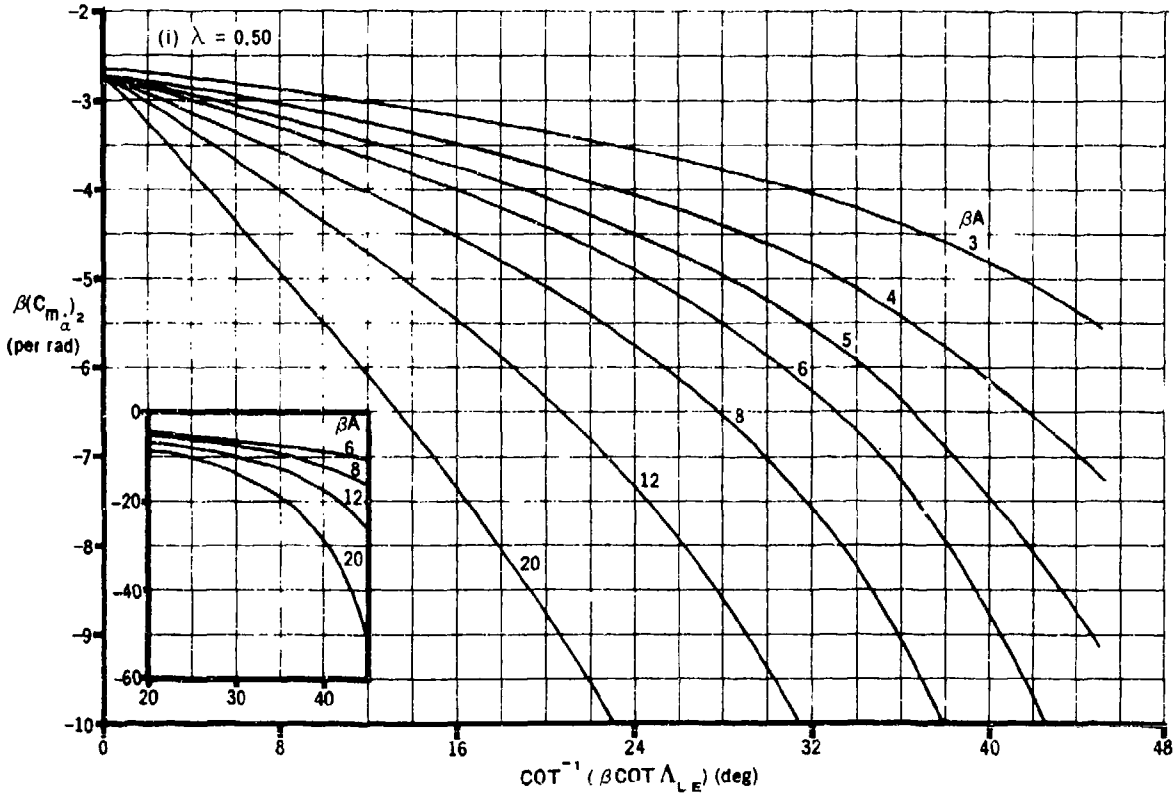

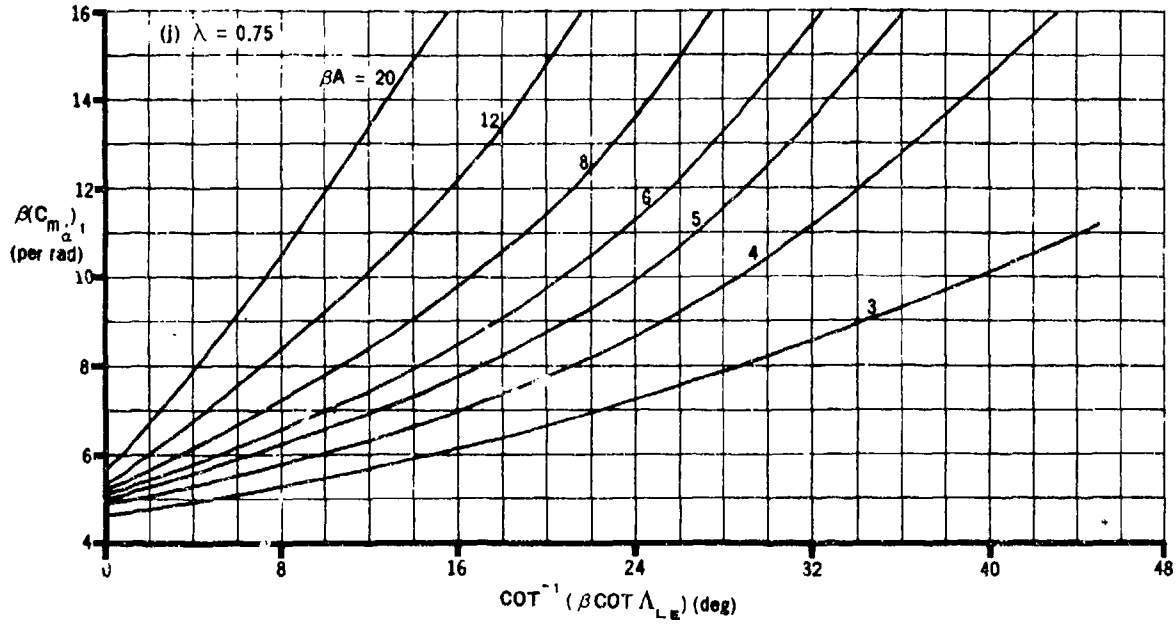

FIGURE 7.1.4.2-13 (CONTD)

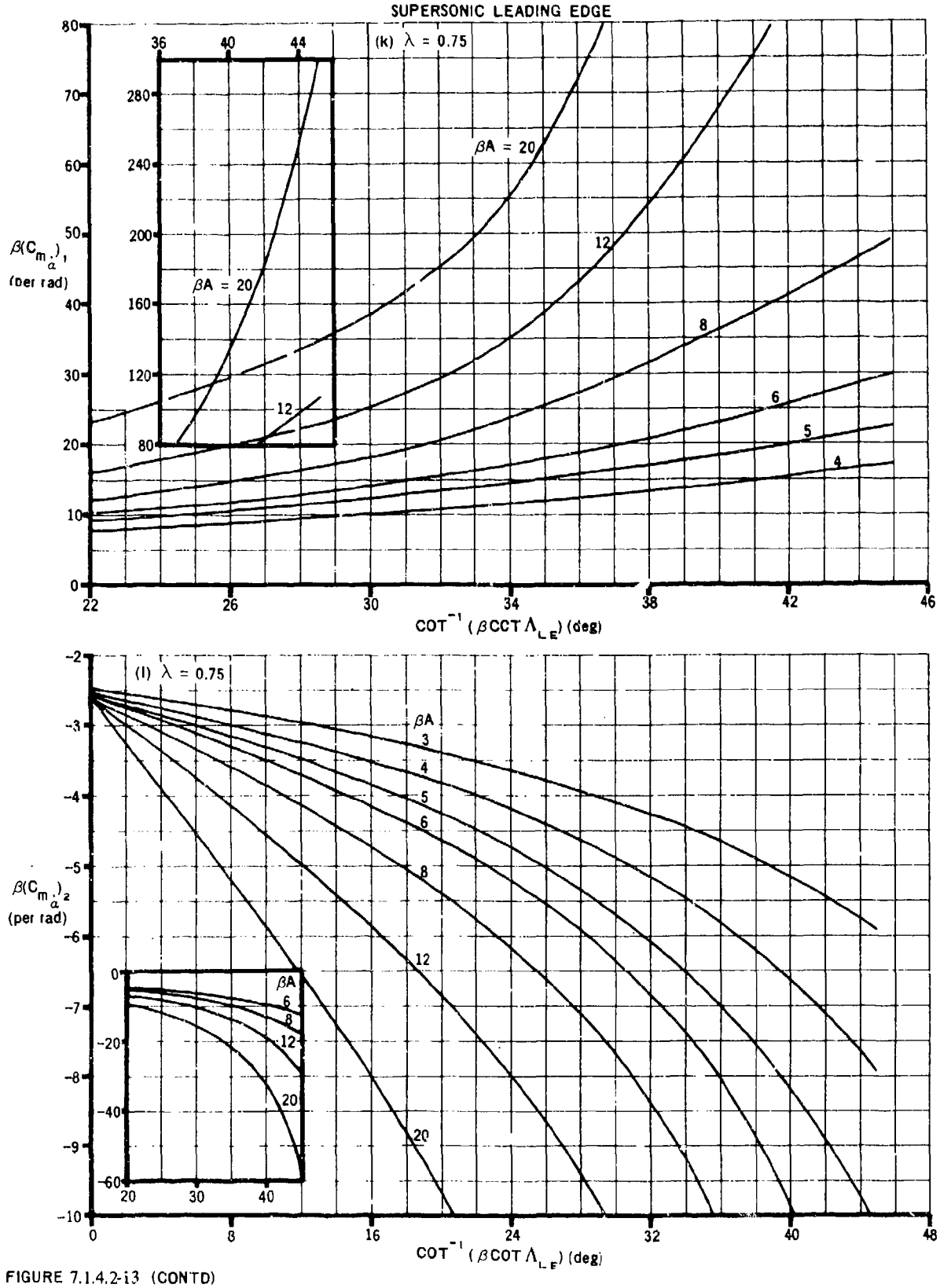

FIGURE 7.1.4.2-13 (CONTD)

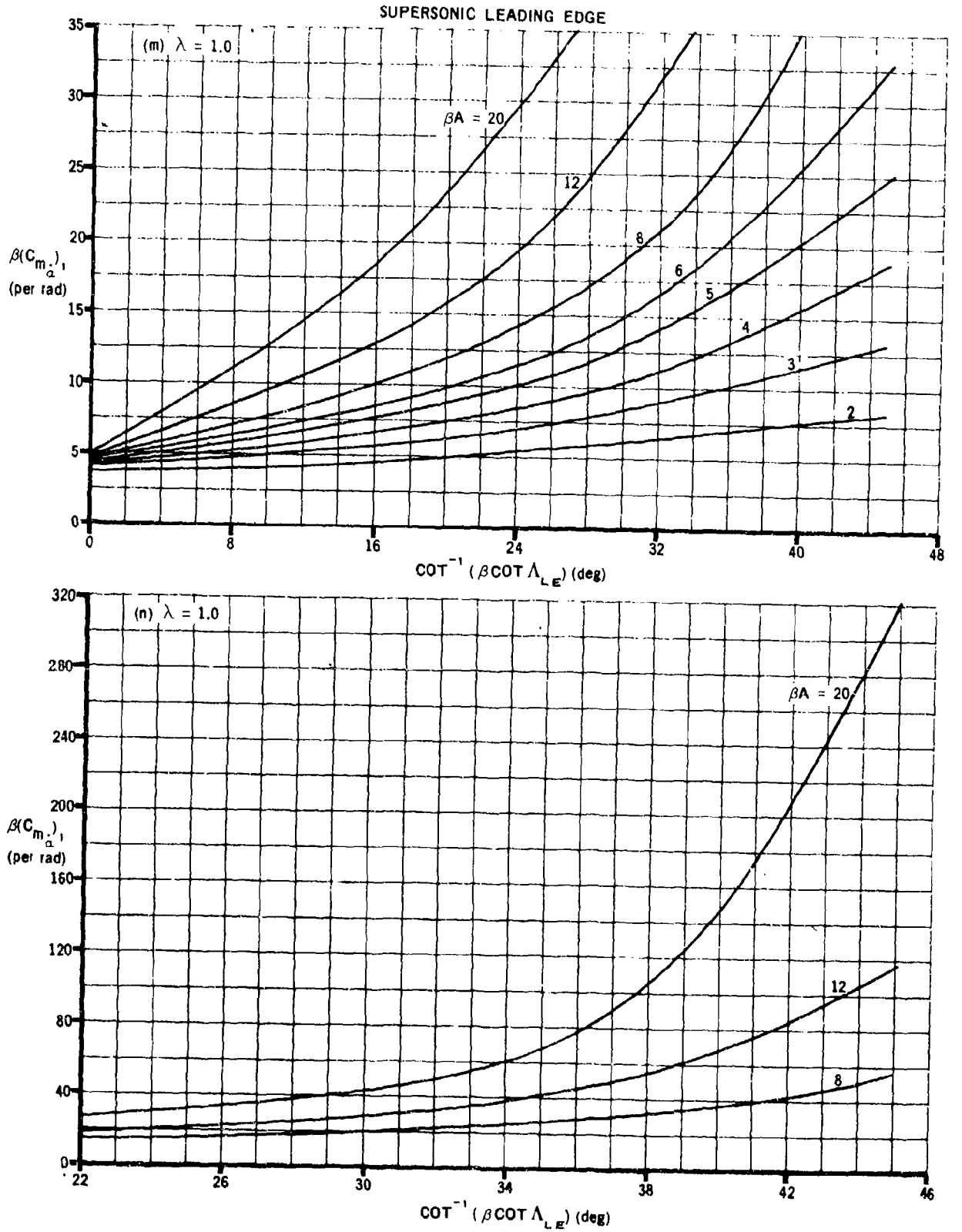

FIGURE 7.1.4.2-13 (CONTD)

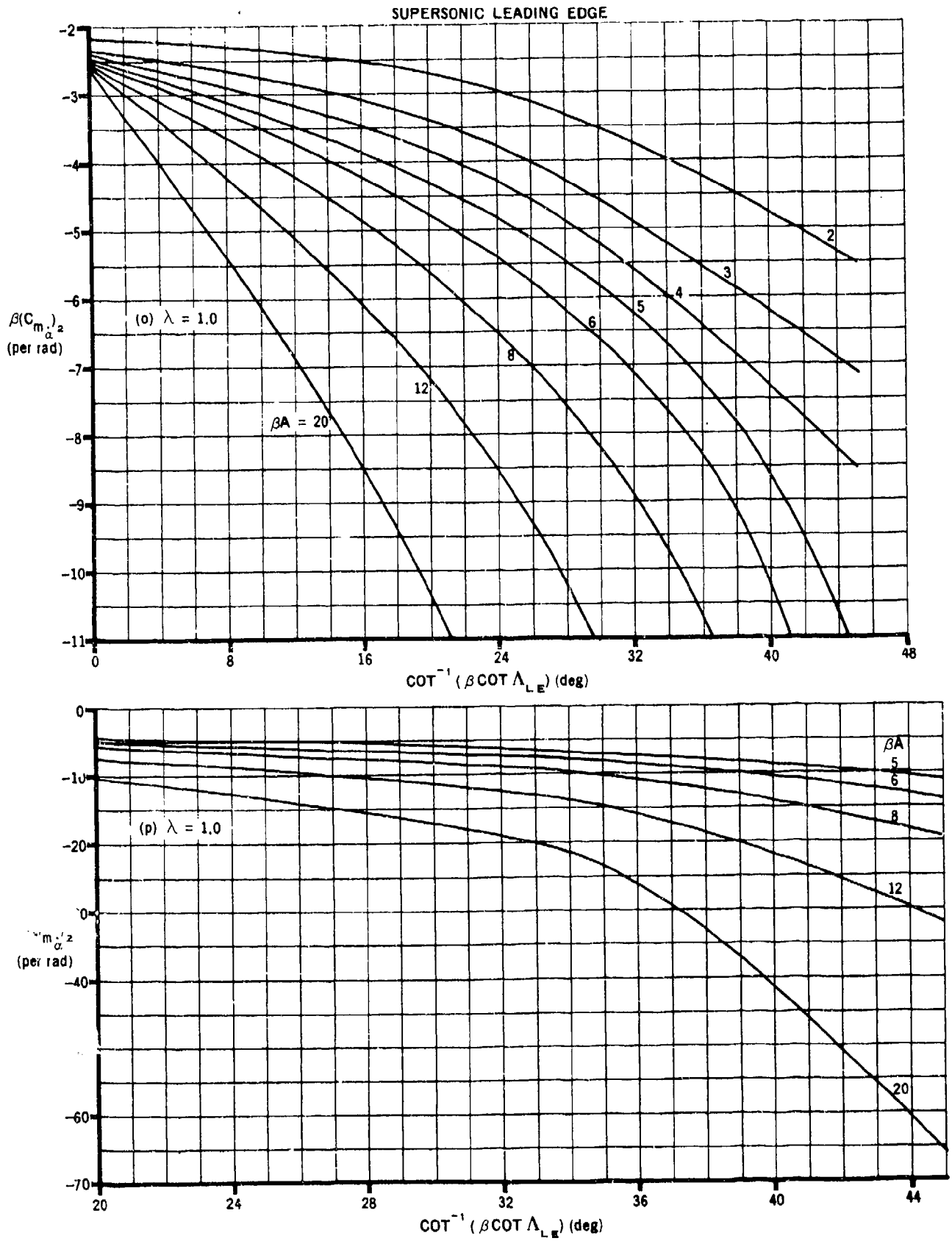

FIGURE 7.1.4.2-13 (CONTD)

7.1.4.3 WING DERIVATIVE $C_{D_{\dot{\alpha}}}$

This section presents a method for estimating the wing contribution to the derivative $C_{D_{\dot{\alpha}}}$ at subsonic speeds. This derivative is the change in drag coefficient due to a change in $\dot{\alpha}$ at a constant pitch rate and is defined as

$$C_{D_{\dot{\alpha}}} = \frac{\partial C_D}{\partial\left(\frac{\dot{\alpha}\bar{c}}{2V}\right)}, \text{ where } C_D \text{ is based on } S_W.$$

In general, this derivative is small and has a negligible effect on longitudinal stability; hence, it is usually neglected.

A. SUBSONIC

DATCOM METHOD

From the two-dimensional unsteady-flow theory of Garrick (Reference 1), the perturbation section drag coefficient of an oscillating surface can be approximated by

$$c_d = \frac{\pi}{2} c \frac{1}{V} [1 + 2C(k)]\, \alpha\dot{\alpha} \qquad 7.1.4.3\text{-a}$$

where

c_d is the drag coefficient per unit span.

c is the wing chord.

V is the free-stream velocity

$C(k)$ is Theodorsen's function, defined as

$$C(k) = F(k) + iG(k) \qquad 7.1.4.3\text{-b}$$

where

$F(k)$, $G(k)$ are Theodorsen's functions obtained from Table 7.1.4.3-A as a function of the reduced frequency k, where k is defined as

$$k = \frac{\omega c}{2V} \qquad 7.1.4.3\text{-c}$$

where c and V are as defined above, and ω is the angular velocity (rad/sec)

Only one part of the complex equation is needed. It is arbitrary whether to use the real or imaginary part. If the wing oscillation can be defined as

$$\alpha = \alpha_1 e^{i\omega t} = \alpha_1 \cos \omega t + i\alpha_1 \sin \omega t \qquad 7.1.4.3\text{-d}$$

where

α is the complex form of the angle of attack of oscillation

α_1 is the amplitude of the oscillation (radians)

t is the time

then by substitution and expansion the imaginary part of Equation 7.1.4.3-a can be shown to be equal to the following:

$$c_d = \frac{\pi}{2} \frac{c}{V} \alpha_1^2 \omega \left\{(1 + 2F)(\cos^2 \omega t - \sin^2 \omega t) - 4G \sin \omega t \cos \omega t\right\}^* \qquad 7.1.4.3\text{-e}$$

where all the terms are defined above and where the oscillation is given by $\alpha = \alpha_1 \sin \omega t$.

The three-dimensional drag may be obtained by

$$C_D = 2 \int_0^{b/2} \frac{c_d c}{S_W} dy \qquad 7.1.4.3\text{-f}$$

where

c_d is the two-dimensional drag from Equation 7.1.4.3-e.

c is the local wing chord.

S_W is the wing reference area.

If the derivative $C_{D_{\dot{\alpha}}}$ is desired, variations in C_D may be calculated for different values of $\dot{\alpha}$. For α as defined by Equation 7.1.4.3-d, the imaginary part of $\dot{\alpha}$ (to be used in conjunction with Equation 7.1.4.3-e) may be expressed as

$$\dot{\alpha} = \alpha_1 \omega \cos \omega t \qquad 7.1.4.3\text{-g}$$

where the terms are defined above.

*The expression in brackets could also be written as $[(1 + 2F) \cos 2\omega t - 2G \sin 2\omega t]$, which would indicate that c_d varies at twice the angular velocity.

Then $C_{D_{\dot{\alpha}}}$ may be approximated by

$$C_{D_{\dot{\alpha}}} = \frac{\partial C_D}{\partial\left(\frac{\dot{\alpha}\bar{c}}{2V}\right)} = \frac{(C_D)_{t_2} - (C_D)_{t_1}}{[(\dot{\alpha})_{t_2} - (\dot{\alpha})_{t_1}]\frac{\bar{c}}{2V}} \qquad 7.1.4.3\text{-h}$$

where

C_D is the three-dimensional drag coefficient obtained by application of Equation 7.1.4.3-f

$\dot{\alpha}$ is the rate of change of angle of attack obtained by application of Equation 7.1.4.3-g

and the subscript t_n refers to a specified time such that $t_2 - t_1$ is the time interval over which C_D and $\dot{\alpha}$ are evaluated.

Sample Problem

Given: The following wing-body combination

Wing Characteristics:

$A = 4$ $\quad \Lambda = 0$ $\quad \lambda = 1.0$ $\quad S_W = 64.0\ ft^2$ $\quad c = 4.0\ ft$

Additional Characteristics:

$V = 200$ ft/sec $\qquad \omega = 2\pi$ rad/sec

$\alpha = \alpha_1 (\cos \omega t + i \sin \omega t) \qquad \alpha_1 = 1^o$

Compute c_d at $t = 1$ sec:

Find the reduced frequency k

$$k = \frac{\omega c}{2V} \qquad \text{(Equation 7.1.4.3-c)}$$

$$= \frac{(2\pi)(4.0)}{2(200)}$$

$$= 0.0628 \text{ rad}$$

$F = 0.8875$
$G = -0.1451$ } Table 7.1.4.3-A (linear interpolation)

$$c_d = \frac{\pi}{2}\frac{c}{V}\alpha_1^2\,\omega\left\{(1 + 2F)(\cos^2\omega t - \sin^2\omega t) - 4G \sin \omega t \cos \omega t\right\} \qquad \text{(Equation 7.1.4.3-e)}$$

$$= \frac{\pi}{2}\left(\frac{4.0}{200}\right)\left(\frac{1}{57.3}\right)^2 2\pi\left\{[1 + 2(0.8876)](1.0 - 0) - 4(-0.1451)(0)(1)\right\}$$

$$= \frac{\pi}{2}\left(\frac{4.0}{200}\right)\left(\frac{1}{57.3}\right)^2 2\pi\left\{[1 + 2(0.8876)]\ 1.0\right\}$$

$$= 0.000167$$

$\dot{\alpha} = \alpha_1 \omega \cos \omega t$ (Equation 7.1.4.3-g)

$$= \frac{1}{57.3}\ (2\pi)(1)$$

$$= 0.110$$

$C_D = 2\int_0^{b/2} \frac{c_d c}{S_W}\, dy$ (Equation 7.1.4.3-f)

$= 2\frac{c_d c}{S_W}\frac{b}{2} = 2\frac{c_d c}{bc}\frac{b}{2} = c_d$ (Rect wing $S_W = bc$)

$C_D = 0.000167$

Compute c_d for t = 1.1 sec:

$c_d = \frac{\pi}{2}\frac{c}{V}\alpha_1^2\ \omega\left\{(1 + 2F)(\cos^2 \omega t - \sin^2 \omega t) - 4G \sin \omega t \cos \omega t\right\}$ (Equation 7.1.4.3-e)

$$= \frac{\pi}{2}\left(\frac{4.0}{200}\right)\left(\frac{1}{57.3}\right)^2 2\pi\left\{[1 + 2(0.8876)]\,[(0.8090)^2 - (0.5878)^2]\right.$$
$$\left. - 4(-0.1451)(0.8090)(0.5878)\right\}$$

$$= 0.0000681$$

$\dot{\alpha} = \alpha_1 \omega \cos \omega t$ (Equation 7.1.4.3-g)

$$= \frac{1}{57.3}\ 2\pi(0.809)$$

$$= 0.0887$$

$$C_D = 2 \int_0^{b/2} \frac{c_d c}{S_W} \, dy \qquad \text{(Equation 7.1.4.3-f)}$$

$$= 2 \frac{c_d c}{S_W} \frac{b}{2} = .2 \frac{c_d c}{bc} \frac{b}{2} = c_d \qquad \text{(Rect Wing } S_W = bc\text{)}$$

$$C_D = 0.0000681$$

Solution:

$$C_{D_{\dot{\alpha}}} = \frac{\partial C_D}{\partial \left(\frac{\dot{\alpha} \bar{c}}{2V} \right)} = \frac{(C_D)_{t_2} - (C_D)_{t_1}}{[(\dot{\alpha})_{t_2} - (\dot{\alpha})_{t_1}] \frac{\bar{c}}{2V}} \qquad \text{(Equation 7.1.4.3-h)}$$

$$= \frac{(0.0000681 - 0.000167)}{(0.0887 - 0.110) \frac{4.0}{2(200)}}$$

$$= 0.464 \text{ per rad}$$

$$= 0.0081 \text{ per deg}$$

B. TRANSONIC

No method is presented.

C. SUPERSONIC

No method is presented.

REFERENCE

1. Garrick, I. E.: Propulsion of a Flapping and Oscillating Airfoil. NACA TR 567, 1936. (U)

TABLE 7.1.4.3-A

THEODORSEN'S FUNCTIONS

k	F	--G
∞	0.5000	0
10.00	0.5006	0.0206
6.00	0.5017	0.0206
4.00	0 5037	0.0305
3.00	0.5063	0.0400
2.00	0.5129	0.0577
1.50	0.5210	0.0736
1.20	0.5300	0.0877
1.00	0.5394	0.1003
0.80	0.5541	0.1165
0.66	0.5699	0.1308
0.60	0.5788	0.1378
0.56	0.5856	0.1428
0.50	0.5979	0.1507
0 44	0.6130	0.1592
0.40	0.6250	0.1650
0.34	0.6469	0.1738
0.30	0.6650	0.1793
0.24	0.6989	0.1862
0.20	0.7276	0.1886
0.16	0.7628	0.1876
0.12	0.8063	0.1801
0.10	0.8320	0.1723
0.08	0.8604	0.1604
0.06	0.8920	0.1426
0.05	0.9090	0.1305
0.04	0.9267	0.1160
0.025	0.9545	0.0872
0.01	0.9824	0.0482
0	1.000	0

7.2 BODY DYNAMIC DERIVATIVES

The methods presented in this section are for estimating pitching and acceleration dynamic derivatives of isolated bodies. The methods and charts of the subsonic, transonic, and supersonic speed ranges are based on a combination of slender-body theory and the theories used in predicting the body-lift-curve slope and pitching-moment-curve slope in Sections 4.2.1.1 and 4.2.2.1, respectively. Newtonian impact theory is used in the hypersonic speed range. The methods are restricted to angles of attack near zero and should yield values suitable for first approximations to dynamic stability.

No test data are available on body dynamic derivatives. Therefore, all theoretical methods must be considered tentative until compared with experimental results. A brief discussion of available theoretical methods is presented.

The starting point of almost all theories is the well-known linearized potential equation. Various methods based on linear theory have been developed for obtaining the flow field about bodies in supersonic flow. The problem of determining the dynamic stability derivatives for bodies has been treated principally within the assumptions of slender-body theory. The application of Munk's slender-body theory to the calculation of the aerodynamic coefficients describing steady motion has been made by a number of authors (see references 1 through 4). In reference 5, slender-body values of the aerodynamic coefficients associated with nonsteady angle of attack have been obtained as a by-product of a linear analysis of the potential equation for nonsteady supersonic flow. However, approximations made in the analysis effectively limit its application to bodies of vanishingly small thickness. The problem of determining the dynamic derivatives for a smooth slender body of arbitrary cross section performing slow maneuvers is treated within the assumptions of slender-body theory by Sacks in reference 6. This approach is novel in slender-body theory in that the squared terms in the pressure relation for slender configurations are retained and all motions of the configuration are treated simultaneously. However, the derivatives are obtained in terms of the mapping functions of the cross sections and are too complex for inclusion in the Datcom.

A method is developed for estimating aerodynamic loads on slender, symmetrical configurations performing small lateral oscillations of limited reduced frequency in sonic and supersonic flow in references 7 and 8, respectively. This method is an extension of an iterative technique originally proposed by Adams and Sears in reference 9, and is a combination of first-order and second-order cross-flow solutions. The results consist of slender-body-theory terms plus higher-order effects of fineness ratio. For sonic flow about a body of revolution, reference 7 shows that by retaining only the first-order terms in reduced frequency the pitching derivatives are given by simple slender-body theory; whereas the acceleration derivatives are influenced by the second-order terms and contain logarithms of the reduced frequency. Under certain limitations on the rapidity of the oscillations, all derivatives in supersonic flow prove to be independent of changes in reduced frequency; consequently the method can be applied to slow time-dependent motions. At present this method is limited to slender bodies of revolution, and in most cases requires a considerable amount of mathematical manipulation to obtain a solution. This method can be applied to bodies of more general cross section; however, the practicality of such an analysis would depend on the possibility of solving the integrals that appear.

In reference 10 an attempt has been made to overcome the slender-body limitation by adapting hybrid theory to the calculation of the body dynamic derivatives. (This method, derived by Van Dyke in reference 11, has proved successful in calculations for the static aerodynamic derivatives.) This method is used to predict the dynamic derivatives of a cone, and the results are consistent with those obtained by impact theory at the higher Mach numbers. In order to extend this method to bodies of more general shape, it is necessary to satisfy the boundary conditions corresponding to the specified body. Unfortunately, the analytical expressions required to do so have been found only for the cone.

The application of simple slender-body theory appears to be the only method of solution warranted at the present time, in view of the large effects of viscosity on the forces acting over slender bodies, the mathematical complexity involved in solution of the linearized equations for general planforms, and the lack of test data.

Since extensive use is made of slender-body-theory results throughout this section, the term "slender" is clarified.* Tsien, in reference 2, pointed out that slender-body theory applies to the flow about inclined, pointed projectiles at supersonic speeds. Subsequently, Jones, in reference 12, indicated that his slender-wing theory (slender-body theory extended to wings) applies to both subsonic and supersonic speeds, at least for pointed planforms. Actually, the meaning of the term "slender" is somewhat different in the various speed regimes. For supersonic Mach numbers "slender" implies that the body lies well within the Mach cone from the body apex. This leads directly to the limitation to pointed bodies. It also leads to the conclusion that relatively blunt bodies may qualify as "slender" at low supersonic speeds; while for hypersonic speeds the method must fail for practical shapes. At subsonic speeds the term "slender" becomes less restrictive as the Mach number increases from 0 to 1, until at sonic speed all bodies become slender. Thus, slender-body theory is seen to apply to at least some body shapes throughout the speed range from low subsonic to hypersonic.

REFERENCES

1. Munk, M. M.: The Aerodynamic Forces on Airship Hulls. NACA TR 184, 1924. (U)

2. Tsien, H. S.: Supersonic Flow Over an Inclined Body of Revolution. Jour. Aero. Sci., Vol. 5, No. 12, October 1938. (U)

3. Laitone, E. V.: Linearized Subsonic and Supersonic Flow About Inclined Slender Bodies of Revolution. Jour. Aero. Sci., Vol. 14, No. 11, November 1947. (U)

4. Tobak, M., Resse, D. E., Jr., and Bean, B. H.: Experimental Damping in Pitch of 45° Triangular Wings. NACA RM A50J26, 1950. (U)

5. Dorrance, W. H.: Nonsteady Supersonic Flow About Pointed Bodies of Revolution. Jour. Aero. Sci., Vol. 18, No. 8, August 1951. (U)

6. Sacks, A. H.: Aerodynamic Forces, Moments, and Stability Derivatives for Slender Bodies of General Cross Section. NACA TN 3283, 1954. (U)

7. Landahl, M. T.: Forces and Moments on Oscillating Slender Wing-Body Combinations at Sonic Speed. MIT Fluid Dynamics Research Group Report No. 56-1, 1956. (U)

8. Zartarian, G., and Ashley, H.: Forces and Moments on Oscillating Slender Wing-Body Combinations at Supersonic Speed. Part I – Basic Theory. MIT Fluid Dynamics Research Group Report No. 57-2, 1957. (U)

*This discussion is essentially quoted from reference 9

9. Adams, M. C., and Sears, W. R.: Slender-Body Theory – Review and Extension. Jour. Aero. Sci., Vol. 20, No. 2, February 1953. (U)

10. Tobak, M., and Wehrend, W. R.: Stability Derivatives of Cones at Supersonic Speeds. NACA TN 3788, 1956. (U)

11. Van Dyke, M. D.: First- and Second-Order Theory of Supersonic Flow Past Bodies of Revolution. Jour. Aero. Sci., Vol. 18, No. 3, March 1951. (U)

12. Jones, R. T.: Properties of Low Aspect Ratio Wings at Speeds Below and Above the Speed of Sound. NACA TR 835, 1946. (U)

7.2.1 BODY PITCHING DERIVATIVES

7.2.1.1 BODY PITCHING DERIVATIVE C_{L_q}

The pitching derivative C_{L_q} is a measure of the lift produced by rotational motion of the airframe about a spanwise axis. This derivative is generally small compared to other terms in the equations of motion and is frequently neglected. However, methods are presented for determining the body contribution to C_{L_q} in the subsonic, transonic, supersonic, and hypersonic speed ranges. The value of C_{N_q} in the hypersonic speed range is used to obtain the value of C_{m_q} in the hypersonic speed range in Section 7.2.1.2.

In the subsonic, transonic, and supersonic speed ranges the Datcom methods are based on the relatively simple results derived from slender-body theory and the assumption that a relationship of corresponding slender-body derivatives may be employed with reasonable accuracy to the case of steady pitching in a manner similar to that of reference 1. This approach to the calculation of body dynamic derivatives has been applied with reasonable success by Walker and Wolowicz in reference 2. It was shown in reference 1 that, although slender-body theory alone does not accurately predict the characteristics of nonslender configurations, the ratio of corresponding slender-body derivatives may be employed with reasonable accuracy in predicting the static forces on nonslender configurations. The body contribution to C_{L_q} is thus given as the product of the lift-curve slope C_{L_α} and the ratio of slender-body derivatives, i.e.,

$$C_{L_q} = C_{L_\alpha}\left(\frac{C_{L_q}}{C_{L_\alpha}}\right)_{\text{slender-body theory}}$$

Slender-body theory states that body force characteristics are independent of Mach number. The effect of Mach number is taken into account by the static force coefficient. Therefore, the limitations of these methods are determined by the limitations of the methods employed in determining the static derivative C_{L_α} in the various speed regimes. Experimental data should be used for the body lift-curve slope when available.

A. SUBSONIC

There is no explicit method available in the literature for obtaining the body dynamic derivatives for general planforms.

The method presented is based on the application of the results of slender-body theory in the manner previously discussed.

DATCOM METHOD

The body contribution to C_{L_q}, based on body base area and body length and referred to the center of rotation, is given by

$$C_{L_q} = 2\,C_{L_\alpha}\left(1 - \frac{x_m}{\ell_B}\right) \quad \text{(per radian)} \qquad 7.2.1.1\text{-a}$$

where

C_{L_α} is the body lift-curve slope from paragraph A of Section 4.2.1.1 multiplied by $\left(V_B^{2/3}/S_b\right)$ (per radian).

x_m is the longitudinal distance from the body vertex to the center of rotation, positive aft.

ℓ_B is the length of the body.

V_B is the total body volume from Section 2.3.

S_b is the body base area.

Sample Problem

Given:

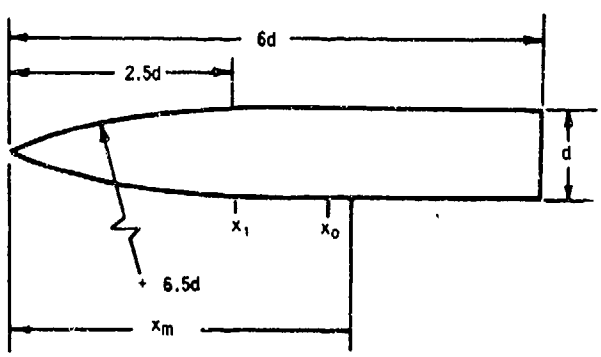

d = 1.0 ft $\quad \ell_B$ = 6.0 ft $\quad$ Fineness Ratio = 6.0 $\quad x_m$ = 3.8 ft

C_{L_α} = 0.548 per rad (based on $V_B^{2/3}$) (Section 4.2.1.1)

$V_B^{2/3}$ = 2.47 sq ft (Section 2.3) $\quad S_b$ = 0.785 sq ft

Compute:

$$C_{L_\alpha} = (0.548)\frac{(V_B)^{2/3}}{S_b} = (0.548)\left(\frac{2.47}{0.785}\right) = 1.724 \text{ per rad (based on } S_b)$$

$$\left(1 - \frac{x_m}{\ell_B}\right) = \left(1 - \frac{3.8}{6}\right) = 0.367$$

Solution:

$$C_{L_q} = 2\, C_{L_\alpha} \left(1 - \frac{x_m}{\ell_B}\right) \quad \text{(equation 7.2.1.1-a)}$$

$$= 2(1.724)\,(0.367)$$

$$= 1.265 \text{ per rad (based on } S_b \ell_B)$$

B. TRANSONIC

The linearization of the transonic flow problem has been accomplished by Landahl, in reference 3, by introducing a small amount of unsteadiness into the motion. This theoretical method is briefly discussed in Section 7.2. By neglecting the second-order effects of reduced frequency the pitching derivatives of a slender body of revolution are those given by slender-body theory. Since slender-body theory does not predict a dependence on configuration parameters, this method cannot be expected to give reasonable approximations for the pitching derivatives of nonslender configurations. Therefore, the method of paragraph A is applied throughout the transonic speed range.

C. SUPERSONIC

Several of the theoretical methods that have been developed for estimating the body pitching derivative C_{N_q} in the supersonic speed range are briefly discussed in Section 7.2. The available theoretical methods are limited to simple slender-body theory, theories treated within the assumptions of slender-body theory, and hybrid theory. The method presented here is based on simple slender-body theory. Theories treated within the assumption of slender-body theory are mathematically complex and restricted to specific body shapes; therefore, no general quantitative results are presented.

The supersonic C_{N_q} for cones can be estimated by the hybrid theory solutions presented in reference 4.

DATCOM METHOD

The method presented here for determining the body contribution to C_{N_q}, based on the cone-cylinder or ogive-cylinder maximum frontal area and body length and referred to the center of rotation, is the same as that of paragraph A and is given by equation 7.2.1.1-a, i.e.,

$$C_{N_q} = 2\, C_{N_\alpha} \left(1 - \frac{x_m}{\ell_B}\right) \quad \text{(per radian)}$$

where C_{N_α} is the body normal-force-curve slope from paragraph C of Section 4.2.1.1, evaluated at the appropriate Mach number and based on the cone-cylinder or ogive-cylinder maximum frontal area (per radian).

D. HYPERSONIC

Simple Newtonian theory is used in this section to estimate the contribution of cone frustum bodies, with or without spherical noses, to the derivative C_{N_q}. Newtonian theory is discussed in paragraph D, Section 4.2.1.1.

DATCOM METHOD

Charts taken from reference 5, based on simple Newtonian theory, are presented for determining C_{N_q} of spherical segments and cone frustums at small angles of attack.

The coefficients of these charts are referred to the body base area and base diameter and to a moment center at the forward face of the segment. By proper use of the data presented, the total C_{N_q} may be determined for bodies composed of multiple cone frustums with or without spherically blunted noses.

The Newtonian value of the derivative C_{N_q} for a complex body is obtained as follows:

Step 1. Compute $C_{N_q}{}'$ for each body segment about its front face using figures 7.2.1.1-9a and 7.2.1.1-9b.

Step 2. Transfer the individual derivatives $C_{N_q}{}'$ to a common reference axis by applying the following transfer equation to each body segment

$$C_{N_q} = C_{N_q} - 2\left(\frac{n}{d}\right)C_{N_\alpha} \qquad 7.2.1.1\text{-b}$$

where

C_{N_α} is the normal-force-curve slope for each segment based on individual base areas from paragraph D, Section 4.2.1.1.

C_{N_q} is the pitching derivative for each segment based on individual base areas and base diameters and referred to a moment center at the forward face of the segment, from figures 7.2.1.1-9a and 7.2.1.1-9b.

n is the distance from the face of a given frustum to the desired moment reference axis of the configuration, positive aft.

d is the base diameter of a given frustum.

Step 3. The transferred derivatives of the individual body segments are converted to a common reference area and diameter and added. The total derivative is given by

$$C_{N_q} = \sum_{n=1}^{m} (C_{N_q})_n \left(\frac{d_n}{d_b}\right)^3 \qquad 7.2.1.1\text{-c}$$

Sample Problem

Given: Same multiple-segment body as sample problem of paragraph D of Sections 4.2.1.1 and 4.2.2.1.

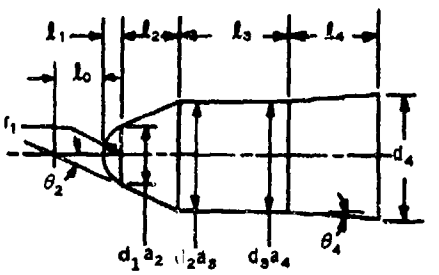

ℓ_0 = 0.55 ft (distance from moment reference center to body nose)

Spherical segment

ℓ_1 = 0.18 ft

r_1 = 0.36 ft

d_1 = 0.62 ft

Forward cone frustum

a_2 = 0.62 ft

d_2 = 1.20 ft

ℓ_2 = 0.72 ft

θ_2 = 22.5°

Cylinder

a_3 = 1.20 ft

d_3 = 1.20 ft

ℓ_3 = 1.20 ft

θ_3 = 0

Rear cone frustum

a_4 = 1.20 ft

d_4 = 1.368 ft

ℓ_4 = 0.96 ft

θ_4 = 5°

Compute:

Spherical segment

$2\ell_1/d_s = \ell_1/r_1 = 0.50$

$C_{N_{q_1}}' = 0.865$ per rad (figure 7.2.1.1-9b)

$n_1 = -\ell_0 = -0.55$ ft

$d_1 = a_2 = 0.62$ ft

$C_{N_{\alpha_1}} = 0.75$ per rad (figure 4.2.1.1-23)

$$C_{N_{q_1}} = C_{N_{q_1}}' - 2\left(\frac{n_1}{d_1}\right)C_{N_{\alpha_1}} \quad \text{(equation 7.2.1.1-b)}$$

$$= 0.865 - 2\left(\frac{-0.55}{0.62}\right)0.75$$

$$= 2.195 \text{ per rad } \left(\text{based on } \frac{\pi d_1^{\,3}}{4}\right)$$

Forward cone frustum

$a_2/d_2 = \lambda_2 = 0.517$

$C_{N_{q_2}}' = 1.22$ per rad (figure 7.2.1.1-9a)

$n_2 = -(\ell_0 + \ell_1) = -0.73$

$C_{N_{\alpha_2}} = 1.250$ per rad (figure 4.2.1.1-26)

$$C_{N_{q_2}} = C_{N_{q_2}}' - 2\left(\frac{n_2}{d_2}\right)C_{N_{\alpha_2}} \quad \text{(equation 7.2.1.1-b)}$$

$$= 1.22 - 2\left(\frac{-0.73}{1.20}\right)1.250$$

$$= 2.74 \text{ per rad} \left(\text{based on } \frac{\pi d_2{}^3}{4}\right)$$

Cylinder

$$a_3/d_3 = \lambda_3 = 1.0$$

$$C_{N_{q_3}}{}' = 0 \text{ (figure 7.2.1.1-9a)}$$

$$n_3 = -(\ell_0 + \ell_1 + \ell_2) = -1.45$$

$$C_{N_{\alpha_3}} = 0 \text{ (figure 4.2.1.1-26)}$$

$$C_{N_{q_3}} = C_{N_{q_3}}{}' - 2\left(\frac{n_3}{d_2}\right)C_{N_{\alpha_3}} \quad \text{(equation 7.2.1.1-b)}$$

$$= 0$$

Rear cone frustum

$$a_4/d_4 = \lambda_4 = 0.877$$

$$C_{N_{q_4}}{}' = 0.36 \text{ per rad} \quad \text{(figure 7.2.1.1-9a)}$$

$$n_4 = -(\ell_0 + \ell_1 + \ell_2 + \ell_3) = -2.65$$

$$C_{N_{\alpha_4}} = 0.450 \text{ per rad} \quad \text{(figure 4.2.1.1-26)}$$

$$C_{N_{q_4}} = C_{N_{q_4}}{}' - 2\left(\frac{n_4}{d_4}\right)C_{N_{\alpha_4}} \quad \text{(equation 7.2.1.1-b)}$$

$$= 0.36 - 2\left(\frac{-2.65}{1.368}\right)0.45$$

$$= 2.10 \text{ per rad} \left(\text{based on } \frac{\pi d_4{}^3}{4}\right)$$

Solution:

Converting the derivative for each segment to a common reference area and diameter, the base area and diameter of the rear cone frustum, and adding

$$C_{N_q} = \sum_{n=1}^{m} \left(C_{N_q}\right)_n \left(\frac{d_n}{d_b}\right)^3 \qquad \text{(equation 7.2.1.1-c)}$$

$$C_{N_q} = C_{N_{q_1}} \left(\frac{d_1}{d_4}\right)^3 + C_{N_{q_2}} \left(\frac{d_2}{d_4}\right)^3 + C_{N_{q_3}} \left(\frac{d_3}{d_4}\right)^3 + C_{N_{q_4}}$$

$$= 2.195 \left(\frac{0.62}{1.368}\right)^3 + 2.74 \left(\frac{1.20}{1.368}\right)^3 + 0 + (2.10)$$

$$= 0.2043 + 1.8494 + 2.10$$

$$= 4.154 \text{ per rad} \quad \left(\text{based on } \frac{\pi d_4{}^3}{4}\right)$$

REFERENCES

1. Pitts, W. C., Nielsen, J. N., and Kaattari, G. E.: Lift and Center of Pressure of Wing-Body-Tail Combinations at Subsonic, Transonic, and Supersonic Speeds. NACA TR 1307, 1959. (U)

2. Walker, H. J., and Wolowicz, C. H.: Theoretical Stability Derivatives for the X-15 Research Airplane at Supersonic and Hypersonic Speeds Including a Comparison with Wind-Tunnel Results. NASA TM X-287, 1960. (U)

3. Landahl, M. T.: Forces and Moments on Oscillating Slender Wing-Body Combinations at Sonic Speed. MIT Fluid Dynamics Research Group Report No. 56-1, 1956. (U)

4. Tobak, M., and Wehrend, W. R.: Stability Derivatives of Cones at Supersonic Speeds. NACA TN 3788, 1956. (U)

5. Fisher, L. R.: Equations and Charts for [illegible]ning the Hypersonic Stability Derivatives of Cone Frustums Computed by Newtonian Impact Theory. NASA TN D-149, 1959. (U)

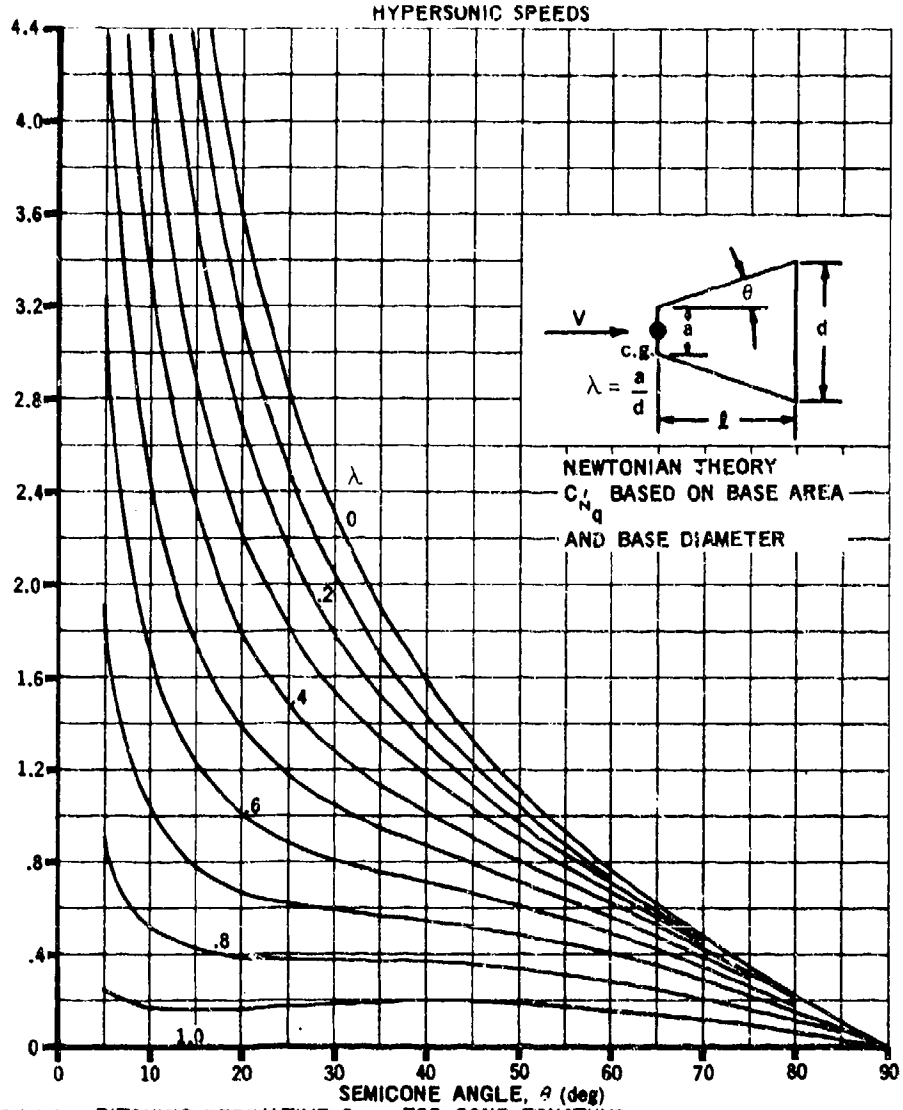

FIGURE 7.2 1.1-9a PITCHING DERIVATIVE C'_{N_q} FOR CONE FRUSTUMS

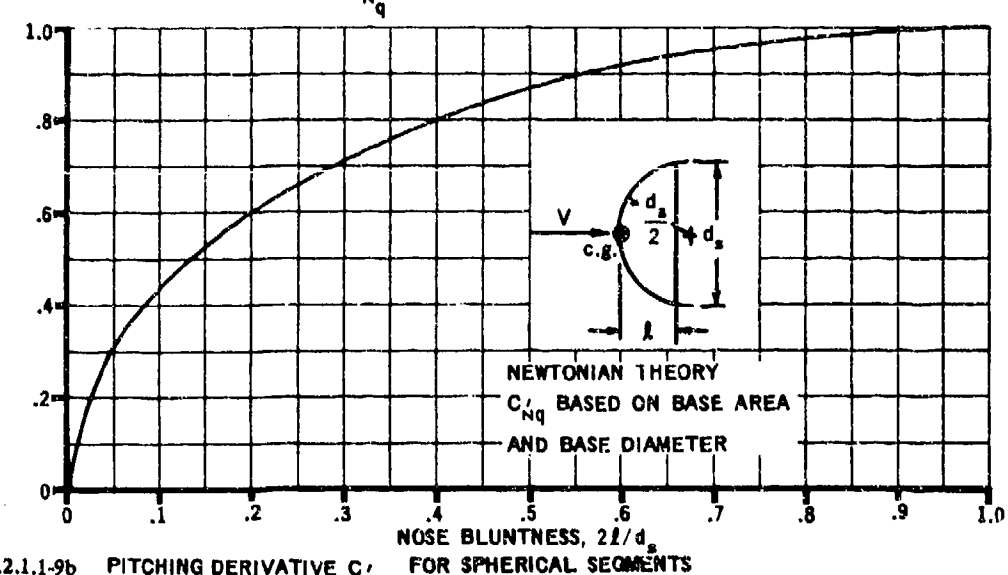

FIGURE 7.2.1.1-9b PITCHING DERIVATIVE C'_{N_q} FOR SPHERICAL SEGMENTS

7.2.1.2 BODY PITCHING DERIVATIVE C_{m_q}

The derivative C_{m_q} is a measure of the pitching moment produced by rotational motion of the airframe about a spanwise axis and is commonly referred to as the pitch-damping derivative. Methods are presented for determining the body contribution to this derivative in the subsonic, transonic, supersonic, and hypersonic speed ranges.

In the subsonic, transonic, and supersonic speed ranges the Datcom methods are based on the same assumption that was made in regard to the body contribution to the derivative C_{L_q}, and the general discussion of Section 7.2.1.1 is directly applicable here.

The body contribution to C_{m_q} is expressed as

$$C_{m_q} = C_{m_\alpha}\left(\frac{C_{m_q}}{C_{m_\alpha}}\right)_{\text{slender-body theory}}$$

The limitations of these methods are determined by the limitations of the methods employed in determining the static derivative C_{m_α} in the various speed regimes. Experimental data should be used for the body pitching-moment-curve slope when available.

A. SUBSONIC

The comments of paragraph A of Section 7.2.1.1 are directly applicable here.

DATCOM METHOD

The body contribution to C_{m_q}, based on body base area and the square of body length and referred to the center of rotation, is given by

$$C_{m_q} = 2\,C_{m_\alpha}\left[\frac{\left(1-\frac{x_m}{\ell_B}\right)^2 - \frac{V_B}{S_b \ell_B}\left(\frac{x_c}{\ell_B}-\frac{x_m}{\ell_B}\right)}{\left(1-\frac{x_m}{\ell_B}\right)-\frac{V_B}{S_b \ell_B}}\right] \qquad 7.2.1.2\text{-a}$$

where

C_{m_α} is the body pitching-moment-curve slope from paragraph A of Section 4.2.2.1, multiplied by $V_B/(S_b \ell_B)$.

V_B is the total body volume from Section 2.3.

S_b is the body base area.

x_c is the longitudinal distance from the vertex to the centroid of the volume and is given by

$$x_c = \frac{\int_0^{\ell_B} S(x)\, x\, dx}{V_B} \qquad 7.2.1.2\text{-b}$$

where

$S(x)$ is the body cross-sectional area at any station. It is not feasible to present generalized design charts of x_c, but the equation can be integrated for any arbitrary body of revolution.

ℓ_B is the length of the body.

x_m is the longitudinal distance from the body vertex to the center of rotation, positive aft.

Sample Problem

Given: Same ogive-cylinder configuration as sample problem of paragraph A of Section 7.2.1.1.

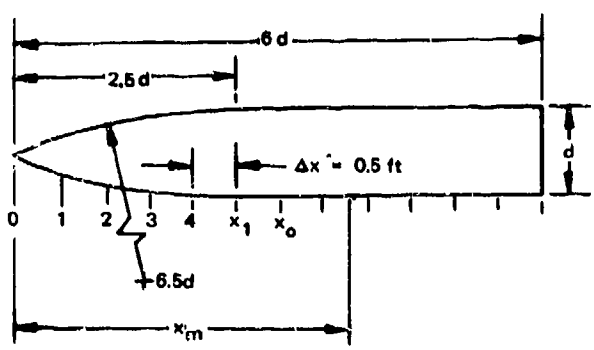

$d = 1.0$ ft $\quad \ell_B = 6.0$ ft $\quad$ Fineness Ratio $= 6.0$ $\quad x_m = 3.8$ ft

$x_1 = 2.5$ ft
$x_o = 3.6$ ft
$(k_2 - k_1) = 0.863$
} (Section 4.2.1.1)

$S_b = 0.785$ sq ft $\quad V_B = 3.88$ cu ft

Compute:

Determine C_{m_α}

Station	d	S_x	$\Delta S_x \approx \frac{dS_x}{dx} \Delta x$	$(x_m - x)^*$	$\frac{dS_x}{dx} (x_m - x) \Delta x$
1	0.4	0.126	0.126	3.467	0.4368
2	0.68	0.363	0.237	3.028	0.7176
3	0.89	0.622	0.259	2.539	0.6576
4	0.98	0.754	0.132	2.046	0.2701
x_1	1.0	0.785	0.031	1.549	0.0480
x_o	1.0	0.785	0	0.75	0

$$\sum_{x=0}^{x_o} \frac{dS_x}{dx} (x_m - x) \Delta x = 2.1301$$

$$C_{m_\alpha} = \frac{2(k_2 - k_1)}{V_B} \sum_{x=0}^{x_o} \frac{dS_x}{dx} (x_m - x) \Delta x \quad \text{(equation 4.2.2.1-a)}$$

$$= \frac{(2)\ (0.863)\ (2.1301)}{3.88}$$

$$= 0.948 \text{ per rad (based on } V_B)$$

$$C_{m_\alpha} = (0.948) \left(\frac{V_B}{S_b \ell_B} \right)$$

$$= (0.948) \left(\frac{3.88}{4.71} \right)$$

$$= 0.781 \text{ per rad (based on } S_b \ell_B)$$

*x is taken to be at the center of volume of each body segment.

Determine x_c

Station	d	S(x)	x*	S(x) x Δx
1	0.4	0.126	0.333	0.0210
2	0.68	0.363	0.772	0.1400
3	0.89	0.622	1.261	0.3920
4	0.98	0.754	1.754	0.6615
5	1.00	0.785	2.251	0.8836
6	1.00	0.785	2.75	1.0795
7	1.00	0.785	3.25	1.2755
8	1.00	0.785	3.75	1.4720
9	1.00	0.785	4.25	1.6680
10	1.00	0.785	4.75	1.8645
11	1.00	0.785	5.25	2.0605
12	1.00	0.785	5.75	2.2570

$$\sum_{x=0}^{\ell_B} S(x)x\,\Delta x = 13.775$$

$$x_c = \frac{\int_0^{\ell_B} S(x)\,x\,dx}{V_B} \quad \text{(equation 7.2.1.2-b)}$$

$$= \frac{13.775}{3.88} = 3.55 \text{ ft}$$

$$\frac{V_B}{S_b \ell_B} = \frac{(3.88)}{(0.785)\,(6.0)} = 0.824$$

$$\left(1 - \frac{x_m}{\ell_B}\right) = 1 - \frac{3.8}{6.0} = 0.367$$

Solution:

$$C_{m_q} = 2\,C_{m_\alpha} \left[\frac{\left(1 - \frac{x_m}{\ell_B}\right)^2 - \frac{V_B}{S_b \ell_B}\left(\frac{x_c}{\ell_B} - \frac{x_m}{\ell_B}\right)}{\left(1 - \frac{x_m}{\ell_B}\right) - \frac{V_B}{S_b \ell_B}} \right] \quad \text{(equation 7.2.1.2-a)}$$

*x is taken to be at the center of volume of each body segment.

$$= (2)(0.781)\left[\frac{(0.367)^2 - (0.824)\left(\frac{3.55}{6.0} - \frac{3.8}{6.0}\right)}{0.367 - 0.824}\right]$$

$$= 1.562\left[\frac{0.135 - (0.824)(-0.0417)}{-0.457}\right]$$

$$= 1.562\left[\frac{0.1693}{-0.457}\right]$$

$$= -0.579 \text{ per rad (based on } S_b \ell_B{}^2)$$

B. TRANSONIC

The comments of paragraph B of Section 7.2.1.1 are directly applicable here. The method of paragraph A is applicable throughout the transonic speed range.

C. SUPERSONIC

The theoretical methods applicable for the estimation of the body contribution to the derivative C_{m_q} parallel those of the body contribution to the derivative C_{L_q}.

Therefore, the general comments of paragraph C of Section 7.2.1.1 are also applicable here.

The supersonic C_{m_q} for cones can be estimated from the hybrid theory solutions presented in reference 1.

DATCOM METHOD

The method presented here for the body contribution to C_{m_q}, based on body base area and the square of body length and referred to the center of rotation, is the same as that of paragraph A and is given by equation 7.2.1.2-a, i.e.,

$$C_{m_q} = 2\,C_{m_\alpha}\left[\frac{\left(1 - \frac{x_m}{\ell_B}\right)^2 - \frac{V_B}{S_b \ell_B}\left(\frac{x_c}{\ell_B} - \frac{x_m}{\ell_B}\right)}{\left(1 - \frac{x_m}{\ell_B}\right) - \frac{V_B}{S_b \ell_B}}\right]$$

where C_{m_α} is the body pitching-moment-curve slope from paragraph C of Section 4.2.2.1 evaluated at the appropriate Mach number.

D. HYPERSONIC

Simple Newtonian theory is used in this section to estimate the derivative C_{m_q} of cone frustum bodies with or without spherical noses. Newtonian theory is discussed in paragraph D, Section 4.2.1.1.

DATCOM METHOD

Charts based on simple Newtonian theory (reference 2) are presented for determining C_{m_q} of spherical segments and cone frustums at small angles of attack. The coefficients of these charts are referred to the base area and the square of the base diameter and to a moment center at the forward face of the segment. By proper use of the data presented, the total C_{m_q} may be determined for bodies composed of multiple cone frustums with or without spherically blunted noses.

The Newtonian value of the stability derivative C_{m_q} for a complex body is obtained as follows:

Step 1. Compute $C_{m_q}{}'$ for each body segment about its own front face using figures 7.2.1.2-12 and 7.2.1.2-13b if the body has a spherically blunted nose, and figures 7.2.1.2-12 and 7.2.1.2-13a if the body nose is a cone frustum.

Step 2. Transfer the individual derivatives $C_{m_q}{}'$ to a common moment center by applying the following axis transfer equation to each body segment:

$$C_{m_q} = C_{m_q}{}' - 2\frac{n}{d} C_{m_\alpha}{}' + \frac{n}{d} C_{N_q}{}' - 2\left(\frac{n}{d}\right)^2 C_{N_\alpha} \qquad 7.2.1.2\text{-c}$$

where

C_{N_α} is the normal-force-curve slope for each segment based on individual base areas from Section 4.2.1.1.

$C_{N_q}{}'$ is the pitching derivative for each segment based on individual base areas and base diameters and referred to a moment center at the forward face of the segment. This derivative is obtained from paragraph D of Section 7.2.1.1.

$C_{m_\alpha}{}'$ is the pitching-moment-curve slope for each segment based on individual base areas and base diameters and referred to a moment center at the forward face of the segment. This derivative is obtained from paragraph D of Section 4.2.2.1.

$C_{m_q}{}'$ is the pitching derivative for each body segment based on individual base areas and the square of base diameters and referred to a moment center at

the forward face of the segment. If a complex body consists of combinations of cone frustums, the derivative for the first frustum must be obtained from figure 7.2.1.2-13a, which accounts for the front face being exposed to the air stream. If the body has a spherically blunted nose, the derivative of the nose is obtained from figure 7.2.1.2-13b. For subsequent frustums the derivatives are obtained from figure 7.2.1.2-12.

Step 3. The transferred derivatives of the individual body segments are added after being converted to a common reference area and squared diameter. The total derivative of the individual body segments is given by

$$C_{m_q} = \sum_{n=1}^{m} \left(C_{m_q}\right)_n \left(\frac{d_n}{d_b}\right)^4 \qquad 7.2.1.2\text{-d}$$

Sample Problem

Given: Same multiple-segment body as sample problems of paragraph D of Sections 4.2.1.1, 4.2.2.1, and 7.2.1.1.

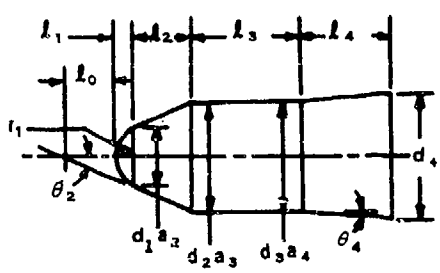

ℓ_0 = 0.55 ft (distance from moment reference center to body nose)

Spherical segment

ℓ_1 = 0.18 ft

r_1 = 0.36 ft

d_1 = 0.62 ft

Forward cone frustum

a_2 = 0.62 ft

d_2 = 1.20 ft

ℓ_2 = 0.72 ft

θ_2 = 22.5°

Cylinder

$a_3 = 1.20$ ft

$d_3 = 1.20$ ft

$\ell_3 = 1.20$ ft

$\theta_3 = 0$

Rear cone frustum

$a_4 = 1.20$ ft

$d_4 = 1.368$ ft

$\ell_4 = 0.96$ ft

$\theta_4 = 5°$

Compute:

Spherical segment

$2\ell_1/d_s = \ell_1/r_1 = 0.50$

$C_{m_{q_1}}' = -0.50$ per rad (figure 7.2.1.2-13b)

$n_1 = -\ell_0 = -0.55$ ft

$d_1 = a_2 = 0.62$ ft

$C_{N_{\alpha_1}} = 0.75$ per rad (figure 4.2.1.1-23)

$C_{m_{\alpha_1}}' = -0.430$ per rad (figure 4.2.2.1-20b)

$C_{N_{q_1}}' = 0.865$ per rad (figure 7.2.1.1-9b)

$$C_{m_{q_1}} = C_{m_{q_1}} - 2\frac{n_1}{d_1} C_{m_{\alpha_1}}' + \frac{n_1}{d_1} C_{N_{q_1}}' - 2\left(\frac{n_1}{d_1}\right)^2 C_{N_{\alpha_1}} \quad \text{(equation 7.2.1.2-c)}$$

$$= -0.50 - (-1.774)(-0.43) + (-0.887)(0.865) - (1.574)(0.75)$$

$$= -0.50 - 0.763 - 0.767 - 1.180$$

$$= -3.210 \text{ per rad} \left(\text{based on } \frac{\pi d_1^4}{4}\right)$$

Forward cone frustum

$a_2/d_2 = \lambda_2 = 0.517$

$C_{m_{q_2}}' = -0.68$ per rad (figure 7.2.1.2-12)

$n_2 = -(\ell_0 + \ell_1) = -0.73$

$C_{N_{\alpha_2}} = 1.250$ per rad (figure 4.2.1.1-26)

$C_{m_{\alpha_2}}' = -0.590$ per rad (figure 4.2.2.1-20a)

$C_{N_{q_2}}' = 1.22$ per rad (figure 7.2.1.1-9a)

$$C_{m_{q_2}} = C_{m_{q_2}}' - 2\frac{n_2}{d_2} C_{m_{\alpha_2}}' + \frac{n_2}{d_2} C_{N_{q_2}}' - 2\left(\frac{n_2}{d_2}\right)^2 C_{N_{\alpha_2}} \quad \text{(equation 7.2.1.2-c)}$$

$$= -0.68 - (-1.217)(-0.590) + (-0.608)(1.22) - (0.74)(1.25)$$

$$= -0.68 - 0.718 - 0.742 - 0.925$$

$$= -3.065 \text{ per rad} \left(\text{based on } \frac{\pi d_2^4}{4}\right)$$

Cylinder

$a_3/d_3 = \lambda_3 = 1.0$

$C_{m_{q_3}}' = 0$ (figure 7.2.1.2-12)

$n_3 = -(\ell_0 + \ell_1 + \ell_2) = -1.45$

$C_{N_{\alpha_3}} = 0$ (figure 4.2.1.1-26)

$C_{m_{\alpha_3}} = 0$ (figure 4.2.2.1-20a)

$C_{N_{q_3}}' = 0$ (figure 7.2.1.1-9a)

$C_{m_{q_3}} = 0$

Rear cone frustum

$a_4/d_4 = \lambda_4 = .0.877$

$C_{m_{q_4}}' = -0.250$ per rad (figure 7.2.1.2-12)

$n_4 = -(\ell_0 + \ell_1 + \ell_2 + \ell_3) = -2.65$

$C_{N_{\alpha_4}} = 0.450$ per rad (figure 4.2.1.1-26)

$C_{m_{\alpha_4}}' = -0.19$ per rad (figure 4.2.2.1-20a)

$C_{N_{q_4}}' = 0.36$ per rad (figure 7.2.1.1-9a)

$$C_{m_{q_4}} = C_{m_{q_4}}' - 2\frac{n_4}{d_4} C_{m_{\alpha_4}}' + \frac{n_4}{d_4} C_{N_{q_4}}' - 2\left(\frac{n_4}{d_4}\right)^2 C_{N_{\alpha_4}} \quad \text{(equation 7.2.1.2-c)}$$

$$= -0.25 - (-3.87)(-0.19) + (-1.94)(0.36) - (7.53)(0.45)$$

$$= -0.25 - 0.735 - 0.698 - 3.388$$

$$= -5.072 \text{ per rad} \left(\text{based on } \frac{\pi d_4^4}{4}\right)$$

Solution:

Converting the derivative for each segment to a common reference area and square of the diameter, the base area and diameter of the rear cone frustum, and adding gives

$$C_{m_q} = C_{m_{q_1}}\left(\frac{d_1}{d_4}\right)^4 + C_{m_{q_2}}\left(\frac{d_2}{d_4}\right)^4 + C_{m_{q_3}}\left(\frac{d_3}{d_4}\right)^4 + C_{m_{q_4}} \quad \text{(equation 7.2.1.2-d)}$$

$$= -3.210\left(\frac{0.62}{1.368}\right)^4 - 3.065\left(\frac{1.20}{1.368}\right)^4 + 0 + (-5.072)$$

$$= -0.1354 - 1.8148 - 5.072$$

$$= -7.022 \text{ per rad} \left(\text{based on } \frac{\pi d_4^4}{4}\right)$$

REFERENCES

1. Tobak, M., and Wehrend, W. R.: Stability Derivatives of Cones at Supersonic Speeds. NACA TN 3788, 1956. (U)

2. Fisher, L. R.: Equations and Charts for Determining the Hypersonic Stability Derivatives of Cone Frustums Computed by Newtonian Impact Theory. NASA TN D-149, 1959. (U)

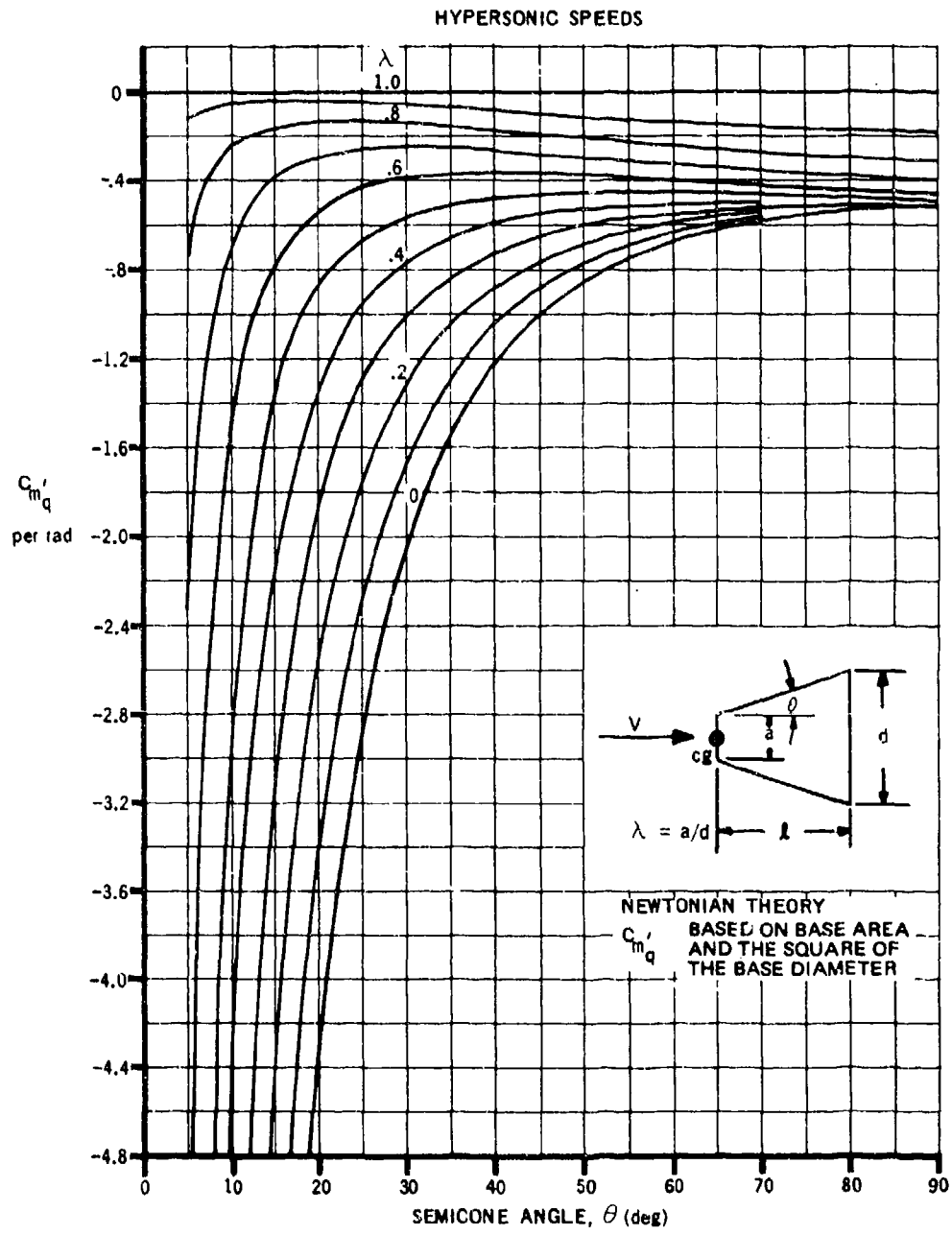

FIGURE 7.2.1.2-12 PITCHING DERIVATIVE $C_{m_q'}$ DUE TO INCLINED SIDES OF CONE FRUSTUMS

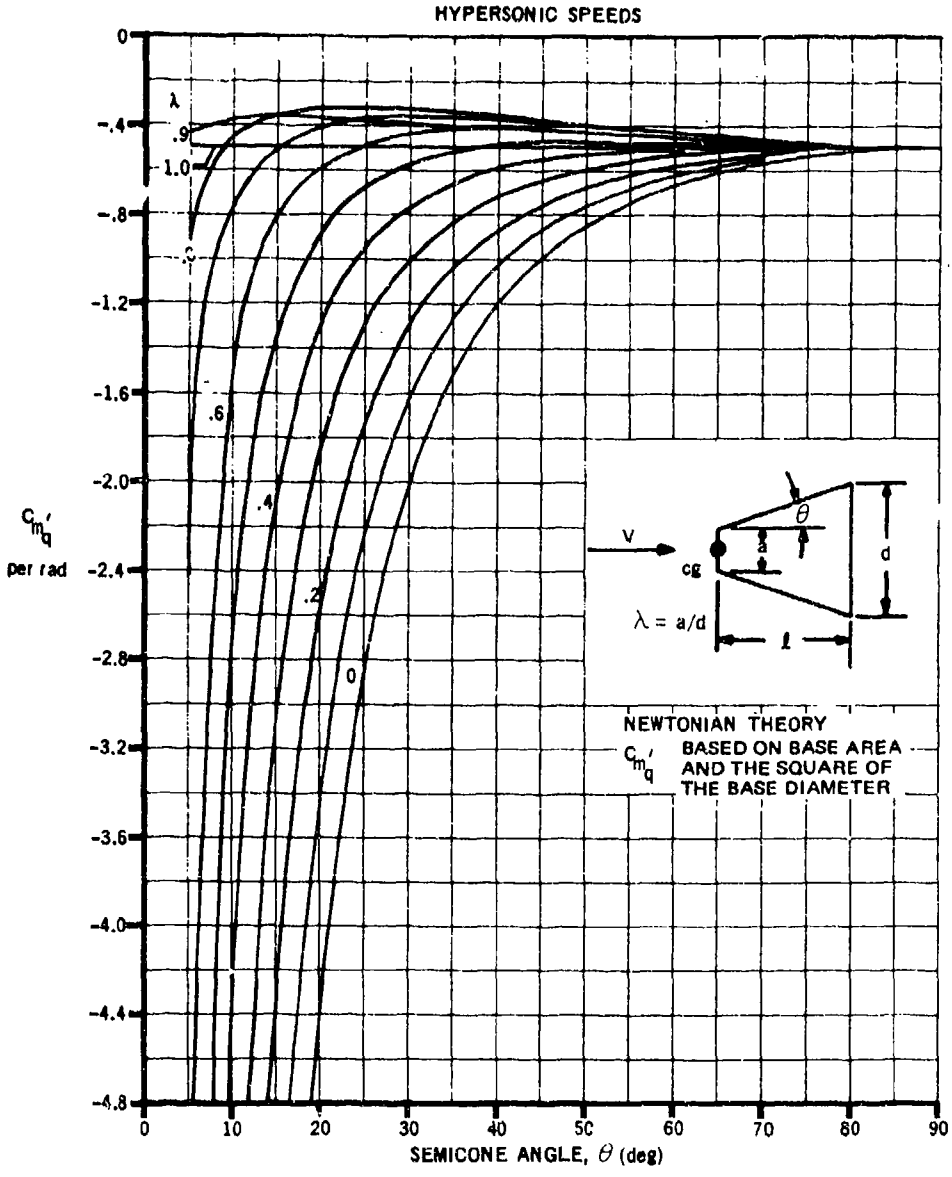

FIGURE 7.2.1.2-13a PITCHING DERIVATIVE C_{m_q}' FOR CONE FRUSTUMS

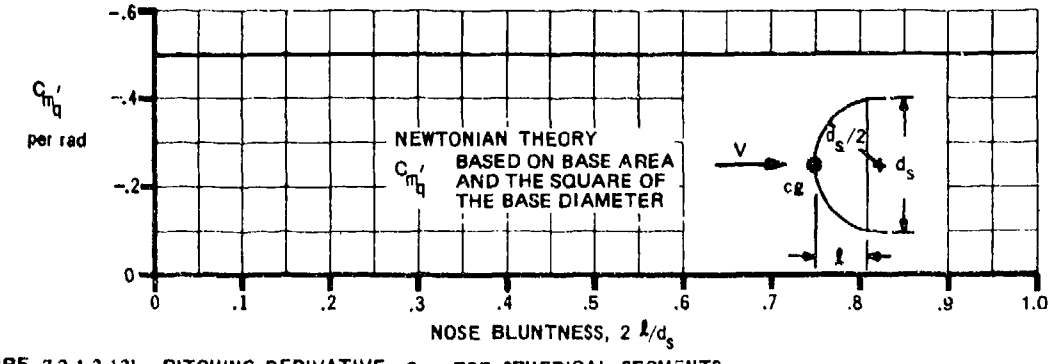

FIGURE 7.2.1.2-13b PITCHING DERIVATIVE C_{m_q}' FOR SPHERICAL SEGMENTS

7.2.2 BODY ACCELERATION DERIVATIVES

7.2.2.1 BODY ACCELERATION DERIVATIVE $C_{L_{\dot{\alpha}}}$

Methods are presented for determining the body contribution to the derivative $C_{L_{\dot{\alpha}}}$ in the subsonic, transonic, and supersonic speed ranges.

Datcom methods are based on the relatively simple results derived from slender-body theory in a manner similar to that used to predict the body pitching derivatives. It is assumed that a relationship of corresponding slender-body derivatives may be applied with reasonable accuracy to the case of vertical acceleration in a manner similar to that of reference 1. This approach to the calculation of body dynamic derivatives has been applied with reasonable success by Walker and Wolowicz in reference 2. It was shown in reference 1 that, although slender-body theory alone does not accurately predict the characteristics of nonslender bodies, the ratio of corresponding slender-body derivatives may be used with reasonable accuracy to predict the static forces on nonslender configurations. The body contribution to $C_{L_{\dot{\alpha}}}$ is then given as the product of the lift-curve slope C_{L_α} and the ratio of slender-body derivatives, i.e.,

$$C_{L_{\dot{\alpha}}} = C_{L_\alpha}\left(\frac{C_{L_{\dot{\alpha}}}}{C_{L_\alpha}}\right)_{\text{slender-body theory}}$$

Since slender-body theory states that body force characteristics are independent of Mach number, the limitations of these methods are determined by the limitations of the methods used in determining the derivative C_{L_α} in the various speed regimes. Experimental data should be used for the body lift-curve slope when available.

A. SUBSONIC

There is no explicit method available in the literature for the estimation of body acceleration derivatives in the subsonic speed range. The method presented below is based on the application of slender-body theory in the manner previously discussed.

DATCOM METHOD

The body contribution to $C_{L_{\dot{\alpha}}}$, based on body base area and body length, is given by

$$C_{L_{\dot{\alpha}}} = 2\,C_{L_\alpha}\left(\frac{V_B}{S_b \ell_B}\right) \quad \text{(per radian)} \qquad 7.2.2.1\text{-a}$$

where

C_{L_α} is the body lift-curve slope from paragraph A of Section 4.2.1.1 multiplied by $(V_B{}^{2/3}/S_b)$, based on S_b (per radian).

V_B is the total body volume from Section 2.3.

S_b is the body base area.

ℓ_B is the length of the body.

Sample Problem

Given: Same ogive-cylinder configuration as sample problem of paragraph A of Section 7.2.1.1.

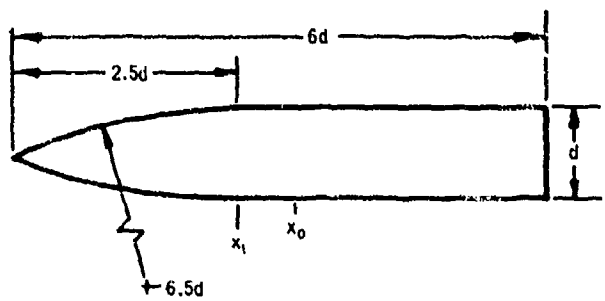

$d = 1$ ft $\quad \ell_B = 6.0$ ft $\quad$ Fineness Ratio $= 6.0$

$V_B = 3.88$ cu ft (Section 2.3) $\quad S_b = 0.785$ sq ft

$C_{L_\alpha} = 1.724$ per rad (based on S_b, Section 7.2.1.1)

Compute:

$$\frac{V_B}{S_b \ell_B} = \frac{(3.88)}{(0.785)\,(6.0)} = 0.824$$

Solution:

$$C_{L_{\dot{\alpha}}} = 2\, C_{L_\alpha} \left(\frac{V_B}{S_b \ell_B}\right) \quad \text{(equation 7.2.2.1-a)}$$

$$= 2(1.724)\,(0.824)$$

$$= 2.84 \text{ per rad (based on } S_b \ell_B)$$

B. TRANSONIC

The only available method for determining the body dynamic stability derivatives at transonic speeds is that of Landahl in reference 3. However, Landahl's results for the acceleration derivatives are frequency-dependent and no quantitative information is presented. Since slender-body theory states that body force characteristics are independent of Mach number, the method of paragraph A is applicable throughout the transonic speed range.

C. SUPERSONIC

Several of the theoretical methods available for estimating the body acceleration derivatives in the supersonic speed range are briefly discussed in Section 7.2. These include simple slender-body theory, theories treated within the assumptions of slender-body theory, and hybrid theory. The method presented here is based on the results of simple slender-body theory. Theories treated within the assumptions of slender-body theory are mathematically complex and restricted to specific planforms; therefore, no general quantitative information of their results is presented.

The supersonic $C_{N_{\dot{\alpha}}}$ of cones may be obtained from the hybrid theory solution of reference 4.

DATCOM METHOD

The method presented here for determining the body contribution to $C_{N_{\dot{\alpha}}}$, based on body base area and body length, is the same as that of paragraph A and is given by equation 7.2.2.1-a, i.e.,

$$C_{N_{\dot{\alpha}}} = 2\, C_{N_{\alpha}} \left(\frac{V_B}{S_b \ell_B} \right)$$

where $C_{N_{\alpha}}$ is the body normal-force-curve slope from paragraph C of Section 4.2.1.1, evaluated at the appropriate Mach number. The other parameters are defined in paragraph A of this section.

D HYPERSONIC

The body contribution to the derivative $C_{N_{\dot{\alpha}}}$ in the hypersonic speed range is shown in reference 5 to be zero when determined by the Newtonian impact theory.

REFERENCES

1. Pitts, W. C., Nielsen, J. N., and Kaattari, G. E.: Lift and Center of Pressure of Wing-Body-Tail Combinations at Subsonic, Transonic, and Supersonic Speeds. NACA TN 1307, 1957. (U)

2. Walker, H. J., and Wolowicz, C. H.: Theoretical Stability Derivatives for the X-15 Research Airplane at Supersonic and Hypersonic Speeds Including a Comparison with Wind-Tunnel Results. NASA TM X-287, 1960. (U)

3. Landahl, M. T.: Forces and Moments on Oscillating Slender Wing-Body Combinations at Sonic Speed. MIT Fluid Dynamics Research Group Report No. 56-1, 1956. (U)

4. Tobak, M., and Wehrend, W. R.: Stability Derivatives of a Cone at Supersonic Speeds. NACA TN 3788, 1956. (U)

5. Fisher, L. R.: Equations and Charts for Determining the Hypersonic Stability Derivatives of Cone Frustums Computed by Newtonian Impact Theory. NASA TN D-149, 1959. (U)

7.2.2.2 BODY ACCELERATION DERIVATIVE $C_{m_{\dot{\alpha}}}$

Methods are presented for determining the body contribution to the acceleration derivative $C_{m_{\dot{\alpha}}}$ in the subsonic, transonic, and supersonic speed ranges.

Datcom methods are based on the same assumptions that were made in regard to the estimation of the body contribution to the derivative $C_{L_{\dot{\alpha}}}$, and the general discussion of Section 7.2.2.1 is directly applicable here. The body contribution to $C_{m_{\dot{\alpha}}}$ is expressed as

$$C_{m_{\dot{\alpha}}} = C_{m_\alpha}\left(\frac{C_{m_{\dot{\alpha}}}}{C_{m_\alpha}}\right)_{\text{slender-body theory}}$$

The limitations of these methods are determined by the limitations of the methods used in estimating the static derivative C_{m_α} in the various speed regimes. Experimental data should be used for the body pitching-moment-curve slope when available.

A. SUBSONIC

The comments of Paragraph A of Section 7.2.2.1 are directly applicable here.

DATCOM METHOD

The body contribution to $C_{m_{\dot{\alpha}}}$, based on body base area and the square of the body length and referred to an arbitrary moment center, is given by

$$C_{m_{\dot{\alpha}}} = 2\,C_{m_\alpha}\frac{\left[\frac{V_B}{S_b \ell_B}\left(\frac{x_c}{\ell_B} - \frac{x_m}{\ell_B}\right)\right]}{\left[\left(1 - \frac{x_m}{\ell_B}\right) - \frac{V_B}{S_b \ell_B}\right]} \qquad 7.2.2.2\text{-a}$$

where

C_{m_α} is the body pitching-moment-curve slope from Paragraph A of Section 4.2.2.1, multiplied by $V_B/(S_b \ell_B)$.

x_c is the longitudinal distance from the vertex to the centroid of the volume and is given by Equation 7.2.1.2-b, i.e.,

$$x_c = \frac{\int_0^{\ell_B} S(x)\, x\, dx}{V_B}$$

x_m is the longitudinal distance from the body vertex to the center of rotation, positive aft.

ℓ_B is the length of the body.

V_B is the total body volume from Section 2.3.

S_b is the body base area.

Sample Problem

Given: Same ogive-cylinder configuration as sample problems of Paragraph A of Sections 7.2.1.2 and 7.2.2.1.

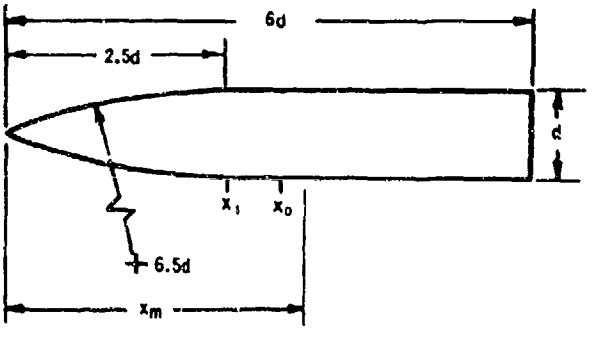

$d = 1$ ft $\quad \ell_B = 6.0$ ft $\quad$ Fineness Ratio $= 6.0$ $\quad x_m = 3.8$ ft

$$\frac{V_B}{S_b \ell_B} = 0.824 \text{ (Section 7.2.2.1)}$$

$$\left.\begin{aligned} C_{m_\alpha} &= 0.781 \text{ per rad} \\ x_c &= 3.55 \text{ ft} \end{aligned}\right\} \text{ (Section 7.2.1.2)}$$

Solution:

$$\left(1 - \frac{x_m}{\ell_B}\right) = \left(1 - \frac{3.8}{6.0}\right) = 0.367$$

$$C_{m_{\dot{\alpha}}} = 2\,C_{m_\alpha} \frac{\left[\frac{V_B}{S_b \ell_B}\left(\frac{x_c}{\ell_B} - \frac{x_m}{\ell_B}\right)\right]}{\left[\left(1 - \frac{x_m}{\ell_B}\right) - \frac{V_B}{S_b \ell_B}\right]} \quad \text{(Equation 7.2.2.2-a)}$$

$$= 2(0.781)\left[\frac{0.824\left(\frac{3.55}{6.0} - \frac{3.8}{6.0}\right)}{0.367 - 0.824}\right]$$

$$= 1.562\left(\frac{-0.0343}{-0.457}\right)$$

$$= 0.117 \text{ per rad (based on } S_b \ell_B^2)$$

B. TRANSONIC

The comments of Paragraph B of Section 7.2.2.1 are directly applicable here. The method of Paragraph A is applicable throughout the transonic speed range.

C. SUPERSONIC

The theoretical methods applicable for the estimation of the body contribution to the derivative $C_{m_{\dot{\alpha}}}$ parallel those of the body contribution to the derivative $C_{L_{\dot{\alpha}}}$. Therefore, the general comments of Paragraph C of Section 7.2.2.1 are also applicable here.

The supersonic $C_{m_{\dot{\alpha}}}$ for a cone can be estimated by the hybrid theory solutions presented in Reference 1.

DATCOM METHOD

The method presented here for the body contribution to $C_{m_{\dot{\alpha}}}$, based on body base area and the square of the body length and referred to an arbitrary moment center, is the same as that of Paragraph A and is given by Equation 7.2.2.2-a, i.e.,

$$C_{m_{\dot{\alpha}}} = 2\,C_{m_\alpha} \frac{\left[\frac{V_B}{S_b \ell_B}\left(\frac{x_c}{\ell_B} - \frac{x_m}{\ell_B}\right)\right]}{\left[\left(1 - \frac{x_m}{\ell_B}\right) - \frac{V_B}{S_b \ell_B}\right]}$$

where C_{m_α} is the body pitching-moment-curve slope from Paragraph C of Section 4.2.2.1, evaluated at the appropriate Mach number. The other parameters are defined in Paragraph A of this section.

D. HYPERSONIC

The body contribution to the derivative $C_{m_{\dot{\alpha}}}$ in the hypersonic speed range is shown in Reference 1 to be zero when determined by the Newtonian impact theory.

REFERENCE

1. Tobak, M., and Wehrend, W. R.: Stability Derivatives of a Cone at Supersonic Speeds. NACA TN 3788, 1956. (U)

7.3 WING-BODY DYNAMIC DERIVATIVES

7.3.1 WING-BODY PITCHING DERIVATIVES

7.3.1.1 WING-BODY PITCHING DERIVATIVE C_{L_q}

The information contained in this section is for estimating the pitching derivative C_{L_q} of wing-body configurations at low angles of attack. In general, it consists of a synthesis of material presented in other sections; however, the method of application is new.

The Datcom methods are based on the assumption that the mutual interferences that occur between components for angle-of-attack variations, determined in references 1 and 2 and presented in Section 4.3.1.2, may be employed with reasonable accuracy to the case of steady pitching. This approach to the calculation of wing-body pitching derivatives has been used with reasonable success by Walker and Wolowicz in reference 3.

A. SUBSONIC

Two methods are presented for determining the pitching derivative C_{L_q} of a wing-body configuration, differing only in their treatment of the mutual interference effects.

DATCOM METHODS

Method 1

For wing-body configurations similar to sketch (d) of Section 4.3.1.2, the pitching derivative C_{L_q}, based on the area and mean aerodynamic chord of the total panel and referred to a moment center at the assumed center of gravity or center of rotation, is given by

$$\left(C_{L_q}\right)_{WB} = \left[K_{W(B)} + K_{B(W)}\right]\left(\frac{S_e}{S}\right)\left(\frac{\bar{c}_e}{\bar{c}}\right)\left(C_{L_q}\right)_e + \left(C_{L_q}\right)_B\left(\frac{S_b}{S}\right)\left(\frac{\ell_B}{\bar{c}}\right) \qquad 7.3.1.1\text{-a}$$

where

$K_{W(B)}$ and $K_{B(W)}$ are the appropriate wing-body interference factors obtained from Section 4.3.1.2.

$\left(C_{L_q}\right)_e$ is the contribution of the exposed panel to the pitching derivative C_{L_q}, obtained from Section 7.1.1.1. (See Section 4.3.1.2 for the definition of exposed surfaces.)

$\left(C_{L_q}\right)_B$ is the contribution of the body to the pitching derivative C_{L_q}, obtained from Section 7.2.1.1.

$\frac{S_e}{S}$ is the ratio of the exposed to the total panel area.

$\frac{S_b}{S}$ is the ratio of the body base area to the total panel area.

$\frac{\bar{c}_e}{\bar{c}}$ is the ratio of the mean aerodynamic chord of the exposed panel to the mean aerodynamic chord of the total panel.

$\frac{\ell_B}{\bar{c}}$ is the ratio of the body length to the mean aerodynamic chord of the total panel.

Moment transfer calculations are included as an integral part of the wing and body derivative estimation methods of Sections 7.1.1.1 and 7.2.1.1, respectively.

Method 2

For wing-body configurations similar to sketch (c) of Section 4.3.1.2, the pitching derivative C_{L_q}, based on the area and mean aerodynamic chord of the total panel and referred to a moment center at the assumed center of gravity or center of rotation, is given by

$$\left(C_{L_q}\right)_{WB} = K_{(WB)}\left(C_{L_q}\right)_W + \left(C_{L_q}\right)_B \left(\frac{S_b}{S}\right)\left(\frac{\ell_B}{\bar{c}}\right) \qquad 7.3.1.1\text{-b}$$

where

$K_{(WB)}$ is the wing-body interference factor, obtained from figure 4.3.1.2-12c of Section 4.3.1.2.

$\left(C_{L_q}\right)_W$ is the contribution of the total panel to the pitching derivative C_{L_q}, obtained from Section 7.1.1.1.

The remaining terms are defined in method 1 above. Moment transfer calculations are included as an integral part of the wing and body derivative estimation methods of Sections 7.1.1.1 and 7.2.1.1, respectively.

Sample Problem

Method 1

Given: An ogive-cylinder-body–triangular-wing configuration

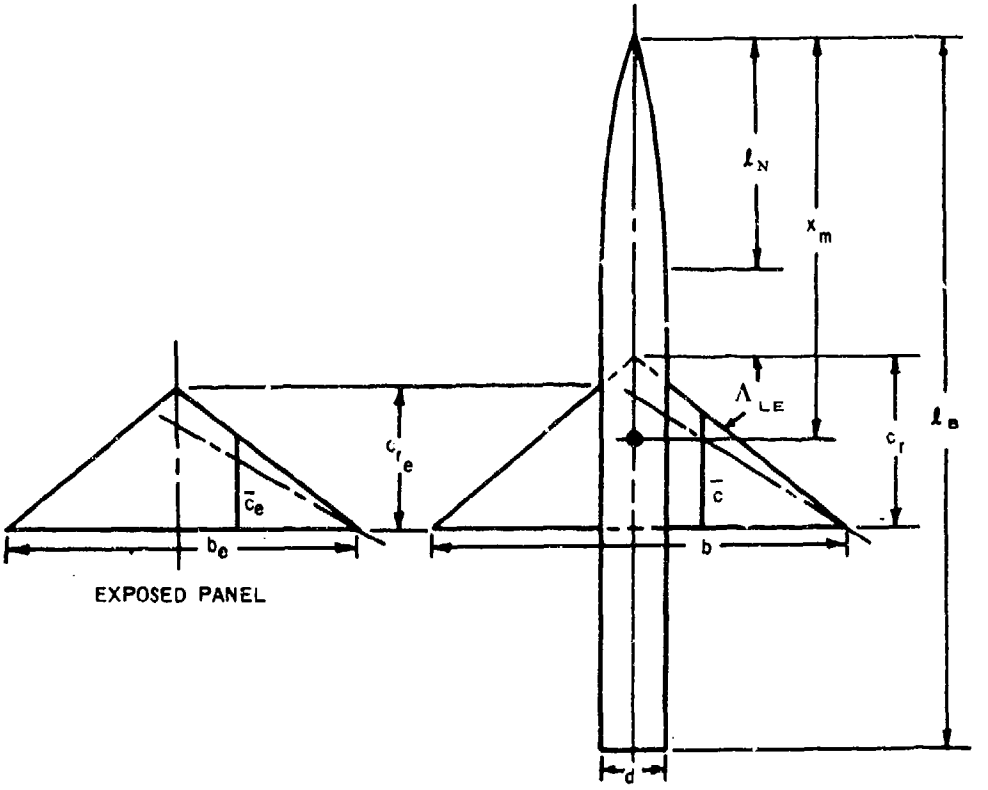

Wing Characteristics:

Total Panel		Exposed Panel	
$A = 5.0$	$\lambda = 0$	$A_e = 5.0$	$\lambda_e = 0$
$\Lambda_{LE} = 38.67°$	$S = 414.0$ sq ft	$b_e = 38.37$ ft	$S_e = 294.50$ sq ft
$i_W = 0$	$c_r = 18.20$ ft	$\Lambda_{c/2} = 21.8°$	$c_{r_e} = 15.375$ ft
$b = 45.50$ ft	$\bar{c} = 12.133$ ft		$\bar{c}_e = 10.25$ ft

NACA 66-206 airfoil section

Body Characteristics:

$\ell_N = 25.0$ ft $\qquad \ell_B = 77.20$ ft $\qquad d = 7.127$ ft

The following ratios based on total panel dimensions:

$\frac{S_e}{S} = 0.7113 \qquad \frac{\bar{c}_e}{\bar{c}} = 0.845 \qquad \frac{S_b}{S} = 0.0963 \qquad \frac{\ell_B}{\bar{c}} = 6.363$

Additional Characteristics:

$M = 0.60$ $\qquad x_m = 43.70$ ft (moment center at $\bar{c}/4$ of total panel)

$\beta = 0.80$ $\qquad \frac{d}{b} = 0.157$

Compute:

Step 1. Pitching derivative C_{L_q} for exposed panel (Section 7.1.1.1)

$c_{\ell_\alpha} = 6.19$ per rad (table 4.1.1-B)

$$\kappa = \frac{c_{\ell_\alpha}}{2\pi} = 0.985$$

$$\frac{A_e}{\kappa}\left[\beta^2 + \tan^2 \Lambda_{c/2}\right]^{1/2} = \frac{5.0}{0.985}\left[0.64 + 0.16\right]^{1/2} = 4.54$$

$$\frac{\left(C_{L_\alpha}\right)_e}{A_e} = 0.90 \text{ per rad} \quad \text{(figure 4.1.3.2-49)}$$

$$\left(C_{L_\alpha}\right)_e = 4.50 \text{ per rad}$$

$$\frac{\tan \Lambda_{LE}}{\beta} = 1.0$$

$$A_e \tan \Lambda_{LE} = 4.0$$

$$\left(\frac{x_{a.c.}}{c_r}\right)_e = 0.560 \quad \text{(figure 4.1.4.2-26a)}$$

$$\left(\frac{x_{c.g.}}{c_r}\right)_e = 0.408 \quad \text{(from planform geometry of exposed panel with c.g. at } \bar{c}/4 \text{ of total panel)}$$

$$\left(\frac{\bar{x}}{\bar{c}}\right)_e = \left(\frac{x_{a.c.}}{\bar{c}} - \frac{x_{c.g.}}{\bar{c}}\right)_e \quad \text{(equation 7.1.1.1-b)}$$

$$= \left(\frac{x_{a.c.}}{c_r} - \frac{x_{c.g.}}{c_r}\right)_e \left(\frac{c_r}{\bar{c}}\right)_e = (0.560 - 0.408)\ 1.50 = 0.228$$

$$\left(C_{L_q}\right)_e = \left(\frac{1}{2} + 2\frac{\bar{x}}{\bar{c}}\right)_e \left(C_{L_\alpha}\right)_e \quad \text{(equation 7.1.1.1-a)}$$

$$= (0.956)\ (4.50)$$

$$= 4.30 \text{ per rad (based on } S_e \bar{c}_e)$$

Step 2. Wing-body interference factors (Section 4.3.1.2)

$$\left.\begin{aligned} K_{W(B)} &= 1.125 \\ K_{B(W)} &= 0.215 \end{aligned}\right\} \text{(figure 4.3.1.2-10)}$$

Step 3. Pitching derivative C_{L_q} for body (Section 7.2.1.1)

$$\frac{\ell}{d} = \frac{77.20}{7.127} = 10.83$$

$$(k_2 - k_1) = 0.947 \quad \text{(figure 4.2.1.1-20a)}$$

$$x_1 = \ell_N = 25.0 \text{ ft}$$

$$\frac{x_1}{\ell_B} = \frac{25.0}{77.2} = 0.324$$

$$\frac{x_o}{\ell_B} = 0.55 \quad \text{(extrapolated using figure 4.2.1.1-20b)}$$

$$x_o = 42.46 \text{ ft}$$

$$S_o = S_1 = 39.88 \text{ sq ft}$$

$$\frac{\ell_N}{d} = \frac{25.0}{7.127} = 3.508$$

$$\frac{V_N}{S_o \ell_N} = 0.535 \quad \text{(figure 2.3-5, ogive)}$$

$$V_N = (0.535)\ (39.88)\ (25.0) = 533.4 \text{ cu ft}$$

$$V_B = (\ell_B - \ell_N)\, S_1 + V_N$$

$$= (77.2 - 25.0)\,(39.88) + 533.4$$

$$= 2615.1 \text{ cu ft}$$

$$V_B^{2/3} = 189.8 \text{ sq ft}$$

$$\left(C_{L_\alpha}\right)_B = \frac{2(k_2 - k_1)\, S_o}{V_B^{2/3}} \quad \text{(equation 4.2.1.1-a)}$$

$$= \frac{2(0.947)\,(39.88)}{189.8}$$

$$= 0.398 \text{ per rad} \quad \text{(based on } V_B^{2/3}\text{)}$$

$$\left(C_{L_\alpha}\right)_B = 0.398\, \frac{V_B^{2/3}}{S_b} = 0.398 \left(\frac{189.8}{39.88}\right) = 1.894 \text{ per rad} \quad \text{(based on } S_b\text{)}$$

$$\left(1 - \frac{x_m}{\ell_B}\right) = \left(1 - \frac{43.70}{77.20}\right) = 0.434$$

$$\left(C_{L_q}\right)_B = 2\left(C_{L_\alpha}\right)_B \left(1 - \frac{x_m}{\ell_B}\right) \quad \text{(equation 7.2.1.1-a)}$$

$$= 2(1.894)\,(0.434)$$

$$= 1.644 \text{ per rad} \quad \text{(based on } S_b \ell_B\text{)}$$

Solution:

$$\left(C_{L_q}\right)_{WB} = \left[K_{W(B)} + K_{B(W)}\right]\left(\frac{S_e}{S}\right)\left(\frac{\bar{c}_e}{\bar{c}}\right)\left(C_{L_q}\right)_e + \left(C_{L_q}\right)_B \left(\frac{S_b}{S}\right)\left(\frac{\ell_B}{\bar{c}}\right) \quad \text{(equation 7.3.1.1-a)}$$

$$= (1.175 + 0.215)\,(0.7113)\,(0.845)\,(4.30) + (1.644)\,(0.0963)\,(6.363)$$

$$= 3.46 + 1.007$$

$$= 4.467 \text{ per rad} \quad \text{(based on the area and mean aerodynamic chord of the total panel and referred to a moment center at } \bar{c}/4 \text{ of the total panel)}$$

B. TRANSONIC

The aerodynamic interference effects for slender wing-body configurations are relatively insensitive to Mach number; consequently, the slender-body interference factors of Section 4.3.1.2 should give reasonable results. For nonslender configurations, transonic interference effects can become quite large and sensitive to minor changes in local contour.

DATCOM METHODS

It is recommended that the methods presented in paragraph A for estimating the pitching derivative C_{L_q} of a wing-body configuration be applied to the transonic speed regime. Care should be taken to estimate the contributions of the lifting panel and body at the appropriate Mach number. The interference factors should be obtained from paragraph C, Section 4.3.1.2.

C. SUPERSONIC

The information included in the Datcom accounts for most of the mutual interferences that occur between components of a wing-body configuration at supersonic speeds. These interference effects have been accounted for by the slender-body interference factors of Section 4.3.1.2.

DATCOM METHODS

The methods presented in paragraph A for estimating the pitching derivative C_{L_q} of a wing-body configuration are also applicable to the supersonic speed range. Care should be taken to estimate the contributions of the lifting panel and body at the appropriate Mach number.

Sample Problem

Method 1

Given: Same configuration as sample problem of paragraph A

$M = 1.4 \qquad \beta = 0.98$

Compute:

Step 1. Pitching derivative C_{L_q} for exposed panel (Section 7.1.1.1)

$$\frac{\tan \Lambda_{LE}}{\beta} = 0.816$$

$$A_e \tan \Lambda_{LE} = 4.0$$

$$\beta \left(C_{N_\alpha}\right)_e = 4.0 \text{ per rad} \quad \text{(figure 4.1.3.2-56a)}$$

$\left(C_{N_\alpha}\right)_e$ = 4.08 per rad

$\left(\frac{x_{a.c.}}{c_r}\right)_e$ = 0.67 (figure 4.1.4.2-26a)

$\left(\frac{x_{c.g.}}{c_r}\right)_e$ = 0.408 (from planform geometry of exposed panel with c.g. at $\bar{c}/4$ of total panel)

$\left(\frac{\bar{x}}{\bar{c}}\right)_e = \left(\frac{x_{a.c.}}{\bar{c}} - \frac{x_{c.g.}}{\bar{c}}\right)_e$ (equation 7.1.1.1-b)

$= \left(\frac{x_{a.c.}}{c_r} - \frac{x_{c.g.}}{c_r}\right)_e \left(\frac{c_r}{\bar{c}}\right)_e$ = (0.67 – 0.408) 1.50 = 0.393

$\beta \cot \Lambda_{LE}$ = 1.225 (supersonic leading edge)

βA_e = 4.90

$\cot^{-1} (\beta \cot \Lambda_{LE})$ = 39.23°

$\left(C_{L_q}'\right)_e$ = 0 (figure 7.1.1.1-11a)

$\left(C_{L_q}\right)_e = \left(C_{L_q}'\right)_e + 2\left(\frac{\bar{x}}{\bar{c}}\right)_e \left(C_{N_\alpha}\right)_e$ (equation 7.1.1.1-c)

= 0 + 2(0.393) (4.08)

= 3.21 per rad (based on $S_e \bar{c}_e$)

Step 2. Wing-body interference factors (Section 4.3.1.2)

$K_{W(B)}$ = 1.125 (figure 4.3.1.2-10)

$\frac{\beta d}{c_{r_e}} = \frac{(0.98)\ (7.127)}{15.375}$ = 0.455

$K_{B(W)}\left[\beta \left(C_{N_\alpha}\right)_e (\lambda_e + 1)\left(\frac{b}{d} - 1\right)\right]$ = 3.90 (figure 4.3.1.2-11a)

$$\left[\beta \left(C_{N_\alpha}\right)_e (\lambda_e + 1) \left(\frac{b}{d} - 1\right)\right] = (0.98)\,(4.08)\,(1)\,(6.38 - 1) = 21.51$$

$$K_{B(W)} = \frac{3.90}{21.51} = 0.181$$

Step 3. Pitching derivative C_{L_q} for body (Section 7.2.1.1)

$$f_A = \frac{\ell_A}{d} = \frac{77.2 - 25.0}{7.127} = 7.32$$

$$f_N = \frac{\ell_N}{d} = \frac{25.0}{7.127} = 3.51$$

$$f_A / f_N = 2.09$$

$$\frac{\beta}{f_N} = \frac{0.98}{3.51} = 0.279$$

$\left(C_{N_\alpha}\right)_B$ = 2.74 per rad (figure 4.2.1.1-21a, extrapolated)

$\left(1 - \frac{x_m}{\ell_B}\right)$ = 0.434 (sample problem, paragraph A)

$$\left(C_{L_q}\right)_B = 2\left(C_{N_\alpha}\right)_B \left(1 - \frac{x_m}{\ell_B}\right) \quad \text{(equation 7.2.1.1-a)}$$

$$= 2(2.74)\,(0.434)$$

$$= 2.378 \text{ per rad (based on } S_b \ell_B)$$

Solution:

$$\left(C_{L_q}\right)_{WB} = \left[K_{W(B)} + K_{B(W)}\right] \left(\frac{S_e}{S}\right) \left(\frac{\bar{c}_e}{\bar{c}}\right) \left(C_{L_q}\right)_e + \left(C_{L_q}\right)_B \left(\frac{S_b}{S}\right) \left(\frac{\ell_B}{\bar{c}}\right)$$

(equation 7.3.1.1-a)

$$= (1.125 + 0.181)\,(0.7113)\,(0.845)\,(3.21) + (2.378)\,(0.0963)\,(6.363)$$

$$= 2.520 + 1.457$$

= 3.977 per rad (based on the area and mean aerodynamic chord of the total panel and referred to a moment center at $\bar{c}/4$ of the total panel)

REFERENCES

1. Pitts, W., Neilsen, J., and Kaattari, G.: Lift and Center of Pressure of Wing-Body-Tail Combinations at Subsonic, Transonic, and Supersonic Speeds. NACA TR 1307, 1959. (U)

2. Spreiter, J.: The Aerodynamic Forces on Slender Plane- and Cruciform-Wing and Body Combinations. NACA TR 962, 1950. (U)

3. Walker, H., and Wolowicz, C.: Theoretical Stability Derivatives for the X-15 Research Airplane at Supersonic and Hypersonic Speeds Including a Comparison with Wind-Tunnel Results. NASA TM X-287, 1960. (U)

7.3.1.2 WING-BODY PITCHING DERIVATIVE C_{m_q}

The information contained in this section is for estimating the pitching derivative C_{m_q} of wing-body configurations at low angles of attack. The derivative C_{m_q} is a measure of the pitching moment produced by rotational motion about a spanwise axis and is commonly referred to as the pitch-damping derivative.

The Datcom methods are based on the same assumption that was made in regard to the pitching derivative C_{L_q} of a wing-body configuration, and the general discussion of Section 7.3.1.1 is directly applicable here.

A. SUBSONIC

Two methods are presented for determining the pitching derivative C_{m_q} of a wing-body configuration, differing only in their treatment of the mutual interference effects.

DATCOM METHODS

Method 1

For wing-body configurations similar to sketch (d) of Section 4.3.1.2, the pitching derivative C_{m_q}, based on the area and the square of the mean aerodynamic chord of the total panel and referred to a moment center at the assumed center of gravity or center of rotation, is given by

$$\left(C_{m_q}\right)_{WB} = \left[K_{W(B)} + K_{B(W)}\right]\left(\frac{S_e}{S}\right)\left(\frac{\bar{c}_e}{\bar{c}}\right)^2\left(C_{m_q}\right)_e + \left(C_{m_q}\right)_B\left(\frac{S_b}{S}\right)\left(\frac{\ell_B}{\bar{c}}\right)^2 \qquad 7.3.1.2\text{-a}$$

where

$\left(C_{m_q}\right)_e$ is the contribution of the exposed panel to the pitching derivative C_{m_q}, obtained from Section 7.1.1.2. (See Section 4.3.1.2 for the definition of exposed surfaces.)

$\left(C_{m_q}\right)_B$ is the contribution of the body to the pitching derivative C_{m_q}, obtained from Section 7.2.1.2.

The remaining terms are defined in paragraph A of Section 7.3.1.1. Moment transfer calculations are included as an integral part of the wing- and body-derivative estimation methods of Sections 7.1.1.2 and 7.2.1.2, respectively.

Method 2

For wing-body configurations similar to sketch (c) of Section 4.3.1.2, the pitching derivative C_{m_q}, based on the area and the square of the mean aerodynamic chord of the total panel and referred to a moment center at the assumed center of gravity or center of rotation, is given by

$$\left(C_{m_q}\right)_{WB} = K_{(WB)}\left(C_{m_q}\right)_W + \left(C_{m_q}\right)_B \left(\frac{S_b}{S}\right)\left(\frac{\ell_B}{\bar{c}}\right)^2 \qquad 7.3.1.2\text{-b}$$

where

$\left(C_{m_q}\right)_W$ is the contribution of the total panel to the pitching derivative C_{m_q}, obtained from Section 7.1.1.2.

The remaining terms are defined in method 1 above and paragraph A of Section 7.3.1.1. Moment transfer calculations are included as an integral part of the wing- and body-derivative estimation methods of Sections 7.1.1.2 and 7.2.1.2, respectively.

Sample Problem

Method 1

Given: Same configuration as sample problem of paragraph A, Section 7.3.1.1. The characteristics are repeated below.

Wing Characteristics:

Total Panel		Exposed Panel	
$A = 5.0$	$\lambda = 0$	$A_e = 5.0$	$\lambda_e = 0$
$\Lambda_{LE} = 38.67°$	$S = 414.0$ sq ft	$b_e = 38.37$ ft	$S_e = 294.50$ sq ft
$i_W = 0$	$c_r = 18.20$ ft	$\Lambda_{c/4} = 30.96°$	$c_{r_e} = 15.375$ ft
$b = 45.50$ ft	$\bar{c} = 12.133$ ft		$\bar{c}_e = 10.25$ ft

NACA 66-206 airfoil section

Body Characteristics:

$\ell_N = 25.0$ ft $\qquad \ell_B = 77.20$ ft $\qquad d = 7.127$ ft

The following ratios based on total panel dimensions:

$$\frac{S_e}{S} = 0.7113 \qquad \left(\frac{\bar{c}_e}{\bar{c}}\right)^2 = 0.7140$$

$$\frac{S_b}{S} = 0.0963 \qquad \left(\frac{\ell_B}{\bar{c}}\right)^2 = 40.49$$

Additional Characteristics:

$M = 0.60$ $\qquad$ $x_m = 43.70$ ft (moment center at $\bar{c}/4$ of total panel)

$\beta = 0.80$ $\qquad$ $\frac{d}{b} = 0.157$

Compute:

Step 1. Pitching derivative C_{m_q} for exposed panel (Section 7.1.1.2)

$$\left.\begin{array}{l} c_{\ell_\alpha} = 6.19 \text{ per rad} \\ \left(\frac{\bar{x}}{\bar{c}}\right)_e = 0.228 \end{array}\right\} \text{ (sample problem, paragraph A, Section 7.3.1.1)}$$

$$\cos \Lambda_{c/4} = 0.8576$$

$$\tan \Lambda_{c/4} = 0.600$$

$$B = \sqrt{1 - M^2 \cos^2 \Lambda_{c/4}} = 0.8575$$

$$\left[\left(C_{m_q}\right)_{M \approx 0.2}\right]_e = -0.7\, c_{\ell_\alpha} \cos \Lambda_{c/4} \left\{ \frac{A_e \left[\frac{1}{2}\frac{\bar{x}}{\bar{c}} + 2\left(\frac{\bar{x}}{\bar{c}}\right)^2\right]_e}{A_e + 2\cos \Lambda_{c/4}} + \frac{1}{24}\left(\frac{A_e^3 \tan^2 \Lambda_{c/4}}{A_e + 6\cos \Lambda_{c/4}}\right) + \frac{1}{8}\right\} \text{ (equation 7.1.1.2-a)}$$

$$= -0.7(6.19)(0.8576)\left\{ \frac{5\left[\frac{1}{2}(0.228) + 2(0.228)^2\right]}{5 + 2(0.8576)} + \frac{1}{24}\left[\frac{(5)^3 (0.6)^2}{5 + 6(0.8576)}\right] + \frac{1}{8}\right\}$$

$$= -3.72\left[\frac{1.090}{6.715} + \frac{1}{24}\left(\frac{45}{10.146}\right) + \frac{1}{8}\right]$$

$$= -3.72(0.4721)$$

$$= -1.76 \text{ per rad (based on } S_e \bar{c}_e{}^2)$$

$$\left(C_{m_q}\right)_e = \left[\frac{\frac{A_e{}^3 \tan^2 \Lambda_{c/4}}{A_e B + 6\cos\Lambda_{c/4}} + \frac{3}{B}}{\frac{A_e{}^3 \tan^2 \Lambda_{c/4}}{A_e + 6\cos\Lambda_{c/4}} + 3}\right]\left[\left(C_{m_q}\right)_{M\approx 0.2}\right]_e \quad \text{(equation 7.1.1.2-b)}$$

$$= \left[\frac{\frac{(5)^3\,(0.6)^2}{(5)\,(0.8575) + 6(0.8576)} + \frac{3}{0.8575}}{\frac{(5)^3\,(0.6)^2}{5 + 6(0.8576)} + 3}\right](-1.76)$$

$$= \left(\frac{4.77 + 3.499}{4.435 + 3}\right)(-1.76)$$

$$= \left(\frac{8.269}{7.435}\right)(-1.76)$$

$$= -1.96 \text{ per rad (based on } S_e \bar{c}_e{}^2)$$

Step 2. Wing-body interference factors (Section 4.3.1.2)

$K_{W(B)} = 1.125$

$K_{B(W)} = 0.215$

} (sample problem, paragraph A, Section 7.3.1.1)

Step 3. Pitching derivative C_{m_q} for body (Section 7.2.1.2)

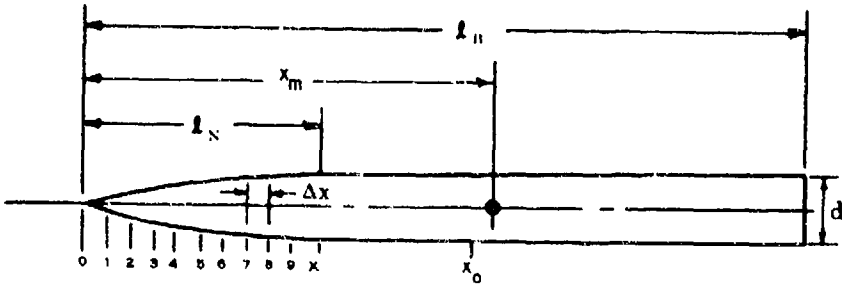

$\Delta x = 2.5$ ft

From sample problem, paragraph A, Section 7.3.1.1:

$(k_2 - k_1) = 0.947$ $\quad V_B = 2615.1$ cu ft $\quad S_b = 39.88$ sq ft

$x_1 = 25.0$ ft $\quad x_o = 42.46$ ft

Determine $\left(C_{m_\alpha}\right)_B$

Station	d ft	S_x sq ft	$\Delta S_x \approx \frac{dS_x}{dx} \Delta x$	$(x_m - x)^*$	$\frac{dS_x}{dx} (x_m - x) \Delta x$
1	1.137	1.016	1.016	42.033	42.71
2	2.600	5.309	4.293	39.787	170.81
3	3.725	10.898	5.589	37.376	208.89
4	4.650	16.982	6.084	34.904	212.36
5	5.450	23.328	6.346	32.417	205.72
6	6.150	29.706	6.378	29.925	190.86
7	6.625	34.472	4.766	27.425	130.71
8	6.950	37.937	3.405	24.940	86.42
9	7.100	39.592	1.655	22.446	37.15
x_1	7.127	39.800	0.288	19.949	5.74
x_o	7.127	39.880	0	9.970	0

$$\sum_{x=0}^{x_o} \frac{dS_x}{dx} (x_m - x) \Delta x = 1291$$

$$\left(C_{m_\alpha}\right)_B = \frac{2(k_2 - k_1)}{V_B} \sum_{x=0}^{x_o} \frac{dS_x}{dx} (x_m - x) \Delta x \quad \text{(equation 4.2.2.1-a)}$$

$$= \frac{2(0.947)\,(1291)}{2615.1} = 0.935 \text{ per rad (based on } V_B)$$

$$\left(C_{m_\alpha}\right)_B = (0.935) \frac{V_B}{S_b \ell_B} = 0.935 \frac{(2615.1)}{(39.88)\,(77.2)} = 0.794 \text{ per rad (based on } S_b \ell_B)$$

*x is taken to be at the center of volume of each body segment.

Determine x_c

Station	d ft	S(x) sq ft	x*	S(x) x Δx
1	1.137	1.016	1.667	4.23
2	2.600	5.309	3.913	51.94
3	3.725	10.898	6.324	172.30
4	4.650	16.982	8.796	373.43
5	5.450	23.328	11.283	658.02
6	6.150	29.706	13.775	1023.00
7	6.625	34.472	16.275	1402.58
8	6.950	37.937	18.760	1779.24
9	7.100	39.592	21.254	2103.72
10	7.127	39.880	23.751	2367.97
ℓ_B	7.127	39.880	51.100	106,377.

$$\sum_{x=0}^{\ell_B} S(x) \times \Delta x = 116{,}313$$

$$x_c = \frac{\int_0^{\ell_B} S(x) \times dx}{V_B} = \frac{116{,}313}{2615.1} = 44.48 \text{ ft} \quad \text{(equation 7.2.1.2-b)}$$

$$\frac{V_B}{S_b \ell_B} = \frac{2615.1}{(39.88)(77.2)} = 0.849$$

$$\left(1 - \frac{x_m}{\ell_B}\right) = 0.434 \quad \text{(sample problem, paragraph A, Section 7.3.1.1)}$$

$$\left(C_{m_q}\right)_B = 2\left(C_{m_\alpha}\right)_B \left[\frac{\left(1 - \frac{x_m}{\ell_B}\right)^2 - \frac{V_B}{S_b \ell_B}\left(\frac{x_c}{\ell_B} - \frac{x_m}{\ell_B}\right)}{\left(1 - \frac{x_m}{\ell_B}\right) - \frac{V_B}{S_b \ell_B}}\right] \quad \text{(equation 7.2.1.2-a)}$$

$$= 2(0.794)\left[\frac{(0.434)^2 - 0.849\left(\frac{44.48 - 43.70}{77.20}\right)}{0.434 - 0.849}\right]$$

*x is taken to be at the center of volume of each body segment.

$$= 1.59\left[\frac{0.1884 - 0.849\,(0.0101)}{-0.415}\right]$$

$$= 1.59\left(\frac{0.1798}{-0.415}\right)$$

$$= -0.689 \text{ per rad (based on } S_b \ell_B{}^2)$$

Solution:

$$\left(C_{m_q}\right)_{WB} = [K_{W(B)} + K_{B(W)}]\left(\frac{S_e}{S}\right)\left(\frac{\bar{c}_e}{\bar{c}}\right)^2 \left(C_{m_q}\right)_e + \left(C_{m_q}\right)_B \left(\frac{S_b}{S}\right)\left(\frac{\ell_B}{\bar{c}}\right)^2$$

(equation 7.3.1.2-a)

$$= (1.125 + 0.215)\,(0.7113)\,(0.7140)\,(-1.96) + (-0.689)\,(0.0963)\,(40.49)$$

$$= -1.334 - 2.687$$

$$= -4.021 \text{ per rad (based on the area and the square of the mean aerodynamic chord of the total panel and referred to a moment center at } \bar{c}/4 \text{ of the total panel)}$$

B. TRANSONIC

The comments of paragraph B of Section 7.3.1.1 are directly applicable here.

DATCOM METHODS

It is recommended that the methods presented in paragraph A for estimating the pitching derivative C_{m_q} of a wing-body configuration be applied to the transonic speed regime. Care should be taken to estimate the contributions of the lifting panel and body at the appropriate Mach number. The interference factors should be obtained from paragraph C, Section 4.3.1.2.

C. SUPERSONIC

The comments of paragraph C of Section 7.3.1.1 are directly applicable here.

DATCOM METHODS

The methods presented in paragraph A for estimating the pitching derivative C_{m_q} of a wing-body configuration are also applicable to the supersonic speed range. Care should be taken to estimate the contributions of the lifting panel and body at the appropriate Mach number.

Sample Problem

Method 1

Given: Same configuration as sample problem of paragraph C, Section 7.3.1.1 and paragraph A of this section.

$M = 1.4 \qquad \beta = 0.98$

Compute:

Step 1. Pitching derivative C_{m_q} for exposed panel (Section 7.1.1.2)

$\left(\frac{\bar{x}}{\bar{c}}\right)_e = 0.393$

$\beta \cot \Lambda_{LE} = 1.225$ (supersonic leading edge)

$A_e \beta = 4.90$

$\cot^{-1} (\beta \cot \Lambda_{LE}) = 39.23°$

$\left(C_{L_q}\right)_e = 3.21$ per rad

} (sample problem paragraph C, Section 7.3.1.1)

$-\beta \left(C_{m_q}'\right)_e = 1.018$ per rad (figure 7.1.1.2-10a)

$\left(C_{m_q}'\right)_e = -1.039$ per rad

$\left(C_{m_q}\right)_e = \left(C_{m_q}'\right)_e - \left(\frac{\bar{x}}{\bar{c}}\right)_e \left(C_{L_q}\right)_e$ (equation 7.1.1.2-d)

$= -1.039 - (0.393)(3.21)$

$= -2.301$ per rad (based on $S_e \bar{c}_e^{\,2}$)

Step 2. Wing-body interference factors (Section 4.3.1.2)

$K_{W(B)} = 1.125$

$K_{B(W)} = 0.181$

} (sample problem, paragraph C, Section 7.3.1.1)

Step 3. Pitching derivative C_{m_q} for body (Section 7.2.1.2)

$f_N = 3.51$

$f_A/f_N = 2.09$

$\frac{\beta}{f_N} = 0.279$

$\left(C_{N_\alpha}\right)_B = 2.74$ per rad

} (sample problem, paragraph C, Section 7.3.1.1)

$x_c = 44.48$ ft

$\frac{V_B}{S_b \ell_B} = 0.849$

$\left(1 - \frac{x_m}{\ell_B}\right) = 0.434$

} (sample problem, paragraph A)

$\frac{x_{c.p.}}{\ell_B} = 0.195$ (figure 4.2.2.1-18a, extrapolated)

$\frac{x_m}{\ell_B} = \frac{43.70}{77.20} = 0.566$

$\left(C_{m_\alpha}\right)_B = \left(\frac{x_m}{\ell_B} - \frac{x_{c.p.}}{\ell_B}\right)\left(C_{N_\alpha}\right)_B$ (equation 4.2.2.1-c)

$= (0.566 - 0.195)\, 2.74$

$= 1.017$ per rad (based on $S_b \ell_B$)

$$\left(C_{m_q}\right)_B = 2\left(C_{m_\alpha}\right)_B \left[\frac{\left(1 - \frac{x_m}{\ell_B}\right)^2 - \frac{V_B}{S_b \ell_B}\left(\frac{x_c}{\ell_B} - \frac{x_m}{\ell_B}\right)}{\left(1 - \frac{x_m}{\ell_B}\right) - \frac{V_B}{S_b \ell_B}}\right]$$ (equation 7.2.1.2-a)

$$= 2(1.017)\left[\frac{(0.434)^2 - (0.849)\left(\frac{44.48 - 43.70}{77.20}\right)}{0.434 - 0.849}\right]$$

$$= 2.034\left(\frac{0.1798}{-0.415}\right)$$

$$= -0.881 \text{ per rad (based on } S_b \ell_B{}^2)$$

Solution:

$$\left(C_{m_q}\right)_{WB} = [K_{W(B)} + K_{B(W)}]\left(\frac{S_e}{S}\right)\left(\frac{\bar{c}_e}{\bar{c}}\right)^2\left(C_{m_q}\right)_e + \left(C_{m_q}\right)_B\left(\frac{S_b}{S}\right)\left(\frac{\ell_B}{\bar{c}}\right)^2$$

(equation 7.3.1.2-a)

$$= (1.125 + 0.181)(0.7113)(0.7140)(-2.301) + (-0.881)(0.0963)(40.49)$$

$$= -1.526 - 3.435$$

$$= -4.961 \text{ per rad (based on the area and the square of the mean aerodynamic chord of the total panel and referred to a moment center at } \bar{c}/4 \text{ of the total panel)}$$

7.3.2.1 WING-BODY ROLLING DERIVATIVE C_{Y_p}

This section presents methods for estimating the wing-body contribution to the rolling derivative C_{Y_p} at subsonic and supersonic speeds. This derivative is the change in side-force coefficient with change in the wing-tip helix angle.

A. SUBSONIC

Experimental evidence indicates that the effect of the fuselage on the side force due to rolling is negligible throughout the angle-of-attack range up to the stall. Therefore, the method of Section 7.1.2.1 for estimating the wing-alone derivative at subsonic speeds is also applicable to wing-body configurations. Available test data are limited to wing-body configurations with body diameters less than about 30 percent of the wing span. Therefore, the application of the wing-alone method is limited to values of $d/b \leqslant 0.3$.

The method consists of determining the value of C_{Y_p} at zero lift and extrapolating this result to high lift coefficients by using experimental values of lift and drag at high lift coefficients. The method also includes the effect of geometric dihedral.

DATCOM METHOD

The variation of the wing-body rolling derivative C_{Y_p} with lift coefficient at subsonic speeds is obtained by using the method of paragraph A of Section 7.1.2.1. In using this method experimental values of wing-body lift and drag are used in evaluating the dimensionless correction factor K. This method is limited to configurations with body diameters less than about 30 percent of the wing span, i.e., $d/b \leqslant 0.3$.

If experimental wing-body lift and drag data are not available, wing-alone test data may be used. If experimental lift and drag data are not available, no attempt should be made to extrapolate the zero-lift value to higher lift coefficients. The negligible importance of the derivative does not warrant the complexities involved in estimating the lift and drag characteristics. Furthermore, no known general method for estimating the variation of the drag coefficient will give results reliable enough to use in determining the correction factor for extrapolating the potential-flow values to higher lift coefficients.

The sample problem presented at the conclusion of paragraph A of Section 7.1.2.1 illustrates the use of this method.

B. TRANSONIC

No generalized method is available in the literature for estimating transonic values of the rolling derivative C_{Y_p}. Furthermore, no known experimental results are available for this derivative at transonic speeds.

C. SUPERSONIC

No generalized method is available in the literature for estimating the effect of the fuselage on the rolling derivative C_{Y_p}.

For the purposes of the Datcom the fuselage effect is considered to be negligible for wing-body

configurations with body diameters less than about 30 percent of the wing span. Therefore, for configurations with d/b $\leqslant$ 0.3 the wing-body rolling derivative C_{Y_p} is estimated by the wing-alone method of paragraph C of Section 7.1.2.1.

No known experimental data are available for this derivative at supersonic speeds. Therefore, the validity of the Datcom application cannot be determined.

DATCOM METHOD

The wing-body rolling derivative C_{Y_p} at supersonic speeds and at low values of the lift coefficient is obtained by using the method of paragraph C of Section 7.1.2.1.

This method is limited to configurations with body diameters less than about 30 percent of the wing span, i.e., d/b $\leqslant$ 0.3.

The sample problem at the conclusion of paragraph C of Section 7.1.2.1 illustrates the use of this method.

7.3.2.2 WING-BODY ROLLING DERIVATIVE C_{l_p}

This section presents methods for estimating the wing-body contribution to the rolling derivative C_{l_p} at subsonic and supersonic speeds. This derivative is the change in rolling-moment coefficient with change in the wing-tip helix angle and is commonly referred to as the roll-damping derivative.

A. SUBSONIC

Experimental evidence indicates that in general for configurations with the ratio of maximum body diameter to wing span less than about 30 percent, i.e., $d/b \leq 0.3$, the effect of the fuselage on the roll damping is negligible over the angle-of-attack range up to the stall. Therefore, the method of Section 7.1.2.2 for estimating the wing-alone derivative at subsonic speeds is applied in this section to estimate the wing-body roll damping at subsonic speeds.

The method consists of first determining the value of C_{l_p} at zero lift based on simplified lifting-surface theory, then assuming that variations in the lift-curve slope will affect C_{l_p} in the same proportion as C_{L_α}, and finally accounting for the drag associated with the additional lift on the outer portion of the wing resulting from flow separation and the attendant formation of a stable leading-edge vortex. The method also accounts for geometric dihedral.

The Datcom method accounts for the variations in wing-body lift-curve slope, drag due to lift, profile drag, and the effect of dihedral. The method requires knowledge of the variation of lift and drag over the angle-of-attack range to the stall. Therefore, the method is quite readily applied if experimental lift and drag data are available.

This method is restricted to configurations with values of $d/b \leq 0.3$.

Although all the bodies of the wing-body configurations analyzed were bodies of circular cross section, the method should give reasonable values for configurations with noncircular cross-section bodies, provided reliable values of the wing-body lift-curve-slope variation are available.

DATCOM METHOD

The variation of the wing-body rolling derivative C_{l_p} with lift coefficient at subsonic speeds is obtained by using the method of Paragraph A of Section 7.1.2.2. In using this method experimental values of wing-body lift and drag are used in evaluating the variations of lift-curve slope and profile drag.

The limitations of the method as applied to wing-alone configurations are equally applicable to the method when applied to a wing-body configuration.

A comparison of the roll-damping derivative calculated by using this method with test results is presented as Table 7.3.2.2-A. Experimental values of wing-body lift and drag have been used in evaluating the roll-damping derivative of all the configurations listed in the table.

If test data for wing-body lift and drag are not available, the wing-alone result should be used for the wing-body roll damping of configurations with $d/b \leq 0.3$. In this case wing-alone test data are preferred, but if they are not available, the wing-alone lift and drag should be estimated as outlined in Section 7.1.2.2. The Datcom methods for estimating the wing-body lift and drag variations with angle of attack have not been substantiated and, therefore, should not be used in evaluating the wing-body roll damping.

The sample problem presented at the conclusion of Paragraph A of Section 7.1.2.2 illustrates the use of this method.

B. TRANSONIC

There are no reliable methods for estimating the derivative C_{l_p} in the transonic region. Although this derivative might be expected to vary with Mach number in the same manner as lift-curve slope, this trend is not exhibited by experimental data. A considerable quantity of wing-body test data is available, however, and reference should be made to Table 7-A.

C. SUPERSONIC

Reference 1 presents a linear-theory method for estimating the roll damping of thin supersonic-leading-edge triangular and rectangular wings mounted on cylindrical bodies. The roll damping of thin subsonic-leading-edge triangular wings mounted on cylindrical bodies is presented in Reference 2 based on slender-wing theory. These theoretical results show that for most of the range of variables the net effect of the body is to decrease the roll damping. The body effect is small for body diameters less than about 30 percent of the wing span ($d/b \leq 0.3$) for both triangular and rectangular wing configurations. However, the body effect increases rapidly as the ratio of body diameter to wing span increases beyond this value. Unfortunately, at the higher values of d/b the theory does not show the same trend with Mach number for the body effects of configurations with triangular and rectangular wings. At these higher values of d/b the body effect increases with increasing Mach number for configurations with rectangular wings; whereas, the body effect decreases with increasing Mach number for configurations with triangular wings. Therefore, at higher values of d/b the theoretical results for triangular and rectangular wings cannot be applied to indicate the general trend of the body effect for configurations with other planforms.

The Datcom uses a design chart, based on the theoretical results of References 1 and 2 and a limited amount of experimental data, to account for the effect of a circular body on the roll damping of a wing-body configuration at zero lift. This chart is applicable to all straight-tapered wing configurations at values of $d/b \leq 0.3$, but is restricted to triangular wing configurations at higher values of d/b.

DATCOM METHOD

The wing-body roll-damping derivative at supersonic speeds, based on the product of the wing area and the square of the wing span $S_W b_W^2$, is given by

$$\left(C_{l_p}\right)_{WB} = \left(C_{l_p}\right)_W \frac{C_{l_p}}{\left(C_{l_p}\right)_{d/b=0}} \quad \text{(per radian)} \qquad 7.3.2.2\text{-a}$$

where $(C_{l_p})_W$ is the wing contribution to the roll-damping derivative at supersonic speeds, obtained by using the method of Paragraph C of Section 7.1.2.2, including the effects of wing thickness, and

$\frac{C_{l_p}}{\left(C_{l_p}\right)_{d/b=0}}$ is the semiempirical body-correction factor obtained from Figure 7.3.2.2-13 as a function of the ratio of maximum body diameter to wing span and the Mach number normal to the leading edge.

Figure 7.3.2.2-13 is applicable to all straight-tapered wing configurations with circular bodies over the range $0 \leq d/b \leq 0.3$. For values of $d/b \geq 0.3$ this chart is applicable only to configurations consisting of triangular wings mounted on cylindrical bodies.

Experimental results reported in Reference 15 for triangular wing-body configurations with d/b = 0.4 and 0.6, and for subsonic, sonic, and supersonic leading edges, show good agreement with the values given by Figure 7.3.2.2-13.

No experimental data are presently available to substantiate the theoretical results of Reference 1 for rectangular wing-body configurations with values of $d/b > 0.3$.

As noted above, the triangular- and rectangular-wing results of References 1 and 2 at values of $d/b > 0.3$ cannot be used to indicate the general trend of the body effects for other planforms.

The supersonic roll-damping derivative in the linear-lift range calculated by this method is compared with test results in Table 7.3.2.2-B. Although all configurations listed in Table 7.3.2.2-B have cylindrical bodies, the method may be applied to configurations having bodies which are not true cylinders, but which are almost cylindrical.

Sample Problem

A triangular wing-body configuration of Reference 14.

$\Lambda_{LE} = 44.9^o$ $\quad \Lambda_{c/2} = 26.7^o$ $\quad A = 4.05$ $\quad \lambda = 0$

$d/b = 0.20$ $\quad M = 1.92 ; \beta = 1.639$

Airfoil: Hexagon, $\delta_\perp = 4.9^o$

Compute:

$\beta A = (1.639)(4.05) = 6.64$

$A \tan \Lambda_{c/2} = (4.05)(\tan 26.7^o) = 2.04$

$$\frac{\left(C_{l_p}\right)_{theory}}{A} = -0.0505 \text{ per rad} \qquad \text{(Figure 7.1.2.2-25a)}$$

$\beta \cot \Lambda_{LE} = (1.639)(\cot 44.9^o) = 1.642$ (supersonic leading edge)

$$\frac{\tan \Lambda_{LE}}{\beta} = \frac{\tan 44.9^o}{1.639} = 0.608$$

$$\frac{C_{l_p}}{\left(C_{l_p}\right)_{theory}} = 0.970 \qquad \text{(Figure 7.1.2.2-27)}$$

$$\frac{C_{l_p}}{(C_{l_p})_{d/b=0}} = 0.970 \qquad \text{(Figure 7.3.2.2-13)}$$

Solution:

$$(C_{l_p})_W = \left[\frac{(C_{l_p})_{theory}}{A}\right] A \frac{C_{l_p}}{(C_{l_p})_{theory}} \qquad \text{(Equation 7.1.2.2-d)}$$

$$= [-0.0505]\ (4.05)\ (0.970)$$

$$= -0.198 \text{ per rad}$$

$$(C_{l_p})_{WB} = (C_{l_p})_W \frac{C_{l_p}}{(C_{l_p})_{d/b=0}} \qquad \text{(Equation 7.3.2.2-a)}$$

$$= (-0.198)\ 0.970$$

$$= -0.192 \text{ per rad} \quad \text{(based on } S_W b_W^2\text{)}$$

This compares with a test value of −0.182 per radian from Reference 14.

REFERENCES

1. Tucker, W. A., and Piland, R. O.: Estimation of the Damping in Roll of Supersonic-Leading-Edge Wing-Body Combinations. NACA TN 2151, 1950. (U)

2. Lomax, H., and Heaslet, M. A.: Damping in Roll Calculations for Slender Swept-Back Wings and Slender Wing-Body Combinations. NACA TN 1950, 1949. (U)

3. Queijo, M. J., and Wells, E. G.: Wind-Tunnel Investigation of the Low-Speed Static and Rotary Stability Derivatives of a 0.13-Scale Model of the Douglas D-558-II Airplane in the Landing Configuration. NACA RM L52G07, 1952. (U)

4. Kuhn, R. E., and Wiggins, J. W.: Wind-Tunnel Investigation to Determine the Aerodynamic Characteristics in Steady Roll of a Model at High Subsonic Speeds. NACA RM L52K24, 1953. (U)

5. Wiggins, J. W.: Wind-Tunnel Investigation at High Subsonic Speeds to Determine the Rolling Derivatives of Two Wing-Fuselage Combinations Having Triangular Wings, Including a Semiempirical Method of Estimating the Rolling Derivatives. NACA RM L53L18e, 1954. (U)

6. Myers, B. C., II, and Kuhn, R. E.: High-Subsonic Damping-In-Roll Characteristics of a Wing With the Quarter-Chord Line Swept Back 35° and With Aspect Ratio 3 and Taper Ratio 0.6. NACA RM L9C23, 1949. (U)

7. Fisher, L. R., and Michael, W. H., Jr.: An Investigation of the Effect of Vertical-Fin Location and Area on Low-Speed Lateral Stability Derivatives of a Semitailless Airplane Model. NACA RM L51A10, 1951. (U)

8. Bird, J. D., Lichtenstein, J. H., and Jaquet, B. M.: Investigation of the Influence of Fuselage and Tail Surfaces on Low-Speed Static Stability and Rolling Characteristics of a Swept-Wing Model. NACA TN 2741, 1952. (U)

9. Goodman, A., and Thomas, D. F., Jr.: Effects of Wing Position and Fuselage Size on the Low-Speed Static and Rolling Stability Characteristics of a Delta-Wing Model. NACA TR 1224, 1955. (U)

10. Letko, W., and Riley, D. R.: Effect of an Unswept Wing on the Contribution of Unswept-Tail Configurations to the Low-Speed Static- and Rolling-Stability Derivatives of a Midwing Airplane Model. NACA TN 2175, 1950. (U)

11. Williams, J. L.: Measured and Estimated Lateral Static and Rotary Derivatives of a 1/12-Scale Model of a High-Speed Fighter Airplane With Unswept Wings. NACA RM L53K09, 1954. (U)

12. Lockwood, V. E.: Effects of Sweep on the Damping-in-Roll Characteristics of Three Sweptback Wings Having an Aspect Ratio of 4 at Transonic Speeds. NACA RM L50J19, 1950. (U)

13. Jaquet, B. M., and Brewer, J. D.: Effects of Various Outboard and Central Fins on Low-Speed Static-Stability and Rolling Characteristics of a Triangular-Wing Model. NACA RM L9E18, 1949. (U)

14. Brown, C. E., and Heinke, H. S., Jr.: Preliminary Wind-Tunnel Tests of Triangular and Rectangular Wings in Steady Roll at Mach Numbers of 1.62 and 1.92. NACA TN 3740, 1956. (U)

15. Bland, W. M., Jr., and Dietz, A. E.: Some Effects of Fuselage Interference, Wing Interference, and Sweepback on the Damping in Roll of Untapered Wings as Determined by Techniques Employing Rocket-Propelled Vehicles. NACA RM L51D26, 1951. (U)

16. Bland, W. M., Jr.: Effect of Fuselage Interference on the Damping in Roll of Delta Wings of Aspect Ratio 4 in the Mach Number Range Between 0.6 and 1.6 as Determined With Rocket-Propelled Vehicles. NACA RM L52E13, 1952. (U)

17. Bland, W. M., Jr., and Sandahl, C. A.: A Technique Utilizing Rocket-Propelled Test Vehicles for the Measurement of the Damping in Roll of Sting-Mounted Models and Some Initial Results for Delta and Unswept Tapered Wings. NACA RM L50D24, 1950. (U)

TABLE 7.3.2.2-A

SUBSONIC WING-BODY ROLLING DERIVATIVE C_{l_p}

DATA SUMMARY

Ref.	A	λ	$\Lambda_{c/4}$ (deg)	Airfoil Section	Γ (deg)	$\frac{d}{b}$	M	$R_\ell \times 10^{-6}$	C_L	C_L Test (per deg)	C_{D_0} Test	C_{l_p} Calc. (per rad)	C_{l_p} Test (per rad)	e Percent Error
4	4.0	0.60	45.0	65A006	0	0.139	0.85	3.44	0	0.116	0.011	−0.317	−0.304	4.3
									0.1			−0.317	−0.310	2.3
									0.2			−0.316	−0.320	− 1.3
									0.3	0.121		−0.328	−0.341	− 4.1
									0.4	0.127		−0.342	−0.358	− 4.5
									0.5	0.120		−0.318	−0.316	0.9
									0.6	0.102		−0.266	−0.232	14.7
									0.7	0.0255		−0.053	−0.175	−69.7
									0.75	0.020		−0.035	−0.175	−80.0
							0.70	3.10	0	0.062	0.011	−0.314	−0.315	− 0.2
									0.1			−0.314	−0.325	− 3.4
									0.2			−0.313	−0.340	− 7.9
									0.3			−0.312	−0.356	−12.4
									0.4	0.065		−0.324	−0.363	−10.7
									0.5	0.065		−0.320	−0.340	− 4.4
									0.75	0.032		−0.142	−0.175	−18.9
5	2.31	0	52.4	65A003	0	0.183	0.50	3.60	0	0.0463	0.008	−0.176	−0.180	− 2.2
									0.1	0.0463		−0.175	−0.195	−10.3
									0.2	0.056		−0.209	−0.200	4.5
									0.3	0.0615		−0.225	−0.200	12.5
									0.4	0.066		−0.197	−0.195	1.0
									0.5	0.051		−0.170	−0.184	− 7.6

TABLE 7.3.2.2-A (CONTD)

Ref.	A	λ	$\Lambda_{c/4}$ (deg)	Airfoil Section	Γ (deg)	$\frac{d}{b}$	M	R_ℓ x 10^{-6}	C_L	C_{l_p} Test (per deg)	C_{D_0} Test	C_{l_p} Calc. (per rad)	C_{l_p} Test (per rad)	e Percent Error
5	2.31	0	52.4	65A003	0	0.183	0.60	3.60	0.6	0.046	0.008	−0.137	−0.152	− 9.9
									0.7	0.051		−0.147	—	—
									0.8	0.051		−0.132	—	—
	4.0	0	36.9	65A006	0	0.139	0.60	2.80	0	0.051		−0.267	−0.260	− 1.2
									0.1			−0.267	−0.256	0.8
									0.2			−0.256	−0.247	3.6
									0.3			−0.255	−0.224	13.8
									0.4	0.053		−0.220	−0.192	14.6
									0.5	0.046		−0.188	−0.150	25.3
									0.6	0.039		−0.155	−0.110	40.9
									0.7	0.035		−0.134	—	—
									0.8	0.014		−0.044	—	—
6	3.0	0.60	35.0	see ref.	0	0.121	0.70	4.26	0	0.065	0.007	−0.270	−0.282	− 4.3
									0.1			−0.270	−0.272	− 0.7
									0.2			−0.269	−0.280	− 3.9
									0.3			−0.267	−0.282	− 5.3
									0.4			−0.265	−0.305	−13.1
									0.5			−0.262	—	—
									0.6			−0.259	—	—
7	3.60	0.455	38.16	0010-64	0	0.067	0.16	1.138	0	0.055	0.018	−0.271	−0.267	1.5
									0.1			−0.271	−0.253	7.1
									0.2			−0.270	−0.295	− 8.5
									0.3	0.062		−0.294	−0.300	− 2.0
									0.4	0.059		−0.286	−0.305	− 6.2
									0.5	0.059		−0.284	−0.302	− 6.0
									0.6	0.0525		−0.249	−0.257	− 3.1

TABLE 7.3.2.2-A (CONTD)

Ref.	A	λ	$\Lambda_{c/4}$ (deg)	Airfoil Section	Γ (deg)	$\frac{d}{b}$	M	R_ℓ x 10^{-6}	C_L	C_{l_p} Test (per deg)	C_{D_0} Test	C_{l_p} Calc. (per rad)	C_{l_p} Test (per rad)	e Percent Error
8	2.61	1.00	45.0	0012(⊥LE)	0	0.178	0.17	1.40	0	0.049	0.029	−0.218	−0.215	1.4
									0.1			−0.218	−0.210	3.8
									0.2			−0.216	−0.212	1.9
									0.3			−0.213	−0.215	− 0.9
									0.4			−0.209	−0.223	− 6.3
									0.5			−0.204	−0.233	−12.4
									0.6			−0.198	−0.248	−20.2
									0.7	0.061		−0.241	−0.275	−12.4
									0.8	0.077		−0.305	−0.330	− 7.6
9	2.31	0	52.4	65A003	0	0.123	0.17	2.06	0	0.044	0.011	−0.170	−0.155	8.8
									0.1			−0.171	−0.156	9.6
									0.2			−0.166	−0.165	0.6
									0.3	0.0465		−0.171	−0.165	3.6
									0.4	0.048		−0.170	−0.167	1.8
									0.5	0.050		−0.169	−0.163	3.7
									0.6			−0.158	−0.161	− 1.9
									0.7			−0.145	−0.155	− 6.5
									0.8	0.044		−0.124	−0.156	−20.5
						0.247			0	0.044	0.020	−0.171	−0.130	31.5
									0.1			−0.170	−0.136	25.0
									0.2			−0.167	−0.140	19.3
									0.3			−0.162	−0.139	16.5
									0.4			−0.156	−0.134	16.4
									0.5	0.046		−0.154	−0.131	17.6
									0.6	0.046		−0.144	−0.136	5.9

TABLE 7.3.2.2-A (CONTD)

Ref.	A	λ	$\Lambda_{c/4}$ (deg)	Airfoil Section	Γ (deg)	$\frac{d}{b}$	M	$R_\ell \times 10^{-6}$	C_L	C_{L_α} Test (per deg)	C_{D_0} Test	C_{ℓ_p} Calc. (per rad)	C_{ℓ_p} Test (per rad)	e Percent Error
9	2.31	0	52.4	65A003	0	0.247	0.17	2.06	0.7	0.046	0.020	−0.127	−0.143	−11.2
↓	↓	↓	↓	↓	↓	↓	↓	↓	0.8	0.0415	↓	−0.099	−0.144	−31.3
10	4.0	0.6	0	65A008	0	0.167	0.166	0.88	0	0.066	0.031	−0.318	−0.330	− 3.6
↓	↓	↓	↓	↓	↓	↓	↓	↓	0.1	↓	↓	−0.318	−0.338	− 5.9
									0.2			−0.318	−0.356	−10.7
									0.3			−0.317	−0.371	−14.6
									0.4	0.069		−0.326	−0.371	−12.1
									0.5	0.063		−0.315	−0.360	−12.5
									0.6	0.0495		−0.236	−0.322	−26.7
									0.7	0.024		−0.094	−0.150	−37.3
11	5.90	0.473	− 3.47	63-210	3.0	0.127	0.17	0.73	0	0.077	0.078	−0.396	−0.370	7.0
↓	↓	↓	↓	↓	↓	↓	↓	↓	0.1	↓	↓	−0.396	−0.372	6.5
									0.2			−0.395	−0.380	3.9
									0.3	0.072		−0.370	−0.375	− 1.3
									0.4	↓		−0.370	−0.370	0
									0.5			−0.369	−0.378	− 2.4
									0.6	0.0673		−0.345	−0.385	−10.4
									0.7	↓		−0.344	−0.386	−10.9
									0.8			−0.343	−0.375	− 8.5
12	4.0	0.6	32.6	65A006	0	0.139	0.6	0.62	0	0.066	0.011	−0.313	−0.345	− 9.3
↓	↓	↓	↓	↓	↓	↓	↓	↓	0.1	0.066	↓	−0.313	−0.350	−10.6
									0.2	0.070		−0.332	−0.363	− 8.5
									0.3	0.0725		−0.342	−0.395	−13.4
									0.4	0.075		−0.352	−0.380	− 7.4
									0.5	0.061		−0.284	−0.290	− 2.1

TABLE 7.3.2.2-A (CONTD)

Ref.	A	λ	$\Lambda_{c/4}$ (deg)	Airfoil Section	Γ (deg)	$\frac{d}{b}$	M	R_ℓ x 10^{-6}	C_L	C_{L_α} Test (per deg)	C_{D_0} Test	C_{l_p} Calc. (per rad)	C_{l_p} Test (per rad)	e Percent Error
13	2.31	0	52.2	$65_{(06)}-006.5$	0	0.178	0.13	1.624	0	0.042	0.020	−0.172	−0.171	0.6
									0.1	0.042		−0.171	−0.169	1.2
									0.2	0.045		−0.180	−0.173	4.0
									0.3			−0.175	−0.184	− 4.9
									0.4			−0.168	−0.184	− 8.7
									0.5			−0.160	−0.177	− 9.6
									0.6	0.040		−0.129	−0.174	−25.9
									0.7			−0.117	−0.177	−33.9
									0.8			−0.102	—	—
									1.0	0.033		−0.039	—	—

Average Error = $\frac{\Sigma \mid e \mid}{n}$ = 10.6%

TABLE 7.3.2.2-8

SUPERSONIC WING-BODY ROLLING DERIVATIVE C_{l_p}

DATA SUMMARY

Ref.	A	λ	Λ_{LE} (deg)	$\frac{d}{b}$	M	$\beta \cot \Lambda_{LE}$	Airfoil Section	δ_1 (deg)	$\left(C_{l_p}\right)_{d/b=0}$ Calc. (per rad)	$\frac{C_{l_p}}{\left(C_{l_p}\right)_{d/b=0}}$	C_{l_p} Calc. (per rad)	C_{l_p} Test (per rad)	e Percent Error
14	1.47	0	39.8	0.23	1.62	0.469	Hexagon	4.9	−0.137	1.000	−0.137	−0.128	7.0
	↓	↓	↓	↓	1.92	0.603	↓	↓	−0.131	1.000	−0.131	−0.119	10.1
	1.86	0	65.0	0.19	1.62	0.577			−0.168	1.000	−0.168	−0.163	3.1
	↓	↓	↓	↓	1.92	0.743			−0.151	1.000	−0.151	−0.145	4.1
	2.13	0	61.5	0.19	1.62	0.692			−0.184	1.000	−0.184	−0.179	2.8
	↓	↓	↓	↓	1.92	0.890			−0.164	1.000	−0.164	−0.158	3.8
	2.38	0	59.5	0.19	1.62	0.751			−0.193	1.000	−0.193	−0.178	8.4
	↓	↓	↓	↓	1.92	0.965			−0.180	1.000	−0.180	−0.150	20.0
	2.60	0	56.9	0.19	1.62	0.830			−0.204	1.000	−0.204	−0.198	3.0
	↓	↓	↓	↓	1.92	1.070			−0.184	1.000	−0.184	−0.175	5.1
	2.85	0	54.6	0.18	1.62	0.905			−0.219	1.000	−0.219	−0.194	12.9
	↓	↓	↓	↓	1.92	1.160			−0.185	0.980	−0.181	−0.169	7.1
	3.06	0	52.4	0.19	1.62	0.980			−0.229	1.000	−0.229	−0.211	8.5
	3.36	0	49.7	0.18	1.62	1.080			−0.236	1.000	−0.236	−0.221	6.8
	↓	↓	↓	↓	1.92	1.390			−0.189	0.980	−0.184	−0.182	1.1
	3.97	0	45.4	0.20	1.92	1.619			−0.199	0.970	−0.193	−0.181	6.6
	4.05	0	44.9	0.20	1.62	1.280			−0.248	0.970	−0.241	−0.234	3.0
	↓	↓	↓	↓	1.92	1.642	↓	↓	−0.198	0.970	−0.192	−0.182	5.5
	2.00	1.00	0	0.26	1.62	∞	Circular Arc	6.8	−0.259	0.945	−0.244	−0.260	− 6.2
	↓	↓	↓	0.19	1.92	↓	↓	↓	−0.235	0.975	−0.229	−0.242	− 5.4
	2.73	1.00	0	0.26	1.62				−0.328	0.945	−0.310	−0.313	− 0.9
	↓	↓	↓	0.19	1.92	↓	↓	↓	−0.280	0.975	−0.273	−0.273	0

TABLE 7.3.2.2-8 (CONTD)

Ref.	A	λ	Λ_{LE} (deg)	$\frac{d}{b}$	M	$\beta \cot \Lambda_{LE}$	Airfoil Section	δ_1 (deg)	$(c_{l_p})_{d/b=0}$ Calc. (per rad)	$\frac{c_{l_p}}{(c_{l_p})_{d/b=0}}$	c_{i_p} Calc. (per rad)	c_{l_p} Test (per rad)	e Percent Error
15	3.70	1.00	0	0.191	1.60	∞	65A009	16.6	−0.374	0.975	−0.364	−0.346	5.2
					1.50				−0.398	0.975	−0.387	−0.355	9.0
					1.414				−0.423	0.975	−0.412	−0.360	14.4
					1.30				−0.457	0.975	−0.450	−0.370	19.0
	3.70	1.00	45.0	0.191	1.60	1.25	65A009	16.6	−0.304	0.975	−0.296	−0.300	− 1.3
					1.50	1.12			−0.308	0.975	−0.300	−0.300	0
					1.414	1.00			−0.302	1.000	−0.302	−0.265	14.0
					1.30	0.83			−0.312	1.000	−0.312	−0.311	0.3
16	4.0	0	45.0	0.40	1.485	1.087	Symmetrical Double Wedge	3.24	−0.280	0.815	−0.228	−0.220	3.6
				0.60						0.530	−0.148	−0.155	− 4.5
				0.40	1.414	1.00			−0.309	0.845	−0.261	−0.233	12.0
				0.60						0.550	−0.170	−0.210	19.0
				0.40	1.05	0.319			−0.380	0.970	−0.378	−0.278	36.0
				0.60						0.675	−0.256	−0.212	20.8
17	4.0	0	45.0	0.20	1.60	1.25	Hexagon	4.9	−0.246	0.970	−0.238	−0.241	− 1.2
					1.50	1.12			−0.271	0.970	−0.263	−0.251	4.8
					1.40	0.98			−0.302	1.000	−0.302	−0.264	14.4
					1.30	0.83			−0.315	1.000	−0.315	−0.279	12.9
					1.20	0.663			−0.344	1.000	−0.344	−0.296	16.2

Average Error = $\frac{\Sigma|e|}{n}$ = 8.3%

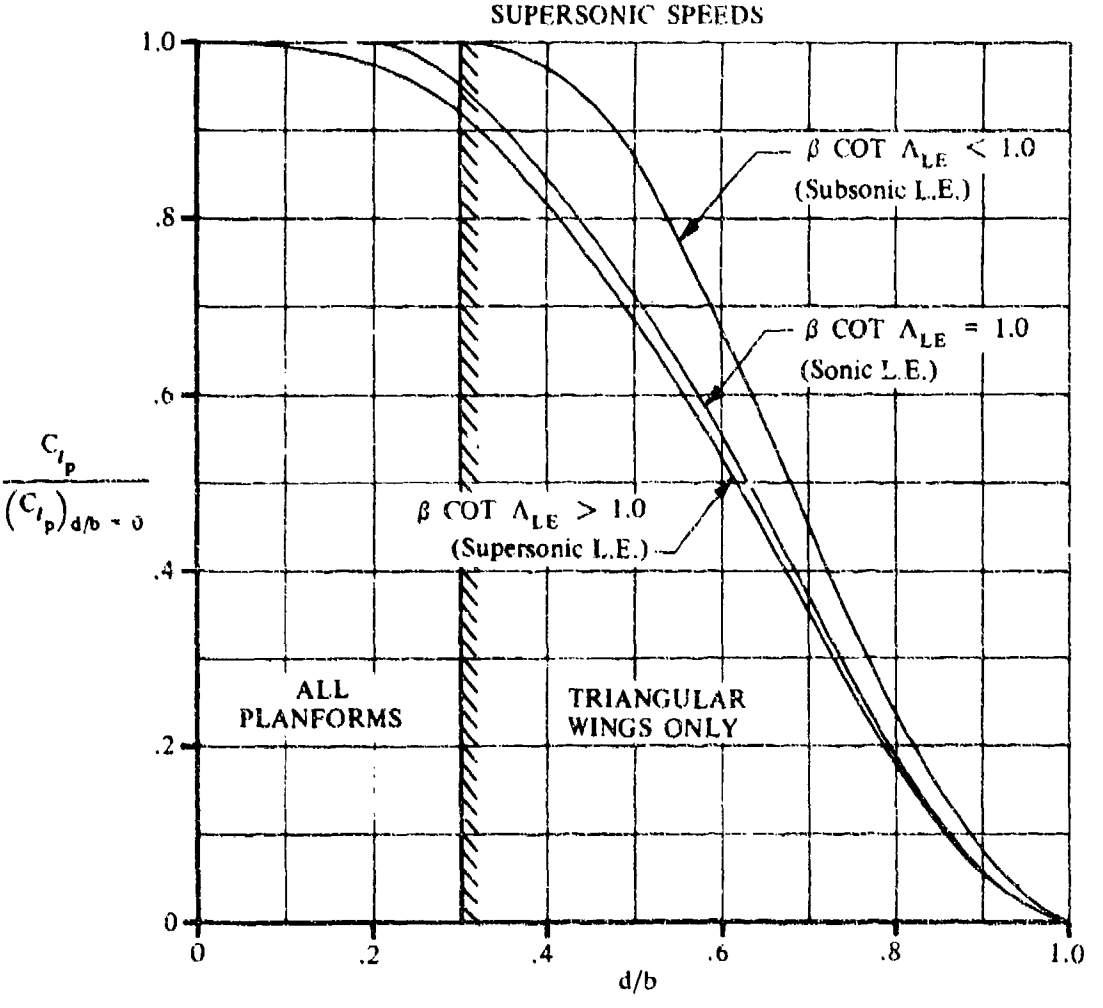

FIGURE 7.3.2.2-13 EFFECT OF THE FUSELAGE ON ROLL DAMPING

7.3.2.3 WING-BODY ROLLING DERIVATIVE C_{n_p}

This section presents methods for estimating the wing-body contribution to the rolling derivative C_{n_p} at subsonic and supersonic speeds. This derivative is the change in yawing-moment coefficient with change in wing-tip helix angle.

A. SUBSONIC

Experimental evidence indicates that the effect of the fuselage on the yawing moment due to rolling is negligible throughout the angle-of-attack range up to the stall. Therefore, the method of Section 7.1.2.3 for estimating the wing-alone derivative at subsonic speeds is also applicable to wing-body configurations. Available test data are limited to wing-body configurations with body diameters less than about 30 percent of the wing span. Therefore, the application of the wing-alone method is limited to values of $d/b \leqslant 0.3$.

The method consists of determining the value of C_{n_p} at zero lift and extrapolating the result to high lift coefficients by using experimental values of lift and drag at high lift coefficients. The method also includes the effects of wing twist and symmetric flap deflection.

DATCOM METHOD

The variation of the wing-body rolling derivative C_{n_p} with lift coefficient at subsonic speeds is obtained by using the method of Paragraph A of Section 7.1.2.3. In using this method experimental values of wing-body lift and drag are used in evaluating the dimensionless correction factor K. This method is limited to configurations with body diameters less than about 30 percent of the wing span, i.e., $d/b \leqslant 0.3$.

If experimental wing-body lift and drag data are not available, wing-alone test data may be used to determine the wing-body rolling derivative C_{n_p}. No attempt should be made to extrapolate the zero-lift value to higher lift coefficients using estimated lift and drag results. No known general method for estimating the variation of drag coefficient will give results reliable enough to use in determining the correction factor for extrapolating the potential-flow values to higher lift coefficients.

The sample problem at the conclusion of Paragraph A of Section 7.1.2.3 illustrates the use of this method.

B. TRANSONIC

No generalized method is available in the literature for estimating transonic values of the rolling derivative C_{n_p}. Furthermore, no known experimental results are available for this derivative at transonic speeds.

C. SUPERSONIC

No generalized method is available in the literature for estimating the effect of the fuselage on the rolling derivative C_{n_p} at supersonic speeds.

For the purpose of the Datcom the fuselage effect is considered to be negligible for wing-body configurations with body diameters less than about 30 percent of the wing span. Therefore, for

configurations with d/b $\leqslant$ 0.3 the wing-body rolling derivative C_{n_p} is estimated by the wing-alone method of Paragraph C of Section 7.1.2.3.

No known experimental data are available for this derivative at supersonic speeds. Therefore, the validity of the Datcom application cannot be determined.

DATCOM METHOD

The wing-body rolling derivative C_{n_p} at supersonic speeds in the range of lift coefficients for which C_{n_p} varies linearly with C_L is obtained by using the method of Paragraph C of Section 7.1.2.3.

This method is limited to configurations with body diameters less than about 30 percent of the wing span, i.e., d/b $\leqslant$ 0.3.

7.3.3 WING-BODY YAWING DERIVATIVES

7.3.3.1 WING-BODY YAWING DERIVATIVE C_{Y_r}

This section recommends methods for estimating the wing-body contribution to the yawing derivative C_{Y_r} at subsonic speeds. However, at subsonic, transonic, and supersonic speeds no generalized methods are available for estimating the wing-body contribution to the yawing derivative C_{Y_r}. This derivative is the change in side-force coefficient with variation in yawing velocity.

A. SUBSONIC

Experimental evidence indicates that the effect of the fuselage on the side force due to yawing is negligible throughout the angle-of-attack range up to the stall. Therefore, the recommendations of Section 7.1.3.1 for estimating the wing-alone derivative at subsonic speeds are also applicable to wing-body configurations.

The recommendations of Section 7.1.3.1 consist of using available experimental data, when applicable, or the method of reference 1 to estimate C_{Y_r}.

B. TRANSONIC

No generalized method is available in the literature for estimating transonic values of the wing-body contribution to the yawing derivative C_{Y_r}. Furthermore, there is a scarcity of experimental data for this derivative at transonic speeds.

C. SUPERSONIC

No generalized method is available in the literature for estimating supersonic values of the wing-body contribution to the yawing derivative C_{Y_r}. Furthermore, there is a scarcity of experimental data for this derivative at supersonic speeds.

REFERENCE

1. Toll, T. A., and Queijo, M. J.: Approximate Relations and Charts for Low-Speed Stability Derivatives of Swept Wings. NACA TN 1581, 1948. (U)

7.3.3.2 WING-BODY YAWING DERIVATIVE C_{l_r}

This section presents a method for estimating the wing-body contribution to the yawing derivative C_{l_r} at subsonic speeds. However, at transonic and supersonic speeds no generalized methods are available for estimating the wing-body contribution to the yawing derivative C_{l_r}. This derivative is the change in rolling-moment coefficient with change in the yawing velocity.

A. SUBSONIC

Experimental evidence indicates that the effect of the fuselage on the rolling moment due to yawing is negligible. Therefore, the method of Section 7.1.3.2 for estimating the wing-alone derivative at subsonic speeds is also applicable to wing-body configurations. Available test data are limited to wing-body configurations with body diameters less than about 30 percent of the wing span. Consequently, the application of the wing-alone method to estimate the wing-body contribution to C_{l_r} is limited to values of $d/b \leq 0.3$.

DATCOM METHOD

The variation of the wing-body yawing derivative C_{l_r} is obtained by using the method of Section 7.1.3.2. The method consists of determining the value of C_{l_r} at zero lift and extending this value to high lift coefficients by using a semiempirical correction factor and test data for C_{l_β}. The method also includes the effect of geometric dihedral, wing twist, and flap deflection. The method is limited to configurations with body diameters less than about 30 percent of the wing span; i.e., $d/b \leq 0.3$.

The sample problem presented at the conclusion of paragraph A of Section 7.1.3.2 illustrates the use of this method.

B. TRANSONIC

No generalized method is available in the literature for estimating transonic values of the wing-body contribution to the yawing derivative C_{l_r}. Furthermore, there is a scarcity of experimental data for this derivative at transonic speeds.

C. SUPERSONIC

No generalized method is available in the literature for estimating supersonic values of the wing-body contribution to the yawing derivative C_{l_r}. Furthermore, there is a scarcity of experimental data for this derivative at supersonic speeds.

7.3.3.3 WING-BODY YAWING DERIVATIVE C_{n_r}

This section presents a method for estimating the wing-body contribution to the yawing derivative C_{n_r} at subsonic speeds. However, at transonic and supersonic speeds no generalized methods are available for estimating the wing-body contribution to the yawing derivative C_{n_r}. This derivative is the change in yawing-moment coefficient with change in the yawing-velocity parameter and is commonly referred to as the yaw damping.

A. SUBSONIC

In general, the wing-fuselage contribution to damping in yaw is small in comparison to the vertical-tail contribution. The contribution from the fuselage depends upon the relative size of the fuselage in comparison to the wing. For configurations in which the fuselage is large relative to the wing, the fuselage contribution is important. Fuselages having flat sides or having a flattened cross section with the major axis vertical can also make a significant contribution (reference 1). Experimental data have also shown that a flattened cross-section fuselage with the major axis horizontal can have negative damping in yaw at moderate and high angles of attack.

No generalized method exists in the literature for predicting the fuselage contribution to yaw damping. Therefore, for the purposes of the Datcom, fuselage effects are considered to be negligible. Consequently, the Datcom method of Section 7.1.3.3 for estimating the wing-alone derivative at subsonic speeds is also applicable to wing-body configurations.

DATCOM METHOD

The estimated value of the wing-body yawing derivative C_{n_r} is obtained by using the method of Section 7.1.3.3. In using this method experimental values of wing profile drag coefficient, evaluated at the appropriate Mach number, are used in conjunction with the lift coefficient. These coefficients are used to evaluate the two major contributions to C_{n_r}; namely, that resulting from the drag due to lift and that resulting from the profile drag. The method does not account for the effects of wing flaps, wing twist, or wing dihedral.

The sample problem presented at the conclusion of paragraph A of Section 7.1.3.3 illustrates the use of this method.

B. TRANSONIC

No generalized method is available in the literature for estimating transonic values of the wing-body contribution to the yawing derivative C_{n_r}. Furthermore, there is a scarcity of experimental data for this derivative at transonic speeds.

C. SUPERSONIC

No generalized method is available in the literature for estimating supersonic values of the wing-body contribution to the yawing derivative C_{n_r}. Furthermore, there is a scarcity of experimental data for this derivative at supersonic speeds.

REFERENCE

1. Campbell, J. P., and McKinney, M. O.: Summary of Methods for Calculating Dynamic Lateral Stability and Response and for Estimating Lateral Stability Derivatives. NACA TR 1098, 1952. (U)

7.3.4 WING-BODY ACCELERATION DERIVATIVES

7.3.4.1 WING-BODY ACCELERATION DERIVATIVE $C_{L_{\dot{\alpha}}}$

The information contained in this section is for estimating the acceleration derivative $C_{L_{\dot{\alpha}}}$ of wing-body configurations at low angles of attack. In general, it consists of a synthesis of material presented in other sections; however, the method of application is new.

Datcom methods are based on the relatively simple results derived from slender-body theory in a manner similar to that used to predict the wing-body pitching derivatives. It is assumed that the mutual interferences that occur between components for angle-of-attack variations, determined in references 1 and 2 and presented in Section 4.3.1.2, may be applied with reasonable accuracy to the case of normal acceleration. This approach to the calculation of wing-body acceleration derivatives has been applied with reasonable success by Walker and Wolowicz in reference 3.

A. SUBSONIC

Two methods are presented for determining the acceleration derivative $C_{L_{\dot{\alpha}}}$ of a wing-body configuration, differing only in their treatment of the mutual interference effects.

DATCOM METHODS

Method 1

For wing-body configurations similar to sketch (d) of Section 4.3.1.2, the acceleration derivative $C_{L_{\dot{\alpha}}}$, based on the area and mean aerodynamic chord of the total panel, is given by

$$\left(C_{L_{\dot{\alpha}}}\right)_{WB} = [K_{W(B)} + K_{B(W)}] \left(\frac{S_e}{S}\right)\left(\frac{\bar{c}_e}{\bar{c}}\right)\left(C_{L_{\dot{\alpha}}}\right)_e + \left(C_{L_{\dot{\alpha}}}\right)_B \left(\frac{S_b}{S}\right)\left(\frac{\ell_B}{\bar{c}}\right) \qquad 7.3.4.1\text{-a}$$

where

$\left(C_{L_{\dot{\alpha}}}\right)_e$ is the contribution of the exposed panel to the acceleration derivative $C_{L_{\dot{\alpha}}}$, obtained from Section 7.1.4.1. (See Section 4.3.1.2 for the definition of exposed surfaces.)

$\left(C_{L_{\dot{\alpha}}}\right)_B$ is the contribution of the body to the acceleration derivative $C_{L_{\dot{\alpha}}}$, obtained from Section 7.2.2.1.

The remaining terms are defined in paragraph A of Section 7.3.1.1.

Method 2

For wing-body configurations similar to sketch (c) of Section 4.3.1.2, the acceleration derivative $C_{L_{\dot{\alpha}}}$, based on the area and mean aerodynamic chord of the total panel, is given by

$$\left(C_{L_{\dot{\alpha}}}\right)_{WB} = K_{(WB)}\left(C_{L_{\dot{\alpha}}}\right)_{W} + \left(C_{L_{\dot{\alpha}}}\right)_{B}\left(\frac{S_b}{S}\right)\left(\frac{\ell_B}{\bar{c}}\right) \qquad 7.3.4.1\text{-b}$$

where $\left(C_{L_{\dot{\alpha}}}\right)_W$ is the contribution of the total panel to the acceleration derivative $C_{L_{\dot{\alpha}}}$, obtained from Section 7.1.4.1, and the remaining terms are defined in paragraph A of Section 7.3.1.1 and method 1 above.

Sample Problem

Method 1

Given: Same configuration as sample problems of paragraph A, Sections 7.3.1.1 and 7.3.1.2. Some of the characteristics are repeated below.

The following ratios based on total panel dimensions:

$$\frac{S_e}{S} = 0.7113 \qquad \frac{\bar{c}_e}{\bar{c}} = 0.845 \qquad \frac{S_b}{S} = 0.0963 \qquad \frac{\ell_B}{\bar{c}} = 6.363$$

Additional Characteristics:

$$M = 0.60 \qquad \beta = 0.80 \qquad A_e = 5.0 \qquad \frac{d}{b} = 0.157 \qquad \ell_B = 77.2 \text{ ft}$$

Compute:

Step 1. Acceleration derivative $C_{L_{\dot{\alpha}}}$ for exposed panel (Section 7.1.4.1)

$$\left.\begin{aligned}\left(\frac{x_{a.c.}}{c_r}\right)_e &= 0.560\\ \left(C_{L_\alpha}\right)_e &= 4.50 \text{ per rad}\end{aligned}\right\} \text{ (sample problem, paragraph A, Section 7.3.1.1)}$$

$$\beta A_e = 4.0$$

$$\frac{-\beta^2 C_L(g)}{\pi A/2} = 0.140 \text{ per rad} \quad \text{(figure 7.1.4.1-6)}$$

$$C_L(g) = -1.718 \text{ per rad}$$

$$\left(C_{L_{\dot{\alpha}}}\right)_e = 1.5\left(\frac{x_{a.c.}}{c_r}\right)_e \left(C_{L_\alpha}\right)_e + 3\,C_L(g) \quad \text{(equation 7.1.4.1-a)}$$

$$= (1.5)\,(0.560)\,(4.50) + 3(-1.718)$$

$$= 3.780 - 5.154$$

$$= -1.374 \text{ per rad (based on } S_e \bar{c}_e)$$

Step 2. Wing-body interference factors (Section 4.3.1.2)

$K_{W(B)} = 1.125$

$K_{B(W)} = 0.215$

} (sample problem, paragraph A, Section 7.3.1.1)

Step 3. Acceleration derivative $C_{L_{\dot{\alpha}}}$ for body (Section 7.2.2.1)

$V_B = 2615.1$ cu ft

$S_b = 39.88$ sq ft

$\left(C_{L_\alpha}\right)_B = 1.894$ per rad (based on S_b)

} (sample problem, paragraph A, Section 7.3.1.1)

$$\left(\frac{V_B}{S_b \ell_B}\right) = \frac{2615.1}{(39.88)\,(77.20)} = 0.849$$

$$\left(C_{L_{\dot{\alpha}}}\right)_B = 2\left(C_{L_\alpha}\right)_B \left(\frac{V_B}{S_b \ell_B}\right) \quad \text{(equation 7.2.2.1-a)}$$

$$= 2(1.894)\,(0.849)$$

$$= 3.216 \text{ per rad (based on } S_b \ell_B)$$

Solution:

$$\left(C_{L_{\dot{\alpha}}}\right)_{WB} = [K_{W(B)} + K_{B(W)}]\left(\frac{S_e}{S}\right)\left(\frac{\bar{c}_e}{\bar{c}}\right)\left(C_{L_{\dot{\alpha}}}\right)_e + \left(C_{L_{\dot{\alpha}}}\right)_B \left(\frac{S_b}{S}\right)\left(\frac{\ell_B}{\bar{c}}\right)$$

(equation 7.3.4.1-a)

$$= (1.125 + 0.215)\,(0.7113)\,(0.845)\,(-1.374) + (3.216)\,(0.0963)\,(6.363)$$

$= -1.107 + 1.971$

$= 0.864$ per rad (based on the area and mean aerodynamic chord of the total panel)

B. TRANSONIC

The aerodynamic interference effects for slender wing-body configurations are relatively insensitive to Mach number; consequently, the slender-body interference factors of Section 4.3.1.2 should give reasonable results. For nonslender configurations transonic interference effects can become quite large and sensitive to minor changes in local contour.

DATCOM METHODS

It is recommended that the methods presented in paragraph A for estimating the acceleration derivative $C_{L_{\dot{\alpha}}}$ of a wing-body configuration be applied to the transonic speed range. Care should be taken to estimate the contributions of the lifting panel and body at the appropriate Mach number. The interference factors should be obtained from paragraph C, Section 4.3.1.2.

C. SUPERSONIC

The information included in the Datcom accounts for most of the mutual interferences that occur between components of a wing-body configuration at supersonic speeds. These interference effects are accounted for by the slender-body interference factors of Section 4.3.1.2.

DATCOM METHODS

The methods presented in paragraph A for estimating the acceleration derivative $C_{L_{\dot{\alpha}}}$ of a wing-body configuration are also applicable to the supersonic speed range. Care should be taken to estimate the contributions to the lifting panel and body at the appropriate Mach number.

Sample Problem

Method 1

Given: Same configuration as sample problems of paragraph C, Sections 7.3.1.1 and 7.3.1.2, and paragraph A of this section.

$M = 1.4$ $\beta = 0.98$ $\frac{d}{b} = 0.157$

Compute:

Step 1. Acceleration derivative $C_{N_{\dot{\alpha}}}$ for exposed panel (Section 7.1.4.1)

$\beta \cot \Lambda_{LE} = 1.225$ (supersonic leading edge)

$\beta A_e = 4.90$

$\cot^{-1} (\beta \cot \Lambda_{LE}) = 39.23°$

} (sample problem, paragraph C, Section 7.3.1.1)

$\beta \left[\left(C_{N_{\dot{\alpha}}}\right)_1\right]_e = 0$ (figure 7.1.4.1-11a)

$\left[\left(C_{N_{\dot{\alpha}}}\right)_1\right]_e = 0$

$\beta\left[\left(C_{N_{\dot{\alpha}}}\right)_2\right]_e = 4.00$ (figure 7.1.4.1-11c)

$\left[\left(C_{N_{\dot{\alpha}}}\right)_2\right]_e = 4.08$ per rad

$$\left(C_{N_{\dot{\alpha}}}\right)_e = \left(\frac{M^2}{\beta^2}\right)\left[\left(C_{N_{\dot{\alpha}}}\right)_1\right]_e - \left(\frac{1}{\beta^2}\right)\left[\left(C_{N_{\dot{\alpha}}}\right)_2\right]_e \text{ (equation 7.1.4.1-c)}$$

$$= \left(\frac{1.4}{0.98}\right)^2 (0) - \left[\frac{1}{(0.98)^2}\right](4.08)$$

$= -4.25$ per rad (based on $S_e \bar{c}_e$)

Step 2. Wing-body interference factors (Section 4.3.1.2)

$K_{W(B)} = 1.125$

$K_{B(W)} = 0.181$

} (sample problem, paragraph C, Section 7.3.1.1)

Step 3. Acceleration derivative $C_{N_{\dot{\alpha}}}$ for body (Section 7.2.2.1)

$$\frac{V_B}{S_b \ell_B} = 0.849 \text{ (sample problem, paragraph A)}$$

$\left(C_{N_\alpha}\right)_B = 2.74$ per rad (sample problem, paragraph C, Section 7.3.1.1)

$$\left(C_{N_{\dot{\alpha}}}\right)_B = 2\left(C_{N_\alpha}\right)_B \left(\frac{V_B}{S_b \ell_B}\right) \quad \text{(equation 7.2.2.1-a)}$$

$$= 2(2.74)\,(0.849)$$

$$= 4.653 \text{ per rad (based on } S_b \ell_B)$$

Solution:

$$\left(C_{N_{\dot{\alpha}}}\right)_{WB} = [K_{W(B)} + K_{B(W)}] \left(\frac{S_e}{S}\right)\left(\frac{\bar{c}_e}{\bar{c}}\right)\left(C_{N_{\dot{\alpha}}}\right)_e + \left(C_{N_{\dot{\alpha}}}\right)_B \left(\frac{S_b}{S}\right)\left(\frac{\ell_B}{\bar{c}}\right)$$

(equation 7.3.4.1-a)

$$= (1.125 + 0.181)\,(0.7113)\,(0.845)\,(-4.25) + (4.653)\,(0.0963)\,(6.363)$$

$$= -3.336 + 2.851$$

$$= -0.485 \text{ per rad (based on the area and mean aerodynamic chord of the total panel)}$$

REFERENCES

1. Pitts, W., Nielsen, J., and Kaattari, G.: Lift and Center of Pressure of Wing-Body-Tail Combinations at Subsonic, Transonic, and Supersonic Speeds. NACA TR 1307, 1959. (U)

2. Spreiter, J.: The Aerodynamic Forces on Slender Plane- and Cruciform-Wing and Body Combinations. NACA TR 962, 1950. (U)

3. Walker, H., and Wolowicz, C.: Theoretical Stability Derivatives for the X-15 Research Airplane at Supersonic and Hypersonic Speeds Including a Comparison with Wind-Tunnel Results. NASA TM X-287, 1960. (U)

7.3.4.2 WING-BODY ACCELERATION DERIVATIVE $C_{m_{\dot{\alpha}}}$

The information contained in this section is for estimating the acceleration derivative $C_{m_{\dot{\alpha}}}$ of wing-body configurations at low angles of attack.

The Datcom methods are based on the same assumption that was made in regard to the acceleration derivative $C_{L_{\dot{\alpha}}}$ of a wing-body configuration, and the general discussion of Section 7.3.4.1 is directly applicable here.

A. SUBSONIC

Two methods are presented for determining the acceleration derivative $C_{m_{\dot{\alpha}}}$ of a wing-body configuration, differing only in their treatment of the mutual interference effects.

DATCOM METHODS

Method 1

For wing-body configurations similar to sketch (d) of Section 4.3.1.2, the acceleration derivative $C_{m_{\dot{\alpha}}}$, based on the area and the square of the mean aerodynamic chord of the total panel and referred to a moment center at the assumed center of gravity, is given by

$$\left(C_{m_{\dot{\alpha}}}\right)_{WB} = [K_{W(B)} + K_{B(W)}] \left(\frac{S_e}{S}\right)\left(\frac{\bar{c}_e}{\bar{c}}\right)^2 \left(C_{\bar{m}_{\dot{\alpha}}}\right)_e + \left(C_{m_{\dot{\alpha}}}\right)_B \left(\frac{S_b}{S}\right)\left(\frac{\ell_B}{\bar{c}}\right)^2 \qquad 7.3.4.2\text{-a}$$

where

$\left(C_{m_{\dot{\alpha}}}\right)_e$ is the contribution of the exposed panel to the acceleration derivative $C_{m_{\dot{\alpha}}}$, obtained from Section 7.1.4.2. (See Section 4.3.1.2 for the definition of exposed surfaces.)

$\left(C_{m_{\dot{\alpha}}}\right)_B$ is the contribution of the body to the acceleration derivative $C_{m_{\dot{\alpha}}}$, obtained from Section 7.2.2.2.

The remaining terms are defined in paragraph A of Section 7.3.1.1. Moment transfer calculations are included as an integral part of the wing- and body-derivative estimation methods of Sections 7.1.4.2 and 7.2.2.2, respectively.

Method 2

For wing-body configurations similar to sketch (c) of Section 4.3.1.2, the acceleration derivative $C_{m_{\dot{\alpha}}}$, based on the area and the square of the mean aerodynamic chord of the total panel and referred to a moment center at the assumed center of gravity, is given by

$$\left(C_{m_{\dot{\alpha}}}\right)_{WB} = K_{(WB)} \left(C_{m_{\dot{\alpha}}}\right)_W + \left(C_{m_{\dot{\alpha}}}\right)_B \left(\frac{S_b}{S}\right)\left(\frac{\ell_B}{\bar{c}}\right)^2 \qquad 7.3.4.2\text{-b}$$

where $(C_{m_{\dot{\alpha}}})_W$ is the contribution of the total panel to the acceleration derivative $C_{m_{\dot{\alpha}}}$, and the remaining terms are defined in paragraph A of Section 7.3.1.1 and method 1 above. Moment transfer calculations are included as an integral part of the wing- and body-derivative estimation methods of Sections 7.1.4.2 and 7.2.2.2, respectively.

Sample Problem

Method 1

Given: Same configuration as sample problems of paragraph A, Sections 7.3.1.1, 7.3.1.2, and 7.3.4.1. Some of the characteristics are repeated below.

The following ratios based on total panel dimensions:

$$\frac{S_e}{S} = 0.7113 \qquad \left(\frac{\bar{c}_e}{\bar{c}}\right)^2 = 0.7140 \qquad \frac{c_{r_e}}{\bar{c}_e} = 1.50$$

$$\frac{S_b}{S} = 0.0963 \qquad \left(\frac{\ell_B}{\bar{c}}\right)^2 = 40.49$$

Additional Characteristics:

$$M = 0.60 \qquad A_e = 5.0 \qquad \frac{d}{b} = 0.157 \qquad \ell_B = 77.20 \text{ ft}$$

$$\beta = 0.80 \qquad x_m = 43.70 \text{ ft (moment center at } \bar{c}/4 \text{ of total panel)}$$

Compute:

Step 1. Acceleration derivative $C_{m_{\dot{\alpha}}}$ for exposed panel (Section 7.1.4.2)

$$\left.\begin{aligned} \left(\frac{x_{a.c.}}{c_r}\right)_e &= 0.560 \\ \left(\frac{x_{c.g.}}{c_r}\right)_e &= 0.408 \\ \left(C_{L_\alpha}\right)_e &= 4.50 \text{ per rad} \end{aligned}\right\} \text{(sample problem, paragraph A, Section 7.3.1.1)}$$

$$\left(\frac{x_{c.g.}}{\bar{c}}\right)_e = \left(\frac{x_{c.g.}}{c_r}\right)_e \left(\frac{c_{r_e}}{\bar{c}_e}\right) = (0.408)\,(1.50) = 0.612$$

$\left(C_{L_{\dot{\alpha}}}\right)_e = -1.374$ per rad (sample problem, paragraph A, Section 7.3.4.1)

$\beta A_e = 4.0$

$\dfrac{\beta^2 C_{m_0}(g)}{\pi A/2} = 0.0767$ per rad (figure 7.1.4.2-8)

$C_{m_0}(g) = 0.941$ per rad

$$\left(C_{m_{\dot{\alpha}}}''\right)_e = -\frac{27}{16}\left(\frac{x_{a.c.}}{c_r}\right)^2 \left(C_{L_\alpha}\right)_e + 3C_{m_0}(g) \quad \text{(equation 7.1.4.2-b)}$$

$$= -\frac{27}{16}\,(0.560)^2\,(4.50) + 3(0.941)$$

$$= -2.381 + 2.823$$

$$= 0.442 \text{ per rad}$$

$$\left(C_{m_{\dot{\alpha}}}\right)_e = \left(C_{m_{\dot{\alpha}}}''\right)_e + \left(\frac{x_{c.g.}}{\bar{c}}\right)_e \left(C_{L_{\dot{\alpha}}}\right)_e \quad \text{(equation 7.1.4.2-a)}$$

$$= 0.442 + (0.612)\,(-1.374)$$

$$= -0.399 \text{ per rad (based on } S_e \bar{c}_e{}^2)$$

Step 2. Wing-body interference factors (Section 4.3.1.2)

$K_{W(B)} = 1.125$

$K_{B(W)} = 0.215$

} (sample problem, paragraph A, Section 7.3.1.1)

Step 3. Acceleration derivative $C_{m_{\dot{\alpha}}}$ for body (Section 7.2.2.2)

$$\frac{V_B}{S_b \ell_B} = 0.849$$

$$\left(1 - \frac{x_m}{\ell_B}\right) = 0.434$$

$$x_c = 44.48 \text{ ft}$$

$$\left(C_{m_\alpha}\right)_B = 0.794 \text{ per rad}$$

} (sample problem, paragraph A, Section 7.3.1.2)

$$\left(C_{m_{\dot{\alpha}}}\right)_B = 2\left(C_{m_\alpha}\right)_B \left[\frac{\frac{V_B}{S_b \ell_B}\left(\frac{x_c}{\ell_B} - \frac{x_m}{\ell_B}\right)}{\left(1 - \frac{x_m}{\ell_B}\right) - \frac{V_B}{S_b \ell_B}}\right] \quad \text{(equation 7.2.2.2-a)}$$

$$= 2(0.794)\left[\frac{0.849\left(\frac{44.48 - 43.70}{77.20}\right)}{0.434 - 0.849}\right]$$

$$= 1.59\left[\frac{(0.849)(0.0101)}{-0.415}\right]$$

$$= -0.0328 \text{ per rad (based on } S_b \ell_B{}^2)$$

Solution:

$$\left(C_{m_{\dot{\alpha}}}\right)_{WB} = \left[K_{W(B)} + K_{B(W)}\right]\left(\frac{S_e}{S}\right)\left(\frac{\bar{c}_e}{\bar{c}}\right)^2\left(C_{m_{\dot{\alpha}}}\right)_e + \left(C_{m_{\dot{\alpha}}}\right)_B\left(\frac{S_b}{S}\right)\left(\frac{\ell_B}{\bar{c}}\right)^2$$

(equation 7.3.4.2-a)

$$= (1.125 + 0.215)(0.7113)(0.7140)(-0.399) + (-0.0328)(0.0963)(40.49)$$

$$= -0.272 - 0.128$$

= −0.400 per rad (based on the area and the square of the mean aerodynamic chord of the total panel and referred to a moment center at $\bar{c}/4$ of the total panel)

B. TRANSONIC

The comments of paragraph B of Section 7.3.4.1 are directly applicable here.

DATCOM METHODS

It is recommended that the methods presented in paragraph A for estimating the acceleration derivative $C_{m_{\dot{\alpha}}}$ of a wing-body configuration be applied to the transonic speed regime. Care should be taken to estimate the contributions of the lifting panel and body at the appropriate Mach number. The interference factors should be obtained from paragraph C, Section 4.3.1.2.

C. SUPERSONIC

The comments of paragraph C of Section 7.3.4.1 are directly applicable here.

DATCOM METHODS

The methods presented in paragraph A for estimating the acceleration derivative $C_{m_{\dot{\alpha}}}$ of a wing-body configuration are also applicable to the supersonic speed range. Care should be taken to estimate the contributions of the lifting panel and body at the appropriate Mach number.

Sample Problem

Method 1

Given: Same configuration as sample problems of paragraph C, Sections 7.3.1.1, 7.3.1.2, and 7.3.4.1, and paragraph A of this section

$M = 1.4$ $\beta = 0.98$ $\frac{d}{b} = 0.157$

Compute:

Step 1. Acceleration derivative $C_{m_{\dot{\alpha}}}$ for exposed panel (Section 7.1.4.2)

$\beta \cot \Lambda_{LE} = 1.225$ (supersonic leading edge)

$\cot^{-1} (\beta \cot \Lambda_{LE}) = 39.23°$

$\beta A_e = 4.90$

} (sample problem, paragraph C, Section 7.3.1.1)

$$\left(\frac{x_{c.g.}}{\bar{c}}\right)_e = 0.612 \quad \text{(sample problem, paragraph A)}$$

$$\left(C_{N_{\dot{\alpha}/e}}\right) = -4.25 \text{ per rad} \quad \text{(sample problem, paragraph C, Section 7.3.4.1)}$$

$$\beta\left[\left(C_{m_{\dot{\alpha}}}\right)_1\right]_e = 9.05 \quad \text{(figure 7.1.4.2-13a)}$$

$$\left[\left(C_{m_{\dot{\alpha}}}\right)_1\right]_e = 9.235 \text{ per rad}$$

$$\beta\left[\left(C_{m_{\dot{\alpha}}}\right)_2\right]_e = -4.52 \quad \text{(figure 7.1.4.2-13c)}$$

$$\left[\left(C_{m_{\dot{\alpha}}}\right)_2\right]_e = -4.612 \text{ per rad}$$

$$\left(C_{m_{\dot{\alpha}}''}\right)_e = \left(\frac{M^2}{\beta^2}\right)\left[\left(C_{m_{\dot{\alpha}}}\right)_1\right]_e + \left(\frac{M^2}{\beta^2} + 1\right)\left[\left(C_{m_{\dot{\alpha}}}\right)_2\right]_e \quad \text{(equation 7.1.4.2-e)}$$

$$= \left(\frac{1.4}{0.98}\right)^2 (9.235) + \left(\frac{1.4^2}{0.98^2} + 1\right)(-4.612)$$

$$= 18.85 - 14.03$$

$$= 4.82 \text{ per rad}$$

$$\left(C_{m_{\dot{\alpha}}}\right)_e = \left(C_{m_{\dot{\alpha}}''}\right)_e + \left(\frac{x_{c.g.}}{\bar{c}}\right)_e \left(C_{L_{\dot{\alpha}}}\right)_e \quad \text{(equation 7.1.4.2-a)}$$

$$= 4.82 + (0.612)(-4.25) \qquad \left(C_{N_{\dot{\alpha}}} \text{ is assumed to be equal to } C_{L_{\dot{\alpha}}}\right)$$

$$= 2.219 \text{ per rad} \quad \left(\text{based on } S_e \bar{c}_e^{\,2}\right)$$

Step 2. Wing-body interference factors (Section 4.3.1.2)

$$\left.\begin{aligned} K_{W(B)} &= 1.125 \\ K_{B(W)} &= 0.181 \end{aligned}\right\} \text{(sample problem, paragraph C, Section 7.3.1.1)}$$

Step 3. Acceleration derivative $C_{m_{\dot{\alpha}}}$ for body (Section 7.2.2.2)

$$\left.\begin{aligned} \frac{V_B}{S_b \ell_B} &= 0.849 \\ \left(1 - \frac{x_m}{\ell_B}\right) &= 0.434 \\ x_c &= 44.48 \text{ ft} \end{aligned}\right\} \text{(sample problem, paragraph A, Section 7.3.1.2)}$$

$\left(C_{m_\alpha}\right)_B = 1.017$ per rad (sample problem, paragraph C, Section 7.3.1.2)

$$\left(C_{m_{\dot{\alpha}}}\right)_B = 2\left(C_{m_\alpha}\right)_B \left[\frac{\frac{V_B}{S_b \ell_B}\left(\frac{x_c}{\ell_B} - \frac{x_m}{\ell_B}\right)}{\left(1 - \frac{x_m}{\ell_B}\right) - \frac{V_B}{S_b \ell_B}}\right] \quad \text{(equation 7.2.2.2-a)}$$

$$= 2(1.017)\left[\frac{(0.849)\left(\frac{44.48 - 43.70}{77.20}\right)}{0.434 - 0.849}\right]$$

$$= 2.034\left[\frac{(0.849)\,(0.0101)}{-0.415}\right]$$

$$= -0.0420 \text{ per rad (based on } S_b \ell_B{}^2)$$

Solution:

$$\left(C_{m_{\dot{\alpha}}}\right)_{WB} = \left[K_{W(B)} + K_{B(W)}\right]\left(\frac{S_e}{S}\right)\left(\frac{\bar{c}_e}{\bar{c}}\right)^2 \left(C_{m_{\dot{\alpha}}}\right)_e + \left(C_{m_{\dot{\alpha}}}\right)_B \left(\frac{S_b}{S}\right)\left(\frac{\ell_B}{\bar{c}}\right)^2$$

(equation 7.3.4.2-a)

$$= (1.125 + 0.181)\,(0.7113)\,(0.7140)\,(2.219) + (-0.0420)\,(0.0963)\,(40.49)$$

$$= 1.472 - 0.164$$

$$= 1.308 \text{ per rad}$$ (based on the area and the square of the mean aerodynamic chord of the total panel and referred to a moment center at $\bar{c}/4$ of the total panel)

7.4 WING-BODY-TAIL DYNAMIC DERIVATIVES

7.4.1 WING-BODY-TAIL PITCHING DERIVATIVES

7.4.1.1 WING-BODY-TAIL PITCHING DERIVATIVE C_{L_q}

The information contained in this section is for estimating the nondimensional pitching derivative C_{L_q} of wing-body-tail combinations at low angles of attack. This derivative represents the lift due to pitching velocity at a constant angle of attack and is defined as

$$C_{L_q} = \frac{\partial C_L}{\partial\left(\frac{q\bar{c}}{2V_\infty}\right)}$$

In general, the methods presented consist of a synthesis of material presented in other sections, although some new information is presented.

The derivative is presented in a manner similar to that used in reference 1 to calculate the lift of a wing-body-tail combination. The complete derivative is the sum of contributions of individual components, treated as isolated surfaces or bodies, and mutual interference effects. The mutual interference effects are assumed to correspond to those due to angle-of-attack variations, established in references 1 and 2 and presented in Section 4.3.1.2.

The horizontal-tail contribution to the derivative C_{L_q} is based on the assumption that instantaneous forces on the tail correspond to the instantaneous angle of attack. This assumption is also the basis used in estimating the horizontal-tail contribution to the derivative C_{m_q} in Section 7.4.1.2. The effect of this assumption is presented in numerous aerodynamic texts, for example, reference 3. The effects of C_{L_q} are generally small and frequently neglected in dynamic analyses.

A. SUBSONIC

Two methods are presented for determining the pitching derivative C_{L_q} of wing-body-tail combinations, differing only in their treatment of the effect of the flow field of the forward surface on the aft surface.

DATCOM METHODS

Method 1: $(b'/b'' \geq 1.5)$

For configurations in which the span of the forward surface is large compared to that of the aft surface, the following approach can be used. This method is to be used when the ratio of the forward-panel span to the aft-panel span is 1.5 or greater. The equation of the nondimensional pitching derivative C_{L_q} of a wing-body-tail configuration, based on the area and mean

aerodynamic chord of the total forward panel and referred to a moment center at the assumed center of gravity or center of rotation, is given by

$$C_{L_q} = \left(C_{L_q}\right)_{WB} + 2\left[K_{W(B)} + K_{B(W)}\right]'' \left(\frac{S_e''}{S'}\right)\left(\frac{x_{c.g.} - x''}{\bar{c}'}\right)\left(\frac{q''}{q_\infty}\right)\left(C_{L_\alpha}\right)_e'' \qquad 7.4.1.1\text{-a}$$

where the primed quantities refer to the forward panel, the double-primed quantities refer to the aft panel, and the subscript e refers to the exposed panel. (See Section 4.3.1.2 for the definition of exposed surfaces.)

$\left(C_{L_q}\right)_{WB}$ is the contribution of the wing-body configuration to the pitching derivative C_{L_q}, obtained from Section 7.3.1.1.

$\left[K_{W(B)} + K_{B(W)}\right]''$ is the appropriate wing-body interference factor obtained from Section 4.3.1.2 for the aft panel.

$\left(C_{L_\alpha}\right)_e''$ is the lift-curve slope of the exposed aft panel, obtained from Section 4.1.3.2.

$\frac{S_e''}{S'}$ is the ratio of the exposed aft panel planform area to the total planform area of the forward panel.

$x_{c.g.} - x''$ is the distance parallel to the longitudinal axis between the moment reference center (usually the vehicle center of gravity) and the quarter-chord point of the mean aerodynamic chord of the total aft horizontal panel.

This parameter is approximated in Section 4.5.2.1 as $x_{c.g.} - x'' = \ell'' + x_{c.g.}$ (equation 4.5.2.1-e) where $x_{c.g.}$ and ℓ'' are defined in figures 4.5.2.1-7a and -7b.

$\frac{q''}{q_\infty}$ is the average dynamic-pressure ratio acting on the aft surface, obtained from Section 4.4.1.

Method 2. ($b'/b'' < 1.5$)

For configurations in which the span of the forward surface is approximately equal to or less than that of the aft surface, the vortex shed from the forward surface interacts directly with the aft surface and the resulting interference effects must be accounted for in the tail terms. This method is to be used when the ratio of the forward-panel span to the aft-panel span is less than 1.5. The equation for the nondimensional pitching derivative C_{L_q} of a wing-body-tail configuration, based on the area and mean aerodynamic chord of the total forward panel and referred to a moment center at the assumed center of gravity or center of rotation, is given by

$$C_{L_q} = \left(C_{L_q}\right)_{WB} + 2.\frac{x_{c.g.} - x''}{\bar{c}'}\left\{\left[K_{W(B)} + K_{B(W)}\right]''\left(\frac{S_e''}{S'}\right)\left(\frac{q''}{q_\infty}\right)\left(C_{L_\alpha}\right)_e'' + \left(C_{L_\alpha}\right)_{W''(v)}\right\}$$

7.4.1.1-b

The parameters in the first two terms on the right-hand side are the same as those in equation 7.4.1.1-a. The last term represents the effect of the forward-panel vortices on the aft panel and is given by

$$\left(C_{L_\alpha}\right)_{W''(v)} = \frac{\left(C_{L_\alpha}\right)_e'\left(\frac{S_e'}{S'}\right)\left(C_{L_\alpha}\right)_e''\left(\frac{q''}{q_\infty}\right)K_{W(B)}'\, I_{v_{W'(W'')}}\left(\frac{b''}{2} - \frac{d''}{2}\right)}{2\pi A_e''\left(\frac{b_v'}{2} - \frac{d'}{2}\right)} \qquad 7.4.1.1\text{-c}$$

where

d' and d'' are the body diameters at the midchord points of the MAC of the forward and aft surfaces, respectively.

b'' is the span of the total aft panel.

$\left(\frac{b_v'}{2} - \frac{d'}{2}\right)$ is obtained from figure 4.4.1-71 as a function of forward-panel geometry.

$I_{v_{W'(W'')}}$ is the vortex interference factor, obtained from Section 4.4.1.

A_e'' is the aspect ratio of the exposed aft panel.

$\left(C_{L_\alpha}\right)_e'$ is the lift-curve slope of the exposed forward panel, obtained from Section 4.1.3.2 (per radian).

$\left(C_{L_\alpha}\right)_e''$ is the lift-curve slope of the exposed aft panel, obtained from Section 4.1.3.2 (per radian).

The remaining terms are defined in method 1 above.

The quantities $\left(C_{L_\alpha}\right)_e'$ and $\left(C_{L_\alpha}\right)_e''$ in the last term of equation 7.4.1.1-b must be expressed in radians. If the result of this term is desired per degree, the conversion must be applied after the term is evaluated.

Because of the similarity of the two methods a sample problem of method 2 is not included. However, evaluation of the term $\left(C_{L_\alpha}\right)_{W''(v)}$ for a wing-body-tail configuration is presented in Section 4.5.1.1.

Sample Problem

Method 1

Given: An ogive-cylinder-body—triangular-wing and triangular-tail configuration. The wing-body configuration is the same as that of the sample problem of Sections 7.3.1 and 7.3.4. Many of the characteristics are repeated below.

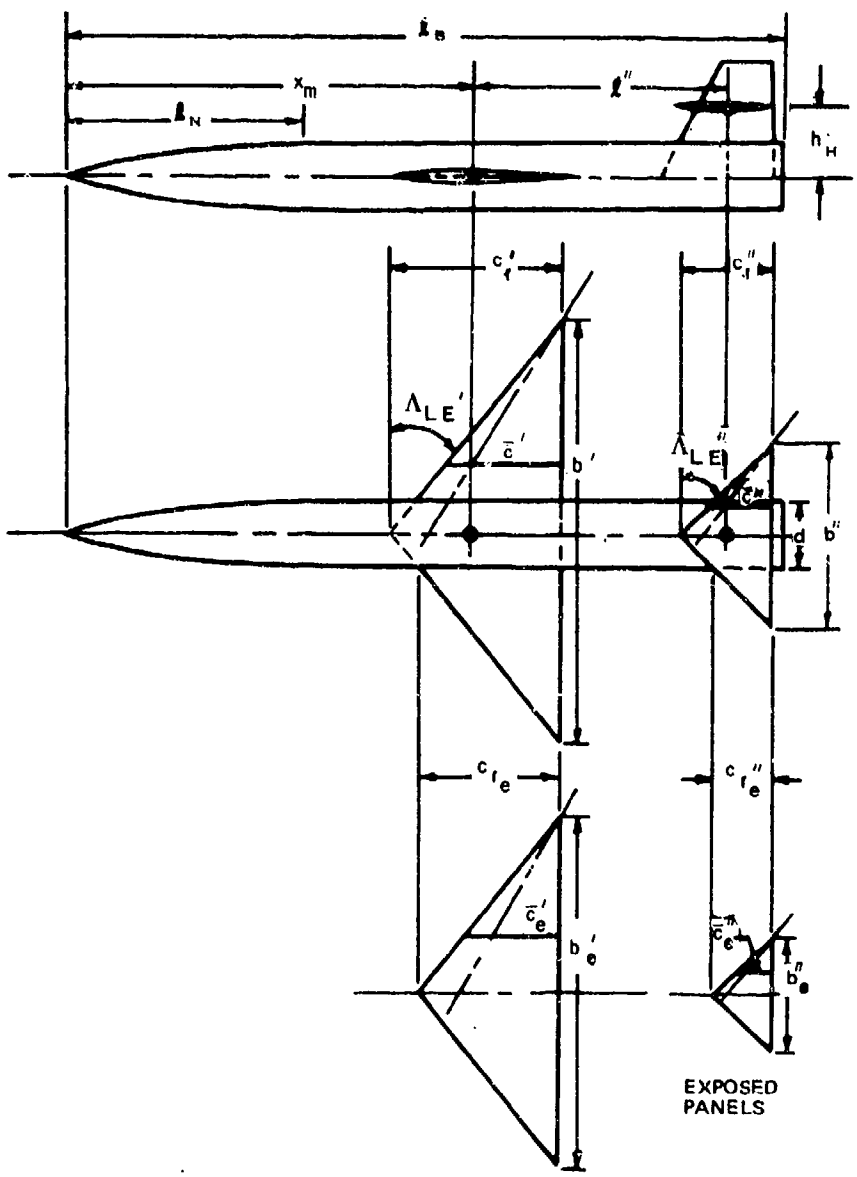

Although a tail has been added to the wing-body configuration of Sections 7.3.1 and 7.3.4, for the sake of simplicity the vehicle center of gravity is taken at $\bar{c}'/4$. Therefore, $x_{c.g.} - x'' = \ell''$, the longitudinal distance from the quarter-chord point of the MAC of the forward surface to the quarter-chord point of the MAC of the aft surface.

Wing Characteristics:

Total Panel		Exposed Panel	
$A' = 5.0$	$\lambda' = 0$	$A_e' = 5.0$	$\lambda_e' = 0$
$\Lambda'_{LE} = 38.67°$	$\Gamma' = 0$	$b_e' = 38.37$ ft	$S_e' = 294.50$ sq ft
$i' = 0$	$c_r' = 18.20$ ft		$c_{r_e}' = 15.375$ ft
$b' = 45.50$ ft	$\bar{c}' = 12.133$ ft		$\bar{c}_e' = 10.25$ ft
$S' = 414.0$ sq ft			

NACA 66-206 airfoil section

Horizontal-Tail Characteristics:

Total Panel		Exposed Panel	
$A'' = 4.0$	$\lambda'' = 0$	$A_e'' = 4.0$	$\lambda_e'' = 0$
$\Lambda''_{LE} = 45°$	$\Gamma'' = 0$	$b_e'' = 12.788$ ft	$S_e'' = 40.90$ sq ft
$i'' = 0$	$c_r'' = 9.958$ ft	$\Lambda''_{c/2} = 26.56°$	$c_{r_e}'' = 6.394$ ft
$b'' = 19.915$ ft	$\bar{c}'' = 6.638$ ft		$\bar{c}_e'' = 4.263$ ft
$S'' = 99.16$ sq ft			

NACA 66-206 airfoil section

Body Characteristics:

$\ell_N = 25.0$ ft $\quad \ell_B = 77.20$ ft $\quad d = 7.127$ ft

The following ratios based on total forward-panel dimensions:

$\frac{\ell''}{\bar{c}'} = 2.26 \quad \frac{S_e''}{S'} = 0.0988$

Additional Characteristics:

$h_H = 7.18$ ft	$\frac{b''}{d''} = 2.794$	$R_\ell = 5.16 \times 10^7$ (based on $\bar{c}'$)
$\ell'' = 27.425$ ft	$M = 0.60$	Sea level
$x = 18.32$ ft*	$\beta = 0.80$	Smooth surfaces
	$\alpha' = 4°$	$\frac{S_{wet}}{S_{ref}} = 2$

Compute:

Step 1. Wing-body C_{L_q} (Section 7.3.1.1)

$$\left(C_{L_q}\right)_{WB} = [K_{W(B)} + K_{B(W)}]' \left(\frac{S_e'}{S'}\right)\left(\frac{\bar{c}_e'}{\bar{c}'}\right)\left(C_{L_q}\right)_e' + \left(C_{L_q}\right)_B \left(\frac{S_b}{S'}\right)\left(\frac{\ell_B}{\bar{c}'}\right)$$

(equation 7.3.1.1-a)

$\left(C_{L_q}\right)_{WB} = 4.467$ per rad (sample problem, paragraph A, Section 7.3.1.1)

Step 2. Lift-curve slope for the exposed horizontal tail panel (Section 4.1.3.2)

$c_{\ell_\alpha} = 6.19$ per rad (table 4.1.1-B)

$$\kappa = \frac{c_{\ell_\alpha}}{2\pi} = 0.985$$

$$\frac{A_e''}{\kappa}\left[\beta^2 + \tan^2 \Lambda_{c/2}''\right]^{1/2} = \frac{4.0}{0.985}[0.64 + 0.25]^{1/2} = 3.83$$

$$\frac{\left(C_{L_{\alpha/e}}\right)''}{A_e''} = 1.00 \quad \text{(figure 4.1.3.2-49)}$$

$$\left(C_{L_\alpha}\right)_e'' = 4.00 \text{ per rad}$$

*x is the longitudinal distance measured from the wing root trailing edge aft. For this problem it is taken equal to ℓ_2 defined in Section 4.4.1.

Step 3. Tail-body interference factors (Section 4.3.1.2)

$$\frac{d''}{b''} = \frac{7.127}{19.915} = 0.358$$

$$\left.\begin{aligned} K_{W(B)}'' &= 1.315 \\ K_{B(W)}'' &= 0.550 \end{aligned}\right\} \text{(figure 4.3.1.2-10)}$$

Step 4. Dynamic pressure ratio (Section 4.4.1)

Obtain value at $\alpha' = 4°$

$C_L' = 0.391$ (sample problem, paragraph A, Section 7.4.4.1)

$$\epsilon = \frac{1.62\, C_L}{\pi A'} \qquad \text{(equation 4.4.1-k)}$$

$$= \frac{1.62\,(0.391)}{5\pi}\, 57.3$$

$$= 2.3°$$

$$\gamma = \tan^{-1}\frac{h_H}{x} = \tan^{-1}\left(\frac{7.18}{18.32}\right) = 21.4° \text{ (see sketch (d), Section 4.4.1)}$$

$$\gamma + \epsilon - \alpha' = 21.4 + 2.3 - 4 = 19.7°$$

$$z = x \tan(\gamma + \epsilon - \alpha') \quad \text{(equation 4.4.1-ℓ)}$$

$$= 18.32\,(0.3581) = 6.56$$

$C_f = 0.00236$ (figure 4.1.5.1-26)

$$C_{D_0} = C_f\left[1 + L\left(\frac{t}{c}\right) + 100\left(\frac{t}{c}\right)^4\right] R_{L.S.}\,\frac{S_{wet}}{S_{ref}} \qquad \text{(equation 4.1.5.1-a)}$$

$$\left[1 + L\left(\frac{t}{c}\right) + 100\left(\frac{t}{c}\right)^4\right] = 1.072 \qquad \text{(figure 4.1.5.1-28a)}$$

$$\cos \Lambda_{(t/c)_{max}} = \cos \Lambda_{.45c} = \cos 23.76° = 0.915$$

$R_{L.S.} = 1.14$ (figure 4.1.5.1-28b)

$$C_{D_0} = (0.00236)\,(1.072)\,(1.14)\,(2) = 0.00577$$

$$\left(\frac{\Delta q}{q}\right)_o = \frac{2.42\left(C_{D_0}\right)^{1/2}}{\frac{x}{\bar{c}} + 0.30} \quad \text{(equation 4.4.1-m)}$$

$$= \frac{2.42\,(0.00577)^{1/2}}{1.51 + 0.30} = 0.102$$

$$\frac{z_w}{\bar{c}} = 0.68\sqrt{C_{D_0}\left(\frac{x}{\bar{c}} + 0.15\right)} \quad \text{(equation 4.4.1-j)}$$

$$= 0.68\sqrt{0.00577\,(1.51 + 0.15)} = 0.0666$$

$$\frac{z}{z_w} = \frac{z/\bar{c}}{z_w/\bar{c}} = \frac{6.56/12.133}{0.0666} = 8.12$$

$$\frac{\Delta q}{q} = \left(\frac{\Delta q}{q}\right)_o \cos^2\left(\frac{\pi}{2}\,\frac{z}{z_w}\right) \quad \text{(equation 4.4.1-n)}$$

$$= (0.102)\cos^2\left[\left(\frac{3.14}{2}\right)(8.12)\,(57.3)\right]$$

$$= (0.102)\,(0.9834)^2$$

$$= 0.099$$

$$\frac{q''}{q_\infty} = 1 - \frac{\Delta q}{q} \quad \text{(equation 4.4.1-o)}$$

$$= 1 - 0.099 = 0.901$$

Solution:

$$C_{L_q} = \left(C_{L_q}\right)_{WB} + 2[K_{W(B)} + K_{B(W)}]''\left(\frac{S_e''}{S'}\right)\left(\frac{x_{c.g.} - x''}{\bar{c}'}\right)\left(\frac{q''}{q_\infty}\right)\left(C_{L_\alpha}\right)_e'' \quad \text{(equation 7.4.1.1-a)}$$

$= 4.467 + 2(1.315 + 0.550)\,(0.0988)\,(2.26)\,(0.901)\,(4.00)$

$= 4.467 + 3.002$

$= 7.47$ per rad (based on the area and mean aerodynamic chord of the total panel and referred to a moment center at $\bar{c}'/4$)

B. TRANSONIC

No accurate methods are available for estimating the characteristics of isolated panels or the dynamic-pressure ratio in the transonic speed regime. The aerodynamic interference "K" factors for slender configurations are relatively insensitive to Mach number; however, for nonslender configurations transonic interference effects can become quite large and sensitive to minor changes in local contour.

DATCOM METHODS

It is recommended that the methods presented in paragraph A above be applied directly to the transonic speed regime. Care should be taken to estimate the various parameters of equations 7.4.1.1-a and -b at the appropriate Mach number. The interference "K" factors should be obtained from paragraph C, Section 4.3.1.2.

C. SUPERSONIC

The information included in the Datcom accounts for most of the mutual interferences that occur between components of wing-body-tail configurations at supersonic speeds.

DATCOM METHODS

The methods presented in paragraph A above are also applicable to the supersonic speed range. Care should be taken to estimate the various parameters of equations 7.4.1.1-a and -b at the appropriate Mach number. Method 3 of paragraph C of Section 4.4.1 should be used to evaluate the last term of equation 7.4.1.1-b.

Sample Problem

Method 1

Given: Same configuration as sample problem of paragraph A. Some of the characteristics are repeated below.

The following ratios based on total forward-panel dimensions:

$$\frac{\ell''}{\bar{c}'} = 2.26 \qquad \frac{S_e''}{S'} = 0.0988$$

Additional Characteristics:

$M = 1.40$	$\alpha' = 4°$	Sea level
$\beta = 0.98$	$\Lambda''_{LE} = 45°$	$R_\ell = 1.2 \times 10^8$ (based on $\bar{c}'$)
$A' = 5.0$	$K = \frac{16}{3}$ (page 4.1.5.1-16)	Smooth surfaces
cg at $\bar{c}'/4$		

Compute:

Step 1. Wing-body C_{L_q} (Section 7.3.1.1)

$$\left(C_{L_q}\right)_{WB} = [K_{W(B)} + K_{B(W)}]' \left(\frac{S_e'}{S'}\right)\left(\frac{\bar{c}_e'}{\bar{c}'}\right)\left(C_{L_q}\right)_e' + \left(C_{L_q}\right)_B \left(\frac{S_b}{S'}\right)\left(\frac{\ell_B}{\bar{c}'}\right)$$

(equation 7.3.1.1-a)

$\left(C_{L_q}\right)_{WB} = 3.977$ per rad (sample problem, paragraph C, Section 7.3.1.1)

Step 2. Lift-curve slope for the exposed horizontal-tail panel (Section 4.1.3.2)

$$\frac{\beta}{\tan \Lambda''_{LE}} = 0.98$$

$A_e'' \tan \Lambda''_{LE} = 4.0$

$\tan \Lambda''_{LE} \left(C_{N_\alpha}\right)_e'' = 4.025$ (figure 4.1.3.2-56a)

$\left(C_{N_\alpha}\right)_e'' = 4.025$ per rad

Step 3. Tail-body interference factors (Section 4.3.1.2)

$\frac{d''}{b''} = 0.358$ (sample problem, paragraph A)

$K_{W(B)}'' = 1.315$ (figure 4.3.1.2-10)

$$\frac{\beta d''}{c_{r_e}''} = \frac{0.98\ (7.127)}{6.394} = 1.092$$

$\beta \cot \Lambda''_{LE} = 0.98$

$K_{B(W)}'' \left[\beta\left(C_{N_\alpha}\right)_e'' (\lambda_e'' + 1)\left(\frac{b''}{d''} - 1\right)\right] = 2.85$ (figure 4.3.1.2-11a)

$\beta\left(C_{N_\alpha}\right)_e'' (\lambda_e'' + 1)\left(\frac{b''}{d''} - 1\right) = 0.98(4.025)\,(1)\,(1.794) = 7.076$

$K_{B(W)}'' = \frac{2.85}{7.076} = 0.4028$

Step 4. Dynamic pressure ratio (Section 4.4.1)

Obtain at $\alpha' = 4°$ Viscous flow field

$\alpha_0' = -1.6°$ (table 4.1.1-B)

$C_{N_\alpha}' = 0.0712$ per deg (sample problem, paragraph C, Section 7.3.1.1)

$C_N' = C_{N_\alpha}'(\alpha' - \alpha_0') = 0.0712[4 - (-1.6)] = 0.399$

$C_f = 0.0018$ (figure 4.1.5.1-26)

$C_{D_f} = C_f \frac{S_{wet}}{S_{ref}}$ (equation 4.1.5.1-i)

$= (0.0018)\,(2) = 0.0036$

$\beta \cot \Lambda_{LE_{bw}} = (0.98)\,(1.25) = 1.225$ (supersonic leading edge)

$C_{D_w} = \frac{K}{\beta}\left(\frac{t}{c}\right)^2_{eff}\left(\frac{S_{bw}}{S_{ref}}\right)$ (equation 4.1.5.1-k)

$= \frac{16}{3(0.98)}\,(0.06)^2\,(1)$

$= 0.0196$

$C_{D_0} = C_{D_f} + C_{D_w}$ (equation 4.1.5.1-h)

$= 0.0036 + 0.0196 = 0.0232$

$$\left(\frac{\Delta q}{q}\right)_o = \frac{2.42\left(C_{D_0}\right)^{1/2}}{\frac{x}{\bar{c}} + 0.30} \qquad \text{(equation 4.4.1-m)}$$

$$= \frac{2.42(0.0232)^{1/2}}{1.51 + 0.30} = 0.204$$

$$\frac{z_w}{\bar{c}} = 0.68\sqrt{C_{D_0}\left(\frac{x}{\bar{c}} + 0.15\right)} \qquad \text{(equation 4.4.1-j)}$$

$$= 0.68\ \sqrt{(0.0232)\ (1.51 + 0.15)}$$

$$= 0.1334$$

$$\epsilon = \frac{1.62\ C_N}{\pi A'} \qquad \text{(equation 4.4.1-k)}$$

$$= \frac{(1.62)\ (0.399)}{5\pi}\ (57.3)$$

$$= 2.36°$$

$\gamma = 21.4°$ (sample problem, paragraph A)

$\gamma + \epsilon - \alpha' = 21.4 + 2.36 - 4 = 19.76°$

$z = x \tan (\gamma + \epsilon - \alpha')$ (equation 4.4.1-ℓ)

$= 18.32(0.3592) = 6.581$

$$\frac{z}{z_w} = \frac{z/\bar{c}}{z_w/\bar{c}} = \frac{6.581/12.133}{0.1334} = 4.07$$

$$\frac{\Delta q}{q} = \left(\frac{\Delta q}{q}\right)_o \cos^2\left(\frac{\pi}{2}\ \frac{z}{z_w}\right) \qquad \text{(equation 4.4.1-n)}$$

$$= (0.204)\cos^2\left[\left(\frac{3.14}{2}\right)(4.07)\ (57.3)\right]$$

$$= (0.204)\ (0.9943)^2 = 0.20$$

$$\frac{q}{q_\infty} = 1 - \frac{\Delta q}{q} \qquad \text{(equation 4.4.1-o)}$$

$$= 1.0 - 0.20 = 0.80$$

Solution:

$$C_{L_q} = \left(C_{L_q}\right)_{WB} + 2[K_{W(B)} + K_{B(W)}]'' \left(\frac{S_e''}{S'}\right) \left(\frac{x_{c.g.} - x''}{\bar{c}'}\right) \left(\frac{q''}{q_\infty}\right) \left(C_{N_\alpha}\right)_e''$$

(equation 7.4.1.1-a)

$$= 3.977 + 2(1.315 + 0.4028)\,(0.0988)\,(2.26)\,(0.80)\,(4.025)$$

$$= 3.977 + 2.47$$

= 6.447 per rad (based on the area and mean aerodynamic chord of the total panel and referred to a moment center at $\bar{c}'/4$)

REFERENCES

1. Pitts, W., Nielsen, J., and Kaattari, G.: Lift and Center of Pressure of Wing-Body-Tail Combinations at Subsonic, Transonic, and Supersonic Speeds. NACA TR 1307, 1959. (U)

2. Spreiter, J.: The Aerodynamic Forces on Slender Plane- and Cruciform-Wing and Body Combinations. NACA TR 962, 1950. (U)

3. Etkin, B.: Dynamics of Flight. John Wiley and Sons, Inc., New York, 1959. (U)

7.4.1.2 WING-BODY-TAIL PITCHING DERIVATIVE C_{m_q}

The information contained in this section is for estimating the nondimensional pitching derivative C_{m_q} of wing-body-tail combinations at low angles of attack. The derivative C_{m_q} is the change in pitching-moment coefficient with varying pitch velocity and is commonly referred to as the pitch-damping derivative. It is expressed as

$$C_{m_q} = \frac{\partial C_m}{\partial\left(\frac{q\bar{c}}{2V_\infty}\right)}$$

This derivative is very important in longitudinal dynamics, since it represents a major portion of the damping of the short-period mode for conventional aircraft.

The Datcom methods are based on the same assumptions that were made for the total pitching derivative C_{L_q} of wing-body-tail combinations, and the general discussion of Section 7.4.1.1 is directly applicable here.

A. SUBSONIC

Two methods are presented for determining the pitching derivative C_{m_q} of wing-body-tail combinations, differing only in their treatment of the effect of the flow field of the forward surface on the aft surface.

DATCOM METHODS

Method 1. ($b'/b'' \geq 1.5$)

For configurations in which the span of the forward surface is large compared to that of the aft surface, the following approach can be used. This method is to be used when the ratio of the forward-panel span to the aft-panel span is 1.5 or greater. The equation for the nondimensional pitching derivative C_{m_q} of a wing-body-tail configuration, based on the area and the square of the mean aerodynamic chord of the total forward panel and referred to a moment center at the assumed center of gravity or center of rotation, is given by

$$C_{m_q} = \left(C_{m_q}\right)_{WB} - 2[K_{W(B)} + K_{(B)W}]'' \left(\frac{S_e''}{S'}\right)\left(\frac{x_{c.g.} - x''}{\bar{c}'}\right)^2 \left(\frac{q''}{q_\infty}\right)\left(C_{L_\alpha}\right)_e'' \qquad 7.4.1.2\text{-a}$$

where the primed quantities refer to the forward panel, the double-primed quantities refer to the aft panel, and the subscript e refers to the exposed panel. (See Section 4.3.1.2 for the definition of exposed surfaces.)

$(C_{m_q})_{WB}$ is the contribution of the wing-body configuration to the pitching derivative C_{m_q}, obtained from Section 7.3.1.2.

The remaining terms are defined in paragraph A of Section 7.4.1.1.

Method 2. $(b'/b'' < 1.5)$

For configurations in which the span of the forward surface is approximately equal to or less than that of the aft surface, the vortex shed from the forward surface interacts directly with the aft surface, and the resulting interference effects must be accounted for in the tail terms. This method is to be used when the ratio of the forward-panel span to the aft-panel span is less than 1.5. The equation for the nondimensional pitching derivative C_{m_q} of a wing-body-tail configuration, based on the area and the square of the mean aerodynamic chord of the total forward panel and referred to a moment center at the assumed center of gravity or center of rotation, is given by

$$C_{m_q} = \left(C_{m_q}\right)_{WB} - 2\left(\frac{x_{c.g.} - x''}{\bar{c}'}\right)^2 \left\{[K_{W(B)} + K_{B(W)}]'' \left(\frac{S_e''}{S'}\right)\left(\frac{q''}{q_\infty}\right)\left(C_{L_\alpha}\right)_e'' + \left(C_{L_\alpha}\right)_{W''(v)}\right\}$$

7.4.1.2-b

All the above terms are defined in paragraph A of Section 7.4.1.1 and method 1 above.

Because of the similarity of the two methods, a sample problem for method 2 is not included. However, evaluation of the term $\left(C_{L_\alpha}\right)_{W''(v)}$ for a wing-body-tail configuration is presented in Section 4.5.1.1.

Sample Problem

Method 1

Given: Same configuration as sample problem of paragraph A, Section 7.4.1.1. Some of the characteristics are repeated below.

The following ratios based on total forward panel dimensions:

$$\frac{\ell''}{\bar{c}'} = 2.26 \qquad \frac{S_e''}{S'} = 0.0988$$

Additional Characteristics:

$M = 0.60$ $\beta = 0.80$ $\alpha' = 4^\circ$ cg at $\bar{c}'/4$

Compute:

Step 1. Wing-body C_{m_q} (Section 7.3.1.2)

$\left(C_{m_q}\right)_{WB}$ = −4.021 per rad (sample problem, paragraph A, Section 7.3.1.2)

Step 2. Lift-curve slope for the exposed horizontal tail (Section 4.1.3.2)

$\left(C_{L_\alpha}\right)_e''$ = 4.0 per rad (sample problem, paragraph A, Section 7.4.1.1)

Step 3. Tail-body interference factors (Section 4.3.1.2)

$K_{W(B)}''$ = 1.315

$K_{B(W)}''$ = 0.550

} (sample problem, paragraph A, Section 7.4.1.1)

Step 4. Dynamic pressure ratio (Section 4.4.1)

$\frac{q''}{q_\infty}$ = 0.901 (sample problem, paragraph A, Section 7.4.1.1)

Solution:

$$C_{m_q} = \left(C_{m_q}\right)_{WB} - 2[K_{W(B)} + K_{B(W)}]'' \left(\frac{S_e''}{S''}\right)\left(\frac{x_{c.g.} - x''}{\bar{c}'}\right)^2 \left(\frac{q''}{q_\infty}\right)\left(C_{L_\alpha}\right)_e''$$

(equation 7.4.1.2-a)

$$= -4.021 - 2(1.315 + 0.550)\,(0.0988)\,(2.26)^2\,(0.901)\,(4.0)$$

$$= -4.021 - 6.78$$

$$= -10.80 \text{ per rad}$$ (based on the area and the square of the mean aerodynamic chord of the total forward panel and referred to a moment center at $\bar{c}'/4$)

B. TRANSONIC

The comments of paragraph B of Section 7.4.1.1 are directly applicable here.

DATCOM METHODS

It is recommended that the methods presented in paragraph A above be applied to the transonic speed regime. Care should be taken to estimate the parameters of equations 7.4.1.2-a and -b at the appropriate Mach number. The interference "K" factors should be obtained from paragraph C, Section 4.3.1.2.

C. SUPERSONIC

The comments of paragraph C of Section 7.4.1.1 are directly applicable here.

DATCOM METHODS

The methods presented in paragraph A above are also applicable to the supersonic speed range. Care should be taken to estimate the parameters of equations 7.4.1.2-a and -b at the appropriate Mach number. Method 3 of paragraph C of Section 4.4.1 should be used to evaluate the last term of equation 7.4.1.2-b.

Sample Problem

Method 1

Given: Same configuration as sample problem of paragraph C Section 7.4.1.1 and paragraph A of this section. Some of the characteristics are repeated below.

The following ratios based on total forward panel dimensions:

$$\frac{S_e''}{S'} = 0.0988 \qquad \frac{\ell''}{\bar{c}'} = 2.26$$

Additional Characteristics:

$M = 1.40$ $\beta = 0.98$ $\alpha' = 4^\circ$ cg at $\bar{c}'/4$

Compute:

Step 1. Wing-body C_{m_q} (Section 7.3.1.2)

$\left(C_{m_q}\right)_{WB} = -4.961$ per rad (sample problem, paragraph C, Section 7.3.1.2)

Step 2. Lift-curve slope for the exposed horizontal tail (Section 4.1.3.2)

$\left(C_{N_\alpha}\right)_e'' = 4.025$ per rad (sample problem, paragraph C, Section 7.4.1.1)

Step 3. Tail-body interference factors (Section 4.3.1.2)

$$\left.\begin{aligned} K_{W(B)}'' &= 1.315 \\ K_{B(W)}'' &= 0.4028 \end{aligned}\right\} \text{ (sample problem, paragraph C, Section 7.4.1.1)}$$

Step 4. Dynamic pressure ratio (Section 4.4.1)

$$\frac{q''}{q_\infty} = 0.80 \text{ (sample problem, paragraph C, Section 7.4.1.1)}$$

Solution:

$$C_{m_q} = \left(C_{m_q}\right)_{WB} - 2[K_{W(B)} + K_{W(B)}]''\left(\frac{S_e''}{S'}\right)\left(\frac{x_{c.g.} - x''}{\bar{c}'}\right)^2 \left(\frac{q''}{q_\infty}\right)\left(C_{N_\alpha}\right)_e''$$

(equation 7.4.1.2-a)

$$= -4.961 - 2(1.315 + 0.4028)\,(0.0988)\,(2.26)^2\,(0.80)\,(4.025)$$

$$= -4.961 - 5.583$$

$$= -10.54 \text{ per rad}$$ (based on the area and the square of the mean aerodynamic chord of the total forward panel and referred to a moment center at $\bar{c}'/4$)

7.4.1.3 WING-BODY-TAIL PITCHING DERIVATIVE C_{D_q}

This section presents a method for estimating the wing-body-tail derivative C_{D_q} at subsonic speeds. This derivative is the change in the drag coefficient due to a change in pitching velocity at a constant angle of attack and is defined as

$$C_{D_q} = \frac{\partial C_D}{\partial\left(\frac{q\bar{c}}{2V}\right)}, \text{ where } C_D \qquad \text{sed on } S_W.$$

In general, this derivative is small and has a negligible effect on longitudinal stability; hence, it is usually neglected.

A. SUBSONIC

The wing-body-tail derivative is obtained by adding the horizontal-tail contribution to the wing-alone contribution developed in Section 7.1.1.3. The body contribution is negligible and has been neglected. The horizontal-tail contribution to C_{D_q} was computed from the tail-damping angle of attack and also from wing-induced downwash at the tail due to pitch rate. The horizontal-tail lift was taken to act normal to the local flow direction at the tail to produce a force component in the direction of the free-stream flow.

DATCOM METHOD

The wing-body-tail derivative C_{D_q} is given by

$$C_{D_q} = C_{D_{q_W}} + \left(C_{D_{q_0}}\right)_H + \left(\frac{\partial C_{D_{q_H}}}{\partial \alpha_F}\right)\alpha_F \qquad 7.4.1.3\text{-a}$$

where

$C_{D_{q_W}}$ is the wing contribution from Section 7.1.1.3-a

$\left(C_{D_{q_0}}\right)_H$ is the horizontal-tail contribution due to zero-angle-of-attack loading given by

$$\left(C_{D_{q_0}}\right)_H = C_{L_{\alpha_H}} \frac{i_H}{57.3}\left(\frac{S_H}{S_W}\right)\left[\epsilon_q - \frac{2(\ell_H \cos\alpha_F + z_H \sin\alpha_F)}{\bar{c}} - \frac{2\,\epsilon_q\,\epsilon}{i_H}\right.$$

$$\left. + \left(\frac{4\epsilon}{i_H}\right)\left(\frac{\ell_H \cos\alpha_F + z_H \sin\alpha_F}{\bar{c}}\right)\right] \text{ (per degree)} \qquad 7.4.1.3\text{-b}$$

where

$C_{L_{\alpha_H}}$ is the horizontal-tail lift-curve slope (based on S_H) obtained from test data or Section 4.1.3.2 (per degree).

i_H is the incidence of the horizontal tail with respect to the fuselage reference line in degrees.

S_H is the horizontal-tail reference area.

S_W is the wing reference area.

ϵ_q is the variation in downwash with respect to pitch rate, $\epsilon_q = \dfrac{\partial \epsilon}{\partial\left(\dfrac{q\bar{c}}{2V}\right)}$

(at $\bar{c}/4$ of the horizontal tail). Design charts are presented in Figures 7.4.1.3-4a through -4x for Mach numbers of 0.2 and 0.8. These charts are presented as a function of wing geometry and the spanwise location of the horizontal-tail MAC relative to the wing span.

ℓ_H is the distance from the moment reference center to the center-of-pressure location of the horizontal stabilizer, measured parallel to the body center line. For Datcom purposes, the horizontal-tail center-of-pressure location is assumed to be at $\bar{c}_H/4$.

z_H is the distance from the moment reference center to the center-of-pressure location of the vertical stabilizer, measured normal to the body center line, positive for the stabilizer above the body.

α_F is the fuselage angle of attack.

$\bar{c}$ is the wing MAC.

ϵ is the downwash of the wing at $\bar{c}/4$ of the horizontal tail, excluding the contribution due to pitch rate. This may be obtained from test data or from Section 4.4.1.

$\dfrac{\partial C_{D_{q_H}}}{\partial \alpha_F}$ is the change in horizontal-tail contribution with angle of attack, obtained by

$$\frac{\partial C_{D_q}}{\partial \alpha_F} = C_{L_{\alpha_H}} \frac{S_H}{S_W} \frac{1}{57.3} \left[\epsilon_q - \frac{2(\ell_H \cos \alpha_F + z_H \sin \alpha_F)}{\bar{c}} \right] \qquad 7.4.1.3\text{-c}$$

where all the terms are defined above.

Sample Problem

Given: Same configuration as sample problem of Paragraph A of Section 7.1.1.3.

Tail Characteristics:

$C_{L_{\alpha_H}} = 0.08$ per deg $\qquad i_H = 1$ deg $\qquad \frac{S_H}{S_W} = 0.37$

$\ell_H = 60.0$ ft $\qquad z_H = 8.0$ ft $\qquad \epsilon = 1.6$ deg

$\frac{y_{\bar{c}_H}}{b/2} = 0.19$

Compute:

$\epsilon_q = -0.02$ (interpolated using Figures 7.4.1.3-4p, −4q, and −4r)

$$\left(C_{D_{q_0}}\right)_H = C_{L_{\alpha_H}} \frac{i_H}{57.3} \frac{S_H}{S_W} \left[\epsilon_q - \frac{2(\ell_H \cos\alpha_F + z_H \sin\alpha_F)}{\bar{c}} - \frac{2\,\epsilon_q\,\epsilon}{i_H} + \frac{4\epsilon}{i_H} \frac{(\ell_H \cos\alpha_F + z_H \sin\alpha_F)}{\bar{c}}\right] \qquad \text{(Equation 7.4.1.3-b)}$$

$$= (0.08)\frac{1}{57.3}\ (0.37)\left\{-0.02 - \frac{2[(60.0)(0.99985) + (8.0)(0.01745)\ ]}{25.0} - \frac{2(-0.02)(1.6)}{1.0} + \frac{4(1.6)}{1.0}\left[\frac{(60.0)(0.99985) + (8.0)(0.01745)}{25.0}\right]\right\}$$

$$= 0.00549 \text{ per deg}$$

$$\frac{\partial C_{D_{q_H}}}{\partial \alpha_F} = C_{L_{\alpha_H}} \frac{S_H}{S_W} \frac{1}{57.3}\left[\epsilon_q - \frac{2(\ell_H \cos\alpha_F + z_H \sin\alpha_F)}{\bar{c}}\right] \qquad \text{(Equation 7.4.1.3-c)}$$

$$= (0.08)(0.37)\frac{1}{57.3}\left[-0.02 - \frac{2[(60.0)(0.99985) + (8.0)(0.01745)]}{25.0}\right]$$

$$= -0.00249 \text{ per deg}^2$$

Solution:

$C_{D_{q_W}} = 0.00272$ per deg (Sample Problem, Paragraph A Section 7.1.1.3)

$$C_{D_q} = C_{D_{q_W}} + \left(C_{D_{q_0}}\right)_H + \left(\frac{\partial C_{D_{q_H}}}{\partial \alpha_F}\right) \alpha_F \qquad \text{(Equation 7.4.1.3-a)}$$

$$= 0.00272 + 0.00549 - (0.00249)\,(1.0)$$

$$= 0.00572 \text{ per deg}$$

B. TRANSONIC

No method is presented.

C. SUPERSONIC

No method is presented.

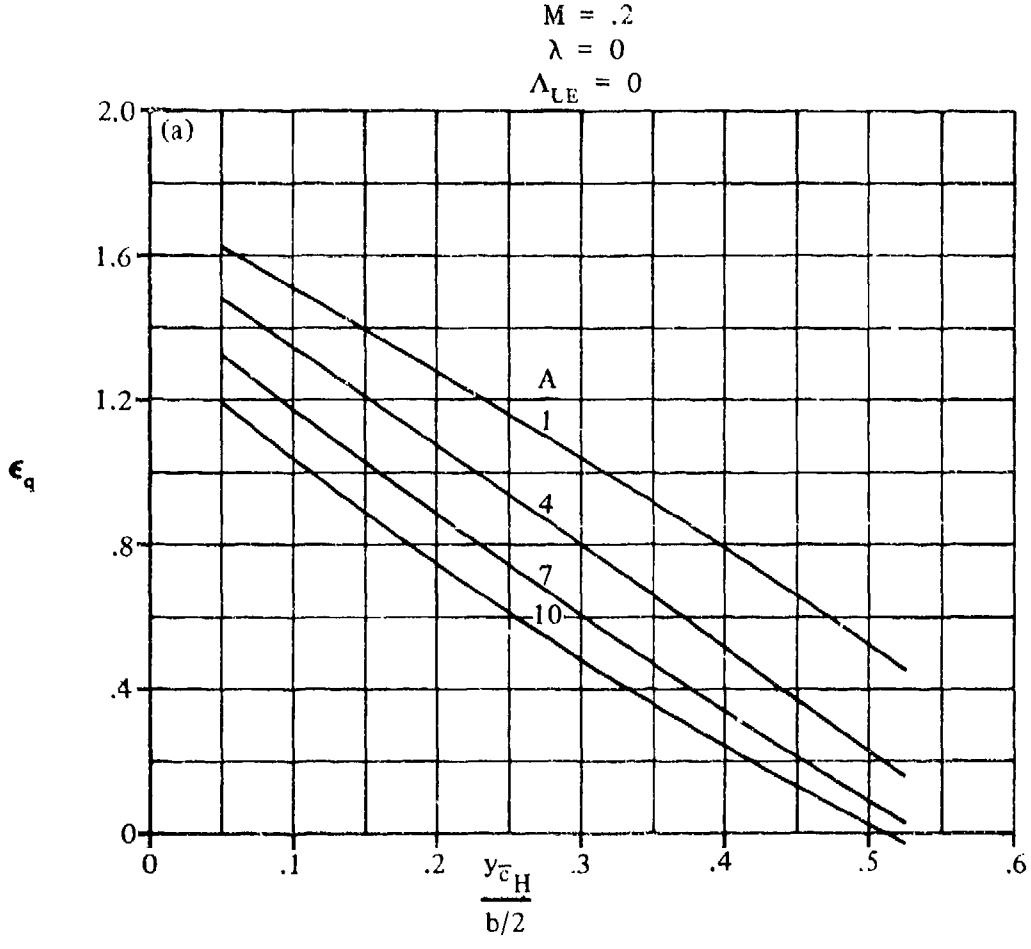

FIGURE 7.4.1.3-4 VARIATION IN DOWNWASH WITH PITCH RATE

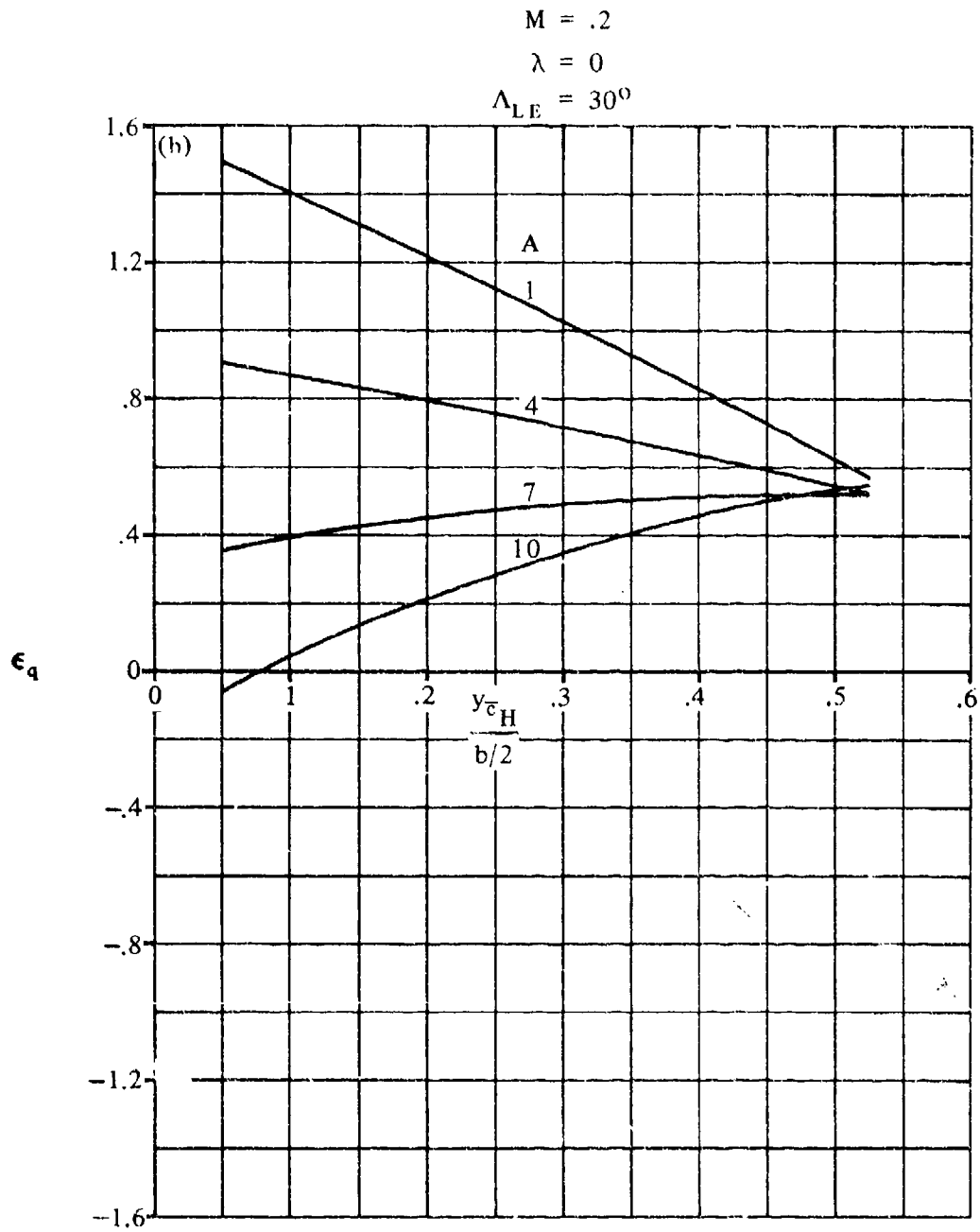

FIGURE 7.4.1.3-4 (CONTD)

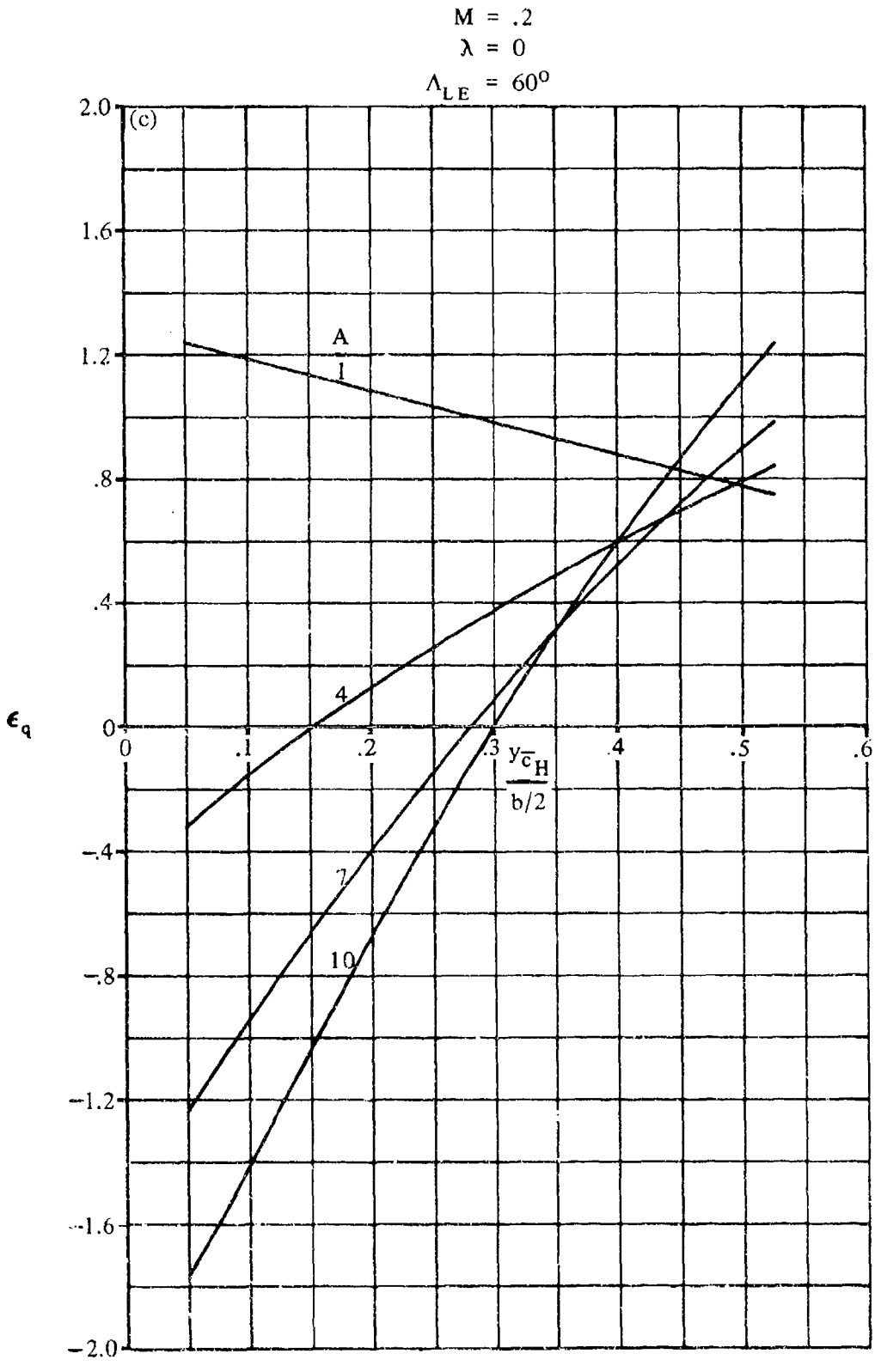

FIGURE 7.4.1.3-4 (CONTD)

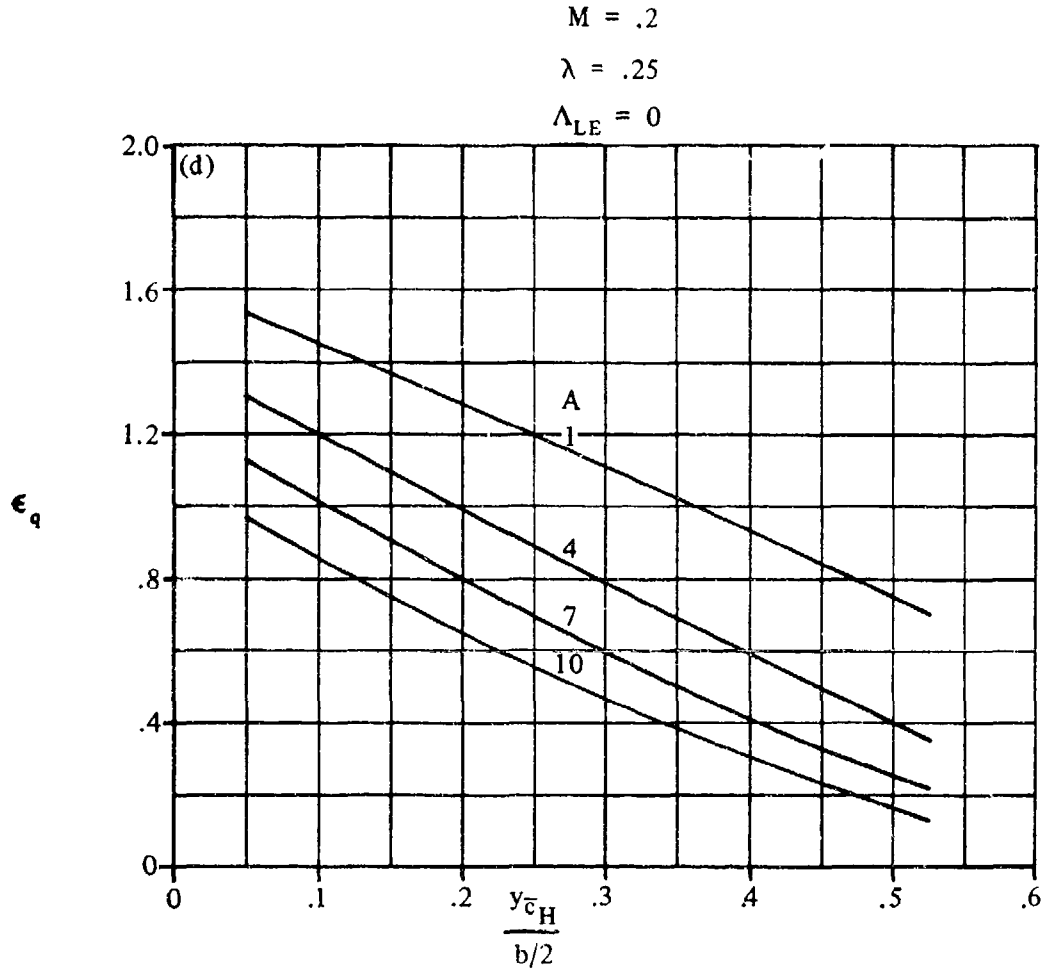

FIGURE 7.4.1.3-4 (CONTD)

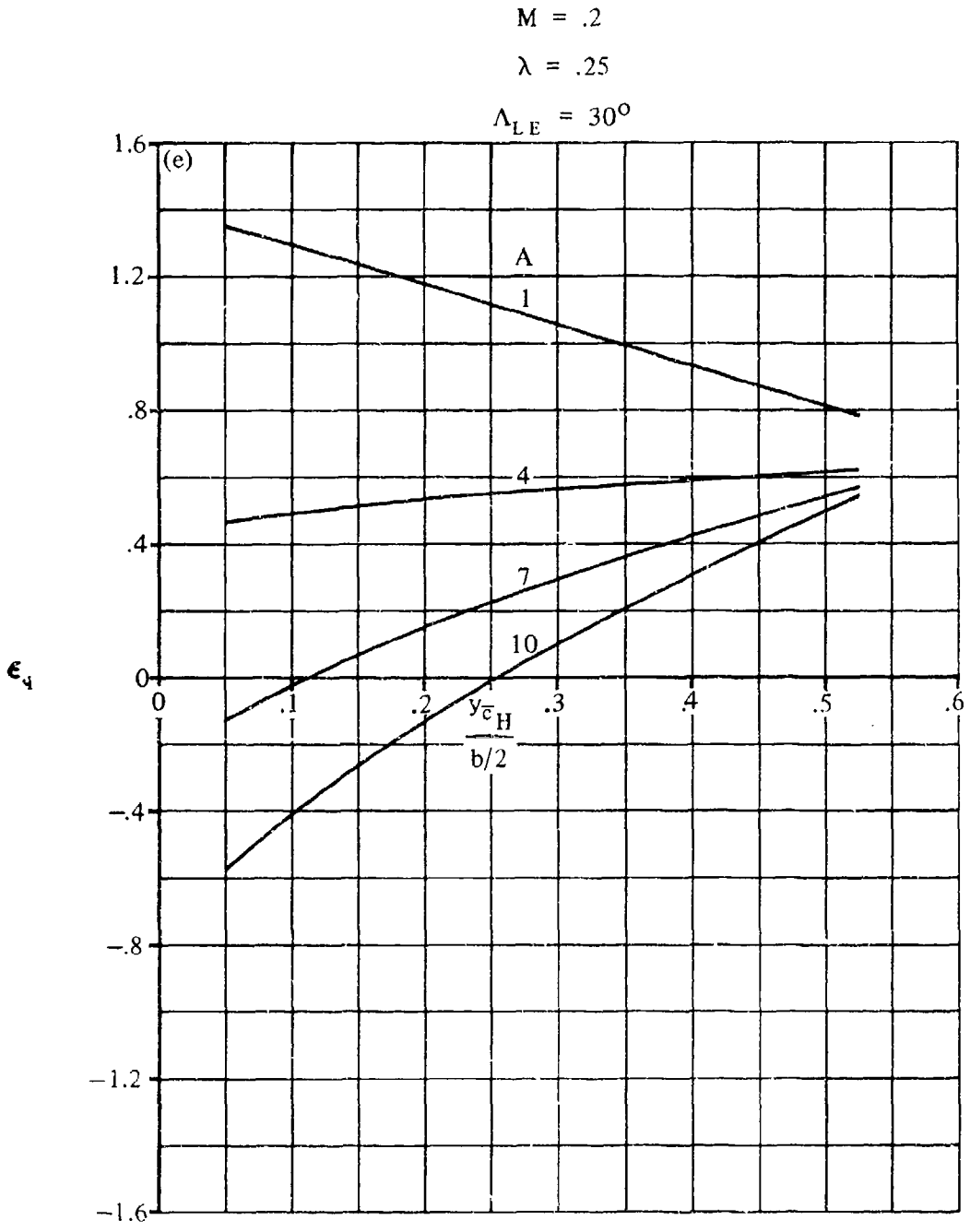

FIGURE 7.4.1.3-4 (CONTD)

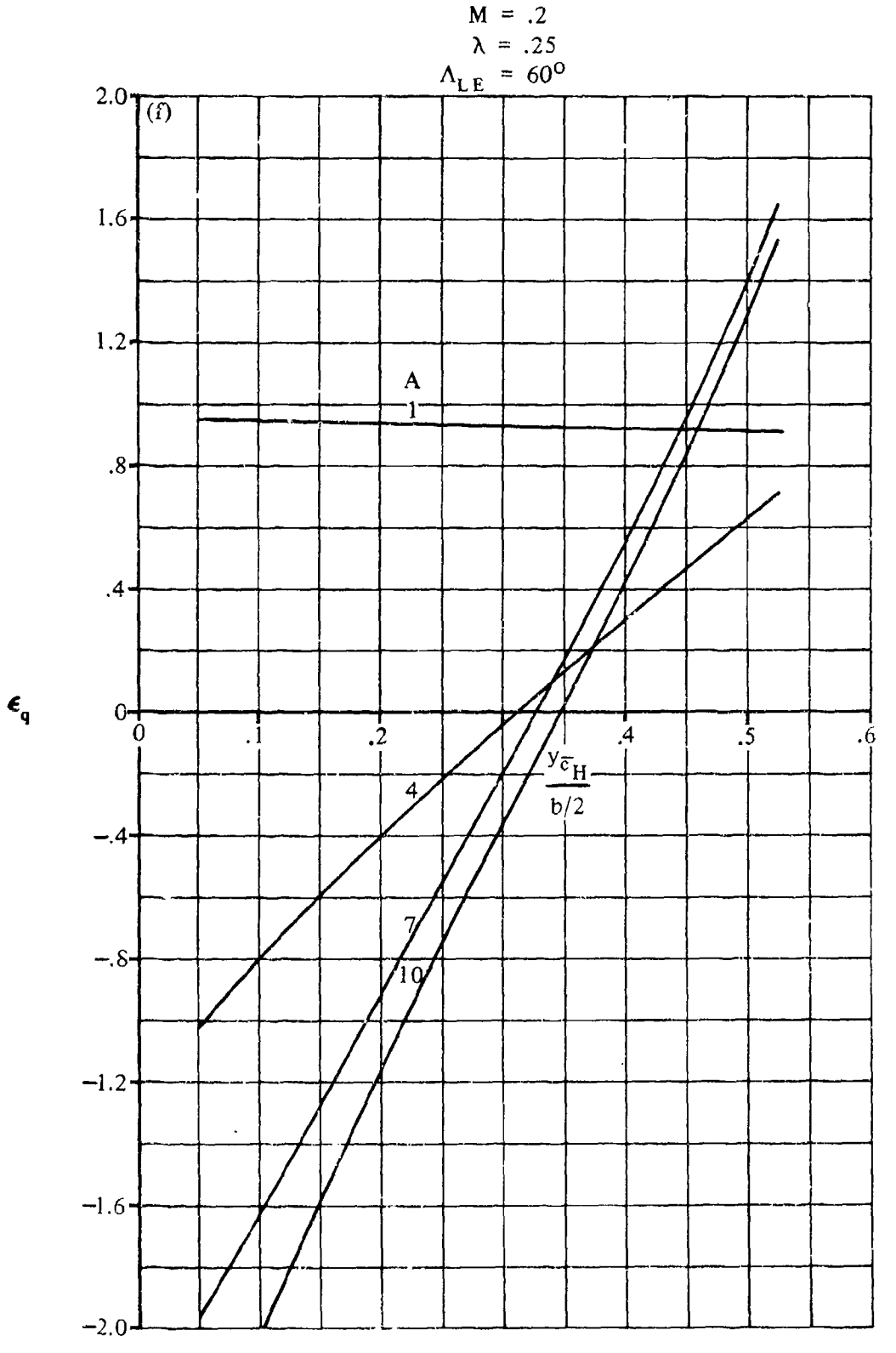

FIGURE 7.4.1.3-4 (CONTD)

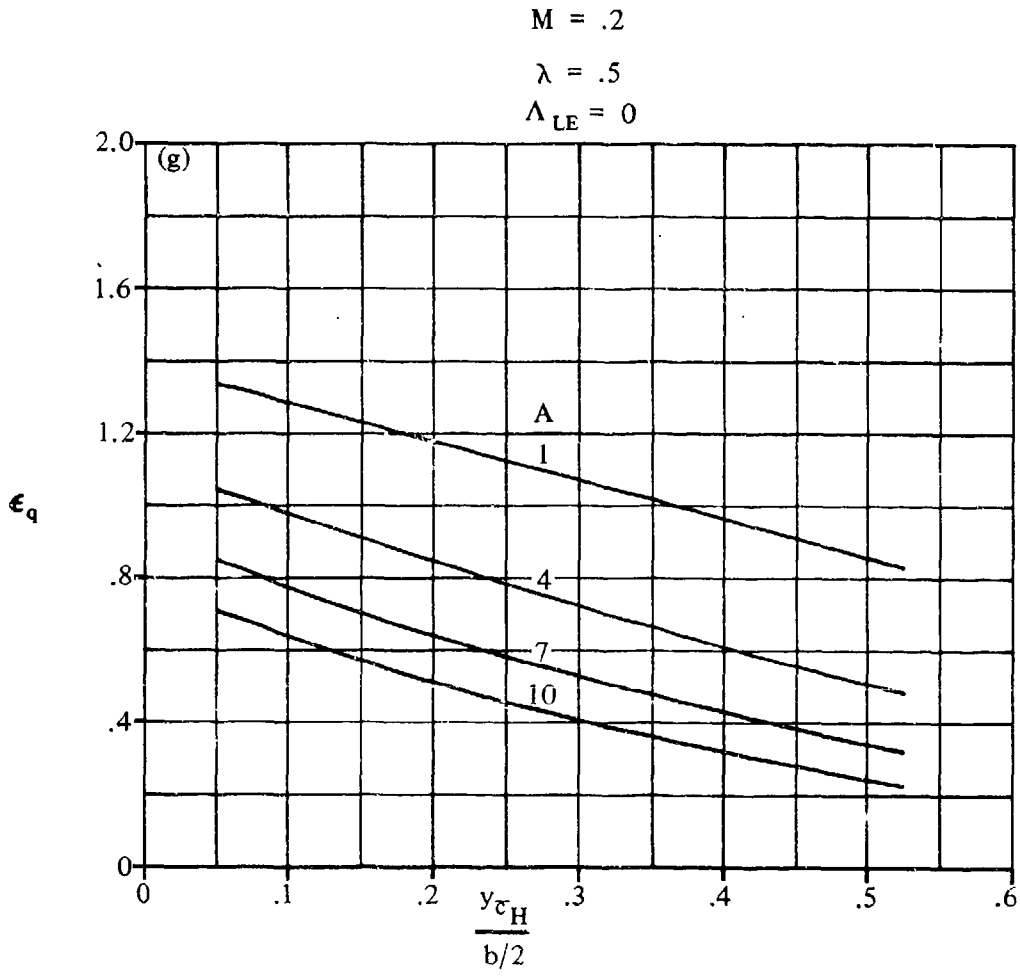

FIGURE 7.4.1.3-4 (CONTD)

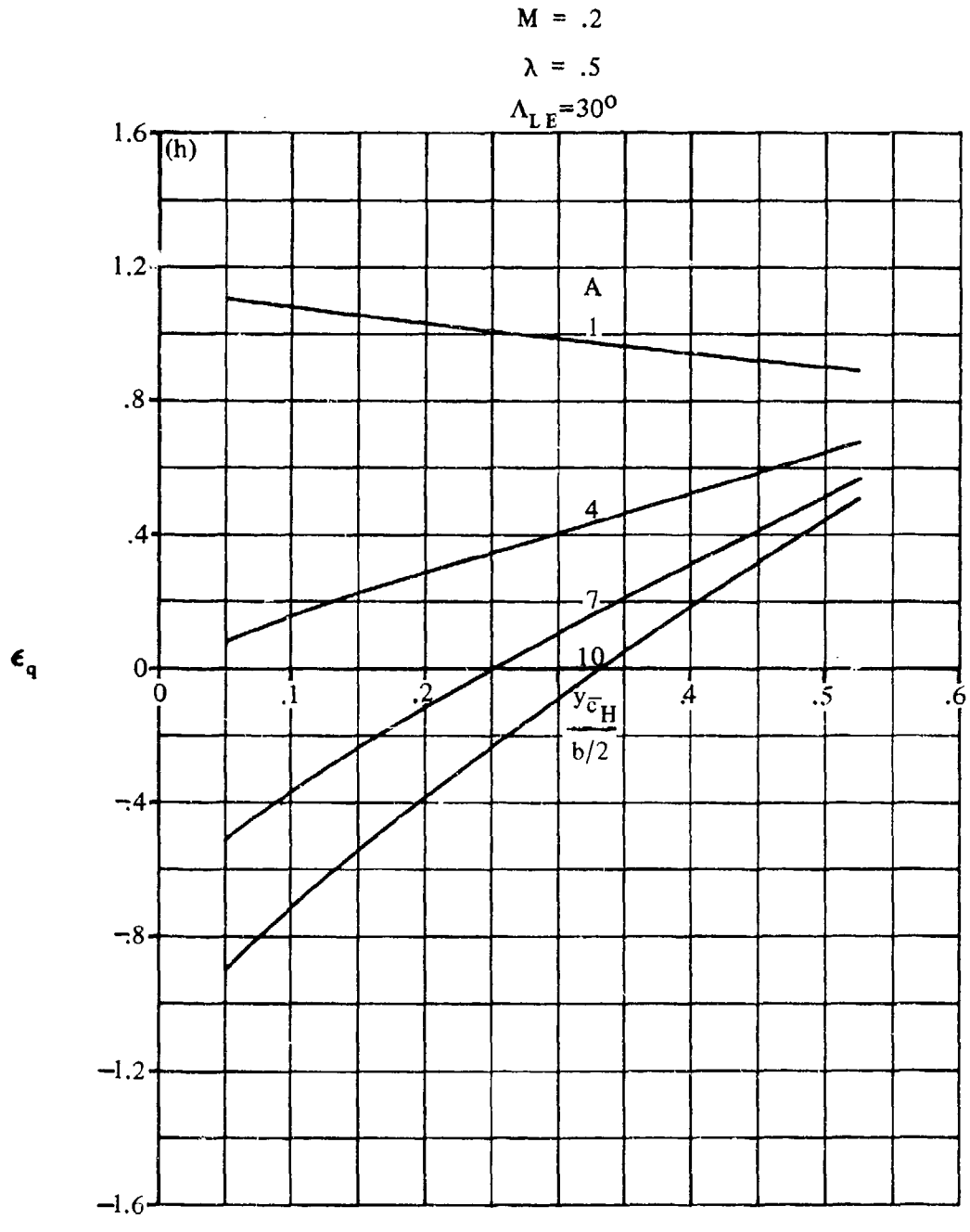

FIGURE 7.4.1.3-4 (CONTD)

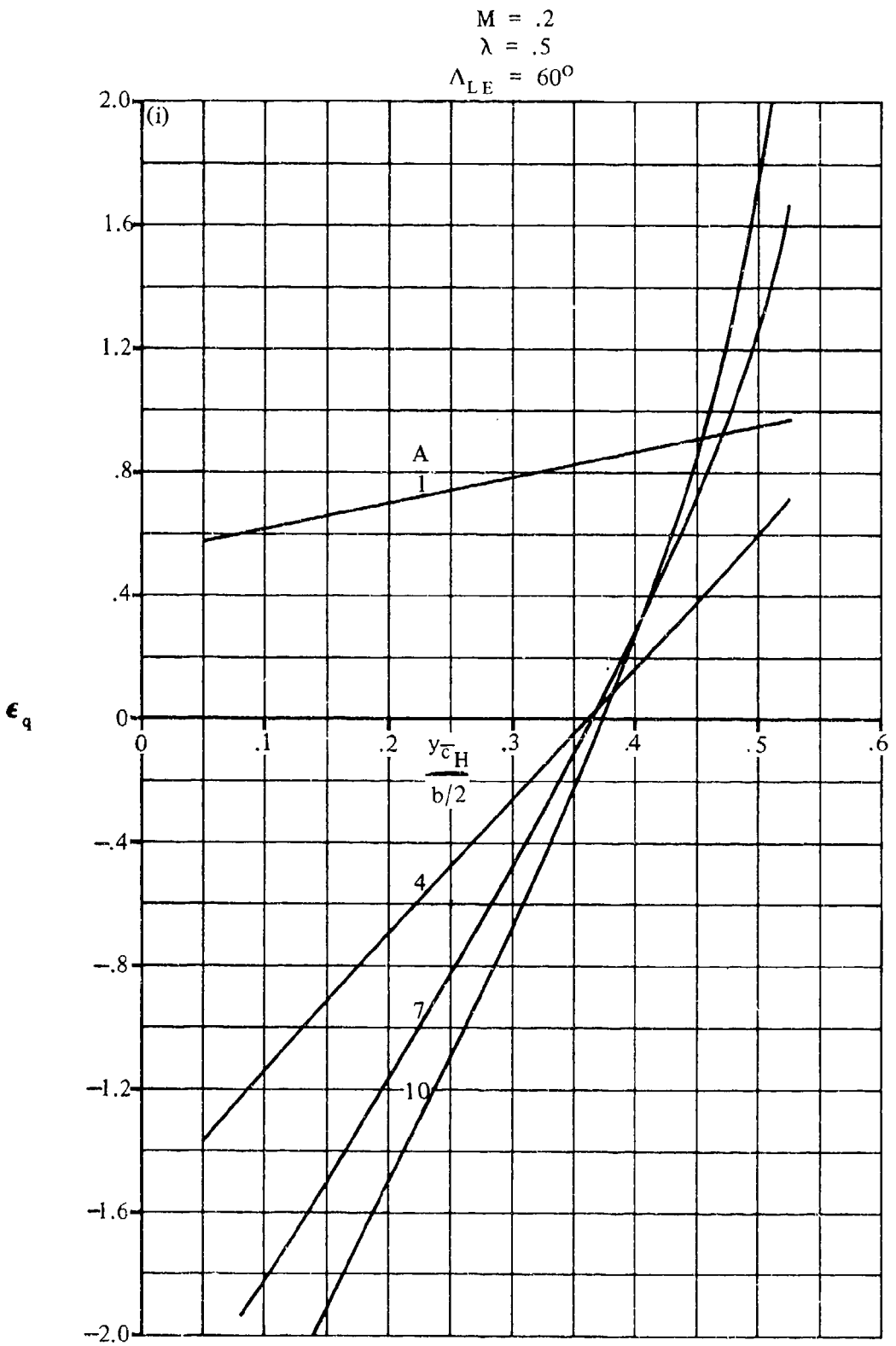

FIGURE 7.4.1.3-4 (CONTD)

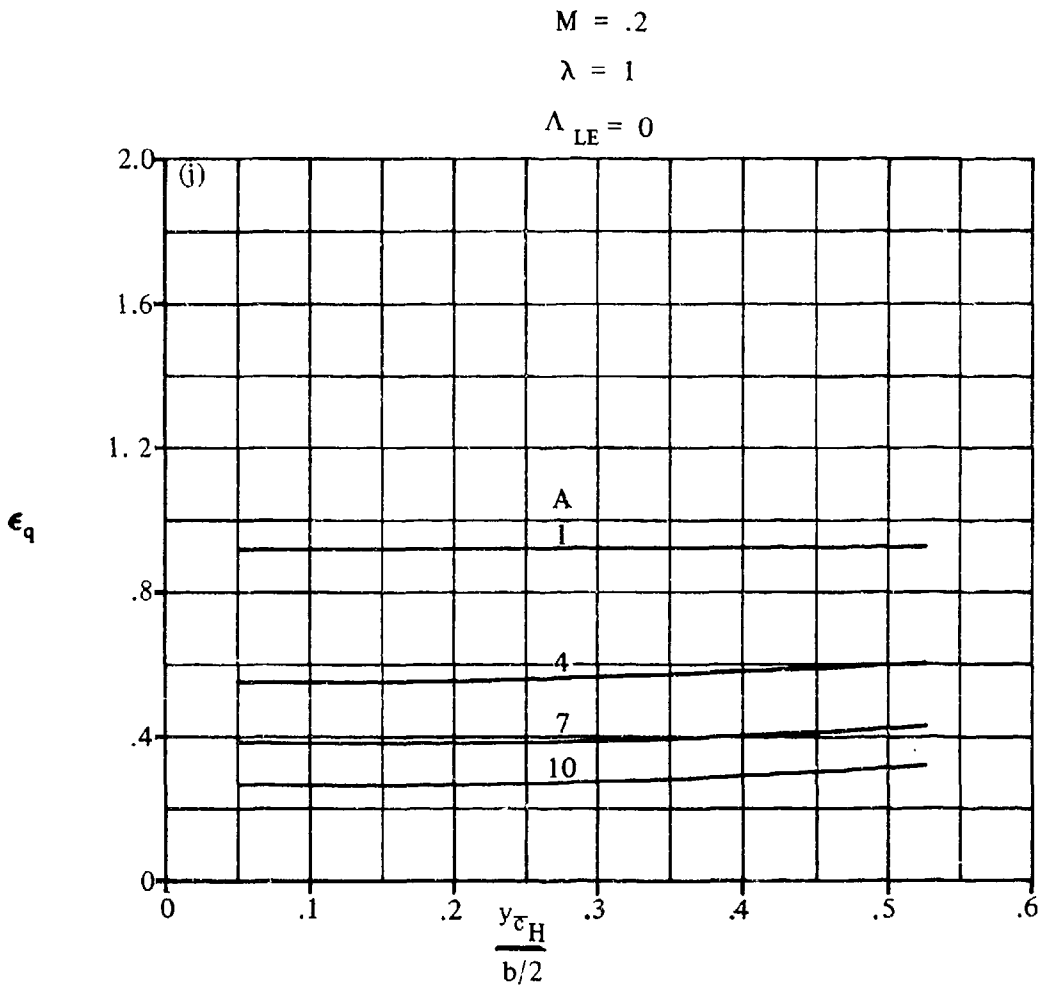

FIGURE 7.4.1.3-4 (CONTD)

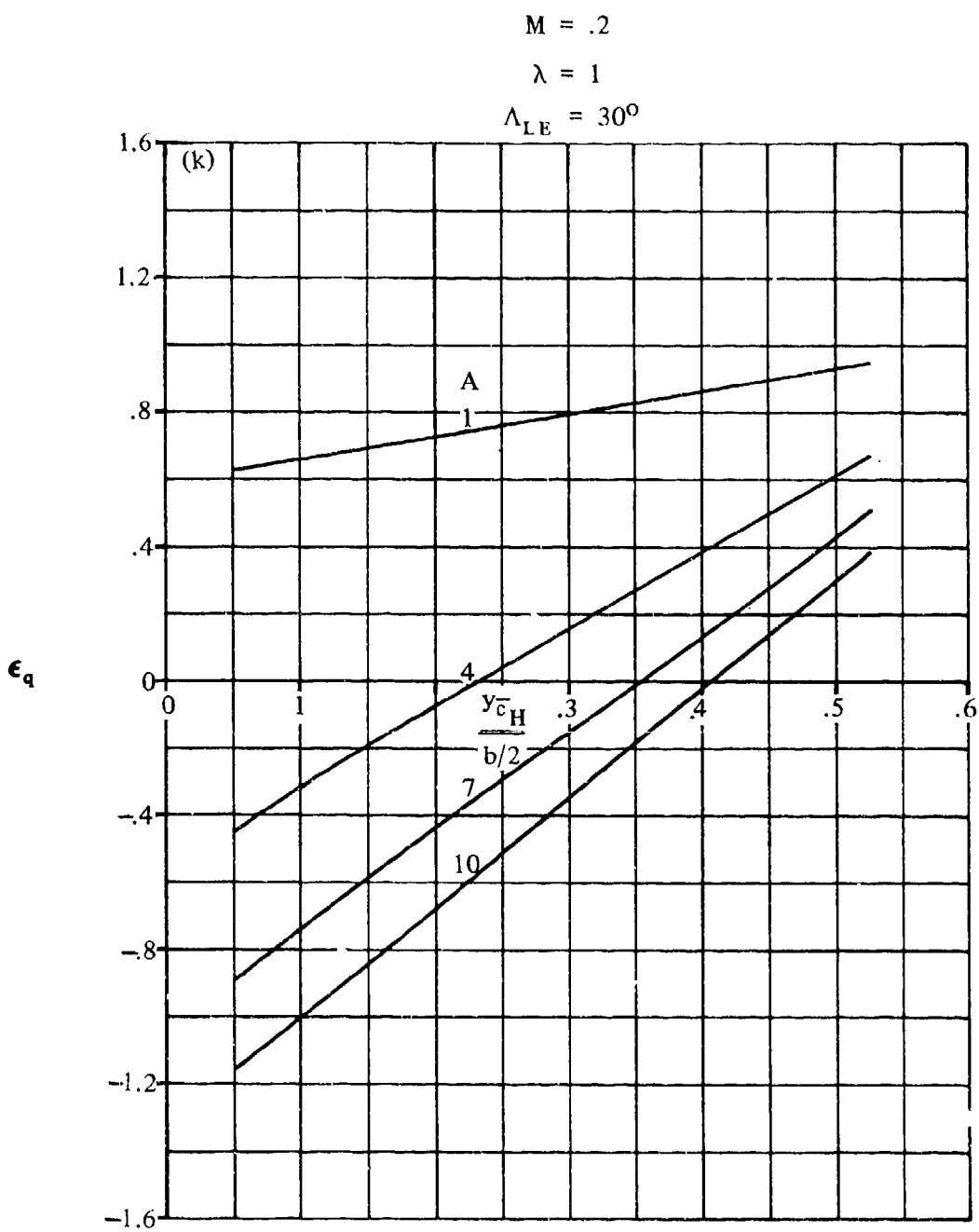

FIGURE 7.4.1.3-4 (CONTD)

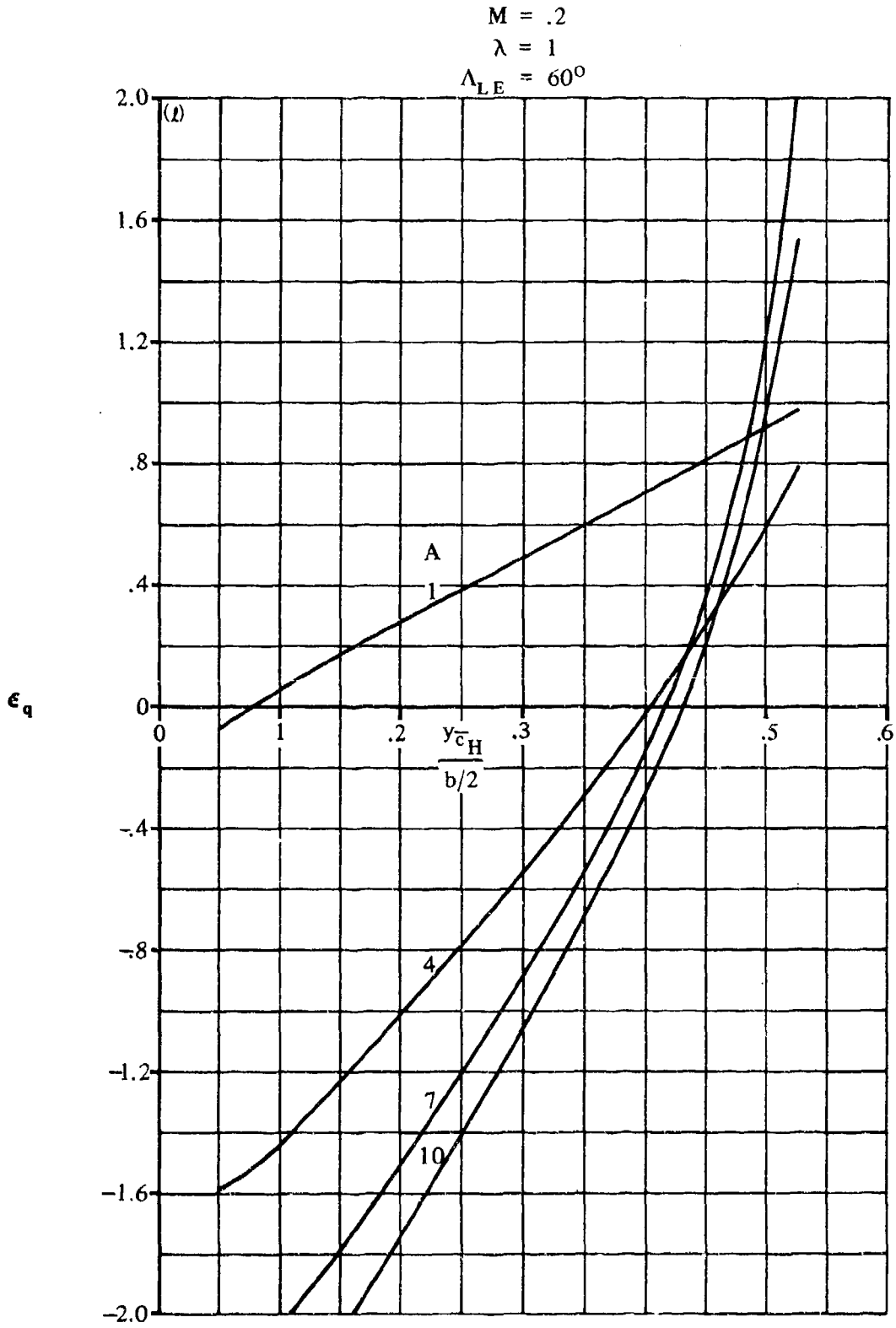

FIGURE 7.4.1.3-4 (CONTD)

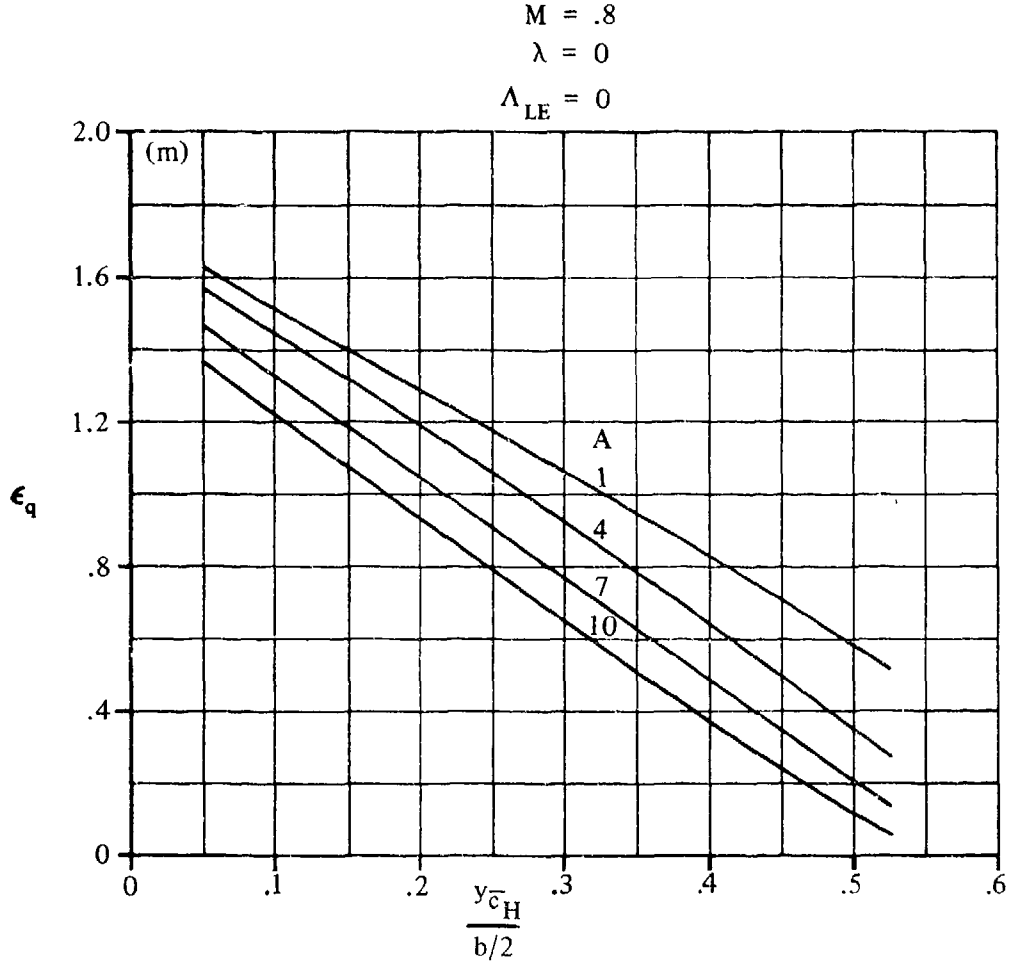

FIGURE 7.4.1.3-4 (CONTD)

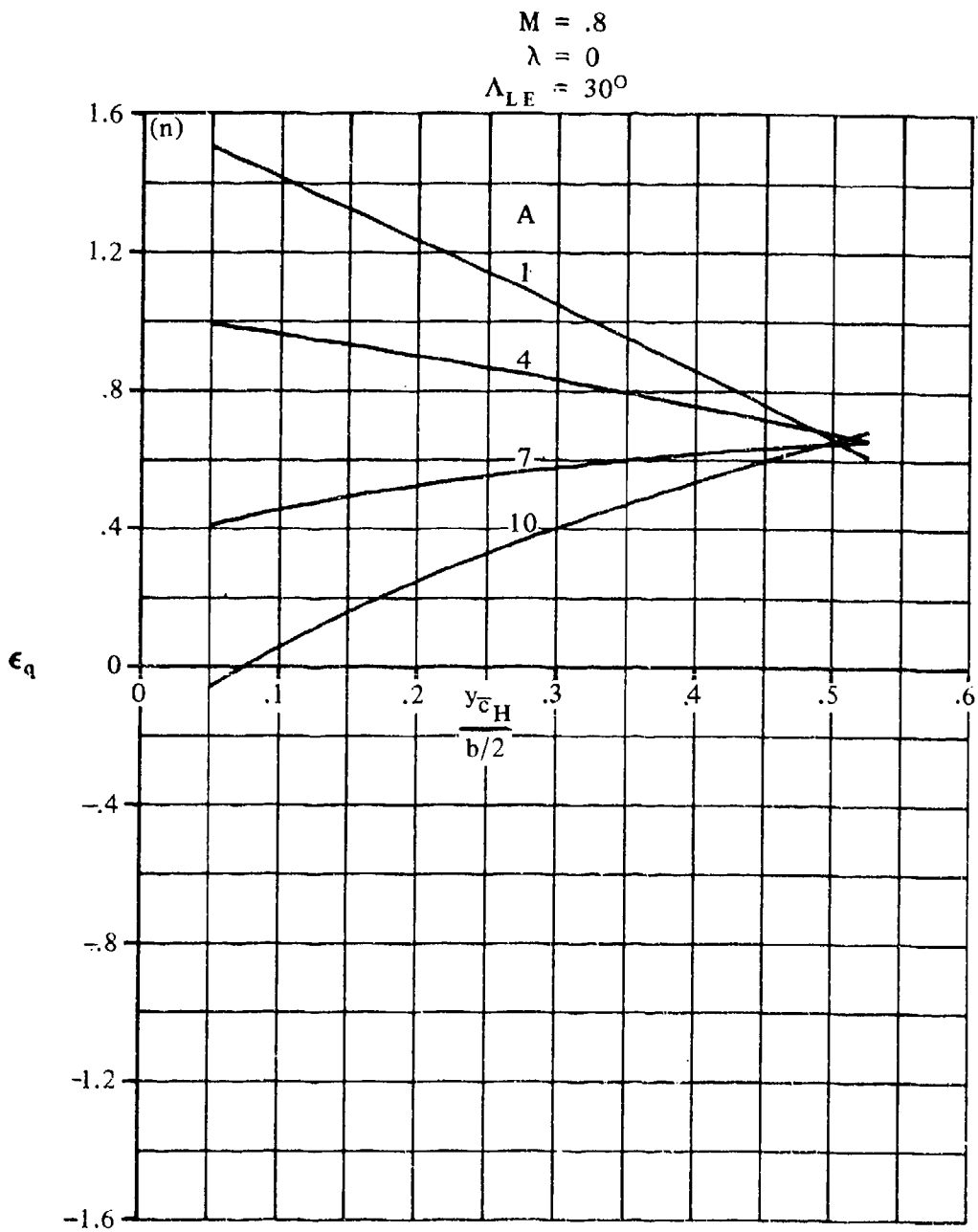

FIGURE 7.4.1.3-4 (CONTD)

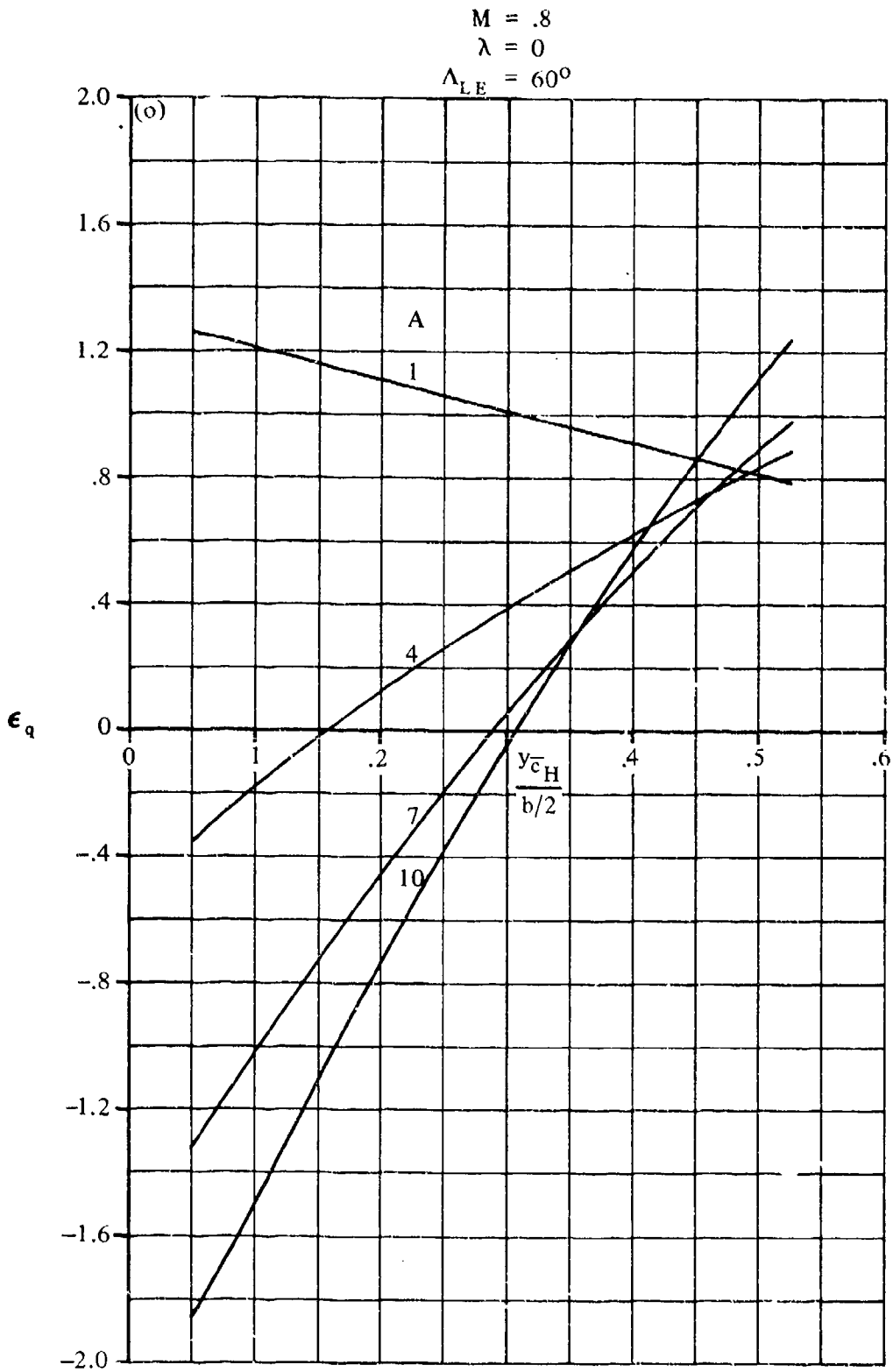

FIGURE 7.4.1.3-4 (CONTD)

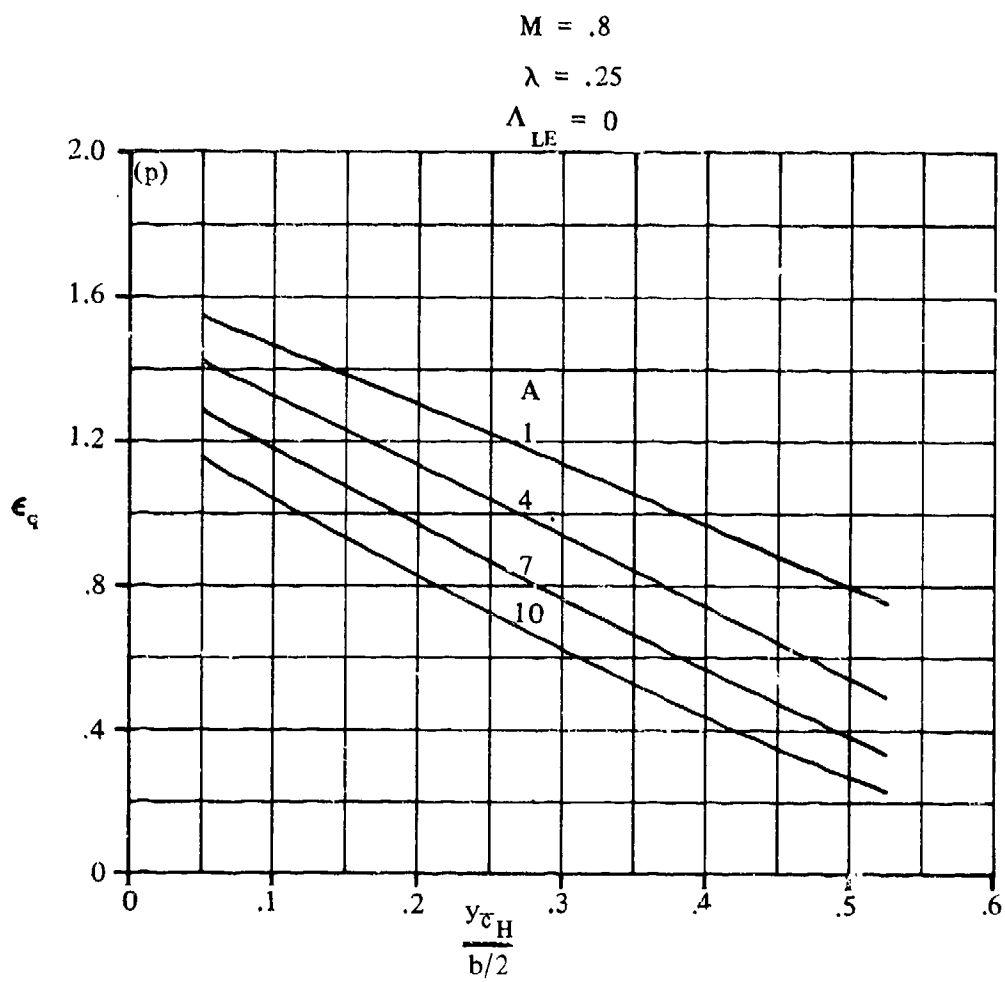

FIGURE 7.4.1.3-4 (CONTD)

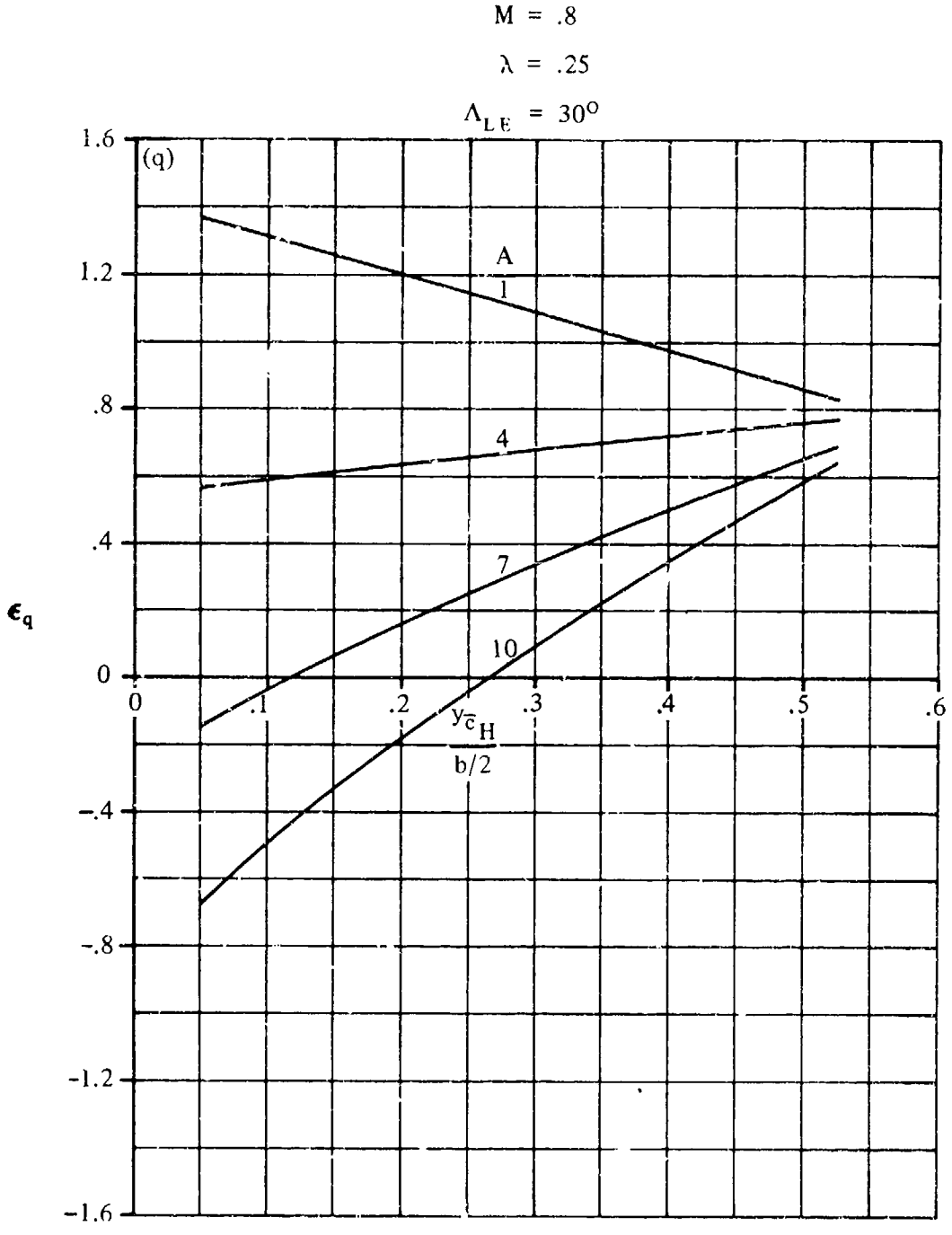

FIGURE 7.4.1.3-4 (CONTD)

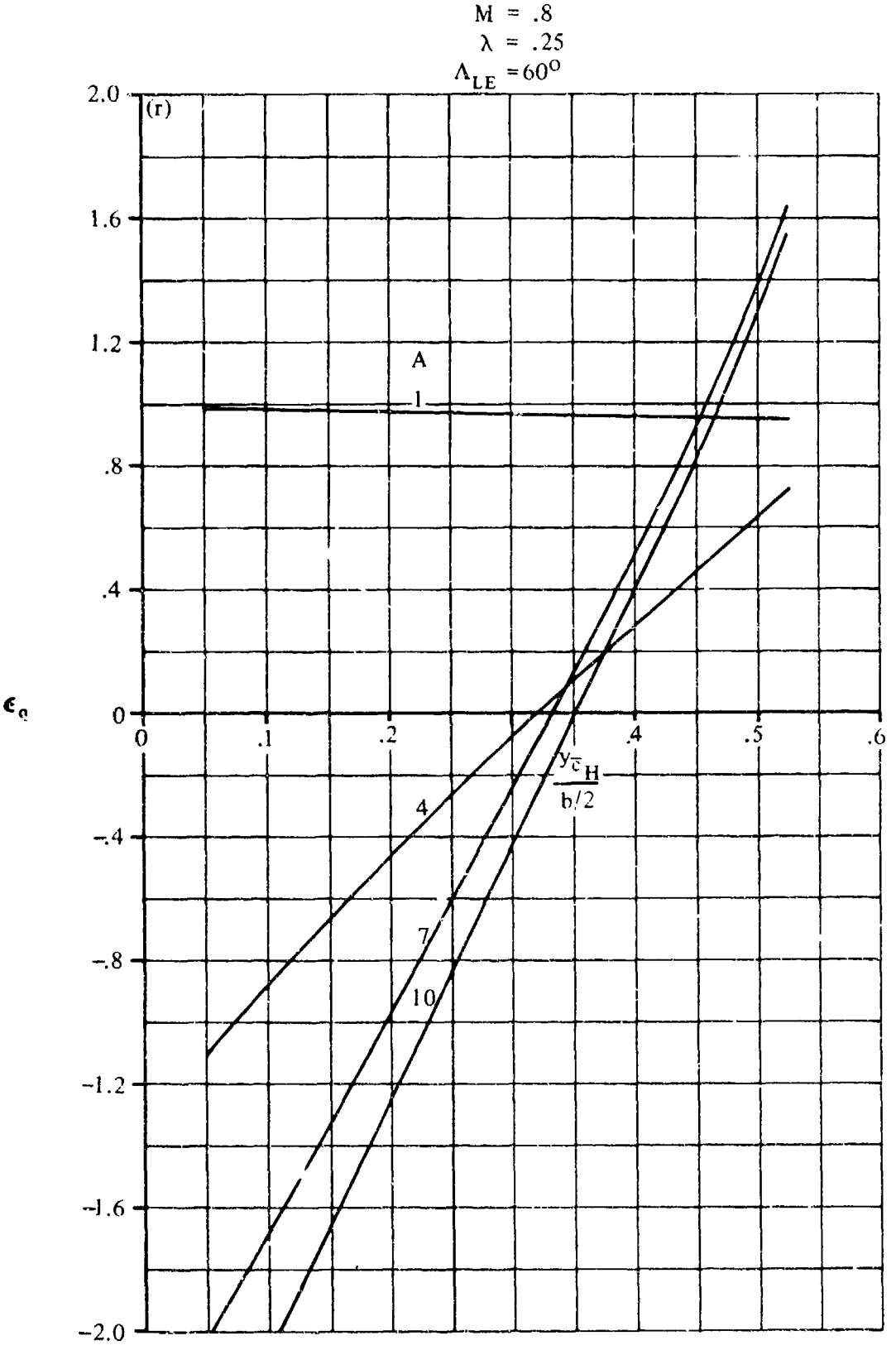

FIGURE 7.4.1.3-4 (CONTD)

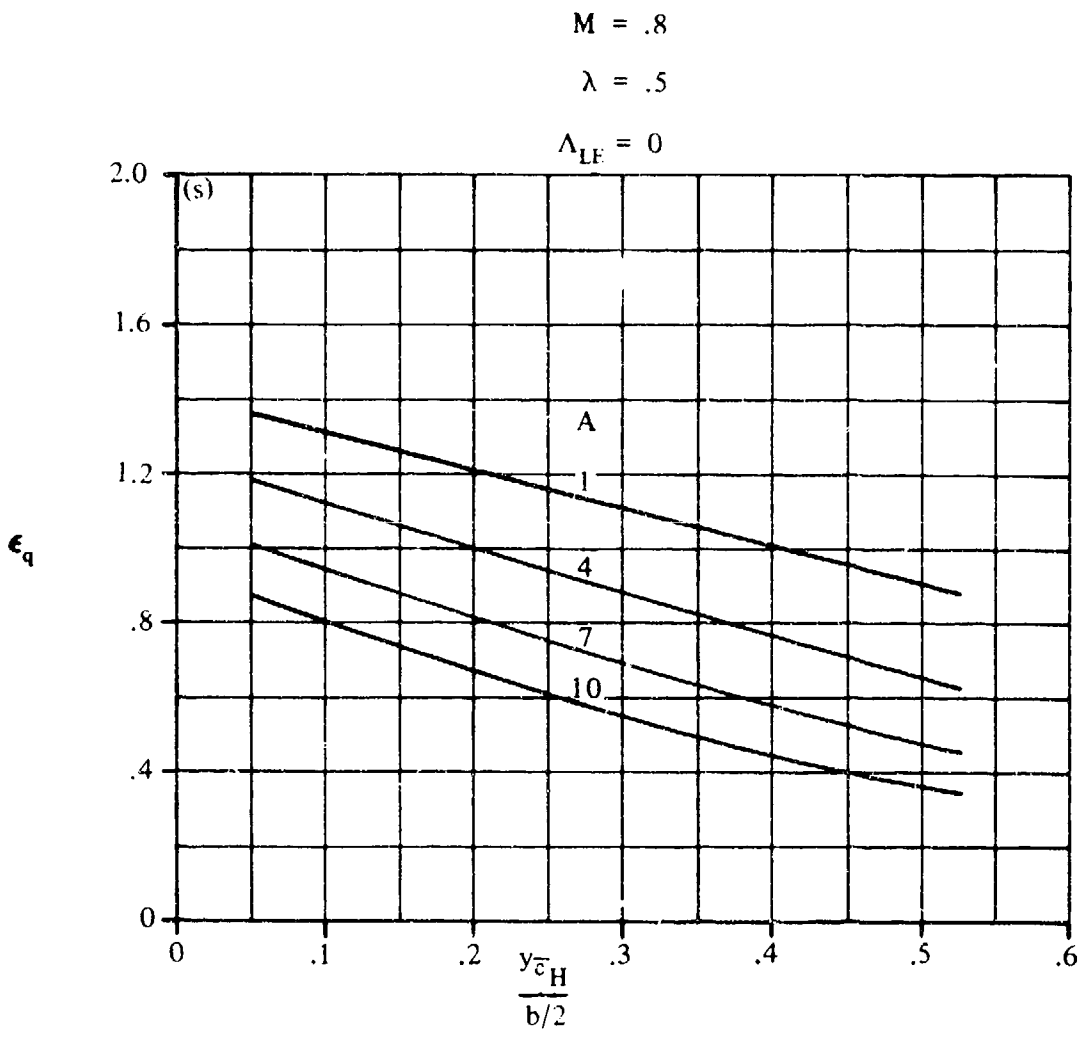

FIGURE 7.4.1.3-4 (CONTD)

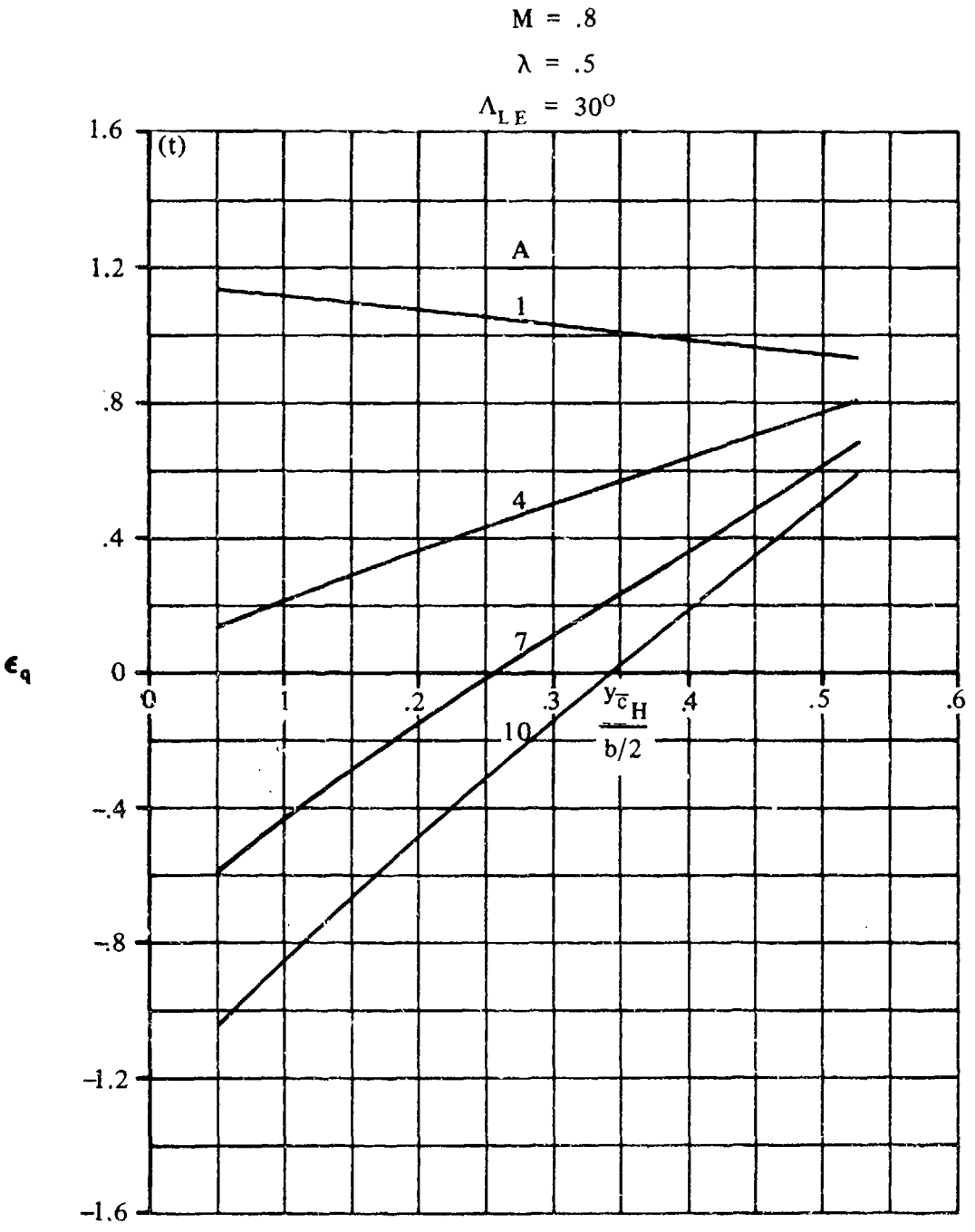

FIGURE 7.4.1.3-4 (CONTD)

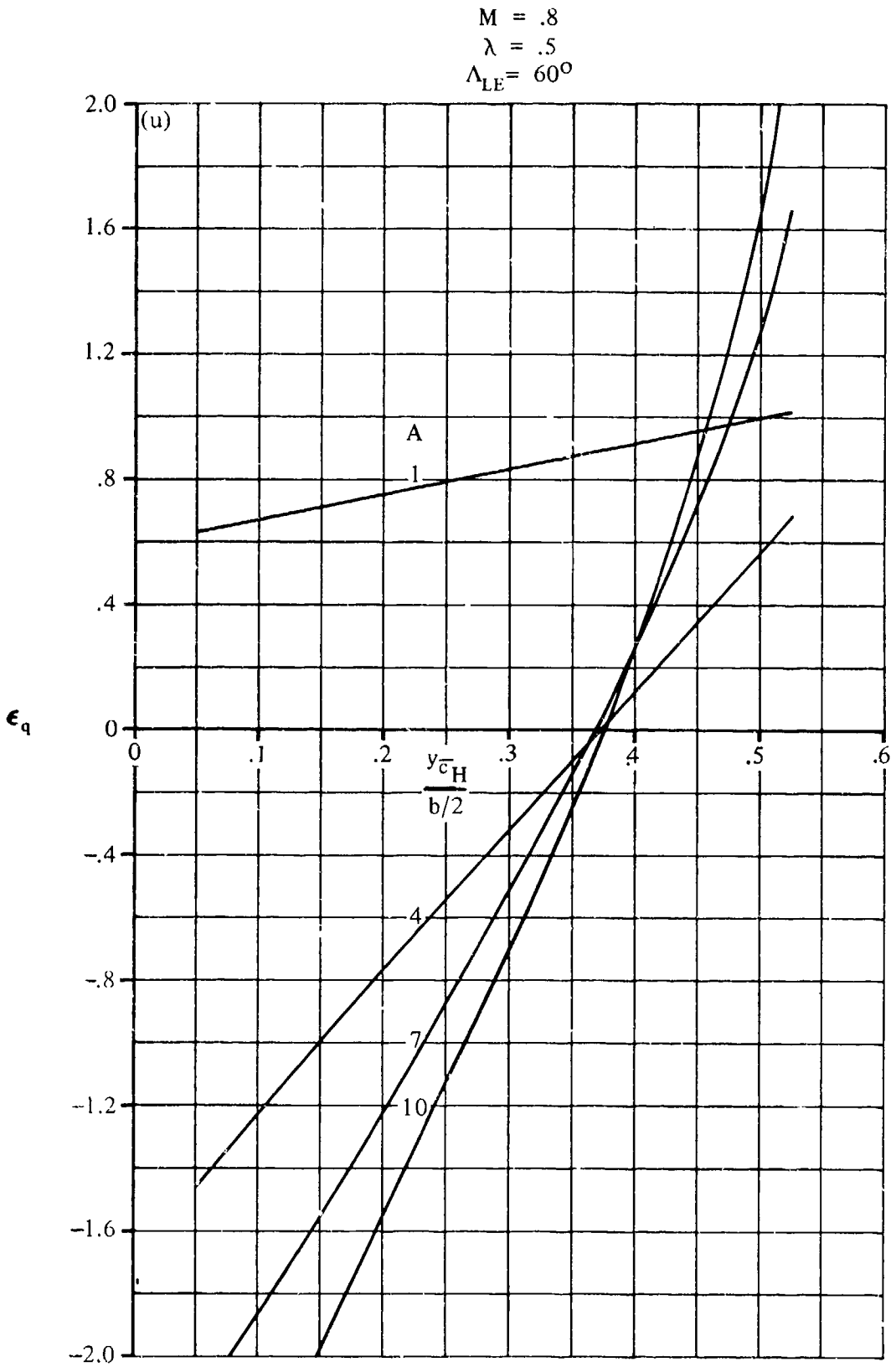

FIGURE 7.4.1.3-4 (CONTD)

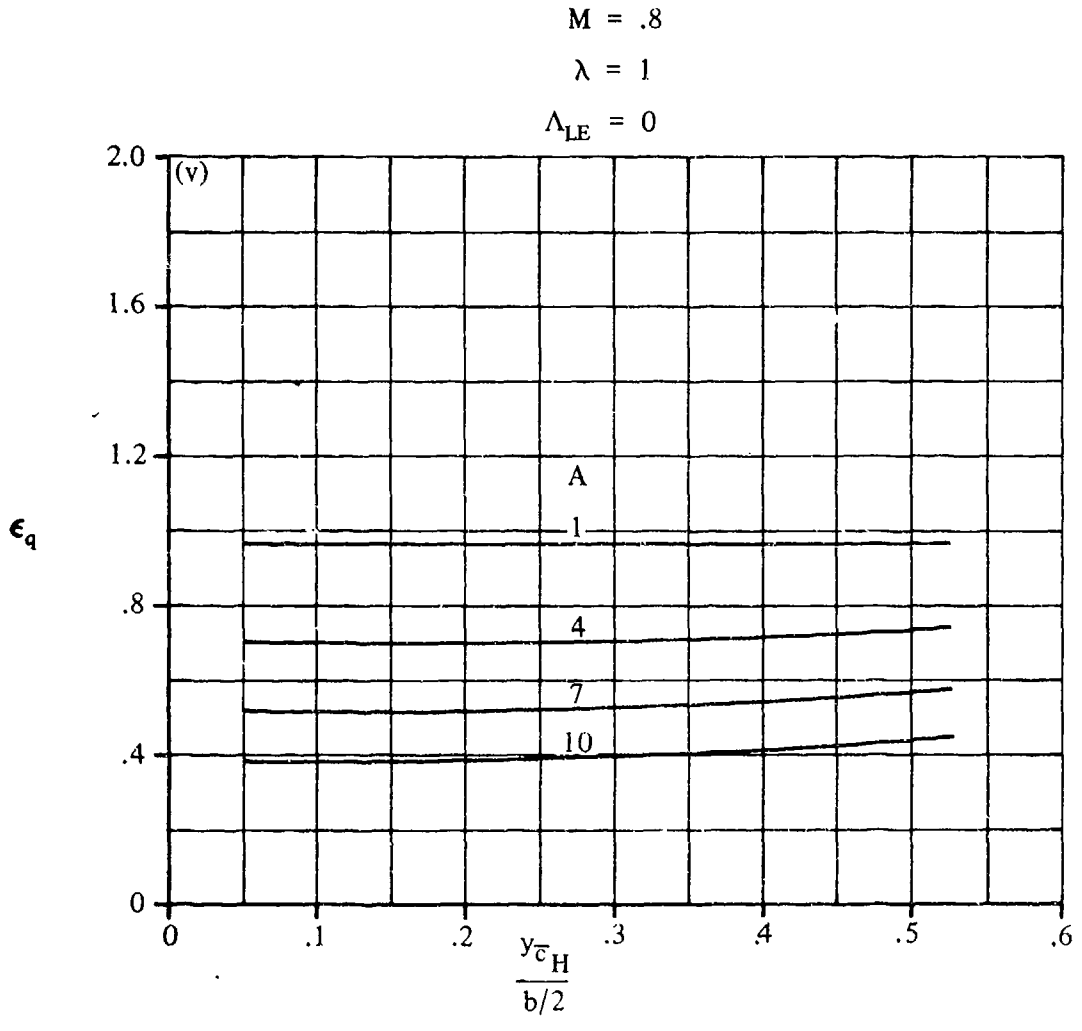

FIGURE 7.4.1.3-4 (CONTD)

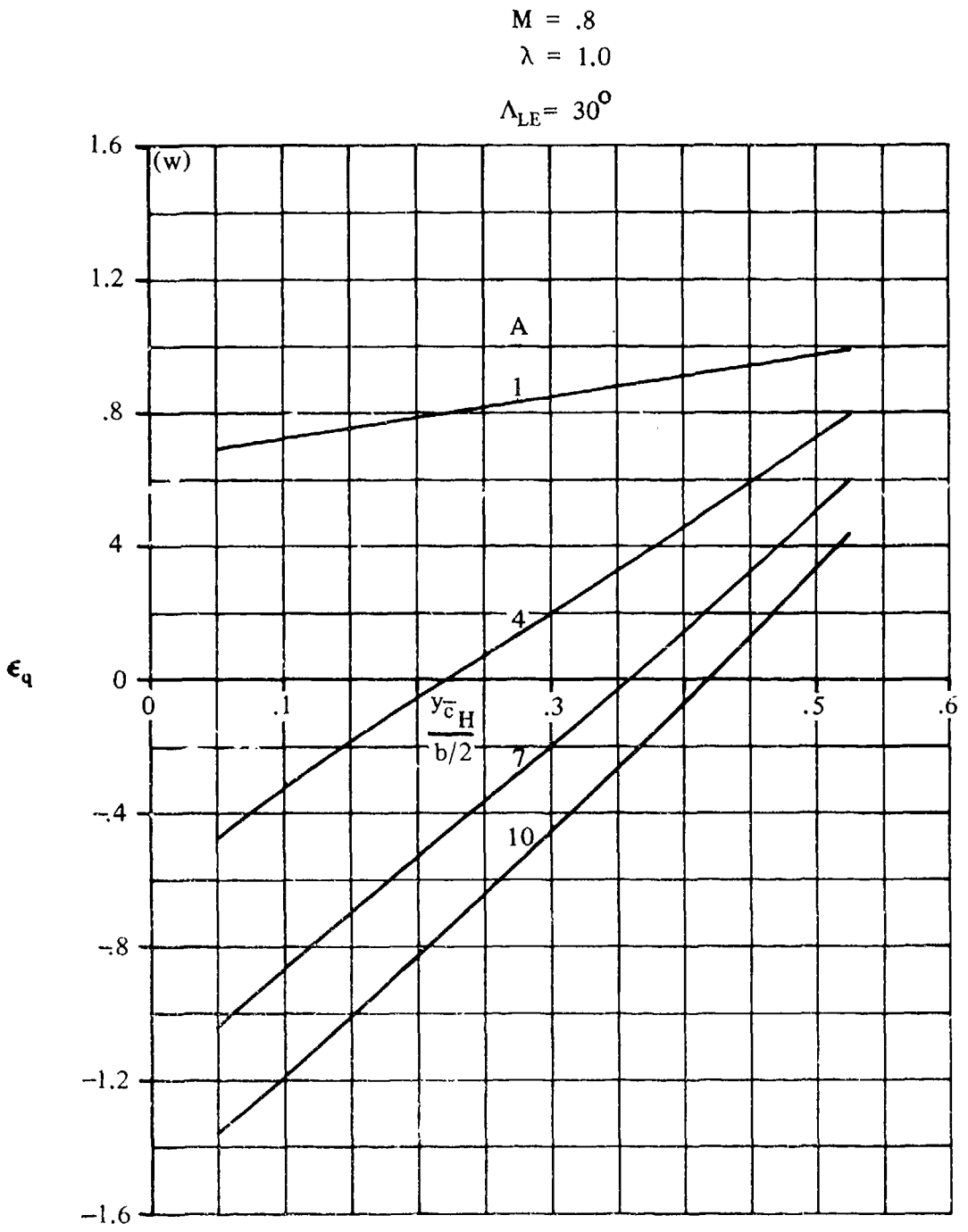

FIGURE 7.4.1.3-4 (CONTD)

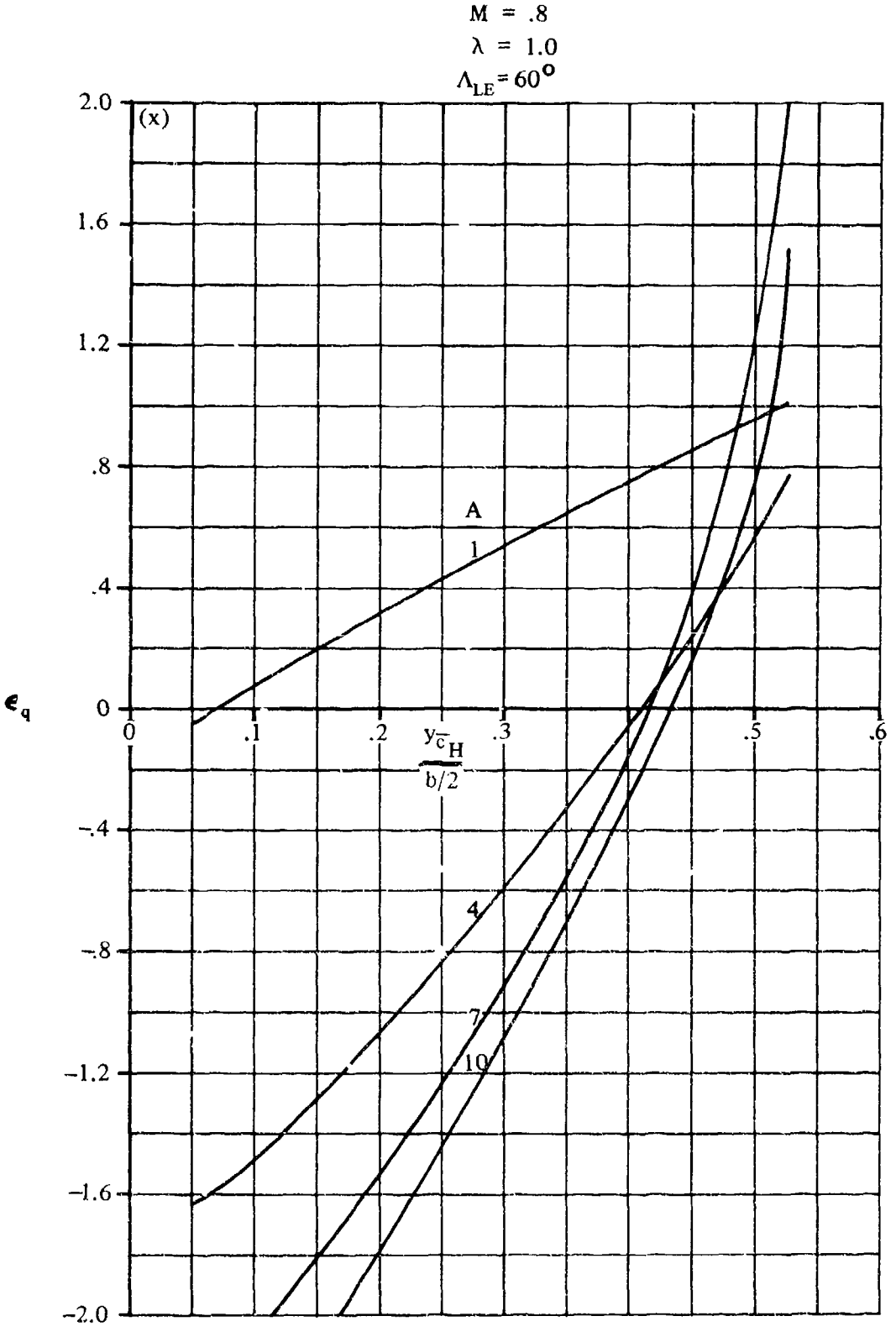

FIGURE 7.4.1.3-4 (CONTD)

7.4.2 WING-BODY-TAIL ROLLING DERIVATIVES

7.4.2.1 WING-BODY-TAIL ROLLING DERIVATIVE C_{Y_p}

This section presents methods for estimating the nondimensional rolling derivative C_{Y_p} of wing-body-tail combinations at subsonic speeds. However, at transonic and supersonic speeds no generalized methods are available for estimating the wing-body-tail rolling derivative C_{Y_p}. The derivative C_{Y_p} is the change in side-force coefficient with change in wing-tip helix angle and is expressed as

$$C_{Y_p} = \frac{\partial C_Y}{\partial\left(\frac{pb}{2V_\infty}\right)}$$

In general, the Datcom methods consist of a synthesis of material presented in Sections 7.1.2.1 and 7.3.2.1, and the vertical-tail contribution based on the methods of reference 1.

The derivative C_{Y_p} arises mainly from the wing and vertical tail. At high angles of attack the vertical-tail contribution predominates. The resultant side force on the vertical tail is generated when the aircraft has a rolling velocity p about its longitudinal body axis and the vertical tail is located either above or below the longitudinal axis. Generally C_{Y_p} is of little importance in lateral dynamics, hence is frequently neglected.

The side force at the vertical tail is created by the effective angle of attack due to the rolling velocity p and the sidewash generated from the wing and fuselage. The sidewash at the vertical tail can significantly alter the tail contribution. This effect is discussed more fully in reference 2. Studies have indicated that the effect of the sidewash varies considerably with tail size, location, and to some extent with wing planform.

A. SUBSONIC

Two methods are presented for determining the rolling derivative C_{Y_p} of the wing-body-tail combination, differing only in their treatment of wing sidewash on the vertical tail. The first method is applicable to conventionally located vertical tails, and the second method applies to tails located directly above, or above and slightly behind the wing. Both methods are based on the assumption that the vertical-tail contribution to C_{Y_p} is zero at $\alpha = 0$ and varies with angle of attack.

For an isolated-tail configuration the vertical-tail value of C_{Y_p} is approximated by

$$\left(C_{Y_p}\right)_V = 2\left(\frac{z}{b_W}\right)\left(\Delta C_{Y_\beta}\right)_{V(WBH)}$$

For a conventionally located vertical tail the effect of wing sidewash on the vertical tail has been approximately accounted for by

$$\left(C_{Y_p}\right)_V = 2\left(\frac{z - z_p}{b_W}\right)\left(\Delta C_{Y_\beta}\right)_{V(WBH)}$$

For configurations with tails located directly above or slightly behind the wing, the effect of wing sidewash has been approximated by using the average of the isolated-tail and conventional-tail values.

DATCOM METHODS

Method 1

For conventionally located vertical tails, the equation for the nondimensional rolling derivative C_{Y_p} of a wing-body configuration, based on the product of wing area and span $S_W b_W$, is given by

$$C_{Y_p} = \left(C_{Y_p}\right)_{WB} + 2\left[\frac{z - z_p}{b_W}\right]\left(\Delta C_{Y_\beta}\right)_{V(WBH)} \text{ (per radian)} \qquad 7.4.2.1\text{-a}$$

where

$\left(C_{Y_p}\right)_{WB}$ is the wing-body contribution to C_{Y_p} obtained from test data or Section 7.3.2.1 and based on the product of wing area and span (per radian).

b_W is the wing span.

z_p is the distance from the moment reference center to the center-of-pressure location of the vertical stabilizer, measured normal to the body center line, positive for the stabilizer above the body. For Datcom purposes, the vertical-tail center-of-pressure location is assumed to be the quarter-chord point of the MAC of the total added panel.

ℓ_p is the distance from the moment reference center to the center-of-pressure location of the vertical stabilizer, measured parallel to the body center line. For Datcom purposes, the vertical-tail center-of-pressure location is assumed to be the quarter-chord point of the MAC of the total added panel.

z is the vertical distance of the vertical-tail center-of-pressure location above or below the moment-reference-center location. This value must be calculated for each angle of attack (see sketch (a)). From sketch (a), z may be expressed as

$$z = z_p \cos\alpha - \ell_p \sin\alpha \qquad 7.4.2.1\text{-b}$$

$\left(\Delta C_{Y_\beta}\right)_{V(WBH)}$ is the tail-body sideslip derivative from test data or Section 5.3.1.1, based on the wing area (per radian). This derivative should include the end-plate effects of the horizontal tail.

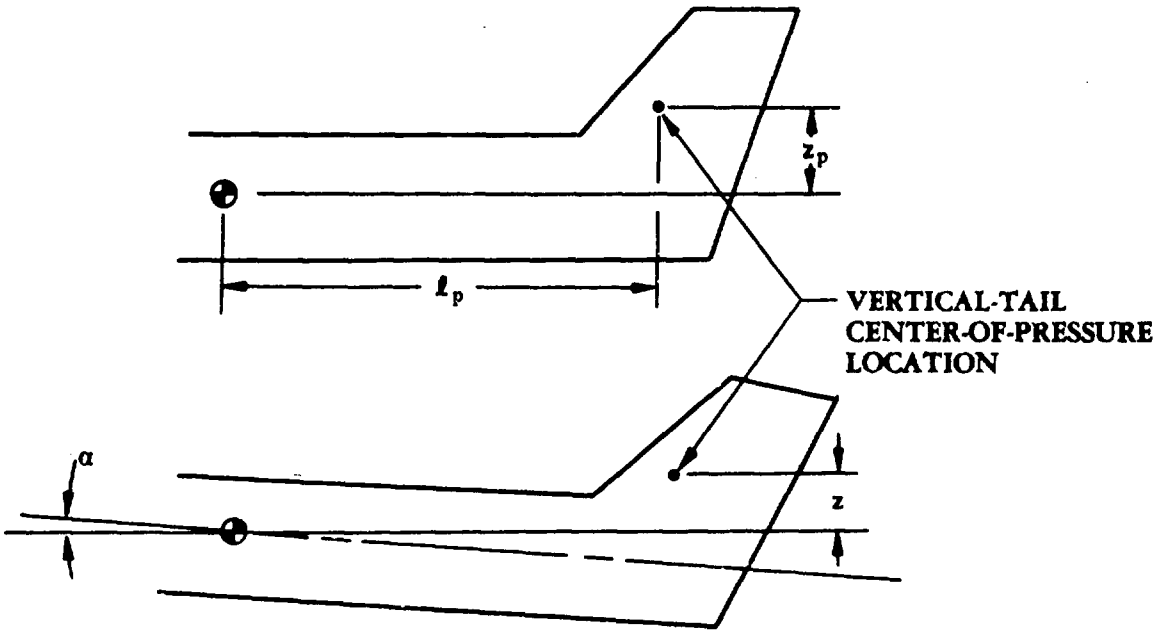

SKETCH (a)

Method 2

For vertical tails located either directly above, or above and slightly behind the wing, the equation for the nondimensional rolling derivative C_{Y_p} of a wing-body-tail configuration, based on the product of wing area and span $S_W b_W$, is given by

$$C_{Y_p} = \left(C_{Y_p}\right)_{WB} + \left[\frac{2z - z_p}{b_W}\right] \left(\Delta C_{Y_\beta}\right)_{V(WBH)} \quad \text{(per radian)} \qquad 7.4.2.1\text{-c}$$

where the components are described in method 1 above.

Sample Problem

Method 1

Given: Model of reference 3

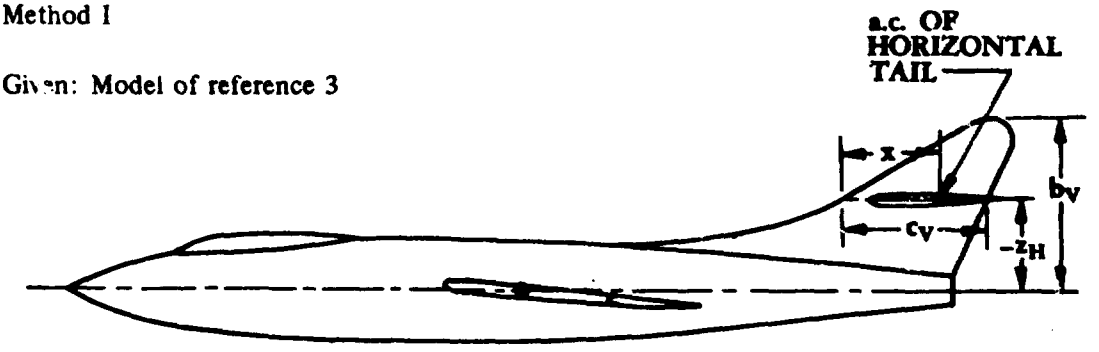

Wing Parameters:

S_W = 428.0 sq in. b_W = 38.84 in. A_W = 3.57

λ = 0.565 $\Lambda_{c/4}$ = 36.2° z_W = 0

Horizontal-Tail Parameters:

S_H = 97.10 sq in. b_H = 18.66 in. A_H = 3.59

λ = 0.50 $-z_H$ = 6.60 in.

Vertical-Tail Parameters:

S_V = 140.5 sq in. b_V = 12.68 in. A_V = 1.15

λ = 0.176 c_V = 11.0 in. $\Lambda_{c/2}$ = 45°

z_p = 5.0 in. ℓ_p = 24.3 in. x = 7.25 in.

Additional Parameters:

α = 8.0° M = 0.17 $\left(C_{Y_p}\right)_{WB}$ = 0.52 per rad (test data)

$2r_1$ = 4.0 in. d = 7.5 in.

Compute:

Calculate the tail-body sideslip derivative $\left(\Delta C_{Y_\beta}\right)_{V\,(WBH)}$ from Section 5.3.1.1

$$\frac{b_V}{2r_1} = \frac{12.68}{4} = 3.17$$

$$\frac{A_{V\,(B)}}{A_V} = 1.29 \quad \text{(figure 5.3.1.1-22a)}$$

$$\frac{z_H}{b_V} = \frac{-6.60}{12.68} = -0.52$$

$$\frac{x}{c_V} = \frac{7.25}{11.0} = 0.659$$

$$\frac{A_{V(HB)}}{A_{V(B)}} = 0.90 \qquad \text{(figure 5.3.1.1-22b)}$$

$$\frac{S_H}{S_V} = \frac{97.1}{140.5} = 0.691$$

$$K_H = 0.76 \qquad \text{(figure 5.3.1.1-22 c)}$$

$$A_{eff} = \frac{A_{V(B)}}{A_V} A_V \left\{1 + K_H \left[\frac{A_{V(HB)}}{A_{V(B)}} - 1\right]\right\} \qquad \text{(equation 5.3.1.1-a)}$$

$$= (1.29)(1.15)\{1 + 0.76\ [0.90 - 1.0]\}$$

$$= (1.29)(1.15)(0.924)$$

$$= 1.37$$

$\kappa = 1$ (assumed)

$$\frac{A_{eff}}{\kappa}\left[\beta^2 + \tan^2 \Lambda_{c/2}\right]^{1/2} = (1.37)\ [0.971 + 1]^{1/2}$$

$$= (1.37)(1.404)$$

$$= 1.923$$

$$\frac{C_{L_\alpha}}{A_{eff}} = 1.315 \qquad \text{(figure 4.1.3.2-49)}$$

$$C_{L_\alpha} = (1.315)(1.37)$$

$$= 1.80 \text{ per rad (based on } S_V)$$

$$\left(1 + \frac{\partial\sigma}{\partial\beta}\right)\frac{q_V}{q_\infty} = 0.724 + 3.06\frac{S_V/S_W}{1 + \cos\Lambda_{c/4}} + \frac{0.4\ z_W}{d} + 0.009A \qquad \text{(equation 5.4.1-a)}$$

$$= 0.724 + 3.06\ \frac{(140.5)/(428.0)}{1.807} + \frac{(0.4)\ 0}{7.5} + (0.009)(3.57)$$

$$= 0.724 + 0.556 + 0.0321$$

$$= 1.312$$

$k = 0.94$ (figure 5.3.1.1-22d)

$$\left(\Delta C_{Y_\beta}\right)_{V\,(WBH)} = -k \left(C_{L_\alpha}\right)_V \left(1 + \frac{\partial \sigma}{\partial \beta}\right) \frac{q_V}{q_\infty} \frac{S_V}{S_W}$$ (equation 5.3.1.1-b)

$$= -(0.94)\,(1.80)\,(1.312)\,\frac{140.5}{428.0}$$

$$= -0.729 \text{ per rad (based on } S_W)$$

Calculate the vertical distance z of the vertical-tail center-of-pressure location above or below the moment-reference-center location

$$z = z_p \cos \alpha - \ell_p \sin \alpha$$ (equation 7.4.2.1-b)

$$= (5.0)\,(0.9903) - (24.3)\,(0.1392)$$

$$= 4.95 - 3.38$$

$$= 1.57 \text{ in.}$$

Calculate the rolling derivative C_{Y_p} for the wing-body-tail configuration

$$C_{Y_p} = \left(C_{Y_p}\right)_{WB} + 2\left[\frac{z - z_p}{b_W}\right]\left(\Delta C_{Y_\beta}\right)_{V\,(WBH)}$$ (equation 7.4.2.1-a)

$$= 0.52 + 2\left[\frac{1.57 - 5.00}{38.84}\right](-0.729)$$

$$= 0.52 + (2)\,(-0.0883)\,(-0.729)$$

$$= 0.52 + 0.129$$

$$= 0.649 \text{ per rad (based on } S_W b_W)$$

This compares with a test value of 0.62 per radian from reference 3.

B. TRANSONIC

No generalized method is available in the literature for estimating transonic values of the rolling derivative C_{Y_p}. Furthermore, only limited experimental data are available for this derivative at transonic speeds (see table 7-A).

C. SUPERSONIC

No generalized method is available in the literature for estimating supersonic values of the rolling derivative C_{Y_p}. Furthermore, there is a scarcity of experimental data for this d ivative at supersonic speeds.

For the purposes of the Datcom the fuselage effect is considered to be negligible for wing-body configurations with body diameters less than about 30 percent of the wing span. Therefore, for configurations with $d/b \leq 0.3$, the wing-body rolling derivative C_{Y_p} is estimated by the wing-alone method of paragraph C of Section 7.1.2.1.

Methods are presented in reference 4 for evaluating the vertical-tail contribution to C_{Y_p}. The stability derivatives presented therein are derived by using supersonic linearized theory for families of thin, isolated vertical tails performing steady rolling motions. Vertical-tail families (half-delta and rectangular planforms) are considered over a broad Mach number range. Also considered are vertical tails with arbitrary sweepback and taper ratio at Mach numbers for which both the leading edge and trailing edge of the tail are supersonic, and triangular vertical tails with a subsonic leading edge and a supersonic trailing edge.

REFERENCES

1. Campbell, J. P., and McKinney, M. O.: Summary of Methods for Calculating Dynamic Lateral Stability and Response and for Estimating Lateral Stability Derivatives. NACA TR 1098, 1952. (U)

2. Michael, W. H. Jr.: Analysis of the Effects of Wing Interference on the Tail Contributions to the Rolling Derivatives. NACA TR 1086, 1952. (U)

3. Queijo, M. J., and Wells, E. G.: Wind-Tunnel Investigation of the Low-Speed Static and Rotary Stability Derivatives of a 0.13-Scale Model of the Douglas D-558-II Airplane in the Landing Configuration. NACA RM L52G07, 1952. (U)

4. Margolis, K., and Bobbitt, P. J.: Theoretical Calculations of the Pressures, Forces, and Moments at Supersonic Speeds due to Various Lateral Motions Acting on Thin Isolated Vertical Tails. NACA TR 1268, 1956. (U)

7.4.2.2 WING-BODY-TAIL ROLLING DERIVATIVE C_{l_p}

This section presents methods for estimating the nondimensional rolling derivative C_{l_p} of wing-body-tail combinations at subsonic speeds. However, at transonic and supersonic speeds no generalized methods are available for estimating the wing-body-tail rolling derivative C_{l_p}. The derivative C_{l_p} is the change in rolling-moment coefficient with change in wing-tip helix angle and is commonly referred to as the roll-damping derivative. It is expressed as

$$C_{l_p} = \frac{\partial C_l}{\partial\left(\frac{pb}{2V_\infty}\right)}$$

In general, the Datcom methods consist of a synthesis of material presented in Sections 7.1.2.2 and 7.3.2.2, and the vertical-tail contribution based on the methods of reference 1.

The derivative C_{l_p} is important in lateral dynamics, since it determines the damping-in-roll characteristics of the vehicle. The derivative is composed of contributions, negative in sign, from the wing, the horizontal tail, and the vertical tail, with the main contribution coming from the wing. The contribution from the vertical tail is usually negligible at low and moderate angles of attack. However, the vertical-tail contribution can become significant at high angles of attack, when the effective moment arm of the tail (z/b_W) becomes a large negative value.

The rolling wing produces a sidewash at the vertical tail, which can significantly alter the vertical-tail contribution. This effect is discussed more fully in reference 2. Studies have indicated that the effect of the sidewash varies considerably with tail size, tail location, and to some extent with wing planform.

Conventional horizontal-tail effects on C_{l_p} are usually small and often neglected, although unusually large horizontal tails can contribute significantly (see references 1 and 3). The horizontal-tail contribution is obtained by using the horizontal-tail geometry and the method of Section 7.1.2.2. The value from Section 7.1.2.2 is then multiplied by a constant, which accounts for the flow rotation produced by the wing, and by the appropriate geometrical parameters to refer the result to the proper reference base.

A. SUBSONIC

Two methods are presented for determining the rolling derivative C_{l_p} of the wing-body-tail combination, differing only in their treatment of wing sidewash on the vertical tail. The first method is applicable to conventionally located vertical tails, and the second method applies to tails located directly above, or above and slightly behind the wing. Both methods are based on the assumption that the vertical-tail contribution to C_{l_p} is zero at $\alpha = 0$ and varies with angle of attack.

For an isolated-tail configuration the vertical-tail value of C_{l_p} is approximated by

$$\left(C_{l_p}\right)_V = 2\left(\frac{z}{b_W}\right)^2 \left(\Delta C_{Y_\beta}\right)_{V(WBH)}$$

For a conventionally located vertical tail the effect of wing sidewash on the vertical tail has been approximately accounted for by

$$\left(C_{l_p}\right)_V = 2\frac{z(z - z_p)}{{b_W}^2} \left(\Delta C_{Y_\beta}\right)_{V(WBH)}$$

For configurations with tails located directly above or slightly behind the wing, the effect of wing sidewash has been approximated by using the average of the isolated-tail and conventional-tail values.

DATCOM METHODS

Method 1

For conventionally located vertical tails, the equation for the nondimensional rolling derivative C_{l_p} of a wing-body-tail configuration, based on the product of wing area and the square of wing span $S_W b_W{}^2$, is given by

$$C_{l_p} = \left(C_{l_p}\right)_{WB} + 0.5\left(C_{l_p}\right)_H \left(\frac{S_H}{S_W}\right)\left(\frac{b_H}{b_W}\right)^2 + \left|2\left(\frac{z}{b_W}\right)\left[\frac{z - z_p}{b_W}\right]\right| \left(\Delta C_{Y_\beta}\right)_{V(WBH)}$$

(per radian) 7.4.2.2-a

where

$\left(C_{l_p}\right)_{WB}$ is the wing-body contribution to C_{l_p}, obtained from test data or Section 7.1.2.2 and based on the product of wing area and the square of wing span (per radian).

$\left(C_{l_p}\right)_H$ is the horizontal-tail contribution obtained from test data or Section 7.1.2.2, based on the horizontal-tail geometry (per radian).

$\frac{S_H}{S_W}\left(\frac{b_H}{b_W}\right)^2$ is the ratio of the horizontal-tail area to the wing area times the square of the ratio of the horizontal-tail span to the wing span.

z is the vertical distance of the vertical-tail center-of-pressure location above or below the moment-reference-center location. This value must be calculated for each angle of attack. (See sketch (a) in Section 7.4.2.1.) From equation 7.4.2.1-b, z is expressed as

$$z = z_p \cos\alpha - \ell_p \sin\alpha$$

ℓ_p is the distance from the moment reference center to the center-of-pressure location of the vertical stabilizer, measured parallel to the body center line (see sketch (a) in Section 7.4.2.1). For Datcom purposes, the vertical-tail center-of-pressure location is assumed to be the quarter-chord point of the MAC of the total added panel.

z_p is the distance from the moment reference center to the center of pressure of the vertical stabilizer, measured normal to the body center line, positive for the stabilizer above the body. For Datcom purposes, the vertical-tail center-of-pressure location is assumed to be the quarter-chord point of the MAC of the total added panel.

$\left(\Delta C_{Y_\beta}\right)_{V(WBH)}$ is the tail-body sideslip derivative obtained from test data or Section 5.3.1.1. It includes the end-plate effects of the horizontal tail and is based on the wing area (per radian).

Method 2

For vertical tails located either directly above, or above and slightly behind the wing, the equation of the nondimensional rolling derivative C_{l_p} of a wing-body-tail configuration, based on the product of wing area and the square of wing span $S_W b_W{}^2$, is given by

$$C_{l_p} = \left(C_{l_p}\right)_{WB} + 0.5\left(C_{l_p}\right)_H \left(\frac{S_H}{S_W}\right)\left(\frac{b_H}{b_W}\right)^2 + \left|\frac{z}{b_W}\left[\frac{2z - z_p}{b_W}\right]\right| \left(\Delta C_{Y_\beta}\right)_{V(WBH)}$$

(per radian) 7.4.2.2-b

where the components are described in method 1 above.

Example Problem

Method 1

Given: Model of reference 4

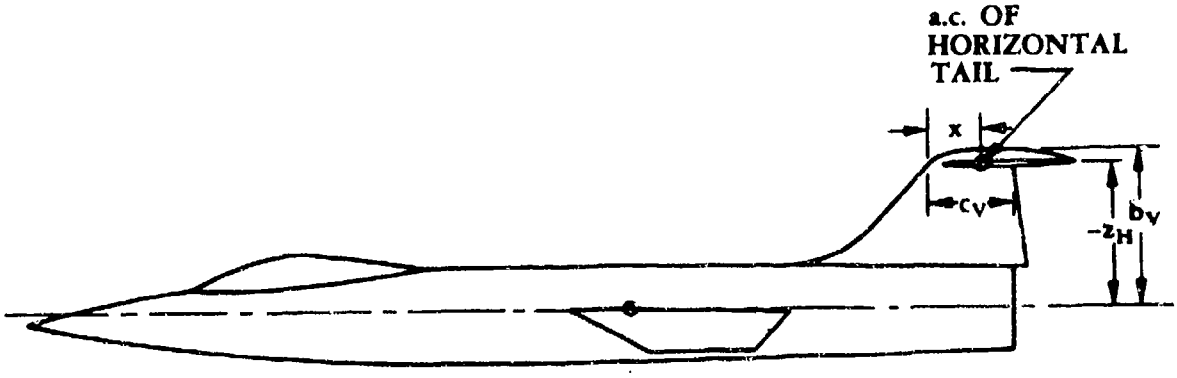

Wing Parameters:

S_W = 1.90 sq ft b_W = 2.16 ft A_W = 2.44 λ = 0.38

Γ = −10° $\bar{c}$ = 0.94 ft $\Lambda_{c/4}$ = 18.0° z_W = 0

Horizontal-Tail Parameters:

S_H = 0.48 sq ft b_H = 1.20 ft A_H = 2.97 λ = 0.31

$\Lambda_{c/4}$ = 10.5° Γ = 0 $\frac{t}{c}$ = 0.05 $\bar{c}$ = 0.44 ft $-z_H$ = 8.30 in.

Vertical-Tail Parameters:

S_V = 0.56 sq ft b_V = 9.0 in. A_V = 0.86 λ_V = 0.37

c_V = 0.42 ft $\bar{c}$ = 0.87 ft $\Lambda_{c/2}$ = 23.25° z_p = 0.308 ft

ℓ_p = 1.25 ft x = 0.25 ft

Additional Parameters:

α = 4.0° M = 0.25 $(C_{l_p})_{WB}$ = −0.30 per rad (test data)

C_L = 0.3 R_ℓ = 1.5 x 10^6 $2r_1$ = 4.88 in.

Compute:

Calculate $\left(C_{l_p}\right)_H$ for the horizontal tail from Section 7.1.2.2

$$\left(C_{l_p}\right)_H = \left(\frac{\beta C_{l_p}}{\kappa}\right)_{C_L=0} \left(\frac{\kappa}{\beta}\right) \frac{\left(C_{L_\alpha}\right)_{C_L}}{\left(C_{L_\alpha}\right)_{C_L=0}} \frac{\left(C_{l_p}\right)_\Gamma}{\left(C_{l_p}\right)_{\Gamma=0}} + \left(\Delta C_{l_p}\right)_{drag}$$

(equation 7.1.2.2-a)

$$\Lambda_\beta = \tan^{-1}\left(\frac{\tan \Lambda_{c/4}}{\beta}\right)$$

$$\beta = \sqrt{1 - M^2} = \sqrt{1 - (.25)^2} = 0.968$$

$$\Lambda_\beta = \tan^{-1}\left(\frac{0.1853}{0.968}\right)$$

$$= \tan^{-1}(0.1914) = 10.8°$$

$\kappa = 1$ (assumed)

$$\frac{\beta A_H}{\kappa} = \frac{(0.968)(2.97)}{1.0} = 2.87$$

$$\left(\frac{\beta C_{l_p}}{\kappa}\right)_{C_L=0} = -0.245 \qquad \text{(figure 7.1.2.2-20b)}$$

$$\frac{\left(C_{L_\alpha}\right)_{C_L}}{\left(C_{L_\alpha}\right)_{C_L=0}} = 1.0 \text{ (assumed)}$$

$$\frac{\left(C_{l_p}\right)_\Gamma}{\left(C_{l_p}\right)_{\Gamma=0}} = 1 \text{ (no dihedral)}$$

$$\left(\Delta C_{l_p}\right)_{drag} = \frac{\left(C_{l_p}\right)_{C_{D_L}}}{C_L{}^2} C_L{}^2 - \frac{1}{8} C_{D_0} \qquad \text{(equation 7.1.2.2-c)}$$

$$\frac{\left(C_{l_p}\right)_{C_{D_L}}}{C_L{}^2} = 0.015 \text{ per rad} \qquad \text{(figure 7.1.2.2-24)}$$

$$C_{D_0} = C_f\left[1 + L\left(\frac{t}{c}\right) + 100\left(\frac{t}{c}\right)^4\right] R_{L.S.} \frac{S_{wet}}{S_{ref}} \qquad \text{(equation 4.1.5.1-a)}$$

$\ell = \bar{c}_H = 0.44$ ft

$k = 0.05 \times 10^{-3}$ in (table 4.1.5.1-A, assume polished wood surface)

$$\frac{\ell}{k} = \frac{(0.44)(12)}{5 \times 10^{-5}} = 1.056 \times 10^5$$

Cutoff Reynolds number, $R_\ell = 7 \times 10^6$ (figure 4.1.5.1-27)

Test Reynolds number, $R_\ell = 1.5 \times 10^6$

$C_f = 0.00410$ (figure 4.1.5.1-26)

$L = 1.2$ (assume $(t/c)_{max}$ is located at $x = .50c$)

$$\left[1 + L\left(\frac{t}{c}\right) + 100\left(\frac{t}{c}\right)^4\right] = 1.06 \quad \text{(figure 4.1.5.1-28a)}$$

$$\cos \Lambda_{(t/c)_{max}} = \cos 0^\circ = 1.0$$

$R_{L.S.} = 1.067$ (figure 4.1.5.1-28b)

$\frac{S_{wet}}{S_{ref}} = 2.0$ (assumed) $\quad S_{ref} = S_{\text{horizontal tail}}$

$$C_{D_0} = C_f \left[1 + L\left(\frac{t}{c}\right) + 100\left(\frac{t}{c}\right)^4\right] R_{L.S.} \frac{S_{wet}}{S_{ref}} \quad \text{(equation 4.1.5.1-a)}$$

$$= (0.00410)\,(1.06)\,(1.067)\,(2.0)$$

$$= 0.00927$$

$$\left(\Delta C_{l_p}\right)_{drag} = \frac{\left(C_{l_p}\right)_{C_{D_L}}}{C_L^{\,2}} C_L^{\,2} - \frac{1}{8} C_{D_0} \text{ (per radian)} \quad \text{(equation 7.1.2.2-c)}$$

$$= (0.015)\,(0.3)^2 - \frac{0.00927}{8}$$

$$= 0.001350 - 0.001159$$

$$= 0.000191 \text{ per rad}$$

$$\left(C_{l_p}\right)_H = \left(\frac{\beta C_{l_p}}{\kappa}\right)_{C_L=0} \left(\frac{\kappa}{\beta}\right) \frac{\left(C_{L_\alpha}\right)_{C_L}}{\left(C_{L_\alpha}\right)_{C_L=0}} \frac{\left(C_{l_p}\right)_\Gamma}{\left(C_{l_p}\right)_{\Gamma=0}} + \left(\Delta C_{l_p}\right)_{drag} \text{ (per radian)}$$

(equation 7.1.2.2-a)

$$\left(C_{l_p}\right)_H = (-0.245)\left(\frac{1.0}{0.068}\right)(1)(1) + 0.000191$$

$$= -0.253 + 0.000191$$

$$\simeq -0.253 \text{ per rad} \quad \text{(based on product of horizontal tail area and the square of tail span } S_H b_H{}^2\text{)}$$

Calculate the vertical distance z of the vertical-tail center-of-pressure location above or below the moment-reference-center location

$$z = z_p \cos\alpha - \ell_p \sin\alpha \qquad \text{(equation 7.4.2.1-b)}$$

$$= (0.308)(0.9976) - (1.25)(0.06976)$$

$$= 0.220 \text{ ft}$$

Calculate the tail-body sideslip derivative $\left(\Delta C_{Y_\beta}\right)_{V\,(WBH)}$ from Section 5.3.1.1

$$\frac{b_V}{2r_1} = \frac{9.0}{4.88} = 1.84$$

$$\frac{A_{V\,(B)}}{A_V} = 1.63 \qquad \text{(figure 5.3.1.1-22a)}$$

$$\frac{z_H}{b_V} = \frac{-8.30}{9.0} = -0.922$$

$$\frac{x}{c_V} = \frac{0.25}{0.42} = 0.595$$

$$\frac{A_{V\,(HB)}}{A_{V\,(B)}} = 1.39 \qquad \text{(figure 5.3.1.1-22b)}$$

$$\frac{S_H}{S_V} = \frac{0.48}{0.56} = 0.857$$

$$K_H = 0.85 \qquad \text{(figure 5.3.1.1-22c)}$$

$$A_{eff} = \frac{A_{V(B)}}{A_V} A_V \left\{1 + K_H \left[\frac{A_{V(HB)}}{A_{V(B)}} - 1\right]\right\} \quad \text{(equation 5.3.1.1-a)}$$

$$= (1.63)(0.86)\ \{1 + 0.85\ [1.39-1]\}$$

$$= (1.63)(0.86)(1.33)$$

$$= 1.86$$

$\kappa = 1$ (assumed)

$$\frac{A_{eff}}{\kappa}\left[\beta^2 + \tan^2 \Lambda_{c/2}\right]^{1/2} = 1.86\ [0.9375 + (0.4296)^2]^{1/2} = 1.86\ (1.06) = 1.97$$

$$\frac{C_{L_\alpha}}{A_{eff}} = 1.30 \quad \text{(figure 4 1.3.2-49)}$$

$$C_{L_\alpha} = (1.30)(1.86)$$

$$= 2.42 \text{ per rad (based on } S_V)$$

$$\left(1 + \frac{\partial\sigma}{\partial\beta}\right)\frac{q_V}{q_\infty} = 0.724 + 3.06\frac{S_V/S_W}{1 + \cos\Lambda_{c/4}} + 0.4\frac{z_W}{d} + 0.009A \quad \text{(equation 5.4.1-a)}$$

$$= 0.724 + 3.06\ \frac{0.56/1.90}{1.9511} + 0 + (0.009)(2.44)$$

$$= 0.724 + 0.462 + 0.022$$

$$= 1.208$$

$k = 0.75$ (figure 5.3.1.1-22d)

$$\left(\Delta C_{Y_\beta}\right)_{V(WBH)} = -k\left(C_{L_\alpha}\right)_V \left(1 + \frac{\partial\sigma}{\partial\beta}\right)\frac{q_V}{q_\infty}\frac{S_V}{S_W} \quad \text{(equation 5.3.1.1-b)}$$

$$= (0.75)(2.42)(1.208)\frac{0.56}{1.90}$$

$$= -0.646 \text{ per rad (based on } S_W)$$

$$C_{l_p} = \left(C_{l_p}\right)_{WB} + 0.5\left(C_{l_p}\right)_H \left(\frac{S_H}{S_W}\right)\left(\frac{b_H}{b_W}\right)^2 + \left|2\left(\frac{z}{b_W}\right)\left[\frac{z - z_p}{b_W}\right]\right|\left(\Delta C_{Y_\beta}\right)_{V(WBH)}$$

(equation 7.4.2.2-a)

$$= -0.30 + (0.5)(-0.253)\left(\frac{0.48}{1.90}\right)\left(\frac{1.20}{2.16}\right)^2 + \left|2\left(\frac{0.22}{2.16}\right)\left[\frac{0.22 - 0.308}{2.16}\right]\right|(-0.646)$$

$$= -0.30 - 0.00986 - 0.00536$$

$$= -0.315 \text{ per rad} \quad \text{(based on the product of wing area and the square of wing span } S_W b_W{}^2\text{)}$$

This compares with a test value of −0.33 per radian from reference 4.

B. TRANSONIC

No generalized reliable method is available in the literature for estimating transonic values of the roll-damping derivative C_{l_p}. However, a considerable quantity of test data is available and reference should be made to table 7-A.

C. SUPERSONIC

No generalized method is available in the literature for estimating supersonic values of the roll-damping derivative C_{l_p}.

The wing-body roll-damping derivative at supersonic speeds is estimated by the wing-body method of paragraph C of Section 7.3.2.2.

Methods are presented in reference 5 for evaluating the vertical-tail contribution to C_{l_p}. The stability derivatives presented therein are derived by using supersonic linearized theory for families of thin isolated vertical tails performing steady rolling motions. Vertical-tail families (half-delta and rectangular planforms) are considered over a broad Mach number range. Also considered are vertical tails with arbitrary sweepback and taper ratio at Mach numbers for which both the leading edge and trailing edge of the tail are supersonic, and triangular vertical tails with a subsonic leading edge and a supersonic trailing edge.

REFERENCES

1. Campbell, J. P., and McKinney, M. O.: Summary of Methods for Calculating Dynamic Lateral Stability and Response and for Estimating Lateral Stability Derivatives. NACA TR 1098, 1952. (U)

2. Michael, W. H. Jr.: Analysis of the Effects of Wing Interference on the Tail Contributions to the Rolling Derivatives. NACA TR 1086, 1952. (U)

3. Booth, K. W.: Effect of Horizontal-Tail Chord on the Calculated Subsonic Span Loads and Stability Derivatives of Isolated Unswept Tail Assemblies in Sideslip and Steady Roll. NASA Memo 4-1-59L, 1959. (U)

4. Buell, D. A., Reed, V. D., and Lopez, A. E.: The Static and Dynamic-Rotary Stability Derivatives at Subsonic Speeds of an Airplane Model with an Unswept Wing and a High Horizontal Tail. NACA RM A56I04, 1956. (U)

5. Margulis, K., and Bobbitt, P. J.: Theoretical Calculations of the Pressures, Forces, and Moments at Supersonic Speeds due to Various Lateral Motions Acting on Thin Isolated Vertical Tails. NACA TR 1268, 1956. (U)

7.4.2.3 WING-BODY-TAIL ROLLING DERIVATIVE C_{n_p}

This section presents methods for estimating the nondimensional rolling derivative C_{n_p} of wing-body-tail combinations at subsonic speeds. However, at transonic and supersonic speeds no generalized methods are available for estimating the wing-body-tail rolling derivative C_{n_p}. This derivative is the change in yawing-moment coefficient with change in wing-tip helix angle and is expressed as

$$C_{n_p} = \frac{\partial C_n}{\partial \left(\frac{pb}{2V_\infty}\right)}$$

In general, the Datcom methods consist of a synthesis of material presented in Sections 7.1.2.3 and 7.3.2.3, and the vertical-tail contribution based on the methods of reference 1.

Contributions to this derivative arise from two sources, the wing and the vertical tail. The wing contribution is usually negative; whereas the tail contribution may be positive or negative depending on vertical-tail geometry, sidewash, and equlibrium angle of attack.

The rolling wing produces a sidewash at the vertical tail, which can significantly alter the vertical-tail contribution. This effect is discussed more fully in reference 2. Studies have indicated that the effect of the sidewash varies considerably with tail size, tail location, and to some extent with wing planform.

The derivative C_{n_p} is important in lateral dynamics because of its influence on Dutch-roll damping. Although for most configurations C_{n_p} is negative, positive values of C_{n_p} are desired to increase the Dutch-roll damping characteristics.

A. SUBSONIC

Two methods are presented for determining the rolling derivative C_{n_p} of the wing-body-tail combination, differing only in their treatment of wing sidewash on the vertical tail. The first method is applicable to conventionally located vertical tails, and the second method applies to tails located directly above, or above and slightly behind the wing.

Both methods are based on the assumption that the vertical-tail contribution to C_{n_p} is zero at $\alpha = 0$ and varies with angle of attack.

For an isolated-tail configuration the vertical-tail value of C_{n_p} is approximated by

$$\left(C_{n_p}\right)_V = 2\left(\frac{z}{b_w}\right)\left(\Delta C_{n_\beta}\right)_p$$

For a conventionally located vertical tail the effect of wing sidewash on the vertical tail has been approximately accounted for by $\left(C_{n_p}\right)_V = 2\left[\frac{z-z_p}{b_W}\right]\left(\Delta C_{n_\beta}\right)_p$. For configurations with tails located directly above or slightly behind the wing, the effect of wing sidewash has been approximated by using the average of the isolated-tail and conventional-tail values.

DATCOM METHODS

Method 1

For conventionally located vertical tails, the equation for the nondimensional rolling derivative C_{n_p} of a wing-body-tail configuration, based on the product of wing area and the square of wing span $S_W b_W{}^2$, is given by

$$C_{n_p} = \left(C_{n_p}\right)_{WB} - \frac{2}{b_W}\left(\ell_p \cos\alpha + z_p \sin\alpha\right)\left[\frac{z - z_p}{b_W}\right]\left(\Delta C_{Y_\beta}\right)_{V\,(WBH)} \text{ (per radian)}$$

7.4.2.3-a

However, if test data for $\left(\Delta C_{n_\beta}\right)_p$ of the empennage are available, the above equation can be rewritten to include the effective tail length, i.e.,

$$C_{n_p} = \left(C_{n_p}\right)_{WB} + 2\left[\frac{z - z_p}{b_W}\right]\left(\Delta C_{n_\beta}\right)_p \text{ (per radian)} \qquad 7.4.2.3\text{-b}$$

where

$\left(C_{n_p}\right)_{WB}$ is the wing-body contribution to C_{n_p}, obtained from test data or Section 7.3.2.3 and based on the product of wing area and the square of wing span (per radian).

ℓ_p is the distance from the moment reference center to the center-of-pressure location of the vertical stabilizer, measured parallel to the body center line (see sketch (a) in Section 7.4.2.1). For Datcom purposes, the vertical-tail center-of-pressure location is assumed to be the quarter-chord point of the MAC of the total added panel.

b_W is the wing span.

z is the vertical distance of the vertical-tail center-of-pressure location above or below the moment-reference-center location. This value must be calculated for each angle of attack. (See sketch (a) in Section 7.4.2.1.) From equation 7.4.2.1-b, z can be expressed as

$$z = z_p \cos\alpha - \ell_p \sin\alpha$$

z_p is the distance from the moment reference center to the center of pressure of the vertical stabilizer, measured normal to the body center line, positive for the stabilizer above the body. For Datcom purposes, the vertical-tail center-of-pressure location is assumed to be the quarter-chord point of the MAC of the total added panel.

$\left(\Delta C_{Y_\beta}\right)_{V(WBH)}$ is the tail-body sideslip derivative from test data or Section 5.3.1.1. It includes the end-plate effects of the horizontal tail and is based on the wing area (per radian).

$\left(\Delta C_{n_\beta}\right)_p$ is the tail-body sideslip derivative from force-test data, where p refers to panels present in the empennage. It is based on the product of wing area and span (per radian).

Method 2

For vertical tails located either directly above, or above and slightly behind the wing, the equation for the nondimensional rolling derivative C_{n_p} of a wing-body-tail configuration, based on the product of wing area and the square of wing span $S_W b_W{}^2$, is given by

$$C_{n_p} = \left(C_{n_p}\right)_{WB} - \left[\frac{\ell_p \cos\alpha + z_p \sin\alpha}{b_W}\right] \left[\frac{2z - z_p}{b_W}\right] \left(\Delta C_{Y_\beta}\right)_{V(WBH)} \text{ (per radian)} \qquad 7.4.2.3\text{-c}$$

However, if test data for $\left(\Delta C_{n_\beta}\right)_p$ of the empennage are available, the equation can be rewritten to include the effective tail length, i.e.,

$$C_{n_p} = \left(C_{n_p}\right)_{WB} + \left[\frac{2z - z_p}{b_W}\right] \left(\Delta C_{n_\beta}\right)_p \text{ (per radian)} \qquad 7.4.2.3\text{-d}$$

where the components are described in method 1 above.

Sample Problem

Method 1

Given: Model of reference 3

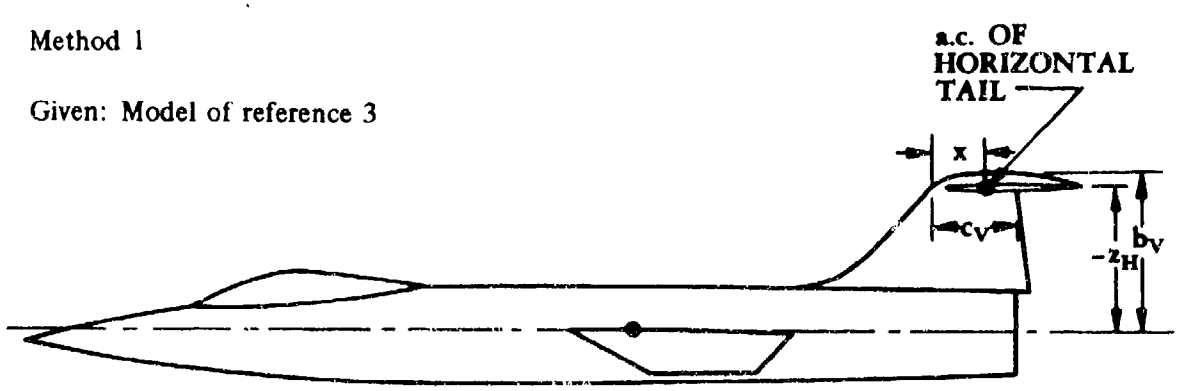

Wing Parameters:

S_W = 1.90 sq ft $\quad b_W$ = 2.16 ft $\quad A_W$ = 2.44

γ = 0.38 $\quad \Lambda_{c/4}$ = 18.0°

Horizontal-Tail Parameters:

S_H = 0.48 sq ft $\quad b_H$ = 1.20 ft $\quad A_H$ = 2.97

γ = 0.31 $\quad -z_H$ = 8.30 in.

Vertical-Tail Parameters:

S_V = 0.56 sq ft $\quad b_V$ = 9.0 in. $\quad A_V$ = 0.86

λ_V = 0.37 $\quad c_V$ = 0.42 ft $\quad \Lambda_{c/2}$ = 23.25°

z_p = 0.308 ft $\quad \ell_p$ = 1.25 ft $\quad x$ = 0.25 ft

Additional Parameters:

α = 6.0° $\quad$ M = 0.25 $\quad \left(C_{n_p}\right)_{WB}$ = 0.02 per rad (test data)

$2r_1$ = 4.88 in.

Compute:

Calculate the tail-body sideslip derivative $\left(\Delta C_{Y_\beta}\right)_{V\,(WBH)}$ from Section 5.3.1.1

$$\frac{b_V}{2r_1} = \frac{9.0}{4.88} = 1.84$$

$$\frac{A_{V\,(B)}}{A_V} = 1.63 \quad \text{(figure 5.3.1.1-22a)}$$

$$\frac{z_H}{b_V} = \frac{8.30}{9.0} = -0.922$$

$$\frac{x}{c_V} = \frac{0.25}{0.42} = 0.595$$

$$\frac{A_{V(HB)}}{A_{V(B)}} = 1.39 \quad \text{(figure 5.3.1.1-22b)}$$

$$\frac{S_H}{S_V} = \frac{0.48}{0.56} = 0.857$$

$$K_H = 0.85 \quad \text{(figure 5.3.1.1-22c)}$$

$$A_{eff} = \frac{A_{V(B)}}{A_V} A_V \left\{1 + K_H \left[\frac{A_{V(HB)}}{A_{V(B)}} - 1\right]\right\} \quad \text{(equation 5.3.1.1-a)}$$

$$= (1.63)(0.85)\{1 + 0.85 \quad [1.39 - 1]\}$$

$$= (1.63)(0.86)(1.33)$$

$$= 1.86$$

$$\kappa = 1 \text{ (assumed)}$$

$$\frac{A_{eff}}{\kappa}\left[\beta^2 + \tan^2 \Lambda_{c/2}\right]^{1/2} = 1.86\,[0.9375 + (0.4296)^2]^{1/2} = 1.86\,(1.06) = 1.97$$

$$\frac{C_{L_\alpha}}{A_{eff}} = 1.30 \quad \text{(figure 4.1.3.2-49)}$$

$$C_{L_\alpha} = (1.30)(1.86)$$

$$= 2.42 \text{ per rad (based on } S_V)$$

$$\left(1 + \frac{\partial\sigma}{\partial\beta}\right)\frac{q_V}{q_\infty} = 0.724 + 3.06\frac{S_V/S_W}{1 + \cos\Lambda_{c/4}} 0.4\frac{z_W}{d} + 0.009A \quad \text{(equation 5.4.1-a)}$$

$$= 0.724 + 3.06\left(\frac{0.56/1.90}{1.9511}\right) + 0 + (0.009)(2.44)$$

$$= 0.724 + 0.462 + 0.022$$

$$= 1.208$$

$$k = 0.75 \quad \text{(figure 5.3.1.1-22d)}$$

$$\left(\Delta C_{Y_\beta}\right)_{V\,(WBH)} = -k\left(C_{L_\alpha}\right)_V \left(1 + \frac{\partial\sigma}{\partial\beta}\right) \frac{q_V}{q_\infty} \frac{S_V}{S_W} \quad \text{(equation 5.3.1.1-b)}$$

$$= -(0.75)\,(2.42)\,(1.208)\left(\frac{0.56}{1.90}\right)$$

$$= -0.646 \text{ per rad (based on } S_W)$$

Calculate the vertical distance z of the vertical-tail center-of-pressure location above or below the moment-reference-center location

$$z = z_p \cos\alpha - \ell_p \sin\alpha \quad \text{(equation 7.4.2.1-b)}$$

$$= (0.308)\,(0.9945) - (1.25)\,(0.1045)$$

$$= 0.176 \text{ ft}$$

$$C_{n_p} = \left(C_{n_p}\right)_{WB} - \frac{2}{b_W}\left(\ell_p \cos\alpha + z_p \sin\alpha\right)\left[\frac{z - z_p}{b_W}\right]\left(\Delta C_{Y_\beta}\right)_{V\,(WBH)}$$

(equation 7.4.2.3-a)

$$= (0.02) - \frac{2}{2.16}\left[(1.25)\,(0.9945) + (0.308)\,(0.1045)\right]\left[\frac{0.176 - 0.308}{2.16}\right](-0.646)$$

$$= 0.02 - \frac{2}{2.16}\,(1.275)\left(\frac{-0.132}{2.16}\right)(-0.646)$$

$$= 0.02 - 0.0466$$

$$= -0.0266 \text{ per rad (based on } S_W b_W{}^2)$$

This compares with a test value of −0.048 per radian from reference 3.

B. TRANSONIC

No generalized method is available in the literature for estimating transonic values of the rolling derivative C_{n_p}.

C. SUPERSONIC

No generalized method is available in the literature for estimating supersonic values of the rolling derivative C_{n_p}.

For the purpose of the Datcom the fuselage effect is considered to be negligible for wing-body configurations with body diameters less than about 30 percent of the wing span. Therefore, for configurations with $d/b \leq 0.3$, the wing-body rolling derivative C_{n_p} is estimated by the wing-alone method of paragraph C of Section 7.1.2.3.

Methods are presented in reference 4 for evaluating the vertical-tail contribution to C_{n_p}. The stability derivatives presented therein are derived by using supersonic linearized theory for families of thin isolated vertical tails performing steady rolling motions. Vertical-tail families (half-delta and rectangular planforms) are considered over a broad Mach number range. Also considered are vertical tails with arbitrary sweepback and taper ratio at Mach numbers for which both the leading edge and trailing edge of the tail are supersonic, and triangular vertical tails with a subsonic leading edge and a supersonic trailing edge.

REFERENCES

1. Campbell, J. P., and McKinney, M. O.: Summary of Methods for Calculating Dynamic Lateral Stability and Response and for Estimating Lateral Stability Derivatives. NACA TR 1098, 1952. (U)

2. Michael, W. H. Jr.: Analysis of the Effects of Wing Interference on the Tail Contributions to the Rolling Derivatives. NACA TR 1086, 1952. (U)

3. Buell, D. A., Reed, V. D., and Lopez, A. E.: The Static and Dynamic-Rotary Stability Derivatives at Subsonic Speeds of an Airplane Model with an Unswept Wing and a High Horizontal Tail. NACA RM A56I04, 1956. (U)

4. Margolis, K., and Bobbitt, P. J.: Theoretical Calculations of the Pressures, Forces, and Moments at Supersonic Speeds due to Various Lateral Motions Acting on Thin Isolated Vertical Tails. NACA TR 1268, 1956. (U)

7.4.3 WING-BODY-TAIL YAWING DERIVATIVES

7.4.3.1 WING-BODY-TAIL YAWING DERIVATIVE C_{Y_r}

This section presents a method for estimating the nondimensional yawing derivative C_{Y_r} of wing-body-tail combinations at subsonic speeds. However, at transonic and supersonic speeds no generalized methods are available for estimating the wing-body-tail yawing derivative C_{Y_r}. This derivative is the change in side-force coefficient with variation in yawing velocity and is expressed as

$$C_{Y_r} = \frac{\partial C_Y}{\partial\left(\frac{rb}{2V_\infty}\right)}$$

In general, the Datcom method consists of a synthesis of material presented in Sections 7.1.3.1 and 7.3.3.1, and the vertical-tail contribution based on the methods of reference 1.

Contributions to the derivative C_{Y_r} arise from two sources, the wing and the vertical tail. The vertical-tail contribution, which constitutes the major portion, is small and positive in sign. Generally C_{Y_r} is of little importance in lateral dynamics, hence it is frequently neglected.

A. SUBSONIC

For the oscillatory mode, the effects due to lag of sidewash in free oscillation are important and hence should be considered. However, no generalized method is available in the literature to account for oscillating sidewash effects on C_{Y_r}; therefore, only the aperiodic mode of C_{Y_r} is presented here.

In the equation for estimating the yawing derivative C_{Y_r}, the sideslip-derivative contribution of the vertical tail should include the end-plate effects of the horizontal tail.

DATCOM METHOD

The equation for the nondimensional yawing derivative C_{Y_r} of a wing-body-tail configuration, based on the product of wing area and wing span $S_W b_W$, is given by

$$C_{Y_r} = \left(C_{Y_r}\right)_{WB} - \frac{2}{b_W}\left(\ell_p \cos\alpha + z_\Gamma \sin\alpha\right)\left(\Delta C_{Y_\beta}\right)_{V(WBH)} \quad \text{(per radian)} \qquad 7.4.3.1\text{-a}$$

However, if test data for $\left(\Delta C_{n_\beta}\right)_p$ of the empennage are available, the above equation can be rewritten to include the effective tail length, i.e.,

$$C_{Y_r} = \left(C_{Y_r}\right)_{WB} + 2\left(\Delta C_{n_\beta}\right)_p \quad \text{(per radian)} \qquad 7.4.3.1\text{-b}$$

where

$(C_{Y_r})_{WB}$ is the wing-body contribution to C_{Y_r} obtained from test data or by using the recommendations of Section 7.1.3.1, based on the product of wing area and wing span (per radian).

b_W is the wing span.

ℓ_p is the distance from the moment reference center to the center-of-pressure location of the vertical stabilizer, measured parallel to the body center line. (See sketch (a) in Section 7.4.2.1.) For Datcom purposes, the vertical-tail center-of-pressure location is assumed to be the quarter-chord point of the MAC of the total added panel.

z_p is the distance from the moment reference center to the center of pressure of the vertical stabilizer, measured normal to the body center line, positive for the stabilizer above the body. For Datcom purposes, the vertical-tail center-of-pressure location is assumed to be the quarter-chord point of the MAC of the total added panel.

$(\Delta C_{Y_\beta})_{V\,(WBH)}$ is the tail-body sideslip derivative obtained from test data or Section 5.3.1.1. It includes the end-plate effects of the horizontal tail and is based on the wing area (per radian).

$(\Delta C_{n_\beta})_p$ is the tail-body sideslip derivative from test data where p refers to panels in the empennage. It is based on the product of wing area and span (per radian).

Sample Problem

Given: Model of reference 2

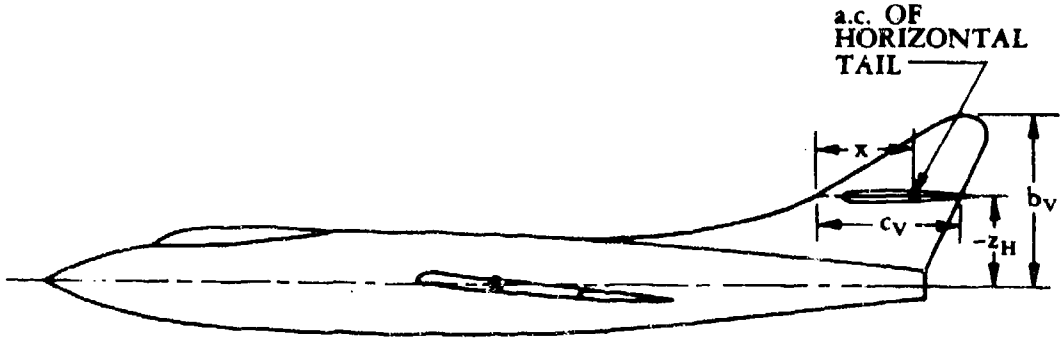

$\alpha = 8.0°$ $\quad (C_{Y_r})_{WB} = -0.10$ per rad (test data) $\quad (\Delta C_{n_\beta})_p = 0.42$ per rad (test data)

Compute:

Calculate the yawing derivative C_{Y_r} for the wing-body-tail configuration

$$C_{Y_r} = \left(C_{Y_r}\right)_{WB} + 2\left(\Delta C_{n_\beta}\right)_p \qquad \text{(equation 7.4.3.1-b)}$$

$$= -0.10 + 2\,(0.42)$$

$$= 0.74 \text{ per rad (based on } S_W b_W)$$

This compares with a test value of 0.50 per radian from reference 2.

B. TRANSONIC

No generalized method is available in the literature for estimating transonic values of the yawing derivative C_{Y_r}. Furthermore, there is a scarcity of experimental data for this derivative at transonic speeds.

C. SUPERSONIC

No generalized method is available in the literature for estimating supersonic values of the yawing derivative C_{Y_r}. Furthermore, there is a scarcity of experimental data for this derivative at supersonic speeds.

REFERENCES

1. Campbell, J. P., and McKinney, M. O.: Summary of Methods for Calculating Dynamic Lateral Stability and Response and for Estimating Lateral Stability Derivatives. NACA TR 1098, 1952. (U)

2. Queijo, M. J., and Wells, E. G.: Wind-Tunnel Investigation of the Low-Speed Static and Rotary Stability Derivatives of a 0.13-Scale Model of the Douglas D-558-II Airplane in the Landing Configuration. NACA RM L52G07, 1952. (U)

7.4.3.2 WING-BODY-TAIL YAWING DERIVATIVE C_{l_r}

This section presents a method for estimating the nondimensional yawing derivative C_{l_r} of wing-body-tail combinations at subsonic speeds. However, at transonic and supersonic speeds no generalized methods are available for estimating the yawing derivative C_{l_r}. This derivative is the change in rolling-moment coefficient with change in the yawing velocity and is expressed as

$$C_{l_r} = \frac{\partial C_l}{\partial\left(\frac{rb}{2V_\infty}\right)}$$

In general, the Datcom method consists of a synthesis of material presented in Sections 7.1.3.2 and 7.3.3.2, and the vertical-tail contribution based on the methods of reference 1.

Contributions to this derivative arise from two sources, the wing and the vertical tail. The wing contribution constitutes the major portion and is positive in sign. The lesser contribution of the vertical tail can be positive or negative, depending upon tail equilibrium angle of attack. This derivative is not of primary importance; however, it is not neglected in lateral dynamic calculations.

A. SUBSONIC

The method presented here is based on the assumption that the wing and fuselage interference effects on tail effectiveness can be determined from geometric dimensions and the sideslip derivatives. This is particularly true if experimental test data are available for $\left(\Delta C_{Y_\beta}\right)_{V(WBH)}$ or $\left(\Delta C_{l_\beta}\right)_p$ in the equations given below.

DATCOM METHOD

The equation for the nondimensional yawing derivative C_{l_r} of a wing-body-tail configuration, based on the product of the wing area and the square of wing span $S_W b_W{}^2$, is given by

$$C_{l_r} = \left(C_{l_r}\right)_{WB} - \frac{2}{b_W{}^2}\left(\ell_p \cos\alpha + z_p \sin\alpha\right)\left(z_p \cos\alpha - \ell_p \sin\alpha\right)\left(\Delta C_{Y_\beta}\right)_{V(WBH)} \quad 7.4.3.2\text{-a}$$

However, if test data for $\left(\Delta C_{l_\beta}\right)_p$ are available, the above equation can be rewritten to approximate the effective vertical-tail center-of-pressure location (the height of the body center line).

$$C_{l_r} = \left(C_{l_r}\right)_{WB} - \frac{2}{b_W}\left(\ell_p \cos\alpha + z_p \sin\alpha\right)\left(\Delta C_{l_\beta}\right)_p \quad 7.4.3.2\text{-b}$$

If test data for $\left(\Delta C_{n_\beta}\right)_p$ and $\left(\Delta C_{Y_\beta}\right)_{V(WBH)}$ are available, the above equation can be rewritten to include the total effective vertical-tail center-of-pressure location.

$$C_{l_r} = \left(C_{l_r}\right)_{WB} + 2\,\frac{\left(\Delta C_{n_\beta}\right)_p}{\left(\Delta C_{Y_\beta}\right)_{V(WBH)}}\left(\Delta C_{l_\beta}\right)_p \text{ (per radian)} \qquad 7.4.3.2\text{-c}$$

where

$\left(C_{l_r}\right)_{WB}$ is the wing-body contribution to C_{l_r} obtained from test data or Section 7.3.3.2, based on the product of wing area and the square of wing span (per radian).

b_W is the wing span.

ℓ_p is the distance from the moment reference center to the center-of-pressure location of the vertical stabilizer, measured parallel to the body center line. (See sketch (a) in Section 7.4.2.1.) For Datcom purposes, the vertical-tail center-of-pressure location is assumed to be the quarter-chord point of the MAC of the total added panel.

z_p is the distance from the moment reference center to the center of pressure of the vertical stabilizer, measured normal to the body center line, positive for the stabilizer above the body. For Datcom purposes, the vertical-tail center-of-pressure location is assumed to be the quarter-chord point of the MAC of the total added panel.

$\left(\Delta C_{Y_\beta}\right)_{V(WBH)}$ is the tail-body sideslip derivative obtained from test data or Section 5.3.1.1. It includes the end-plate effects of the horizontal tail and is based on the wing area (per radian).

$\left(\Delta C_{l_\beta}\right)_p$ is the tail-body sideslip derivative from test data, where p refers to the panels in the empennage. It is based on the product of wing area and span (per radian).

$\left(\Delta C_{n_\beta}\right)_p$ is the tail-body sideslip derivative from test data, where p refers to the panels in the empennage. It is based on the product of wing area and span (per radian).

Sample Problem

Given: Model of reference 2

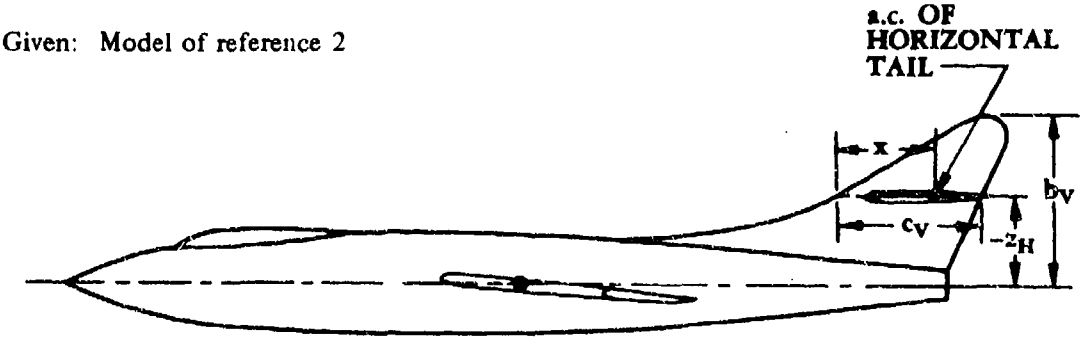

$\alpha = 6.0°$ $\quad b_W = 38.84$ in. $\quad \ell_p = 24.3$ in. $\quad z_p = 5.0$ in.

$\left(C_{l_r}\right)_{WB} = 0.10$ per rad (test data) $\quad \left(C_{Y_\beta}\right)_{V(WBH)} = -0.64$ per rad (test data)

Compute:

Calculate the yawing derivative C_{l_r} for the wing-body-tail configuration

$$C_{l_r} = \left(C_{l_r}\right)_{WB} - \frac{2}{b_W{}^2}\left(\ell_p \cos\alpha + z_p \sin\alpha\right)\left(z_p \cos\alpha - \ell_p \sin\alpha\right)\left(\Delta C_{Y_\beta}\right)_{V(WBH)}$$

(equation 7.4.3.2-a)

$$= 0.10 - \frac{2}{(38.84)^2}\left[(24.3)(0.0045) + (5.0)(0.1045)\right]$$

$$\left[(5.0)(0.0045) - (24.3)(0.1045)\right](-0.64)$$

$$= 0.10 + 0.051$$

$$= 0.151 \text{ per rad (based on } S_W b_W{}^2)$$

This compares with a test value of 0.15 per radian from reference 2.

B. TRANSONIC

No generalized method is available in the literature for estimating transonic values of the yawing derivative C_{l_r}. Furthermore, there is a scarcity of experimental data for this derivative at transonic speeds.

C. SUPERSONIC

No generalized method is available in the literature for estimating supersonic values of the yawing derivative C_{l_r}. Furthermore, there is a scarcity of experimental data for this derivative at supersonic speeds.

REFERENCES

1. Campbell, J. P., and Goodman, A.: A Semiempirical Method for Estimating the Rolling Moment Due to Yawing of Airplanes. NACA TN 1984, 1949. (U)

2. Queijo, M. J., and Wells, E. G.: Wind-Tunnel Investigation of the Low-Speed Static and Rotary Stability Derivatives of a 0.13-Scale Model of the Douglas D-558-II Airplane in the Landing Configuration. NACA RM L52G07, 1952. (U)

7.4.3.3 WING-BODY-TAIL YAWING DERIVATIVE C_{n_r}

This section presents a method for estimating the nondimensional yawing derivative C_{n_r} of wing-body-tail combinations at subsonic speeds. However, at transonic and supersonic speeds no generalized methods are available for estimating the wing-body-tail yawing derivative C_{n_r}. This derivative is the change in yawing-moment coefficient with change in the yawing-velocity parameter. It is commonly referred to as the yaw damping and is expressed as

$$C_{n_r} = \frac{\partial C_n}{\partial\left(\frac{rb}{2V_\infty}\right)}$$

In general, the Datcom method consists of a synthesis of material presented in Sections 7.1.3.3 and 7.3.3.3, and the vertical-tail contribution based on the methods of reference 1.

Contributions to this derivative arise from the wing, the fuselage, and the vertical tail. The vertical-tail contribution usually constitutes the major portion and is negative in sign (positive damping).

The derivative C_{n_r} is very important in lateral dynamics because of the important contribution it makes to the damping of the Dutch-roll oscillatory mode. Its contribution to the spiral-mode damping is also important. It is desirable to have a large negative value of C_{n_r} for each mode.

A. SUBSONIC

For the oscillatory mode, the effects due to lag of sidewash in free oscillation are important and hence should be considered. However, no generalized method is available in the literature to account for oscillating sidewash effects on C_{n_r}; therefore, only the aperiodic mode of C_{n_r} is presented here.

In the equation for determining the yawing derivative C_{n_r}, the sideslip-derivative contribution of the vertical tail should include the end-plate effects of the horizontal tail.

DATCOM METHOD

The equation for the nondimensional yawing derivative C_{n_r} of a wing-body-tail configuration, based on the product of wing area and the square of wing span $S_W b_W{}^2$, is given by

$$C_{n_r} = \left(C_{n_r}\right)_{WB} + \frac{2}{b_W{}^2}\left(\ell_p \cos\alpha + z_p \sin\alpha\right)^2 \left(\Delta C_{Y_\beta}\right)_{V(WBH)} \quad \text{(per radian)} \qquad 7.4.3.3\text{-a}$$

However, if test data for ΔC_{n_β} are available, the above equation can be expressed as

$$C_{n_r} = \left(C_{n_r}\right)_{WB} + 2\frac{\left(\Delta C_{n_\beta}\right)_p{}^2}{\left(\Delta C_{Y_\beta}\right)_{V(WBH)}} \quad \text{(per radian)} \qquad 7.4.3.3\text{-b}$$

where

$\left(C_{n_r}\right)_{WB}$ is the wing-body contribution to C_{n_r} obtained from test data or Section 7.3.3.3, based on the product of wing area and the square of wing span (per radian).

b_W is the wing span.

ℓ_p is the distance from the moment reference center to the center-of-pressure location of the vertical stabilizer, measured parallel to the body center line. (See sketch (a) in Section 7.4.2.1.) For Datcom purposes, the vertical-tail center-of-pressure location is assumed to be the quarter-chord point of the MAC of the total added panel.

z_p is the distance from the moment reference center to the center of pressure of the vertical stabilizer, measured normal to the body center line, positive for the stabilizer above the body. For Datcom purposes, the vertical-tail center-of-pressure location is assumed to be the quarter-chord point of the MAC of the total added panel.

$\left(\Delta C_{Y_\beta}\right)_{V(WBH)}$ is the tail-body sideslip derivative from test data or Section 5.3.1.1 and is based on the wing area (per radian).

$\left(\Delta C_{n_\beta}\right)_p$ is the tail-body sideslip derivative from test data, where p refers to the panels in the empennage. It is based on the product of wing area and span (per radian).

Sample Problem

Given: Model of reference 2

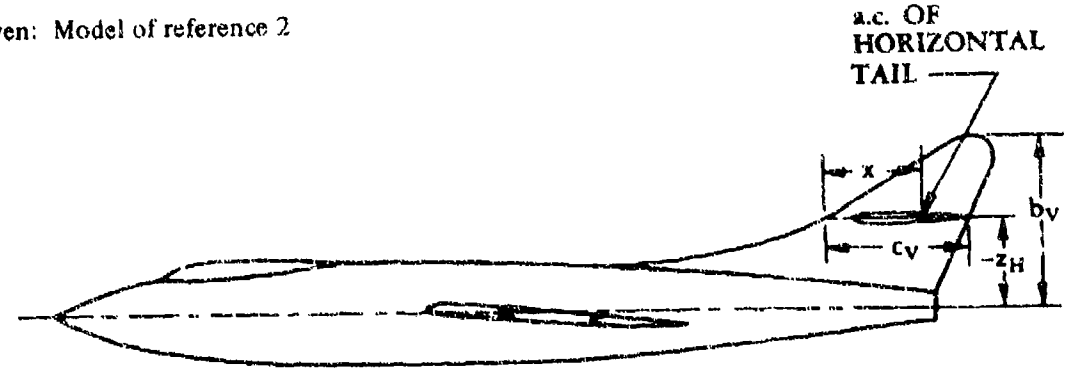

$\alpha = 6^\circ$ $\left(C_{n_r}\right)_{WB} = -0.15$ per r[illegible] (test dat

$\left(\Delta C_{n_\beta}\right)_p = 0.43$ per rad (test data) $\left(\Delta C_{Y_\beta}\right)_{V(WBH)} = -0.64$ per (test data)

Compute:

Calculate the yawing derivative C_{n_r} for the wing-body-tail configuration

$$C_{n_r} = \left(C_{n_r}\right)_{WB} + 2 \frac{\left(\Delta C_{n_\beta}\right)_p^2}{\left(\Delta Y_\beta\right)_{V(WBH)}} \quad \text{(equation 7.4.3.3-b)}$$

$$= -0.15 + (2) \frac{(0.43)^2}{(-0.64)}$$

$$= -0.15 - 0.578$$

$$= -0.728 \text{ per rad (based on } S_W b_W^2)$$

This compares with a test value of −0.60 per radian from reference 2.

B. TRANSONIC

No generalized method is available in the literature for estimating transonic values of the yawing derivative C_{n_r}. Furthermore, there is a scarcity of experimental data for this derivative at transonic speeds.

C. SUPERSONIC

No generalized method is available in the literature for estimating supersonic values of the yawing derivative C_{n_r}. Furthermore, there is a scarcity of experimental data for this derivative at supersonic speeds.

REFERENCES

1. Campbell, J. P., and McKinney, M. O.: Summary of Methods for Calculating Dynamic Lateral Stability and Response and for Estimating Lateral Stability Derivatives. NACA TR 1098, 1952. (U)

2. Queijo, M. J., and Wells, E. G.: Wind-Tunnel Investigation of the Low-Speed Static and Rotary Stability Derivatives of a 0.13-Scale Model of the Douglas D-558-II Airplane in the Landing Configuration. NACA RM L52G07, 1952. (U)

7.4.4 WING-BODY-TAIL ACCELERATION DERIVATIVES

7.4.4.1 WING-BODY-TAIL ACCELERATION DERIVATIVE $C_{L_{\dot{\alpha}}}$

The information contained in this section is for estimating the nondimensional acceleration derivative $C_{L_{\dot{\alpha}}}$ of wing-body-tail combinations at low angles of attack. This derivative is the change in lift coefficient with rate of change of angle of attack and is expressed as

$$C_{L_{\dot{\alpha}}} = \frac{\partial C_L}{\partial\left(\frac{\dot{\alpha}\bar{c}}{2V_\infty}\right)}$$

In general, the methods presented consist of a synthesis of material presented in other sections, although some new information is presented.

This derivative is presented in a manner similar to that used in reference 1 to calculate the lift of a wing-body-tail combination. The complete derivative is the sum of contributions of individual components, treated as isolated surfaces or bodies, and mutual interference effects. The mutual interference effects are assumed to correspond to those due to angle-of-attack variations, established in references 1 and 2 and presented in Section 4.3.1.2.

The horizontal-tail contribution to the derivative $C_{L_{\dot{\alpha}}}$ is based on the concept of the lag of the downwash. The nonstationary character of the lift response of the tail to changes in tail angle of attack is neglected, and the result is attributed entirely to the fact that the downwash at the tail does not respond instantaneously to changes in wing angle of attack. This concept is also the basis used in estimating the horizontal-tail contribution to the derivative $C_{m_{\dot{\alpha}}}$ in Section 7.4.4.2. The result of this concept is presented in numerous aerodynamic texts, for example, reference 3. The effect of $C_{L_{\dot{\alpha}}}$ on longitudinal stability is usually unimportant and is therefore frequently neglected in dynamic analyses.

A. SUBSONIC

Two methods are presented for determining the acceleration derivative $C_{L_{\dot{\alpha}}}$ of wing-body-tail combinations, differing only in their treatment of the effect of the flow field of the forward surface on the aft surface

DATCOM METHODS

Method 1. ($b'/b'' \geq 1.5$)

For configurations in which the span of the forward surface is large compared to that of the aft surface, the following approach can be used. This method is to be used when the ratio of the forward-panel span to the aft-panel span is 1.5 or greater. The equation of the nondimensional acceleration derivative $C_{L_{\dot{\alpha}}}$ of a wing-body-tail configuration, based on the area and mean

aerodynamic chord of the total forward panel and referred to a moment center at the assumed center of gravity or center of rotation, is given by

$$C_{L_{\dot{\alpha}}} = \left(C_{L_{\dot{\alpha}}}\right)_{WB} + 2\left[K_{W(B)} + K_{B(W)}\right]'' \left(\frac{S_e''}{S'}\right)\left(\frac{x_{c.g.} - x''}{\bar{c}'}\right)\left(\frac{q''}{q_\infty}\right)\left(\frac{\partial \bar{\epsilon}}{\partial \alpha}\right)\left(C_{L_\alpha}\right)_e''$$

7.4.4.1-a

where the primed quantities refer to the forward panel, the double-primed quantities refer to the aft panel, and the subscript e refers to the exposed panel. (See Section 4.3.1.2 for the definition of exposed surfaces.)

$\left(C_{L_{\dot{\alpha}}}\right)_{WB}$ is the contribution of the wing-body configuration to the acceleration derivative $C_{L_{\dot{\alpha}}}$, obtained from Section 7.3.4.1.

$\frac{\partial \bar{\epsilon}}{\partial \alpha}$ is the downwash gradient averaged over the aft surface, obtained from Section 4.4.1.

The remaining terms are defined in paragraph A of Section 7.4.1.1.

Method 2. $(b'/b'' < 1.5)$

For configurations in which the span of the forward surface is approximately equal to or less than that of the aft surface, the vortex shed from the forward surface interacts directly with the aft surface and the resulting interference effects must be accounted for in the tail terms. This method is to be used when the ratio of the forward-panel span to the aft-panel span is less than 1.5. The equation for the nondimensional acceleration derivative $C_{L_{\dot{\alpha}}}$ of a wing-body-tail configuration, based on the area and mean aerodynamic chord of the total forward panel and referred to a moment center at the assumed center of gravity or center of rotation, is given by

$$C_{L_{\dot{\alpha}}} = \left(C_{L_{\dot{\alpha}}}\right)_{WB} - 2\left(\frac{x_{c.g.} - x''}{\bar{c}'}\right)\left(C_{L_\alpha}\right)_{W''(v)}$$

7.4.4.1-b

All the terms are defined in paragraph A of Section 7.4.1.1 and method 1 above.

Because of the similarity of the two methods a sample problem for method 2 is not included. However, evaluation of the term $\left(C_{L_\alpha}\right)_{W''(v)}$ for a wing-body-tail configuration is presented in Section 4.5.1.1.

Sample Problem

Method 1

Given: Same configuration as sample problems of paragraph A, Sections 7.4.1.1 and 7.4.1.2. Some of the characteristics are repeated below. Note that for the sake of simplicity the vehicle center of gravity has been taken at $\bar{c}'/4$ and $x_{c.g.} - x'' = \ell''$.

The following ratios based on total forward panel dimensions:

$$\frac{b''}{b'} = 0.4377 \qquad \frac{2\ell_2}{b'} = 0.8053 \qquad \frac{\ell_{eff}}{b'} = 0.4026 \qquad \frac{h_H}{b'} = 0.1578$$

$$\frac{\ell''}{\bar{c}'} = 2.26 \qquad \frac{\ell_3}{b'} = 0.2667 \qquad \frac{S_e''}{S'} = 0.0988$$

Additional Characteristics:

$h_H = 7.18$ feet	$M = 0.60$	$R_\ell = 5.16 \times 10^7$ (based on $\bar{c}'$)
$\ell_{eff} = \ell_2 = 18.32$ feet	$\beta = 0.80$	Sea level
$\ell_3 = \bar{c}' = 12.133$ feet	$\alpha' = 4°$	Smooth surfaces
$\ell'' = 27.425$ feet	$\Gamma = 0$	NACA 66-206 airfoil sections
$\Lambda'_{c/4} = 30.97°$		

Compute:

Step 1. Wing-body $C_{L_{\dot{\alpha}}}$ (Section 7.3.4.1)

$\left(C_{L_{\dot{\alpha}}}\right)_{WB} = 0.864$ per rad (sample problem, paragraph A, Section 7.3.4.1)

Step 2. Lift-curve slope for the exposed horizontal-tail panel (Section 4.1.3.2)

$\left(C_{L_\alpha}\right)_e'' = 4.0$ per rad (sample problem, paragraph A, Section 7.4.1.1)

Step 3. Tail-body interference factors (Section 4.3.1.2)

$K_{W(B)}'' = 1.315$

$K_{B(W)}'' = 0.550$

(sample problem, paragraph A, Section 7.4.1.1)

Step 4. Dynamic pressure ratio (Section 4.4.1)

$\frac{q''}{q_\infty} = 0.901$ (sample problem, paragraph A, Section 7.4.1.1)

Step 5. Downwash parameter (Section 4.4.1)

Obtain value for $\alpha' = 4°$ at M = 0.2 and correct for Mach number effects by equation 4.4.1-g

$\alpha_0' = -1.6°$ (table 4.1.1-B)

$\tan \Lambda_{c/2} = 0.4003$

$$\frac{A'}{\kappa}\left(\beta^2 + \tan^2 \Lambda_{c/2}\right)^{1/2} = \frac{5}{0.985}\left[0.98 + (0.4003)^2\right]^{1/2} = 5.43$$

$\frac{C_{L_\alpha}}{A} = 0.80$ (figure 4.1.3.2-49)

$C_{L_\alpha}' = 4.00$ per rad $= 0.0698$ per deg

$$\left(C_{L_\alpha}'\right)_{\alpha'=4°} = C_{L_{\alpha'}}(\alpha' - \alpha_0') = 0.0698\,[4 - (-1.6)] = 0.391$$

$\alpha'_{C_{L_{max}}} = 21.0°$ (Section 4.1.3.4)

$$\frac{\alpha' - \alpha_0}{\alpha'_{C_{L_{max}}} - \alpha_0'} = \frac{4 - (-1.6)}{21.0 - (-1.6)} = 0.248$$

$\frac{A'_{eff}}{A'} = 1.0$

$\frac{b'_{eff}}{b'} = 1.0$

(figure 4.4.1-66)

$A'_{eff} = 5.0$

$b'_{eff} = 45.50$ ft

$$\left(\frac{\partial \epsilon}{\partial \alpha}\right)_{\infty} = 0.40$$

$$\left(\frac{\partial \epsilon}{\partial \alpha}\right)_{v} = 0.49$$

(figure 4.4.1-67)

$\Delta y = 1.10$ (figure 2.2.1-8)

Type of flow separation: Leading-edge separation is predominant (figure 4.4.1-68a)

$$a = h_H - (\ell_2 + \ell_3)\left(\alpha - \frac{0.41 C_L}{\pi A_{eff}}\right) - \frac{b_{eff}}{2} \tan \Gamma \quad \text{(equation 4.4.1-d)}$$

$$= 7.18 - (18.32 + 12.133)\left(\frac{4}{57.3} - \frac{(0.41)(0.391)}{(3.14)(5.0)}\right) - \frac{45.50}{2}(0)$$

$$= 7.18 - (30.453)(0.0596) = 5.37$$

$$\xi_{ru} = \frac{0.56 A'}{C_L'} = \frac{0.56(5.0)}{0.391} = 7.16 \text{ (See page 4.4.1-6)}$$

$$b_{v_{ru}} = [0.78 + 0.10(\lambda' - 0.4) + 0.003 \Lambda'_{c/4}]\, b'_{eff} \quad (\Lambda_{c/4} \text{ in deg}) \quad \text{(equation 4.4.1-f)}$$

$$= (0.833)(45.50)$$

$$= 37.90 \text{ ft}$$

$$b_v = b'_{eff} - \left(b'_{eff} - b_{v_{ru}}\right)\left[\frac{2\ell_{eff}}{b' \xi_{ru}}\right]^{1/2} \quad \text{(equation 4.4.1-e)}$$

$$= 45.5 - (45.5 - 37.9)\left[\frac{36.64}{(45.5)(7.16)}\right]^{1/2}$$

$$= 45.5 - 2.5 = 43.0$$

$$\frac{b_H}{b_v} = \frac{b''}{b_v} = \frac{19.915}{43.0} = 0.463$$

$$\frac{2a}{b_v} = \frac{2(5.37)}{43.0} = 0.25$$

$$\frac{\left(\frac{\partial \bar{\epsilon}}{\partial \alpha}\right)}{\left(\frac{\partial \epsilon}{\partial \alpha}\right)_v} = 0.93 \quad \text{(figure 4.4.1-68b)}$$

$$\left(\frac{\partial \bar{\epsilon}}{\partial \alpha}\right)_{\substack{\text{low} \\ \text{speed}}} = \frac{\left(\frac{\partial \bar{\epsilon}}{\partial \alpha}\right)}{\left(\frac{\partial \epsilon}{\partial \alpha}\right)_v} \left(\frac{\partial \epsilon}{\partial \alpha}\right)_v = (0.93)(0.49) = 0.4557$$

$$\left(C_{L_\alpha}{}'\right)_{M=0.6} = 4.50 \quad \text{(sample problem, paragraph A, Section 7.3.1.1)}$$

$$\left(\frac{\partial \bar{\epsilon}}{\partial \alpha}\right)_{M=0.6} = \left(\frac{\partial \bar{\epsilon}}{\partial \alpha}\right)_{\substack{\text{low} \\ \text{speed}}} \frac{\left(C_{L_\alpha}{}'\right)_{M=0.6}}{\left(C_{L_\alpha}{}'\right)_{\substack{\text{low} \\ \text{speed}}}} \quad \text{(equation 4.4.1-g)}$$

$$= (0.4557)\left(\frac{4.50}{4.00}\right)$$

$$= (0.513)$$

Solution:

$$C_{L_{\dot{\alpha}}} = \left(C_{L_{\dot{\alpha}}}\right)_{WB} + 2[K_{W(B)} + K_{B(W)}]'' \left(\frac{S_e''}{S'}\right)\left(\frac{x_{c.g.} - x''}{\bar{c}'}\right)\left(\frac{\partial \bar{\epsilon}}{\partial \alpha}\right)\left(\frac{q''}{q_\infty}\right)\left(C_{L_\alpha}\right)_e''$$

(equation 7.4.4.1-a)

$$= 0.864 + 2(1.315 + 0.550)(0.0988)(2.26)(0.513)(0.901)(4.0)$$

$$= 0.864 + 1.540$$

$$= 2.404 \text{ per rad} \quad \text{(based on the area and mean aerodynamic chord of the total forward panel and referred to a moment center at } \bar{c}'/4)$$

B. TRANSONIC

No accurate methods are available for estimating the characteristics of isolated panels, the dynamic-pressure ratio, or the downwash gradient in the transonic speed regime. The aerodynamic interference "K" factors for slender configurations are relatively insensitive to Mach number; however, for nonslender configurations transonic interference effects can become quite large and sensitive to minor changes in local contour.

DATCOM METHODS

It is recommended that the methods presented in paragraph A above be applied directly to the transonic speed regime. Care should be taken to estimate the various parameters of equations 7.4.4.1-a and -b at the appropriate Mach number. The interference "K" factors should be obtained from paragraph C, Section 4.3.1.2.

C. SUPERSONIC

The information included in the Datcom accounts for most of the mutual interferences that occur between components of wing-body-tail configurations at supersonic speeds.

DATCOM METHODS

The methods presented in paragraph A above are also applicable to the supersonic speed range. Care should be taken to estimate the various parameters of equations 7.4.4.1-a and -b at the appropriate Mach number. Method 3 of paragraph C of Section 4.4.1 should be used to evaluate the last term of equation 7.4.4.1-b.

Sample Problem

Method 1

Given: Same configuration as sample problems of paragraph C, Sections 7.4.1.1 and 7.4.1.2, and paragraph A of this section. Some of the characteristics are repeated below.

The following ratios based on total forward panel dimensions:

$$\frac{\ell''}{\bar{c}'} = 2.26 \qquad \frac{S_e''}{S'} = 0.0988$$

Additional Characteristics:

$h_H = 7.18$ ft $M = 1.40$ $\alpha' = 4°$

$A' = 5.0$ $\beta = 0.98$ cg at $\bar{c}'/4$

Compute:

Step 1. Wing-body $C_{N_{\dot{\alpha}}}$ (Section 7.3.4.1)

$$\left(C_{N_{\dot{\alpha}}}\right)_{WB} = \left[K_{W(B)} + K_{B(W)}\right]' \left(\frac{S_e'}{S'}\right)\left(\frac{\bar{c}_e'}{\bar{c}'}\right)\left(C_{L_{\dot{\alpha}}}\right)_e + \left(C_{L_{\dot{\alpha}}}\right)_B \left(\frac{S_b}{S'}\right)\left(\frac{\ell_B}{\bar{c}'}\right)$$

(equation 7.3.4.1-a)

$\left(C_{N_{\dot{\alpha}}}\right)_{WB}$ = -0.485 per rad (sample problem, paragraph C, Section 7.3.4.1)

Step 2. Lift-curve slope for the exposed horizontal-tail panel (Section 4.1.3.2)

$\left(C_{N_\alpha}\right)_e''$ = 4.025 per rad (sample problem, paragraph C, Section 7.4.1.1)

Step 3. Tail-body interference factors (Section 4.3.1.2)

$K_{W(B)}''$ = 1.315

$K_{B(W)}''$ = 0.4028

(sample problem, paragraph C, Section 7.4.1.1)

Step 4. Dynamic pressure ratio (Section 4.4.1)

$\frac{q''}{q_\infty}$ = 0.80 (sample problem, paragraph C, Section 7.4.1.1)

Step 5. Downwash parameter (Section 4.4.1)

Obtain value in the plane of symmetry at $\frac{\bar{c}''}{4}$

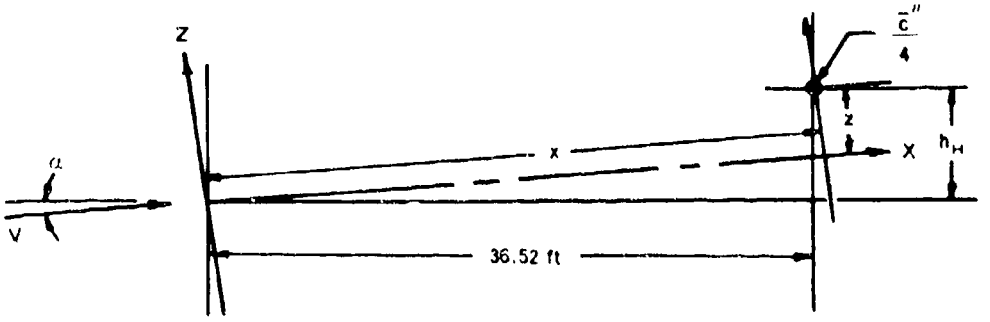

x, y, and z referred to wind axes:

$x = h_H \sin\alpha + (36.52)\cos\alpha = 36.93$

$y = 0$ (plane of symmetry)

$z = h_H \cos\alpha - (36.52)\sin\alpha = 4.615$

$$\frac{2x}{\beta b'} = 1.656 \qquad \frac{2z}{b'} = 0.2029 \qquad \frac{2y}{b'} = 0$$

$\beta A' = 4.90$

$$\frac{2h}{\alpha'\beta b'} = 1.0^* \quad \text{(figure 4.4.1-74a)}$$

$$\left(\frac{2z}{b'}\right)_{eff} = \frac{2z}{b'} + \frac{2h}{\alpha'\beta b'}\,\alpha'\beta \quad (\alpha' \text{ in rad})$$

$$= 0.2029 + (1.0)(0.0684)$$

$$= 0.2713$$

$$\frac{\partial\bar{\epsilon}}{\partial\alpha} = 0.29^* \quad \text{(figure 4.4.1-76a)}$$

Solution:

$$C_{L_{\dot{\alpha}}} = \left(C_{L_{\dot{\alpha}}}\right)_{WB} + 2[K_{W(B)} + K_{B(W)}]'' \left(\frac{S_e''}{S'}\right)\left(\frac{x_{c.g.} - x''}{\bar{c}'}\right)\left(\frac{q''}{q_\infty}\right)\left(\frac{\partial\bar{\epsilon}}{\partial\alpha}\right)\left(C_{N_\alpha}\right)_e''$$

(equation 7.4.4.1-a)

$$= -0.485 + 2(1.315 + 0.4028)(0.0988)(2.26)(0.80)(0.29)(4.025)$$

$$= -0.485 + 0.716$$

$$= 0.231 \text{ per rad} \quad \text{(based on the area and mean aerodynamic chord of the total forward panel and referred to a moment center at } \bar{c}'/4)$$

REFERENCES

1. Pitts, W., Neilsen, J., and Kaattari, G.: Lift and Center of Pressure of Wing-Body-Tail Combinations at Subsonic, Transonic, and Supersonic Speeds. NACA TR 1307, 1959. (U)

2. Spreiter, J.: The Aerodynamic Forces on Slender Plane- and Cruciform-Wing and Body Combinations. NACA TR 962, 1950. (U)

3. Etkin, B.: Dynamics of Flight. John Wiley and Sons, Inc., New York, 1959. (U)

*The data obtained from figures 4.4.1-74a and 4.4.1-76a for triangular planforms have been extrapolated to $\beta A' = 4.90$. (See reference 14, Section 4.4.1.)

7.4.4.2 WING-BODY-TAIL ACCELERATION DERIVATIVE $C_{m_{\dot{\alpha}}}$

The information contained in this section is for estimating the nondimensional acceleration derivative $C_{m_{\dot{\alpha}}}$ of wing-body-tail combinations at low angles of attack. This derivative is the change in pitching-moment coefficient with rate of change of angle of attack and is expressed by

$$C_{m_{\dot{\alpha}}} = \frac{\partial C_m}{\partial\left(\frac{\dot{\alpha}\bar{c}}{2V_\infty}\right)}$$

This derivative is important in longitudinal dynamics, since it is involved in the damping of the short-period mode.

The Datcom methods are based on the same assumptions that were made for the total pitching derivative $C_{L_{\dot{\alpha}}}$ of the wing-body-tail combinations, and the general discussion of Section 7.4.4.1 is directly applicable here.

A. SUBSONIC

Two methods are presented for determining the acceleration derivative $C_{m_{\dot{\alpha}}}$ of wing-body-tail combinations, differing only in their treatment of the effect of the flow field of the forward surface on the aft surface.

DATCOM METHODS

Method 1. ($b'/b'' \geq 1.5$)

For configurations in which the span of the forward surface is large compared to that of the aft surface, the following approach can be used. This method is to be used when the ratio of the forward-panel span to the aft-panel span is 1.5 or greater. The equation for the nondimensional acceleration derivative $C_{m_{\dot{\alpha}}}$ of a wing-body-tail configuration, based on the area and the square of the mean aerodynamic chord of the total forward panel and referred to a moment center at the assumed center of gravity or center of rotation, is given by

$$C_{m_{\dot{\alpha}}} = \left(C_{m_{\dot{\alpha}}}\right)_{WB} - 2[K_{W(B)} + K_{B(W)}]'' \left(\frac{S_e''}{S'}\right)\left(\frac{x_{c.g.} - x''}{\bar{c}'}\right)^2 \left(\frac{q''}{q_\infty}\right)\left(\frac{\partial\bar{\epsilon}}{\partial\alpha}\right)\left(C_{L_\alpha}\right)_e''$$

7.4.4.2-a

where the primed quantities refer to the forward panel, the double-primed quantities refer to the aft panel, and the subscript e refers to the exposed panel. (See Section 4.3.1.2 for the definition of exposed surfaces.)

$(C_{m_{\dot{\alpha}}})_{WB}$ is the contribution of the wing-body configuration to the acceleration derivative $C_{m_{\dot{\alpha}}}$, obtained from Section 7.3.4.2.

$\frac{\partial \bar{\epsilon}}{\partial \alpha}$ is the downwash gradient averaged over the aft panel, obtained from Section 4.4.1.

The remaining terms are defined in paragraph A of Section 7.4.1.1.

Method 2. $(b'/b'' < 1.5)$

For configurations in which the span of the forward surface is approximately equal to or less than that of the aft surface, the vortex shed from the forward surface interacts directly with the aft surface, and the resulting interference effects must be accounted for in the tail- or aft-surface-contribution terms. This method is to be used when the ratio of the forward-panel span to the aft-panel span is less than 1.5. The equation for the nondimensional acceleration derivative $C_{m_{\dot{\alpha}}}$ of a wing-body-tail configuration, based on the area and the square of the mean aerodynamic chord of the total forward panel and referred to a moment center at the assumed center of gravity or center of rotation, is given by

$$C_{m_{\dot{\alpha}}} = \left(C_{m_{\dot{\alpha}}}\right)_{WB} + 2\left(\frac{x_{c.g.} - x''}{\bar{c}'}\right)^2 \left(C_{L_\alpha}\right)_{W''(v)} \qquad 7.4.4.2\text{-b}$$

All the above terms are defined in paragraph A of Section 7.4.1.1 and method 1 above.

Because of the similarity of the two methods a sample problem for method 2 is not included. However, evaluation of the term $(C_{L_\alpha})_{W''(v)}$ for a wing-body-tail configuration is presented in Section 4.5.1.1.

Sample Problem

Method 1

Given: Same configuration as sample problems of paragraph A, Sections 7.4.1.1, 7.4.1.2, and 7.4.4.1. Some of the characteristics are repeated below.

The following ratios based on total forward-panel dimensions:

$$\frac{\ell''}{\bar{c}'} = 2.26 \qquad \frac{S_e''}{S'} = 0.0988$$

Additional Characteristics:

$M = 0.60$ $\beta = 0.80$ $\alpha' = 4^\circ$ cg at $\bar{c}'/4$

Compute:

Step 1 Wing-body $C_{m_{\dot{\alpha}}}$ (Section 7.3.4.2)

$$\left(C_{m_{\dot{\alpha}}}\right)_{WB} = [K_{W(B)} + K_{B(W)}]' \left(\frac{S_e'}{S'}\right)\left(\frac{\bar{c}_e'}{\bar{c}'}\right)^2 \left(C_{m_{\dot{\alpha}}}\right)_e' + \left(C_{m_{\dot{\alpha}}}\right)_B \left(\frac{S_b}{S'}\right)\left(\frac{\ell_B}{\bar{c}'}\right)^2$$

(equation 7.3.4.2-a)

$\left(C_{m_{\dot{\alpha}}}\right)_{WB}$ = −0.400 per rad (sample problem, paragraph A, Section 7.3.4.2)

Step 2. Lift-curve slope for the exposed horizontal-tail panel (Section 4.1.3.2)

$\left(C_{L_\alpha}\right)_e''$ = 4.0 per rad (sample problem, paragraph A, Section 7.4.1.1)

Step 3. Tail-body interference factors (Section 4.3.1.2)

$K_{W(B)}'' = 1.315$

$K_{B(W)}'' = 0.550$

} (sample problem, paragraph A, Section 7.4.1.1)

Step 4. Dynamic pressure ratio (Section 4.4.1)

$\frac{q''}{q_\infty}$ = 0.901 (sample problem, paragraph A, Section 7.4.1.1)

Step 5. Downwash parameter (Section 4.4.1)

$\frac{\partial \bar{\epsilon}}{\partial \alpha}$ = 0.513 (sample problem, paragraph A, Section 7.4.4.1)

Solution:

$$C_{m_{\dot{\alpha}}} = \left(C_{m_{\dot{\alpha}}}\right)_{WB} - 2[K_{W(B)} + K_{B(W)}]'' \left(\frac{S_e''}{S'}\right)\left(\frac{x_{c.g.} - x''}{\bar{c}'}\right)^2 \left(\frac{q''}{q_\infty}\right)\left(\frac{\partial \bar{\epsilon}}{\partial \alpha}\right)\left(C_{L_\alpha}\right)_e''$$

(equation 7.4.4.2-a)

$= -0.400 - 2(1.315 + 0.550)\,(0.0988)\,(2.26)^2\,(0.901)\,(0.513)\,(4.0)$

$= -0.400 - 3.48$

$= -3.88$ per rad (based on the area and the square of the mean aerodynamic chord of the total forward panel and referred to a moment center at $\bar{c}'/4$)

B. TRANSONIC

The comments of paragraph B of Section 7.4.4.1 are directly applicable here.

DATCOM METHODS

It is recommended that the methods presented in paragraph A above be applied to the transonic speed regime. Care should be taken to estimate the parameters of equations 7.4.4.2-a and -b at the appropriate Mach number. The interference "K" factors should be obtained from paragraph C, Section 4.3.1.2.

C. SUPERSONIC

The comments of paragraph C of Section 7.4.4.1 are directly applicable here.

DATCOM METHODS

The methods presented in paragraph A above are also applicable to the supersonic speed range. Care should be taken to estimate the parameters of equations 7.4.4.2-a and -b at the appropriate Mach number. Method 3 of paragraph C of Section 4.4.1 should be used to evaluate the last term of equation 7.4.4.2-b.

Sample Problem

Method 1

Given: Same configuration as sample problems of paragraph C, Sections 7.4.1.1, 7.4.1.2, and 7.4.4.1, and paragraph A of this section. Some of the characteristics are repeated below.

The following ratios based on total forward-panel dimensions:

$$\frac{\ell''}{\bar{c}'} = 2.26 \qquad \frac{S_e''}{S'} = 0.0988$$

Additional Characteristics:

$M = 1.4 \qquad \beta = 0.98 \qquad \alpha' = 4^\circ \qquad$ cg at $\bar{c}/4$

Compute:

Step 1. Wing-body $C_{m_{\dot{\alpha}}}$ (Section 7.3.4.2)

$$\left(C_{m_{\dot{\alpha}}}\right)_{WB} = [K_{W(B)} + K_{B(W)}]' \left(\frac{S_e'}{S'}\right)\left(\frac{\bar{c}_e'}{\bar{c}'}\right)^2 \left(C_{m_{\dot{\alpha}}}\right)_e' + \left(C_{m_{\dot{\alpha}}}\right)_B \left(\frac{S_b}{S'}\right)\left(\frac{\ell_B}{\bar{c}'}\right)^2$$

(equation 7.3.4.2-a)

$\left(C_{m_{\dot{\alpha}}}\right)_{WB}$ = 1.308 per rad (sample problem, paragraph C, Section 7.3.4.2)

Step 2. Lift-curve slope for the exposed horizontal-tail panel (Section 4.1.3.2)

$\left(C_{N_\alpha}\right)_e''$ = 4.025 per rad (sample problem, paragraph C, Section 7.4.1.1)

Step 3. Tail-body interference factors (Section 4.3.1.2)

$K_{W(B)}'' = 1.315$

$K_{B(W)}'' = 0.4028$

} (sample problem, paragraph C, Section 7.4.1.1)

Step 4. Dynamic pressure ratio (Section 4.4.1)

$\frac{q''}{q_\infty}$ = 0.80 (sample problem, paragraph C, Section 7.4.1.1)

Step 5. Downwash parameter (Section 4.4.1)

$\frac{\partial \bar{\epsilon}}{\partial \alpha}$ = 0.29 (sample problem, paragraph C, Section 7.4.4.1)

Solution:

$$C_{m_{\dot{\alpha}}} = \left(C_{m_{\dot{\alpha}}}\right)_{WB} - 2[K_{W(B)} + K_{B(W)}]'' \left(\frac{S_e''}{S'}\right)\left(\frac{x_{c.g.} - x''}{\bar{c}'}\right)^2 \left(\frac{q''}{q_\infty}\right)\left(\frac{\partial \bar{\epsilon}}{\partial \alpha}\right)\left(C_{N_\alpha}\right)_e''$$

(equation 7.4.4.2-a)

$= 1.308 - 2(1.315 + 0.4028)\,(0.0988)\,(2.26)^2\,(0.80)\,(0.29)\,(4.025)$

$= 1.308 - 1.619$

$= -0.31$ per rad (based on the area and the square of the mean aerodynamic chord of the total forward panel and referred to a moment center at $\bar{c}'/4$)

7.4.4.3 WING-BODY-TAIL DERIVATIVE $C_{D_{\dot{\alpha}}}$

This section presents a method for estimating the wing-body-tail derivative $C_{D_{\dot{\alpha}}}$ at subsonic speeds. This derivative is the change in the drag coefficient due to a change in $\dot{\alpha}$ at a constant pitch rate and is defined as

$$C_{D_{\dot{\alpha}}} = \frac{\partial C_D}{\partial \left(\frac{\dot{\alpha}\bar{c}}{2V}\right)}, \text{ where } C_D \text{ is based on } S_W.$$

In general, this derivative is small and has a negligible effect on longitudinal stability; hence, it is usually neglected.

A. SUBSONIC

The wing contribution to $C_{D_{\dot{\alpha}}}$ can be estimated using unsteady-flow theory. The body contribution is small and has been neglected. The tail contribution is computed from conventional downwash-lag theory. The horizontal-tail lift due to $\dot{\alpha}$ was taken to act normal to the local flow direction at the tail, to produce a force component in the direction of the free-stream.

DATCOM METHOD

The wing-body-tail derivative is given by

$$C_{D_{\dot{\alpha}}} = \left(C_{D_{\dot{\alpha}}}\right)_W + \left(C_{D_{\dot{\alpha}_0}}\right)_H + \left(\frac{\partial C_{D_{\dot{\alpha}}}}{\partial \alpha_F}\right)_H \alpha_F \qquad 7.4.4.3\text{-a}$$

where

$\left(C_{D_{\dot{\alpha}}}\right)_W$ is the wing contribution to $C_{D_{\dot{\alpha}}}$ obtained from Section 7.1.4.3.

$\left(C_{D_{\dot{\alpha}_0}}\right)_H$ is the horizontal-tail contribution independent of angle of attack, obtained by

$$\left(C_{D_{\dot{\alpha}_0}}\right)_H = \frac{1}{57.3} C_{L_{\alpha_H}} \frac{S_H}{S_W} \frac{(\ell_H \cos\alpha_F + z_H \sin\alpha_F)}{\bar{c}/2} \frac{\partial \epsilon}{\partial \alpha} (2\epsilon_0 - i_H) \qquad 7.4.4.3\text{-b}$$

where

$C_{L_{\alpha_H}}$ is the horizontal-tail lift-curve slope (based on S_H) obtained from test data or from Section 4.1.3.2 (per degree).

S_H is the horizontal-tail reference area.

S_W is the wing reference area.

ℓ_H is the distance from the momen reference center to the center-of-pressure location of the horizontal stabilizer, measured parallel to the body center line. For Datcom purposes, the horizontal-tail center-of-pressure location is assumed to be at the quarter-chord point of the MAC of the total added panel.

z_H is the distance from the moment reference center tc the center-of-pressure location of the horizontal stabilizer, measured normal to the body center line, positive for the stabilizer above the body. For Datcom purposes, the horizontal-tail center-of-pressure location is assumed to be at the quarter-chord point of the MAC of the total added panel.

α_F is the fuselage angle of attack.

$\frac{\partial \epsilon}{\partial \alpha}$ is the downwash gradient at $\bar{c}/4$ of the horizontal tail, obtained from test data or from Section 4.4.1.

$\bar{c}$ is the wing MAC.

ϵ_0 is the downwash angle at $\bar{c}/4$ of the horizontal tail at $\alpha_F = 0$.

i_H is the horizontal-tail incidence with respect to the fuselage reference line.

$\left(\frac{\partial C_{D_\alpha}}{\partial \alpha_F}\right)_H$ is the change in horizontal-tail contribution with angle of attack, obtained by

$$\left(\frac{\partial C_{D_\alpha}}{\partial \alpha_F}\right)_H = \frac{1}{57.3} C_{L_{\alpha_H}} \frac{S_H}{S_W} \frac{(\ell_H \cos \alpha_F + z_H \sin \alpha_F)}{\bar{c}/2} \frac{\partial \epsilon}{\partial \alpha} \left(2 \frac{\partial \epsilon}{\partial \alpha} - 1\right) \qquad 7.4.4.3\text{-c}$$

where all of the terms are defined above.

Sample Problem

Given: Same configuration as sample problem of Paragraph A of Section 7.1.4.3.

Tail Characteristics:

$C_{L_{\alpha_H}} = 0.05$ per deg $\qquad S_H = 16$ ft^2

$\ell_H = 8$ ft $\qquad z_H = 0 \qquad \frac{\partial \epsilon}{\partial \alpha} = 0.32$

$\epsilon_0 = 1^o \qquad i_H = 0$

Compute:

$$\left(C_{D_{\alpha_0}}\right)_H = \frac{1}{57.3} C_{L_{\alpha_H}} \frac{S_H}{S_W} \frac{(\ell_H \cos \alpha_F + z_H \sin \alpha_F)}{\bar{c}/2} \frac{\partial \epsilon}{\partial \alpha} (2 \epsilon_0 - i_H) \qquad \text{(Equation 7.4.4.3-b)}$$

$$= \left(\frac{1}{57.3}\right)(0.05)\left(\frac{16.0}{64.0}\right)\frac{[(8.0)(0.9998)+0]}{4/2}(0.32)[2(1.0)-0]$$

$$= 0.000558$$

$$\left(\frac{\partial C_{D_{\dot{\alpha}}}}{\partial \alpha_F}\right)_H = \frac{1}{57.3} C_{L_{\alpha_H}} \frac{S_H}{S_W} \frac{(\ell_H \cos\alpha_F + z_H \sin\alpha_F)}{\bar{c}/2} \frac{\partial \epsilon}{\partial \alpha}\left(2\frac{\partial \epsilon}{\partial \alpha} - 1\right) \qquad \text{(Equation 7.4.4.3-c)}$$

$$= \left(\frac{1}{57.3}\right)(0.05)\left(\frac{16.0}{64.0}\right)\frac{[(8.0)(0.9998)+0]}{4/2}(0.32)[2(0.32)-1]$$

$$= -0.000100$$

Solution:

$$C_{D_{\dot{\alpha}}} = \left(C_{D_{\dot{\alpha}}}\right)_W + \left(C_{D_{\dot{\alpha}_0}}\right)_H + \left(\frac{\partial C_{D_{\dot{\alpha}}}}{\partial \alpha_F}\right)_H \alpha_F \qquad \text{(Equation 7.4.4.3-a)}$$

$\left(C_{D_{\dot{\alpha}}}\right)_W$ = 0.0085 per deg (Sample Problem, Paragraph A, Section 7.1.4.3)

$$C_{D_{\dot{\alpha}}} = 0.0085 + 0.000558 + (-0.000100)\,1.0$$

$$= 0.00896 \text{ per degree}$$

B. TRANSONIC

No method is presented.

C. SUPERSONIC

No method is presented.

7.4.4.4 WING-BODY-TAIL DERIVATIVE $C_{Y_{\dot{\beta}}}$

This section presents a method for estimating the contribution of the vertical tail, in the presence of the wing and body, to the derivative $C_{Y_{\dot{\beta}}}$ at subsonic speeds. This derivative is the change in side-force coefficient with variations in the rate of change of sideslip angle at a constant yaw rate and is defined as

$$C_{Y_{\dot{\beta}}} = \frac{\partial C_Y}{\partial\left(\frac{\dot{\beta} b}{2V}\right)} \text{, where } C_Y \text{ is based on } S_W.$$

In general, at low to moderate angles of attack, this derivative is small and has a negligible effect on lateral stability; hence, it is usually neglected.

A. SUBSONIC

A wing contribution to $C_{Y_{\dot{\beta}}}$ can be evaluated by using unsteady-flow theory, but at low to moderate angles of attack it is generally considered small and is neglected. At low angles of attack and for attached-flow conditions, the largest contributor to $C_{Y_{\dot{\beta}}}$ is the vertical tail. The method herein applies a sidewash-lag theory in an analogous manner to the downwash-lag theory that is used in finding the horizontal-tail contribution to $C_{L_{\dot{\alpha}}}$. The body contribution is small and has been neglected.

For a brief discussion of the physical flow phenomena at high angles of attack, i.e., leading-edge vortex sheets and flow separation, and a comprehensive bibliography on related subject matter, the reader is referred to Reference 1.

DATCOM METHOD

Design charts for predicting the change of wing sidewash angle with the change of sideslip angle are presented as a function of wing geometry, i.e., aspect ratio, sweep, and taper ratio, at Mach numbers 0.2 and 0.8. These design charts were generated from wing loadings in sideslip by using the theory presented in References 2 and 3.

The vertical-tail contribution to the derivative $C_{Y_{\dot{\beta}}}$ at low to moderate angles of attack is given by

$$C_{Y_{\dot{\beta}}} = 2\, C_{L_{\alpha_V}}\, \sigma_\beta \frac{S_V}{S_W} \frac{(\ell_p \cos\alpha_F + z_p \sin\alpha_F)}{b_W} \qquad 7.4.4.4\text{-a}$$

where

$C_{L_{\alpha_V}}$ is the lift-curve slope of the vertical tail obtained from test data or Section 4.1.3.2.

σ_β is the change of sidewash angle (due only to the wing, i.e., no sidewash due to fuselage cross flow) with respect to the change in the sideslip angle. This factor can be estimated by

$$\sigma_\beta = \sigma_{\beta_\alpha}\alpha_F + \frac{\sigma_{\beta_\Gamma}}{57.3}\Gamma - \sigma_{\beta_\theta}\theta + \sigma_{\beta_{WB}} \qquad 7.4.4.4\text{-b}^*$$

where

σ_{β_α} is the sidewash contribution due to angle of attack, obtained from Figures 7.4.4.4-6a through -6p as a function of $\frac{z_V}{b/2}$ and wing geometry. z_V is the distance between the wing $\bar{c}/4$ point and the vertical-stabilizer center-of-pressure location, measured normal to the free-stream direction. For Datcom purposes the vertical-tail center-of-pressure location is assumed to be at the quarter-chord point of the MAC of the total added panel.

$$z_V = z_p \cos\alpha_F - \ell_p \sin\alpha_F \qquad 7.4.4.4\text{-c}$$

where z_p and ℓ_p are defined below.

α_F is the fuselage angle of attack in degrees.

σ_{β_Γ} is the sidewash contribution due to wing dihedral, obtained from Figures 7.4.4.4-22a through -22d as a function of $\frac{z_V}{b/2}$ and wing geometry.

Γ is the wing dihedral in degrees.

σ_{β_θ} is the sidewash contribution due to wing twist, obtained from Figures 7.4.4.4-26a through -26p as a function of $\frac{z_V}{b/2}$ and wing geometry.

θ is the wing twist in degrees between the root and tip sections, negative for washout (see Figure 5.1.2.1-30b).

$\sigma_{\beta_{WB}}$ is the sidewash contribution due to the body effect on the wing loading. It is presented as a function of $\frac{z_V}{b/2}$ and wing geometry, at three different body-radius-to-wing-span ratios of 0.06, 0.12, and 0.24. In addition, the wing position on the body has an effect on this term. However, for Datcom considerations a low-wing position was assumed as shown in Sketch (a). For a high-wing position as shown in Sketch (b), the sign of $\sigma_{\beta_{WB}}$ in Figures 7.4.4.4-42a through -42p becomes negative.

*A more accurate result can be obtained from the equation

$$\sigma_\beta = \frac{1}{S_V}\int_o^{b_V} \sigma_{\beta_{local}} c_V \, dz$$

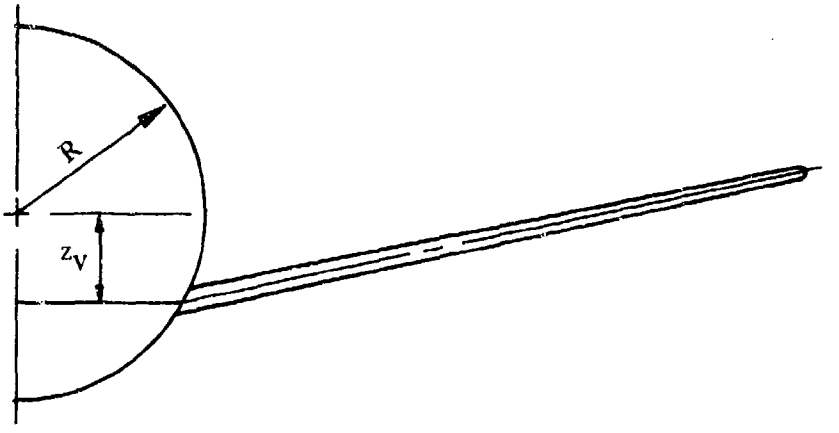

SKETCH (a)

high-wing position as shown in sketch (b), the sign of $\sigma_{\beta WB}$ in Figures 7.4.4.4-42a through -42p becomes negative.

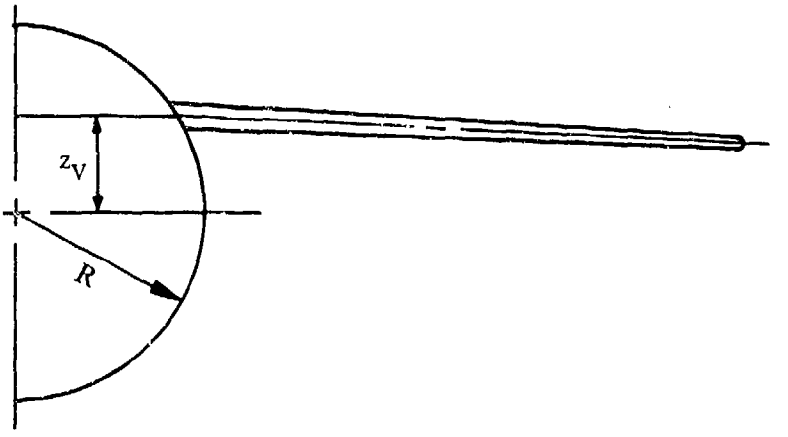

SKETCH (b)

S_V is the vertical-tail area, consistent with the vertical-tail area used to define $C_{L_{\alpha_V}}$.

S_W is the wing reference area.

ℓ_p is the distance from the wing quarter-chord point to the center-of-pressure location of the vertical stabilizer, measured parallel to the body center line. For Datcom purposes, the vertical-tail center-of-pressure location is assumed to be at the quarter-chord point of the MAC of the total added panel. (See Sketch (a) of Section 7.4.2.1.)

z_p is the distance from the wing quarter-chord point to the center-of-pressure location of the vertical stabilizer, measured normal to the body center line, positive for the stabilizer above the body. For Datcom purposes, the vertical-tail center-of-pressure location is assumed to be at the quarter-chord point of the MAC of the total added panel.

b_W is the wing span.

Sample Problem

Given: The following wing-body-tail configuration

Wing Characteristics:

$A = 7$ $\quad \lambda = 0.25$ $\quad \Lambda_{LE} = 35^o$ $\quad$ Low wing

$S_W = 3500\ ft^2$ $\quad b_W = 156.52\ ft$ $\quad \theta = -5^o$ $\quad \Gamma = 3^o$

Vertical-Tail Characteristics:

$C_{L_{\alpha_V}} = 0.055$ per deg $\quad S_V = 600\ ft^2$

$\frac{z_V}{b/2} = 0.242$

Additional Characteristics:

$\ell_p = 60.0\ ft$ $\quad z_p = 20.0\ ft$ $\quad \alpha_F = 1^o$

$M = 0.8$ $\quad \frac{\text{Body Radius}}{b/2} = 0.12$

Compute:

Determine σ_β

$$\sigma_\beta = \sigma_{\beta_\alpha}\alpha_F + \frac{\sigma_{\beta_\Gamma}}{57.3}\Gamma - \sigma_{\beta_\theta}\theta + \sigma_{\beta_{WB}} \qquad \text{(Equation 7.4.4.4-b)}$$

$\sigma_{\beta_\alpha} = -0.013$ (Figure 7.4.4.4-6ℓ)

$\sigma_{\beta_\Gamma} = -0.56$ (Figure 4.4.4.4-22d)

$\sigma_{\beta_\theta} = -0.0113$ (Figure 7.4.4.4-26ℓ)

$\sigma_{\beta_{WB}} = 0.07$ (Figure 7.4.4.4-42ℓ)

$$\sigma_\beta = (-0.013)(1) + \left(\frac{-0.56}{57.3}\right)3 - (-0.0113)(-5) + (0.07)$$

$$= -0.013 - 0.0293 - 0.0565 + 0.07$$

$$= -0.0288$$

Solution:

$$C_{Y_{\dot\beta}} = 2\,C_{L_{\alpha_V}}\,\sigma_\beta\,\frac{S_V}{S_W}\,\frac{(\ell_p\cos\alpha_F + z_p\sin\alpha_F)}{b_W} \qquad \text{(Equation 7.4.4.4-a)}$$

$$= 2(0.055)(-0.0288)\,\frac{600}{3500}\left[\frac{(60)(0.9998)+(20)(0.01745)}{156.52}\right]$$

$$= -0.000209 \text{ per deg}$$

B. TRANSONIC

No method is presented.

C. SUPERSONIC

No method is presented.

REFERENCES

1. Coe, P. L., Jr., Graham, A. B., and Chambers, J. R.: Summary of Information on Low-Speed Lateral-Directional Derivatives Due to Rate of Change of Sideslip $\dot\beta$. NASA TN D-7972, 1975. (U)

2. De Young, J., and Harper, C. W.: Theoretical Symmetric Span Loading at Subsonic Speeds for Wings Having Arbitrary Planform. NACA TR 921, 1948. (U)

3. Queijo, M. J.: Theoretical Span Loading Distribution and Rolling Moments for Sideslipping Wings of Arbitrary Planform in Incompressible Flow. NACA TR 1269, 1956. (U)

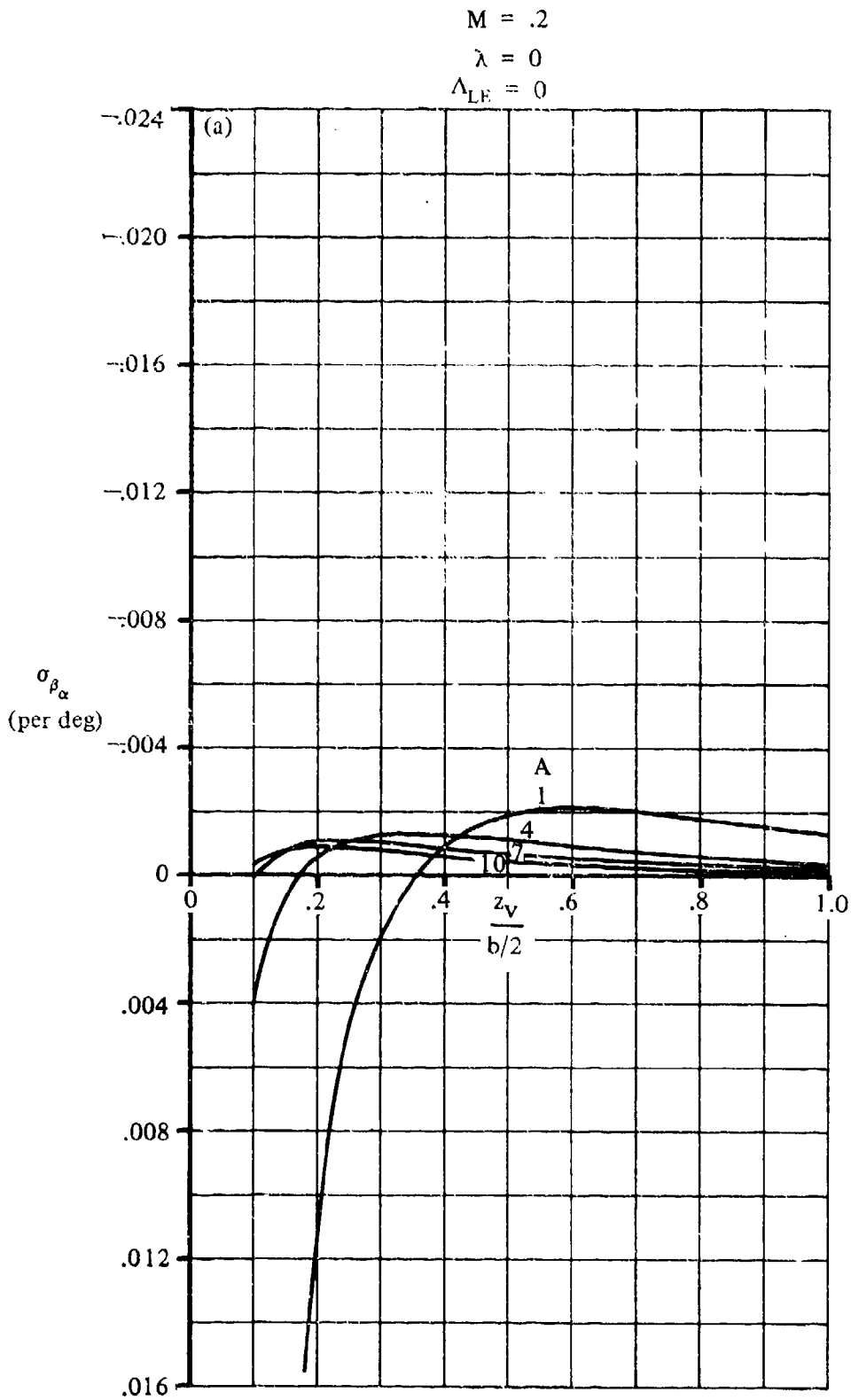

FIGURE 7.4.4.4-6 SIDEWASH CONTRIBUTION DUE TO ANGLE OF ATTACK

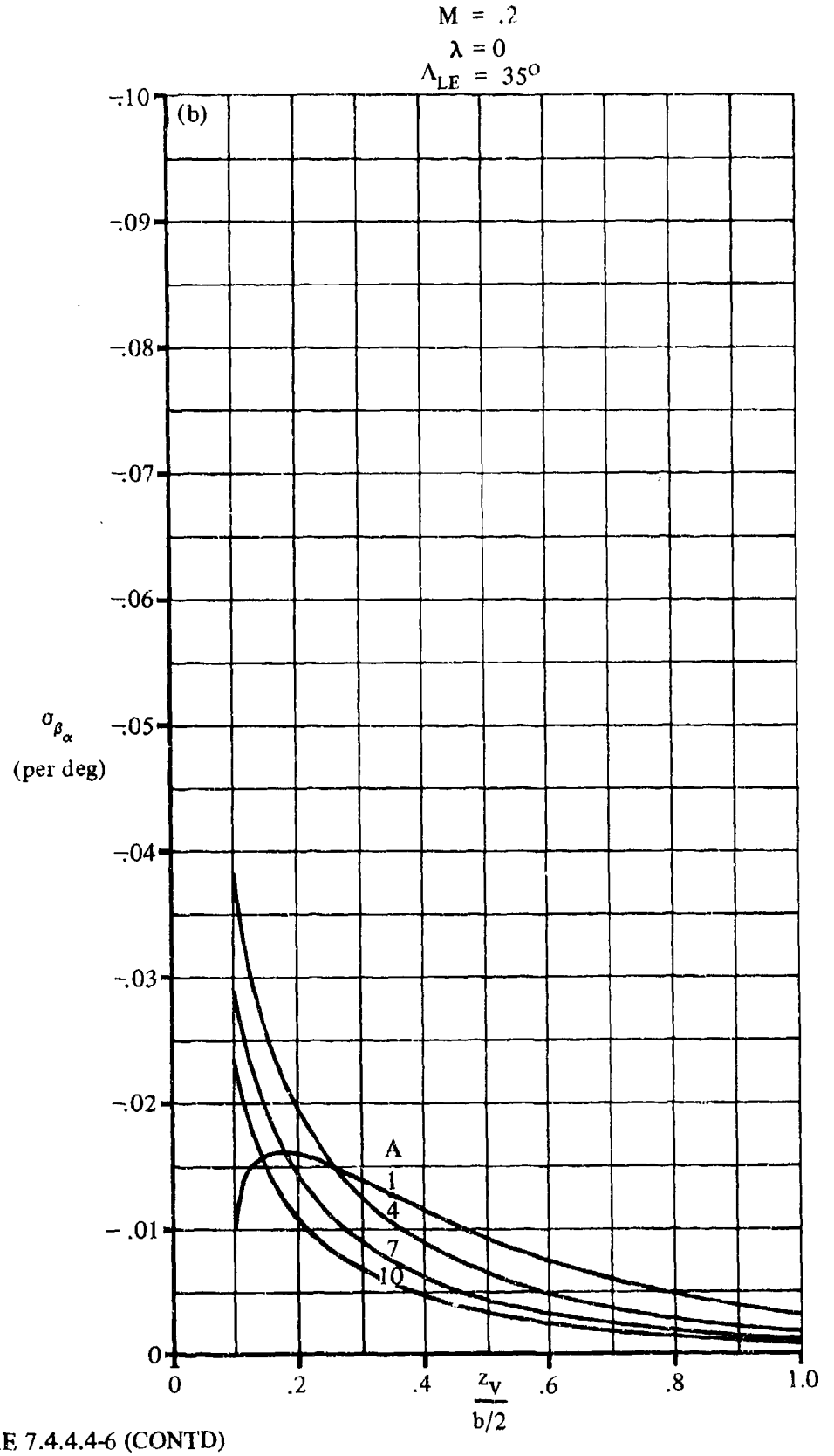

FIGURE 7.4.4.4-6 (CONTD)

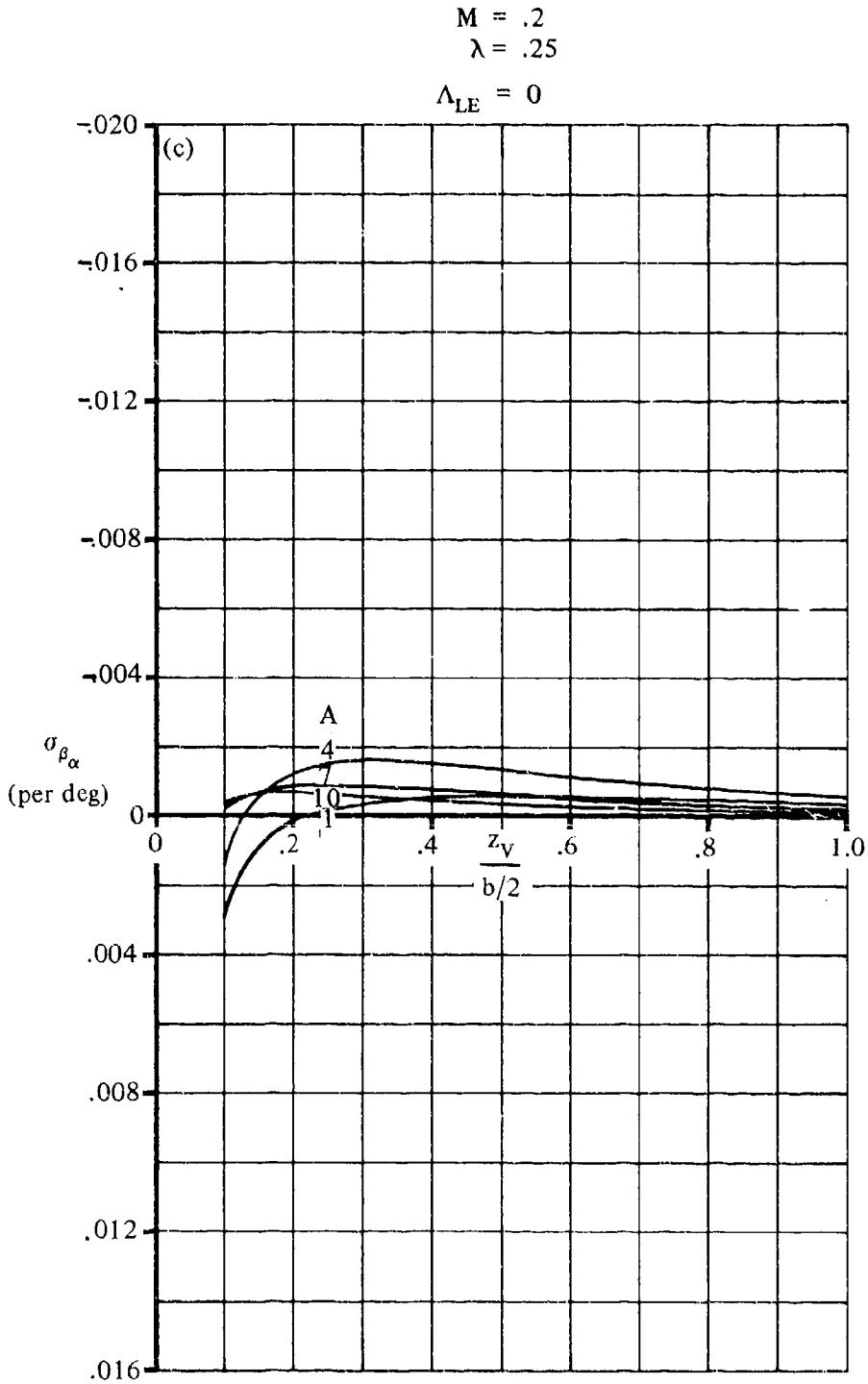

FIGURE 7.4.4.4-6 (CONTD)

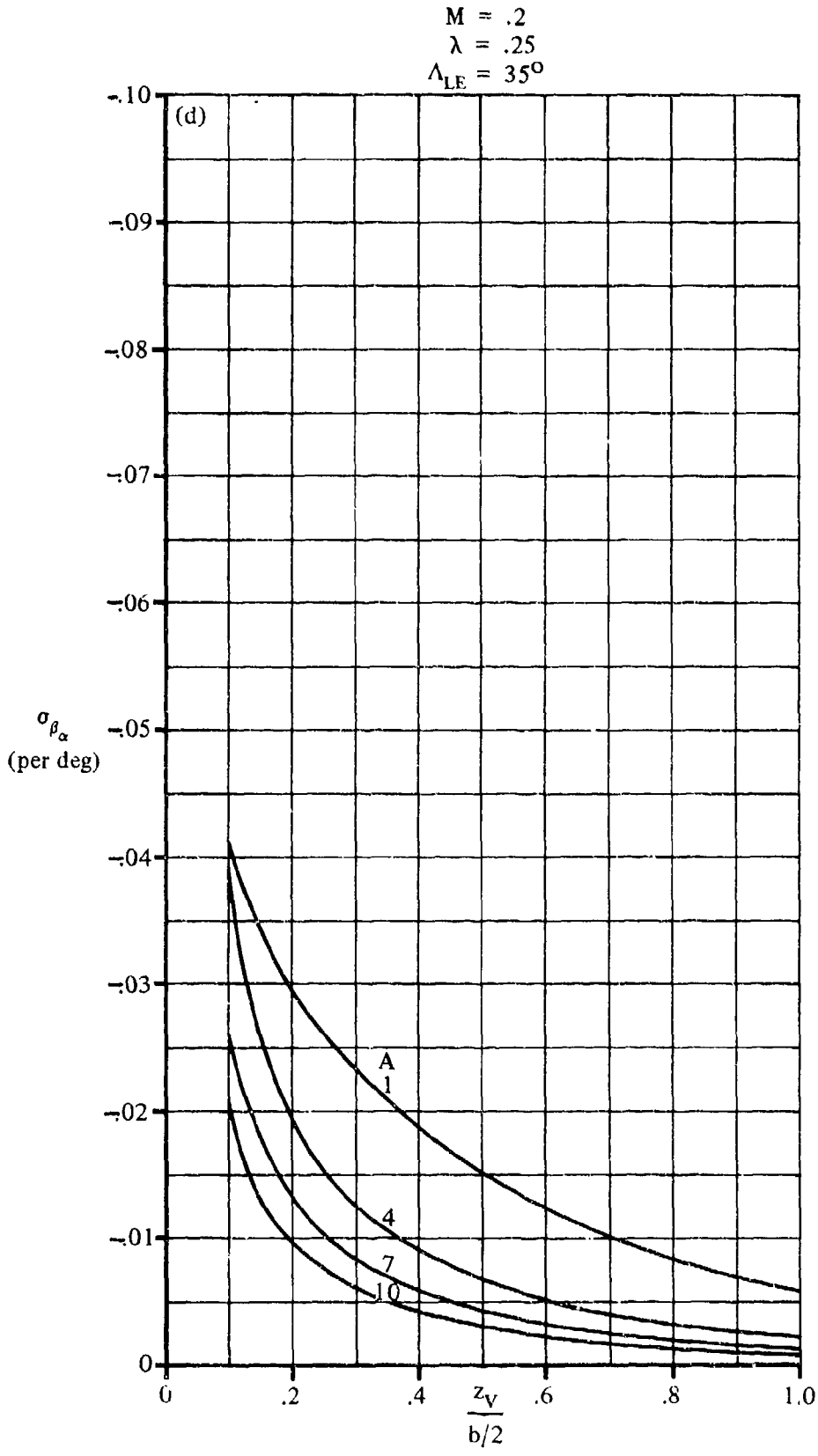

FIGURE 7.4.4.4-6 (CONTD)

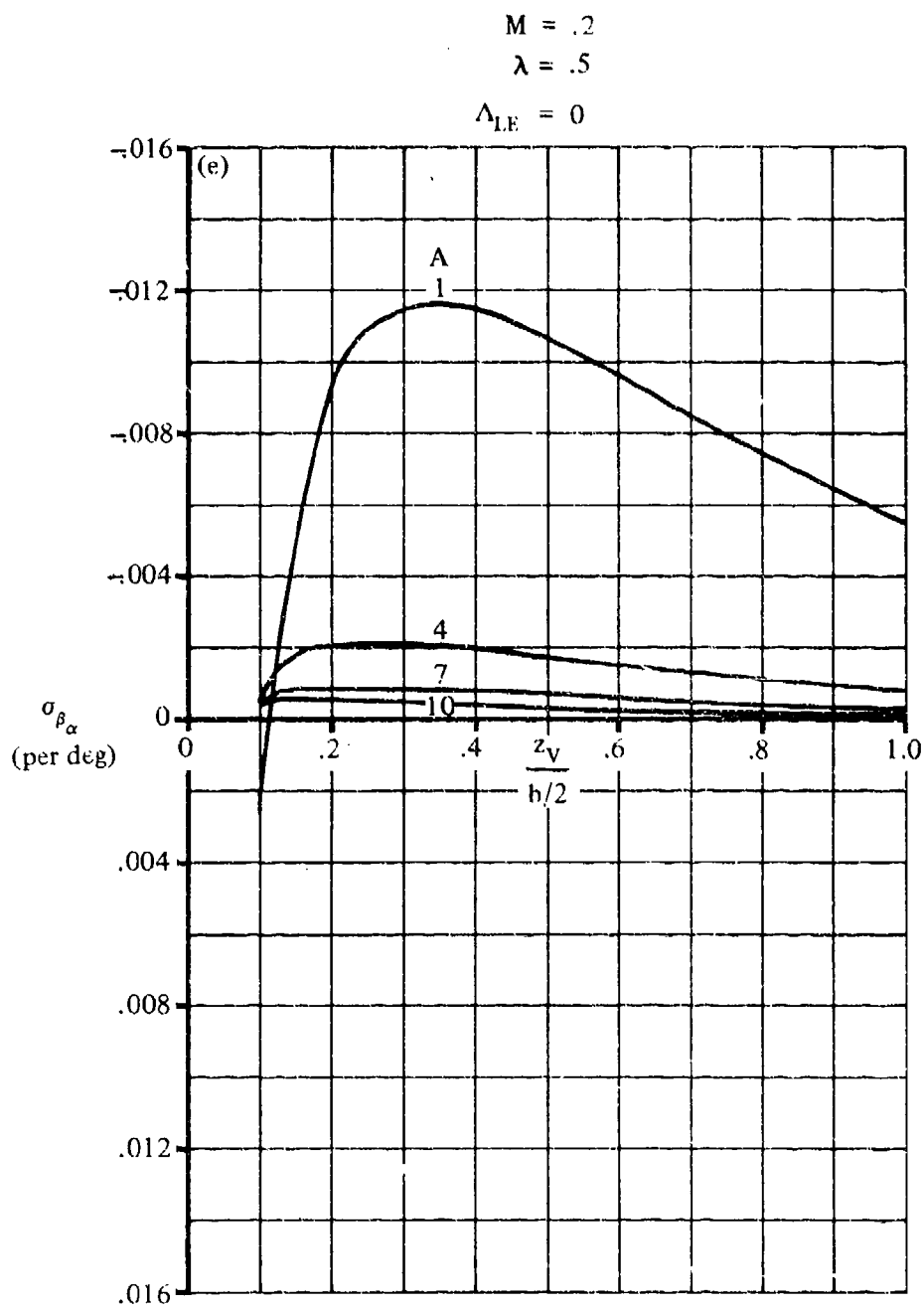

FIGURE 7.4.4.4-6 (CONTD)

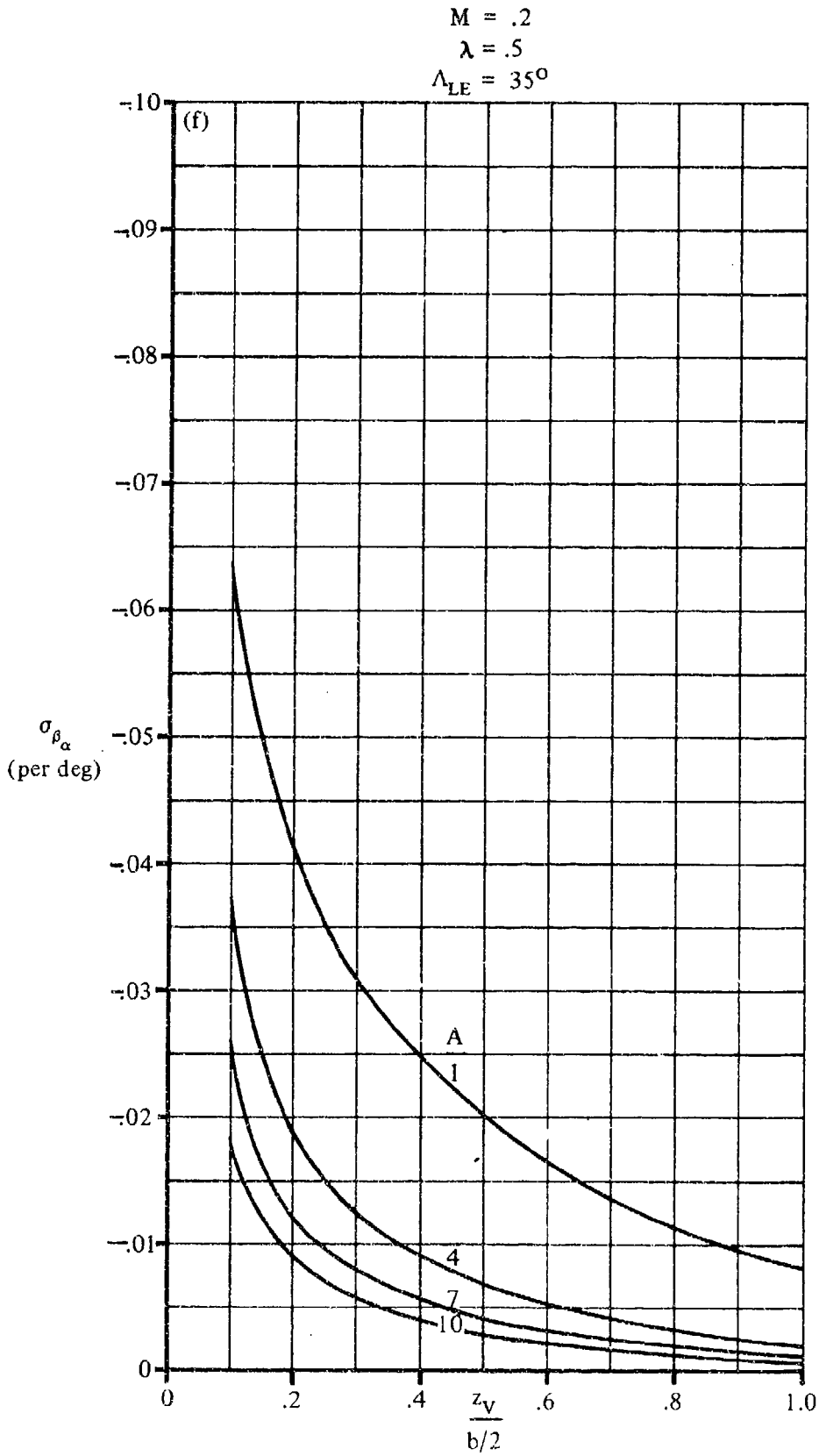

FIGURE 7.4.4.4-6 (CONTD)

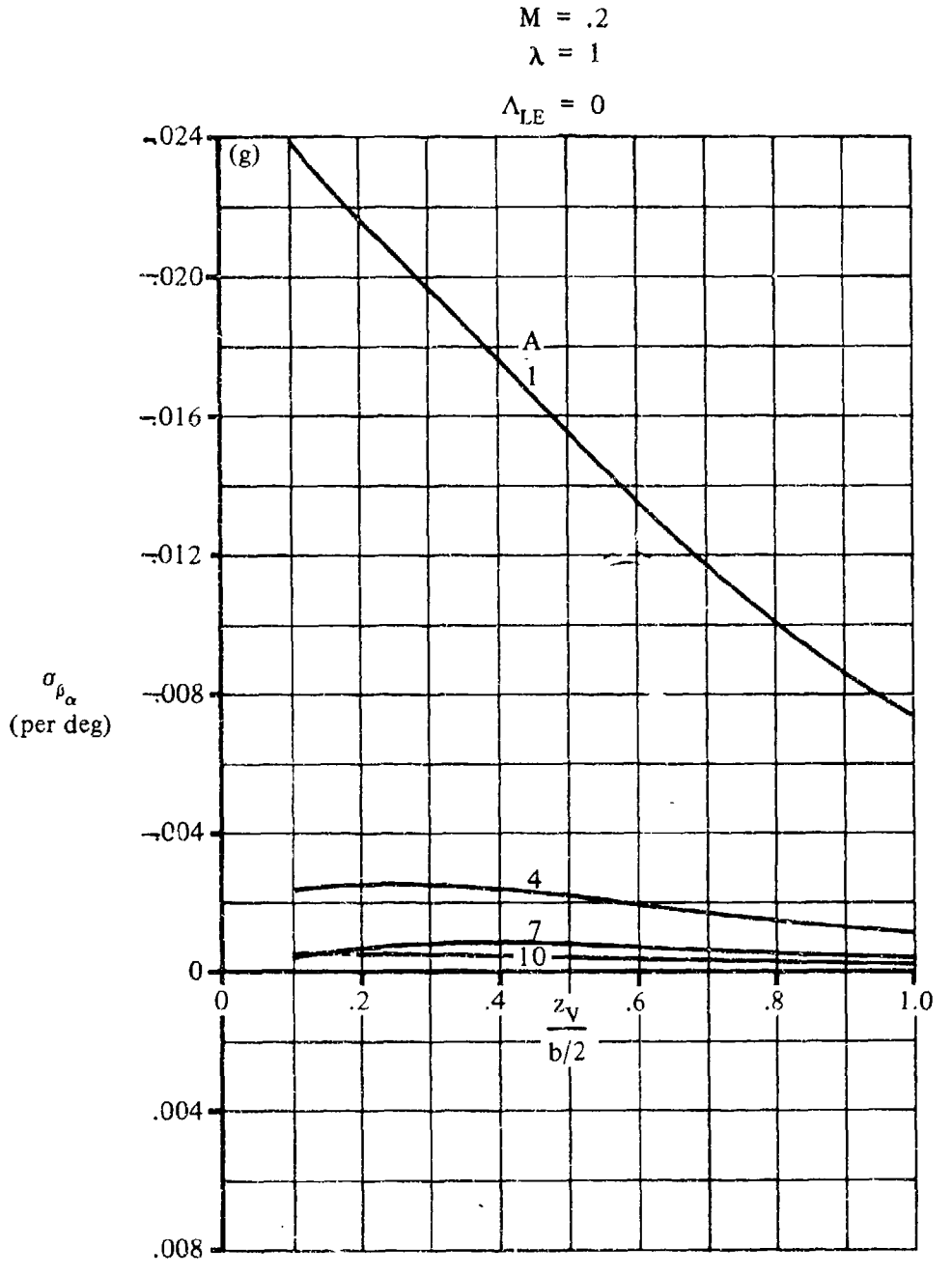

FIGURE 7.4.4.4-6 (CONTD)

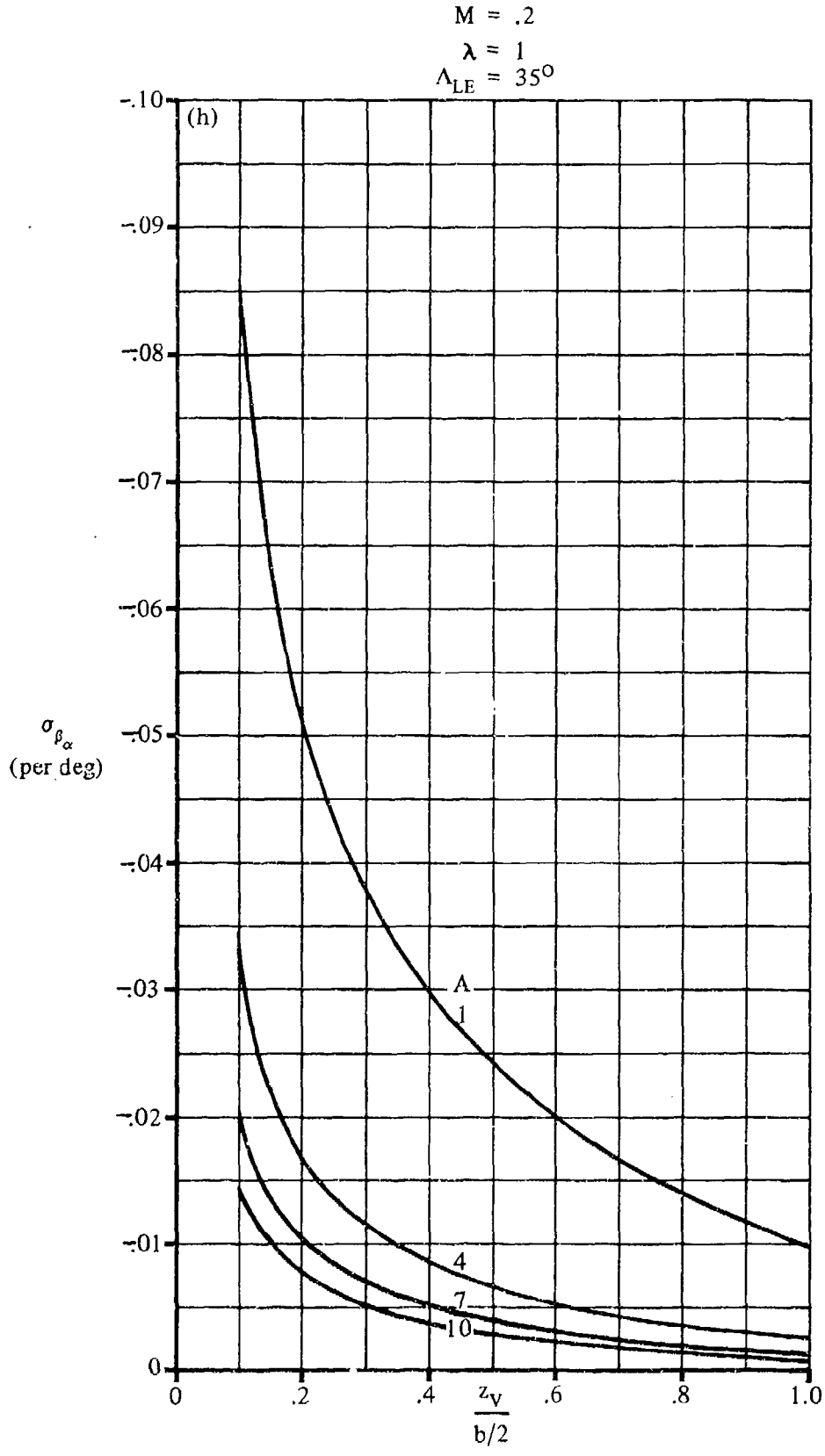

FIGURE 7.4.4.4-6 (CONTD)

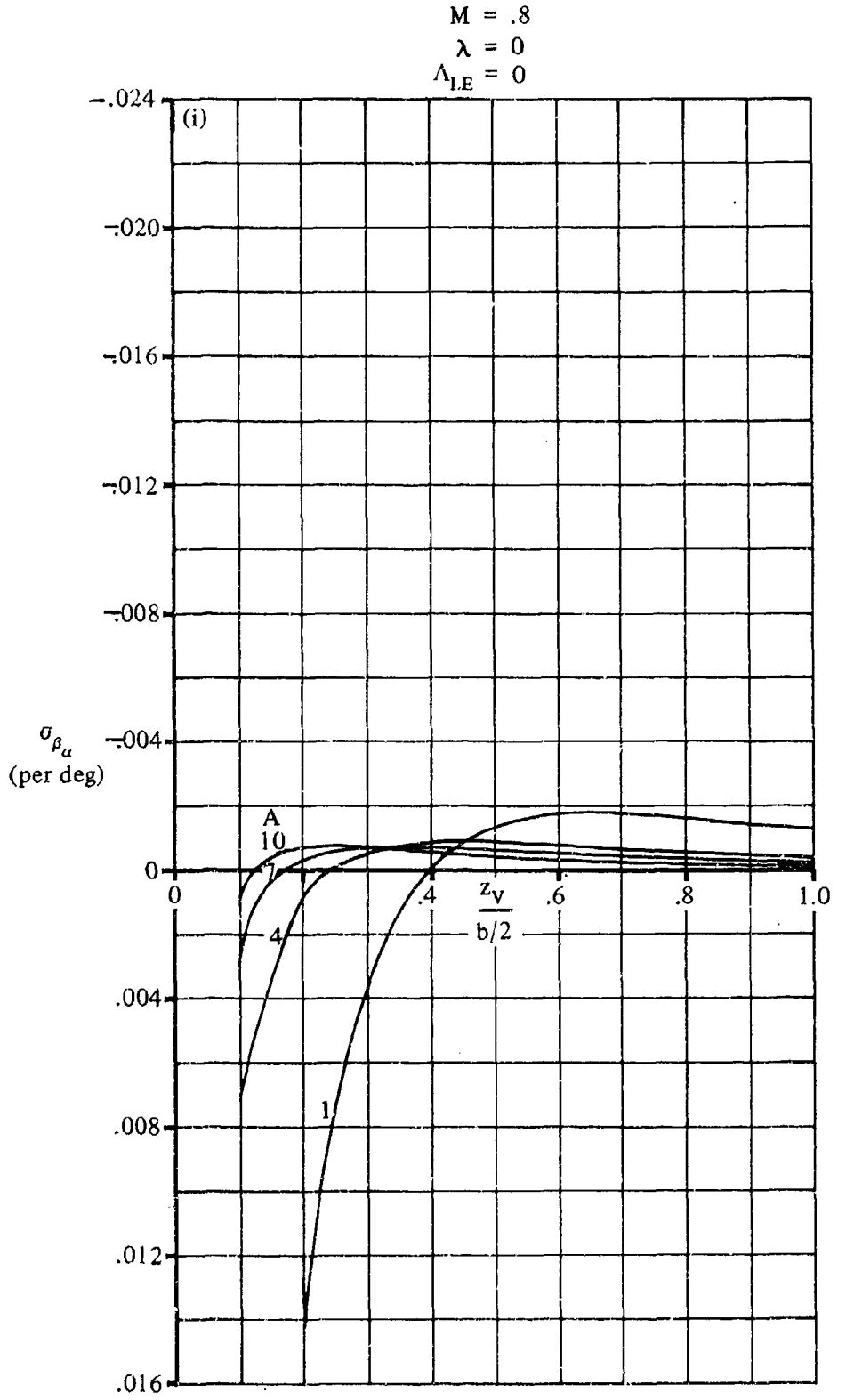

FIGURE 7.4.4.4-6 (CONTD)

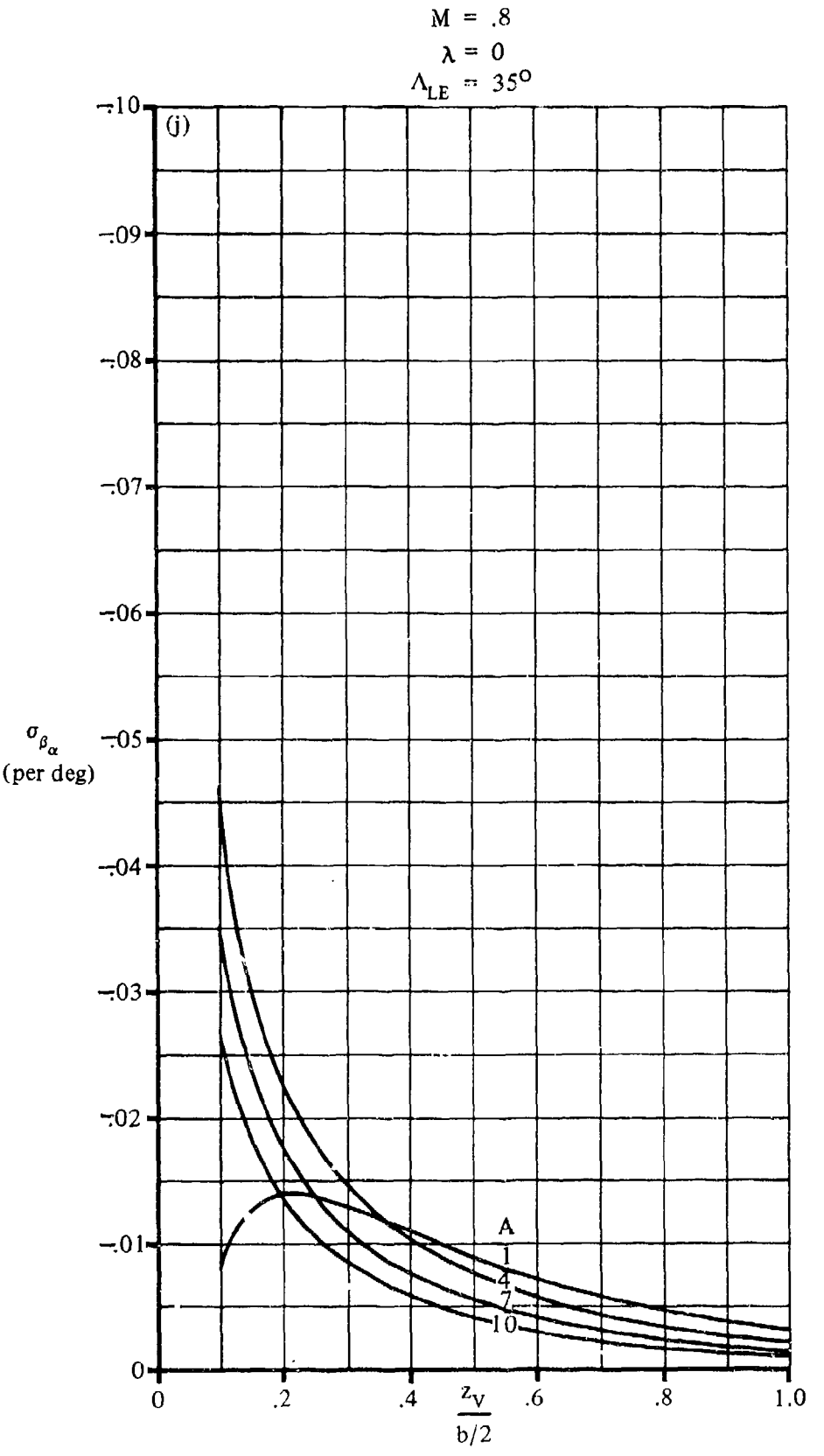

FIGURE 7.4.4.4-6 (CONTD)

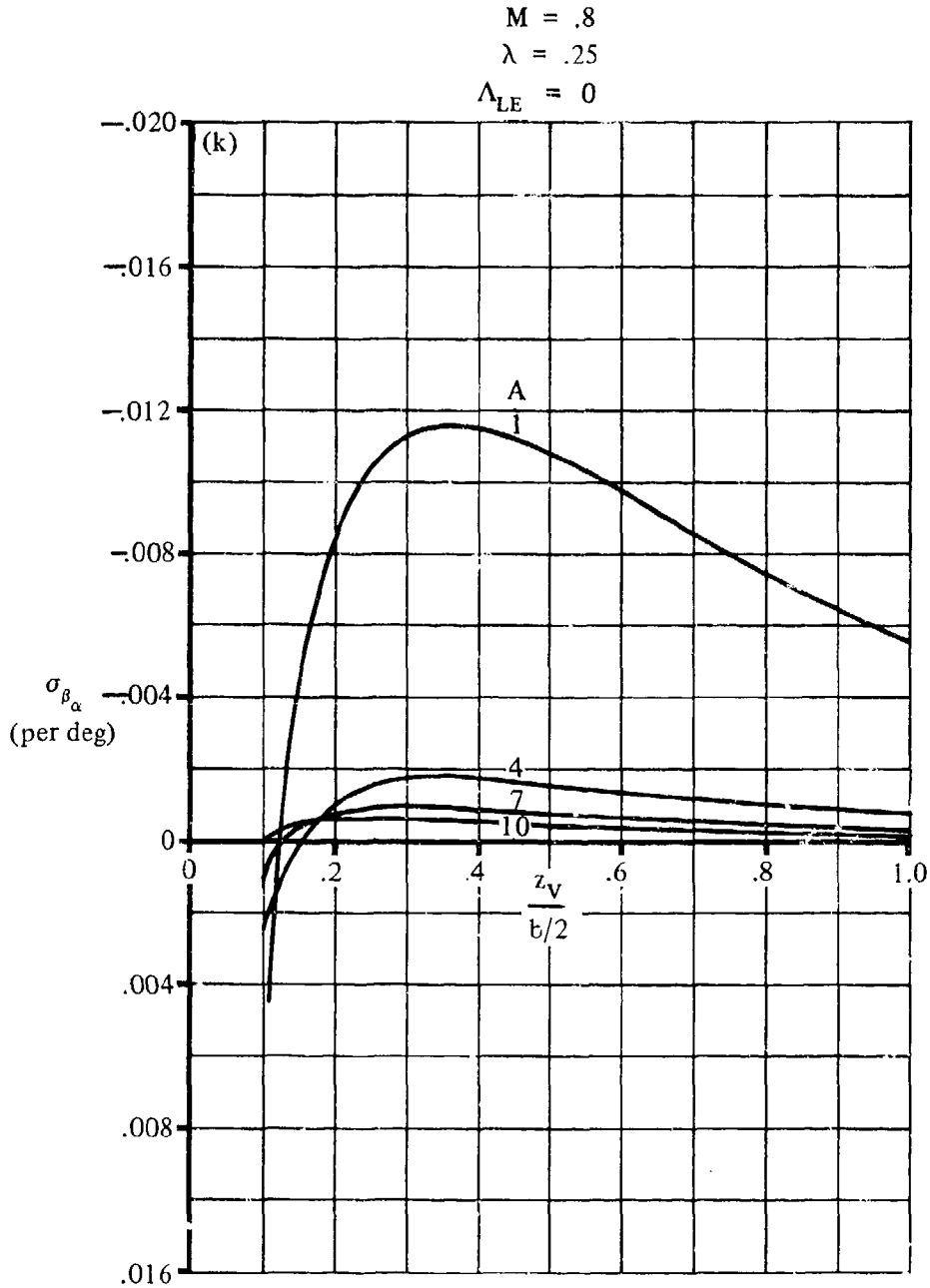

FIGURE 7.4.4.4-6 (CONTD)

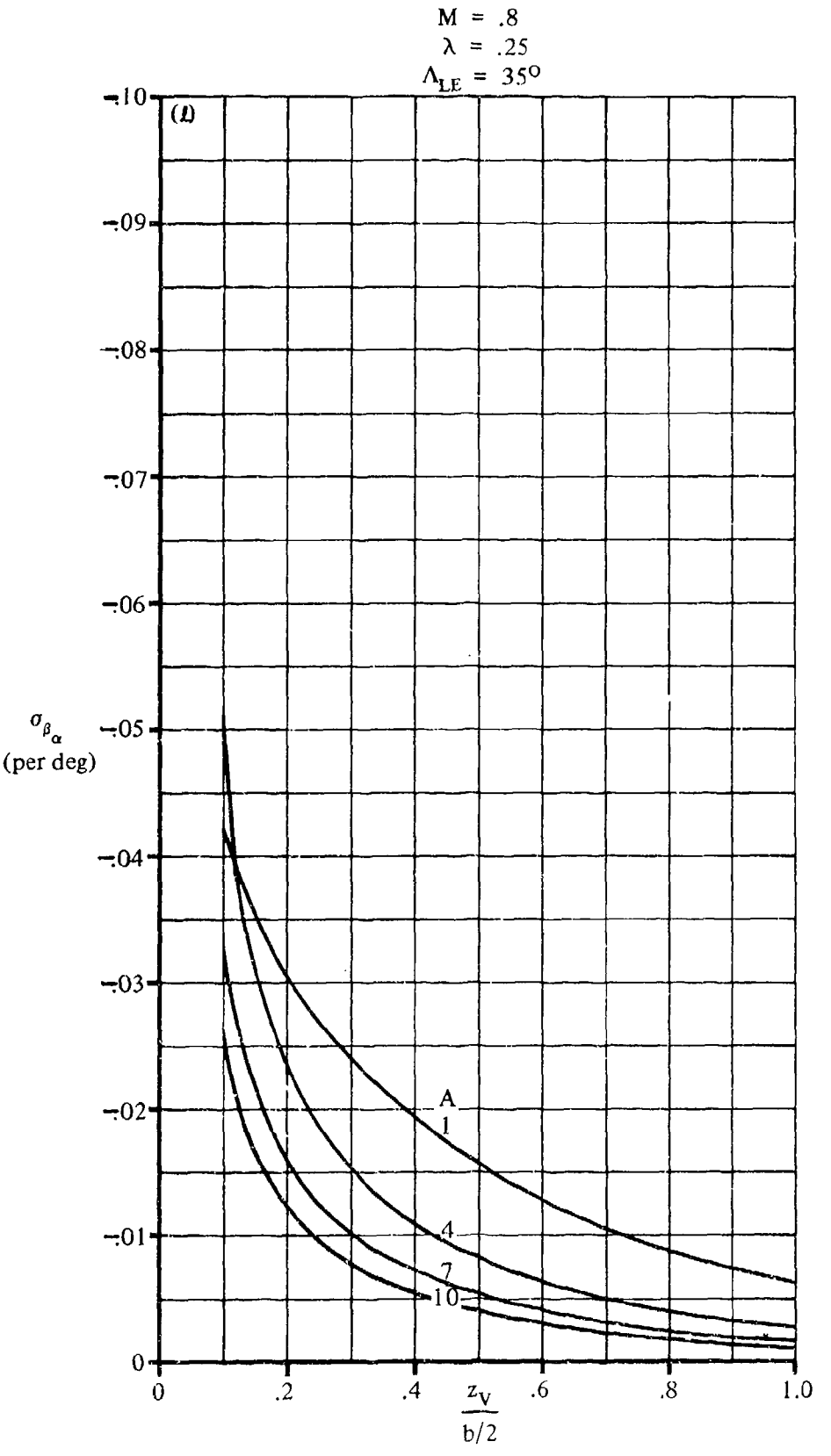

FIGURE 7.4.4.4-6 (CONTD)

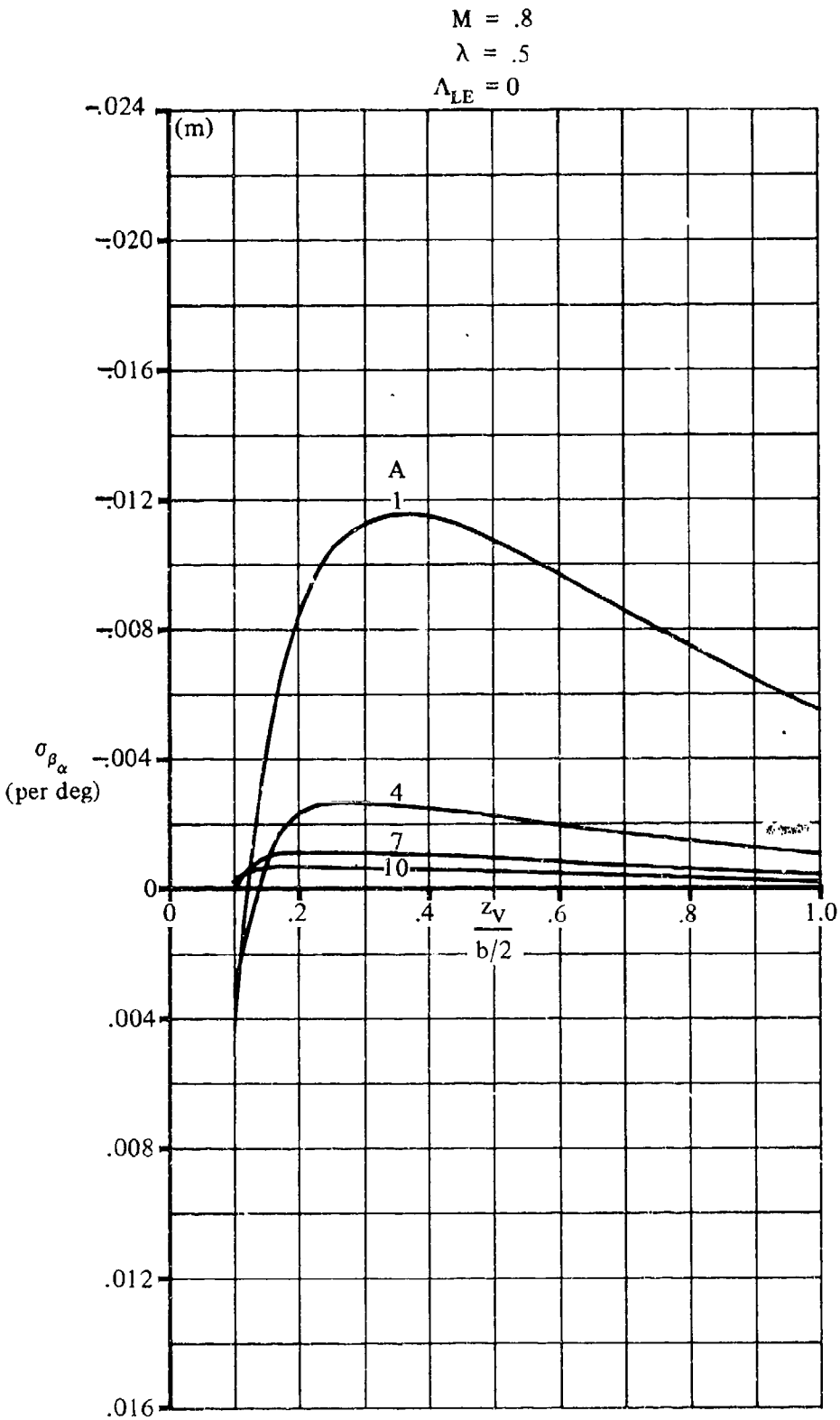

FIGURE 7.4.4.4-6 (CONTD)

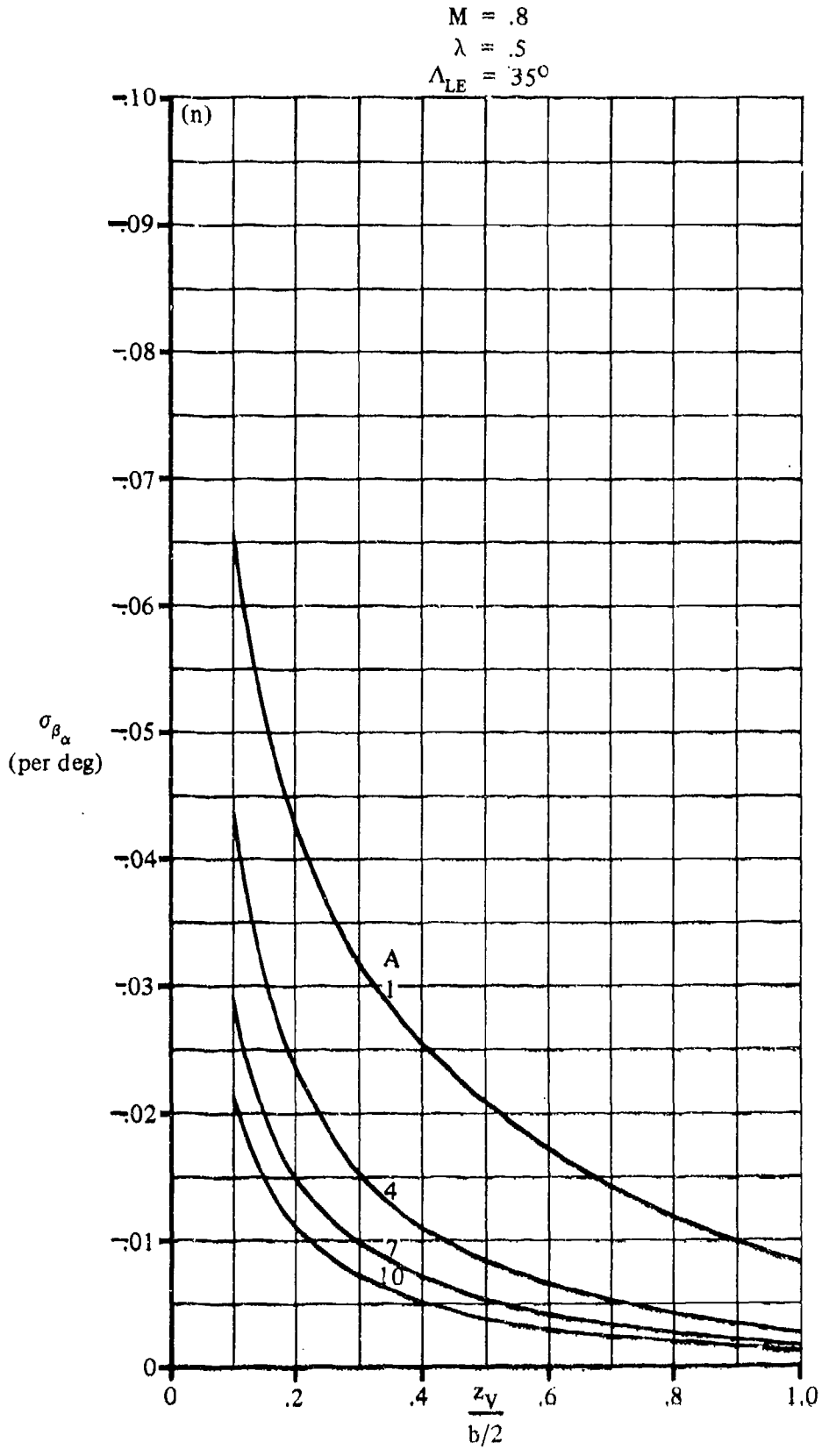

FIGURE 7.4.4.4-6 (CONTD)

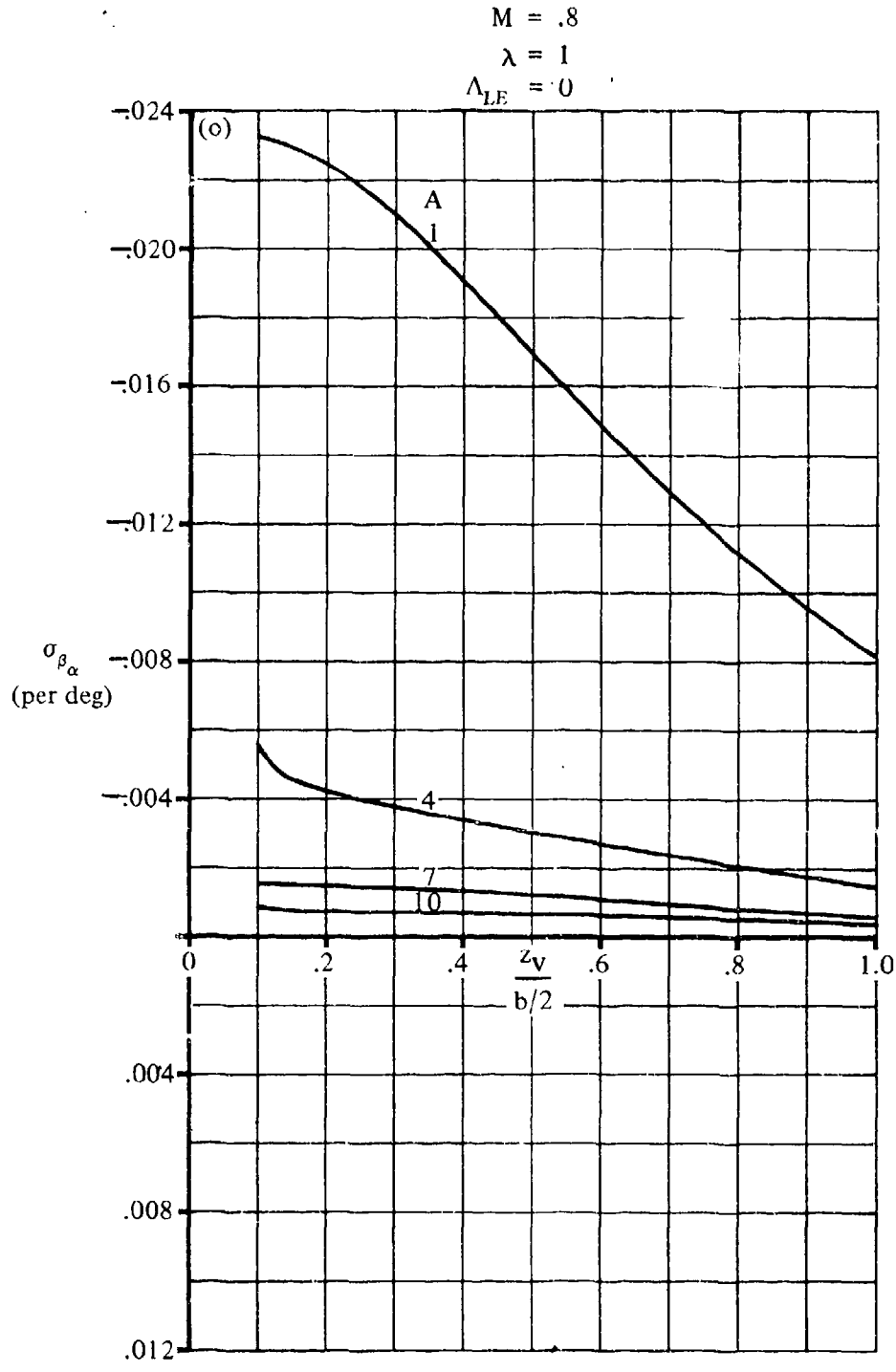

FIGURE 7.4.4.4-6 (CONTD)

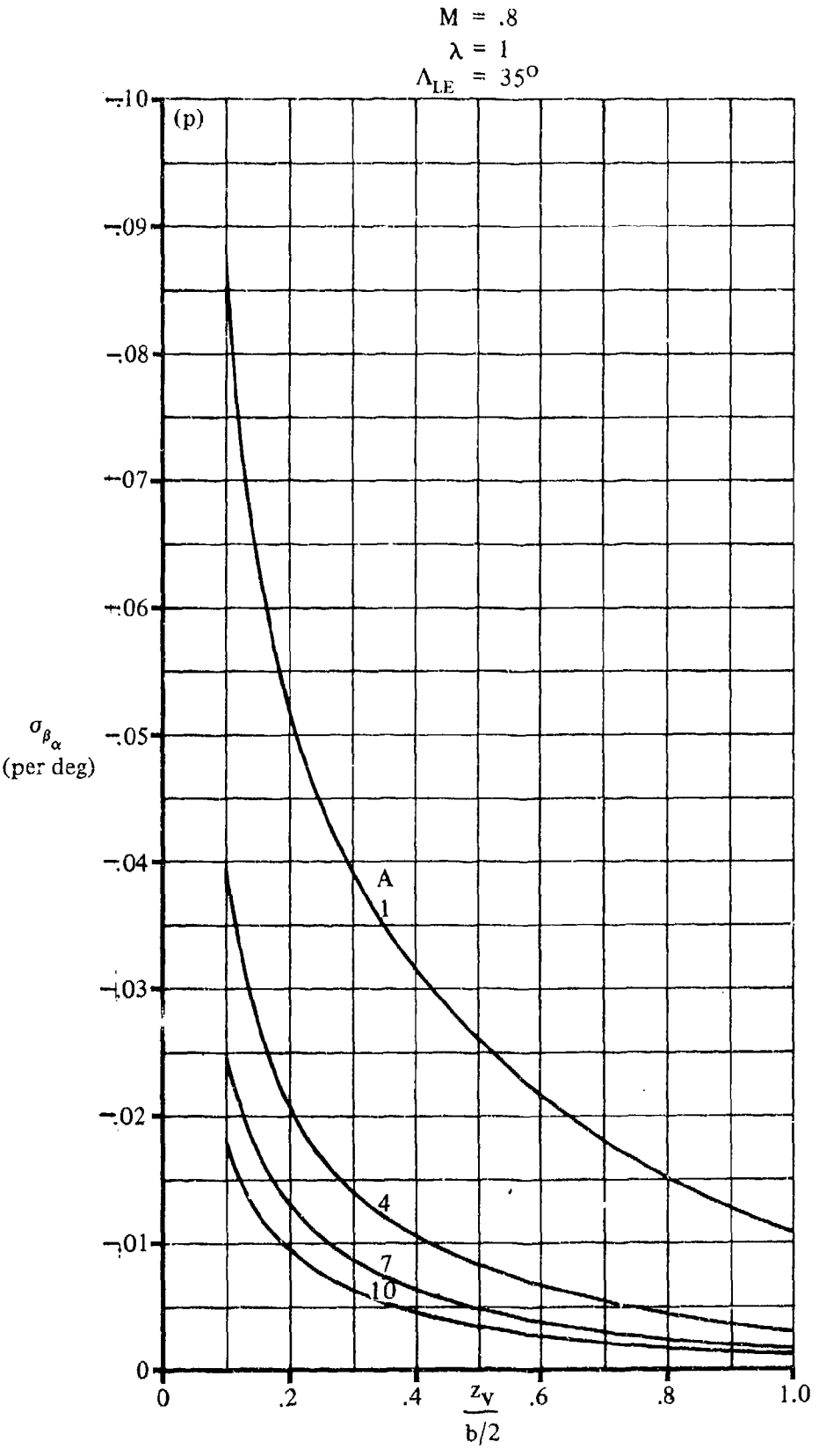

FIGURE 7.4.4.4-6 (CONTD)

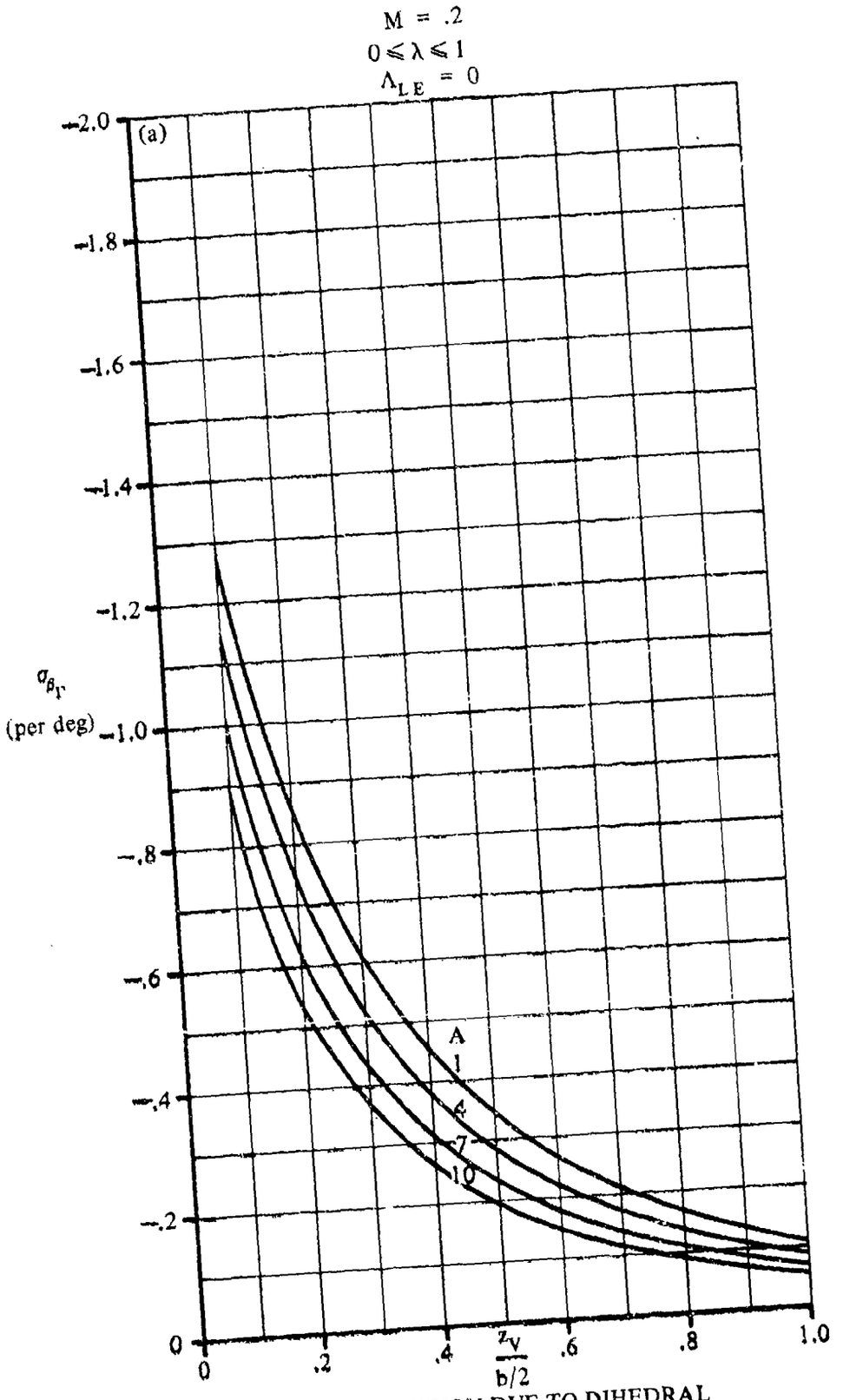

FIGURE 7.4.4.4-22 SIDEWASH CONTRIBUTION DUE TO DIHEDRAL

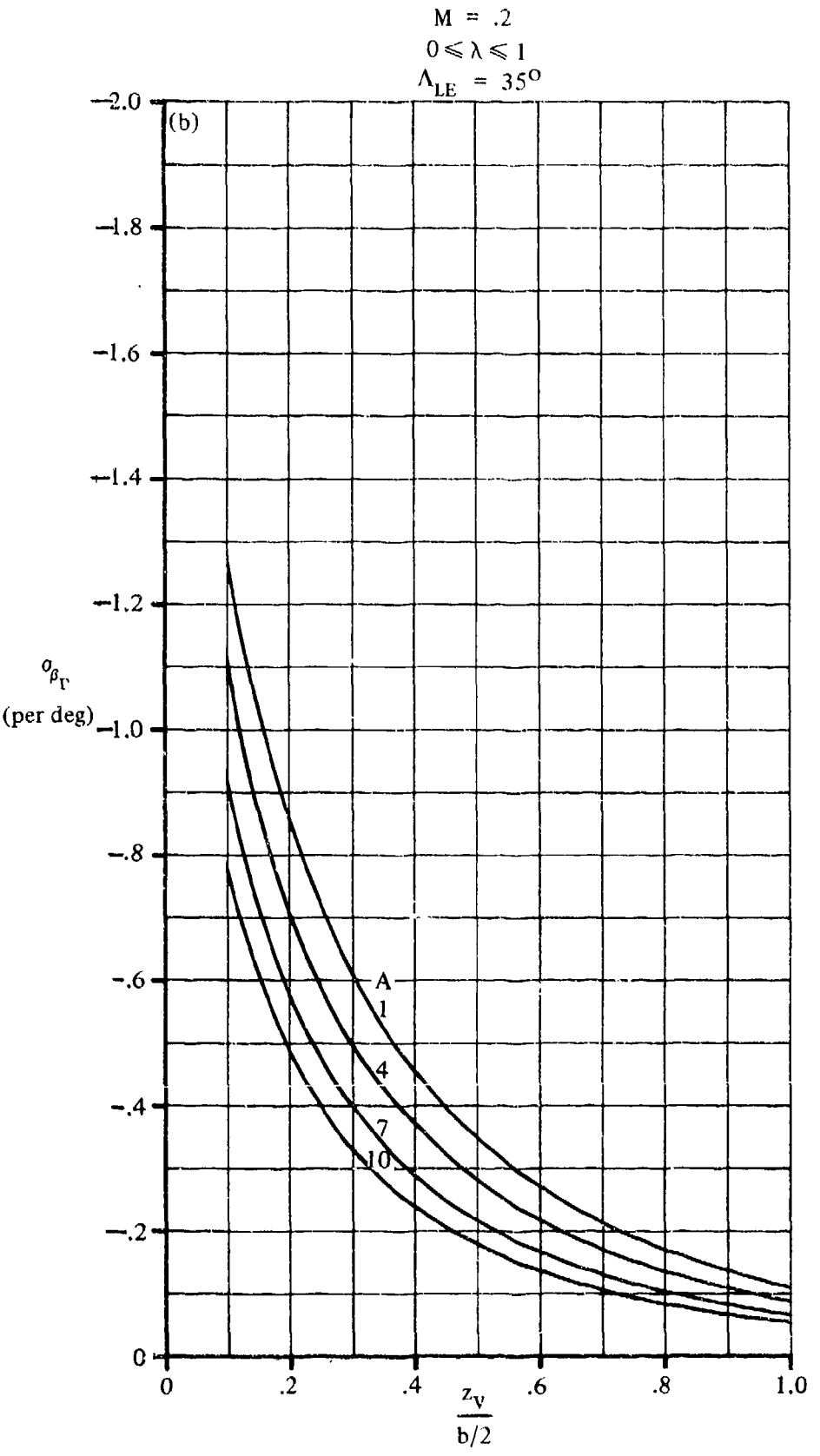

FIGURE 7.4.4.4-22 (CONTD)

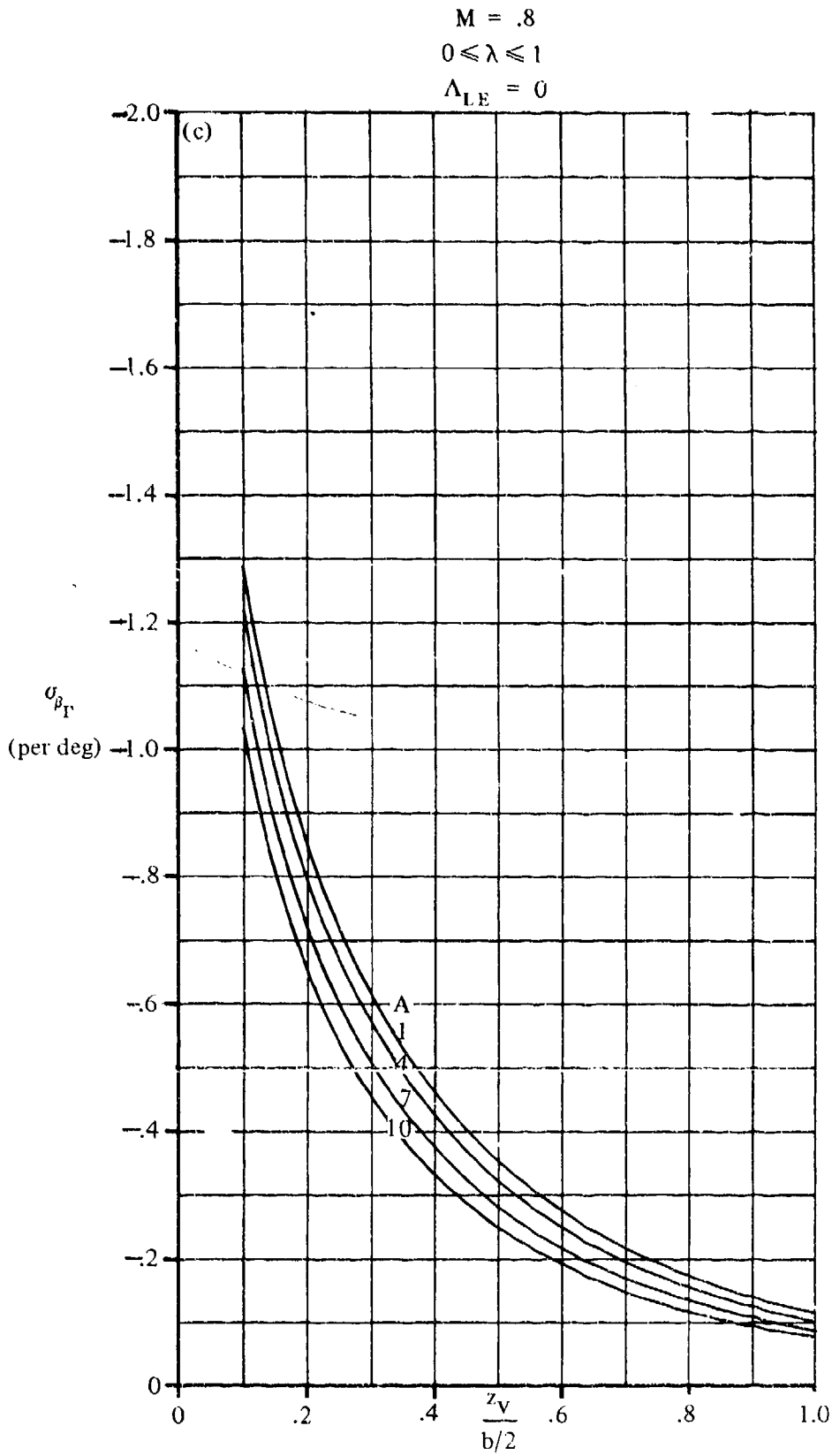

FIGURE 7.4.4.4-22 (CONTD)

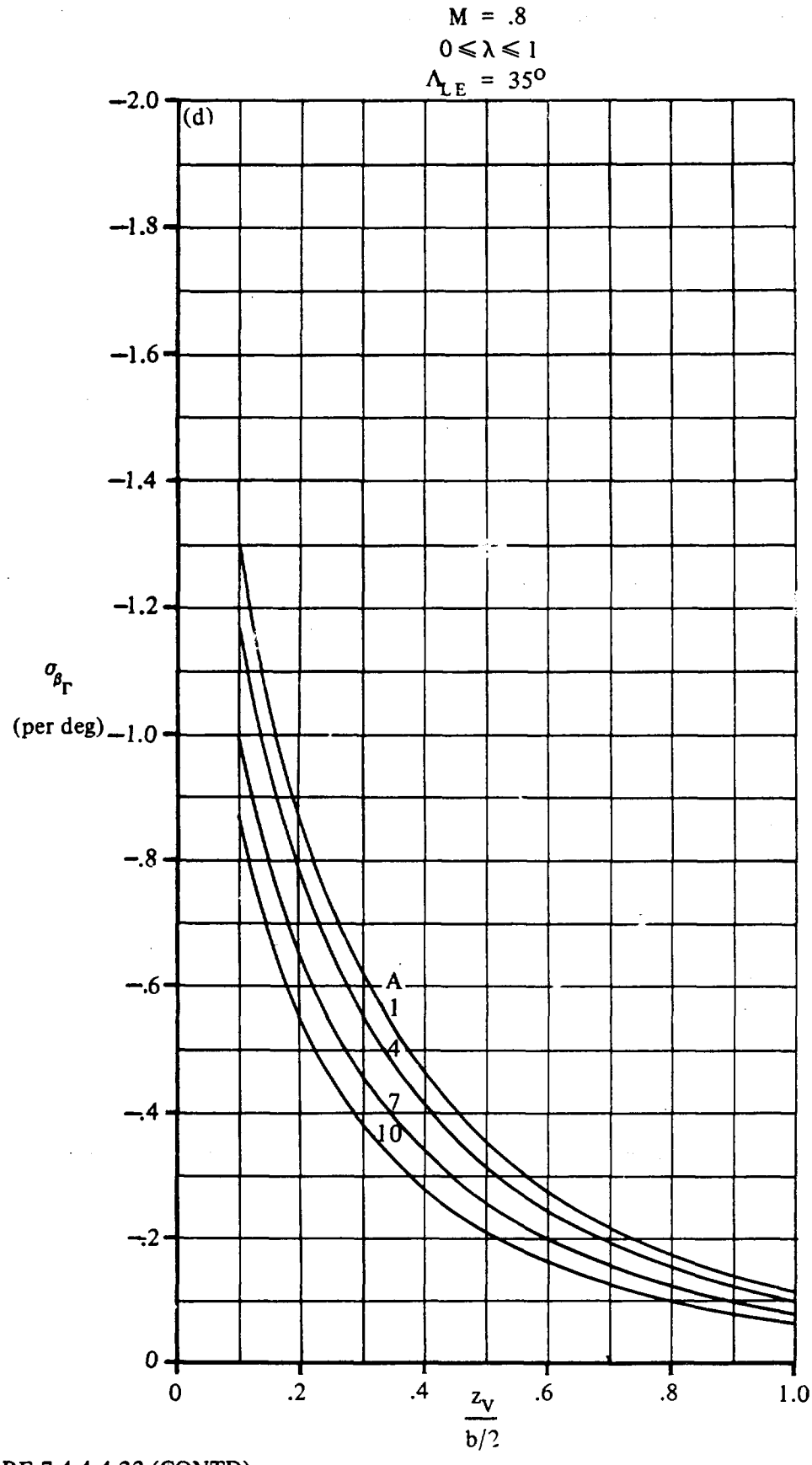

FIGURE 7.4.4.4-22 (CONTD)

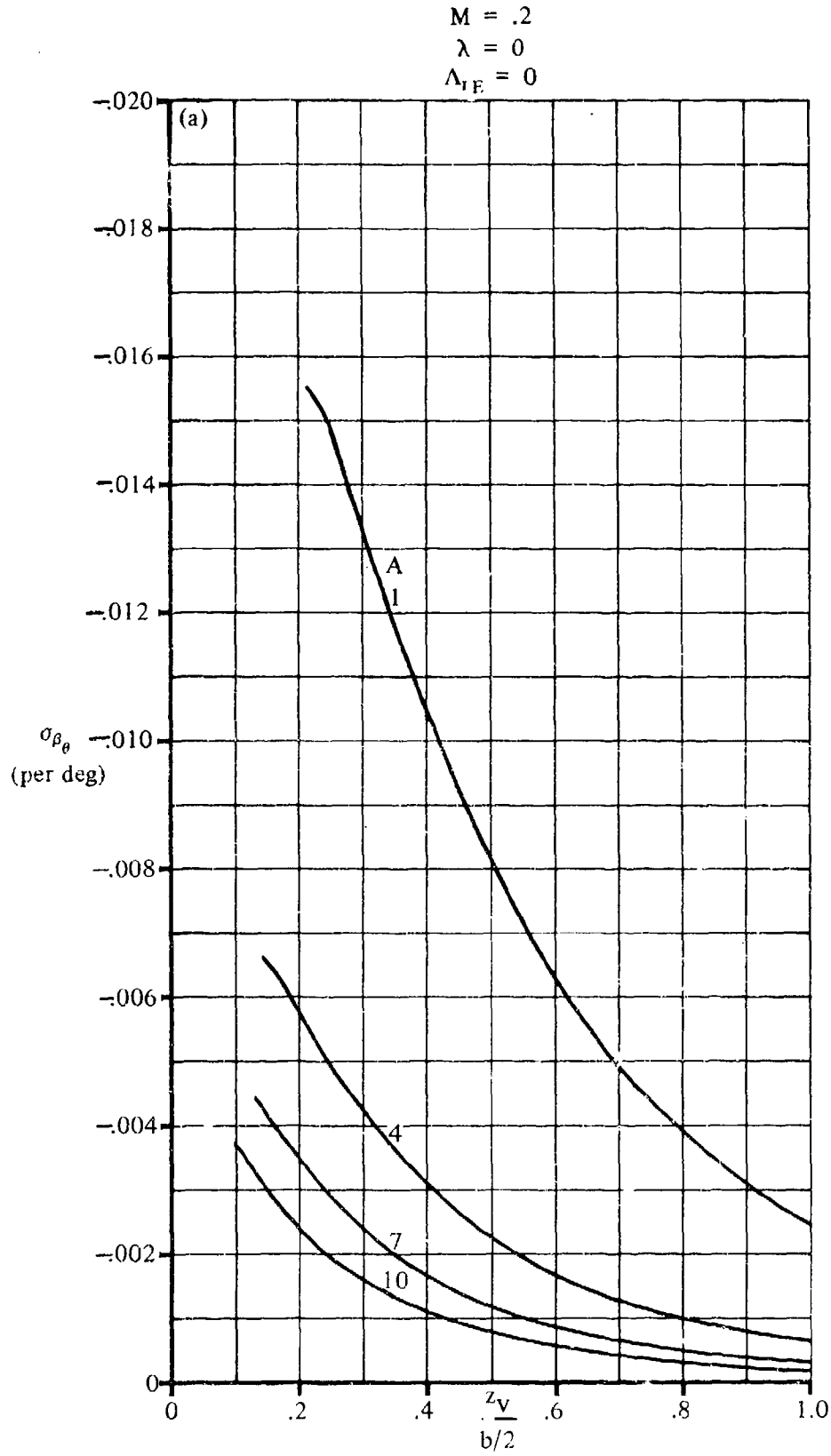

FIGURE 7.4.4.4-26 SIDEWASH CONTRIBUTION DUE TO WING TWIST

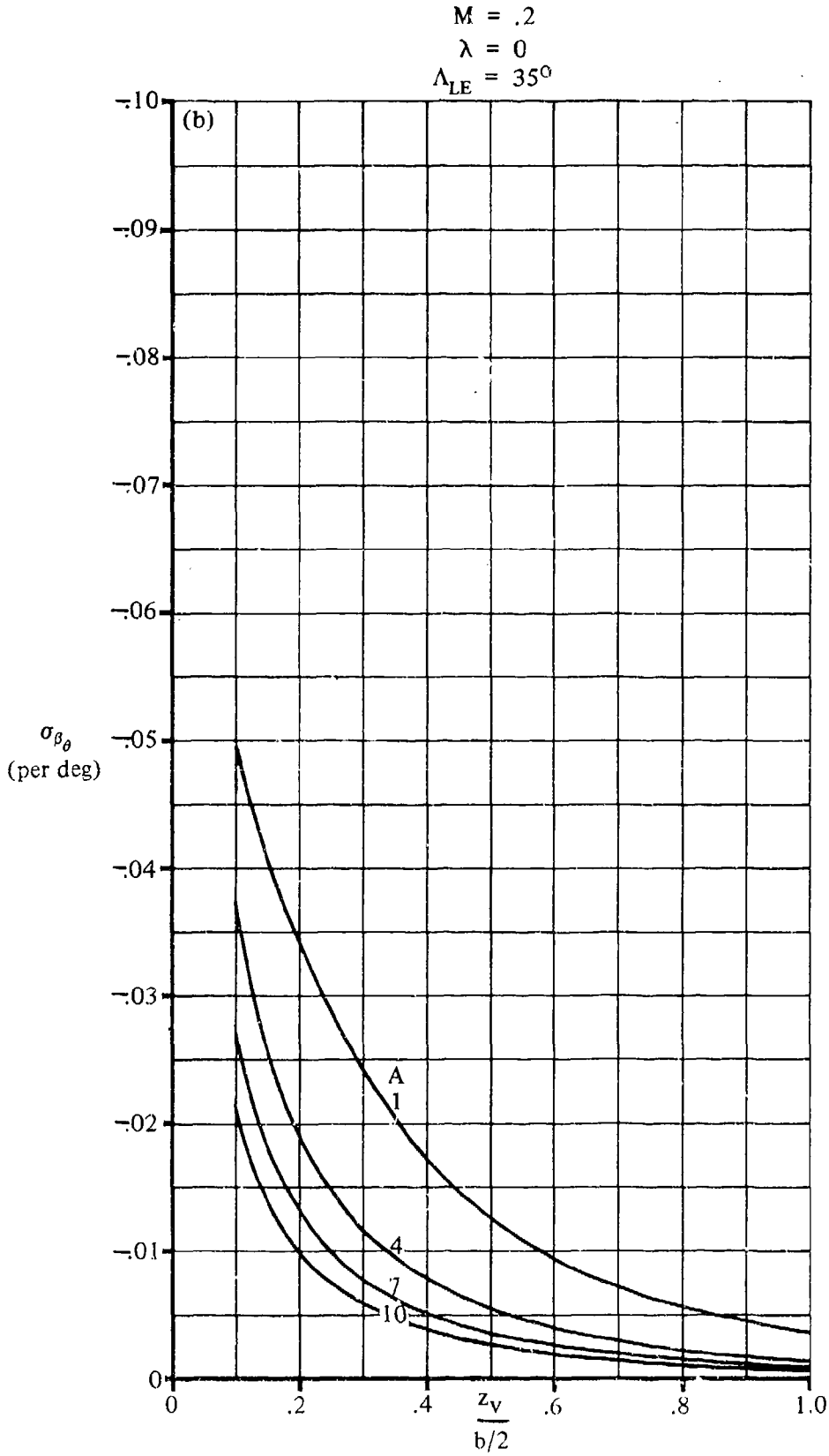

FIGURE 7.4.4.4-26 (CONTD)

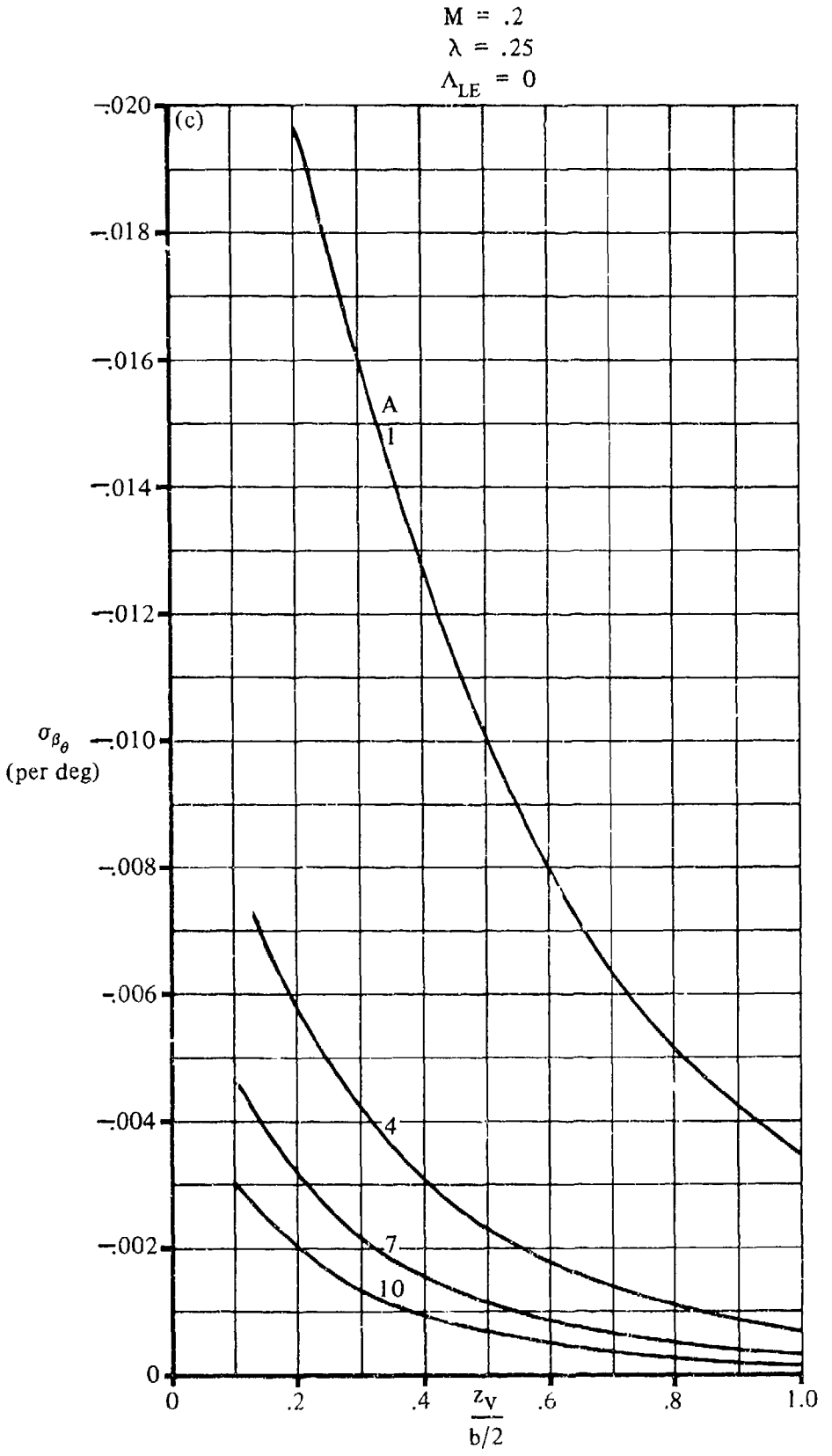

FIGURE 7.4.4.4-26 (CONTD)

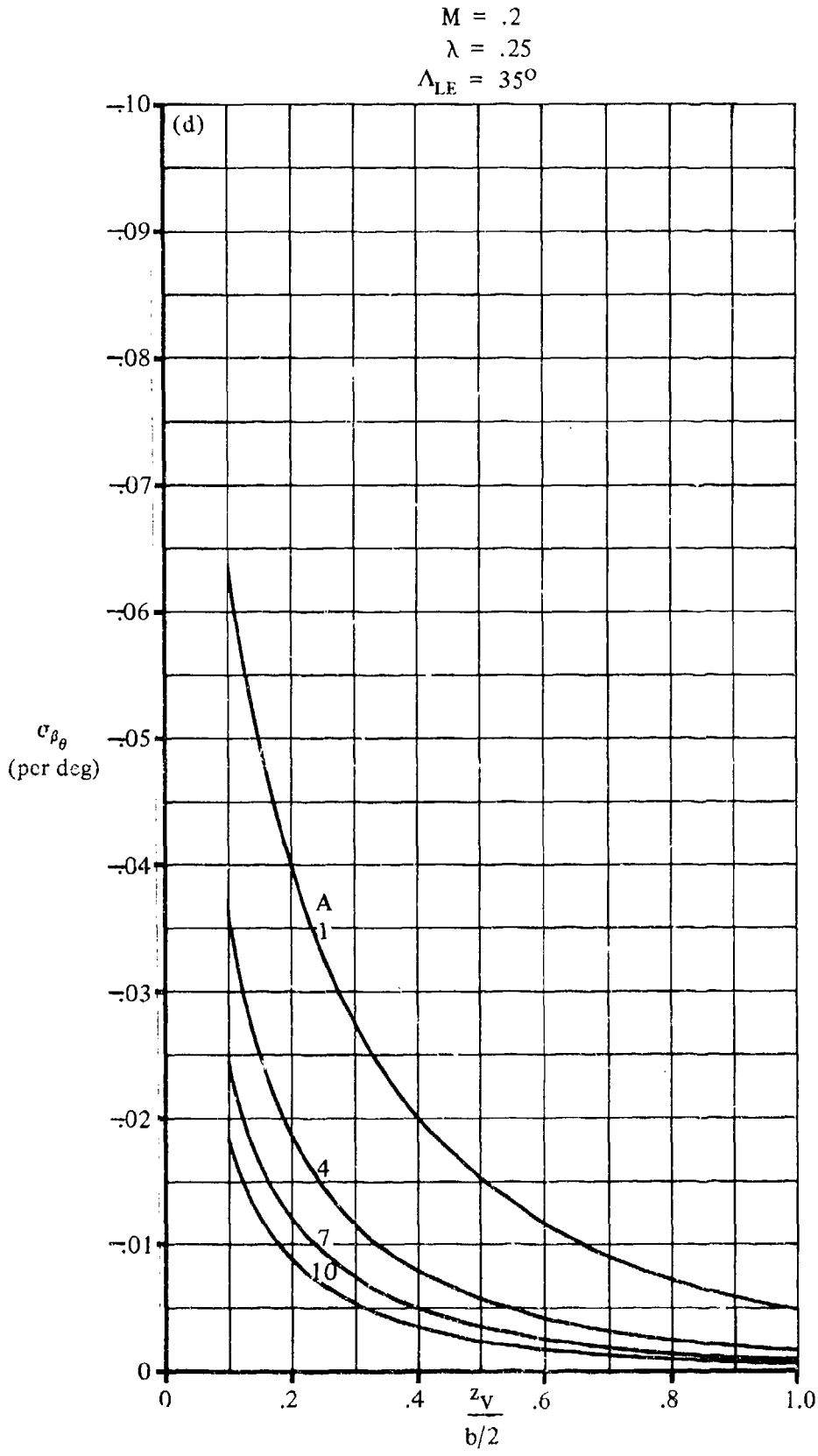

FIGURE 7.4.4.4-26 (CONTD)

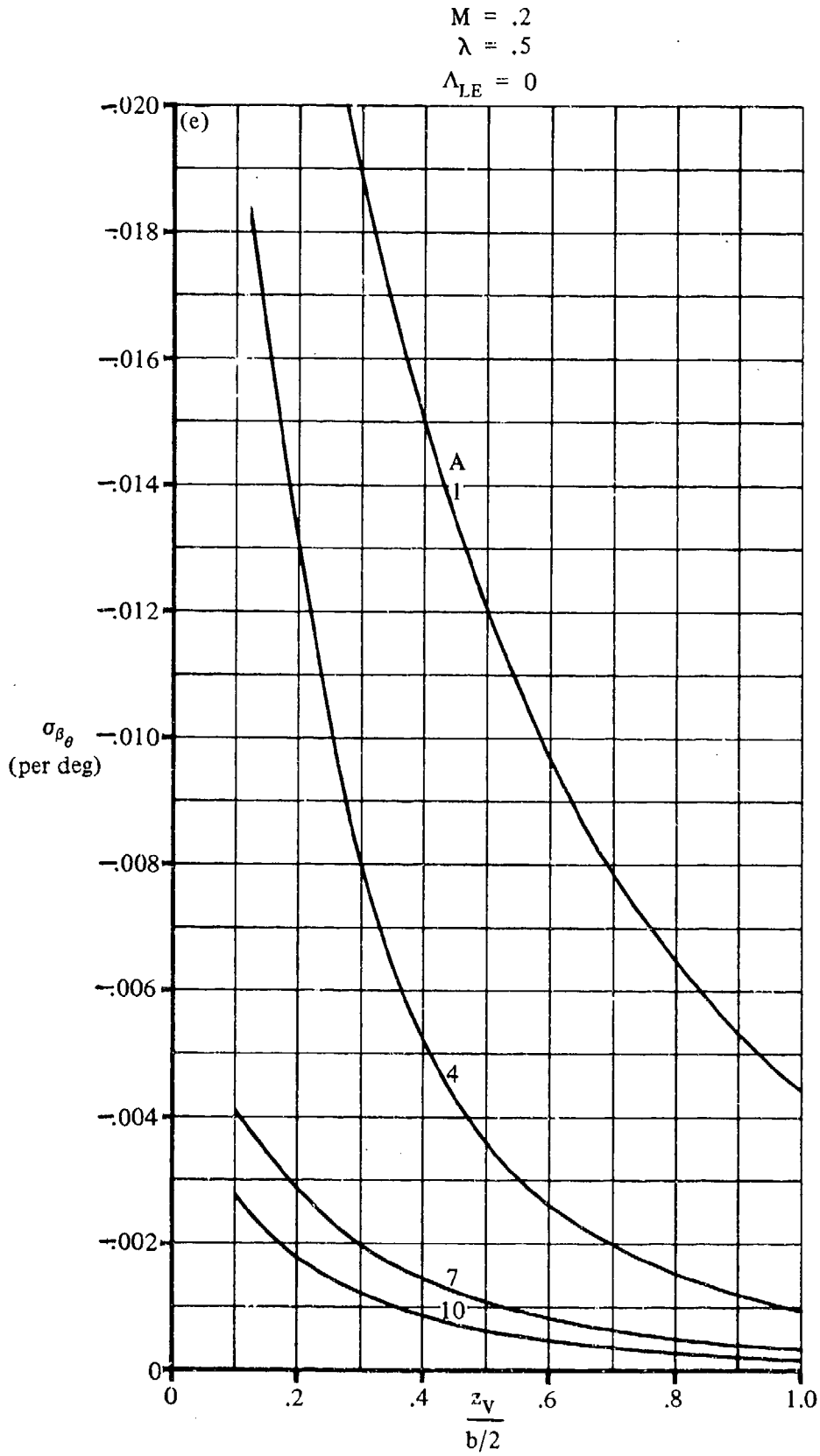

FIGURE 7.4.4.4-26 (CONTD)

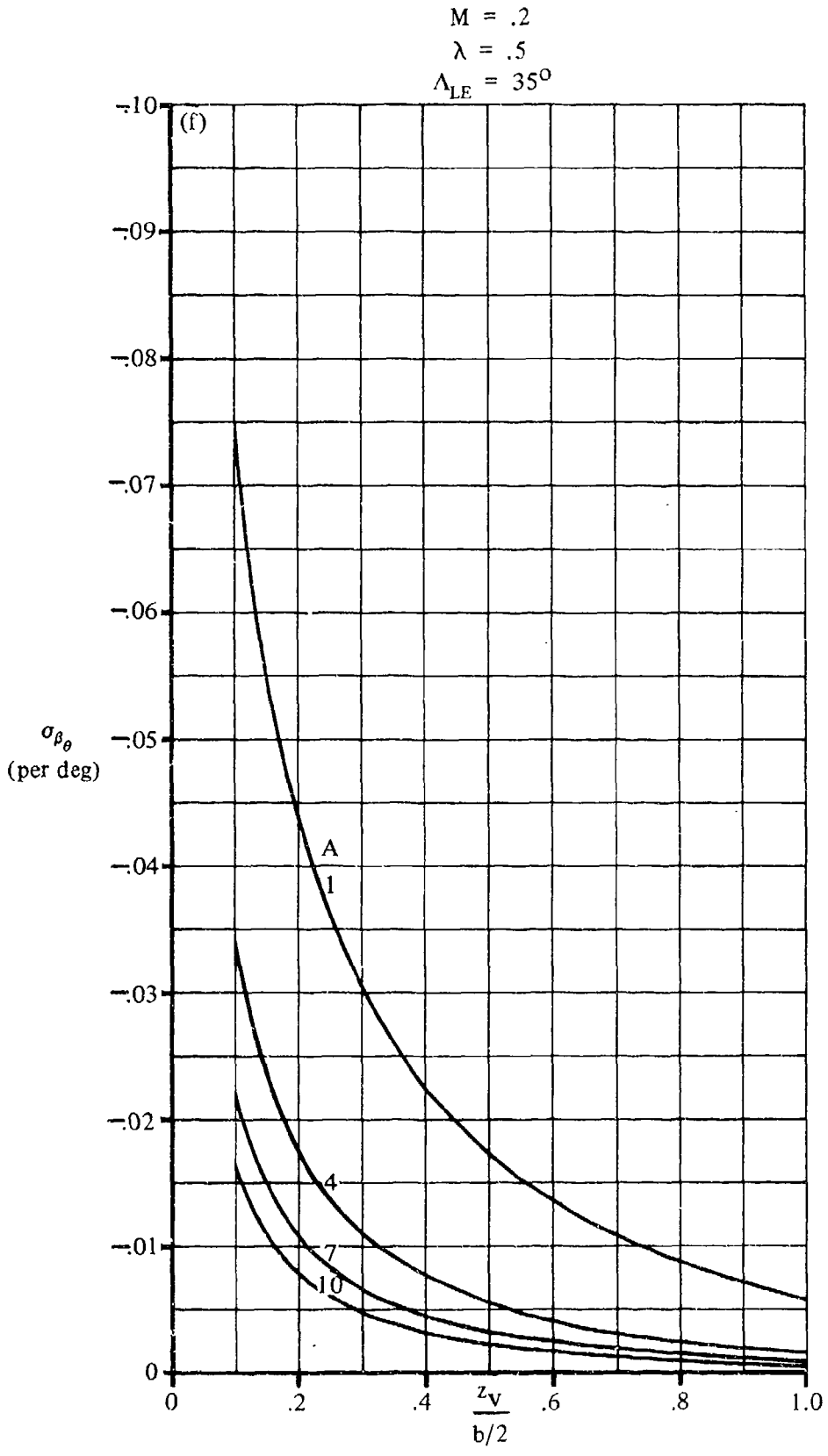

FIGURE 7.4.4.4-26 (CONTD)

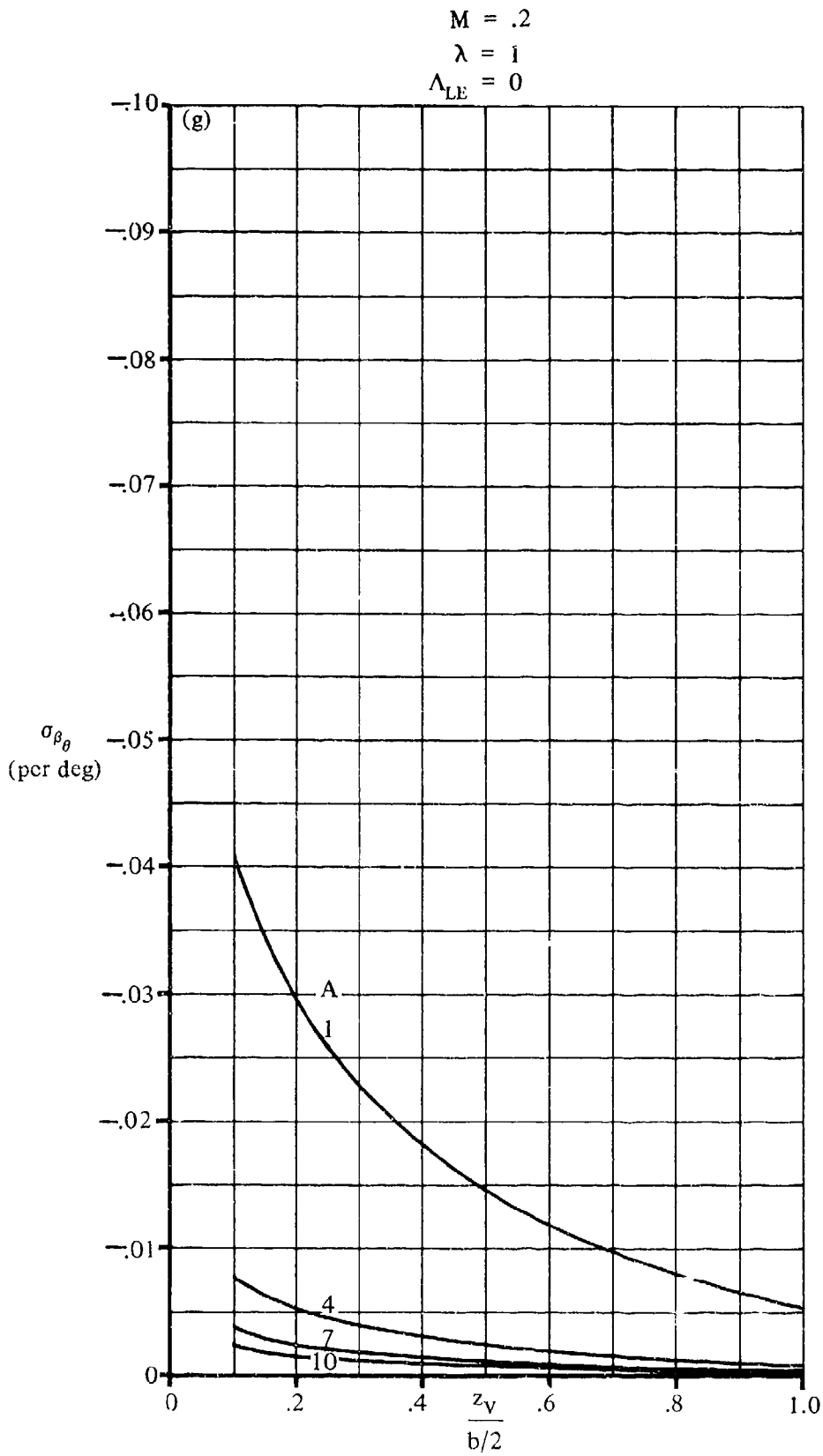

FIGURE 7.4.4.4-26 (CONTD)

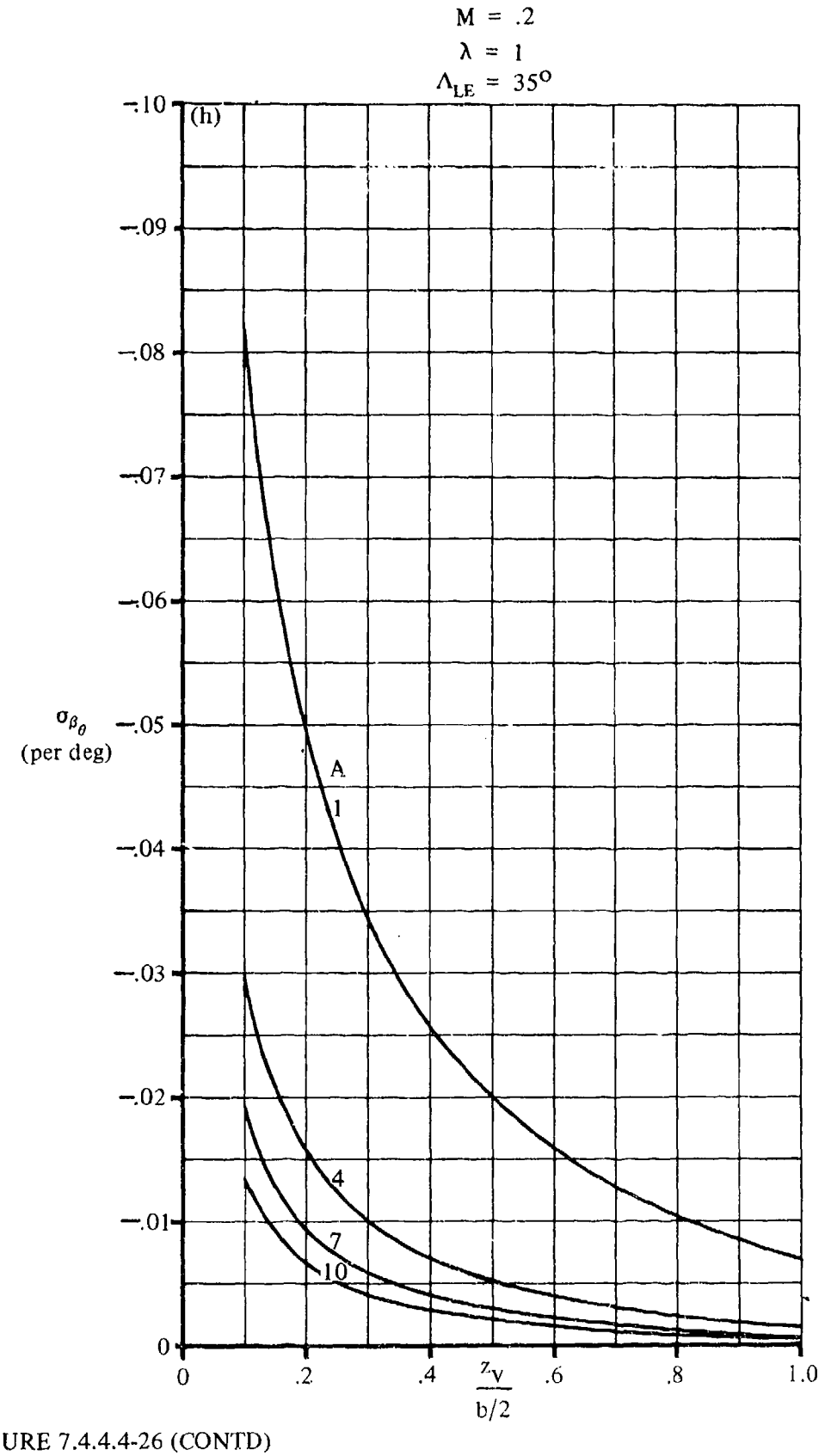

FIGURE 7.4.4.4-26 (CONTD)

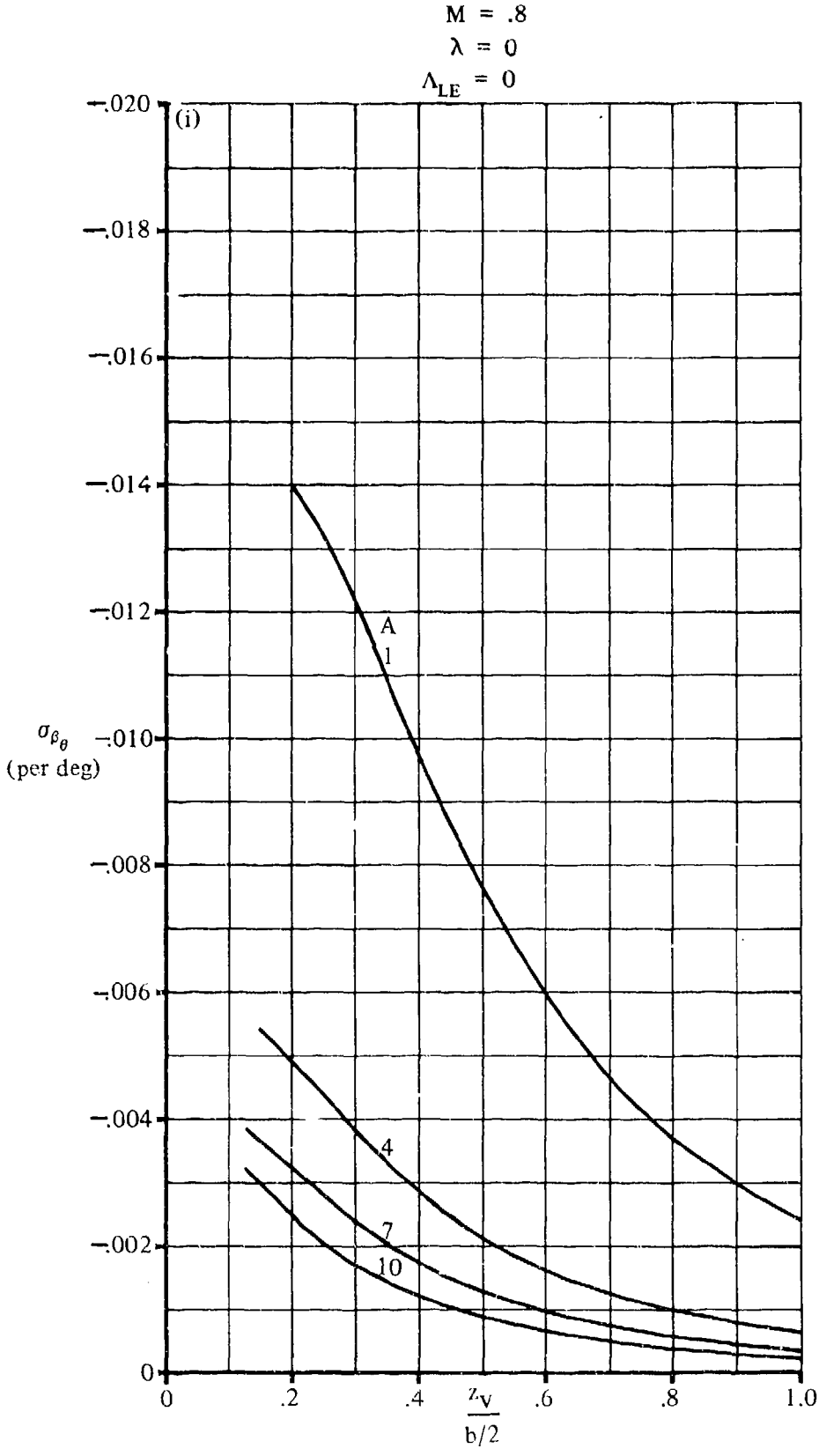

FIGURE 7.4.4.4-26 (CONTD)

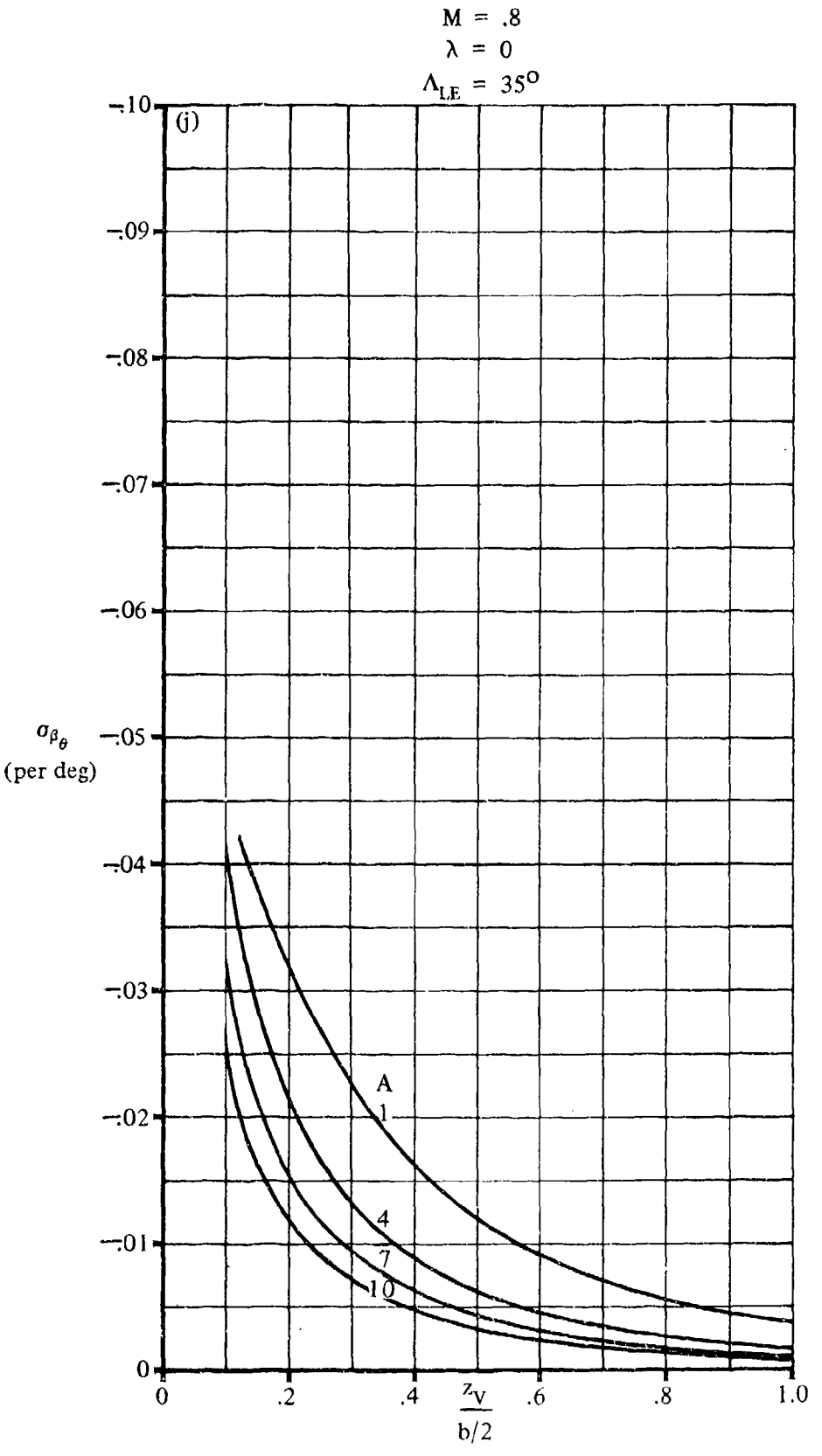

FIGURE 7.4.4.4-26 (CONTD)

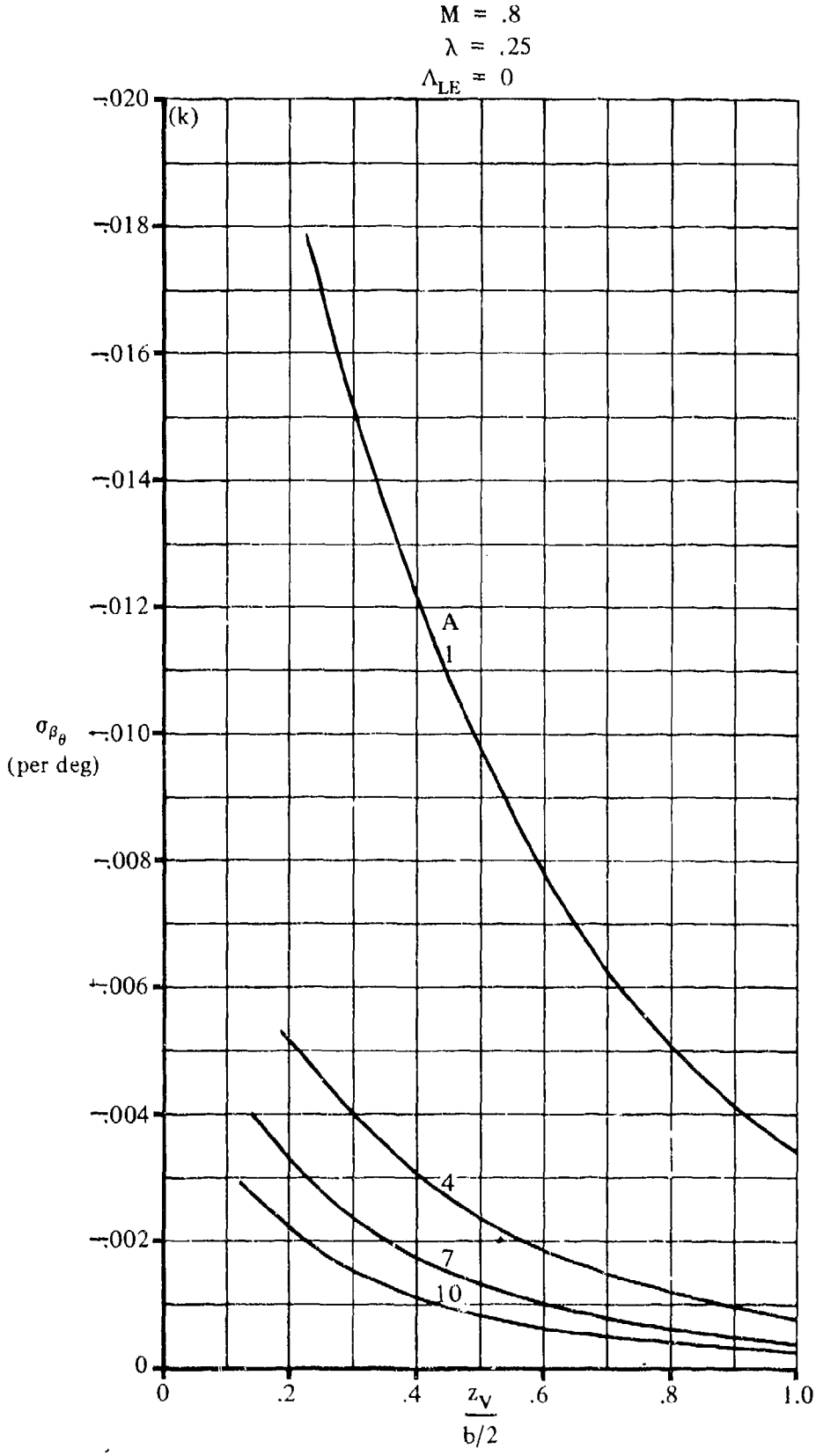

FIGURE 7.4.4.4-26 (CONTD)

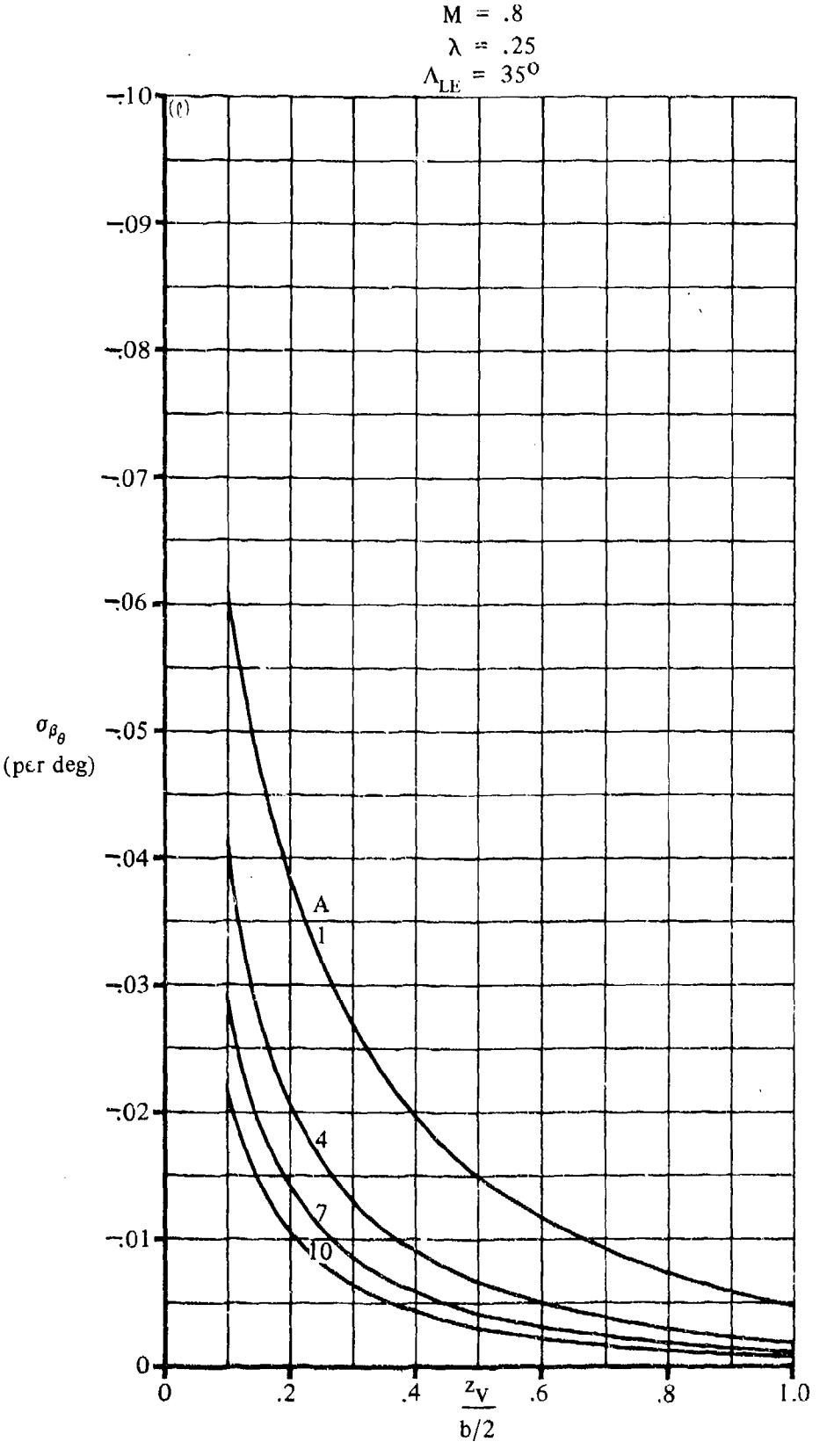

FIGURE 7.4.4.4-26 (CONTD)

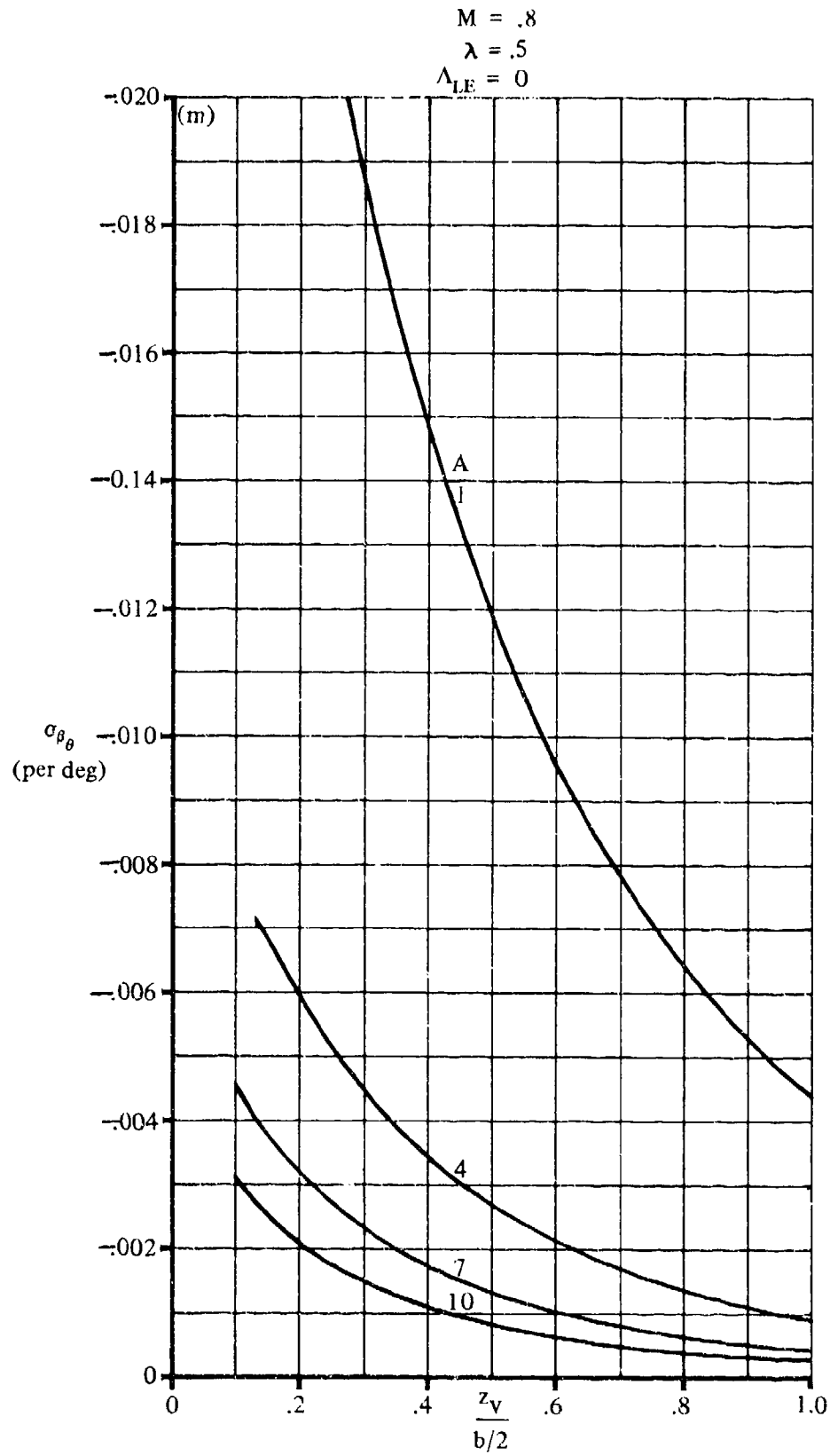

FIGURE 7.4.4.4-26 (CONTD)

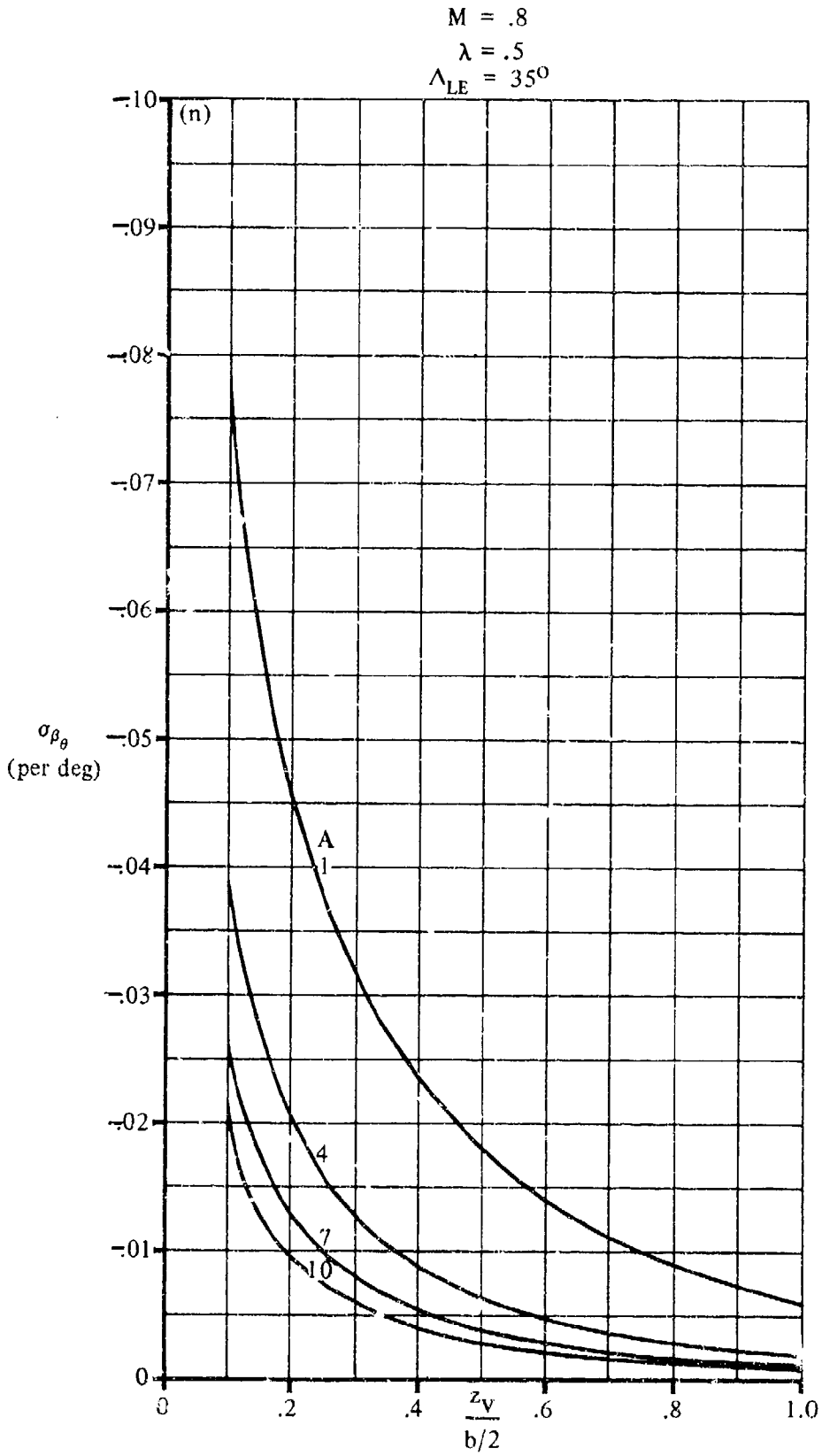

FIGURE 7.4.4.4-26 (CONTD)

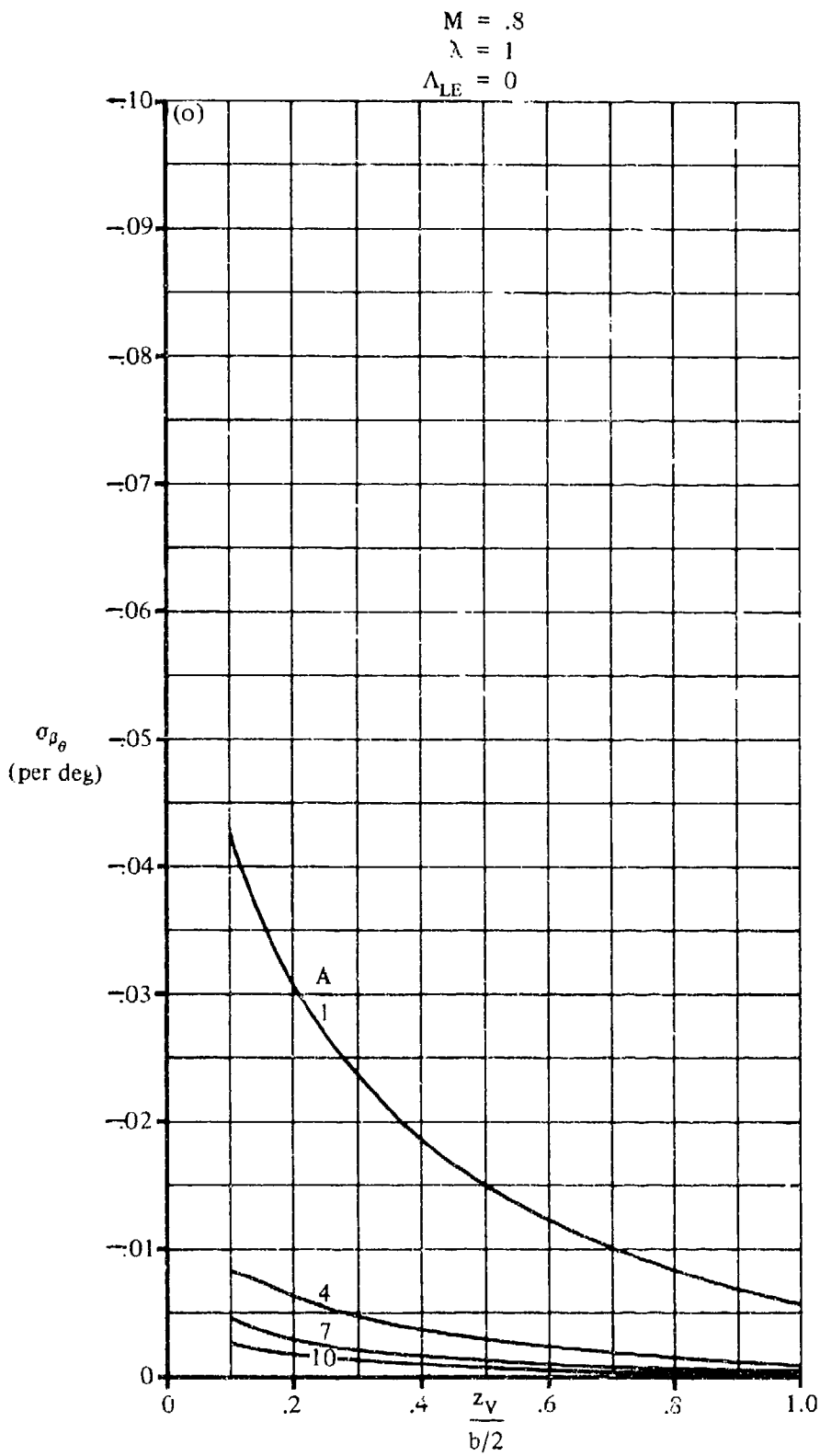

FIGURE 7.4.4.4-26 (CONTD)

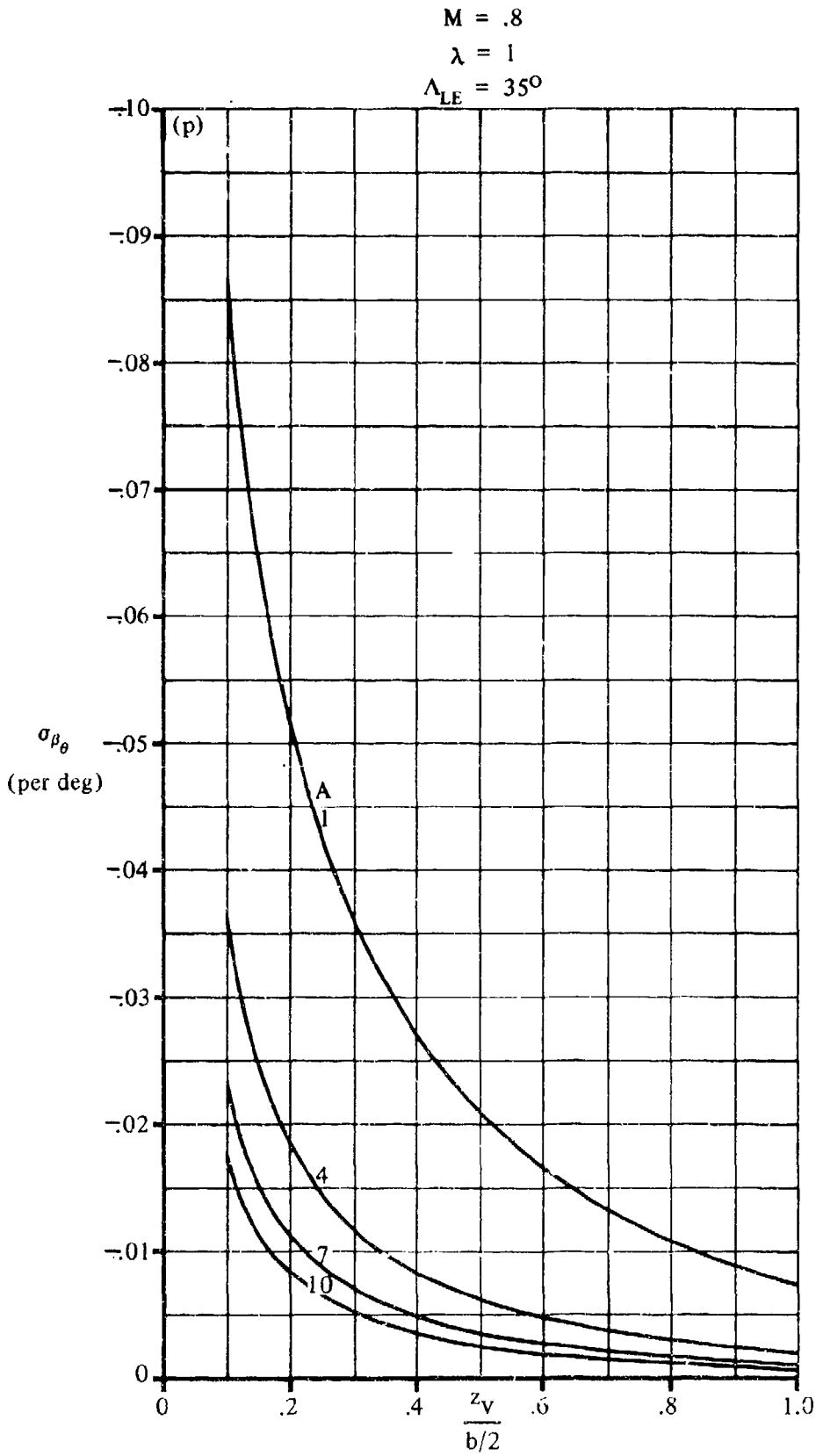

FIGURE 7.4.4.4-26 (CONTD)

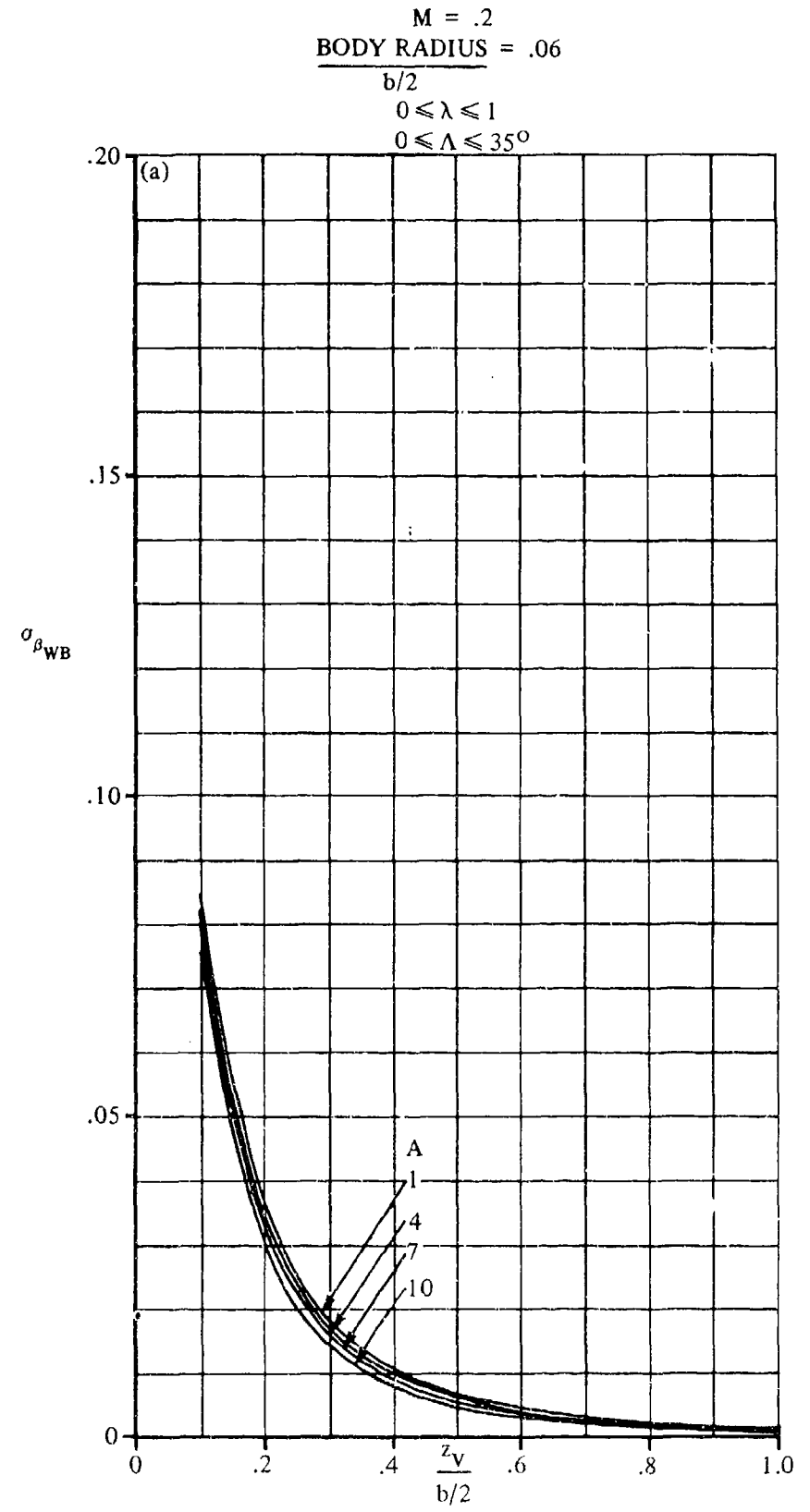

FIGURE 7.4.4.4-42 SIDEWASH CONTRIBUTION DUE TO BODY EFFECT

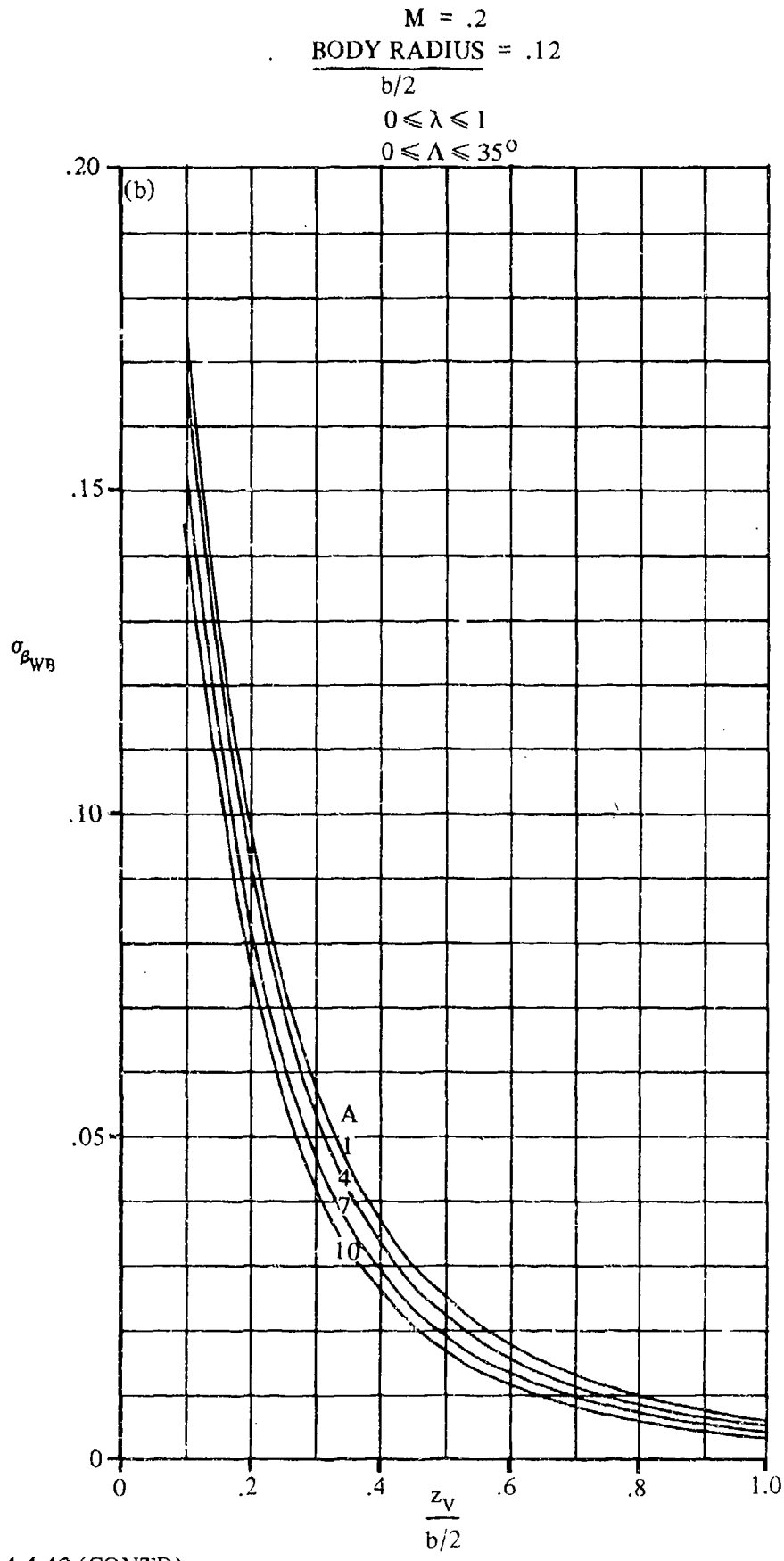

FIGURE 7.4.4.4-42 (CONTD)

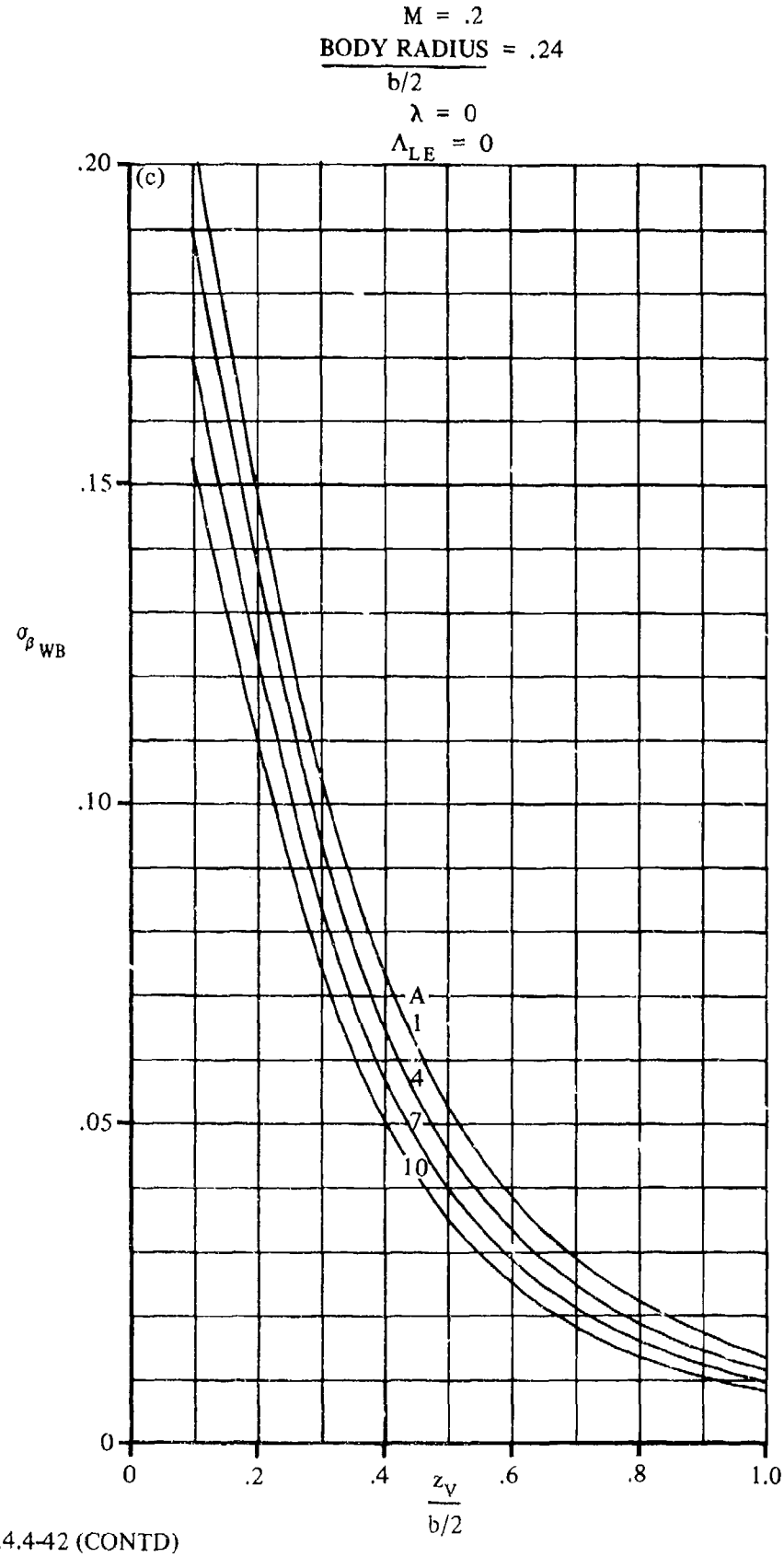

FIGURE 7.4.4.4-42 (CONTD)

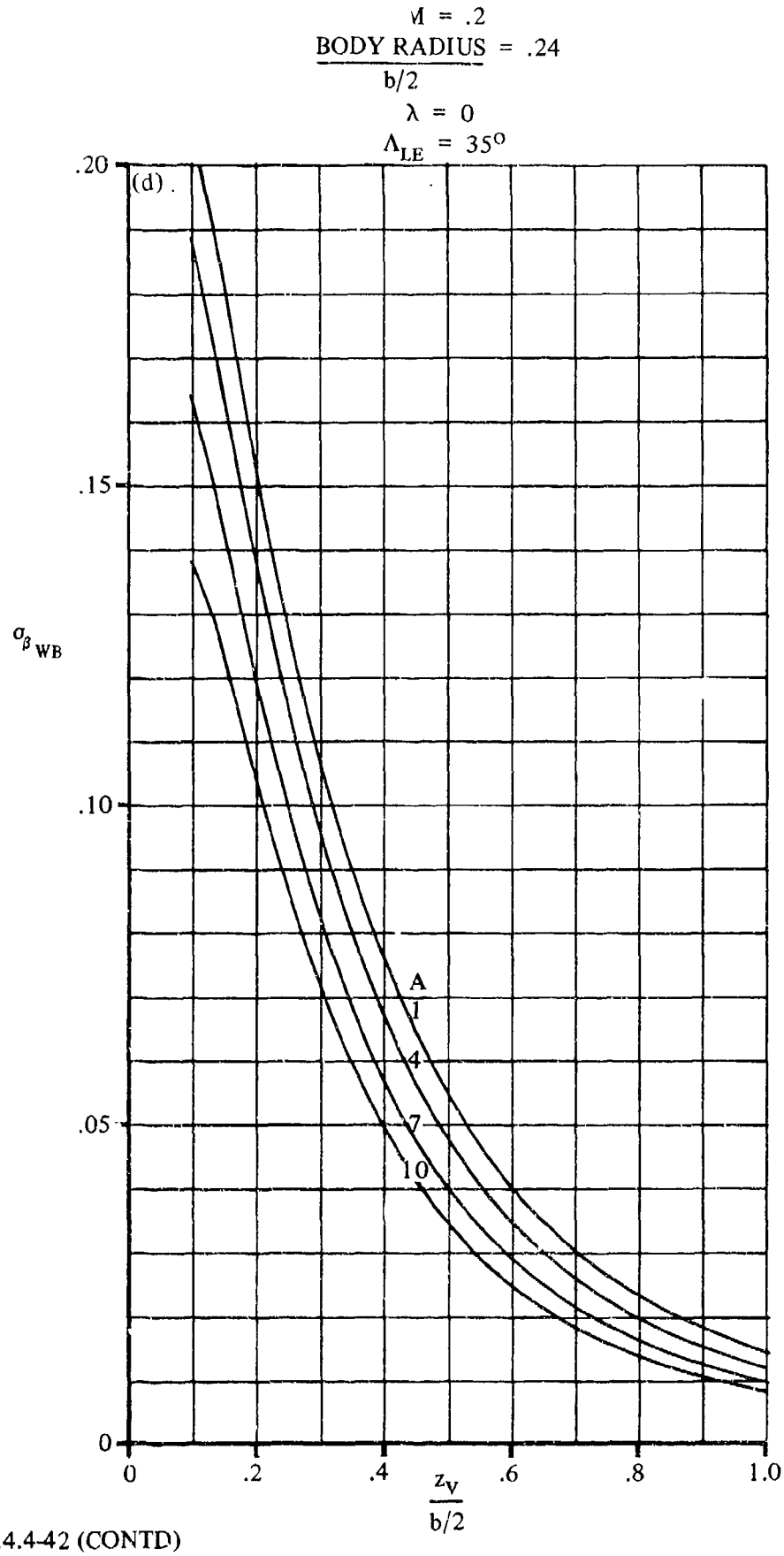

FIGURE 7.4.4.4-42 (CONTD)

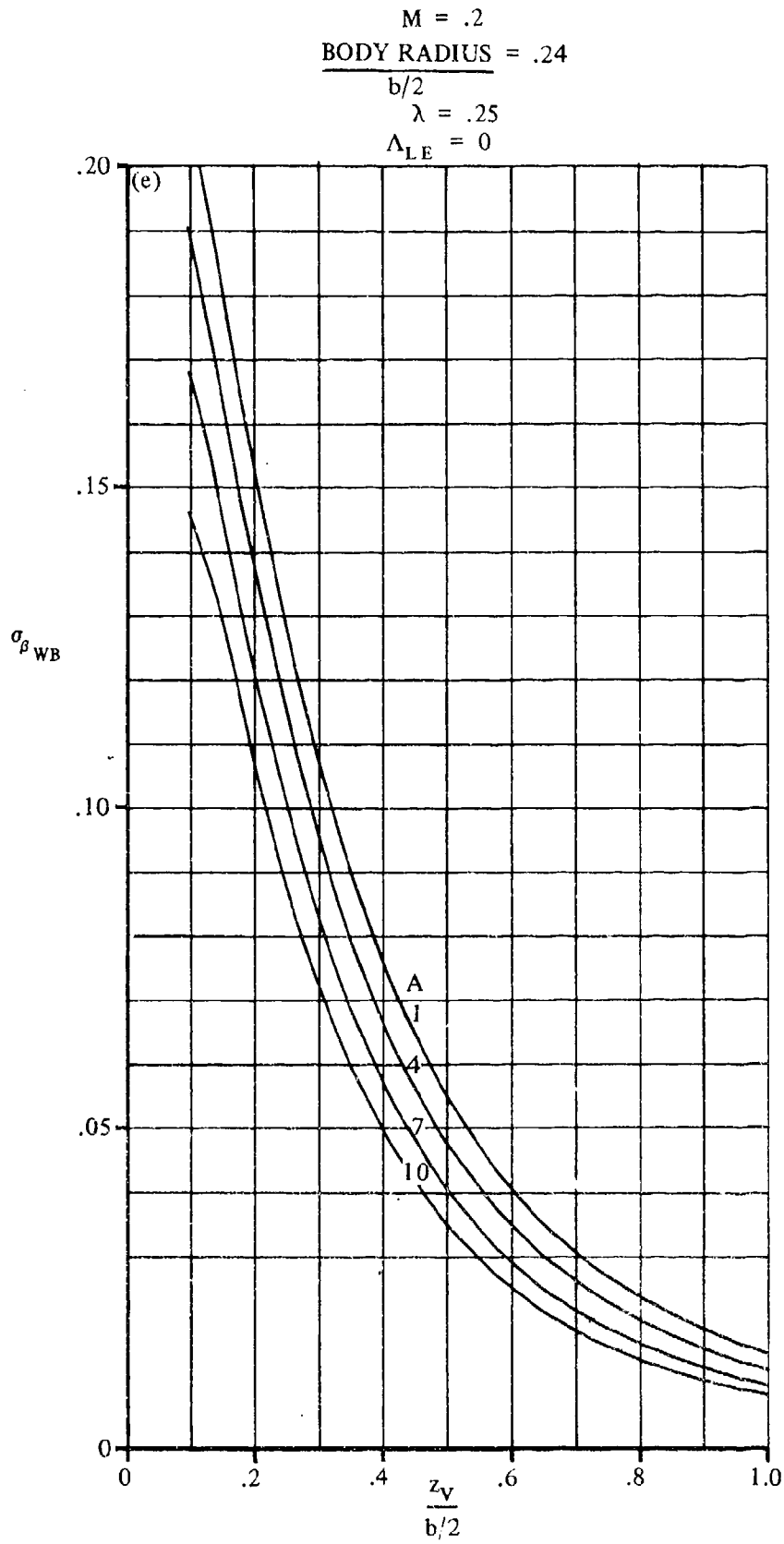

FIGURE 7.4.4.4-42 (CONTD)

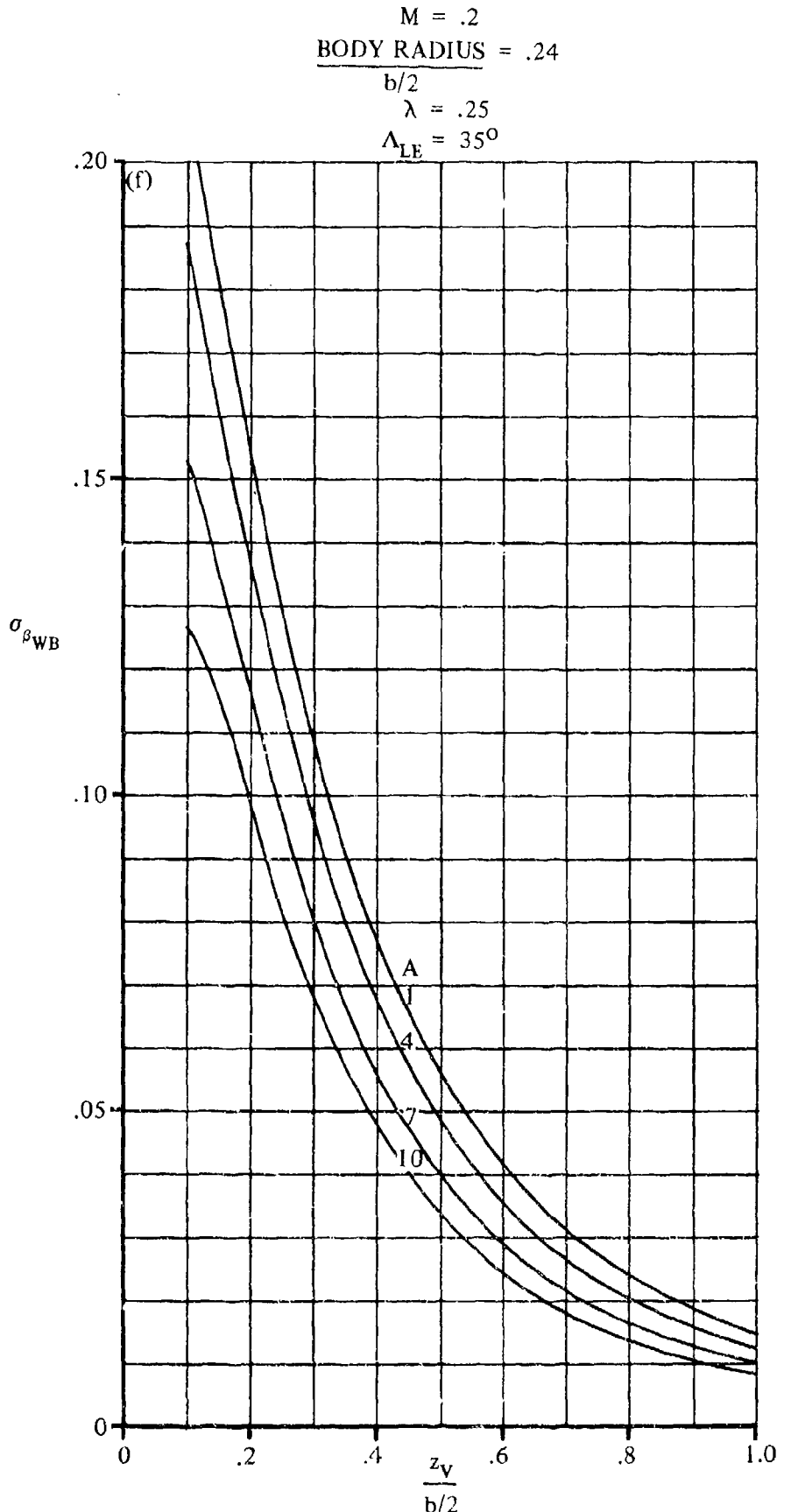

FIGURE 7.4.4.4-42 (CONTD)

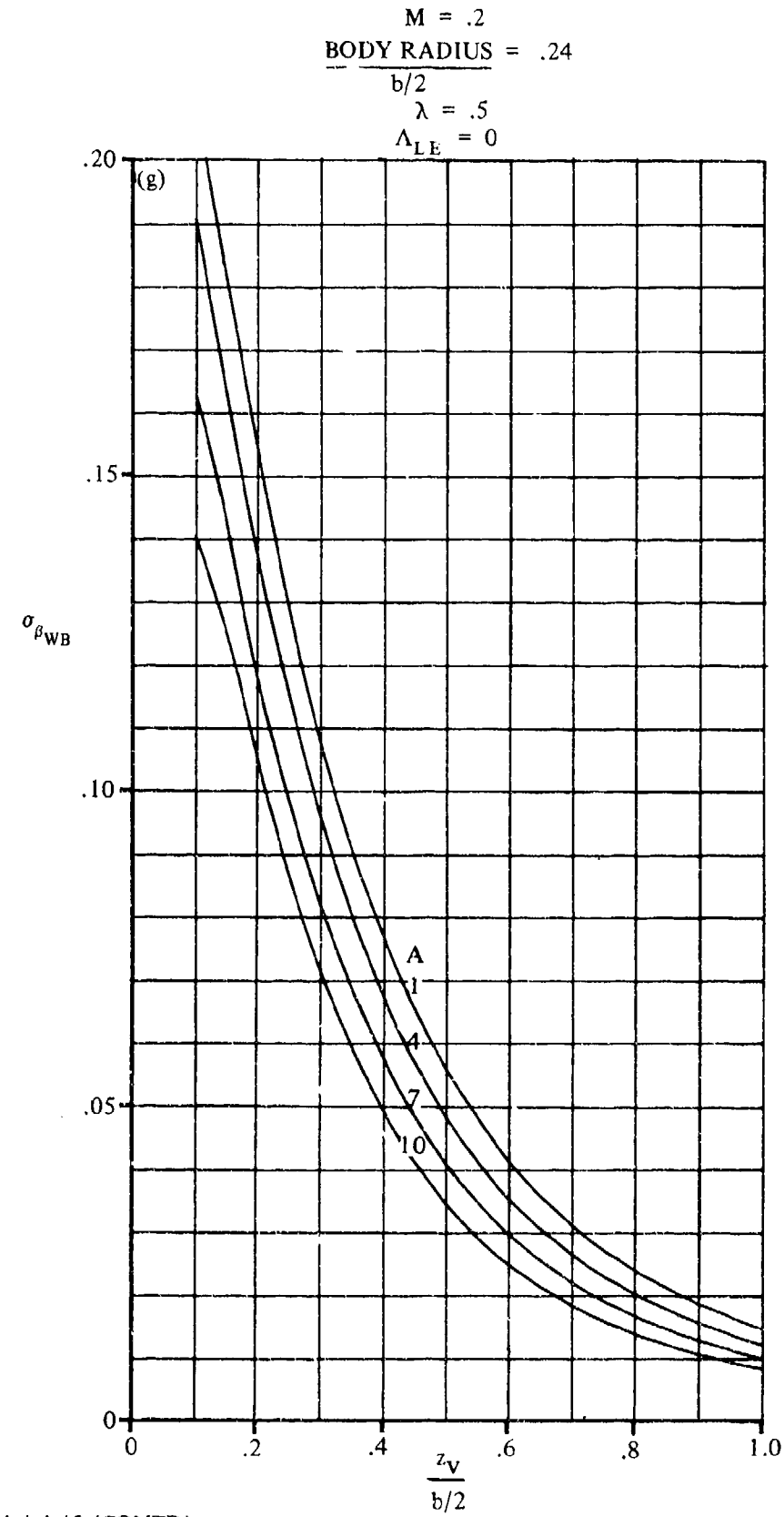

FIGURE 7.4.4.4-42 (CONTD)

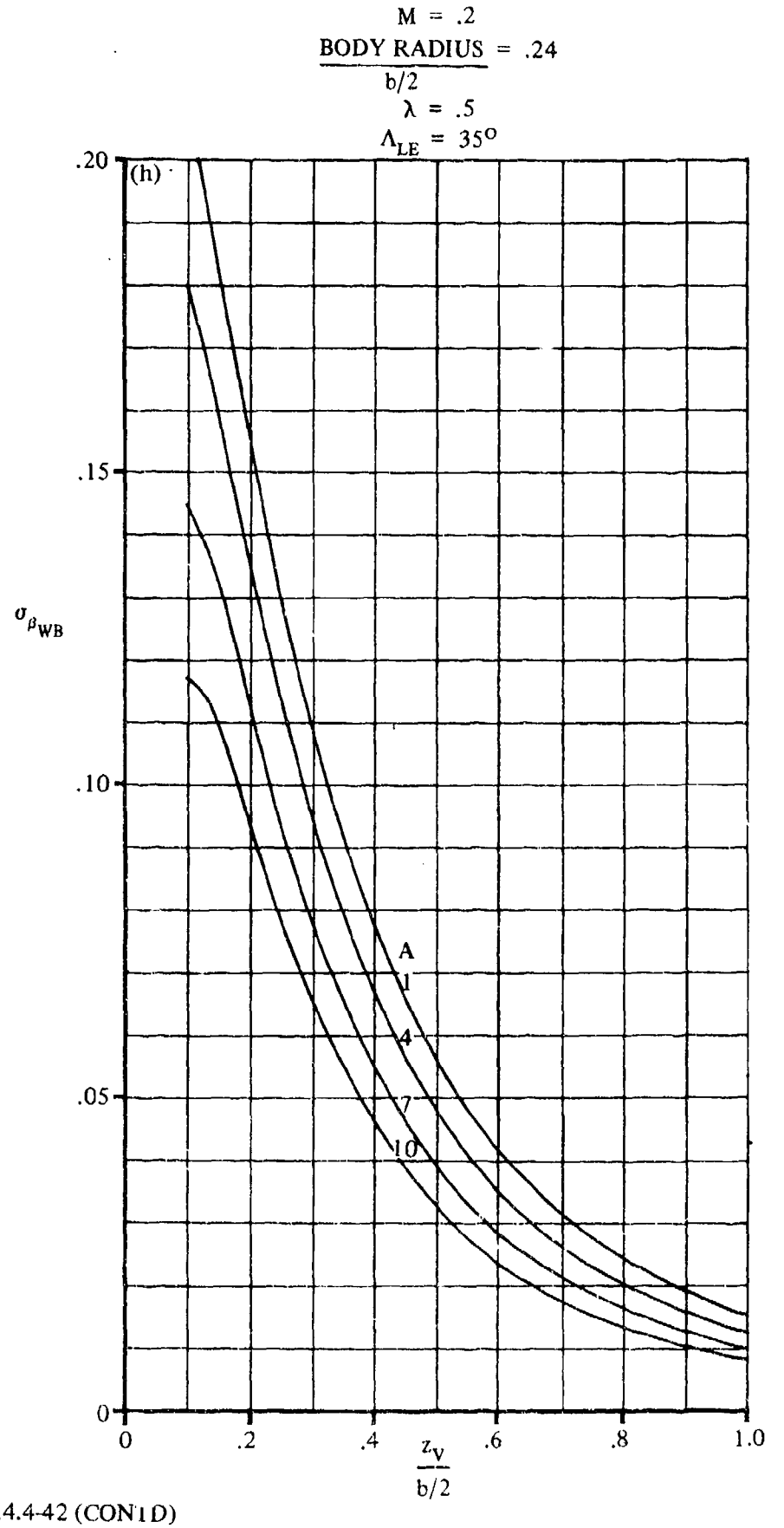

FIGURE 7.4.4.4-42 (CONTD)

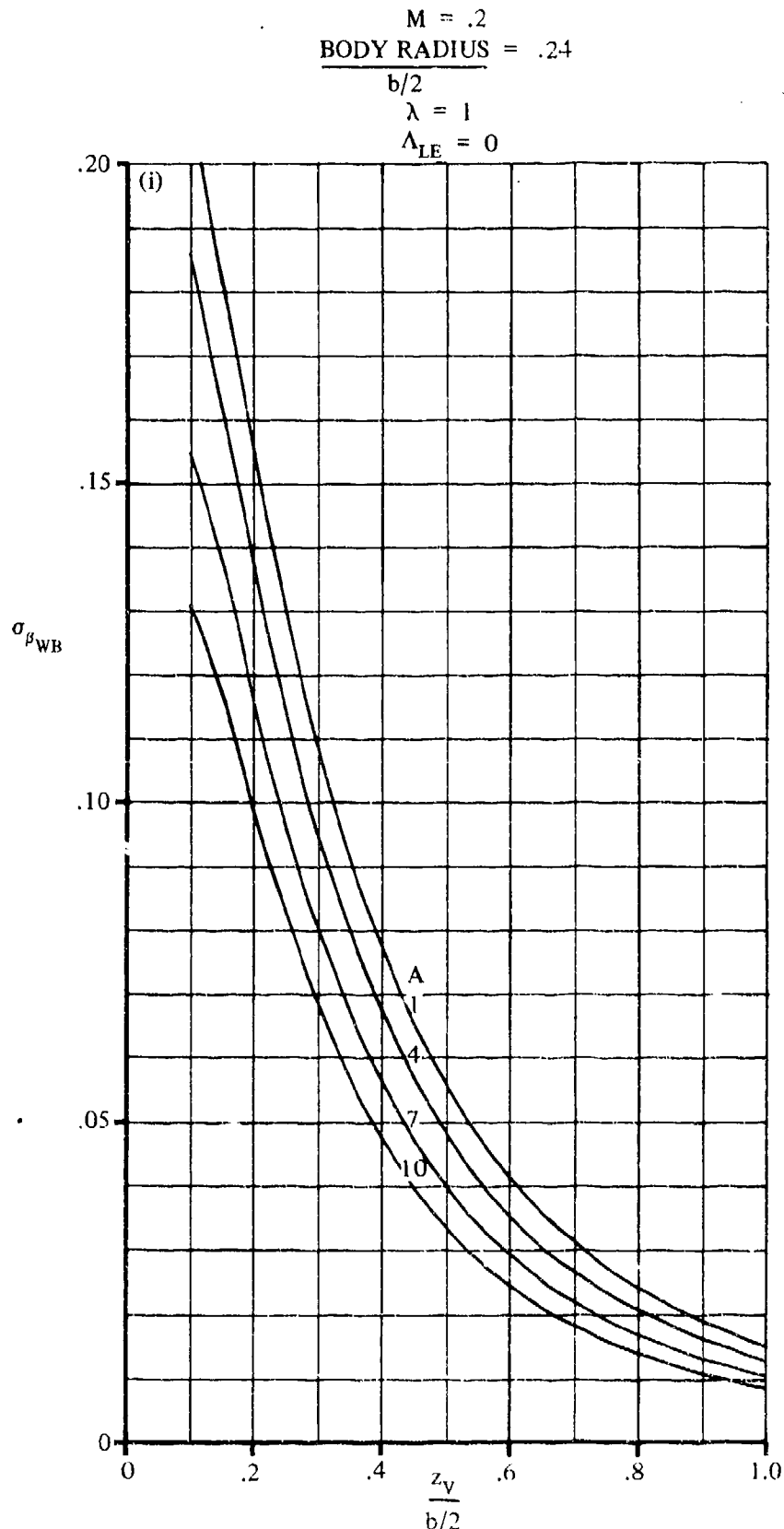

FIGURE 7.4.4.4-42 (CONTD)

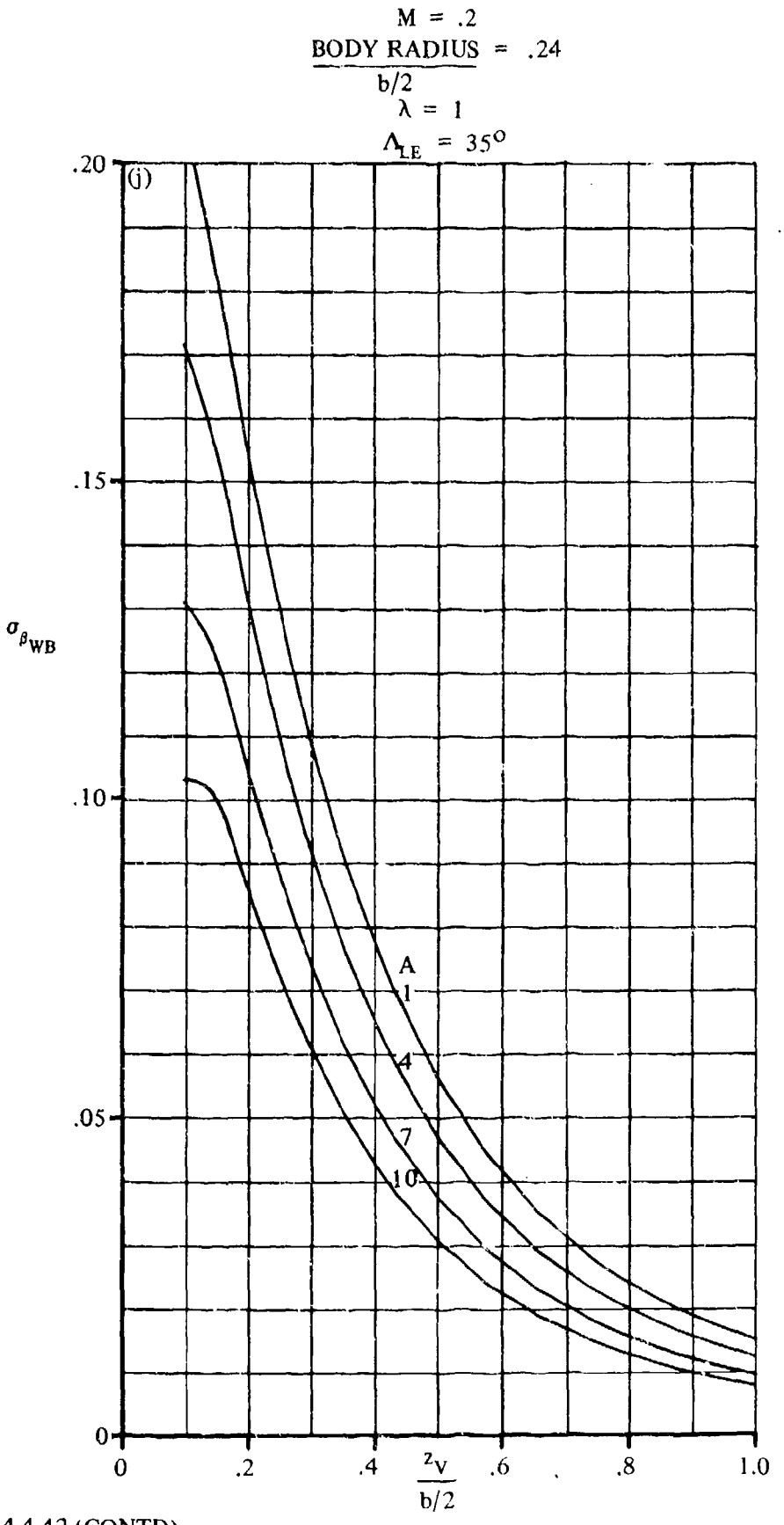

FIGURE 7.4.4.4-42 (CONTD)

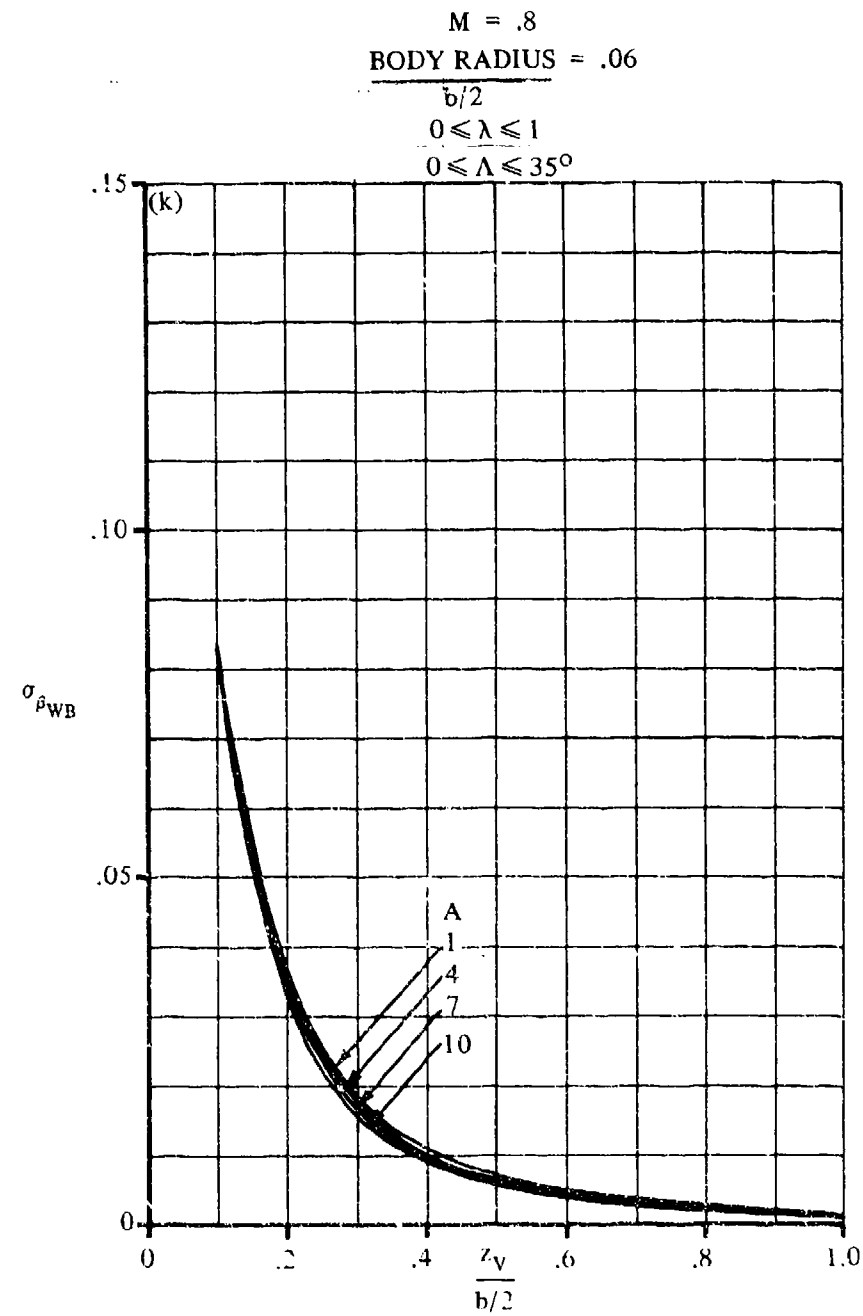

FIGURE 7.4.4.4-42 (CONTD)

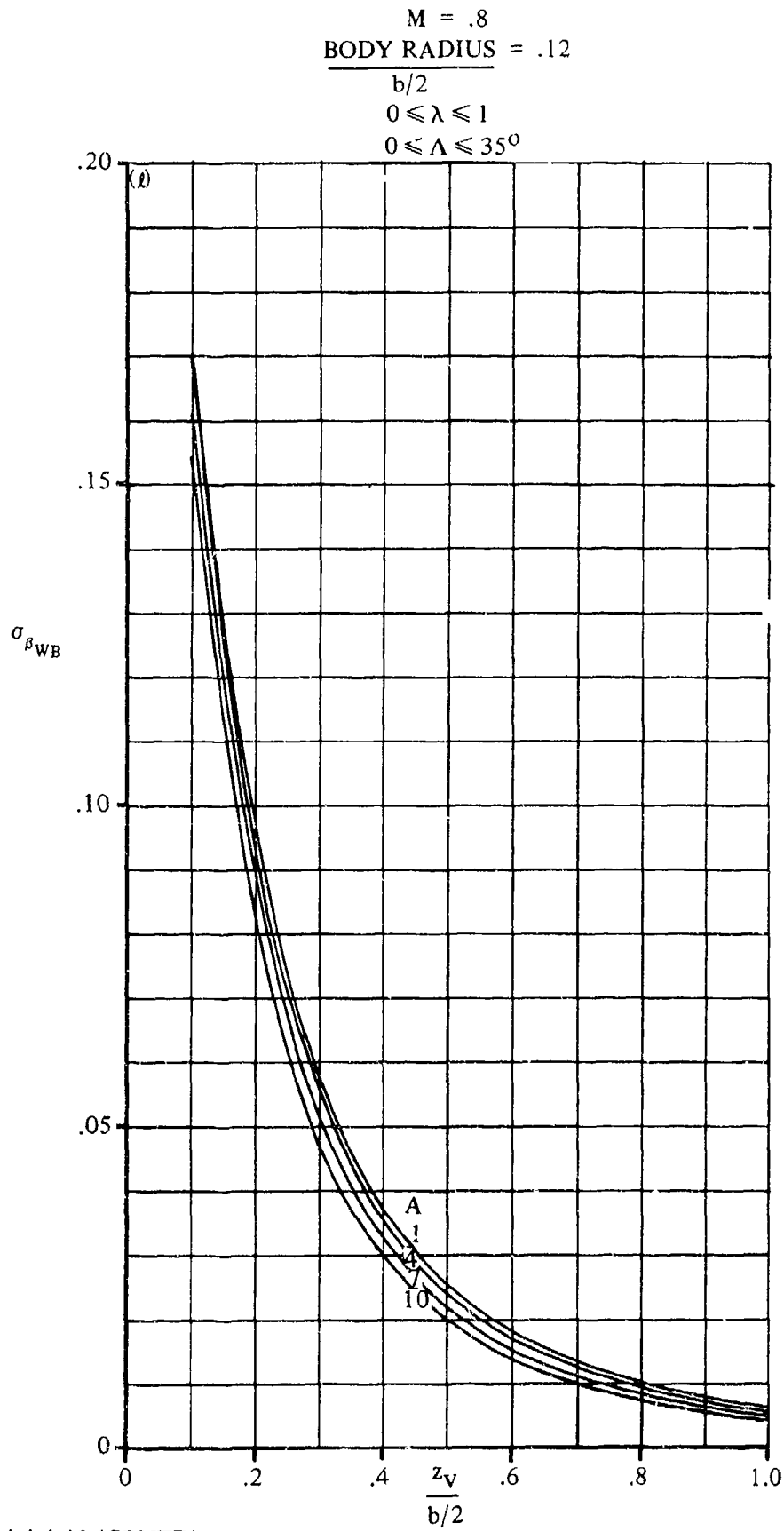

FIGURE 7.4.4.4-42 (CONTD)

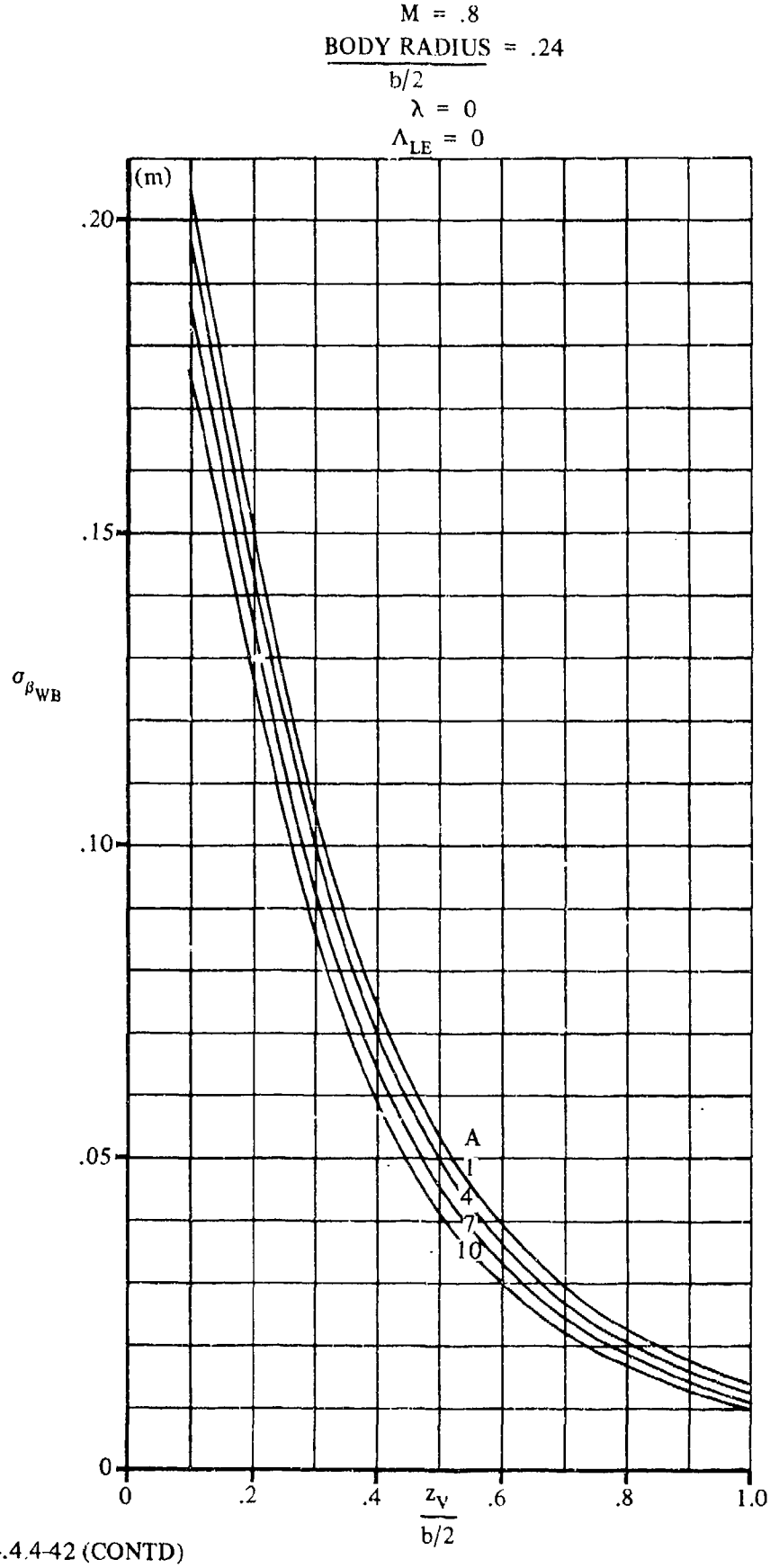

FIGURE 7.4.4.4-42 (CONTD)

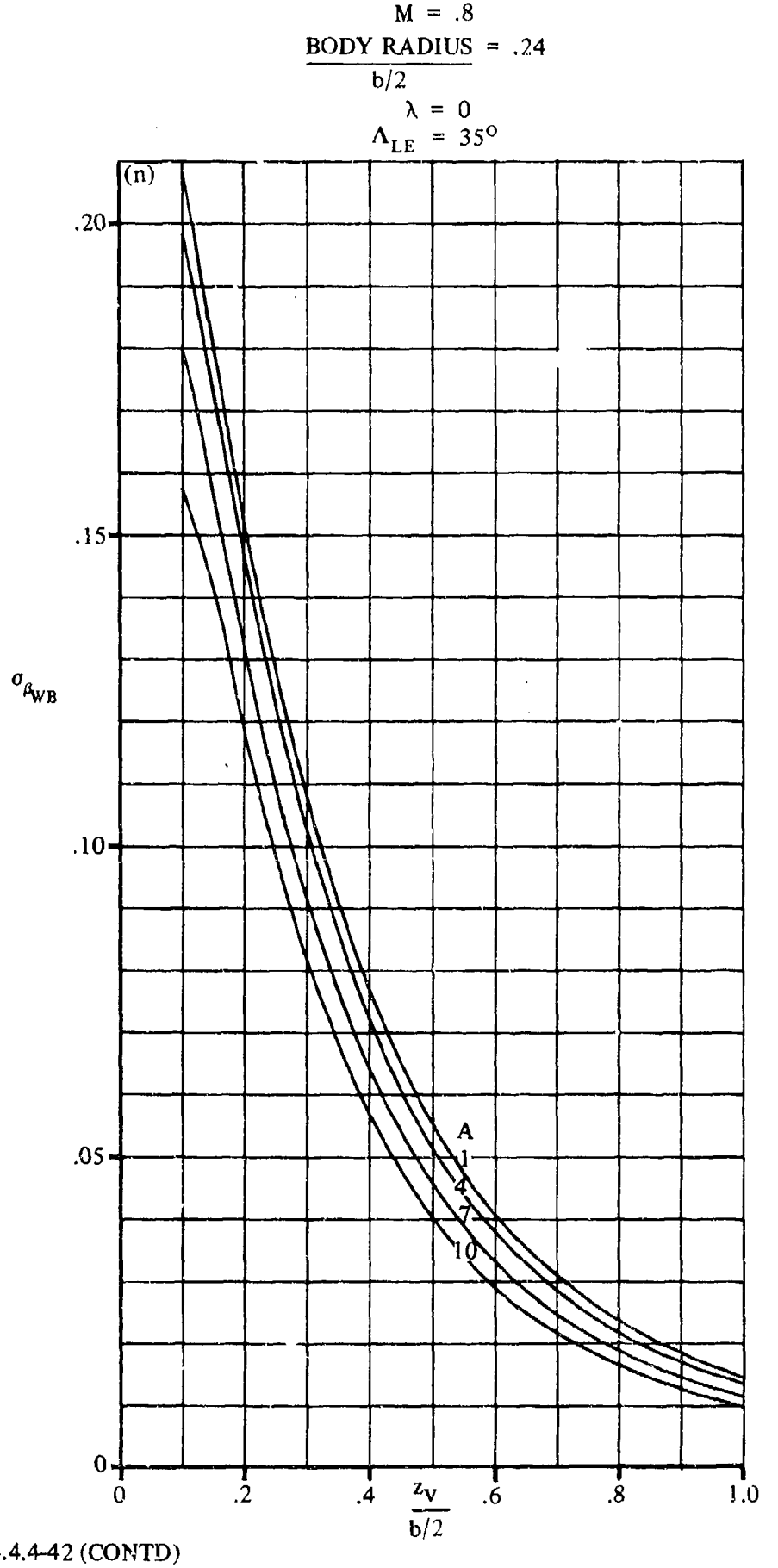

FIGURE 7.4.4.4-42 (CONTD)

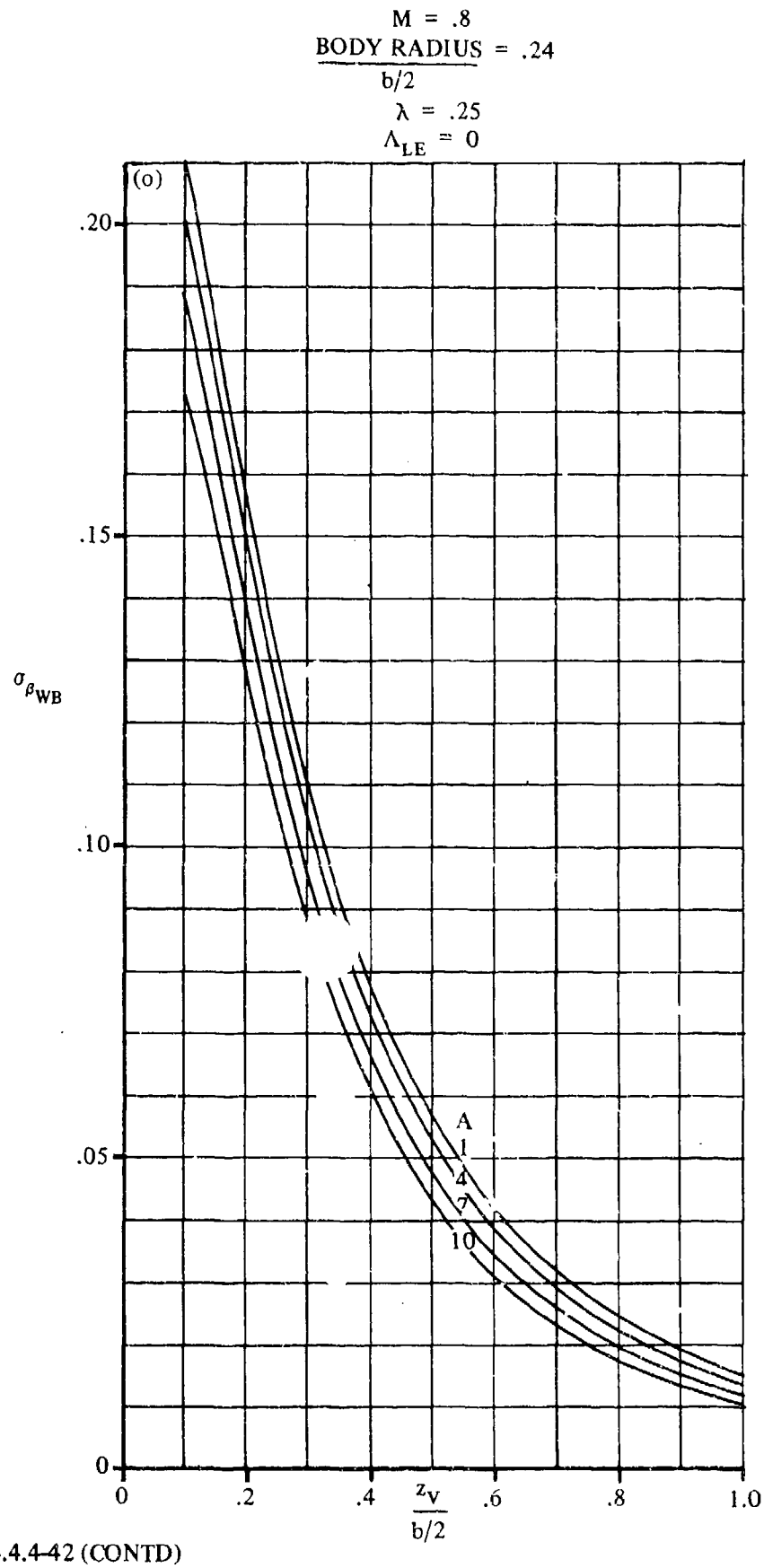

FIGURE 7.4.4.4-42 (CONTD)

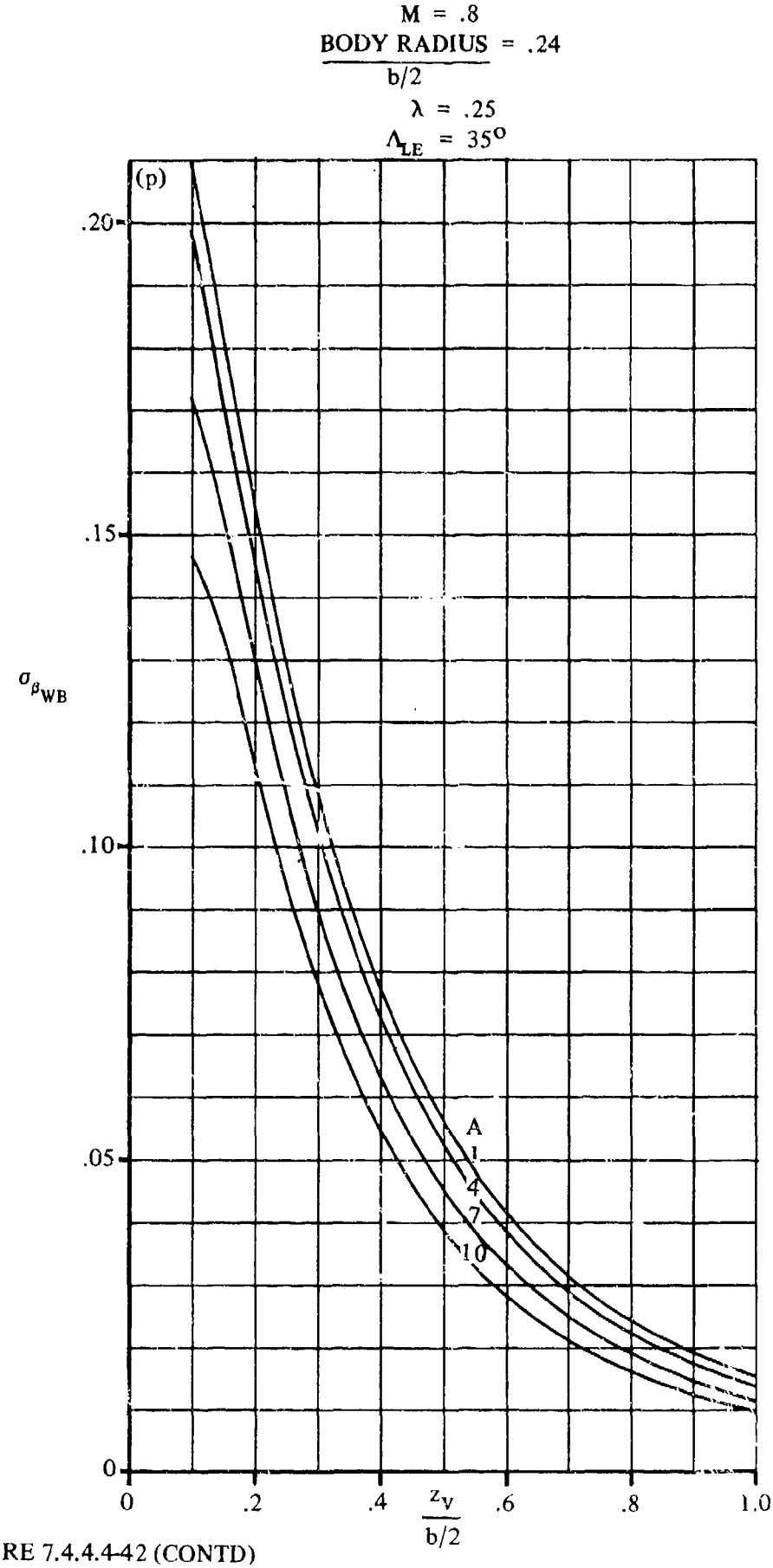

FIGURE 7.4.4.4-42 (CONTD)

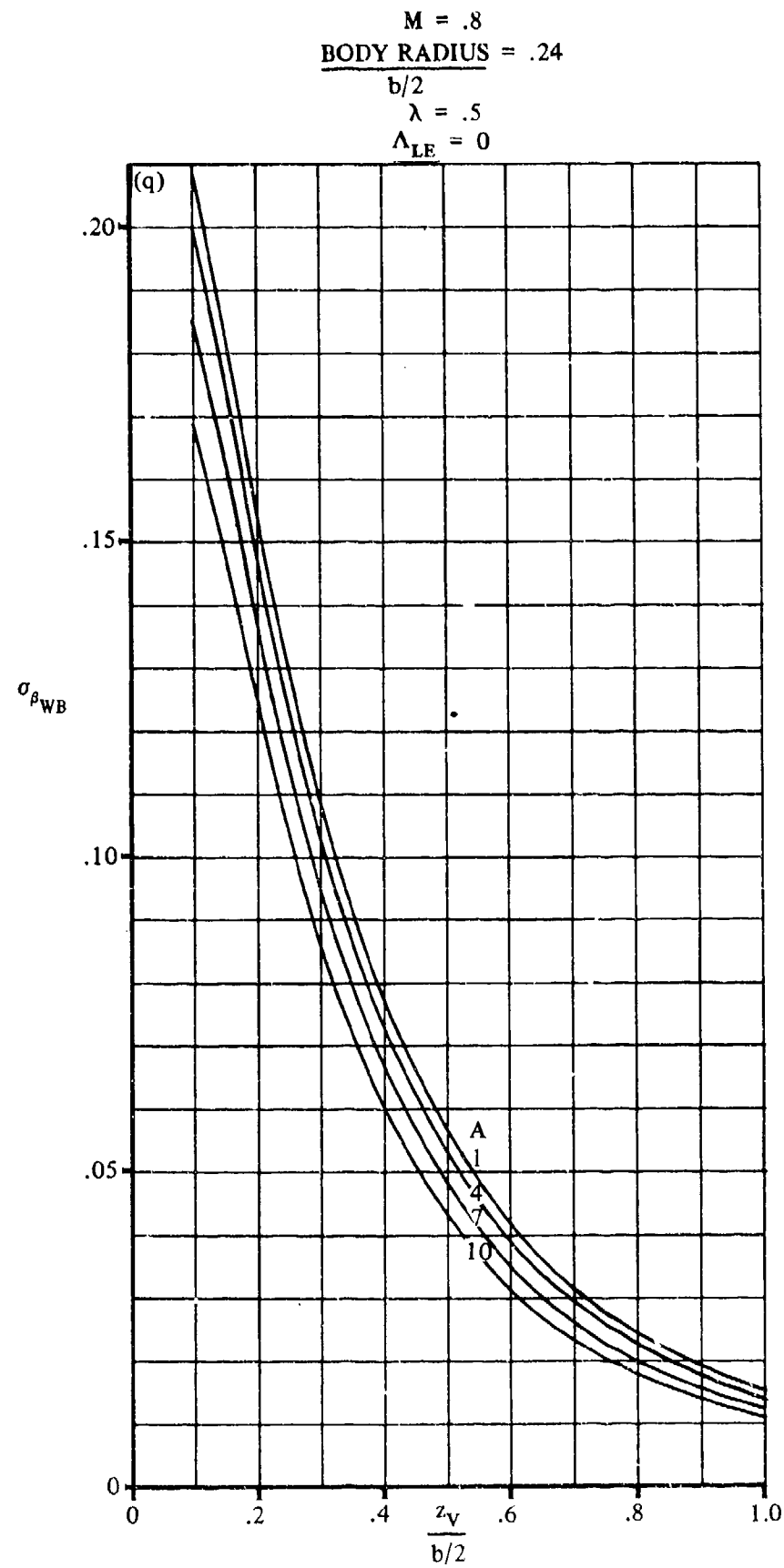

FIGURE 7.4.4.4-42 (CONTD

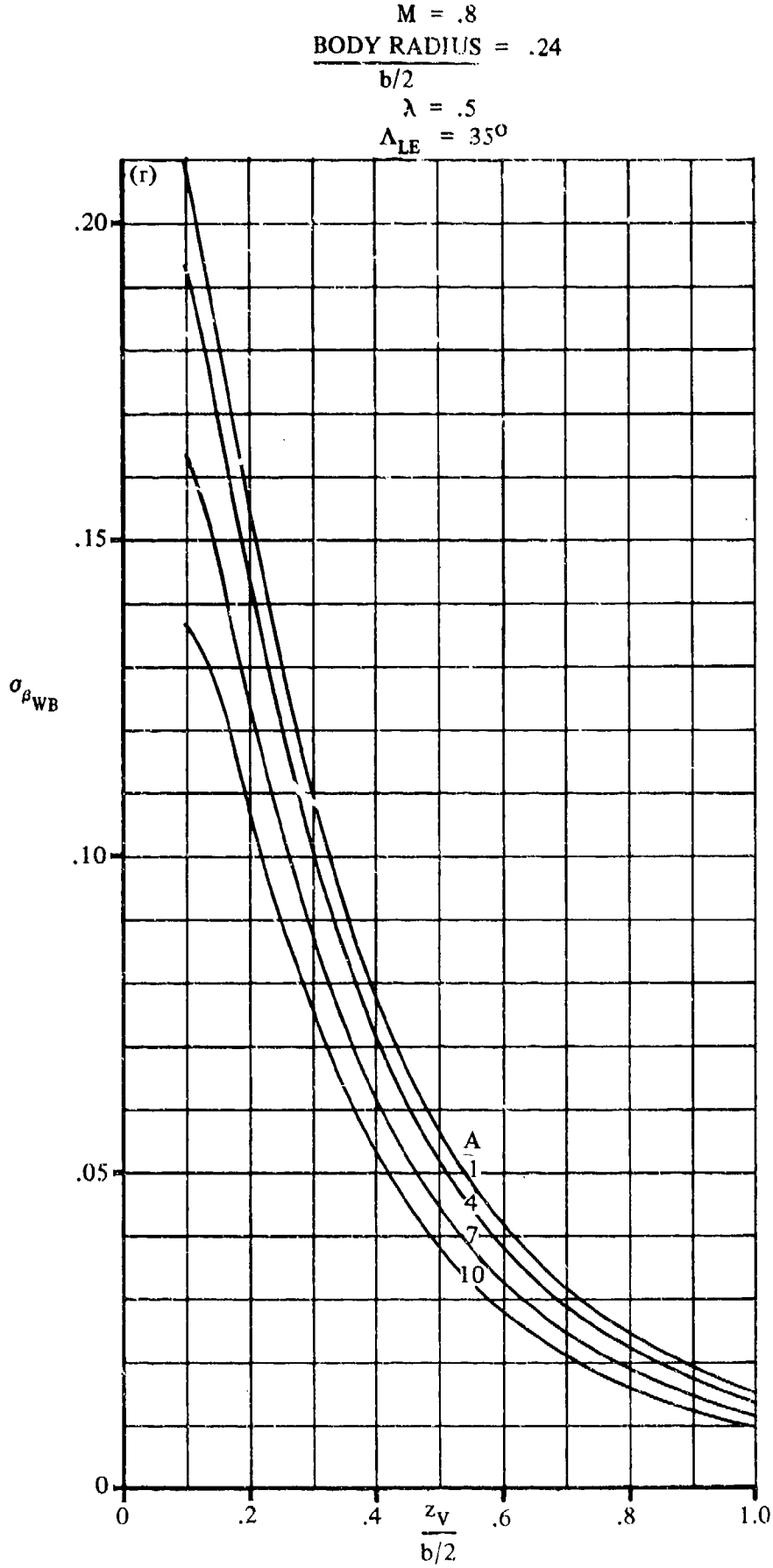

FIGURE 7.4.4.4-42 (CONTD)

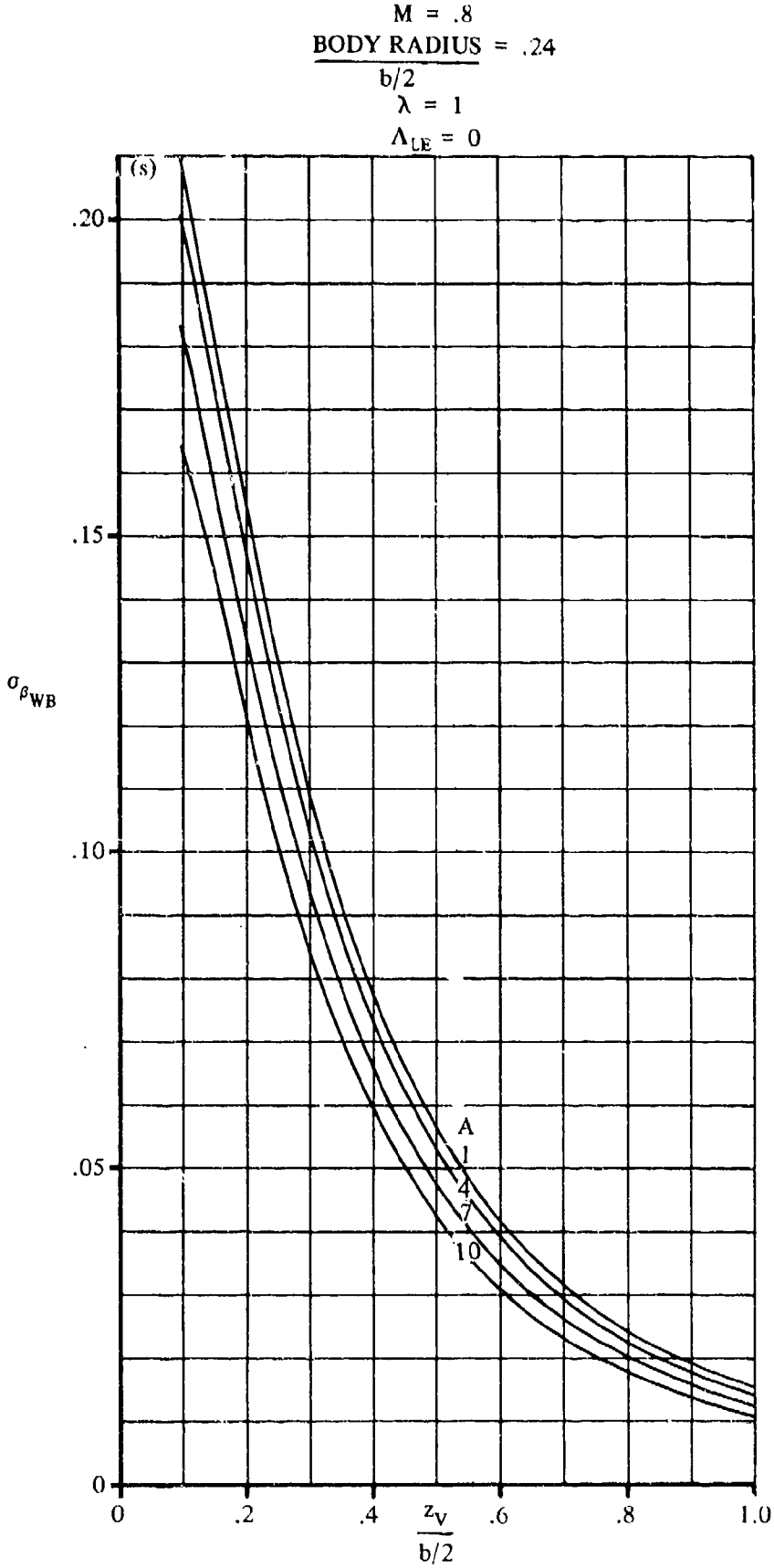

FIGURE 7.4.4.4-42 (CONTD)

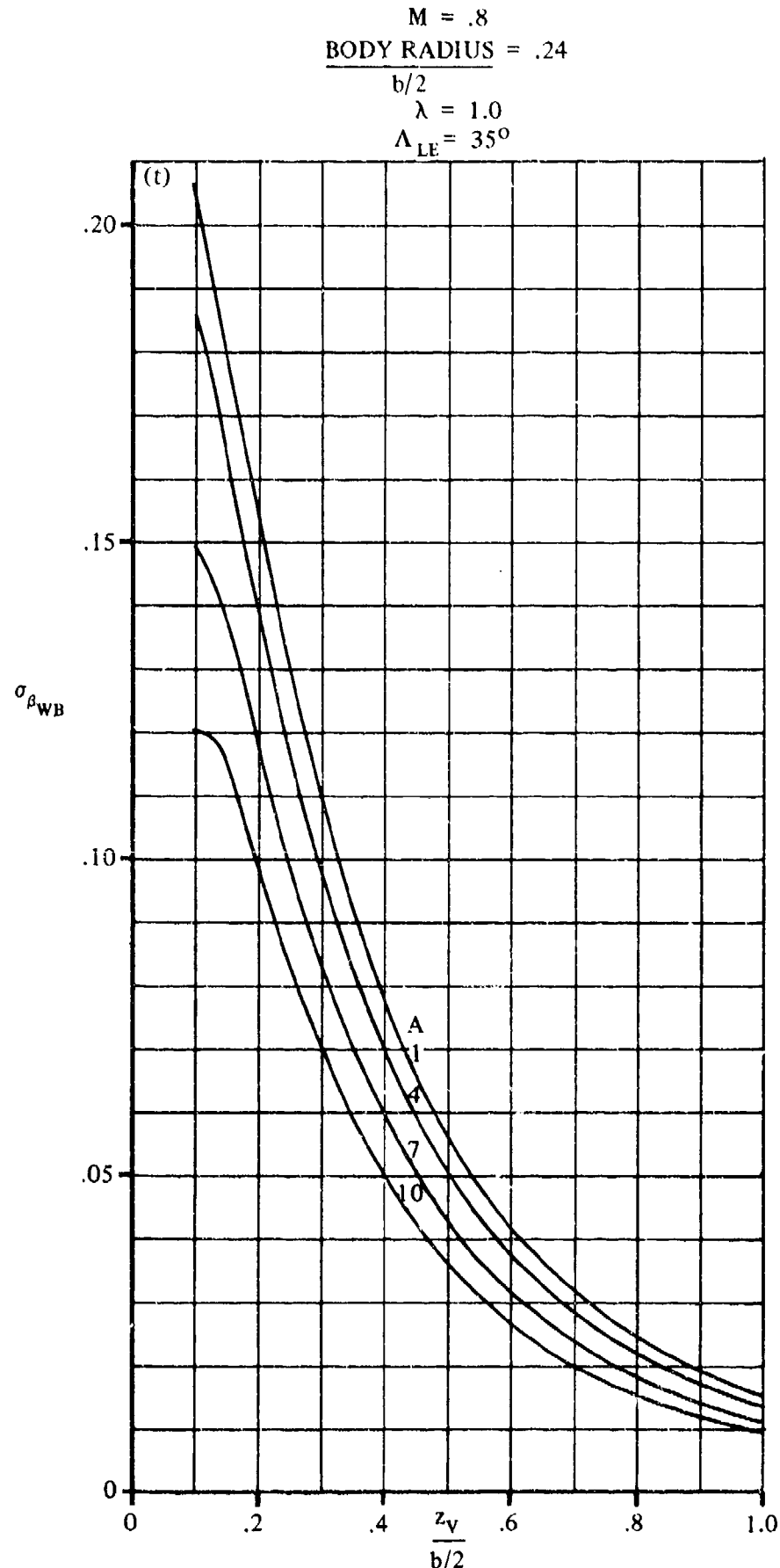

FIGURE 7.4.4.4-42 (CONTD)

7.4.4.5 WING-BODY-TAIL DERIVATIVE $C_{l_{\dot{\beta}}}$

This section presents a method for estimating the contribution of the vertical tail, in the presence of the wing and body, to the derivative $C_{l_{\dot{\beta}}}$ at subsonic speeds. This derivative is the change in rolling-moment coefficient with variation in the rate of change of sideslip angle at a constant yaw rate and is defined as

$$C_{l_{\dot{\beta}}} = \frac{\partial C_l}{\partial\left(\frac{\dot{\beta} b}{2V}\right)}, \text{ where } C_l \text{ is based on } S_W b_W .$$

In general, at low to moderate angles of attack, this derivative is small and has a negligible effect on lateral stability; hence, it is usually neglected.

A. SUBSONIC

The wing contribution to $C_{l_{\dot{\beta}}}$ can be evaluated by using unsteady-flow theory, but at low to moderate angles of attack it is generally considered small and is neglected. At low angles of attack and for attached-flow conditions, the largest contributor to $C_{l_{\dot{\beta}}}$ is the vertical tail. The rolling moment produced on the airframe by the vertical tail is due to the sidewash time-lag effects from the wing. The body contribution is small and has been neglected.

For a brief discussion of the physical flow phenomena at high angles of attack, i.e., leading-edge vortex sheets and flow separation, and a comprehensive bibliography on related subject matter, the reader is referred to Reference 1. Reference 1 also discusses the inadequacy of oscillating-airfoil theory and sidewash-lag theory for predicting the vertical-tail contribution to $C_{l_{\dot{\beta}}}$ at high angles of attack. However, a modified flow-field-lag theory is discussed in Reference 1 that appears to give qualitative agreement with experimental data for a current twin-jet fighter configuration.

DATCOM METHOD

The vertical-tail contribution to the derivative $C_{l_{\dot{\beta}}}$ at low to moderate angles of attack is given by

$$C_{l_{\dot{\beta}}} = C_{Y_{\dot{\beta}}} \left(\frac{z_p \cos\alpha_F - \ell_p \sin\alpha_F}{b_W}\right) \qquad 7.4.4.5\text{-a}$$

where

$C_{Y_{\dot{\beta}}}$ is the vertical-tail contribution to the derivative $C_{Y_{\dot{\beta}}}$ obtained from Section 7.4.4.4.

z_p is the distance from the wing quarter-chord point to the center-of-pressure location of the vertical stabilizer, measured normal to the body center line, positive for the stabilizer above the body. For Datcom purposes, the vertical-tail center-of-pressure location is assumed to be the quarter-chord point of the MAC of the total added panel.

ℓ_p is the distance from the wing quarter-chord point to the center-of-pressure location of the vertical stabilizer, measured parallel to the body center line. For Datcom purposes, the vertical-tail center-of-pressure location is assumed to be at the quarter-chord point of the MAC of the total added panel. (See Sketch (a) of Section 7.4.2.1.)

α_F is the fuselage angle of attack.

b_W is the wing span.

Sample Problem

Given: Same configuration as sample problem of Paragraph A of Section 7.4.4.4.

Compute:

$$C_{Y_{\dot{\beta}}} = -0.000209 \qquad \text{(Sample Problem, Paragraph A, Section 7.4.4.4)}$$

$$C_{l_{\dot{\beta}}} = C_{Y_{\dot{\beta}}} \left(\frac{z_p \cos \alpha_F - \ell_p \sin \alpha_F}{b_W} \right) \qquad \text{(Equation 7.4.4.5-a)}$$

$$C_{l_{\dot{\beta}}} = (-0.000209) \left[\frac{(20)(0.9998) - (60)(0.0175)}{156.52} \right]$$

$$= -0.0000253 \text{ per deg}$$

B. TRANSONIC

No method is presented.

C. SUPERSONIC

No method is presented.

REFERENCE

1. Coe, P. L., Jr., Graham, A. B., and Chambers, J. R.: Summary of Information on Low-Speed Lateral-Directional Derivatives Due to Rate of Change of Sideslip $\dot{\beta}$. NASA TN D-7972, 1975. (U)

7.4.4.6 WING-BODY-TAIL DERIVATIVE $C_{n_{\dot{\beta}}}$

This section presents a method for estimating the contribution of the vertical tail, in the presence of the wing and body, to the derivative $C_{n_{\dot{\beta}}}$ at subsonic speeds. This derivative is the change in yawing-moment coefficient with variation in the rate of change of sideslip angle at a constant yaw rate and is defined as

$$C_{n_{\dot{\beta}}} = \frac{\partial C_n}{\partial\left(\frac{\dot{\beta} b}{2V}\right)}, \text{ where } C_n \text{ is based on } S_W\, b_W .$$

For most configurations at low to moderate angles of attack, $C_{n_{\dot{\beta}}}$ is rather small and can be neglected in lateral dynamic calculations. However, at high angles of attack for swept- and delta-wing configurations, $C_{n_{\dot{\beta}}}$ can approach the magnitude of C_{n_r} and consequently have large effects on the calculated dynamic stability of these configurations.

A. SUBSONIC

The wing contribution to $C_{n_{\dot{\beta}}}$ can be evaluated by using unsteady-flow theory, but at low to moderate angles of attack it is generally considered small and is neglected. At low angles of attack and for attached-flow conditions, the largest contributor to $C_{n_{\dot{\beta}}}$ is the vertical tail. The yawing moment produced on the airframe by the vertical tail is due to the sidewash time-lag effects from the wing. The body contribution is small and has been neglected.

For a brief discussion of the physical flow phenomena at high angles of attack, i.e., leading-edge vortex sheets and flow separation, and a comprehensive bibliography on related subject matter, the reader is referred to Reference 1. Reference 1 also discusses the inadequacy of oscillating-airfoil theory and sidewash-lag theory for predicting the vertical-tail contribution to $C_{n_{\dot{\beta}}}$ at high angles of attack. However, a modified flow-field-lag theory is discussed in Reference 1 that appears to give qualitative agreement with experimental data for a current twin-jet fighter configuration.

DATCOM METHOD

The vertical-tail contribution to the derivative $C_{n_{\dot{\beta}}}$ at low to moderate angles of attack is given by

$$C_{n_{\dot{\beta}}} = -C_{Y_{\dot{\beta}}}\left(\frac{\ell_p \cos\alpha_F + z_p \sin\alpha_F}{b_W}\right) \qquad 7.4.4.6\text{-a}$$

where

$C_{Y_{\dot{\beta}}}$ is the vertical-tail contribution to the derivative $C_{Y_{\dot{\beta}}}$ obtained from Section 7.4.4.4.

ℓ_p is the distance from the moment reference center to the center-of-pressure location of the vertical stabilizer, measured parallel to the body center line. (See Sketch (a) in Section 7.4.2.1.) For Datcom purposes the vertical-tail center-of-pressure location is assumed to be at the quarter-chord point of the MAC of the total added panel.

z_p is the distance from the moment reference center to the center of pressure of the vertical stabilizer, measured normal to the body center line, positive for the stabilizer above the body. For Datcom purposes, the vertical-tail center-of-pressure location is assumed to be at the quarter-chord point of the MAC of the total added panel.

b_W is the wing span.

α_F is the fuselage angle of attack.

Sample Problem

Given: Same configuration as sample problem of Paragraph A of Section 7.4.4.4.

Compute:

$C_{Y_{\dot{\beta}}} = -0.000209$ (Sample Problem, Paragraph A, Section 7.4.4.4)

$$C_{n_{\dot{\beta}}} = -C_{Y_{\dot{\beta}}}\left(\frac{\ell_p \cos\alpha_F + z_p \sin\alpha_F}{b_W}\right) \qquad \text{(Equation 7.4.4.6-a)}$$

$$= -(-0.000209)\left[\frac{(60)(0.9998) + (20)(0.01745)}{156.52}\right]$$

$$= +0.0000805 \text{ per deg}$$

B. TRANSONIC

No method is presented.

C. SUPERSONIC

No method is presented.

REFERENCE

1. Coe, P. L., Jr., Graham, A. B., and Chambers, J. R.: Summary of Information on Low-Speed Lateral-Directional Derivatives Due to Rate of Change of Sideslip $\dot{\beta}$. NASA TN D-7972, 1975. (U)

8. MASS AND INERTIA

Performance, stability, control, and strength analyses of airborne vehicles depend not only on the mass of the vehicle but on the distribution of the mass within the vehicle. This concept of mass distribution is reflected in the property of the vehicle called moment of inertia. This Section discusses moment of inertia determination for two types of airborne vehicles — manned aircraft and missiles.

8.1 AIRCRAFT MASS AND INERTIA

The purpose of this Section is to furnish the engineer with a method for rapidly but accurately estimating the moment of inertia of manned aircraft during the preliminary-design period. Such inertias are needed in order that dynamic load and stability characteristics of the aircraft may be evaluated.

The following pages present basic moment-of-inertia theory, a discussion of inertia methods in general with the assumptions and conclusions used in evolving the Datcom method, and a discussion of the Datcom method in detail, with a summary showing the step-by-step procedure to follow when using this method.

This method applies to all existing combat and transport aircraft including those of unconventional* design. If radically different airplane configurations evolve, the present methods will have to be altered. The tools needed are a weight-and-balance statement, a three-view drawing, and some knowledge of the design characteristics of the airplane. A total time of approximately three hours for one man is needed to estimate inertia by this method, and the accuracy obtained is within the tolerance required for any preliminary-design project.

Basic Moment-of-Inertia Theory

Moment of inertia is the measure of resistance to angular acceleration, as mass is the measure of resistance to linear acceleration. Moment of inertia may be mathematically derived as follows:

If torque is expressed as the product of force and radius

$$T = Fr$$

and the following substitutions are made:

$$F = ma \quad \text{and} \quad a = \alpha r$$

then

$$T = mar$$

or

$$T = mr^2\alpha \tag{8.1-a}$$

where

a is the linear acceleration
α is the angular acceleration
m is the mass

The term mr^2 is defined as the moment of inertia (I) and equation 8.1-a may be written

$$T = I\alpha \tag{8.1-b}$$

If a body of mass m is caused to rotate about a remote axis y (see sketch (a)) the following relationship exists:

$$I_y = mr^2 = m(x^2 + z^2) \tag{8.1-c}$$

However, since mass m not only offers resistance to rotation about the y axis but also offers resistance to rotation about its own centroidal axis, the total inertia of m about y is

$$I_y = mr^2 + I_{oy} \tag{8.1-d}$$

where I_{oy} is the inertia of m about its own centroidal axis.

---

*The term unconventional as used herein refers chiefly to extreme locations of the wing, fuselage, tail and power plant sections with respect to each other, and to the size and mass of these sections. However, when the shape and mass distribution of any of the sections change considerably over present state of the art design, the method for computing inertia as described herein should be altered accordingly.

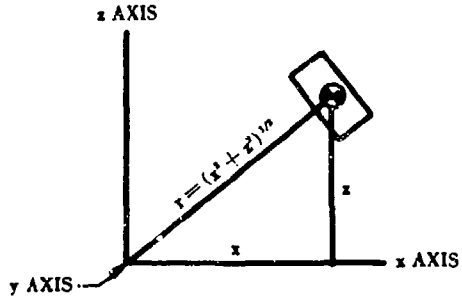

SKETCH (s)

If mass m is divided into several parts, $m_1, m_2, \ldots m_n$, then the total inertia of the sum of these parts about y is

$$I_y = m_1 r_1^2 + I_{oy_1} + m_2 r_2^2 + I_{oy_2} + \ldots m_n r_n^2 + I_{oy_n}$$

or

$$I_y = \sum_{i=1}^{n} (m_i r_i^2 + I_{oy_i}) \qquad 8.1\text{-e}$$

Finally, if the total inertia about a remote axis is computed from equation 8.1-e, the inertia of the total mass about its own centroidal axis can be computed from equation 8.1-d, or

$$I_{oy} = I_y - m\bar{r}^2 \qquad 8.1\text{-f}$$

where $\bar{r}$ is the distance from the y axis to the centroid of the total mass.

$$\bar{r} = \frac{\sum_{i=1}^{n} m_i r_i}{\sum_{i=1}^{n} m_i} \qquad 8.1\text{-g}$$

Inertia Methods in General

As equation 8.1-d indicates, the inertia of a body about a remote axis depends on three basic factors: (1) mass, (2) the distance of the mass from the remote axis, and (3) the inertia of the mass about its own centroidal axis. If any one of these factors is ignored, the inertia derived will not be accurate.

A common method is to divide the airplane into many sections, so that the I_o values may be calculated easily and accurately. The total airplane inertia about the remote axis may then be derived by equation 8.1-e, and the total inertia about the aircraft's centroidal axis by equation 8.1-f. Unfortunately, however, this method requires a detail breakdown of the masses and centroids of the components of the aircraft as well as a large time expenditure. Therefore the method does not lend itself to successful application at the preliminary design level.

Another method for computing inertia is one in which the total mass and dimensional data of the aircraft are used as parameters in an empirical inertia equation. However, the equations have to be based on aircraft with mass distribution similar to that of the proposed aircraft, since the mass and locations of the wing, fuselage, tail, and engines can vary greatly between aircraft. This means that a large amount of statistical data has to be available, and this type of method is almost useless for aircraft of unconventional design, where there is a lack of statistical data.

Obviously neither of these two methods fulfills the requirements for one rapid but accurate method independent of airplane type or conventional nature. But consideration of a few facts about inertia methods in general shows which method is preferable in a particular situation. These facts are:

(1) When statistical data are not available —

(a) The time required to compute inertia and the accuracy of the answer are directly proportional to the number of sections into which the airplane is divided.

(b) The number of sections into which the airplane is divided is dependent on the amount of detail information available.

(2) When statistical data are available —

(a) Time is inversely proportional to parametric correlation, which is the mutual relationship of the inertia of the proposed aircraft to statistical data by means of parameters such as size, shape, and mass.

(b) Accuracy is dependent upon the extent to which parametric correlation is applied. This means that, if these correlations are carried beyond the bounds of mass distribution similarity, the accuracy is affected adversely; if carried only as far as these bounds, the accuracy is affected only slightly.

Therefore the method evolved is one that divides the airplane into the least number of sections necessary to maintain sufficient mass distribution similarity to permit valid parametric correlation. Thus the accuracy obtained is within the tolerance required for preliminary-design studies. After careful consideration, these five major sections were chosen:

(1) Wing
(2) Fuselage
(3) Horizontal Stabilizer
(4) Vertical Stabilizer
(5) Power Plant (Engine and Nacelle)

The inertias for fuel, cargo, and other variable items may also be added, as shown in the sample problem.

DATCOM METHOD

The method consists of determining the mass and centroids for each of the major sections and then, by equations involving the parameters of size, shape, mass, and centroids, calculating the I_o values for each of these sections. Once this is completed, the inertias about the remote axis may be derived by equation 8.1-e, and hence the inertias about the airplane centroids by equation 8.1-f.

The I_o formulas are based on aircraft in a gear-up configuration with expendable and variable items, such as fuel, cargo, and passengers, deleted. Since it is impossible to predict the aircraft configurations for which inertia will be needed, the inertia for the expendable and variable items comprising these configurations must be added to the basic inertia derived from the method.

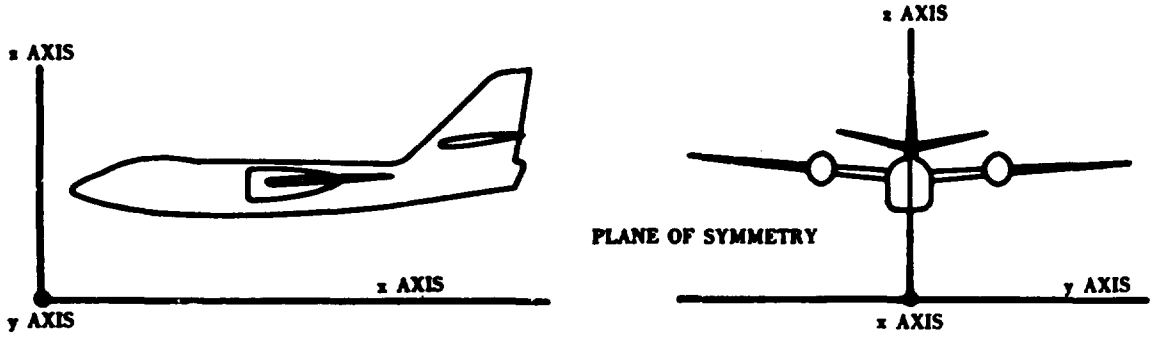

SKETCH (b)

Step 1. Selection of remote axes — Three remote axes are chosen so that inertia in pitch, roll, and yaw may be calculated. The origin of these axes should be located so that distances to the centroids of the major sections are positive and should be located on the plane of symmetry of the airplane. This type of location simplifies calculations and minimizes errors. An example of a remote-axis selection is shown in sketch (b). The "x" axis is the axis along which longitudinal distances are measured; the y axis is the axis along which the lateral distances are measured; the z axis is the axis along which vertical distances are measured.

Step 2. Mass and centroid determinations for the major sections — With the aid of a weight-and-balance statement, the three-view drawing, and a knowledge of the locations of the group items, the mass and corresponding centroids for each of the five sections are determined. These values are then recorded on a form similar to the one shown in the sample problem.

For single-engine aircraft with the engine mounted on the aircraft plane of symmetry and with the nacelle structure in part integral with the fuselage, only the engine is considered as a separate section, and the nacelle and other engine items are considered with the fuselage section. Only x and z distances are recorded for all sections mounted on the aircraft plane of symmetry. However, for noncenterline-mounted vertical stabilizers and power-plant sections y distances are recorded in addition to x and z values, since the I_o values are calculated about the centroids of each section For example, the power-plant sections for a four-engine aircraft are analyzed as follows:

The masses of both inboard power-plant sections are added together and recorded. The lateral distance from the aircraft plane of symmetry to the centerline of one of the inboard power plants is recorded along with the distances from the other two axes. The outboard power plants are analyzed similarly, except that the lateral distance recorded is measured from the aircraft plane of symmetry to the centerline of one of the outboard power plant sections.

Care must be taken to use consistent units for mass and distance throughout the entire calculation. Since most group components are listed by pounds, this unit of weight may be used for all calculations. The resulting inertias may then be converted to units involving mass by dividing by the acceleration due to the force of gravity at the desired altitude. An example of such a conversion is included in the sample problem.

Step 3. Calculations of I_o for the major sections — The I_o values for the major sections are determined by first considering an "ideal" formula that closely correlates with the shape of the section. These formulas are labeled "ideal," since they are based on sound mathematical principles, a prerequisite for any school, and since they assume a homogeneous mass distribution throughout the section. The result from the "ideal" formula is then multiplied by a K factor that accounts for deviations in the homogeneous nature of the mass of the section. These factors are based on statistical data. It is found that for some sections a constant factor may be used. For other sections, where the mass distribution may vary considerably, it is found that the K factor varies primarily with the centroid location of the section. Graphs showing the variable K factors, along with substantiating correlation plots, are included as figures. The I_o calculations for each section follow:

(a) Wing Pitching I_o

The wing pitching I_o formulas are listed in the summary. The formulas are based on a consideration of three basic wing shapes (see figure 8.1-22). A constant K factor ($K_o = 0.703$) is used for all wing designs.

(b) Wing Rolling I_o

Because of the large span of the wing with respect to other sections of the aircraft, the wing rolling I_o calculations has the greatest effect on the rolling inertia of the aircraft. The variable K factor (K_I) shown in figure 8.1-23 is based primarily on the lateral centroid of half the wing. As this centroid approaches the aircraft plane of symmetry, more weight must be concentrated in the inboard section of the wing, thereby lowering its I_o value.

(c) Wing Yawing I_o

As is shown by statistical data and by an analysis of the inertias of flat plates, the wing yawing I_o is equal to the sum of the wing pitching and rolling I_o's.

(d) Fuselage Pitching I_o

The fuselage pitching I_o formula is based on that of a combination cylindrical shell and conical shell. The formula provides that as the ratio of the fuselage wetted area to the theoretical wetted area of the fuselage as a two-way cone increases, the inertia approaches that of a cylindrical shell. The fuselage I_o is probably the most difficult to correlate parametrically, since parameters are not available to accurately predict the location of large mass items such as landing gear, electronic equipment, etc. However, statistical data show that the longitudinal centroid location has a definite bearing on the inertia, and therefore the variable K factor (K_x) uses this centroid location as its basic parameter (see figure 8.1-24). It should also be noted that the fuselage pitching I_o has the greatest effect on the pitching inertia of the airplane.

(e) Fuselage Rolling I_o

The formula is based on that of a cylindrical shell of an average diameter determined by consideration of the fuselage wetted area. The fuselage diameter and the ratio of the fuselage structural mass to the total fuselage section mass are the parameters by which K is computed. As the fuselage diameter decreases, the I_o approaches that of a solid cylinder, since the solidity of the equipment items is more effective. Therefore the fuselage diameter is directly proportional to the I_o value since the rolling I_o of the solid circular cylinder is less than that of a cylindrical shell.

The ratio of the fuselage structural mass to the total fuselage-section mass is also directly proportional to the I_o result, since as the value of the ratio decreases, the effect of the solidity of equipment items increases, which decreases the final I_o result. The graph for determining the variable K factor (K_o) is shown as figure 8.1-25.

(f) Fuselage Yawing I_o

As is shown by statistical data and by an analysis of the inertias of cylindrical bodies, the fuselage yawing I_o is equal to the fuselage pitching I_o.

(g) Tail Section I_o

The tail section I_o determinations are similar to those discussed for the wing. Note that the constant K factor used in evaluating tail section I_o's differs from the wing K_o value. For horizontal or vertical stabilizers $K_o = 0.771$.

(h) Power-Plant Pitching and Rolling I_o

The power-plant pitching and rolling formulas are based on that of a solid circular cylinder. The pitching I_o formula accounts for differences in length between the nacelle structure and the engine. Both formulas include a constant factor that may be used for all designs. These formulas are given in the Datcom Summary.

(i) Power-Plant Yawing I_o

As is shown by statistical data and an analysis of the inertias of cylindrical bodies, the power plant yawing I_o is equal to the power plant pitching I_o.

Step 4. Total airplane inertia — When the data discussed above and similar data for the expendable or variable load items have been itemized, the total airplane inertias in pitch, roll, and yaw can be determined from equations 8.1-e and 8.1-f. For further illustration, see the sample problem.

Ten aircraft were analyzed in detail, in order to substantiate the method and the choice of major sections. These aircraft were chosen for their availability of data, for the degree in which they could be analyzed in detail, and for the large cross section of configurations, which include (1) those with a weight empty of from 7,000 to 125,000 pounds, (2) swept and nonswept wing designs, (3) combat, cargo, and passenger types for Air Force, Navy, and commercial uses, (4) reciprocal and jet, both multiple- and single-engine designs, (5) wing and fuselage engine locations, (6) wing and fuselage main-landing-gear locations, (7) fuselage and nonfuselage fuel locations, and (8) all types of tail configurations, including those having wing-mounted elevons instead of horizontal stabilizers.

DATCOM METHOD — SUMMARY

1. Notation*

I_y	pitching moment of inertia about a remote axis
I_x	rolling moment of inertia about a remote axis
I_z	yawing moment of inertia about a remote axis
I_{oy}	pitching moment of inertia about the centroidal axis of the body
I_{ox}	rolling moment of inertia about the centroidal axis of the body
I_{oz}	yawing moment of inertia about the centroidal axis of the body
W_w	weight of wing section including wing carry-through structure
$\bar{y}_w$	lateral centroidal distance of half-wing from aircraft plane of symmetry
C_a, C_b, C_c	wing parameters measured parallel to plane of symmetry (see figure 8.1-22 and page 8.1-7)
c_r	root chord of wing (at ℄)
c_t	tip chord of wing
Λ_{LE}	sweepback angle of wing leading edge
W_f	weight of fuselage section
W_{fs}	weight of fuselage structure
$\bar{x}_f$	longitudinal centroidal distance of fuselage from nose
l_B	length of fuselage
d	average maximum diameter of fuselage $= \frac{\text{max. diameter} + \text{max. width}}{2}$
S_s	fuselage wetted area
W_H	weight of horizontal stabilizer section
$\bar{y}_H$	lateral centroidal distance of half horizontal stabilizer from aircraft plane of symmetry
c_{r_H}	root chord of horizontal stabilizer (at ℄)
c_{t_H}	tip chord of horizontal stabilizer
b_H	span of horizontal stabilizer
Λ_{LE_H}	sweepback angle of horizontal-stabilizer leading edge
W_V	weight of vertical stabilizer
$\bar{z}_V$	vertical centroidal distance of vertical stabilizer from theoretical root chord (at fuselage)
c_{r_V}	root chord of vertical stabilizer (at fuselage)

* Since the values used for W in this section are those of weight instead of mass, the solution of the equations is more general and applicable to any altitude. Consequently, the inertias throughout the problem are in lb-in.^{2}, but are converted at the end of the problem to slug-ft^2 by using the value of gravity at the particular altitude.

c_{t_V} tip chord of vertical stabilizer

b_{v_1} span of vertical stabilizer (tip to fuselage)

Λ_{LE_V} sweepback angle of vertical stabilizer leading edge

W_P weight of power plant section

W_e weight of engine and propeller (if applicable)

l_e length of engine including propeller (if applicable)

d_e average maximum diameter of engine

l_p length of nacelle structure

ρ ratio of weight to chord for wing shapes

2. Select three remote axes and an origin location for these axis.

3. Determine mass and centroids for all sections and applicable expendable and variable load items and record on a convenient form.

4. From the information determined by item 3, calculate and record mass times centroid and mass times centroid squared.

5. Determine the I_o figures for the major sections as follows:

a. Wing pitching I_o (see figure 8.1-22 for development of equations)

if: $$W_W = \frac{\rho}{2}(-C_a + C_b + C_c) \qquad 8.1\text{-h}$$

$$W_W x = \frac{\rho}{6}(-C_a^2 + C_b^2 + C_c C_b + C_c^2) \qquad 8.1\text{-i}$$

$$I = \frac{\rho}{12}(-C_a^3 + C_b^3 + C_c^3 C_b + C_c C_b^2 + C_c^3) \qquad 8.1\text{-j}$$

$$I_{oy} = K_o\left[I - \frac{(W_w x)^2}{W_W}\right] \qquad 8.1\text{-k}$$

where:

$K_o = 0.703$

C_a is the smallest of the following values:

$$c_r \;;\; \frac{b_W \tan \Lambda_{LE}}{2} \;;\; c_t + \frac{b_W \tan \Lambda_{LE}}{2} \qquad 8.1\text{-}\ell$$

C_b is the intermediate value

C_c is the largest value

b. Wing Rolling I_o

$$I_{ox} = \frac{W_w b_W^2 K_1}{24}\left(\frac{c_r + 3c_t}{c_r + c_t}\right) \qquad 8.1\text{-m}$$

where K_1 is obtained from figure 8.1-23.

c. Wing Yawing I_o

$$I_{oz} = I_{oy} + I_{ox} \qquad 8.1\text{-n}$$

d. Fuselage Pitching I_o

$$I_{oy} = \frac{W_f S_s K_2}{37.68}\left(\frac{3d}{2l_B} + \frac{l_B}{d}\right) \qquad 8.1\text{-}o$$

where K_2 is obtained from figure 8.1-24.

e. Fuselage Rolling I_o

$$I_{ox} = \frac{W_f K_3}{4}\left(\frac{S_s}{\pi l_B}\right)^2 \qquad 8.1\text{-}p$$

where K_3 is obtained from figure 8.1-25.

f. Fuselage Yawing I_o

$$I_{oz} = I_{oy} \qquad 8.1\text{-}q$$

g. Horizontal Stabilizer Pitching I_o

Use same equations as wing pitching I_o

$K_o = 0.771$

h. Horizontal Stabilizer Rolling I_o

$$I_{ox} = \frac{W_H b_H^2 K_4}{24}\left(\frac{c_{r_H} + 3c_{t_H}}{c_{r_H} + c_{t_H}}\right) \qquad 8.1\text{-}r$$

where K_4 is obtained from figure 8.1-26.

i. Horizontal Stabilizer Yawing I_o

$$I_{oz} = I_{oy} + I_{ox} \qquad 8.1\text{-}s$$

j. Vertical Stabilizer Rolling I_o

$$I_{ox} = \frac{W_v b_{v_1}^2 K_5}{18}\left[1 + \frac{2c_{r_V} c_{t_V}}{(c_{r_V} + c_{t_V})^2}\right] \qquad 8.1\text{-}t$$

where K_5 is obtained from figure 8.1-27.

k. Vertical Stabilizer Yawing I_o

Use same equations as wing pitching I_o (use twice the vertical stabilizer span as the value of b in the equations for wing pitching I_0)

$K_o = 0.771$

Vertical Stabilizer Pitching I_o

$$I_{oy} = I_{oz} + I_{ox} \qquad 8.1\text{-}u$$

m. Power Plant Pitching I_o

$$I_{oy} = 0.061\left[\frac{3}{4} W_p d_e^2 + W_e l_e^2 + (W_p - W_e) l_p^2\right] \qquad 8.1\text{-}v$$

n. Power Plant Rolling I_o

$$I_{ox} = 0.083\, W_p d_e^2 \qquad 8.1\text{-}w$$

o. Power Plant Yawing I_o

$$I_{oz} = I_{oy} \qquad \text{8.1-x}$$

6. Determine the I_o value for the expendable and variable load items by considering the conventional inertia formulas which closely match the shape of these load items. (See sample problem.)

7. Determine the total airplane inertias in pitch, roll, and yaw by using equations 8.1-e and 8.1-f. (See sample problem.)

Sample Problem

Given:

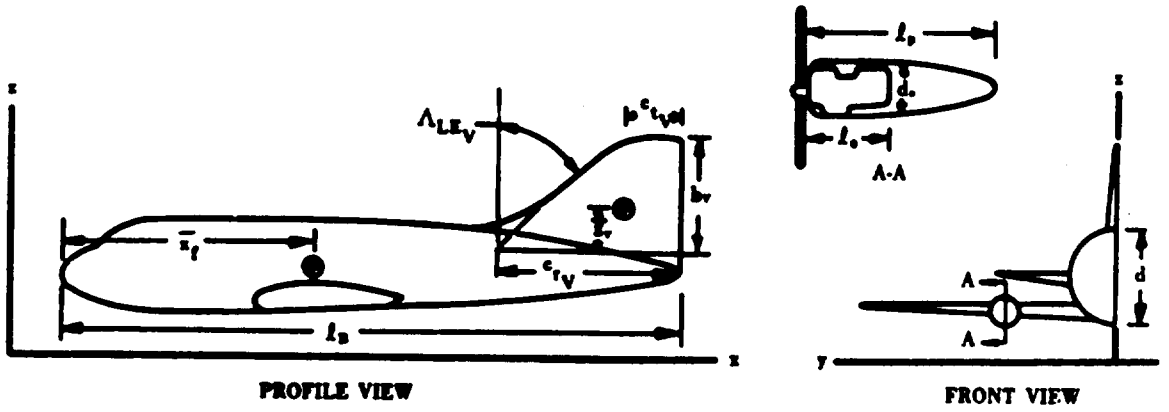

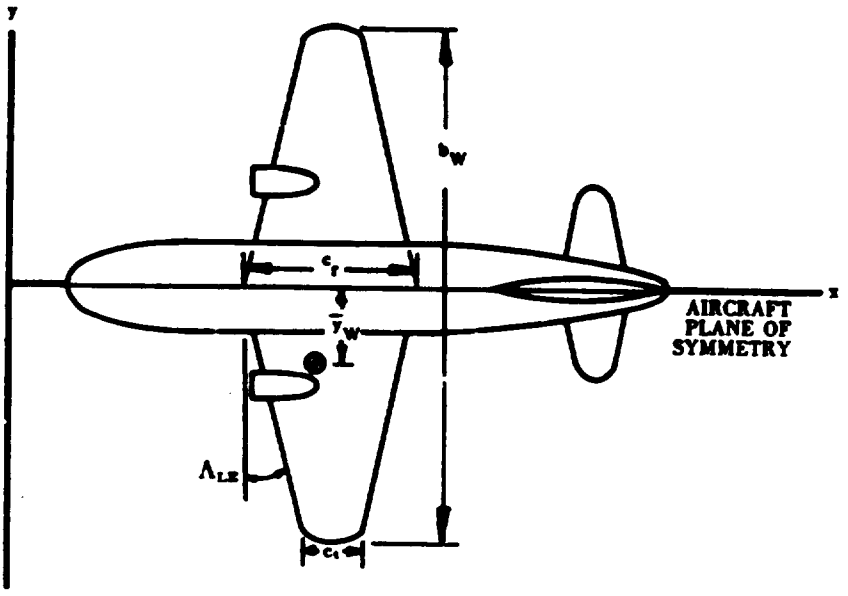

Wing

$\Lambda_{LE} = 12.1°$

$b_W = 10$

$c_r = 300$ in.

$c_t = 100$ in.

$\bar{y}_W = 150$ in.

Hor. Stab.

$\Lambda_{LE_H} = 12°$

$b_H = 400$ in.

$c_{r_H} = 100$ in.

$c_{t_H} = 50$ in.

$\bar{y}_H = 80$ in.

Ver. Stab.

$\Lambda_{LE_V} = 37°$

$b_{V_1} = 200$ in.

$c_{r_V} = 250$ in.

$c_{t_V} = 100$ in.

$\bar{z}_V = 75$ in.

Fuselage

$l_n = 1200$ in.

$d = 150$ in.

$\bar{x}_f = 500$ in.

$S_s = 400{,}000$ sq in.

$W_{f_s} = 8000$ lb

Power Plant

$l_p = 200$ in.

$l_e = 100$ in.

$d_e = 50$ in.

$W_e = 7000$ lb

SECTION	WEIGHT (lbs)	x (in.)	z (in.)	y (in.)
Wing	15,000	650	150	
Fuselage	20,000	600	200	
H. Stab.	1000	1150	200	
V. Stab.	300	1200	300	
P. Plant	10,000	520	150	200
Fuel	20,000	650	150	
Cargo	10,000	500	200	

Compute:

1. Calculate and tabulate the products of weight and centroid location and the products of weight and centroid location squared.

2. Determine the I_o values for the major sections.

   a. Wing pitching I_o

$$C_a = \frac{b_W \tan \Lambda_{LE}}{2} = \frac{(1000) \tan 12.1°}{2} = 107 \text{ in.}$$

$$C_b = c_t + \frac{b_W \tan \Lambda_{LE}}{2} = 100 + 107 = 207 \text{ in.}$$

$$C_c = c_r = 300 \text{ in.}$$

(equation 8.1-ℓ)

$K_o = 0.703$ (constant for any wing)

$$\rho = \frac{W_W}{.5\,(-C_a + C_b + C_c)} \quad \text{(equation 8.1-h)}$$

$$= \frac{15{,}000}{.5\,(-107 + 207 + 300)} = 75 \text{ lb/in.}$$

$$W_W x = \frac{\rho}{6}[-C_a^2 + C_b^2 + C_c C_b + C_c^2] \quad \text{(equation 8.1-i)}$$

$$= 12.5\,[-(107)^2 + (207)^2 + (300)(207) + (300)^2] = 2{,}293{,}750 \text{ lb-in.}$$

$$I = \frac{\rho}{12}[C_r^3 + C_r^2 C_t + C_r C_t^2 + C_t^3] \quad \text{(equation 8.1-j)}$$

$$= 0.23[(107)^3 + (207)^2 + (300)^2(207) + (300)(207)^2 + (300)^3] = 413,308,750 \text{ lb-in.}^2$$

$$I_{oy} = K_o\left[I - \frac{(W_w \bar{x})^2}{W_w}\right] \text{(equation 8.1-k)}$$

$$= (0.703)\left[413,308,750 - \frac{(2,293,750)^2}{15,000}\right] = 43,976,971 \text{ lb-in.}^2$$

b. Wing Rolling I_o

$$\frac{\bar{y}_w}{\frac{b_w}{6}\frac{c_r + 2c_t}{c_r + c_t}} = \frac{150}{208} = 0.72$$

$K_1 = 0.67$ (figure 8.1-23)

$$I_{ox} = \frac{W_w b_w^2 K_1}{24}\left(\frac{c_r + 3c_t}{c_r + c_t}\right) \quad \text{(equation 8.1-m)}$$

$$= \frac{(15,000)(1000)^2(0.67)}{24}\left(\frac{300 + 300}{300 + 100}\right) = 628,125,000 \text{ lb-in.}^2$$

c. Wing Yawing I_o

$$I_{oz} = I_{oy} + I_{ox} \quad \text{(equation 8.1-n)}$$

$$= 43,976,971 + 628,125,000 = 672,101,971 \text{ lb-in.}^2$$

d. Fuselage Pitching I_o

$$\frac{\left|\frac{\ell_B}{2} - \bar{x}_f\right|}{\frac{\ell_B}{2}} = \frac{|600 - 500|}{600} = 0.17$$

$K_2 = 0.83$ (figure 8.1-24)

$$I_{oy} = \frac{W_f S_o K_2}{37.68}\left(\frac{3d}{2\ell_B} + \frac{\ell_B}{d}\right) \quad \text{(equation 8.1-o)}$$

$$= \frac{(20,000)(400,000)(0.83)}{37.68}\left(\frac{450}{2400} + \frac{1200}{150}\right) = 1,442,807,855 \text{ lb-in.}^2$$

e. Fuselage Rolling I_o

$$\frac{(d)^{1/2}(W_{fs})}{W_f} = \frac{(150)^{1/2}(8,000)}{20,000} = 4.9$$

$K_3 = 0.97$ (figure 8.1-25)

$$I_{ox} = \frac{W_f K_3}{4}\left(\frac{S_1}{\pi \ell_B}\right)^2 \quad \text{(equation 8.1-p)}$$

$$= \frac{(20,000)(0.97)}{4}\left(\frac{400,000}{1200\pi}\right)^2 = 54,600,860 \text{ lb-in.}^2$$

f. Fuselage Yawing I_o

$$I_{oz} = I_{oy} = 1,422,807,855 \text{ lb-in.}^2$$

g. Horizontal Stabiliser Pitching I_α

$$C_a = \frac{b_H \tan \Lambda_{LE_H}}{2} = \frac{(400) \tan 12°}{2} = 43 \text{ in.}$$

$$C_b = c_{t_H} + \frac{b_H \tan \Lambda_{LE_H}}{2} = 50 + 43 = 93 \text{ in.}$$

$$C_c = c_{t_H} = 100 \text{ in.}$$

(equation 8.1-*l*)

$K_\alpha = 0.771$ (constant for any tail surface)

$$\rho = \frac{W_H}{.5(-C_a + C_b + C_c)} \quad \text{(equation 8.1-h)}$$

$$= \frac{1000}{.5(-43 + 93 + 100)} = 13.3 \text{ lb/in.}$$

$$Wx = \frac{\rho}{6}[-C_a^2 + C_b^2 + C_cC_b + C_c^2] \quad \text{(equation 8.1-i)}$$

$$W_Hx = 2.2[-(43)^2 + (93)^2 + (100)(93) + (100)^2] = 57{,}420 \text{ lb-in.}$$

$$I = \frac{\rho}{12}[-C_a^3 + C_b^3 + C_c^2C_b + C_cC_a^2 + C_c^3] \quad \text{(equation 8.1-j)}$$

$$= 1.1[-(43)^3 + (93)^3 + (100)^2(93) + (100)(93)^2 + (100)^3] = 3{,}871{,}725 \text{ lb-in.}^2$$

$$I_{\alpha y} = K_\alpha\left[I - \frac{W_Hx^2}{W_H}\right] \quad \text{(equation 8.1-k)}$$

$$= (0.771)\left[3{,}871{,}725 - \frac{(57{,}420)^2}{1000}\right] = 443{,}070 \text{ lb-in.}^2$$

h. Horizontal Stabiliser Rolling I_α

$$\frac{\bar{y}_H}{\frac{b_H}{6}\left(\frac{c_{r_H} + 2c_{t_H}}{c_{r_H} + c_{t_H}}\right)} = \frac{80}{\frac{400}{6}\left(\frac{100 + 100}{100 + 50}\right)} = 0.90$$

$K_\alpha = 0.740$ (figure 8.1-26)

$$I_{\alpha x} = \frac{W_H b_H^2 K_\alpha}{24}\left(\frac{c_{r_H} + 3c_{t_H}}{c_{r_H} + c_{t_H}}\right) \quad \text{(equation 8.1-r)}$$

$$= \frac{(1000)(400)^2(0.74)}{24}\left(\frac{100 + 150}{100 + 50}\right) = 8{,}222{,}222 \text{ lb-in.}^2$$

i. Horizontal Stabiliser Yawing I_α

$$I_{\alpha z} = I_{\alpha y} + I_{\alpha x} \quad \text{(equation 8.1-s)}$$

$$= 443{,}070 + 8{,}222{,}222 = 8{,}665{,}292 \text{ lb-in.}^2$$

j. Vertical Stabiliser Rolling I_α

$$\frac{\bar{z}_V}{\frac{b_V}{3}\left(\frac{c_{r_V} + 2c_{t_V}}{c_{r_V} + c_{t_V}}\right)} = \frac{75}{\frac{200}{3}\left(\frac{250 + 200}{250 + 100}\right)} = 0.87$$

$K_\alpha = 0.930$ (figure 8.1-27)

$$I_{\alpha z} = \frac{W_V b_V^2 K_\alpha}{18}\left[1 + \frac{2c_{r_V}c_{t_V}}{(c_{t_V} + c_{t_V})^2}\right] \quad \text{(equation 8.1-t)}$$

$$= \frac{(300)(200)^2(0.93)}{18}\left[1 + \frac{2(250)(100)}{(250+100)^2}\right] = 872{,}960 \text{ lb-in.}^2$$

k. Vertical Stabilizer Yawing I_o

$$\left.\begin{aligned} C_a &= b_{V_1} \tan \Lambda_{LE_V} = (200) \tan 37^\circ = 150 \text{ in.} \\ C_b &= c_{t_V} + b_{V_1} \tan \Lambda_{LE_V} = 100 + 150 = 250 \text{ in.} \\ C_c &= c_{t_V} = 250 \text{ in.} \end{aligned}\right\} \text{ (equation 8.1-}\ell\text{)}$$

$K_o = 0.771$ (constant for any tail surface)

$$\rho = \frac{W_V}{.5(-C_a + C_b + C_c)} \text{ (equation 8.1-h)}$$

$$= \frac{300}{.5(-150+250+250)} = 1.7 \text{ lb/in.}$$

$$W_V x = \frac{\rho}{6}[-C_a^2 + C_b^2 + C_c C_b + C_c^2] \text{ (equation 8.1-i)}$$

$$= 0.28[-(150)^2 + (250)^2 + (250)(250) + (250)^2] = 46{,}200 \text{ lb-in.}$$

$$I = \frac{\rho}{12}[-C_a^3 + C_b^3 + C_c^2 C_b + C_c C_b^2 + C_c^3] \text{ (equation 8.1-j)}$$

$$= 0.14[-(150)^3 + (250)^3 + (250)^2(250) + (250)(250)^2 + (250)^3] = 8{,}277{,}500 \text{ lb-in.}^2$$

$$I_{ox} = K_o\left[I - \frac{(W_V x)^2}{W_V}\right] \text{ (equation 8.1-k)}$$

$$= (0.771)\left[8{,}277{,}500 - \frac{(46{,}200)^2}{300}\right] = 896{,}442 \text{ lb-in.}^2$$

l. Vertical Stabilizer Pitching I_o

$$I_{oy} = I_{ox} + I_{oz} \text{ (equation 8.1-u)}$$

$$= 872{,}960 + 896{,}442 = 1{,}769{,}402 \text{ lb-in.}^2$$

m. Power Plant Pitching I_o

$$I_{oy} = 0.061\left[\frac{3}{4} W_e d_o^2 + W_e \ell_e^2 + (W_p - W_e)\ell_p^2\right] \text{ (equation 8.1-v)}$$

$$= 0.061\left[\frac{3}{4}(10{,}000)(50)^2 + (7000)(100)^2 + (10{,}000-7000)(200)^2\right]$$

$$= 12{,}733{,}750 \text{ lb-in.}^2$$

n. Power Plant Rolling I_o

$$I_{oz} = 0.083 W_p d_o^2 \text{ (equation 8.1-w)}$$

$$= (0.083)(10{,}000)(50)^2 = 2{,}075{,}000 \text{ lb-in.}^2$$

o. Power Plant Yawing I_o

$$I_{ox} = I_{oy} = 12{,}733{,}750 \text{ lb-in.}^2 \text{ (equation 8.1-x)}$$

3. Determine the I_o values for the expendable and variable loads items

a. Fuel I_o

Estimate fuel volume as a rectangular flat plate

Span = 600 in. Chord = 150 in. Thickness = 8 in.

Using the conventional inertia formula for a rectangular parallelopiped

$$I_{oy} = \frac{W}{12}(c^2 + t^2) = \frac{20{,}000}{12}[(150)^2 + (8)^2] = 37{,}606{,}667 \text{ lb-in.}^2$$

$$I_{ox} = \frac{W}{12}(b^2 + t^2) = \frac{20{,}000}{12}[(600)^2 + (8)^2] = 600{,}106{,}667 \text{ lb-in.}^2$$

$$I_{oz} = \frac{W}{12}(c^2 + b^2) = \frac{20{,}000}{12}[(150)^2 + (600)^2] = 637{,}500{,}000 \text{ lb-in.}^2$$

where W is the fuel weight

b. Cargo I_o

*Cargo Distribution

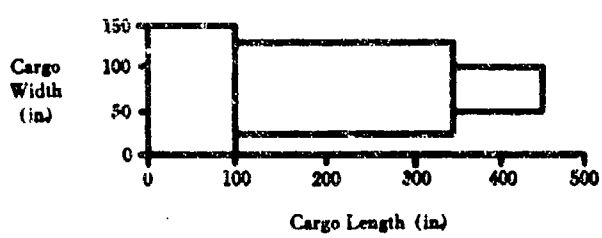

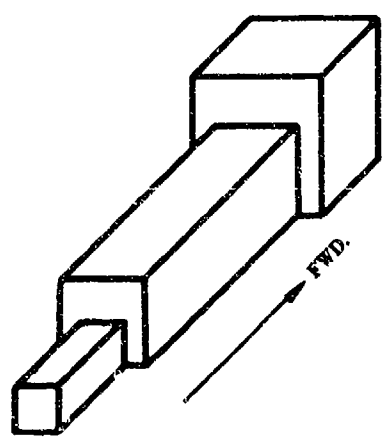

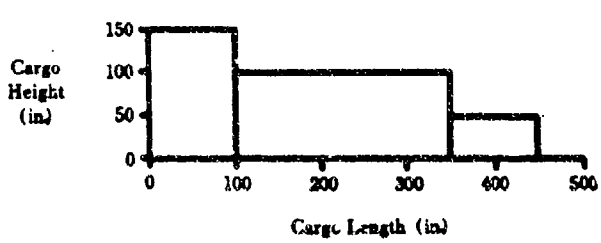

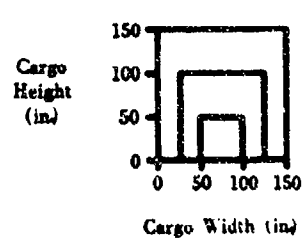

*Indicated as a sample only to show an approach to cargo inertia determinations, and may not reflect actual cargo distributions.

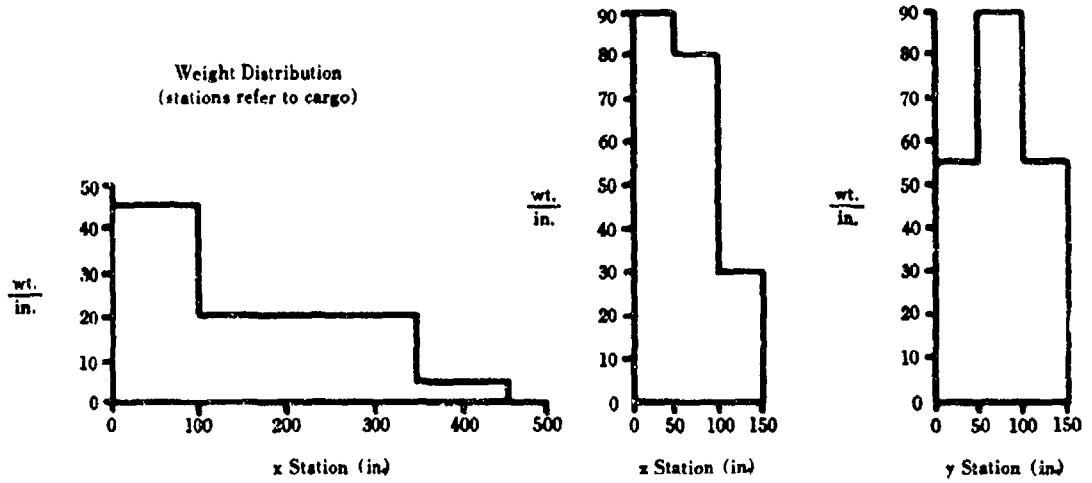

Centroids:*

$$\bar{x} = \frac{\int_0^{100} 45\,x\,dx + \int_{100}^{350} 20\,x\,dx + \int_{350}^{450} 5\,x\,dx}{10{,}000} = 155.0$$

$$\bar{z} = \frac{\int_0^{50} 90\,z\,dz + \int_{50}^{100} 80\,z\,dz + \int_{100}^{150} 30\,z\,dz}{10{,}000} = 60.0$$

$$\bar{y} = \frac{\int_0^{50} 55\,y\,dy + \int_{50}^{100} 90\,y\,dy + \int_{100}^{150} 55\,y\,dy}{10{,}000} = 75.0$$

Second Moments:*

$$Wx^2 = \int_0^{100} 45\,x^2dx + \int_{100}^{350} 20\,x^2dx + \int_{350}^{450} 5\,x^2dx = 374{,}583{,}333$$

$$Wz^2 = \int_0^{50} 90\,z^2dz + \int_{50}^{100} 80\,z^2dz + \int_{100}^{150} 30\,z^2dz = 50{,}833{,}333$$

$$Wy^2 = \int_0^{50} 55\,y^2dy + \int_{50}^{100} 90\,y^2dy + \int_{100}^{150} 55\,y^2dy = 72{,}083{,}333$$

$I_{oy} = I_y - W\bar{r}^2$ (equation 8.1-f)

$= Wx^2 - W\bar{x}^2 + Wz^2 - W\bar{z}^2$ (Substituting equation 8.1-c in 8.1-f)

$= 374{,}583{,}333 - (10{,}000)(155)^2 + 50{,}833{,}333 - (10{,}000)(60)^2$

$= 149{,}166{,}666$ lb-in.^{2}

* The x, y, and z distances, as well as the Wx^2, Wz^2, and Wy^2 terms in the equations for Centroids and Second Moments, refer only to these calculations and are not to be confused with the distances and moment terms in Table 8.1-A.

$$I_{ox} = I_x - W\bar{r}^2 \quad \text{(equation 8.1-f)}$$

$$= Wx^2 - W\bar{z}^2 + Wy^2 - W\bar{y}^2$$

$$= 50{,}833{,}334 - (10{,}000)(60)^2 + 72{,}083{,}335 - (10{,}000)(75)^2$$

$$= 30{,}666{,}666 \text{ lb-in.}^2$$

$$I_{oz} = I_z - W\bar{r}^2 \quad \text{(equation 8.1-f)}$$

$$= Wy^2 - W\bar{y}^2 + Wx^2 - W\bar{x}^2$$

$$= 72{,}083{,}333 - (10{,}000)(75)^2 + 374{,}583{,}333 - (10{,}000)(155)^2$$

$$= 150{,}166{,}666 \text{ lb-in.}^2$$

4. Determine the total airplane inertias in pitch, roll, and yaw. All of the values calculated in 1, 2, and 3 are tabulated in Table 8.1-A and each column is totaled.

   a. Inertia about the remote axis

$$I_y = \sum (Wr^2 + I_{oy}) \quad \text{(equation 8.1-e)}$$

$$= \sum [W(x^2 + z^2) + I_{oy}]$$

$$= (28{,}946{,}000 + 2{,}279{,}500)\,10^3 + (1{,}688{,}505)\,10^3$$

$$= 32{,}914{,}005 \times 10^3 \text{ lb-in.}^2$$

$$I_x = \sum (Wr^2 + I_{ox}) \quad \text{(equation 8.1-e)}$$

$$= \sum [W(y^2 + z^2) + I_{ox}]$$

$$= (400{,}000 + 2{,}279{,}500)\,10^3 + (1{,}324{,}670)\,10^3$$

$$= 4{,}004{,}170 \times 10^3 \text{ lb-in.}^2$$

$$I_z = \sum (Wr^2 + I_{oz}) \quad \text{(equation 8.1-e)}$$

$$= \sum [W(y^2 + x^2) + I_{oz}]$$

$$= (400{,}000 + 28{,}946{,}000)\,10^3 + (2{,}924{,}872)\,10^3$$

$$= 32{,}270{,}872 \times 10^3 \text{ lb-in.}^2$$

   b. Inertia about the airplane centroid

Pitching $I_o = I_y - W\bar{r}^2$ (equation 8.1-f)

where $\bar{r} = \dfrac{\sum Wr}{\sum W}$ (equation 8.1-g)

$$I_o = I_y - \left[\frac{\sum (Wx)^2 + \sum (Wz)^2}{\sum W}\right]$$

$$= 32{,}914{,}005 \times 10^3 - \left[\frac{(46{,}460{,}000)^2 + (13{,}040{,}000)^2}{76{,}300}\right]$$

$$= 2{,}395{,}352 \times 10^3 \text{ lb-in.}^2$$

Rolling $I_o = I_x - W\bar{r}^2$ (equation 8.1-f)

$$= I_x - \left[\frac{\sum (Wy)^2 + \sum (Wz)^2}{\sum W}\right]$$

$$= 4{,}004{,}170 \times 10^3 - \frac{(2{,}000{,}000)^2 + (13{,}040{,}000)^2}{76{,}300}$$

$$= 1{,}723{,}153 \times 10^3 \text{ lb-in.}^2$$

Yawing $I_w = I_z - Wf^2$ (equation 8.1-f)

$$= I_z - \left[\frac{\sum (Wx)^2 + \sum (Wy)^2}{\sum W}\right]$$

$$= 32{,}270{,}872 \times 10^3 - \frac{(46{,}460{,}000)^2 + (2{,}000{,}000)^2}{76{,}300}$$

$$= 3{,}928{,}387 \times 10^3 \text{ lb-in.}^2$$

See Table 8.1-A for tabulated results and conversion to units of mass times distance squared.

TABLE 8.1-A

SECTION	WEIGHT (lbs)	x (in.)	z (in.)	y (in.)	$Wx \times 10^{-3}$ (lb-in.)	$Wz \times 10^{-3}$ (lb-in.)	$Wy \times 10^{-3}$ (lb-in.)	$Wx^2 \times 10^{-3}$ (lb-in.^{2})	$Wz^2 \times 10^{-3}$ (lb-in.^{2})	$Wy^2 \times 10^{-3}$ (lb-in.^{2})
Wing	15,000	650	150		9750	2250		6,337,500	337,500	
Fuselage	20,000	600	200		12,000	4000		7,200,000	800,000	
H. Stab.	1000	1150	200		1150	200		1,322,500	40,000	
V. Stab.	300	1200	300		360	90		432,000	27,000	
P. Plant	10,000	520	150	200	5200	1500	2000	2,704,000	225,000	400,000
Fuel	20,000	650	150		13,000	3000		8,450,000	450,000	
Cargo	10,000	500	200		5000	2000		2,500,000	400,000	
Subtotal	76,300	608.91	170.90	—	46,460	13,040	2000	28,946,000	2,279,500	400,000

SECTION	PITCH $I_{yy} \times 10^{-3}$ (lb-in.^{2})	ROLL $I_{xx} \times 10^{-3}$ (lb-in.^{2})	YAW $I_{zz} \times 10^{-3}$ (lb-in.^{2})
Wing	43,977	628,125	672,102
Fuselage	1,442,808	54,601	1,442,808
H. Stab.	443	8222	8665
V. Stab.	1769	873	896
P. Plant	12,734	2075	12,734
Fuel	37,607	600,107	637,500
Cargo	149,167	30,667	150,167
Subtotal	1,688,505	1,324,670	2,924,872
Total I_{--} ~ lb-in.^{2}	2,395,352	1,723,153	3,928,397
Total I_{--} ~ slug-ft^2*	517	372	848

*For conversion to slug-ft^2, multiply lb-in.^{2} by $\left(\frac{1 \text{ ft}^2}{144 \text{ in.}^2}\right)\left(\frac{1}{32.17 \text{ ft/sec}^2}\right)$ $\left(\frac{1 \text{ ft}^2}{4632.48 \text{ in.}^2\text{-ft/sec}^2}\right)$

This conversion factor gives an inertia value at sea level, since the value of 32.17 ft/sec^2 is the standard acceleration of gravity at sea level.

REFERENCES

1. Marsh, Daniel: Mass Moment of Inertia Estimation Methods. Society of Aeronautical Weight Engineers Technical Paper 313, May 1962. (U)

2. Society of Aeronautical Weight Engineers, Texas Chapter: An Introduction to Aeronautical Weight Engineering. First Edition, Chance Vought Aircraft, Inc., Dallas, Texas; Chapter 21, 1959. (U)

3. Anon: S.A.W.E. Weight Handbook, Volume 1: Third Edition, Society of Aeronautical Weight Engineers, Inc., 1944. (U)

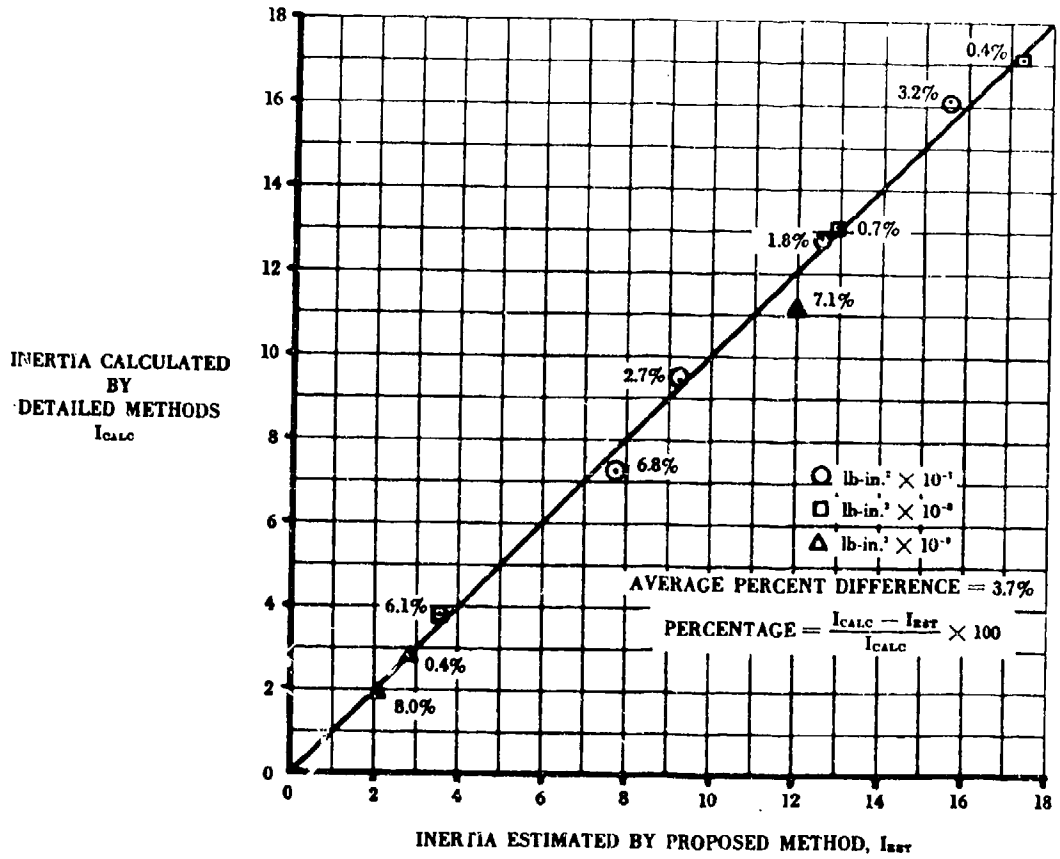

FIGURE 8.1-19 TOTAL AIRPLANE PITCHING INERTIA CORRELATION

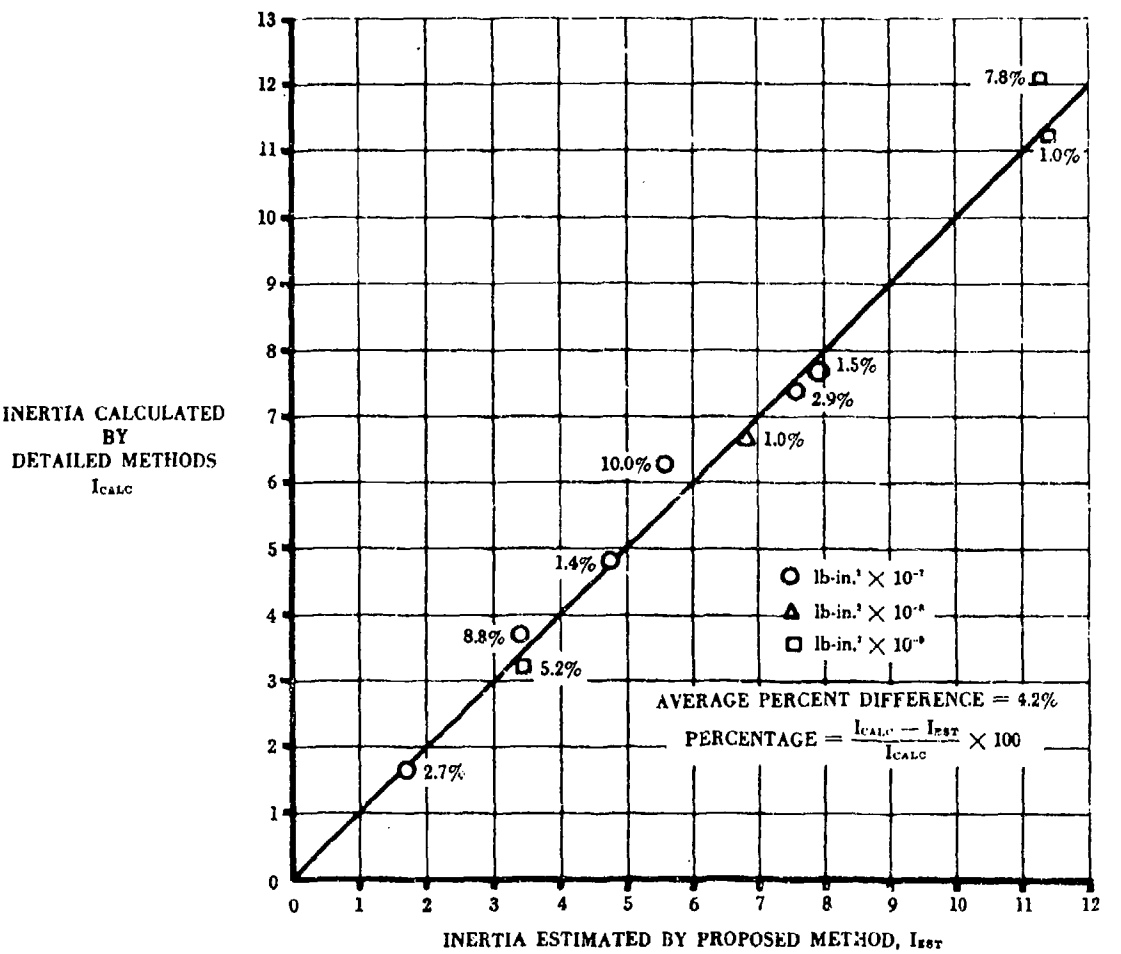

FIGURE 8.1-20 TOTAL AIRPLANE ROLLING INERTIA CORRELATION

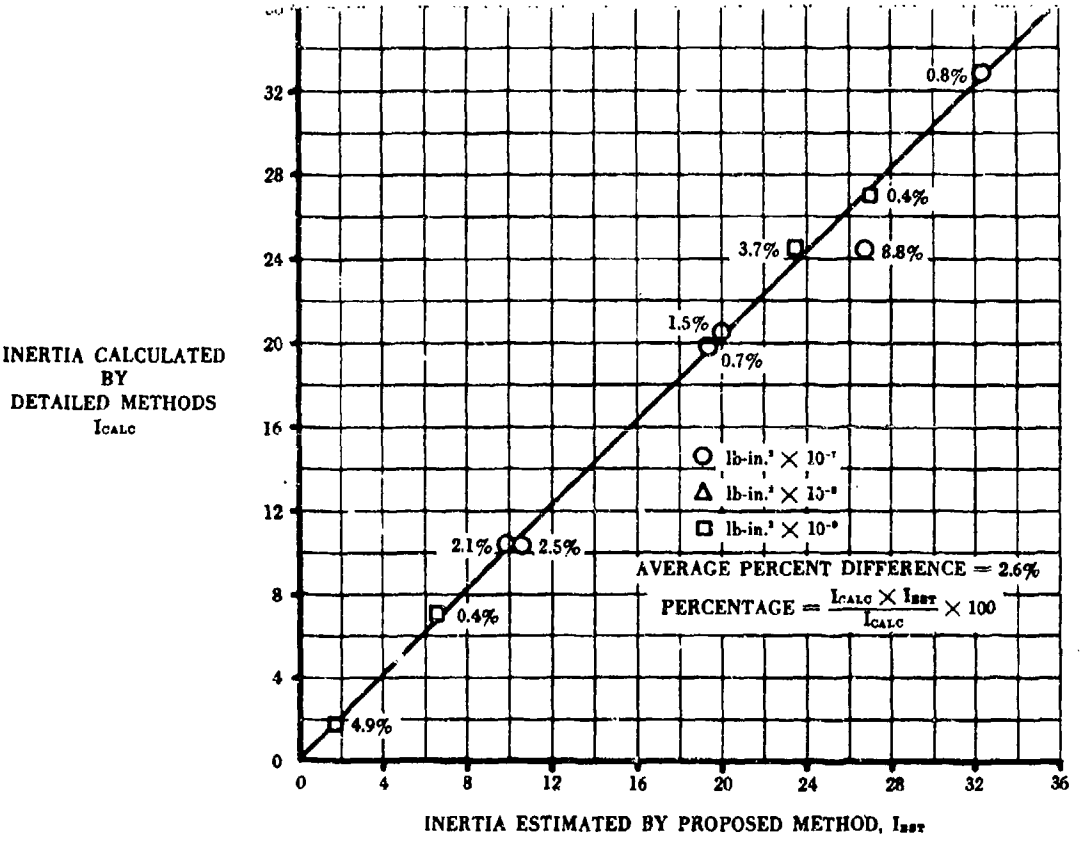

FIGURE 8.1-21 TOTAL AIRPLANE YAWING INERTIA CORRELATION

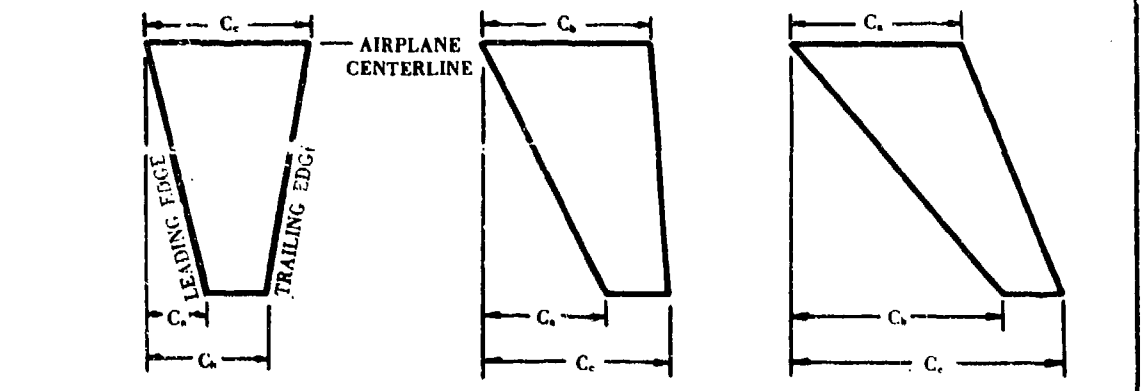

WING SHAPES

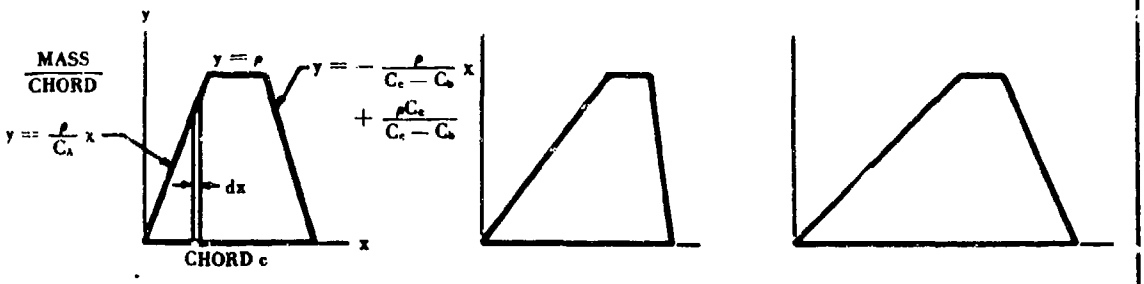

MASS DISTRIBUTIONS

$$\Sigma m = \int_0^{C_a} \frac{\rho}{C_a} x\,dx + \int_{C_a}^{C_b} \rho\,dx - \int_{C_b}^{C_c} \frac{\rho}{C_c - C_b} x\,dx + \int_{C_b}^{C_c} \frac{\rho C_c}{C_c - C_b} dx = \frac{\rho(-C_a + C_b + C_c)}{2}$$

$$\Sigma mx = \int_0^{C_a} \frac{\rho}{C_a} x^2 dx + \int_{C_a}^{C_b} \rho x\,dx - \int_{C_b}^{C_c} \frac{\rho}{C_c - C_b} x^2 dx + \int_{C_b}^{C_c} \frac{\rho C_c}{C_c - C_b} x\,dx = \frac{\rho(-C_a^2 + C_b^2 + C_c C_b + C_c^2)}{6}$$

$$I = \Sigma mx^2 = \int_0^{C_a} \frac{\rho}{C_a} x^3 dx + \int_{C_a}^{C_b} \rho x^2 dx - \int_{C_b}^{C_c} \frac{\rho}{C_c - C_b} x^3 dx + \int_{C_b}^{C_c} \frac{\rho C_c}{C_c - C_b} x^2 dx$$

$$= \frac{\rho(-C_a^3 + C_b^3 + C_c^2 C_b + C_c C_b^2 + C_c^3)}{12}$$

$$I_{oy} = K_o \left[I - \frac{(\Sigma mx)^2}{\Sigma m} \right]$$

where

$K_o = 0.703$ for any wing

$K_o = 0.771$ for any horizontal or vertical stabilizer

FIGURE 8.1-22 WING PITCHING INERTIA CONSIDERATIONS

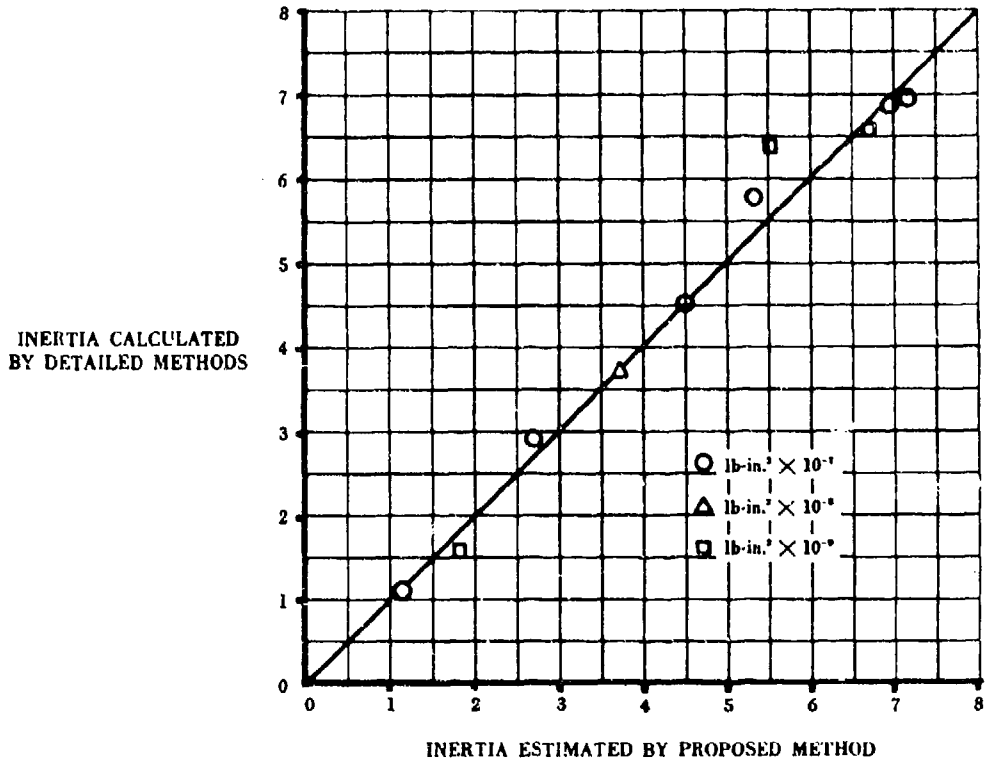

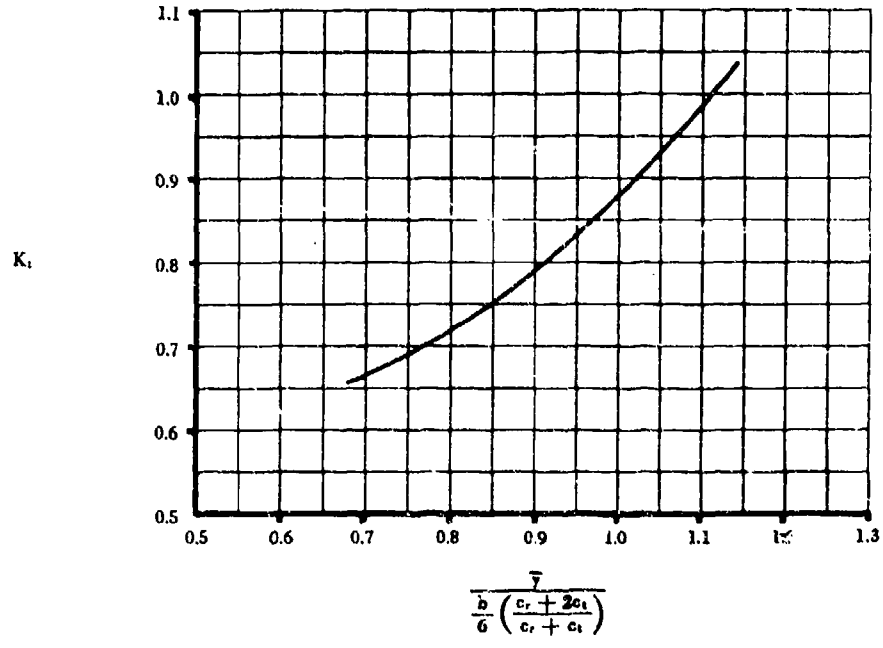

FIGURE 8.1-23 WING ROLLING I, CORRELATION AND K FACTOR

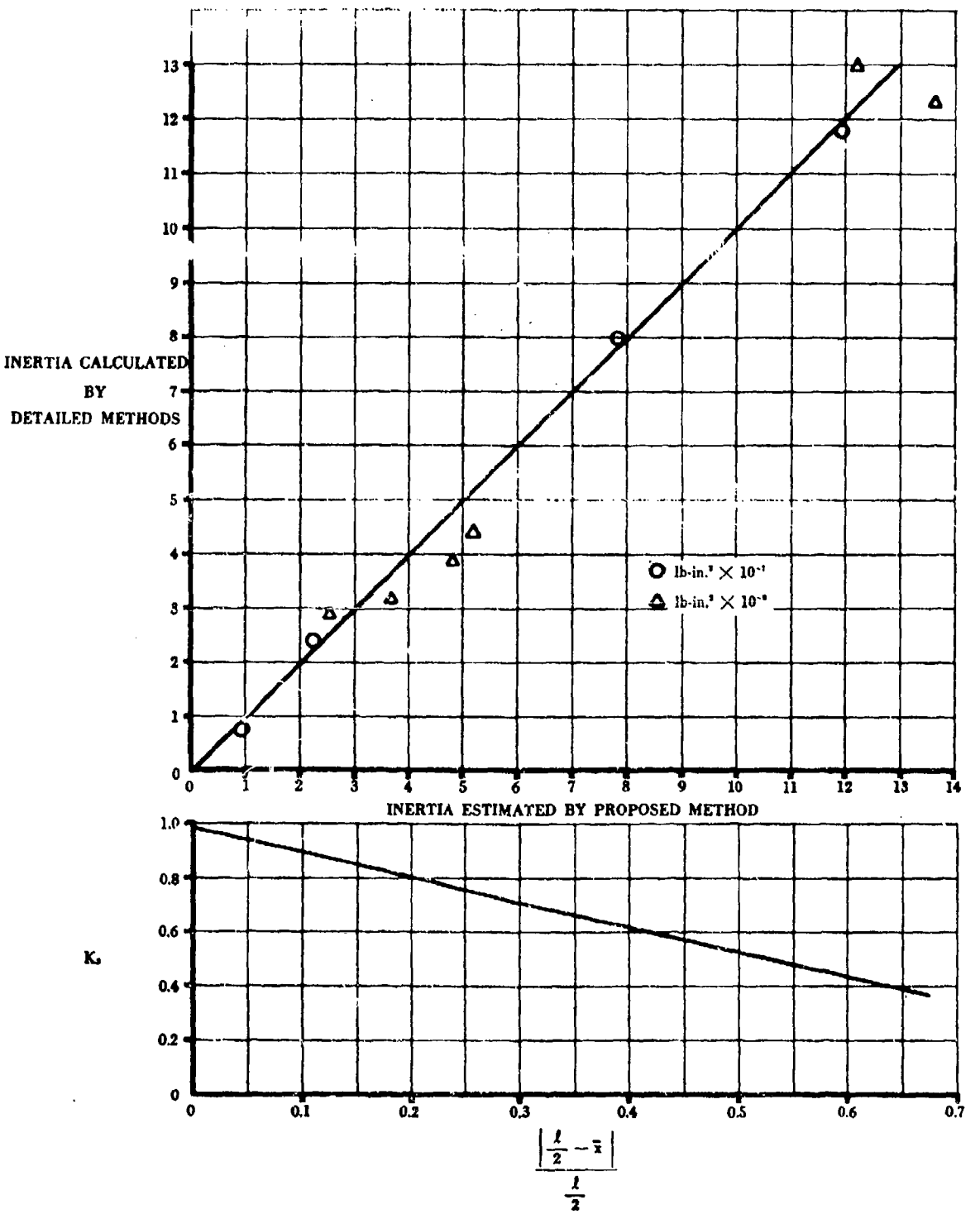

FIGURE 8.1-24 FUSELAGE PITCHING I, CORRELATION AND K FACTOR

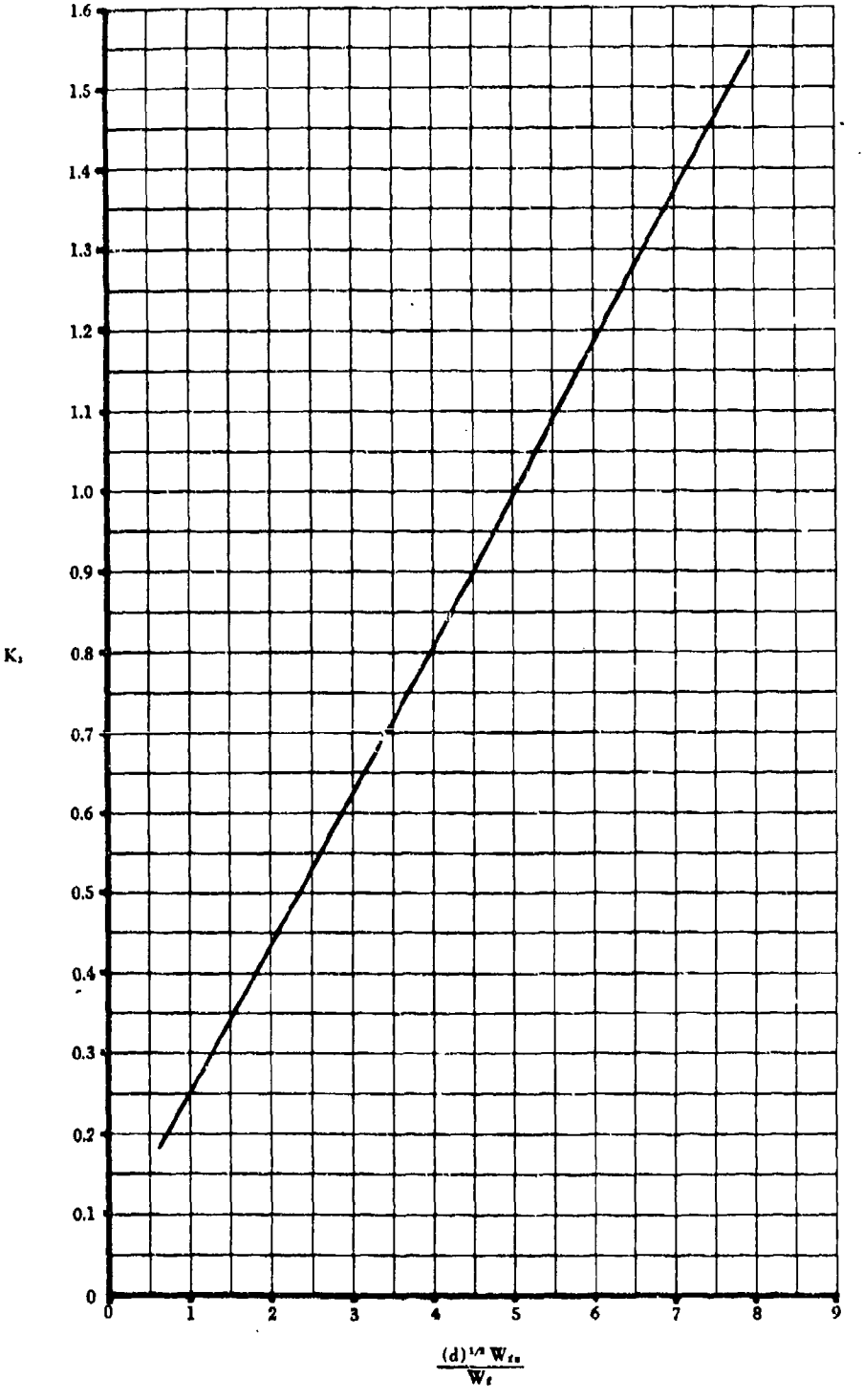

FIGURE 8.1-25 FUSELAGE ROLLING I. K FACTOR

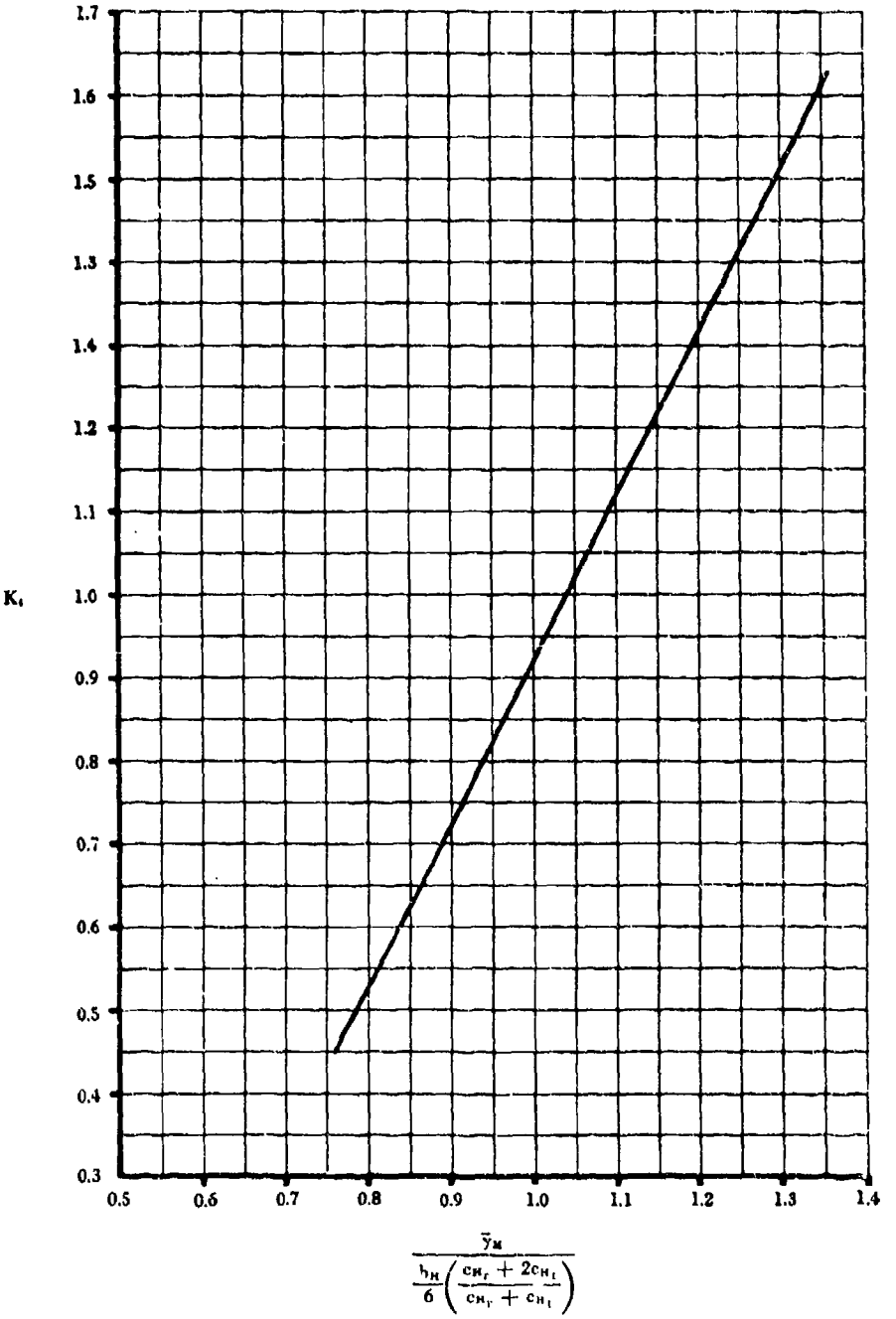

FIGURE 8.126 HORIZONTAL STABILIZER ROLLING I. K FACTOR

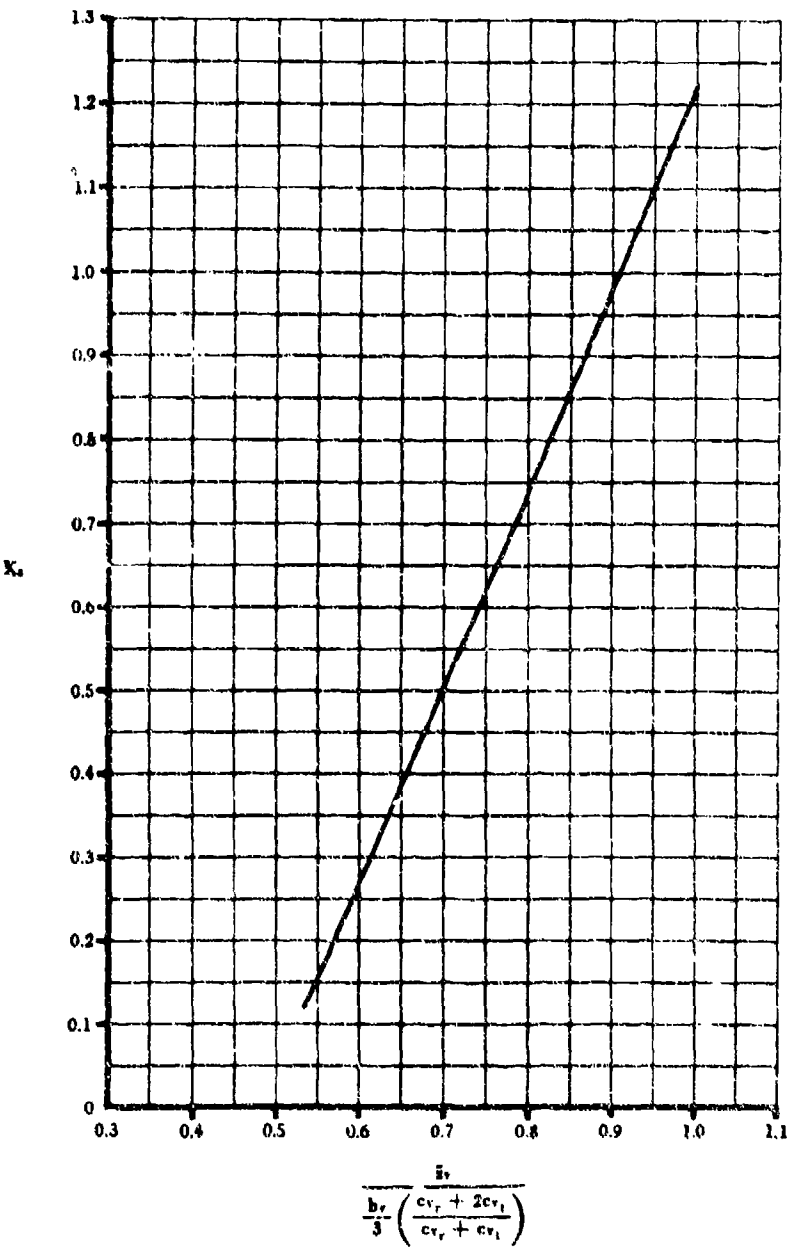

FIGURE 8.1-27 VERTICAL STABILIZER ROLLING I, K FACTOR

8.2 MISSILE MASS AND INERTIA

Two methods of estimating missile mass and inertia, each limited by the initial assumptions and input data, are presented in this section. The method selected will depend on the desired accuracy related to the problem at hand.

The first method, more sophisticated than the second, requires an estimated weight and center-of-gravity breakdown of the vehicle. Although the results are presented in the Datcom for hand calculations, they are most expeditiously programed for a small-capacity computer. The hand computations may be long and tedious, but they are not complicated.

The second method presents the procedure, based on estimates of gross stage weight and profile, for determining the order of magnitude of pitch and roll moments of inertia of a vehicle.

DATCOM METHODS

Method 1

This method assumes that the basic body being analyzed is symmetrical about one axis, as illustrated in the axis-system diagram of sketch (a). This leads to the assumption that the center of gravity of the body lies on the longitudinal axis of the vehicle. However, this assumption does not eliminate handling of missile components that are not symmetrical.

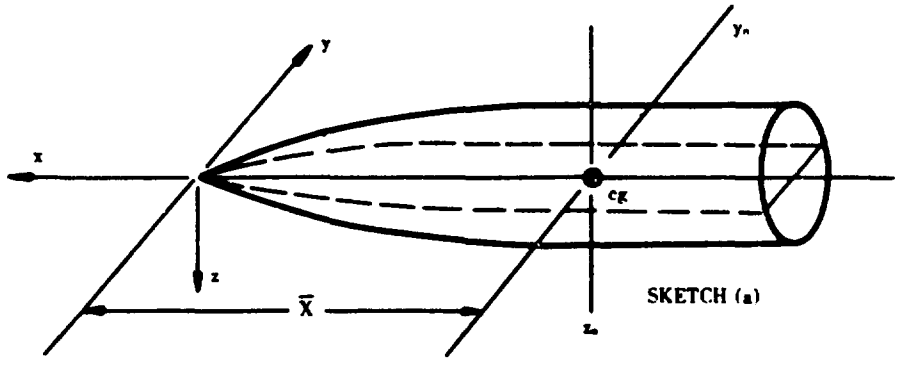

SKETCH (a)

A second assumption is that the moment of inertia with respect to the z_o axis is equal to the moment of inertia with respect to the y_o axis. (yaw moment of inertia = pitch moment of inertia). This assumption is reasonable for most missile bodies and will be in the range of accuracy desired for moment-of-inertia values of vehicles in the preliminary-design phase.

A third assumption is that all components can be approximated by a linear mass distribution along the longitudinal axis as shown in sketch (b). This assumption forces the following limitation: $l/3 \leq l_{c.g.} \leq 2l/3$, where l is the length of the component and l_{cg} is the center of gravity of the component measured from the beginning station of the component. The weight per unit length of element is denoted by w.

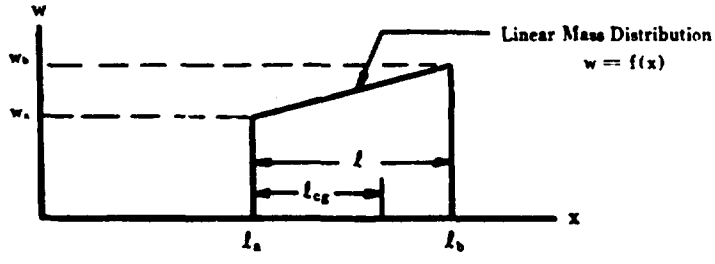

SKETCH (b)

A fourth assumption is that the diameters of any component can be approximated by a linear distribution along the longitudinal axis as shown in sketch (c).

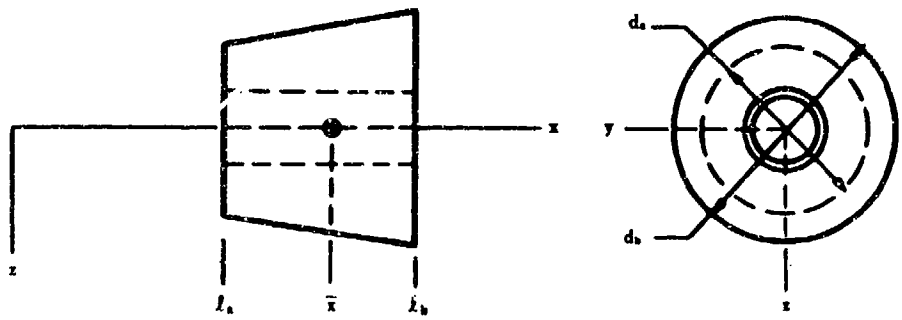

SKETCH (c)

It will be assumed that W, $\bar{x}$, ℓ_a, ℓ_b, d_a and d_b are given or can be estimated and tabulated for each symmetrical component of the missile, where W is the weight of a given component and $\bar{x}$ is the longitudinal station of the center of gravity of that component with respect to the missile nose apex.

The values w_a and w_b are then estimated for each component from the equations

$$w_a = \frac{W}{\ell_b - \ell_a}\left[4 - \frac{6(\bar{x} - \ell_a)}{\ell_b - \ell_a}\right] \qquad 8.2\text{-a}$$

$$w_b = \frac{W}{\ell_b - \ell_a}\left[\frac{6(\bar{x} - \ell_a)}{\ell_b - \ell_a} - 2\right] \qquad 8.2\text{-b}$$

The pitch and yaw moments of inertia (I_{yy}' and I_{zz}') of each solid (nonliquid) component can then be estimated from

$$I_{yy}' = I_{zz}' = (\ell_b^4 - \ell_a^4)\left(\frac{m}{4} + \frac{mT^2}{4K}\right) + (\ell_b^3 - \ell_a^3)\left(\frac{b}{3} + \frac{2mTN + bT^2}{3K}\right) + (\ell_b^2 - \ell_a^2)\left(\frac{mN^2 + 2bTN}{2K}\right) + (\ell_b - \ell_a)\frac{bN^2}{K} - W\bar{x}^2 \qquad 8.2\text{-c}$$

where

$$m = \frac{w_b - w_a}{\ell_b - \ell_a}$$

$$T = \frac{d_b - d_a}{\ell_b - \ell_a}$$

$$b = w_a - \ell_a\left(\frac{w_b - w_a}{\ell_b - \ell_a}\right)$$

$$N = d_a - \ell_a\left(\frac{d_b - d_a}{\ell_b - \ell_a}\right)$$

$K = \dfrac{16}{1 + \left(\dfrac{d_o}{d}\right)^2}$ for elements symmetrical about the longitudinal axis (use figure 8.2-5)

$= \dfrac{1}{\left(\dfrac{\bar{z}}{d}\right)^2 + \left(\dfrac{\rho_{y_o}}{d}\right)^2}$ for unsymmetrical solid elements in pitch (use figure 8.2-6)

$$= \frac{1}{\left(\frac{\bar{y}}{d}\right)^2 + \left(\frac{\rho_{z_o}}{d}\right)^2}$$ for unsymmetrical solid elements in yaw (use figure 8.2-6)

$\bar{x}, \bar{y}, \bar{z}$ are measured to the c.g. of the element as shown in sketch (d)

$\rho_{x_o}, \rho_{y_o}, \rho_{z_o}$ are the radii of gyration of the element

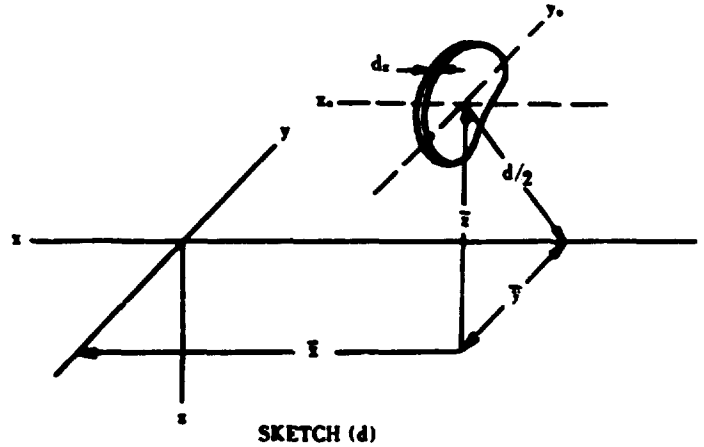

SKETCH (d)

The corresponding roll moment of inertia of a given solid element is

$$I_{xx}' = \frac{2}{C}\left[(l_b^4 - l_a^4)\frac{mT^2}{4} + (l_b^3 - l_a^3)\left(\frac{2mTN + bT^2}{3}\right) + (l_b^2 - l_a^2)\frac{mN^2 + 2bTN}{2} + (l_b - l_a)\,bN^2\right] \qquad 8.2\text{-d}$$

where

$$C = \frac{16}{1 + \left(\frac{d_o}{d}\right)^2}$$ for symmetrical elements (same as K, use figure 8.2-5)

$$= \frac{2}{\frac{1}{4} + \left(\frac{\rho_{x_o}}{d}\right)^2}$$ for unsymmetrical elements (use figure 8.2-7)

and the other symbols are as defined for equation 8.2-c.

For liquid components, the pitch and yaw moments of inertia are

$$I_{yy}' = I_{zz}' = K_L\left[(l_b^4 - l_a^4)\left(\frac{m}{4} + \frac{mT^2}{64}\right) + (l_b^3 - l_a^3)\left(\frac{b}{3} + \frac{2mTN + bT^2}{48}\right) + (l_b^2 - l_a^2)\frac{mN^2 + 2bTN}{32} + (l_b - l_a)\frac{bN^2}{16} - W\bar{x}^2\right] \qquad 8.2\text{-e}$$

where

K_L is given by figure 8.2-8 as a function of the fineness ratio of the element.

The corresponding roll moment of inertia of a liquid element is assumed to be zero.

$$I_{xx}' = 0 \qquad 8.2\text{-f}$$

The pitch and yaw moments of inertia of the complete vehicle are obtained by using the parallel-axis theorem to sum the contribution of each element. Thus

$$I_{yy} = I_{zz} = \sum I_{yy}' + \sum W\bar{x}^2 - (\sum W)\bar{X}^2 \qquad 8.2\text{-g}$$

where the sums are taken over the entire set of elements comprising the configuration and $\bar{X}$ is the longitudinal position of the vehicle center of gravity. This latter term is obtained from the equation

$$\bar{X} = \frac{\sum \bar{x} W}{\sum W} \qquad 8.2\text{-h}$$

The corresponding roll moment of inertia for the complete vehicle is

$$I_{xx} = \sum I_{xx}' \qquad 8.2\text{-i}$$

where again the sum extends over all components.

Certain common vehicle components not satisfying the basic assumptions can be handled exactly by replacing them by equivalent shapes that do satisfy the assumptions.

The spherical segment shell, which does not have a linear diameter variation, can be replaced by an equivalent cylindrical shell as illustrated in figure 8.2-9. The moment of inertia of the cylindrical shell can be computed by the derived equations.

The dimensions of an equivalent solid cylinder for a hemispherical solid are given as

$$d = 0.894\ D \qquad \ell_a = \bar{x} - 0.2105\ D$$

$$L = 0.421\ D \qquad \ell_b = \bar{x} + 0.2105\ D$$

where the symbols are defined in sketch (e).

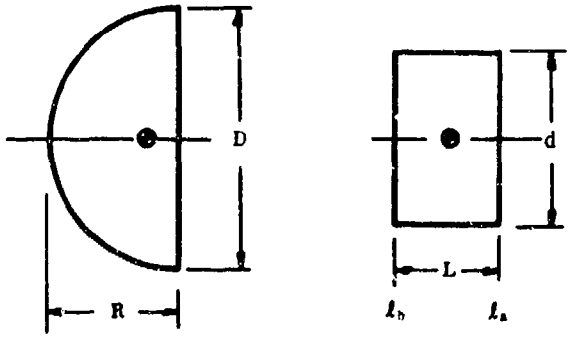

SKETCH (e)

Method 2

For order-of-magnitude determinations, figures 8.2-10 and 8.2-11 summarize the pitch (and yaw) and roll radii of gyration, respectively, of a number of actual missile configurations. This information will allow a determination of these parameters within perhaps ±20 percent. The moments of inertia are then

$$I_{y_{c.g.}} = I_{yy} = I_{zz} = \rho_P^2 \sum W \qquad 8.2\text{-j}$$

$$I_{x_{c.g.}} = I_{xx} = \rho_R^2 \sum W \qquad 8.2\text{-k}$$

where $\sum W$ is the total weight of the vehicle

ρ_P and ρ_R are obtained from figures 8.2-10 and 8.2-11, respectively.

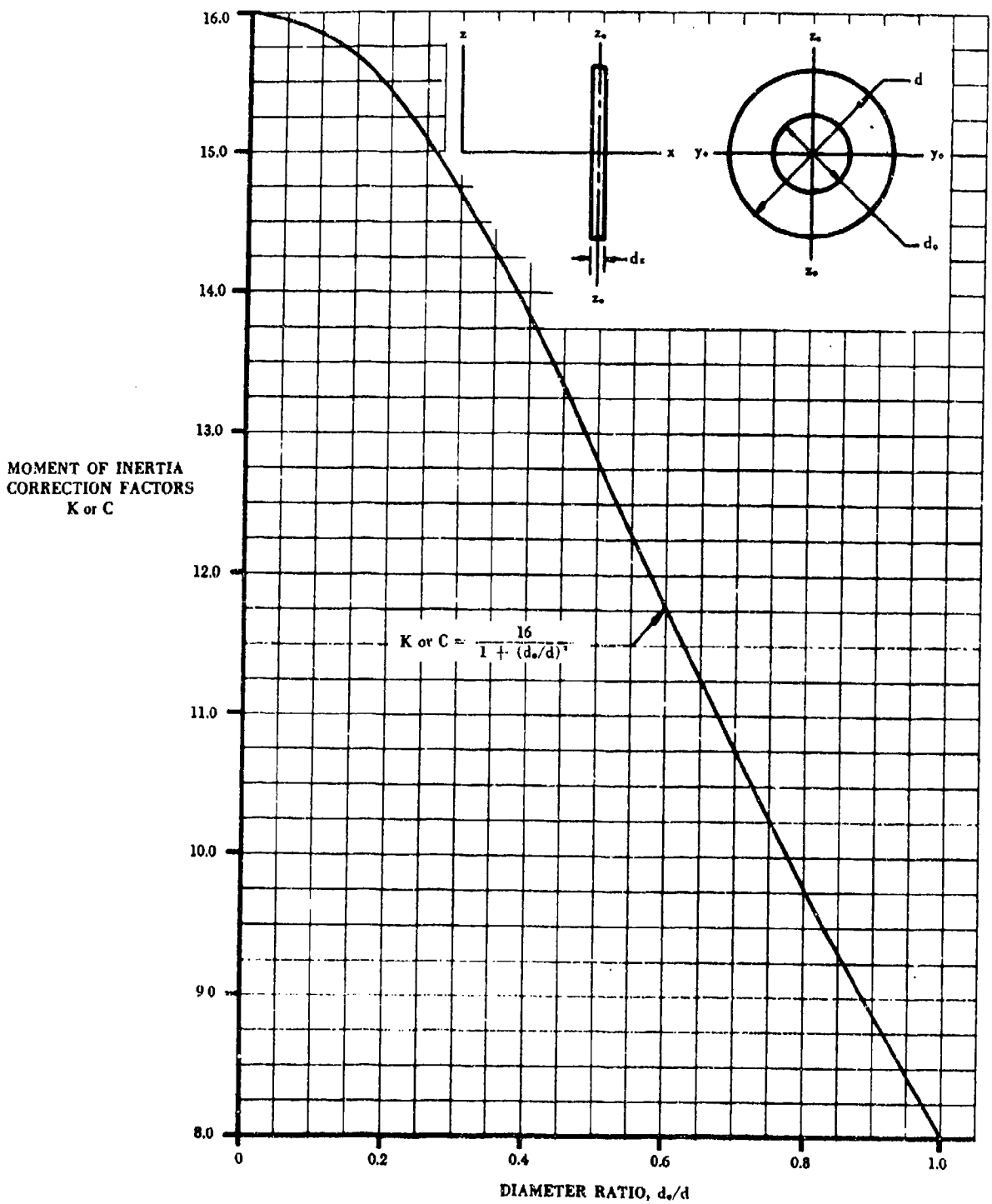

FIGURE 8.2-5 SYMMETRICAL SOLID COMPONENT
MOMENT OF INERTIA CORRECTION FACTORS K AND C

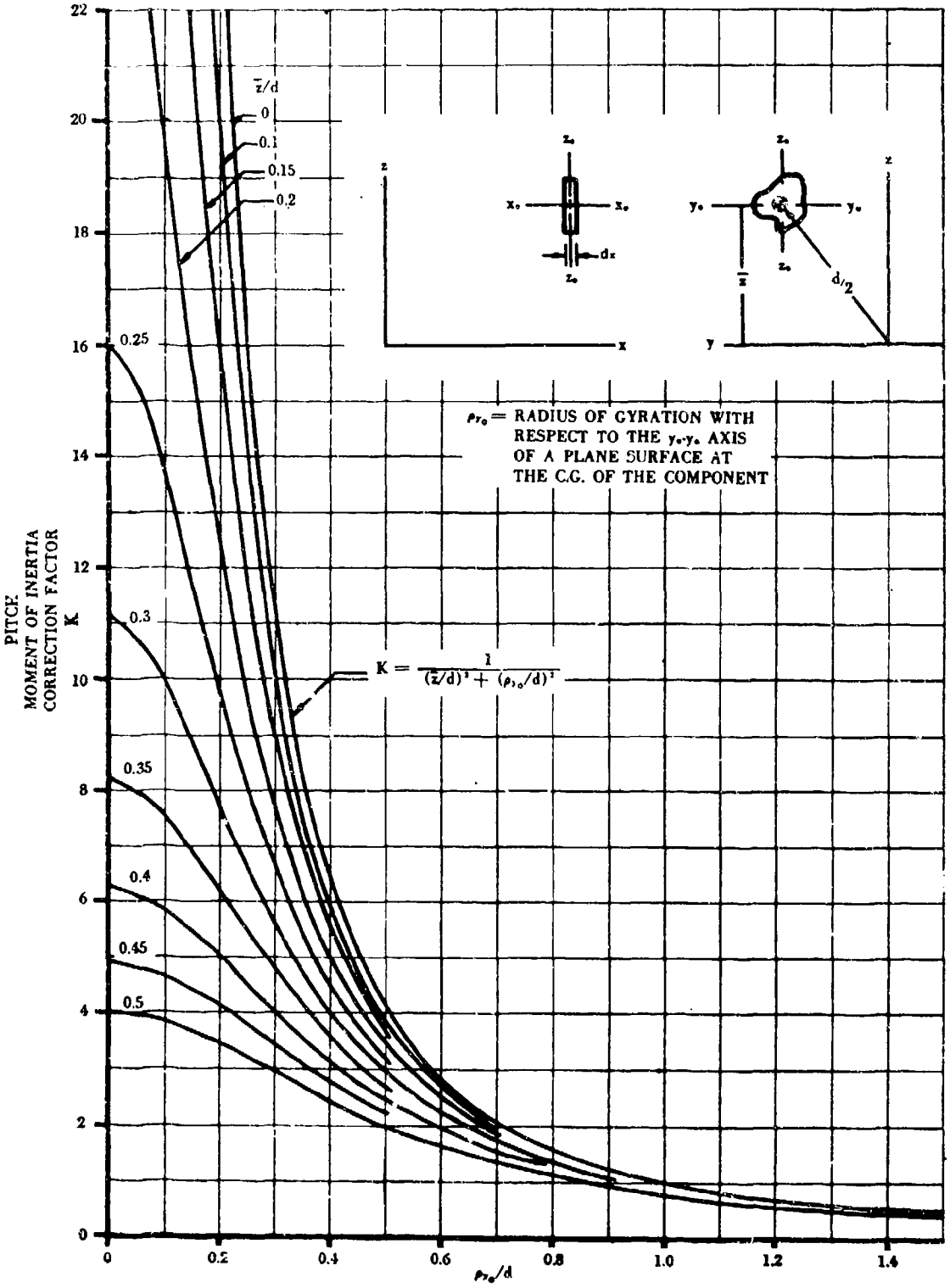

FIGURE 8.2-6 UNSYMMETRICAL SOLID COMPONENT
PITCH MOMENT OF INERTIA CORRECTION FACTOR K

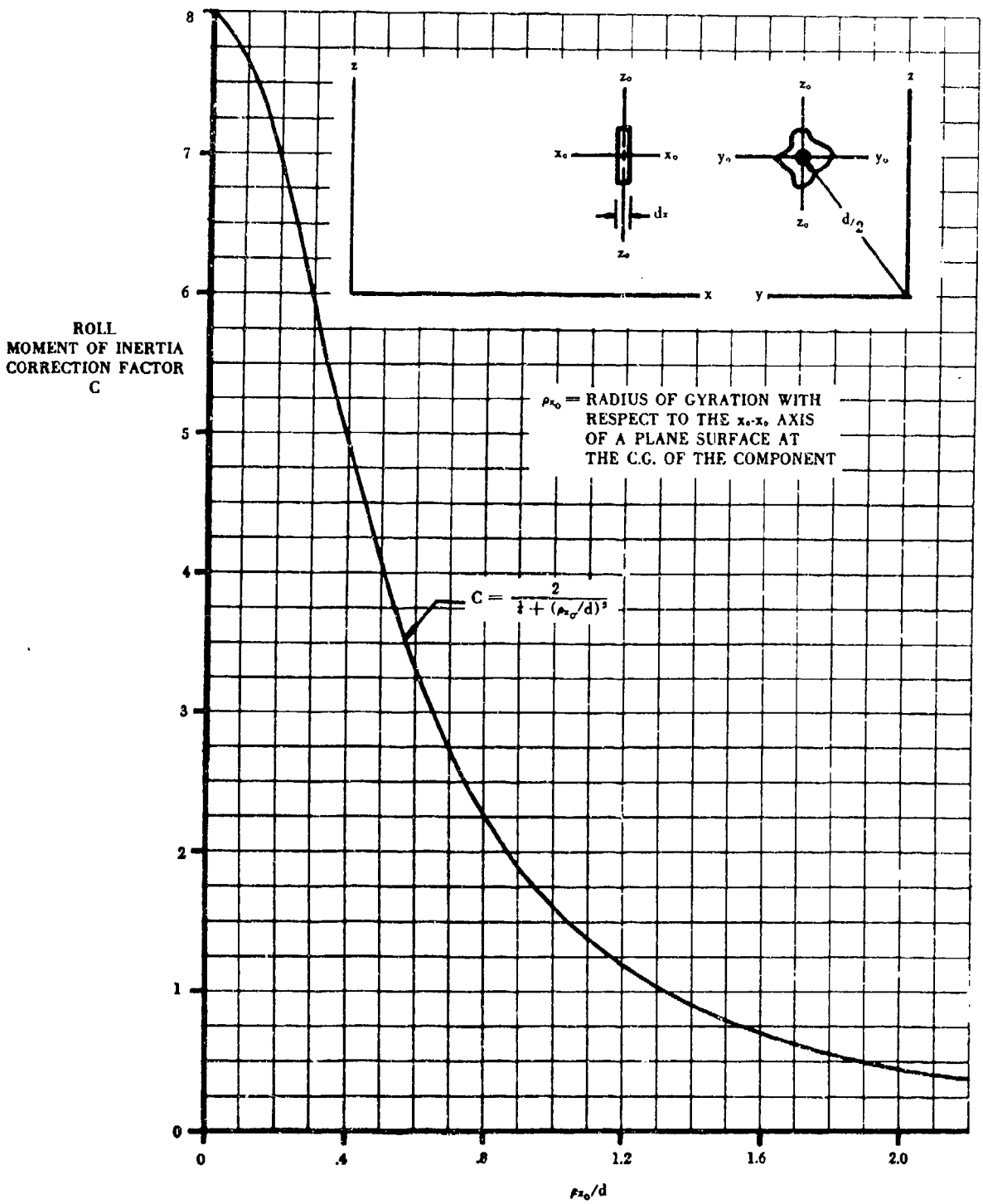

FIGURE 8.2-7 UNSYMMETRICAL SOLID COMPONENT ROLL MOMENT OF INERTIA CORRECTION FACTOR C

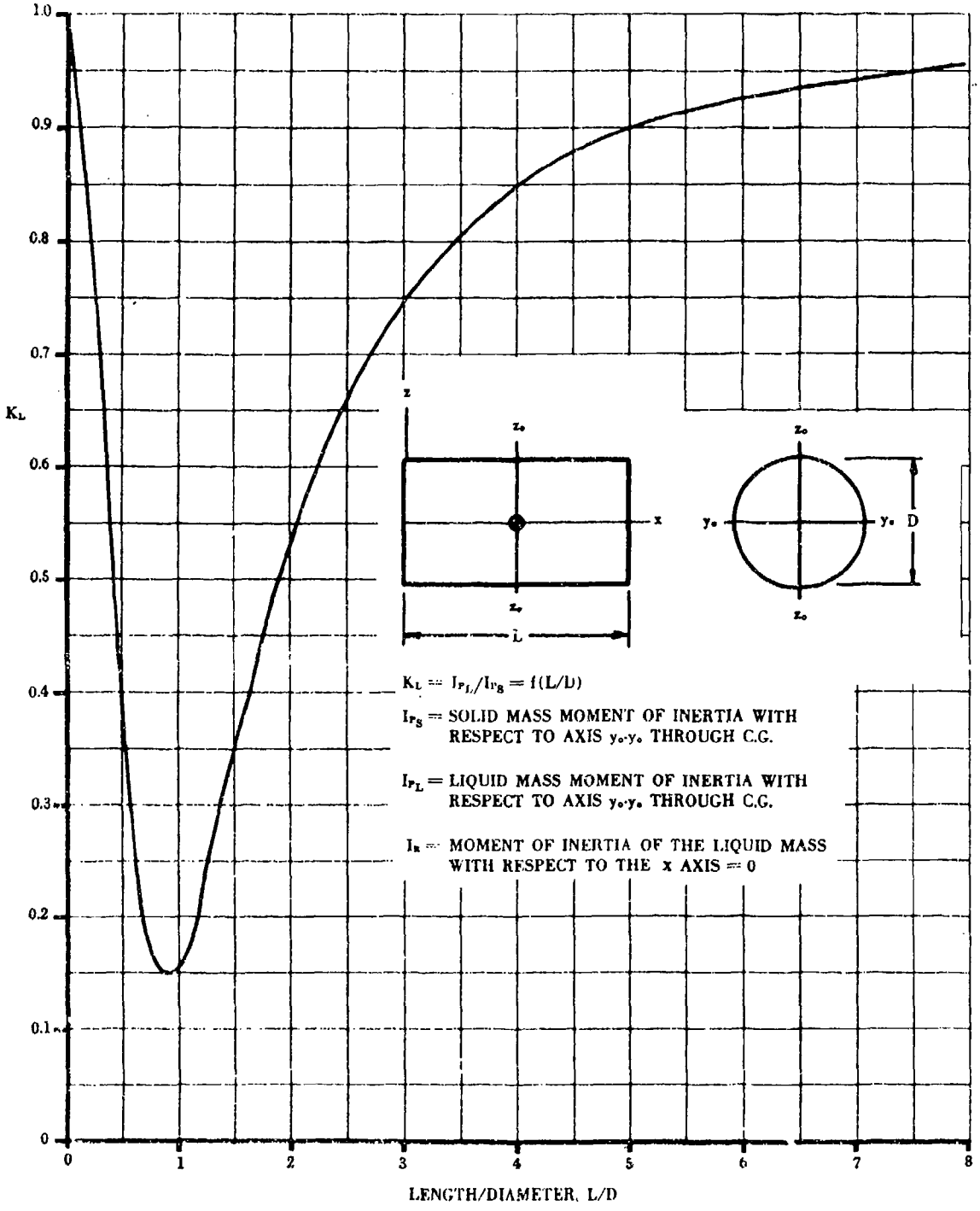

FIGURE 8.2-8 LIQUID MASS COMPONENT
PITCH MOMENT OF INERTIA CORRECTION FACTOR K_L

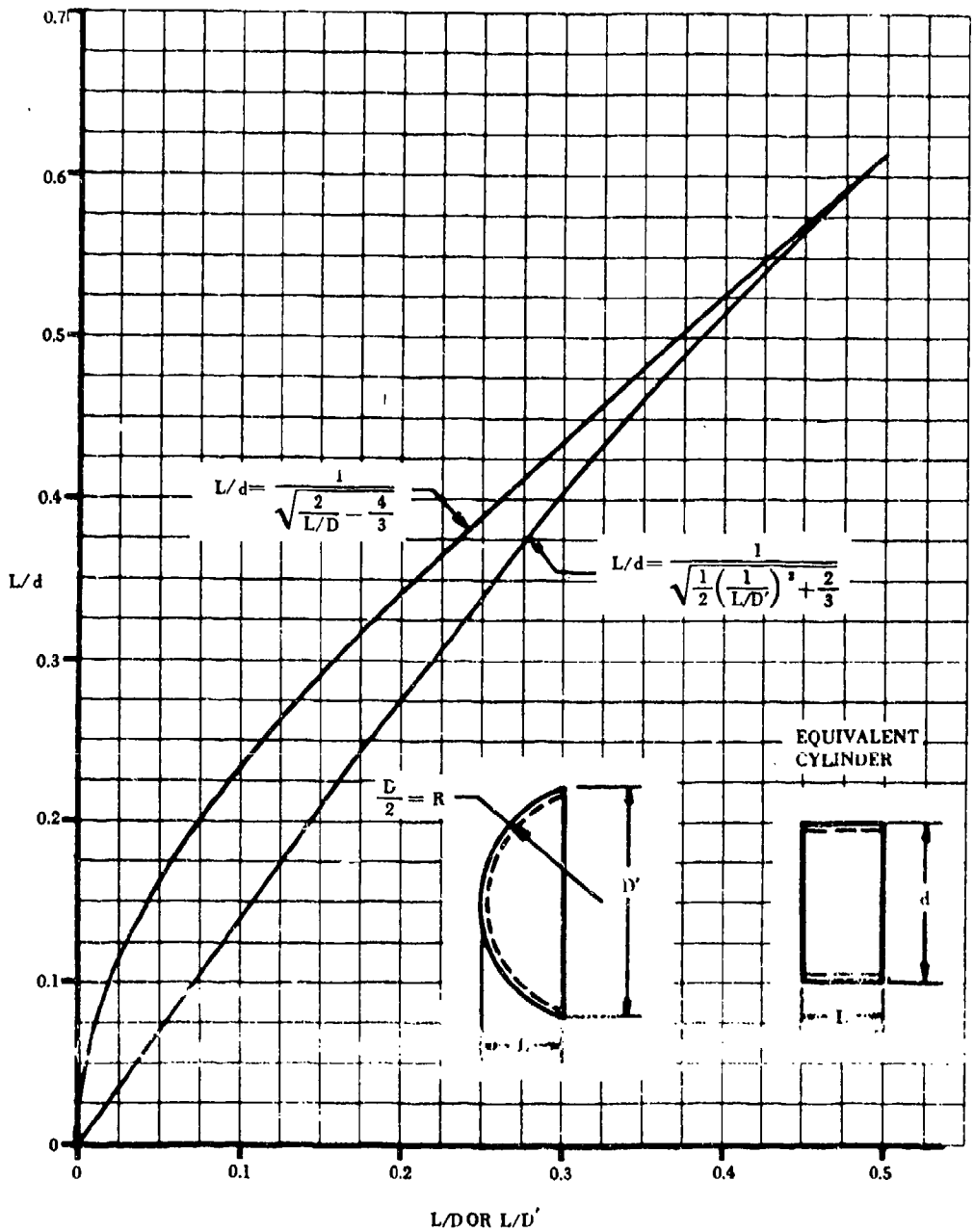

FIGURE 8.2-9 SPHERICAL SEGMENT SHELL EQUIVALENT CYLINDER FOR MOMENTS OF INERTIA

PITCH RADIUS OF GYRATION
STAGE LENGTH

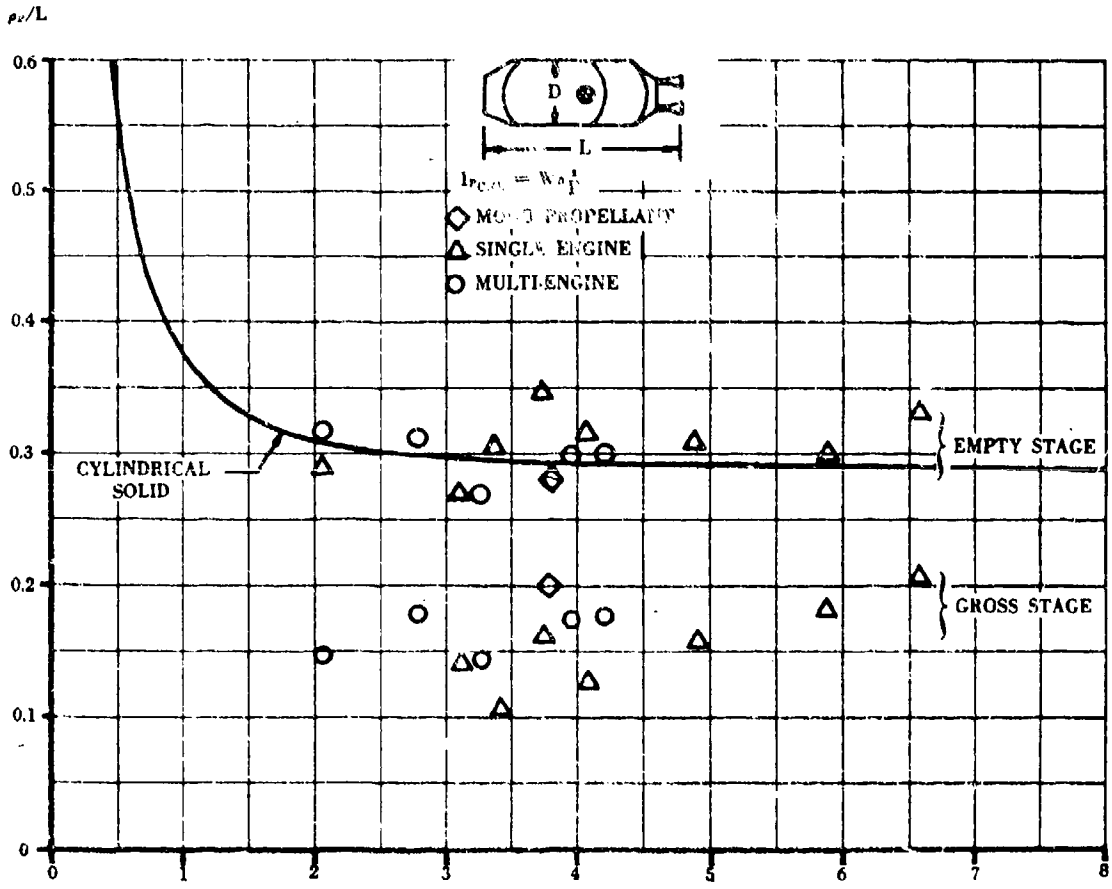

FIGURE 8.2-10 LIQUID PROPELLANT STAGE
PITCH RADIUS OF GYRATION

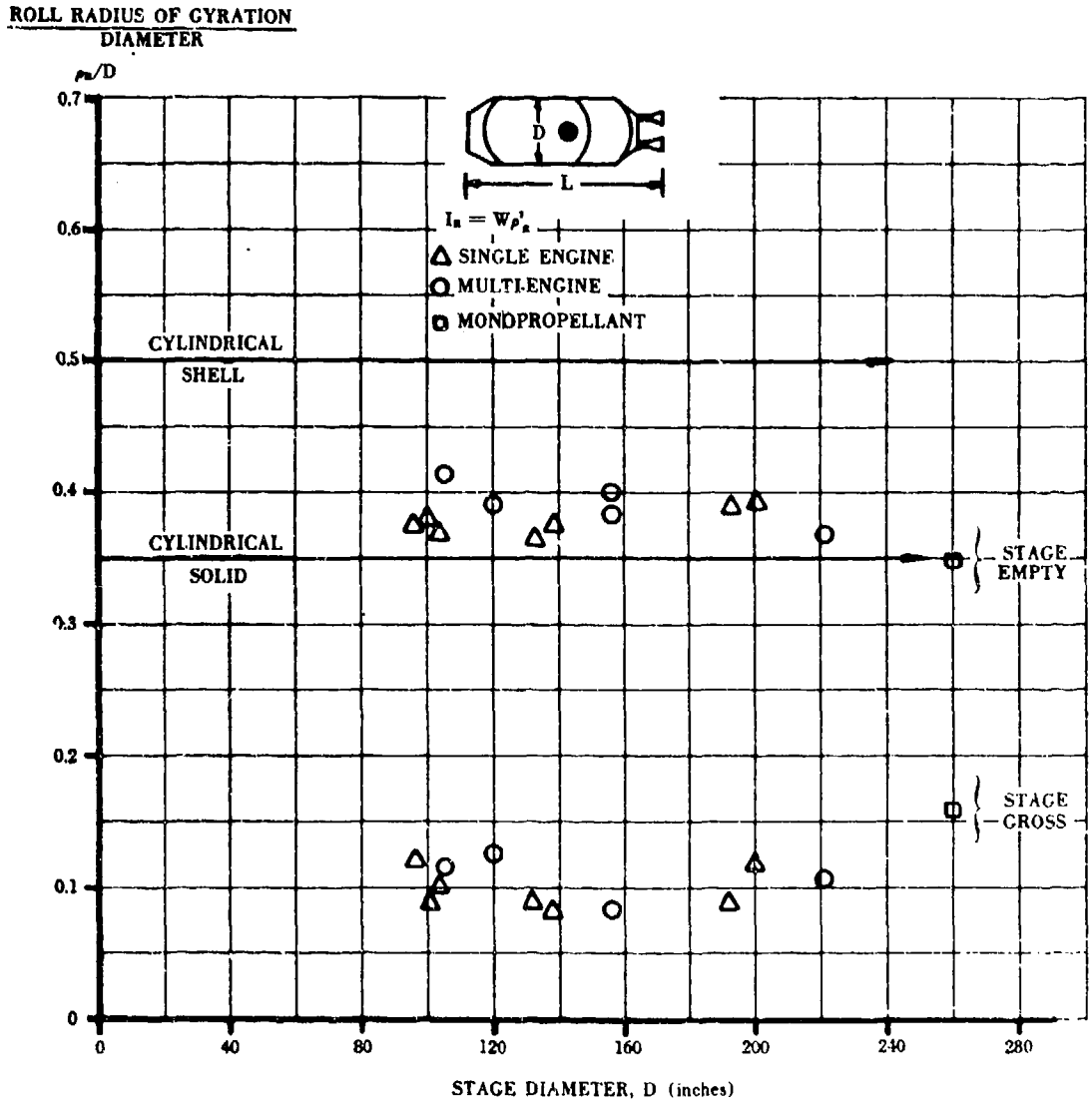

FIGURE 8.2-11 LIQUID PROPELLANT STAGE
ROLL RADIUS OF GYRATION

9. CHARACTERISTICS OF VTOL-STOL AIRCRAFT

The interest in a wide variety of aircraft having VTOL-STOL capability has created the need for establishing preliminary-design methods for the prediction of the aerodynamic characteristics of such vehicles.

The terms VTOL, STOL, and V/STOL appear many times in the literature. VTOL means "vertical take-off and landing." STOL means "short take-off and landing," and vehicles of this classification do not have vertical take-off and landing capability. V/STOL means the capability to perform both vertical and short take-offs and landings. The many ways of achieving VTOL-STOL capability are exhibited in the proposed and existing vehicles of this family. There are four basic VTOL-STOL principles involved for accomplishing the conversion from hovering to cruise flight; namely, aircraft tilting, thrust tilting, thrust deflection, and dual-propulsion. These four conversion principles are coupled with four different propulsion methods; namely, rotor, propeller, fan, and jet, to give the family of basic V/STOL types. In the broad sense the material presented in this section does not include all V/STOL concepts. Specifically, the methods presented in Section 9 are applicable to predicting the forces and moments on free propellers (Section 9.1), power-on lift and drag forces of propeller-wing combinations (Section 9.2), and the forces and moments on isolated ducted propellers as functions of power and angle of attack (Section 9.3). No discussion or methodology is presented for rotor-type V/STOL aircraft. In addition to the material presented in this section, there are additional methods pertaining to STOL aircraft given in Section 6. Specifically, these methods pertain to jet-flap configurations; i.e., both internally-blown flaps (IBF) and externally-blown flaps (EBF).

Because of the unusual low-speed configurations and the effects of power and high angles of attack in the low-speed flight regime, which are typical of VTOL-STOL vehicles, conventional methods of predicting aerodynamic characteristics at low speeds are not applicable in most cases. In cruise flight, VTOL-STOL vehicles can usually be analyzed by conventional methods. Therefore, the primary problem is the prediction of characteristics that exist as a result of high-velocity slipstreams, high angles of attack, and geometry variations in the hover and transition flight regimes.

Because of the scope of VTOL-STOL aerodynamics and the scarcity of verified theoretical methods and design charts, a literature summary is presented as Table 9-A, accompanied by a subject index on page 9-34, a "key" to the summary table on page 9-35, and a bibliography on pages 9-3 through 9-33.

V/STOL aircraft are characterized by the following four basic and unique characteristics:

1. High power requirements in hover and transition
2. High-velocity slipstreams in hover and transition
3. Inherent deficiencies in aerodynamic stability and control in hover and low-speed flight
4. Special provisions for performing the conversion from the hovering to the cruise configuration

The high power required in hovering and transition is not of primary concern to the stability and control engineer and is not considered in the Datcom. However, it should be noted that the engine-operation problems are extremely significant in the design of a V/STOL vehicle. The high power required in hovering and transition results in both higher fuel consumption and greater noise.

The magnitude of these increases depends on the type of propulsion system used. Both fuel consumption and noise level progressively increase from the rotor to the propeller, the fan, and the jet.

The high-velocity slipstream required in hovering and transition flight introduces problems due to surface erosion, recirculation of dust and debris, ingestion of foreign objects, and slipstream recirculation, which can result in adverse aerodynamic effects and ingestion of hot gases into the engine, resulting in a serious reduction in engine thrust. Only the aerodynamic effects of the slipstream are considered in this section. Slipstream recirculation can affect the pressure on the airframe, which can cause significant changes in the vertical lift. When a single high-velocity slipstream exhausts in still air, suctions are generated on the surrounding surface because of the entrainment into the high-velocity slipstream. This "suckdown" effect is a pressure reduction and reduces the vertical lift. This lift loss is evident during hovering near the ground for a configuration with a single vertical slipstream or a close cluster of vertical slipstreams. On the other hand, when several vertical slipstreams are dispersed over the planform, the high-velocity slipstreams tend to meet on the ground between the exits, and the consequent upflow can produce positive-pressure regions between the exits to counterbalance the "suckdown" generated by the entrainment. Unfortunately, this upward flow of air is not very steady or symmetrical and can result in random upsetting motions. In addition, for configurations with a tail behind the slipstreams, additional interference effects on longitudinal trim and stability can occur during transition flight. (Strong downwash and sidewash fields can develop in the region aft of the exits as a result of the rearward deflection and distortion of the slipstreams together with the entrainment of the free-stream flow.) References pertaining to the aerodynamic effects of high-velocity slipstreams are listed under one or more of the following specialized categories in table 9-A:

5.5 Ground Effects

5.10 Jet-Wake or Propeller-Slipstream Effects

5.11 Jet-Induced Effects

An important aspect of V/STOL hovering and low-speed flight is the inherently low level of aerodynamic stability and control. Aerodynamic control and static and dynamic stability vary with dynamic pressure in the free stream, and they all drop off rapidly as the flight speed is decreased. In hovering there is no aerodynamic control effectiveness (unless the control surface is in a high-velocity slipstream), and it is usually necessary to provide an additional control system for hovering and low-speed flight. In hovering flight the static stability is neutral (no stability of attitude) for all V/STOL types. The dynamic stability in hover is about neutral for jet-V/STOL types, but other types are usually dynamically unstable in the form of unstable pitching and rolling oscillations. Almost any system that will provide control for the pilot under these conditions can also be used to augment stability. However, the way in which this should be accomplished has not been clearly settled for any V/STOL type. The cost, complexity, reliability, and maintainability of any augmentation system must be weighed against the improvements in handling qualities and the potential reductions in control requirements. The problem immediately becomes more complex, since there is still a great deal of controversy regarding control-system requirements and handling-quality criteria. References pertaining to the aerodynamic stability and control deficiencies in hovering and low-speed flight may be found

under one or more of the following specialized categories in table 9-A:

5.1 General Static Stability and Control

5.2 Dynamic Stability

5.3 Handling Criteria

5.4 Handling Qualities

5.7 Stabilization

5.8 Zero or Low-Airspeed Control and/or Control Systems

Although wind-tunnel tests cover a wide variety of V/STOL configurations, they are often of questionable accuracy because of wall interference effects and/or data-accuracy limitations at the low tunnel velocities required to simulate low-speed flight. Large flow-deflection angles are required for flight at very low speeds, and when these conditions are duplicated by a powered model in a wind tunnel, the presence of the tunnel walls have a first-order effect on tunnel flow conditions. Most existing low-speed wind tunnels are inadequate for the simulation of powered-lift low-speed flight because of their size limitations. The test section must be large compared to model dimensions to minimize the adverse effects of the wind-tunnel walls on the flow field. Simply testing models of smaller scale in an effort to avoid wall-interference effects often has not proved satisfactory, because of the significant errors in test data associated with low Reynolds number and the problems encountered in the design and manufacture of a powered model to a small scale. There appears to be a limit, which is a function of the tunnel test-section size and shape, model size, flow deflection angle, and model configuration, at which the tunnel-wall constraint causes a complete flow breakdown. The effects of all these variables on the accuracy of the wind-tunnel data are quite complex and some are not yet clearly understood. However, one fact has become very clear, and that is that most existing wind tunnels are simply too small for simulation of V/STOL flight.* References pertaining to wind-tunnel test techniques are listed under category 5.12 in table 9-A.

REFERENCES

1. Abbott, W. A.: Studies of Flow Fields Created by Vertical and Inclined Jets When Stationary or Moving over a Horizontal Surface. ARC CP-911,1964. (AD-809897) (U)

2. A'Harrah, R. C., and Kwiatkowski, S. F.: A New Look at V/STOL Flying Qualities. IAS Paper 61-62, 1961. (U)

3. Alexander, A. J.: Experiments on Jet-Flap Delta Wing in Ground Effect. College of Aeronautics, Cranfield, G. B., CoA Rept. Aero 164, 1963. (U)

4. Alexander, A. J., and Williams, J.: Wind-Tunnel Experiments on a Rectangular-Wing Jet-Flap Model of Aspect-Ratio 6. ARC R&M 3329, 1961. (U)

5. Alford, W. J., Jr., and Harris, R. V., Jr.: Cruise Performance and Stability Considerations for Jet V/STOL Aircraft, 1966. (N66-24617) (U)

*A number of new low-speed wind tunnels are presently being planned or built, and their designs have been influenced by the requirements of V/STOL model testing.

6. Alvarez-Calderon, A.: VTOL and the Rotating Cylinder Flap. Annals of the N. Y. Academy of Sciences, Vol. 107, Art. I, 1963. (U)

7. Anderson, S. B.: An Examination of Handling-Qualities Criteria for V/STOL Aircraft. NASA TN D-331, 1960. (AD-241025) (U)

8. Anderson, S. B., and Tapscott, R. J.: A Review of V/STOL Handling-Qualities Criteria. Unpublished NASA Report, 1963. (U)

9. Anderson, S. B., Quigley, H. C., and Innis, R. C.: Stability and Control Considerations for STOL Aircraft. AIAA P-65-715, 1965. (U)

10. Anderton, D. A.: Auxiliary Surfaces Boost STOL Control. Aviation Week and Space Technology, Vol. 76, 1962. (U)

11. Anon.: AeCAN Data Sheet-Breguet 941. The Aeroplane and Commercial Aviation News, Vol. 104, 1962. (U)

12. Anon.: Aerodynamic Problems Associated With V/STOL Aircraft, Vol. II. Propulsion Interference Aerodynamics. CAL Symposium, 1966. (AD-657563) (N67-86835) (U)

13. Anon.: Aerodynamic Problems Associated with V/STOL Aircraft. Vol. IV. Panels on Recommended V/STOL Aerodynamic Research. CAL/USAAVLABS Symposium Proceedings, 1966. (AD-657565) (U)

14. Anon.: The Aerodynamics of V/STOL Aircraft. AGARDograph 126, 1968. (N69-29645) (U)

15. Anon.: AIAA Aerodynamic Testing Conference, 1964. (N64-17013) (U)

16. Anon.: Application of a Mechanical Gyroscopic Stabilizer to VTOL Aircraft. Kellett Aircraft Corporation Report 220A90-2, 1963. (U)

17. Anon.: Aspects of V/STOL Aircraft Development. Agard-Advisory-13, 1967. (N68-23761) (U)

18. Anon.: Auto-Trim VTOL Feasibility Study Final Report. Goodyear Report GER-10409, 1961. (U)

19. Anon.: Comparative Performance Charts for Ducted Propellers. Hiller Aircraft Corporation Report ARD-257, 1960. (U)

20. Anon.: Conference on V/STOL and STOL Aircraft. NASA SP-116, 1966. (N66-24606) (U)

21. Anon.: The Development of an All Mechanical Control System for VTOL-STOL Aircraft. Northrop Corporation NOR 62-237, 1963. (C) Title Unclassified

22. Anon.: Estimated Static Stability and Control Characteristics. G. E. Rept. 146, 1964. (AD-639236) (U)

23. Anon.: Extracts from the First and Second Recommendations of the ACOA to the Technical Advisory Panel of the National Aeronautical Research Committee, 1964. (AD-474541) (N65-10909) (U)

24. Anon.: Final Systems Analysis and Flight Simulation Report. Vol. II. G. E. Rept. 157, Vol. 2, 1965. (AD-639230) (U)

25. Anon.: Flight-Testing Experiments with the Tilt-Wing Aircraft. IAS Paper 59-8, 1959. (U)

26. Anon.: Full-Scale Tests of the XV-4A Hummingbird in the Ames 40 x 80 Foot Wind Tunnel. G. E. Report ER-7634, 1965. (AD-654783) (U)

27. Anon.: Full Scale Wind-Tunnel Test Report. G. E. Report 153, 1966. (AD-654043) (U)

28. Anon.: Integration of Propulsion Systems in Airframes. AGARD CP-27, 1967. (AD-672073) (N68-28850) (U)

29. Anon.: An Investigation Into the Loss of Thrust Occurring in a Wing-Fan System Due to Ground Effects. Boulton Paul Aircraft Ltd., T.N. 10, 1959. (U)

30. Anon.: Lift on a Wing in a Propeller Slipstream as Related to Low-Speed Flight. IAS Preprint 643, 1956. (U)

31. Anon.: Low-Speed Free-Air Tests of a Powered .166-Scale Four-Engine Tilt-Wing V/STOL Model. North American Aviation, 1962. (U)

32. Anon.: NASA Conference on V/STOL Aircraft. Compilation of the papers presented at Langley Research Center, Nov. 1960. (N63-14683) (U)

33. Anon.: The P-1127 Analysed. Flight International, October 11, 1962. (U)

34. Anon.: Phase I Flight Test Results (XV-5A), Vol. I. G. E. Report 166, Vol. 1, 1966. (AD-639231) (N67-13030) (U)

35. Anon.: Phase I Flight Test Results (XV-5A), Vol. II. G. E. Report 166, Vol. 2, 1966. (AD-639232) (N67-13031) (U)

36. Anon.: Phase I Flight-Test Results (XV-5A), Vol. III. G. E. Report 166, Vol. 3, 1966. (AD-639233) (N67-13907) (U)

37. Anon.: A Preliminary Study of V/STOL Transport Aircraft and Bibliography of NASA Research in the VTOL-STOL Field. NASA TN D-624, 1961. (U)

38. Anon.: Proceedings of a NASA Briefing on VTOL/STOL Aircraft Research. U.S. Army Transportation Research Command, 1959. (U)

39. Anon.: Provisional Recommendations for V/STOL Handling Qualities. AGARD Flt. Mech. Panel Working Group on V/STOL Handling Qualities, 1962. (U)

40. Anon.: Recommendations for V/STOL Handling Qualities with an Addendum Containing Comments on the Recommendations. AGARD 408A, 1964. (AD-661748) (N65-28861) (U)

41. Anon.: Results of Static Test of a Full-Scale Wing-Mounted Tip-Turbine-Driven Lift Fan. TREC TR-62-21, 1962. (AD-285037) (N64-31128) (U)

42. Anon.: Results of Wind-Tunnel Tests of a Full-Scale Fuselage-Mounted, Tip-Turbine-Driven Lift Fan, Vol. 2. G. E. TR-61-15-V2, 1961. (AD-263450) (U)

43. Anon.: Results of Wind-Tunnel Tests of a Full-Scale Wing-Mounted, Tip-Turbine-Driven Lift Fan. ATRECOM TR-63-21, 1963. (AD-426785) (U)

44. Anon.: Review of NASA-Ames Research Program on VTOL/STOL Aircraft Concepts. NASA-Ames Research Center, 1960. (U)

45. Anon.: STOL Light-Intratheater-Transport Study. Vol. 2. Design. Part 2. Performance, Stability and Control. Boeing D-8-2113, Vol. 2, Pt. 2, 1968. (AD-393112) (U)

46. Anon.: Symposium on Vertical and Short Take-off and Landing Aircraft. Parts I and II. AGARDograph 46, 1970. (U)

47. Anon.: Tentative Airworthiness Standards for Verticraft/Powered Lift-Transport Category Aircraft. Federal Aviation Admin., 1968. (U)

48. Anon.: Theoretical Investigation and Examination by Measuring Tests of the Thrust Control by Rudders Uniformly Tilted at the Outlet of a Duct. Bureau Technique Zborowski, 1959. (U)

49. Anon.: Vertical Take-off Planes. A DDC Bibliography. Vol. I, 1968. (AD-683500) (N69-24602) (U)

50. Anon.: Vertical Take-off Planes. Vol. II. DDC-TAS-68-65, 1968. (AD-849500) (U)

51. Anon.: Vertical Take-off Planes. Vol. V. Experimental and Research Models. DDC-TAS-68-68, 1968. (AD-849501) (U)

52. Anon.: The Vertodyne VTOL Aircraft Study Semi-Span Model Tests in Hovering and Forward Flight. Vertol Division, Boeing Aircraft Company Report R-158, 1960. (U)

53. Anon.: V/STOL Control System Design Unveiled. Aviation Week and Space Technology, April 1961. (U)

54. Anon.: VTOL-1968. AIAA Paper 68-977, 1968. (A68-44931) (U)

55. Anon.: Wind-Tunnel-Test Report, Lift-Fan Powered-Scale Model. G. E. Report 137, 1963. (AD-647386) (U)

56. Anon.: XV-5A Lift-Fan Flight Research Aircraft Program; Estimated Dynamic Stability Characteristics. G. E. Report 151, 1964. (AD-639235) (U)

57. Anon.: XV-5A Lift-Fan Flight Research Aircraft Program; Estimated Static Stability and Control Characteristics. G. E. Report 146, 1964. (AD-639236) (U)

58. Aoyagi, K., Hickey, D. H., and deSavigny, R. A.: Aerodynamic Characteristics of a Large-Scale Model with a High Disk-Loading Lifting Fan Mounted in the Fuselage. NASA TN D-775, 1961. (AD-266252) (N62-71349) (U)

59. Archino, D. T.: Simplified Approximations of Interference Effects on Jet V/STOL Aircraft. AFIT Report No. GAM/AE/68-2, 1968. (AD-833270) (U)

60. Asmus, F. J.: Design and Development of the Tip-Turbine Lift Fan. Annals of the N.Y. Academy of Sciences, Vol. 107, Art. I, 1963. (A63-14980) (U)

61. Augustine, N. R.: An Investigation of the Fundamental Parameters Which Govern the Aerodynamics of Various Wing-Propeller Combinations as Related to Vectored-Slipstream Aircraft. Princeton University Report 37, 1958. (U)

62. Barche, J., et al: Jet Problems with V/STOL Aircrafts. Meeting Report of WGLR Tech. Comm. on Aerodyn., 1967. (N68-13985) (U)

63. Barrack, J. P., and Kirk, J. V.: Low-Speed Characteristics of High-Performance Lift-Engine V/STOL Aircraft. SAE Paper 680644, 1968. (A68-45072) (U)

64. Basile, G., Fitzpatrick, J. E., and Zon, J.: Estimated Flying Qualities of the Kaman K-16B VTOL/STOL Aircraft. Kaman Aircraft Corp., G-113-4, 1959. (AD-219400) (U)

65. Bates, W. R., Lovell, P. M., Jr., et al: Additional Studies of the Stability and Controllability of an Unswept-Wing Vertically-Rising Airplane Model in Hovering Flight Including Studies of Various Tethered Landing Techniques. NACA RM L51I07a, 1949. (U)

66. Bates, W. R., Lovell, P. M., Jr., et al: Dynamic Stability and Control Characteristics of a Vertically-Rising Airplane Model in Hovering Flight. NACA RM L50J16, 1951. (U)

67. Beilman, J. L.: X-22A Variable Stability System. Presented at First National V/STOL Symposium, Nov. 1965. (U)

68. Benner, S. D.: The Coanda Effect at Deflection Surfaces Widely Separated from the Jet Nozzle. TRECOM TR-64-70, 1965. (AD-610525) (N65-17862) (U)

69. Beppu, G., and Curtiss, H. C., Jr.: An Analytical Study of Factors Influencing The Longitudinal Stability of Tilt-Wing VTOL Aircraft. Princeton University R756, USAAVLABS TR-66-53, 1966. (AD-640945) (U)

70. Biermann, D., and Conway, R. N.: The Selection of Propellers for High Thrust at Low Airspeed. NACA WR L-483, 1941. (U)

71. Biermann, D., Gray, W. H., et al: Wind-Tunnel Tests of Single- and Dual-Rotating Tractor Propellers of Large Blade Width. NACA WR L-685, 1942. (U)

72. Black, D. M., Wainauski, H. S., and Rohrbach, C.: Shrouded-Propeller — A Comprehensive Performance Study. AIAA Paper 68-994, 1968. (U)

73. Black, D. M., and Wainauski, H. S.: Shrouded-Propeller Test Program Data Analysis. Hamilton Standard Report HSER 4348, Vol. 1, 1967. (AD-820759) (U)

74. Black, E. L., and Booth, G. C.: Correlation of Aerodynamic Stability and Control Derivatives Obtained from Flight Tests and Wind-Tunnel Tests on the XC-142A Airplane. AFFDL TR-68-167, 1968. (AD-854018) (X69-17816) (U)

75. Blakeslee, D. J.: Empirical Relationships for Jet-Flap Lift and Drag Prediction. Aerospace Eng., Nov. 1960. (U)

76. Bock, G., Klug, H. G., and Spintzyk, H: VTOL/STOL Aircraft — First Supplement 1961/62. AGARD Report, 1963. (AD-427826) (U)

77. Bock, G., and Spintzyk, H.: VTOL/STOL Aircraft Bibliography. Institut Fur Luftfahrttechnik, for AGARD, 1961. (AD-266061) (U)

78. Borst, H. V.: Design and Development Considerations of the X-19 VTOL Aircraft. Annals of the N.Y. Academy of Sciences, Vol. 107, Art. I, 1963. (U)

79. Botrel, A., et al: Recommendations for V/STOL Handling Qualities. AGARD R-408, 1962. (AD-410323) (N63-13660) (U)

80. Boyden, R. P., and Curtiss, H. C., Jr.: Investigation of the Lateral-Directional Stability Characteristics of a Four-Propeller, Tilt-Wing VTOL Model at Low Speeds. Princeton Univ. Rept. 743, USAAVLABS TR-68-19. (AD-673147) (N68-35391) (U)

81. Bradbury, L. J. S., and Wood, M. N.: Static-Pressure Distribution Around a Circular Jet Exhausting Normally From a Plane Wall Into an Airstream. RAE TN Aero 2978, 1964. (AD-453315) (U)

82. Brady, W. G., and Ludwig, G.: Theoretical and Experimental Studies of Impinging Uniform Jets. American Helicopter Society Journal, Vol. 8, 1963. (A63-17411) (U)

83. Brenckmann, M.: Experimental Investigation of the Aerodynamics of a Wing in a Slipstream. Univ. of Toronto, Institute of Aeropnysics, TN 11, 1957. (U)

84. Brenckmann, M.: Improvements in Longitudinal Stability and Control During the Landing Approach of STOL Aircraft. AIAA-CASI Paper 64-804, 1964. (A64-27416) (U)

85. Breul, H. T.: A Simulator Study of Low-Speed VTOL Handling Qualities in Turbulence. Grumman Aircraft Engineering Corporation Final Research Report RE-238, 1966. (AD-477949) (N66-24861) (U)

86. Breul, H. T.: A Simulator Study of Tilt-Wing Handling Qualities. Grumman Aircraft Engineering Corporation Report RE-162, 1963. (AD-402774) (N63-15725) (U)

87. Brogan, E., Casey, G., et al: Vertodyne Fan-in-Wing VTOL Aircraft. Vertol Aircraft Corp. Final Summary Report R-254, 1961. (AD-265569) (U)

88. Brogan, E., Casey, G., et al: The Vertodyne VTOL Aircraft Study Semi-Span Model Tests in Hovering and Forward Flight. Vertol Aircraft Rept. R-158, 1960. (AD-234751) (U)

89. Burgan, E. T., and Matthews, J. T.: Wind-Tunnel Tests of a 1/8-Scale Powered Model K-16B Kaman VTOL/STOL Airplane. DTMB Report 998, 1961. (AD-254940) (U)

90. Burkhardt, W.: Optimization of VTOL-Flight-Control Characteristics in Hovering. EWR-89-63, 1963. (N64-10900) (U)

91. Butler, L., Goland, L., and Huang, K. P.: An Investigation of Propeller Slipstream Effects on V/STOL Aircraft Performance and Stability. USAAVLABS TR-65-81, 1966. (AD-629637) (N66-22604) (U)

92. Butler, S. F. J., Moy, B. A., and Hutchins, G. D.: Low-Speed Wind-Tunnel Tests of Aspect-Ratio-9 Jet-Flap Model, With Ground Simulation by Moving Belt Rig. ARC CP-849, 1966. (U)

93. Butler, S. F. J., Guyett, M. B., and Moy, B. A.: Six-Component Low-Speed Tunnel Tests of Jet-Flap Complete Models with Variation of Aspect Ratio, Dihedral, Sweep, Including Influence of Ground Proximity. ARC R&M 3441, 1967. (U)

94. Butz, J. S.: Army Attempts Major STOL Advance. Aviation Week Including Space Technology, No. 22, 1959. (U)

95. Cahn, M. S.: The Design and Performance of Shrouded Propellers. SAE Preprint 587C, 1962. (U)

96. Campbell, G. S.: Turbulence in the Wake of a Thin Airfoil at Low Speeds. NACA TM 1427, 1957. (U)

97. Campbell, W. S., and Von Ohain, H.: Thrust Augmentation – Application to Jet Wing V/STOL Aircraft. Aerospace Research Labs., W-PAFB, OAR-607-3, Vol. 2, 1967. (AD-383444) (X68-10381) (C) Title Unclassified

98. Carpenter, D. O., and Jenny, R. B.: Statistical Approach to Low-Speed Control Criteria for V/STOL Aircraft. AIAA Paper 64-286, 1964. (U)

99. Carter, A. W.: Effects of Jet-Exhaust Longitudinal Aerodynamic Characteristics of a Jet V/STOL Model. NASA TN D-5333, 1969. (N69-33210) (U)

100. Castle, R. A., Gray, A. L., and McIntyre, W.: Simulation of Helicopter and V/STOL Aircraft – Computational Methods Analog – Study, Equations of Motion of Vertical/Short Take-Off and Landing Operational Flight/Weapon System Trainers. Navy, Naval Training Device Center Report 1205-3, Vol. III, Pt. I, 1964. (AD-607737) (N65-11379) (U)

101. Chambers, J. R., and Grafton, S. B.: Calculation of the Dynamic Longitudinal Stability of a Tilt-Wing V/STOL Aircraft and Correlation with Model Flight Tests. NASA TN D-4344, 1968. (N68-15941) (U)

102. Chambers, J. R., and Grafton, S. B.: Static and Dynamic Longitudinal Stability Derivatives of a Powered 0.18-Scale Model of a Fan-in-Wing VTOL Aircraft. NASA TN D-4322, 1968. (N68-15894) (U)

103. Chambers, J. R., and Grafton, S. B.: Static and Dynamic Longitudinal Stability Derivatives of a Powered 1/9-Scale Model of a Tilt-Wing V/STOL Transport. NASA TN D-3691, 1966. (U)

104. Chinn, H. W.: Results of Flight Tests on the Short SC1 VTOL Research Aircraft with Particular Reference to Handling Qualities in the Hover and Transition Regimes. AGARD-527, 1965. (N67-14110) (U)

105. Church, R. M. W.: A Method for the Calculation of Force, Moment, and Power Coefficients of Propellers in Forward Flight of Tilt Angles from 0 to 90°. AL-119, 1969. (AD-855562) (U)

106. Cincotta, G. A., and Dunn, H. S.: The Static and Dynamic Stability of a Deflected-Slipstream Vehicle. Princeton Univ. Report 407, 1958. (U)

107. Clark, J. W., Miller, D. P., and Gallant, R. A.: Investigation of Control and Stability Augmentation Requirements for Tandem-Tilting Ducted-Propeller VTOL Transports. UAC R-1624-5, 1963. (AD-419126) (N63-22245) (U)

108. Clark, J. W., and Miller, D. P.: Research on Methods for Presenting VTOL Aircraft Handling-Qualities Criteria for Unstable Systems. UAR-B175, 1964. (N64-14141) (U)

109. Coles, A. V.: Control Characteristics of Vectored-Thrust V/STOL Vehicles in the Transition Regime. American Helicopter Society Journal, Vol. 13, 1968. (A68-30961) (U)

110. Colin, P. E.: Experimental Investigation of Some Ground-Proximity Problems Associated with ACV and VTOL Types of Vehicles. Von Karman Institute for Fluid Dynamics, Final Technical Report, 1966. (AD-801819L) (U)

111. Colin, P. E.: Ground Proximity and the VTOL Aircraft. AGARD Report 409, 1962. (AD-422560) (N64-10133) (U)

112. Colin, P. E.: Powered-Lift-Model Testing for Ground-Proximity Effects. Report No. TCEA TN-14, 1963. (AD-437657) (N64-25031) (U)

113. Colin, P. E.: A Preliminary Investigation on V/STOL Model Testing for Ground-Proximity Effects. Wissenschaftlichen Gesellschraft fur Luftfahrt Paper No. 30, 1962. (N63-10028) (U)

114. Colin, P. E.: The Wall Jet Beneath a Counter-Flowing Stream. Final Report VKIFD, 1968. (AD-673200) (N68-35705) (U)

115. Conway, H. G.: The Development of the SC-1. Flight, June 1960. (U)

116. Conway, J. A.: The Augmentor Wing: A New Approach to Jet STOL. SAWE Tech. Paper 624, 1967. (U)

117. Corden, C. D., and Everett, W. L.: Simulation Approach to Development of the XV-5A Lift-Fan V/STOL Aircraft. SAE Paper 755A, 1963. (A63-25844) (U)

118. Cornish, J. J., III, and Tanner, R. F.: High-Lift Techniques for STOL Aircraft. SAE P-670245, 1967. (U)

119. Coward, K. S.: Propeller Selection for High-Static and Forward-Flight Efficiency for VTOL Aircraft. Aero. Eng. Rev., July 1957. (U)

120. Coward, K. S.: Propeller Static Thrust. Aerospace Eng., March 1959. (U)

121. Cox, M., and Abbott, W. A.: Studies of the Flow Fields Created by Single Vertical Jets Directed Downwards upon a Horizontal Surface. ARC CP-912, 1967. (AD-813962) (U)

122. Crabtree, L. G.: The Rotating Flap as a High-Lift Device. (Incl App. II: Kirby, D. A.: Power Required to Rotate the Flap of a Typical Four-Engined Transport). ARC CP-480, 1960. (U)

123. Crabtree, L. G., and Kirby, D. A.: The Rotating Flap as a High-Lift Device. Appendix I. Theory of an Aerofoil with Rotating Flap. Appendix II. Power Required to Rotate the Flap of a Typical Four-Engined Transport. RAE TN Aero 2492, 1957. (U)

124. Craig, S. J., and Campbell, A.: Analysis of VTOL Handling-Qualities Requirements, Part 1 — Longitudinal Hover and Transition. AFFDL TR-67-179, Part 1, 1968. (AD-845165) (U)

125. Craig, S. J.: Survey of Lateral Hover Mode Satisfactory and Unacceptable Dynamics. STI Working Paper 171-3, 1968. (U)

126. Crigler, J. L., and Gilman, J.: Calculation of Aerodynamic Forces on a Propeller in Pitch or Yaw. NACA TN 2585, 1952. (U)

127. Crim, A. D.: Hovering and Low-Speed Controllability of VTOL Aircraft. Jour. of the American Helicopter Soc., January 1959. (U)

128. Cromwell, C. H., III, and Payne, H. E., III: A Stability Analysis of Tilt-Wing Aircraft (Analytical). Princeton Univ. Report 477, 1960. (A61-881) (U)

129. Cumberbatch, E.: A Lifting-Surface Theory for Wings at High Angles of Attack Extending Through Multiple Jets. VRC Report No. 9, 1963. (AD-423274) (U)

130. Curnutt, R. A., and Curtiss, H. C., Jr.: Comparison of Longitudinal Stability Characteristics of Three Tilt-Wing VTOL Aircraft Designs. Princeton Univ. R749, USAAVLABS TR-66-64, 1968. (AD-667983) (N68-26700) (U)

131. Currie, M. M., and Dunsby, J. A.: Pressure Distribution and Forces Measurements on a VTOL Tilting Wing-Propeller Model. Part II: Analysis of Results. NRC LR-284, 1960. (U).

132. Curry, P. R., and Matthews, J. T., Jr.: Suggested Requirements for V/STOL Flying Qualities. USAAVLABS TR-65-45, 1965. (AD-617748) (U)

133. Curtiss, H. C., Jr.: An Analytical Study of the Dynamics of Aircraft in Unsteady Flight. USAAVLABS TR-65-48, 1965. (AD-627370) (N66-20863) (U)

134. Curtiss, H. C., Jr., and Struble, R. W.: Downwash Tests of the Dual-Tandem Ducted-Propeller VTOL Research Aircraft Configurations to Evaluate Engine Inlets, Protection Devices and Study Aerodynamic Interference. Kellett Aircraft Corporation Report 179T80-12, 1965. (N66-21906) (U)

135. Curtiss, H. C., Jr.: Dynamic Stability of V/STOL Aircraft at Low Speeds. AIAA Paper 69-194, 1969. (A69-19566) (U)

136. Curtiss, H. C., Jr., Putman, W. F., and Lebacqz, J. V.: An Experimental Investigation of the Longitudinal Dynamic Stability Characteristics of a Four-Propeller Tilt-Wing VTOL Model. Princeton Univ. R 774, USAAVLABS TR-66-80, 1967. (AD-663848) (U)

137. Curtiss, H. C., Jr., Putman, W. F.: General Description of the Princeton Dynamic-Model Track. USAAVLABS TR-66-73, 1966. (AD-645883) N67-22608) (U)

138. Curtiss, H. C., Jr.: An Investigation of the Dynamic Stability Characteristics of a Quad Configuration, Ducted-Propeller V/STOL Model. Vol. IV. The Longitudinal Stability Characteristics of a Quad Configuration, Ducted-Propeller V/STOL Model at High Duct Incidence. USAAVLABS TR-68-49D, 1968. (AD-859276) (U)

139. Curtiss, H. C., Jr., and Putman, W. F.: Results of Experimental Correlation of Model and Full-Scale Helicopter and VTOL Longitudinal Dynamics. Princeton Univ. Report 543, 1961. (U)

140. Curtiss, H. C., Jr.: Some Basic Considerations Regarding Longitudinal Dynamics of Aircraft and Helicopters. Princeton Univ. Report 562, 1961. (U)

141. Czinczenheim, J.: Aerodynamic Design and Flight Development of the Breguet 941 STOL Aircraft. RAE LT-1063, No. 3, 1964. (AD-443858) (U)

142. Dathe, H. M.: Review of Hovering Control Requirements for VTOL Aircraft by a Flight-Dynamics Analysis. AGARD 472, 1963. (AD-438878) (N64-19855) (U)

143. Davenport, E. E., and Spreemann, K. P.: Thrust Characteristics of Multiple Lifting Jets in Ground Proximity. NASA TN D-513, 1960. (U)

144. Davenport, E. E., and Spreemann, K. P.: Transition Characteristics of a VTOL Aircraft Powered by Four Ducted-Tandem Propellers. NASA TN D-2254, 1964. (U)

145. Davenport, E. E., and Kuhn, R. E.: Wind-Tunnel-Wall Effects and Scale Effects on a VTOL Configuration with a Fan Mounted in the Fuselage. NASA TN D-2560, 1965. (N65-13574) (U)

146. Davidson, J. K.: Aerodynamics of the Propulsive Wing. Presented at AF V/STOL Technology and Planning Conf., Sept. 1969. (U)

147. Davidson, J. K.: LTV Low-Speed Wind-Tunnel-Test Number 190, Follow-On Test of High-Mass-Rate Vectored-Propulsion Flow Model. LTV Report 2-53310/5R-2217, 1965. (AD-621578) (U)

148. Daw, D. F., Gould, D. G., and McGregor, D. M.: A Flight Investigation of the Effects of Weathercock Stability on V/STOL Aircraft Directional Handling Qualities. NRC LR-400, 1964. (AD-442252) (U)

149. Deckert, W. H., Page, V. R., and Dickinson, S. O.: Large-Scale Wind-Tunnel Tests of Descent Performance of an Airplane Model with a Tilt-Wing and Differential Propeller Thrust. NASA TN D-1857, 1964. (U)

150. deDecker, R. W.: Investigation of an Isolated Monocyclic V/STOL Propeller Performance and Oscillatory Stress. USAAVLABS TR-65-80, 1966. (U)

151. dePontfaracy, B., and Labussiere, A.: Investigation on the STOL – Starting from the Airplane Breguet 941. Wissenschaftliche Gesellschaft fur Luftfahrt Jahrbuch, 1960. (U)

152. de-Richemont, G.: Methods Utilized for Perfecting the Breguet 940 Blown-Wing Airplane. AGARD-371, 1961. (N62-15540) (U)

153. deSavigny, R. A., and Hickey, D. H.: Aerodynamic Characteristics in Ground Effect of a Large-Scale Model with a High Disk-Loading Lifting Fan Mounted in the Fuselage. NASA TN D-1557, 1963. (N63-11617) (U)

154. DeYoung, J.: Force and Moment Derivatives Due to Propellers of Arbitrary Configuration Inclined with Respect to Free Stream. Grumman ADR 01-03-64.1, 1964. (U)

155. DeYoung, J.: Propellers at High Incidence. Jour. of Aircraft, May-June, 1965. (U)

156. DeYoung, J.: Symmetric Loading of a Wing in a Wide Slipstream. Grumman Rept. ADR 01-04-66.1, 1966. (U)

157. Dickerman, F. N., and Branson, C. F.: Lockheed BLC Hercules – A Practical STOL Transport. SAE S-259, 1960. (U)

158. Dickinson, S. O., Page, C. R., and Deckert, W. H.: Large-Scale Wind-Tunnel Investigation of an Airplane Model with a Tilt Wing of Aspect Ratio 8.4, and Four Propellers, in the Presence of a Ground Plane. NASA TN D-4493, 1968. (N68-20370) (U)

159. Dixon, C. J.: Lift Augmentation by Lateral Blowing Over a Lifting Surface. AIAA Paper 69-193, 1969. (U)

160. Dods, J. B., Jr., and Watson, E. C.: The Effects of Blowing Over Various Trailing-Edge Flaps on an NACA 0006 Airfoil Section, Comparisons with Various Types of Flaps on Other Airfoil Sections, and an Analysis of Flow and Power Relationships for Blowing Systems. NACA RM A56C01, 1956. (U)

161. Dolbin, B. H., Jr.: Investigation of Lateral-Directional Handling Qualities of V/STOL Airplanes. Cornell Aeronautical Laboratory Report FDM 348, 1963. (U)

162. Dornier, S.: The STOL Experimental Aircraft Do. 29. AGARD Symposium, Paris, June 1960. (U)

163. Down, H. W., Jr., Jones, G. E., and Satterwhite, J. J.: XC-142A Limited Category II Stability and Control Tests. AFFTC-TR-68-9, 1968. (AD-840552) (U)

164. Draper, J. W., and Kuhn, R. E.: Investigation of the Aerodynamic Characteristics of a Model Wing-Propeller Combination and of the Wing and Propeller Separately at Angles of Attack up to 90°. NACA TN 3304, 1954. (U)

165. Draper, J. W., and Kuhn, R. E.: Some Effects of Propeller Operation and Location on Ability of a Wing with Plain Flaps to Deflect Propeller Slipstreams Downward for Vertical Take-off. NACA TN 3360, 1955. (U)

166. Drinkwater, F. J., III.: Operational Technique for Transition of Several Types of V/STOL Aircraft. NASA TN D-774, 1961. (AD-252988) (U)

167. Dukes, T. A., Carballal, J. M., et al: Some Dynamic Aspects of Stability in Low-Speed Flying Machines. TRECOM TR-63-56, 1963. (AD-431566) (U)

168. Dunsby, J. A., Currie, M. M., et al: Pressure Distribution and Force Measurements on a VTOL Tilting Wing-Propeller Model. Part I: Description and Tabulated Results. NRC LR-252, 1959. (AD-225870) (U)

169. Duvivier, J. F., and McCallum, R. B.: Investigation of Tilting-Duct and Fan-Wing in Transition Flight. TREC TR-61-19, 1960. (U)

170. Ellis, D. R., and Carter, G. A.: A Preliminary Study of the Dynamic Stability and Control Response Desired for V/STOL Aircraft. Princeton Univ. Report 611, 1962. (AD-289561) (U)

171. Erickson, J. C., Jr.: New Considerations of the Fluctuating Flow Field in Propeller Theory. CAL-BB-2670-S-1, 1968. (AD-680232) (U)

172. Erickson, J. C., Jr.: The Pitching-Moment Coefficient of a Jet-Flapped Airfoil. Jour. Aero. Sci., Dec. 1962. (U)

173. Erickson, J. C., Jr., Borst, H. V., and Ladden, R. M.: A Theory for VTOL Propeller Operation in a Static Condition. USAAVLABS TR-65-69, 1965. (AD-623527) (U)

174. Erlandsen, P., Zercard, J. G., and Olcott, J. W.: Wind-Tunnel Correlation Study of North American Tilt-Wing Model Tested in the NACA L 14' x 16' Tunnel and the Airship Model Test Facility. Naval Air Station, Lakehurst, N. J., 1962. (U)

175. Ernst, G., and Jardinier, J.: Influence Des Effets Gyroscopiques d'un Turboreacteur sur un Avion Decollant a la Verticale. Extrait de Docaero No. 48, 1958. (U)

176. Ernst, G.: A Method of Artificially Stabilizing Jet-Sustained Aircraft. Wissenschaftliche Gesellschaft fur Luftfahrt Jahrbuch, 1960. (U)

177. Ernst, G., and Jardinier, J.: Stabilization of VTOL Aircraft in Vertical Flight. RAE LT-892, 1962. (AD-272521) (U)

178. Fay, C. B.: A Cursory Analysis of the VTOL Tilt-Wing Performance and Control Problems. Annals of the N.Y. Academy of Sciences, Vol. 107, Art. I, 1963. (U)

179. Faye, A. E., Jr.: Attitude Control Requirements for Hovering Determined Through the Use of a Piloted Flight Simulator. NASA TN D-792, 1961. (U)

180. Feistel, T. W., Gerdes, R. M., and Fry, E. B.: An Investigation of a Direct Side-Force Maneuvering System on a Deflected-Jet VTOL Aircraft. NASA TN D-5175, 1969. (U)

181. Fimple, W. R.: An Experimental Investigation of the Aerodynamic Forces and Moments on a Jet-Flapped Wing in the Presence of a Propeller Slipstream and a Free Stream. Princeton Univ. Report 571, 1961. (AD-270966) (U)

182. Fink, M. P.: Aerodynamic Characteristics, Temperature, and Noise Measurement of Large-Scale, External-Flow Jet-Augmented-Flap Model with Turbojet Engines Operating. NASA TN D-943, 1961. (U)

183. Fink, M. P.: Aerodynamic Data on Large Semispan Tilting Wing with 0.4-Diameter Chord, Single-Slotted Flap, and Single Propeller 0.22 Chord Below Wing. NASA TN D-5016, 1969. (N69-17312) (U)

184. Fink, M. P., Mitchell, R. G., et al: Aerodynamic Data on a Large Semispan Tilting Wing with 0.5-Diameter Chord, Double-Slotted Flap, and Both Left- and Right-Hand Rotation of a Single Propeller. NASA TN D-3375, 1966. (U)

185. Fink, M. P.: Aerodynamic Data on a Large Semispan Tilting Wing with a 0.5-Diameter Chord, a Double-Slotted Flap, and Left- and Right-Hand Rotation of a Single Propeller, in Presence of Fuselage. NASA TN D-3674, 1966. (U)

186. Fink, M. P., and Mitchell, R. G.: Aerodynamic Data on a Large Semispan Tilting Wing with a 0.5-Diameter Chord, a Single-Slotted Flap, and Both Left- and Right-Hand Rotation of a Single Propeller. NASA TN D-3754, 1967. (U)

187. Fink, M. P.: Aerodynamic Data on Large Semispan Tilting Wing with 0.5-Diameter Chord, Single-Slotted Flap, and Single Propeller 0.08 Chord Below Wing. NASA TN D-4030, 1967. (U)

188. Fink, M. P.: Aerodynamic Data on Large Semispan Tilting Wing with 0.5-Diameter Chord, Single-Slotted Flap, and Single Propeller 0.19 Chord Below Wing. NASA TN D-3884, 1967. (U)

189. Fink, M. P., Mitchell, R. G., and White, L. C.: Aerodynamic Data on a Large Semispan Tilting Wing with 0.6-Diameter Chord, Fowler Flap, and Single Propeller Rotating Up at Tip. NASA TN D-2180, 1964. (N64-14729) (U)

190. Fink, M. P., Mitchell, R. G., and White, L. C.: Aerodynamic Data on Large Semispan Tilting Wing with 0.6-Diameter Chord, Single-Slotted Flap, and Single Propeller Rotating Down at Tip. NASA TN D-2412, 1964. (N64-28325) (U)

191. Fink, M. P., Mitchell, R. G., and White, L. C.: Aerodynamic Data on Large Semispan Tilting Wing with 0.6-Diameter Chord, Single-Slotted Flap, and Single Propeller Rotating Up at Tip. NASA TN D-1586, 1964. (N64-31221) (U)

192. Fink, M. P., and Smith, C. C., Jr.: Pressure Distribution of a Large Semispan Tilting Wing with 0.4-Diameter Chord, Single-Slotted Flap, and a Single Propeller 0.22 Chord Below Wing. NASA TN D-5481, 1969. (U)

193. Fink, M. P.: Static Tests of an External-Flow Jet-Augmented-Flap Test Bed with a Turbojet Engine. NASA TN D-124, 1959. (U)

194. Finnestead, R. L., Welter, W. L., and Ferrell, K. R., et al: Engineering Flight Research Evaluation of the XV-5A Lift-Fan Aircraft – Part 1, Stability and Control, Final Report. U.S. Army, Test and Evaluation Command Project 4-5-1220-01, Part 1, 1966. (AD-800973L) (U)

195. Fisher, I. A.: Testing the Kestrel. AGARD Report 518, 1965. (N67-19243) (U)

196. Fitch, C. R.: Three-Dimensional Aerodynamic Representation of V/STOL Wings by the Vortex-Lattice Method. AEDC-TR-68-6, 1968. (AD-826007) (U)

197. Fitzpatrick, J. E.: Longitudinal Characteristics of the K-168 Aircraft Based on 1/8-Scale Model Wind-Tunnel-Test Results. Kaman Report No. G-113-31, 1961. (U)

198. Fletcher, H. S.: Experimental Investigation of Lift, Drag, and Pitching Moment of Five Annular Airfoils. NACA TN 4117, 1957. (U)

199. Fletcher, J.: Aerodynamic Design Problems of Jet-Lift VTOL Aircraft. Aircraft Eng., July 1962. (U)

200. Flinn, E. H., and Statler, I. C.: V/STOL Aerodynamic Stability and Control. Presented at AF V/STOL Technology and Planning Conf., Sept. 1969. (U)

201. Foody, J. J.: The Control System of the S. C. 1. Shell Aviation News, No. 283, 1962. (U)

202. Foody, J. J.: Controlling VTOL Aircraft at Transition Speeds. Control, Part I, II, III, September, October, and November 1960. (U)

203. Fry, E. B., Greif, R. K., and Gerdes, R. M.: Use of a Six-Degree-of-Freedom Motion Simulator for VTOL Hovering Tasks. NASA TN D-5383, 1969. (N69-35359) (U)

204. Fuetterer, H., and Harms, L.: Jet-Interference Measurements on a V/STOL Model with Jet Simulation by Fans. AGARD CP-22, 1967. (N68-22500) (U)

205. Gainer, G.: Low-Speed Wind-Tunnel Investigation to Determine the Aerodynamic Characteristics of a Rectangular Wing Equipped with a Full-Span and an Inboard Half-Span Jet-Augmented Flap Deflected 55°. NASA Memo 1-27-59L, 1959. (U)

206. Garner, J. E.: A Review of Jet-Efflux Studies Applicable to V/STOL Aircraft. AEDC TR-67-163, 1967. (AD-658432) (N67-39617) (U)

207. Garren, J. F., Jr., and Kelly, J. R.: Description of an Analog-Computer Approach to V/STOL Simulation Employing a Variable-Stability Helicopter. NASA TN D-1970, 1964. (U)

208. Garren, J. F., Jr.: Effects of Coupling Between Pitch and Roll-Control Inputs on the Handling Qualities of VTOL Aircraft. NASA TN D-1233, 1962. (AD-273086) (U)

209. Garren, J. F., Jr., Kelley, J. R., and Reeder, J. P.: Effects of Gross Changes in Static Directional Stability on V/STOL Handling Characteristics Based on a Flight Investigation. NASA TN D-2477, 1964. (U)

210. Garren, J. F., Jr.: Effects of Gyroscopic Cross Coupling Between Pitch and Roll on the Handling Qualities of VTOL Aircraft. NASA TN D-812, 1961. (AD-255198) (U)

211. Garren, J. F., Jr.: Effects of Gyroscopic Cross Coupling Between Pitch and Yaw on the Handling Qualities of VTOL Aircraft. NASA TN D-973, 1961. (U)

212. Garren, J. F., Jr., Kelly, J. R., et al: A Visual Flight Investigation of Hovering and Low-Speed VTOL Control Requirements. NASA TN D-2788, 1965. (U)

213. Garren, J. F., Jr., and Assadourian, A.: VTOL Height-Control Requirements in Hovering as Determined from Motion Simulator Study. NASA TN D-1488, 1962. (U)

214. Gentry, G. L., and Margason, R. J.: Jet-Induced Lift Losses on VTOL Configurations Hovering In and Out of Ground Effect. NASA TN D-3166, 1966. (U)

215. George, M., and Kisielowski, E.: Investigation of Propeller-Slipstream Effects on Wing Performance. Final Report. Dynasciences Corp. Report, DCR-234, USAAVLABS TR-67-67, 1967. (AD-666247) (N68-21564) (U)

216. Gerdes, R. M.: A Piloted Motion-Simulator Investigation of VTOL Height-Control Requirements. NASA TN D-2451, 1964. (U)

217. Gerdes, R. M., and Weick, R. F.: A Preliminary Piloted Simulator and Flight Study of Height-Control Requirements for VTOL Aircraft. NASA TN D-1201, 1962. (U)

218. Gibson, M. M., and Norbury, J. F.: Nomogram Analysis for Ducted Fans with Pre-Rotation. Aircraft Eng., 1960. (U)

219. Gill, W. J.: Wind-Tunnel Tests of Several Ducted Propellers in Non-Axial Flow. Hiller Aircraft Corporation, Report ARD-224, 1959. (U)

220. Gilman, J.: Static Thrust and Torque Characteristics of Single and Dual-Rotating Tractor Propellers. NACA Memo Report L-750, 1955. (U)

221. Girard, P. F.: The Handling Qualities of VTOL Aircraft at Low Speed. IAS Preprint 843, 1958. (U)

222. Girard, P. F., and Everett, W. J.: A Test-Pilot Report on the X-13 Vertijet and VZ3RY Vertiplane. Annals of the N.Y. Academy of Sciences, Vol. 107, Art. I, 1963. (U)

223. Giulianetti, D. J., Biggers, J. C., and Maki, R. L.: Longitudinal Aerodynamic Characteristics in Ground Effect of a Large-Scale, V/STOL Model with Four Tilting Ducted Fans Arranged in a Dual-Tandem Configuration. NASA TN D-4218, 1967. (N67-39980) (U)

224. Giulianetti, D. J., Biggers, J. C., and Maki, R. L.: Longitudinal and Lateral-Directional Aerodynamic Characteristics of a Large-Scale, V/STOL Model with Four Tilting Ducted Fans Arranged in a Dual-Tandem Configuration. NASA TN D-3490, 1966. (N66-29218) (U)

225. Gobetz, F. W.: A Review of the Wing-Slipstream Problem with Experiments on a Wing Spanning a Circular Jet. Princeton Univ. Report 489, 1960. (U)

226. Goland, L., Miller, N., and Butler, L.: Effects of Propeller Slipstream on V/STOL Aircraft Performance and Stability. TRECOM TR-64-47, 1964. (AD-608186) (U)

227. Goldberger, S.: On the Relative Importance of the Low-Speed Control Requirement for V/STOL Aircraft. AEDC TR-66-205, 1966. (AD-644191) (N67-20708) (U)

228. Goldsmith, R., and Hickey, D. H.: Characteristics of Aircraft with Lifting-Fan Propulsion Systems for V/STOL. IAS Paper 63-27, 1963. (A63-11581) (U)

229. Goodson, K. W., and Grunwald, K. J.: Aerodynamic Characteristics of a Powered Semi-Span Tilting Shrouded-Propeller VTOL Model in Hovering and Transition Flight. NASA TN D-981, 1962. (U)

230. Goodson, K. W.: Effect of Ground Proximity on the Longitudinal, Lateral, and Control Aerodynamic Characteristics of a Tilt-Wing Four-Propeller V/STOL Model. NASA TN D-4237, 1967. (N68-11519) (U)

231. Goodson, K. W.: Ground Effects on a Four-Propeller Tilt-Wing Configuration Over a Fixed and a Moving Ground Plane. NASA TN D-3938, 1967. (N67-23820) (U)

232. Goodson, K. W.: Longitudinal Aerodynamic Characteristics of a Flapped Tilt-Wing Four-Propeller V/STOL Transport Model. NASA TN D-3217, 1966. (N66-16924) (U)

233. Gould, D. G.: Results of Recent Investigations of V/STOL Control and Response Requirements Using Variable-Stability Helicopters. AGARD-519, 1965. (N66-33488) (U)

234. Grabe, W.: Ground-Effect Experiments on a Fan-in-Wing Configuration at Zero Forward Speed. NRCC MET-369, 1962. (AD-292102) (U)

235. Grady, W. T.: Some Aerodynamic Aspects of Propellers for VTOL Aircraft. American Helicopter Soc., 3rd Annual Western Forum, October, 1956. (U)

236. Grasmann, K.: Jet Deflection for the Purpose of Thrust-Vector Control in V/STOL Aircraft. Wissenschaftliche Gesellschaft fur Luftfahrt Paper 29, 1962. (N63-10027) (U)

237. Greenberg, M. D., and Ordway, D. E.: The Ducted Propeller in Static and Low-Speed Flight. Therm Advanced Research TAR-TR-6407, 1964. (AD-608526) (N65-16112) (U)

238. Greenberg, M. D., Ordway, D. E., and Lo, C. F.: A Three-Dimensional Theory for the Ducted Propeller at Angle of Attack. Therm Advanced Research TAR-TR-6509, 1965. (AD-480994) (U)

239. Gregory, N., and Walker, W. S.: Measurement of Lift and Ground Interference on a Lifting-Fan Wing at Zero Forward Speed. ARC R&M 3263, 1962. (N62-10193) (U)

240. Gregory, N., and Love, E. M.: Wind-Tunnel Tests on a Nacelle Fitted with Two Lifting Fans in Tandem. ARC R&M 3494, 1967. (N68-12756) (U)

241. Greif, R. K., Fry, E. B., et al: Simulator Investigations of Various Control Systems for VTOL Aircraft. Conf. on V/STOL and STOL Aircraft, 1966. (N66-24623) (U)

242. Greif, R. K., Fry, E. B., et al: VTOL Control System Studies on a 6 Degree of Freedom Motion Simulator. ICAS-66-9, 1966. (U)

243. Griffin, J. M., et al: V/STOL Flying-Qualities Criteria. Presented at AF V/STOL Technology and Planning Conf., Sept. 1969. (U)

244. Griffin, R. N., Holzhauser, C. A., and Weiberg, J. A.: Large-Scale Wind-Tunnel Tests of an Airplane Model with an Unswept, Aspect-Ratio-10 Wing, Two Propellers, and Blowing Flaps. NASA Memo 12-3-58A, 1958. (U)

245. Griffith, J. H.: Proposed VTOL Flight Requirements. Annals of the N.Y. Academy of Sciences, Vol. 107, Art. I, 1963. (U)

246. Grose, R. M.: Wind-Tunnel Tests of Shrouded Propellers at Mach Numbers from 0 to 0.6. WADC TR-58-604, 1958. (U)

247. Grunwald, K. J.: Aerodynamic Characteristics of a Four-Propeller Tilt-Wing VTOL Model with Twin Vertical Tails Including Effects of Ground Proximity. NASA TN D-901, 1961. (U)

248. Grunwald, K. J., and Goodson, K. W.: Aerodynamic Loads on an Isolated Shrouded-Propeller Configuration for Angles of Attack from -10° to 110°. NASA TN D-995, 1962. (AD-268842) (U)

249. Grunwald, K. J., and Goodson, K. W.: Division of Aerodynamic Loads on a Semispan Tilting-Ducted-Propeller Model in Hovering and Transition Flight. NASA TN D-1257, 1962. (U)

250. Grunwald, K. J.: Experimental Study of Wind-Tunnel-Wall Effects and Wall Corrections for a General-Research V/STOL Tilt-Wing Model with Flap. NASA TN D-2887, 1965. (U)

251. Grunwald, K. J.: Investigation of Long-tudinal and Lateral Stability Characteristics of a Six-Propeller Deflected-Slipstream VTOL Model with Boundary-Layer Control Including Effects of Ground Proximity. NASA TN D-445, 1961. (AD-249651) (U)

252. Grunwald, K. J.: Investi[illegible]of a Semispan Tilt-Wing VTOL Model to Determine Ground Effect on Full-Span Flaps Used for Yaw Control in Hovering. NASA TN D-3437, 1966. (N66-27730) (U)

253. Guerrieri, M. A., and Stuart, J., III.: A Simplified Theoretical Investigation of a Wing-Propeller Combination Through a Range of Angles of Attack from 0° to 90° and a Comparison with Experimental Results. Hiller Helicopters Eng. Report. 461.31, 1955. (AD-103341) (U)

254. Gustafson, F. B., Pegg, R. J., and Kelley, H. L.: Aerodynamic Observations from Flight Tests of Two VTOL Aircraft. NASA Conference on V/STOL Aircraft, Langley Research Center, 1960. (BW-C-20000) (U)

255. Gyorgyfalvy, D.: Flight Investigation of Leading-Edge-Suction Boundary-Layer Control on a Liaison Type STOL Aircraft. Mississippi State Univ. Report 31, 1961. (U)

256. Hacker, T.: Problems of the Dynamics and Control of VTOL Aircraft: Optimum Guidance and Stability. Library Translation RAE-1186, 1966. (AD-810440) (N67-24586) (U)

257. Hafer, X.: V/TOL Control Systems, Especially Controlled by Thrust Modulation. AGARDograph 89-1, 1964. (N65-22900) (U)

258. Hall, L. P., Hickey, D. H., and Kirk, J. V.: Aerodynamic Characteristics of a Large-Scale V/STOL Transport Model with Lift and Lift-Cruise Fans. NASA TN D-4092, 1967. (N67-33454) (U)

259. Halley, D. H.: The Development of a Simplified Analytical Approach for Evaluation of the Dynamic Stability Characteristics of a Ducted-Propeller VTOL Aircraft in Transition. Princeton Univ. Aerospace and Mechanical Science Report 850, 1968. (U)

260. Ham, N. D., and Moser, H. H.: Preliminary Investigation of a Ducted Fan in Lifting Forward Flight. IAS Preprint 827, 1958. (U)

261. Hammond, A. D., and McLemore, H. E.: Hot-Gas Ingestion and Jet Interference Effects for Jet V/STOL Aircraft. NASA TM X-60449, 1967. (N68-26194) (U)

262. Hargraves, C. R.: An Analytical Study of the Longitudinal Dynamics of a Tilt-Wing VTOL. Princeton Univ. Report 561, 1961. (U)

263. Hartunian, R. A., Sowydra, A., and Vidal, R. J.: The Aerodynamic Appraisal of STOL/VTOL Configurations. IAS Paper 60-37, 1960. (U)

264. Hayes, W. C., Kuhn, R. E., and Sherman, I. R.: Effects of Propeller Position and Overlap on the Slipstream Deflection Characteristics of a Wing-Propeller Configuration Equipped with a Sliding and Fowler Flap. NACA TN 4404, 1958. (U)

265. Heinle, D. R.: The Use of Piloted Simulators in the Study of VTOL Flight. NASA Conference on V/STOL Aircraft, Langley Research Center, November 1960. (N63-14700) (U)

266. Helmbold, H. B.: Compressibility Effect on a Shrouded Propeller. Fairchild Aircraft Division, Eng. Report R221-012, 1955. (U)

267. Helmbold, H. B.: Performance Diagrams for Free and Ducted Propellers. Fairchild Aircraft Division, Eng. Report R221-013, 1956. (U)

268. Henderson, C., Kroll, J., and Hesby, A.: Control Characteristics of V/STOL Aircraft in Transition. Bell Aerosystems R-2023-917002, 1962. N66-81695) (U)

269. Henshaw, D. H., and Colavincenzo, O. M. S.: The Steady-State Lateral-Control Equations with Particular Reference to STOL Aircraft. Canadian Aeronautics and Space Jour., Vol. 10, 1964. (A64-15877) (U)

270. Herbst, W.: Calculation of the Aerodynamic Coefficients of a Finite Fan-in-Wing Airfoil. VDI Zeitschrift, Vol. 108, No. 27, 1966. (A66-43050) (U)

271. Hesby, A., and Sherman, E. W., Jr.: Wind-Tunnel-Test Data Report for the Full-Scale Powered-Duct Model. Bell Aerosystems R-2127-921007, 1965. (AD-487970L) (U)

272. Heyson, H. H.: Linearized Theory of Wind-Tunnel Jet-Boundary Corrections and Ground Effects for VTOL-STOL Aircraft. NASA TR R-124, 1962. (AD-269611) (N63-10219) (U)

273. Heyson, H. H.: Nomographic Solution of the Momentum Equation for VTOL-STOL Aircraft. NASA TN D-814, 1961. (N62-71388) (U)

274. Heyson, H. H.: Some Considerations in Wind-Tunnel Tests of V/STOL Models. NASA TM X-60772, 1967 (N68-13016) (U)

275. Heyson, H. H.: Wind-Tunnel Wall Effects at Extreme Force Coefficients. Annals of N.Y. Academy of Sci., Vol. 154, Art. 2, 1968. (U)

276. Hickey, D. H., and Hall, A. H.: Aerodynamic Characteristics of a Large-Scale Model with Two High Disk-Loading Fans Mounted in the Wing. NASA TN D-1650, 1963. (N63-13100) (U)

277. Hickey, D. H., and Cook, W. L.: Aerodynamics of V/STOL Aircraft Powered by Lift Fans. NASA TM X-60455, 1967. (N68-27435) (U)

278. Hickey, D. H., and Goldsmith, R. H.: Characteristics of Aircraft with Lifting-Fan Propulsion Systems for V/STOL. IAS Paper 63-27, 1963. (N63-12889) (U)

279. Hickey, D. H., and Cook, W. L.: Correlation of Wind-Tunnel and Flight-Test Aerodynamic Data for Five V/STOL Aircraft. AGARD Report 520, 1965. (N67-29536) (U)

280. Hickey, D. H.: Preliminary Investigation of the Characteristics of a Two-Dimensional Wing and Propeller with the Propeller Plane of Rotation in the Wing-Chord Plane. NASA RM A57F03, 1957. (U)

281. Hickey, D. H., and Ellis, D. R.: Wind-Tunnel Tests of a Semi-Span Wing with a Fan Rotating in the Plane of the Wing. NASA TN D-88, 1959. (U)

282. Hill, T. G.: Some Fundamentals for Efficient VTOL Aircraft Hover Control. American Helicopter Society Journal, Vol. 11, No. 1, Jan. 1966. (A66-23258) (U)

283. Hink, G. R., Gilbert, R. F., and Sundstrom, K. A.: General Method for Determining the Aerodynamic Characteristics of Fan-in-Wing Configurations. Vol. II. USAAVLABS TR-67-61B, Vol. 2, 1967. (AD-667981) (N68-26344) (U)

284. Hinz, E. R.: Stability and Control Characteristics of the Vertical-Attitude VTOL Aircraft. Canadian Aeronautical Institute — Institute of the Aeronautical Sciences Preprint 763, Canadian Aero. Journal, 1958. (U)

285. Hoehne, V. O., and Monical, R. E.: A Method of Design of Shrouded Propellers. Univ. of Wichita, Dept. of Eng. Research Report 213-8, 1959. (U)

286. Hoehne, V. O., and Wattson, R. K., Jr.: Shrouded-Propeller Investigations. Univ. of Wichita, Dept. of Eng. Research Reports 213-1-7, 9-11, 1958-60. (U)

287. Hoehne, V. O.: Shrouded-Propeller Investigations: Aerodynamic Characteristics of a Shroud with Centerbody. Univ. of Wichita, Dept. of Eng. Research Report 337, 1959. (U)

288. Hoffert, F.: The Dornier D031 Jet-Lift Concept, A Light Military Transport with VTOL Capability. SAE-864C, 1964. (U)

289. Holden, K. J.: The Effects of Introducing a Restoring Moment Proportional to Stick Velocity on the Hovering of an Unstabilized Jet-Lift Aircraft. Aeronautical Quarterly, Vol. 15, Feb. 1964. (A64-15303) (U)

290. Holladay, W. L., and Campbell, J. E.: VTOL Flight-Control Design Considerations for IFR Landings. Presented at AF V/STOL Technology and Planning Conf., Sept. 1969. (U)

291. Holzhauser, C. A., Innis, R. C., et al: A Flight and Simulator Study of the Handling Qualities of a Deflected-Slipstream STOL Seaplane Having Four Propellers and Boundary-Layer Control. NASA TN D-2966, 1965. (U)

292. Hough, G. R., and Kaskel, A. L.: A Comparison of Ducted-Propeller Theory with Bell X-22A Experimental Data. Therm Advanced Research Report TR-6510, 1965. (AD-480995) (X66-18702) (U)

293. Huang, K. P., Goland, L., et al: Charts for Estimating Aerodynamic Forces on STOL Aircraft Wings Immersed in Propeller Slipstreams. Dynasciences Corporation Report DCR-161, 1965. (AD-634722) (N66-34885) (U)

294. Huggett, D. J.: The Ground Effect on the Jet-Flap in Two Dimensions. ARC 19713, 1957. (AD-161226) (U)

295. Huston, R. J., and Winston, M. M.: Data from a Static-Thrust Investigation of a Large-Scale General Research VTOL-STOL Model in Ground Effect. NASA TN D-397, 1960. (AD-241018) (U)

296. Huston, R. J., Ward, J. F., and Winston, M. M.: Wing and Flap Loads Obtained from a Wind-Tunnel Investigation of a Large-Scale V/STOL Model. NASA TN D-1634, 1963. (U)

297. Iakovlevskii, O. V., and Krasheninnikov, S. I. U.: Propagation of a Turbulent Jet Colliding with a Flat Surface. Mekhanika Zhidkosti I Gaza, July-August 1966. (A66-41737) (U)

298. Illingworth, J. K. B., and Chinn, H. W.: Variable Stability and Control Tests on the S.C.1. Aircraft in Jet-Borne Flight, with Particular Reference to Desirable V.T.O.L. Flying Qualities. RAE TN Aero 2895, 1963. (AD-342066) (C) Title Unclassified

299. Illingworth, J. K. B., and Chinn, H. W.: Variable Stability and Control Tests on the S.C.1 Aircraft in Jet-Borne Flight, with Particular Reference to Desirable VTOL Flying Qualities. ARC R&M 3584, 1969. (AD-851181) (U)

300. Innis, R. C., and Quigley, H. C.: A Flight Examination of Operating Problems of V/STOL Aircraft in STOL-Type Landing and Approach. NASA TN D-862, 1961. (AD-257800) (U)

301. Isakson, G., and Buning, H.: A Study of Problems in the Flight Simulation of VTOL Aircraft. WADC TN-59-305, 1960. (U)

302. James, H. A., and Saunders, K. L.: Fan-in-Wing V/STOL Aircraft. Astronautics and Aerospace Eng., Vol. 1, June 1963. (N63-17562) (U)

303. James, H. A.: Generalized Characteristics of Vertifan Aircraft in the Fan Mode. Annals of the N. Y. Academy of Sciences, Vol. 107, Art. I, 1963. (U)

304. James, H. A., Wingrove, R. C., et. al: Wind-Tunnel and Piloted-Flight-Simulator Investigation of a Deflected-Slipstream VTOL Airplane, the Ryan VZ-3RY. NASA TN D-89, 1959. (U)

305. Jeffrey, N. E.: A Simple Method for Predicting Propeller Aerodynamic Forces and Moment with Inflow Angles from 0^{o} to 90^{o}. Canadair Ltd. Report RAA 62-103, 1958. (U)

306. Johnson, A. E.: A Mears of Improving the Static Performance of Cruise-Designed Shrouded Propellers. Journal-of the Aero Space Sciences, August 1958. (U)

307. Johnson, A. E.: Wind-Tunnel Investigation of the Effects of Thrust, Shroud Length, and Shroud Camber on the Static Stability Characteristics of Shrouded Propellers. DTMB Aero 1073, 1964. (AD-601989) (U)

308. Johnston, G. W.: Recent Advances in STOL Aircraft Design and Operation. AIAA Paper 64-183, 1964. (U)

309. Johnston, J. F., and Friend, C. F.: Effect of Size on VTOL Aircraft Hover and Low-Speed Handling Qualities. 1st Nat. VTOL A/C Symposium, W-PAFB, Nov. 3-4, 1965. (A66-16813) (U)

310. Johnston, J. F., Culver, I. H., and Friend, C. F.: Study of Size Effects on VTOL Handling-Qualities Criteria. USAAVLABS TR-65-24, 1965. (AD-622579) (N66-11993) (U)

311. Jordinson, R.: Flow in a Jet Directed Normal to the Wind. ARC R&M 3074, 1956. (U)

312. Kakol, S. J.: Flight Tests of the First Dual-Tandem Ducted-Fan V/STOL. Soc. of Experimental Test Pilots Annual Report to the Aerospace Profession (Tenth), 1968. (U)

313. Kaplan, D. H.: Development of Quad Control for VTOL. Proceedings of the American Helicopter Soc. 15th Annual Nat'l Forum, 1959. (U)

314. Katzenberger, E. F., Ulisnik, H. D., and Adler, A.: Some Considerations of Direct-Lift V/STOL Aircraft. N. Y. Acad. of Sci. Annals, Vol. 107, Art. 1, 1963. (A63-14992) (U)

315. Keller, R. P., and Green, D. C.: A Preliminary Analysis of the XV-4B VTOL Aircraft Computer Simulation. AFIT Report No. GAM/AE-68-4, 1968. (AD-838777) (U)

316. Kelley, H. L., and Champine, R. A.: Flight Operating Problems and Aerodynamic and Performance Characteristics of a Fixed-Wing, Tilt-Duct, VTOL Research Aircraft. NASA TN D-1802, 1963. (U)

317. Kelley, H. L.: Transition and Hovering Flight Characteristics of a Tilt-Duct VTOL Research Aircraft. NASA TN D-1491, 1962. (U)

318. Kelly, J. R., and Garren, J. F., Jr.: Study of the Optimum Values of Several Parameters Affecting Longitudinal Handling Qualities of VTOL Aircraft. NASA TN D-4624, 1968. (N68-28153) (U)

319. Kelly, M. W.: Analysis of Some Parameters Used in Correlating Blowing-Type Boundary-Layer Control Data. NACA RM A56F12, 1956. (U)

320. Kelly, M. W.: Large-Scale Wind-Tunnel Studies of Several VTOL Types. NASA Conference on V/STOL Aircraft, 1960. (U)

321. Kemper, E. H., et al: Design Study – CV-7A Transport Aircraft Modification to Provide an Augmentor-Wing Jet STOL Research Aircraft. North American Rockwell Rept., 1969. (N69-25291) (U)

322. Kerney, K. P.: An Asymptotic Theory of the High-Aspect-Ratio Jet Flap. Ph.D. Thesis, Cornell Univ., 68-881, 1967. (N69-12940) (U)

323. Key, D. L.: Study to Develop Equations of Motion Suitable for Analyses of VTOL Dynamics During Hover and Transition. CAL TB-2312-F, 1966. (U)

324. Key, D. L., and Reed, L. E.: VTOL Transition Dynamics and Equations of Motion with Application to the X-22A. CAL TB-2312-F-1, 1968. (AD-835996) (U)

325. Kind, R. J., and Maull, D. J.: An Experimental Investigation of a Low-Speed Circulation-Controlled Aerofoil. Aeronautical Quarterly, Vol. 19, 1968. (A68-31596) (U)

326. King, K. P., and McPherson, A.: A Piloted-Simulator Study of a Jet VTOL Aircraft in Partially Jet-Borne Flight. RAE TR-68301, 1968. (AD-856991) (U)

327. Kirby, R. H.: Aerodynamic Characteristics of Propeller-Driven VTOL Aircraft. NASA TN D-730, 1961. (N62-71304) (U)

328. Kirby, R. H., and Chambers, J. R.: Flight Investigation of Dynamic Stability and Control Characteristics of a 0.18-Scale Model of a Fan-in-Wing VTOL Airplane. NASA TN D-3412, 1966. (N66-32941) (U)

329. Kirby, R. H., Schade, R. O., and Tosti, L. P.: Force-Test Investigation of a 1/4-Scale Model of the Modified VZ-2 Aircraft. NASA TN D-2382, 1964. (N64-26773) (U)

330. Kirby, R. H.: Hovering and Transition Flight Tests of a Supersonic Fan-in-Fuselage VTOL Fighter Model. NASA TM X-424, 1961. (AD-324937) (C) Title Unclassified

331. Kirchner, E.: Testing Slipstream Deflection for VTO Transports (Cascades). Aviation Age, September 1955. (U)

332. Kirk, J. V., Hickey, D. H., and Hall, L. P.: Aerodynamic Characteristics of a Full-Scale Fan-in-Wing Model Including Results in Ground Effect with Nose-Fan Pitch Control. NASA TN D-2368, 1964. (U)

333. Kirk, J. V., and Hickey, D. H.: Full-Scale Wind-Tunnel Investigation of a VTOL Aircraft with a Jet-Ejector System for Lift Augmentation. NASA TN D-3725, 1966. (N67-32321) (U)

334. Kirk, J. V., Hodder, B. K., and Hall, L. P.: Large-Scale Wind-Tunnel Investigation of a V/STOL Transport Model with Wing-Mounted Lift Fans and Fuselage-Mounted Lift-Cruise Engines for Propulsion. NASA TN D-4233, 1967. (N67-40198) (U)

335. Kirk, J. V., Hickey, D. H., and Aoyagi, K.: Large-Scale Wind-Tunnel Investigation of a Model with an External Jet-Augmented Flap. NASA TN D-4278, 1967. (N68-11627) (U)

336. Kliner, W. J., and Craig, S. J.: Study of VTOL Control Requirements During Hovering and Low-Speed Flight Under IFR Conditions. IAS Psper 61-60, 1961. (A61-1639) (U)

337. Kline, S. J.: On the Nature of Stall. Stanford Univ. Dept. of Mech. Eng., Air Force Office of Scientific Research TN 58-637, 1958. (U)

338. Koch, J. J.: Summary of the VTOL State of the Art. American Helicopter Soc. Newsletter, Vol. 7, September 1961. (U)

339. Korbacher, G. K.: Jet-Flap Characteristics for High-Aspect-Ratio Wings. AIAA Journal, Vol. 2, No. 1, Jan. 1964. (U)

340. Korbacher, G. K.: The Jet Flap and STOL. Univ. of Toronto, Institute of Aerophysics, Decennial Symposium Proceedings, Part II, 1959. (U)

341. Korbacher, G. K.: Performance and Operation of Quasi, Two-Dimensional Jet Flaps. UTIA Rept. 90, 1963. (U)

342. Korbacher, G. K.: Performance, Operation, and Use of Low-Aspect-Ratio Jet-Flapped Wings. UTIAS Rept. 97, 1964. (AD-448444) (U)

343. Korbacher, G. K., and Sridhar, K.: A Review of Jet Flap. Univ. of Toronto, Institute of Aerophysics Review 14, 1960. (U)

344. Kraft, R. M., and Neville, R. W. F.: An Analysis of the Stick-Fixed Dynamic Stability of a Typical VTOL Aircraft During Transition Flight out of Ground Effect. Naval Post-Graduate School, 1965. (AD-475341) (U)

345. Krenz, G., and Barche, J.: Jet Influence on V/STOL Aircraft in the Transitional and High-Speed Flight Regime. AGARD CP-27, 1967. (N68-28852) (U)

346. Kriebel, A. R., and Mendenhall, M. R.: Predicted and Measured Performance of Two Full-Scale Ducted Propellers. NACA CR-678, 1966. (U)

347. Kriebel, A. R., Sacks, A. H., and Nielsen, J. N.: Theoretical Investigation of Dynamic Stability Derivatives of Ducted Propellers. Vidya TR 63-65, 1963. (U)

348. Kriebel, A. R.: Theoretical Investigation of Static Coefficients, Stability Derivatives, and Interference for Ducted Propellers. ITEK Report 112, 1964. (AD-602269) (U)

349. Kriebel, A. R.: Theoretical Stability Derivatives for a Ducted Propeller. AIAA Preprint 64-170, 1964. (U)

350. Kroeger, R. A., and Osborn, R. F.: Aerodynamic Analysis of High-Disc-Loading V/STOL Aircraft. Presented at AF V/STOL Technology and Planning Conf., Sept., 1969. (U)

351. Kroll, J., Jr.: Initial VTOL Flight-Control Design Criteria Development – Discussion of Selected Handling-Qualities Topics; First Yearly Report. CAL Rept. BB-2249-F-1, 1967. (AD-825471) (U)

352. Kroll, J., Jr.: VTOL Flying-Qualities Bibliography. CAL Rept. FDM-407, 1968. (AD-829747L) (X68-17203) (U)

353. Kruger, W.: On Wind-Tunnel Tests and Computations Concerning the Problem of Shroud Propellers. NACA TM 1202, 1944. (U)

354. Kuhn, R. E., and Draper, J. W.: Investigation of the Aerodynamic Characteristics of a Model Wing-Propeller Combination and of the Wing and Propeller Separately at Angle of Attack up to 90°. NACA TR 1263, 1956. (U)

355. Kuhn, R. E., and Draper, J. W.: Investigation of Effectiveness of Large-Chord Slotted Flaps in Deflecting Propeller Slipstreams Downward for Vertical Take-Off and Low-Speed Flight. NACA TN 3364, 1955. (U)

356. Kuhn, R. E.: Investigation of Effectiveness of a Wing Equipped with a 50-Percent-Chord Sliding Flap, a 30-Percent-Chord Slotted Flap, and a 30-Percent-Chord Slat in Deflecting Propeller Slipstreams Downward for Vertical Take-Off. NACA TN 3919, 1959. (U)

357. Kuhn, R. E.: Investigation of the Effects of Ground Proximity and Propeller Position on the Effectiveness of a Wing with Large-Chord Slotted Flaps in Redirecting Propeller Slipstreams Downward for Vertical Take-Off. NACA TN 3629, 1956. (U)

358. Kuhn, R. E., and Draper, J. W.: An Investigation of a Wing-Propeller Configuration Employing Large-Chord Plain Flaps and Large-Diameter Propellers for Low-Speed Flight and Vertical Take-Off. NACA TN 3307, 1954. (U)

359. Kuhn, R. E.: Investigation at Zero Forward Speed of a Leading-Edge Slat as a Longitudinal-Control Device for Vertically-Rising Airplanes that Utilize the Redirecting-Slipstream Principle. NACA TN 3692, 1956. (U)

360. Kuhn, R. E., and Grunwald, K. J.: Lateral Stability and Control Characteristics of a Four-Propeller Deflected-Slipstream VTOL Model Including the Effects of Ground Proximity. NASA TN D-444, 1961. (AD-250017) (U)

361. Kuhn, R. E., and Grunwald, K. J.: Longitudinal Aerodynamic Characteristics of a Four-Propeller Deflected-Slipstream VTOL Model Including the Effects of Ground Proximity. NASA TN D-248, 1960. (U)

362. Kuhn, R. E., and McKinney, M. O., Jr.: NASA Research on the Aerodynamics of Jet-VTOL Engine Installation. NASA TM X-56820, 1965. (N65-34998) (U)

363. Kuhn, R. E., and Spreemann, K. P.: Preliminary Investigation of the Effectiveness of a Sliding Flap in Deflecting a Propeller Slipstream Downward for Vertical Take-Off. NACA TN 3693, 1956. (U)

364. Kuhn, R. E.: Review of Basic Principles of V/STOL Aerodynamics. NASA TN D-733, 1961. (N62-71307) (U)

365. Kuhn, R. E.: Semiempirical Procedure for Estimating Lift and Drag Characteristics of Propeller-Wing-Flap Configurations for Vertical- and Short-Take-Off-and-Landing Airplanes. NASA Memo 1-16-59L, 1959. (U)

366. Kuhn, R. E., and Naeseth, R. L.: Tunnel-Wall Effects Associated with VTOL/STOL Model Testing. AGARD Rept. 303, 1959. (N62-15912) (U)

367. Kuhn, R. E., and Hayes, W. C.: Wind-Tunnel Investigation of Effect of Propeller Slipstream on Aerodynamic Characteristics of a Wing Equipped with a 50-Percent-Chord Sliding Flap and a 30-Percent-Chord Slotted Flap. NACA TN 3918, 1957. (U)

368. Kuhn, R. E., and Hayes, W. C.: Wind-Tunnel Investigation of Longitudinal Aerodynamic Characteristics of Three Propeller-Driven VTOL Configurations in the Transition Speed Range; Including Effects of Ground Proximity. NASA TN D-55, 1960. (U)

369. Kurata, T., Ohara, N., et al: Dynamic Stability Tests of V/STOL Model. Mitsubishi Technical Review, Vol. 5, No. 5, 1968. (A69-17091) (U)

370. Kutyna, D. J.: Low-Speed Aerodynamic Characteristics of Jet-VTOL Aircraft at Angles of Attack. MIT M.S. Thesis, 1965. (AD-620442) (N66-11330) (U)

371. LaPlant, P. C., and Baldwin, R. L.: Flight Evaluation of the XV-5A V/STOL Aircraft. AFFTC-TR-66-30, 1967. (AD-810922) (X67-18167) (U)

372. Lasbrey, I. K. B.: Lift Compensation in the S.C.-1. Control, Vol. 5, February 1962. (U)

373. Laschka, B., Mueller, A., and Ebeling, P.: A Contribution on the Determination of Overall Forces of Inclined Propellers. AGARD CP-22, 1967. (N68-22490) (U)

374. Lavi, R., Hall, G. R., and Stark, W. W.: Full-Scale Ground-Proximity Investigation of a VTOL Fighter Model Aircraft. NASA CR-1098, 1968. (N68-28233) (U)

375. Lavi, R.: Parametric Investigation of VTOL Hot-Gas Ingestion and Induced-Jet Effects in Ground Proximity. Northrop Corp., NOR-67-32, 1967. (AD-809224) (U)

376. Lecomte, P. E.: Recent French Experience in the Field of V/STOL Aircraft. SAE Paper 6708, 1963. (U)

377. Levinsky, E. S., Thommen, H. U., et al: Lifting-Surface Theory and Tail-Downwash Calculations for V/STOL Aircraft in Transition and Cruise — Final Report. USAAVLABS TR-68-67, 1968. (AD-680969) (N69-20533) (U)

378. Lissaman, P. B. S.: Design Data for the Jet Flap in Ground Effect. Jour. of Aircraft, Vol. 4, No. 6, 1967. (U)

379. Lissaman, P. B. S.: A Linear Theory for Jet Flap in Ground Effect. AIAA Paper 67-2, 1967. (A68-36681) (U)

380. Lo, C. F., and Binion, T. W., Jr.: A V/STOL Wind-Tunnel-Wall Interference Study. AIAA Paper 69-171, 1969. (U)

381. Lockwood, V. E., Turner, T. R., and Riebe, J. M.: Wind-Tunnel Investigation of Jet-Augmented Flaps on a Rectangular Wing to High Momentum Coefficients. NACA TN 3865, 1956. (U)

382. Lollar, T. E., Bus, F. J., and Dolliver, D. M.: Control Requirements and Control Methods for Large V/STOL Aircraft. SAE Paper 650808, 1965. (A65-34838) (U)

383. Lollar, T. E.: A Rationale for the Determination of Certain VTOL Handling-Qualities Criteria. AGARD Report 471, 1963. (N64-19854) (U)

384. Lollar, T. E., and Kriechbaum, G. K. L.: VTOL Handling Qualities Criteria and Control Requirements. Analysis and Experiments. Am. Heli. Soc. Jour., Vol. 13, 1968. (A68-37051) (U)

385. Longhurst, W. S.: A Report on Stability and Control Testing of a Tilt-Wing V/STOL Aircraft. SAE Paper 660315, 1966. (U)

386. Lovell, P. M., Jr., and Parlett, L. P.: Effects of Wing Position and Vertical-Tail Configuration on Stability and Control Characteristics of a Jet-Powered Delta-Wing Vertically-Rising Aircraft Model. NACA TN 3899, 1957. (U)

387. Lovell, P. M., Jr., and Parlett, L. P.: Flight Tests of a Model of a High-Wing Transport Vertical Take-Off Aeroplane with Tilting Wing and Propellers and with Jet Controls at the Rear of the Fuselage for Pitch and Yaw Control. NACA TN 3912, 1957. (U)

388. Lovell, P. M., Jr., and Parlett, L. P.: Hovering-Flight Tests of a Model of a Transport Vertical-Take-Off Airplane with Tilting Wing and Propellers. NACA TN 3630, 1956. (U)

389. Lovell, P. M., Jr., and Parlett, L. P.: Transition-Flight Tests of a Model of a Low-Wing Transport Vertical-Take-Off Airplane with Tilting Wing and Propellers. NACA TN 3745, 1956. (U)

390. Lowry, J. G., Riebe, J. M., and Campbell, J. P.: The Jet-Augmented Flap. Preprint No. 715, S.M.F. Fund Paper, Inst. Aero. Sci., January 1957. (U)

391. Lowry, J. G., and Vogler, R. D.: Wind-Tunnel Investigation at Low Speeds to Determine the Effect of Aspect Ratio and End Plates on a Rectangular Wing with Jet Flaps Deflected 85°. NACA TN 3863, 1956. (U)

392. Ludwig, G. R.: An Investigation of the Flow in Uniform and Nonuniform Jets Impinging Normally on a Flat Surface. AIAA Paper 64-796, 1964. (A64-26517) (U)

393. Madden, J., Kroll, J., and Neil, D.: A Study of V/STOL Flying-Qualities Requirements. Bell Aerosystems Report No. 2023-917001, 1960. (AD-245368) (U)

394. Maguire, W. B.: A Wind-Tunnel Investigation of Some Short-Chord Low-Solidity Shrouded Propellers in the Cruise Condition. DTMB Aero-1083, 1964. (AD-612184) (U)

395. Maki, R. L., and Giulianetti, D. J.: Aerodynamic Stability and Control of Ducted-Propeller Aircraft. Conf. on V/STOL and STOL Aircraft, 1966. (N66-24615) (U)

396. Maki, R. L., and Hickey, D. H.: Aerodynamics of a Fan-in-Fuselage Model. NASA TN D-789, 1961. (AD-256074) (N62-71363) (U)

397. Margason, R. J., and Gentry, G. L., Jr.: Aerodynamic Characteristics of a Five-Jet VTOL Configuration in the Transition Speed Range. NASA TN D-4812, 1968. (N68-36081) (U)

398. Margason, R. J.: Jet-Induced Effects in Transition Flight. NASA SP-116, 1966. (N66-24619) (U)

399. Margason, R. J., Hammond, A. D., et al: Longitudinal Stability and Control Characteristics of a Powered Model of a Twin-Propeller Deflected-Slipstream STOL Airplane Configuration. NASA TN D-3438, 1966. (U)

400. Margason, R. J.: The Path of a Jet Directed at Large Angles to a Subsonic Free Stream. NASA TN D-4919, 1968. (N69-11634) (U)

401. Martin, E. E.: The Lift Produced by a Wing-Mounted Lift Fan at Flight Speeds Below Transition. American Helicopter Society, Vol. 9, April 1964. (A64-17610) (U)

402. Martin, J. F., and Michaelsen, O. E.: The Aerodynamic Approach to Improved Flying Qualities of Tilt-Wing Aircraft. AIAA/CASI/RAeS Paper 63-484, 1963. (A63-24595) (U)

403. Martin, J. F.: Investigation of Longitudinal Handling-Qualities Requirements and the Development of Piloting Techniques for Tilt-Wing V/STOL Aircraft in Normal and Emergency Conditions. AIAA, 1963. (A63-20569) (U)

404. Matsuoka, K., Takahashi, M., and Yonezawa, M.: Aerodynamic Characteristics of Propeller-Wing-Flap Systems. Osaka Univ., Eng. and Natural Sci. Bulletin, Series A, Vol. 17, No. 1, 1968. (A69-22278) (U)

405. McCormick, B. W.: Aerodynamics of V/STOL Flight. Academic Press, New York, 1967. (U)

406. McEachern, N. V., and Currie, M. M.: A Vortex-Lattice Lifting-Surface Theory for Wings with Submerged Fans. NRL LR-311 or NRC Rept. 6480, 1961. (AD-266780) (U)

407. McGregor, D. M.: A Flight Investigation of the Influence of Various Levels of Dihedral Effect on V/STOL Aircraft Directional Handling Qualities. NRC LR-412, NRCC 8281, 1964. (AD-461879) (U)

408. McGregor, D. M.: A Flight Investigation of Various Stability-Augmentation Systems for a Jet-Lift V/STOL Aircraft (Hawker-Siddeley P1127) Using an Airborne Simulator. NAE-LR-500, 1968. (AD-675766) (U)

409. McGregor, D. M.: The Influence of Aircraft Size on Control-Power and Control-Sensitivity Requirements. NAE-LR-459, 1966. (AD-805418) (U)

410. McGregor, D. M.: An Investigation of the Effects of a Lateral-Directional Control Cross-Coupling on Flying Qualities Using a V/STOL Airborne Simulator. NRC LR-390, NRCC 7778, 1963. (AD-428236) (U)

411. McGregor, D. M.: Simulation of the Canadair CL-84 Tilt-Wing Aircraft Using an Airborne V/STOL Simulator. NRC LR-435, 1965. (U)

412. McIntyre, W.: Simulation of Helicopter and V/STOL Aircraft. Vol. II – V/STOL Analysis Report. Study, Equations of Motion of Vertical/Short Take-Off and Landing Operational-Flight/Weapon System Trainers. NAVTRADEVCEN 1205-2, 1963. (AD-602427) (N64-21244) (U)

413. McKinney, M. O., Jr., Kirby, R. H., and Newsom, W. A.: Aerodynamic Factors to Be Considered in the Design of Tilt-Wing V/STOL Airplanes. Annals of the N. Y. Academy of Sciences, Vol. 107, Art. I, 1963. (U)

414. McKinney, M. O., Jr., Kuhn, R. E., and Reeder, J. P.: Aerodynamic and Flying Qualities of Jet V/STOL Airplanes. SAE-864A, 1964. (N64-23378) (U)

415. McKinney, M. O., Jr., Parlett, L. P., and Newsom, W. A., Jr.: An Approach to Efficient Low-Speed Flight for Fan-Powered Aircraft. NASA SP-116, 1966. (N66-24616) (U)

416. McKinney, M. O., Tosti, L. P., and Davenport, E. E.: Dynamic Stability and Control Characteristics of a Cascade-Wing Vertically-Rising Airplane Model in Take-Offs, Landings, and Hovering Flight. NACA TN 3198, 1954. (U)

417. McKinney, M. O., Jr.: Dynamic Tests of V/STOL Transport Models. NASA TM X-51790, 1965. (N65-22183) (U)

418. McKinney, M. O., and Newsom, W. A.: Experimental Research on 4-Duct Tandem VTOL Aircraft Configurations. American Helicopter Society Paper, 1962. (N62-11441) (U)

419. McKinney, M. O., and Newsom, W. A.: Fan V/STOL Aircraft. NASA TM X-59739, 1967. (N68-25278) (U)

420. McKinney, M. O.: Low-Speed Wind-Tunnel Investigation of a Wingless Jet VTOL Transport Model. NASA TN D-57, 1959. (U)

421. McKinzie, G. A., Bradfield, E. N., Jr., et al: P-1127 (XV-6A) V/STOL Handling-Qualities Evaluation. AFFTC-TR-68-10, 1968. (AD-839849) (U)

422. McLemore, H. C., and Peterson, J. B., Jr.: Aerodynamic Characteristics of a Large-Scale Unswept Wing-Body-Tail Configuration with Blowing Applied Over the Flap and Wing Leading Edge. NASA TN D-407, 1960. (U)

423. McLemore, H. C., and Cannon, M. D.: Aerodynamic Investigation of a Four-Blade Propeller Operating Through an Angle-of-Attack Range From 0° to 180°. NACA TN 3228, 1954. (U)

424. McLemore, H. C.: Jet-Induced Lift Loss of Jet VTOL Configurations in Hovering Condition. NASA TN D-3435, 1966. (U)

425. McWherter, R. C.: VTOL Wind-Tunnel Testing Techniques and Facilities. SAE Paper 370A, 1961. (A62-8744) (U)

426. Meagher, G., and Billington, I. J.: Canada's Entry in the New Family of Large Wind Tunnels for V/STOL Aircraft Development. Engineering Inst. of Canada, Congress of Canadian Engineers, May-June 1967. (A68-12525) (U)

427. Mertaugh, L. J., Jr., and Davidson, J. K.: Analysis of a Follow-On Low-Speed Wind-Tunnel Test of a High-Mass-Rate Vectored-Propulsion Flare Model. LTV Rept. 2-53310/5R-2206, 1965. (AD-619578) (N65-34528) (U)

428. Mertaugh, L. J., Jr.: Data Report for LTV Low-Speed Wind-Tunnel-Test Number 172. Test of High-Mass-Rate Vectored-Propulsion Flow Model. LTV 2-53310/5R-2172, 1965. (AD-612927) (U)

429. Michaels, J. L.: Study and Evaluation of V/STOL Ground-Based Simulation Techniques for the X-22A Aircraft. Bell Aerosystems, TR BA-7356-927001, USAAVLABS TR-69-40, 1969. (AD-859290) (U)

430. Michaelson, O. E.: The CL-84 V/STOL Flight Simulation — A Comparison With Reality. ICAS Paper 66-18, 1966. (A66-42493) (U)

431. Miller, D. P., and Vinje, E. W.: Fixed-Base Flight-Simulator Studies of VTOL Aircraft Handling Qualities in Hovering and Low-Speed Flight. AFFDL TR-67-152, 1968. (AD-831446) (U)

432. Mitchell, R. G.: Full-Scale Wind-Tunnel Test of the VZ-2 VTOL Airplane With Particular Reference to the Wing-Stall Phenomena. NASA TN D-2013, 1963. (N64-11550) (U)

433. Miyai, Y., and Kida, T.: An Approximate-Calculating Method of the Flow for a Thin Jet-Flapped Wing With a Small Deflection Angle in Proximity of the Ground. Japan Soc. for Aero. & Space Sci., Transactions, Vol. 9, No. 15, 1966. (A67-29308) (U)

434. Monical, R. E.: A Method of Representing Fan-Wing Combinations for Three-Dimensional Potential-Flow Solutions. Jour. of Aircraft, Vol. 2, No. 6, 1965. (U)

435. Morel, J. P., and Lissaman, P.B.S.: The Jet-Flap Diffuser: A New Thrust Augmenting Device. AIAA Paper 69-777, 1969. (U)

436. Mort, K. W., and Yaggy, P. F.: Aerodynamic Characteristics of a 4-Foot Diameter Ducted-Fan Mounted on the Tip of a Semispan Wing. NASA TN D-1301, 1962. (N62-11045) (U)

437. Mort, K. W., and Yaggy, P. F.: Aerodynamic Characteristics of a Full-Scale Propeller Tested with Both Rigid and Flapping Blades and with Cyclic Pitch Control. NASA TN D-1774, 1963. (U)

438. Mort, K. W., and Gamse, B.: A Wind-Tunnel Investigation of a 7-Foot-Diameter Ducted Propeller. NASA TN D-4142, 1967. (U)

439. Moser, H. H., and Linvingston, C. L.: Experimental and Analytical Study of the Ducted Fan and Fan-in-Wing in Hovering and Forward Flight. MIT TR 79-1, 1959. (AD-213316) (U)

440. Murphy, R. D.: Wind-Tunnel Boundary Effects Studies for VTOL/STOL Data Using a Four-Propeller, Ducted-Fan, Generalized Transport Design. DTMB Test AL-4, 1966. (AD-480760L) (U)

441. Murphy, R. D.: Wind-Tunnel Tests of a 1/16-Scale Model of a Rotorable-Wing Seaplane. Part III. Analysis of the Test Data. DTMB Aero. Report 902, 1960. (U)

442. Neal, B.: The Design and Testing of Three 6-Foot-Diameter Ducted Propellers With Their Rotational Axes Normal to the Free Stream. NRCC 8483, LR-426, 1965. (AD-464741) (U)

443. Neal, B.: The Static and Forward-Speed Testing of a Flapped Wing With Boundary-Layer Control for Use in Deflecting Propeller Slipstreams Downward for Vertical Take-off. Part 2. Tests at Incidence and Ground-Proximity Effects. NRC LR-383, 1963. (AD-417969) (U)

444. Neal, B., and Slack, W. E.: Static and Forward-Speed Tests on Several Six-Foot-Diameter Tractor and Pusher Ducted Propellers. NRC LR-445, 1965. (AD-482539) (U)

445. Newsom, W. A., Jr.: Aerodynamic Characteristics of a Four-Duct Tandem VTOL-Aircraft Configuration. NASA TN D-1481, 1963. (U)

446. Newsom, W. A., Jr.: Effect of Ground Proximity on the Aerodynamic Characteristics of a Four-Engine Vertical-Take-Off-and-Landing Transport Aircraft Model with Tilting Wing and Propellers. NACA TN 4124, 1957. (U)

447. Newsom, W. A., Jr.: Effect of Ground Proximity on Aerodynamic Characteristics of Two Horizontal-Attitude Jet Vertical-Take-Off-and-Landing Airplane Models. NACA RM L57G16, 1957. (U)

448. Newsom, W. A., Jr.: Effects of Ground Proximity on Aerodynamic Characteristics of Two Horizontal-Attitude Jet Vertical-Take-Off-and-Landing Airplane Models. NASA TN D-419, 1960. (AD-144809) (U)

449. Newsom, W. A., Jr.: Effect of Propeller Location and Flap Deflection on the Aerodynamic Characteristics of a Wing-Propeller Combination for Angles of Attack from 0° to 80°. NACA TN 3917, 1957. (U)

450. Newsom, W. A., Jr.: Experimental Investigation of the Lateral Trim of a Wing-Propeller Combination at Angles of Attack up to 90° with All Propellers Turning in the Same Direction. NACA TN 4190, 1958. (U)

451. Newsom, W. A., Jr.: Flight Investigation of the Longitudinal and Control Characteristics of a Four-Propeller Tilt-Wing VTOL Model with a Programmed Flap. NASA TN D-1390, 1962. (U)

452. Newsom, W. A., Jr., and Kirby, R. H.: Flight Investigation of Stability and Control Characteristics of a 1/9-Scale Model of a Four-Propeller Tilt-Wing V/STOL Transport. NASA TN D-2443, 1964. (U)

453. Newsom, W. A., Jr., and Freeman, D. C., Jr.: Flight Investigation of Stability and Control Characteristics of a 0.18-Scale Model of a Four-Duct Tandem V/STOL Transport. NASA TN D-3055, 1966. (U)

454. Newsom, W. A., Jr.: Force-Test Investigation of the Stability and Control Characteristics of a Four-Propeller Tilt-Wing VTOL Model with a Programmed Flap. NASA TN D-1389, 1962. (U)

455. Newsom, W. A., Jr., and Tosti, L. P.: Force-Test Investigation of the Stability and Control Characteristics of a 1/4-Scale Model of a Tilt-Wing Vertical-Take-Off-and-Landing Aircraft. NASA Memo 11-3-58L, 1958. (AD-208821) (U)

456. Newsom, W. A., Jr., and Tosti, L. P.: Slipstream Flow Around Several Tilt-Wing VTOL Aircraft Models Operating Near the Ground. NASA TN D-1382, 1962. (U)

457. Newsom, W. A., Jr.: Wind-Tunnel Investigation of a Deflected-Slipstream Cruise-Fan V/STOL Aircraft Wing. NASA TN D-4262, 1967. (N68-11036) (U)

458. Nicholson, R., and Lowry, R. B.: XV-4A VTOL-Research-Aircraft Program. USAAVLABS TR-66-45, 1966. (AD-635106) (U)

459. Norland, S. A.: An Investigation of the Lift Produced by a Fan in a Two-Dimensional Wing. American Helicopter Society Jour. Vol. 7, Oct. 1962. (A63-10240) (U)

460. Notess, C. B., and Whitcomb, D. W.: A Review and Study of Flying Qualities to Aid Design of a Variable Stability VTOL Aircraft. CAL-TE-1865-F-2, 1963. (AD-816032) (U)

461. Olcott, J. W.: A Survey of V/STOL Wind-Tunnel Wall Corrections and Test Techniques. Princeton Univ. Aerospace and Mechanical Science Report 725, 1965. (N66-30290) (U)

462. O'Malley, J. A., Jr.: Problems of Stability and Control for VTOL Aircraft. IAS Preprint 729, 1957. (U)

463. Ordway, D. E., Sluyter, M. M., and Sonnerup, B. O. U.: Three-Dimensional Theory of Ducted Propellers. Therm Advanced Research TAR-TR-602, 1960. (AD-245846) (U)

464. Otis, J. H., Jr.: Induced Interference Effects on a Four-Jet VTOL Configuration with Various Wing Planforms in the Transition Speed Range. NASA TN D-1400, 1962. (N62-15319) (U)

465. Page, V. R., Dickinson, S. O., and Deckert, W. H.: Large-Scale Wind-Tunnel Tests of a Deflected-Slipstream STOL Model With Wings of Various Aspect Ratio. NASA TN D-4448, 1968. (N68-18771) (U)

466. Page, V. R., and Soderman, P. T.: Wing Surface Pressure Data From Large-Scale Wind-Tunnel Tests of a Propeller-Driven STOL Model. NASA TM X-1527, 1968. (N68-19065) (U)

467. Parlett, L. P.: Aerodynamic Characteristics of a Small-Scale Shrouded Propeller at Angles of Attack from 0^{o} to 90^{o} NACA TN 3547, 1955. (U)

468. Parlett, L. P.: Experimental Investigation of Some of the Parameters Related to the Stability and Control of Aerial Vehicles Supported by Ducted Fans. NASA TN D-616, 1960. (U)

469. Parlett, L. P.: Stability and Control Characteristics of a Model of an Aerial Vehicle Supported by Four Ducted Fans. NASA TN D-937, 1961. (U)

470. Parlett, L. P.: Stability and Control Characteristics of a Small-Scale Model of an Aerial Vehicle Supported by Two Ducted Fans. NASA TN D-920, 1961. (AD-260541) (U)

471. Parlett, L. P., and Kirby, R. H.: Test Techniques Used by NASA for Investigating Dynamic Stability Characteristics of V/STOL Models. AIAA, 1964. (A64-14526) (U)

472. Parlett, L. P.: Wind-Tunnel Investigation of a Small-Scale Model of an Aerial Vehicle Supported by Ducted Fans. NASA TN D-377, 1960. (U)

473. Parlett, L. P., and Shivers, J. P.: Wind-Tunnel Investigation of an STOL Aircraft Configuration Equipped With an External-Flow Jet Flap. NASA TN D-5364, 1969. (N69-33275) (U)

474. Patierno, J., and Isca, J. A.: Instrument Flight-Simulator Study of the VTOL Controllability Control-Power Relationship. Aerospace Eng., Vol. 21, 1962. (U)

475. Paxhia, V. B., and Sing, E. Y.: Design and Development of a Dual-Tandem Ducted-Propeller VTOL Aircraft. IAS Paper 63-30, 1963. (U)

476. Payne, H. E., III.: Application of Small-Scale Propeller Test Data to V/STOL Aircraft Design. Princeton Univ. Report 503, 1961. (AD-270110) (U)

477. Payne, H. E., III.: Propeller Effects on the Stability and Control of VTOL Aircraft. Aerospace Eng., March 1960. (U)

478. Payne, H. E., III, and Cromwell, C. H., III: A Stability Analysis of Tilt-Wing Aircraft (Experimental). Princeton Univ. Report 478, 1960. (U)

479. Peake, D. J.: The Pressures on a Surface Surrounding a Jet Issuing Normal to a Mainstream. NRL Report LR-410, 1964. (AD-463295) (U)

480. Pegg, R. J., Kelley, H. L., and Reeder, J. P.: Flight Investigation of VZ-2 Tilt-Wing Aircraft With Full-Span Flap. NASA TN D-2680, 1965. (N65-18211) (U)

481. Pegg, R. J.: Flight-Test Investigation of Ailerons as a Source of Yaw Control on the VZ-2 Tilt-Wing Aircraft. NASA TN D-1375, 1962. (U)

482. Pegg, R. J.: Summary of Flight-Test Results of the VZ-2 Tilt-Wing Aircraft. NASA TN D-989, 1962. (U)

483. Perry, D. H., and Chinn, H. W.: A Preliminary Flight-Simulation Study of Jet-Borne VTOL Aircraft Handling Qualities. ARC CP-902, 1965. (AD-809892) (N67-24038) (U)

484. Peterson, J. M.: Lift-Fan V/STOL Concept for Future Applications. Jour. of Aircraft, Mar-Apr. 1965. (U)

485. Pitkin, M.: Free-Flight-Tunnel Investigation of the Effect of Mode of Propeller Rotation Upon the Lateral-Stability Characteristics of a Twin-Engine Airplane Model With Single Vertical Tails of Different Size. NACA WR L-354, 1943. (U)

486. Pivko, S.: The Annular Aerofoil with Central Body and Propeller. Aircraft Eng., Vol. 29, No. 345, 1957. (U)

487. Pivko, S.: Predicting the Performance of Jet-Flap Configurations. Semiempirical Theory and Comparison With Available Test Results. Aircraft Engineering, Jan. 1962. (U)

488. Plaskowski, Z.: Annular Airfoils. Report given at 4th International Astronautical Congress, Zurich, Switzerland, 1953. (U)

489. Platt, R. J., Jr.: Static Tests of Four Two-Blade NACA Propellers Differing in Camber and Solidity. NACA RM L8H25a, 1948. (U)

490. Platt, R. J., Jr.: Static Tests of a Shrouded and an Unshrouded Propeller. NACA RM L7H25, 1948. (U)

491. Pokorny, V.: The Effects of Nonlinearities in Lift and Pitching-Moment Curves on Longitudinal Motion of an Aircraft. 'Zprava Vzlu, Dec. 1964. (A66-26285) (U)

492. Pruyn, R. A.: Effects of Airframe Geometry on Downwash Problems of Tandem Ducted-Propeller VTOL Aircraft. Kellett Aircraft Corporation Report 179T80-6, 1964. (AD-452792) (U)

493. Przedpelski, Z. J.: Results of Wind-Tunnel Tests of a Full-Scale Fuselage-Mounted Tip-Turbine-Driven Lift Fan, Vol. 3. General Electric Company, TREC TR 61-15, 1962. (AD-275711) (N62-12414) (U)

494. Putman, W. F.: An Experimental Investigation of Ground Effect on a Four-Propeller Tilt-Wing V/STOL Model. USAAVLABS TR-68-45, 1968. (AD-673824) (U)

495. Putman, W. F., Traybar, J. J., et al: An Investigation of the Dynamic Stability Characteristics of a Quad Configuration, Ducted-Propeller V/STOL Model – Volume 1, Phase I; Hovering. Princeton Univ. Report 835, USAAVLABS TR-68-49A, 1968. (AD-679134) (N69-17670) (U)

496. Putman, W. F., and Traybar, J. J.: An Investigation of the Dynamic Stability Characteristics of a Quad Configuration, Ducted-Propeller V/STOL Model – Volume 2, Phase II, Longitudinal Dynamics at High Duct Incidence Data Report. Princeton Univ. Report 836, USAAVLABS TR-68-49B, 1968. (AD-676861) (N69-13715) (U)

497. Putman, W. F., Traybar, J. J., et al: An Investigation of the Dynamic Stability Characteristics of a Quad Configuration, Ducted-Propeller V/STOL Model – Volume 3, Final Data Report, Phase 3, Lateral/Directional Dynamics at High Duct Incidences. USAAVLABS TR-68-49C, 1968. (AD-682749) (N69-25070) (U)

498. Putman, W. F.: An Investigation of the Lateral-Directional Dynamic Stability Characteristics of a Tilt-Wing V/STOL Transport Model in Simulated Low-Speed Descending Flight. USAAVLABS TR-69-46, 1969. (AD-859807) (U)

499. Putman, W. F.: Results of Experiments on a Tilt-Wing VTOL Aircraft Using the Princeton University Forward Flight Facility. Princeton Univ. Rept. 542, 1961. (AD-270217) (U)

500. Quigley, H. C., Innis, R. C., and Holzhauser, C. A.: A Flight Investigation of the Performance, Handling Qualities, and Operational Characteristics of a Deflected-Slipstream STOL Transport Airplane Having Four Interconnected Propellers. NASA TN D-2231, 1964. (U)

501. Quigley, H. C., Innis, R. C., et al: A Flight and Simulator Study of Directional Augmentation Criteria for a Four-Propellered STOL Airplane. NASA TN D-3909, 1967. (N67-24619) (U)

502. Quigley, H. C., and Innis, R. C.: Handling Qualities and Operational Problems of a Large Four-Propeller STOL Transport Airplane. NASA TN D-1647, 1963. (N63-12247) (U)

503. Quigley, H. C., and Lawson, H. F., Jr.: Simulator Study of the Lateral-Directional Handling Qualities of a Large Four-Propellered STOL Transport Airplane. NASA TN D-1773, 1963. (U)

504. Ramnath, R. V.: Transition Dynamics of VTOL Aircraft. AIAA Paper 69-130, 1969. (A69-18157) (U)

505. Rampy, J. M.: Important V/STOL Aircraft Stability Derivatives in Hover and Transition. AFFTC-TR-66-29, 1966. (AD-641371) (N67-17673) (U)

506. Reeder, J. P.: Handling-Qualities Experience with Several VTOL Research Aircraft. NASA TN D-735, 1961. (U)

507. Reichert, J. B., and Ulyate, J. R.: Final Report Doak Model 16. Doak Aircraft Company Rept. DS-215, 1960. (U)

508. Rethorst, S., Royce, W. W., et al: Development of Methods for Predicting V/STOL Aircraft Characteristics. VRC Rept 5, 1961. (AD-244736) (U)

509. Rethorst, S., Royce, W. W., and Wu, Y.: Lift Characteristics of Wings Extended Through Propeller Slipstreams. VRC Rept 1., 1958. (PB-146592) (U)

510. Rethorst, S., and Royce, W. W.: Lifting Systems for VTOL Vehicles. VRC Rept. 2; IAS Paper 59-123, 1959. (U)

511. Ribner, H. S.: On the Lift and Induced Drag Associated with Large Downwash Angles. Univ. of Toronto, Institute of Aerophysics, TN 19, 1958. (U)

512. Ribner, H. S.: Propellers in Yaw. NACA TR 820, 1945. (U)

513. Ribner, H. S.: The Ring Airfoil in Non-Axial Flow. Jour. Aero. Sci., Vol. 14, No. 9, 1947. (U)

514. Ribner, H. S.: Theory of Wings in Slipstreams. Univ. of Toronto, Institute of Aerophysics, Rept. 60, 1959. (U)

515. Ricard G., Czinczenheim, J., et al: The Breguet Family of STOL Aircraft. SAE Preprint 428A, 1961. (U)

516. Riebe, J. M.: A Correlation of Two-Dimensional Data on Lift Coefficient Available with Blowing-, Suction-, and Plain-Flap High-Lift Devices. NACA RM L55D29a, 1955. (U)

517. Robertson, J. L.: Exploratory Full-Scale Ground and Flight-Test Evaluation of the Robertson Ultra-Low-Speed Flight-Control System. Skycraft Inc. TCREC TR 62-23, 1962. (AD-282123) (U)

518. Robinson, D. W., Jr.: Design Consideration for a Propeller-Driven VTOL. Jour. of American Helicopter Soc., January 1959. (U)

519. Rogallo, F. M., and Swanson, R. S.: Wind-Tunnel Tests of a Twin-Engine Model to Determine the Effect of Propeller Rotation of the Static-Stability Characteristics. NACA WR L-295, 1943. (U)

520. Rolls, L. S.: Characteristics of a Deflected-Jet VTOL Aircraft. NASA Conference on V/STOL Aircraft, 1960. (U)

521. Rolls, L. S., Drinkwater, F. J., III, and Innis, R. C.: Effects of Lateral-Control Characteristics on Hovering a Jet-Lift VTOL Aircraft. NASA TN D-2701, 1965. (U)

522. Rolls, L. S., and Drinkwater, F. J., III.: A Flight Determination of the Attitude Control Power and Damping Requirements of a Visual Hovering Task in the Variable Stability and Control X-14A Research Vehicle. NASA TN D-1328, 1962. (U)

523. Rosenthal, G., et al: Aircraft Preliminary-Design Report V/STOL-Jet-Operations Research-Airplane Design Study, Part 2. NASA CR 66422, 1967. (N67-33826) (U)

524. Ross, A. J.: The Theoretical Evaluation of the Downwash Behind Jet-Flapped Wings. ARC R&M 3119, 1961. (U)

525. Rubbert, P. E., Saaris, G. R., et al: A General Method for Determining the Aerodynamic Characteristics of Fan-in-Wing Configurations, Volume I, Theory and Application. USAAVLABS TR-67-61A, Vol 1, 1967. (AD-667980) (U)

526. Rubbert, P. E., and Saaris, G. R.: A General Three-Dimensional Potential-Flow Method Applied to V/STOL Aerodynamics. SAE Paper 680304, 1968. (A68-31326) (U)

527. Sacks, A. H., and Burnell, J. A.: Ducted Propellers – A Critical Review of the State of the Art. Progress in Aeronautical Sciences, Vol 3, Pergamon Press, New York, 1962. (U)

528. Sadoff, M., McFadden, N. M., and Heinle, D. R.: A Study of Longitudinal Control Problems at Low and Negative Damping and Stability with Emphasis on Effects of Motion Cues. NASA TN D-348, 1961. (U)

529. Salmirs, S., and Tapscott, R. J.: The Effects of Various Combinations of Damping and Control Power on Helicopter Handling Qualities During Both Instrument and Visual Flight. NASA TN D-58, 1959. (U)

530. Saunders, G. H.: Development of a Flying-Qualities Specification for Military V/STOL Aircraft. American Helicopter Society Paper 363, 1969. (A69-33520) (U)

531. Schade, R. O., and Kirby, R. H.: Effect of Wing Stalling in Transition on a 1/4-Scale Model of the VZ-2 Aircraft. NASA TN D-2381, 1964. (N64-26840) (U)

532. Schade, R. O.: Ground Interference Effects. NASA TN D-727, 1961. (AD-253626) (U)

533. Schlichting, H., et al: Discussion on Aerodynamic Aspects of V/STOL Aeroplanes. AGARD DFL-151, Report 61/22, 1961. (AD-852414) (U)

534. Scholes, J. F., and Patterson, G. N.: On Wind-Tunnel Tests on Ducted Contra-Rotating Fans. Australian Council for Aeronautics Report -14, 1944. (U)

535. Schuck, G. I.: An Analysis of Results from Army-Sponsored VTOL Research Aircraft. TRECOM TR-61-3, 1961. (AD-250924) (U)

536. Schuler, J. M., Kroll, J., Jr., and Key, D. L.: VTOL Flying-Qualities and the Flight-Research Use of VTOL Variable-Stability Airplanes. AIAA Paper 65-706, 1965. (U)

537. Schulz, R. J.: Simulation of Jet Entrainment in a Potential Field. AEDC-TR-67-217, 1967. (AD-822341) (U)

538. Schwantes, E.: Survey on the Ground Effect of V/STOL Aircraft With Jet Propulsion. DLR-Mitt-68-28, 1968. (N69-27640) (U)

539. Schweizer, G., Seelmann, H., and Weischedel, H.: Control of VTOL Aircraft in Hovering Flight. Presented at Wiss. Ges. Fur Luft-und Raumfahrt Meeting, Munich, 1963. (N64-13925) (U)

540. Schweizer, G.: Pilot Behavior in VTOL Aircraft. AGARD Report 521, 1965. (N67-13399) (U)

541. Seckel, E., Traybar, J. J., and Miller, G. E.: Longitudinal Handling Qualities for Hovering. Princeton Univ. R-594, 1961. (N62-12215) (U)

542. Seibold, W.: The Mechanics of Flow on Annular Wings. Interavia, No. 1, 1955. (U)

543. Shanks, R. E., and Smith, C. C., Jr.: Low-Speed Measurements of Static and Oscillatory Lateral Stability Derivatives of 1/5-Scale Model of a Jet-Powered Vertical-Attitude VTOL Research Airplane. NASA TN D-433, 1960. (U)

544. Shen, Y. C.: Theoretical Analysis of Jet Ground-Plane Interaction. IAS Paper 62-144, 1962. (N62-13384) (U)

545. Shenkman, A. M.: Generalized Performance of Conventional Propellers for VTOL/STOL Aircraft. Hamilton Standard Division, United Aircraft Corporation Report HS-1829, 1958. (U)

546. Shumpert, P. K., and Tibbetts, J. G.: Model Tests of Jet-Induced-Lift Effects on a VTOL Aircraft in Hover. NASA CR-1297, 1969. (N69-21477) (U)

547. Sinacori, J. B., and Lange, A.: Theoretical Investigation of Ducted Propeller Aerodynamics. Vol. IV. Republican Aviation TCREC TR 61-120, 1961. (AD-266422) (U)

548. Sinacori, J. B.: V/STOL Ground-Based Simulation Techniques. USAAVLABS TR-67-55, 1967. (N68-20774) (U)

549. Skelton, G. B.: Investigation of the Effects of Gusts on V/STOL Craft in Transition and Hover. AFFDL TR-68-85, 1968. (AD-679593) (N69-17823) (U)

550. Skifstad, J. G.: Aerodynamics of Jets Pertinent to VTOL Aircraft. AFAPL TR-69-28, 1969. (AD-853494) (U)

551. Sleeman, W. C., Jr., and Linsley, E. L.: Low-Speed Wind-Tunnel Investigation of the Effects of Propeller Operation at High Thrust on the Longitudinal Stability and Trim of a Twin-Engine Airplane Configuration. NACA RM L52D04, 1952. (U)

552. Smelt, R., and Davis, H.: Estimation of Increase in Lift Due to Slipstream. ARC R&M 1788, 1937. (U)

553. Smith, C. C., Jr., and Parlett, L. P.: Flight Tests of a 0.13-Scale Model of a Vectored-Thrust Jet VTOL Transport Airplane. NASA TN D-2285, 1964. (U)

554. Smith, C. C., Jr.: Hovering and Transition Flight Tests of a 1/5-Scale Model of a Jet-Powered Vertical-Attitude VTOL Research Airplane. NASA Memo 10-27-58L. 1958. (U)

555. Smith, C. C., Jr.: Hovering and Transition Flight Tests of a 1/5-Scale Model of a Jet-Powered Vertical-Attitude VTOL Research Airplane. NASA TN D-404, 1961. (U)

556. Smith, C. C., Jr.: Wind-Tunnel Investigation of a Small-Scale Model of an Aerial Vehicle Supported by Tilting Ducted Fans. NASA TN D-409, 1960. (U)

557. Smith, R. E.: A Comparison of V/STOL Aircraft Directional-Handling-Qualities Criteria for Visual and Instrument Flight Using an Airborne Simulator. NRC LR-465, 1966. (U)

558. Solarski, A. H.: Survey and Study of VTOL-STOL Stability and Control Characteristics. WADC TR-59-357, 1959. (AD-314894) (C) Title Unclassified

559. Spence, D. A.: The Lift Coefficient of a Thin, Jet-Flapped Wing. I. Royal Soc. of London Proc. (A) Vol. 238, Dec-Jan 1956-1957. (U)

560. Spence, D. A.: The Lift Coefficient of a Thin, Jet-Flapped Wing. II. A Solution of the Integro-Differential Equation for the Slope of the Jet. Royal Soc. of London Proc. (A) Vol. 261, 1961. (U)

561. Speth, R. F.: Aerodynamic-Test-Data Report for Ground-Effect Model, X-22A. Bell Aerosystems Corp. Rept. 2127-921004, 1963. (AD-472814) (U)

562. Spreemann, K. P.: Effectiveness of Boundary-Layer Control Obtained by Blowing Over a Plain Rear Flap in Combination with a Forward Slotted Flap, in Deflecting a Slipstream Downward for Vertical Take-off. NACA TN 4200, 1958. (U)

563. Spreemann, K. P., and Sherman, I. R.: Effects of Ground Proximity on the Thrust of a Simple Downward-Directed Jet Beneath a Flat Surface. NACA TN 4407, 1958. (U)

564. Spreemann, K. P.: Free-Stream Interference Effects on Effectiveness of Control Jets Near the Wing Tip of a VTOL Aircraft Model. NASA TN D-4084, 1967. (U)

565. Spreemann, K. P.: Induced Interference Effects on Jet and Buried Fan VTOL Configurations in Transition. NASA TN D-731, 1961. (AD-253303) (U)

566. Spreemann, K. P., and Davenport, E. E.: Investigation of the Aerodynamic Characteristics of a Combination Jet-Flap and a Deflected-Slipstream Configuration at Zero and Low Forward Speeds. NASA TN D-363, 1960. (U)

567. Spreemann, K. P., and Kuhn, R. E.: Investigation of the Effectiveness of Boundary-Layer Control by Blowing Over a Combination of Sliding and Plain Flaps in Deflecting a Propeller Slipstream Downward for Vertical Take-off. NACA TN 3904, 1956. (U)

568. Spreemann, K. P.: Investigation of the Effects of Propeller Diameter on the Ability of Flapped Wing With and Without Boundary-Layer Control, to Deflect a Propeller Slipstream Downward for Vertical Take-off. NACA TN 4181, 1957. (U)

569. Spreemann, K. P.: Investigation of Interference of a Deflected Jet with Free Stream and Ground on Aerodynamic Characteristics of a Semispan Delta-Wing VTOL Model. NASA TN D-915, 1961. (AD-261369) N62-71489) (U)

570. Spreemann, K. P.: Investigations of a Semispan Tilting-Propeller Configuration and Effects of Ratio of Wing Chord to Propeller Diameter on Several Small-Chord Tilting-Wing Configurations at Transition Speeds. NASA TN D-1815, 1963. (U)

571. Spreemann, K. P.: Wind-Tunnel Investigation of Lateral Aerodynamic Characteristics of a Powered 4-Duct-Propeller VTOL Model in Transition. NASA TN D-4343, 1968. (N68-17023) (U)

572. Spreemann, K. P.: Wind-Tunnel Investigation of Longitudinal Aerodynamic Characteristics of a Powered 4-Duct-Propeller VTOL Model in Transition. NASA TN D-3192, 1966. (U)

573. Stalter, J. L., and Wattson, R. K.: Circulation-Control Research Wind-Tunnel Tests of a Powered-Blowing Type, Circulation-Control Research Airplane Model. II: Effect of Power on the Aerodynamic Characteristics of a Circulation-Control Research Model. University of Wichita, Dept. Eng. Res. Report 187-2, 1957. (U)

574. Stancil, R. T., and Mertaugh, L. J., Jr.: Analysis of a Low-Speed Wind-Tunnel Test of a High-Mass-Rate Vectored-Propulsion Flow Model. LTV Report No. 2-53310/4R-2166, 1965. (AD-613198) (U)

575. Stapleford, R. L., Wolkovitch, J., et al: An Analytical Study of V/STOL Handling Qualities in Hover and Transition. AFFDL-TR-65-73, 1965. (AD-625599) (N66-16671) (U)

576. Staufenbiel, R., and Girlatschek, S.: Automatic Stabilization and Safety of VTOL Aircraft. Wissenschaftliche Gesellschaft Fur Luftfahrt Paper 31, 1962. (U)

577. Steils, W. T., Jr.: V/STOL Hover-Control System Analysis. Jour. of Aircraft, Vol. 3, 1966. (A66-40985) (U)

578. Stenning, T. A., and Dolan, J. A.: Lateral/Directional Simulation of the CL-84 V/STOL Aircraft in the Transition Regime. AIAA Paper 64-806, 1964. (A64-27095) (U)

579. Stepniewski, W. Z., and Dancik, P. J.: Flight-Testing Experiments with the Tilt-Wing Aircraft. Aerospace Eng., February, 1959, IAS Preprint 59-8, 1959. (U)

580. Stockman, N. O., and Lieblein, S.: Theoretical Analysis of Flow in VTOL Lift-Fan Inlets Without Crossflow. NASA TN D-5065, 1969. (N69-17831) (U)

581. Stouffer, C. G.: Analysis of Wind-Tunnel Test Results of the Fairchild M-243 Jet-Flap Model. Fairchild Aircraft and Missiles Div., R243-006, 1960. (U)

582. Strand, T.: Inviscid-Incompressible Flow Theory of Normal and Slightly Oblique Impingement of a Static Round Jet on the Ground. AROD-5274-3, 1967. (AD-648500) (N67-26496) (U)

583. Streiff, H. G.: Study, Survey of Helicopter and V/STOL Aircraft-Simulator Trainer Dynamic Response; Vol. II — Dynamic-Response Criteria for V/STOL Aircraft Trainers. Navy, Naval Training Device Center Report 1753-2, 1967. (AD-668006) (U)

584. Swaim, R. L., and Connors, A. J.: Effects of Gust-Velocity Spatial Distributions on Lateral-Directional Response of a VTOL Aircraft. AFFDL-TR-67-93, 1967. (AD-657321) (U)

585. Swain, W. N.: Wind-Tunnel Test of a 0.16-Scale XV-4B Model in the NASA Langley 17-Foot Low-Speed Wind Tunnel and the 7 x 10-Foot High-Speed Wind Tunnel. Lockheed-Georgia Report ER 9061, 1968. (U)

586. Sweeney, T. E. (compiler): A Summary of the Princeton University — U.S. Army ALART (Army Low-Speed Aeronautical Research Task) Program. Princeton University Final Report 566, 1962. (U)

587. Tapscott, R. J.: Criteria for Control and Response Characteristics of Helicopters and VTOL Aircraft in Hovering and Low-Speed Flight. IAS Preprint 60-51, 1960. (U)

588. Tapscott, R. J.: Criteria for Primary Handling-Qualities Characteristics of VTOL Aircraft in Hovering and Low-Speed Flight. NASA Conference on V/STOL Aircraft, 1960. (U)

589. Tapscott, R. J., and Kelley, H. L: A Flight Study of the Conversion Maneuvers of a Tilt-Duct VTOL Aircraft. NASA TN D-372 1960. (AD-246130) (U)

590. Taylor, A. S.: A Theoretical Investigation of the Longitudinal Stability, Control, and Response Characteristics of Jet-Flap Aircraft. Parts I and II. ARC R&M 3272, 1960. (U)

591. Taylor, R. T.: Wind-Tunnel Investigation of Effects of Ratio of Wing Chord to Propeller Diameter with Addition of Slats on the Aerodynamic Characteristics of Tilt-Wing VTOL Configurations in the Transition Speed Range. NASA TN D-17, 1959. (U)

592. Templin, R. J.: Recent Trends in Low-Speed Wind-Tunnel Design and Techniques. ICSA, New York Academy of Sciences, Annals, Vol. 154, 1968. (A69-15573) (U)

593. Theisen, J. G.: V/STOL Stability and Control in Turbulence. American Meterological Society, 1968. (A68-35131) (U)

594. Theodorsen, T.: Theoretical Investigation of Ducted-Propeller Aerodynamics, Vol I. Dept. National Defense, DDD Technical Library Account 71999, 1960. (AD-240956) (U)

595. Theodorsen, T.: Theoretical Investigation of Ducted-Propeller Aerodynamics, Vol II. Dept. National Defense, DDD Technical Library Account 72000, 1960. (AD-240849) (U)

596. Theodorsen, T., and Nomicos, G.: Theoretical Investigation of Ducted-Propeller Aerodynamics, Vol III. Republic Aviation TCREC TR 61-119, 1961. (AD-266411) (U)

597. Thomas, F.: Investigation of the Increase of Lift of Lifting Wings by Means of Boundary-Layer Control by Blowing. Z. Flugwiss. (10), Heft 2, 1962. (U)

598. Thomas, L. P.: A Flight Study of the Conversion Maneuver of a Tilt-Wing VTOL Aircraft. NASA TN D-153, 1959. (U)

599. Thompson, J. F., Jr.: An Experimental Investigation of the Effect of Forward and Rearward Motion on the Thrust of a Shrouded Propeller. USAAVLABS TR-66-65, Miss. State University RR-65, 1966. (U)

600. Tosti, L. P.: Aerodynamic Characteristics of a 1/4-Scale Model of a Tilt-Wing VTOL Aircraft at High Angles of Wing Incidence. NASA TN D-390, 1960. (AD-241926) (U)

601. Tosti, L. P.: Flight Investigation of Stability and Control Characteristics of a 1/8-Scale Model of a Tilt-Wing Vertical-Take-Off-and-Landing Airplane. NASA TN D-45, 1960. (U)

602. Tosti, L. P.: Flight Investigation of the Stability and Control Characteristics of a 1/4-Scale Model of a Tilt-Wing Vertical-Take-Off-and-Landing Aircraft. NASA Memo 11-4-58L, 1959. (U)

603. Tosti, L. P.: Force-Test Investigation of the Stability and Control Characteristics of a 1/8-Scale Model of a Tilt-Wing Vertical-Take-Off-and-Landing Airplane. NASA TN D-44, 1960. (U)

604. Tosti, L. P., and Davenport, E. E.: Hovering Flight Tests of a Four-Engine Transport Vertical-Take-Off Airplane Model Utilizing a Large Flap and Extensible Vanes for Redirecting the Propeller Slipstream. NACA TN 3440, 1955. (U)

605. Tosti, L. P.: Longitudinal Stability and Control of a Tilt-Wing VTOL Aircraft Model with Rigid and Flapping Propeller Blades. NASA TN D-1365, 1962. (U)

606. Tosti, L. P.: Rapid-Transition Tests of a 1/4-Scale Model of the VZ-2 Tilt-Wing Aircraft. NASA TN D-946, 1961. (U)

607. Tosti, L. P.: Transition-Flight Investigation of a Four-Engine-Transport Vertical-Take-Off Airplane Model Utilizing a Large Flap and Extensible Vanes for Redirecting the Propeller Slipstream. NASA TN 4131, 1957. (U)

608. Traybar, J. J.: Aerodynamic Characteristics of a General Tilt-Wing/Propeller Model Tested at Slow Speeds and High Angles of Attack. USAAVLABS TR-67-79, 1968. (AD-671666) (N68-33646) (U)

609. Trebble, W. J. G., and Williams, J.: Exploratory Wind-Tunnel Investigations on a Bluff Body Containing a Lifting Fan. ARC CP-597, 1962. (N62-15845) (U)

610. Trebble, W. J. G.: Low-Speed Wind-Tunnel Investigation of the Roll Stability of a 1/5-Scale Model of the Short SC-1 at Large Sideslip. ARC CP-994, 1967. (AD-837313) (N68-13424) (U)

611. Trebble, W. J. G.: Techniques for the Aerodynamic Testing of V/STOL Models. RAE TM-Aero 1080, 1968. (AD-856976) (U)

612. Trebble, W. J. G.: Wind-Tunnel Experiments on a Simple Lifting-Jet Body with and Without Wings. ARC CP-718, 1964. (N65-17894) (U)

613. True, H. C.: Advanced Lift-Fan System (LFX) Study Continuation. USAAVLABS TR-67-45, GE R-66-RPD-342, 1967. (U)

614. Turner, H. L., and Drinkwater, F. J., III: Longitudinal-Trim Characteristics of a Deflected-Slipstream V/STOL Aircraft During Level Flight at Transition Flight Speeds. NASA TN D-1430, 1962. (U)

615. Turner, H. L., and Drinkwater, F. J., III: Some Flight Characteristics of a Deflected-Slipstream V/STOL Aircraft. NASA TN D-1891, 1963. (N63-18663) (U)

616. Turner, R. C., and Sparkes, D. W.: An Investigation Into the Effect of Ground Proximity on the Performance of Lifting Fans. National Gas Turbine Establishment Memo M 353, 1962. (AD-329625) (C) Title Unclassified

617. Turner, T. R.: Ground Influence on a Model Airfoil With a Jet-Augmented Flap as Determined by Two Techniques. NASA TN D-658, 1961. (U)

618. Uberti, B. J., and Reichert, J. B.: Design Philosophy and Test Experience of a VTOL Aircraft. IAS Paper 59-122, 1959. (U)

619. Vanderlip, E. G., and Schneider, J. J.: Design and Development of the Shaft-Driven Fan-in-Wing VTOL Aircraft. Annals of the N.Y. Academy of Sciences, Vol 107, Art. I, 1963. (U)

620. Vidal, R. J., Curtis, J. T., and Hilton, J. H.: The Influence of Two-Dimensional Stream Shear on Airfoil Maximum Lift. CAL Rept A1-1190-A-7, 1961. (U)

621. Vidal, R. J.: A Theory of Wing-Propulsion Combination in Slow Flight. CAL Rept A1-1190-A-1, 1959. (U)

622. Vidal, R. J., Hilton, J. H., and Curtis, J. T.: The Two-Dimensional Effects of Slipstream Shear on Airfoil Characteristics. CAL Rept A1-1109-A-5 1960. (AD-246522) (U)

623. Vinje, E. W., and Miller, D. P.: Analytical and Flight-Simulator Studies to Develop Design Criteria for VTOL Aircraft Control Systems. AFFDL TR-68-165, 1969. (U)

624. Vogler, R. D.: Ground Effects on Single- and Multiple-Jet VTOL Models at Transition Speeds over Stationary and Moving Ground Planes. NASA TN D-3213, 1966. (U)

625. Vogler, R. D.: Interference Effects of Single- and Multiple-Round or Slotted Jets on a VTOL Model in Transition. NASA TN D-2380, 1964. (N64-26628) (U)

626. Vogler, R. D., and Kuhn, R. E.: Longitudinal and Lateral Stability Characteristics of Two Four-Jet VTOL Models in the Transition Speed Range. NASA TM X-1092, 1965. (N66-22925) (U)

627. Vogler, R. D.: Surface Pressure Distributions Induced on a Flat Plate by a Cold-Air Jet Issuing Perpendicularly from the Plate and Normal to a Low-Speed Free-Stream Flow. NASA TN D-1629, 1963. (U)

628. Vogler, R. D., and Turner, T.R.: Wind-Tunnel Investigation at Low Speeds to Determine Flow-Field Characteristics and Ground Influence on a Model with Jet-Augmented Flaps. NACA TN 4116, 1957. (U)

629. Von Glahn, U. H.: Exploratory Study of Ground-Proximity Effects on Thrust of Annular and Circular Nozzles. NACA TN 3982, 1957. (U)

630. Vrana, J. C.: On Gyroscopic Inherent Stability of VTOL Aircraft Near the Hover Condition. Canadian Aeronautics and Space Journal, Vol 9, 1963. (U)

631. Wainauski, H. S.: Variable-Geometry Shrouded-Propeller Test Program. Vol I. Data Analysis. HSER-5062-Vol 1, 1968. (AD-835089L) (U)

632. Ward, J. P., and Jones, G. E.: Lessons Learned from the XC-142 Program. Presented at AF V/STOL Technology and Planning Conf, September 1969. (U)

633. Wardlow, R. L., and Templin, R. J.: Some Aerodynamic Characteristics of Wing-Mounted Lifting Fans for VTOL Applications. Canadian Aeronautical Institute Preprint 10/12, 1958. (U)

634. Wardlow, R. L., and McEachern, N. V.: Some Aerodynamic Characteristics of Wing-Mounted Lifting Fans for VTOL Applications. Canadian Aero. Journal March 1959. (U)

635. Wardlow, R. L., and McEachern, N. V.: A Wing-Submerged Lifting Fan: Wind-Tunnel Investigations and Analysis of Transition Performance. NRC LR-243, 1959. (AD-225858) (U)

636. Wattson, R. K., Jr.: Note on Blade-Tip Effects in Shrouded Propellers. University of Wichita Dept. of Eng. Research Report 333, 1959. (U)

637. Weiberg, J. A., and Page, V. R.: Large-Scale Wind-Tunnel Tests of an Airplane Model with an Unswept, Aspect-Ratio-10 Wing, Four Propellers, and Blowing Flaps. NASA TN D-25, 1959. (U)

638. Weiberg, J. A., Griffin, R. M., Jr., and Florman, G. L.: Large-Scale Wind-Tunnel Tests of an Airplane Model with an Unswept, Aspect-Ratio-10 Wing, Two Propellers, and Area-Suction Flaps. NACA TN 4365, 1958. (U)

639. Weiberg, J. A., and Holzhauser, C. A.: Large-Scale Wind-Tunnel Tests of an Airplane Model with an Unswept, Tilt-Wing of Aspect Ratio 5.5 and with Four Propellers and Blowing Flaps. NASA TN D-1034, 1961. (AD-257858) (U)

640. Weiberg, J. A., and Giulianetti, D. J.: Large-Scale Wind-Tunnel Tests of an Airplane Model With an Unswept Tilt Wing of Aspect Ratio of 5.5, and With Various Stall-Control Devices. NASA TN D-2133, 1964. (N64-14728) (U)

641. Weiberg, J. A., and Holzhauser, C. A.: STOL Characteristics of a Propeller-Driven, Aspect-Ratio-10, Straight-Wing Airplane with Boundary-Layer-Control Flaps, as Estimated from Large-Scale Wind-Tunnel Tests NASA TN D-1032, 1961. (AD-258268) (U)

642. Weiberg, J. A., and Giulianetti, D. J.: Wind-Tunnel Investigation of a Tilt-Wing VTOL Airplane With Articulated Rotors. NASA TN D-2538, 1965. (U)

643. Weitz, P.: A Qualitative Discussion of the Stability and Control of VTOL Aircraft During Hover (out of ground effect), and Transition. Naval Postgraduate School Report, 1964. (AD-622205) (N66-12060) (U)

644. White, H. E.: Wind-Tunnel Tests of an Aerodynamically Controlled Tilting-Wing VTOL Configuration. DTMB Aero-1057, 1963. (AD-420239) (N63-22769) (U)

645. Whittley, D. C.: The Augmentor-Wing Research Program; Past, Present, and Future. AIAA Paper 67-0741, 1967. (U)

646. Wickens, R. H.: Aerodynamic Force and Moment Characteristics of a Four-Bladed Propeller Yawed Through 120 Degrees. NRC LR-454, 1966. (U)

647. Wickens, R. H., and Gartshore, I. S.: Observations on the Flow Near a Lifting Propeller. NRC 6705, LR-325, 1961. (U)

648. Williams, J., and Wood, M. N.: Aerodynamic Interference Effects With Jet-Lift Schemes on V/STOL Aircraft at Forward Speeds. RAE TM Aero 912, 1965. (U)

649. Williams, J., and Wood, M. N.: Aerodynamic-Interference Effects with Jet-Lift V/STOL Aircraft under Static and Forward-Speed Conditions. RAE TR-66403, 1966. (AD-813258) (X67-19040) (U)

650. Williams, J., Butler, S. F. J., and Wood, M. N.: The Aerodynamics of Jet Flaps. RAE Rept. Aero 2646, 1961. (AD-253915) (U)

651. Williams, J.: Comments on Some Recent Basic Research on V/STOL Aerodynamics. RAE TN-Aero-2795, 1961. (AD-328280L) (N65-29640) (U)

652. Williams, J., and Butler, S. F. J.: Further Developments in Low-Speed Wind-Tunnel Techniques for V/STOL and High-Lift Model Testing. RAE TN-Aero-2944, 1964. (AD-436352) (U)

653. Williams, J.: Recent Basic Research on V/STOL Aerodynamics at R.A.E., Ministry of Aviation, Zeitschrift Fur Flugwissenschaften, Vol. 14, 1966. (A66-35364) (U)

654. Williams, P. G.: A Note on the Lift of a Jet-Flap Aerofoil Near the Ground. ARC 23821, 1962. (U)

655. Williamson, G. G.: Dynamic Stability Analysis of a VTOL Vectored-Slipstream Vehicle During Transition. Princeton Univ. Report 535, 1961. (AD-260719) (U)

656. Wilson, R. K., and Westbrook, C. B.: Handling Qualities of VTOL Aircraft. AIAA Paper 64-777, 1964. (A64-25313) (U)

657. Wimpress, J. K.: Shortening the Takeoff and Landing Distances of High-Speed Aircraft. AGARD 501, 1965. (N66-21022) (U)

658. Winston, M. M., and Huston, R. J.: Propeller-Slipstream Effects as Determined from Wing-Pressure Distribution on a Large-Scale Six-Propeller VTOL Model at Static Thrust. NASA TN D-1509, 1962. (U)

659. Winston, M. M.: Wind-Tunnel Data From a 0.16-Scale V/STOL Model with Direct-Lift and Lift-Cruise Jets. NASA TM X-1758, 1969. (N69-20016) (U)

660. Winston, M. M., and Huston, R. J.: Wing-Pressure Measurements Within the Propeller Slipstream for a Large-Scale V/STOL Wind-Tunnel Model Simulating Transition. NASA TN D-2014, 1963. (U)

661. Winters, C. P.: The Approximate Longitudinal Stability Derivatives of a Vectored-Thrust VTOL. AFIT Rept. GAM/AE68-11, 1968. (AD-833396) (U)

662. Wolkovitch, J.: Approximate Factors for Longitudinal Transfer Function Denominators of the Vertol VZ-2 Tilt-Wing VTOL Airplane. STI TM 128-1, 1962. (U)

663. Wolkovitch, J.: The Calculation of Lateral Stability Derivatives for the Doak VZ-4 VTOL Configuration. STI TM 128-5, 1963. (U)

664. Wolkovitch, J.: The Calculation of Longitudinal Stability Derivatives for the Doak VZ-4 VTOL Configuration. STI TM 128-3, 1963. (U)

665. Wolkovitch, J.: An Introduction to Hover Dynamics. SAE Paper 660576, 1966. (A67-10570) (U)

666. Wolkovitch, J., and Walton, R. P.: VTOL and Helicopter Approximate Transfer Functions and Closed-Loop Handling Qualities. STI TR-128-1, 1965. (U)

667. Wood, M. N.: Jet V/STOL Aircraft Aerodynamics. New York Academy of Sciences, Annals, Vol. 154, 1968. (A69-15566) (U)

668. Wooler, P. T., Burghart, G. H., and Gallagher, J. T.: Pressure Distribution on a Rectangular Wing with a Jet Exhausting Normally into an Airstream. Jour. of Aircraft, Vol. 4, No. 6, 1967. (U)

669. Wu, J. C., Mosher, D. K., and Wright, M. A.: Experimental and Analytical Investigation of Jets Exhausting Into a Deflecting Stream. AIAA Paper 69-223, 1969. (U)

670. Wu, T. Y.: A Lifting-Surface Theory for Wings at High Angles of Attack Extending Through Inclined Jets, Pt. 3. VRC Rept. 9A, 1963. (N64-17121) (U)

671. Wyatt, L. A.: Tests on the Loss of Vertical-Jet Thrust Due to Ground Effect on Two Simple VTOL Planforms, With Particular Reference to the Short SC-1 Aircraft. ARC R&M 3313, 1958. (N63-17120) (U)

672. Wygnanski, I.: The Effect of Jet Entrainment on Loss of Thrust for a Two-Dimensional Symmetrical Jet-Flap Aerofoil. McGill Univ. Rept. 64-13, DRB G-9551-12, 1964. (N64-31243) (U)

673. Yaggy, P. F., and Goodson, K. W.: Aerodynamics of a Tilting Ducted-Fan Configuration. NASA TN D-785, 1961. (U)

674. Yaggy, P. F., and Mort, K. W.: A Wind-Tunnel Investigation of a Four-Foot-Diameter Ducted Fan Mounted on the Tip of a Semi-Span Wing. NASA TN D-776, 1961. (U)

675. Yaggy, P. F., and Rogallo, V. L.: A Wind-Tunnel Investigation of Three Propellers Through an Angle-of-Attack Range from 0^{o} to 85^{o}. NASA TN D-318, 1960. (U)

676. Yaggy, P. F., and Mort, K. W.: Wind-Tunnel Tests of Two VTOL Propellers in Descent. NASA TN D-1766, 1963. (U)

677. Yen, K. T.: On the Thrust Hypothesis for the Jet Flap Including Jet-Mixing Effects. Jour. Aero. Sci., Aug. 1960. (U)

678. Zeganoski, B. A.: A Generalized Experimental Study of Inlet Temperature Rise and Lift-Thrust of Jet VTOL Aircraft in Ground Effect. Bell Rept. 2099/928002, 1964. (AD-447906) (N64-32551) (U)

679. Zon, J., Giansanti, N., and Fitzpatrick, J. E.: Estimated Flying Qualities of the Kaman K-16B VTOL/STOL Aircraft. Part 2 – Dynamic Stability in Transitional Flight. Kaman Aircraft Corp., G-113-7, 1959. (AD-238648) (U)

VTOL-STOL SUBJECT INDEX

1. Propeller-Driven Aircraft and Component Combinations

    1.1 Boundary-Layer Control
    1.2 Tilting Wing
    1.3 Deflected Slipstream
    1.4 Ducted Propeller
    1.5 Tilting Propeller
    1.6 Tailsitter

2. Jet-Driven Aircraft and Component Combinations

    2.1 Deflected Jet (Vectored Jet)
    2.2 Lift Plus Propulsion
    2.3 Tailsitter
    2.4 Tilting Engine
    2.5 Boundary-Layer Control

3. Fan-Driven (Lifting System) Aircraft and Component Combinations

    3.1 Fan in Wing
    3.2 Fan in Fuselage

4. Individual Components

    4.1 Free Propeller
    4.2 Ducted Propeller
    4.3 Plane Wing
    4.4 Annular Wing
    4.5 Jet Flaps or Jet-Augmented Flaps

5. Specialized Categories

    5.1 General Static Stability and Control
    5.2 Dynamic Stability
    5.3 Handling Criteria
    5.4 Handling Qualities
    5.5 Ground Effects
    5.6 Gyroscopic Effects
    5.7 Stabilization
    5.8 Zero or Low-Airspeed Control and/or Control Systems
    5.9 Propeller-Rotation-Direction Effects
    5.10 Jet-Wake or Propeller-Slipstream Effects
    5.11 Jet-Induced Effects
    5.12 Wind-Tunnel Test Techniques
    5.13 Miscellaneous Effects

6. Bibliographies and Compilations

KEY TO VTOL-STOL SUMMARY TABLE

Column Heading	Abbreviation	Definition
V/STOL Concept	BLC	Boundary-Layer Control
	DJ	Deflected Jet (Vectored Jet)
	DP	Ducted Propeller
	DSS	Deflected Slipstream
	FIF	Fan in Fuselage
	FIW	Fan in Wing
	FP	Free Propeller
	HL	High Lift (Flaps, Slots, Slats)
	JF	Jet Flap or Jet-Augmented Flap
	L+P	Lift-Plus-Propulsion Engine
	RF	Rotating Flap
	S	Several
	TE	Tilting Engine
	TP	Tilting Propeller
	TS	Tailsitter
	TW	Tilting Wing
Nature of Report Material	A	Analytical
	BIB	Bibliography
	D	Description
	DS	Design Study
	E	Experimental
	PR	Pilot Report
	R	Research Summary
	S	Several
	T	Theoretical
Flight Regime or Air Flow	Ax	Axial Flow
	C	Cruise
	H	Hover
	LS	Low Speed
	N-Ax	Nonaxial Flow
	S	Several
	St	Static
	T	Transition
Test Article	C	Component
	E	Existing Aircraft (Production Aircraft)
	M	Model
	P	Prototype
	PM	Prototype Model
	S	Several
	Sim	Simulator
Type of Test	F	Flight Test
	S	Several
	Sim	Simulator
	St	Static
	T	Princeton Dynamic Model Track
	WT	Wind Tunnel

TABLE 9-A*

VTOL-STOL SUMMARY

Subject Index Classification	Reference Number	Year of Publication	V/STOL Concept	Nature of Report Material	Flight Regime or Airflow	Test Article	Type of Test	Areas of Investigation or Analysis: Force and Moment	Wing	Free Propeller	Ducted Propeller	Two-Dimensional Data	Pressure Data	Max. Lift or Tm-ing	Ground Effect	Propeller Slipstream Direction	Stability and Control: General	Longitudinal	Lateral-Directional	Dynamic	Stabilization	Mechanisms	Crossover Effects / Low Airspeed	Handling Qualities	Handling Qualities Criteria	COMMENTS
1.1	94	59	BLC/DP	D	S	–	–	X							X											
	157	60	BLC/DSS	R/D	LS	–	–																			DEVELOPMENT PROGRAM FOR LOCKHEED BLC C-130
	158	60	BLC	E/D	LS	M	WT																			LIFT AUGMENTATION BY SPANWISE BLOWING OVER A LIFTING SURFACE
	244	58	BLC/DSS	E/A	LS	M	WT	X																		LIFTING EFFECTIVENESS, FLOW REQ OF BLOWING BLC APPLIED TO PROPELLER-DRIVEN AIRPLANE
	256	61	BLC	E/A	LS	R	F	X																		LIAISON AIRCRAFT
	291	66	BLC/DSS	E/PR/A	LS	PM	F/SIM										X	X	X		X		X	X		HANDLING QUALITIES OF STOL SEAPLANE
	443	63	BLC/DSS	E/A	LS	M	WT/ST	X							X		X									TEST OF FLAPPED WING IMMERSED IN SLIPSTREAM OF 4 PROPELLERS, GRD PROXIMITY, BLC
	502	63	BLC/DSS	E/A/PR	LS	P	F										X	X	X				X	X		MODIFIED C-130. STOL PERFORMANCE: BLC FLAP, AILERONS, ELEVATOR, RUDDER
	503	63	BLC/HL	E/A/PR	LS	SIM	SIM											X	X		X			X		C-130
	562	58	BLC/DSS	E/A	ST	C	ST	X	X	X				X												WING PLUS PROPELLERS
	567	56	BLC/DSS	E/A	ST	C	ST	X	X	X					X											WING PLUS PROPELLERS. SLAT, END PLATES, PROPELLER-POSITION VARIATIONS
	568	57	BLC/DSS	E/A	ST	C	ST	X	X	X				X												WING PLUS PROPELLERS
	573	57	BLC	E/A	LS	M	WT	X																		CIRCULATION-CONTROL RESEARCH MODEL
	597	62	BLC/JF	T/E/A	LS	M	WT	X				X	X													INCR OF LIFT DUE TO BLOWING BLC. JET MOMENTUM REQ TO PREVENT SEP. SURVEY ON SYSTEMATIC MEAS.
	637	59	BLC	E/A	LS	M	WT	X					X				X									46-FT-SPAN MODEL LIKE C-143 BUT 4 PROPELLERS, BLOWING FLAPS
	638	58	BLC	E/A	LS	M	WT	X					X													46-FT-SPAN MODEL LIKE C-143, AREA SUCTION FLAPS, LE FLAP
	639	61	BLC/TW	E/A	T/C	M	WT	X							X											LARGE MODEL, 4 PROPELLERS, BLC TRAILING-EDGE FLAP
	641	61	BLC	E/A	S	M	WT	X									X	X					X			AR-10 WING, DUAL ROTATION PROPELLERS LIKE C-143 BUT 4 PROPELLERS
1.2	25	59	TW	E/A	H/T	F	F	X																		VZ-2
	31	62	TW	E/A	LS	M	F										X	X	X							FREE-AIR TESTS, 4-PROPELLER MODEL
	69	66	TW/DSS	A	T	–	–																			ANALYTICAL METHOD FOR PREDICTING STABILITY CHAR OF TILT-WING VTOL AIRCRAFT
	74	69	TW/DSS	R/A	H/T/C	M/PM	WT/F	[illegible]																		WT – FLIGHT-TEST CORRELATION PROGRAM TO DETERMINE STATIC WT TEST TECHNIQUES
	80	68	TW	E/A	T	M	WT											X	X							4-PROPELLER TILT-WING VTOL. STATIC AND DYNAMIC DERIVATIVES
	86	63	TW	E/D/PR	H/T	SIM	SIM										X	X	X		X		X	X	X	SIMULATOR STUDY OF TILT-WING HANDLING QUALITIES, 2 DEGREES OF FREEDOM

* See table 9B for key to summary

TABLE 9-A (CONTD)*

SUBJECT INDEX CLASSIFICATION	REFERENCE NUMBER	YEAR OF PUBLICATION	V/STOL CONCEPT	NATURE OF REPORT MATERIAL	FLIGHT REGIME OR AIRFLOW	TEST ARTICLE	TYPE OF TEST	AREAS OF INVESTIGATION OR ANALYSIS: Forces and Moments	Wing	Free Propeller	Ducted Propeller	Two-Dimensional Data	Pressure Data	Max. Lift or Turning	Gen. g Effect	Propeller Rotation Direction	Gen. Jet	STABILITY AND CONTROL: Longitudinal	Lateral Directional	Dynamic	Stabilization	Stabilizers	Dynamic Effects	Type or Use Augment Control System	Handling Qualities	Handling Qualities Criteria	COMMENTS
1.2 (CONT)	89	61	TW/DSS	E/A	T/C	PM	WT	X																			KAMAN K-16B MODEL
	101	68	TW	A	T	–	–										X		X								IMPORTANT FACTORS INFLUENCING DYNAMIC LONG STAB OF TILT-WING V/STOL AIRCRAFT
	103	66	TW	E/A	H/T/C	M	WT	X		X							X		X								STATIC AND DYNAMIC LONG STAB DERIVATIVES
	128	60	TW/DSS	T/A	H/T/C	–	–									X											METHODS FOR PREDICTING AERO STAB DERIVS OF PROPELLER-DRIVEN TILT-WING V/STOL AIRCRAFT
	130	68	TW	A	H/T	M	WT										X		X								EXPERIMENTAL VALUES OF LONG STAB DERIVS OF 3 TILT-WING AIRCRAFT VARIED TO ANALYZE CHARACTERISTIC ROOTS AND TRANSIENT RESPONSE
	131	60	TW	A	T	M	WT	X				X															DISCUSSION OF SLIPSTREAM EFFECTS
	135	59	DP/TW	A	LS	–	–	X								X	X		X								ASPECTS OF LONG DYNAMIC STAB CHAR OF PROPELLER-DRIVEN V/STOL AIRCRAFT ANALYZED
	136	67	TW/DSS	E/A	T	M	T										X		X								XC-142A MODEL, LONGITUDINAL DYNAMICS AT HIGH WING INCIDENCE
	138	61	TW	A/E	T	M/E	F										X		X								PRINCETON FREE-FLIGHT FACILITY (VZ-2)
	149	64	TW/DSS	E/A	T	M	WT	X								X	X										TILT-WING V/STOL TRANSPORT. STALL, PERFORMANCE, LONGITUDINAL STAB AND CONTROL CHARACTERISTICS
	156	66	TW/DSS	T	H/T	-	–							X		X											WING LOADING OF ARBITRARY PLANFORM EQUAL TO OR LESS THAN SPAN OF PROPELLER JET
	158	68	TW/DSS	E/A	LS	M	WT	X						X		X											AERO CHAR OF LARGE-SCALE MODEL OF 4-PROPELLER TILT-WING CONFIG. GROUND EFFECTS
	163	68	TW/DSS	E/PR/A	–	PM	F									X											RESULTS OF CATEGORY II FLT TESTS OF XC-142, CATEGORY I DATA INCLUDED
	164	54	TW	E/A	H/T/C	M	WT	X	X	X							X										AERO CHARACTERISTICS OF WING - PROPELLER, WING ALONE, AND PROPELLER ALONE
	168	59	TW	E/A	T	M	WT	X				X															TWIN-ENGINE MODEL
	174	62	TW	E/A	T	M	WT	X																			
	178	63	TW	D/A/E	S	S	S	X						X										X			REVIEW STUDY (VZ-2)
	183	65	TW/DSS	E/A	LS	M	WT								X		X										LONG AERO CHARACTERISTICS. EFFECT OF PROPELLER-ROTATION DIRECTION
	184	66	TW	E	LS	M	WT	X	X						X	X	X										EFFECT OF PROPELLER-ROTATION DIRECTION, FLAPS, SLATS, FENCES, ON AERO AND FLOW CHARACTERISTICS
	185	66	TW	E	LS	M	WT	X	X						X	X	X										EFFECT OF PROPELLER-ROTATION DIRECTION, FLAPS, SLATS, FENCES, ON AERO AND FLOW CHARACTERISTICS
	186	67	TW	E	LS	M	WT	X	X						X	X	X										EFFECT OF PROPELLER-ROTATION DIRECTION, FLAPS, SLATS, FENCES, ON AERO AND FLOW CHARACTERISTICS
	187	67	TW	E	LS	M	WT	X	X						X	X	X										EFFECT OF PROPELLER-ROTATION DIRECTION, FLAPS, SLATS, FENCES, ON AERO AND FLOW CHARACTERISTICS
	188	67	TW	E	LS	M	WT	X	X						X	X	X										EFFECT OF PROPELLER-ROTATION DIRECTION, FLAPS, SLATS, FENCES, ON AERO AND FLOW CHARACTERISTICS
	189	64	TW/DSS	E	LS	M	WT	X									X										LONG AERO CHARACTERISTICS WING STALLING CHARACTERISTICS

* See table 9B for key to summary

TABLE 9-A (CONTD)*

SUBJECT INDEX CLASSIFICATION	REFERENCE NUMBER	YEAR OF PUBLICATION	V/STOL CONCEPT	NATURE OF REPORT MATERIAL	FLIGHT REGIME OR AIRFLOW	TEST ARTICLE	TYPE OF TEST	AREAS OF INVESTIGATION OR ANALYSIS: Force and Moment	Wing	Free Propeller	Ducted Propeller	Two Dimensional Data	Pressure Data	Max. Lift or Turning	Ground Effect	Propeller Slipstream Deflection Effects	Controls	STABILITY AND CONTROL: Longitudinal	Lateral-Directional	Dynamic	Stabilization	Stabilization	Gyroscopic Effects	Term or Low Airspeed Control/Attitude	Handling Qualities	Handling Qualities Criteria	COMMENTS
1.2 (CONT)	190	64	TW/DSS	E	LS	M	WT	X									X										LONG AERO CHARACTERISTICS. WING STALLING CHARACTERISTICS
	191	64	TW	E	LS/H	M	WT	X	X							X	X										EFFECT OF SLATS AND LE AND TE FLAPS ON AERO AND FLOW CHARACTERISTICS
	192	69	TW/DSS	E	LS	M	WT					X			X												SEMISPAN MODEL. WING SURFACE PRESSURES OVER α FROM 5° TO 80° FOR THRUST COEFF .3, .6, .8, .9 AND δ_f = 0, 20°, 40°, 60°. PROP-ROTATION-DIRECTION EFFECTS.
	197	61	TW/DSS	E/A	T	PH	WT										X										KAMAN K-16B MODEL
	230	67	TW/DSS	E/A	LS	M	WT	X						X			X	X						X			LONG, LAT AND CONTROL CHAR OF 4-PROPELLER TW MODEL IN GRD EFF, RECIRCULATION EFFECTS MOVING-BELT GROUND PLANE. THOROUGH REPT
	231	67	TW	E/A	T	M	WT	X						X		X	X										GROUND EFFECTS ON TILT-WING AIRPLANE
	232	66	TW/DSS	E/A	T	M	WT							X		X	X										EXPERIMENTAL STUDY OF LONG AERO PROBS OF FLAPPED 4-PROPELLER V/STOL TRANSPORT
	247	61	TW	E/A	H/T	M	WT	X						X				X	X								AO 1 CONVERSION TO 4-PROPELLER TILT WING (MOHAWK)
	253	65	TW	T/A/E	N-Ax	C	WT	X	X	X																	WING PLUS PROPELLERS
	254	60	TW/DP	D/E	H/T	P	F	X						X		X											VZ-2, VZ-4
	262	61	TW	T/A	T	–	–										X		X								
	295	60	TW/DSS	E/A	ST	M	ST	X				X		X													
	298	63	TW/DSS	E/A	T	M	WT	X				X															WING AND FLAP LOADS
	313	59	TW	E/A	T	M	U									X								X			4-POINT CONTROL
	327	61	TW/DSS	R/D/A	H/T	–	–	X								X	X										DISCUSSION OF TW AND DSS, PROPELLER-DRIVEN VTOL AIRCRAFT
	329	64	TW/DSS	E/A	T	M	WT										X										VZ-2. FORCE TEST TO DETERMINE LONG AERO CHAR AND AILERON CONTROL CHAR. EFF OF LE DROOP
	354	56	TW	E/A	0-80°	C	WT	X	X	X																	WING PLUS PROPELLER, AND SEPARATELY
	368	60	TW/DSS	E	T	M	WT	X	X					X			X										AERO CHAR OF TILT-WING, DEFLECTED SLIPSTREAM, AND TW + DES VTOL AIRCRAFT
	369	68	TW	–	LS	M	WT												X						X		RESULTS OF DYNAMIC STAB TESTS. EFFECT OF STAB DERIVS ON DYNAMIC STAB
	377	68	TW/TP	T	T/C	–	–										X										LARGE TILT-ANGLE LIFTING-SURFACE THEORY. DOWNWASH ANGLES AT TAIL NOT ACCURATELY PREDICTED AT HIGH ANGLES.
	385	66	TW	R	H/T/C	–	–										X	X			X			X	X	X	SUMMARY OF TEST PROGRAM ON CL-84 V/STOL PROTOTYPE AND 2 TYPES OF SIMULATORS TO ASSESS QUALITATIVELY HANDLING QUALITIES
	387	67	TW	E/A	T	M	F									X											4-PROPELLER MODEL
	388	65	TW	E/A	H	M	F										X	X	X								4-PROPELLER MODEL
	389	66	TW	E/A	T	M	F										X	X	X								4-PROPELLER MODEL

* See table 9B for key to summary

TABLE 9-A (CONTD)*

SUBJECT INDEX CLASSIFICATION	REFERENCE NUMBER	YEAR OF PUBLICATION	V/STOL CONCEPT	NATURE OF REPORT MATERIAL	FLIGHT REGIME OR AIRFLOW	TEST ARTICLE	TYPE OF TEST	AREAS OF INVESTIGATION OR ANALYSIS: Force and Moment	Wing	Tilt Propeller	Ducted Propeller	Two-Dimensional Data	Pressure Data	Aero Lift or Turning	Ground Effect	Propeller Rotation Direction Effects	STABILITY AND CONTROL: General	Longitudinal	Lateral Directional	Dynamic	Stabilization	Simulation	Gyroscopic Effects	Term or Low Airspeed Control/Station	Handling Qualities	Handling Qualities Criteria	COMMENTS
1.2 (CONT)	602	58	TW	E/A	S	PM	F										X	X	X				X				VZ-2 MODEL FLIGHT TEST
	603	60	TW	E/A	S	PM	WT	X					X				X	X									X-18 MODEL (FORCE TEST)
	605	61	TW	E/A	H/T	PM	F										X		X					X			VZ-2, 1/4-SCALE MODEL, RIGID AND FLAPPING PROPELLER BLADES
	606	61	TW	E/A	T	PM	F										X		X				X				VZ-2, 1/4-SCALE MODEL
	608	68	TW	E	H/T	M	WT	X								X	X										PRINCETON DYNAMIC MODEL TRACK FACILITY. A GENERAL TILT-WING-PROPELLER MODEL
	632	65	TW	R/D	H/T/C	–	–						X			X											TECH. AND OPERATIONAL LESSONS FROM XC-142 PROGRAM. WT AND FLT-TEST RESULTS COMPARED. PROP. PITCH MOM. AT HIGH INFLOW ANGLES
	639	61	TW DSS	E	T	M	WT	X					X			X											LARGE-SCALE WT TEST OF TILT-WING AND DEFLECTED-SLIPSTREAM MODEL
	640	64	TW/DSS	E/A	LS	M	WT	X							X	X											EFFECTS OF HIGH-LIFT D VICES ON FLOW SEPARATION, BUFFET, AND DESCENT CHAR
	642	65	TW	E	T/H	M	WT/ST	X								X	X	X	X								PERFORMANCE AND CONTROL CHAR. OF VTOL AIRPLANE
	644	63	TW	E/A	LS	M	WT	X									X										VTOL CONFIG WITH FREE-PIVOTED TILTING WING WITH AERODYNAMICALLY CONTROLLED TILT ANGLE. EFF OF PIVOT LOC ON ABILITY TO TRIM
	658	62	TW DSS	E A	ST	M	ST					X															6-PROPELLER MODEL. PROPELLER SLIPSTREAM EFFECTS INVESTIGATED
	662	62	TW	T/A/E	S	PM	F/WT										X		X								VZ-2 STABILITY DERIVATIVES
	670	63	TW/DSS	T	H/T	–	–			X			X															METHOD FOR ASSESSING NONUNIFORM FLOW FIELDS OF WING-PROPELLER SLIPSTREAM AERODYNAMICS. METHODS FOR SPANWISE LIFT DISTRIBUTION AND INDUCED DRAG
	11	62	DSS	D	LS	P	F	X																			BREGUET 941 DESCRIPTION
	61	58	DSS	E A	T	C	U	X	X	X																	WING PLUS PROPELLERS (VARIOUS COMBINATIONS)
	69	66	TW DSS	A	T		–																				ANALYTICAL METHOD PREDICTING STAB CHAR. OF VTOL AIRCRAFT
	74	66	TW DSS	R A	H/T/C	M/PM	WT/F																				WT-FLT-TEST PROGRAM TO DETERMINE STATUS OF WT TEST TECHNIQUES
	89	61	TW DSS	E/A	U	PM	WT	X																			KAMAN K-16B
	106	58	DSS	T/A/E	H/T	M	WT	X											X								STATIC AND DYNAMIC STABILITY (VZ-3)
	28	60	TW DSS	T/A	H/T/C	–	–									X											METHODS PREDICTING AERO STAB DERIVS OF PROPELLER-DRIVEN V/STOL AIRCRAFT
	141	64	DSS	A	C	–	–									X	X	X	X					X	X		BREGUET 941 LOW-SPEED FLYING QUALITIES COMPARED WITH AGARD REQUIREMENTS FOR V/STOL
	139	54	TW DSS	E/A	T	M	WT	X								X	X										STALL PERFORMANCE AND LONG STAB. AND CONTROL CHAR. OF V/STOL TRANSPORT
	51	60	DSS	D	S	P	F	X																			BREGUET 941 AND 942
	152	61	DSS	D	H/T/C	M/PM/ SIM	W/F/ SIM												X								DISCUSSION OF COORDINATED METHODS USED TO PERFECT DYNAMIC BEHAVIOR OF BREGUET 940

* See table 9B for key to summary

TABLE 9-A (CONTD)*

SUBJECT MATTER CLASSIFICATION	REFERENCE NUMBER	YEAR OF PUBLICATION	V/STOL CONCEPT	NATURE OF REPORT MATERIAL	FLIGHT REGIME OR ARRFLOW	TEST ARTICLE	TYPE OF TEST	AREAS OF INVESTIGATION OR ANALYSIS: Vert and Horizont	Wing	Free Propeller	Ducted Propeller	Two-Dimensional Data	Pressure Data	Aero Lift or Torque	Ground Effect	Propeller Rotation Direction Effects	STABILITY AND CONTROL: General	Longitudinal	Lateral-Directional	Dynamic	Stabilization	Simulations	Gyroscopic Effects	Loss or Gain Airspeed Control System	Handling Qualities	Hovering Conditions Criteria	COMMENTS
1.2 (CONT)	413	63	TW	A/D/E	S	S	S	X						X		X	X	X	X				X				REVIEW STUDY OF TILT-WING V/STOL AERODYNAMICS
	432	63	TW/DSS	E/A	T	M	WT	X									X							X			VZ-2 WING STALLING PHENOMENA STUDIED. LIFT AND DRAG CORRELATED WITH FLT-TEST RESULTS. FLYING QUALITIES PROBLEMS CORRELATED WITH WING STALL. TUFT STUDY
	441	60	TW	E/A	T	M	WT										X	X						X				DAVID TAYLOR MODEL BASIN, STOL MODEL
	446	57	TW	E/A	ST	M	ST	X						X														4-PROPELLER MODEL
	450	58	TW/DSS	E/A	T	M	WT	X										X										4-PROPELLER MODEL
	451	62	TW	E/A	H/T	M	F										X		X									4-PROPELLER MODEL WITH PROGRAMMED FLAPS (FLT TEST)
	452	64	TW	E/A	H/T/C	M	WT/ST							X			X	X	X		X		X					FREE-FLIGHT TESTS OF 1/8-SCALE MODEL OF 4-PROPELLER V/STOL TRANSPORT
	454	62	TW	E/A	S	M	WT										X	X										4-PROPELLER MODEL WITH PROGRAMMED FLAPS (FORCE TEST)
	455	58	TW	E/A	T	PM	WT	X									X	X										VZ-2
	486	62	TW	E/A	H	M	ST							X														SLIPSTREAM FLOW AROUND VZ-2, X-18, AND ARB CONFIG MODELS
	480	66	TW	PR/A	H/LS	PM	F							X			X	X	X					X	X			FULL-SCALE FLIGHT INVESTIGATION OF MODIFIED VZ-2 OPERATIONAL AND AERO ASPECTS
	481	62	TW	E/A	H/T	P	F																	X				AILERON FOR YAW CONTROL INVESTIGATION (VZ-2)
	482	52	TW	E/A	S	P	F	X						X			X	X	X					X	X			FLIGHT-TEST RESULT SUMMARY (VZ-2)
	494	68	TW/DSS	E/A	T	M	T/WT	X						X														XC-142A MODEL. GROUND EFFECTS ON LONG. FORCES AND PITCHING MOMENT
	498	69	TW	E/A	T	M	T	X										X	X									XC-142A MODEL TESTED IN 3° OF LAT-DIR FREEDOM IN MID-TRANSITION FLT COND. CONTROL EFFECTIVENESS. CONTROL MIXING REQUIREMENTS
	498	61	TW	E/A	T	M	T	X									X		X									PRINCETON UNIV FORWARD FLIGHT FACILITY
	513	59	TW/DSS	D	S	P	–																					KAMAN K-16B DESCRIPTION
	531	64	TW/DSS	E/A	T	M	SIM								X		X	X	X									DYNAMIC LAT STAB AND CONT CHAR OF THE VZ-2, SIM FLT-TEST EVALUATION TRANSITION RANGE WHERE WING STALLING OCCURS
	570	63	TP/TW	E/A	T/LS/C	M	WT	X							X	X												DETERMINATION OF LIMITING VALUES ON TRANSITION STALLING CHAR RATIO OF WING CHORD TO PROP DIAM VARIED
	578	64	TW/DSS	E/A	T	SIM	SIM											X	X		X							PROB AREAS IN SIM OF LAT-DIR DYN BEHAVIOR OF STOL AIRCRAFT EQ OF MOTION. TURBULENCE EFFECTS
	591	59	TW	E/A	T	C	WT	X	X	X							X											WING CHORD TO PROPELLER DIAMETER RATIO. WING PLUS PROPELLER. SLATS
	598	58	TW	E/A	S	P	F	X																				VZ-2 CONVERSION MANEUVER
	600	60	TW	E/A	T	PM	WT	X									X	X	X									VZ-2
	601	60	TW	E/A	S	PM	F							X			X	X	X					X				X-18 MODEL (FLIGHT TEST)

* See table 9B for key to summary

TABLE 9-A (CONTD)*

SUBJECT INDEX CLASSIFICATION	REFERENCE NUMBER	YEAR OF PUBLICATION	V/STOL CONCEPT	NATURE OF REPORT MATERIAL	FLIGHT REGIME OR AIRFLOW	TEST ARTICLE	TYPE OF TEST	AREAS OF INVESTIGATION OR ANALYSIS: Forces and Moments	Wing	Free Propeller	Ducted Propeller	Two-Dimensional Data	Pressure Data	Max. Lift or Turning	Ground Effect	Propeller Rotation Direction Effects	STABILITY AND CONTROL: General	Longitudinal	Lateral-Directional	Dynamic	Stabilization	Simulation	Gyroscopic Effects	Turn or Low Airspeed Control/Systems	Handling Qualities Rating/Qualities Criteria	COMMENTS
1.3 (CONT)	156	66	TW/DSS	T	H/T	–	–							X		X										WING LOADING OF ARBITRARY PLANFORM EQUAL TO OR LESS THAN SPAN OF PROPELLER JET
	157	60	BLC/DSS	R/D	LS	–	–																			DESCRIPTION OF THE DEVELOPMENT PROGRAM FOR LOCKHEED BLC C-130 AIRCRAFT
	158	66	TW/DSS	E/A	LS	M	WT	X						X		X										AERO CHAR OF A LARGE-SCALE MODEL OF 4-PROPELLER CONFIG. GROUND EFF.
	163	66	TW/DSS	E/PR/A	–	PM	F									X										RESULTS OF CATEGORY II FLT TESTS OF XC-142. CATEGORY I DATA INCLUDED
	166	56	DSS	E/A	ST	C	ST	X	X	X			X													WING PLUS PROPELLERS
	183	69	TW/DSS	E/A	LS	M	WT								X		X									LONG AERO CHAR. EFFECT OF PROPELLER-ROTATION-DIRECTION EFFECTS
	189	64	TW/DSS	E	LS	M	WT	X									X									LONG AERO CHAR. WING STALLING CHAR
	190	64	TW/DSS	E	LS	M	WT	X									X									LONG AERO CHAR. WING STALLING CHAR
	192	69	TW/DSS	E	LS	M	WT					X			X											SEMISPAN MODEL. WING SURFACE PRESSURES OVER α FROM 5° TO 80° FOR THRUST COEFF .3, .6, .8, .9, AND δ_f = 0, 20°, 40°, 60°. PROP.-ROTATION DIRECTION EFFECTS
	197	61	TW/DSS	E/A	T	PM	WT										X									KAMAN K-16B MODEL
	222	63	DSS/TS	PR	S	P	F	X						X			X		X	X		X				VZ-3 AND X-13
	230	67	TW/DSS	E/A	LS	M	WT	X						X			X	X						X		LONG., LAT., AND CONTROL CHAR. OF 4-PROPELLER TW MODEL IN GRD EFF. RECIRCULATION EFFECTS. MOVING-BELT GROUND PLANE. THOROUGH REPT.
	232	66	TW/DSS	E/A	T	M	WT							X		X	X									EXPERIMENTAL STUDY OF LONG AERO PROPS OF FLAPPED 4-PROPELLER V/STOL TRANSPORT
	244	58	BLC/DSS	E/A	LS	M	WT	X																		LIFTING EFFECTIVENESS, FLOW REQ OF BLOWING BLC APPLIED TO PROPELLER-DRIVEN AIRPLANE
	251	61	BLC/DSS	E/A	S	M	WT							X			X	X								6 PROPELLERS, T-TAIL
	264	66	DSS	E/A	H	C_a	ST		X	X						X										WING PLUS PROPELLERS, PROPELLER POSITION EFFECTS
	291	65	DSS/BLC	E/PR/A	LS	PM	F/SIM										X	X	X		X			X	X	HANDLING QUALITIES OF A STOL SEAPLANE
	295	60	DSS/TW	E/A	ST	M	ST	X					X		X											6 PROPELLERS, 35-FT SPAN, AR=8, DOUBLE-SLOTTED FLAPS
	296	63	DSS/TW	E/A	T	M	WT	X					X													WING AND FLAP LOADS
	304	59	DSS	E/A	S	P/SIM	WT/SIM	X						X			X	X						X	X	AMES 40 x 80 WT TEST OF PROTOTYPE PLUS SIMULATOR (VZ-3)
	327	61	TW/DSS	R/D/A	H/T	–	–	X								X	X									DISCUSSION OF TW AND DSS, PROPELLER-DRIVEN VTOL AIRCRAFT
	328	64	TW/DSS	E/A	T	M	WT										X									VZ-2. FORCE TEST TO DETERMINE LONG AERO CHAR AND AILERON CONTROL CHAR. EFF OF LE DROOP
	331	55	DSS	E/A	LS	C	S																			SUMMARY OF NACA FLAP AND VANE INVESTIGATIONS
	365	55	DSS	E/A	H/T	C	WT	X	X	X			X													WING PLUS PROPELLERS, TURNING EFFECTIVENESS

* See table 9B for key to summary

TABLE 9-A (CONTD)*

	SUBJECT INDEX CLASSIFICATION	REFERENCE NUMBER	YEAR OF PUBLICATION	V/STOL CONCEPT	NATURE OF REPORT MATERIAL	FLIGHT REGIME OR SUBTOW	TEST ARTICLE	TYPE OF TEST	AREAS OF INVESTIGATION OR ANALYSIS: Parts and Material	Wing	Fans Propellers	Ducted Propeller	Two-Dimensional Data	Pressure Data	Misc. Lift or Turning	Ground Effect	Propeller Position	Blowing Effects	Control	STABILITY AND CONTROL: Longitudinal	Lateral-Directional	Dynamic	Stabilization	Manipulation	Gyroscopic Effects	Jets or Low Airspeed	Control Powered	Handling Qualities	Transition Corridor Criteria	COMMENTS
1.3 (CONT)	356	57	DSS	E/A	ST	C	ST	X	X	X				X	X														WING PLUS PROPELLERS, TURNING EFFECTIVENESS
	357	58	DSS	E/A	ST	C	ST	X	X	X				X	X														WING PLUS PROPELLERS, PROPELLER POSITION EFFECTS
	358	54	DSS	E/A	0-80°	C	WT	X	X	X				X															4-PROPELLER MODEL. WING PLUS PROPELLERS, TURNING EFFECTIVENESS
	359	54	DSS	E/A	ST	C	ST	X	X	X								X							X				WING PLUS PROPELLERS, LE SLAT
	360	61	DSS	E/A	T	PM	WT	X							X					X									LARGE POWER EFFECTS ON DIR STAB. (VZ-8)
	361	60	DSS	E/A	S	M	WT	X							X			X											4 PROPELLERS, PROPELLER EFFECTS, SLAT, TAIL FAN OPERATION
	363	56	DSS	E/A	ST	C	ST	X	X	X				X	X														WING PLUS PROPELLERS, TURNING EFFECTIVENESS
	365	59	DSS	T/A/E	H/T	C	WT	X	X	X																			WING PLUS PROPELLERS, LIFT AND DRAG ESTIMATION METHODS
	367	57	DSS	E/A	T	M	WT	X																					LARGE WALL CORRECTIONS NOT REMOVED
	368	60	TW/DSS	E	T	M	WT	X	X					X				X											AERO CHAR OF TILT-WING, DEFLECTED SLIPSTREAM, AND TW + DSS VTOL AIRCRAFT
	398	66	DSS	E/A	LS	M	WT	X								X	X												STAB AND CONTROL DATA ON 2-PROPELLER STOL AIRCRAFT
	416	54	DSS	E/A	H	M	F													X									4 CASCADE WINGS, 4 PROPELLERS
	443	63	BLC/DSS	E/A	LS	M	WT/ST	X						X		X													TEST OF FLAPPED WING IMMERSED IN SLIPSTREAM OF 4 PROPELLERS. GRD PROXIMITY. BLC
	448	57	DSS	E/A	0-80°	C	WT	X	X	X																			WING PLUS PROPELLERS. PROPELLER LOCATION EFFECTS
	450	58	DSS or TW	E/A	T	M	WT	X											X						X				4 PROPELLERS
	457	57	DSS	E/A	H/T	M	WT		X		X																		WING WITH DUCTED FANS AND DOUBLE-SLOTTED FLAP. DUCT POSITION AND DUCT EXIT CONFIG VARIED. FLAP TURNING EFFECTIVENESS
	465	66	DSS	E/A	LS	M	WT	X						X		X													LONG FORCE CHAR OF STOL MODEL. WING SPAN VARIED. PROP-ROTATION-DIRECTION EFFECTS. SPANWISE VARIATION OF PROP THRUST
	466	66	DSS	E/A	LS	M	WT	X				X			X		X												WING PRESSURE DISTRIBUTION DATA ON STOL MODEL. WING SPAN VARIED. PROP-ROTATION-DIRECTION EFFECTS. SPANWISE VARIATION OF PROP THRUST
	500	64	DSS	E/A	LS	P	F											X	X	X					X	X			BREGUET 941. RESULTS OF FLT TEST OF PERFORMANCE, HANDLING QUALITIES, AND OPERATIONAL CHAR
	502	63	BLC/DSS	E/A/PR	LS	P	F											X	X	X					X	X			MODIFIED C-130. STOL PERFORMANCE: BLC FLAP, AILERONS, ELEVATOR, RUDDER
	515	61	DSS	D	LS/C	P	F																						BREGUET STOL AIRCRAFT
	518	59	DSS/TW	D	S	P	–																						KAMAN K-16B, DESCRIPTION IN JAHS
	563	60	DSS/JF	E	H/LS	C	WT	X	X	X			X		X														SEMISPAN WING PLUS 2 PROPELLERS, WING TIP BEYOND SLIPSTREAM
	567	58	DSS/BLC	E/A	ST	M	F	X												X									4-ENGINE TRANSPORT

* See table 9B for key to summary

TABLE 9-A (CONTD)*

SUBJECT MODE CLASSIFICATION	REFERENCE NUMBER	YEAR OF PUBLICATION	V/STOL CONCEPT	NATURE OF REPORT MATERIAL	FLIGHT REGIME OR AIRFLOW	TEST CYCLE	TYPE OF TEST	AREAS OF INVESTIGATION OR ANALYSIS: Force and Moment	Wing	Ejector Propeller	Ducted Propeller	Two Dimensional Data	Pressure Data	Misc. Lift or Control	Ground Effect	Propeller Rotation Direction Effects	STABILITY AND CONTROL: General	Longitudinal	Lateral-Directional	Dynamic	Stabilization	Simulation	Gyroscopic Effects	Yaw or Yaw Attitude Control Systems	Handling Qualities or Handling Qualities Criteria	COMMENTS
1.3 (CONT)	568	61	BLC/DSS	E/A	ST	C	ST	X	X	X				X													EFFECTS OF PROP DIAM ON ABILITY OF FLAPPED WING TO DEFLECT SLIPSTREAM DOWNWARD
	578	64	TW/DSS	E/A	T	SIM	SIM												X	X		X					PROB AREAS IN SIM OF LAT-DIR DYN BEHAVIOR OF STOL AIRCRAFT, EQ OF MOTION TURBULENCE EFFECTS
	579	59	DSS	D/A/E	S	P	F	X								X				X				X			VZ-2
	604	56	DSS	E/A	H	M	F	X											X								4-ENGINE TRANSPORT, LARGE FLAP AND EXTENSIBLE VANES
	607	57	DSS	E/A	T	M	F	X									X	X	X								4-ENGINE TRANSPORT, LARGE FLAP AND EXTENSIBLE VANES
	614	62	DSS	E/A	T	P	F							X			X							X	X		VZ-3
	615	63	DSS	E/A	LS	PM	F																		X		FLIGHT TEST OF RYAN VZ-34R V/STOL VEHICLE. EVALUATION OF DSS CONCEPT FOR VTOL AND STOL
	639	61	TW/DSS	E	T	M	WT	X						X		X											LARGE-SCALE WT TEST OF TILT-WING AND DEFLECTED SLIPSTREAM MODEL
	640	64	TW/DSS	E/A	LS	M	WT	X							X	X											EFFECTS OF HIGH-LIFT DEVICES ON FLOW SEPARATION, BUFFET, AND DESCENT CHAR
	656	61	DSS	T/A	T	–	–												X								6 EQUATIONS OF MOTION DEVELOPED AND EXAMINED
	658	62	TW/DSS	E/A	ST	M	ST				X																6-PROPELLER MODEL. SLIPSTREAM EFFECTS
	670	63	TW/DSS	T	H/T	–	–			X			X														METHOD FOR ASSESSING NON-UNIFROM FLOW FIELDS OF WING-PROPELLER SLIPSTREAM AERODYNAMICS METHODS FOR SPANWISE LIFT DISTRIBUTION AND INDUCED DRAG
1.4	27	66	DP	E	C/T/H	M	WT	X								X	X							X			XV-5A, HOVER TO 100 KNOTS IN CONVENTIONAL AND FAN POWER MODES. SUMMARY OF AERO PERF
	55	63	DP	E	C/T/H	M	H/T	X	X			X		X		X	X	X						X			XV-5A
	94	59	DP/BLC	D	LS/C	P	–	X																				
	107	63	DP	E/A	H/T/LS	–	–										X	X	X	X				X	X	X	CONTROL AND STAB AUGMENTATION REQUIREMENTS. THEOR AND ANALOG COMPUTER INVESTIGATIONS
	134	65	DP	E/A	H	PM	ST			X				X										X			DOWNWASH TESTS OF DUAL TANDEM DUCTED-PROP VTOL
	135	69	DP/TW	A	LS	–	–	X								X	X		X								LONG DYN STAB CHAR
	139	68	DP	P/A	T	–	–										X	X									LONG DYNAMICS ANALYZED TO DETERMINE STAB DERIVS
	144	64	DP	E/A	T	M	WT	X									X							X			TRANSITION CHAR OF DUAL TANDEM CONFIG, TRIM AND CONTROL
	194	66	DP	PR/A	H/T/C	E	F	X								X	X	X									XV-5A STAB AND CONTROL FLT-TEST EVALUATION
	223	67	DP	E/A	H/T/C	M	WT							X			X							X			LONG AERO CHAR IN GROUND EFFECT, 3 GROUND HEIGHTS, VTOL AND STOL OPERATION
	224	68	DP	E/A	H/T/C	M	WT	X								X	X	X						X			LONG AND LAT-DIR AERO CHAR, PERFORMANCE STAB AND CONTROL, EFF OF DUCT STALL
	229	62	DP	E/A	H/T	C	WT	X	X		X			X			X										VZ-4 4 TAIL LOCATIONS, LIP MODIFICATION, WING PLUS DUCTED PROPELLER

* See table 9B for key to summary

TABLE 9-A (CONTD)*

SUBJECT INDEX CLASSIFICATION	REFERENCE NUMBER	YEAR OF PUBLICATION	V/STOL CONCEPT	NATURE OF REPORT MATERIAL	FLIGHT REGIME OR AIRFLOW	TEST ARTICLE	TYPE OF TEST	AREAS OF INVESTIGATION OR ANALYSIS: Forces and Moments	Wing	Free Propeller	Ducted Propeller	Two Dimensional Data	Pressure Data	Max. Lift or Trimming	Ground Effect	Propeller Rotation Direction Effects	STABILITY AND CONTROL: General	Longitudinal	Lateral-Directional	Dynamic	Stabilization	Aerodynamic Effects	Fore or Aft Vertical Control System	Handling Qualities	Handling Qualities Criteria	COMMENTS
14 (CONT)	238	66	DP	T	AX	–	–	X		X						X										INVISCID THEORY FOR STEADY AERO LOADING ON DUCTED PROPELLER IN FORWARD FLIGHT
	249	62	DP	E/A	H/T	M	WT	X	X	X																DIVISION OF AERO LOADS. WING PLUS DUCTED PROPELLER
	254	60	TW/DP	D/E	H/T	P	F	X						X		X								X		ANALYSIS OF FLT CHAR (VZ-4 AND VZ-2)
	259	63	DP	A	T	–	–			X									X							SIMPLIFIED ANALYTICAL APPROACH FOR EVALUATING DYN STAB CHAR OF VTOL CONFIG
	312	68	DP	E/A/PR	H/T	P	F									X										DEVELOPMENT FLT TESTS OF X-22A
	317	67	DP	E/A	H/T	P	F	X																	X	TRANSITION AND HOVER FLT CHAR (VZ-4)
	324	68	DP	A	T	–	–										X	X	X							X-22A DYNAMICS IN TRANSITION. EQ OF MOTION FOR FLT-TEST PARAMETER IDENTIFICATION
	336	61	DP	T	H/LS	–	–										X	X	X				X	X		HOVERING IN STILL AIR AND GUST COND, GLIDE APPROACHES AT LOW SPEED. DAMPING AND SENSITIVITY
	395	66	DP	D/R	T	–	–							X			X	X	X	X			X			REVIEW OF TEST RESULTS WITH EMPHASIS ON STAB AND CONT CHAR.
	418	62	DP	E/A	H/T/C	M	WT	X									X	X								STATIC STAB AND CONT CHAR OF CONFIG WITH 4 TILTING DUCTED PROPS, MOUNTED IN TANDEM PAIRS
	419	68	FIW; DP/DJ	D	H/T/C	–	–	X						X		X										PROBS ENCOUNTERED BY FAN V/STOL AIRCRAFT
	429	69	DP	R/PR/A	H/T	SIM	SIM									X					X				X	3 TYPES OF GROUND-BASED SIMULATORS OF THE X-22A EVALUATED AND COMPARED WITH ACTUAL FLIGHT
	436	62	DP	E/A	S	C	WT	X	X	X							X									WING PLUS DUCTED PROPELLERS, EXTENSIVE DUCT TESTS (VZ-4)
	445	63	DP	E/A	S	M	WT	X									X	X								4-DUCT TANDEM VTOL CONFIG
	453	66	DP	E/A	H/T/C	M	WT							X			X	X	X		X		X			FREE-FLT TESTS OF A 1/18-SCALE MODEL OF A 4-DUCT TANDEM V/STOL TRANSPORT
	469	61	DP	E/A	H/T	M	F										X	X	X	X						4-DUCT MODEL
	470	61	DP	E/A	H/T	M	F												X	X						2-DUCT MODEL
	472	60	DP	E/A	T	M	WT	X									X									JEEP-TYPE VEHICLE
	475	63	DP	D/E	S	M	WT	X								X										X-22A DESIGN DESCRIPTION
	492	64	DP	E	S	M	WT							X												FULL-SCALE, HALF-MODEL SIMULATION OF A DUAL TANDEM DUCTED PROPELLER AIRCRAFT. DOWNWASH ALLEVIATION
	495	68	DP	E/A	H	M	WT	X		X							X	X	X							MODEL SIMILAR TO X-22A. LONG AND LAT TRANSIENT RESPONSE USING A DYNAMIC MODEL. COMPARISON OF L, DRAG, PITCH MOM OF ISOLATED DUCT
	496	68	DP	E/A	T	M	WT										X		X							MODEL SIMILAR TO X-22A. LONG TRANSIENT RESPONSE USING A DYNAMIC MODEL. TIME HISTORIES OF MODEL MOTION IN VARIOUS LONG DEGREES OF FREEDOM
	497	68	DP	E/A	LS	M	WT											X	X							X-22A, LAT-DIR DYN STAB OF DUCTED-PROP, QUAD CONFIG, TIME HISTORIES
	507	60	DP	E/D	S	P	F	X						X		X	X	X	X				X			FLIGHT-TEST REPORT (VZ-4)

* See table 9B for key to summary

TABLE 9-A (CONTD)*

SUBJECT INDEX CLASSIFICATION	REFERENCE NUMBER	YEAR OF PUBLICATION	V/STOL CONCEPT	NATURE OF REPORT MATERIAL	FLIGHT REGIME OR AIRFLOW	TEST ARTICLE	TYPE OF TEST	AREAS OF INVESTIGATION OR ANALYSIS: Force and Moment	Wing	Free Propeller	Ducted Propeller	Two Dimensional Data	Pressure Data	Aero Lift in Turning	Ground Effect	Propeller Race Characteristics	Blockage Effects	STABILITY AND CONTROL: General	Longitudinal	Lateral-Directional	Dynamic	Stabilization	Simulation	Gyroscopic Effects	Take-off or Low Airspeed Control Systems	Handling Qualities	Handling Qualities Criteria	COMMENTS
1.6 (CONT)	556	60	DP	E/A	T	M	WT	X										X									JEEP-TYPE VEHICLE
	561	63	DP	E/A	H	M	WT	X						X				X	X								TRENDS IN LIFT, PITCHING MOM., AND ROLLING MOM. DUE TO GROUND EFFECT
	571	48	DP	E/A	T	M	WT												X					X			LAT AND DIR CHAR OF 4.4-DUCT-PROPELLER VTOL MODEL IN GROUND EFFECT
	572	56	DP	E/A	H/T/C	M	WT	X		X						X	X	X	X					X			LONG. AERO AND CONTROL CHAR. OF DUCTED-PROP. VTOL MODEL
	585	60	DP	E.A	S	P	F	X								X								X			CONVERSION MANEUVER (VZ-4)
	618	59	DP	D/E	S	P	ST F	X								X											DESCRIPTION AND INITIAL FLT-TEST FINDINGS (VZ-4)
	660	63	DP	A/T/E	T/C	P/C	F/WT												X	X							LAT STAB. DERIVS (VZ-4)
	664	53	DP	A/T/E	T/C	P/C	F/WT											X		X							LONG STAB. DERIVS (VZ-4)
	673	51	DP	E/A	S	C	WT	X	X		X							X									WING PLUS DUCTED PROPELLER. GENERAL OVERALL DATA (VZ-4)
	674	61	DP	E/	T	C	WT	X	X		X							X									WING PLUS DUCTED PROPELLER. TRANSITION CONDITIONS (VZ-4)
1.6	64	59	TP	A/E	S	–	–																		X		FLYING QUALITIES REPORT FOR KAMAN K-168
	78	63	TP	D/A	S	P	–	X											X					X	X		X-19 (DUAL-TANDEM FREE-TILTING PROPELLERS)
	162	60	TP	D	LS	P PM	F/WT																				DORNIER DO-29 (AGARD SYMPOSIUM PAPER)
	257	64	S	R/D	H/LS	–	–														X			X			LOW SPEED CONT SYS REQ FOR VTOL. GUIDANCE, FREQ, ATTITUDE CONT. GENERATION OF MOM DISCUSSED STABILIZATION DEVICES. CONT SYS OF GER VJ101 TILT-ENGINE CONFIG DESCRIBED
	373	67	TP	T	H/T	–	–	X		✓																	FORCES AND MOMENTS ON PROPELLER AT ANGLE OF ATTACK
	377	68	TW/TP	T	T/C	–												X									LARGE-TILT-ANGLE LIFTING-SURFACE THEORY. DOWNWASH ANGLES AT TAIL NOT ACCURATELY PREDICTED AT HIGH ANGLES
	570	53	TP/TW	E/A	T/LS/C	M	WT	X							X	X											DETERMINATION OF LIM VALUES ON TRANSITION STALLING CHAR. RATIO OF WING CHORD TO PROP. DIAM VARIED
	679	59	TP	A/E	T	–	–												X						X		FLYING-QUALITIES REPORT FOR KAMAN K-168. DYN STAB. IN TRANSITIONAL FLT.
1.6	65	51	TS	E/A	H	M	F												X					X			LOCKHEED "POGO" (XFV-1)
	66	51	TS	E/A	H	M	F												X					X			LOCKHEED "POGO" (XFV-1)
	284	58	TS	R/A	H/T	–		X								X						X		X		X	STAB. AND CONT CHAR. OF TAILSITTER AIRCRAFT
2.1	5	66	DJ/L+P	A/D	H/T/C	–																					COND NECESSARY FOR GOOD PERFORMANCE AND STAB. AND CONTROL CHAR. FOR JET V/STOL AIRCRAFT
	33	62	DJ	PR	S	P	F										X							X			HAWKER P.1127. HOVER TIME HISTORY
	59	68	DJ/L+P	T.A	H/T	–								X													SEMI EMPIRICAL APPROACH PREDICTING PERF. LOSSES AND PITCH MOM. DUE TO JET INTERFERENCE EFFECTS

* See table 9B for key to summary

TABLE 9-A (CONTD)*

SUBJECT INDEX CLASSIFICATION	REFERENCE NUMBER	YEAR OF PUBLICATION	V/STOL CONCEPT	NATURE OF REPORT MATERIAL	FLIGHT PROGRAM OR AIRFLOW	TEST ARTICLE	TYPE OF TEST	AREAS OF INVESTIGATION OR ANALYSIS: Parts and Material	Wing	Fan Propeller	Ducted Propeller	Thru-Blanketed Duct	Pressure Data	Aero Lift or Turning	Ground Effect	Propeller Rotation Direction Effects	Control	STABILITY AND CONTROL: Longitudinal	Lateral-Directional	Dynamic	Modification	Stimulation	Gyroscopic Effects	Jets or Gas Impinged Control Systems	Handling Qualities Operating Problems Criteria	COMMENTS
2.1 (CONT)	81	64	DJ/L+P	E/A	H	M	WT					X														STATIC PRESS DISTRIB ON WALL AROUND A CIRC JET EXHAUSTING NORMALLY FROM PLANE WALL INTO AIRSTREAM
	86	66	DJ	E/A	T	M	WT	X				X														JET LOCATION INTERFERENCE EFFECTS ON LONG. AERO CHAR. OF A JET VTOL MODEL
	168	66	DJ	R/A	T	–	–																			REORGANIZATION OF THRUST MANAGEMENT CONTROLS FOR VECTORED-THRUST V/STOL VEHICLES DISCUSSED
	112	63	DJ	E	H	M	WT	X					X											X	X	
	180	69	DJ	E/A/P/R	H	P	F/SIM										X									SINGLE- AND DOUBLE-JET MODELS. GROUND EFFECTS ON PERFORMANCE
	196	65	DJ	D/PR	H/T/C	PM	F									X								X	X	X-14A. UTILITY OF DIRECT SIDE-FORCE MANEUVERING DEVICE FOR VTOL AIRCRAFT
	236	62	DJ	E/A	ST/LS	C	ST/WT							X												P-1127 (KESTREL). LOS TECHNIQUES, STAB. IN HOVER AND ACCELERATING TRANSITION, ROUGH GRD OPERATION, NIGHT FLYING
	286	64	DJ/L+P	R	S	–	–								X									X		JET DEFLECTOR TESTS AND COMMENTS
	288	64	DJ/L+P	A	H	–	–									X										DORNIER DO-31. JET-LIFT CONCEPT
	314	63	FIW/ DJ/L+P	R/D	H/T/C	–	–																	X		"MIXED" CONTROL SYSTEM TO HOVER UNSTABILIZED JET-LIFT AIRCRAFT. CONTROL-SYSTEM MOM A FUNCTION OF STICK POS AND RATE OF CHANGE OF STICK POS
	316	68	DJ	A	S	SIM	SIM							X										X	X	DESIGN OPTIMIZATION OF V/STOL DIRECT-LIFT TRANSPORT. DESIGN PROBS OF PROPULSION, HANDLING QUALITIES, TRIM IN HOVER AND TRANSITION, GRD EFFECTS
	333	66	DJ	E/A	H/T/C	M	WT	X									X	X	X							EFFECT OF VARYING AERO DERIVS FOR 4 FLT COND ON STAB AND CONTROL OF XV-4B
	350	69	FIW/ DJ/L+P	A/D	H	–	–									X	X	X						X		AERO CHAR OF VTOL AIRPLANE WITH JET EJECTOR FOR AUGMENTING LIFT
	382	66	DJ/L+P	R/D	H	–	–					X														JET LIFT AND/OR LIFT-FAN V/STOL AERO ANALYZED. SIM MODEL OF JET EFFLUX SUPERIMPOSED ON REP OF VEH GEOM. VORTEX LATTICE TECHNIQUE DISCUSSED, APPL TO P-1127. THEO AND TEST COMP
	397	68	DJ/L+P	E/A	T	M	WT	X						X		X										AERODYNAMICS OF JET VTOL ENGINE INSTALLATIONS. JET INDUCED EFF. EFF OF JET WAKE, GRD. AND INLET L/P SHAPE
	408	66	DJ	E/A	LS	SIM	SIM							X			X	X								AERO CHAR OF A 5-JET VTOL CONFIG. HORIZ-TAIL POSITION EFFECTS. GRD PROXIMITY
	414	64	DJ/L+P	R/D	LS	–	–											X	X		X				X	FLT INVESTIGATION OF STAB AUGMENTATION SYSTEMS FOR P-1127 JET-LIFT V/STOL AIRCRAFT, WITH VARIABLE-STAB HELICOPTER
	19	68	FIW/ DP/DJ	D	H/T/C	–	–	X							X										X	AERODYNAMICS AND FLYING QUALITIES. JET INTERFERENCE. EFF OF MULTIPLE JETS AND WING PLANFORM. INLET EFFECTS. INGESTION CONTROL POWER
	421	68	DJ	E/A/P/R	H/T/C	E	F							X		X										PROBS OF FAN V/STOL AIRCRAFT
	438	65	DJ/L+P	E	LS	M	WT	X									X	X	X	X				X	X	FLT EVALUATION OF P-1127 (XV-6A)
	488	66	DJ	R/D	H/T/C	–	–									X	X	X								SEMI SPAN MODEL OF CLOSE-SUPPORT VTOL. INTEGRATED PROPULSION AND/OR LIFTING-SURFACE SYSTEM
	484	62	DJ/L+P	E/A	H	M	WT	X									X										SUMMARY OF XV-4A VTOL RESEARCH. RESULTS OF FLT TEST. DESIGN SYSTEMS SMALL- AND LARGE-SCALE WT TEST
	820	60	DJ	D/E	S	P	F	X									X										MUTUAL INTERFERENCE BETWEEN NOZZLE SYS, W-B COMBINATIONS, AND FREE STREAM. BASIC FUS AND SERIES OF WINGS. JET-INDUCED DOWNLOAD AND PITCH MOM. OUT OF GRD EFF
	983	64	DJ	E/A	H/T/C	M	SIM						X				X	X	X				X				BELL X-14
																											DYN STAB AND CONT CHAR. OF A VECTORED-THRUST V/STOL MODEL. FLT SIMULATION

* See table 9B for key to summary

TABLE 9-A (CONTD)*

SUBJECT INDEX CLASSIFICATION	REFERENCE NUMBER	YEAR OF PUBLICATION	V/STOL CONCEPT	NATURE OF REPORT MATERIAL	FLIGHT REGIME OR AIRFLOW	TEST ARTICLE	TYPE OF TEST	AREAS OF INVESTIGATION OR ANALYSIS: Forces and Moments	Wing	Free Propeller	Ducted Propeller	Two-Dimensional Data	Pressure Data	Max. Lift or Turning	Ground Effect	Propulsion System Operational Effects	STABILITY AND CONTROL: General	Longitudinal	Lateral-Directional	Dynamic	Stabilization	Simulation	Gyroscopic Effects	Low or Zero Airspeed Control Systems	Handling Qualities	Handling Qualities Criteria	COMMENTS
2.1 (CONT)	589	61	DJ	E/A	H/T	M	WT	X					X														JET INTERFERENCE EFFECTS ON DELTA-WING MODEL
	574	65	JF/L+P	A	H/C	M	WT	X								X											INTEGRATED PROPULSION LIFTING SURFACE SYSTEM. COMPARISONS WITH THEORY
	626	65	DJ	E/A	T	–	–	X									X	X					X				LONG. AND LAT-DIR CHAR. OF 2.4 JET VECTORED-THRUST-TYPE VTOL MODELS
	653	66	S	R/D	H/T/C	–	–																				V/STOL AERO. RESEARCH AT RAE, 1962-66. JET LIFT, FAN LIFT, BLC, JET FLAPS, GRD SIM., WT TEST TECHNIQUES
	661	66	DJ	A	H/T	–	–									X											STAB. INVESTIGATION OF VECTORED-THRUST P-1127. EXPRESSIONS DERIVED FOR STAB. DERIVS
	667	68	DJ/L+P	R/A	H/LS	–	–	X					X			X											AERO. INTERFERENCE EFF. DUE TO JET EFFLUX. STATIC INTERFERENCE EFF. FWD-SPEED INTERFERENCE EFF. THEORY FOR JET-EFFLUX INTERFERENCE
2.2	5	66	DJ/L+P	A/D	H/T/C	–	–																				COND. NECESSARY FOR GOOD PERFORMANCE AND STAB. AND CONTROL CHAR. FOR JET V/STOL AIRCRAFT
	59	68	DJ/L+P	T/A	H/T	–	–						X														SEMIEMPIRICAL APPROACH PREDICTING PERF. LOSSES AND PITCH MOM. DUE TO JET INTERFERENCE EFFECTS
	81	64	DJ/L+P	E/A	H	M	WT					X															STATIC PRESS. DISTRIB. ON WALL AROUND A CIRC. JET EXHAUSTING NORMALLY FROM PLANE WALL INTO AIRSTREAM
	104	65	L+P	A/PR	H/T/C	PM	F																			X	SHORT SC-1. PERFORMANCE, STAB., AND CONTROL, ESPECIALLY IN HOVER AND TRANSITION
	115	60	L+P	D	S	P	F														X			X			SHORT SC-1. DETAILED AIRCRAFT SCHEMATIC
	199	62	L+P	D	H/T	P	F	X					X			X					X			X			SHORT SC-1
	201	62	L+P	D	H/T	P	F	X													X						SHORT SC-1
	288	64	DJ/L+D	R	S	–	–									X											DORNIER DO-31. JET-LIFT CONCEPT
	289	64	DJ/L+D	A	H	–	–																	X			"MIXED" CONTROL SYSTEM TO HOVER UNSTABILIZED JET-LIFT AIRCRAFT. CONTROL-SYSTEM MOM. A FUNCTION OF STICK POS AND RATE OF CHANGE OF STICK POS
	298	63	L+P	E/A/D	H/LS	P	F						X				X	X	X	X			X	X			RESEARCH FLT-TEST RESULTS ON SC-1. FLYING QUALITIES
	299	69	L+P	R	H/LS	–	–						X		X	X	X	X					X	X			SERIES OF TESTS ON SC-1 VARIABLE-STAB. VTOL
	314	63	FIW/ DJ/L+P	R/D	H/T/C	–	–						X										X	X			DESIGN OPTIMIZATION OF V/STOL DIRECT-LIFT TRANSPORT. DESIGN PRORS OF PROPULSION, HANDLING QUALITIES. TRIM IN HOVER AND TRANSITION, GRD EFFECTS
	350	69	FIW/ DJ/L+P	A/D	H	–	–					X															JET LIFT AND/OR LIFT FAN V/STOL AERODYNAMICS ANALYZED. SIM MODEL OF JET EFFLUX SUPERIMPOSED ON REPRESENTATION OF VEHICLE GEOM. VORTEX LATTICE TECHNIQUE DISCUSSED, APPLIED TO P-1127, THEORY AND TEST COMPARED
	362	66	DJ/L+P	R/D	H	–	–						X			X											AERODYNAMICS OF JET VTOL ENGINE INSTALLATIONS. JET INDUCED EFF. EFF OF JET WAKE, GRD, AND INLET LIP SHAPE
	372	62	L+P	D	T	P	F														X						SHORT SC-1
	387	68	DJ/L+P	E/A	T	M	WT	X					X				X	X									AERO. CHAR. OF A JET VTOL CONFIG. HORIZ-TAIL POSITION EFFECTS. GRD PROXIMITY
	414	64	DJ/L+P	R/D	LS	–	–									X										X	AERODYNAMICS AND FLYING QUALITIES. JET INTERFERENCE EFF OF MULTIPLE JETS AND WING PLANFORM. INLET EFFECTS. INGESTION. CONTROL POWER
	427	54	L+P	A/E	LS	M	WT	X				X		X													SEMISPAN MODEL. INTEGRATED PROPULSION-LIFTING-SURFACE SYSTEM

* See table 9-B for key to summary

TABLE 9-A (CONTD)*

SUBJECT INDEX CLASSIFICATION	REFERENCE NUMBER	YEAR OF PUBLICATION	V/STOL CONCEPT	NATURE OF REPORT MATERIAL	FLIGHT REGIME OR AIRFLOW	TEST ARTICLE	TYPE OF TEST	AREAS OF INVESTIGATION OR ANALYSIS: Force and Moment	Wing	Tilt Propeller	Ducted Propeller	Two-Dimensional Data	Pressure Data	Aero. Lift or Turning	Ground Effect	Propeller Rotation Direction Effect	STABILITY AND CONTROL: General	Longitudinal	Lateral Directional	Dynamic	Stabilization	Simulations	Gyroscopic Effects	Take or Low Airspeed Control System	Handling Qualities	Handling Qualities Criteria	COMMENTS
2.2 (CONT)	428	65	DJ/L+P	E	LS	M	WT	X								X	X	X									SEMISPAN MODEL OF CLOSE-SUPPORT VTOL INTEGRATED PROPULSION AND/OR LIFTING SURFACE SYSTEM
	464	62	DJ/L+P	E/A	H	M	WT	X									X										MUTUAL INTERFERENCE BETWEEN NOZZLE SYS, W-B COMBINATIONS, AND FREE STREAM. BASIC FUS PLUS SERIES OF WINGS. JET-INDUCED DOWN LOAD AND PITCH MOMENT OUT OF GRD EFF
	577	66	L+P	A	H	–	–																X				PROPULSION SYS AND/OR CONTROL SYS INTERFACE FOR HOVER CONTROL CONCEPTS, USING LIFT PLUS LIFT-CRUISE PROPULSION
	585	68	L+P	E/A	H/T/C	M	WT	X						X			X	X									XV-4B POWERED INTERFERENCE EFFECTS IN AND OUT OF GRD IN LANGLEY LOW-SPEED TUNNEL. BASIC DATA IN CRUISE IN LANGLEY HIGH-SPEED TUNNEL
	610	68	L+P	E/A	T	M	WT	X										X						X			
	575	64	L+P	E/A	LS	M	WT	X						X			X										ROLL STAB OF SHORT SC-1
	653	66	S	R/D	H/T/C	–	–	?																			INTERFERENCE EFF BETWEEN LIFTING JETS, FREE-STREAM VELOCITY, AND MODEL SURFACES AT LOW FWD SPEEDS. EFF ON LONG. AERO CHAR. VARIOUS JET CONFIG AND WING HEIGHTS. GRD EFF
	659	69	L+P	E/A	T/C	M	WT							X			X	X						X			V/STOL AERO RESEARCH AT RAE, 1962-66. JET LIFT, FAN LIFT, BLC, JET FLAPS, GRD SIM, W T TEST TECHNIQUES
	667	68	DJ/L+P	R/A	H/LS	–	–	X						X	X												LONG. AND LAT-DIR CHAR OF JET-LIFT MODEL. GRD EFF, CONTROL EFFECTIVENESS. EFF OF POWER VARIATIONS OF LIFT JETS
	671	63	L+P	E/A	H/LS	M	WT							X													AERO INTERFERENCE EFF DUE TO JET EFFLUX. STATIC INTERFERENCE EFF. FWD-SPEED INTERFERENCE EFF. THEORY FOR JET-EFFLUX INTERFERENCE
2.3	222	63	YS/DSS	PR	S	2P	F	X						X				X	X	X	X		X				SHORT SC-1. THRUST LOSS AS FUNCTION OF WING HT ABOVE GRD FOR JET-LIFT SCHEMES. THRUST LOSS REDUCTION
	284	58	TS	R/D	H	–	–									X											X-13 AND VZ-3
	386	57	TS	E/A	H/T	PM	F/WT									X		X	X	X							STAB AND CONTROL CHAR OF VERTICAL-ALTITUDE VTOL AIRCRAFT
	543	60	TS	E/A	LS	PM	WT											X	X								X-13, WING POSITION AND VERTICAL-TAIL POSITION VARIED
	554	58	TS	E/A	H/T	PM	WT									X							X				X-13
	556	61	TS	E/A	H/T	PM	F									X	X	X		X			X				X-13
2.4	420	59	TE	E/A	LS	M	WT	X									X	X									WINGLESS JET VTOL TRANSPORT MODEL
2.5	159	69	BLC	E/D	LS	M	WT																				LIFT AUGMENTATION BY SPANWISE BLOWING OVER A LIFTING SURFACE
	422	60	BLC	E/A/T	LS	M	WT	X				X					X	X					X				SIMILAR TO F104 LE AND FLAP BLOWING
	473	69	JF	E/A	LS/C	M	WT	X									X	X									STOL AIRCRAFT EQUIPPED WITH EXTERNAL-FLOW JET FLAP
	597	62	BLC/JF	T/E/A	LS	M	WT	X			X	X															INCR OF LIFT BY BLOWING BLC JET MOMENTUM TO PREVENT SEP. SURVEY ON SYSTEMATIC MEAS.
	653	66	S	R/D	H/T/C	–	–																				V/STOL AERO RESEARCH AT RAE, 1962-66. JET LIFT, FAN LIFT, BLC, JET FLAP, GRD SIM, W-T TEST TECHNIQUES
3.1	24	65	FIW	E/PR/A	H	SIM	SIM													X	X						XV-5A FLT SIM STUDY OF HOVERING UNDER GUSTY COND. OPTIMIZATION OF STAB AUGMENTATION GAINS
	26	66	FIW	E	H/T/C	M	WT	X								X	X	X					X				XV-4A. FULL SCALE. CONTROL EFFECTIVENESS IN ALL 3 MODES

* See table 9B for key to abbreviations

TABLE 9-A (CONTD)*

SUBJECT INDEX CLASSIFICATION	REFERENCE NUMBER	YEAR OF PUBLICATION	V/STOL CONCEPT	NATURE OF REPORT MATERIAL	FLIGHT REGIME OR AIRFLOW	TEST ARTICLE	TYPE OF TEST	AREAS OF INVESTIGATION OR ANALYSIS: Force and Moment	Wing	Free Propeller	Ducted Propeller	Two-Dimensional Data	Pressure Data	L/D or Trimming	Ground Effect	Propeller Location Blockage Effects	STABILITY AND CONTROL: General	Longitudinal	Lateral-Directional	Dyn. s.c.	Stabilization	Simulations	Gyroscopic Effects	Take or Low Airspeed Control Systems	H. Jolling Operations	Handling Qualities Criteria	COMMENTS
3.1 (CONT)	29	59	F/W	E/A		M	ST																				
	34	66	F/W	E/PR/A	H/T/C	P	F																				INVESTIGATION OF THRUST LOSS
	35	66	F/W	E/PR/A	H/T/C	P	F																				XV-5A FAN-IN-WING V/STOL AIRCRAFT
	36	66	F/W	E/PR/A	H/T/C	P	F																				XV-5A FAN-IN-WING V/STOL AIRCRAFT
	41	62	F/W	E/A	ST	M	ST	X																			APPENDIX OF PLOTTED GRAPHS PERTAINING TO VOLS I AND II OF G.E. REPT 166
	43	63	F/W	E/A	–	M	WT/ST	X			X		X			X	X										
	52	60	F/W	E/D/A	H/T	M	WT	X				X	X														LARGE-SCALE TEST DATA
	56	64	F/W	E/T/A	C	M	WT																				VERTOL
	57	64	F/W	E/A/T	H/T/C	M	WT										X	X	X								DYN STAB CHAR OF XV-5A BASED ON THEOR AND EMPIRICAL EST OF DYN AND STATIC DERIVS FROM WT TESTS. CONVENTIONAL FLT.
	60	63	F/F/F/W	D	LS	–	–									X											XV-5A. EST STATIC STAB AND CONTROL
	87	61	F/W	E/A	H/T	M	ST/WT	X				X	X		X												TIP-TURBINE-DRIVEN LIFT FAN SYS. F/F STATIC PERF, WT EVALUATION, GRD-EFF EVALUATION. F/W STATIC PERF, WT EVALUATION, WT RESEARCH
	88	60	F/W	E/A	ST/C	M	ST/WT	X			X																WT TESTS OF VERTODYNE RESEARCH AIRCRAFT. FAN-THRUST VARIATION. GRD EFF WING SURFACE PRESSURES
	102	68	F/W	E/A	T/LS	M	WT										X		X								VERTODYNE. STATIC AND FWD-SPEED TESTS. WING SURFACE PRESSURES, FORCES AND MOM
	117	63	F/W	R/D/A	H/T/C	–	–														X			X	X		STATIC AND DYN LONG. STAB OF VTOL AIRCRAFT
	189	60	DP/F/W	E/A/T	T	M	WT	X			X		X														XV-5A SIMULATION PROGRAM. DESIGN PROBS SOLVED BY SIMULATION
	198	68	F/W	D	T	–	–																				DUCTED FAN AS LIFTING DEVICE IN FWD FLT
	204	67	F/W	E/D/A	LS	M	WT	X																			TECHNIQUE AND COMPUTATION FOR POTENTIAL-FLOW SOLUTION OF 3-DIM V/STOL AIRCRAFT. TRANSITIONAL SIM STUDY
	228	63	F/F/F/W	E/A	H/T/C	M	WT	X								X			X				X				INFLUENCE OF FAN EFFLUX FLOW ON LIFT AND PITCH MOMENT OF FUS, WING, AND TAILPLANE
	234	62	F/W	E/A	H	M	ST		X				X														LARGE-SCALE CONFIGURATION TESTED AND ANALYZED. GEN STATIC AND DYN STAB AND CONT. STRIKE AIRCRAFT AND ASSAULT TRANSPORT ANALYZED.
	239	62	F/W	E/A	ST	M	ST	X					X														GRD EFF ON F/W CONFIG
	266	67	F/W	E/A	LS	M	WT	X																			WING SIZE VARIED
	269	68	F/W	E/A	T	C	WT	X									X	X	X					X			EFF OF LIFT-FAN AND CRUISE-FAN VARIABLES ON AERO CHAR
	270	66	F/W	T	LS	–	–										X	X									
	276	63	F/W	E	LS	M	WT							X				X									CALCULATION OF AERO COEFF OF F/W AIRFOIL
																											AERO CHAR OF DIRECT-LIFT FANS IN WING PANELS. EFF OF FAN OPERATION, THRUST CONTROL BY FAN EFFLUX ON LONG. CHAR. DOWNWASH AT TAIL

* See table 9B for key to summary

TABLE 9-A (CONTD)*

SUBJECT INDEX CLASSIFICATION	REFERENCE NUMBER	YEAR OF PUBLICATION	V/STOL CONCEPT	NATURE OF REPORT MATERIAL	FLIGHT REGIME OR AIRFLOW	TEST ARTICLE	TYPE OF TEST	AREAS OF INVESTIGATION OR ANALYSIS: Forces and Moments	Whirl	Free Propeller	Ducted Propeller	Two-Dimensional Data	Powered Data	Trans. Lift or Landing	Ground Effect	Propeller Effects on Wing/Body	Control	STABILITY AND CONTROL: Longitudinal	Lateral-Directional	Dynamic	Maneuvering	Manipulation	Cryogenic Effects	Effects of Fuel Jettison	Handling Qualities	Control Systems	COMMENTS
3.1 (CONT)	277	67	FIW/FIF	D	T	–	–	X						X		X											COMPREHENSIVE EXPER RESEARCH PROGRAM TO DEFINE AERO CHAR OF LIFT-FAN V/STOL AIRCRAFT
	278	63	FIW/FIF	A/E	T	M	WT	X									X										PERFORMANCE ESTIMATION METHODS GIVEN
	280	57	FIW	E	H/LS	M	ST/WT				X	X		X													INITIAL INVESTIGATION OF FIW CONCEPT
	281	59	FIW	E/A	ST/T	C	WT	X	X	X		X		X													PROPELLER ALSO TESTED SEPARATELY
	283	67	FIW	T	H/T/C	–	–									X											DIGITAL COMPUTER PROGRAM TO STUDY AERO CHAR. FLOW CHARTS, INPUT DATA FORMATS
	302	63	FIW	R/D	S	–	–	X								X	X										SURVEY OF TECHNOLOGICAL STATE-OF-THE-ART FOR FIW CONCEPT
	303	63	FIW	T/A/D/E	H/T	M	WT	X																			MANY PERF DESIGN GRAPHS
	314	63	FIW/ DJ/L+P	R/D	H/T/C	–	–							X											X	X	DESIGN OPTIMIZATION OF V/STOL DIRECT-LIFT TRANSPORT. DESIGN PROBS OF PROPULSION, HANDLING QUALITIES, TRIM IN HOVER AND TRANSITION, GRD EFFECTS
	323	66	FIW	E	H/T/C	M	WT	X						X			X	X	X		X		X				STAB AND CONT CHAR IN HOVERING AND TRANSITION ON FIW MODEL
	332	64	FIW	E/A	H/T	M	WT	X						X			X	X					X				LARGE-SCALE INVESTIGATION OF FIW CONCEPT. GEN AERO CHAR IN AND OUT OF GRD EFF
	334	67	FIW	E/A	LS			X									X	X									AERO CHAR OF V/STOL TRANSPORT. EFF OF ENGINE PLACEMENT. 8 WING FANS AND 2 LIFT-CRUISE ENGINES IN PLIS. FAN FLOW-FIELD INTERFERENCE
	344	65	FIW	A	T	–	SIM												X								ANALOG SIMULATION OF XV-5A DYN STAB CHAR
	360	69	FIW/ DJ/F+P	A/D	H	–	–					X															JET LIFT AND/OR LIFT-FAN V/STOL AERODYANAMICS ANALYZED. SIM MODEL OF JET EFFLUX SUPERIMPOSED ON REPRESENTATION OF VEHICLE GEOM. VORTEX LATTICE TECHNIQUE DISCUSSED, APPLIED TO P-1127. THEORY AND TEST COMPARED
	371	67	FIW	E/PR/A	H/T/C	PM	F							X		X									X		FLIGHT EVALUATION OF HANDLING QUALITIES OF XV-5A
	401	64	FIW	T/A	T	–	–		X							X											THREE-DIMENSIONAL ANALYSIS OF FIW LIFT
	408	61	FIW	T	LS	–	–																				LIFTING-SURFACE THEORY
	416	66	FIW	E/A	LS	M	WT									X											EXPLORATORY TESTS OF FAN-POWERED V/STOL CONFIG, EFFICIENTLY PRODUCING LARGE-LIFT FORCES AT LOW SPEEDS
	419	66	FIW/ DP/DJ	D	H/T/C	–	–	X						X		X											PROBS OF FAN V/STOL AIRCRAFT
	434	65	FIW	A	–	–	–																				METHOD FOR STUDYING EFF ON AERO CHAR OF WINGS IN VICINITY OF LIFTING PROPULSION DEVICES, STAB AND CONT, GRD EFF, AND W-T CORRECTIONS
	439	66	DP/FIW	A/E	AX/N-AX	C	WT	X	X		X																
	488	62	FIW	T	LS	–	–		X								X										TWO-DIM TREATMENT OF DECR IN LIFT AT LOW FWD SPEEDS. COMPARED WITH 2-DIM TEST DATA
	484	66	FIW/FIF	R/D	S	–	–																				LIFT-FAN CONCEPT
	525	67	FIW	T	H/T	–	–									X											INCOMPRESSIBLE POTENTIAL-FLOW THEORY FOR DETERMINING AERO CHAR. THEORY AND APPLICATION
	580	69	FIW	A/T	S	–	–																				ANALYSIS OF AXISYMMETRIC FLOW IN LIFT FAN IN STATIC OPERATION BASED ON DOUGLAS INCOMPRESSIBLE POTENTIAL-FLOW COMPUTER PROGRAM

* See table 9B for key to summary

TABLE 9-A (CONTD)*

SUBJECT WORK CLASSIFICATION	REFERENCE NUMBER	YEAR OF PUBLICATION	V/STOL CONCEPT	NATURE OF REPORT MATERIAL	FLIGHT REGIME OR AIRFLOW	TEST ARTICLE	TYPE OF TEST	AREAS OF INVESTIGATION OR ANALYSIS: Parts and Material	Wing	Free Propeller	Ducted Propeller	Two-Dimensional Data	Pressure Data	Aero Lift in Turning	Ground Effect	Propeller Rotation Direction Effects	General	STABILITY AND CONTROL: Longitudinal	Lateral-Directional	Dynamic	Stabilization	Simulations	Gyroscopic Effects	Jets w/ Low Airspeed	Control Systems	Handling Qualities	Rendering Qualities Criteria	COMMENTS
31 (CONT)	613	67	FIW	A	H/T/C	–	–	X				X											X				PRELIM "IN-DEPTH" DESIGN OF ADVANCED LIFT FAN PROPULSION SYSTEM
	618	62	FIW	E/A	H	M	WT	X						X													GRD EFF ON PERF OF LIFTING FAN
	619	63	FIW	D	T	P	WT	X																			SHAFT-DRIVEN FAN IN WING (VANGUARD)
	633	58	FIW	A/D	H/T	–	–	X																			
	634	59	FIW	E/A/T	H/T	C	WT	X	X			X															
	635	59	FIW	E/A/T	H/T	C	WT	X	X			X	X														INCLUDES WATER VISUALIZATION
	653	66	S	R/D	H/T/C	–	–																				BASIC RESEARCH ON V/STOL AERODYNAMICS AT RAE, 1962-66, JET LIFT, FAN LIFT, BLC, JET FLAPS, GRD SIM, W-T TEST TECHNIQUES
3.2	42	61	FIF	E/A	H/T	M	WT	X																			
	58	61	FIF	E/A	H/T	M	WT	X				X					X										LONG CHAR OF LARGE-SCALE MODEL. FAN SUPPORTED FLT FROM 0 TO 100 KNOTS STATIC PRESS. DISTRIB. DOWN WASH AT HORIZ TAIL
	60	63	FIF/FIW	D	LS	–	–																				TIP-TURBINE-DRIVEN LIFT-FAN SYS. FIF STATIC PERF, WT EVALUATION, GRD EFF EVALUATION, FIW STATIC PERF, WT EVALUATION, WT RESEARCH
	145	65	FIF	E/A	LS	M	WT	X				X				X	X						X				EFF OF SCALE AND WT WALLS ON AERO CHAR. POWER ON AND POWER OFF PITCH. MOM., NORMAL FORCE, AND AXIAL FORCE. PRESSURE DATA
	153	63	FIF	E/A	LS	M	WT	X				X		X			X										AERO CHAR IN GRD EFF. DOWNWASH AT HORIZ TAIL PLUS AREA INDICATED
	228	63	FIW/FIF	E/A	H/T/C	M	WT	X								X			X				X				LARGE-SCALE CONFIGS TESTED AND ANALYZED. GEN STATIC AND DYN STAB. AND CONT STRIKE AIRCRAFT AND ASSAULT TRANSPORT ANALYZED
	277	67	FIW/FIF	D	T	–	–	X						X		X											COMPREHENSIVE EXPER RESEARCH PROGRAM TO DEFINE AERO CHAR OF LIFT FAN V/STOL AIRCRAFT
	278	63	FIW/FIF	A/E	T	M	WT	X																			PITCH-MOM ESTIMATION METHOD GIVEN
	330	61	FIF	D/E	H/T	M	F									X											SUPERSONIC FIGHTER DESIGN. CONFID PEPT. NO PLOTS
	370	65	FIF	E	LS/T	M	WT	X									X										
	386	60	FIF	E/A	T	M	WT	X																			
	484	65	FIW/FIF	R/D	S	–	–																				LIFT-FAN CONCEPT
	483	62	FIF	E/D	LS	M	WT							X													PROPULSION, PERF, AND GRD EFF
	612	63	FIF	E/A	LS	M	WT	X																			INTERFERENCE LOADS DUE TO INTERACTION BETWEEN MAINSTREAM AND EFFLUX. EFF ON LIFT AND PITCH MOMENT
	653	66	S	R/D	H/T/C	–	–																				BASIC RESEARCH ON V/STOL AERODYNAMICS AT RAE, 1962-66, JET LIFT, FAN LIFT, BLC, JET FLAPS, GRD SIM, WT TEST TECHNIQUES
4.1	70	41	–	E/A	AX/LS	C	WT		X	X																	LOW-SPEED, HIGH-THRUST PROPELLERS, OUT OF ROTATION
	71	42	–	E/A	AX	C	WT			X																	SINGLE AND DUAL-TRACTOR PROPELLERS WIDE BLADES

* See table 9B for key to summary

TABLE 9-A (CONTD)*

SUBJECT INDEX CLASSIFICATION	REFERENCE NUMBER	YEAR OF PUBLICATION	V/STOL CONCEPT	NATURE OF REPORT MATERIAL	FLIGHT REGIME OR WINDTUNN	TEST ARTICLE	TYPE OF TEST	AREAS OF INVESTIGATION OR ANALYSIS: Force and Moment	Wing	Free Propeller	Ducted Propeller	Free Dimensional Data	Pressure Data	Max. Lift or Transit	General Effect	Propeller Rotation Slip Stream Effects	STABILITY AND CONTROL: General	Longitudinal	Lateral Directional	Dynamic	Stabilization	Simulation	Cross-coupling Effects	Type of Tail Arrangement	Control Systems	Handling Qualities	Handling Qualities Criteria	COMMENTS
4.1 (CONT)	105	69	FP	T	T	–	–	X		X								X	X									METHOD FOR CALCULATING FORCE, MOM, AND POWER COEFFS OF PROPELLERS IN OBLIQUE FLOW
	119	57	–	T/A	ST/AX	–	–			X																		V/STOL PROPELLER SELECTION
	120	59	–	T/A	ST	–	–			X																		PROPELLER STATIC THRUST
	126	52	–	T/A	N-AX	–	–	X		X																		PROPELLER IN YAW (PITCH)
	150	68	FP	E/A	H/T	C	ST			X								X						X				MONOCYCLIC PROPELLER PITCH FOR LONG. CONTROL
	154	64	–	T	LS	–	–	X		X							X											FORCE AND MOM DERIVS DUE TO FREE PROPELLER INCLINED TO FREE STREAM
	156	66	TP	T	H/T/C	–	–	X		X								X	X									GEN FORCE AND MOM EQ DEVELOPED FOR MOD TO HIGH ANGLES OF INCIDENCE
	171	68	S	T	C/ST	–	–																					RESEARCH ON PROP FLOW FIELD ASSOCIATED WITH TYPICAL V/STOL OPERATIONS, CRUISE FLT AND STATIC OPERATION
	173	66	FP	T	ST	–	–			X																		GEN THEORY FOR PERF CALCULATIONS OF VTOL PROPELLERS OPERATING IN STATIC COND
	220	44	–	E/A	ST	C	ST			X																		THRUST AND TORQUE, SINGLE- AND DUAL-TRACTOR PROPELLERS
	235	56	–	D/A	LS	–	–	X		X																		AERO ASPECTS OF VTOL PROPELLERS
	287	56	FP/DF	T/A	LS	–	–			X	X																	PERF DIAGRAMS
	305	58	–	T	0-90°	–	–			X																		SIMPLE METHOD TO PREDICT PROP FORCES AND PITCH MOM
	373	67	TP	T	H/T	–	–	X		X																		APPROACH TO DETERMINE FORCES AND MOM ON PROPS AT HIGH ANGLES OF ATTACK
	423	54	–	E/A	0-180°	C	WT	X		X																		4-BLADED PROPELLER
	437	63	TP	E/A	H/T/C	M	ST			X														X				EFFECTIVENESS OF MONOCYCLING VARYING BLADE ANGLE FOR LONG CONTROL. BASIC AERO CHAR OF SAME PROP IN A FLAPPING AND RIGID CONFIG
	476	61	S	T/A/R	LS	–	–																					APPLICATION OF SMALL-PROP DATA
	489	48	–	E/A	ST	C	ST			X																		4 DIFFERENT 2-BLADED PROPS TESTED
	490	48	FP/DP	E/A	ST	C	ST	X		X	X																	
	512	45	–	T/A	N-AX	–	–	X		X																		"PROPELLERS IN YAW" (R. BNER)
	545	58	S	T/A	AX/N-AX	–	–	X		X																		GENERALIZED PROP PERF
	646	66	FP	E/A	LS	M	W/T	X		X								X	X									FORCES AND MOM ACTING ON PROP CENTER WERE TESTED FOR WIDE RANGE OF ADVANCE RATIO, PROPELLER ATTITUDE, AND BLADE PITCH SETTINGS
	647	61	–	E/A/T	N-AX	M				X																		WATER-TUNNEL PROP AXIS NORMAL TO FLOW, PHOTOS
	675	60	–	E/A	0-85°	C	WT	X		X																		3 PROPS TESTED EXTENSIVE POWER DATA

* See table 9B for key to summary

TABLE 9-A (CONTD)*

SUBJECT INDEX CLASSIFICATION	REFERENCE NUMBER	YEAR OF PUBLICATION	V/STOL CONCEPT	NATURE OF REPORT MATERIAL	FLIGHT REGIME OR AIRFLOW	TEST ARTICLE	TYPE OF TEST	AREAS OF INVESTIGATION OR ANALYSIS: Forces and Moments: Wing	Fixed Propeller	Locked Propeller	Two-Dimensional Data	Pressure Data	Max Lift or Trim Limiting	Ground Effect	Propeller Rotation Direction Effects	STABILITY AND CONTROL: General	Longitudinal	Lateral-Directional	Dynamic	Stabilization	Simulations	Compressibility Effects	Jets or Low Airspeed Control Systems	Handling Qualities	Flutter Considerations	COMMENTS
4.1 (CONT)	676	63	-	E/A	LS	C	WT	X		X																TWO VTOL PROPS IN DESCENT
4.2	19	60	DP	E/A	S	C	WT/ST	X			X															PERF CHARTS. WATER TESTS ALSO
	72	68	DP	R/A	—	—	—	X			X		X			X										SUMMARY OF TEST RESULTS OF EXTENSIVE RESEARCH PROGRAM ON SHROUDED PROPS
	73	67	DP	E/A	H/T/C	M	WT/ST	X			X		X			X										EXTENSIVE SHROUDED-PROP RESEARCH PROGRAM
	95	62	DP	T/A/E	S	C	WT/ST	X			X		X													
	169	60	DP/FIW	E/A/T	T	M	WT	X			X		X													THE DUCTED FAN AS A LIFTING DEVICE IN FWD FLT
	21	60	DP	T	—	—	—				X															NOMOGRAM ANALYSIS
	219	61	DP	E/A	ST/N-AX	C	WT	X	X		X		X													RING-WING AND SEVERAL DUCTED PROPS IN NONAXIAL FLOW
	237	64	DP	T	LS/ST	—	—				X		X													THEORY FOR STEADY AERO LOADING ON DUCTED PROP IN STATIC AND LOW-SPEED FLT SHROUD THRUST AND SURFACE PRESS
	246	58	DP	E/A	S	C	ST/WT	X			X															DATA FORM = 0 TO 0.6, MAX ANGLE OF ATTACK = 6°
	248	67	DP	E/A	N-AX	M	WT	X			X															α_D = -10° TO 110°
	266	55	DP	T	C	—	—				X															COMPRESSIBILITY EFFECTS
	267	58	PP/DP	T/A	F-X	—	—			X	X															PERF DIAGRAM
	271	65	JP	E/A	H/T/C	M	WT	X			X		X													POWERED-DUCT MODEL OF X-22A VTOL AIRCRAFT. FORCES AND MOM ON COMPLETE UNIT AND SHROUD ALONE. SHROUD INTERNAL AND EXTERNAL PRESS DISTRIB
	285	59	DP	E/A	S	C	WT	X			X															DUCTED-PROP DESIGN METHOD (UNIV OF WICHITA)
	286	58	DP	E/A	ST/N-AX	C	ST/WT				X		X													SEVERAL REPTS. FAMILY OF DUCTED PROPS (UNIV OF WICHITA)
	292	66	DP	E/T/A	C	M	WT				X		X													COMPARISON OF THEOR PREDICTIONS OF DUCT PRESS DISTRIB IN FWD FLT AND TEST RESULTS FOR X-22A DUCTED-PROP UNIT
	306	58	DP	E/A	ST	C	ST	X			X															STATIC THRUST IMPROVEMENT METHOD
	307	64	DP	E/A	H/T	M	WT	X			X															RELATED THRUST PROFILES TESTED TO DETERMINE EFF OF GEOM VARIABLES AND THRUST COEFF ON LIFT AND PITCH MOM.
	346	64	DP	E/T	LS	M	WT	X			X		X													LARGE-SCALE DUCTED PROPS USED TO EVAL THEOR METHODS THRUST, NORMAL FORCE, PITCH MOM., DUCT PRESS.
	347	63	DP	T	H/T/C	—	—	X			X					X			X							THEOR METHOD TO PREDICT FORCES, MOM, STAB DERIVS (STATIC AND DYN) OF ISOLATED DUCTED PROP AT ALL α's
	348	64	DP	A/T	AX/T/C	—	—	X			X						X	X	X							FORCE AND MOM COEFF AND DYN PITCH DERIVS PREDICTED BY POTENTIAL FLOW ANALYSIS
	349	64	DP	A/T	H/T/C	—	—	X			X					X	X		X							THEOR STAB DERIVS
	353	44	DP	E/A/T	ST/AX	C	ST/WT	X			X															

* See table 9B for key to summary

TABLE 9-A (CONTD)*

SUBJECT INDEX CLASSIFICATION	REFERENCE NUMBER	YEAR OF PUBLICATION	V/STOL CONCEPT	NATURE OF REPORT MATERIAL	FLIGHT REGIME OR AIRFLOW	TEST ARTICLE	TYPE OF TEST	Forces and Moments	Wing	AREAS OF INVESTIGATION OR ANALYSIS: Free Propeller	Ducted Propeller	Two-Dimensional Data	Pressure Data	Aux. Lift or Turning	Ground Effect	Propeller Rotation Direction Effects	STABILITY AND CONTROL: General	Longitudinal	Lateral-Directional	Dynamic	Stabilization	Transitions	Gyroscopic Effects	Loss or Low Airspeed Control Systems	Hovering Conditions	Hovering Conditions Effects	COMMENTS
4.2 (CONT)	394	64	DP	E/A	C	M	WT				X																	SHORT-CHORD LOW-SOLIDITY DUCTED PROPS. IN CRUISE COND. PERF DATA IN PITCH
	430	67	DP	E/A	AX/N-AX	C	WT	X			X																	X-22A COMPONENT
	439	59	DP/FIW	E/A	AX/N-AX	C	WT	X	X		X																	
	442	65	DP	E/A	H/C	M	ST/WT	X																				FORCE AND MOM. DATA FOR 3 DUCTED-PROP CONFIG (SAME DUCT). STATIC AND FWD SPEED COND
	444	65	DP	E/A	H/LS	M	ST/WT				X		X															PERF, DUCT PRESS. DISTRIB, AND PROP. INFLOW DATA FOR TRACTOR AND PUSHER PROPELLERS
	463	60	DP	T	AX	–	–																					3-DIM. THEORY. EFF OF BLADE NO., CIRCULATION PROFILE AND STRENGTH, PROP ADV RATIO, TIP CLEARANCE
	467	60	DP	E/A	0-90°	C	WT	X	X		X																	DUCT (WITH AND WITHOUT PROP.)
	488	60	DP	E/A	ST/N-AX	C	WT				X			X			X											STAB. AND CONT. INVESTIGATION. STATIC-TYPE SHROUD
	486	57	DP	T/A	AX	–	–				X																	RING WING WITH CENTER BODY AND PROP
	490	48	FR/DP	E/A	ST	C	ST	X		X	X		X															
	527	59	DP	T/A/D	S	–	–	X			X																	REVIEW AND BIBLIOGRAPHY ON DUCTED PROPS. THROUGH 1959
	534	44	DP	A	AX	–	–				X																	
	547	61	DP/S	T/D/E	S	P	F				X																	APPENDIX PRESENTS PERF. DATA ON 20 VTOL'S, 6 JEEPS
	556	60	DP	E/A	T	M	WT	X			X						X											JEEP-TYPE VEHICLE
	594	60	DP	T	H/LS	–	–																					PROBS OF DUCTED FAN AND ITS APPLICATION. THEOR RESULTS FOR THRUST, MOM., AND MOM OF MOMENTUM
	595	60	DP	R/A	H/T/C	M	ST/WT																					REVIEW AND ANALYSIS OF EXPER RESULTS. STATIC, AXIAL AND NONAXIAL
	596	61	DP	T	AX	–	–	X			X																	
	599	66	DP	E	H	C	ST						X															FLOW PATTERN AND PRESS. DISTRIB ABOUT THE SHROUD, REARWARD MOTION AND FWD MOTION
	631	68	DP	A																								DUCTED-PROP TEST PROGRAM – DATA ANALYSIS
	636	59	DP	E/A	–	M	WT				X																	BLADE TIP EFFECTS
4.3	8	63	KL	E/A	–	M	WT	X	X			X		X														ROTATING-CYLINDER FLAP
	83	57	TW	T/E/A	T	M	WT	X	X																			WING ALONE IN PROP. SLIPSTREAM, "DESTALLING" EFFECTS ANALYZED
	122	60	RF	T/A	LS	–	–	X	X																			ROTATING FLAP AS HIGH-LIFT DEVICE
	123	57	RF	T/E/A	LS	M	WT	X	X																			APPENDIX I AND II (THEORY AND POWER REQ. (SEE REF. 122)

* See table 9B for key to summary

TABLE 9-A (CONT'D)*

Subject Index Classification	Reference Number	Year of Publication	V/STOL Concept	Nature of Report Material	Flight Regime of Airflow	Test Article	Type of Test	Force and Moment	Wing	Free Propeller	Ducted Propeller	Two-Dimensional Jets	Pressure Data	Max Lift or Turning	Ground Effect	Propeller Rotation Direction Effects	Co-axial	Stability and Control: Longitudinal	Lateral-Directional	Dynamic	Stabilization	Simulations	Gyroscopic Effects	Tare or Fan Analyzed Control/Systems	Handling Qualities Criteria	Comments
4.3 (CONT)	160	56	BLC	E/A/T/R	LS	C	WT	X	X			X	X	X												BLOWING OVER NOSE OF TE FLAPS, POWER REQ
	205	58	JF	E/A	LS	C	WT	X	X																	FULL-SPAN AND HALF-SPAN BLOWING, AR=8.3
	225	60	–	T/A/E	–	C	WT/ST		X																	WING IN SLIPSTREAM STUDY
	319	56	BLC	T/E	LS	C	WT	X	X			X														BLOWING TYPE BLC
	337	58	HL	A/E	LS	C	ST	X	X																	VISUAL DATA INCLUDED, "ON THE NATURE OF STALL"
	511	54	HL	T	LS	–	–		X																	LIFT AND INDUCED DRAG WITH LARGE DOWNWASH ANGLES
	514	36	–	T	–	–	–		X																	WING IN SLIPSTREAMS
	518	56	BLC/HL	R/T/E/A	LS	C	WT	X	X			X														BLOWING, SUCTION, SLOTTED, PLAIN FLAP, HIGH-LIFT DEVICES
	542	58	DSS/BLC	E/A	ST	C	ST	X	X					X	X											WING IN PROP SLIPSTREAM
	620	61	DSS/TW	E/A	LS	C	WT		X			X		X												PROP TO WING CHORD RELATIONSHIP
	621	56	S	T	LS	–	–		X																	THEORY OF WING-PROPULSION SYSTEMS
	522	60	–	T/A	–	–	–		X																	SLIPSTREAM SHEAR ON AIRFOIL CHAR
	528	57	JF	E/A	LS	C	WT	X	X						X			X								ε AND dε/dα FOR VARIOUS TAIL LOCATIONS, η_t
4.4	199	57	DP	E/A	LS	M	WT	X	X																	LIFT, DRAG, AND PITCH MOM OF FAMILY OF ANNULAR AIRFOILS. EST LIFT-CURVE SLOPES AND INDUCED DRAG COMPARED WITH TEST
	287*	58	–	E/A	N-AX	C	WT	X	X																	RING WING WITH CENTERBODY
	488	53	–	T/A	N-AX	–	–		X																	
	513	47	–	T	N-AX	–	–		X																	
	542	55	DP	A/R/D	LS	–	–																			SPECIAL PROBS DUE TO ANNULAR-WING CONCEPT, FROM POINT OF VIEW OF FLOW MECHANICS
4.5	3	63	JF	E/A	LS	M	WT	X	X						X		X									EFF OF GRD PROXIMITY ON DELTA WING WITH AND WITHOUT JET BLOWING AT TE
	4	61	JF	E/A	LS	M	WT/ST	X																		THRUST, FLOW VISUALIZATION, DOWNWASH MEAS, JET TRAVERSING COMPARISON WITH THEORY
	75	60	JF	T	LS	–	–	X																		EMPIRICAL RELATIONS FOR LIFT AND DRAG OF UNSWEPT 3-DIM JET-FLAPPED WINGS
	92	66	JF	E/A	LS	M	SIM	X							X											JET-FLAP MODEL WITH MOVING BELT RIG FOR GRD SIMULATION
	93	67	JF	E/A	LS	M	WT	X					X		X			X	X							BASIC AERO CHAR, INCLUDING GRD EFF
	97	67	JF	T/A	LS	–	–																			PROPOSED JET-WING FOR V/STOL AIRCRAFT THRUST AUGMENTATION CONCEPTS ASSESSED, TEST APPARATUS AND RESULTS DESCRIBED

* See table 9B for key to summary

TABLE 9-A (CONTD)*

SUBJECT INDEX CLASSIFICATION	REFERENCE NUMBER	YEAR OF PUBLICATION	V STOL CONCEPT	NATURE OF REPORT MATERIAL	FLIGHT REGIME OR AIRFLOW	TEST ARTICLE	TYPE OF TEST	AREAS OF INVESTIGATION OR ANALYSIS: Forces and Moments	Wing	Thru Propeller	Ducted Propeller	Thru Downstream Duct	Pressure Duct	Jet Lift or Turning	Ground Effect	Propeller Rotation Direction Effect	Control	STABILITY AND CONTROL: Longitudinal	Lateral Directional	Dynamic	Stabilization	Simulation	Crosswind Effects	Type of Jet Actuated Control System	Handling Qualities	Handling Qualities Criteria	COMMENTS
45 (CONT)	116	67	JF	D	LS	–	–																				JET AUGMENTOR WING PRINCIPLE DISCUSSED
	146	59	JF	D	LS	–	–	X	X								X										COMMENTS ON AERODYNAMICS OF PROPULSIVE-WING CONCEPT LIFT, SPAN EFFICIENCY &C, DRAG DIVERGENCE
	147	65	JF	E/A	LS	M	WT							X				X	X								SEMISPAN JET-AUGMENTED-FLAP MODEL, WITH AND WITHOUT GRD BOARD
	172	62	JF	T	LS	–	–	X																			THEOR SOLUTION FOR PITCH MOM OF 2-DIM JET-FLAPPED WING
	181	61	JF	E/A	LS	M	WT	X																			AERO FORCES AND MOM ON JET FLAPPED WING IN PRESENCE OF PROP SLIPSTREAM AND FREE STREAM
	182	61	JF	E/A	LS	M	WT	X									X										LARGE-SCALE EXTERNAL FLOW JET-AUGMENTED-FLAP MODEL
	193	59	JF	E	H	C	ST	X	X					X													FLATTENED TAILPIPE EXHAUSTED OVER FLAP
	294	57	JF	E/A	LS	M	WT					X	X		X												GRD EFF ON HIGH LIFT COEFFS
	321	69	JF	D/A	LS	M	WT	X									X	X	X	X	X			X	X		DESIGN STUDY OF AUGMENTOR-WING JET STOL RESEARCH AIRCRAFT ENGINE SURVEY CONFIG DEVELOPMENT PERF COMPARISONS CONF G SELECTION, SYS, AERODYNAMICS
	322	67	JF	T	LS	–	–	X																			ASYMPTOTIC THEORY OF HIGH ASPECT RATIO JET FLAP LIFT INDUCED DRAG AND PITCH MOM COEFFS COMPARISON WITH EARLIER THEORIES
	325	68	JF	E/A	LS	M	WT	X				X						X									LOW-SPEED CIRCULATION-CONTROLLED AIRFOIL LIFT DRAG AND PITCH MOM AS FUNCTIONS OF BLOWING MOMENTUM COEFF TWO DIM
	335	67	JF	E/A	LS	M	WT	X										X	X								MODEL WITH EXTERNAL JET AUGMENTED FLAP
	339	64	JF	T/A	LS	–	–	X																			THRUST HYPOTHESIS AND ITS VERIFICATION APPLICATION OF JET FLAP PRINCIPLE TO STOL AIRCRAFT
	340	59	JF	A/D	LS	–	–										X										JET FLAP APPLICATION FOR STOL
	341	63	JF	T	LS	–	–		X			X					X											CHAR OF JET-FLAPPED WINGS AT ANGLES OF ATTACK
	342	64	JF	T/D	–	–	–																	X			CHAR OF JET FLAPPED WING EVALUATED FOR STOL APPLICATION
	378	67	–	T	LS	–	–							X													LINEAR THEORY SOLUTION FOR JET FLAP IN GRD EFF
	379	67	JF	T/A	LS	–	–							X													LINEAR THEORY FOR JET FLAP IN GRD EFF GEN LINEAR CASE OF AN ARBITRARY AIRFOIL AND JET COEFF
	381	56	JF	E/D	LS	M	WT																				PRELIM INVESTIGATION OF JET FLAPS IN 7 X 10' LOW-SPEED TUNNEL
	390	57	JF	A/D	LS	–	–							X		X	X										HIST OF JET AUGMENTATION PRINCIPLE INTEGRATION OF PROPULSION AND LIFTING SYSTEMS PREDICTING AERO CHAR OF WINGS WITH JET AUG FLAPS GRD EFF AND DOWNWASH FIELD BEHIND WING LONGITUDINAL S AND C
	391	56	JF	E/A	LS	M	WT																				EFF OF ASPECT RATIO AND END PLATES ON AERO CHAR OF WING WITH JET FLAP CHART FOR EST JET-CIRCULATION LIFT
	427	65	JF	A	LS	M	WT	X			X		X														DATA ANALYSIS OF SEMISPAN VTOL MODEL INTEGRATED PROPULSION LIFTING SURF FLOW ANGULARITY MEAS AT TAIL
	433	66	JF	T	LS	–								X													FLOW PATTERN OF THIN JET-FLAPPED 2-DIM WING IN GRD EFF
	436	68	JF	T	LS	–	–																				ANALYSIS OF A JET SHEET AS AN ALTERNATIVE TO A RIGID DIFFUSER FOR MOMENTUM PROPULSION

* See table 9B for key to summary

TABLE 9-A (CONTD)*

Subject Index Classification	Reference Number	Year of Publication	V/STOL Concept	Nature of Report Material	Flight Regime or Airflow	Test Article	Type of Test	Force and Moment	Wing	Free Propeller	Ducted Propeller	Two-Dimensional Data	Pressure Data	Max Lift or Turning	Ground Effect	Propeller Slipstream / Downwash Effects	Stability and Control: General	Longitudinal	Lateral-Directional	Dynamic	Stabilization	Simulation	Operational Effects	Zero or Low Airspeed / Control Systems	Handling Qualities Criteria	COMMENTS
4.6 (CONT)	473	66	JF	E/A	LS/C	M	WT	X									X	X								STOL AIRCRAFT EQUIPPED WITH EXTERNAL-FLOW JET FLAP
	487	62	JF	T/A/R	LS	–	–	X																		SEMIEMPIRICAL METHOD FOR DETERMINING JET-FLAP PERF. COMPARISON WITH TEST DATA
	526	61	JF	T	LS	–	–																			EVALUATION OF DOWNWASH BEHIND JET FLAPPED WING
	538	57	JF	T/A	LS	–	–	X				X	X													THEOR SOLUTION FOR 2-DIM JET-FLAPPED WING. COMPARISON WITH EXPERIMENT
	540	61	JF	T/A	LS	–	–	X				X	X													THEOR SOLUTION FOR 2-DIM JET-FLAPPED WING
	565	60	DSB/JF	E	H/LS	C	WT	X	X	X			X		X											WING-PROPELLER CONFIG JET FLAP PLUS DEFLECTED SLIPSTREAM
	573	6[illegible]	JF	E/A	LS	M	WT	X																		POWERED BLOWING-TYPE CIRCULATION CONTROL
	574	65	L+P/JF	A	HC	M	WT	X								X										ANALYSIS OF SELECTED DATA. INTEGRATED PROPULSION-LIFTING-SURFACE SYSTEM COMPARISON WITH THEORY
	581	60	JF	E	LS	M	WT	X						X			X	X								EFF OF WING JET THRUST ON AERO CHAR
	590	62	JF	T	LS	–	–										X		X							LONG STAB, CONTROL, AND RESPONSE CHAR OF JET-FLAP AIRCRAFT
	597	62	BLC/JF	T/E/A	LS	M	WT	X				X	X													INCR OF LIFT BY BLOWING BLC. JET MOMENTUM REQ TO PREVENT SEP. SURVEY ON SYSTEMATIC MEAS
	617	61	JF	E	LS	M	WT/SIM		X				X		X											FREE-FLT INVESTIGATION TO EVALUATE GRD EFF ON JET-FLAPPED WING
	628	57	JF	E/A	LS	C	WT	X	X						X		X									FLOW-FIELD CHAR. AND GRD INFLUENCE ON MODEL WITH JET AUGMENTED FLAPS. DOWNWASH AND DOWNWASH GRADIENTS
	646	67	JF	D	LS	–	–	X								X	X						X			PROGRESS REPT THROUGH LATE 1967 ON AUGMENTOR-WING RESEARCH
	660	61	JF	T	LS	–	–	X						X		X										AERODYNAMICS OF JET FLAPS
	663	66	S	R/D	H/T/C	–	–																			BASIC RESEARCH ON V/STOL AERODYNAMICS AT RAE, 1962-66. JET LIFT, FAN LIFT, BLC, JET FLAPS, GRD SIM, W-T TEST TECHNIQUES
	664	62	JF	T/A	LS	–	–							X												A FORMULA DERIVED BY CONFORMAL TRANSFORMATION FOR LIFT INDUCED BY 90-DEGREE JET FLAP IN GRD EFF. COMPARISON WITH OTHER THEORY AND EXPERIMENT
	672	64	JF	A	LS	–	–																			THEOR TREATMENT OF 2-DIM INCOMPRESSIBLE JET. EFF OF JET ENTRAINMENT ON LOSS OF THRUST FORCE
	677	60	JF	T	LS	–	–																			THEOR METHOD FOR THRUST DEVELOPED BY JET FLAP
8.1	22	64	F/W	T/A	H/T/C	M	WT										X	X					X			EST OF XV-6A AERO CHAR
	47	66	S	R/D/PR/A	S	–	–									X	X	X	X	X			X	X	X	AIRWORTHINESS STANDARDS FROM RECOMMENDATIONS OF AEROSPACE INDUSTRIES ASSN. FAA DRAFT DISCUSSED
	128	60	TW/DSB	T/A	H/T/C	–	–									X										METHODS PREDICTING AERO STAB DERIVS OF PROP-DRIVEN TILT-WING V/STOL AIRCRAFT
	200	66	S	R/A/D	S	–	–										X	X	X	X			X	X	X	PROGS IN EST STAB AND CONT CHAR OF V/STOL AIRCRAFT. REC ANALYTICAL STUDIES. MATH MODELS DISCUSSED
	208	62	–	E/A	H/T	F	F																X	X	X	EFF OF LOW-SPEED-CONTROL CROSS COUPLING. HELICOPTER TEST BED

* See Table 9B for key to summary

TABLE 9-A (CONTD)*

SUBJECT WORK CLASSIFICATION	REFERENCE NUMBER	YEAR OF PUBLICATION	V/STOL CONCEPT	NATURE OF REPORT MATERIAL	FLIGHT REGIME OR AIRFLOW	TEST ARTICLE	TYPE OF TEST	AREAS OF INVESTIGATION OR ANALYSIS: Factors Involved: Wing	Free Propeller	Ducted Propeller	Two-Dimensional Data	Pressure Data	Abs. Lift or Thrust	Ground Effect	Propeller Slipstream Blocking Effect	Control	STABILITY AND CONTROL: Longitudinal	Lateral-Directional	Dynamic	Stabilization	Simulation	Gyroscopic Effects	Type or Type Airplane Control Systems	Handling Qualities Rating/Pilot Opinion	Handling Qualities Criteria	COMMENTS
5.1 (CONT)	215	57	TW/DSS	T/E/A	LS	M	WT	X								X										EFF OF PROP SLIPSTREAM ON WING PERF. VARIATION IN SLIPSTREAM VELOCITY
	284	58	DSS	E/A	H	C	ST		X	X					X											WING PLUS PROPELLER, PROP-POSITION EFF
	273	61	–	T	LS	–	–								X											GEN NOMOGRAPHIC SOLUTION FOR INDUCED VELOCITIES AND WAKE SKEW
	293	66	DSS	A	LS	–	–																			EQS AND CHARTS FOR LIFT AND LONG FORCE COEFFS OF WINGS IMMERSED IN PROP SLIPSTREAMS. SAMPLE CALC
	345	67	–	R/D	H/T/C	–	–						X		X											AERO PROBS IN V/STOL. CHANGES IN FORCES AND MOM DURING TRANSITION AND IN STOL WITH GRD INTERFERENCE
	361	60	DSS	E/A	S	M	WT	X					X			X										PROP EFF, LE SLAT, TAIL FAN OPERATION
	430	66	TW/DSS	A	S	SIM	TM								X	X	X	X	X	X						REVIEW OF V/STOL FLT SIM AT CANADAIR THROUGH FLT TESTING THE CL-84
	468	60	DP	E/A	ST/N-AX	C	WT									X										STAB AND CONT INVESTIGATION. STATIC-TYPE SHROUD
	473	69	JF	E/A	LS/C	M	WT	X								X	X									STOL AIRCRAFT EQUIPPED WITH EXTERNAL-FLOW JET FLAP
	523	67	–	A	H/T/C	–	–								X			X								RESEARCH AIRPLANE DESIGN STUDY. STAB AND CONT SUMMARIES. FLT DYN ANALYSIS
	861	52	–	E/A	LS	M	WT	X								X										PROP THRUST, TAIL LOCATION VARIED, q_t/q_∞ $d\epsilon/d\alpha$
	585	61	S	D/E	T	M/C	WT								X	X										JET INTERFERENCE EFF, SEVERAL CONFIGS
	595	68	L-P	E/A	H/T/C	M	WT	X					X			X	X									XV-4B. POWERED INTERFERENCE EFFECTS IN AND OUT OF GRD IN LANGLEY LOW-SPEED TUNNEL. BASIC DATA IN CRUISE IN LANGLEY HIGH-SPEED TUNNEL
	830	63	–	A/D	H/LS	–	–								X				X		X					STAB DUE TO GYROSCOPIC FORCES
	843	64	–	R/D	H/T	–	–								X							X	X	X		QUALITATIVE DISCUSSION OF STAB AND CONT PROBS OF VTOL AIRCRAFT
	661	68	DJ	A	H/T	–	–								X											STAB OF VECTORED-THRUST P-1127. EXPRESSIONS FOR STAB DER.VS
5.2	31	62	TW	E/A	LS	M	F									X	X	X								4 PROPS., FREE-AIR TESTS
	47	66	S	R/D/PR/A	S	–	–								X	X	X	X	X			X	X	X		AIRWORTHINESS STANDARDS FROM RECOMMENDATIONS OF AEROSPACE INDUSTRIES ASSN, FAA DRAFT DISCUSSED
	56	64	DP	A/T	C/T	–	–											X								XV-6A. ANALYSIS OF CONVENTIONAL FLT CHAR. NATURAL DAMPING CONTRIB TO FLT IN LIFT-FAN MODE
	85	51	TS	E/A	H	M	F											X					X			LOCKHEED "POGO" (XFV-1)
	86	51	TS	E/A	H	M	F											X					X			LOCKHEED "POGO" (XFV-1)
	101	68	TW	A	T	–	–									X		X								FACTORS INFLUENCING DYN LONG STAB OF A TILT-WING V/STOL AIRCRAFT
	103	68	TW	E/A	H/T/C	M	WT	X		X						X		X								STATIC AND DYN LONG STAB DERIVS
	106	58	DSS	T/A/E	H/T	M	WT	X										X								ALSO STATIC STAB (VZ-3)

* See table 9B for key to summary

TABLE 9-A (CONTD)*

3.2 (CONT)	REFERENCE NUMBER	YEAR OF PUBLICATION	V/STOL CONCEPT	NATURE OF REPORT MATERIAL	FLIGHT REGIME OR AIRFLOW	TEST ARTICLE	TYPE OF TEST	AREAS OF INVESTIGATION OR ANALYSIS: Parts and Assembl	Wing	Free Propeller	Ducted Propeller	Trans-Sonic/Sonic Data	Pressure Data	Max. Lift or Turning	Ground Effect	Propeller Rotation Direction Effects	General	STABILITY AND CONTROL: Longitudinal	Lateral-Directional	Dynamic	Stabilization	Simulations	Cross-coupling Effects	Take-off, Low Airspeed Control Systems	Handling Qualities	Handling Criteria	COMMENTS
	124	68	S	R/A	H/T	–	–												X				X	X	X		DYN AND CONT REQUIREMENTS FOR VTOL, BASED ON HANDLING-QUALITY EXPERIMENTS LONG HOVER AND TRANSITION
	126	68	–	R/A	H	–	–											X	X								LAT HOVER-MODE DYNAMICS, SATISFACTORY AND UNACCEPTABLE
	128	60	TW/DSS	T/A	H/T/C	–	–									X											METHODS PREDICTING AERO STAB DERIVS OF PROP-DRIVEN TILT-WING V/STOL AIRCRAFT
	130	68	TW	A	H/T	M	WT										X		X								EXPER VALUES OF LONG STAB DERIVS OF 3 TILT-WING AIRCRAFT VARIED TO ANALYZE CHARACTERISTIC ROOTS AND TRANSIENT RESPONSE
	133	66	–	T	LS	–	–												X								DYN RESPONSE OF VTOL AIRCRAFT WITH VARYING FLT VELOCITY
	136	69	OP/TW	A	LS	–	–	X								X	X		X								ASPECTS OF LONG. DYN STAB CHAR OF PROP-DRIVEN V/STOL AIRCRAFT ANALYZED
	136	67	TW/DSS	E/A	T	M	T										X		X								XC-142A MODEL LONG DYNAMICS AT HIGH WING INCIDENCE
	137	68	–	D	LS	–	–										X	X	X								DESCRIPTION OF PRINCETON DYNAMIC MODEL TRACK (VTOL MODEL TESTING)
	139	61	TW/H	E/A	T	M/E	T/F										X		X								PRINCETON FORWARD FLIGHT FACILITY, VZ-2 AND HELICOPTER
	140	61	S	T/A	H/LS	–	–												X								ANALYSIS OF LONG EQS OF MOTION
	152	61	DSS	D	H/T/C	M/PM/ SIM	W/F/ SIM												X								DISCUSSION OF COORDINATED METHODS USED TO PERFECT DYN BEHAVIOR OF BREGUET 940
	167	63	–	A	T	–	–										X		X								LINEAR TIME-VARYING APPROXIMATION TO DYNAMICS OF LOW-SPEED FLYING MACHINES, APPLICATION TO LONG DYNAMICS OF VTOL AIRCRAFT DURING TRANSITION
	170	62	–	T/A	H/T	–	–										X		X	X	X						RESPONSE DESIRED OF V/STOL AIRCRAFT
	200	69	S	R/A/D	S	–	–										X	X	X	X			X	X	X		PROBS IN EST STAB AND CONT CHAR OF V/STOL AIRCRAFT, REQ ANALYTICAL STUDIES MATH MODELS DISCUSSED
	202	60	L+P	A/T	H/T	P	F										X	X	X	X		X	X	X	X		SHORT SC-1
	256	66	–	T	H	–	–												X								THEORY OF DYN STAB. OF VTOL AIRCRAFT, CHAR. OF DISTURBED MOTION IN HOVER, CONTROLLED TRANSITIONAL FLT DISCUSSED
	259	68	DP	A	T	–	–		X										X								SIMPLIFIED ANALYTICAL APPROACH FOR EVALUATING DYN STAB CHAR OF VTOL CONFIG
	282	61	TW	T/A	T	–	–										X		X								EQS OF MOTION FOR UNCONVENTIONAL FLT CHAR
	301	60	–	T/A/D	H/T	–	–												X								
	315	68	DJ	A	S	SIM	SIM										X	X	X								XV-4B, EFF ON STAB AND CONT OF VARYING AERO DERIVS, 4 FLT COND
	323	66	–	T	H/T	–	–												X								DEVEL OF EQS OF MOTION FOR ANALYZING VTOL DYNAMICS DURING HOVER AND TRANSITION
	324	62	DP	A	T	–	–										X	X	X								X-22A DYNAMICS IN TRANSITION, EQS OF MOTION FOR IDENTIFYING FLT-TEST PARAMETERS
	344	66	FIW	A	T	–	SIM												X								ANALOG SIM OF XV-5A DYN STAB CHAR
	369	68	TW		LS	M	WT												X					X			DYN STAB TESTS, EFF OF STAB DERIVS ON DYN STAB

* See table 9B for key to summary

TABLE 9-A (CONTD)*

SUBJECT INDEX CLASSIFICATION	REFERENCE NUMBER	YEAR OF PUBLICATION	V/STOL CONCEPT	NATURE OF REPORT MATERIAL	FLIGHT REGIME OR AIRFLOW	TEST ARTICLE	TYPE OF TEST	AREAS OF INVESTIGATION OR ANALYSIS: Tests and Measurements	Wing	Free Propeller	Ducted Propeller	Two-Dimensional Data	Pressure Data	Aero Lift or Turning	Ground Effect	Propeller Operation	Ducted Effects	STABILITY AND CONTROL: General	Lo Bi-Lateral Lateral-Directional	Dynamic	Instrumentation	Simulations	Gyroscopic Effects	Aero or Low Airspeed Control Systems	Handling Qualities	Handling Qualities Criteria	COMMENTS
5.2 (CONT)	388	56	TW	E/A	H/T	M	F											X	X	X							4-PROP VTOL
	389	56	TW	E/A	T	M	F													X							4-CASCADE WINGS, 4 PROPS.
	412	63	–	A	–	–	–													X							ANALYSES FOR SIM AND DEVEL OF EQS OF MOTION. EQS OF MOTION FOR X-19, XV-5A, AND P-1127
	416	54	DSS	E/A	H	M	F							X						X							
	417	64	TW/DJ/FW	R/D	H/LS	–	–											X	X	X	X			X	X		DYN TESTS OF FREE-FLT MODELS OF 3 V/STOL CONCEPTS DYN STAB AND CONT PROBS.
	451	62	TW	E/A	H/T	M	F											X		X							4-PROP TILT-WING WITH FLAPS
	469	61	DP	E/A	H/T	M	F											X	X	X	X						4-DUCT VEHICLE
	470	61	DP	E/A	H/T	M	F													X	X						2-DUCT VEHICLE
	471	64	–	A/R	LS	–	-													X							DISCUSSION AND RESULTS OF 3 MODEL TEST TECHNIQUES USED BY NASA FOR DYN STAB TESTS
	491	64	–	R/A/D	LS	–	–											X		X							EFF OF TYP NONLINEARITIES IN LIFT AND PITCH MOM CURVES ON LONG MOTION. APPLIC TO V/STOL AIRCRAFT
	495	68	DP	E/A	H	M	WT	X			X							X	X	X							MODEL SIMILAR TO X-22A. LONG AND LAT TRANSIENT RESPONSE USING DYN MODEL. COMPARISON OF LIFT, DRAG, AND PITCH MOM OF ISOLATED DUCT
	496	68	DP	E/A	T	M	WT											X		X							MODEL SIMILAR TO X-22A. LONG TRANSIENT RESPONSE USING DYN MODEL. TIME HISTORIES OF MODEL MOTION IN VARIOUS LONG DEGREES OF FREEDOM
	498	69	TW	E/A	T	M	T	X											X	X							XC-142A MODEL TESTED IN 3 DEGREES OF LAT DIR FREEDOM IN MIDTRANSITION FLT COND. CONTROL EFFECTIVENESS. CONTROL MIXING REQUIREMENTS
	499	61	TW	E/A	T	M	T/F	X										X		X							PRINCETON FORWARD FLIGHT FACILITY (VZ-2 MODEL)
	504	66	–	A	T	–	–											X		X							ASYMPTOTIC APPROX USING MULTIPLE TIME SCALES FOR LONG DYN OF VTOL VEHICLES
	512	67	–	A	H/T/C	–	–										X			X							RESEARCH AIRPLANE DESIGN STUDY. STAB AND CONT SUMMARIES FLT DYN ANALYSIS
	531	64	TW/DSS	E/A	T	M	SIM								X			X	X	X							DYN LAT STAB AND CONT CHAR OF THE VZ-2 SIM FLT-TEST EVALUATION. TRANSITION RANGE WHERE WING STALLING OCCURS
	543	60	TS	E/A	LS	PM	WT												X	X							X-13
	553	64	DJ	E/A	H/T/C	M	SIM							X				X	X	X				X			DYN STAB AND CONT CHAR OF A VECTORED-THRUST V/STOL MODEL FLT SIMULATION
	578	64	TW/DSS	E/A	T	SIM	SIM												X	X		X					PROB AREAS IN SIM OF LAT-DIR DYN BEHAVIOR OF STOL AIRCRAFT EQ OF MOTION. TURBULENCE EFFECTS
	593	68	–	T/A	T	–	–							X				X	X	X							DEVEL OF DYN MODEL FOR ANALYZING V/STOL TRANSPORTS IN LOW-ALT TURBULENCE IN TRANSITION FACTORS AFFECTING RESPONSE TO TURBULENCE
	600	60	TW	E/A	T	PM	WT	X										X	X	X							VZ-2
	601	80	TW	E/A	S	PM	F							X				X	X	X				X			X-18
	602	58	TW	E/A	S	PM	F													X							VZ-2

* See table 9B for key to abbreviations

TABLE 9-A (CONTD)*

SUBJECT INDEX CLASSIFICATION	REFERENCE NUMBER	YEAR OF PUBLICATION	V/STOL CONCEPT	NATURE OF REPORT MATERIAL	FLIGHT REGIME OR AIRFLOW	TEST ARTICLE	TYPE OF TEST	AREAS OF INVESTIGATION OR ANALYSIS: Force and Moment	Wing	Tilting Propeller	Ducted Propeller	Two-Dimensional Data	Pressure Data	Max. Lift or Turning	Ground Effect	Propeller Rotation Direction Effects	General	STABILITY AND CONTROL: Longitudinal	Lateral-Directional	Dynamic	Stabilization	Manual/Auto	Oppositeness Effects	Zero or Low Airspeed Control Systems	Handling Qualities	Handling Qualities Criteria	COMMENTS
6.2 (CONT.)	304	55	DSS	E/A	H	M	F	X											X								
	607	57	DSS	E/A	T	M	F	X									X	X	X									4-ENGINE TRANSPORT CONFIG, EXTENSIBLE VANES
	665	61	DSS	T/A	T	–	–												X								4-ENGINE TRANSPORT CONFIG, EXTENSIBLE VANES
	682	62	TW	T/A/E	S	P/M	F/WT										X		X								6 EQS OF MOTION DEVELOPED AND EXAMINED
	663	63	DP	A/T/E	T/C	P/C	F/WT											X	X								STAB DERIVS (VZ-2)
	684	63	DP	A/T/E	T/C	P/C	F/WT										X		X								LAT STAB DERIVS (VZ-4)
	668	66	–	T/A	H	–	–			X	X								X								LONG STAB DERIVS (VZ-4)
5.3	2	61	–	A	H/T	–	–												X		X					X	TECHNIQUE FOR ASSESSING EFF OF CONFIG GEOM, SIZE, AND MASS ON DYNAMICS OF HOVERING VEHICLES. EQ OF MOTION. THEORY COMPARED WITH TEST DATA ON DUCTED PROPS AND FREE PROPS
	7	60	–	E/A	H/T	S	S																	X	X		
	8	63	S	E/A	H/T	S/SIM	S/SIM										X	X			X			X	X		HELICOPTER, AIRPLANE, V/STOL COMPARISON
	39	62	–	D	H/T	–	–																		X	X	SEVERAL AIRCRAFT, UNPUBLISHED
	47	58	S	R/D/PR/A	S	–	–									X	X	X	X	X				X	X	X	AGARD RECOMMENDATIONS AS OF 1962
	79	62	–	D	H/T	–	–																			X	AIRWORTHINESS STANDARDS FROM RECOMMENDATIONS OF AEROSPACE INDUSTRIES ASSN, FAA DRAFT DISCUSSED
	86	63	TW	E/D/PR	H/T	SIM	SIM										X	X	X		X			X	X	X	AGARD RECOMMENDATIONS
	107	53	DP	E/A	H/T/LS	–	–										X	X	X	X				X	X	X	STUDY OF TILT-WING HANDLING QUALITIES. 2° OF FREEDOM
	108	63	–	E/A	LS	SIM	SIM														X					X	CONT AND STAB AUGMENTATION REQUIREMENTS. THEOR AND ANALOG-COMPUTER INVESTIGATIONS
	124	58	S	R/A	H/T	–	–												X					X	X	X	STUDY TO DETERMINE METHOD OF PRESENTING HANDLING QUALITIES CRITERIA FOR UNSTABLE MODELS
	132	66	–	Q/R	H/T/C	–	–									X	X	X	X					X	X	X	DYN AND CONT REQUIREMENTS FOR VTOL, BASED ON HANDLING-QUALITY EXPERIMENTS. LONG HOVER AND TRANSITION
	148	64	–	PR/A	H/LS	SIM	F/SIM											X						X	X	X	SUGGESTIONS FOR FLYING-QUALITY SPECIFICATIONS FOR VTOL AIRCRAFT
	179	61	–	E/A	H	SIM	SIM												X		X	X			X	X	EFF OF WEATHERCOCK STAB ON DIR HANDLING QUALITIES. SYNTHETIC TURBULENCE. VAR-STAB HELICOPTER TESTED
	200	66	S	R/A/D	S	–	–										X	X	X	X				X	X	X	PILOTED 1 D.O.F. FLT SIMULATOR, ALTITUDE
	207	64	–	E/A	T	SIM	SIM														X						PROBS IN EST STAB AND CONT CHAR OF V/STOL AIRCRAFT. REQ ANALYTICAL STUDIES. MATH MODELS DISCUSSED
	213	62	–	E/A	H	SIM	SIM							X					X	X	X			X	X	X	DESCRIPTION OF ANALOG COMPUTER APPROACH TO V/STOL SIMULATION
	216	64	–	E/A/PR	H	SIM	SIM													X	X			X	X	X	HEIGHT CONTROL 1 D.O.F. SIMULATOR
																											HEIGHT-CONTROL REQ FOR VTOL AIRCRAFT DURING HOVER

* See table 9B for key to summary

TABLE 9-A (CONTD)*

SUBJECT UNDER CLASSIFICATION	REFERENCE NUMBER	YEAR OF PUBLICATION	V/STOL CONCEPT	NATURE OF REPORT MATERIAL	FLIGHT REGIME OR AIRFLOW	TEST ARTICLE	TYPE OF TEST	AREAS OF INVESTIGATION OR ANALYSIS: Forces and Moments: Wing	Fan Propeller	Ducted Propeller	Two-Dimensional Data	Pressure Data	Max. Lift or Turning	Ground Effect	Propeller Rotation Direction Effects	Stability and Control: General	Longitudinal	Lateral-Directional	Dynamic	Stabilization	Simulation	Operational Effects	Type or Low Authority Control Systems	Handling Qualities	Handling Qualities Criteria	COMMENTS
S (CONT)	217	62	–	E/A	H	SIM/E	SIM/F						X					X	X	X		X	X	X		HEIGHT CONTROL, FIXED-BASE SIMULATOR AND AIRCRAFT FLIGHT CHECKS
	243	69	–	A	H/T/C	–	–																X	X		PROGRESS IN DEVELOPMENT OF HANDLING QUALITY SPEC FOR MILITARY V/STOL AIRPLANES
	245	63	–	D	H/T	–	–																	X		FAA PROPOSED VTOL FLIGHT REQUIREMENTS
	262	66	–	A	H	–	–																			FACTORS AFFECTING EFFICIENCY OF HOVER CONTROL SYSTEM FOR VTOL CONTROL EFFECTIVENESS, CONTROL CRITERIA
	290	69	S	R/A	C/T/H	SIM	SIM													X	X		X	X	X	NO. AMERICAN ROCKWELL RESEARCH IN V/STOL FLT CONT, VTOL FLT CONTROL DESIGN WITH IFR CAPABILITY, VTOL LDG PROB FROM CONVENTIONAL FLT TO HOVER
	310	65	J/L+F	R/A	H/LS	–	–																	X	X	EFF OF VEHICLE SIZE ON HANDLING QUALITIES OF VTOL AIRCRAFT AT HOVER AND LOW SPEEDS
	318	68	–	A	LS	–	–									X		X						X	X	LONG HANDLING QUALITIES DATA ANALYZED IN TERMS OF PILOT RATING TRENDS ASSOC WITH VARIATIONS IN IMPORTANT PARAMETERS
	351	67	–	R/D	S	–	–																	X	X	DEVEL OF VTOL FLYING-QUALITIES CRITERIA AREAS FOR FURTHER RESEARCH
	383	63	–	R/D	LS	SIM	SIM													X				X	X	VTOL HANDLING QUALITIES USING FIXED-BASE SIMULATORS, SIM TECHNIQUES BOUNDARIES OF DAMPING AND CONT SENSITIVITY
	393	60	–	E/A	H/T	SIM	SIM																		X	
	403	62	TW	E/A	H/T/LS	SIM	SIM									X					X			X	X	FLT SIM TO DETERMINE LONG HANDLING QUALITIES AND PILOT TECHNIQUES NORMAL AND EMERGENCY CONDITIONS
	407	64	–	E/PR/A	H/LS	SIM	SIM/F										X	X						X	X	DIHEDRAL EFF ON DIR-HANDLING QUALITIES, AIRBORNE SIMULATOR (VAR STAB HELICOPTER) ANGULAR RATE DAMPING, CONTROL SENSITIVITY
	408	66	–	E/PR/A	H/LS	SIM	SIM									X	X	X	X				X	X	X	FLT RESEARCH TO DETERMINE CONT POWER AND CONT SENSITIVITY REQUIREMENTS DURING VISUAL HOVERING AND LOW-SPEED APPROACH (VARIABLE-STAB HELICOPTERS)
	412	63	–	A	–	–	–											X								V/STOL ANALYSES FOR SIM AND DEVEL OF EQS OF MOTION, EQS OF MOTION FOR X-19, XV-5A, AND P-1127
	505	66	–	E/A	H/T	SIM	SIM									X	X	X		X					X	PARAMETERS IDENTIFIED TO SPECIFY HANDLING-QUALITIES CRITERIA, DERIVS DEFINED
	522	67	DJ	E/A	H	P	F											X	X			X	X	X	X	HOVERING CONT REQUIREMENTS OF VARIABLE STAB AND CONT X-14A
	528	61	–	E/A	H/T	SIM/E	SIM/F									X		X	X	X				X	X	LONG CONT PROBS AT LOW DAMPING
	529	59	H	E/A	H/LS	E	F											X	X	X		X	X	X	X	DAMPING AND CONT POWER EFF ON HELICOPTER HANDLING QUALITIES
	530	69	–	R/D/A	H/T/C	–	–																	X	X	RESEARCH AND PROGRESS TO 1969 IN DEVEL OF V/STOL FLYING-QUALITIES SPEC, PERTINENT AREAS DISCUSSED
	540	66	–	E/PR/A	H	SIM	F																	X		RESULTS OF FLT TESTS IN HOVERING RIG TO INVESTIGATE HANDLING QUALITIES
	557	66	–	E/A	T	SIM	SIM										X	X		X					X	DIR HANDLING-QUALITIES CRITERIA FOR INSTRUMENT APPROACH
	583	67	–	R	H/T/C	–	–											X	X	X				X		DYN RESPONSE CRITERIA FOR V/STOL AIRCRAFT SIMULATOR
	587	60	–	A	H/T	–	–																		X	
	588	60	–	A	H/T	–	–											X	X					X	X	

* See table 9B for key to summary

TABLE 9-A (CONTD)*

SUBJECT MODEL CLASSIFICATION	REFERENCE NUMBER	YEAR OF PUBLICATION	V/STOL CONCEPT	NATURE OF REPORT MATERIAL	FLIGHT REGIME OR AIRFLOW	TEST ARTICLE	TYPE OF TEST	AREAS OF INVESTIGATION OR ANALYSIS: Forces and Moments	Wing	Free Propeller	Ducted Propeller	Two Dimensional Data	Pressure Data	Max Lift or Turning	Ground Effect	Propeller Operation Disturbed Effects	STABILITY AND CONTROL: General	Longitudinal	Lateral-Directional	Dynamic	Stabilization	Simulators	Gyroscopic Effects	Turn or Low Airspeed Control/Attitude	Handling Qualities	Handling Qualities Criteria	COMMENTS
5.3 (CONT)	623	69	-	PR/A	H/LS	SIM	SIM										X	X	X	X	X		X	X	X		CRITERIA FOR VTOL DYN RESPONSE IN HOVER AND LOW-SPEED FLT LONG., LAT, HEIGHT, AND DIR HANDLING QUALITIES REQUIREMENTS
	643	64	-	R/D	H/T	-	-									X							X	X	X		QUALITATIVE DISCUSSION OF STAB AND CONT PROBS OF VTOL AIRCRAFT
5.4	7	60	-	E/A	H/T	S	S																	X	X		HELICOPTER, AIRPLANE, V/STOL COMPARISON
	8	63	S	E/A	H/T	S/SIM	S/SIM										X	X			X			X	X		SEVERAL AIRCRAFT, UNPUBLISHED
	9	65	DSS/ DSS+BLC	R/A	LS	-	-									X		X					X	X			LIFT PERF, LIMITATIONS IN LOW-SPEED OPERATION, AND HANDLING QUALITIES PROBS OF STOL AIRCRAFT
	40	64	-	R/D	H/T/C	-	-																	X			FLYING QUALITIES FOR MIL V/STOL VEHICLES RECOMMENDED BY AGARD FLT MECH PANEL
	47	66	S	R/D-PR/A	S	-	-									X	X	X	X	X			X	X	X		AIRWORTHINESS STANDARDS FROM RECOMMENDATIONS OF AEROSPACE INDUSTRIES ASSN, FAA DRAFT DISCUSSED
	69	59	TP	E/A	S	-	-																	X			FLYING QUALITIES REPT FOR KAMAN K 158
	84	64	DSS	A	LS	SIM	SIM										X		X		X		X	X			OTTEF, AIRCRAFT, SHORT-FIELD LDG CHAR OF STOL AIRCRAFT FROM PERF STUDIES, MANEUVER DYN ANALYSES AND FLT SIM
	85	66	-	P/D/E/A	H/T	SIM	SIM																	X			EFF OF SOME DERIVS, TURBULENCE, AND CONT POWER ON VTOL HANDLING QUALITIES
	96	63	TW	E/D/PR	H/T	SIM	SIM										X	X	X		X		X	X	X		TILT-WING HANDLING QUALITIES, 2° OF FREEDOM
	90	63	-	E/PR	H	M	F													X			X	X	X		CRITICAL DEMANDS ON VTOL ATTITUDE IN HOVER APPLICATION OF MANEUVERING CRITERIA IN VAR STAB AIRCRAFT
	101	68	TW	A	T	-	-										X		X								FACTORS INFLUENCING DYN LONG STAB OF TILT-WING V/STOL AIRCRAFT
	104	65	L+P	A/PR	H/T/C	PM	F																	X			SHORT SC-1, PERF, STAB., AND CONT, ESPECIALLY IN HOVER AND TRANSITION
	117	63	FIW	R/D/A	H/T/C	-	-														X			X	X		XV-5A SIMULATION PROGRAM, DESIGN PROBS SOLVED BY SIMULATION
	124	68	S	R/A	H/T	-	-												X				X	X	X		DYN AND CONT REQUIREMENTS FOR VTOL, BASED ON HANDLING-QUALITY EXPERIMENTS, LONG HOVER AND TRANSITION
	141	64	DSS	A	C	-	-									X	X	X	X					X	X		BREGUET 941, LOW-SPEED FLYING QUALITIES COMPARED WITH AGARD REQUIREMENTS FOR V/STOL
	145	64	-	PR/A	H/LS	SIM	F/SIM											X						X	X		EFF OF WEATHERCOCK STAB ON DIR HANDLING QUALITIES SYNTHETIC TURBULENCE VAR-STAB HELICOPTER TESTED
	151	69	DSS	D	LS/C	P	F	X																X			BREGUET 941 AND 942
	161	63																X						X			LAT-DIR HANDLING QUAL OF V/STOL AIRPLANES
	166	61	S	P/D	T	P	F																	X			SEVERAL PROTOTYPES
	180	69	D	E/A/PR	H	P	F/SIM											X						X	X		X-14A UTILITY OF DIRECT SIDE-FORCE MANEUVERING DEVICE FOR VTOL AIRCRAFT
	200	69	S	R/A/D	S	-	-										X		X	X				X	X	X	PROBS IN EST STAB AND CONT CHAR OF V/STOL AIRCRAFT, REG ANALYTICAL STUDIES, MATH MODELS DISCUSSED
	202	69	L+P	A/T/E	H/T	P	F										X	X	X	X		X	X	X	X		SHORT SC-1

* See table 9-B for key to summary

TABLE 9-A (CONTD)*

SUBJECT INDEX CLASSIFICATION	REFERENCE NUMBER	YEAR OF PUBLICATION	V/STOL CONCEPT	NATURE OF REPORT MATERIAL	FLIGHT REGIME OR SIMULOW	TEST ARTICLE	TYPE OF TEST	AREAS OF INVESTIGATION OR ANALYSIS: Force and Moment	Wing	Free Propeller	Ducted Propeller	Two-Dimensional Data	Pressure Data	Max. Lift or Turning	Ground Effect	Propeller Rotation Direction Effects	STABILITY AND CONTROL: General	Longitudinal	Lateral-Directional	Dynamics	Stabilization	Stabilizers	Gyroscopic Effects	Free or Tow Airborne	Control Systems	Handling Qualities	Handling Qualities Criteria	COMMENTS
5.4 (CONT)	203	68	–	A/O/PR	H	SIM	SIM									X					X			X				6°-OF-FREEDOM MOTION SIMULATOR EVALUATED ON ITS ABILITY TO SIMULATE VTOL VISUAL HOVER TC
	208	62	–	E/A	H/T	E	F														X			X				LOW-SPEED CONTROL CROSS COUPLING HELICOPTER SIMULATOR
	209	64	–	PR/A	LS/P	E	F																X	X				EFF OF CHANGES IN STATIC DIR STAB ON HANDLING QUALITIES AND ON DIR SENSITIVITY AND DAMPING
	210	61	–	E/A	H/T	SIM	SI															X		X				GYROSCOPIC CROSS COUPLING, PITCH-ROLL
	211	61	–	E/A	H/T	SIM	SIM															X		X				GYROSCOPIC CROSS COUPLING, PITCH-YAW
	213	62	–	E/A	H	SIM	SIM						X					X	X	X			X	X	X			HEIGHT CONTROL, 1 D.O.F. SIMULATOR
	217	62	–	E/A	H	SIM/E	SIM/F						X					X	X	X			X	X	X			HEIGHT CONTROL, FIXED-BASE SIMULATOR AND AIRCRAFT FLIGHT CHECKS
	221	58	–	D	H/T	–	–													X			X	X				HANDLING QUALITIES, PILOTING TECHNIQUES, AND HUMAN FACTORS OF VTOL
	233	65	–	T/E/PR	LS	SIM	SIM									X	X	X	X	X			X	X				VTOL CONT AND RESPONSE REQUIREMENTS USING VAR-STAB HELICOPTER AS SIMULATOR. C_{rg} VARIED CONTROL SENSITIVITY AND CONT POWER REQUIREMENTS. SIMULATED TURBULENCE
	241	66	–	E/A	H	SIM	SIM														X		X	X				6°-OF-FREEDOM MOTION SIMULATOR USED TO INVESTIGATE CONT-SYS REQUIREMENTS. EMPHASIS ON HOVERING. SIMULATOR CHAR
	242	66	–	E/A	H/T	SIM	SIM														X		X	X				6°-OF-FREEDOM MOTION SIMULATOR. LOW-SPEED CONT SYS CONCEPTS RELATING TO HANDLING QUALITIES AND CONT POWER REQUIREMENTS
	245	69	–	A	H/T/C	–	–																	X	X			PROGRESS IN DEVEL OF HANDLING-QUALITY SPEC FOR MIL V/STOL AIRPLANES
	265	60	–	D/A	–	SIM	SIM														X							REVIEW STUDY ON SIMULATORS
	268	62	S	E/A	T	SIM	SIM									X								X	X			3 CONFIGS, DP, TR, AND TW WITH FLAPS
	269	64	–	T/A	LS	–	–												X					X	X			EVALUATION OF LAT-CONT EQS FOR APPLICATION TO STOL AIRCRAFT
	282	66	–	A	H	–	–																					FACTORS AFFECTING EFFICIENCY OF HOVER CONTROL SYS FOR VTOL. CONTROL EFFECTIVENESS, CONTROL CRITERIA
	290	69	S	R/A	H/T/C	SIM	SIM													X	X		X	X	X			NO. AMERICAN ROCKWELL RESEARCH IN V/STOL FLT COND, V TOL FLT-CONT DESIGN WITH IFR CAPABILITY. VTOL LOG PROB FROM CONVENTIONAL FLT TO HOVER
	291	65	DSS/BLC	E/PR/A	LS	PM	F/SIM									X	X	X		X			X	X				HANDLING QUALITIES OF A STOL SEAPLANE
	298	63	L+P	E/A/O	H/LS	P	F						X			X	X	X	X				X	X				RESEARCH FLT-TEST RESULTS ON SC-1 FLYING QUALITIES
	299	63	L+P	R	H/LS	–	–						X		X	X	X	X					X	X				SERIES OF TESTS ON SC-1 VARIABLE-STAB VTOL
	300	61	HL	D/R/A	LS	E	F									X	X							X				FLIGHT EXAMINATION OF STOL APPROACH
	304	59	DSS	E/A	S	P/SIM	WT/SIM	X					X			X	X						X	X				VZ-3 PROTOTYPE WT AND SIMULATOR STUDY
	309	65	DJ/L+P	R/A	H/LS	–	–																	X				EFF OF SIZE ON VTOL AIRCRAFT HOVER AND LOW-SPEED HANDLING QUALITIES
	316	63	DP	E/A PR	T/LS	P	F									X	X						X	X				RESULTS OF COMBINATIONS OF AIRCRAFT ATTITUDE, AIRSPEED, AND ANGLE OF ATTACK IN SIMULATED GRD-CONTROLLED LOG APPROACHES

* See table 9B for key to summary

TABLE 9-A (CONTD)*

SUBJECT INDEX CLASSIFICATION	REFERENCE NUMBER	YEAR OF PUBLICATION	V/STOL CONCEPT	NATURE OF REPORT MATERIAL	FLIGHT REGIME OR AIRFLOW	TEST ARTICLE	TYPE OF TEST	AREAS OF INVESTIGATION OR ANALYSIS: Force and Moment	Wing	Free Propeller	Ducted Propeller	Two-Dimensional Data	Pressure Data	Man, Life or Training	Ground Effect	Propeller Rotation Direction Effects	STABILITY AND CONTROL: Control	Longitudinal	Lateral-Directional	Dynamic	Stabilization	Simulations	Gyroscopic Effects	Tests on Low Aircraft Control Systems	Handling Qualities	Handling Qualities Criterion	COMMENTS
5.4 (CONT)	318	68	–	A	LS	–	–										X		X					X	X	LONG HANDLING-QUALITIES DATA ANALYZED IN TERMS OF PILOT RATING TRENDS ASSOCIATED WITH VARIATIONS IN IMPORTANT PARAMETERS
	326	68	DJ		T	SIM	SIM													X		X				SIM OF PRINCIPLES OF CONTROLLING SMALL JET VTOL AIRCRAFT
	336	61	DP	T	H/LS	–	–										X	X	X				X	X		HOVERING IN STILL AIR AND GUST COND, GLIDE APPROACHES AT LOW SPEED. DAMPING AND SENSITIVITY
	351	67	–	R/D	S	–	–																	X	X	DEVEL OF VTOL FLYING-QUALITIES CRITERIA, AREAS FOR FURTHER RESEARCH
	369	68	TW		LS	M	WT												X					X		DYN STAB TESTS, EFF OF STAB DERIVS ON DYN STAB
	371	67	TW	E/PR/A	H/T/C	PM	F							X		X								X		FLT EVALUATION OF HANDLING QUALITIES OF XV-5A
	376	63	S	D	H/T	P	F																	X	X	FRENCH V/STOLS (BREGUET 941, BALZAC)
	383	63	–	R/D	LS	SIM	SIM													X				X	X	VTOL HANDLING QUALITIES USING FIXED-BASE SIMULATORS. SIM TECHNIQUES. BOUNDARIES OF DAMPING AND CONT SENSITIVITY
	394	68	L+P	E/A	T/LS	E	–																X	X	X	HANDLING QUALITIES OF VTOL AIRCRAFT. CONT MODES COMPARED IN TERMS OF PILOT ACCEPTANCE AND CONT POWER REQ
	395	66	TW	R	H/T/C	–	–										X	X			X			X	X	SUMMARY OF TEST PROGRAM ON CL-84 V/STOL PROTOTYPE AND 2 TYPES OF SIMULATORS TO ASSESS QUALITATIVELY HANDLING QUALITIES
	402	63	TW	R/A	H/T	–	–										X						X	X		LONG FLT CONT, FLOW SEPARATION, PITCH MOM, CONT SYS
	403	63	TW	E/A	H/T/LS	SIM	SIM										X				X			X	X	FLT SIM TO DETERMINE LONG HANDLING QUALITIES AND PILOTING TECHNIQUES. NORMAL AND EMERGENCY CONDITION
	407	64	–	E/PR/A	H/LS	SIM	SIM/F												X	X				X	X	DIHEDRAL EFF ON DIR HANDLING QUALITIES. AIRBORNE SIMULATOR (VAR-STAB HELICOPTER). ANGULAR RATE DAMPING CONTROL SENSITIVITY
	408	65	DJ	E/A	LS	SIM	SIM												X	X	X			X		FLT INVESTIGATION OF STAB AUGMENTATION SYS FOR P-1127 JET-LIFT V/STOL AIRCRAFT, WITH VAR-STAB HELICOPTER
	409	66	–	E/PR/A	H/LS	SIM	SIM										X	X	X	X			X	X	X	FLT RESEARCH TO DETERMINE CONT POWER AND CONT SENSITIVITY REQUIREMENTS DURING VISUAL HOVER AND LOW-SPEED APPROACH (VAR-STAB HELICOPTERS)
	410	63	–	A/D/E/PR	H/T/N–AX	SIM	SIM										X							X		HOVER, TRANSITION, AND STEEP APPROACHES. CONT CROSS-COUPLING EFF
	411	65	TW	E/A/PR	H/T/C	SIM	SIM								X						X			X	X	CANADAIR CL-84 SIMULATED BY AIRBORNE SIMULATOR
	414	64	DJ/L+P	R/D	LS	–	–								X									X		AERODYNAMICS AND FLYING QUALITIES. JET INTERFERENCE. EFF OF MULTIPLE JETS AND WING PLANFORM. INLET EFF. INGESTION CONT POWER
	417	64	TW/ FIW/DJ	R/D	H/LS	–	–										X	X	X	X			X	X		DYN TESTS OF FREE-FLT MODELS OF 3 V/STOL CONCEPTS. DYN STAB AND CONT PROBS
	421	68	DJ	E/A/PR	H/T/C	E	F										X	X	X	X			X	X		FLT EVALUATION OF P-1127 (XV-6A)
	429	69	DP	R/PR/A	H/T	SIM	SIM								X						X			X		3 TYPES OF GBD-BASED SIMULATORS OF THE X-22A EVALUATED AND COMPARED WITH ACTUAL FLIGHT
	431	68	–	R/A	H/LS	–	–														X			X		
	432	63	TW/DSB	E/A	T	M	WT	X									X							X		VZ-2. WING STALLING PHENOMENA STUDIED. LIFT AND DRAG CORRELATED WITH FLT-TEST RESULTS. FLYING QUALITIES PROBS CORRELATED WITH WING STALL, TUFT STUDY
	460	63	–	R/A	H/T/C	–	–																	X		PILOTING TASKS DEFINED. HANDLING QUALITIES OF VTOL AND CONVENTIONAL AIRCRAFT CONTRASTED

* See table 9B for key to summary

TABLE 9-A (CONTD)*

Subject Index Classification	Reference Number	Year of Publication	V/STOL Concept	Nature of Report Material	Flight Regime or Airflow	Test Article	Type of Test	Force and Moment	Wing	Free Propeller	Ducted Propeller	Two-Dimensional Data	Pressure Data	Max. Lift or Turning	Ground Effect	Propeller Rotation/Download Effects	Stability and Control: General	Longitudinal	Lateral-Directional	Dynamic	Stabilization	Simulation	Gyroscopic Effects	Low or Low Airspeed Control/Dynamics	Handling Qualities Criteria	COMMENTS
5.4 (CONT)	462	57	–	T/A	T	–	–									X			X					X		
	474	62	–	E/A	H	SIM	SIM													X	X		X	X	X	INSTRUMENT FLT SIMULATOR STUDY, HOVER CONTROL POWERS
	482	62	TW	E/A	S	P	F	X						X			X	X	X				X	X		SUMMARY OF FLT-TEST RESULTS (VZ-2)
	483	65	–	E/P/A	H/LS	SIM	SIM										X	X	X				X	X		FLT SIMULATOR STUDY OF ATTITUDE CONT REQUIREMENTS FOR JET VTOL AIRCRAFT
	500	64	DSS	E/A	LS	P	F										X	X	X				X	X		BREGUET 941, RESULTS OF FLT TEST OF PERF, HANDLING QUALITIES, AND OPERATIONAL CHAR
	501	67	–	E/PR/A	LS	SIM/PM	SIM/F											X						X		DIR AUGMENTATION FOR SATISFACTORY HANDLING QUALITIES OF STOL AT LOW APPROACH SPEEDS
	502	63	BLC/DSS	E/A/PR	LS	P	F										X	X	X				X	X		MODIFIED C-130, STOL PERF, BLC FLAP, AILERONS, ELEVATOR, RUDDER
	503	63	BLC/HL	E/A/PR	LS	SIM	SIM											X	X		X			X		LAT-DIR HANDLING QUALITIES OF THE C-130
	505	66	–	E/A	H/T	SIM	SIM										X	X	X		X				X	PARAMETERS IDENTIFIED TO SPECIFY HANDLING-QUALITIES CRITERIA, DERIVS DEFINED
	506	61	S	PR	S	P	F							X										X		SEVERAL VTOL AIRCRAFT
	522	62	D	E/A	H	P	F												X	X		X	X	X	X	HOVERING CONTROL REQUIREMENT OF VAR STAB AND CONTROL X-14A
	528	[illegible]	–	E/A	H/T	SIM/E	SIM/F										X		X	X	X			X	X	LONG CONT PROB AT LOW DAMPING
	529	56	H	E/A	H/LS	E	F												X	X	X		X	X	X	DAMPING AND CONT POWER EFF ON HELICOPTER HANDLING QUALITIES
	530	6-	–	R/D/A	H/T/C		–																	X	X	RESEARCH AND PROGRESS TO 1969 IN DEVEL OF V/STOL FLYING-QUALITIES SPEC, PERTINENT AREAS DISCUSSED
	535	5'	S	D/A	S	S	F																			BELL XV-3, VERTOL VZ-2PH, DOAK VZ-4DA, MCDONNELL XV-1, HANDLING QUALITIES DEFICIENCIES AND RECOMMENDED CORRECTIONS
	536	66		R/A/D	H/T/C	–	–									X								X		VTOL FLYING QUALITIES AND VAR-STAB AIRCRAFT IN FLYING-QUALITIES RESEARCH
	539	62	–	E	H	SIM	SIM										X	X	X	X	X		X	X	X	AUTO PILOT IN HOVERING CONT, CONT SYS NONLINEARITIES, SIMULATOR TEST METHOD FOR ANALYZING STAB AND CONT CHAR OF AUTOPILOT
	545	56	–	E/PR/A	C	SIM	F																	X		FLT TESTS IN HOVERING RIG TO INVESTIGATE HANDLING QUALITIES
	547	6	–	E/PR/A	H	SIM	F										X				X		X	X		VAR-STAB HELICOPTER USED TO DETERMINE EFF OF PARAMETERS ON LONG HANDLING QUALITIES
	548	67	–	R/D	H/T	SIM	SIM														X			X		SIMULATORS AND THEIR CAPABILITY FOR V/STOL VISUAL FLT SIM
	555	62	–	A	H/T	–	–														X			X		STATISITICAL MODELS FOR GUST ENVIRONMENT TO DETERMINE GUST RESPONSE CHAR
	558	59	S	R/A	S	–	–										X	X	X	X			X	X		V/STOL FLYING-QUALITIES CHAR STATE OF THE ART TO 1960
	575	65	DP/TW+DSS	A	H/T	–	–																	X		USE OF PILOT TRANSFER-FUNCTION MODEL AND OTHER ANALYTICAL TECHNIQUES

* See Table 9B for key to summary

TABLE 9-A (CONT'D)*

Subject Index Classification	Reference Number	Year of Publication	V/STOL Concept	Nature of Report Material	Flight Regime or Airflow	Test Article	Type of Test	Force and Moment	Wing	Free Propeller	Ducted Propeller	Two-Dimensional Data	Pressure Data	Max Lift or Turning	Ground Effect	Propeller Rotation Slipstream Effects	Stability and Control: General	Longitudinal	Lateral-Directional	Dynamic	Stabilization	Simulations	Gyroscopic Effects	Zero or Low Airspeed Control/Systems	Handling Qualities	Handling Qualities Criteria	Comments
F.4 (CONT'D)	584	67	–	A	H	–	–	x											x	x					x		EFF OF GUST VEL DISTRIBUTIONS ON LAT-DIR RESPONSE OF HOVERING VTOL AIRCRAFT
	606	[illegible]	TW	E/A	H/T	PM	F											x		x					x		RIGID VS FLAPPING-PROP BLADES ON VZ-2 MODEL
	614	62	DSS	E/A	T	P	F								x			x						x	x		LONG TRIM CHAR (VZ-3)
	[illegible]23	[illegible]	–	PR/A	H/LS	SIM	SIM											x	x	x	x	x		x	x	x	CRITERIA FOR VTOL DYN RESPONSE IN HOVER AND LOW-SPEED FLT. LONG, LAT, HEIGHT, AND DIR HANDLING-QUALITIES REQUIREMENTS
	[illegible]	[illegible]	–	[illegible]	[illegible]	–	–										x							x	x	x	QUALITATIVE DISCUSSION OF STAB AND CONT PROBS OF VTOL AIRCRAFT
	656	5[illegible]	–	D/A	H/T/C	–	–													x					x	x	PROB AREAS IN DESIGN OF VTOL RELATED TO HANDLING QUALITIES AND NEEDED RESEARCH
	[illegible]	[illegible]	–	A	H/T/C	–	–											x	x	x				x	x		VTOL APPROX TRANSFER FUNCTIONS AND CLOSED-LOOP HANDLING QUALITIES. SAMPLE CALCULATIONS
	679	59	TP	E/A	T	–	–													x					x		FLYING-QUALITIES REPT FOR KAMAN K-16B. DYN STAB IN TRANSITIONAL FLT
5.5	3	63	JF	E/A	LS	M	WT	x	x						x		x										EFF OF GRD PROXIMITY ON A DELTA WING WITH AND WITHOUT JET BLOWING AT TE
	29	59	FF[illegible]	E/A	ST	M	S								x												
	92	66	JF	E/A	LS	M	SIM	x							x												JET-FLAP MODEL WITH MOVING BELT RIG FOR GRD SIM
	93	67	JF	E/A	LS	M	WT	x					x		x			x	x								BASIC AERO CHAR OF JET-FLAP AIRCRAFT INCLUDING GRD EFF
	110	66	–	E/A	H	M	WT								x		x										INVESTIGATION OF VTOL GRD-PROXIMITY PROBS. EFF OF GRD ON AERO CHAR
	111	62	S	R	H	–	–						x		x												VTOL AIRCRAFT IN GRD PROXIMITY. GRD EROSION, RECIRCULATION, AND PRESS DISTRIB ON AIRCRAFT
	112	63	DJ	E	H	M	WT	x							x												SINGLE- AND DOUBLE-JET MODELS. GRD EFF ON PERF
	113	62	–	E/A	H/T	M	WT								x												INVESTIGATION OF V/STOL MODEL TESTING FOR GRD EFF
	114	63	DJ/L+P	E/A	LS/H	M	WT								x												RECIRCULATION PROB OF JET-LIFT AIRCRAFT FLYING OR HOVERING IN WIND IN GRD PROXIMIT[illegible]
	143	60	–	E/A	ST	M	ST	x							x												MULTIPLE LIFTING JETS
	147	65	JF	E/A	LS	M	WT								x			x	x								SEMISPAN JET-AUGMENTED-FLAP MODEL, WITH AND WITHOUT GRD BOARD
	153	63	FIF	E/A	LS	M	WT	x					x		x			x									AERO CHAR IN GRD EFF. DOWNWASH AT HORIZ TAIL PLUS AREA INDICATED
	158	66	TW/DSS	E/A	LS	M	WT	x							x		x										AERO CHAR OF LARGE-SCALE MODEL OF 4-PROP TILT-WING CONFIG GRD EFF
	214	66	DJ/L+F	E/T/A	H	M	ST						x		x												LIFT LOSS DUE TO SUCTION PRESS INDUCED BY ENTRAINMENT OF VERTICAL EFFLUX FROM LIFTING JETS HOVERING IN AND OUT OF GRD
	223	67	DP	E/A	H/T/C	M	WT								x			x						x			LONG. AERO CHAR IN GRD EFF 3 GRD HEIGHTS. VTOL AND STOL OPERATION
	230	57	TW/DSS	E/A	LS	M	WT	x							x			x	x					x			LONG, LAT, AND CONT CHAR OF 4-PROP TILT-WING MODEL IN GRD EFF. RECIRCULATION EF-MOVING-BELT GRD PLANE. THOROUGH REPT

* See table 9B for key to summary

TABLE 9-A (CONTD)*

SUBJECT INDEX CLASSIFICATION	REFERENCE NUMBER	YEAR OF PUBLICATION	V/STOL CONCEPT	NATURE OF REPORT MATERIAL	FLIGHT REGIME OR AIRFLOW	TEST ARTICLE	TYPE OF TEST	AREAS OF INVESTIGATION OR ANALYSIS: Force and Moment	Wing	Fan Propeller	Ducted Propeller	Two-Dimensional Data	Pressure Data	Max. Lift or Turning	Ground Effect	Propeller Rotation	Deflected Slipstream	STABILITY AND CONTROL: General	Longitudinal	Lateral-Directional	Dynamic	Stabilization	Simulation	Gyroscopic Effects	Zero or Low Airspeed Control Systems	Handling Qualities	Handling Qualities Criteria	COMMENTS
55 (CONT)	231	67	TW	E/A	T	M	WT	x						x		x	x											GRD EFF ON TILT-WING AIRPLANE
	234	62	FIW	E/A	H	M	ST		x					x														GRD EFF ON FAN-IN-WING CONFIG
	239	62	FIW	E/A	ST	M	ST	x						x														WING SIZE VARIED
	247	61	TW	E/A	H/T	M	WT	x						x			x	x										A0-1 CONVERSION TO 4-PROP TILT-WING AIRCRAFT (MOHAWK). AERO CHAR INCLUDING GRD EFF
	251	61	DSS/BLC	E/A	S	M	WT	x						x			x	x										6-PROP VTOL MODEL
	252	66	TW	E/A	H	M	ST	x				x		x				x							x			GRD EFF ON PLAIN, SINGLE-SLOTTED, AND DOUBLE-SLOTTED FULL-SPAN FLAPS USED FOR YAW CONTROL
	272	62	S	T/A/R	LS	–	–							x														LINEARIZED THEORY OF WIND-TUNNEL JET-BOUNDARY CORRECTIONS AND GRD EFF INTERFERENCE FACTORS AS A FUNCTION OF WAKE DEFLECTION
	294	57	JF	E/A	LS	M	WT				x	x		x														GRD EFF ON HIGH-LIFT COEFF OF A JET-FLAP AIRFOIL
	296	60	TW/DSS	E/A	ST	M	ST	x				x		x														
	314	63	FIW/ DJ/L+P	R/D	H/T/C	–	–							x											x	x		DESIGN OPTIMIZATION OF V/STOL DIRECT-LIFT TRANSPORT. DESIGN PROBS OF PROPULSION, HANDLING QUALITIES, TRIM IN HOVER AND TRANSITION, GRD EFF
	337	64	FIW	E/A	H/T	M	WT	x						x			x	x							x			LARGE-SCALE INVESTIGATION OF FIW CONCEPT. GEN AERO CHAR IN AND OUT OF GRD EFF
	357	56	DSS	E/A	ST	C	ST	x	x	x			x	x														EFF OF GRD PROXIMITY AND PROP POSITION ON EFFECTIVENESS OF TURNING THE PROP SLIPSTREAM
	360	61	DSS	E/A	S	M	WT	x						x				x										LAT STAB AND CONT CHAR INCLUDING EFF OF GRD PROXIMITY ON A 4-PROP DSS AIRCRAFT
	361	60	DSS	E/A	S	M	WT	x						x			x											LONG. AERO CHAR INCLUDING EFF OF GRD PROXIMITY ON A 4-PROP DSS AIRCRAFT
	368	60	TW	E/A	T	M	WT							x			x											LONG. AERODYNAMICS OF 3 PROP-DRIVEN VTOL AIRCRAFT. GRD EFF
	371	67	FIW	E/PR/A	H/T/C	PM	F							x	x										x			FLT EVALUATION OF XV-5A HANDLING QUALITIES
	374	68	L+P	E/A	H/LS	PM	ST	x						x														EXHAUST GAS INGESTION CHAR AND INDUCED AERODYNAMICS FOR VTOL FIGHTER MODEL IN GRD PROXIMITY. STATIC TEST OF FULL-SCALE AIRCRAFT
	375	57	L+P	E/A	H	M	S							x														PARAMETRIC DATA ON GAS INGESTION AND JET EFF IN JET-POWERED VTOL VEHICLES IN GRD PROXIMITY
	378	67	?	T	LS	–	–							x														LINEAR-THEORY SOLUTION FOR JET FLAPS IN GRD EFF
	379	67	JF	T/A	LS	–	–							x														LINEAR THEORY FOR JET FLAP IN GRD EFF. GEN LINEAR CASE OF AN ARBITRARY AIRFOIL AND JET COEFF
	392	64	DF, FIW, FIF	E/A	H/LS	M	WT/ST							x														FLOW UNDER NORMALLY IMPINGING JET INVESTIGATED. PROPERTIES OF FLOW NEAR GRD. ROTORS AND DUCTED FANS
	427	66	JF	A	LS	M	WT	x				x		x														DATA ANALYSIS OF SEMISPAN VTOL MODEL. INTEGRATED PROPULSION-LIFTING SURF. FLOW ANGULARITY MEAS AT TAIL
	433	66	JF	T	LS	–	–							x														THEOR CONSIDERATIONS OF FLOW PATTERN OF THIN JET-FLAPPED 2-DIM WING IN GRD EFF
	434	66	FIW	A	–	–	–																					METHOD FOR STUDYING EFF ON AERO CHAR OF WINGS OF LIFTING-PROPULSION DEVICES, STAB AND CONT, GRD EFF, AND W-T CORRECTIONS

* See table 9B for key to symbols

TABLE 9-A (CONTD)*

SUBJECT INDEX CLASSIFICATION	REFERENCE NUMBER	YEAR OF PUBLICATION	V/STOL CONFIG*	NATURE OF REPORT MATERIAL	FLIGHT REGIME OR AIRFLOW	TEST ARTICLE	TYPE OF TEST	AREAS OF INVESTIGATION OR ANALYSIS: Factor and Aspect	W/Wo	1 or 2 Propeller	Ducted Propeller	Two Dimensional Data	Pressure Data	Jets Lift or Turning	General Effect	Propeller Tilting	Direction Effects	STABILITY AND CONTROL: General	Longitudinal	Lateral Directional	Dynamic	Stabilization	Simulators	Compressibility Effects	Ferry or Tow Attached	Control Systems	Handling Qualities	Hazardous Conditions	Criteria	COMMENTS
SE CONT.	446	57	TW	E A	ST	M	ST	X						X															4-PROP CONFIGURATION
	447	57	TW/DJ	E A	H	M	WT	X						X															QUANTITATIVE MEASURE OF GRD EFF ON 2 JET VTOL AIRCRAFT
	448	60	TW+E DJ	E A	H	M	ST	X						X															INCLUDES TUFT STUDIES
	456	62	TW	E A	H	M	ST							X															SLIPSTREAM FLOW AROUND VZ 2 X 18, AND ARB CONFIG
	492	64	TF	F	H	M	WT							X															FULL SCALE, HALF-MODEL SIMULATION OF A DUAL TANDEM DUCTED-PROP AIRCRAFT, DOWNWASH ALLEVIATION
	494	68	TW/DSS	E/A	T	M	TWT	X						X															XC-142A MODEL GRD EFF ON LONG FORCES AND PITCH MOM
	532	59	S	E.A	S	S	F							X															GRD INTERFERENCE STUDY
	538	68	DJ/L+P	R	H/LS	-	-							X															TABULAR SURVEY OF 132 REPORTS ON GRD EFF ON JET LIFT V/STOL AIRCRAFT, REGION OF DEFLECTED JET DESCRIBED
	546	69	DJ L+P	E.A	H	M	ST	X						X															JET-INDUCED LIFT EFF ON VTOL AIRCRAFT, JET DECAY PROFILES, NOZZLE LAT SPACING, 5 JET ARRANGEMENTS
	550	69	DJ L+P	E T A	H LS	M	WT/ST							X															THEOR AND TEST DATA FOR CIRCULAR, SUBSONIC JETS, AERO EFF SINGLE AND MULTIPLE JETS IN AND OUT OF GRD, INFLUENCE OF EXTERNAL FLOWS
	561	63	DF	E/A	H	M	WT	X						X				X	X										TRENDS IN LIFT, PITCH MOM., AND ROLLING MOM. DUE TO GRD EFF
	563	68	DJ	E	H	M	ST						X	X															GRD EFF ON SIMPLE JET EXHAUSTING BENEATH A FLAT SURFACE
	566	60	DSS JF	E A	ST/LS	M	WT	X	X	X		X		X						X									AERO CHAR OF A COMBINATION OF JET-FLAP AND DEFLECTED SLIPSTREAM CONFIG
	585	68	L+P	E/A	H T/C	M	WT	X						X				X	X										XV-4B POWERED INTERFERENCE EFF IN AND OUT OF GRD IN LANGLEY LOW-SPEED TUNNEL
	593	68	-	T/A	T	-	-							X					X	X	X								BASIC DATA IN CRUISE IN LANGLEY HIGH-SPEED TUNNEL
	616	67	FW	E/A	H	M	WT	X						X															DEVEL OF DYN MODEL FOR ANALYZING V/STOL TRANSPORTS IN LOW-ALT TURBULENCE IN TRANSITION, FACTORS AFFECTING RESPONSE TO TURBULENCE
	617	61	JF	E	LS	M	WT/S.M	X				X		X															GRD EFF ON PERF OF LIFTING FAN
	624	66	DJ L+P	E.A	LS	M	WT	X						X		X	X							X	X				FREE-FLT INVESTIGATION TO EVALUATE GRD EFF ON JET FLAPPED WING
	625	64	L+P	S/A	LS	M	WT	X						X			X												EFF OF GRD AND JET FREE-STREAM INTERFERENCE ON LONG CHAR
	628	57	JF	E A	LS	C	WT	X	X					X			X												INTERFERENCE EFF BETWEEN LIFTING JETS, FREE STREAM VELOCITY, AND MODEL SURFACES AT LOW FWD SPEEDS, EFF ON LONG AERO CHAR, VARIOUS JET CONFIG AND WING HEIGHTS GRD EFF
	629	57	-	E/A	ST	C	ST							X															FLOW-FIELD CHAR AND GRD INFLUENCE ON MODEL WITH JET AUGMENTED FLAPS, DOWNWASH AND DOWNWASH GRADIENTS
	634	28	TW	R/C	H T/C	-	-							X															GRD EFF ON CIRCULAR AND ANNULAR NOZZLES
	653	66	S	R D	H T C	-	-							X															TECH AND OPERATIONAL LESSONS FROM XC-142 PROGRAM, W T and FLT TEST RESULTS COMPARED, PROP PITCH MOM AT HIGH INFLOW ANGLES
	654	62	JF	T A	LS	-	-							X															V/STOL AERO RESEARCH AT RAE 1962-66, JET LIFT, FAN LIFT, BLC, JET FLAPS, GRD SIM, W-T TEST TECHNIQUES
														X															A FORMULA DERIVED BY CONFORMAL TRANSFORMATION FOR LIFT INDUCED BY 90° JET FLAP IN GRD EFF, COMPARISON WITH OTHER THEORY AND EXPERIMENT

* See list of abbreviations (p. 9-3)

TABLE 9-A (CONTD)*

SUBJECT INDEX CLASSIFICATION	REFERENCE NUMBER	YEAR OF PUBLICATION	V/STOL CONCEPT	NATURE OF REPORT MATERIAL	FLIGHT REGIME OR AIRFLOW	TEST ARTICLE	TYPE OF TEST	AREAS OF INVESTIGATION OR ANALYSIS: Wing	Free Propeller	Ducted Propeller	Tip Downstream Data	Pressure Data	Jet Lift or Turning	General Effect	Propeller Rotation	Downwash Effects	STABILITY AND CONTROL: Control	Longitudinal	Lateral Directional	Dynamic	Stabilization	Simulation	Gyroscopic Effects	Loss or Less Accurate Control Systems	Modeling Equations	Handling Qualities Criteria	COMMENTS
5.5 (C[illegible])	669	69	L+P	E/A	T/C	M	WT						X			X	X						X			LONG AND LAT DIR CHAR OF JET-LIFT MODEL GRD EFF CONTROL EFFECTIVENESS EFF OF POWER VARIATION OF LIFT JETS
	671	63	L+P	E A	H/LS	M	WT						X														SHORT SC 1 THRUST LOSS AS FUNCTION OF WING HEIGHT ABOVE GRD FOR JET-LIFT SCHEMES THRUST LOSS REDUCTION
	678	64	L+P	E/A	H	M	ST						X		X												INLET TEMPERATURE RISE IN GRD EFF AND ITS EFF ON LIFT
5.6	175	58	–	T/A	S	–	–													X		X					
	210	61	–	E/A	H/T	SIM	SIM															X		X			GYROSCOPIC CROSS COUPLING, PITCH-ROLL
	211	61	–	E/A	H/T	SIM	SIM															X		X			GYROSCOPIC CROSS COUPLING PITCH-YAW
	222	63	TS/DSS	PR	S	P	F	X					X			X		X		X		X					X-13 AND VZ 3
	554	58	TS	E/A	H/T	PM	WT								X							X					X-13
	630	63	–	A/D	H/LS	–	–								X					X		X					STAB DUE TO GYROSCOPIC FORCES
5.7	16	63	TR	A/E	H/T	–	–									X		X		X		X	X	X			MECHANICAL GYROSCOPIC STABILIZER APPLIED TO TILT-WING VTOL AIRCRAFT DESIGN CRITERIA PERF, DESIGN FEATURES
	18	61	–	DS	H/T	–	–									X				X							FEASIBILITY STUDY
	24	66	F/W	E/PR/A	H	SIM	SIM													X	X						XV-5A FLT SIMULATOR STUDY OF HOVERING IN GUSTY COND OPTIMIZATION OF STAB AUGMENTATION GAINS
	53	61	–	D	H/T	–	–													X							V/STOL CONT SYS DESIGN
	57	66	DP	D	H/T/C	–	–									X	X	X		X	X		X	X			DESCRIPTION OF X-22A VAR STAB SYS
	176	60	–	A	H	–	–													X							
	177	62	–	A/D	H	S/M/F	–													X							
	201	62	L+P	T	H/T	P	F	X												X				Y			SHORT SC 1 CONTROL SYS
	202	60	L+P	A/T/E	H/T	P	F									X	X	X		X		X	X	X	X	X	SHORT SC-1
	245	60	S	A/E/PR	S	SIM	SIM													X	X						FACTORS AFFECTING PILOTED FLT SIM USE OF SIMULATORS TO STUDY FLT TECHNIQUES
	288	64	DJ L+P	A	H	–	–																	X			"MIXED" CONT SYS TO HOVER UNSTABILIZED JET LIFT AIRCRAFT CONTROL SYS MOM A FUNCTION OF STICK POS AND RATE OF CHANGE OF STICK POS
	372	62	L+P	D	T	P	F													X							SHORT SC-1 LIFT COMPENSATION
	527	66	DJ	E/PR	H/LS	E	F											X						X			HOVERING VTOL AIRCRAFT (X-14A) WITH VARIATION IN CONT POWER AND STICK TRAVEL
	576	62	–	A	H/T	–	–													X							
	636	63	–	A/D	H/LS	–	–								X					X		X					STAB DUE TO GYROSCOPIC FORCES

* See [illegible] for key to abbreviations

TABLE 9A (CONTD)*

Subject Index Classification	Reference Number	Year of Publication	V/STOL Concept	Nature of Report Material	Flight Regime or Airflow	Test Article	Type of Test	Aero and Interference	Wing	Free Propeller	Ducted Propeller	Fan-Submerged Data	Pressure Data	Max Lift or Turning	Ground Effect	Propeller Reactions / Blockage Stalls	Stability and Control: General	Longitudinal	Lateral-Directional	Dynamic	Stabilization	Simulators	Gyroscopic Effects	Tests at Low Airspeed / Control Systems	Handling Qualities	Handling Qualities Criteria	Comments
5.8	10	62	–	O	LS	F	F	X										X	X					X			SKYLARK (SINGLE-ENGINE LIGHT AIRCRAFT)
	16	63	TW	A/E	H/T	–	–											X	X	X	X		X	X	X		MECHANICAL GYROSCOPIC STABILIZER APPLIED TO TILT-WING VTOL AIRCRAFT DESIGN CRITERIA, PERF, DESIGN FEATURES
	21	63	–	O	H/T	SIM	SIM														X			X			MECHANICAL V/STOL CONT SYS
	47	[illegible]	S	R/D/PR/A	S	–	–										X	X	X	X	X			X	X	X	AIRWORTHINESS STANDARDS FROM RECOMMENDATIONS OF AEROSPACE INDUSTRIES ASSN. FAA DRAFT DISCUSSED
	48	58	DP	T/E	H	C	ST	X			X																THRUST CONTROL BY RUDDERS AT DUCT OUTLETS
	84	6[illegible]	DSS	A	LS	SIM	SIM											X		X		X		X	X		OTTER AIRCRAFT. SHORT-FIELD LDG CHAR OF STOL AIRCRAFT FROM PERF STUDIES, MANEUVER DYN ANALYSES, AND FLT SIM
	90	62	–	E/PR	H	M	F														X			X	X	X	CRITICAL DEMANDS ON VTOL ATTITUDE. APPLICATION OF MANEUVERING CRITERIA USING VAR-STAB AIRCRAFT
	98	64	–	R/A	LS	–	–																	X			VTOL CONT CRITERIA. DATA FROM INDUSTRY AND NASA CORRELATED. COMPARISON WITH CRITERIA FROM HELICOPTER MIL SPEC, AGARD 408, AND MIL-F-8785
	134	[illegible]	S	R/A	H/T	–	–													X				X	X	X	DYN AND CONT REQUIREMENTS FOR VTOL, BASED ON HANDLING-QUALITY EXPERIMENTS. LONG HOVER AND TRANSITION
	127	56	S	D/A	H/T	P	F											X	X					X	X		SEVERAL TEST-BED AIRCRAFT
	142	63	S	A	H	–	–																	X	X	X	HANDLING QUALITIES, EST OF CONT POWER, AND CONT THRUST REQ. CONTROL SYS DESIGN CRITERIA
	150	[illegible]	FP	E/A	H/T	C	ST			X								X						X			MONOCYCLIC PROP PITCH FOR LONG CONT
	180	69	DJ	E/A/PR	H	P	F/SIM												X					X	X		X-14A. UTILITY OF DIRECT SIDE-FORCE MANEUVERING DEVICE FOR VTOL AIRCRAFT
	202	60	L+P	A/T	H/T	P	F											X	X	X	X		X	X	X	X	SHORT SC-1
	208	64	–	PR/A	LS/H	E	F																	X	X		EFF OF STATIC DIR STAB ON HANDLING QUALITIES AND DIR SENSITIVITY AND DAMPING
	212	65	–	PR	H/C	E	F											X	X			X		X	X		SIM OF VTOL CONT REQUIREMENTS USING VAR-STAB HELICOPTER
	227	[illegible]	FIW/FIC	R/A	H/T	–	–											X	X	X	X	X		X	X		CLOSED-LOOP DYN RESPONSE OF VTOL AIRPLANE, PILOT, AND AUTOSTABILIZATION SYS SHOWING IMPORTANCE OF LOW-SPEED CONT REQUIREMENTS
	236	62	DJ	E/A	ST/LS	C	ST/WT																	X			JET DEFLECTOR TESTS AND COMMENTS
	241	66	–	E/A	H	SIM	SIM															X		X	X		6°-OF-FREEDOM MOTION SIMULATOR FOR STUDYING CONT SYS REQUIREMENTS. SIMULATOR CHAR
	252	56	TW	* E/A	H	M	ST	X					X		X				X					X			GRD EFF ON PLAIN, SINGLE-SLOTTED, AND DOUBLE-SLOTTED FULL-SPAN FLAPS USED FOR YAW CONT
	257	64	S	R/D	H/LS	–	–														X			X			LOW-SPEED CONT SYS REQ FOR VTOL. GUIDANCE, FREQUENCIES, ATTITUDE CONT. GENERATION OF MOMENTS DISCUSSED. STABILIZATION DEVICES. CONT SYS OF GER VJ101 TILT-ENGINE CONFIG DESCRIBED
	288	54	DJ/L+P	A	H	–	–																	X			"MIXED" CONT SYS TO HOVER UNSTABILIZED JET-LIFT AIRCRAFT. CONT-SYS MOM A FUNCTION OF STICK POS AND RATE OF CHANGE OF STICK POS.
	290	[illegible]	S	R/A	C/T/H	SIM	SIM														X	X		X	X	X	NO AMER ROCKWELL RESEARCH IN FLT-CONT AREA. STUDY OF VTOL FLT-CONT DESIGN WITH IFR CAPABILITY. LONG PROB FROM CONVENTIONAL FLT TO HOVER
	313	59	TW	E/A	T	M											X							X			4-POINT CONTROL

* See table 9B for key to summary

TABLE 9-A (CONTD)*

Subject Index Classification	Reference Number	Year of Publication	V/STOL Concept	Nature of Report Material	Flight Regime or Air-flow	Test Article	Type of Test	Areas of Investigation or Analysis: Forces and Moment	Wing	Free Propeller	Ducted Propeller	Two-Dimensional Data	Pressure Data	Max Lift or Turning	Ground Effect	Propeller Rotation Direction Effects	General	Stability and Control: Longitudinal	Lateral-Directional	Dynamic	Stabilization	Simulators	Gyroscopic Effects	Zero or Low Airspeed Control/Systems	Handling Qualities	Handling Qualities Criteria	Comments
5.8 (CONT)	336	61	DP	T	H/LS	–	–											X	X	X				X	X		HOVERING IN STILL AIR AND GUST COND, GLIDE APPPOACHES AT LOW SPEED. DAMPING AND SENSITIVITY
	359	56	DSS	E/A	ST	C	ST	X	X	X								X						X			WING PLUS PROPS, LE SLAT
	382	65	–	A	LS	–	–														X			X			CONT PROBS OF LARGE V/STOL TRANSPORTS. CONT POWER REQ, THEIR INFLUENCE ON HARDWARE DESIGN AND AIRCRAFT WEIGHT
	384	68	L+P	E/A	T/LS	E	–																	X	X	X	VTOL HANDLING QUALITIES. CONT MODES COMPARED IN TERMS OF PILOT ACCEPTANCE AND CONT POWER REQ
	409	66	–	E/PR/A	H/LS	SIM	SIM											X	X	X	X			X	X	X	FLT-RESEARCH PROGRAM TO DETERMINE CONT POWER AND CONT SENSITIVITY REQ DURING VISUAL HOVER AND LOW-SPEED APPROACH (VAR STAB HELICOPTERS)
	422	60	BLC	E/A/T	LS	M	WT	X					X					X	X					X			LIKE F 104. SEVERAL SPOILERS, 2 AILERON CONFIGS, 3 TAIL HEIGHTS
	481	62	TW	E/A	H/T	P	F																	X			AILERONS FOR YAW CONTROL (VZ-2)
	517	62	HL	D	LS	P	F											X	X					X	X		ULTRA LOW-SPEED CONT SYS
	522	62	DJ	E/A	H	P	E													X	X		X	X	X	X	HOVERING CONT REQUIREMENTS OF VAR STAB AND CONT.
	539	63	–	A	H	SIM	SIM											X	X	X	X	X		X	X	X	AUTOPILOT FOR VTOL HOVER CONT. CONT-SYS NONLINEARITIES, METHOD FOR ANALYZING STAB AND CONT CHAR OF AUTOPILOT
	564	67	–	E/A	LS	M	WT						X						X					X			JET AND FREE-STREAM INTERFERENCE EFF ON ROLL CONT OF V/STOL AIRCRAFT IN TRANSITION
	572	66	DP	E/A	H/T/C	M	WT	X			X						X	X	X					X			LONG AERO AND CONT CHAR OF DUCTED-PROP VTOL MODEL
	577	65	L+P	[illegible]	H	–	–																	X			PROPULSION SYS AND/OR CONT SYS INTERFACE FOR HOVER CONT CONCEPTS USING LIFT + LIFT CRUISE PROPULSION
	593	68	–	T/A	T	–	–								X			X	X	X							DEVEL OF DYN MODEL FOR ANALYZING V/STOL TRANSPORTS IN A LOW-ALT TURBULENCE IN TRANSITION FACTORS AFFECTING RESPONSE TO TURBULENCE
	514	62	DSS	E/A	T	P	F								X			X						X	X		LONG TRIM CHAR (VZ-3)
	643	64	–	R/D	H/T	–	–										X							X	X	X	QUALITATIVE DISCUSSION OF STAB AND CONT PROBS OF VTOL AIRCRAFT
	658	69	L+P	E/A	T/C	M	WT								X			X	X					X			LONG AND LAT-DIR CHAR OF JET-LIFT MODEL. GRD EFF CONT EFFECTIVENESS. EFF OF POWER VARIATION OF LIFT JETS
5.9	183	69	TW/DSS	E/A	LS	M	WT									X		X									LONG AERO CHAR,EFF OF PROP-ROTATION DIRECTION
	184	66	TW	E	LS	M	WT	X	X							X	X	X									EFF OF PROP-ROTATION DIRECTION, FLAPS, SLATS, AND FENCES ON AERO AND FLOW CHAR
	185	66	TW	E	LS	M	WT	X	X							X	X	X									EFF OF PROP-ROTATION DIRECTION, FLAPS, SLATS, AND FENCES ON AERO AND FLOW CHAR
	186	67	TW	E	LS	M	WT	X	X							X	X	X									EFF OF PROP-ROTATION DIRECTION, FLAPS, SLATS, AND FENCES ON AERO AND FLOW CHAR
	187	67	TW	E	LS	M	WT	X	X							X	X	X									EFF OF PROP-ROTATION DIRECTION, FLAPS, SLATS, AND FENCES ON AERO AND FLOW CHAR
	188	67	TW	E	LS	M	WT	X	X							X	X	X									EFF OF PROP-ROTATION DIRECTION, FLAPS, SLATS, AND FENCES ON AERO AND FLOW CHAR
	486	43	–	E/A	LS/C	M	F									X			X	X							EFF OF PROP-ROTATION DIRECTION ON LAT STAB CHAR

* See table 9B for key to summary

TABLE 9-A (CONTD)*

AIRCRAFT MODEL CLASSIFICATION	REFERENCE NUMBER	YEAR OF PUBLICATION	V/STOL CONCEPT	NATURE OF REPORT MATERIAL	FLIGHT REGIME OR AIRFLOW	TEST ARTICLE	TYPE OF TEST	AREAS OF INVESTIGATION OR ANALYSIS: Force and Moment	Wing	Tilt Propeller	Ducted Propeller	Two-Dimensional Data	Pressure Data	Max. Lift or Trailing	Powered Lift	Propeller Wakes (Including Effects)	Powered	STABILITY AND CONTROL: Longitudinal	Lateral Directional	Dynamic	Stabilization	Simulations	Gyroscopic Effects	Forces on V/STOL Aircraft	Control Systems	Handling Qualities	Handling Qualities Criterion	Secrets	COMMENTS
5.8 (CONT)	619	43	–	E/A	LS/C	PM	WT	X							X		X	X										EFF OF PROP-ROTATION DIRECTION ON STATIC STAB
	631	64	TW/DSC	E/A	T	M	F								X		X	X	X									DYN LAT STAB AND CONT. REMOTE-CONTROL MODEL EFF OF WING STALLING AND STALL-CONTROL DEVICES
5.10	30	56	FP	R/D/A	LS	–	–		X	X				X														LIFT ON A WING IN PROP SLIPSTREAM
	89	68	DJ/L+P	T/A	H/T	–	–								X													SEMIEMPIRICAL APPROACH TO PREDICTING PERF LOSSES AND PITCH MOM. CAUSED BY JET INTERFERENCE
	91	63	TW/DSS	R/A	T	–	–																					WING STALL DURING TRANSITION, STALL-FREE TRANSITION, EFF OF SLIPSTREAM ON PITCH MOM
	120	63	TW/DSS	T	LS	–	–																					METHOD PREDICTING WING-SLIPSTREAM INTERACTIONS. LIFTING-SURFACE THEORY
	158	66	TW/DSS	T	H/T	–	–								X		X											WING LOADING OF ARBITRARY PLANFORM EQUAL TO OR LESS THAN SPAN OF PROP JET
	171	68	S	T	C/ST	–	–																					RESEARCH ON PROP FLOW FIELD ASSOCIATED WITH TYPICAL V/STOL OPERATIONS
	181	61	JF	E/A	LS	M	WT	X																				AERO FORCES AND MOM ON JET-FLAPPED WING IN PRESENCE OF PROP SLIPSTREAM AND FREE STREAM
	183	69	TW/DSS	E/A	LS	M	WT								X		X											LONG AERO CHAR, EFF OF PROP-ROTATION DIRECTION
	228	64	DSS	A	LS	–	–									X												AERO FORCES ON WING-PROP COMBINATIONS INCL SLIPSTREAM EFF THEORY APPLIED TO 2- AND 4-PROP V/STOL CONFIG
	293	65	DSS	A	LS	–	–																					EQ AND CHARTS FOR LIFT AND LONG - FORCE COEFFS OF WINGS IN PROP SLIPSTREAMS, SAMPLE CALCULATIONS
	311	68	DJ/L+P	E/A	LS	M	WT					X																FLOW IN JETS EJECTED NORMAL TO THE WIND
	382	65	DJ/L+P	R/D	H	–	–							X		X												AERO OF JET VTOL ENGINE INSTALLATIONS. JET INDUCED EFF. EFF OF GRD, JET WAKE, AND INLET LIP SHAPE
	388	66	DJ/L+P	R/D	T	M	WT	X								X												CHAR OF JET-POWERED VTOL FIGHTER CONFIGS. INTERFERENCE EFF DUE TO INTERACTION BETWEEN FREE STREAM AND JET WAKES
	400	68	DJ/L+P	E/A	LS	M	WT																					PATH AND SHAPE OF WAKE FROM A SINGLE JET EXITING AT LARGE ANGLES TO FREE STREAM
	401	68	DSS	E/T/A	LS	M	WT	X								X												AERO CHAR OF PROP-WING-FLAP SYS. EQ FOR EST AERO FORCES. PROP SLIPSTREAM EFF. COMPARISON OF TEST AND THEORY
	457	67	DSS	E/A	H/T	M	WT		X		X																	WING WITH DUCTED FANS AND DOUBLE-SLOTTED FLAPS. DUCT POS AND DUCT EXIT CONFIG VARIED. FLAP TURNING EFFECTIVENESS
	477	60	FP	R/D	LS	–	–										X											PROP EFFECTS ON STAB AND CONT OF VTOL AIRCRAFT
	509	58	FP/TW	E/A	LS	–	–																					LIFT-GENERATING CAPABILITIES OF WINGS EXTENDING THROUGH PROP SLIPSTREAMS
	562	37	FP	A	LS	–	–		X	X																		METHOD CALCULATING INCR IN LIFT OF WING DUE TO PROP SLIPSTREAM. COMPARISON WITH TEST
	584	67	–	E/A	LS	M	WT					X							X						X			JET AND FREE-STREAM INTERFERENCE EFF ON ROLL CONTROL OF V/STOL AIRCRAFT IN TRANSITION
	612	63	FIF	E/A	LS	M	WT	X																				INTERFERENCE LOADS DUE TO INTERACTION BETWEEN MAINSTREAM AND EFFLUX EFF ON LIFT AND PITCH MOM.
	620	61	TW/DSS	E/A	LS	C	WT		X			X		X															EFF OF 2-DIM STREAM-SHEAR FLOW ON AIRFOIL MAX LIFT. PROP TO WING CHORD RELATIONSHIP

* See table 9B for key to summary

TABLE 9-A (CONTD)*

SUBJECT INDEX CLASSIFICATION	REFERENCE NUMBER	YEAR OF PUBLICATION	V/STOL CONCEPT	NATURE OF REPORT MATERIAL	FLIGHT REGIME OR AIRFLOW	TEST ARTICLE	TYPE OF TEST	AREAS OF INVESTIGATION OR ANALYSIS: Fuses and Nacelles	Wing	Free Propeller	Ducted Propeller	Two-Dimensional Data	Pressure Data	Aero Lift or Turning	Ground Effect	Propeller Ingestion	Reaction Effects	General	STABILITY AND CONTROL: Longitudinal	Lateral-Directional	Dynamics	Stabilization	Simulation	Gyroscopic Effects	Aero or Jet Augmented Control Systems	Handling Qualities	Handling Qualities Criteria	COMMENTS
5.10 (CONT)	622	60	–	T/A	–	–	–				X																	2-DIM EFF OF SLIPSTREAM SHEAR ON AIRFOIL CHAR
	624	66	DJ/L+P	E/A	LS	M	WT	X						X		X	X								X	X		EFF OF GRD AND FREE-STREAM INTERFERENCE ON LONG CHAR
	656	62	TW/DSS	E/A	ST	M	ST						X															PROP SLIPSTREAM EFF OF 6-PROP VTOL MODEL AT STATIC THRUST
	660	63	TW/DSS	E/A	T	M	WT	X				X																EFF OF NONUNIFORM FLOW AND SLIPSTREAM – FREE STREAM INTERACTION ON WING AERODYNAMICS
	670	63	TW/DSS	T	H/T/C	–	–			X			X															LIFTING-SURFACE THEORY FOR WINGS EXTENDING THROUGH INCLINED JETS SPANWISE LIFT DISTRIBUTION AND INDUCED DRAG
5.11	1	67	–	E/A	ST/LS	M	ST/LS																					RECIRCULATION EFF OF VERT AND INCLINED JETS ON HORIZ SURF
	39	68	DJ/L+P	T/A	H/T	–	–							X														SEMIEMPIRICAL APPROACH TO PREDICTING PERF LOSSES AND PITCH MOMENTS CAUSED BY JET INTERFERENCE
	82	67	–	R/D	H/T	–	–																					AERO INTERFERENCE EFFECTS OF JET LIFT SYSTEMS
	83	68	L+P/DJ	R/A	H/T	–	–	X						X		X												PROPULSION SYSTEM – AIRFRAME INTERFERENCE EFF, LIFT-ENGINE-INLET-FLOW DISTORTION, EXHAUST GAS REINGESTION
	88	68	–	E/D	LS	–	–					X																COANDA EFF AT WIDELY SEPARATED DEFLECTION SURFACES
	91	64	DJ/L+P	E/A	H	M	WT					X																STATIC PRESS DISTRIB ON WALL AROUND A CIRCULAR JET EXHAUSTING NORMALLY FROM A PLANE WALL INTO AN AIRSTREAM
	92	63	DJ	A/T/E	H/LS	M	WT					X		X														FLOW FIELD UNDER A UNIFORM CIRCULAR JET NORMAL TO AND IMPINGING ON GRD, JET-GRD-PLANE INTERACTION
	99	69	DJ	E/A	T	M	WT	X				X																JET LOCATION INTERFERENCE EFF ON LONG AERO CHAR OF JET VTOL MODEL
	114	63	DJ/L+P	E/A	LS/H	M	WT							X														RECIRCULATION PROB OF JET-LIFT AIRCRAFT FLYING OR HOVERING IN WIND IN GRD PROXIMITY
	121	67	–	E/A	ST	M	ST																					RECIRCULATION EFF OF VERT JET DIRECTED DOWNWARD ON HORIZ SURF
	204	67	F/W	E/D A	LS	M	WT	X																				INFLUENCE OF FAN EFFLUX FLOW ON LIFT AND PITCH MOMENTS OF FUS, WING, AND TAILPLANE
	208	67	–	–	–	–	–																					REVIEW OF JET-EFFLUX STUDIES. ANALYTICAL DESCRIPTION OF FLOW FIELD CREATED BY V/STOL AIRCRAFT
	214	66	DJ/L+P	E/T/A	H	M	ST					X		X														LIFT LOSS DUE TO SUCTION PRESS INDUCED BY ENTRAINMENT OF VERT EFFLUX FROM LIFTING JETS HOVERING IN AND OUT OF GRD
	240	67	F/W F/F	E/A	LS	M	WT	X																				NACELLE WITH 2 LIFTING FANS IN TANDEM, EFF OF EFFLUX ON LIFT
	701	67	DJ/L+P	E/A	LS	M	WT																					HOT GAS INGESTION, AERO SUCK-DOWN, JET INTERFERENCE IN TRANSITION
	287	66	DJ/L+P	T/A	H/LS	–	–																					FORMULAS FOR APPROX CALC OF FLOW PHENOMENA FOR A TURBULENT JET COLLIDING WITH A FLAT SURF
	350	69	F/W/ DJ/L+P	A/D	H	–	–					X																JET LIFT AND/OR LIFT FAN V/STOL AERODYNAMICS ANALYZED. SIM MODEL OF JET EFFLUX SUPERIMPOSED ON REPRESENTATION OF VEHICLE GEOM. VORTEX LATTICE TECHNIQUE DISCUSSED, APPLIED TO P 1127. THEORY AND TEST COMPARED
	362	66	DJ/L+P	R/D	H	–	–							X		X												AERODYNAMICS OF JET VTOL ENGINE INSTALLATIONS. JET INDUCED EFF, EFF OF GRD, JET WAKE, AND INLET LIP SHAPE
	375	67	L+P	E/A	H	M	S							X														PARAMETRIC DATA ON GAS INGESTION AND JET EFF IN JET-POWERED VTOL VEHICLES IN GRD PROXIMITY

* See table 9B for key to summary

TABLE 9-A (CONTD)*

SUBJECT INDEX CLASSIFICATION	REFERENCE NUMBER	YEAR OF PUBLICATION	V/STOL CONCEPT	NATURE OF REPORT MATERIAL	FLIGHT REGIME OR AIRFLOW	TEST ARTICLE	TYPE OF TEST	AREAS OF INVESTIGATION OR ANALYSIS: Forces and Moments	Wing	Free Propeller	Ducted Propeller	Two-Dimensional Data	Pressure Data	Jet Lift w. Turning	Ground Effect	Propeller Ingestion Distortion Effects	General	STABILITY AND CONTROL: Longitudinal	Lateral-Directional	Dynamic	Stabilization	Simulations	Gyroscopic Effects	Take or Low Airspeed	Control Systems	Handling Qualities	Manned Qualities Criteria	COMMENTS
5.11 (CONT)	392	64	DP/ FIW/FIF	E/A	H/LS	M	WT/ST							X														FLOW UNDER NORMALLY IMPINGING JET INVESTIGATED. PROPERTIES OF FLOW NEAR GRD ROTORS AND DUCTED FANS
	397	66	DJ/L+P	E/A	T	M	WT	X						X			X	X										AERO CHAR OF A 5-JET VTOL CONFIG. HORIZ-TAIL-POSITION EFFECTS. GRD PROXIMITY
	400	66	DJ/L+P	E/A	LS	M	WT																					PATH AND SHAPE OF WAKE FROM A SINGLE JET EXITING AT LARGE ANGLES TO FREE STREAM
	414	64	DJ/L+P	R/D	LS	–	–									X											X	AERODYNAMICS AND FLYING QUALITIES. JET INTERFERENCE EFF OF MULTIPLE JETS AND WING PLANFORM. INLET EFFECTS. INGESTION.CONTROL POWER
	424	66	DJ/L+P	–	H	M	ST					X																JET INDUCED LIFT LOSSES OF JET-VTOL CONFIGURATIONS
	434	65	FIW	A	–	–	–																					METHOD FOR STUDYING EFF ON AERO CHAR OF WINGS IN VICINITY OF LIFTING PROPULSION DEVICES, STAB AND CONT, GRD EFF, AND W T CORRECTIONS
	464	62	DJ/L+P	E/A	H	M	WT	X									X											MUTUAL INTERFERENCE BETWEEN NOZZLE SYS, W-B COMBINATIONS, AND FREE STREAM. BASIC FUS PLUS SERIES OF WINGS. JET-INDUCED DOWNLOAD AND PITCH MOMENTS. OUT-OF-GRD EFF
	479	64	DJ/ L+P/FIW	E/A	LS	M	WT					X																MEAS OF PRESS ON WING SURF WITH A JET ISSUING NORMALLY FROM THE SURF INTO A MAINSTREAM
	537	67	DJ/L+P	A	H/LS	–	–																					METHOD OF SIMULATING 3-DIM ENTRAINING JET EXHAUSTING INTO LOW-VEL CROSS WIND. EFF OF ENTRAINMENT ON POTENTIAL FLOW FIELD
	544	62	DJ/L+P	T	H/LS	–	–							X														ANALYSIS OF JET – GRD-PLANE INTERACTION. (VERT AXISYMMETRICAL JET)
	548	69	DJ/L+P	E/A	H	M	ST	X						X														JET-INDUCED LIFT EFF ON VTOL AIRCRAFT. JET DECAY PROFILES. NOZZLE LAT SPACING. 5 JET ARRANGEMENTS
	550	69	DJ/L+P	E/T/A	H/LS	M	WT/ST							X														THEOR AND TEST DATA FOR CIRCULAR, SUBSONIC JETS. AERO EFF. SINGLE AND MULTIPLE JETS IN AND OUT OF GRD. INFLUENCE OF EXTERNAL FLOWS
	563	58	DJ	E	H	M	ST					X		X														GRD EFF ON SIMPLE JET EXHAUSTING BENEATH A FLAT SURFACE
	585	61	S	R/D	T	–	–									X	X											JET-INDUCED EFF. DUE TO JET EFFLUX
	589	61	DJ	E/A	H/T	M	WT	X						X														JET-INDUCED INTERFERENCE EFF. INTERACTION OF DEFLECTED JET WITH FREE STREAM AND GRD
	582	67	DJ/L+P	T	H	–	–							X														THEORY FOR OBLIQUE IMPINGEMENT OF STATIC ROUND JET ON GRD. VEL DISTRIB ALONG GRD AND ACROSS JET AXIS. THRUST RATIOS. COMPARISON WITH BENCH TEST
	586	68	L+P	E/A	H/T/C	M	WT	X						X			X	X										XV-4B. POWERED INTERFERENCE EFF IN AND OUT OF GRD IN LANGLEY LOW-SPEED TUNNEL. BASIC DATA IN CRUISE IN LANGLEY HIGH-SPEED TUNNEL
	609	62	FIF	E/A	H	M	WT	X									X											EFF OF FAN IN FUSELAGE ON LONG. AERO CHAR
	626	64	L+P	E/A	LS	M	WT	X						X			X											INTERFERENCE EFF BETWEEN LIFTING JETS, FREE-STREAM VEL, AND MODEL SURFACES AT LOW FWD SPEEDS. EFF ON LONG. AERO CHAR. VARIOUS JET CONFIGS AND WING HEIGHTS. GRD EFF
	626	65	DJ	E/A	T			X									X	X					X					LONG. AND LAT-DIR CHAR OF TWO 4-JET VECTORED-THRUST-TYPE VTOL MODELS
	627	67	DJ/L+P	E/A	LS	M	WT					X																PRESS DISTRIB ON SURF OF FLAT PLATE INDUCED BY A ROUND COLD-AIR JET EXITING NORMAL TO LOW-SPEED FREE STREAM
	643	65	T.W/FIF/ L+P/DJ	R/A	S	–	–	X				X		X														AERO INTERFERENCE EFF THAT ARISE WITH JET AND LIFT-FAN V/STOL SCHEMES
	649	66	FIW/FIF/ L+P/DJ	R/A	H/T	–	–	X						X														AERO FEATURES DUE TO ADVERSE FLOWS INDUCED AROUND THE AIRFRAME
	667	68	DJ/L+P	R/A	H/LS	–	–	X						X	X													AERO INTERFERENCE EFF DUE TO JET EFFLUX. STATIC INTERFERENCE EFF. FWD-SPEED INTERFERENCE EFF. THEORY FOR JET-EFFLUX INTERFERENCE

* See table 9B for key to summary

TABLE 9-A (CONTD)*

SUBJECT INDEX CLASSIFICATION	REFERENCE NUMBER	YEAR OF PUBLICATION	V/STOL CONCEPT	NATURE OF REPORT MATERIAL	FLIGHT REGIME OR AIRFLOW	TEST ARTICLE	TYPE OF TEST	AREAS OF INVESTIGATION OR ANALYSIS: Force and Moment	Wing	Tilt Propeller	Ducted Propeller	Two-Dimensional Data	Pressure Data	Max Lift or Turning	Ground Effect	Propeller Rotation Effective Efflux	Control	STABILITY AND CONTROL: Longitudinal	Lateral-Directional	Dynamic	Stabilization	Simulations	Gyroscopic Effect	Zero or Low Airspeed Control System	Handling Qualities Handling Qualities Criteria	COMMENTS
5.11 (CONT)	668	67	DJ/L+P	T	LS	–	–					X														INTERACTION BETWEEN A JET EXHAUSTING NORMALLY FROM A LIFTING SURF INTO A UNIFORM STREAM. COMPARISON WITH TEST
	669	68	–	T/E/A	LS	M	WT					X														POTENTIAL-FLOW MODEL OF A CIRCULAR JET ISSUING NORMALLY FROM AN INFINITE FLAT PLATE INTO A DEFLECTING STREAM. FLOW SURVEY. COMPARISON WITH TEST
5.12	15	64	–	R/D	S	–	–																			SEVERAL REPORTS ON V/STOL MODEL TESTING. WT, PRINCETON DYNAMIC MODEL TRACK, NASA TECHNIQUES
	74	69	TW/DSS	R/A	H/T/C	M/PM	WT/F																			W-T-FLT-TEST PROGRAM TO DETERMINE STATUS OF W-T TEST TECHNIQUES
	137	66	–	D	LS	–	–										X	X	X							DESCRIPTION OF PRINCETON DYNAMIC MODEL TRACK (VTOL MODEL TESTING)
	145	66	FIF	E/A	LS	M	WT	X				X				X	X							X		EFF OF SCALE AND TUNNEL WALLS ON AERO CHAR
	174	62	TW	E/A	T	M	WT	X																		W-T DATA CORRELATION
	250	65	TW/DSS	E/A	T	M	WT	X									X	X						X		TUNNEL-WALL EFF ON DEFLECTED-SLIPSTREAM AND TILT-WING MODELS
	272	62	S	T/A/R	LS	–	–							X												LINEARIZED THEORY OF W-T JET-BOUNDARY CORRECTIONS AND GRD EFF. INTERFERENCE FACTORS AS A FUNCTION OF WAKE DEFLECTION
	274	67	–	D	LS	–	–																			FEATURES TO BE CONSIDERED IN APPLYING WALL-INTERFERENCE CORRECTIONS TO V/STOL DATA
	275	63	–	R/D/T	LS	–	–																			W-T WALL EFF AT EXTREME FORCE COEFFS. EFF OF NONUNIFORM INTERFERENCE GRADIENTS
	279	65	S	R/D	T	M/PM	WT/F										X									CORRELATION OF W-T AND FLT-TEST DATA ON 5 V/STOL AIRCRAFT. W-T WALL CORRECTIONS. SIZING CRITERIA
	366	59	S	D	LS	–	–																			W-T WALL EFFECTS IN V/STOL TESTING FROM EXP[illegible] OF LANGLEY RESEARCH CENTER
	380	69	–	E/A	–	S	WT																			THEOR AND EXPERIMENTAL STUDY TO DEVELOP V/STOL W-T WALLS
	425	61	–	D	H/T/C	–	–																			WIND TUNNEL FOR LOW FWD SPEED, HOVER, AND TRANSITION TESTING
	426	67	–	D	H/T/C	–	–																			LARGE-SCALE, CANADIAN V/STOL TUNNEL
	440	68	DP	E/A	H/T	M	WT																			W-T BOUNDARY EFFECTS RELATED TO V/STOL DATA
	461	65	–	R/D	LS	–	–																			W-T BOUNDARY CORRECTIONS APPLICABLE TO VTOL MODEL TESTING
	471	64	L	A/R	LS	–	–												X							3 MODEL TEST TECHNIQUES USED BY NASA TO INVESTIGATE DYN STAB OF V/STOL MODELS, AND TEST RESULTS
	478	60	TW	R/D	H/T	–	–																			W-T TEST METHODS FOR POWERED V/STOL MODELS. PROP EFF ON STAB AND CONT OF VTOL AIRCRAFT
	592	68	S	D	S	–	–																			LOW-SPEED W-T DESIGN AND TECHNIQUES. SIZE AND TEST SECTION REQ'D. NEW TUNNELS
	611	68	–	R/T	H/T	–	–							X												TECHNIQUES FOR TESTING LIFTING-JET OR LIFTING-FAN MODELS
	652	64	–	T	LS	–	–							X												METHODS TO E[illegible]ITE W-T TESTING OF JET AND LIFT-FAN MODELS
	853	66	S	R/D	H/T/C	–	–																			V/STOL AERO RE[illegible]RCH AT RAE, 1962-66. JET LIFT, FAN LIFT, BLC, JET FLAPS, GRD SIM, W-T TEST TECHNIQUES

* See table 9B for key to summary

TABLE 9-A (CONTD)*

SUBJECT INDEX CLASSIFICATION	REFERENCE NUMBER	YEAR OF PUBLICATION	V/STOL CONCEPT	NATURE OF REPORT MATERIAL	FLIGHT REGIME OR AIRFLOW	TEST ARTICLE	TYPE OF TEST	AREAS OF INVESTIGATION OR ANALYSIS										STABILITY AND CONTROL									COMMENTS
								Tests and Material	Wing	Free Propeller	Ducted Propeller	Two-Dimensional Data	Pressure Data	Max. Lift or Turning	Ground Effect	Propeller Tandem Slipstream Effects	General	Longitudinal	Lateral-Directional	Dynamic	Stabilization	Simulation	Gyroscopic Effects	Ease of Low Airspeed Control/Stabilization	Handling Qualities	Handling Qualities Criteria	
5.13	14	68	S	R/D	H/T/C	–	–																				AERO PROBS AND REQ FOR V/STOL AIRCRAFT
	17	67	–	R/D	H/T/C	–	–																				SURVEY OF FLT MECHANICS OF VTOL AIRCRAFT, INCL TECHNOLOGY, EFF OF VEHICLE CHAR
	28	67	–	R/A	H/T/C	–	–																				SURVEY PAPERS, THRUST FOR HOVER CONTROL, GRD EFF, JET-INDUCED EFF, REINGESTION
	44	60	S	R/D	S	–	–									X											NASA-AMES RESEARCH THROUGH 1960
	54	68	S	R/A	H/T/C	–	–																				PROMISING V/STOL CONFIGS. LIFT SYS, PROPULSION, AIRFRAME SYS, DYN AND AERO CHAR, CONTROL SYS
	96	57	S	E/A	LS	M	WT		X			X															NATURE OF TURBULENCE IN WAKE OF 2-DIM AIRFOIL
	100	64	–	–	–	SIM	SIM																				METHODS OF MECHANIZING EQ OF MOTION USING ANALOG COMPUTER
	118	67	S	A	LS	–	–							X													METHODS PRODUCING HIGH LIFT, COMPARISON ON BASIS OF MAX LIFT
	263	60	S	A/R/D	H/T/LS	–	–																				EST OF V/STOL CHAR, INTERACTION BETWEEN LIFTING SYS AND PROPULSION WAKES, JET AND PROP SLIPSTREAM INTERACTIONS
	273	61	S	A	LS	–	–																				GEN NOMOGRAPHIC SOLUTION FOR INDUCED VEL AND WAKE SKEW ANGLE
	308	64	VSS/JF	R/D	LS	–	–										X	X					X				BASIC STOL PERF AND LOW-SPEED CONT AND HANDLING DEVEL, de HAVILAND AIRCRAFT CO
	338	61	S	R/A/D	S	–	–									X											SUMMARY OF VTOL STATE OF THE ART THROUGH 1961
	364	61	S	D	H/T/C	–	–																				PRINCIPLES OF V/STOL AERODYNAMICS REGARDING DESIGN FOR GOOD PERF
	508	60	DP/FP	A	LS	–	–																				PREDICTION OF OPTIMUM PERF CHAR
	510	59	S	T/A	LS	–	–																				LIFT-GENERATING SYSTEMS COMPARED. FIXED WING, ACTUATOR DISK, DUCTED PROP, ANNULAR WING, THEORY AND TEST COMPARED
	526	68	FIW/FIF	T	H/T	–	–	X			X																NUMERICAL SOLUTION OF 3-DIM INCOMPRESSIBLE FLOW PROBS, ITS APPLICATION TO V/STOL CONFIGS
	651	61	S	D	S	–	–									X											AERO ASPECTS OF V/STOL SYS, RESEARCH AT RAE THROUGH 1961, ESPECIALLY DIRECT-LIFT JET, PROP LIFT, JET FLAPS, BLC
	657	65	–	A	LS	–	–																				RELATIONSHIPS INVOLVED IN SHORTENING TAKEOFF AND LANDING DIST OF HIGH-SPEED AIRCRAFT
8.0	12	66	S	R/A/T/D	S	–	–	X	X		X			X		X											AERO PROBS OF V/STOL AIRCRAFT
	13	68	S	R/A	S	–	–																				RECOMMENDATIONS FOR V/STOL AERO RESEARCH
	20	66	S	S	H/T/C	S	S				X			X		X					X			X			PAPERS OF VTOL-STOL CONF, 1966
	23	64	S	A/R	S	–	–			X	X			X					X						X	X	RESEARCH AND RECOMMENDATIONS ON V/STOL AERODYNAMICS
	32	60	S	S	S	S	S	X						X		X	X	X	X	X	X		X	X	X		NASA CONF ON V/STOL AIRCRAFT (26 PAPERS)
	37	61	S	BIB	S	–	–																				NASA V/STOL REPT, BIBLIOGRAPHY AND V/STOL TRANSPORT STUDY

* See table 9B for key to summary

TABLE 9-A (CONTD)*

SUBJECT INDEX CLASSIFICATION	REFERENCE NUMBER	YEAR OF PUBLICATION	V-STOL CONCEPT	NATURE OF REPORT MATERIAL	FLIGHT REGIME OR AIRFLOW	TEST ARTICLE	TYPE OF TEST	AREAS OF INVESTIGATION OR ANALYSIS: Tests and Manuals	Wing	Free Propeller	Ducted Propeller	Two Dimensional Data	Pressure Data	Max. Lift or Turning	Ground Effect	Propeller Rotation Direction Effects	General	STABILITY AND CONTROL: Longitudinal	Lateral Directional	Dynamic	Stabilization	Simulation	Cross-axis Effects	Two or Four Axis Control System	Handling Qualities Criteria	COMMENTS
(CONTD)	38	59	S	BIB	S	P	F	X								X								X		3 ARTICLES ON V/STOL, NASA BIBLIOGRAPHY, REF 37
	46	60	S	S	S	S	S	X						X		X										AGARD SYMPOSIUM ON V/STOL AIRCRAFT
	50	68	S	R	S	–	–																			DDC VTOL BIBLIOGRAPHY, 1953 – JUNE 1968
	51	68	S	R	S	–	–																			DDC VTOL BIBLIOGRAPHY, EXPERIMENTAL VTOL MODELS, XV-5, XC-142, X-22, ETC., 1953 – JUNE 1968
	54	68	S	R/D	H/T/C	–	–									X								X	X	VTOL STATE OF THE ART, LIFT SYS, PROPULSION, AIRFRAME SYS, DYN AND AERO CHAR, CONT SYS OF PROMISING VTOL CONFIGS
	76	63	S	BIB	S	–	–																			V/STOL LITERATURE SURVEY COVERING 1961-62
	77	61	S	BIB	S	–	–																			AGARD V/STOL BIBLIOGRAPHY THROUGH 1960
	320	60	S	E/A/D	S	M	WT																			LARGE-SCALE, WT STUDIES OF VTOL TYPES, NASA CONF ON V/STOL AIRCRAFT
	343	60	JF	R/BIB	LS	–	–	X																		DETAILED JET FLAP REVIEW, THEORIES, DATA BIBLIOGRAPHY
	352	68	S	BIB	S	–	–																		X	VTOL FLYING-QUALITIES BIBLIOGRAPHY
	405	67	S	T/E/A/D	S	–	–																			CLASSROOM TEXT ON AERODYNAMICS OF V/STOL FLIGHT
	527	59	DP	R/BIB	S	–	–	X		X																REVIEW AND BIBLIOGRAPHY
	533	61	BLC/JF	S	LS	S	S	X						X												AERO ASPECTS OF V/STOL AIRPLANES
	538	68	DJ/L+P	R	H/LS	–	–							X												TABULAR SURVEY OF 132 REPORTS ON GRD EFF OF JET-LIFT V/STOL AIRCRAFT, REGION OF DEFLECTED JET
	586	62	–	BIB/D	LS	–	–																			BIBLIOGRAPHY OF PRINCETON LOW-SPEED WORK

* See table 9B for key to summary

9.1 FREE-PROPELLER CHARACTERISTICS

The methods of this Section are for estimating forces and moments on propellers. The primary purpose of this work is to provide information for analysis of direct propeller effects during the transition flight phase of V/STOL aircraft.

Operation of a propeller in an unsymmetrical flow field results in unsymmetrical loading on the blades as a function of their rotational position, which, in turn, produces forces normal to the thrust axis resulting in pitching and yawing moments. Flow field asymmetries result from either thrust-axis tilt or from flow angles induced by the airplane lifting surfaces. The propellers on V/STOL aircraft will encounter greater asymmetries than those of conventional aircraft because of the greater thrust-axis tilt and greater induced upwash of more effective high-lift devices.

Methods for the prediction of forces and moments on propellers inclined with respect to the free stream are developed by DeYoung in reference 1. DeYoung has generalized existing small-incidence theory (references 2 and 3) using a propeller solidity based on average blade chord. Simple expressions are thus developed for propeller normal (or side) force and some of the principal derivatives. DeYoung develops these expressions by first determining approximate equations of propeller geometry and operating parameters from the theory presented by Ribner in references 2 and 3, and then establishing by statistical means the equation constants and slightly altered functions from computed data of given blade shapes.

DeYoung also derives expressions for the ratio of normal force at high incidence to normal-force derivative at zero incidence, and the ratios of thrust, torque, and power at high incidence to the zero-incidence values.

Reference 5 presents results of a propeller test for three full-scale propellers of different design at nine angles of incidence ranging from 0 to 85 degrees. The operating conditions were selected to simulate the take-off, landing, and transition regimes of V/STOL aircraft. From the data of this reference certain generalizations can be made regarding propeller characteristics likely to be encountered in transition flight. It is shown that the thrust coefficients for given values of blade angle and advance ratio are nearly constant over a large range of thrust-axis angles of attack and that this range decreases with increasing advance ratio. Furthermore, it is shown that, over the same range of thrust-axis angles, the variations of propeller normal force and pitching moment are nearly linear. Using these generalizations it is possible to present approximate methods for the estimation of propeller forces and moments at large angles of inclination from experimental data at small angles of inclination for certain transition programs.

A general notation list is included in this Section for all free-propeller Sections.

The positive direction of forces and moments is shown in figure 9.1-4.

Notation List

A	wing aspect ratio
a_o	blade section lift-curve slope, per rad
B	number of blades

Notation List (continued)

b'	propeller blade chord, ft
$\bar{b}'$	average blade chord, ft
$b'_{.25}, _{.50}, \cdots$	blade chord at $\frac{r}{R} = .25, .50, \cdots$, ft
C_N'	normal-force coefficient based on free-stream velocity and propeller disk area, $\frac{N}{q_\infty S_p}$
C_N	normal-force coefficient, $\frac{N}{\rho n^2 D^4} = \frac{\pi J^2}{8} C_N'$
C_T	thrust coefficient, $\frac{T}{\rho n^2 D^4} = \frac{\pi J^2}{8} T_c$
c_r	wing root chord, ft
D	propeller diameter, ft
J	advance ratio, $\frac{V_\infty}{nD}$
J'	modified advance ratio, $J \cos \alpha$
J_{0T}	advance ratio at zero thrust
J_{0P}	advance ratio at zero power
N	propeller normal force, lb
n	propeller rotational speed, rps
q_∞	free-stream dynamic pressure, lb/sq ft
R	propeller radius, ft
R_{fus}	maximum fuselage radius forward of propeller plane
r	radial distance to blade element, ft
S_p	propeller disk area, $\frac{\pi}{4} D^2$, sq ft
T	propeller thrust, lb
T_c	thrust coefficient based on free-stream velocity and propeller disk area, $\frac{T}{q_\infty S_p} = \frac{8}{\pi J^2} C_T$
x	longitudinal coordinate measured positive forward from wing leading edge, ft
y	lateral coordinate measured positive to right of plane of symmetry, f
Δ_y	lateral distance from thrust axis of one propeller blade to element of another, ft

Notation List (continued)

V_∞	free-stream velocity, ft/sec
α	wing angle of attack measured from zero lift, deg
α_{in}	inflow angle at propeller disk, deg
β	blade angle at .75R blade station, deg
$\epsilon_{z_{slip}}$	upwash induced by propeller slipstream, positive downward, deg
σ	propeller solidity, ratio of blade element area to annulus area at .75R
σ_e	effective propeller solidity (propeller solidity based on average blade chord)
δ_f	force phase angle, deg

Subscripts

α_{in}	differentiation with respect to inflow angle, α_{in}
$L_{.75}$	left blade position at three-quarters radius point
$R_{.75}$	right blade position at three-quarters radius point
fus	fuselage

REFERENCES

1. DeYoung, J.: Force and Moment Derivatives Due to Propellers of Arbitrary Configuration Inclined with Respect to Free Stream. AIAA Preprint No. 64-169, 1964. (U)

2. Ribner, H. S.: Formulas for Propellers in Yaw and Charts of the Side-Force Derivative. NACA TR 819, 1945. (U)

3. Ribner, H. S.: Propellers in Yaw. NACA TR 820, 1945. (U)

4. Ribner, H. S.: Notes on the Propeller and Slipstream in Relation to Stability. NACA ARR L4I12a, 1944. (U)

5. Yaggy, P. F., and Rogallo, V. L.: A Wind-Tunnel Investigation of Three Propellers Through an Angle-of-Attack Range From 0° to 85°. NASA TN D-318, 1960. (U)

6. McLemore, H. C., and Cannon, M. D.: Aerodynamic Investigation of a Four-Blade Propeller Operating Through an Angle-of-Attack Range From 0° to 180°. NACA TN 3228, 1954. (U)

7. Draper, J. W., and Kuhn, R. E.: Investigation of the Aerodynamic Characteristics of a Model Wing-Propeller Combination and of the Wing and Propeller Separately at Angles of Attack Up to 90°. NACA TN 3304, 1954. (U)

8. LaMont, C. W.: Theoretical Forces on Tilted Propellers (Unpublished) Douglas Aircraft Company, Inc., 1961. (U)

9. Dong, J. C.: A Method of Estimating the Propeller Shaft Loads Induced by First Order Excitations. Curtiss-Wright Report C-2378, 1952. (U)

10. Dong, J. C.: Some Theoretical and Experimental Procedures for Determination of the Propeller First-Order Excitation Factor, Aq. Curtiss-Wright Report C-2640, 1956. (U)

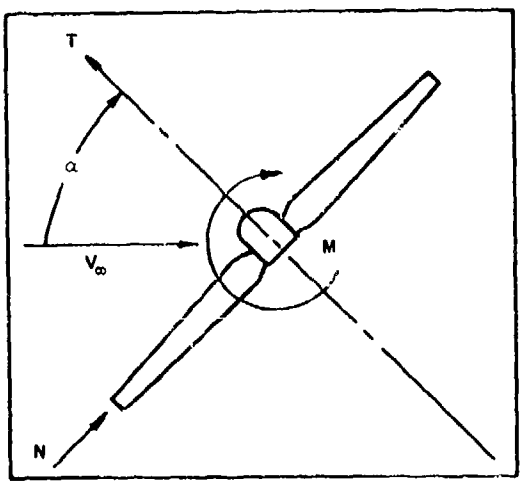

FIGURE 9.1-4 CONVENTIONS USED TO DEFINE POSITIVE SENSE OF FORCES AND MOMENTS

9.1.1 PROPELLER THRUST VARIATION WITH ANGLE OF ATTACK

Two methods are presented in this Section for estimating the thrust of a propeller at high angles of incidence. The first method is that of reference 1 and provides thrust relative to the zero-incidence value. This ratio is approximately proportional to the square of the tangent of the angle of incidence with a constant advance ratio, determined from the velocity normal to the propeller disk. In the theory the thrust is represented by the phase-angle change of the resultant velocity at the blade and takes into account both the angle-of-attack changes and the dynamic-pressure changes. A 90-degree incidence level is formulated from helicopter theory to provide a relatively small correction to the propeller theory. This thrust ratio is dependent on blade angle and advance ratio but, except for a small dependence on solidity, is independent of propeller geometry.

In the absence of complete data on a particular propeller, a second method is given that can be used to approximate the thrust at large incidence angles from experimental data at small incidence angles. This approach is formulated in reference 2, wherein it is demonstrated that certain VTOL transition programs can lie within the region of linear slope of the propeller forces and moments.

The methods presented herein are for an isolated propeller where the thrust-axis angle of attack is the angle between the free-stream velocity and the propeller thrust axis. For airplane installations this angle is often affected by flow induced by the wing, fuselage, and other propellers; however, the results of references 3 and 4 indicate that the major effects of induced flow on propeller thrust occur under conditions that are not likely to be of practical interest (high forward speed at high angles of attack).

DATCOM METHODS

Method 1

The variation of propeller thrust with angle of attack is given relative to the value at zero angle of attack, provided equal advance ratios exist as determined from the velocity normal to the propeller disk. This thrust ratio is given in reference 1 as

$$\frac{C_T(\alpha,J')}{C_T(0,J')} = 1 + \frac{3\left(\frac{J'}{J_{\alpha_T}}\right)^2}{4\left(1-\frac{J'}{J_{\alpha_T}}\right)} \sin(\beta+5)\left[\tan(\beta+5) + \sigma_e\left(1+\sqrt{1+\frac{2}{\sigma_e}\tan(\beta+5)}\right)(1-\cos\alpha)\right]\tan^2\alpha \qquad 9.1.1\text{-a}$$

where all parameters are defined in the general notation list of Section 9.1 and the positive direction of forces and angles is shown in figure 9.1-4.

The procedure to be followed in evaluating equation 9.1.1-a is outlined in the following steps.

Step 1. Determine the propeller effective solidity σ_e by

$$\sigma_e = \frac{\bar{b}'}{b'_{.75}} \sigma = \frac{4B\bar{b}'}{3\pi D} \qquad 9.1.1\text{-b}$$

where

$\bar{b}' = \frac{1}{0.8} \int_{.2}^{1} b' \, dx'$, which may be approximated by

$$\bar{b}' = 0.16 \left(\frac{5}{4} b'_{.25} + 2b'_{.50} + 2b'_{.75} + b'_{.95} \right) \qquad 9.1.1\text{-c}$$

$b'_{.25, .50, \ldots}$ are obtained from the propeller blade planform curve at $\frac{r}{R} = 0.25, 0.50, \ldots$

Step 2. The advance ratio at zero-thrust J_{O_T} is obtained from figure 9.1.1-7 as a function of β. This functional relationship is given in reference 1 as

$$J_{O_T} = 2.2 \tan(\beta + 5) \qquad 9.1.1\text{-d}$$

Step 3. Using equation 9.1.1-a obtain $\frac{C_T(\alpha,J')}{C_T(0,J')}$ with the σ_e and J_{O_T} values obtained in Steps 1 and 2. With this result values of the thrust ratio can be computed for a range of angles of attack and modified advance ratios.

Step 4. Determine the propeller thrust coefficient at selected angles of attack and modified advance ratios by

$$C_T(\alpha,J') = \frac{C_T(\alpha,J')}{C_T(0,J')} C_T(0,J')$$

where $C_T(0,J')$ is the propeller thrust coefficient at zero angle of attack, but with the velocity equal to $V_\infty \cos\alpha$. This parameter will normally be a known quantity.

Figures 9.1.1-8a-g and 9.1.1-11a-d present a comparison of experimental data from reference 2 with the Datcom method as computed from equation 9.1.1-a.

Method 2

This method is suggested in reference 2 for estimating propeller thrust at high angles of attack when experimental data at zero angle of attack are available.

The experimental data of reference 2 show that the thrust coefficient for given values of blade angle and advance ratio is practically constant over a wide angle-of-attack range at low advance ratios, and that this range diminishes with increasing advance ratio. Using these observations, it is possible to identify these ranges in VTOL transition programs.

The boundary of this region, presented in figure 9.1.1-13, has been determined on the basis of five-percent thrust-coefficient increases from the zero-angle-of-attack values for two propellers at a constant blade angle, tested in reference 2. The region varies with blade angle. The boundary curve of figure 9.1.1-13 is defined for a 12-degree blade angle, typical for maximum propeller efficiency in very low-speed flight. The characteristics of the two test propellers are presented in table 9.1.1-A.

As a simple rule of thumb, the propeller thrust at high angles of attack may be assumed to equal the value at zero angle of attack if the modified advance ratio falls below the boundary of figure 9.1.1-13.

A 1-g transition program for a hypothetical airplane described in reference 3 is also shown in figure 9.1.1-13. This program is based on the data obtained for propeller 1 of reference 2. The modified advance ratio lies well below the boundary curve. However, for conditions of steep descent or rapidly decelerating transition the boundary could be exceeded.

Sample Problem

Method 1

Given: The three-bladed propeller designated as propeller number 1 of reference 2. The following example is based on four values of the modified advance ratio over a thrust-axis angle-of-attack range from 0 to 85°.

$B = 3$ $\quad D = 12$ ft $\quad \beta = 12^{\circ}$

r/R	0.25	0.50	0.75	0.95
b', ft	0.89	1.115	1.175	1.18

J'	0.1	0.2	0.4	0.6
$C_T(0,J')$	0.132	0.121	0.083	0.032

Compute:

Step 1. Determine the effective propeller solidity σ_e.

$$\bar{b}' = 0.16\left[\frac{5}{4}b'_{.25} + 2b'_{.50} + 2b'_{.75} + b'_{.95}\right] \quad \text{(equation 9.1.1-c)}$$

$$= 0.16\left[\frac{5}{4}(0.89) + (2)(1.115) + (2)(1.175) + 1.18\right]$$

$$= 0.16\,(6.87) = 1.10$$

$$\sigma_e = \frac{4B\bar{b}'}{3\pi D} = \frac{(4)(3)(1.10)}{(3)(12)\pi} = 0.117 \quad \text{(equation 9.1.1-b)}$$

Step 2. Determine the advance ratio at zero-thrust J_{O_T} from figure 9.1.1-7 at $\beta = 12^o$.

$$J_{O_T} = 0.6725$$

Solution:

Determine the ratio of the thrust coefficient at inclination to the thrust coefficient at zero angle of incidence.

$$\frac{C_T(\alpha,J')}{C_T(0,J')} = 1 + \frac{3\left(\frac{J'}{J_{O_T}}\right)^2}{4\left(1 - \frac{J'}{J_{O_T}}\right)} \sin(\beta + 5)\left|\tan(\beta + 5)\right.$$

$$+ \sigma_e \left(1 + \sqrt{1 + \frac{2}{\sigma_e}\tan(\beta + 5)}\right)(1-\cos\alpha)\left|\right. \tan^2\alpha$$

(equation 9.1.1-a)

$$= 1 + \frac{3\left(\frac{J'}{0.6725}\right)^2}{4\left(1 - \frac{J'}{0.6725}\right)} \sin(17)\left|\tan(17)\right.$$

$$+ 0.117\left(1+\sqrt{1+\frac{2}{0.117}\tan(17)}\right)(1-\cos\alpha)\left|\right. \tan^2\alpha$$

$$= 1 + \frac{6.64\,J'^2}{4 - 5.95J'}\,(0.2924)\left|0.3057 + 0.409(1-\cos\alpha)\right|\tan^2\alpha$$

$$= 1 + \frac{1.939J'^2}{4 - 5.95J'}\left|0.3057 + 0.409\,(1-\cos\alpha)\right|\tan^2\alpha$$

Using this result obtain $\frac{C_T(\alpha,J')}{C_T(0,J')}$ as a function of J' and α. This is calculated below for seven angles of attack. Note that at $J' = 0$, $\frac{C_T(\alpha,J')}{C_T(0,J')} = 1.0$; and at $J' = J_{O_T}$, $\frac{C_T(\alpha,J')}{C_T(0,J')} \longrightarrow \infty$

				$\left[C_T(\alpha,J')/C_T(0,J')\right]$ -1						
①	②	③	④	$\alpha=85^\circ$	79.5°	75°	67.5°	60°	45°	30°
J'	4-5.95J'	1.939J'^{2}	③ / ②	88.68 ④	18.63 ④	8.465 ④	3.252 ④	1.531 ④	.4255 ④	.1206 ④
.05	3.7025	.0048	.00130	.1152	.0244	.0111	.0042	.0020	.00056	.00016
.10	3.405	.0194	.00570	.505	.1062	.0482	.0185	.0087	.0024	.00069
.15	3.1075	.0436	.01404	1.245	.2619	.1190	.0456	.0215	.0060	.0017
.20	2.810	.0776	.02760	2.447	.5142	.2336	.0898	.0423	.0117	.0033
.30	2.215	.1745	.07879	6.987	1.468	.6669	.2562	.1206	.0335	.0095
.40	1.620	.3102	.1915	16.983	3.568	1.621	.6228	.2931	.0815	.0231
.50	1.025	.4848	.4729	41.934	8.811	4.003	1.538	.7239	.2012	.0570
.60	0.430	.6980	1.6233	143.95	30.24	13.740	5.279	2.485	.6907	.1958
.65	0.1325	.8192	6.1829	548.30	115.19	52.340	20.107	9.464	2.631	.7457

The calculated values of the thrust ratio are compared with the experimental results from reference 1 in figure 9.1.1-14.

The thrust coefficient at angle of inclination and given advance ratio is then

$$C_T(\alpha,J') = C_T(0,J') \frac{C_T(\alpha,J')}{C_T(0,J')}$$

	$C_T(\alpha,J')$			
α	J'=.1	J'=.2	J'=.4	J'=.6
0	0.132	0.121	0.083	0.032
30	0.1321	0.1214	0.0849	0.0383
45	0.1323	0.1224	0.0898	0.0541
60	0.1331	0.1261	0.1073	0.1115
67.5	0.1344	0.1319	0.1347	0.2009
75	0.1384	0.1493	0.2175	0.4717
79.5	0.1462	0.1832	0.3791	0.9997
85	0.1987	0.4171	1.4926	4.6384

The calculated values of the thrust coefficients are compared with the experimental results from reference 1 in figure 9.1.1-15. The results may be converted to thrust in pounds by

$$-T(\alpha,J') = \frac{8}{\pi(J')^2} C_T(\alpha,J') \quad q_\infty \; S_p$$

REFERENCES

1. DeYoung, J.: Force and Moment Derivatives Due to Propellers of Arbitrary Configuration Inclined with Respect to Free Stream. AIAA Preprint No. 64-169, 1964. (U)

2. Yaggy, P. F., and Rogallo, V. L.: A Wind-Tunnel Investigation of Three Propeller Through an Angle-of-Attack Range From 0° to 85°. NASA TN D-318, 1960. (U)

3. Draper, J. W., and Kuhn, R. E.: Investigation of the Aerodynamic Characteristics of a Model Wing-Propeller Combination and of the Wing and Propeller Separately at Angles of Attack. NACA TN 3304, 1957. (U)

4. Kuhn, R. E., and Hayes, W. C., Jr.: Wind-Tunnel Investigation of Longitudinal Aerodynamics of Three Propeller-Driven VTOL Configurations in the Transition Speed Range, Including Effects of Ground Proximity. NASA TN D-55, 1960. (U)

TABLE 9.1.1-A
Reference 2

Propeller	No. 1 Curtiss C6345-C500	No. 2 Curtiss C6345-C300
Diameter	12.0 ft	10.0 ft
No. of blades	3	3
Airfoil section	NACA 16 series	NACA 64 series
Blade designation	858-7C4-36	X100188
Activity factor/blade	150	188
Solidity	0.124	0.183

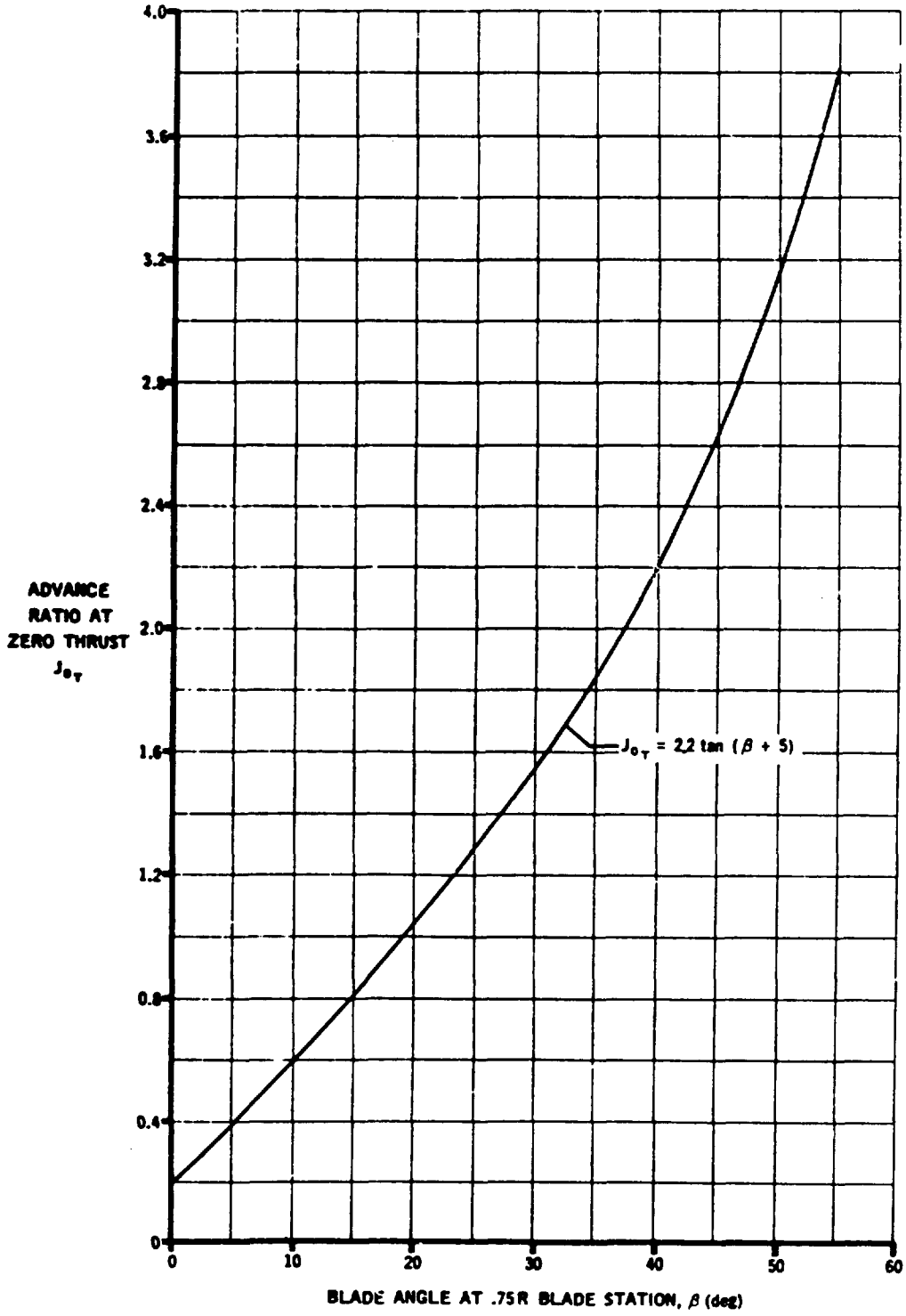

FIGURE 9.1.1-7 ADVANCE RATIO AT ZERO THRUST

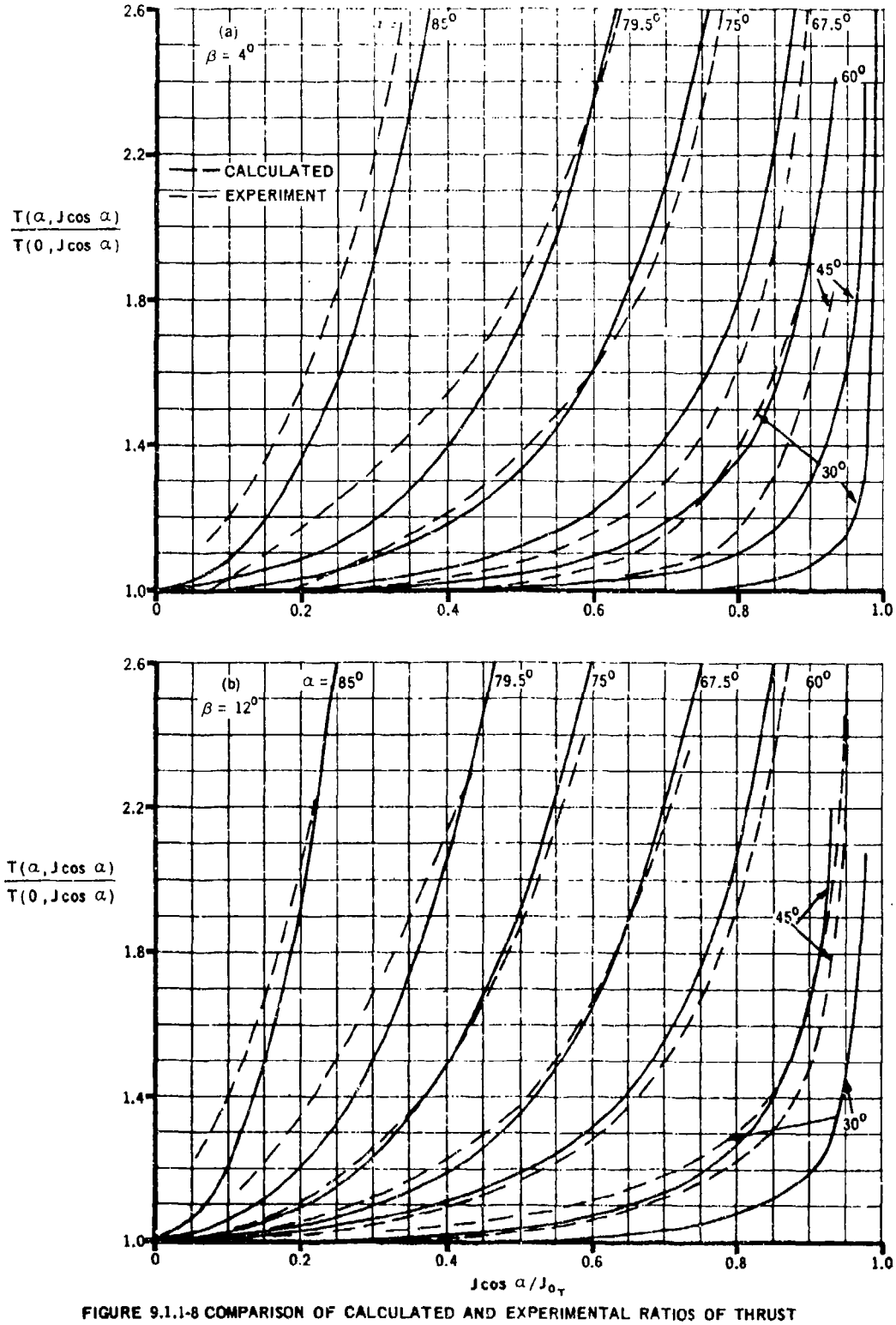

FIGURE 9.1.1-8 COMPARISON OF CALCULATED AND EXPERIMENTAL RATIOS OF THRUST AT PROPELLER THRUST-AXIS ANGLE OF ATTACK TO THRUST AT ZERO THRUST-AXIS ANGLE OF ATTACK FOR PROPELLER 1 OF REFERENCE 2

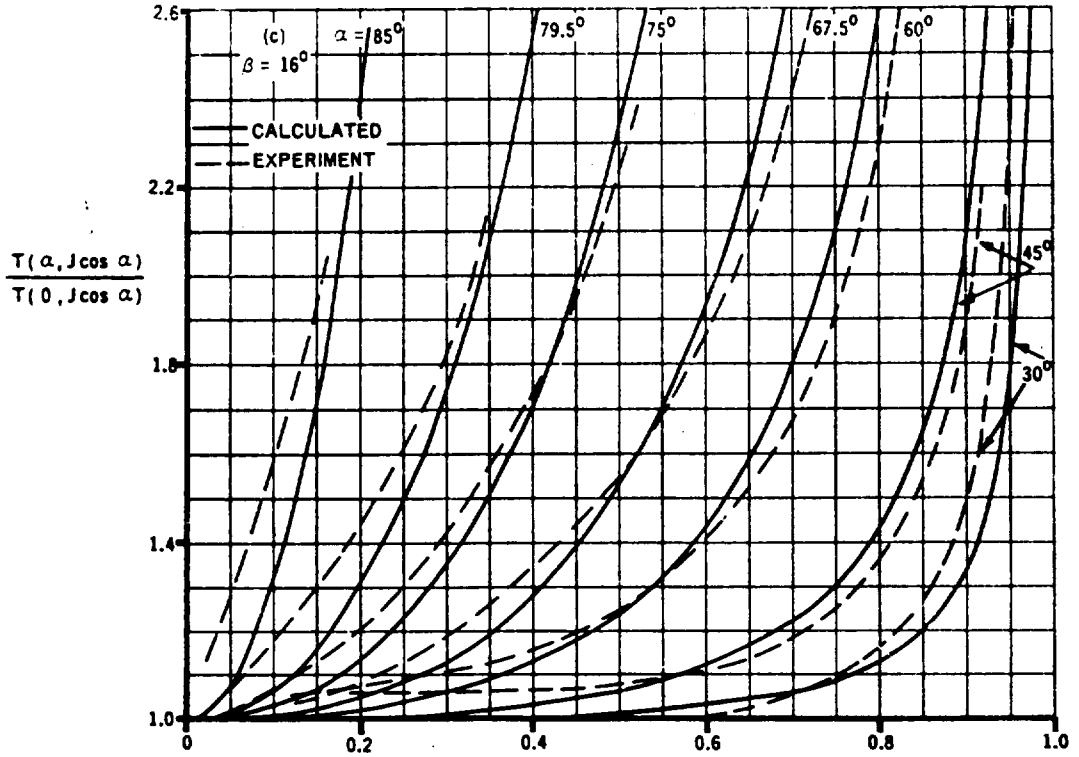

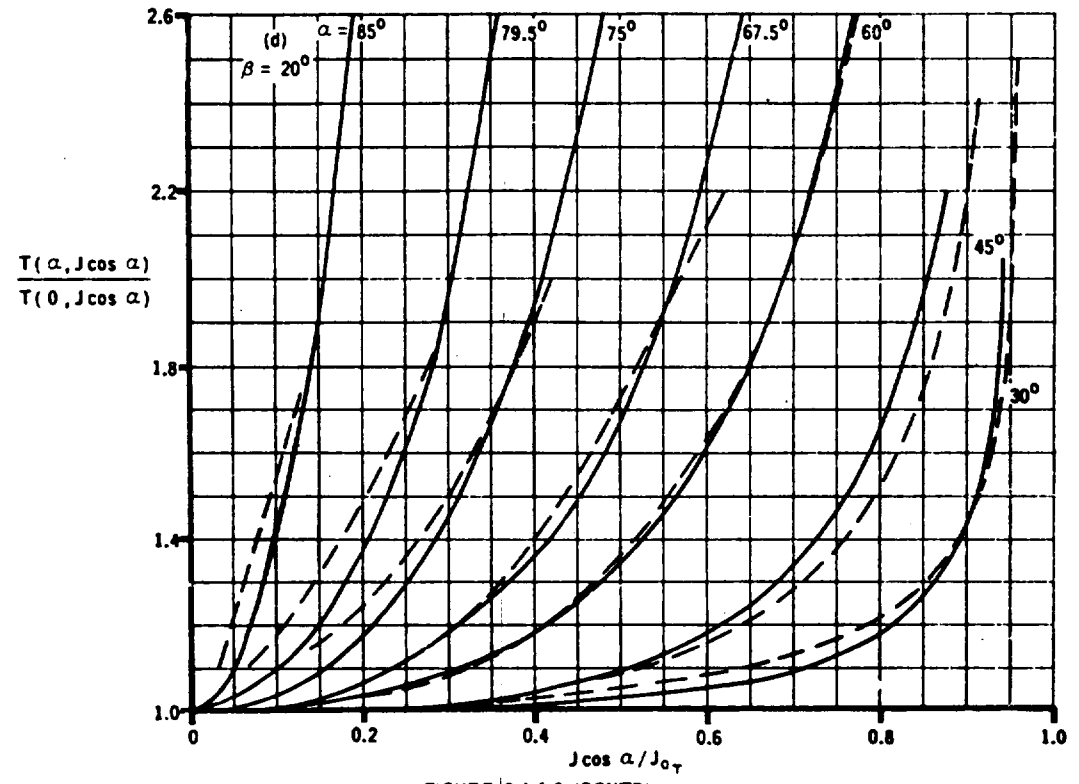

FIGURE 9.1.1-8 (CONTD)

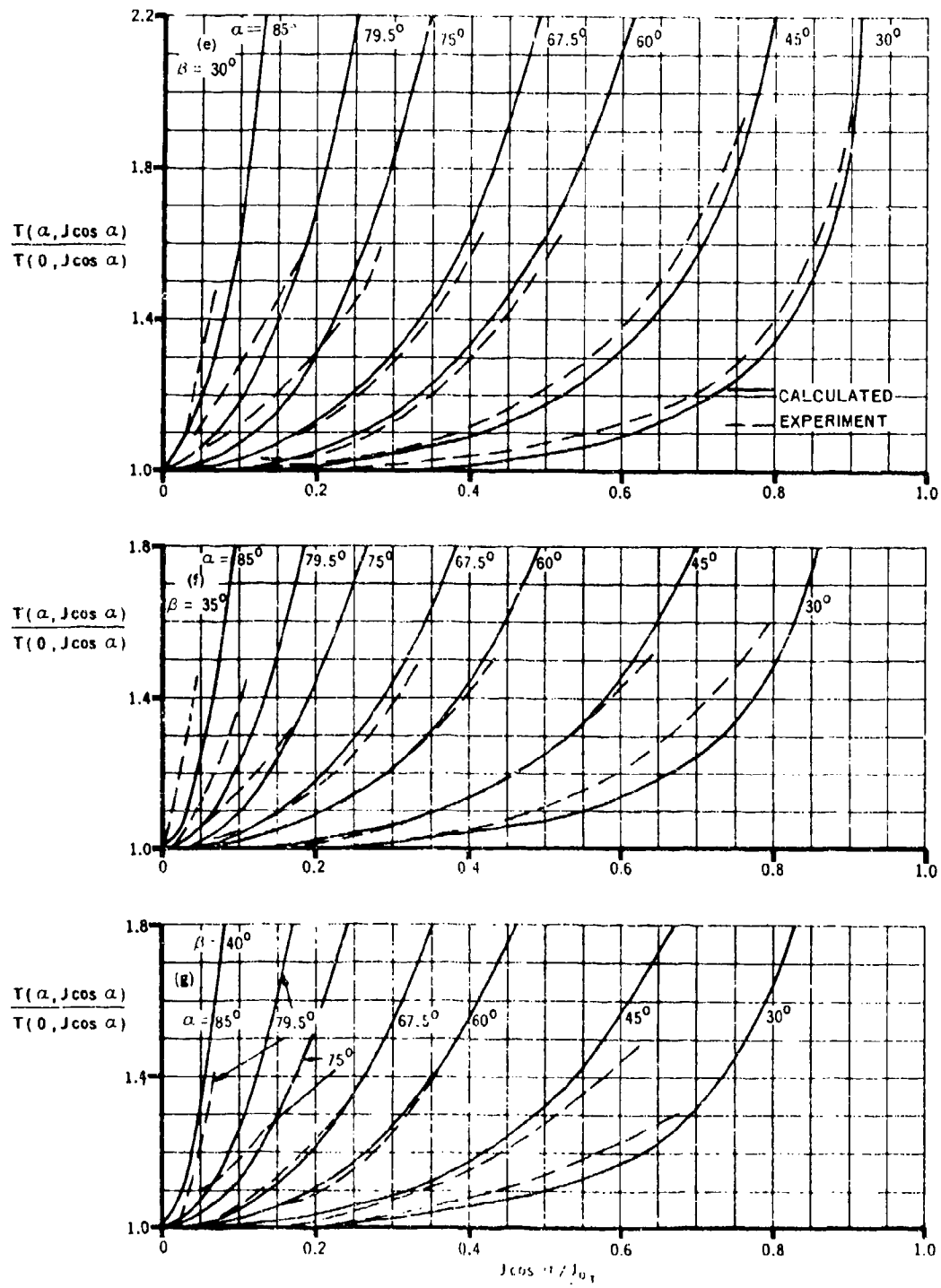

FIGURE 9.1.1-8 (CONTD)

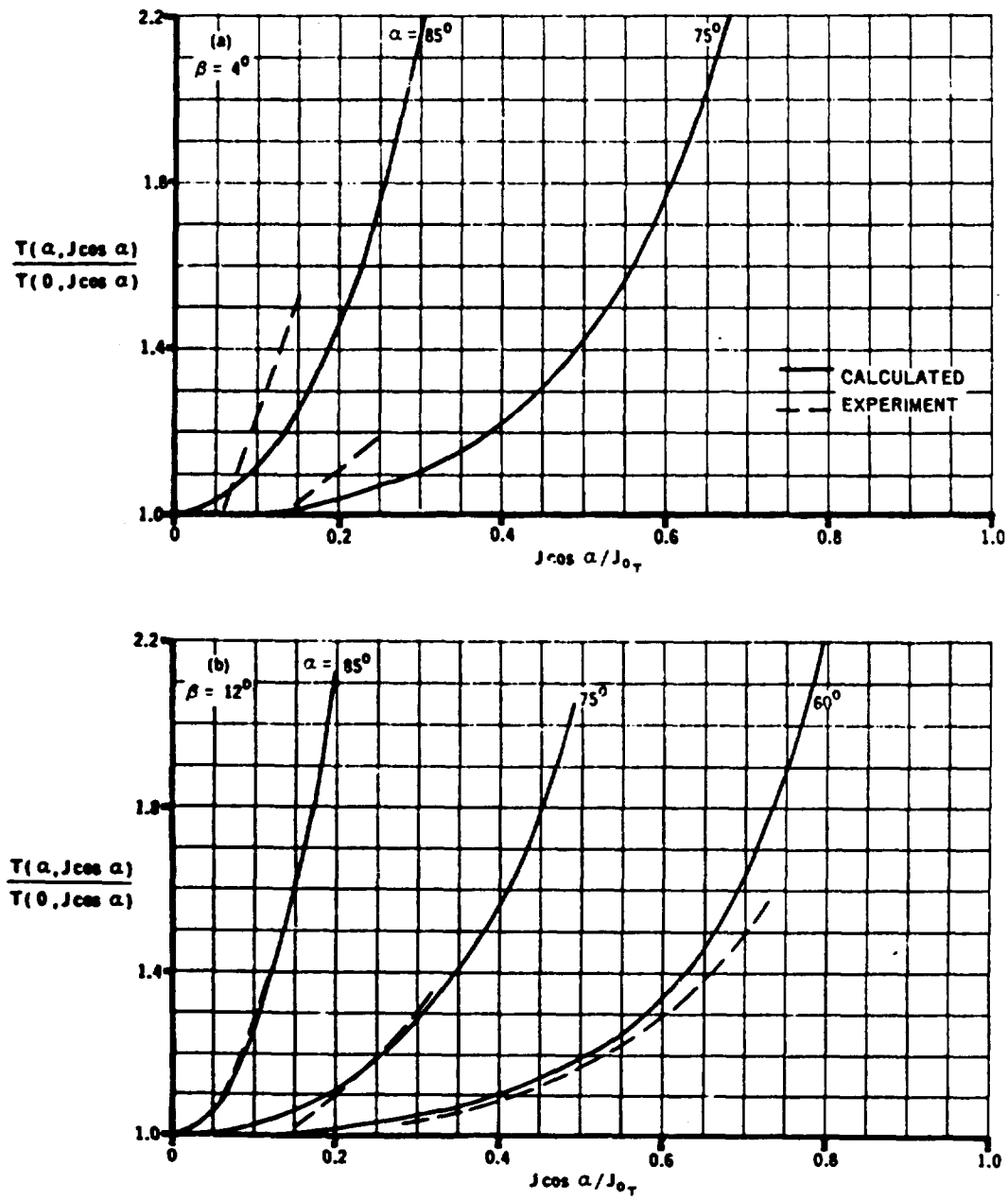

FIGURE 9.1.1-11 COMPARISON OF CALCULATED AND EXPERIMENTAL RATIOS OF THRUST AT PROPELLER THRUST-AXIS ANGLE OF ATTACK TO THRUST AT ZERO THRUST-AXIS ANGLE OF ATTACK FOR PROPELLER 2 OF REFERENCE 2

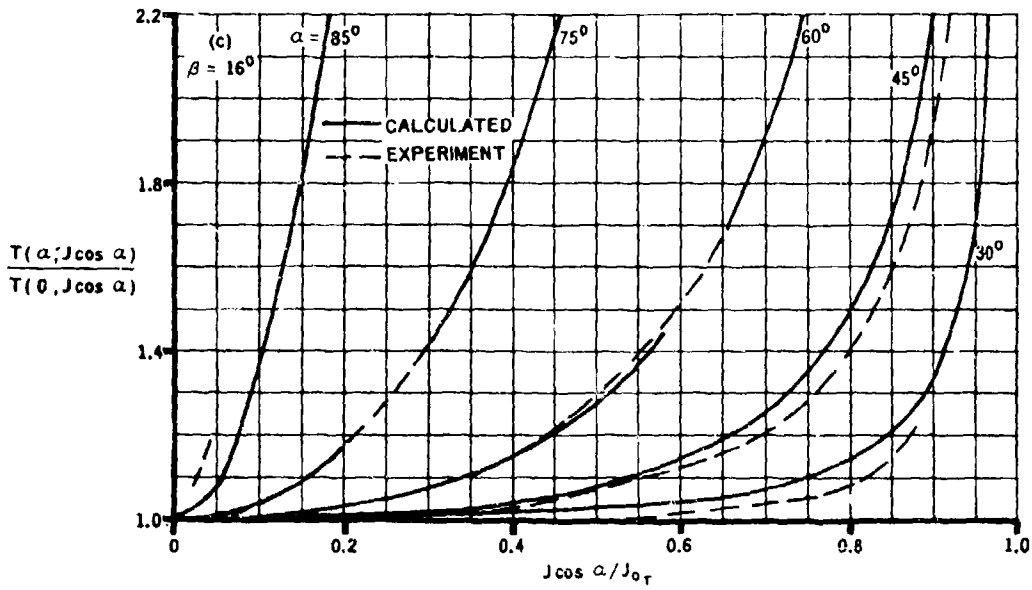

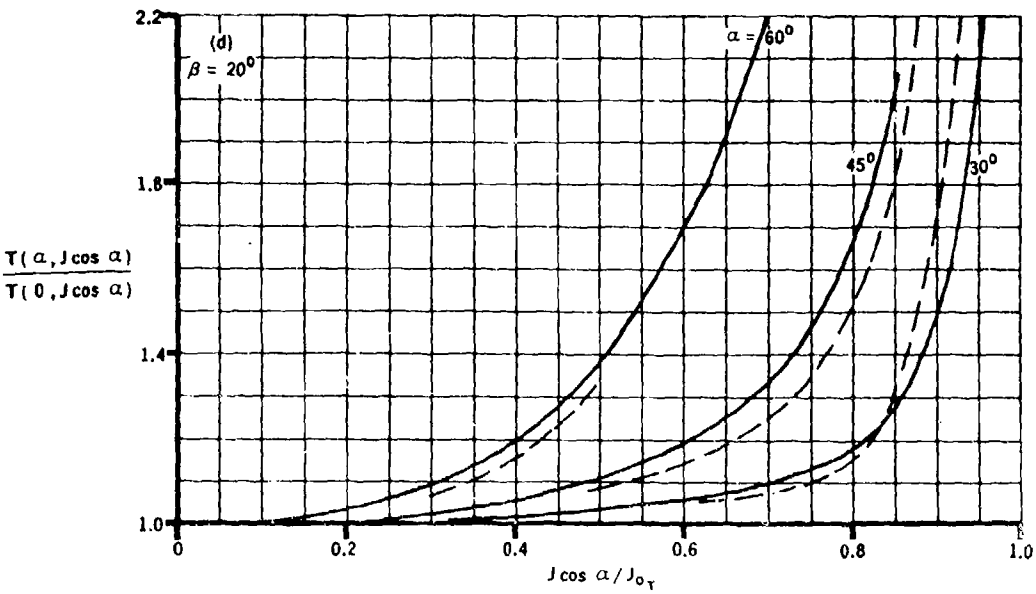

FIGURE 9.1.1-11 (CONTD)

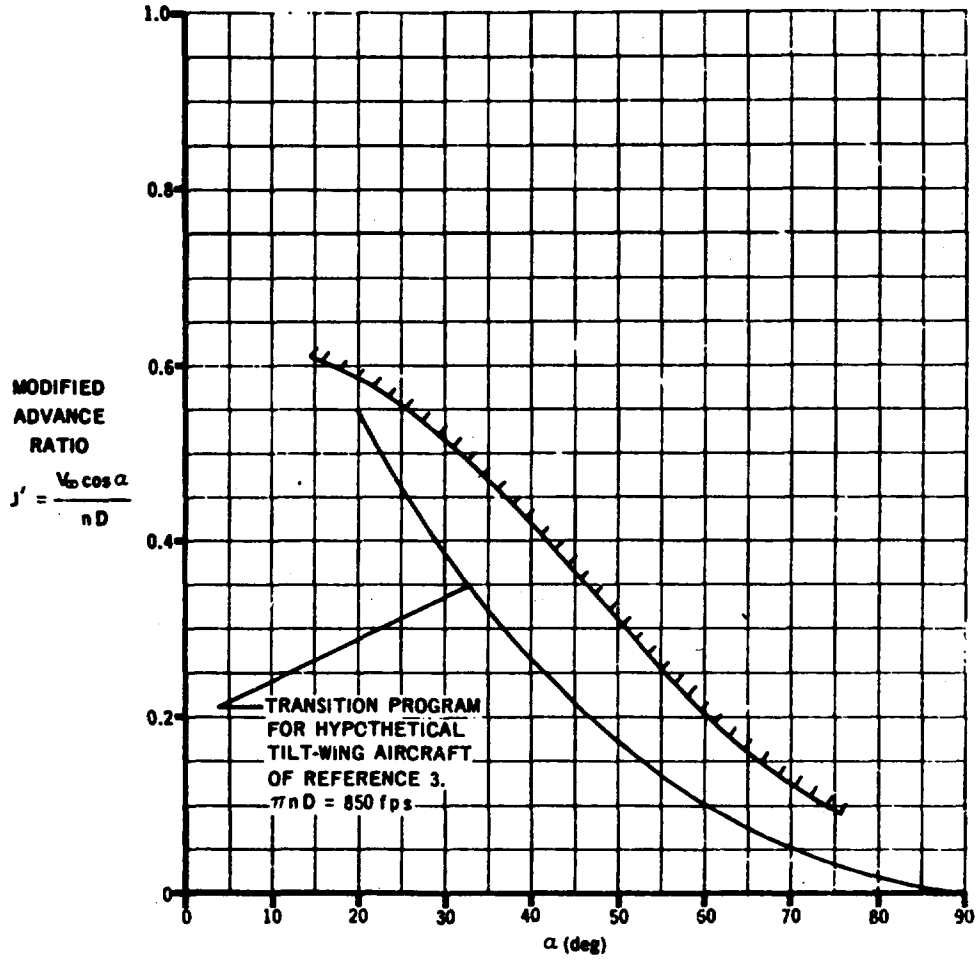

FIGURE 9.1.1-13 BOUNDARY CURVE FOR 5-PERCENT INCREASE OF COEFFICIENT OVER VALUE AT ZERO THRUST-AXIS ANGLE OF ATTACK

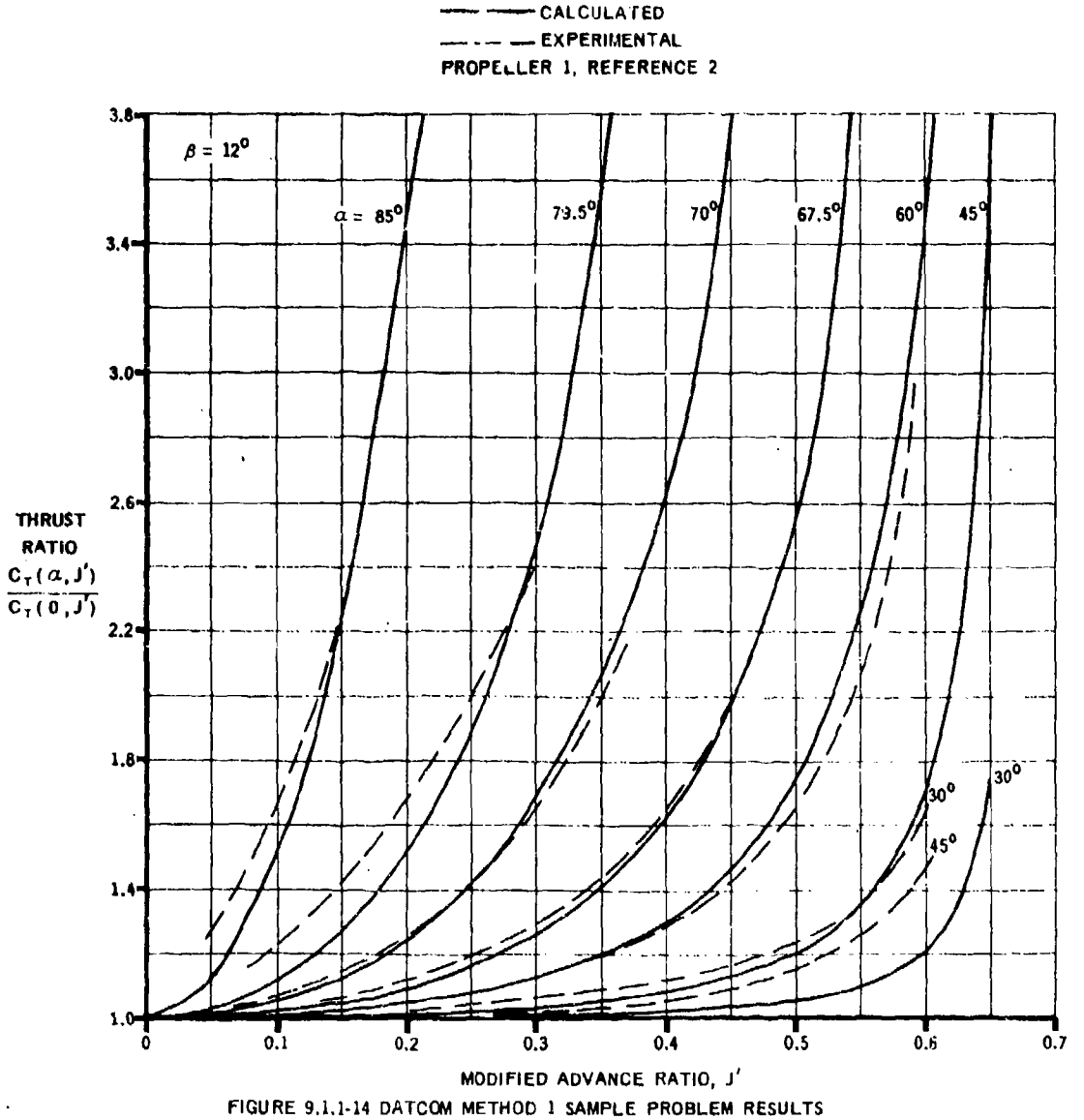

FIGURE 9.1.1-14 DATCOM METHOD 1 SAMPLE PROBLEM RESULTS

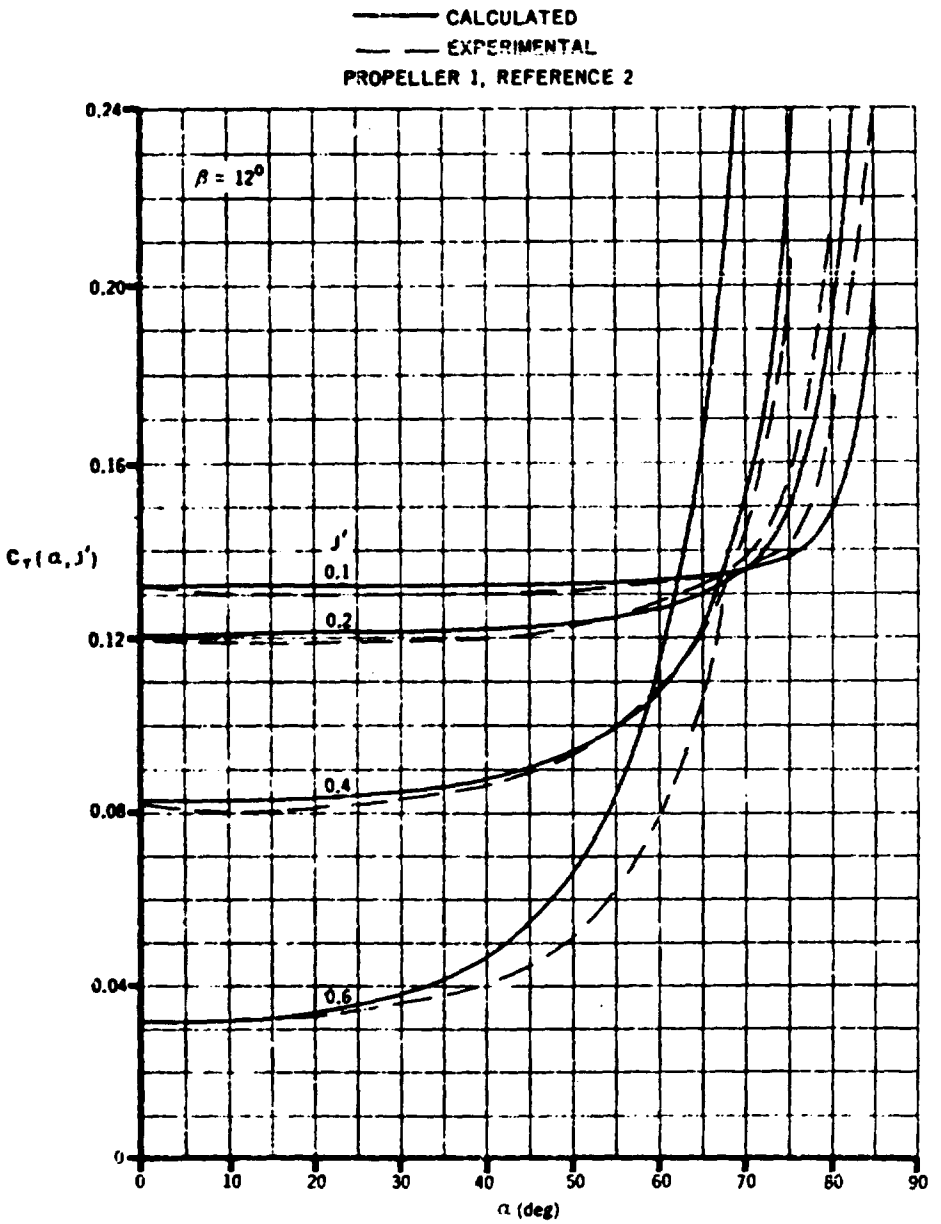

FIGURE 9.1.1-15 DATCOM METHOD 1 SAMPLE PROBLEM RESULTS

9.1.2 PROPELLER PITCHING-MOMENT VARIATION WITH POWER AND ANGLE OF ATTACK

At the present there are no theoretical or semi-empirical methods available in the literature for the prediction of propeller pitching moments at high angles of attack. The method presented herein is empirical and requires experimental data at two moderate angles of attack.

Experimental data indicate that there is an appreciable direct pitching moment on the propeller during operation at angle of attack. This pitching moment may be regarded as being due to the fact that the center of thrust is some distance away from the center of rotation. Figures 9.1.2-3 and 9.1.2-4 show the direct propeller pitching moment expressed as an effective thrust-axis shift for the propeller and the propeller-wing combination of reference 1 and for propeller 1 of reference 2, respectively. These data indicate an increase in propeller pitching moment with increasing angle of attack and a more pronounced shift of the effective thrust axis at the lower thrust coefficients. The data of figure 9.1.2-3 further show that the propeller pitching moment was approximately doubled when the propeller was operated in the presence of the wing because of the upwash induced by the wing.

The Datcom method which follows is based on observations of the large body of test data presented in reference 2.

DATCOM METHOD

This method is suggested in reference 2 for estimating propeller pitching moment at high thrust-axis angles of attack when experimental data are available at two angles of attack, such as zero and 15 degrees.

The experimental data of reference 2 show that the propeller pitching moment for given values of blade angle and advance ratio have nearly a constant slope over wide angle-of-attack ranges at low advance ratio and that the width of these ranges diminishes with increasing advance ratio.

It is not possible to define the limits of the regions of linearity of propeller pitching moments from the experimental data as was done for the propeller thrust in Section 9.1.1. However, in view of the fact that the angle-of-attack ranges of pitching-moment linearity are essentially those over which the thrust is constant, it is assumed that, to a first approximation, the boundary, defined in figure 9.1.1-13, also applies to pitching moments. As noted in Section 9.1.1, this boundary varies with blade angle. It is defined for a blade angle typical of maximum propeller efficiency in very low-speed flight.

As a simple rule of thumb, the propeller pitching moment at high angles of attack may be obtained with accuracy acceptable for preliminary design analysis by a linear extrapolation of experimental data at moderate angles of attack, provided the modified advance ratio falls below the boundary of figure 9.1.1-13 .

REFERENCES

1. Draper, J. W., and Kuhn, R. E.: Investigation of the Aerodynamic Characteristics of a Model Wing-Propeller Combination and of the Wing and Propeller Separately at Angles of Attack Up to 90°. NACA TN 3304, 1954. (U)

2. Yaggy, P. F., and Rogallo, V. L.: A Wind-Tunnel Investigation of Three Propellers Through an Angle-of-Attack Range From 0° to 85°. NASA TN D-318, 1960. (U)

3. McLemore, H. C., and Cannon, M. D.: Aerodynamic Investigation of a Four-Blade Propeller Operating Through an Angle-of-Attack Range From 0° to 180°. NACA TN 3228, 1954. (U)

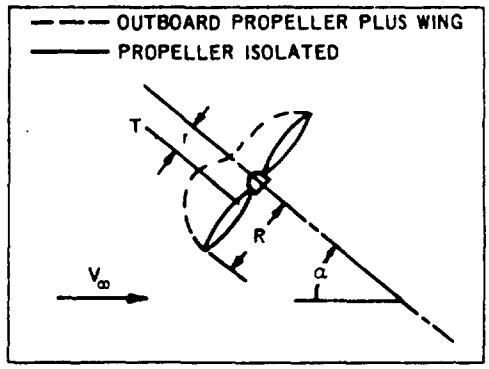

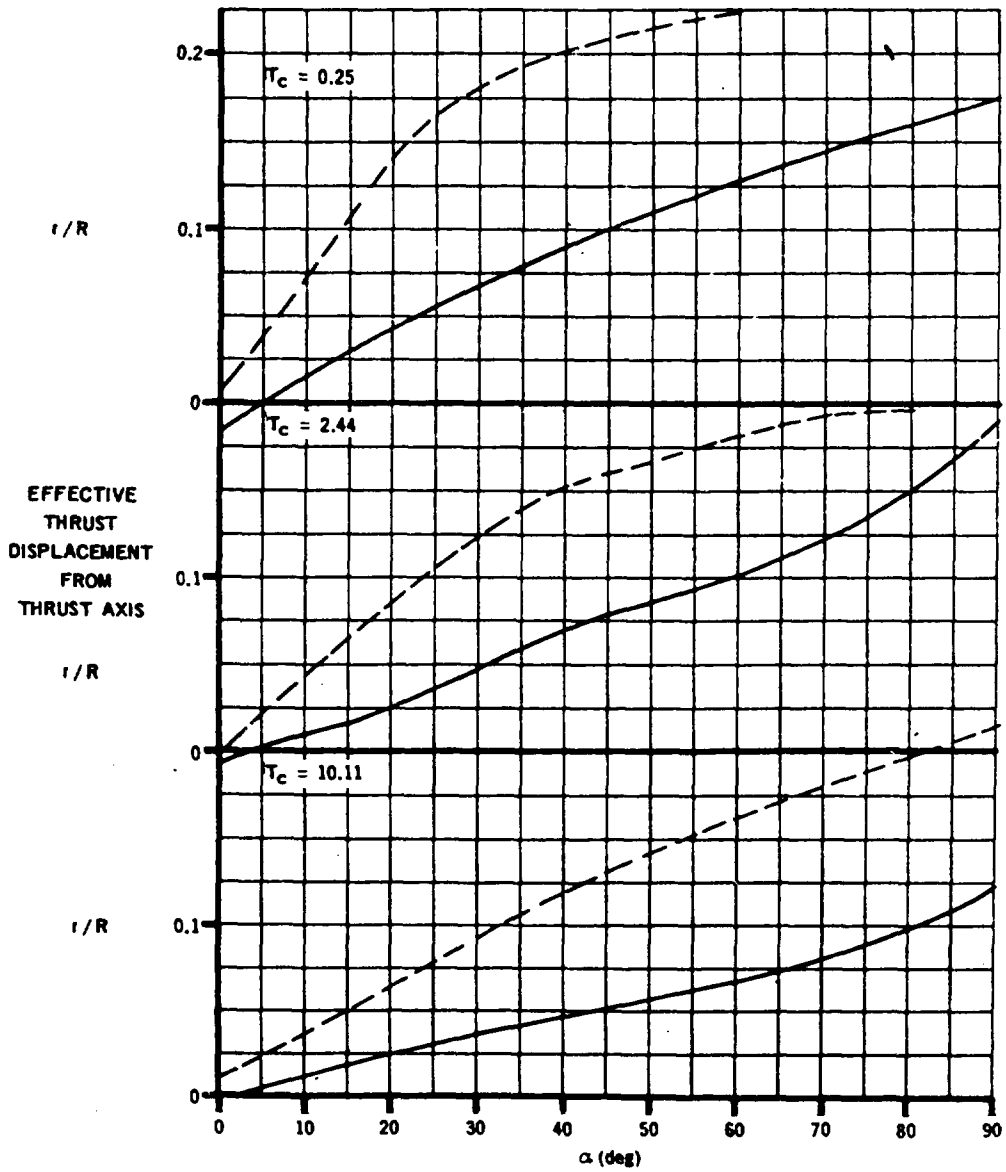

FIGURE 9.1.2-3 EFFECT OF ANGLE OF ATTACK ON EFFECTIVE THRUST DISPLACEMENT FROM THRUST AXIS FOR THE PROPELLER OF REFERENCE 1

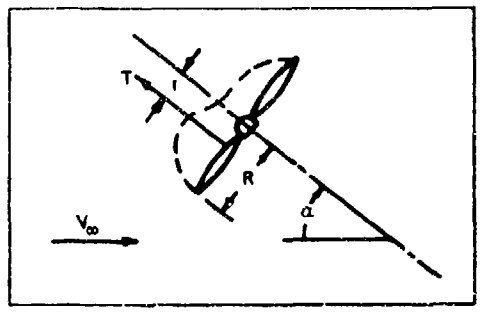

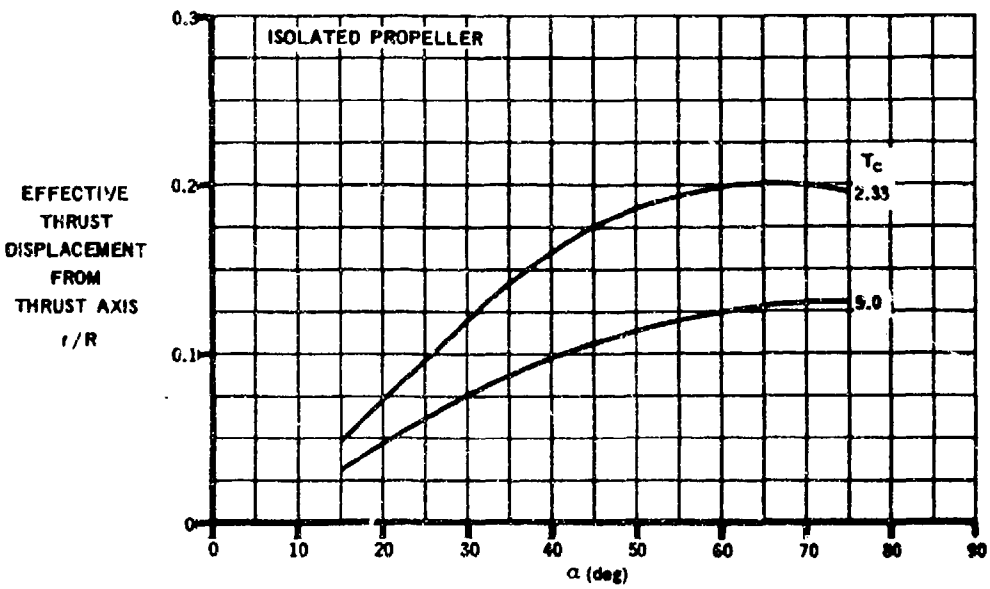

FIGURE 9.1.2-4 EFFECT OF ANGLE OF ATTACK ON EFFECTIVE THRUST DISPLACEMENT FROM THRUST AXIS FOR PROPELLER 1 OF REFERENCE 2

9.1.3 PROPELLER NORMAL-FORCE VARIATION WITH POWER AND ANGLE OF ATTACK

Two methods are presented in this Section for estimating the propeller normal force at high angles of attack .

The first method, developed by DeYoung in reference 1, provides the normal-force coefficient at high angles of attack relative to the linear relation $\left(\frac{dC_N}{d\alpha}\right)_{\alpha=0}$ This ratio is equal to the tangent of the angle of attack, provided equal advance ratios, as determined from the velocity normal to the propeller disk, exist. In theory, the normal force is considered to be proportional to the torque difference due to angle of incidence between the down-going blade and the up-going blade.

The essential part of Datcom method 1 is the estimation of $\left(\frac{dC_N}{d\alpha}\right)_{\alpha=0}$. This involves determining the normal-force derivative with respect to the local angle of attack, the local angle-of-attack gradient, and a correction for phase-angle shift.

DeYoung, in reference 1, has obtained a simple relationship for the normal-force derivative with respect to local angle of attack in the manner described in Section 9.1. A general expression for this derivative as a function of propeller geometry and operating parameters is obtained from the analysis of Ribner in references 2 and 3 and the assumption of a blade section lift-curve slope of $c_{l_\alpha} = 0.95(2\pi)$ per radian. The constants of the resulting expression are evaluated by statistical means from the computed data of the given blade shapes of reference 4.

The normal-force derivative with respect to wing angle of attack is given as the product of the normal-force derivative with respect to the local propeller angle of attack and the local angle-of-attack gradient $\frac{d\alpha_{in}}{d\alpha}$, obtained in reference 1 by an analysis of the upwash due to the wing, fuselage, and other propellers.

Propellers operating at high angles of attack experience appreciable angle-of-attack variation on the blades. Lift increases and decreases in a harmonic fashion. As the angle of attack is increased, circulation increases, and a starting vortex is shed which induces a downwash and changes the buildup of circulation. This unsteady motion causes the lift cycle to be out of phase with the angle-of-attack cycle; consequently, the propeller forces and moments have components in both the lateral and vertical directions. The normal force at incidence is then the product of the normal force computed for zero phase angle and the cosine of the phase angle. In Datcom method 1 the effect of this phase-angle shift is applied to the computed linear relation $\left(\frac{dC_N}{d\alpha}\right)_{\alpha=0}$.

In the theory of reference 1 the propeller phase angle is approximated by an analogous wing unsteady solution, assuming that the propeller forces and blade angle of attack are analogous to those of a wing that is harmonically pitching about its quarter-chord line.

A second method is given which, in the absence of complete data on a particular propeller, can be used to approximate the normal force at large angles of attack from experimental data at small angles of attack. This approach is formulated in reference 5, wherein it is demonstrated that certain VTOL transition programs can lie within the region of linear slope of the propeller forces and moments.

DATCOM METHODS

Method 1

The variation of propeller normal force with angle of attack is given relative to $\left(\frac{dC_N}{d\alpha}\right)_{\alpha=0}$, provided equal advance ratios, as determined from the velocity normal to the propeller disk, exist. This ratio is given in reference 1 as

$$\frac{C_N(\alpha,J')}{C_{N_\alpha}(0,J')} = \tan\alpha \qquad 9.1.3\text{-a}$$

The positive normal-force and angle-of-attack senses are shown in figure 9.1-4, and the required parameters are defined in the general notation list of Section 9.1.

This method is essentially one of determining the denominator values in the form of C_{N_α}' where

$$C_{N_\alpha}' = C_{N_{\alpha_{in}}}' \frac{d\alpha_{in}}{d\alpha} \text{ per rad} \qquad 9.1.3\text{-b}$$

In computing these values the J or thrust in the relation for $C_{N_{\alpha_{in}}}'$ must be taken at J' and velocity at $V_\infty \cos\alpha$.

The derivatives C_{N_α}' and C_{N_α} are related by

$$C_{N_\alpha}(0,J') = \frac{\pi}{8}(J')^2 C_{N_\alpha}'(0,J') \text{ per rad} \qquad 9.1.3\text{-c}$$

The procedure to be followed in evaluating the normal force is outlined in the following steps.

Step 1. Determine at zero phase angle the propeller normal-force derivative with respect to the local angle of attack at the propeller disk by

$$C_{N_{\alpha_{in}}}' = \frac{4.25\,\sigma_e}{1+2\,\sigma_e}\sin(\beta+8)\left(1+\frac{3T_c}{8\sqrt{1+(2/3)T_c}}\right) \text{ per rad} \qquad 9.1.3\text{-d}$$

for single-rotation propellers, and by

$$C_{N_{\alpha_{in}}}' = \frac{3.86\,\sigma_e}{1+\sigma_e}\sin(\beta+14)\left(1+\frac{3T_c}{8\sqrt{1+(2/3)T_c}}\right) \text{per rad} \qquad 9.1.3\text{-d}'$$

for counter-rotating propellers;

where σ_e is obtained as outlined in Step 1 of Datcom method 1 of Section 9.1.1 and the thrust values are taken at J', with velocity equal to $V_\infty \cos\alpha$. The thrust values will normally be known.

Step 2. Determine the local angle-of-attack gradient $\frac{d\alpha_{in}}{d\alpha}$ by

$$\frac{d\alpha_{in}}{d\alpha} = \frac{1 + \frac{2A}{9(A+10)}\left(\frac{1}{\frac{x_{L\ .75}}{c_r} + \frac{1}{10}} + \frac{1}{\frac{x_{R\ .75}}{c_r} + \frac{1}{10}}\right) + \frac{1}{2}\left[\left(\frac{R_{fus}}{y_{L\ .75}}\right)^2 + \left(\frac{R_{fus}}{y_{R\ .75}}\right)^2\right]}{1 - \frac{1}{4}\sum_{\text{other props}}\left[\left(\frac{R}{\Delta y_{L\ .75}}\right)^2 + \left(\frac{R}{\Delta y_{R\ .75}}\right)^2\right]\frac{d\epsilon_{z\ slip}}{d\alpha_{in}}} \qquad 9.1.3\text{-e}$$

where the first two terms in the numerator are the average upwash at the propeller .75R station due to the wing, and the third term in the numerator is the average upwash at the propeller .75R station due to the fuselage.

The summation term in the denominator is the average downwash in the propeller slipstream at the propeller .75R station. For propellers operating near each other this downwash must be considered in predicting the local angle-of-attack gradient. This downwash may be neglected if a fuselage separates the propellers or if adjacent propellers are sufficiently far apart so that $\Delta y > 2R$. The slipstream gradient is given by

$$\frac{d\epsilon_{z_{slip}}}{d\alpha_{in}} = \frac{T_c}{4 + \frac{8}{7}T_c} + \frac{\left(C_{N'_{\alpha_{in}}}\right)_{T_c=0}\sqrt{1 + 1.3\,T_c}}{4 + 2T_c} \qquad 9.1.3\text{-f}$$

Step 3. Determine the propeller normal-force derivative with respect to wing angle of attack at zero phase angle using the terms obtained in Steps 1 and 2 and equation 9.1.3-b

$$C_{N'_\alpha} = C_{N'_{\alpha_{in}}}\frac{d\alpha_{in}}{d\alpha} \text{ per rad}$$

Step 4. Correct the $C_{N'_\alpha}$ value obtained for zero phase angle (Step 3) for phase-angle shift by

$$C_{N'_\alpha}(\delta) = C_{N'_\alpha}\cos\delta_f \text{ per rad} \qquad 9.1.3\text{-g}$$

The phase angle is determined by

$$\delta_f = 0.825 \tan^{-1} \frac{15\ \sigma_e}{B\sqrt{2\ J_{o_P}\ J' - (J')^2}} \qquad 9.1.3\text{-h}$$

where

$$J_{o_P} = J_{o_T} + \frac{16}{\sin(\beta + 5)\cos^4(\beta + 5)} \left(\frac{\sigma_e}{B}\right)^2 \qquad 9.1.3\text{-i}$$

and J_{o_T} is obtained as a function of β from Figure 9.1.1-7.

Step 5. Convert the C_{N_α}' results of Step 4 to C_{N_α} using equation 9.1.3-c.

$$C_{N_\alpha}(0,J') = \frac{\pi}{8} (J')^2\ C_{N_\alpha}'(0,J') \quad \text{per rad}$$

Step 6. Determine the normal force at selected wing angles of attack and modified advance ratios using

$$C_N(\alpha,J') = C_{N_\alpha}(0,J') \tan\alpha$$

A comparison of normal-force derivative at zero thrust, computed using equations 9.1.3-d and 9.1.3-d', with the theory of reference 4 is presented in Table 9.1.3-A. The percentage difference shown has been taken with respect to the values of reference 4. The comparison includes data with two blade shapes and wide variations of solidity, blade pitch angles, and number of blades. The percentage difference is considered to be within the accuracy of detailed propeller theory.

The normal-force ratio given by equation 9.1.3-a is compared with experimental data from reference 5 in figure 9.1.3-14.

Method 2

This method is suggested in reference 5 for estimating the propeller normal force at high angles of attack when experimental data are available at two angles of attack, such as zero and 15 degrees. This is an empirical method based on observations of a large body of test data in reference 5. The method is analogous to the method of Section 9.1.2 for estimating propeller pitching moments and provides acceptable accuracy for preliminary-design analysis. The method merely states that the propeller normal force at high angles of attack may be obtained by linear extrapolation of experimental data, provided the modified advance ratio falls below the boundary of figure 9.1.1-13.

Sample Problem

Method 1

Given: The hypothetical four-propeller, tilt-wing airplane of reference 6 with linear dimensions six times those of the model. The propellers are those designated as propeller 1 of reference 5. The following example is computed for four values of the modified advance ratio over an angle-of-attack range from 0 to 80 degrees.

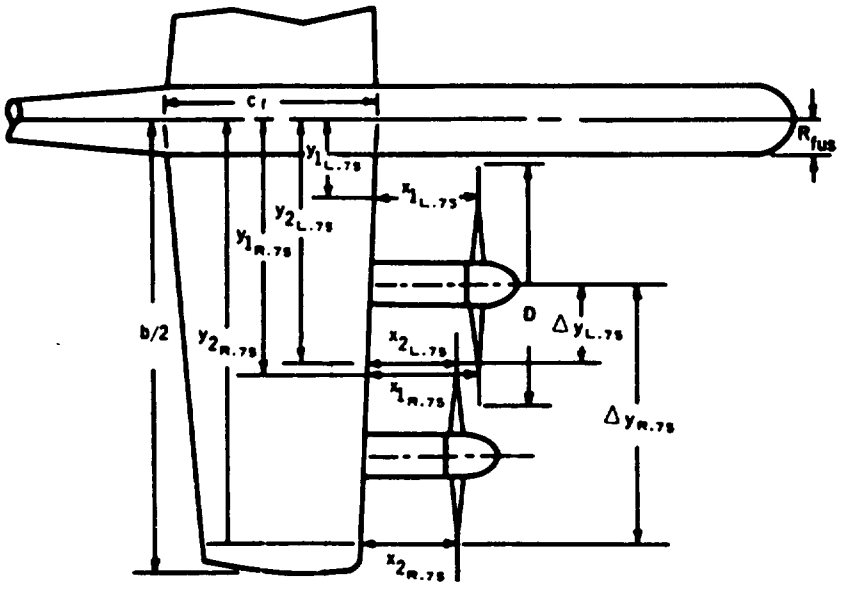

Propeller Characteristics

The propellers are the same as those of the sample problem of Section 9.1.1.

B = 3 D = 12 ft $\beta = 12^{\circ}$ $\sigma_e = 0.117$ $J_{OT} = 0.6725$

J'	0.1	0.2	0.4	0.6
T_c (0, J')	33.61	7.703	1.321	0.2267

These T_c (0,J') values have been obtained from the C_T (0,J') values given in the sample problem of Section 9.1.1 by

$$T_c\ (0,J') = \frac{8}{\pi\ (J')^2}\ C_T\ (0,J')$$

Airplane Characteristics

c_r = 10.0 ft A = 4.89 R_{fus} = 1.25 ft

Propeller 1 (Inboard)		Propeller 2 (Outboard)	
$x_{L\ .75}$ = 5.25 ft	$y_{L\ .75}$ = 3.25 ft	$x_{L\ .75}$ = 4.50 ft	$y_{L\ .75}$ = 11.75 ft
$x_{R\ .75}$ = 5.60 ft	$y_{R\ .75}$ = 12.25 ft	$x_{R\ .75}$ = 4.80 ft	$y_{R\ .75}$ = 20.75 ft

$\Delta y_{L\ .75}$ = 4.0 ft

$\Delta y_{R\ .75}$ = 13.0 ft

Compute:

Step 1. Determine the propeller normal-force derivatives at zero phase angle with respect to the local angle of attack at the propeller disk $C_{N'_{\alpha_{in}}}$

$$C_{N'_{\alpha_{in}}} = \frac{4.25\ \sigma_e}{1 + 2\ \sigma_e} \sin(\beta + 8) \left(1 + \frac{3T_c}{8\sqrt{1 + (2/3)T_c}}\right) \text{per rad}$$

(equation 9.1.3-d)

$$= \frac{(4.25)(0.117)}{1 + 2\ (0.117)} \sin(12 + 8) \left(1 + \frac{3T_c}{8\sqrt{1 + (2/3)T_c}}\right)$$

$$= 0.138 + \frac{0.0517T_c}{\sqrt{1 + (2/3)T_c}}$$

TABLE I

①	②	③	④	⑤	⑥
J'	T_c	$0.0517T_c$ / 0.0517 ②	$\sqrt{1 + (2/3)\ T_c}$ / $\sqrt{1 + (2/3)}$ ②	$C_{N'_{\alpha_{in}}}$ -0.138 ③/④	$C_{N'_{\alpha_{in}}}$ (1/rad) 0.138 + ⑤
0.1	33.61	1.74	4.84	0.3600	0.498
0.2	7.703	0.398	2.48	0.1600	0.298
0.4	1.321	0.0683	1.371	0.0498	0.1878
0.6	0.2267	0.0117	1.072	0.0109	0.1489

Step 2. Determine the local angle-of-attack gradient $d\alpha_{in}/d\alpha$.

For this configuration $\Delta y < 2R$ and the propeller downwash effect on the local angle-of-attack gradient must be considered.

$$\frac{d\alpha_{in}}{d\alpha} = \frac{1 + \frac{2A}{9(A+10)}\left(\frac{1}{\frac{x_{L\ .75}}{c_r} + \frac{1}{10}} + \frac{1}{\frac{x_{R\ .75}}{c_r} + \frac{1}{10}}\right) + \frac{1}{2}\left[\left(\frac{R_{fus}}{y_{L\ .75}}\right)^2 + \left(\frac{R_{fus}}{y_{R\ .75}}\right)^2\right]}{1 - \frac{1}{4}\sum_{prop\ 1}^{prop\ 2}\left[\left(\frac{R}{\Delta y_{L\ .75}}\right)^2 + \left(\frac{R}{\Delta y_{R\ .75}}\right)^2\right]\frac{d\epsilon_{z\ slip}}{d\alpha_{in}}} \qquad \text{(equation 9.1.3-e)}$$

Propeller 1 (Inboard)

$$\left(\frac{d\alpha_{in}}{d\alpha}\right)_1 = \frac{1 + \frac{2(4.89)}{9(4.89+10)}\left(\frac{1}{\frac{5.25}{10} + \frac{1}{10}} + \frac{1}{\frac{5.60}{10} + \frac{1}{10}}\right) + \frac{1}{2}\left[\left(\frac{1.25}{3.25}\right)^2 + \left(\frac{1.25}{12.25}\right)^2\right]}{1 - \frac{1}{4}\left[\left(\frac{6.0}{4.0}\right)^2 + \left(\frac{6.0}{13.0}\right)^2\right]\frac{d\epsilon_{z_{slip}}}{d\alpha_{in}}}$$

$$= \frac{1 + 0.073\left(\frac{1}{0.625} + \frac{1}{0.660}\right) + \frac{1}{2}(0.148 + 0.0104)}{1 - 0.25\ (2.25 + 0.213)\ \frac{d\epsilon_{z_{slip}}}{d\alpha_{in}}}$$

$$= \frac{1 + 0.073\ (3.115) + 0.0792}{1 - 0.25\ (2.463)\ \frac{d\epsilon_{z_{slip}}}{d\alpha_{in}}}$$

$$= \frac{1.3067}{1 - (0.616)\ \frac{d\epsilon_{z_{slip}}}{d\alpha_{in}}}$$

Propeller 2 (Outboard)

$$\left(\frac{d\alpha_{in}}{d\alpha}\right)_2 = \frac{1 + 0.073\ \left(\frac{1}{\frac{4.50}{10} + \frac{1}{10}} + \frac{1}{\frac{4.80}{10} + \frac{1}{10}}\right) + \frac{1}{2}\left[\left(\frac{1.25}{11.75}\right)^2 + \left(\frac{1.25}{20.75}\right)^2\right]}{1 - (0.616)\ \frac{d\epsilon_{z_{slip}}}{d\alpha_{in}}}$$

$$= \frac{1 + 0.073\left(\frac{1}{0.550} + \frac{1}{0.580}\right) + \frac{1}{2}(0.0113 + 0.0036)}{1 - (0.616)\frac{d\epsilon_{z_{slip}}}{d\alpha_{in}}}$$

$$= \frac{1 + 0.073\ (3.542) + 0.00745}{1 - (0.616)\ \frac{d\epsilon_{z_{slip}}}{d\alpha_{in}}}$$

$$= \frac{1.266}{1 - (0.616)\ \frac{d\epsilon_{z_{slip}}}{d\alpha_{in}}}$$

$\left(C_{N_{\alpha'_{in}}}\right)_{T_c=0} = 0.138$ (step 1 with $T_c=0$)

$$\frac{d\epsilon_{z_{slip}}}{d\alpha_{in}} = \frac{T_c}{4 + \frac{8}{7}T_c} + \frac{\left(C_{N'_{\alpha_{in}}}\right)_{T_c=0}\sqrt{1 + 1.3\ T_c}}{4 + 2\ T_c}$$ (equation 9.1.3-f)

$$= \frac{T_c}{4 + \frac{8}{7}T_c} + \frac{0.138\sqrt{1 + 1.3\ T_c}}{4 + 2\ T_c}$$

TABLE II

①	②	③	④	⑤	⑥	⑦	⑧
J'	T_c	$4 + \frac{8}{7}T_c$	$\frac{T_c}{③}$	$\sqrt{1 + 1.3\ T_c}$	$4 + 2\ T_c$	$\frac{0.138\ ⑤}{⑥}$	$d\epsilon_{z_{slip}}/d\alpha_{in}$ ④ + ⑦
0.1	33.61	42.41	0.7925	6.69	71.22	0.0130	0.8055
0.2	7.703	12.80	0.6018	3.32	19.41	0.0236	0.6254
0.4	1.321	5.51	0.2397	1.65	6.642	0.0343	0.2740
0.6	0.2267	4.259	0.0532	1.14	4.453	0.0353	0.0885

Using the $\frac{d\epsilon_{z_{slip}}}{d\alpha_{in}}$ values from Table II calculate $\frac{d\alpha_{in}}{d\alpha}$ for propellers 1 and 2.

TABLE III

① J'	② $\frac{d\epsilon_{z_{slip}}}{d\alpha_{in}}$	③ 1 - (0.616) ②	④ $(d\alpha_{in}/d\alpha)_1$ 1.3067/ ③	⑤ $(d\alpha_{in}/d\alpha)_2$ 1.266/ ③
0.1	0.8055	0.5038	2.594	2.513
0.2	0.6254	0.6148	2.125	2.059
0.4	0.2740	0.3312	1.572	1.523
0.6	0.0885	0.9455	1.382	1.339

Step 3. Determine the propeller normal-force derivatives at zero phase angle with respect to wing angle of attack $C_{N'_\alpha}$

$$C_{N'_\alpha} = C_{N'_{\alpha_{in}}} \frac{d\alpha_{in}}{d\alpha} \quad \text{per rad} \quad \text{(equation 9.1.3-b)}$$

TABLE IV

① J'	② $C_{N'_{\alpha_{in}}}$ (1/rad) Col. ⑥, Table I	③ $(C_{N'_\alpha})_1$ (1/rad) Col. ④, Table III x ②	④ $(C_{N'_\alpha})_2$ (1/rad) Col. ⑤, Table III x ②
0.1	0.498	1.292	1.251
0.2	0.298	0.633	0.614
0.4	0.1878	0.295	0.286
0.6	0.1489	0.206	0.199

Step 4. Correct the $C_{N'_\alpha}$ values obtained in step 3 for phase-angle shift.

$$J_{o_P} = J_{o_T} + \frac{16}{\sin(\beta + 5)\cos^4(\beta + 5)} \left(\frac{\sigma_e}{B}\right)^2 \quad \text{(equation 9.1.3-i)}$$

$$= 0.6725 + \frac{16}{\sin(17)\cos^4(17)} \left(\frac{0.117}{3}\right)^2$$

$$= 0.6725 + \frac{16}{(0.2924)(0.9563)^4} (0.00152)$$

$$= 0.6725 + 0.0995$$

$$= 0.772$$

$$\delta_f = 0.825 \tan^{-1} \frac{15\ \sigma_e}{B\sqrt{2\ J_{o_p}\ J' - (J')^2}} \qquad \text{(equation 9.1.3-h)}$$

$$= 0.825 \tan^{-1} \frac{15(0.117)}{3\sqrt{2(0.772)(J') - (J')^2}}$$

$$= 0.825 \tan^{-1} \frac{0.585}{\sqrt{1.544\ J' - (J')^2}}$$

TABLE V

①	②	③	④	⑤	⑥	⑦	⑧
J'	$(J')^2$ ①^2	1.544 J' 1.544 ①	1.544 $J' - (J')^2$ ③ − ②	$\sqrt{④}$	0.585 ⑤	$\tan^{-1}$ ⑥ (deg)	δ_f (deg) 0.825 ⑦
0.1	0.01	0.1544	0.1444	0.3800	1.535	57.0	47.0
0.2	0.04	0.3088	0.2688	0.5180	1.129	48.5	40.0
0.4	0.16	0.6176	0.4576	0.6760	0.865	40.9	33.7
0.6	0.36	0.9264	0.5664	0.7530	0.777	37.8	31.2

The $C_{N'_\alpha}$ values are corrected for phase-angle shift by

$$C_{N'_\alpha}(\delta) = C_{N'_\alpha} \cos \delta_f \quad \text{per rad} \qquad \text{(equation 9.1.3-g)}$$

TABLE VI

①	②	③	④	⑤	⑥
J'	$(C_{N'_\alpha})_1$ (1/rad) Col. ③, Table IV	$(C_{N'_\alpha})$ (1/rad) Col. ④, Table IV	$\cos \delta_f$	$(C_{N'_\alpha})_1 \cos \delta_f$ ② ④	$(C_{N'_\alpha})_2 \cos \delta_f$ ③ ④
0.1	1.292	1.251	0.6820	0.881	0.853
0.2	0.633	0.614	0.7660	0.485	0.470
0.4	0.295	0.286	0.8320	0.245	0.238
0.6	0.206	0.199	0.8554	0.176	0.170

Step 5. Convert the $C_{N'_\alpha}$ values obtained in Step 4 to C_{N_α}.

$$C_{N_\alpha}(0, J') = \frac{\pi}{8} (J')^2\ C_{N'_\alpha}(0, J') \quad \text{per rad} \qquad \text{(equation 9.1.3-c)}$$

TABLE VII

① J'	② $(J')^2$ ①^2	③ $\pi/8\ (J')^2$ $(\pi/8)$ ②	④ $C_{N_\alpha}\ (0, J')_1$ (1/rad) ③ x Col. ⑤, Table VI	⑤ $C_{N_\alpha}\ (0, J')_2$ (1/rad) ③ x Col. ⑥, Table VI
0.1	0.01	0.00393	0.00346	0.00335
0.2	0.04	0.0157	0.00761	0.00738
0.4	0.16	0.0628	0.0154	0.0149
0.6	0.36	0.1414	0.0249	0.0240

Solution:

The variation of propeller normal-force coefficient with angle of attack at the chosen values of J' is tabulated below using

$$C_N(\alpha, J') = C_{N_\alpha}(0, J') \tan \alpha \quad \text{(equation 9.1.3-a)}$$

for both the inboard and outboard propellers.

$C_N(\alpha, J')$

		Propeller 1 (Inboard)				Propeller 2 (Outboard)			
α	tan α	$J' = 0.1$	0.2	0.4	0.6	$J' = 0.1$	0.2	0.4	0.6
0	0	0	0	0	0	0	0	0	0
10	0.1763	0.00061	0.00134	0.00272	0.00439	0.00059	0.00130	0.00263	0.00423
20	0.3640	0.00126	0.00277	0.00561	0.00906	0.00122	0.00269	0.00542	0.00874
30	0.5774	0.00200	0.00439	0.00889	0.01438	0.00193	0.00426	0.00860	0.01386
40	0.8391	0.00290	0.00639	0.01292	0.02089	0.00281	0.00619	0.01250	0.02014
50	1.1918	0.00412	0.00907	0.01835	0.0297	0.00399	0.00880	0.0178	0.0286
60	1.7321	0.00599	0.0132	0.0267	0.0431	0.00580	0.0128	0.0258	0.0416
70	2.7475	0.00951	0.0209	0.0423	0.0684	0.00920	0.0203	0.0409	0.0659
80	5.6713	0.0196	0.0432	0.0873	0.1412	0.0190	0.0419	0.0845	0.1361

The calculated values of the normal-force coefficients for both the inboard and outboard propellers are plotted in figure 9.1.3-15.

REFERENCES

1. DeYoung, J.: Force and Moment Derivatives Due to Propellers of Arbitrary Configuration Inclined with Respect to Free Stream. AIAA Preprint No. 64-169, 1964. (U)

2. Ribner, H. S.: Formulas for Propellers in Yaw and Charts of the Side-Force Derivative. NACA TR 819, 1945. (U)

3. Ribner, H. S.: Propellers in Yaw. NACA TR 820, 1945. (U)

4. Ribner, H. S.: Notes on the Propeller and Slipstream in Relation to Stability. NACA ARR L4I12a, 1944. (U)

5. Yaggy, P. F., and Rogallo, V. L.: A Wind-Tunnel Investigation of Three Propellers Through an Angle-of-Attack Range From 0° to 85°. NASA TN D-318, 1960. (U)

6. Kuhn, R. E., and Hayes, W. C., Jr.: Wind-Tunnel Investigation of Effect of Propeller Slipstreams on Aerodynamic Characteristics of a Wing Equipped with a 50-Percent-Chord Sliding Flap and a 30-Percent-Chord Slotted Flap. NACA TN 3918, 1957. (U)

TABLE 9.1.3-A
COMPARISON OF NORMAL-FORCE DERIVATIVE AT ZERO THRUST
COMPUTED BY DATCOM METHOD I WITH THEORY OF REFERENCE 4

Hamilton Standard 3155-6

$\frac{r}{R}$	.25	.50	.75	.95
$\frac{b'}{b'_{.75}}$	0.615	1.03	1.00	0.57
	$(C_{N'\alpha_{in}})_{T_c=0}$			
σ , σ_e	β (deg)	ref. 4	Datcom Method 1	% Diff.
σ = .061	25	.079	.079	0
σ_e = .0527	25	.111	.109	-1.8
2	35	.134	.137	2.2
Blades	45	.158	.160	1.3
	55	.177	.179	1.1
σ = .091	15	.112	.112	0
σ_e = .079	25	.155	.156	0.6
3	35	.194	.196	1.0
Blades	45	.229	.230	0.4
	55	.258	.256	-0.8
σ = .121	15	.142	.144	1.4
σ_e = .1054	25	.198	.200	1.0
4	35	.249	.250	0.4
Blades	45	.295	.293	-0.7
	55	.332	.328	-1.2
σ = .182	15	.192	.197	2.6
σ_e = .158	25	.271	.276	1.8
6	35	.346	.346	0
Blades	45	.413	.406	-1.7
	55	.471	.452	-4.0
Counter-Rotation				
σ = .182	15	.250	.253	1.2
σ_e = .158	25	.332	.329	-0.9
6	35	.393	.392	-0.3
Blades	45	.446	.448	0.4
	55	.490	.490	0

NACA 10-3062-045

$\frac{r}{R}$	.25	.50	.75	.95
$\frac{b'}{b'_{.75}}$	1.03	1.03	1.00	0.765
	$(C_{N'\alpha_{in}})_{T_c=0}$			
σ , σ_e	β (deg)	ref. 4	Datcom Method 1	% Diff.
σ = .083	20	.143	.139	-2.8
σ_e = .081	25	.162	.161	-0.6
2	35	.204	.202	-1.0
Blades	45	.235	.236	0.4
	55	.260	.263	1.1
σ = .124	20	.196	.194	-1.0
σ_e = .122	25	.226	.225	-0.4
3	35	.284	.281	-1.0
Blades	45	.333	.330	-0.9
	55	.372	.368	-1.1
σ = .165	20	.243	.244	0.4
σ_e = .162	25	.280	.282	0.7
4	35	.352	.353	0.3
Blades	45	.416	.414	-0.5
	55	.471	.462	-1.9
Counter-Rotation				
σ = .248	15	.363	.364	0.4
σ_e = .244	25	.478	.473	-1.0
6	35	.567	.566	-0.2
Blades	45	.634	.642	1.3
	55	.689	.699	1.4

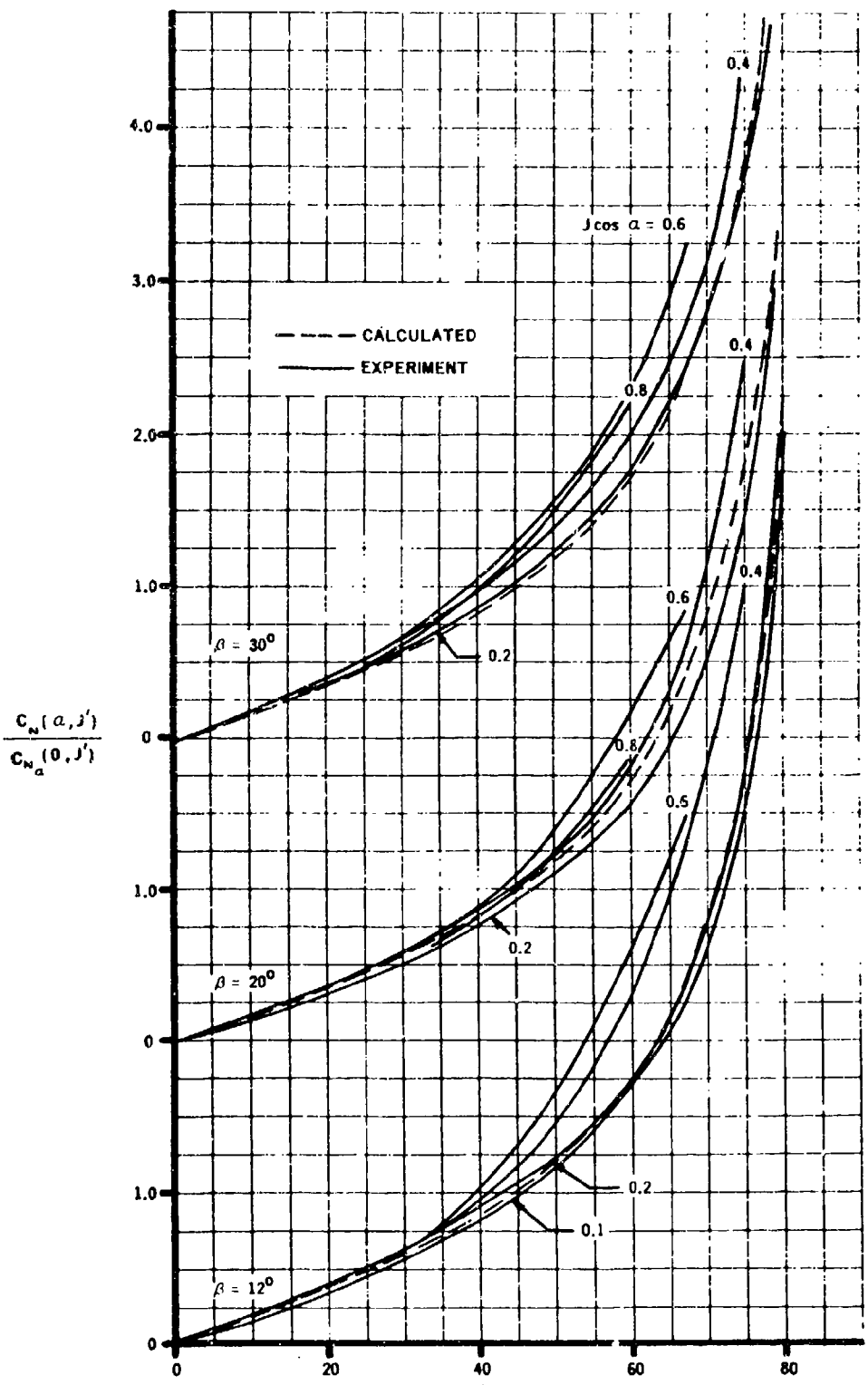

FIGURE 9.1.3-14 COMPARISON OF CALCULATED AND EXPERIMENTAL NORMAL-FORCE RATIO WITH PROPELLER THRUST-AXIS ANGLE OF ATTACK FOR PROPELLER 1 OF REFERENCE 5

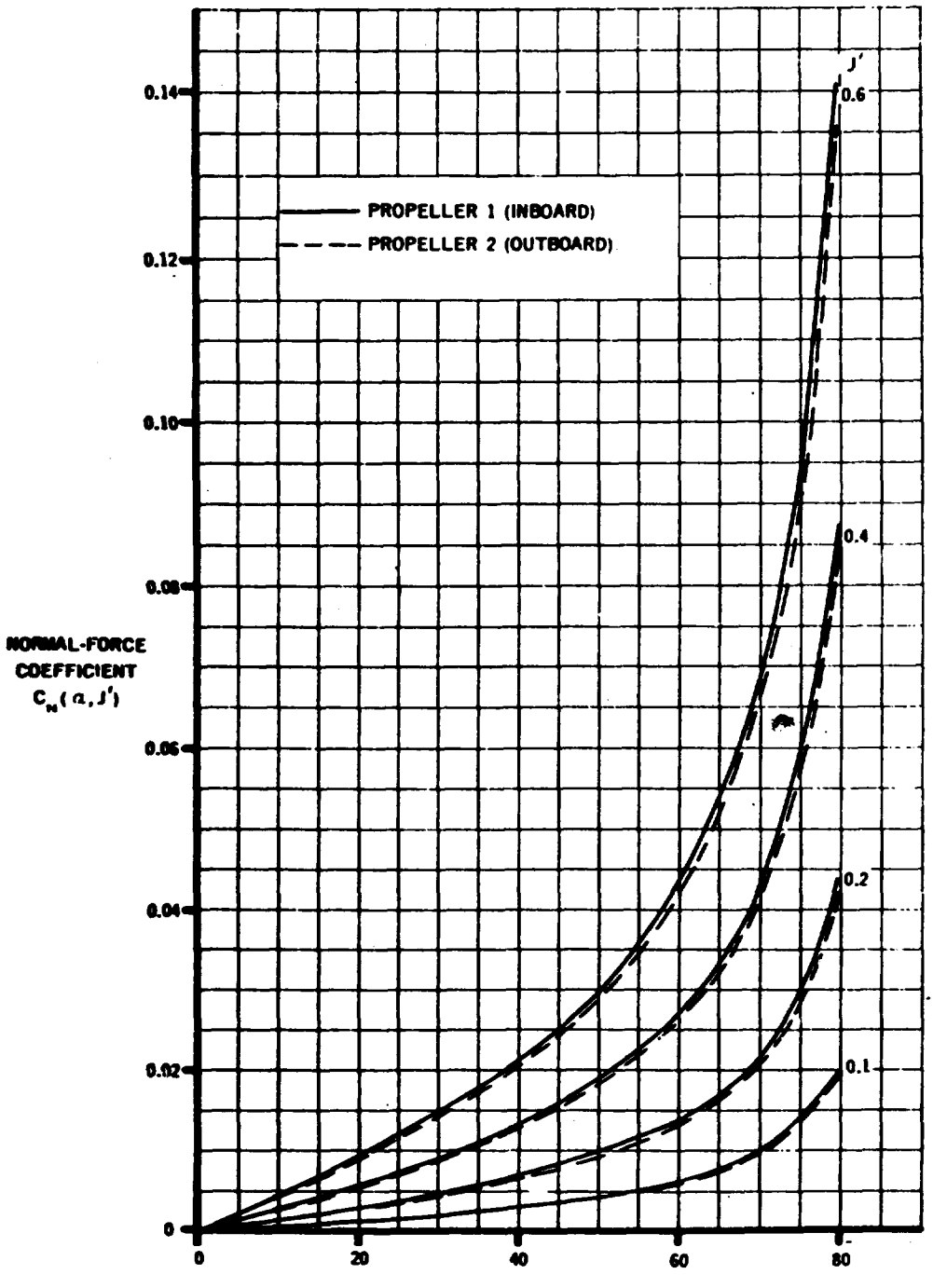

FIGURE 9.1.3-15 VARIATION OF PROPELLER NORMAL-FORCE COEFFICIENT WITH ANGLE OF ATTACK AND MODIFIED ADVANCE RATIO FOR INBOARD AND OUTBOARD PROPELLERS OF A HYPOTHETICAL 4-PROPELLER TILT-WING AIRPLANE. SAMPLE PROBLEM, METHOD 1

9.2 PROPELLER-WING CHARACTERISTICS

The methods of this section are for prediction of the power-on lift and drag forces of propeller-wing combinations of V/STOL aircraft and deal primarily with the low-speed, high-power flight regime where wing stalling tendencies at high angles of attack are delayed by power effects.

The usual approach to attaining V/STOL capabilities is to use power plant thrust to obtain lift at low speeds. Propeller-driven V/STOL configurations, other than those employing ducted propellers, consist basically of three types:

1. Deflected slipstream
2. Tilt wing
3. Combination tilt wing–deflected slipstream

These configurations differ in detail, but each employs interacting wing and thrust systems. In treating such configurations in the low-speed, high-power flight regime we must abandon the familiar distinction between lifting and thrusting systems and combine them.

Several factors dealing with propeller slipstream flow over a wing are of special significance. The local angles of attack of a propeller-wing combination in transition are determined by vector addition of the free-stream and propeller slipstream velocities. The propeller slipstream is a strong factor in reducing the local angles of attack and thereby minimizing the tendency of wing stall. Stalls may occur even in the presence of the slipstream if the slipstream velocity is low.

Since the velocity of the slipstream relative to that of the free stream is increased by increased disk loading, stalling tendencies are decreased by increasing the propeller disk loading. Wing stall can be avoided entirely by immersing the entire wing in the propeller slipstream, provided sufficient thrust is generated by the propellers.

Experimental studies have been conducted to determine the spanwise distribution of the lift increase due to the slipstream at different angles of attack with various free-stream-to-slipstream velocity ratios. The results of these tests, reported in reference 7, indicate that the lift increment due to the passage of a slipstream over a wing consists of two parts:

1. A direct lift gain which can be accurately predicted by potential flow theory.
2. A lift increment due to a "destalling" or boundary-layer-control effect. This "destalling" effect extends to portions of the wing outside the propeller slipstream and improves the wing stalling behavior.

The results also indicate that the limits of the direct slipstream influence are sharply defined and do not vary with wing angle of attack and slipstream strength.

Both references 7 and 61 indicate that the rotation of the propeller slipstream causes an upwash over the wing behind the upward moving blade. This area will generally be the first to stall on a wing that is fully immersed in propeller slipstreams. The effect of propeller rotation on maximum lift was investigated in reference 20, wherein it is concluded that slightly larger values of maximum lift can be generated when propellers rotate with the inboard tips moving up. This lift increase is attributed to a reduction in tip losses resulting from the propeller rotating in such a manner as to oppose the wing-tip vortex and to the fact that the upwash behind the upward moving blade is not entirely cancelled by the downflow at the wing tip.

Propeller-wing combinations in the transition region do not lend themselves to theoretical analysis. The Datcom methods for the prediction of lift and drag forces at forward speed with power on comprise semiempirical expressions from reference 52. These methods employ momentum theory as a starting point. They are based on power-off data and a correlation of slipstream-deflection data at zero forward speed. The correlation of slipstream-deflection data is based on numerous static investigations of a limited number of wing-flap systems. Effects of various parameters on the slipstream-deflection characteristics are summarized in reference 52.

The methods are applicable only in the unstalled flight regime. Comparison of experimental results with calculations made using the Datcom methods indicate that, in general, the estimation procedures give reasonably good results for steady level flight and for climbing flight. Through judicious use of the Datcom methods the lift and drag forces can be estimated for deflected-slipstream, tilt-wing, and combination tilt-wing – deflected-slipstream configurations. At the present time there are no methods available for the prediction of the pitching moment of a propeller-wing configuration in the transition flight regime.

Numerous static and forward speed investigations have been conducted on propeller-driven V/STOL configurations. However, the number of specific designs tested has been so limited that the substantiation of any semiempirical method developed for the prediction of forces and moments has not been possible. Furthermore, excessive wind-tunnel wall effects during simulated low-speed, high-power flight conditions invalidate many investigations.

A comprehensive tabulation of pertinent propeller-wing experimental data is presented as table 9.2-A. This table provides a brief outline of the test data contained in each report and indicates the basic parametric changes made. Additional reports, dealing with complete configurations, can be found in the VTOL-STOL summary table of Section 9.

A general notation list is included in this section for all propeller-wing combination sections. Coefficients are based on the dynamic pressure in the propeller slipstream unless otherwise noted. The conversion from coefficients based on slipstream dynamic pressure to coefficients based on free-stream dynamic pressure is presented at the end of the notation list.

The positive direction of forces and angles is shown in figure 9.2-9.

NOTATION

c	average wing chord, ft
ΔC_D	zero-lift drag increment due to flap deflection based on free-stream velocity
C_{D_f}	power-off zero-lift drag coefficient based on free-stream velocity
C_{D_o}	power-off drag coefficient based on free-stream velocity, $\frac{\text{Drag}}{q_\infty S}$
c_f	average flap chord, ft
C_{F_x}	negative-drag coefficient based on free-stream velocity, $\frac{F_x}{q_\infty S}$
C_{F_x}''	negative-drag coefficient based on slipstream velocity, $\frac{F_x}{q'' S}$
C_{L_o}	power-off lift coefficient based on free-stream velocity, $\frac{L}{q_\infty S}$
C_L''	lift coefficient based on slipstream velocity, $\frac{L}{q'' S}$
D	propeller diameter, ft
e	span efficiency factor
F	resultant force, lb
F_x	horizontal force, lb
$\frac{F}{T}$	thrust-recovery factor
i_W	wing incidence measured between thrust axis and wing chord plane, deg
J	advance ratio, $\frac{V_\infty}{nD}$
K	number of propellers

L lift, lb

q_∞ free-stream dynamic pressure, lb/sq ft

q'' slipstream dynamic pressure, $q_\infty + \frac{T}{S_p}$, lb/sq ft

S wing area, sq ft

S_p propeller disk area, $\frac{\pi}{4} D^2$, sq ft

T thrust per propeller or total thrust when used in thrust-recovery factor, lb

T_c propeller thrust coefficient based on free-stream velocity and wing area, $\frac{KT}{q_\infty S}$

T_c'' propeller thrust coefficient based on slipstream velocity and propeller disk area, $\frac{T}{q'' S_p}$

α angle of attack measured between free stream and thrust axis, deg

δ flap deflection, deg

δ_e equivalent flap deflection due to wing camber and incidence, deg

θ slipstream turning angle measured from thrust axis, deg

θ_f slipstream turning angle adjusted to the condition of zero camber and zero incidence, deg

$\Delta\theta$ increment of slipstream turning angle due to wing camber and incidence, deg

Conversion between systems:

(Unprimed coefficients are based on free-stream dynamic pressure.)

$$C_D = \frac{-C_{F_x}''}{1 - T_c''} \qquad C_{F_x}'' = \frac{-C_D}{1 + T_c \frac{S}{KS_p}} \qquad T_c = \frac{T_c''}{1 - T_c''} \frac{KS_p}{S}$$

$$C_L = \frac{C_L''}{1 - T_c''} \qquad C_L'' = \frac{C_L}{1 + T_c \frac{S}{KS_p}} \qquad T_c'' = \frac{T_c}{T_c + \frac{KS_p}{S}}$$

$$q_\infty = q'' (1 - T_c'')$$

REFERENCES

1. Anderson, S. B., Quigley, H. C., and Innis, R. C.: Stability and Control Considerations for STOL Aircraft. AIAA Paper 65-715, 1965. (U)

2. Anon: Application of a Mechanical Gyroscopic Stabilizer to VTOL Aircraft. Kellett Aircraft Corp. Report 220A90-2, 1963. (U)

3. Anon: Conference on V/STOL and STOL Aircraft. NASA SP-116, 1966. (U)

4. Beppu, G., and Curtiss, H. C., Jr.: An Analytical Study of Factors Influencing the Longitudinal Stability of Tilt-Wing VTOL Aircraft. Princeton Univ. R 756, USAAVLABS TR-66-53, 1966. (U)

5. Black, E. L., and Booth, G. C.: Correlation of Aerodynamic Stability and Control Derivatives Obtained From Flight Tests and Wind-Tunnel Tests on the XC-142A Airplane. AFFDL TR-68-167, 1968. (U)

6. Boyden, R. P., and Curtiss, H. C., Jr.: Investigation of the Lateral-Directional Stability Characteristics of a Four-Propeller Tilt-Wing VTOL Model at Low Speeds. Princeton Univ. R 743, USAAVLABS TR-68-19, 1968. (U)

7. Brenckmann, M. E.: Experimental Investigation of the Aerodynamics of a Wing in a Slipstream. Jour. Aero. Sci., Vol. 25, No. 5, May 1958. (U)

8. Chambers, J. R., and Grafton, S. B.: Calculation of the Dynamic Longitudinal Stability of a Tilt-Wing V/STOL Aircraft and Correlation With Model Flight Tests. NASA TN D-4344, 1968. (U)

9. Chambers, J. R., and Grafton, S. B.: Static and Dynamic Longitudinal Stability Derivatives of a Powered 1/9-Scale Model of a Tilt-Wing V/STOL Transport. NASA TN D-3591, 1966. (U)

10. Cromwell, C. H., III, and Payne, H. E., III: A Stability Analysis of Tilt-Wing Aircraft (Analytical). Princeton Univ. R 477, 1960. (U)

11. Curnutt, R. A., and Curtiss, H. C., Jr.: Comparison of Longitudinal Stability Characteristics of Three Tilt-Wing VTOL Aircraft Designs. Princeton Univ. R 749, USAAVLABS TR-66-64, 1968. (U)

12. Curtiss, H. C., Jr.: Dynamic Stability of V/STOL Aircraft at Low Speeds. AIAA Paper 69-194, 1969. (U)

13. Curtiss, H. C., Jr., Putman, W. F., and Lebacqz, J. V.: An Experimental Investigation of the Longitudinal Dynamic Stability Characteristics of a Four-Propeller Tilt-Wing VTOL Model. Princeton Univ. R 774, USAAVLABS TR-66-80, 1967. (U)

14. Czinczenheim, J.: Aerodynamic Design and Flight Development of the Breguet 941 STOL Aircraft. RAE-LT-1063, No. 3, 1964. (U)

15. Deckert, W. H., Page, V. R., and Dickinson, S. O.: Large-Scale Wind-Tunnel Tests of Descent Performance of an Airplane Model With a Tilt Wing and Differential Propeller Thrust. NASA TN D-1857, 1964. (U)

16. De Young, J.: Symmetric Loading of a Wing in a Wide Slipstream. Grumman Report ADR-01-04-66.1, 1966. (U)

17. Dickinson, S. O., Page, V. R., and Deckert, W. H.: Large-Scale Wind-Tunnel Investigation of an Airplane Model With a Tilt Wing of Aspect Ratio 8.4 and Four Propellers in the Presence of a Ground Plane. NASA TN D-4493, 1968. (U)

18. Down, H. W., Jr., Jones, G. E., and Satterwhite, J. J.: XC-142A Limited Category II Stability and Control Tests. AFFTC TR-68-9, 1968. (U)

19. Draper, J. W., and Kuhn, R. E.: Investigation of the Aerodynamic Characteristics of a Model Wing-Propeller Combination and of the Wing and Propeller Separately at Angles of Attack Up to 90°. NACA TN 3304, 1954. (U)

20. Draper, J. W., and Kuhn, R. E.: Some Effects of Propeller Operation and Location on Ability of a Wing with Plain Flaps to Deflect Propeller Slipstreams Downward for Vertical Take-Off. NACA TN 3360, 1955. (U)

21. Erlandsen, P., Zarcard, J. G., and Olcott, J. W.: Wind-Tunnel Correlation Study of North American Tilt-Wing Model Tested in the NACA L 14' x 16' Tunnel and the Airship Model Test Facility. Naval Air Station, Lakehurst, N. J., 1962. (U)

22. Fink, M. P.: Aerodynamic Data on Large Semispan Tilting Wing With 0.4-Diameter Chord, Single-Slotted Flap, and Single Propeller 0.22 Chord Below Wing. NASA TN D-5016, 1969. (U)

23. Fink, M. P., Mitchell, R. G., and White, L. C.: Aerodynamic Data on a Large Semispan Tilting Wing With 0.5-Diameter Chord, Double-Slotted Flap, and Both Left- and Right-Hand Rotation of a Single Propeller. NASA TN D-3375, 1966.(U)

24. Fink, M. P.: Aerodynamic Data on a Large Semispan Tilting Wing With a 0.5-Diameter Chord, a Double-Slotted Flap, and Left- and Right-Hand Rotation of a Single Propeller, in Presence of Fuselage. NASA TN D-3674, 1966. (U)

25. Fink, M. P., and Mitchell, R. G.: Aerodynamic Data on a Large Semispan Tilting Wing With a 0.5-Diameter Chord, a Single-Slotted Flap, and Both Left- and Right-Hand Rotation of a Single Propeller. NASA TN D-3754, 1967. (U)

26. Fink, M. P.: Aerodynamic Data on Large Semispan Tilting Wing With 0.5-Diameter Chord, Single-Slotted Flap, and Single Propeller 0.08 Chord Below Wing. NASA TN D-4030, 1967. (U)

27. Fink, M. P.: Aerodynamic Data on Large Semispan Tilting Wing With 0.5-Diameter Chord, Single-Slotted Flap, and Single Propeller 0.19 Chord Below Wing. NASA TN D-3884, 1967. (U)

28. Fink, M. P., Mitchell, R. G., and White, L. C.: Aerodynamic Data on a Large Semispan Tilting Wing With 0.6-Diameter Chord, Fowler Flap, and Single Propeller Rotating Up at Tip. NASA TN D-2180, 1964. (U)

29. Fink, M. P., Mitchell, R. G., and White, L. C.: Aerodynamic Data on Large Semispan Tilting Wing With 0.6-Diameter Chord, Single-Slotted Flap, and Single Propeller Rotating Down at Tip. NASA TN D-2412, 1964. (U)

30. Fink, M. P., Mitchell, R. G., and White, L. C.: Aerodynamic Data on Large Semispan Tilting Wing With 0.6-Diameter Chord, Single-Slotted Flap, and Single Propeller Rotating Up at Tip. NASA TN D-1586, 1964. (U)

31. Fink, M. P. and Smith, C. C., Jr.: Pressure Distribution of a Large Semispan Tilting Wing With 0.4-Diameter Chord, Single-Slotted Flap, and a Single Propeller 0.22 Chord Below the Wing. NASA TN D-5481, 1969. (U)

32. George, M., and Kisielowsky, E.: Investigation of Propeller Slipstream Effects on Wing Performance. Dynasciences Corp. Report DCR-234, USAAVLABS TR-67-67, 1967. (U)

33. Goland, L., Miller, N., and Butler, L.: Effects of Propeller Slipstream on V/STOL Aircraft Performance and Stability. TRECOM TR-64-47, 1964. (U)

34. Goodson, K. W.: Effect of Ground Proximity on the Longitudinal, Lateral, and Control Aerodynamic Characteristics of a Tilt-Wing Four-Propeller V/STOL Model. NASA TN D-4237, 1967. (U)

35. Goodson, K. W.: Ground Effects on a Four-Propeller Tilt-Wing Configuration Over a Fixed and a Moving Ground Plane. NASA TN D-3938, 1967. (U)

36. Goodson, K. W.: Longitudinal Aerodynamic Characteristics of a Flapped Tilt-Wing Four-Propeller V/STOL Transport Model. NASA TN D-3217, 1966. (U)

37. Griffin, R. N., Holzhauser, C. A., and Weiberg, J. A.: Large-Scale Wind-Tunnel Tests of an Airplane Model With an Unswept, Aspect-Ratio-10 Wing, Two Propellers, and Blowing Flaps. NASA Memo 12-3-58A, 1958. (U)

38. Grunwald, K. J.: Experimental Investigation of Wind-Tunnel Wall Effects and Wall Corrections for a General-Research V/STOL Tilt-Wing Model With Flap. NASA TN D-2887, 1965. (U)

39. Grunwald, K. J.: Investigation of a Semispan Tilt-Wing VTOL Model to Determine Ground Effect on Full-Span Flaps Used for Yaw Control in Hovering. NASA TN D-3437, 1966. (U)

40. Hayes, W. C., Jr., Kuhn, R. E., and Sherman, I. R.: Effects of Propeller Position and Overlap on the Slipstream Deflection Characteristics of a Wing-Propeller Configuration Equipped with a Sliding and Fowler Flap. NACA TN 4404, 1958. (U)

41. Holzhauser, C. A., Innis, R. C., and Vomaske, R. F.: A Flight and Simulator Study of the Handling Qualities of a Deflected Slipstream STOL Seaplane Having Four Propellers and Boundary-Layer Control. NASA TN D-2966, 1965. (U)

42. Huang, K. P., Goland, L., and Bolin, I.: Charts for Estimating Aerodynamic Forces on STOL Aircraft Wings Immersed in Propeller Slipstreams. Dynasciences Corp. Report DCR-161, 1965. (U)

43. Kirby, R. H.: Aerodynamic Characteristics of Propeller-Driven VTOL Aircraft. NASA TN D-730, 1961. (U)

44. Kirby, R. H., Schade, R. O., and Tosti, L. P.: Force-Test Investigation of a 1/4-Scale Model of the Modified VZ-2 Aircraft. NASA TN D-2382, 1964. (U)

45. Kuhn, R. E., and Draper, J. W.: Investigation of the Aerodynamic Characteristics of a Model Wing-Propeller Combination and of the Wing and Propeller Separately at Angles of Attack Up to 90°. NACA TR 1263, 1956. (U)

46. Kuhn, R. E., and Draper, J. W.: Investigation of Effectiveness of Large-Chord Slotted Flaps in Deflecting Propeller Slipstreams Downward for Vertical Take-Off and Low-Speed Flight. NACA TN 3364, 1955. (U)

47. Kuhn, R. E.: Investigation of Effectiveness of a Wing Equipped With a 50-Percent-Chord Sliding Flap, a 30-Percent-Chord Slotted Flap, and a 30-Percent-Chord Slat in Deflecting Propeller Slipstreams Downward for Vertical Take-Off. NACA TN 3919, 1957. (U)

48. Kuhn, R. E.: Investigation of the Effects of Ground Proximity and Propeller Position on the Effectiveness of a Wing with Large-Chord Slotted Flaps in Redirecting Propeller Slipstreams Downward for Vertical Take-Off. NACA TN 3629, 1956. (U)

49. Kuhn, R. E., and Draper, J. W.: An Investigation of a Wing-Propeller Configuration Employing Large-Chord Plain Flaps and Large-Diameter Propellers for Low-Speed Flight and Vertical Take-Off. NACA TN 3307, 1954. (U)

50. Kuhn, R. E.: Investigation at Zero Forward Speed of a Leading-Edge Slat as a Longitudinal Control Device for Vertically Rising Airplanes That Utilize the Redirected-Slipstream Principle. NACA TN 3692, 1956. (U)

51. Kuhn, R. E., and Spreemann, K. P.: Preliminary Investigation of the Effectiveness of a Sliding Flap in Deflecting a Propeller Slipstream Downward for Vertical Take-Off. NACA TN 3693, 1956. (U)

52. Kuhn, R. E.: Semiempirical Procedure for Estimating Lift and Drag Characteristics of Propeller-Wing-Flap Configurations for Vertical- and Short-Take-Off-and-Landing Airplanes. NASA Memo 1-16-59L, 1959. (U)

53. Kuhn, R. E., and Hayes, W. C., Jr.: Wind-Tunnel Investigation of Effect of Propeller Slipstreams on Aerodynamic Characteristics of a Wing Equipped With a 50-Percent-Chord Sliding Flap and a 30-Percent-Chord Slotted Flap. NACA TN 3918, 1957. (U)

54. Kuhn, R. E., and Hayes, W. C., Jr.: Wind-Tunnel Investigation of Longitudinal Aerodynamic Characteristics of Three Propeller-Driven VTOL Configurations in the Transition Speed Range, Including Effects of Ground Proximity. NASA TN D-55, 1960. (U)

55. LaMont, C. W.: Power-On Lift and Drag of Tractor Propeller Tilt-Wing and Deflected Slipstream Configurations. (Unpublished Report) Douglas Aircraft Company, 1963. (U)

56. Levinsky, E. S., Thommen, H. U., et al: Lifting Surface Theory and Tail Downwash Calculations for V/STOL Aircraft in Transition and Cruise. USAAVLABS TR-68-67, 1968. (U)

57. Longhurst, W. S.: A Report on Stability and Control Testing of a Tilt Wing V/STOL Aircraft. SAE Paper 660315, 1966. (U)

58. Margason, R. J., Hammond, A. D., and Gentry, G. L.: Longitudinal Stability and Control Characteristics of a Powered Model of a Twin-Propeller Deflected-Slipstream STOL Airplane Configuration. NASA TN D-3438, 1966. (U).

59. Matsuoka, K., Takahashi, M., and Yonezawa, M.: Aerodynamic Characteristics of Propeller-Wing-Flap Systems. Osaka Univ., Eng. and Natural Sci. Bulletin, Series A, Vol. 17, No. 1, 1968. (U)

60. Michaelcen, D. E.: The CL-84 V/STOL Flight Simulation – A Comparison With Reality. ICAS Paper 66-18, 1966. (U)

61. Mitchell, R. G.: Full-Scale Wind-Tunnel Test of the VZ-2 VTOL Airplane With Particular Reference to the Wing Stall Phenomena. NASA TN D-2013, 1963. (U)

62. Neal, B.: The Static and Forward-Speed Testing of a Flapped Wing With Boundary-Layer Control for Use in Deflecting Propeller Slipstreams Downward for Vertical Take-Off, Part II: Tests at Incidence and Ground Proximity Effects. NRC LR-383, 1963. (U)

63. Newsom, W. A., Jr., and Kirby, R. H.: Flight Investigation of Stability and Control Characteristics of a 1/9-Scale Model of a Four-Propeller Tilt-Wing V/STOL Transport. NASA TN D-2443, 1964. (U)

64. Page, V. R., Dickinson, S. O., and Deckert, W. H.: Large-Scale Wind-Tunnel Tests of a Deflected-Slipstream STOL Model With Wings of Various Aspect Ratio. NASA TN D-4448, 1968. (U)

65. Payne, H. E., III, and Cromwell, C. H., III: A Stability Analysis of Tilt-Wing Aircraft (Experimental). Princeton Univ. Rept. 478, 1960. (U)

66. Pegg, R. J., Kelley, H. L., and Reeder, J. P.: Flight Investigation of the VZ-2 Tilt-Wing Aircraft With Full-Span Flap. NASA TN D-2680, 1965. (U)

67. Putman, W. F.: An Experimental Investigation of Ground Effect of a Four-Propeller Tilt-Wing V/STOL Model. USAAVLABS TR-68-45, 1968. (U)

68. Putman, W. F.: An Investigation of the Lateral-Directional Dynamic Stability Characteristics of a Tilt-Wing V/STOL Transport Model in Simulated Low-Speed Descending Flight. USAAVLABS TR-69-46, 1969. (U)

69. Quigley, H. C., Innis, R. C., and Holzhauser, C. A.: A Flight Investigation of the Performance, Handling Qualities, and Operational Characteristics of a Deflected Slipstream STOL Transport Airplane Having Four Interconnected Propellers. NASA TN D-2231, 1964. (U)

70. Quigley, H. C., and Innis, R. C.: Handling Qualities and Operational Problems of a Large Four-Propeller STOL Transport Airplane. NASA TN D-1647, 1963. (U)

71. Schade, R. O., and Kirby, R. H.: Effect of Wing Stalling in Transition on a 1/4-Scale Model of the VZ-2 Aircraft. NASA TN D-2381, 1964. (U)

72. Spreemann, K. P.: Effectiveness of Boundary-Layer Control, Obtained by Blowing Over a Plain Rear Flap in Combination With a Forward Slotted Flap, in Deflecting a Slipstream Downward for Vertical Take-Off. NACA TN 4200, 1958. (U)

73. Spreemann, K. P., and Davenport, E. E.: Investigation of the Aerodynamic Characteristics of a Combination Jet-Flap and Deflected-Slipstream Configuration at Zero and Low Forward Speeds. NASA TN D-363, 1960. (U)

74. Spreemann, K. P., and Kuhn, R. E.: Investigation of the Effectiveness of Boundary-Layer Control by Blowing Over a Combination of Sliding and Plain Flaps in Deflecting a Propeller Slipstream Downward for Vertical Take-Off. NACA TN 3904, 1956. (U)

75. Spreemann, K. P.: Investigation of the Effects of Propeller Diameter on the Ability of a Flapped Wing, With and Without Boundary-Layer Control, to Deflect a Propeller Slipstream Downward for Vertical Take-Off. NACA TN 4181, 1957. (U)

76. Spreemann, K. P.: Investigation of a Semispan Tilting-Propeller Configuration and Effects of Ratio of Wing Chord to Propeller Diameter on Several Small-Chord Tilting-Wing Configurations at Transition Speeds. NASA TN D-1815, 1963. (U)

77. Stapleford, R. L., Wolkovitch, J., et al: An Analytical Study of V/STOL Handling Qualities in Hover and Transition. AFFDL-TR-65-73, 1965. (U)

78. Stenning, T. A., and Dolan, J. A.: Lateral-Directional Simulation of the CL-84 V/STOL Aircraft in the Transition Regime. AIAA Paper 64-806, 1964. (U)

79. Taylor, R. T.: Wind-Tunnel Investigation of Effect of Ratio of Wing Chord to Propeller Diameter With Addition of Slats on the Aerodynamic Characteristics of Tilt-Wing VTOL Configurations in the Transition Speed Range. NASA TN D-17, 1959. (U)

80. Traybar, J. J.: Aerodynamic Characteristics of a General Tilt-Wing Propeller Model Tested at Slow Speeds and High Angles of Attack. Princeton Univ. R 807, USAAVLABS TR-67-79, 1968. (U)

81. Turner, H. L., and Drinkwater, F. J.: Some Flight Characteristics of a Deflected Slipstream V/STOL Aircraft. NASA TN D-1891, 1963. (U)

82. Weiberg, J. A., and Holzhauser, C. A.: Large-Scale Wind-Tunnel Tests of an Airplane Model With an Unswept, Tilt Wing of Aspect Ratio 5.5, and With Four Propellers and Blowing Flaps. NASA TN D-1034, 1961. (U)

83. Weiberg, J. A., and Giulianetti, D. J.: Large-Scale Wind-Tunnel Tests of an Airplane Model With an Unswept Tilt Wing of Aspect Ratio 5.5, and With Various Stall Control Devices. NASA TN D-2133, 1964. (U)

84. Weiberg, J. A., and Giulianetti, D. J.: Wind-Tunnel Investigation of a Tilt-Wing VTOL Airplane With Articulated Rotors. NASA TN D-2538, 1965. (U)

85. White, H. E.: Wind-Tunnel Tests of an Aerodynamically Controlled Tilting-Wing VTOL Configuration. DTMB Aero-1057, 1963. (U)

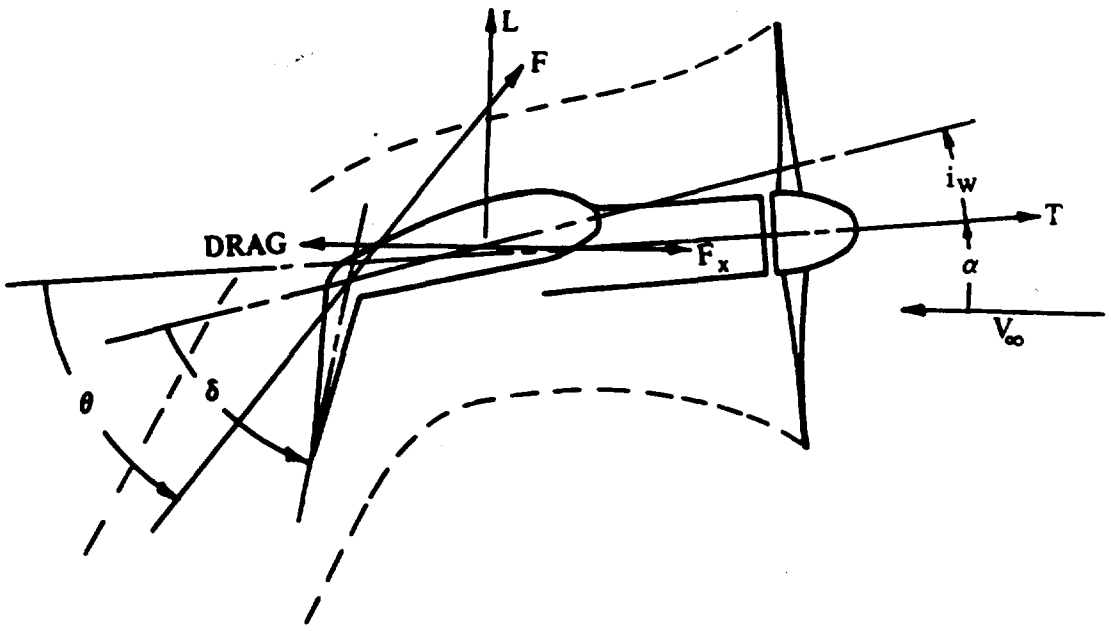

FIGURE 9.2-9 CONVENTIONS USED TO DEFINE POSITIVE SENSE OF FORCES AND ANGLES

TABLE 9.2-A
SUMMARY OF EXPERIMENTAL PROPELLER-WING DATA

			CONFIGURATION GEOMETRY									TEST CONDITIONS					TEST DATA						
REFERENCE NO.	YEAR OF PUBLICATION	WING ASPECT RATIO	WING AIRFOIL SECTION	TYPE OF FLAP	FLAP CHORD TO AIRFOIL CHORD RATIO (FLAP RETRACTED)	PROPELLER DIAMETER (FT)	BLADES PER PROPELLER	NUMBER PROPELLERS PER SEMISPAN	AUXILIARY TURNING AIDS	PROPELLER DIAMETER WING CHORD	α RANGE	MAX. ADVANCE RATIO	SLIPSTREAM DYNAMIC PRESSURE (lb/ft²)	SLIPSTREAM REYNOLDS NUMBER (BASED ON WING MAC)	STATIC TURNING EFFECTIVENESS	TRANSITION PERFORMANCE	GROUND EFFECTS	PROPELLER FORCES	PROPELLER LOCATION VARIED	PROPELLER ROTATION MODE	SLIPSTREAM DYN. PRESS. SURVEY	DOWNWASH SURVEY	POWER	COMMENTS
4	66	8.53	NACA 63-316	DOUBLE SLOTTED	–	1.55	4	2	–	1.92	−15° → 15°				x	x		x				x	FULL-SPAN, TILT WING, 1/10-SCALE XC-142A, PROPELLERS OVERLAPPED. EFFECT OF AERODYNAMIC DERIVATIVES ON STABILITY CHARACTERISTICS. RESULTS OF ANALYTICAL APPROACH COMPARED WITH TEST IN PRINCETON DYNAMIC MODEL TRACK.
5	66	8.53	NACA 63-318	DOUBLE SLOTTED	.33	1.55	4	2	LE SLAT	1.88			(a) .463, .543 (b) – (c) –			x		x					.11-SCALE MODEL OF TILT-WING XC-142A IN 3 TEST SECTIONS OF VOUGHT AERONAUTICS DIV. TUNNEL: (A) 7 x 10 FT, (B) 15 x 20 FT, (c) 21 x 23 FT PROPELLER OVERLAPPED. TUFT STUDIES OF FLOW FIELDS ON WING AND OF RECIRCULATION. EFFECT OF REYNOLDS NUMBER, WING INCIDENCE, PROPELLER BLADE PITCH ANGLE, TUNNEL WALL CORRECTIONS, AND TUFTS ON AERO CHAR. EFFECT OF RECIRCULATION ON PROPELLER THRUST. WIND-TUNNEL WALL CORRECTIONS EVALUATED. FLIGHT-TEST AND WIND-TUNNEL RESULTS COMPARED.
6	66	8.53	NACA 63-318	DOUBLE SLOTTED	.33	1.55	4	2	KRUGER FLAP	78									x					*1/10-SCALE XC-142 TILT-WING MODEL IN PRINCETON DYNAMIC MODEL TRACK.* PROPELLERS OVERLAPPED. STATIC AND DYNAMIC TESTS IN HOVER AND FORWARD FLIGHT TO DETERMINE LATERAL-DIRECTIONAL STABILITY CHARACTERISTICS.
7	58	4	NACA 64A418	–	–	.57	2	1/ SPAN		1.0	0 → 17°				x			x						STRAIGHT WING WITH ONE PROPELLER IN PUSHER CONFIGURATION, SPANNING THE UTIA 32- x 48-IN. LOW-SPEED TUNNEL. DEFLECTED-SLIPSTREAM TYPE. EFFECT OF SLIPSTREAM AND RATIO OF FREE-STREAM TO SLIPSTREAM VELOCITIES ON LIFT.
d	66	8.53	NACA 63_3-318	DOUBLE SLOTTED	.47	1.72	4	2	LE SLAT	1.92														*FREE-FLIGHT TESTS OF 1/9-SCALE TILT-WING VSTOL.* PROPELLERS OVERLAPPED. STATIC AND DYNAMIC STABILITY DERIVATIVES IN HOVER AND TRANSITION. CORRELATION WITH CALCULATED VALUES. QUALITATIVE MEASUREMENTS.
9	66	8.53	NACA 63_3-318	DOUBLE SLOTTED	.47	1.72	4	2	LE SLAT	1.92	−30° → 30°				x									1/9-SCALE, FULL-SPAN, TILT-WING MODEL. PROPELLERS OVERLAPPED. STATIC LONGITUDINAL, AND IN-PHASE AND OUT-OF-PHASE OSCILLATORY DERIVATIVES.
10	60	4.58	NACA 0015			1.17	3	1		1.77	0 → 40°			.064 TO .4					x					METHODS PREDICTING AERO STABILITY DERIVATIVES OF TILT-WING VTOL AIRCRAFT. TEST DATA FOR AERO FORCES ON WING ALONE AND FUSELAGE ALONE FOR VARIOUS THRUST COEFFICIENTS.
11	66	(a) 5.3 (b) 6.7 (c) 6.5				(a) 9.5 (b) 2.4 (c) 1.72	(a) 3 (b) 4 (c) 4	(a) 1 (b) 1 (c) 2		(a) 2.0 (b) – (c) 1.92														(A) VZ-2 RESEARCH PLANE IN FULL-SCALE TUNNEL AND 1/4-SCALE MODEL IN LANGLEY 30- x 60-FT TUNNEL; (B) 1/10-SCALE VTOL IN PRINCETON DYNAMIC MODEL TRACK; (C) 4-PROPELLER-OVERLAPPING MODEL IN LTV AND 1/9-SCALE NASA TEST COMPARED. LONG STABILITY DERIVATIVES. ANALOG COMPUTER STUDY ALSO COMPARED.
12	66	–	–	–	–	–	–	1, 2	–	–	–	–	–	–										LONGITUDINAL DYNAMIC CHARACTERISTICS OF 2 FULL-SPAN MODELS: (A) QUAD DUCTED PROPELLER MODEL; (B) 2-PROPELLER AND 4-PROPELLER TILTING-WING MODELS. PROPELLERS OVERLAPPED IN LATTER. EQUATIONS FOR DERIVATIVES COMPARED WITH PRINCETON TRACK TESTS.
13	67	8.53	NACA 63-318	DOUBLE SLOTTED	.33	1.55	4	2	KRUGER FLAPS	1.92	−15° → 15°													FULL-SPAN 1/10-SCALE MODEL OF THE LTV XC-142. PROPELLERS OVERLAPPED. TILT WING. LONGITUDINAL DYNAMIC STABILITY AT HIGH WING INCIDENCE MEASURED IN PRINCETON DYNAMIC MODEL TRACK. TUFT STUDY. PRIMARILY 2° OF FREEDOM MOTIONS, ALSO 1° AND 3° OF FREEDOM.
14	64	6.52	NACA 63A416	TRIPLE SLOTTED	.386	14.76	3	2	AILERONS	1.21														BREGUET 941, A DEFLECTED-SLIPSTREAM STOL. INTERCONNECTED PROPELLERS. NO PROPELLER OVERLAP. STATIC AND DYNAMIC STABILITY AND CONTROL, PERFORMANCE, TAKEOFF AND LANDING TECHNIQUES. FLYING QUALITIES COMPARED WITH AGARD REQ.
15	64	8.35	NACA 23017 WITH LE OF NACA 63-318	DOUBLE SLOTTED	.33	9.3	3	2	LE SLATS, KRUGER FLAPS	1.86	−16° → 22°				x									.6-SCALE TILT-WING XC-142 IN AMES 40- x 80-FOOT TUNNEL. PROPELLERS OVERLAPPED. LONG STABILITY AND CONTROL. EFFECT OF SPAN OF LE DEVICES ON ONSET OF AIR FLOW SEPARATION. EFFECT OF PROPELLER THRUST ON DESCENT PERFORMANCE. EFFECT OF WING TILT ANGLE, FLAP DEFLECTION AND LE DEVICES ON LONG CHAR.

TABLE 9.2-A (CONTD)

REFERENCE NO.	YEAR OF PUBLICATION	WING ASPECT RATIO	CONFIGURATION GEOMETRY: WING AIRFOIL SECTION	TYPE OF FLAP	FLAP CHORD TO AIRFOIL CHORD RATIO (FLAP RETRACTED)	PROPELLER DIAMETER (FT)	BLADES PER PROPELLER	NUMBER PROPELLERS PER SEMISPAN	AUXILIARY TURNING AIDS	PROPELLER DIAMETER / WING CHORD	α RANGE	TEST CONDITIONS: MAX. ADVANCE RATIO	SLIPSTREAM DYNAMIC PRESSURE (lb/ft²)	SLIPSTREAM REYNOLDS NUMBER (BASED ON WING MAC)	STATIC TURNING EFFECTIVENESS	TRANSITION PERFORMANCE	GROUND EFFECTS	TEST DATA: PROPELLER FORCES	PROPELLER LOCATION VARIED	PROPELLER ROTATION MODE	SLIPSTREAM DYN. PRESS. SURVEY	DOWNWASH SURVEY	POWER	COMMENTS
17	68	8.35	MOD NACA 23017	DOUBLE SLOTTED	.33	9.3	3	2	LE SLATS	1.86						X			X					LARGE-SCALE TILT-WING V/STOL TRANSPORT IN AMES 40- x 80-FT TUNNEL. PROPELLERS OVERLAPPED, FIXED GROUND PLANE. EFFECT OF GROUND HEIGHT ON FLAP EFFECTIVENESS AND YAW CONTROL IN HOVER. EFFECT OF GROUND HEIGHT, FLAPS, SLATS, WING TILT ON LONG AERO CHAR. PRESSURE DATA AT VARIOUS GROUND HEIGHTS, WING TILT ANGLES, THRUST COEFFICIENTS, AND PROPELLER RPM.
18	68	8.53	NACA 63-318	DOUBLE SLOTTED	.33	16.625	4	2	LE SLATS	1.94									X					FLIGHT TESTS ON XC-142A PROTOTYPE, A TILT-WING, DEFLECTED-SLIPSTREAM CARGO ASSAULT AIRCRAFT AT EDWARDS AFB. PROPELLERS OVERLAPPED. CATEGORY II PERFORMANCE EVALUATION OF STATIC AND DYNAMIC LONG STABILITY, LATERAL-DIRECTIONAL STABILITY, MANEUVERING STABILITY, TAKEOFF, CONVERSIONS, ETC.
19	54	4.55	NACA 0015	PLAIN	.30	2	3	2	–	1.32	$-10^\circ \rightarrow 90^\circ$	.122	8	.8			X			X			X	SEMISPAN WING IN SLIPSTREAM OF 2 LARGE-DIAM PROPELLERS. PROPELLERS OVERLAPPED. TILT WING AND PROPELLER TEST SEPARATELY AND IN COMBINATION IN LANGLEY 300-MPH 7- x 10-FT TUNNEL. PROPELLER-EFFICIENCY DATA. EFFECT OF PROPELLERS, THRUST, AND NACELLES ON AERO CHAR. EFFECT OF SLIPSTREAM ON VARIATION OF LIFT-CURVE SLOPE WITH THRUST.
20	55	4.55	NACA 0015	PLAIN	.60 .30	2	3	2, 1	2 VANES	1.33	–	0	8	–	X			X	X		X			SEMISPAN MODEL. PROPELLERS OVERLAPPED. EFFECTS OF PROPELLER BLADE ANGLE, MODE OF PROPELLER ROTATION, PROPELLER LOCATION, AND RATIO OF WING CHORD TO PROPELLER DIAMETER ON TURNING EFFECTIVENESS. LONG AND VERTICAL POSITION OF PROPELLERS VARIED. EFFECT OF WING CHORD FROM FLAT PLATE WINGS. SOME DATA WITH AUX VANES.
22	69	6.14	NACA 4420	SINGLE SLOTTED	.40	5.67	4	1	LE SLAT	2.5	$5^\circ \rightarrow 80^\circ$			1.9				X						LARGE-SCALE, SEMISPAN TILT-WING AND FUSELAGE IN LANGLEY FULL-SCALE TUNNEL. EFFECT OF PROPELLER ROTATION DIRECTION, FENCES, SLATS, AND FLAP DEFLECTION ON AERO DATA. TABULATED AND PLOTTED. TUFT STUDIES.
23	66	4.88	NACA 4415	DOUBLE SLOTTED	.35	5.67	4	1	LE SLAT	2.0	$-20^\circ \rightarrow 90^\circ$			2.32, 1.91		X			X					LARGE-SCALE, SEMISPAN TILT-WING IN LANGLEY FULL-SCALE TUNNEL. EFFECT OF FENCES, SLATS IN 2 POSITIONS, FLAP DEFLECTION, AND PROPELLER ROTATION DIRECTION ON AERO CHAR. TUFT STUDIES.
24	66	4.88	NACA 4415	DOUBLE SLOTTED	.35	5.67	4	1	LE SLATS	2.0	$0 \rightarrow 90^\circ$			2.38, 1.95		X			X					LARGE SEMISPAN TILT-WING AND FUSELAGE IN LANGLEY FULL-SCALE TUNNEL. EFFECT OF FENCES, SLATS IN 2 POSITIONS, FLAP DEFLECTION, AND PROPELLER ROTATION DIRECTION ON AERO CHAR. TUFT STUDIES. LOADS ON FUSELAGE (LIFT ONLY).
25	67	4.88	NACA 4415	SINGLE SLOTTED	.40	5.67	4	1	LE SLATS	2.0	$0 \rightarrow 85^\circ$			2.38		X			X					LARGE-SCALE SEMISPAN TILT-WING AND FUSELAGE IN LANGLEY FULL-SCALE TUNNEL. EFFECT OF FENCES, SLATS, FLAP DEFLECTION, AND PROPELLER ROTATION DIRECTION ON LONG AERO CHAR. TUFT STUDIES. LOADS ON FUSELAGE (LIFT ONLY).
26	67	4.88	NACA 4415	SINGLE SLOTTED	.40	5.67	4	1	LE SLATS	2.0	$5^\circ \rightarrow 85^\circ$			2.38		X			X					LARGE-SCALE SEMISPAN TILT-WING AND FUSELAGE IN LANGLEY FULL-SCALE TUNNEL. EFFECT OF FENCES, SLATS IN 2 POSITIONS, FLAP DEFLECTION, AND PROPELLER ROTATION DIRECTION ON LONG AERO CHAR. TUFT STUDIES. LOADS ON FUSELAGE (LIFT ONLY)
27	67	4.88	NACA 4415	SINGLE SLOTTED	.40	5.67	4	1	LE SLATS	2.0	$5^\circ \rightarrow 85^\circ$			2.38		X			X					LARGE-SCALE SEMISPAN TILT-WING AND FUSELAGE IN LANGLEY FULL-SCALE TUNNEL. EFFECT OF FENCES, SLATS, FLAP DEFLECTION, AND PROPELLER ROTATION DIRECTION ON LONG AERO CHAR. TUFT STUDIES. LOADS ON FUSELAGE (LIFT ONLY).
28	64	4.05	NACA 4415	FOWLER	.40	5.67	4	1	LE SLAT, DROOP NOSE, KRUEGER FLAP	1.67	$-20^\circ \rightarrow 90^\circ$					X								LARGE-SCALE SEMISPAN TILT-WING IN LANGLEY FULL-SCALE TUNNEL. EFFECT OF VARIOUS LE DEVICES AND FLAP DEFLECTION ON LONG AERO CHAR. TUFT STUDIES.

TABLE 9.2-A (CONTD)

REFERENCE NO.	YEAR OF PUBLICATION	WING ASPECT RATIO	CONFIGURATION GEOMETRY: WING AIRFOIL SECTION	CONFIGURATION GEOMETRY: TYPE OF FLAP	CONFIGURATION GEOMETRY: FLAP CHORD TO AIRFOIL CHORD RATIO (FLAP RETRACTED)	CONFIGURATION GEOMETRY: PROPELLER DIAMETER (FT)	CONFIGURATION GEOMETRY: BLADES PER PROPELLER	CONFIGURATION GEOMETRY: NUMBER PROPELLERS PER SEMISPAN	CONFIGURATION GEOMETRY: AUXILIARY TURNING AIDS	CONFIGURATION GEOMETRY: PROPELLER DIAMETER / WING CHORD	CONFIGURATION GEOMETRY: α RANGE	TEST CONDITIONS: MAX. ADVANCE RATIO	TEST CONDITIONS: SLIPSTREAM DYNAMIC PRESSURE (LB/FT²)	TEST CONDITIONS: SLIPSTREAM REYNOLDS NUMBER (BASED ON WING MAC)	TEST CONDITIONS: STATIC TURNING EFFECTIVENESS	TEST CONDITIONS: TRANSITION PERFORMANCE	TEST CONDITIONS: GROUND EFFECTS	TEST DATA: PROPELLER FORCES	TEST DATA: PROPELLER LOCATION VARIED	TEST DATA: PROPELLER ROTATION MODE	TEST DATA: SLIPSTREAM DYN. PRESS. SURVEY	TEST DATA: PROPELLER RPM	TEST DATA: DOWNWASH SURVEY	TEST DATA: POWER	COMMENTS
29	64	4.05	NACA 4415	SINGLE SLOTTED	.40	5.67	4	1	LE SLAT, DROOP NOSE, KRUEGER FLAP	1.67	−20° → 90°			2.8, 2.3		X										LARGE-SCALE SEMISPAN TILT-WING IN LANGLEY FULL-SCALE TUNNEL. EFFECT OF VARIOUS LE DEVICES AND FLAP DEFLECTION ON LONG. AERO CHAR. TUFT STUDIES
30	64	4.05	NACA 4415	SINGLE SLOTTED	.40	5.67	4	1	LE SLAT, KRUEGER FLAP	1.67	−20° → 90°			2.8, 2.3		X										LARGE-SCALE SEMISPAN TILT-WING IN LANGLEY FULL-SCALE TUNNEL. EFFECT OF LE SLATS AND KRUEGER FLAPS ON LONG. AERO CHAR. TUFT STUDIES
31	69	6.1	NACA 4420	SINGLE SLOTTED	.40	5.67	4	1	LE SLAT	2.5	5° → 80°			1.9					X							SEMISPAN TILT-WING AND FUSELAGE IN LANGLEY TUNNEL. TABULATED PRESSURE DISTRIBUTION SHOWING EFFECT OF FLAP DEFLECTION, PROPELLER ROTATION DIRECTION, SLATS, AND FENCES. TUFT STUDIES. PLOTS OF TYPICAL CHORDWISE PRESSURE DISTRIBUTION, SPANWISE SECTION NORMAL-FORCE COEFFICIENTS, AND CHORDWISE PRESSURE DISTRIBUTION AT VARIOUS SPANWISE STATIONS.
32	67	6.37	NACA 0015	SPLIT	.33	3.25	2			2.17	0 → 80°		8								X				SEMISPAN SEGMENTED WING ON SEMIFUSELAGE IN LOW-SPEED NAA TUNNEL. EFFECT OF PROPELLER SLIPSTREAM ON SPANWISE DISTRIBUTION OF LIFT, DRAG, PITCHING MOMENTS, AND TOTAL WING FORCES AND MOMENTS. STALL CHAR. OF WING IMMERSED IN SLIPSTREAM. SURVEY OF VELOCITY FIELD IN PROPELLER SLIPSTREAM. EFFECTS OF FLAPS, THRUST, AND PROPELLER GEOMETRY. TUFT STUDIES. COMPUTER PROGRAM. THEORETICAL AND EXPERIMENTAL DATA COMPARED.
33	64						1, 2																		ANALYTIC INVESTIGATION OF AERO FORCES ON WING-PROPELLER COMBINATION. RESULTS APPLIED TO VISTOL AIRCRAFT. EFFECT OF PROPELLER SLIPSTREAM ON WING STALL, TAKE-OFF AND LANDING PERFORMANCE.
34	67	8.51	NACA 63-318	DOUBLE SLOTTED	.33	1.41	4	2	LE SLAT	1.92			10	.51			X		X	X					1/11-SCALE TILT-WING IN LANGLEY 300-MPH 7- x 10-FT TUNNEL. PROPELLERS OVERLAPPED. MOVING-BELT GROUND PLANE. SMOKE-FLOW STUDY. EFFECT OF GROUND, GROUND HEIGHT, WING TILT ANGLE, FLAP DEFLECTION, HORIZONTAL-TAIL INCIDENCE, AND PROPELLER ROTATION DIRECTION ON AERO CHAR. EFFECT OF NOSE STRAKES, ASYMMETRIC RPM, AILERON DEFLECTION, AND SPOILERS.
35	67	8.28	NACA 63-318	DOUBLE SLOTTED	.33	1.41	4	2	LE SLAT	1.92	−8° → 24°		.10	.51			X			X					FULL-SPAN 1/11-SCALE TILT-WING MODEL IN LANGLEY 300-MPH 7- x 10-FT TUNNEL. PROPELLERS OVERLAPPED. MOVING-BELT GROUND PLANE. EFFECT OF THRUST, GROUND, GROUND HEIGHT, MOVING GROUND PLANE, WING INCIDENCE, AND HORIZONTAL-TAIL INCIDENCE ON AERO CHAR.
36	66	8.28	NACA 63-318	DOUBLE SLOTTED	.33	1.41	4	2	LE SLAT, DROOP NOSE	1.92	−30° → 40°		10	.51		X	X	X		X					1/11-SCALE TILT-WING IN LANGLEY 300-MPH 7- x 10-FT TUNNEL. PROPELLERS OVERLAPPED. FIXED GROUND BOARD. EFFECT OF THRUST, WING INCIDENCE, HORIZONTAL-TAIL INCIDENCE, PROPELLER BLADE ANGLE, FLAPS, SLATS, NOSE DROOP, AND GROUND ON LONG. AERO CHAR.
37	58	9.66	NACA 23017	SLOTTED		6.75	4	1	LE FLAP, BLOWING BLC, DROOPED AILERON	1.43	−8° → 20°													X	LARGE-SCALE, STRAIGHT-WING MODEL IN AMES 40- x 80-FT TUNNEL. EFFECT OF THRUST, STABILIZER INCIDENCE, NOZZLE HEIGHT, FLAP AND AILERON JET MOMENTUM, FLAPS, AND LE FLAPS ON AERO CHAR. EFFECT OF DROOPED AILERON ON LATERAL CONTROL.
38	66	2.82	NACA 0015	SINGLE SLOTTED	.30	2	3	1		1.33	0 → 90°			.63						X					TILT-WING IN LANGLEY 300-MPH 7- x 10-FT TUNNEL, 17-FT SECTION OF 7- x 10-FT TUNNEL, AND FULL-SCALE TUNNEL. EFFECT OF TUNNEL SIZE, REYNOLDS NUMBER, AND FLAPS ON LONG. AERO CHAR. DATA FROM FIRST 2 TUNNELS CORRECTED BY THEORY AND COMPARED WITH DATA FROM FULL-SCALE TUNNEL TO DETERMINE WALL EFFECTS AND VALIDITY OF WALL-CORRECTION THEORY (GIVEN IN APP. I).

TABLE 9.2-A (CONTD)

REFERENCE NO.	YEAR OF PUBLICATION	WING ASPECT RATIO	WING AIRFOIL SECTION	TYPE OF FLAP	FLAP CHORD TO AIRFOIL CHORD RATIO (FLAP RETRACTED)	PROPELLER DIAMETER (FT)	BLADES PER PROPELLER	NUMBER PROPELLERS PER SEMISPAN	AUXILIARY TURNING AIDS	PROPELLER DIAMETER / WING CHORD	α RANGE	HALF ADVANCE RATIO	SLIPSTREAM DYNAMIC PRESSURE (LB/FT²)	SLIPSTREAM REYNOLDS NUMBER (BASED ON WING MAC)	STATIC TURNING EFFECTIVENESS	TRANSITION PERFORMANCE	GROUND EFFECTS	PROPELLER FORCES	PROPELLER LOCATION / VARIED	PROPELLER ROTATION MODE	SLIPSTREAM DYN. PRESS. SURVEY	DOWNWASH SURVEY	POWER	COMMENTS
39	66	7.64	NACA 4415	(a),(b),(c) PLAIN (d) SINGLE SLOTTED (e),(f) DOUBLE SLOTTED	(a) .15 (b) .25 (c) .375 (d) .40 (e) .22 (f) .44	2	3	2	1.67						X		X				X	X			A SEMISPAN TILT-WING VTOL MODEL WITH 6 FLAPS USED FOR YAW CONTROL. NO PROPELLER OVERLAP. TUFT STUDIES. EFFECT OF FLAP-CHORD-TO-PROPELLER-DIAMETER RATIO, TYPE OF FLAP, LENGTH OF FLAP CHORD, FLAP DEFLECTION, AILERON CUTOUTS, AND GROUND PROXIMITY ON AERO CHAR.
40	66	7.66	NACA 4415	SLIDING, FOWLER (SLOTTED)	.40	2.0	3	2, 1	LE SLAT	1.67	VARIES	0	8	–	X		X		X		X				SEMISPAN MODEL. EFFECTS OF PROPELLER POSITION AND OVERLAP ON SLIPSTREAM DEFLECTION CHAR (EFFECTS OF PROPELLER VERTICAL POSITION, CHORDWISE POSITION, AND OVERLAP). EFFECTS OF LE SLAT, NACELLE SIZE, EXTENSION OF NACELLES THROUGH FLAPS (FLAP SEGMENTATION), AND NUMBER OF PROPELLERS. EFFECT OF GROUND PROXIMITY ON PROPELLER STATIC THRUST EFFICIENCY. ANGLE BETWEEN THRUST AXIS AND GROUND PLANE VARIES WITH FLAP DEFLECTION.
41	66	7.67	NACA 23017, NACA 23012		.26	(a) 11.0 (b) 9.3		2	BLC, LE SLAT	(a) 1.02 (b) .87														FLIGHT AND SIMULATOR TESTS OF STOL SEAPLANE LIF-X8 COMPARED. DEFLECTED-SLIPSTREAM TYPE. NO PROPELLER OVERLAP. MOVING-BASE SIMULATOR. AUTOMATIC STABILIZATION EQUIPMENT IN PLANE. COMPARISON WITH FLIGHT TESTS OF OTHER STOL VEHICLES AND WITH BREGUET 941 SIMULATOR STUDIES. HANDLING QUALITIES RATHER THAN PERFORMANCE OF CHIEF CONSIDERATION.
42	65	–	–	–	–	–	–	–	–	–	–	–	–	–											EQUATIONS ESTIMATING LIFT AND LONG. FORCE COEFFICIENTS FOR STOL AND WINGS IN PROPELLER SLIPSTREAMS. COMPARISON WITH TEST DATA. EFFECTS OF PROPELLER SLIPSTREAM, PROPELLER THRUST, TAPER RATIO, SLATS, FLAP-CHORD-TO-WING-CHORD RATIO, PROPELLER-DIAMETER-TO-CHORD RATIO, AND WING CAMBER.
43	61			SLOTTED				2	LE SLAT						X	X					X			TILT-WING AND DEFLECTED-SLIPSTREAM CONFIG. NO PROPELLER OVERLAP. AERO CHAR. OF VTOL IN HOVER AND TRANSITION. EFFECTS OF WING CHORD, SLATS, AND FLAPS ON POWER REQUIRED.
44	64	4.78	MOD NACA 4415	SLIDING	.33	2.33	3	1	LE DROOP	1.78	$-10^0 \rightarrow 20^0$													1/4-SCALE, FULL-SPAN MODEL OF VZ-2. FULL-SPAN AILERONS. EFFECT OF FLAPS AND LE DROOP ON LONG. AERO CHAR. EFFECT OF FLAP DEFLECTION ON FLOW PATTERNS. TUFT TESTS. AILERON CONTROL EFFECTIVENESS.
45	66	4.86	NACA 0015	–	–	2.0	3	2	–	1.33	$-10^0 \rightarrow 80^0$	.80	6	.80	X	X		X			X			X	SEMISPAN TILT-WING MODEL. PROPELLERS OVERLAPPED. INVESTIGATION OF WING-PROPELLER COMBINED AND SEPARATELY. NACELLE EFFECTS. PROPELLER EFFICIENCY. SPINNER CHARACTERISTICS. PITCHING-MOMENT INCREMENT DUE TO PROPELLERS. APPENDIXES: (1) TUNNEL-WALL CORRECTIONS, (2) SLIPSTREAM CHARACTERISTICS, (3) PERFORMANCE CALCULATIONS.
46	66	4.85	NACA 0015	SLOTTED	.60, .30	2.0	3	2, 1	VANE	1.33	$-40^0 \rightarrow 80^0$	–	6	–	X	X			X						SEMISPAN DEFLECTED-SLIPSTREAM MODEL. PROPELLERS OVERLAPPED. TURNING EFFECTIVENESS OF LARGE-CHORD SLOTTED FLAPS. FORWARD-SPEED TEST WITH INBOARD PROPELLER ONLY. EFFECTS OF VANE AND WING INCIDENCE ON TURNING EFFECTIVENESS. COMPARISON OF TURNING EFFECTIVENESS AND PITCHING MOMENTS OF WING WITH PLAIN FLAPS VS SLOTTED FLAPS. EFFECT OF PROPELLER BLADE ANGLE ON STATIC CONDITION.
47	67	4.78	NACA 4415	SLIDING, SLOTTED	.60 .30	2.0	–	2	LE SLAT	1.33			4.8	–	X		X			X	X				SEMISPAN MODEL. PROPELLERS OVERLAPPED. EFFECTS OF FLAP DEFLECTION, GROUND PROXIMITY, LE SLAT, END PLATES, AND MODE OF PROPELLER ROTATION. EFFECT OF ATTITUDE OF THRUST AXIS TO GROUND PLANE FROM 0 TO 20^0.
48	66	4.85	NACA 0015	SLOTTED	.60, .30	2.0	3	2, 1	VANE	1.33		0	4.8	–	X		X	X	X		X			X	SEMISPAN MODEL. PROPELLERS OVERLAPPED. EFFECTS OF GROUND PROXIMITY AND PROPELLER POSITION ON TURNING EFFECTIVENESS OF WING WITH LARGE-CHORD SLOTTED FLAPS. TUFT STUDIES DISCUSSED. GROUND EFFECT ON ISOLATED PROPELLER THRUST. WING INCIDENCE VARIED. 20^0 ANGLE BETWEEN THRUST AXIS AND GROUND PLANE.

TABLE 9.2-A FOOTNOTE

REFERENCE NO.	YEAR OF PUBLICATION	WING ASPECT RATIO	WING AIRFOIL SECTION	TYPE OF FLAP	FLAP CHORD TO AIRFOIL CHORD RATIO (FLAP RETRACTED)	PROPELLER DIAMETER (FT)	BLADES PER PROPELLER	NUMBER PROPELLERS PER SEMISPAN	AUXILIARY TURNING AIDS	PROPELLER DIAMETER / WING CHORD	α RANGE	MAX. ADVANCE RATIO	SLIPSTREAM DYNAMIC PRESSURE RATIO (TYP.)	SLIPSTREAM DEFLECTION ANGLE BASED ON WING AOA	STATIC TURNING EFFECTIVENESS	TRANSITION PERFORMANCE	GROUND EFFECTS	PROPELLER FORCES	PROPELLER LOCATION VARIED	PROPELLER ROTATION VARIED	SLIPSTREAM DYN. PRESS. SURVEY	DOWNWASH SURVEY	POWER	COMMENTS
49	54	4.55	NACA 0015	PLAIN	.60, .30	2.0	3	2, 1	2 VANES	1.33	−30° → 90°	–	6	80	X	X		X			X					SEMISPAN MODEL. TILT-WING AND DEFLECTED-SLIPSTREAM CONFIG. PROPELLERS OVERLAPPED. TURNING VANES ABOVE NOSE OF FIRST FLAP. EFFECT OF NO. OF PROPELLERS ON AERO CHAR. EFFECTS OF FLAP DEFLECTION AND ANGLE OF ATTACK ON PROPELLER NORMAL FORCE AND PITCHING MOMENTS. PERFORMANCE CALCULATIONS. EFFECT OF VANES.
50	56	4.55	NACA 0015	SLOTTED	.60, .30	2.0	3	2, 1	LE SLAT	1.33		0	4.8	–	X		X		X		X				SEMISPAN MODEL. PROPELLERS OVERLAPPED. EFFECT OF LE SLAT AS A LONG. CONTROL DEVICE. SLAT POSITION VARIED. EFFECTS OF PROPELLER LOCATION. EFFECTS OF ONE AND TWO PROPELLERS IN GROUND-EFFECT REGION COMPARED. TUFT STUDIES DISCUSSED. 20° ANGLE BETWEEN THRUST AXIS AND GROUND PLANE.
51	56	2.67	NACA 4415	SLIDING, PLAIN	.50, .25	2.0	–	1	LE SLAT, END PLATE	1.33		0	4.8	–	X		X			X					SEMISPAN MODEL. TURNING EFFECTIVENESS OF A WING EQUIPPED WITH A SLIDING FLAP AND A LE SLAT. EFFECT OF SLIDING FLAP ON PITCHING MOMENTS. COMPARISON OF CHAR. OF SLIDING-FLAP WING AND SLOTTED-FLAP WING OF REF. 48 AND 46. 20° ANGLE BETWEEN THRUST AXIS AND GROUND PLANE.
53	57	4.89	NACA 4415	SLIDING, SLOTTED	.50, .30	2.0	–	2	LE SLAT	1.33	−40° → 120°	1.5	4.8	62	X	X		X			X				X	SAME MODEL AS REF 47. AERO CHAR. OF HYPOTHETICAL V/STOL MODEL. EFFECTS OF LE SLAT AND HORIZONTAL STABILIZER. NO CORRECTION FOR TUNNEL-WALL EFFECTS.
54	60	7.66	NACA 4415	SLIDING, FOWLER (SLOTTED)	.40	2.0	3	2, 1	LE SLAT	1.67	−70° → 90°	1.10	8	63		X	X				X	X	X	X	SEMISPAN MODEL. NO PROPELLER OVERLAP. SAME MODEL AS REF 40. LONG. AERO CHAR. OF TILT-WING, DEFLECTED-SLIPSTREAM CONFIG. PROPELLER-ALONE AND WING-ALONE DATA. EFFECT OF SLAT POSITION, FLAP DEFLECTION, GROUND PROXIMITY, AND DOWNWASH. EST PERFORMANCE OF HYPOTHETICAL AIRPLANE. APP ON CHAR OF 17-FT SECTION OF LANGLEY 300-MPH 7- x 10-FT TUNNEL.
56	68	–	–	–	–	–	–	–	–	–	–	–	–	–											WING LIFTING-SURFACE THEORY WITH INCLINED SLIPSTREAMS, INCLINED ACTUATOR DISC THEORY, AND FORTRAN COMPUTER PROGRAM, COMPARED WITH TEST DATA: SLIPSTREAM DOWNWASH ANGLE, SLIPSTREAM ROTATION ANGLE, SPAN LOAD DISTRIBUTION, AND DOWNWASH ANGLE. DESIGN CHARTS FOR 7-SLIPSTREAM AND 4-SLIPSTREAM CONFIG AT VARIOUS PROPELLER ANGLE OF ATTACK, FLAP DEFLECTION, ADVANCE RATIO, ANGLE OF ATTACK, AND THRUST COEFFICIENT.
58	66	5.42	NACA 4415	DOUBLE SLOTTED	.40	2	3	1		1.56	−4° → 44°		7.5	65				X			X				DEFLECTED-SLIPSTREAM WING-BODY STOL MODEL IN LANGLEY 300-MPH 7- x 10-FT TUNNEL. EFFECT OF TAIL AREA, TAIL HEIGHT, THRUST, AND TAIL INCIDENCE ON LONG. AERO CHAR.
59	68																								WIND-TUNNEL TEST ON PROPELLER-WING-FLAP MODEL USED IN DEFLECTED-SLIPSTREAM STOL AIRCRAFT EQUATIONS FOR EST AERO FORCES AND COMPARISON WITH TEST DATA.
61	63	5.24	NACA 4415	–	–	9.5	3	1	LE SLAT, LE DROOP	2.0	−12° → 34°														VZ-2 TILT-WING IN LANGLEY FULL-SCALE TUNNEL. EFFECT OF SLATS, NOSE DROOP, AND WING INCIDENCE ON AERO CHAR. TUFT STUDIES. STALL DIAGRAMS.
62	63	4.0	NACA 0015	SLOTTED	.50, .30	3.5	4	2	BLC	1.167	0 → 30°	–	7	–	X	X	X	X		X				X	LARGE FULL-SCALE MODEL (12-FT SPAN). NO PROPELLER OVERLAP. MOBILE TEST RIG. EFFECTS OF BLOWING OVER NOSE OR REAR FLAP (.30C). GROUND-PROXIMITY EFFECTS OVER FIXED AND MOVING GROUND. q VARIED FOR FORWARD-SPEED TESTS. THRUST MEASURED. POWER RATIO GIVEN.
63	64	8.53	NACA 63_3-318	DOUBLE SLOTTED	.47	1.72	4	2	LE SLAT	1.91							X								1/8-SCALE TILT-WING V/STOL IN LANGLEY FULL-SCALE TUNNEL. PROPELLERS OVERLAPPED. FREE-FLIGHT TESTS IN HOVERING, FORWARD LEVEL FLIGHT, AND DESCENT AT VARIOUS ANGLES OF DESCENT AND WING INCIDENCES, AS WELL AS FORCE TESTS. EFFECTS OF GROUND PROXIMITY.
64	68	(a) 5.71 (b) 6.52 (c) 8.06	NACA 63_2-416	TRIPLE SLOTTED	~.24	9.3	3	2	LE SLAT	(a) 1.19 (b) 1.22 (c) 1.27															LARGE-SCALE DEFLECTED-SLIPSTREAM STOL IN AMES 40- x 80-FT TUNNEL. NO PROPELLER OVERLAP. 3 WING SPANS. EFFECTS ON LONG. AERO CHAR. OF WING SPAN, FLAP DEFLECTION, SLATS, PROPELLER ROTATION DIRECTION, AND SPANWISE VARIATION OF PROPELLER THRUST.

TABLE 9.2-A (CONTD)

REFERENCE NO.	YEAR OF PUBLICATION	WING ASPECT RATIO	CONFIGURATION GEOMETRY: WING AIRFOIL SECTION	CONFIGURATION GEOMETRY: TYPE OF FLAP	CONFIGURATION GEOMETRY: FLAP CHORD TO AIRFOIL CHORD RATIO (FLAP RETRACTED)	CONFIGURATION GEOMETRY: PROPELLER DIAMETER (FT)	CONFIGURATION GEOMETRY: BLADES PER PROPELLER	CONFIGURATION GEOMETRY: NUMBER PROPELLERS PER SEMISPAN	CONFIGURATION GEOMETRY: AUXILIARY TURNING AIDS	CONFIGURATION GEOMETRY: PROPELLER DIAMETER / WING CHORD	CONFIGURATION GEOMETRY: α RANGE	TEST CONDITIONS: MAX. ADVANCE RATIO	TEST CONDITIONS: SLIPSTREAM DYNAMIC PRESSURE (LB/FT²)	TEST CONDITIONS: SLIPSTREAM REYNOLDS NUMBER (BASED ON WING MAC)	TEST CONDITIONS: STATIC TURNING EFFECTIVENESS	TEST CONDITIONS: TRANSITION PERFORMANCE	TEST CONDITIONS: GROUND EFFECTS	TEST DATA: PROPELLER FORCES	TEST DATA: PROPELLER LOCATION VARIED	TEST DATA: PROPELLER ROTATION MODE	TEST DATA: SLIPSTREAM DYN. PRESS. SURVEY	TEST DATA: PROPELLER RPM	TEST DATA: DOWNWASH SURVEY	TEST DATA: POWER	COMMENTS
65	60	4.58	NACA 0015	–		1.167	3	1	–	1.76	0 → 90°			.0644 → .4				X		X						TILT-WING ASSAULT TRANSPORT MODEL IN OPEN-END TUNNEL TO GET STAB DERIVS FOR EQ OF MOTION. PROPELLER EFFECTS DURING HOVER AND TRANSITION.
66	65	4.74	NACA 4415	SINGLE SLOTTED	.34	9.67	3	1	DROOPED LE	1.84					X	X									FLIGHT TEST OF VZ-2 TILT-WING VTOL IN LANGLEY FULL-SCALE TUNNEL. FULL-SPAN AILERONS. EFFECT OF FULL-SPAN FLAPS ON RATE OF DESCENT. GROUND EFFECTS.
67	68	8.53	NACA 63-318	DOUBLE SLOTTED	.33	1.55	4	2	LE SLAT	1.92			VAR-IES			X			X						1/10-SCALE TILT-WING MODEL IN PRINCETON DYNAMIC MODEL TRACK. SAME AS LTV XC-142A OF REF 13 WITH LE SLATS ADDED. PROPELLERS OVERLAPPED. GROUND EFFECTS, GROUND HEIGHT, THRUST COEFF, WING INCIDENCE, FLAP DEFLECTION, AND HORIZONTAL VELOCITY VARIED. LIFT, DRAG, PITCHING MOMENT IN STOL TAKE-OFF AND LANDING. COMPARISON OF WIND-TUNNEL AND MOVING-BELT TESTS.
68	68	8.53	NACA 63-318	DOUBLE SLOTTED	.33	1.55	4	2	LE SLAT	1.92									X						1/10-SCALE TILT-WING V/STOL OF XC-142A IN PRINCETON DYNAMIC MODEL TRACK. PROPELLERS OVERLAPPED. LAT-DIR DYNAMIC STAB CHAR IN DESCENT CONDITION. TIME HISTORIES OF RESPONSE TO VARIATIONS IN PROPELLER PITCH, FUSELAGE PITCH ATTITUDE, DESCENT ANGLE, VELOCITY, AND DEGREES OF FREEDOM.
69	64	6.52	NACA 63A416	TRIPLE SLOTTED	.385	14.76	3	2	–	1.21															FLIGHT TEST OF BREGUET 941 PROTOTYPE ASSAULT TRANSPORT (DSS). NO PROPELLER OVERLAP. INTERCONNECTED PROPELLERS. STOL PERFORMANCE, HANDLING QUALITIES, AND OPERATIONAL TECHNIQUES. LIFT AND DRAG AT VARIOUS THRUST COEFFICIENTS IN TAKE-OFF, LANDING, AND WAVE-OFF CONFIGURATIONS.
70	63	10.09	NACA 64A318 (ROOT), 64A412 (TIP)		.25	13.5	4	2	BLOWING BLC, DROOPED AILERONS	.985	−8° → 12°															FLIGHT TESTS OF MODIFIED LOCKHEED C-130S (DSS). NO PROPELLER OVERLAP. STOL PERFORMANCE, HANDLING QUALITIES, AND OPERATIONAL TECHNIQUES. LIFT, DRAG, INCLUDING EFFECT OF BLC IN TAKE-OFF AND LANDING.
71	64	4.78	MOD NACA 4415	SINGLE SLOTTED	.33	2.33	3	1	KRUGER-TYPE FLAP	1.79										X					FLIGHT TESTS OF 1/4-SCALE VZ-2 TILT-WING VTOL IN LANGLEY FULL-SCALE TUNNEL. TIME HISTORIES AND PILOT RATINGS OF DYNAMIC LATERAL CONTROL IN DESCENT.
72	58	2.67	NACA 4415	SLOTTED, PLAIN	.67 .33	2.0	–	1	BLC	1.33		0	4.8	–	X		X			X				X	SEMISPAN MODEL. EFFECTIVENESS OF BLOWING A JET SHEET OF AIR OVER A PLAIN REAR FLAP COMBINED WITH A SLOTTED FORWARD FLAP IN DEFLECTING PROPELLER SLIPSTREAM DOWNWARD. AIR EXHAUSTED OVER REAR FLAP ONLY. EFFECTS OF GROUND PROXIMITY. BLOWING SYSTEM CHARACTERISTICS. 20° ANGLE BETWEEN THRUST AXIS AND GROUND PLANE.
73	60	7.0	NACA 63A412	SLIDING, TE EXTENSION	.385	1.33	3	2	BLC	1.0	−30° → 80°	.6	8	–	X	X	X			X				X	SEMISPAN MODEL. NO PROPELLER OVERLAP. PROPELLERS DO NOT SPAN ENTIRE WING. NO DATA ANALYSIS. AERO CHAR OF JET-FLAPPED AND DEFLECTED-SLIPSTREAM CONFIG. PRESS SURVEY DATA. EFFECT OF GROUND PROXIMITY FOR STATIC AND FORWARD-SPEED CONDITIONS.
74	58	2.67	NACA 4415	SLIDING, PLAIN	.50, .25	2.0	–	1	LE SLAT, BLC, END PLATE	1.33		0	4.8	–	X		X		X	X					SEMISPAN MODEL. EFFECTIVENESS OF BLOWING A JET OF AIR OVER FLAPS IN DEFLECTING PROPELLER SLIPSTREAM DOWNWARD. EFFECTS OF LE SLAT, GROUND PROXIMITY, END PLATE, AND PROPELLER POSITION. BLOWING SYSTEM CHAR. RATIO OF RESULTANT FORCE OBTAINED BY BLOWING VS THAT OBTAINED BY USING EQUAL POWER IN THE PROPELLER. 20° ANGLE BETWEEN THRUST AXIS AND GROUND PLANE.
75	57	4.0	NACA 4415	PLAIN	.50, .20	2.0, 1.67, 1.33	–	1	BLC	2.00		0	4.8	.39, .47, .59	X		X								SEMISPAN MODEL. EFFECTS OF PROPELLER DIAMETER ON ABILITY OF FLAPPED WING, WITH AND WITHOUT BLC TO DEFLECT PROPELLER SLIPSTREAM DOWNWARD. BLOWING SYSTEM CHAR. EFFECTS OF GROUND PROXIMITY. 20° ANGLE BETWEEN THRUST AXIS AND GROUND PLANE. R_f VARIES WITH PROPELLER DIAMETER.

TABLE 9.2-A (CONTD)

REFERENCE NO.	YEAR OF PUBLICATION	CONFIGURATION GEOMETRY: WING ASPECT RATIO	WING AIRFOIL SECTION	TYPE OF FLAP	FLAP CHORD TO AIRFOIL CHORD RATIO (FLAP RETRACTED)	PROPELLER DIAMETER (FT)	BLADES PER PROPELLER	NUMBER PROPELLERS PER SEMISPAN	AUXILIARY TURNING AIDS	PROPELLER DIAMETER / WING CHORD	α RANGE	TEST CONDITIONS: MAX. ADVANCE RATIO	SLIPSTREAM DYNAMIC PRESSURE (LB/FT²)	SLIPSTREAM REYNOLDS NUMBER (BASED ON WING MAC)	STATIC TURNING EFFECTIVENESS	TRANSITION EFFECTIVENESS	GROUND PERFORMANCE	TEST DATA: PROPELLER FORCES	PROPELLER LOCATION VARIED	PROPELLER ROTATION MODE	SLIPSTREAM DYN. PRESS. SURVEY	DOWNWASH SURVEY	POWER	COMMENTS
76	63	(a) 4.62 (b) 7.38 (c) 12.31	(a),(b) NACA 4415 (c) NACA 4424	(a) SINGLE SLOTTED (b),(c) –	(a) 40 (b) – (c) –	2.0		1	LE SLAT	(a) 3 (b) 4.8 (c) 8	0 → 10°		8	(a) .350 (b) .218 (c) .131					X						3 SEMISPAN TILT-PROPELLER VTOL MODELS IN LANGLEY 300-MPH 7- x 10-FT TUNNEL. EFFECT OF WING-CHORD-TO-PROPELLER-DIAMETER RATIO, PROPELLER ROTATION DIRECTION, PROPELLER INCIDENCE, THRUST COEFF., AND FLAP DEFLECTION ON AERO CHAR. EFFECT OF WING-CHORD-TO-PROPELLER-DIAMETER RATIO, WING SPAN, PROPELLER ROTATION DIRECTION, WING ANGLE OF ATTACK, PROPELLER INCIDENCE, AND LE SLAT ON POWER REQUIRED, PITCHING MOMENT, AND THRUST ANGLE OF ATTACK. TRANSITION REGIME.
79	59	(a) 7.5 (b) 5.0 (c) 3.33	NACA 0015	–	–	2.0	–	1	LE SLAT	2.96	−10° → 110°	1.0	8	(a) .362 (b) .53 (c) .795		X				X				X	SEMISPAN MODEL. EFFECT OF CHANGES IN WING CHORD AND LE SLATS ON LONG. AERO CHAR. OF WING-PROPELLER TILT-WING CONFIG. TUFT-GRID PHOTOGRAPHS. PROPELLER EFFICIENCY, R_L VARIES WITH WING CHORD.
90	68	2.82	NACA 0015	–	–	2.0	3	1	–	1.33															TILT WING ON PRINCETON DYNAMIC MODEL TRACK (PROPELLER + NACELLE). AERO CHAR IN TRANSITION AND HOVER. GRAPHS OF LIFT, HORIZ FORCE, AND PITCHING MOMENT VS THRUST FOR VARIOUS WING ANGLES.
92	61	5.54	NACA 23017	SINGLE SLOTTED	–	4.77	3	2	BLC, LE SLAT	.92						X									LARGE-SCALE TILT-WING, DEFLECTED-SLIPSTREAM VTOL. NO PROPELLER OVERLAP. EFFECTS ON AERO CHAR OF WING TILT, LE FLAP, GROUND HEIGHT, THRUST-COEFFICIENT VARIATION, FLAP DEFLECTION, AND BLOWING.
83	64	5.54	NACA 23017	SINGLE SLOTTED	–	4.77	3	2	LE SLAT, BLC ON TE, BLC NOSE FLAP	.92	−28° → 28°						X	X							LARGE-SCALE TILT-WING, DEFLECTED-SLIPSTREAM VTOL. NO PROPELLER OVERLAP. WING FLOW PATTERNS FROM TUFT STUDIES. EFFECTS OF THRUST, FLAPS, SLATS, BLOWING, AND WING TILT ON AERO CHAR. EFFECTS OF WING TILT, FLAPS, SLATS, PROPELLER ROTATION DIRECTION, AND STALL CONTROL DEVICES ON BUFFET BOUNDARY AND DESCENT CHAR.
84	66	5.0	NACA 23021	FOWLER	.40	15.17	3	1	LE SLAT, DROOPED LE	2.21					X	X			X						TILT-WING MODIFIED GRUMMAN JRF-5 VTOL IN AMES 40- x 80-FT TUNNEL. GROUND TEST STAND. EFFECTS OF WING TILT, FLAPS, BLADE FLAP DEFLECTION, VELOCITY, AND LE DEVICES ON LONG CHAR IN TRANSITION. TUFT STUDIES. EFFECT OF ROTOR CYCLIC CONTROL ON LONG AND LATERAL CHAR.
85	63	(a) 6.04 (b) 7.64	–	SINGLE SLOTTED	.30	1.633	3	1		(a) 1.96 (b) 2.40	0 → 90°						X								SEMISPAN TILT WING AND FUSELAGE. EFFECTS OF FLAP DEFLECTION, THRUST COEFFICIENT, AND NACELLE SHAPE ON AERO CHAR.

9.2.1 PROPELLER-WING-FLAP LIFT VARIATION WITH POWER AND ANGLE OF ATTACK

The methods for calculating power-on lift and drag forces of tilt-wing and deflected-slipstream configurations are those developed by Kuhn in reference 1. The methods treat the flow system of a propeller-wing-flap configuration as two separate mass flows, each deflected through a different angle by the wing. The two mass flows are (1) the mass flow deflected downward by the wing through small to moderate angles and (2) the mass flow in slipstreams created by the action of the propellers and deflected downward through large angles by either tilting the thrust axis or deflecting the flaps. These flow systems are illustrated in sketch (a).

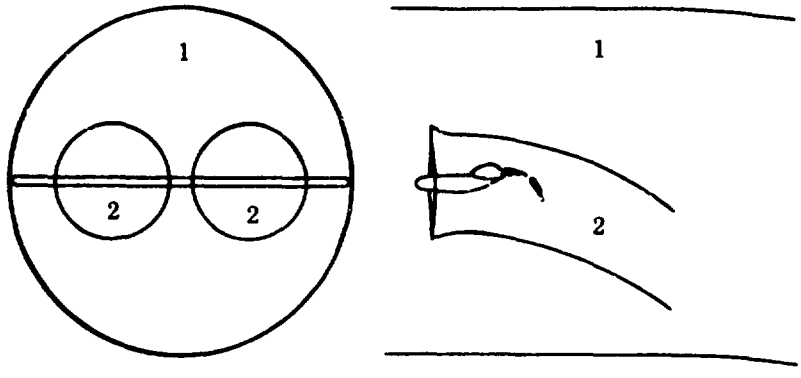

SKETCH (a)

The forces generated in deflection of these mass flows are the familiar lift, induced drag, and profile drag of a wing in a free stream; the propeller thrust which accelerates the propeller slipstream; and a force which accounts for deflection of the propeller slipstream by the wing. Kuhn has analyzed the forces arising from the deflection of each mass flow separately and combined them to arrive at a semiempirical method based on simple momentum theory to estimate the lift and drag forces of propeller-wing-flap configurations. The method uses static slipstream deflection data and power-off wing-flap data as the basis for the calculations.

Kuhn develops expressions for both the lift and drag forces in cruising and high-speed flight by neglecting the forces due to the propeller slipstream and treating the deflection of the mass flow affected by the wing within the assumption of simple momentum thoery. Using this assumption at very low cruising speeds requires that the stream tube be deflected through large angles with a minimum loss in order to produce enough lift to support the airplane. Although the validity of extrapolation of simple momentum theory to large angles appears to be a rather gross assumption, the theory gives reasonable results as long as stall can be avoided.

At zero forward speed, only the propeller slipstreams are available to produce thrust and lift. At this end of the speed range Kuhn develops expressions for the lift and drag forces from available static experimental data on the effectiveness of wing-flap systems in deflecting propeller slipstreams. These expressions are presented in terms of propeller thrust, slipstream characteristics, and the turning effectiveness parameters θ and $\frac{F}{T}$. The slipstream characteristics are obtained using simple momentum theory as applied to propellers.

At transition speeds both flow regions are considered. The resulting expressions approach the power-off wing expressions as velocity is increased and thrust reduced to zero, and approach the zero-forward-speed expressions as the speed is reduced to zero. The method thus provides a logical means of interpolating between these end points.

In treating the flow in the two systems, the fact that the propeller slipstreams occupy space within the large wing stream tube is compensated for by assuming the propeller slipstream to be fully contracted at the wing and that the contraction does not alter the diameter of the stream tube affected by the wing.

To determine the velocity increments necessary to calculate momentum changes, Kuhn assumes that the propeller slipstreams are deflected through the turning angle θ obtained at zero forward speed, that the stream tube affected by the wing is deflected through the downwash angle ϵ obtained under power-off conditions, and that both θ and ϵ remain constant with changes in speed and power.

In order to apply the Datcom methods, it is necessary to have experimental results for or to be able to estimate power-off lift and drag-force characteristics of the wing, as well as slipstream deflection characteristics of the propeller-wing-flap configuration at zero forward speed. The slipstream deflection characteristics for a given propeller-wing-flap configuration require experimental static-thrust data, which will more than likely not be available during the preliminary design phase. Therefore design charts, taken from reference 1, for the slipstream deflection characteristics are provided.

The method presented in this Section is for estimation of the lift of propeller-wing-flap configurations at combined forward speed and power-on conditions. The method is applicable only in the unstalled region of flight.

DATCOM METHOD

The lift of a propeller-wing-flap configuration at combined forward speed and power-on conditions is given in reference 1 as

$$C_L'' = C_{L_o} (1 - T_c'') + \frac{F}{T} T_c'' \frac{KS_p}{S} \sin(\theta + \alpha) \left[1 + 1.6 (1 - T_c'')^{1/2} \right] \quad 9.2.1\text{-a}$$

where all the parameters are defined in the general notation list of Section 9.2. The coefficients, except for C_{L_o}, are based on the dynamic pressure in the propeller slipstream, and the positive direction of forces and angles is shown in Figure 9.2-6.

The first term of equation 9.2.1-a represents the power-off lift contribution. The last term represents both the direct propeller thrust contribution and the lift augmentation of the wing due to the propeller slipstream. The significance of these terms is illustrated in sketch (b).

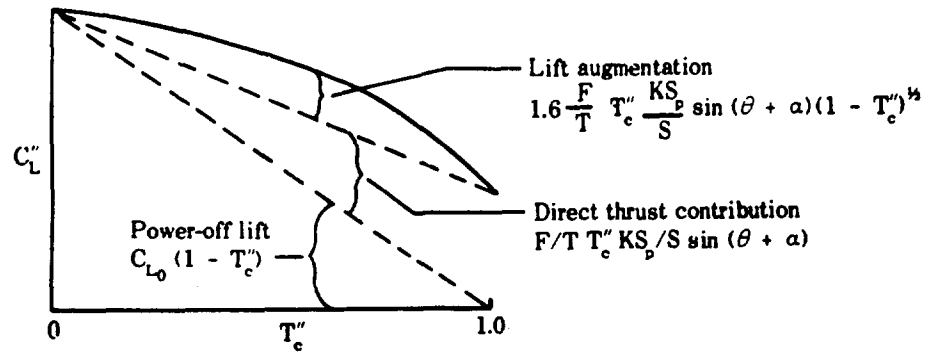

SKETCH (b)

The procedure to be followed in evaluating equation 9.2.1-a is outlined in the following steps.

Step 1. Determine the slipstream turning angle θ by

$$\theta = \theta_f + \Delta\theta \qquad 9.2.1\text{-b}$$

where

θ_f is the slipstream turning angle under conditions of zero incidence and zero camber

$\Delta\theta$ is the slipstream turning-angle increment due to wing camber and incidence between the wing-chord plane and the thrust axis

θ_f is obtained by

$$\theta_f = \frac{\theta}{\delta}\,\delta \qquad 9.2.1\text{-c}$$

where $\frac{\theta}{\delta}$ is obtained from figure 9.2.1-18a as a function of the ratio of the total extended flap chord to the propeller diameter $\frac{c_f}{D}$, and δ is the total flap deflection. For a multiple-flapped configuration the total flap deflection is the sum of the flap deflection of each individual flap.

$\Delta\theta$ is obtained by

$$\Delta\theta = \frac{\theta}{\delta}\,\delta_e \qquad 9.2.1\text{-d}$$

where $\frac{\theta}{\delta}$ is obtained from Figure 9.2.1-18a as a function of the ratio of the wing chord to the propeller diameter $\frac{c}{D}$, and δ_e is an equivalent flap deflection angle defined as the angle between the thrust axis and the mean camber line at the wing trailing edge (see sketch (c)).

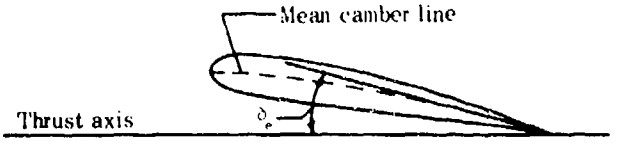

SKETCH (c)

In using this procedure to determine the slipstream turning angle, it is necessary that the value be obtained over the linear part of the curve of variation of turning angle with flap deflection.

In order to define the region of linearity for a given flap configuration, a curve of the variation of the maximum turning angle θ_{max} with the ratio of the total flap chord to the propeller diameter $\frac{c_f}{D}$ is given as figure 9.2.1-18b. A comparison of Figures 9.2.1-18a and 9.2.1-18b indicates that the slope $\frac{\theta}{\delta}$ is dependent only on the total flap chord; whereas the maximum turning angle is dependent upon both the total flap chord and the type of flap. The slope $\frac{\theta}{\delta}$ will become nonlinear as θ_{max} for a given flap configuration is approached. For the purpose of the Datcom the range of the linear variation of θ with δ is defined as

$$\frac{\theta_f}{\theta_{max}} \leq 0.95$$

Step 2. Determine the thrust-recovery factor $\frac{F}{T}$ from figure 9.2.1-19 as a function of the turning angle θ (obtained in Step 1), the flap configuration, and the propeller arrangement.

Step 3. Determine the power-off lift coefficient C_{L_o}.

A wing which is stalled in the power-off condition would frequently be unstalled at some moderate to high propeller thrust coefficient. In order to estimate the power-on data in this region, it is necessary to use the lift values that would exist if the wing were unstalled in the power-off condition. Where possible, experimental power-off data should be used and extrapolated for this purpose. Under these conditions the power-off lift coefficient can be estimated by

$$C_{L_o} = C_{L_{\alpha_o}} 57.3 \sin (\alpha - \alpha_o) \qquad 9.2.1\text{-e}$$

where $C_{L_{\alpha_o}}$ is the extrapolated power-off lift-curve slope of the wing-flap configuration, per degree, and α_o is the extrapolated power-off zero-lift angle of attack.

If power-off data for the given configuration are not available or if the power-off data do not exhibit any region of unstalled flow, the following procedure can be used:

(a) Determine the unflapped wing zero-lift angle of attack from Section 4.1.3.1.

(b) Determine the wing-flap incremental lift from Section 6.1.4.1.

(c) Determine the power-off lift-curve slope of the flapped wing from Section 6.1.4.2.

(d) Using the parameters determined in (a), (b), and (c) construct the power-off lift curve of the flapped wing to obtain α_o.

(e) The power-off lift coefficient of the flapped wing at angle of attack is then obtained using equation 9.2.1-e.

Step 4. The propeller thrust coefficient T_c'' will usually be specified; however, if necessary this parameter can be estimated using the method of Section 9.1.1. $\left(\text{Note that } T_{c_{9.2.1}} = T_{c_{9.1.1}} \frac{S_p}{S}, \text{ and } T_c'' = \frac{T_{c_{9.1.1}}}{T_{c_{9.1.1}} + K}.\right)$

Step 5. The lift coefficient is then obtained from equation 9.2.1-a.

The sample problems illustrate the use of the Datcom method in estimating the lift coefficients of both deflected-slipstream and tilt-wing configurations.

Comparison of experimental data, in the unstalled flight regime, with calculations made using the Datcom method is presented for deflected-slipstream and tilt-wing configurations in Table 9.2.1-A.

Sample Problems

1. Deflected-Slipstream Configuration

Given: A propeller-wing-flap deflected-slipstream configuration of reference 2.

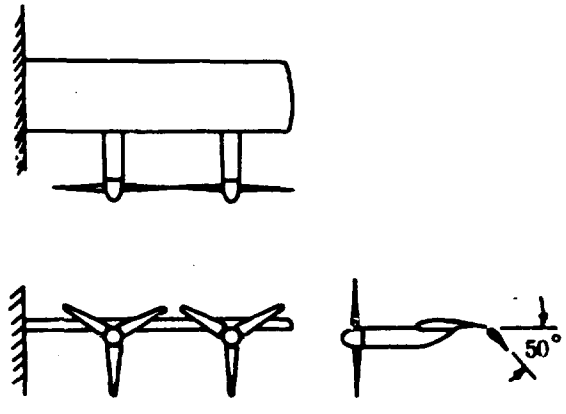

Wing Characteristics

$S = 10.96$ sq ft $A = 7.66$ NACA 4415 airfoil section

$i_w = 0^\circ$ $c = 1.2$ ft (flap retracted) $c = 1.68$ ft (Fowler flap extended)

Flap Characteristics

Fowler flap $\frac{c_f}{c} = 0.286$ (flap extended) $\delta = 50^\circ$

Propeller Characteristics

$K = 4$ (2 propellers per semispan, no overlap) $D = 2.0$ ft

$S_p = 3.14$ sq ft

Additional Characteristics

$T_c" = 0.90$ $\delta_e = 7.4^\circ$

Compute:

Step 1. Determine the slipstream turning angle θ.

$$\frac{c_f}{D} = \frac{c_f}{c}\,\frac{c}{D} = (0.286)\left(\frac{1.68}{2.0}\right)$$

$$= 0.24$$

$\frac{\theta}{\delta} = 0.50$ (figure 9.2.1-18a at $\frac{c_f}{D} = 0.24$)

$\theta_f = \frac{\theta}{\delta}\,\delta = (0.50)(50)$ (equation 9.2.1-c)

$= 25^\circ$

Assuming the wing to be a large-chord flap

$\frac{c}{D} = \frac{1.2}{2.0} = 0.60$

$\frac{\theta}{\delta} = 0.803$ (figure 9.2.1-18a at $\frac{c}{D} = 0.6$)

$\Delta\theta = \frac{\theta}{\delta}\,\delta_e = (0.803)(7.4)$ (equation 9.2.1-d)

$= 5.94$

$\theta = \theta_f + \Delta\theta = 25 + 5.94$ (equation 9.2.1-b)

$= 30.94^\circ$

Determine if the $\frac{\theta}{\delta}$ value for this wing-flap configuration is in the linear range.

$\theta_{max} = 26.5^{o}$ (figure 9.2.1-18b at $\frac{cf}{D} = 0.24$)

$\frac{\theta_f}{\theta_{max}} = \frac{25}{26.5} = 0.943$ which is within the range of the linear variation of θ with δ as defined by the Datcom.

Step 2. Determine the thrust-recovery $\frac{F}{T}$.

$\frac{F}{T} = 0.96$ (figure 9.2.1-19)

Step 3. Determine the power-off lift coefficient C_{L_o}.

The experimental power-off lift curve is extrapolated to obtain

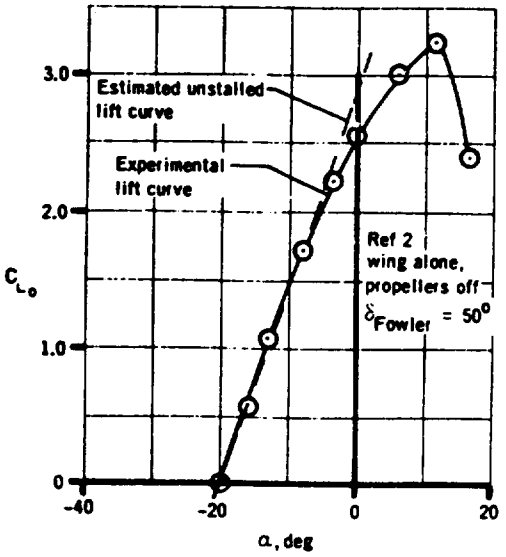

$\alpha_o = -20^{o}$

$C_{L_{\alpha_o}} = 0.145$ per deg

The lift curve that would exist if the wing were unstalled in the power-off condition is estimated by

$C_{L_o} = C_{L_{\alpha_o}} 57.3 \sin(\alpha - \alpha_o)$ (equation 9.2.1-e)

α deg	$(\alpha - \alpha_o)$ deg	$\sin(\alpha - \alpha_o)$	C_{L_o}
-20	0	0	0
-10	10	0.1736	1.442
0	20	0.3420	2.842
10	30	0.5000	4.154
20	40	0.6428	5.341

Solution:

$$C_L'' = C_{L_o}(1 - T_c'') + \frac{F}{T} T_c'' \frac{KS_p}{S} \sin(\theta + \alpha) \left[1 + 1.6(1 - T_c'')^{1/2}\right] \text{(equation 9.2.1-a)}$$

$$= C_{L_o}(1 - 0.9) + (0.96)(0.9) \frac{(4)(3.14)}{(10.96)} \sin(\theta + \alpha) \left[1 + 1.6(1 - 0.9)^{1/2}\right]$$

$$= 0.10\, C_{L_o} + 1.491 \sin(\theta + \alpha)$$

①	②	③	④	⑤	⑥	⑦
α deg	C_{L_o}	$(\theta + \alpha)$ deg	sin $(\theta + \alpha)$ sin ③	0.10 C_{L_δ} 0.10 ②	1.491 ④	$C_{L''}$ ⑤ + ⑥
-20	0	10.94	0.1898	0	0.2830	0.2830
-10	1.442	20.94	0.3574	0.1442	0.5329	0.6771
0	2.842	30.94	0.5141	0.2842	0.7665	1.0507
10	4.154	40.94	0.6553	0.4154	0.9771	1.3925
20	5.341	50.94	0.7764	0.5341	1.1576	1.6917

These results are compared with experimental data in table 9.2.1-A.

2. Deflected-Slipstream Configuration

Given: A propeller-wing-flap deflected-slipstream configuration of reference 2.

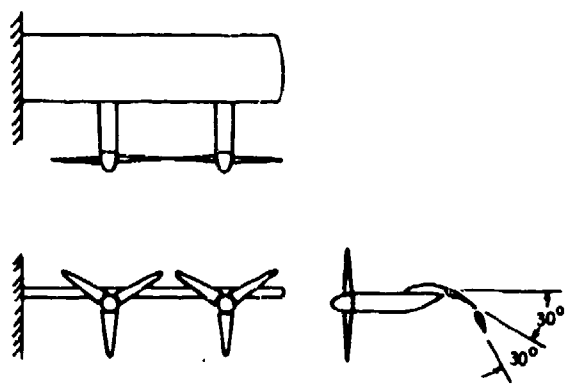

Wing Characteristics

S = 10.96 sq ft A = 7.66 NACA 4415 airfoil section

i_W = 0 c = 1.2 ft (flaps retracted)

c = 1.68 ft (sliding flap and Fowler flap extended)

Flap Characteristics

Combination sliding and Fowler flap

$\frac{c_f}{c}$ = 0.566 (sliding flap and Fowler flap extended; effective chord of sliding flap measured to flap knee)

$\left.\begin{aligned} \delta_{sliding} &= 30^o \\ \delta_{Fowler} &= 30^o \end{aligned}\right\} \delta = \delta_{sliding} + \delta_{Fowler} = 60^o$

Propeller Characteristics

K = 4 (2 propellers per semispan, no overlap) D = 2.0 ft

S_p = 3.14 sq ft

Additional Characteristics

$T_c" = 0.90$ $\delta_e = 7.4^\circ$

Compute:

Step 1. Determine the slipstream turning angle θ.

$$\frac{c_f}{D} = \left(\frac{c_f}{c}\right)\left(\frac{c}{D}\right) = (0.566)\left(\frac{1.68}{2.0}\right)$$

$$= 0.475$$

$\frac{\theta}{\delta} = 0.72$ (figure 9.2.1-18a at $\frac{c_f}{D} = 0.475$)

$\theta_f = \frac{\theta}{\delta}\,\delta = (0.72)(60)$ (equation 9.2.1-c)

$= 43.2^\circ$

Assuming the wing to be a large-chord flap

$\frac{c}{D} = \frac{1.2}{2.0} = 0.60$

$\frac{\theta}{\delta} = 0.803$ (figure 9.2.1-18a at $\frac{c}{D} = 0.60$)

$\Delta\theta = \frac{\theta}{\delta}\,\delta_e$ (0.803)(7.4) (equation 9.2.1-d)

$= 5.94^\circ$

$\theta = \theta_f + \Delta\theta = 43.2 + 5.94$ (equation 9.2.1-b)

$= 49.14^\circ$

Determine if the $\frac{\theta}{\delta}$ value for this wing-flap configuration is in the linear range.

$\theta_{max} = 53.5^\circ$ (upper curve of figure 9.2.1-18b at $\frac{c_f}{D} = 0.475$)

$\frac{\theta_f}{\theta_{max}} = \frac{43.2}{53.5} = 0.807$ which is within the range of linear variation of θ with δ as defined by the Datcom.

Step 2. Determine the thrust-recovery factor $\frac{F}{T}$.

$\frac{F}{T} = 0.90$ (figure 9.2.1-19)

Step 3. Determine the power-off lift coefficient C_{L_o}.

The experimental power-off lift curve is extrapolated to obtain

$\alpha_o = -35^o$

$C_{L_{\alpha_o}} = 0.180$ per deg

The lift curve that would exist if the wing were unstalled in the power-off condition is estimated by

$$C_{L_o} = C_{L_{\alpha_o}} 57.3 \sin (\alpha - \alpha_o)$$ (equation 9.2.1-e)

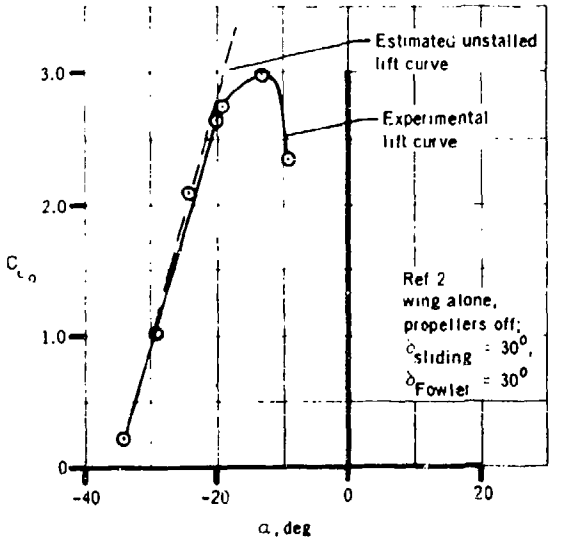

α deg	$\alpha - \alpha_o$ deg	$\sin (\alpha - \alpha_o)$	C_{L_o}
-40	-5	-0.0872	-0.8990
-35	0	0	0
-20	15	0.2588	2.6693
-10	25	0.4226	4.3587
0	35	0.5736	5.9161
10	45	0.7071	7.2930
20	55	0.8192	8.4492

Solution:

$$C_L'' = C_{L_o} (1 - T_c'') + \frac{F}{T} T_c'' \frac{KS_p}{S} \sin (\theta + \alpha) \left[1 + 1.6(1 - T_c'')^{1/2}\right]$$ (equation 9.2.1-a)

$$= C_{L_o} (1 - 0.9) + (0.90)(0.90) \frac{(4)(3.14)}{(10.96)} \sin (\theta + \alpha) \left[1 + 1.6(1 - 0.9)^{1/2}\right]$$

$$= 0.10\, C_{L_o} + 1.3978 \sin (\theta + \alpha)$$

① α deg	② C_{L_o}	③ $(\theta + \alpha)$ deg	④ sin ③	⑤ 0.10 ②	⑥ 1.3978 ④	⑦ ⑤ + ⑥ C_L''
-40	-0.8990	9.14	0.1588	-0.0899	0.2220	0.1321
-35	0	14.14	0.2443	0	0.3415	0.3415
-20	2.6693	29.14	0.4869	0.2669	0.6806	0.947
-10	4.3587	39.14	0.6312	0.4359	0.8823	1.318
0	5.9161	49.14	0.7563	0.5916	1.0571	1.649
10	7.2930	59.14	0.8585	0.7293	1.2000	1.929
20	8.4492	69.14	0.9344	0.8449	1.3061	2.151

These results are compared with experimental data in table 9.2.1-A.

3. Tilt-Wing Configuration

Given: The propeller-wing configuration of reference 5.

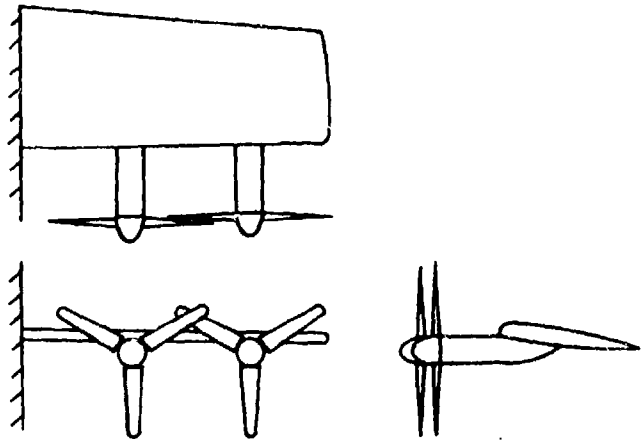

Wing Characteristics

$S = 11.0$ sq ft $\quad A = 4.89 \quad i_w = 5^\circ \quad$ NACA 4415 airfoil section

$c = 1.5$ ft

Propeller Characteristics

$K = 4$ (2 propellers per semispan, overlapped) $\quad D = 2.0$ ft

$S_p = 3.14$ sq ft

Additional Characteristics

$T_c'' = 0.69 \quad \delta_e = 12.4^\circ$

Compute:

Step 1. Determine the slipstream turning angle θ.

$\theta_f = 0$

$\frac{c}{D} = \frac{1.5}{2.0} = 0.75$

$\frac{\theta}{\delta} = 0.89$ (figure 9.2.1-18a at $\frac{c}{D} = 0.75$)

$\Delta\theta = \frac{\theta}{\delta}\delta_e = (0.89)(12.4)$ (equation 9.2.1-d)

$= 11.0^\circ$

$\theta = \theta_f + \Delta\theta$ (equation 9.2.1-b)

$= 11.0^\circ$

Step 2. Determine the thrust-recovery factor $\frac{F}{T}$.

$\frac{F}{T} = 1.0$ (figure 9.2.1-19)

Step 3. Determine the power-off lift coefficient C_{L_o}.

The experimental power-off lift curve is extrapolated to obtain

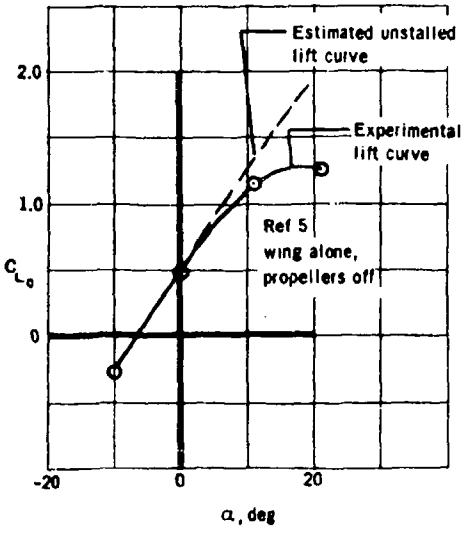

$\alpha_o = -6.5^\circ$

$C_{L_{\alpha_o}} = 0.075$ per deg

The lift curve that would exist if the wing were unstalled in the power-off condition is estimated by

$C_{L_o} = C_{L_{\alpha_o}} 57.3 \sin(\alpha - \alpha_o)$ (equation 9.2.1-

α deg	$(\alpha - \alpha_o)$ deg	$\sin(\alpha - \alpha_o)$	C_{L_o}
-10	-3.5	-0.0611	-0.2624
-6.5	0	0	0
0	6.5	0.1132	0.4865
10	16.5	0.2840	1.2205
20	26.5	0.4462	1.9175

Solution:

$$C_L'' = C_{L_o}(1 - T_c'') + \frac{F}{T} T_c'' \frac{KS_p}{S} \sin(\theta + \alpha) \quad 1 + 1.6(1 - T_c'')^{1/2} \quad \text{(equation 9.2.1-a}$$

$$= C_{L_o}(1 - 0.69) + (1.0)(0.69) \frac{(4)(3.14)}{(11.0)} \sin(\theta + \alpha) \quad 1 + 1.6(1-0.69)^{1/2}$$

$$= 0.31\, C_{L_o} + 1.4897 \sin(\theta + \alpha)$$

① α deg	② C_{L_o}	③ $(\theta + \alpha)$ deg	④ $\sin(\theta + \alpha)$ $\sin$ ③	⑤ $0.31\, C_{L_o}$ 0.31 ②	⑥ 1.4897 ④	⑦ C_L'' ⑤ + ⑥
-10	-0.2624	1.0	0.0175	-0.0813	0.0261	-0.0552
-6.5	0	4.5	0.0785	0	0.1169	0.1169
0	0.4865	11.0	0.1908	0.1508	0.2842	0.4350
10	1.2205	21.0	0.3584	0.3784	0.5339	0.9123
20	1.9175	31.0	0.5150	0.5944	0.7672	1.3616

These results are compared with experimental data in table 9.2.1-A.

REFERENCES

1. Kuhn, R. E.: Semiempirical Procedure for Estimating Lift and Drag Characteristics of Propeller-Wing-Flap Configurations for Vertical- and Short-Take-off-and-Landing Airplanes. NASA Memo 1-16-59L, 1959. (U)

2. Kuhn, R. E., and Hayes, W. C., Jr.: Wind-Tunnel Investigation of Longitudinal Aerodynamic Characteristics of Three Propeller-Driven VTOL Configurations in the Transition Speed Range, Including Effects of Ground Proximity. NASA TN D-55, 1960. (U)

3. Kuhn, R. E., and Draper, J. W.: Investigation of Effectiveness of Large-Chord Slotted Flaps in Deflecting Propeller Slipstreams Downward for Vertical Take-Off and Low-Speed Flight. NACA TN 3364, 1955. (U)

4. Kuhn, R. E., and Draper, J. W.: An Investigation of a Wing-Propeller Configuration Employing Large-Chord Plain Flaps and Large Diameter Propellers for Low-Speed Flight and Vertical Take-Off. NACA TN 3307, 1954. (U)

5. Kuhn, R. E., and Hayes, W. C., Jr.: Wind-Tunnel Investigation of Effect of Propeller Slipstreams on Aerodynamic Characteristics of a Wing Equipped with a 50-Percent-Chord Sliding Flap and a 30-Percent-Chord Slotted Flap. NACA TN 3918, 1957. (U)

TABLE 9.2.1-A
DATA SUMMARY AND SUBSTANTIATION
PROPELLER-WING-FLAP LIFT COEFFICIENT

Ref.	Configuration Characteristics	T_c"	α deg	C_{L_o}*	C_L" Calc	C_L" Test	ΔC_L" (Calc-Test)
2	Deflected-slipstream configuration	0.6	-20	0	0.2520	0.34	-0.09
	Wing		-10	1.442	1.0514	1.25	-0.20
	S = 10.96 sq ft		0	2.842	1.8195	1.90	-0.08
	A = 7.66		10	4.154	2.5318	2.41	-0.12
	Airfoil: NACA 4415	0.9	-20	0	0.2830	0.28	0
	i_W = 0		-10	1.442	0.6771	0.71	-0.03
	$\frac{c}{D}$ = 0.60		0	2.842	1.0507	1.07	-0.02
	δ_e = 7.4°		10	4.154	1.3925	1.39	0
			20	5.341	1.6917	1.62	0.07
	Propeller	0.95	-20	0.	0.2693	0.26	0.01
	K = 4 (no overlap)		-10	1.442	0.5792	0.59	-0.01
	D = 2.0 ft		0	2.842	0.8716	0.87	0
	Flap		10	4.154	1.1375	1.14	0
	Fowler flap		20	5.341	1.3687	1.35	0.02
	$\frac{c_f}{D}$ = 0.24 (flap extended)						
	δ = 50°						
	Additional						
	$\frac{F}{T}$ = 0.96						
	θ = 30.96°						
2	Deflected-slipstream configuration	0.6	-40	-0.8990	-0.162	-0.20	0.04
	Wing		-20	2.6693	1.674	1.56	0.11
	S = 10.96 sq ft		-10	4.3587	2.529	2.21	0.32
	A = 7.66	0.9	-40	-0.8990	0.132	-0.05	0.18
	Airfoil: NACA 4415		-20	2.6693	0.947	0.91	0.04
	i_W = 0		-10	4.3587	1.318	1.28	0.04
	$\frac{c}{D}$ = 0.60		0	5.9161	1.649	1.56	0.09
	δ_e = 7.4°		10	7.2930	1.929	1.71	0.22
			20	8.4492	2.151	1.70	0.45
	Propeller	0.95	-40	-0.8990	0.166	0.02	0.15
	K = 4 (no overlap)		-20	2.6693	0.781	0.68	0.10
	D = 2.0 ft		-10	4.3587	1.004	1.0	0
	Flap		0	5.9161	1.302	1.26	0.04
	Sliding + Fowler flap		10	7.2930	1.506	1.46	0.05
	$\frac{c_f}{D}$ = 0.475 (flaps extended)		20	8.4492	1.665	1.53	0.13
			30	9.3476	1.773	1.48	0.29
	δ sliding = 30°						
	δ Fowler = 30°						
	Additional						
	$\frac{F}{T}$ = 0.90						
	θ = 49.14°						

* Estimated unstalled power-off lift coefficient

TABLE 9.2.1-A (CONTD)

Ref.	Configuration Characteristics	T_c"	α deg	C_{L_o}*	C_L" Calc	C_L" Test	ΔC_L" (Calc-Test)
3	Deflected-slipstream configuration	0.5	-20	-0.1600	0.009	0	0.01
	Wing		-10	0.6380	0.515	0.50	0.01
	S = 10.25 sq ft		0	1.4165	1.004	1.075	-0.03
	A = 4.55		10	2.1522	1.464	1.575	-0.11
	Airfoil: NACA 0015		20	2.8224	1.878	1.775	0.10
	i_W = 0		30	3.4064	2.236	-	-
	$\frac{c}{D}$ = 0.755	0.71	-20	-0.1600	0.064	0.10	-0.04
			-10	0.6380	0.428	0.47	-0.04
	δ_e = 0		0	1.4165	0.778	0.95	-0.17
	Propeller		10	2.1522	1.105	1.24	-0.14
	K = 2		20	2.8224	1.398	1.375	0.02
	D = 2.0 ft		30	3.4064	1.649	-	-
	Flap	0.91	-20	-0.1600	0.099	0.12	-0.02
	Slotted flap		-10	0.6380	0.305	0.325	-0.02
	$\frac{c_f}{D}$ = 0.226		0	1.4165	0.502	0.55	-0.05
			10	2.1522	0.684	0.75	-0.07
	δ = 60°		20	2.8224	0.845	0.875	-0.03
	Additional		30	3.4064	0.980	0.895	0.08
	$\frac{F}{T}$ = 0.96						
	θ = 28.2°						
4	Deflected-slipstream configuration	0.5	-20	0.43	0.536	0.655	-0.12
	Wing		-10	0.81	0.929	0.93	0
	S = 10.25 sq ft		0	1.162	1.293	1.30	-0.01
	A = 4.55		10	1.482	1.618	1.52	0.10
	Airfoil: NACA 0015		20	1.755	1.894	1.65	0.24
	i_W = 0	0.71	-20	0.43	0.522	0.600	-0.08
	$\frac{c}{D}$ = 0.755		-10	0.81	0.855	1.07	-0.18
			0	1.162	1.220	1.23	-0.01
	δ_e = 0		10	1.482	1.518	1.565	-0.05
	Propeller		20	1.755	1.769	1.515	0.25
	K = 4 (overlapped)	0.91	-20	0.43	0.444	0.420	0.02
	D = 2.0 ft		-10	0.81	0.735	0.70	0.04
	Flap		0	1.162	1.004	0.935	0.07
	Two plain flaps (60-percent-chord flap and 30-percent-chord flap)		10	1.482	1.242	1.175	0.07
			20	1.755	1.442	1.38	0.06
	$\frac{c_f}{D}$ = 0.453						
	δ_{60}=30°						
	δ_{30}=20°						
	Additional						
	$\frac{F}{T}$ = 0.94						
	θ = 35°						

* Estimated unstalled power-off lift coefficient

TABLE 9.2.1-A (CONTD)

Ref	Configuration Characteristics	T_c"	α deg	C_{L_o} *	C_L" Calc	C_L" Test	ΔC_L" (Calc-Test)
4	Tilt-wing configuration	0.5	-10	-0.6217	-0.538	-0.55	0.01
	Wing		0	0	0	0.08	-0.08
	S = 10.25 sq ft		10	0.6217	0.538	0.63	-0.09
	A = 4.55		20	1.2248	1.059	1.08	-0.02
	Airfoil: NACA 0015		30	1.7906	1.548	1.33	0.22
	i_W = 0	0.71	-10	-0.6217	-0.461	-0.46	0
	$\frac{c}{D}$ = 0.75		0	0	0	0.08	-0.08
			10	0.6217	0.461	0.55	-0.09
	δ_e = 0		20	1.2248	0.909	0.98	-0.07
	Propeller		30	1.7906	1.329	1.27	0.06
	K = 4 (overlapped)		40	2.3020	1.709	1.40	0.31
	D = 2.0 ft	0.91	-10	-0.6217	-0.342	-	-
	Additional		0	0	0	0.08	-0.08
	$\frac{F}{T}$ = 1.0		10	0.6217	0.342	0.42	-0.08
			20	1.2248	0.675	0.73	-0.06
	θ = 0		30	1.7906	0.986	1.00	-0.01
			40	2.3020	1.260	1.21	0.07
			50	2.7432	1.511	1.27	0.24
2	Tilt-wing configuration	0.6	-20	-1.102	-0.7760	-	-
	Wing		-10	-0.418	-0.2651	-	-
	S = 10.96 sq ft		0	0.279	0.2548	0.17	0.08
	A = 7.66		10	0.9676	0.7669	0.78	-0.01
	Airfoil: NACA 4415		20	1.627	1.256	1.23	0.03
	i_W = 0		30	2.237	1.707	1.44	0.27
	$\frac{c}{D}$ = 0.60	0.9	-20	-1.102	-0.4865	-0.56	0.07
			-10	-.418	-0.1518	-0.28	0.13
	δ_e = 7.4°		0	0.279	0.1886	0.08	0.11
	Propeller		10	0.9676	0.5233	0.45	0.07
	K = 4 (no overlap)		20	1.627	0.8421	0.78	0.06
	D = 2.0 ft		30	2.237	1.135	1.05	0.09
	Additional		40	2.779	1.394	1.20	0.19
	$\frac{F}{T}$ = 1.0	0.95	-20	-1.102	-0.4133	-	-
			-10	-.418	-0.1256	-	-
	θ = 5.94°		0	0.279	0.1669	0.07	0.10
			10	0.9676	0.4543	0.34	0.11
			20	1.627	0.7279	0.59	0.14
			30	2.237	0.9796	0.80	0.18
			40	2.779	1.201	0.97	0.23

*Estimated unstalled power-off lift coefficient

TABLE 9.2.1-A (CONTD)

Ref	Configuration Characteristics	T_c"	α deg	C_{L_o}*	C_L" Calc	C_L" Test	ΔC_L" (Calc-Test)
5	Tilt-wing configuration	0.49	-10	-0.2623	-0.109	-0.20	0.09
	Wing		0	0.4865	0.481	0.40	0.08
	S = 11.0 sq ft		10	1.2205	1.056	0.95	0.11
	A = 4.85		20	1.9175	1.599	1.52	0.08
	Airfoil: NACA 4415	0.69	-10	-0.2624	-0.0552	-0.20	0.15
	$i_w = 5^o$		0	0.4865	0.4350	0.32	0.12
	$\frac{c}{D} = 0.75$		10	1.2205	0.9123	0.86	0.05
	$\delta_e = 12.40^o$		20	1.9175	1.3616	1.29	0.07
	Propeller						
	K = 4 (overlapped)						
	D = 2.0 ft						
	Additional						
	$\frac{F}{T} = 1.0$						
	$\theta = 11.0^o$						

*Estimated unstalled power-off lift coefficient Av error = $\frac{\sum |\Delta C_L"|}{n} = 0.092$

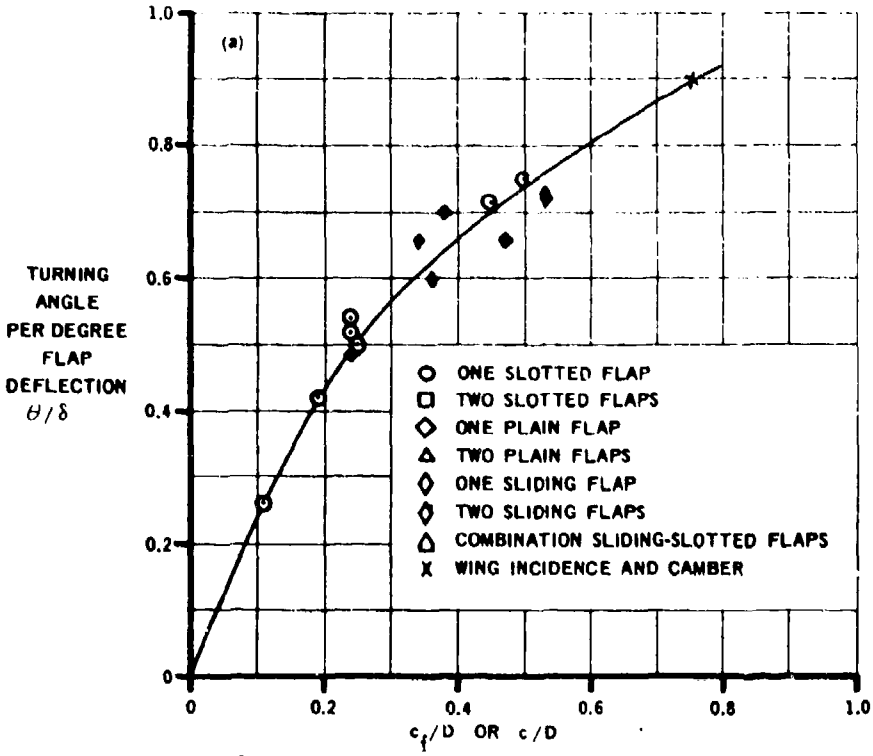

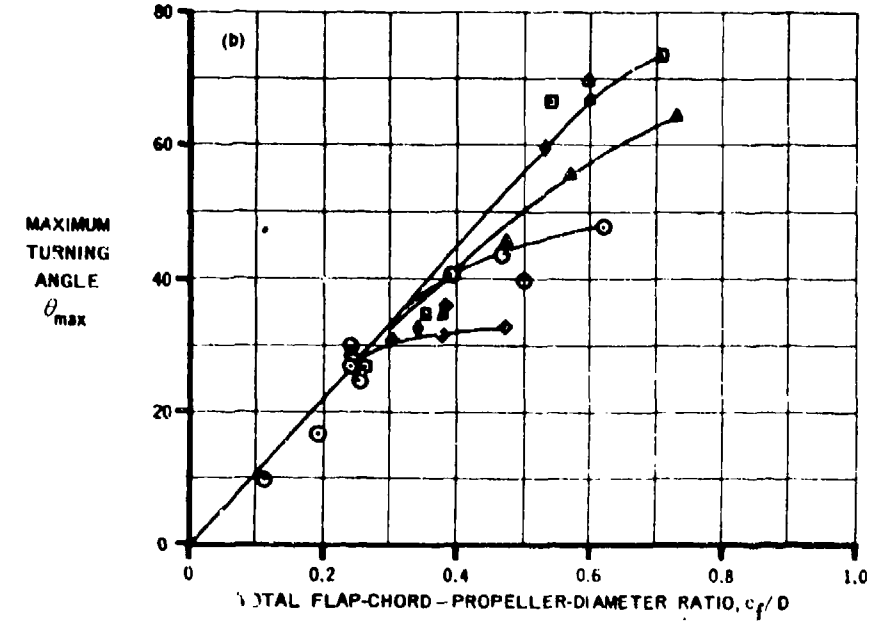

FIGURE 9.2.1-18 VARIATION OF TURNING ANGLE WITH THE RATIO OF TOTAL FLAP CHORD TO PROPELLER DIAMETER FOR VARIOUS CONFIGURATIONS

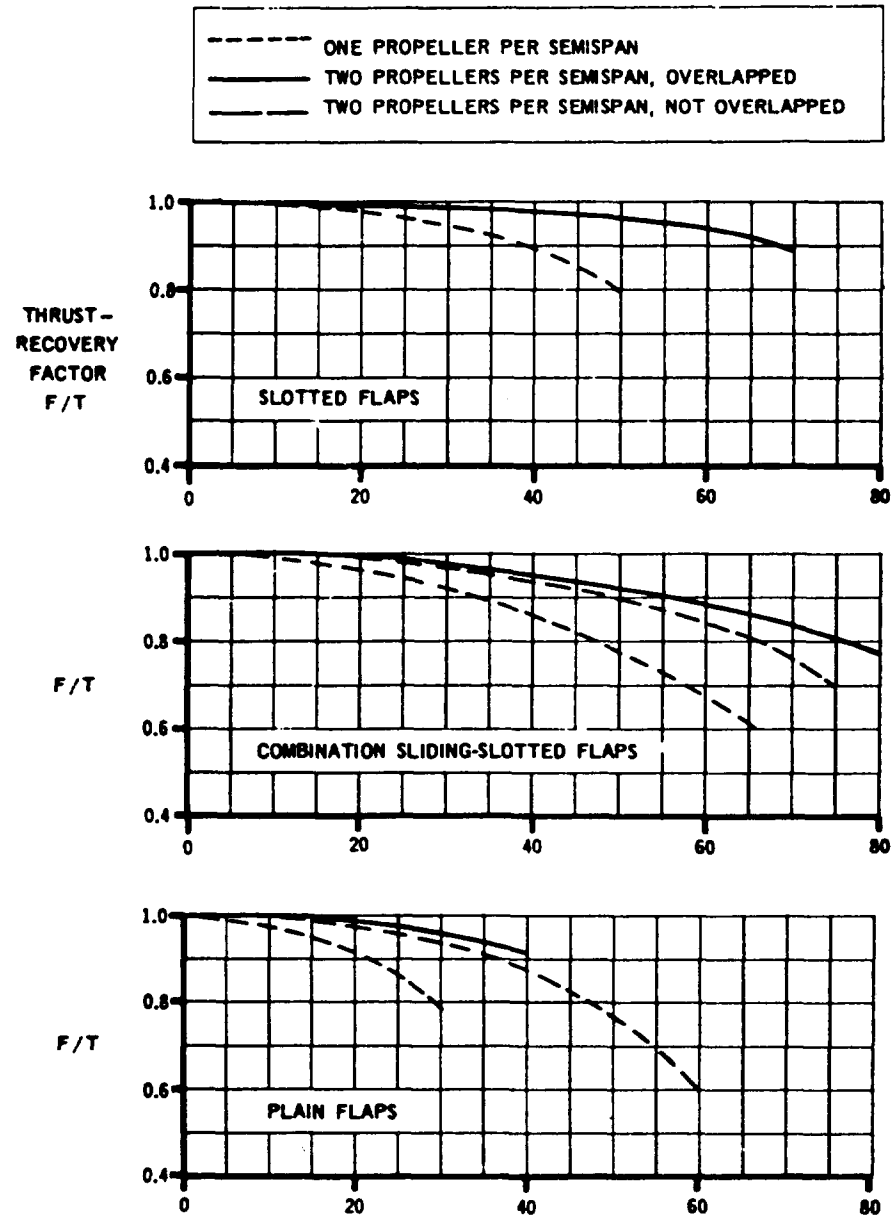

FIGURE 9.2.1-19 VARIATION OF THE AVERAGE THRUST-RECOVERY FACTOR FOR VARIOUS FLAP AND PROPELLER CONFIGURATIONS

9.2.3 PROPELLER-WING-FLAP DRAG VARIATION WITH POWER AND ANGLE OF ATTACK

This Section presents a method for estimating the drag force of propeller-wing-flap configurations at combined forward speed and power-on conditions. The method is applicable only in the unstalled region of flight. The discussion in Section 9.2.1 is directly applicable to this Section, and the reader is referred to that discussion for a general description of the fundamental phenomena.

DATCOM METHOD

The negative drag force of a propeller-wing-flap configuration at combined forward speed and power-on conditions is given in reference 1 as

$$C_{F_X}'' = -C_{D_o}(1 - T_c'') + \frac{F}{T} T_c'' \frac{KS_p}{S} \cos(\theta + \alpha)$$

$$-1.6 \frac{F}{T} T_c'' \frac{KS_p}{S} \left|1 - \cos(\theta + \alpha)\right| (1 - T_c'')^{1/2} \qquad 9.2.3\text{-a}$$

where all the parameters are defined in the general notation list of Section 9.2. The coefficients, except for C_{D_o}, are based on the dynamic pressure in the propeller slipstream, and the positive direction of forces and angles is shown in Figure 9.2-6.

The first term of equation 9.2.3-a represents the power-off drag contribution, the second term represents the component of thrust opposing the drag, and the third term represents the drag resulting from the lift augmentation due to the propeller slipstream. The significance of these terms is illustrated in sketch (a).

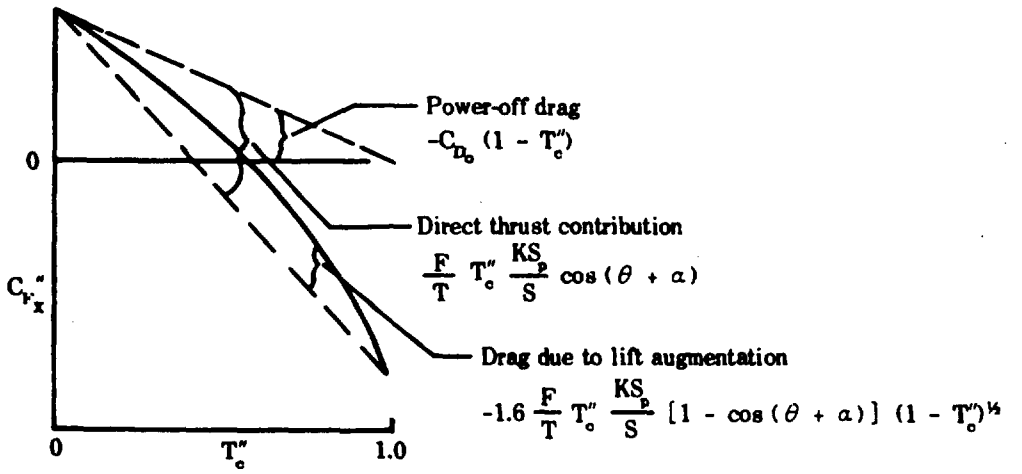

SKETCH (a)

The procedure to be followed in evaluating equation 9.2.3-a is outlined in the following steps.

Step 1. Determine the slipstream turning angle θ as in Step 1 of the method outline of Section 9.2.1.

In using this procedure to determine the slipstream turning angle it is necessary that the value be obtained over the linear part of the curve of variation of turning angle with flap deflection. The range of linear variation is defined in Step 1 of the method outline of Section 9.2.1.

Step 2. Determine the thrust-recovery factor $\frac{F}{T}$ as in Step 2 of the method outline of Section 9.2.1.

Step 3. Determine the power-off drag coefficient C_{D_o}.

A wing which is stalled in the power-off condition would frequently be unstalled at some moderate to high propeller thrust coefficient. In order to estimate the power-on data in this region, it is necessary to use the drag values that would exist if the wing were unstalled in the power-off condition. Where possible, experimental power-off data should be used for this purpose. Under these conditions the power-off drag coefficient can be estimated by

$$C_{D_o} = C_{D_f} + \frac{C_{L_o}^2}{\pi A e} \qquad 9.2.3\text{-b}$$

where

C_{D_f} is the power-off zero-lift drag coefficient. (For the purpose of the Datcom this coefficient is taken as the minimum experimental power-off drag coefficient in order to simplify the definition of the drag polar.)

C_{L_o} is the power-off lift coefficient obtained as in Step 3 of the method outline of Section 9.2.1

e is the span efficiency factor for the configuration. For the purpose of the Datcom e = 0.85.

If power-off data for the given configuration are not available or if power-off test data do not exhibit any region of unstalled flow, the following procedure should be used:

(a) Determine the power-off lift variation and α_o as in Step 3 of the method outline of Section 9.2.1.

(b) Determine the power-off zero-lift drag coefficient for the unflapped wing from Section 4.1.5.1.

(c) Determine the zero-lift drag increment due to flap deflection from Section 6.1.7.

then

$$C_{D_f} = C_{D_{f(4.1.5.1)}} + (\Delta C_D)_{(6.1.7)} \qquad 9.2.3\text{-c}$$

(d) The power-off drag coefficient of the flapped wing at angle of attack is then obtained from equation 9.2.3-b.

Step 4. The propeller thrust coefficient T_c'' will usually be specified; however, if necessary this parameter can be estimated using the method of Section 9.1.1.

$$\left(\text{Note that } T_{c_{9.2.1}} = T_{c_{9.1.1}} \frac{S_p}{S}, \text{ and } T_c'' = \frac{T_{c_{9.1.1}}}{T_{c_{9.1.1}} + K}.\right)$$

Step 5. The drag force coefficient is then obtained from equation 9.2.3-a.

The sample problems illustrate the use of the Datcom method in estimating the horizontal-force coefficients of both deflected-slipstream and tilt-wing configurations.

Comparison of experimental data, in the unstalled flight regime, with calculations made using the Datcom method is presented for deflected-slipstream and tilt-wing configurations in Table 9.2.3-A.

Sample Problems

1. Deflected-Slipstream Configuration

Given: A propeller-wing-flap deflected-slipstream configuration of reference 2. This is the same configuration as that of sample problem 1 of Section 9.2.1. The characteristics are repeated below.

Wing Characteristics

$S = 10.96$ sq ft $A = 7.66$ NACA 4415 airfoil section

$i_w = 0$ $c = 1.2$ ft (flap retracted) $c = 1.68$ ft (Fowler flap extended)

Flap Characteristics

Fowler flap $\frac{c_f}{c} = 0.286$ (flap extended) $\delta = 50^\circ$

Propeller Characteristics

$K = 4$ (2 propellers per semispan, no overlap) $D = 2.0$ ft

$S_p = 3.14$ sq ft

Additional Characteristics

$T_c'' = 0.90$ $\delta_e = 7.4^\circ$

Compute:

Step 1. Determine the slipstream turning angle θ.

$\theta = 30.94^\circ$ (sample problem 1, Section 9.2.1)

Also note that the variation of θ with δ for this wing-flap configuration was shown to be within the range of linear variation as defined by the Datcom.

Step 2. Determine the thrust-recovery factor $\frac{F}{T}$.

$\frac{F}{T} = 0.96$ (sample problem 1, Section 9.2.1)

Step 3. Determine the power-off drag coefficient C_{D_o}.

The power-off drag coefficient is obtained using the experimental zero-lift drag coefficient, and the power-off lift coefficient at angle of attack as determined in sample problem 1 of Section 9.2.1.

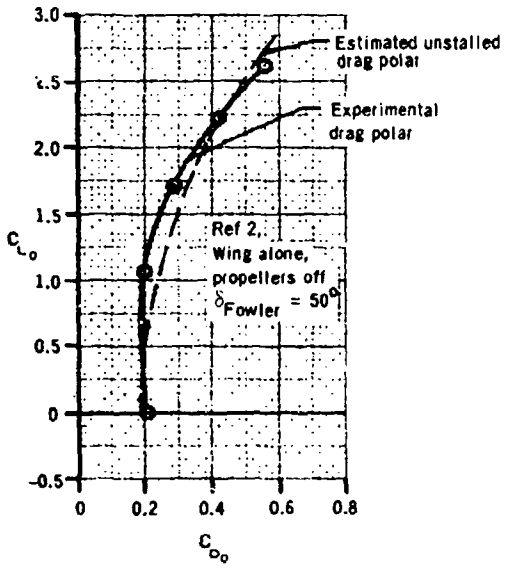

$C_{D_f} = 0.19$ (minimum experimental power-off drag coefficient)

The drag polar that would exist if the wing were unstalled in the power-off condition is estimated by

$$C_{D_o} = C_{D_f} + \frac{C_{L_o}^2}{\pi Ae} \quad \text{(equation 9.2.3-b)}$$

α deg	C_{L_o} Problem 1 9.2.1	$\frac{C_{L_o}^2}{\pi Ae}$	C_{D_o}
-20	0	0	0.1900
-10	1.422	0.1017	0.2917
0	2.842	0.3949	0.5849
10	4.154	0.8436	1.0336
20	5.341	1.3946	1.5846

Solution:

$$C_{F_x}'' = -C_{D_o}(1 - T_c'') + \frac{F}{T} T_c'' \frac{KS_p}{S} \cos(\theta + \alpha)$$

$$- 1.6 \frac{F}{T} T_c'' \frac{KS_p}{S} \left|1 - \cos(\theta + \alpha)\right| (1 - T_c'')^{1/2} \quad \text{(equation 9.2.3-}$$

$$= -C_{D_o}(1 - 0.9) + (0.96)(0.9) \frac{(4)(3.14)}{(10.96)} \cos(\theta + \alpha)$$

$$-1.6(0.96)(0.9) \frac{(4)(3.14)}{(10.96)} \left|1 - \cos(\theta + \alpha)\right| (1 - 0.9)^{1/2}$$

$$= -0.10\, C_{D_o} + 0.990 \cos(\theta + \alpha) - 0.501 \left|1 - \cos(\theta + \alpha)\right|$$

①	②	③	④	⑤	⑥	⑦	⑧
α deg	C_{D_o}	$(\theta + \alpha)$ deg	$\cos(\theta + \alpha)$ $\cos$ ③	0.10 ②	0.990 ④	$\cdot\left[1 - ④\right]^{0.501}$	C_{F_x}" $-⑤ + ⑥ - ⑦$
-20	0.1900	10.94	0.9818	0.0190	0.9720	0.0091	0.9439
-10	0.2917	20.94	0.9340	0.0292	0.9247	0.0331	0.8624
0	0.5849	30.94	0.8578	0.0585	0.8492	0.0712	0.7195
10	1.0336	40.94	0.7555	0.1034	0.7479	0.1225	0.5220
20	1.5846	50.94	0.6302	0.1585	0.6239	0.1853	0.2801

These results are compared with experimental data in table 9.2.3-A.

2. Deflected-Slipstream Configuration

Given: A propeller-wing-flap deflected-slipstream configuration of reference 2. This is the same configuration as that of sample problem 2 of Section 9.2.1. The characteristics are repeated below.

Wing Characteristics

$S = 10.96$ sq ft $\quad A = 7.66$ $\quad$ NACA 4415 airfoil section

$i_w = 0$ $\quad c = 1.2$ ft (flaps retracted) $\quad c = 1.68$ ft (sliding flap and Fowler flap extended)

Flap Characteristics

$\frac{c_f}{c} = 0.566$ (sliding flap and Fowler flap extended; effective chord of sliding flap measured to flap knee)

$$\left.\begin{aligned} \delta_{sliding} &= 30^\circ \\ \delta_{Fowler} &= 30^\circ \end{aligned}\right\} \delta = \delta_{sliding} + \delta_{Fowler} = 60^\circ$$

Propeller Characteristics

$K = 4$ (2 propellers per semispan, no overlap) $\quad D = 2.0$ ft

$S_p = 3.14$ sq ft

Additional Characteristics

$T_c" = 0.90 \qquad \delta_e = 7.4^\circ$

Compute:

Step 1. Determine the slipstream turning angle θ.

$\theta = 49.14^\circ$ (sample problem 2, Section 9.2.1) Also note that the variation of θ with δ for this wing-flap configuration was shown to be within the range of linear variation as defined by the Datcom.

Step 2. Determine the thrust-recovery factor $\frac{F}{T}$.

$\frac{F}{T} = 0.90$ (sample problem 1, Section 9.2.1)

Step 3. Determine the power-off drag coefficient C_{D_o}.

The power-off drag coefficient is obtained using the experimental zero-lift drag coefficient, and the power-off lift coefficient at angle of attack determined in sample problem 2 of Section 9.2.1.

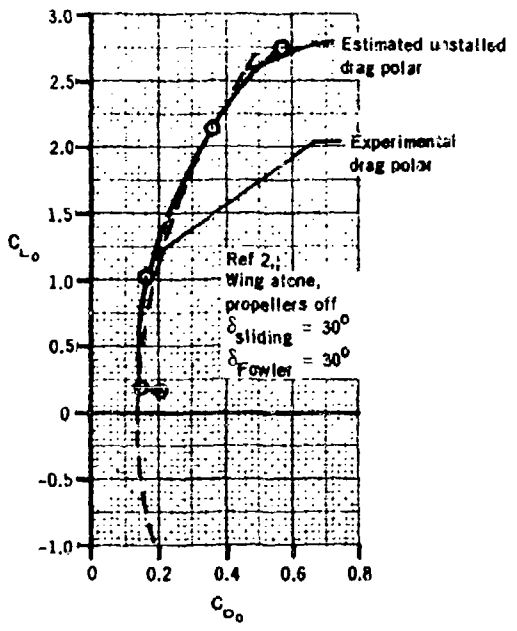

$C_{D_f} = 0.14$ (minimum experimental power-off drag coefficient)

The drag polar that would exist if the wing were unstalled in the power-off condition is estimated by

$$C_{D_o} = C_{D_f} + \frac{C_{L_o}^2}{\pi Ae} \quad \text{(equation 9.2.3-b)}$$

α deg	C_{L_o} Problem 2 9.2.1	$\frac{C_{L_o}^2}{\pi Ae}$	C_{D_o}
-40	-0.8990	0.0395	0.1795
-35	0	0	0.1400
-20	2.6693	0.3483	0.4883
-10	4.3587	0.9288	1.0688
0	5.9161	1.7111	1.8511
10	7.2930	2.6002	2.7402
20	8.4492	3.4900	3.6301

Solution:

$$C_{F_x}" = -C_{D_o}(1 - T_c") + \frac{F}{T} T_c" \frac{KS_p}{S} \cos(\theta + \alpha) - 1.6 \frac{F}{T} T_c" \frac{KS_p}{S} \left[1 - \cos(\theta + \alpha)\right] (1 - T_c")^{1/2}$$

(equation 9.2.3-a)

$$= -C_{D_o}(1 - 0.9) + (0.90)(0.90) \frac{(4)(3.14)}{(10.96)} \cos(\theta + \alpha) - 1.6\,(0.90)(0.90) \frac{(4)(3.14)}{(10.96)} \left[1 - \cos(\theta + \alpha)\right] (1 - 0.9)^{1/2}$$

$$= -0.10\, C_{D_o} + 0.9282 \cos(\theta + \alpha) - 0.4697 \left[1 - \cos(\theta + \alpha)\right]$$

①	②	③	④	⑤	⑥	⑦	⑧
α deg	C_{D_o}	$(\theta + \alpha)$ deg	$\cos(\theta + \alpha)$ $\cos$ ③	0.10 ②	0.9282 ④	0.4697 $\lvert 1 -$ ④ $\rvert$	C_{F_x}'' -⑤ + ⑥ - ⑦
-40	0.1795	9.14	0.9873	0.0180	0.9164	0.0060	0.8924
-35	0.1400	14.14	0.9697	0.0140	0.9001	0.0142	0.8719
-20	0.4883	29.14	0.8734	0.0488	0.8107	0.0595	0.7024
-10	1.0688	39.14	0.7756	0.1069	0.7199	0.1054	0.5076
0	1.8511	49.14	0.6542	0.1851	0.6072	0.1624	0.2597
10	2.7402	59.14	0.5129	0.2740	0.4761	0.2288	-0.0267
20	3.6301	69.14	0.3561	0.3630	0.3305	0.3024	-0.3349

These results are compared with experimental data in table 9.2.3-A

3. Tilt-Wing Configuration

Given: The propeller-wing configuration of reference 5. This is the same configuration as that of sample problem 3 of Section 9.2.1. The characteristics are repeated below.

Wing Characteristics

$S = 11.0$ sq ft $\quad A = 4.89 \quad i_w = 5^\circ$ NACA 4415 airfoil section

$c = 1.5$ ft

Propeller Characteristics

$K = 4$ (2 propellers per semispan, overlapped) $\quad D = 2.0$ ft

$S_p = 3.14$ sq ft

Additional Characteristics

$T_c'' = 0.69 \quad \delta_e = 12.4^\circ$

Compute:

Step 1. Determine the slipstream turning angle θ.

$\theta = 11.0^\circ$ (sample problem 3, Section 9.2.1)

Step 2. Determine the thrust-recovery factor $\frac{F}{T}$.

$\frac{F}{T} = 1.0$ (sample problem 3, Section 9.2.1)

Step 3. Determine the power-off drag coefficient C_{D_o}

The power-off drag coefficient is obtained using the experimental zero-lift drag coefficient, and the power-off lift coefficient at angle of attack determined in sample problem 3 of Section 9.2.1.

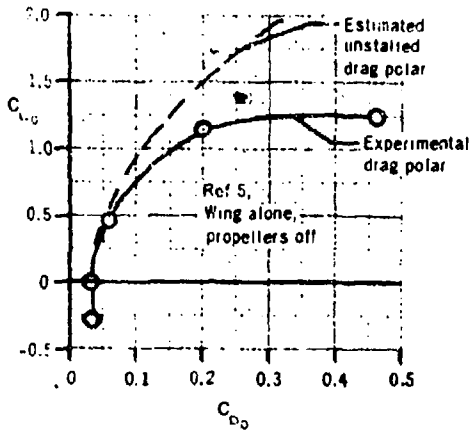

$C_{D_f} = 0.035$

The drag polar that would exist if the wing were unstalled in the power-off condition is estimated by

$$C_{D_o} = C_{D_f} + \frac{C_{L_o}^2}{\pi Ae} \quad \text{(equation 9.2.3-b)}$$

α deg	C_{L_o} Problem 3 9.2.1	$\frac{C_{L_o}^2}{\pi Ae}$	C_{D_o}
-10	-0.2624	0.0053	0.0403
-6.5	0	0	0.0350
0	0.4865	0.0181	0.0531
10	1.2205	0.1141	0.1491
20	1.9175	0.2816	0.3166

Solution:

$$C_{F_x}'' = -C_{D_o}(1 - T_c'') + \frac{F}{T} T_c'' \frac{KS_p}{S} \cos(\theta + \alpha) - 1.6 \frac{F}{T} T_c'' \frac{KS_p}{S} \left[1 - \cos(\theta + \alpha)\right] (1 - T_c'')^{1/2}$$

(equation 9.2.3-a)

$$= -C_{D_o}(1 - 0.69) + (1.0)(0.69) \frac{(4)(3.14)}{(11.0)} \cos(\theta + \alpha) - (1.6)(1.0)(0.69) \frac{(4)(3.14)}{(11.0)} \left[1 - \cos(\theta + \alpha)\right] (1 - 0.69)^{1/2}$$

$$= -0.31\, C_{D_o} + 0.7879 \cos(\theta + \alpha) - 0.7018 \left[1 - \cos(\theta + \alpha)\right]$$

① α deg	② C_{D_o}	③ $(\theta + \alpha)$ deg	④ $\cos(\theta + \alpha)$ cos ③	⑤ 0.31 ②	⑥ 0.7879 ④	⑦ 0.7018 [1 - ④]	⑧ C_{F_x}'' - ⑤ + ⑥ - ⑦
-10	0.0403	1.0	0.9998	0.0125	0.7877	0.0001	0.7751
-6.5	0.0350	4.5	0.9969	0.0109	0.7855	0.0022	0.7724
0	0.0531	11.0	0.9816	0.0165	0.7734	0.0129	0.7440
10	0.1491	21.0	0.9336	0.0462	0.7356	0.0466	0.6428
20	0.3166	31.0	0.8572	0.0981	0.6754	0.1002	0.4771

These results are compared with experimental data in table 9.2.3-A.

REFERENCES

1. Kuhn, R. E.: Semiempirical Procedure for Estimating Lift and Drag Characteristics of Propeller-Wing-Flap Configurations for Vertical- and Short-Take-off-and-Landing Airplanes. NASA Memo 1-16-59L, 1959. (U)

2. Kuhn, R. E., and Hayes, W. C., Jr.: Wind-Tunnel Investigation of Longitudinal Aerodynamic Characteristics of Three Propeller-Driven VTOL Configurations in the Transition Speed Range, Including Effects of Ground Proximity. NASA TN D-55, 1960. (U)

3. Kuhn, R. E., and Draper, J. W.: Investigation of Effectiveness of Large-Chord Slotted Flaps in Deflecting Propeller Slipstreams Downward for Vertical Take-Off and Low-Speed Flight. NACA TN 3364, 1955. (U)

4. Kuhn, R. E., and Draper, J. W.: An Investigation of a Wing-Propeller Configuration Employing Large-Chord Plain Flaps and Large Diameter Propellers for Low-Speed Flight and Vertical Take-Off. NACA TN 3307, 1954. (U)

5. Kuhn, R. E., and Hayes, W. C., Jr.: Wind-Tunnel Investigation of Effect of Propeller Slipstreams on Aerodynamic Characteristics of a Wing Equipped with a 50-Percent-Chord Sliding Flap and a 30-Percent-Chord Slotted Flap. NACA TN 3918, 1957. (U)

TABLE 9.2.3-A

DATA SUMMARY AND SUBSTANTIATION

PROPELLER-WING-FLAP DRAG COEFFICIENT

Ref	Configuration Characteristics	T_c"	α deg	C_{D_o}*	C_{F_x}" Calc	C_{F_x}" Test	ΔC_{F_x}" (Calc-Test)
2	Deflected-slipstream configuration (See reference 2, table 9.2.1-A)	0.6	-20	0.1900	0.552	0.43	0.12
			-10	0.2917	0.448	0.37	0.08
			0	0.5849	0.229	0.19	0.04
			10	1.0336	-0.086	-0.19	0.10
		0.9	-20	0.1900	0.944	0.84	0.10
			-10	0.2917	0.862	0.79	0.07
			0	0.5849	0.720	0.65	0.07
			10	1.0336	0.522	0.43	0.09
			20	1.5846	0.280	0.11	0.17
		0.95	-20	0.1900	1.009	0.92	0.09
			-10	0.2917	0.936	0.87	0.07
			0	0.5849	0.813	0.75	0.06
			10	1.0336	0.645	0.57	0.07
			20	1.5846	0.440	0.32	0.12
2	Deflected-slipstream configuration (See reference 2, table 9.2.1-A)	0.6	-40	0.1795	0.545	0.27	0.27
			-20	0.4883	0.323	0.18	0.14
			-10	1.0688	-0.012	-0.05	0.04
		0.9	-40	0.1795	0.892	0.72	0.17
			-20	0.4883	0.702	0.68	0.02
			-10	1.0688	0.508	0.53	-0.02
			0	1.8511	0.260	0.30	-0.04
			10	2.7402	-0.027	0	-0.03
			20	3.6301	-0.335	-0.20	0.14
		0.95	-40	0.1795	0.968	0.83	0.14
			-20	0.4883	0.847	0.78	0.07
			-10	1.0688	0.709	0.65	0.06
			0	1.8511	0.526	0.45	0.08
			10	2.7402	0.309	0.18	0.13
			20	3.6301	0.068	-0.06	0.13
			30	4.4117	-0.187	-0.21	0.02

*Estimated unstalled power-off drag coefficient

TABLE 9.2.3-A (CONTD)

Ref	Configuration Characteristics	T_c''	α deg	C_{D_o}*	C_{F_x}'' Calc	C_{F_x}'' Test	$\Delta C_{F_x}''$ (Calc Test)
3	Deflected-slipstream configuration (See reference 3, table 9.2.1-A)	0.5	-20	0.1521	0.212	0.17	0.04
			-10	0.1835	0.171	0.15	0.02
			0	0.3151	0.062	0.045	0.02
			10	0.5312	-0.106	-0.145	0.04
			20	0.8056	-0.318	-0.37	0.05
			30	1.1050	-0.555	-0.49	-0.06
		0.71	-20	0.1521	0.366	0.285	0.08
			-10	0.1835	0.326	0.275	0.05
			0	0.3151	0.234	0.19	0.04
			10	0.5312	0.097	0.025	0.07
			20	0.8056	-0.075	-0.15	0.07
			30	1.1050	-0.271	-0.25	-0.02
		0.91	-20	0.1521	0.513	0.425	0.09
			-10	0.1835	0.479	0.40	0.08
			0	0.3151	0.413	0.345	0.07
			10	0.5312	0.318	0.23	0.09
			20	0.8051	0.199	0.08	0.12
			30	1.1050	0.061	-0.02	0.08
4	Deflected-slipstream configuration (See reference 4, table 9.2.1-A)	0.5	-20	0.1652	0.4571	0.46	0
			-10	0.2040	0.3638	0.36	0
			0	0.2611	0.2272	0.23	0
			10	0.3308	0.0532	0.08	-0.03
			20	0.4035	-0.1487	-0.21	0.06
		0.71	-20	0.1652	0.7261	0.72	0.01
			-10	0.2040	0.6232	0.65	-0.03
			0	0.2611	0.4726	0.50	-0.03
			10	0.3308	0.2799	0.275	0
			20	0.4035	0.0534	0.18	-0.13
		0.91	-20	0.1652	0.9910	0.97	0.02
			-10	0.2040	0.8941	0.885	0.01
			0	0.2611	0.7524	0.76	-0.01
			10	0.3308	0.5703	0.60	-0.03
			20	0.4035	0.3545	0.38	-0.03

*Estimated unstalled power-off drag coefficient

TABLE 9.2.1-A (CONTD)

Ref	Configuration Characteristics	T_c"	α deg	C_{D_o}*	C_{F_x}" Calc	C_{F_x}" Test	ΔC_{F_x}" (Calc-Test)
4	Tilt-wing configuration (See reference 4, table 9.2.1-A)	0.5	-10	0.04181	0.572	0.57	0
			0	0.01	0.608	0.62	-0.01
			10	0.04181	0.572	0.58	-0.01
			20	0.1335	0.467	0.41	0.06
			30	0.2739	0.301	0.1	0.20
		0.71	-10	0.04181	0.833	0.80	0.03
			0	0.01	0.867	0.82	0.05
			20	0.1335	0.734	0.66	0.07
			30	0.2739	0.574	0.42	0.15
			40	0.4461	0.362	0.14	0.22
		0.91	-10	0.04181	1.086	1.08	0.01
			0	0.01	1.114	1.08	0.03
			10	0.04181	1.086	1.05	0.04
			20	0.1335	1.004	0.94	0.06
			30	0.2739	0.869	0.76	0.11
			40	0.4461	0.689	0.55	0.14
			50	0.6294	0.469	0.32	0.15
2	Tilt-wing configuration (See reference 2, Table 9.2.1-A)	0.6	-20	0.0794	0.6145	-	-
			-10	0.0285	0.6727	0.56	0.11
			0	0.0238	0.6706	0.57	0.10
			10	0.0658	0.6080	0.46	0.15
			20	0.1494	0.4885	0.21	0.28
			30	0.2647	0.3183	-0.11	0.43
		0.9	-20	0.0794	0.9770	0.76	0.22
			-10	0.0285	1.0247	0.86	0.16
			0	0.0238	1.0206	0.92	0.10
			10	0.0658	0.9650	0.86	0.11
			20	0.1494	0.8601	0.71	0.15
			30	0.2647	0.7092	0.50	0.21
			40	0.3976	0.5185	0.26	0.26
		0.95	-20	0.0794	1.0405	-	-
			-10	0.0285	1.0836	-	-
			0	0.0238	1.0795	0.93	0.15
			10	0.0658	1.0285	0.88	0.15
			20	0.1494	0.9324	0.79	0.14
			30	0.2647	0.7940	0.65	0.14
			40	0.3976	0.6186	0.46	0.16

*Estimated unstalled power-off drag coefficient

TABLE 9.2.3-A (CONTD)

Ref	Configuration Characteristics	T_c"	α deg	C_{D_o}*	C_{F_x}" Calc	C_{F_x}" Test	ΔC_{F_x}" (Calc-Test)
5	Tilt-wing configuration (See reference 5, table 9.2.1-A)	0.49	-10	0.0403	0.539	0.54	0
			0	0.0531	0.510	0.52	-0.01
			10	0.1491	0.402	0.40	0
			20	0.3166	0.225	0.16	0.06
		0.69	-10	0.0403	0.775	0.75	0.02
			0	0.0531	0.744	0.71	0.03
			10	0.1491	0.643	0.64	0
			20	0.3166	0.477	0.43	0.05

*Estimated unstalled power-off drag coefficient Av. Error = $\frac{\sum \Delta C_{F_x}"}{n}$ = 0.082

9.3 DUCTED-PROPELLER CHARACTERISTICS

The estimation of ducted-propeller aerodynamics can be approached in three phases, each representing a VTOL aircraft flight regime. These are static operation (hovering), axial flow (approximately zero duct angle of attack as in cruise or vertical climb), and nonaxial flow (high duct angles of attack as in transition). The most important and most difficult problem is the prediction of the aerodynamic characteristics in the presence of strong power effects at high angles of attack and low speeds during transition.

The methods presented in this section are for predicting forces and moments on isolated ducted propellers as functions of power and angle of attack. The static and axial-flow regimes are trivial, and no attempt is made to deal with the characteristics in these regimes. It is virtually impossible to present quantitative information on the effects of the various geometric and aerodynamic variables involved because of the complexity of the problem and the general lack of appropriate data. However, a qualitative discussion of the ducted-propeller problem is given with primary emphasis on the nonaxial flow regime.

A ducted propeller consists of a propeller enclosed in an axially symmetric duct as shown in figure 9.3-12. The purpose of the duct is to increase the thrust-generating capability of the entire unit in the static and low subsonic speed regimes for a given propeller diameter and power input. If the chordwise cross section of the duct is reasonably faired, the unit can function as a ring wing as well as a thrusting propeller.

Differing from flying platforms or "flying jeeps," ducted-propeller units are typically mounted on the tips of low-aspect-ratio wings with the capability of rotating from 0 to 90 degrees. Since much of the ducted-propeller work has been the application to particular vehicle designs, the emphasis has been on propeller design and development of auxiliary devices to augment thrust and to provide control moments. This work is thus of little interest here because the lift and pitching moments are not affected significantly. The development of various auxiliary devices is reported in reference 84, and additional information pertaining to experimental investigations is given in table 9.3-A.

The duct complicates the problem of predicting the aerodynamic characteristics because of the strong mutual interference effects and the increased number of geometric variables. A preliminary list of geometric variables includes duct aspect ratio, duct section parameters (thickness ratio, camber, leading-edge radius, etc.), diffuser angle, propeller activity factor, propeller pitch setting, propeller solidity, propeller section parameters (twist, camber, taper, thickness, etc.), blade tip clearance, center-body location relative to the duct, center-body shape, ratio of hub diameter to propeller diameter, and propeller location within the duct. Aside from this seemingly endless list of geometric variables, there are the aerodynamic variables of angle of attack, Reynolds number, advance ratio, and Mach number.

The ducted propeller in the nonaxial flow regime has received very little theoretical attention in comparison to that given to the static and axial-flow regimes. The theoretical work available in the literature is generally classified under one of three general categories of analysis: (1) method of singularities, (2) momentum considerations, and (3) methods which seek to avoid the

mathematical complexities of the method of singularities and yet yield more detailed results than simple momentum theory. The method of singularities is relatively complex, and almost all solutions in the literature are restricted to special classes of duct profiles. The method involves replacing the annular airfoil by a vortex distribution on its camber line, determining the axial and radial velocity components induced by this vortex distribution, and relating these velocity components to the shape of the airfoil by satisfying the potential flow streamline condition. Two approaches to the problem can be defined: (1) given the vortex distribution, find the corresponding shape and determine its aerodynamic characteristics, and (2) given the shape, find the corresponding vortex distribution, from which the aerodynamic characteristics can be determined. In either case, an iteration process is required if other than a first approximation is desired. The effects of geometric parameters and propellers are induced by the use of additional distributed singularities. The theoretical basis on which the method of singularities rests is developed and discussed in reference 57.

An approximate theory for nonaxial flow, based on the method of singularities, is developed by Burggraf in reference 1. Burggraf represents the ducted propeller as a short, thin, cylindrical duct with a uniformly loaded actuator disk across its exit plane. Each section of the duct is treated as a thin two-dimensional airfoil, and solutions are obtained by means of conformal transformations. An analysis with less restricted geometry has been made by Kriebel and summarized in reference 55. Kriebel treats the duct as a thin cylinder (but not necessarily short) and represents the propeller as a uniformly loaded actuator disk located at the duct inlet. The vorticity distribution bound to the duct and trailing from it is found in terms of a Fourier series by the method of singularities. The results are obtained by solving for the coefficients of the Fourier series representing the duct-bound vorticity distribution. Both Burggraf and Kriebel include the nonaxial flow case by assuming the vorticity shed by both the actuator disk and the duct to be concentrated on a circular cylinder which extends axially downstream, even at angles of attack. Because of this assumption, the exit velocity must be large relative to the cross-flow component of the free-stream velocity, i.e.,

$$V_e >> V_\infty \sin \alpha_D ,$$

a restriction which requires high actuator disk loadings at high angles of attack.

Momentum theory in itself is not sufficient to predict the performance of a ducted propeller, since the relationships between thrust and power are in terms of the area and velocity of the final wake. At the present time, there appears to be no available way of relating wake characteristics to duct design without using the method of singularities. To avoid this difficulty some assumption must be made which relates the duct exit characteristics to the final wake. The most common assumption, forming what is generally termed "simple momentum theory," is that the final wake area is equal to the duct exit area. This implies that the exit velocity profile is uniform and the static pressure at the exit is equal to that at infinity. The nonaxial flow case is generally based on the additional assumption that the internal mass flow exits parallel to the duct axis, an assumption which is valid only for low duct aspect ratios and high exit-velocity ratios. Examples of simple momentum theory as applied to nonaxial flow are given in references 85 and 58.

Moser and Livingston, in reference 70, develop semiempirical expressions for the aerodynamic characteristics of ducted propellers in nonaxial flow by adapting blade element theory and modifications to it to take some account of duct influence. This method is shown to be reasonable for analyzing ducted-propeller characteristics where the deflection of the airstream is relatively small.

Minassian, in reference 65, treats the ducted propeller in nonaxial flow as a ring wing. He assumes that the propeller causes the internal pressures on the duct to cancel one another and then applies two-dimensional airfoil characteristics to predict normal-force variation with angle of attack. This work is restricted to rough approximations at low angles of attack and high advance ratios.

Wind-tunnel tests cover a wide variety of ducted propellers in the nonaxial flow regime; however, the data are often of questionable accuracy because of wall-interference effects and data accuracy limitations at the tunnel speeds required to simulate low-speed flight. Testing small models in an effort to avoid wall-interference effects has not proved satisfactory because of the errors associated with low Reynolds numbers and balance-system sensitivity. The uncertainties of wind-tunnel test data, coupled with the geometric and aerodynamic variables involved, preclude generalization and verification of any valid prediction methods. Although a large number of experimental investigations have been conducted, it is still difficult to draw any general conclusions pertaining to the effects of geometric or aerodynamic variations. However, the results that are available can serve at least to give a practical orientation to some aspects of the ducted propeller problem. Accordingly, a qualitative discussion of the effects of a number of the important variables is given.

Duct Leading-Edge Radius

The duct leading-edge radius is critical in that it must be large enough to prevent inlet flow separation at high power and/or angle of attack and yet not so large as to produce an excessive drag penalty in cruise flight. Leading-edge lip stall reduces lift and pitching moment and increases the power required.

Diffuser

A properly designed diffuser increases the diameter of the fully developed stream tube, thereby increasing the static thrust and efficiency of a given ducted propeller. Tests of two unpowered ducts (reference 36) in nonaxial flow indicate that diffusion of the duct afterbody results in an appreciable increase in lift-curve slope and maximum-lift stall angle of attack. Reference 36 also indicates that diffusion causes the center of pressure to move forward. These effects can be attributed to the increased internal mass flow through the duct resulting from increased positive circulation.

Although substantial diffusion may be beneficial in the static flow regime, it can lead to internal flow separation during essentially axial flow with an attendant drag increase.

Exit Stators

In addition to providing a structural tie between the center body and the duct, exit stators, because of twist and camber, also serve as guide vanes to eliminate the slipstream rotation resulting from the high thrust loading of the ducted propeller. This flow straightening converts the rotational kinetic energy to pressure and increased axial velocity. If flow straightening is not provided, the propeller efficiency is severely reduced.

Propeller Twist

The effect of propeller twist on static performance has been a source of controversy. The results reported in references 12 and 64 indicate that a relatively flat, untwisted blade is best for static and low-speed operation, because of the better match with the theoretical ring vortex circulation about the duct, resulting in gains in static efficiency. However, these reports make no statement regarding blade pitch optimization, and it is difficult to distinguish between the effects of blade twist and those of blade pitch. On the other hand, the results reported in references 19 and 56, which did use blade pitch optimization, show no such corresponding improvement and indicate that blade twist is relatively unimportant. Moser and Livingston, in reference 70, also indicate that the effects of blade twist are relatively unimportant except at the highest collective pitch tested.

Propeller Tip Clearance

Ducted-propeller efficiency increases with decreasing tip clearance. Excessive tip clearance will aggravate a condition of flow reversal that occurs on the duct in the propeller plane even for small tip clearances. At moderate to high angles of attack, the flow reversal condition on the lower inside surface of the duct can cause premature inlet lip separation, resulting in reductions in both lift and pitching moment accompanied by increased power requirements.

Propeller Position

The effect of propeller position on ducted-propeller forces and moments in nonaxial flow is relatively undefined. Reference 19 indicates that at a given thrust level, moving the propeller forward reduces the lift and pitching-moment coefficients. However, data of reference 57 indicate that forward movement of the propeller plane increases the radial variation in duct velocity distribution (greater velocities near the duct), which would be expected to increase the pitching moments in nonaxial flow.

It is stated in reference 55 that analytical results indicate that in axial flow the pressure jump acting upon the internal duct surface downstream of the propeller plane is maximum when the propeller plane is located at the minimum duct internal cross-sectional area. For this location of the propeller in axial flow, the disk area and disk thrust are minimum for a given disk loading, and the duct-to-disk thrust ratio and the propulsive efficiency are maximum.

Exit-Velocity Ratio and Angle of Attack

The exit-velocity ratio and angle of attack determine the basic flow pattern for a given ducted propeller. As the duct angle of attack is increased beyond the unpowered stall angle, the exit-velocity ratio must be increased to prevent stalling of the duct lower leading edge. Because of the predominance of power effects as duct angle of attack is increased, the separation that occurs on the top aft portion of the duct usually has a minor effect on force and moment data.

Reynolds Number

Reynolds-number effects are of extreme importance in ducted-propeller design because of the low airspeed of operation and the short streamwise lengths of ducted-propeller elements. The separation that occurs on the lower inside surface of the duct leading edge at high angles of attack and low exit-velocity ratios is a low Reynolds-number characteristic. At low Reynolds number, laminar flow is followed by separation rather than by attached turbulent flow, resulting in substantial losses in both lift and pitching moment at a given power setting.

A comprehensive tabulation of pertinent ducted-propeller experimental data in the nonaxial flow regime is presented as table 9.3-A. This table provides a brief outline of the test data contained in each report and indicates the basic parametric changes. Similar tables pertaining to the static- and axial-flow regimes are given in reference 84. It should be recognized that the ducted propeller problem cannot be satisfactorily handled by treating isolated effects with all other variables fixed. The effect of a geometric or aerodynamic variation on the characteristics of a ducted propeller of different design will very likely be quite different from that indicated by the test results of available reports.

A general notation list is included in this section for all ducted propeller sections. Figures 9.3-12 and 9.3-13 illustrate the geometric data required by the methods of these sections. Figure 9.3-13 also illustrates the positive sense of forces, moments, and angles.

NOTATION

A_D duct aspect ratio, $\frac{d_e}{c}$

c duct chord, ft

C_{D_e} external duct drag coefficient, $\frac{-F_{x_e}}{q_\infty S_D}$

C_{F_x} duct negative-drag coefficient, $\frac{F_x}{q_\infty S_D}$

$C_{F_{x_e}}$ external duct negative-drag coefficient, $\frac{F_{x_e}}{q_\infty S_D}$

C_L duct lift coefficient, $\frac{L}{q_\infty S_D}$

C_m duct pitching-moment coefficient, $\frac{M}{q_\infty S_D \, c}$

d_{CB} duct center-body diameter at the exit plane, ft

d_e duct exit diameter, ft

d_p propeller diameter, ft

F_x duct negative-drag force, lb $\left(F_x = C_{F_x} q_\infty S_D\right)$

J advance ratio, $\frac{V_\infty}{nd_p}$

L duct lift force, lb ($L = C_L \, q_\infty \, S_D$)

M duct pitching moment, ft-lb ($M = C_m \, q_\infty \, S_D \, c$)

m_i duct internal mass flow, $\frac{\text{slugs}}{\text{sec}}$

N ducted-propeller normal force, lb

n propeller rotational speed, rps

q_∞ free-stream dynamic pressure, $\frac{\text{lb}}{\text{sq ft}}$

S_D duct planform area, sq ft ($S_D = d_e \, c$)

T ducted-propeller thrust, lb

T_i total internal thrust, lb

T_{net} total net thrust, lb ($T_{net} = T_i - C_{D_e} \, q_\infty \, S_D$)

V_e duct exit velocity, $\frac{ft}{sec}$

V_i velocity increment of internal mass flow due to power, $\frac{ft}{sec}$

V_{i_o} internal mass-flow velocity with power off, $\frac{ft}{sec}$

V_∞ free-stream velocity, $\frac{ft}{sec}$

$\frac{V_e}{V_\infty}$ exit-velocity ratio

$\bar{x}$ chordwise distance from the reference center to the unstalled duct center of pressure, positive for the center of pressure ahead of the reference center, ft

x_{cp} chordwise distance from the duct leading edge to the center of pressure of the unstalled duct, positive aft of the duct leading edge, ft

x_m chordwise distance from the duct leading edge to the reference center, positive aft of the duct leading edge, ft

α_D angle of attack between duct axis and free-stream direction, deg

δ_{i_f} net turning angle of the internal flow including power effects, deg

δ_{i_o} turning angle of the internal flow with power off, deg

REFERENCES

1. Anon.: Aerial Jeep Phase I, Final Report Vol. I and II. Aerophysics Development Corp. Report 520-3/R24/46, 1957. (U)

2. Anon.: Comparative Performance Charts for Ducted Propellers. Hiller Aircraft Corp. Report ARD-257, 1960. (U)

3. Anon.: Full Scale Wind Tunnel Test Report. G. E. Report 153, 1966. (U)

4. Anon.: Theoretical Investigation and Examination by Measuring Tests of the Thrust Control by Rudders Uniformly Tilted at the Outlet of a Duct. Bureau Technique Zborowski, 1959. (U)

5. Anon.: Wind-Tunnel-Test Report, Lift-Fan Powered Scale Model. G. E. Report 137, 1963. (U)

6. Anon.: XV-5A Lift-Fan Flight-Research Aircraft Program; Estimated Dynamic Stability Characteristics. G. E. Report 151, 1964. (U)

7. Beilman, J. L.: X-22A Variable Stability System. Presented at First National V/STOL Symposium, Nov. 1965. (U)

8. Black, D. M., Wainauski, H. S., and Rohrbach, C.: Shrouded Propellers – A Comprehensive Performance Study. AIAA Paper 68-994, 1968. (U)

9. Black, D. M. and Wainauski, H. S.: Shrouded-Propeller Test Program Data Analysis. Hamilton Standard Report HSER 4348, Vol. 1, 1967. (U)

10. Cahn, M. S.: The Design and Performance of Shrouded Propellers. SAE Preprint 587C, 1962. (U)

11. Clancy, G., and Cowgill, R.: Truck Test Stand Tests of Hiller Airborne Personnel Platform. Phase II. Hiller Aircraft Corporation, Eng. Report 680.2, 1955. (U)

12. Colton, R. F.: Preliminary Engineering Report on the .4 Scale Aerodyne Model Static Tests. Collins Aeronautical Research Laboratory, Report CER-924, 1959. (U)

13. Curtiss, H. C., Jr., and Struble, R. W.: Downwash Tests of the Dual-Tandem Ducted-Propeller VTOL Research Aircraft Configurations to Evaluate Engine Inlets, Protection Devices and Study Aerodynamic Interference. Kellett Aircraft Corp. Report 179T80-12, 1965. (U)

14. Curtiss, H. C., Jr.: Dynamic Stability of V/STOL Aircraft at Low Speeds. AIAA Paper 69-194, 1969. (U)

15. Davenport, E. E., and Spreemann, K. P.: Transition Characteristics of a VTOL Aircraft Powered by Four Ducted-Tandem Propellers. NASA TN D-2254, 1964. (U)

16. Duvivier, J. F., and McCallum, R. B.: Investigation of Tilting-Duct and Fan-Wing in Transition Flight. TREC TR-61-19, 1960. (U)

17. Finnestad, R. L., Welter, W. L., Ferrell, K. R., et al: Engineering Flight Research Evaluation of the XV-5A Lift-Fan Aircraft – Part I, Stability and Control, Final Report. USATREC Project 4-5-1220-01, Part 1, 1966. (U)

18. Fletcher, H. S.: Experimental Investigation of Lift, Drag, and Pitching Moment of Five Annular Airfoils. NACA TN 4117, 1957. (U)

19. Gill, W. J.: Wind-Tunnel Tests of Several Ducted Propellers in Non-Axial Flow. Hiller Aircraft Corp. Report ARD-224, 1959. (U)

20. Gill, W. J.: Airborne Personnel Platform. Hiller Aircraft Corp. Report ARD-236, 1959. (U)

21. Giulianetti, D. J., Biggers, J. C., and Maki, R. L.: Longitudinal Aerodynamic Characteristics in Ground Effect of a Large-Scale, V/STOL Model with Four Tilting Ducted Fans Arranged in a Dual Tandem Configuration. NASA TN D-4218, 1967. (U)

22. Giulianetti, D. J., Biggers, J. C., et al: Longitudinal and Lateral-Directional Aerodynamic Characteristics of a Large-Scale, V/STOL Model with Four Tilting Ducted Fans Arranged in a Dual Tandem Configuration. NASA TN D-3490, 1966. (U)

23. Goodson, K. W., and Grunwald, K. J.: Aerodynamic Characteristics of a Powered Semispan Tilting Shrouded Propeller VTOL Model in Hovering and Transition Flight. NASA TN D-981, 1962. (U)

24. Gorton, J. V., and Hamel, L. A.: Aerial Jeep Vehicle Project – Phase I, Final Report. Chrysler Corporation, Contract DA44-177-TC-448, 1958. (U)

25. Greenberg, M. D., and Ordway, D. E.: The Ducted Propeller in Static and Low-Speed Flight. Therm Advanced Research TAR-TR-6407, 1964. (U)

26. Greenberg, M. D., Ordway, D. E., and Lo, C. F.: A Three-Dimensional Theory for the Ducted Propeller at Angle of Attack. Therm Advanced Research TAR-TR-6509, 1965. (U)

27. Grose, R. M.: Wind-Tunnel Tests of Shrouded Propellers at Mach Numbers from 0 to .6. WADC TR 58-604, 1958. (U)

28. Grunwald, K. J., and Goodson, K. W.: Aerodynamic Loads on an Isolated Shrouded-Propeller Configuration for Angles of Attack from -10° to 110°. NASA TN D-995, 1962. (U)

29. Grunwald, K. J., and Goodson, K. W.: Division of Aerodynamic Loads on a Semispan Tilting-Ducted-Propeller Model in Hovering and Transition Flight. NASA TN D-1257, 1962. (U)

30. Halley, D. H.: The Development of a Simplified Analytical Approach for Evaluation of the Dynamic Stability Characteristics of a Ducted-Propeller VTOL Aircraft in Transition. Princeton Univ. Aerospace and Mech. Sci. Report 850, 1968. (U)

31. Ham, N. D., and Moser, H. H.: Preliminary Investigation of a Ducted Fan in Lifting Forward Flight. IAS Preprint 827, 1958. (U)

32. Heaby, A., and Sherman, E. W., Jr.: Wind-Tunnel-Test Data Report for the Full-Scale Powered-Duct Model. Bell Aerosystems R-2127-921007, 1965. (U)

33. Hoehne, V. O.: Investigation of Shrouded Propellers, Progress Report for 1 December 1957 through 31 December 1957. University of Wichita, Dept. of Eng. Research Report 305, 1958. (U)

34. Hoehne, V. O., and Monical, R. E.: A Method of Design of Shrouded Propellers. University of Wichita, Dept. of Eng. Research Report 213-8, 1959. (U)

35. Hoehne, V. O.: Progress Report for 1 July 1956 through 31 October 1957 on Wind-Tunnel Investigation of Shrouded Propellers. University of Wichita, Dept. of Eng. Research Report 300, 1957. (U)

36. Hoehne, V. O.: Shrouded Propeller Investigations: Aerodynamic Characteristics of a Shroud with Centerbody. University of Wichita, Dept. of Eng. Research Report No. 337, 1959. (U)

37. Hoehne, V. O.: Shrouded Propeller Investigations: Shroud and Centerbody Pressure Distributions of a Shrouded Propeller with a 17-Bladed Rotor, Inlet and Exit Stators and Long-Chord Shroud. University of Wichita, Dept. of Eng. Research Report No. 213-9, 1959. (U)

38. Hoehne, V. O.: Shrouded Propeller Investigations: Shroud and Centerbody Pressure Distributions of a Shrouded Propeller with a 10-Bladed Rotor, Exit Stators and Long-Chord Shroud. University of Wichita, Dept. of Eng. Research Report No. 213-10, 1960. (U)

39. Hoehne, V. O., and Wattson, R. K., Jr.: Shrouded Propeller Investigations: Static Performance of Two Highly-Loaded Shrouded Propellers as Measured in the Walter H. Beech Memorial Wind Tunnel. University of Wichita, Dept. of Eng. Research Report No. 213-4, 1958. (U)

40. Hoehne, V. O.: Shrouded Propeller Investigations: Wind-Tunnel Tests of a Shrouded Propeller with a 17-Bladed Rotor, Inlet and Exit Stators, and Long-Chord Shroud with Modified Static Inlet and No Diffusion. University of Wichita, Dept. of Eng. Research Report No. 213-3, 1958. (U)

41. Hoehne, V. O., and Wattson, R. K., Jr.: Shrouded Propeller Investigations: Wind-Tunnel Tests of a Shrouded Propeller with a 17-Bladed Rotor, Inlet and Exit Stators, and Long-Chord Shroud with Static Inlet and No Diffusion. University of Wichita, Dept. of Eng. Research Report No. 213-2, 1958. (U)

42. Hoehne, V. O., and Wattson, R. K., Jr.: Shrouded Propeller Investigations: Wind-Tunnel Tests of a Shrouded Propeller with a 17-Bladed Rotor, Inlet and Exit Stators, and Long Shroud with High-Speed Inlet and No Exit Diffusion. University of Wichita, Dept. of Eng. Research, Report No. 213-1, 1958. (U)

43. Hoehne, V. O.: Shrouded Propeller Investigations: Wind-Tunnel Tests of a Shrouded Propeller with a 10-Bladed Propeller, Exit Stators, and Long-Chord Shroud with High-Speed Inlet and No Exit Diffusion. University of Wichita, Dept. of Eng. Research Report No. 213-5, 1959. (U)

44. Hoehne, V. O.: Shrouded Propeller Investigations: Wind-Tunnel Tests of a Shrouded Propeller with a 10-Bladed Propeller, Exit Stators, and Long-Chord Shroud with a Modified Static Inlet and No Diffusion. University of Wichita, Dept. of Eng. Research Report No. 213-7, 1959. (U)

45. Hoehne, V. O.: Shrouded Propeller Investigations: Wind-Tunnel Tests of a Shrouded Propeller with a 10-Bladed Propeller, Exit Stators, and Long-Chord Shroud with Static Inlet and No Diffusion. University of Wichita, Dept. of Eng. Research Report No. 213-6, 1959. (U)

46. Hoehne, V. O.: Shrouded Propeller Investigations: Wind Tunnel Tests of a 2-Bladed Shrouded-Propeller Model. University of Wichita, Dept. of Eng. Research Report No. 213-11, 1960. (U)

47. Hough, G. R., and Kaskel, A. L.: A Comparison of Ducted Propeller Theory with Bell X-22A Experimental Data. Therm Advanced Research Report TR-6510, 1965. (U)

48. Johnson, A. E.: Wind-Tunnel Investigation of the Effects of Thrust, Shroud Length, and Shroud Camber on the Static Stability Charactoristics of Shrouded Propellers. DTMB Aero 1073, 1964. (U)

49. Kakol, S. J.: Flight Tests of the First Dual Tandem Ducted Fan V/STOL. Soc. of Experimental Test Pilots Annual Report to the Aerospace Profession (Tenth), 1968. (U)

50. Kelley, H. L., and Champine, R. A.: Flight Operating Problems and Aerodynamic and Performance Characteristics of a Fixed-Wing, Tilt-Duct, VTOL Research Aircraft. NASA TN D-1802, 1963. (U)

51. Key, D. L., and Reed, L. E.: VTOL Transition Dynamics and Equations of Motion with Application to the X-22A. CAL-TB-2312-F-1, 1968. (U)

52. Kriebel, A. R., and Mendenhall, M. R.: Predicted and Measured Performance of Two Full-Scale Ducted Propellers. NACA CR-578, 1966. (U)

53. Kriebel, A. R., Sacks, A. H., and Nielsen, J. N.: Theoretical Investigation of Dynamic Stability Derivatives of Ducted Propellers. Vidya TR 63-95, 1963. (U)

54. Kriebel, A. R.: Theoretical Investigation of Static Coefficients, Stability Derivatives, and Interference for Ducted Propellers. ITEK Report No. 112, 1964. (U)

55. Kriebel, A. R.: Theoretical Stability Derivatives for a Ducted Propeller. AIAA Preprint 64-170, Journal of Aircraft, Vol. 1, No. 4, 1964. (U)

56. Krüger, W.: On Wind Tunnel Tests and Computations Concerning the Problem of Shrouded Propellers. NACA TM 1202, 1949. (U)

57. Küchemann, D., and Weber, J.: Aerodynamics of Propulsion. McGraw-Hill Book Company, Inc., New York, 1956. (U)

58. Lippisch, A. M.: Theoretical Investigation of the Shrouded Propeller in Forward Flight. ONR, Air Branch, Contract No. NOnr 701 (00). Collins Aeronautical Research Laboratory, 1954. (U)

59. Maguire, W. B.: A Wind-Tunnel Investigation of Some Short-Chord Low-Solidity Shrouded Propellers in the Cruise Condition. DTMB Aero-1083, 1964. (U)

60. Maki, R. L., and Giulianetti, D. J.: Aerodynamic Stability and Control of Ducted-Propeller Aircraft. Conf. on V/STOL and STOL Aircraft. NASA SP-116, 1966. (U)

61. McKinney, M. O., Parlett, L. R., and Newsom, W. A., Jr.: An Approach to Efficient Low-Speed Flight for Fan-Powered V/STOL Aircraft. Conf. on V/STOL and STOL Aircraft. NASA SP-116, 1966. (U)

62. McKinney, M. O., and Newsom, W. A.: Experimental Research on 4-Duct Tandem VTOL Aircraft Configurations. Amer. Helicopter Soc. Paper, 1962. (U)

63. McLemore, H. C., and Cannon, M. D.: Aerodynamic Investigation of a Four-Blade Propeller Operating Through an Angle-of-Attack Range from 0° to 180°. NASA TN 3228, 1954. (U)

64. McNay, D. E.: Study of the Effects of Various Propeller Configurations on the Flow About a Shroud. Mississippi State College, Research Report 14, 1958. (U)

65. Minassian, B.: Analytical Study of Shrouded Propellers. Longren Aircraft Company, Rpt. Nos. Pr-2-4, 1955, Rpt. Nos. Pr-5, Lr-501, 1956. (U)

66. Monical R. E: Progress Report for 1 January 1958 through 30 November 1958 on Wind-Tunnel Investigation of Shrouded Propellers. Univ. of Wichita, Dept. of Eng. Research Report 331, 1958. (U)

67. Mort, K. W., and Yaggy, P. J.: Aerodynamic Characteristics of a 4-Foot Diameter Ducted Fan Mounted on the Tip of a Semispan Wing. NASA TN D-1301, 1962. (U)

68. Mort, K. W.: Summary of Large-Scale Tests of Ducted Fans. Conf. on V/STOL and STOL Aircraft. NASA SP-116, 1966. (U)

69. Mort, K. W., and Gamse, B.: A Wind-Tunnel Investigation of a 7-Foot-Diameter Ducted Propeller. NASA TN D-4142, 1967. (U)

70. Moser, H. H., and Livingston, C. L.: Experimental and Analytic Study of the Ducted Fan and Fan-in-Wing in Hovering and Forward Flight. MIT TR 79-1, 1959. (U)

71. Neal, B.: The Design and Testing of Three 6-Foot Diameter Ducted Propellers with Their Rotational Axes Normal to the Free Stream. NRC 8483, LR-426, 1965. (U)

72. Neal, B., and Slack, W. E.: Static and Low Forward-Speed Tests on Several Six-Foot-Diameter Tractor and Pusher Ducted Propellers. NRC LR-445, 1965. (U)

73. Newsom, W. A., Jr.: Aerodynamic Characteristics of Four-Duct Tandem VTOL-Aircraft Configurations. NASA TN D-1481, 1963. (U)

74. Newsom, W. A., Jr., and Freeman, D. C., Jr.: Flight Investigation of Stability and Control Characteristics of a 0.18-Scale Model of a Four-Duct Tandem V/STOL Transport. NASA TN D-3055, 1966. (U)

75. Newsom, W. A., Jr.: Wind-Tunnel Investigation of a Deflected-Slipstream Cruise-Fan V/STOL Aircraft Wing. NASA TN D-4262, 1967. (U)

76. Ordway, D. E., Sluyter, M. M., and Sonnerup, B. O. U.: Three-Dimensional Theory of Ducted Propellers. Therm Advanced Research TAR-TR-602, 1960. (U)

77. Parlett, L. P.: Aerodynamic Characteristics of a Small-Scale Shrouded Propeller at Angles of Attack from 0° to 90° NACA TN 3547, 1955. (U)

78. Parlett, L. P.: Experimental Investigation of Some of the Parameters Related to the Stability and Control of Aerial Vehicles Supported by Ducted Fans. NASA TN D-616, 1960. (U)

79. Platt, R. J., Jr.: Static Tests of a Shrouded and an Unshrouded Propeller. NACA RM L7H25, 1948. (U)

80. Pruyn, R. A.: Effects of Airframe Geometry on Downwash Problems of Tandem Ducted-Propeller VTOL Aircraft. Kellett Aircraft Corp. Report 179T80-6, 1964. (U)

81. Putman, W. F., Traybar, J. J., et al: An Investigation of the Dynamic Stability Characteristics of a Quad Configuration, Ducted-Propeller V/STOL Model – Volume 1, Phase 1, Hovering. Princeton Univ. Report 835, USAAVLABS TR-68-49A, 1968. (U)

82. Putman, W. F., and Traybar, J. J.: An Investigation of the Dynamic Stability Characteristics of a Quad Configuration, Ducted-Propeller V/STOL Model – Volume 2, Phase 2, Longitudinal Dynamics at High Duct Incidence Data Report. Princeton Univ. Report 836, USAAVLABS TR-68-49B, 1968. (U)

83. Putman, W. F., Traybar, J. J., et al: An Investigation of the Dynamic Stability Characteristics of a Quad Configuration, Ducted-Propeller V/STOL Model – Volume 3, Phase 3, Lateral-Directional Dynamics at High Duct Incidences. USAAVLABS TR-68-49C, 1968. (U)

84. Sacks, A. H., and Burnell, J. A.: Ducted Propellers – A Critical Review of the State of the Art. Progress in Aeronautical Sciences, Vol. 3, edited by Ferri, A., Küchemann, D., and Stern, L. H. G., Pergamon Press, New York, 1962. (U)

85. Sacks, A. H.: The Flying Platform as a Research Vehicle for Ducted Propellers. IAS Preprint No. 832, 1958. (U)

86. Speth, R. F.: Aerodynamic Test Data Report for Ground Effect Model, X-22A. Bell Aerosystems Corp. Report 2127-921004, 1963. (U)

87. Spreemann, K. P.: Wind-Tunnel Investigation of Lateral Aerodynamic Characteristics of a Powered Four-Duct-Propeller VTOL Model in Transition. NASA TN D-4343, 1968. (U)

88. Spreemann, K. P.: Wind-Tunnel Investigation of Longitudinal Aerodynamic Characteristics of a Powered 4-Duct-Propeller VTOL Model in Transition. NASA TN D-3192, 1966. (U)

89. Stapleford, R. L., Wolkovitch, J., et al: An Analytical Study of V/STOL Handling Qualities in Hover and Transition. TR-140-1, AFFDL-TR-65-73, 1965. (U)

90. Tapscott, R. J., and Kelley, H. L.: A Flight Study of the Conversion Maneuver of the Tilt-Duct VTOL Aircraft. NASA TN D-372, 1960. (U)

91. Theodorsen, T.: Theoretical Investigation of Ducted-Propeller Aerodynamics, Vol. I. Dept. National Defense, DOD Tech. Library Account 71999, 1960. (U)

92. Theodorsen, T.: Theoretical Investigation of Ducted-Propeller Aerodynamics, Vol. II. Dept. National Defense, DOD Tech. Library Account 72000, 1960. (U)

93. Thompson, J. F., Jr.: An Experimental Investigation of the Effect of Forward and Rearward Motion on the Thrust of a Shrouded Propeller. Miss. State Univ. RR-65, USAAVLABS TR-66-55, 1966. (U)

94. Wainauski, H. S.: Variable-Geometry Shrouded-Propeller Test Program. Vol. 1. Data Analysis. HSER-5062, Vol. 1, 1968. (U)

95. Wattson, R. K., Jr.: Shrouded Propeller Investigations at the University of Wichita. University of Wichita, Dept. of Eng. Research Report No. 306, 1958. (U)

96. Yaggy, P. F., and Goodson, K. W.: Aerodynamics of a Tilting-Ducted Fan Configuration. NASA TN D-785, 1961. (U)

97. Yaggy, P. F., and Mort, K. W.: A Wind-Tunnel Investigation of a 4-Foot Diameter Ducted Fan Mounted on the Tip of a Semispan Wing. NASA TN D-776, 1961. (U)

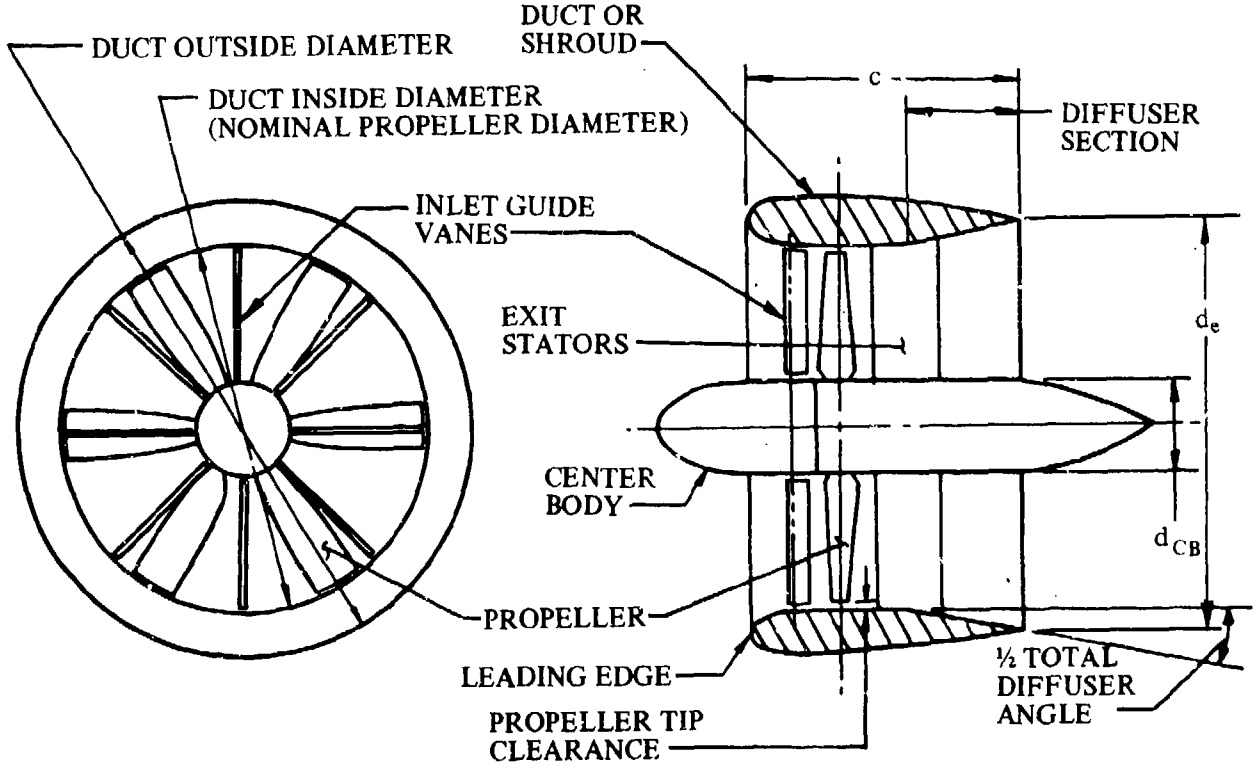

FIGURE 9.3-12 DUCTED-PROPELLER GEOMETRY

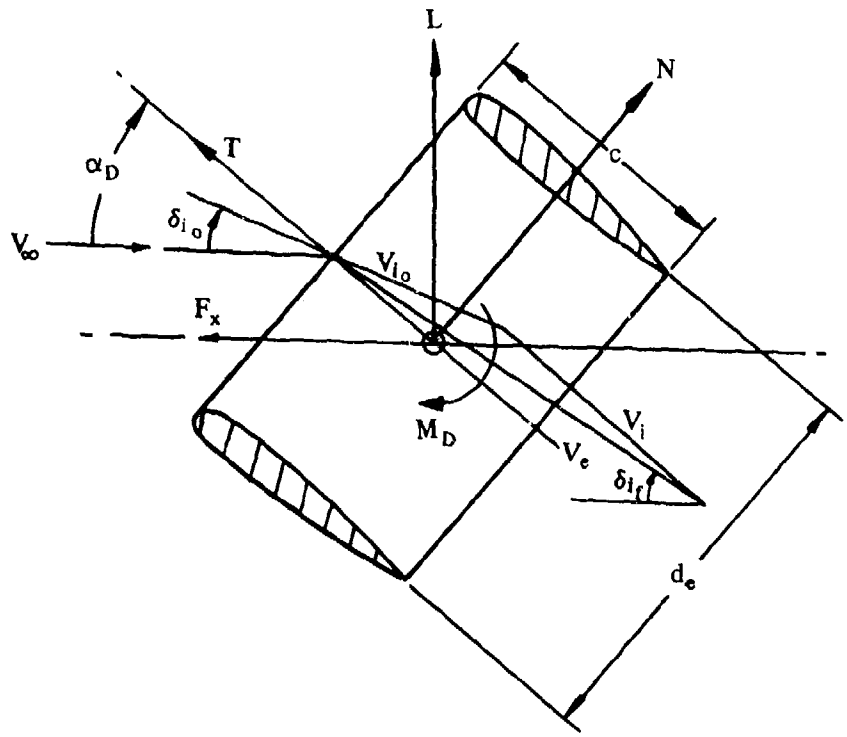

FIGURE 9.3-13 DEFINITION SKETCH FOR DUCTED-PROPELLER FLOW GEOMETRY – WIND-AXIS SYSTEM

TABLE 9.3-A
SUMMARY OF EXPERIMENTAL DUCTED PROPELLER DATA
NON-AXIAL FLOW

REFERENCE NO.	YEAR OF PUBLICATION	DUCT SHAPE*	GEOMETRY: DUCT ASPECT RATIO	GEOMETRY: TOTAL NO. PROP. BLADES PER DUCT	GEOMETRY: NOMINAL PROP. DIAM. (FT)	GEOMETRY: PROP. DISK AREA / TUNNEL AREA (%)	TUNNEL DATA: MAX. $\dot{m}$ / MIN. $\dot{m}_{TUNNEL}$ (%)	TEST CONDITIONS: α RANGE	TEST CONDITIONS: MAX. TESTED Δ/OR DESIGN DISK LOADING (LB/FT^2)	TEST CONDITIONS: MAX. V_o / V_∞	TEST CONDITIONS: MAX. ADVANCE RATIO J	TEST CONDITIONS: R_j RANGE $\times 10^{-6}$	DATA IN ADDITION TO L, D, M, RPM, & POWER: DUCT FORCE, MOMENTS	PROP. FORCES, MOMENTS	DUCT PRESS. DISTRIBUTION	VELOCITY SURVEY	STATIC DATA	PROP.-REMOVED DATA	EXIT-VANE TESTS	INLET GUIDE VANE TEST	COMMENTS
2	60	–	–	–	–	–	–	–	–	–	–	–									REVIEW AND CONSTRUCTION OF COMPARATIVE PERFORMANCE CHARTS USING DATA FROM A MAJORITY OF THE REPORTS ON THE REFERENCE LIST. HOVERING, TRANSITION, AND CRUISE. 2-DIMENSIONAL WATER-FLOW STUDIES.
8	68	MA	1.575, 1.647, 1.714, 2.103	3,4	2.5	1.83, 9.26	–	–	–	–	~2	–	X	X	.X	X	X		X	X	SINGLE SHROUDED PROPELLER TESTED IN UAC 18-FT OCTAGONAL TUNNEL FOR HOVER UP TO M = .2 AND IN 9-FT TUNNEL FOR CRUISE. BLADE PITCH 20° – 56°. DIFFUSION ANGLE NOT GIVEN. RPM MEASURED. EFFECTS OF DUCT EXIT AREA RATIO, LIP SHAPE, DUCT CHORD LENGTH, PROPELLER POSITION, DUCT EXTERNAL SHAPE, INLET-VANE ANGLES, EXIT-VANE ANGLES, AND PROPELLER PARAMETERS, SUCH AS PLANFORM DISTRIBUTION, NO. OF BLADES, AND TIP CLEARANCE TESTS RUN THROUGH RANGE OF PROP POWER LOADINGS AND FREE-STREAM MACH NOS. EFFECT OF EACH PARAMETER SEPARATELY.
9	67	MA	1.575, 1.647, 1.714, 2.103	3,4	2.5	1.83, 9.26	–	–	–	1.875 → 1.08	–	–	X	X	X	X	X		X	X	SAME CONFIG. AS ABOVE. 15° → 42° BLADE TWIST. DIFFUSION VARIED UP TO 12° (HALF-ANGLE) POWER SURVEY. THRUST DATA ONLY. EFFECTS ON PERFORMANCE OF DUCT EXIT AREA, DUCT CHORD LENGTH, PROPELLER POSITION, SHROUD EXTERNAL SHAPE, INLET-VANE ANGLES, EXIT-VANE ANGLES, AND PROPELLER PARAMETERS, SUCH AS PLANFORM DISTRIBUTION, NO. OF BLADES, AND TIP CLEARANCE. PRESSURE AND VELOCITY DATA USED TO COMPUTE PROP THRUST AND POWER-LOADING DISTRIBUTION AND DUCT DRAG AND SLIPSTREAM CONTRACTION. PRESS. DATA SHOW EFFECT OF BLADE ANGLE, MACH NO., AND TIP SPEED. MAX AND MIN DUCT EXIT VELOCITIES GIVEN FOR BASIC CONFIG. AND ALSO TO SHOW EFF. OF VARYING RPM, BLADE ANGLE, MACH NO., DUCT EXIT AREA, DUCT CHORD LENGTH, INLET VANES, TIP CLEARANCE, NO. OF BLADES, AND PROP PLANFORM.
10	62	–	–	3	2.5	–	–	–	–	–	–	–	X	X	X		X	X			A DUCTED PROPELLER WITH FORWARD AND AFT GUIDE VANES AND BLC TESTED IN UAC TUNNEL. HAMILTON STANDARD VARIABLE CAMBER PROPELLER. DIFFUSION VARIES → 11° (HALF-ANGLE) AND 30° WITH BLC. PROP EFF. PLOTS. THRUST FOR DUCT, PROP, AND TOTAL. ADVANTAGES OF DUCTED PROPELLER, METHODS OF DETERMINING PERFORMANCE, AND TEST DATA VERIFYING PREDICTED PERFORMANCE. HOVER, CRUISE, AND TRANSITION.
13	65	MA	2.26	3	8	–	–	0, 90°	76.5	–	–	–	X	X		X	X				FULL-SCALE HALF-MODEL SIMULATION OF DUAL TANDEM DUCTED-PROP VTOL AIRCRAFT TESTED OVER SAND AND STONE TO TEST ENGINE PROTECTIVE DEVICES. ISOLATED DUCT ALSO TESTED. 19°, 22.5°, 26° BLADE PITCH. DIFFUSION ANGLE NOT GIVEN. GROUND EFFECT, STATIC PRESSURE. EFFECTS OF PROP BLADE ANGLE, DUCT HEIGHT, POWER, AND DISTANCE BETWEEN DUCTS. THRUST AND TORQUE SHOW EFFECT OF RPM ALSO. APPENDIX INCLUDES PROP BLADE STRESS STUDIES MADE IN KELLETT DOWNWASH TEST FACILITY SHOWING EFF. OF GROUND AND ADJACENT COMPONENTS ON VIBRATORY STRESSES ON BLADES OF DUCTED PROP.
14	69	MA	1.90	3	1.017	–	–	50° → 80°	–	–	–	–	X								3 TILT-WING CONFIG. LONG STABILITY CHAR. (HORIZ.-FORCE, VERTICAL-FORCE, PITCHING, AND VELOCITY-STABILITY DERIVS.) COMPARED WITH QUAD-DUCTED PROP CONFIG. AND 2 HELICOPTERS. RPM MEASURED. HOVER AND TRANSITION EQ. FOR DERIVS.
15	64	MA	1.77	4	1.146	–	–	0° → 90°	–	–	–	–	X								VTOL CONFIG. WITH 4 TILTING DUCTED PROPELLERS IN TANDEM. LIFT, LONG. FORCE, AND PITCHING MOMENTS. RPM MEASURED. DIFFUSION ANGLE NOT GIVEN. EFFECT OF DIFFERENTIAL THRUST AND DIFFERENTIAL INCIDENCE ON AERO. STAB. AND CONTROL CHAR. IN TRANSITION. TUFT GRID PICTURES.
16	80	BM	2.88	2	1.5	–	–	–10° → 90°	–	–	–	–			X	X					A TILTING DUCTED PROP. AND A FAN-IN-WING IN MIT 7-1/2- x 10-FT TUNNEL. INCREMENTS IN LIFT, DRAG, AND PITCHING MOMENT, AND POWER COEFFICIENT TABULATED FOR TILT ANGLES OF –10° TO 90°, A BLADE PITCH SETTING OF 20°, AND TUNNEL VELOCITY OF 0 TO 40 MPH. MAX. MASS FLOW VARIES FROM .288 TO .887 SLUGS/SEC. NO DIFFUSION. RPM MEASURED. TRANSITION REGIME. DUCT INFLOW VELOCITIES AND INLET PRESS. DISTRIB. TUFT STUDY.
18	57	MA	.333, .667, 1.0, 1.5, 3.0	0	–	–	–	–4° → 90°	–	–	–	704 → 2.11				X	X				5 ANNULAR AIRFOILS OF EQUAL PROJECTED AREAS IN LANGLEY 8- x 8-FT TUNNEL. NO DIFFUSION. LOW-SPEED STATIC LONG. STAB. CHAR. MAX. L/D, LIFT-CURVE SLOPES AND DRAG POLARS COMPARED WITH CALC. VALUES. TUFT GRID TESTS.

*MA = Modified Airfoil; BM = Bellmouth; NBM = Notched Bellmouth; +D = Plus Diffuser; TWC = Thin Walled Cylinder

TABLE 9.3-A (CONTD)

REFERENCE NO.	YEAR OF PUBLICATION	DUCT SHAPE*	GEOMETRY: DUCT ASPECT RATIO	GEOMETRY: TOTAL NO. PROP. BLADES PER DUCT	GEOMETRY: NOMINAL PROP. DIAM. (FT)	GEOMETRY: PROP. DISK AREA / TUNNEL AREA (%)	TUNNEL DATA: MAX. q_o / MIN. q_o (%)	TEST CONDITIONS: α_s RANGE	TEST CONDITIONS: MAX. TESTED L/QR DESIGN / DISK LOADING (LB/FT²)	TEST CONDITIONS: MAX. V_o/V_{tip}	TEST CONDITIONS: MAX. ADVANCE RATIO J	TEST CONDITIONS: α_s RANGE × 10^{-6}	DATA IN ADDITION TO L, D, M, RPM, & POWER: DUCT FORCE, MOMENTS	DATA IN ADDITION TO L, D, M, RPM, & POWER: PROP. FORCES, MOMENTS	DATA IN ADDITION TO L, D, M, RPM, & POWER: DUCT PRESS. DISTRIBUTION	DATA IN ADDITION TO L, D, M, RPM, & POWER: VELOCITY SURVEY	DATA IN ADDITION TO L, D, M, RPM, & POWER: STATIC DATA	DATA IN ADDITION TO L, D, M, RPM, & POWER: PROP.-REMOVED DATA	DATA IN ADDITION TO L, D, M, RPM, & POWER: EXIT-VANE TESTS	DATA IN ADDITION TO L, D, M, RPM, & POWER: INLET GUIDE VANE TEST	COMMENTS
19	59	MA, MA+D, BM, MA	4.0, 4.04, 4.0, 6.66	4.6	2.0	0.83	6.6	0 → 90°	82/26	7.4	0.47	.072 → .37	X			X	X	X	X		2- AND 3-BLADED COUNTER ROTATING PROPELLERS. PROP TWIST AND BLADE PITCH VARIED. SPINNER ROTATES. PROP TIP CLEARANCE, CENTER-BODY LENGTH, PROP LOCATION, AND EXIT-VANE EFFECTIVENESS INVESTIGATED. EXIT-VELOCITY SURVEY DATA. TEST POINTS PRIMARILY AROUND HORIZ-FORCE EQUILIBRIUM CONDITION.
20	59																				SUMMARY PLOTS OF TRANSITION DATA FROM REF 19 AND STATIC TEST DATA OF A HIGH-ASPECT-RATIO DUCT (DUCT 3 OF REF 19).
21	67	MA	1.844	8	4	0.44	–	0 → 90°	–	–	0.95	–	X	X			X		X		FULL-SCALE V/STOL MODEL WITH 4 TILTING DUCTED FANS IN DUAL-TANDEM ARRANGEMENT IN AMES 40- × 80-FT. TUNNEL. BLADE PITCH ANGLE 22° (AT TIP). 11° DIFFUSION ANGLE (HALF-ANGLE). EFFECT OF GROUND HEIGHT ON LONG AERO CHAR IN HOVER, TRANSITION, AND CRUISE, AT VARIOUS DUCT DEFLECTION, FORWARD SPEEDS, ADVANCE RATIOS, AND DUCT VANE DEFLECTIONS. RPM MEASURED. THRUST COEFF FOR ISOLATED DUCTED FAN AS FUNCTION OF ADVANCE RATIO AND DUCT DEFLECTION. EFFECT OF GROUND HEIGHT ON POWER AT VARIOUS DUCT DEFLECTIONS, FORWARD SPEEDS, AND ADVANCE RATIOS. PITCH CONTROL EFFECTIVENESS OF DUCT EXIT VANES.
22	66	MA	1.844	8	4	0.44	–	20° → 90°	338.8/–	–	1.23	–	X				X	X	X	X	LARGE-SCALE V/STOL MODEL WITH 4 TILTING DUCTED FANS IN DUAL-TANDEM ARRANGEMENT IN AMES 40- BY 80-FT TUNNEL. BLADE PITCH ANGLE 22° (AT TIP). 11° DIFFUSION (HALF-ANGLE). RPM MEASURED. THRUST COEFF OF ISOLATED DUCTED PROP AS FUNCTION OF ADVANCE RATIO AND DUCT INCIDENCE. EFFECTS ON LONG AERO CHAR IN HOVER, TRANSITION, AND CRUISE, OF DUCT INCIDENCE, DIFFERENTIAL FORE-AFT DUCT INCIDENCE, MOMENT CENTER, FRONT DUCT THRUST, WING TIPS OUTBOARD OF REAR DUCTS, DUCT STALL, AT VARIOUS ADVANCE RATIOS AND DUCT INCIDENCES. EFF OF SIDESLIP, VERTICAL TAIL, DIFFERENTIAL LEFT-RIGHT DUCT EXIT-VANE DEFLECTION ON LAT-DIR AERO CHAR AT VARIOUS ADVANCE RATIOS AND DUCT INCIDENCES. DUCT INCIDENCE, POWER, AND DIFFERENTIAL EXIT-VANE DEFLECTIONS REQ FOR TRANSITION, MAX DESCENT VELOCITIES AND DUCT STALL MARGINS IN TRANSITION. CONTROL POWER VARIATION WITH DUCT EXIT-VANE SETTINGS.
23	62	MA	1.46	3	1.25	0.43	6.4	0 → 90°	28/–	15.0	0.80	.037 → .72					X	X			5/16-SCALE MODEL OF VZ4 DUCT AND SEMISPAN WING EXCEPT DUCT INTERNAL ELEMENTS (PROP, VANES, ETC.). ALL DATA INCLUDE WING LOADS. NO BLADE PITCH VARIATION GROUND EFFECT DATA. SPINNER ROTATES. 11° DIFFUSION (HALF-ANGLE).
27	58	MA, BM	2.0	4	2.5	9.5, 1.89	9.6	0 → 6°	37/– 103/–	1.0+	4.3	1.4 → 4.2	X	X			X	X			NEARLY AXIAL FLOW, M = 0 TO 0.6. DUCT LE AT OPEN END OF 16-FT OCTAGONAL W-T TEST SECTION. PROP NORMAL FORCE NOT MEASURED. ONLY STATIC DATA ON BELLMOUTH DUCT. BLADE PITCH VARIED. SPINNER ROTATES. 6° DIFFUSION. SHARP-RADIUS INLET.
28	62	MA	1.84	3	1.25	0.43	8.2	–10° → 110°	26/–	18.0	.886	.042 → .78		X			X	X			5/16-SCALE MODEL OF VZ4 DUCT. DIVISION OF LOADS BETWEEN PROP AND DUCT. LOWER FORWARD LE RADIUS INCREASED DURING TEST TO PREVENT SEPARATION. NO BLADE PITCH VARIATION. 11° DIFFUSION. (HALF-ANGLE)
29	62	MA, BM	1.74	8	1.12	0.34	4.8	0 → 90°	61/–	12.4	0.70	.098 → .70		X			X	X	X		SEMISPAN MODEL. DIVISION OF LOADS INVESTIGATION. BELLMOUTH CONFIG IS A MODIFICATION OF MOD AIRFOIL CONFIG. NO BLADE PITCH VARIATION. GROUND-EFFECT DATA. SPINNER ROTATES. 11° DIFFUSION.
32	65	MA	1.80	3	7.0	.084		0 → 100°			2.1		X	X	X		X				FULL-SCALE, DUCTED-FAN MODEL OF X-22A IN AMES 40- × 80-FT TUNNEL. TRANSITION, HOVER, AND CRUISE. BLADE ANGLE 15° – 60° (.75R). 8° DIFFUSION (ONE SIDE). THRUST PRESS., LIFT, DRAG, AND PITCHING MOMENT. HINGE MOMENTS. EFF OF ELEVONS.
35	67	BM															X			X	PROGRESS REPT. DUCT OF REF 41 DISCUSSED. INLET-GUIDE-VANE TEST PLOTS.
36	59	MA, MA, MA+D	1.46, 2.0, 2.16	–[1]	1.16	1.51	–	0 → 90°	–	–	–	.54 → .73						X			PROPELLER-OUT DATA FOR MA DUCT OF REFS 42 AND 43, AND MA AND MA+D DUCTS OF REF 46. HUB DIAMETER AND NOSE LENGTH INVESTIGATED.
37	59	MA, BM, NBM													X						DUCT AND CENTER-BODY SURFACE PRESSURE SURVEYS OF DUCTS OF REFS 40, 41, AND 42.

*MA = Modified Airfoil; BM = Bellmouth; NBM = Notched Bellmouth; +D = Plus Diffuser; TWC = Thin Walled Cylinder

TABLE 9.3-A (CONTD)

Reference No.	Year of Publication	Duct Shape*	Geometry: Duct Aspect Ratio	Geometry: Total No. Prop. Blades per Duct	Geometry: Nominal Prop. Diam. (ft)	Geometry: Prop. Disk Area / Tunnel Area	Tunnel Data: Max. π_t / Min. π_{tunnel} (%)	Test Conditions: α_p Range	Test Conditions: Max. Tested β/r or Design Disk Loading (lb/ft²)	Test Conditions: Max. V_o/V_{tip}	Test Conditions: Max. Advance Ratio J	Test Conditions: β_t Range x 10^{-4}	Data in Addition to L, D, M, RPM, & Power: Duct Force, Moments	Data in Addition to L, D, M, RPM, & Power: Prop. Forces, Moments	Data in Addition to L, D, M, RPM, & Power: Duct Press. Distribution	Data in Addition to L, D, M, RPM, & Power: Velocity Survey	Data in Addition to L, D, M, RPM, & Power: Static Data	Data in Addition to L, D, M, RPM, & Power: Prop.-Removed Data	Data in Addition to L, D, M, RPM, & Power: Exit-Vane Tests	Data in Addition to L, D, M, RPM, & Power: Inlet Guide Vane Test	Comments
18	60	MA, BM, NBM													X						DUCT AND CENTER-BODY SURFACE PRESSURE SURVEYS OF DUCTS OF REFS 43, 44, AND 46.
40	58	NBM	1.29	17	1.16	1.51	16.6	0 → 90°	227/227	11.0	7.0	.18 → .79	X								THRUST ONLY. NOTCHED INLET VERSION OF DUCT IN REF 42. NO BLADE PITCH VARIATION. SPINNER ROTATES. NO DIFFUSION.
41	58	BM	1.29	17	1.16	1.51	16.6	0 → 90°	227/227	11.0	5.0	.18 → .79	X			X					THRUST ONLY. BELLMOUTH INLET VERSION OF DUCT OF REF 42. NO BLADE PITCH VARIATION. SPINNER ROTATES. NO DIFFUSION.
42	58	MA	1.46	17	1.16	1.51	16.6	0 → 30°	227/227	7.2	5.0	.22 → 1.16	X			X					THRUST ONLY. NO BLADE PITCH VARIATION. NO DIFFUSION.
43	59	MA	1.46	10	1.16	1.51	8.36	0 → 30°	160/160	5.5	5.0	.22 → 1.24	X								THRUST ONLY. BLADE PITCH VARIED. SPINNER ROTATES. NO DIFFUSION.
44	59	NBM	1.29	10	1.16	1.51	8.36	0 → 90°	160/160	8.15	4.0	.18 → .79	X								THRUST ONLY. NOTCHED INLET VERSION OF DUCT OF REF. 43. BLADE PITCH VARIED. SPINNER ROTATES. NO DIFFUSION.
45	59	BM	1.29	10	1.16	1.51	8.36	0 → 90°	160/160	8.15	6.3	.18 → .79	X								THRUST ONLY. BELLMOUTH INLET VERSION OF DUCT OF REF 43. BLADE PITCH VARIED. SPINNER ROTATES. NO DIFFUSION.
46	60	MA, MA+D BM, BM+D	2.0, 2.15, 2.0, 2.15	2	1.16	1.51	5.86	0 → 40°	70/35	3.9	2.2	.18 → 1.55	X			X	X				THRUST ONLY. BLADE PITCH VARIED. SPINNER ROTATES. MODIFIED AI[illegible]HL AND BELLMOUTH DUCTS WITH AND WITHOUT DIFFUSION. BELLMOUTH DUCTS RUN STATICALLY ONLY.
47	65	TWC	1.90	3	(a) 3.8, (b) 9.9	– –	– –	– –	– –	– –	(a) .302, (b) .249	– –			X		X				THEORETICAL PREDICTIONS OF DUCT PRESSURE DISTRIBUTIONS COMPARED WITH DATA FROM (a) 1/3-SCALE AND (b) FULL-SCALE MODELS OF BELL X-22A TESTED IN DTMB 8- x 10-FT TUNNEL AND AMES 40- x 80-FT TUNNEL, RESPECTIVELY. STATIC PRESS DISTRIBUTION ON INNER AND OUTER SURFACES OF DUCT, ALSO FOR DUCT WITH PROPELLER REMOVED, AND WITH PROPELLER AND HUB REMOVED. SPEED, ANGLE OF ATTACK, AND POWER INPUT VARIED.
48	64	(a) TWC (b) MA (c) MA (d) MA (e) MA (f) MA	a. 5.03 b) 2.98 c) 2.00 d) 1.38 e) 1.95 f) 2.05	3	1.333	–	–	−10° → 10°	–	–	1.65	–	X			X					ADJUSTABLE-PITCH PROPELLER AND SPINNER WITH 6 DUCTS, SOME UNCAMBERED WITH VARIED CHORD-DIAM RATIOS, AND SOME WITH POSITIVE AND NEGATIVE CAMBER AND A CONSTANT CHORD-DIAM RATIO.(a) HAS NO DIFFUSION. EFFECTS OF THRUST, DUCT LENGTH, AND CAMBER ON STATIC STAB CHAR, LIFT AND LONGITUDINAL-FORCE COEFF, PITCHING MOMENT, C_{L_α} AND [illegible] COMPARISON WITH THEORY. POWER SURVEY. PROPULSIVE EFFICIENCY. EQ FOR FORCES AND MOMENTS IN APPENDIX.
52	66	MA	a) 1.645 b) 1.904	(a) 8 (b) 3	(a) 4 (b) 7.06	(a) .44 (c) 1.37	–	–	–	–	(a) .541 (b) .682	.13 → 1.06	X	X	X	X	X	X	X	X	2 LARGE-SCALE DUCTED-PROPELLER MODELS OF DOAK VZ-4DA AND BELL X-22A TESTED IN AMES 40- x 80-FT TUNNEL. 15° BLADE PITCH AT TIP IN (a), VARIABLE BLADE PITCH IN (b). [illegible]° DIFFUSION (HALF-ANGLE). THRUST OF DUCTED PROPELLER, DUCT, AND PROPELLER FOR VARIED ADVANCE RATIOS. NORMAL FORCE AND PITCHING MOMENT. PRESS FOR RANGE OF ANGLE OF ATTACK, ADVANCE RATIOS, AND DUCTED-PROPELLER THRUST COEFF. COMPUTED AND MEASURED B-L THICKNESS. DUCT STALL BOUNDARY FOR (a) FROM TUFTS, SOUND, AND PITCHING-MOMENT DATA. EFFECTS OF ELEVONS (ACROSS DUCT EXIT PLANE) AND PROP BLADE PITCH ON THRUST AND PRESS FOR (b).
53	60	–	–	–	–	–	–	–	–	–	–	–		X			X				STATIC AND DYN STAB DERIVS OF DUCTED PROPS IN HOVER AND CRUISE PREDICTED. EXPER DATA (FROM REFS 18, 27, 58, 70, 79, et al.) ON PROP THRUST COEFF, DUCT NORMAL FORCE, AND PROPULSIVE EFFICIENCY COMPARED WITH THEORY.
56	49	MA	1.60	8	.7875	~27	–	–	–	–	1.6	→1.2	X	X	X	X	X	X	X		2 PROPELLERS DIFFERING IN BLADE TWIST PLUS NACELLE PLUS 15 DUCTS, WHICH DIFFER IN CHORD LENGTH, EXTENDED CHORD, THICKNESS RATIO, AND CAMBER. BLADE PITCH 15° TO 85°. NO DIFFUSION. THRUST, SOME DRAG, AND TORQUE. EFFECT OF SHAPE OF PROPELLER AND SHROUD SEPARATELY, OF NOSE SPLIT-RING FLAP, OF EXIT STATORS PRIMARILY ON POWER AND THRUST AS A FUNCTION OF ADVANCE RATIO AND BLADE PITCH. RPM MEASURED. CALC AND EXPER VALUES OF EFFICIENCY AND STATIC THRUST FACTOR OF MERIT COMPARED. PHOTOS OF SMOKE TESTS.

*MA = Modified Airfoil; BM = Bellmouth; NBM = Notched Bellmouth; +D = Plus Diffuser; TWC = Thin Walled Cylinder

TABLE 9.3-A (CONTD)

REFERENCE NO.	YEAR OF PUBLICATION	DUCT SHAPE*	GEOMETRY: DUCT ASPECT RATIO	GEOMETRY: TOTAL NO. PROP BLADES PER DUCT	GEOMETRY: NOMINAL PROP DIAM. (FT)	GEOMETRY: PROP DISK AREA / TUNNEL AREA (%)	TUNNEL DATA: MAX. α_T / MIN. α_{TUNNEL} (%)	TEST CONDITIONS: α_T RANGE	TEST CONDITIONS: MAX. TESTED β/FOR DESIGN DISK LOADING (LB/FT^2)	TEST CONDITIONS: MAX $V_\infty/V_{\infty_{HOVER}}$	TEST CONDITIONS: MAX. ADVANCE RATIO J	TEST CONDITIONS: β_T RANGE x 10^{-3}	DATA IN ADDITION TO L, D, M, RPM, & POWER: DUCT FORCE MOMENTS	DUCT PROP FORCES, MOMENTS	DUCT PRESS. DISTRIBUTION	VELOCITY SURVEY	STATIC DATA	PROP REMOVED DATA	EXIT VANE TESTS	INLET GUIDE VANE TEST	COMMENTS
58	64	MA	a) 10.2 b) 5.75	2,3	2	–	–	$-10^\circ \rightarrow 10^\circ$	–	–	–	–	X								2 DUCTS, EACH TESTED WITH 2 PROPS IN DTMB 8- x 10-FT TUNNEL. $15^\circ \rightarrow 35^\circ$ BLADE PITCH ANGLE DIFFUSION ANGLE NOT GIVEN. CRUISE, LIFT, PITCHING MOMENT, THRUST PROPULSIVE EFFICIENCY
60	66	MA	–	8	a) 4 b) ~1.2	a) .44 b) –	–	$180 \rightarrow 700$	–	–	1.30	–	X							X	LARGE DUAL-TANDEM, TILTING DUCTED-PROPELLER VTOL MODEL OF DOAK VZ-4DA IN AMES FULL-SCALE TUNNEL, AND A .3-SCALE MODEL OF THE SAME IN THE LANGLEY TUNNEL. DIFFUSION ANGLE NOT GIVEN. PITCHING MOMENT IN TRANSITION. SIDE-FORCE, YAWING MOMENT, AND ROLL-YAW COUPLING. DUCT ANGLE AND POWER REQUIRED AS FUNCTION OF FLIGHT SPEED. GROUND EFFECT. SOME DATA IN HOVER AND CRUISE ALSO.
61	66	–	–	–	0.5	–	–	–	–	–	–	–	X								SEMISPAN MODEL WITH 2 DUCTED PROPELLERS MOUNTED AHEAD OF A WING WITH DOUBLE-SLOTTED FLAPS IN LANGLEY TUNNEL. DIFFUSION ANGLE NOT GIVEN. EFFECTS OF EXHAUST SPLIT, SLIPSTREAM DEFLECTION, AND FENCES ON LIFT-THRUST AND DRAG-THRUST RATIOS IN HOVER. EFFECT OF FENCES ON JET-INDUCED LIFT THRUST REQUIRED IN TRANSITION.
63	54	–	–	4	5.33	–	–	$0 \rightarrow 180^\circ$	–	–	–	0 → 1.8		X							1/3-SCALE MODEL PROPELLER IN LANGLEY FULL-SCALE TUNNEL. EFFECT OF BLADE ANGLE (0 TO 26° AT .75R) ON THRUST AND POWER COEFF. IN HOVER. EFFECTS OF BLADE ANGLE (0 → 67.8°), ADVANCE RATIO, AND PROP ANGLE OF ATTACK ON THRUST AND POWER COEFFICIENTS, PROPELLER EFFICIENCY, NORMAL-FORCE, YAWING-MOMENT, AND PITCHING-MOMENT COEFFICIENTS. COMPARISON OF THEORY AND EXPER. PROP NORMAL-FORCE, THRUST, AND POWER COEFFICIENTS AND PROP EFFICIENCY FOR VARIOUS BLADE ANGLES, ADVANCE RATIOS, AND ANGLES OF ATTACK. CRUISE, TRANSITION, AND HOVER
67	62	MA	1.64	8	4.0	0.38	1.8	$0 \rightarrow 80^\circ$	125/100	4.8	0.91	.86 → 3.07									VZ4 SEMISPAN WING PLUS DUCT (PROTOTYPE COMPONENTS). DUCT AND DUCT-WING DATA TAKEN AT 4 WING ANGLE-OF-ATTACK SETTINGS. DUCT STALL BOUNDARIES DEFINED. 2 BLADE PITCH ANGLES TESTED. 11° DIFFUSION (HALF-ANGLE).
68	66	–	–	a) – b) – c) 3	a) 3 b) 5 c) 7	–	–	–	–	–	1.2	–	X					X	X		2 SIZES OF ISOLATED DUCTED PROPELLERS IN AMES TUNNEL. THE 7-FT PROPELLER A FULL-SCALE MODEL OF THOSE IN X-22A. THE 3-FT PROPELLER WITH 3 LIPS. VARIABLE BLADE PITCH. DIFFUSION ANGLE NOT GIVEN. PRESSURE LOSSES FOR 3- AND 5-FT PROPELLERS. NACELLE DRAG FOR 3-FT PROPELLER AND ITS EFFECT ON THRUST. EFFECT OF TIP CLEARANCE ON THRUST AND POWER COEFFICIENTS AND ON STATIC PERFORMANCE. DUCT ANGLE OF ATTACK FOR INNER AND OUTER TIP STALL.
69	67	MA	1.80	3	7	1.40	–	$0 \rightarrow 90^\circ$	–	–	2.17	–	X		X		X	X	X		LARGE-SCALE DUCTED PROPELLER LIKE THOSE ON BELL X-22A TESTED IN AMES 40- x 80-FT TUNNEL. $14^\circ \rightarrow 48^\circ$ BLADE PITCH. 9° DIFFUSION (HALF-ANGLE). RPM MEASURED. TOTAL THRUST, POWER COEFF., AND PROPULSIVE EFFICIENCY FOR RANGE OF BLADE ANGLES AND ADVANCE RATIOS. TOTAL LIFT, DRAG, AND PITCHING MOMENT. ALSO WITH PROP REMOVED. STATIC EFFICIENCY SHOWN AS FIGURE OF MERIT. THRUST VALUES COMPARED WITH THEORY. DUCT LIP STALL.
70	68	BM	3.0	2	1.5	3.22	10.9	$70^\circ \rightarrow 100^\circ$	23/–	3.4	0.27	.08 → 0.14			X	X	X				ARTICULATED BLADES WITH OFFSET LAG HINGES. BLUNT AFTERBODY, NO SPINNER. ANALYSIS OF DUCTED PROPS. BLADE PITCH VARIED. NO DIFFUSION. GROUND-EFFECT DATA
71	68	MA	4.0	a) 4 b) 2 c) 2	6	–	–	90°	a) 22/– b) 23/– c) 23/–	–	–	–	X	X	X	X	X			X	FULL-SCALE DUCT AND 3 PROPELLERS ON MOBILE TEST RIG. BLADE PITCH AT .75R FOR (a) $8.8^\circ \rightarrow 11.8^\circ$, (b) 13.8°, (c) 13.3°, 13.8°. BLADE TWIST. NO DIFFUSION. RPM MEASURED. TOTAL THRUST AND FOR PROP ALONE. TOTAL PITCHING MOMENT. EFFECT OF DUCT, ENGINE COWLINGS, THRUST VECTORING VANES, DUCT LIP EXTENSION, TIP CLEARANCE, BLADE TWIST, AND GROUND PROXIMITY. DUCT PRESSURES COMPARED WITH THEORY. EFFECT OF VANES ON AIR-TURNING ANGLE. HOVER CONDITION.
72	68	MA	a) 2.48 b) 2.48 c) 2.37 d) 2.24 e) 2.62 f) 2.38 g) 2.32	2	5	–	–	α, β°	a) 38.8/– b) 39.4/– c) 38.0/– d) 34.1/– e) 41.0/– f) 36.0/– g) 36.8/–	–	–	–	X	X	X	X		X			TRACTOR AND PUSHER DUCTED PROPELLERS WITH 4 PROPELLERS IN NAE MOBILE TEST RIG. TRACTOR DUCTS HAVE MODIFIED LE AND 8° AND 10° DIFFUSION (HALF-ANGLE). PUSHER DUCTS OF 5.7 PERCENT THICKNESS-CHAM RATIO HAVE 3° DIFFUSION (HALF-ANGLE). OF 8.3 PERCENT THICKNESS-DIAM RATIOS, 8° AND 10° DIFFUSION (HALF-ANGLE). BLADE TWIST. RPM MEASURED. HOVER AND CRUISE CONDITIONS. THRUST FOR DUCTED AND PROP. ALONE AND COMBINED. EFFECTS OF DUCT, DIFFUSER ANGLE, AND MODEL INCIDENCE, PROP LOCATION, TIP CLEARANCE, AND TIP CHORD OF BLADES.

*MA = Modified Airfoil; BM = Bellmouth; NBM = Notched Bellmouth; +D = Plus Diffuser; TWC = Thin Walled Cylinder

TABLE 9.3-A (CONTD)

REFERENCE NO.	YEAR OF PUBLICATION	GEOMETRY: DUCT SHAPE*	GEOMETRY: DUCT ASPECT RATIO	GEOMETRY: TOTAL NO. PROP. BLADES PER DUCT	GEOMETRY: NOMINAL PROP. DIAM. (FT)	GEOMETRY: PROP. DISK AREA / TUNNEL AREA (%)	TUNNEL DATA: MAX. $\frac{q_0}{q_{min}}$ (%)	TEST CONDITIONS: α_0 RANGE	TEST CONDITIONS: MAX. TESTED T/S OR DESIGN DISK LOADING (LB/FT²)	TEST CONDITIONS: MAX. V_0/V_e	TEST CONDITIONS: MAX. ADVANCE RATIO J	TEST CONDITIONS: β_0 RANGE x 10^{-6}	DATA IN ADDITION TO L, D, M, RPM, & POWER: DUCT FORCE, MOMENTS	PROP. FORCES, MOMENTS	DUCT PRESS. DISTRIBUTION	VELOCITY SURVEY	STATIC DATA	PROP.-REMOVED DATA	EXIT-VANE TESTS	INLET GUIDE VANE TEST	COMMENTS
72	63	MA	1.77	4	1.146	–	–	0 → 75°	–	–	–	–	x						x		4 VTOL CONFIGS WITH TILTING DUCTED PROPS IN TANDEM PAIRS IN LANGLEY 12-FT OCTAGONAL TEST SECTION. BLADE PITCH FIXED. DIFFUSION ANGLE NOT GIVEN. EFFECTS OF VARIOUS LAT AND VERT POSITIONS OF DUCTS, DUCT INCIDENCE, WING INCIDENCE, AND POWER ON LONG CHAR., WITH AND WITHOUT PROPS IN CRUISE AND TRANSITION. EFFECTS OF VERT TAIL, DUCT INCIDENCE, AND ANGLE OF ATTACK ON LATERAL CHARACTERISTICS.
74	66	MA	1.90	4	1.4	–	–	0 → 80°	–	–	–	–	x								MOSTLY FREE-FLIGHT TESTS OF AN 18-SCALE MODEL OF 4-DUCT TANDEM V/STOL TRANSPORT IN LANGLEY FULL-SCALE TUNNEL. DIFFUSION ANGLE NOT GIVEN. EFFECTS OF GROUND PROXIMITY ON LIFT, ROLLING AND PITCHING MOMENTS, AND AILERON YAW CONTROL EFFECTIVENESS IN HOVER AND TRANSITION. EFFECTS OF VERT-TAIL SIZE, YAW DAMPER, VORTEX GENERATORS, AND LE SLATS ON PITCHING. TUFT STUDIES OF DUCT STALL. ROLL AND YAW CONTROL BY DIFFERENTIALLY DEFLECTING AILERONS IN DUCTS. EFFECT OF DUCT INCIDENCE ON THRUST COEFF AT VARIOUS DESCENT RATES.
75	67	MA	–	4	0.5	–	–	0 → 20°	–	–	–	–	x		x						SEMISPAN WING WITH DOUBLE-SLOTTED FLAP AND DUCTED PROPELLERS IN LANGLEY FULL-SCALE AND LOW-SPEED 12-FT. OCTAGONAL TEST SECTION. NO DIFFUSION. EFFECTS OF 1 OR 2 FANS, SPANWISE DUCT LOCATION, DUCT-EXIT SPLIT FENCES, FLAP DEFLECTION, AND MOMENTUM COEFF. LIFT, DRAG, PITCHING MOMENT AND TOTAL PRESS AT FORWARD SPEED AND STATIC THRUST CONDITIONS. LIFT INDUCED BY JET FLAP ACTION COMPARED WITH CALC VALUES. THRUST REQUIRED IN TRANSITION. SLIPSTREAM ROTATION AND TURNING CONTROLLED BY VANES, FENCES, AND FLAPS.
77	55	TWC	1.47	2	1.90	1.48	9.6	0 → 90°	3.4/–	6.4	.213	.066 → .53					x	x			VERY LOW DISC LOADING. BLUNT CENTERBODY. 5 SMALL CIRCULAR LEADING RADII TESTED. NO DIFFUSION.
78	40	BM	2.33, 3.06		2.33	0.24	4.1	80° → 80°	8.9/–	17.4	.84	.017 → .20					x	x		x	2-, 3-, AND 4-BLADED PROPELLERS, BLADE PITCH VARIED. NO DIFFUSION. GROUND EFFECTS. ISOLATED-DUCT STATIC STAB., LE-RADIUS EFFECTS, AND INLET-GUIDE-VANE THRUST CONTROL.
79	48	MA	(a) 1.6 (b) 1.7 (c) 1.4	12	4	–	–	–	(a) 107/– (b) 119/– (c) –	–	–	–	x	x	x	x	x	x			2 HIGH-SOLIDITY PROPELLERS, ONE TESTED WITH 3 DUCTS, TESTED OUTDOORS. BLADE PITCH: 18° → 40° (UNSHROUDED PROP.) 35° → 45° (DUCTED PROP.) DIFFUSION ANGLE (BOTH SIDES): (a) 7°, (b) 22.4°, (c) 14.4°. RPM MEASURED. ONLY THRUST AND POWER FOR COMPONENTS AND VARIOUS BLADE ANGLES. HOVER CONDITION.
80	64	MA	2.26	3	8	–	–	75° → 106°	60/–	–	–	–			x						A FULL-SCALE HALF-MODEL OF DUAL-TANDEM DUCTED-PROP. VTOL TESTED OVER SAND AND WATER IN HOVER. 31.5° BLADE PITCH AT .75R. APPROX 8° DIFFUSION (HALF-ANGLE). RPM MEASURED. EFFECTS OF GROUND PROXIMITY, DUCT INCLINATION, AFT DUCT LOCATION, DISC LOADING, AND TERRAIN TYPE ON POWER LOADING, INGESTION, AND RECIRCULATION.
81	68	MA	1.90	3	1.02	–	–	40° → 90°	–	–	.44	–	x				x				ISOLATED DUCT AND COMPLETE .145-SCALE QUAD-CONFIG., DUCTED-PROP. V/STOL SIMILAR TO BELL X-22A IN PRINCETON DYNAMIC MODEL TRACK. STATIC TESTS AT FIXED BLADE ANGLE OF 19.1° (AT .75R); DYNAMIC TESTS AT BLADE ANGLES OF 25.6° → 29.2° (.75R) AND WITH DIFFERENTIAL BLADE ANGLES OF FRONT AND REAR PROPELLERS. DIFFUSION ANGLE APPROX 9° (HALF-ANGLE). RPM MEASURED. STATIC TESTS ON ISOLATED DUCT LIFT, DRAG, AND PITCHING MOMENT COMPARED WITH FULL-SCALE DATA. TIME HISTORIES OF TRANSIENT RESPONSE CHAR. IN HOVER OF COMPLETE MODEL FOR 1°, 2°, AND 3° OF FREEDOM ROLL, YAW, SIDE VELOCITY AND VERT. VELOCITY MOTIONS
82	68	MA	1.90	3	1.02	–	–	–	–	–	–	–									.143-SCALE QUAD-CONFIG., DUCTED-PROPELLER V/STOL SIMILAR TO BELL X-22A IN PRINCETON DYNAMIC MODEL TRACK. DIFFUSION APPROX 9° (HALF-ANGLE). BLADE ANGLE VARIED 23.7° → 28° AT .75R, DIFFERENTIAL BLADE ANGLE BETWEEN FRONT AND REAR PROPS. RPM MEASURED. LONG. DYNAMIC STAB. CHAR. AT LOW SPEED AND HIGH INCIDENCES (50° – 80°). TIME HISTORIES OF TRANSIENT RESPONSES TO 3° OF FREEDOM (PITCH, HORIZ. AND VERTICAL VELOCITY), TO 2° OF FREEDOM (PITCH AND HORIZ. VELOCITY, AND PITCH AND VERT. VELOCITY), AND TO 1° OF FREEDOM IN PITCH.
83	68	MA	1.90	3	1.02	–	–	–	–	–	–	–									.143-SCALE QUAD-CONFIG. DUCTED-PROPELLER V/STOL SIMILAR TO BELL X-22A IN PRINCETON DYNAMIC MODEL TRACK. DIFFUSION APPROX 9° (HALF-ANGLE). BLADE ANGLE VARIED FROM 24.8° → 29.6° AT .75R. LAT.-DIR. DYNAMIC STAB. CHAR. AT LOW SPEEDS AND HIGH INCIDENCES (50° – 80°). TIME HISTORIES OF TRANSIENT RESPONSES TO 3° OF FREEDOM (ROLL, YAW, LATERAL VELOCITY), TO 2° OF FREEDOM (ROLL AND YAW, AND ROLL AND LATERAL VELOCITY), AND 1° OF FREEDOM (ROLL ONLY AND YAW ONLY). RPM MEASURED.

*MA = Modified Airfoil; BM = Bellmouth; NBM = Notched Bellmouth; +D = Plus Diffuser, TWC = Thin Walled Cylinder

TABLE 9.3-A (CONTD)

REFERENCE NO.	YEAR OF PUBLICATION	GEOMETRY: DUCT SHAPE*	GEOMETRY: DUCT ASPECT RATIO	GEOMETRY: TOTAL NO. PROP. BLADES PER DUCT	GEOMETRY: NOMINAL PROP. DIAM. (FT)	GEOMETRY: PROP. DISK AREA / TUNNEL AREA	TUNNEL DATA: MAX. q_t / MIN. q_{tunnel} (%)	TEST CONDITIONS: α RANGE	TEST CONDITIONS: MAX. TESTED T_j/A OR DESIGN DISK LOADING (LB/FT²)	TEST CONDITIONS: MAX. V_∞ / V_j	TEST CONDITIONS: MAX. ADVANCE RATIO	TEST CONDITIONS: β_j RANGE × 10^{-4}	DATA IN ADDITION TO L, D, M, RPM, & POWER: DUCT FORCE, MOMENTS	DUCT PROP. FORCES, MOMENTS	DUCT PRESS. DISTRIBUTION	VELOCITY SURVEY	STATIC DATA	PROP.-REMOVED DATA	EXIT-VANE TESTS	INLET GUIDE VANE TEST	COMMENTS
84	59	–	–	–	–	–	–	–	–	–	–	–									
86	63	MA	1.80	3	1.02	–	–	–	–	1.62	–	–	X								
87	88	MA	1.9	3	1.40	–	–	−5° → 90°	–	–	–	.066 → .48	X	X				X			
89	88	MA	1.9	3	1.40	–	–	−5° → 90°	–	–	–	.066 → .48	X					X			
90	60	–	–	8	4	–	–	0 → 90°	–	–	–	–	X							X	
22	60	–	–	–	–	–	–	–	–	–	–	–	X				X				
83	66	MA	2.48	3	2.21	–	–	–	–	–	–	–	X	X							
95	58																				
96	61	MA	–	–	4	–	–	0 → 90°	250/–	–	–	–	X					X			
97	61	MA	1.64	8	4.0	0.38	2.64	0 → 90°	125/100	6.75	0.91	.59 → 4.06				X		X		X	

124 REPORTS LISTED PERTAINING TO DUCTED PROPELLERS. A TABLE OF 29 REPORTS CONTAINING EXPERIMENTAL DATA IN HOVER, CRUISE, AND TRANSITION FLIGHT SHOW THE PARAMETERS VARIED, WITH ADDITIONAL COMMENTS, SIMILAR TO THE ANALYSIS IN THIS TABLE

1/31.27-SCALE MODEL OF X-22A. DIFFUSION ANGLE APPROX 9° (HALF-ANGLE). EFFECT OF GROUND AND ANGLE OF ATTACK ON LIFT, PITCHING MOMENT, AND ROLLING MOMENT IN HOVERING

1/5-SCALE VTOL MODEL WITH 4 DUCTED PROPELLERS IN 17-FT TEST SECTION OF LANGLEY 300-MPH, 7- x 10-FT TUNNEL. DIFFUSION ANGLE NOT GIVEN. HOVER, CRUISE, AND TRANSITION FLIGHT. EFFECTS OF ANGLE OF ATTACK, POWER, VERT-TAIL SIZE AND ASPECT RATIO, AND VERT. FINS ON SIDE-FORCE, YAWING AND ROLLING MOMENTS. PROPELLER THRUST COEFFICIENTS. YAW AND ROLL CONTROL BY EXIT VANES.

1/5-SCALE VTOL MODEL WITH 4 DUCTED PROPELLERS IN 17-FT TEST SECTION OF LANGLEY 300-MPH, 7- x 10-FT TUNNEL. DIFFUSION ANGLE NOT GIVEN. HOVER, CRUISE, AND TRANSITION FLIGHT. EFFECT OF GROUND ON LIFT, DRAG, AND PITCHING MOMENT.

EFFECTS OF HORIZ. TAIL, DUCT FAIRINGS, DUCT LOCATION, DUCT DEFLECTION, DUCT LIP, DIFFERENTIAL DUCT DEFLECTION, PROPELLER PROP ROTATION DIRECTION, NACELLES, VANE DEFLECTION, AND POWER ON LIFT, DRAG, AND PITCHING MOMENT OF MODEL. ALSO ISOLATED DUCTED PROP DATA. DUCT STALL. TUFT STUDIES AT VARIOUS THRUST COEFF., DUCT DEFLECTION ANGLES, AND ANGLES OF ATTACK.

VTOL CONFIG WITH TILTING DUCTED FANS ON EACH WING-TIP (DOAK 16) IN FLIGHT TEST. TIME HISTORIES OF AIRCRAFT MOTIONS IN ROLL, PITCH, AND YAW, CONTROL POSITIONS, AND DUCT PITCHING-MOMENT VARIATIONS IN HOVER AND TRANSITION.

84 REF. LISTED CONTAINING TEST DATA ON DUCTED PROPS. 17 REF. ANALYZED, INCLUDING 18, 27, 40 THROUGH 45, 56, 63, 70, AND 79, AND PRESENTED ON PLOTS OF STATIC EFFICIENCY AND SHROUD THRUST IN HOVER, THRUST COEFFICIENT AS A FUNCTION OF ADVANCE RATIO AND BLADE ANGLE, PROPULSIVE EFFICIENCY, AND SHROUD THRUST IN CRUISE; AND LIFT, DRAG, AND POWER COEFF. AND PITCHING AND ROLLING MOMENTS IN TRANSITION.

SHROUDED PROPELLER IN HOVER, REARWARD MOTION, AND FORWARD MOTION. BLADE PITCH VARIED FROM 5° TO 26°. BLADE TWIST ZERO. DIFFUSION APPROX. 15° (HALF-ANGLE). RPM MEASURED. SHROUD PRESS DISTRIBUTION, STAGNATION-LINE LOCATION, AND SHROUD THRUST FOR 3 CASES OF MOTION AT SEVERAL PROP PITCH ANGLES, PROP ROTATIONAL SPEEDS, AND VEHICLE LINEAR SPEEDS. TUFT STUDIES OUTSIDE OF DUCT.

PROGRAM SUMMARY OF UNIV. OF WICHITA DUCTED PROPELLER RESEARCH. NO DATA BUT SOME MODEL GEOMETRIC CHARACTERISTICS GIVEN.

SEMISPAN WING WITH DOAK DUCTED FAN MOUNTED ON WING TIP IN AMES 40- x 80-FT TUNNEL. DIFFUSION ANGLE NOT GIVEN. EFFECT OF WING ANGLE OF ATTACK ON DOWNWASH. EFFECTS OF EXIT VANE DEFLECTION, AIRPLANE WEIGHT AND DISC LOADING, AND LIP STALL ON DUCT PITCHING MOMENT FROM HOVER TO CRUISE. LIFT AND PITCHING MOMENT FOR DUCT AND DUCT PLUS WING.

VZ4 SEMISPAN WING PLUS DUCT (PROTOTYPE COMPONENTS). NO BLADE PITCH VARIATION TRANSITION CONDITIONS. WING-ALONE DATA. DOWNWASH INVESTIGATION AT HORIZ. LOCATION. EXIT-VANE PITCHING-MOMENT CONTROL INVESTIGATED. 11° DIFFUSION (HALF-ANGLE).

*MA = Modified Airfoil; BM = Bellmouth; NBM = Notched Bellmouth; +D = Plus Diffuser; TWC = Thin Walled Cylinder

1,100 - March 1971 - LO139 - 25-71-[illegible]

9.3.1 DUCTED-PROPELLER LIFT VARIATION WITH POWER AND ANGLE OF ATTACK

The primary purpose of enclosing a propeller in a duct is to increase the thrust-generating capability in the static and low subsonic speed regimes for a given propeller diameter and power input. Because of strong mutual interference effects, the ducted-propeller aerodynamic characteristics are vastly different from those of a free propeller and an annular airfoil. The forces and moments acting on a ducted propeller may be considered as arising from the propeller forces, the duct forces, and the mutual interference of the duct and propeller.

As a consequence of the input of mechanical energy to a propeller delivering positive thrust, there is a pressure rise at the propeller disk, which is subsequently transformed into kinetic energy in the slipstream. If the propeller is enclosed within a fairing, a further velocity increment is produced at the propeller, which must be superimposed on the propeller flow. If this velocity increment is positive, the mass flow and consequently the total thrust are increased. This increase in force acts on the duct, and its magnitude depends upon the velocity increment due to the duct and the propeller loading. In addition, the mutual interference of the duct and propeller and other bodies which may be present results in an induced circulation, which may either increase or decrease the internal mass flow.

The Datcom methods presented for estimating forces and moments on ducted-propeller configurations require knowledge of only the total internal axial thrust rather than the thrust due to the propeller and to the duct at angle of attack. However, the fundamental phenomenon of ducted-propeller aerodynamics may be clarified somewhat by an analysis of the division of loads between the duct and the propeller.

The results of an investigation of the division of the forces and moments between a duct and a propeller of a ducted propeller are reported in reference 6. The investigation covered an angle-of-attack range and an advance-ratio range typical of the transition of a tilt-duct VTOL aircraft.

Figures 9.3.1-10a and 9.3.1-10b, reproduced from reference 6, present a comparison of the normal force, thrust force, and pitching moment on the propeller with the total model forces and moments, for an unstalled and a stalled duct, respectively. The unstalled configuration is the basic symmetrical duct shape modified by the addition of leading-edge fairings. These results show that the normal force and pitching moment acting on the propeller and spinner are relatively small in comparison with the total normal force and pitching moment of either the stalled or unstalle unit and that the duct is the primary source of normal force and pitching moment.

Figure 9.3.1-12, reproduced from reference 6, presents the variation of propeller thrust relative to total thrust with angle of attack for both the unstalled and the stalled duct configurations. In hovering ($V/nd_p = 0$), the propeller carries approximately 40 percent of the total thrust. At the highest value of the advance ratio tested, the propeller carries approximately 70 percent of the total thrust when α is near 0^o. For the unstalled operation, the propeller thrust ratio generally decreases with increasing angle of attack at a constant advance ratio. Beyond the stall the propeller thrust ratio increases with increasing angle of attack at a constant advance ratio. The increase can be attributed to the reduction in duct thrust caused by the lip stall.

Unpowered conditions correspond to a duct exit-velocity ratio of approximately 1.0. The exact value depends on the circulation about the duct. Annular wing reports, such as reference 2, may be used to estimate the forces and moments on an unpowered ducted propeller at angle of attack.

For convenience, the methods presented in subsequent Sections provide wind-axis aerodynamic force coefficients: conventional lift and drag coefficients normal and parallel to the free stream. The aerodynamic force and moment coefficients are referred to free-stream dynamic pressure.

Ducted propeller forces and moments are compared with those predicted by the Datcom methods in this and the following Sections. The experimental data represent a wide variation of duct and propeller variables over angle-of-attack and advance-ratio ranges typical of the transition range of a tilting duct VTOL aircraft. Experimental axial-thrust values have been used in the Datcom method calculations. A comparison of some of the pertinent geometric and aerodynamic parameter variations of the test configurations can be made by referring to the reference list of this Section and the reference list and table 9.3-A of Section 9.3. The Datcom methods are based on modifications to simple momentum theory and do not account for the possible wide variation in design parameters.

The lift predicted by the Datcom method of this Section compares favorably with test results throughout the range of the investigation. On the other hand, the pitching moment and drag predicted by the Datcom methods of Sections 9.3.2 and 9.3.3, respectively, vary noticeably from experimental results.

The method presented in this Section for the estimation of the lift of a ducted propeller is expressed as the sum of the lift components resulting from the internal and external mass flows. The internal-mass-flow component is estimated on the basis of simple momentum theory with empirical flow-turning corrections as a function of the duct aspect ratio and the duct exit-velocity ratio. The external-mass-flow component is estimated on the basis of empirical modifications of the data of references 1 and 2.

DATCOM METHOD

The method presented for the estimation of ducted-propeller lift coefficient is expressed as the sum of the components resulting from the internal and external mass flows. This approach is summarized by

$$C_L = \frac{L}{q_\infty S_D} = C_{L_i} + C_{L_e}$$

$$= \frac{\pi A_D}{2}\left[1 - \left(\frac{d_{CB}}{d_e}\right)^2\right]\left(\frac{V_e}{V_\infty}\right)^2 \sin \delta_{1_f} + C_{L_e} \qquad 9.3.1\text{-a}$$

where

C_{L_i} is the lift coefficient resulting from the internal mass flow

C_{L_e} is the lift coefficient resulting from the external mass flow. It is obtained from figure 9.3.1-13 as a function of duct aspect ratio and angle of attack. Figure 9.3.1-13 is based on empirical modifications of the data of references 1 and 2.

δ_{i_f} is the net turning angle of the internal flow including power effects.

The basic approach to the solution of equation 9.3.1-a is as follows:

1. Determine the turning angle of the internal flow neglecting the effects of power.
2. Determine the exit-velocity ratio V_e/V_∞.
3. Determine the net turning angle of the internal flow including power effects.
4. Evaluate the internal-flow lift contribution using the terms obtained in steps 2 and 3 above.

The results of reference 2 indicate that the lift-curve slope of annular wings is twice that of plane unswept wings of the same aspect ratio. Based on simple momentum theory, the usual small-angle approximation, and the assumption of no lip separation, the turning angle of the internal flow, neglecting power effects, is

$$\delta_{i_o} \approx \sin^{-1}\left(\frac{C_{L_\alpha}\,\alpha}{\pi\, A_D}\right) \qquad 9.3.1\text{-b}$$

The unpowered, internal-flow turning angle relative to duct angle of attack is presented in figure 9.3.1-14 as a function of duct aspect ratio. Figure 9.3.1-14 is based on the unstalled test data of reference 2 and equation 9.3.1-b.

Addition of power causes further turning of the internal flow. This turning occurs forward of the propeller plane because of the closed boundaries of the duct. The flow is assumed to pass through the duct normal to the propeller plane, and the total velocity increase imparted to the internal flow (V_i) is assumed to be the difference between the duct exit velocity and the free-stream velocity. This results in the following expression for the net turning angle of the internal flow, including power effects (see figure 9.3-11b).

$$\delta_{i_f} \approx \sin^{-1}\left[\frac{V_\infty \sin\delta_{i_o} + (V_e - V_\infty)\sin\alpha_D}{V_e}\right] \qquad 9.3.1\text{-c}$$

The total lift contribution of a ducted propeller is obtained from the procedure outlined in the following steps:

Step 1. Determine the turning angle of the internal flow, neglecting power effects, by

$$\delta_{i_o} = \alpha_D\left(\frac{\Delta\delta_{i_o}}{\Delta\alpha_D}\right) \qquad 9.3.1\text{-d}$$

where $\frac{\Delta\delta_{i_o}}{\Delta\alpha_D}$ is obtained from figure 9.3.1-14 as a function of duct aspect ratio.

Step 2. Determine the exit-velocity ratio $\frac{V_e}{V_\infty}$ using

$$\frac{V_e}{V_\infty} = \frac{1 + \sqrt{1 + \frac{2T_i}{q_\infty S_e}}}{2} \qquad 9.3.1\text{-e}$$

where

S_e is the flow area at the duct exit plane $= \frac{\pi d_e^2}{4}\left[1 - \left(\frac{d_{CB}}{d_e}\right)^2\right]$

T_i is the total internal axial thrust ($\alpha_D = 0$), obtained as the sum of the net axial thrust T_{net} and the external duct drag.

$$T_i = T_{net} + C_{D_e}\, q_\infty\, S_D \qquad 9.3.1\text{-f}$$

Estimation of the net axial thrust is a ducted-propeller performance problem and is consequently outside the scope of the Datcom. A propulsion engineer should be consulted for this parameter.

The external duct drag C_{D_e} is obtained from figure 9.3.3-4 at $\alpha_D = 0^\circ$, where $C_{D_e} = -C_{F_{x_e}}$

Step 3. Using equation 9.3.1-e, obtain δ_{i_f} with the δ_{i_o} and $\frac{V_e}{V_\infty}$ values from Steps 1 and 2 above.

Step 4. Determine the internal-mass-flow lift-coefficient contribution by

$$C_{L_i} = \frac{\pi A_D}{2}\left[1 - \left(\frac{d_{CB}}{d_e}\right)^2\right]\left(\frac{V_e}{V_\infty}\right)^2 \sin\delta_{i_f} \qquad 9.3.1\text{-g}$$

Step 5. Obtain the lift coefficient C_{L_e} from figure 9.3.1-13 as a function of the duct aspect ratio and angle of attack.

Step 6. The total lift coefficient is given by equation 9.3.1-a

$$C_L = C_{L_i} + C_{L_e}$$

A comparison of test data with ducted-propeller lift coefficients computed by this method is shown in Table 9.3.1-A.

Sample Problem

Given: The ducted propeller configuration of reference 1

$d_e = 4.525$ ft $\quad d_{CB} = 1.208$ ft $\quad c = 2.75$ ft $\quad S_D = 12.45$ sq ft

Additional Characteristics

$V_\infty = 93.5$ ft/sec $\quad \alpha_D = 30^\circ \quad T_{net} = 635$ lb $\quad$ Sea level $\quad q_\infty = 10.4$ lb/sq ft

Compute:

Step 1. Determine the turning angle of the internal mass flow without power effects.

$$A_D = \frac{d_e}{c} = \frac{4.525}{2.75} = 1.645$$

$$\frac{\Delta\delta_{i_o}}{\Delta\alpha_D} = 0.830 \quad \text{(figure 9.3.1-14)}$$

$$\delta i_o = \alpha_D \left(\frac{\Delta\delta_{i_o}}{\Delta\alpha_D}\right) \quad \text{(equation 9.3.1-d)}$$

$$= (30)(0.830)$$

$$= 24.9 \text{ deg}$$

Step 2. Determine the exit-velocity ratio

$$C_{D_e} = -C_{F_{x_e}} = 0.022 \quad \text{(figure 9.3.3-4, at } \alpha_D = 0)$$

$$T_i = T_{net} + C_{D_e}\, q_\infty\, S_D \quad \text{(equation 9.3.1-f)}$$

$$= 635 + (0.022)(10.4)(12.45)$$

$$= 637.7 \text{ lb}$$

$$S_e = \frac{\pi d_e^2}{4}\left[1 - \left(\frac{d_{CB}}{d_e}\right)^2\right] = \frac{\pi(4.525)^2}{4}\left[1 - \left(\frac{1.208}{4.525}\right)^2\right]$$

$$= 16.10 \quad (0.9295)$$

$$= 14.97 \text{ sq ft}$$

$$\frac{V_e}{V_\infty} = \frac{1 + \sqrt{1 + \dfrac{2T_i}{q_\infty\, S_e}}}{2} \quad \text{(equation 9.3.1-e)}$$

$$= \frac{1 + \sqrt{1 + (2)\dfrac{637.7}{(10.4)(14.97)}}}{2}$$

$$= \frac{1 + \sqrt{1 + 8.19}}{2}$$

$$\frac{V_e}{V_\infty} = 2.02$$

Step 3. Determine the net turning angle of the internal mass flow, including power effects.

$$\delta_{i_f} \approx \sin^{-1}\left[\frac{V_\infty \sin \delta_{i_o} + (V_e - V_\infty) \sin \alpha_D}{V_e}\right] \text{(equation 9.3.1-c)}$$

$$= \sin^{-1}\left[\frac{(93.5)(0.421) + (189 - 93.5)(0.50)}{189}\right]$$

$$= \sin^{-1} (0.4609)$$

$$= 27.45 \text{ deg}$$

Step 4. Determine the lift-coefficient contribution of the internal mass flow.

$$C_{L_i} = \frac{\pi A_D}{2}\left[1 - \left(\frac{d_{CB}}{d_e}\right)^2\right]\left(\frac{V_e}{V_\infty}\right)^2 \sin \delta_{i_f} \quad \text{(equation 9.3.1-g)}$$

$$= \frac{\pi(1.645)}{2} (0.9295)(2.02)^2(0.4604)$$

$$= 4.53$$

Step 5. Determine the lift-coefficient contribution of the external mass flow.

$$C_{L_e} = 0.69 \quad \text{(figure 9.3.1-13)}$$

Solution:

$$C_L = C_{L_i} + C_{L_e} \quad \text{(equation 9.3.1-a)}$$

$$= 4.53 + 0.69$$

$$= 5.22$$

This corresponds to an experimental value of 5.40 obtained from reference 1.

REFERENCES

1. Mort, K. W., and Yaggy, P. F.: Aerodynamic Characteristics of a Four-Foot Diameter Ducted Fan Mounted on the Tip of a Semi-Span Wing. NASA TN D-1301, 1962. (U)

2. Fletcher, H. S.: Experimental Investigation of Lift, Drag, and Pitching Moment of Five Annular Airfoils. NACA TN 4117, 1957. (U)

3. Hoehne, V. O.: Shrouded Propeller Investigations: Wind-Tunnel Test of a Shrouded Propeller with a 10-Bladed Propeller, Exit Stators, and Long-Chord Shroud with High Speed Inlet and No Exit Diffusion. University of Wichita, Dept. of Eng. Research Rpt. No. 213-5, 1959. (U)

4. Hoehne, V. O.: Shrouded Propeller Investigations: Wind Tunnel Test of a Shrouded Propeller with a 10-Bladed Propeller, Exit Stators, and Long-Chord Shroud with Static Inlet and No Diffusion. University of Wichita, Dept. of Eng. Research Rpt. No. 213-6, 1959. (U)

5. Hoehne, V. O.: Shrouded Propeller Investigations: Wind Tunnel Tests of a 2-Bladed Shrouded Propeller Model. University of Wichita, Dept. of Eng. Research Rpt. No. 213-11, 1960. (U)

6. Grunwald, K. J., and Goodson, K. W.: Aerodynamic Loads on an Isolated Shrouded-Propeller Configuration for Angles of Attack From -10° to 110°. NASA TN D-995, 1962. (U)

TABLE 9.3.1-A

DATA SUMMARY AND SUBSTANTIATION

DUCTED PROPELLER LIFT COEFFICIENT

Reference	α_D deg	J	V_∞ fps	T_i lb	$\frac{V_e}{V_\infty}$	δ_{1_o} deg	δ_{1_f} deg	C_L Calc	C_L Test	$\frac{\epsilon}{\%}$ Error
1*	15	0.62	165.5	251.6	1.21	12.4	12.85	1.31	1.3	.8
c = 2.75 ft	|	0.48	128.0	456.3	1.52	|	13.28	1.79	1.8	-.6
d_e = 4.525 ft	30	0.62	165.5	251.6	1.21	24.9	25.78	2.23	2.6	-14.2
A_D = 1.645	|	0.48	128.0	456.3	1.52	|	26.61	3.16	3.6	-12.2
d_{CB} = 1.208 ft	|	0.35	93.5	637.7	2.02	|	27.45	5,22	5.4	-3.3
	|	0.28	74.8	743.9	2.49	|	27.93	7.69	8.3	-7.3
	45	0.48	128.0	456.3	1.52	37.3	39.82	4.17	5.3	-21.3
	|	0.35	93.5	637.7	2.02	|	41.10	7.07	8.0	-11.6
	|	0.28	74.8	743.9	2.49	|	41.80	10.59	12.4	-14.6
	|	0.22	58.8	820.0	3.13	|	42.44	16.52	18.0	-8.2
	60	0.42	112.0	535.1	1.70	49.7	53.65	6.06	8.0	-24.2
	|	0.28	74.8	743.9	2.49	|	55.54	12.77	14.8	-13.7
	|	0.22	58.8	820.0	3.13	|	56.41	20.06	23.4	-14.3
	|	0.17	45.4	894.0	4.03	62.2	57.18	33.26	32.0	3.9
	75	0.35	93.5	637.7	2.02	|	67.77	9.28	11.2	-17.1
	|	0.22	58.8	743.9	3.13	|	70.03	22.34	25.4	-12.0
	90	0.22	58.8	743.9	3.13	74.6	81.30	23.28	27.5	-15.3
3										
c = 0.794 ft	30	0.35	75.0	88.2	3.18	25.6	28.60	10.77	11.56	-6.8
d_e = 1.16 ft	|	0.35	100.0	256.0	3.85	|	28.84	15.60	16.24	-3.9
A_D = 1.46	|	0.70	|	53.2	2.11	|	27.90	5.01	5.26	-4.8
d_{CB} = 0.348 ft										
4	30	0.35	100.0	262.5	3.93	26.25	29.03	14.49	15.49	-6.5
c = 0.895 ft	|	0.50	|	115.4	2.80	|	28.65	7.59	8.20	-7.4
d_e = 1.16 ft	|	0.70	|	45.0	1.99	|	28.10	4.09	4.78	-14.4
A_D = 1.296	45	0.25	75.0	323.9	5.55	39.38	43.95	40.11	40.27	-.4
d_{CB} = 0.348 ft	|	0.35	|	147.6	3.93	|	43.52	20.26	21.59	-6.2
	|	0.50	|	64.9	2.80	|	42.93	10.47	11.55	-9.4
	60	0.20	50.0	146.4	5.59	52.5	58.54	49.68	50.46	-1.5
	|	0.30	|	57.7	3.72	|	57.8	22.12	23.04	-4.0
	|	0.40	|	28.8	2.80	|	57.15	12.39	13.18	-6.0
	75	0.20	40.0	93.7	5.59	65.63	72.96	55.40	49.00	13.1
	|	0.30	|	36.8	3.72	|	71.73	24.39	25.39	-3.9
	|	0.40	|	18.5	2.80	|	71.14	13.90	14.55	-4.5
	90	0.20	30.0	52.7	5.59	78.75	85.30	57.35	55.99	2.4
	|	0.30	|	20.7	3.72	|	84.00	25.4	26.18	-3.0
	|	0.40	|	10.4	2.80	|	83.25	14.39	14.77	-2.6
5	20	0.39	100.0	75.53	2.26	15.10	17.81	5.53	5.73	-3.5
c = 0.58 ft	|	0.292	|	141.20	2.86	|	18.27	8.62	9.31	-7.4
d_e = 1.246 ft	|	0.25	|	194.86	3.25	|	18.48	11.08	12.48	-11.2
A_D = 2.15	30	0.39	|	75.53	2.26	22.65	26.69	7.85	7.59	3.4
d_{CB} = 0.348 ft	|	0.292	|	141.20	2.86	|	27.38	12.39	12.99	-4.6
	|	0.25	|	194.86	3.25	|	27.69	15.99	17.60	-9.1

*Test results include wing-duct interference effects.

TABLE 9.3.1-A (CONTD)

Reference	α_D deg	J	V_∞ fps	T_i lb	$\frac{V_e}{V_\infty}$	δi_o deg	δi_f deg	C_L Calc	C_L Test	e % Error
5 (con't)	20	0.39	100.0	73.89	2.37	15.56	18.11	5.64	5.21	8.3
c = 0.58 ft		0.292		132.35	2.96		18.49	8.59	8.61	-.2
		0.25		177.20	3.33		18.65	10.79	10.80	-.1
d_e = 1.160 ft	30	0.39		73.89	2.37	23.34	27.14	8.02	7.22	11.1
A_D = 2.0		0.292		132.35	2.96		27.71	12.34	12.29	.4
d_{CB} = 0.348 ft		0.25		177.20	3.33		27.96	15.56	15.92	-2.3
	40	0.39		73.89	2.37	31.12	36.13	10.12	8.66	16.9
		0.292		132.35	2.96		36.89	15.69	14.52	8.1
		0.25		177.20	3.33		37.23	19.84	18.60	6.7
6	10	0.595	100.0	18.8	1.39	8.30	8.80	1.08	1.06	1.7
c = 0.859 ft	15					12.50	13.18	1.59	1.59	0
d_e = 1.41 ft	20					16.60	17.56	2.03	1.95	4.1
A_D = 1.64	30					24.90	26.30	2.75	2.75	0
d_{CB} = 0.358 ft	40					33.20	35.00	3.32	3.39	-2.1
	45					37.40	39.37	3.58	3.59	-.3

Average error = $\frac{\sum |e|}{n}$ = 7.1%

(a) UNSTALLED CONFIGURATION

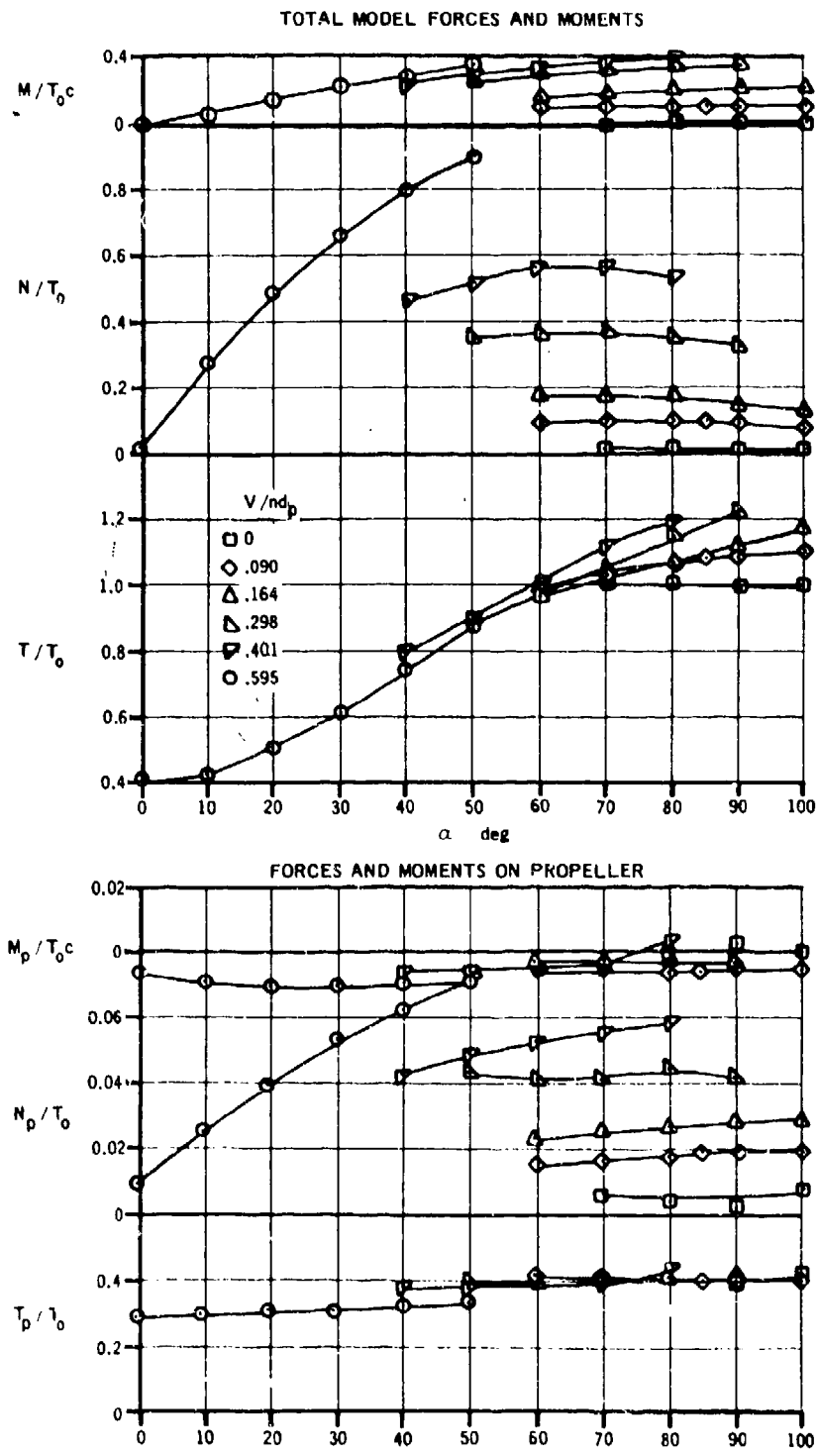

FIGURE 9.3.1-10 COMPARISON OF FORCES AND MOMENTS ON THE PROPELLER WITH TOTAL FORCES AND MOMENTS FOR THE DUCTED PROPELLER CONFIGURATION OF REFERENCE 6

(b) STALLED CONFIGURATION

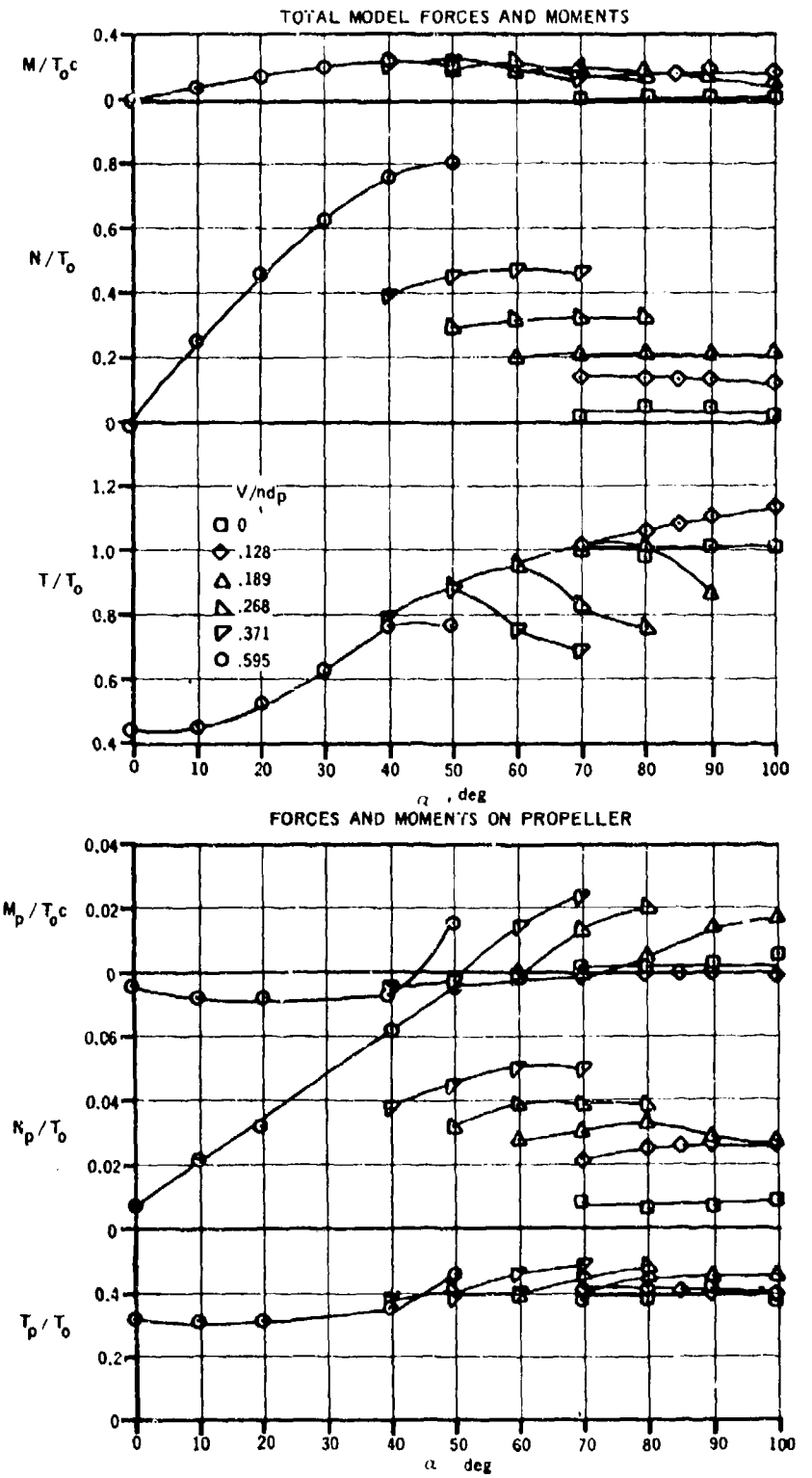

FIGURE 9.3.1-10 (CONTD)

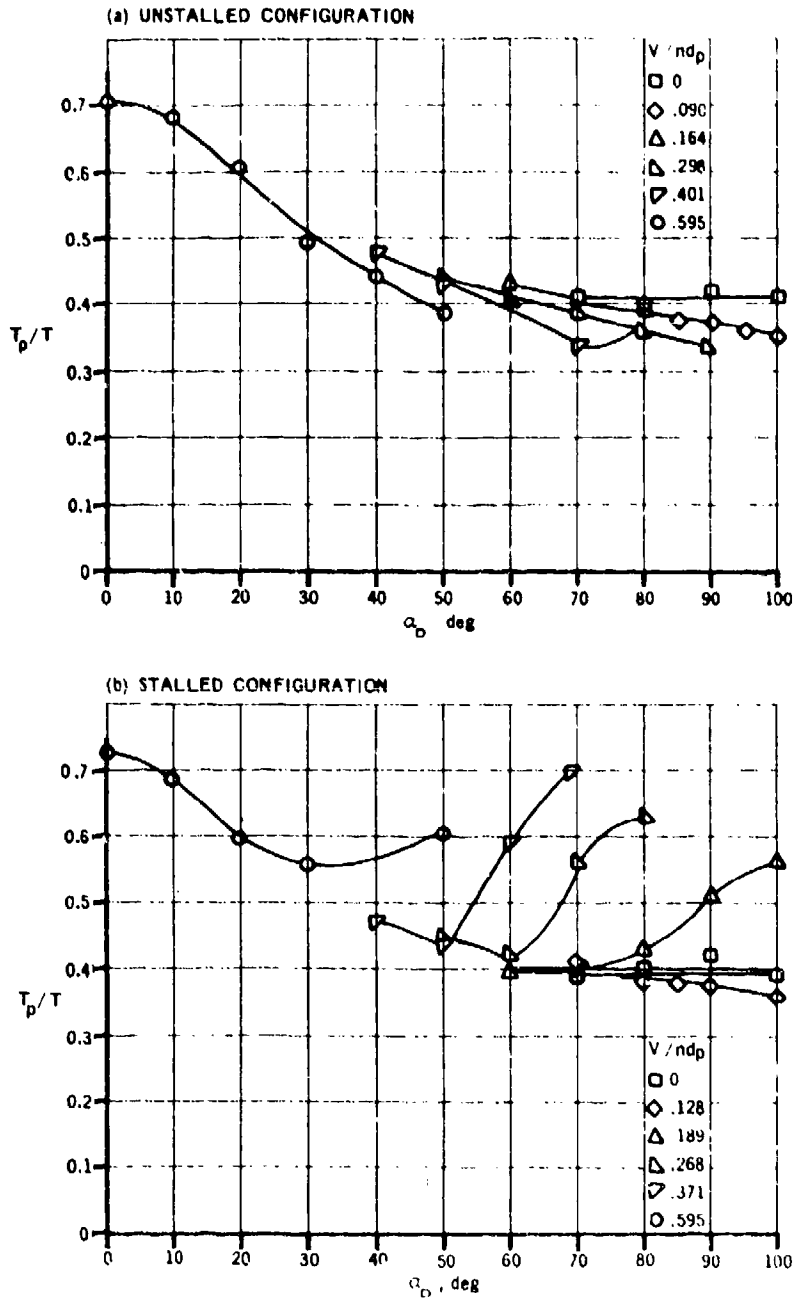

FIGURE 9.3.1-12 VARIATION OF THE RATIO OF PROPELLER THRUST TO TOTAL THRUST WITH ANGLE OF ATTACK FOR THE DUCTED PROPELLER CONFIGURATION OF REFERENCE 6

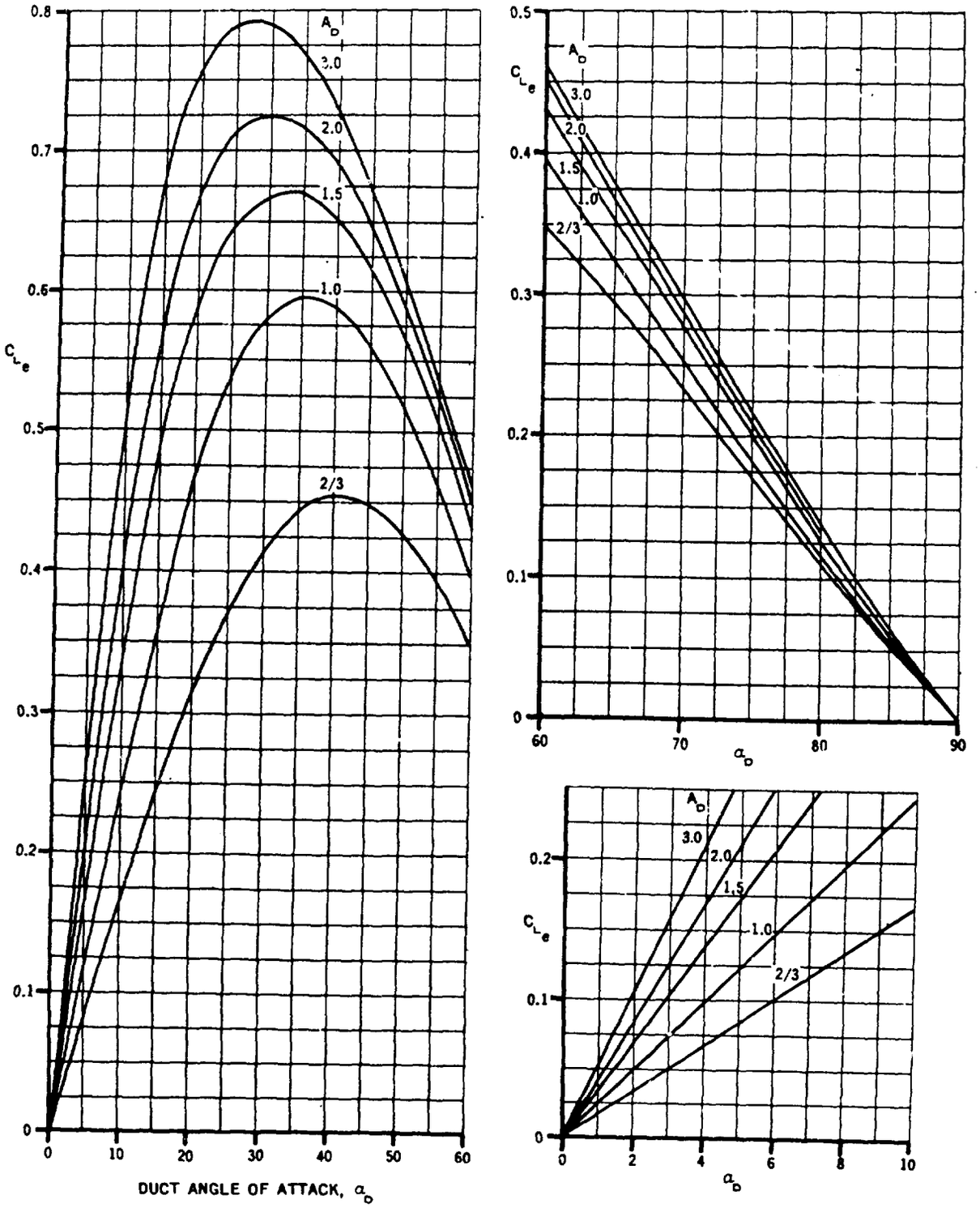

FIGURE 9.3.1-13 EXTERNAL MASS FLOW LIFT COEFFICIENT

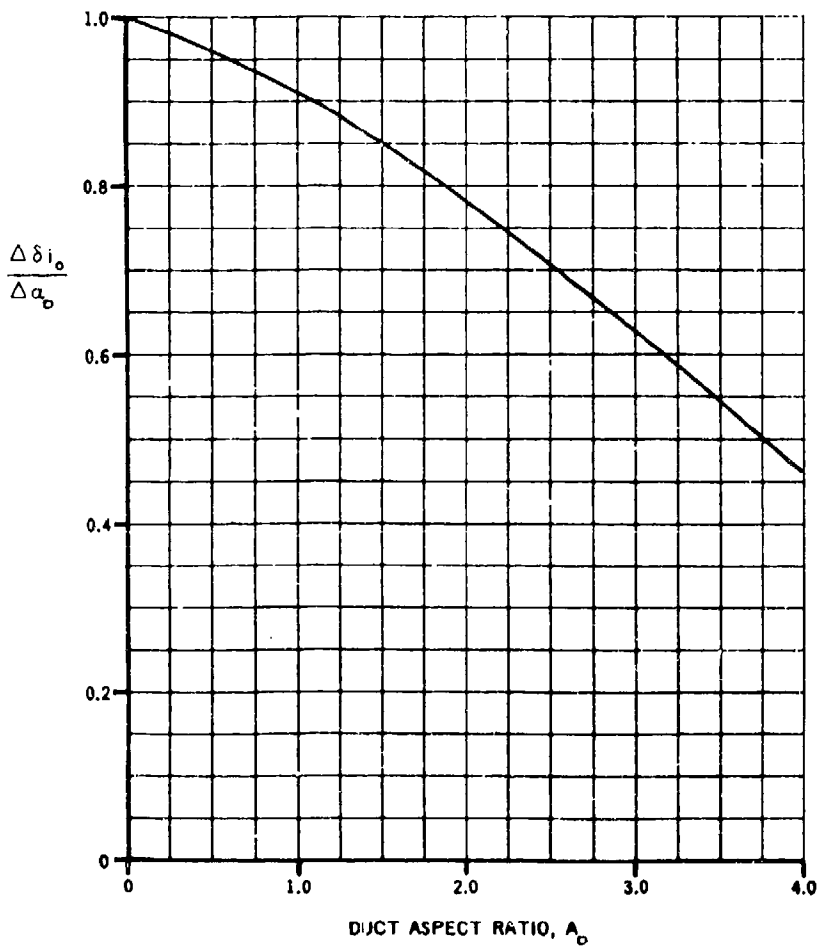

FIGURE 9.3.1-14 RATIO OF UNPOWERED DUCT INTERNAL MASS FLOW TURNING ANGLE TO DUCT ANGLE OF ATTACK

9.3.2 DUCTED-PROPELLER PITCHING-MOMENT VARIATION WITH POWER AND ANGLE OF ATTACK

This Section presents a method for estimating ducted-propeller pitching moments as functions of power and angle of attack. The basic discussion in Section 9.3.1 is directly applicable to this Section, and the reader is referred to that discussion for a general description of the fundamental phenomenon.

DATCOM METHOD

The method presented for estimating ducted-propeller pitching moments is based on ring vortex and simple momentum theories with empirical modifications.

The pitching moment consists of three component parts:

(1) A circulation-induced moment which in effect causes a shift in axial duct forces (essentially a shift in thrust axis.)
(2) A moment due to the lift component
(3) A moment due to the negative drag component

The circulation-induced moment is always positive (nose-up) and increases with increasing power. The last two components also increase in magnitude with power but may be positive or negative depending upon the location of the ducted-propeller center of pressure. This method assumes the center-of-pressure location to be independent of power and angle of attack and to be on the duct axis at the unstalled center-of-pressure location of the undiffused annular wings of reference 2.

The pitching-moment contribution of a ducted-propeller configuration, based on the duct planform area and duct chord and referred to an arbitrary moment center, is given by

$$C_m = \frac{\pi A_D}{2}\left(\frac{V_e}{V_\infty} - \cos \delta_{i_f}\right) \sin \alpha_D + \frac{\bar{x}}{c}\left(C_L \cos \alpha_D - C_{F_x} \sin \alpha_D\right) \qquad 9.3.2\text{-a}$$

where the first term on the right-hand side is the circulation-induced moment as derived by Sacks in reference 1, modified by the empirical relation for the net turning angle of the internal flow, discussed in Section 9.3.1. The last two terms are the components due to lift and drag.

$\frac{V_e}{V_\infty}$ is the exit-velocity ratio, obtained from equation 9.3.1-e

δ_{i_f} is the internal-flow turning angle, including the effects of power, obtained from equation 9.3.1-c

C_L is the total lift coefficient of the ducted propeller, obtained from Section 9.3.1

C_{F_x} is the total negative drag coefficient of the ducted propeller, obtained from Section 9.3.3

$\frac{\bar{x}}{c} = \left(\frac{x_m}{c} - \frac{x_{cp}}{c}\right)$, the chordwise distance, in duct chords, from the reference center to the unstalled duct center of pressure, positive for the center of pressure ahead of the reference center

$\frac{x_m}{c}$ is the chordwise distance, in duct chords, from the duct leading edge to the reference center, positive aft of the duct leading edge

$\frac{x_{cp}}{c}$ is the chordwise distance, in duct chords, from the duct leading edge to the center of pressure of the unstalled duct, positive aft of the duct leading edge. It is obtained as a function of duct aspect ratio from figure 9.3.2-6.

A comparison of test data with ducted propeller pitching-moment coefficients computed by this method is shown in table 9.3.2-A.

Because of the number of variables involved in the ducted propeller problem and the design parameters not considered in the Datcom method, the comparison between theory and experiment cannot be analyzed by examining the isolated effect of one variable. However, it is felt that one important factor pertaining to the test conditions of the available data, namely scale effect, should be considered before assessing the accuracy of this method. The data presented in reference 1 of table 9.3.2-A are the only available test results of a large-scale ducted propeller in the non-axial flow regime. Although experimental data on similar models of different scale are needed for the proper evaluation of the scale effect, it is felt that the low Reynolds numbers of small scale tests will appreciably affect the stalling characteristics of the duct. Therefore, comparison of calculated and large-scale experimental results of reference 1 in table 9.3.2-A is more indicative of the accuracy of the method than comparison with the other reference data.

Sample Problem

Given: Same ducted propeller configuration as sample problem of Section 9.3.1. Some of the characteristics are repeated below.

$d_e = 4.525$ ft $\quad d_{CB} = 1.208$ ft $\quad c = 2.75$ ft

$A_D = 1.645$ $\quad S_D = 12.45$ sq ft

Additional Characteristics

$V_\infty = 93.5$ ft/sec $\quad \alpha_D = 30^\circ$ $\quad$ Sea level

Moment reference center at 0.49c $\quad q_\infty = 10.4$ lb/sq ft

Compute:

$\frac{V_e}{V_\infty} = 2.02$

$\delta_{1_f} = 27.45^\circ$

$C_L = C_{L_i} + C_{L_e} = 5.22$

(sample problem Section 9.3.1)

C_{F_x} = 3.455 (sample problem Section 9.3.3)

$\frac{x_{cp}}{c}$ = 0.266 (figure 9.3.2-6)

$\frac{\bar{x}}{c} = \frac{x_m}{c} - \frac{x_{cp}}{c}$

$= (0.49 - 0.266)$

$= 0.224$

Solution:

$$C_m = \frac{\pi A_D}{2}\left(\frac{V_e}{V_\infty} - \cos \delta_{i_f}\right) \sin \alpha_D + \frac{\bar{x}}{c}\left(C_L \cos \alpha_D - C_{F_x} \sin \alpha_D\right) \text{ (equation 9.3.2-a)}$$

$$= \frac{\pi(1.645)}{2}(2.02 - 0.8874)(0.50) + 0.224\left[(5.22)(0.866) - (3.455)(0.50)\right]$$

$$= (2.58)(1.1326)(0.50) + 0.224\ (2.792)$$

$$= 2.085$$

This corresponds to an experimental value of 1.899 obtained from reference 1.

REFERENCES

1. **Sacks, A. H.: The Flying Platform as a Research Vehicle for Ducted Propellers. Institute of Aeronautical Sciences Preprint No. 832, 1958. (U)**

2. **Fletcher, H. S.: Experimental Investigation of Lift, Drag, and Pitching Moment of Five Annular Airfoils. NACA TN 4117, 1957. (U)**

TABLE 9.3.2-A[a]

DATA SUMMARY AND SUBSTANTIATION

DUCTED PROPELLER PITCHING-MOMENT COEFFICIENT

Ref[b]	α_D deg	J	$\frac{V_e}{V_\infty}$	C_L Table 9.3.1-A	C_{F_x} Table 9.3.3-A	$\frac{\bar{x}}{c}$	C_m Calc	C_m Test	e % Error
1[c]	15	0.62	1.21	1.31	0.38	0.224	0.42	0.50	-16.0
		0.48	1.52	1.79	1.61		0.67	0.70	-4.3
	30	0.62	1.21	2.23	-0.135		0.84	1.00	-16.0
		0.48	1.52	3.16	0.915		1.32	1.10	20.0
		0.35	2.02	5.22	3.46		2.035	1.90	9.5
		0.28	2.49	7.69	6.79		2.81	2.60	8.1
	45	0.48	1.52	4.17	-0.010		2.02	2.10	-3.8
		0.35	2.02	7.07	1.91		3.12	2.85	9.5
		0.28	2.49	10.59	4.49		4.15	4.35	-4.6
		0.22	3.13	16.52	9.22		5.52	5.20	6.2
	60	0.42	1.70	6.06	-0.724		3.29	3.30	-0.3
		0.28	2.49	12.77	1.69		5.41	5.10	6.1
		0.22	3.13	20.06	4.75		7.08	6.50	8.9
		0.17	4.03	33.26	10.72		9.44	7.80	21.0
	75	0.35	2.02	9.28	-1.90		5.03	4.45[s]	13.0
		0.22	3.13	22.34	-0.237		8.29	7.90	4.9
	90	0.22	3.13	23.28	-4.60		8.72	8.50[s]	2.5
3	30	0.35	3.18	10.77	12.70	0.283	3.40	2.95	15.6
		0.35	3.85	15.60	20.60		4.29	3.24	32.4
		0.70	2.11	5.01	3.80		2.02	1.71	18.1
4	30	0.35	3.93	14.49	17.33	0.353	4.48	3.86	16.1
		0.50	2.80	7.59	7.18		3.01	2.52	19.4
		0.70	1.99	4.09	2.42		1.95	1.68	16.1
	45	0.25	5.55	40.11	30.2		9.43	7.93[s]	18.9
		0.35	3.93	20.26	12.86		6.45	5.71	13.0
		0.50	2.80	10.47	4.84		4.38	3.76	16.5
	60	0.20	5.59	49.68	19.14		11.83	9.74[s]	21.5
		0.30	3.72	22.12	6.04		7.69	6.55[s]	17.4
		0.40	2.80	12.39	1.98		5.55	4.94[s]	12.3
	75	0.20	5.59	55.40	5.89		13.45	10.08[s]	33.4
		0.30	3.72	24.39	0.435		8.79	7.15[s]	22.9
		0.40	2.80	13.90	-1.205		6.53	5.54[s]	17.9
	90	0.20	5.59	57.35	-6.22	0.353	13.38	13.26	0.9
		0.30	3.72	25.40	-4.82		9.08	8.40	8.1
		0.40	2.80	14.39	-4.08		6.89	6.31	9.2

a Refer to Table 9.3.1-A for additional characteristics
b These references are found in Section 9.3.1
c Test results include wing-duct interference effects
s Stalled

TABLE 9.3.2-A[a] (CONTD)

Ref[b]	α_D deg	J	$\frac{V_e}{V_\infty}$	C_L Table 9.3.1-A	C_{F_x} Table 9.3.3-A	$\frac{\bar{x}}{c}$	C_m Calc	C_m Test	e % Error
5	20	0.39	2.26	5.53	7.79	0.208	2.01	1.59	26.4
		0.292	2.86	8.62	15.17		2.79	1.91	46.1
		0.25	3.25	11.08	20.76		3.32	1.99	66.8
	30	0.39	2.26	7.85	6.69		2.99	2.20	35.9
		0.292	2.86	12.39	13.19		4.15	2.90	43.1
		0.25	3.25	15.99	18.53		4.91	3.31	48.3
	20	0.39	2.37	5.64	8.20		2.05	1.33	54.1
		0.292	2.96	8.59	15.01		2.78	1.82	52.7
		0.25	3.33	10.79	20.23		3.24	2.19	47.9
	30	0.39	2.37	8.02	7.05		3.04	1.81	68.0
		0.292	2.96	12.34	13.25		4.11	2.54	61.8
		0.25	3.33	15.56	18.02		4.78	2.79	71.3
	40	0.39	2.37	10.12	5.58		4.02	2.34	71.8
		0.292	2.96	15.69	10.96		5.40	3.31	61.3
		0.25	3.33	19.84	15.11		6.27	5.72	65.5
6	10	0.595	1.39	1.08	1.19	0.174	0.403	0.219	84.0
	15			1.59	1.05		0.593	0.359	65.2
	20			2.03	0.87		0.77	0.47	63.8
	30			2.75	0.43		1.09	0.72	51.4
	40			3.32	-0.90		1.41	0.94	50.0
	45			3.58	-0.37		1.52	1.064	42.9

Average error = $\frac{\sum |e|}{n}$ = 29.5%

a Refer to Table 9.3.1-A for additional characteristics
b These references are found in Section 9.3.1

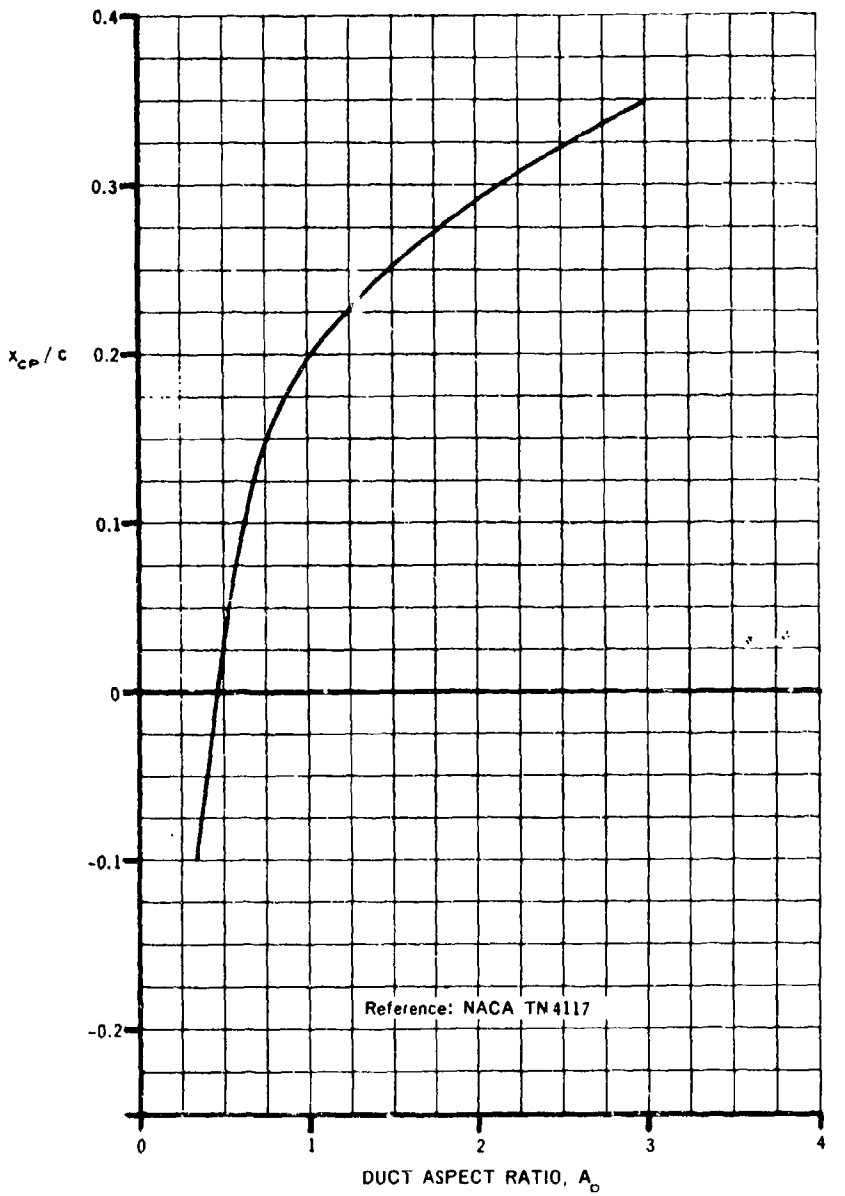

FIGURE 9.3.2-6 DUCT CENTER OF PRESSURE LOCATION

9.3.3 DUCTED-PROPELLER DRAG VARIATION WITH POWER AND ANGLE OF ATTACK

This Section presents a method for estimating ducted-propeller drag as a function of power and angle of attack. The basic discussion in Section 9.3.1 is directly applicable to this Section, and the reader is referred to that discussion for a general description of the fundamental phenomenon.

DATCOM METHOD

The method presented for estimating ducted-propeller drag is expressed as the sum of the components resulting from the internal and external mass flows. The theoretical basis of this method is the same as that of the Datcom lift-estimation method of Section 9.3.1.

The negative drag coefficient of a ducted propeller is given by

$$C_{F_x} = \frac{\pi A_D}{2}\left[1 - \left(\frac{d_{CB}}{d_e}\right)^2\right]\left[\left(\frac{V_e}{V_\infty}\right)^2 \cos\delta_{i_f} - \left(\frac{V_e}{V_\infty}\right)\right] + C_{F_{x_e}} \qquad 9.3.3\text{-a}$$

where the first term on the right-hand side is due to internal flow and is estimated on the basis of simple momentum theory modified by the empirical relation for the net internal-flow turning angle, discussed in Section 9.3.1.

$\frac{V_e}{V_\infty}$ is the exit-velocity ratio, obtained from equation 9.3.1-e

δ_{i_f} is the net turning angle of the internal flow, obtained from equation 9.3.1-c

$C_{F_{x_e}}$ is the external negative drag coefficient, resulting from the external flow, obtained from figure 9.3.3-4 as a function of duct aspect ratio and angle of attack. Figure 9.3.3-4 is based on empirical modifications of the data of references 1 and 2.

A comparison of test data with ducted-propeller drag coefficients computed by this method is shown in table 9.3.3-A. The measurement of drag involves the difference between the components of the thrust force and the normal force and is inherently less accurate than the measurement of the lift force. At a tunnel velocity near that for steady level flight ($C_{F_x} = 0$), slight errors in drag measurement can result in test values with an opposite sign than that predicted by theory; and percent error becomes incalculable, although the actual magnitude of the difference may be less than that for lift. Consequently, a comparison of theory and experiment in this area may be misleading when presented in terms of percent error. Therefore, a summary of the results presented in table 9.3.3-A is presented as a weighted error.

Sample Problem

Given: Same ducted-propeller configuration as sample problem of Section 9.3.1. Some of the characteristics are repeated below.

$d_e = 4.525$ ft $\qquad d_{CB} = 1.208$ ft $\qquad c = 2.75$ ft

$A_D = 1.645$ $\qquad S_D = 12.45$ sq ft

Additional Characteristics

V_{∞} = 93.5 ft/sec — Sea level

α_D = 30° — q_{∞} = 10 lb/sq ft

Compute:

$$\left.\begin{aligned}\frac{V_e}{V_{\infty}} &= 2.02\\ \delta_{1_f} &= 27.45^{\circ}\end{aligned}\right\} \quad \text{(sample problem Section 9.3.1)}$$

$$\left[1 - \left(\frac{d_{CB}}{d_e}\right)^2\right] = 0.9295$$

$$C_{F_{x_e}} = -0.395 \quad \text{(figure 9.3.3-4)}$$

Solution:

$$C_{F_x} = \frac{\pi A_D}{2}\left[1-\left(\frac{d_{CB}}{d_e}\right)^2\right]\left[\left(\frac{V_e}{V_{\infty}}\right)^2 \cos\delta_{1_f} - \left(\frac{V_e}{V_{\infty}}\right)\right] + C_{F_{x_e}} \quad \text{(equation 9.3.3-a)}$$

$$= \frac{\pi(1.645)}{2}(0.9295)\left[(2.02)^2(0.8874)-(2.02)\right] + (-0.395)$$

$$= (2.41)(1.60) - 0.395$$

$$= (3.455)$$

This corresponds to an experimental value of 3.785 obtained from reference 1.

REFERENCES

1. Mort, K. W., and Yaggy, P. F.: Aerodynamic Characteristics of a Four-Foot Diameter Ducted Fan Mounted on the Tip of a Semi-Span Wing. NASA TN D-1301, 1962. (U)

2. Fletcher, H. S.: Experimental Investigation of Lift, Drag, and Pitching Moment of Five Annular Airfoils. NACA TN 4117, 1957. (U)

TABLE 9.3.3-A[a]

DATA SUMMARY AND SUBSTANTIATION

DUCTED-PROPELLER DRAG COEFFICIENT

Ref[b]	α_D deg	J	$\frac{V_e}{V_\infty}$	C_{F_x} Calc	C_{F_x} Test	e % Error
1[c]	15	0.62	1.21	0.38	0.40	-5.0
		0.48	1.52	1.61	1.70	-5.3
	30	0.62	1.21	-0.135	0.10	-
		0.48	1.52	0.915	1.30	-29.6
		0.35	2.02	3.46	3.80	-9.1
		0.28	2.49	6.79	7.50	-10.6
	45	0.48	1.52	-0.01	0.20	-
		0.35	2.02	1.91	2.10	-9.0
		0.28	2.49	4.49	5.30	-15.3
		0.22	3.13	9.22	11.20	-17.7
	60	0.42	1.70	-0.724	-0.50	44.8
		0.28	2.49	1.69	1.40	20.7
		0.22	3.13	4.75	5.90	-19.5
		0.17	4.03	10.72	10.40	3.1
	75	0.35	2.02	-1.90	-2.40	-20.8
		0.22	3.13	-0.237	-0.60	-60.5
	90	0.22	3.13	-4.60	-7.30	-37.0
3	30	0.35	3.18	12.70	10.90	16.5
		0.50	3.85	20.60	16.90	21.9
		0.70	2.11	3.80	2.69	41.3
4	30	0.35	3.93	17.33	17.39	-0.3
		0.50	2.80	7.18	6.94	3.5
		0.70	1.99	2.42	2.63	-8.0
	45	0.25	5.55	30.2	28.65	5.4
		0.35	3.93	12.86	12.50	2.9
		0.50	2.80	4.84	4.58	5.7
	60	0.20	5.59	19.14	18.36	4.2
		0.30	3.72	6.04	5.19	16.4
4	60	0.40	2.80	1.98	1.02	94.1
	75	0.20	5.59	5.89	2.40	145.4
		0.30	3.72	0.435	-0.63	-
		0.40	2.80	-1.205	-2.22	-45.7
	90	0.20	5.57	-6.22	-12.34	-49.6
		0.30	3.72	-4.82	-7.91	-29.1
		0.40	2.80	-4.08	-6.35	-35.7
5	20	0.39	2.26	7.79	6.70	16.3
		0.292	2.86	15.17	13.50	12.4
		0.25	3.25	20.76	19.09	8.7
	30	0.39	2.26	6.69	4.66	43.6
		0.292	2.86	13.19	10.80	22.1
		0.25	3.25	18.53	15.30	21.1
	20	0.39	2.37	8.20	5.87	39.7
		0.292	2.96	15.01	12.10	24.0
		0.25	3.33	20.23	16.94	19.4
	30	0.39	2.37	7.05	4.38	61.0
		0.292	2.96	13.25	9.73	36.2
		0.25	3.33	18.02	13.73	31.2
	40	0.39	2.37	5.58	2.70	106.7
		0.242	2.96	10.96	7.03	55.9
		0.25	3.33	15.11	8.66	74.5
6	10	0.595	1.39	1.19	1.204	-1.2
	15			1.05	1.126	-6.7
	20			0.87	1.00	-13.0
	30			0.43	0.704	39.8
	40			-0.90	0.188	-
	45			-0.37	-0.303	18.2

$$\text{Weighted error} = \frac{\sum\left(|e|\,|C_{F_{x_{Test}}}|\right)}{\sum|C_{F_{x_{Test}}}|} = 21.8\%$$

a Refer to Table 9.3.1-A for additional characteristics
b These references are found in Section 9.3.1
c Test results contain wing-duct interference effects

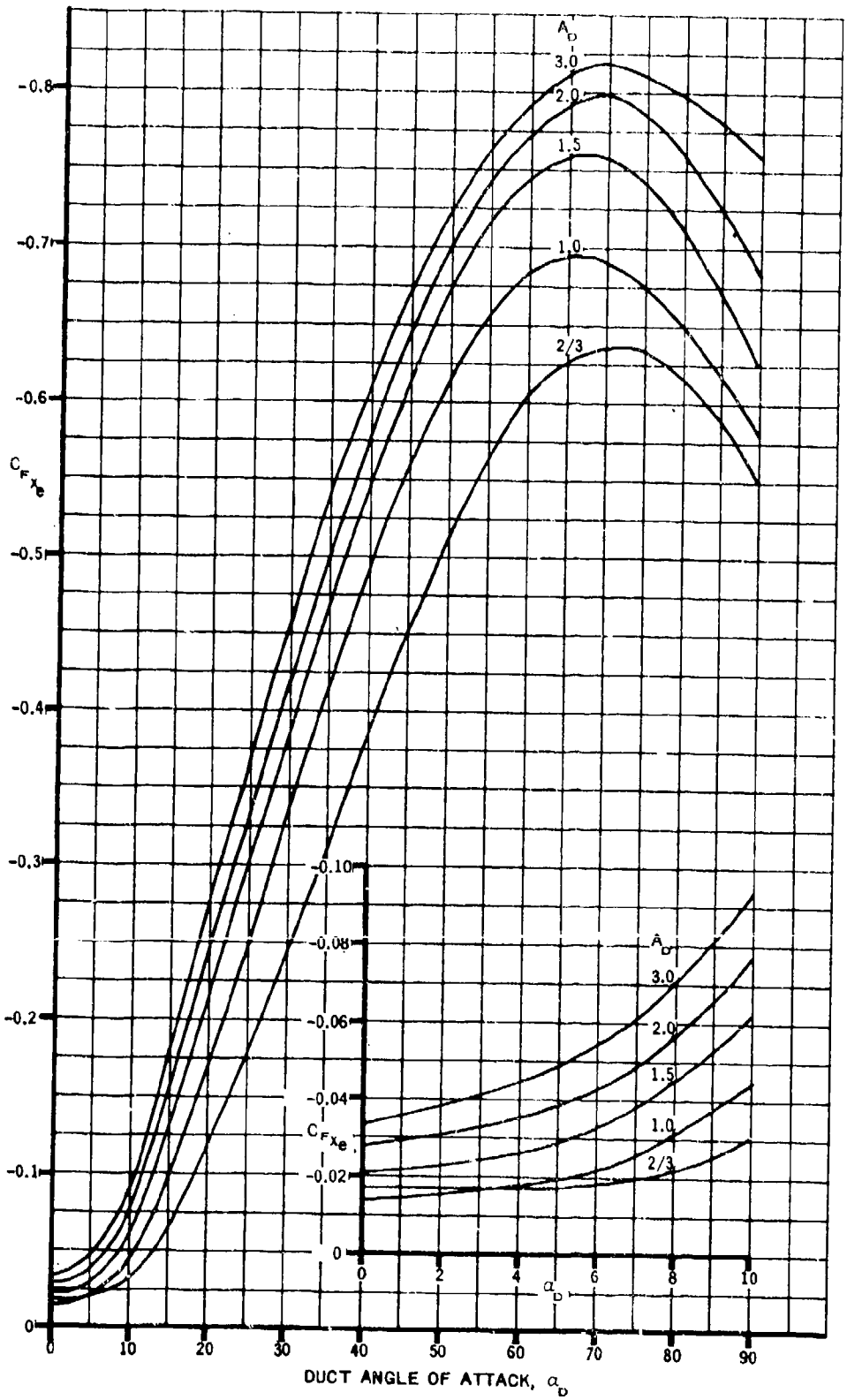

FIGURE 9.3.3-4 EXTERNAL MASS FLOW NEGATIVE DRAG COEFFICIENT

*U.S. GOVERNMENT PRINTING OFFICE: 1980/657-150/6303